THIRD EDITION 3

ABDOMINAL-PELVIC MRI

RICHARD C. SEMELKA

WILEY-BLACKWELL

ABDOMINAL-PELVIC MRI

Volume 1

ABDOMINAL-PELVIC MRI

Third Edition

Volume 1

Richard C. Semelka, M.D.
Director, Magnetic Resonance Services
Professor, Vice Chairman of Clinical Research and
Vice Chairman of Quality and Safety
Department of Radiology
University of North Carolina at Chapel Hill

WILEY-BLACKWELL
A JOHN WILEY & SONS, INC., PUBLICATION

Copyright 2010 by John Wiley & Sons, Inc. All rights reserved

Wiley-Blackwell is an imprint of John Wiley & Sons, formed by the merger of Wiley's global Scientific, Technical, and Medical business with Blackwell Publishing.

Published by John Wiley & Sons, Inc., Hoboken, New Jersey
Published simultaneously in Canada

No part of this publication may be reproduced, stored in a retrieval system, or transmitted in any form or by any means, electronic, mechanical, photocopying, recording, scanning, or otherwise, except as permitted under Section 107 or 108 of the 1976 United States Copyright Act, without either the prior written permission of the Publisher, or authorization through payment of the appropriate per-copy fee to the Copyright Clearance Center, Inc., 222 Rosewood Drive, Danvers, MA 01923, (978) 750-8400, fax (978) 750-4470, or on the web at www.copyright.com. Requests to the Publisher for permission should be addressed to the Permissions Department, John Wiley & Sons, Inc., 111 River Street, Hoboken, NJ 07030, (201) 748-6011, fax (201) 748-6008, or online at http://www.wiley.com/go/permission.

Limit of Liability/Disclaimer of Warranty: While the publisher and author have used their best efforts in preparing this book, they make no representations or warranties with respect to the accuracy or completeness of the contents of this book and specifically disclaim any implied warranties of merchantability or fitness for a particular purpose. No warranty may be created or extended by sales representatives or written sales materials. The advice and strategies contained herein may not be suitable for your situation. You should consult with a professional where appropriate. Neither the publisher nor author shall be liable for any loss of profit or any other commercial damages, including but not limited to special, incidental, consequential, or other damages.

For general information on our other products and services or for technical support, please contact our Customer Care Department within the United States at (800) 762-2974, outside the United States at (317) 572-3993 or fax (317) 572-4002.

Wiley also publishes its books in a variety of electronic formats. Some content that appears in print may not be available in electronic formats. For more information about Wiley products, visit our web site at www.wiley.com.

ISBN 978-0-470-48775-4

Library of Congress Cataloging-in-Publication Data is available

Printed in the United States of America

10 9 8 7 6 5 4 3 2 1

This book is dedicated to all the patients whose images we have used to illustrate MR findings. I hope that the MR studies offered positive impact on their lives. Furthermore, I hope that many, many more patients worldwide will benefit from the knowledge conferred to their physicians by the information contained herein.

—Richard Semelka

Christ seated, disputing with the doctors. Etching, 1654. Rembrandt. This etching describes evolution in human thought. New individuals challenge prevailing wisdom, and the end result is the improvement of the human condition.

Christ driving the money-changers from the temple. Etching, 1635. Rembrandt. This etching describes the necessity of being ever vigilant against the excesses of greed. We must constantly challenge ourselves and others that this is not a prime motivation for conduct.

CONTENTS

Volume 1

Preface xi
Contributors xiii

1. DIAGNOSTIC APPROACH TO PROTOCOLING AND INTERPRETING MR STUDIES OF THE ABDOMEN AND PELVIS 1
Puneet Sharma, Diego R. Martin, Brian M. Dale, Busakorn Vachiranubhap, and Richard C. Semelka

2. LIVER 45
Larissa Braga, Diane Armao, Mohamed El Azzazi, and Richard C. Semelka

3. GALLBLADDER AND BILIARY SYSTEM 455
Ersan Altun, Till Bader, Jorge Elias, Jr., Faiq Shaikh, and Richard C. Semelka

4. PANCREAS 535
Ersan Altun, Jorge Elias, Jr., Diane Armao, Busakorn Vachiranubhap, and Richard C. Semelka

5. SPLEEN 677
Ersan Altun, Jorge Elias, Jr., Young Hoon Kim, and Richard C. Semelka

6. GASTROINTESTINAL TRACT 725
Diego R. Martin, Ersan Altun, Jorge Elias, Jr., Mohamed Elazzazi, Miguel Ramalho, Chang-Hee Lee, and Richard C. Semelka

Index I-1

Volume 2

Preface xi
Contributors xiii

7. PERITONEAL CAVITY 901
Ersan Altun, N. Cem Balci, Jorge Elias, Jr., Young Mi Ku, and Richard C. Semelka

8. ADRENAL GLANDS 963
Ersan Altun, Nikolaos L. Kelekis, Jorge Elias, Jr., Penampai Tannaphai, Waqas Qureshi, and Richard C. Semelka

9. KIDNEYS 1025
Larissa Braga, Ersan Altun, Jorge Elias, Jr., Diego R. Martin, Sang Soo Shin, and Richard C. Semelka

10. RETROPERITONEUM AND BODY WALL 1193
Diego R. Martin, Ersan Altun, Jorge Elias, Jr., Young Mi Ku, and Richard C. Semelka

11. BLADDER 1297
Ersan Altun, Corinne Deurdulian, Jorge Elias, Jr., Penampai Tannaphai, and Richard C. Semelka

12. MALE PELVIS 1343
Ersan Altun, Tara Noone, Jorge Elias, Jr., Milena Spirovski, Rahel A. Kubik, Young Mi Ku, and Richard C. Semelka

13. FEMALE URETHRA AND VAGINA 1401
Lara B. Eisenberg, Jorge Elias, Jr., Waqas Qureshi, Young Mi Ku, and Richard C. Semelka

14. UTERUS AND CERVIX 1433
Michèle A. Brown, Sameer A. Patel, Caroline Reinhold, Waqas Qureshi, and Richard C. Semelka

15. ADNEXA 1499
Michèle A. Brown, Mihaela I. Pop, Susan M. Ascher, Mohamed Elazzazi, and Richard C. Semelka

16. PREGNANCY AND FETUS 1559
Lorene Romine, Reena Chopra, Katarina Koprivsek, Waqas Qureshi, Richard C. Semelka, and Michèle A. Brown

17. PEDIATRICS 1637
Waqas Qureshi, Naciye Turan, Thuy Vu, Mohamed Elazzazi, Carlos Gonzalez, Rafael de Campos, and Richard C. Semelka

18. CHEST 1653
Ersan Altun, Jorge Elias, Jr., Katherine R. Birchard, Busakorn Vachiranubhap, Vasco Heredia, and Richard C. Semelka

19. BREAST 1687
Dragana Djilas-Ivanović, Helmuth Schultze-Haack, Dag Pavic, and Richard C. Semelka

20. CONTRAST AGENTS 1767
Ersan Altun, Diego R. Martin, and Richard C. Semelka

Index I-1

PREFACE

Much change has occurred in imaging since the writing of the previous edition of this work. The entity of nephrogenic systemic fibrosis (NSF) has been identified and its association with gadolinium-based contrast agents (GBCAs), especially the linear nonionic agents, has been recognized. Further recognition by the main-stream radiological community of the detrimental nature of excessive medical radiation, that may result in malignancy, and contrast-induced-nephropathy related to the use of iodine-based contrast agents (IBCAs) have simultaneously occurred. These lapses in attention on the subject of safety by the radiology community serve to remind ourselves of our duty to patients of Primum Non Nocere, emphasizing the age-old wisdom of "everything in moderation" and the importance of being ever vigilant when it comes to patient welfare. Positive steps have been taken by individual radiologists and radiological societies and equipment manufacturers to lessen the potential harmful effects of what we have previously assumed to be innocuous imaging studies. Almost all centers have adopted a restrictive GBCA policy that has largely vanquished NSF, and will progressively make the elimination of this condition complete. Policies and programs related to medical radiation, currently foremost amongst them being the Image Gently campaign, a program designed to minimize the amount of radiation sustained by pediatric patients in imaging studies, and operated as a joint venture between many of the large radiology societies, have been developed and instituted.

At the same time, positive advances in MRI have occurred. These include the more widespread adoption and development of 3 T MRI to study diseases of the chest, abdomen and pelvis. 3T possesses higher signal-to-noise, greater image quality especially with 3D-gradient echo imaging, greater sensitivity to GBCA enhancement, and thinner section acquisition. This has allowed further expansion of MRI into more applications in torso imaging.

In recognition of these changes in the imaging terrain, this current edition addresses many of these above mentioned issues and advances. A new chapter on Contrast Agents is included to address the use of MR contrast agents, but also describes GBCA and IBCA issues and safe practice. New chapters on Fetus and Pediatric imaging draw attention to the capacity of MRI to accurately investigate young subjects, to ameliorate the problems with excess medical radiation in this group, who are the most sensitive to radiation damage. Breast imaging has also come of age and is included as a new chapter in this work. Additionally, many of the new images throughout the book are 3T images, emphasizing the high image quality provided at ultrahigh field strength, and illustrating its growing importance.

Despite all these changes, the principles of this book remain unchanged. The emphasis remains on short duration imaging studies that combine comprehensive information and consistent image quality. The major step to widespread implementation of MRI in replacement of other modalities, remains reproducibility and generalizability of information acquired. MRI has to replicate CT images and studies need to be generated with comparable and not excessively longer duration, and image quality must be reliable and consistent, but with the addition of greater and more comprehensive information, and greater safety. Although we touch on new applications in Chapter 1, such as diffusion-weighted imaging and MR elastography, at present I do not consider their roles established in main-stream MRI practice, paying attention to the above mentioned principles, and I recommend that at present their use be restricted to research centers. This text again emphasizes multiple examples of disease processes both rare and common, so that the reader has guidance on the appearances of virtually all diseases processes in the abdomen, pelvis, chest and breast, to compare their own cases against. With all the advances in MRI, and perhaps despite the advances in CT, coupled with the recognition of the hazards intrinsic to CT, especially CT performed with multiple passes of the torso, this work aims to show that much of imaging of these areas can be performed with MRI, by virtue of the depth and breadth of disease processes that can be evaluated well. In many organ systems, as this book reveals, MRI performs extremely well at diagnosing most disease entities, and outperforms CT in many areas, notably the liver. MRI may be the best tool to evaluate cancers in most of the organs described in this text, and much of

the inflammatory diseases. CT remains dominant for major trauma, diffuse lung parenchymal diseases, and renal stone diseases. What remains exciting is that despite the comprehensiveness of this work, it is not the omega work of MRI. We anticipate further exciting advances that may further alter imaging management, perhaps especially, making inroads into more indications in trauma. Those developments may need to wait for the future next edition. With further exciting advances we have to remain vigilant on the subject of safety, MRI is not an innocuous tool, and as we move to even higher field strengths, safety must be cautiously assessed.

RICHARD SEMELKA, M.D.

CONTRIBUTORS

ERSAN ALTUN, M.D., Department of Radiology, University of North Carolina, Chapel Hill, Chapel Hill, North Carolina

DIANE ARMAO, M.D., Department of Radiology, University of North Carolina, Chapel Hill, Chapel Hill, North Carolina

SUSAN M. ASCHER, M.D., Department of Radiology, Georgetown University, Washington, DC

TILL BADER, M.D., Associate Professor of Radiology, Medical University of Vienna, Austria

N. CEM BALCI, M.D., Department of Radiology, St. Louis University, St. Louis, Missouri

KATHERINE R. BIRCHARD, M.D., Department of Radiology, University of North Carolina, Chapel Hill, North Carolina

LARISSA BRAGA, M.D. Ph.D, M.P.H., Department of Radiology, University of Nebraska Medical Center, Omaha, Nebraska

MICHÈLE A. BROWN, M.D., Associate Professor of Radiology, University of California, San Diego, California

REENA CHOPRA, M.D., Clinical Fellow, Department of Radiology, University of California, San Diego, California

BRIAN M. DALE, Ph.D., Siemens Medical Solutions, Inc., Morrisville, North Carolina

RAFAEL DE CAMPOS, M.D., Clinical Research Scholar, MR Section, Department of Radiology, University of North Carolina, Chapel Hill, North Carolina

CORINNE DEURDULIAN, M.D., Imaging Department, VA Medical Center, Salisbury, North Carolina

DRAGANA DJILAS-IVANOVIĆ, M.D., Ph.D., Associate Professor of Radiology, University of Novi Sad, Oncology Institute of Vojvodina, Sremska Kamenica, Serbia

LARA B. EISENBERG, M.D., Chairman of Radiology, Suburban Hospital, Bethesda, Maryland

MOHAMED ELAZZAZI, M.D., Ph.D., Clinical Research Scholar, MR Section, Department of Radiology, University of North Carolina, Chapel Hill, North Carolina; Professor of Radiology, Al-Azhar University, Cairo, Egypt

JORGE ELIAS, JR., M.D., Ph.D., Professor of Radiology, Faculty of Medicine of Ribeirao Preto, University of Sao Paulo, Brazil

CARLOS GONZALEZ, M.D., Clinical Research Scholar, MR Section, Department of Radiology, University of North Carolina, Chapel Hill, North Carolina

VASCO HEREDIA, M.D., Clinical Research Scholar, MR Section, Department of Radiology, University of North Carolina, Chapel Hill, Chapel Hill, North Carolina

NIKOLAOS L. KELEKIS, M.D., Associate Professor of Radiology, National and Kapodistrian University of Athens, General University Hospital "ATTIKON," Athens, Greece

YOUNG HOON KIM, M.D., Clinical Research Scholar, MR Section, Department of Radiology, University of North Carolina, Chapel Hill, North Carolina; Seoul National University College of Medicine and Seoul National University Bundang Hospital, Seongnam-si, Gyeonggi-do, Korea

KATARINA KOPRIVSEK, M.D., Ph.D., Associate Professor of Radiology, University of Novi Sad, Diagnostic Imaging Center, Oncology Institute of Vojvodina, Sremska Kamenica, Serbia

YOUNG MI KU, M.D., Clinical Research Scholar, MR Section, Department of Radiology, University of North Carolina, Chapel Hill, North Carolina; Assistant Professor, Department of Radiology, Uijongbu St. Mary's Hospital, Catholic University of Korea, Uijongu, Korea

RAHEL A. KUBIK, M.D., M.P.H., Department of Medical Services, Cantonal Hospital, Baden, Switzerland

CHANG-HEE LEE, M.D., Ph.D., Clinical Research Scholar, MR Section, Department of Radiology, University of North Carolina, Chapel Hill, North Carolina; Associate

Professor, Department of Radiology, Korea University Guro Hospital, Korea University College of Medicine, Seoul, Korea

DIEGO R. MARTIN, M.D., Professor and Director of MR, Department of Radiology, Emory University, Atlanta, Georgia

TARA NOONE, M.D., President, SEA Imaging, LLC, Mt. Pleasant, South Carolina; Clinical Associate Professor, Medical University of South Carolina, Charleston, South Carolina

SAMEER A. PATEL, M.D., Clinical Fellow, Department of Radiology, University of California, San Diego, California

DAG PAVIC, M.D., Assistant Professor of Radiology, University of North Carolina, Chapel Hill, North Carolina

MIHAELA I. POP, M.D., Clinical Fellow, Department of Radiology, University of California, San Diego, California

WAQAS QURESHI, M.D., Clinical Research Scholar, MR Section, Department of Radiology, University of North Carolina, Chapel Hill, North Carolina

MIGUEL RAMALHO, M.D., Clinical Research Scholar, MR Section, Department of Radiology, University of North Carolina, Chapel Hill, North Carolina

CAROLINE REINHOLD M.D., M.Sc., Professor of Radiology, Gynecology, and Internal Medicine; Director, MR Imaging, McGill University Health Center, Montréal, Québec, Canada

LORENE ROMINE, M.D., Assistant Professor of Radiology, University of California, San Diego, California

HELMUTH SCHULTZE-HAACK, Siemens Medical Solutions USA, Inc., Santa Ana, California

RICHARD C. SEMELKA, M.D., Professor of Radiology, University of North Carolina, Chapel Hill, North Carolina

FAIQ SHAIKH, M.D., Clinical Research Scholar, MR Section, Department of Radiology, University of North Carolina, Chapel Hill, North Carolina

PUNEET SHARMA, Ph.D., Clinical MR Physicist, Department of Radiology, Emory Healthcare, Inc., Atlanta, Georgia

SANG SOO SHIN, M.D., Clinical Research Scholar, MR Section, Department of Radiology, University of North Carolina, Chapel Hill, North Carolina; Assistant Professor, Department of Radiology, Chonnam National University Medical School, Gwanju, Korea

MILENA SPIROVSKI, M.D., Diagnostic Imaging Center, Oncology Institute of Vojvodina, Sremska Kamenica, Serbia

PENAMPAI TANNAPHAI, M.D., Clinical Research Scholar, MR Section, Department of Radiology, University of North Carolina, Chapel Hill, North Carolina

NACIYE TURAN, M.D., Resident, Department of Radiology, University of North Carolina, Chapel Hill, North Carolina

BUSAKORN VACHIRANUBHAP, M.D., Clinical Research Scholar, MR Section, Department of Radiology, University of North Carolina, Chapel Hill, North Carolina

THUY VU, M.D., Resident, Department of Radiology, University of North Carolina, Chapel Hill, Chapel Hill, North Carolina

CHAPTER

1

DIAGNOSTIC APPROACH TO PROTOCOLING AND INTERPRETING MR STUDIES OF THE ABDOMEN AND PELVIS

PUNEET SHARMA, DIEGO R. MARTIN, BRIAN M. DALE, BUSAKORN VACHIRANUBHAP, AND RICHARD C. SEMELKA

High image quality, reproducibility of image quality, and good conspicuity of disease require the use of sequences that are robust and reliable and avoid artifacts [1–5]. Maximizing these principles to achieve high-quality diagnostic MR images usually requires the use of fast scanning techniques, with the overall intention of generating images with consistent image quality that demonstrate consistent display of disease processes. The important goal of shorter examination time may also be achieved with the same principles that maximize diagnostic quality. With the decrease of imaging times for individual sequences, a variety of sequences may be employed to take advantage of the major strength of MRI, which is comprehensive information on disease processes.

Respiration and bowel peristalsis are the major artifacts that have lessened the reproducibility of MRI. Breathing-independent sequences and breath-hold sequences form the foundation of high-quality MRI studies of the abdomen. Breathing artifact is less problematic in the pelvis and high-spatial and contrast-resolution imaging have been the mainstay for maximizing image quality for pelvis studies.

Disease conspicuity depends on the principle of maximizing the difference in signal intensities between diseased tissues and the background tissue. For disease processes situated within or adjacent to fat, this is readily performed by manipulating the signal intensity of fat, which can range from low to high in signal intensity on both T1-weighted and T2-weighted images. For example, diseases that are low in signal intensity on T1-weighted images, such as peritoneal fluid or retroperitoneal fibrosis, are most conspicuous on T1-weighted sequences in which fat is high in signal intensity (i.e., sequences without fat suppression). Conversely, diseases that are high in signal intensity on T1-weighted images, such as subacute blood or proteinaceous fluid, are more conspicuous if fat is rendered low in signal intensity with the use of fat suppression techniques. On T2-weighted images, diseases that are low in signal intensity, such as fibrous tissue, are most conspicuous on sequences in which background fat is high in signal intensity, such as single-shot echo-train spin-echo sequences (fig. 1.1). Diseases that are moderate to high in signal intensity, such as lymphadenopathy or ascites, are most conspicuous on sequences in

Abdominal-Pelvic MRI, Third Edition, edited by Richard C. Semelka. Copyright © 2010 John Wiley & Sons, Inc.

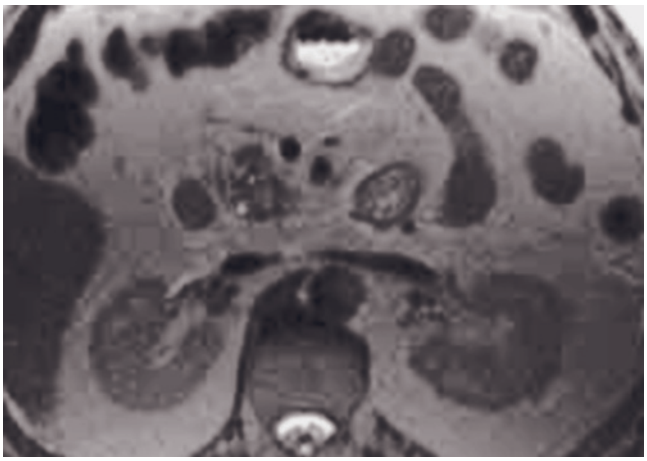

(*a*)

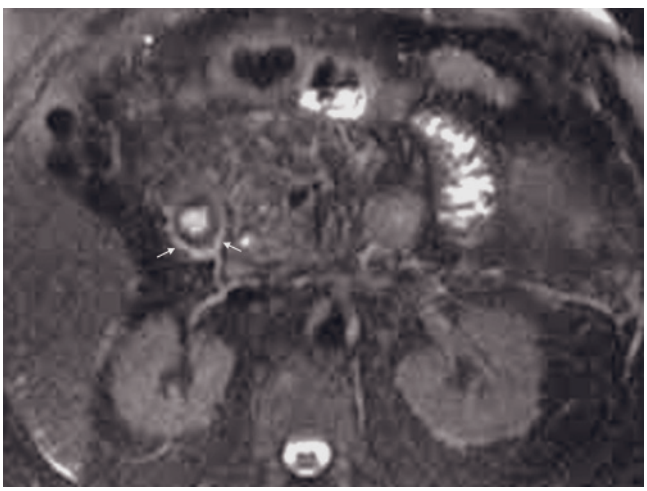

(*b*)

FIG. 1.1 Maximizing contrast between abnormal and background tissue. T2-weighted single-shot echo-train spin-echo, standard (*a*) and fat-suppressed (*b*) in a patient with mild pancreatitis. On the non-fat-suppressed image (*a*), the small-volume peripancreatic fluid is most clearly seen because background fat is high signal and of comparable signal intensity. With application of fat suppression (*b*), fat is rendered dark and the small-volume fluid surrounding the pancreatic head and duodenum (arrows, *b*) is readily appreciated.

which fat signal intensity is low, such as fat-suppressed sequences.

Gadolinium chelate enhancement may be routinely useful since it provides at least two further imaging properties that facilitate detection and characterization of disease, specifically the pattern of blood delivery (i.e., capillary enhancement) and the size and/or rapidity of drainage of the interstitial space (i.e., interstitial enhancement) [6]. Capillary phase image acquisition is achieved by using a short-duration sequence initiated immediately after gadolinium injection. Two- or three-dimensional (2D or 3D) gradient echo sequences, performed as multisection acquisition, are an ideal sequence to use for capillary phase imaging. The majority of focal mass lesions are best evaluated in the capillary phase of enhancement, particularly lesions that do not distort the margins of the organs in which they are located (e.g., focal liver, spleen, or pancreatic lesions). Images acquired 1.5–10 min after contrast administration are in the interstitial phase of enhancement, with the optimal window being 2–5 min after contrast administration. Diseases that are superficially spreading or inflammatory in nature are generally well shown on interstitial phase images. The concomitant use of fat suppression serves to increase the conspicuity of disease processes characterized by increased enhancement on interstitial phase images including peritoneal metastases, cholangiocarcinoma, ascending cholangitis, inflammatory bowel disease, and abscesses [7, 8].

The great majority of diseases can be characterized by defining their appearance on T1, T2, and early and late postgadolinium images. Throughout this text the combination of these four parameters for the evaluation of abdomino-pelvic disease will be stressed.

T1-WEIGHTED SEQUENCES

T1-weighted sequences are routinely useful for investigating diseases of the abdomen, and they supplement T2-weighted images for investigating disease of the pelvis. The primary information that precontrast T1-weighted images provide includes 1) information on abnormally increased fluid content or fibrous tissue content that appears low in signal intensity on T1-weighted images and 2) information on the presence of subacute blood or concentrated protein, which are both high in signal intensity. T1-weighted sequences obtained without fat suppression also demonstrate the presence of fat as high-signal-intensity tissue. The routine use of an additional fat attenuating technique permits reliable characterization of fatty lesions.

In the abdomen and pelvis, gradient echo (GE) sequences including spoiled gradient echo (SGE) or three-dimensional gradient echo (3D-GE) sequences are preferred to spin-echo sequences. Gradient-echo sequences have a number of advantages:

1. With GE sequences, T1 tissue contrast can be generated similar to that of spin-echo sequences with much shorter scan times. The scan time reduction can be achieved either by exciting all required slices within one TR (multislice) or exciting one slice per very short TR (single slice). The spoiling in the SGE minimizes the influence of T2 weighting.
2. The shorter scan time of GE sequences allows breath-hold imaging to minimize motion artifacts. Breath holding obviates other, often time-consuming,

methods of artifact reduction such as signal averaging and phase reordering.

3. GE sequences allow chemical shift imaging for the detection of relatively small amounts of fat in organs (e.g., fatty infiltration of the liver) and lesions (e.g., adrenal adenomas, liver cell adenomas). In contrast, frequency-selective fat-suppression methods suppress the signal in tissues or lesions with larger amounts of fat like intraperitoneal fat or dermoid cysts.
4. SGE, which is a two-dimensional (2D) technique, allows multislice imaging that acquires central k-space lines, which determine tissue contrast, of 20–24 slices within 4–5 s. 3D-GE can also acquire central k-space lines volumetrically, in a segmented fashion within the early portion of data acquisition. These properties are useful to perform contrast-enhanced dynamic exams of the upper abdomen with distinct arterial, portal, and venous phases in breath hold times.
5. Currently, 3D-GE sequences, in combination with robust segmented fat suppression techniques, overlapping reconstruction, and in-plane as well as through-plane interpolation of the MR data, allow high-quality imaging with larger volume coverage in breath hold times. 3D-GE sequences can be obtained with sufficient anatomic coverage, very thin sections, and high spatial resolution matrices in scan times of only 15–20 s. 3D-GE is particularly suitable for dynamic contrast-enhanced MR imaging because of its excellent inherent fat suppression and sensitivity to enhanced tissues and abnormalities. The spatial resolution depends on matrix size, section thickness, and field of view (FOV). In 3D-SGE, the actual spatial resolution depends on the chosen FOV and is often different in three orthogonal dimensions: spatial resolution$_x$ = FOV$_x$/N$_x$; spatial resolution$_y$ = FOV$_y$/N$_y$; spatial resolution$_z$ = section thickness. Currently, most of the 3D-GE sequences used for dynamic gadolinium-enhanced MR exams employ sequential k-space filling as opposed to the sequences with centric or elliptic-centric k-space filling used in MR angiography in most centers. The 3D-GE sequences with sequential k-space filling can be combined with segmented fat suppression techniques that result in very reliable and homogenous fat suppression without significant increase in scan time. These beneficial features, in combination with clinically viable acquisition breath hold times, makes 3D-GE the primary technique over 2D-SGE for dynamic contrast-enhanced imaging of the abdomen and pelvis.

Gradient Echo (GE) Sequences

The most commonly used gradient echo sequences for routine abdominal imaging are SGE and 3D-GE sequences.

SGE sequences are one of the most important and versatile sequences for studying abdominal disease. SGE sequences are two-dimensional sequences and can also be used as a single (breathing independent) or multiacquisition (breath hold) technique. They provide true T1-weighted imaging and, with the use of phased-array multicoil imaging, may be used to replace longer-duration sequences such as T1-weighted spin-echo (SE) sequence. Image parameters for breath-hold SGE sequences involve: 1) relatively long repetition time (TR) (approximately 150 ms) and 2) the shortest in-phase echo time (TE) (approximately 6.0 ms at 1.0 T, 4.4 ms at 1.5 T, 2.2 ms at 3.0 T), both to maximize signal-to-noise ratio and the number of sections that can be acquired in one multisection acquisition [2]. For routine T1-weighted images, in-phase TE are preferable to the shorter out-of-phase echo times (4.0 ms at 1.0 T and 2.2 ms at 1.5 T, 1.1 ms at 3.0 T), to avoid both phase-cancellation artifact around the borders of organs and fat-water phase cancellation in tissues containing both fat and water protons. Flip angle should be approximately 70–90° to maximize T1-weighted information. With the body coil, the signal-to-noise ratio of 2D-SGE sequences is usually suboptimal, with section thickness less than 8 mm, whereas with the phased-array multicoil, section thickness of 5 mm results in diagnostically adequate images. On new MRI machines, more than 22 sections may be acquired in a 20-second breath hold.

An important feature of multisection acquisition of SGE is that the central phase encoding steps (which determine the bulk signal in the image) are acquired over 6 s for both the entire data set and each individual section. The data acquisition, therefore, is sufficiently short to isolate a distinct phase of enhancement (e.g., hepatic arterial dominant phase), while at the same time the data acquisition of each individual section is sufficiently long to compensate for slight variations in patient cardiac output, peak lesion enhancement, and injection technique.

In addition to its use as precontrast T1-weighted images, SGE may be routinely used for capillary-phase image acquisition after gadolinium administration for investigation of the liver, spleen, pancreas, and kidneys.

In single-shot techniques, all of the k-space lines for one slice are acquired before acquiring the lines for another slice, that is, in sequential rather than interleaved fashion. SGE may be modified to a single-shot technique, by minimizing TR, to achieve breathing-independent images for noncooperative patients.

GE sequences can be performed as a 3D acquisition, which can be used both for volumetric imaging of organs such as the liver and for pre- and postgadolinium administration.

A 3D-GE sequence is typically performed with minimum TR and TE and a flip angle between 10° and

15°. The flip angle is related to the TR to maximize T1 signal. With a minimum TR, flip angle can also be relatively low and still achieve good T1 contrast. As TR and TE of these sequences have minimum values (TR < 5 ms and TE < 2.5 ms), the flip angle will mainly determine the contrast in the images. In 3D-GE, a volume of data is obtained rather than individual slices. There are several advantages of 3D versus 2D gradient echo sequences:

1. Higher inherent signal-to-noise ratio (SNR) than 2D gradient echo sequences
2. Higher in-plane resolution with larger matrices (>192 × >256)
3. Contiguous, thinner sections for higher through-plane resolution, which facilitates reformats in other planes; thin sections are often possible because of interpolation of the MR data in the *z*-direction.
4. Homogenous fat-suppression (most vendors apply segmented fat suppression, i.e., fat suppression pulse is applied after every *n*th k-space lines [*n* can typically be up to 60–70]; this allows scan times that are still short enough to perform breath-hold imaging with fat suppression.
5. The enhancement of vessels and tissues with gadolinium is more obvious because of the fat suppressed nature of the sequence.

Gadolinium-enhanced 3D-GE sequences also are the most clinically effective techniques for MR angiography (MRA) of the body (see Chapter 10, *Retroperitoneum and Body Wall*).

Fat-Suppressed Gradient Echo Sequences

Fat-suppressed (FS) SGE sequences are routinely used as precontrast images for evaluating the pancreas and for the detection of subacute blood. Image parameters are similar to those for standard SGE; however, it is advantageous to employ a lower out-of-phase echo time (2.2–2.5 ms at 1.5 T), which benefits from additional fat-attenuating effects and also increases signal-to-noise ratio and the number of sections per acquisition. On state-of-the-art MRI machines, FS-SGE may acquire 22 sections in a 20-s breath hold with reproducible uniform fat suppression.

Fat-suppressed-SGE images are often used to acquire interstitial-phase gadolinium-enhanced images. The complementary roles of gadolinium enhancement, which generally increases the signal intensity of disease tissue, and fat suppression, which diminishes the competing high signal intensity of background fat, are particularly effective at maximizing conspicuity of diseased tissue. The principle of maximizing signal difference between diseased tissue and background tissue is achieved in the majority of MRI examinations with this approach. Fat-suppressed 3D-GE sequences can also be routinely used for the acquisition of fat-suppressed precontrast T1-weighted images. Although the contrast resolution of fat-suppressed 3D-GE is mildly lower compared to fat-suppressed SGE, the acquisition of thin sections with higher matrices is advantageous.

If fat-suppressed-GE sequences cannot be performed on an MRI system, then fat-suppressed spin-echo sequences can be substituted, with little loss of diagnostic information.

Out-of-Phase Gradient Echo Sequences

Out-of-phase (opposed-phase) SGE images are useful for demonstrating diseased tissue in which fat and water protons are present within the same voxel. A TE of 2.2 ms is advisable at 1.5 T, 4 ms at 1.0 T, and 1.1 ms at 3T. A TE of 6.6 ms is also out of phase at 1.5 T, but the shorter TE of 2.2 ms is preferable as more sections can be acquired per sequence acquisition, signal is higher, the sequence is more T1-weighted, and in combination with a T2-weighted sequence, it is easier to distinguish fat and iron in the liver. At TE = 6.6 ms both fat and iron in the liver result in signal loss relative to the TE = 4.4 ms in-phase sequence, while on TE = 2.2 ms out-of-phase sequences fat is darker and iron is brighter relative to TE = 4.4 ms, facilitating their distinction (fig. 1.2). At 3.0 T, the shortest in-phase and out-of-phase values are 2.2 ms and 1.1 ms, respectively. It is challenging to acquire the first echoes at these optimal in-phase and out-of-phase TE times due to gradient capabilities unless imaging bandwidth is increased, or highly asymmetric echoes are utilized in a single scan. With these adjustments, asymmetric TE values can achieve low in-phase (2.5 ms) and out-of-phase (1.58 ms) echoes. These values vary depending on the vendor. When acquiring in-phase/out-of-phase GE sequences, it is essential to use an opposed-phase TE that is less than the in-phase TE. Additionally, it is also possible to acquire in-phase and out-of-phase 3D-GE sequences, although this technique is still developing.

The most common indications for an out-of-phase sequence are to detect the presence of fat within the liver and lipid within adrenal masses to characterize them as adenomas. Another useful feature is that the generation of a phase-cancellation artifact around high-signal-intensity masses, located in water-based tissues, confirms that these lesions are fatty. Examples of this include angiomyolipomas of the kidney and ovarian dermoids. In addition to out-of-phase effects, the different TE, for the out-of-phase sequence compared to the in-phase sequence, provides information on magnetic susceptibility effects that increase with increase in TE. This can be used to distinguish iron-containing structures (e.g., surgical clips, Gamna–Gandy bodies in the

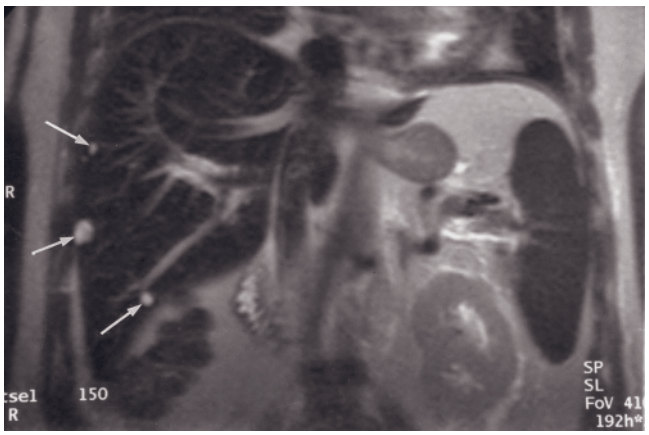

(*a*)

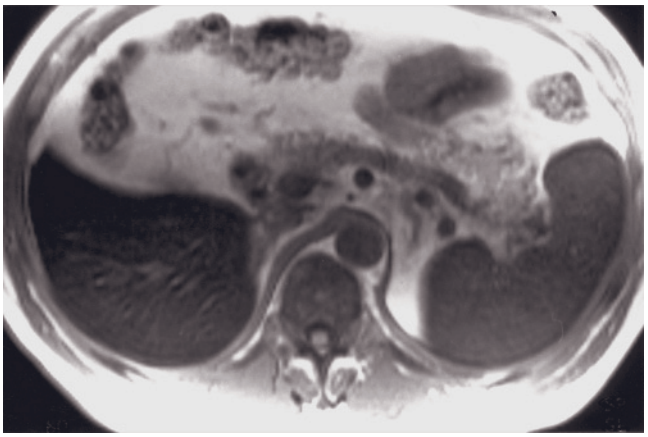

(*b*)

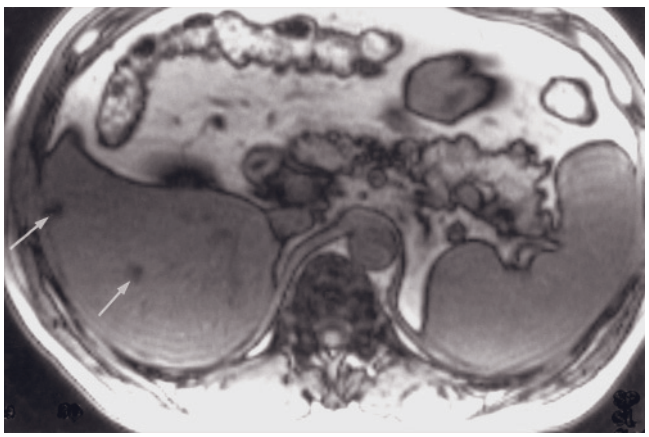

(*c*)

FIG. 1.2 Iron effects. Coronal T2-weighted single-shot echo-train spin-echo (*a*), TE = 4 ms in-phase (*b*), and TE = 2 ms out-of-phase (*c*) sequences. Iron in the reticuloendothelial system from transfusional siderosis results in low signal of the liver and spleen on T2-weighted images (*a*). The liver and spleen are low signal on the longer-TE in-phase sequence (*b*) and increase in signal on the shorter-TE out-of-phase (*c*) sequence, because of decreasing susceptibility effects on the shorter-TE sequence. Note the excellent conspicuity of small liver cysts on the T2-weighted image (arrows, *a*). The high fluid content of cysts in a background of iron-deposited liver renders them very high in signal. On T1-weighted images, the low signal of cysts results in no signal difference from liver on the TE = 4 ms in-phase sequence because of the concurrent low signal of liver. On the TE = 2 ms sequence, liver becomes higher in signal and the cysts are visible (arrows, *c*).

spleen) from nonmagnetic signal-void structures (e.g., calcium). To illustrate this point, the signal void susceptibility artifact from surgical clips increases in size, from a shorter TE (e.g., 2.2 ms) out-of-phase sequence to a longer TE (e.g., 4.4 ms) in-phase sequence, whereas the signal void from calcium remains unchanged.

Magnetization-Prepared Rapid-Acquisition Gradient Echo (MP-RAGE) Sequences

MP-RAGE sequences include turbo fast low-angle shot (turboFLASH). In 2D, multisection varieties, these techniques are generally performed as a single shot, with image acquisition duration of 1–2 s, which renders them relatively breathing independent. Magnetization preparation is currently performed with a 180° inversion pulse to impart greater T1-weighted information. The inversion pulse may be either slice or non-slice selective. Slice-selective means that only the tissue section that is being imaged experiences the inverting pulse, while non-slice-selective means that all the tissue in the bore of the magnet experiences the inverting pulse. The advantage of a non-slice-selective inversion pulse is that no time delay is required between acquisition of single sections in multiple single-section acquisition. A stack of single-section images can be acquired in a rapid fashion. This is important for dynamic gadolinium-enhanced studies. A non-slice-selective inversion pulse results in slightly better image quality, particularly because flowing blood is signal void (fig. 1.3). Approximately 3 s of tissue relaxation is required between acquisition of individual sections, which limits the usefulness of this sequence for dynamic gadolinium-enhanced acquisitions. Current versions of MP-RAGE are limited because of low signal-to-noise ratio, varying signal intensity and contrast between sections, unpredictable bounce-point boundary artifacts due to signal-nulling effects caused by the inverting 180° pulse, and unpredictable nulling of tissue enhanced with gadolinium. Research is ongoing to alleviate these problems with MP-RAGE so that it may assume a more important clinical role. Routine use of a high-quality MP-RAGE sequence would further increase the reproducibility of MR image quality by obviating the need for breath holding, particularly in patients unable to suspend

FIG. 1.3 Non-slice -selective 180° magnetization prepared gradient echo. A coronal image through the liver demonstrates good T1 weighting, evidenced by a moderately high-signal-intensity liver and moderately low-signal-intensity spleen. The infracardiac portion of the left lobe is artifact free. Blood vessels in the liver and the cardiac chambers are seen as signal void.

respiration. 3.0T MR imaging particularly improves the image quality of MP-RAGE sequences due to higher signal-to-noise ratio and greater spectral separation [9].

T2-WEIGHTED SEQUENCES

The predominant information provided by T2-weighted sequences are 1) the presence of increased fluid in diseased tissue, which results in high signal intensity, 2) the presence of chronic fibrotic tissue, which results in low signal intensity, and 3) the presence of iron deposition, which results in very low signal intensity.

Echo-Train Spin-Echo Sequences

Echo-train spin-echo (ETSE) sequences are termed fast spin-echo, turbo spin-echo, or rapid acquisition with relaxation enhancement (RARE) sequences. The principle of ETSE sequences is to summate multiple echoes within the same repetition time interval to decrease examination time, increase spatial resolution, or both. ETSE has achieved widespread use because of these advantages. Conventional T2 spin-echo sequences are lengthy and suffer from patient motion and increased examination time, factors that are lessened with ETSE. In addition, ETSE sequences allow higher matrices within relatively shorter acquisition times. One of the disadvantages of echo-train sequences is that T2 differences between tissues are reduced, in part because of averaging of T2 echoes, which has the greatest effect of diminishing contrast between background organs and focal lesions with minimal T2 differences. This generally is not problematic in the pelvis because of the substantial differences in the T2 values between diseased and normal tissue. In the liver, however, the T2 difference between diseased (solid tissue) and background liver may be small and the T2-averaging effects of summated multiple echoes blur this T2 difference. These effects are most commonly observed with hepatocellular carcinoma. Fortunately, diseases with T2 values similar to those of liver generally have longer T1 values than liver, so that lesions poorly visualized on ETSE are generally apparent on precontrast GE as low-signal lesions or on postgadolinium GE images as low- or high-signal lesions depending on enhancement features.

ETSE, and T2-weighted sequences in general, are important for evaluating the liver and pelvis. T2-weighted sequences are often useful for the pancreas, in demonstrating the pancreatic and common bile ducts, evaluating cystic masses and pseudocysts, and detecting islet cell tumors. Breathing-independent single-shot T2-weighted sequences are useful for the investigation of bowel and peritoneum. Use of the single-shot technique for many applications of a T2 sequence is recommended, because the image quality is consistent, in large part because of the breathing-independent nature of these sequences. Although the detection of lesions with subtle T2 difference from background organ/tissue is compromised (e.g., hepatocellular carcinoma), the major role for T2-weighted sequences is to provide information on fluid content of disease processes for disease characterization. This information is reliably provided by single-shot echo-train spin-echo.

Fat is high in signal intensity on ETSE sequences, in comparison to conventional spin-echo sequences in which fat is intermediate in signal intensity. The MR imaging determination of recurrent malignant disease versus fibrosis for pelvic malignancies illustrates this difference. Recurrent malignant disease in the pelvis (e.g., cervical, endometrial, bladder, or rectal cancer) generally appears high in signal intensity on conventional spin-echo sequences because of the higher signal intensity of the diseased tissue relative to the moderately low-signal-intensity fat. In contrast, fat is high in signal intensity on ETSE images, and recurrent disease will commonly appear relatively lower in signal intensity. The fact that abnormal tissue is not high signal on T2-weighted images relative to fat cannot be relied

upon to exclude recurrence. Caution must therefore be exercised not to misinterpret recurrent disease as fibrotic tissue, by making the assumption that recurrence is higher in signal intensity than background fat. Fat may also be problematic in the liver because fatty liver will be high in signal intensity on ETSE sequences, thereby diminishing contrast with the majority of liver lesions, which are generally high in signal intensity on T2-weighted images. It may be essential to use fat suppression on T2-weighted ETSE sequences for liver imaging. Alternative fat-suppressed T2-weighted sequences for the liver such as echo-planar imaging have also been employed at some centers (further description is provided in the 3T section of this chapter).

ETSE sequences, acquired as contiguous thin 2D sections, as 3D thin sections, or as a thick 3D volume slab, form the basis for MR cholangiography (see Chapter 3, *Gallbladder and Biliary System*) and MR urography (see Chapter 9, *Kidneys*). The greatest concern with high-resolution 3D ETSE sequences is the significant increase in specific absorption rate (SAR). This is particularly relevant since most 3D implementations must increase the echo-train length compared to 2D varieties because of the added data that need to be acquired. Recently, newer MR systems, in combination with advances in gradient and software design, have allowed the development of efficient long echo-train 3D ETSE using variable flip angle refocusing pulses. Concerns of SAR are offset by using smaller (constant or variable) flip angles during data acquisition. With this strategy, T2 information can be maintained throughout the echo train, or used more effectively, for high-SNR imaging. Efficiency is further aided by implementing an additional "restore" pulse at the end of data collection to expedite magnetization recovery, allowing shorter TRs (~1200 ms) to be used for T2 imaging. These recent modifications to conventional 3D-ETSE imaging have made high-resolution isotropic (1 mm^3) T2 imaging of the pelvis and biliary system feasible in a relatively short acquisition time (~5 min).

Single-Shot Echo-Train Spin-Echo Sequence

Single-shot echo-train spin-echo sequence [e.g.,: half-Fourier acquisition single shot turbo spin-echo (HASTE), single-shot fast or turbo spin echo (SSFSE or SSTSE), or single-shot echo-train spin echo (SS-ETSE)] is a breathing-independent T2-weighted sequence that has had a substantial impact on abdominal imaging [3]. Typical imaging involves a 400-ms image acquisition time, in which k-space is completely filled using half-Fourier reconstruction. Shorter effective echo time (e.g., 60 ms) is recommended for bowel-peritoneal disease, and longer effective echo time (e.g., 100 ms and greater) is recommended for liver-biliary disease. Since the technique is single shot, the echo train length is typically greater than 100 echoes, while the effective TR for one slice is infinite. A stack of sections should be acquired in single-section mode in one breath hold to avoid slice misregistration; however, the method lends itself to free-breathing application under uncooperative imaging circumstances. Recently, 3D versions of this technique have been implemented. Motion artifacts from respiration and bowel peristalsis are obviated; chemical-shift artifact is negligible; and susceptibility artifact from air in bowel, lungs, and other locations is minimized, such that bowel wall is clearly demonstrated. Similarly, susceptibility artifact from metallic devices such as surgical clips or hip prostheses is minimal (fig. 1.4). All of these effects render SS-ETSE an attractive sequence for evaluating abdomino-pelvic disease. In patients with implanted metallic devices and extensive surgical clips, SS-ETSE is the sequence least affected by metal susceptibility artifact.

Fat-Suppressed (FS) Echo-Train Spin-Echo Sequences

Fat suppression in spin-echo sequences may be useful for investigating focal liver disease to attenuate the high signal intensity of fatty infiltration, if present. Fatty liver is high in signal intensity on ETSE, in particular single-shot versions, which lessens the conspicuity of high-signal-intensity liver lesions. Diminishing fat signal intensity with fat suppression accentuates the high signal intensity of focal liver lesions (fig. 1.5). FS SS-ETSE is also useful for evaluating the biliary tree. Fat suppression appears to diminish the image quality of bowel because of susceptibility artifact from air-bowel wall interface and is not recommended for bowel studies, although bowel-related extraluminal disease (such as appendical abscess) may be well shown with this technique.

Fat suppression in ETSE is achieved through either spectral-selective or non-spectral-selective preparation pulses. Non-spectral-selective fat suppression, which is termed short-tau inversion recovery (STIR), is performed with a slice-selective inversion pulse timed to suppress the T1 of fat (TI = 150 ms at 1.5 T). Since the pulse is broadband, both water and fat are magnetization prepared, resulting in suppression of fat signal, alteration of contrast from water signal, and depression of water signal from equilibrium. While fat signal is uniformly suppressed (given ideal inversion pulses and consistent T1 over the imaging FOV), the remaining soft tissue (water signal) has lower signal as a direct consequence of the inversion pulse. Since soft tissue in the abdomen has long T1 relative to fat, adequate SNR is still maintained. Although STIR is sensitive to nonuniform

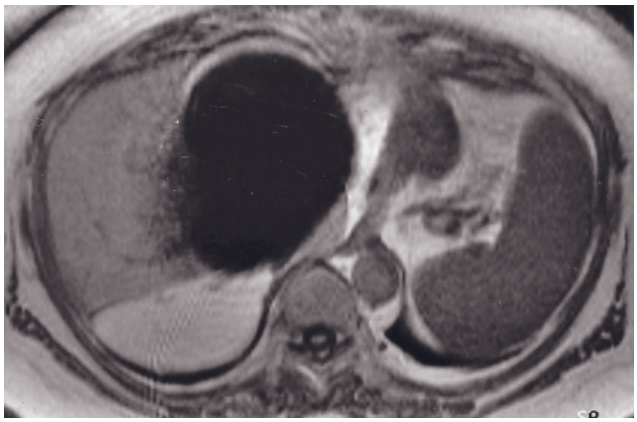

(*a*)

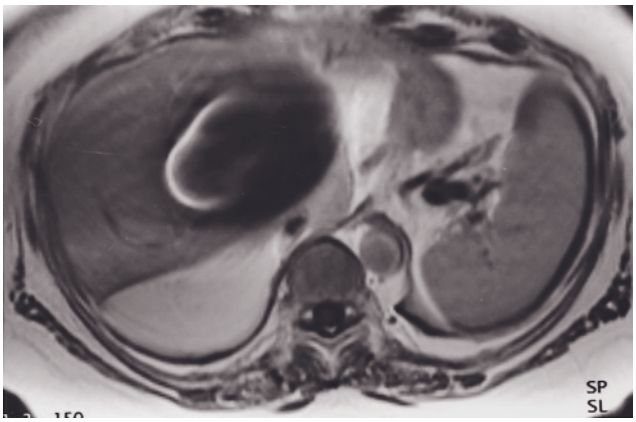

(*b*)

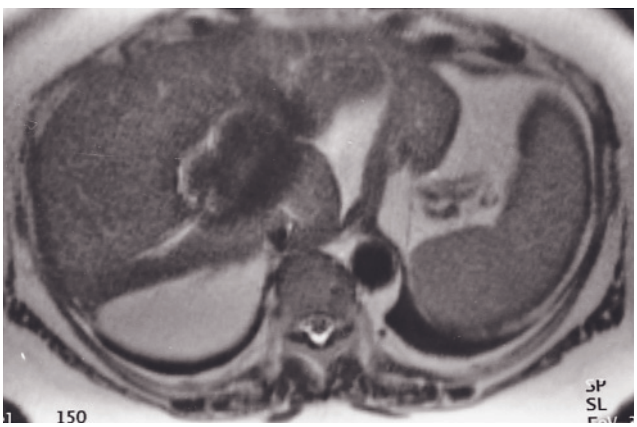

(*c*)

FIG. 1.4 Metallic susceptibility artifact. SGE (*a*), T1 spin-echo (T1-SE) (*b*), and HASTE (*c*) images. Severe susceptibility artifact is present on the SGE image (*a*), with the result that the images of the liver are not interpretable. T1-SE (*b*) is relatively resistant to image degradation by susceptibility artifact; however, substantial artifact still renders much of the liver uninterpretable. The HASTE image (*c*) is the least sensitive MR sequence, and less sensitive than CT imaging for artifacts generated by metallic devices. Only a small portion of the liver is not interpretable with HASTE (*c*).

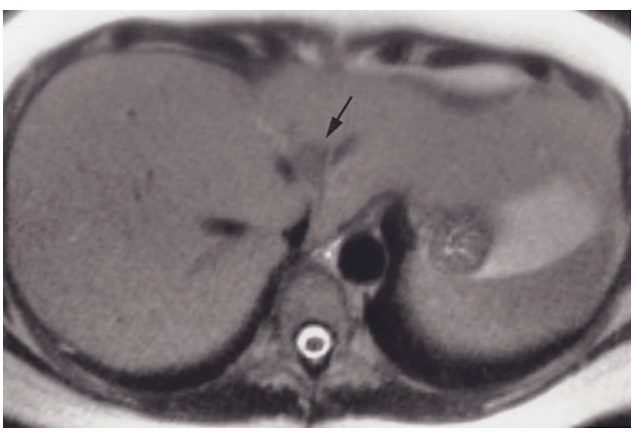

(*a*)

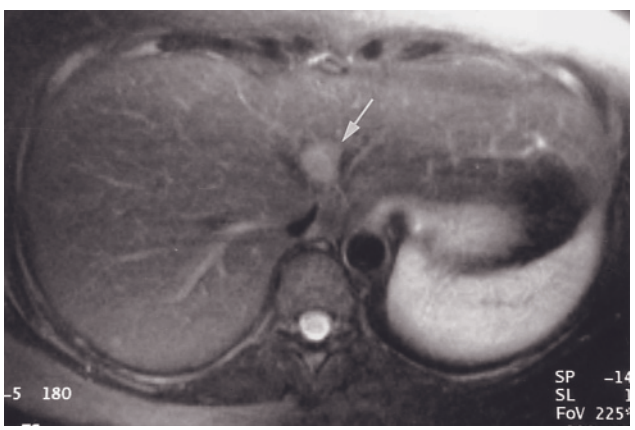

(*b*)

FIG. 1.5 Focal liver lesion in a fatty liver. Single-shot echo-train spin-echo (SS-ETSE) (*a*) and fat-suppressed (FS)-SS-ETSE (*b*) images. The liver appears high in signal intensity on the SS-ETSE image (*a*) because of the presence of fatty liver. A focal liver lesion (focal nodular hyperplasia, arrow, *a*) is identified that is mildly lower in signal intensity than liver parenchyma. On the FS-SS-ETSE image (*b*), the liver has decreased in signal intensity, and the liver lesion (arrow, *b*) now appears moderately high in signal intensity relative to liver. Good liver-spleen contrast is also apparent on the fat-suppressed image (*b*), with no liver-spleen contrast on the nonsuppressed sequence (*a*).

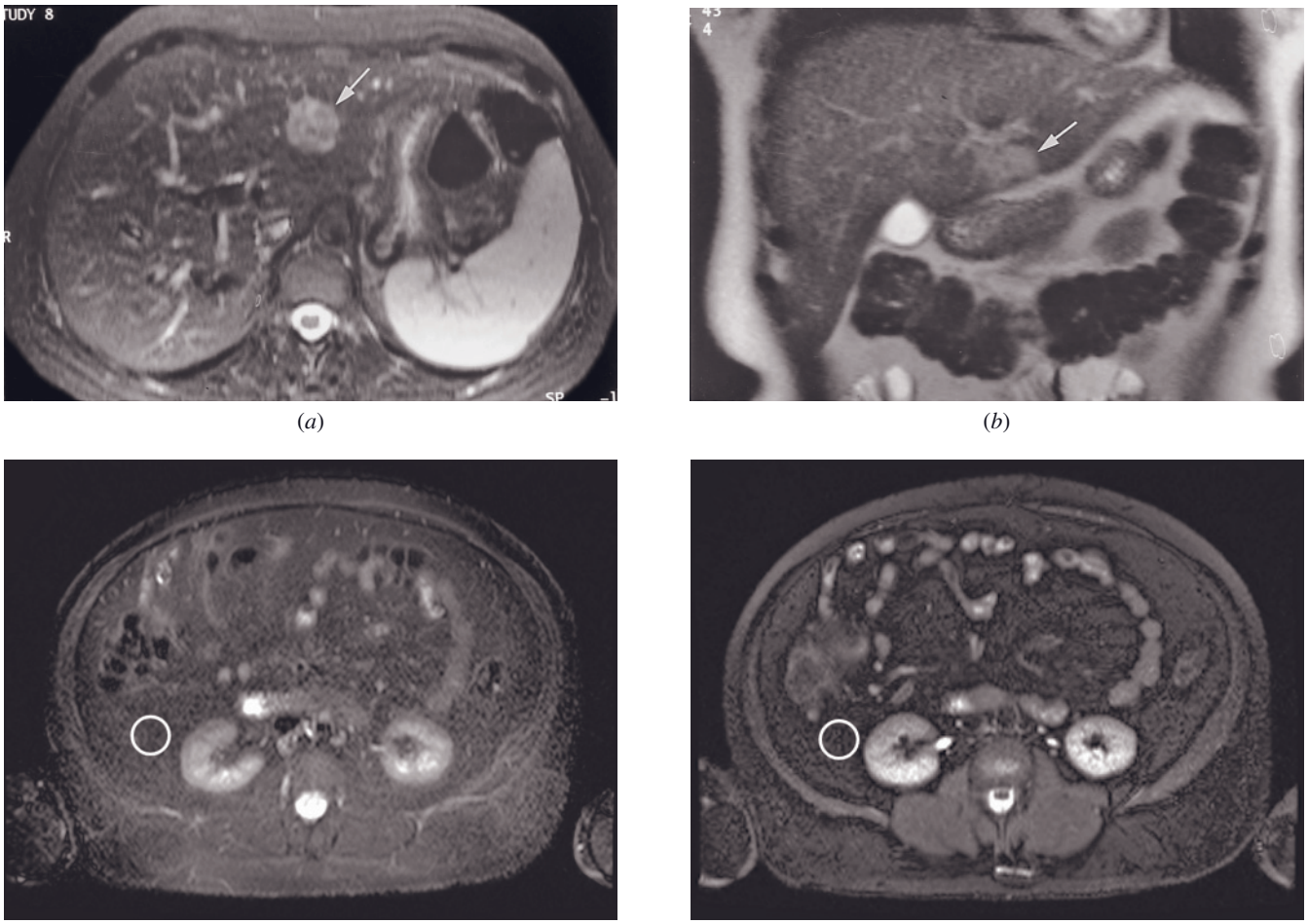

FIG. 1.6 Echo-train STIR and SS-ETSE. Transverse echo-train STIR (*a*) and coronal SS-ETSE (*b*) images in a patient with colon cancer liver metastases. A moderately high-signal-intensity metastasis is present in the left lobe of the liver on the echo-train STIR (arrow, *a*). Background fat is nulled. The liver metastasis is also shown on the coronal SS-ETSE image (arrow, *b*). Background fat is high in signal intensity. Variations in the signal intensity of the background fat provide differing contrast relationships. Comparison of axial STIR (*c*) and SPAIR (*d*) fat suppression on SS-ETSE. The bowel and kidneys are more defined on SPAIR because of the preservation of water signal. Region-of-interest measures (white circle, *c*, *d*) reveal a significant difference in soft tissue SNR and CNR ($P < 0.01$).

inversion (due to B1 field effects), the method is well-accepted as a robust technique for fat suppression in the abdomen using spin echo-based sequences. As the sequence is fundamentally different from SS-ETSE, it may be useful to combine both short-duration sequences for the liver in place of longer, breathing-averaged ETSE (fig. 1.6).

An alternate method of fat suppression involves spectral selection of fat resonances exclusively. Preparation pulses (inversion or saturation) can be spectrally tuned to fat signal, while avoiding undue suppression or alteration of water signal, as seen with STIR techniques. Conceptually, the technique is similar to STIR, in which magnetization (in this case, only fat) is prepared with an inversion pulse timed to suppress fat. Ideally, other soft tissue will remain unaffected, preserving high contrast-to-noise ratio. Since spectral fat suppression is frequency-specific, it is sensitive to spatial susceptibility, which creates an inhomogeneous magnetic field. The water and fat resonances are not clearly delineated in this circumstance, causing fat-water frequency "overlap," and potentially a significant number of fat spins to be unsuppressed. This effect is also prevalent at the edges of the FOV, or any regions away from the magnet isocenter.

Further improvement in uniform fat suppression can be achieved by incorporating adiabatic pulses, which are a specially designed class of RF pulses that provide B1-insensitive spin nutation. Recently, spectral (fat)-selective adiabatic inversion pulses, termed "SPAIR," have been used in T2-weighted imaging of the abdomen [10]. The uniformity of fat suppression is more

robust than traditional spectral-selective techniques, making it the method of choice for liver and bowel imaging. Moreover, its inherent high CNR provides important diagnostic advantages over STIR, since soft tissue signal is preserved. The effects of inhomogeneous main magnetic field still pose challenges for SPAIR, due to spectral overlap. But the improved inversion profile and frequency cutoff of SPAIR alleviates the degree of poor fat suppression (fig. 1.6). Implementation of SPAIR fat suppression takes longer than its other counterparts, because of the longer pulse length required for the adiabatic condition. This may increase scan times for segmented T2 and T1 acquisitions.

GADOLINIUM-ENHANCED T1-WEIGHTED SEQUENCES

Gadolinium contrast agent is most effective when it is administered as a rapid bolus, with imaging performed with T1-weighted SGE or 3D-GE sequences obtained in a dynamic serial fashion. After the intravenous injection of gadolinium, a minimum of two postcontrast sequences are needed, one acquired in the hepatic arterial dominant phase, within 30 s of contrast administration, and the second in the hepatic venous or interstitial phase at approximately 2–5 min. For liver imaging, an intermediate-timed third pass, termed portal venous or early hepatic venous, at 1 min postcontrast, is useful as well [6]. Little additional information is provided if more than four sequences are acquired. Features of these phases of enhancement are as follows.

Hepatic Arterial Dominant (Capillary) Phase

The hepatic arterial dominant (capillary) phase is the single most important data set when using a nonspecific extracellular gadolinium chelate contrast agent [6]. This technique is essential for imaging the liver, spleen, and pancreas, and it provides useful information on the kidneys, adrenals, vessels, bladder, and uterus. The timing for this phase of enhancement is the only timing for postcontrast sequences that is crucial. It is essential to capture the "first pass" or capillary bed enhancement of tissues during this phase. Demonstration of gadolinium in hepatic arteries and portal veins and absence of gadolinium in hepatic veins are reliable landmarks (fig. 1.7). At this phase of enhancement, although contrast is present in portal veins, the majority of the gadolinium present in the liver has been delivered by hepatic arteries. The absolute volume of hepatic artery-delivered gadolinium is greater in this phase of enhancement than acquiring the data when gadolinium is only present in hepatic arteries; therefore, more hepatic arterial enhancement information is available. This is important since most focal liver lesions, especially metastases and hepatocellular carcinoma, are fed primarily by hepatic arteries. Imaging slightly earlier than this, when only hepatic arteries are opacified (hepatic arteries-only phase) may approach the diagnostic utility of the hepatic arterial dominant phase if the injection rate of contrast is very fast (e.g., 5 ml/s) and data are acquired late in the hepatic arteries-only phase (within 1 or 2 s of gadolinium appearing in the portal veins). It is very difficult to achieve these objectives in the hepatic arteries-only phase, and it is also difficult to judge whether image acquisition is too early in this phase, when the liver is essentially unenhanced. Appropriate timing, as judged by vessel enhancement, also is important for the evaluation of surrounding organs. Too little pancreatic enhancement is consistent with pancreatic fibrosis or chronic pancreatitis, and too little enhancement of renal cortex may imply ischemic nephropathy or acute cortical necrosis. This can be reliably judged on hepatic arterial dominant phase images, because of the fixed landmarks of contrast in portal veins and absence in hepatic veins. In the hepatic arteries-only phase, minimal enhancement of pancreas or renal cortex may reflect too early image acquisition rather than disease process. Since this immediate postgadolinium phase of enhancement is also used to diagnose adequate perfusion of these organs, it is oxymoronic to use enhancement of these organs as the determination of the appropriateness of the phase of image acquisition timing. Although

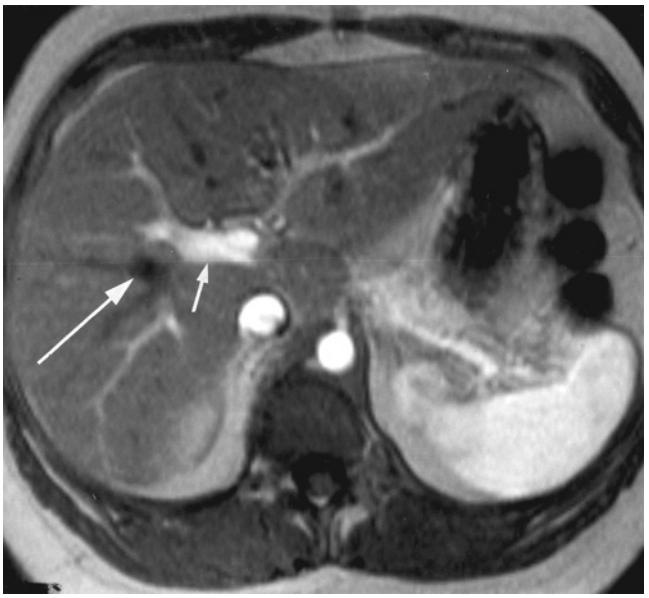

FIG. 1.7 Hepatic arterial dominant phase. Image demonstrates gadolinium in portals veins (short arrow) and lack of contrast in hepatic veins (long arrow).

enhancement of pancreas or renal cortex is used as ancillary information for assessment of timing, it is not the major determinant, since the extent of enhancement of these organs is also evaluated at this phase. In the liver, imaging too early in the hepatic arteries-only phase diminishes the ability to recognize the distinctive patterns of lesion enhancement for different lesion types, because the absolute volume of hepatic artery-delivered contrast may be too small and may cause lesions to be mischaracterized (fig. 1.8).

On hepatic arterial dominant phase T1-weighted SGE or 3D-GE images, various types of liver lesions have distinctive enhancement patterns: Cysts show lack of enhancement, hemangiomas show peripheral nodules of enhancement in a discontinuous ring, nonhemorrhagic adenomas and focal nodular hyperplasia show intense uniform enhancement, metastases show ring enhancement, and hepatocellular carcinomas show diffuse heterogeneous enhancement. The ability to use this information to characterize lesions as small as 1 cm may be unique to MRI. Appearances of less common liver lesions on immediate postgadolinium images have also been reported, many of which show overlap with the above-described patterns of common liver lesions. To a somewhat lesser extent, appreciation of the capillary phase enhancement of lesions in the pancreas, spleen, and kidneys provides information on lesion characterization that will be described in the respective chapters of these organ systems. Clinical history is often important, despite the high diagnostic accuracy of current MRI imaging protocols. In addition, many different histologic types of liver lesions when they measure less than 1 cm, demonstrate virtually identical uniform enhancement, for example, hemangiomas, adenomas, focal nodular hyperplasia, metastases, and hepatocellular carcinoma. Ancillary information to assist in characterization of lesions is crucial, which includes T2-weighted images that demonstrate lesion fluid content (e.g., high for hemangioma and often high for hypervascular metastases, and relatively low for adenoma, focal nodular hyperplasia, and hepatocellular carcinoma), appearance of other concomitant large lesions, and clinical history (e.g., history of known primary tumor that can result in hypervascular metastases, such as gastrointestinal leiomyosarcoma).

Various enhancement patterns of liver and other organ parenchyma are also demonstrated on hepatic arterial dominant phase images. One of the most common perfusion abnormalities observed in the liver is transient increased segmental enhancement in liver segments with compromised portal venous flow due to compression or thrombosis. Other hepatic diseases that demonstrate perfusion abnormalities on immediate postgadolinium images include Budd–Chiari syndrome, with different enhancement patterns for acute, subacute, and chronic disease, and severe acute hepatitis with hepatocellular injury. Perfusion abnormalities of the kidneys are also relatively common and are clearly shown on early- and late-phase gadolinium-enhanced images.

Examination for liver metastases may be the most common indication for liver MR examination. Liver metastases have been classified as hypovascular (typical examples are colon cancer and transitional cell carcinoma) or hypervascular (typical examples are islet cell tumors, renal cell carcinoma, and breast cancer). A third category of vascularity has not been described well in the past and this is near-isovascular with liver. Near-isovascular refers to lesion enhancement that is very comparable to that of liver on early and late postgadolinium images. Near isovascularity is most readily appreciated when lesions are poorly seen on postgadolinium images but well seen on precontrast images (fig. 1.9). Liver metastases from primaries of colon, thyroid, and endometrium may show this type of enhancement pattern. The most common setting is postchemotherapy, although this may also be observed in untreated patients. Fortunately, many of these tumors are moderately low signal intensity on T1-weighted images, rendering them readily apparent, and on occasion they may also be moderately high signal intensity on T2-weighted images. Rarely they may also be near isointense on T1-weighted and T2-weighted images, and therefore can escape detection. The rarity of this occurrence illustrates one of the great strengths of MRI over sonography and computed tomography: The greater the number of distinctly different data sets that are acquired, the less likely it is for disease to escape detection. MRI has more acquisitions of different types of data than ultrasound or CT.

Chemotherapy-treated liver metastases deserve special mention in that chemotherapy is routinely given to the majority of patients with liver metastases and chemotherapy alters the imaging features of metastases. Chemotherapy induces change in the signal intensity and imaging features of metastases such that they may resemble cysts, hemangiomas, or scar tissue [6]. As mentioned above, they may also become near isovascular on postgadolinium images.

Portal Venous Phase or Early Hepatic Venous Phase

This phase is acquired at 45–60 s after initiation of gadolinium injection. In this phase hepatic parenchyma is maximally enhanced so hypovascular lesions (cysts, hypovascular metastases, and scar tissue) are best shown as regions of lesser enhancement. Patency or thrombosis of hepatic vessels are also best shown in this phase.

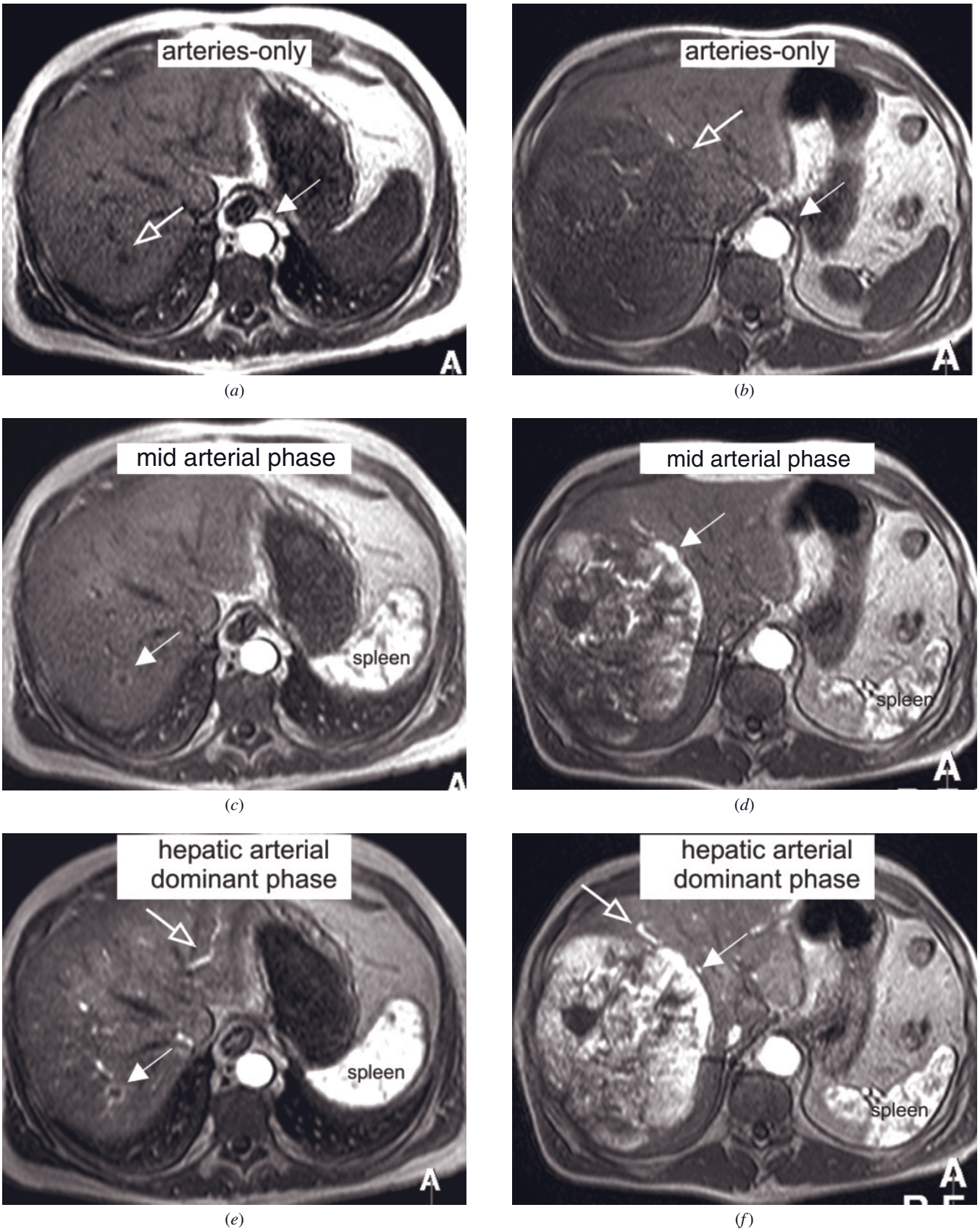

FIG. 1.8 Hepatic arteries-only, hepatic early arterial phase and hepatic arterial dominant phase. Images from a series of time-resolved 2D dynamic gadolinium-enhanced spoiled gradient echo with parallel imaging (parallel MRI acceleration factor 2; scan time of 7 s per image) in two different patients with a neuroendocrine metastasis (*a*, *c*, *e*) and with a pathology-proved hepatocellular carcinoma (HCC) in a noncirrhotic liver (*b*, *d*, *f*), respectively. Very early after the injection of gadolinium, only the arteries are visible (arrows in *a* and *b*). In the following phase, little enhancement of the lesions is present (arrows in *c* and *d*). In the hepatic arterial dominant phase, optimal enhancement difference is visible between the liver and the lesions because of more enhancement of the lesions (solid arrows in *e* and *f*). Note also the enhancement of the portal vessels in this phase (open arrows in *e* and *f*). Data acquisition in the arterial phase provided better diagnostic information on the enhancement features of the two hepatic lesions.

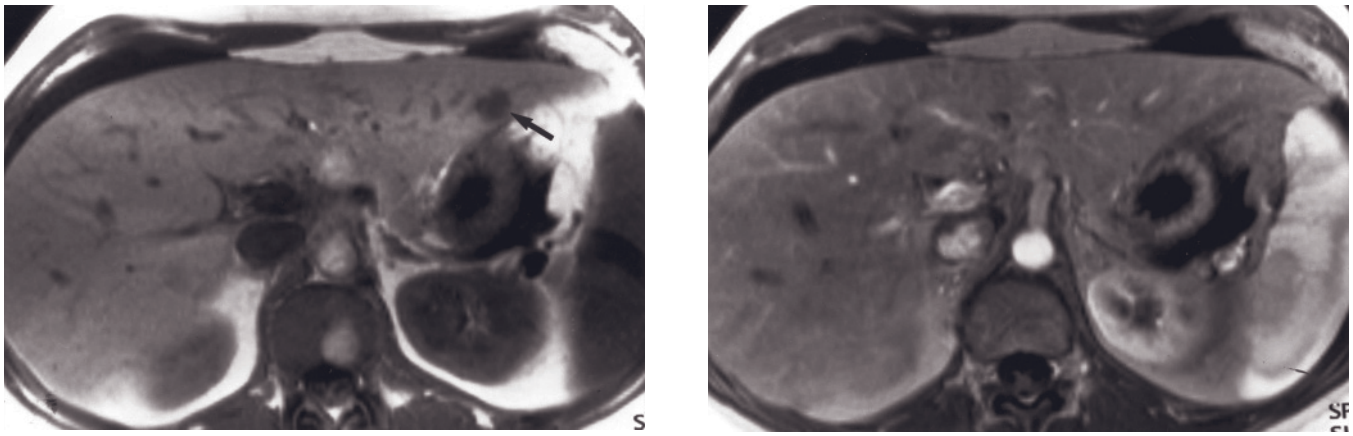

(*a*) (*b*)

FIG. 1.9 Near-isovascular liver metastases. SGE (*a*) and hepatic arterial phase gadolinium-enhanced SGE (*b*) images. In this patient with liver metastases who is at 9 months after initiation of chemotherapy, liver metastases are clearly shown on noncontrast T1-weighted images (arrow, *a*) but poorly seen after gadolinium administration. This enhancement pattern, termed near-isovascular, is most commonly observed in liver metastases in a subacute phase of response to chemotherapy.

Hepatic Venous (Interstitial) Phase

Hepatic venous phase or interstitial phase is acquired 90 s to 5 min after initiation of contrast injection. Late enhancement features of focal liver lesions are shown that aid in lesion characterization, such as persistent lack of enhancement of cysts, coalescence and centripetal progression of enhancing nodules in hemangiomas, homogeneous fading of enhancement of adenomas and focal nodular hyperplasia to near isointensity with liver, late enhancement of central scar in some focal nodular hyperplasias, peripheral or heterogeneous washout of contrast in liver metastases, washout to hypointensity with liver in small liver metastases and hepatocellular carcinoma, heterogeneous washout of hepatocellular carcinoma, and delayed capsule enhancement in hepatocellular carcinoma (less commonly adenoma). Enhancement of peritoneal metastases, inflammatory disease, bone metastases (fig. 1.10) and circumferential, superficial spreading cholangiocarcinoma are also well shown at this time frame. Concomitant use of fat suppression is essential for optimized demonstration of these findings. Additional documentation of vascular thrombosis is also provided on these images.

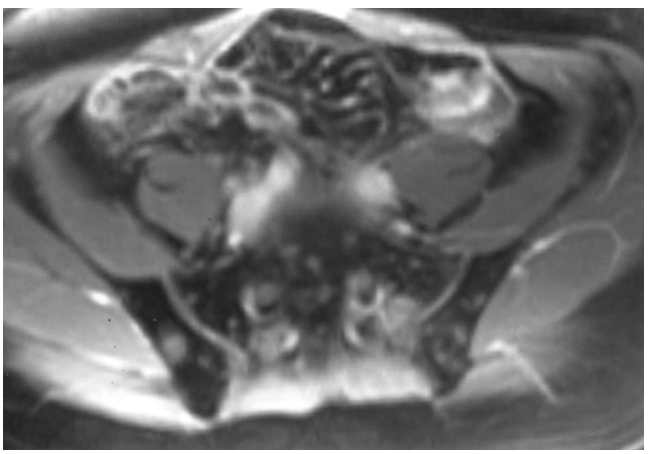

FIG. 1.10 Bone metastases. Two-minute gadolinium-enhanced T1-weighted fat-suppressed SGE image demonstrates multiple rounded enhancing bone metastases that are clearly defined in a background of suppressed fatty marrow.

MULTIPLE IMAGING VARIABLES

On MR images, it is common that multiple imaging properties are concurrently present. The contributions of these various properties must be separately determined so that appropriate diagnosis is made. Common potentially competing imaging characteristics include T2 and fat suppression effects; T1 out-of-phase and magnetic susceptibility effects; and gadolinium washout and fat suppression effects. T2 and fat suppression effects can usually be separated by employing both nonsuppressed and fat-suppressed T2-weighted sequences. Low signal due to fat suppression effects can be correctly ascertained by the demonstration of higher signal intensity of the structure on non-fat-suppressed T2 sequences relative to the T2 fat-suppressed sequences. Out-of-phase and magnetic susceptibility signal loss can be separated by observing that susceptibility effects increase with increasing TE on SGE sequences and are generally also observed as low signal on T2-weighted sequences, whereas out-of-phase lipid signal effects cycle with in- and out-of-phase echo times. Distinction between gadolinium washout and fat suppression effects on the 2-min postgadolinium T1-weighted

fat-suppressed GE sequence must also be established. In problem cases, there is the observation of low signal of a structure on later postgadolinium fat-suppressed sequences, that appeared high signal on early postgadolinium nonsuppressed sequences. The question arises whether this reflects a fat suppression effect rather than a gadolinium washout effect. In the liver, this can usually be distinguished by the observation that a fatty lesion is low signal on a 2-min postgadolinium fat-suppressed sequence, while isointense or hyperintense on both the immediate and the 1-min nonsuppressed portal venous phase SGE sequences. Generally, if a liver lesion washes out at 2 min, it has most often shown evidence of washout already by 1 min on the portal venous phase non-fat-suppressed SGE images. Further supportive information of a fat effect is evidence that the lesion appears fatty on any of the other sequences employed in the imaging protocol (e.g., out-of-phase or noncontrast fat-suppressed sequences). Figure 1.11 illustrates many of these combined imaging properties in one situation.

With MR imaging, it is possible to acquire images in any desirable anatomic orientation (i.e., transverse, coronal, sagittal, or oblique) without moving the patient. The choice of the plane of data acquisition is influenced by the familiarity of image interpretation using different planes, type of MR equipment used, and the sequence employed. In general terms, the majority of the imaging is acquired in the transverse plane, which can be explained for a number of reasons, including lesser problems with partial volume effects and general familiarity of radiologists with this plane from experience with CT. In the upper abdomen, we routinely supplement the transverse plane by one or two (or more) acquisitions in the coronal plane, and in the pelvis with sagittal plane imaging. Additional planes may be obtained, but as a general principle, our view is to maintain as few possible data acquisitions to achieve the balanced effect of sufficient redundancy but not excessive data acquisition (mainly for time and patient cooperation reasons). In some organ systems, our routine practice of acquiring the primary sequences in the transverse plane and supplementing them with an additional plane is modified when employing the thin-section data acquisition capability of 3D-GE, which facilitates reconstruction in different planes from a single acquired data set. As an example, with imaging of the kidneys using SD-SGE sequences, our approach has been to acquire transverse images and supplement them with sagittal plane images. Using 3D-SGE, our tendency has been to acquire data in the coronal plane, which also facilitates simultaneous assessment of the renal arteries. In the end, since studies often must be viewed at other facilities, radiologists are generally familiar with transverse plane from CT, and comparison must often be made with CT studies, it seems prudent to use the transverse plane as the primary imaging plane.

SIGNAL INTENSITY OF VESSELS

Inhomogeneous signal intensity of vessels is a diagnostic problem not infrequently encountered on MR images. In general, we have found that image acquisition between 1 and 2 min postgadolinium using GE results in consistently high signal of patent arteries and veins. Unfortunately, data acquisition often falls beyond this range, particularly in the setting of acquiring images of the pelvis after images of the abdomen. If patency of vessels is a particular diagnostic concern, then we employ sequences that consistently show high signal in patent vessels, often by combining intrinsic in-flow effects and gadolinium effects. Sequences we employ include gadolinium-enhanced slice-selective 180° MP-RAGE (particularly useful for noncooperative patients), gadolinium-enhanced water excitation SGE, and gradient echo sequences with gradient echo refocusing (without gadolinium) (e.g., true FISP, GRASS). Acquisition of additional planes is also useful, for example, coronal plane of the liver postgadolinium and sagittal plane of the pelvis postgadolinium.

IMAGING STRATEGIES

High diagnostic accuracy can be achieved by describing the T1-, T2-, capillary and interstitial phase gadolinium-enhanced T1-weighted sequence appearance of various disease processes. In practice, it is also important to recognize which technique is the most consistent in demonstrating various lesions in order to target these lesions in an imaging protocol. Table 1.1 lists the MR sequences on which certain disease processes are consistently shown.

A major strength of MRI is the variety of types of information that the modality is able to generate. As a result, MRI is able to provide comprehensive information on organ systems and disease entities. The use of a diverse group of sequences, acquired in multiple planes, minimizes the likelihood of not detecting disease or misclassifying disease. This is a reflection of the fact that the more different information that is acquired, the less likely it is that disease will escape detection. Attention to length of examination is critical because longer examinations result in fewer patients who can be examined and a decrease in patient cooperation. Ideally, many of the different sequences employed should be of short duration and breath hold or breathing-independent. An attempt should be made to achieve

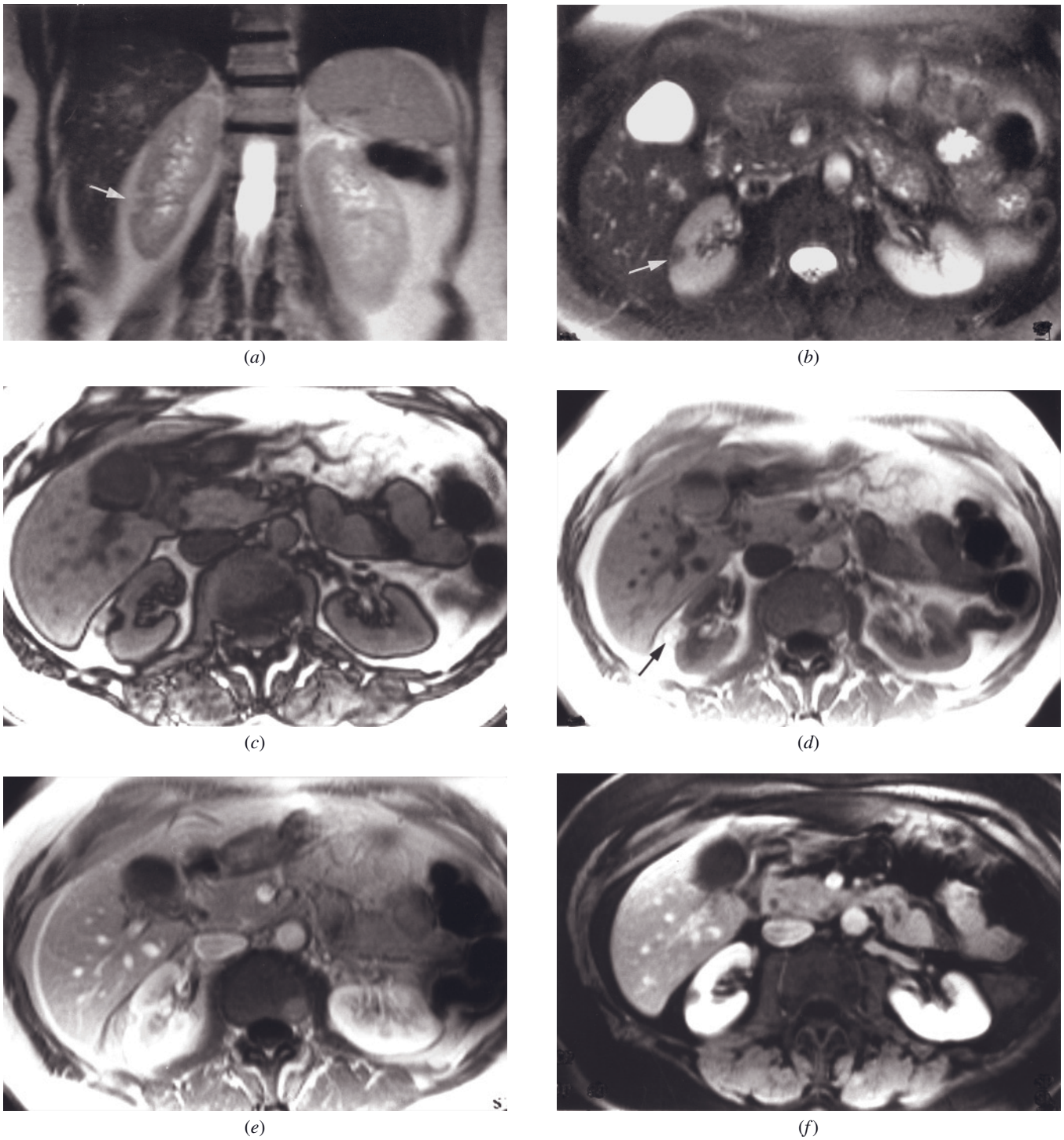

FIG. 1.11 Fat effects, gadolinium effects, and their distinction. Coronal T2-weighted single-shot echo-train spin-echo (*a*), T2-weighted fat suppressed single-shot echo-train spin-echo (*b*), T1-weighted out-of-phase SGE (*c*), T1-weighted in-phase SGE (*d*), 1-min postgadolinium SGE (*e*), and 1.5-min gadolinium-enhanced fat-suppressed SGE (*f*) images. It is always useful to compare noncontrast nonsuppressed (*a*) and fat suppressed (*b*) sequences to ascertain whether high-signal structures observed on nonsuppressed sequences represent fat, or lower-signal structures observed on fat-suppressed sequences represent fat and not low-fluid-content solid masses. Comparing out-of-phase (*c*) to in-phase (*d*) sequences also permits characterization of fatty tumors. In this patient, a right renal angiomyolipoma is present that on the basis of the fat-suppressed T2-weighted sequence alone (arrow, *b*) may be considered a possible renal cancer or hemorrhagic cyst because of its low signal. Comparison with the non-fat-suppressed sequence (*a*) reveals that the tumor is high signal intensity in the absence of suppression (arrow, *a*), showing that it represents fat. Another approach is to show that the high-signal mass on the in-phase image (arrow, *d*) develops a phase cancellation black ring interface with renal parenchyma on the out-of-phase image (*c*). By noting that the mass is fatty, then high signal on early post-gadolinium images (arrow, *d*) can be recognized as a fat effect, and not enhancement, and loss of signal on the 1.5-min gadolinium-enhanced fat-suppressed image is not misinterpreted as washout, but correctly observed as a fat suppression effect.

Table 1.1 MR Imaging Sequences That Show Consistent Display of Various Disease Processes

Sequences	Disease Process	Appearance
T1	Fluid	↓↓
T1 out of phase	Adrenal adenoma, fatty liver	↓
T1 fat suppressed	Normal pancreas Subacute hematoma Endometriosis (subacute blood)	↑
T2	Fluid	↑↑
T2	Iron (including hemosiderin)	↓↓
T2	Uterine cervix, prostate	Zonal anatomy, cancer
Capillary phase Gad	Focal lesions of liver, spleen, pancreas	Distinctive patterns
Capillary phase? Gad	Inflammatory disease	↑
Capillary phase Gad	Arterial compromise	↓
Capillary phase? Gad	Portal vein compromise	↑
Interstitial phase Gad	Inflammatory disease, peritoneal metastases, bone metastases, lymphadenopathy	↑

this goal in protocol design. Another consideration is reproducibility of examination protocols. Efficient operation of an MRI system requires the use of set protocols, which serves to speed up examinations, render exams reproducible, and increase utilization by familiarity with a standard approach. A useful approach is to have sufficient redundancy in sequences that if one or two sequences are unsatisfactory there still is enough information for the study to be diagnostic, while at the same time not to have too much redundancy that study times are long and patient cooperation diminishes towards the latter part of the study. The diminishing patient cooperation toward the latter part of the study also implies that the most important sequences should be acquired as early as possible in the exam. MRI techniques are in continuous evolution, and when new sequences are developed it is important to replace older sequences with newer sequences, rather than simply adding new sequences onto an existing protocol. Speed of data acquisition, image quality, disease display, and consistency of image quality are all important considerations when evaluating new sequences. For example, it is well-accepted that the image quality of contrast-enhanced 3D T1-weighted GE imaging has exceeded the point that it is now superior to 2D imaging. Hence, for dynamic contrast imaging, all SGE sequences in our protocols have been replaced with 3D imaging. It is anticipated that this transition may also extend to opposed-phase imaging, with 3D acquisitions being the preferred imaging method. On older MR systems, one may still want to implement SGE technique because of its robustness. On the newest MR systems, the rationale to utilize 3D imaging includes thinner-section data acquisition, lesser problems with motion and phase artifact, and the ability to use the same data set to generate an MRA exam [11, 12].

The protocoling of MRI studies that investigate the abdomen and pelvis in the same setting may be rendered most efficient by acquiring a complete study of the upper abdomen initially, using precontrast SGE and FS 3D-GE and/or FS SGE, T2-weighted single shot ETSE and single shot FS-ETSE, and serial postgadolinium FS 3D-GE or SGE and FS-SGE images, then acquiring the pelvis study, including postgadolinium FS-SGE or FS 3D-GE followed by T2-weighted sequences (fig. 1.12). Comprehensive examination of all organs and tissues in the abdomen and pelvis can be achieved with this approach, which permits detection of a full range of disease, including unsuspected disease (fig. 1.13). This strategy minimizes table motion and repositioning of the phased-array coil, which are time-consuming procedures. Newer MR systems now allow simultaneous planning of abdomen and pelvis regions, such that each acquisition can be conducted in series. With this capability, all precontrast T2 and T1 imaging can be acquired together without disrupting the specifically-timed T1 postcontrast images. This strategy allows increased exam efficiency, since one can migrate specific T2-weighted precontrast sequences, such as SSFP or MRCP, to postcontrast slots, especially between the portal venous phase (1–2 min post) and delayed interstitial phase (3+ min post). Although it is not generally desired to acquire T2-weighted images after gadolinium, we have not observed significant degradation of T2-weighted images of the pelvis after gadolinium. The presence of concentrated low-signal-intensity gadolinium in the bladder on T2-weighted images may in fact be beneficial by increasing conspicuity of bladder

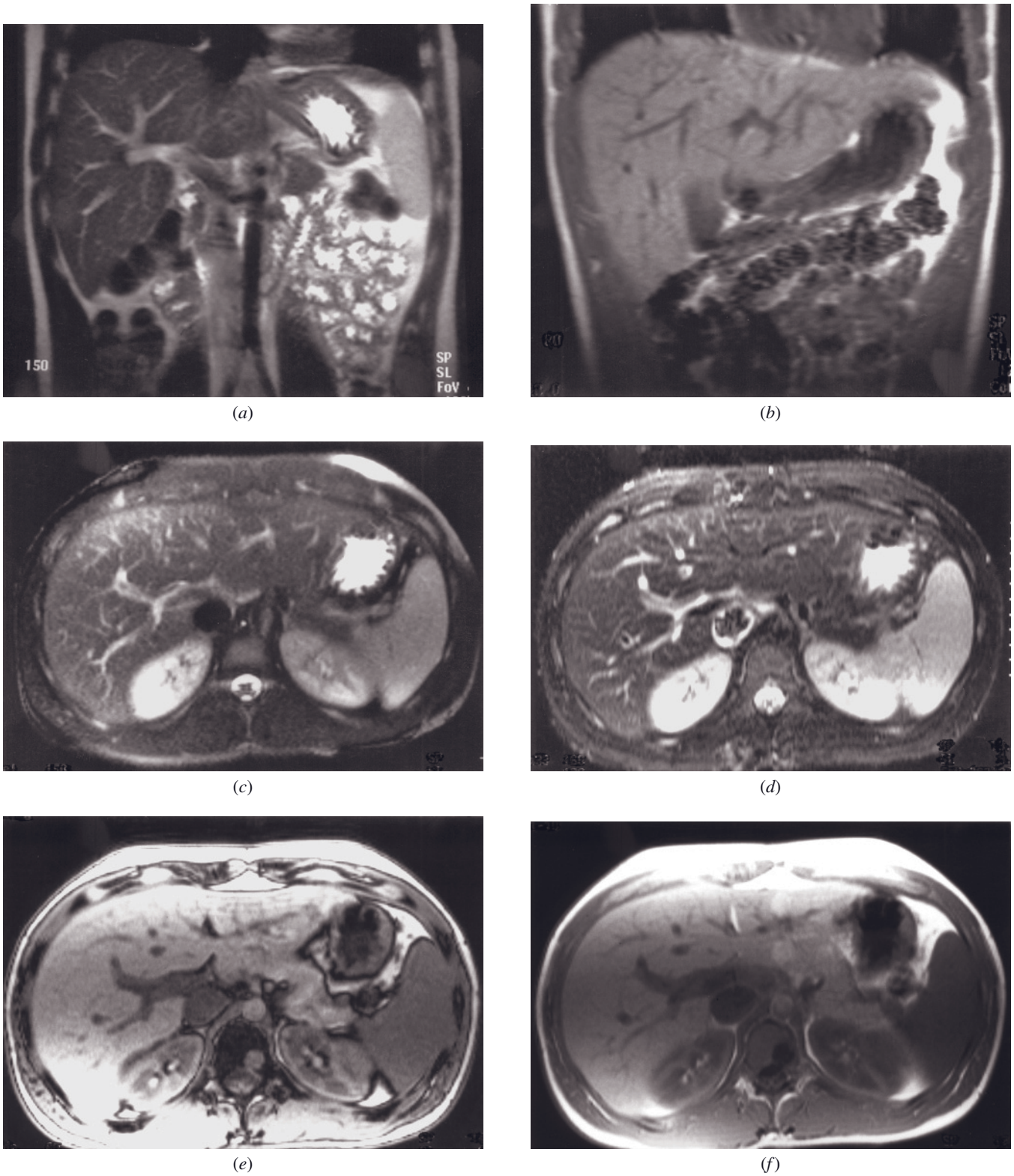

(*a*) (*b*) (*c*) (*d*) (*e*) (*f*)

FIG. 1.12 Liver and pelvis protocol. Coronal T2-weighted single-shot echo-train spin-echo (*a*), coronal T1-weighted SGE (*b*), T2-weighted fat-suppressed single-shot echo-train spin-echo (*c*), T2-weighted breath-hold STIR (*d*), T1-weighted out-of-phase SGE (*e*), T1-weighted in-phase SGE (*f*), hepatic arterial dominant phase SGE (*g*), 1-min postgadolinium SGE (*h*), 1.5-min postgadolinium

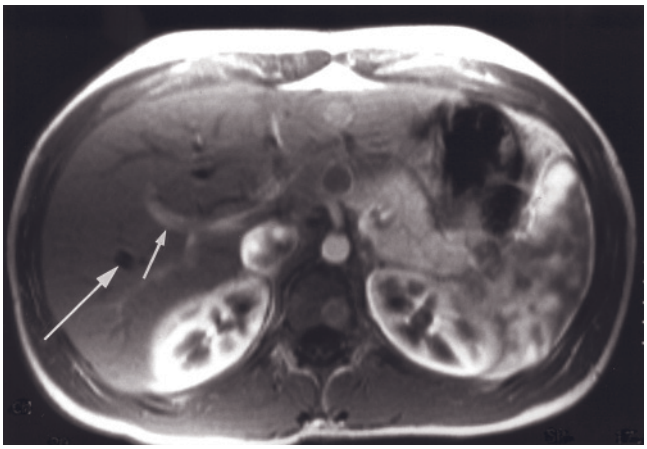

(*g*)

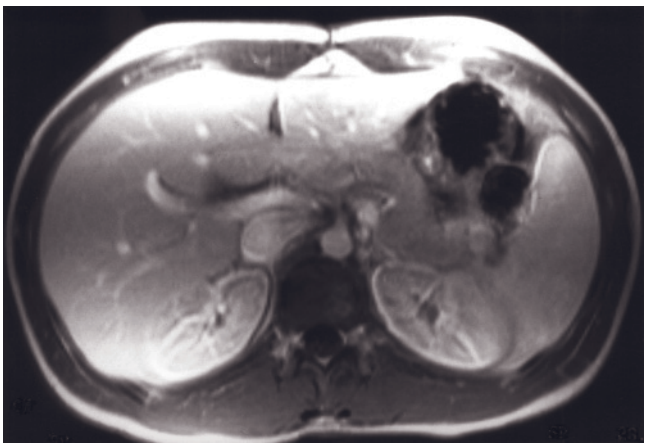

(*h*)

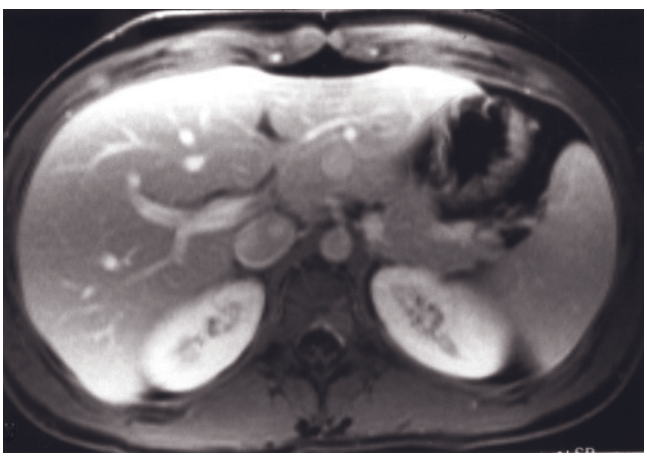

(*i*)

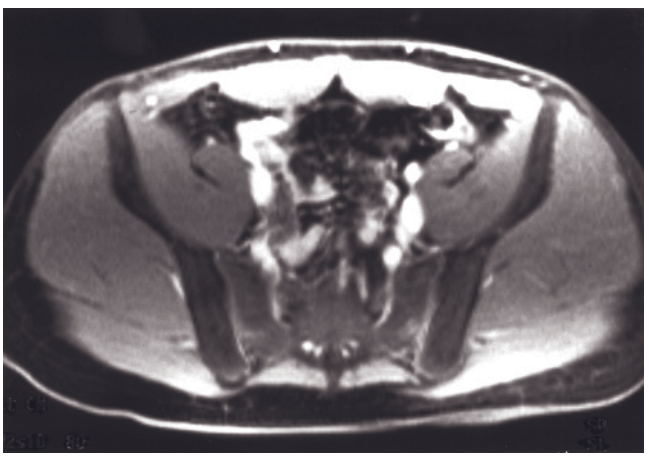

(*j*)

(*k*)

FIG. 1.12 (*Continued*) fat-suppressed SGE (*i*), transverse (*j*) and sagittal (*k*) 4-min postgadolinium fat-suppressed SGE, transverse (*l*) and sagittal (*m*) T2-weighted single-shot echo-train spin-echo images. Pre- and postgadolinium multiplanar T1- and

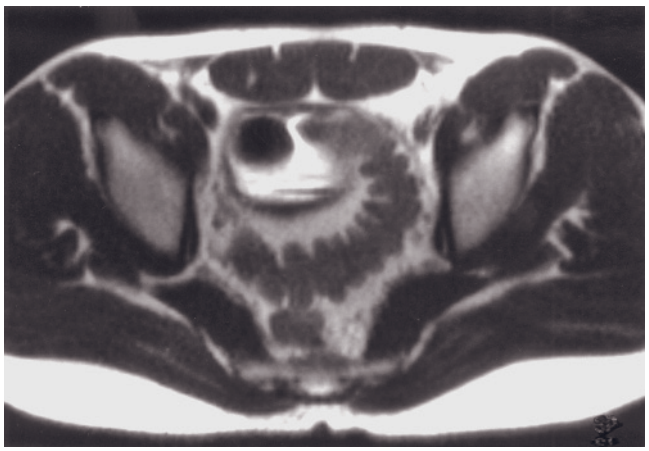

(*l*)

(*m*)

FIG. 1.12 (*Continued*) T2-weighted images of the pelvis (*j–m*). A combination of breath-hold (*b*, *d*, *e–k*) and breathing-independent (*a*, *c*, *l*, *m*) sequences are used to ensure consistent image quality in cooperative patients, combined with short study duration, typically 30–40 min. On the hepatic arterial dominant phase image, note the presence of gadolinium in portal veins (short arrow, *g*) and not hepatic veins (long arrow, *g*).

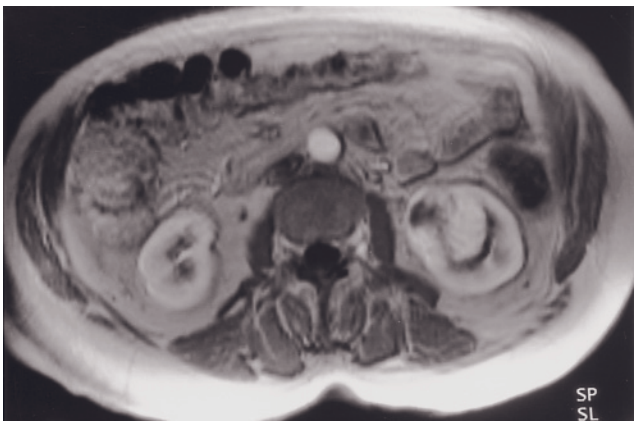

(*a*)

(*b*)

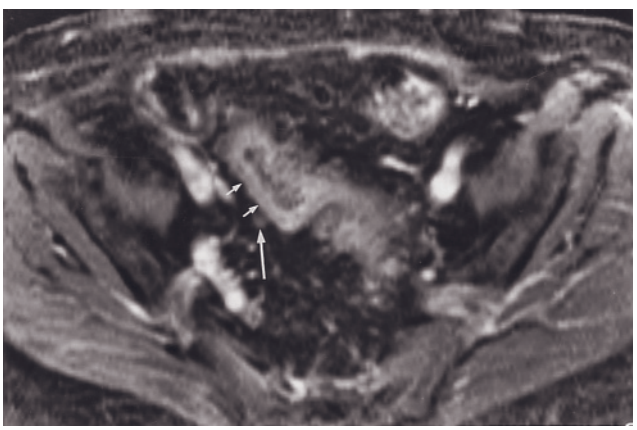

(*c*)

FIG. 1.13 Concurrent renal cell cancer and colon cancer. Immediate postgadolinium SGE (*a*), 90-s postgadolinium fat-suppressed SGE (*b*), and 3-min postgadolinium fat-suppressed SGE (*c*) images. Selected images from a liver pelvis protocol in a patient evaluated for colon cancer demonstrate an incidental left renal tumor that enhances intensely on immediate postgadolinium images (*a*) and washes out (arrow, *b*) on the fat-suppressed image, diagnostic for renal cell cancer. Thickening of the sigmoid colon representing cancer (small arrows, *c*) is appreciated on images acquired of the pelvis. A small regional involved lymph node (long arrow, *c*) is well shown on the gadolinium-enhanced fat-suppressed image.

involvement from malignant pelvic diseases. The liver is the organ that benefits the most from immediate postgadolinium imaging, and imaging protocols should be designed in a fashion to image the liver immediately after gadolinium administration. If, however, liver metastases are unlikely and the pelvis is the major focus of investigation, studies can be structured to acquire immediate postgadolinium images of the pelvis (e.g., for the evaluation of bladder tumors).

Patient setup can be performed as follows. The phased-array coil is initially placed over the upper abdomen, and image acquisition is centered over the liver. After precontrast sequences, with the patient positioned in the bore of the magnet, gadolinium is injected as a forceful hand bolus injection over 5 s, followed by injection of a normal saline flush over 3 s. Image acquisition is initiated immediately after the normal saline flush with the SGE sequence. Another approach, using a power injector, is to administer contrast at 2 ml/s and to initiate the scan 17 s after the start of contrast injection. Other researchers have also recommended using a timing bolus to increase the reproducibility of data acquisition in a correct phase of enhancement [12].

Accuracy and reproducibility of arterial-phase acquisition is of vital importance, as discussed earlier in this section. It is reasonable to assert that individual arterial transit times from the point of contrast administration to hepatic arteries vary in patients with a range of liver disease. Therefore, customized arterial timing is preferred to fixed timing methods, assuming it also provides efficient implementation for users. To this end, a real-time ("on-the-fly") bolus-tracking method for liver imaging has been utilized by some centers to eliminate the need for test-bolus timing injections. This timing method incorporates a strategy similar to MRA timing, in which a fast (~0.5 s), single-slice SGE, with real-time reconstruction, is used to image the arrival of contrast medium into a region-of-interest, whereupon the user performs a breath-hold command and triggers the next acquisition. Extension of real-time bolus tracking to liver timing application involves redefining the specific elements of execution, namely, 1) the trigger point-of-interest to stop bolus tracking and 2) subsequent time delay to commence arterial-phase acquisition with 3D GE. Current clinical implementation utilizes the descending aorta at the level of the diaphragm (celiac axis) as an appropriate stopping point, since it is easily visualized and occurs upstream enough from the hepatic arterial dominant phase to allow adequate delay for breath-hold commands. The precise time for this delay is a matter of continued investigation. In a strict sense, the delay should signify the duration from celiac axis to peak tumor signal contrast in liver. Preliminary perfusion MR data have shown an average duration of approximately 10 s [13]. Using this strategy, it is intended to time 3D GE at peak tumor contrast, which refers to the center of k-space, not the start of the scan. Therefore, the delay following bolus detection in the descending aorta must be adapted according to the pulse sequence (i.e., 6 s). For certain 3D GE configurations, the effective center of k-space may not occur near the beginning of the acquisition, as seen with 3D MRA sequences. This may limit the capacity to perform adequate breath-hold commands. In this scenario, the user may choose a vascular reference trigger point further upstream to compensate. It should be emphasized, however, that "optimal delay of 10 s" refers to the duration to "peak" tumor contrast, which can be tempered by realizing there naturally exists a finite window of "high tumor contrast," allowing the user a margin of error in 3D GE timing acquisition. The real-time bolus-tracking strategy has been shown to be a highly efficient and reproducible method for capturing the time-sensitive arterial phase over fixed-timing techniques, and without the need for multiple injections, as with a separate timing bolus. Additionally, a separate timing bolus will inevitably result in a small amount of contrast enhancement characteristic of the interstitial phase, which will contaminate the desired perfusion information of the earlier phases.

On the most recent MR systems, remote table motion, performed at the imaging console, and the ability to use either two phased-array torso coils overlying the abdomen and pelvis or one extended-coverage torso coil covering the abdomen and pelvis, are available. This permits time-efficient imaging of the abdomen and pelvis such that precontrast imaging of the pelvis can be performed as well, if needed.

A number of authors have described the use of oral contrast in evaluating the abdomen and pelvis, especially when the primary organ of interest is the small bowel [14]. Reflecting our overall view of wanting to keep MR studies simple to perform, we have generally not routinely advocated or used oral contrast agents, with the one exception that if one knows in advance that the organ of primary interest is the stomach, it is useful to distend the stomach (water suffices for this purpose) and to use a parenteral injection of a hypotonic agent. This is not, however, to say that the use of oral contrast may not be helpful, especially if the interpreting radiologists do not have much experience with bowel studies on MRI. Also, if one is to perform MR colonography, it is likely important to distend the colon with rectally administered fluid.

Tables 1.2–1.11 show the current protocols that are useful for the investigation of abdominopelvic disease when imaging at 1.5 T with a phased-array multicoil.

The sequence protocols are designed for a Siemens system. However, the terms used are generic, as current systems produced by all manufacturers can generate

Table 1.2 General Abdomen

Sequence	Plane	TR	TE	Flip	Thickness/Gap	FOV	Matrix
Localizer	3-plane						
SS-ETSE	Coronal	1500*	85	170	8–10 mm/20%	350–400	192 × 256
SS-ETSE	Axial	1500*	85	170	8–10 mm/20%	350–400	192 × 256
SS-ETSE fat-suppressed	Axial	1500*	85	170	8–10 mm/20%	350–400	192 × 256
T1 SGE in/out-of-phase	Axial	170	2.2/4.4	70	7 mm/20%	350–400	192 × 320
SS-ETSE MRCP	Coronal	5000	700	180	50 mm	300	224 × 384
T1 3D GE FS pre	Axial	3.8	1.7	10	3 mm	350–400	160 × 256
Contrast							
T1 3D GE FS arterial	Axial	3.8	1.7	10	3 mm	350–400	160 × 256
T1 3D GE FS venous	Axial	3.8	1.7	10	3 mm	350–400	160 × 256
T1 3D GE FS delayed	Axial	3.8	1.7	10	3 mm	350–400	160 × 256

*TR between slice acquisitions.

Table 1.3 Motion-Resistant Abdomen

Sequence	Motion	Plane	TR	TE	Flip	Thickness/Gap	FOV	Matrix
Localizer		3-plane						
SS-ETSE	FB or RT	Coronal	1500*	85	170	8–10 mm/20%	350–400	192 × 256
SS-ETSE	FB or RT	Axial	1500*	85	170	8–10 mm/20%	350–400	192 × 256
SS-ETSE fat-suppressed	FB or RT	Axial	1500*	85	170	8–10 mm/20%	350–400	192 × 256
T1 SGE in/out-of-phase	RT	Axial	170	2.2/4.4	70	7 mm/20%	350–400	192 × 320
SS-ETSE MRCP	FB	Coronal	5000	700	180	50 mm	300	224 × 384
SSFP	FB	Axial	3.5	1.2	60	8 mm/0%	350–400	224 × 256
2D MP-RAGE fat suppressed	FB	Axial	3.5	1.2	15	8 mm/20%	350–400	150 × 256
Contrast								
2D MP-RAGE 15 s post	FB	Axial	3.5	1.2	15	8 mm/20%	350–400	150 × 256
2D MP-RAGE 1 min	FB	Axial	3.5	1.2	15	8 mm/20%	350–400	150 × 256
2D MP-RAGE 5 min	FB	Axial	3.5	1.2	15	8 mm/20%	350–400	150 × 256

*TR between slice acquisitions; FB = free breathe; RT = respiratory triggered; SSFP = steady-state free precession.

Table 1.4 Pelvis

Sequence	Plane	TR	TE	Flip	Thickness/Gap	FOV	Matrix
Localizer	3-plane						
SS-ETSE	Coronal	1500*	85	170	8–10 mm/20%	350–400	192 × 256
SS-ETSE	Axial	1500*	85	170	8–10 mm/20%	350–400	192 × 256
SS-ETSE	Sagittal	1500*	85	170	8–10 mm/20%	350	192 × 256
SS-ETSE fat-suppressed	Axial	1500*	85	170	8–10 mm/20%	350–400	192 × 256
T1 SGE in/out-of-phase	Axial	170	2.2/4.4	70	7 mm/20%	350–400	192 × 320
T2 3D ETSE	Axial	1200	120	150	1.5 mm	250	256 × 256
T1 3D GE FS pre	Axial	3.8	1.7	10	3 mm	350–400	160 × 256
Contrast							
T1 3D GE FS 30 s	Axial	3.8	1.7	10	3 mm	350–400	160 × 256
T1 3D GE FS 1 min	Axial	3.8	1.7	10	3 mm	350–400	160 × 256
T1 2D ETSE fat suppressed	Axial	600	11	180	5 mm/20%	250	224 × 256

*TR between slice acquisitions.

Table 1.5 General Abdomen-Pelvis

Sequence	Coverage	Plane	TR	TE	Flip	Thickness/Gap	FOV	Matrix
Localizer		3-plane						
SS-ETSE	Abd-Pel	Coronal	1500*	85	170	8–10 mm/20%	350–400	192 × 256
SS-ETSE	Abd-Pel	Axial	1500*	85	170	8–10 mm/20%	350–400	192 × 256
SS-ETSE	Pelvis	Sagittal	1500*	85	170	8–10 mm/20%	350	192 × 256
SS-ETSE fat-suppressed	Abd-Pel	Axial	1500*	85	170	8–10 mm/20%	350–400	192 × 256
T1 SGE in/out-of-phase	Abd	Axial	170	2.2/4.4	70	7 mm/20%	350–400	192 × 320
SS-ETSE MRCP	Abd	Coronal	5000	700	180	50 mm	300	224 × 384
T2 3D ETSE	Pel	Axial	1200	120	150	1.5 mm	250	256 × 256
T1 3D GE FS pre	Abd-Pel	Axial	3.8	1.7	10	3 mm	350–400	160 × 256
Contrast								
T1 3D GE FS arterial	Abd	Axial	3.8	1.7	10	3 mm	350–400	160 × 256
T1 3D GE FS 1 min	Abd-Pel	Axial	3.8	1.7	10	3 mm	350–400	160 × 256
T1 3D GE FS 3 min	Abd-Pel	Axial	3.8	1.7	10	3 mm	350–400	160 × 256
T1 2D ETSE fat suppressed	Pel	Axial	600	11	180	5 mm/20%	250	224 × 256

*TR between slice acquisitions.

Table 1.6 Gastric Bowel

Sequence	Coverage	Plane	TR	TE	Flip	Thickness/Gap	FOV	Matrix
Localizer		3-plane						
SS-ETSE	Abd-Pel	Coronal	1500*	85	170	8–10 mm/20%	350–400	192 × 256
SS-ETSE	Abd-Pel	Axial	1500*	85	170	8–10 mm/20%	350–400	192 × 256
SS-ETSE fat-suppressed	Abd-Pel	Coronal	1500*	85	170	8–10 mm/20%	350–400	192 × 256
SS-ETSE	Pelvis	Sagittal	1500*	85	170	8–10 mm/20%	350	192 × 256
SS-ETSE fat-suppressed	Abd-Pel	Axial	1500*	85	170	8–10 mm/20%	350–400	192 × 256
T1 SGE in/out-of-phase	Abd	Axial	170	2.2/4.4	70	7 mm/20%	350–400	192 × 320
SS-ETSE MRCP	Abd	Coronal	5000	700	180	50 mm	300	224 × 384
T2 3D ETSE	Pel	Axial	1200	120	150	1.5 mm	250	256 × 256
T1 3D GE FS pre	Abd-Pel	Axial	3.8	1.7	10	3 mm	350–400	160 × 256
Contrast								
T1 3D GE FS arterial	Abd	Axial	3.8	1.7	10	3 mm	350–400	160 × 256
T1 3D GE FS 1 min	Abd-Pel	Axial	3.8	1.7	10	3 mm	350–400	160 × 256
T1 3D GE FS 3 min	Abd-Pel	Axial	3.8	1.7	10	3 mm	350–400	160 × 256

*TR between slice acquisitions.

Table 1.7 Chest

Sequence	Plane	TR	TE	Flip	Thickness/Gap	FOV	Matrix
Localizer	3-plane						
SS-ETSE	Coronal	1500*	85	170	8–10 mm/20%	350–400	192 × 256
SS-ETSE	Axial	1500*	85	170	8–10 mm/20%	350–400	192 × 256
SS-ETSE fat suppressed	Axial	1500*	85	170	8–10 mm/20%	350–400	192 × 256
bSSFP	Axial	3.5	1.2	60	8 mm/0%	350–400	224 × 256
T1 3D GE FS pre	Axial	3.8	1.7	10	3 mm	350–400	160 × 256
Contrast							
T1 3D GE FS 20 s	Axial	3.8	1.7	10	3 mm	350–400	160 × 256
T1 3D GE FS 1 min	Axial	3.8	1.7	10	3 mm	350–400	160 × 256
T1 3D GE FS 3 min	Coronal	3.8	1.7	10	3 mm	350–400	160 × 256

*TR between slice acquisitions; SSFP = steady-state free precession.

Table 1.8 Chest/Abd/Pel

Sequence	Coverage	Plane	TR	TE	Flip	Thickness/Gap	FOV	Matrix
Localizer		3-plane						
SS-ETSE	Chest-Abd-Pel	Coronal	1500*	85	170	8–10 mm/20%	350–400	192 × 256
SS-ETSE	Chest-Abd-Pel	Axial	1500*	85	170	8–10 mm/20%	350–400	192 × 256
SS-ETSE	Pelvis	Sagittal	1500*	85	170	8–10 mm/20%	350	192 × 256
SS-ETSE fat-suppressed	Chest-Abd-Pel	Axial	1500*	85	170	8–10 mm/20%	350–400	192 × 256
T1 SGE in/out-of-phase	Abd	Axial	170	2.2/4.4	70	7 mm/20%	350–400	192 × 320
bSSFP	Chest	Axial	3.5	1.2	60	8 mm/0%	350–400	224 × 256
SS-ETSE MRCP	Abd	Coronal	5000	700	180	50 mm	300	224 × 384
T2 3D ETSE	Pel	Axial	1200	120	150	1.5 mm	250	256 × 256
T1 3D GE FS pre	Chest-Abd-Pel	Axial	3.8	1.7	10	3 mm	350–400	160 × 256
Contrast								
T1 3D GE FS arterial	Abd	Axial	3.8	1.7	10	3 mm	350–400	160 × 256
T1 3D GE FS 1 min	Chest-Abd-Pel	Axial	3.8	1.7	10	3 mm	350–400	160 × 256
T1 3D GE FS 3 min	Chest-Abd-Pel	Axial	3.8	1.7	10	3 mm	350–400	160 × 256
T1 3D GE FS 5 min	Chest-Abd	Coronal	3.8	1.7	10	3 mm	350–400	160 × 256
T1 2D ETSE fat suppressed	Pel	Axial	600	11	180	5 mm/20%	250	224 × 256

*TR between slice acquisitions; SSFP = steady-state free precession.

Table 1.9 Whole Body (Brain/Chest/Abd/Pel)

Sequence	Coverage	Plane	TR	TE	Flip	Thickness/Gap	FOV	Matrix
Localizer		3-plane						
T2 ETSE (FLAIR)	Brain	Axial	8000	120	180	4 mm/20%	230	192 × 256
3D GE (COW)	Brain	Axial	40	7.0	20	0.9 mm	200	256 × 512
SS-ETSE	Chest-Abd-Pel	Coronal	1500*	85	170	8–10 mm/20%	350–400	192 × 256
SS-ETSE	Chest-Abd-Pel	Axial	1500*	85	170	8–10 mm/20%	350–400	192 × 256
SS-ETSE	Pelvis	Sagittal	1500*	85	170	8–10 mm/20%	350	192 × 256
SS-ETSE fat-suppressed	Chest-Abd-Pel	Axial	1500*	85	170	8–10 mm/20%	350–400	192 × 256
T1 SGE in/out-of-phase	Abd	Axial	170	2.2/4.4	70	7 mm/20%	350–400	192 × 320
bSSFP	Chest	Axial	3.5	1.2	60	8 mm/0%	350–400	224 × 256
SS-ETSE MRCP	Abd	Coronal	5000	700	180	50 mm	300	224 × 384
T1 3D GE FS pre	Chest-Abd-Pel	Axial	3.8	1.7	10	3 mm	350–400	160 × 256
Contrast								
T1 3D GE FS arterial	Abd	Axial	3.8	1.7	10	3 mm	350–400	160 × 256
T1 3D GE FS 1 min	Chest-Abd-Pel	Axial	3.8	1.7	10	3 mm	350–400	160 × 256
T1 3D GE FS 3 min	Chest-Abd-Pel	Axial	3.8	1.7	10	3 mm	350–400	160 × 256
T1 3D GE FS 5 min	Chest-Abd	Coronal	3.8	1.7	10	3 mm	350–400	160 × 256
T1 3D GE fat suppressed	Neck-Brain	Axial	3.8	1.7	10	3 mm	250–275	224 × 256

similar sequences. Vendor specific sequence names are indicated in Table 1.12, and vendor-specific variations in imaging parameters should be employed as needed. Variations in TR/TE/flip angle for SGE sequences, especially in the same patient study, should generally be avoided. Imaging parameters of ETSE sequences are more flexible, with minor changes resulting in no substantial loss of diagnostic information. With the use of phased-array multicoils both slice thickness and FOV can be substantially modified for many protocols (e.g., slice thickness of 5 mm for the pancreas, adrenals, and pelvis and FOV of 200 mm for the pelvis).

Table 1.10 3T General Abdomen

Sequence	Plane	TR	TE	Flip	Thickness/Gap	FOV	Matrix
Localizer	3-plane						
SS-ETSE	Coronal	1500*	70	170	6–8 mm/20%	350–400	192 × 256
SS-ETSE	Axial	1500*	70	170	6–8 mm/20%	350–400	192 × 256
SS-ETSE fat-suppressed	Axial	1500*	70	170	6–8 mm/20%	350–400	192 × 256
T1 SGE in/out-of-phase	Axial	170	1.1/2.2	60	6 mm/20%	350–400	192 × 320
SS-ETSE MRCP	Coronal	5000	700	180	50 mm	300	224 × 384
T1 3D GE FS pre	Axial	3.3	1.2	10	2.5 mm	350–400	180 × 288
Contrast							
T1 3D GE FS arterial	Axial	3.3	1.2	10	2.5 mm	350–400	180 × 288
T1 3D GE FS venous	Axial	3.3	1.2	10	2.5 mm	350–400	180 × 288
T1 3D GE FS delayed	Axial	3.3	1.2	10	2.5 mm	350–400	180 × 288

*TR between slice acquisitions.

Table 1.11 3T Motion-Resistant Abdomen

Sequence	Motion	Plane	TR	TE	Flip	Thickness/Gap	FOV	Matrix
Localizer		3-plane						
SS-ETSE	FB or RT	Coronal	1500*	70	160	6–8 mm/20%	350–400	192 × 256
SS-ETSE	FB or RT	Axial	1500*	70	160	6–8 mm/20%	350–400	192 × 256
SS-ETSE fat-suppressed	FB or RT	Axial	1500*	70	160	6–8 mm/20%	350–400	192 × 256
T1 SGE in/out-of-phase	RT	Axial	170	1.1/2.2	60	6 mm/20%	350–400	192 × 320
SS-ETSE MRCP	FB	Coronal	5000	700	170	50 mm	300	224 × 384
bSSFP	FB	Axial	3.5	1.2	60	6 mm/0%	350–400	224 × 256
2D WE SS-SGE	FB	Axial	3.2	1.1	12	8 mm/20%	350–400	150 × 256
Contrast								
2D WE SS-SGE 15 s	FB	Axial	3.2	1.1	12	8 mm/20%	350–400	150 × 256
2D WE SS-SGE 1 min	FB	Axial	3.2	1.1	12	8 mm/20%	350–400	150 × 256
2D WE SS-SGE 3 min	FB	Axial	3.2	1.1	12	8 mm/20%	350–400	150 × 256

*TR between slice acquisitions; bSSFP = balanced steady-state free precession; WE SS-SGE = water-excited single-shot spoiled gradient echo.

Table 1.12 Vendor-Specific Terms for Common Abdominal Pulse Sequences

Sequence		Siemens	GE	Philips
ETSE	Echo train spin echo	TSE	FSE	TSE
SS-ETSE	Single-shot echo train spin echo	HASTE	SS-FSE	SS-TSE
SGE	Spoiled gradient echo	FLASH	SPGR	T1-FFE
3D GE	3D spoiled gradient echo	VIBE	LAVA	THRIVE
SSFP	Steady-state free precession	FISP	GRASS	FFE
bSSFP	Balanced steady-state free precession	TrueFISP	FIESTA	Balanced FFE
MP-RAGE	Magnetization-prepared rapid acquisition gradient echo	TurboFLASH	Fast SPGR	TFE

SERIAL MRI EXAMINATION

MRI is currently considered the most expensive imaging modality, which has hampered its appropriate utilization. The expense of MRI studies can be dramatically reduced by decreasing study time and the number of sequences employed. This may be done most reasonably in the setting of follow-up examinations. Depending on the amount of information needed, a follow-up study that employs coronal SS-ETSE, transverse precontrast 2D or 3D gradient echo, immediate and 45-s

postgadolinium 2D or 3D GE, and 2-min postgadolinium fat-suppressed 2D or 3D gradient echo provides relatively comprehensive information in a 10-min study time [5]. Even more curtailed examination can be performed if the only indication is the change in size. An adrenal mass or lymphadenopathy may be adequately followed by precontrast SGE alone or, in the case of an adrenal adenoma, in combination with out-of-phase SGE.

NONCOOPERATIVE PATIENTS

It is crucial to recognize that separate protocols are required for noncooperative patients. In general, noncooperative patients fall into two categories: 1) those who cannot suspend respiration but can breathe in a regular fashion and 2) those who cannot suspend respiration and cannot breathe in a regular fashion. The most common patient population that fits into the first group are sedated pediatric patients. Agitated patients are the most commonly encountered who fit into the second group. Optimal imaging strategies differ for each.

In sedated patients, substitution of breath-hold images (e.g., SGE) can be made readily with breathing-averaged ETSE images, the image quality of which is improved by using fat suppression. Both 2D SGE and ETSE have the ability to be gated to respiration. Since SGE utilizes spoiling gradients within each TR interval, T1 information is preserved between respiratory periods, while T2 ETSE exploits the respiratory period into its inherent T2-weighting. With sedation, breathing is in a more regular pattern than that observed for all other patients. Additionally, breathing-independent T2-weighted SS-ETSE is useful, as is T1-weighted MP-RAGE, if dynamic gadolinium-enhanced images are required (fig. 1.14).

In patients who are agitated, only single-shot techniques should be used, including breathing-independent T2-weighted SS-ETSE and T1-weighted MP-RAGE pre- and postgadolinium administration (fig. 1.15).

EMERGING DEVELOPMENTS IN MRI

There are several emerging developments in MR imaging that are important for body MR imaging. These include 1) recent technical developments, 2) parallel MR imaging, 3) introduction of 3.0 T MR systems as whole body magnets; and 4) whole body MR imaging for screening. MR imaging has undergone major improvements in its diagnostic capability and clinical applications since its introduction in the clinical setting in the 1980s. These developments have mainly occurred in the following areas:

1. Increased main magnetic field strength (from less than 0.3 T to more than 3.0 T)
2. Improved radiofrequency coil design (from large single body or a single surface coil to arrays of multiple smaller (phased-array) coils containing 4–8 elements now, and 16–32 elements or higher in the near future):
3. Improved bandwidth per receiver channel (3 MHz) with advances in digital electronics for faster readouts and faster reconstructions of k-space data sets
4. Increased gradient performance (from gradients of <10 mT/m with switching rates of >1 ms to gradients with >50 mT/m and with switching rates in the order of 100 μs; these gradients can achieve lower TR and TE values, allow better spatial and temporal coverage, and drastically reduce the dead time periods during which no MR signal is acquired.
5. Newer and faster acquisition methods and sequences, like SGE; SS-SGE; bSSFP; ETSE; and SS-ETSE; EPI; and parallel imaging.

As a consequence of these technical improvements, most state-of-the-art MR systems (3.0 T and lower) currently operate just below the physiological barriers of dB/d*t*, acoustic noise, specific absorption rate (SAR), and perhaps also main magnetic field strength. Beyond these boundaries, regulations on patient safety will limit acquisition speed. For instance, negligible further improvements of imaging speed can be achieved by decreasing interecho spacing or repetition time through gradient performance alone. In this respect, the development and implementation of parallel MR imaging methods in combination with multiple coil arrays provides important means to further improve the diagnostic capability of MR imaging without violating physiological barriers.

Parallel MR Imaging

Parallel MR imaging is comprised of a number of methods that can be used in combination with the majority of the MR imaging sequences to reduce scan time by acquiring less data than would otherwise be necessary to avoid aliasing. Currently, several vendor-specific terms are in use for parallel imaging (Table 1.13). Since 1987, several authors have proposed ideas to reduce scan time in MR imaging by using some form of parallel imaging [15–24]. The first successful in vivo implementation of parallel imaging was demonstrated by Sodickson and colleagues in 1997 based on the simultaneous acquisition of spatial harmonics (SMASH) and coil sensitivities. Currently, sensitivity encoding

(*a*)

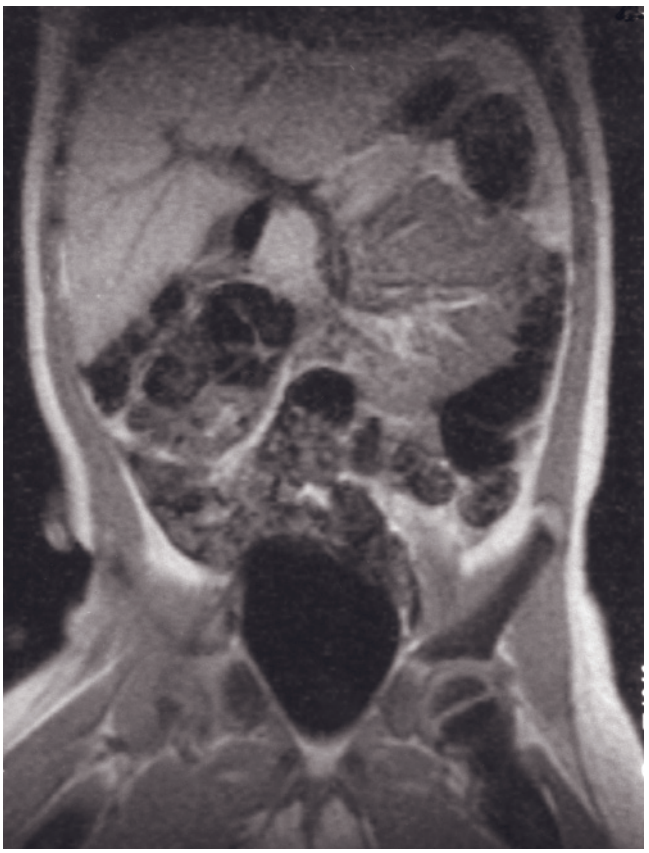

(*b*)

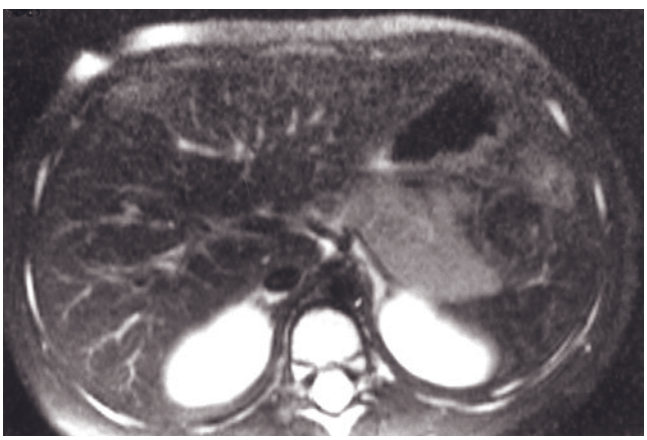

(*c*)

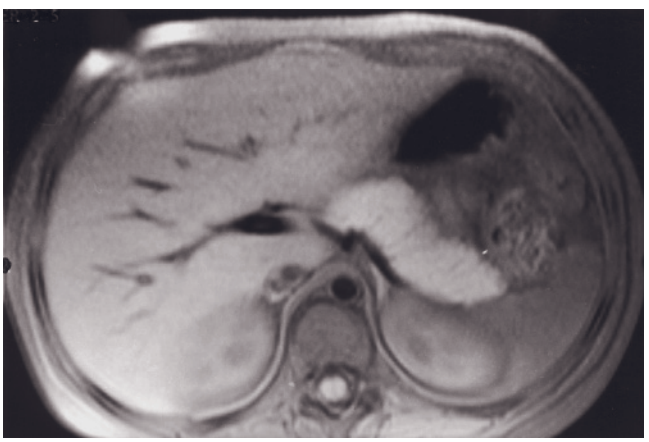

(*d*)

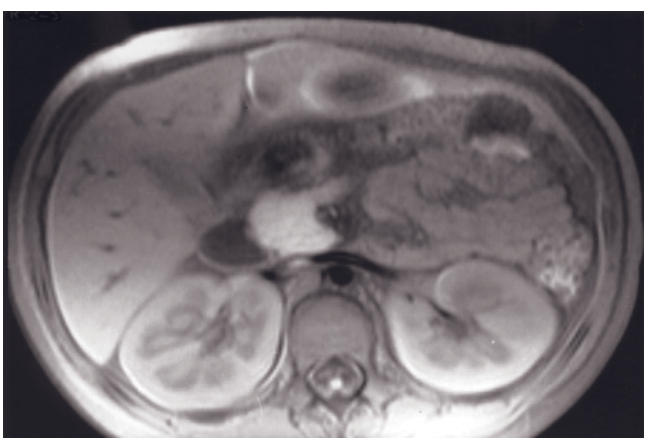

(*e*)

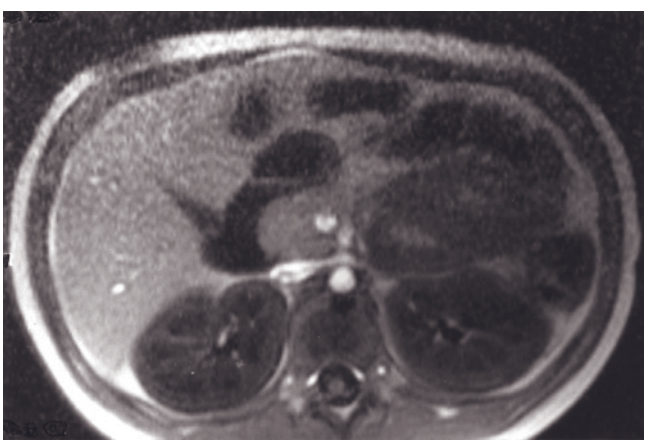

(*f*)

FIG. 1.14 Sedated patient protocol, abdomen and pelvis. Coronal T2-weighted single-shot echo-train spin-echo (*a*), coronal T1-weighted single-shot non-slice-selective 180° magnetization-prepared gradient echo (*b*), T2-weighted fat-suppressed echo-train spin-echo (*c*), T1-weighted fat-suppressed spin-echo (*d*, *e*), immediate postgadolinium T1-weighted slice-selective 180° magnetization-prepared gradient-echo (*f*), 1-min postgadolinium T1-weighted slice-selective 180° magnetization-prepared gradient-echo (*g*),

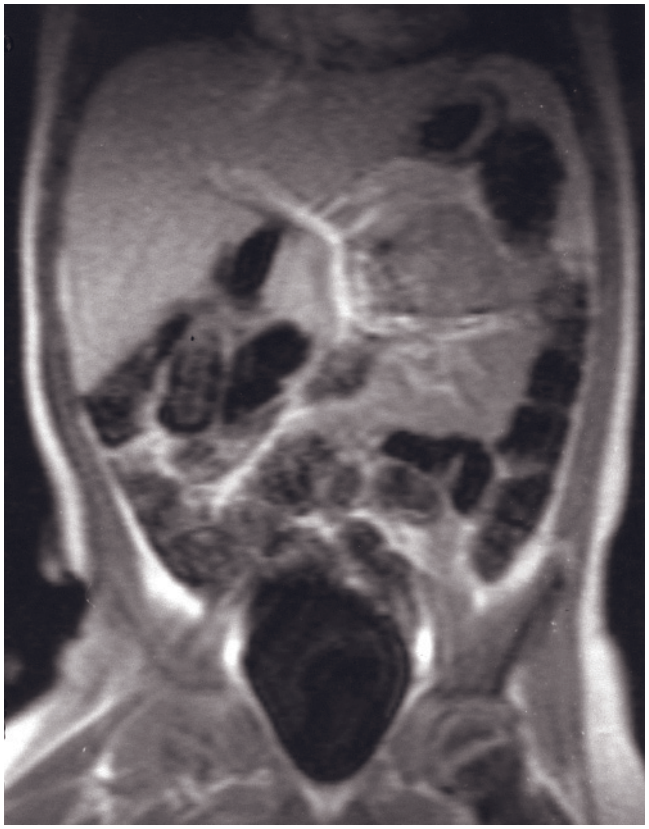

(*g*)

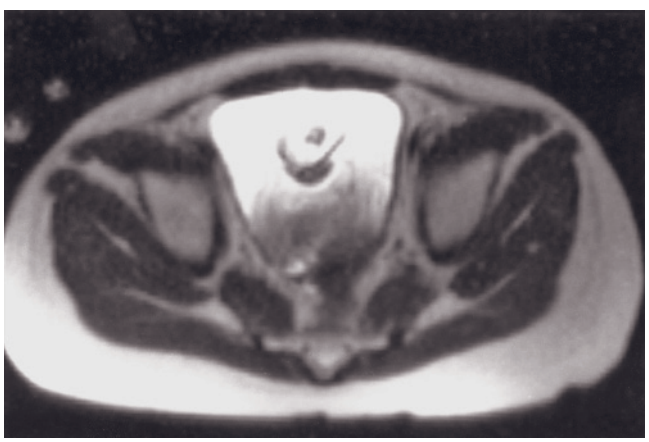

(*j*)

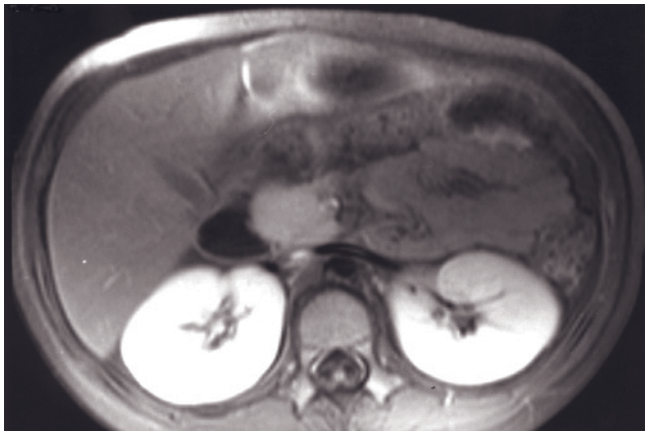

(*h*)

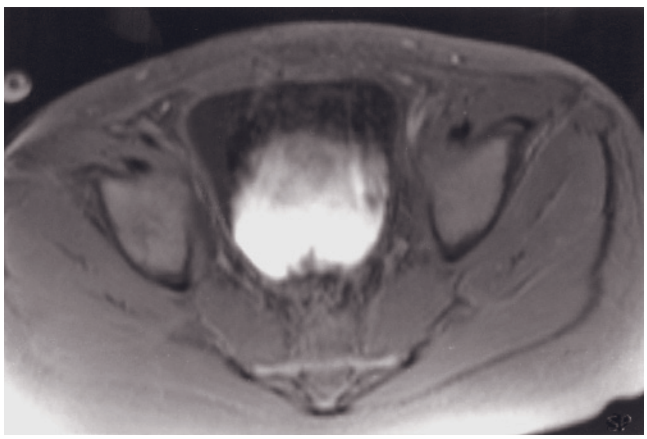

(*i*)

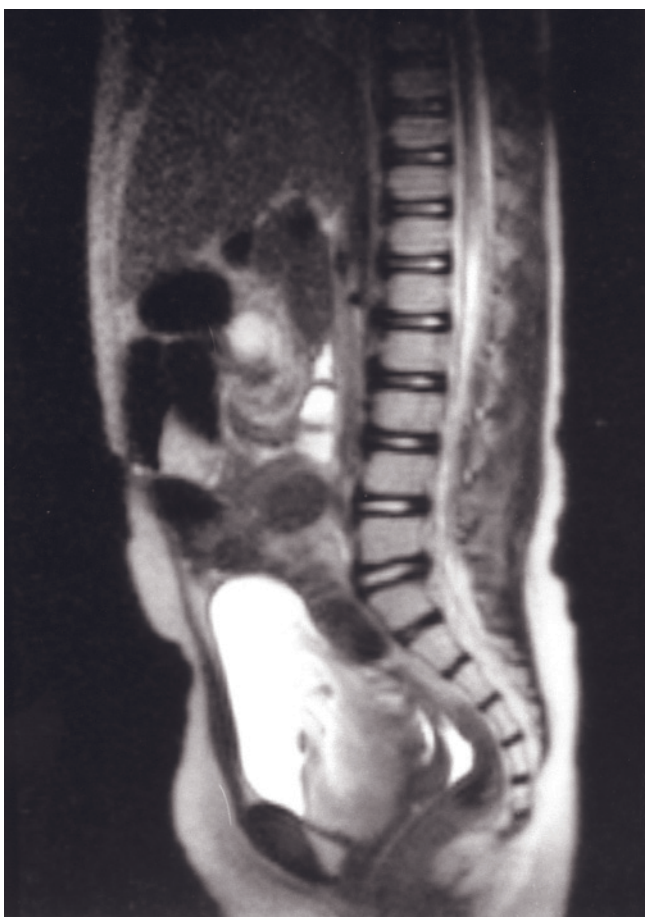

(*k*)

Fig. 1.14 (*Continued*) 1.5-min gadolinium-enhanced T1-weighted fat-suppressed spin-echo (*b*), 5-min gadolinium-enhanced T1-weighted fat-suppressed spin-echo (*i*), and transverse (*j*) and sagittal (*k*) T2-weighted single-shot echo-train spin-echo images. Images of the abdomen are acquired first, pre- and postgadolinium (*a–b*), followed by imaging of the pelvis (*i–k*). In sedated patients, a combination of longer duration, breathing-averaged sequences (*c–e*, *h*, *i*) and breathing-independent single-shot techniques (*a*, *b*, *f*, *g*, *j*, *k*) are used. In this patient the T2-weighted images of the pelvis were acquired with single-shot technique. If there was a high index of suspicion of pelvic disease, breathing-averaged sequences could have been performed. Note the excellent demonstration of the pancreas on the noncontrast breathing-averaged fat-suppressed T1-weighted spin-echo images (*d*, *e*).

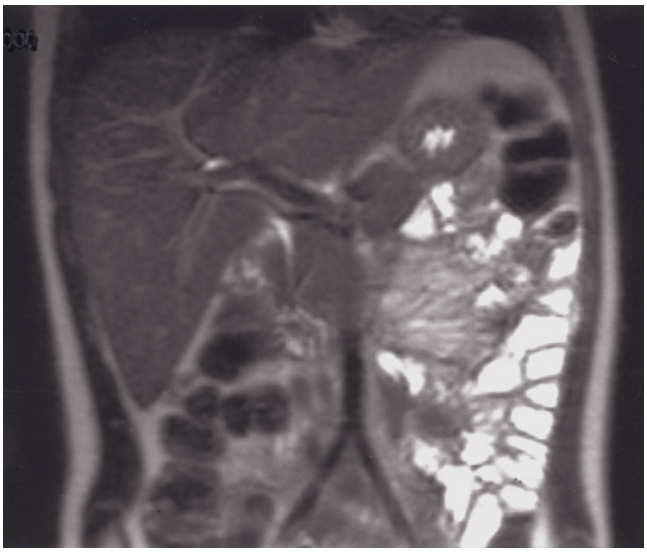

(*a*)

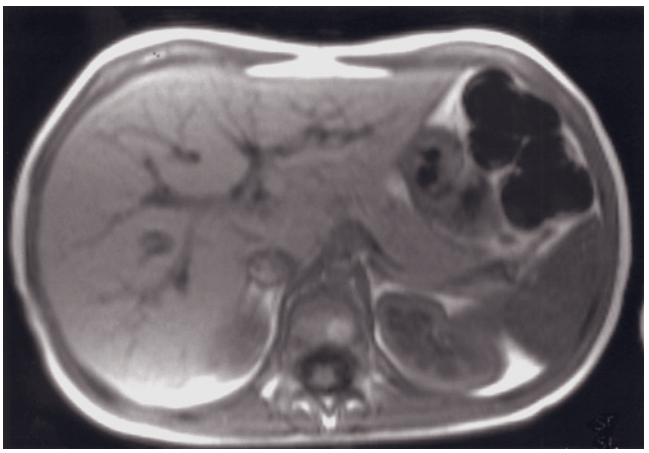

(*b*)

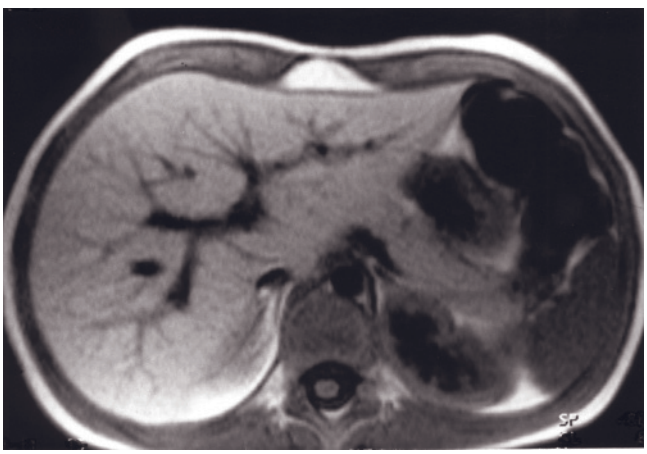

(*c*)

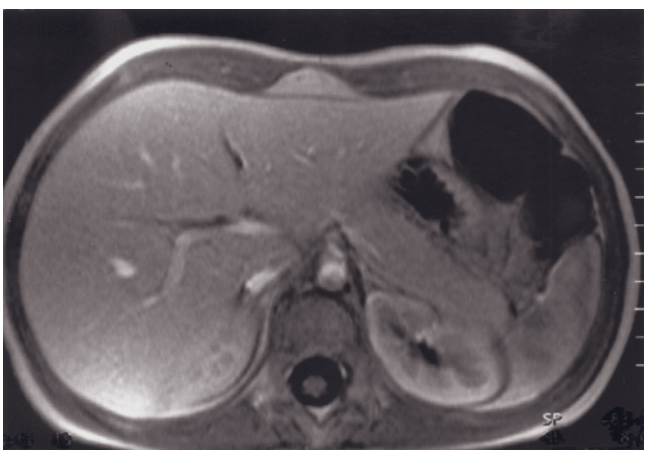

(*d*)

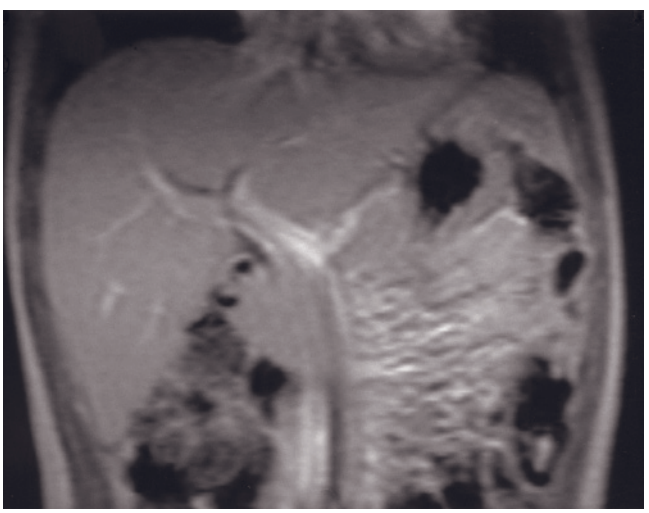

(*e*)

FIG. 1.15 Noncooperative patient protocol. Coronal T2-weighted single-shot echo-train spin-echo (*a*), reduced-matrix (96 × 128) shortened TR (100 ms) SGE (*b*), non-slice-selective 180° magnetization-prepared gradient-echo (*c*), immediate postgadolinium slice-selective 180° magnetization-prepared gradient-echo (*d*), and coronal 1-min postgadolinium slice-selective 180° magnetization-prepared gradient-echo (*e*) images. An imaging protocol for a patient who cannot suspend respiration or breathe in a regular fashion includes breathing-independent sequences (*a*, *c*–*e*). Attempt should be made, as in this patient, to reduce matrix size, field of view, and TR time on the SGE sequence to render it a 10-s breath hold. In this patient, this reduced-parameter SGE sequence (*b*) resulted in acceptable image quality for this acquisition, but was not reproducible. The study was switched to perform only breathing-independent sequences (*c*–*e*). Note the comparison between SGE (*b*) and non-slice-selective 180° magnetization-prepared gradient-echo (*c*) images. The former sequence has mirror artifacts from the aorta (arrow, *b*); the latter sequence has very nice signal void in vessels, no mirror artifacts, and strong T1 weighting, as evidenced by excellent liver-spleen contrast. Drawbacks of non-slice-selective 180° magnetization-prepared gradient echo include low signal-to-noise ratio, lengthy total imaging time, and variable image quality outside the liver.

Table 1.13 Vendor-Specific and Other Terms Used for Various Parallel MR Imaging Methods

ASSET	= Array Spatial Sensitivity Encoding Technique (GE Medical Systems)
GRAPPA	= Generalized Auto-calibrating Partially Parallel Acquisition
iPAT	= integrated Parallel Acquisition Technique (Siemens Medical Systems)
SENSE	= SENSitivity Encoding (Philips Medical Systems)
SMASH	= SiMultaneous Acquisition of Spatial Harmonics
SPACE RIP	= Sensitivity Profiles from an Array of Coils for Encoding and Reconstruction In Parallel

(SENSE), which was introduced in 1999 by Pruessmann and colleagues, is the most versatile method of parallel imaging. There are several differences in SMASH and SENSE types of methods. SMASH is considered a k-space-based method, whereas SENSE is an image-domain method. Parallel imaging methods are still evolving, and improvements in the existing and new methods are published on a regular basis. With the introduction of higher-field (>1.5 T) MR systems as well as multiple coil arrays (>8 coils), the role of parallel imaging will become even more important in the near future. One or a combination of several of the current parallel imaging methods may evolve, and eventually the original concept of Hutchinson and colleagues of "massive" parallel MR imaging [in which the number of coil elements equals the number of k-space lines (15)], may become a reality.

In general, parallel imaging methods require the use of suitable phased-array coils, a "reference" or a "calibration" scan, and vendor-specific software to reduce scan time. Each element of the phased-array coil has its own sensitivity profile, which can be measured based on the "reference" scan data. Parallel MR imaging exploits the calculated sensitivities of the coils and allows acquisition of less k-space data than otherwise necessary to avoid aliasing. The undersampling results in heavily aliased k-space data sets that can then be unfolded, using spatial sensitivity maps of the coils (SENSE method).

In the SMASH method, the same field of view (FOV) with the same spatial resolution as in conventional MRI can be obtained with reduced number of phase-encoding steps based—in part—on the sensitivity profiles of the coils and—in part—on the simultaneous acquisition of spatial harmonics.

The key feature of parallel imaging methods is the application of multiple independent receiver coils with distinct sensitivities across the object being imaged. In conventional MR imaging, the role of phased-array coils is merely to improve the signal-to-noise ratio (SNR), whereas in parallel imaging the phased-array coils are also used to reduce the scan time. The application of parallel imaging allows 1) higher temporal resolution (faster imaging; e.g., MRI exams in noncooperative patients, time-resolved MR angiography, and perfusion studies), 2) higher spatial resolution (larger matrices, thinner slices; e.g., high-resolution MRA) (fig. 1.16), 3) reduced effective interecho spacing (less image blurring and image distortion in ETSE and echo planar imaging; e.g., high-quality MRCP and single-shot EPI of the abdomen), and/or 4) reduced specific absorption rate (SAR) due to shorter echo trains (important for optimization of body MRI sequences at 3 T).

There are several limitations of parallel imaging, including

1. Decreased signal-to-noise ratio (SNR): As SNR is proportional to the square root of the total sampling time, there is an intrinsic loss of SNR with the square root of the acceleration factor. Advances in receiver technology, e.g., scanning with torso phased-array coils with eight or higher number of receivers, can significantly improve the SNR. In contrast-enhanced studies (i.e., dynamic imaging of the liver or MR angiography), an increase in the rate of contrast injection can also compensate for the loss of SNR. In contrast to the iodine-contrast media for CT exams, gadolinium-based contrast media have much lower viscosity. Therefore, unlike CT, the higher injection rates of MR contrast media, for instance with 4 ml/s, do not require the use of larger-bore intravenous catheters.
2. Parallel MR imaging foldover artifact: It should be emphasized that parallel imaging does not correct for foldover artifacts that occur if the FOV is chosen too small for the anatomy. In conventional abdominal MR imaging, a slightly smaller FOV, often in combination with a rectangular FOV, improves the spatial resolution in the phase encoding direction without significant increase in scan time. In such cases, the aliased body part projects on the opposite side of the patient, generally outside of the region of interest. With the application of parallel imaging, such artifacts are projected in the center of the image (fig. 1.17), resulting in severely degraded image quality. To avoid such artifacts, a full FOV should always be applied for any parallel imaging acquisition.
3. Reliability of parallel imaging in daily clinical practice: Depending on the imaging sequence and application, the reliability of the parallel imaging is reduced (for instance, with the appearance of artifacts due to image reconstruction errors) if the acceleration factor reaches an assigned value. Therefore

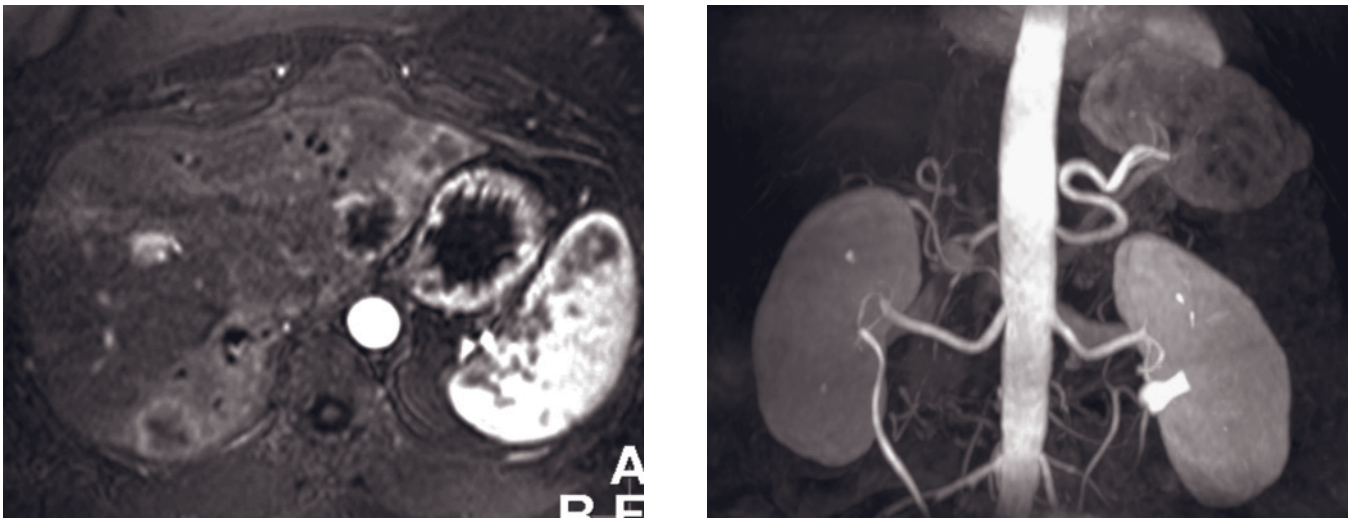

(*a*) (*b*)

FIG. 1.16 Application of parallel imaging (acceleration factor 2) at 1.5 T. Axial fat-suppressed arterial dominant (*a*) image of a 3D gradient-echo image (2-mm sections interpolated to 1-mm sections; parallel imaging acceleration factor of 2; scan time 15 s to cover the entire liver). Based on the thin sections of the arterial dominant phase data set, a MR angiography was additionally reconstructed (*b*). This "free" MRA was used to determine the vasculature of the liver for planning chemoperfusion of the liver, which is the choice of treatment at our hospital for patients with colorectal liver metastases who cannot be treated with surgery or other minimally invasive therapies, such as radiofrequency ablation.

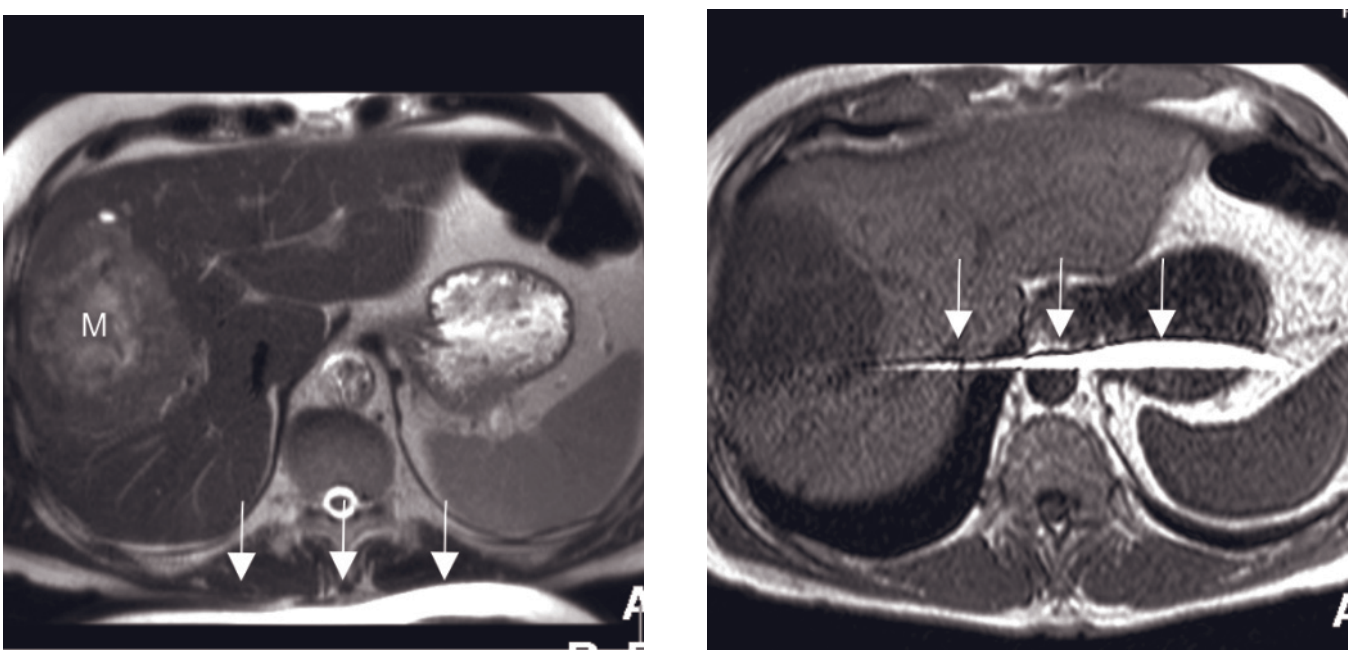

(*a*) (*b*)

FIG. 1.17 Aliasing (foldover artifact) with and without parallel imaging. Axial T2-weighted single-shot echo-train spin-echo image without pMRI (*a*) shows the foldover artifact originating from the anterior abdominal wall projected on the opposite side of the image (arrows). A large metastasis is present in the liver (M). Axial SGE image with parallel imaging acceleration factor 2 (*b*) shows the foldover artifact projected in the center of the image (arrows).

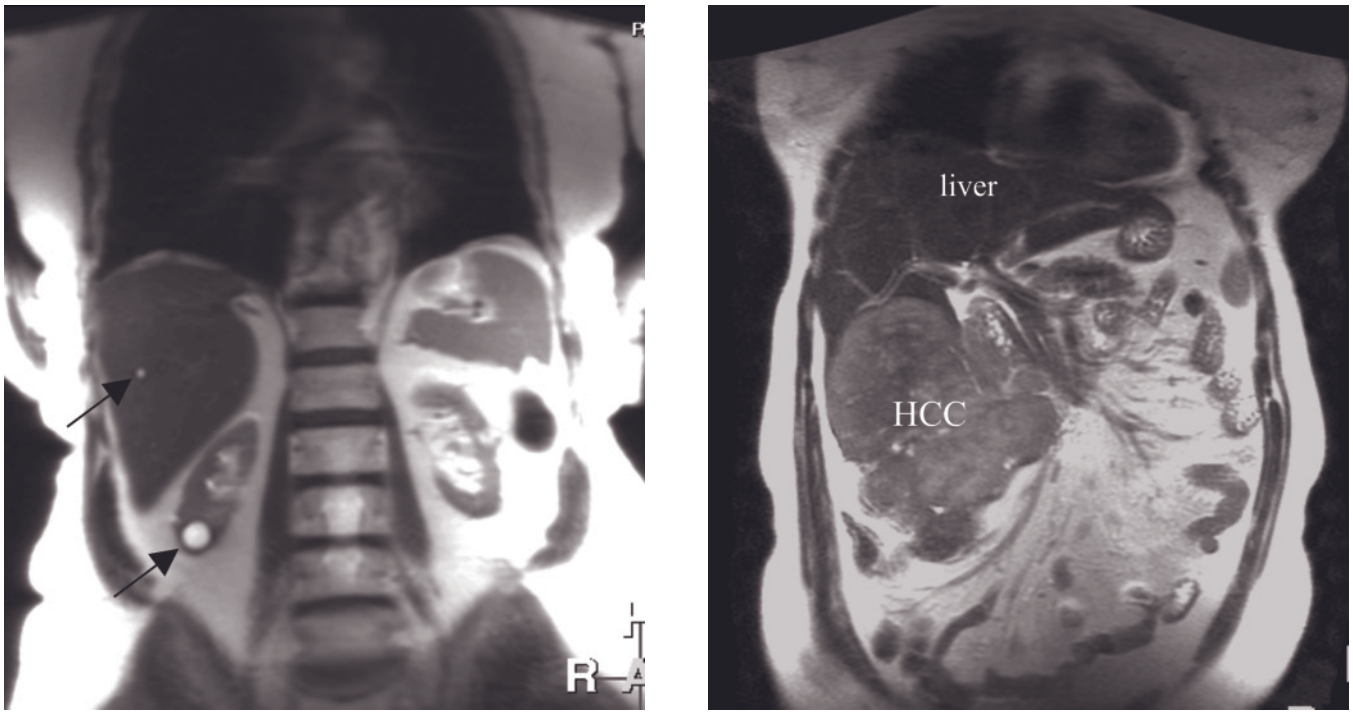

(*a*) (*b*)

FIG. 1.18 8-Channel phased-array torso coil at 3T. Coronal T2-weighted single-shot echo-train spin-echo images in a patient with liver and renal cysts (arrows) (*a*) and in a patient with a large hepatocellular carcinoma (HCC) (*b*). In both cases, the large coverage with sufficient SNR over the entire anatomy was possible with the use of the 8-channel phased-array torso coil.

caution needs to be exercised when applying parallel imaging protocols with the highest acceleration factor possible. In particular, if the individual sequences are not robust, the examination may have to be repeated. This is especially critical for contrast-enhanced exams, where repeating the sequence (e.g., hepatic arterial dominant phase sequence) may not be feasible in the same MR study sessions.

Body MR Imaging at 3 T: General Considerations Compared to 1.5 T

A major advantage of a 3T system compared to 1.5T is that the signal-to-noise ratio (SNR) at 3T is approximately two times higher. At the present time, research is ongoing to develop imaging approaches that take advantage of the higher SNR. In exploring the use of body imaging at 3T, reference must be made to the image quality of state-of-the-art abdominal MR imaging that is achievable at 1.5T, in order to determine the future role of 3T imaging.

Currently, in several centers state-of-the-art 3T MR imaging systems are equipped with eight-channel torso phased-array coils and parallel MR imaging capability. The availability of parallel imaging at 3T is essential for reducing SAR. The eight-channel torso phased-array coils facilitate larger FOV and anatomic coverage in combination with better SNR distribution as compared to four-channel phased-array torso coils at 1.5T (fig. 1.18). Several issues must be considered when developing body MRI for a 3T system:

- **Radio-frequency (RF) power deposition is ~4×:** This follows from the following equation: $\nu = \gamma B_o$ [i.e., frequency (ν) is equal to the product of the gyromagnetic ratio (γ) and the main magnetic field (B_o)]. If B_o increases with a factor of 2, the frequency at which the protons can be excited will also be doubled. Therefore, at 3T RF pulses with 4× higher energy are needed to excite the protons. This results in increased RF heating and higher specific absorption rate (SAR). The limitation of SAR will be greatest for RF-intensive sequences, such as ETSE sequences. At 3T, these limitations result in a lower number of slices per TR and hence smaller anatomic coverage.
- **Chemical shift and susceptibility artifact is ~2×:** The higher chemical shifts and susceptibility may result in artifacts on the gradient-echo and echo planar imaging. For equivalent imaging bandwidth, the fat-water spatial shift is doubled at 3T. These artifacts can be reduced by using higher bandwidths than at 1.5T. At 3T, bandwidths with a value two

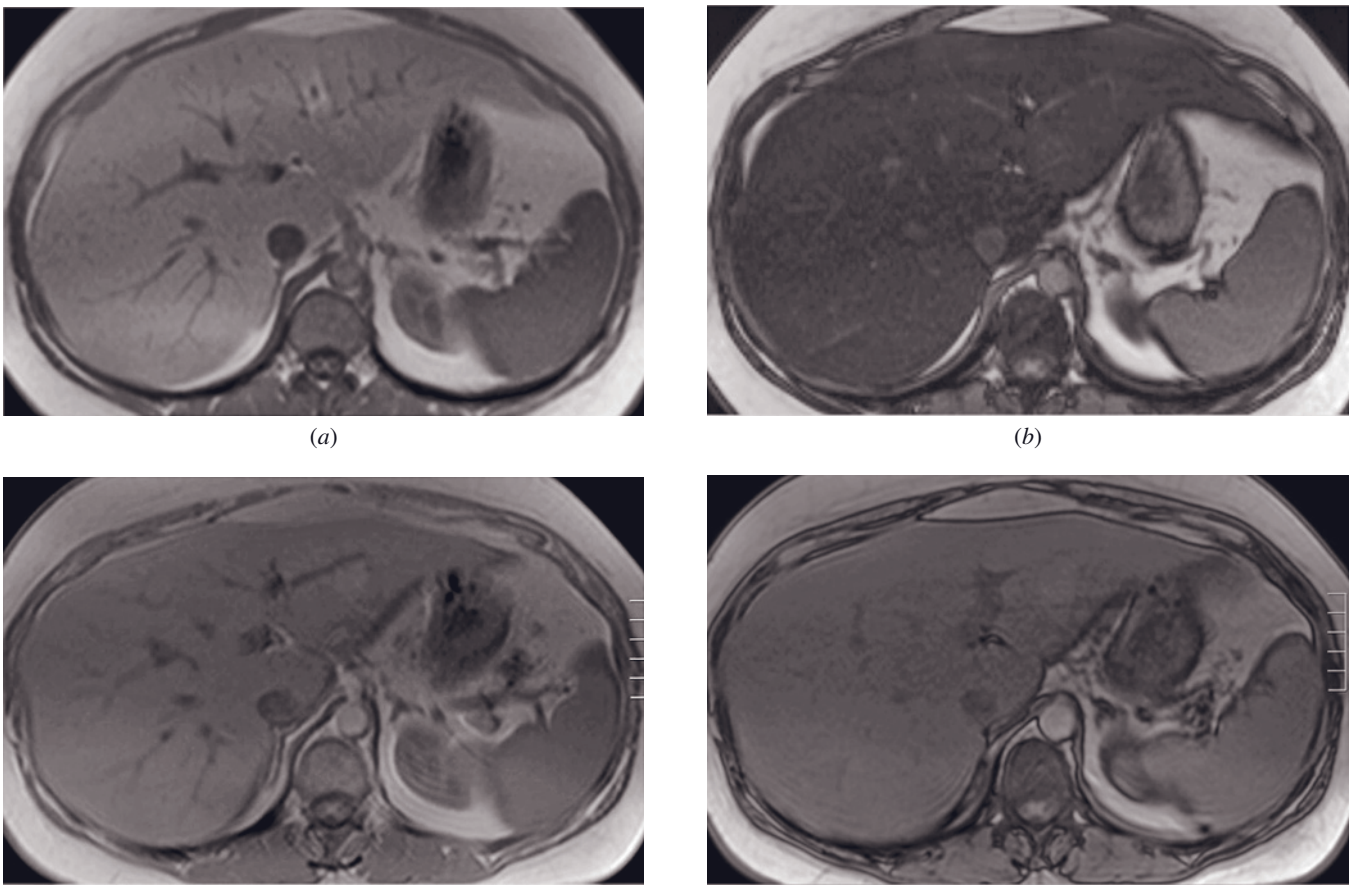

(*a*) (*b*) (*c*) (*d*)

FIG. 1.19 Comparison of T1 contrast at 1.5T and 3T. Axial in-phase and opposed-phase SGE at 1.5T (*a*, *b*) and 3T (*c*, *d*). The inherent prolongation of T1 values at 3T reduces T1 contrast between soft tissues, as seen by comparing in-phase images (*a*, *c*) and opposed-phase images (*b*, *d*). This assumes identical flip angle and TR between field strengths. However, modifications of pulse sequence parameters, such as lengthening TR or decreasing flip angle, may alleviate low T1 contrast at 3T.

times higher than at 1.5T may be required. Higher chemical shift is also an advantage, for instance, for MR spectroscopy. Spectra with resolution similar to that at 1.5T may be acquired in shorter times, and spectrally selective fat suppression techniques also require less time at 3T.

- **T1 relaxation times are longer (e.g., liver has 30% longer T1):** This leads to increased signal saturation effects, especially for rapid GE imaging, which ultimately decreases T1 contrast on T1-weighted images (fig. 1.19). T1 weighting could be improved by different combinations of repetition times (TR), echo time (TE), and flip angle from those at 1.5T. But it is also noteworthy that T1 information can be constrained at 3T, such that alternative methods need to be employed to reveal contrast similar to 1.5T. On some 3T systems, for instance, dual echo SGE allows the shortest in-phase TE of 2.2 ms but, because of SAR, gradient capabilities, and other issues, the systems may only allow an opposed-phase TE of 5.8 ms (which is the fourth opposed-phase TE value at 3T). The shortest in- and opposed-phase TE values (i.e., 1.1 ms and 2.2 ms) with less susceptibility and inflow effects are possible if the imaging bandwidth is increased, and one employs asymmetric echoes. Despite an SNR trade-off, this latter strategy is recommended at 3T, in order to distinguish between iron and fat effects, which may compete on later echoes. In addition to the decreased T1 weighting, inflow effects in abdominal vessels are more pronounced, which has a detrimental effect on the image quality of GE at 3T. The ability of gadolinium-based contrast agents to reduce T1 (known as the relaxivity, r1) is slightly lower at 3T [25]. However, the impact may not be observable with typical administered doses, stemming from the inherent difficulty of distinguishing very low T1 (<150 ms) from one another. The intrinsic differences in T1 between 1.5T and 3T are

lessened postcontrast, such that a greater change in T1, and therefore greater contrast enhancement, is expected at 3T, especially in the blood pool [26].

- **T2* of tissues and other structures is shorter (T2 remains practically unchanged):** This can be solved by echo trains with shorter effective interecho spacing or shorter echo trains. This can be achieved by applying parallel MR imaging. The use of parallel imaging has the additional advantage of reducing SAR.
- **3T safety concerns for body imaging:** Increased magneto-hydrodynamic effect results in a peaked T-wave of the electrocardiograms (ECG) during rapid systolic blood flow. In addition, there are 1) increased risk of RF burns from ECG leads, RF coils, and implanted wires, 2) increased torque on ferromagnetic implants, and 3) 6-dB intrinsic increase in acoustic noise.
- **B1 field inhomogeneities, dielectric resonances, RF penetration, and shape of the torso and abdomen have impact at 3T:** B1 inhomogeneities are particularly problematic, and they result in variations in the signal distribution over the region of interest, which appear to be related to the shape and size of the anatomy. For instance, at the level of the pelvis, B1 inhomogeneities cause darkening in the anterior and posterior parts of the abdomen and pelvis. This is evidence of a "field-focusing" effect, which becomes more prevalent as the RF wavelength becomes on the order of the human torso, as seen at 3T. B1 inhomogeneities, in combination with the intrinsic properties of fat suppression and refocusing pulses in ETSE sequences (Shinnar–Le Roux pulses), may also be responsible for poor quality of fat suppression (fig. 1.20). To reduce SAR and acquire T2-weighted sequences with better fat suppression, alternative fat suppression techniques and T2-weighted imaging sequences must be optimized at 3T (fig. 1.21). The use of spectral-selective adiabatic inversion pulses for fat suppression, such as with SPAIR, has been effective at 3T (fig. 1.21)

Ultimately, the general framework and objectives for abdominal imaging at 3T should remain consistent with 1.5T. At a basic level, the sequence-types depicted in Table 1.2 should be transferred to 3T; however, from a sequence parameter perspective, adjustments must be made. Currently, it seems that the greatest advantage of the higher SNR of 3T, eight-channel torso phased-array coils, and the possibility of higher (>2) parallel imaging acceleration factors is observed in 3D GE gadolinium-enhanced sequences (fig. 1.22). It is highly anticipated that the newly available 32-channel coil will further accelerate 3D GE. This is of great importance at 3T, not only because inherent signal sensitivity increase allows increase in parallel imaging factors with less SNR loss (relative to 1.5T), but it also aids in achieving ultrashort dynamic 3D imaging following bolus contrast administration. This creates new possibilities for acquiring multi-dynamic phases within a single breath hold, or

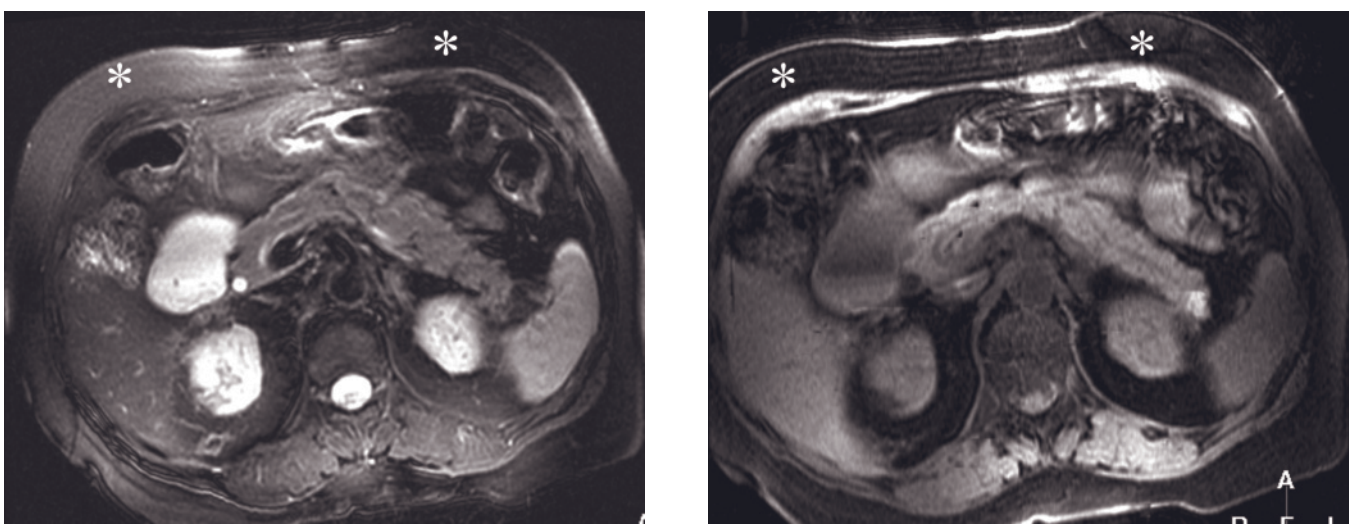

(*a*) (*b*)

FIG. 1.20 Fat suppression in echo-train spin-echo versus SGE sequences at 3T. Axial fat-suppressed T2-weighted echo-train turbo spin-echo sequence (*a*) with inhomogenous fat suppression (*), probably due to multiple refocusing pulses and the MR physics nature of these pulses. Axial fat-suppressed T1-weighted SGE (*b*) shows homogenous fat suppression (*) at the same anatomic level.

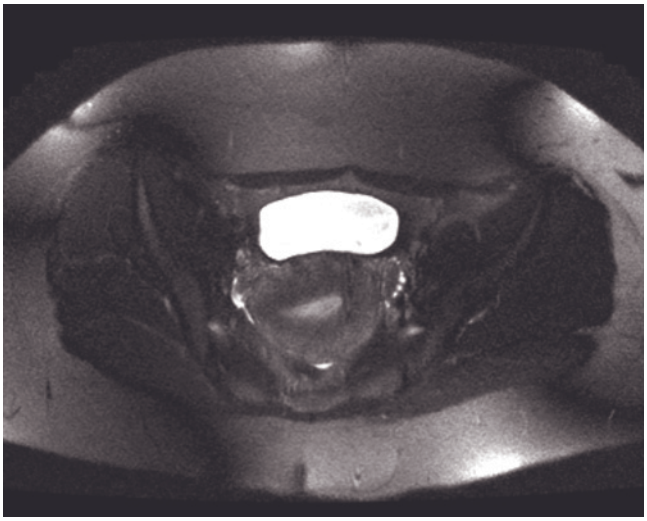

(*a*)

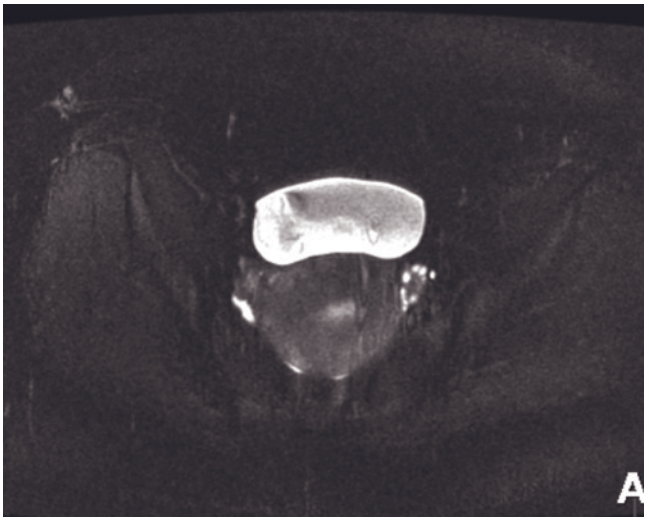

(*b*)

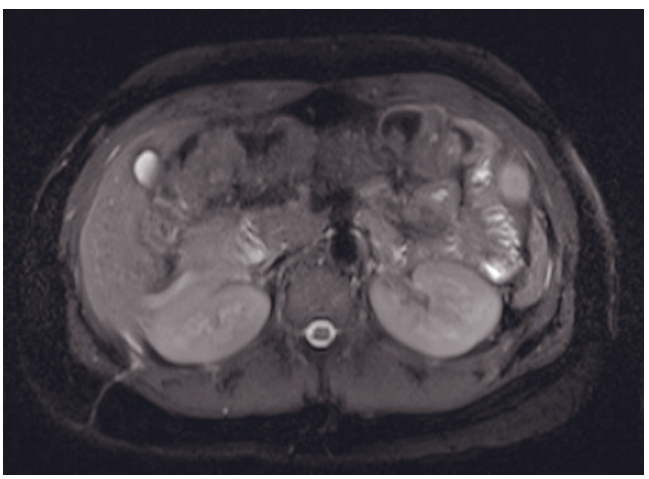

(*c*)

FIG. 1.21 Fat suppression in single-shot echo-train spin-echo versus single-shot echo planar imaging at 3T. Axial fat-suppressed single-shot T2-weighted echo-train turbo spin-echo sequence (*a*) with insufficient fat suppression. Axial fat-suppressed diffusion-weighted single-shot T2-weighted echo planar imaging (*b*) shows homogeneous fat suppression at the same anatomic level. In another patient, application of SSETSE with SPAIR (*c*) reveals robust fat suppression, with maintenance of water signal.

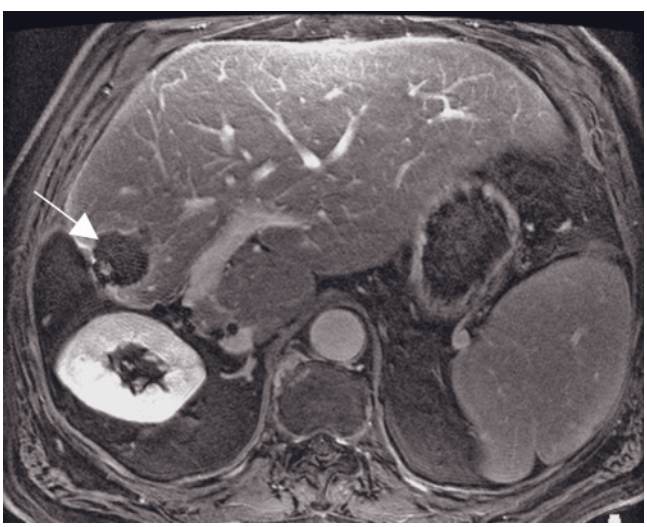

(*a*)

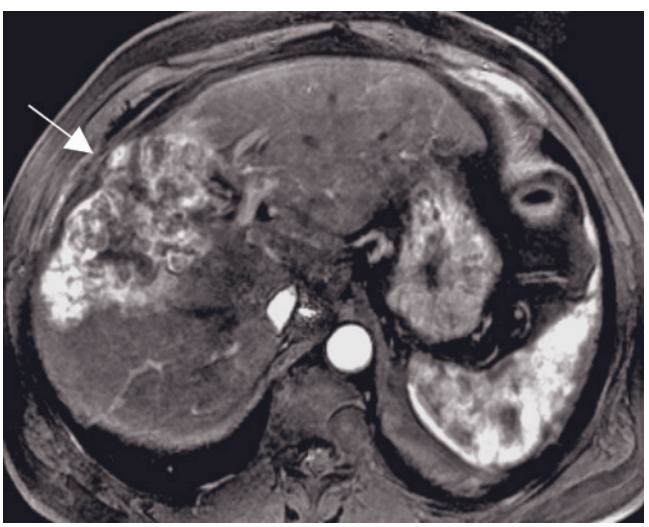

(*b*)

FIG. 1.22 4-Channel versus 8-channel torso phased-array coil at 3T. Axial fat-suppressed 3D gradient echo (4-channel torso phased-array coil; 4-mm section zero-interpolated to 2-mm sections; matrix 320 × 384; parallel imaging acceleration factor 2; scan time 25 s) (*a*) in a patient with status post right liver resection and a radiofrequency ablation of the recurrent metastasis at the resection plane (arrow). Axial fat-suppressed 3D gradient echo (8-channel torso phased-array coil; matrix 512 × 512; parallel imaging acceleration factor 3; other parameters were similar to the previous image) (*b*) in a patient with a recurrent gallbladder carcinoma (arrow).

investigating signal change behavior in the liver. Similarly, the promise of SNR gains at 3T implies the use of thinner sections and higher in-plane resolution with standard single-phase 3D GE. It is often apparent at 1.5T that artifacts due to lower through- and in-plane resolution impair visualization of subtle features of liver disease. This improvement in resolution costs time, effectively negating reasonable breath hold acquisitions. Parallel imaging with multichannel coils will be integral to reducing scan times under 20s. For individuals who still may be stressed from lengthy breath holds, parallel imaging can be further exploited to obtain diagnostic 3D GE at breath hold times between 10 and 15s depending on acceleration factors. As with 1.5T, robust motion insensitivity is vital for maximal diagnostic accuracy (fig. 1.23). Even in extreme cases, 3T still provides comparable, if not superior, robustness to breathing artifacts by utilizing rapid magnetization-prepared single-shot GE, which can eliminate the need for breath holding in noncooperative patients. Figure 1.23 shows clear depiction of a renal cyst on water-excited single-shot GE, in comparison to conventional breath-held 3D GE, which suffers from motion artifact.

For non-fat-suppressed and fat-suppressed T2-weighted MR imaging sequences, the best image quality is currently possible with SS-ETSE and diffusion-weighted single-shot echo planar imaging, respectively (fig. 1.24). Imaging of the pancreas and biliary tree in

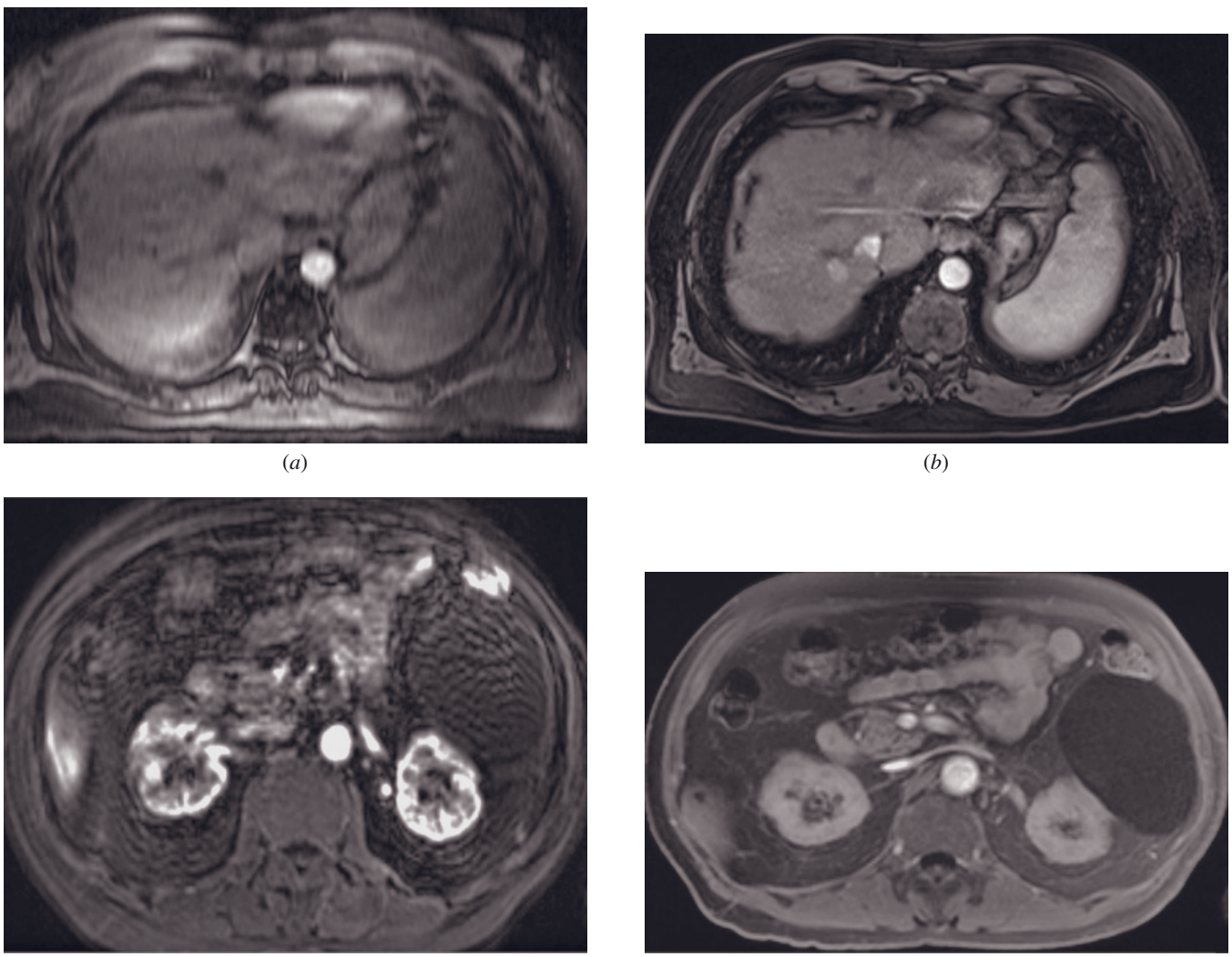

FIG. 1.23 Motion sensitivity at 1.5T and 3T. The importance of patient breath holding is revealed in two 3D GE acquisitions obtained on separate imaging days (*a*, *b*). The initial exam shows the impact of motion on an arterial acquisition, in which no lesion is visible (*a*). On subsequent repeat scanning, proper breath holding reveals a small arterial-enhancing liver lesion (*b*). When patient noncooperation is extreme, a water-excited SS-SGE is utilized, as shown in the depiction of a renal cyst at 3T, with conventional breath-held 3D GE (*c*) and with water-excited SS-SGE (*d*).

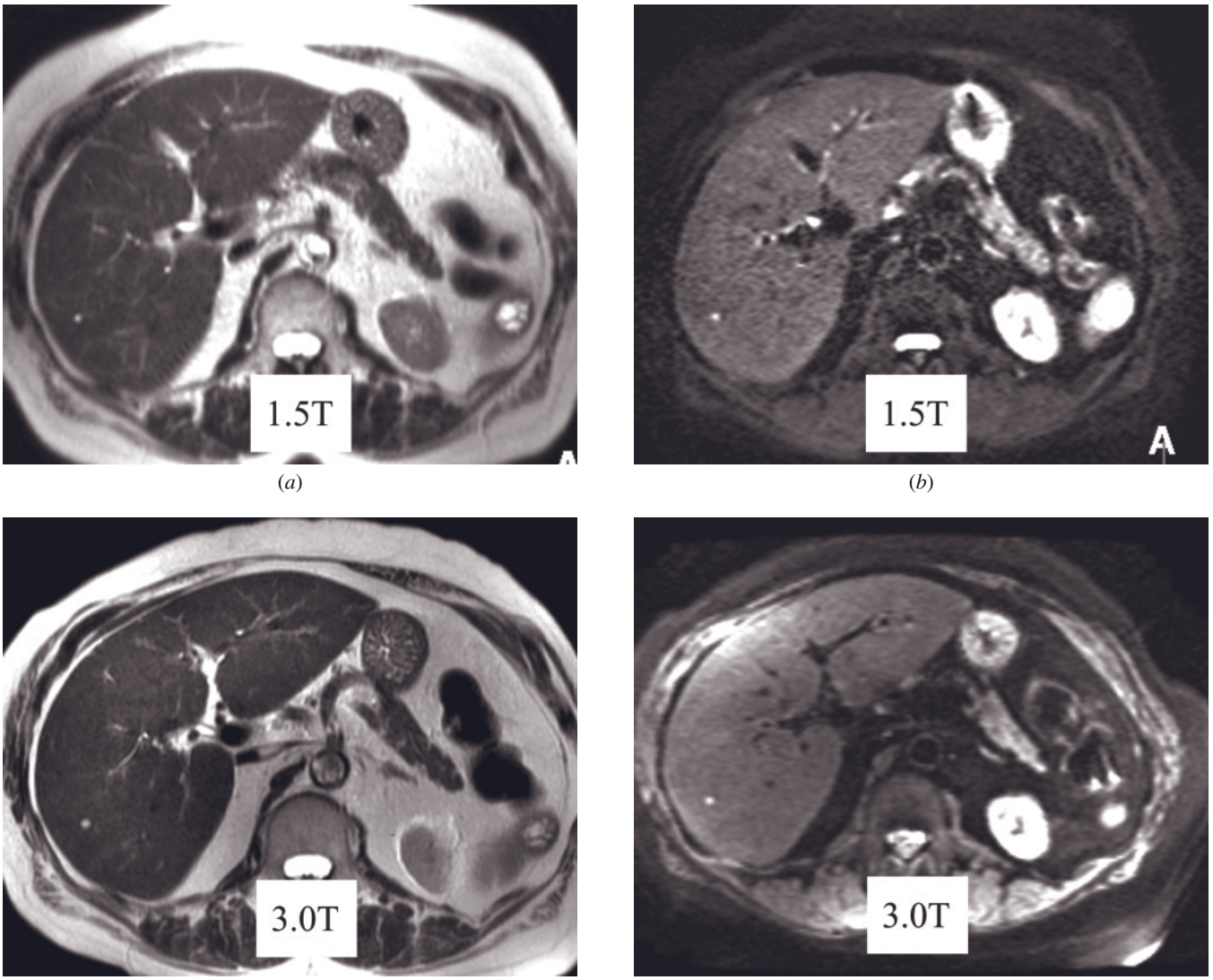

FIG. 1.24 1.5T versus 3.0T. Axial single-shot T2-weighted echo-train spin-echo (*a*) and fat-suppressed diffusion-weighted single-shot echo planar imaging (*b*) sequences at 1.5T (acquired with 4-channel torso phased-array coil and parallel imaging acceleration factor of 2 for echo planar imaging) show a small cyst in the right liver. Axial single-shot T2-weighted echo-train spin-echo (*c*) and fat-suppressed diffusion-weighted single-shot echo planar imaging (*d*) sequences at 3T (acquired with 8-channel torso phased-array coil and parallel imaging acceleration factor of 2 for both sequences) show a slightly better image quality with improved SNR and reduced image blurring.

particular may benefit from the use of eight-channel torso coil and parallel imaging (figs. 1.25 and 1.26). SS-ETSE sequences require parallel imaging, for the reduction of SAR and image blurring (by reducing the effective interecho spacing), whereas echo planar imaging mainly requires parallel imaging for the reduction of anatomic distortion (27). In the near future, a greater number of coil elements may allow higher (>2) parallel imaging acceleration factors that might be advantageous for T2-weighted sequences for better anatomic coverage, less image blurring, and less image distortion. At present, noncontrast T1-weighted sequence such as 2D SGE, as well as T2-weighted ETSE sequences, especially with fat suppression, need further optimization.

Whole Body MRI: Faster and Better

Whole body MRI is a fast, reliable, safe, and accurate means of detecting disease throughout the entire body (figs. 1.27–1.31). This has been well shown in a recent article [28] in which the authors demonstrated that a screening MR protocol showed various disease processes with almost equal accuracy to a variety of comparison "gold standard" diagnostic tests. That article

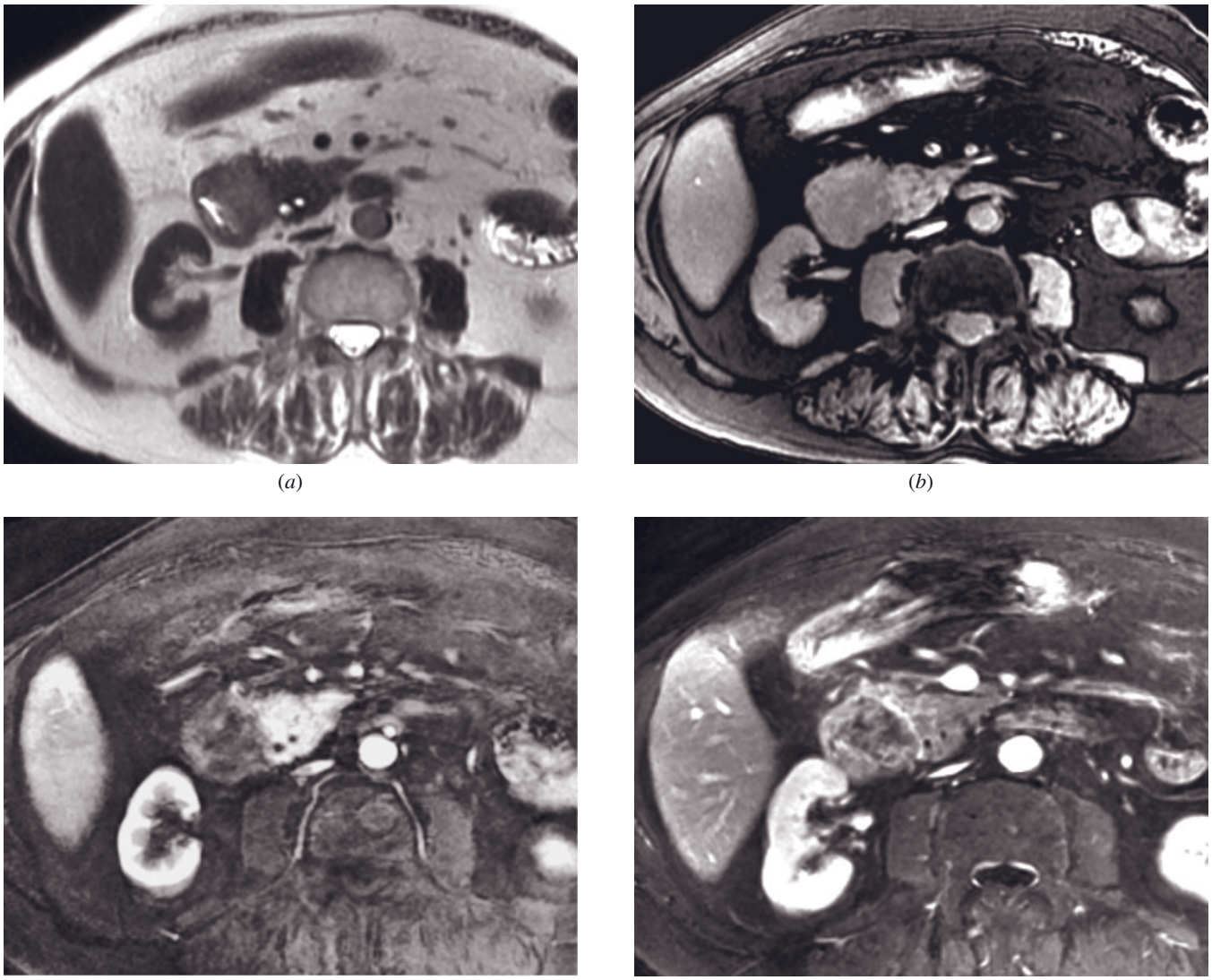

FIG. 1.25 Pancreas imaged with an 8-channel torso coil at 3T. Axial single-shot T2-weighted echo-train spin-echo (*a*), fat-suppressed 2D spoiled gradient echo (*b*), and gadolinium-enhanced 3D gradient echo (parallel imaging acceleration factor 3) in the arterial (*c*) and delayed (*d*) phases shows clearly the pancreas, the pancreatic duct, the peripancreatic vessels, as well as a duodenal tumor, because of the unique combination of a high in-plane spatial (matrix 512 × 512) and the intrinsic tissue-contrast of MRI at 3T.

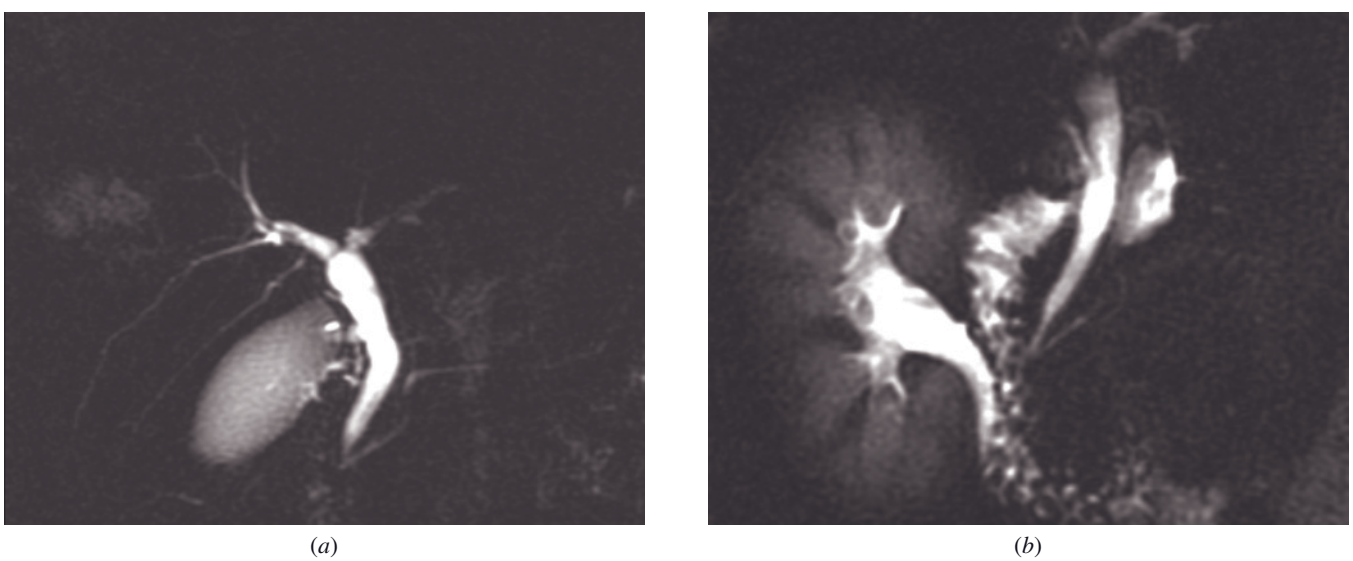

FIG. 1.26 MRCP with an 8-channel torso coil at 3T. A thick-slab (slice thickness 40 mm; 512 × 512 matrix; pMRI acceleration factor 2) shows an overview of the biliary tree (*a*) and a detailed view of the papillary region and the renal collecting system (*b*).

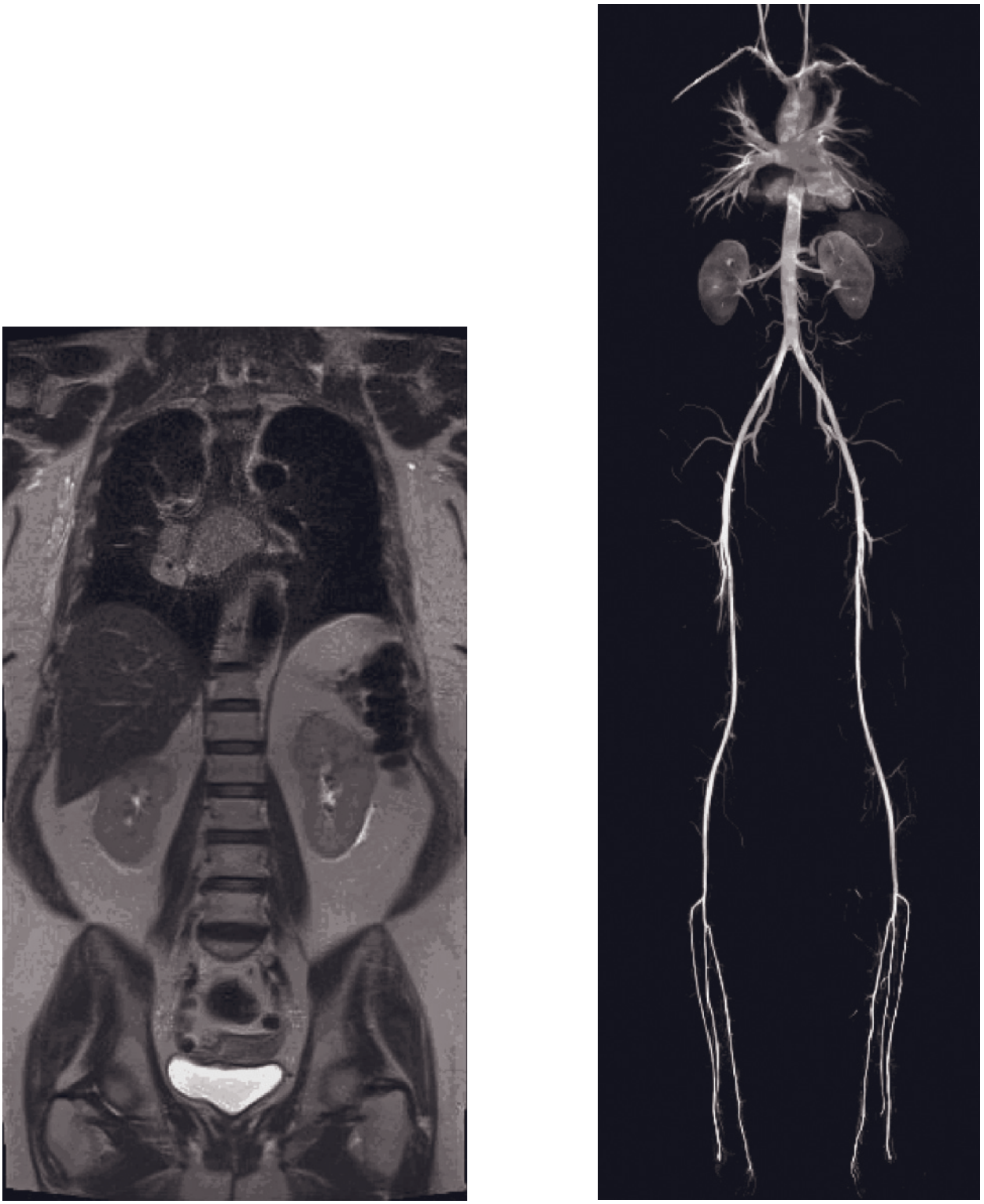

(*a*) (*b*)

FIG. 1.27 Large field-of-view imaging. Coronal large FOV acquisition using table recentering. Routine multislice inspection of the chest through pelvis using T2 single-shot ETSE is possible in one acquisition (*a*). The technique can be modified to acquire axial slices over the same regions of interest, with user-specified automatic table movements. Similar strategies can be used to perform whole body MRA using a single bolus injection (*b*).

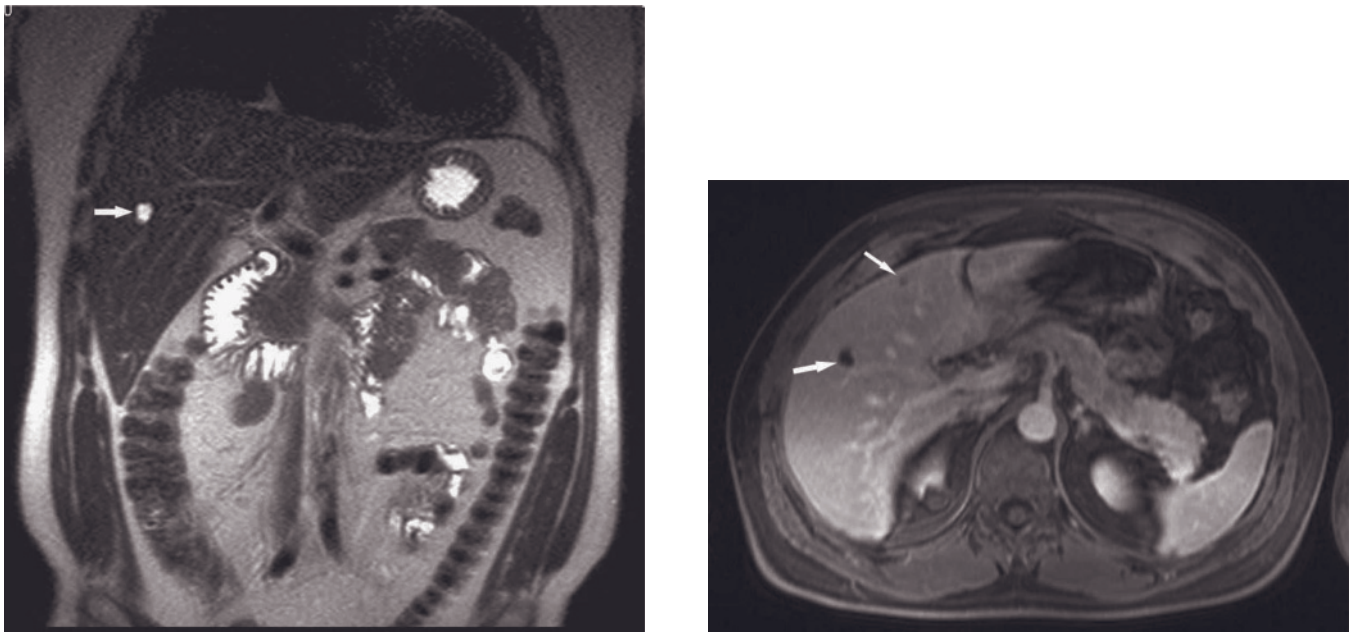

(*a*) (*b*)

FIG. 1.28 Liver. Coronal T2-weighted single-shot echo-train spin-echo image (*a*) shows a high-signal-intensity lesion consistent with biliary hamartoma (arrow). Axial T1-weighted fat-suppressed postgadolinium 3D gradient echo image (*b*) shows the biliary hamartomas with low signal intensity (arrows).

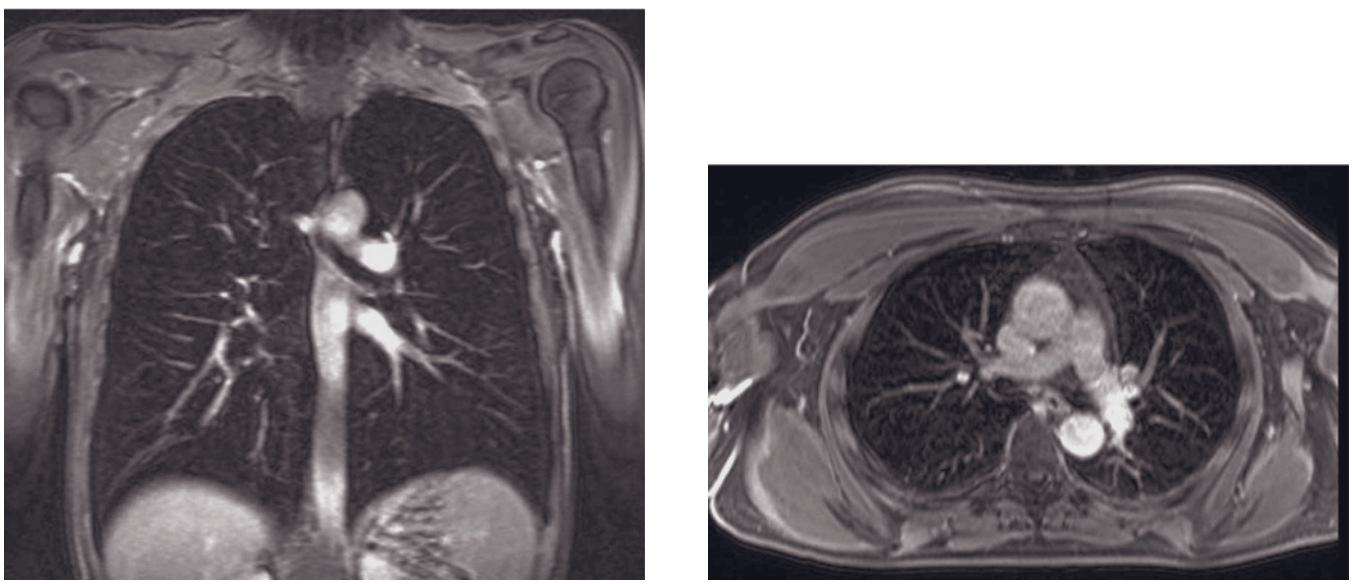

(*a*) (*b*)

FIG. 1.29 Chest. Coronal (*a*) and axial (*b*) T1-weighted fat-suppressed 3D gradient-echo postgadolinium (b) images clearly show enhanced pulmonary vessels that can be traced into the periphery of both lungs.

emphasized one component of whole body MRI, which is the use of gadolinium enhanced 3D GE. There are, however, five major technical advances that have rendered whole body screening with MRI a viable method, which include:

1. Remote movement of the imaging table from the imaging console
2. Multiple input channels that allow simultaneous use of multiple localized, specialized surface coils that generate high-spatial-resolution images of multiple

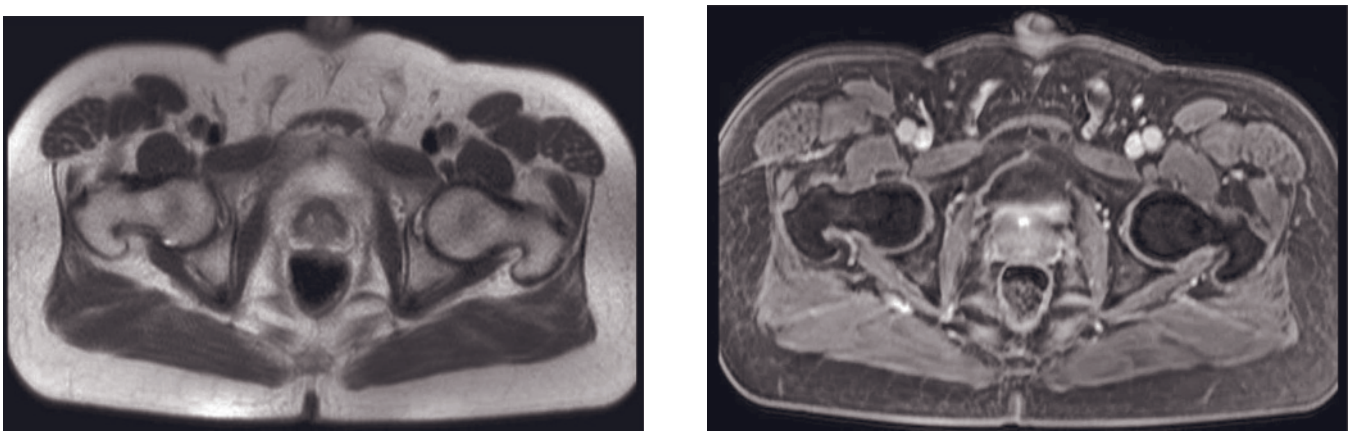

(*a*) (*b*)

FIG. 1.30 Pelvis. Axial T2-weighted single-shot echo-train spin-echo (*a*) and axial T1-weighted fat suppressed 3D gradient echo postgadolinium (*b*) images clearly show the pelvic anatomy.

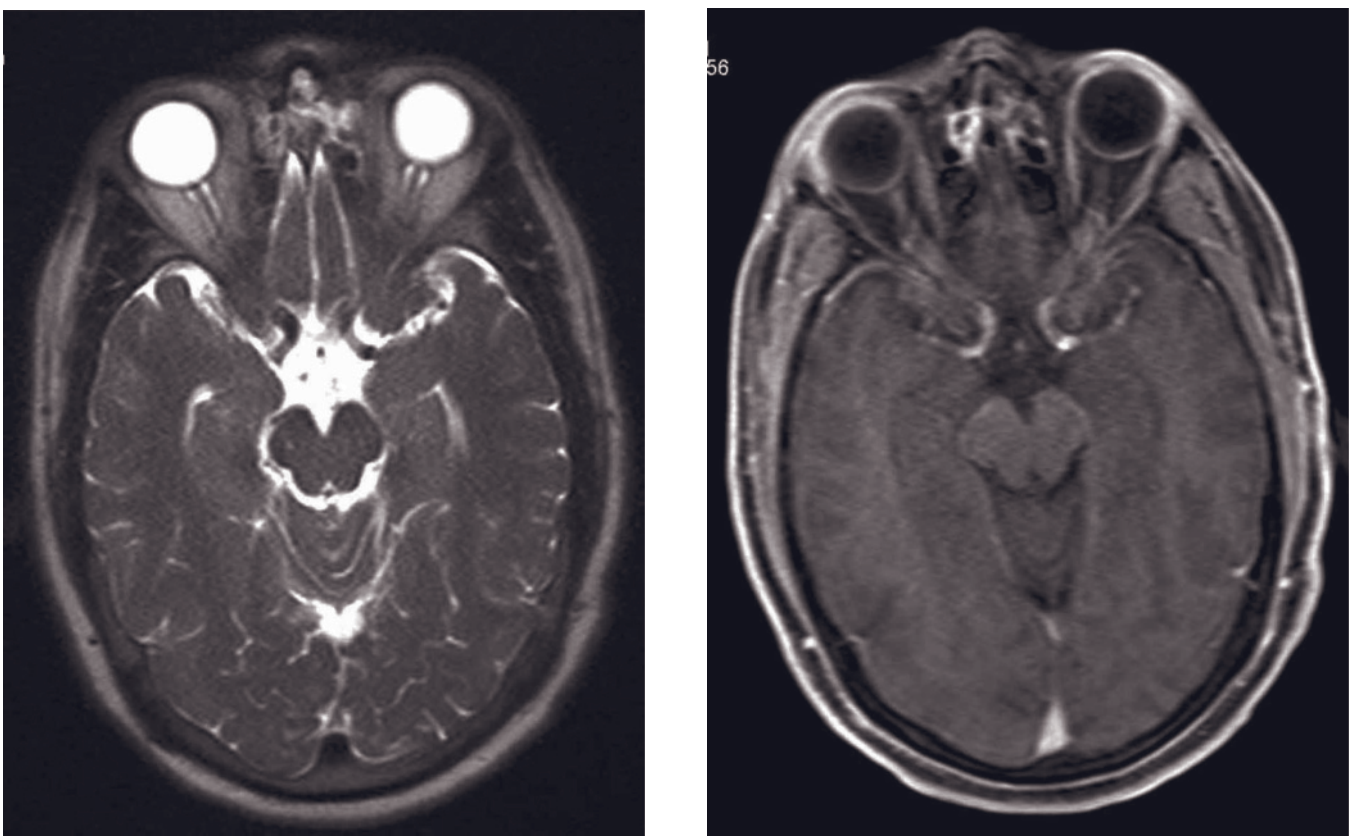

(*a*) (*b*)

FIG. 1.31 Brain. Axial T2-weighted fat-suppressed single-shot echo-train spin-echo (*a*) and axial T1-weighted fat-suppressed 3D gradient-echo postgadolinium (*b*) images provide a detailed view of the intra- and extracranial anatomic structures.

regions of the body, without the delay of coil exchange and setup

3. Specialized surface coils that are designed for independent operation of the individual coil elements
4. Concurrent development of sequence (data acquisition) technology that operates in conjunction with the new specialized coils, such as parallel imaging
5. Development of high-image-quality 3D T1-weighted gradient echo with short echo time (TE) that facilitates acceptable imaging quality of various organ systems, most notably the lungs

The combined effect of all these above innovations has allowed, among other things, full body imaging to be performed more rapidly (because of remote table movement and new short data acquisitions), with maintenance of high image quality (simultaneous use of multiple specialized coils), and with the ability to image the lungs with adequate image quality (3D T1-weighted gradient echo imaging). The result is that the entire body can be imaged in a matter of 10–15 min, with high image quality maintained (Table 1.9).

To use an imaging study to screen for disease, it must be able to detect disease accurately and reliably while avoiding describing normal parts of the body as diseased. Since whole body CT and MRI screening are relatively new procedures, limited data have been collected comparing the two methods. There is growing concern in the medical community that whole body CT screening leads to a large number of questionable findings, requiring additional procedures, including surgery, and creating added risks and costs for the individual (29). Most of the information comparing the performance of CT and MRI has been gathered through diagnostic studies, that is, imaging studies ordered for the detection of suspected disease. Overall, MRI has been found to discover more lesions and correctly characterize more disease, whether benign or malignant, than CT. In these capacities, MRI has been shown to be superior to CT for examining specific regions of the body, for example, head, spine, musculoskeletal, abdomen, and pelvis [30–36]. In the past, the sole exception to this rule has been imaging of the lungs, which is performed better by CT than MRI, although new MRI techniques show promising results [28, 37].

Cost of the imaging study is also an important consideration. Because of the nature of the complexity of the imaging system and intrinsic maintenance costs, MRI is unavoidably a more expensive test than CT. The machinery has many more components, and the requirement for liquid helium and liquid nitrogen to be continuously replenished renders it intrinsically more expensive. The real cost of MRI is greater than that of CT: An approximate estimate is that studies are about 20% more expensive.

Regarding safety, MRI is a safer modality than CT, both the imaging system itself and the intravenous contrast agent employed [38–42]. The powerful magnetic field and radiofrequency energy of MRI has not been shown to cause cancer or fetal abnormalities, unlike the ionizing radiation used in CT that is a known cause of cancer and fetal anomalies. It is important to note that although X-rays are known to cause cancer, the exact risk of cancer from receiving CT scans, and even repeat CT exams, is unknown. A more in-depth discussion on cancer risks from radiation exposure in CT and other X-ray procedures has recently been published [43]. The intravenous contrast agents used routinely in MRI, gadolinium-containing agents, are also considerably safer than the analogous intravenous agents employed in contrast-enhanced CT, which are iodine-based agents. There is a much lesser association with kidney injury with the MRI contrast agents, and much lesser association with allergic reactions, including severe allergic reactions that can lead to death [44–46]. That is why in general individuals who are undergoing diagnostic imaging studies will have an MRI study rather than CT if they have poor kidney function or a history of allergies. Other very compelling aspects of the use of intravenous contrast agents with MRI are that the diameter of the intravenous catheter inserted is much smaller with MRI, the volume of contrast material that is injected intravenously is 10 times less than with CT (the rapid injection of the large volume of contrast with CT can create a strong sense of nausea), and the injection rate is slower with MRI than with CT. Additionally, the chance of the injected contrast agent not going into the vein but into the surrounding tissues is also greater with CT, which is a problem compounded by the large volume of the fluid injected.

Therefore, if MRI is superior to CT for finding small-volume disease, correctly classifying disease, demonstrating that normal structures are intact and not diseased, and safer and less painful (smaller needle stick with MRI), then why is MRI still not considered the method of choice for whole body screening? Historically, the primary reason for this is that MRI is much slower to perform than CT, and imaging of the lungs was suboptimal. Recently, the MR systems that are manufactured have imaging capability that allows them to image the entire body much faster, while maintaining high image quality that even machines made in 2003 did not possess. Basically new designs of transmit-receiver coils, easier movement of the imaging table, and new data acquisition techniques have allowed rapid imaging of the entire body, and also acceptable image quality of the lungs. High-quality whole body MRI imaging that would take 2 hours even in 2003, now can be done in 10–15 min, making the technique very suitable for rapid, highly accurate whole body imaging in an easily tolerable time frame.

Although at present reliability and accuracy of MR imaging at detecting diseases of certain organs including liver, brain, spine, pancreas, and kidneys is extremely high and imaging of the lungs is reasonable, optimal imaging of the heart, breast, and colon still requires further development to achieve consistent image quality and consistent accurate display of small-volume disease. Nonetheless, imaging of all the latter mentioned organs is currently at a diagnostically acceptable level.

Currently manufactured MR systems have evolved to the point that the equipment can image through the

entire body with good image quality and sensitivity to detect disease within a 15-min period. Whole body, high-quality, MRI screening is now feasible.

REFERENCES

1. Brown MA, Semelka RC. *MRI: Basic Principles and Applications*. Second Edition. New York: Wiley-Liss, 1999.
2. Semelka RC, Willms AB, Brown MA, Brown ED, Finn JP. Comparison of breath-hold T1-weighted MR sequences for imaging of the liver. *J Magn Reson Imaging* 4: 759–765, 1994.
3. Semelka RC, Kelekis NL, Thomasson D, Brown MA, Laub GA. HASTE MR imaging: description of technique and preliminary results in the abdomen. *J Magn Reson Imaging* 6: 698–699, 1996.
4. Gaa J, Hutabu H, Jenkins RL, Finn JP, Edelman RR. Liver masses: replacement of conventional T2-weighted spin echo MR imaging with breath-hold MR imaging. *Radiology* 200: 459–464, 1996.
5. Semelka RC, Balci NC, Op de Beeck B, Reinhold C. Evaluation of a 10-minute comprehensive MR imaging examination of the upper abdomen. *Radiology* 211: 189–195, 1999.
6. Semelka RC, Helmberger T. Contrast enhanced MRI of the liver: state-of-the-art. *Radiology* 2001.
7. Low RN, Semelka RC, Worawattanakul S, Alzate GD. Extrahepatic abdominal imaging in patients with malignancy: comparison of MR imaging and helical CT in 164 patients. *J Magn Reson Imaging* 12: 269–277, 2001.
8. Low RN, Semelka RC, Worawwattanakul S, Alzate GD, Sigeti JS. Extrahepatic abdominal imaging in patients with malignancy: comparison of MR imaging and helical CT, with subsequent surgical correlation. *Radiology* 210: 625–632, 1999.
9. Altun E, Semelka RC, Dale BM, Elias J Jr.. Water excitation MPRAGE: an alternative sequence for postcontrast imaging of the abdomen in noncooperative patients at 1.5 Tesla and 3.0 Tesla MRI. *J Magn Reson Imaging* 27: 1146–1154, 2008.
10. Lauenstein TC, Sharma P, Hughes T, Heberlein K, Tudorascu D, Martin DR. Evaluation of optimized inversion-recovery fat-suppression techniques for T2-weighted abdominal MR imaging. *J Magn Reson Imaging* 27(6): 1448–1454, 2008.
11. Rofsky NM, Lee VS, Laub G, Pollack MA, Krinsky GA, Thomasson D, Ambrosino MM, Weinreb JC. Abdominal MR imaging with a volumetric interpolated breath-hold examination. *Radiology* 212: 876–884, 1999.
12. Lee VS, Lavelle MT, Rofsky NM, Laub G, Thomasson DM, Krinsky GA, Weinreb JC. Hepatic MR imaging with a dynamic contrast-enhanced isotropic volumetric interpolated breath-hold examination: feasibility, reproducibility, and technical quality. *Radiology* 215: 365–372, 2000.
13. Sharma P, Salman K, Burrow B, Lauenstein T, Martin D. Quantification of arterial-phase perfusion kinetics in the liver. In: *Proceedings of the 15th Annual Meeting of ISMRM*, Berlin, 2007 (abstract 2980).
14. Low RN, Francis IR, Politoske D, Bennett M. Crohn's disease evaluation: comparison of contrast-enhanced MR imaging and single-phase helical CT scanning. *J Magn Reson Imaging* 11: 127–135, 2000.
15. Hutchinson M, Raff U. Fast MRI data acquisition using multiple detectors. *Magn Reson Med* 6: 87–91, 1988.
16. Kelton JR, Magin RL, Wright SM. An algorithm for rapid image acquisition using multiple receiver coils. In: *Proceedings 8th Annual Meeting of SMRM*, p. 1172.
17. Ra JB, Rim CY. Fast imaging using subencoding data sets from multiple detectors. *Magn Reson Med* 30: 142–145, 1993.
18. Carlson JW, Minemura T. Imaging time reduction through multiple receiver coil data acquisition and image reconstruction. *Magn Reson Med* 29: 681–688, 1993.
19. Kwiat D, Einav S. Preliminary experimental evaluation of an inverse source imaging procedure using a decoupled coil detector array in magnetic resonance imaging. *Med Eng Phys* 17: 257–263, 1995.
20. Sodickson DK, Manning WJ. Simultaneous acquisition of spatial harmonics (SMASH): fast imaging with radio-frequency coil arrays. *Magn Reson Med* 38: 591–603, 1997.
21. Jakob PM, Griswold MA, Edelman RR, Sodickson DK. AUTO-SMASH, a self-calibrating technique for SMASH imaging. *MAGMA* 7: 42–54, 1998.
22. Pruessmann KP, Weiger M, Scheidigger MB, Boesiger P. SENSE: sensitivity encoding for fast MRI. *Magn Reson Med* 42: 952–962, 1999.
23. Kyriakos WE, Panych LP, Kacher DK et al. Sensitivity profiles from an array of coils for encoding and reconstruction in parallel (SPACE RIP). *Magn Reson Med* 44: 301–308, 2000.
24. Griswold MA, Jakob PM, Heidemann RM et al. Generalized auto-calibrating partially parallel acquisition (GRAPPA). *Magn Reson Med* 47: 1202–1210, 2002.
25. Ramalho M, Altun E, Heredia V, Zapparoli M, Semelka R. Liver MR imaging: 1.5T versus 3T. *Magn Reson Imaging Clin N Am* 15: 321–347, 2007.
26. Goncalves Neto JA, Altun E, Elazzazi M, Vaidean G, Chaney M, Semelka RC. Enhancement of abdominal organs on hepatic arterial phase: quantitative comparison between 1.5T and 3.0T MRI. *Magn Reson Imaging* 2009, In press.
27. Hussain SM, De Becker J, Hop WCJ, Dwarkasing S, Wielopolski PA. Can a single-shot black-blood T2-weighted spin-echo echo planar imaging sequence with sensitivity encoding replace the respiratory-triggered turbo spin-echo sequence for the liver? An optimization and a feasibility study. *J Magn Reson Imaging* 21: 219–229, 2005.
28. Lauenstein TC, Goehde SC, Herborn CU, Goyen M, Oberhoff C, Debatin JF, Ruehm SG, Barkhausen J. Whole-body MR imaging: evaluation of patients for metastases. *Radiology* 233: 139–148, 2004.
29. Ko J, Casola G. Whole Body MR Screening Found Feasible. Whole Body CT Screening. http://www.rsna.org/publications/rsnanews/febo4/mri-1.html
30. Gillman S. Imaging the brain: second of two parts. *N Engl J Med* 338(13): 889–896, 1998.
31. Semelka R, Martin D, Balci C, Lance T. Focal liver lesions: comparison of dual-phase CT and multisequence multiplanar MR imaging including dynamic gadolinium enhancement. *J Magn Reson Imaging* 13: 397–401, 2001.
32. Low R, Semelka R, Woranwattanakul S, Alzate G, Sigeti J. Extrahepatic abdominal imaging in patients with malignancy: comparison of MR imaging and helical CT, with subsequent surgical correlation. *Radiology* 210: 625–632, 1999.
33. Low R, Semelka R, Woranwattanakul S, Alzate G. Exrahepatic abdominal imaging in patients with malignancy: comparison of MR imaging and helical CT in 164 patients. *J Magn Reson Imaging* 12: 269–277, 2000.
34. Semelka RC, Kelekis NL, Molina PL, Sharp TJ, Calvo B. Pancreatic masses with inconclusive findings on spiral CT: Is there a role for MRI? *J Magn Reson Imaging* 6: 585–588, 1996.
35. Sheridan MB, Ward J, Guthrie JA, Spencer JA, Craven CM, Wilson D, Guillou P, Robinson P. Dynamic contrast-enhanced MR imaging and dual-phase helical CT in the preoperative assessment of suspected pancreatic cancer: a comparative study with receiver operating characteristic analysis. *AJR Am J Roentgenol* 173: 583–590, 1999.
36. Semelka RC, Martin D, Balci C, Lance T. Focal liver lesions: comparison of dual-phase CT and multisequence multiplanar MR

imaging Including dynamic gadolinium enhancement. *J Magn Reson Imaging* 13: 397–401, 2001.
37. Bader T, Semelka R, Pedro M, Armao D, Brown M, Molina P. Magnetic resonance imaging of pulmonary parenchymal disease using a modified breath-hold 3D gradient-echo technique: Initial observations. *J Magn Reson Imaging* 15: 31–38, 2002.
38. Budinger TF. Nuclear magnetic resonance (NMR) in vivo studies: known thresholds for health effects. *J Comp Assist Tomogr* 5: 800–811, 1981.
39. Reid A, Smith FW et al. Nuclear magnetic resonance imaging and its safety implications: follow-up of 181 patients. *Br J Radiol* 55: 784–786, 1982.
40. McRobbie D, Foster MA. Pulsed magnetic field exposure during pregnancy and implications for NMR fetal imaging: a study with mice. *Magn Reson Imaging* 3: 231–234, 1985.
41. Heinrichs WL, Fong P et al. Midgestational exposure of pregnant BALB/c mice to magnetic resonance imaging conditions. *Magn Reson Imaging* 6: 305–313, 1988.
42. Terens WL, Gluck R, Golimbu M, Rofsky NM. Use of gadolinium-DTPA-enhancement MRI to characterize renal masses in patient with renal insufficiency. *Urology* 40: 152–154, 1992.
43. Berrington de González A, Darby S. Risk of cancer from diagnostic X-rays: estimates for the UK and 14 other countries. *Lancet* 363: 345–351, 2004.
44. Brezis M, Epsetein FH. A closer look at radiocontrast-induced nephropathy. *N Engl J Med* 323: 179–181, 1989.
45. Berns AS. Nephrotoxicity of contrast media. *Kidney Int* 35: 730–740, 1989.
46. Parfrey PS, Griffths SM, Barrett BJ et al. Contrast material-induced renal failure in patients with diabetes mellitus, renal insufficiency or both; a prospective controlled study. *N Engl J Med* 323: 143–149, 1989.

CHAPTER

2

LIVER

LARISSA BRAGA, DIANE ARMAO, MOHAMED ELAZZAZI, AND RICHARD C. SEMELKA

NORMAL ANATOMY

The liver is the most massive of the viscera and commands the right upper quadrant of the abdomen. The current classification system of liver segmental anatomy, as refined by Couinaud [1], describes the liver as divided into eight independent functioning units or segments, each of which is served by its own vascular pedicle (arterial, portal venous, and lymphatic) and biliary drainage. This improved understanding of the intrahepatic architecture has fueled technical progress in liver surgery and transplantation. Vessels are clearly discernible with MRI, which makes this technique ideally suited to the study of the functional segmental anatomy of the liver (fig. 2.1).

With respect to the imaging features of liver, there are three fissures that help define functional right and left hepatic lobes and the major hepatic segments. The interlobar fissure, located on the inferior liver margin, is oriented along a line passing through the gallbladder fossa inferiorly and the middle hepatic vein superiorly. Although well defined in some patients, the interlobar fissure is usually difficult to identify. The left intersegmental fissure (fissure for the ligamentum teres) forms a well-defined sagitally oriented cleft in the caudal aspect of the left hepatic lobe, serving to divide the lobe into medial and lateral segments. The ligamentum teres, or obliterated vestige of the left umbilical vein, normally ensconced in a small amount of fat, runs through this fissure after entering it via the free margin of the falciform ligament. The third fissure, or fissure for the ligamentum venosum, is oriented in a coronal or oblique plane between the posterior aspect of the left lateral hepatic segment and the anterior aspect of the caudate lobe. This fissure forms a continuum with the intersegmental fissure. The fissure for the ligamentum venosum cuts deeply anterior to the caudate lobe and contains the two layers of the lesser omentum.

The porta hepatis is a deep transverse fissure situated between the medial segment anteriorly and the caudate process posteriorly. At the porta hepatis, the portal vein, hepatic artery, and hepatic nerve plexus enter the liver and the right and left hepatic ducts and lymphatic vessels emerge from it. The caudate lobe stands at the watershed between right and left portobiliary arterial territories. Because the caudate lobe drains directly into the inferior vena cava, it may escape injury from venous outflow obstruction [2]. Whereas branches of the hepatic artery, the portal vein, and

Abdominal-Pelvic MRI, Third Edition, edited by Richard C. Semelka. Copyright © 2010 John Wiley & Sons, Inc.

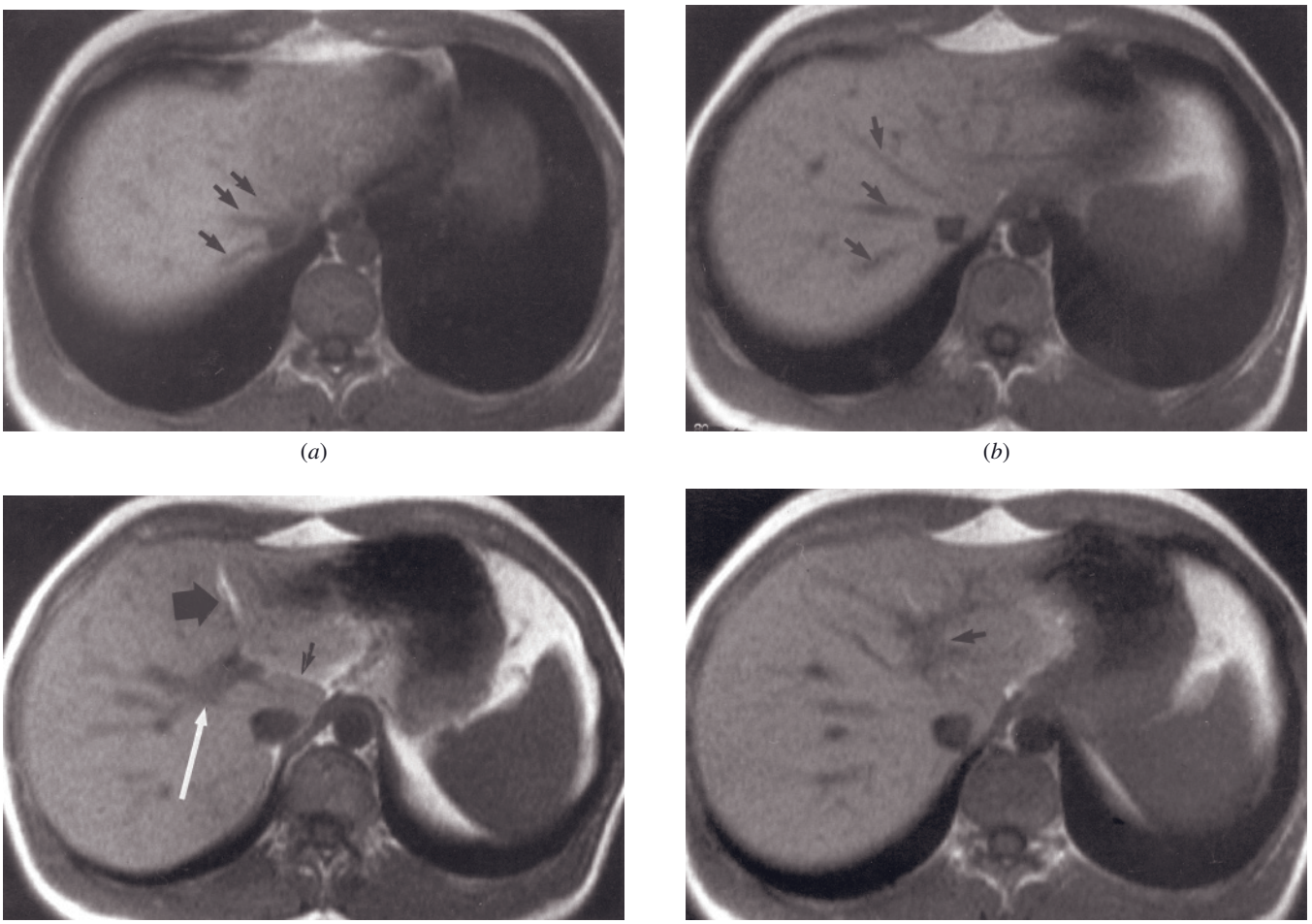

FIG. 2.1 Normal anatomy. Transverse SGE images (*a–d*). The vascular anatomy of the liver includes the hepatic venous system—superior, middle, and inferior hepatic veins (arrows, *a*, *b*) and portal venous system—right portal vein(long white arrow, *c*) and left portal vein (arrow, *d*). Note the caudate lobe, the fissure for the ligamentum venosum (small black arrow, *c*), and the fissure for the ligamentum teres (large black arrow, *c*).

tributaries of the bile ducts travel together serving segments of the liver, hepatic veins run independently and are intersegmental (fig. 2.2). The close relationship of the hepatic artery portal vein and bile ducts on a macroscopic level is mirrored on a microscopic level by the presence of portal triads comprising hepatic arterioles, portal venules, and interlobular bile ducts.

MRI TECHNIQUE

The current standard MRI examination of the liver includes a T2-weighted sequence, a T1-weighted sequence, and a dynamic contrast-enhanced sequence (fig. 2.3). The most comprehensive contrast administration approach is the use of gadolinium chelate, as a rapid bolus injection with serial imaging using spoiled gradient echo (SGE), 3D gradient echo, or a combination of both. A variety of sequences exist that generate T2- and T1-weighted images. Field strength and gradient factors of the MRI machine generally dictate the type of sequences employed. At lower field strength (<1.0 T) spin-echo sequences are generally used because of gradient strength and signal-to-noise ratio (SNR) limitations. At high field strength (3.0 T) echo-train sequences are used for T2-weighted sequences, and gradient-echo sequences are generally used for T1-weighted sequences. At 3.0 T the higher SNR significantly improves the image quality of postcontrast 3D-GE sequences, mainly to depict and characterize small liver nodules in chronic disease. However, new sequences are needed to improve image quality before contrast and reduce artifacts [3]. See Chapter 1 for a more complete description of standard liver imaging protocols. The vast majority of liver diseases can be characterized by the combined information provided by T2, T1, and early (hepatic arterial dominant) and late (hepatic venous) gradient echo images (figs. 2.4–2.6). A recent study [4] stressed that

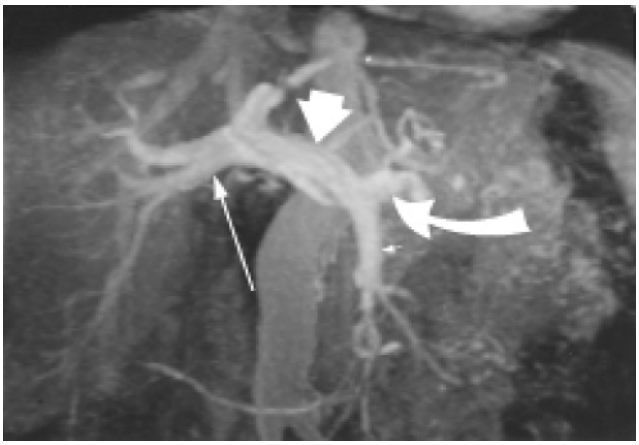

FIG. 2.2 Portal venous system. Anteroposterior projection from 3D MIP reconstruction of a set of coronal gadolinium-enhanced 2-mm 3D MRA source images. Superior mesenteric vein (small arrow), splenic vein (curved arrow), main portal vein (large arrow), and intrahepatic portal veins (long arrow) are well defined on this gadolinium-enhanced 3D MRA source image.

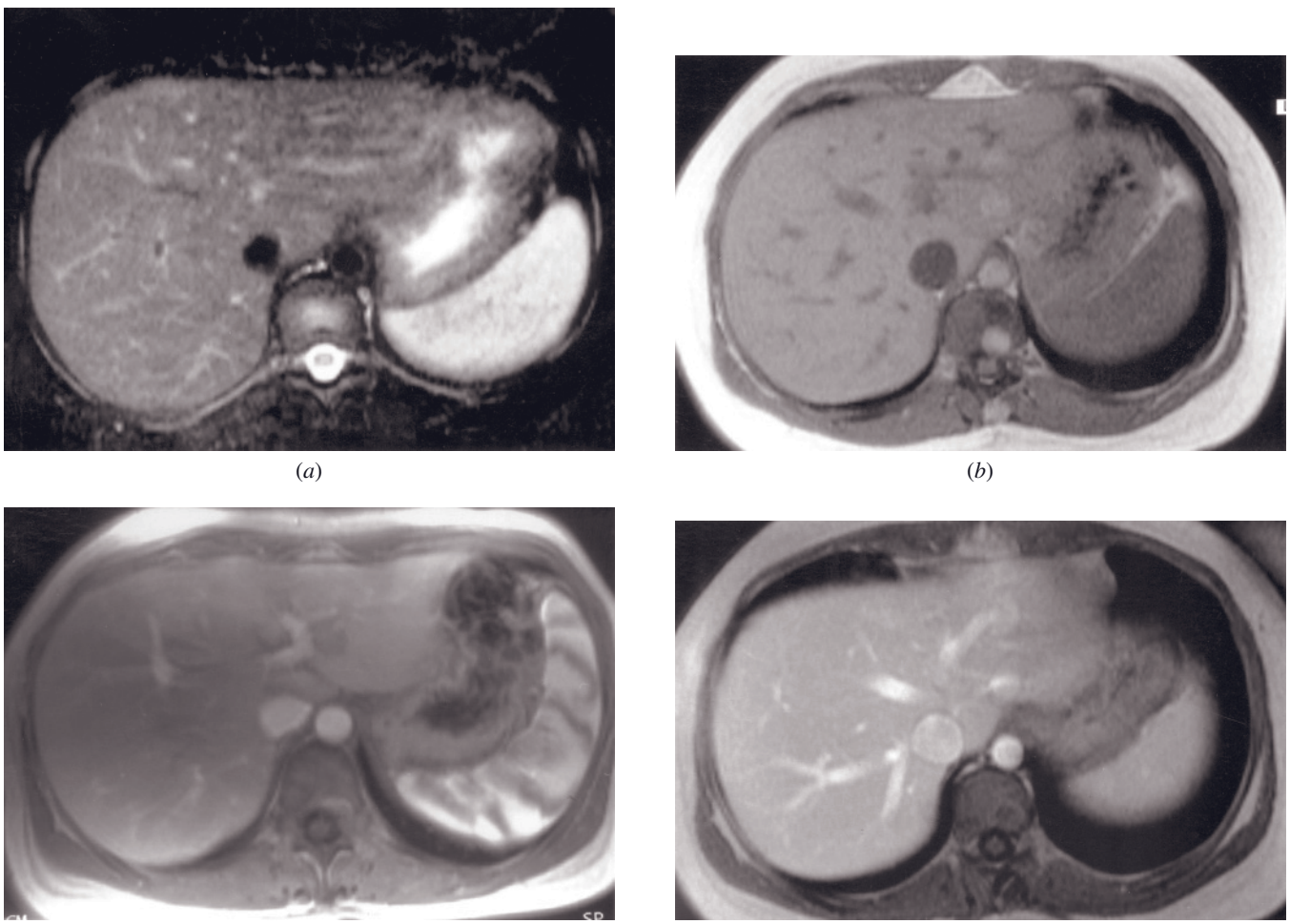

FIG. 2.3 Normal liver and sequences. T2-weighted fat-suppressed SS-ETSE (*a*), SGE (*b*), and immediate (*c*), 45-s (*d*), and 90-s fat-suppressed (*e*) postgadolinium SGE images. Liver is lower in signal than normal, non-iron-deposited spleen on the T2-weighted (*a*) and higher in signal intensity than spleen on the T1-weighted (*b*) images. A liver imaging protocol should include noncontrast T2-weighted (*a*) and T1-weighted (*b*) sequences and hepatic arterial dominant phase (*c*), early hepatic venous phase (*d*), and hepatic venous phase fat-suppressed (*e*) sequences.

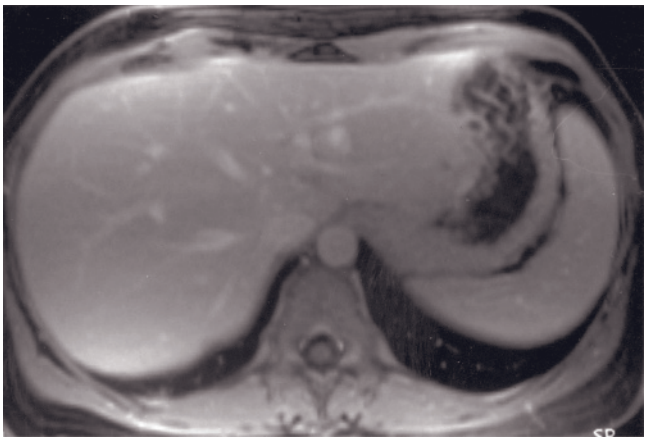

(*e*)

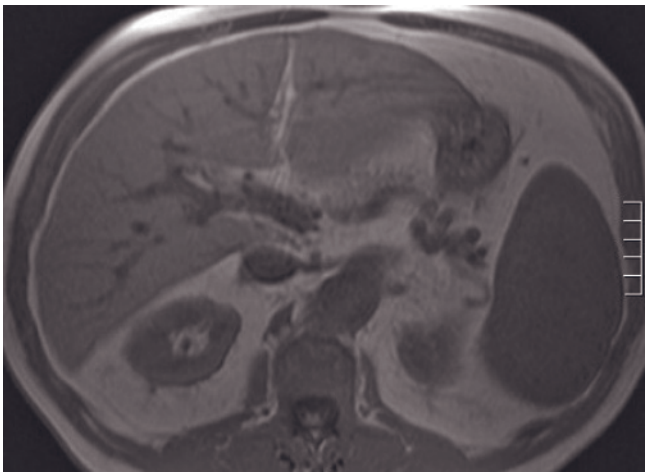

(*f*)

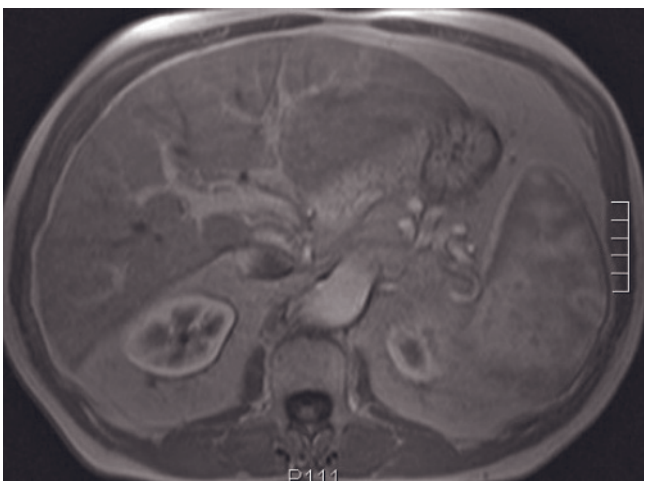

(*g*)

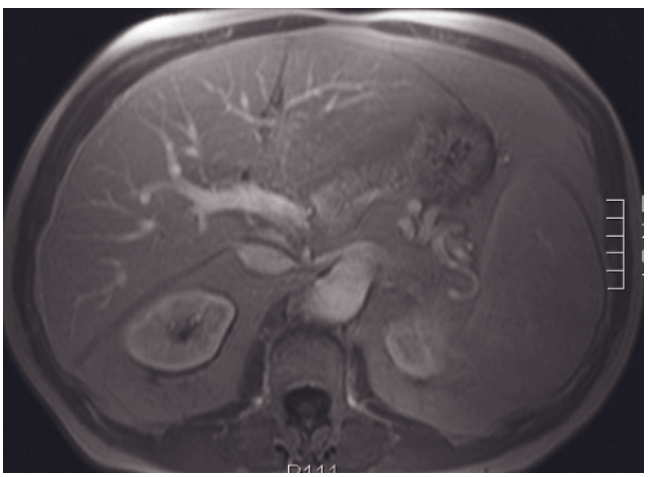

(*h*)

(*i*)

FIG. 2.3 (*Continued*) SGE (*f*) and immediate (*g*), 45-s (*h*), and 90-s (*i*) fat-suppressed postgadolinium SGE images in a second patient at a lower tomographic level than the first patient. Note the presence of contrast in the main portal vein and branches but not in the branches of hepatic veins on the immediate postgadolinium image (*g*), denoting that the sequence was acquired in the perfect timing of the contrast. At 45 s after gadolinium (*h*), the liver is homogeneously enhanced with all vessels opacified, which persists on 90-s images (*i*).

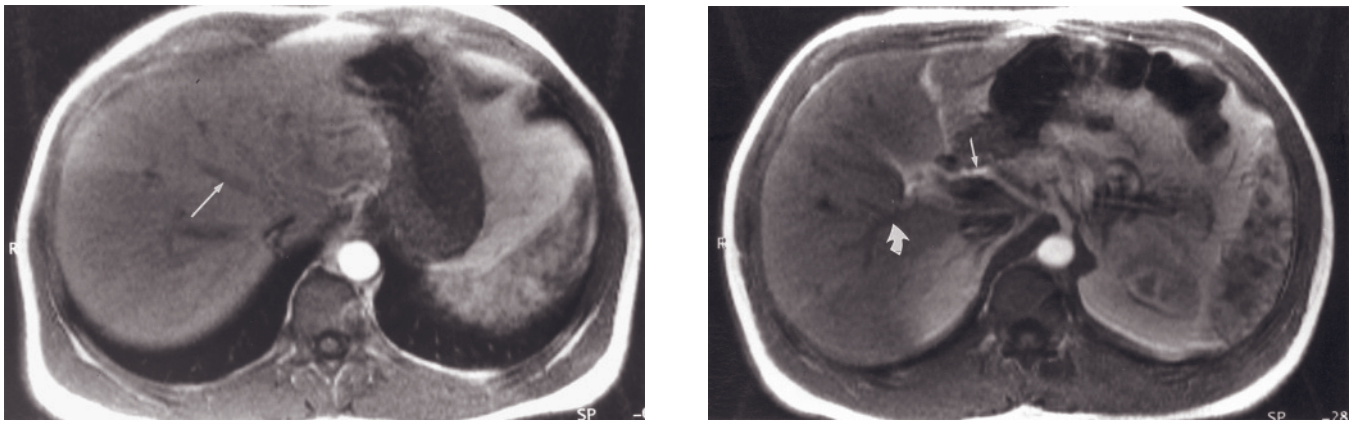

(*a*) (*b*)

FIG. 2.4 Hepatic arterial-phase gadolinium-enhanced SGE images. Transverse hepatic arterial-phase images from the level of the hepatic veins (*a*) and portal vein (*b*). The hepatic artery (thin arrow, *b*) is enhanced. Hepatic veins (arrow, *a*) and portal vein (curved arrow, *b*) are not enhanced. Some enhancement is appreciated in the splenic parenchyma and superior aspect of the left kidney, showing that these images were acquired in approximately the middle of the hepatic arterial enhancement phase.

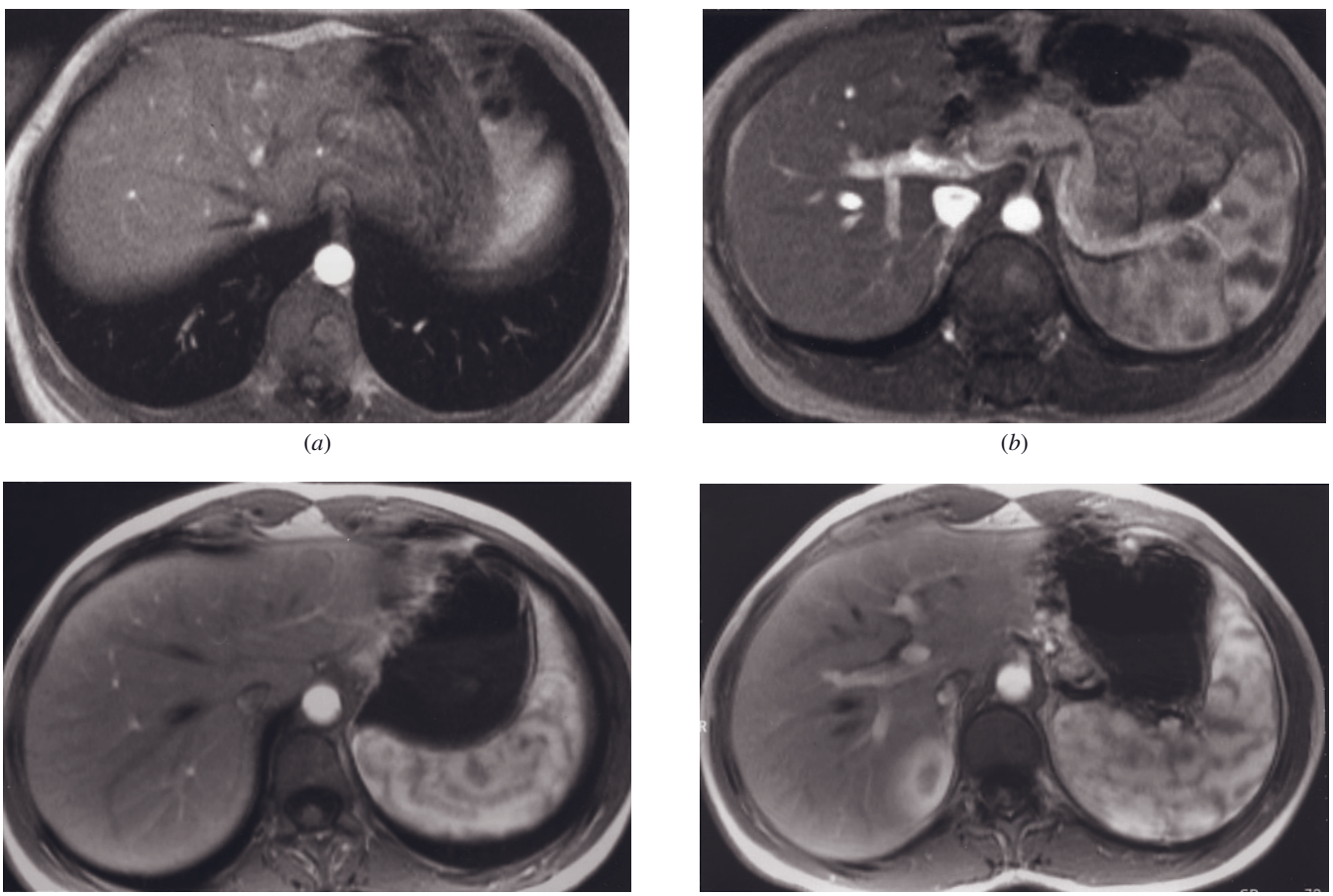

(*a*) (*b*)

(*c*) (*d*)

FIG. 2.5 Hepatic arterial dominant-phase gadolinium-enhanced SGE images. Immediate postgadolinium SGE images in 2 patients (*a* and *b*, and *c* and *d*, respectively). Images acquired from the higher tomographic sections (*a*, *c*) demonstrate absence of gadolinium in hepatic veins and images acquired from the more inferior tomographic sections (*b*, *d*) demonstrate presence of gadolinium in hepatic arteries and portal veins.

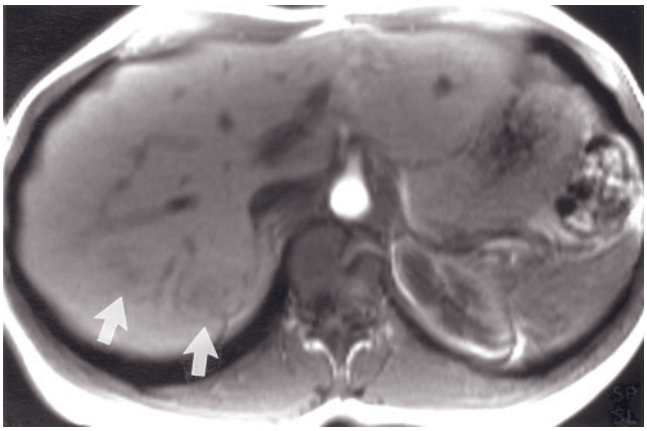

(*a*)

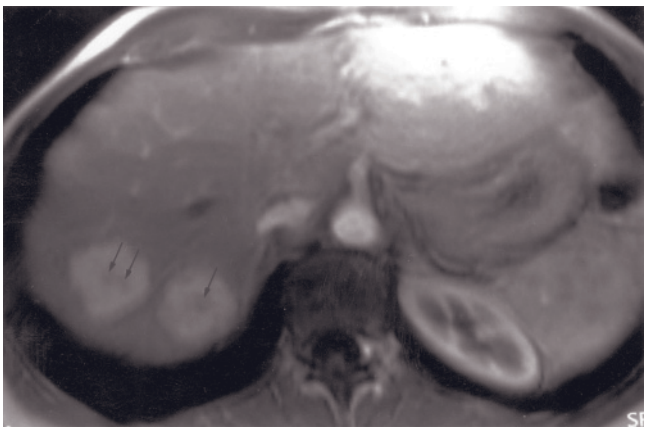

(*b*)

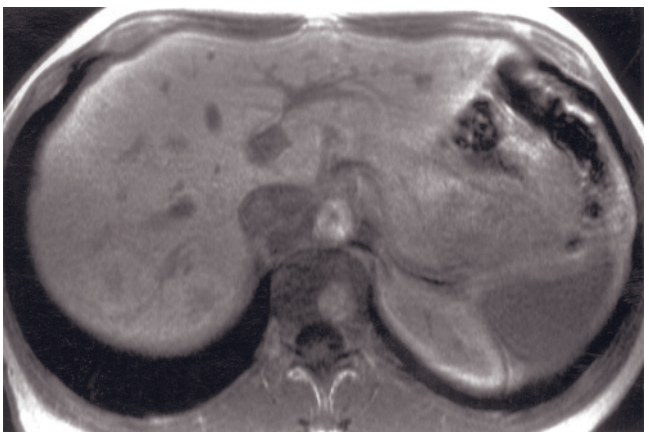

(*c*)

FIG. 2.6 Hepatic arterial, hepatic arterial dominant phase, and Mn-DPDP-enhanced SGE images. Hepatic arterial (*a*), hepatic arterial dominant-phase postgadolinium (*b*), and Mn-DPDP-enhanced SGE (*c*) images. Two lobular lesions are seen in the right hepatic lobe and demonstrate moderate high signal after manganese administration (*c*). Hepatic arterial phase (*a*) shows faint heterogeneous enhancement that may suggest a hepatocellular carcinoma. The intense blush on hepatic arterial dominant phase (*b*), with a central scar (arrows, *b*) is, however, characteristic for a FNH. Note that on hepatic arterial phase the lesions are not so evident (arrows, *a*) as in hepatic arterial dominant phase (*b*). Note that uptake of Mn-DPDP by the lesions is consistent with FNHs (*c*).

the arterial phase can be divided in five subgroups as follows: early hepatic arterial phase, mid-hepatic arterial phase, late hepatic arterial phase, splenic-vein-only hepatic arterial dominant phase, and hepatic arterial dominant phase, based on the presence of contrast in major abdominal vessels, as well as renal cortex, spleen, pancreas, and liver parenchyma. The importance of this subdivision is the impact of detection of hypervascular liver lesions based upon the phase where images were acquired. Table 2.1 describes the appearance of common focal liver lesions with this approach.

LIVER CONTRAST AGENTS

Intravenously administered contrast agents have been used in clinical magnetic resonance imaging of the liver since 1988. The need for more accurate detection and characterization of the full spectrum of liver pathology has been the major impetus for continued development in intravenous contrast agents [4, 5]. The first category of contrast agents to be used in clinical practice was that of nonspecific extracellular gadolinium chelates. Since then, other classes of contrast agents have been developed for liver MR studies. There are two histologically and functionally distinct populations of cells in the liver. Liver epithelial cells, or hepatocytes, carry out the major metabolic activities. Hepatocyte function is assisted by another major class of cells, the reticuloendothelial system (RES), which possess storage, phagocytic, and mechanically supportive functions. In recent years, hepatocyte-selective contrast agents and RES-specific contrast agents have targeted these cell populations and added a new dimension to hepatic MR imaging. Clinically available liver contrast agents can be categorized as follows: 1) nonspecific extracellular contrast: gadolinium chelates; 2) hepatocyte-selective: Mn-DPDP (mangafodipir trisodium); 3) agents with combined early nonspecific extracellular and late hepatocyte-selective properties: Gd-EOB-DTPA (gadolinium ethoxybenzyl diethylenetriaminepentaacetic acid) and Gd-DTPA-BOPTA (gadolinium benzyloxypropionictetraacetate); 4) RES-specific: superparamagnetic iron oxide particles (SPIO); 5) agents with combined early blood pool and late RES-specific properties: ultrasmall paramagnetic iron oxide particles.

Table 2.1 Liver lesion pattern recognition

	T1	T2	EARLY GD	LATE GD	OTHER FEATURES
Cyst	↓↓	↑↑	○	○	Well defined
Hamartoma	↓↓	↑↑	Thin rim	Thin rim	<1 cm
Hemangioma	↓↓	↑↑	Peripheral nodules	Nodules coalesce, retain contrast	<1.5-cm lesion may enhance homogeneously
FNH	↓–Ø	Ø–↑	Homogeneous intense, negligible scar enhancement	Homogeneous washout, late scar enhancement	Central scar, liver is commonly fatty
Adenoma	↓–↑	Ø–↑	Homogeneous intense	Homogeneous washout	Uniform signal loss on out-of-phase T1, hemorrhage not uncommon
Metastases	↓	↑	Ring	Progressive with heterogeneous washout	<1.5-cm lesion may enhance homogeneously
HCC	↓–↑	Ø–↑	Diffuse heterogeneous	Heterogeneous late washout, capsule enhancement	<1.5-cm lesion may enhance homogeneously
Bacterial abscess	↓↓	↑–↑↑	Perilesional enhancement, capsule enhancement	Perilesional enhancement fades, capsule remains enhanced	Resemble metastases but no progressive lesion enhancement
Lymphoma, secondary	↓	↑	Ring	Progressive mild enhancement	Resemble metastases
Lymphoma, primary	↓	↑	Diffuse heterogeneous	Progressive with heterogeneous washout	Resemble HCC
Regenerative nodule	↓–Ø	↓–Ø	Negligible	Negligible	Lesions generally <1.5 cm and homogeneous
Mildly dysplastic nodule	↓–↑	—	Minimal	Minimal	Lesions generally <1.5 cm and homogeneous
Severely dysplastic nodule	↓–↑	—	Homogeneous intense	Fade to isointensity with liver	Lesions generally <1.5 cm, homogeneous, and no capsule

↓↓ Moderately decreased signal intensity, ↓ Mildly decreased signal intensity, Ø Isointense, ↑ Mildly increased signal intensity, ↑↑ Moderately increased signal intensity, ○ No enhancement

Nonspecific extracellular gadolinium chelates are the standard contrast agents to image liver and other organs and tissues in patients evaluated with MR imaging for a diverse range of indications. These paramagnetic contrast agents provide important information about tumor perfusion, which is a key factor in the assessment of liver masses [6–8]. Gadolinium chelates are optimally used when they are administered as a rapid bolus and imaging is performed with a T1-weighted gradient-echo sequence that is repeated in a dynamic serial fashion. This is best achieved at high field strength. The elimination is 100% renal. The most important phase of enhancement may be termed the hepatic arterial dominant phase, with contrast present in hepatic arteries and portal veins and before contrast appears in hepatic veins (figs. 2.5 and 2.6). The hepatic arterial phase has contrast present only in the hepatic arteries (see fig. 2.4). See Chapter 1 for a more complete description.

Hepatocyte-selective contrast agents undergo uptake by hepatocytes and are eliminated through the renal and biliary system [9–11]. This category of contrast agents—Mn-DPDP (mangofodipir), Gd-EOB-DTPA (primivist), and Gd-BOPTA (multiHance)—are all T1-relaxation-enhancing agents that are taken up by and result in an increase in the signal intensity of normal liver tissue and hepatocyte-containing tumors. Gd-EOB-DTPA and Gd-BOPTA exhibit early perfusional information as well. These contrast agents are not taken up by non-hepatocyte-containing masses (e.g., hemangioma, metastases) on late, >10-min, postcontrast images; therefore, they leave signal unchanged in these entities on T1-weighted images. Non-hepatocyte-containing masses are rendered more conspicuous by the increase in signal of background liver tissue. Advantages of T1 relaxation agents include the following: 1) Use of gradient echo (as 2D or 3D sequences with or without fat suppression) results in robust, reproducible image quality with complete liver coverage in one breath hold, and 2) they do not result in artifacts, such as susceptibility artifact, that can mask small lesions. Mangofodipir and multiHance are licensed by the FDA for use in humans. Mangofodipir is administered as a slow (1 min) intravenous infusion, and the maximal imaging window is between 15 min and 4 h [5, 12, 13]. Dynamic images

cannot be obtained with this agent, and therefore it is not necessary that the MR machine have high field strength. At this stage of clinical use, this agent appears to be safe and well tolerated. At present, the best clinical role for Mn-DPDP is to improve detection of the number and extension of focal liver metastases from colon cancer in patients in whom hepatic resection is being contemplated [5, 13, 14]. The combined use of conventional gadolinium chelates and Mn-DPDP has been described [13]. This approach combines the perfusional information of gadolinium with the hepatocyte uptake information of Mn-DPDP (fig. 2.7). In selected cases, the combination of gadolinium chelates and liver-specific contrast agents may provide additional information. This combined-agent approach may not be necessary any more since multiHance, which possesses both early perfusional and late hepatocellular activity, is now licensed for use.

Gd-EOB-DTPA (fig. 2.8) and Gd-BOPTA are combined extracellular/hepatocyte agents that can be used to acquire early perfusional information similar to standard gadolinium chelates. Gd-EOB-DTPA demonstrates diagnostically useful hepatocyte enhancement at 10–15 min after injection, whereas Gd-BOPTA requires a delay of 1 h after injection for hepatocyte selection enhancement [15–21]. The early perfusional information is very important for lesion characterization, with the additional benefit of improved detection, particularly for hypervascular lesions. The late images may be used for lesion detection with some additional information to distinguish hepatocyte-containing from non-hepatocyte-containing tumors. Although hepatocyte-specific agents

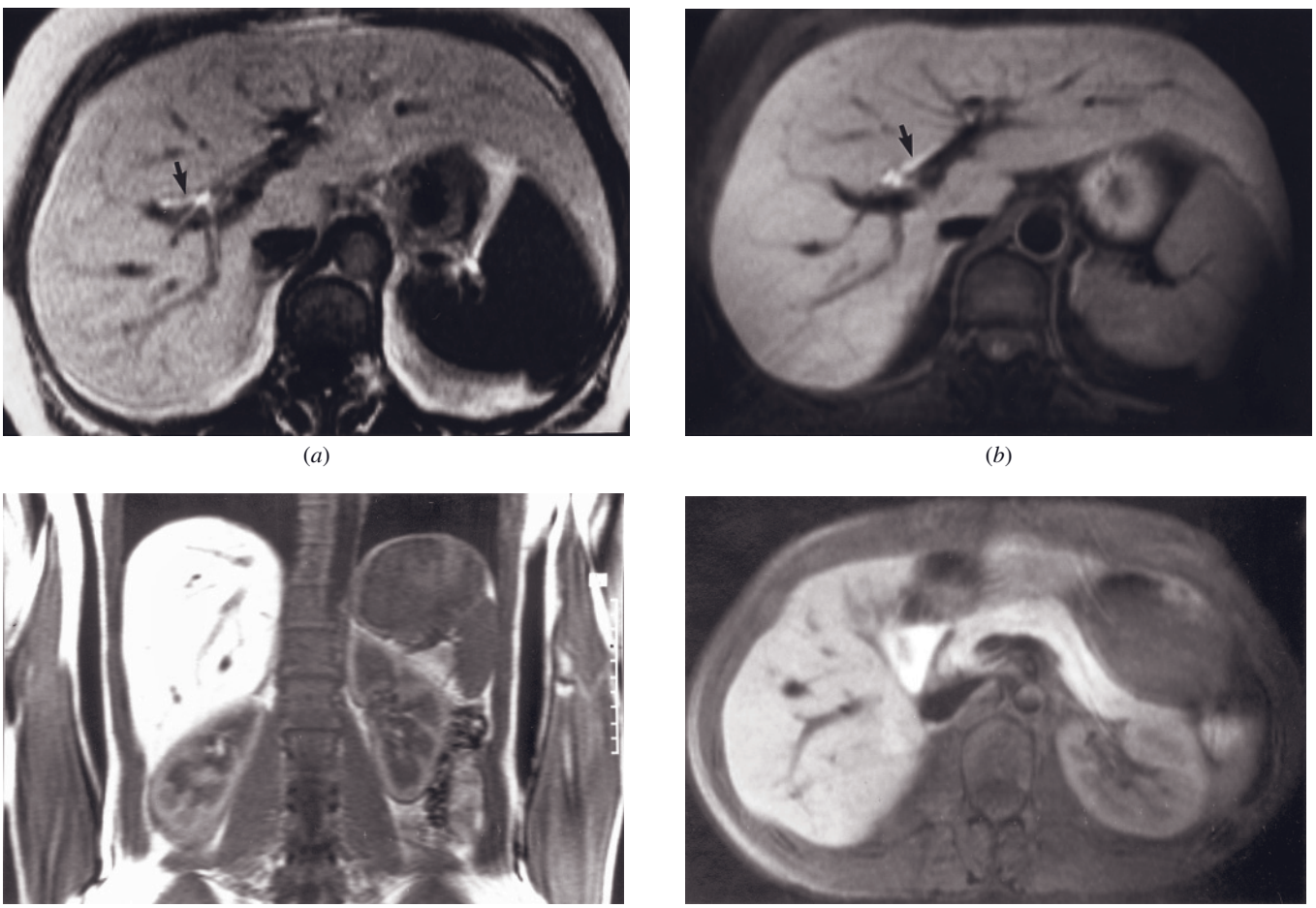

FIG. 2.7 Mn-DPDP-enhancement. Mn-DPDP-enhanced SGE (*a*) and Mn-DPDP-enhanced T1-weighted fat-suppressed SE (*b*) images in a normal patient. Normal liver homogeneously enhances with Mn-DPDP because of its T1-shortening effect. Excretion of Mn-DPDP in the biliary system is shown as high-signal-intensity fluid in biliary ducts (arrow, *a*, *b*).

Coronal Mn-DPDP-enhanced SGE (*c*) and transverse Mn-DPDP-enhanced T1-weighted fat-suppressed spin-echo (*d*) images in a second patient. Note the increased signal intensity of normal liver tissue after administration of Mn-DPDP.

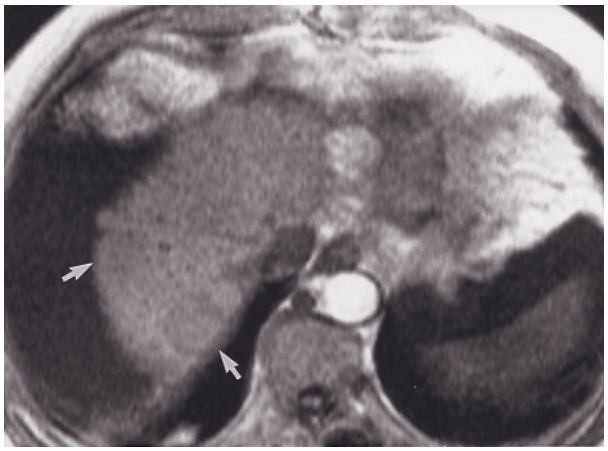

(*e*)

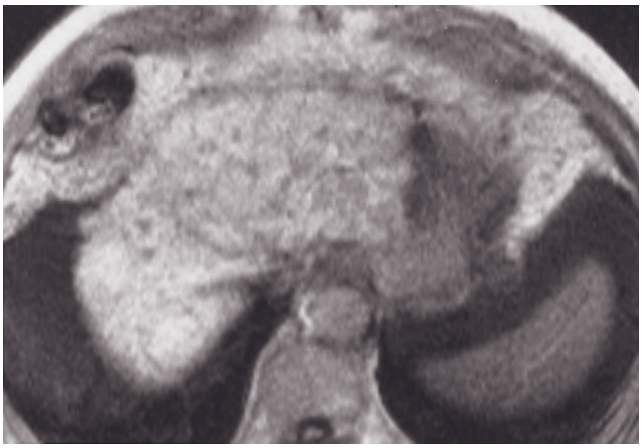

(*f*)

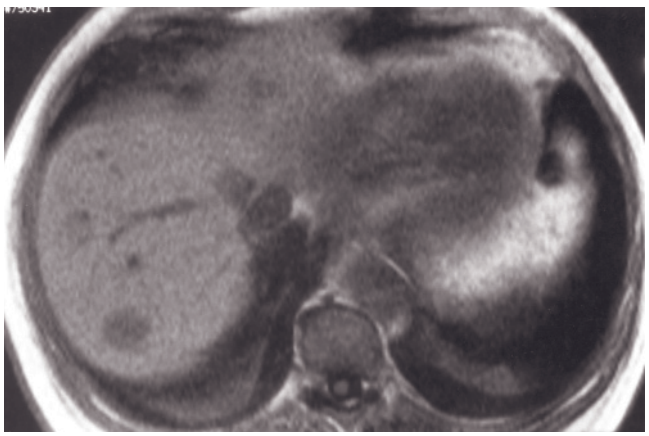

(*g*)

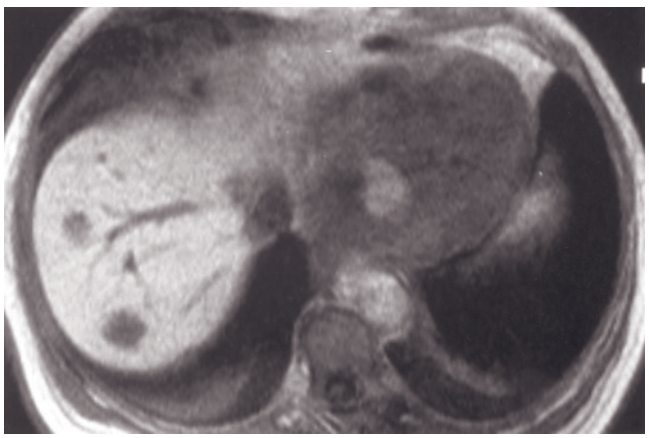

(*h*)

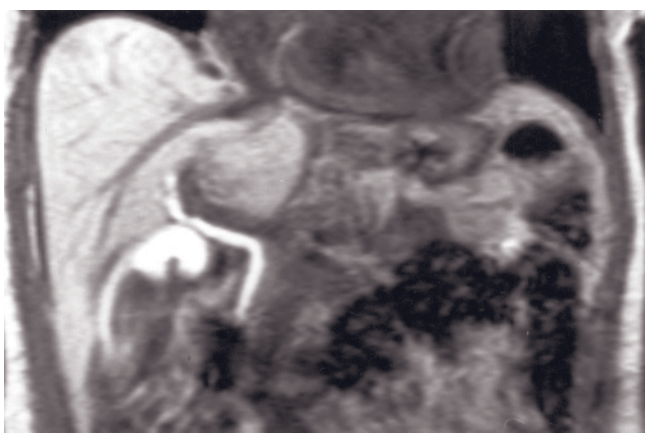

(*i*)

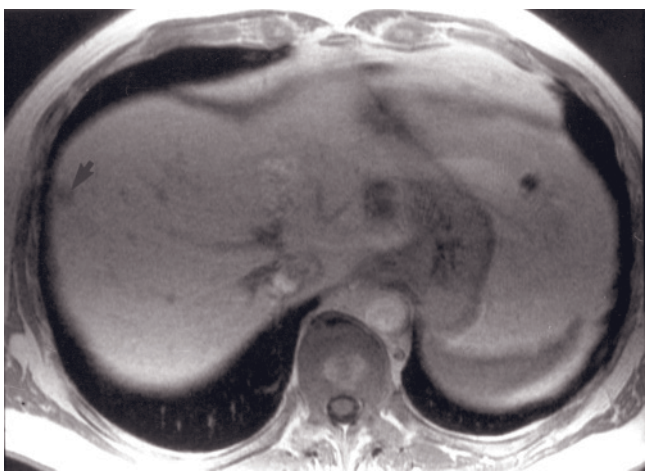

(*j*)

FIG. 2.7 (*Continued*) SGE (*e*) and 30-min post-Mn-DPDP SGE (*f*) images in a third patient. Subtle low-signal-intensity mass lesions are apparent on the precontrast image (arrows, *e*). After Mn-DPDP enhancement (*f*) the HCCs enhance slightly more intensely than background liver, rendering the tumors minimally hyperintense. A pseudocapsule is appreciated around the more posterior tumor on both the precontrast and postcontrast images.

Transverse noncontrast SGE (*g*) and 10-min post-Mn-DPDP-enhanced SGE (*h*) and coronal 10-min Mn-DPDP-enhanced SGE (*i*) images in a fourth patient with liver metastases. The liver increases in signal from pre (*g*)- to post (*h*)-Mn images, increasing the conspicuity of the metastases. Note the excretion of Mn-DPDP into the biliary system (*i*).

Mn-DPDP-enhanced 512-resolution SGE image (*j*) in a fifth patient who has a liver metastasis (arrow, *j*). The liver detail is greater than usual, reflecting the use of 512 matrix.

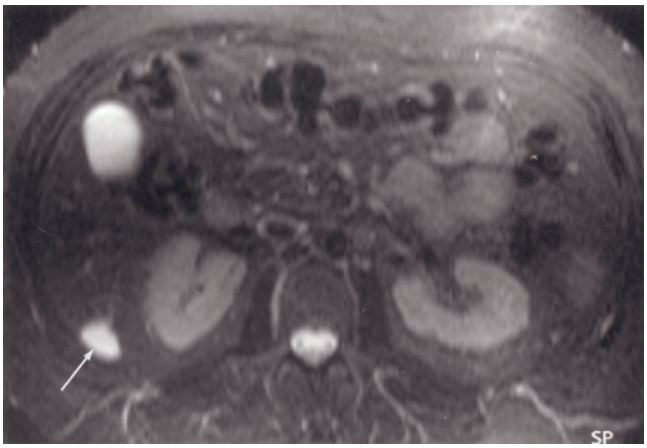

(*a*)

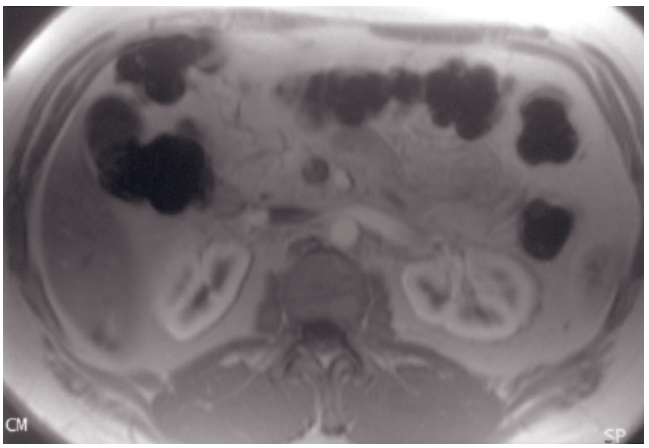

(*b*)

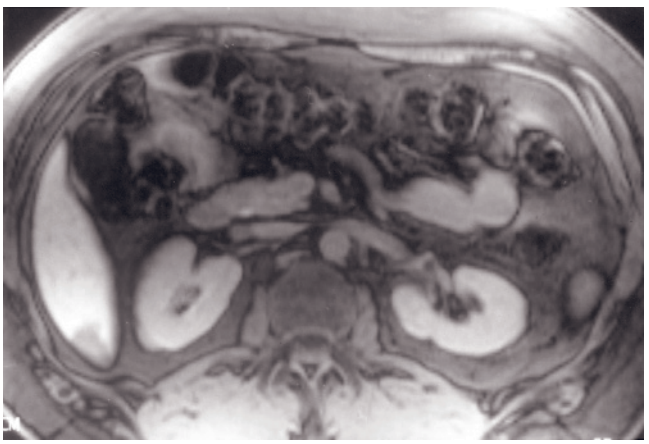

(*c*)

FIG. 2.8 Hemangioma, Gd-EOB-DTPA-enhanced. Echo-train STIR (*a*) and immediate (*b*) and 10-min post-Gd-EOB-DTPA (*c*) images. There is a lobular lesion in the tip of the right lobe (arrow, *a*) that is high signal intensity on the T2-weighted image (*a*) and exhibits peripheral nodular enhancement immediately after the administration of contrast (*b*) and hepatocellular uptake and washout of the lesion at 5 min. This lesion is consistent with a hemangioma based on the well-defined lobular margins, high signal on T2, and early peripheral nodular enhancement.

permit distinction between hepatocyte-containing tumors (e.g., adenoma, focal nodular hyperplasia, hepatocellular carcinoma) and non-hepatocyte-containing tumors (e.g., hemangioma, metastases), it is generally more important to distinguish between benign and malignant tumors. Early perfusional information generally achieves this goal. Gd-BOPTA provides distinction between FNH, which demonstrates delayed 1-h enhancement, and hepatic adenoma and moderately poorly differentiated HCC, which do not exhibit late enhancement (fig. 2.9).

Iron oxide particle agents are selectively taken up by RES in the liver, spleen, and bone marrow. This class of contrast agent is also termed superparamagnetic iron oxide (SPIO), and the first of these agents licensed for use in the United States are the ferumoxides. RES cell-specific contrast agents are T2 relaxation-enhancing agents that lower the signal intensity of normal RES cell-containing liver tissue on T2-weighted images and do not alter the signal intensity of mass lesions that do not contain RES cells (e.g., metastases) [22–24]. Blood pool effects may be observed with hemangiomas, which can result in T1 shortening on T1-weighted sequences [25, 26]. This results in an increase in detection and in the conspicuity of liver tumors that are moderately high in signal intensity on T2-weighted images [25] (fig. 2.10). The patient group in which this role for SPIO may be the most applicable is patients with liver metastases from colon cancer and HCC who are considered to be candidates for hepatic resection or liver transplant [5, 27, 28]. Studies have shown that SPIO-enhanced T2-weighted MR imaging has performance comparable to that of CT during arterial portography for the demonstration of liver metastases [29, 30]. However, other reports demonstrated that SPIO-enhanced MRI has a higher sensitivity and accuracy to detect hepatic malignancies than helical CT [31–34]. A cautionary note for this agent is that susceptibility artifact may potentially interfere with detection of sub-centimeter lesions such as metastases. A number of sequences have been employed to improve image quality, including gradient-echo sequences with a longer TE (≥6 ms), single-shot or breath-hold echo-train spin echo, and breathing-averaged proton density echo-train spin echo. Combined

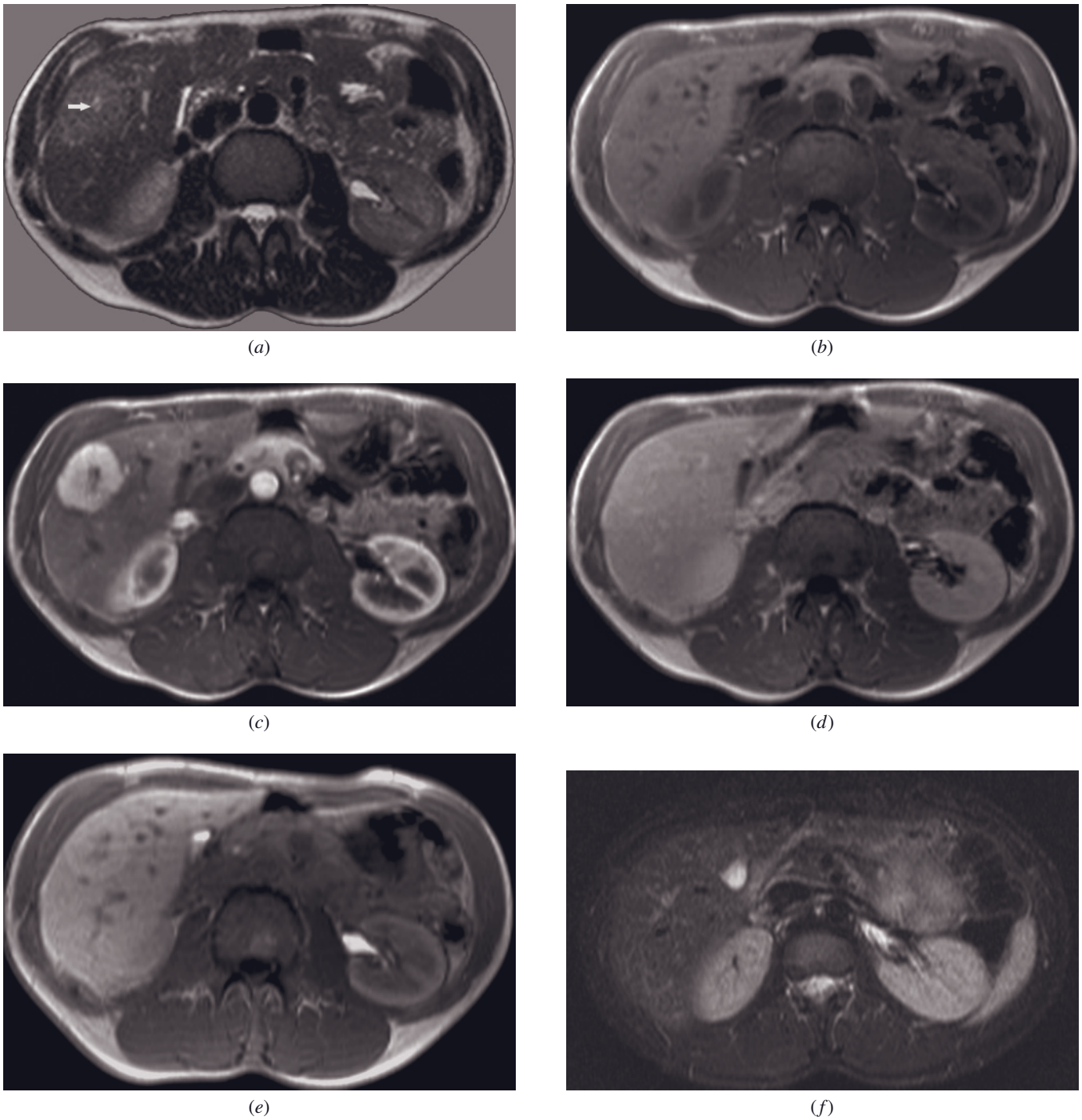

FIG. 2.9 FNH, Gd-BOPTA-enhanced. SS-ETSE (*a*), SGE (*b*), and immediate (*c*), 90-s (*d*), and 1-h (*e*) postinjection Gd-BOPTA contrast images. There is a lesion in the right hepatic lobe that exhibits slightly high signal intensity on T2-weighted image (*a*), isointensity on T1-weighted image (*b*), and intense enhancement on immediate post contrast image (*c*) and fades as the background parenchyma on 90-s postcontrast image (*d*). This lesion has a central scar that is well seen on the T2-weighted image (arrow, *a*) and on the immediate postcontrast image (*c*). On 90-s postcontrast image (*d*) the scar enhances and acquires signal intensity comparable to the lesion. The lesion shows higher signal intensity than the background parenchyma 1 h after administration of contrast (*e*), and the scar demonstrates lower signal intensity than the lesion, consistent with lesional contrast uptake in this phase. (Courtesy of Guenther Schneider, M.D., Ph.D., Dept. of Diagnostic and Interventional Radiology, University Hospital Homburg/Saar, Germany.)

T2-weighted SS-ETSE (*f*), SGE (*g*), and immediate (*h*), 90-s fat-suppressed (*i*), and 1-h (*j*) postcontrast SGE images in a second patient show similar findings. The tumor enhances intensely on immediate postcontrast images (arrow, *h*) and shows 1-h delayed

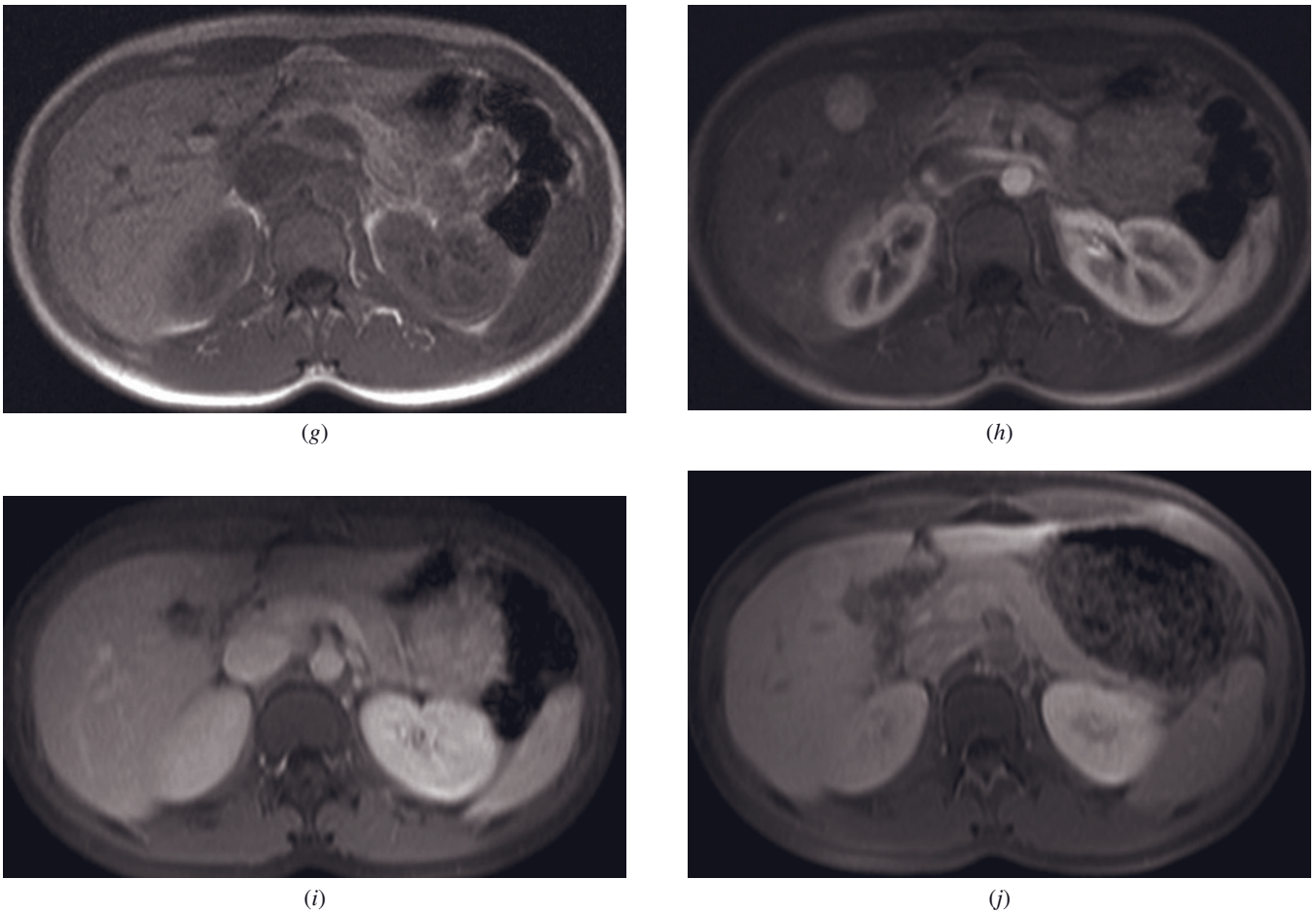

FIG. 2.9 (*Continued*) enhancement, consistent with and FNH. The central scar is not as well defined as in the first patient.

use of SPIO and conventional gadolinium chelates has been described [35]. This approach combines the perfusional information of gadolinium with the RES information of SPIO. It may be expected that their combined use would be more effective for detection and characterizing focal lesions than either contrast agent alone [35]. The long infusion period (30 min) is an inconvenient aspect of this agent, which necessitates two imaging sessions for nonenhanced and enhanced images. Attractive features of the agent include the long imaging window (1–4 h), no need for precise dynamic image acquisition related to contrast material administration, and acceptable image quality with machines of various field strengths. Although serious adverse events are rare, approximately 3% of patients will experience severe back pain while the contrast agent is being administered. This back pain appears to be a side effect of particulate agents in general and develops in patients in whom the contrast agent is administered too rapidly [35]. This agent can also be administered as a small-volume rapid bolus, which is greatly advantageous over the larger particulate agent superparamagnetic iron oxide.

Ultrasmall paramagnetic iron oxide particles have blood pool effects that may be helpful in detecting or characterizing vascular lesions such as hemangiomas [36] and provide bright vessel enhancement in the vascular phase, which can be used for MR angiography [5].

Other tissue-specific contrast agents are under development such as those targeted to cell membrane antigens [37]. The application and role of new contrast agents will ultimately depend on how they compare with nonspecific extracellular gadolinium chelates. Prior studies have compared contrast agents in an attempt to define clinical uses [12, 17, 38–42]. Defined clinical roles are under development for these new agents. It is likely that the majority of these agents cannot replace extracellular gadolinium entirely because of its broad applicability.

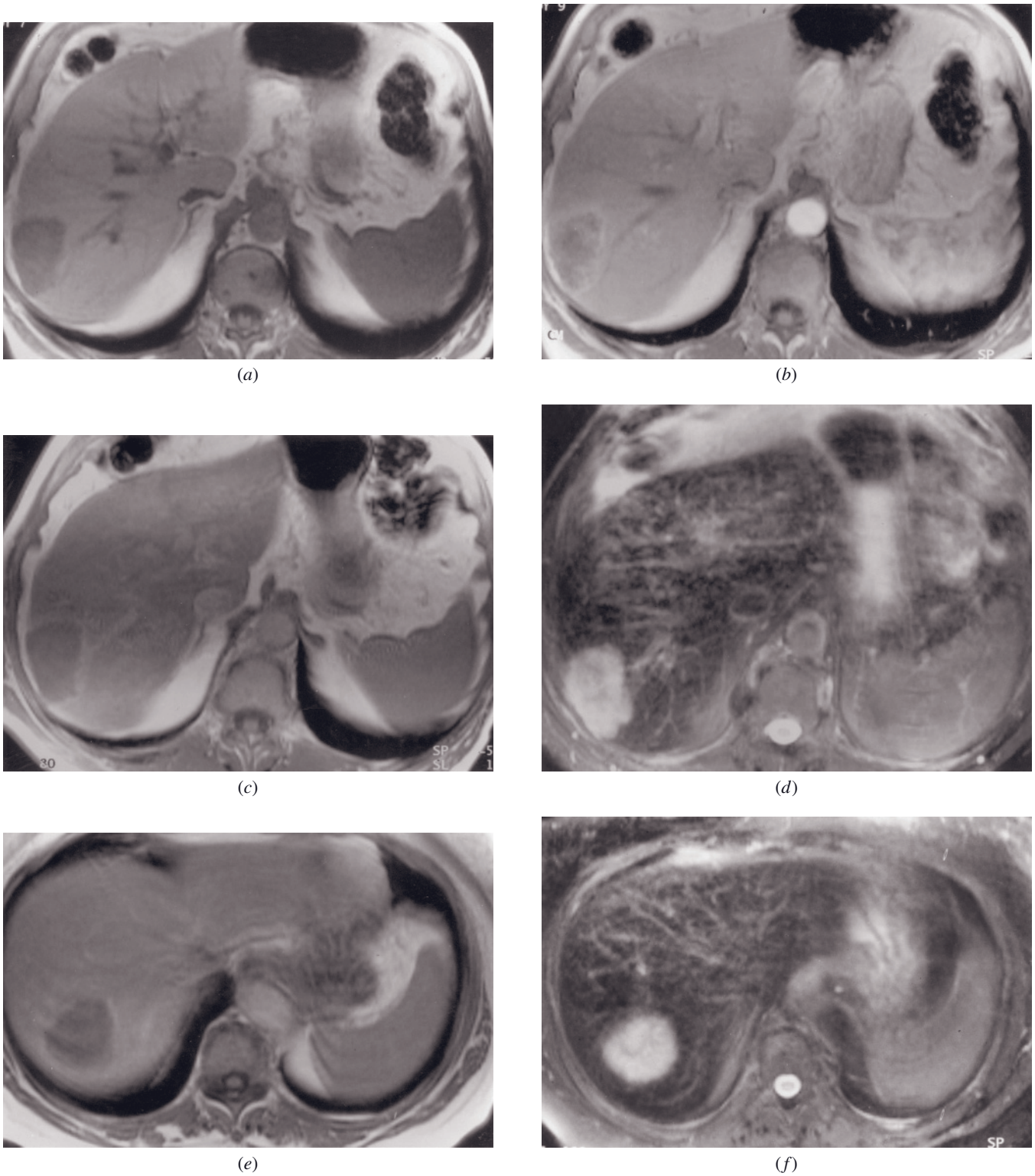

FIG. 2.10 Gadolinium and iron oxide. Noncontrast SGE (*a*), immediate postgadolinium SGE (*b*), iron oxide-enhanced SGE (*c*), and iron oxide-enhanced T2-weighted fat-suppressed (*d*) images in a patient with colon carcinoma imaged with a gadolinium study performed 19 days before an iron oxide study. A 3-cm metastasis is seen in the right hepatic lobe, which is moderately low signal on the noncontrast SGE image (*a*) and demonstrates a peripheral ring enhancement on the immediate postgadolinium SGE image (*b*), consistent with metastasis. On the iron oxide-enhanced SGE image (*c*), a lowered signal intensity in the liver and spleen is noted, diminishing the conspicuity of the metastasis. On the iron oxide-enhanced T2-weighted image (*d*), the signal intensity of the liver and spleen are markedly lower, increasing the conspicuity of the metastasis.

Iron oxide-enhanced SGE (*e*), iron oxide-enhanced T2-weighted fat-suppressed (*f*), and immediate postgadolinium iron oxide-enhanced SGE (*g*) images in a second patient with colon carcinoma imaged with iron oxide and gadolinium contrast agents, with iron oxide imaged first in a combined protocol. A lesion is present in the right hepatic lobe, which is low signal intensity on the iron oxide-enhanced SGE image (*e*) and high signal intensity on the iron oxide-enhanced T2-weighted image (*f*). The lesion enhances

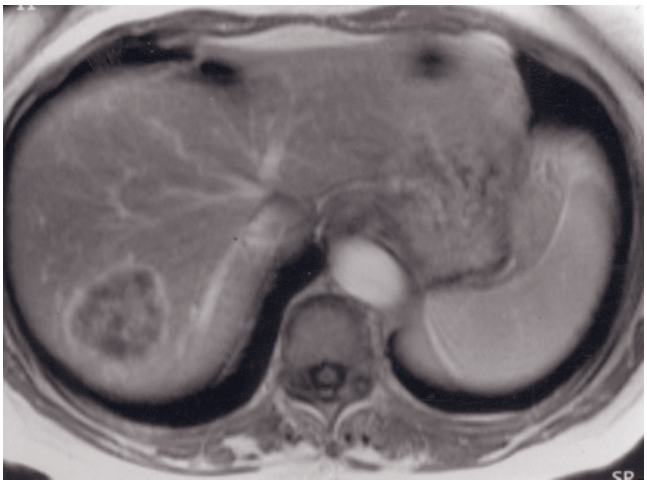

(*g*)

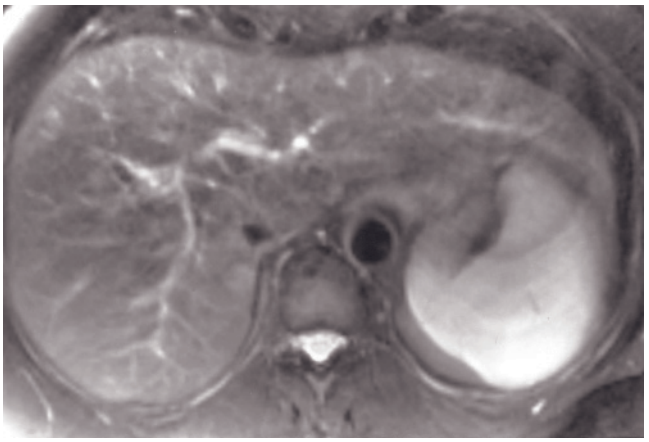

(*h*)

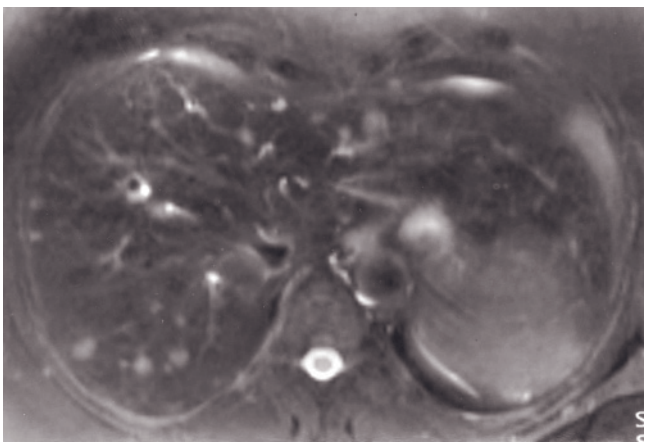

(*i*)

FIG. 2.10 (*Continued*) with a peripheral ring pattern consistent with a metastasis on the immediate postgadolinium iron oxide-enhanced SGE image (*g*). Lesion conspicuity is high on the postgadolinium iron oxide-enhanced image because of the lowered signal intensity of the background liver parenchyma and intense early enhancement of the neoplasm. (Reproduced with permission from Semelka RC, Lee JKT, Worawattanakul S, Noone TC, Patt RH, Asher SM. Sequential use of ferumoxide particles and gadolinium chelate for the evaluation of focal liver lesions on MRI. *J Magn Reson Imaging* 8: 670–674, 1998).

Nonenhanced (*h*) and iron oxide particulate-enhanced (*i*) T2-weighted fat-suppressed ETSE images in a third patient, who has liver metastases. After contrast administration (*i*), a greater number of <1-cm metastases are identified in the liver.

NORMAL VARIATIONS

A number of normal variations in liver size and shape occur. Common variations include horizontal elongation of the lateral segment of the left lobe, hypoplasia of the left lobe, and vertical elongation of the right lobe, termed the Riedel lobe. The Riedel lobe is fairly common and is characterized by a downward tonguelike projection of the right lobe. This anatomic variation is more frequent in women [43]. Correct identification of a Riedel lobe is necessary to avoid confusion with hepatomegaly. Transverse and coronal images are effective at demonstrating this variant, and coronal images are useful for excluding an exophytic mass lesion such as hepatic adenoma or HCC (fig. 2.11).

An elongated lateral segment may wrap around the anterior aspect of the upper abdomen and extend laterally to the spleen. This variation is also more common in women. A clear distinction between liver and spleen may be made with T2-weighted images, in which normal spleen is high in signal intensity and distinct from the lower-signal-intensity liver (fig. 2.12). Hypoplasia of the left lobe does not generally result in diagnostic difficulties, although it may simulate a left hepatectomy, which clinical history readily establishes.

Diaphragmatic insertions are not an uncommon finding along the lateral aspect of the liver. They tend to be multiple and closely related to overlying ribs, having wedge-shaped margins with the capsular surface of the liver (fig. 2.13). Insertions are low in signal on T2- and T1-weighted images. These features help to distinguish diaphragmatic insertions from peripheral mass lesions.

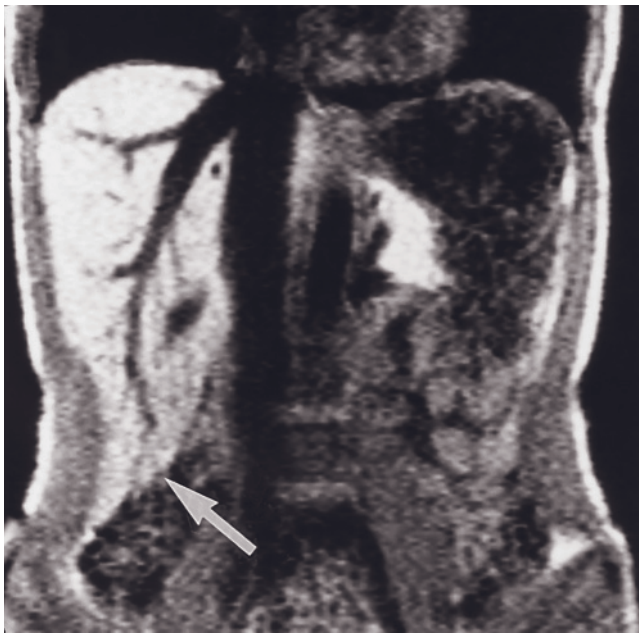

(*a*)

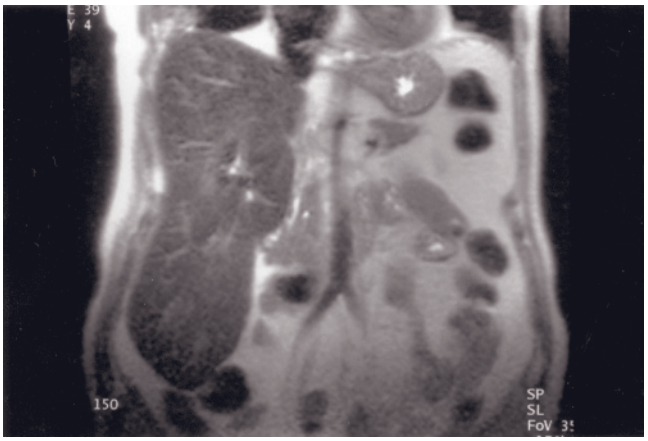

(*b*)

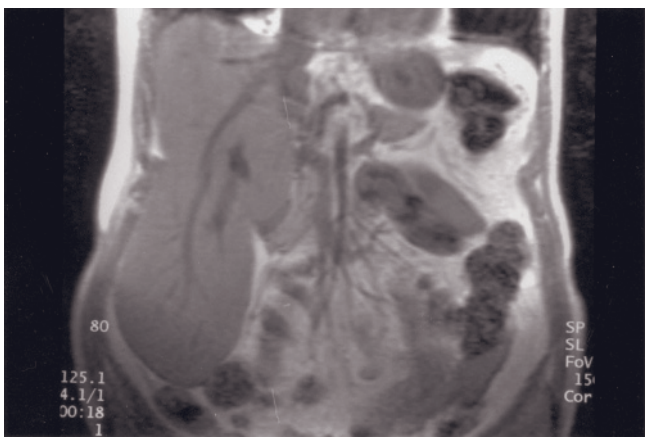

(*c*)

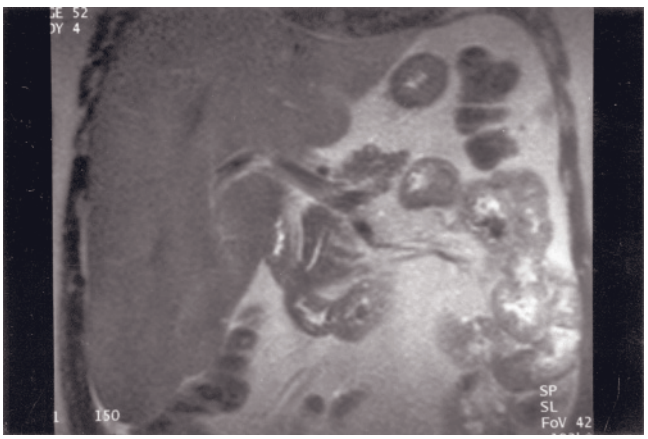

(*d*)

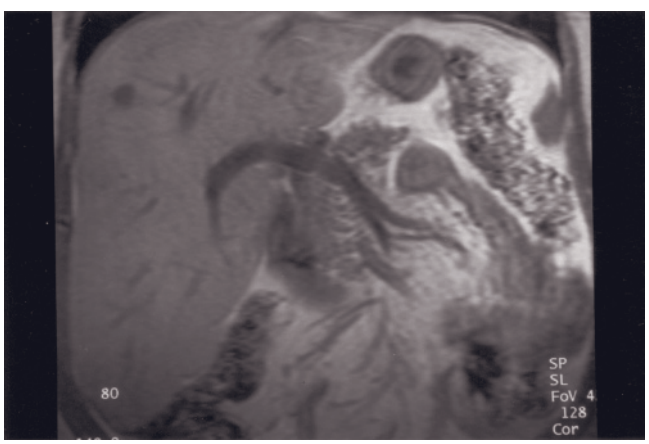

(*e*)

FIG. 2.11 Riedel lobe. Coronal snap-shot magnetization-prepared gradient-echo image (*a*) demonstrates elongation of the inferior aspect of the right lobe of the liver (arrow, *a*) consistent with Riedel lobe.

Coronal T2-weighted SS-ETSE (*b*) and SGE (*c*) images in a second patient exhibit a Riedel lobe with bulbous inferior aspect.

Coronal T2-weighted SS-ETSE (*d*) and SGE (*e*) images in a third patient demonstrate hypertrophy of the Riedel lobe, with a convex medial border.

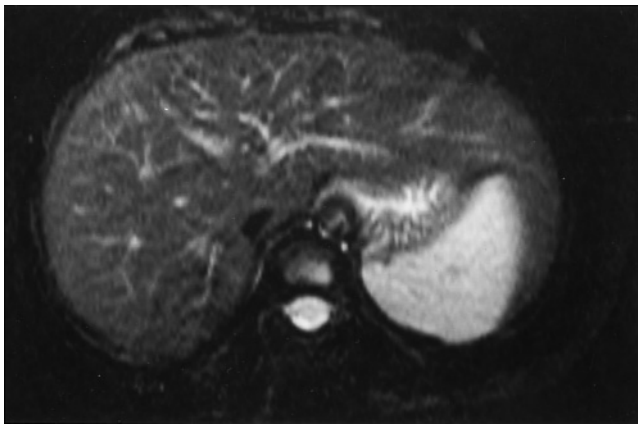

FIG. 2.12 Elongated lateral segment of the left lobe. T2-weighted fat-suppressed ETSE image demonstrates an elongated lateral segment that extends lateral to the spleen. Clear distinction is made between lower-signal-intensity liver and moderately high-signal-intensity spleen on T2-weighted images.

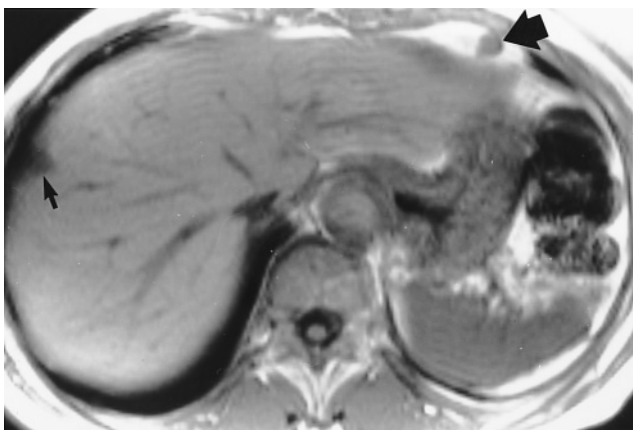

FIG. 2.13 Diaphragmatic insertion. SGE image demonstrates a wedge-shaped defect along the lateral superior margin of the liver (arrow). Diaphragmatic insertions are usually multiple but may be single as in this case. Incidental note is made of a subdiaphragmatic lymph node (large arrow).

DISEASE OF THE HEPATIC PARENCHYMA

Benign Masses

Solitary (Nonparasitic) Cysts

Hepatic cysts are common lesions and are usually divided into unilocular (95 %) or multilocular varieties. Although the pathogenesis of these cysts is not clear, developmental and acquired causes are postulated. Acquired cysts are thought to represent retention cysts of bile ductule derivation [44]. Pathologically, the lining of the cyst shows a single layer of cuboidal to columnar epithelial cells. Lining epithelium rests on an underlying fibrous stroma.

On imaging, cysts are homogeneous, well-defined lesions that possess a sharp margin with liver. Although slight variations are common, cysts are usually oval-shaped [45]. Occasionally, cysts are so closely grouped that they resemble a multicystic mass. Simple cysts are low in signal intensity on T1-weighted images and high in signal intensity on T2-weighted images, and thus retain signal intensity on longer echo time (e.g. >120 ms) T2-weighted images. Because cysts do not enhance with gadolinium on MR images, delayed postgadolinium images (up to 5 min) may be useful to ensure that lesions are cysts and not poorly vascularized metastases that show gradual enhancement (figs. 2.14–2.17) [46]. Rarely, a simple cyst may bleed because of trauma or malformation within or nearby the cyst wall. On T2- and T1-weighed precontrast images, the hemorrhagic cysts may show variable findings according to the age of hemorrhage (see trauma section) (fig. 2.18). Fluid-fluid level within the cyst cavity and a thickened and irregular wall are often observed in the hemorrhagic cyst [47]. Negligible enhancement of the cyst walls is generally present when the cysts do not exhibit inflammatory or fibrotic changes.

An advantage of MRI over computed tomography (CT) imaging in the characterization of cysts is that on gadolinium-enhanced MR images cysts are nearly signal void, whereas cysts on contrast-enhanced CT images are a light gray in attenuation. Single-shot breathing-independent T2-weighted sequences (e.g., SS-ETSE) are especially effective at showing small (≤5 mm) cysts. MRI is particularly valuable when lesions are small and the patient has a known primary malignancy.

Ciliated Hepatic Foregut Cysts

Foregut cysts are an uncommon type of solitary unilocular cyst. These congenital lesions are believed to arise from the embryonic foregut and to differentiate toward bronchial tissue in the liver. Pathologically, the cyst wall consists of four layers: pseudostratified ciliated columnar epithelium with mucous cells, subepithelial connective tissue, abundant smooth muscle, and an outermost fibrous capsule. These cysts are most frequently located at the anterosuperior margin of the liver, but may be situated elsewhere, superficially along the external surface of the liver, typically at intersegmental locations.

On MRI, foregut cysts characteristically bulge the liver contour and show hyperintensity on T2-weighted images and range from hypo- to hyperintense on T1-weighted images [48, 49]. The presence of mucin in these cysts results in high signal intensity on T1-weighted images, with the extent of increase in signal intensity dependent on the concentration of mucin (fig. 2.19).

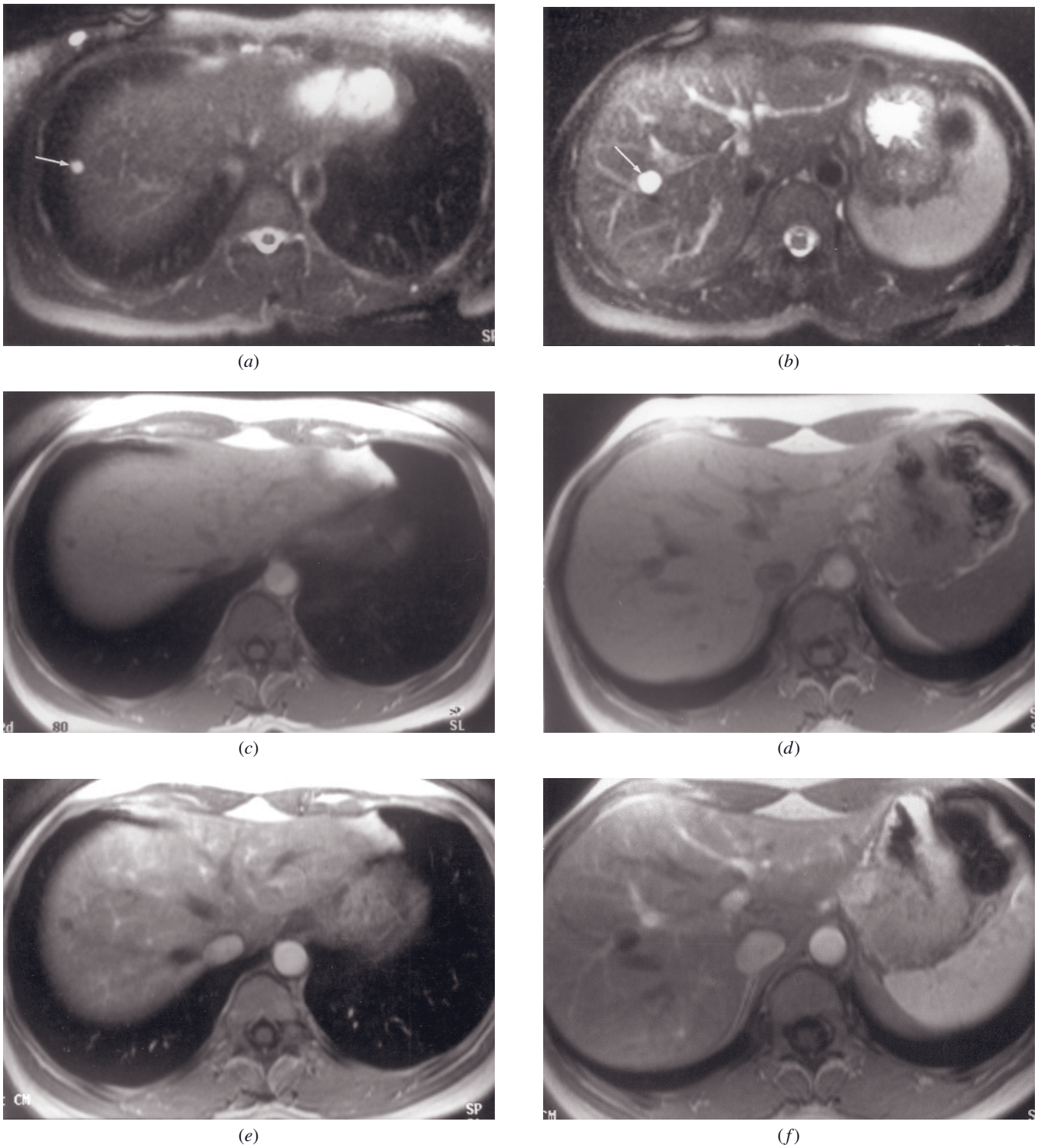

FIG. 2.14 Simple unilocular cysts. T2-weighted SS-ETSE (*a, b*), SGE (*c, d*), and immediate (*e, f*) and 90-s fat-suppressed (*g*, *h*) postgadolinium SGE images in the same patient but at different levels. There are two well-defined lesions (arrow, *a*, *b*) that are homogeneously high signal on T2-weighted images (*a, b*) and homogeneously low signal on T1-weighted images (*c, d*) and show no enhancement after administration of gadolinium (*e–h*), consistent with simple liver cysts.

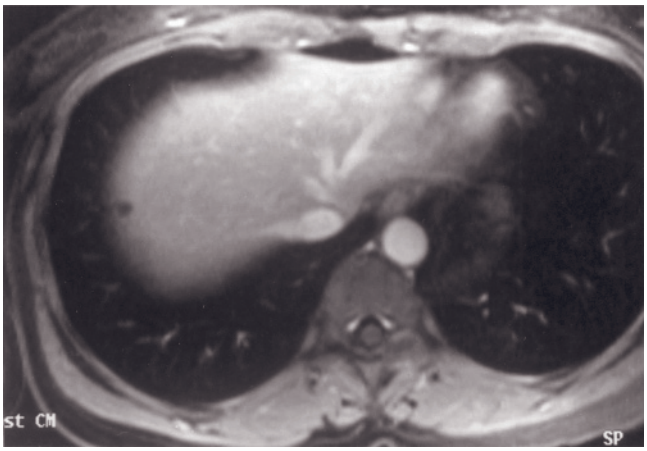

(*g*)

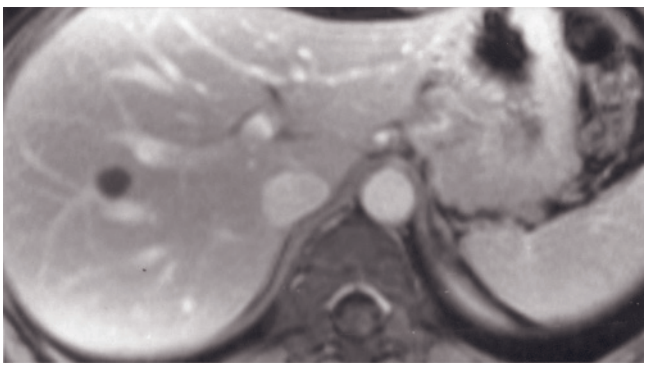

(*h*)

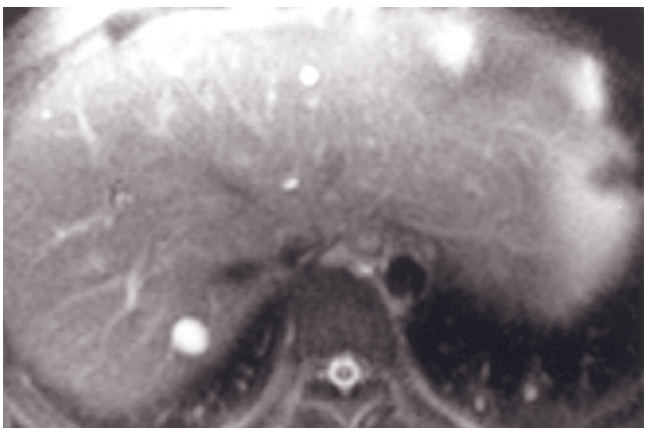

(*i*)

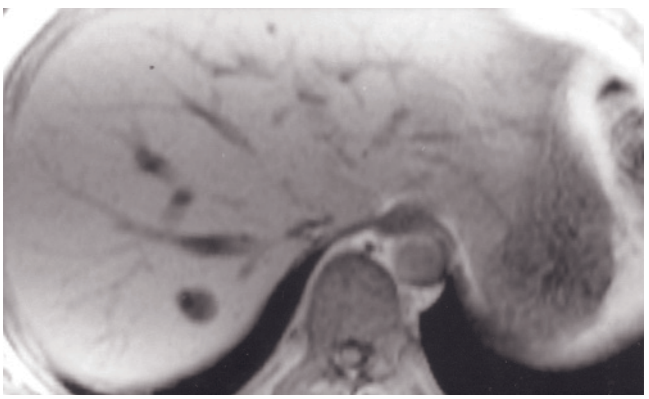

(*j*)

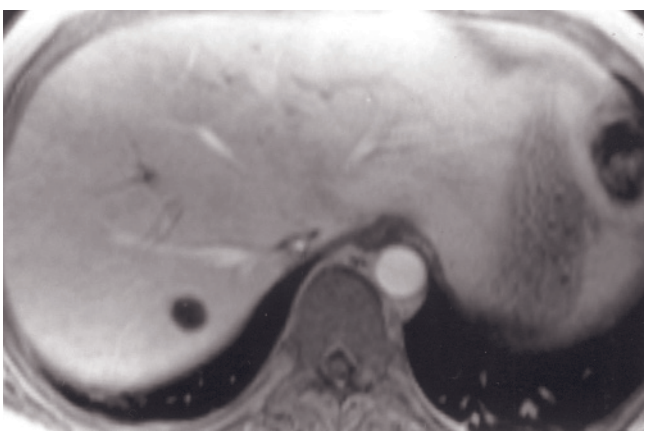

(*k*)

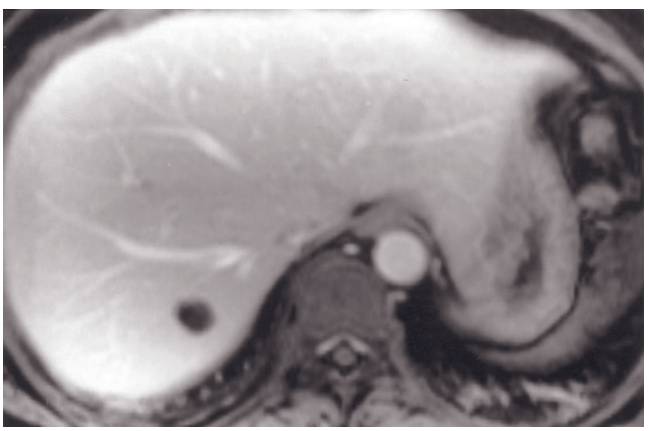

(*l*)

FIG. 2.14 (*Continued*) T2-weighted SS-ETSE (*i*), SGE (*j*), and immediate (*k*) and 90-s fat-suppressed (*l*) postgadolinium images in a second patient that demonstrate a small cyst in the right hepatic lobe with the same MRI characteristics as described above.

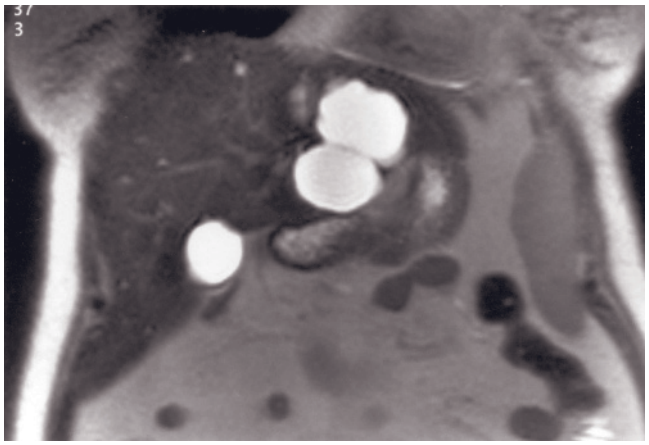

(*m*)

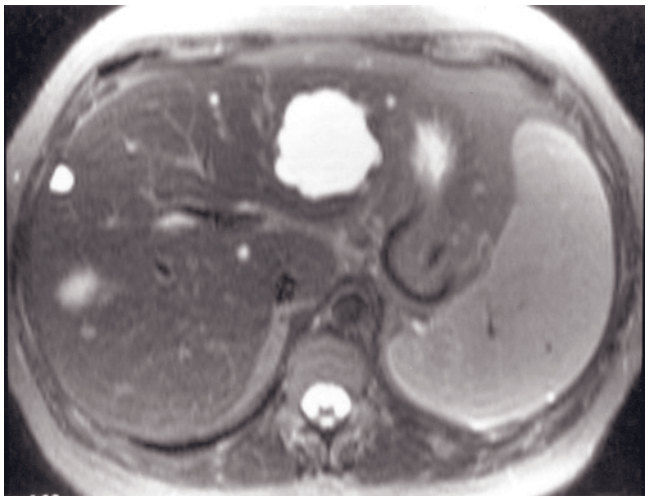

(*n*)

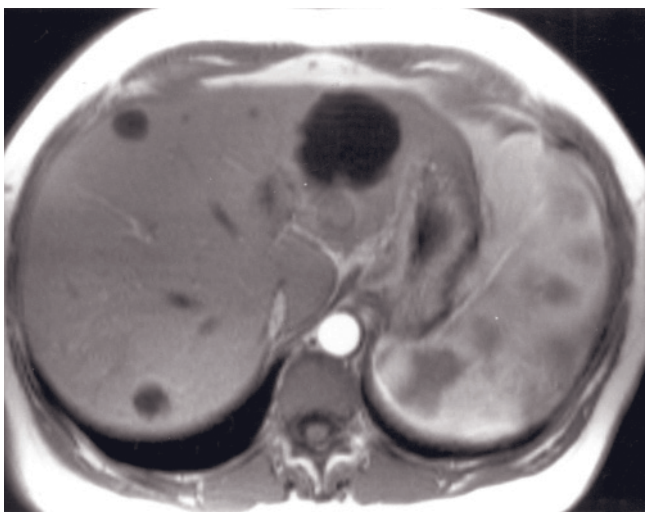

(*o*)

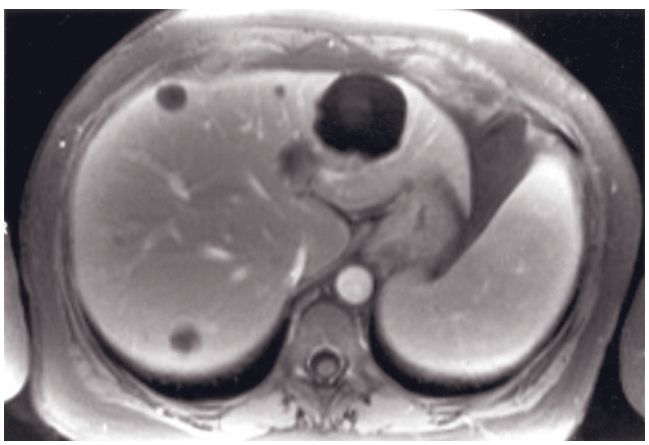

(*p*)

FIG. 2.14 (*Continued*) Coronal T2-weighted SS-ETSE (*m*), transverse echo train-STIR (*n*), and immediate (*o*) and 90-s fat-suppressed (*p*) postgadolinium SGE images in a third patient. Multiple simple cysts of different sizes are scattered throughout the hepatic parenchyma.

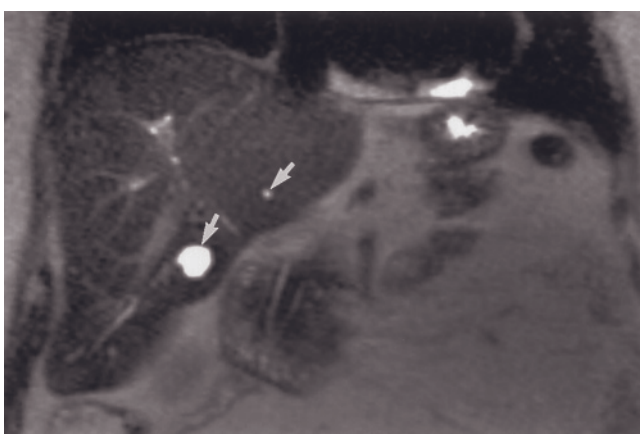

(*a*)

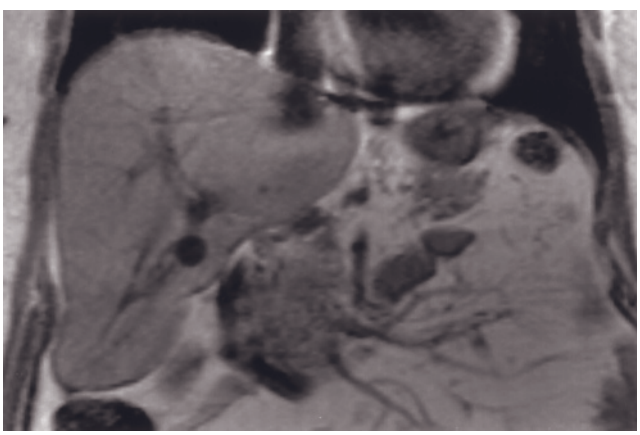

(*b*)

FIG. 2.15 Small simple cysts. Coronal T2-weighted SS-ETSE (*a*), SGE (*b*), and immediate (*c*) and 90-s fat-suppressed (*d*) post-gadolinium SGE images. Two cysts, 2 mm and 10 mm, are present in this patient. Cysts measuring <5 mm are most clearly shown

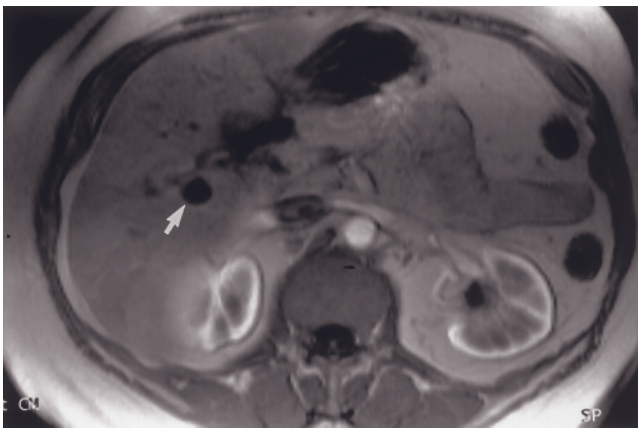

(*c*)

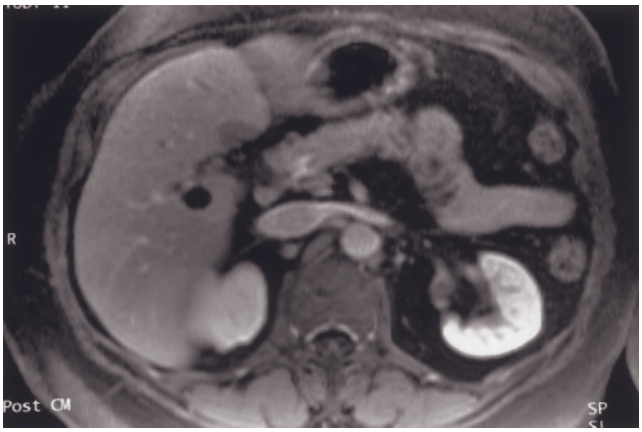

(*d*)

FIG. 2.15 (*Continued*) on T2-weighted images (arrows, *a*). The 10-mm cyst is signal void on early (arrow, *c*) and late (*d*) post-gadolinium images.

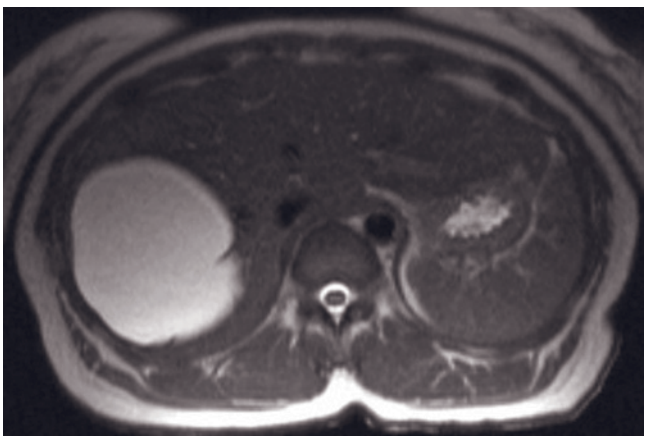

(*a*)

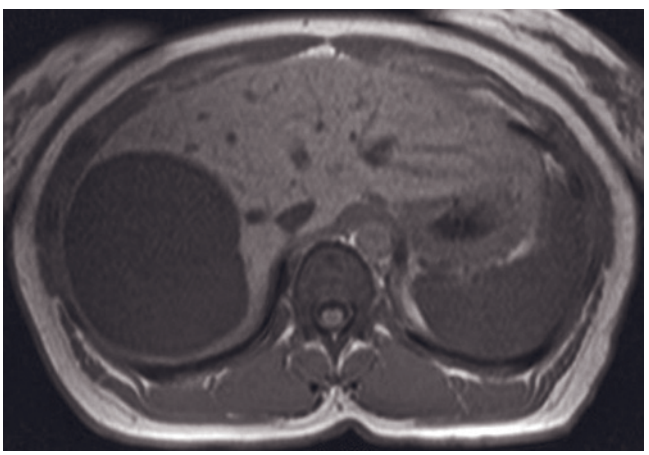

(*b*)

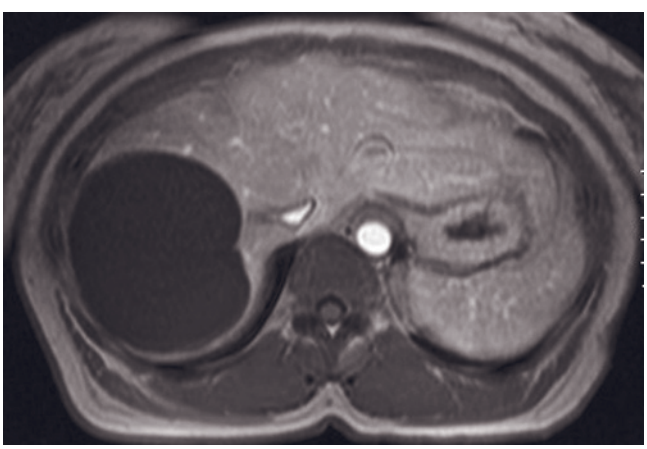

(*c*)

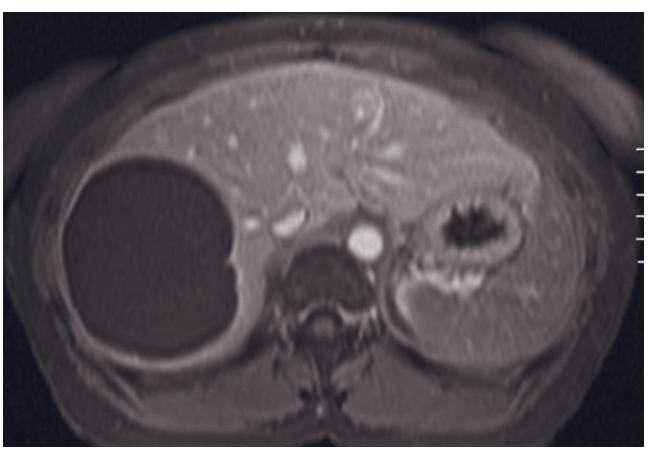

(*d*)

FIG. 2.16 Large simple cyst. T2-weighted SS-ETSE (*a*), SGE (*b*), and immediate (*c*) and 90-s fat-suppressed (*d*) postgadolinium SGE images. A large cyst is seen in the right hepatic lobe, which shows high signal intensity on the T2-weighted image (*a*), low signal intensity on the T1-weighted image (*b*), and lack of enhancement on early (*c*)- and late (*d*)-phase images.

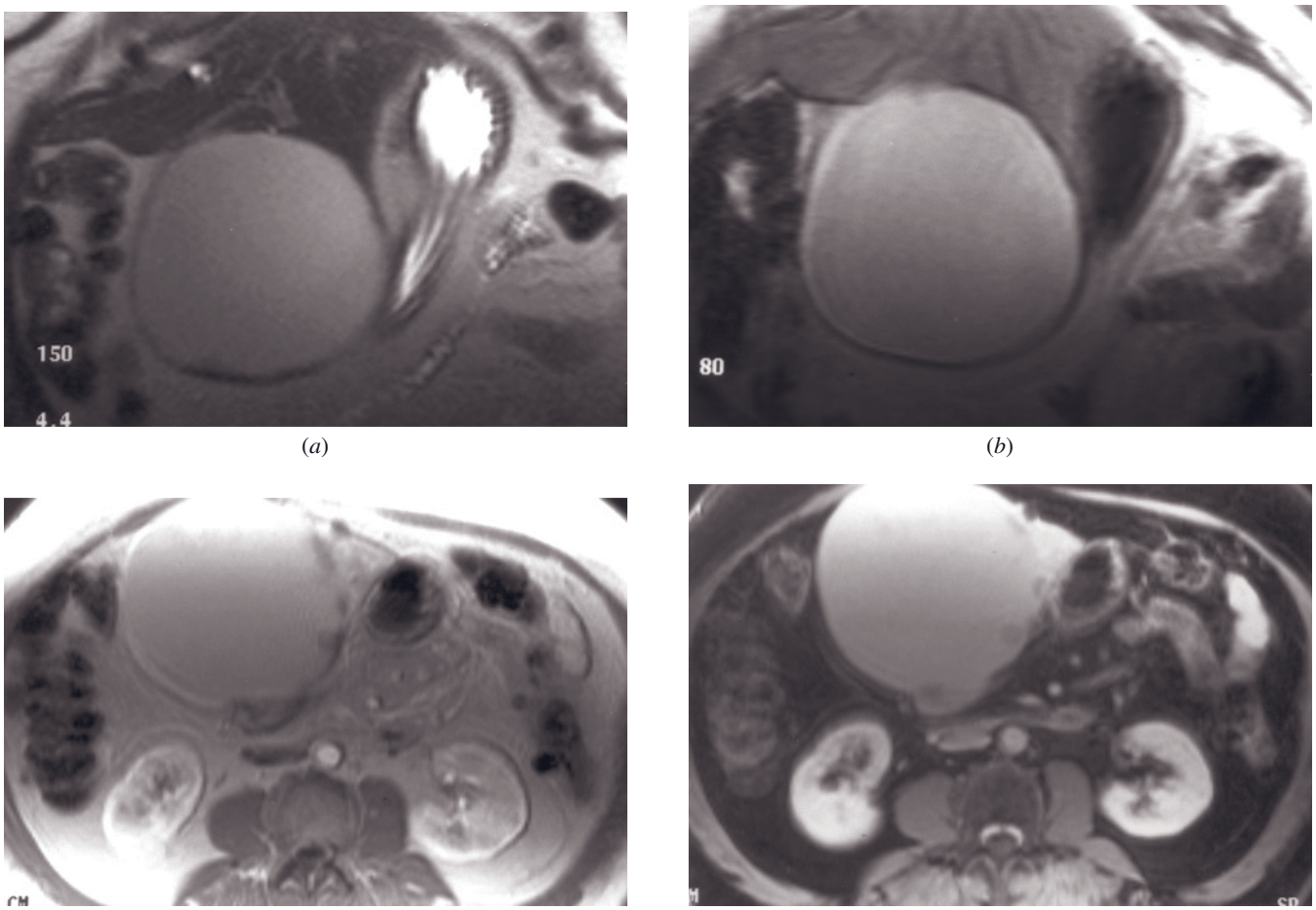

(*a*) (*b*)

(*c*) (*d*)

FIG. 2.17 Hemorrhagic cyst. Coronal T2-weighted SS-ETSE (*a*), transverse SGE (*b*), and transverse immediate (*c*) and 90-s fat-suppressed(*d*) postgadolinium images. A large cystic mass with thickened and irregular wall arises from the lateral segment of the liver and demonstrates high signal on both T2-weighted (*a*) and T1-weighted (*b*) images and lack of enhancement on early (*c*) and late (*d*) postcontrast images. A blood-filled cyst was proven by histopathology.

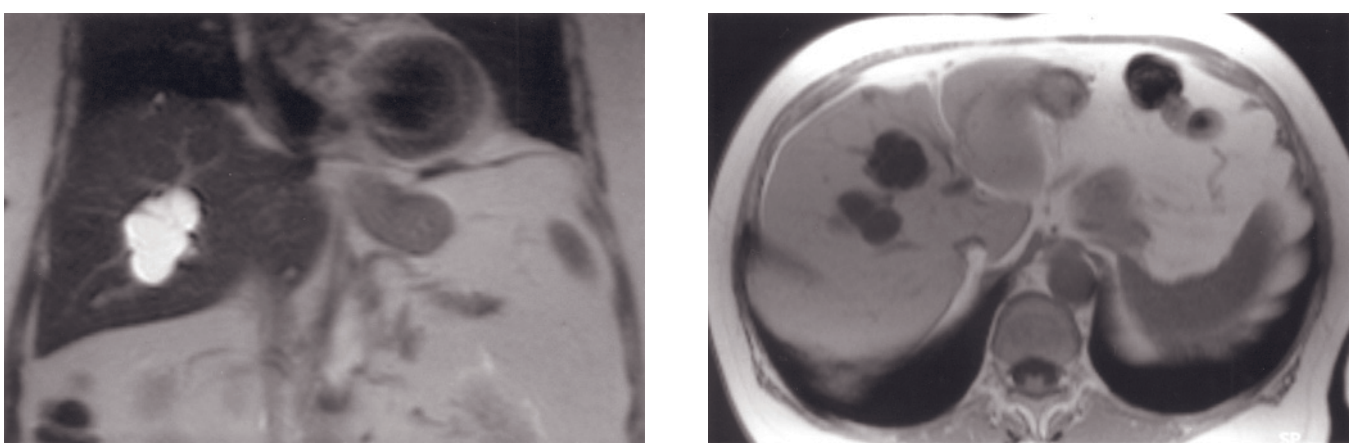

(*a*) (*b*)

FIG. 2.18 Multilocular cyst. Coronal T2-weighted SS-ETSE (*a*), transverse SGE (*b*), and immediate (*c*) and 90-s fat-suppressed (*d*) postgadolinium SGE images. Multiple cystic lesions, some with internal septations, are present in the liver parenchyma.

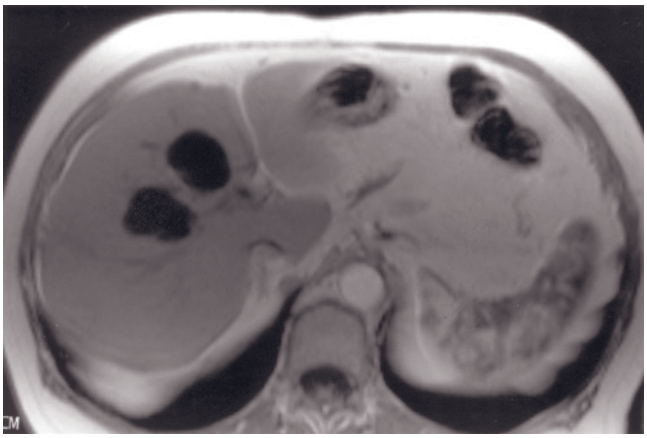

(*c*)

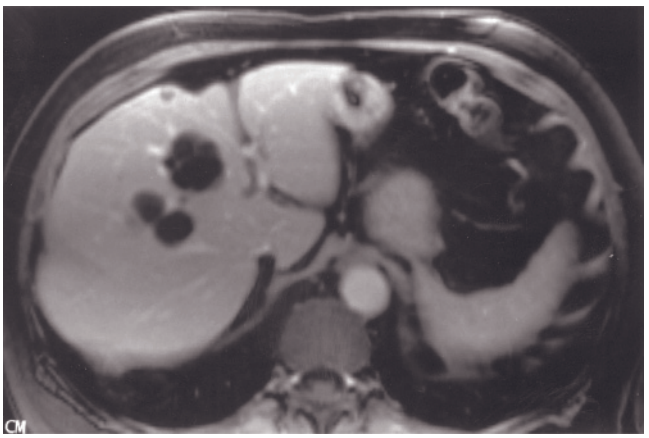

(*d*)

FIG. 2.18 (*Continued*)

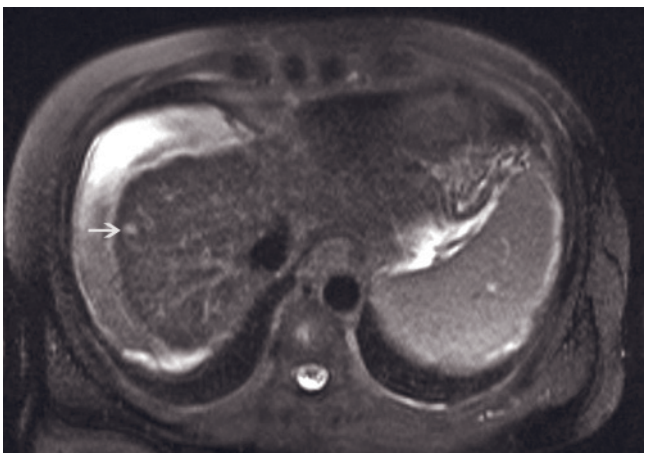

(*a*)

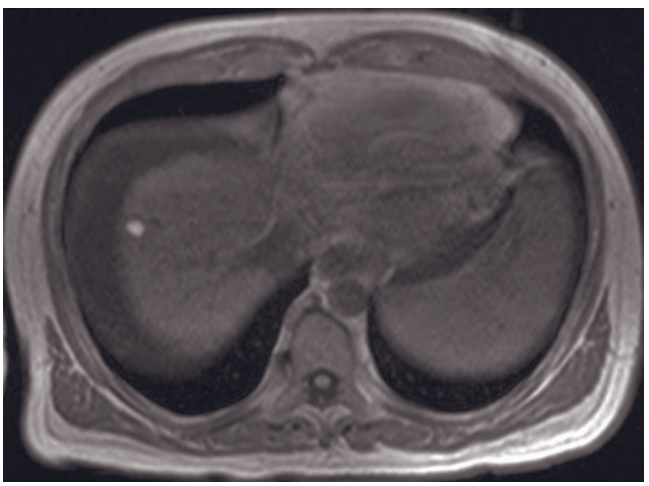

(*b*)

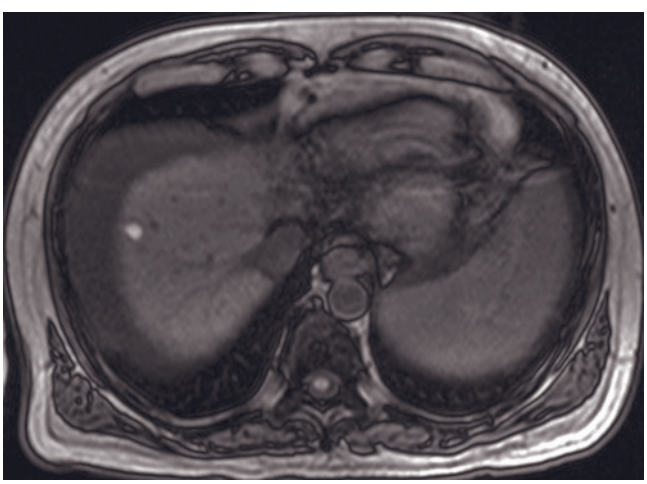

(*c*)

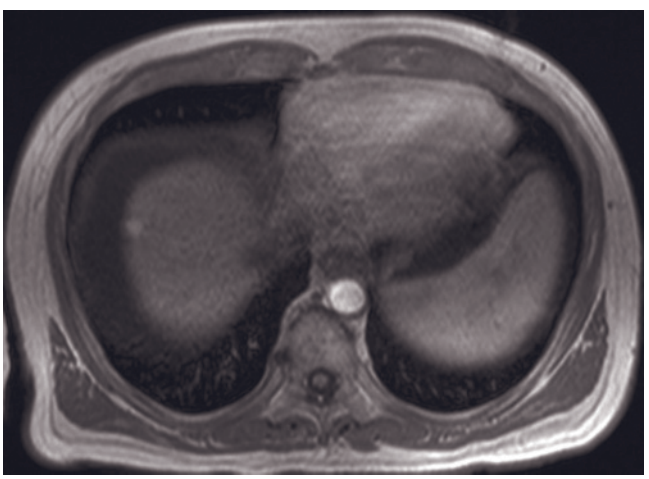

(*d*)

FIG. 2.19 Small foregut cyst. T2-weighted fat-suppressed SS-ETSE (*a*), SGE (*b*), out-of-phase SGE (*c*), and immediate postgadolinium SGE (*d*) images. A small lesion is seen superiorly in the liver (arrow, *a*) that exhibits high signal intensity on all sequences (*a–d*). Note that on the out-of-phase image (*c*) the lesion signal intensity does not drop, confirming that the high signal intensity on the in-phase T1-weighted image represents mucin (proteinaceous material) rather than fat within the lesion.

On the serial dynamic enhanced images, there is a lack of lesional enhancement but a subtle perceptible enhancing cyst wall is noticed (figs. 2.20 and 2.21). The presence of a cystic lesion with an enhancing wall and extension beyond the contour of the liver may also be observed in some forms of metastatic disease such as hepatic metastasis from ovarian malignancies. For this reason, a diagnosis of foregut cyst on imaging studies should only be made in the absence of peritoneal disease and a clinical history of malignancy.

Autosomal Dominant Polycystic Kidney Disease

In autosomal dominant polycystic kidney (ADPKD) disease, the liver is the most common extrarenal organ in which cysts occur. It is estimated that up to 75% of patients with ADPKD have hepatic involvement. Although these cysts vary in number and size, they tend to be multiple and smaller than the renal cysts, measuring up to 4 cm [50]. However, extensive hepatic replacement with large cysts has been described [51]. Liver cysts in ADPKD generally do not distort hepatic architecture or undergo hemorrhage, in contrast to kidney cysts in this entity. Liver cysts in the setting of ADPKD exhibit the same MR features as simple cysts, mentioned above in this section (figs. 2.22 and 2.23). Occasionally, hemorrhage may be observed in cysts. Massive involvement of the liver with large cysts, which are sometimes hemorrhagic, may result in right upper quadrant pain [50].

Biliary Hamartoma

Biliary hamartomas (or von Meyenburg complexes) are benign biliary malformations, which are currently considered as part of the spectrum of fibropolycystic diseases of the liver due to ductal plate malformation [52]. This entity is common and estimated to be present in approximately 3% of patients. Tumors may be solitary or multiple, and multiple tumors can be extensive.

Histopathologically biliary hamartomas consist of a collection of small, sometimes dilated, irregular and branching bile ducts embedded in a fibrous stroma. A few of the ducts may contain inspissated bile. In general, biliary hamartomas contain no or few vascular channels.

On MR images, lesions are small (usually <1 cm) and well defined. The high fluid content renders these lesions high signal on T2-weighted images, low signal on T1-weighted images, and negligible lesional enhancement on early and late postgadolinium images. Although this appearance resembles simple cysts, biliary hamartomas demonstrate a subtle thin rim of enhancement on early and late postcontrast images (figs. 2.24 and 2.25). The major potential diagnostic error is to misclassify these lesions as metastases because of the presence of the rim enhancement. The thin enhancing rim of biliary hamartomas, visualized on imaging, may be correlated histopathologically with the presence of compressed hepatic parenchyma bordering the lesion [52]. In contrast, the pattern of ring enhancement displayed by metastases relates histopathologically with the outer, most vascularized portion of the tumor. Peritumoral enhancement is also observed in some metastases as described in the next section. MR imaging further corroborates the different histologic profiles of the two processes through the observation that enhancement in biliary hamartoma does not progress centrally, whereas enhancement in metastases most often progresses centrally (fig. 2.26).

Biliary Cystadenoma/Cystadenocarcinoma

Although rare, benign and malignant cystic tumors of biliary origin may arise in the liver. There is a peak incidence of these lesions in the fifth decade, with a great predominance in women. Pathologically, on gross inspection, tumors are typically large and multiloculated and filled with clear or mucinous fluid. Mural nodules may be a component of some cysts. Histologically, cystic and stromal components are present to variable degrees. Malignant lesions will exhibit pronounced cytologic atypia with evidence of stromal invasion [53–56].

On imaging, these tumors frequently have solid nodules associated with cystic components (fig. 2.27) [57]. Occasionally, mucin content renders these tumors high in signal intensity on T1-weighted images [53, 56]. Solid components of the tumor demonstrate early heterogeneous enhancement in a pattern consistent with tumors of hepatic origin. Enhancement is often minimal in intensity, distinguishing these tumors from the extensive enhancement of HCC [58].

Extramedullary Hematopoiesis

Focal intrahepatic extramedullary hematopoiesis (EH) is an unusual condition that may appear as focal hepatic masses in the setting of hereditary disorders of hematopoiesis or in longstanding hematologic malignancies. EH is a compensatory phenomenon that occurs when erythrocyte production is diminished or destruction is accelerated [59]. EH is usually microscopic and commonly involves the liver, spleen, and lymph nodes. Rarely, the involvement may be macroscopic [59]. The focal hepatic disease can manifest as solitary or multiple lesions [60]. The masses tend to be homogeneously moderate high signal intensity on T2- and T1-weighted images and usually enhance in a diffuse homogeneous fashion on immediate postgadolinium images (fig. 2.28). A histopathological specimen is required for definitive diagnosis.

Angiomyolipomas

Angiomyolipomas of the liver are uncommon benign mesenchymal tumors. Histologically, the tumor is

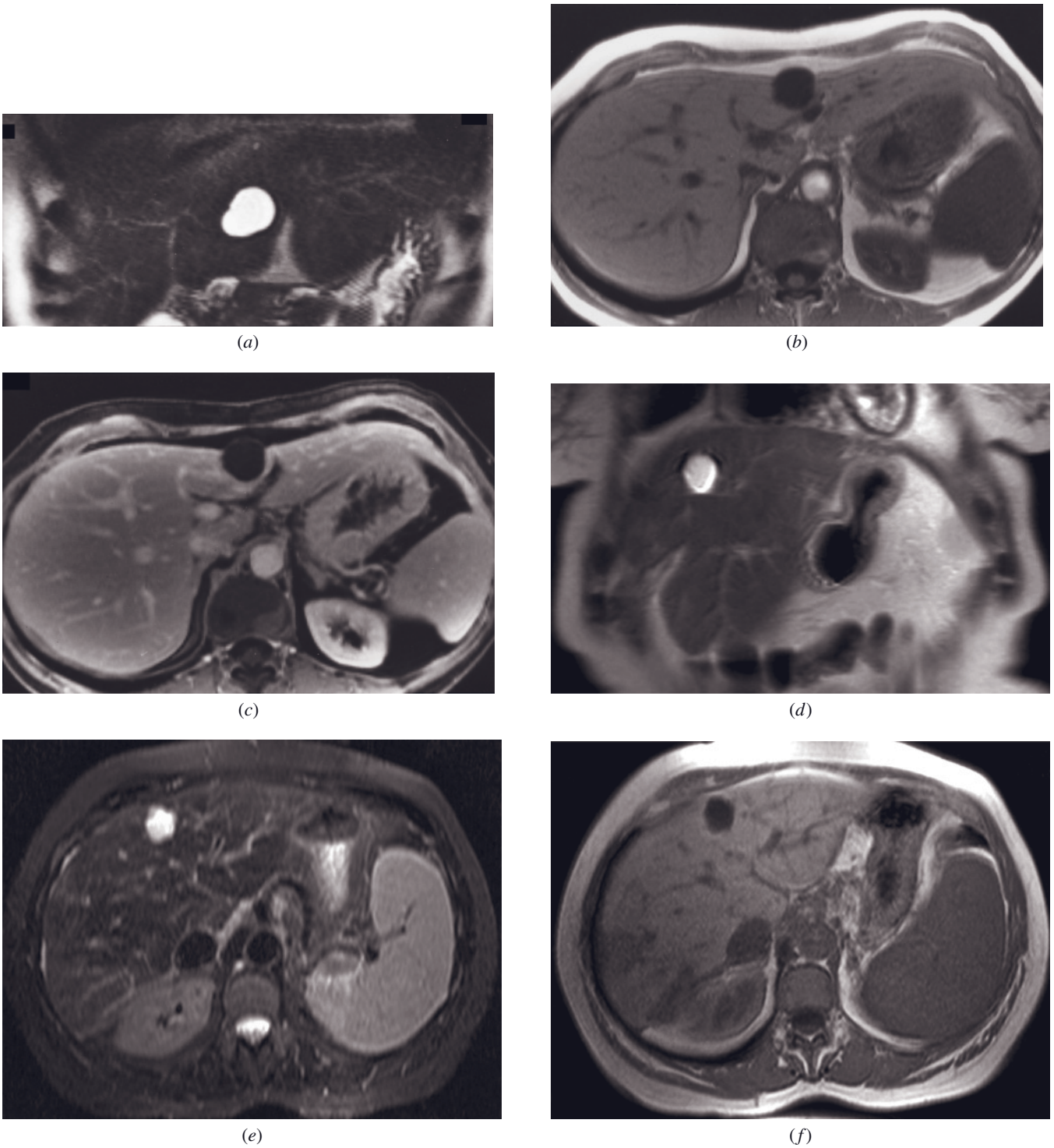

FIG. 2.20 Foregut cysts. Coronal T2-weighted SS-ETSE (*a*), transverse SGE (*b*), and 90-s fat-suppressed postgadolinium SGE (*c*) images. A 3-cm cystic lesion is noted superiorly on the border between medial and lateral segments. The lesion extends beyond the contour of the liver and has a thin perceptible wall, features that are characteristic of foregut cysts.

Coronal T2-weighted SS-ETSE (*d*), transverse T2-weighted fat-suppressed SS-ETSE (*e*), SGE (*f*), and immediate (*g*) and 90-s fat-suppressed (*h*) postgadolinium SGE images in a second patient. A cystic lesion is seen in segment 4 of the liver, consistent with a foregut cyst. Note faint enhancement of the cyst wall best appreciated on the late-phase image (*h*).

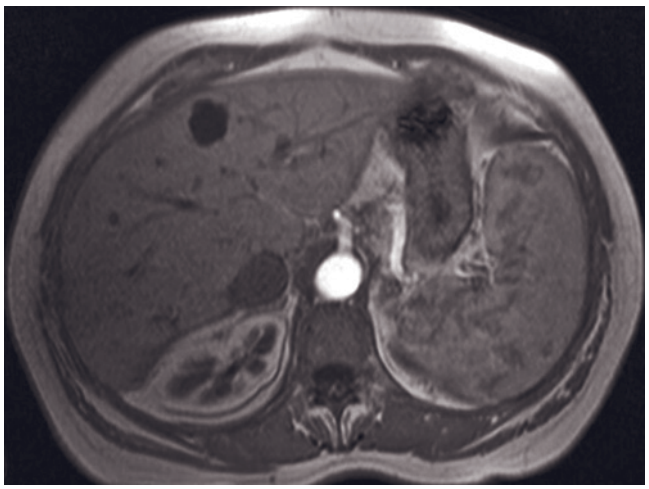

(*g*)

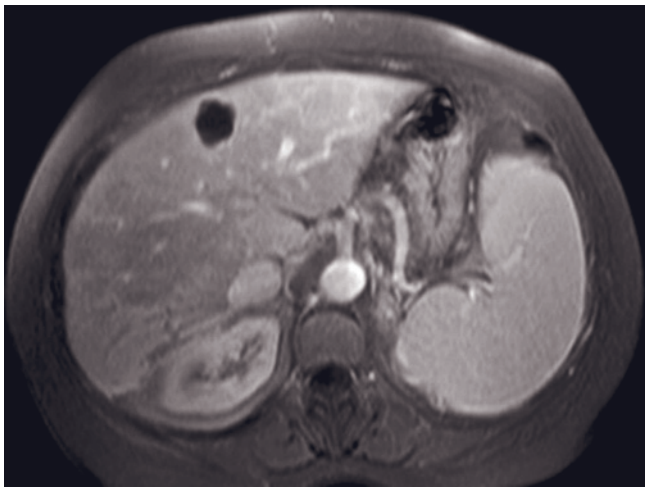

(*h*)

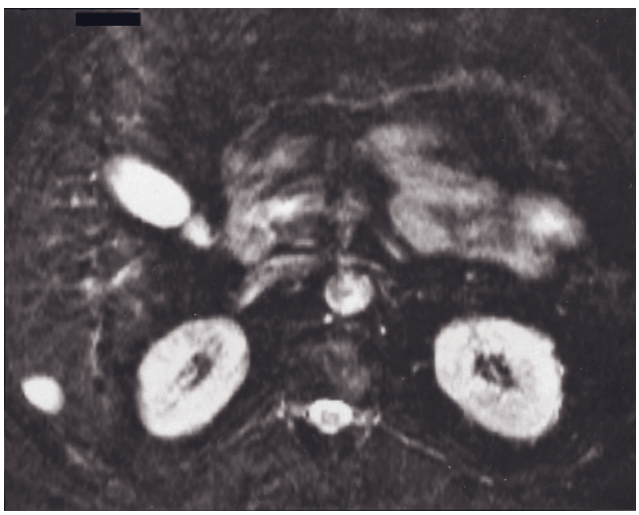

(*i*)

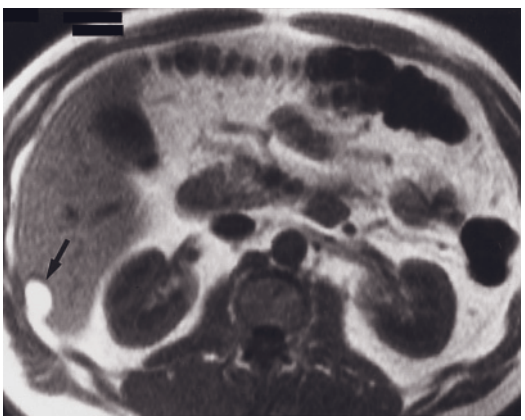

(*j*)

(*k*)

FIG. 2.20 (*Continued*) T2-weighted fat-suppressed SS-ETSE (*i*), SGE (*j*), and immediate postgadolinium SGE (*k*) images in a third patient demonstrate a 1.5-cm lesion along the lateral inferior aspect of the right lobe of the liver (arrow, *j*). The lesion is sharply demarcated, is high in signal intensity on the T2-weighted (*i*) and T1-weighted (*j*) images, and does not change in shape or appearance after gadolinium administration (*k*). The high concentration of mucin in the cyst accounts for the high signal intensity on the T1-weighted (*j*) images. Note also that the lesion extends beyond the contour of the liver, which is characteristic of foregut cysts.

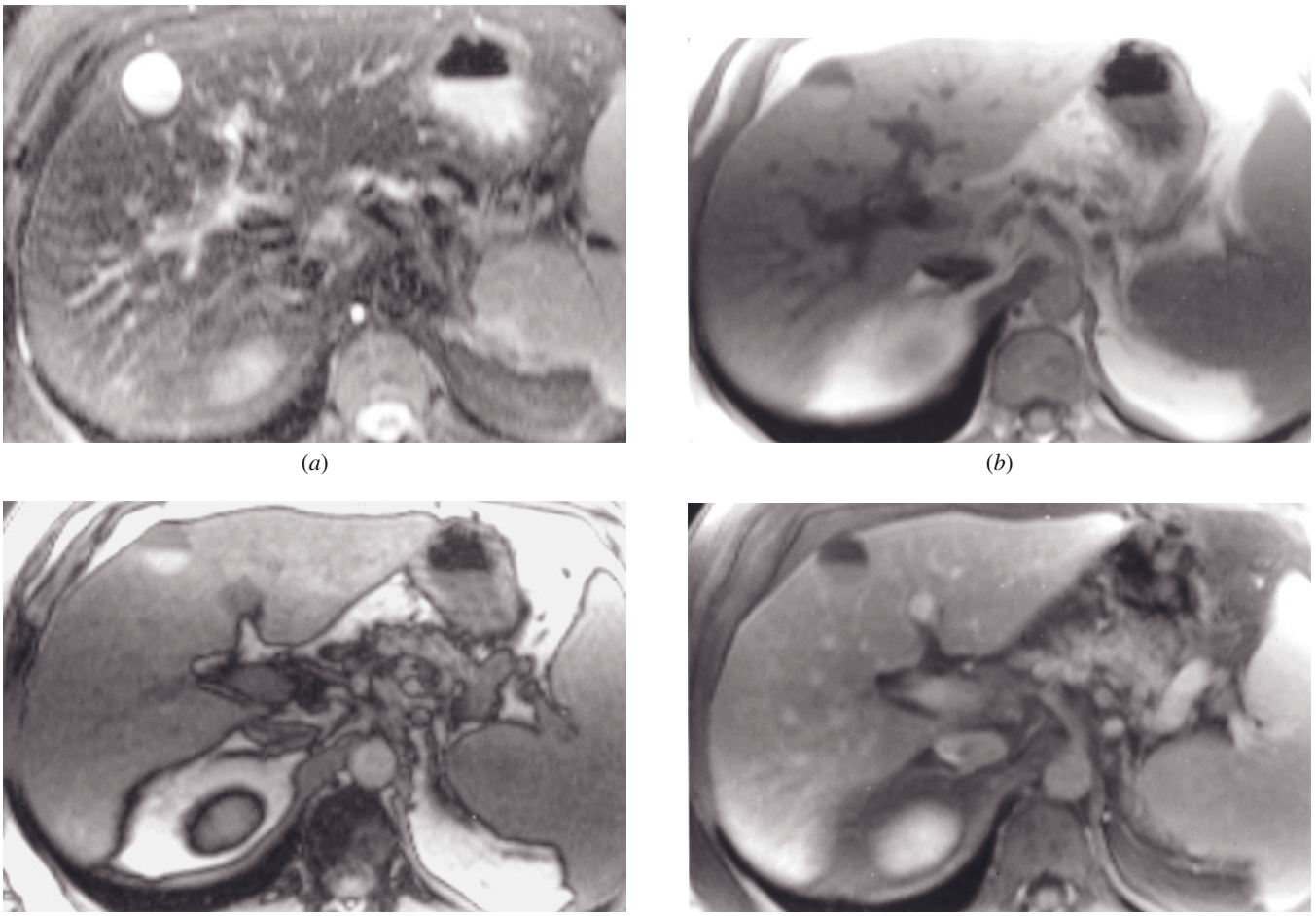

(*a*) (*b*) (*c*) (*d*)

FIG. 2.21 Foregut cyst with layering. Echo train-STIR (*a*), SGE (*b*), out-of-phase SGE (*c*), and 90-s fat-suppressed postgadolinium SGE (*d*) images. A cystic lesion is identified in segment 4 and distorts the anterior liver contour. The lesion is homogeneously high signal on T2-weighted image (*a*) and shows layering with high signal intensity on T1-weighted image (*b*), which does not lose signal on out-of-phase image (*c*), consistent with proteinaceous material (mucin) observed in these cysts.

composed of mature fat, blood vessels, and smooth muscle. Some tumors may contain foci of extramedullary hematopoiesis (angiomyomyelolipomas). Some patients have tuberous sclerosis [61], although the association is less strong than with renal angiomyolipomas.

Angiomyolipomas are well-defined, sharply marginated masses that frequently have a high fat content, and therefore are high in signal intensity on T1-weighted images and low in signal intensity on fat-suppressed images. Angiomyolipomas may also have a low fat content and appear moderately high in signal on T2-weighted images and low in signal intensity on T1-weighted images and exhibit a diffuse heterogeneous enhancement on immediate postgadolinium SGE images (figs. 2.29 and 2.30) [62]. A similar enhancement pattern is observed in well-differentiated hepatocellular carcinoma, and this enhancement reflects the appearance of well-defined tumors of hepatic origin. The pattern of enhancement of angiomyolipomas tends to be much more orderly than well-differentiated hepatocellular carcinomas.

Lipomas

Hepatic lipomas are rarer than angiomyolipomas. On imaging, tumors are commonly multiple and appear as fatty tumors that are high in signal intensity on T1-weighted sequences and low in signal intensity with fat-suppressed techniques [63]. These lesions show negligible enhancement on postgadolinium images (fig. 2.31).

Hemangiomas

Hemangiomas are the most common benign hepatic neoplasm, with an autopsy incidence between 0.4 and 20% [64, 65]. Hemangiomas are more frequent in females, rarely produce symptoms, and are usually detected incidentally.

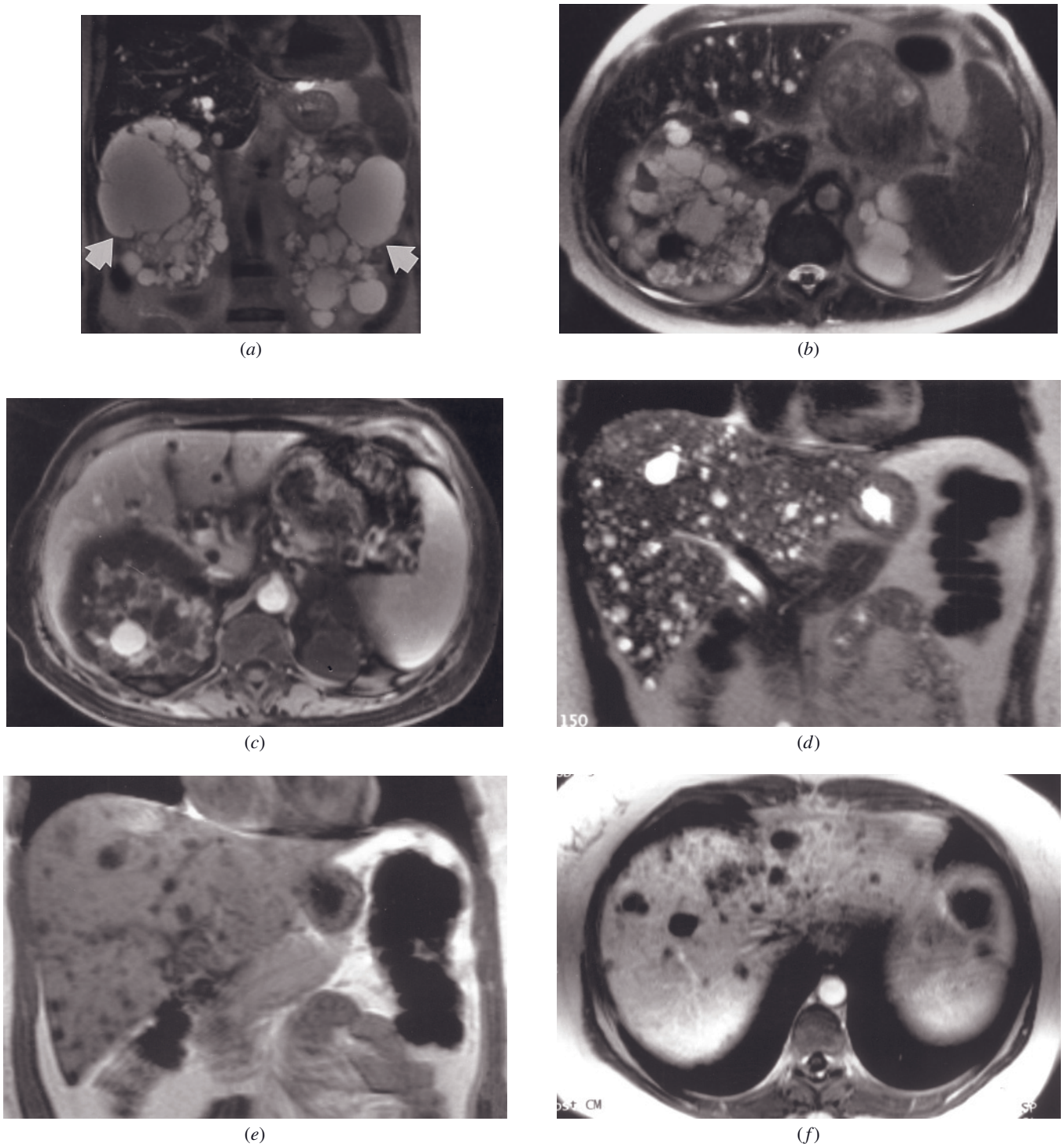

FIG. 2.22 Liver cysts in polycystic kidney disease. Coronal (*a*) and transverse (*b*) T2-weighted SS-ETSE and 90-s fat-suppressed postgadolinium SGE (*c*) images. The kidneys are massively enlarged and contain multiple cysts of varying size with no definable renal parenchyma (arrows, *a*). Multiple <1-cm cysts are present and scattered throughout the liver that are high in signal intensity on T2-weighted images (*a*, *b*) and do not enhance after gadolinium administration (*c*).

Coronal T2-weighted SS-ETSE (*d*) and SGE (*e*) and transverse 1-min postgadolinium SGE (*f*) images in a second patient show cysts scattered throughout the liver parenchyma with no evidence of hemorrhage or distortion of hepatic architecture.

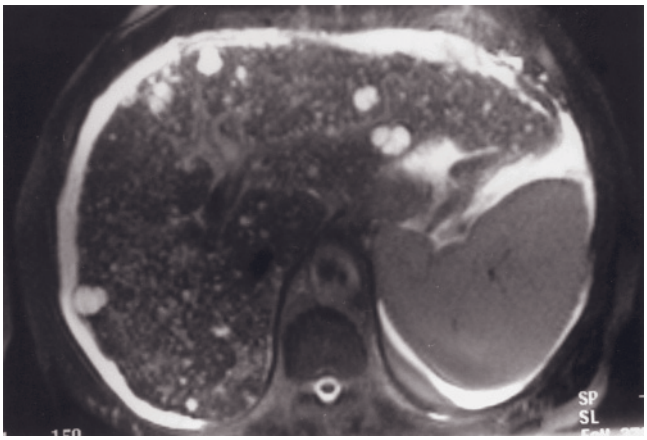

(*a*)

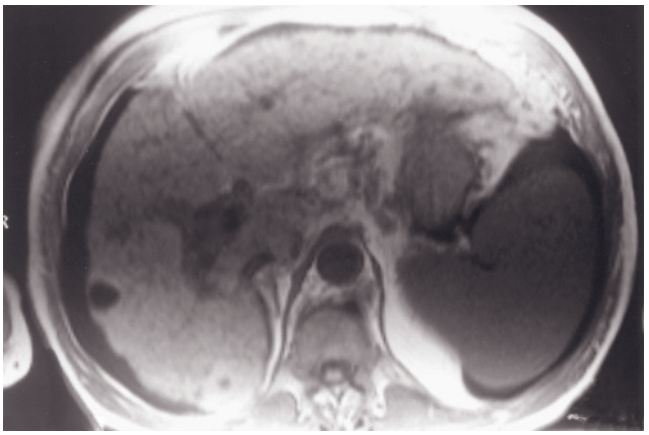

(*b*)

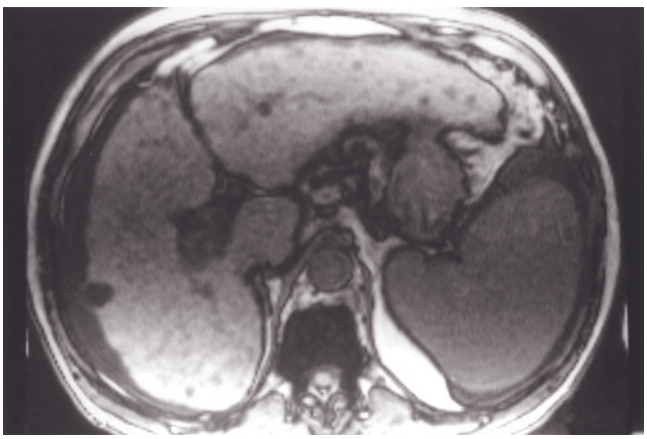

(*c*)

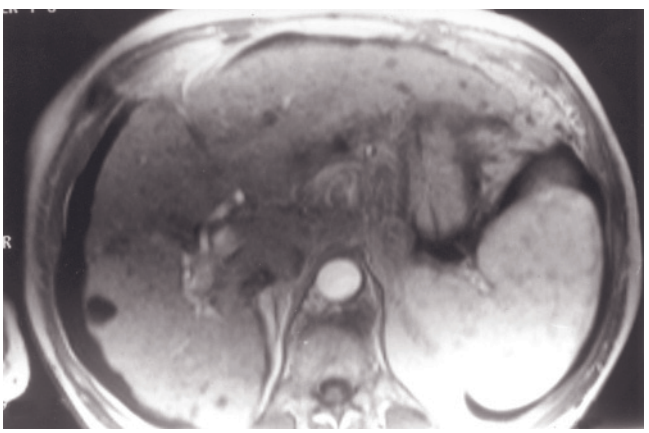

(*d*)

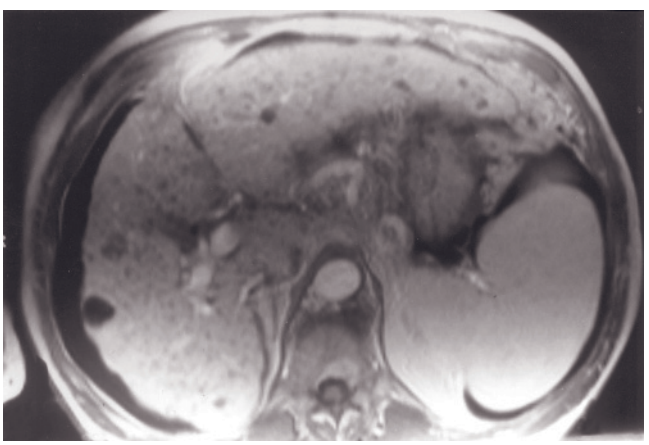

(*e*)

FIG. 2.23 Polycystic liver disease and cirrhosis. T2-weighted fat-suppressed SS-ETSE (*a*), SGE (*b*), out-of-phase SGE (*c*), and immediate (*d*) and 45-s fat-suppressed (*e*) postgadolinium SGE images in a patient who has a history of polycystic liver disease. The liver is small, with an irregular contour consistent with cirrhosis. Multiple small cysts are scattered throughout the liver, compatible with liver cysts seen in autosomal dominant polycystic kidney disease.

Pathologically, hemangiomas are characterized grossly as well-circumscribed, spongelike blood-filled mesenchymal tumors. Microscopically, hemangiomas reveal numerous large vascular channels lined by a single layer of flat endothelial cells, separated by slender fibrous septa. Foci of thrombosis, extensive fibrosis, and calcification may be present. The great majority of these benign vascular lesions are cavernous hemangiomas, but in rare instances they may represent capillary telangiectasias. Cavernous hemangiomas are composed primarily of large vascular lakes and channels. Some of the vascular channels undergo thrombosis and fibrous organization [66].

Hemangiomas are usually multiple (fig. 2.32). Small hemangiomas typically appear round, whereas larger

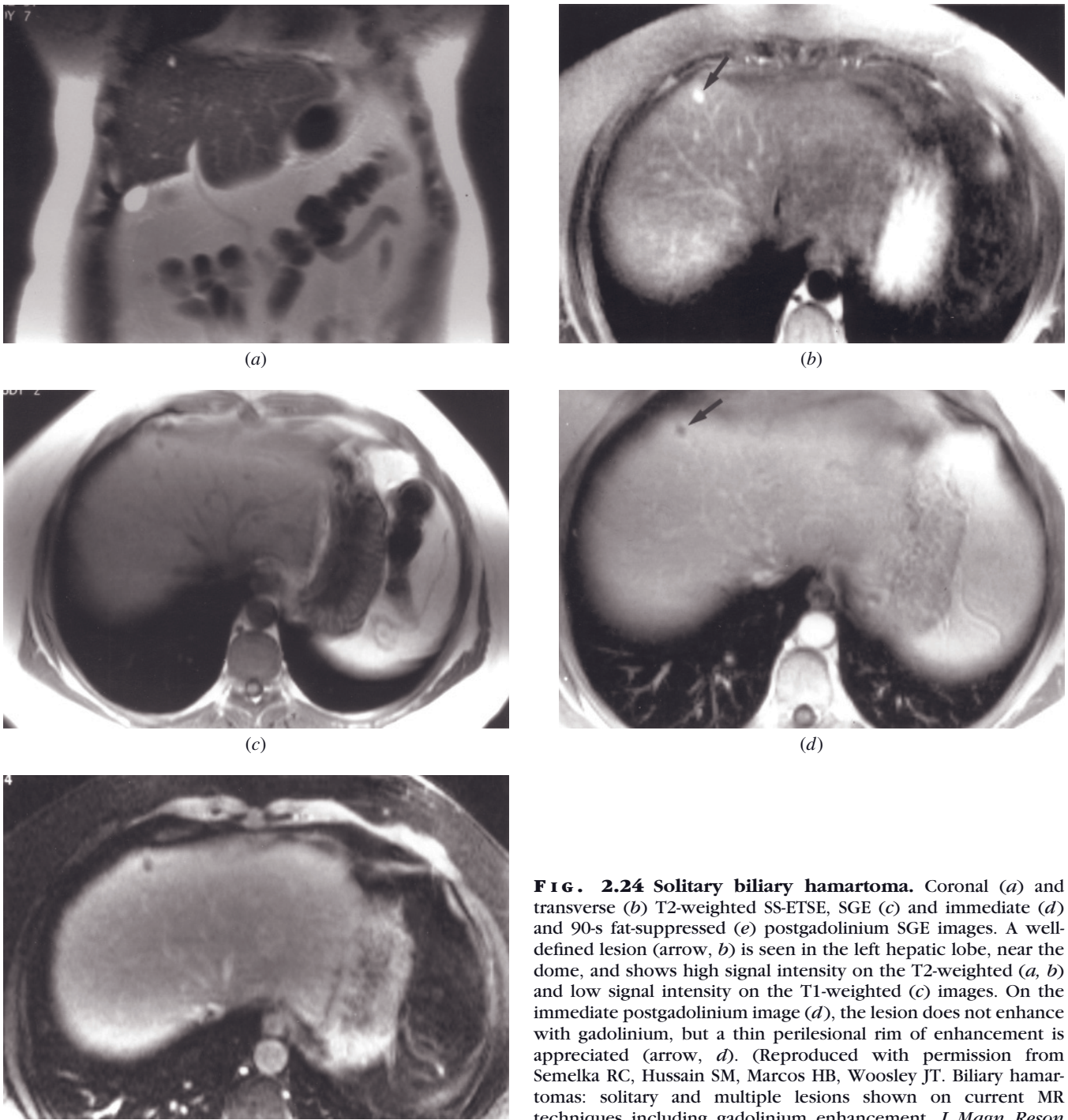

FIG. 2.24 Solitary biliary hamartoma. Coronal (*a*) and transverse (*b*) T2-weighted SS-ETSE, SGE (*c*) and immediate (*d*) and 90-s fat-suppressed (*e*) postgadolinium SGE images. A well-defined lesion (arrow, *b*) is seen in the left hepatic lobe, near the dome, and shows high signal intensity on the T2-weighted (*a, b*) and low signal intensity on the T1-weighted (*c*) images. On the immediate postgadolinium image (*d*), the lesion does not enhance with gadolinium, but a thin perilesional rim of enhancement is appreciated (arrow, *d*). (Reproduced with permission from Semelka RC, Hussain SM, Marcos HB, Woosley JT. Biliary hamartomas: solitary and multiple lesions shown on current MR techniques including gadolinium enhancement. *J Magn Reson Imaging* 10: 196–201, 1999).

lesions have either a well-defined round or lobular margin.

On MRI, hemangiomas have long T2 and T1 values, so they are high in signal intensity on T2-weighted images and low in signal intensity on T1-weighted images, maintaining signal intensity on longer echo times (e.g., >120 ms) [67, 68]. T2 measurements are less than those of cysts. On dynamic serial postcontrast images, hemangiomas typically enhance on a peripheral nodular fashion, which enlarge, coalesce, and slowly progress centripetally to complete or nearly complete fill-in of the entire lesion by 10 min [69–72]. Hemangiomas may fade

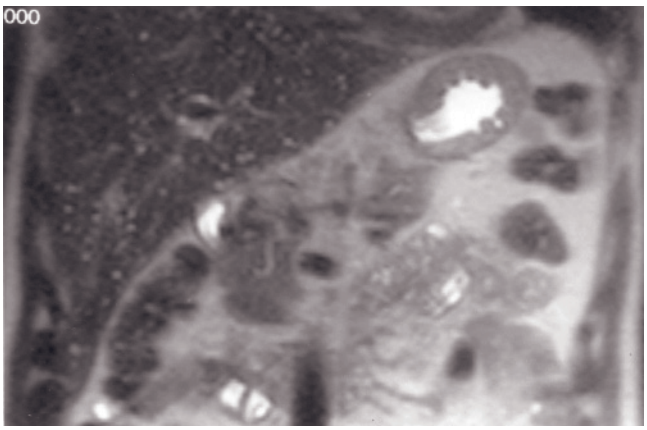

(*a*)

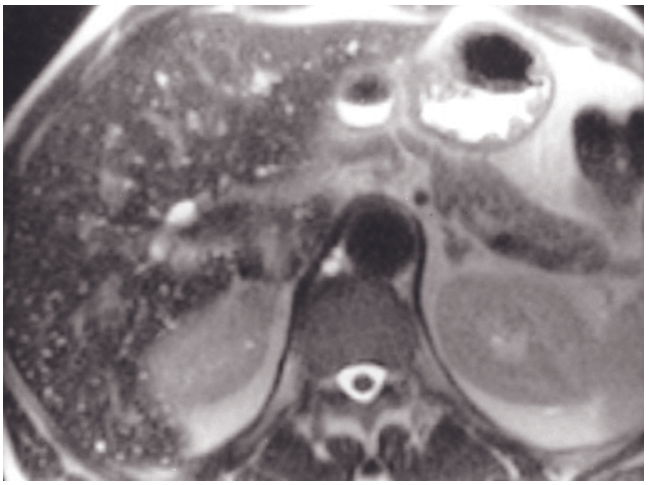

(*b*)

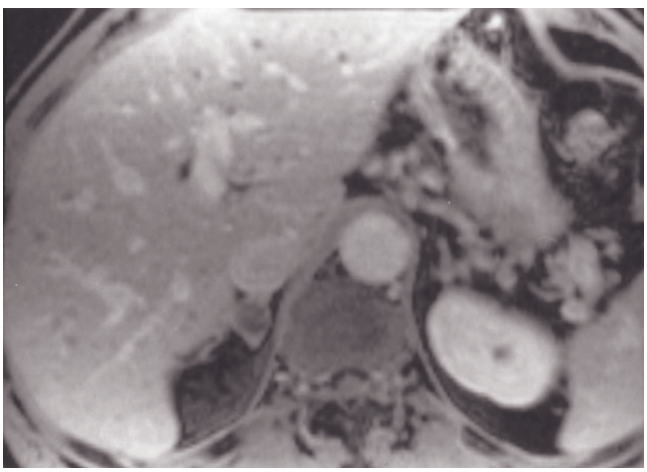

(*c*)

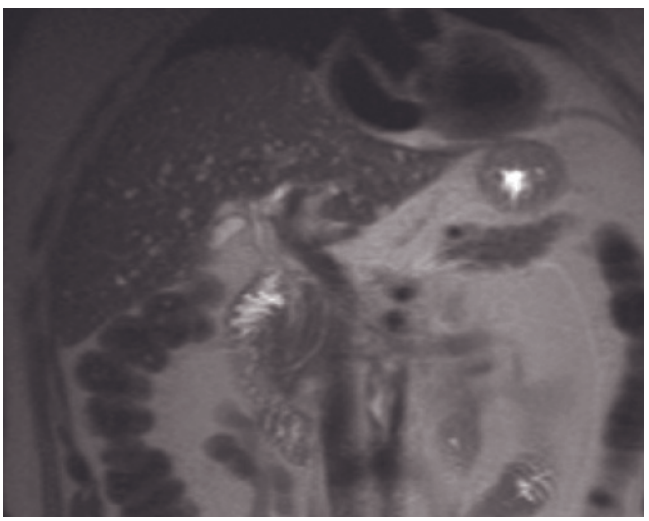

(*d*)

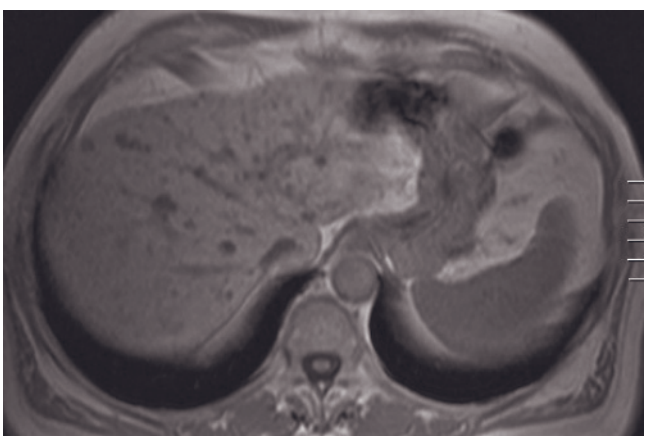

(*e*)

FIG. 2.25 Multiple biliary hamartomas. Coronal (*a*) and transverse (*b*) T2-weighted SS-ETSE and 90-s postgadolinium fat-suppressed SGE (*c*) images in one patient and coronal T2-weighted SS-ETSE (*d*), SGE (*e*), and immediate (*f*) and 90-s fat-suppressed (*g*) SGE images in a second patient. In both patients there are multiple well-defined lesions, <1cm, scattered throughout the liver. They are high signal intensity on T2-weighted (arrows, *d*)

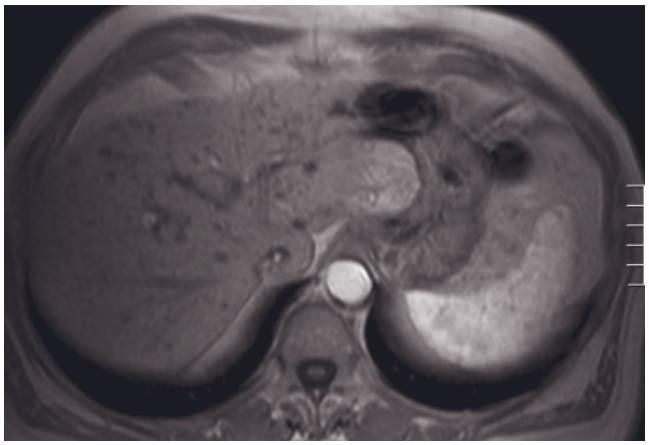

(*f*)

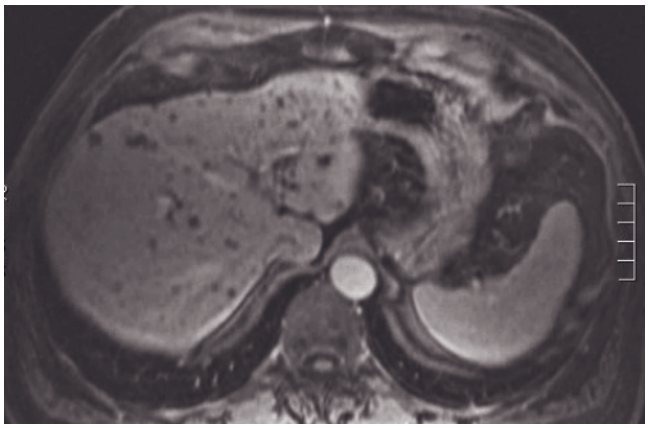

(*g*)

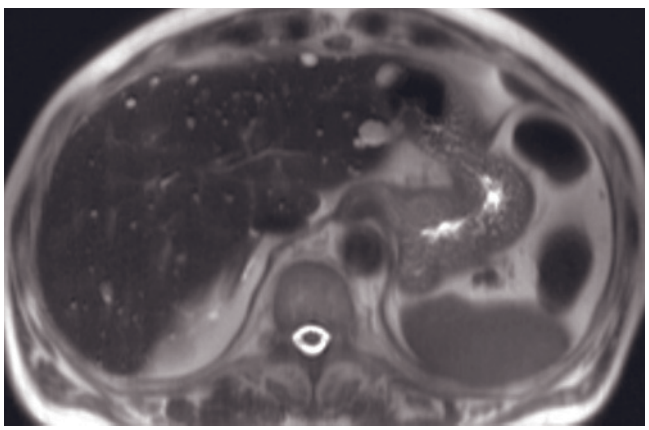

(*h*)

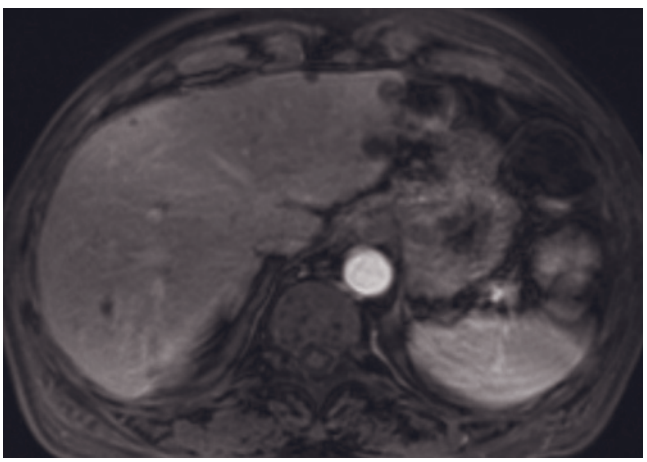

(*i*)

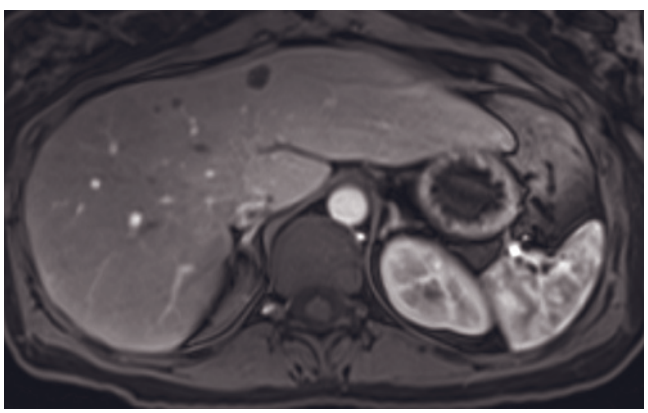

(*j*)

Fig. 2.25 (*Continued*) and low signal intensity on noncontrast T1-weighted (*e*) images and demonstrate thin perilesional rim enhancement on postgadolinium images. 3T images in a third (*h*, *i*) and a fourth (*j*) patient with biliary hamartoma, with imaging features similar to those previously described.

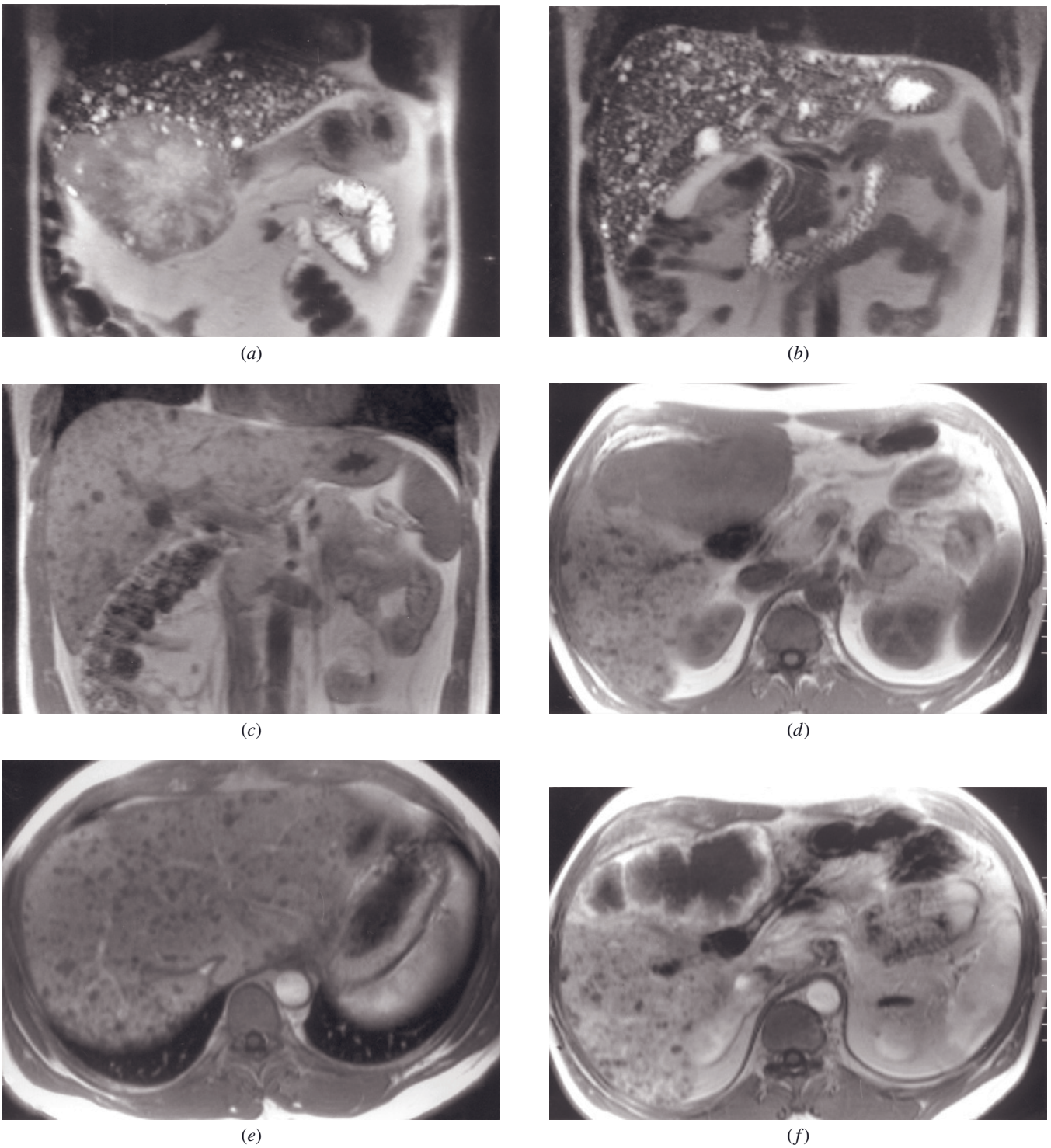

FIG. 2.26 Multiple biliary hamartomas and colon cancer metastasis. Coronal T2-weighted SS-ETSE (*a, b*), coronal (*c*) and transverse (*d*) SGE, and immediate (*e, f*) and 90-s fat-suppressed (*g, h*) postgadolinium SGE images in a patient who has a history of colon cancer. There is a large hepatic mass in segments 4/5 that demonstrates heterogeneous and moderately high signal on

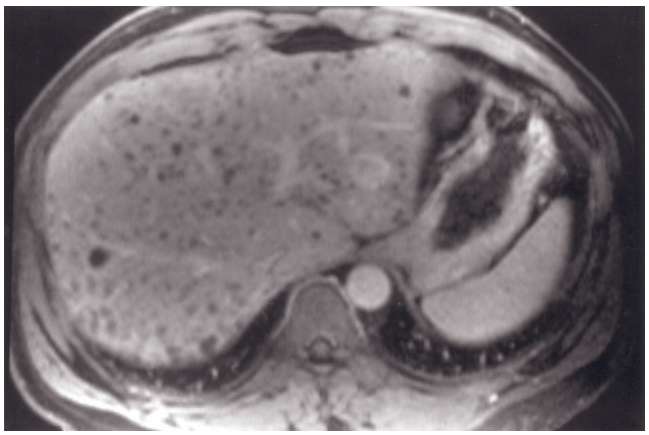

(*g*)

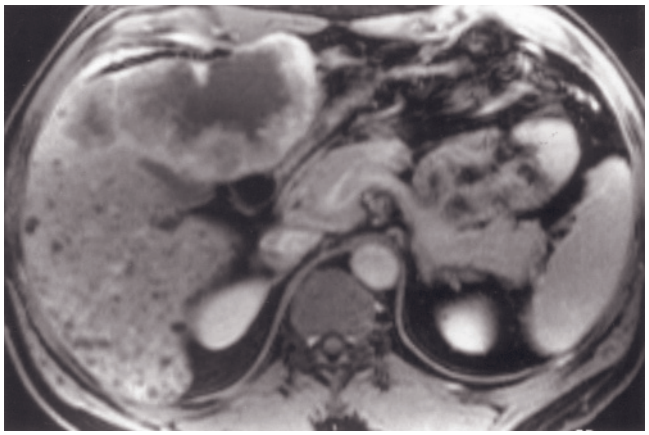

(*h*)

FIG. 2.26 (*Continued*) T2-weighted image (*a*) and moderately low signal on T1-weighted image (*d*) and ring enhancement after administration of contrast (*f, h*), consistent with a metastasis. The liver is riddled with many small well-defined lesions, measuring <1 cm, that also demonstrate ring enhancement after contrast, consistent with biliary hamartomas. Note that the metastasis progresses in enhancement from early (*f*) to late (*h*) images, whereas biliary hamartomas show identical ring enhancement on early and late images with no progressive enhancement.

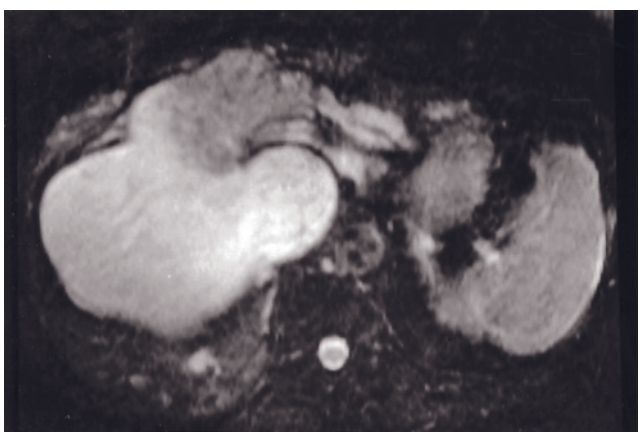

(*a*)

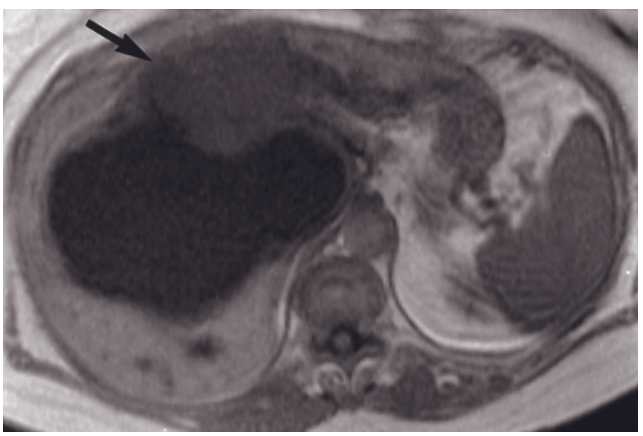

(*b*)

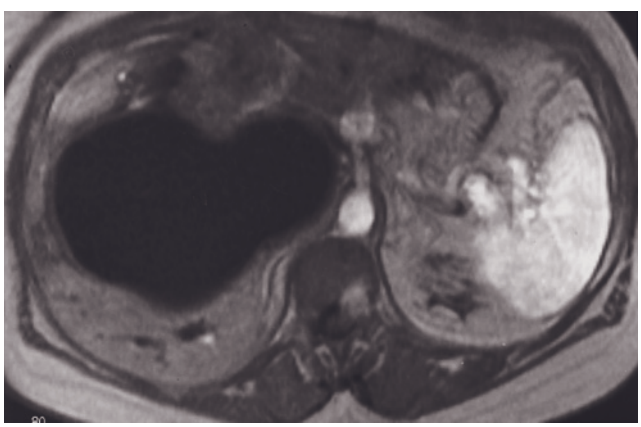

(*c*)

FIG. 2.27 Biliary cystadenoma. T2-weighted fat-suppressed ETSE (*a*), SGE (*b*), and immediate postgadolinium SGE (*c*) images. A large cystic mass with a 5-cm solid nodular component (arrow, *b*) is present in the liver. The nodular component is moderately hyperintense on the T2-weighted image (*a*) and slightly hypointense on the T1-weighted image (*b*) and enhances in a diffuse heterogeneous fashion on the immediate postgadolinium image (*c*). Diffuse heterogeneous enhancement on immediate postgadolinium images is a feature of tumors of hepatic origin.

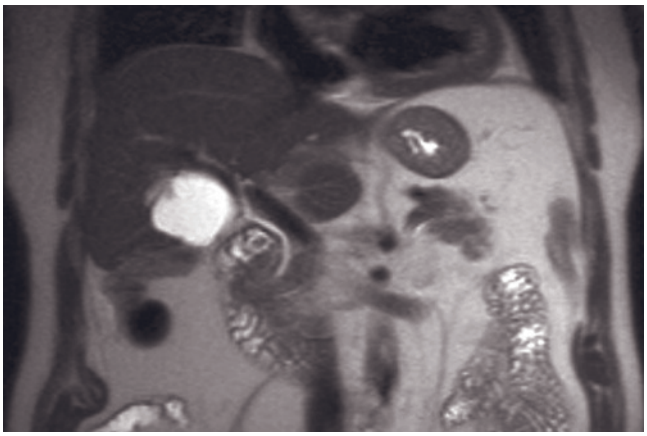

(*d*)

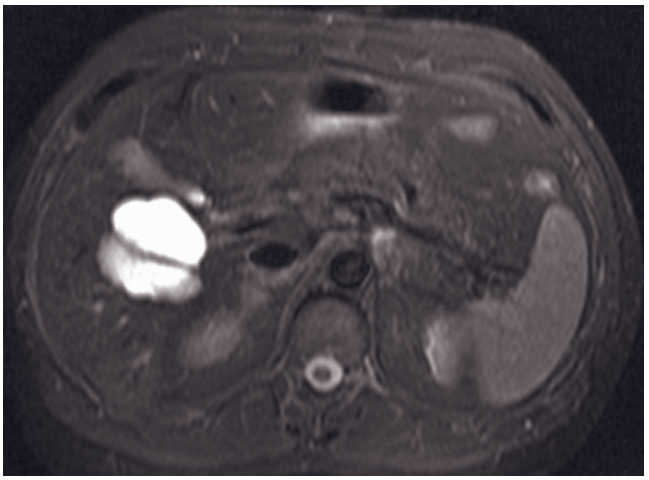

(*e*)

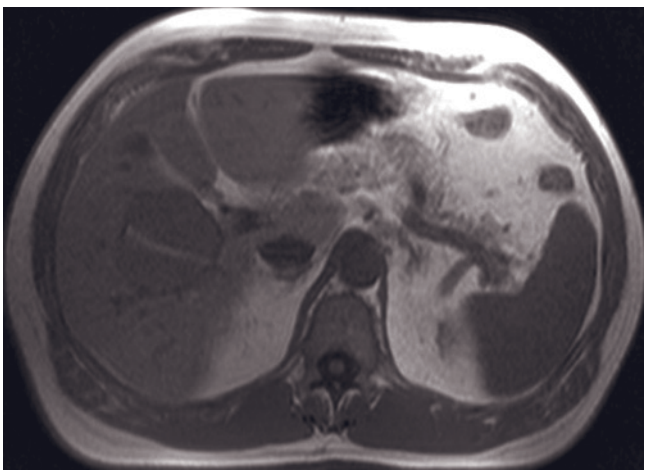

(*f*)

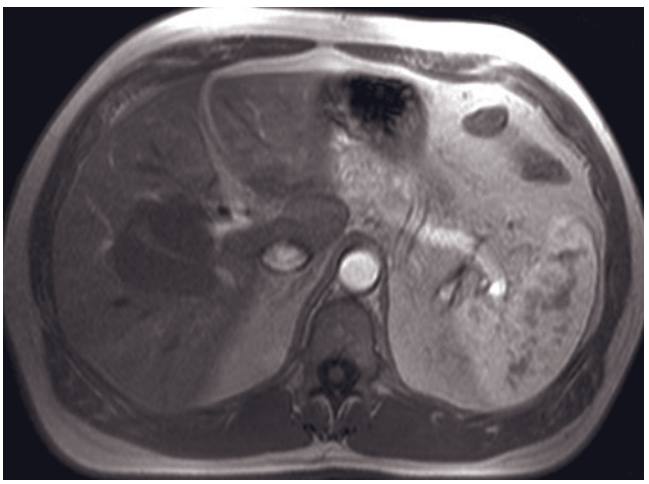

(*g*)

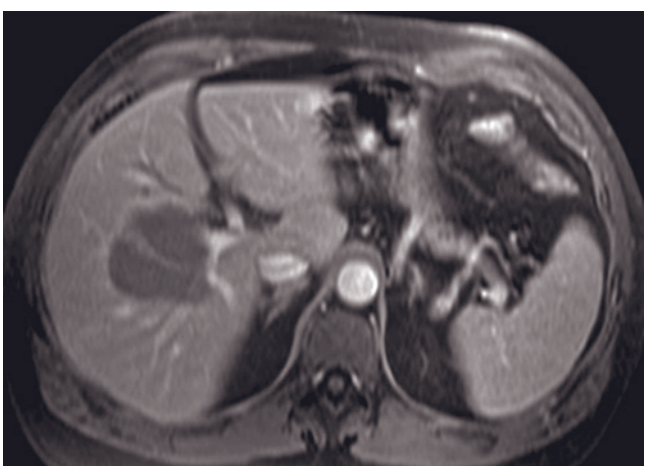

(*h*)

FIG. 2.27 (*Continued*) Coronal T2-weighted SS-ETSE (*d*), transverse fat-suppressed T2-weighted SS-ESTSE (*e*), SGE (*f*), and immediate (*g*) and 90-s fat-suppressed (*h*) postgadolinium SGE images. A cystic lesion with a thick internal septum is seen in segments 5 and 8 of the liver. This lesion shows high signal on the T2-weighted image (*d*, *e*), low signal on the T1-weighted image (*f*), and lack of enhancement except for the septum on postcontrast images (*g*, *h*). Histopathology was consistent with a biliary cystadenoma.

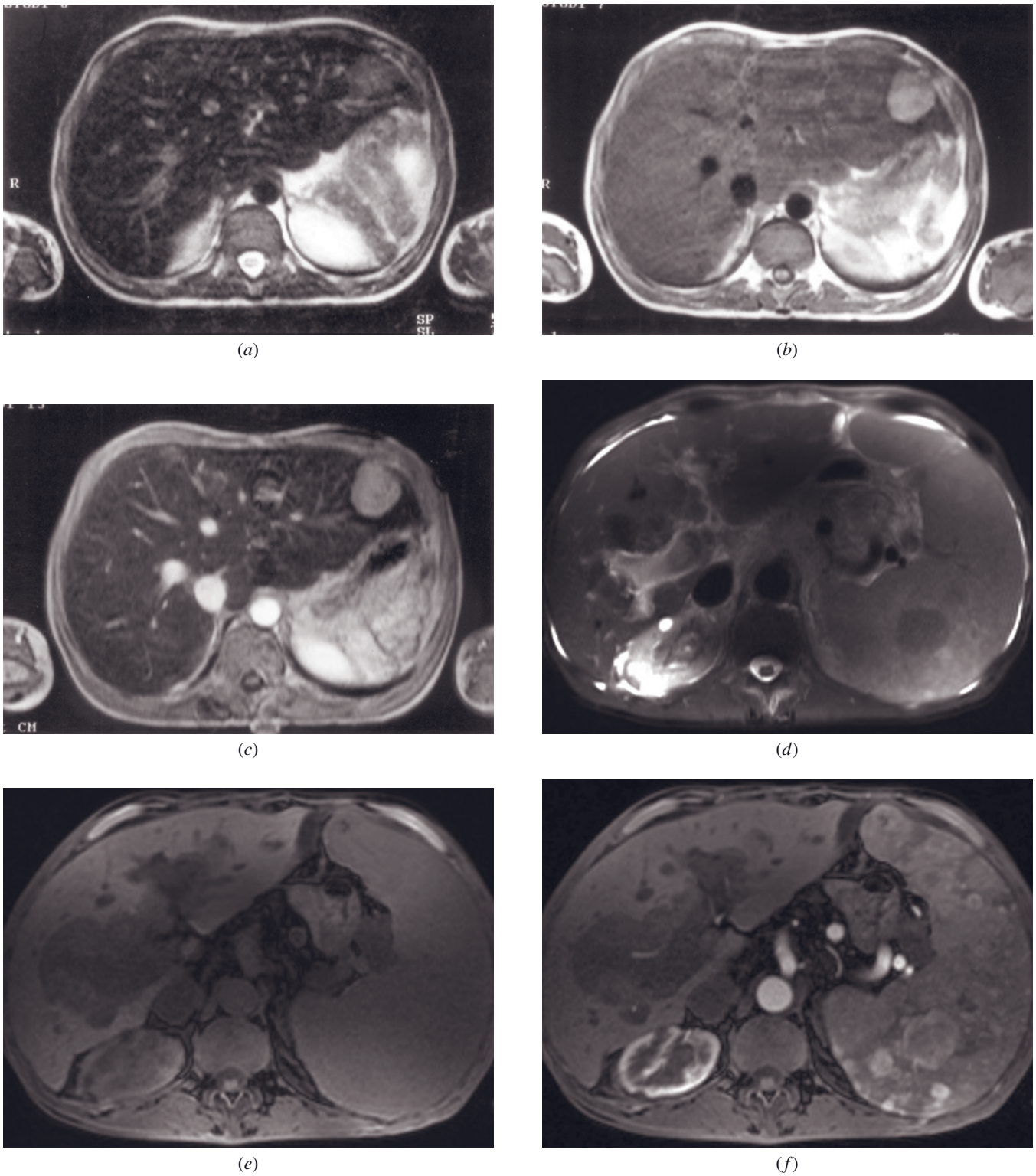

(*a*) (*b*) (*c*) (*d*) (*e*) (*f*)

FIG. 2.28 Extramedullary hematopoiesis. T2-weighted SS-ETSE (*a*), T1-weighted spin-echo (*b*), and 1-min postgadolinium SGE (*c*) images. A rounded lesion is present in the left lobe that demonstrates moderate increase in signal intensity on T2-weighted (*a*) and T1-weighted (*b*) images and mild diffuse homogeneous enhancement after administration of gadolinium (*c*). (Courtesy of Cem Balci, M.D).

T2-weighted SS-ETSE fat-suppressed (*d*), T1-weighted SGE (*e*), and immediate (*f*) and 90-s fat-suppressed (*g*) postgadolinium SGE 3T images in a second patient with the diagnosis of extramedullary hematopoiesis. The liver is irregular in contour with

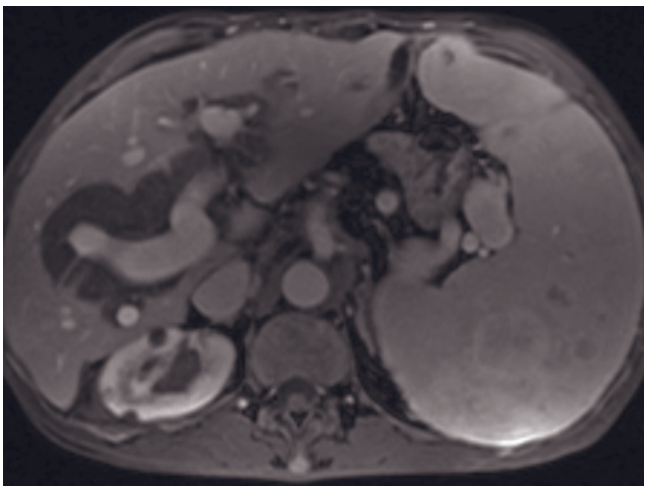

(*g*)

FIG. 2.28 (*Continued*) prominence of periportal area that is intermediate signal intensity on T2-weighted images (*d*) and low signal intensity on T1-weighted images (*e*) and shows minimal enhancement after contrast administration (*f*, *g*), reflecting infiltration by hypovascular tissue which is well-demarcated. The spleen is massively enlarged in size with multiple hypervascular lesions on immediate postcontrast images (*f*). This patient has coexistent cirrhosis and periportal extramedullary hematopoiesis.

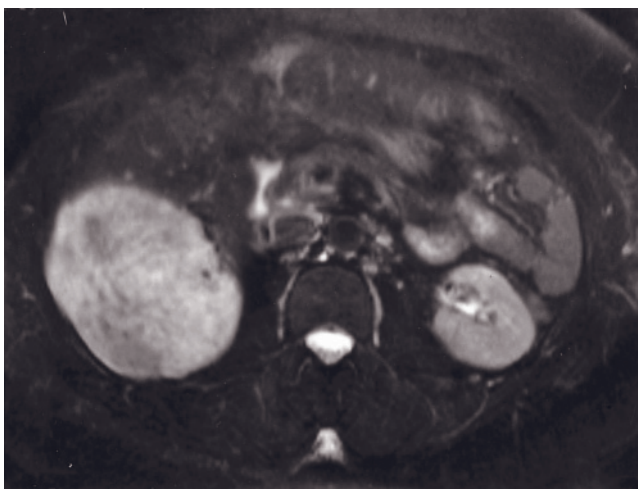

(*a*)

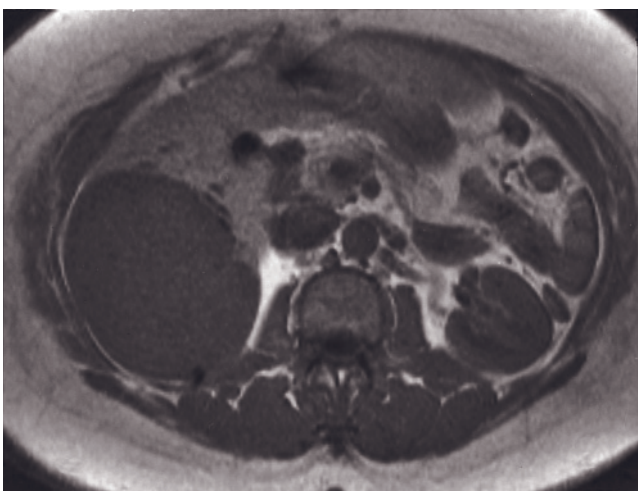

(*b*)

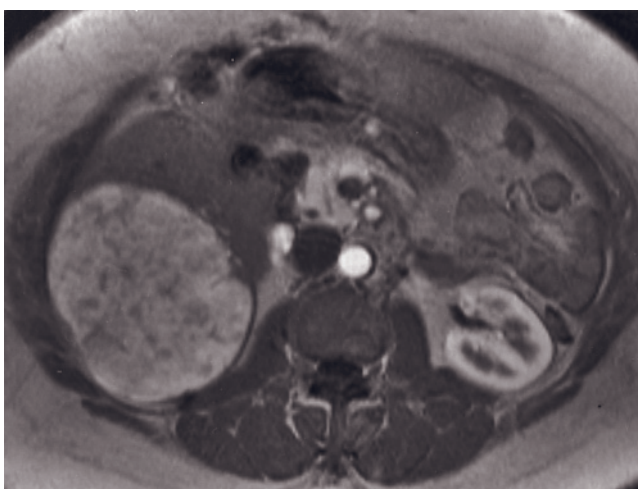

(*c*)

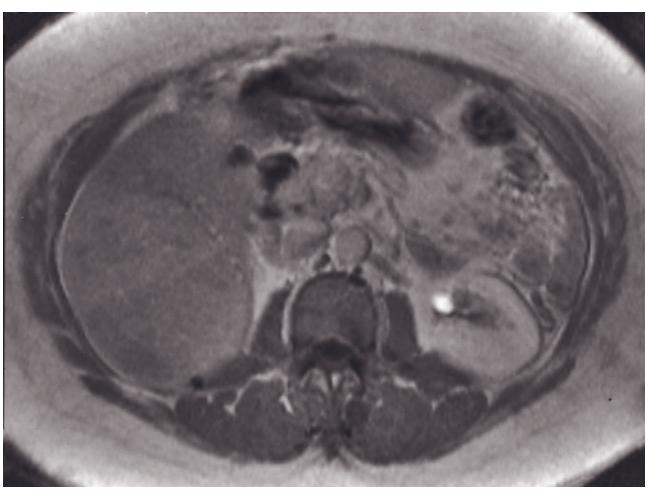

(*d*)

FIG. 2.29 Angiomyolipoma with minimal fat. T2-weighted fat-suppressed ETSE (*a*), SGE (*b*), and immediate (*c*) and 90-s (*d*) postgadolinium SGE images. The angiomyolipoma is moderately hyperintense with slight heterogeneity on the T2-weighted image (*a*) and moderately hypointense on the T1-weighted image (*b*) and enhances intensely in a diffuse heterogeneous fashion on the immediate postgadolinium image (*c*). On the 90-s image (*d*), the lesion has faded in signal intensity to slightly higher than background liver. This angiomyolipoma is unusual in that it contains minimal fat. The diffuse heterogeneous enhancement is typical of tumors of hepatic origin.

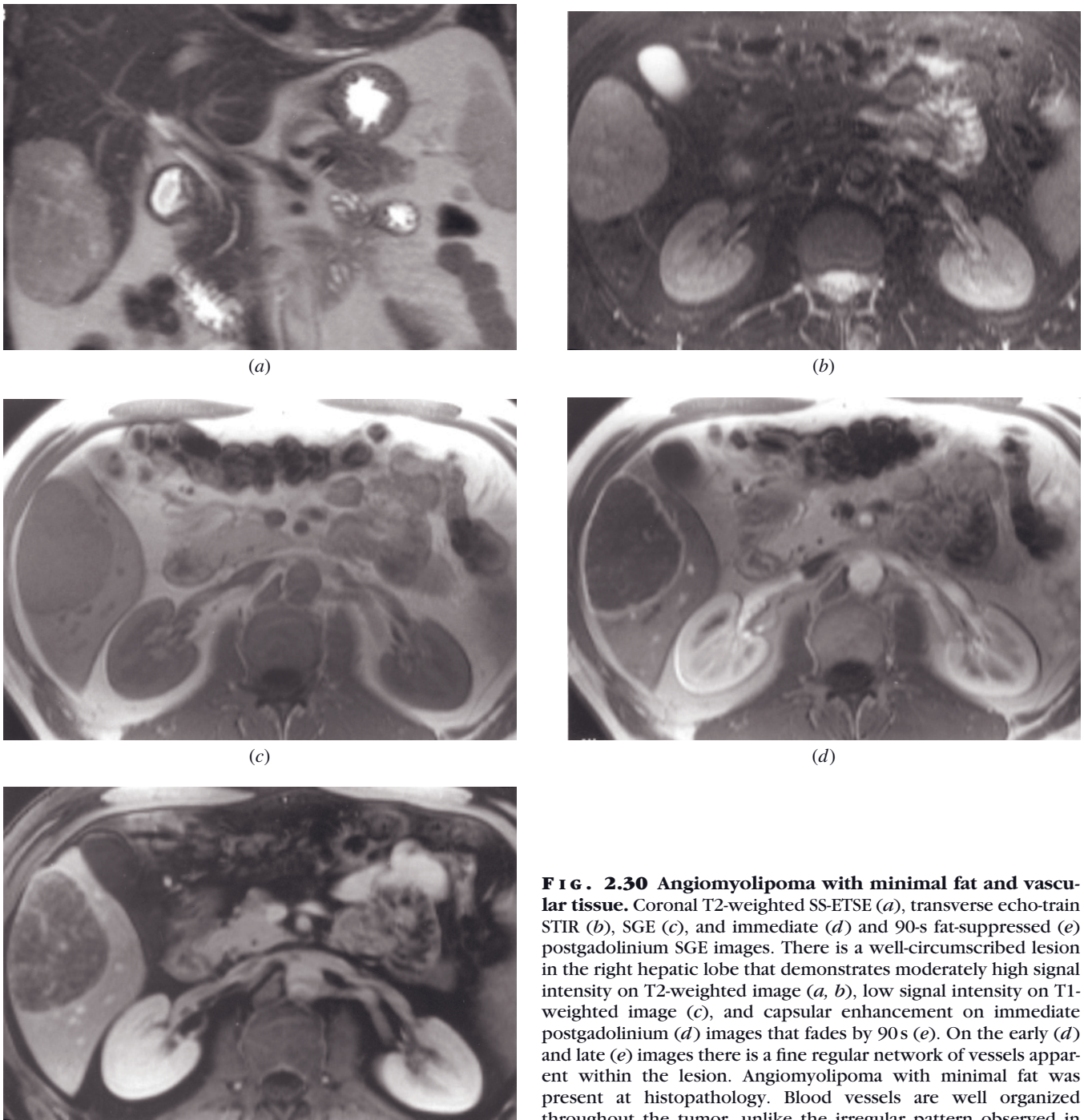

FIG. 2.30 Angiomyolipoma with minimal fat and vascular tissue. Coronal T2-weighted SS-ETSE (*a*), transverse echo-train STIR (*b*), SGE (*c*), and immediate (*d*) and 90-s fat-suppressed (*e*) postgadolinium SGE images. There is a well-circumscribed lesion in the right hepatic lobe that demonstrates moderately high signal intensity on T2-weighted image (*a, b*), low signal intensity on T1-weighted image (*c*), and capsular enhancement on immediate postgadolinium (*d*) images that fades by 90 s (*e*). On the early (*d*) and late (*e*) images there is a fine regular network of vessels apparent within the lesion. Angiomyolipoma with minimal fat was present at histopathology. Blood vessels are well organized throughout the tumor, unlike the irregular pattern observed in HCC. There is also a paucity of vascular tissue in this tumor.

away in signal intensity toward parenchyma isointensity over time, but they will fade in a homogeneous fashion with no evidence of peripheral or heterogeneous lesional washout [73].

The most distinctive imaging feature of hemangiomas is the demonstration of a discontinuous ring of nodules immediately after contrast administration [73]. Nodular enhancement is most frequently eccentric in location and may originate from the superior or inferior aspect of the hemangioma, simulating central enhancement on transverse images (fig. 2.33). True central enhancement may rarely occur. The appearance of central enhancement is rare for all histologic types of tumors and occurs by early filling of a large central lake by a narrow feeding vessel.

The MRI appearances of small (<1.5 cm), medium (1.5–5.0 cm), and large (>5.0 cm) hemangiomas have

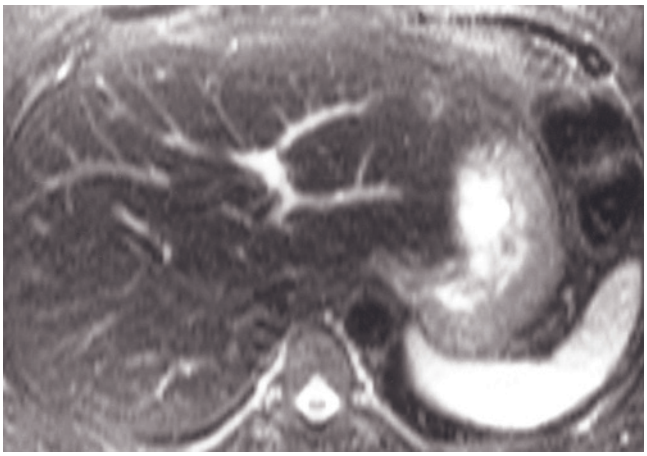

(*a*)

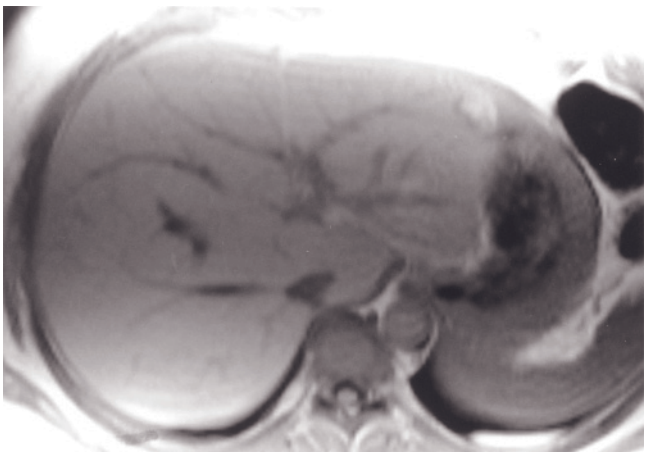

(*b*)

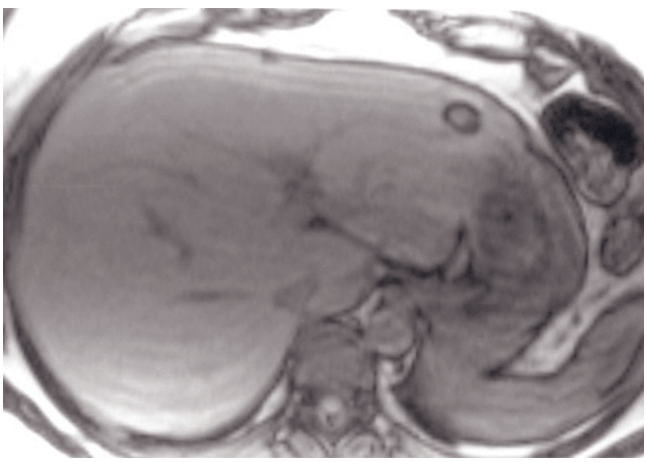

(*c*)

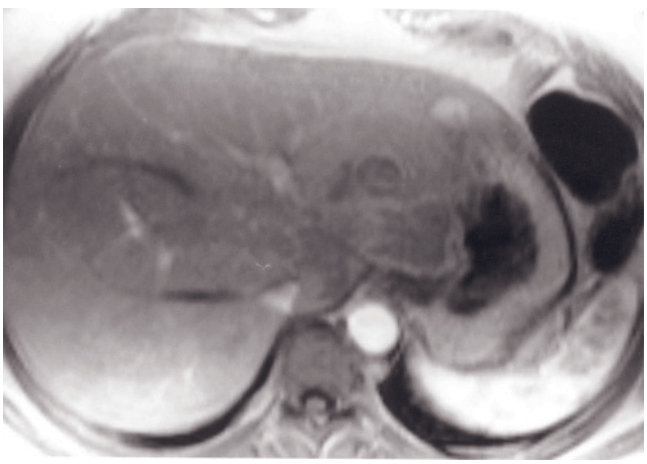

(*d*)

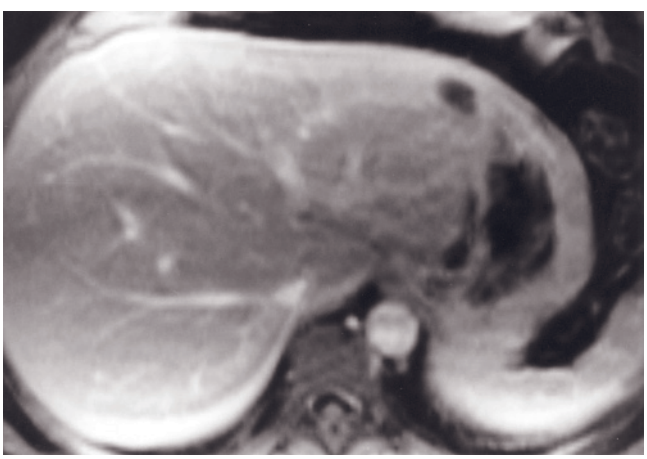

(*e*)

FIG. 2.31 Lipoma. T2-weighted fat-suppressed SS-ETSE (*a*), SGE (*b*), out-of-phase SGE (*c*), and immediate (*d*) and 90-s fat-suppressed (*e*) postgadolinium SGE images. A 2.5-cm lipoma (*b*) is present in the left lobe that demonstrates the same signal as fat on all imaging sequences. Note the development of a phase cancellation artifact on the out-of-phase image (*c*), which shows that the high-signal lesion is fatty. Care should be exercised not to attribute the high signal of fat as enhancement in fatty lesion on gadolinium-enhanced nonsuppressed images (*d*) or attribute the effect of fat suppression as washout on later fat-suppressed images (*e*).

been reported in a multi-institutional study [73]. Among the 154 hemangiomas in 66 patients, 52.6 % (81/154) lesions were small, 36.4% (56/154) medium, and 11% (17/154) large. Hemangiomas were multiple in 68% of patients. All lesions were high in signal intensity on T2-weighted images. Three types of enhancement patterns were observed: uniform high signal intensity immediately after contrast (Type 1); peripheral nodular enhancement with centripetal progression to uniform high signal intensity (Type 2); and peripheral nodular enhancement with centripetal progression and a persistent central scar (Type 3). Type 1 enhancement was observed only in

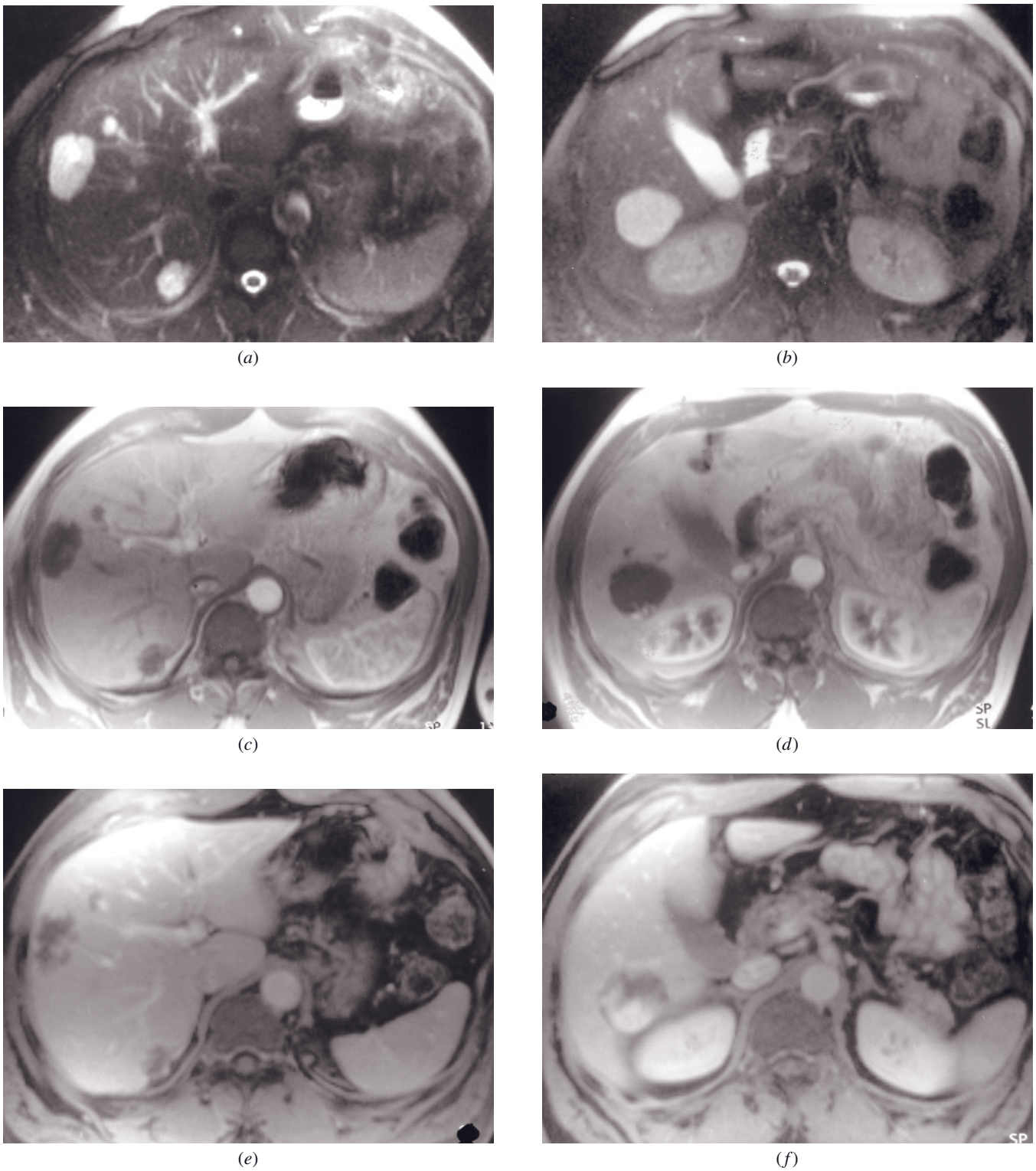

FIG. 2.32 Multiple hemangiomas. T2-weighted fat-suppressed SS-ETSE (*a*, *b*) and immediate (*c*, *d*) and 90-s fat-suppressed (*e*, *f*) postgadolinium images. Multiple hemangiomas are appreciated throughout the liver. All of these lesions show increased signal intensity on T2-weighted images (*a*, *b*), peripheral nodular enhancement after contrast administration (*c*, *d*), and enlargement and coalescence of nodules on delayed postcontrast images (*e*, *f*), consistent with multiple hemangiomas.

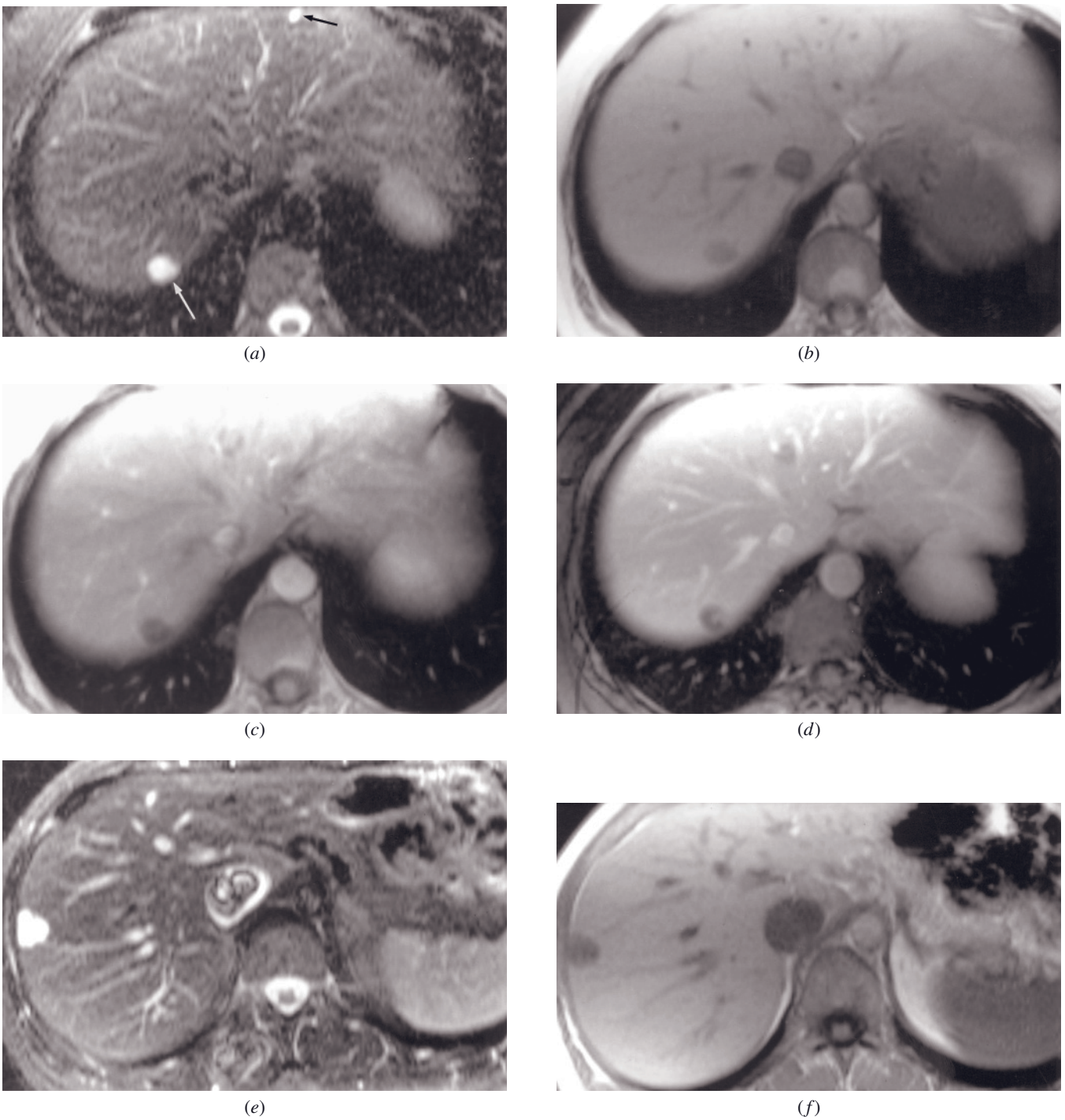

FIG. 2.33 Hemangioma with central filling. T2-weighted fat-suppressed SS-ETSE (*a*), SGE (*b*), and immediate (*c*) and 90-s fat-suppressed (*d*) postgadolinium SGE images. There are two lesions (arrows, *a*) located in the left and right hepatic lobe. The lesion in the right lobe shows increased signal intensity on T2-weighted image (*a*) and decreased signal intensity on T1-weighted image (*b*). On both early (*c*)- and late (*d*)-phase images the lesion demonstrates peripheral and central enhanced nodules. The small left lobe lesion lobe is hyperintense on the T2-weighted image (black arrow, *a*) and is barely perceptible on any of the other sequences. This is not uncommon with <1-cm hemangiomas with type 1 enhancement, in which enhancement may be minimally greater comparable in intensity to background liver on immediate postgadolinium images and lesions fade to isointensity by 1-2 min. Note the presence of a phase encoding mirror artifact from the IVC, which should not be mistaken for a lesion (*c*).

Echo train-STIR (*e*), SGE (*f*), and immediate (*g*) and 90-s fat-suppressed (*h*) postgadolinium SGE images in a second patient.

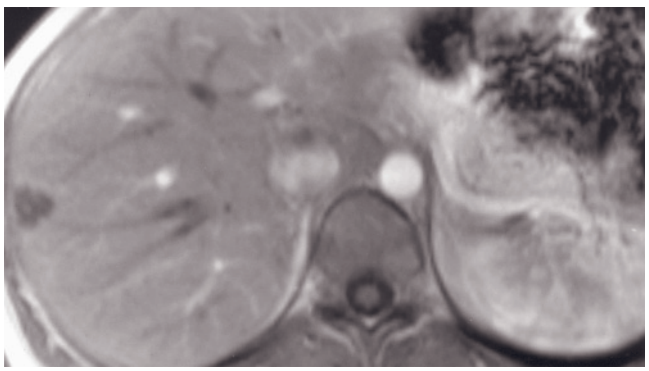

(*g*)

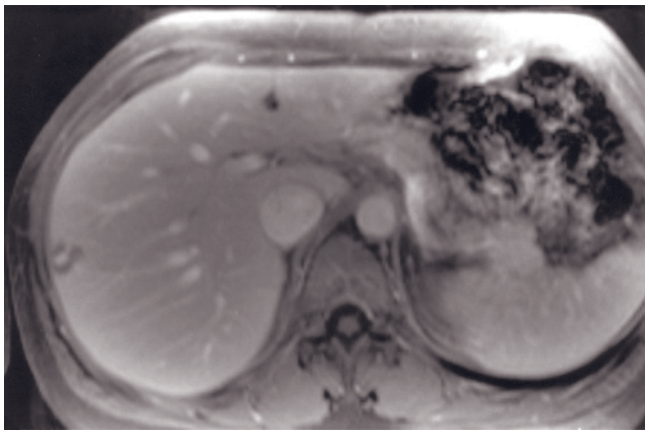

(*h*)

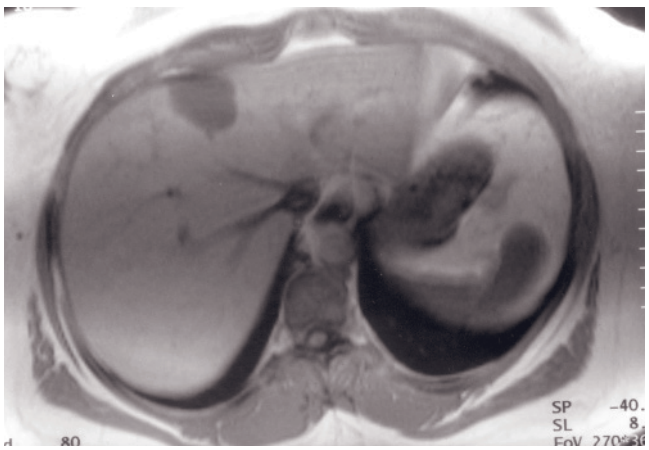

(*i*)

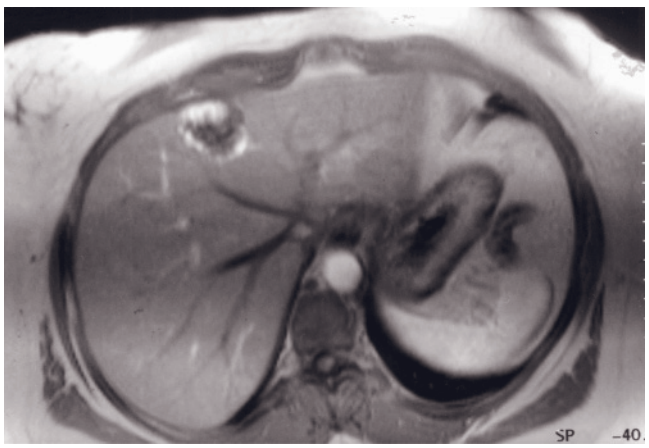

(*j*)

(*k*)

Fig. 2.33 (*Continued*) A lobulated lesion is seen along the lateral edge of the right hepatic lobe and demonstrates peripheral and central nodular filling enhancement, which progresses on late-phase image (*h*).

SGE (*i*) and immediate (*j*) and 90-s fat-suppressed (*k*) post-gadolinium SGE images in a third patient. There is a lobular hemangioma in the left lobe that demonstrates high signal intensity on T2-weighted image (not shown) and low signal on T1-weighted image (*i*), enhances in a peripheral nodular pattern on early-phase image (*j*), and fills in completely on late-phase image (*k*).

small tumors. Type 2 and Type 3 enhancements were observed in all size categories. Type 3 enhancement was observed in 16 of 17 large tumors.

Small hemangiomas most commonly demonstrate Type 2 enhancement. The peripheral nodules of enhancement are typically very small (fig. 2.34). Type 1 enhancement is the next most common pattern (fig. 2.35), whereas Type 3 enhancement is uncommonly noted (fig. 2.36). Small hemangiomas are difficult to distinguish from other types of liver lesions, specifically hypervascular liver metastases, and MRI follow-up is generally required.

The great majority of medium-sized hemangiomas exhibit Type 2 enhancement (fig. 2.37 and 2.38) and

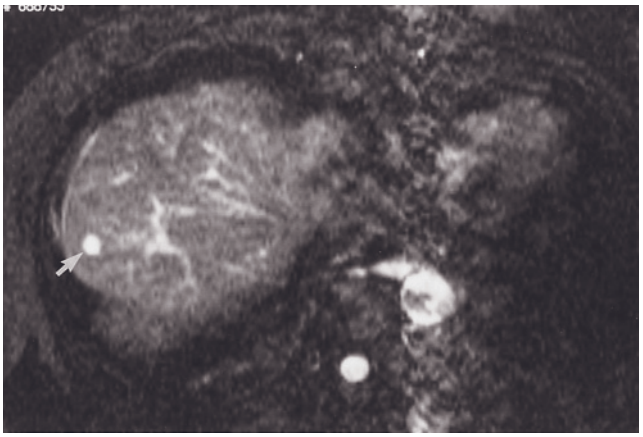

(*a*)

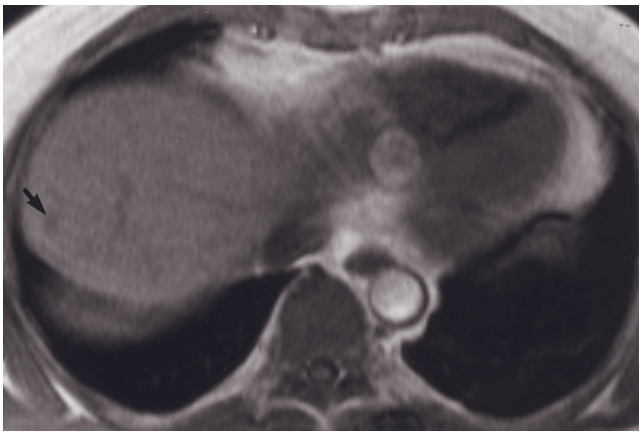

(*b*)

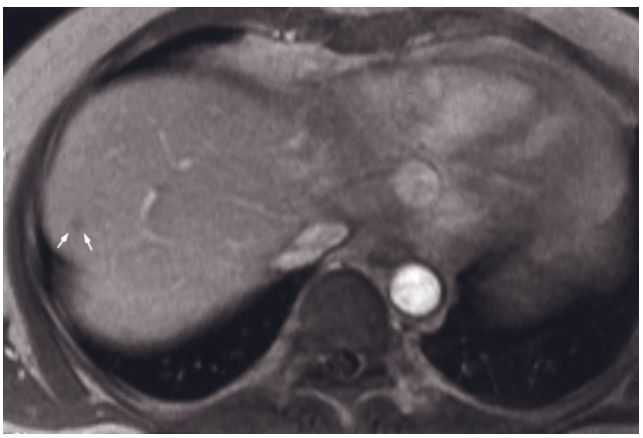

(*c*)

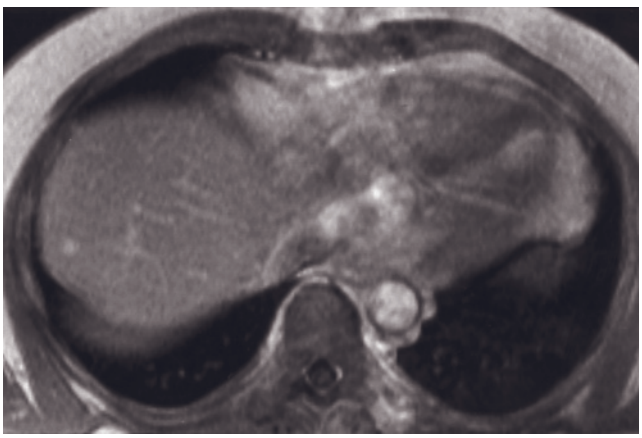

(*d*)

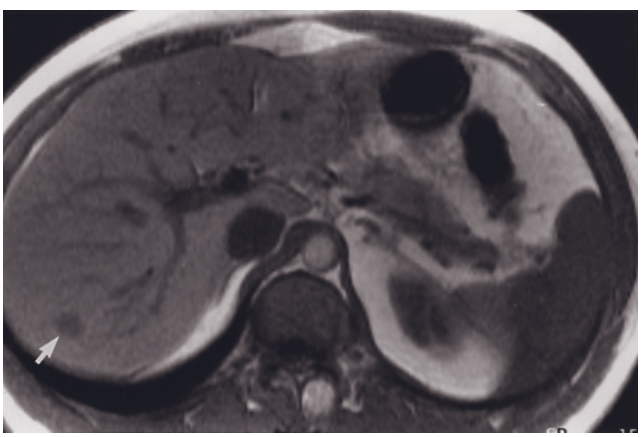

(*e*)

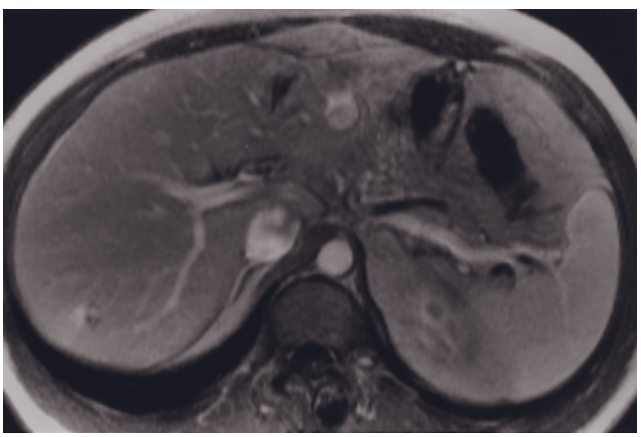

(*f*)

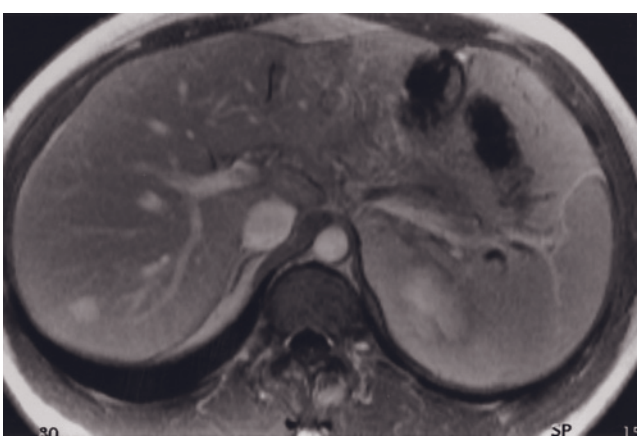

(*g*)

Fig. 2.34 Small hemangiomas, Type 2 enhancement. T2-weighted fat-suppressed ETSE (*a*), SGE (*b*), and immediate (*c*) and 5-min (*d*) postgadolinium SGE images. A 1-cm hemangioma is present in the right lobe that is high in signal intensity on T2-weighted image (arrow, *a*) and low in signal intensity on T1-weighted image (arrow, *b*), demonstrates peripheral nodular enhancement on early image (arrows, *c*), and is uniformly homogeneous and moderately high in signal intensity on delayed image (*d*). T1-weighted SGE (*e*), immediate (*f*) and 90-s (*g*) SGE images in a second patient show similar findings for a small hemangioma (arrow *e*).

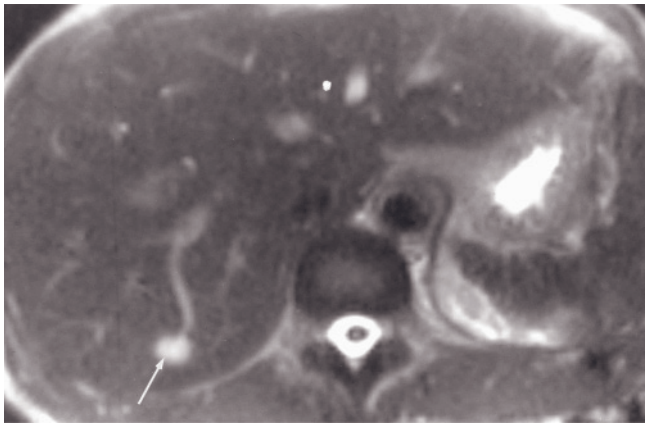

(*a*)

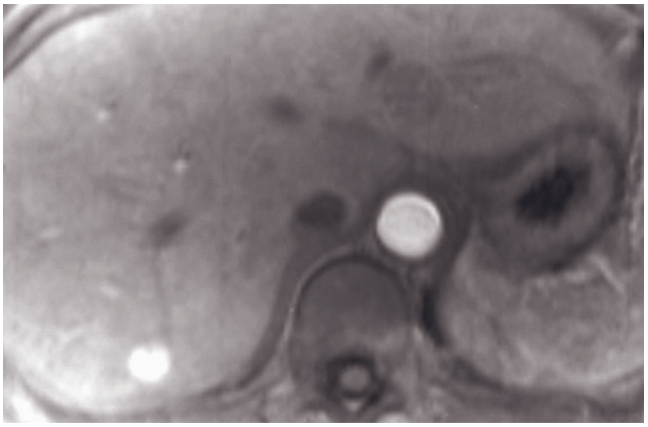

(*b*)

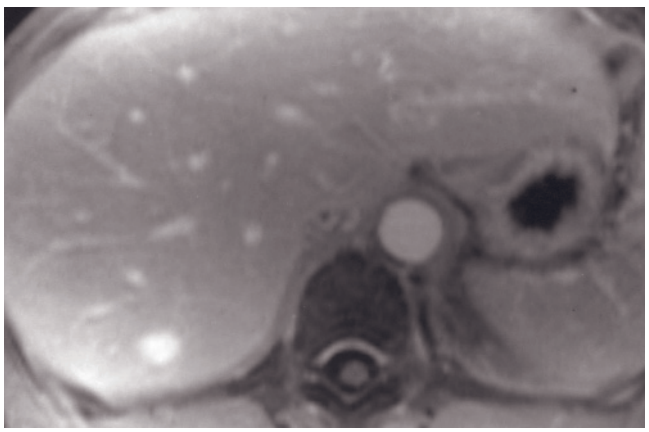

(*c*)

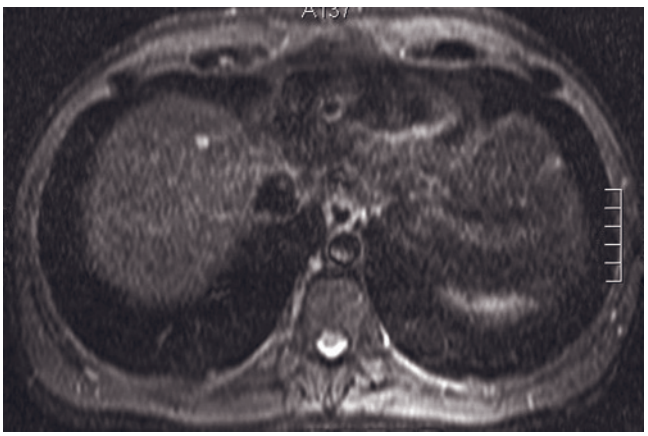

(*d*)

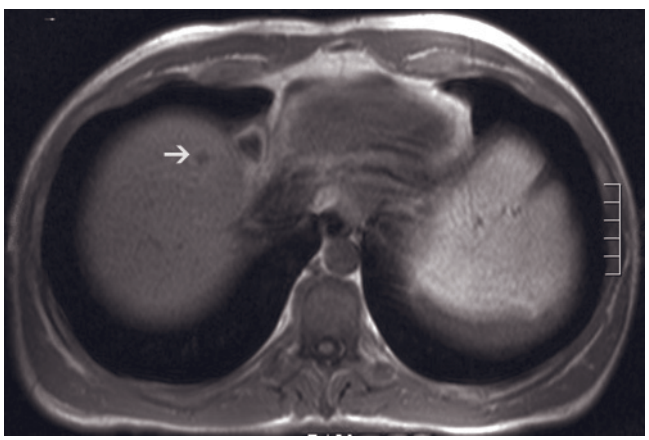

(*e*)

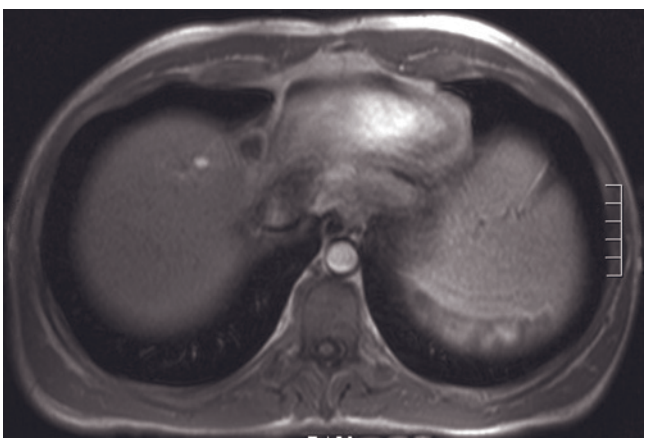

(*f*)

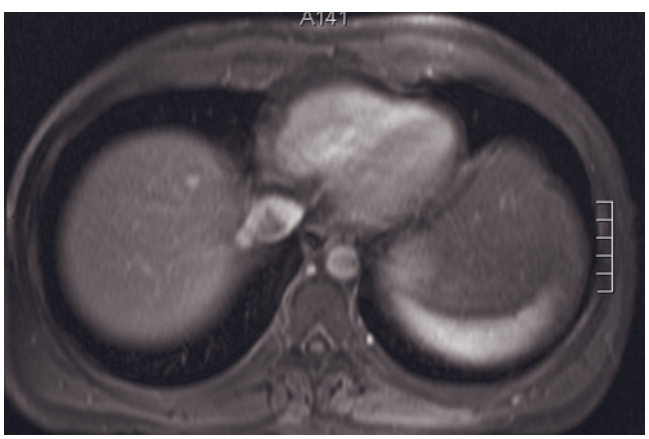

(*g*)

Fig. 2.35 Small hemangioma, Type 1 enhancement. Transverse T2-weighted SS-ETSE (*a*) and immediate (*b*) and 90-s fat-suppressed (*c*) postgadolinium SGE images. A lesion (arrow, *a*) is present in the right hepatic lobe that shows high signal on T2-weighted image (*a*), low signal on T1-weighted image (not shown), and intense uniform enhancement immediately after administration of gadolinium (*b*) that persists at 90-s image (*c*). These findings represent a Type 1 hemangioma.

T2-weighted fat-suppressed SS-ETSE (*d*), SGE (*e*), and immediate (*f*) and 90-s fat-suppressed (*g*) postgadolinium SGE image in a second patient. A tiny lesion is seen in segment 4 of the liver that shows high signal intensity on the T2-weighted image, low signal intensity on the T1-weighted image (arrow, *e*), and homogeneous enhancement on early phase (*f*) that remains on the late phase image (*g*), consistent with Type 1 hemangioma.

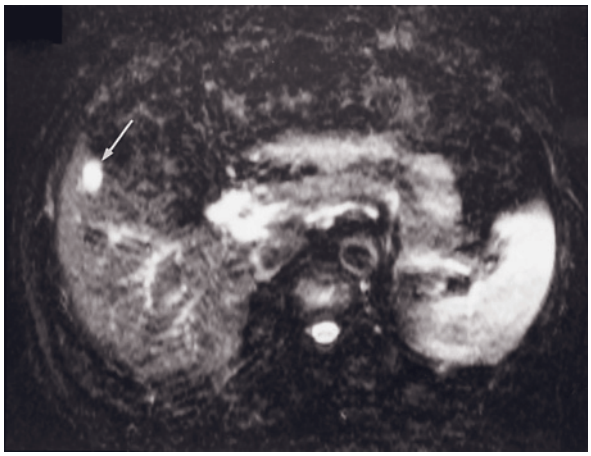

(*a*)

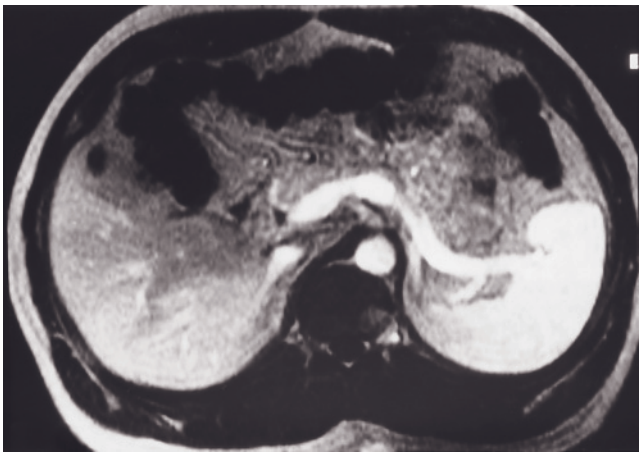

(*b*)

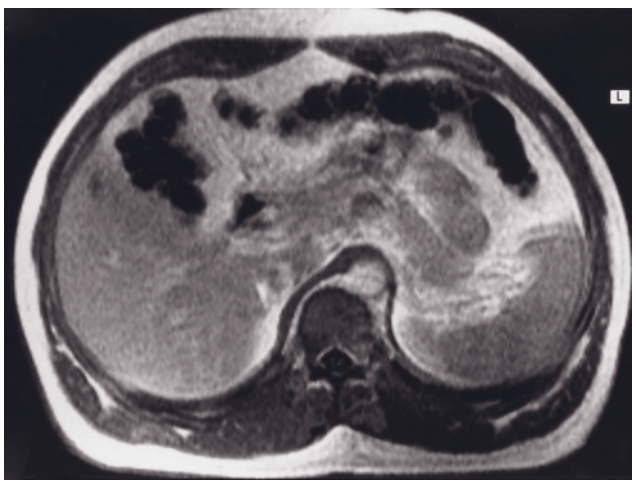

(*c*)

FIG. 2.36 Small hemangioma, Type 3 enhancement. T2-weighted fat-suppressed SS-ETSE (*a*) and immediate (*b*) and 10-min (*c*) postgadolinium SGE images. A 1.5-cm lesion is present in the right lobe that is high in signal intensity on the T2-weighted image (arrow, *a*) and nearly signal void with subtle small peripheral nodules on the early image (*b*) and shows peripheral enhancement with persistence of central low signal intensity on the late image (*c*), consistent with a central scar.

represent the classic hemangiomas. Type 3 enhancement is the next most common enhancement pattern (figs. 2.39–2.41), whereas Type 1 enhancement is exceedingly rare. Lesions > 1.5 cm with Type 1 enhancement represent either well-differentiated tumors of hepatocellular origin or hypervascular liver metastases.

Giant hemangiomas most frequently have a central scar, and virtually all giant hemangiomas have Type 3 enhancement (fig. 2.42) [73–75]. Absence of a central scar should raise the concern that the mass may represent another lesion. Giant hemangiomas often have a multiloculated appearance with mildly complex signal intensity on T2-weighted images and the common presence of low-signal strands, which reflects the internal network of fibrous stroma that is observed histologically (fig. 2.43) [75]. In rare instances, large hemangiomas may compress adjacent portal veins, resulting in transient segmental increased enhancement on immediate postgadolinium images secondary to autoregulatory increased hepatic arterial supply (fig. 2.44). On rare occasions, large hemangiomas may also undergo hemorrhage.

Hemangiomas vary in the rate and completeness of tumor enhancement. A variation in the Type 2 or 3 enhancement pattern consists of enhancement that spreads at a fairly rapid rate with complete enhancement at 1–2 min [73]. Rapidity of enhancement has been determined on 90-s images as slow (approximately 25% of tumor enhancement at the maximum transverse diameter), medium (approximately 50% enhancement), and fast (approximately 75% enhancement) [73, 76]. Tumors at all sizes may enhance very slowly to very quickly, and enhance minimally to complete enhancement, with the exception that >5-cm tumors almost invariably demonstrate lack of central enhancement [73].

Slow enhancement of hemangiomas permits distinction from most tumors. The only other neoplasm that may show comparable slow enhancement is chemotherapy-treated metastases (as described below). Fast-enhancing hemangiomas show enhancement

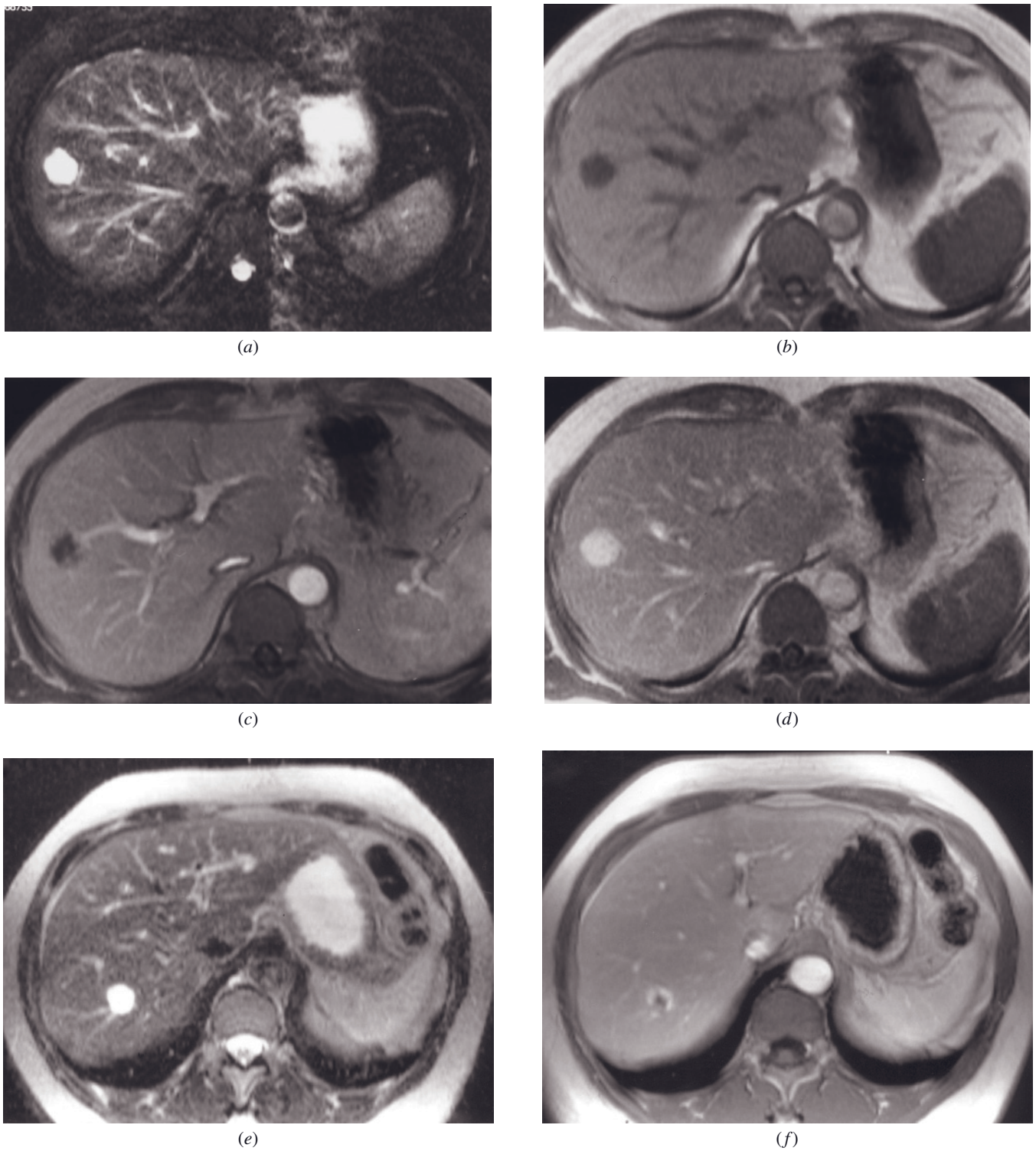

FIG. 2.37 Medium-sized hemangioma, Type 2 enhancement. T2-weighted fat-suppressed ETSE (*a*), SGE (*b*), and immediate (*c*) and 5-min (*d*) postgadolinium SGE images demonstrate a well-defined, round lesion that is high signal on T2-weighted image (*a*) and moderately low signal on T1-weighted image (*b*) and enhances in a peripheral nodular fashion on early image (*c*) with complete filling of the entire lesion on the late image (*d*), consistent with hemangioma.

T2-weighted fat-suppressed ETSE (*e*) and immediate (*f*) and 90-s fat-suppressed (*g*) postgadolinium SGE images in a second patient. A 2.1-cm hemangioma is present in the right hepatic lobe, and it shows high signal intensity on T2-weighted image (*e*) and

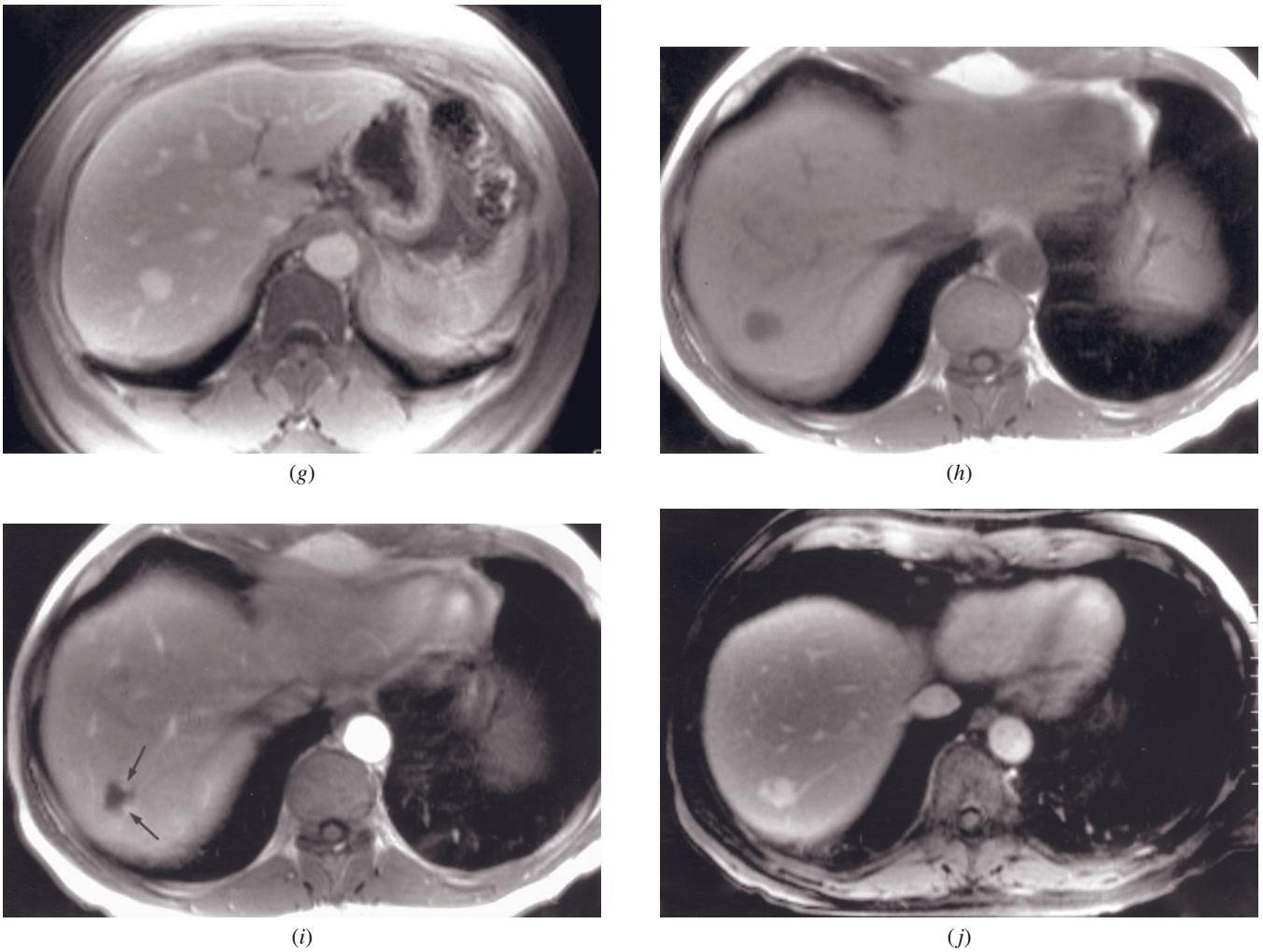

FIG. 2.37 (*Continued*) low signal intensity on T1-weighted image (not shown) and enhances in a peripheral nodular fashion on early image (*f*), which fills in on late image (*g*).

SGE (*h*) and immediate (*i*) and 90-s fat-suppressed (*j*) postgadolinium SGE images in a third patient showing the same findings as the second patient.

patterns that can resemble other tumors, with metastases being the most difficult to distinguish. Transient increased perilesional enhancement may occur, and is seen most often in small capsule-based hemangiomas (fig. 2.45). This phenomenon may reflect recruitment of capsular vessels. These findings are rare in hemangiomas and are more commonly observed in metastases, especially colon cancer metastases. A study [77] correlated the temporal parenchyma enhancement surrounding hepatic cavernous hemangiomas with the rapidity of intratumoral contrast material enhancement and tumor volume. Thirty-two of the 167 (19%) hemangiomas had temporal peritumoral enhancement, and this was more common in hemangiomas with rapid enhancement (41%). However, there was no statistically significant relationship between peritumoral enhancement and tumor volume. The mean diameter of hemangiomas with peritumoral enhancement was not significantly different from that of hemangiomas without peritumoral enhancement.

Hemangiomas not uncommonly coexist with focal nodular hyperplasia (FNH) lesions, particularly in the setting of the multiple FNH syndrome [78]. Hemangiomas are a common finding in patients with breast cancer. An early report [79] showed that among all benign liver lesions observed in patients with breast cancer who underwent screening examinations, hemangiomas were the most frequent type. This is important information since small metastases from breast cancer are hypervascular and may mimic the appearance of type 1 hemangiomas on early-phase postgadolinium images. However, late-phase demonstrates distinction between these entities: small hypervascular metastases tend to

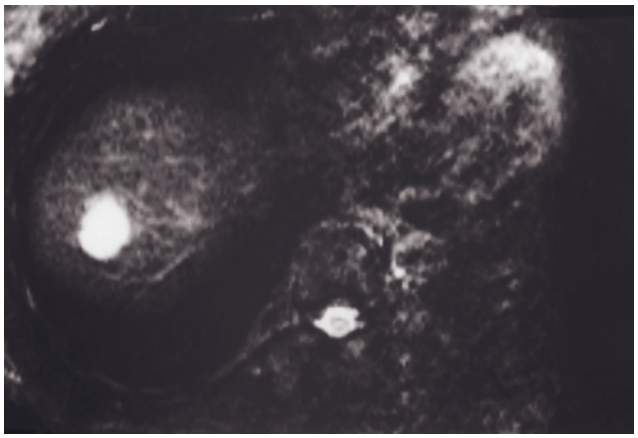

(*a*)

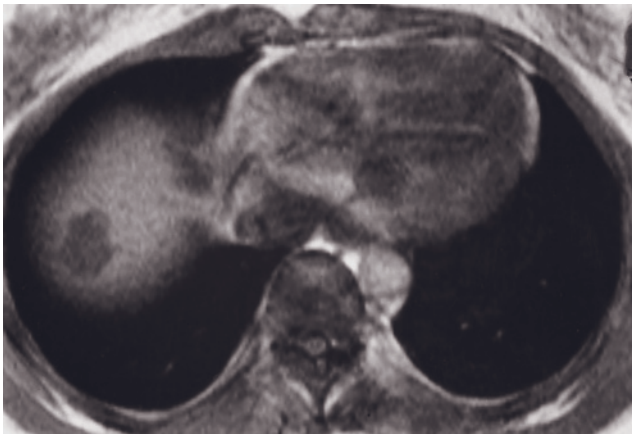

(*b*)

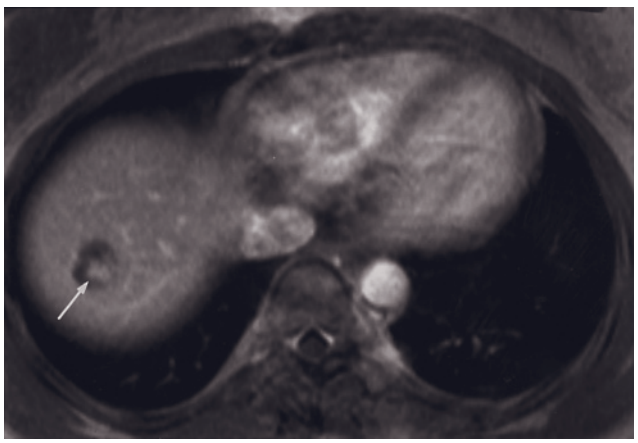

(*c*)

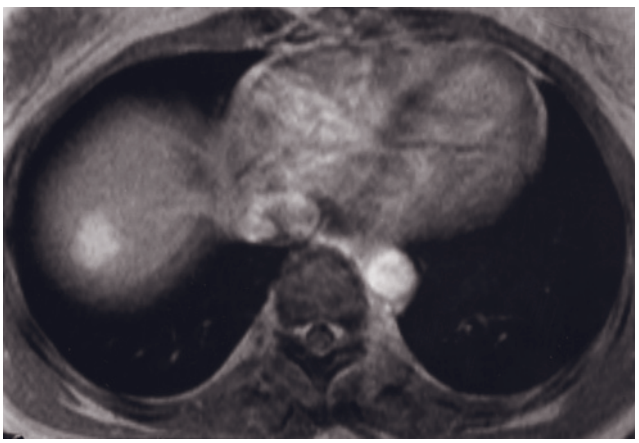

(*d*)

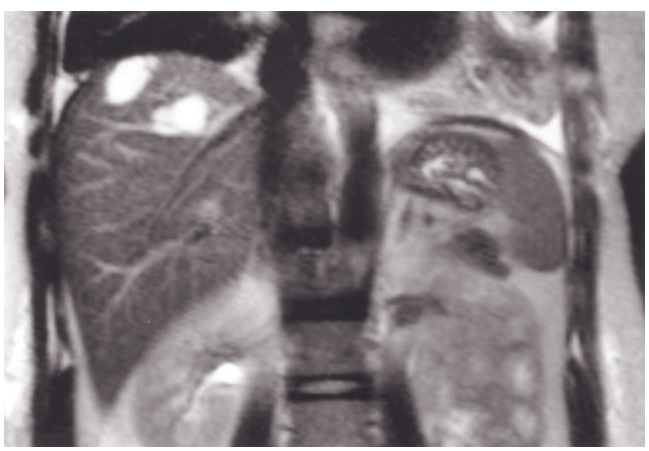

(*e*)

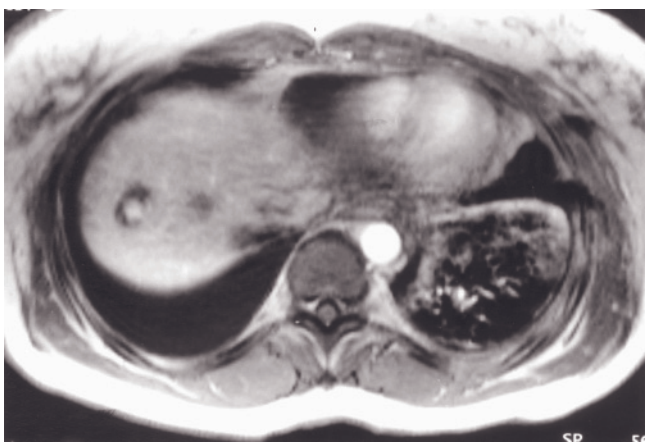

(*f*)

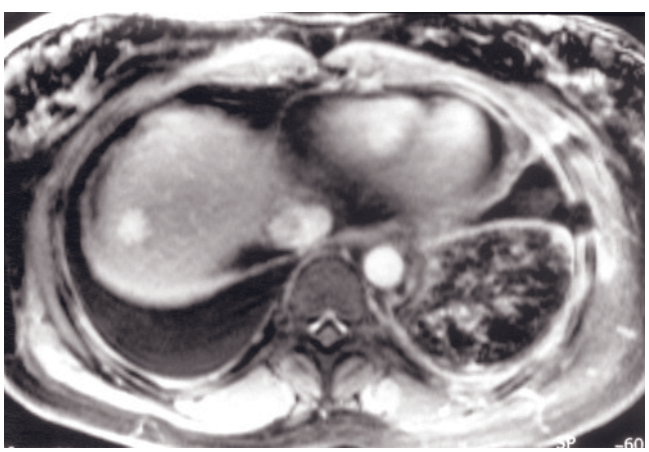

(*g*)

Fig. 2.38 Medium-sized hemangiomas, Type 2 enhancement with central nodular enhancement. T2-weighted fat-suppressed ETSE (*a*), SGE (*b*), and immediate (*c*) and 10-min (*d*) postgadolinium SGE images. A 2.5-cm hemangioma is present in segments 8 and 7 of the liver, and it demonstrates high signal on T2-weighted image (*a*), moderately low signal on T1-weighted image (*b*), and nodular progressive enhancement after contrast administration (*c*) with complete fill in with contrast on the late image (*d*). The early image (arrow, *c*) demonstrates one predominant enhancing nodule that is almost central in location.

Coronal T2-weighted SS-ETSE (*e*) and transverse immediate (*f*) and 90-s fat-suppressed (*g*) postgadolinium SGE images in a second patient demonstrate two hemangiomas with the same features described in the first patient. Note that on early image (*f*) one of the hemangiomas has a central enhancing nodule.

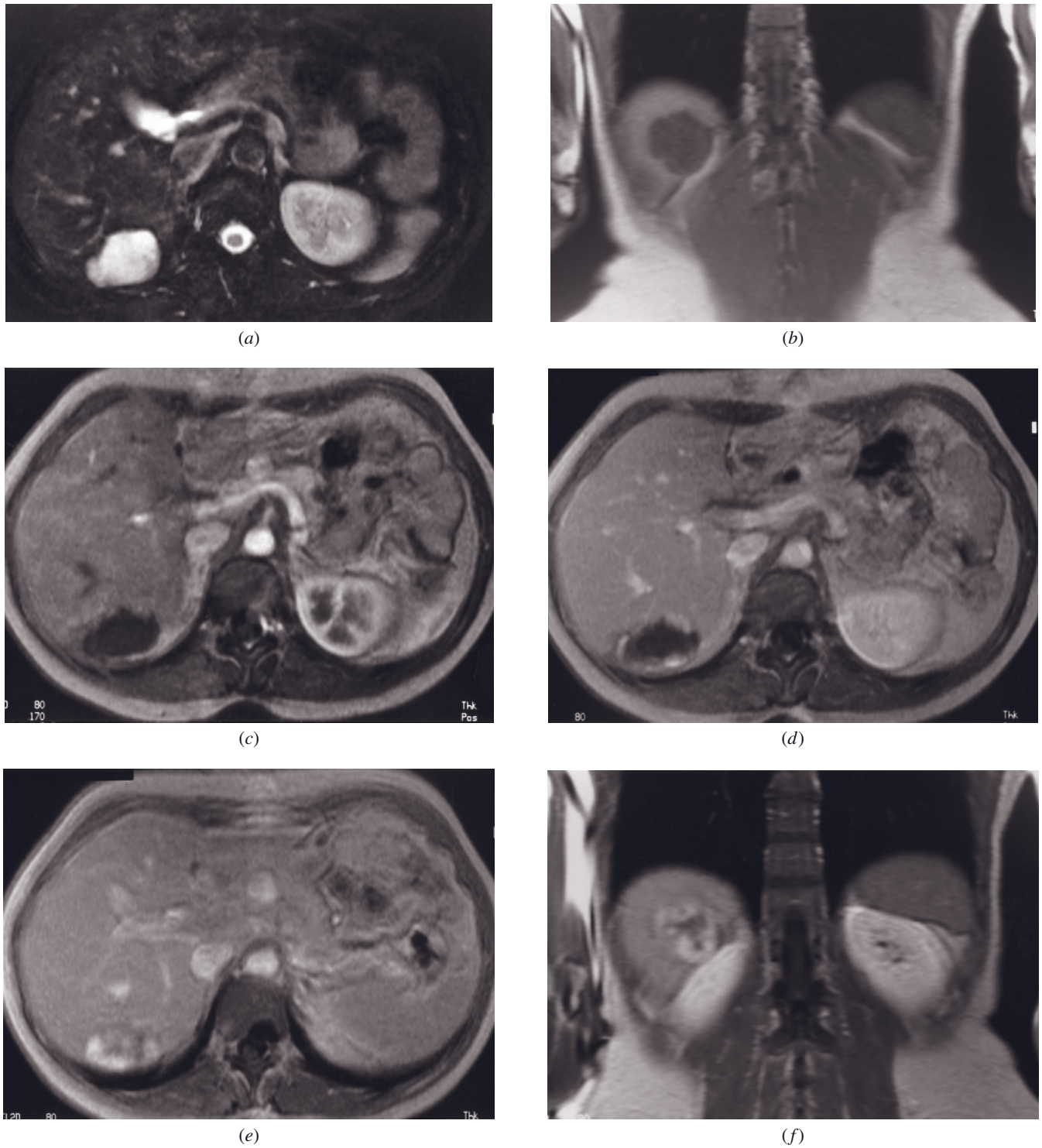

FIG. 2.39 Medium-sized hemangioma, Type 3 enhancement. T2-weighted fat-suppressed ETSE (*a*), coronal SGE (*b*), immediate (*c*) and 45-s (*d*) postgadolinium SGE images, and transverse (*e*) and coronal (*f*) 10-min postgadolinium SGE images. The hemangioma is high in signal intensity on the T2-weighted image (*a*) and moderately low in signal intensity on the T1-weighted image (*b*) and demonstrates peripheral nodular enhancement (*c*) that progresses centripetally (*d*). Note the persistence of a central scar on delayed images (*e*, *f*).

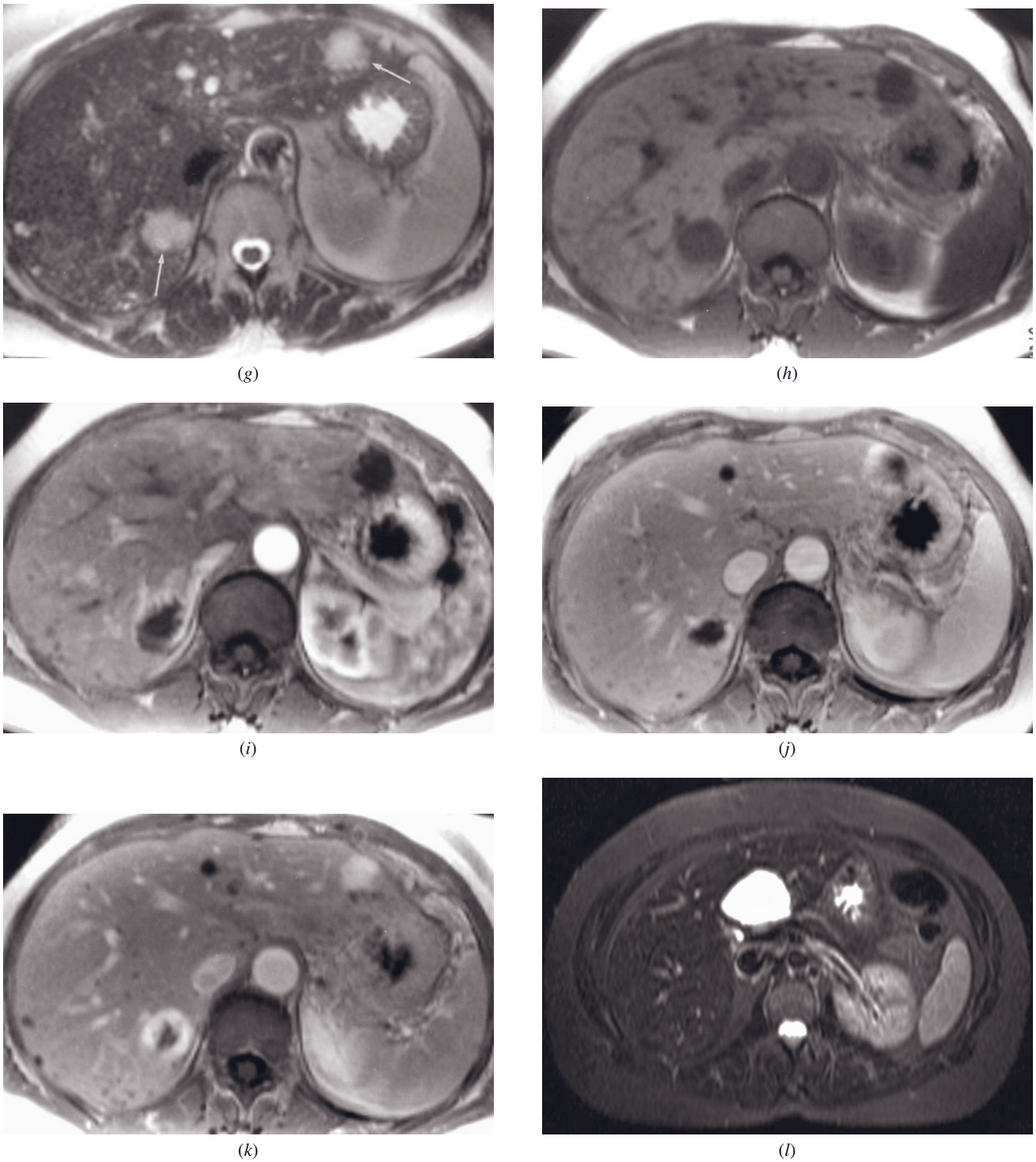

FIG. 2.39 (*Continued*) Transverse T2-weighted SS-ETSE (*g*), SGE (*h*), and immediate (*i*), 45-s (*j*), and 5-min (*k*) postgadolinium SGE images in a second patient. There are two lobular lesions that appear high in signal intensity on T2-weighted image (arrows, *g*) and low in signal intensity on T1-weighted (*h*) images. The first lesion is situated in the left lobe, demonstrates peripheral nodular enhancement after administration of gadolinium, and gradually fills in completely on delayed images (*k*), consistent with a Type 2 hemangioma. The other lesion is situated in the right hepatic lobe and shows peripheral nodular enhancement that progresses centripetally but with persistence of a central scar on the delayed image consistent with a Type 3 hemangioma. Note also multiple tiny lesions throughout the hepatic parenchyma consistent with biliary hamartomas.

T2-weighted fat-suppressed SS-ETSE (*l*), SGE (*m*), and immediate (*n*), 45-s (*o*), and 90-s fat-suppressed (*p*) postgadolinium SGE images in a third patient with a Type 3 hemangioma in the left lobe.

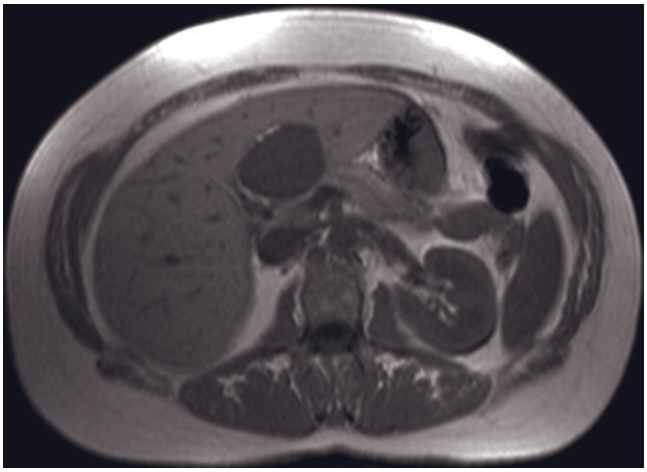

(*m*)

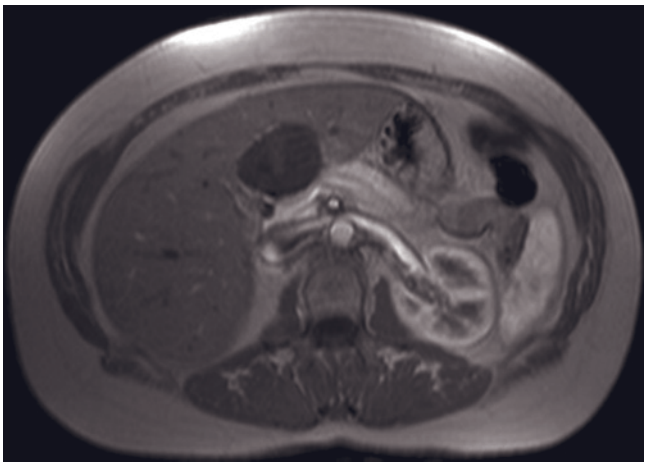

(*n*)

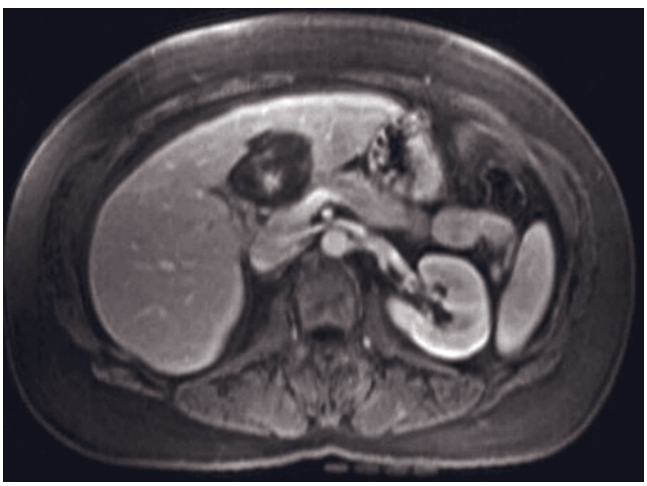

(*o*)

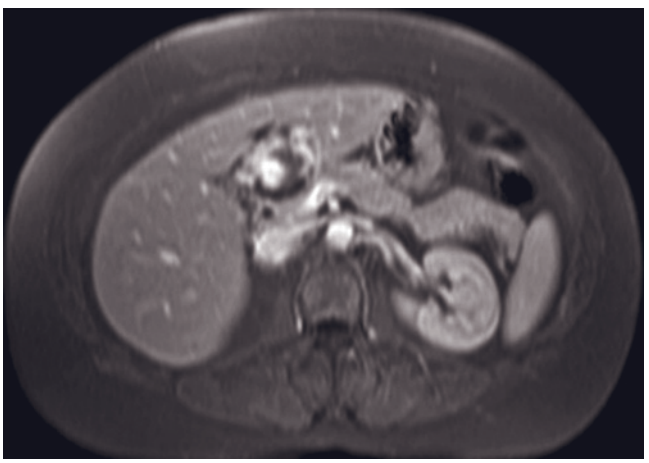

(*p*)

FIG. 2.39 (*Continued*)

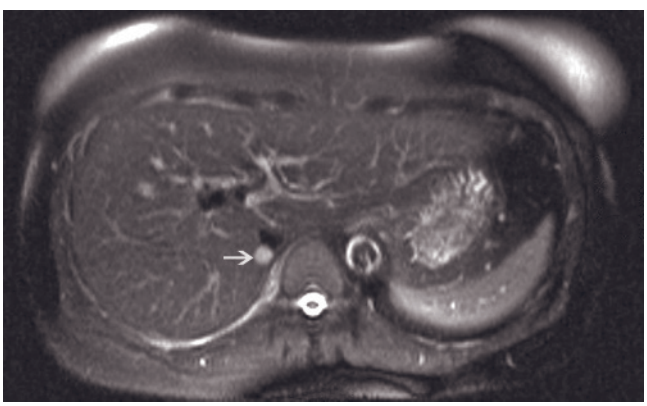

(*a*)

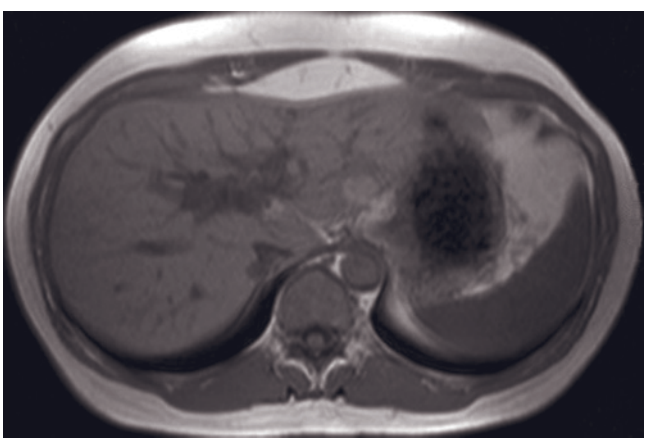

(*b*)

FIG. 2.40 Small-sized slow-enhancing hemangioma. T2-weighted fat-suppressed SS-ETSE (*a*), SGE (*b*), and immediate (*c*) and 90-s fat-suppressed (*d*) postgadolinium SGE images. There is a small hepatic lesion adjacent to the inferior vena cava that shows

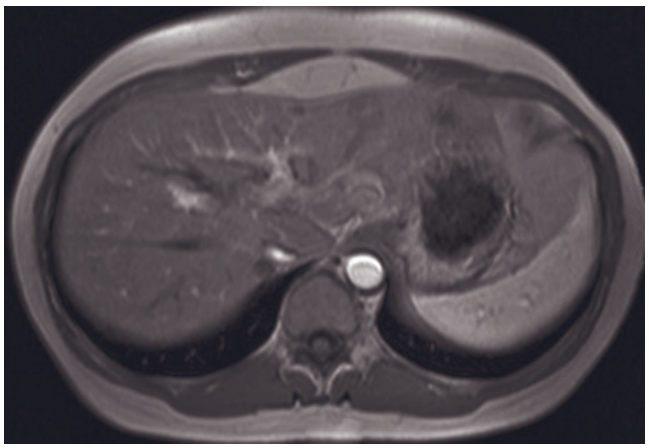

(*c*)

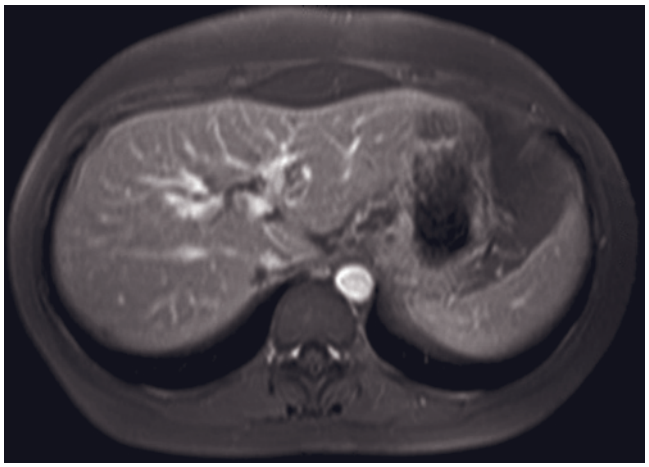

(*d*)

FIG. 2.40 (*Continued*) high signal intensity on the T2-weighted image (arrow, *a*), low signal intensity on T1-weighted image (*b*), a lack of enhancement on early image (*c*) and peripheral globular enhancement on late image (*d*) compatible with a slow-enhancing hemangioma. Slow enhancement is a feature that suggests the diagnosis of a hemangioma.

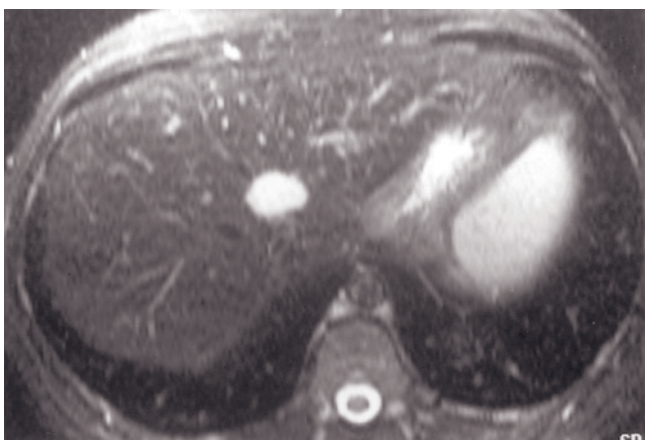

(*a*)

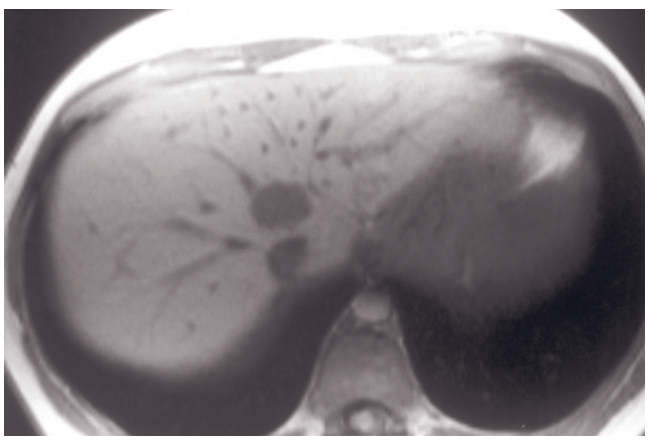

(*b*)

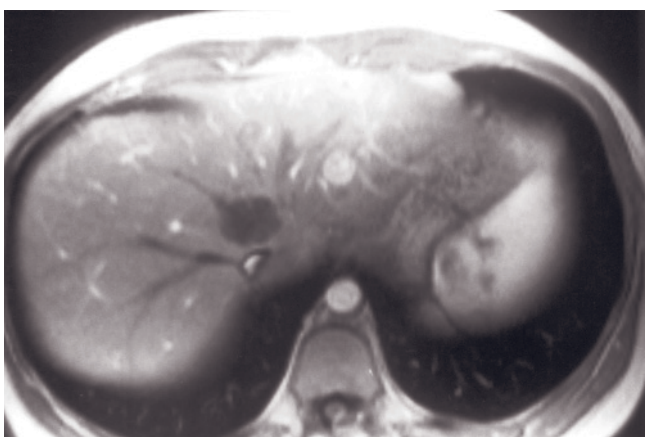

(*c*)

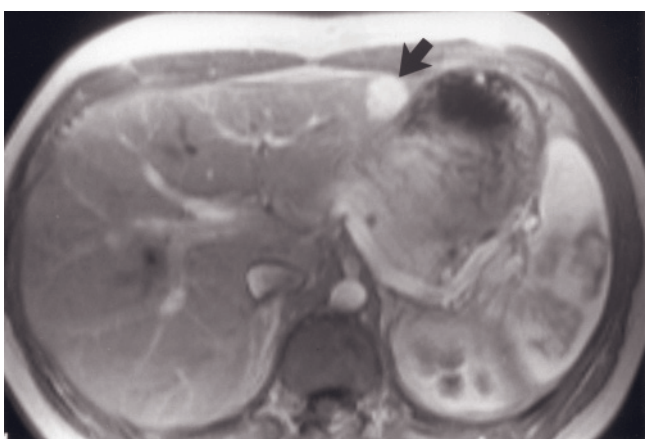

(*d*)

FIG. 2.41 Medium-sized slow-enhancing hemangioma, Type 3 enhancement. Echo train-STIR (*a*), SGE (*b*), and immediate (*c*, *d*) and 90-s fat-suppressed (*e*) postgadolinium SGE images. A lobular lesion is present that demonstrates moderately high signal intensity on the T2-weighted image (*a*) and moderately low signal intensity on the T1-weighted image (*b*), small peripheral nodules

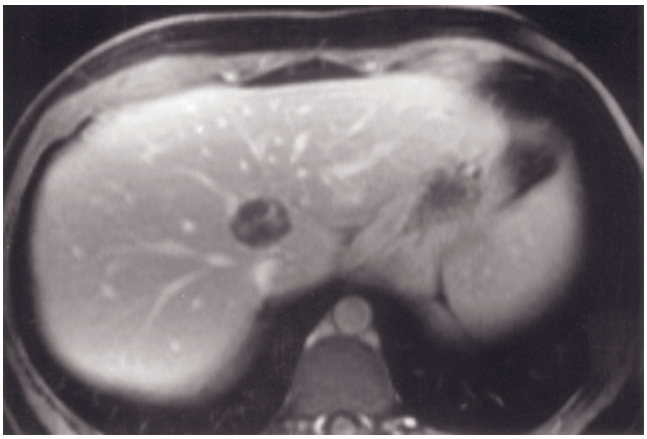

(*e*)

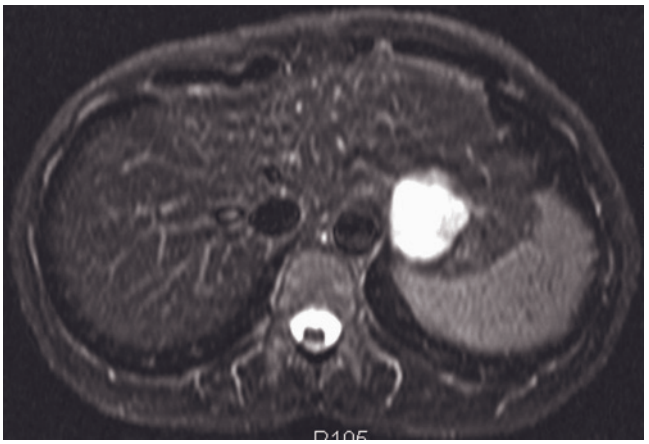

(*f*)

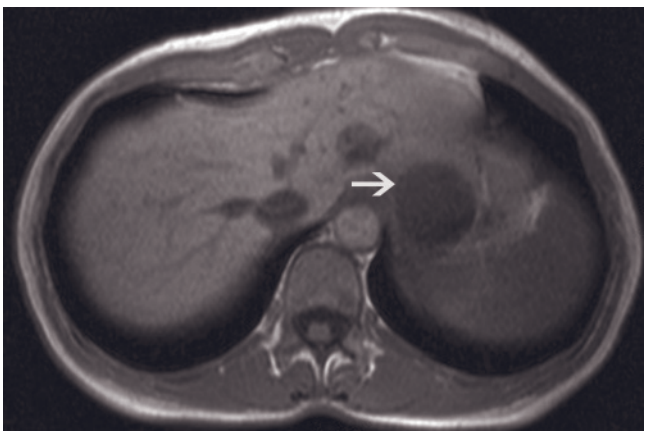

(*g*)

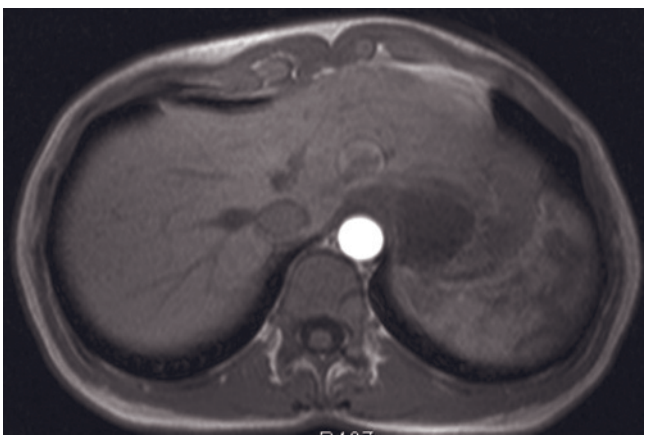

(*h*)

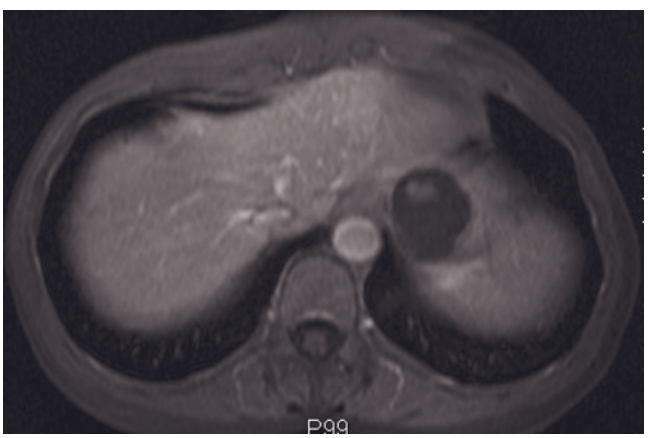

(*i*)

FIG. 2.41 (*Continued*) of enhancement immediately after contrast administration (*c*), and lack of progression of enhancement on the late-phase image (*e*), consistent with a hemangioma Type 3 enhancement. There is another rounded lesion in the tip of the left lobe that shows intense enhancement on the immediate postgadolinium image (arrow, *d*), consistent with focal nodular hyperplasia.

Echo train-STIR (*f*), SGE (*g*), and immediate (*h*) and 90-s fat-suppressed (*i*) SGE images in a second patient. A hemangioma is seen in the left hepatic lobe that appears moderately high signal intensity on the T2-weighted image (*f*), moderately low signal intensity on T1-weighed image (arrow, *g*), a lack of enhancement on early phase (*h*), and a globular focus of enhancement on the late postcontrast image (*i*), consistent with a slow-enhancing hemangioma.

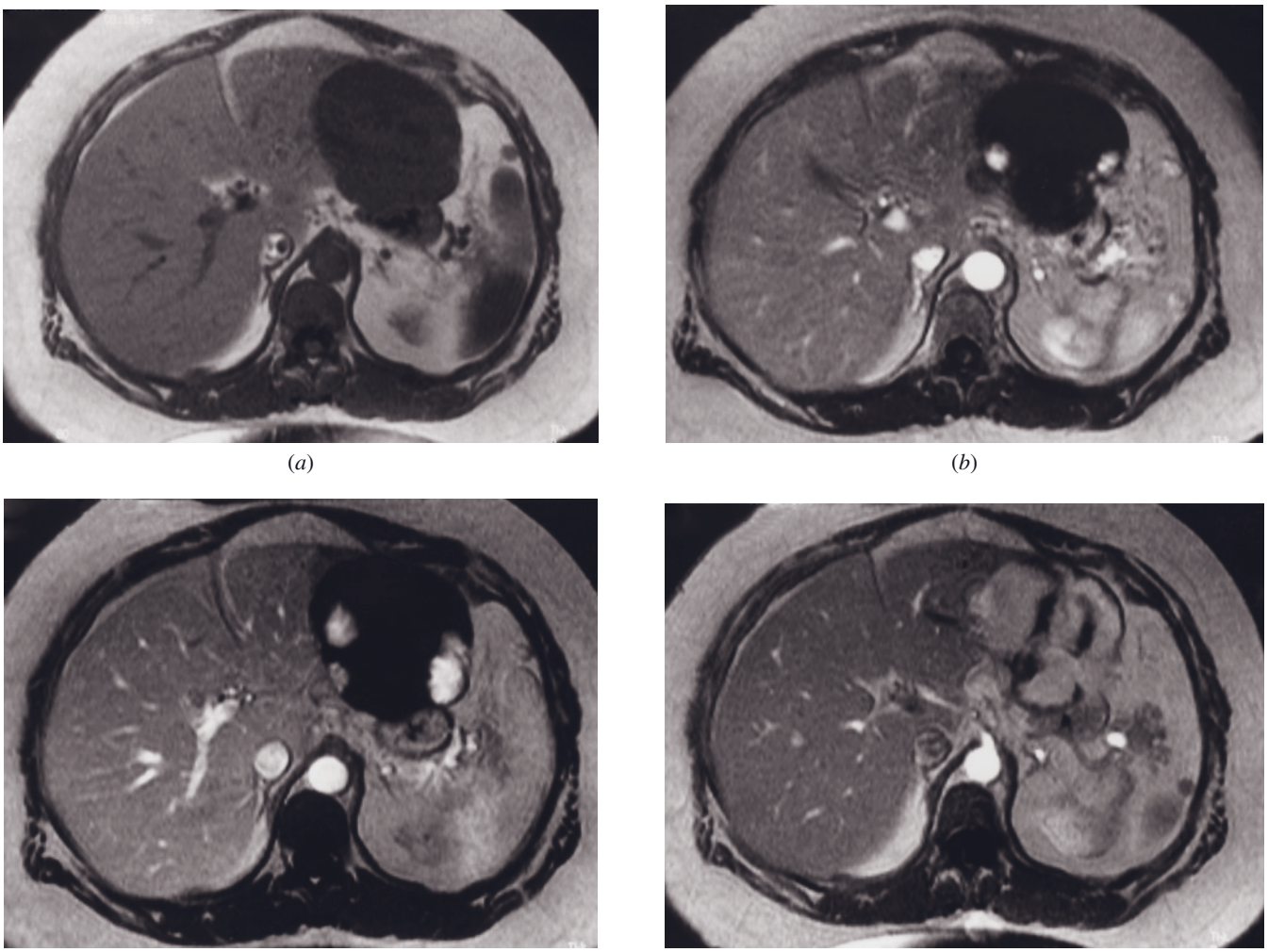

FIG. 2.42 Giant hemangioma. SGE (*a*) and immediate (*b*), 90-s (*c*), and 10-min (*d*) postgadolinium SGE images. A hemangioma is present in the left lobe that is moderately low in signal intensity on T1-weighted image (*a*), demonstrates peripheral nodular enhancement in a discontinuous ring on the early image (*b*), and gradually enhances in a centripetal fashion (*c*) with persistent low signal intensity central scar on delayed image (*d*).

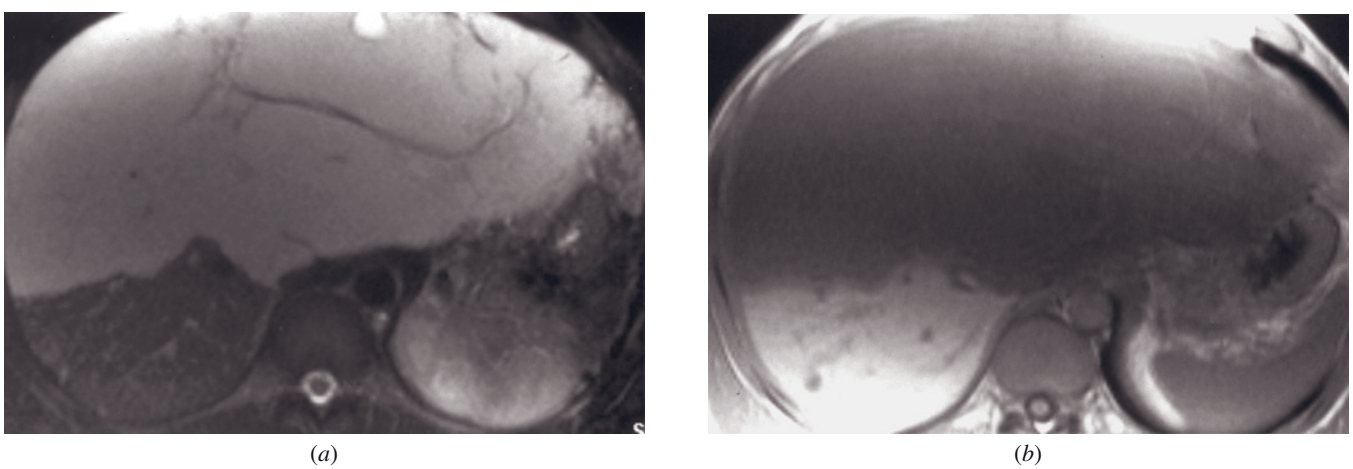

FIG. 2.43 Massive hemangiomas. Echo train-STIR (*a*), SGE (*b*), and immediate (*c*) and 90-s fat-suppressed (*d*) postgadolinium SGE images. A massive tumor replaces the majority of the liver, with sparing of segments 6 and 7 in the right hepatic lobe. After administration of gadolinium, this lesion demonstrates discontinuous peripheral nodular enhancement with enlargement and coalescence of the nodules. The appearance is consistent with a massive hemangioma.

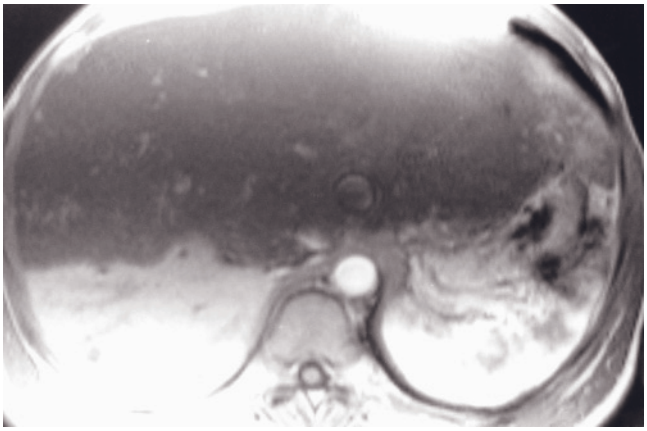

(*c*)

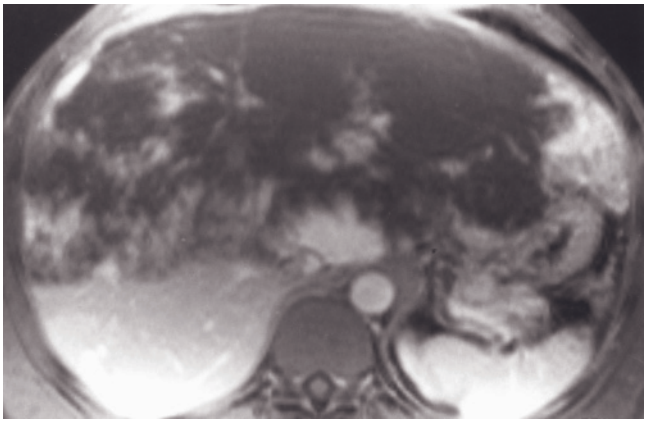

(*d*)

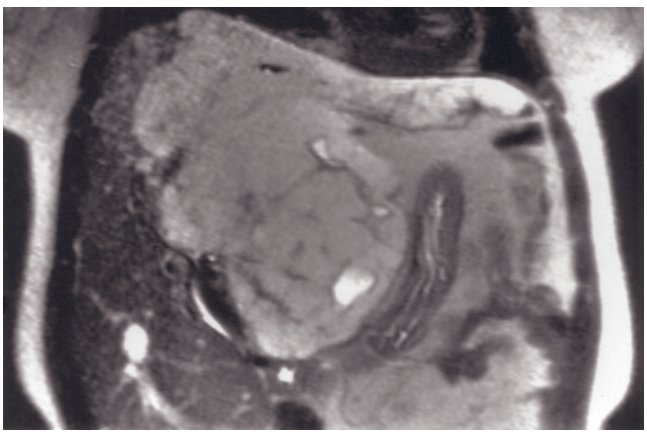

(*e*)

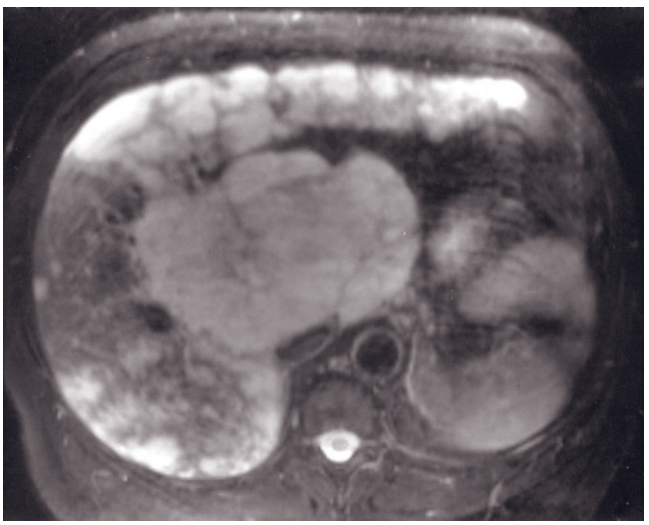

(*f*)

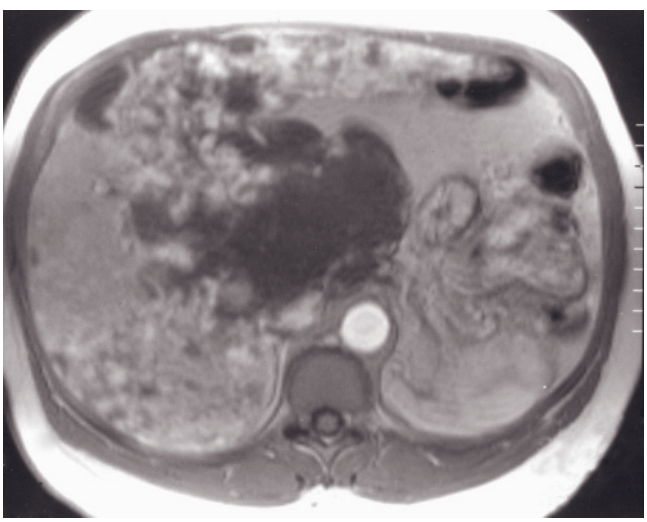

(*g*)

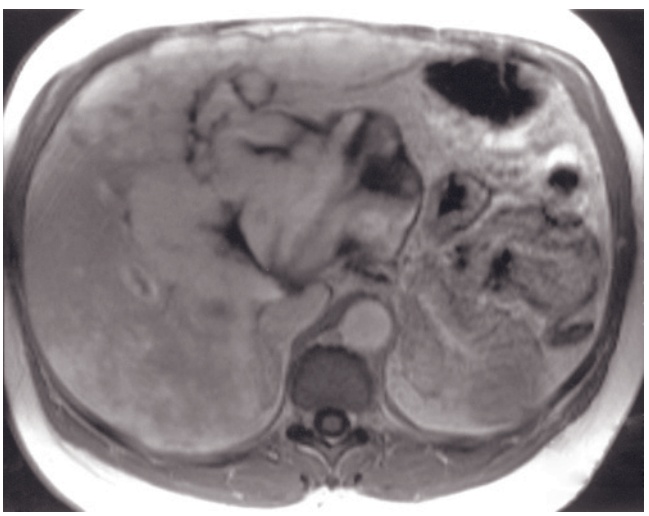

(*h*)

Fig. 2.43 (*Continued*) Coronal T2-weighted SS-ETSE (*e*), transverse echo-train STIR (*f*), and immediate (*g*) and 5-min (*h*) post-gadolinium SGE images in a second patient. A massive lobulated lesion is present in the liver parenchyma that is predominantly high signal intensity on T2-weighted images (*e*, *f*), but with multiple low-signal strands, and demonstrates discontinuous nodular enhancement (*g*) with centripetal progression (*h*) after the administration of gadolinium. Regions of hypointense central scar persist on the late images (*h*). Low-signal-intensity linear strands are common on T2-weighted images in giant hemangiomas and represent bands of collagenous tissue. This patient underwent liver transplantation because of the extensive hepatic replacement by hemangiomas.

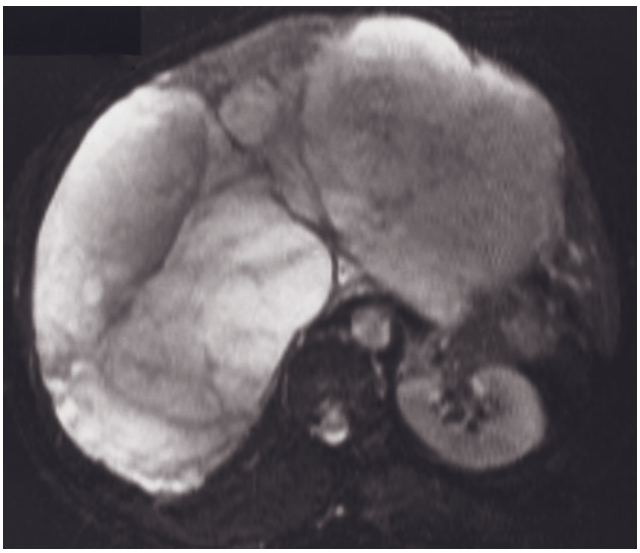

(*i*)

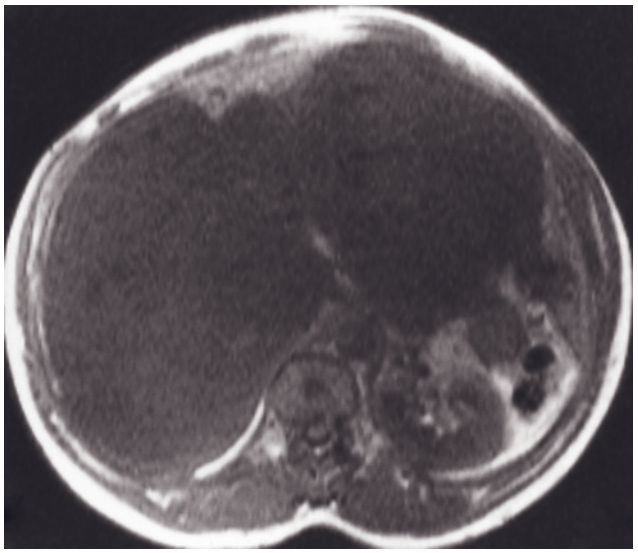

(*j*)

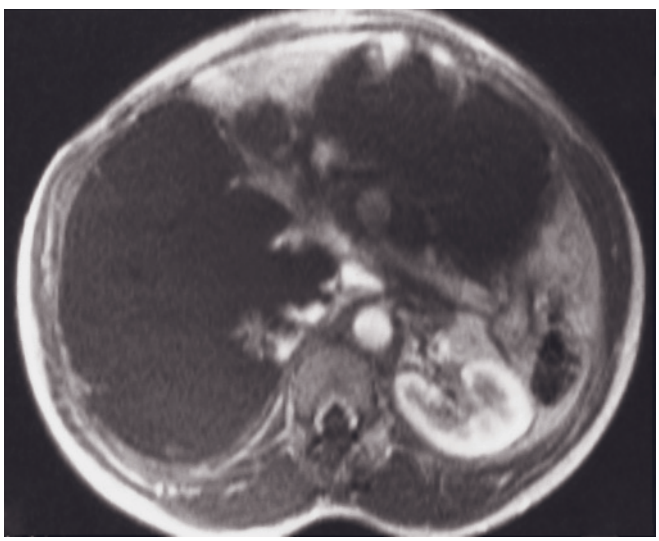

(*k*)

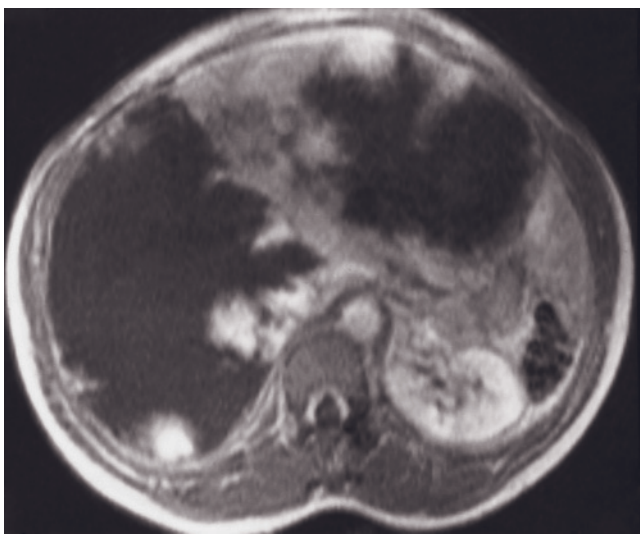

(*l*)

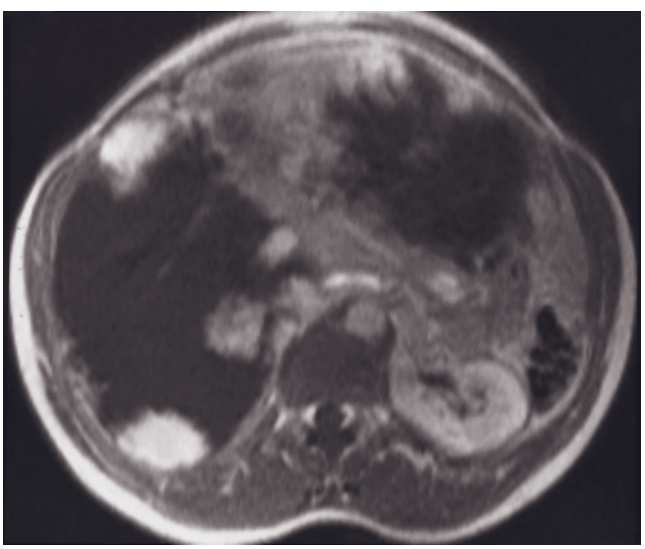

(*m*)

Fig. 2.43 (*Continued*) T2-weighted fat-suppressed ETSE (*i*), SGE (*j*), and immediate (*k*), 90-s (*l*), and 5-min (*m*) postgadolinium SGE images in a third patient who has the liver largely replaced by massive hemangiomas. The findings appreciated in this patient are similar to those in the second patient.

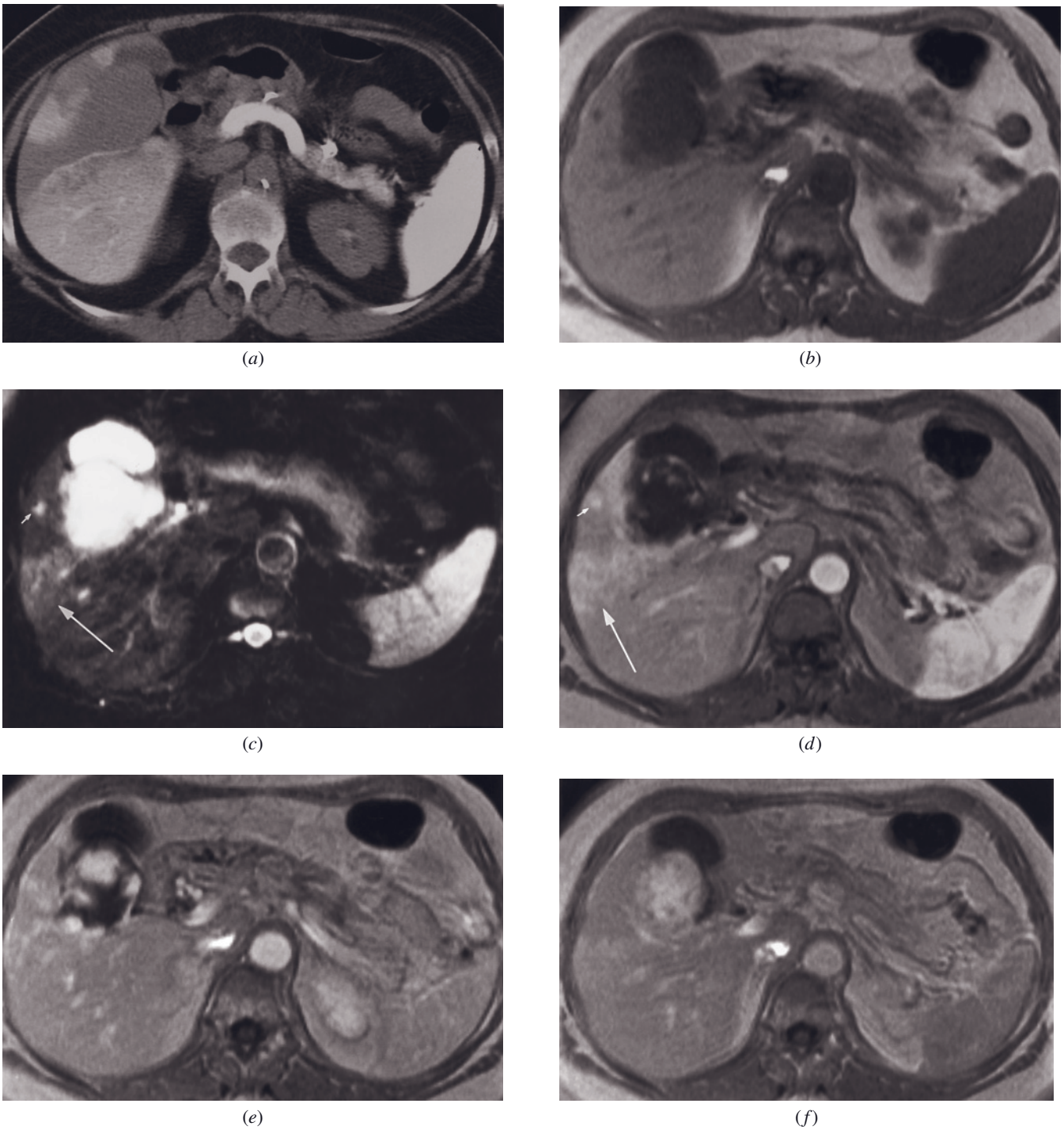

FIG. 2.44 Hemangioma compressing portal vein. Spiral CTAP (*a*), SGE (*b*), T2-weighted fat-suppressed ETSE (*c*), and immediate (*d*), 90-s (*e*), and 10-min (*f*) postgadolinium SGE images. A 6-cm lesion is present in the anterior segment of the right lobe that causes distal wedge-shaped diminished portal venous perfusion on the CTAP image (*a*), findings that were considered consistent with a malignant tumor. The tumor is moderately low in signal intensity on T1-weighted image (*b*) and high in signal intensity on T2-weighted image (*c*) and has perilesional and peripheral nodular enhancement on early-phase image (*d*) that progressively fills in a centripetal fashion on late and delayed images (*e*, *f*). The perfusion defect observed on the CTAP image (*a*) is noted to be wedge-shaped and mildly hyperintense on T2-weighted image (long arrow, *c*) and enhances in a transient fashion greater than adjacent liver on the early-phase image (long arrow, *d*), findings consistent with portal vein compression. Additional note is made of a 6-mm hemangioma lateral to the large hemangioma (small arrow, *c*), which enhances intense and homogeneously on early-phase image (small arrow, *d*), compatible with a Type 1 pattern of enhancement.

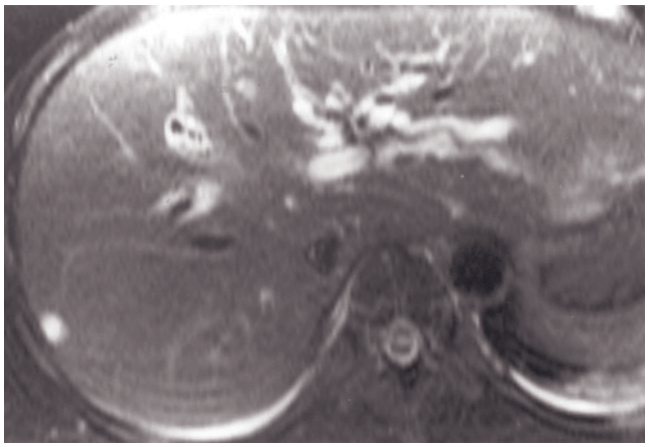

(*a*)

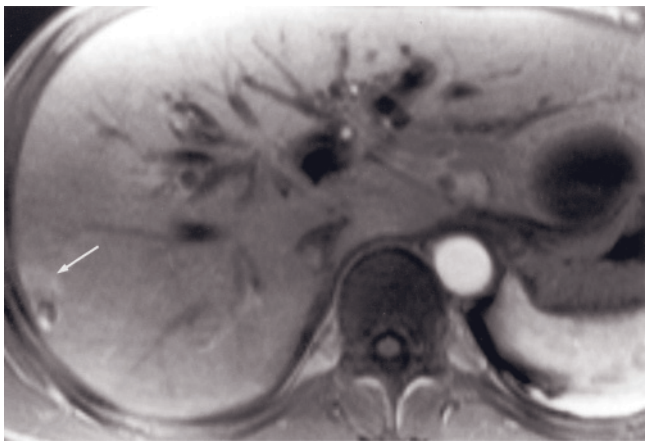

(*b*)

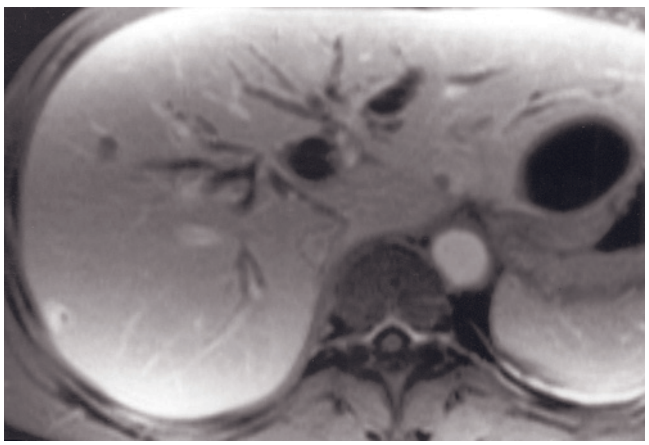

(*c*)

FIG. 2.45 Hemangioma with perilesional enhancement. T2-weighted SS-ETSE (*a*) and immediate (*b*) and 90-s fat-suppressed (*c*) postgadolinium SGE images. This patient, who has an inflammatory pseudotumor arising in the common hepatic duct that causes dilatation of the biliary tree, also demonstrates a round, well-defined lesion, which is hyperintense on T2-weighted image (*a*) and shows peripheral nodular enhancement on the immediate postcontrast image (*b*) with nearly complete fill-in of the lesion on the delayed image (*c*). Note the transient ill-defined increased perilesional enhancement (arrow, *b*) on the immediate postcontrast image (*b*). Perilesional enhancement.

washout and the type 1 hemangioma are more likely to maintain the signal intensity or to fade away toward background isointensity. In this setting, a large lesion is usually present that will exhibit the enhancement features of either a hemangioma or a metastasis, so that the histology of the small lesions may be inferred. Reports have shown that hemangiomas may be reliably distinguished from metastases on T2-weighted images based on the smooth lobular margins and the higher calculated T2 values of hemangiomas (mean of 140 ms) [80]. Although this may be true in the majority of patients, cumulative experience from many centers has shown that T2-weighted images alone may not allow characterization of small tumors or allow reliable distinction between hemangiomas and metastases from hypervascular malignant tumors. For this reason, long-TE T2-weighted sequences for hemangiomas are not performed at our institution because some diagnostically difficult lesions, such as hypervascular metastases, may also show long T2 values. The routine combination of T2-weighted information with serial gadolinium-enhanced SGE is useful to increase observer confidence for establishing the correct diagnosis and also to maximize evaluation of other hepatic and extrahepatic diseases (fig. 2.46) [72, 81].

Chemotherapy-treated liver metastases may resemble the appearance of hemangiomas when chemotherapy treatment has occurred within a 2- to 12-month period before MRI. A less aggressive enhancement pattern that develops in chemotherapy-treated liver metastasis may be reflective of underlying histologic changes associated with a salutary response to chemotherapy, that is, antiangiogenic effect with altered vascularity [82].

Few studies to date have reported the imaging findings of hemangiomas in the setting of cirrhosis or chronic liver disease. It is suggested that the incidence of hemangiomas in patients with chronic liver disease is up to 9% [83]. Hemangiomas in this setting are more likely to be solitary and subcapsular [84, 85]. It has been suggested that hemangiomas tend to decrease in size with the progression of liver disease due to fibrotic

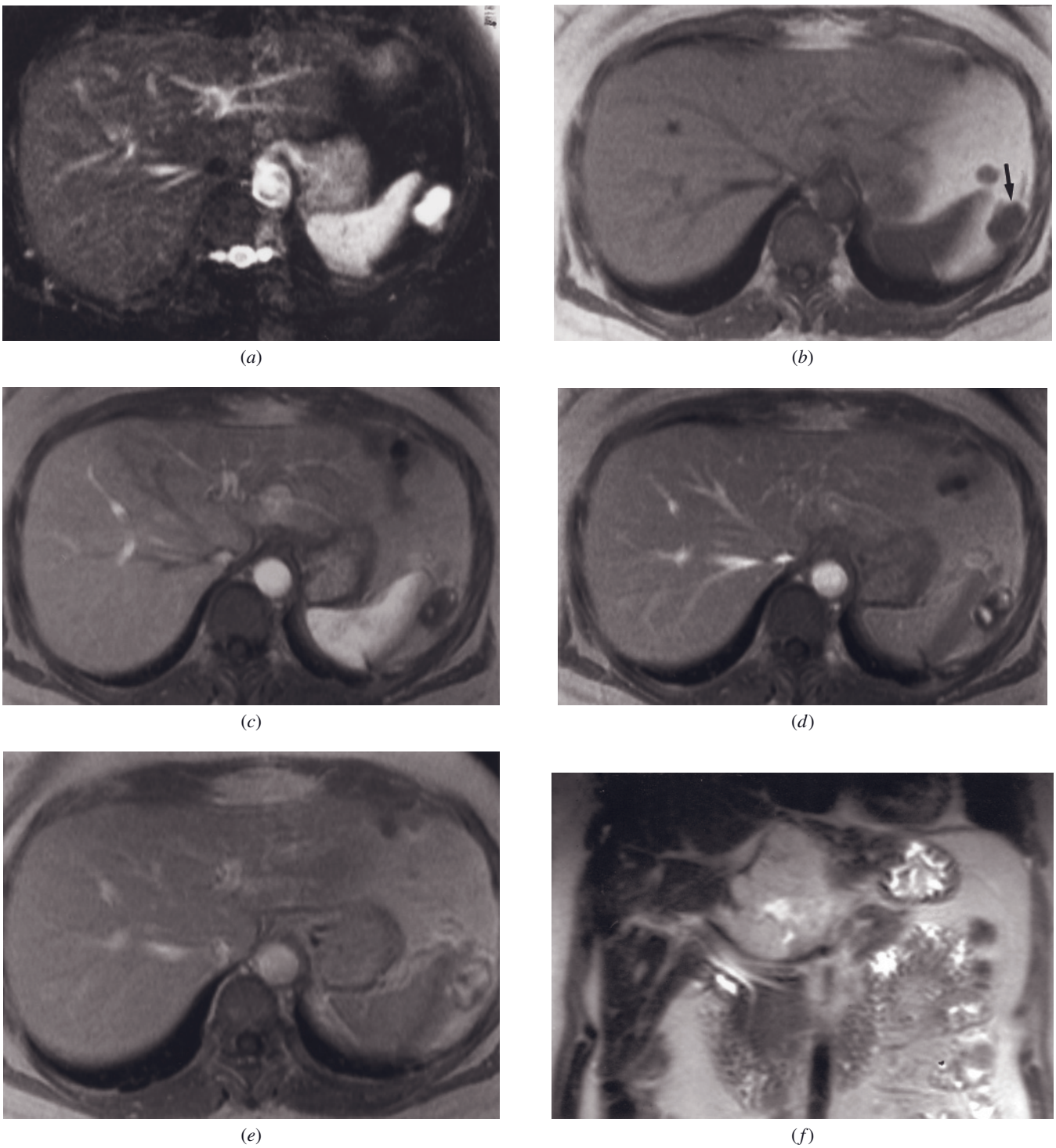

FIG. 2.46 Exophytic hemangioma. T2-weighted fat-suppressed ETSE (*a*), SGE (*b*), and immediate (*c*), 90-s (*d*), and 10-min (*e*) postgadolinium SGE images. A pedunculated 2.5-cm hemangioma (arrow, *b*) arises from the tip of the lateral segment of the liver. The hemangioma is high in signal intensity on T2-weighted image (*a*) and moderately low in signal intensity on T1-weighted image (*b*), enhances in a peripheral nodular fashion on the early-phase image (*c*), and shows centripetal progression on late (*d*) and delayed (*e*) images. Despite the thin stalk of the hemangioma, it exhibits circumlesional peripheral nodular enhancement, comparable to standard intraparenchymal hemangiomas.

Coronal (*f*, *g*) and transverse (*h*) T2-weighted SS-ETSE, T1-weighted fat-suppressed SGE (*i*), and immediate (*j*) and 90-s fat-suppressed (*k*) postgadolinium SGE images in a second patient. There is a mass arising from segment 1 of the liver, with extension

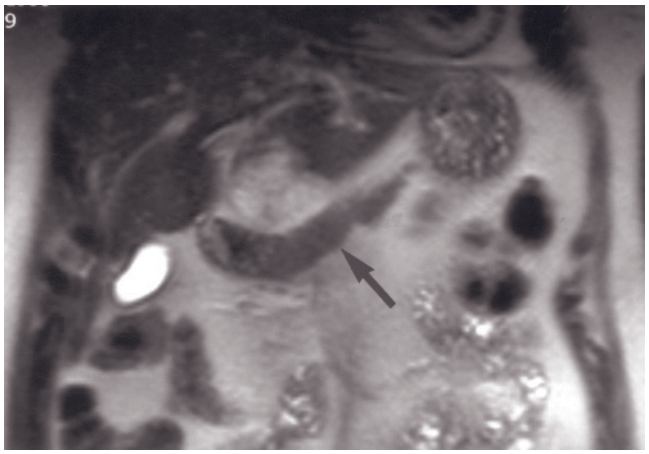

(*g*)

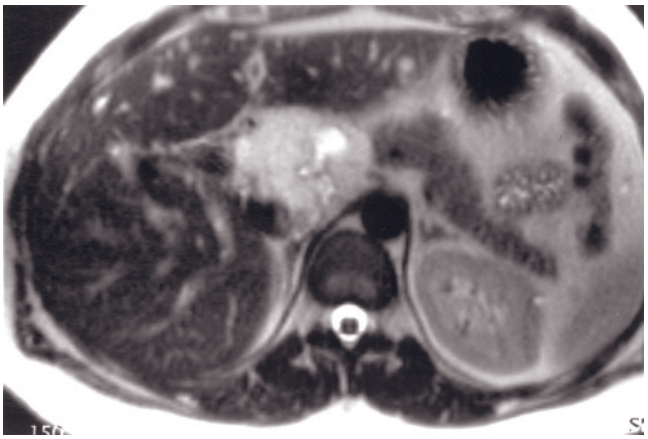

(*h*)

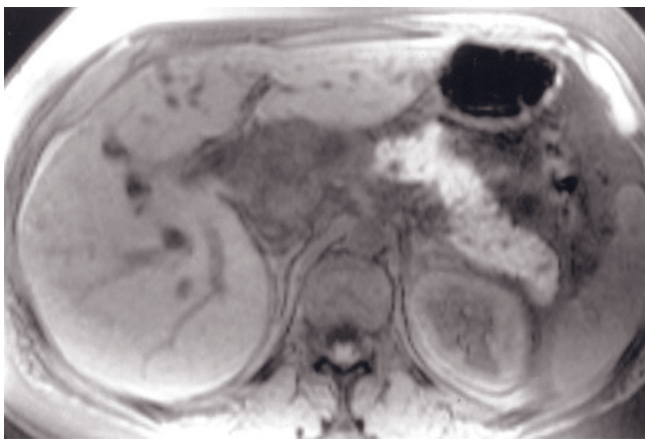

(*i*)

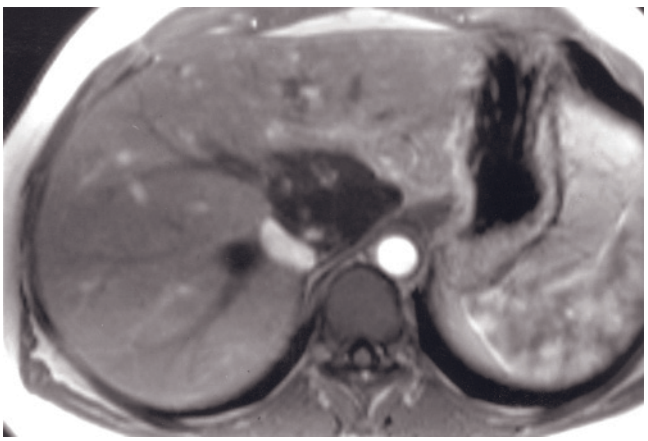

(*j*)

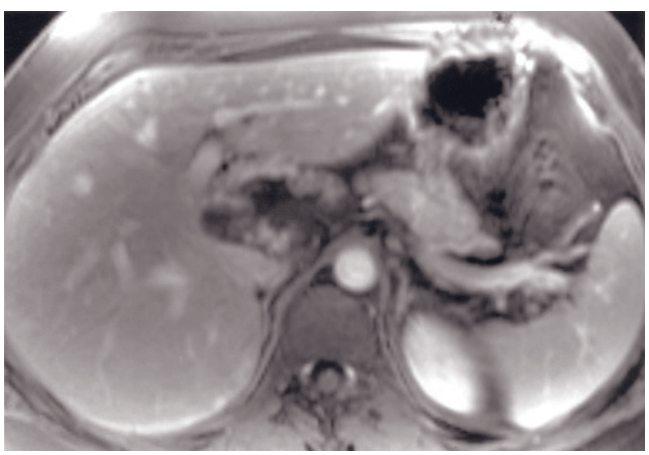

(*k*)

Fig. 2.46 (*Continued*) into the porta hepatis, that demonstrates high signal on T2-weighted images (*f*, *g*, *h*) and low signal on T1-weighted image (*i*). Immediately after gadolinium administration (*j*), multiple peripheral enhancing nodules are identified that enlarge and coalesce on later images (*k*), consistent with an exophytic hemangioma. On an outside CT examination this was thought to arise from the pancreas. The coronal T2-weighted image (*g*) demonstrates inferior displacement of an intact pancreas (arrow, *g*). Additionally, the pancreas distal to the mass exhibits normal high signal on the T1-weighted fat-suppressed image (*i*), which essentially excludes a pancreatic adenocarcinoma.

degeneration, thrombosis, or hemorrhage [83–85]. Mastropasqua and colleagues [84] also have shown that there is no statistically significant difference between the size of small and medium hemangiomas in unaffected livers and in cirrhotic or chronic liver disease, although there was a tendency for cirrhotic livers to have small hemangiomas and no giant hemangiomas were observed in cirrhosis (fig. 2.47). This observation may reflect the fact that, in severely fibrotic livers, these is a paucity of vascular tissue available to support the growth of hemangiomas to a large size. On MRI, the signal intensity of hemangiomas on T2- and T1-weighted images pre- and postcontrast in patients with cirrhosis or chronic liver disease is similar to that in patients with

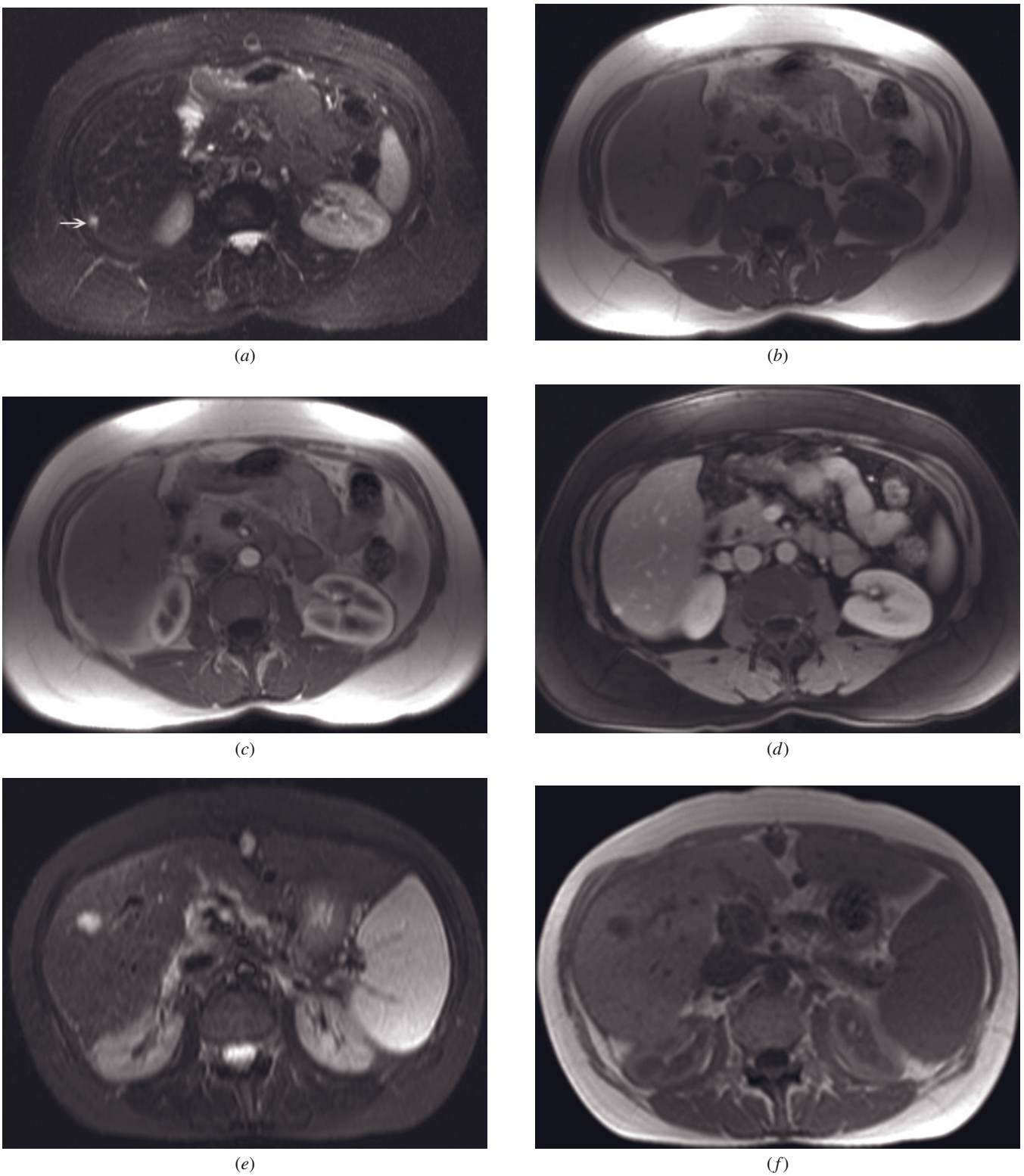

FIG. 2.47 Hemangioma in the setting of chronic liver disease. T2-weighted SS-ETSE (*a*), SGE (*b*), and immediate (*c*) and 90-s fat-suppressed (*d*) postgadolinium SGE images in a patient with chronic liver disease patient. There is an hepatic lesion in segment 6 that demonstrates moderately high signal intensity on the T2-weighted image (arrow, *a*), moderately low signal intensity on the T1-weighted image (*b*), and enhancement of a peripheral focus on the early-phase image (*c*) that fills in on the late-phase image (*d*), consistent a with Type 2 hemangioma.

T2-weighted SS-ETSE (*e*), SGE (*f*), and immediate (*g*) and 90-s fat-suppressed (*h*) postgadolinium SGE images in a second patient with a history of acute on chronic hepatitis. There is a hemangioma in segment 5 of the liver that shows high signal intensity on

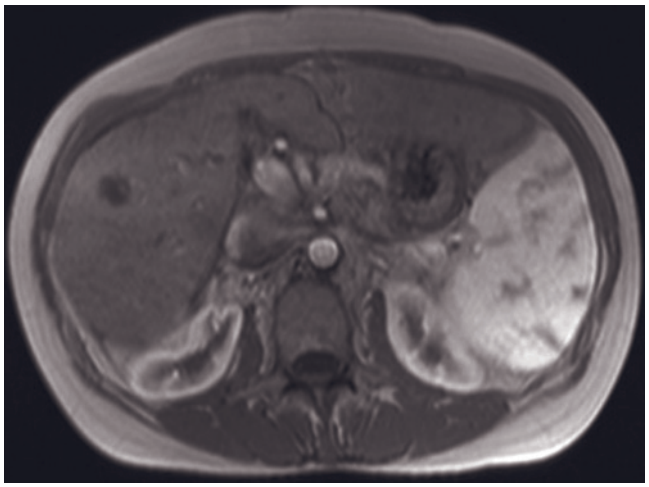

(*g*)

(*h*)

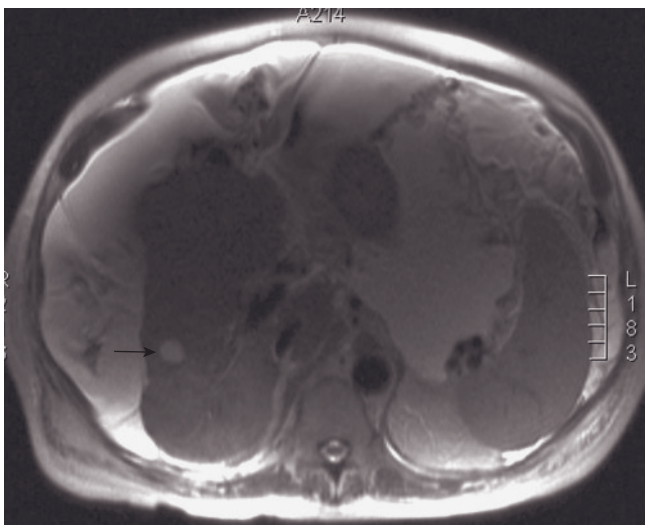

(*i*)

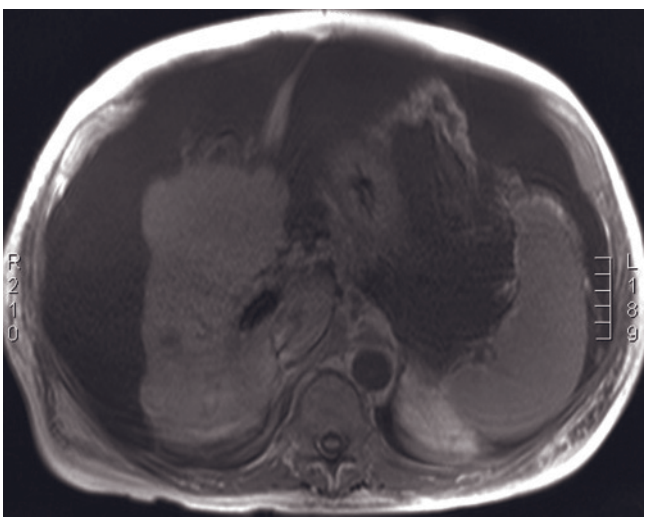

(*j*)

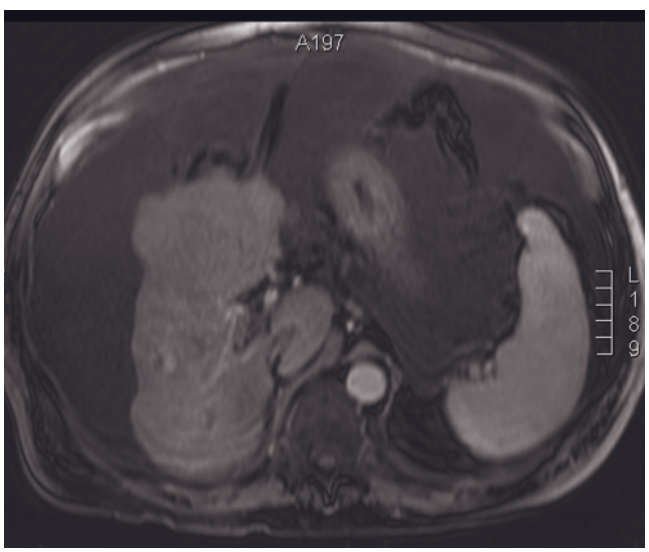

(*k*)

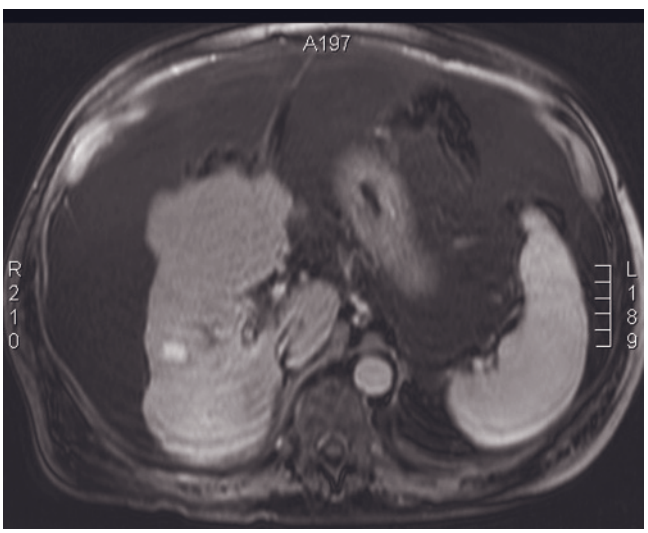

(*l*)

FIG. 2.47 (*Continued*) the T2-weighted image, low signal intensity on the T1-weighted image (*f*), and globular enhancement on early-phase image (*g*) that persists on late-phase (*h*) images. Increased perilesional enhancement surrounding the hemangioma is appreciated on the early-phase image (*g*). Additionally, the parenchyma enhances in a patchy fashion on early- and late-phase images, consistent with acute on chronic hepatitis.

T2-weighted SS-ETSE (*i*), SGE (*j*), and immediate (*k*) and 90-s fat-suppressed (*l*) postgadolinium SGE images in a third patient with end-stage chronic liver disease and a Type 2 hemangioma (arrow, *i*).

nonaffected livers. Regardless of the size, hemangiomas are more likely to show a fast lesional fill-in after contrast. The recognition of the MR features of hemangioma type 1 is useful since it may be indistinguishable from HCC in early phase because both entities exhibit homogeneous moderately intense enhancement. The signal intensity on T2-weighted images may help in this differentiation, because small HCCs are often near isointensity in contrast to the moderately high signal of hemangiomas.

Advantages of MRI over CT imaging in the evaluation of hemangiomas include: 1) the greater ability to image the entire liver in the same phase of contrast enhancement, which is particularly useful when multiple lesions are present; 2) greater lesion enhancement on contrast-enhanced images such that lesions are comparatively brighter than background liver (fig. 2.48); 3) superior detection of small hemangiomas; and 4) effective lesion detection and characterization with T2-weighted images, which CT does not have an analogous technique.

Infantile Hemangioendothelioma

Infantile hemangioendotheliomas (IHE) are congenital lesions and the most common mesenchymal tumor of the liver in childhood [86]. Although infantile heman-

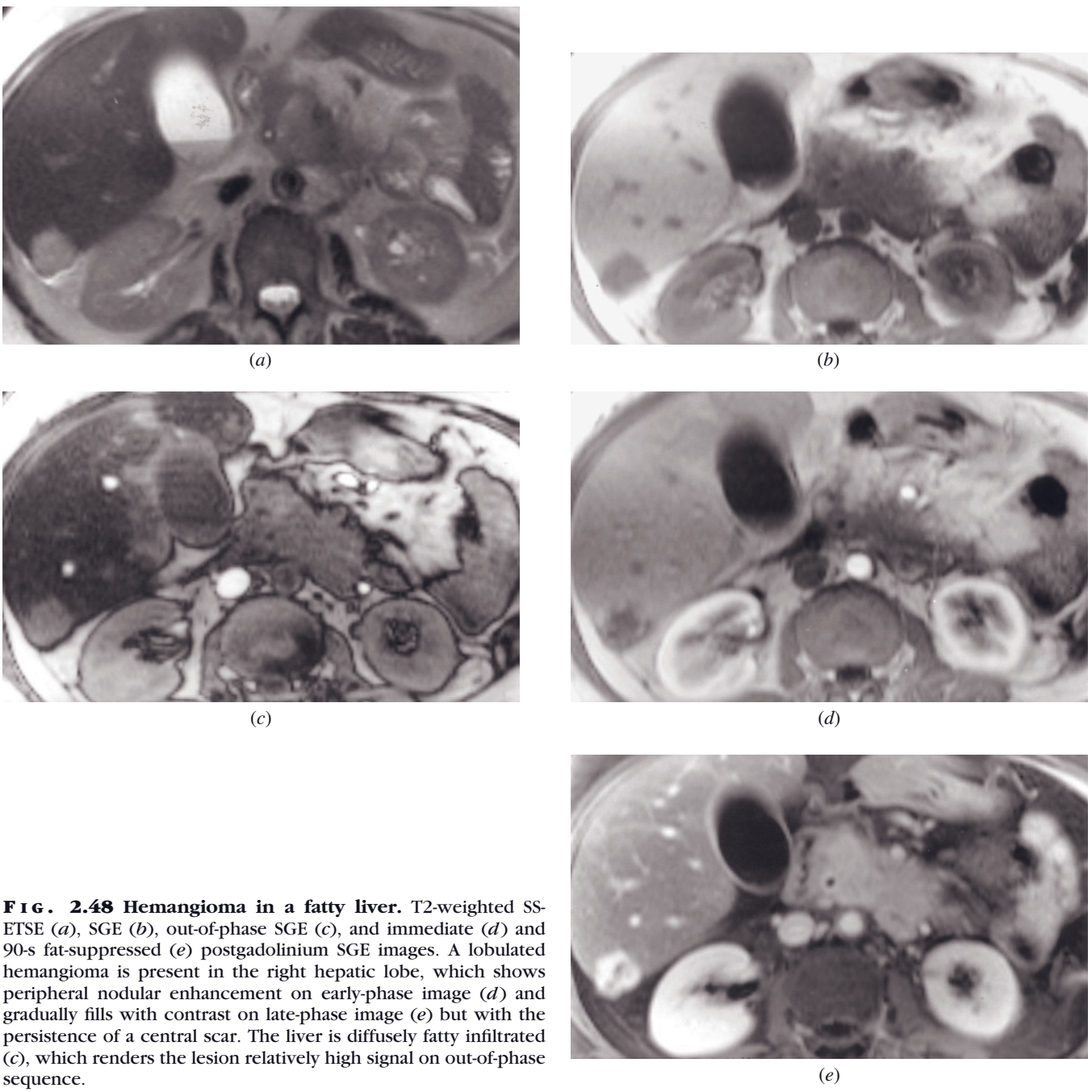

FIG. 2.48 Hemangioma in a fatty liver. T2-weighted SS-ETSE (*a*), SGE (*b*), out-of-phase SGE (*c*), and immediate (*d*) and 90-s fat-suppressed (*e*) postgadolinium SGE images. A lobulated hemangioma is present in the right hepatic lobe, which shows peripheral nodular enhancement on early-phase image (*d*) and gradually fills with contrast on late-phase image (*e*) but with the persistence of a central scar. The liver is diffusely fatty infiltrated (*c*), which renders the lesion relatively high signal on out-of-phase sequence.

gioendotheliomas are histologically benign, they may lead to death within months secondary to heart or liver failure. Spontaneous regression of the lesions tends to occur after 8 months of age [87, 88]. Pathologic examination shows a multinodular tumor involving both lobes. Microscopically, numerous dilated vascular channels are lined by multiple layers of plump endothelial cells. Cavernous vascular channels are frequent.

On imaging, these lesions tend to be numerous similar-size tumors that are uniformly moderately to markedly hyperintense on T2-weighted images and hypointense on T1-weighted images and enhance homogeneously on interstitial-phase gadolinium-enhanced images (fig. 2.49) [89].

Hepatocellular Adenoma

Hepatocellular adenomas (HCA) are benign epithelial neoplasms [2]. Approximately 90% of HCAs occur in young women [90]. These lesions are associated with the use of oral contraceptive steroids [2]. Tumors will involute spontaneously after patients withdraw from birth control pill. Other much less frequent associations include the use of anabolic steroids and disorders associated with abnormal carbohydrate metabolism, such as familial diabetes mellitus, galactosemia, and glycogen storage disease type Ia [91–93]. Patients may present with acute abdominal pain, related to hemorrhage into the tumor [94]. Rarely, rupture into the peritoneal cavity may occur that requires emergency intervention. Malignant transformation is sporadic [95].

Pathologically, HCA are most commonly solitary tumors characterized as a bulging mass with dilated blood vessels traversing the surface. HCA are partially or completely enclosed by a pseudocapsule derived from compressed and collapsed hepatic parenchyma. Sectioning reveals a spherical, well-demarcated, richly vascular lesion, frequently with areas of hemorrhage or necrosis. Focal scar formation is indicative of remote infarction. The histologic hallmark consists of clusters of benign hepatocytes arranged in slender plates of two- to three-cell thickness. Steatosis may be prominent. Neoplastic hepatocytes are separated by slitlike sinusoids and numerous thin-walled veins. Bile ducts are absent [87].

The typical MR appearance of HCA is homogeneously mild hyperintensity on T2-weighted images, homogeneously mild hypointensity or isointensity on T1-weighted images, and transient homogeneous blush immediately after contrast that uniformly fades to isointensity with liver parenchyma by 1 min. The intensity and heterogeneity of signal on T2- and T1-weighted images may vary and reflect the quantity of fat, hemorrhage, and necrosis within the tumor (figs. 2.50 and 2.51) [53, 96, 97]. The arrangement of vessels and stroma in HCA may result in an intense marbled pattern of enhancement that may be difficult to distinguish from HCC on arterial dominant phase. However, the presence of lesional washout and complete capsule enhancement on late phase suggest the diagnosis of HCC. HCA may decrease homogeneously in signal intensity on out-of-phase or fat-suppressed images because of their fat content, which is commonly uniform (fig. 2.52).

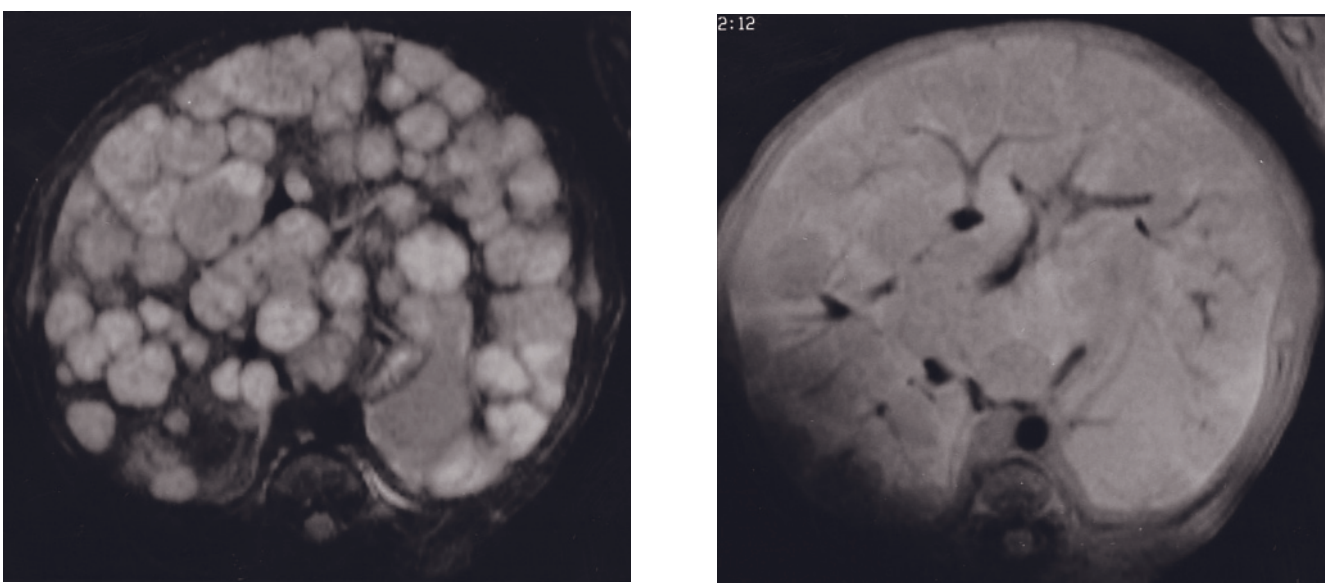

(*a*) (*b*)

FIG. 2.49 Infantile hemangioendothelioma. T2-weighted fat-suppressed ETSE (*a*), T1-weighted fat-suppressed SE (*b*), and T1-weighted interstitial-phase fat-suppressed gadolinium-enhanced SE (*c*) images. The liver in this 9-month-old boy is extensively replaced with focal mass lesions, smaller than 1 cm, that are high in signal intensity on the T2-weighted image (*a*) and mildly low in signal intensity on the T1-weighted image (*b*) and enhance homogeneously on the interstitial-phase gadolinium-enhanced image (*c*). This appearance is characteristic for hemangioendothelioma in neonatal patients.

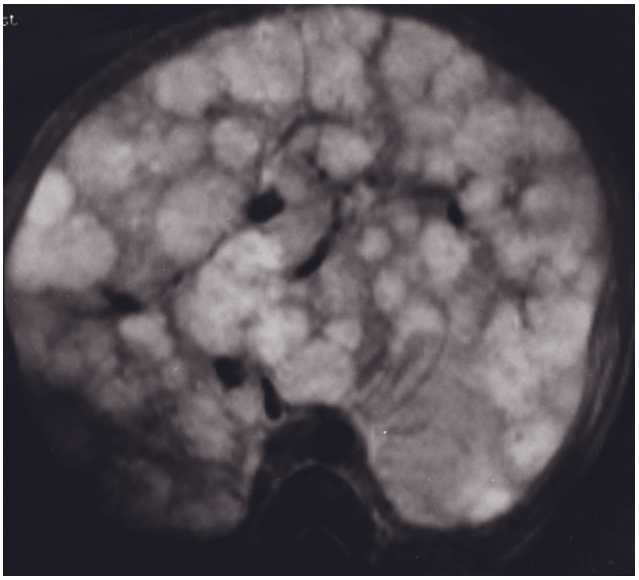

(*c*)

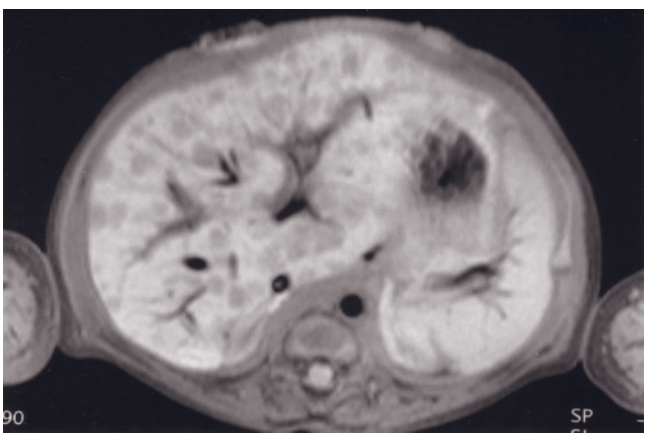

(*e*)

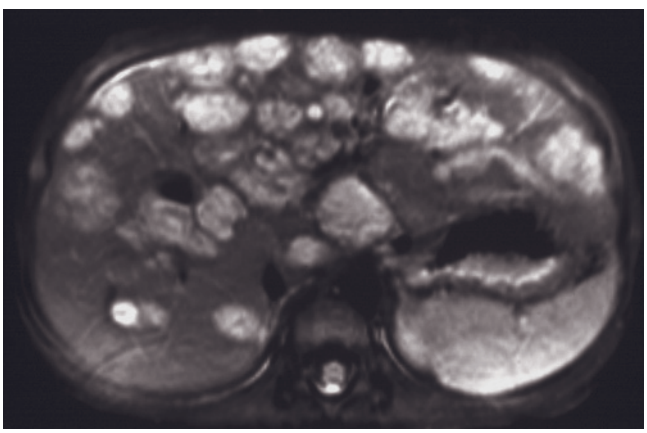

(*g*)

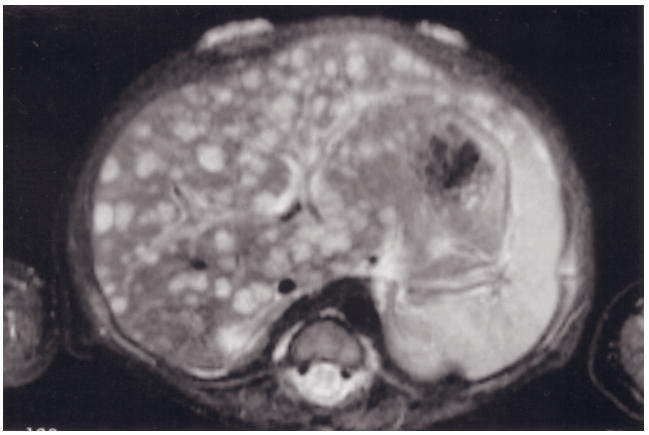

(*d*)

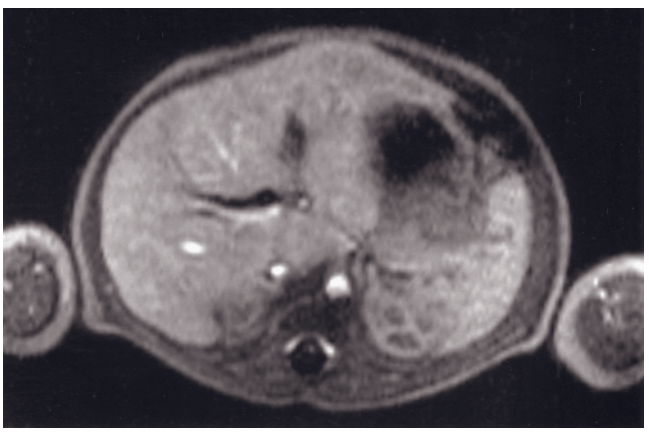

(*f*)

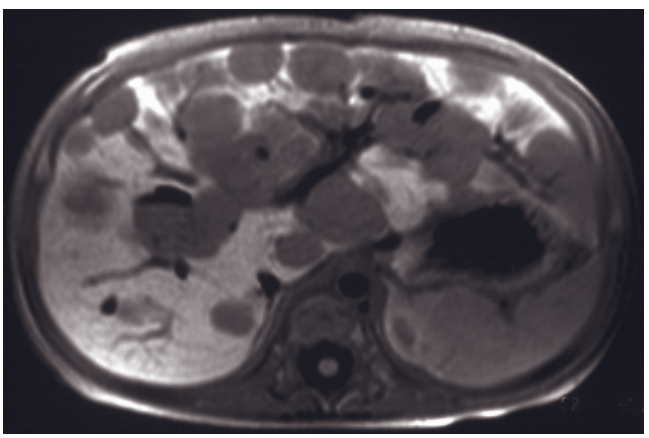

(*h*)

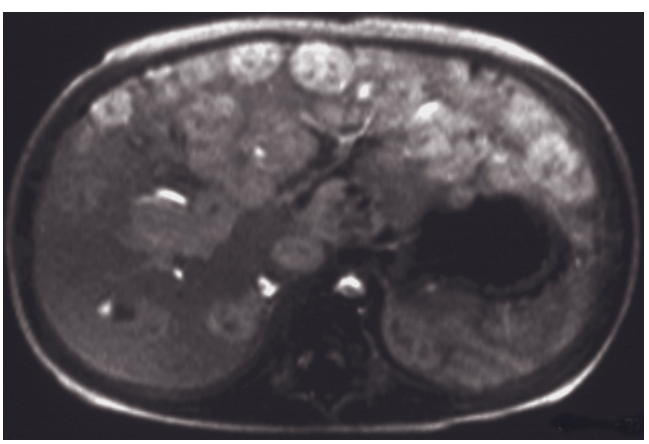

(*i*)

Fig. 2.49 (*Continued*) T2-weighted fat-suppressed ETSE (*d*), T1-weighted fat-suppressed SE (*e*), and T1-weighted immediate postgadolinium magnetization-prepared gradient-echo (*f*) images in a second patient who is 2 years old. The liver has multiple small foci of increased signal on T2-weighted images (*d*), decreased signal on T1-weighted images (*e*), and intense uniform or nodular enhancement after administration of gadolinium, consistent with infantile hemangioendothelioma.

T2-weighted fat-suppressed SS-ETSE (*g*), T1-weighted fat-suppressed SGE (*h*), and immediate (*i*) and 90-s (*j*) postgadolinium SGE images in a third patient show findings similar to those in the second patient.

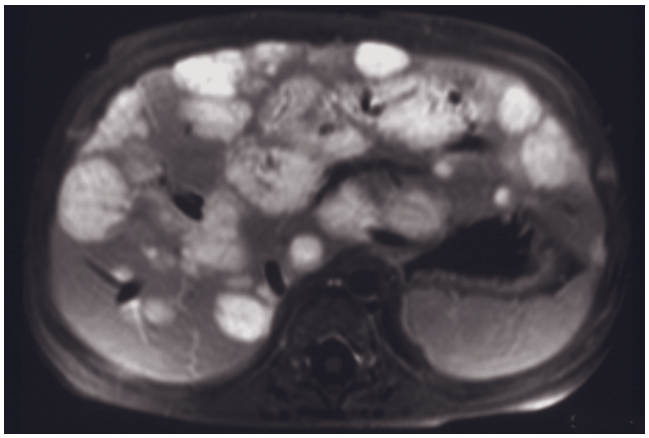

(*j*)

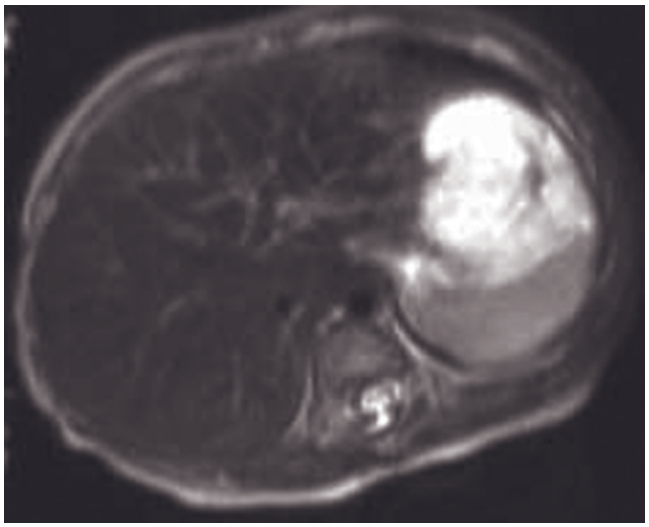

(*k*)

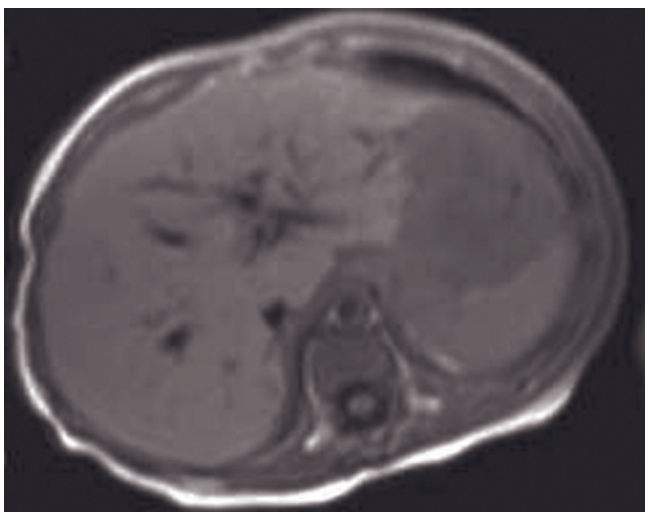

(*l*)

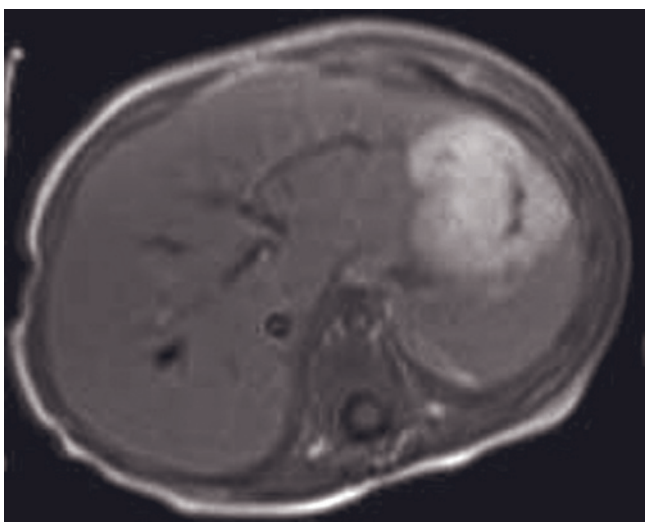

(*m*)

FIG. 2.49 (*Continued*) T2-weighted SS-ETSE (*k*), SGE (*l*), and immediate postgadolinium SGE (*m*) images in a fourth patient demonstrate a lobular lesion in the tip of the left lobe that shows moderately high signal intensity on the T2-weighted image (*k*), low signal on the T1-weighted image (*l*), and intense enhancement after administration of contrast (*m*). Histopathology was consistent with infantile hemangioendothelioma.

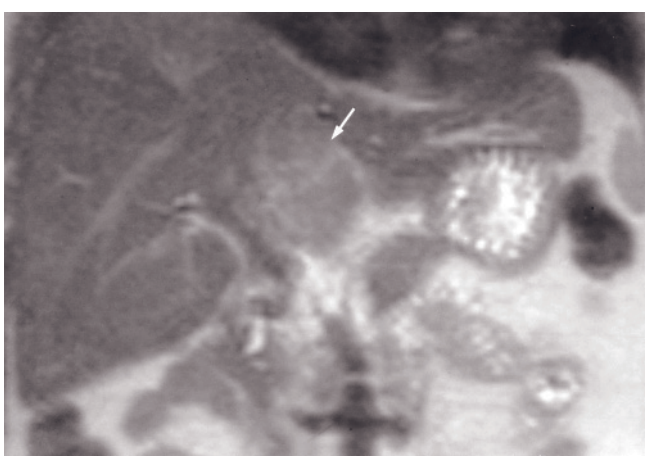

(*a*)

FIG. 2.50 Hepatic adenoma. Coronal T2-weighted SS-ETSE (*a*), SGE (*b*), out-of-phase SGE (*c*), and immediate (*d*) and 90-s fat-suppressed (*e*) postgadolinium SGE images. There is a lesion in

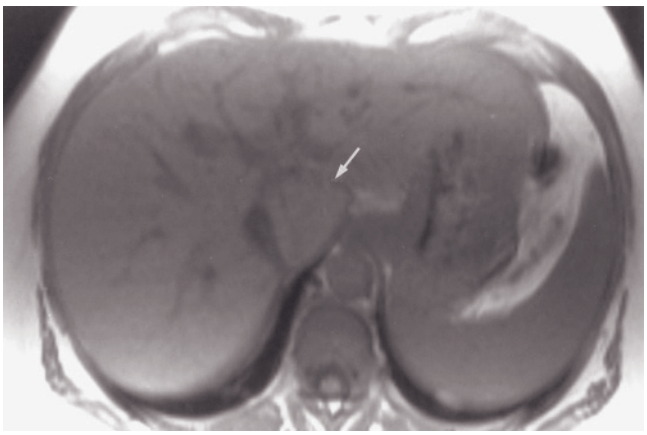

(*b*)

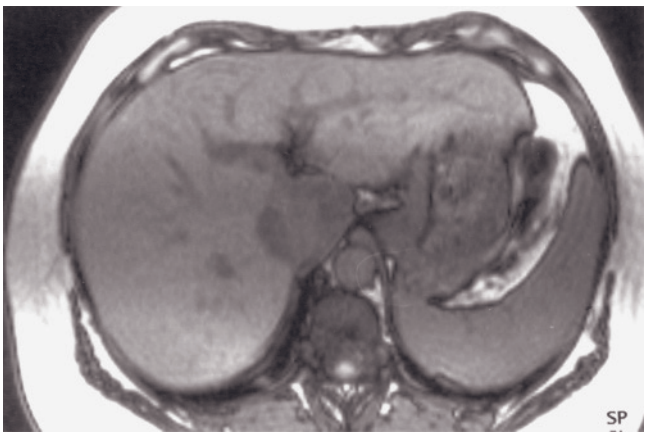

(*c*)

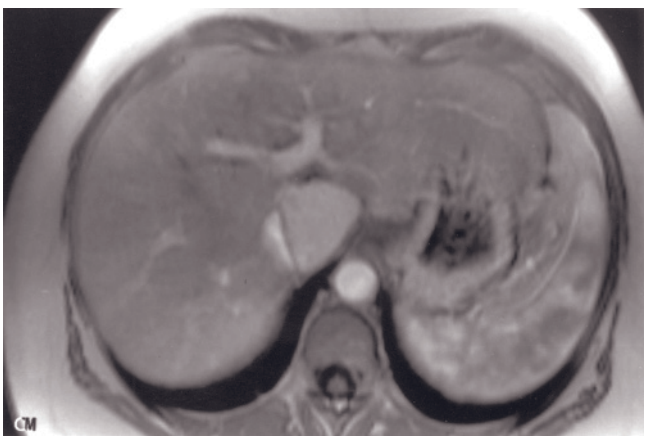

(*d*)

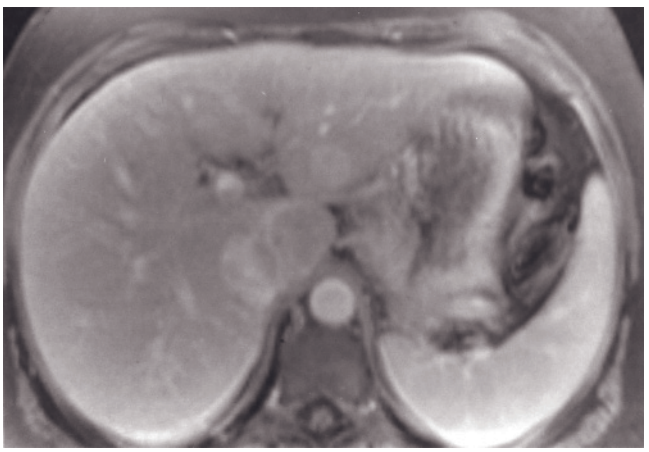

(*e*)

FIG. 2.50 (*Continued*) the caudate lobe (arrow, *a*, *b*) characterized by mild increased signal on T2-weighted image (*a*) and T1-weighted image (*b*), drop in signal on out-of-phase images (*c*), diffuse intense homogeneous enhancement on early-phase image (*d*), and fading to near isointensity on late-phase image (*e*). Loss of signal on out-of-phase image (*c*) is characteristic of hepatic adenoma. Late capsular enhancement (*e*), as observed in this case, may be occasionally observed in hepatic adenomas.

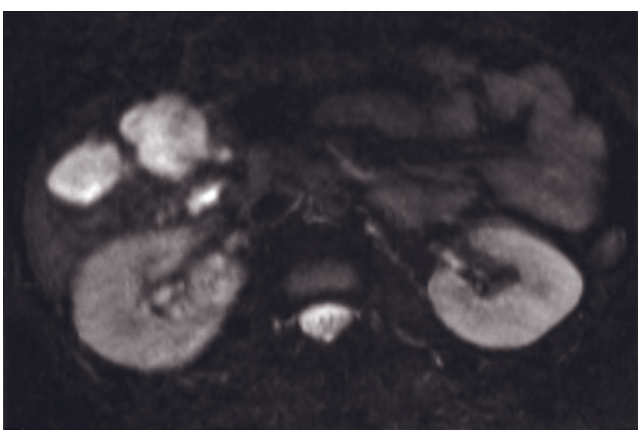

(*a*)

FIG. 2.51 Hepatic adenoma complicated by hemorrhage. T2-weighted fat-suppressed ETSE (*a*), SGE (*b*), and immediate post-gadolinium SGE (*c*) images. An 8-cm mass arises from the inferior aspect of the right hepatic lobe. Regions within the mass possess high signal intensity on T2-weighted image (*a*) and high signal intensity peripheral rims on T1-weighted image (arrows, *b*) consistent with blood. Heterogeneous enhancement of the nonhemorrhagic portions of the mass is identified on early phase image (*c*). The patient discontinued birth control pills and on the 3-month follow-up study the mass had decreased in size to 3.5-cm (not shown).

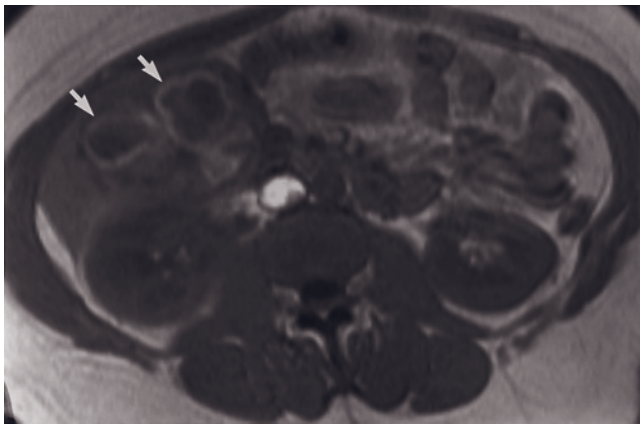

(*b*)

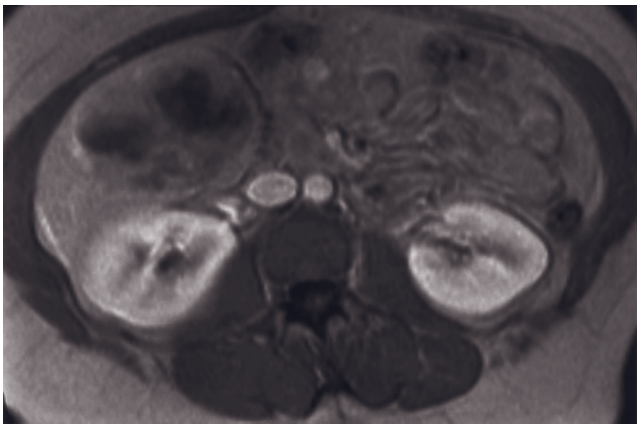

(*c*)

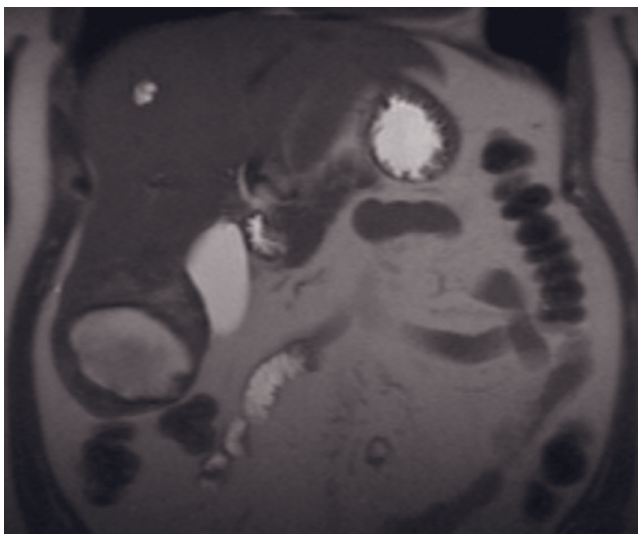

(*d*)

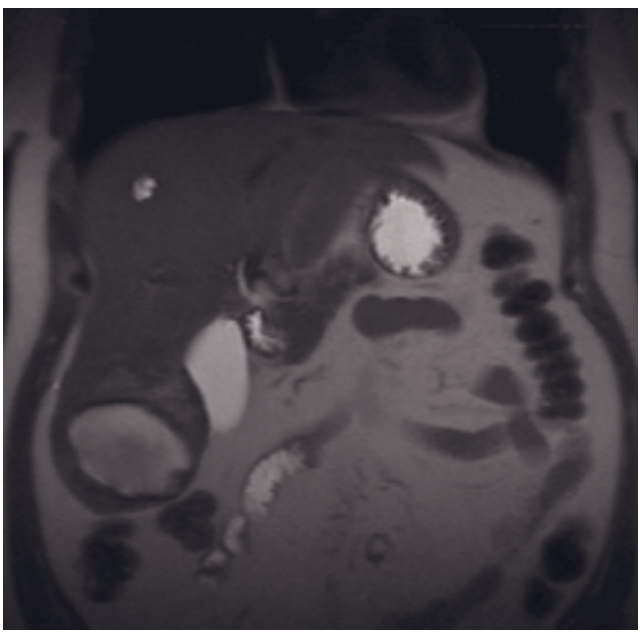

(*e*)

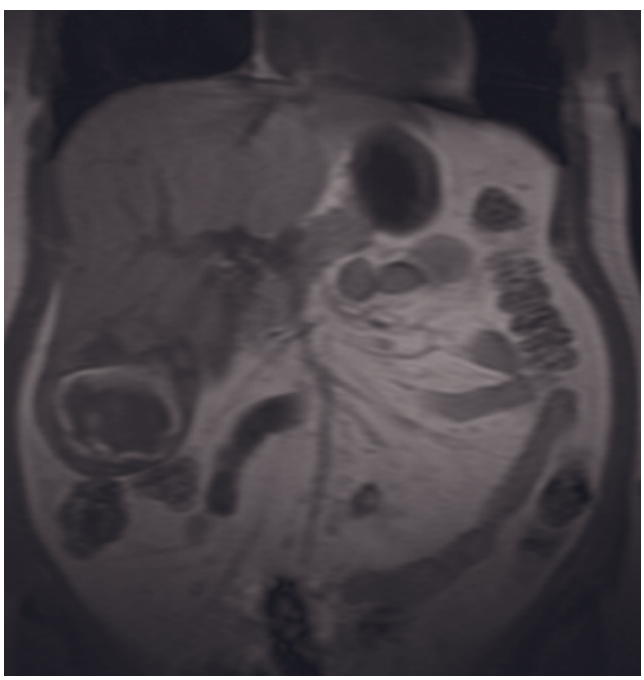

(*f*)

Fig. 2.51 (*Continued*) Coronal T2-weighted fat-suppressed ETSE (*d*), 3D-gradient echo (*e*), and late phase postgadolinium 3D-gradient echo (*f*) 3T images of a complicate adenoma in segment 6 of the liver **at 3T** in a second patient. Note the heterogeneous signal intensity on T2-weighted (*d*) and high signal intensity on T1-weighted (*e*) consistent with various age hemorrhage.

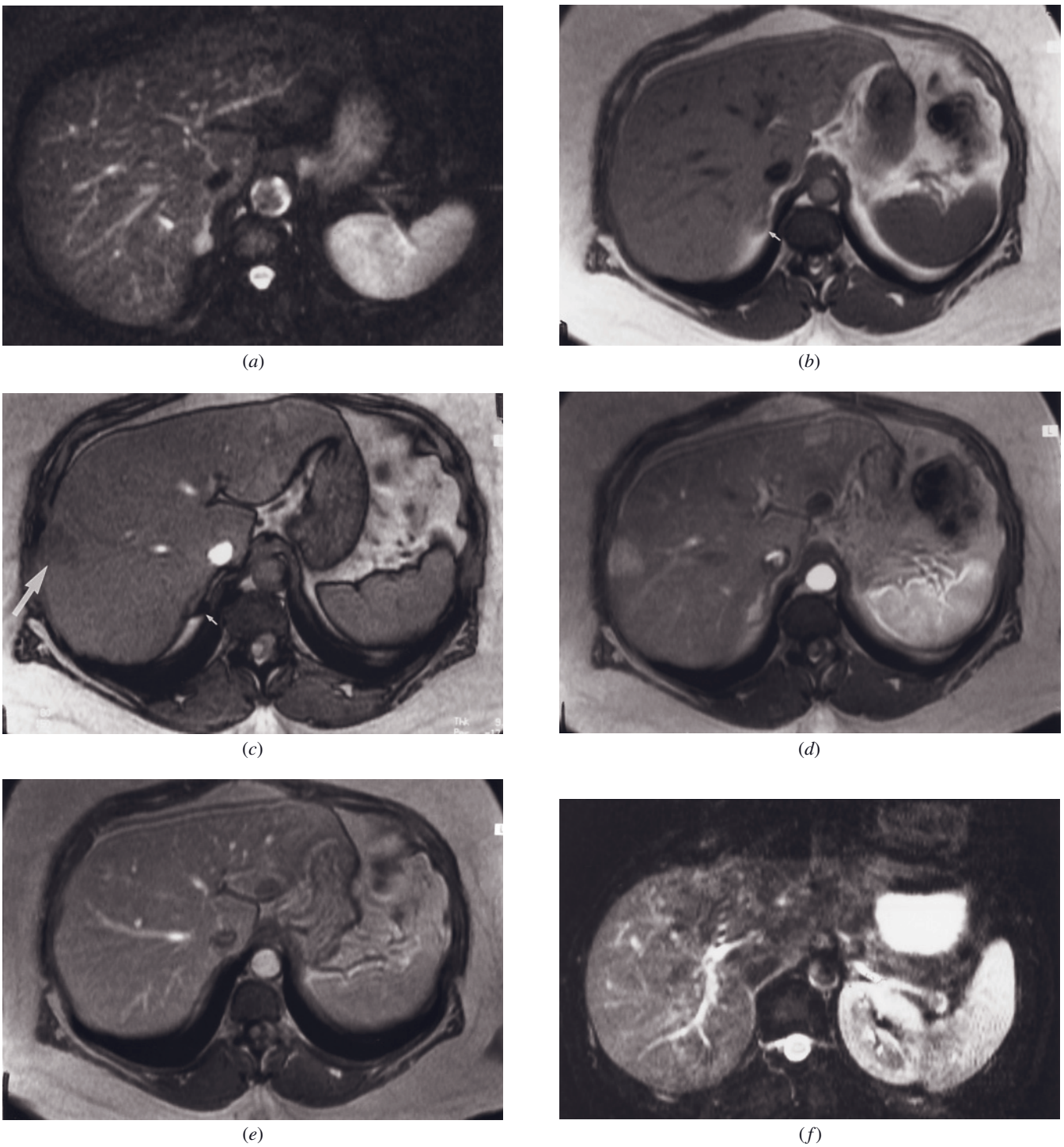

FIG. 2.52 Hepatic adenoma with fat. T2-weighted fat-suppressed ETSE (*a*), SGE (*b*), out-of-phase SGE (*c*), and immediate (*d*) and 90-s (*e*) postgadolinium SGE images. No focal liver lesions are apparent on the T2-weighted image (*a*) or the T1-weighted image (*b*). On out-of-phase image the adenoma is shown as a low-signal mass (arrow, *c*) because of signal drop caused by the presence of fat within the tumor. The adenoma enhances with a characteristic uniform hepatic arterial dominant-phase blush (*d*), which rapidly fades, rendering the tumor isointense with liver by 90 s. Incidental note is made of a right adrenal mass (small arrow, *b, c*) that drops in signal intensity from in-phase (*b*) to out-of-phase (*c*) images, which is diagnostic for adrenal adenoma.

T2-weighted fat-suppressed ETSE (*f*), SGE (*g*), out-of-phase SGE (*h*), and immediate postgadolinium SGE (*i*) images in a second patient. A 4-cm hepatic adenoma is nearly isointense on T2-weighted (*f*) and T1-weighted (*g*) images, drops in signal intensity on

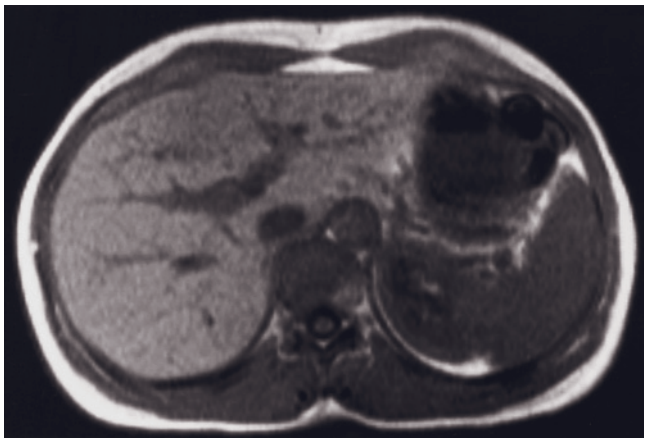

(*g*)

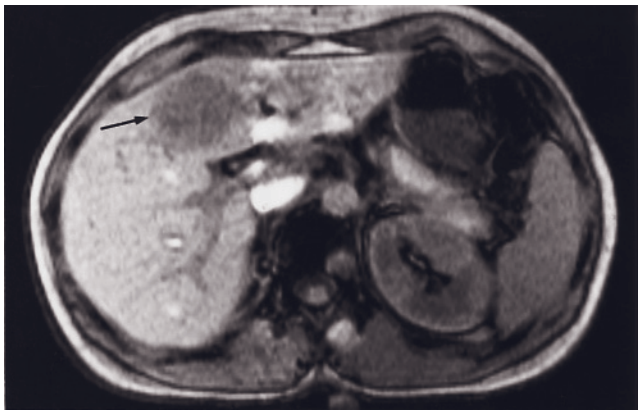

(*h*)

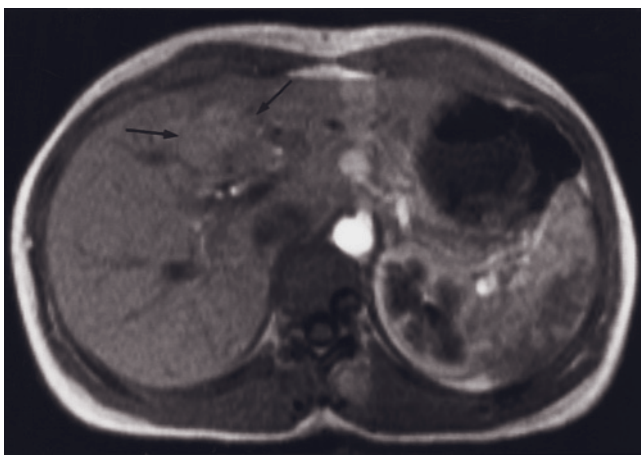

(*i*)

FIG. 2.52 (*Continued*) out-of-phase image (arrow, *h*), and possesses a faint blush on early-phase image (arrows, *i*) greater than that of adjacent liver. The uniform hepatic arterial dominant-phase blush of adenomas permits distinction from focal fatty infiltration, which enhances less than or equal to adjacent liver.

The drop in signal intensity is a relatively common feature of fat-containing HCA and is rarely observed in HCC. Occasionally, the presence of central fibrosis may cause diagnostic confusion with FNH. Although the signal intensity on T2- and T1-weighted precontrast images and the pattern of enhancement of both entities may be quite similar, the presence of fat or hemorrhage within the lesion is suggestive of HCA. Moreover, FNH rarely contains fat or blood, and is more likely to exist in the setting of fatty liver.

Similar to FNH, hepatic adenomas tend to involute with age. In part, this may reflect age-related changes, but this may also reflect hormone-related changes. Unlike FNH, which maintain a well-organized, nonaggressive rounded configuration as they involute, hepatic adenomas tend to have more irregular margins and more irregular signal on all sequences, which mimics the appearance of more aggressive tumors such as metastases and HCC. The explanation for the more heterogenous signal and irregular morphology of these lesions is that they presumably have more fibrosis and perhaps internal hemorrhage as they involute, rendering a more aggressive appearance. A lesion with strikingly irregular spiculated margins within the liver suggests the presence of fibrosis, which may be either spontaneous or the result of therapy. Hence, if a lesion has this appearance, but the patient has no history of chemotherapy for primary malignancy or local therapy for malignant liver lesion, then spontaneous fibrosis should be considered. The lesions with the greatest propensity for spontaneous fibrosis are myofibroblastic tumor (see *Inflammatory Myofibroblastic Tumor* below) and hepatic adenoma.

Rarely, HCA may arise in men, often related to the use of anabolic steroids or an underlying genetic disorder, although sporadic cases with no underlying cause may be observed. The majority of these HCA are asymptomatic and are discovered incidentally during a routine examination. The MR findings of HCA in men are not well established because of their rarity. Preliminary reports suggest that only 25% of the cases will demonstrate the typical findings of HCA as observed in women; notably, in most cases of HCA in men, uniform fat content is not present [98]. The presence

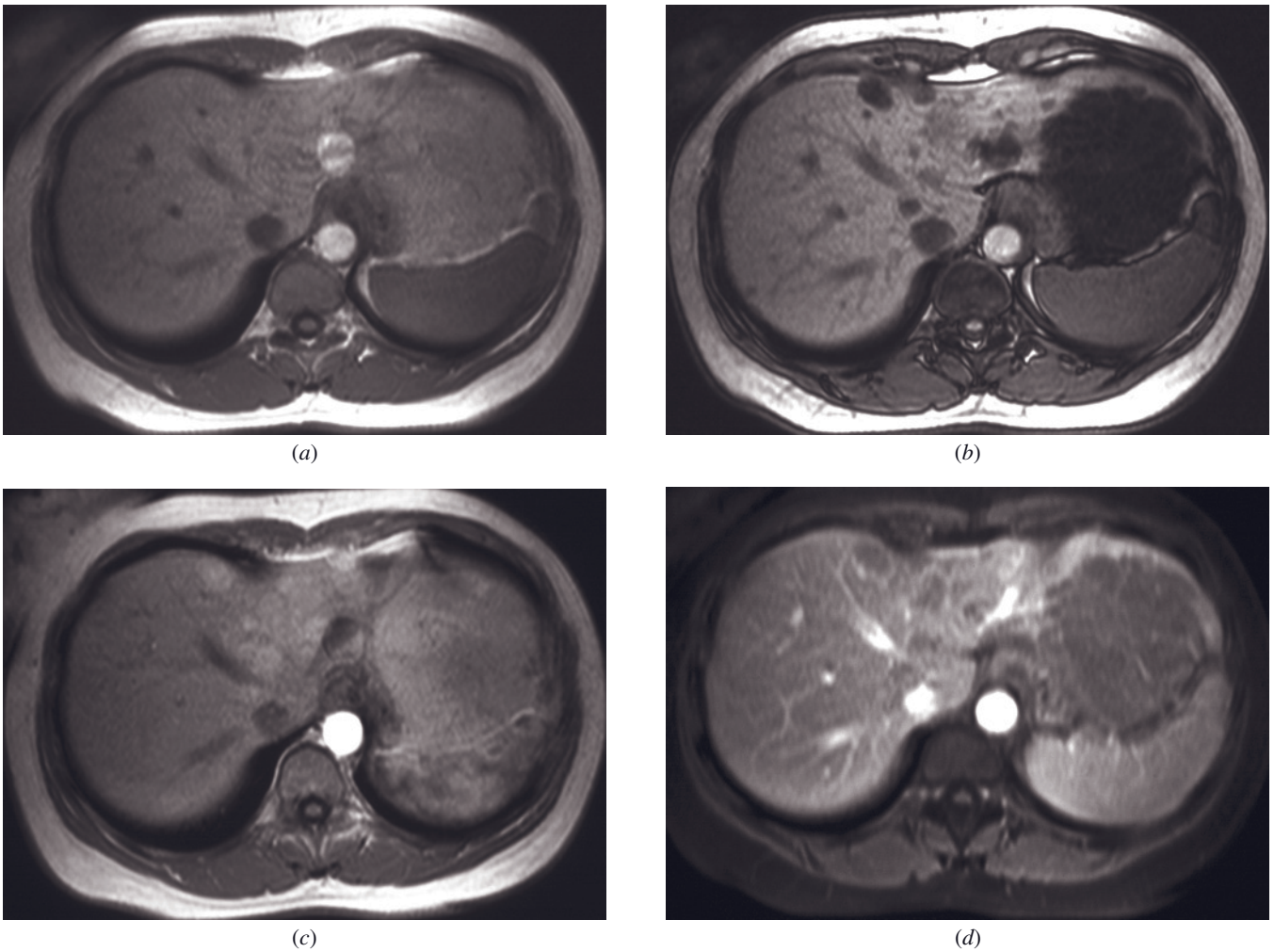

FIG. 2.53 Fat containing adenomatosis. SGE (*a*), out-of-phase SGE (*b*), and immediate (*c*) and 90-s fat-suppressed (*d*) post-gadolinium SGE images. Multiple lesions with varying sizes are seen predominantly present in the left hepatic lobe that show isointensity on T1-weighted images (*a*) and drop in signal intensity on out-of-phase images (*b*) and show a faint homogeneous enhancement on early-phase images (*c*) compatible with fat-containing adenomatosis. On the late-phase image (*d*) some lesions show lower signal intensity than background parenchyma, which may reflect a fat suppression effect, lesion washout, or a combination of both.

and extent of fat, hemorrhage, and necrosis are responsible for the variation in the signal intensity on MRI. The major differential diagnosis to be considered in this setting is HCC. Histopathology is crucial to distinguish these entities. Because hepatocellular adenomas contain hepatocytes, hepatocyte-specific contrast agents (e.g., Mn-DPDP) will be taken up by these tumors [5, 13, 99, 100].

Liver adenomatosis is an uncommon condition first described by Flejou and colleagues in 1985 [101]. As a separate clinical entity, liver adenomatosis may be distinguished from liver cell adenoma by the presence, in the former, of numerous adenomas (>10), lack of correlation with steroid medication, equal involvement in men and women, abnormal liver function tests, and a higher incidence of hemorrhage and malignant transformation. HCAs in the setting of adenomatosis tend to exhibit a more heterogeneous appearance on all MR sequences and more variable enhancement on arterial dominant-phase images when compared to solitary HCAs (figs. 2.53–2.56) [102–104].

Peliosis Hepatis

Peliosis hepatis is characterized by the presence of grossly visible cystic blood-filled spaces in the liver [2, 3]. Peliosis occurs most commonly in the liver, but can occasionally occur in other parts of the reticuloendothelial system including the spleen or bone marrow [105]. Risk factors for peliosis include chronic wasting illnesses such as AIDS, tuberculosis, and cancer [106]

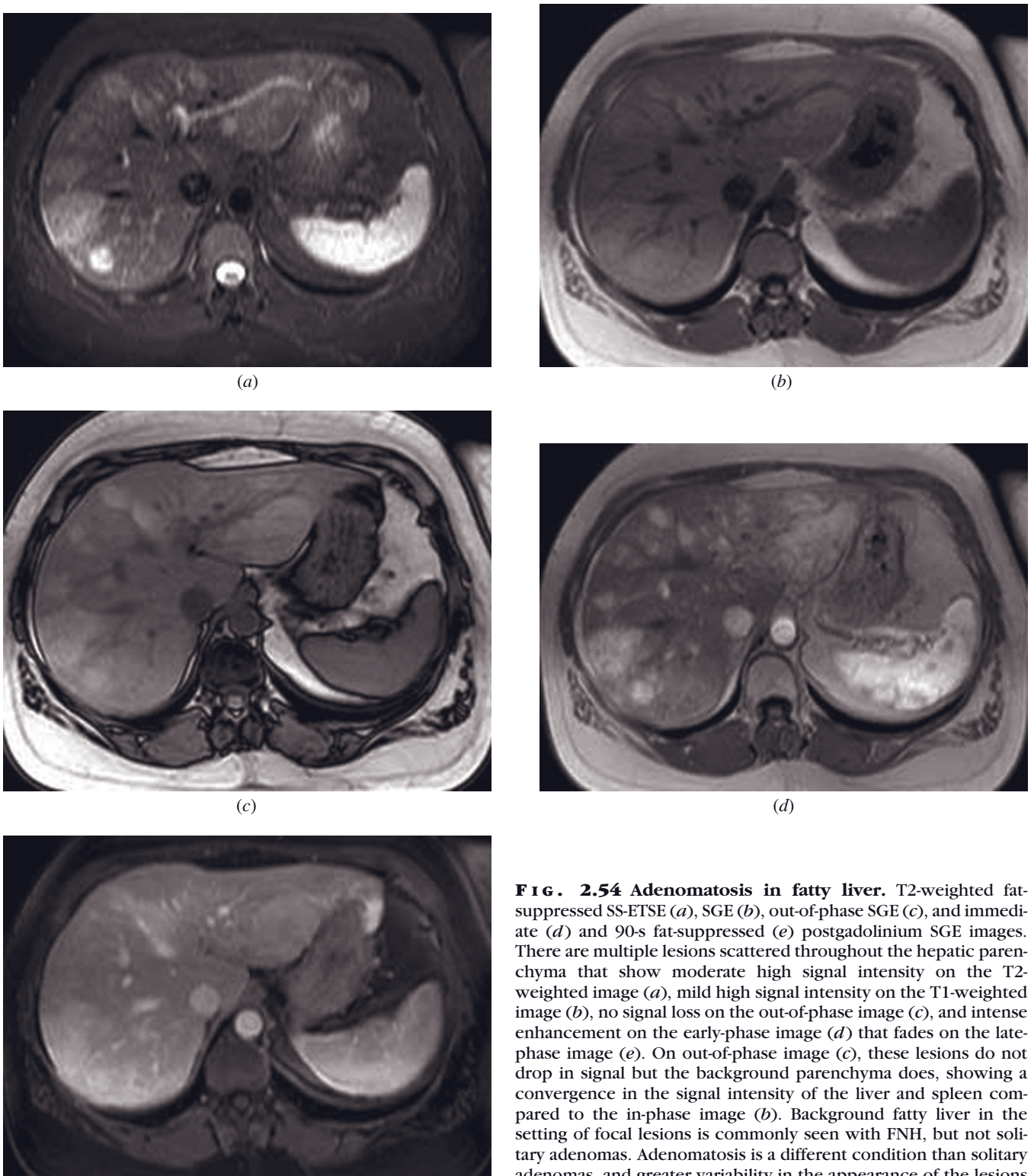

FIG. 2.54 Adenomatosis in fatty liver. T2-weighted fat-suppressed SS-ETSE (*a*), SGE (*b*), out-of-phase SGE (*c*), and immediate (*d*) and 90-s fat-suppressed (*e*) postgadolinium SGE images. There are multiple lesions scattered throughout the hepatic parenchyma that show moderate high signal intensity on the T2-weighted image (*a*), mild high signal intensity on the T1-weighted image (*b*), no signal loss on the out-of-phase image (*c*), and intense enhancement on the early-phase image (*d*) that fades on the late-phase image (*e*). On out-of-phase image (*c*), these lesions do not drop in signal but the background parenchyma does, showing a convergence in the signal intensity of the liver and spleen compared to the in-phase image (*b*). Background fatty liver in the setting of focal lesions is commonly seen with FNH, but not solitary adenomas. Adenomatosis is a different condition than solitary adenomas, and greater variability in the appearance of the lesions and liver is observed.

and drugs such as androgenenic anabolic steroids and oral contraceptives. The term was originally ascribed to macroscopic lesions (*peliosis* = dusky or purple), which may be several centimeters in diameter. The ectatic blood-filled spaces lack an endothelial lining when viewed microscopically. Peliosis hepatis may occur within hepatic neoplasms, including adenomas and hepatocellular carcinoma [2, 3].

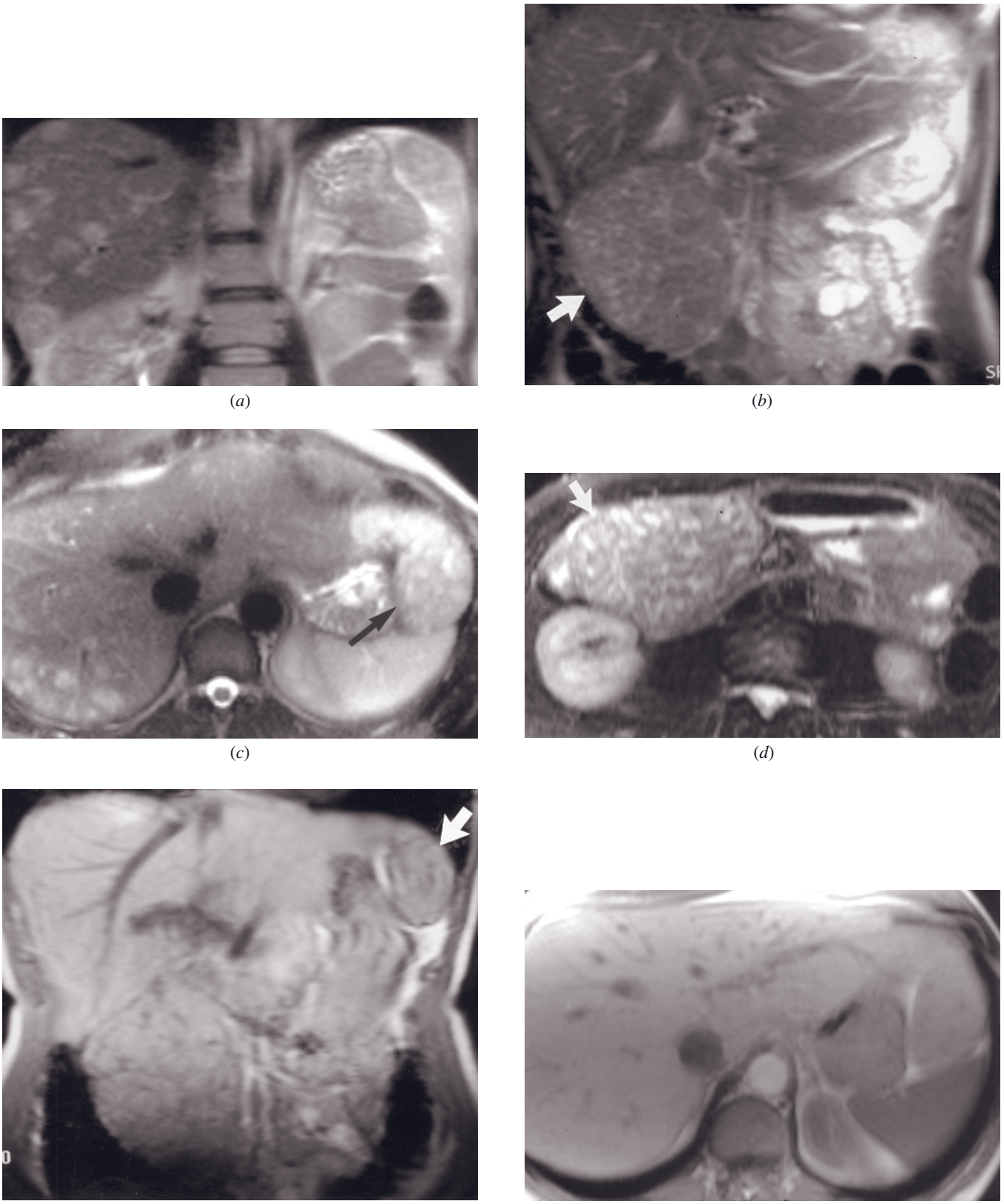

FIG. 2.55 Adenomatosis. Coronal (*a*, *b*) and transverse (*c*, *d*) T2-weighted SS-ETSE, coronal (*e*) and transverse (*f*, *g*) SGE, out-of-phase SGE (*h*, *i*), and immediate (*j*, *k*) and 90-s fat-suppressed (*l*, *m*) postgadolinium SGE images. Multiple small lesions are

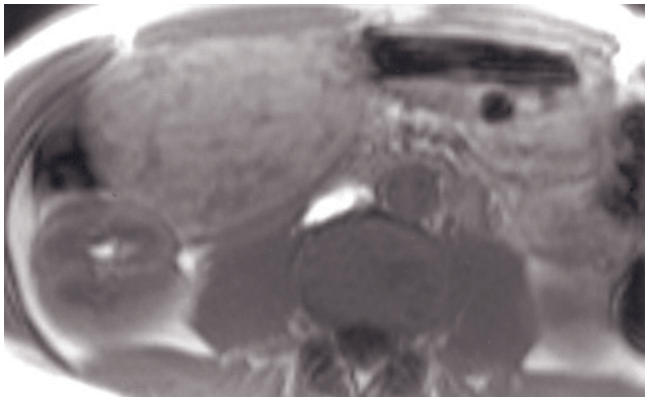

(*g*)

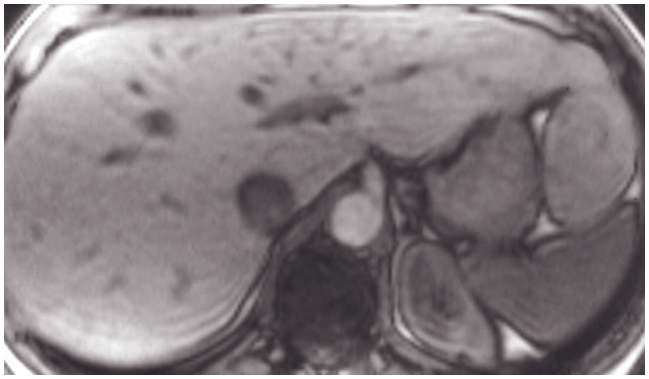

(*h*)

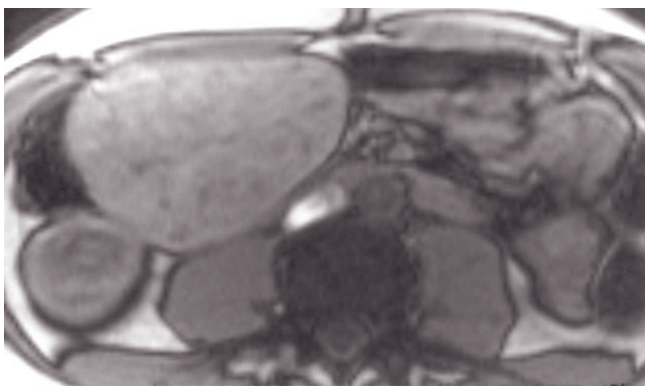

(*i*)

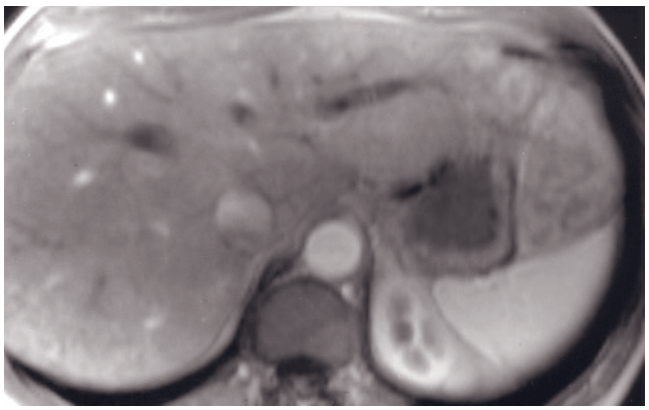

(*j*)

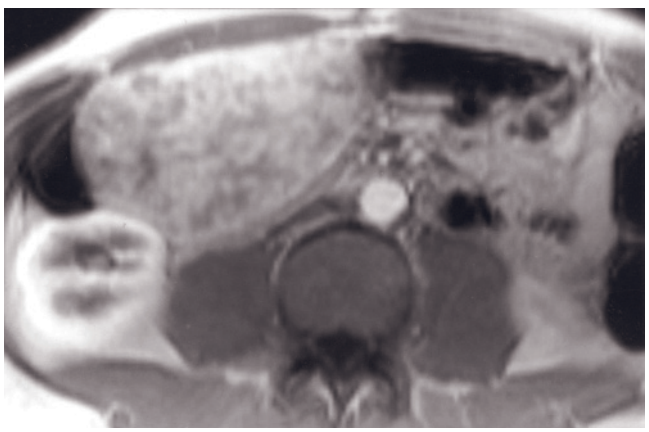

(*k*)

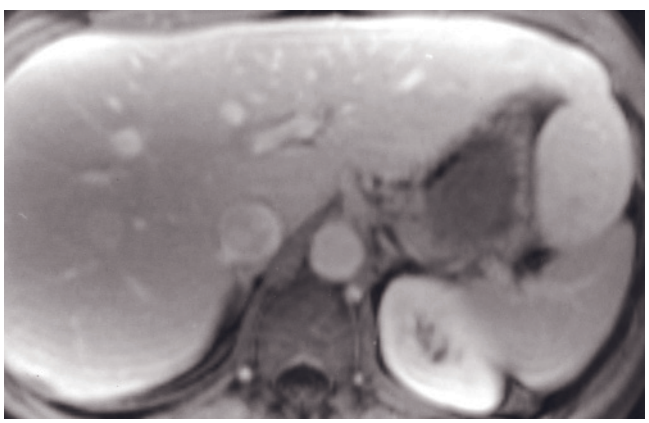

(*l*)

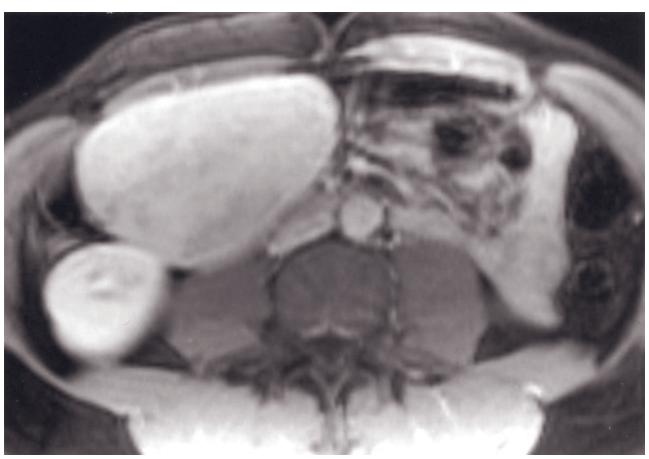

(*m*)

FIG. 2.55 (*Continued*) scattered throughout the hepatic parenchyma, predominantly in the right lobe, that demonstrate slight high signal on T2-weighted images (*a*, *c*), near isointensity on T1-weighted image (*f*), and mildly intense homogeneous enhancement immediately after administration of contrast (*j*, *k*) and become isointense with the liver by 90 s (*l*, *m*). Two exophytic lesions are seen, one of them in the tip of the left lobe (arrow, *c, e*) and the other an 8-cm tumor (arrow, *b, d*), in the right lobe. Both lesions demonstrate mildly heterogeneous signal intensity on T2-weighted images (*a–d*) and T1-weighted images (*e–g*). On early-phase images (*j*, *k*) the lesions enhance in a heterogeneous variegated fashion and become homogeneous on late-phase images (*l*, *m*). The intense heterogeneous variegated regular pattern on the early-phase images is rare for adenomas and raises the suspicious of hepatocellular carcinoma. It may be that adenomas in the setting of adenomatosis may be more heterogeneous than standard adenomas.

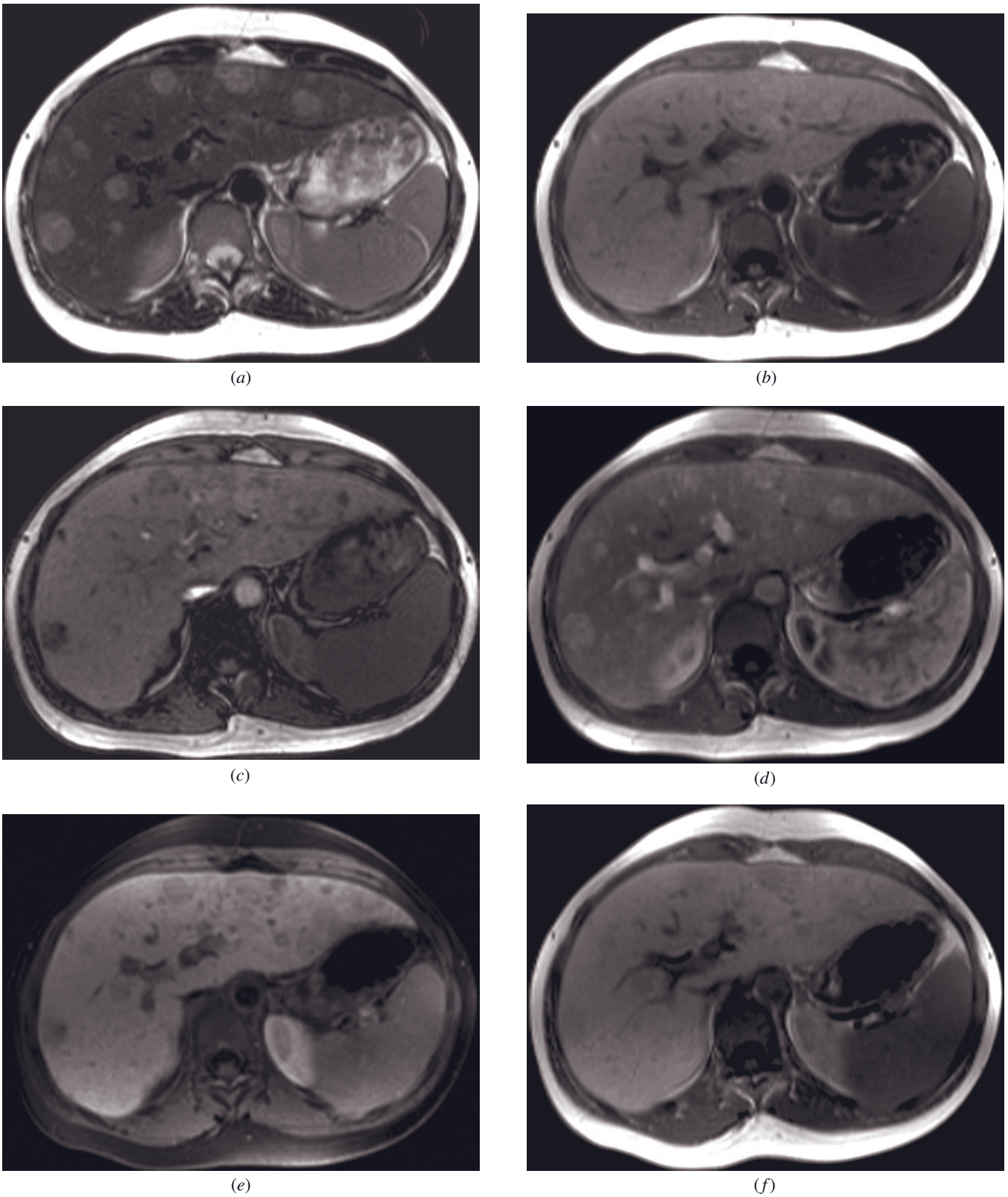

FIG. 2.56 Adenomatosis, Gd-BOPTA. T2-weighted SS-ETSE (*a*), SGE (*b*), out-of-phase SGE (*c*), and immediate (*d*), 90-s fat-suppressed (*e*), and 1-h (*f*) SGE after administration of Gd-BOPTA. Multiple lesions with varying sizes are seen in the hepatic parenchyma. These lesions demonstrate moderately high signal intensity on the T2-weighted image (*a*), isointensity on the T1-weighted image (*b*), drop in signal intensity on the out-of-phase image (*c*), and intense enhancement on the early phase image (*d*). On the late-phase image (*e*) these lesions show low signal intensity partially due to the fat suppression effect of this sequence. One hour (*f*) after administration of contrast, the lesions are low signal relative to liver, suggesting that there is no uptake of the contrast by the hepatocytes. This finding is consistent with adenomatosis and rules against multiple FNHs. (Courtesy of Guenther Schneider, M.D., Ph.D., Dept. of Diagnostic and Interventional Radiology, University Hospital Homburg/Saar, Germany).

The MR imaging appearance of peliosis hepatis is not well established. It has been described that peliosis hepatis may demonstrate varying signal intensity on T2-weighted and T1-weighted images according to the stage of hemorrhage. After contrast administration, peliosis hepatis may show moderate to intense enhancement on arterial dominant-phase images [107–111]. It is not clear to date whether the MR findings reflect this entity itself or the appearance of coexistent focal lesions, such as hepatic adenomas (fig. 2.57).

Focal Nodular Hyperplasia

Focal nodular hyperplasia (FNH) is an uncommon lesion defined by a localized region of hyperplasia within otherwise normal liver [2]. Although the lesion may occur in all age groups and both sexes, FNH predominantly is found in women during the third to fifth decades of life; after that age they tend to show progressive involution and are rarely observed in individuals beyond age 60, reflecting the frequency of this age-related involution. In contrast to hepatocellular adenomas (HCA), FNH does not appear to have a clear-cut association with oral contraceptive use [92]. Generally, FNH is a solitary lesion and tends to involute while maintaining its rounded configuration. Multicentric lesions may be encountered as part of the multiple FNH syndrome including other lesions such as liver hemangioma, meningioma, astrocytoma, telangiectasias of the brain, berry aneurysm, dysplastic systemic arteries, and portal vein atresia [78]. FNH does not exhibit malignant potential [93].

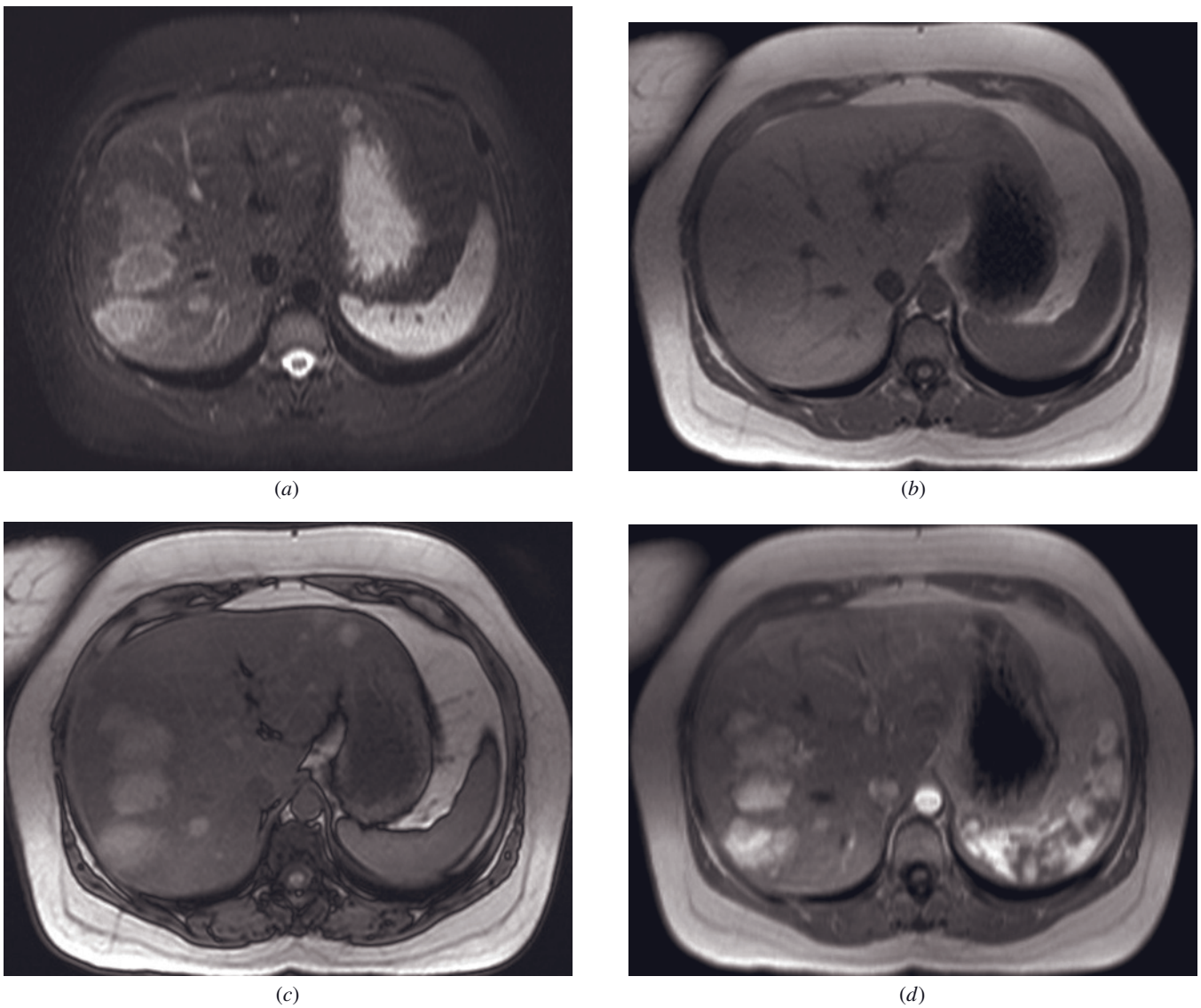

Fig. 2.57 Peliosis. Fat-suppressed T2-weighted SS-ETSE (*a*), SGE (*b*), out-of-phase SGE (*c*), and immediate (*d*) and 90-s fat-suppressed (*e*) postgadolinium SGE images. There are multiple liver lesions that demonstrate moderately high signal intensity on

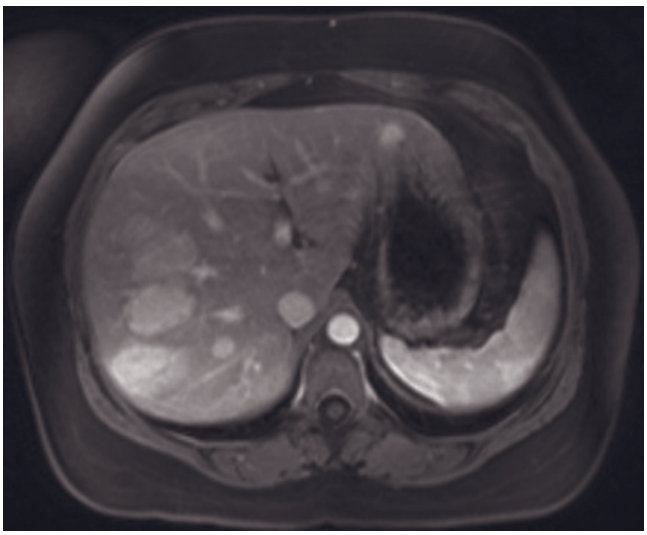

(*e*)

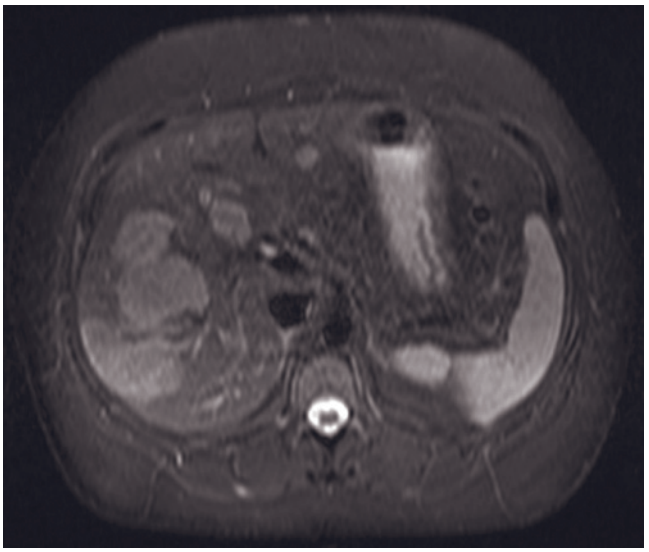

(*f*)

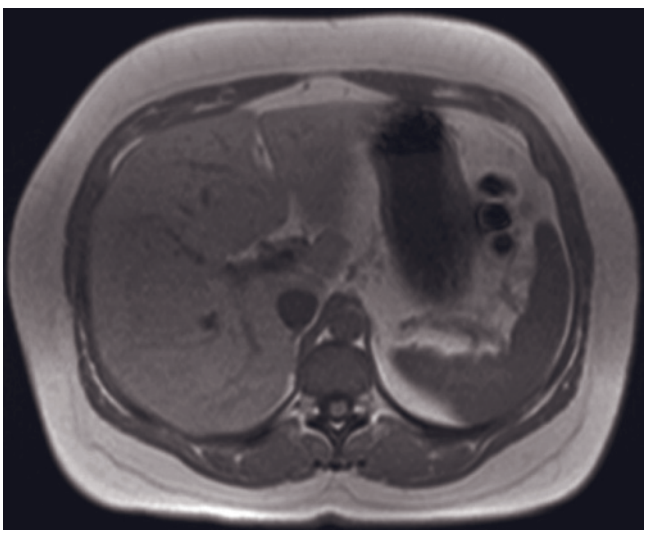

(*g*)

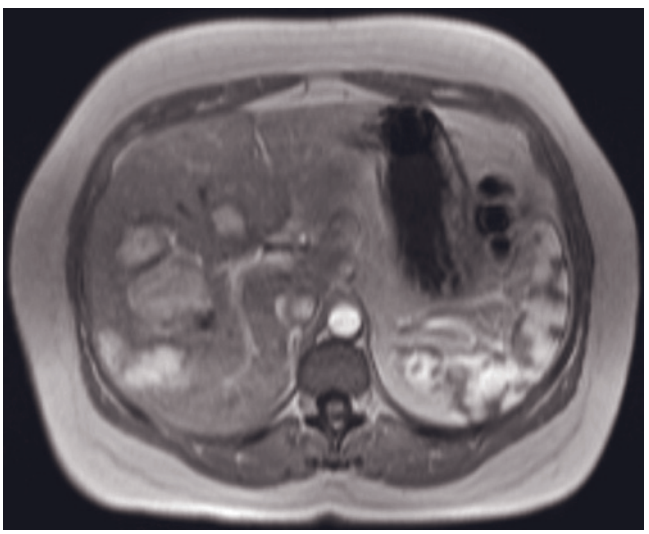

(*h*)

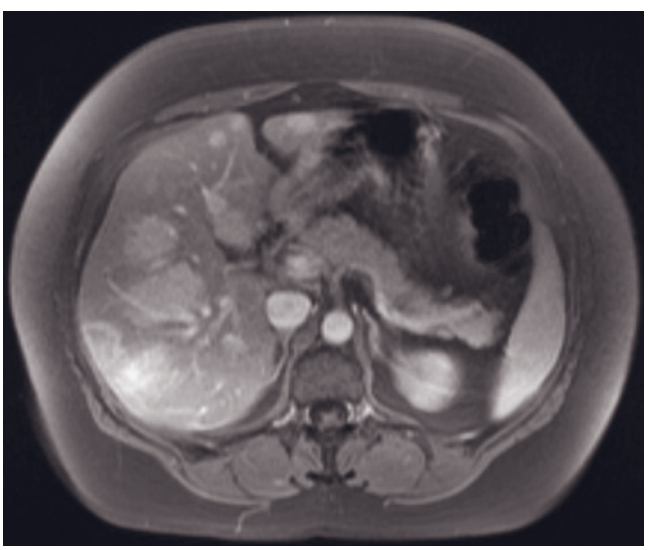

(*i*)

FIG. 2.57 (*Continued*) T2-weighted images (*a*), isointensity to background parenchyma on T1-weighted images (*b*), and intense enhancement on early-phase images (*d*) that persists on late-phase images (*e*). On out-of-phase image, the liver drops in signal intensity, which is compatible with fat replacement. Histopathology was consistent with peliosis. At the present time it is not clear whether in all cases the MR imaging appearance of peliosis hepatis reflects this entity itself or the appearance of coexistent focal lesions, such as hepatic adenomas.

T2-weighted fat-suppressed SS-ETSE (*f*), SGE (*g*), and immediate (*h*) and 90-s fat-suppressed (*i*) postgadolinium SGE images in a second patient showing features similar to those previously described.

Although the pathoetiology of FNH is incompletely understood, it has been proposed that the lesion is developmental in origin, consisting of a hyperplastic response of hepatic parenchyma to a preexisting arterial malformation [112]. From a pathologic perspective, FNH is characterized grossly as a sharply circumscribed, but unencapsulated, rounded or lobulated mass. The cut surface reveals a central stellate scar, often containing large, malformed blood vessels. It is postulated that the spiderlike branches of the anomalous vessels provide excellent blood supply to the component nodules; hence these tumors are usually homogeneous (with internal necrosis and hemorrhage being rare events) [113]. Microscopically, fibrous septa radiating from the central scar contain vascular channels, exuberant bile duct proliferation, and intense inflammation. Parenchyma between the septa shows benign hepatocytes.

Two subtypes of FNH have been described: 1) solid type, which is most common and is characterized by the presence of a central fibrous scar containing enlarged malformed arteries that may be inconspicuous or absent in lesions <1 cm, and 2) telangiectatic type, which is characterized by the presence of centrally located multiple dilated blood-filled spaces. This subtype is enriched with more abundant and smaller arteries than the solid type. The telangiectatic type of FNH is more commonly associated with the multiple FNH syndrome [78, 93].

The most common appearance on noncontrast MR images is mild hyperintensity on T2-weighted images and mild hypointensity on T1-weighted images, although tumors may be nearly isointense on both of these sequences. Unlike HCA, FNH rarely has higher signal intensity than liver on T1-weighted images; hemorrhage is uncommon, encountered most often in large lesions [92, 114–116]. FNH enhances with an intense uniform blush on immediate postgadolinium images and fades rapidly to near isointensity (typically at 1 min after contrast) (fig. 2.58). Commonly, small (<1.5 cm) FNH is isointense on all precontrast images and may be appreciated only on the immediate postgadolinium SGE images.

The central scar in FNH has a typical appearance of a relatively small size with sharp angular margins. Thin radial septations are also often present. High signal intensity on T2-weighted images of the central scar is a characteristic feature of FNH but is observed in only 10–49% of patients [114, 117–121]. The hyperintense appearance of the central scar on T2-weighted images may correlate with the presence of vascular channels, bile ducts, fibrosis, chronic inflammation, and edema noted histopathologically. When observed, the central scar exhibits lack of enhancement on immediate postgadolinium images, and the majority show gradual enhancement to hyperintensity over time (figs. 2.59 and 2.60). This enhancement pattern is that of scar tissue independent of location. In small FNH (<1.5 cm), the central scar is often not apparent. Larger FNH has a tendency to have central scars that show only partial enhancement on delayed images, which may reflect more mature, less vascularized scar tissue.

On imaging, background fatty liver may be more common in FNH than that observed with other focal liver lesions, except metastases. A collar of higher-concentration perilesional fatty infiltration may rarely be present [122], which differs from the perilesional fatty sparing of metastasis. In the setting of diffuse fatty liver the tumor may be mildly hypointense on in-phase T1-weighted images and hyperintense on out-of-phase images (figs. 2.61 and 2.62). Fatty infiltration of FNH is rare and only sporadically mentioned in the literature [115, 116]. Unlike the situation with HCA, we have not observed signal drop of FNH on out-of-phase images. In previous reports describing the presence of fat in FNH, fatty infiltration of the lesion was interpreted as an extension of the patient's underlying disease, that is, hepatic steatosis. In theory, intralesional steatosis in FNH may be encountered in several types of hepatic injury associated with steatosis, including alcoholic toxicity, obesity, diabetes, and malnutrition [114].

FNH may also occur as exophytic lesions and the attachment to liver may be a thin stalk. Even exophytic tumors possess the characteristic imaging appearance (fig. 2.63) [103].

There are several imaging features that help to distinguish between FNA and HCA. A central scar that shows delayed enhancement is typical for FNH, whereas pseudocapsule, internal hemorrhage, focal necrosis, and intralesional fat are features more commonly noted in HCA. Both lesions have an uniform transient tumor blush on early gadolinium enhanced images that fades away toward parenchyma isointensity on late images. Also, both lesions may take up Mn-DPDP [96, 99, 121, 123, 124].

Hepatocyte-selective contrast agents may distinguish between hypervascular metastases and atypical FNHs. However, a uniform capillary blush and uptake of Mn-DPDP must be cautiously interpreted because they are features of well-differentiated tumors of hepatocellular origin, including well-differentiated or small HCC. On Gd-EOB-DTPA- and Gd-BOPTA-enhanced images, FNH will show an early capillary blush and late hepatocellular uptake, and the late uptake is not observed with HCA (figs. 2.64 and 2.65) [5, 125].

Malignant Masses

Liver Metastases

Metastases are the most common malignant tumors of the liver in western countries. The most common primary tumors metastatic to the liver originate from the

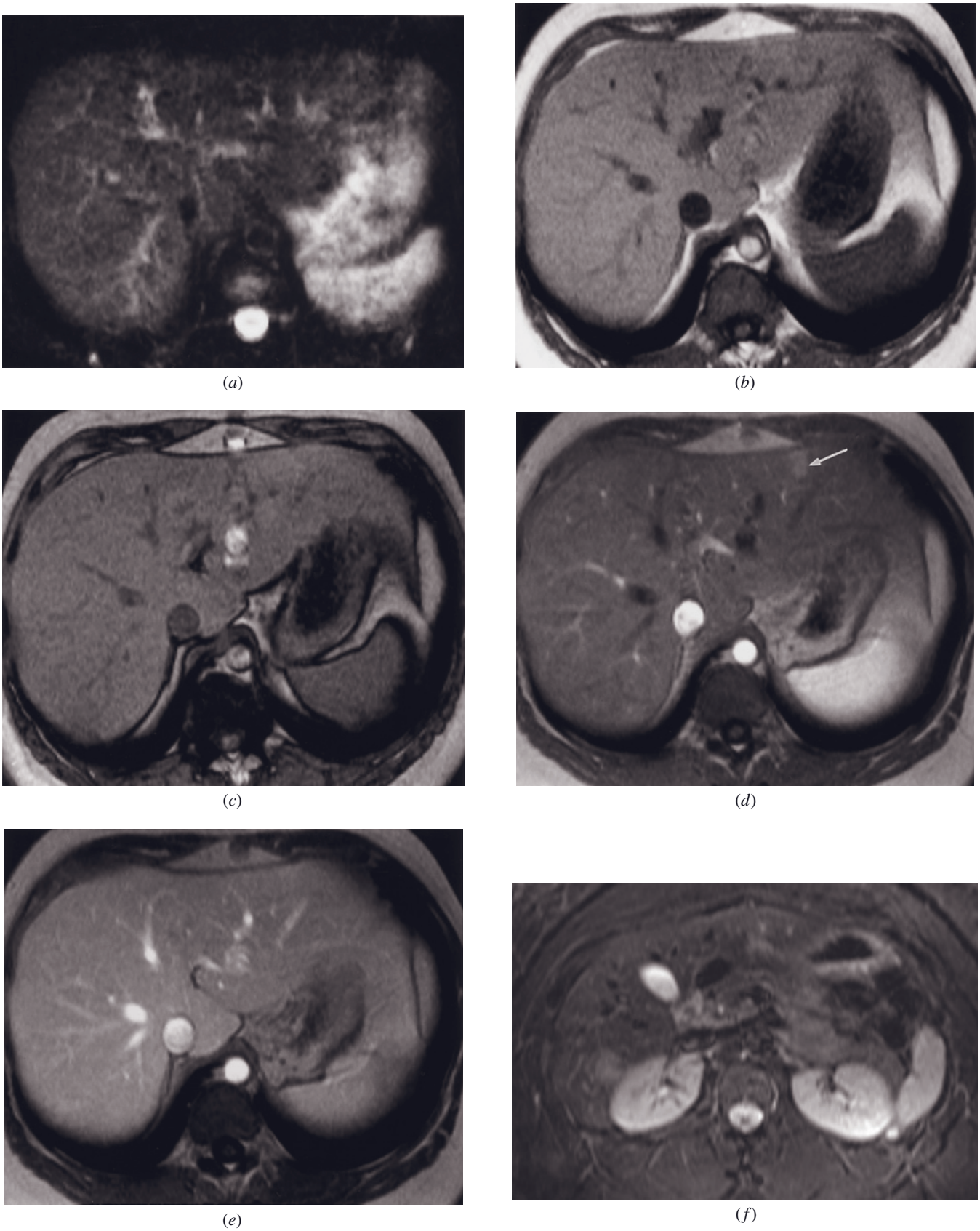

FIG. 2.58 Small-sized FNH. T2-weighted fat-suppressed ETSE (*a*), SGE (*b*), out-of-phase SGE (*c*), and immediate (*d*) and 90-s (*e*) postgadolinium SGE images. A 1.5-cm FNH is present in the lateral hepatic segment, and it is isointense on T2-weighted image (*a*) and near isointense on T1-weighted image (*b*) and does not drop in signal on out-of-phase images (*c*). The tumor is only visualized on the immediate postgadolinium SGE image by the presence of a hepatic arterial dominant blush (arrow, *d*). The tumor fades by 90 s to isointensity with background liver (*e*).

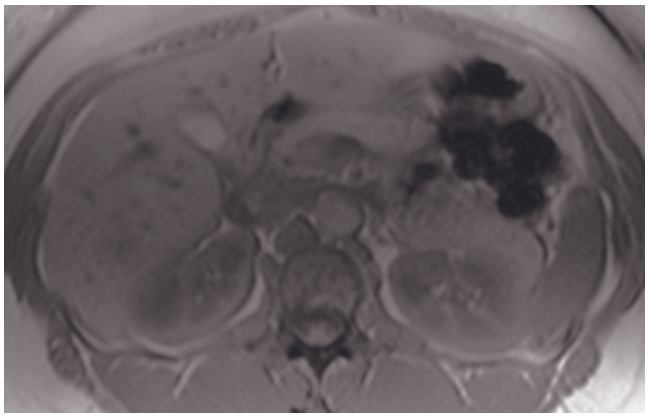

(*g*)

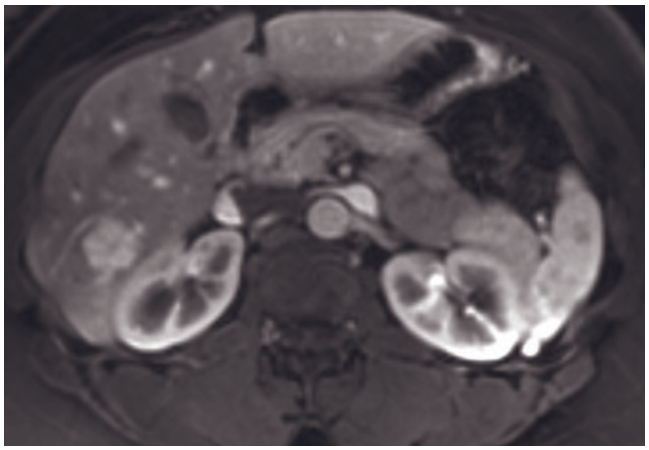

(*h*)

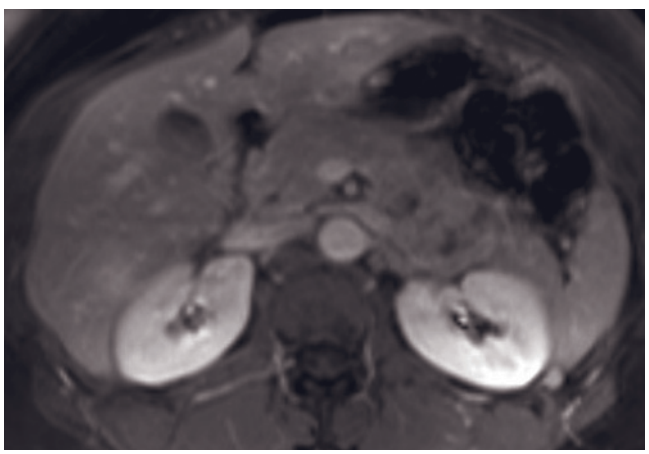

(*i*)

FIG. 2.58 (*Continued*) T2-weighted fat-suppressed SS-ETSE (*f*), 3D-gradient echo (*g*), and immediate (*h*) and 90-s fat-suppressed (*i*) postgadolinium 3D-gradient echo images obtained **at 3T** in a third patient with an FNH showing findings similar to those previously described.

Small, 1-cm, FNH may be only visible on hepatic arterial dominant-phase images. A central scar is often not visualized in small FNHs.

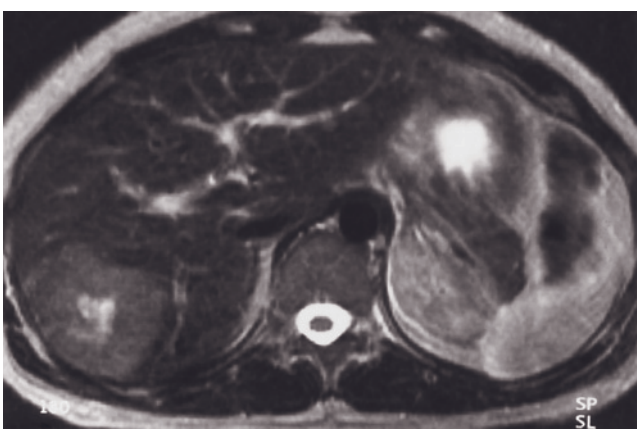

(*a*)

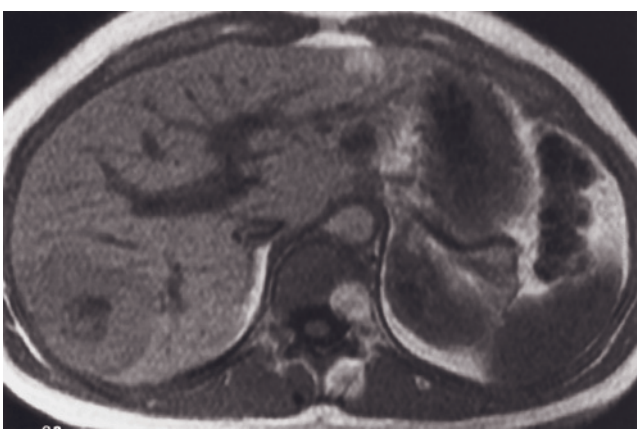

(*b*)

FIG. 2.59 Medium-sized FNH. T2-weighted ETSE (*a*), SGE (*b*), and immediate (*c*) and 5-min (*d*) postgadolinium SGE images.

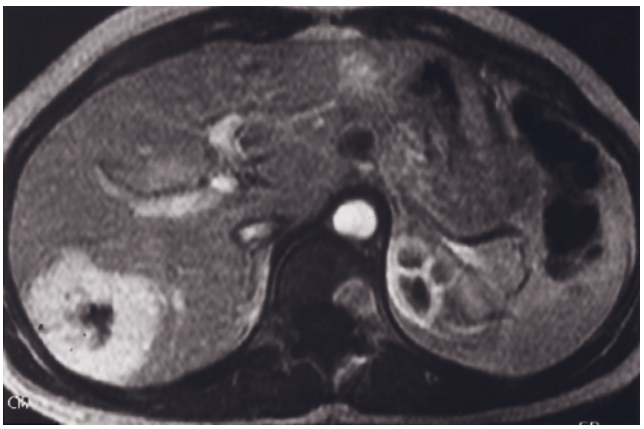

(*c*)

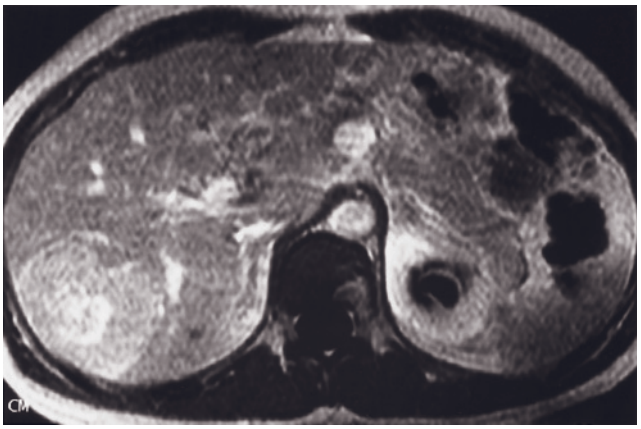

(*d*)

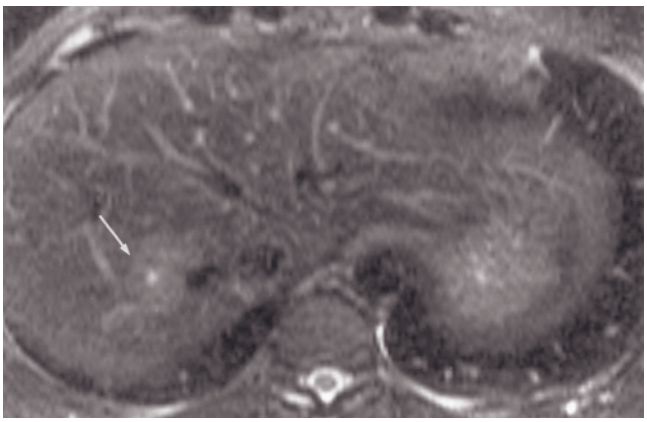

(*e*)

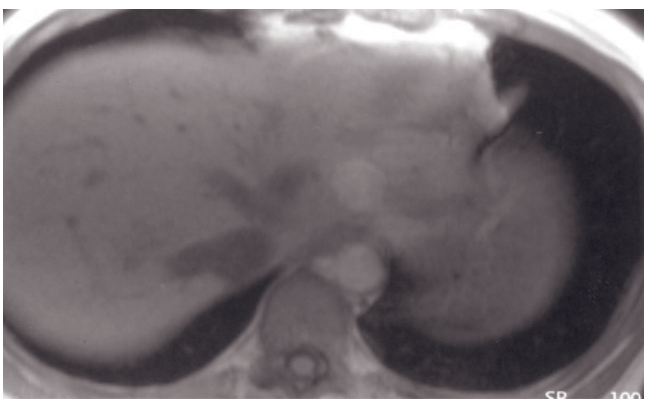

(*f*)

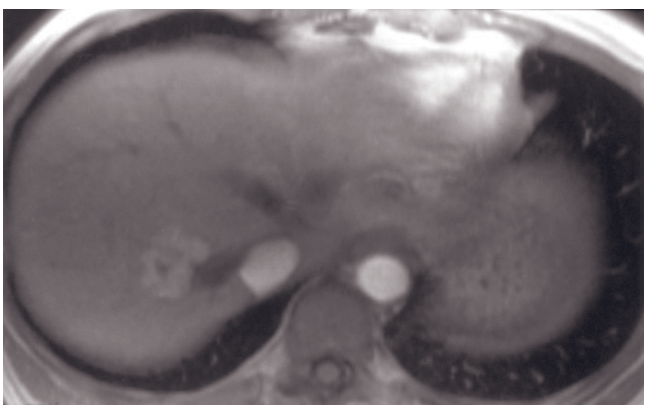

(*g*)

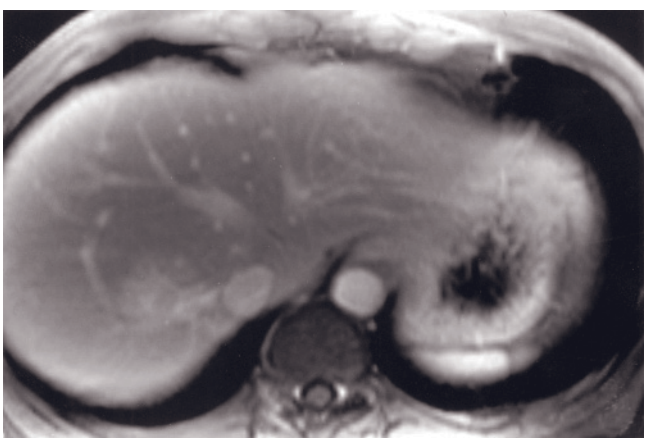

(*h*)

FIG. 2.59 (*Continued*) A 5.5-cm mass is present in the right hepatic lobe, and it shows mildly hyperintense on T2-weighted image (*a*) and mildly hypointense on the T1-weighted image (*b*). A central scar is present that is high in signal intensity on T2 (*a*) and low in signal intensity on T1 (*b*). On the immediate postgadolinium image (*c*), the tumor enhances with a uniform capillary blush, whereas the central scar remains low in signal intensity. On the late-phase image (*d*), the tumor fades to near isointensity with background parenchyma, whereas the central scar shows delayed enhancement (Courtesy of Susan M. Ascher, M.D., Department of Radiology, Georgetown University Medical Center.)

Echo train-STIR (*e*), SGE (*f*), and immediate (*g*) and 90-s (*h*) postgadolinium SGE images in a second patient. There is a lesion in the right hepatic lobe (arrow, *e*) that demonstrates minimally high signal on the T2-weighted image (*e*) and isointensity on the T1-weighted image (*f*), enhances with a uniform blush on early-phase image (*g*), and fades to near isointensity on the late-phase image (*h*). Note the small central scar that is high signal on T2-weighted image (*e*) and low signal intensity on T1-weighted image (*f*) and demonstrates negligible enhancement on early-phase image (*g*) and moderate enhancement over time (*h*).

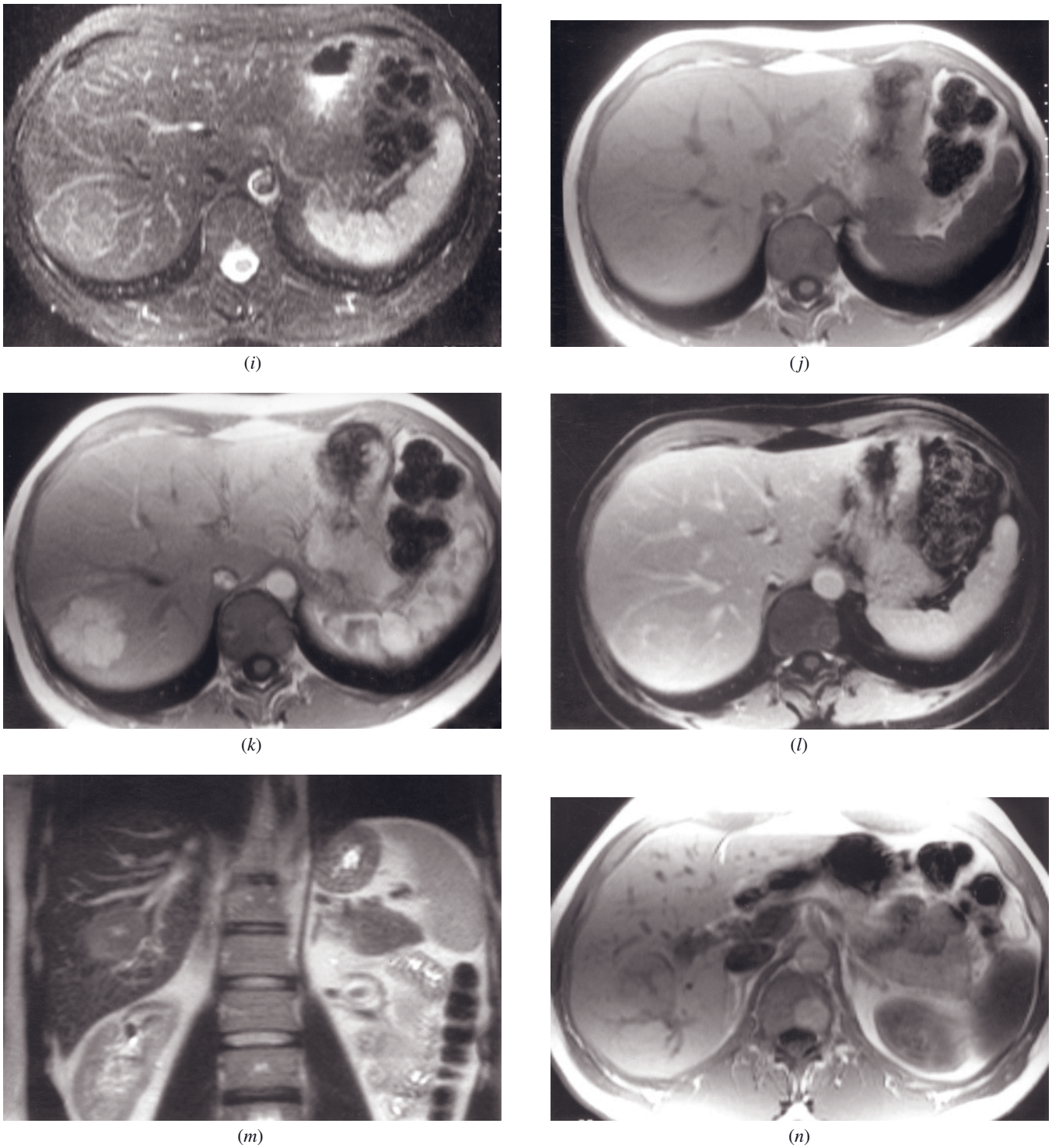

FIG. 2.59 (*Continued*) Echo train-STIR (*i*), SGE (*j*), and immediate (*k*) and 90-s fat-suppressed (*l*) postgadolinium SGE images in a third patient. There is a lobular lesion in the right hepatic lobe that has minimally increased signal on T2-weighted image (*i*) and near isointensity on T1-weighted image (*j*), demonstrates intense uniform enhancement on the early-phase image (*k*), and fades to near isointensity on the late-phase image (*l*). There is a small central scar best seen as a low-signal linear structure on the immediate postcontrast image (*k*).

Coronal T2-weighted SS-ETSE (*m*), SGE (*n*), and immediate (*o*) and 90-s fat-suppressed (*p*) postgadolinium SGE images in a fourth patient. The 3.5-cm FNH has a partial pseudocapsule (arrow, *o*). The pseudocapsule and central scar show partial enhancement on the late-phase image (*p*). The lesion otherwise has a typical MRI appearance for a FNH.

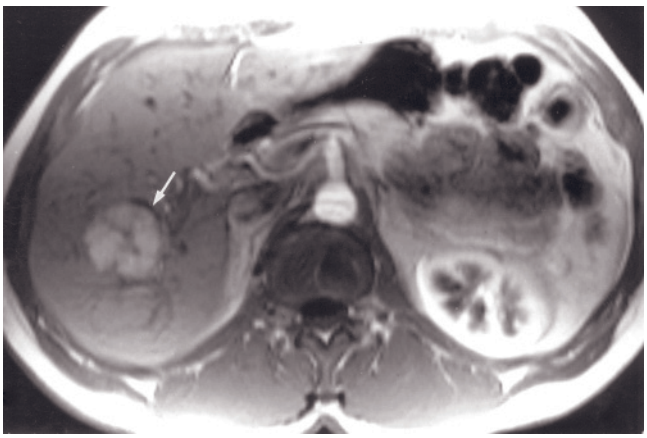

(*o*)

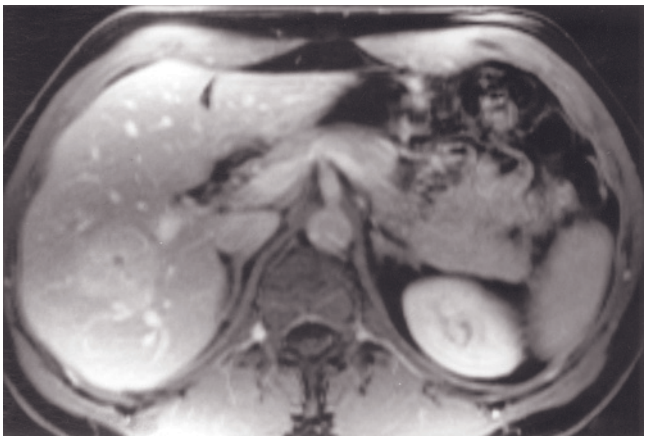

(*p*)

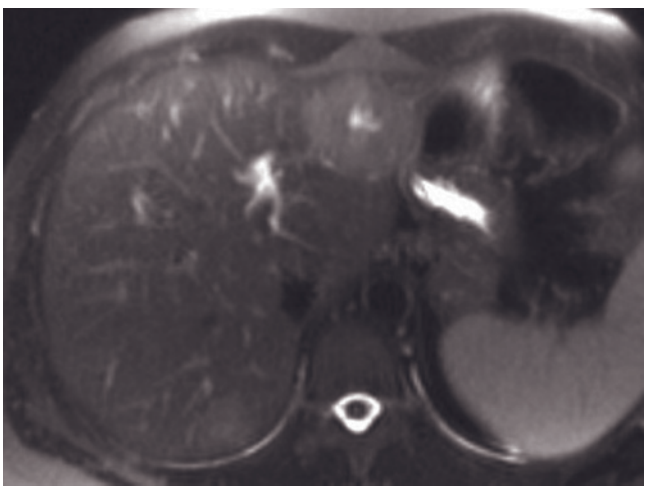

(*q*)

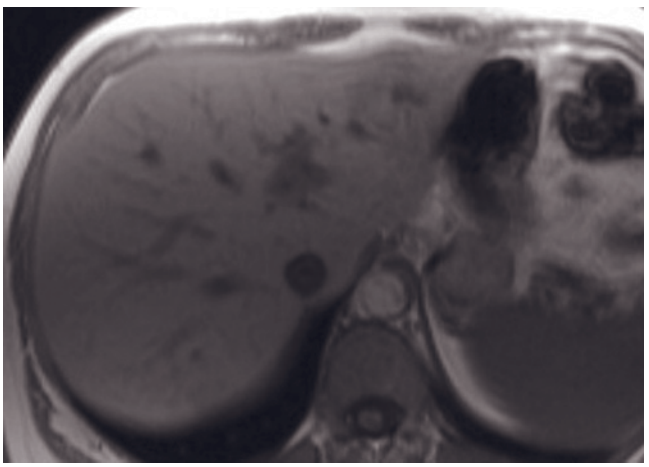

(*r*)

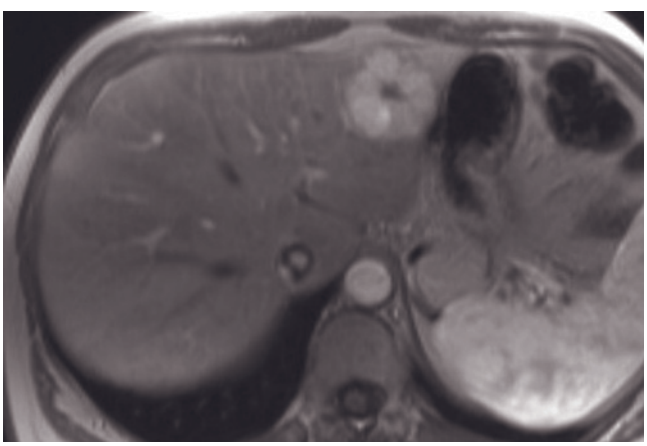

(*s*)

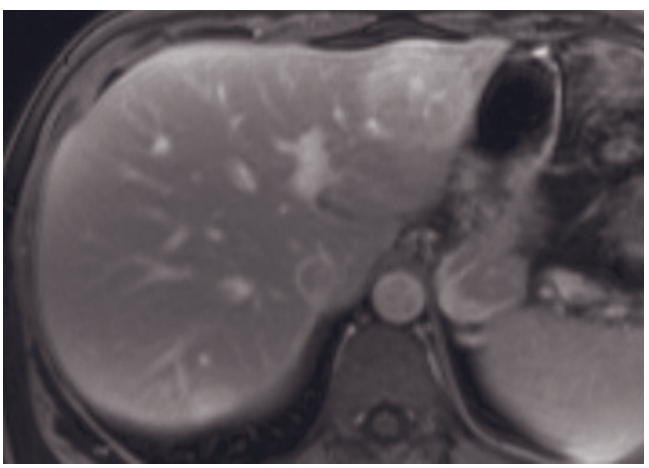

(*t*)

FIG. 2.59 (*Continued*) T2-weighted SS-ETSE (*q*), SGE (*r*), and immediate (*s*) and 90-s fat-suppressed (*t*) postgadolinium SGE images in a fifth patient with a typical FNH in the left lobe.

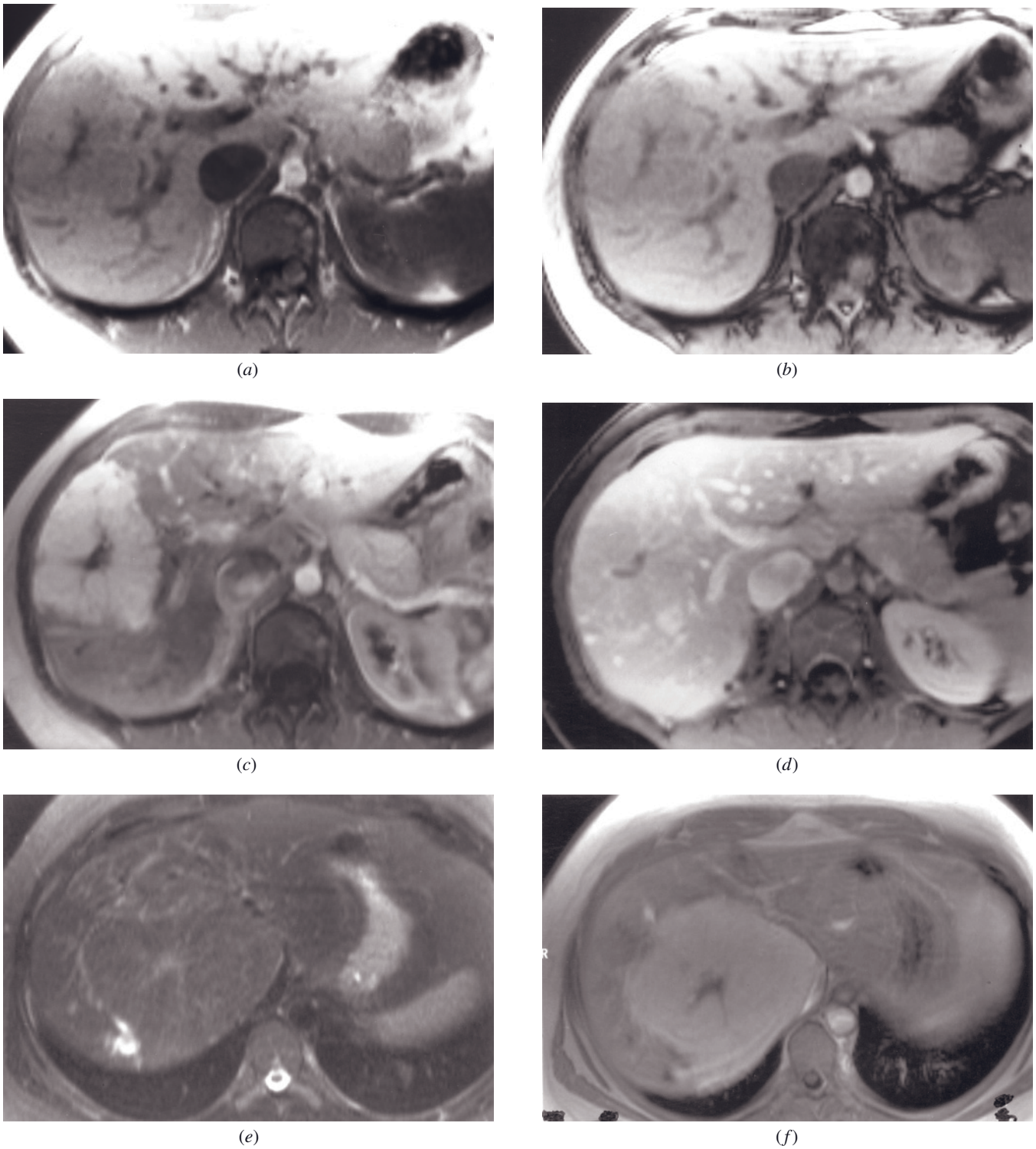

FIG. 2.60 Large-sized FNH. SGE (*a*), out-of-phase SGE (*b*), and immediate (*c*) and 90-s fat-suppressed (*d*) postgadolinium SGE images. A large lesion is seen in the right hepatic lobe that is mildly hypointense on T1-weighted image (*a*), does not drop in signal intensity on out-of-phase image (*b*), and shows intense homogeneous enhancement on early-phase image (*c*) that fades away on late-phase image (*d*). The central scar exhibits lack of enhancement on early-phase image (*c*) but enhances partially on late-phase image (*d*). The central scar in FNH is commonly small in size with angular margins. FNH almost never drop in signal on out-of-phase images, unlike adenomas, which commonly do.

Echo-train STIR (*e*) and immediate (*f*) and 90-s fat-suppressed (*g*) postgadolinium SGE images in a second patient. There is a

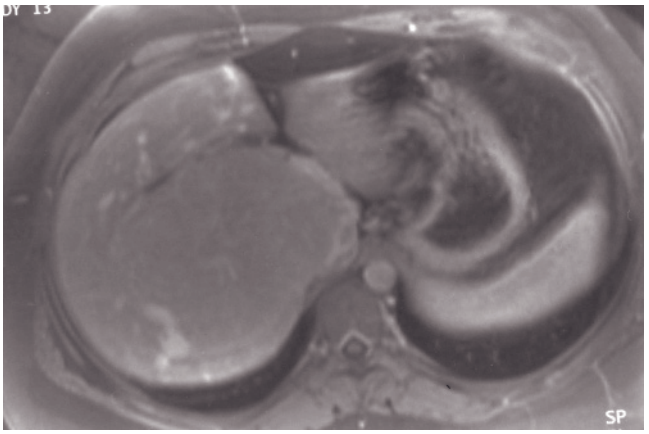

(*g*)

FIG. 2.60 (*Continued*) FNH with a small central scar and lobular margins in the right hepatic lobe. The tumor has signal comparable to surrounding liver on T2-weighted image (*e*) and shows moderate homogeneous enhancement on early-phase image (*f*) that fades away on late-phase image (*g*). The central scar is slightly hyperintense on the T2-weighted image (*e*), exhibits negligible enhancement on the early-phase image (*f*), but enhances over time (*g*).

lung, gastrointestinal tract, and breast [2, 3]. Pathologically, liver metastases usually appear as solitary or multiple nodules, with rare appearances including confluent masses or small, infiltrative lesions mimicking cirrhosis. Lesion shape is influenced by its size. Small metastases tend to be round or oval, and large metastases may adopt a more irregular morphology. Borders are commonly ill defined but may be sharp. Metastasis may be complicated by hemorrhage, central necrosis, or cystic change.

Role of MRI in the Detection and Characterization of Liver Metastases. Optimal hepatic imaging evaluation involves both detection and characterization of focal lesions [69, 124, 126, 127]. The detection of focal liver lesions by imaging is achieved through signal intensity differences between the lesion and the surrounding parenchyma. Detection involves identification of the presence of lesions and the segmental extent of liver involvement [126]. Demonstration that malignant disease has limited hepatic involvement may have a substantial impact on patient management. Survival of patients with colorectal metastases may be improved by partial hepatectomy, if metastases are localized to three or fewer segments [128, 129]. Tantamount to detection by imaging is characterization of lesions as benign or malignant, and in cases where initial imaging assessment is uncertain, histologic diagnosis or follow-up imaging.

An imaging protocol including T2-weighted images, T1-weighted gradient-echo precontrast images, and dynamic serial gadolinium-enhanced gradient-echo images acquired with whole liver coverage per acquisition achieves good lesion detection (T2-weighted and immediate postgadolinium gradient echo images) and characterization (T2-weighted and serial postgadolinium gradient echo images) (fig. 2.66).

The use of fat suppression on T2-weighted sequences is advisable because it facilitates detection of subcapsular lesions [130]. Fat suppression is especially important to apply on echo-train spin-echo sequences, because fatty liver results in a bright liver on nonsuppressed T2-weighted echo-train sequences that can obscure liver metastases. In addition to histologic features of the metastases themselves, histologic changes often occur in uninvolved portions of liver.

Dynamic serial gadolinium-enhanced MR images are particularly important for lesion detection and characterization in patients with known hypervascular primary tumors (fig. 2.67). The hepatic arterial dominant phase of enhancement is the most important phase of image acquisition both for detection and characterization.

On out-of-phase gradient echo images, liver metastases may appear high in signal intensity because of signal drop of background liver parenchyma (fig. 2.68). On occasion, this may facilitate lesion detection, particularly if lesions are intrinsically high in signal intensity on T1-weighted images (fig. 2.69). More often, however, lesions are rendered less conspicuous on short TE because the lowered signal of the liver reduces the contrast with low-signal focal liver lesions on in-phase images. Pathologically, in the setting of liver metastasis, surrounding parenchyma may show compression or atrophy of hepatocyte cords, scattered foci of chronic inflammation replacing lost hepatocytes, and the absence of fatty change. On out-of-phase images, this zone of compressed liver parenchyma bordering on the metastasis appears as a moderately bright rim. This finding is relatively common in the setting of colon cancer metastases with background fatty liver, and may occasionally be seen in other lesions including hemangiomas.

The acquisition of at least one sequence in the coronal plane may be of value in evaluating the superior and inferior margins of the liver, particularly the infracardiac portion of the left lobe [131]. Short-duration techniques such as SS-ETSE, T1-weighted gradient echo, or both are useful for this purpose (fig. 2.70).

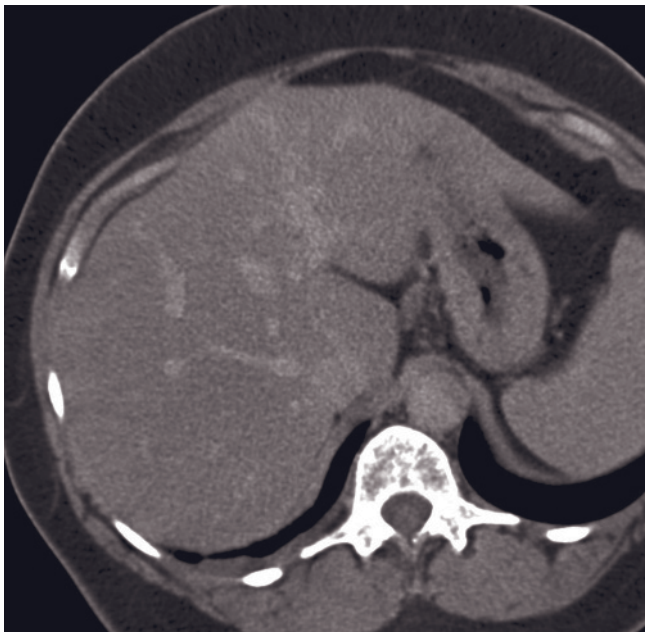

(*a*)

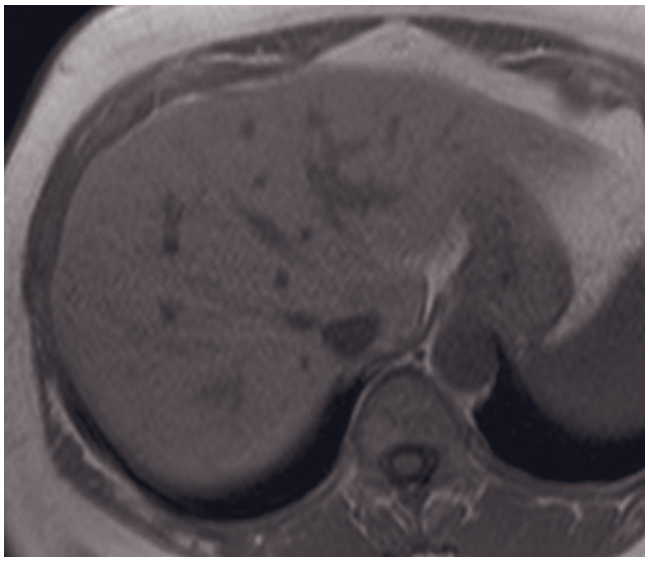

(*b*)

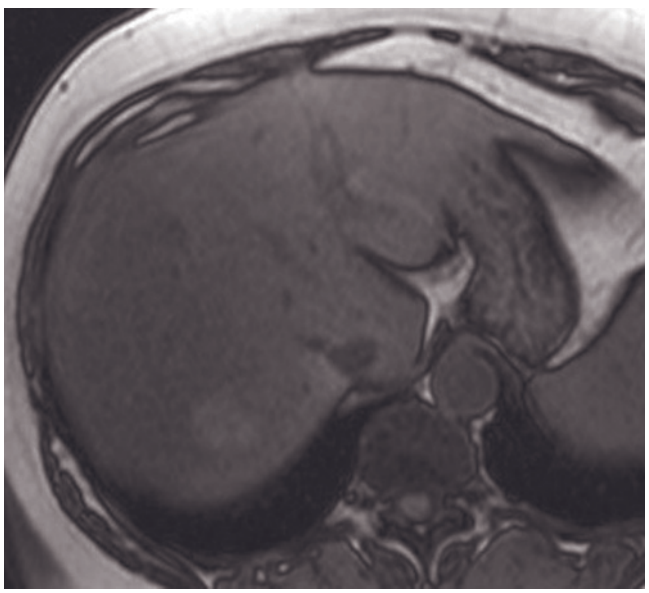

(*c*)

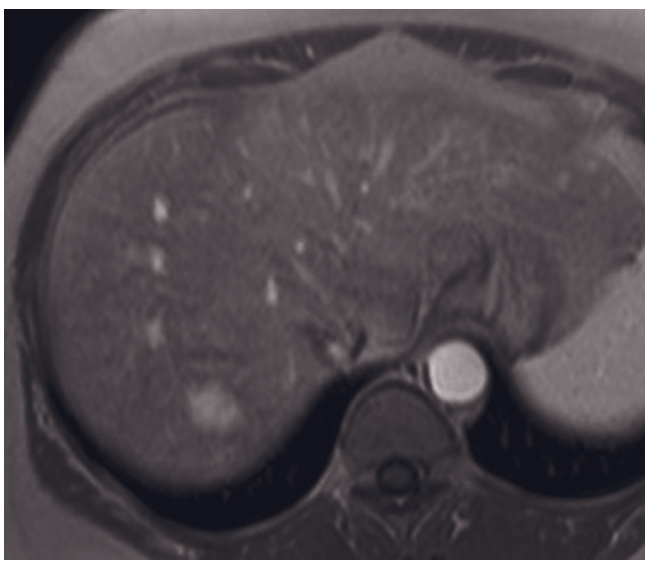

(*d*)

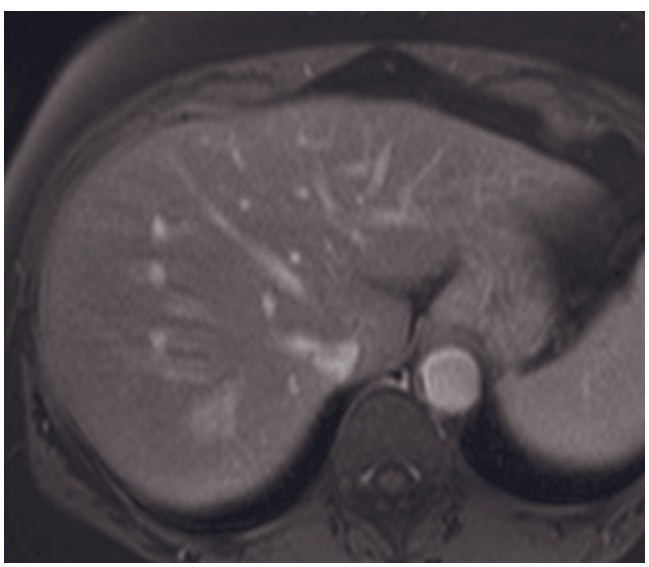

(*e*)

Fig. 2.61 FNH in a fatty liver—comparison between CT and MRI. Dynamic contrast-enhanced CT (*a*), SGE (*b*), out-of-phase SGE (*c*), and immediate (*d*) and 90-s fat-suppressed (*e*) postgadolinium SGE images. A FNH is situated in segment 6 of the liver and demonstrates isointensity with the background parenchyma on T1-weighted image (*b*) and intense and homogeneous enhancement on the immediate post contrast image (*d*) and remains enhanced on late-phase image (*e*). Note that the signal intensity of the liver parenchyma is isointense to the signal intensity of the spleen on out-of-phase image (*c*), suggesting the presence of moderate fat liver replacement, but the lesion does not drop in signal. In contrast to MRI, the CT examination is unremarkable.

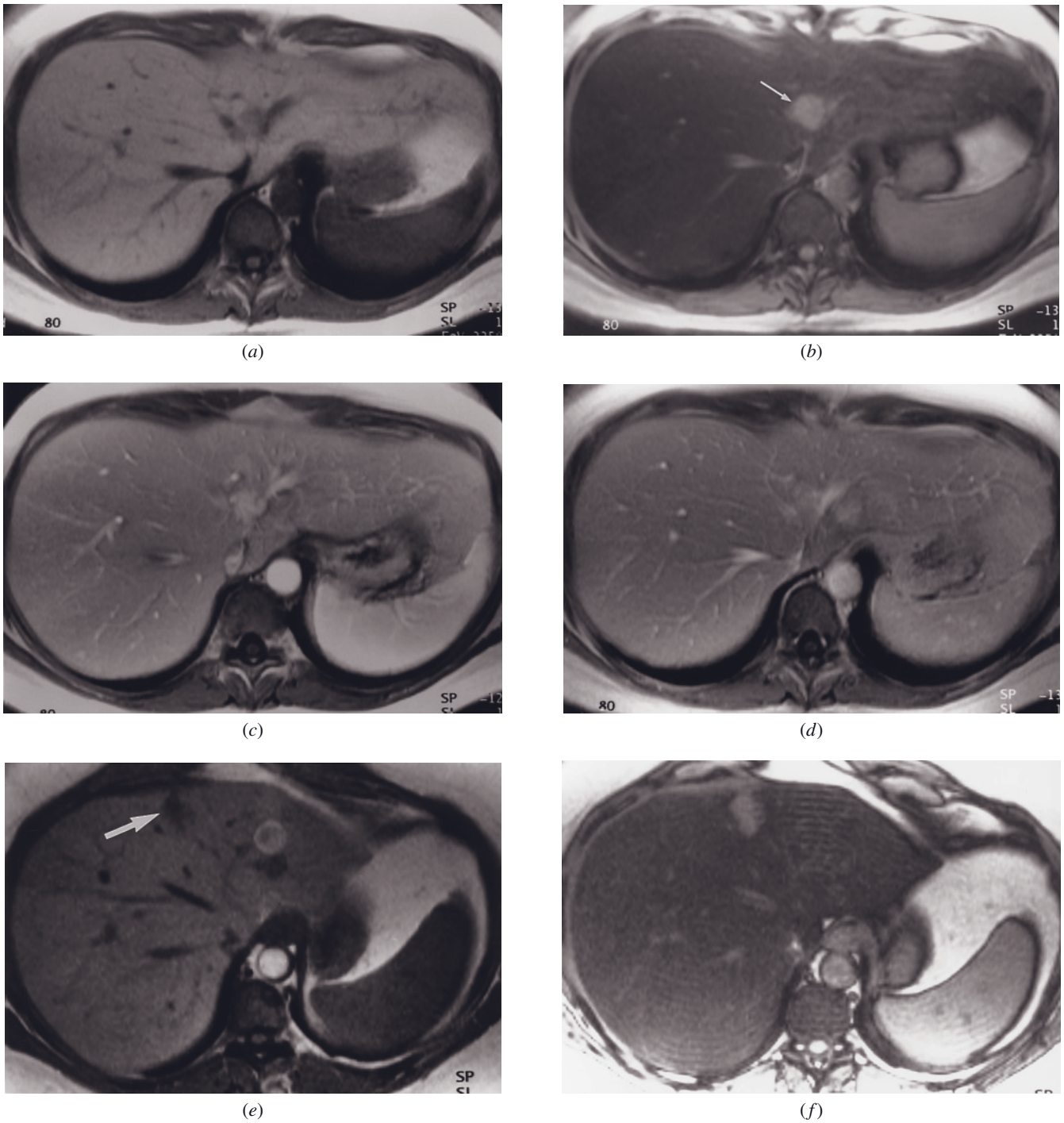

FIG. 2.62 FNH with surrounding fatty infiltration. SGE (*a*), out-of-phase SGE (*b*), and immediate (*c*) and 90-s (*d*) postgadolinium SGE images. A 2-cm focal nodular hyperplasia is present in the medial segment that is hypointense on in-phase (*a*) and hyperintense on out-of-phase (arrow, *b*) images because of signal dropout of the fatty liver. The tumor enhances with a uniform blush on the early-phase image (*c*) and fades in signal intensity on the late-phase image (*d*).

SGE (*e*), out-of-phase SGE (*f*), and immediate (*g*) and 90-s (*h*) postgadolinium SGE images in a second patient, who has diffuse fatty infiltration of the liver and a 2-cm FNH in the medial segment (arrow, *e*). Imaging findings identical to those shown in the first patient are present.

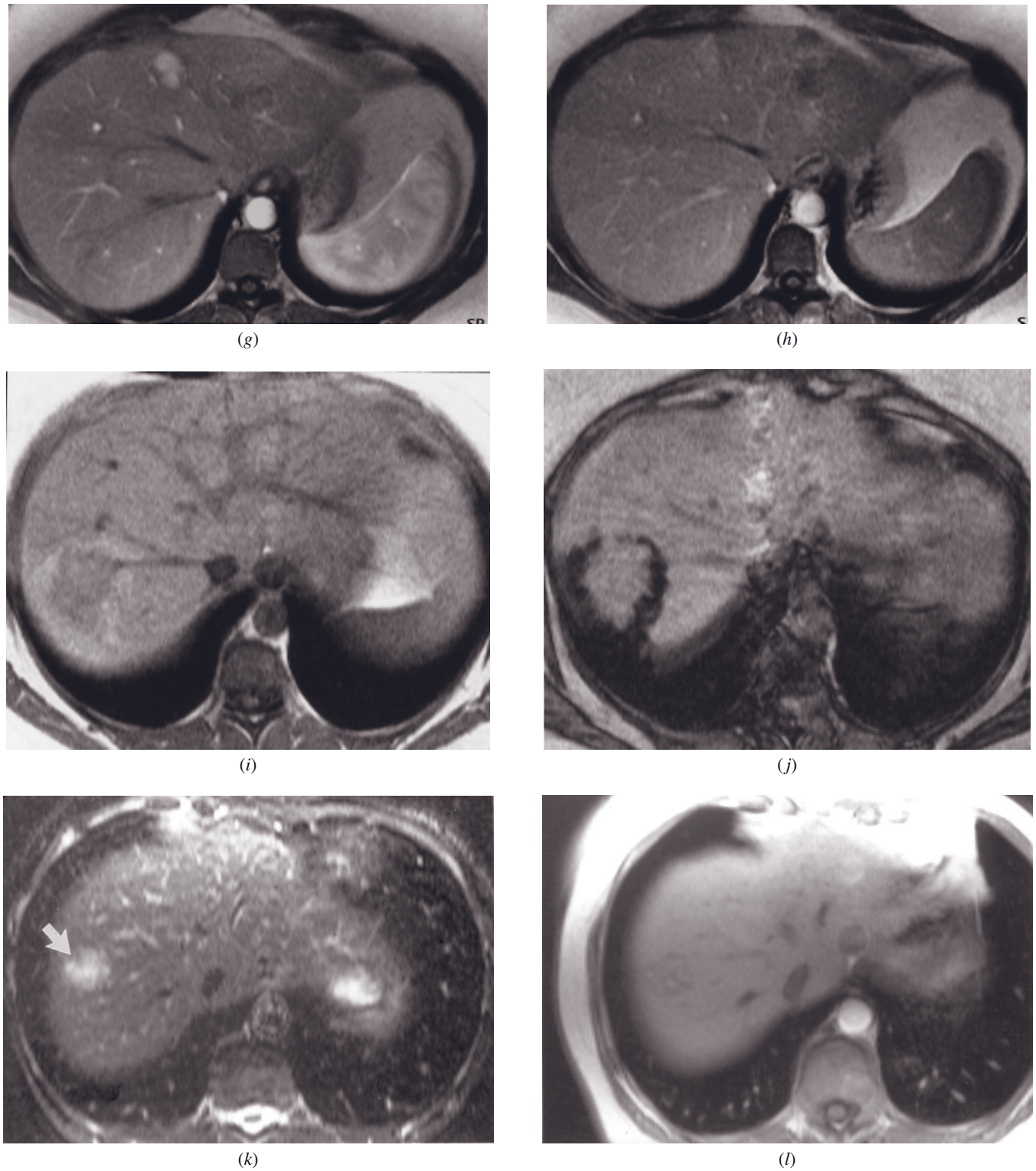

FIG. 2.62 (*Continued*) SGE (*i*) and out-of-phase SGE (*j*) images in a third patient. A 4-cm FNH demonstrates a collar of condensed fatty infiltration. The perilesional fat is moderately high in signal intensity on in-phase image (*i*) and drops to nearly signal void on out-of-phase image (*j*).

Echo-train STIR (*k*), SGE (*l*), out-of-phase SGE (*m*), and immediate (*n*) and 90-s (*o*) postgadolinium SGE images in a fourth patient, who has minimal fatty liver infiltration. The FNH in the right hepatic lobe (arrow, *k*) has mildly high signal intensity on T2-weighted image (*k*) and mildly low signal intensity on T1-weighted image (*l*) and becomes near isointense on the out-of-phase image (*m*), reflecting slight drop in signal of background liver. Note that the pseudocapsule appears slightly hyperintense on out-of-phase image. This lesion exhibits a central scar more evident, as a low-signal linear structure, on early-phase image (*n*).

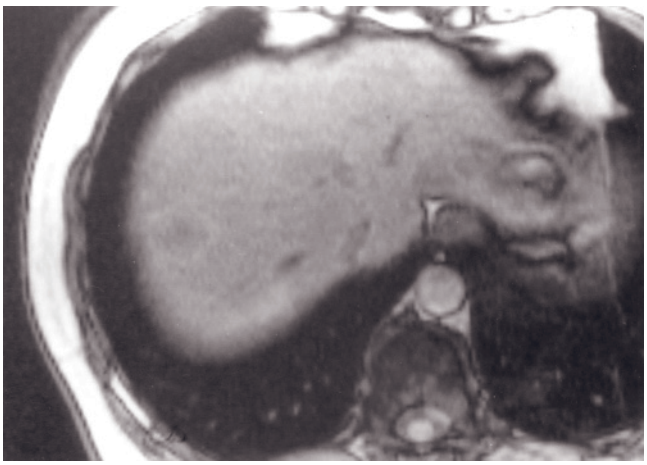

(*m*)

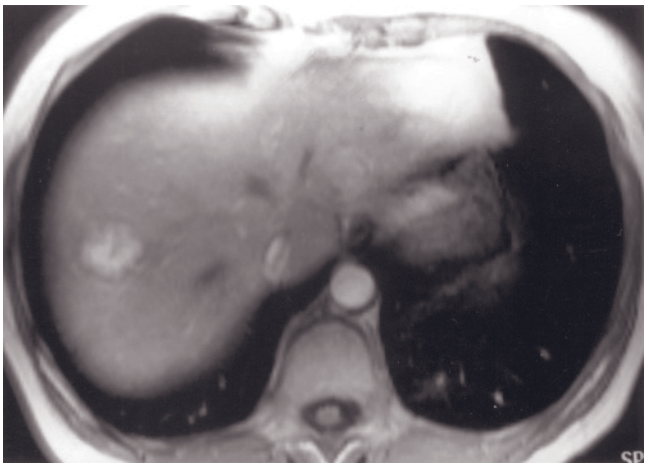

(*n*)

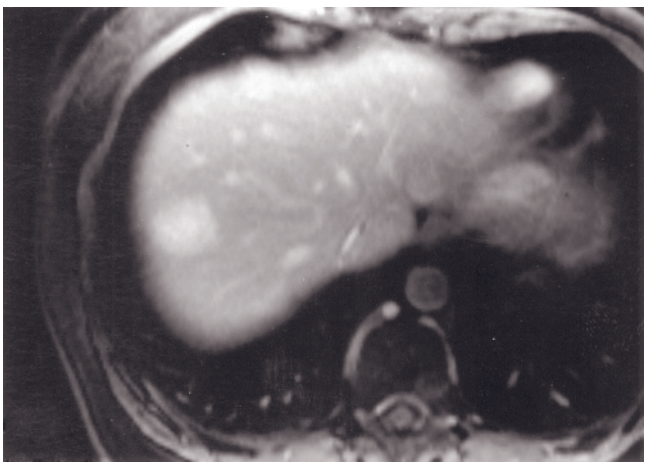

(*o*)

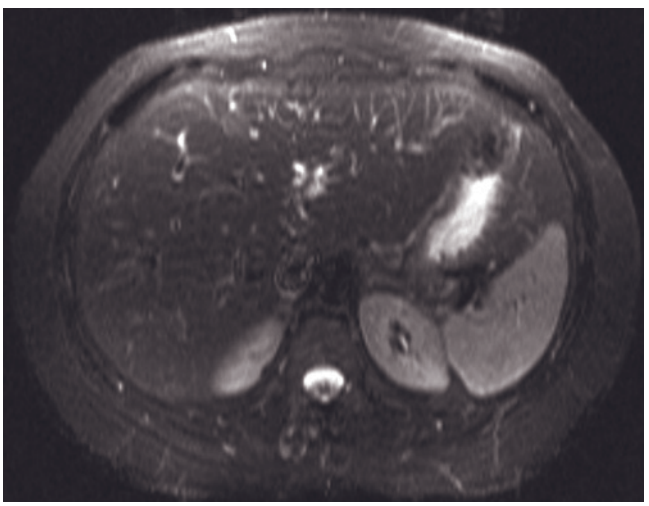

(*p*)

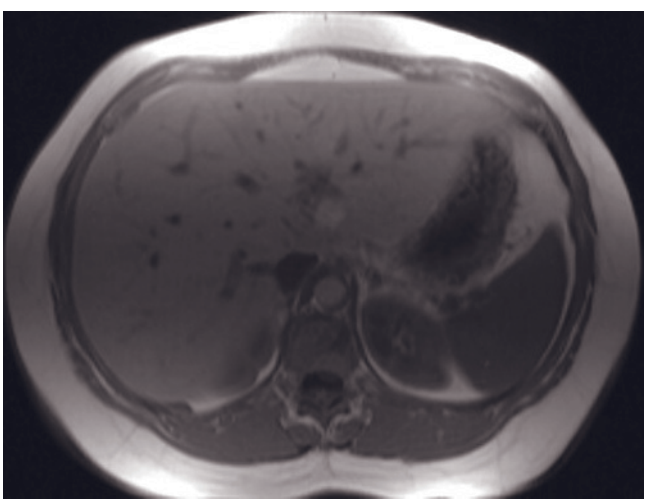

(*q*)

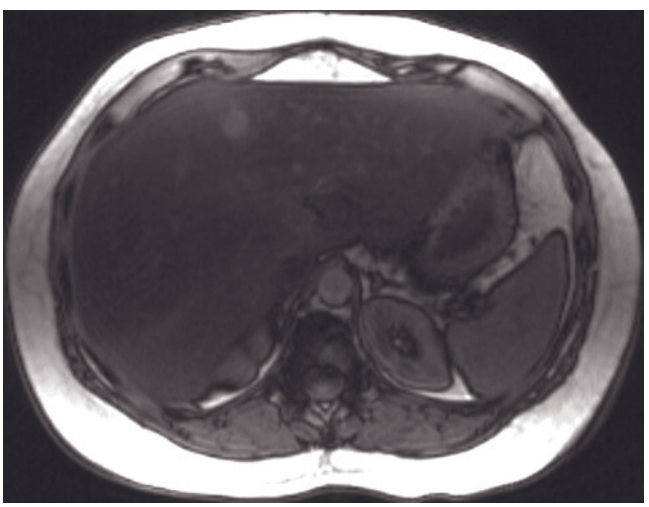

(*r*)

FIG. 2.62 (*Continued*) The lesions remains hyperintense on late-phase fat-suppressed image (*o*), which may reflect signal loss in background liver more than retention of contrast in the lesion.

T2-weighted fat-suppressed SS-ETSE (*p*), SGE (*q*), out-of-phase SGE (*r*), and immediate (*s*) and 90-s fat-suppressed (*t*) post-gadolinium images in a fifth patient show a FNH in a fatty liver.

These cases illustrate that fatty infiltration of background liver is not uncommon in the setting of focal nodular hyperplasia.

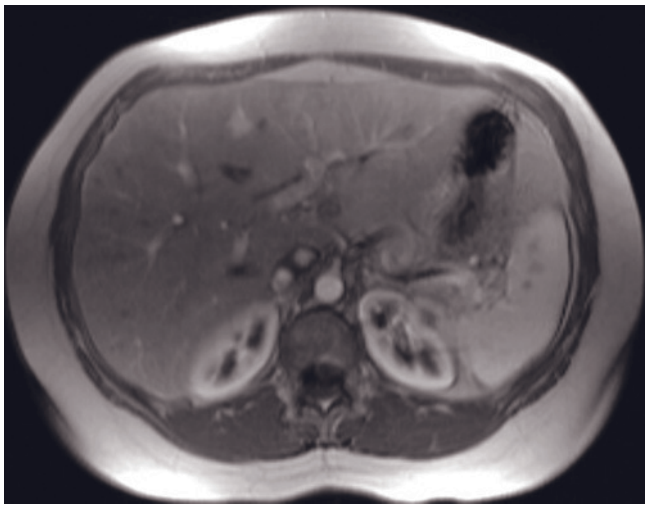

(*s*)

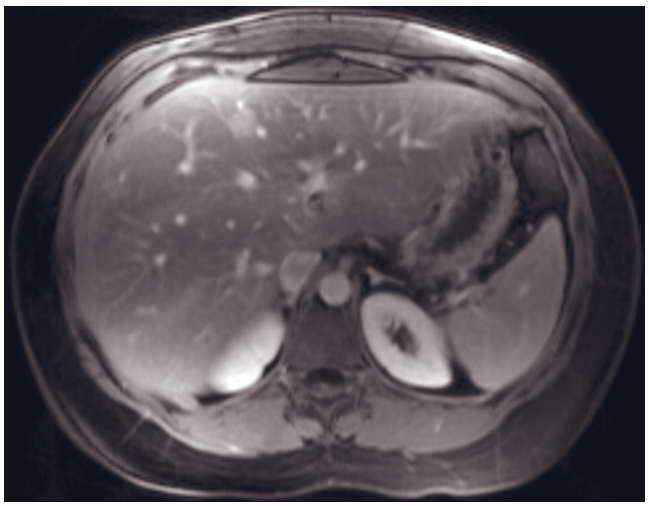

(*t*)

FIG. 2.62 (*Continued*)

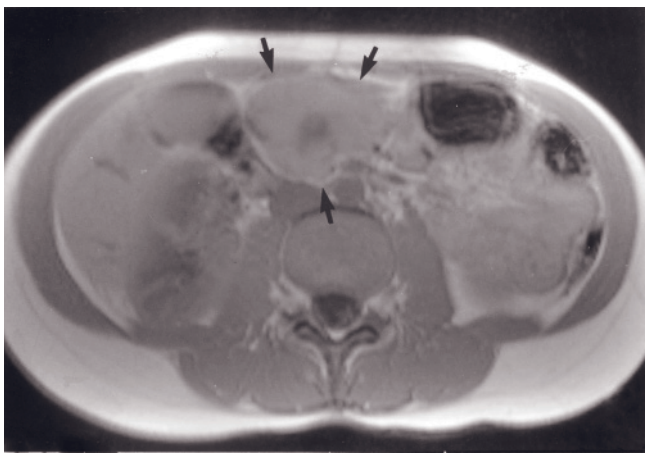

(*a*)

(*b*)

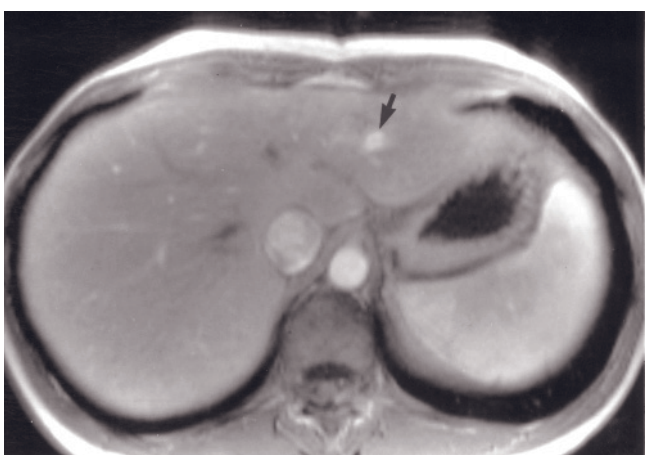

(*c*)

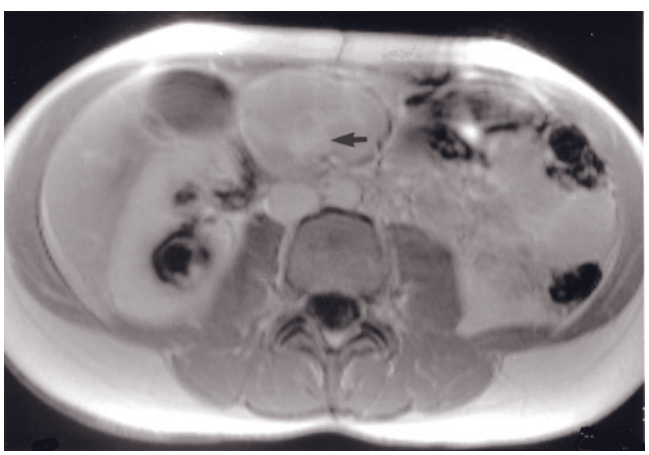

(*d*)

FIG. 2.63 Exophytic FNH. SGE (*a*), immediate (*b*, *c*) and 3-min (*d*) postgadolinium SGE images. There is a lobular mass with a central scar in the anterior upper abdomen, which abuts the left hepatic lobe. This lesion is isointense on T1-weighted image (arrows, *a*) and demonstrates a transient blush on the immediate postgadolinium image with lack of enhancement of the central scar (*b*). Note early filling of the left hepatic vein (arrow, *c*) that drains the tumor, confirming its hepatic origin. Transverse (*d*)

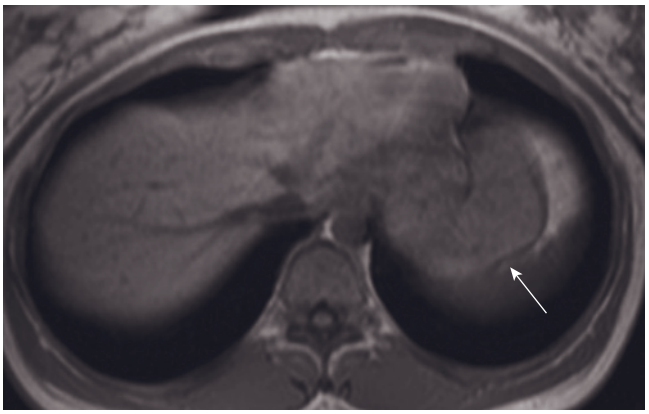

(*e*)

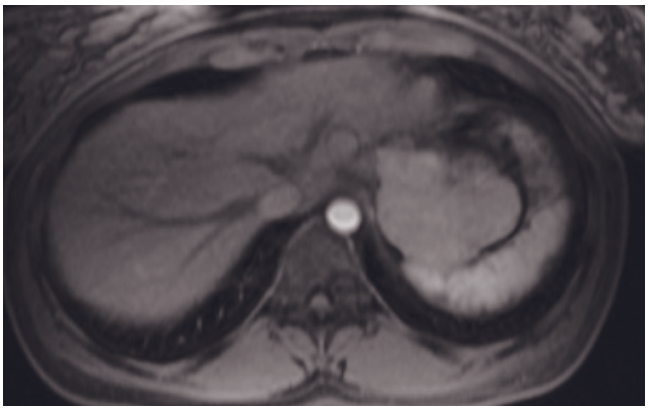

(*f*)

(*g*)

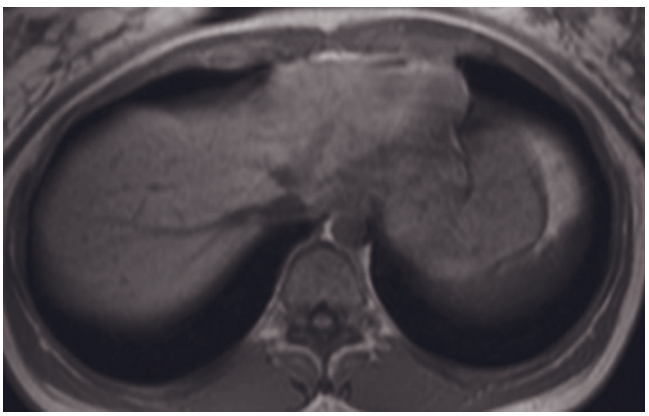

(*h*)

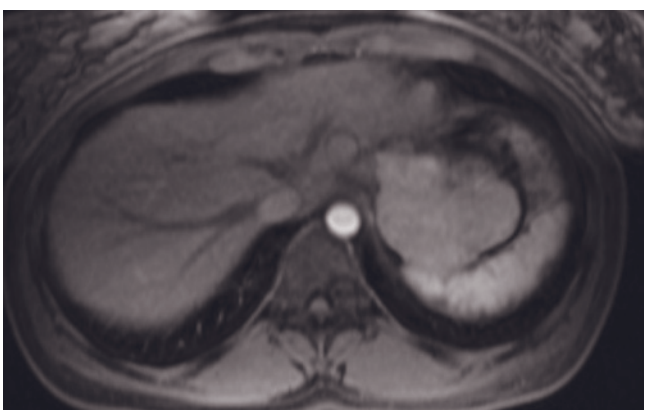

(*i*)

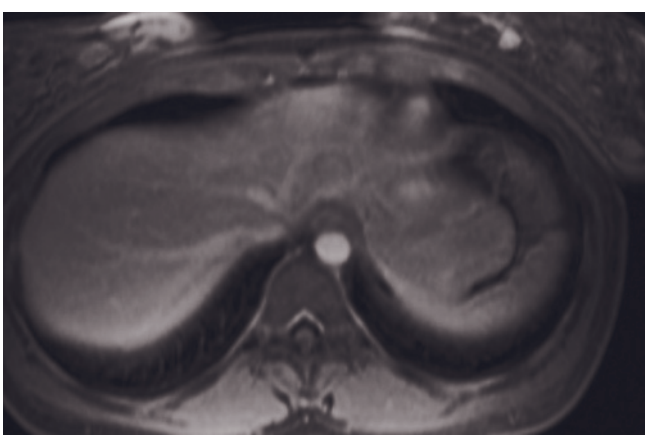

(*j*)

FIG. 2.63 (*Continued*) delayed image demonstrates late enhancement of the central scar. Despite its completely exophytic origin to the liver, the tumor exhibits the classic imaging features of FNH, which establishes the diagnosis.

Immediate (*e*) and 90-s fat-suppressed (*f*) postgadolinium SGE images in a second patient with an exophytic FNH (arrow, *e*). No central scar is appreciated in this lesion.

Coronal SS-ETSE (*g*), 3D-gradient echo (*h*), and immediate (*i*) and 90-s (*j*) fat-suppressed 3D-gradient echo images obtained **at 3T** reveal an exophytic FNH arising from the left lobe, adjacent to the spleen, in another patient.

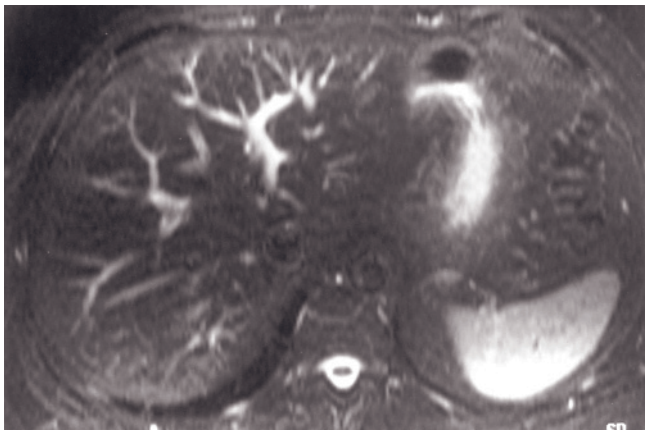

(*a*)

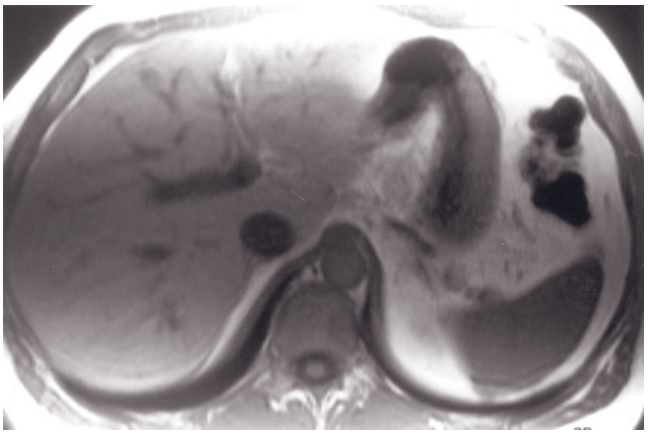

(*b*)

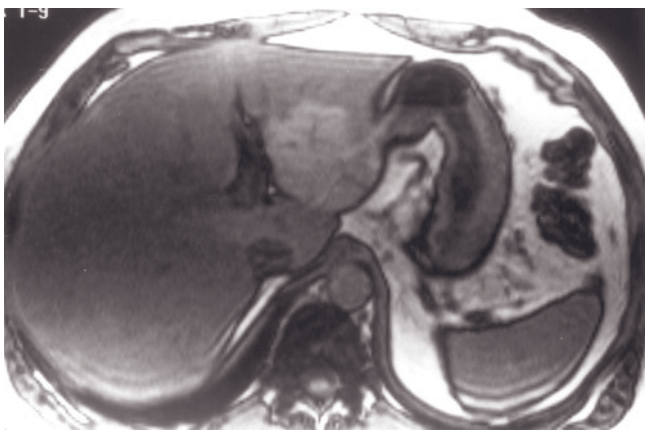

(*c*)

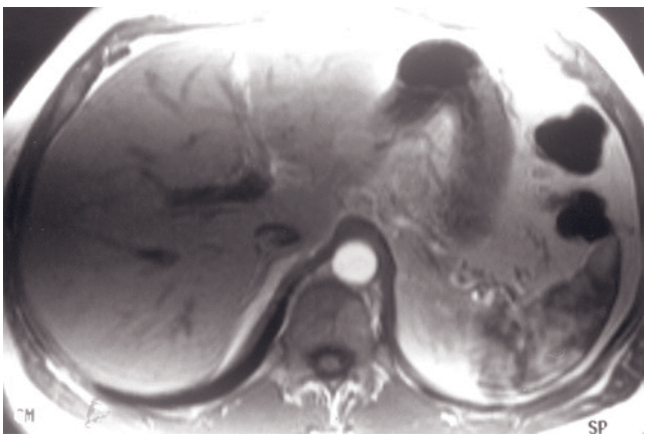

(*d*)

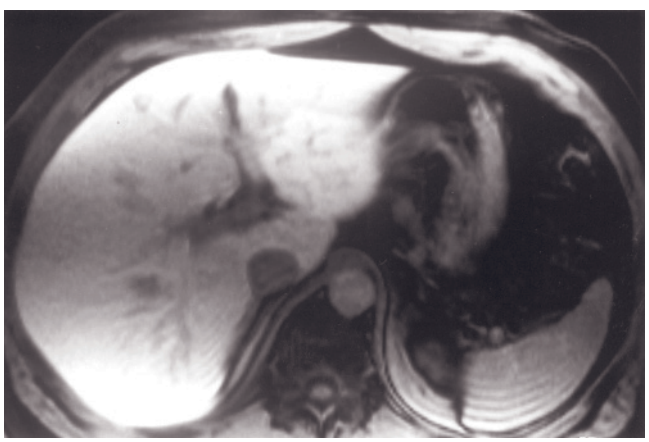

(*e*)

FIG. 2.64 Atypical FNH imaged with Gd-EOB-DTPA. Echo-train STIR (*a*), SGE (*b*), out-of-phase SGE (*c*), and immediate (*d*) and 12-min hepatocyte phase fat-suppressed (*e*) post-Gd-EOB-DTPA SGE images. There is a lobular mass that is isointense on T2-weighted image (*a*) and T1-weighted image (*b*), but it is well seen on out-of-phase image (*c*) as a high-signal mass because of signal drop of surrounding fatty liver. Atypical for FNH is negligible enhancement immediately after gadolinium administration (*d*). Note the high signal of the mass on the hepatocyte phase fat-suppressed image (*e*) that reflects both signal loss in the fatty liver and Gd-EOB-DTPA uptake in the hepatocytes of the FNH.

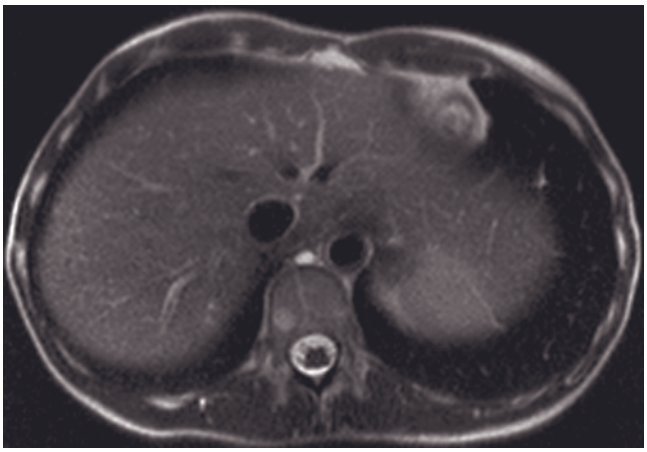

(*a*)

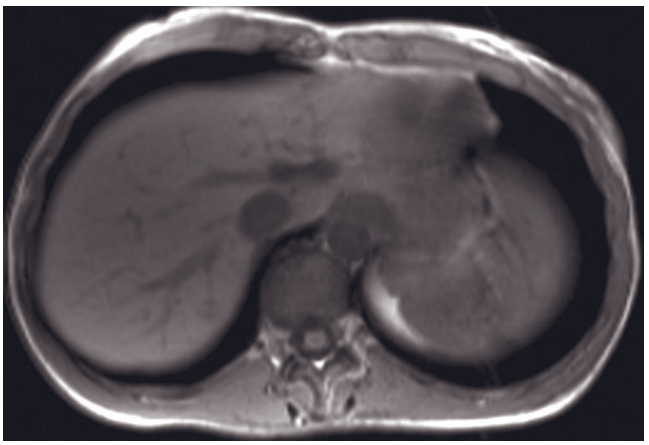

(*b*)

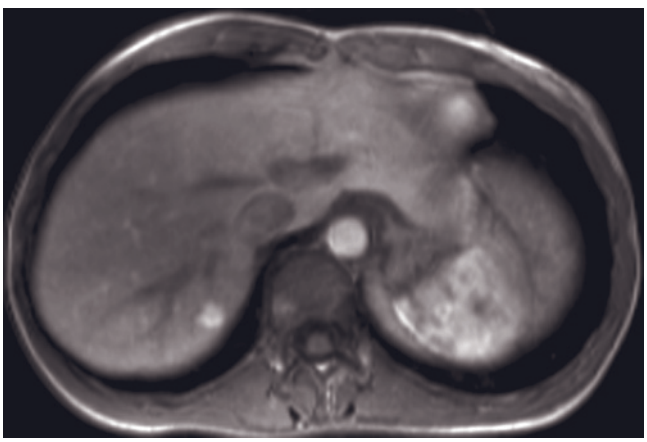

(*c*)

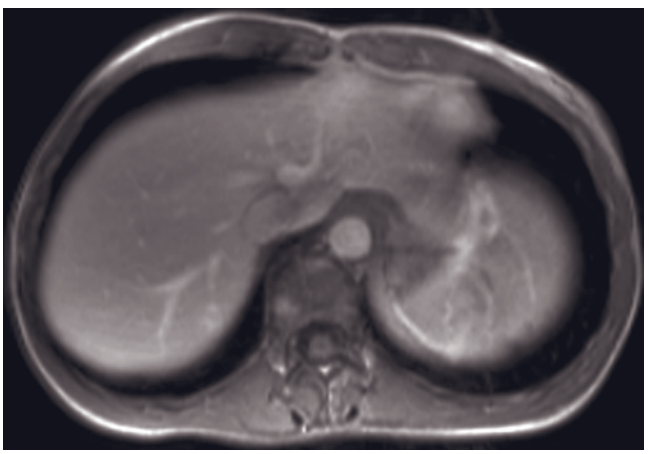

(*d*)

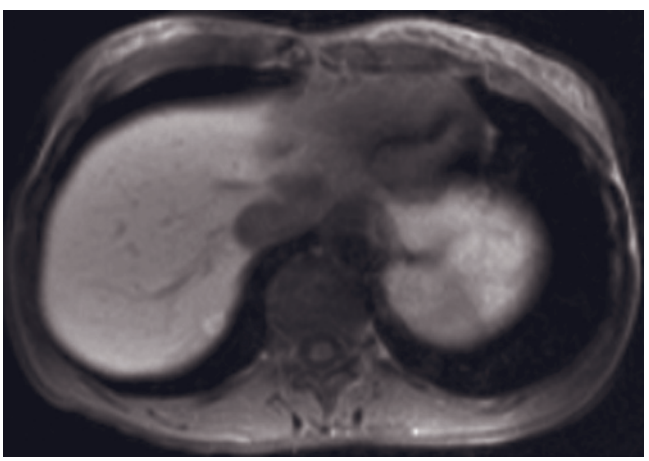

(*e*)

FIG. 2.65 FNH imaged with Gd-BOPTA. T2-weighted SS-ETSE (*a*), SGE (*b*), and immediate (*c*), 90-s (*d*), and 1-h fat-suppressed (*e*) postcontrast SGE images. There is a small lesion in segment 7 of the liver that demonstrates mildly high signal intensity on the T2-weighted image (*a*) and low signal on the T1-weighted image (*b*), enhances in an intense fashion on the early-phase image (*c*), and fades to background parenchyma on the late-phase image (*d*). On the 1-h postcontrast image (*e*) the lesion is increased in signal relative to background liver, reflecting hepatocyte uptake and retention of Gd-BOPTA (Courtesy of Guenther Schneider M.D., Ph.D.; Dept. of Diagnostic and Interventional Radiology, University Hospital Homburg/Saar, Germany).

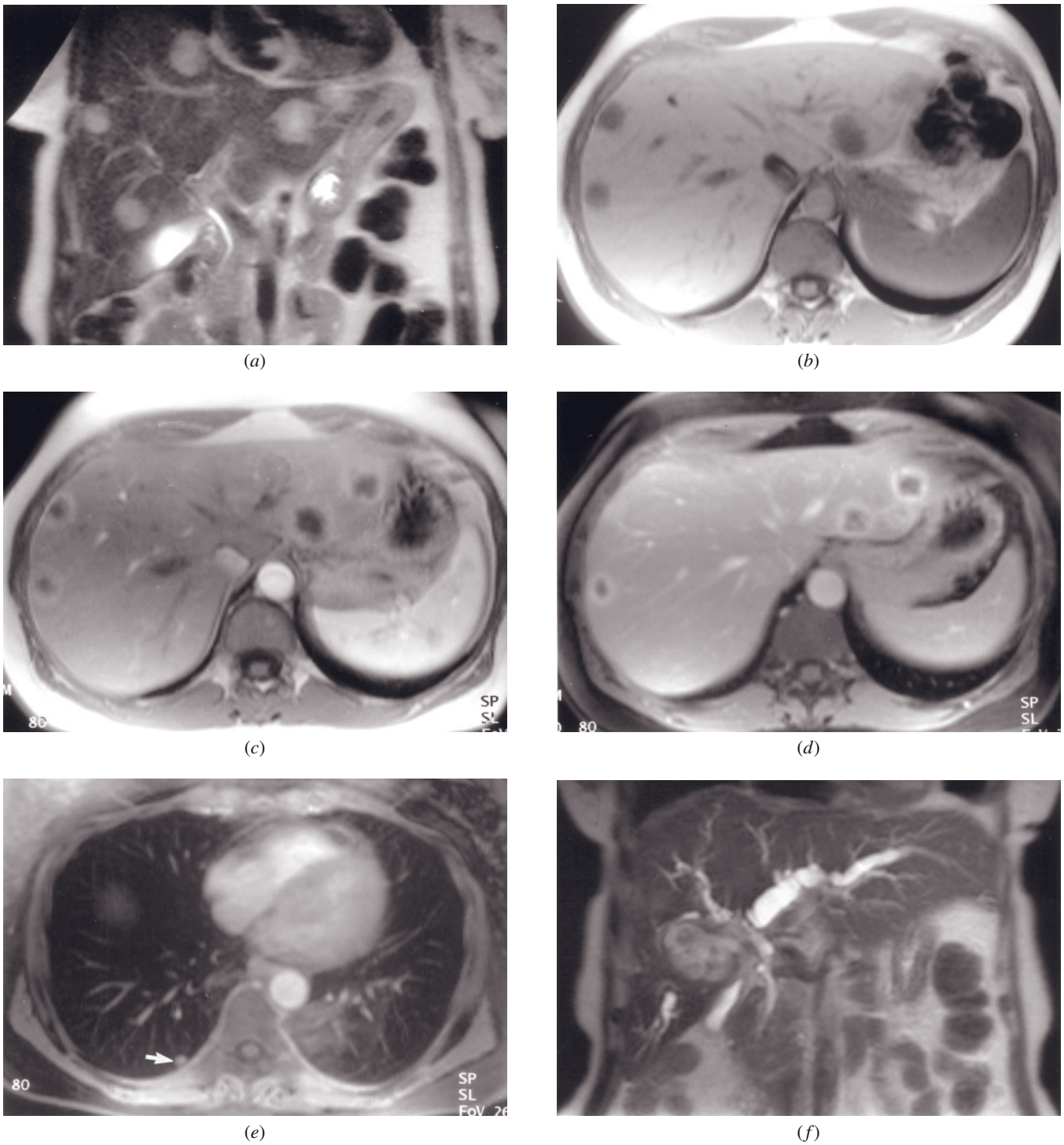

FIG. 2.66 Metastases—illustrating sequences. Coronal T2-weighted SS-ETSE (*a*), SGE (*b*), and immediate (*c*) and 90-s fat-suppressed (*d, e*) postgadolinium images in a patient with metastases from cloacogenic carcinoma. A MR study of the liver should include coronal (*a*) in addition to transverse plane images, T2 (*a*), T1 (*b*), and immediate (*c*) and 90-s fat-suppressed (*d*) images. Multiple metastases are present throughout the liver. Well-defined ring enhancement is appreciated on immediate postgadolinium images (*c*). Attention to lung bases must be made to evaluate for lung metastases (arrow, *e*).

Coronal T2-weighted SS-ETSE (*f*) and transverse echo-train STIR (*g*), SGE (*h*), and immediate (*i*) and 90-s fat-suppressed (*j*) postgadolinium SGE images in a second patient with capsule-based metastases who has colon cancer. Two capsule-based metastases are present that demonstrate scalloping of the liver margin. A large metastasis in segment 5 is also present, which obstructs the common hepatic duct (*f*).

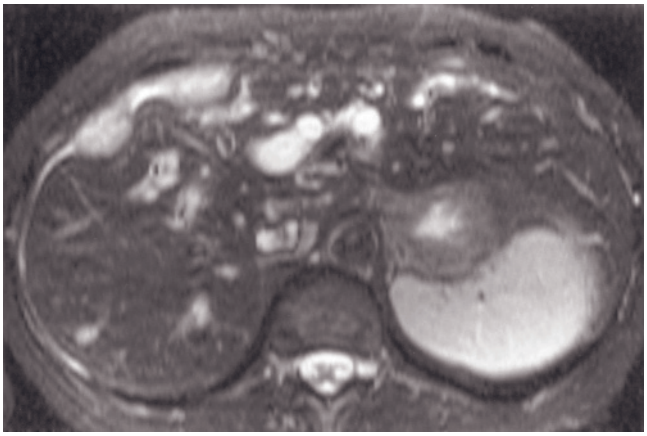

(*g*)

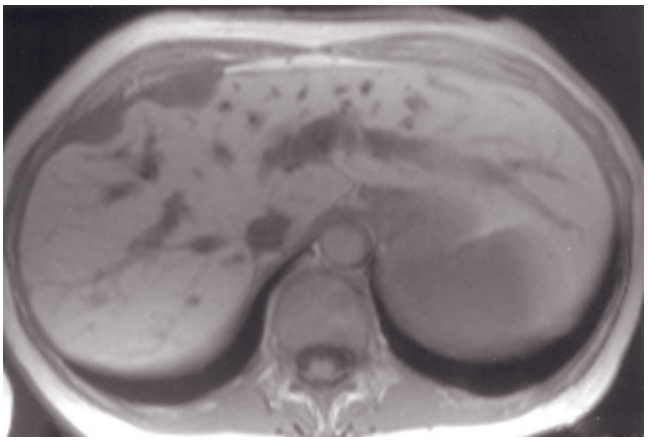

(*h*)

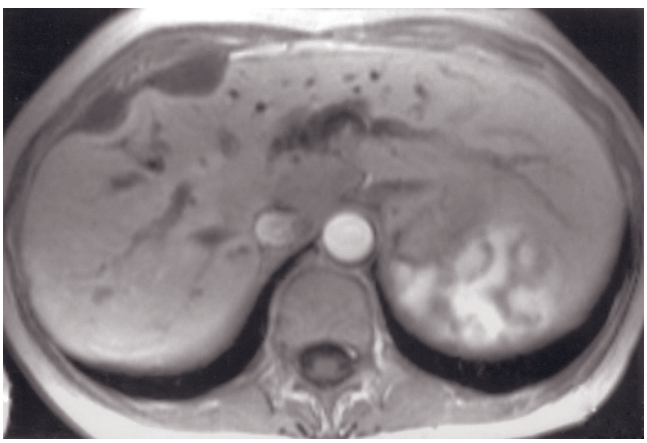

(*i*)

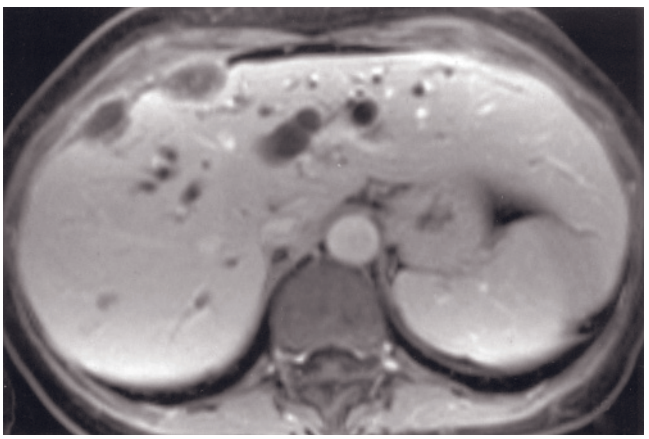

(*j*)

FIG. 2.66 (*Continued*)

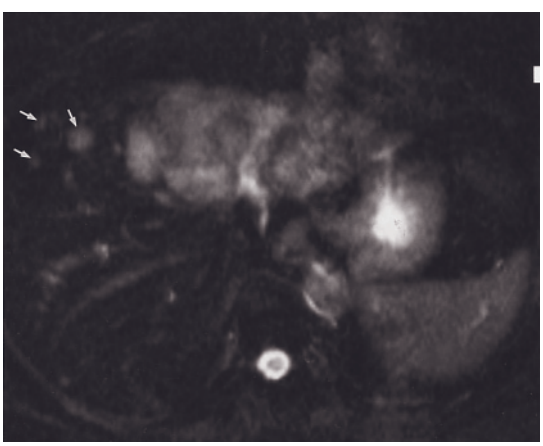

(*a*)

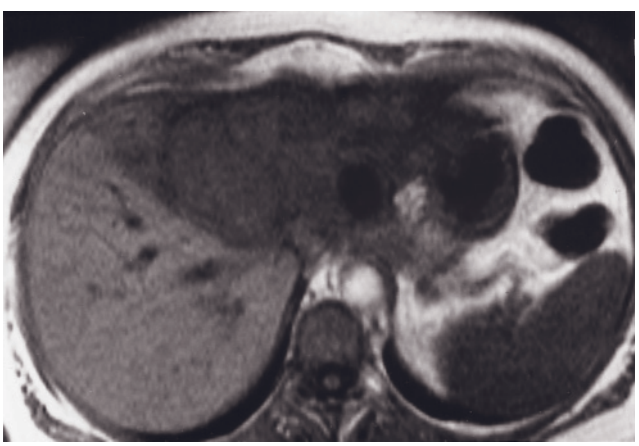

(*b*)

FIG. 2.67 Hypervascular liver metastases. Fat-suppressed T2-weighted ETSE (*a*), SGE (*b*), and immediate (*c*) and 90-s (*d*) postgadolinium SGE images. A 7-cm metastasis is identified in the left lobe of the liver (*a–d*). Several metastases smaller than 1 cm

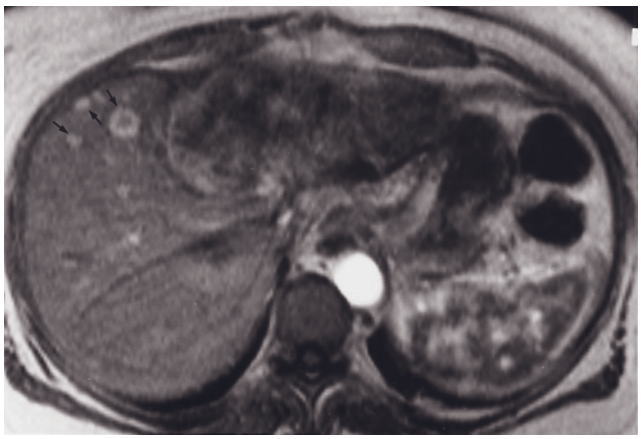

(*c*)

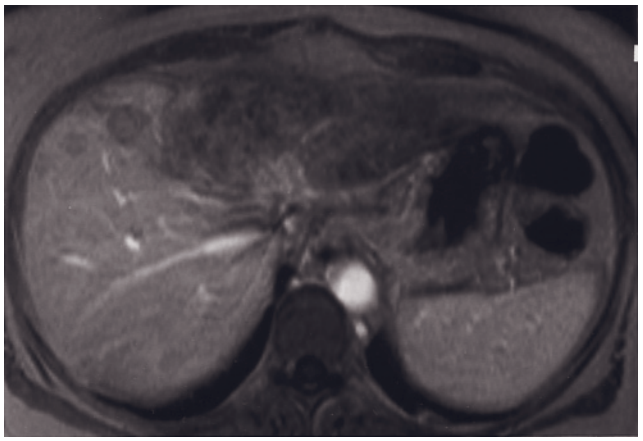

(*d*)

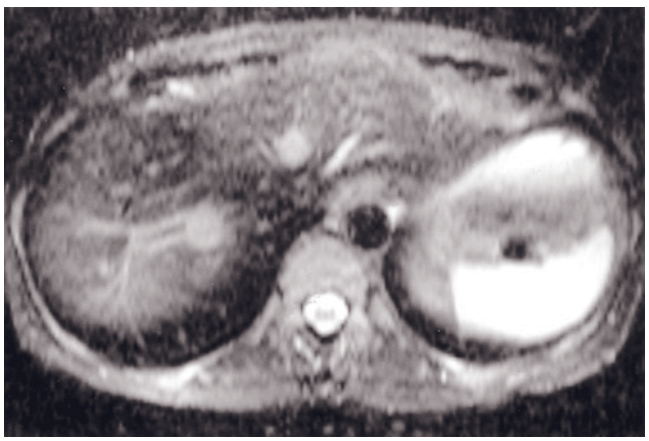

(*e*)

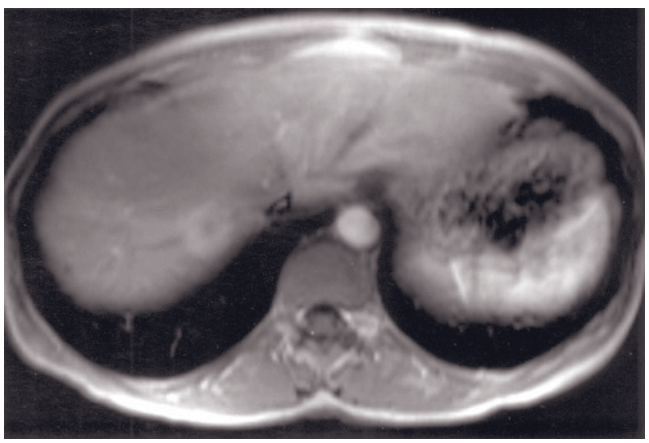

(*f*)

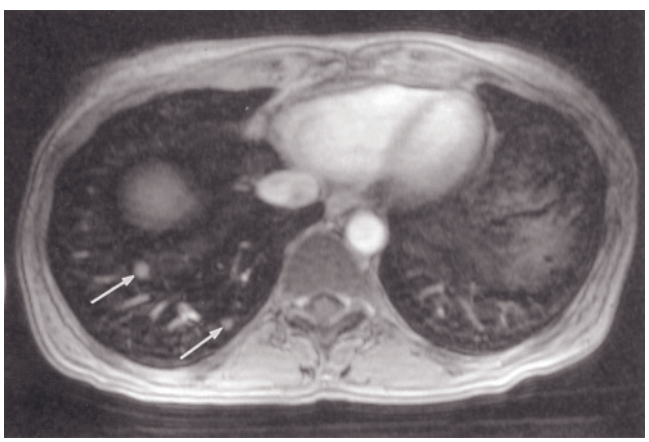

(*g*)

FIG. 2.67 (*Continued*) are present in the medial and anterior segments. These small metastases are moderately high in signal intensity on T2 (arrows, *a*) and not visible on T1 (*b*), enhance intensely on immediate postgadolinium images (arrows, *c*), and wash out to lower signal intensity than liver on 90-s postgadolinium images (*d*). On the immediate postgadolinium image (*c*) the smallest lesions enhance homogeneously, whereas the 1-cm metastasis has ring enhancement.

Echo-train STIR (*e*) and immediate (*f*) and 90-s fat-suppressed (*g*) postgadolinium SGE images in a second patient, who has a history of thyroid cancer. Two lesions are seen in the liver that are high signal on T2 (*e*) and enhance intensely on immediate postgadolinium images (*f*), consistent with hypervascular metastases. Note also the presence of lung metastases (arrows, *g*).

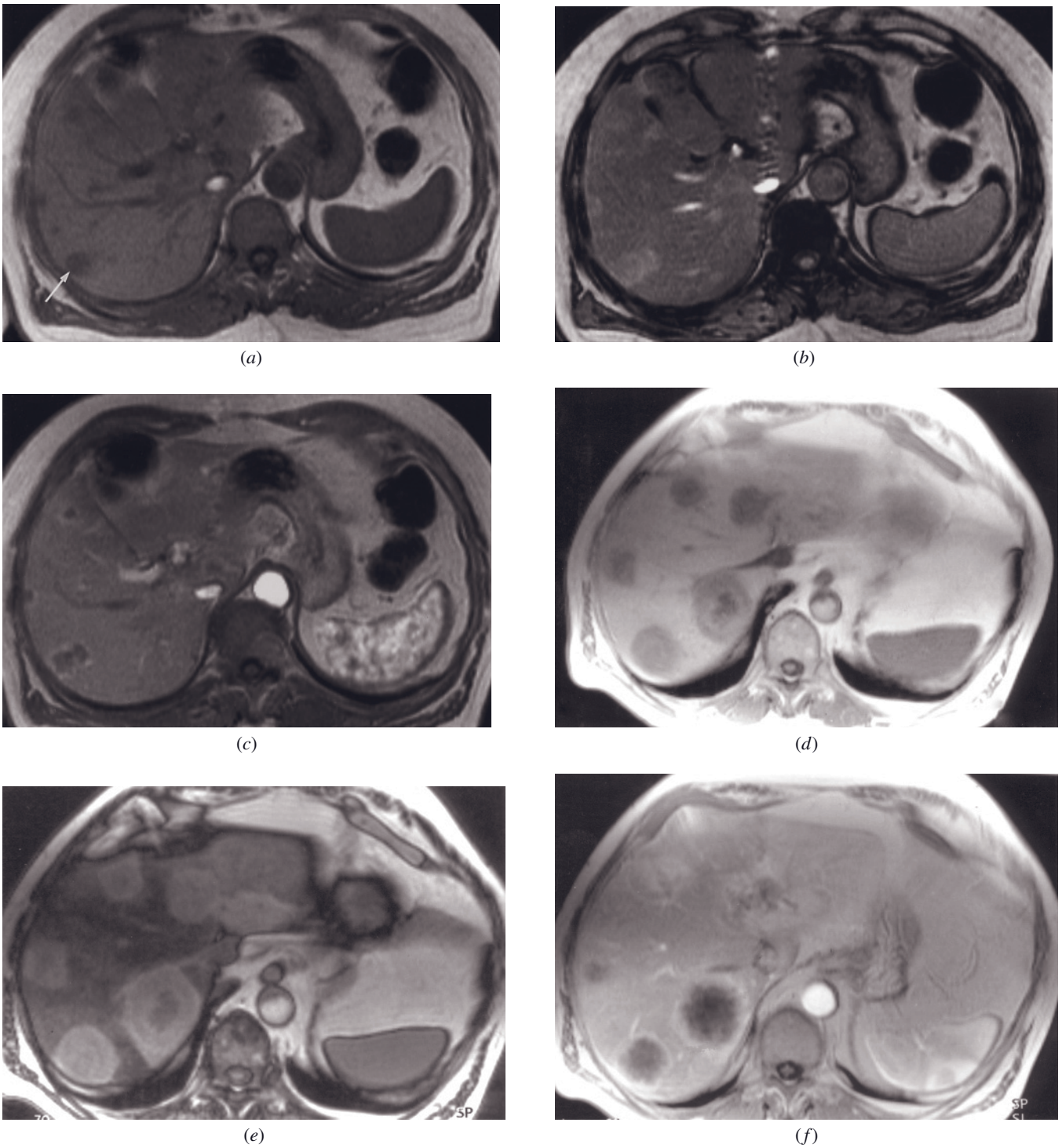

FIG. 2.68 Liver metastases in fatty liver. SGE (*a*), out-of-phase SGE (*b*), and immediate postgadolinium SGE (*c*) images. Multiple low-signal-intensity metastases are present in the liver on the in-phase T1-weighted image (arrow, *a*). On the out-of-phase T1-weighted image (*b*), the liver diminishes in signal intensity, rendering the metastases mildly high in signal intensity relative to liver. The immediate postcontrast image (*c*) shows that the lesions enhance in a peripheral ring fashion, consistent with metastases.

SGE (*d*), out-of-phase SGE (*e*), and immediate postgadolinium SGE (*f*) images in a second patient with colon cancer liver metastases. Fatty liver may arise as a response to the presence of liver metastases or also as a response to the chemotherapy directed at the metastases.

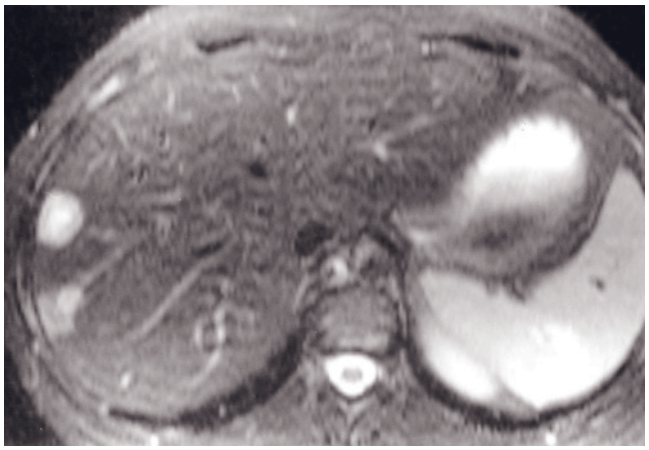

(*g*)

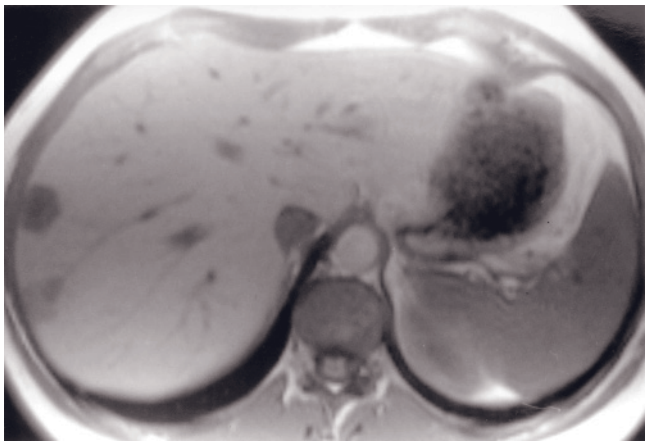

(*h*)

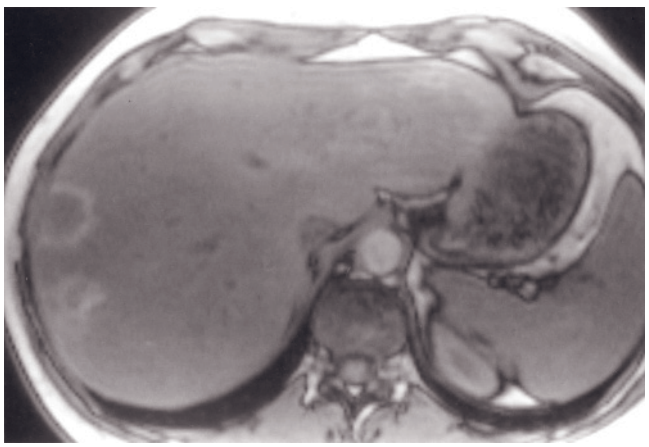

(*i*)

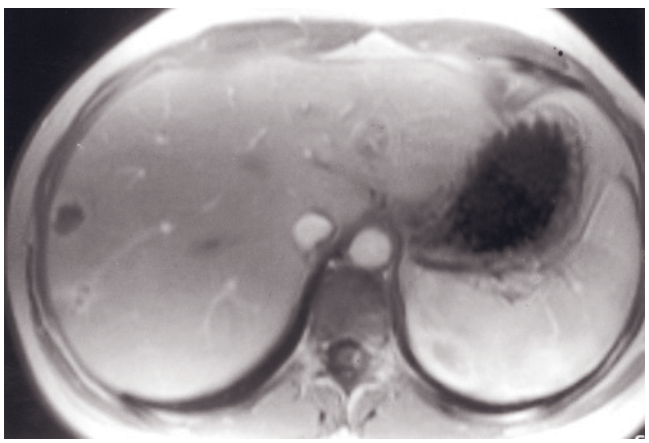

(*j*)

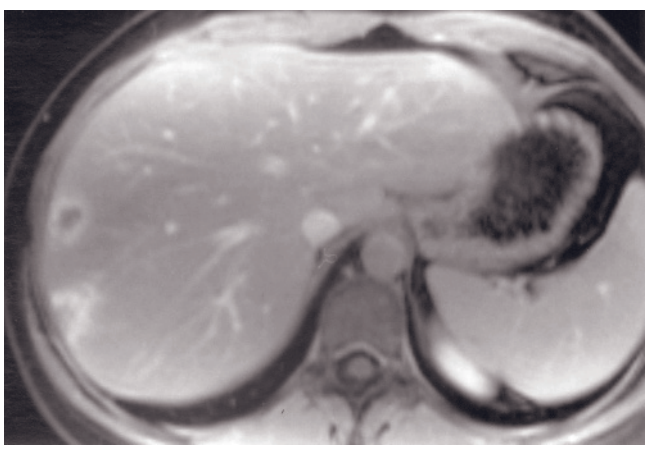

(*k*)

FIG. 2.68 (*Continued*) Echo train-STIR (*g*), SGE (*h*), out-of-phase SGE (*i*), and immediate (*j*) and 90-s fat-suppressed (*k*) postgadolinium images in a third patient, who has breast cancer. There are two lesions in the right hepatic lobe that demonstrate high signal on T2 (*g*), low signal on T1 (*h*), and ring enhancement after contrast administration (*j, k*), consistent with metastases. Note that the liver drops moderately in signal on the out-of-phase image (*i*) and a bright rim is present around the lesions, consistent with compressed liver parenchyma, which is unable to accumulate intracytoplasmic lipid.

MRI versus CT. MRI is superior to CT imaging in the evaluation of the liver [69, 132–136]. The current challenge is whether the superior performance of MRI translates into a beneficial effect on patient management, disease outcome, and health care costs. New MR sequences, phased-array surface coils, and tissue-specific MR contrast agents suggest that MRI may further exceed the diagnostic ability of CT imaging.

An earlier study [69] compared the efficacy of non-spiral dynamic contrast-enhanced CT imaging and MRI employing T2-weighted fat-suppressed spin-echo, T1-weighted precontrast gradient-echo, and dynamic serial

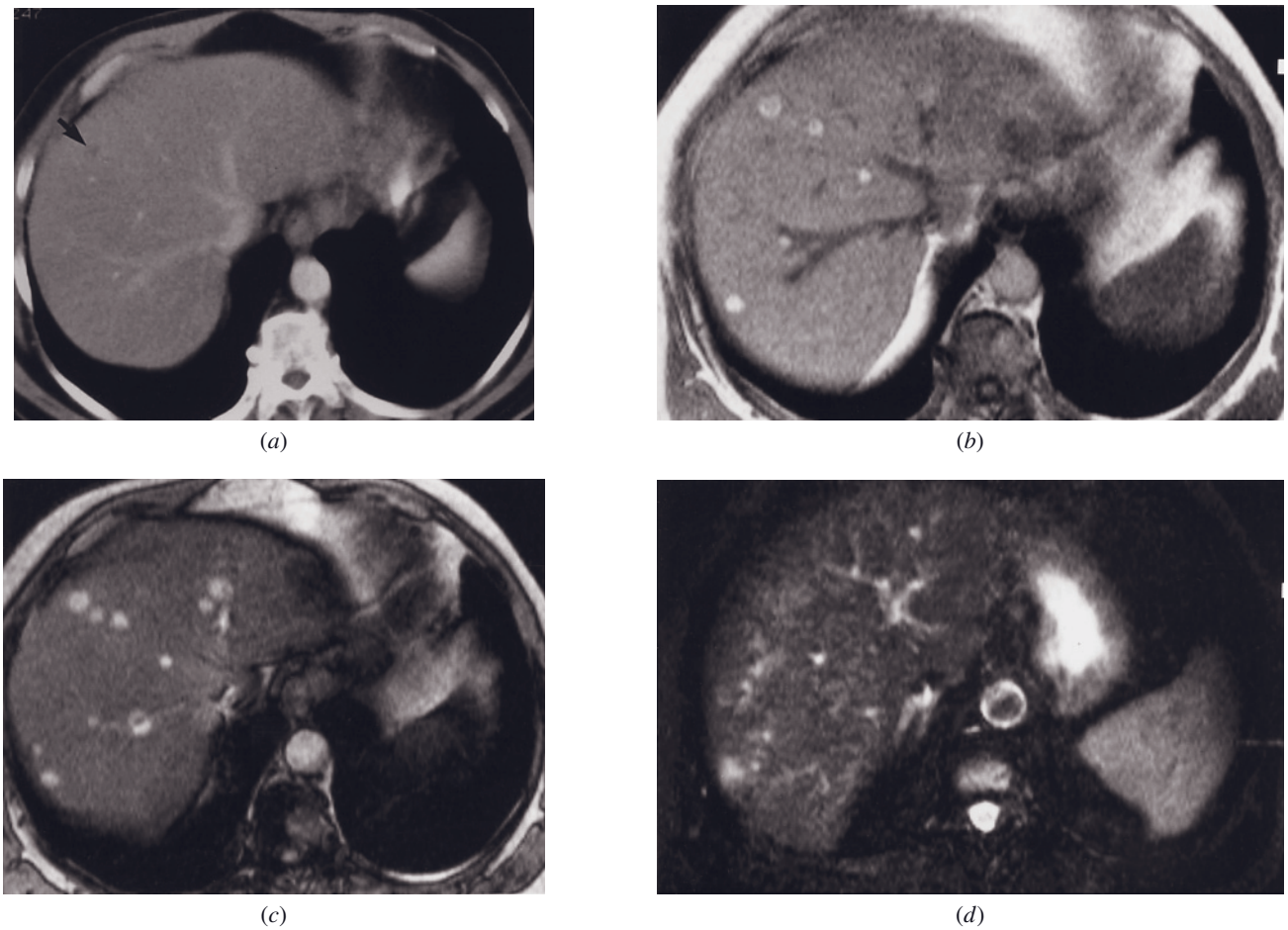

FIG. 2.69 Melanoma metastases in a fatty liver—comparison of spiral CT imaging and MRI. Spiral CT (*a*), SGE (*b*), out-of-phase SGE (*c*), and fat-suppressed T2-weighted ETSE (*d*) images. A solitary melanoma metastasis is apparent on the spiral CT image (arrow, *a*). Multiple mildly hyperintense metastases smaller than 1 cm are identified on the SGE image (*b*), and these high-signal-intensity lesions become more conspicuous on the out-of-phase image (*c*). Lesions are apparent on the T2-weighted images (*d*) but are not as clearly shown as on the out-of-phase images (*c*). The presence of fatty infiltration of the liver has resulted in a signal drop on out-of-phase images (*c*), which has increased the conspicuity of the high T1-weighted signal intensity liver metastases.

postgadolinium gradient-echo images in 73 patients with clinically suspected liver disease. The results demonstrated a statistically significant difference in lesion detection ($P < 0.03$) and characterization ($P < 0.01$) by dynamic MRI (fig. 2.71). A follow-up study [133] compared these MRI sequences to dynamic nonspiral contrast-enhanced CT images in 20 patients with solitary hepatic metastases detected by CT imaging and demonstrated that MRI depicted more than one lesion in 30% (6 of 20) of patients.

The authors reported [137] a comparison between MRI using T2-weighted fat-suppressed echo-train spin echo and immediate postgadolinium spoiled gradient echo with single-phase spiral CT for the detection and characterization of hepatic lesions in 89 patients. The results demonstrated a statistically significant difference in the detection ($P < 0.001$) and characterization ($P < 0.001$) of lesions by MR images on a patient-by-patient basis. No patients had true-positive lesions shown on spiral CT that were not shown on MRI. Regarding effect on patient management, findings on MRI provided information that altered care compared to findings on spiral CT in 64% of patients. A follow-up study [138] comparing dual-phase spiral CT and the above-described MRI sequences in 22 patients also showed the superiority of MR over dual-phase spiral CT in the detection and characterization of lesions. Our current clinical experience with 16-row multidetector CT and MRI shows similar findings that reveal the superiority of MRI in liver imaging. As MRI and CT both evolve as modalities, MRI has consistently shown superiority over CT, including comparison to current CT techniques. In fact, our impression is that with increasing numbers of rows of detectors, although spatial resolution may improve,

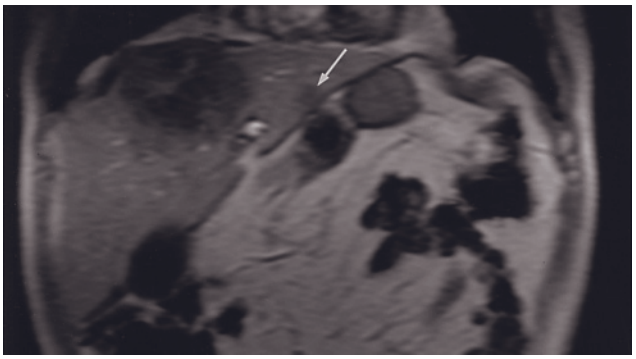

(*a*)

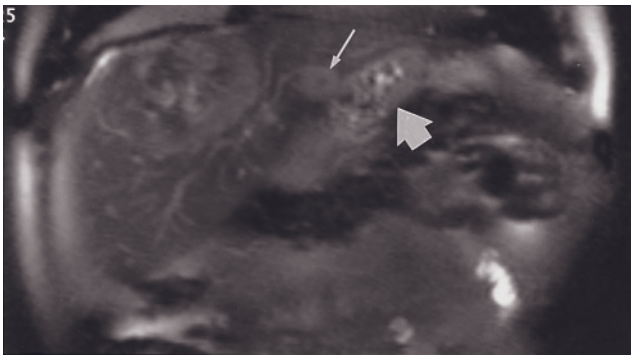

(*b*)

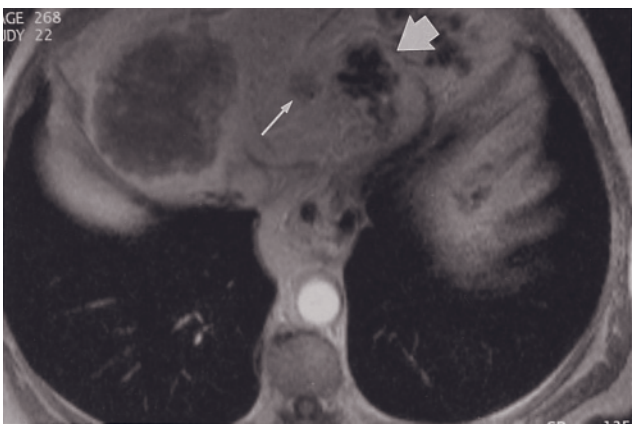

(*c*)

FIG. 2.70 Liver metastases, coronal images. Coronal magnetization-prepared gradient-echo (*a*), coronal T2-weighted SS-ETSE (*b*), and 45-s postgadolinium SGE (*c*) images. A 6-cm colon cancer metastasis is present in the medial segment that is heterogeneous and low in signal intensity on the T1-weighted image (*a*) and heterogeneous and mildly hyperintense on the T2-weighted image (*b*). A 1-cm capsule-based metastasis is identified in the lateral segment (arrows *a, b*) that has signal intensity features similar to those of the larger metastasis. Close proximity to the stomach (large arrow, *b*) is appreciated. The transverse postgadolinium image (*c*) demonstrates ring enhancement around the large heterogeneously low-signal-intensity metastasis. Ring enhancement is also appreciated around the small lesion (arrow, *c*). This lesion could easily be mistaken for a partial volume artifact with the nearby stomach (large arrow, *c*) on transverse sections. At least one coronal acquisition is recommended to minimize potential errors of ascribing lesions on the superior and inferior edges of the liver as partial volume effects.

contrast resolution, which is essential to detect small malignant tumors, may actually suffer.

MRI versus CTAP. Comparison between spiral CT arterial portography (CTAP) and current MRI techniques for diagnostic accuracy, cost, and effect on patient management has been studied using a population of 26 patients referred for hepatic surgery with suspected malignant liver lesions [139]. Regarding lesion detection, CTAP and MRI, respectively, showed 185 and 176 true-positive malignant lesions, 15 and 0 false-positive malignant lesions, 0 and 18 true-negative malignant lesions, and 13 and 22 false-negative malignant lesions. Regarding segmental involvement, CTAP and MRI, respectively, showed 107 and 105 true-positive segments, 11 and 0 false-positive segments, 80 and 91 true-negative segments, and 4 and 6 false-negative segments. A statistically significant difference in specificity of segmental involvement was observed between MRI and CTAP ($P < 0.03$). Total procedural charges were twofold higher for CTAP than for MRI. Findings at MR imaging altered patient treatment in seven patients, whereas findings at CTAP did not impact on patient treatment in any of the cases; this result was statistically significant ($P = 0.015$). The results of this study demonstrated that MRI has higher diagnostic accuracy and greater effect on patient management than spiral CTAP and is 64% less expensive. A follow-up study [140] comparing spiral CTAP and MRI in 20 surgically staged patients showed a trend that MR was superior for lesion detection and segmental involvement. CTAP and MR images demonstrated, respectively, 54 and 60 true-positive lesions, six and one false-positive lesions, 15 and 22 true-negative (i.e., benign) lesions, and eight and two false-negative lesions. CTAP and MR images demonstrated, respectively, 57 and 62 true-positive segmental involvement, six and one false-positive segmental involvement, 89 and 95 true-negative segmental involvement, and eight and two false-negative segmental involvement. A major problem with CTAP is the frequent occurrence of perfusion defects that can resemble a focal mass or can mask the presence of metastases on CTAP images. Perfusion defects are rarely problematic on MR images (figs. 2.72 and 2.73).

MR Features of Liver Metastases. Metastases vary substantially in appearance on T2- and T1-weighted images. Generally, they are moderately high in signal

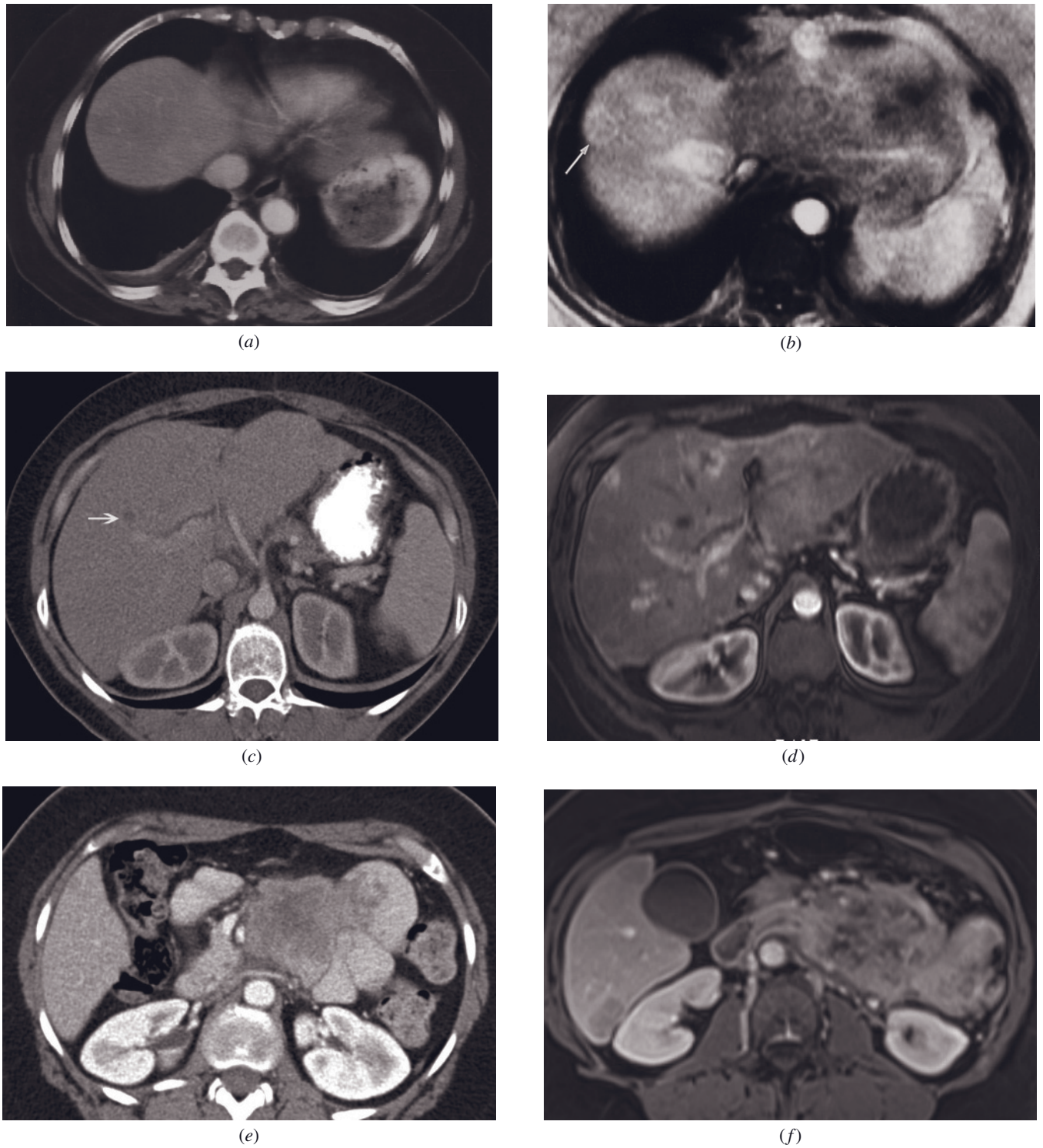

FIG. 2.71 Liver metastases, spiral and multidetector CT imaging versus MRI. Spiral contrast-enhanced CT (*a*), and immediate post gadolinium SGE (*b*) image. No lesions in the liver dome are apparent on the spiral CT image, while uniform ring enhancing lesions are evident on the immediate postgadolinium SGE image (arrow, *b*).

Multidetector contrast-enhanced CT (*c*) and immediate fat-suppressed postgadolinium SGE (*d*) images in a patient with liver metastases from carcinoid tumor. Note that extensive metastases are observed on the early-phase postcontrast MR image (*d*), while only one lesion (arrow, *c*) is appreciated on the multidetector CT image.

Multidetector contrast-enhanced CT (*e*) and immediate postgadolinium fat-suppressed 3D-gradient obtained **at 3T** (*f*) images in a patient with a large pancreatic tumor. No liver lesion is detected on CT (*e*), but on the MR image a metastasis is apparent in segment 6.

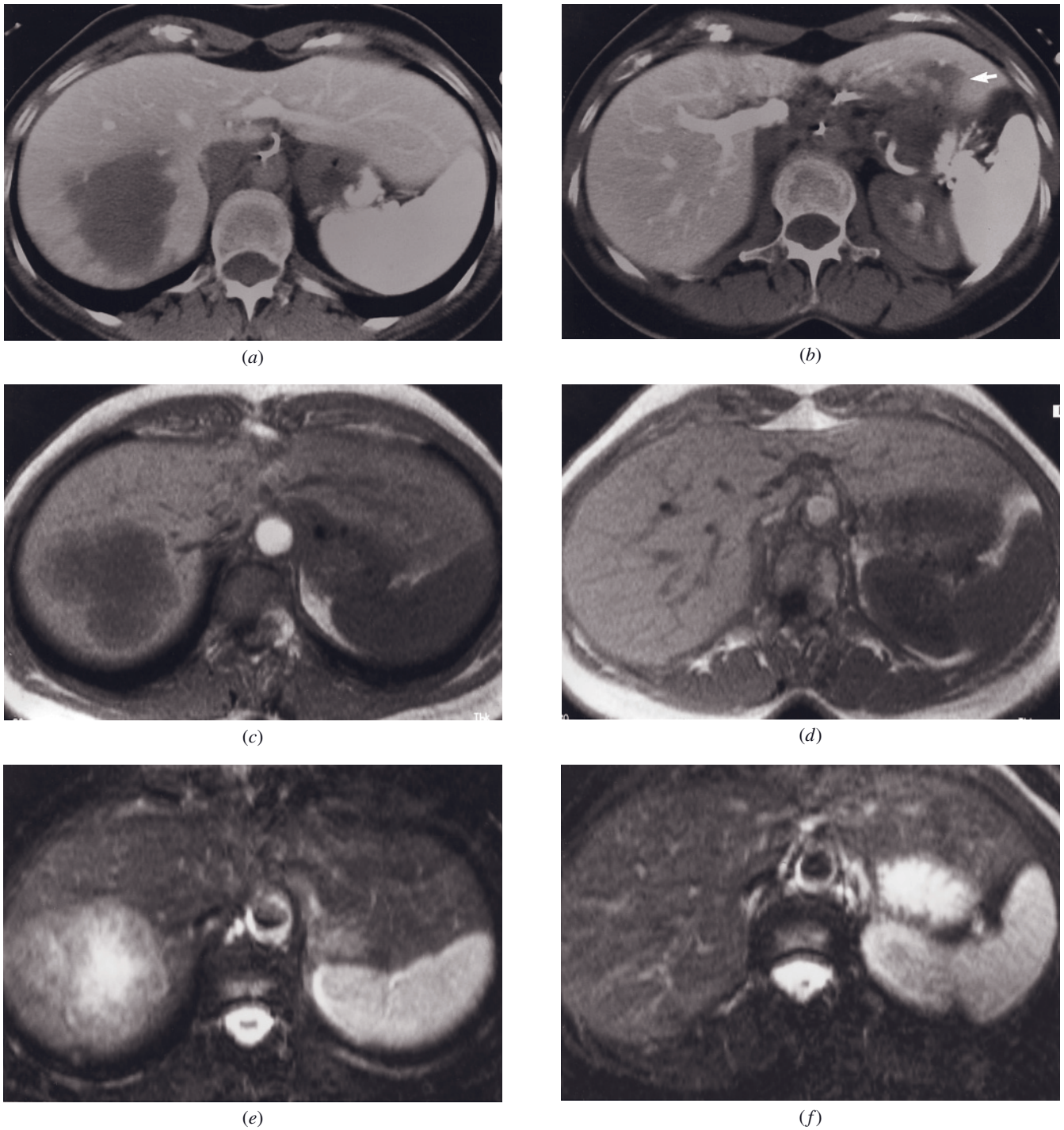

FIG. 2.72 Liver metastases—spiral CT arterial portography versus MRI. Spiral CTAP (*a*, *b*), SGE (*c*, *d*), fat-suppressed T2-weighted SS-ETSE (*e*, *f*) and immediate postgadolinium SGE (*g*, *h*) images from superior (*a*, *c*, *e*, *g*) and more inferior (*b*, *d*, *f*, *h*) tomographic sections. A large metastasis is present in the right lobe of the liver shown on all imaging techniques (*a*, *c*, *e*, *g*). A second metastasis was suspected on the CTAP image (arrow, *b*) in the lateral segment. No lesion was identified in this location on any MRI sequence. CTAP findings would have precluded surgery. However, the decision to operate was based on MRI findings. No liver metastasis was identified in the lateral segment by surgical palpation or intraoperative sonography. The patient is disease-free for more than 5 years since right hepatectomy. MRI was more accurate and had a greater impact on patient management and outcome than CTAP.

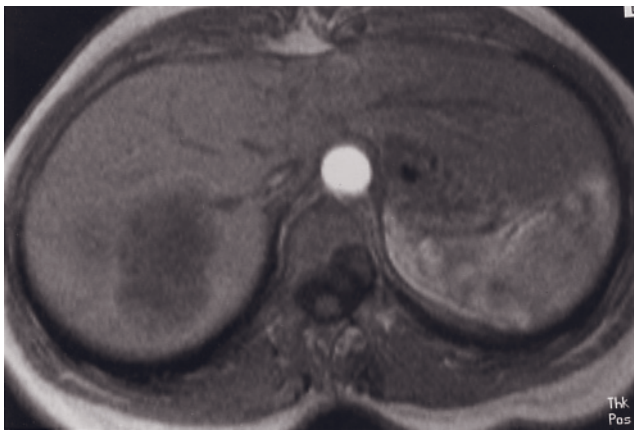

(*g*)

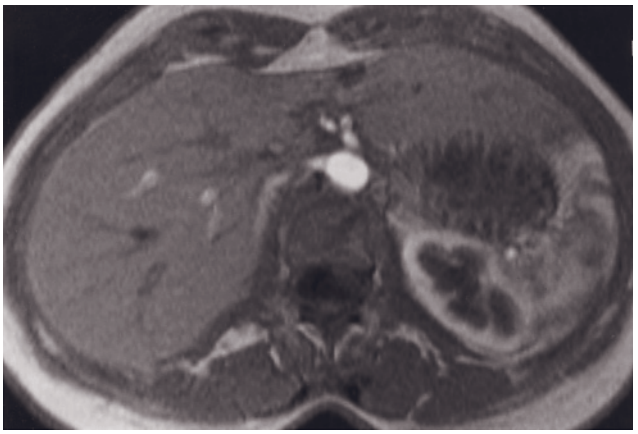

(*h*)

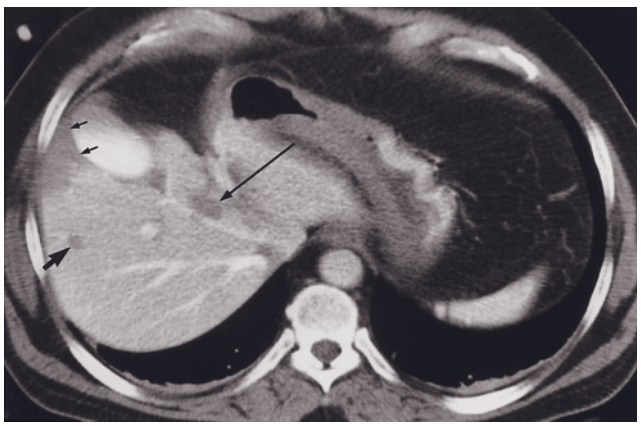

(*i*)

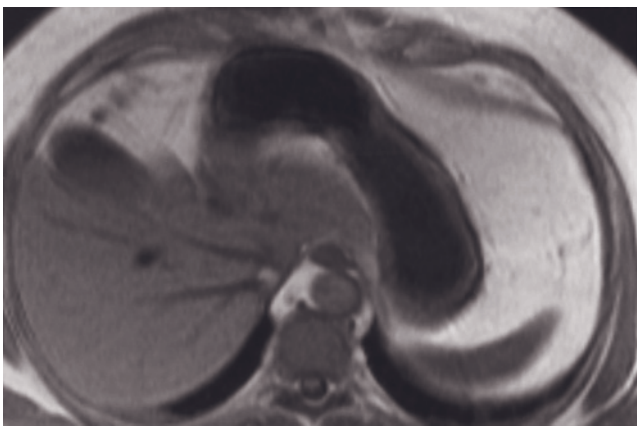

(*j*)

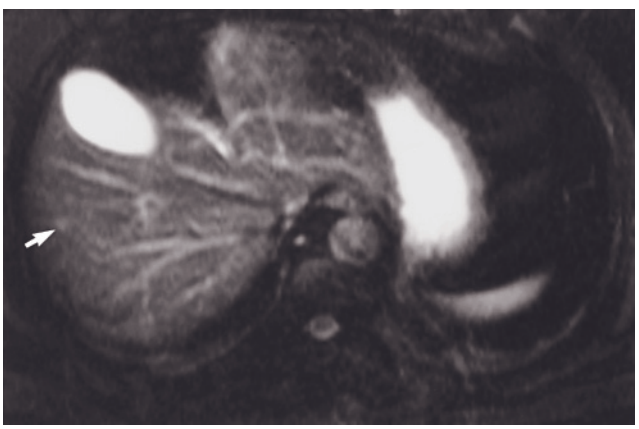

(*k*)

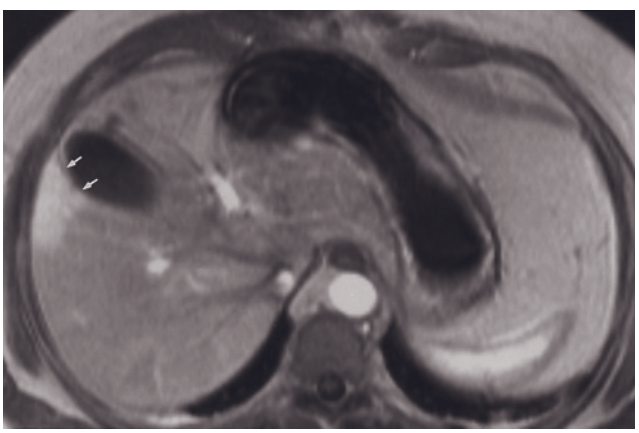

(*l*)

FIG. 2.72 (*Continued*) Spiral CTAP (*i*), SGE (*j*), fat-suppressed T2-weighted SS-ETSE (*k*), and immediate (*l*) images in a second patient with liver metastases from colon cancer. Spiral CTAP and MR images demonstrate an 8-mm metastasis in the anterior segment of the right lobe (arrow, *i, k*) and a perfusional abnormality related to a metastasis in the anterior segment of the right lobe (short arrows, *i, l*). A focal defect interpreted as metastasis on the CTAP image (long arrow, *i*) is apparent in the medial segment, but is not identified on any of the MR images (*j–l*). No metastasis in this location was identified at surgery and intraoperative sonography.

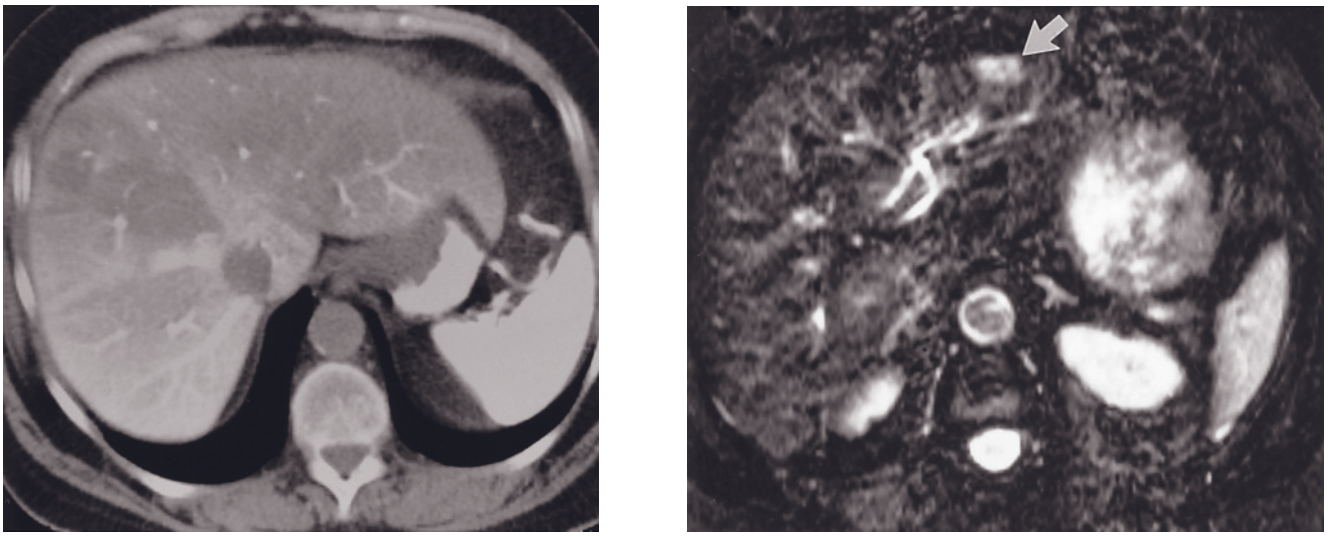

(*a*) (*b*)

FIG. 2.73 Liver metastases—perfusional defect. Spiral CTAP (*a*) and fat-suppressed T2-weighted SS-ETSE (*b*) images. Multiple large perfusional defects are present on the CTAP image (*a*), with the entire left lobe exhibiting diminished perfusion. A 1.5-cm liver metastasis is present on the T2-weighted image (arrow, *b*), which was masked by the perfusion defect on the CTAP image.

intensity on T2-weighted images and moderately low in signal intensity on T1-weighted images.

Lesional and Perilesional Enhancement. Enhancement is considered lesional when the size of the metastases on T1-weighted precontrast images and on arterial dominant-phase images is equal, and generally the outer margin of enhancement is well defined. Perilesional enhancement is described when the enhancement occurs beyond the margins of the lesion delineated on precontrast images, and the outer margin of enhancement is generally ill defined or wedge shaped.

The pattern of lesional enhancement of liver metastases has a strong association with the size of the lesion. Liver metastases can be classified according to the following features based on the pattern of enhancement on arterial dominant-phase images and the size of metastases: 1) homogeneous, usually when the lesion is ≤1.5-cm in the transverse diameter; 2) heterogeneous (uncommon), usually when the lesion is >1.5 cm in the transverse diameter; and 3) ring enhancement, commonly when the lesion is >1.5 cm in transverse diameter [141, 142]. It should be noted that homogeneity of enhancement occurring in lesions >1.5 cm is not rare, particularly when the primary tumor is hypervascular. Heterogeneity observed on early-phase images may reflect necrosis within the metastases. Diffuse heterogeneous enhancement observed in >1.5-cm hypervascular metastases may possess a radial spoke-wheel appearance with thin radial strands of lesser enhancement.

The ring enhancement pattern on early-phase images is the most characteristic appearance of liver metastases (fig. 2.74) [72, 81, 141, 143–145]. On arterial dominant-phase images, the outer margin of the metastasis enhances prominently and the inner portion has negligible enhancement, reflecting the underlying pathophysiology that the most vascularized outer portion of the tumor enhances more intensely. On interstitial-phase images there is an equilibration of enhancement as the less vascularized central tumor gradually receives its blood supply. The outer margin demonstrates a decrease in the degree of enhancement that may appear as heterogeneous fading to near isointensity or washout, and the inner area shows an increase in the degree of enhancement. The centripetal enhancement with the washout of the outer margin observed in the interstitial phase is highly suggestive of malignancy [145]. It is suggested that the lesional washout occurs because the peripheral margin of the metastasis is more vascularized, and therefore contrast enters and leaves this region more rapidly, while the inner portion is less well vascularized, ischemic, and fibrotic and thus receives a decreased amount of contrast but retains it to a longer extent [145–149]. The outer margin has a high ratio between intravascular and interstitial space, but the inner portion has a decreased intravascular space and an increased interstitial space [145, 146]. As a consequence, the blood supply is decreased in the inner portion of the metastases [145] and the clearance of the gadolinium is slower [150]. Well-defined peripheral washout with centripetal enhancement is most typical of hypervascular metastases, with gastrinoma being the most common.

Perilesional enhancement can be classified based on the shape of parenchymal enhancement as follows:

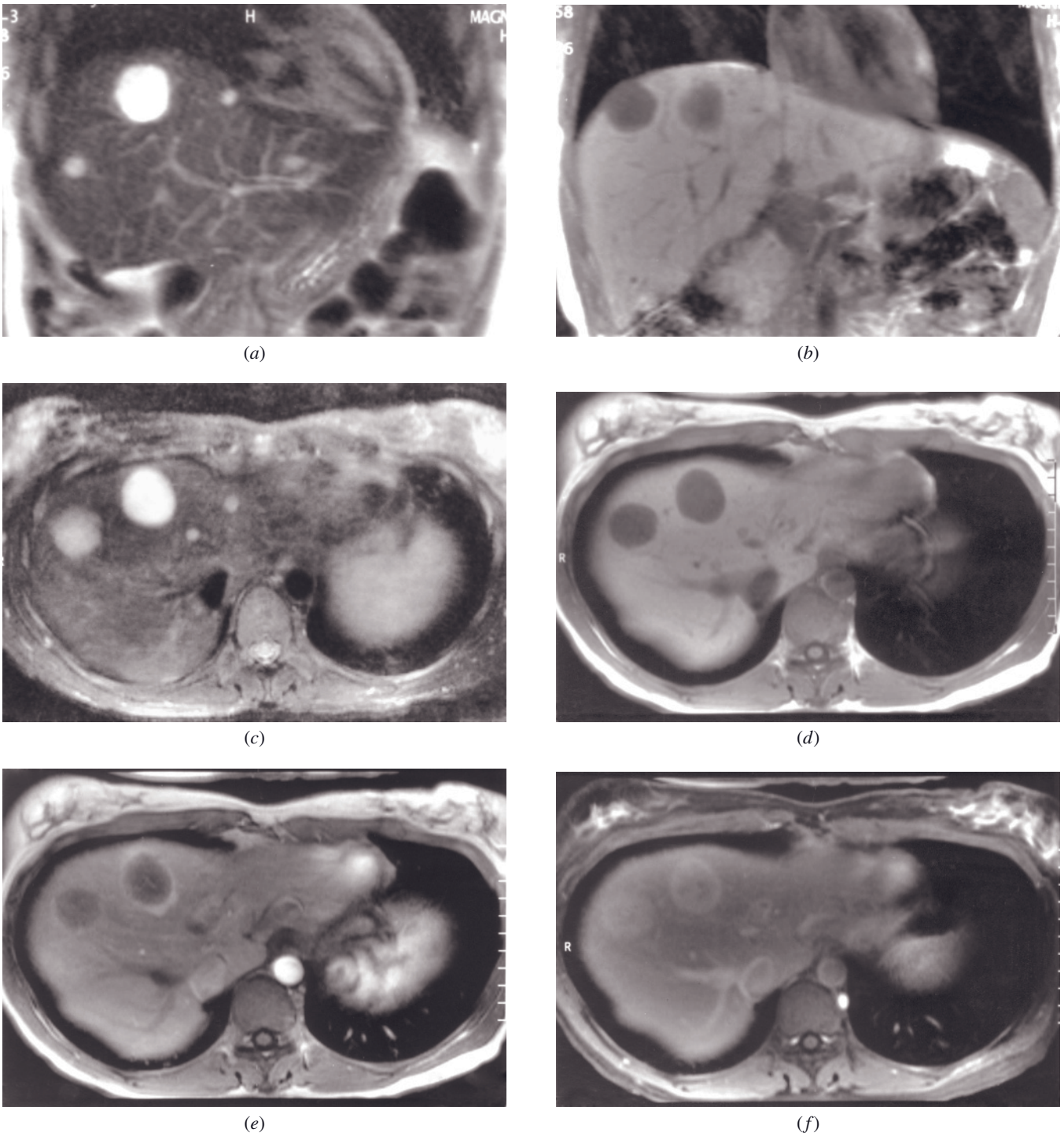

FIG. 2.74 Gastrointestinal stromal sarcoma—metastases that mimic hemangiomas on T2. Coronal T2-weighted SS-ETSE (*a*), coronal SGE (*b*), fat-suppressed T2-weighted ETSE (*c*), SGE (*d*), and immediate (*e*) and 90-s (*f*) fat-suppressed postgadolinium SGE images. There are two lesions that are well-defined and demonstrate high signal on T2-weighted images (*a*, *c*) and low signal on T1-weighted images (*b*, *d*). The high signal on T2-weighted images (*a*, *c*) resembles hemangiomas. Ring enhancement is shown on immediate postgadolinium images (*e*), diagnostic for metastases.

1) Circumferential enhancement is more typically ill-defined and better demonstrated on the arterial dominant phase with fading on interstitial-phase images; commonly observed in colon cancer metastases, and 2) wedge-shaped enhancement that is more sharply demarcated and often observed on metastases from pancreatic ductal adenocarcinoma [151].

Perilesional enhancement is uncommonly observed in other metastases apart from colorectal and pancreatic ductal adenocarcinoma [141, 151–153]. Perilesional enhancement is uncommon in hypervascular tumors such as islet cell tumors or renal cell carcinomas, implying that increased hepatic arterial supply is not the cause of perilesional enhancement. A study [151] reported that microscopic examination of liver tissue surrounding metastases showed variable degrees of hepatic parenchyma compression, desmoplastic reaction, inflammatory infiltrates, and neovascularization. This histopathologic zone, surrounding the metastasis, was termed the tumor border. Tumors with more extensive perilesional enhancement had a thicker tumor border. The area of perilesional enhancement observed on imaging was, however, broader than the tumor border noted on histopathologic inspection, suggesting the possibility that vascular changes extended beyond the outer confines of compressed liver tissue. Hypothetically, hepatocellular damage induced by the presence of nearby tumor or secretion of tumor metabolites into the vicinity adjacent to tumor may have incited an inflammatory response and neovascularization, contributing to the perilesional enhancement seen on MR images (fig. 2.75).

Association Between Vascularity of Liver Metastases and Degree of Enhancement. Liver metastases are fed primarily by arterial blood supply. The degree of enhancement of liver metastases on arterial dominant-phase images is determined by the size and number of vessels and the capillary permeability within the lesion. Moreover, the presence of fibrosis, necrosis, or confluent dense cellularity may also influence the degree of enhancement of liver metastases (fig. 2.76).

On the basis of the degree of enhancement of both arterial dominant- and interstitial-phase images, and on the lesion conspicuity on the interstitial-phase images, liver metastases by MRI may be categorized as follows: 1) avascular when there is a lack of lesional enhancement on arterial dominant- and interstitial-phase images; 2) hypovascular when the lesion demonstrates a lack of or faint enhancement on arterial dominant phase, comparable with the signal intensity of the pancreas and/or renal cortex, and becomes more conspicuous on interstitial-phase images; 3) isovascular when the lesion demonstrates similar enhancement as the background parenchyma on arterial dominant-phase images and may become more conspicuous on interstitial phase; and 4) hypervascular when the lesion shows moderate or intense enhancement on arterial dominant-phase images more accentuated than the background parenchyma and similar to the signal intensity of the pancreas and/or renal cortex and less conspicuous on interstitial phase [5, 142].

To analyze the degree of enhancement on arterial dominant-phase images, it is crucial to determine whether the sequence was acquired in the "perfect timing of enhancement." Perfect timing of enhancement is considered when contrast is seen in hepatic arteries and portal veins but not in hepatic veins [5]. Normal pancreas and/or renal cortex are used as referent organs to establish the degree of lesional enhancement on arterial dominant-phase images. These structures are highly vascularized and are located in close proximity to the liver, facilitating this analysis.

Avascular metastases appear as completely cystic or necrotic metastases. They are characterized by high signal intensity on T2-weighted images, low signal intensity on T1-weighed images, and lack of enhancement on arterial dominant- and interstitial-phase images. A thin lesional or perilesional enhancement in the margin of the metastases is often demonstrated in one of the phases postcontrast. Metastases from ovarian cancer and after treatment (chemotherapy, chemoembolization, or ablation) may demonstrate avascularity on dynamic postcontrast images (fig. 2.77). Avascular metastases may mimic the appearance of benign cysts (fig. 2.78). Sometimes, the delayed postgadolinium images demonstrate indistinct borders of metastatic lesions and a decrease in size due to peripheral enhancement. This feature distinguishes avascular metastases from true cysts since the latter lesions remain sharply circumscribed with no change in size on late postcontrast images.

Hypovascular metastases are characterized by near isointensity or high signal intensity on T2-weighted images and low signal on T1-weighted images. After contrast, hypovascular metastases demonstrate minimal enhancement on arterial dominant-phase images that tends to be more conspicuous on interstitial-phase images [154]. Primary tumors that commonly result in hypovascular metastases include colorectal carcinoma (fig. 2.79), transitional cell carcinoma (fig. 2.80) [5], pancreatic ductal adenocarcinoma, small bowel adenocarcinoma, pulmonary carcinoma, bladder carcinoma, and prostate carcinoma [141, 152].

Isovascular metastases are characterized by lesional enhancement similar to background parenchyma on arterial dominant-phase images. On interstitial-phase images, isovascular metastases often, but not always, show decrease in the degree of enhancement (washout), becoming more conspicuous. Isovascular metastases are

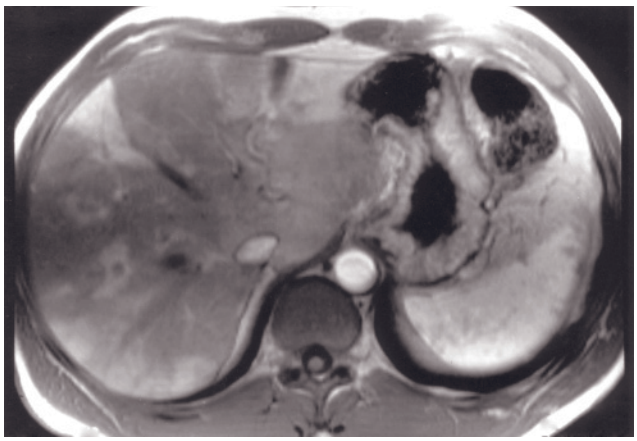

(*a*)

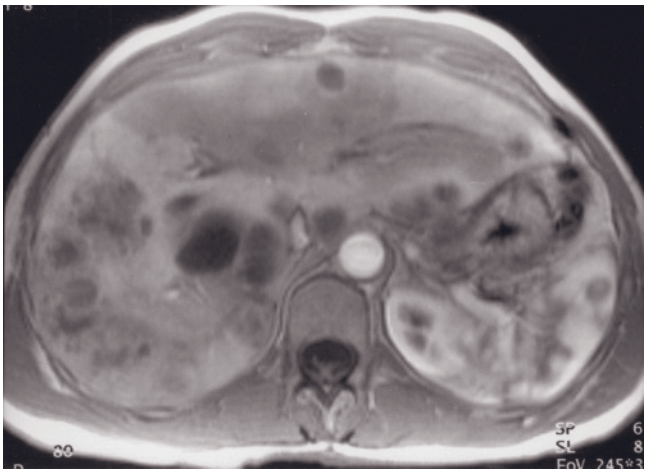

(*b*)

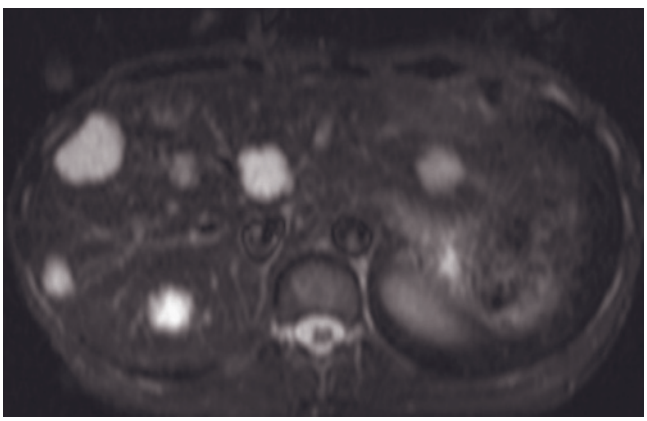

(*c*)

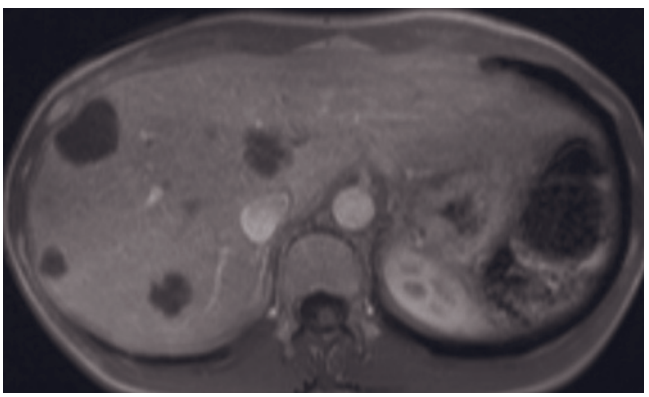

(*d*)

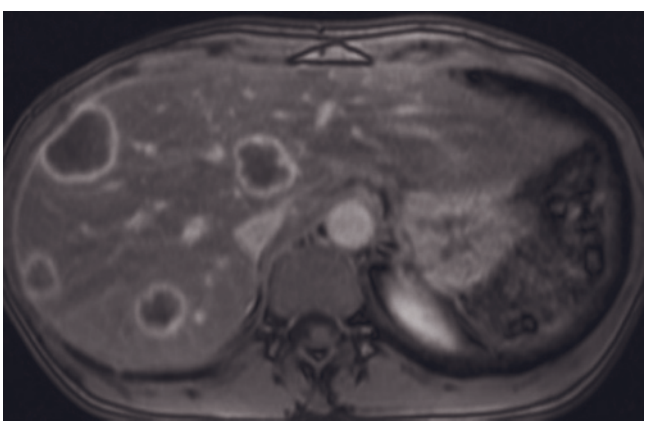

(*e*)

FIG. 2.75 Liver metastases with perilesional enhancement. Immediate postgadolinium SGE images (*a*,*b*) in two patients demonstrating perilesional enhancement. The first patient has pancreatic cancer and metastases exhibit wedge-type enhancement, while the second has gastric cancer, and shows circumferential perilesional enhancement.

T2-weighted fat-suppressed SS-ETSE (*c*) and T1-weighted fat-suppressed immediate- (*d*) and 90-s-phase (*e*) postgadolinium images obtained **at 3T** in a third patient demonstrate perilesional enhancement on delayed phase images that is characteristic for colon cancer metastases.

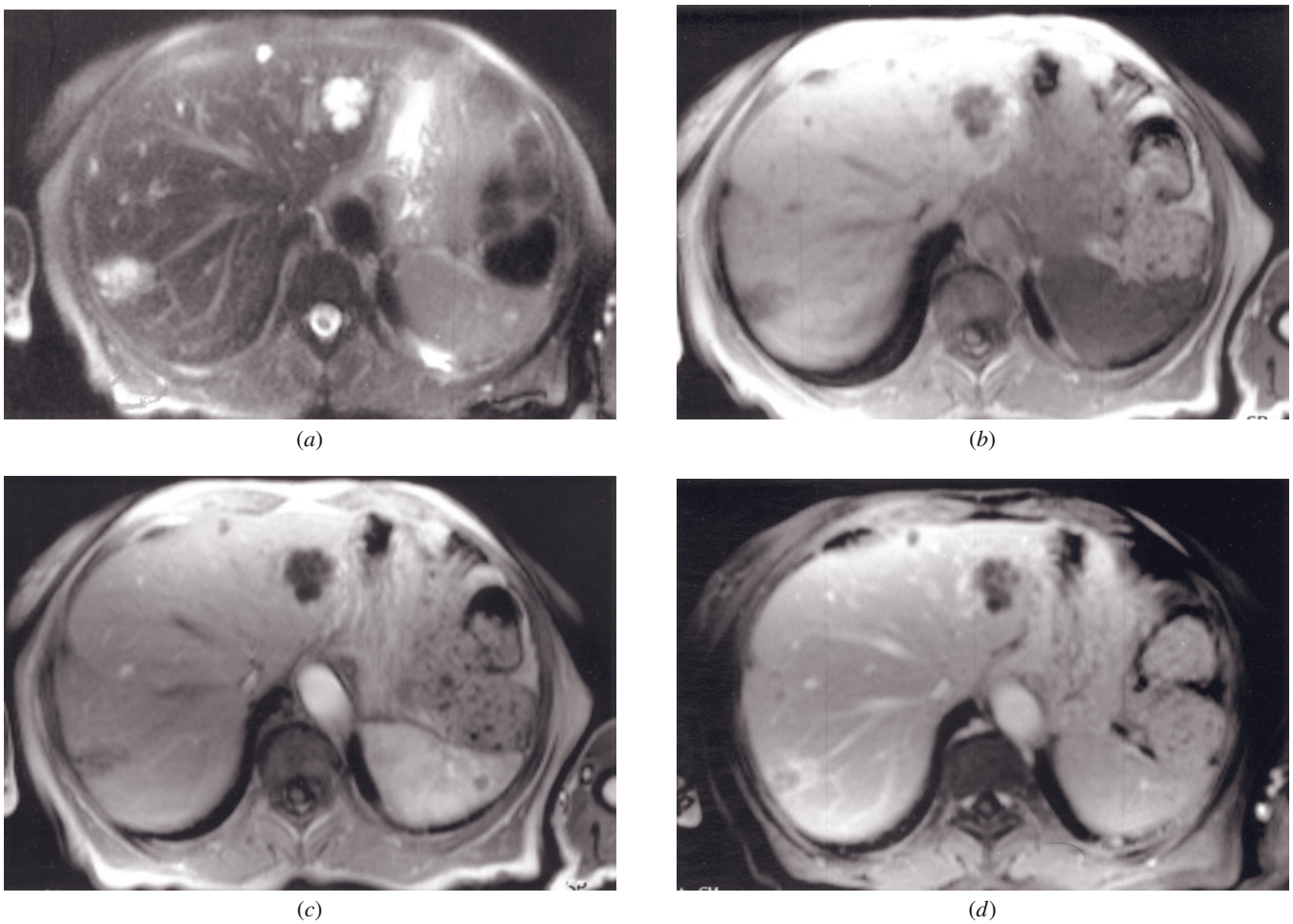

FIG. 2.76 Endometrial cancer with liver metastases. Echo-train STIR (*a*), SGE (*b*), and immediate (*c*) and 90-s fat-suppressed postgadolinium SGE(*d*) images in a patient who has endometrial cancer. There are multiple lesions that demonstrate high signal on T2 (*a*)- and low signal on T1 (*b*)-weighted images and exhibit ring enhancement and perilesional enhancement on immediate postgadolinium images (*c*). Ring enhancement persists on interstitial-phase images (*d*).

generally well-demonstrated on precontrast images as high signal intensity on T2-weighted images, low signal on T1-weighted images, or both. This appearance is most often observed in metastases after chemotherapy, presumably reflecting an antiangiogenic effect. Most commonly, metastases from colon, thyroid, and endometrium may demonstrate isovascularity [5, 150].

Hypervascular metastases are generally high in signal intensity on T2-weighted images and low in signal intensity on T1-weighted images and possess a moderate or intense peripheral ring of enhancement on early-phase images, comparable with the extent of enhancement of the pancreas and/ or renal cortex. On interstitial-phase images these metastases are the most likely to show centripetal enhancement and peripheral washout (figs. 2.81–2.84) [72, 143, 144]. Hypervascular metastases are more conspicuous on arterial dominant-phase images because of the great signal difference between intensely enhanced lesions and minimal enhancement of the background parenchyma.

Small (<1.5 cm) hypervascular metastases are commonly homogeneously high in signal intensity on T2-weighted images and homogeneously low in signal intensity on T1-weighted images and show either fading to background or washout. Often, small hypervascular metastases (especially those <1.0 cm) are only evident on hepatic arterial dominant-phase images; that is, the lesion is isointense on T2- and T1-weighed images and interstitial-phase postcontrast images [143].

The malignancies that most commonly result in hypervascular liver metastases include breast cancer, renal cell carcinoma, carcinoid tumor, islet cell tumor, thyroid carcinoma, adenocarcinoma of unknown primary site, leiomyosarcoma, and malignant melanoma. Other malignancies that occasionally result in hypervascular liver metastases include colon carcinoma, pancreatic

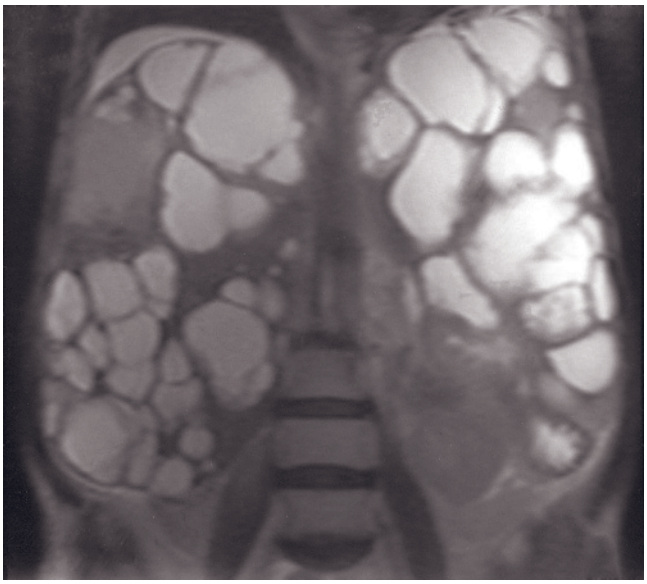

(*a*)

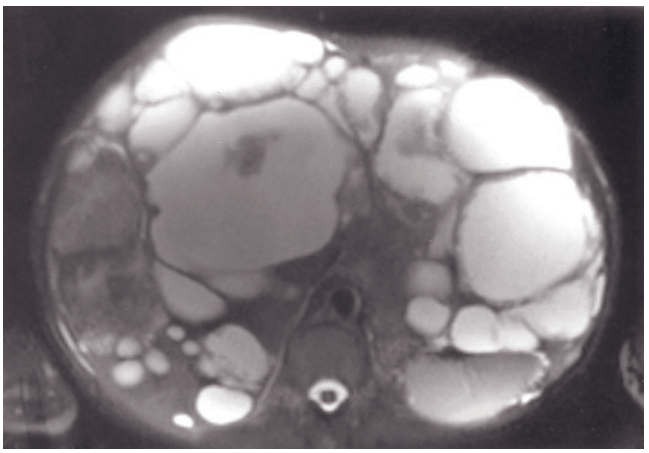

(*b*)

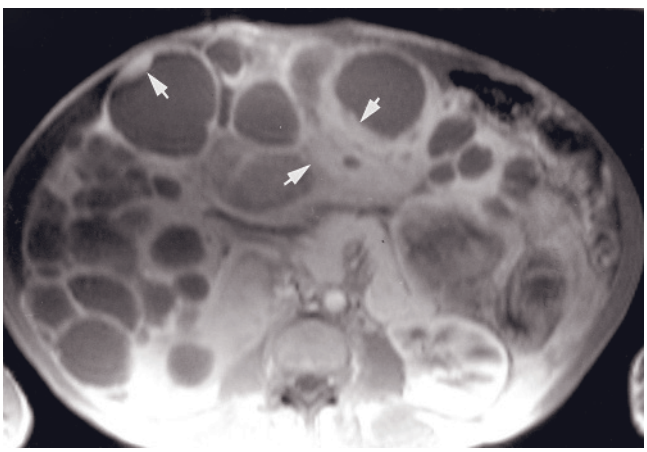

(*c*)

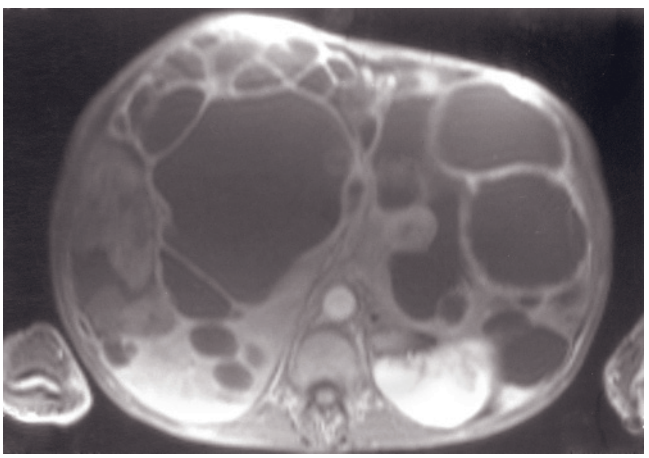

(*d*)

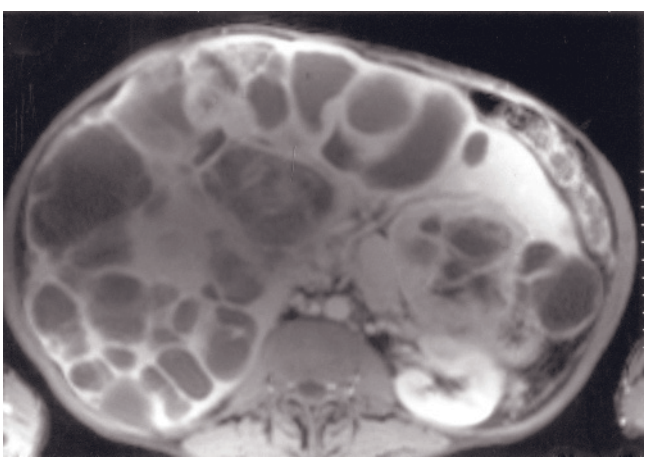

(*e*)

FIG. 2.77 Hypovascular cystic metastases. Coronal T2-weighted SS-ETSE (*a*), fat-suppressed T2-weighted SS-ETSE (*b*), and immediate (*c*) and 90-s fat-suppressed (*d*, *e*) postgadolinium SGE images. The liver is massively expanded with multiple cysts of varying sizes that replace the parenchyma. Some of these cysts have relatively uniform walls, some contain debris, and some cystic lesions have mural nodules (arrows, *c*) and intervening tumor stroma. On interstitial phase images (*d*, *e*), some progressive enhancement of tumor stroma is appreciated. The metastases are from epithelioid stromal tumor.

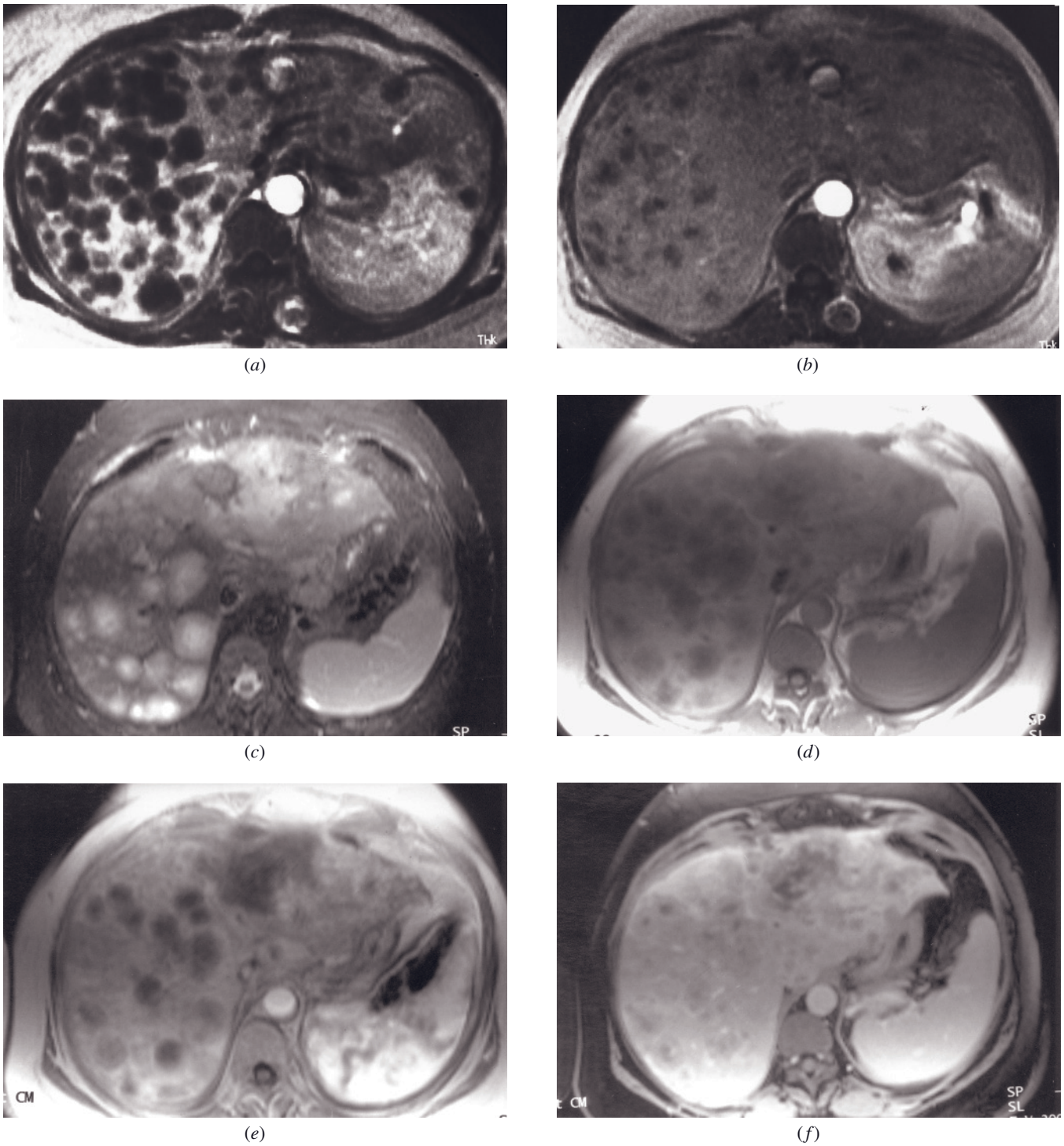

FIG. 2.78 Hypovascular liver metastases with high fluid content from adenocarcinoma of unknown primary. Immediate (*a*) and 10-min (*b*) postgadolinium SGE images. Hypovascular liver metastases with a high fluid content are low in signal intensity on T1 (not shown) and high in signal intensity on T2 (not shown) images. On immediate postgadolinium images (*a*), they may appear well defined and nearly signal void, mimicking the appearance of cysts. On delayed postgadolinium images (*b*) these lesions will partially enhance and decrease in size, permitting correct characterization (Reproduced with permission from Semelka RC, Shoenut JP, Greenberg HM, Micflikier AB. The liver. In: Semelka RC, Shoenut JP, eds. *MRI of the Abdomen with CT Correlation*. New York: Raven Press, 1993. p.13–41).

Echo-train STIR (*c*), SGE (*d*), and immediate (*e*) and 90-s fat-suppressed (*f*) postgadolinium SGE images in a second patient with adenocarcinoma of unknown primary. There are multiple metastases scattered throughout the liver that exhibit high signal on T2-weighted images (*c*), low signal on T1-weighted images (*d*), and mild ring enhancement on immediate postgadolinium images (*e*) with progressive enhancement of the lesions on delayed images (*f*).

As these cases illustrate, patients with adenocarcinoma of unknown primary often have extensive liver metastases that also may be of relatively low vascularity.

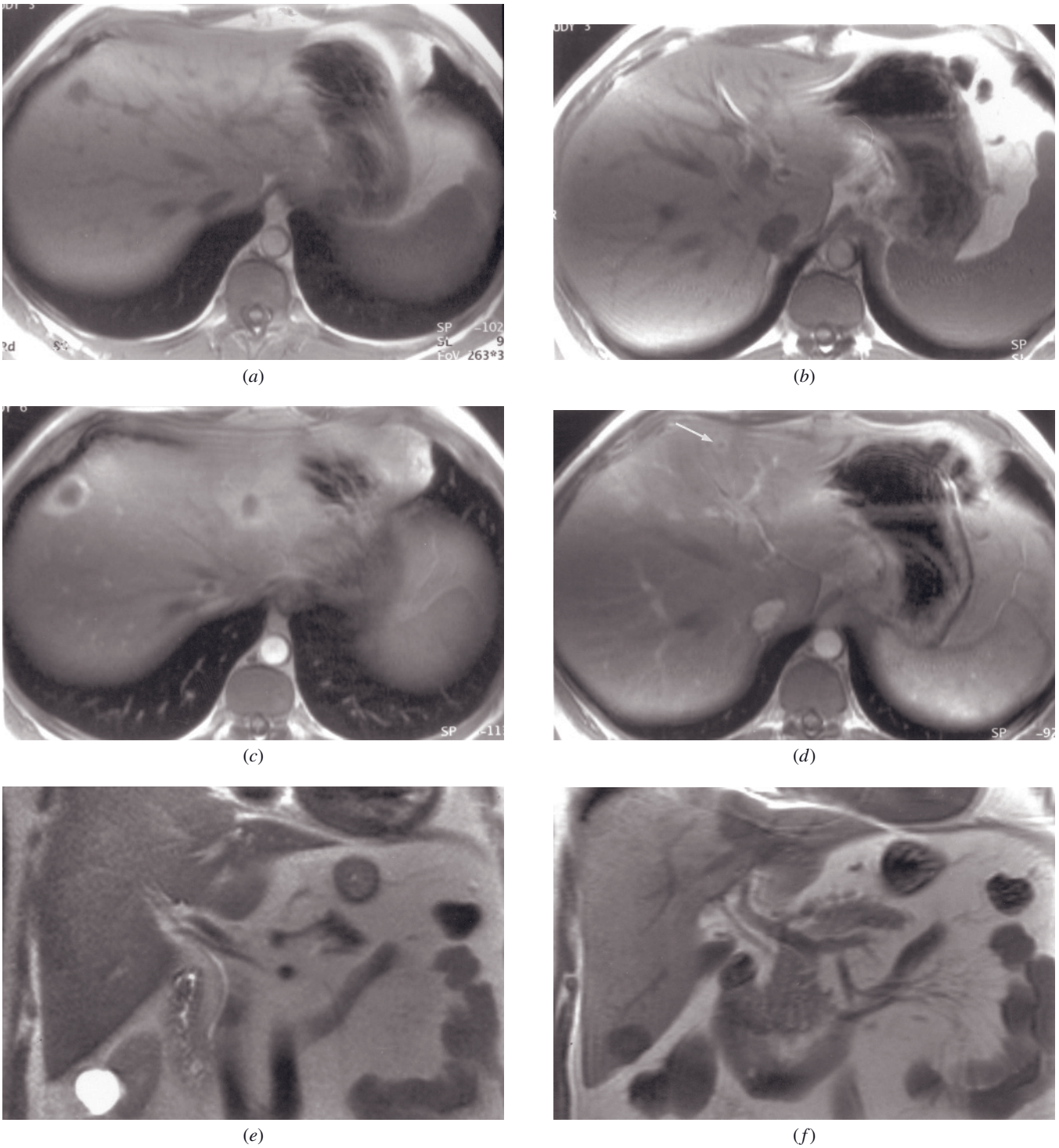

FIG. 2.79 Low-fluid-content colon cancer metastases. SGE (*a*, *b*) and immediate postgadolinium SGE (*c*, *d*) images. Lesions, especially small lesions, are difficult to discern on noncontrast T2 (not shown)- and T1 (*a*, *b*)-weighted images. On immediate postgadolinium images (*c*, *d*), lesions are rendered conspicuous because of ring enhancement. Lesions <1 cm in size may be detected and characterized with this technique.

Coronal fat-suppressed T2-weighted SS-ETSE (*e*), coronal SGE (*f*), transverse T2-weighted SS-ETSE (*g*), and transverse immediate postgadolinium SGE (*h*) images in a second patient. There are multiple metastases in the liver that are near isointense on T2 (*e*, *g*)

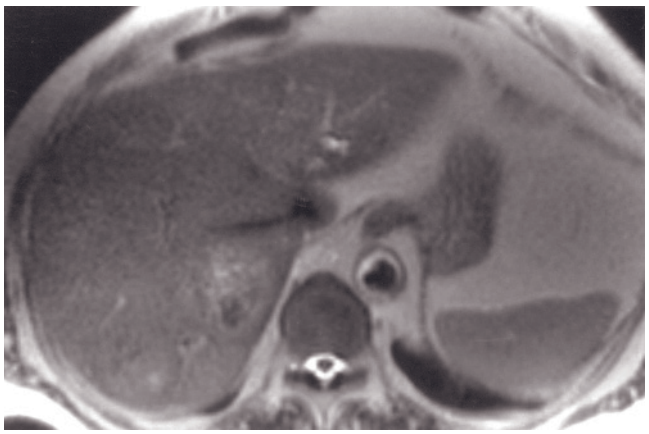

(*g*)

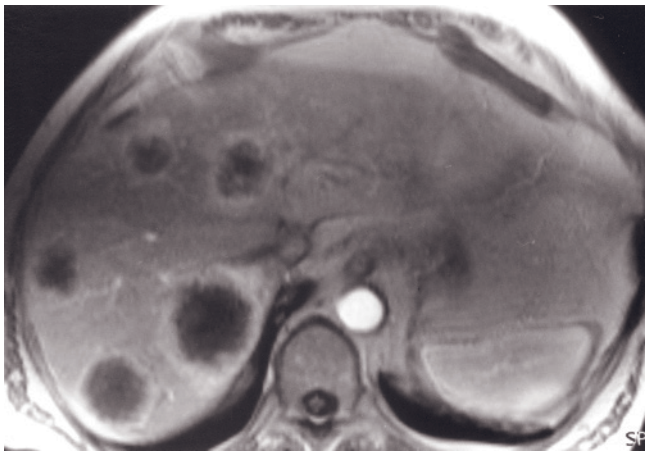

(*h*)

FIG. 2.79 (*Continued*) and hypointense on T1-weighted images (*f*), and demonstrate ring enhancement on postgadolinium images (*h*). These liver metastases are poorly seen on T2 (*e*, *g*), well seen on T1 (*f*), and very well shown on immediate postgadolinium images (*h*).

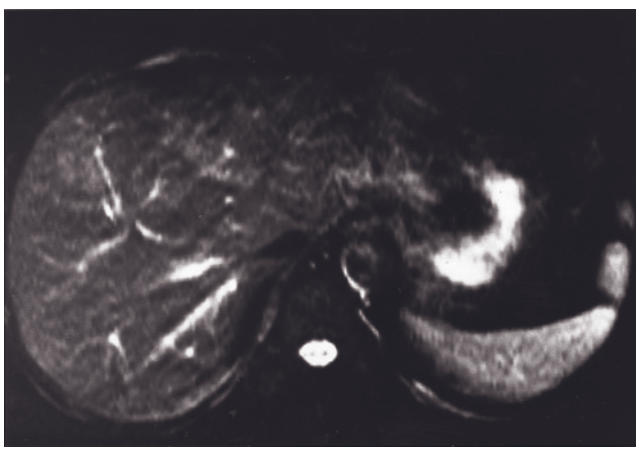

(*a*)

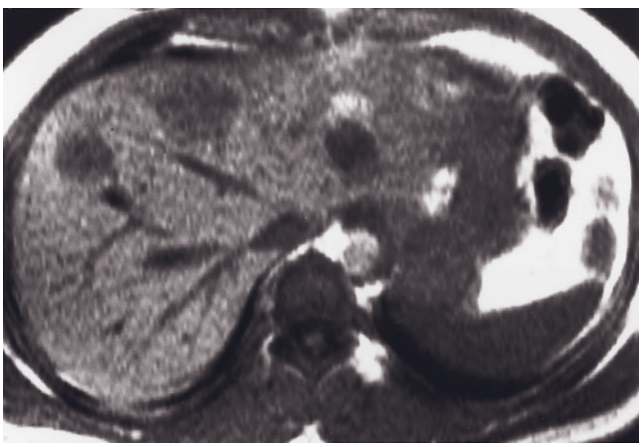

(*b*)

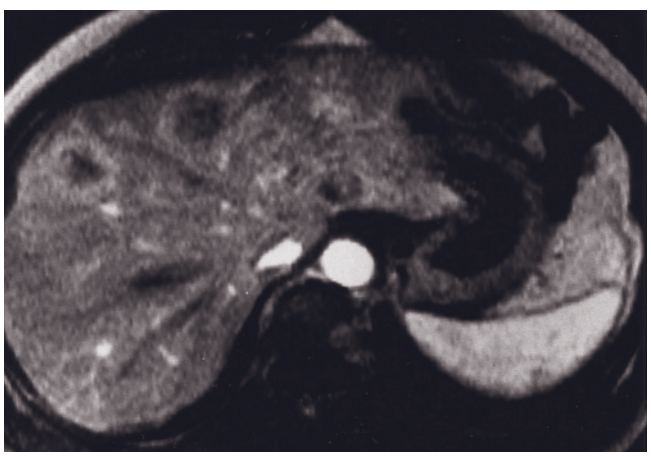

(*c*)

FIG. 2.80 Hypovascular liver metastases with low fluid content. Fat-suppressed T2-weighted ETSE (*a*), SGE (*b*), and immediate postgadolinium SGE (*c*) images. Hypovascular liver metastases with low fluid content are usually low in signal intensity on T2- and T1-weighted images, which renders them isointense to minimally hyperintense in signal intensity relative to liver on T2-weighted images (*a*) and low in signal relative to liver on T1-weighted images (*b*). Hypovascular liver metastases with low fluid content possess imaging features comparable to those of fibrous tissue. Despite their hypovascularity, these metastases exhibit faint peripheral rim enhancement on the immediate image (*c*) (Reproduced with permission from Semelka RC, Shoenut JP, Greenberg HM, Micflikier AB. The liver. In: Semelka RC, Shoenut JP, eds. *MRI of the Abdomen with CT Correlation*. New York: Raven Press, 1993, p.13–41).

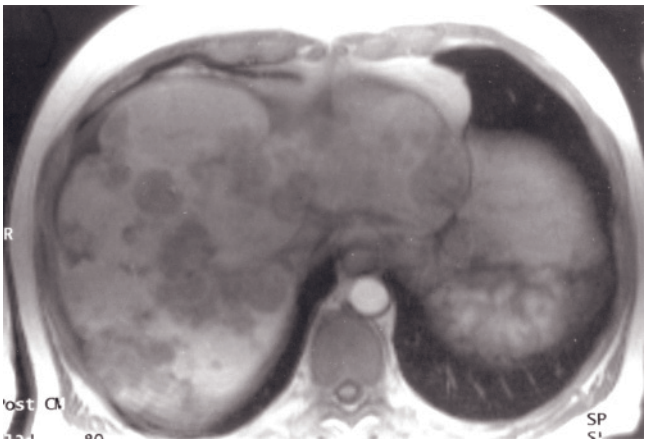

(*d*)

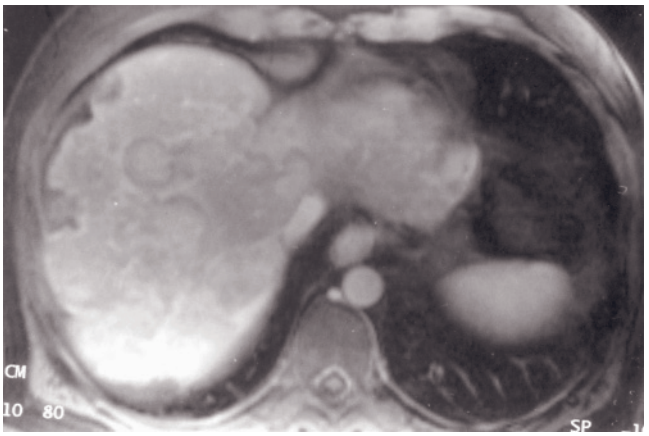

(*e*)

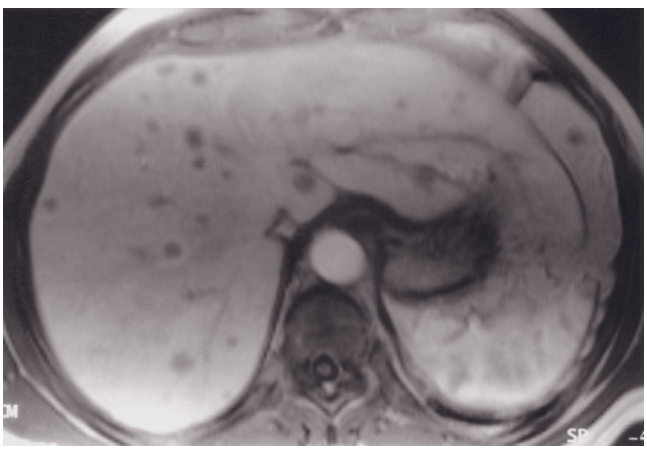

(*f*)

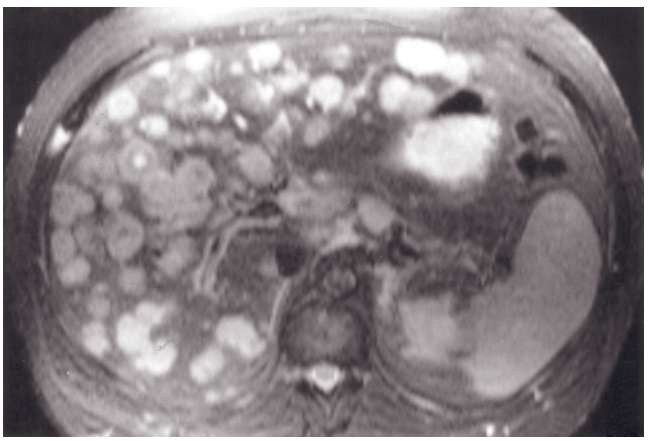

(*g*)

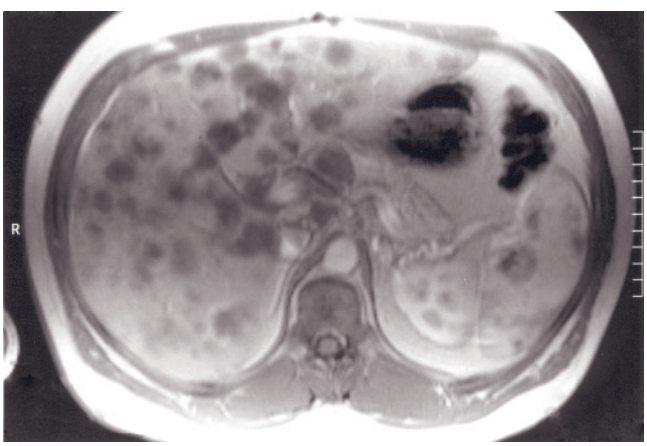

(*h*)

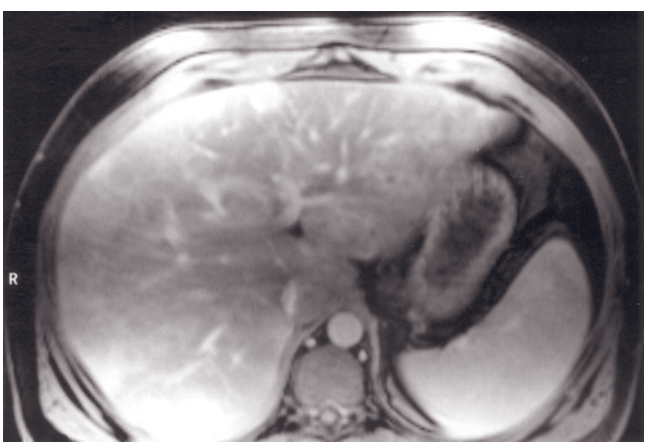

(*i*)

FIG. 2.80 (*Continued*) Immediate (*d*) and 90-s fat-suppressed (*e*) postgadolinium SGE images in a second patient, who has a history of bladder carcinoma. On the immediate postgadolinium image (*d*), the lesions exhibit negligible enhancement, and on the interstitial-phase image (*e*), they become heterogeneously isointense with liver.

Immediate postgadolinium SGE (*f*) image in a third patient. Multiple hypointense lesions with faint ring enhancement are seen in the hepatic parenchyma, consistent with metastases.

Echo-train STIR (*g*) and immediate (*h*) and 90-s fat-suppressed (*i*) postgadolinium SGE images in a fourth patient. Extensive metastases are scattered throughout the liver that appear moderately high signal on T2 (*g*) and moderately low signal on T1 (not shown), show ring enhancement on immediate postgadolinium images (*h*), and enhance to near isointensity on late images (*i*).

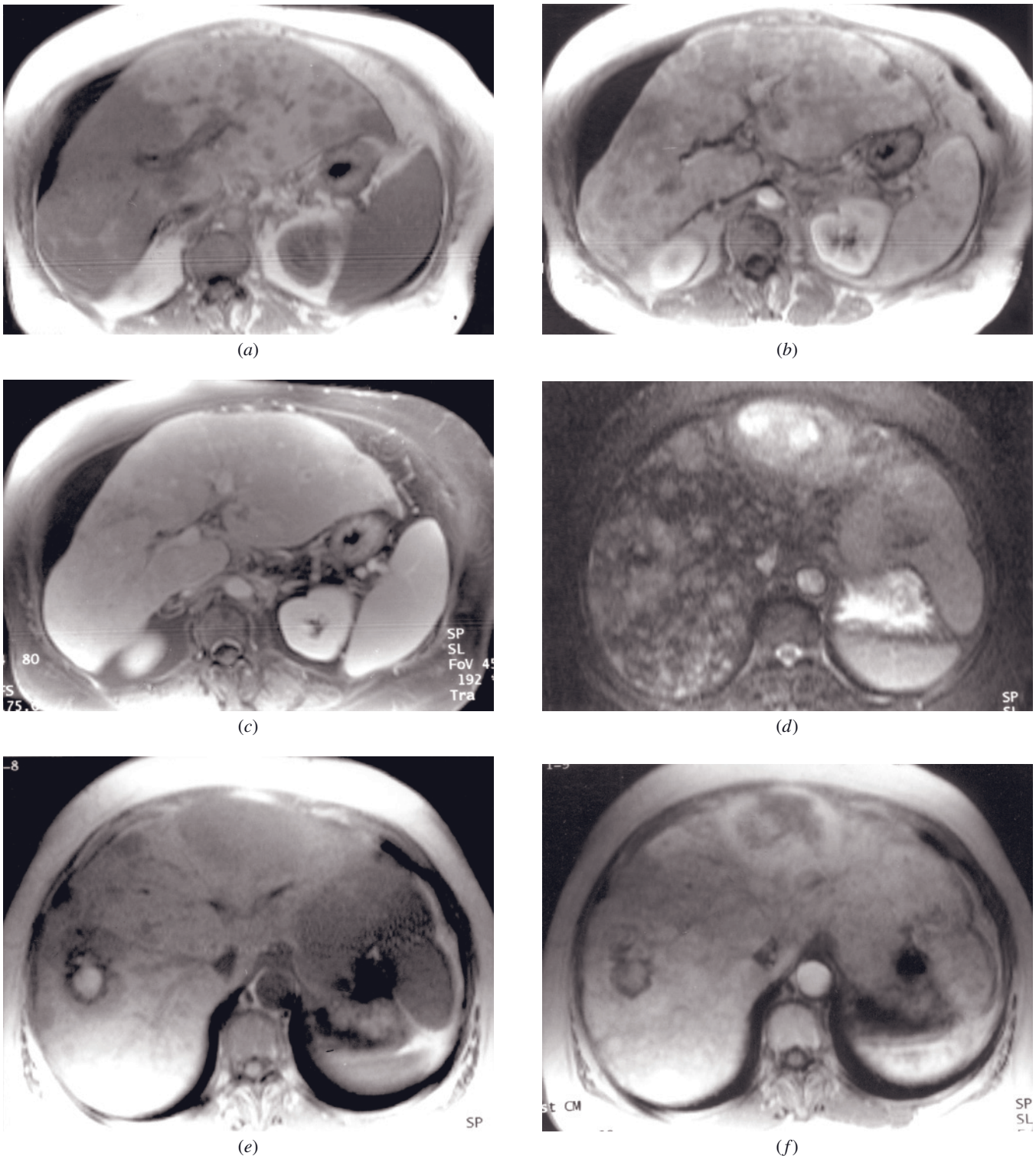

FIG. 2.81 Hypervascular liver metastases from adenocarcinoma of unknown primary. SGE (*a*) and immediate (*b*) and 90-s fat-suppressed postgadolinium SGE (*c*) images. There are numerous lesions scattered throughout the hepatic parenchyma, which are low signal on T1-weighted image (*a*), exhibit ring enhancement immediately after gadolinium administration (*b*), and enhance to near isointensity with liver on interstitial-phase images (*c*).

Echo-train STIR (*d*), SGE (*e*) and immediate postgadolinium SGE (*f*) images in a second patient. There are numerous metastases in the liver. One lesion has mildly increased signal on T2-weighted image (*d*) and high signal on T1-weighted image (*e*), consistent with hemorrhage. Note that many of the <1-cm metastases exhibit moderately intense uniform enhancement (*f*).

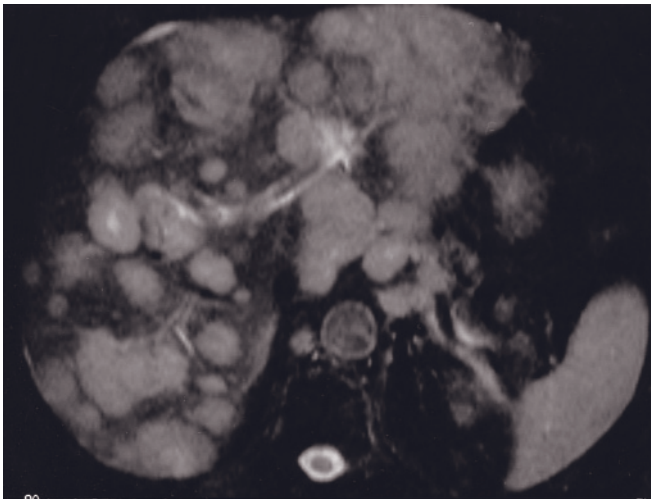

(*g*)

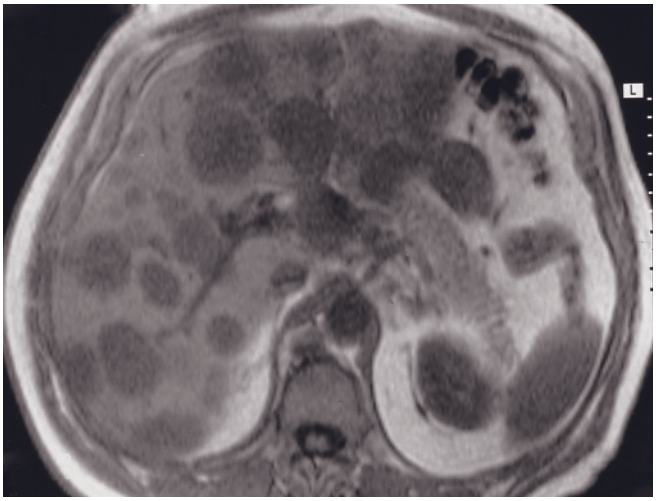

(*h*)

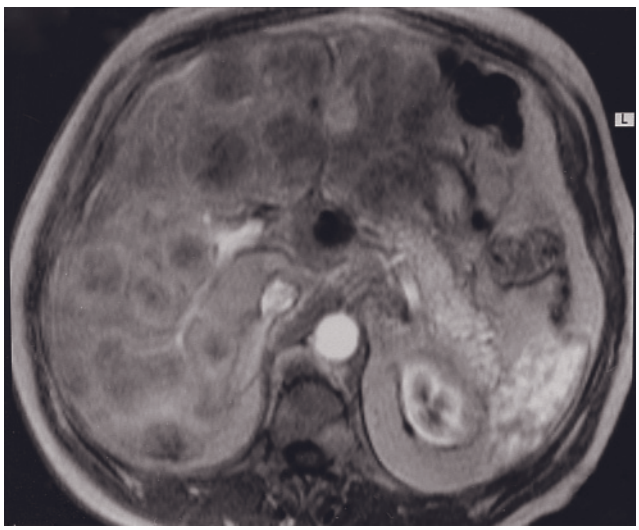

(*i*)

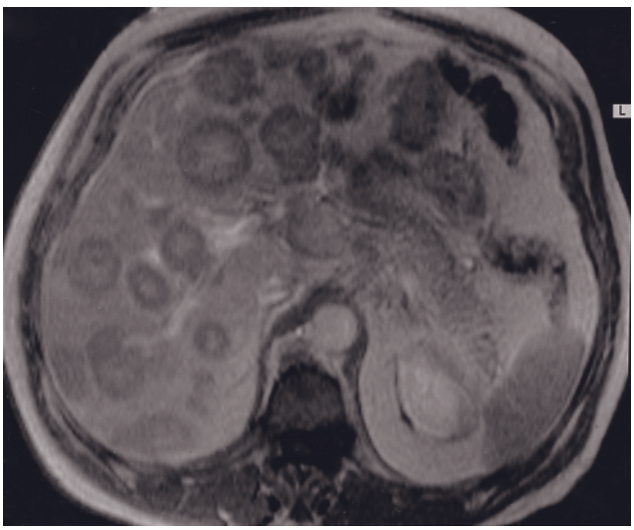

(*j*)

FIG. 2.81 (*Continued*) Fat-suppressed T2-weighted ETSE (*g*), SGE (*h*), and immediate (*i*) and 2-min (*j*) postgadolinium SGE images. The liver contains numerous metastases scattered throughout all segments that are moderately high in signal intensity on T2 (*g*) and well defined and moderately low in signal intensity on T1 (*h*) and have prominent thick uniform rings of enhancement on immediate postgadolinium images (*i*). Peripheral washout with centripetal progression of enhancement is noted on the delayed postcontrast image (*j*). Peripheral washout is common in hypervascular tumors that possess uniform intense rings of enhancement on immediate postgadolinium images.

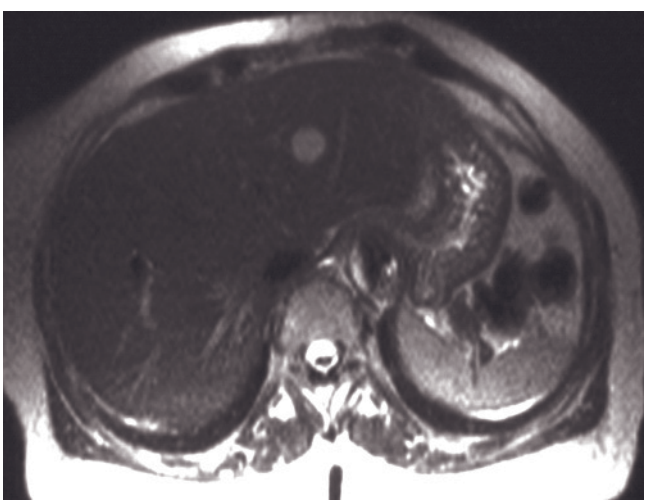

(*a*)

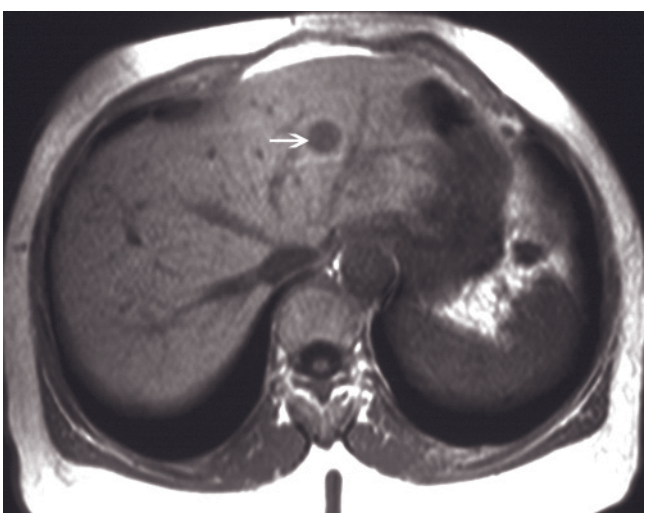

(*b*)

FIG. 2.82 Liver metastases from ovarian cancer. T2-weighted SS-ETSE (*a*), SGE (*b*), and immediate (*c*) and 90-s fat-suppressed (*d*) SGE images. A rounded lesion is seen in the left hepatic lobe that shows high signal intensity on the T2-weighted image (*a*),

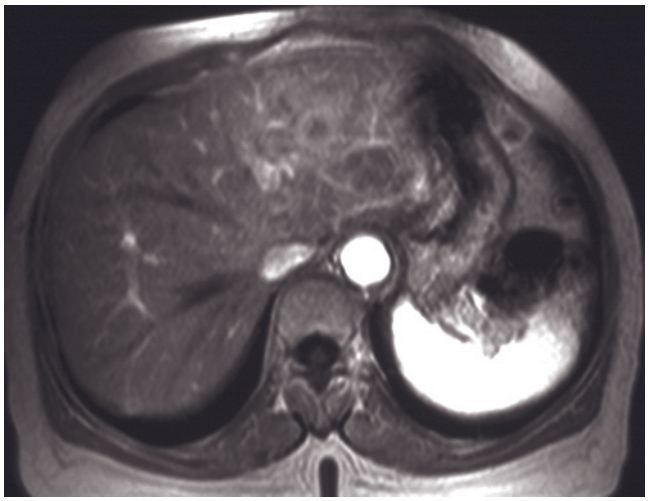

(*c*)

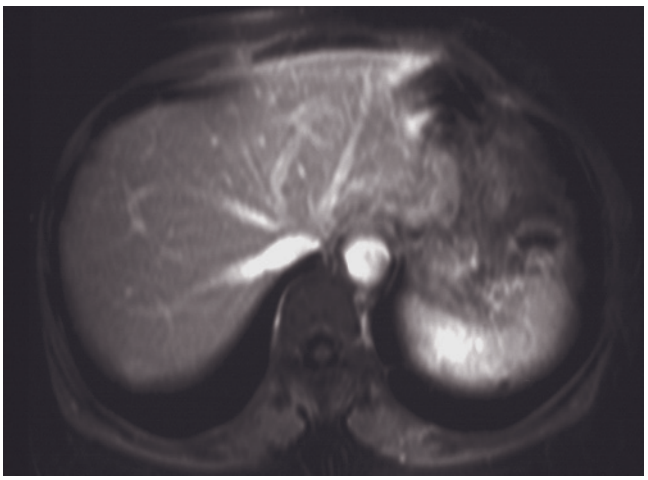

(*d*)

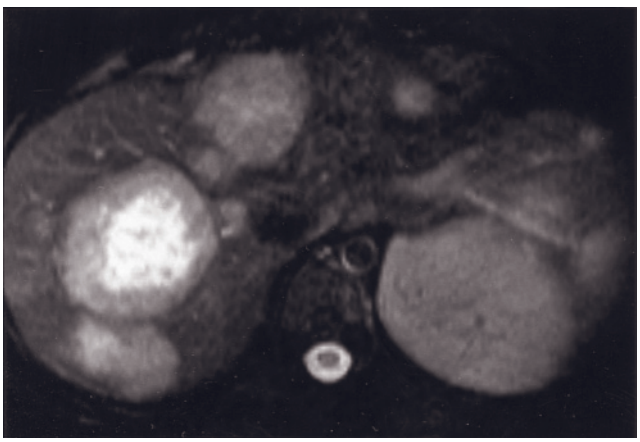

(*e*)

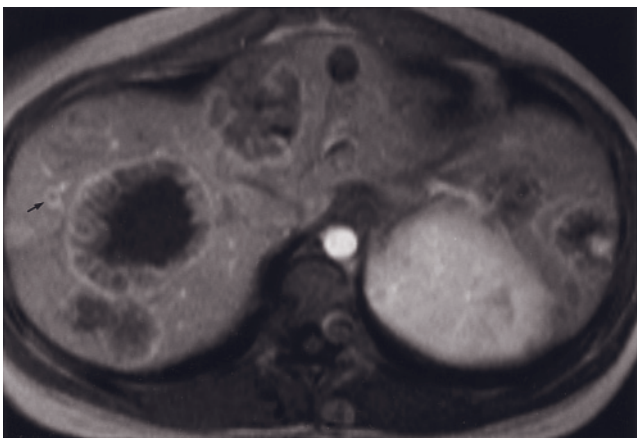

(*f*)

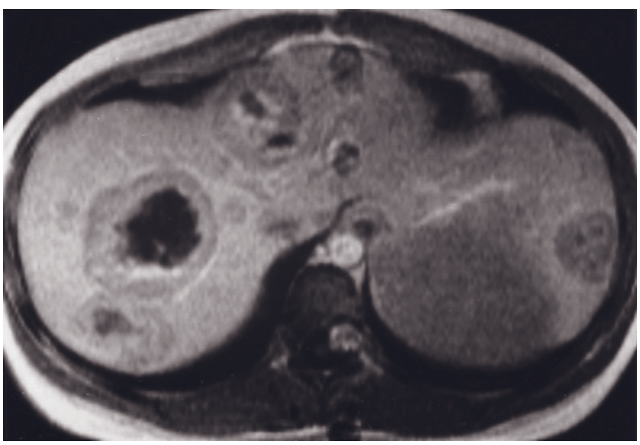

(*g*)

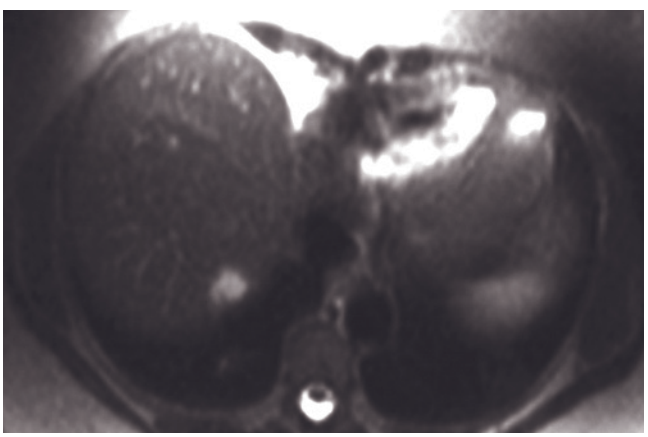

(*h*)

FIG. 2.82 (*Continued*) low signal intensity on the T1-weighted image (arrow, *b*), and faint ring enhancement and perilesional enhancement on the early-phase image (*c*) that become less conspicuous on the late-phase image (*d*), consistent with a metastasis.

Fat-suppressed T2-weighted ETSE (*e*) and immediate (*f*) and 10-min (*g*) postgadolinium SGE images in a second patient with ovarian cancer. Multiple varying-sized metastases are scattered throughout the liver. The largest metastasis is high in signal intensity centrally on the T2-weighted image (*e*) because of central necrosis. Metastases are better shown on the immediate postgadolinium image and appear as multiple hypervascular lesions with ring enhancement. Ring enhancement is appreciated in metastases as small as 6 mm (arrow, *f*). Peripheral washout of metastases is apparent on the 10-min postgadolinium image (*g*).

T2-weighted SS-ETSE (*h*) and immediate (*i*) and 90-s fat-suppressed (*j*) postgadolinium SGE images in a third patient demonstrates a liver metastasis that is high signal intensity on the T2-weighted image (*h*) and low signal intensity on the T1-weighted image (not shown) and shows a faint thin ring enhancement on the early-phase image (*i*) that becomes more conspicuous on the late-phase image (*j*).

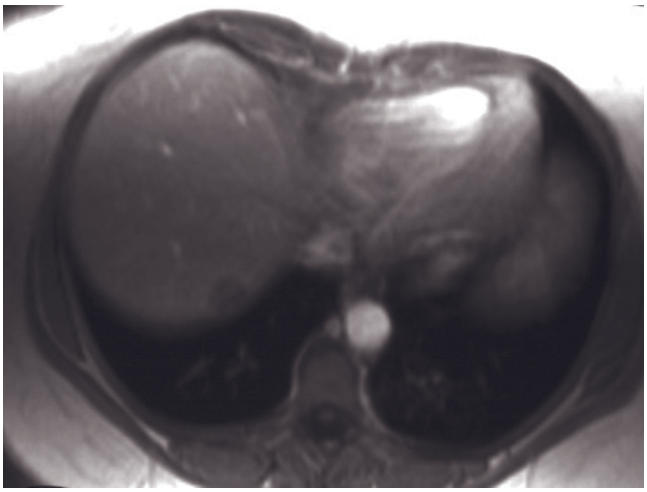

(*i*)

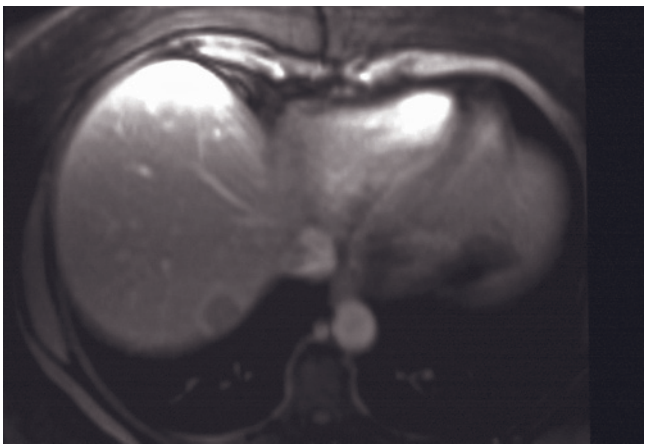

(*j*)

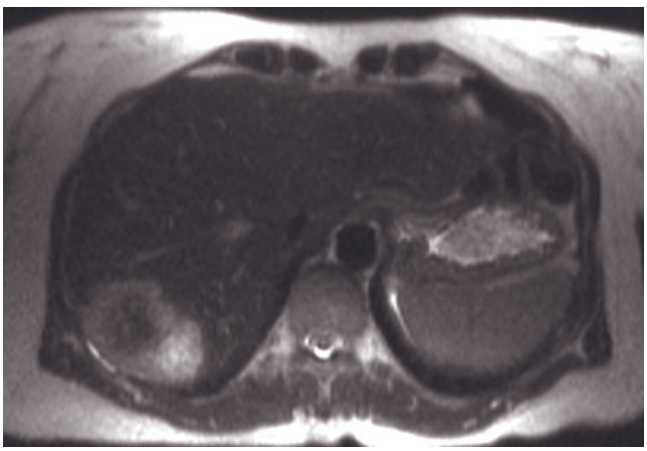

(*k*)

(*l*)

(*m*)

FIG. 2.82 (*Continued*) T2-weighted SS-ETSE (*k*) and immediate (*l*) and 90-s fat-suppressed (*m*) postgadolinium SGE images in a fourth patient with liver metastases from ovarian cancer demonstrate metastases that are heterogeneously high signal intensity on T2-weighted images (*k*) and moderately low signal intensity on T1-weighted images (not shown) and show moderate ring enhancement on early-phase images (*l*) that becomes less conspicuous on late-phase images (*m*).

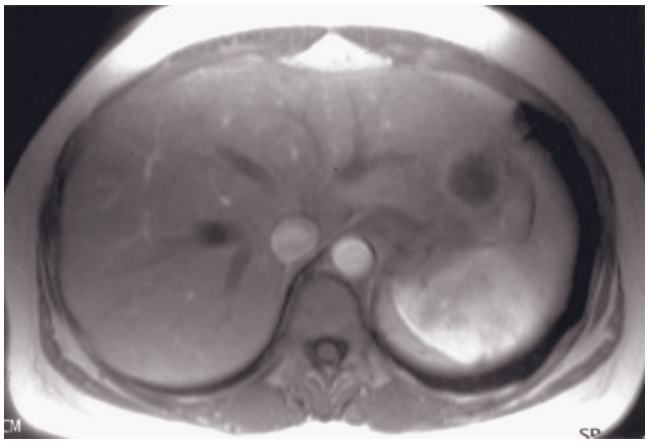

(*a*)

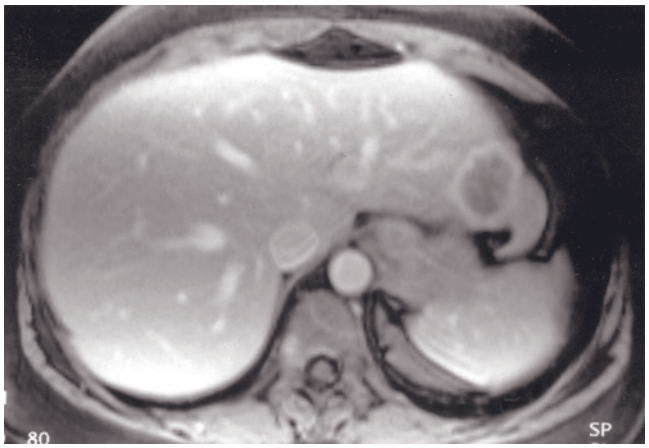

(*b*)

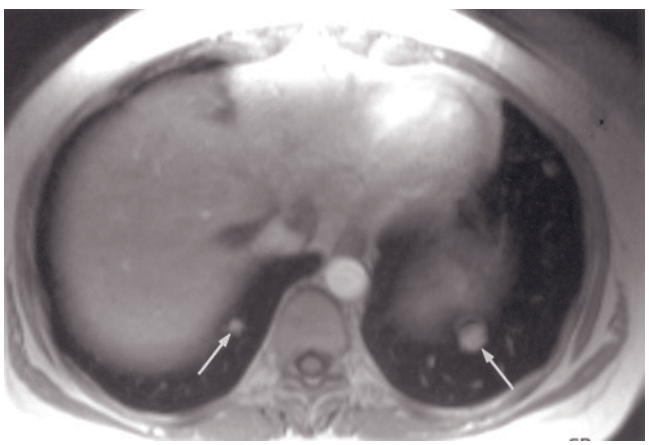

(*c*)

FIG. 2.83 Lung and liver metastases. Immediate (*a*, *c*) and 90-s fat-suppressed (*b*) postgadolinium SGE images in a patient who has a history of carcinoma of the sphenoid sinus. A metastasis in the left hepatic lobe is present, which demonstrates peripheral rim enhancement following administration of contrast (*a*) that persists on the late image (*b*), consistent with a metastasis. Note that lung metastases are also present (arrows, *c*).

ductal carcinoma, and lung cancer [143, 155]. The most commonly observed extremely hypervascular metastases are of neuroendocrine origin (i.e., carcinoid and islet cell tumor).

Enhancement of hypervascular metastases is better shown on MR than on CT images because of the higher sensitivity of MRI for gadolinium chelates, the more compact bolus of contrast delivered to the hepatic parenchyma, and the better temporal resolution for dynamic image acquisition (fig. 2.85).

MR Features of Liver Metastases According to Primary Site. Certain histologic types of metastases may display distinctive morphology or patterns of enhancement (figs. 2.86–2.88).

Metastases from colon cancer are commonly hypovascular. As a characteristic histopathologic finding, these tumors have a thin zone of fibrous tissue and inflammatory cells that translates in a thin peripheral ring of enhancement on MR images that enhances on early-phase images and remains enhanced on late-phase images [141]. When tumors exceed 3 cm in diameter, metastases from colorectal cancer typically develop a cauliflower-type appearance. It is suggested that this appearance is due to the presence of fibrous tissue strands and inflammatory cells that extend into the lesions, surrounded by islets of tumoral cells that arise with tumor growth and bulge through portions of the fibrous encapsulation [141]. This creates areas of peripheral enhancement that extend into the periphery of the tumor, creating the cauliflower-type appearance. Large solitary metastases are most commonly observed in colon carcinoma. This imaging observation may in part reflect the fact that colon cancer is the most frequently encountered liver metastasis. Minimal involvement of the liver with metastatic disease explains why colon cancer is one of the few malignancies amenable to curative surgical resection of liver metastases. Colorectal metastases may exhibit coagulative necrosis, which may produce central low signal intensity on T2-weighted images surrounded by higher-signal-intensity viable tumor [156].

Multiple small subcapsular metastases are observed in approximately one-third of patients with liver metastases from colon cancer. These metastases may only

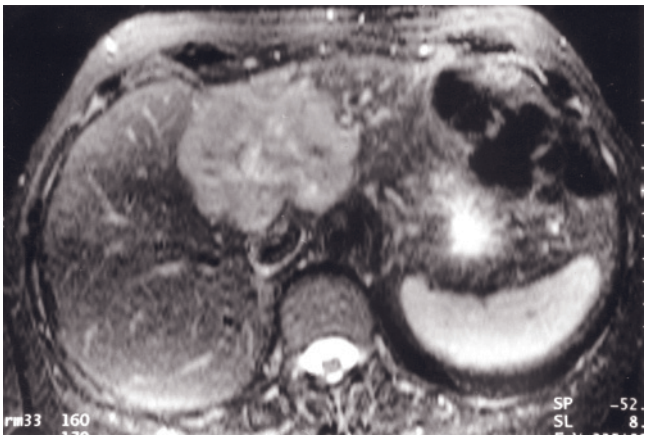

(*a*)

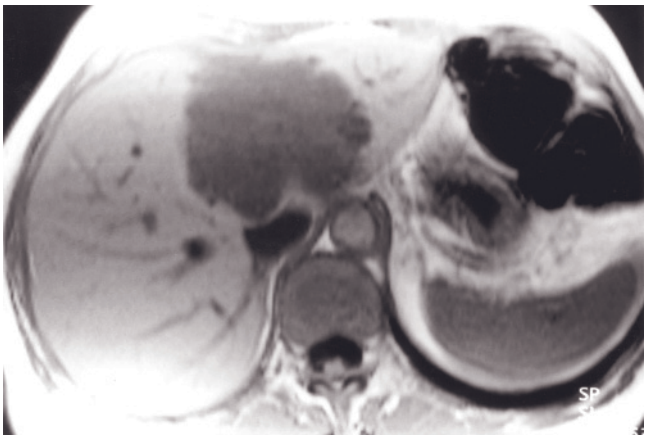

(*b*)

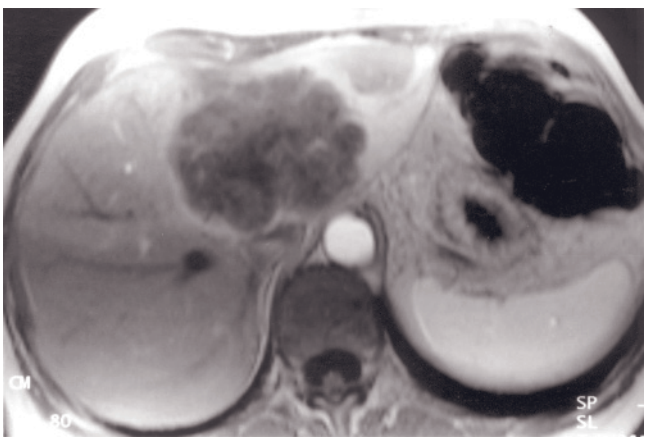

(*c*)

FIG. 2.84 Cauliflower-shaped metastasis from ovarian cancer. Echo-train STIR (*a*), SGE (*b*), and immediate postgadolinium SGE (*c*) images. A large mass is seen in the left hepatic lobe, which demonstrates high signal on T2-weighted (*a*), low signal on T1-weighted (*b*), and ring and perilesional enhancement on immediate postgadolinium images (*c*). Note that the lesion resembles a colon cancer metastasis because of its cauliflower shape.

be apparent on immediate postgadolinium images (fig. 2.89).

Metastases from breast cancer are characterized as hypervascular. Breast cancer liver metastases have a greater range of MR findings than other common types of liver metastases. These patterns include ring, miliary, and confluent segmental (figs. 2.90–2.92). Confluent segmental involvement is more typical of breast cancer than of any other cancer. [141, 142].

Metastases from pancreatic ductal adenocarcinoma are commonly hypovascular, but hypervascularity is not rare. Lesions tend to be multiple and scattered throughout the parenchyma or capsule based. Circumferential or wedge-shaped perilesional enhancement is not uncommon. On T2-weighted images, lesions show moderately high signal intensity, and on T1-weighted images lesions exhibit mildly low signal intensity or isointensity, particularly when ≤1.5 cm. In approximately 20% of patients, the only liver metastases present are small (<1.5 cm) and capsule based and are only seen transiently on hepatic arterial dominant-phase images as hypervascular lesions [152].

Metastases from squamous cell lung cancer are generally characterized as well-defined rounded masses that have a high-signal-intensity rim and a low-signal-intensity center on T2-weighted images and show intense enhancement of the outer rim on early postcontrast images (fig. 2.93). Squamous cell carcinomas from other sites of origin also tend to be rounded and have uniform ring enhancement on immediate postcontrast SGE images (fig. 2.93).

Metastases from unknown primary site are commonly hypervascular and multiple. However, hypovascular lesions and solitary lesions are not uncommon [152]. Hypervascular metastases appear high in signal intensity on T2-weighted images and moderately low signal intensity on T1-weighted images and show intense enhancement on immediate postgadolinium images that becomes less evident on interstitial-phase images.

Poorly differentiated adenocarcinomas frequently demonstrate numerous metastases <2 cm scattered throughout the entire liver. These metastases are typically high in signal intensity on T2-weighted images and

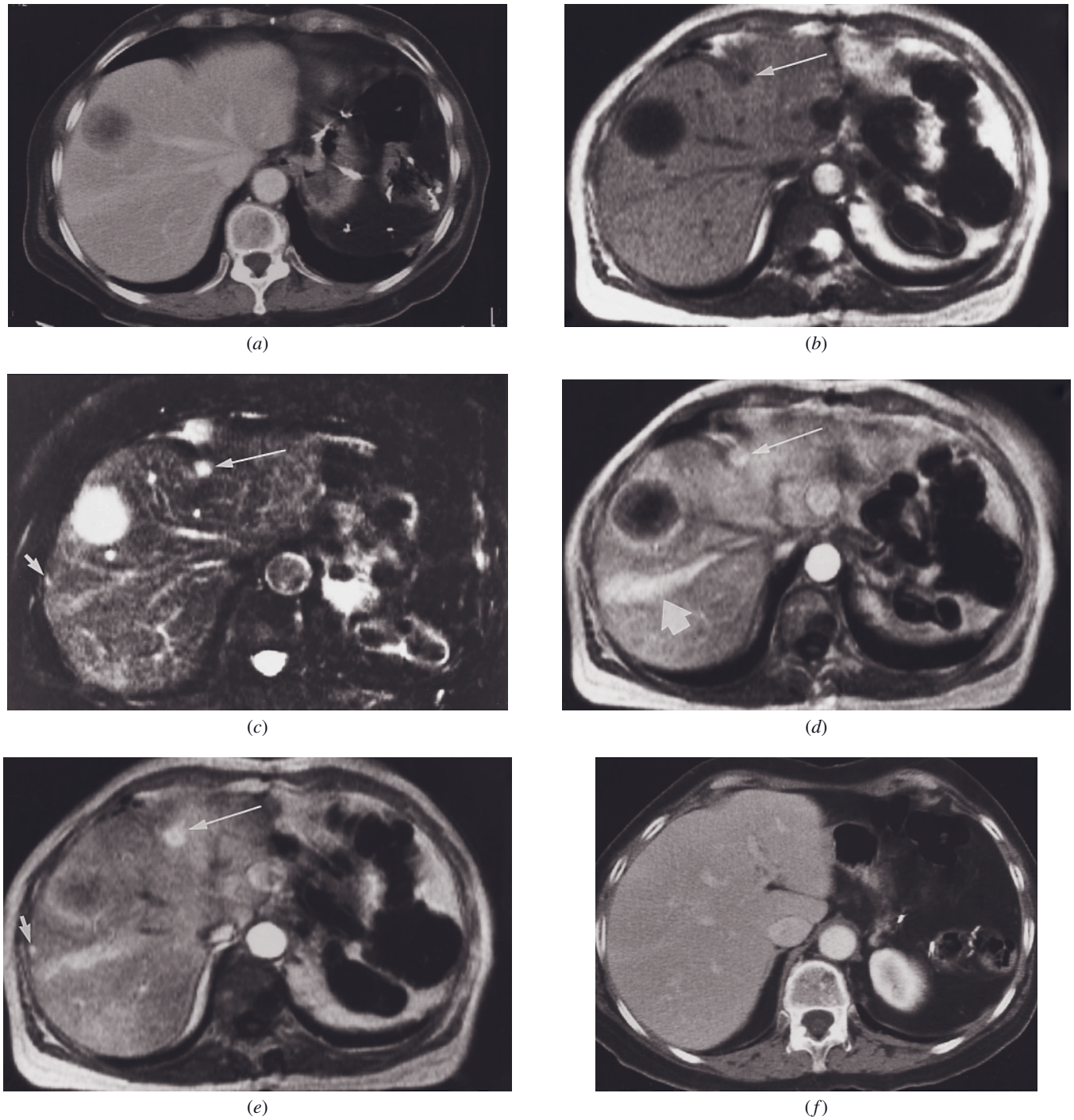

FIG. 2.85 Hypervascular liver metastases from small bowel leiomyosarcoma. Dynamic contrast-enhanced CT (*a*), SGE (*b*), fat-suppressed T2-weighted SE (*c*), and immediate postgadolinium SGE (*d*, *e*) images. A 4-cm metastasis was appreciated on the CT imaging study (*a*). The SGE image (*b*) demonstrated a second 8-mm lesion in the lateral segment (arrow, *b*). The fat-suppressed T2-weighted SE image (*c*) demonstrated the lesion in the lateral segment (long arrow, *c*) and a 5-mm subcapsular lesion in the anterior segment (short arrow, *c*). Immediate images (*d*, *e*) demonstrate ring enhancement around the 4-cm metastases and uniform enhancement of the 8-mm metastases in the lateral segment (long arrow, *d*, *e*) and of the 5-mm subcapsular metastases (short arrow, *e*). Wedge-shaped transient increased enhancement is present in the posterior segment (large arrow, *d*), which is also faintly apparent on the CT image (*a*). Dynamic contrast enhanced CT (*f*), SGE (*g*), fat-suppressed T2-weighted SE (*h*), and immediate (*i*) and 45-s (*j*) postgadolinium SGE images from the midhepatic level in the same patient. A 7-mm metastasis is present in the right lobe

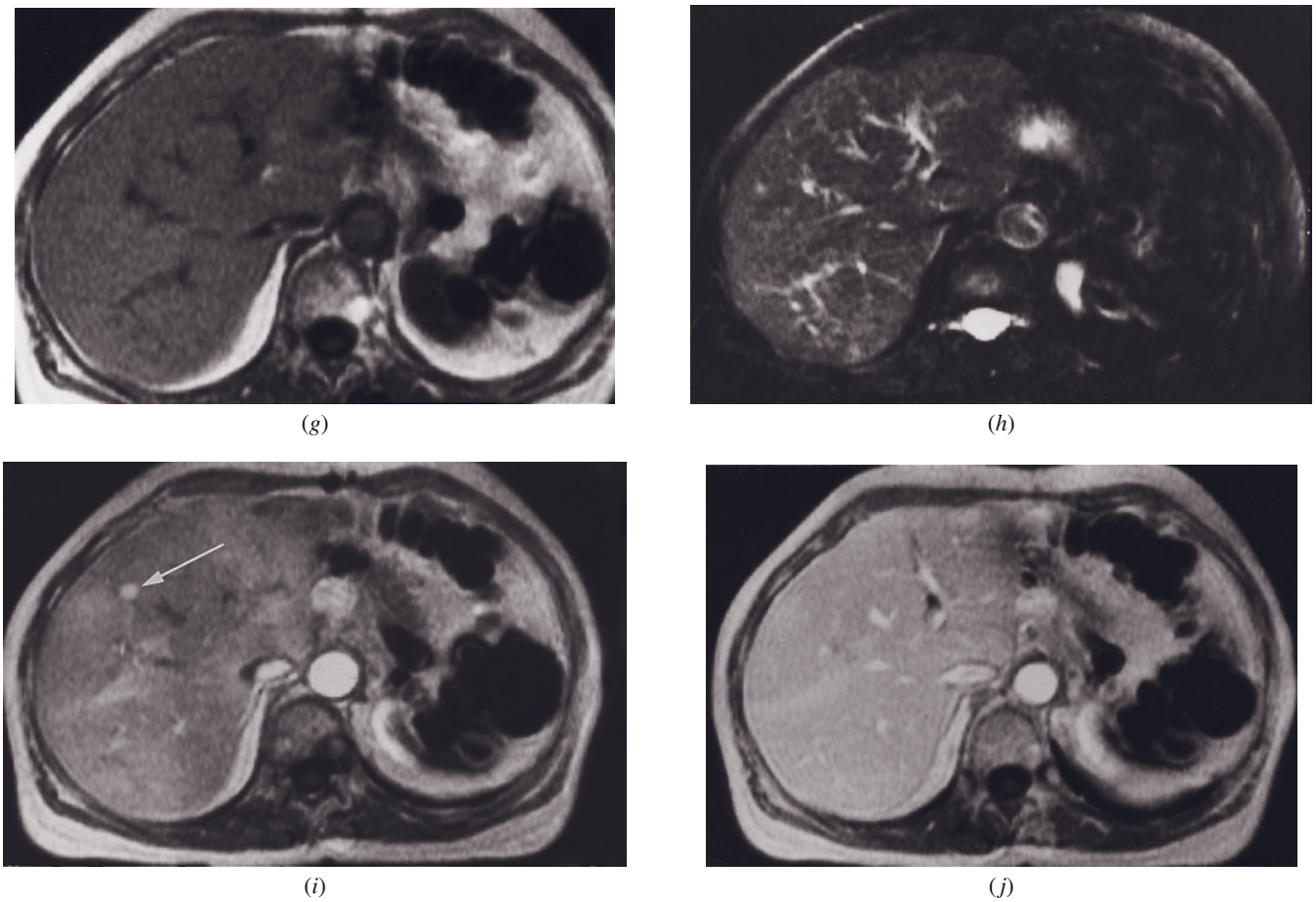

FIG. 2.85 (*Continued*) of the liver that is not visualized on the CT (*f*) or noncontrast T1-weighted (*g*) or T2-weighted (*h*) images, but is well shown as a uniformly enhancing lesion (arrow, *i*) on the immediate image (*i*). The metastasis washes out rapidly and becomes isointense with liver by 45 s (*j*). Small hypervascular malignant lesions commonly are shown only on hepatic arterial dominant-phase images.

show peripheral ring enhancement on immediate postgadolinium images. These metastases range from hypovascular to very hypervascular. Small cell and other aggressive nonsquamous cell lung cancers have similar imaging findings (figs. 2.94 and 2.95).

Metastases from gastrinomas exhibit a uniform moderately intense peripheral ring pattern of enhancement on arterial dominant-phase images and have a particular propensity to washout peripherally on late-phase images (fig. 2.96). Gastrinoma metastases often appear as a relatively uniform population of lesions. Metastases may also be extremely extensive despite relatively mild patient symptomatology.

Metastases from melanoma may represent a mixture of high- and low-signal-intensity lesions on T2- and T1-weighted images because of the paramagnetic property of melanin (fig. 2.97). Melanoma metastases must be highly pigmented, well-differentiated lesions to produce this paramagnetic effect. Amelanocytic malignant melanomas or poorly-differentiated tumors do not contain melanin and therefore will not produce the paramagnetic effect and will appear mildly hyperintense on T2-weighted images and mildly hypointense on T1-weighted images. Melanoma metastases may be hypervascular and may also be very extensive.

Metastases from carcinoid tumor commonly demonstrate high signal intensity on T2-weighted images, low signal intensity on T1-weighted images, and moderate or intense enhancement after contrast administration, suggesting hypervascularity (fig. 2.98) [157]. On late-phase images, metastases from carcinoid tumor either wash out or fade to isointensity. Not uncommonly, they are only appreciated on immediate postgadolinium images. In addition, carcinoid metastases may resemble HCC as they can also be high signal intensity on noncontrast T1-weighed images (reflecting protein synthesis) and can show washout with capsule enhancement on late-phase images. In approximately 90% of patients with liver metastases, the lesions are hypervascular, and in 10% they can be hypovascular [158].

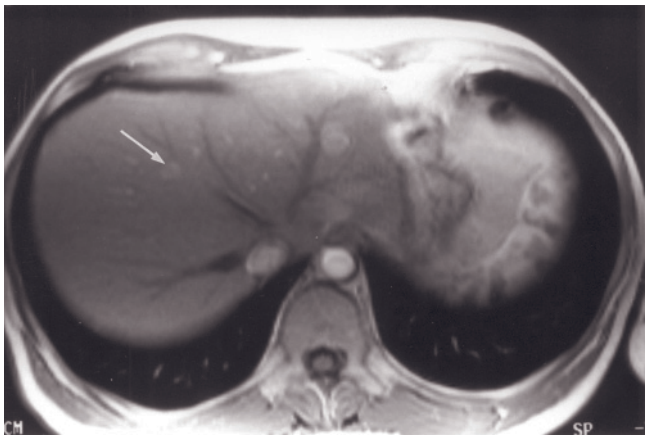

(*a*)

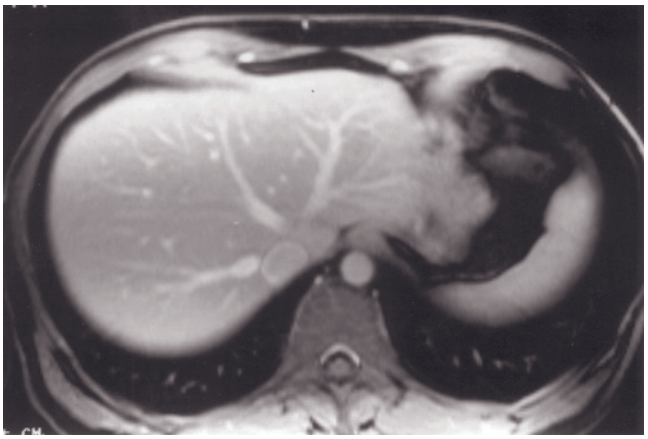

(*b*)

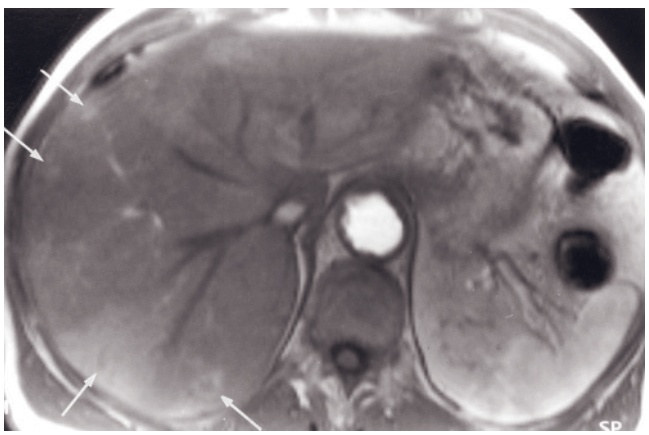

(*c*)

FIG. 2.86 Small colon cancer metastases. Immediate (*a*) and 90-s fat-suppressed postgadolinium SGE (*b*) images. On the immediate postgadolinium SGE image (*a*), a 1-cm ring enhancing metastasis is identified in segment 8 (arrow, *a*) that equilibrates with background liver on the interstitial-phase image (*b*)

Immediate postgadolinium SGE image (*c*) in a second patient shows multiple small subcapsular metastases (arrows) from colon cancer.

Metastases from mucin-producing tumors such as ovarian cancer or mucinous cystadenocarcinoma of the pancreas may result in liver metastases that are high in signal intensity on T1-weighted images because of the protein content (fig. 2.99).

Metastases that are active in protein synthesis, such as in the production of enzymes or hormones (e.g., carcinoid tumors) may also be high in signal intensity on T1-weighted images because of the presence of a high concentration of protein (fig. 2.100).

Capsule-based metastases frequently occur in the setting of tumors that metastasize by intraperitoneal spread (fig. 2.101). Ovarian cancer most commonly results in capsule-based metastases (fig. 2.102) followed by colon cancer. A prior study [152] reported that 81% (13/16) of patients with liver metastases from pancreatic ductal adenocarcinoma showed capsule-based metastases, among them, 19% (3/16) exhibit only capsule-based metastases. A variety of other malignancies can also produce capsule-based metastases (fig. 2.103).

Hemorrhagic metastases result in varying high- and low-signal-intensity lesions on T2- and T1-weighted images.

Distinction Between Liver Metastases and Benign Lesions.

METASTASES VERSUS HEMANGIOMAS. On T2-weighted images small (≤1.5 cm) hypervascular liver metastases, particularly from islet cell tumors, leiomyosarcoma, gastrointestinal stromal tumors, pheochromocytoma and renal cell carcinoma, and small avascular metastases, necrotic or cystic metastases from ovarian cancer, may mimic the appearance of hemangiomas [67, 132, 144, 159].

Small (<1.5 cm) hypervascular metastases often enhance in an intense homogeneous fashion on arterial dominant-phase images and tend to wash out below the signal intensity of the background parenchyma on interstitial-phase images [144]. Type I hemangiomas may enhance in similar fashion on arterial dominant-phase images; however, they tend to retain contrast or fade to isointensity with the background parenchyma on interstitial-phase images. Often at least one lesion greater than 2 cm in diameter is present that possesses the typical enhancement features of a metastasis or hemangioma, allowing inference of the nature of the smaller lesions.

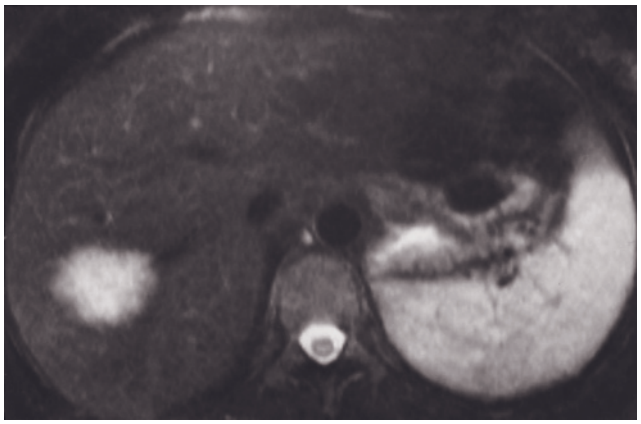

(*a*)

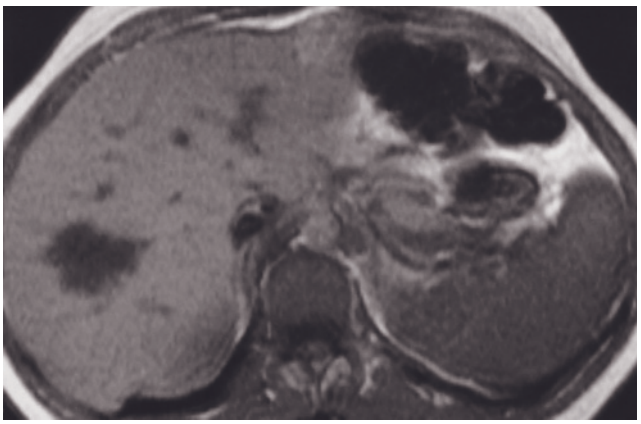

(*b*)

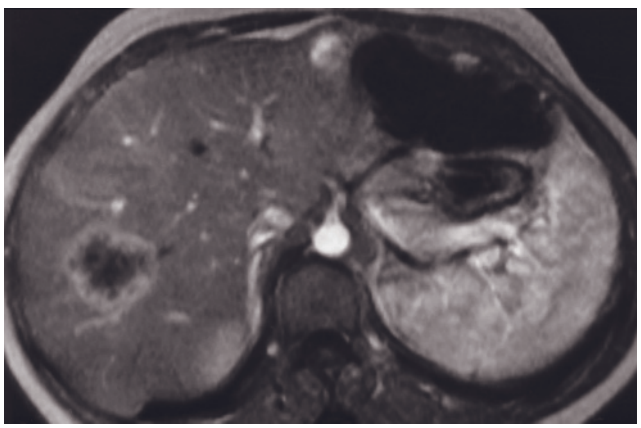

(*c*)

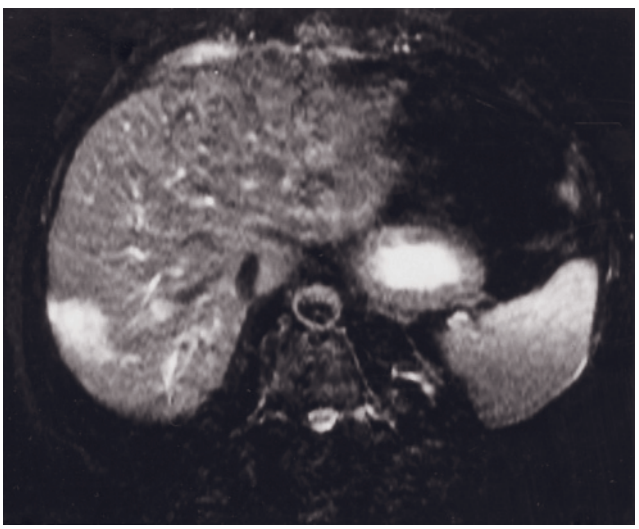

(*d*)

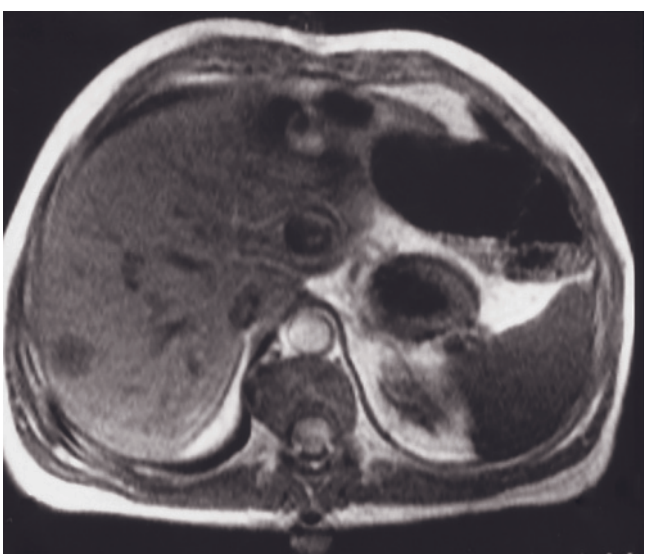

(*e*)

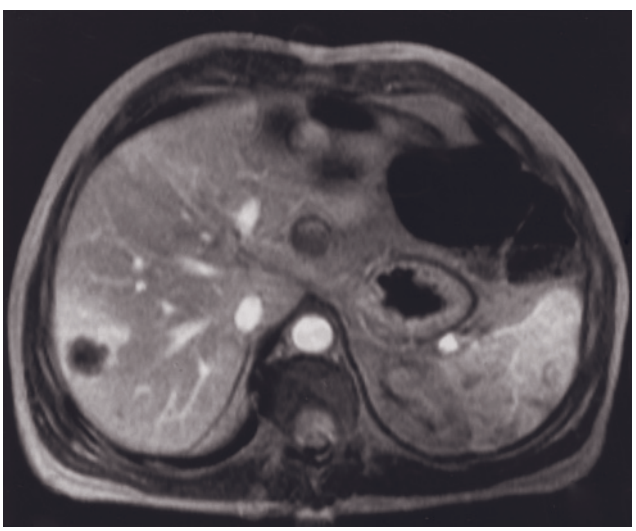

(*f*)

FIG. 2.87 Medium-sized liver metastases from colon cancer. Fat-suppressed T2-weighted ETSE (*a*), SGE (*b*), and immediate postgadolinium SGE (*c*) images. An irregularly marginated mass is present in the right lobe that is moderately high in signal intensity on the T2-weighted image (*a*) and moderately low in signal intensity on the T1-weighted image (*b*) and demonstrates intact ring enhancement on the immediate postgadolinium image (*c*) with an irregular inner margin to the ring. A faint region of ill-defined transient increased enhancement is present on the immediate postgadolinium image (*c*).

Fat-suppressed T2-weighted SS-ETSE (*d*), SGE (*e*), and immediate (*f*) and 90-s (*g*) postgadolinium SGE images in a second patient.

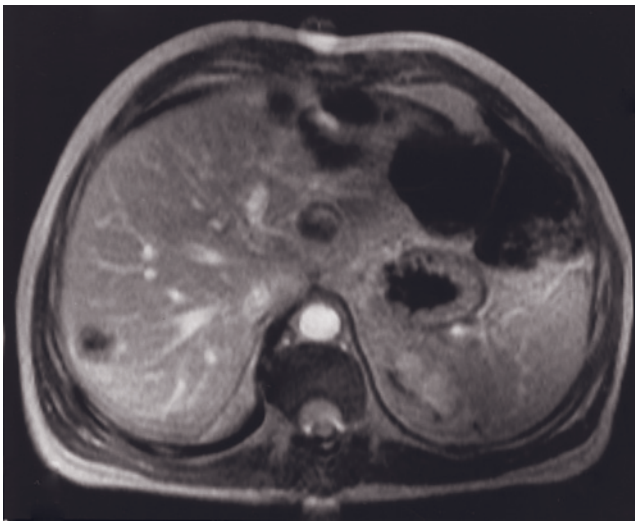

(*g*)

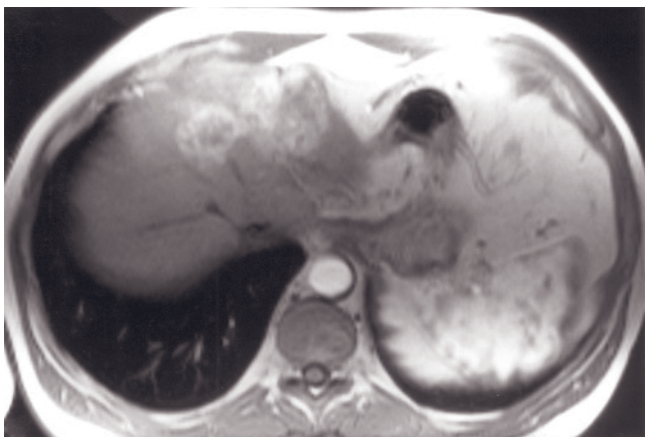

(*h*)

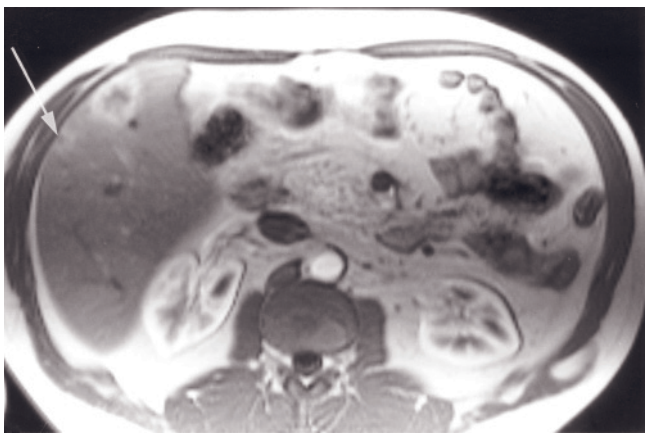

(*i*)

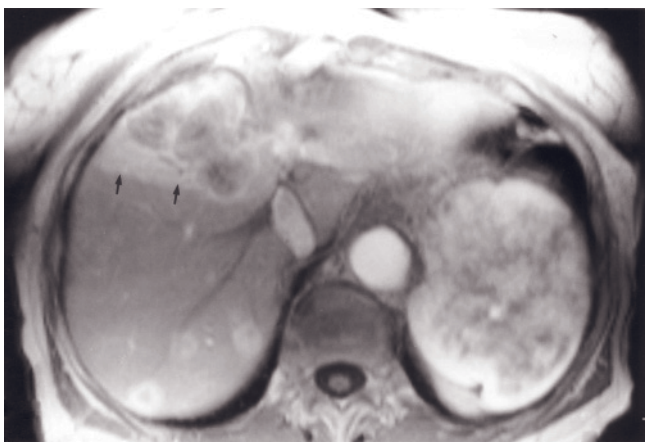

(*j*)

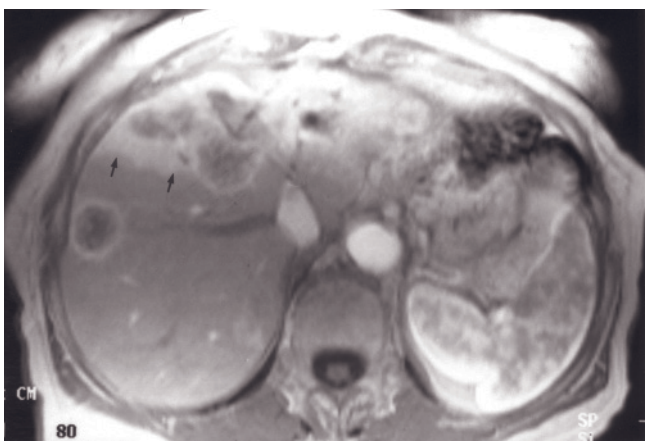

(*k*)

Fig. 2.87 (*Continued*) A 2-cm liver metastasis is present in the right lobe of the liver that is moderately high in signal intensity on the T2-weighted image (*d*) and moderately low in signal intensity on the T1-weighted image (*e*) and demonstrates ring enhancement on the immediate postgadolinium image (*f*) with ill-defined perilesional enhancement. Ill-defined perilesional enhancement resolves at 90 s after gadolinium (*g*).

Immediate images (*h*, *i*) in a third patient demonstrate irregular ring enhancement lesions consistent with metastases. Even metastases <1 cm often exhibit ring enhancement (arrow, *i*).

Immediate postgadolinium SGE images (*j*, *k*) in a fourth patient with colon cancer demonstrate multiple metastatic foci, several small rounded masses, and one large cauliflower-shaped lesion, all with ring enhancement. Note ill-defined perilesional enhancement (arrows, *j*, *k*) around the cauliflower-shaped metastasis, characteristic for colon cancer metastases.

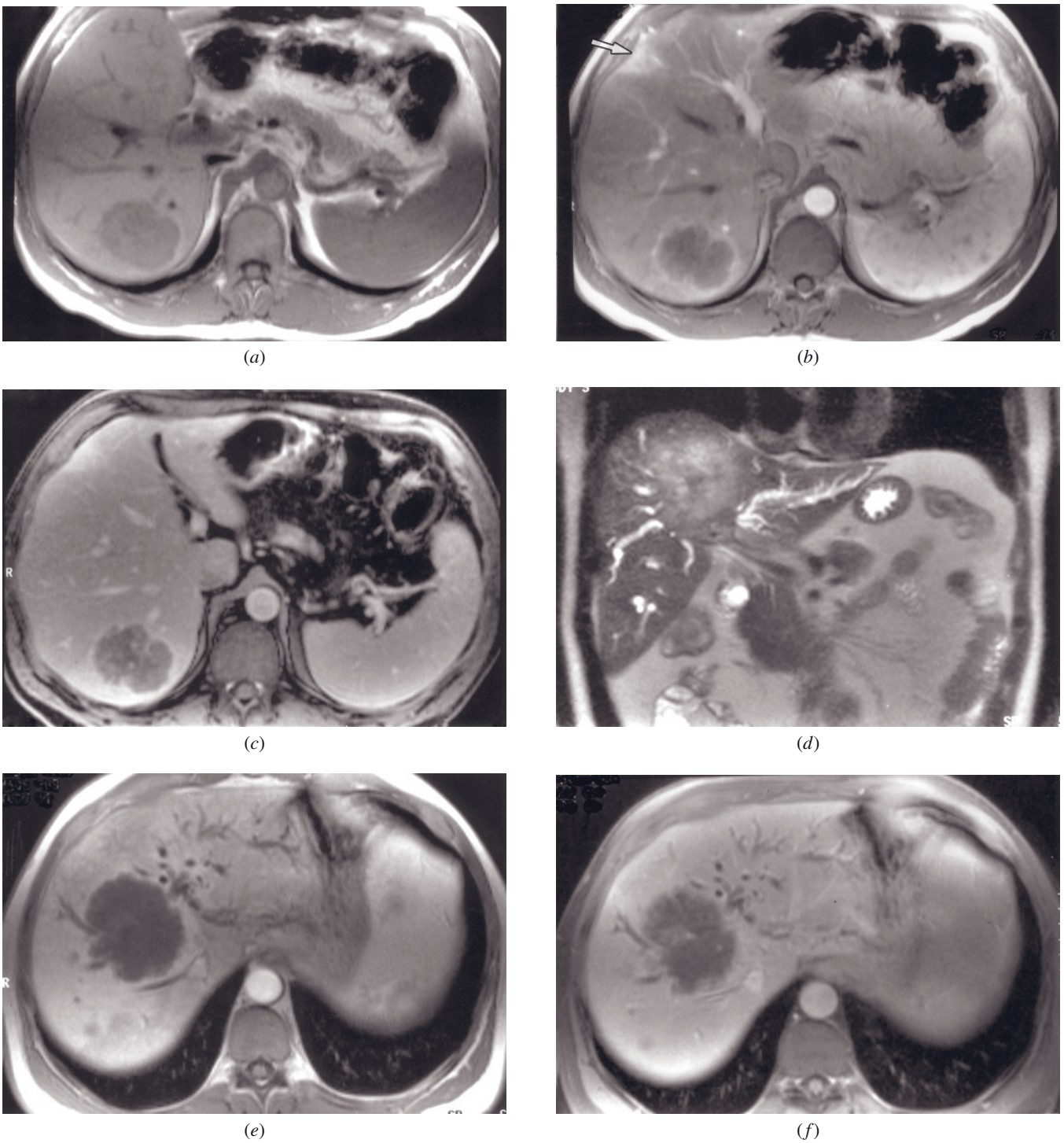

FIG. 2.88 Large colon cancer liver metastases—cauliflower shape. SGE (*a*) and immediate (*b*) and 90-s (*c*) fat-suppressed postgadolinium SGE images demonstrate a colon cancer metastasis with a cauliflower shape. A small peripheral metastasis with intense wedge-shaped perilesional enhancement (arrow, *b*) is present.

Coronal T2-weighted SS-ETSE (*d*) and transverse immediate (*e*) and 90-s fat-suppressed (*f*) postgadolinium SGE images in a second patient demonstrate a large, centrally located metastasis that has a cauliflower shape. Note that the central location of the metastases has resulted in bile duct obstruction (*d*).

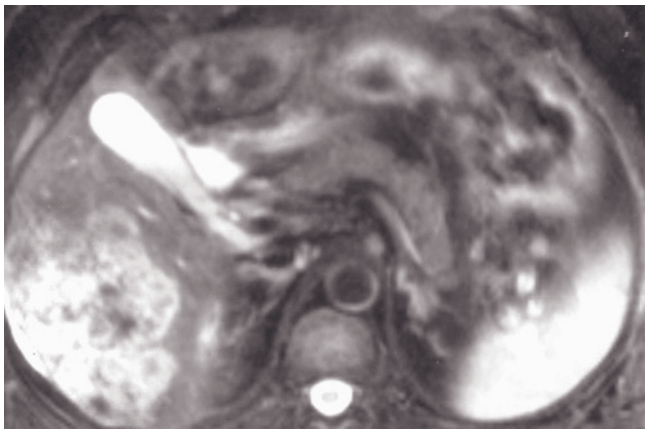

(*g*)

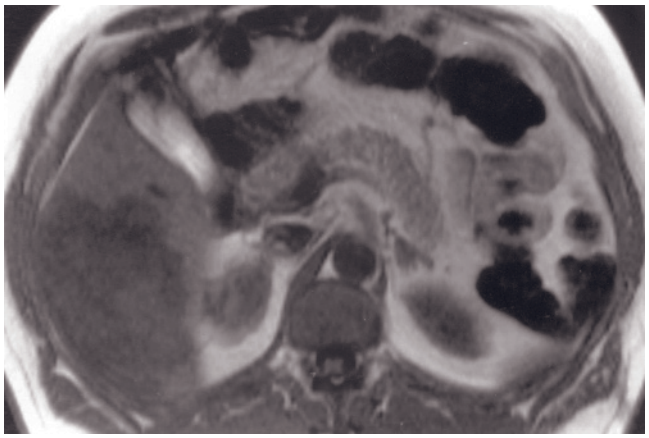

(*h*)

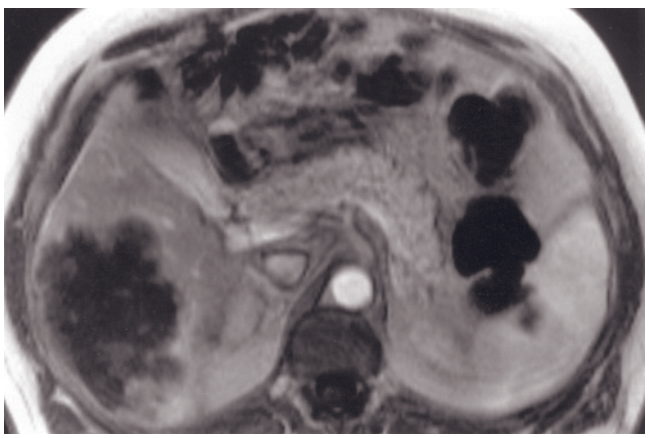

(*i*)

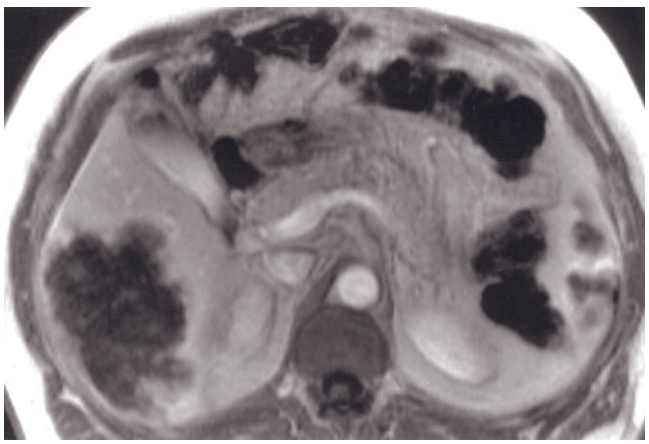

(*j*)

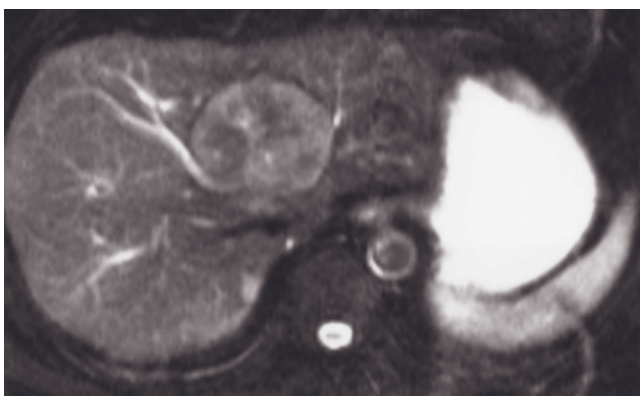

(*k*)

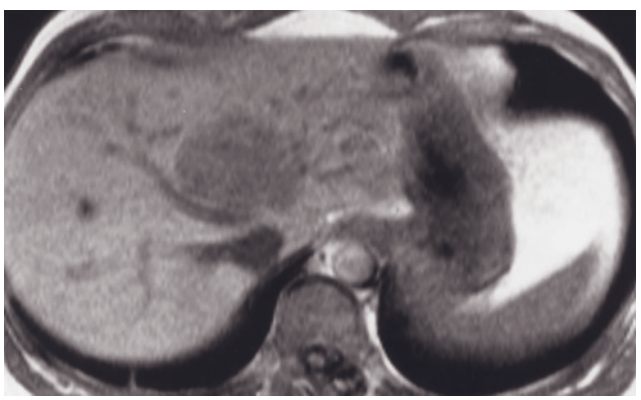

(*l*)

FIG. 2.88 (*Continued*) Fat-suppressed T2-weighted SS-ETSE (*g*), SGE (*h*), and immediate (*i*) and 45-s (*j*) postgadolinium SGE images in a third patient demonstrate a large cauliflower-shaped metastasis that has ring enhancement with perilesional enhancement. Note that arcs of peripheral enhancement extend into the lesion.

Fat-suppressed T2-weighted SS-ETSE (*k*), SGE (*l*), and immediate postgadolinium SGE (*m*) images in a fourth patient. This lesion possesses the typical imaging features of a colon cancer metastasis. The metastasis is heterogeneous and moderately hyperintense on the T2-weighted image (*k*) and mildly hypointense on the T1-weighted image (*l*) and has ring enhancement with perilesional enhancement on the immediate postgadolinium SGE image (*m*).

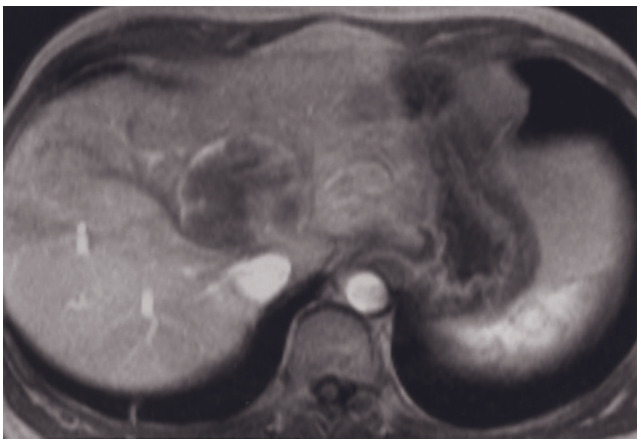

(*m*)

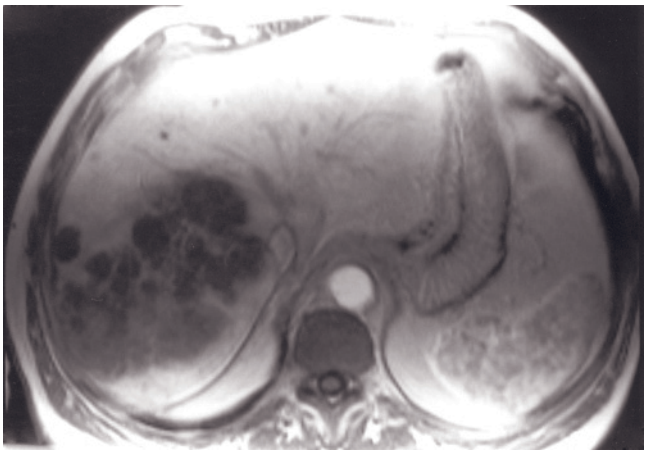

(*n*)

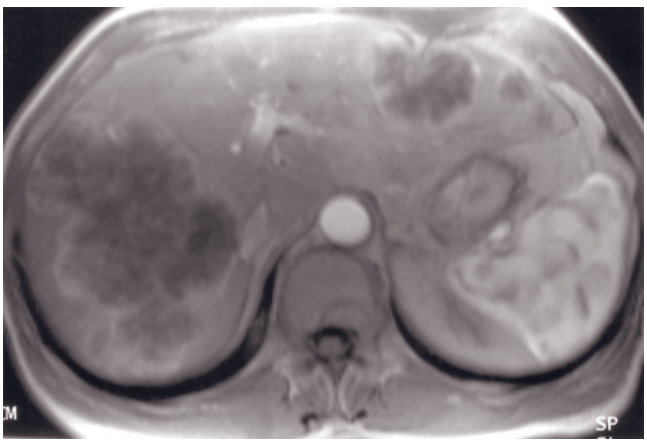

(*o*)

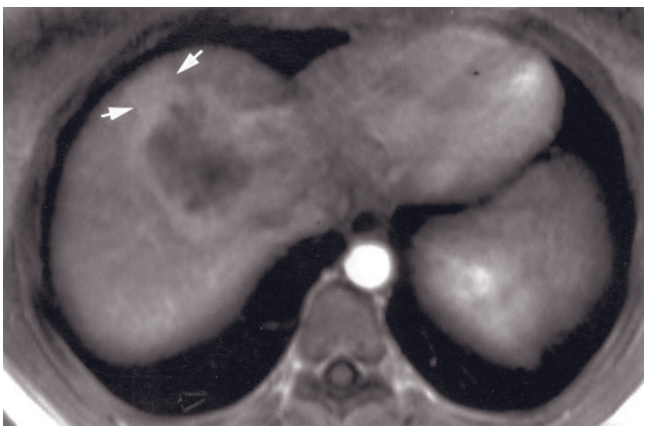

(*p*)

FIG. 2.88 (*Continued*) Immediate postgadolinium SGE images (*n–p*) in three additional patients with large metastases that exhibit the characteristic cauliflower shape of colon cancer metastases. Ill-defined perilesional enhancement (arrows, *p*) is observed in the last of these patients.

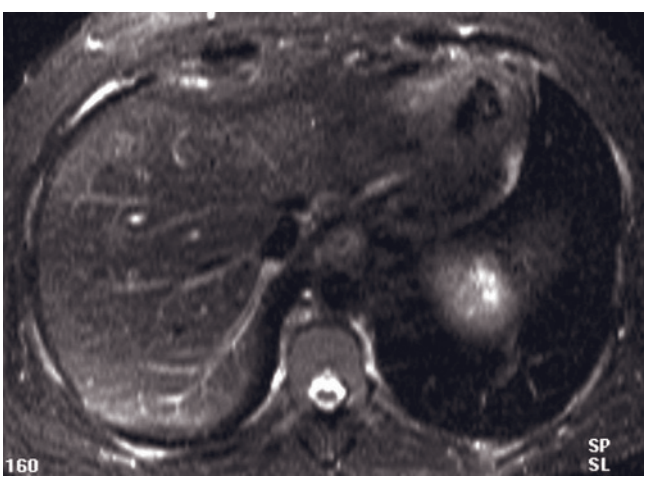

(*a*)

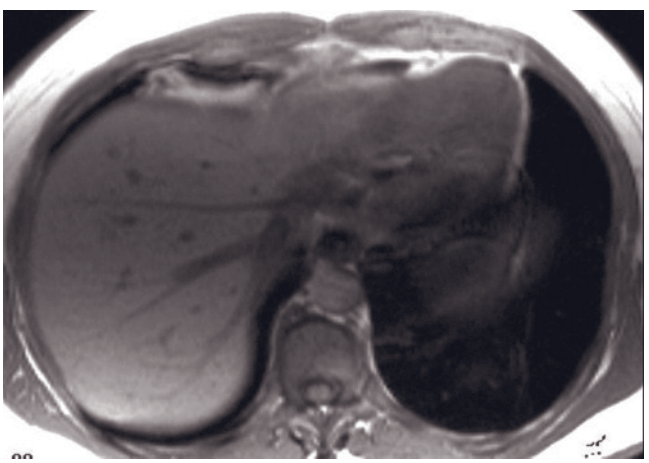

(*b*)

FIG. 2.89 Small hypervascular colon cancer metastases. T2-weighted SS-ETSE (*a*), SGE (*b*), and immediate (*c*) and 90-s fat-suppressed (*d*) postgadolinium SGE images. Multiple small lesions are seen scattered throughout the parenchyma that show

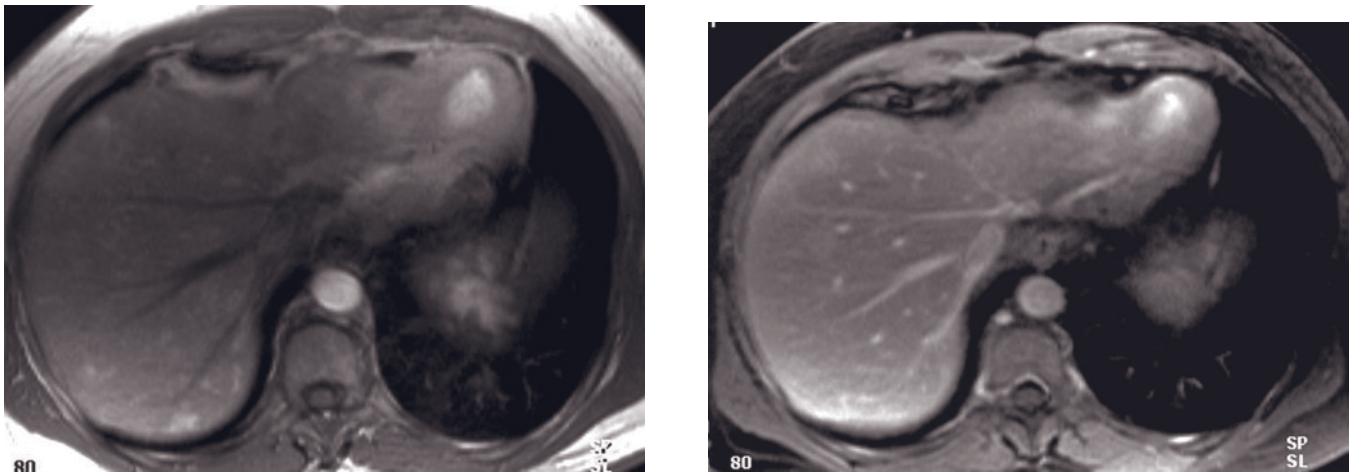

(*c*) (*d*)

FIG. 2.89 (*Continued*) isointensity on T2-weighted (*a*) and T1-weighted (*b*) images and intense enhancement on early-phase images (*c*) that fade to background parenchyma on late-phase images (*d*).

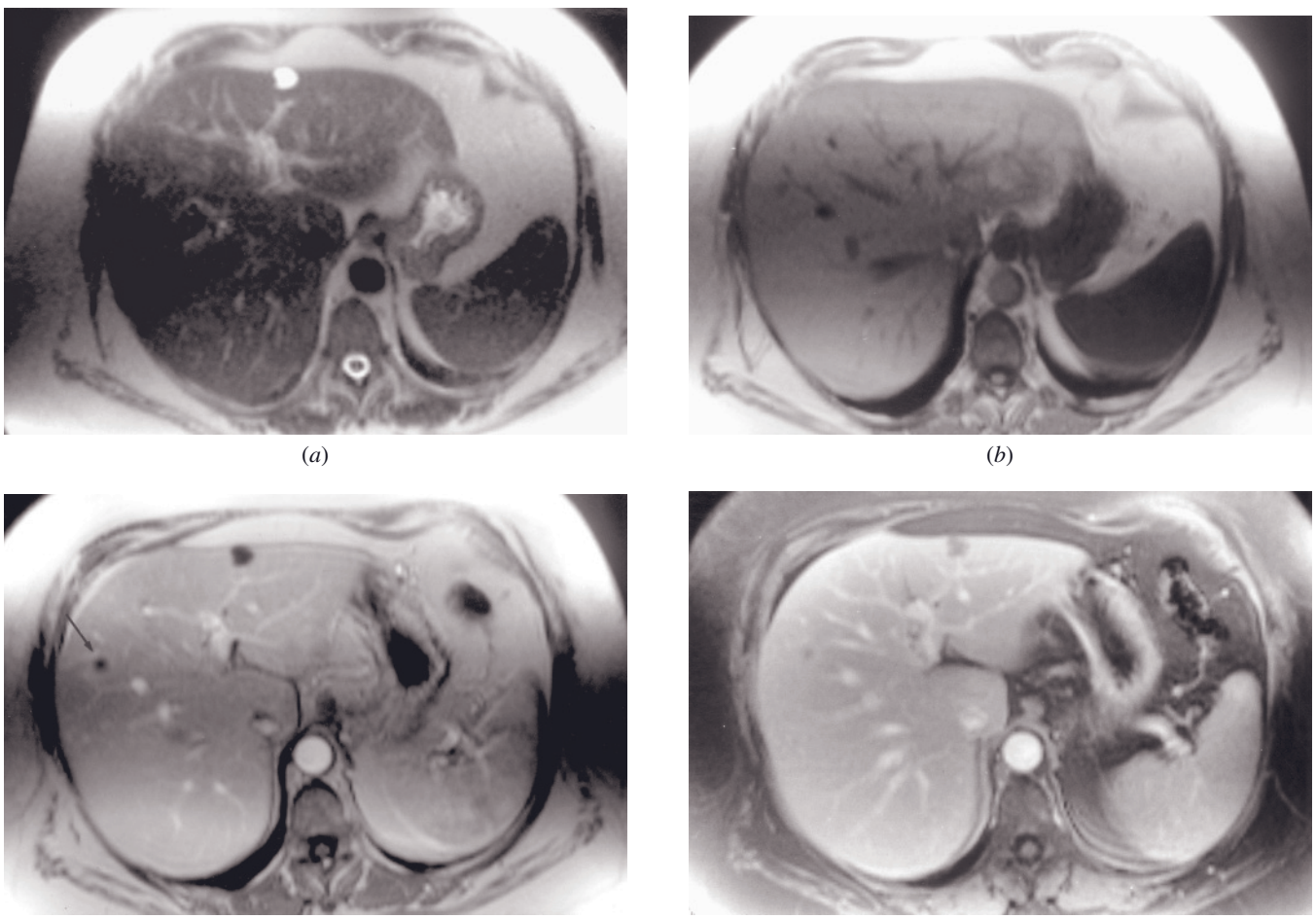

(*a*) (*b*)

(*c*) (*d*)

FIG. 2.90 Breast cancer liver metastases—ring enhancement. T2-weighted SS-ETSE (*a*), SGE (*b*), and immediate (*c*) and 90-s fat-suppressed (*d*) postgadolinium SGE images. There is a small lesion in the right lobe that is almost imperceptible on T2 (*a*) and T1 (*b*) images. The metastasis exhibits mild ring enhancement (arrow, *c*) on immediate postgadolinium images that renders it conspicuous. The metastasis fades on the interstitial-phase image (*d*). This lesion was not seen on spiral CT (not shown). Note also a ciliated hepatic foregut cyst between segments 4 and 2 anteriorly.

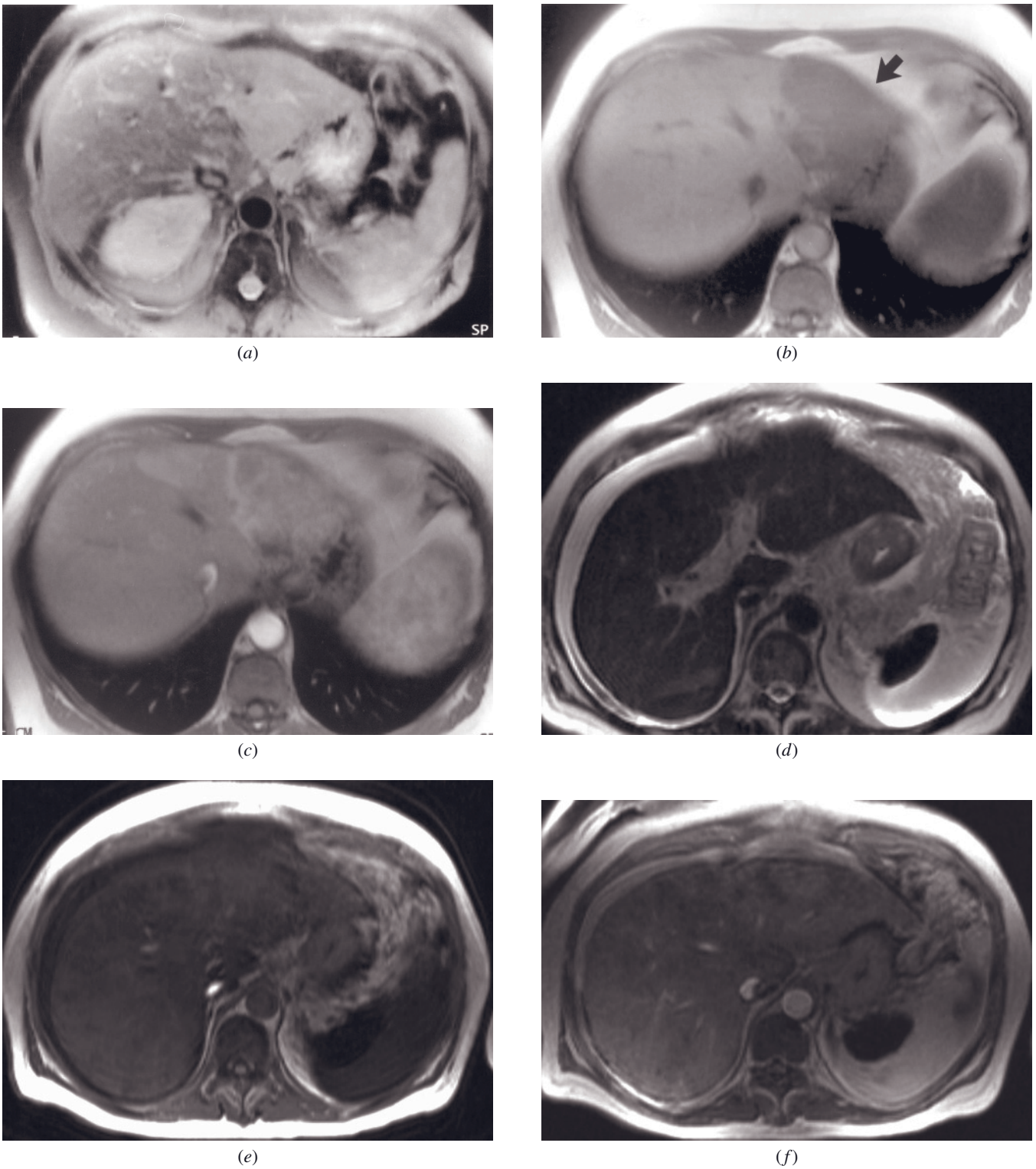

FIG. 2.91 Breast cancer liver metastases—infiltrative pattern. Fat-suppressed T2-weighted SS-ETSE (*a*), SGE (*b*), and immediate postgadolinium SGE (*c*) images. There is a mass (arrow, *b*) in the left hepatic lobe that demonstrates slightly increased signal on T2-weighted (*a*), decreased signal on T1-weighted (*b*), and heterogeneous enhancement on immediate postgadolinium SGE (*c*) images, consistent with metastatic disease. The confluent involvement of a segment, as in this case, is characteristic of breast cancer but represents an uncommon pattern.

T2-weighted SS-ETSE (*d*), SGE (*e*) and immediate postgadolinium SGE (*f*) images in a second patient. The liver shows normal signal intensity on both T2 (*d*)- and T1 (*e*)-weighted images, but diffuse increased parenchymal enhancement in a heterogeneous fashion on early-phase images (*f*) reflects infiltrative metastatic disease. The liver signal intensity becomes more homogeneously enhanced on late-phase images (not shown).

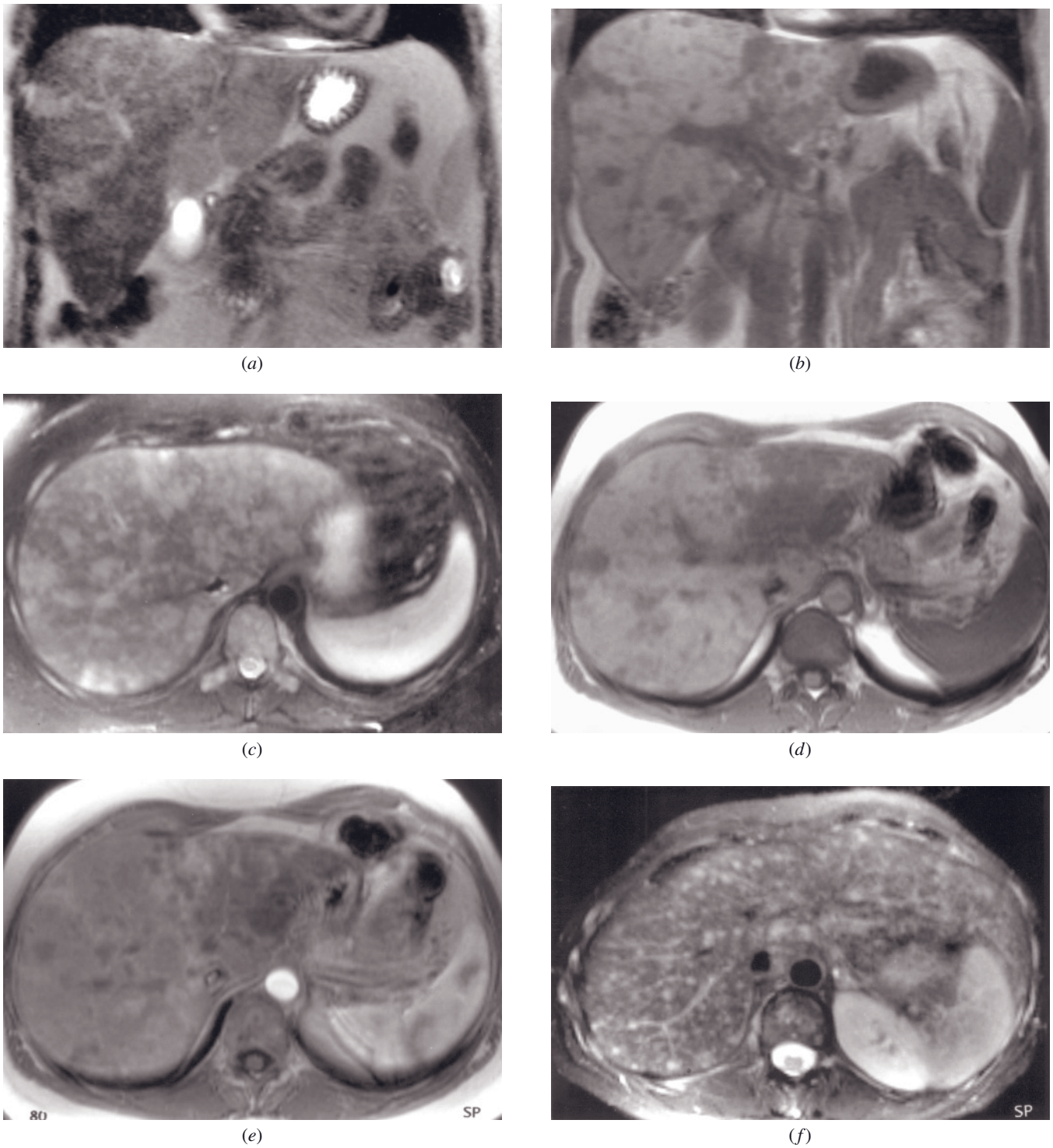

FIG. 2.92 Breast cancer liver metastases—miliary pattern. Coronal T2-weighted SS-ETSE (*a*), coronal SGE (*b*), transverse fat-suppressed T2-weighted ETSE (*c*), SGE (*d*), and immediate postgadolinium SGE (*e*) images. There are numerous lesions scattered throughout the hepatic parenchyma that demonstrate moderate signal on T2 (*a*, *c*) and moderately low signal on T1 (*b*, *d*) and show mild ring enhancement on immediate postgadolinium (*e*) images, consistent with metastases.

Fat-suppressed T2-weighted SS-ETSE (*f*), SGE (*g*), and immediate (*h*) and 90-s fat-suppressed (*i*) postgadolinium SGE images in a second patient. Extensive liver metastases, <5 mm in size, are present throughout the liver with a miliary pattern of involvement. The lesions show high signal on T2-weighted images (*f*), low signal on T1-weighted images (*g*), and a mild ring enhancement

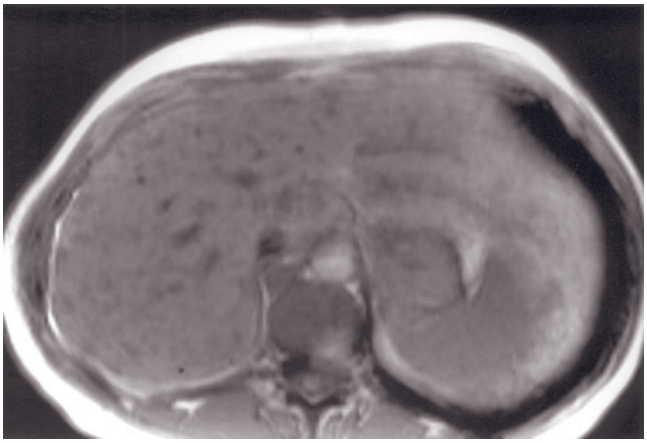

(*g*)

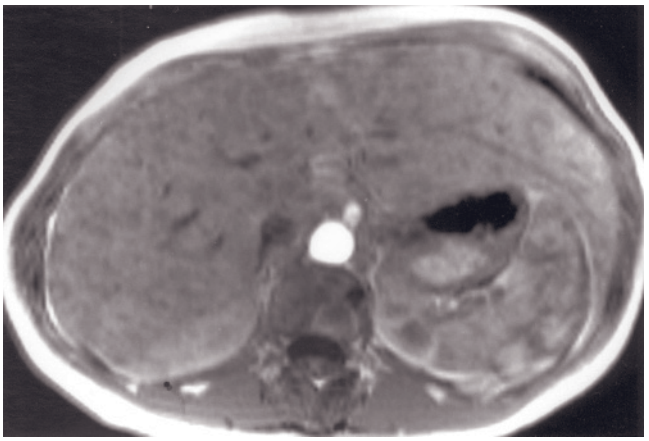

(*h*)

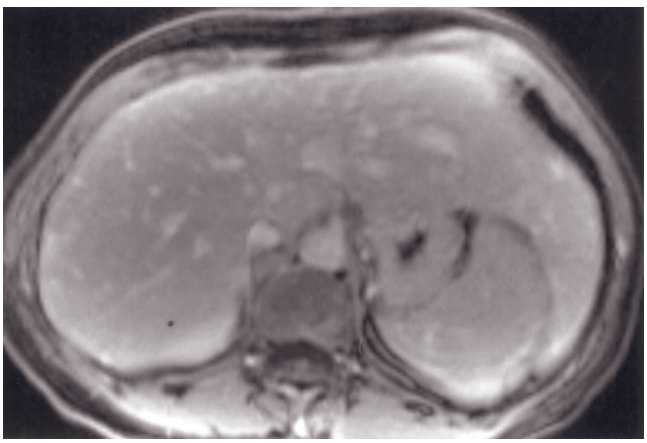

(*i*)

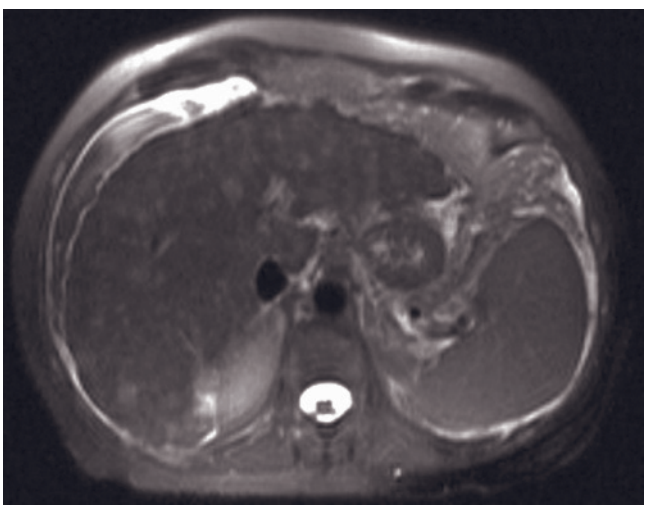

(*j*)

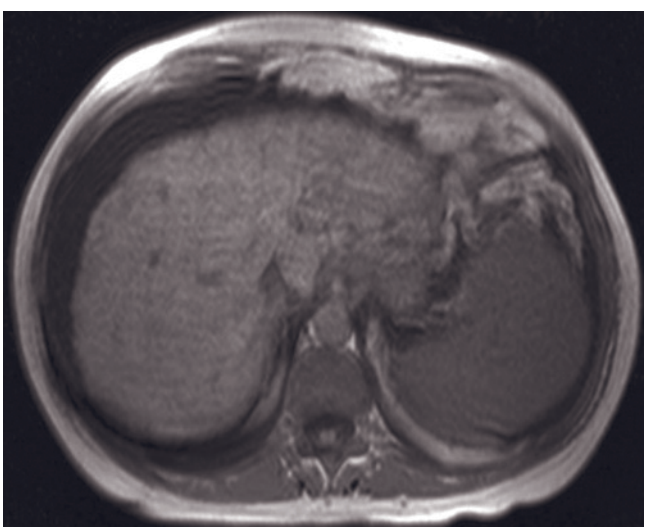

(*k*)

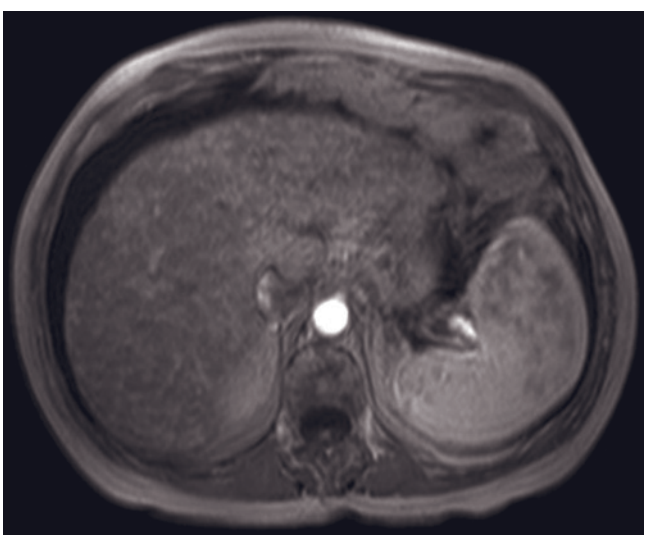

(*l*)

FIG. 2.92 (*Continued*) on immediate postgadolinium image (*h*) and fades on late image (*i*). Note that the metastases are best seen on T2-weighted images (*f*) and not definable on late phase (*i*).

T2-weighted SS-ETSE (*j*), SGE (*k*), and immediate (*l*) and 90-s fat-suppressed (*m*) postgadolinium SGE images in a third patient demonstrate similar findings.

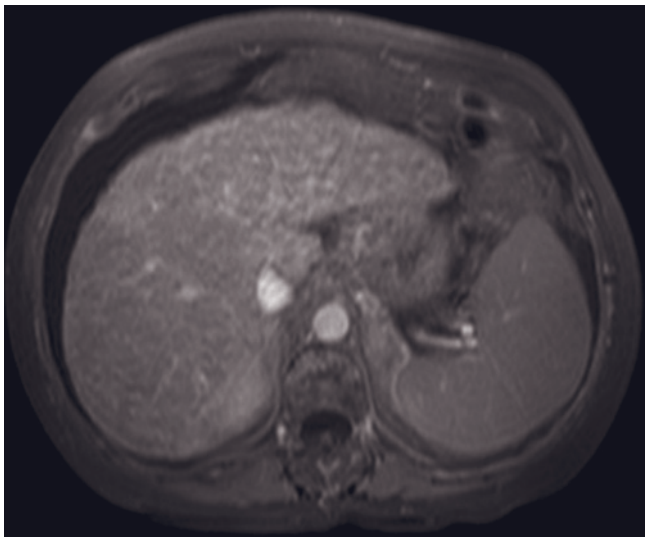

(*m*)

FIG. 2.92 (*Continued*) Miliary involvement of the liver with metastases is an uncommon but characteristic appearance for breast cancer liver metastases. Note that coexistent bone metastases are common in vertebral bodies, and they appear as high-signal small foci on fat-suppressed T2 and exhibit uniform enhancement on interstitial-phase fat-suppressed SGE images. If the liver metastases in patients with miliary involvement respond to chemotherapy, the liver develops extensive fibrosis with an appearance that resembles cirrhosis.

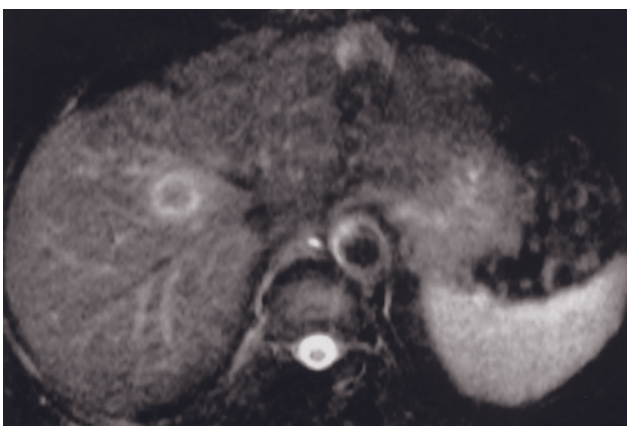

(*a*)

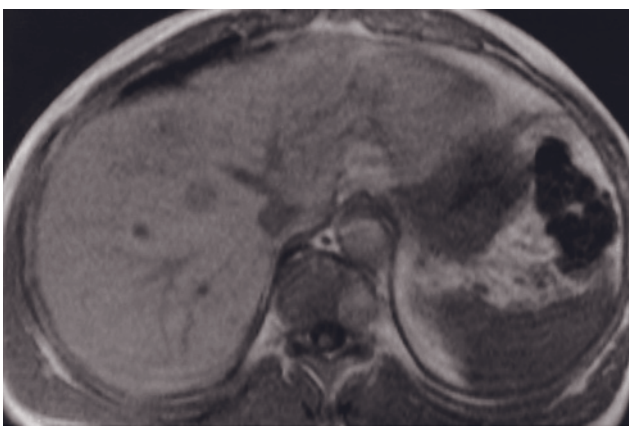

(*b*)

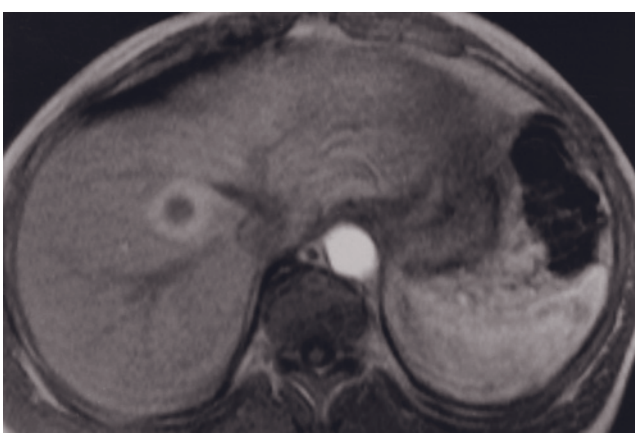

(*c*)

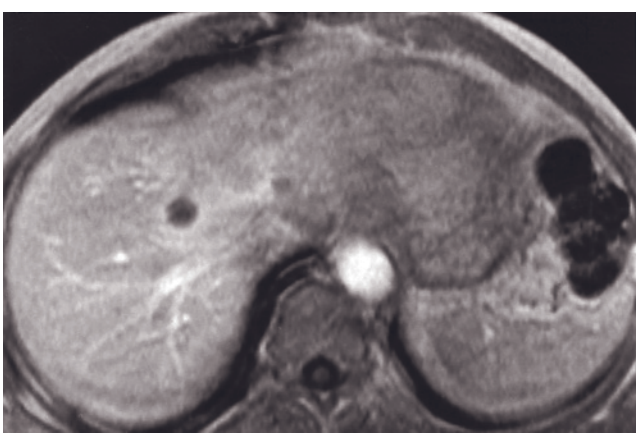

(*d*)

FIG. 2.93 Liver metastases, squamous cell type. Fat-suppressed T2-weighted ETSE (*a*), SGE (*b*), and immediate (*c*) and 45-s (*d*) postgadolinium SGE images. A well-defined 2-cm metastasis is present in the anterior segment of the right lobe that appears as a moderately high-signal intensity ring with central isointensity on the T2 (*a*) and mildly low in signal intensity on the T1 (*b*) images, has a uniform ring enhancement on the immediate image (*c*), and fades over time with negligible central enhancement (*d*). The enhancing ring on the immediate postgadolinium image (*c*) corresponds to the high-signal-intensity rim on the T2-weighted image (*a*). This is a typical appearance for liver metastases from squamous cell lung cancer.

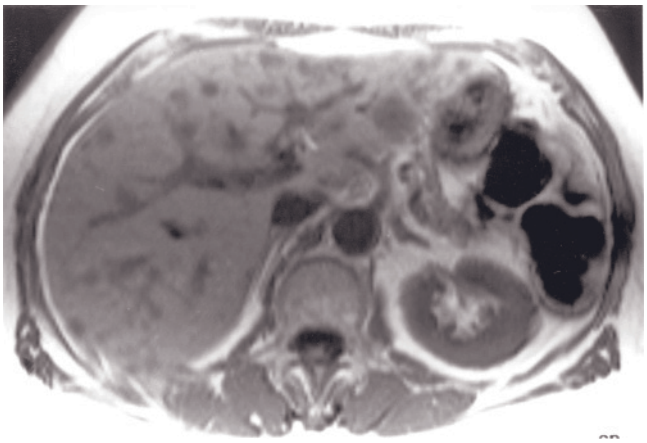

(*e*)

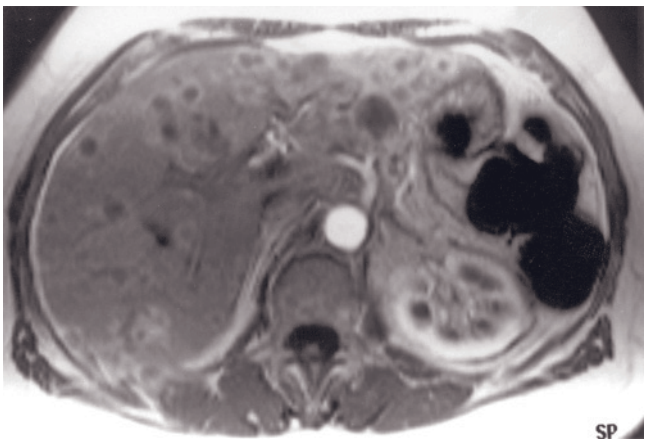

(*f*)

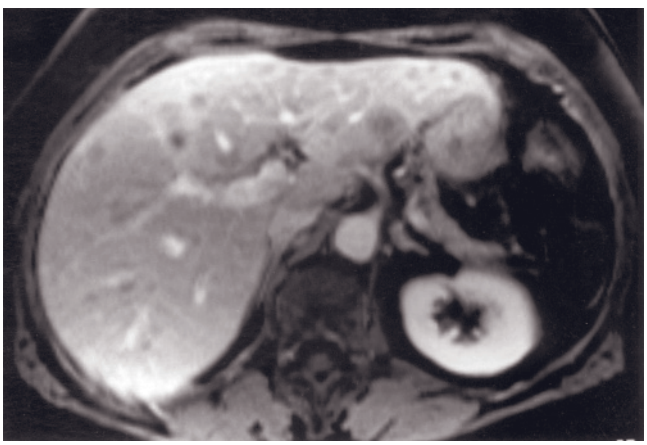

(*g*)

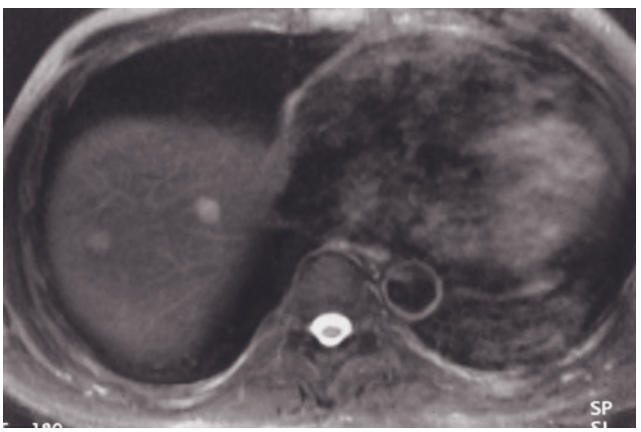

(*h*)

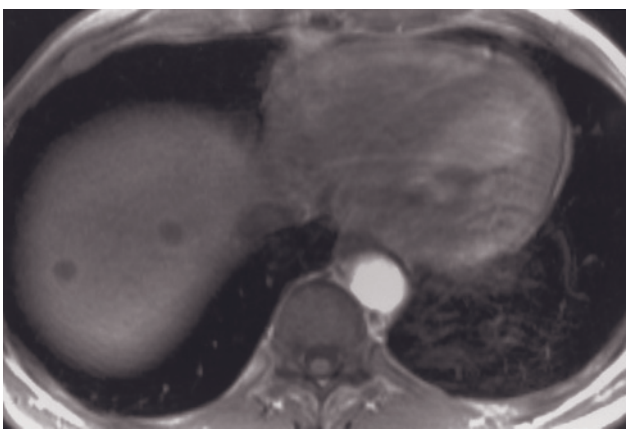

(*i*)

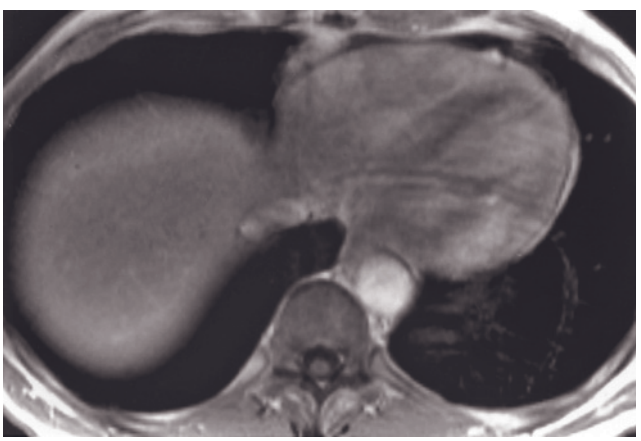

(*j*)

FIG. 2.93 (*Continued*) SGE (*e*) and immediate (*f*) and 90-s fat-suppressed (*g*) postgadolinium SGE images in a second patient with squamous cell lung cancer. There are multiple rounded lesions scattered throughout the liver that demonstrate low signal on T1-weighted images (*e*) and ring enhancement immediately after gadolinium administration (*f*), consistent with metastases.

Fat-suppressed T2-weighted SS-ETSE (*h*) and immediate (*i*) and 90-s (*j*) postgadolinium SGE images in a third patient, who has liver metastases from esophageal squamous cell cancer. The metastases are round, well-defined, and high in signal on the T2-weighted image (*h*), enhance with uniform rings on the early-phase image (*i*), and become isointense with liver on the late-phase image (*j*).

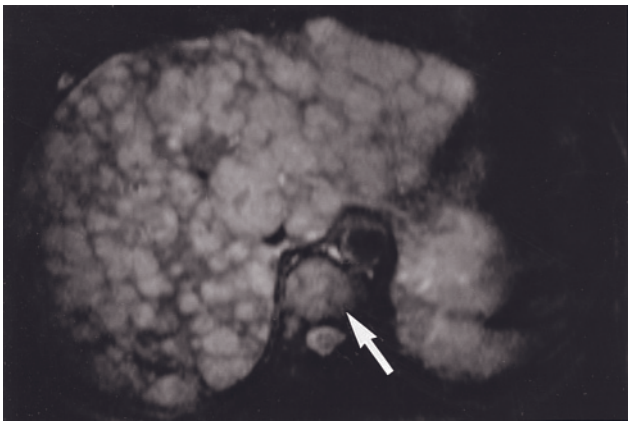

(*a*)

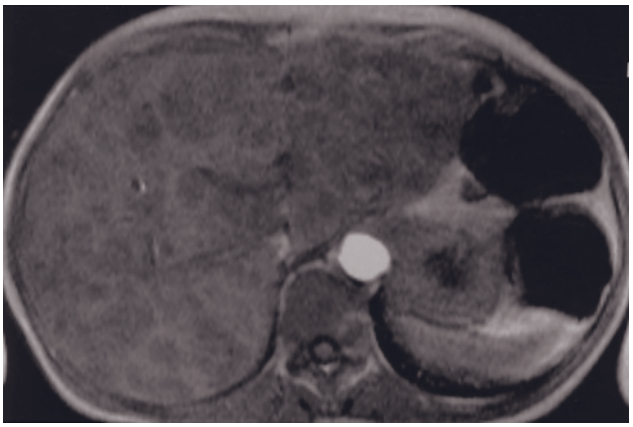

(*b*)

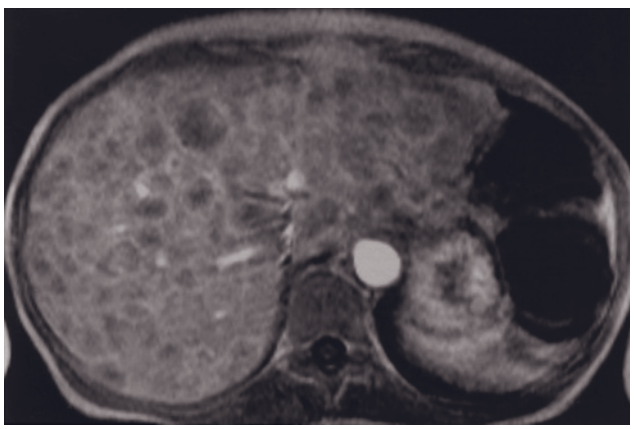

(*c*)

FIG. 2.94 Liver metastases, poorly-differentiated small cell type. Fat-suppressed T2-weighted ETSE (*a*), SGE (*b*), and immediate postgadolinium SGE (*c*) images. The liver is extensively replaced by numerous metastatic lesions smaller than 2 cm. Lesions are high in signal intensity on the T2-weighted image (*a*) and mildly low in signal intensity on the T1-weighted image (*b*) and demonstrate ring enhancement on the immediate postgadolinium images (*c*). High signal intensity is also apparent in the bone marrow on the T2-weighted image (arrow, *a*), which represents bone metastases. Poorly-differentiated or anaplastic malignancies not uncommonly result in this pattern of liver metastases. This patient has small cell lung cancer.

The distinction between liver metastases treated with systemic chemotherapy and rapid-enhancing type II or III hemangiomas is challenging. Chemotherapy-treated metastases demonstrate high signal intensity on T2-weighted images and peripheral irregular enhancement that may resemble globular enhancement [82]. Clinical history of liver metastases with recent initiation of chemotherapy is critical. Attention should be paid to unusual features such as partial washout pattern of enhancement and jagged rather than nodular inner margin of enhancement.

We reported [79] the occurrence of benign liver lesions in a consecutive population of women with newly diagnosed breast cancer and suspected liver metastases who were referred to MRI. A total of 32% (11 of 34) patients had benign lesions; 62% (21 of 34) had malignant lesions, two of whom had coexistent benign lesions. Characterization of focal liver lesions as benign or malignant is important because patients with known primary malignancies commonly have small hepatic lesions that are benign cysts or hemangiomas. The whole organ coverage per acquisition of spoiled gradient echo permits optimal evaluation of the entire liver in distinct phases of enhancement with serial image acquisition after gadolinium administration. In the presence of multiple liver lesions, the distinction of benign and malignant lesions is of critical importance and is well performed by MRI (fig. 2.104).

Lesion characterization is critical in assessing and staging patients with primary nonhepatic malignancies, as benign liver lesions are common, even in these patients. One previous report [160] described the detection of small (<15 mm) lesions in 254 of 1454 patients who underwent CT examination. The majority of patients (82%) with liver lesions in this study had a known primary tumor, yet lesions in 51% of these patients were benign. Another report [161] described a large series of cancer patients in whom 41.8% of detected focal liver lesions were benign.

METASTASIS VERSUS FNH AND HCA. Hypervascular metastases may demonstrate a homogeneous intense enhancement on arterial dominant-phase images similar to FNH and HCA. Small hypervascular metastases (<1.5 cm) may also be isointense on noncontrast T2- and T1-weighted images. Large hypervascular metastases

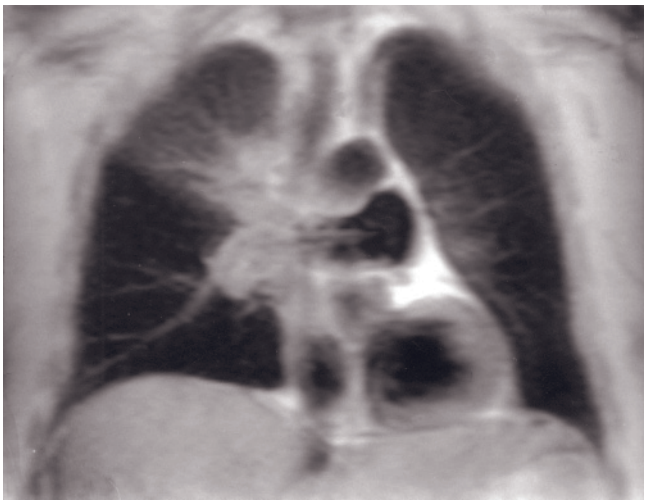

(*a*)

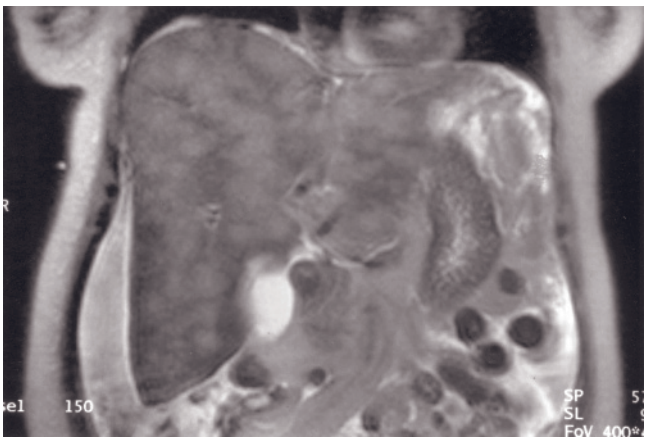

(*b*)

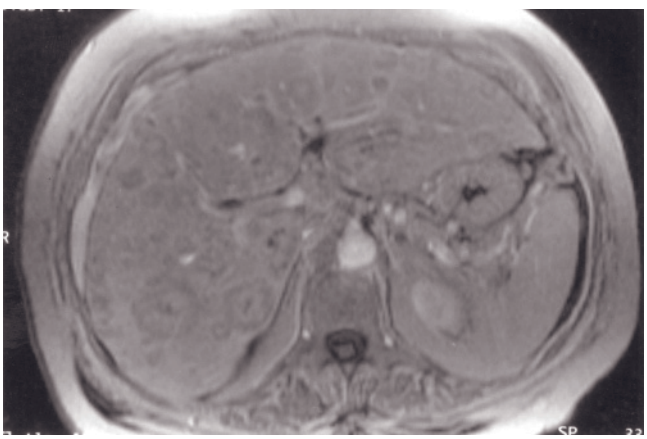

(*c*)

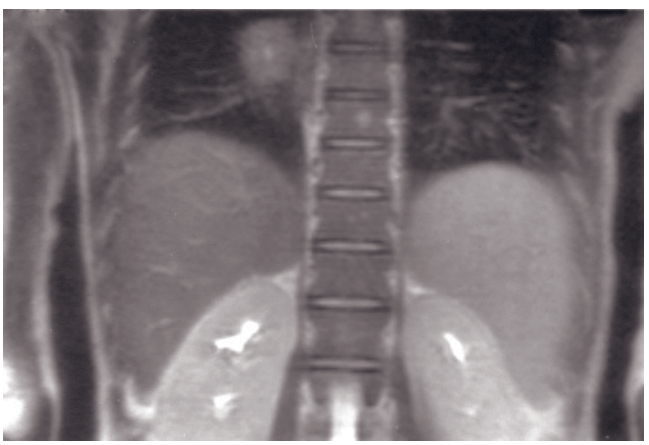

(*d*)

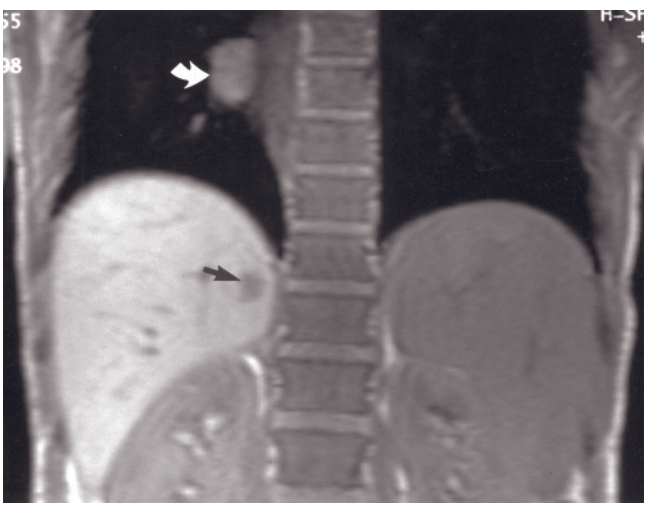

(*e*)

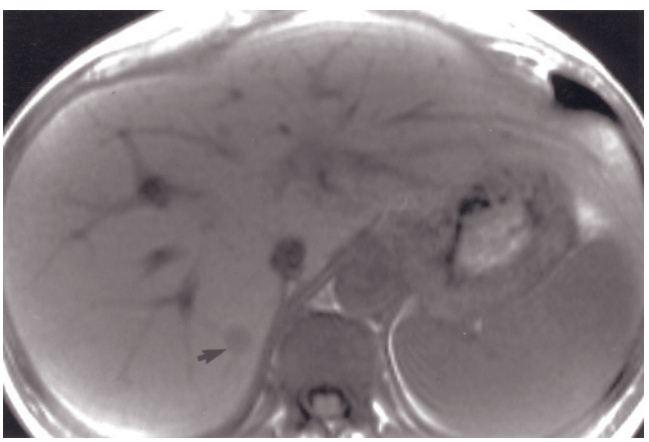

(*f*)

FIG. 2.95 Metastases from lung cancer. Coronal T2-weighted SS-ETSE (*a*, *b*) and transverse immediate postgadolinium magnetization-prepared gradient-echo (*c*) images. Multiple lesions are scattered throughout the liver, which appear high signal on T2-weighted images (*b*) and show ring enhancement on immediate postgadolinium images (*c*). Note the right hilar mass associated with an alveolar infiltrate due to postobstructive pneumonia (*a*).

Coronal T2-weighted SS-ETSE (*d*), coronal SGE (*e*), SGE (*f*), and immediate postgadolinium (*g*) images in a second patient. A small lesion is seen in the right hepatic lobe (arrow, *e, f*) and demonstrates low signal on T1-weighted image (*e*, *f*) and thin ring enhancement immediately after contrast administration (*g*), consistent with a metastasis. Note the right infrahilar mass in the lung (curved arrow, *e*).

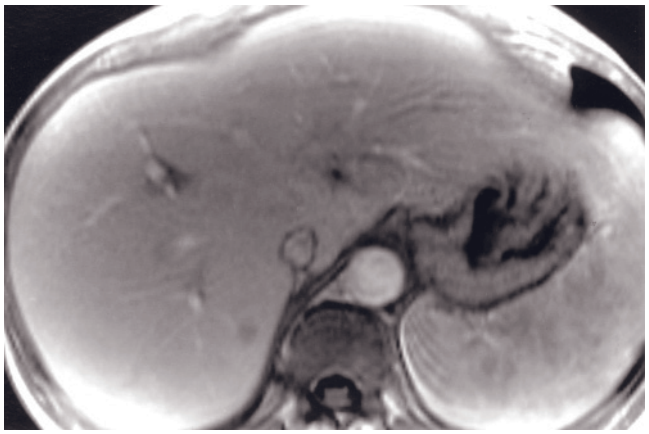

(*g*)

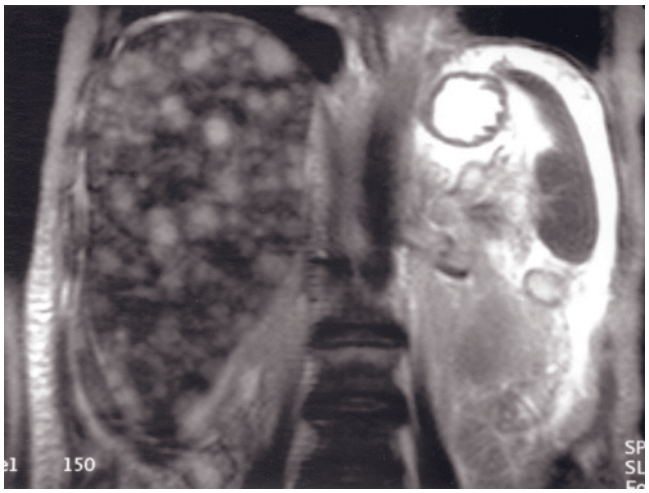

(*h*)

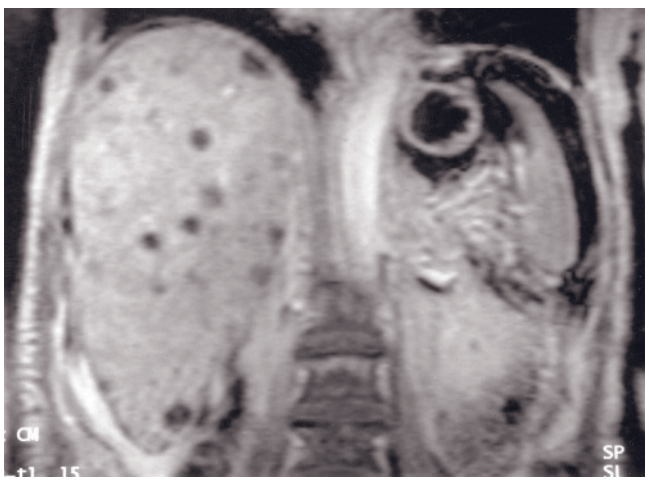

(*i*)

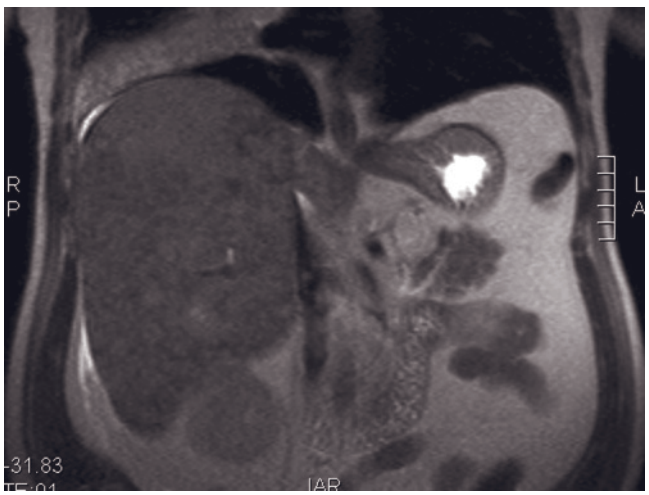

(*j*)

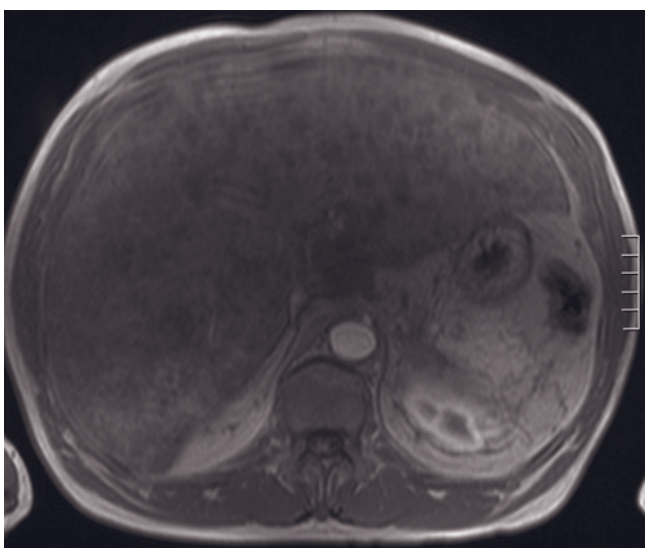

(*k*)

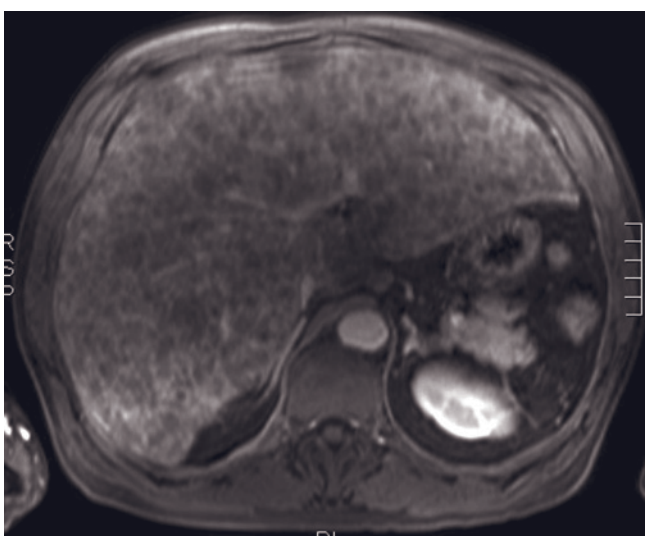

(*l*)

FIG. 2.95 (*Continued*) Coronal T2-weighted SS-ETSE (*h*) and coronal immediate postgadolinium magnetization prepared gradient-echo (*i*) images in a third patient. There are numerous metastases scattered throughout the liver, which exhibit high signal on T2-weighted image (*h*) and ring enhancement after gadolinium administration (*i*), consistent with metastases from non-small cell carcinoma.

Coronal T2-weighted SS-ETSE (*j*) and immediate (*k*) and 90-s fat-suppressed (*l*) postgadolinium SGE images in a fourth patient that show similar findings.

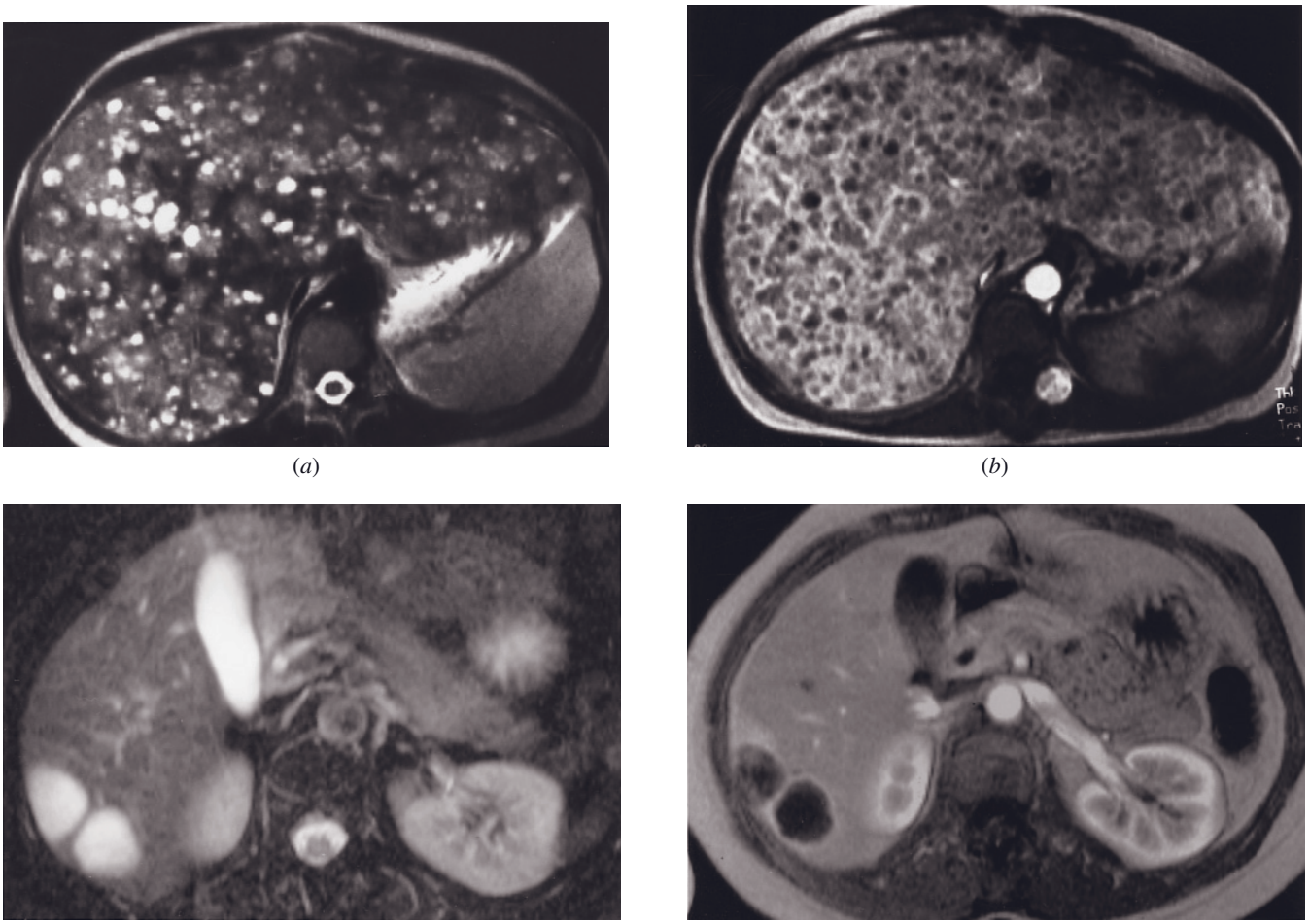

(*a*) (*b*) (*c*) (*d*)

FIG. 2.96 Hypervascular liver metastases from islet cell tumors. Transverse 512-resolution ETSE (*a*) and immediate postgadolinium SGE (*b*) images in a patient with gastrinoma. Numerous metastases smaller than 1 cm are scattered throughout all segments, many of which are well defined and high in signal intensity on the T2-weighted image (*a*). The immediate postgadolinium image (*b*) demonstrates that the metastases have intact ring enhancement.

Fat-suppressed T2-weighted ETSE (*c*) and immediate postgadolinium SGE (*d*) images in a second patient who has an untyped islet cell tumor. The metastases are well-defined round masses that are high in signal intensity on the T2-weighted image (*c*) and have calculated T2 values of 160 ms. On the immediate postgadolinium image (*d*), the lesions possess intact rings of enhancement that are a feature of metastases and not of hemangiomas. Prior outside MRI performed with conventional spin-echo techniques and original outside interpretation of percutaneous biopsy specimen suggested the diagnosis of hemangiomas. On the gadolinium-enhanced images, hypervascular cystic liver metastases and a 2-cm islet cell tumor in the head of the pancreas were shown. The histology specimen was re-examined, and the diagnosis of islet cell tumor was confirmed.

(>1.5 cm) often possess a radial spoke-wheel appearance with thin radial strands of lesser enhancement on arterial-phase images. Also, FNH and HCA, independent of lesion size, almost invariably show isointensity or mild hyperintensity on T2-weighted images and isointensity or mild hypointensity on T1-weighted images. Larger hypervascular metastases are generally moderately high in signal on T2-weighted images. On interstitial-phase images, FNH and HCA show enhancement that fades to isointensity with surrounding parenchyma. Hypervascular metastases commonly show lesion washout, although small lesions may fade on late post-contrast images [69, 72, 81, 113, 121, 132, 162]. Clinical history of a primary hypervascular tumor is usually present, facilitating the correct diagnosis.

Secondary Infection of Liver Metastases. Secondary infection of metastases may occur and is most commonly observed with colon cancer metastases. It is postulated that the high content of intraluminal bacteria within the colon may be conducive to embolization of coliform bacteria with tumor cells. Experimental data suggests that certain anaerobic bacteria grow selectively in tumor nodules but not in the

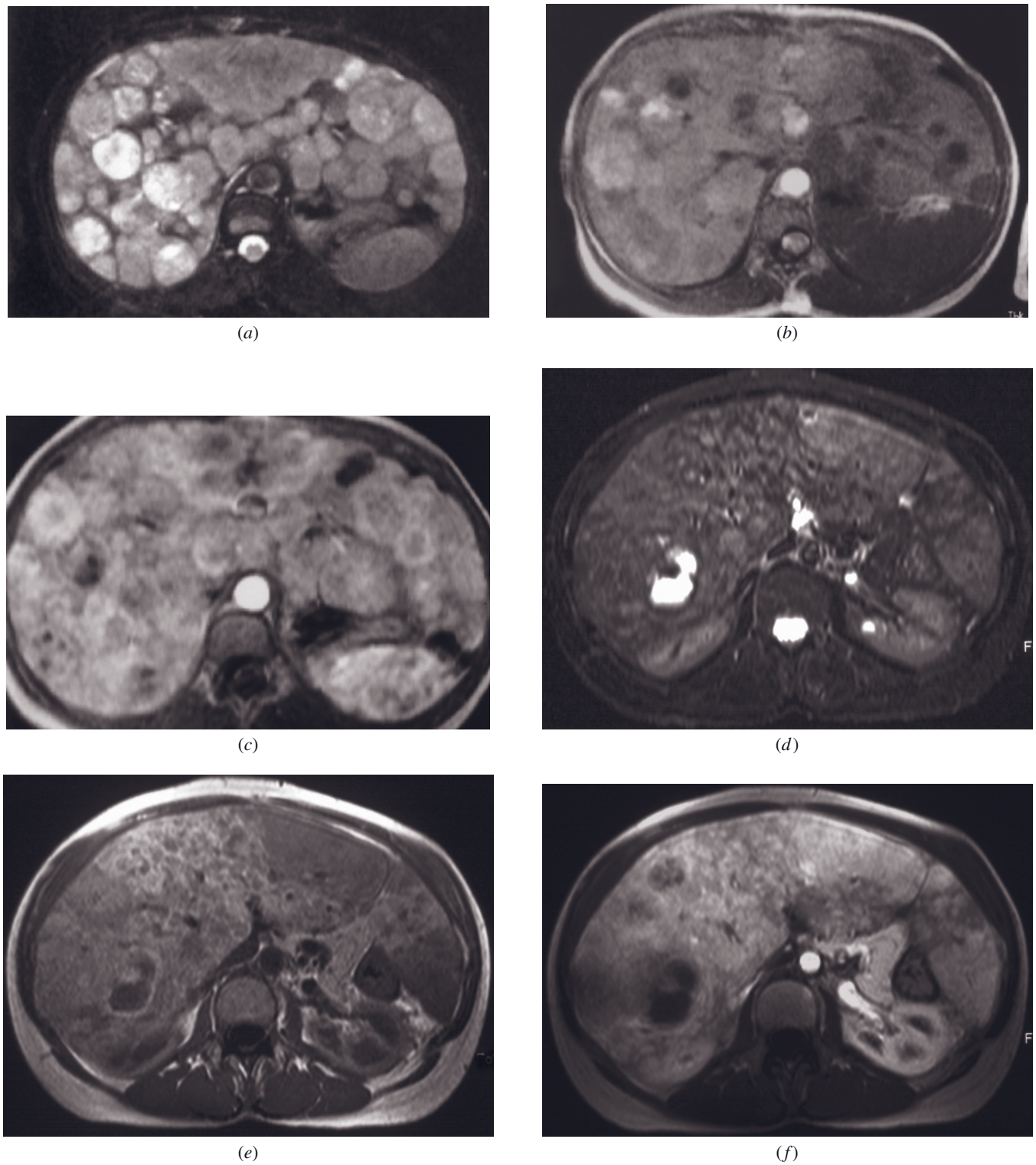

FIG. 2.97 Melanoma metastases. Fat-suppressed T2-weighted ETSE (*a*), SGE (*b*), and immediate postgadolinium SGE (*c*) images. Melanoma metastases are a mixed population of low- to high-signal intensity lesions on T2 (*a*)- and T1 (*b*)-weighted images. This reflects the paramagnetic properties of melanin. Intense ring enhancement is present on the immediate postgadolinium SGE image (*c*), demonstrating the hypervascularity of these metastases.

Fat-suppressed T2-weighted SS-ETSE (*d*), SGE (*e*), and immediate (*f*) and 90-s fat-suppressed (*g*) postgadolinium SGE images in a second patient. There are multiple lesions scattered throughout hepatic parenchyma that show heterogeneous high signal on the

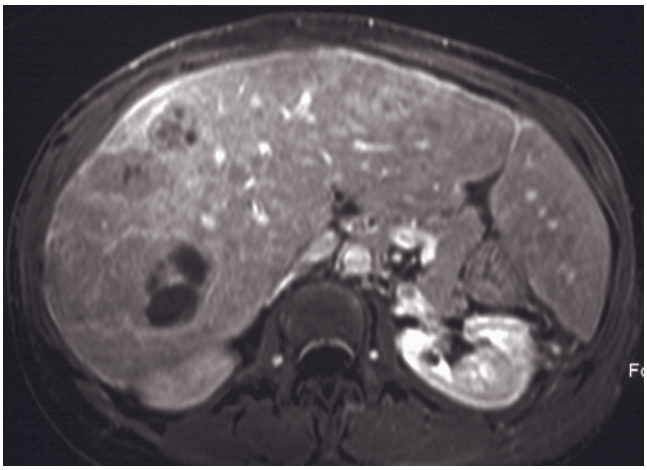

(*g*)

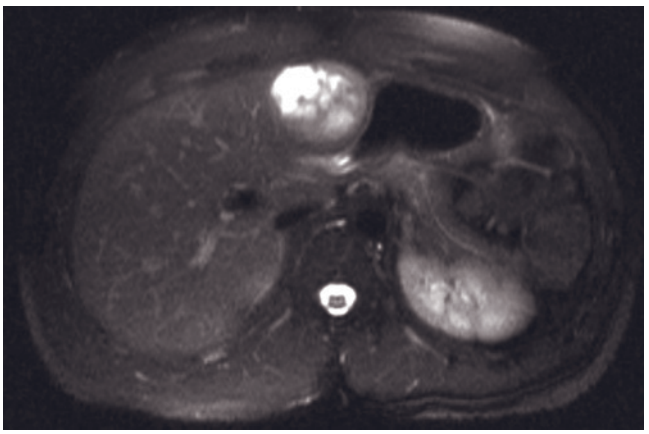

(*h*)

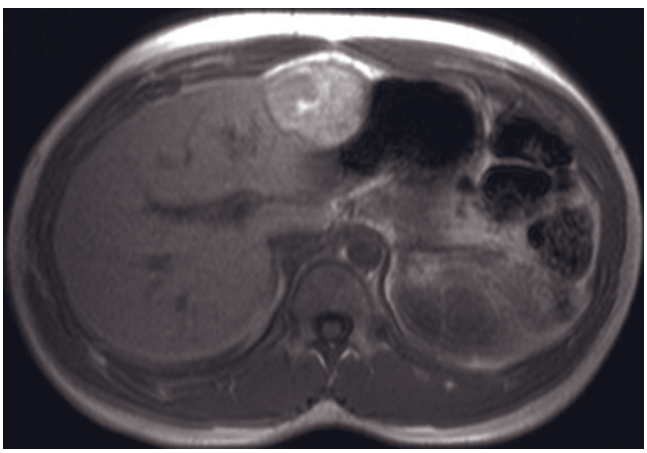

(*i*)

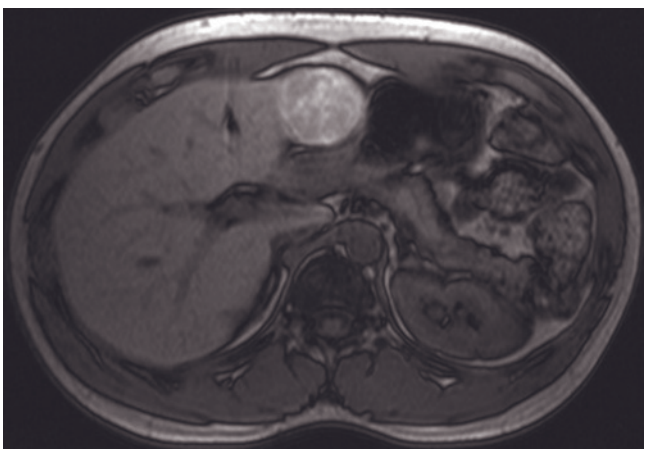

(*j*)

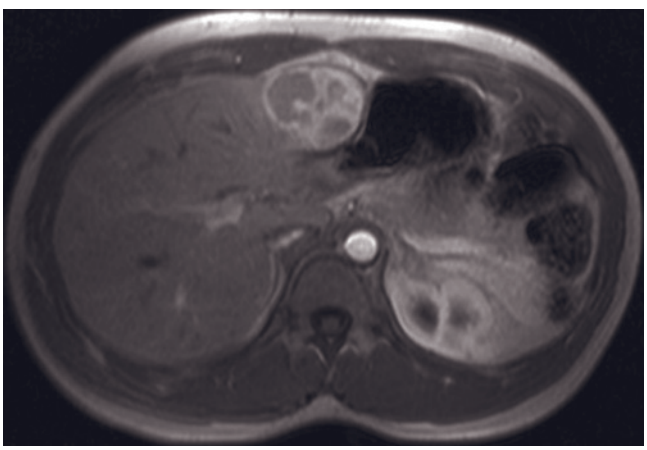

(*k*)

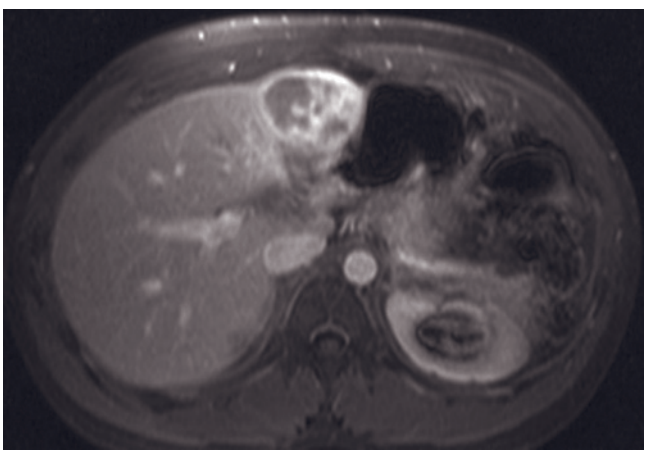

(*l*)

FIG. 2.97 (*Continued*) T2-weighted (*d*) and the T1-weighted (*e*) images and intense heterogeneous enhancement on the early-phase image (*f*) that becomes more homogeneous on the late-phase image (*g*). The high signal intensity on both the T2- and T1-weighted images reflects the presence of melanin.

Fat-suppressed T2-weighted SS-ETSE (*h*), SGE (*i*), out-of-phase SGE (*j*), and immediate (*k*) and 90-s fat-suppressed (*l*) SGE images in a third patient show similar features.

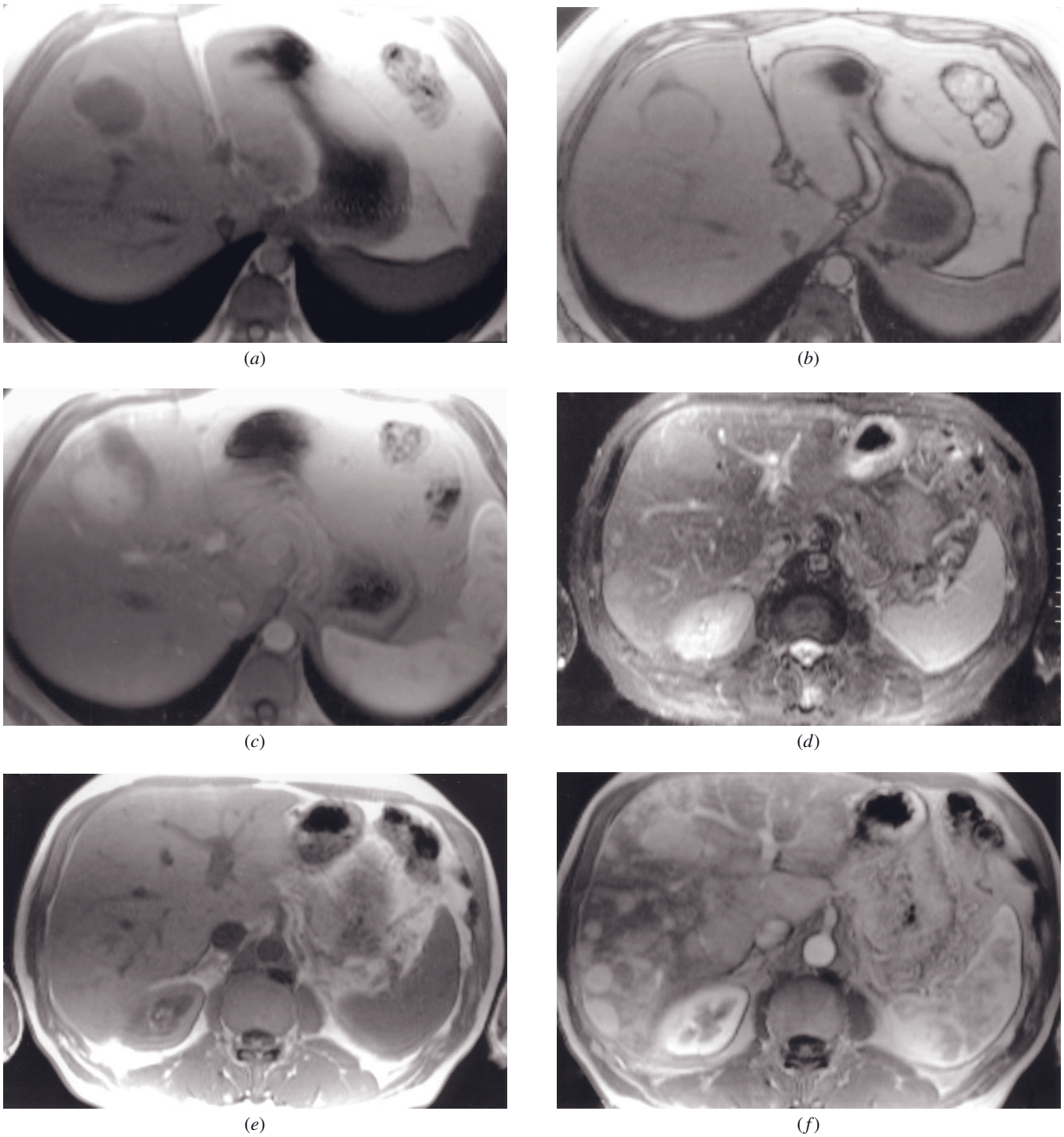

FIG. 2.98 Hypervascular liver metastases from carcinoid tumor. SGE (*a*), out-of-phase SGE (*b*), and immediate postgadolinium SGE (*c*) images. There is a rounded lesion in the right hepatic lobe that demonstrates low signal intensity on T1-weighted image (*a*), the lesion and liver become comparable in signal on out-of-phase image (*b*) due to signal loss in background fatty liver—note the rim of greater fat content. The lesion shows intense and homogeneous enhancement after gadolinium administration (*c*), consistent with a hypervascular metastasis. Carcinoid tumor was present at histopathology.

Echo train-STIR (*d*), SGE (*e*), and immediate (*f*) and 90-s fat-suppressed (*g*) postgadolinium SGE images in a second patient. Numerous metastases are scattered throughout the hepatic parenchyma that demonstrate near-isointense signal on T2 (*d*)- and T1 (*e*)-weighted images and intense enhancement on immediate postgadolinium images (*f*) that wash out on later images (*g*), consistent with hypervascular metastases. The difference in lesion conspicuity between immediate postgadolinium images and other sequences, including noncontrast T2- and T1-weighted images and late postgadolinium images, is particularly impressive in the setting of hypervascular malignant disease.

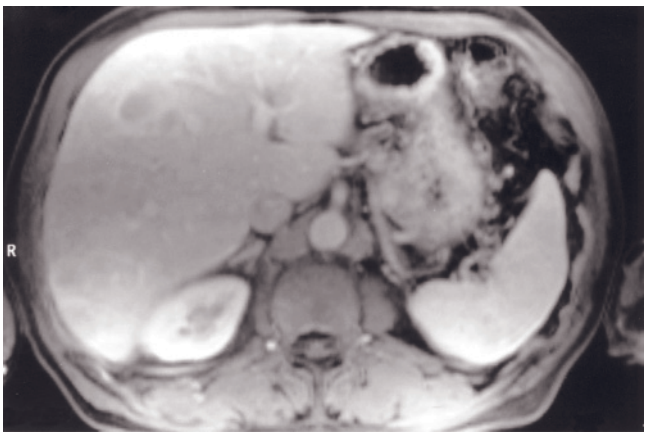

(*g*)

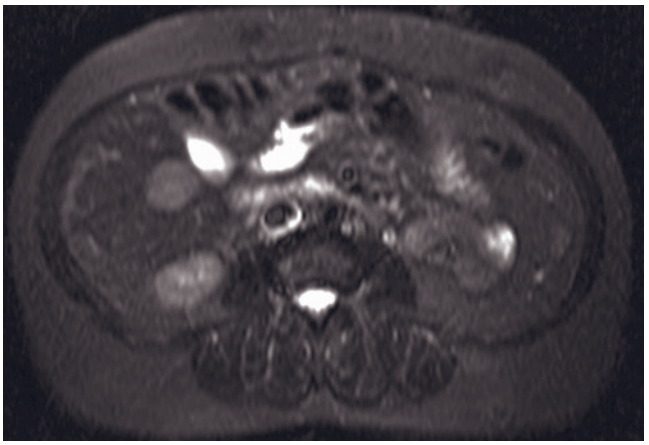

(*h*)

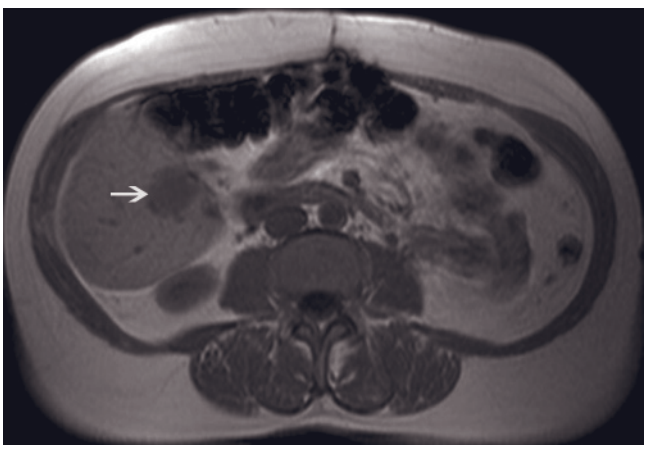

(*i*)

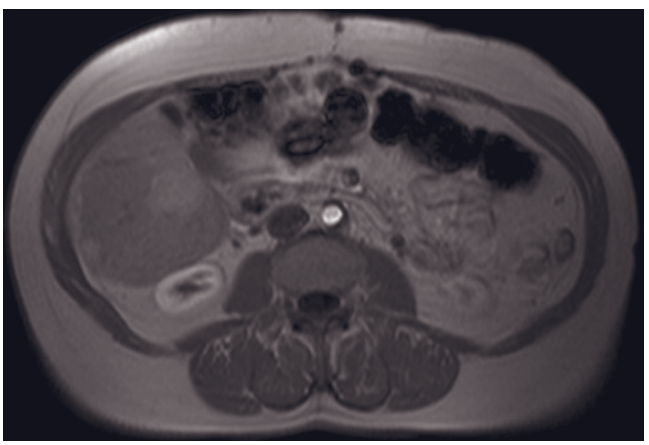

(*j*)

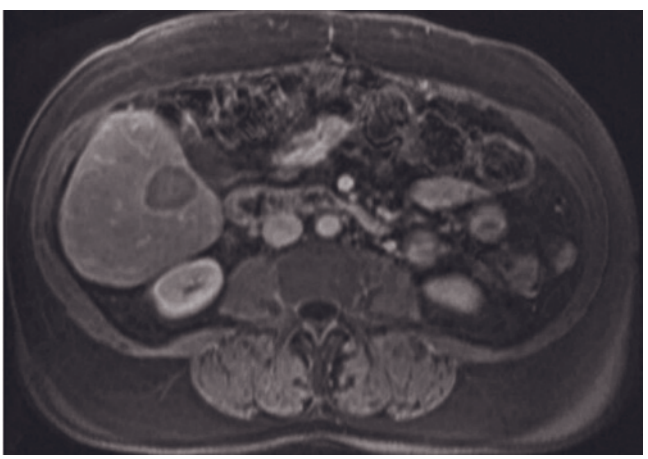

(*k*)

FIG. 2.98 (*Continued*) Fat-suppressed T2-weighted SS-ETSE (*h*), SGE (*i*), and immediate (*j*) and 90-s fat-suppressed (*k*) post-gadolinium SGE images in a third patient. There is a metastasis that shows high signal intensity on T2-weighted images (*h*), low signal intensity on T1-weighted images (arrow, *i*), and a moderate enhancement on early-phase images (*j*) that washes out with persistent ring enhancement on late-phase images (*k*).

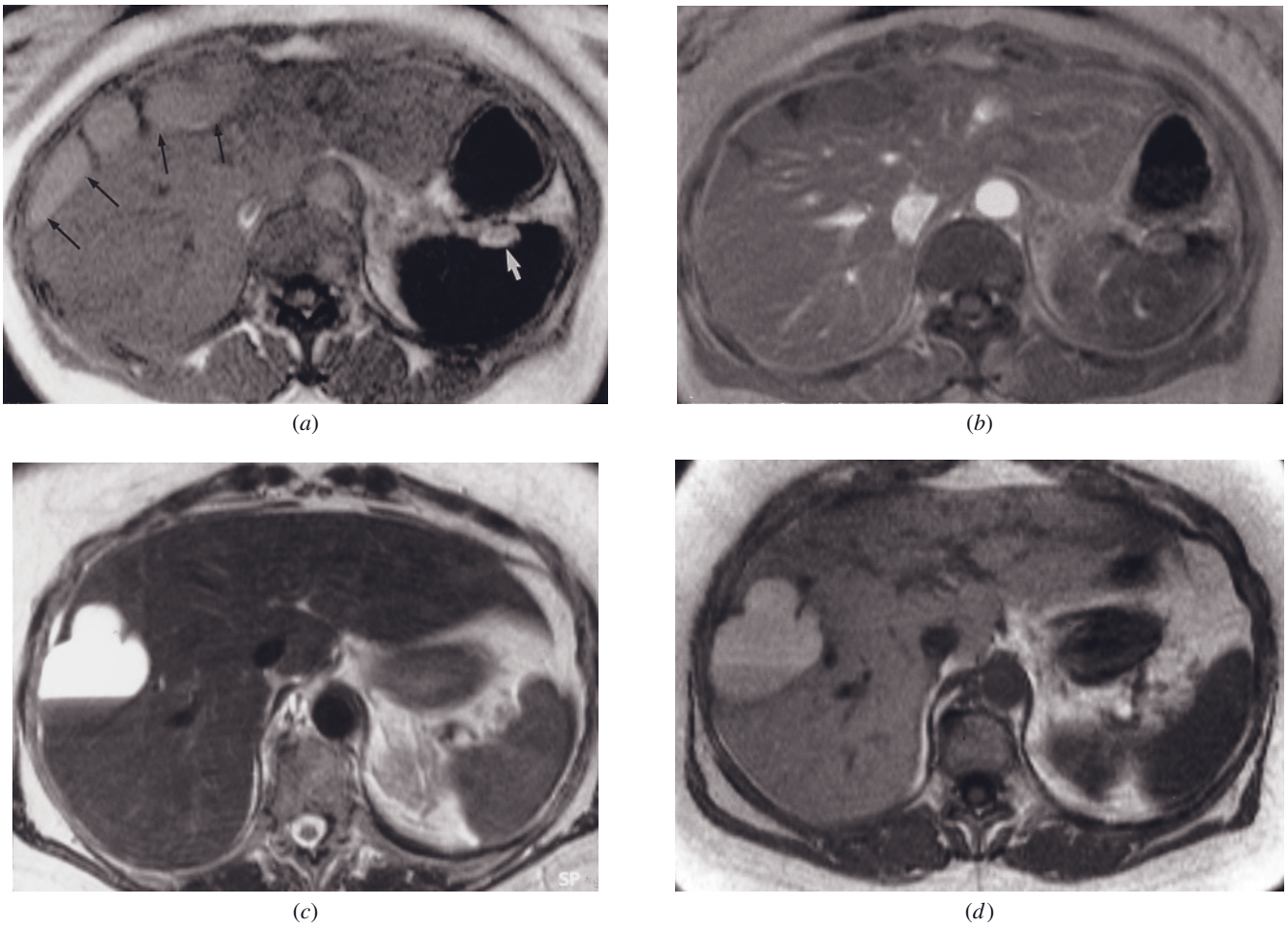

FIG. 2.99 High T1 signal mucin-producing liver metastases, ovarian cancer. SGE (*a*) and 90-s postgadolinium SGE (*b*) images. A large capsule-based metastasis is present along the lateral margin of the liver (black arrows, *a*), and a smaller subcapsular metastasis is present in the spleen (white arrow, *a*). The metastases are high in signal intensity on T1-weighted image, reflecting high mucin content. Enhancement of cyst walls is present on postgadolinium images (*b*). The spleen is nearly signal void on these T1-weighted images because of transfusional hemosiderosis.

T2-weighted ETSE (*c*) and SGE (*d*) images in a second patient demonstrate a cystic ovarian metastasis located superficially in the right lobe of the liver. On the T2-weighted image (*c*), low-signal-intensity material layers in the dependent portion of the metastasis. The high mucin content of the cystic metastasis renders it high in signal intensity on the T1-weighted image (*d*).

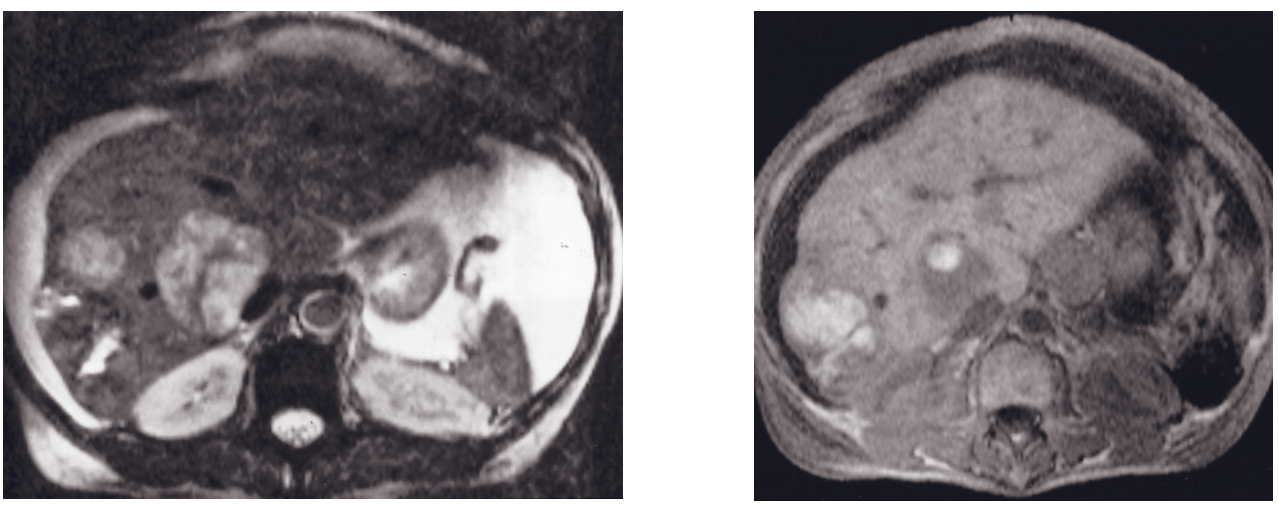

FIG. 2.100 Carcinoid liver metastases. Fat-suppressed T2-weighted ETSE (*a*) and SGE (*b*) images. Metastases are heterogeneous with mixed high-signal intensity on T2 (*a*) and T1 (*b*) images. The high signal intensity on the T1-weighted image (*b*) reflects a high protein concentration due to protein synthesis from hormone production. The high signal on T1-weighted image (*b*) is an uncommon appearance for carcinoid metastases.

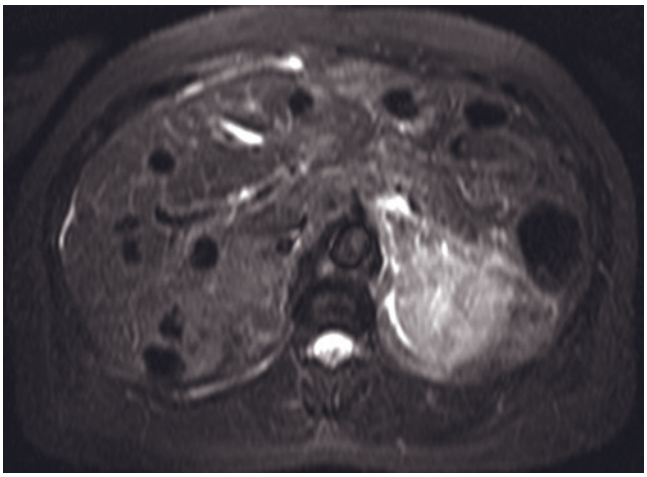

(*c*)

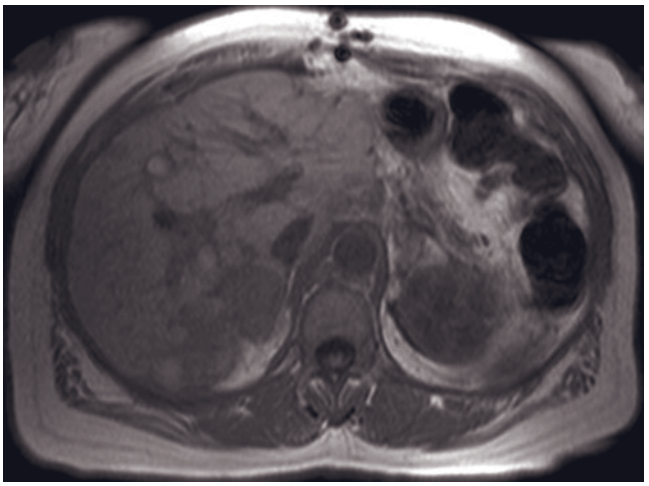

(*d*)

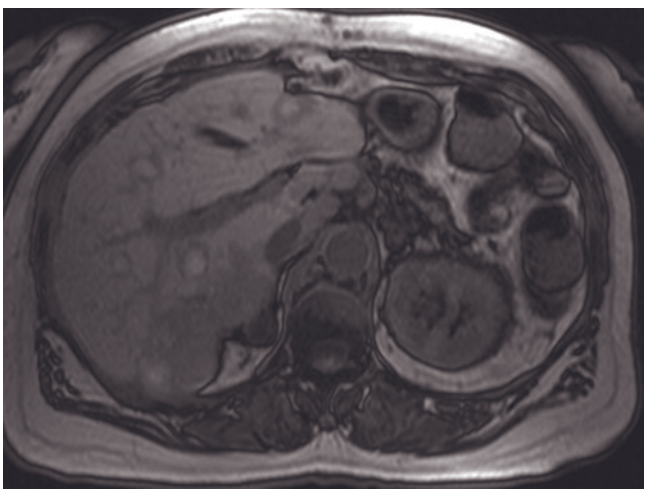

(*e*)

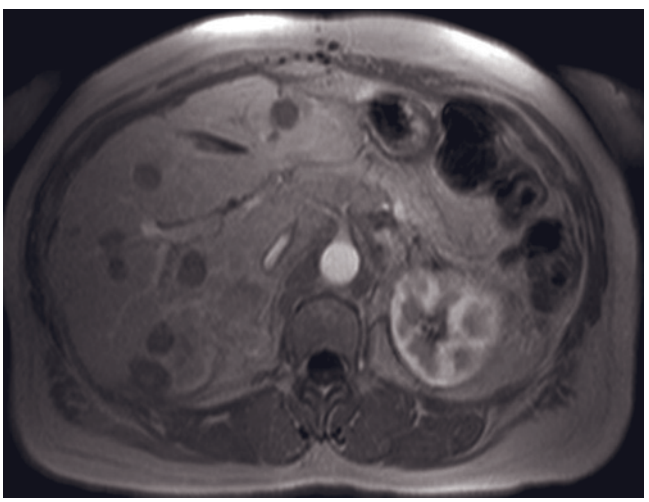

(*f*)

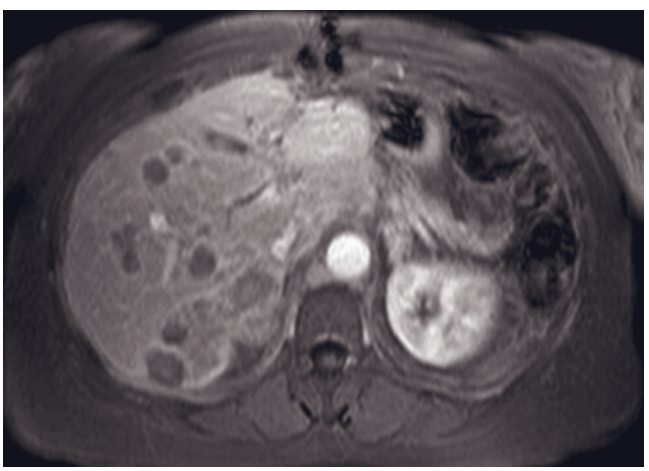

(*g*)

FIG. 2.100 (*Continued*) Fat-suppressed T2-weighted SS-ETSE (*c*), SGE (*d*), out-of-phase SGE (*e*), and immediate (*f*) and 90-s fat-suppressed (*g*) SGE images in a second patient. Multiple rounded lesions are scattered throughout the hepatic parenchyma that are low signal on T2-weighted images (*c*) and high signal intensity on T1-weighted images (*d*), and show no loss in signal intensity on out-of-phase images (*e*) and ring enhancement on early-phase images (*f*), with persistent appearance on late-phase images (*g*).

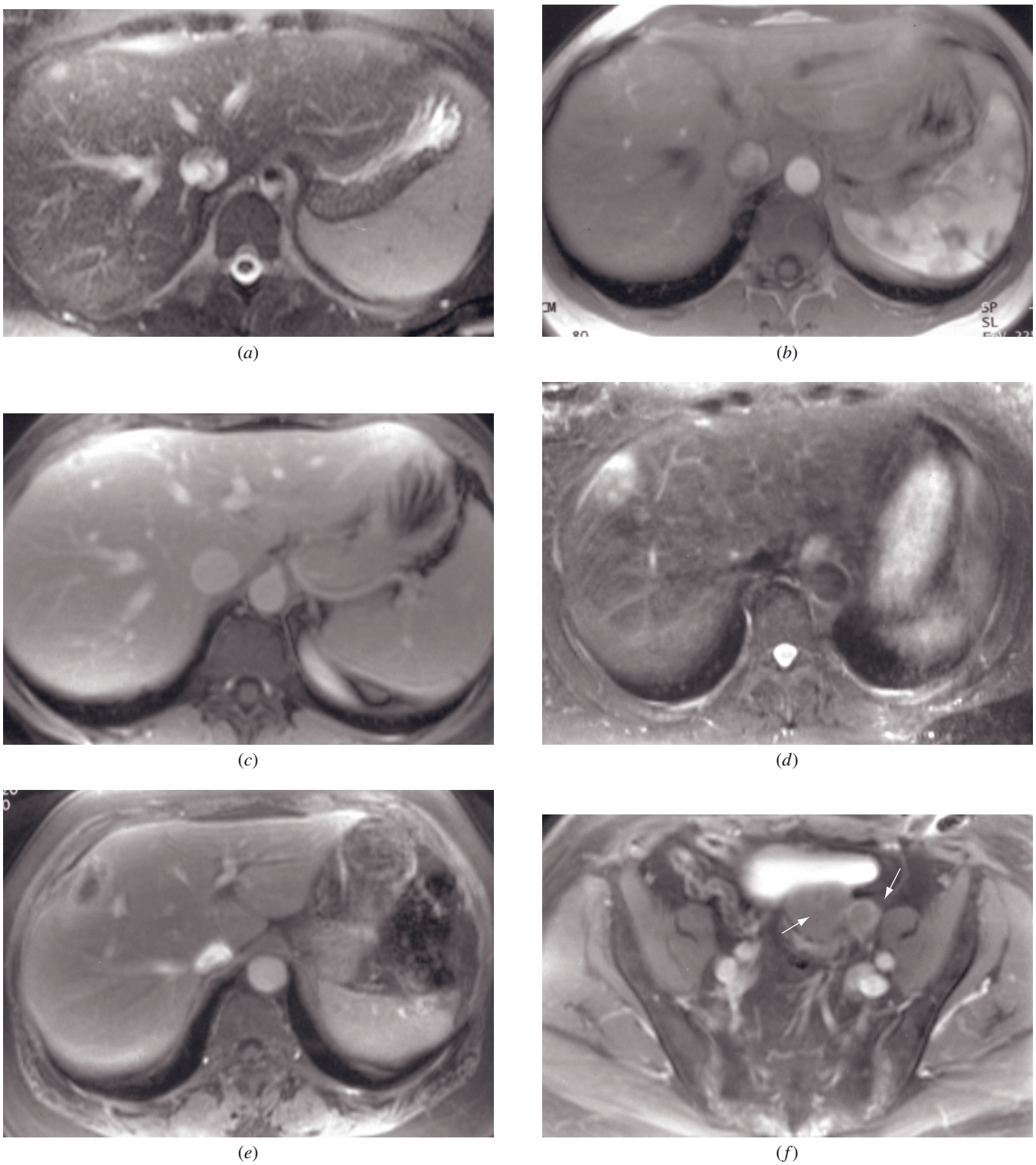

FIG. 2.101 Liver and peritoneal metastases from ovarian tumor. Echo-train STIR (*a*) and immediate (*b*) and 90-s fat-suppressed (*c*) postgadolinium SGE images in one patient and echo-train STIR (*d*) and 90-s fat-suppressed postgadolinium SGE (*e*, *f*) images in a second patient, both of whom have ovarian cancer and peritoneal metastases. Both patients demonstrate liver metastases characterized by high signal on T2-weighted images (*a*, *d*) and ring enhancement on early (*b*) and late (*c*, *e*) postgadolinium images. Note the presence of recurrent pelvic tumor (arrows, *f*) in the second patient.

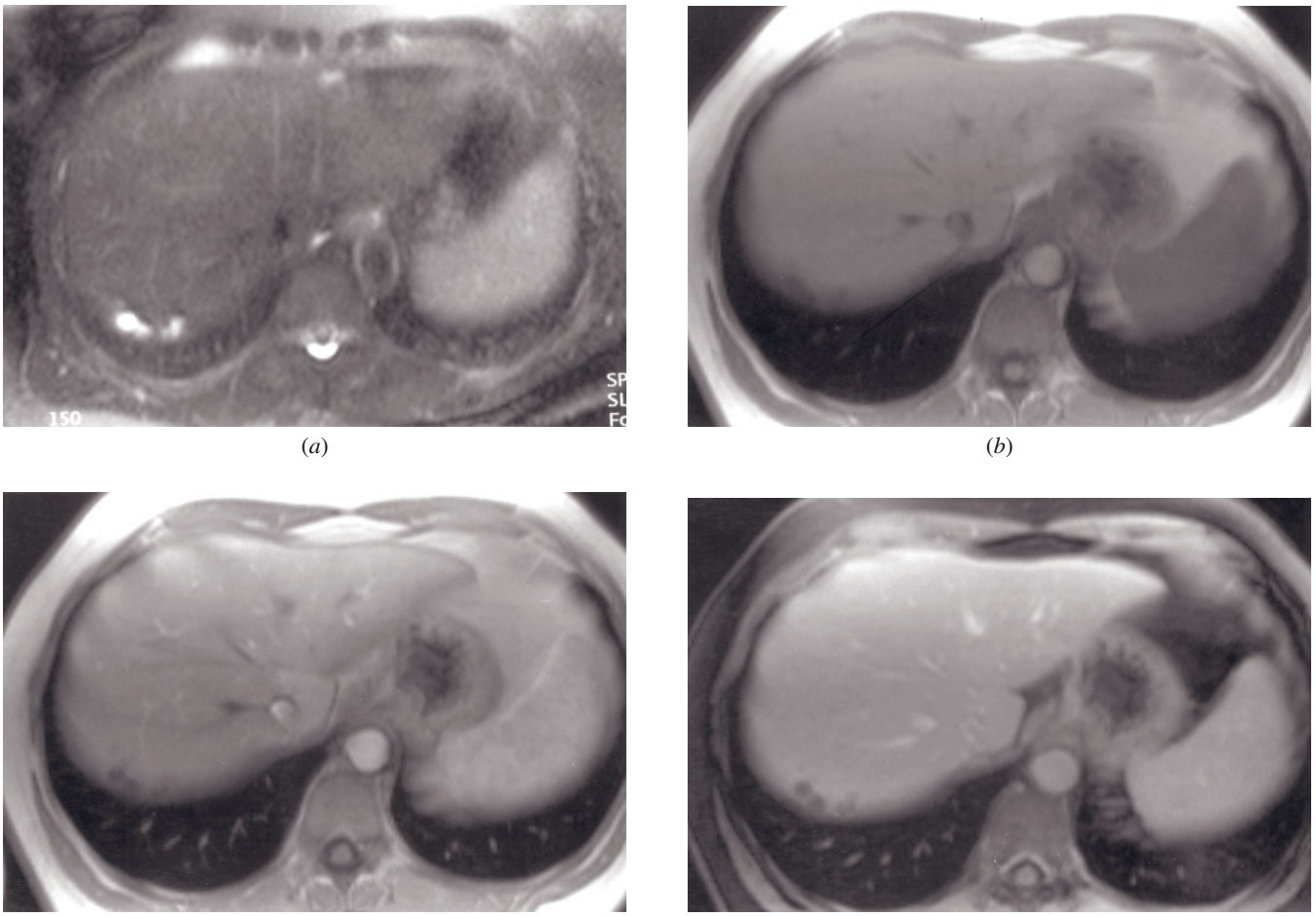

FIG. 2.102 Ovarian subcapsular metastases. Echo-train STIR (*a*), SGE (*b*), and immediate (*c*) and 90-s fat-suppressed (*d*) postgadolinium SGE images. There is a cluster of small lesions in a subcapsular location along the dome of the liver, which demonstrate high signal on T2 (*a*), low signal on T1 (*b*), and faint ring enhancement on early (*c*) and late (*d*) postgadolinium images consistent with capsule-based metastatic implants. This is the most common pattern of involvement of the liver with ovarian cancer and represents part of the generalized process of intraperitoneal seeding and spread.

normal tissues of a tumor-bearing host [163]. Secondary infection of liver metastases after chemoembolization of these lesions has been reported [164]. Infected metastases may simulate both the clinical and imaging features of liver abscesses.

On MRI, infected metastases tend to have thickened, irregular walls and heterogeneous intermediate signal intensity on T2-weighted images and show some progressive central stromal enhancement on delayed images (fig. 2.105). Abscesses tend to have thinner walls and higher signal intensity on T2-weighted images and do not demonstrate progressive central lesion stromal enhancement over time, even in abscesses with thick walls and internal septations. Both types of lesions will show transient, ill-defined perilesional enhancement reflecting an inflammatory hyperemic response in the liver.

Hepatocellular Carcinoma

Hepatocellular carcinoma (HCC) is the most common primary malignancy of the liver and usually develops in patients with cirrhosis [165]. It should be recognized that HCC does occur in the noncirrhotic liver as well. HCC is the fifth most common cancer in the world and accounts for up to 1 million deaths annually worldwide [166]. Incidence of HCC is particularly high in patients with cirrhosis from chronic hepatitis C infection, chronic hepatitis B infection, and alcoholic liver disease [165]. Men are affected three times more frequently than women [167]. The 5-year survival rate for untreated symptomatic HCC is <5% [167]. This statistic is in sharp contrast to the survival rate in patients with cirrhosis with small (<2 cm) HCC who have undergone liver transplantation, where the 5-year survival is 80% [165]. Thus detection of small HCC is imperative for improved

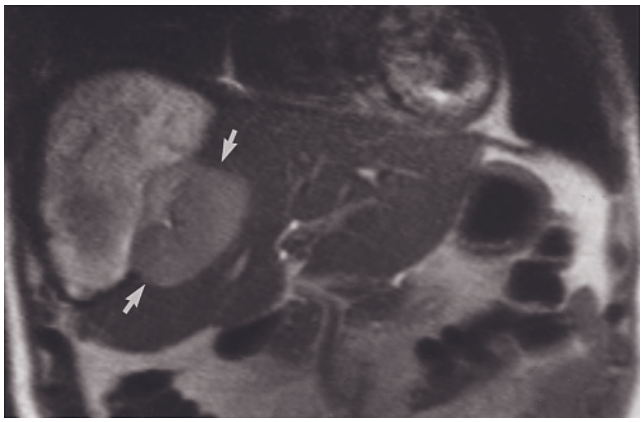

(*a*)

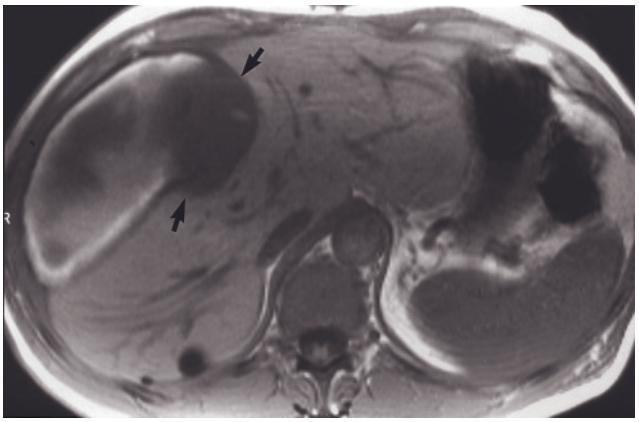

(*b*)

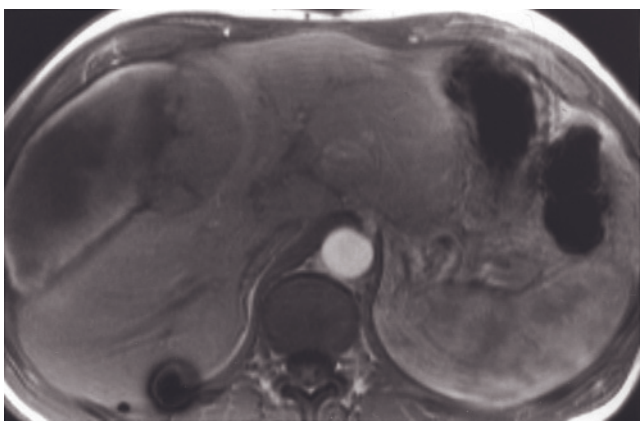

(*c*)

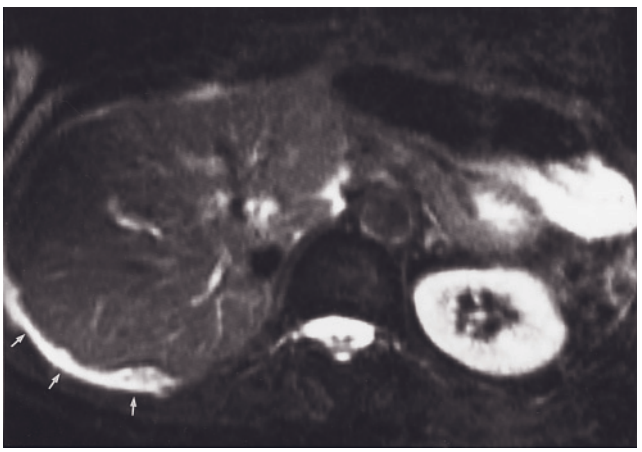

(*d*)

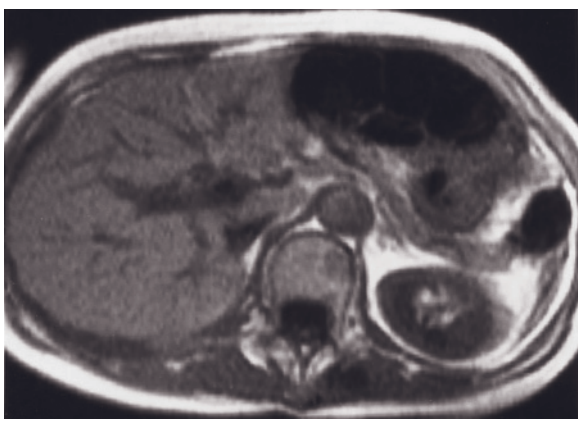

(*e*)

FIG. 2.103 Capsule-based liver metastases. Coronal T2-weighted SS-ETSE (*a*), transverse SGE (*b*), and immediate postgadolinium SGE (*c*) images. A large capsule-based metastasis is present along the lateral margin of the liver with a solid tumor component (arrows, *a, b*) from synovial sarcoma. Hemorrhage is heterogeneous on the T2-weighted image (*a*). On the noncontrast T1-weighted image (*b*), a peripheral rim of high signal intensity is present from recent hemorrhage. On the immediate postgadolinium image (*c*), the solid tumor component enhances uniformly.

Fat-suppressed T2-weighted SS-ETSE (*d*) and SGE (*e*) images in a second patient with capsule-based metastases from colon cancer. Capsule-based metastases are very conspicuous on the fat-suppressed T2-weighted image (arrows, *d*) because of the intrinsic high signal intensity of the masses and removal of the competing signal of fat. They are subtle on the T1-weighted image (*e*).

outcomes. In North America, most HCCs are large at the time of diagnosis, although with increasing surveillance of patients with liver cirrhosis and/or chronic hepatitis, detection of earlier stage neoplasms appears to be occurring more often [168].

Hepatocarcinogenesis is attributed to genetic predisposition and epigenetic changes that accumulate over time [169]. Liver cancer is considered a linear process beginning with the development of benign, hyperplastic foci of hepatocytes, or regenerative nodules (RNs), then evolving through premalignant stages of dysplastic nodules (DNs), and finally culminating in malignant HCC [169]. Continuous inflammation and hepatocyte regeneration provide the optimal setting for

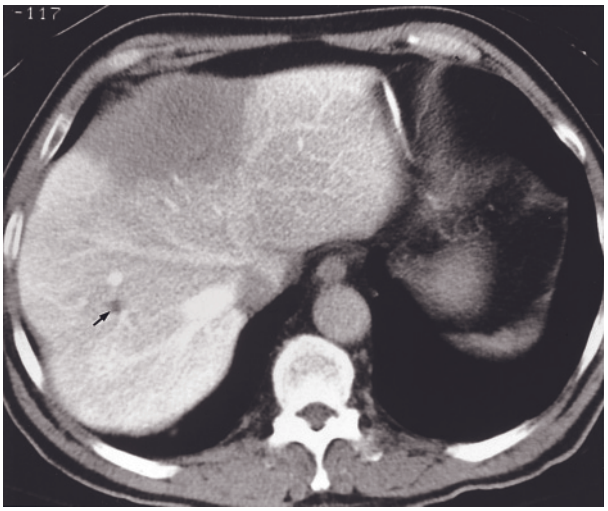

(*a*)

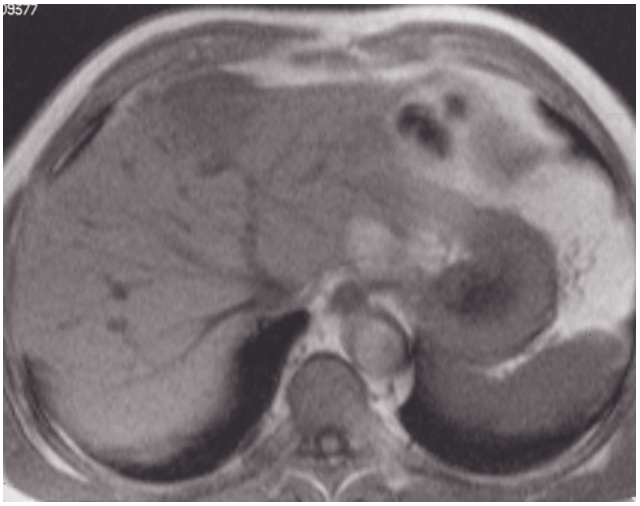

(*b*)

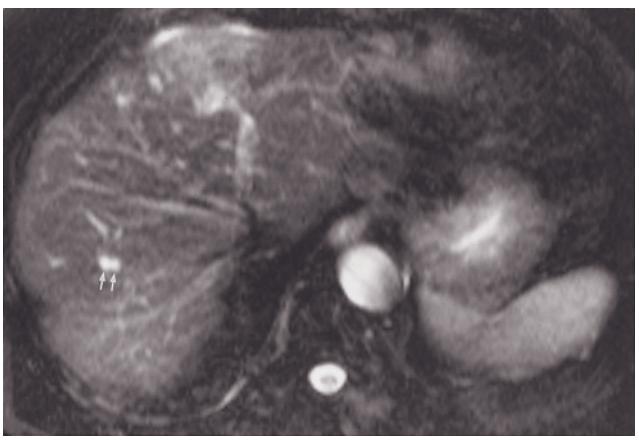

(*c*)

(*d*)

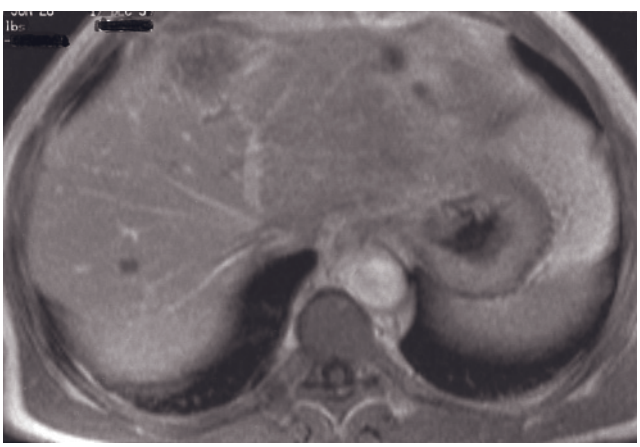

(*e*)

FIG. 2.104 Liver metastasis with coexistent cysts—spiral CTAP and MRI comparison. Spiral CTAP (*a*), SGE (*b*), fat-suppressed T2-weighted ETSE (*c*), and immediate (*d*) and 5-min (*e*) postgadolinium SGE images. The CTAP image (*a*) demonstrates a large perfusional defect in the medial segment related to a colon cancer metastasis. A 6-mm lesion in the anterior segment (arrow, *a*) was interpreted as one of several similar-appearing small lesions consistent with metastases scattered throughout the remainder of the liver. The MR images demonstrate a 4-cm mass in the medial segment with the imaging features of a colon cancer metastasis, including transient ill-defined perilesional enhancement on the immediate postgadolinium image (*d*). The lesion in the anterior segment represents two 3-mm juxtaposed cysts (arrows, *c*) that are small, sharply marginated, low in signal intensity on the T1-weighted image (*b*), and high in signal intensity on the T2-weighted image (*c*). Lack of enhancement on early (*d*) and later (*e*) postgadolinium-enhanced images is diagnostic for cysts. The remaining small liver lesions scattered throughout the liver were all shown to be cysts on MR images. The patient was operated on based on the MRI findings of a solitary liver metastases and multiple coexistent cysts. Intraoperative sonography-guided aspiration demonstrated that these small lesions were cysts. MRI was more diagnostically accurate than CTAP and had a greater effect on patient management.

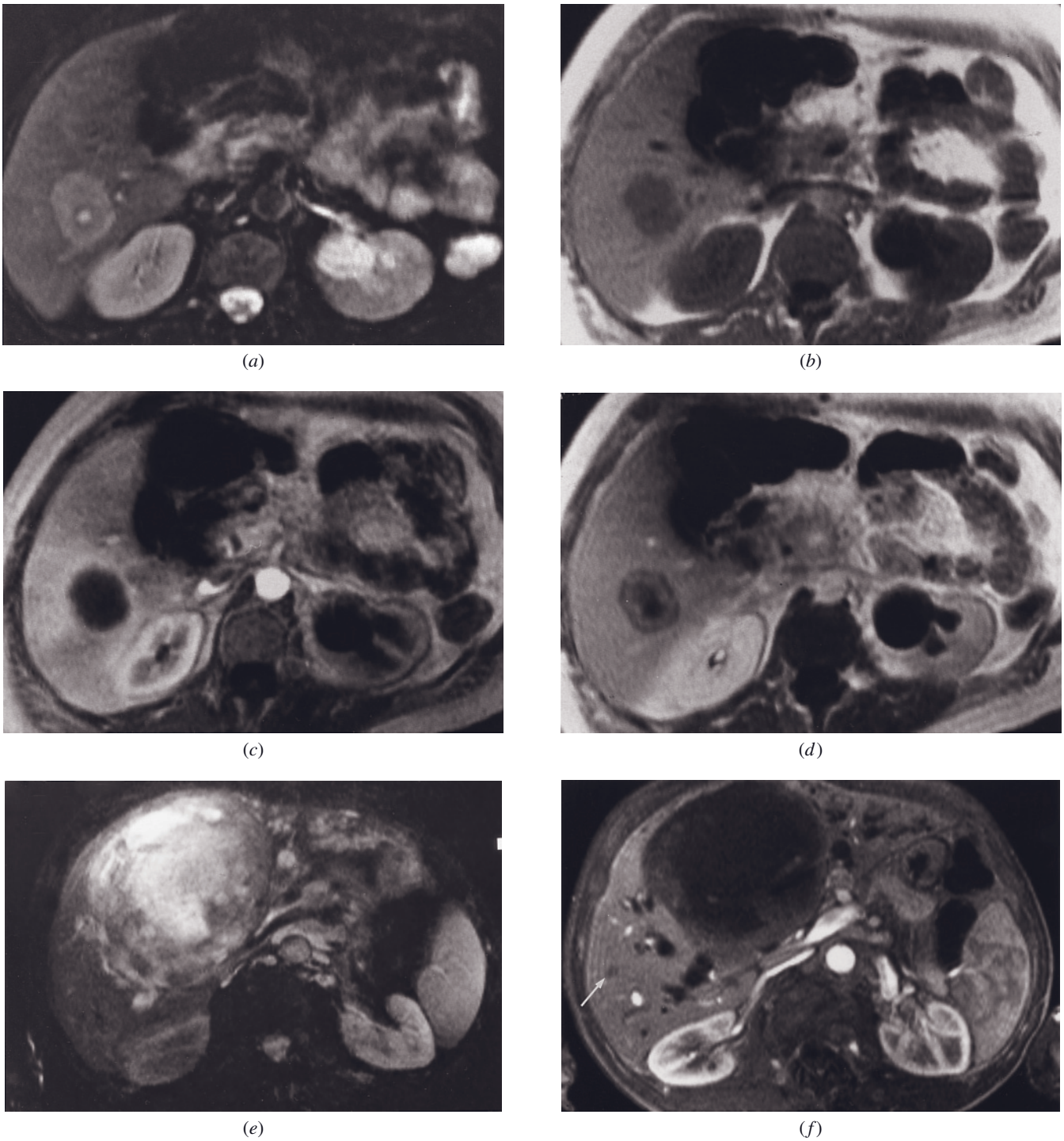

FIG. 2.105 Infected liver metastases. Fat-suppressed T2-weighted SE (*a*), SGE (*b*), and immediate (*c*) and 10-min (*d*) postgadolinium SGE images. This patient with colon cancer and clinical findings of sepsis has a 4-cm infected metastasis in the right lobe of the liver. The tumor has ill-defined margins and is minimally hyperintense on T2 (*a*) with a small central focus of high signal intensity and moderately low in signal intensity on T1 (*b*), and on the immediate postgadolinium image (*c*) the infected metastasis shows ring enhancement with prominent ill-defined perilesional enhancement. The 10-min postcontrast image (*d*) shows some centripetal enhancement with peripheral washout resulting in a low-signal-intensity outer border. Chronic obstruction of the left renal collecting system is caused by entrapment of the ureter in the pelvis by the carcinoma arising in the sigmoid colon.

Fat-suppressed T2-weighted ETSE (*e*) and immediate (*f*) and 2-min (*g*) postgadolinium SGE images in a second patient. A 14-cm

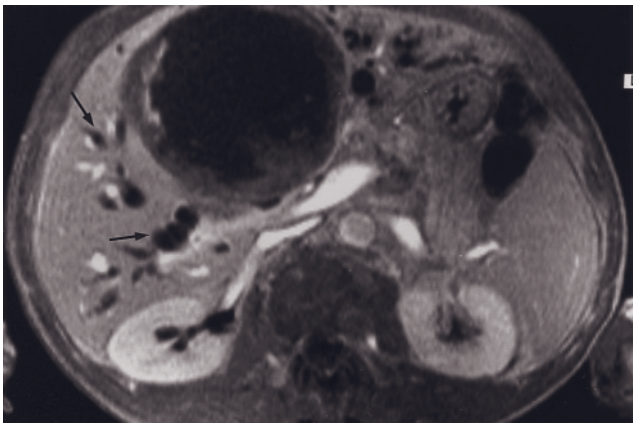

(*g*)

FIG. 2.105 (*Continued*) metastasis superinfected by *Listeria* is present in the left lobe of the liver. The infected metastasis is heterogeneous and high in signal intensity on T2-weighted image (*e*) and demonstrates enhancement of the thick irregular wall on the immediate postgadolinium image (*f*), with progressive enhancement on the interstitial-phase image (*g*). Additional metastases <1 cm are evident only on the immediate postgadolinium images (arrow, *f*). The mass causes obstruction of the biliary tree at the level of the porta hepatis, resulting in substantial intrahepatic biliary dilatation (arrows, *g*).

critical molecular alterations to become established in the genome [170]. Therefore, HCC is much more common in individuals with chronic liver disease, such as chronic viral hepatitis and cirrhosis, than it is in the population at large [169].

Statistics from the National Liver Cancer Network reveal that 87% of patients with HCC have underlying chronic liver disease and 52% have hepatitis C virus [171]. In part because of the increasing incidence of hepatitis C infection, HCC is the fastest growing malignancy in the U.S. [171]. Although cirrhosis of any etiology increases the risk of developing HCC, cirrhosis from viral hepatitis, alcohol, or hereditary hemochromatosis carries significantly more increased risk [170, 172, 173].

From a pathologic perspective, HCC forms soft, hemorrhagic, occasionally bile-stained nodules and masses with a propensity for necrosis [2]. On gross inspection, HCC may present as a single mass, as multiple nodules, as diffuse liver involvement, or as a large mass replacing most of the liver. In our experience, on MRI HCC is solitary in approximately 50% of cases (fig. 2.106), multifocal in approximately 40% (figs. 2.107 and 2.108), and diffuse in less than 10% of cases.

Histologically, malignant cells usually form trabeculae or plates of varying thickness, separated by a rich network of sinusoidal spaces filled with arterial blood. HCCs are fed by the hepatic arterial blood supply, but both hepatic and portal veins proliferate alongside tumors and cavernous structures develop in collaterals. As a consequence of these intrahepatic vascular changes, intra- and extrahepatic spread may occur by a number of routes including hepatic veins, inferior vena cava, and portal system (figs. 2.109–2.112).

Detection and characterization of focal liver lesions by imaging examination are closely related to the tumor size. Several reports describe the sensitivity and specificity of CT and MRI in the depiction of HCCs. The results vary widely, presumably because of the high frequency of bias in these studies, including the bias of greater experience with one or other modality. In general, there is a consensus that MRI is superior to CT in the detection of HCC, especially tumors that are <2.0 cm. (figs. 2.113 and 2.114) [174–179]. The superiority of MR imaging to detect and characterize liver lesions is due to its inherent excellent contrast resolution, combination of multiplanar T2- and T1-weighted images, and serial dynamic imaging after gadolinium administration. All sequences are necessary because tumors vary in signal intensity on non-contrast images [143, 180, 181], and this combination of sequences increases observer confidence.

A retrospective analysis examined the rate of HCC undetected by MRI in a large medical center transplant service over a 1-year period [182]. After review of imaging studies and pathologic diagnoses in explanted livers, there were 4 cases out of 279 MRI examinations in which HCC was not detected by MRI. Explanations for the presence of HCC undetected by MRI included patient motion, the misclassification of HCC as high-grade dysplastic nodules, and isovascular HCC. These results show the outstanding performance of MRI in detecting HCC.

Small HCCs (<2 cm) are frequently isointense on T2-weighted images [183–187]. Isointensity on T2-weighted images may correlate with a more favorable histology for well-differentiated HCC (fig. 2.115) [188]. Signal intensity on T1-weighted image varies from moderately low to moderately high signal. High signal intensity on T1-weighted images may reflect the presence of fat or protein (figs. 2.116 and 2.117) [185, 188, 189]. The majority of HCCs do not contain fat, and high protein content is most commonly responsible for the high signal intensity of these lesions (fig. 2.118) [189]. The most sensitive sequence for detecting small HCCs is hepatic arterial dominant-phase images, in which the majority of small tumors will enhance moderately; and not uncommonly these tumors may only be apparent

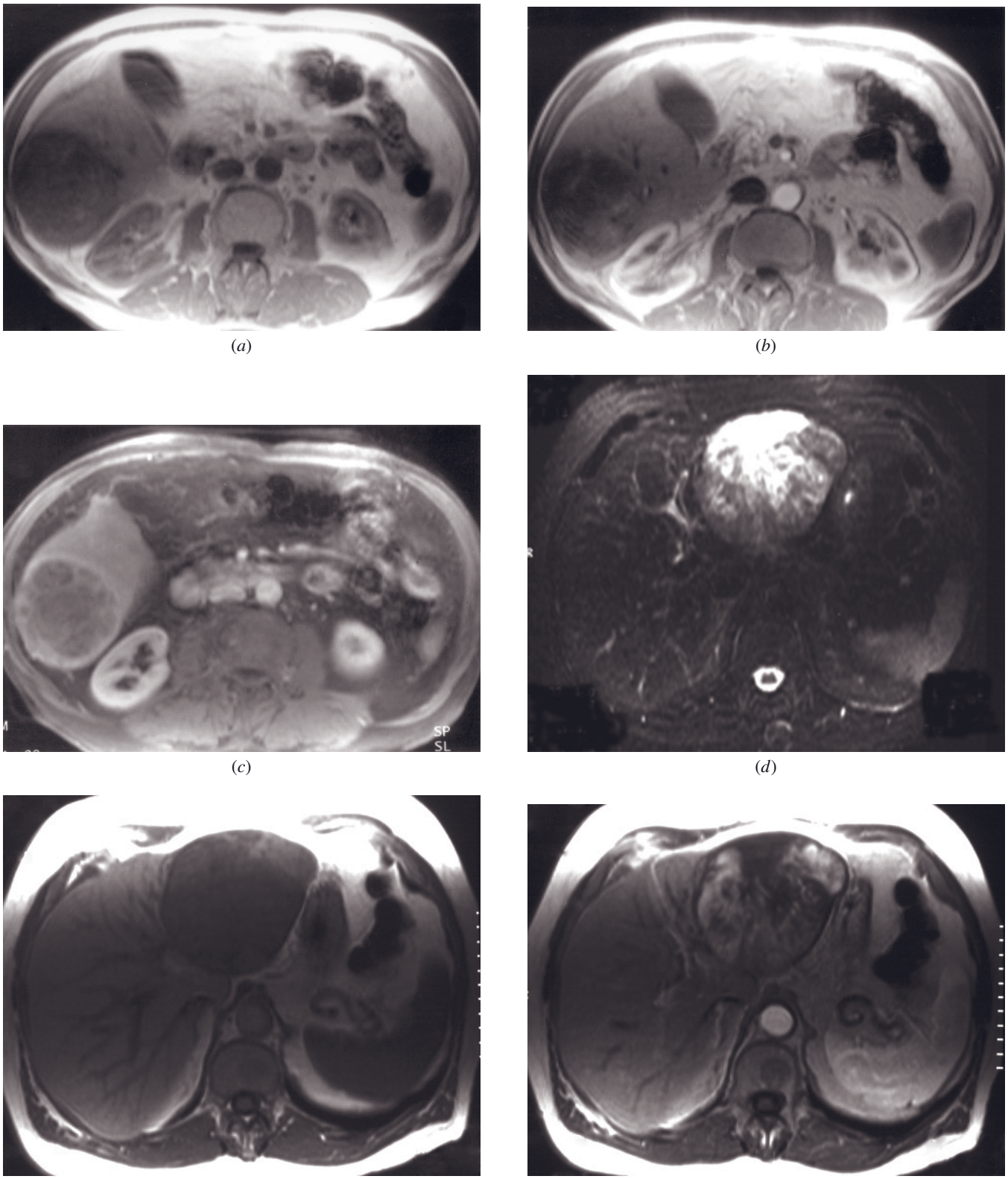

FIG. 2.106 Hepatocellular carcinoma, solitary hypovascular tumor. SGE (*a*) and immediate (*b*) and 90-s fat-suppressed (*c*) postgadolinium SGE images. There is an 8-cm mass arising from the inferior aspect of the right lobe that is low signal on the T1-weighted image (*a*) and demonstrates minimal heterogeneous enhancement immediately after gadolinium administration (*b*) and late mild and heterogeneous enhancement with a pseudocapsule (*c*) consistent with hypovascular HCC.

Fat-suppressed T2-weighted SS-ETSE (*d*), SGE (*e*), and immediate (*f*) and 90-s fat-suppressed (*g*) SGE images in a second patient with a small HCC that shows minimal tumor enhancement after contrast administration (*f*), consistent with hypovascular HCC.

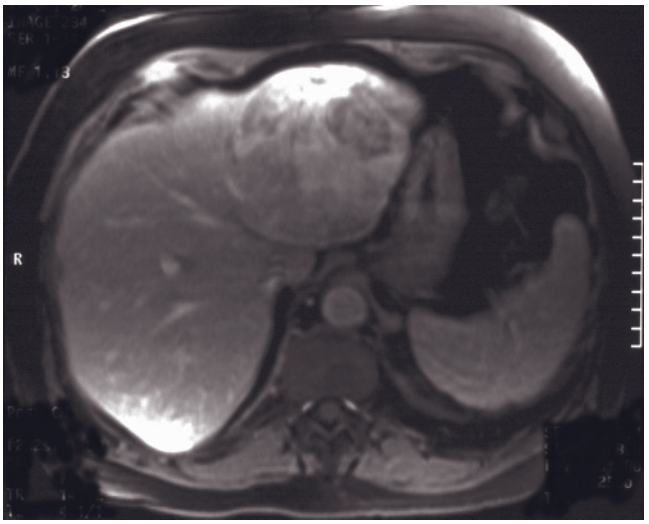

FIG. 2.106 (*Continued*) (*g*)

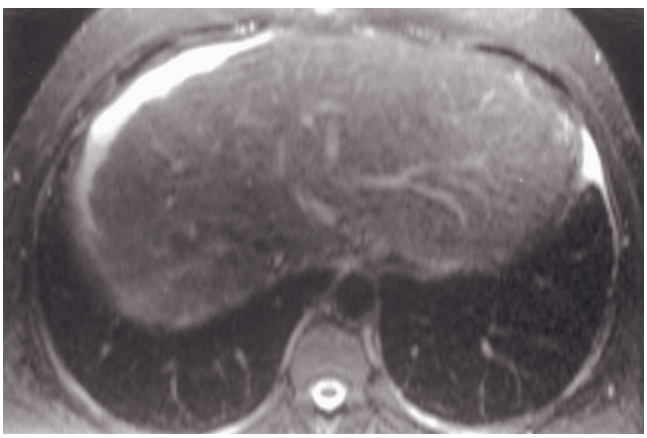

(*a*)

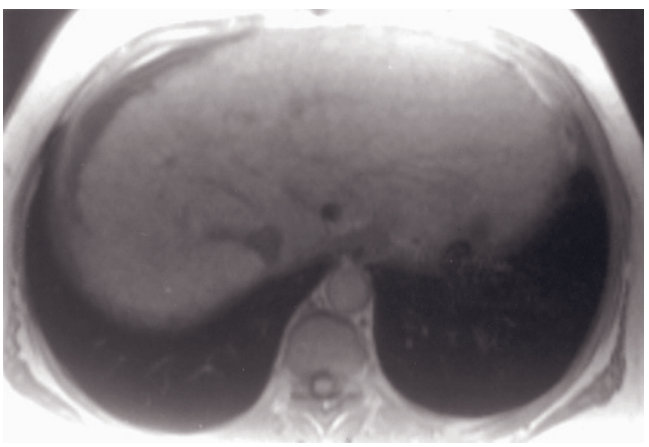

(*b*)

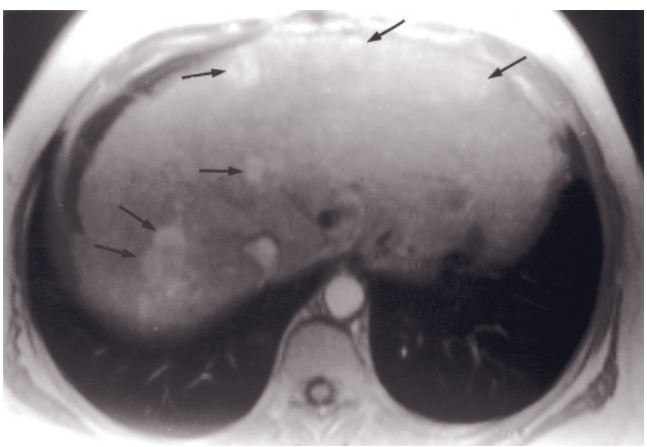

(*c*)

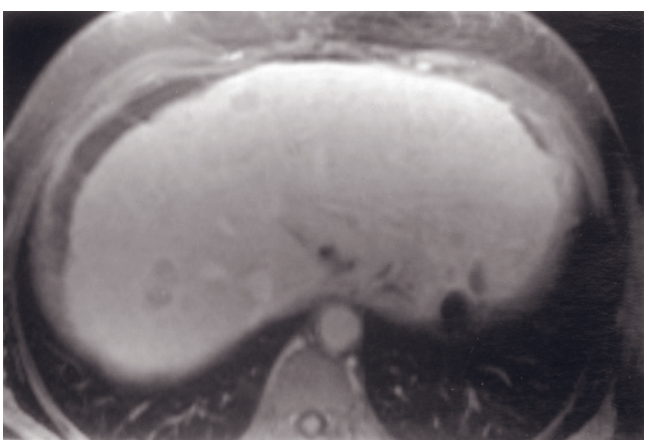

(*d*)

FIG. 2.107 Multifocal small HCC. Echo-train STIR (*a*), SGE (*b*), and immediate (*c*) and 90-s fat-suppressed (*d*) postgadolinium SGE images. There are multiple small HCCs (arrows, *c*) scattered throughout the hepatic parenchyma. These lesions are isointense on T2 (*a*)- and T1 (*b*)-weighted images and show homogeneous moderate enhancement after contrast administration (*c*) and lesion washout with pseudocapsule enhancement on late images (*d*).

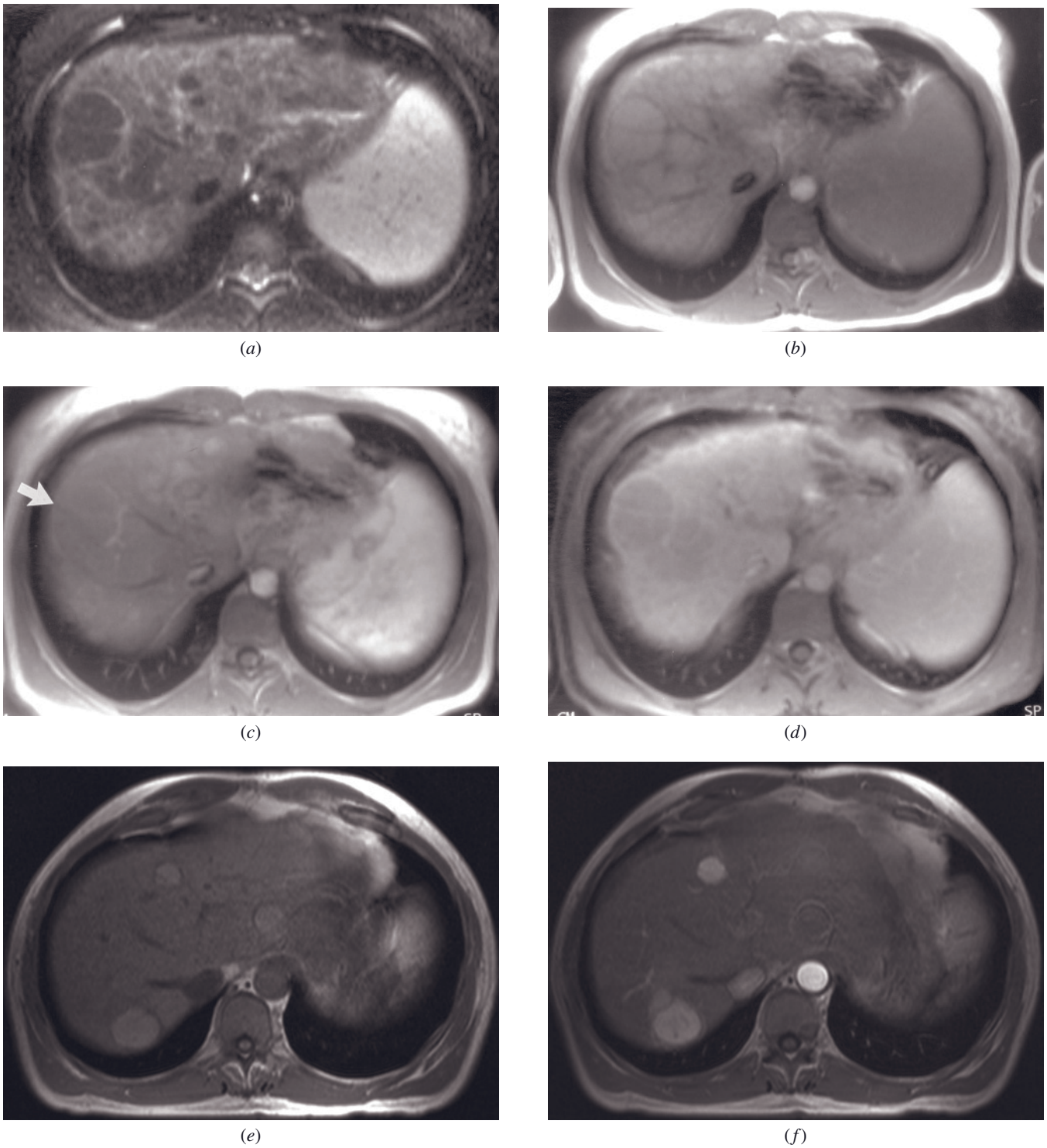

FIG. 2.108 Multifocal HCC. Echo-train STIR (*a*), SGE (*b*), and immediate (*c*) and 90-s fat-suppressed (*d*) postgadolinium SGE images. Multiple HCCs are present that are moderately hypointense on T2 (*a*)- and mildly hyperintense on T1 (*b*)-weighted images. The smaller lesions possess mildly intense homogeneous enhancement, and the 4-cm tumor (arrow, *c*) shows isointense enhancement immediately after gadolinium administration (*c*). Lesional washout along with pseudocapsule enhancement is observed on interstitial-phase images (*d*).

SGE (*e*) and immediate (*f*) and 90-s fat-suppressed (*g*) postgadolinium SGE images in a second patient. There are multiple rounded lesions that show mildly high signal intensity on T1-weighted images (*e*), intense enhancement on early-phase images (*f*),and washout with capsular enhancement on late-phase images (*g*), compatible with mutifocal HCC.

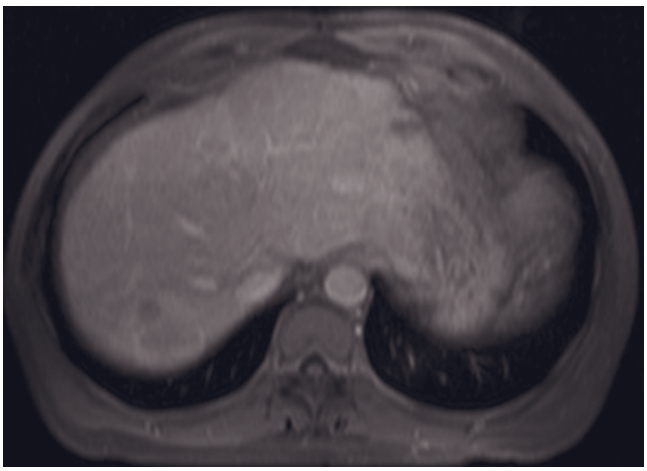

(*g*)

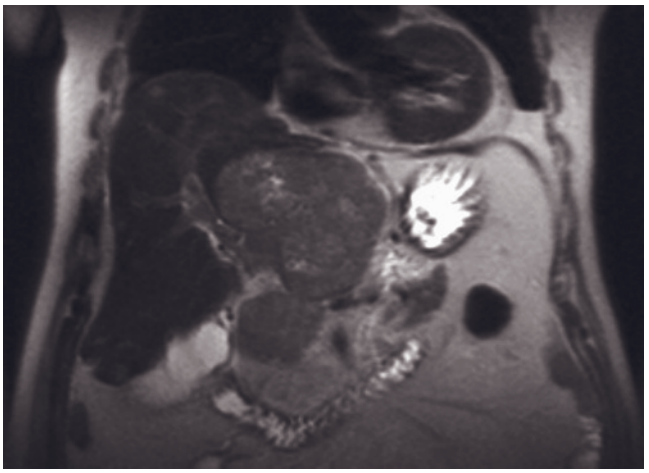

(*h*)

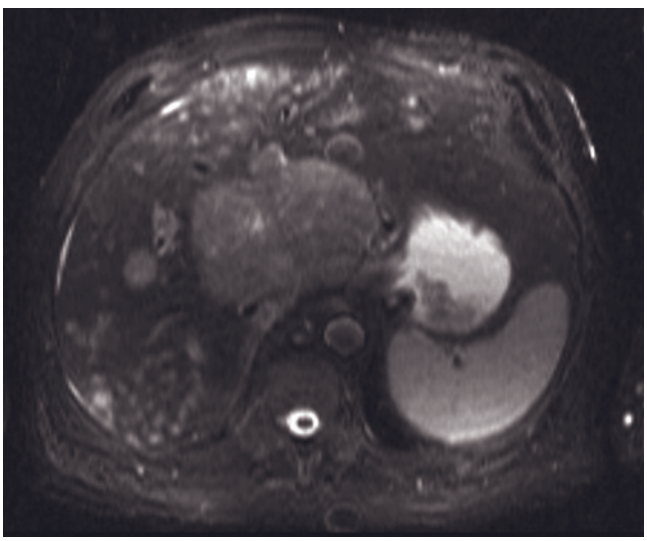

(*i*)

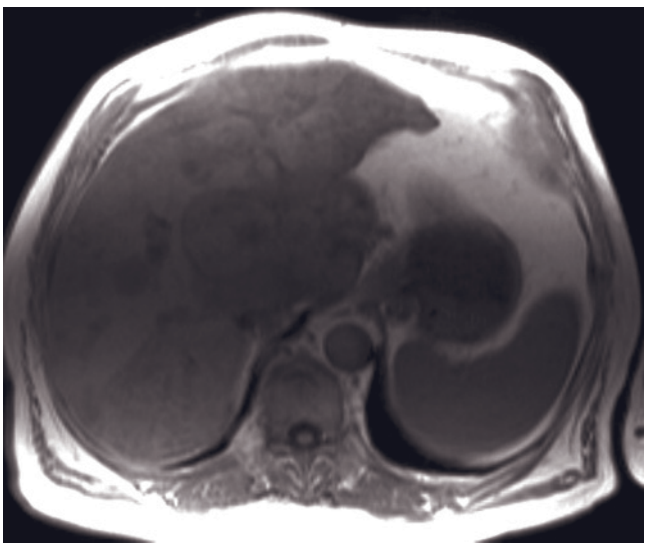

(*j*)

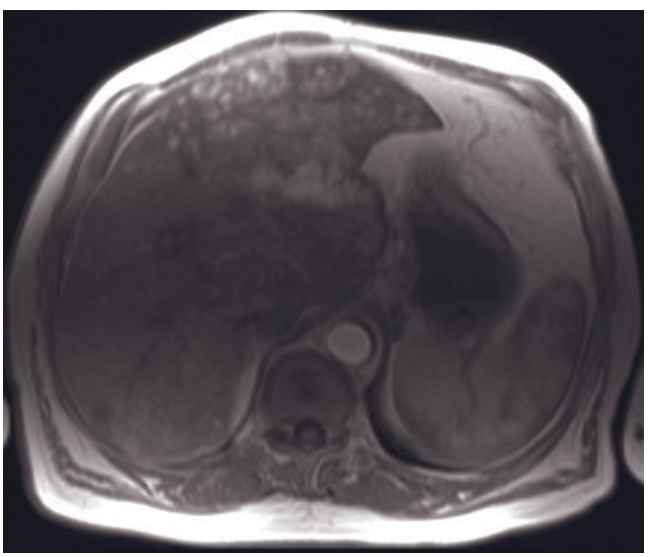

(*k*)

FIG. 2.108 (*Continued*) Coronal (*h*) and transverse (*i*) fat-suppressed T2-weighted SS-ETSE, SGE (*j*), and immediate (*k*) and 90-s fat-suppressed (*l*) postgadolinium SGE images in a third patient. There is a mass in the porta hepatis that demonstrates mildly high signal intensity on the T2-weighted image (*h*, *i*), mildly low signal intensity on the T1-weighted image (*j*), and partial enhancement on the early-phase image (*k*) that progresses over time. On the late-phase image (*l*) the mass demonstrates washout with capsule enhancement, which is compatible with HCC. Additional multiple small lesions are scattered throughout the hepatic parenchyma, consistent with multifocal HCCs.

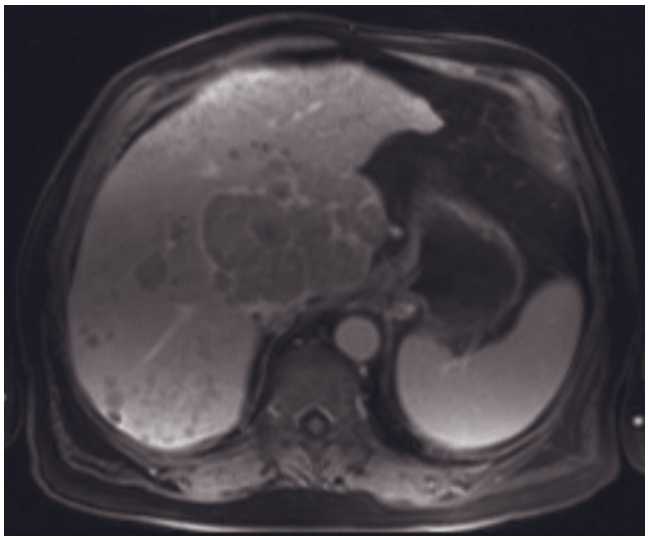

(*l*)

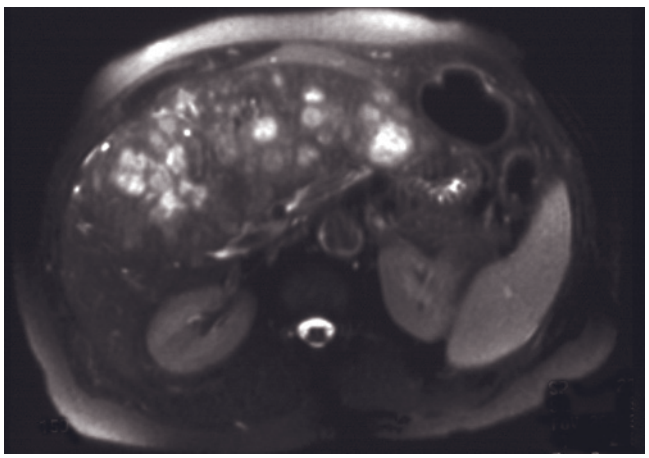

(*m*)

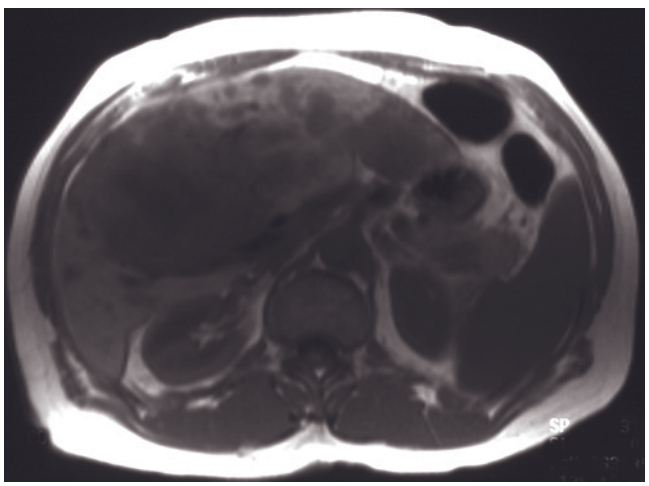

(*n*)

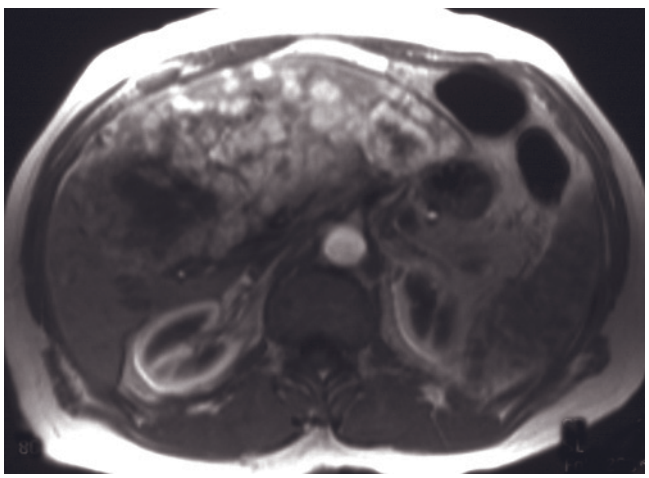

(*o*)

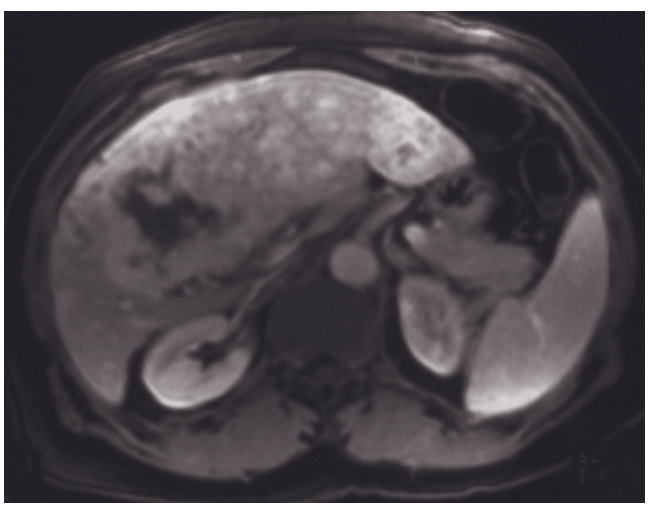

(*p*)

FIG. 2.108 (*Continued*) T2-weighted SS-ETSE (*m*), SGE (*n*), and immediate (*o*) and 90-s fat-suppressed (*p*) postgadolinium SGE images in a fourth patient show similar findings.

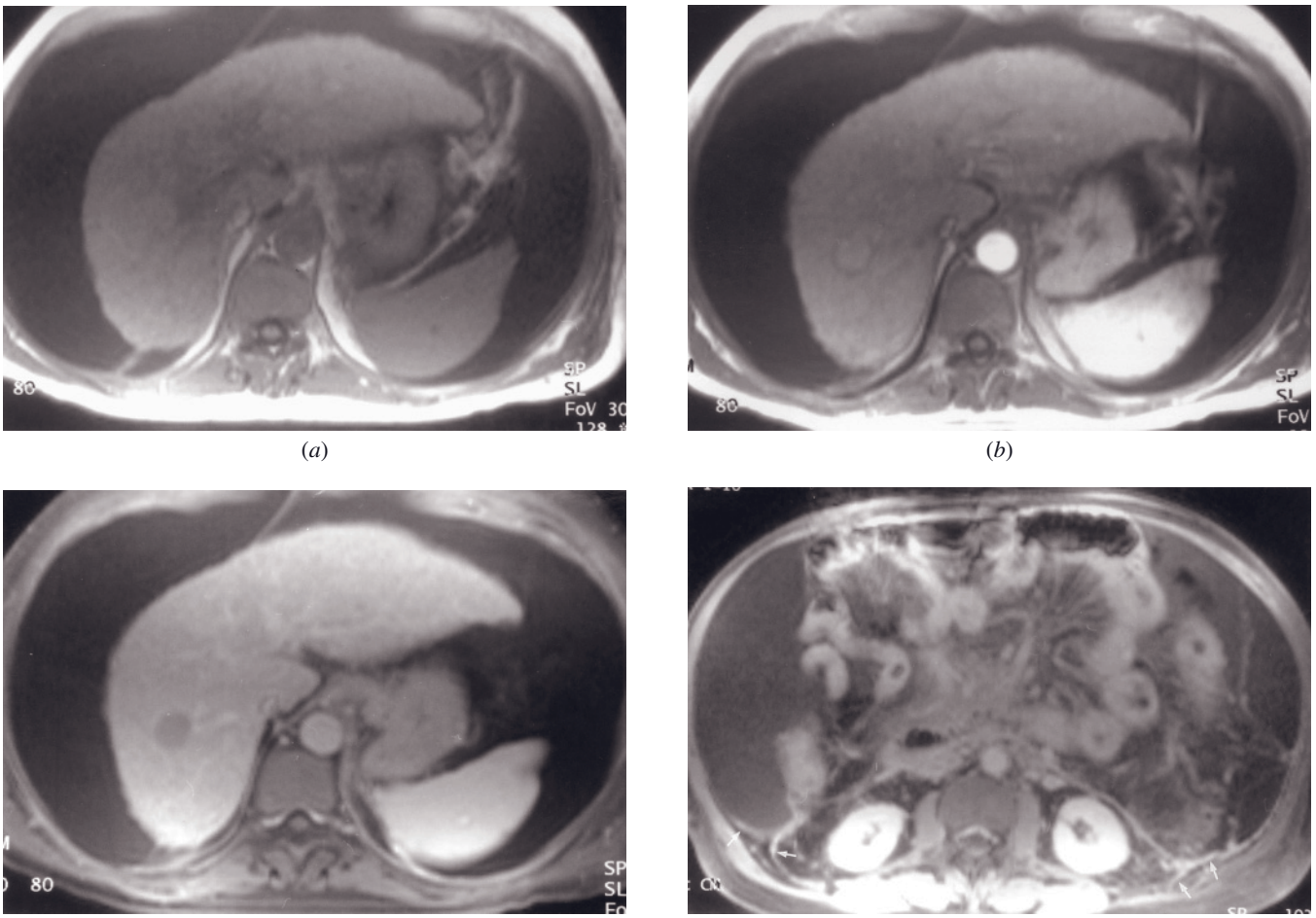

FIG. 2.109 HCC and microvarices in peritoneum. SGE (*a*) and immediate (*b*) and 90-s fat-suppressed (*c*, *d*) postgadolinium images. There is a 2-cm tumor centrally located in the right hepatic lobe that is not seen on the precontrast image (*a*) and demonstrates homogeneous moderate enhancement on the immediate postcontrast image (*b*) with washout and capsular enhancement on the late image (*c*), consistent with a small HCC. Note extensive varices throughout the peritoneal cavity (arrows, *d*). Varices typically show extension of small curvilinear structures deep to the peritoneum, as observed in this patient. Peritoneal metastases stay confined to the peritoneal surface and within the peritoneal cavity. A small well-defined central HCC, as in this patient, would also not be expected to have peritoneal metastases. Note the micronodular contour of the liver and the large volume of ascites.

on this set of images[183, 190, 191]. Intense enhancement revealed on early-phase images is not specific to HCC as high-grade DNs may also show similar findings. Rarely, small HCCs may be hypovascular, shown by minimal extent of enhancement on arterial dominant-phase images (fig. 2.119) [181, 183]. Isovascular HCCs on arterial-phase images have been reported, and attention should be paid to interstitial-phase images that may show washout of the tumors with capsule enhancement [182, 192]. At present it is not known how often washout and late capsule enhancement are observed in small hypo- or isovascular HCCs.

The distinction between small hypovascular HCC with washout and late capsule enhancement on interstitial-phase images must be made from regenerative liver surrounded by fibrosis. Late enhancement of fibrosis generally appears as reticular stromal with more angular margins and is also part of an extensive pattern in the liver of similar findings, whereas the capsule of HCCs is more rounded, and the appearance is distinctly different from surrounding bands of fibrous tissue (if fibrosis is present); for example, the capsule may be thicker or enhance more intensely.

Large HCC (≥2-cm) may range from hypo- to hyperintensity on T2- and T1-weighted images. The most frequent appearance is mildly high signal intensity on T2-weighted images and minimally low signal intensity on T1-weighted images [180, 181, 184–186, 193–196]. The hyperintensity on T2-weighted images and hypointensity on T1-weighted images are highly suggestive of moderately differentiated HCC [188]. The primary hepatic origin of HCC presumably results in a blood

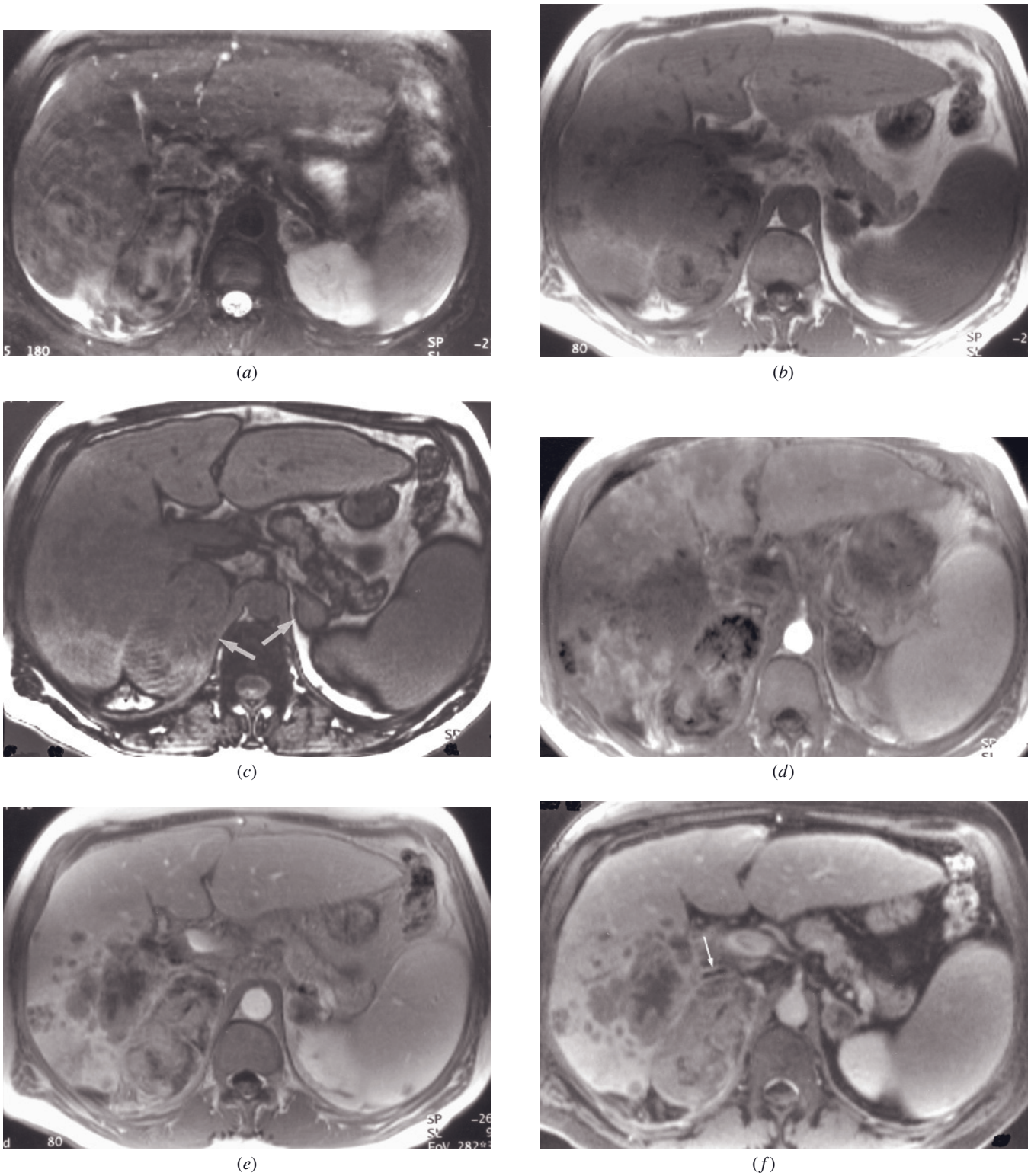

FIG. 2.110 HCC and adrenal metastases. Fat-suppressed T2-weighted ETSE (*a*), SGE (*b*), out-of-phase SGE (*c*), and immediate (*d*), 45-s (*e*), and 90-s fat-suppressed postgadolinium SGE (*f*) images. There are multiple lesions throughout the liver, which are high signal on T2 (*a*) and low signal on T1 (*b*) and demonstrate a mixed population of lesions that enhance in a diffuse heterogeneous or peripheral ring fashion on immediate postgadolinium images (*d*), consistent with multifocal HCC. Ring enhancement in many of these lesions presumably represents intrahepatic metastases. Bilateral adrenal masses (arrows, *c*) are present that demonstrate mixed signal intensity on T1 (*b*), do not drop in signal on out-of-phase (*c*), and enhance heterogeneously after contrast administration (*d–f*) consistent with metastases. Abnormal signal in the IVC (arrow, *f*) represents thrombus.

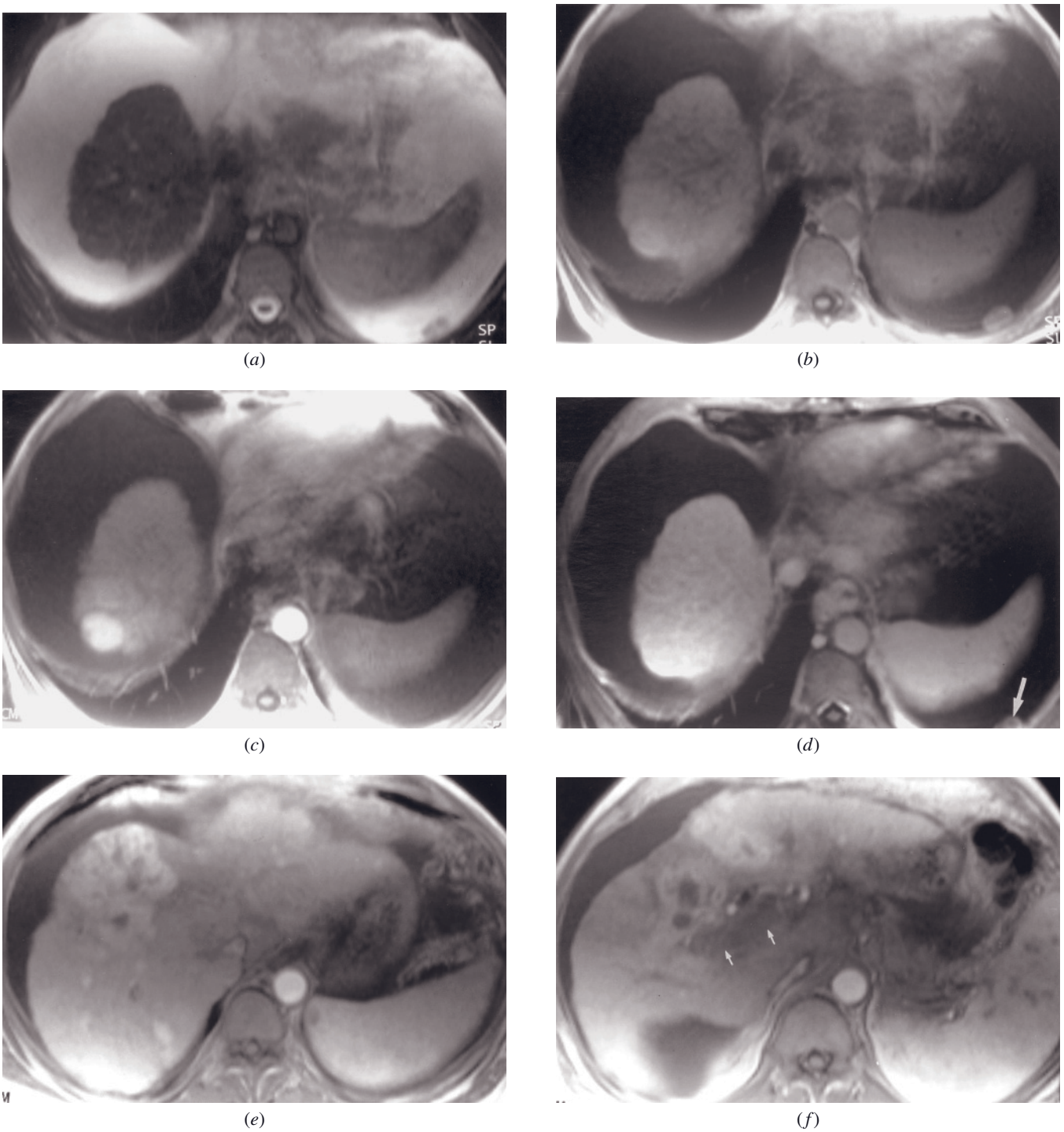

FIG. 2.111 HCC with peritoneal spread. Fat-suppressed T2-weighted SS-ETSE (*a*), SGE (*b*), and immediate (*c*) and 90-s fat-suppressed postgadolinium SGE (*d*) images. The liver is small and irregular in contour, compatible with cirrhosis. There is a small exophytic HCC in the right hepatic lobe that demonstrates isointensity on T2 (*a*), slight hyperintensity on T1 (*b*), intense enhancement immediately after contrast administration (*c*), and washout with capsular enhancement on the late image (*d*), consistent with HCC. Note the peritoneum-based mass (arrow, *d*) in the left upper abdomen, near the spleen, consistent with a peritoneal metastasis from HCC.

Immediate (*e*, *f*) and 90-s fat-suppressed postgadolinium SGE (*g*) images in a second patient. The liver is nodular in contour and demonstrates a reticular pattern of enhancement compatible with cirrhosis. There is a large HCC in the dome of the liver that bulges the liver contour and shows intense heterogeneous enhancement immediately after gadolinium (*e*, *f*). Other smaller HCCs are also identified. Note that the main portal vein is expanded with tumor thrombus (arrows, *f*). Peritoneal thickening and enhancement is observed within the paracolic gutters (arrows, *g*), consistent with peritoneal metastases.

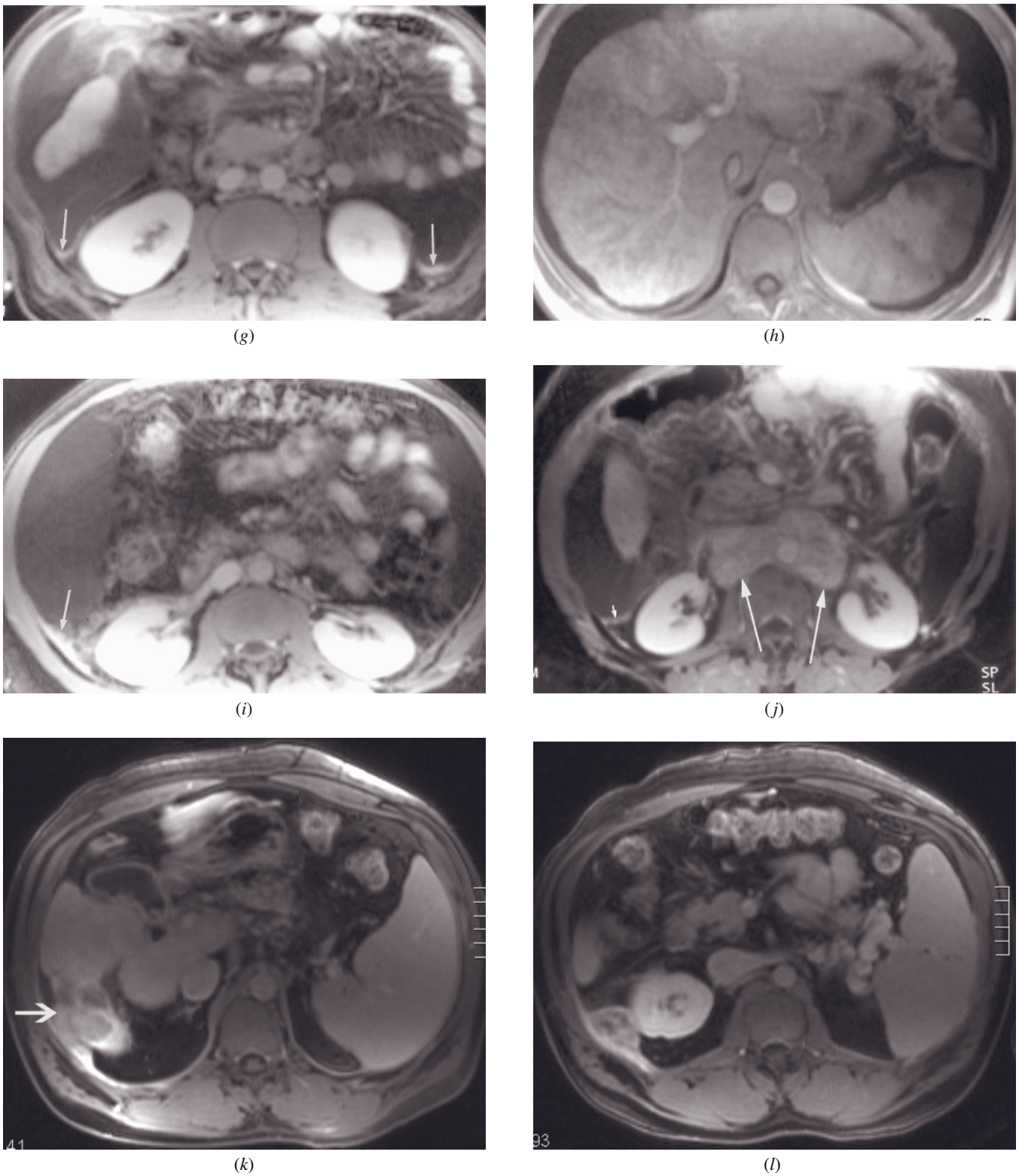

FIG. 2.111 (*Continued*) Immediate (*h*) and 90-s fat-suppressed postgadolinium SGE (*i*) images in a third patient. There is heterogeneous mottled enhancement of the hepatic parenchyma after the administration of gadolinium, consistent with diffuse HCC. Note the infiltrative peritoneal thickening and enhancement compatible with small tumoral implants (arrow, *i*).

Transverse 90-s fat-suppressed postgadolinium SGE image (*j*) in a fourth patient. This patient with HCC has thickening of the peritoneum in the right paracolic gutter (small arrow, *j*) and multiple, enlarged aortocaval and retroaortic lymph nodes (long arrows, *j*).

90-s fat-suppressed postgadolinium SGE images (*k*, *l*) in a fifth patient show nodular peritoneal metastases from HCC.

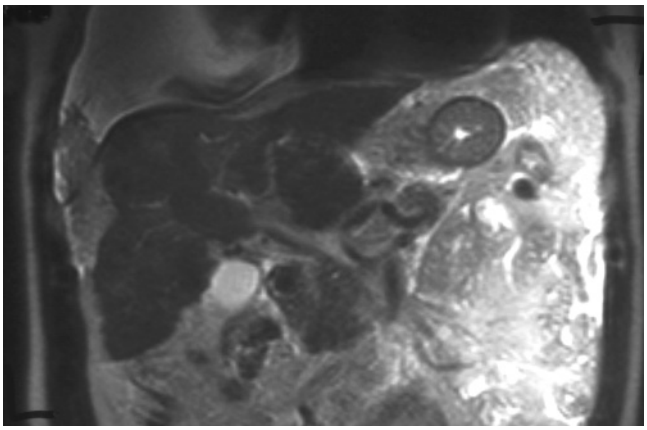

FIG. 2.112 HCC with pleural metastases. Coronal T2-weighted SS-ETSE image shows tumor extension through the diaphragm resulting in pleural metastases.

supply similar to and in continuity with background liver, explaining the diffuse heterogeneous enhancement on arterial dominant-phase images [143, 197, 198]. In the interstitial phase, large HCCs tend to demonstrate washout below the signal intensity of background parenchyma, and capsule enhancement, which may only be apparent around some portions of the tumor (fig. 2.120) [183].

It is postulated that small well-differentiated HCCs are vascularized by a mixture of arterial and portal blood supply, with predominance of arterial supply, while moderate and poorly differentiated HCCs are supplied only by hepatic arteries [199–201]. In a previous study [202], the authors demonstrated a correlation between the presence of vascular endothelial growth factor (VEGF) in hepatic nodules and high signal intensity on T2- and T1-weighted images, but a similar relationship was not shown with the degree of enhancement on arterial dominant-phase and interstitial-phase images. The authors postulated that VEGF is present in highest concentration early in the process of transformation of large regenerative or dysplastic hepatic nodules into well-differentiated HCCs in order to stimulate vessel growth. VEGF may then be downregulated at the last stages of development into hypervascular HCC (fig. 2.121–2.123).

Important ancillary features of HCC include late capsule enhancement and venous thrombosis [203]. In histopathologic analysis, 60–87% of large HCC have a fibrosis tumor capsule [204]. The typical signal intensity of a capsule is mild hyperintensity on T2-weighted images, hypointensity on T1-weighted images, and negligible mild enhancement on immediate postgadolinium images that becomes more intense on interstitial phase images (fig. 2.124).

Tumor extension occurs most commonly into portal veins (figs. 2.125 and 2.126); however, hepatic venous extension also occurs (fig. 2.127). Although tumor thrombus is observed in fewer than 50% of cases, it is common in the setting of large and advanced tumors. The appearance on hepatic arterial dominant-phase gadolinium-enhanced images often permits distinction between HCC and metastatic disease when tumors are ≥1.5 cm in diameter, because HCCs typically demonstrate enhancing stroma throughout the entire tumor, whereas metastases have ring enhancement [143]. However, there is an overlap of MR features between small HCCs (<1.5 cm) and hypervascular metastases. Both entities commonly show homogeneous moderate or intense enhancement on arterial dominant phase and lesional washout on late phase. The presence of capsule enhancement on late phase and the presence of underlying chronic hepatic disease or cirrhosis are supportive features of HCC. Ring enhancement observed on hepatic arterial dominant-phase images in HCCs, especially in patients with underlying hepatitis C, may represent an aggressive appearance of the neoplasm. Explosive growth has been observed in some of these tumors. The ring enhancement is a pattern of enhancement most typical for metastases, and its presence in HCCs may reflect a more aggressive blood supply, with recruitment of additional surrounding vessels to the tumor (fig. 2.128).

In the setting of viral hepatitis, the hepatic architecture tends to be less distorted than in patients with cirrhosis. As livers may not appear cirrhotic, a high index of suspicion for HCC is recommended in patients with focal liver masses and underlying viral hepatitis.

Higher doses of gadolinium or higher flow rates may improve visualization of HCCs that may possess minimal increased vascularity [5]. Newer contrast agents with higher T1 relaxivity may aid in lesion detection of hypovascular, isovascular, or minimally hypervascular tumors. Also, new techniques such as parallel imaging may improve detection of HCCs in debilitated patients unable to suspend breathing for 20 s with conventional spoiled gradient echo sequences [205, 206].

Overlap exists between the appearance of high-grade dysplastic nodules and HCC, as HCC may also exhibit the classic appearance described for high-grade dysplastic nodules; which is near isointense on T2-weighted and noncontrast T1-weighted images and moderately intense enhancement on early postgadolinium images that fades to isointensity on late postgadolinium images. The great majority of these lesions can be correctly classified using the following ancillary features: 1) in the presence of a coexistent large HCC, the small lesions are more likely satellite HCCs; 2) interval growth of lesion by greater than 30% in transverse dimension in a 3-month interval is consistent with HCC;

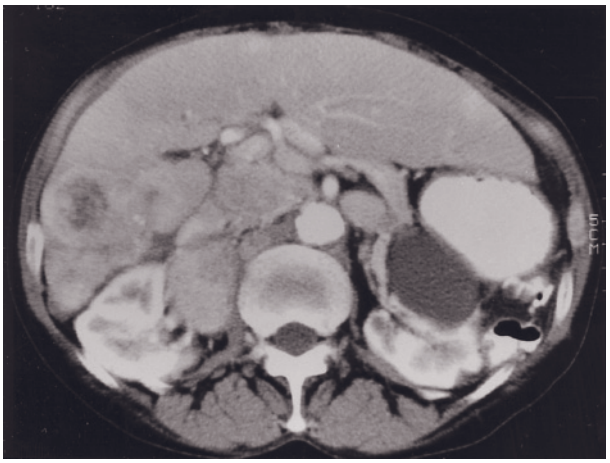

(*a*)

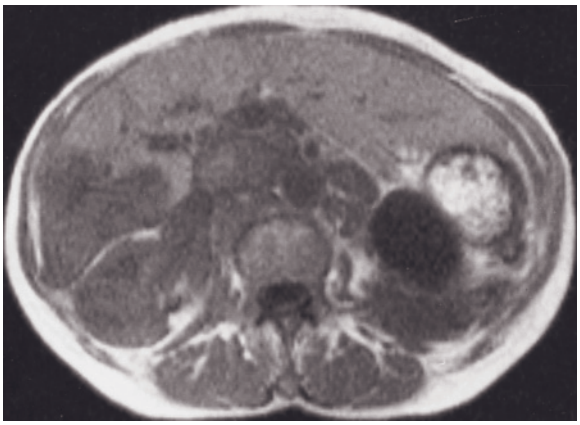

(*b*)

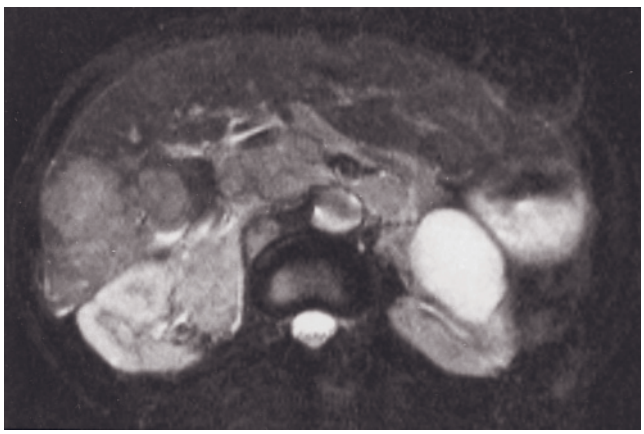

(*c*)

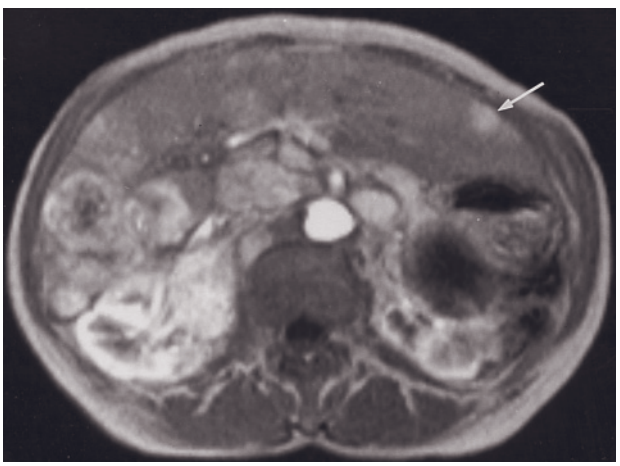

(*d*)

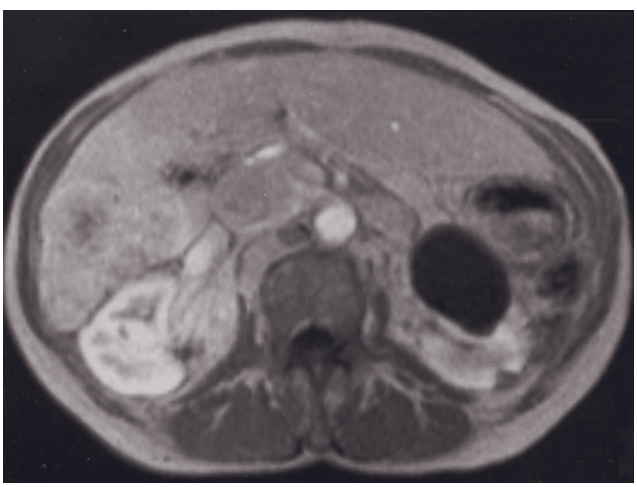

(*e*)

FIG. 2.113 Multifocal HCC with adenopathy—spiral CT imaging and MRI comparison. Spiral CT (*a*), SGE (*b*), fat-suppressed T2-weighted ETSE (*c*), and immediate (*d*) and 45-s (*e*) postgadolinium SGE images. On the CT image (*a*), an HCC is identified in the right lobe with multiple nodes in the porta hepatis and retroperitoneum. Precontrast SGE image (*b*) demonstrates the HCC as a moderately low-signal-intensity mass in the right lobe and the lymph nodes as moderately low in signal intensity. The T2-weighted image (*c*) demonstrates the tumor and lymph nodes as moderately high in signal intensity. On the immediate image (*d*), the HCC in the right lobe demonstrates intense diffuse heterogeneous enhancement. Multiple additional HCCs smaller than 1 cm are also apparent (arrow, *d*) that were not visible on spiral CT images (*a*) or on noncontrast T1 (*b*)- and T2 (*c*)-weighted images. The small HCCs wash out to isointensity with the liver by 45 s (*e*), at a time when renal CMD is still pronounced. Intense enhancement of the associated adenopathy is also present on the immediate postgadolinium image (*d*).

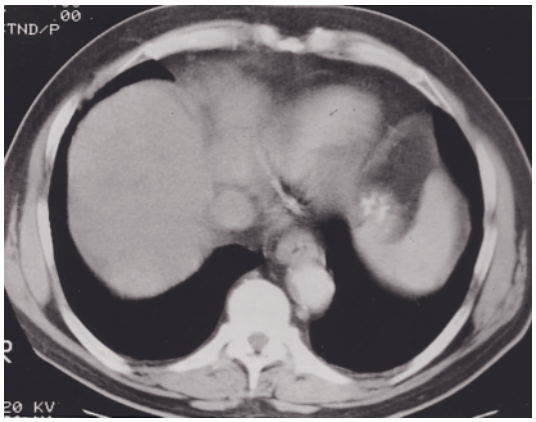

(*a*)

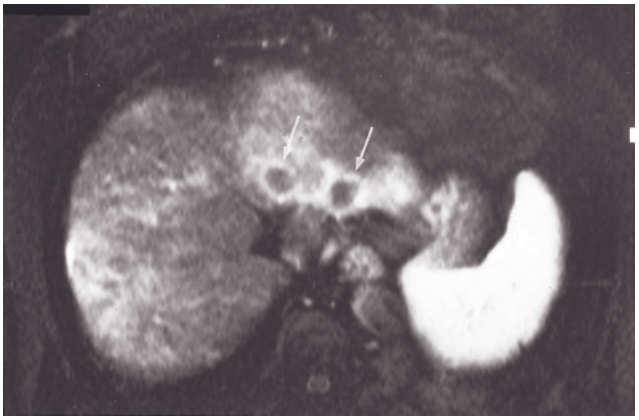

(*b*)

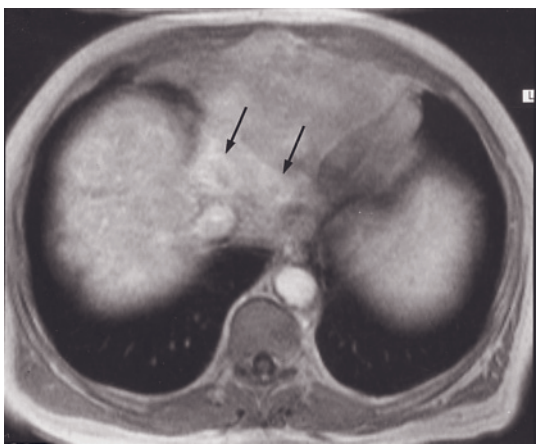

(*c*)

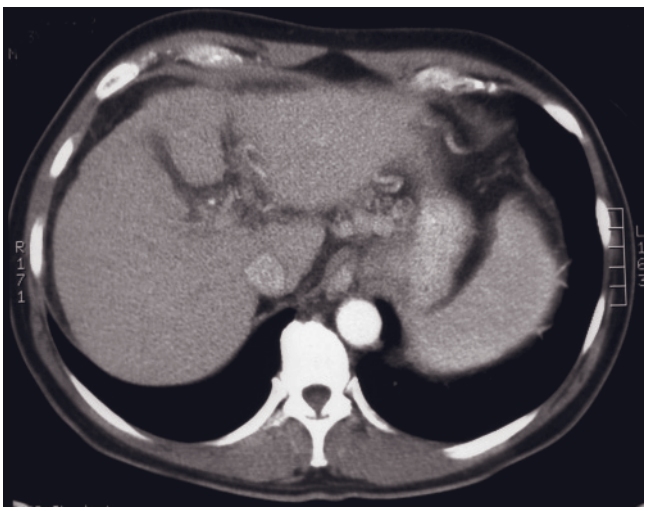

(*d*)

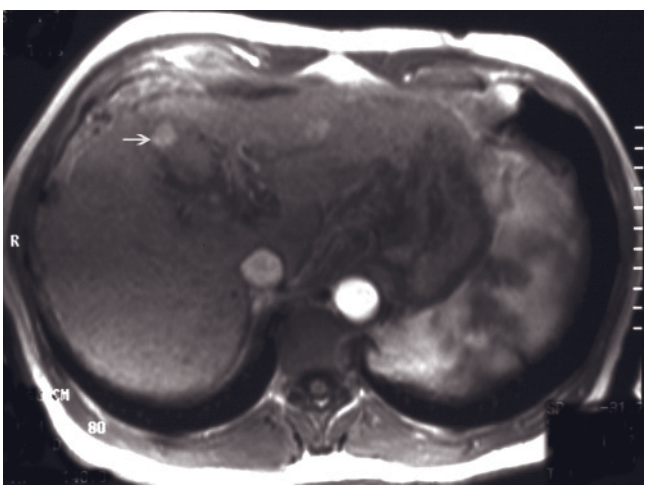

(*e*)

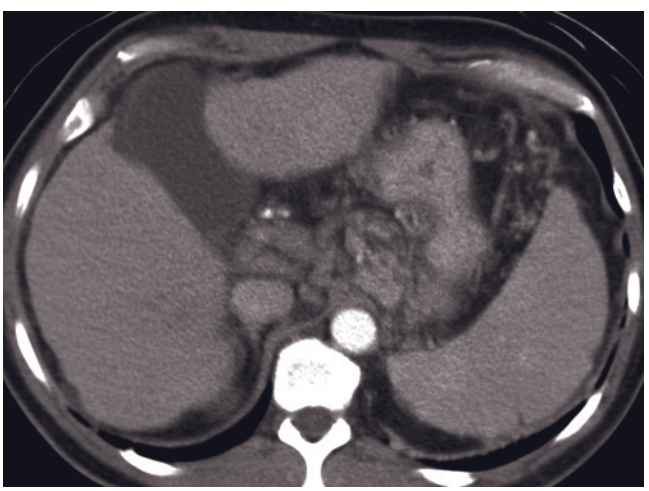

(*f*)

FIG. 2.114 Multifocal HCC-spiral and multidetector CT and MR comparison. Spiral CT (*a*), fat-suppressed T2-weighted ETSE (*b*), and immediate postgadolinium SGE (*c*) images. The spiral CT image demonstrates a solitary HCC in a patient with 8 HCCs shown on MRI tumors. No tumors are evident on CT at this tomographic level (*a*). The T2-weighted image (*b*) demonstrates two 1.8-cm HCCs at this level that have high-signal-intensity peripheral rims and are isointense centrally (arrows, *b*). On immediate postgadolinium image (*c*), these tumors enhance in a predominantly ring fashion (arrows, *c*).

Multidetector CT (*d*, *f*) and immediate postgadolinium SGE (*e*, *g*) images in a second patient at two tomographic levels. Note

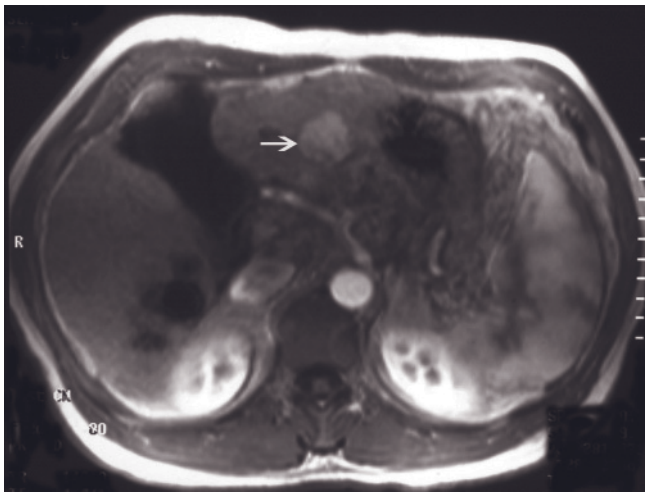

(*g*)

FIG. 2.114 (*Continued*) that the HCCs are more evident on early-phase postgadolinium MR images (arrow, *e, g*) than on the multidetector CT images.

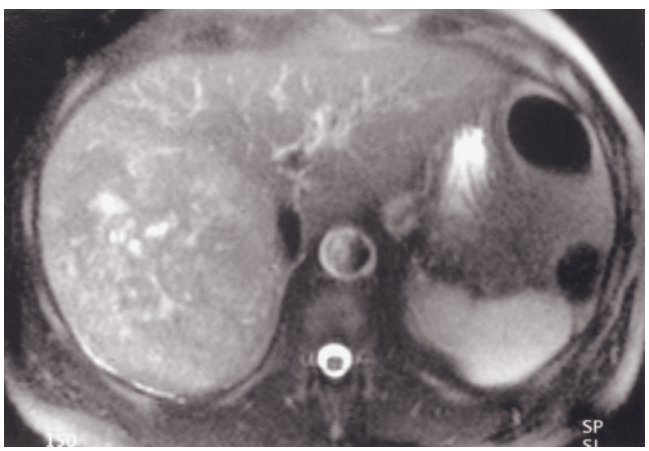

(*a*)

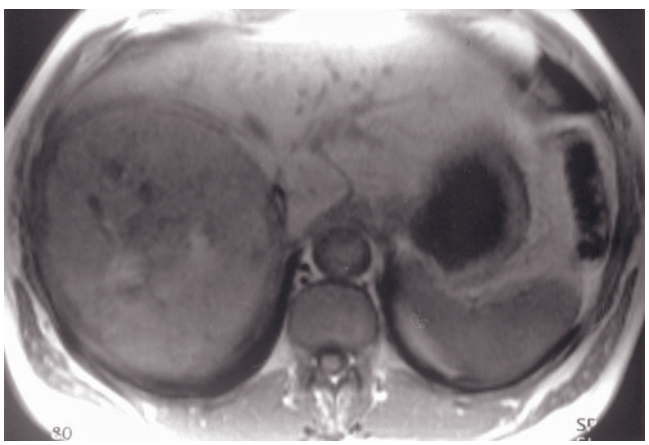

(*b*)

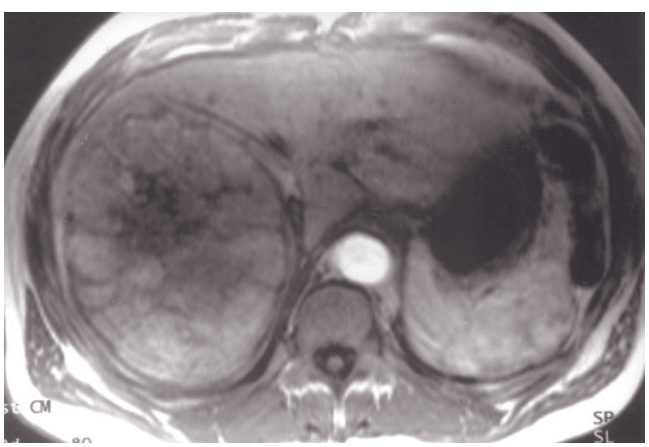

(*c*)

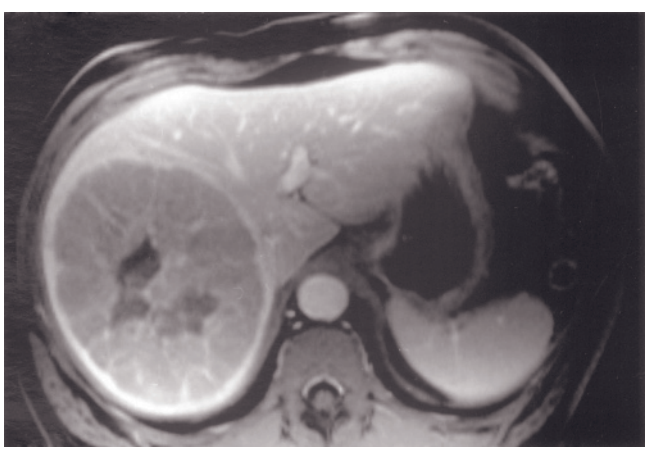

(*d*)

FIG. 2.115 Large well-differentiated HCC. Fat-suppressed T2-weighted SS-ETSE (*a*), SGE (*b*), immediate (*c*) and 90-s fat-suppressed (*d*) postgadolinium SGE images. There is a large well-defined mass in the right hepatic lobe that demonstrates slightly increased and heterogeneous signal intensity on T2 (*a*), moderately decreased signal intensity on T1 (*b*), heterogeneous enhancement on immediate postgadolinium images (*c*), and heterogeneous washout with late enhancement of a pseudocapsule (*d*).

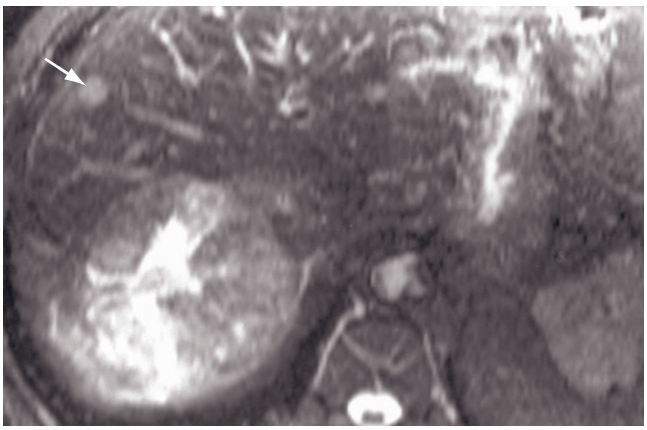

(*e*)

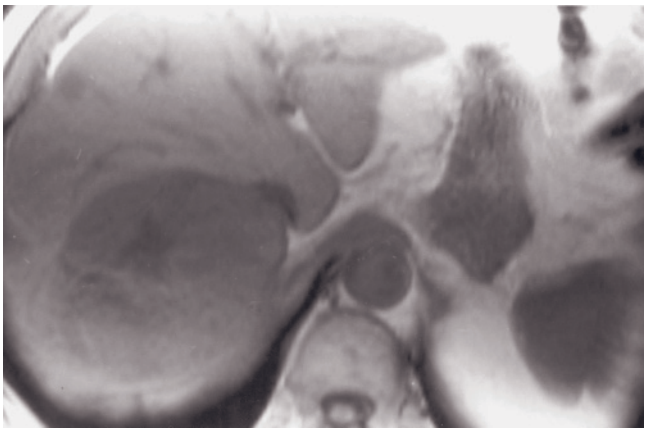

(*f*)

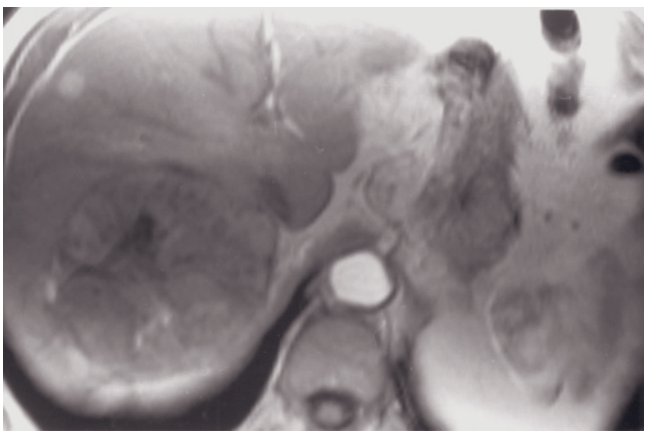

(*g*)

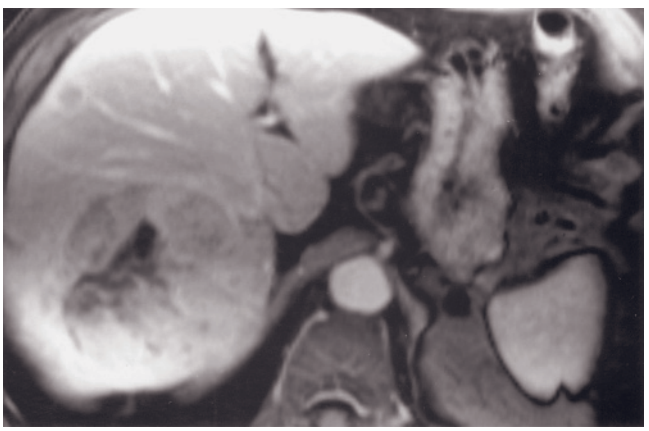

(*h*)

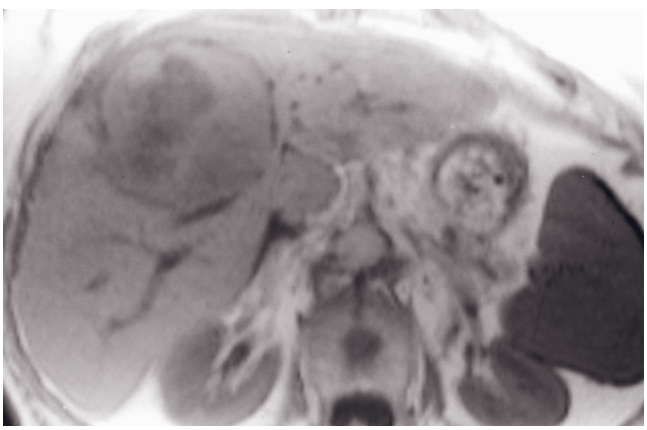

(*i*)

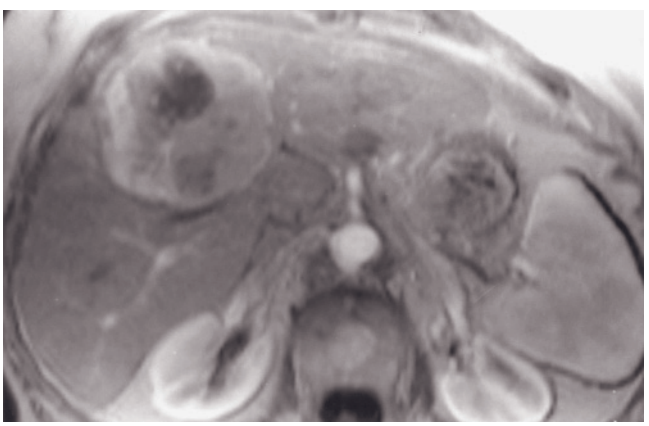

(*j*)

FIG. 2.115 (*Continued*) Echo-train STIR (*e*), SGE (*f*), and immediate (*g*) and 90-s fat-suppressed (*h*) postgadolinium SGE images in a second patient. There is a large mass in the right hepatic lobe that is moderately and heterogeneously hyperintense on T2-weighted image (*e*) and mildly hypointense on T1-weighted image (*f*) and demonstrates heterogeneous enhancement on immediate postgadolinium images (*g*) and washout with pseudocapsular enhancement on late image (*h*). Note a small satellite lesion (arrow, *e*) that exhibits high signal on T2 (*e*), low signal on T1 (*f*), homogeneous intense enhancement on hepatic arterial dominant phase (*g*), and washout with pseudocapsule enhancement on late image (*h*). Both lesions are consistent with HCC.

SGE (*i*) and immediate (*j*) and 90-s fat-suppressed (*k*) postgadolinium SGE images in a third patient. There is a large HCC that demonstrates heterogeneous mainly hypo- to isointense signal on T1 (*i*), heterogeneous enhancement immediately after contrast administration (*j*), and washout with an enhanced pseudocapsule on late images (*k*), consistent with HCC.

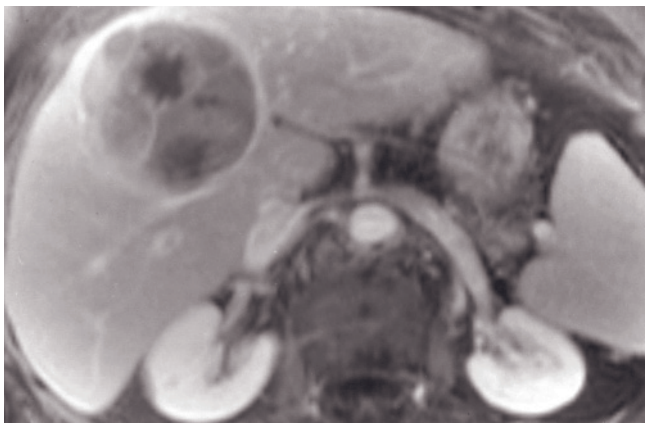

(*k*)

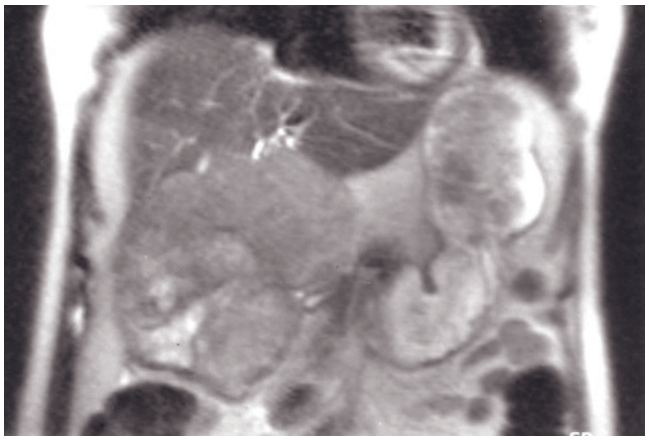

(*l*)

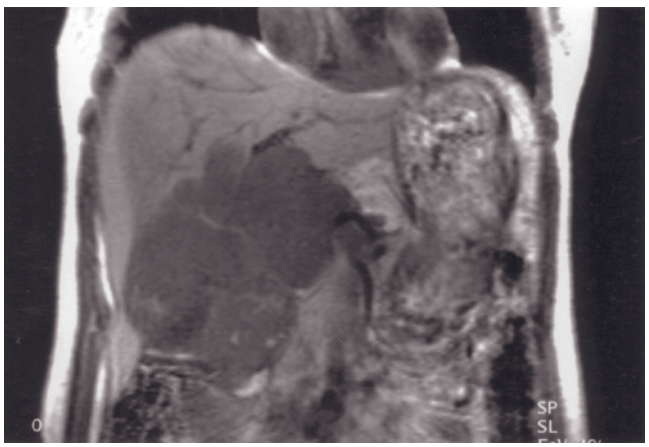

(*m*)

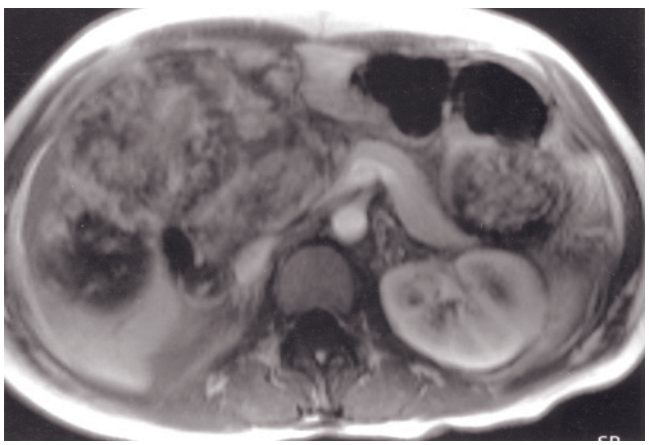

(*n*)

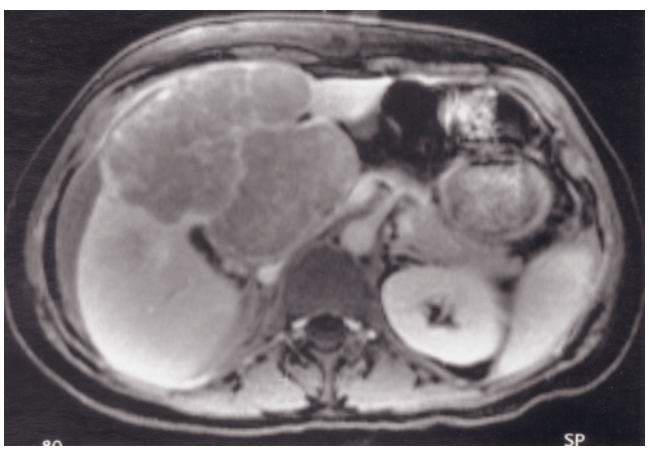

(*o*)

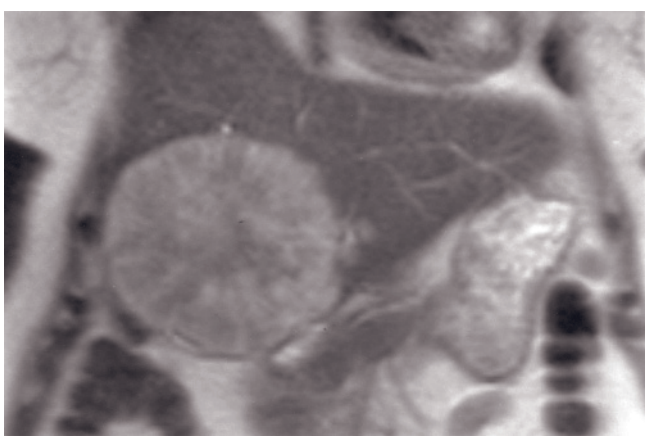

(*p*)

Fig. 2.115 (*Continued*) Coronal T2-weighted SS-ETSE (*l*), coronal SGE (*m*), and immediate (*n*) and 90-s fat-suppressed (*o*) postgadolinium SGE images in a fourth patient. A large mass is present that demonstrates heterogeneous moderately high signal intensity on T2 (*l*), moderate low signal intensity on T1 (*m*), heterogeneous enhancement immediately after contrast administration (*n*), and washout with an enhanced pseudocapsule on interstitial-phase image (*o*).

Coronal T2-weighted SS-ETSE (*p*), transverse fat-suppressed T2-weighted ETSE (*q*), SGE (*r*), and immediate (*s*) and 5-min (*t*) postgadolinium SGE images in a fifth patient. An 8-cm mass is present in the right hepatic lobe with heterogeneous and moderately

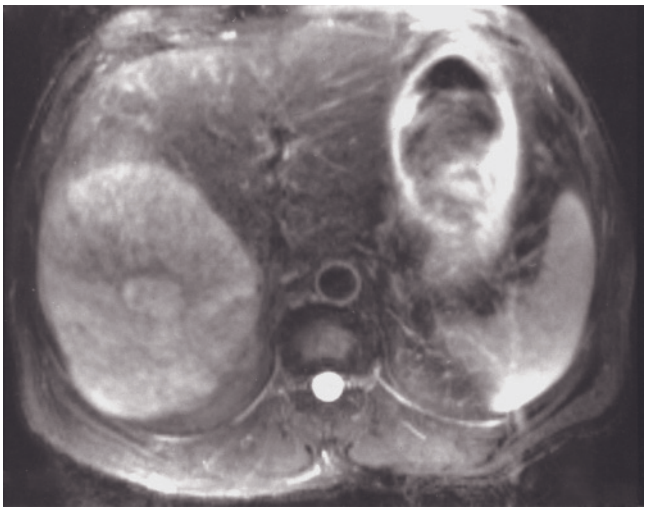

(*q*)

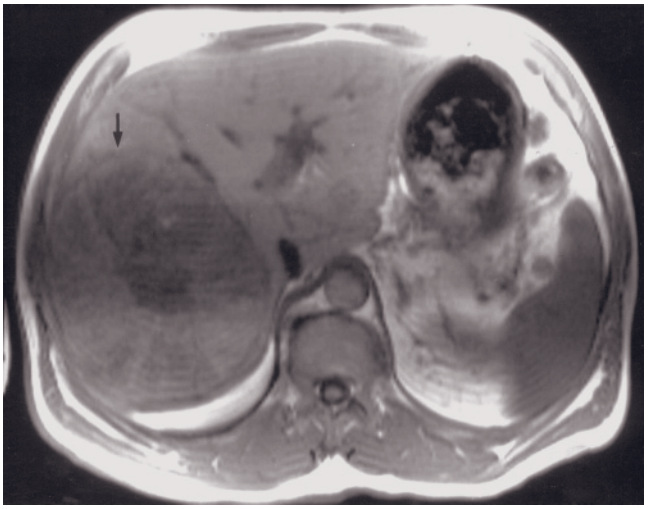

(*r*)

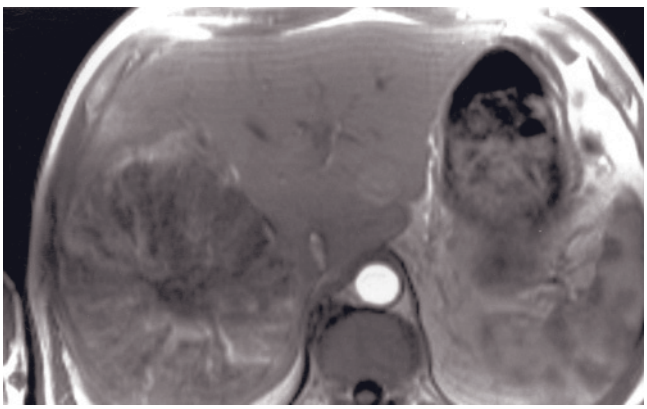

(*s*)

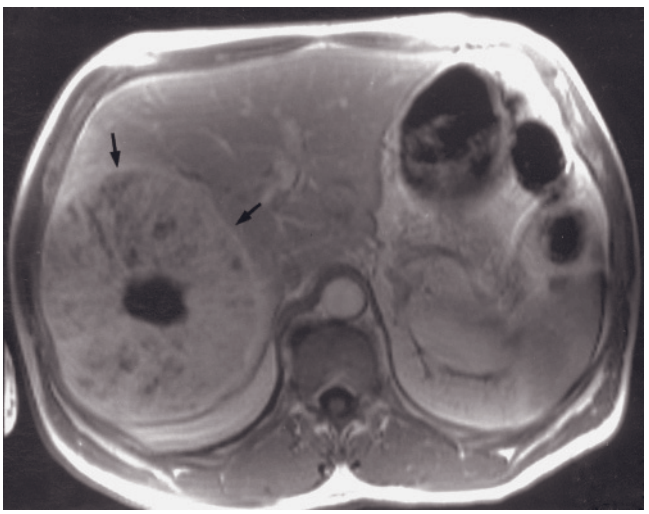

(*t*)

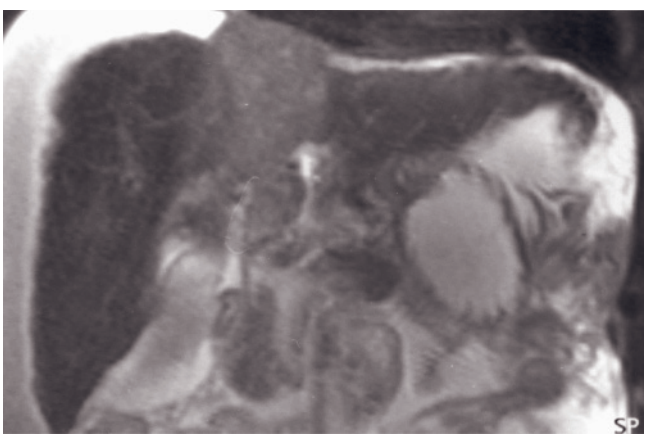

(*u*)

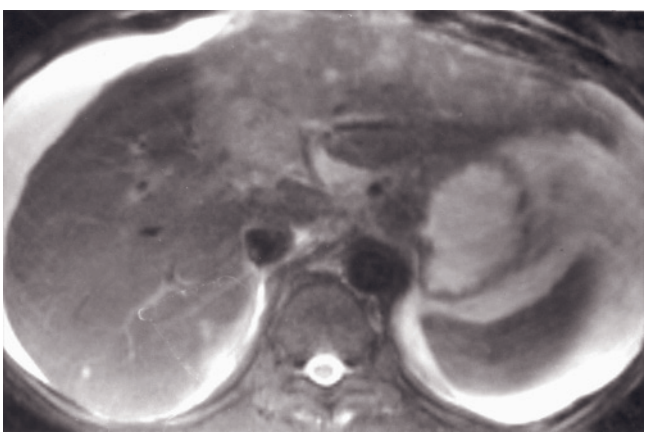

(*v*)

Fig. 2.115 (*Continued*) high signal on T2 (*p*, *q*), heterogeneous low signal intensity on T1-weighted images (*r*), and diffuse heterogeneous enhancement on immediate (*s*) and late (*t*) postgadolinium images. A tumor capsule is evident, which is hypointense on SGE (arrow, *r*) and immediate postgadolinium images, and enhances on late images (arrows, *t*). A large and dark central scar is best seen on late image (*t*) (Reproduced with permission from Kelekis NL, Semelka RC, Worawattanakul S, Lange EE, et al. Hepatocellular carcinoma in North America: a multiinstitutional study of appearance on T1-weighted, T2-weighted, and serial gadolinium-enhanced gradient-echo images. *AJR Am J Roentgenol* 170: 1005–1013, 1998).

Coronal T2-weighted SS-ETSE (*u*), transverse fat-suppressed T2-weighted ETSE (*v*), SGE (*w*), and immediate (*x*) and 90-s fat-suppressed (*y*) postgadolinium SGE images in a sixth patient. There is a large tumor mass occupying the majority of the left lobe

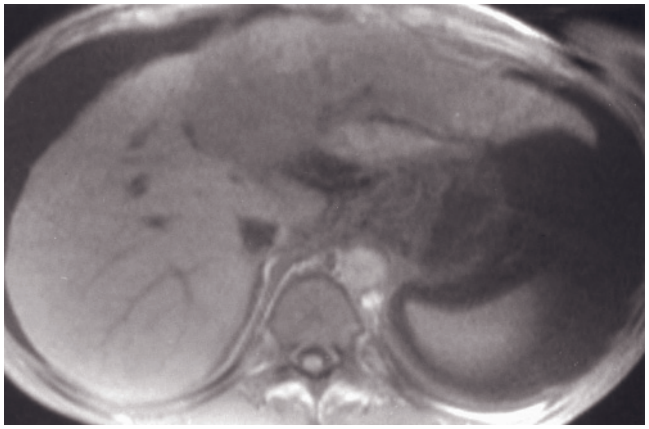

(*w*)

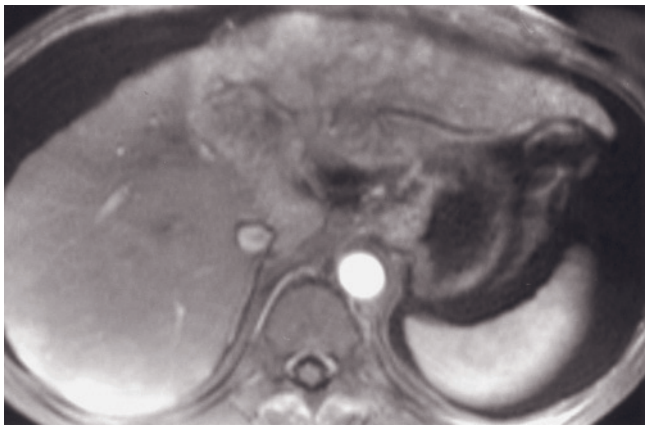

(*x*)

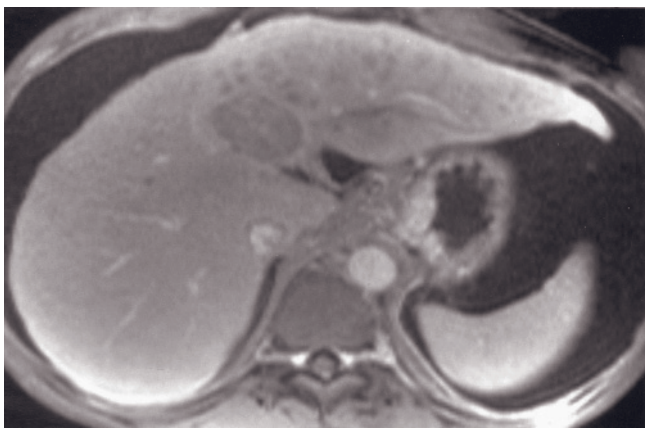

(*y*)

FIG. 2.115 (*Continued*) that is mildly and heterogeneously hyperintense on T2 (*u*, *v*) and moderately hypointense on T1 (*w*) and shows diffuse heterogeneous enhancement on immediate postgadolinium images (*x*) and washout with capsular enhancement on interstitial-phase images (*y*), consistent with a large HCC. Note the ascites, irregular liver contour, and varices along the lesser gastric curvature.

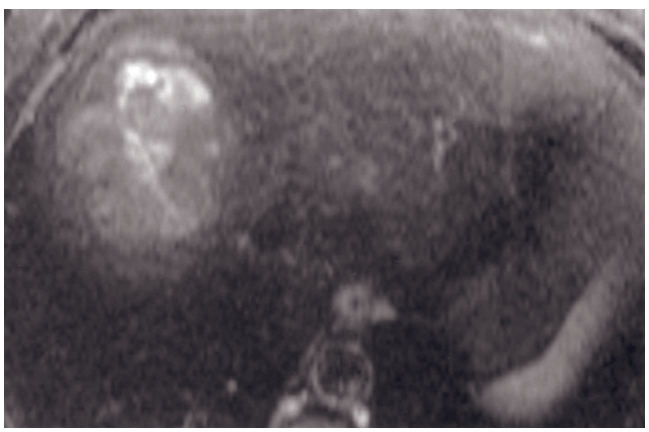

(*a*)

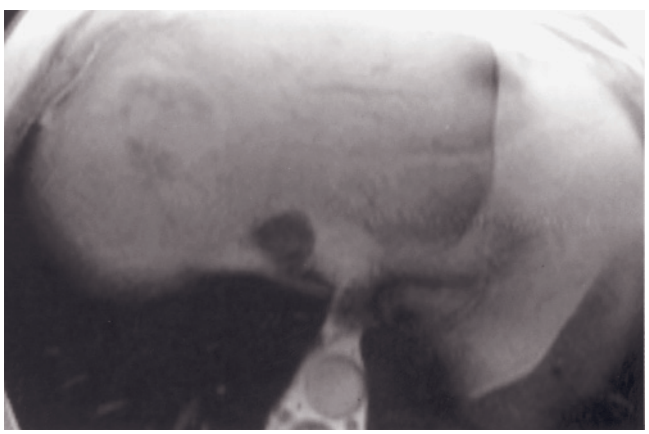

(*b*)

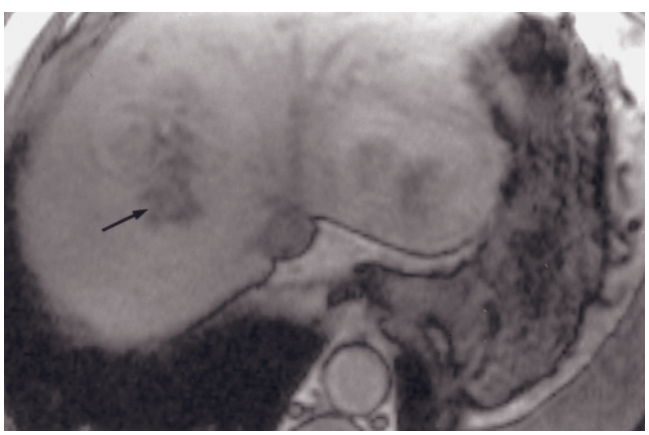

(*c*)

FIG. 2.116 Fat-containing well-differentiated HCC. Echo-train STIR (*a*), SGE (*b*), out-of-phase SGE (*c*), and immediate (*d*) and 90-s fat-suppressed (*e*) postgadolinium SGE images. There is

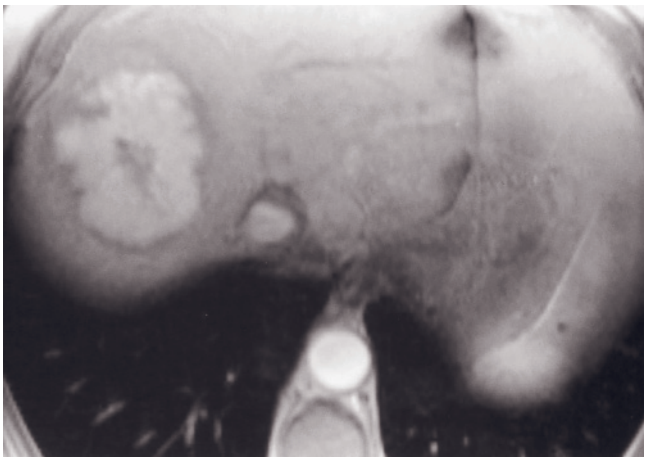

(*d*)

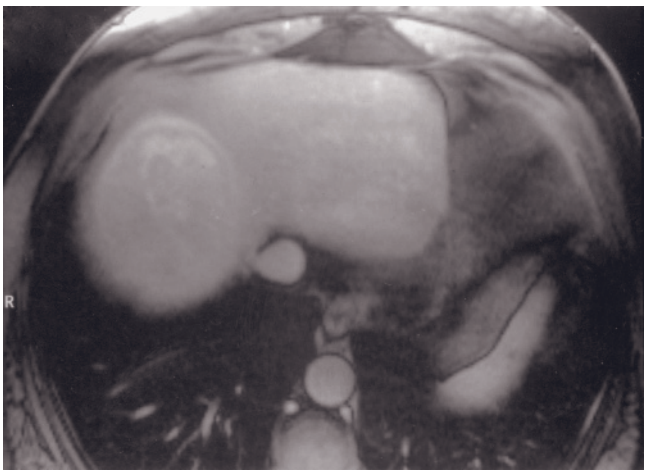

(*e*)

(*f*)

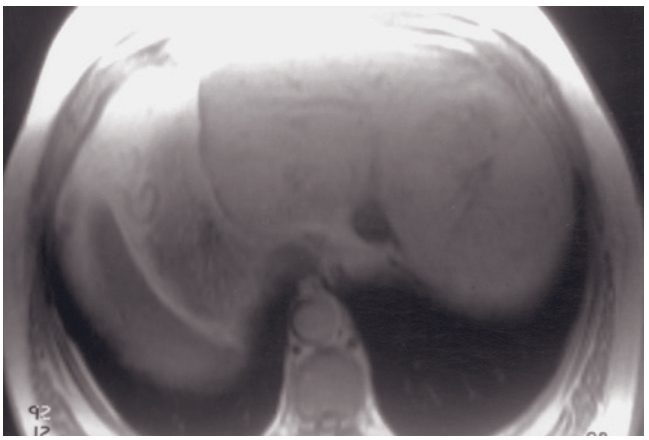

(*g*)

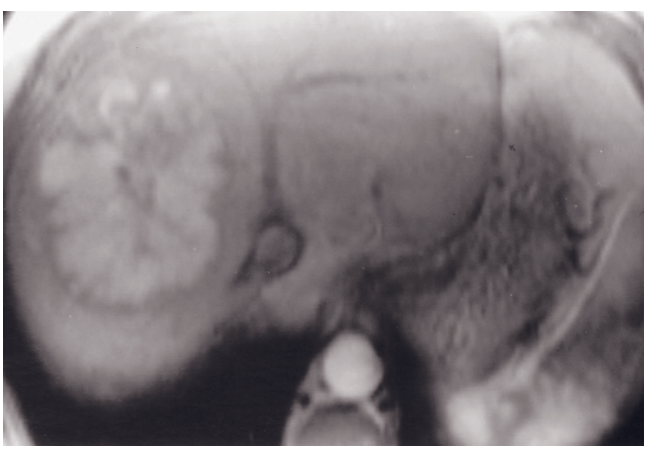

(*h*)

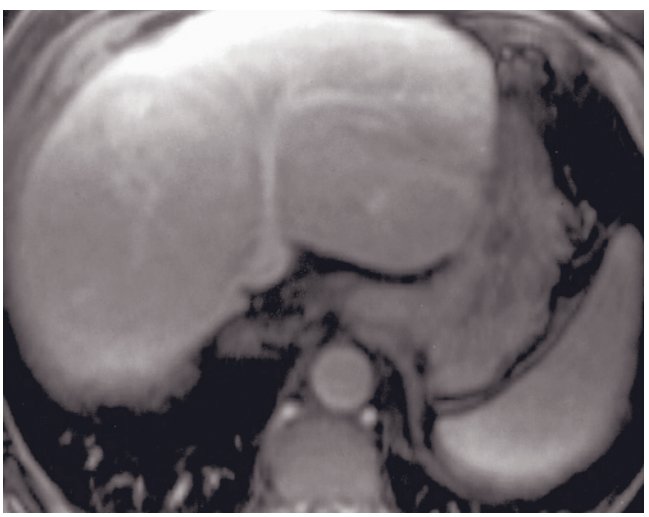

(*i*)

FIG. 2.116 (*Continued*) a lobular mass in the right hepatic lobe that demonstrates high signal on T2 (*a*), isointensity on T1 (*b*), partial loss of signal on out-of-phase image (*c*), intense immediate enhancement after contrast (*d*), and washout (*e*). On late images (*e*), the pseudocapsule is high signal and well visualized. Note a small central scar that is high signal on T2 (*a*), and hypointense immediately after gadolinium (*d*) and shows late enhancement (*e*). Superficially this well-differentiated HCC resembles an FNH. A distinguishing feature is the regions of signal heterogeneity on all MR sequences; FNH should be homogeneous on all sequences. Note also that the lesion demonstrates a peripheral region of signal loss (arrow, *c*) on the out-of-phase sequence consistent with fat. Presence of fat is a feature of well-differentiated HCC and not FNH, and irregular regions of fatty infiltration distinguish it from adenoma, which most commonly shows uniform fatty infiltration. Echo train-STIR (*f*), SGE (*g*), and immediate (*h*) and 90-s fat-suppressed postgadolinium SGE (*i*) images in the same patient, 4 months later. The lesion has increased in size, reflecting its malignant behavior.

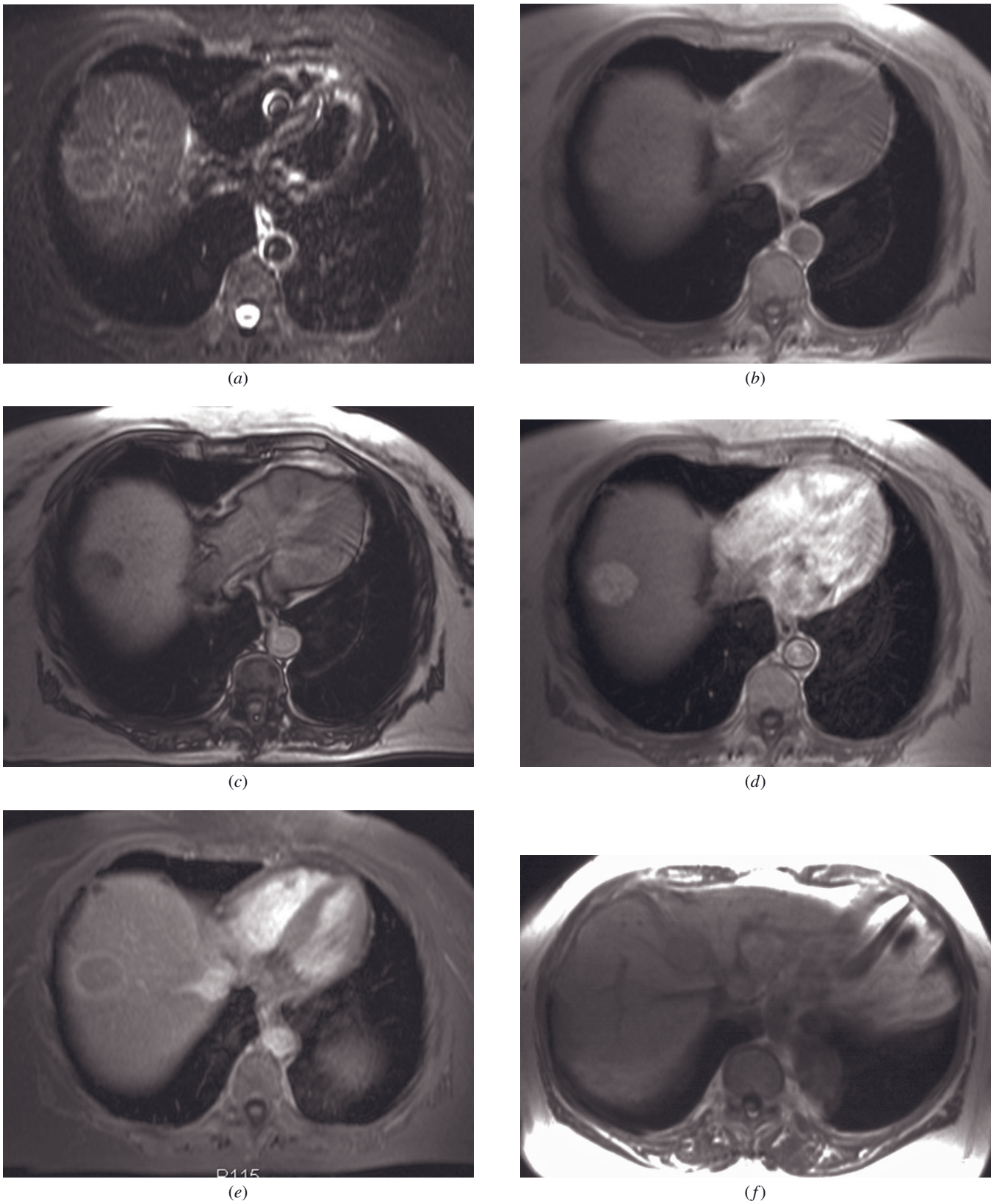

FIG. 2.117 Fat-containing well-differentiated HCC. T2-weighted SS-ETSE (*a*), SGE (*b*), out-of-phase (*c*), and immediate (*d*) and 90-s fat-suppressed (*e*) postgadolinium SGE images. A mass is present in the segment 8 of the liver that shows signal intensity similar to background parenchyma on the T2-weighted image (*a*), slightly higher signal intensity on the T1-weighted image (*b*), heterogeneous loss in signal intensity on the out-of-phase image (*c*), intense enhancement the on the early-phase image (*d*), and washout with late capsule enhancement on the late-phase image (*e*), but with the persistence of the capsule enhancement.

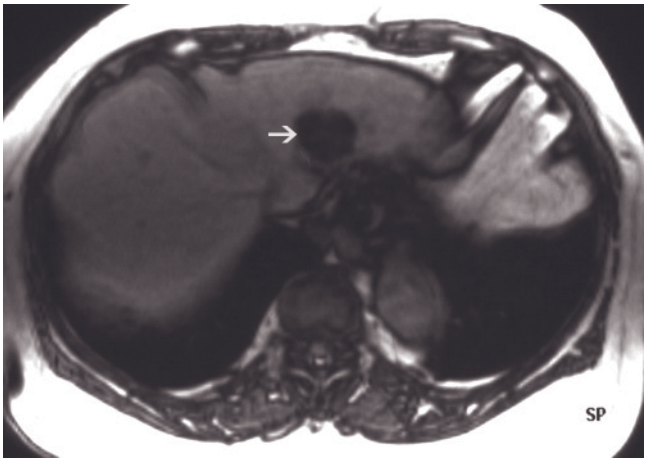

(*g*)

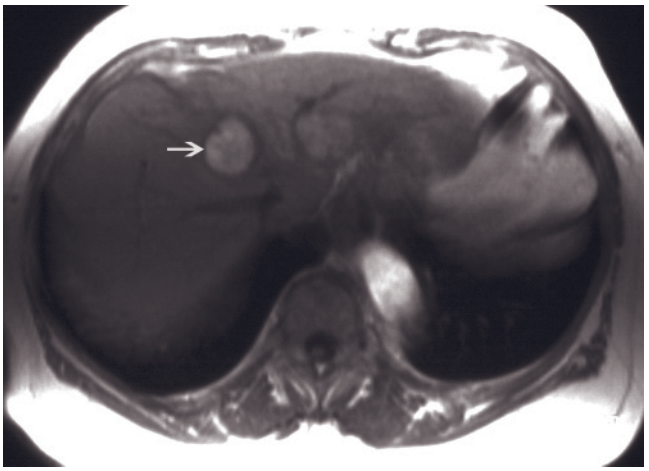

(*h*)

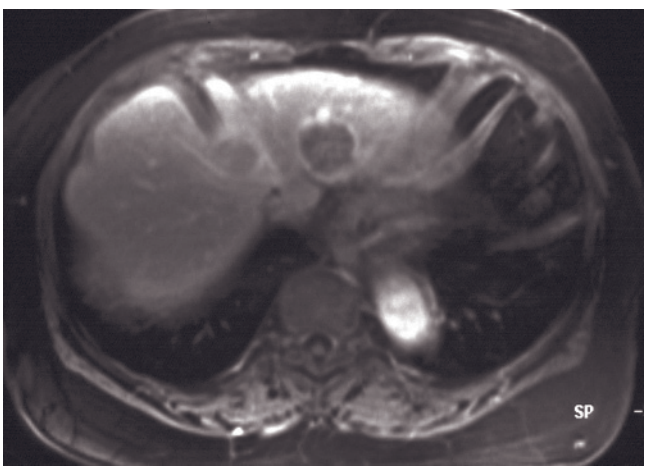

(*i*)

FIG. 2.117 (*Continued*) SGE (*f*), out-of-phase SGE (*g*), and immediate (*h*) and 90-s fat-suppressed (*i*) postgadolinium SGE image in a second patient. There are two rounded lesions situated side by side in the left hepatic lobe. The nodule adjacent to the middle hepatic vein demonstrates low signal intensity on T1-weighted image, intense enhancement on early-phase image (arrow, *h*), and washout with capsule enhancement on late-phase image (*i*). This HCC does not show drop in signal intensity on out-of-phase image (*g*). The tumor located near the left hepatic vein has similar imaging features, but it drops in signal intensity on the out-of-phase image (arrow, *g*), consistent with the presence of fat within the HCC.

3) stability of lesion over a 1-year period is suggestive of high-grade dysplastic nodule, although HCC can still develop; 4) regression of lesion on follow-up MR studies is suggestive of dysplastic nodule; 5) size of nodule <1.5 cm (in combination with absence of a large coexistent HCC) is consistent with high-grade dysplastic nodule; and 6) size of nodule >2 cm is worrisome for HCC.

The most reliable feature that raises the concern for high likelihood of HCC is interval growth. It may be prudent to identify the presence of all nodules, even those <1 cm, that show moderately intense early enhancement, even though recognizing that many lesions <1 cm will diminish in enhancement or resolve on serial follow-up MR studies. At the present time, it may not be possible to predict which <1-cm lesions will resolve, and patients with chronic liver disease at high risk for development of HCC (e.g., hepatitis C or alcohol related) may have a greater tendency for these lesions to continue to grow into HCCs.

Diffuse HCC

The diffuse type of HCC is a permeative hepatic tumor that involves at least 50% of the hepatic parenchyma and occurs in approximately 13% of patients with HCC [207]. The most common appearance of diffuse infiltrative HCC is extensive hepatic parenchymal involvement with mottled, punctate mildly to moderate high signal intensity on T2-weighted images and mildly to moderate low signal on T1-weighted images. The MR features on unenhanced images are nonspecific, that is, similar to those in cirrhotic livers without tumor involvement. Patchy or miliary pattern of enhancement is often observed on immediate postgadolinium images with tumor washout and segments of late capsule enhancement on late images (fig. 2.129). Miliary enhancement on early phase is a relatively specific MR finding of diffuse HCCs and may represent the enhancement of extensive micronodules as shown on histopathology [207, 208].

Diffuse HCC may also appear as irregular linear strands that are iso- to moderately hyperintense on

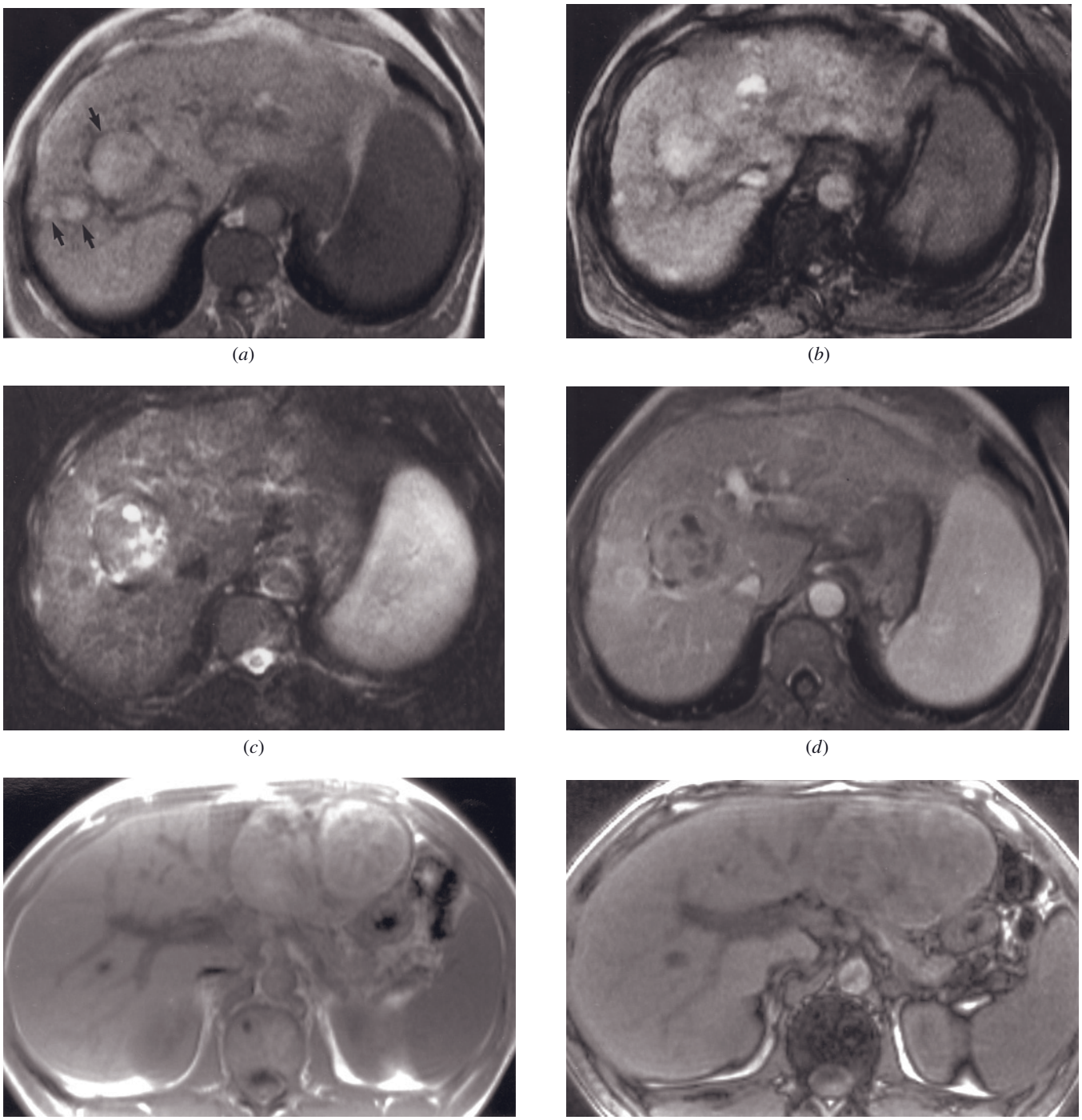

FIG. 2.118 Hepatocellular carcinoma, multifocal with high signal intensity, not representing fat, on T1-weighted images. SGE (*a*), out-of-phase SGE (*b*), fat-suppressed T2-weighted ETSE (*c*), and immediate (*d*) postgadolinum SGE images. Multiple HCCs are present that are high in signal intensity on T1 in-phase images (arrows, *a*) and do not drop in signal or develop a phase-cancellation artifact on the out-of-phase image (*b*), which excludes the presence of fat. The small HCCs are isointense with liver on T2 (*c*), whereas the large tumor is heterogeneous and mildly hyperintense. On the immediate postgadolinium image (*d*), the small HCCs exhibit predominantly peripheral enhancement, whereas the larger HCC has diffuse heterogeneous enhancement. A low-signal-intensity pseudocapsule is appreciated around the larger HCC on all imaging sequences.

SGE (*e*), out-of-phase SGE (*f*), and immediate postgadolinium SGE (*g*) images in a second patient. There is a large HCC with high signal intensity on T1-weighted image (*e*), which does not drop in signal on out-of-phase images (*f*) and shows diffuse heterogeneous enhancement on immediate postcontrast images (*g*). This lesion is consistent with a nonfatty HCC.

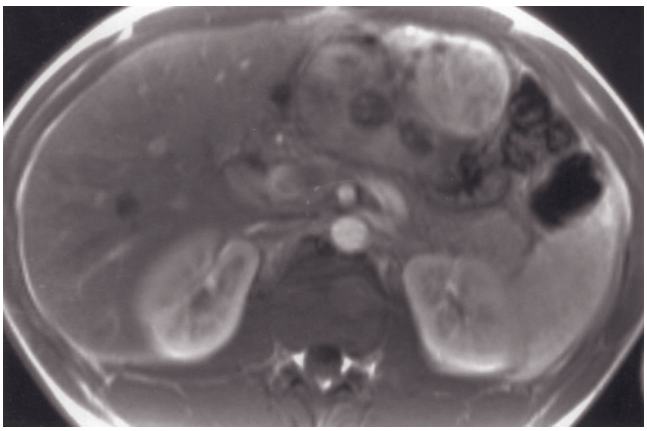

(*g*)

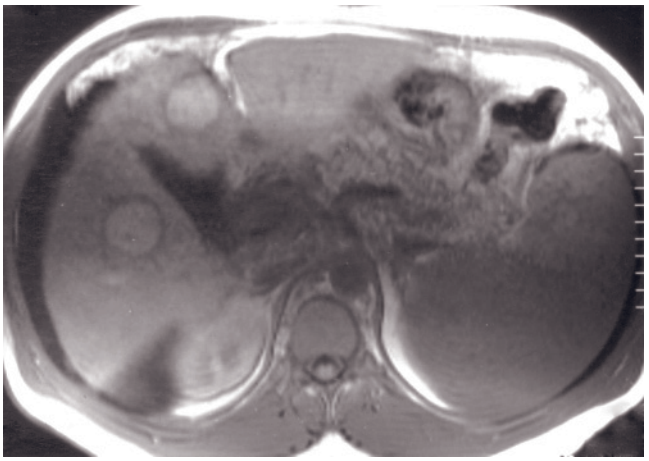

(*h*)

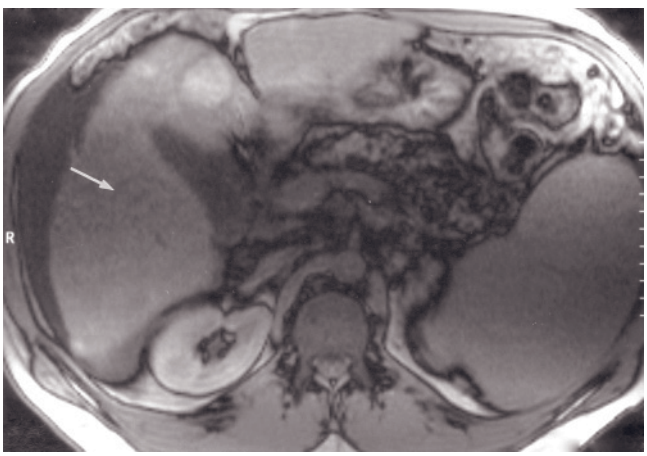

(*i*)

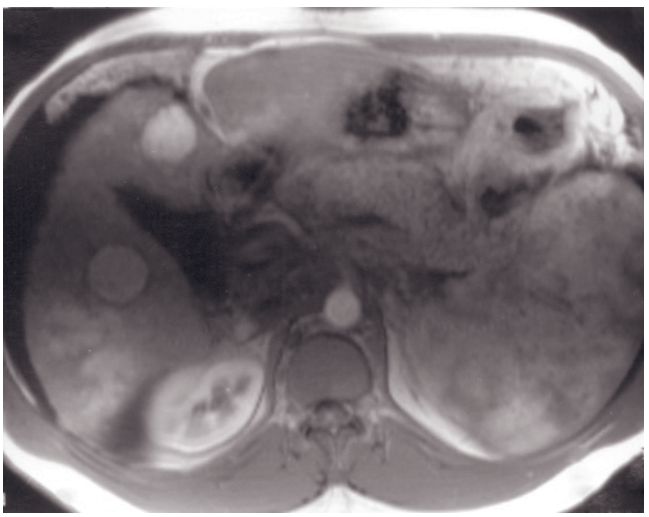

(*j*)

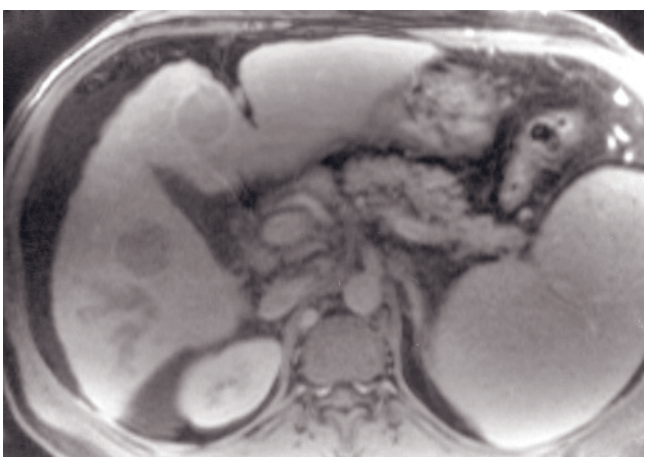

(*k*)

FIG. 2.118 (*Continued*) SGE (*h*), out-of-phase SGE (*i*), and immediate (*j*) and 90-s fat-suppressed (*k*) postgadolinium SGE images in a third patient. There are two rounded lesions, both with high signal on in-phase images (*h*). The more posterior mass (arrow, *i*) loses signal on out-of-phase image, reflecting the presence of fat. The anterior lesion does not lose signal, consistent with the absence of fat. Both HCCs enhance intensely on immediate postgadolinium images (*j*) and washout with late capsule enhancement on interstitial-phase images (*k*).

As these cases illustrate, high signal on T1-weighted images is relatively common in HCC, but in the majority of cases it does not reflect the presence of fat. The high signal is most often on the basis of high protein content.

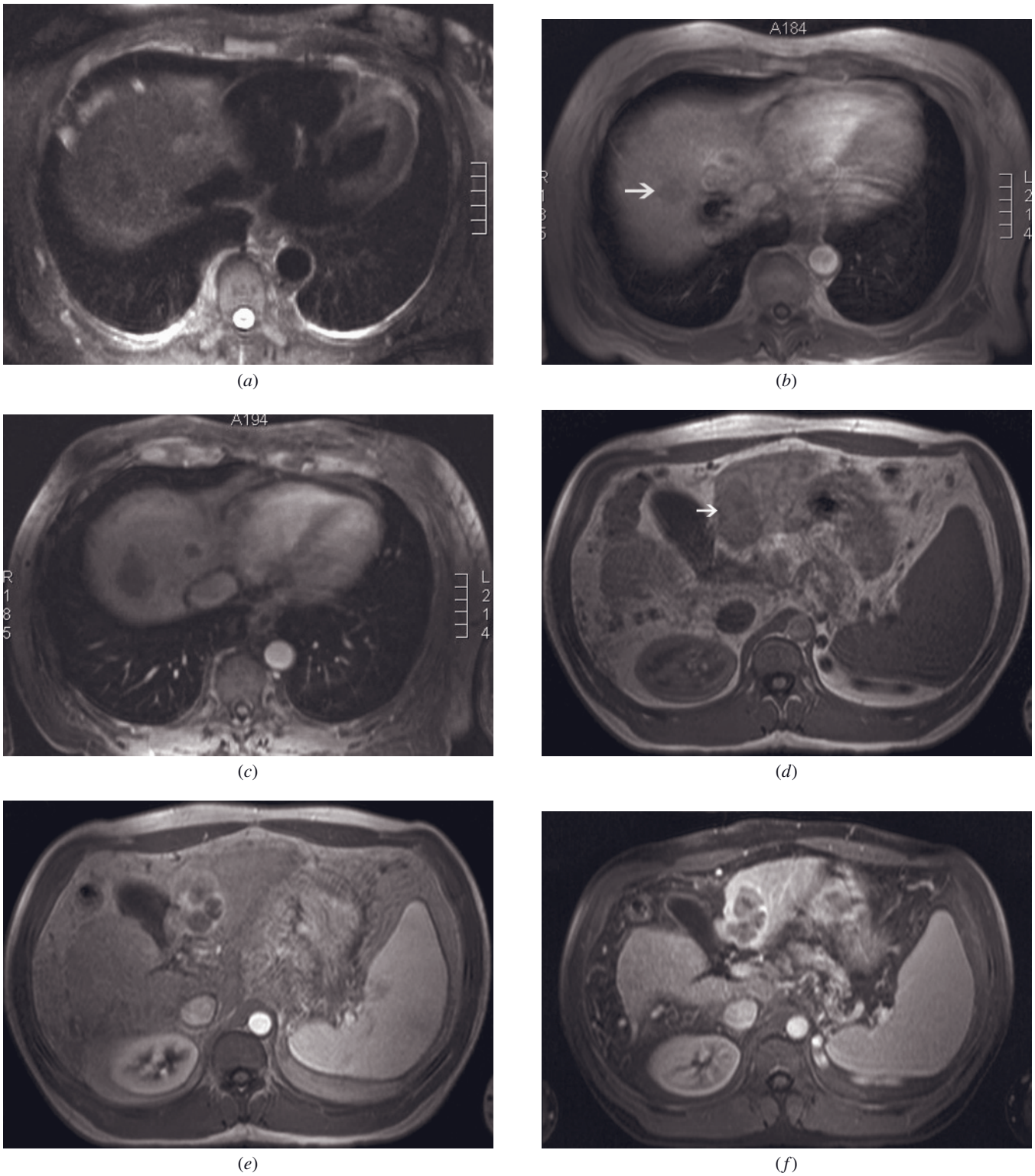

FIG. 2.119 Hypovascular and isovascular HCC. Fat-suppressed T2-weighted SS-ETSE (*a*) and immediate (*b*) and 90-s fat-suppressed (*c*) postgadolinium SGE images. There are two nodular lesions in the top of the liver. The largest one (arrow, *b*) shows low signal intensity on T2-weighted image (*a*) and minimal enhancement on early-phase image (*b*) that decreases over time (*c*), compatible with hypovascular HCC. Nearby the hypovascular HCC, there is a smaller lesion that shows high signal intensity on T2-weighted image (*a*) and ring and perilesional enhancement on early-phase image (*b*) that becomes more conspicuous on late-phase image (*c*), consistent with metastasis from the HCC.

SGE (*d*) and immediate (*e*) and 90-s fat-suppressed (*f*) postgadolinium SGE images in a second patient. A HCC is present in the liver that is moderately low signal intensity on the T1-weighted image (arrow, *d*), shows partial faint enhancement on the early-phase image (*e*) and partially washes out on late-phase image (*f*), consistent with hypovascular HCC.

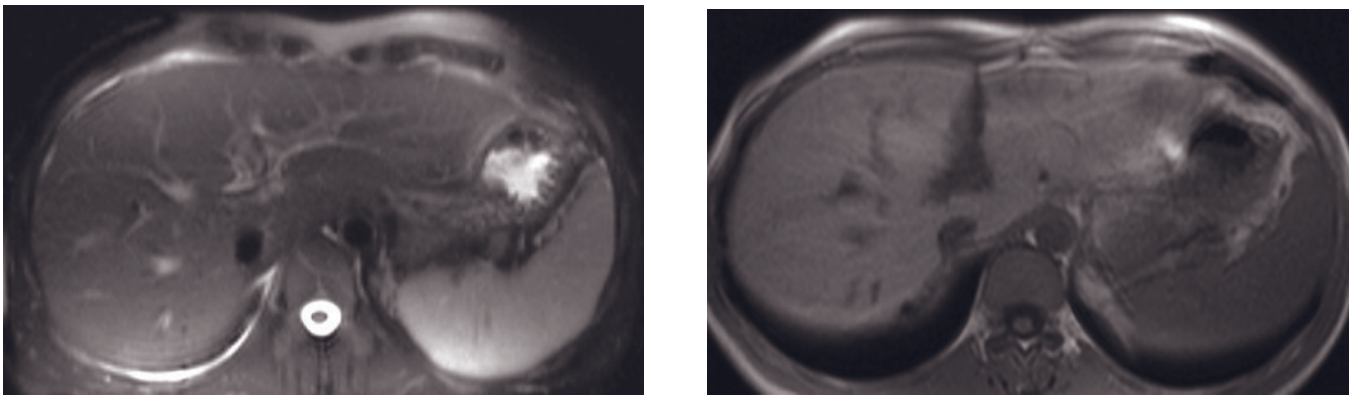

(*g*)

(*h*)

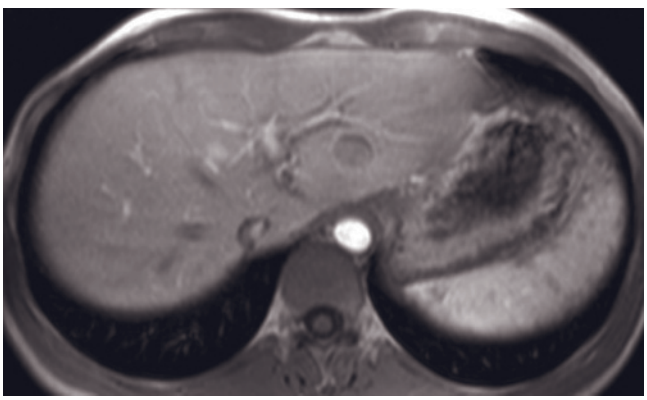

(*i*)

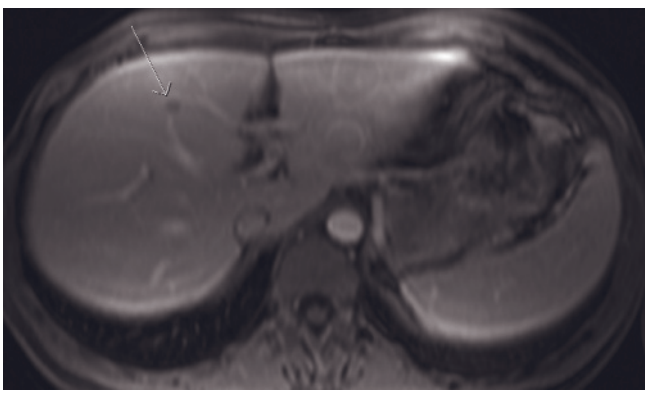

(*j*)

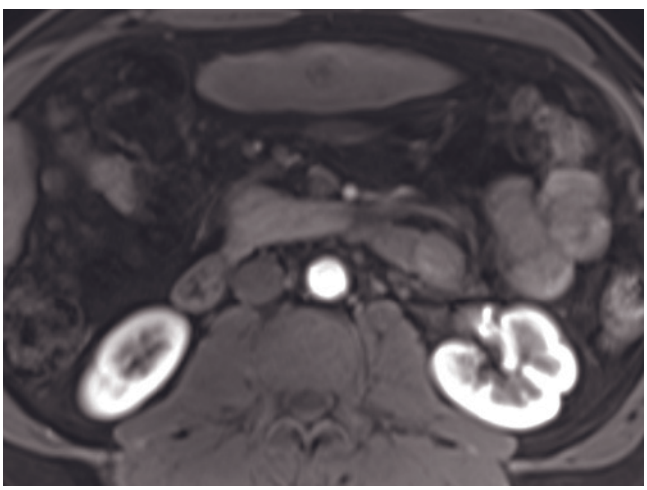

(*k*)

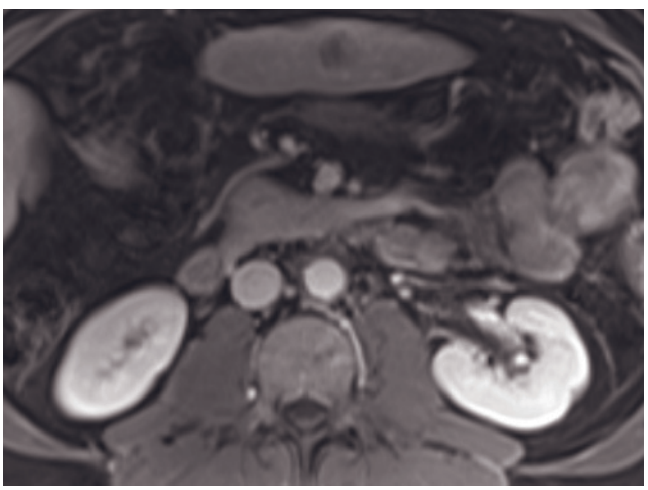

(*l*)

FIG. 2.119 (*Continued*) T2-weighted fat-suppressed SS-ETSE (*g*), SGE (*h*), and immediate (*i*, *k*) and 90-s (*j*, *l*) postgadolinium fat-suppressed 3D-gradient echo images obtained **at 3T** show similar findings with multiple hypovascular HCCs.

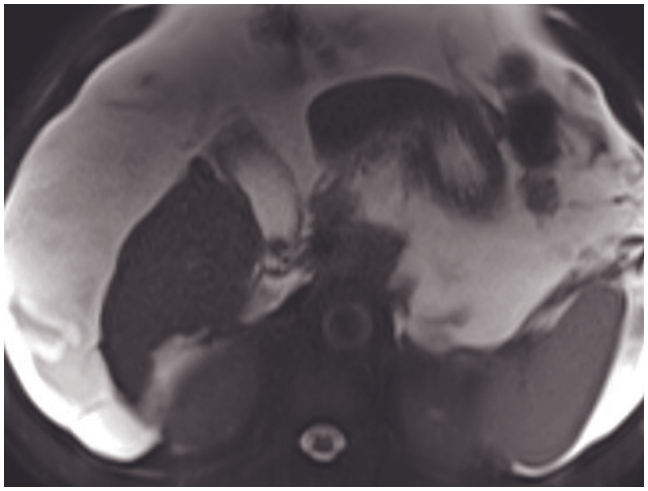

(*m*)

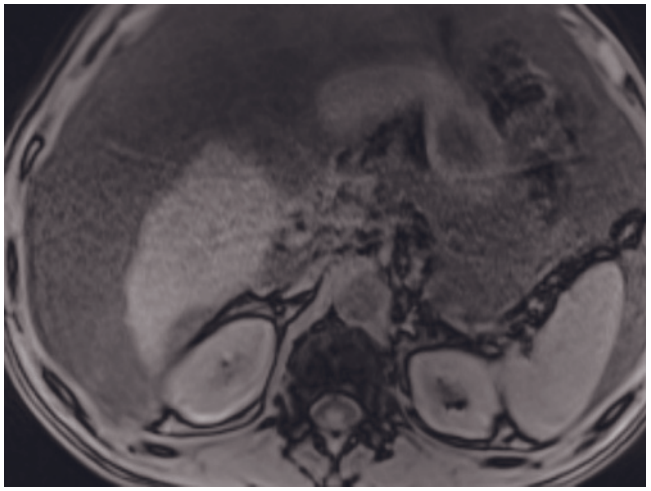

(*n*)

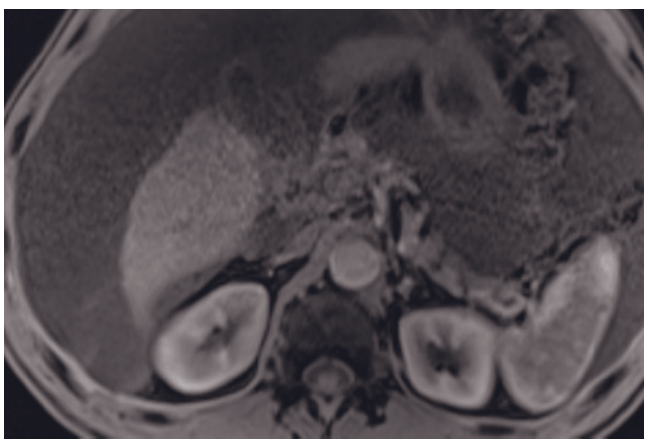

(*o*)

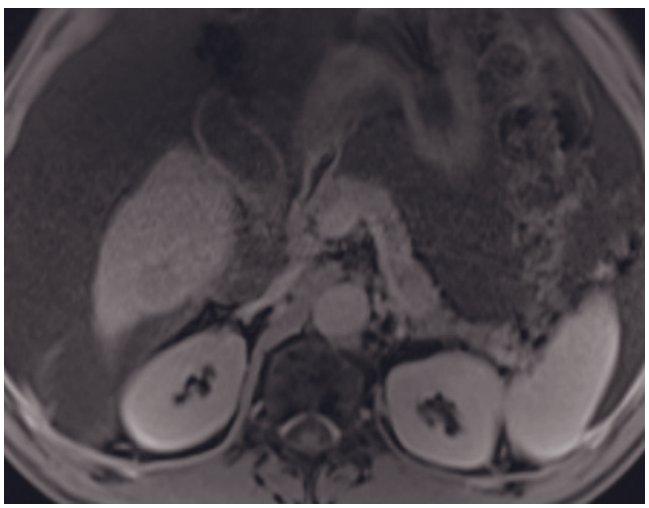

(*p*)

FIG. 2.119 (*Continued*) T2-weighted SS-ETSE fat-suppressed (*m*), SGE (*n*), and immediate (*o*) and 90-s (*p*) postgadolinium fat-suppressed 3D gradient echo images obtained **at 3T** show a hypointense lesion on T2 (*m*)- and T1 (*n*)-weighted images, that enhances in an isointense fashion on early phase (*o*) and demonstrates washout with capsular enhancement on late phase (*p*), compatible with isovascular HCC.

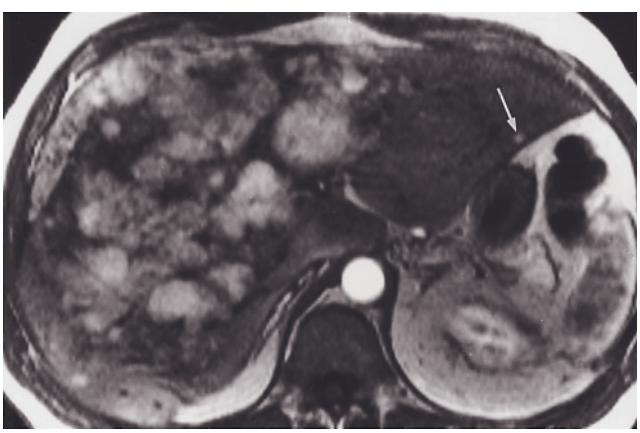

(*a*)

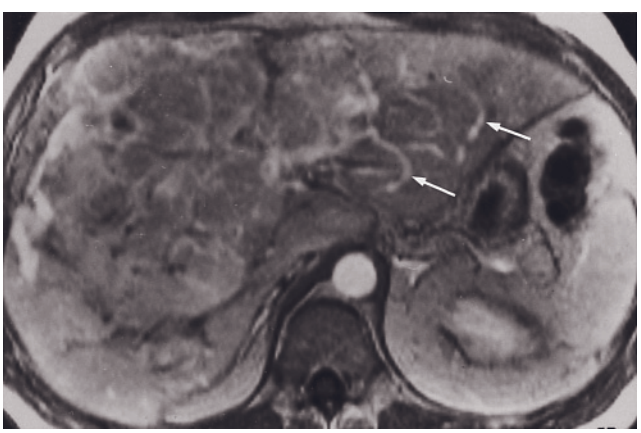

(*b*)

FIG. 2.120 Hypervascular HCC with small satellite tumors. Immediate (*a*) and 90-s (*b*) postgadolinium SGE images. Intense diffuse heterogeneous enhancement of a 15-cm HCC is present on the immediate postgadolinium image (*a*). Multiple additional small HCCs are apparent, including tumors as small as 3 mm (arrow, *a*). By 90 s after gadolinium (*b*), the large tumor has washed out in a heterogeneous fashion with prominent abnormal curvilinear hepatic veins apparent (arrows, *b*). The small HCC has become isointense with liver at this time.

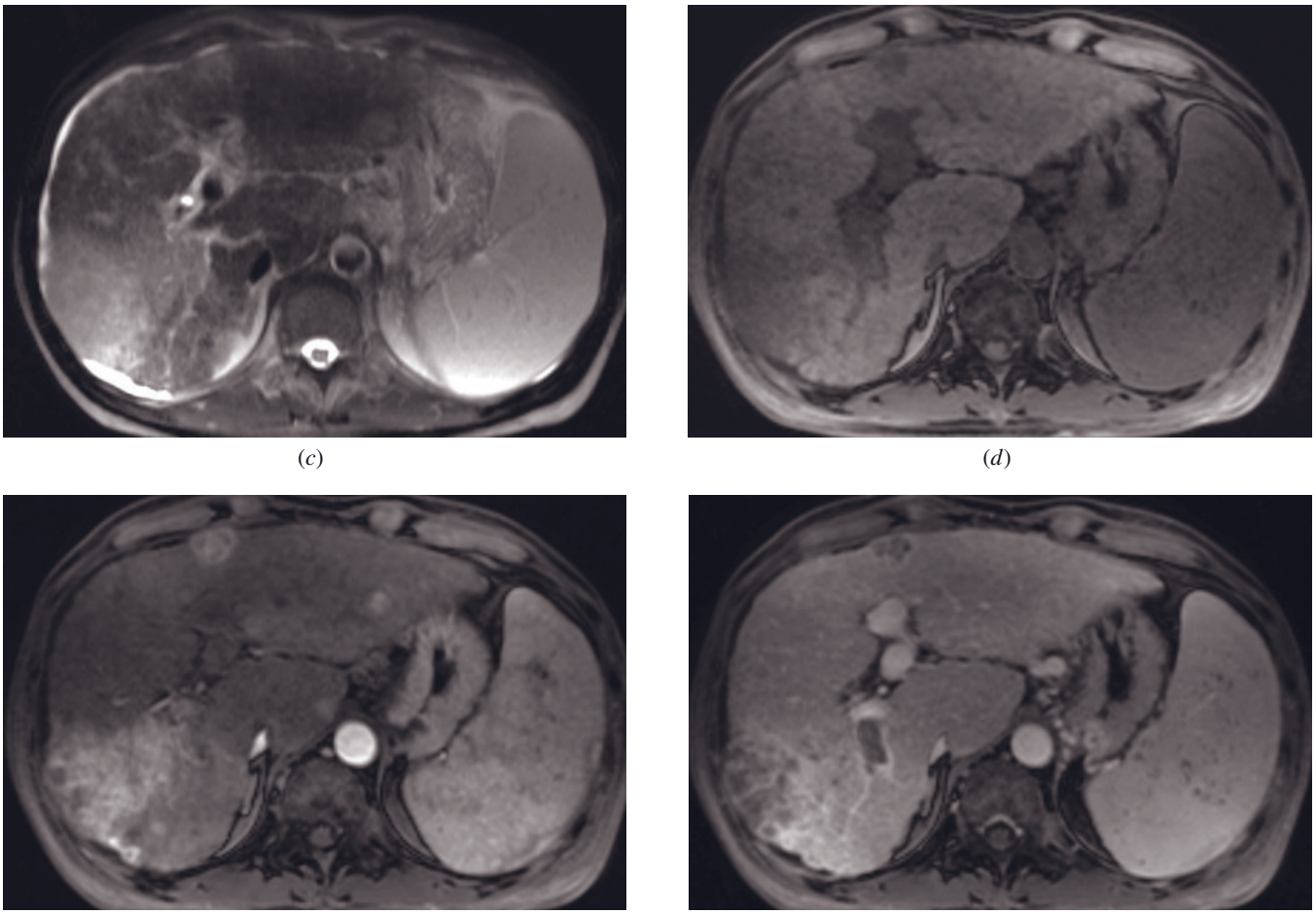

(*c*) (*d*)

(*e*) (*f*)

FIG. 2.120 (*Continued*) T2-weighted fat-suppressed SS-ETSE (*c*), SGE (*d*), and immediate (*e*) and 90-s postcontrast (*f*) fat suppressed 3D-gradient echo images obtained **at 3T** show multiple hypervascular lesions on early phase image (*e*) with washout and capsular enhancement on late phase (*f*) compatible with HCCs in a second patient. Note tumor thrombosis of the right branch of the portal vein (*f*).

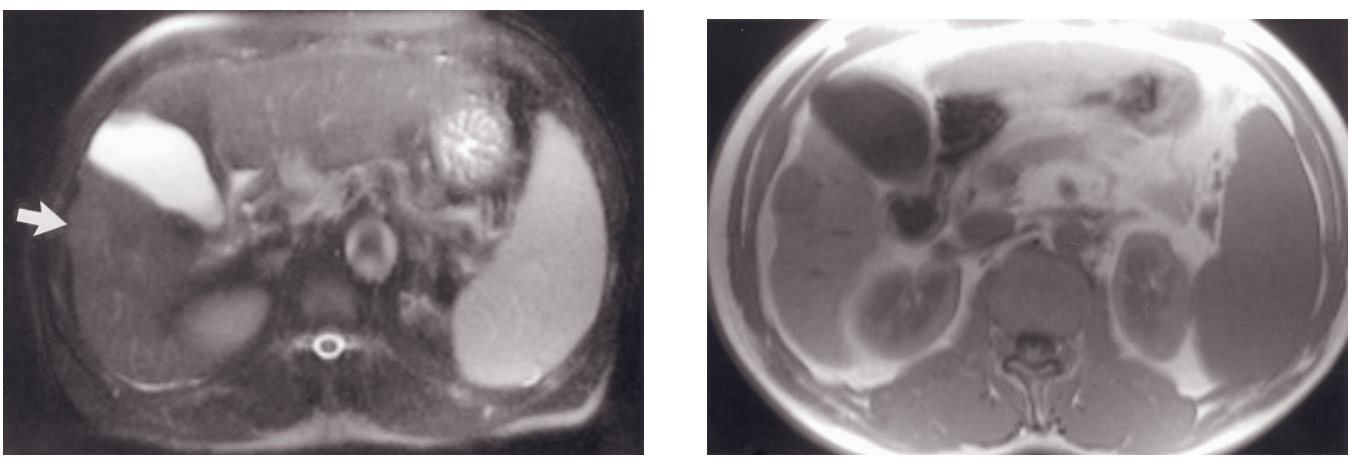

(*a*) (*b*)

FIG. 2.121 Solitary small hypervascular HCC. Fat-suppressed T2-weighted SS-ETSE (*a*), SGE (*b*), and immediate (*c*) and 90-s fat-suppressed postgadolinium SGE (*d*) images. There is a 2-cm mass that bulges the liver contour slightly in the right lobe. The mass is minimally hyperintense on T2 (*a*) and mildly hypointense on T1 (*b*), demonstrates intense uniform enhancement on the immediate postgadolinium image (*c*), and fades to hypointensity by 90 s (*d*) with late enhancement of a pseudocapsule. Intense hepatic arterial dominant-phase enhancement is the most sensitive technique for the detection of small HCCs. Washout to hypointensity with late capsular enhancement is the most specific.

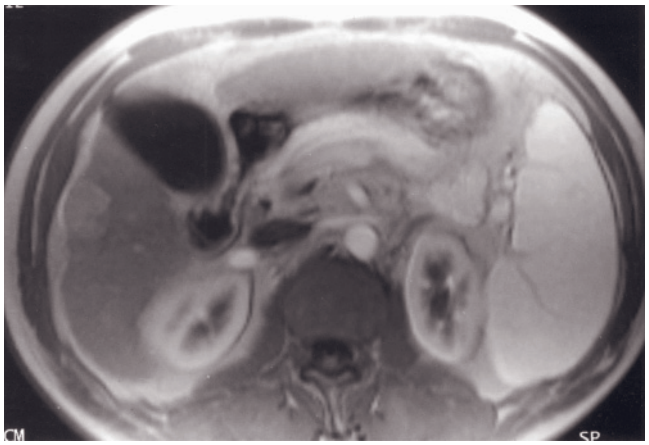

(*c*)

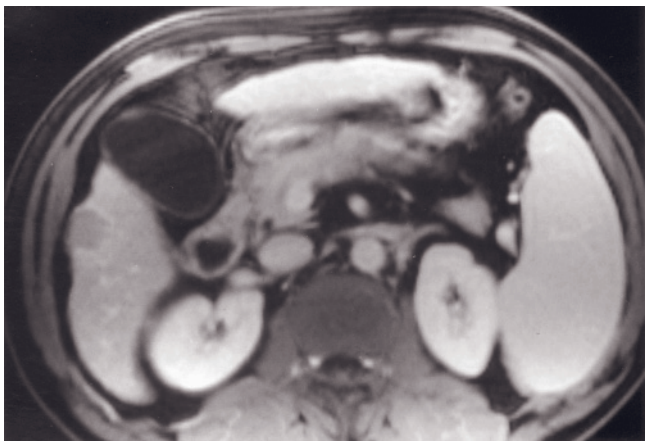

(*d*)

FIG. 2.121 (*Continued*)

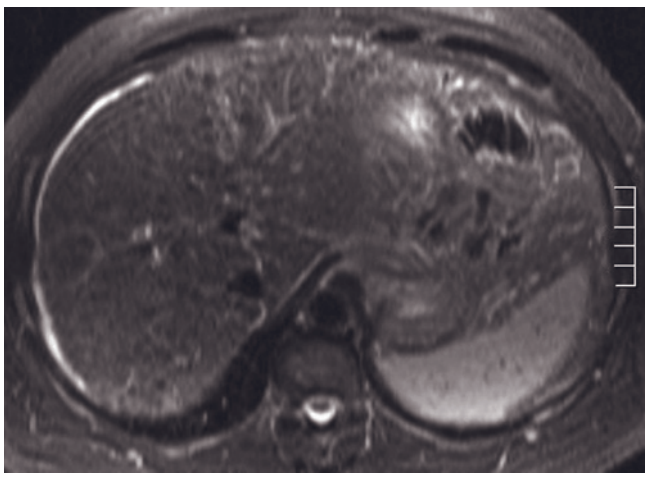

(*a*)

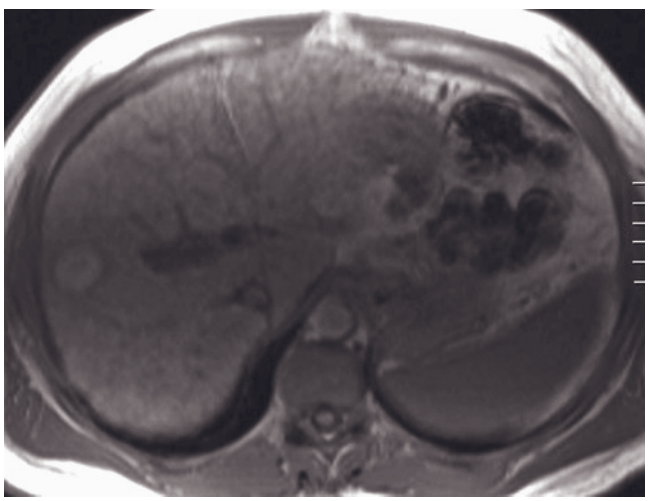

(*b*)

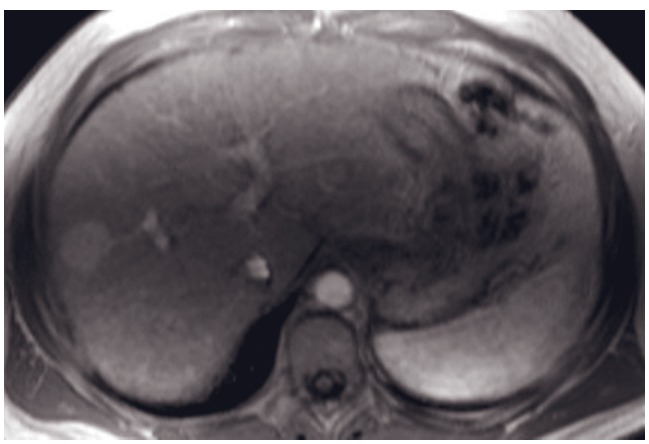

(*c*)

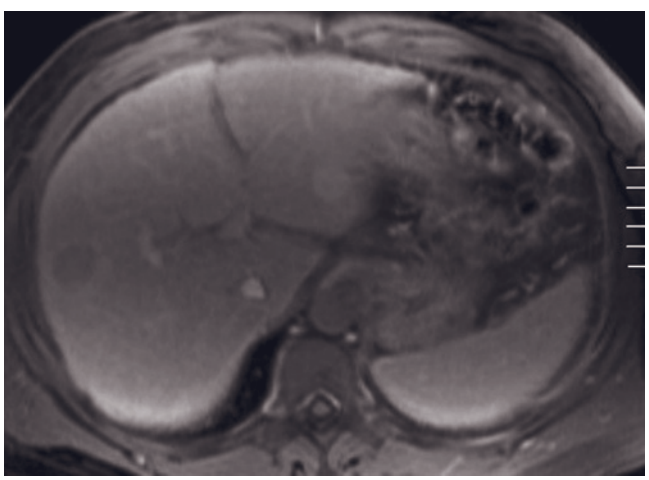

(*d*)

FIG. 2.122 Small hypervascular HCC. T2-weighted SS-ETSE (*a*), SGE (*b*), immediate (*c*) and 90-s fat-suppressed (*d*) post-gadolinium SGE in one patient; T2-weighted SS-ETSE (*e*), SGE (*f*), out-of-phase SGE (*g*), and immediate (*h*) and 90-s fat-suppressed

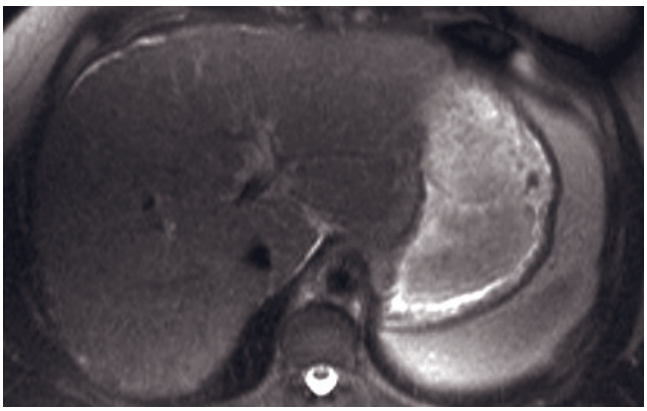

(*e*)

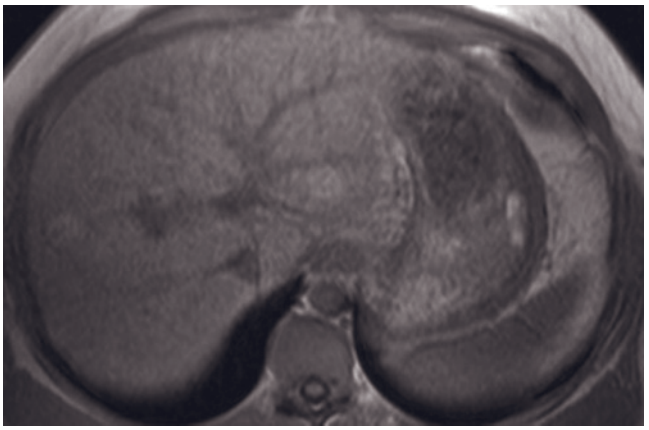

(*f*)

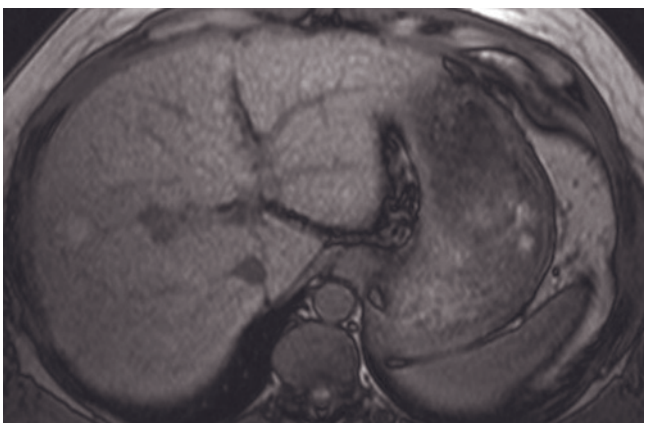

(*g*)

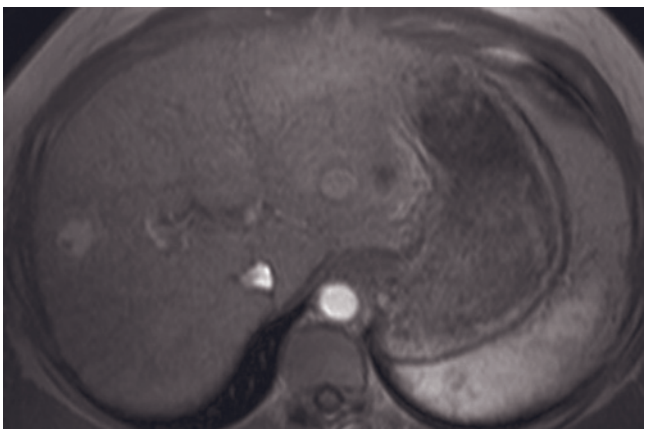

(*h*)

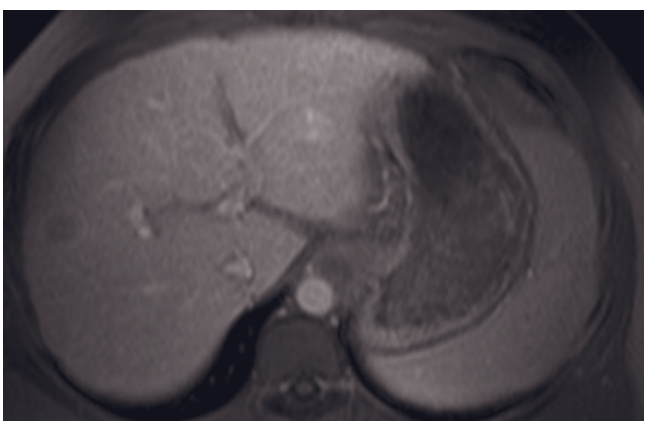

(*i*)

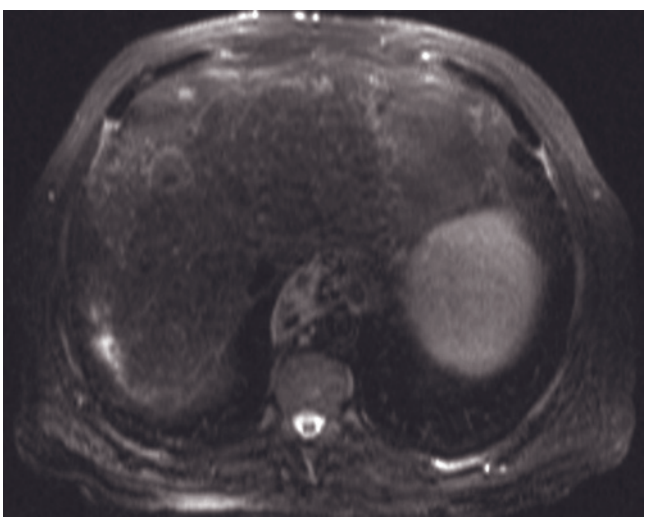

(*j*)

FIG. 2.122 (*Continued*) (*i*) postgadolinium SGE in a second patient; and T2-weighted SS-ETSE (*j*), SGE (*k*), out-of-phase SGE (*l*), and immediate (*m*) and 90-s fat-suppressed (*n*) postgadolinium SGE in a third patient, all with a small hypervascular HCC. Note that in all cases the tumor has intense enhancement on early-phase images and washout with late capsule enhancement on late-phase images.

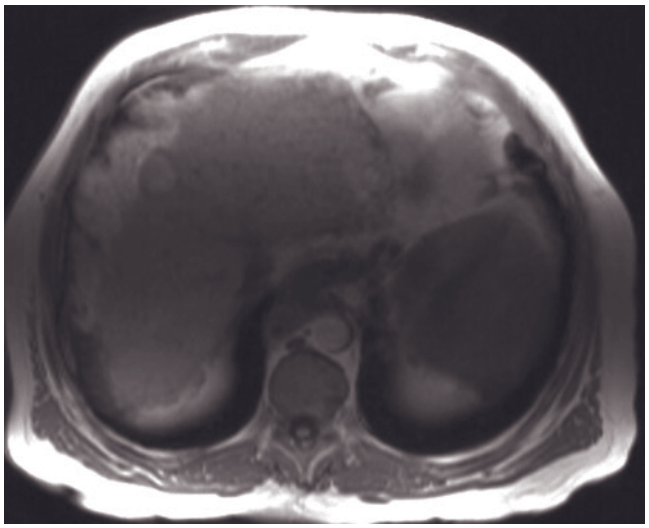

(*k*)

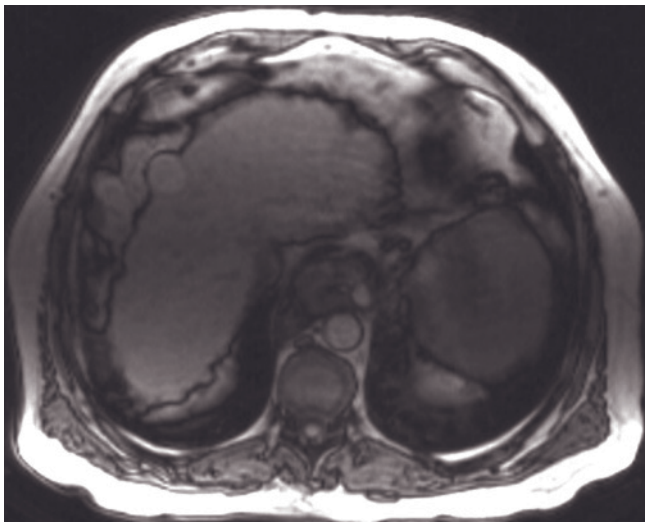

(*l*)

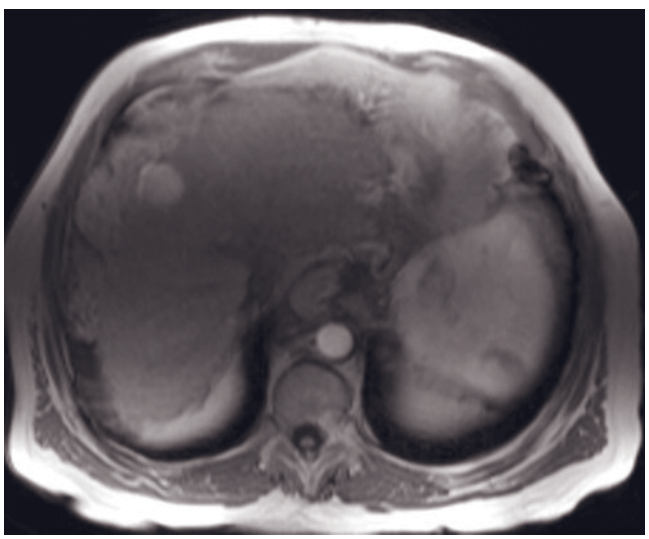

(*m*)

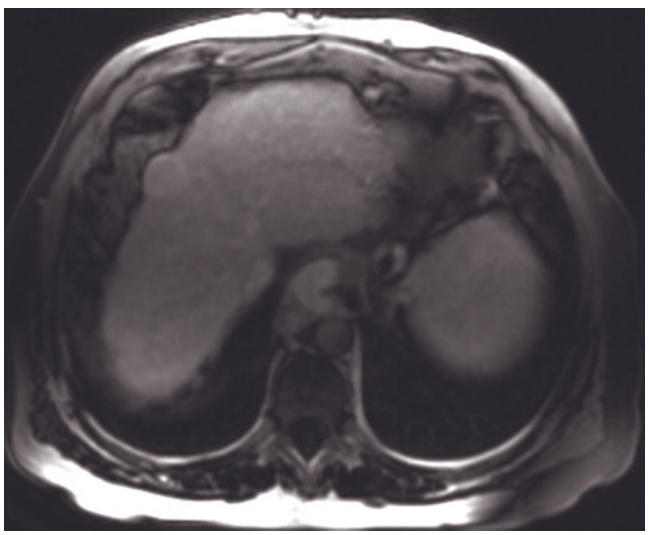

(*n*)

Fig. 2.122 (*Continued*)

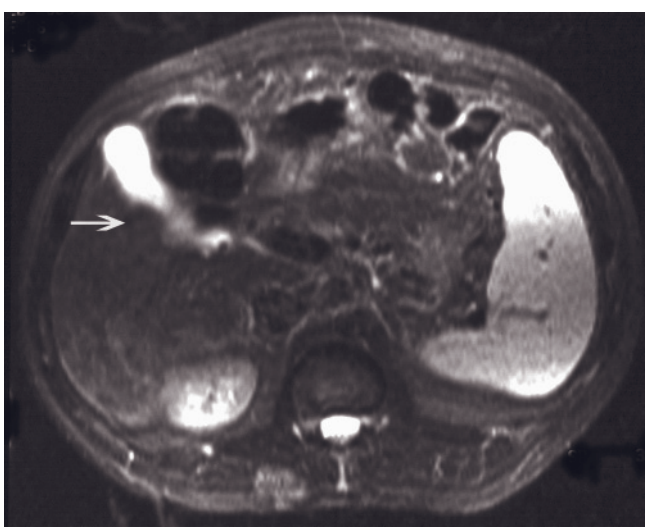

(*a*)

Fig. 2.123 Hypervascular HCC. Fat-suppressed T2-weighted SS-ETSE (*a*), SGE (*b*), and immediate (*c*) and 90-s fat-suppressed (*d*) postgadolinium SGE images. There is a lesion that bulges into the gallbladder fossa that appears mildly low signal intensity on the T2-weighted image (arrow, *a*), mildly high signal intensity on the T1-weighted image (*b*), intense enhancement on the early-phase image (*c*), and washout with capsule enhancement on the late-phase image (*d*), consistent with an HCC.

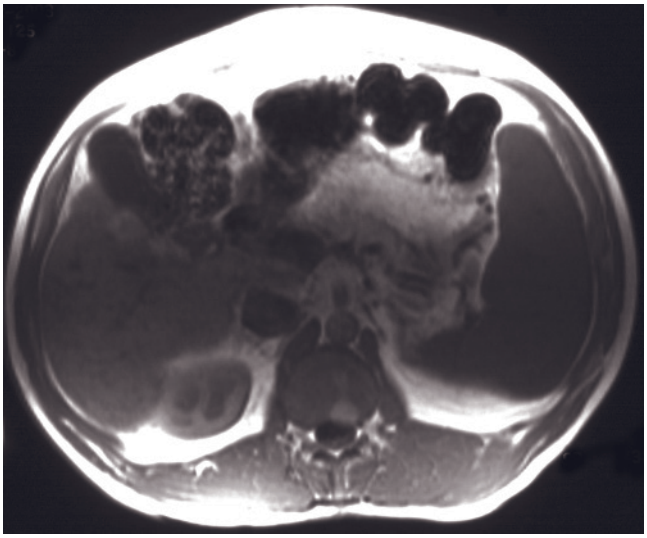

(*b*)

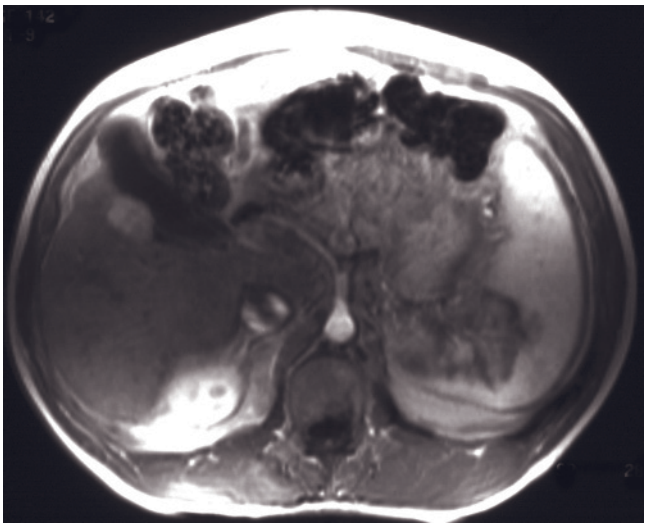

(*c*)

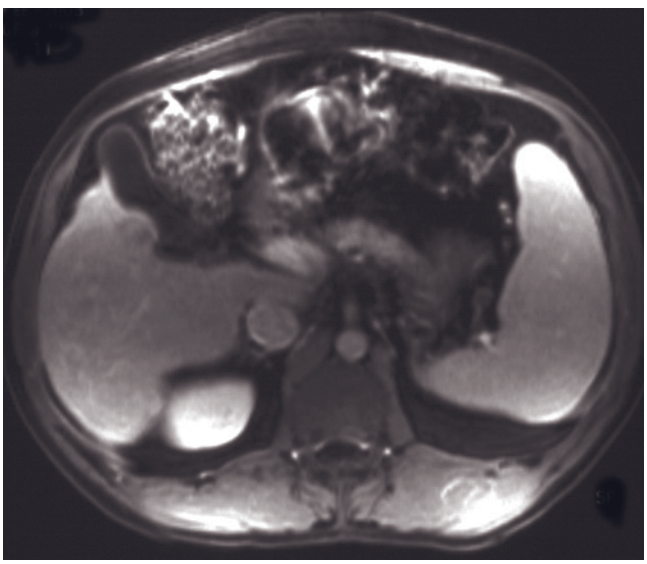

(*d*)

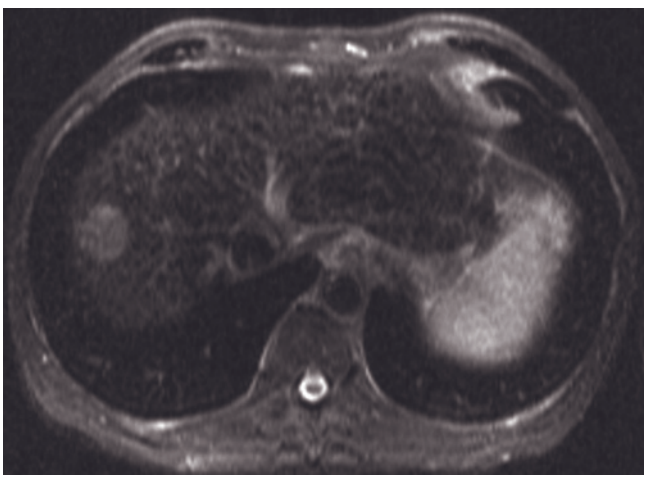

(*e*)

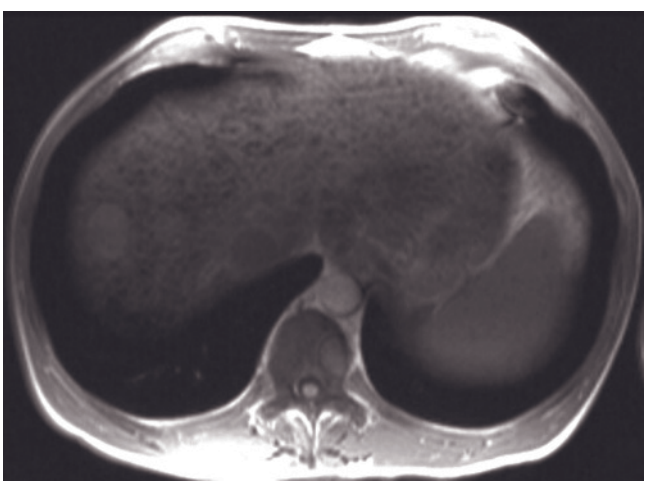

(*f*)

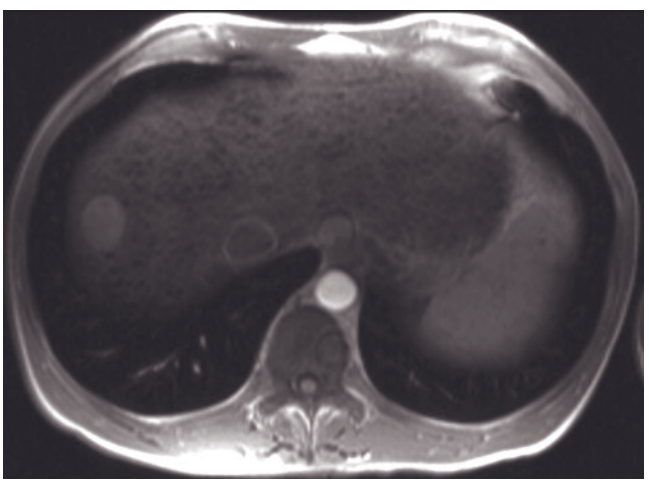

(*g*)

FIG. 2.123 (*Continued*) Fat-suppressed T2-weighted SS-ETSE (*e*), SGE (*f*), and immediate (*g*), 45-s (*h*), and 90-s fat-suppressed (*i*) postgadolinium SGE images in a second patient with a tumor located in segment 8. This mass shows mildly high signal intensity on the T2-weighted image (*e*), mildly high signal intensity on the T1-weighted image (*f*), moderate enhancement on the early phase (*g*), and washout and capsule enhancement on 45-s image (*h*) that persist on late-phase image (*i*), consistent with HCC. Note that washout occurs by 1 min postgadolinium for HCCs, and excellent renal corticomedullary enhancement is still present when the tumor has washed out.

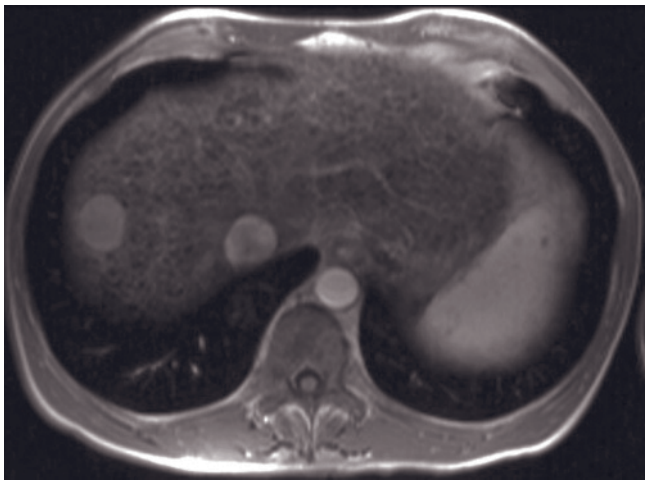

(*h*)

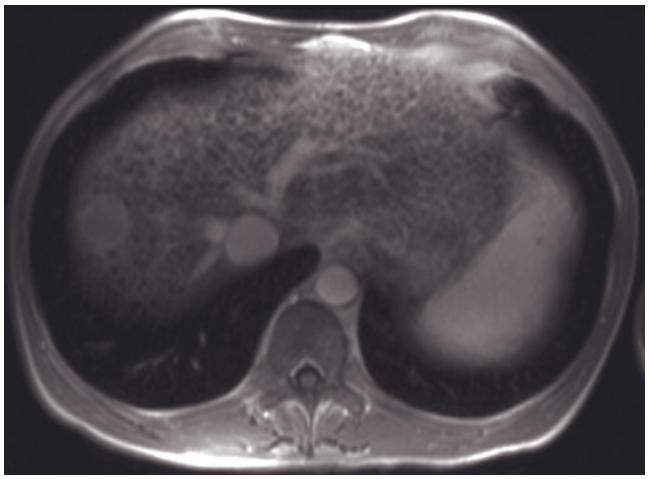

(*i*)

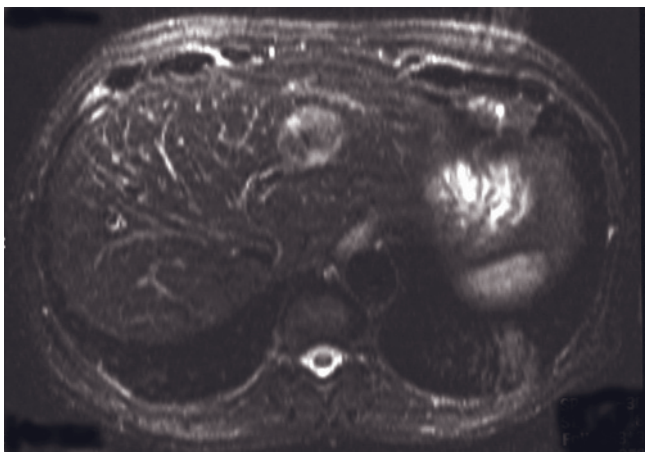

(*j*)

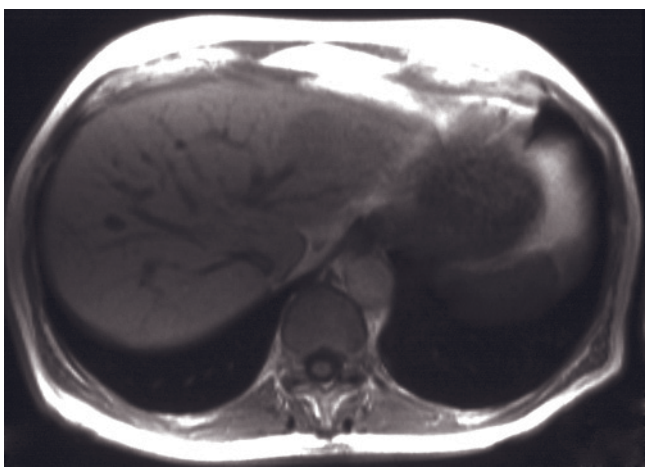

(*k*)

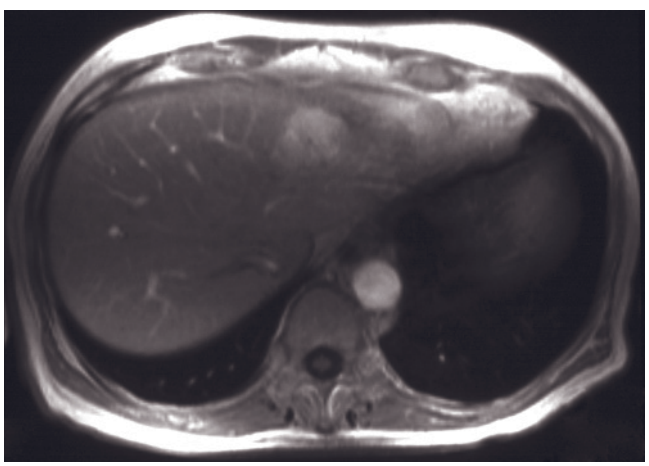

(*l*)

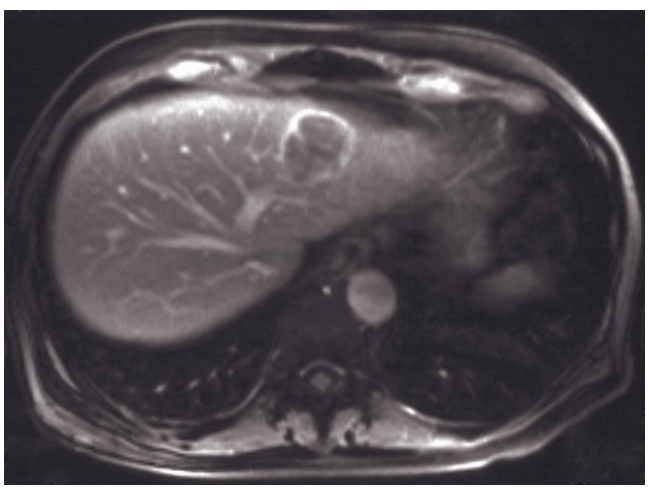

(*m*)

FIG. 2.123 (*Continued*) Fat-suppressed T2-weighted SS-ETSE (*j*), SGE (*k*), and immediate (*l*) and 90-s fat-suppressed (*m*) post-gadolinium SGE images in an additional patient with HCC shows similar findings.

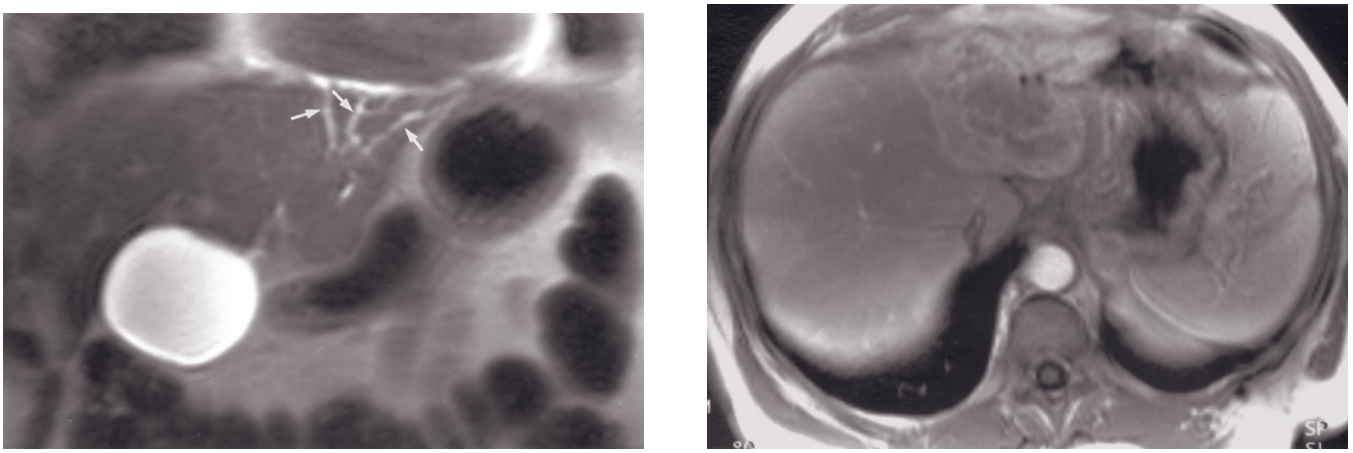

(*a*) (*b*)

FIG. 2.124 Focal HCC with bile duct obstruction. Coronal T2-weighted SS-ETSE (*a*) and immediate postgadolinium SGE (*b*) images. There is a large lesion in the left hepatic lobe that demonstrates minimally hyperintense signal on T2-weighted images (*a*) and moderate heterogeneous enhancement immediately after gadolinium administration (*b*), consistent with a large HCC. Note that the mass causes ductal obstruction (arrows, *a*) of the biliary tree in segment 2 of the left lobe.

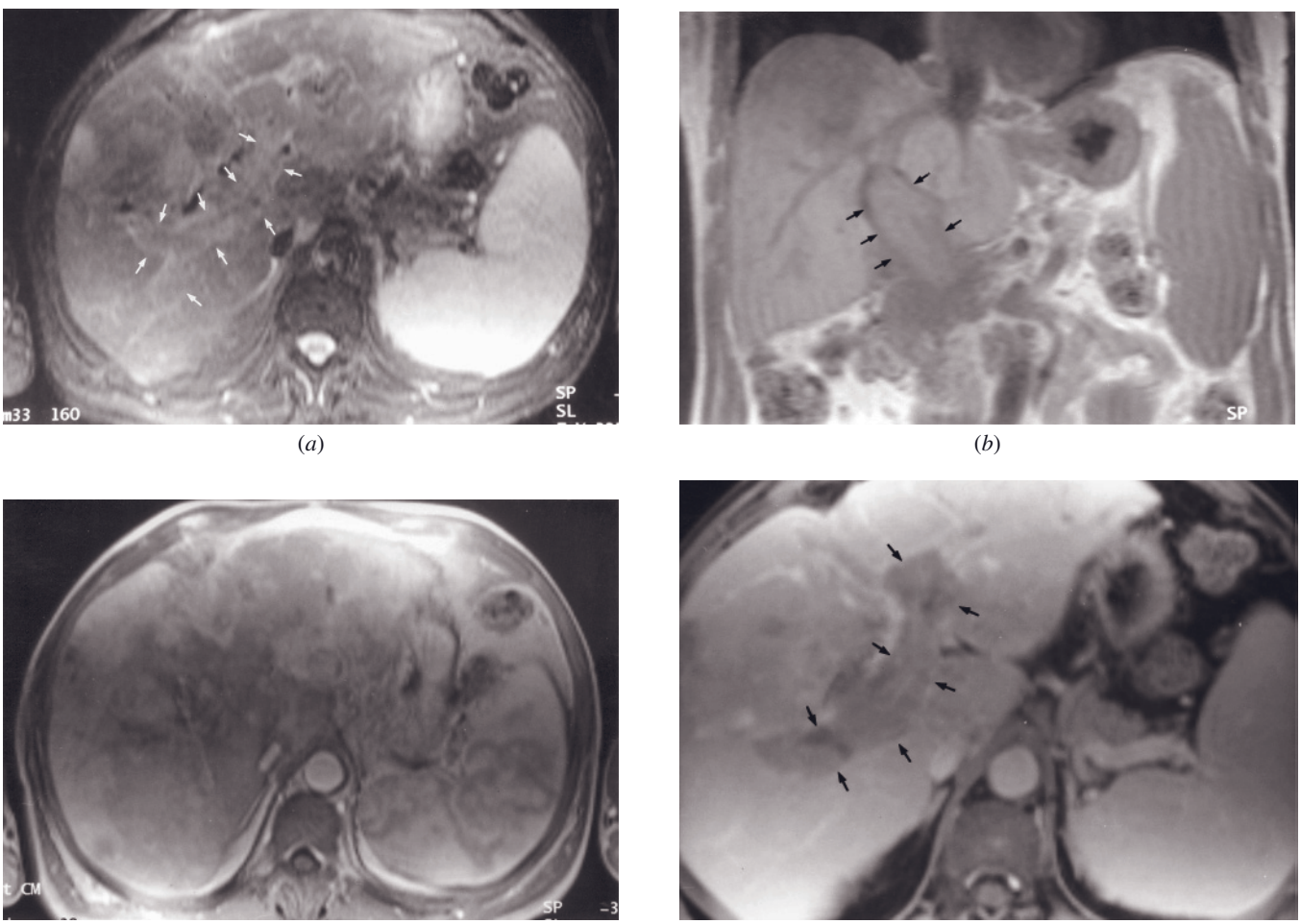

(*a*) (*b*)

(*c*) (*d*)

FIG. 2.125 Multifocal HCC with tumor thrombus. Echo-train STIR (*a*), coronal SGE (*b*), and immediate (*c*) and 90-s fat-suppressed postgadolinium SGE (*d*) images. There are multiple irregular, ill-defined multifocal HCCs scattered throughout all hepatic segments that demonstrate mildly decreased signal on T1 (*a*), mildly increased signal on T2 (*b*), and heterogeneous moderate enhancement on hepatic arterial dominant-phase images (*c*), with late washout and capsular enhancement (*d*). The portal vein is expanded with tumor thrombus (arrows, *a, b, d*). The thrombus is not well seen on the immediate postgadolinium image (*c*), as it enhances in a comparable fashion to background liver. Portions of tumor show late washout and capsule enhancement as observed in focal HCC.

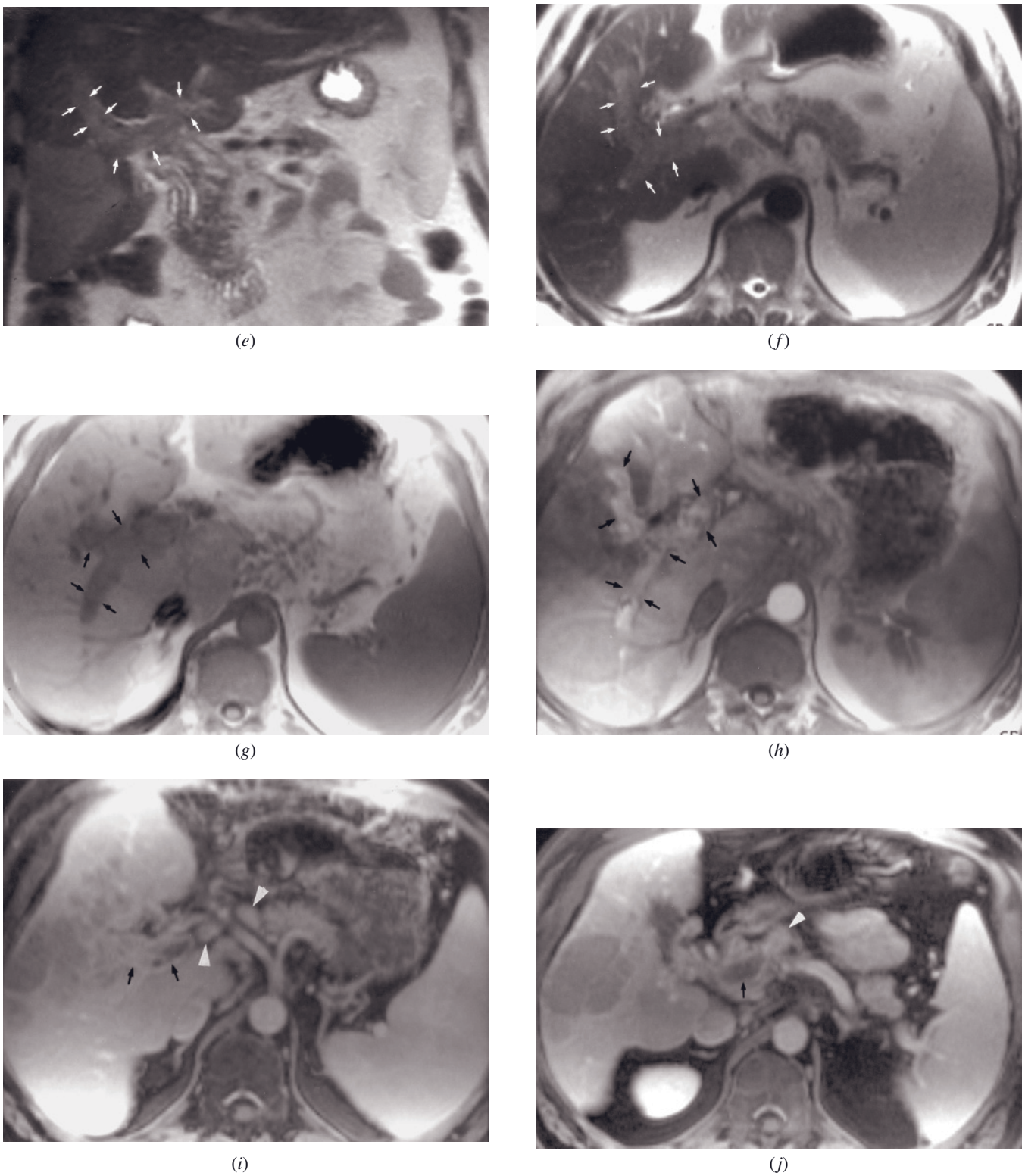

FIG. 2.125 (*Continued*) Coronal (*e*) and transverse (*f*) T2-weighted SS-ETSE, SGE (*g*), and immediate (*h*) and 90-s fat-suppressed (*i–l*) postgadolinium SGE images in a second patient. There is a large irregular mass occupying the majority of segments 5 and 6 of the right hepatic lobe, with tumor thrombus (small arrows, *e–j*) extending into the right, left, and main portal veins. Interstitial-phase gadolinium-enhanced images clearly depict multiple lymph nodes (arrowheads, *i–l*).

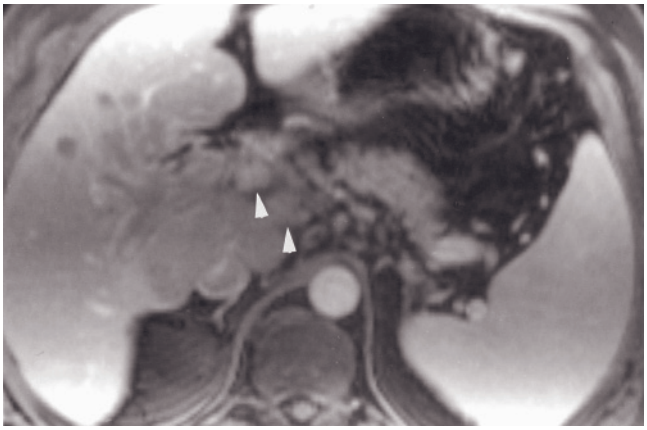

(*k*)

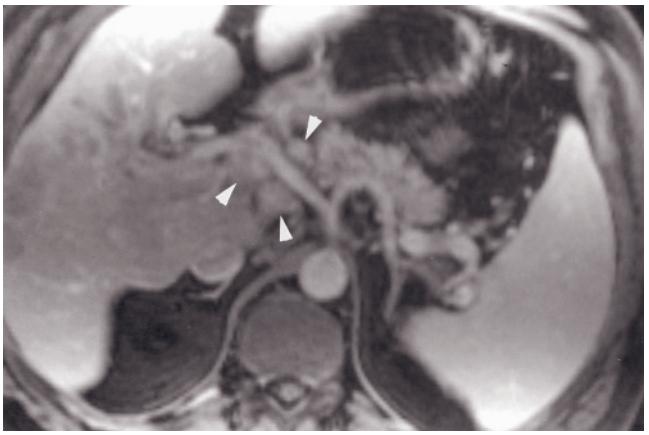

(*l*)

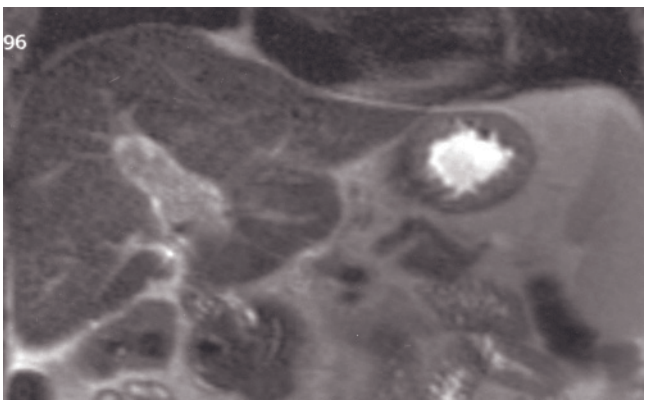

(*m*)

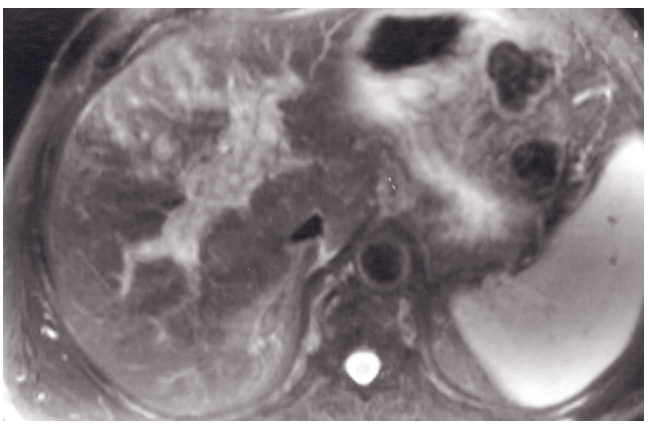

(*n*)

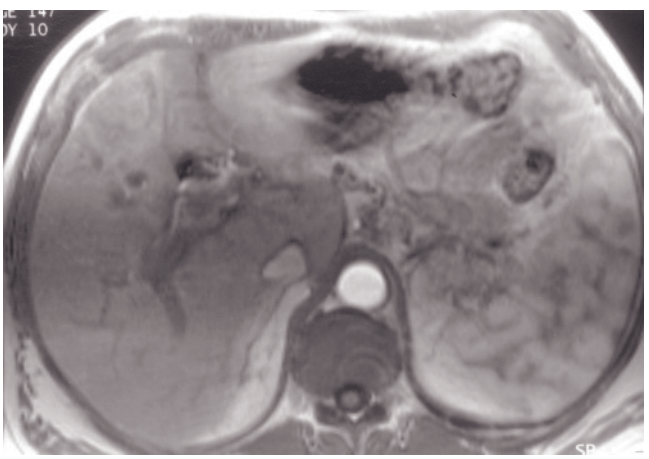

(*o*)

FIG. 2.125 (*Continued*) Coronal T2-weighted SS-ETSE (*m*), echo-train STIR (*n*), and immediate postgadolinium SGE (*o*) images in a third patient. There is expansion of the right and left portal veins consistent with tumor thrombus. Heterogeneous tumor is identified in segment 4.

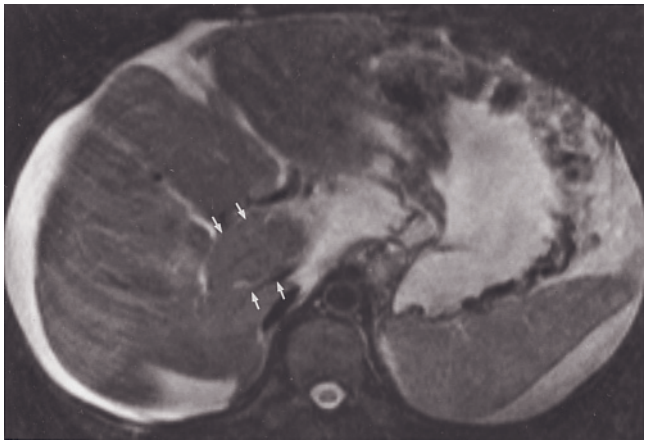

(*a*)

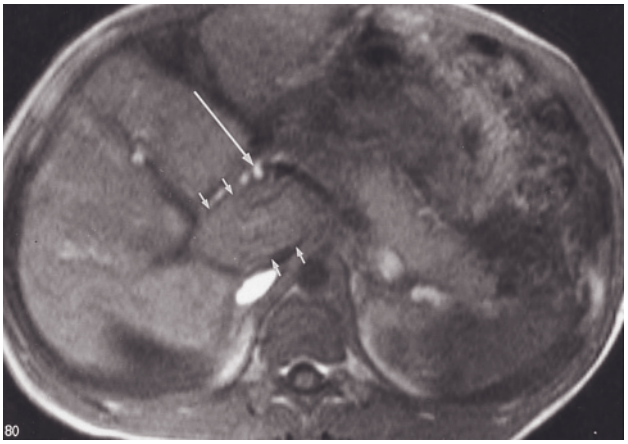

(*b*)

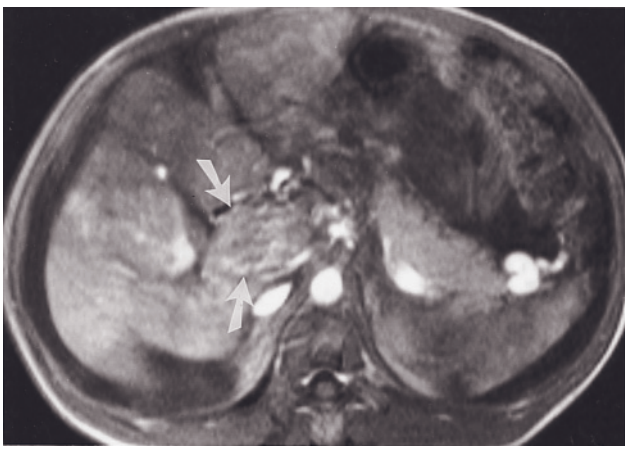

(*c*)

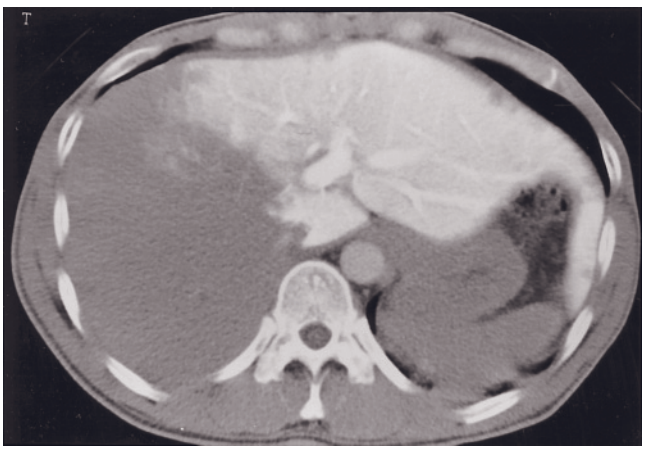

(*d*)

(*e*)

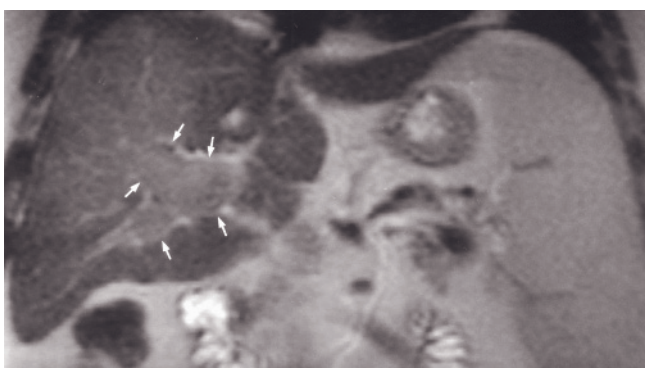

(*f*)

FIG. 2.126 Diffuse hepatocellular carcinoma with portal vein thrombosis. Fat-suppressed T2-weighted ETSE (*a*), SGE (*b*), and immediate postgadolinium SGE (*c*) images. The portal vein is expanded with tumor thrombus (small arrows, *a, b*), which is nearly isointense with liver on T2 (*a*) and T1(*b*) images. Tumor thrombus enhances in a diffuse heterogeneous fashion (arrows, *c*) on the immediate postgadolinium image (*c*). The hepatic artery is identified as a small high-signal tubular structure on the precontrast and immediate images (long arrow, *b*). Heterogeneous enhancement of the liver on the immediate postgadolinium image (*c*) reflects a combination of vascular abnormality from portal vein thrombosis and heterogeneous enhancement of diffusely infiltrative HCC. A substantial volume of ascites is present that is high in signal intensity on T2-weighted images (*a*) and low in signal intensity on pre- and postcontrast T1-weighted images (*b*, *c*).

Portal vein thrombosis in a second patient with diffuse HCC shown on spiral CTAP (*d*) and immediate postgadolinium SGE (*e*) images. On the CTAP image (*d*), nonopacification of the right hemiliver because of thrombosis of the right portal vein is noticed. The immediate postgadolinium image demonstrates a tumor thrombus that expands the right portal vein (arrow, *e*). Diffuse heterogeneous mottled enhancement of the right lobe of the liver is present on the MR image (*e*), which is a typical appearance for diffusely infiltrative HCC.

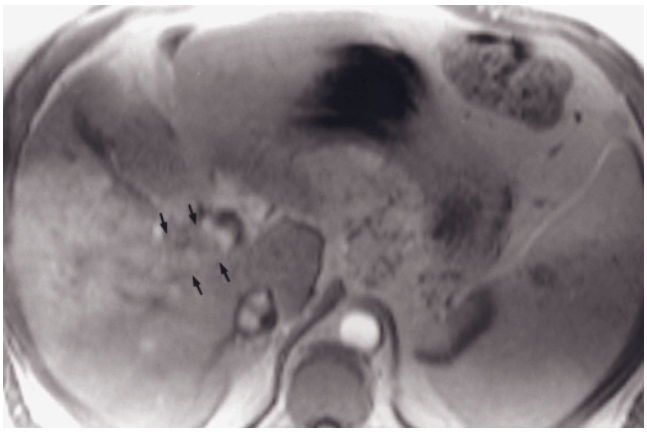

(*g*)

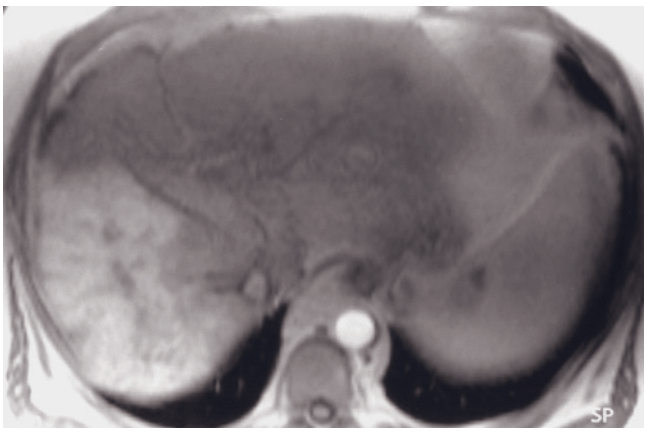

(*h*)

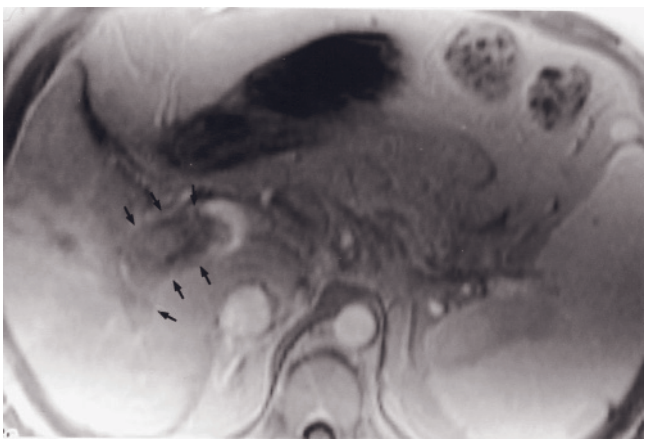

(*i*)

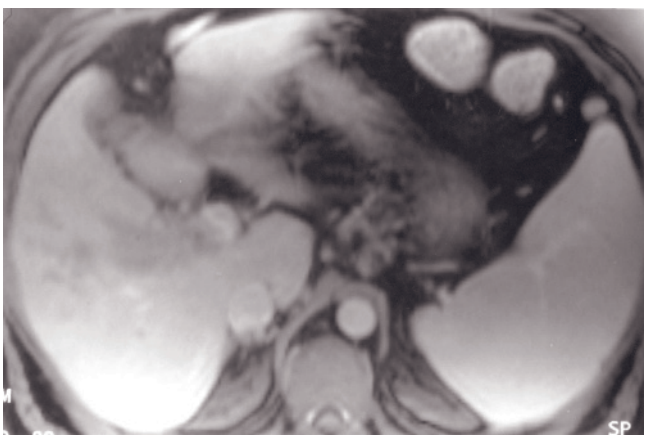

(*j*)

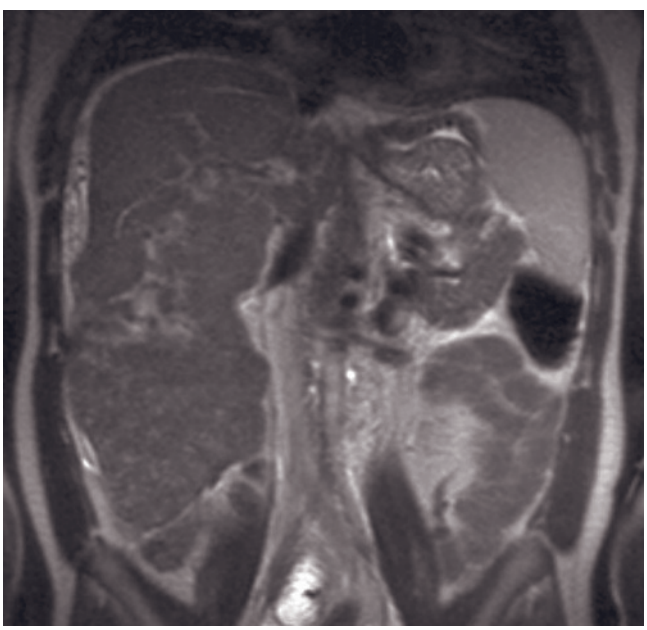

(*k*)

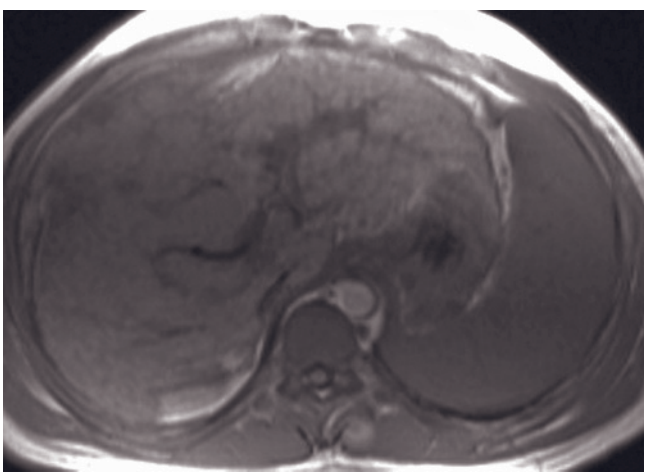

(*l*)

FIG. 2.126 (*Continued*) Coronal T2-weighted SS-ETSE (*f*), transverse immediate (*g*, *h*) and 45-s postgadolinium SGE (*i*) and 90-s fat-suppressed postgadolinium SGE (*j*) images in a second patient. There is an infiltrative HCC in the right hepatic lobe that demonstrates mild high signal intensity on the T2-weighted image (*f*) and heterogeneous intense enhancement immediately after gadolinium administration (*g*, *h*). The portal vein is expanded with tumor thrombus (arrows, *f*, *g*, *i*), which enhances in a diffuse fashion after contrast.

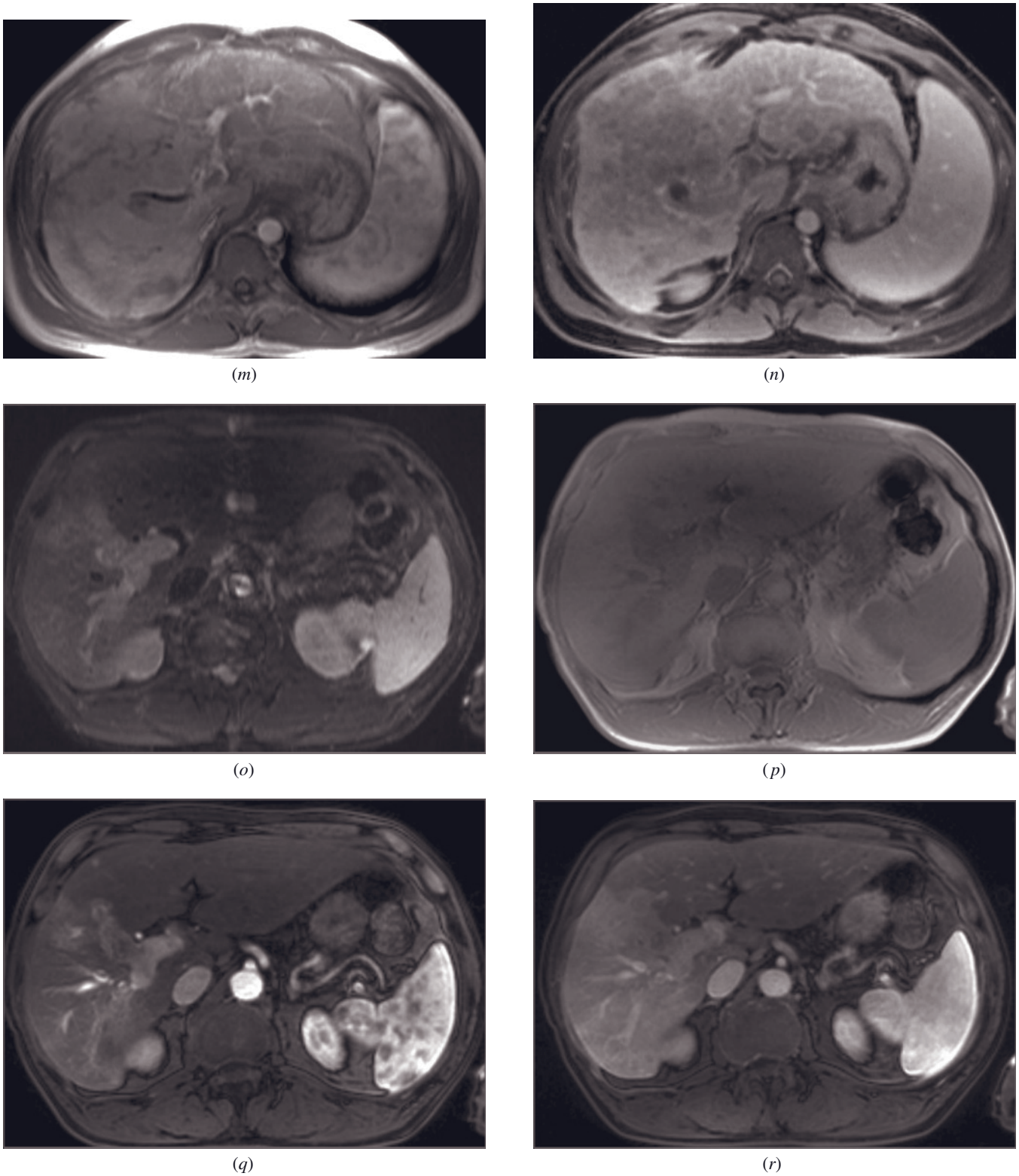

FIG. 2.126 (*Continued*) Coronal T2-weighted SS-ETSE (*k*), SGE (*l*), and immediate (*m*) and 90-s fat-suppressed (*n*) postgadolinium SGE images in a third patient with a diffuse HCC and tumor thrombus of the right portal vein. T2-weighted fat-suppressed SS-ETSE (*o*), SGE (*p*) and immediate (*q*) and 90s postcontrast fat-suppressed 3D-gradient echo images **at 3T** demonstrate poorly defined diffuse HCC in the right lobe. Note intense early enhancement of the tumor thrombus (*q*).

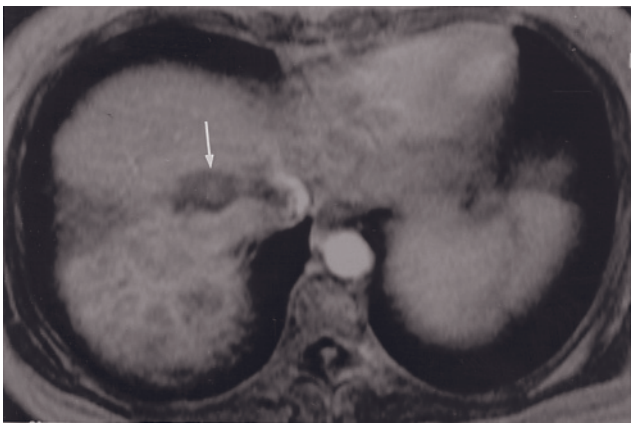

(*a*)

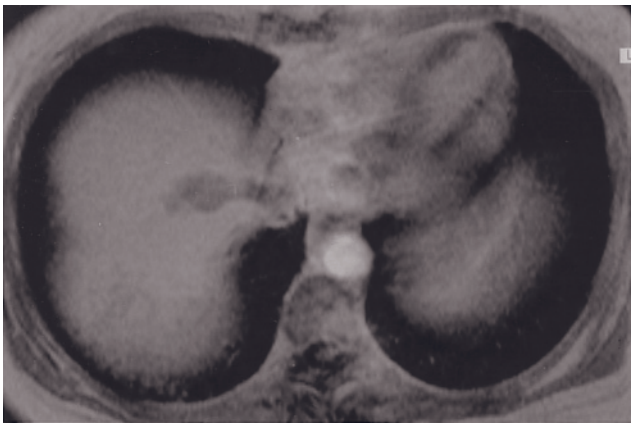

(*b*)

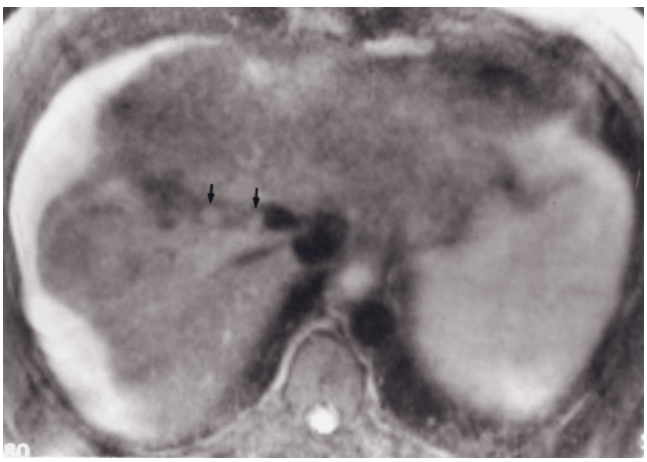

(*c*)

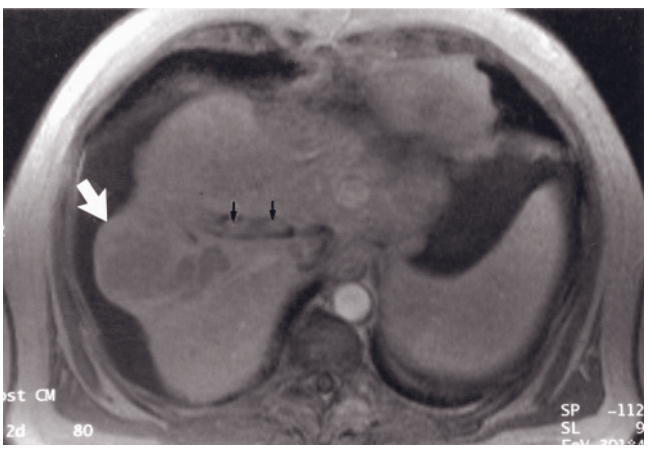

(*d*)

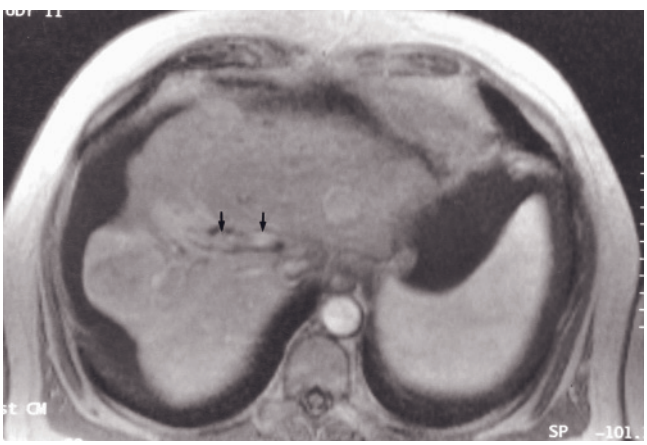

(*e*)

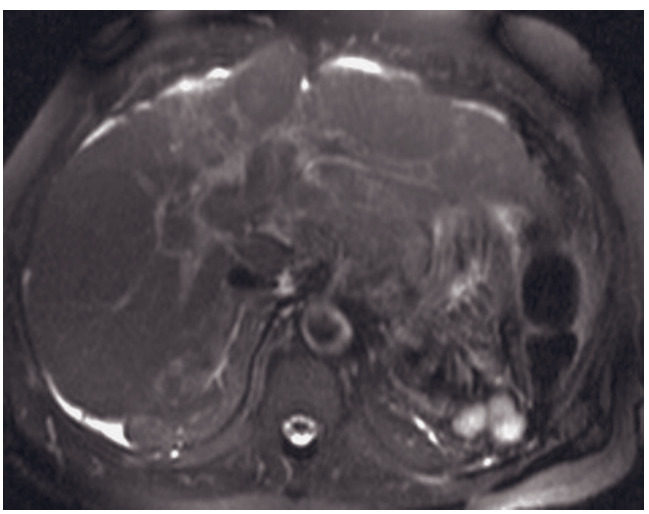

(*f*)

FIG. 2.127 Hepatocellular carcinoma with hepatic-vein thrombosis. Transverse 45-s (*a*) and 90-s (*b*) postgadolinium SGE images. On the 45-s postgadolinium image (*a*) tumor thrombus is apparent in the middle hepatic vein as low-signal-intensity material that expands the vein (arrow, *a*). Diffuse heterogeneous enhancement is noted in the right lobe that represents diffuse infiltrative HCC. Distal to the thrombosed hepatic vein, a wedge-shaped perfusion defect is identified. On the 90-s image (*b*) the tumor thrombus maintains low signal intensity compared to liver. However, the perfusion defect resolved, and the diffuse HCC is more isointense with background liver.

Fat-suppressed T2-weighted ETSE (*c*), SGE (*d*), and immediate postgadolinium SGE (*e*) images in a second patient. A 5-cm HCC (large arrow, *d*) is present in the right hepatic lobe that appears isointense on T2 (*c*)- and mildly hypointense on T1 (*d*)-weighted images and exhibits mild enhancement on hepatic dominant-phase image (*e*). A thin tumor capsule is identified on the precontrast T1-weighted image (*d*). In the middle hepatic vein there is an abnormal soft tissue with isointense signal intensity on T1- and T2-weighted images (arrows, *c, d*, *e*) and moderate enhancement after gadolinium administration (arrow, *e*). A perfusional abnormality adjacent to middle hepatic vein is related to the presence of tumor thrombus.

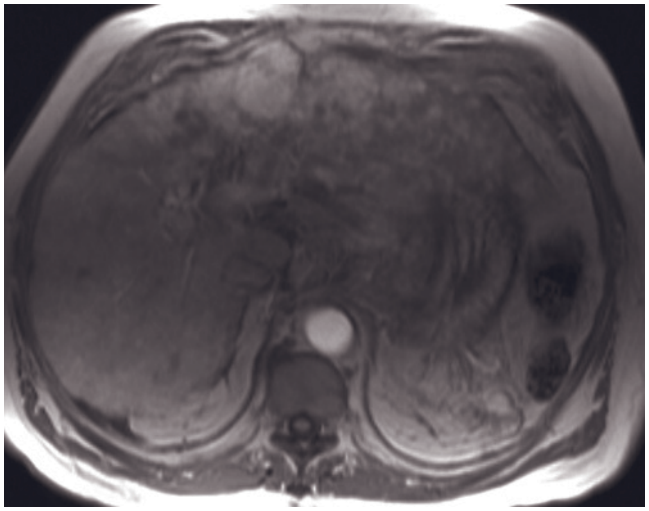

(*g*)

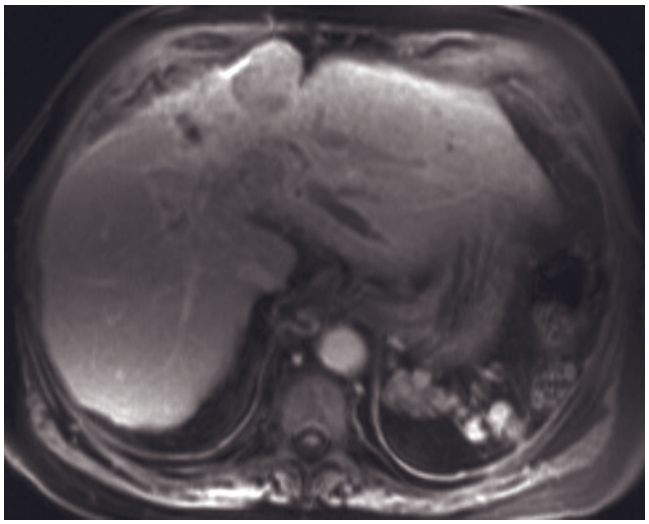

(*h*)

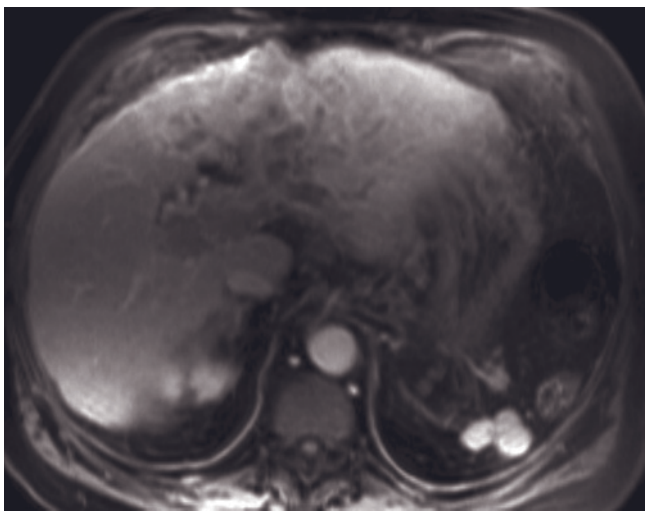

(*i*)

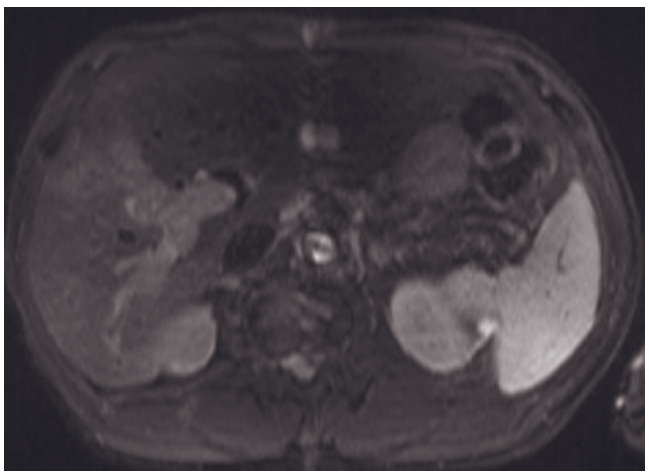

(*j*)

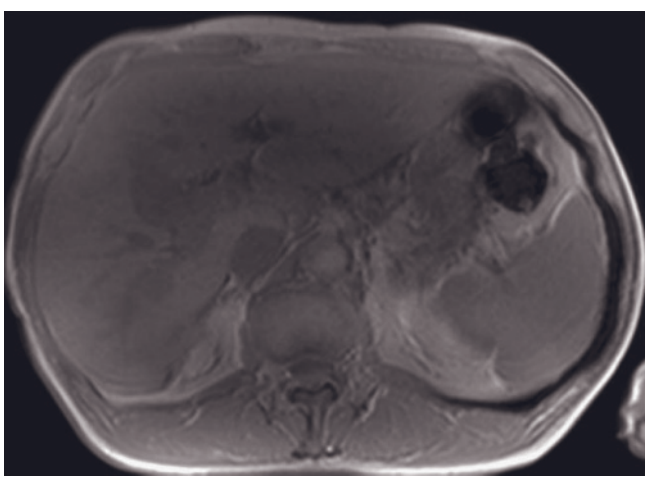

(*k*)

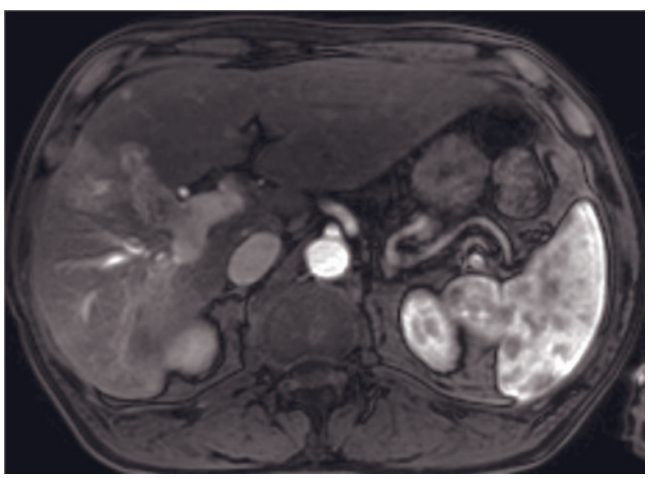

(*l*)

FIG. 2.127 (*Continued*) T2-weighted SS-ETSE (*f*) and immediate (*g*) and 90-s fat-suppressed (*h*, *i*) postgadolinium SGE images in a third patient. The left hepatic lobe and part of the right hepatic lobe show irregularity of the contour and distortion of the normal architecture due to the presence of a large tumor. On T2-weighted image (*f*), this tumor demonstrates mildly high signal intensity, on T1-weighted images (not shown) it shows low signal intensity, and after administration of contrast there is a moderate and heterogeneous enhancement on early-phase images (*g*) that fades to background signal intensity on late-phase images (*h*, *i*). Tumor thrombus is present in the main branches of the portal vein, which enhances on late-phase images. Note the biliary dilatation due to tumor compression.

T2-weighted SS-ETSE fat-suppressed (*j*), SGE (*k*), and immediate (*l*) and 90-s (*m*) fat-suppressed postgadolinium fat-suppressed 3D-gradient echo images **at 3T** images in a fourth patient. Tumor thrombus is apparent in the main portal vein as well right and left branches with features similar to those previously described. Note the perfusional parenchymal abnormality adjacent to the right portal vein.

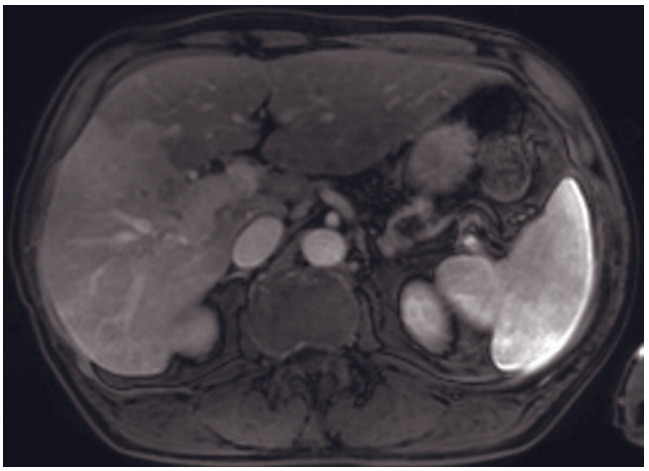

(*m*)

FIG. 2.127 (*Continued*)

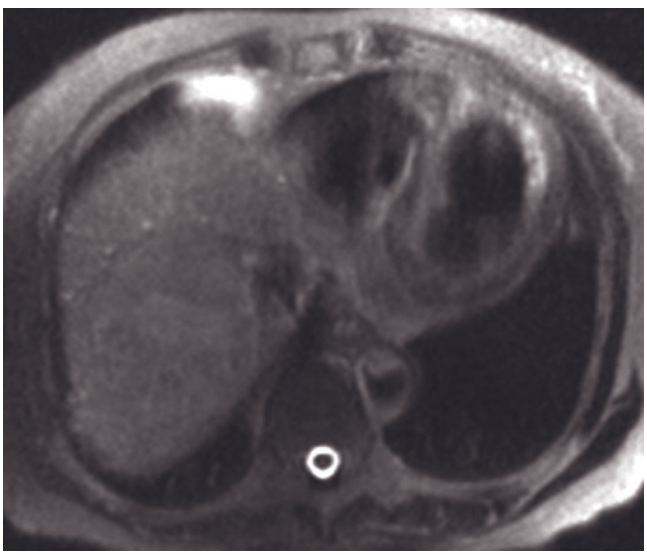

(*a*)

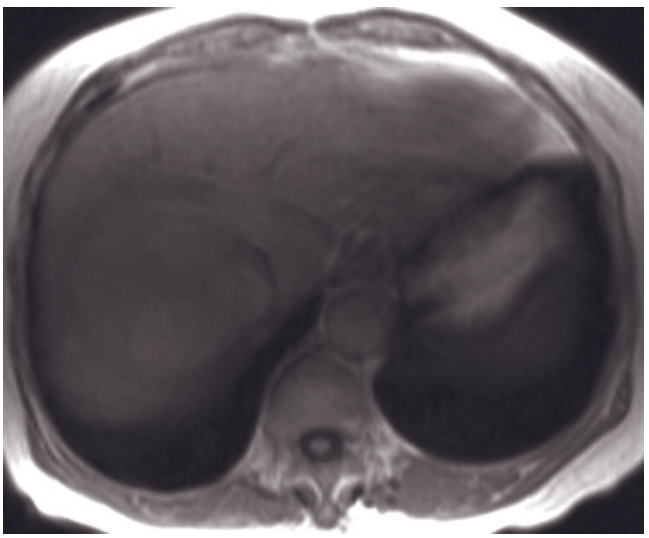

(*b*)

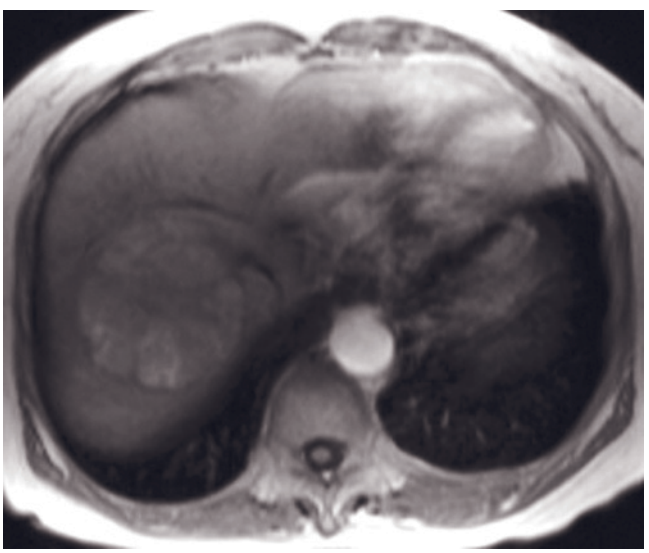

(*c*)

FIG. 2.128 T2-weighted SS-ETSE (*a*), T1-weighted SGE (*b*), and immediate (*c*) and 90-s post gadolinium fat-suppressed (*d*) SGE images; immediate (*e*) and 90-s (*f*) postgadolinium fat-suppressed 3D gradient-echo **at 3T** demonstrate a large hypervascular HCC.

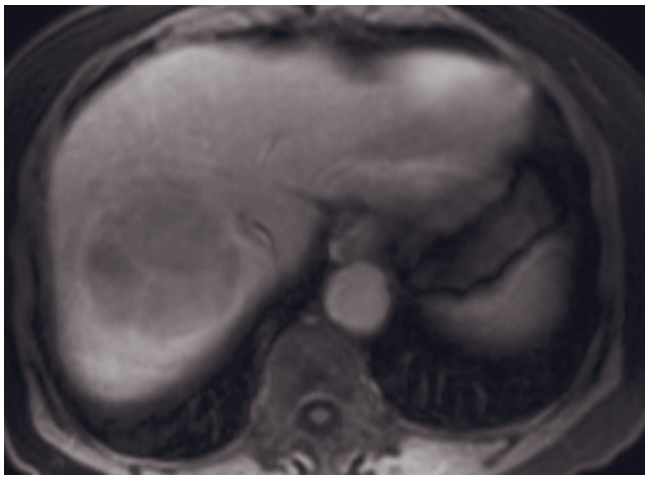

(*d*)

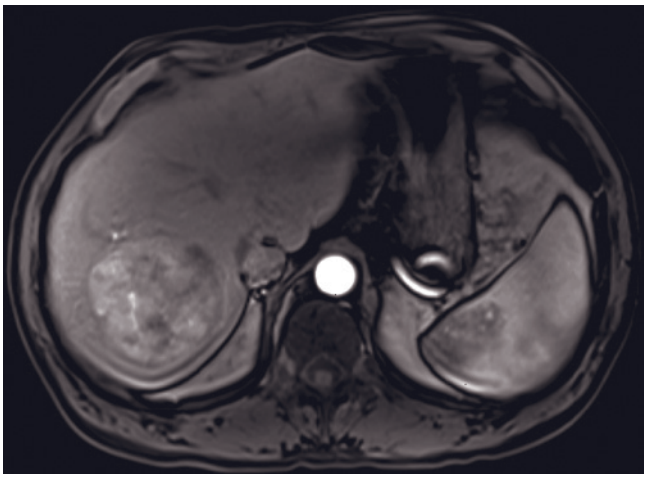

(*e*)

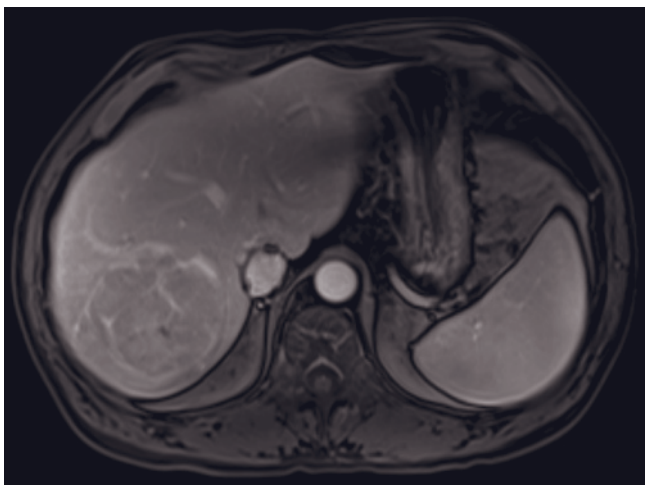

(*f*)

(*g*)

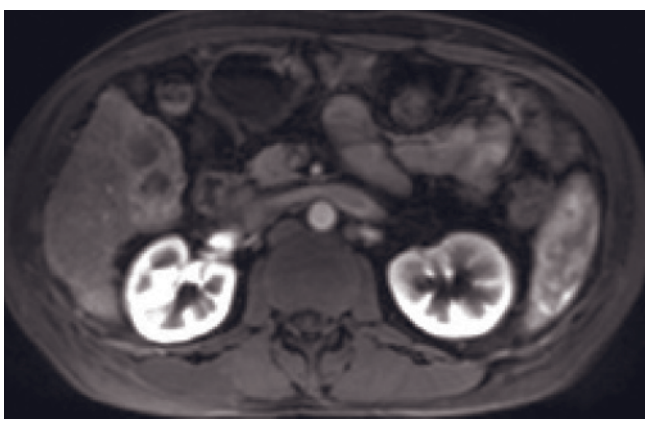

(*h*)

FIG. 2.128 (*Continued*) **Ring enhancing HCC.** T1-weighted fat-suppressed 3D-gradient echo immediate post gadolinium images obtained **at 3T** in a 6-month interval between studies (*g*, *h*). Note the ring pattern of enhancement best observed on 6-month follow-up exam, which mimics the enhancement pattern of metastases. Ring enhancement may be a sign of a more aggressive HCC.

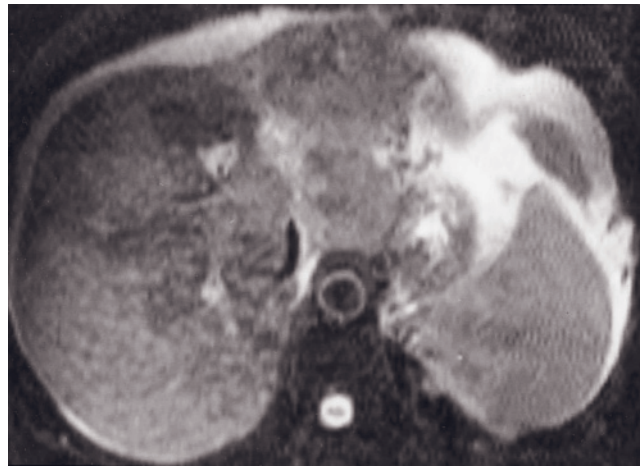

(*a*)

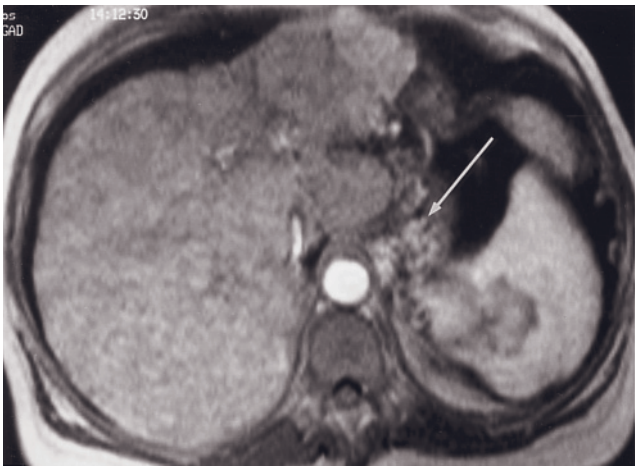

(*b*)

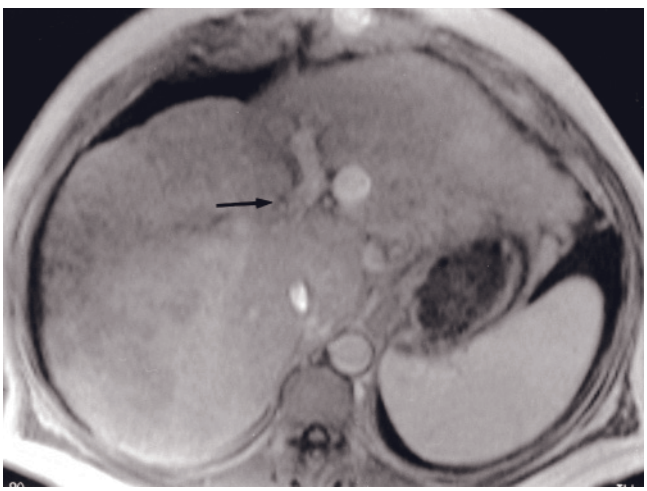

(*c*)

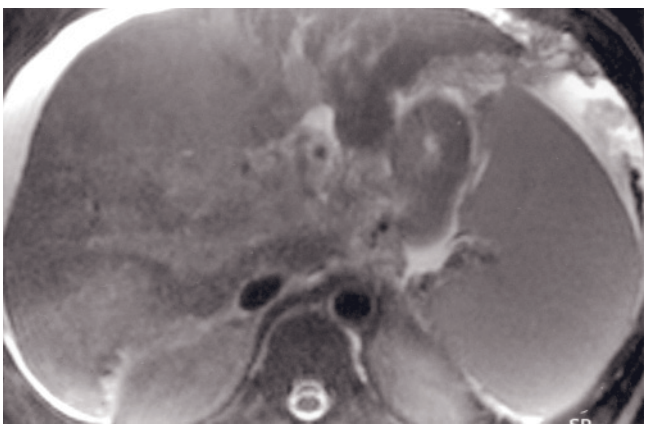

(*d*)

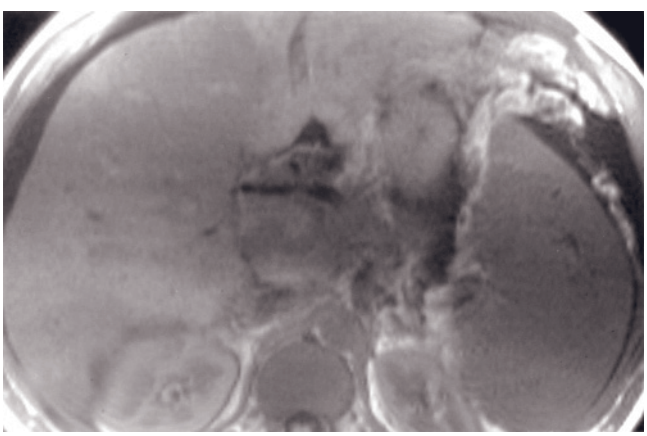

(*e*)

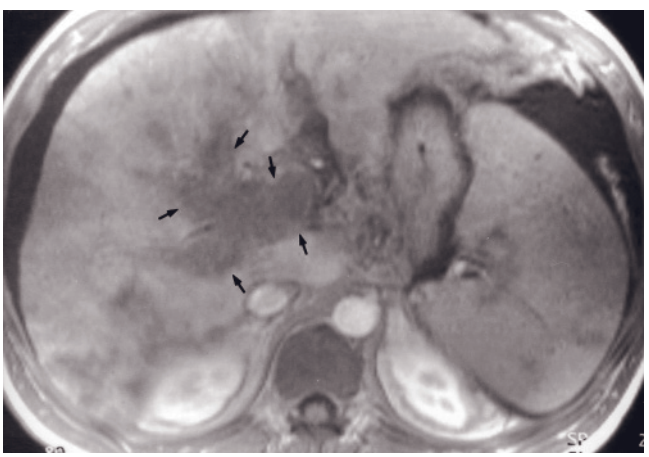

(*f*)

FIG. 2.129 Hepatocellular carcinoma, diffuse infiltrative type. Fat-suppressed T2-weighted ETSE (*a*) and immediate postgadolinium SGE (*b*) images. Mottled diffuse high signal intensity is present throughout the liver on the T2-weighted image (*a*). Diffuse mottled heterogeneous enhancement is appreciated on the immediate postgadolinium image (*b*). These findings represent diffuse infiltrative HCC. Mottled signal intensity is the most common MRI appearance for diffuse infiltrative HCC. Occasionally, diffuse infiltrative HCC will appear as low in signal intensity on T2-weighted images and very low in signal intensity on postgadolinium images. Prominent varices are present along the lesser curvature of the stomach (arrow, *b*).

Transverse 45-s postgadolinium SGE (*c*) in a second patient. There is a large heterogeneous region of mottled enhancement throughout the right lobe of the liver, consistent with an infiltrating HCC. Note the irregularity of liver contour. Tumor thrombus of the right portal vein (arrow, *c*) is also present.

Transverse fat-suppressed T2-weighted SS-ETSE (*d*), SGE (*e*), and immediate postgadolinium SGE (*f*) images in a third patient. The liver is diffusely heterogeneous in appearance on both T2 (*d*)- and T1 (*e*)-weighted images and shows mild diffuse heterogeneous enhancement after contrast (*f*), consistent with infiltrative HCC. The main, right, and left portal veins are distended with tumor thrombus (arrows, *f*). Note ascites and splenomegaly.

These cases illustrate the mottled heterogeneity of infiltrative HCC and illustrate that tumor thrombus in veins is almost invariably present. A third important feature is that α-fetoprotein is frequently extremely high.

T2-weighted images and hypo isointense on T1-weighted images. Immediate postcontrast images, tumor strands enhance variably. Late imperceptible enhancement or increased enhancement of tumor strands may reflect a high fibrous composition (fig. 2.130).

Venous thrombosis, almost always portal veins, sometimes in combination with hepatic venous thrombosis, is virtually invariably present. Very high serum α-fetoprotein (AFP) levels are commonly observed with diffuse HCC, with 78% of patients reported as presenting with increased AFP levels. AFP levels can be normal or near normal in a sizable minority of patients. A prior study [207] reported that 100% (22 of 22) of patients with diffuse HCC presented with portal vein thrombosis. Tumor thrombus is commonly high signal intensity on T2-weighted images and enhances with gadolinium; meanwhile, bland thrombus is low in signal intensity on T2-weighted images and does not enhance after gadolinium.

Diffuse HCC may simulate the appearance of acute on chronic hepatitis or recent-onset fibrosis on imaging studies. Acute on chronic hepatitis tends to fade to background parenchyma rather than washing out on late postcontrast images and does not have expansive thrombus. AFP levels for acute on chronic hepatitis are usually relatively low. Major differential diagnoses to be considered are cholangiocarcinoma and metastases. Commonly, cholangiocarcinoma has better defined margins and does not exhibit tumor venous thrombus. Infiltrative metastases such as from breast cancer also have a more clearly focal pattern of involvement than diffuse HCC, and the primary tumor is almost always

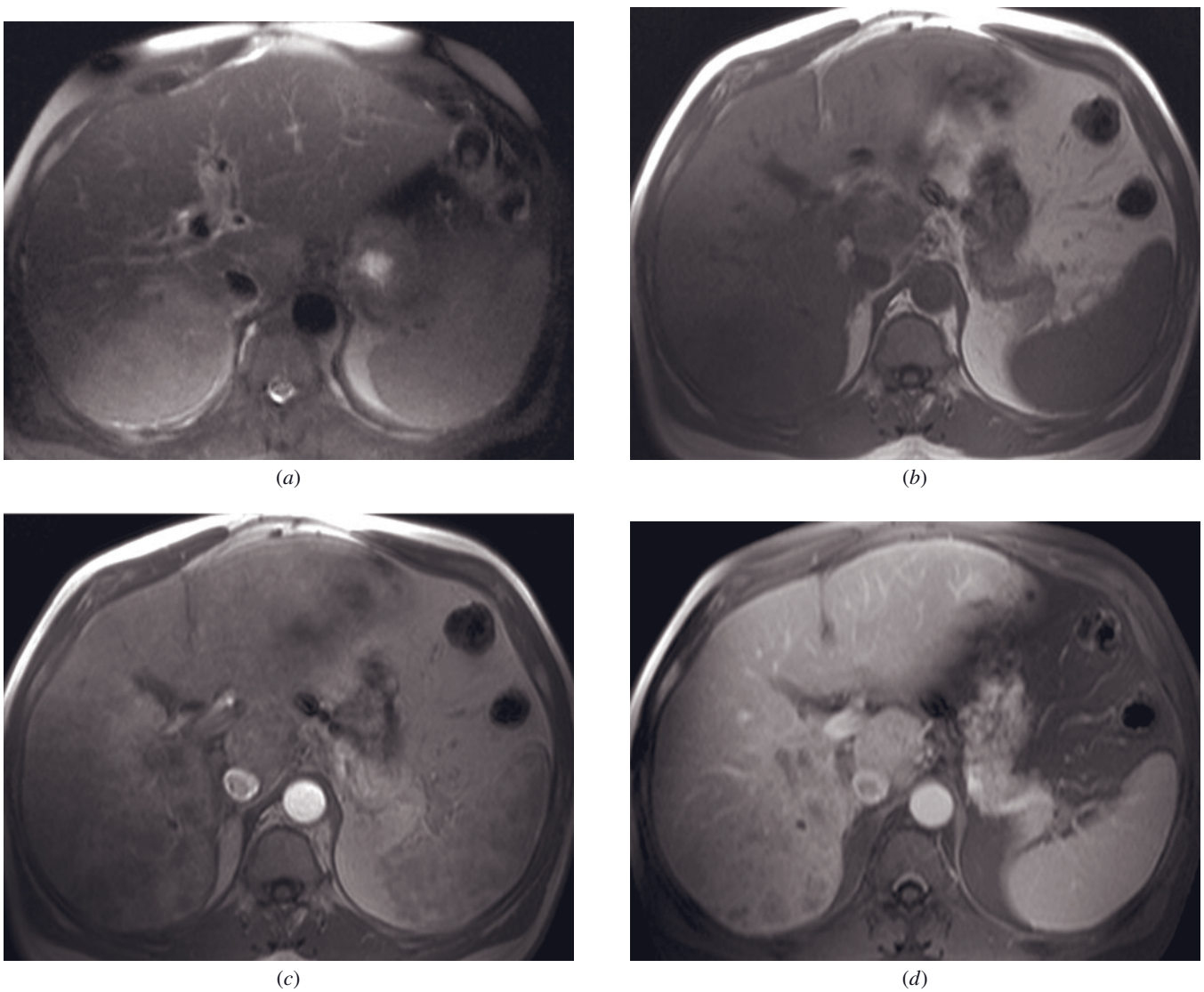

FIG. 2.130 Diffuse Infiltrative HCC. Fat-suppressed T2-weighted SS-ETSE (*a*), SGE (*b*), and immediate (*c*) and 90-s fat-suppressed (*d*) postgadolinium SGE images; fat-suppressed T2-weighted SS-ETSE (*e*) and immediate (*f*) and 90-s fat-suppressed (*g*)

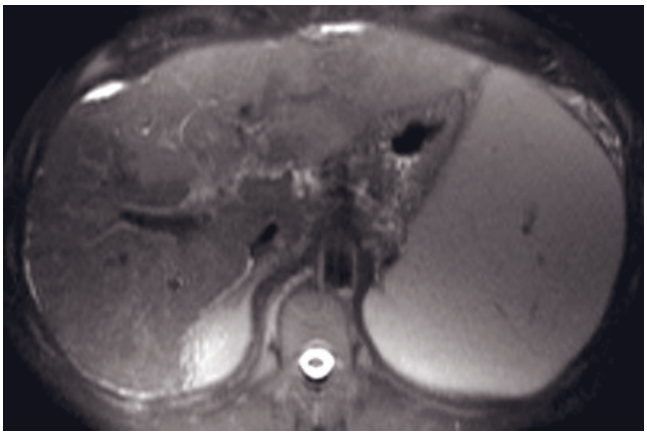

(*e*)

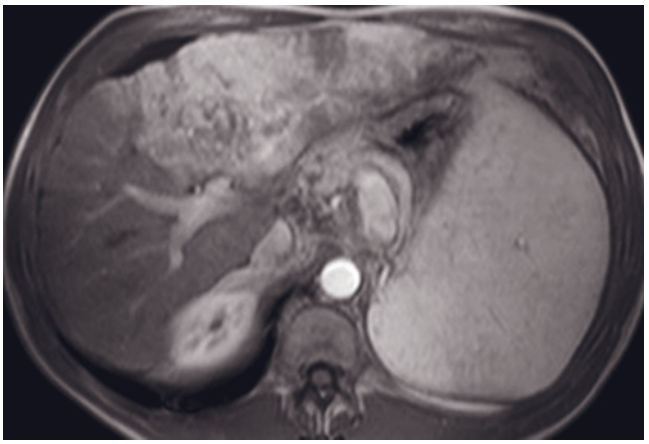

(*f*)

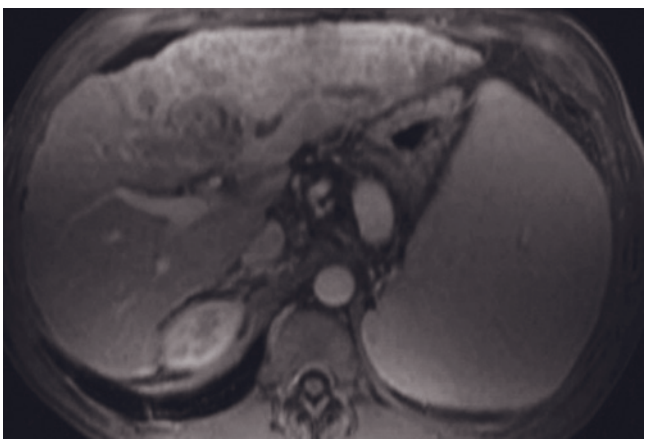

(*g*)

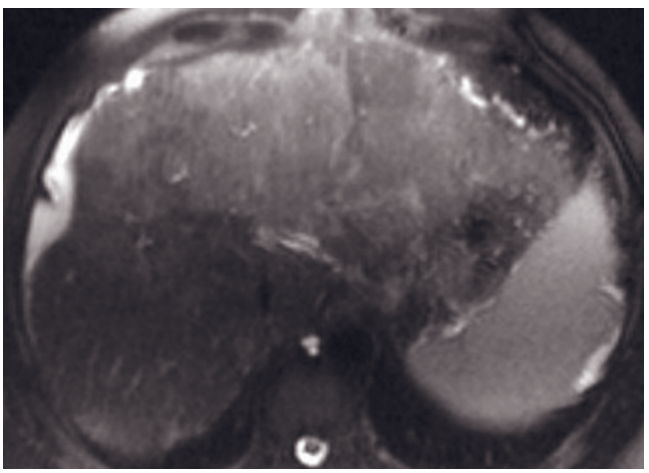

(*h*)

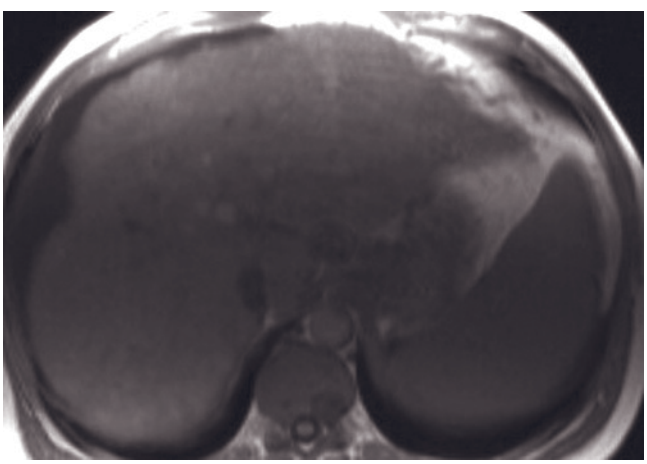

(*i*)

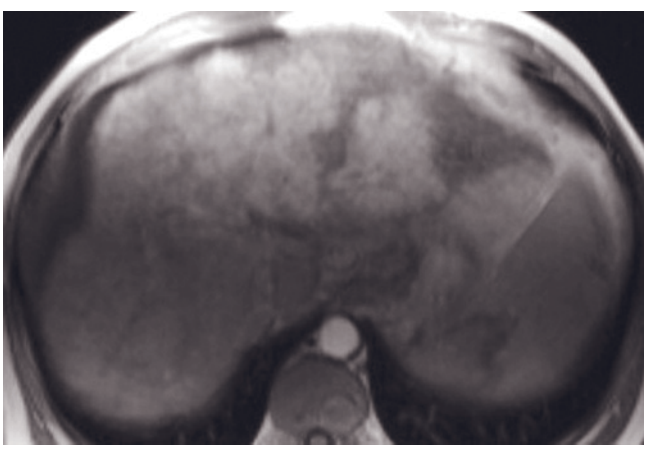

(*j*)

FIG. 2.130 (*Continued*) postgadolinium SGE images; fat-suppressed T2-weighted SS-ETSE (*h*), SGE (*i*), and immediate (*j*) and 90-s fat-suppressed (*k*) postgadolinium SGE images.

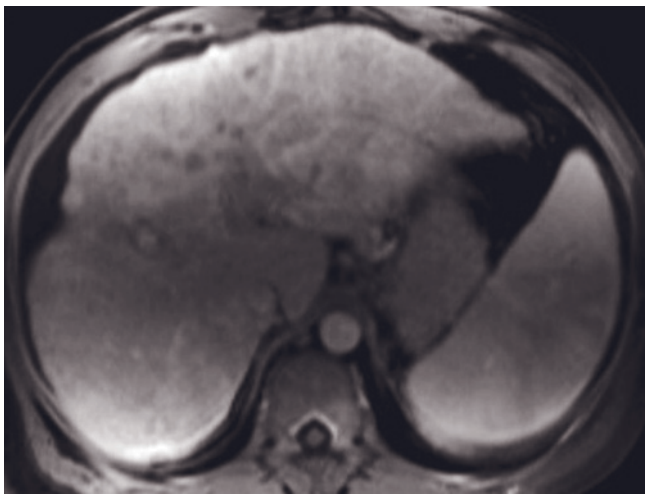

(*k*)

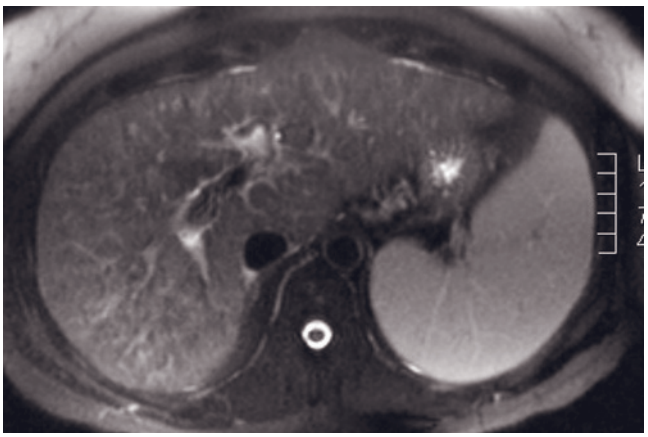

(*l*)

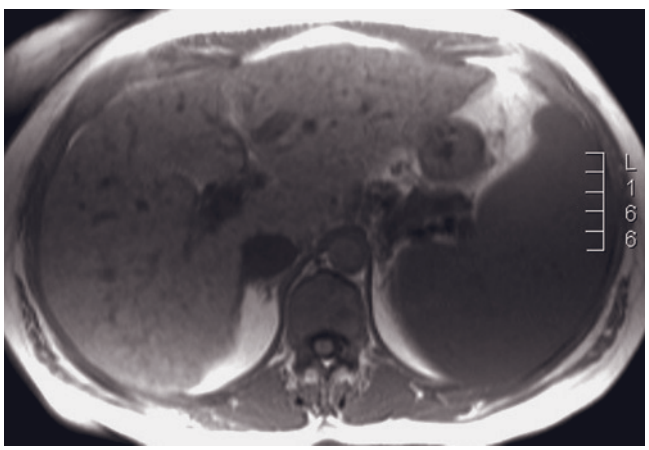

(*m*)

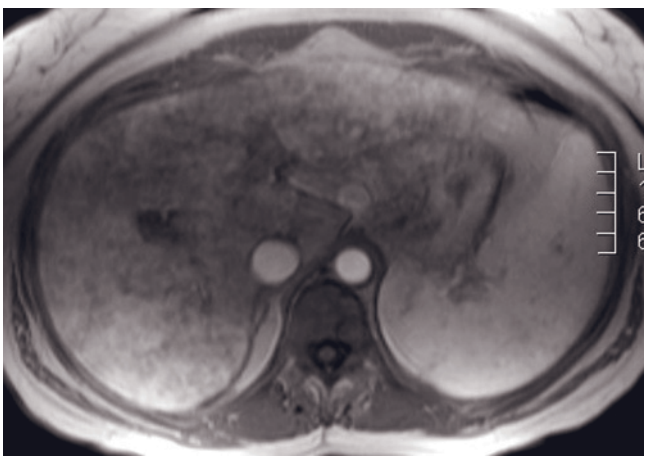

(*n*)

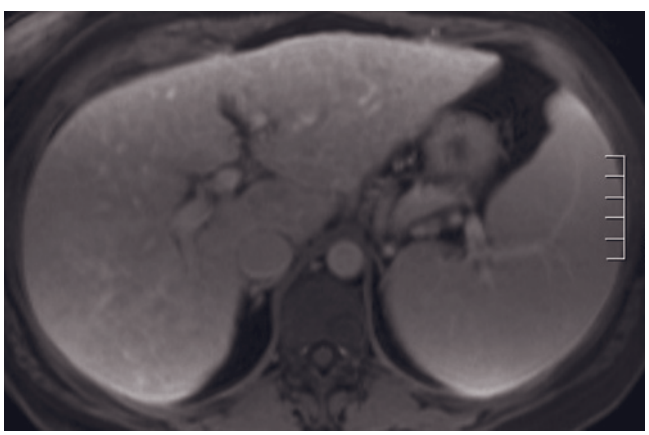

(*o*)

FIG. 2.130 (*Continued*) Fat-suppressed T2-weighted SS-ETSE (*l*), SGE (*m*), and immediate (*n*) and 90-s fat-suppressed (*o*) post-gadolinium SGE images in four different patients with infiltrative HCC. In all cases, the tumor shows an intense heterogeneous enhancement on early-phase images (*e*, *f*, *j*, *n*) that becomes less evident but with persistent enhancement (*d*, *g*, *k*) or imperceptible (*o*) on late-phase images.

known [207]. Venous tumor thrombus rarely may occur in the setting of metastases.

Fibrolamellar Carcinoma

Fibrolamellar carcinoma is a distinct morphologic subtype of liver cell carcinoma. This tumor occurs in younger patients, frequently females, without underlying cirrhosis or chronic liver disease. Fibrolamellar carcinoma is biologically distinct from other HCCs because it exhibits slow growth and is associated with a favorable prognosis [209]. From a pathologic viewpoint, the tumor is oftentimes large, usually solitary and well defined [2]. Macroscopically, the tumor shows a lobular architecture with intervening fibrous septa or a central stellate scar. Microscopically, tumor cells are polygonal, large, and eosinophilic. An extensive meshwork of collagenous stroma surrounding nests of tumor cells is the sine qua non for pathologic diagnosis. The rich fibrous network that incarcerates tumor has been credited for the slow, indolent growth of fibrolamellar carcinoma in contrast with ordinary HCC, which has a richly vascularized stroma permissive for intra- and extrahepatic spread [2].

On imaging, fibrolamellar carcinomas are generally large, solitary tumors that are heterogeneous and moderately high in signal intensity on T2-weighted images and heterogeneous and moderately low in signal intensity on T1-weighted images. Enhancement of the tumor is diffuse heterogeneous and moderately intense on immediate postgadolinium images. A huge central scar with radiating appearance is present. The central scar is variable in signal and has large low-signal components on T2-weighted images that enhance negligibly on delayed gadolinium-enhanced images (fig. 2.131) [210, 211]. On MR imaging, the scar is characterized by a complex arborizing pattern, radiating from a central focus and extending out to the tumor periphery. This profile is distinctly different from the appearance of FNH, in which the scar occupies a small central portion of the tumor and exhibits more uniform signal enhancement characteristics on late images [210].

Lymphoma

Secondary involvement of the liver by Hodgkin and non-Hodgkin lymphoma is common in stage IV disease [212]. On imaging, non-Hodgkin lymphoma more frequently results in focal hepatic lesions than Hodgkin disease. Lesions vary in signal intensity from low to moderately high on T2-weighted images and are typically low in signal intensity on T1-weighted images. Enhancement on immediate postgadolinium images tends to parallel the signal intensity on T2-weighted images; lesions that are low in signal intensity on T2-weighted images tend to enhance minimally (fig. 2.132), whereas lesions that are high in signal intensity tend to enhance in a substantial fashion (fig. 2.133) [213]. As with liver metastases, enhancement on immediate postgadolinium images usually is predominantly peripheral. Lesions of malignant lymphoma may possess transient, ill-defined perilesional enhancement on immediate postgadolinium images independent of the degree of enhancement of the lesions themselves (fig. 2.134). Rarely tumors may directly invade vessels producing an angiotropic pattern of involvement (fig. 2.135). Histopathologically, secondary involvement of the liver by malignant lymphoma is heralded by tumor deposits within the portal tracts. A clinical correlate with this microscopic appearance may be reflected on MR imaging with the appearance of periportal tumor tracking. This particular pattern may be very difficult to diagnose but is best visualized on a combination of T2-weighted fat-suppressed images and hepatic venous-phase gadolinium-enhanced fat-suppressed images. On both techniques, periportal tumor is moderately high in signal intensity (fig. 2.136).

Primary hepatic lymphoma is considerably rarer than secondary involvement, and histologically the majority are non-Hodgkin lymphomas. Most tumors are characterized grossly as a large solitary mass, but they may vary in appearance from multiple nodules to diffuse involvement. Tumors are mild to moderately high in signal on T2-weighted images and moderately low in signal intensity on T1-weighted images and show relatively diffuse heterogeneous enhancement on immediate postgadolinium gradient-echo images (figs. 2.137 and 2.138), analogous to primary hepatic tumors of other histologic types.

Multiple Myeloma

Focal deposits of multiple myeloma rarely occur in the liver and most often in the setting of disseminated disease. Pathologically, hepatic lesions are characterized by tumor cell infiltration of sinusoids and portal tracts. Focal hepatic lesions are observed most commonly in light-chain multiple myeloma. Lesions are often small, measuring approximately 1 cm in diameter. They are moderately hyperintense on T2-weighted images and iso- to mildly hyperintense on T1-weighted images [214]. The hyperintensity on T1-weighted images may reflect the increased production of monoclonal protein. Multiple myeloma lesions are sufficiently rare that is difficult to establish their enhancement characteristics; many, however, appear to be hypervascular (fig. 2.139).

Intrahepatic or Peripheral Bile Duct Carcinoma (Cholangiocarcinoma)

Intrahepatic or peripheral cholangiocarcinoma are terms applied to lesions that originate in the ducts proximal to (i.e., above) the hilum of the liver. Malignant tumors arising from intrahepatic bile ducts are much less

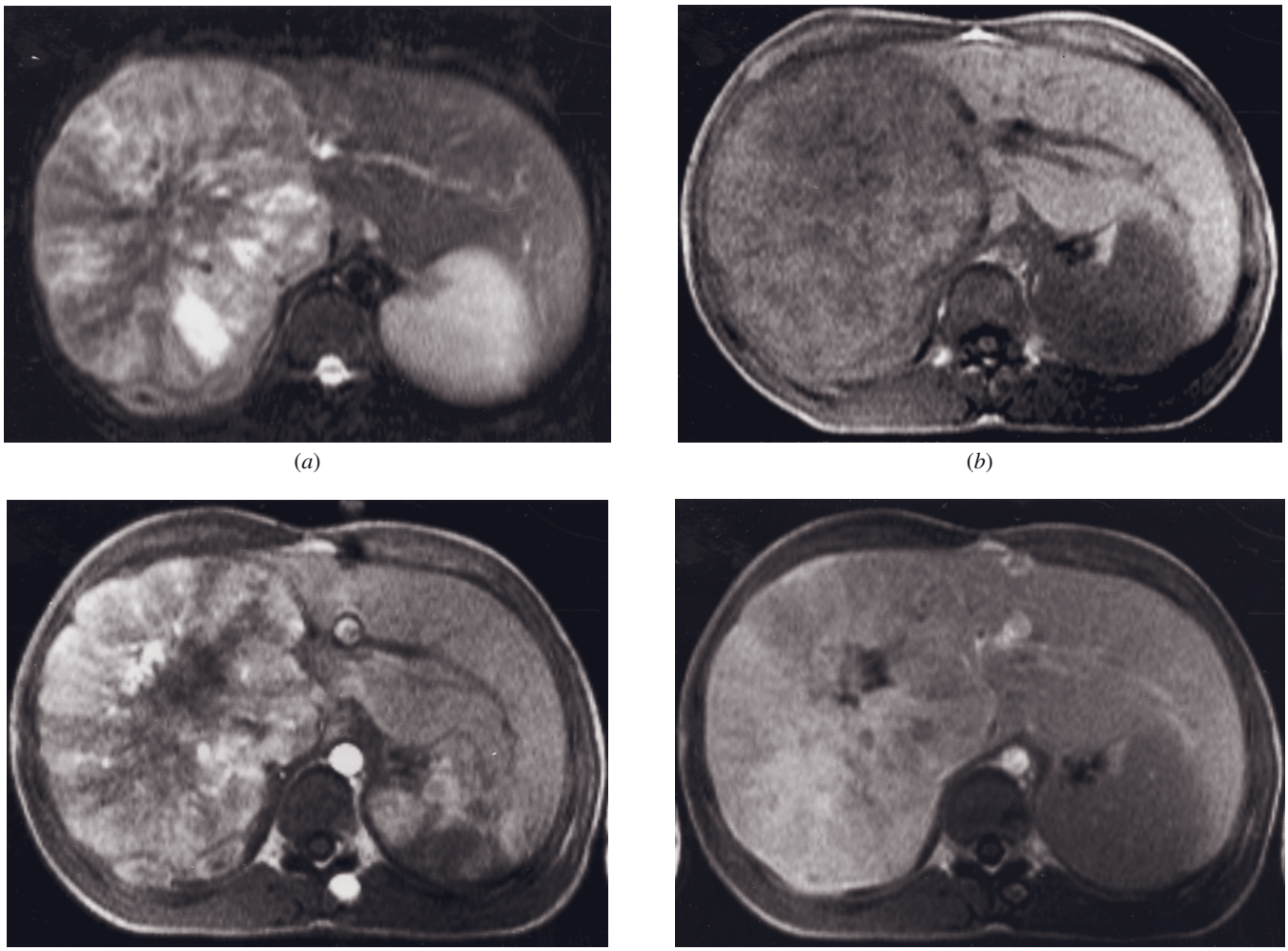

(*a*) (*b*) (*c*) (*d*)

FIG. 2.131 Fibrolamellar carcinoma. Fat-suppressed T2-weighted ETSE (*a*), SGE (*b*), and immediate (*c*) and 10-min postgadolinium SGE (*d*) images. A 14-cm fibrolamellar hepatocellular carcinoma is present in this adolescent male with no history of liver disease and 1-yr duration of gynecomastia. The tumor is heterogeneously hyperintense on the T2-weighted image (*a*) with the central radiating scar largely low in signal intensity and hypointense on the T1-weighted image (*b*) with the central scar also low in signal intensity. On the immediate image (*c*), the tumor exhibits diffuse moderate heterogeneous enhancement with negligible enhancement of the radiating scar. On the 10-min image (*d*), the bulk of the tumor has become isointense with background liver. Portions of the central scar are higher in signal intensity than surrounding tissue, whereas other parts remain low in signal. In contrast to FNH, the scar in fibrolamellar HCC is much larger and exhibits more heterogeneous signal on T2 and early and late postgadolinium images.

common than those arising from hepatocytes and have no direct association with cirrhosis [215]. Most cases of cholangiocarcinoma occur after the age of 60 years. Pathologically, the tumor is generally better circumscribed and of firmer consistency than hepatocellular carcinoma. The microscopic picture is characterized by glandular configurations surrounded by abundant, dense fibrous stroma. The prominent sinusoidal pattern of HCC is not present [22].

The tumor is frequently large at presentation [216]. Cholangiocarcinoma resembles HCC with moderate high signal intensity on T2-weighted images and low signal intensity on T1-weighted images. High signal on T1-weighted images, pseudocapsule, and invasion into portal and hepatic veins are common with HCC and rarely seen with cholangiocarcinoma. Also, biliary and extrinsic portal vein obstruction are more common with cholangiocarcinoma. Enhancement with gadolinium varies from minimal to intense diffuse heterogeneous enhancement immediately after contrast administration (fig. 2.140). Minimal enhancement is most commonly observed. Persistent enhancement on delayed images is relatively common [217]. The intrahepatic origin of the tumor likely explains the early diffuse heterogeneous

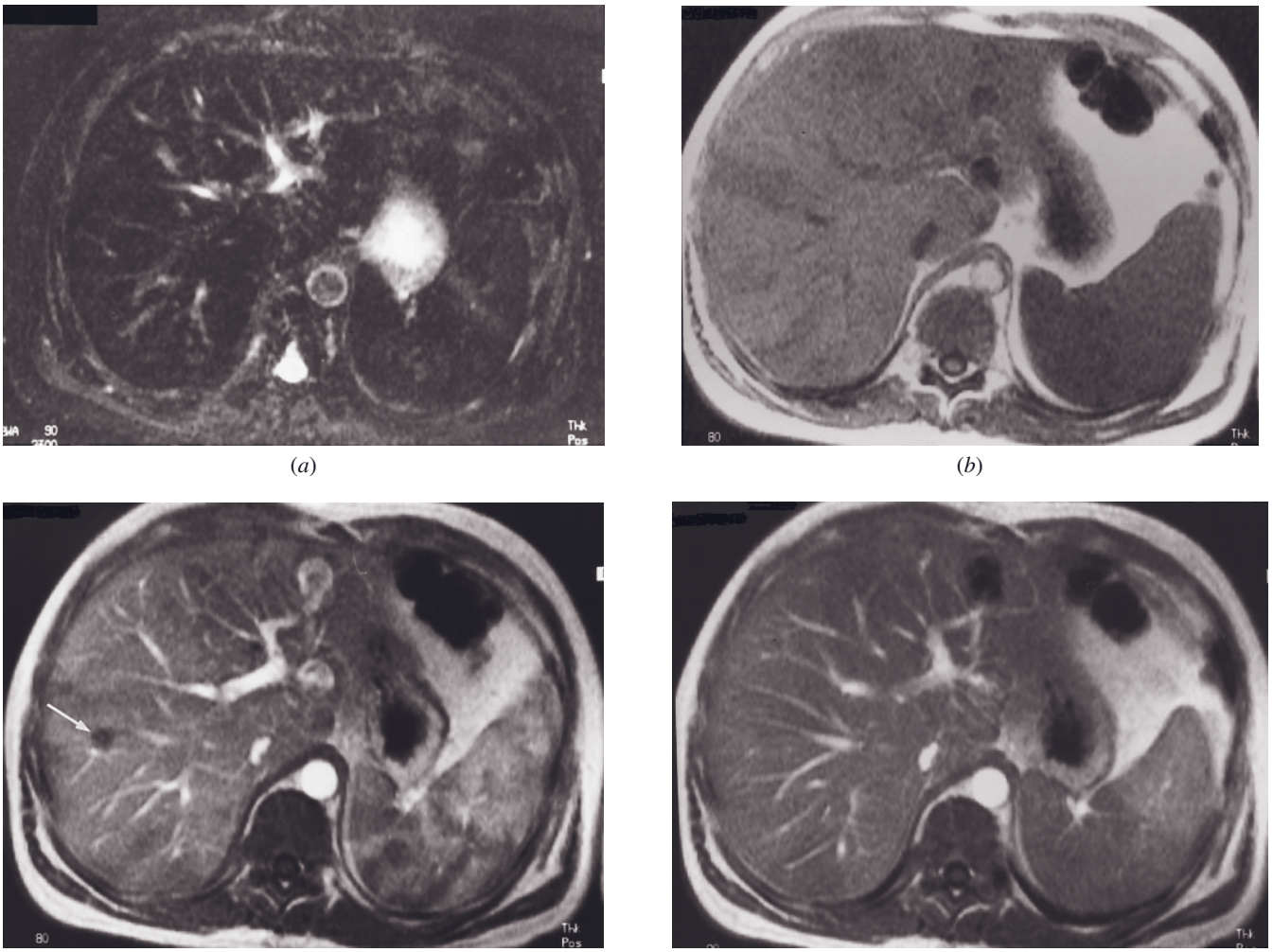

(*a*) (*b*) (*c*) (*d*)

FIG. 2.132 Hepatic lymphoma, low T2-weighted signal. Fat-suppressed T2-weighted SE (*a*), SGE (*b*), and immediate (*c*) and 90-s (*d*) postgadolinium SGE images. On the T2-weighted image (*a*), the liver and spleen demonstrate transfusional siderosis with low signal intensity of the liver and spleen. The SGE image (*b*) demonstrates wedge-shaped regions of low signal intensity representing increased iron deposition. On the immediate postgadolinium image (*c*), focal low-signal intensity masses (arrow, *c*) of diffuse histiocytic lymphoma are shown. These masses enhance to isointensity with hepatic parenchyma on interstitial-phase images.

enhancement. (For a more complete description of cholangiocarcinoma see Chapter 3, *Gallbladder and Biliary System*).

Malignant tumors of mixed liver cell and bile duct differentiation are rare. Mixed HCC-cholangiocarcinoma may occur, and the imaging appearance is generally indistinguishable from that of HCC (fig. 2.141). These tumors tend to be multifocal and hypervascular.

Angiosarcoma

Angiosarcoma is the most common sarcoma arising in the liver and accounts for 1.8% of all liver cancers. An increased risk for the development of this tumor in adults has been documented in the following settings: 1) cirrhosis; 2) vinyl chloride exposure; 3) thorium dioxide exposure (Thorotrast) for radiographic purposes; and 4) arsenic exposure. This tumor is usually encountered in middle-aged patients and occurs more commonly in men. Pathologically, angiosarcomas appear most commonly as multicentric nodules diffusely involving the liver. Occasionally, tumor may present as a solitary, large mass. Microscopically, angiosarcoma is characterized by ill-defined clusters of malignant endothelial cells lining and expanding the sinusoids. Internal hemorrhage is relatively common [218].

On MRI, angiosarcoma usually appears as a multifocal process, but an infiltrative pattern is also described [219, 220]. Angiosarcoma may be high signal intensity

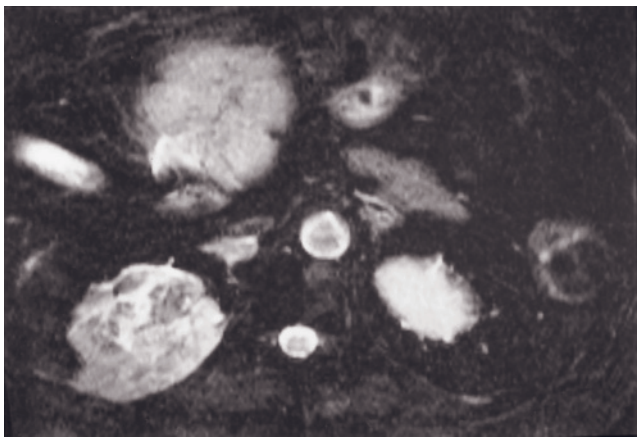

(*a*)

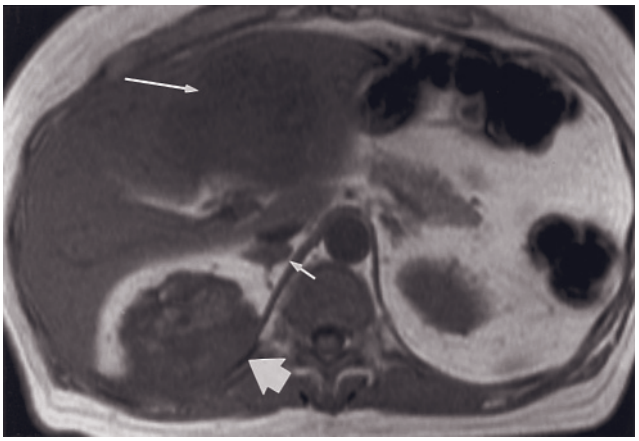

(*b*)

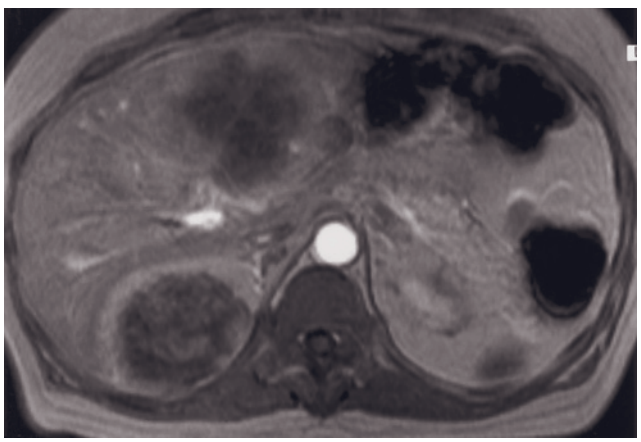

(*c*)

FIG. 2.133 Hepatic lymphoma, after transplant. Fat-suppressed T2-weighted SE (*a*), SGE (*b*), and immediate postgadolinium SGE (*c*) images. In this patient with post-heart transplant lymphoma, and 8-cm hepatic mass (long arrow, *b*), a 1-cm adrenal mass (short arrow, *b*), and a 6-cm peritoneum-based mass (large arrow, *b*) are present. The hepatic mass is moderately hyperintense on the T2-weighted image (*a*) and moderately hypointense on the T1-weighted image (*b*) and demonstrates predominantly peripheral enhancement on the immediate postgadolinium image (*c*). Minimal heterogeneous enhancement of the peritoneal and adrenal masses is present on the immediate postgadolinium image (*c*).

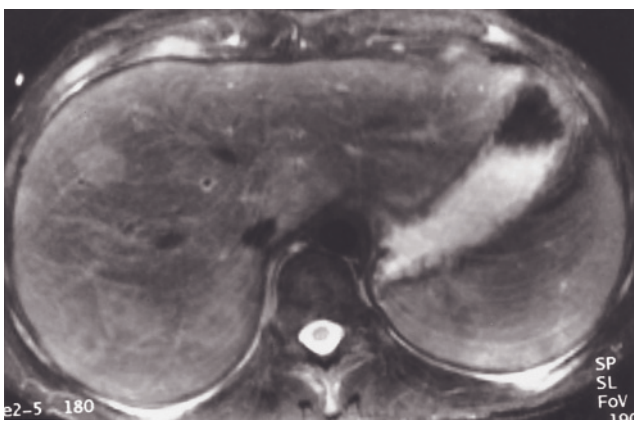

(*a*)

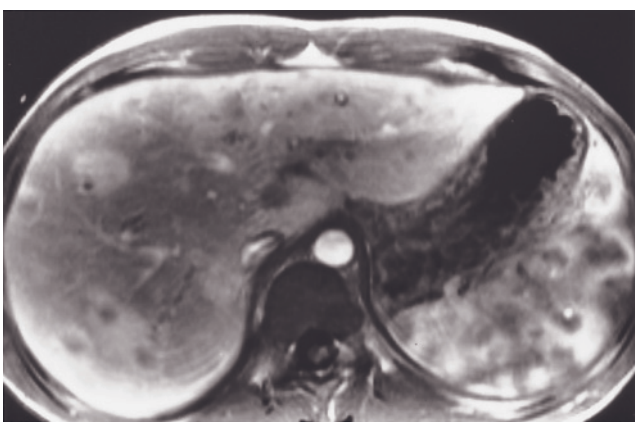

(*b*)

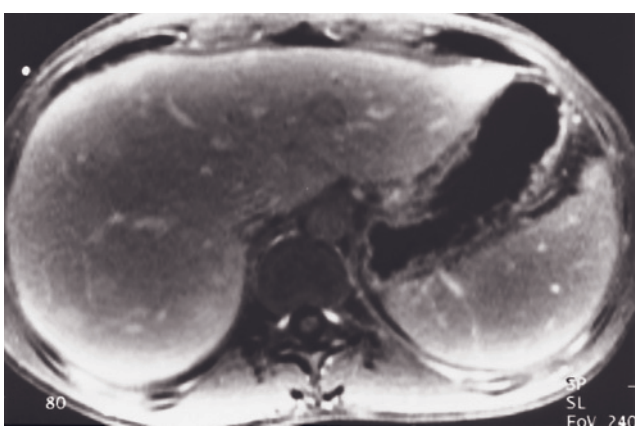

(*c*)

FIG. 2.134 Hodgkin lymphoma. Fat-suppressed T2-weighted ETSE (*a*) and immediate (*b*) and 90-s fat-suppressed postgadolinium SGE (*c*) images. Multiple focal mass lesions smaller than 2 cm are present throughout the liver, many of which show mildly hyperintense tumor periphery on T2 (*a*) and demonstrate ring enhancement with ill-defined perilesional enhancement on immediate postgadolinium images (*b*). Arciform enhancement of the spleen is present on the immediate postgadolinium image, with no evidence of focal low-signal-intensity masses (*b*). By 90 s after gadolinium (*c*), many of the hepatic masses have become isointense with the liver.

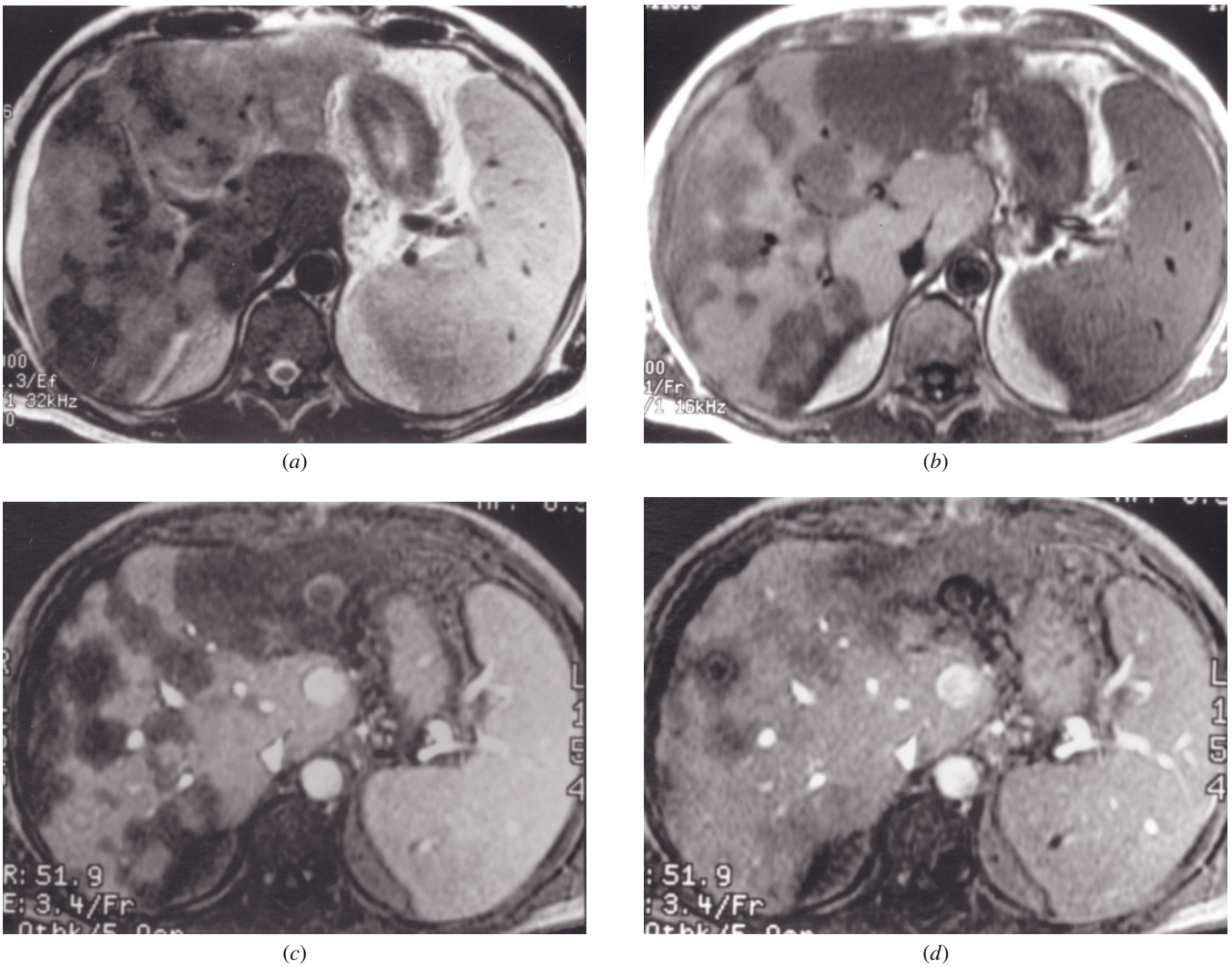

FIG. 2.135 Angiotropic intravascular lymphoma. T2-weighted ETSE (*a*), SGE (*b*), and immediate (*c*) and 90-s (*d*) postgadolinium SGE images. There is an irregular geographic pattern of liver involvement that represents angiotropic intravascular lymphoma. The vascular involvement causes moderately high signal on T2 (*a*), moderately low signal on T1 (*b*), and negligible early enhancement (*c*) with delayed enhancement (*d*) (Courtesy of Evan Siegelman, M. D., Dept. Radiology, Hospital of the University of Pennsylvania.)

on T2-weighted images and low signal on T1-weighted images. The frequent presence of hemorrhage results in focal areas of low signal intensity on T2-weighted images and high signal on T1-weighted images. After contrast, angiosarcoma may demonstrate peripheral nodular enhancement with centripetal progression, mimicking the appearance of hemangioma (fig. 2.142) [220]. The frequent presence of hemorrhage, which results in low signal intensity on T2-weighted images, high signal on T1-weighted images, and lack of central enhancement due to hemorrhage, fibrosis, or necrosis are distinguishing features [219, 220]. Mild to moderate heterogeneous enhancement on arterial dominant phase that increases in the extent of enhancement on delayed-phase images has also been reported [219].

Malignant Mesothelioma

Malignant mesothelioma of the liver is a rare soft tissue tumor that occurs most commonly in men, with peak incidence beginning in the fifth decade of life. Asbestos exposure is suggested to be a risk factor. Malignant mesotheliomas of the liver are large tumors, oftentimes greater than 10 cm, solid and well-circumscribed. The cut surface shows cystic areas with interlacing septations [221].

Malignant mesothelioma exhibits heterogeneous high signal intensity on T2-weighted images and heterogeneous low signal on T1-weighted images. Heterogeneity on both T2- and T1-weighted images usually reflects the presence of hemorrhage. Diffuse heterogeneous enhancement is commonly observed (fig. 2.143).

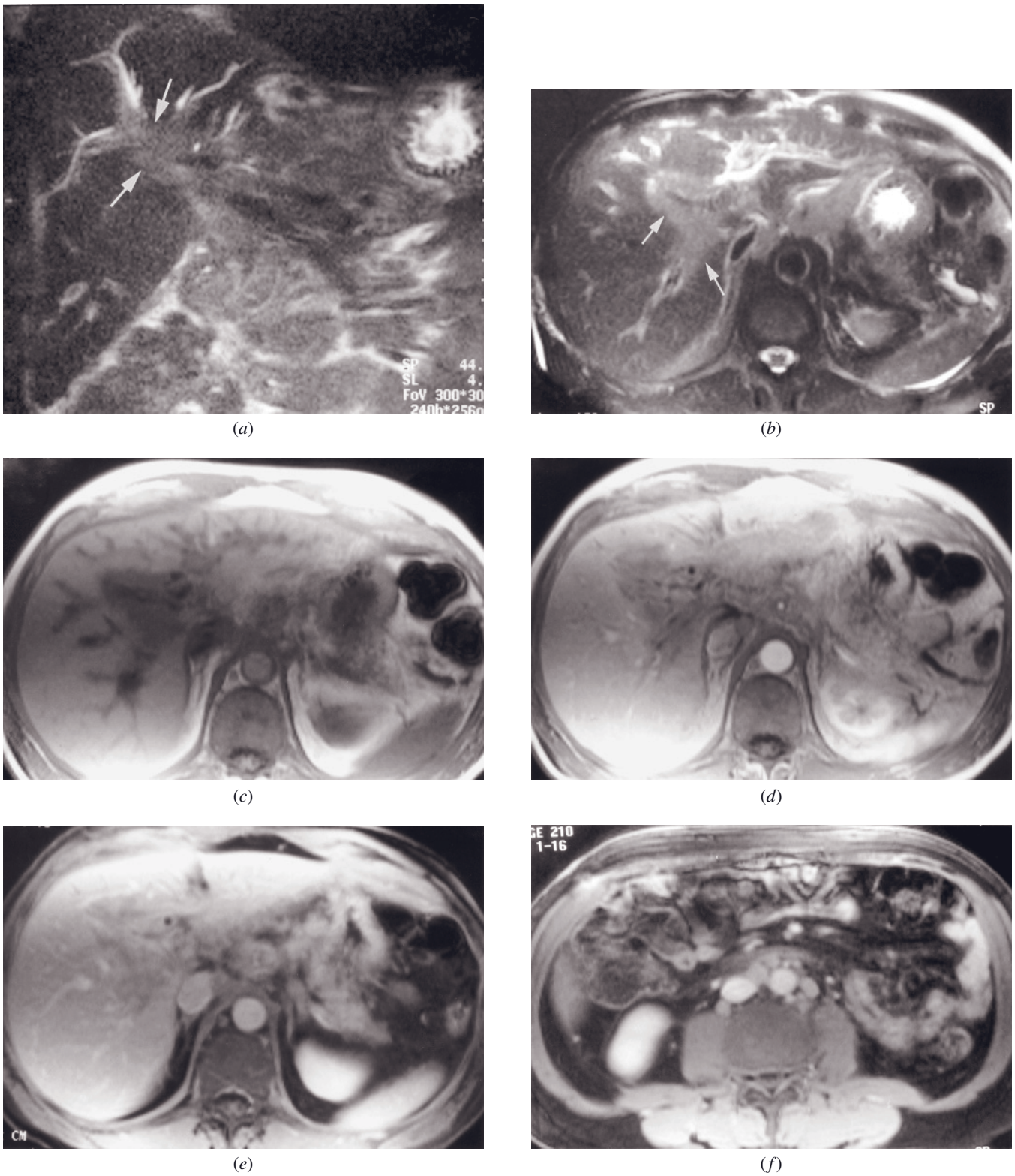

(*a*) (*b*) (*c*) (*d*) (*e*) (*f*)

FIG. 2.136 Burkitt lymphoma with periportal infiltration. Coronal T2-weighted SS-ETSE (*a*), fat-suppressed T2-weighted SS-ETSE (*b*), SGE (*c*), and immediate (*d*) and 90-s fat-suppressed postgadolinium SGE (*e*, *f*) images. There is extensive soft tissue infiltration in the porta hepatis with periportal extension (arrows, *a, b*). Periportal tumor infiltration is more common with lymphoma than with other forms of malignant disease. Retroperitoneal nodes are also present (*f*).

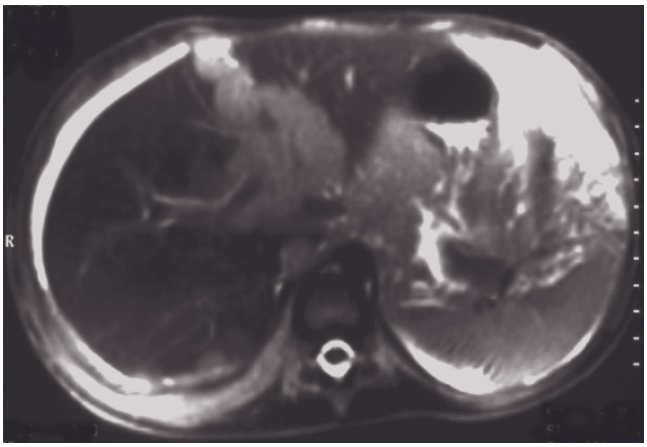

(*g*)

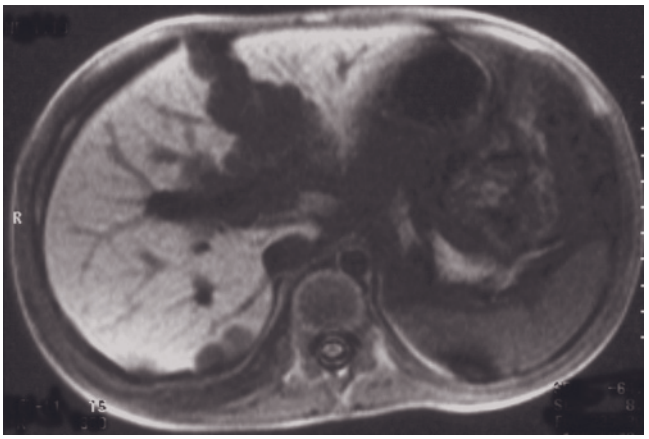

(*h*)

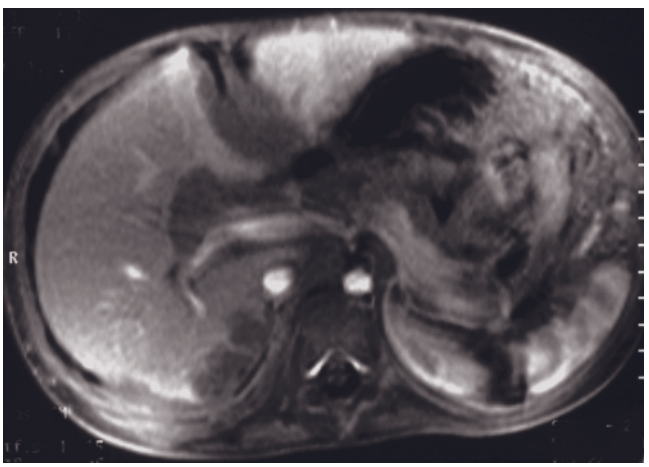

(*i*)

Fig. 2.136 (*Continued*) Fat-suppressed T2-weighted ETSE (*g*), SGE (*h*), and 45-s postgadolinium SGE (*i*) images in a second patient. Note the presence of ascites.

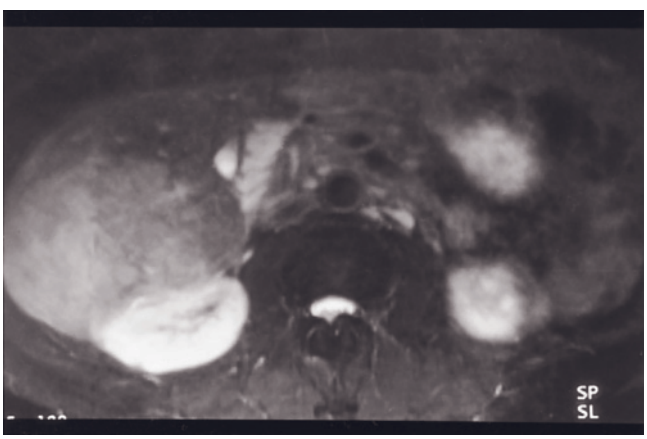

(*a*)

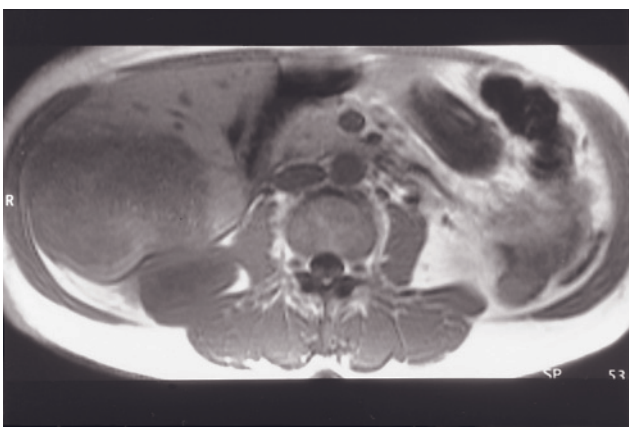

(*b*)

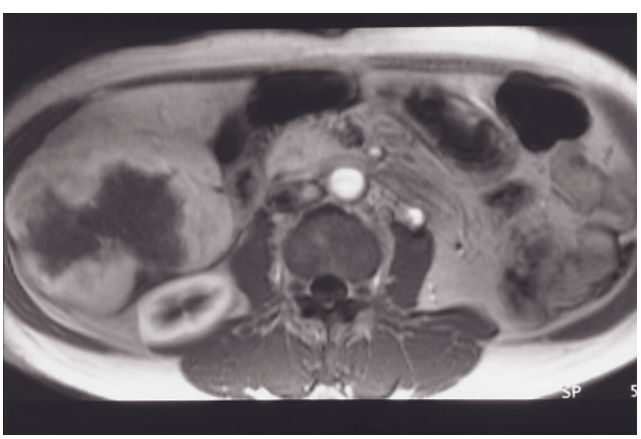

(*c*)

Fig. 2.137 Primary hepatic lymphoma. Fat-suppressed T2-weighted ETSE (*a*), SGE (*b*), and immediate postgadolinium SGE (*c*) images. An 8-cm primary hepatic lymphoma is present in the right lobe of the liver. The tumor is mildly hyperintense on T2 (*a*) and moderately hypointense on T1 (*b*) and demonstrates thick, irregular multilayered peripheral enhancement on immediate postgadolinium images (*c*).

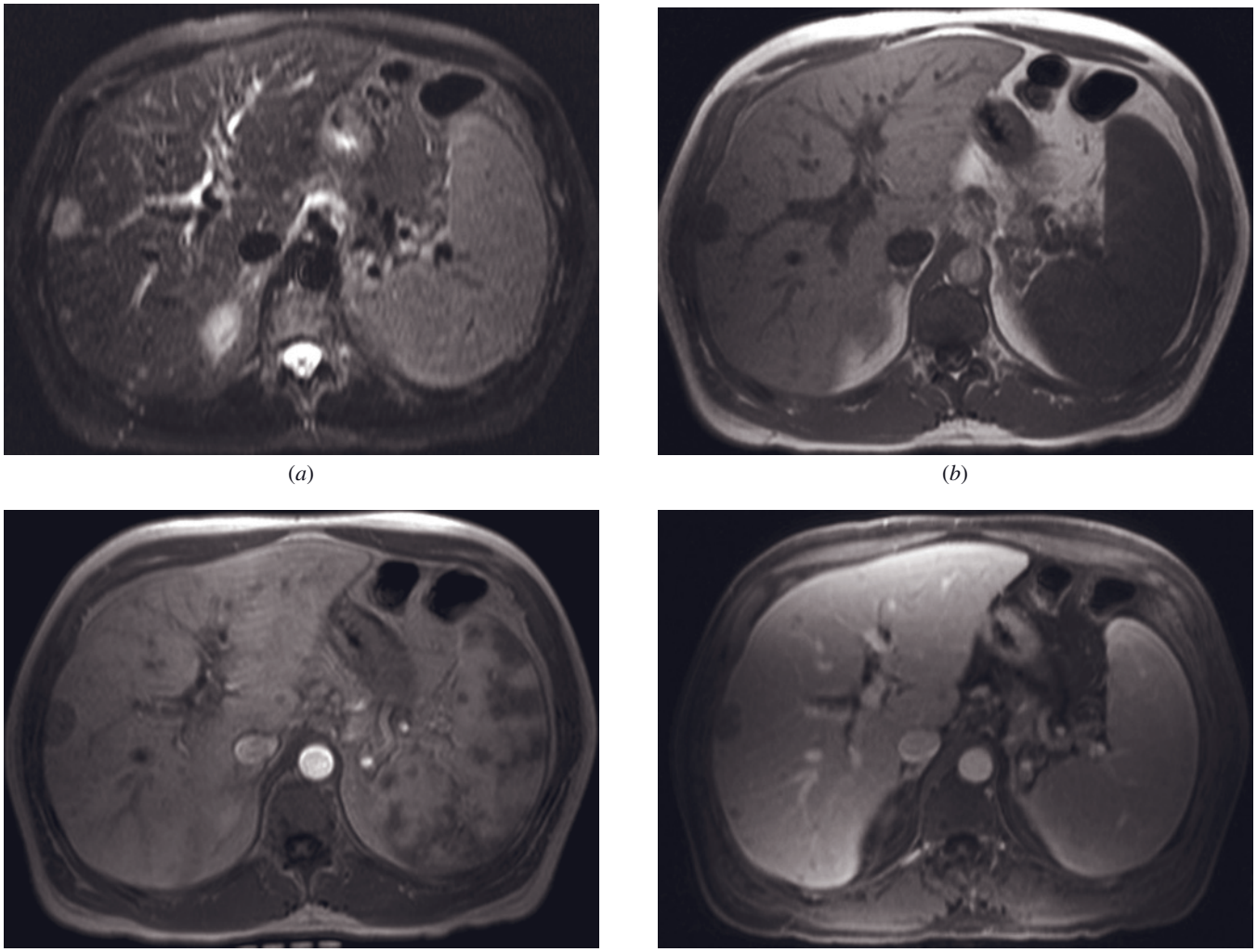

(*a*) (*b*)

(*c*) (*d*)

Fig. 2.138 Liver lymphoma in a HIV patient. T2-STIR (*a*), SGE (*b*), immediate postgadolinium SGE (*c*), and 90-s fat-suppressed postgadolinium SGE (*d*) images in a patient with HIV. Multiple focal lesions are present throughout the liver that are mildly hyperintense on T2 (*a*) and moderately hypointense on T1 (*b*) and demonstrate minimal early enhancement with perilesional enhancement (*c*), with mild progression of lesion enhancement and fading of the perilesional enhancement. A variety of etiologies of liver disease occurs in HIV patients in greater frequency than in patients with normal immune systems, including infectious and neoplastic disease. In this patient, multiple foci of lymphoma are present throughout the liver. Note also abnormal signal intensity of the bone marrow of the spine consistent with disease involvement in this location as well.

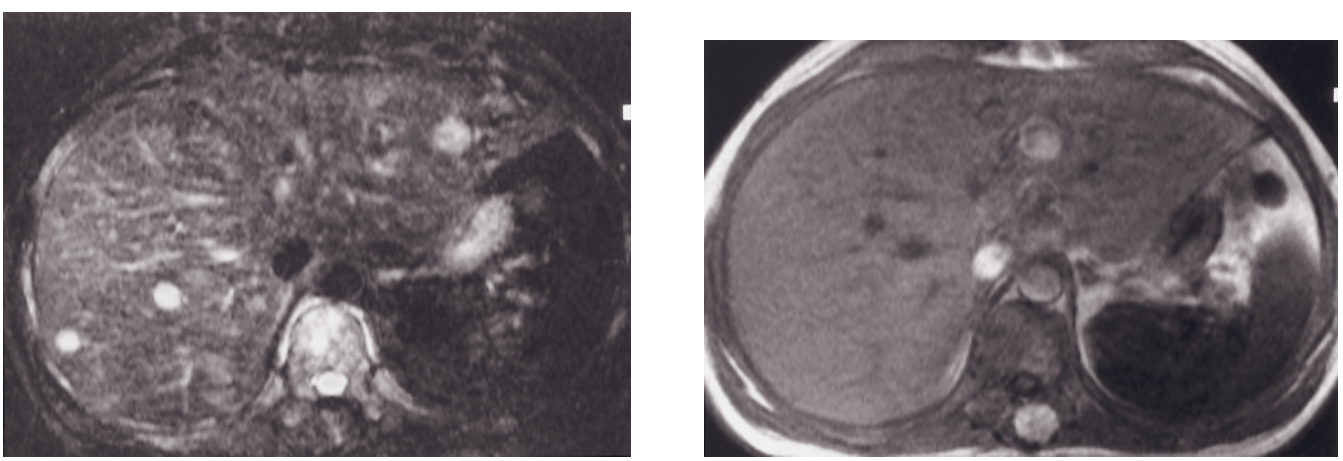

(*a*) (*b*)

Fig. 2.139 Multiple myeloma. Fat-suppressed T2-weighted ETSE (*a*), SGE (*b*), and T1-weighted fat-suppressed spin-echo (*c*) images. Multiple focal masses <1.5 cm are present in the liver that are moderately hyperintense on T2 image (*a*), nearly isointense

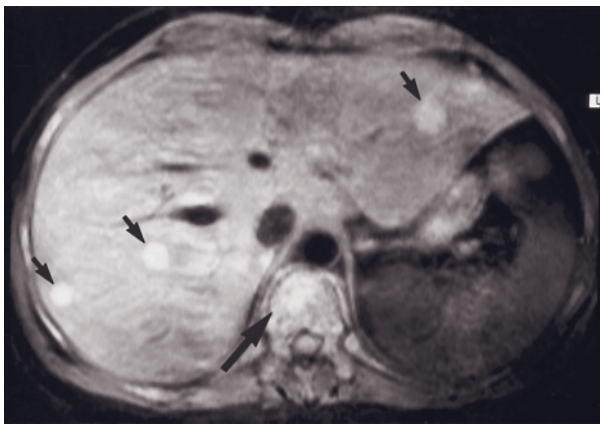

(*c*)

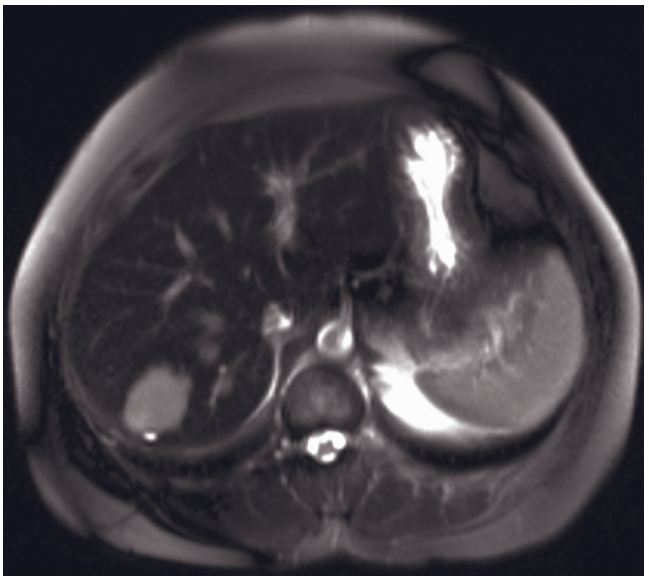

(*d*)

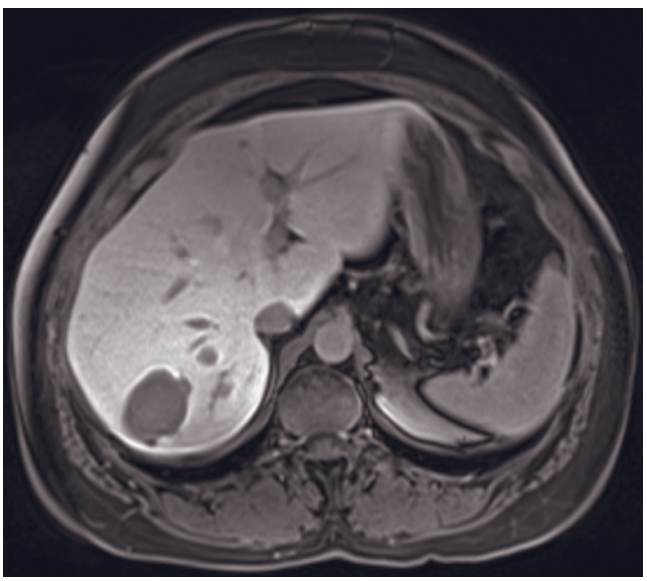

(*e*)

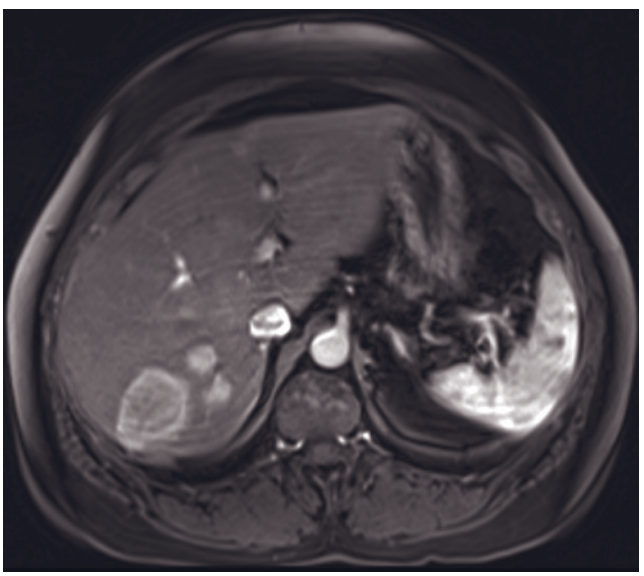

(*f*)

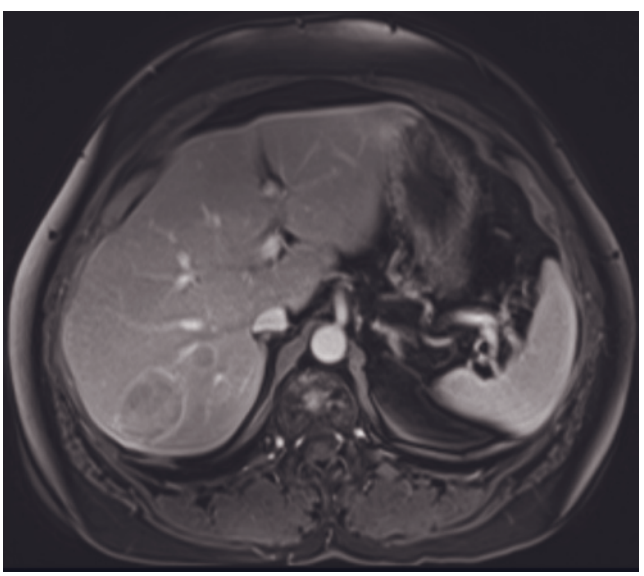

(*g*)

Fig. 2.139 (*Continued*) on T1-weighted image (*b*), and moderately hyperintense on T1-weighted fat-suppressed spin-echo image (small arrows, *c*). High signal intensity on T1- and T2-weighted images is also present in vertebral bodies (large arrow, *c*) because of myelomatous involvement.

Fat-suppressed T2-weighted ETSE (*d*), fat-suppressed 3D-gradient echo (*e*), and immediate (*f*) and 90-s fat-suppressed (*g*) postgadolinium fat-suppressed 3D-gradient echo images obtained **at 3T** in a second patient with multiple myeloma. Multiple focal lesions on the right hepatic lobe are moderately hyperintense on T2 (*d*) and hypointense on SGE (*e*), enhance in an intense diffuse heterogeneous fashion on immediate images (*f*), with lesional washout and thin rim enhancement on delayed images (*g*).

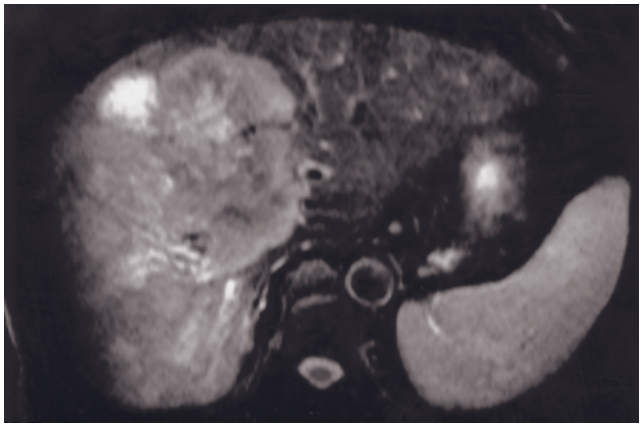

(*a*)

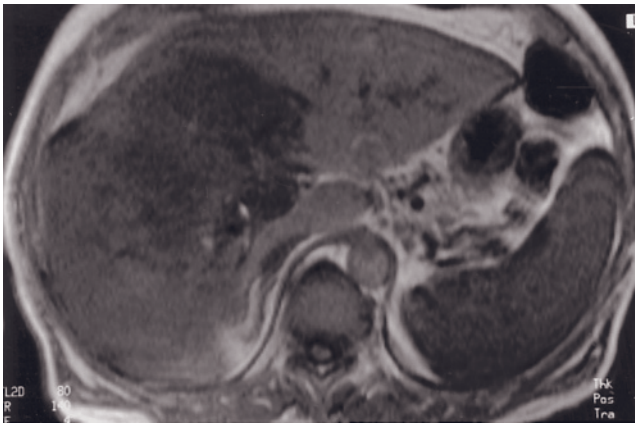

(*b*)

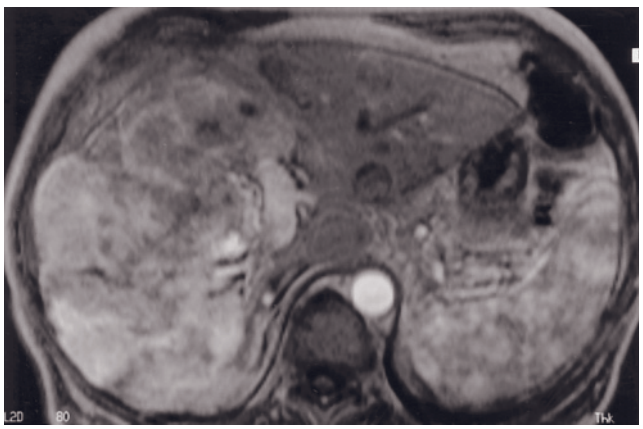

(*c*)

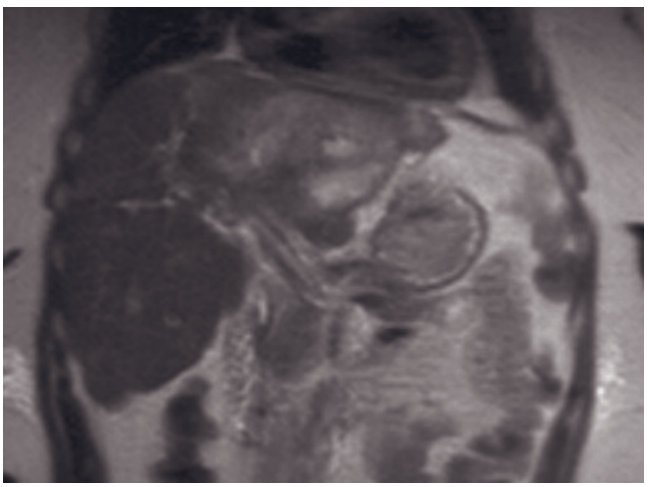

(*d*)

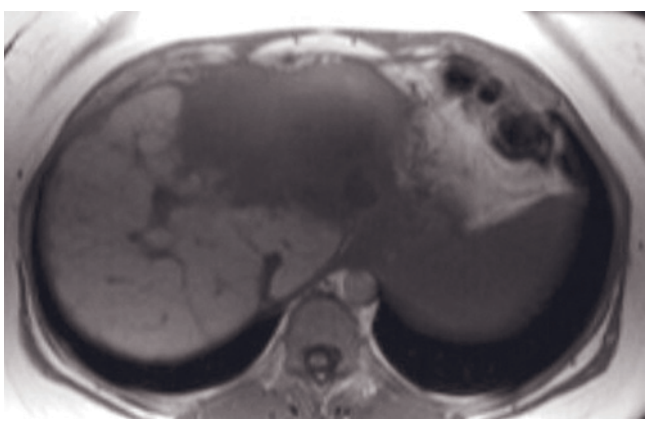

(*e*)

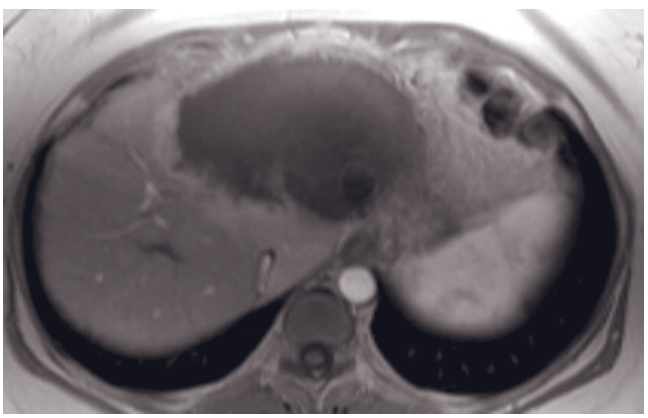

(*f*)

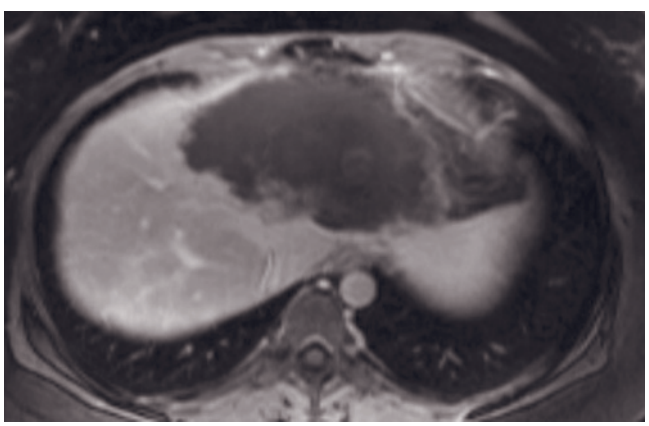

(*g*)

FIG. 2.140 Intrahepatic cholangiocarcinoma. Fat-suppressed T2-weighted ETSE (*a*), SGE (*b*), and immediate post-gadolinium SGE (*c*) images. A 14-cm tumor is present in the right lobe of the liver that is moderately high in signal intensity on the T2-weighted image (*a*) and moderately low in signal intensity on the T1-weighted image (*b*) and enhances in an intense, diffuse heterogeneous fashion on the immediate image (*c*). The appearance resembles that of an HCC.

Coronal T2-weighted SS-ETSE (*d*), SGE (*e*), and immediate (*f*) and 90-s fat-suppressed (*g*) postgadolinium SGE images in a second patient. There is a mass in the left hepatic lobe that demonstrates heterogeneous high signal intensity on T2-weighted image (*d*), low signal intensity on T1-weighted images (*e*), and perilesional enhancement on early-phase images (*f*) that fades on late phase images (*g*). Minimal lesional enhancement is appreciated in this case. Histopathology was consistent with intrahepatic cholangiocarcinoma.

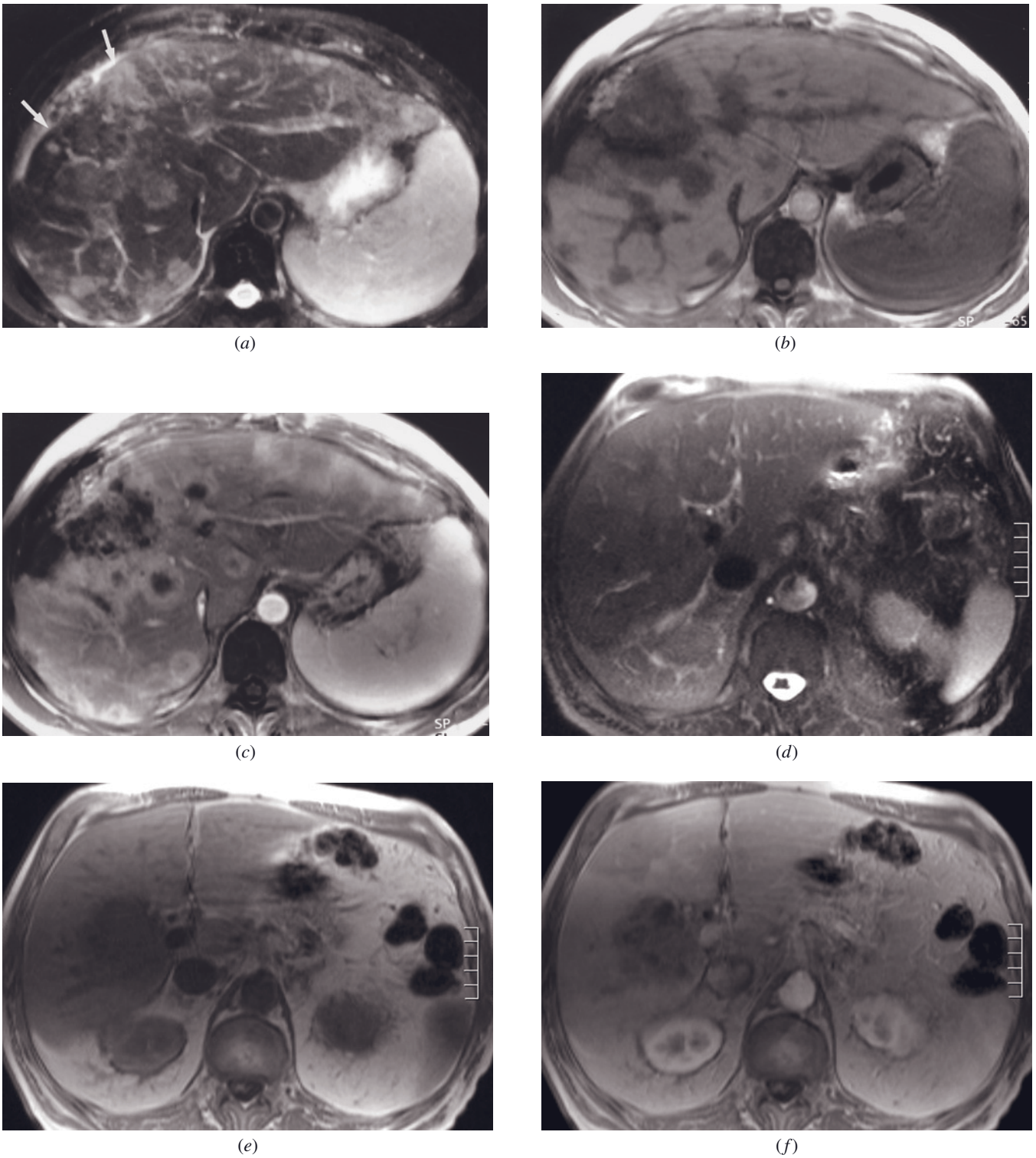

FIG. 2.141 Mixed HCC-cholangiocarcinoma. Fat-suppressed T2-weighted ETSE (*a*), SGE (*b*), and immediate postgadolinium SGE (*c*) images. A large 14-cm tumor is centered in the anterior segments 4/8, and multiple small satellite lesions are scattered throughout the remainder of the liver. The tumors are moderately high in signal on the T2-weighted image (*a*) and moderately low in signal intensity on the T1-weighted image (*b*) and enhance intensely immediately after gadolinium administration (*c*). Capsular retraction is also noted (arrows, *a*).

T2-weighted SS-ETSE (*d*), SGE (*e*), and immediate (*f*) and 90-s fat-suppressed (*g*) postgadolinium SGE images in a second patient. A mass is present adjacent to the porta hepatis. This lesion is isointense with background parenchyma on T2-weighted images (*d*) and moderately low signal intensity on T1-weighted images (*e*), shows moderate heterogeneous enhancement on early-phase images (*f*), and demonstrates washout on late-phase images (*g*).

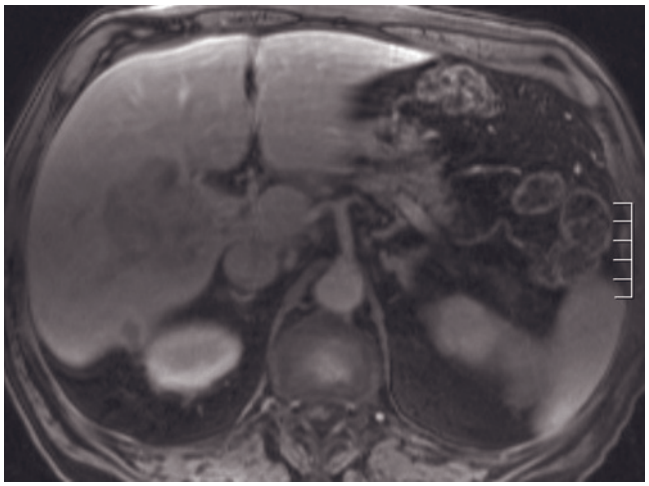

(*g*)

FIG. 2.141 (*Continued*)

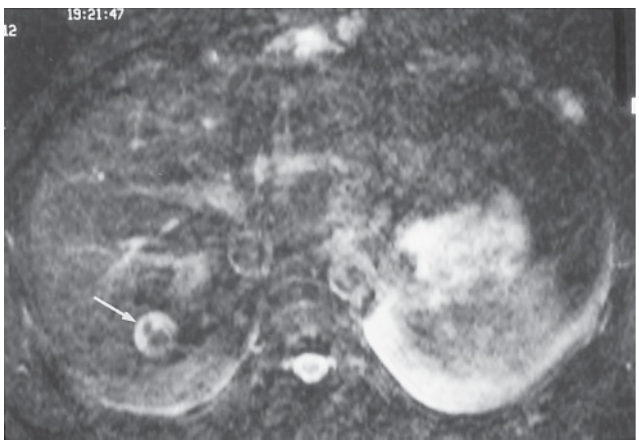

(*a*)

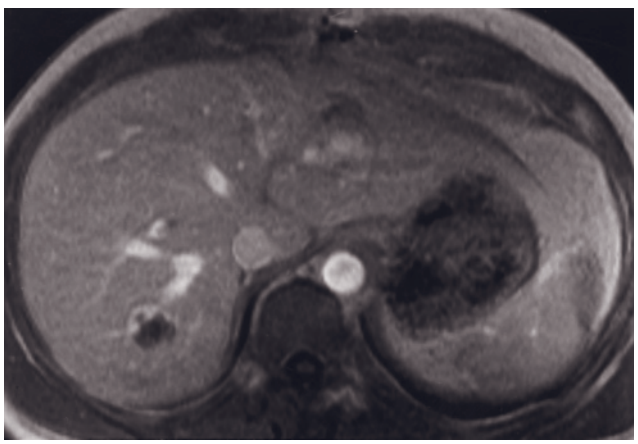

(*b*)

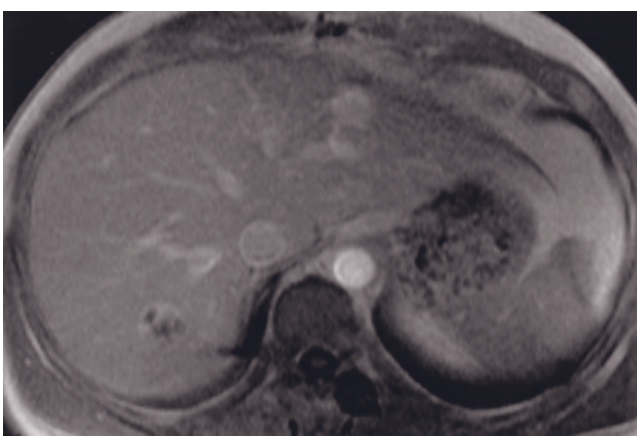

(*c*)

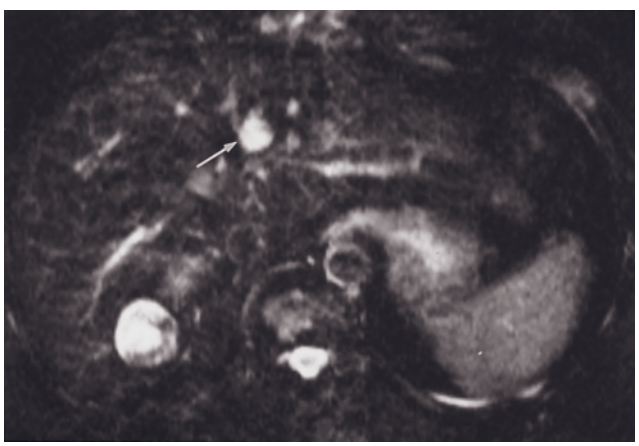

(*d*)

FIG. 2.142 Angiosarcoma. Fat-suppressed T2-weighted ETSE (*a*) and 90-s (*b*) and 10-min (*c*) postgadolinium SGE images. A 2-cm angiosarcoma is present in the right lobe of the liver. The mass is well defined and largely hyperintense on the T2-weighted image (arrow, *a*) with a central region of low signal intensity due to hemorrhage. On the 90-s postgadolinium image (*b*), peripheral nodular enhancement is present. By 10 min after contrast (*c*), nodular enhancement has progressed centripetally, with a central nonenhanced area that corresponds to the region of hemorrhage on the T2-weighted image. Angiosarcomas mimic the appearance of hemangiomas. The presence of hemorrhage in this case is a common finding in angiosarcomas and rare in hemangiomas. Interval increase in size of this tumor is identified on a follow-up study obtained 1 month later, shown on fat-suppressed T2-weighted SS-ETSE image (*d*). Increase in size of a second tumor is also present. Rapid growth is compatible with angiosarcomas and not with hemangiomas. A change in the signal intensity of the larger mass on the T2-weighted image (*d*) is also noted between studies because of aging of the central hemorrhage.

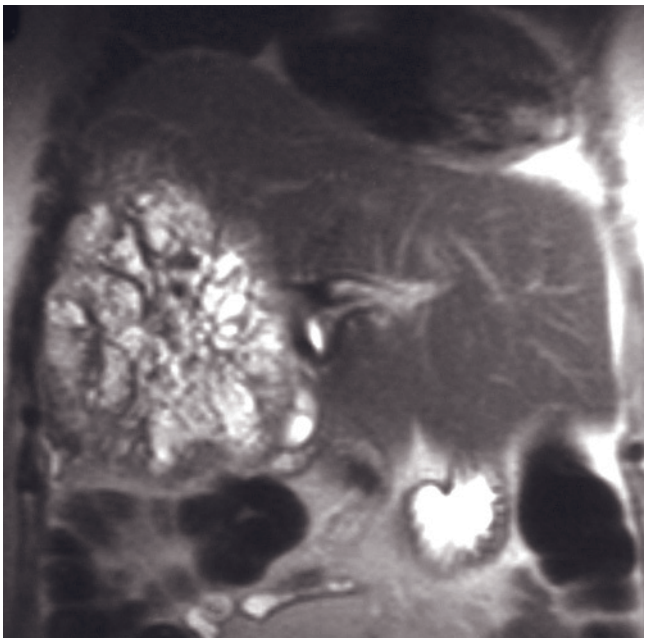

(*a*)

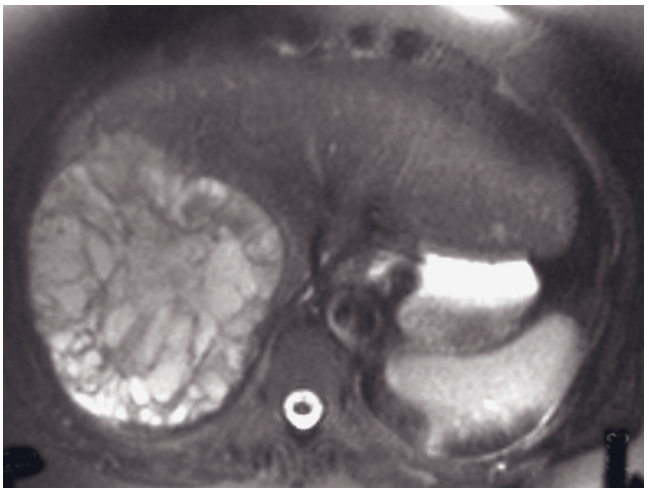

(*b*)

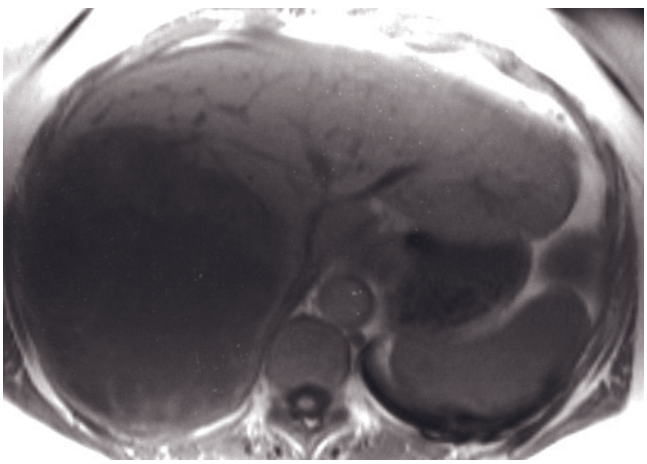

(*c*)

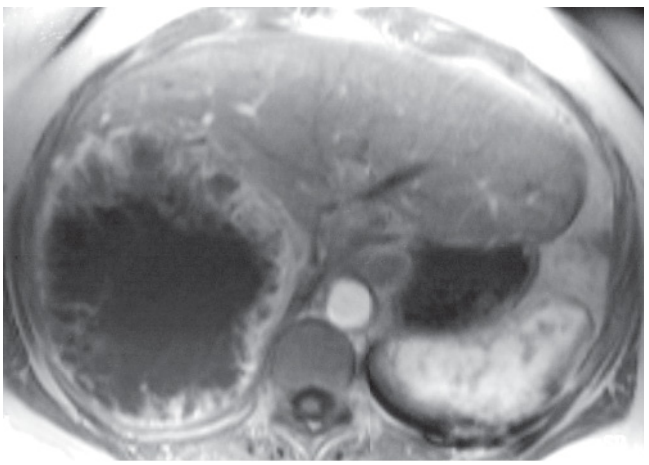

(*d*)

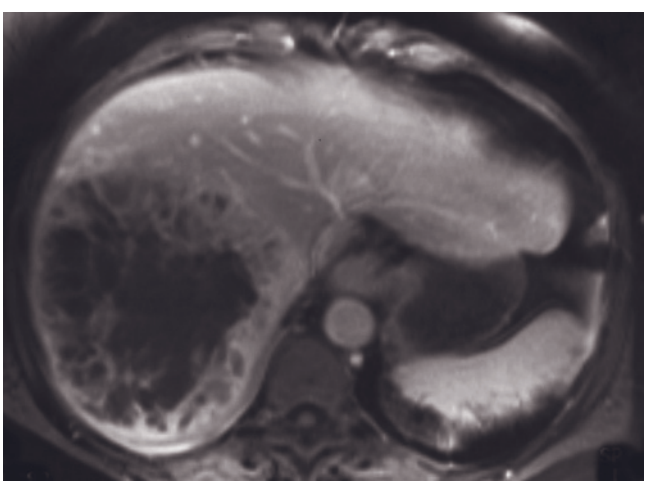

(*e*)

FIG. 2.143 Mesothelioma. Coronal (*a*) and transverse (*b*) T2-weighted SS-ETSE, SGE (*c*), and immediate (*d*) and 90-s fat-suppressed (*e*) postgadolinium SGE images. There is a large mass that measures 120 mm localized in the right hepatic lobe that shows high signal intensity on T2-weighted image within strips with moderately low signal intensity (*a*, *b*). On precontrast T1-weighted image, this mass exhibits low signal intensity. Intense predominantly peripheral enhancement is observed on early-phase images that tends to fill in at late-phase images. Note that multiple septations are well appreciated on late-phase images.

Septations demonstrate mild to moderate enhancement on early phase that tend to be more intense on delayed-phase images. Lack of central enhancement is common, reflecting central necrosis [222]. (See also Chapter 7, *Peritoneal Cavity*, on mesothelioma.)

Epithelioid Hemangioendothelioma

Epithelioid hemangioendothelioma (EHE) is a malignant, slow-growing vascular tumor, usually occurring in middle-aged patients. Females predominate over males in a 2-to-1 ratio, and oral contraceptives have been implicated as possible causative agents in younger patients [223]. Pathologically, lesions tend to be multiple, tough, fibrous masses distributed throughout the liver. Microscopically, there is characteristically abundant stroma with scattered clumps of neoplastic cells invading sinusoids and vessels [2]. Tumors tend to be low-grade malignancies with a much more favorable prognosis than for angiosarcoma. EHE are moderately high signal on T2-weighted images and moderately low signal on T1-weighted images and show a mild heterogeneous enhancement on early-phase images. The MRI findings described above are consistent with the predominance of stroma and relatively less conspicuous areas of sinusoid and blood vessel infiltration by tumor cells [224]. EHE can also appear as moderately high signal intensity on T2-weighted images and moderately intense diffuse heterogeneous enhancement on immediate postcontrast images (fig. 2.144). This appearance is similar to that of hepatocellular carcinoma, particularly in tumors with aggressive growth patterns.

Hepatoblastoma

Hepatoblastoma is the most common primary malignant tumor of the liver in children and may occur from the newborn to adolescent period and rarely older. The tumor is most often detected by 3 years of age, with a median age of 1 year. Hepatoblastoma occurs more often in boys than in girls, with a ratio of 3:2. On gross inspection, hepatoblastoma is a solid, well-defined, occasionally lobulated mass surrounded by a pseudocapsule. Although it is usually solitary, multiple lesions can be seen in less than 20% of cases. Areas of necrosis and calcifications are frequently present [225].

On MR imaging, hepatoblastoma resembles hepatocellular carcinoma in that the tumor shows diffuse heterogeneous enhancement on immediate postgadolinium images (fig. 2.145).

Undifferentiated Sarcoma of the Liver

Undifferentiated sarcoma of the liver (USL) is a rare mesenchymal tumor occurring most frequently in pediatric patients [226]. Pathologically, USL appears as a solitary, large mass with internal septations, commonly surrounded by a fibrous pseudocapsule. USL is mainly a solid tumor, with large cystic areas consistent with hemorrhage and necrosis. Histologically, USL demonstrates typically a myxoid stroma containing undifferentiated cells similar to embryonic cells [226–228].

On MRI, USL has a cystic appearance due to the presence of hemorrhagic and necrotic portions along with the high water content of myxoid stroma in the solid portion of the tumor [227, 228]. On T2-weighted images, USL is heterogeneously high signal intensity, and on T1-weighted images the tumor is heterogeneously low signal intensity. After gadolinium, solid areas enhance heterogeneously. Areas with lack of enhancement are consistent with hemorrhage or necrosis. Septations may show mild or moderate enhancement on arterial dominant-phase images that persists on late-phase images (fig. 2.146) [227–230].

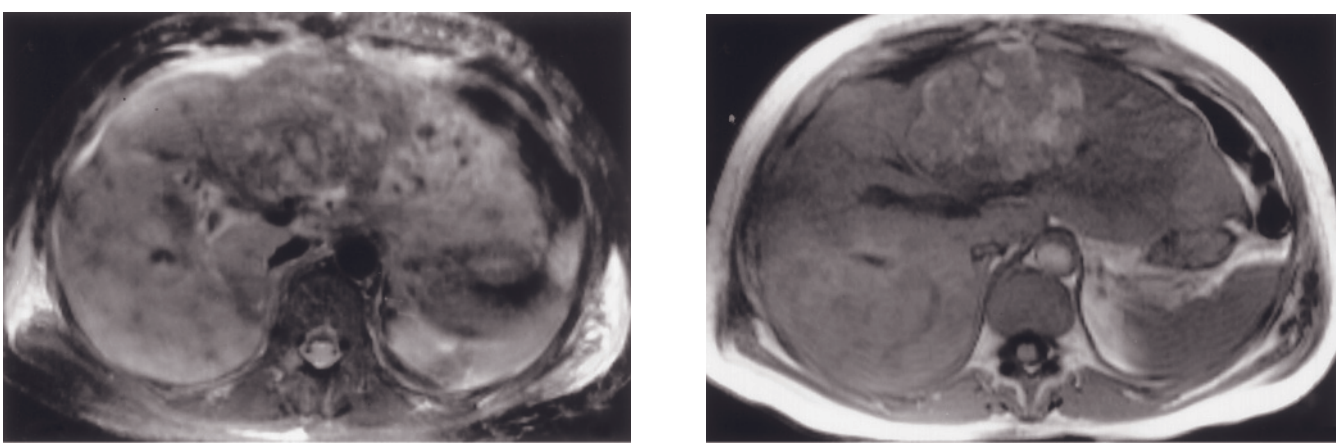

(*a*) (*b*)

FIG. 2.144 Epithelioid hemangioendothelioma. Fat-suppressed T2-weighted ETSE (*a*), SGE (*b*), and immediate (*c*) and 90-s fat-suppressed (*d*) postgadolinium SGE images in an adult patient with epithelioid hemangioendotheliosarcoma. Extensive liver

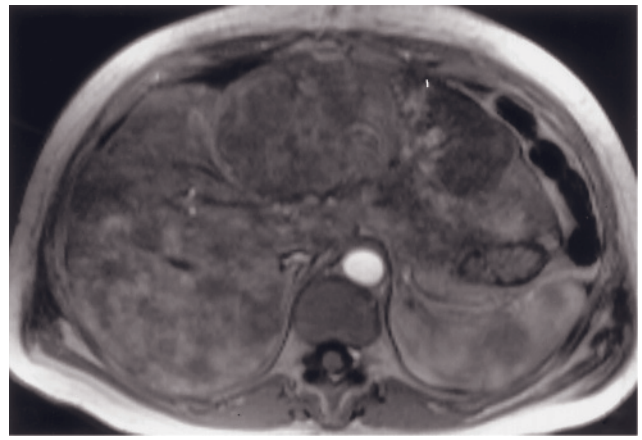

(*c*)

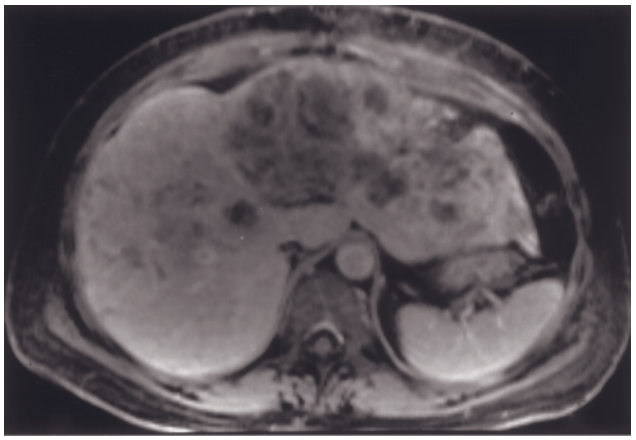

(*d*)

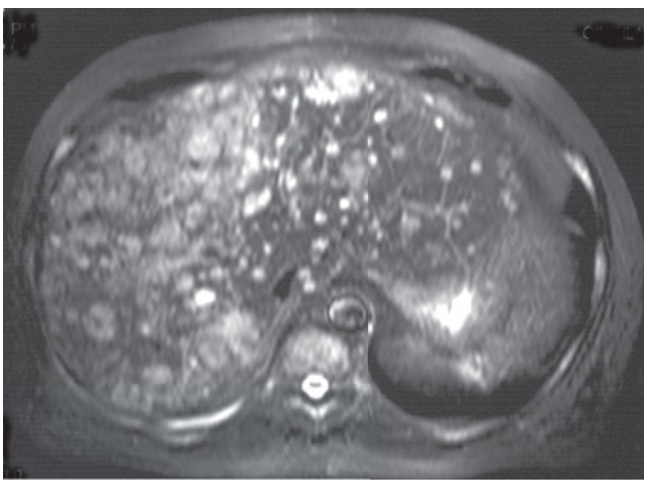

(*e*)

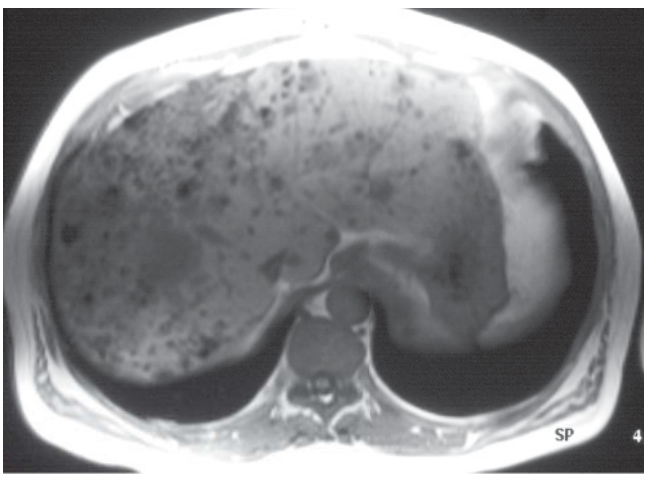

(*f*)

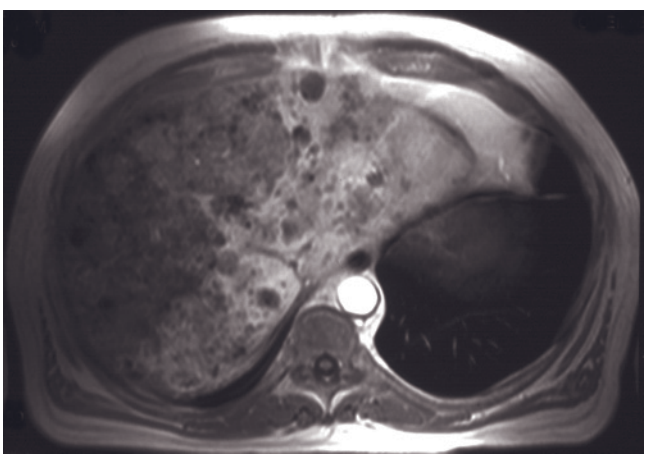

(*g*)

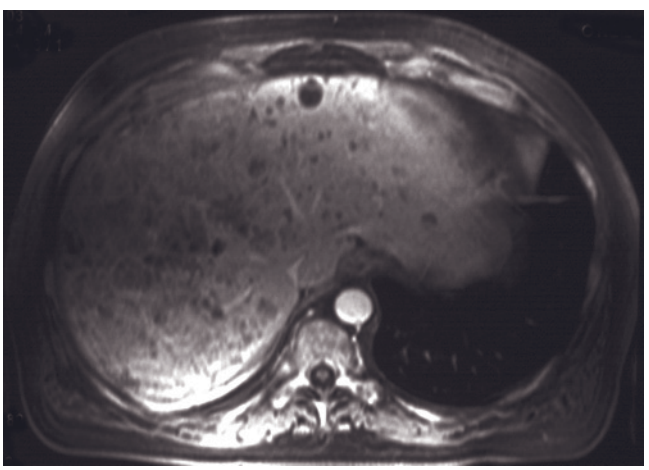

(*h*)

FIG. 2.144 (*Continued*) involvement with a multifocal malignant epithelioid hemangioendotheliosarcoma is present. The tumor is heterogeneous and isointense to minimally hyperintense on the T2-weighted image (*a*). Regions of high signal intensity are present in the largest mass on the T1-weighted image (*b*). Enhancement is diffuse heterogeneous on the immediate postgadolinium image (*c*), with heterogeneous washout on the 90-s postcontrast image (*d*). The MRI appearance of this epitheloid hemangioendothelioma resembles HCC.

Fat-suppressed T2-weighted SS-ETSE (*e*), SGE (*f*), and immediate (*g*) and 90-s fat-suppressed (*h*) postgadolinium SGE images in a second patient. There are multiple focal rounded liver lesions, some of them confluent, that have moderately high signal intensity on T2-weighted images (*e*), moderately low signal intensity on T1-weighed images (*f*), and mild diffuse heterogeneous enhancement on early-phase images (*g*) that remains on late-phase images (*h*). Histopathology was epithelioid hemangioendothelioma.

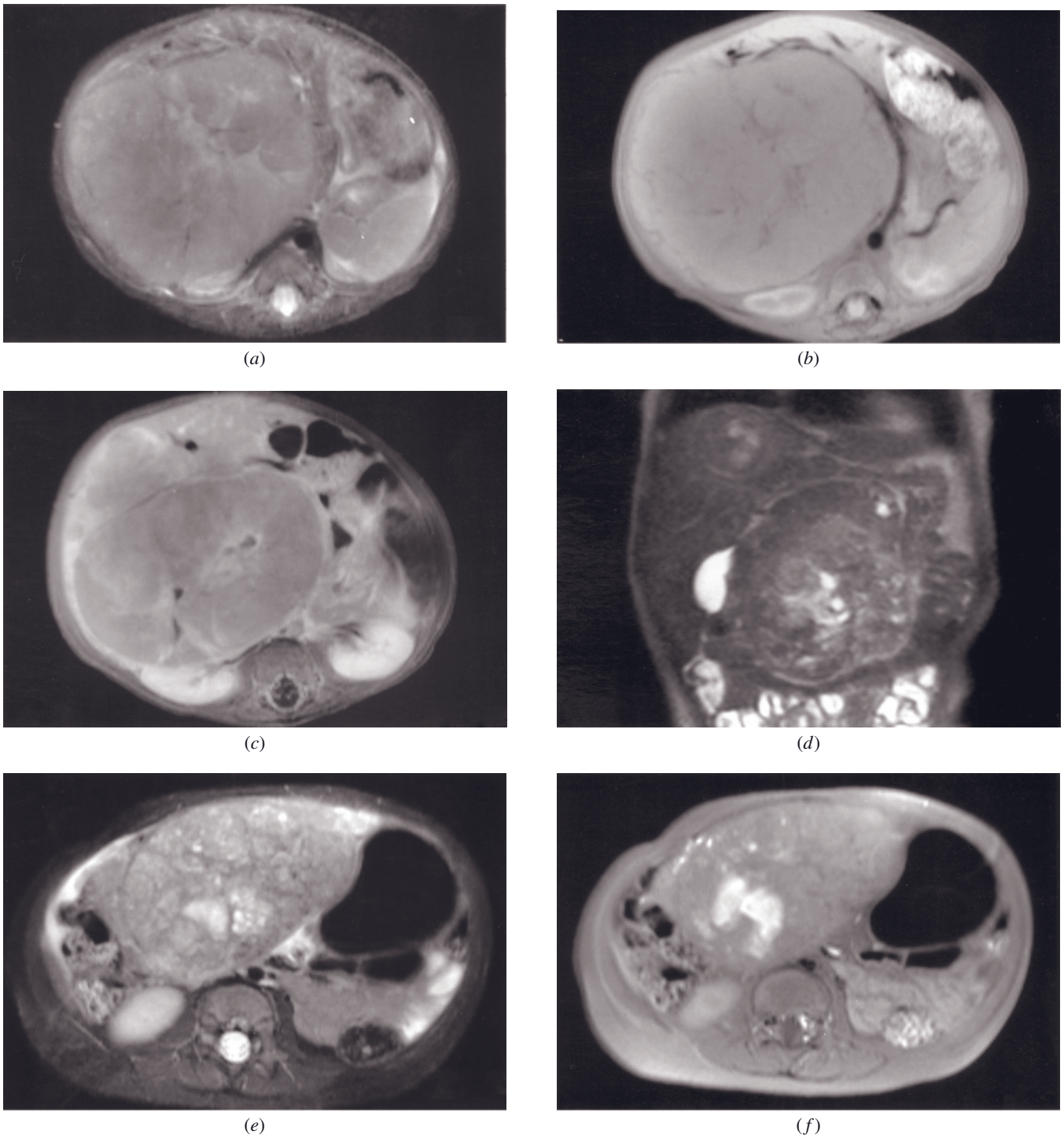

FIG. 2.145 Hepatoblastoma. Fat-suppressed T2-weighted ETSE (*a*), T1-weighted fat-suppressed SE (*b*), and T1-weighted 90-s fat-suppressed SE (*c*) images in a 2-month-old boy. There is a large, slightly lobulated mass arising from the liver, which demonstrates slightly increased signal intensity on T2 (*a*), mildly decreased signal intensity on T1(*b*), and mildly heterogeneous enhancement on interstitial-phase gadolinium-enhanced (*c*) images. Note that the mass displaces the celiac axis, the right kidney, aorta, inferior vena cava, and pancreas.

Coronal T2-weighted SS-ETSE (*d*), transverse fat-suppressed T2-weighted ETSE (*e*), T1-weighted fat-suppressed SE (*f*), and immediate postgadolinium SE (*g*) images in a second (1-year old) patient with hepatoblastoma. There is a large mass arising from

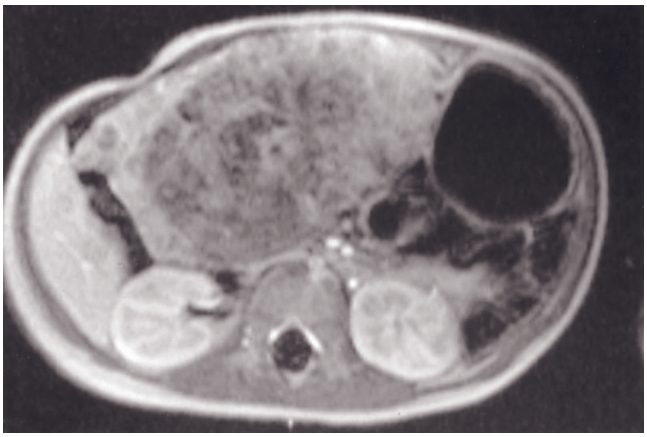

(*g*)

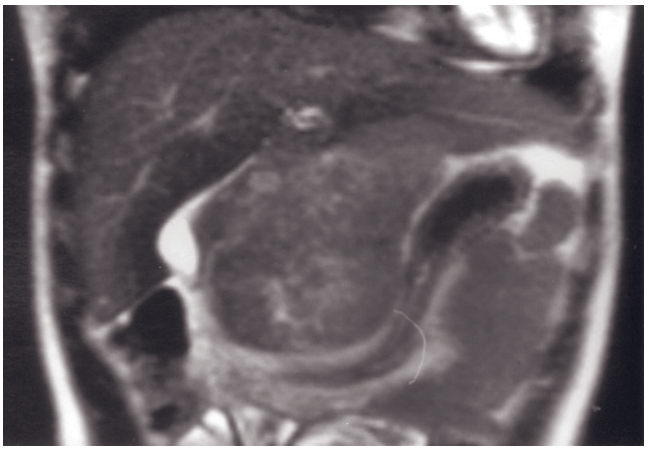

(*h*)

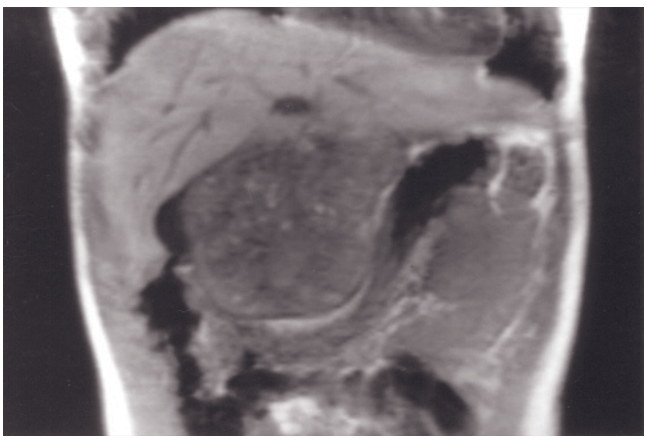

(*i*)

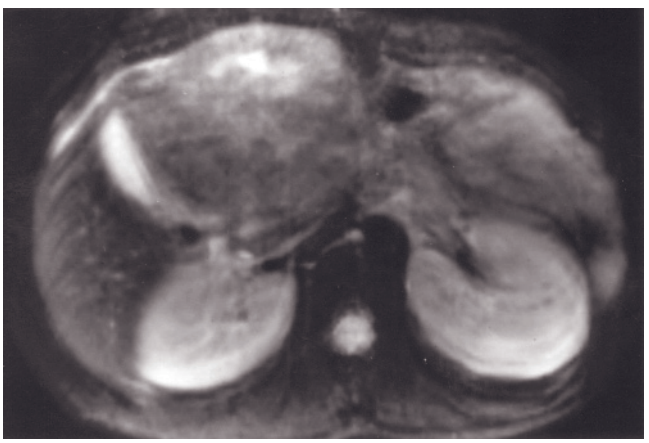

(*j*)

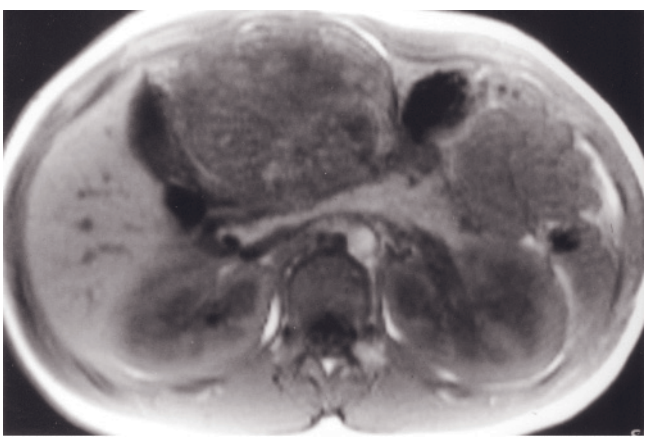

(*k*)

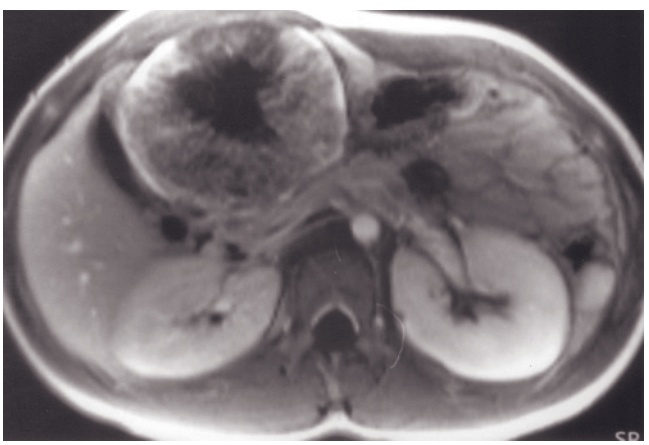

(*l*)

FIG. 2.145 (*Continued*) the left hepatic lobe inferiorly, that demonstrates heterogeneous signal on T2 (*d*, *e*) and T1 (*f*) images. On the T1-weighted image (*f*) there are also several focal areas of high signal consistent with hemorrhage. The tumor enhances in a diffuse heterogeneous fashion (*g*).

Coronal T2-weighted SS-ETSE (*h*), coronal SGE (*i*), fat-suppressed T2-weighted SS-ETSE (*j*), SGE (*k*), and immediate (*l*) and 90-s fat-suppressed (*m*) postgadolinium SGE in a 14-year-old girl. There is a large tumor that is heterogeneous and moderately

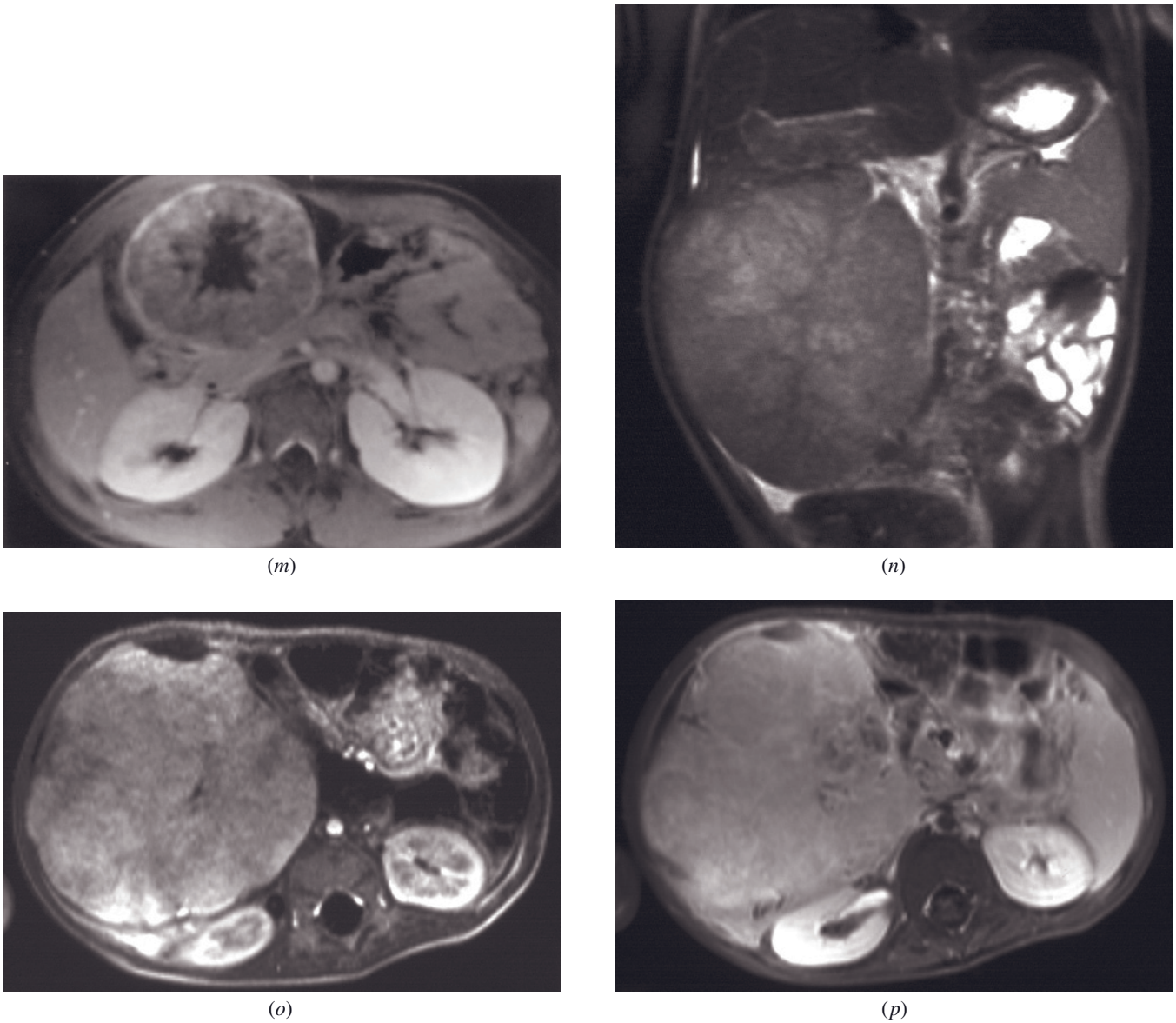

(*m*) (*n*)

(*o*) (*p*)

FIG. 2.145 (*Continued*) hyperintense on T2 (*h*, *j*). The tumor shows diffuse heterogeneous enhancement on immediate post-gadolinium images (*l*), which fades by 90 s (*m*). The central region does not enhance, consistent with fibrous tissue.

Coronal T2-weighted SS-ETSE fat suppressed (*n*) and immediate (*o*) and 90-s fat-suppressed (*p*) postgadolinium SGE images. There is large exophytic lobular hepatic mass (12 cm in the longest axis) with mildly high signal intensity on T2-weighted images (*n*), moderately high signal intensity on T1-weighted images (not shown), and heterogeneous enhancement on early-phase images (*o*) that becomes more homogeneous on late-phase images (*p*). Note the posterior displacement of the kidney by the mass.

The most common primary liver malignancy changes from hepatoblastoma to hepatocellular carcinoma in the adolescent period between 14 and 16 years of age. This last patient is at the upper age range of hepatoblastoma.

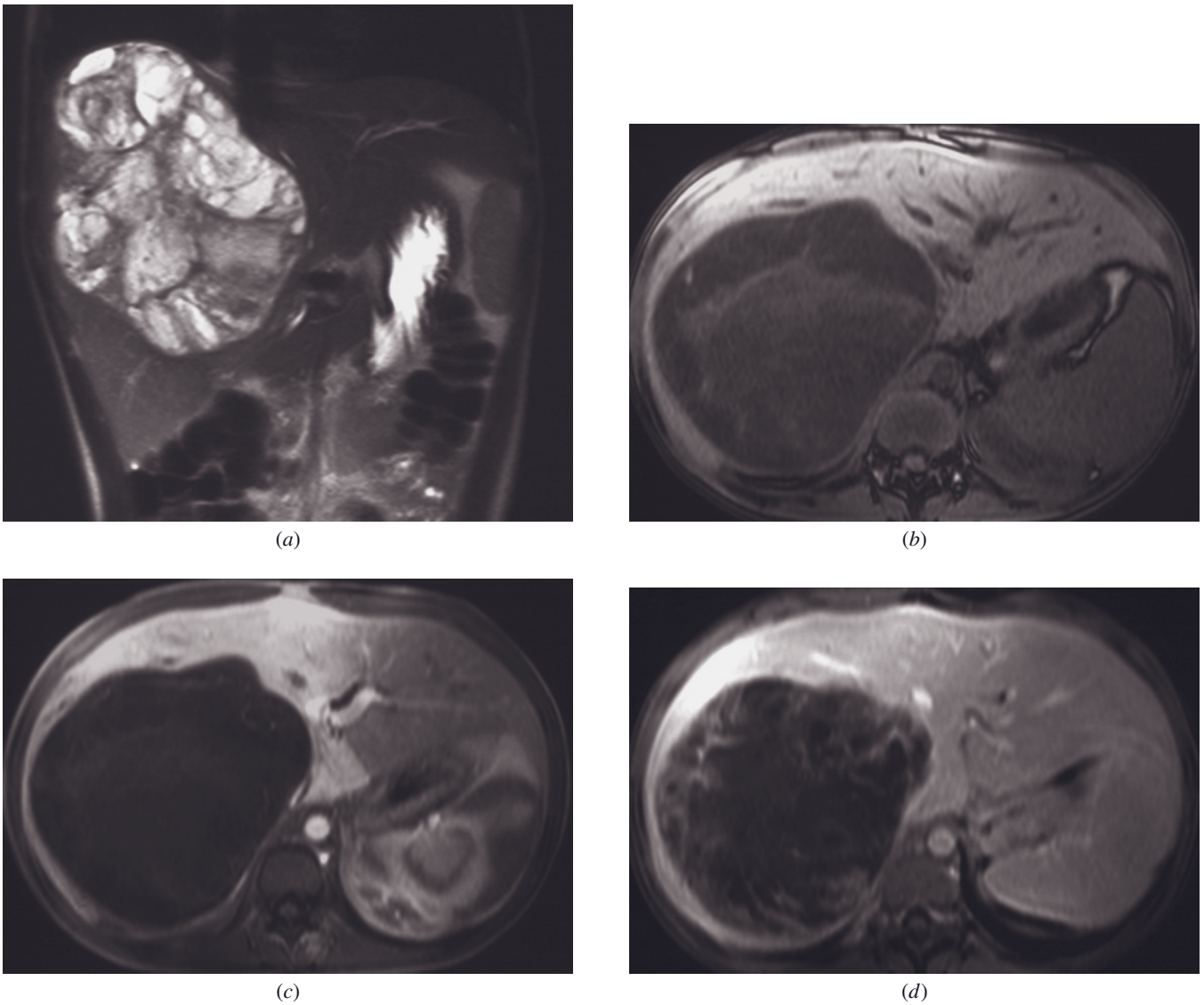

FIG. 2.146 Undifferentiated sarcoma of the liver. Coronal T2-weighted SS-ETSE (*a*), SGE (*b*), and immediate (*c*) and 90-s fat-suppressed (*d*) postgadolinium SGE images. There is a large mass in the right hepatic lobe that measures 12 cm in the longest axis and demonstrates moderately high signal intensity on T2-weighted images (*a*) and moderately low signal intensity on T1-weighted images (*b*), and shows negligible enhancement on early-phase images (*c*) and moderate enhancement of the outer margin of the tumor on late-phase images (*d*). At histopathology, the mass was undifferentiated sarcoma of the liver.

Posttreatment Lesions

Malignant liver lesions may be treated by a number of interventions, including surgical resection, radiation therapy, systemic chemotherapy, transcatheter arterial chemoembolization, ablative therapy, and liver transplantation [231–251]. The appearance of hepatic parenchyma and malignant liver lesions after therapeutic interventions has been previously described [233–240, 242, 244–248]. In the evaluation of posttreatment liver, the time course of benign posttreatment tissue changes, primarily tissue injury and development and maturation of granulation tissue, and the appearance of persistent or recurrent disease must be ascertained. Certain features of treatment-related changes depend on the form of therapy. The following discussion describes many of those features.

Resection. Surgical removal with resection of negative margins remains the optimal therapy for primary and secondary liver tumors. However, only up to 25% of patients are eligible for curative resection [252–254].

Within the first 3–5 months after resection, the parenchyma and surgically resected margins often appear as high signal intensity on T2-weighted images and low signal intensity on T1-weighted images and

display homogeneously mild to moderately increased enhancement on arterial dominant-phase images that fades to background parenchyma on interstitial-phase images [231, 255] (fig. 2.147). These focal areas reflect edema and granulation tissue in the liver parenchyma, and they may appear linear, circular, oval, or serpiginous in configuration [255].

Hyperplasia of the remaining liver may be appreciated as early as 3 months after surgery. Within 1 year, general enlargement of the remaining liver occurs. After right hepatectomy, hypertrophy of the medial segment may create the appearance of a pseudo-right lobe (fig. 2.148). Magnetic susceptibility artifact, related to surgical clips, is often present along the resection margin of the liver.

After surgery, malignancy may recur along the margin of resection or separate focal lesions may develop in the remainder of the liver (figs. 2.149 and 2.150) [239]. Tumor recurrence has an appearance similar to untreated malignant lesions.

Postradiation Therapy. As with postradiation changes in other tissues and organ systems, the distinction between benign and malignant disease usually can be made with certainty beyond 1 year after treatment. At this time point, benign disease usually exhibits regular or linear margins, low signal intensity on T2-weighted image, and mild or negligible enhancement on immediate postgadolinium images. In comparison, malignant disease tends to appear more irregular, nodular, or masslike, with moderately high signal intensity on T2-weighted images and moderate or intense enhancement on hepatic arterial dominant-phase images. Radiation changes generally exhibit linear margins that do not conform to segmental anatomy but rather conform to expected radiation portals. Within the first 3 months, radiation changes generally exhibit features of edema (i.e., moderately high signal on T2-weighted images and moderately low signal on T1-weighted images). Beyond 3 months, radiation changes may show increased granulation tissue progressing to fibrosis (fig. 2.151). Often, immediate postcontrast images effectively define pathophysiological changes that reflect successful response or recurrence.

Systemic Chemotherapy. A number of chemotherapeutic agents are currently utilized in the treatment of focal liver malignancies. The number of agents and their cytotoxic effectiveness continue to progress dramatically. The mechanisms of tumor cell control are complex and probably involve a number of pathways. However, studies have focused on the antiangiogenic activity of some of these agents.

Tumor response after systemic chemotherapy is assessed by evaluating the number and size of the tumors before and after systemic chemotherapy. The time course and variation in imaging appearance of metastases that have responded to chemotherapy have not been fully elucidated. However, it has been reported that in after as little as 2 weeks of therapy there is a decrease in the tumor size and vascularity if tumor shows a good response [256].

We have previously described the appearance of liver metastases 2 to 7 months after initiation of chemotherapy [82]. In that report, liver metastases became better defined and higher in signal intensity on T2-weighted images, showing peripheral nodular enhancement with progressive enhancement that remained on 10-min delayed images (fig. 2.152). The appearance was considered to mimic that of hemangiomas. Explanations for this change in appearance are related to altered physiology and blood supply of metastatic tumors treated with chemotherapy. The less aggressive enhancement patterns of metastasis after chemotherapy might be ascribed to chemo-induced tumor antiangiogenesis (fig. 2.153). Continued resolution of metastatic lesions results in a progressive decrease in signal intensity on T2-weighted images and progressive decrease in contrast enhancement (fig. 2.154). One report described the appearance of liver metastases treated by intravenous chemotherapy in 34 patients on serial MRI studies [234]. In that report, a good prognosis was associated with decreased signal intensity on T2-weighted images and increased signal intensity of the lesions on T1-weighted images, essentially approaching the signal intensity of the liver.

The vascularity of liver metastases, that is, hypervascularity and hypovascularity, can be assessed based on the degree of enhancement on arterial dominant-phase images (fig. 2.155). This is an important imaging feature since evidence points to a close association between tumor vascularity and patients' response to therapy. A prior study [142] demonstrated that breast cancer patients with persistently hypervascular liver metastases after systemic chemotherapy were more likely to have disease progression compared to patients whose liver metastases became hypovascular.

The appearance of chronic healed metastases is comparable to the appearance of treated focal lesions of other causes, such as infection. The chronic healed phase of lesion response usually develops at least 1.5 years after initiation of treatment. Chronic healed lesions possess an irregular, angular, polygonal margin frequently associated with retraction of surrounding liver parenchyma. In superficial lesions, capsule retraction may develop, creating a puckered appearance on imaging studies. Chronic healed lesions contain mature fibrous tissue that has a low fluid content and is hypovascular. These lesions appear as low signal intensity or isointensity on T2-weighted images and moderately

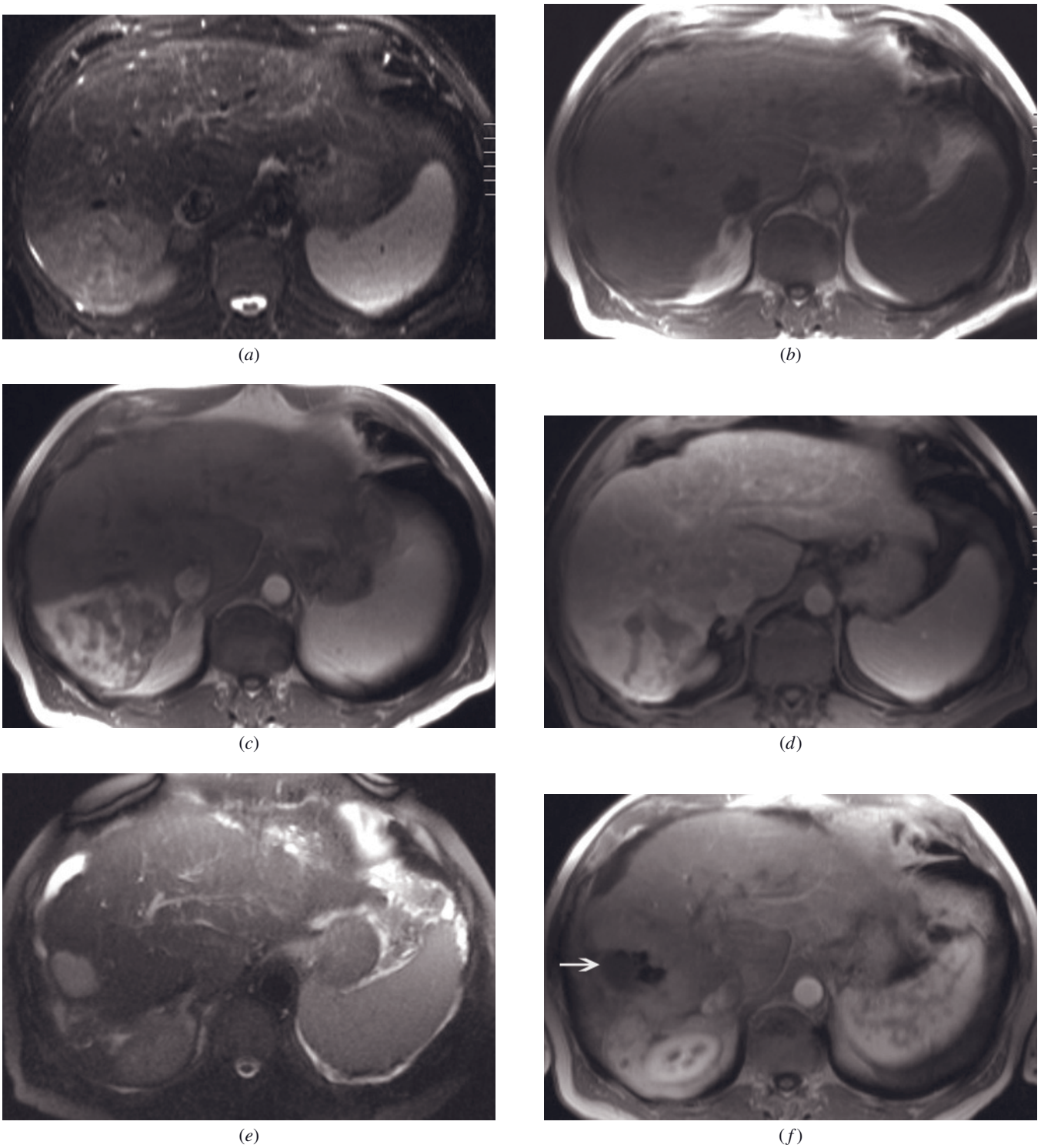

FIG. 2.147 Before and after liver resection. T2-weighted SS-ETSE (*a*, *e*), SGE (*b*), and immediate (*c*, *f*) and 90-s fat-suppressed (*d*, *g*) postgadolinium SGE images. The images before resection (*a–d*) show a 9-cm HCC in the right hepatic lobe. After resection, a small biloma is present (arrow, *f*). Note the heterogeneous mildly increased enhancement along the resection margin on early-phase images (*f*) that fades on late-phase images (*g*), features of early granulation tissue and mild inflammation.

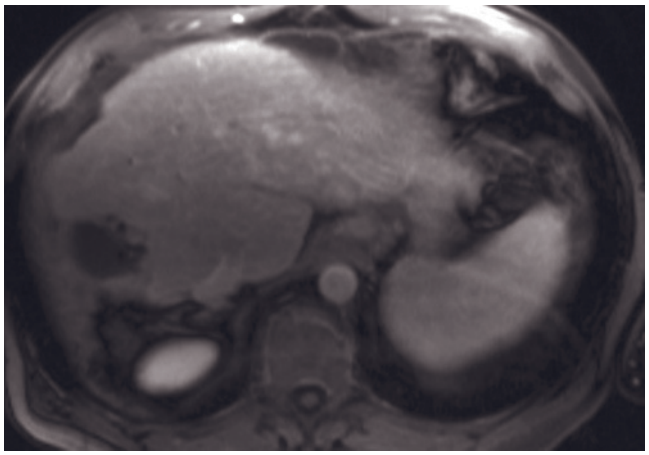

(*g*)

FIG. 2.147 (*Continued*)

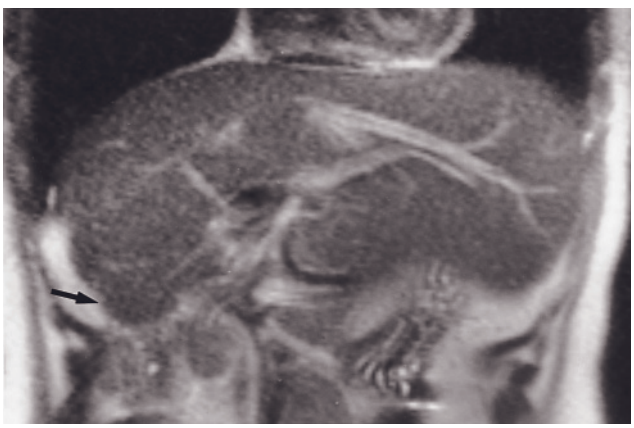

(*a*)

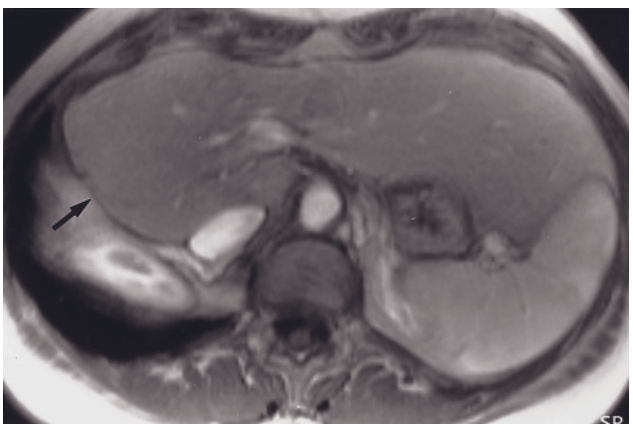

(*b*)

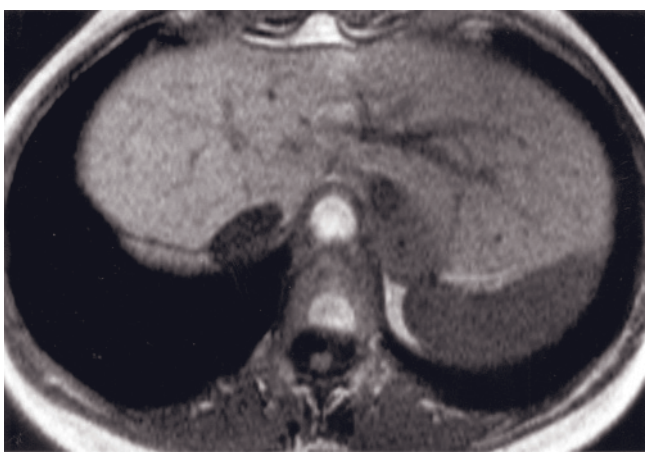

(*c*)

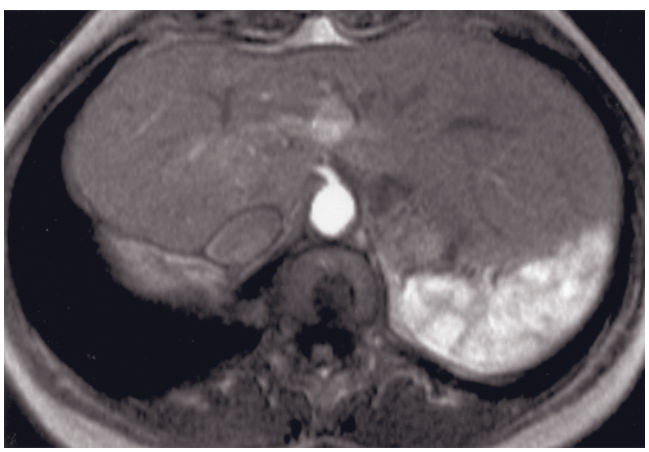

(*d*)

FIG. 2.148 Liver regeneration after right hepatectomy. Coronal T2-weighted SS-ETSE (*a*) and immediate postgadolinium SGE (*b*) images. The lateral segment of the left lobe is enlarged and rounded in contour (*a*, *b*). Hypertrophy of the medial segment results in an appearance of a pseudo-right lobe (arrow, *a*). A relatively sharp resection margin is noted (arrow, *b*) with no abnormal tissue apparent.

Transverse SGE (*c*) and immediate postgadolinium SGE (*d*) images in a second patient with hypertrophy of the left liver lobe after right lobectomy. Note that the lateral segment of the left lobe is enlarged but there is a clear distinction between the liver and the spleen.

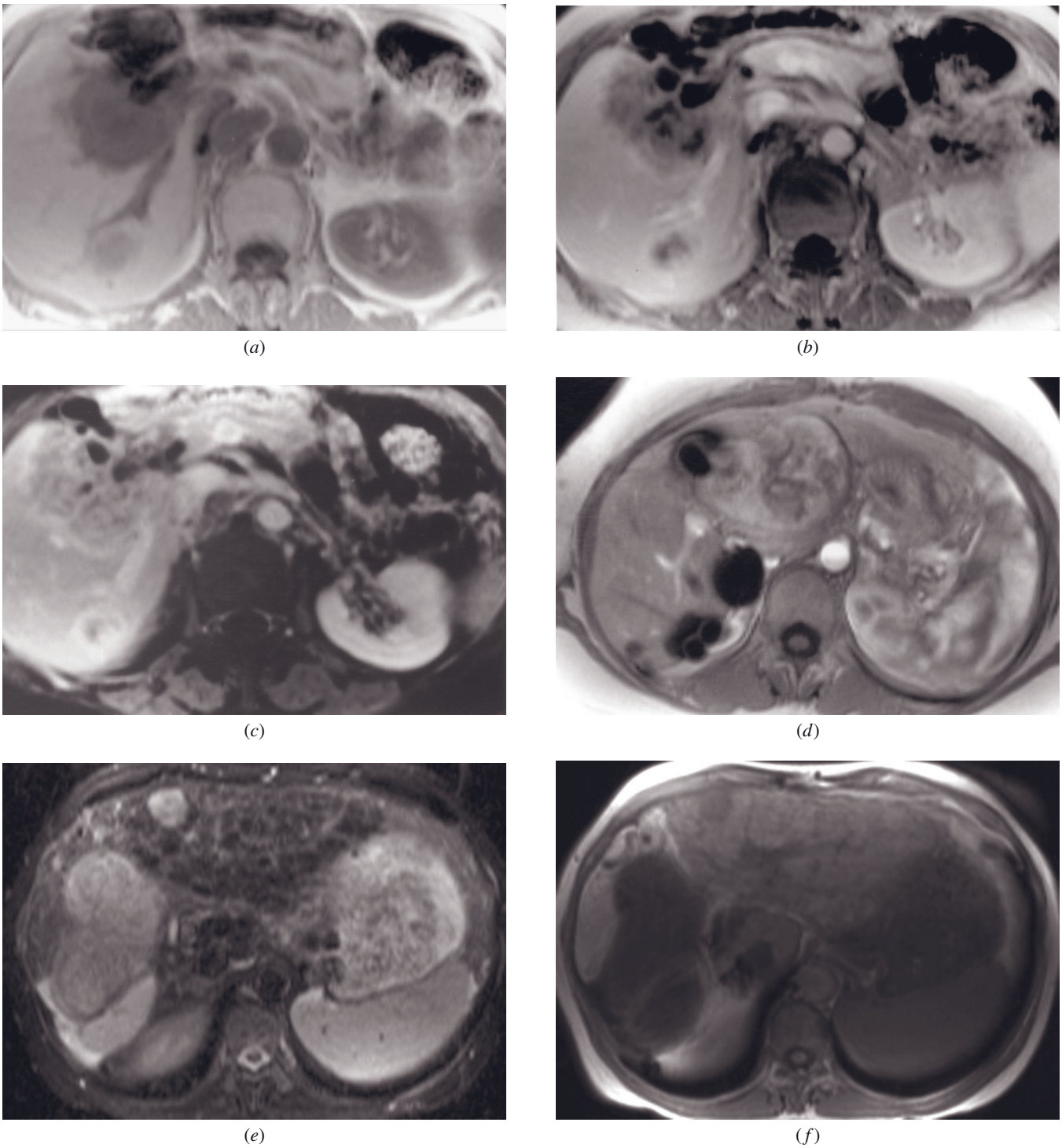

FIG. 2.149 Recurrent HCC. SGE (*a*), 45-s postgadolinium SGE (*b*), and 90-s fat-suppressed postgadolinium SGE (*c*) images. This patient had previously undergone a left hepatic lobe resection for HCC. There are multiple lesions throughout the right lobe, all of which appear low signal on T1-weighted images (*a*) and exhibit lesional enhancement after gadolinium (*b*, *c*), consistent with recurrent disease. Note the large volume of tumor along the resection margin consistent with incomplete excision.

Immediate postgadolinium SGE (*d*) image in a second patient with a history of HCC, and left hepatectomy. There is a large mass that enhances heterogeneously on immediate postgadolinium images, consistent with recurrent HCC. The recurrence is along the resection margin, compatible with incomplete excision. Note the surgical clips along the liver edge from prior resection.

T2-weighted fat-suppressed SS-ETSE (*e*), SGE (*f*), and immediate (*g*) and 90-s fat-suppressed (*h*) postgadolinium SGE images in a third patient with recurrence of HCC after liver resection show similar findings.

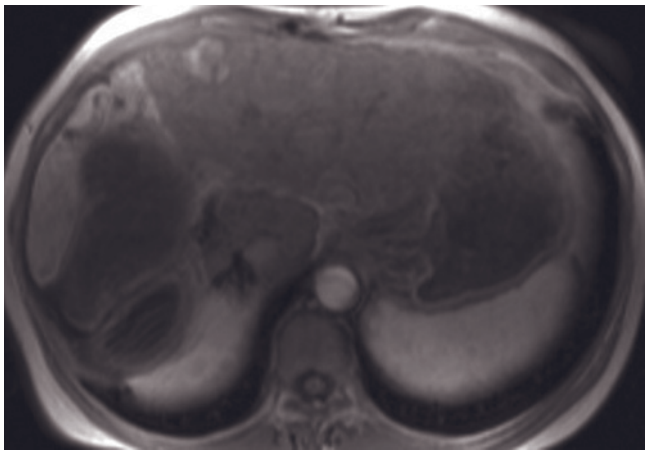

(*g*)

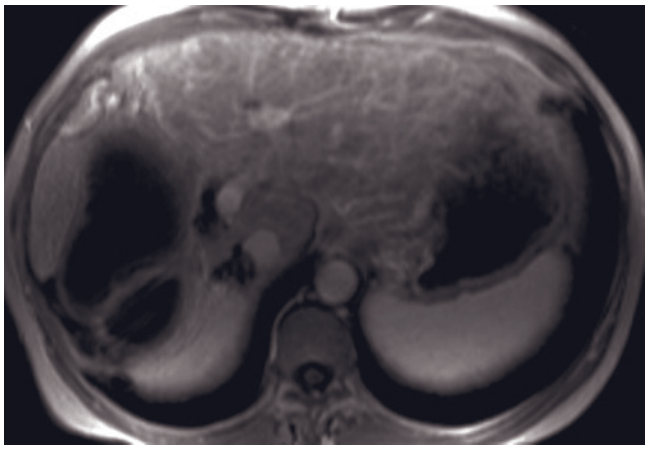

(*h*)

FIG. 2.149 (*Continued*)

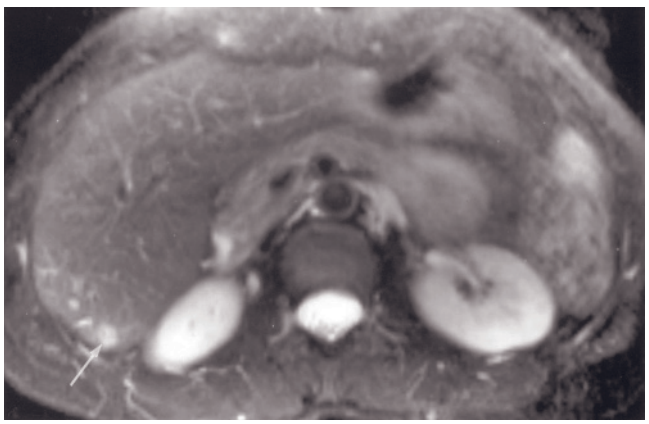

(*a*)

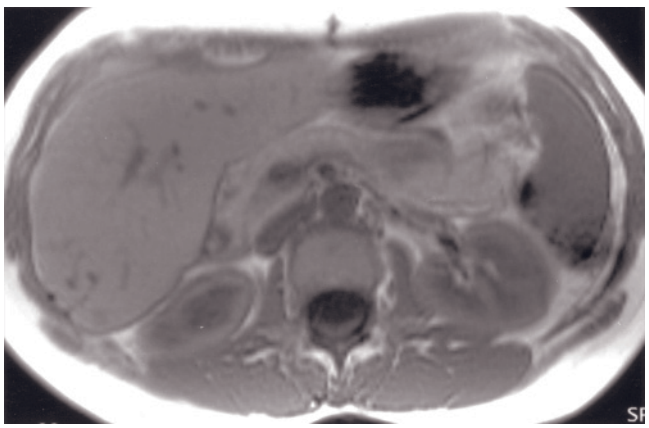

(*b*)

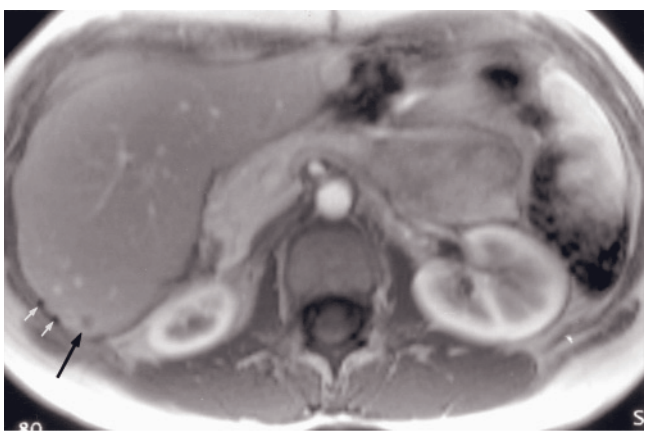

(*c*)

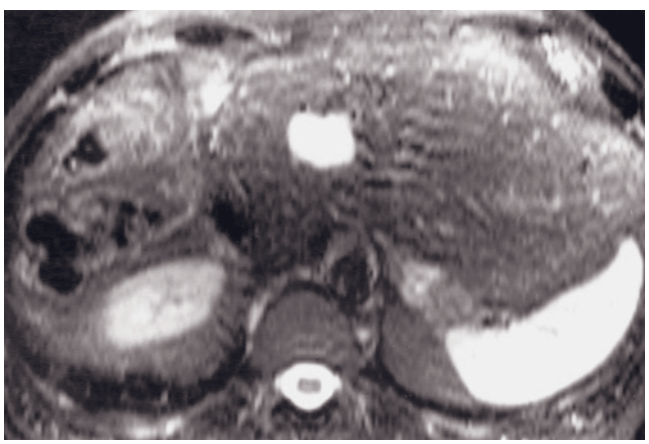

(*d*)

FIG. 2.150 Recurrent metastases after resection. Echo-train STIR (*a*), SGE (*b*) and immediate postgadolinium SGE (*c*) images in a patient who has a history of colon cancer and previous resection of liver metastases. There is a small lesion that demonstrates moderately high signal on T2 (arrow, *a*), mildly low signal on T1 (*b*), and ring enhancement (arrow, *c*) after gadolinium administration, consistent with a recurrent metastasis. Note the surgical clips (small arrows, *c*) adjacent to the lesion.

Echo-train STIR (*d*), SGE (*e*), immediate postgadolinium SGE (*f*), and 90-s fat-suppressed postgadolinium SGE (*g*) images in a second patient, who has a history of gastrointestinal stromal sarcoma and right hepatectomy 15 months earlier for liver metastasis.

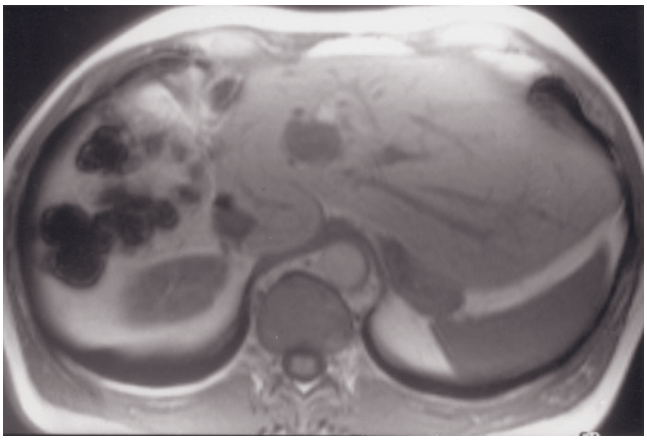

(*e*)

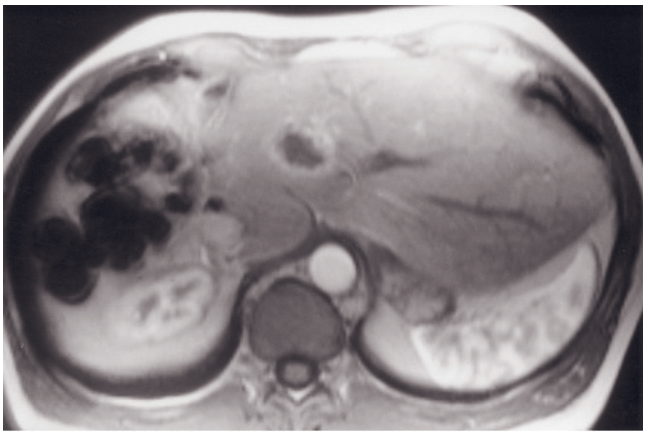

(*f*)

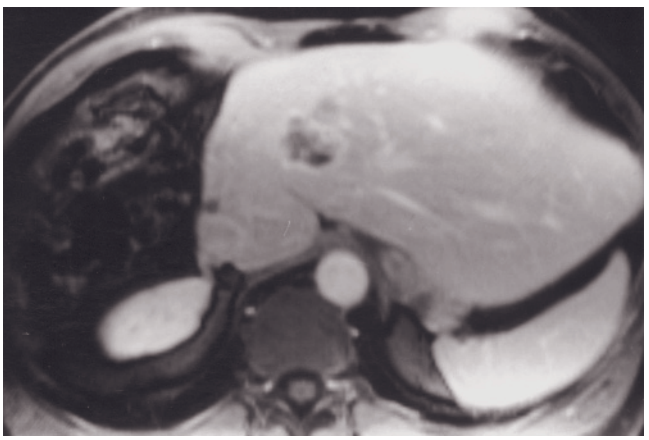

(*g*)

FIG. 2.150 (*Continued*) There is a lesion in the left lobe that demonstrates high signal on T2 (*d*), low signal on T1 (*e*), lesional ring enhancement immediately after gadolinium administration (*f*), and central progression of enhancement on the late image (*g*).

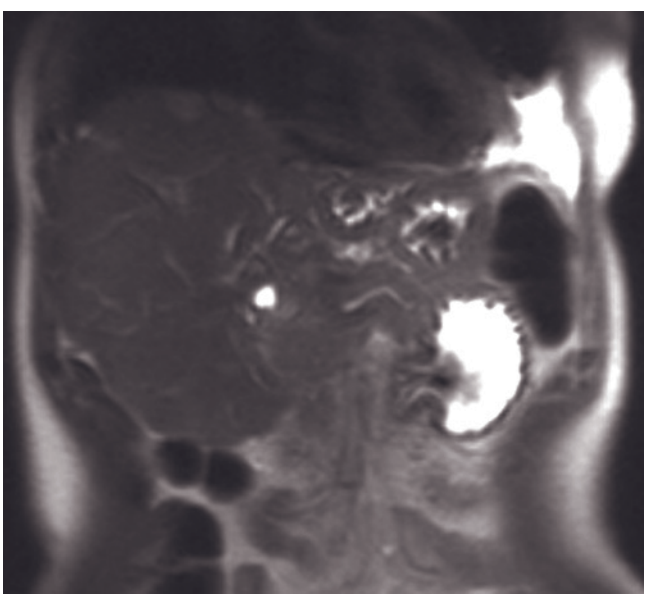

(*a*)

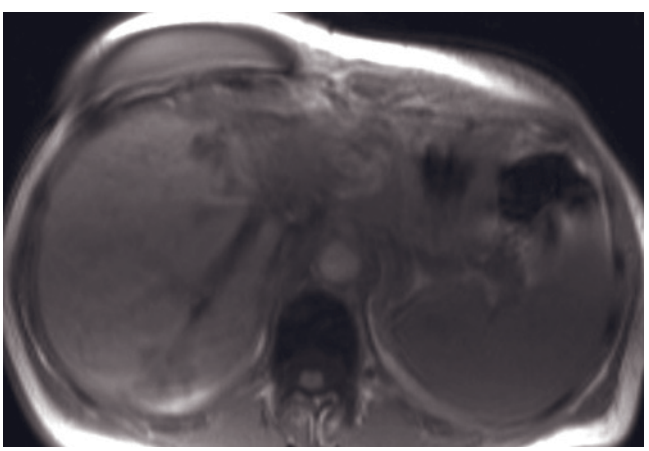

(*b*)

FIG. 2.151 Liver metastasis from breast cancer after radiation. Coronal T2-weighted SS-ETSE (*a*), immediate (*b*), 45-s (*c*), and 90-s fat-suppressed (*d*) postgadolinium SGE images, and sagittal 90-s fat-suppressed post gadolinium SGE image (*e*) in a patient with liver and bone metastases from breast cancer after breast radiation therapy. The left lobe of the liver is shrunken, causing

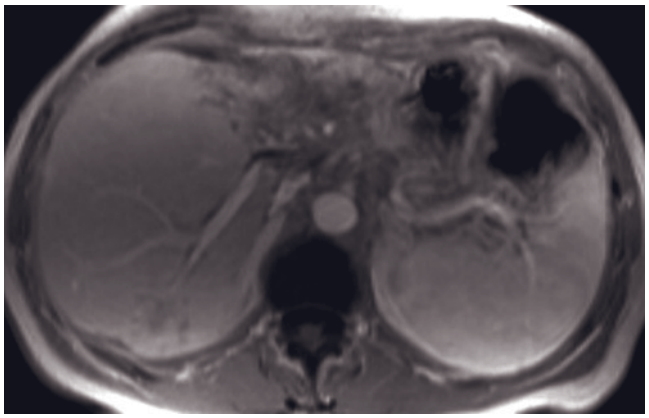

(*c*)

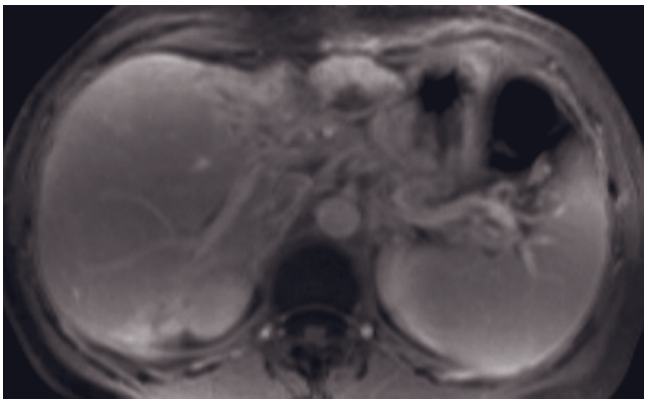

(*d*)

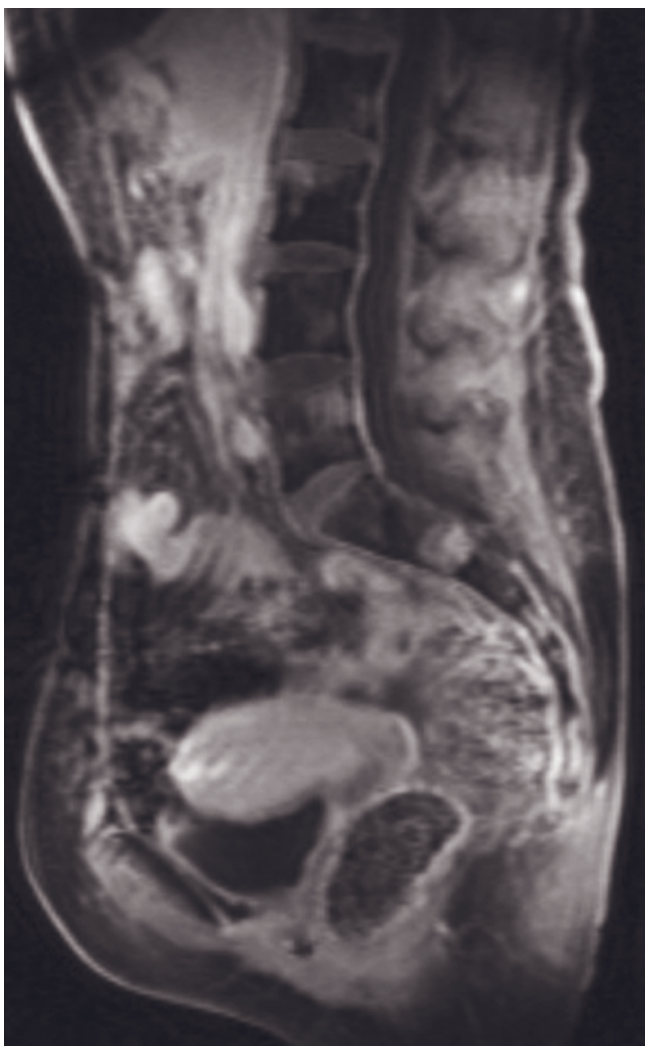

(*e*)

Fig. 2.151 (*Continued*) distortion in the normal hepatic architecture. The affected area shows isointensity on T2-weighted image (*a*), low signal intensity on T1-weighted images (*b*), negligible enhancement on early-phase images (*b*) and 45-s images (*c*), and homogeneous increased enhancement on late-phase images (*d*) compatible with fibrosis after radiation therapy. Note also the presence of bone metastasis in the sagittal plane (*e*).

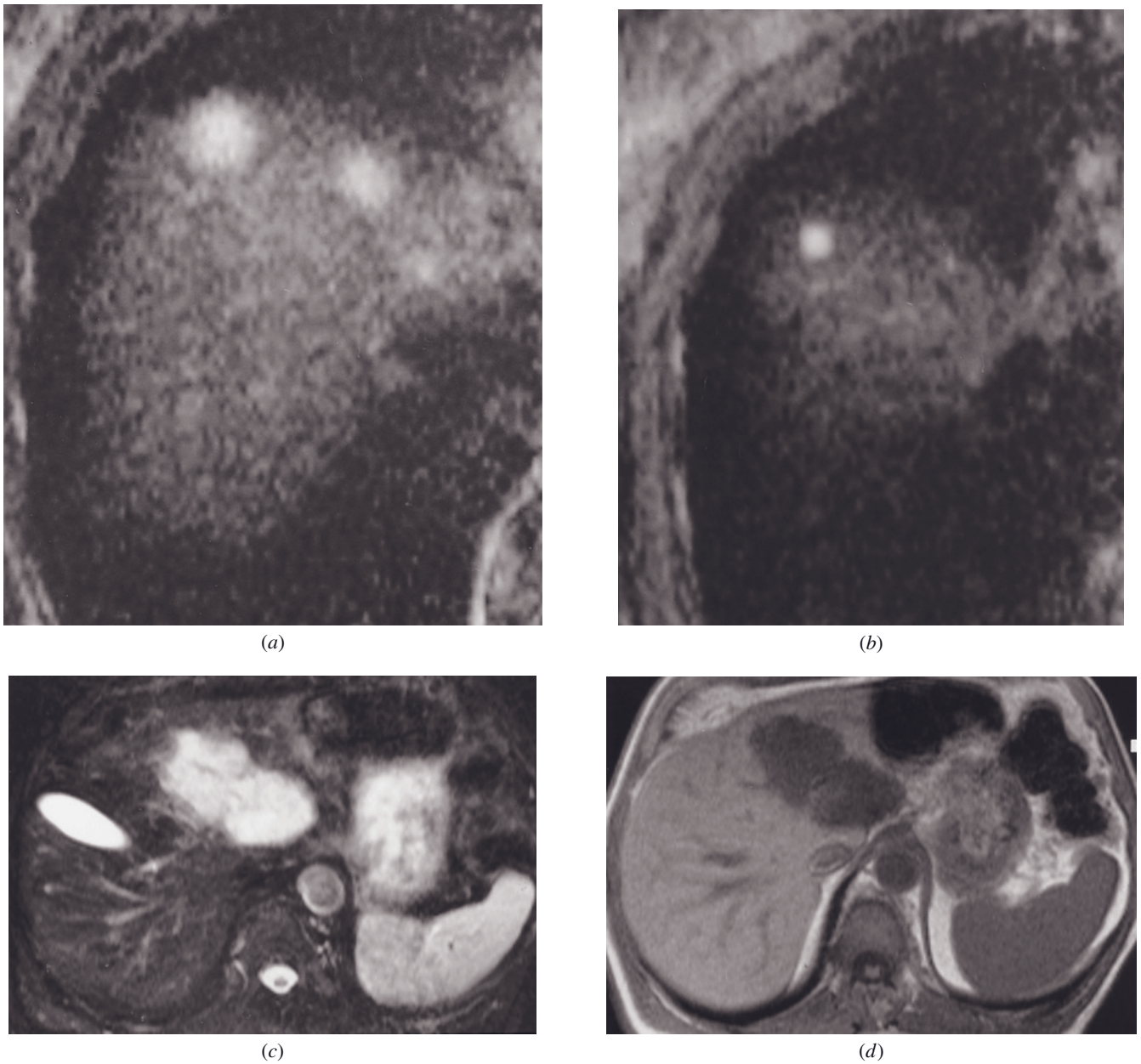

FIG. 2.152 Chemotherapy-treated metastases. Chemotherapy-treated liver metastases imaged within 7 months of therapy initiation. T2-weighted fat-suppressed ETSE image before (*a*) and 3 months after (*b*) initiation of chemotherapy. On the pretreatment examination (*a*), two metastases (1.5 cm and 1 cm) are evident in the dome of the liver. The metastases have slightly ill-defined margins and are moderately high in signal intensity. Three months after initiation of chemotherapy, the larger metastasis has decreased in size to 4 mm, has well-defined margins, and appears more hyperintense (*b*).

T2-weighted fat-suppressed SS-ETSE (*c*), SGE (*d*), and 90-s (*e*) and 10-min (*f*) postgadolinium SGE images in a second patient demonstrate two 4-cm metastases. The metastases are well-defined, moderately high in signal intensity on T2-weighted images (*c*), and moderately low in signal intensity on T1-weighted image (*d*) and demonstrate peripheral irregular enhancement (*e*) that progresses centripetally. The lesions appear hyperintense relative to liver with a low-signal intensity central scar at 10 min (*f*).

In both patients, the appearance of these subacute treated metastases (2–7 months after initiation of chemotherapy) mimics the appearance of hemangiomas. History of chemotherapy treatment for liver metastasis is critical to obtain in patients with lesions that resemble hemangiomas.

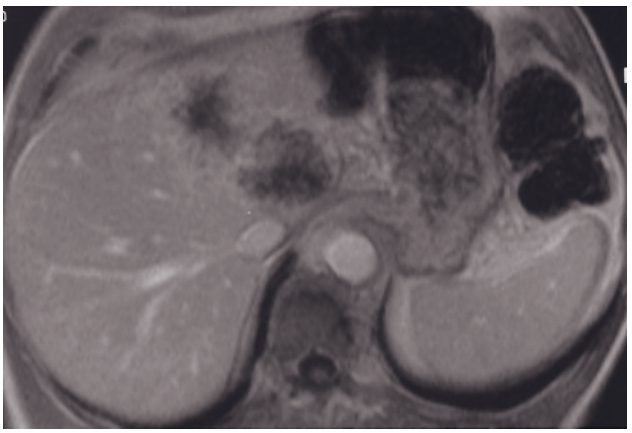

(*e*)

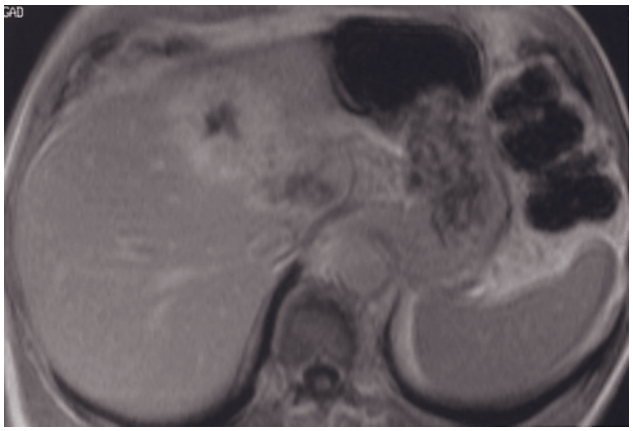

(*f*)

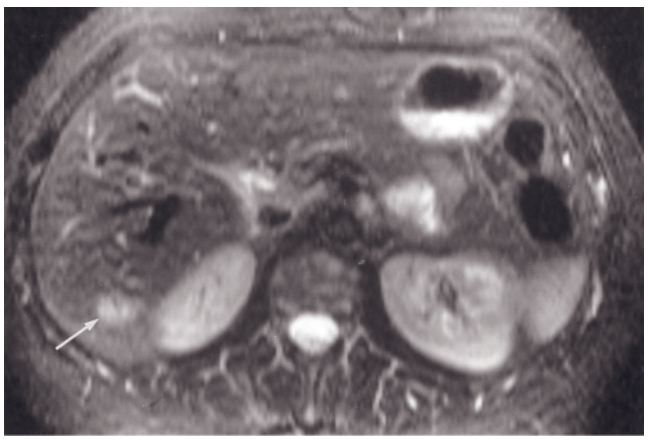

(*g*)

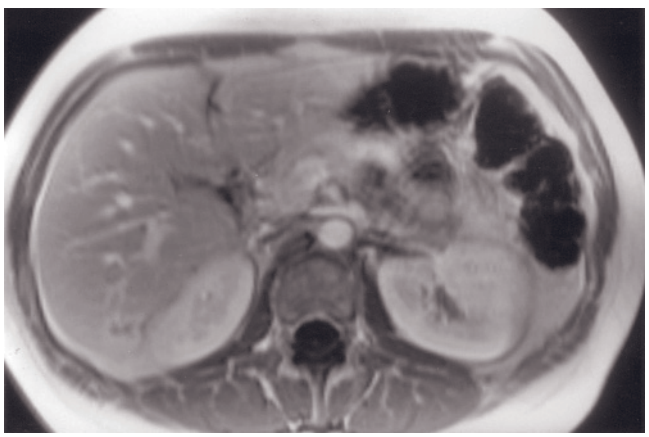

(*h*)

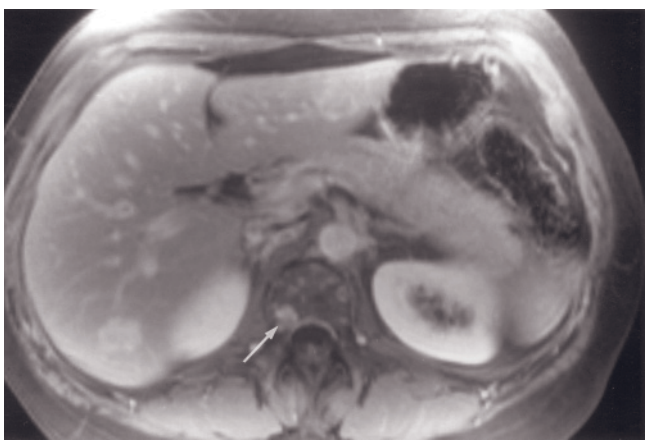

(*i*)

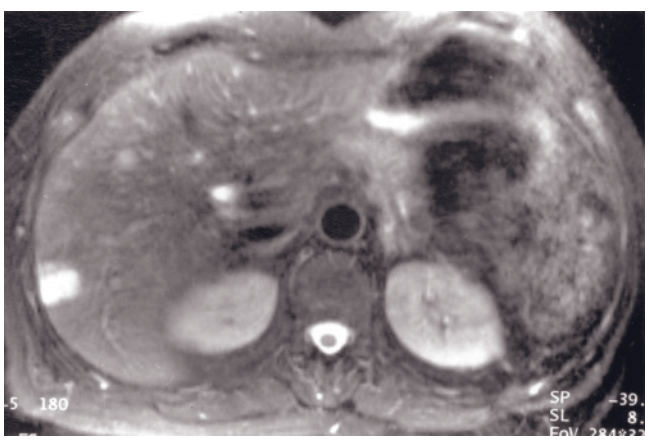

(*j*)

FIG. 2.152 (*Continued*) Echo-train STIR (*g*) and 45-s (*h*) and 90-s fat-suppressed (*i*) postgadolinium SGE images in a patient who has a history of liver metastases from breast cancer, treated with chemotherapy 2 years before this MR study. There is a lesion in the right hepatic lobe that demonstrates high signal on T2 (arrow, *g*), peripheral ring enhancement on the 45-s (*h*), and complete fill-in on the delayed image (*i*), consistent with a subacute chemotherapy-treated metastasis with features suggestive of hemangioma. Note also multiple bone metastases (arrow, *i*).

Echo-train STIR (*j*), SGE (*k*), and immediate (*l*) and 45-s (*m*) postgadolinium SGE images in a patient who has liver metastases from ovarian cancer. A lobular lesion is present in the right hepatic lobe that demonstrates high signal on T2 (*j*), low signal intensity

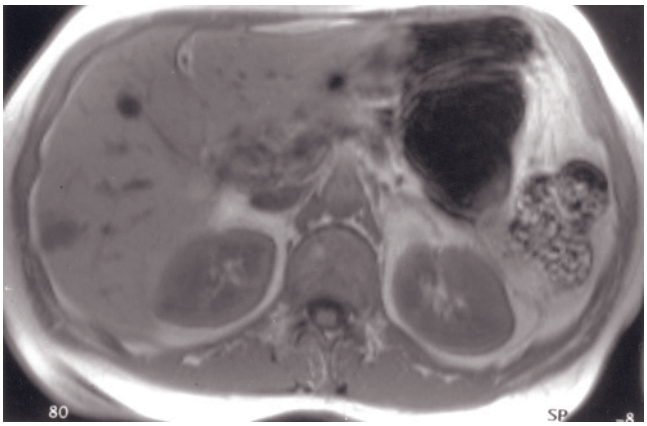

(*k*)

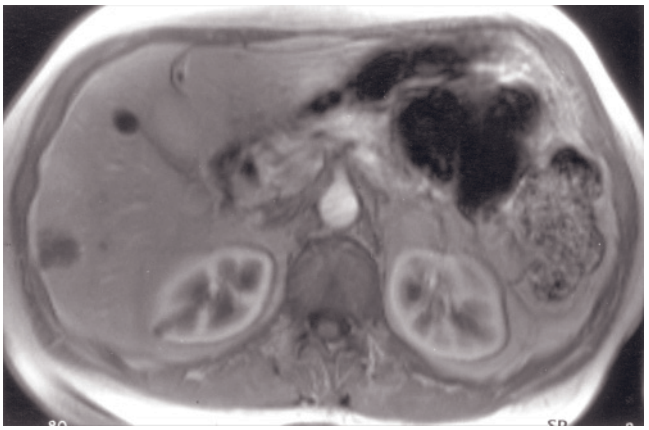

(*l*)

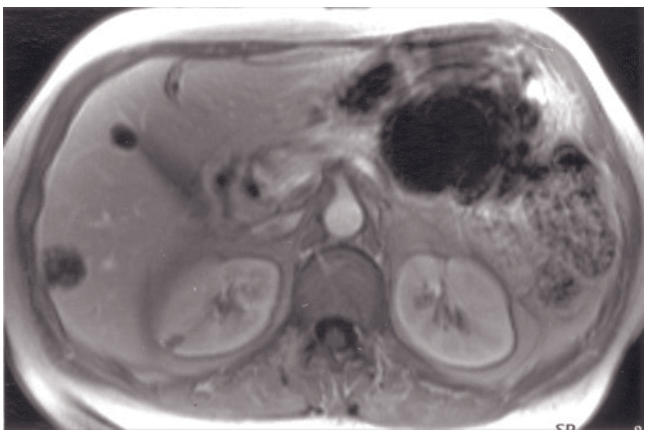

(*m*)

FIG. 2.152 (*Continued*) on T1-weighted images (*k*), negligible enhancement immediately after gadolinium administration (*l*), and small central nodules on the 45-s image (*m*).

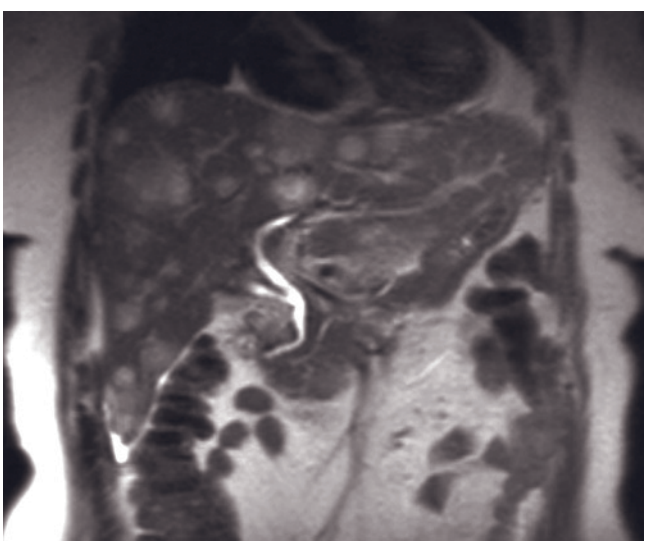

(*a*)

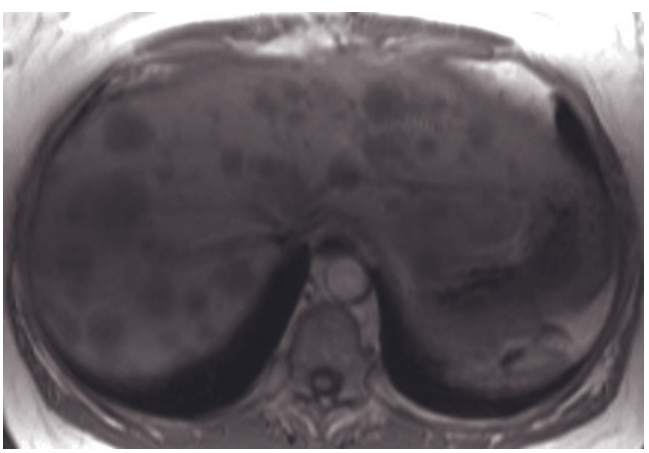

(*b*)

FIG. 2.153 Metastases from breast cancer before and after chemotherapy. Coronal T2-weighted SS-ETSE (*a*), SGE (*b*), and immediate (*c*) and 90-s fat-suppressed (*d*) postgadolinium SGE images. Multiple lesions are seen throughout the liver that appear

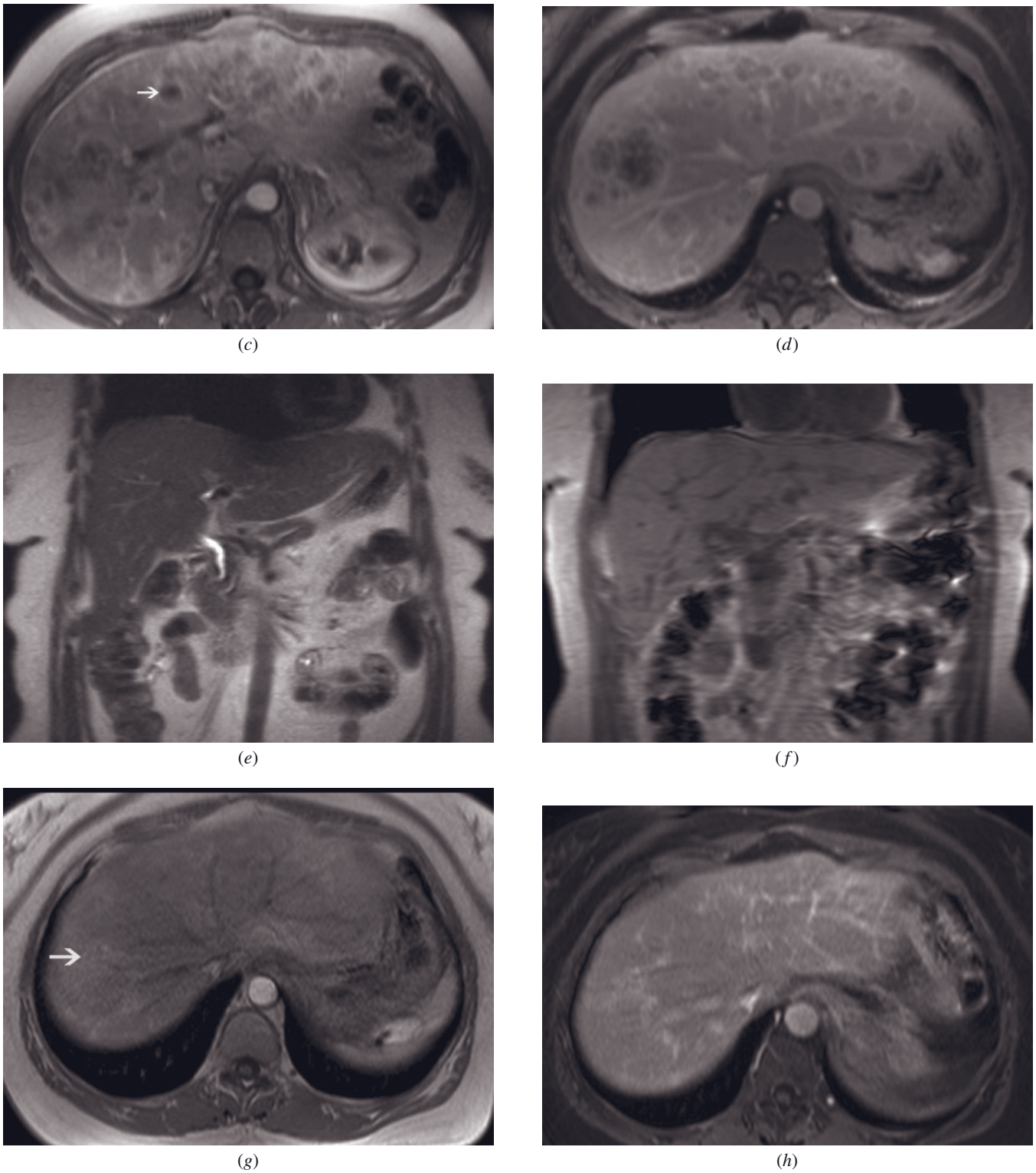

FIG. 2.153 (*Continued*) moderately high signal intensity on T2-weighted images (*a*) and moderately low signal intensity on T1-weighted image (*b*) and show ring enhancement on early-phase image (arrow, *c*) that become less conspicuous on the late-phase image (*d*). Coronal T2-weighted SS-ETSE (*e*) and T1-weighted SGE (*f*) and transverse immediate (*g*) and 90-s fat-suppressed (*h*) postgadolinium SGE images in the same patient after a course of cycles of chemotherapy. Only patchy enhancement on early-phase images can be appreciated (arrow, *g*). The remaining sequences are unremarkable.

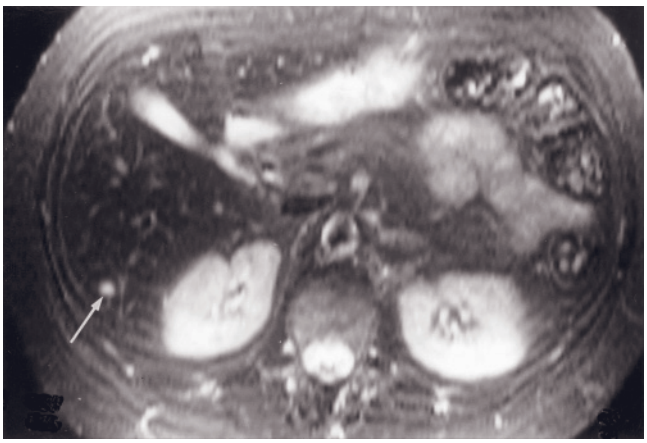

(*a*)

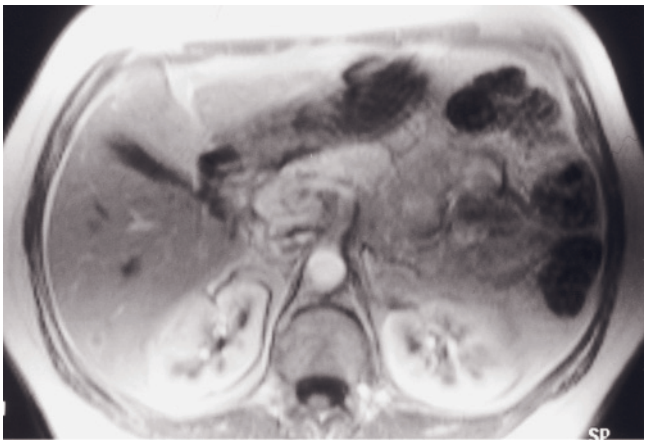

(*b*)

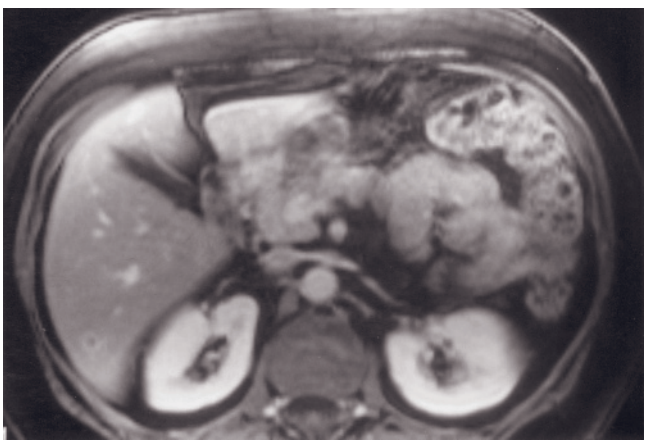

(*c*)

FIG. 2.154 Metastases from breast cancer—after chemotherapy. Echo-train STIR (*a*) and immediate (*b*) and 90-s fat-suppressed (*c*) postgadolinium SGE images. There is a small lesion in the right lobe that exhibits high signal on T2 (arrow, *a*) and ring enhancement on the immediate postgadolinium image (*b*) that persists on the late image (*c*). High signal on T2-weighted images may be observed as an early response (<1 year) to chemotherapy.

low signal intensity on T1-weighted images. After contrast, these lesions exhibit negligible early enhancement with progressive enhancement on later postcontrast images (fig. 2.156).

The fibrotic process of chronic healed metastases may be very extensive in the presence of numerous liver metastases, such that a cirrhosis-type liver appearance may develop [238, 240]. This appearance is most commonly observed in breast cancer patients with a miliary pattern of hepatic metastases, who have subsequently shown a salutary response to chemotherapy (fig. 2.157).

During the course of chemotherapy, lesions develop acute granulation tissue that may mask the appearance of coexistent viable tumor. Successful resolution of metastases should not be considered until lesions are in the chronic healed phase.

Transcatheter Arterial Chemoembolization. Chemoembolic therapy is based on the pathophysiologic premise that hypervascular malignant tumors receive a disproportionately greater blood supply from hepatic arteries than surrounding intact liver and thus cytotoxic agents are preferentially delivered to malignant cells (figs. 2.158–2.162) [242]. Within 1 month after chemoembolization, complete response is demonstrated by the lack of enhancing tumor stroma. In one report [232], 27 tumors treated with chemoembolization were low in signal on T2-weighted image and showed lack of enhancement after contrast administration. All of these tumors were necrotic at biopsy. Partial response shows increased signal intensity on T2-weighted images and enhancement on immediate postgadolinium images of residual tumor (fig. 2.163). Substantial variation does occur, reflecting variation in the degree of response and the time course of healing. One series correlated serial changes of liver lesions on T2, T1, and dynamic postgadolinium images before and after chemoembolization (figs. 2.158 and 2.160) [257]. On pretreatment MR studies, homogeneous intense enhancement on hepatic arterial dominant-phase images combined with small malignant lesion size were the best predictors of successful response. Lesions that showed good response became low signal on T2-weighted images immediately

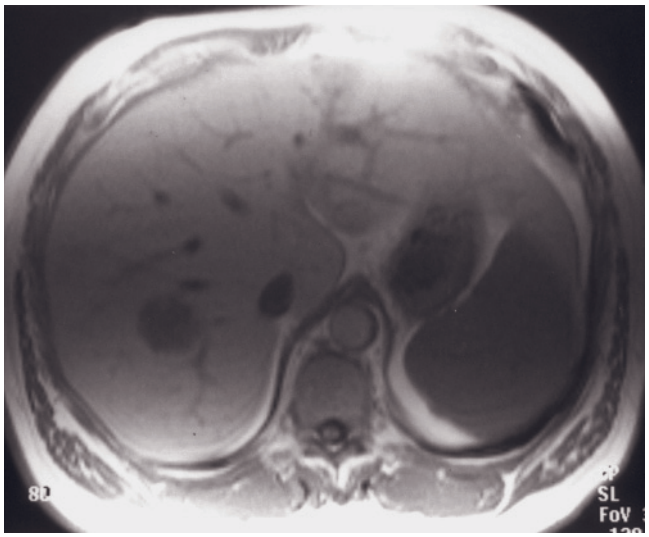

(*a*)

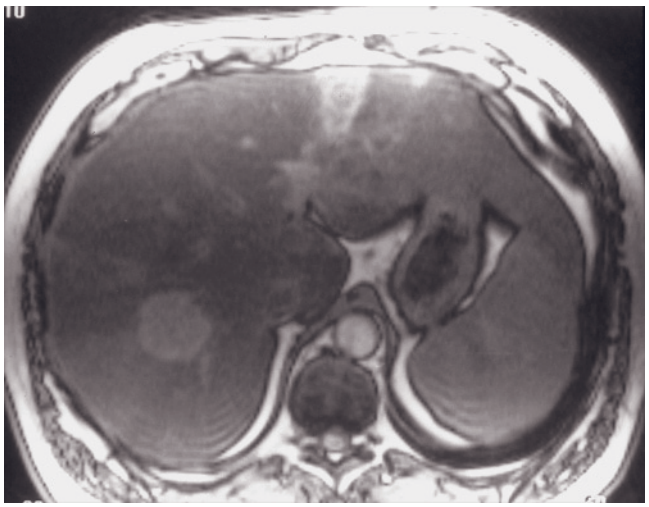

(*b*)

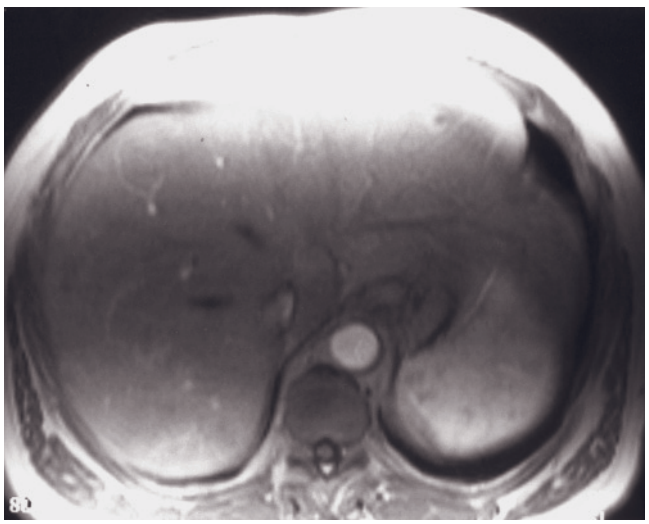

(*c*)

FIG. 2.155 Colon cancer metastases after chemotherapy. SGE (*a*), out-of-phase SGE (*b*), and immediate postgadolinium SGE (*c*) images. Chemotherapy-treated metastases are present that demonstrate low signal on T1-weighted image (*a*) and near-isointense enhancement immediately after gadolinium administration (*c*). Near-isointense enhancement is a feature observed in chemotherapy-treated metastases. Fatty infiltration of the liver (*b*) may reflect a response to the metastases or may be secondary to chemotherapy. Note that the liver metastases are conspicuous as high-signal lesions in a suppressed background of fatty liver on out-of-phase images (*b*).

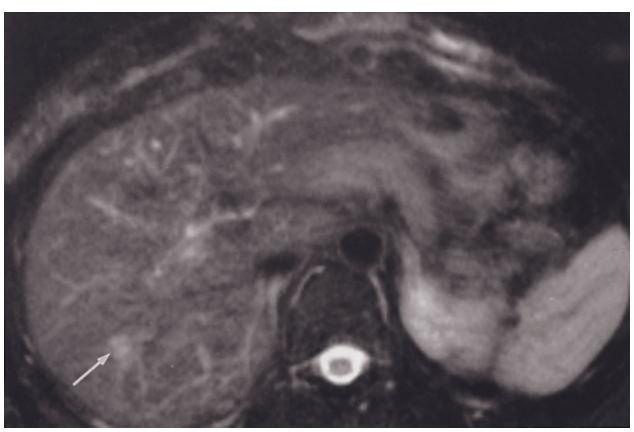

(*a*)

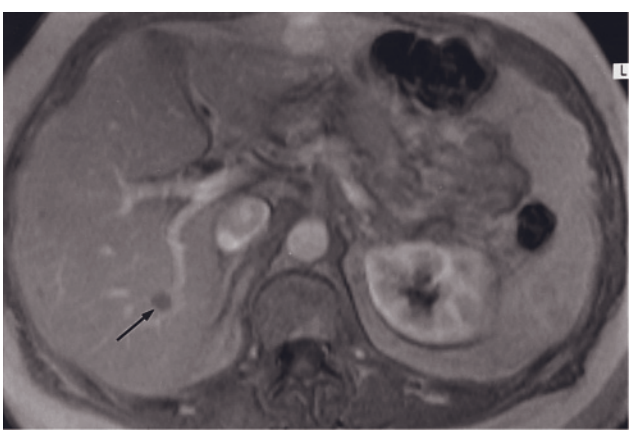

(*b*)

FIG. 2.156 Liver metastases, chronic (11 years) after chemotherapy treatment. T2-weighted fat-suppressed ETSE (*a*) and immediate postgadolinium SGE (*b*) images. A 7-mm lesion is present in the right lobe of the liver that is minimally hyperintense on the T2-weighted image (arrow, *a*) and demonstrates negligible enhancement on the immediate postgadolinium SGE image (arrow, *b*).

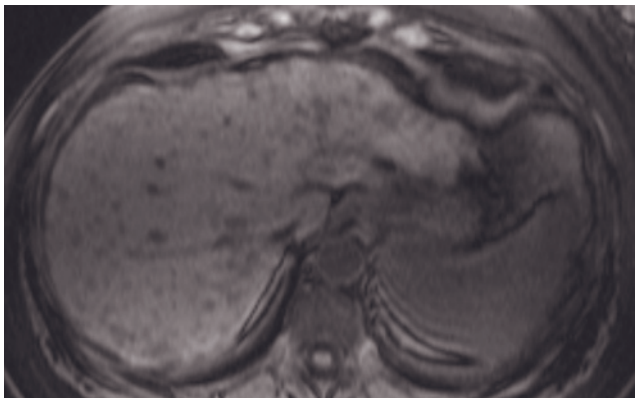

(*a*)

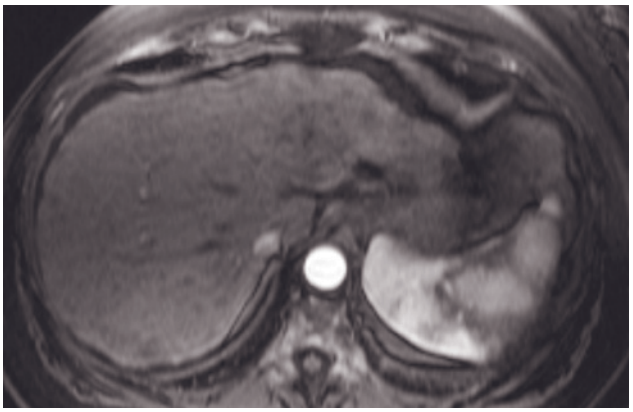

(*b*)

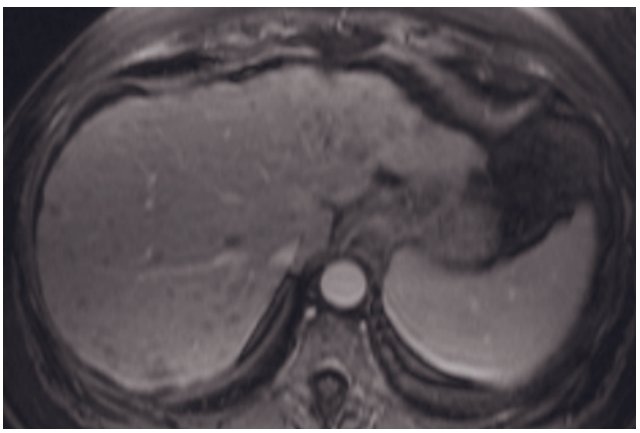

(*c*)

FIG. 2.157 Chronic treated metastases simulating cirrhosis. Non-contrast T1-weighted fat-suppressed 3D-gradient echo (*a*), immediate (*b*) and 2 min (*c*) postgadolinium fat-suppressed 3D gradient echo images. The liver has an irregular contour and contains numerous angular-marginated focal lesions, many with adjacent linear stranding, and some associated with capsule retraction. The lesions are low signal intensity on T1-weighted images (*a*) and show negligible enhancement on early (*b*) and late (*c*) postgadolinium images, consistent with focal masses of low biological activity. The appearance of these lesions is diagnostic for chronic fibrotic lesions, in this case, chronically fibrosed breast cancer liver metastases. The background hepatic fibrosis that may develop in patients who have breast cancer with chronically treated liver metastases, reflects a marked fibrogenic response, and may simulate the appearance of hepatic cirrhosis. Clinical history and the presence of numerous larger angular marginated defects (the latter may not always be present) establishes the correct diagnosis.

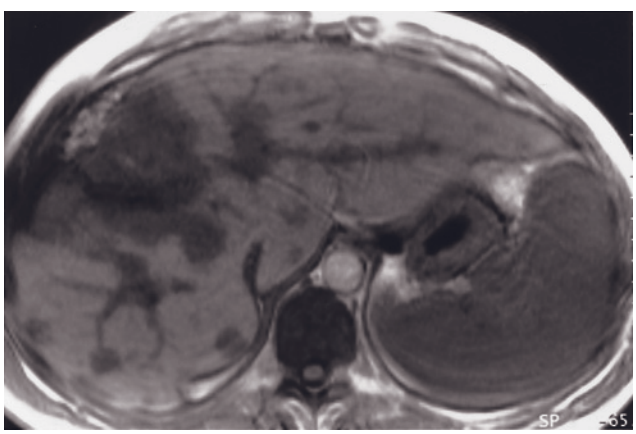

(*a*)

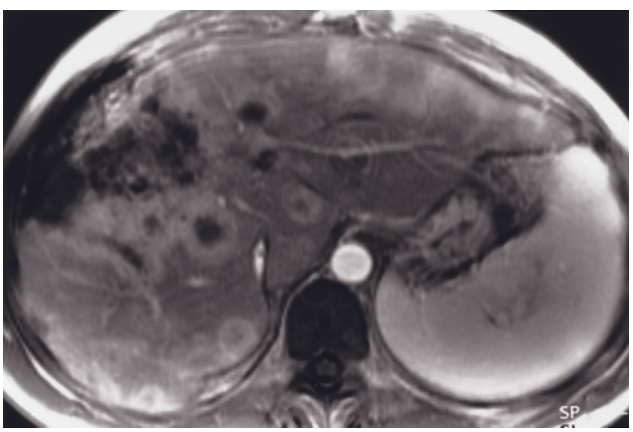

(*b*)

FIG. 2.158 Liver metastases, before and after chemoembolization. SGE (*a*) and immediate postgadolinium SGE (*b*) images before chemoembolization and immediate postgadolinium SGE image (*c*) 1 month after chemoembolization. On the pretreatment images (*a*, *b*), an 8-cm tumor and multiple tumors <2.5 cm are present throughout the liver. Prominent ring enhancement is present in these tumors (*b*). One month after chemoembolization (*c*), lesions have decreased in size and number and mural enhancement has markedly diminished.

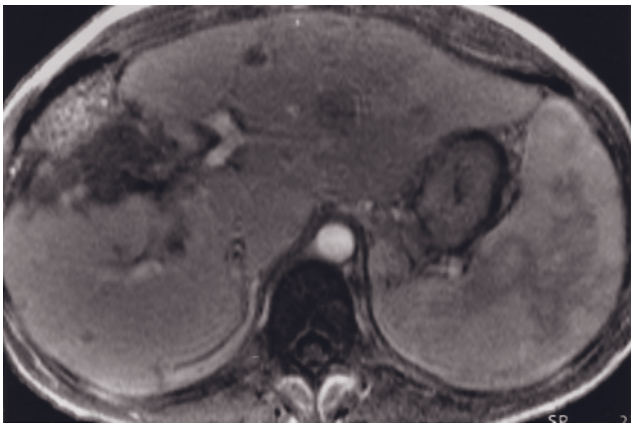

(*c*)

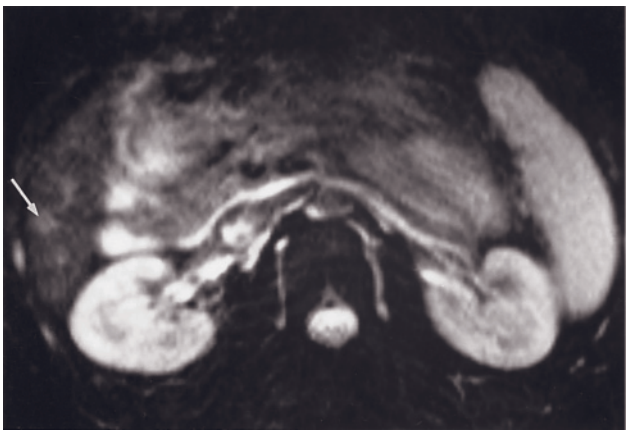

(*d*)

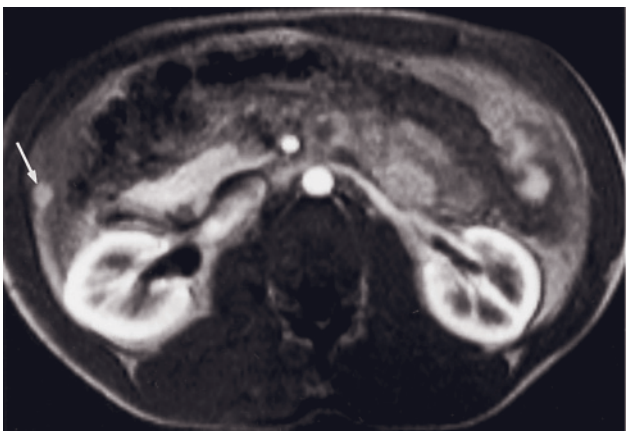

(*e*)

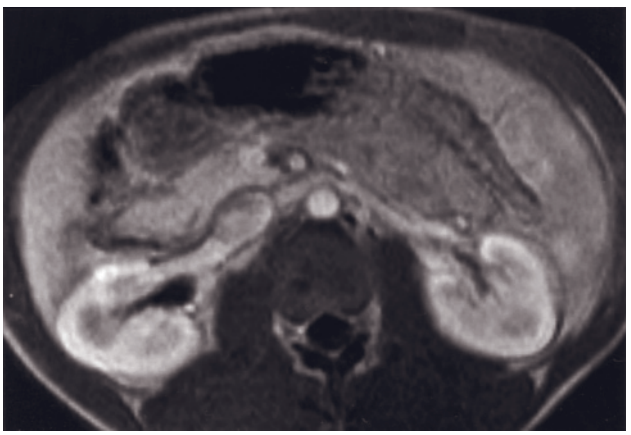

(*f*)

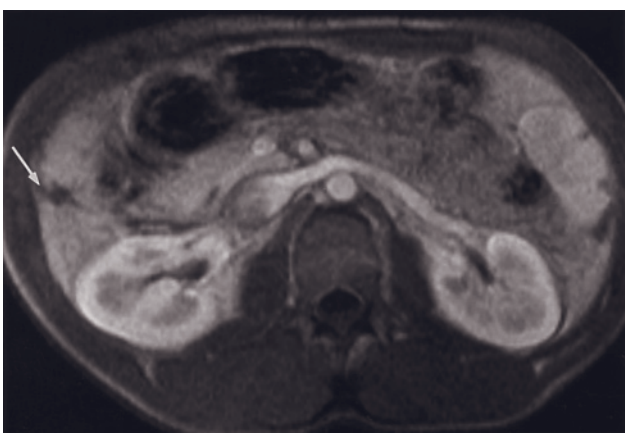

(*g*)

FIG. 2.158 (*Continued*) T2-weighted fat-suppressed ETSE (*d*) and immediate (*e*) and 45-s (*f*) postgadolinium SGE images in a second patient before chemoembolization. This patient with recurrent fibrolamellar HCC possesses multiple liver lesions that are moderately high in signal intensity on T2-weighted images (arrow, *d*), show intense uniform enhancement immediately after gadolinium administration (arrow, *e*), and fade rapidly to isointensity with liver by 45 s (*f*). Immediate postgadolinium SGE image acquired 1 month after chemoembolization (*g*) shows complete lack of enhancement of the lesion, which now has polygonal angular margins (arrow, *g*), consistent with scarring.

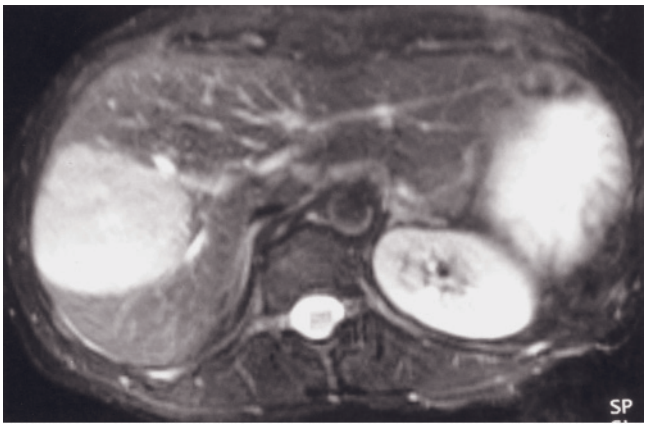

(*a*)

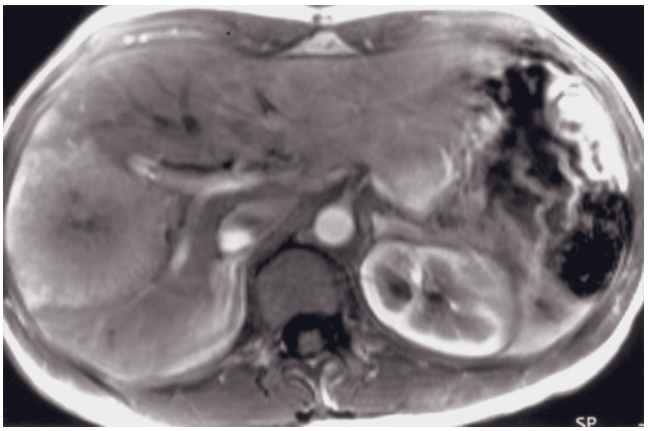

(*b*)

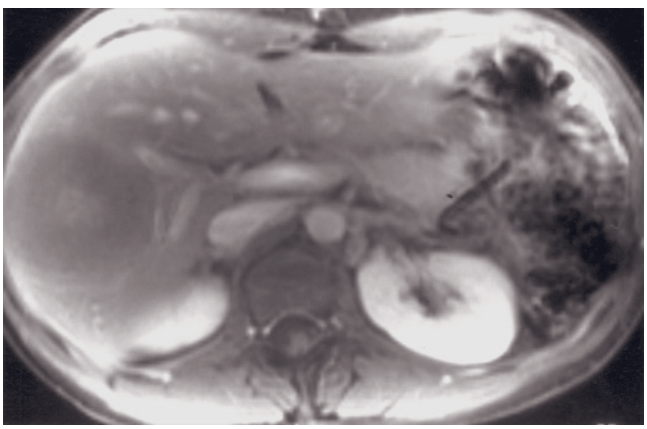

(*c*)

(*d*)

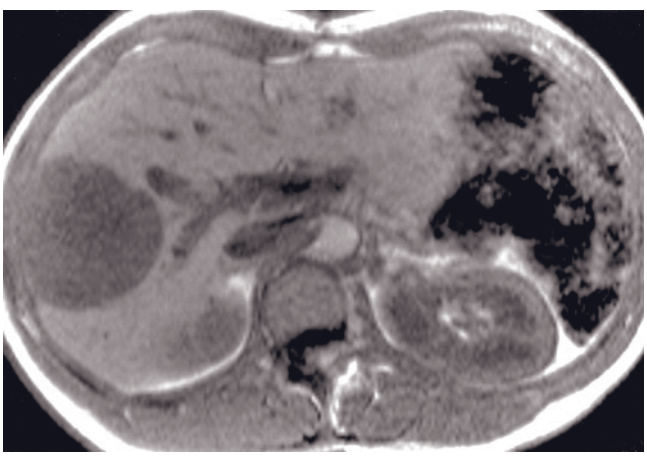

(*e*)

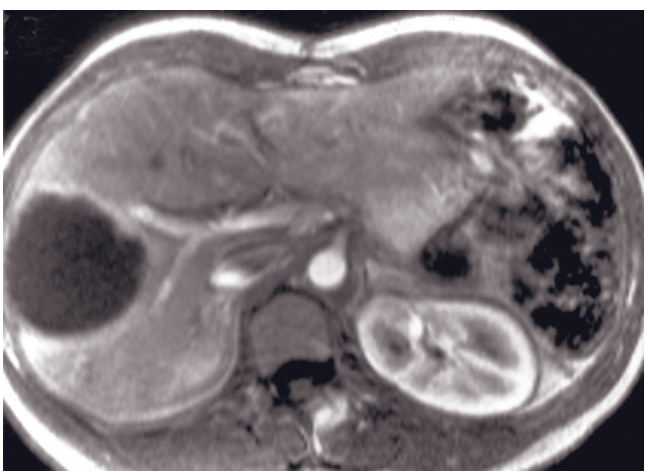

(*f*)

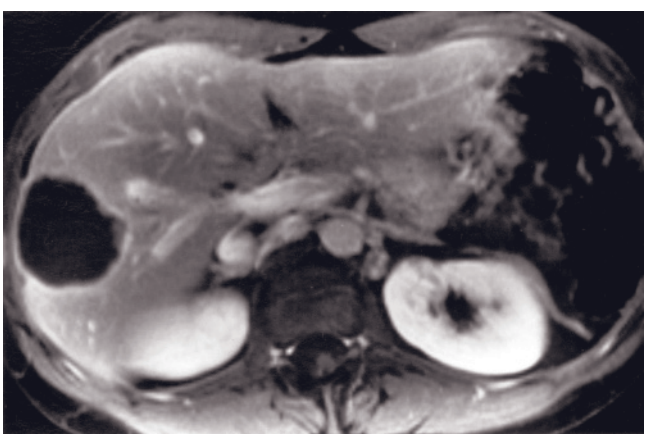

(*g*)

FIG. 2.159 Metastases from gastrinoma—before and after chemoembolization. Echo-train STIR (*a*) and immediate (*b*) and 90-s fat-suppressed (*c*) postgadolinium SGE images. There is a large mass in the right hepatic lobe that demonstrates high signal on the T2-weighted image (*a*) and moderate enhancement on the early-phase image (*b*) with washout on the late-phase image (*c*), consistent with a hypervascular metastasis.

Echo-train STIR (*d*), SGE (*e*), and immediate (*f*) and 90-s fat-suppressed (*g*) postgadolinium SGE images after chemoembolization. The lesion has decreased slightly in size, with the most prominent feature being lack of enhancement on the immediate postgadolinium image (*f*). Note a thin rim of enhancement on early (*f*)- and late (*g*)-phase images. A distinctive feature of chemoembolization-treated lesions is the relatively low signal on T2-weighted images immediately after treatment, reflecting devascularization. Most other treatments methods result in increased signal on T2-weighted images in the acute phase.

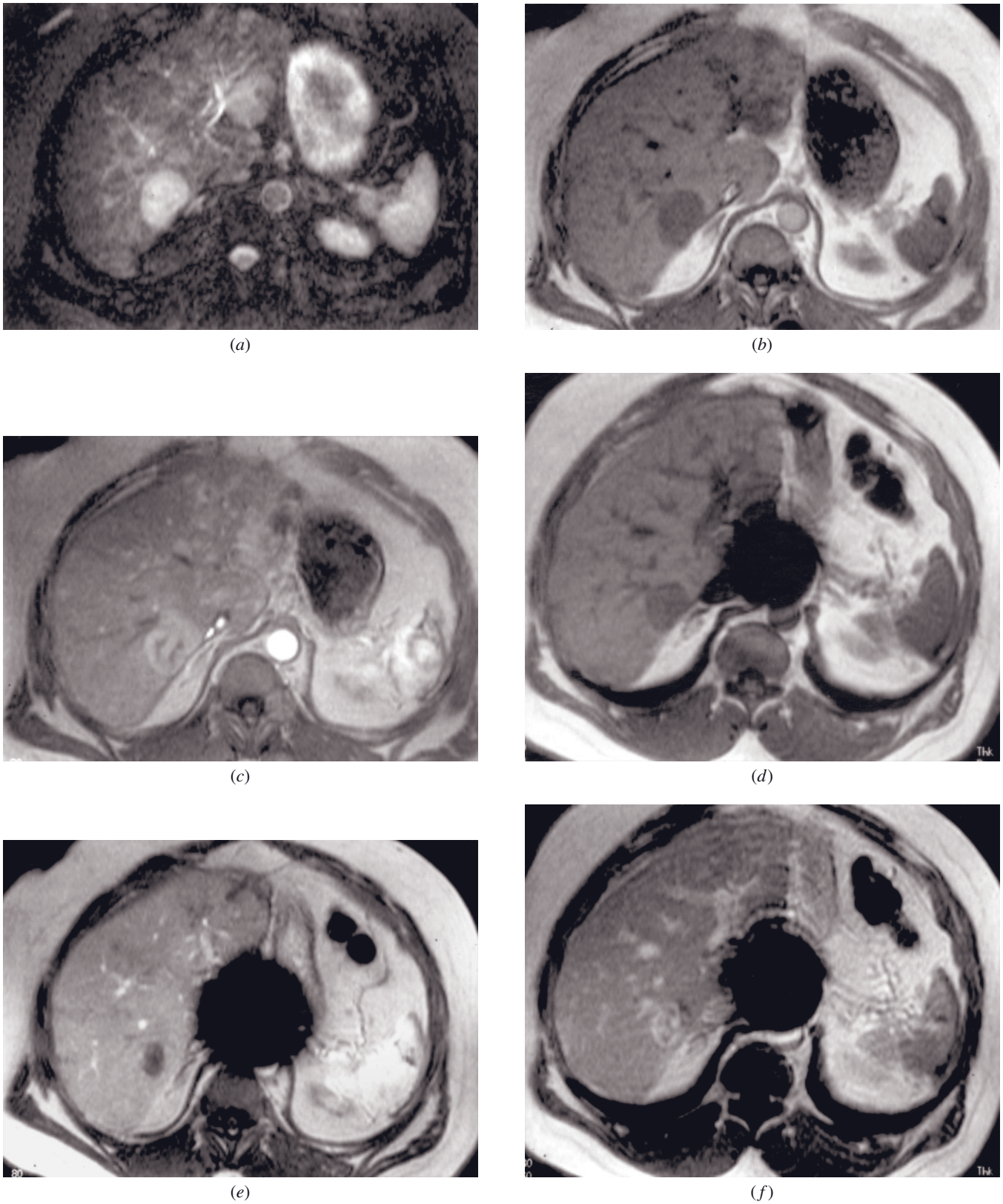

FIG. 2.160 Metastasis from carcinoid—before and after chemoembolization. T2-weighted fat-suppressed ETSE (*a*), SGE (*b*), and immediate postgadolinium SGE (*c*) images. A 4-cm metastasis is present in the right lobe and a second 4-cm lesion in the lateral segment. They appear moderately high signal intensity on T2-weighted image (*a*) and moderately low signal intensity on T1-weighted image (*b*) and show intense enhancement on early-phase image (*c*).

SGE (*d*) and immediate (*e*) and 45-s (*f*) postgadolinium SGE images in the same patient after chemoembolization. Note that the lesion has decreased in size and shows minimal enhancement on the immediate postgadolinium image (*e*), with progressive enhancement on later images. This enhancement pattern is consistent with fibrosis. Note the large metal artifact in the porta hepatis that represents a metal coil placed at the time of chemoembolization.

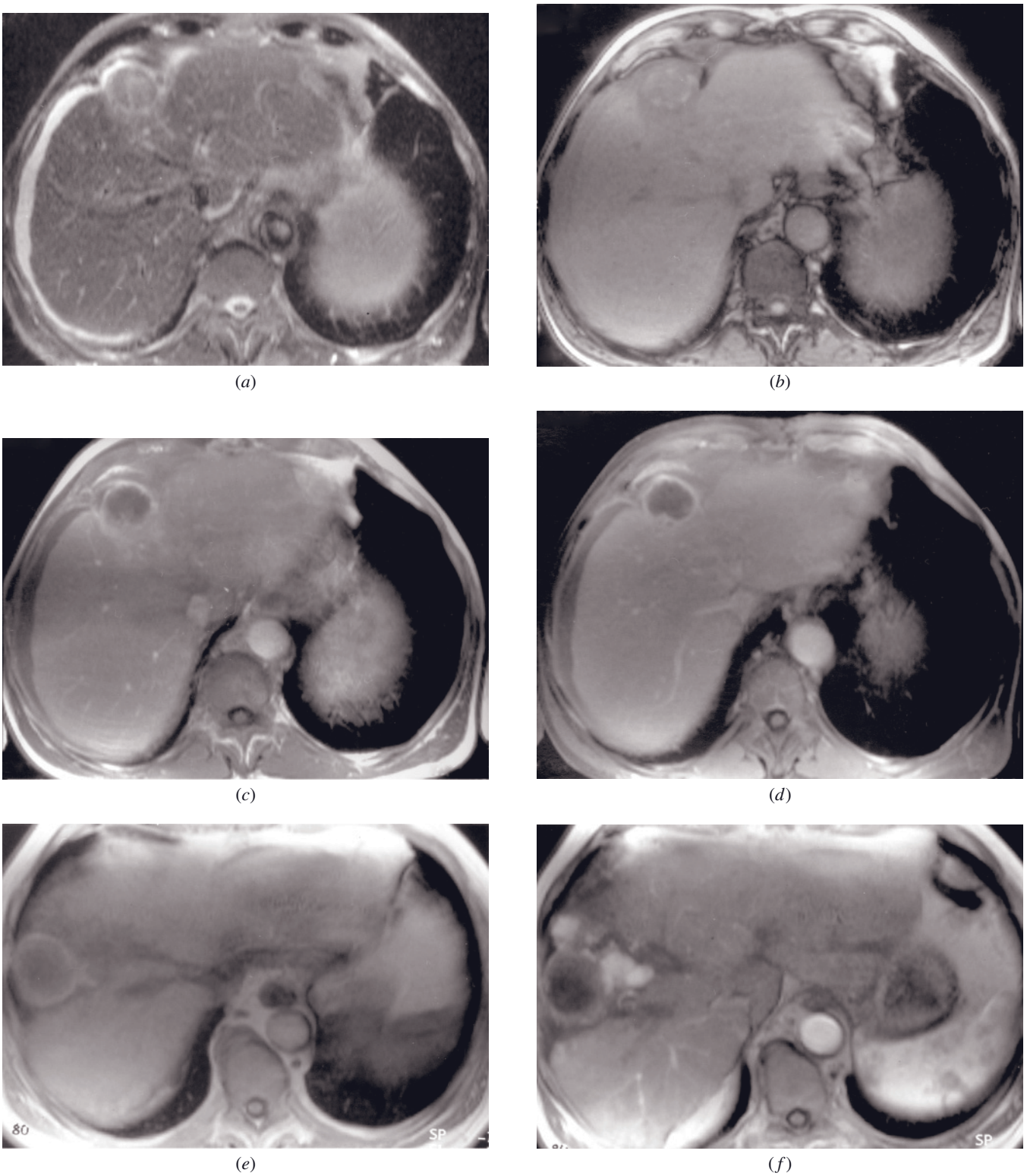

FIG. 2.161 HCC and chemoembolization. Echo-train STIR (*a*), out-of-phase SGE (*b*), and 45-s (*c*) and 90-s fat-suppressed (*d*) postgadolinium SGE images. A rounded lesion is seen in the left hepatic lobe that demonstrates minimal high signal intensity on T2 (*a*), minimal low signal intensity with a high signal rim on T1 (*b*), capsular enhancement after gadolinium (*c*, *d*) with lack of tumor enhancement. The combination of isointensity on T2 with lack of central enhancement on postgadolinium T1-weighted images is consistent with devascularization of tumor, which occurs after chemoembolization.

SGE (*e*), immediate postgadolinium SGE (*f*), and 90-s fat-suppressed postgadolinium SGE (*g*) images in a second patient. There is an oval lesion located in the right hepatic lobe that shows decreased signal intensity centrally and increased signal intensity

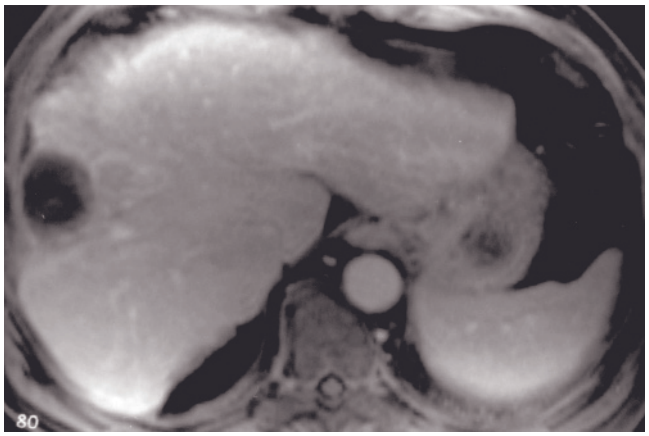

(*g*)

FIG. 2.161 (*Continued*) peripherally on the noncontrast T1-weighted image (*e*). On the immediate postgadolinium image (*f*), there is intense enhancement with well-defined margins anterior to the ablation site. This persistent tumor washes out and shows late capsule enhancement on interstitial phase images (*g*). The central devascularized ablation site does not enhance on early or late postcontrast images. The high-signal material on the precontrast T1-weighted image (*e*) represents extracellular methemoglobin.

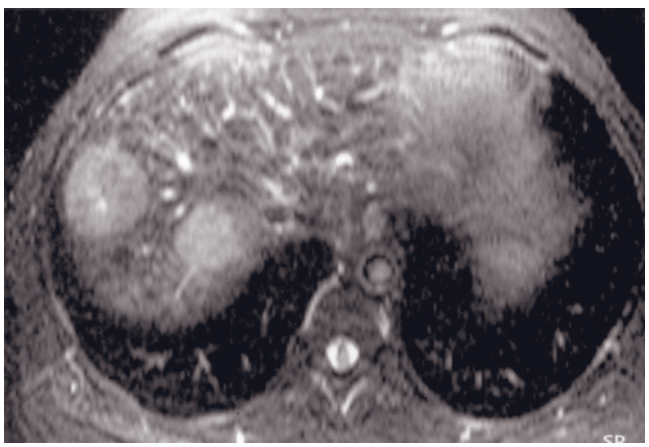

(*a*)

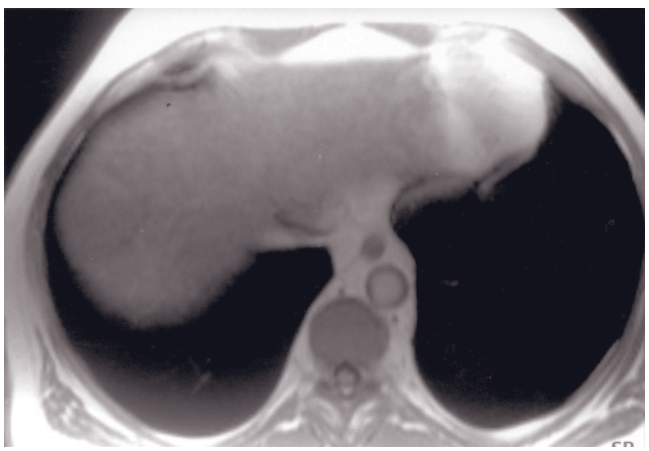

(*b*)

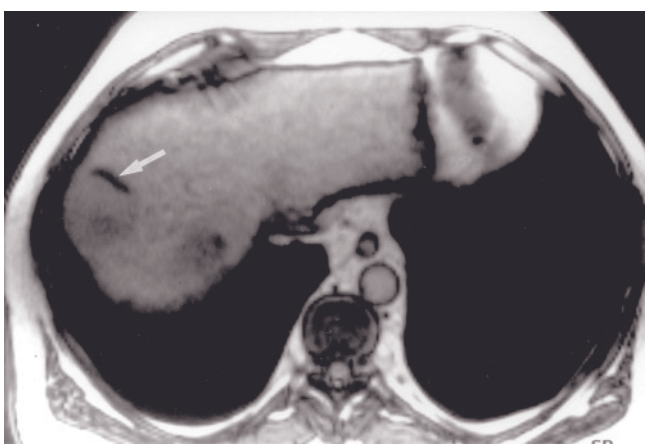

(*c*)

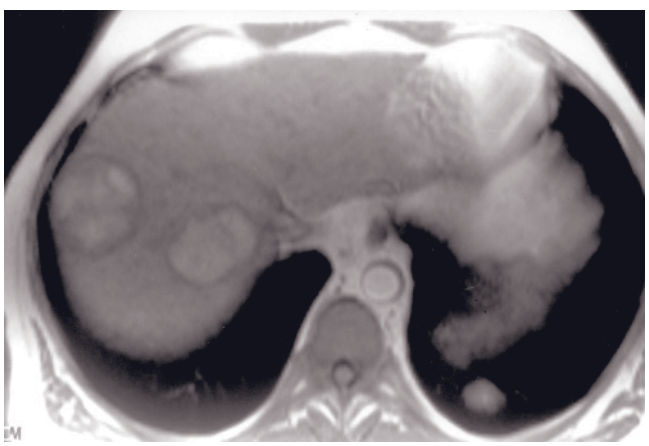

(*d*)

FIG. 2.162 HCC after chemoembolization—poor response. Echo-train STIR (*a*), SGE (*b*), out-of-phase SGE (*c*), and immediate (*d*) and 90-s fat-suppressed (*e*) postgadolinium SGE images. There are two rounded lesions that are mildly high signal on T2 (*a*) and minimally low signal on T1 (*b*) and demonstrate intense heterogeneous enhancement immediately after gadolinium (*d*), with washout and capsular enhancement on the late image (*e*), consistent with HCC. Note that one of the lesions demonstrates a small focus (arrow, *c*) that exhibits signal drop on the out-of-phase image, consistent with fat.

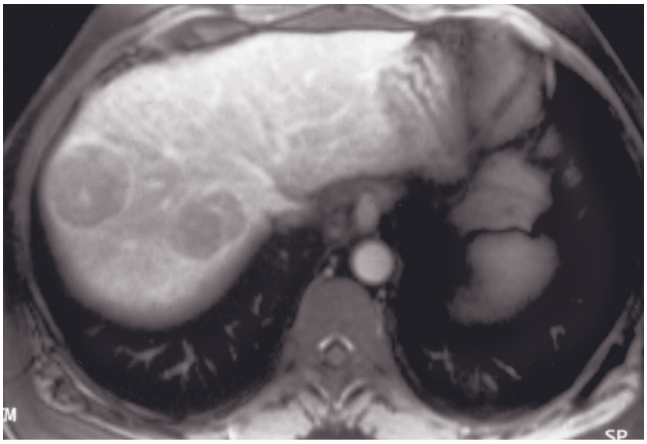

(*e*)

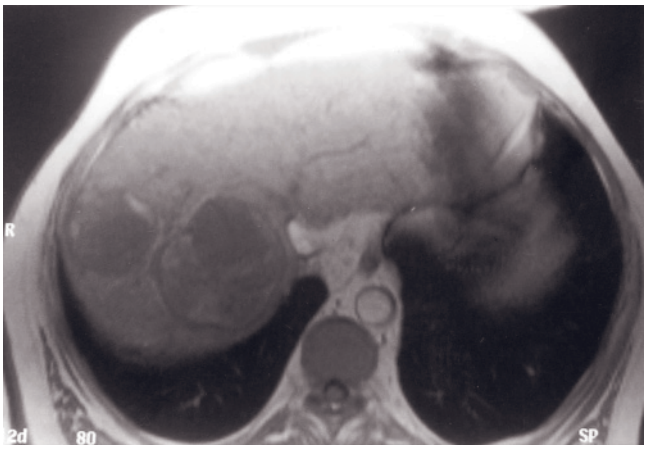

(*f*)

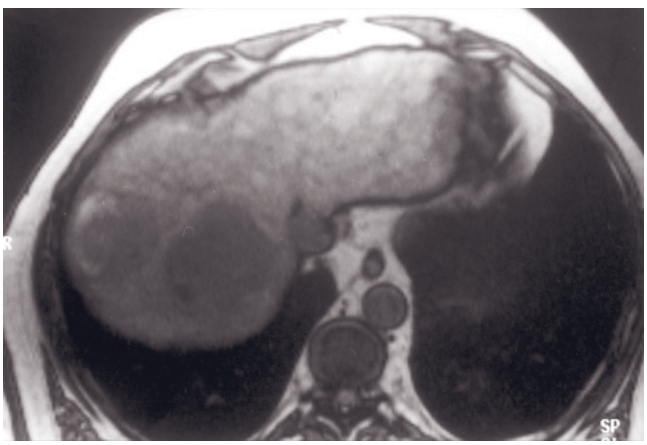

(*g*)

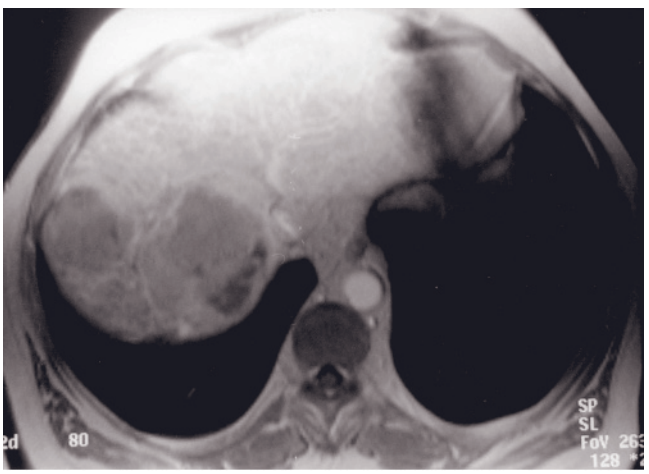

(*h*)

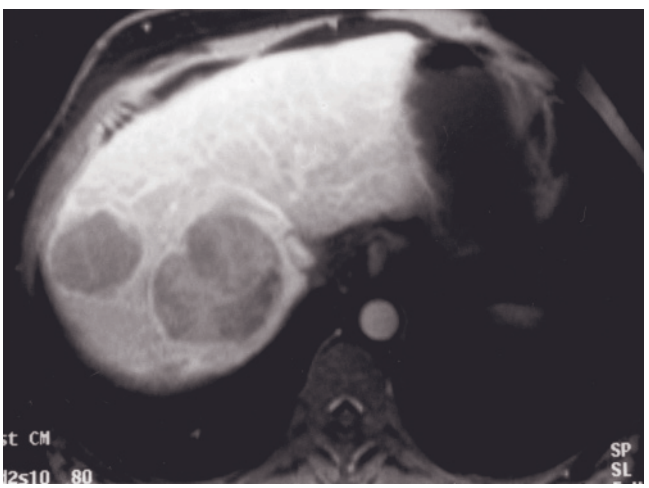

(*i*)

FIG. 2.162 (*Continued*) SGE (*f*), out-of-phase SGE (*g*), immediate postgadolinium SGE (*h*), and 90-s postgadolinium fat-suppressed SGE (*i*) images in the same patient 7 months later. Note the increased size of the lesions. The lesions demonstrate diminished enhancement on early (*h*) and late (*i*) images, reflecting central desvascularization from chemoembolization.

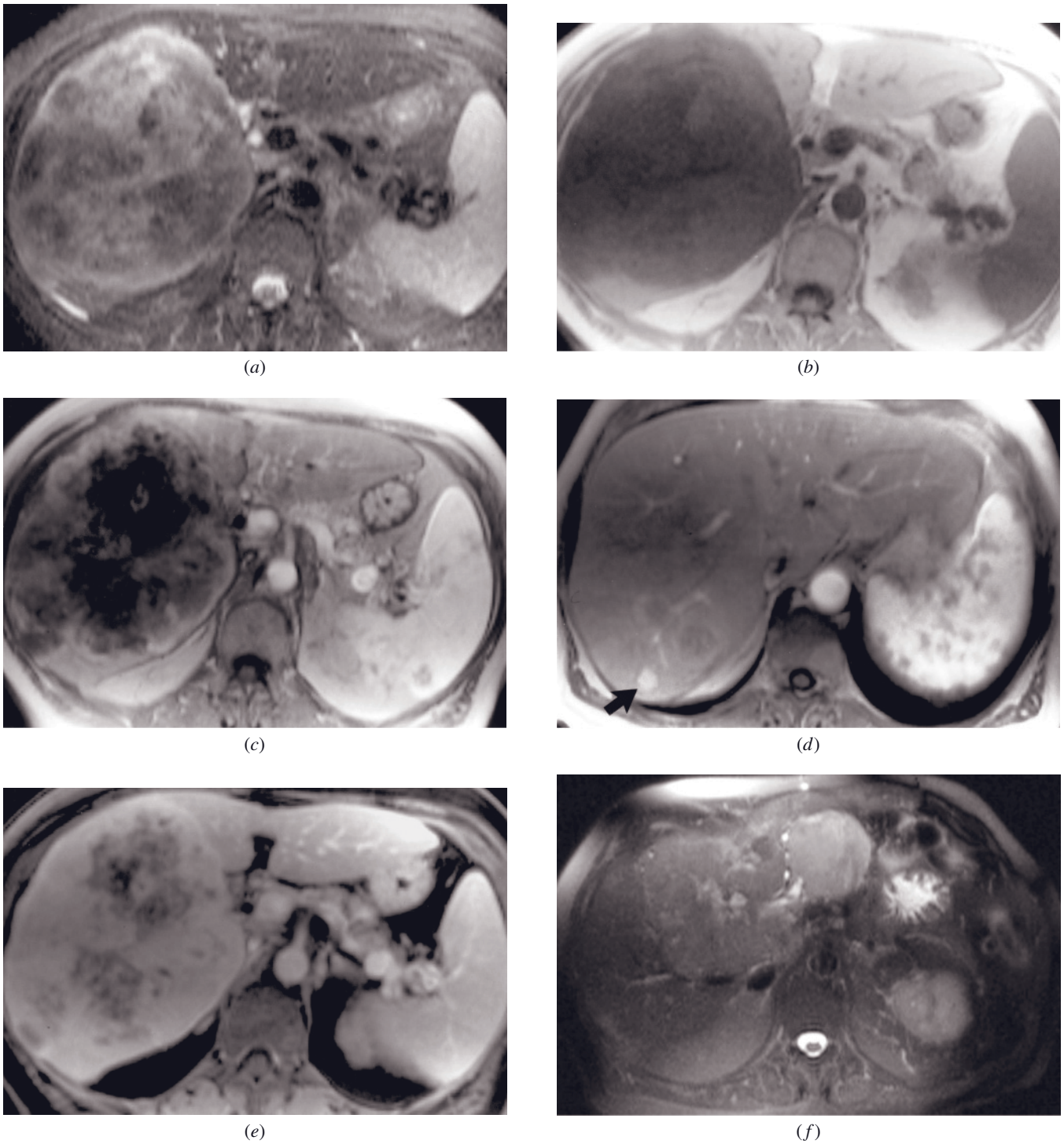

FIG. 2.163 Partial response of HCC after chemoembolization. Echo-train STIR (*a*), SGE (*b*), and immediate (*c*, *d*) and 90-s fat-suppressed (*e*) postgadolinium SGE images. There is a huge mass that shows high signal intensity on T2-weighted image (*a*) and low signal intensity on T1-weighted image (*b*). Immediately after gadolinium, it shows intense heterogeneous enhancement (*c*) with large regions of low signal centrally within the tumor consistent with necrosis, reflecting a partial response to chemoembolization. On a higher tomographic section, a small satellite HCC (arrow, *d*) is present, which demonstrates intense uniform enhancement.

T2-weighted fat-suppressed SS-ETSE (*f*), SGE (*g*), and immediate (*h*) and 90-s fat-suppressed (*i*) postgadolinium SGE images in a second patient. There is a lesion mainly on the left lobe of the liver that shows moderate high signal intensity on T2-weighted

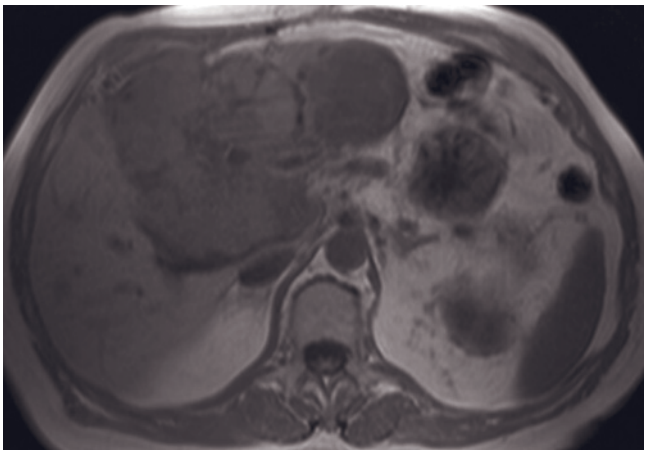

(*g*)

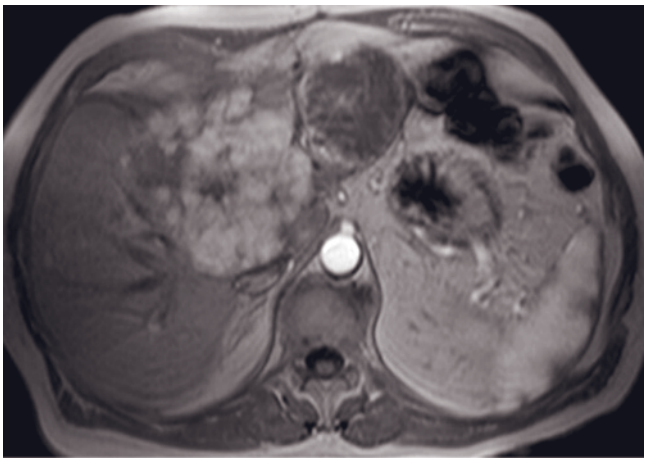

(*h*)

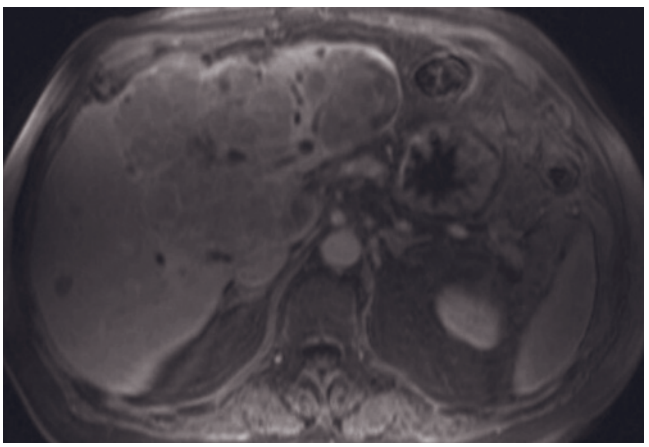

(*i*)

FIG. 2.163 (*Continued*) image (*f*), low signal intensity on T1-weighted image (*g*), and a partial enhancement on early-phase image (*h*) that washes out on late-phase image (*i*). The enhanced portion corresponds to viable tumor and the nonenhanced area to necrosis.

after treatment, reflecting the devascularization of tumor. Low signal intensity on T2-weighted images early after therapy is distinctive for chemoembolization. This differs from local therapy techniques (e.g., RF ablation), which result in high T2 signal early after therapy. The best indication of good response is negligible enhancement on hepatic arterial dominant-phase images after chemoembolization.

Ablative Therapies. Radiofrequency (RF) ablation, cryoablation, ethanol ablation, microwave ablation, and laser ablation are alternative methods to treat focal liver malignancies when curative resection is not feasible (figs. 2.164–2.166) [235].

Successful treatment occurs when the entire tumor is destroyed with mild injury of the surrounding parenchyma. The best predictor of successful ablation is the size of the necrotic cavity after intervention. The ablated area must exceed the tumor margins by approximately 1.0 cm [258]. Over time, the ablated zone might either regress in dimensions or retain similar size to pretreatment [259, 260]. Small necrotic areas may disappear completely. Enlargement of the ablated area on follow-up examinations is suggestive of unsuccessful intervention [261, 262].

Up to 1 week after ablation, the signal intensity on T2-weighted and T1-weighted images is determined by the stage of hemorrhage and the presence of either liquefactive or coagulative necrosis [259, 262, 263]. In a successful procedure, lack of contrast enhancement is observed. Initially after intervention, an ill-defined perilesional rim is often observed, measuring up to 1 cm in thickness, that appears mildly high signal intensity on T2-weighted images and exhibits moderate to intense enhancement on arterial dominant-phase images [259, 262, 263]. The thickness of this perilesional rim regresses over time in successfully treated lesions, which additionally shows decrease in the extent of enhancement on early-phase images and gradually disappears by 6 months after ablation (figs. 2.167 and 2.168) [258, 260, 263, 264]. At histopathology, the perilesional rim corresponds to intense inflammatory reaction and hemorrhage, which gradually are replaced by granulation tissue [258, 263, 265].

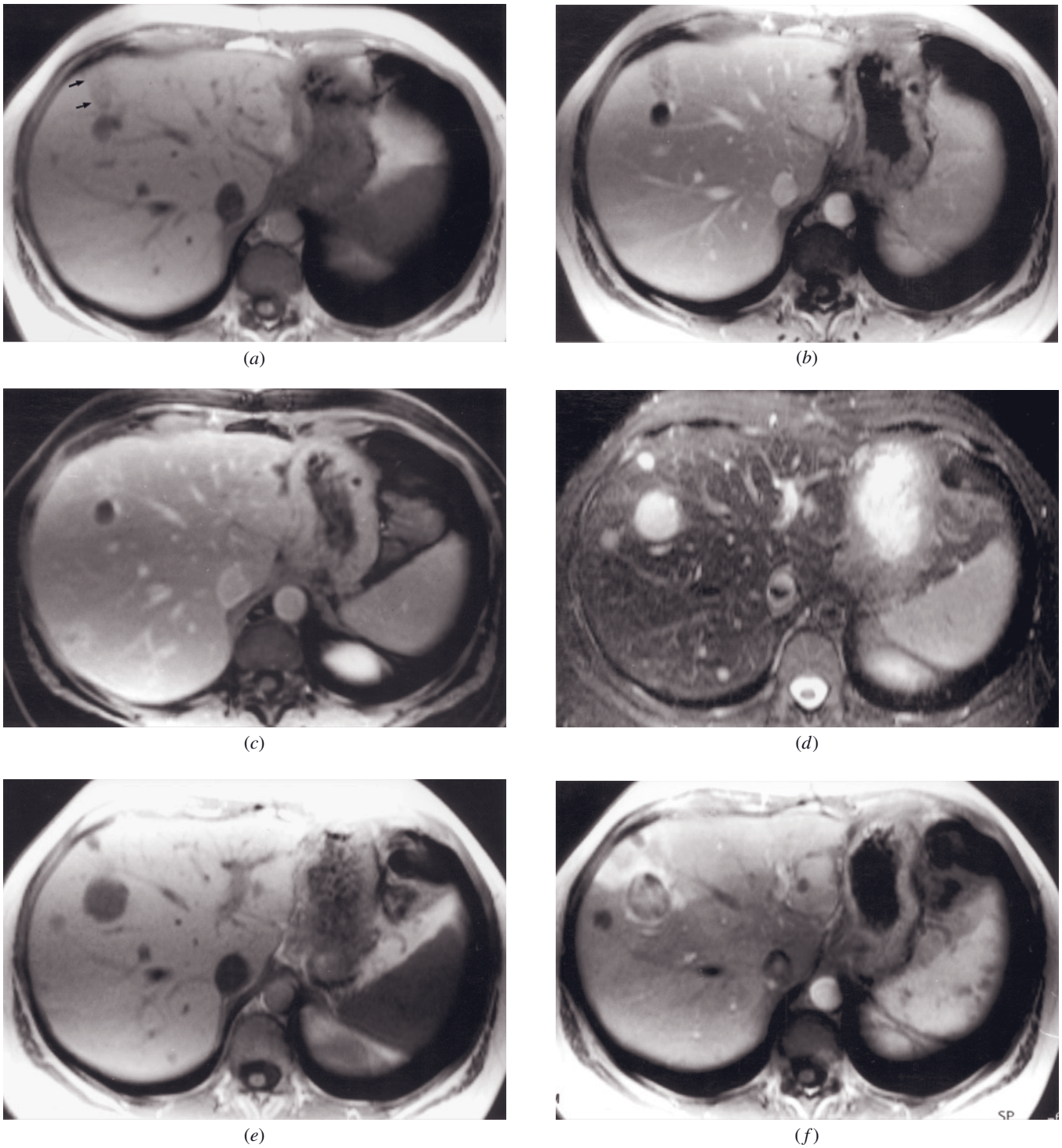

FIG. 2.164 Radiofrequency ablation. SGE (*a*), 45-s postgadolinium SGE (*b*), and 90-s postgadolinium fat-suppressed SGE (*c*) images in a patient, who has a history of a liver metastasis from retroperitoneum leiomyosarcoma that has been treated with radiofrequency ablation. There is a rounded lesion in the right hepatic lobe that demonstrates low signal on T1 (*a*), negligible enhancement immediately after gadolinium administration (*b*), and a thin rim of enhancement on the late image (*c*). Note that the track of the radiofrequency probe is visible as a linear defect extending from the liver surface to the lesion (arrows, *a*).

Echo-train STIR (*d*), SGE (*e*), and immediate (*f*) and 90-s fat-suppressed (*g*) postgadolinium SGE images in the same patient 2 months later. More lesions are appreciated in the hepatic parenchyma. The largest lesion, which was present on the first exam, demonstrates diffuse heterogeneous enhancement on the immediate postgadolinium image (*f*) that persists on the later image (*g*), in comparison to the findings from the earlier study in which no central lesion enhancement was observed. Note the presence of perilesional enhancement on the immediate postgadolinium image (*f*).

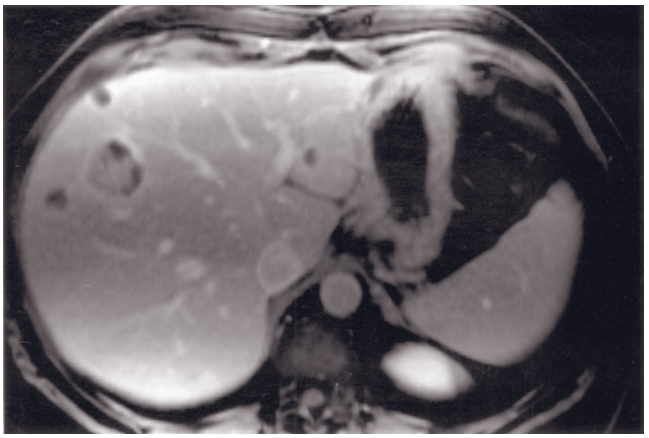

FIG. 2.164 (*Continued*) (*g*)

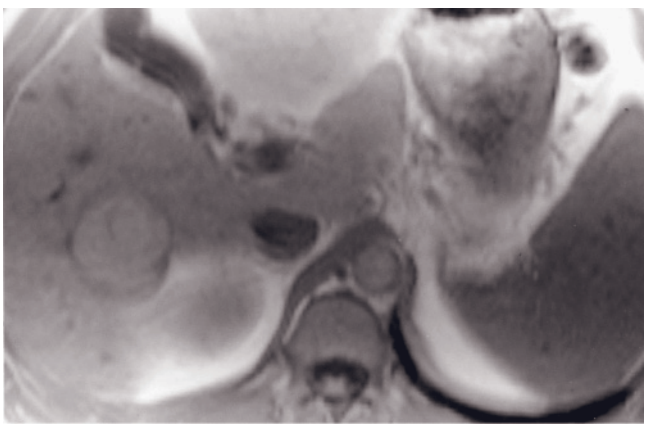

(*a*)

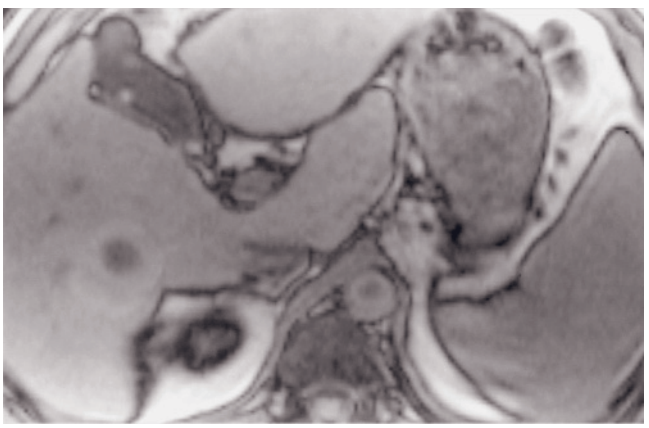

(*b*)

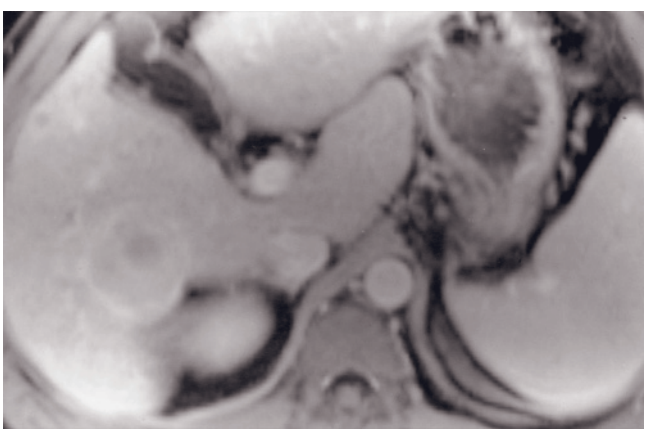

(*c*)

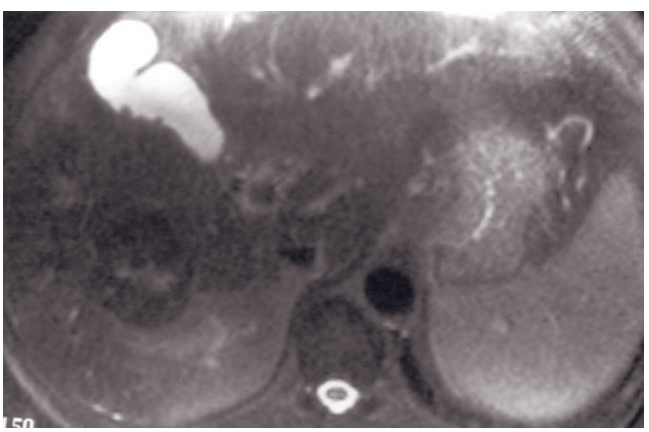

(*d*)

FIG. 2.165 HCC before and after RF ablation. SGE (*a*), out-of-phase SGE (*b*), and 90-s postgadolinium fat-suppressed SGE (*c*) images. There is an HCC in the right hepatic lobe that is isointense on T1 (*a*), contains a central focus that drops in signal on out-of-phase (*b*), and demonstrates heterogeneous enhancement on interstitial-phase images. The central focus that loses signal on out-of-phase represents fat.

T2-weighted fat-suppressed SS-ETSE (*d*), SGE (*e*), out-of-phase SGE (*f*), 45-s postgadolinium SGE (*g*), and 90-s postgadolinium fat-suppressed SGE (*h*) images in the same patient 5 months later, after radiofrequency ablation. The HCC has increased in size, is

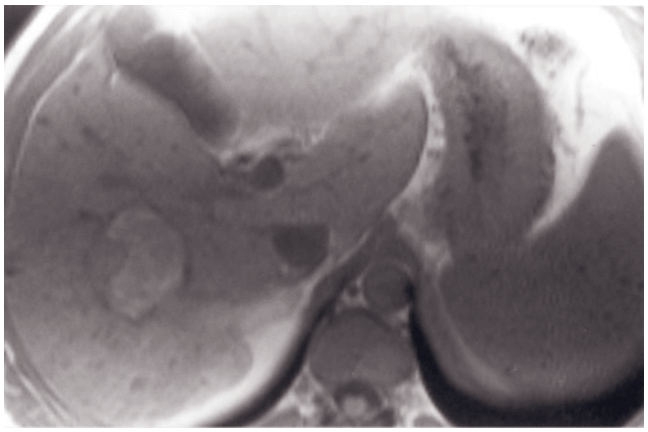

(*e*)

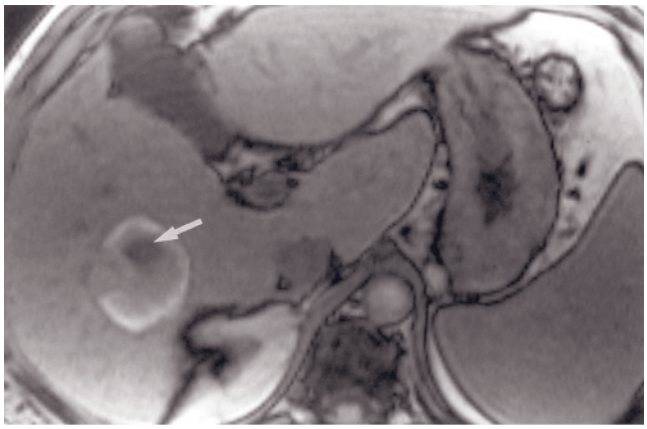

(*f*)

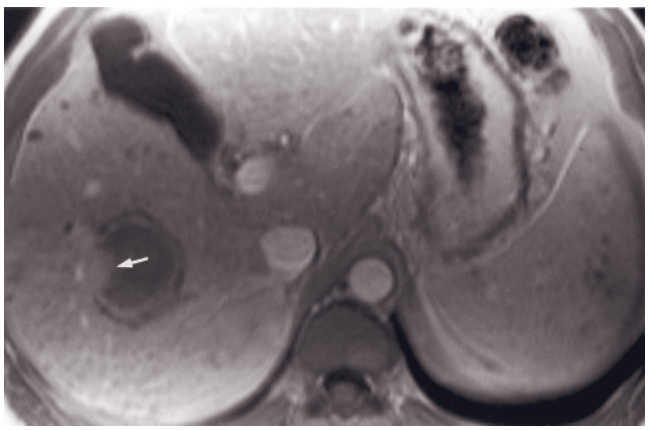

(*g*)

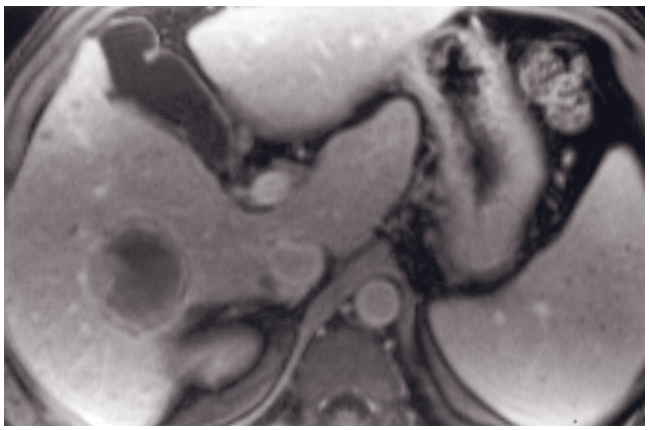

(*h*)

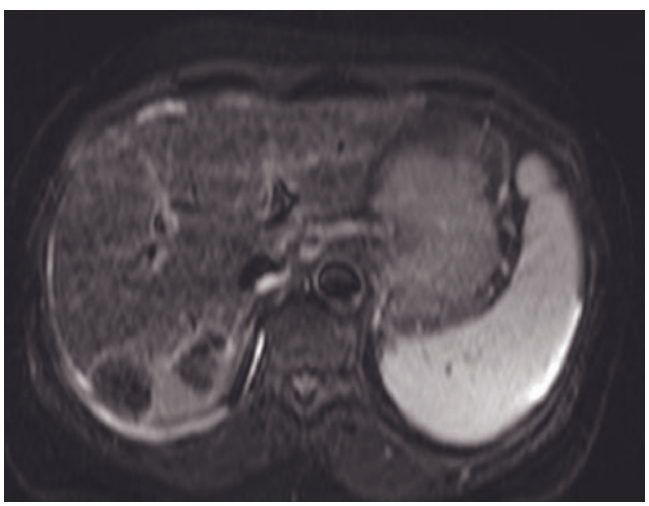

(*i*)

FIG. 2.165 (*Continued*) mildly hypointense on T2 (*d*) and mildly hypertense on T1 (*e*), and contains a small focus that drops in signal on out-of-phase image (arrow, *f*). After gadolinium administration, there is a thin rim of enhancement surrounding the entire lesion, with lack of enhancement of the majority of the lesion on early (*g*) and late (*h*) images. A mural nodule (arrow, *g*) is present along the lateral wall of the lesion that demonstrates moderate contrast enhancement consistent with residual tumor.

T2-weighted fat-suppressed SS-ETSE (*i*), SGE (*j*), and immediate (*k*) and 90-s fat-suppressed (*l*) postgadolinium 3D-gradient

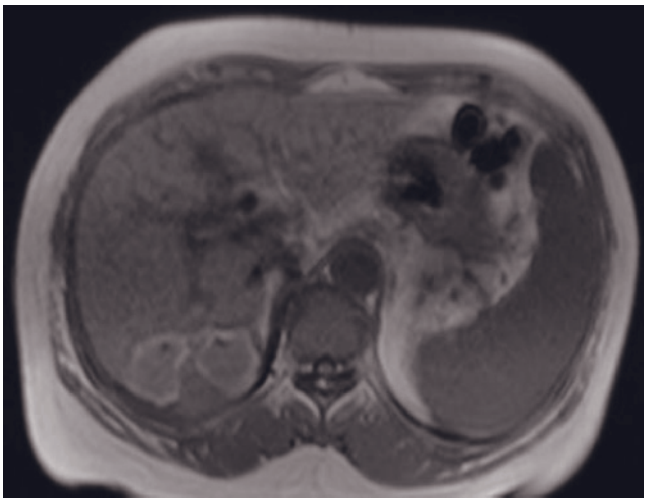

(*j*)

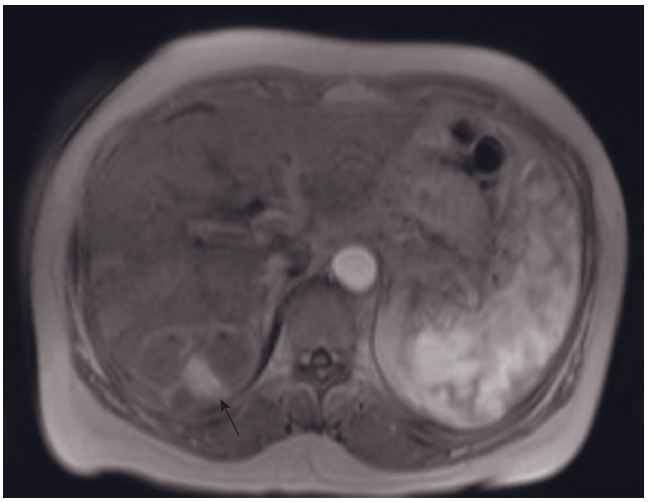

(*k*)

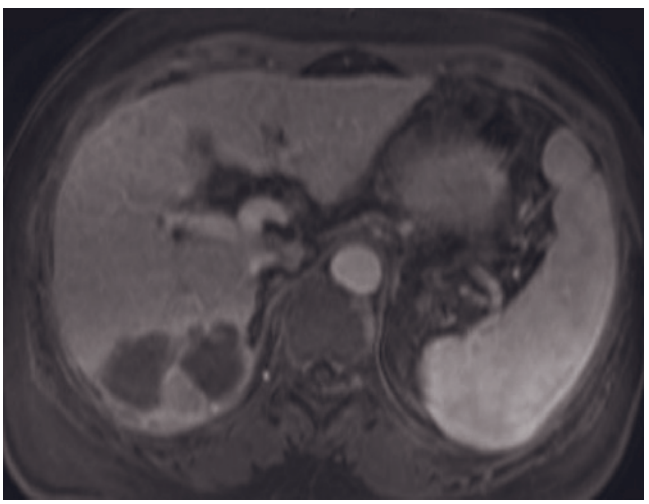

(*l*)

FIG. 2.165 (*Continued*) echo images obtained after RF ablation. The central portion of the lesion is hyperintense signal on T2 (arrow, *i*) and intermediate signal on T1-weighted precontrast (*j*), but with enhancement on immediate phase (arrow, *k*) and washout on late phase (*l*), consistent with residual/recurrent tumor.

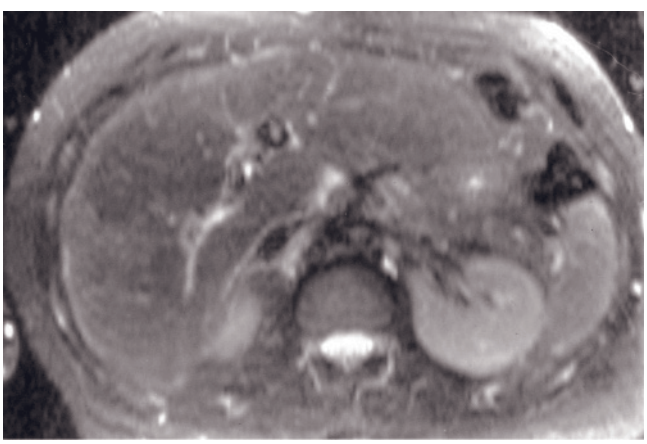

(*a*)

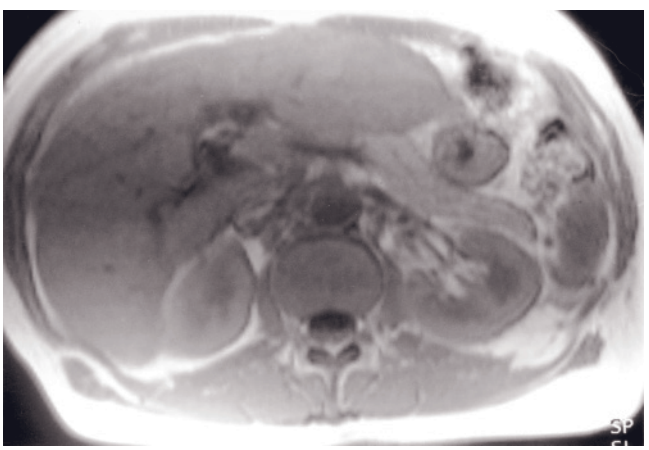

(*b*)

FIG. 2.166 HCC before and after RF ablation. Echo-train STIR (*a*), SGE (*b*), immediate postgadolinium SGE (*c*), and 90-s postgadolinium fat-suppressed SGE (*d*) images. There is a small lesion in the right hepatic lobe that is near isointense on T2 (*a*)

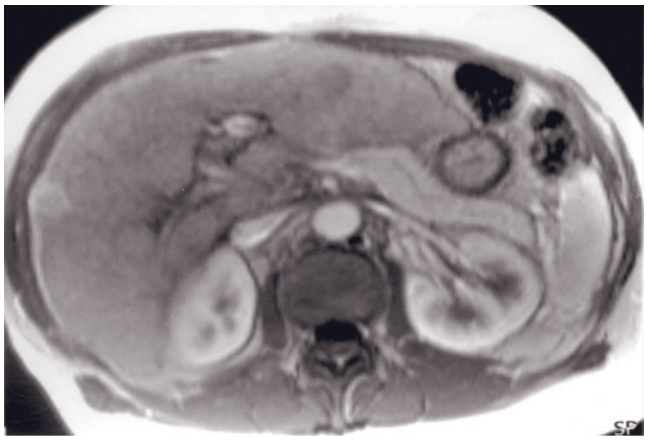

(*c*)

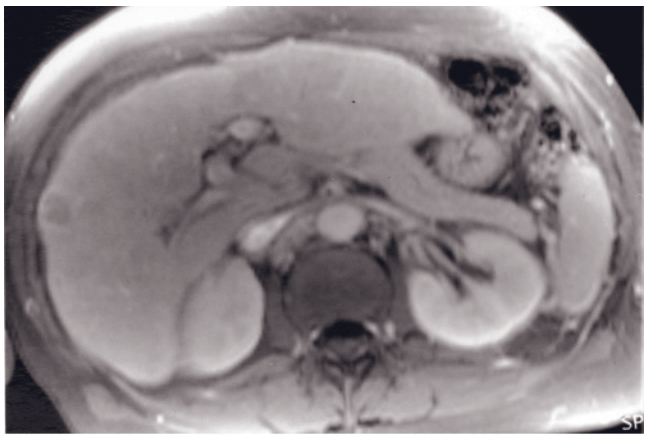

(*d*)

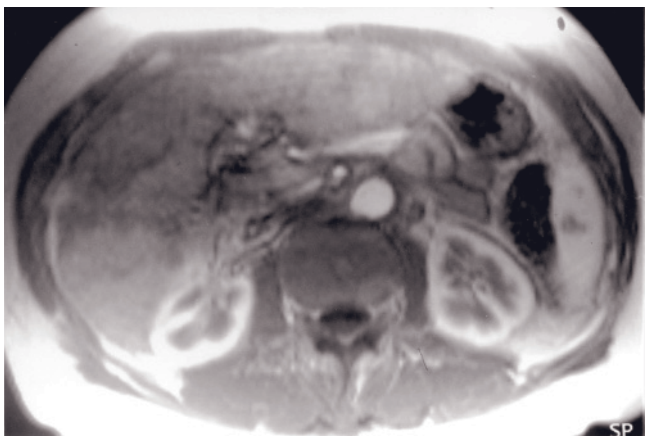

(*e*)

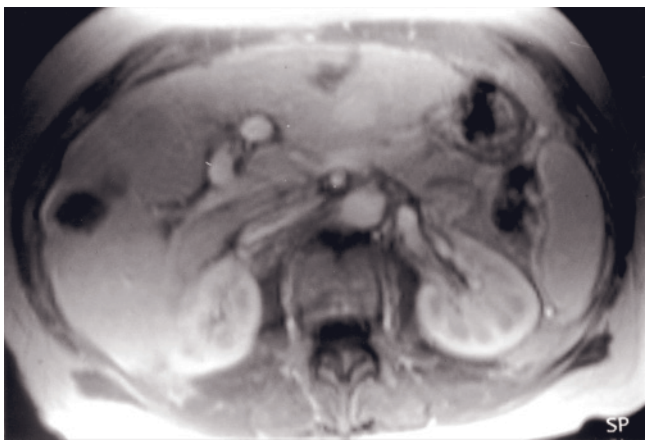

(*f*)

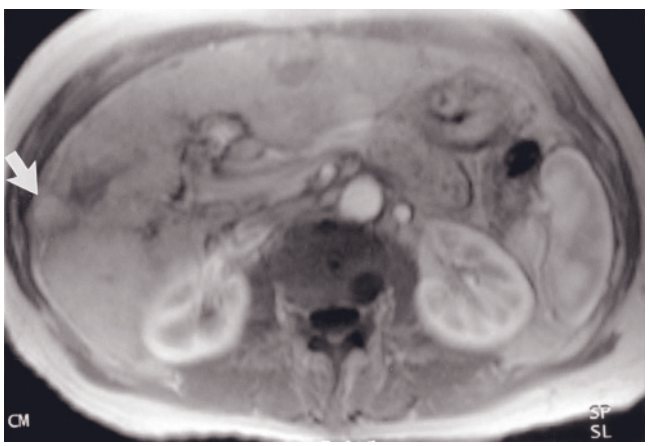

(*g*)

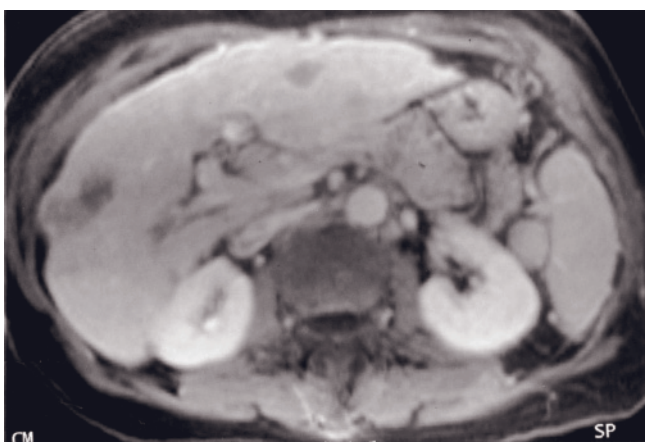

(*h*)

Fig. 2.166 (*Continued*) and T1 (*b*) images and demonstrates early heterogeneous enhancement (*c*) and late washout with capsule enhancement (*d*), consistent with a small HCC. Immediate (*e*) and 45-s (*f*) postgadolinium SGE images in the same patient 1 week after radiofrequency ablation show a necrotic lesion with thick ring enhancement on the 45-s postcontrast administration image (*f*). Immediate postgadolinium SGE (*g*) and 90-s postgadolinium fat-suppressed SGE (*h*) images 2 months after radiofrequency ablation. In the interval, a soft tissue mass (arrow, *g*) has developed on the lateral aspect of the tumor consistent with recurrence. The recurrent nodule shows moderate enhancement on the immediate postgadolinium images (*g*) with heterogeneous washout at 90 s (*h*).

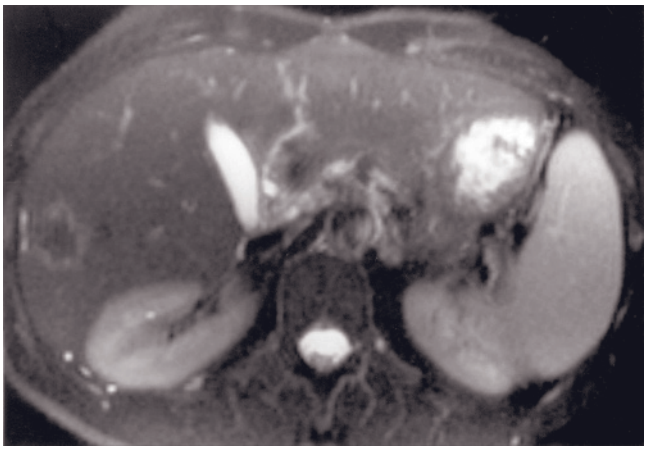

(*i*)

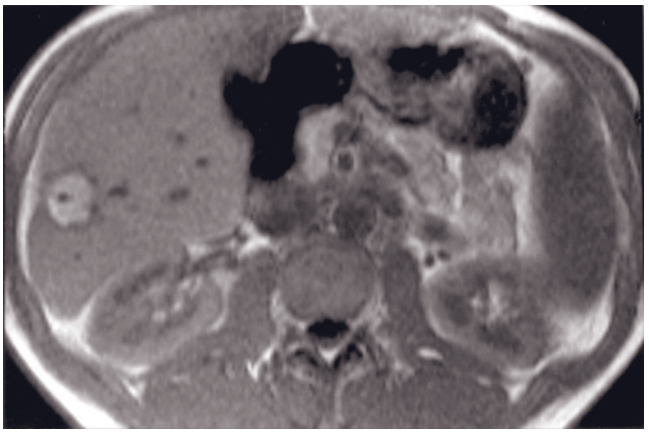

(*j*)

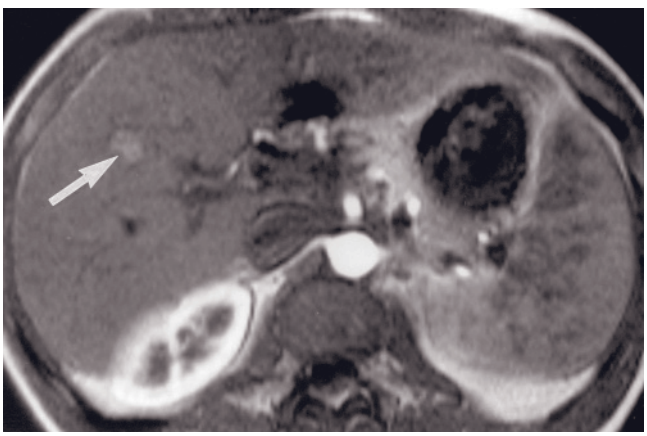

(*k*)

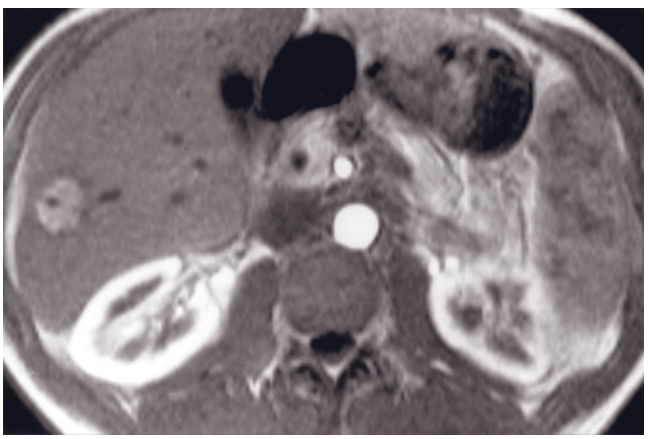

(*l*)

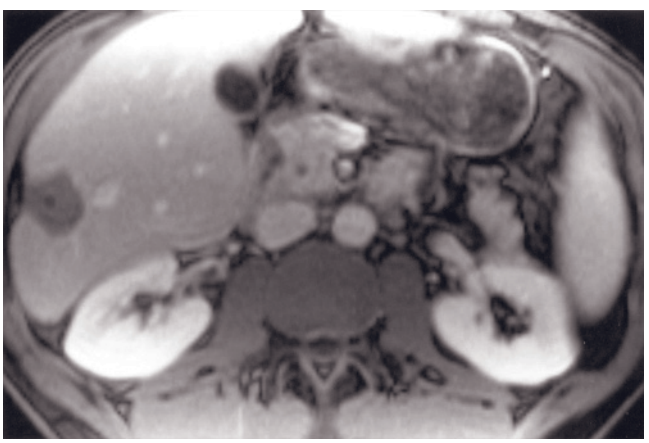

(*m*)

FIG. 2.166 (*Continued*) Echo-train STIR (*i*), SGE (*j*), and immediate (*k*, *l*) and 90-s fat-suppressed (*m*) postgadolinium SGE images in a second patient. There is a lesion in segment 6 of the right hepatic lobe that demonstrates isointensity on T2 (*i*), hyperintensity on T1 (*j*), and negligible enhancement immediately after administration of gadolinium (*k*, *l*), consistent with a hemorrhagic nonviable lesion after RF ablation. Note the puckering of the liver capsule adjacent to the lesion along the track of the radiofrequency probe. A small satellite lesion (arrow, *k*) has developed in the interval between radiofrequency ablation and this MR study.

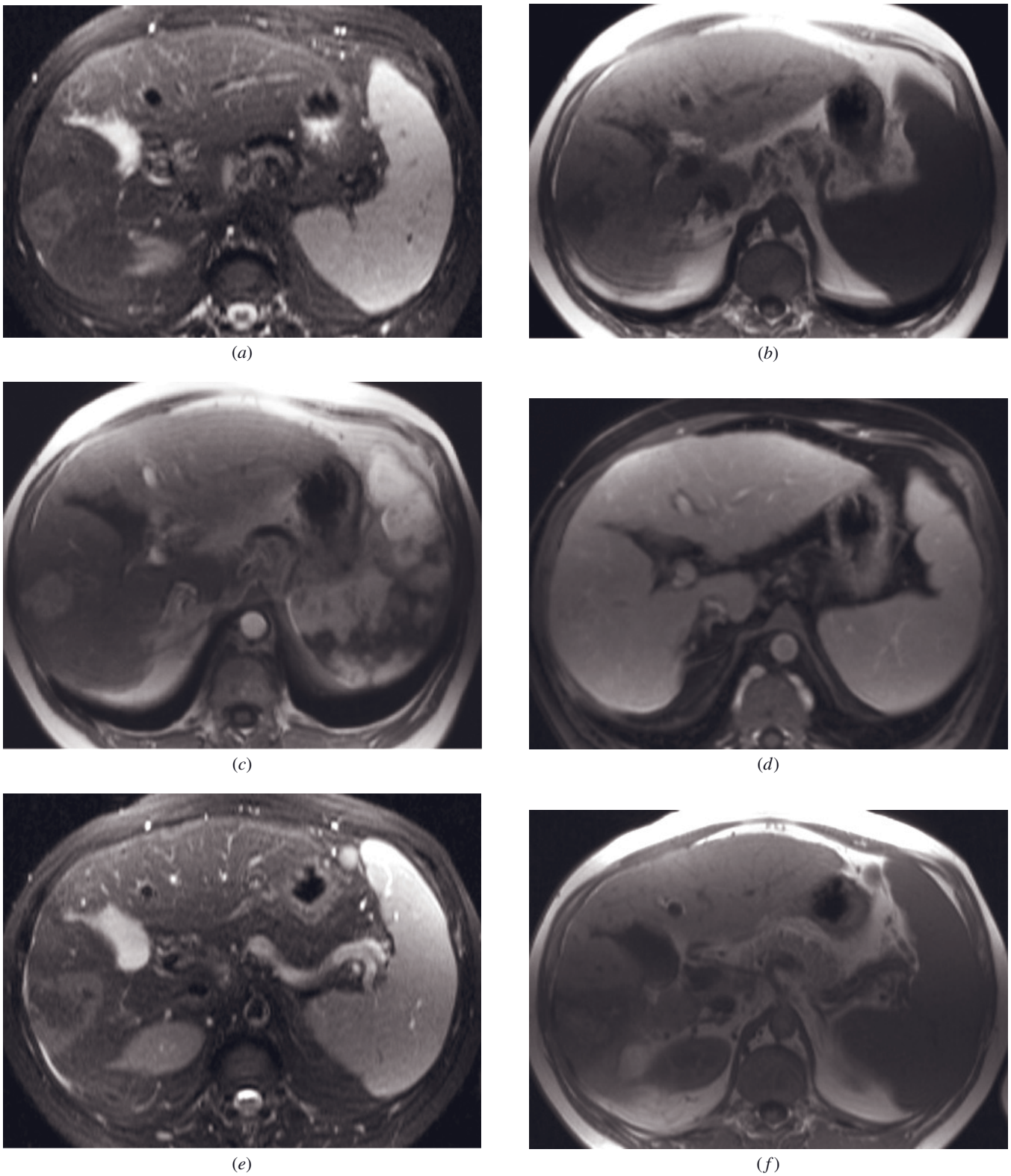

FIG. 2.167 HCC before and after RF ablation—early changes. T2-weighted SS-ETSE (*a*, *e*), SGE (*b*, *f*), and immediate (*c*, *g*) and 90-s fat-suppressed (*d*, *h*) postgadolinium SGE images. Before RF ablation (*a–d*), a lesion is appreciated in the right hepatic lobe that shows mildly high signal intensity on T2-weighted image (*a*), mildly low signal intensity on T1-weighted image (*b*), and intense enhancement on early-phase image (*d*) that fades with capsule enhancement on late-phase image (*d*), consistent with an HCC. At 1 week after RF ablation (*e–h*), the ablated area demonstrates isointensity on T2-weighted image (*e*), high signal intensity on T1-weighted image (*f*), and lack of enhancement on early (*g*)- and late (*h*)-phase images. Surrounding the ablated area, there is

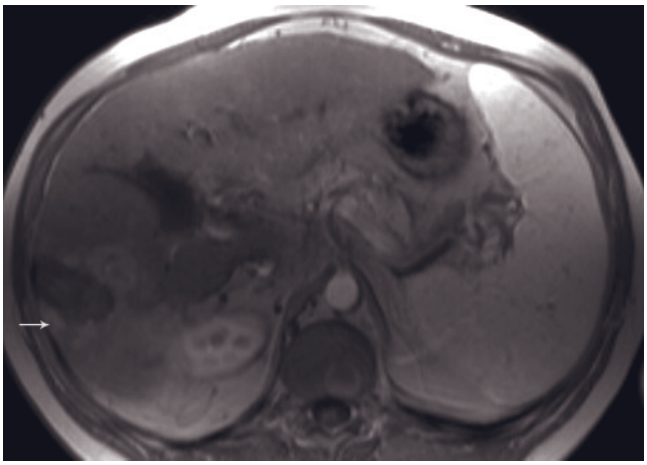

(*g*)

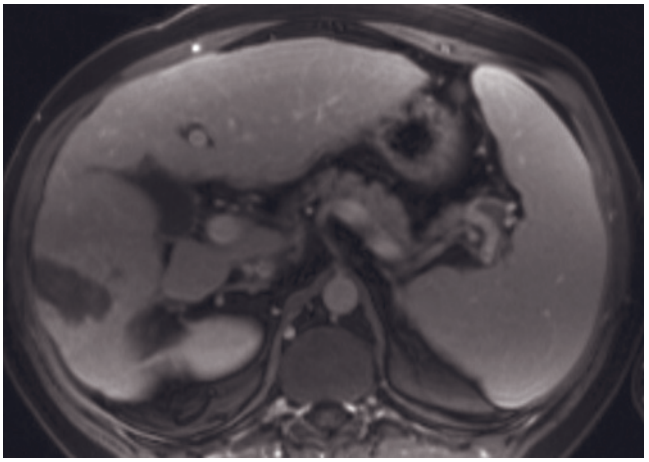

(*h*)

FIG. 2.167 (*Continued*) a parenchymal reaction due to the intervention, and it demonstrates high signal intensity on T2-weighted image (*e*), low signal intensity on T1-weighted image (*f*), and moderate enhancement on early-phase image (arrow, *g*) that fades on late-phase image (*b*). This inflammatory reaction is normal early after RF ablation.

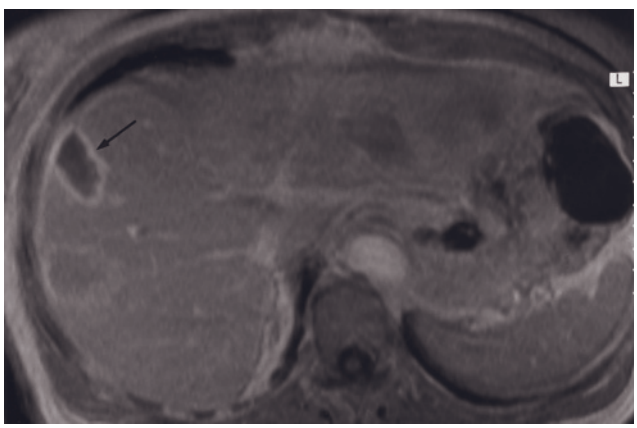

(*a*)

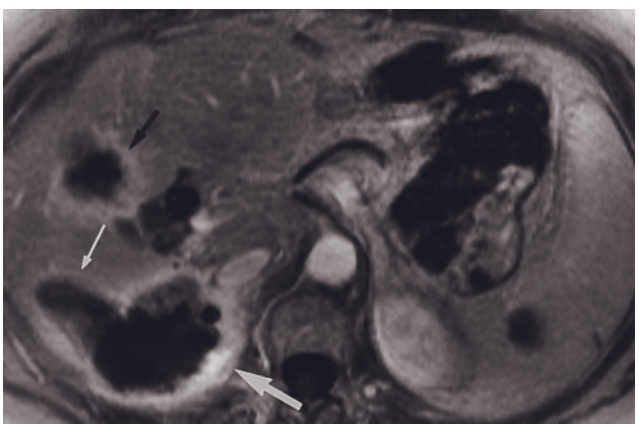

(*b*)

FIG. 2.168 Liver metastases after cryotherapy—acute changes. Transverse 90-s postgadolinium SGE images (*a*, *b*) in two patients. In the first patient (*a*), a cryotherapy defect is present in the right lobe (arrow, *a*) that has a uniform-thickness enhancing wall in continuity with enhancing liver capsule of similar thickness. In the acute stage, this appearance is compatible with tumor ablation and formation of acute granulation tissue along the cavity wall. The oblong shape of the defect corresponds to the direction of placement of the cryotherapy device. In the second patient (*b*), a cryotherapy tract (thin white arrow, *b*) is noted in continuity with a necrotic cavity. Portions of the cavity wall are thick and irregular (large white arrow, *b*). A second cryotherapy defect is noted in a more anterior location (black arrow, *b*). The cavity wall is thick and irregular. The presence of thick irregular walls after treatment is consistent with persistent disease.

The presence of a nodular focus distorting the internal contour within the ablated area is indicative of residual or recurrent tumor [258, 259, 263, 266]. Residual or recurrent tumor shows moderately high signal intensity on T2-weighted images and moderate to intense enhancement on arterial dominant-phase images, which may persist on late-phase images (fig. 2.169).

Gas bubbles present within the necrotic cavity immediately after the intervention are a common feature and tend to disappear within the first month [264, 267, 268]. Gas bubbles appear signal void on both T2- and T1-weighted images and show lack of enhancement after contrast administration.

Perfusional parenchymal abnormalities may be seen after ablation, and they may be due to arterial-venous

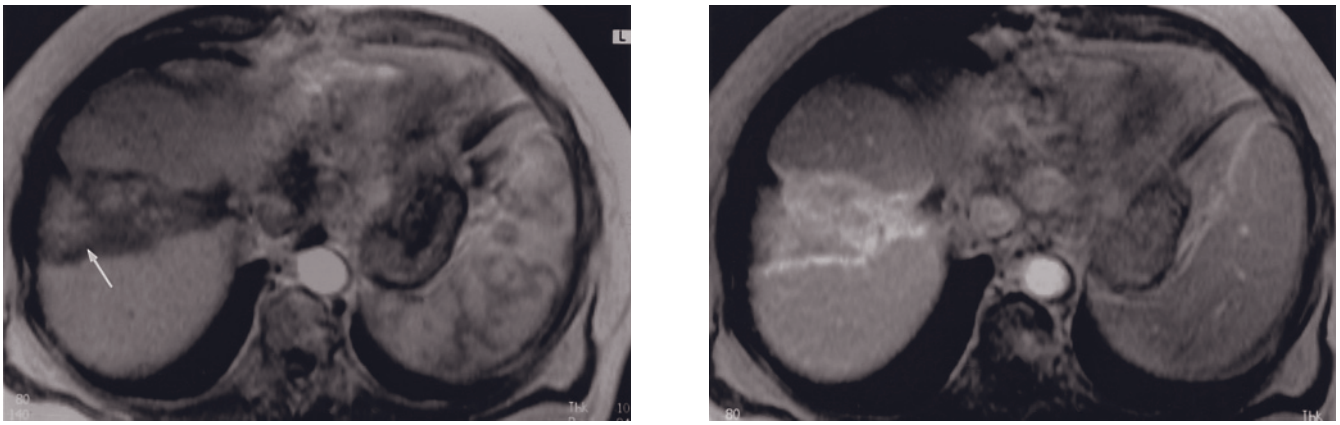

(*a*) (*b*)

FIG. 2.169 Liver metastases after cryotherapy—chronic changes with recurrent disease. Immediate (*a*) and 10-min (*b*) postgadolinium SGE images. A large wedge-shaped defect is present in the superior aspect of the liver that enhances minimally on the immediate postgadolinium image (*a*) and shows delayed enhancement at 10 min (*b*). This enhancement pattern is consistent with fibrosis. Focal irregular regions of soft tissue are identified within the wedge-shaped tissue (arrow, *a*) that represent recurrent adenocarcinoma.

shunts or obstructed vascular structures. Often, the perfusional abnormalities vanish by 1 month after the procedure [264, 269]. On MRI, perfusional abnormalities are seen as wedge-shaped enhancing areas on early-phase images that fade on late-phase images.

HEPATIC TRANSPLANTATION

Liver disease is the tenth leading cause of death in the United States, and transplantation has become the treatment of choice for end-stage disease [270]. Major recent advances and technical progress in liver surgery and transplantation have been based, in large part, on improved understanding of the internal architecture of the liver. Toward this end, MRI provides valuable information for preoperative and postoperative liver evaluation of both donors and recipients. The increased utilization of adult-to-adult living related hemi-liver donation has resulted in an increased role for MRI in the preoperative evaluation, reflecting the comprehensive nature of the information provided by MRI. Donors may undergo a liver MR protocol with MRCP and MRA (figs. 2.170–2.172). The usual surgical procedure involves resecting the right lobe for donation and retaining the left lobe in the donor. The resection plane is approximately 1 cm into the right lobe from the middle hepatic vein and extends inferiorly to the bifurcation between the right and left portal veins [271], so that the donor retains the middle hepatic vein. Evaluation is made of relative size of right and left lobes and anomalies of the biliary or vascular system. Contraindications for transplant include focal mass lesions, depending on size and type (e.g., malignant), or preexistent diffuse liver disease that may be the same type as that in the recipient (e.g., chronic hepatitis, primary sclerosing cholangitis). After surgery, donors are assessed for surgical complications of transplantation (e.g., abscess, biloma, transection or stenosis of vessels on bile duct) and for hypertrophy of the left lobe (figs. 2.173 and 2.174).

In recipients, preoperatively, patency of the inferior vena cava, portal vein, hepatic artery, and common bile duct are evaluated, and the presence of malignant disease is determined. Patients with malignant tumors evaluated for possible transplantation are evaluated for extent of hepatic involvement and for the presence of porta hepatis nodes or distant disease. Recipients may receive living related partial livers (lateral segment for small pediatric patients, right lobe for adult-to-adult recipients) (fig. 2.175) or cadaveric whole or partial livers (fig. 2.176).

The most common cause of early liver graft failure is rejection. The incidence of rejection is as high as 64% in some published series [272]. Early diagnosis is essential to allow modification of immunosuppressive therapy [273]. The differential diagnosis of rejection includes biliary obstruction, cholangitis, ischemic injury, viral infection, and drug toxicity.

Vascular complications are important causes of graft failure [274, 275]. Hepatic artery thrombosis is the most frequent and severe complication, occurring in up to 12% of adult patients [276, 277]. Hepatic artery patency can be documented by MRI in most cases. Technical

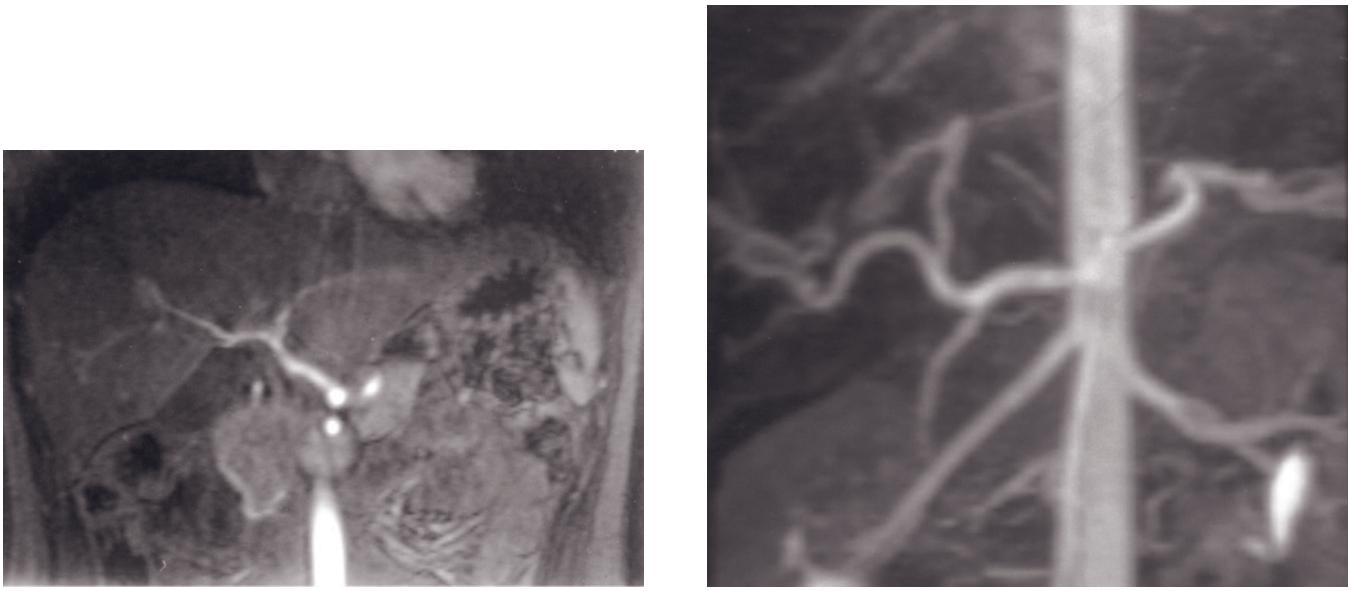

(*a*) (*b*)

FIG. 2.170 Liver donor MRA. Coronal 3D gradient-echo 2-mm source image (*a*) and MIP reconstruction of the 2-mm 3D gradient-echo sections (*b*) in two different patients show the hepatic artery arising from the celiac axis.

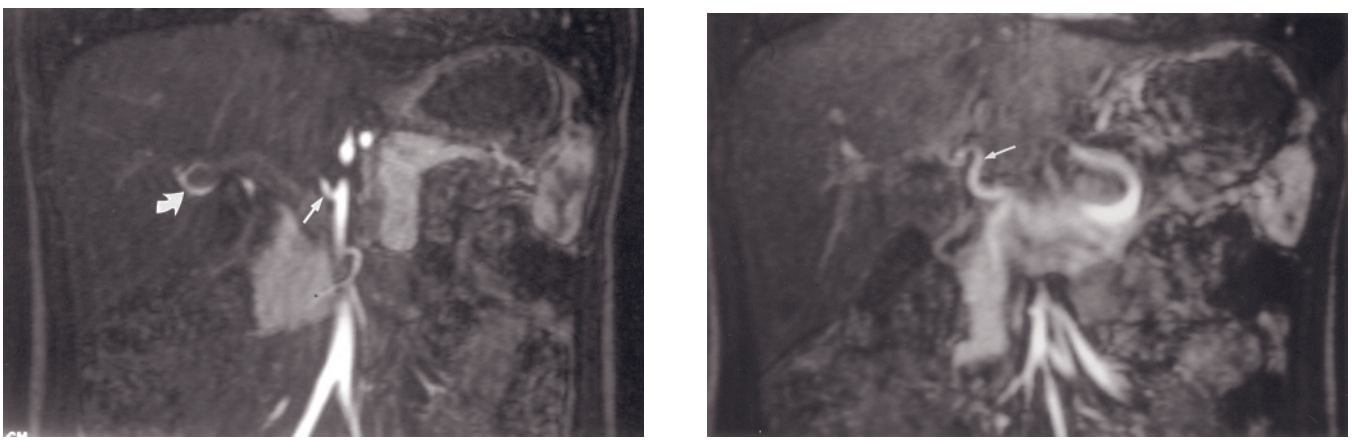

(*a*) (*b*)

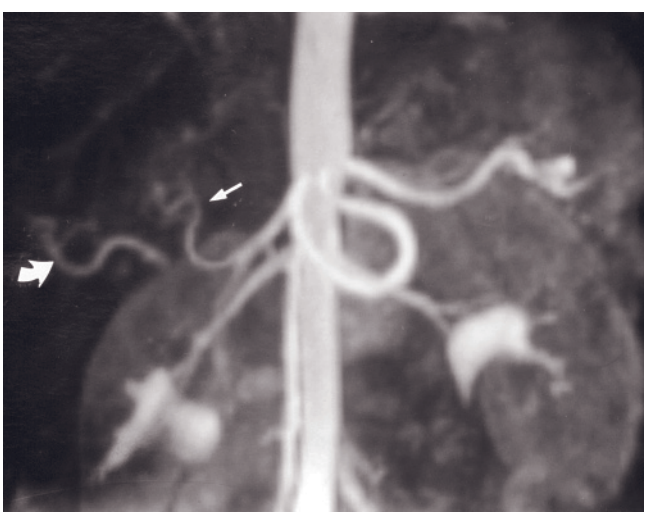

(*c*)

FIG. 2.171 Liver donor MRA—replaced right hepatic artery. Coronal 3D gradient echo 2-mm source images (*a, b*) and MIP reconstruction of the 2-mm 3D gradient-echo sections (*c*) images that demonstrate the left hepatic artery arising from the celiac trunk (short arrows, *b, c*) and the right hepatic artery (curved arrows, *a, c*) arising from the SMA.

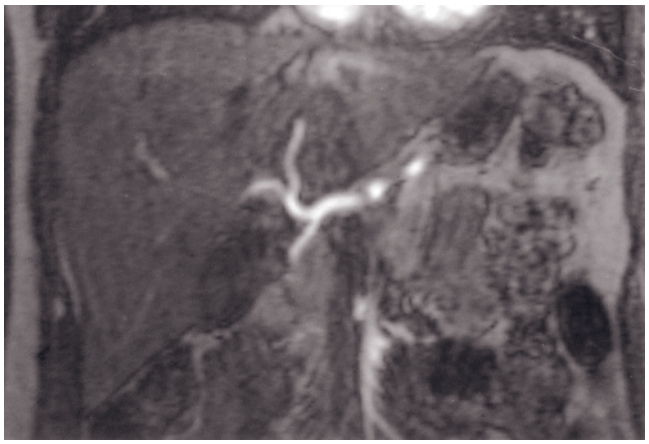

(*a*)

(*b*)

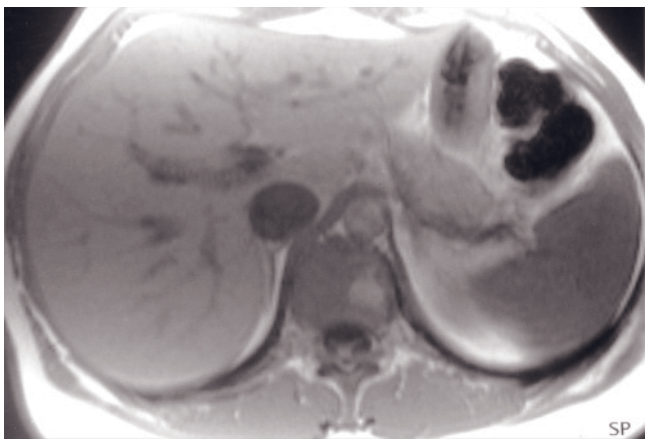

(*c*)

FIG. 2.172 Liver donor evaluation before transplant. Coronal 3D gradient-echo 2-mm source image (*a*), source image from a MRCP study (*b*), and transverse SGE image (*c*) demonstrate three MR techniques used to evaluate liver donors: MRA, MRCP, and tissue imaging sequences.

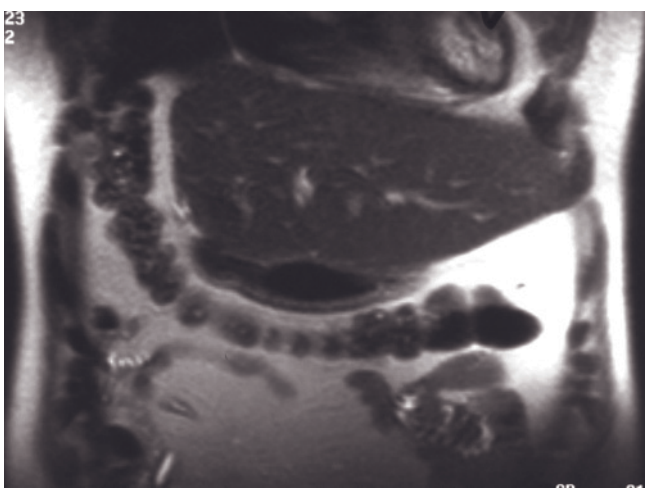

(*a*)

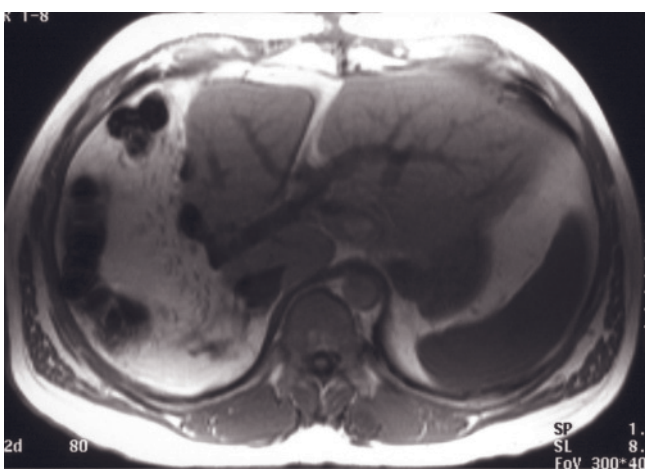

(*b*)

FIG. 2.173 Hemi-liver donor after transplant. Coronal T2-weighted SS-ETSE (*a*), SGE (*b*), and immediate (*c*) and 90-s fat-suppressed (*d*) postgadolinium SGE images with an unremarkable examination of the retained left lobe after right hemiliver donation.

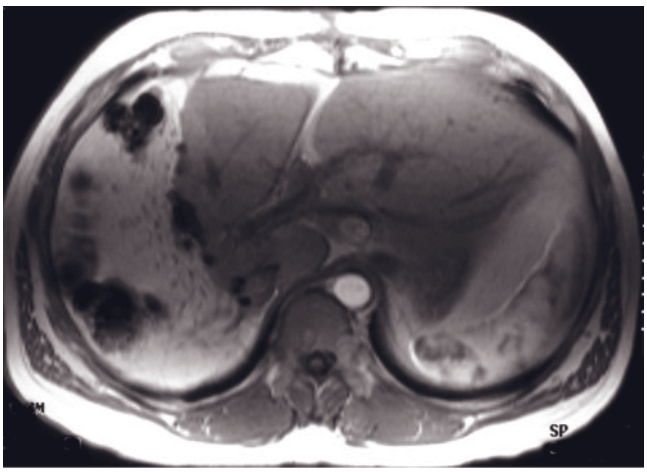

(*c*)

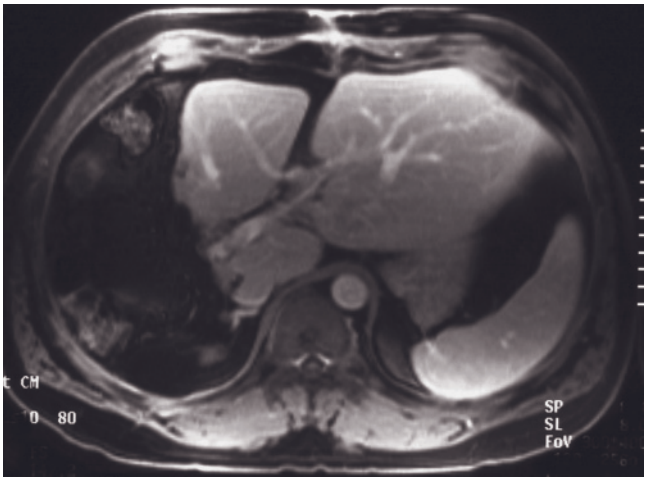

(*d*)

FIG. 2.173 (*Continued*)

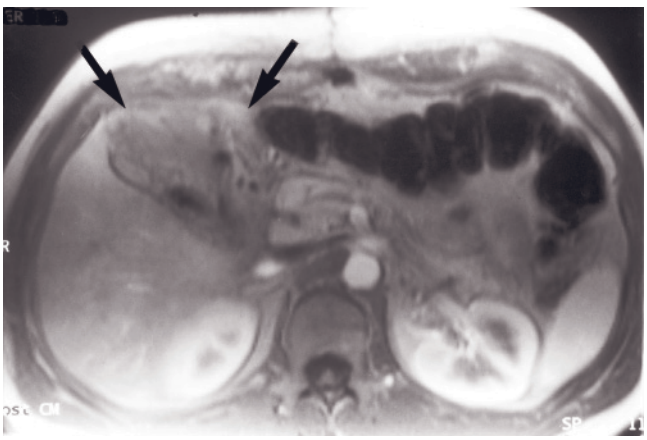

(*a*)

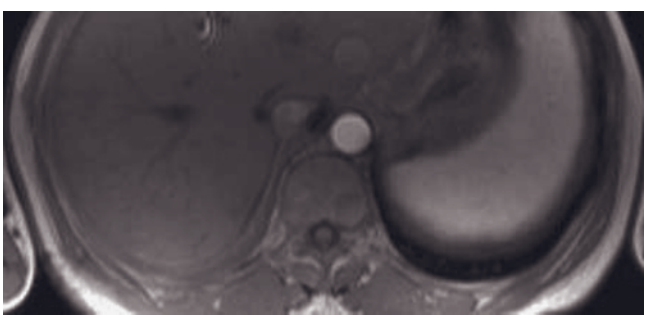

(*c*)

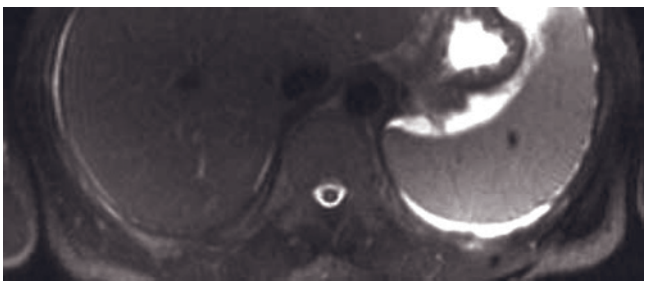

(*b*)

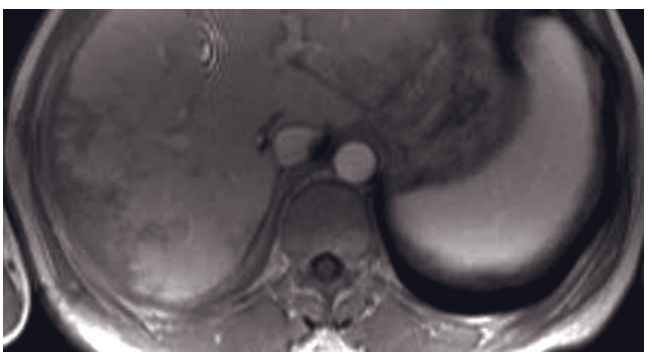

(*d*)

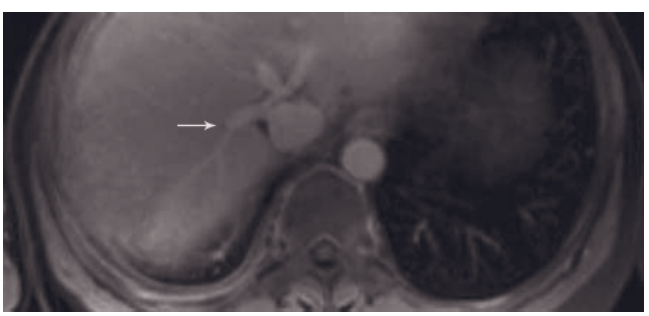

(*e*)

FIG. 2.174 Ischemic changes. Immediate postgadolinium image (*a*) in a lateral segment liver donor patient demonstrates heterogeneous areas with diminished enhancement in segment 4 (arrows), reflecting postsurgical injury.

T2-weighted fat-suppressed SS-ETSE (*b*), and immediate (*c*), 45-s (*d*), and 90-s fat-suppressed (*e*) postgadolinium SGE images in a second patient. There is an irregular area in the periphery of the right lobe of the liver that is not evident on T2-weighted image (*b*) or on early-phase image (*c*) but becomes evident on 45-s image (*d*), reflecting greater contrast between the enhanced normal parenchyma and the nonenhanced ischemic portion. On late-phase image, a stricture in the right hepatic vein is appreciated (arrow, *e*).

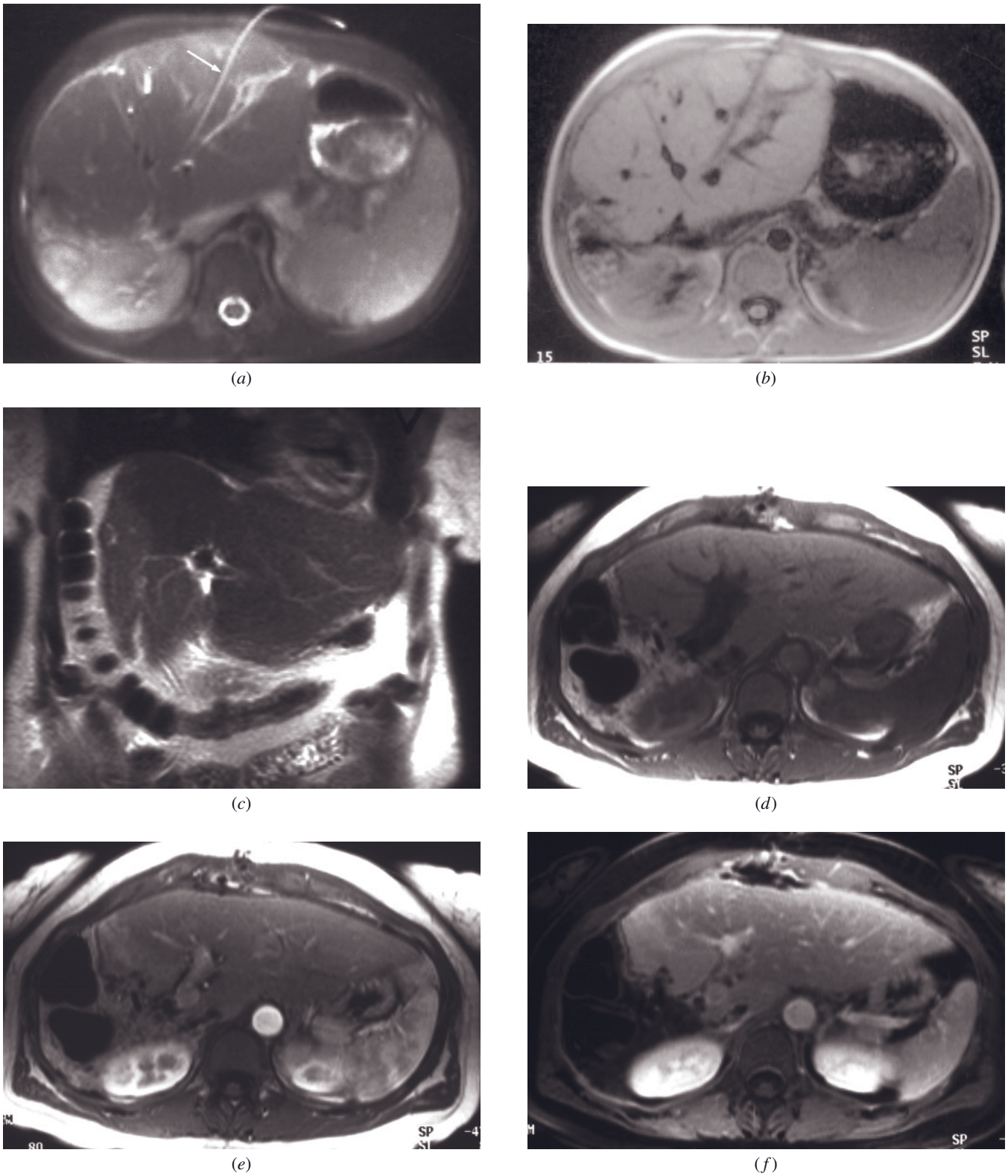

FIG. 2.175 Transplanted liver recipient—lateral segment; and left lobe in a donor. T2-weighted fat-suppressed SS-ESTE (*a*) and SGE (*b*) images in a pediatric patient who had undergone liver transplantation of a lateral segment 6 years earlier. The liver has developed a rounded configuration through hyperplasia. Note a percutaneous biliary drain (arrow, *a*).

Coronal T2-weighted SS-ETSE (*c*), SGE (*d*), and immediate (*e*) and 90-s fat-suppressed (*f*) SGE images in a second patient. Along the resection margin, there is an abnormal area that shows higher signal intensity on T2-weighted image (*c*) and demonstrates a faint enhancement after contrast (*e*, *f*) compatible with inflamation and granulation tissue.

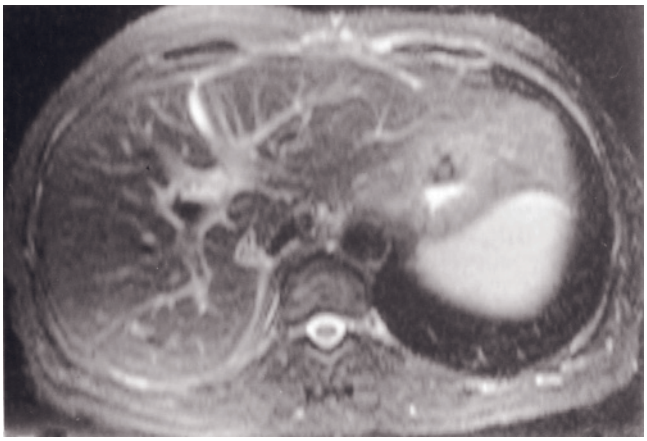

(*a*)

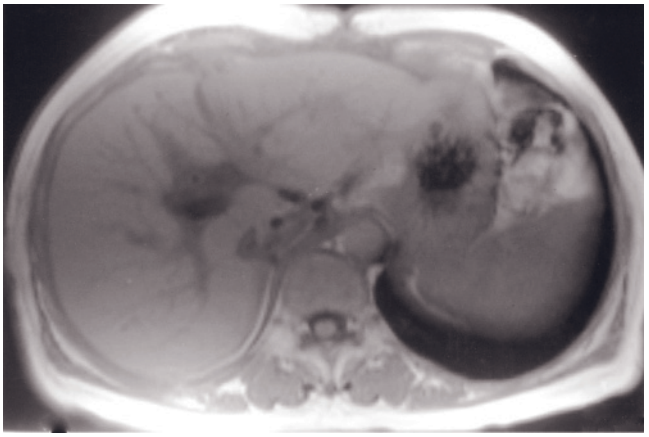

(*b*)

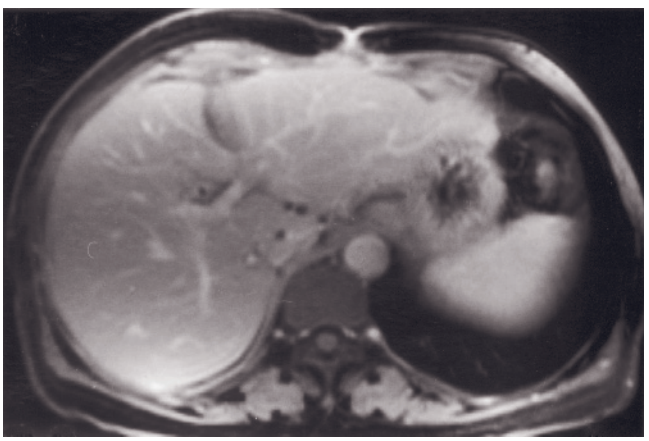

(*c*)

FIG. 2.176 Cadaveric liver transplant recipient. Echo train-STIR (*a*), SGE (*b*) and 90-s postgadolinium fat-suppressed SGE (*c*) images in a patient after transplant of a cadaveric liver. The liver showed normal signal without evidence for mass lesions or abnormal enhancement. No perihepatic fluid is identified. Note the clip artifacts in the porta hepatis and adjacent to the IVC, which are observed in patients with cadaveric liver transplant.

modifications of the gadolinium-enhanced 3D MRA technique to demonstrate small-vessel stenosis is undergoing continued refinement. One report that compared 3D gadolinium-enhanced MR angiograms with conventional angiography and surgery found that gadolinium-enhanced 3D MRA achieved accurate results in 58 (94%) of the 62 vessels analyzed [278]. Breathing-arrested protocols have recently been developed and show promise in examining for patency of the hepatic artery in patients, especially young children, who are unable to suspend respiration for a high-quality breath-hold MRA examination. High-spatial-resolution noninvasive arterial studies of small vessels are at present best performed with multidetector CT. The incidence of venous complications—portal vein and inferior vena cava thrombosis/stenosis—is lower than that of arterial complication [274–276]. Portal vein and IVC patency can be diagnosed reproducibly on MR images (fig. 2.177) [278, 279].

Fluid collections are commonly observed after hepatic transplantation and include hematomas (figs. 2.178 and 2.179), seromas, bilomas (fig. 2.180), abscesses, and simple ascites. Bile leaks may develop at the anastomosis for technical reasons or may be secondary to bile duct necrosis in those patients with hepatic artery thrombosis [276].

Strictures of the biliary tree are often a late complication of liver transplantation and usually occur at the anastomosis secondary to scar formation. Stenosis or obstruction of the biliary tree (fig. 2.181) may be shown with techniques that render bile low in signal, high in signal (MR cholangiography), or a combination of both. Mucocele of the cystic duct remnant is a rare cause of biliary obstruction and may appear as a focal fluid collection adjacent to the hepatic duct [276, 280]. MRI is able to distinguish between hematomas and other fluid collections in hepatic transplants. In the acute phase (7–72 h), deoxyhemoglobin has distinctive very low signal on T2-weighted images. In the period spanning several days to several months after surgery, intra- or extracellular methemoglobin in subacute hematoma is higher in signal on T1-weighted images than other fluid.

Periportal signal abnormalities are frequently present in transplanted livers. The typical appearance is tissue that is low in signal intensity on T1-weighted images and high in signal intensity on T2-weighted

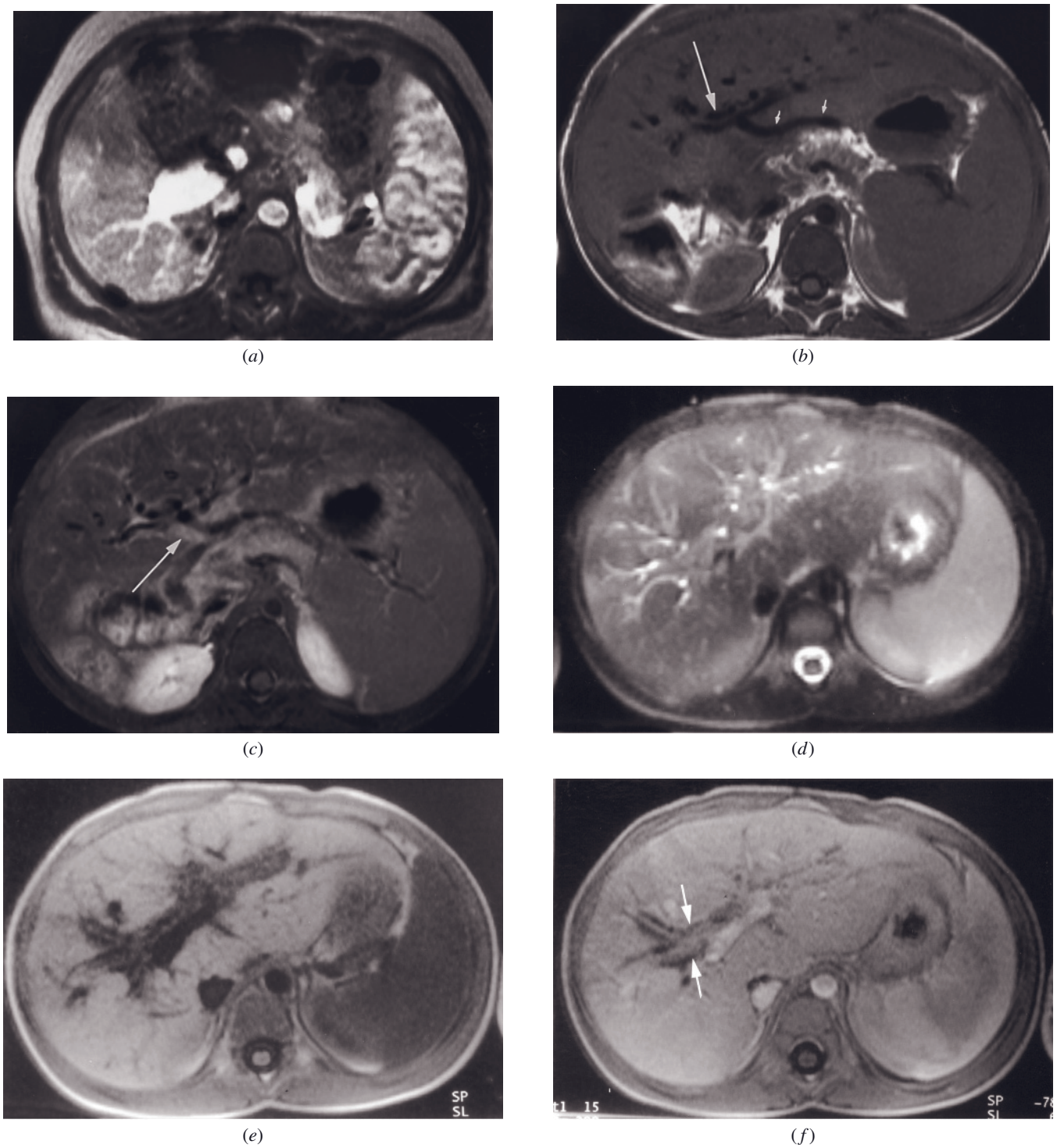

FIG. 2.177 Hepatic transplant—portal vein complications. Immediate postgadolinium SGE image (*a*) demonstrates dilatation of the right portal vein secondary to anastomotic stenosis.

T1-weighted SE (*b*) and interstitial-phase gadolinium-enhanced T1-weighted fat-suppressed SE (*c*) images in a pediatric patient with a trisegmental transplant. Patent hepatic arterial graft (small arrows, *b*) and biliary ducts (long arrow, *b*) are evident. There is no evidence of a patent portal vein. Enhancing inflammatory tissue is present in the porta hepatis and in the expected location of the portal vein (long arrow, *c*).

Echo train-STIR (*d*), SGE (*e*), and immediate postgadolinium SGE (*f*) images in a 6-year-old girl, 14 months after transplant. There is an abnormal decreased signal intensity seen in the distal right portal vein (arrows, *f*) on the post-contrast image with slight expansion of the portal vein and patchy enhancement to this segment of the liver. These features are consistent with thrombosis of the right portal vein. Note also that mild intrahepatic ductal dilatation is present (*d*).

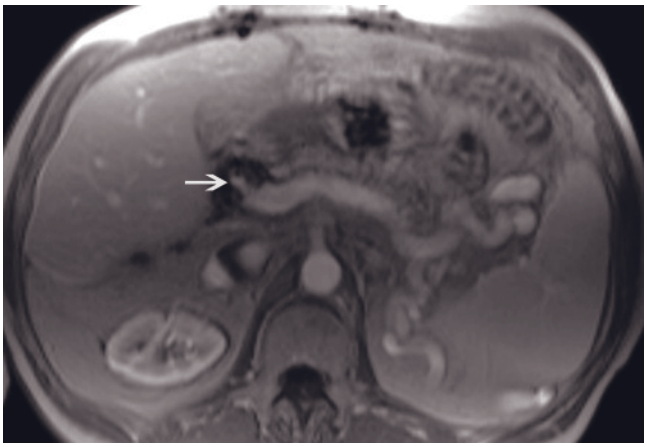

(*g*)

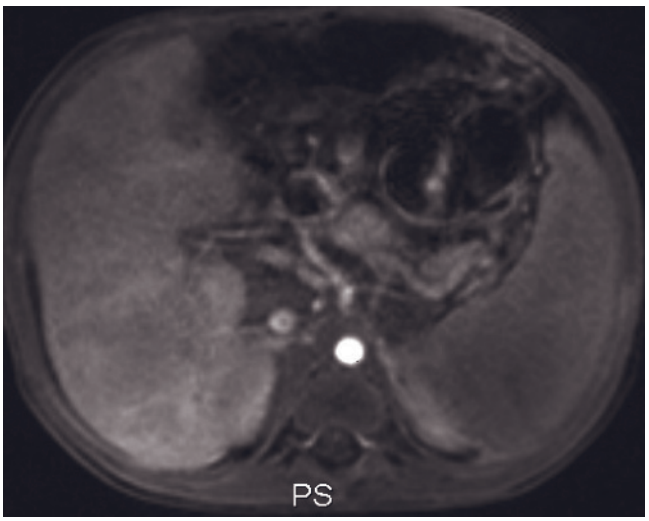

(*h*)

FIG. 2.177 (*Continued*) Immediate (*g*) postgadolinium SGE images in a fourth patient who has a stricture of the portal vein distal to its bifurcation (arrow, *g*).

Breathing-arrested postgadolinium 3D-gradient echo **at 3T** in an infant demonstrates extremely narrowed but patent portal vein (*b*).

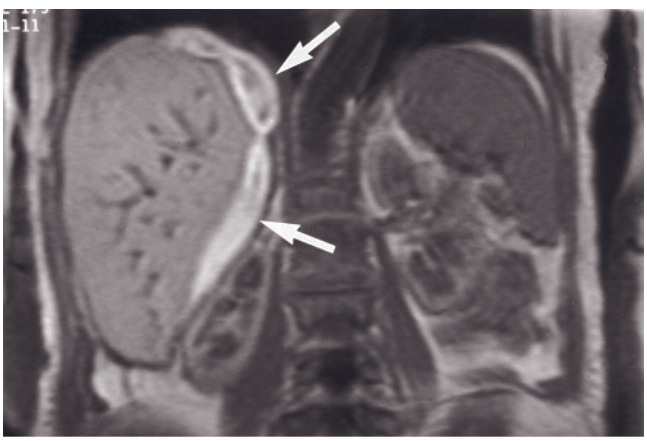

(*a*)

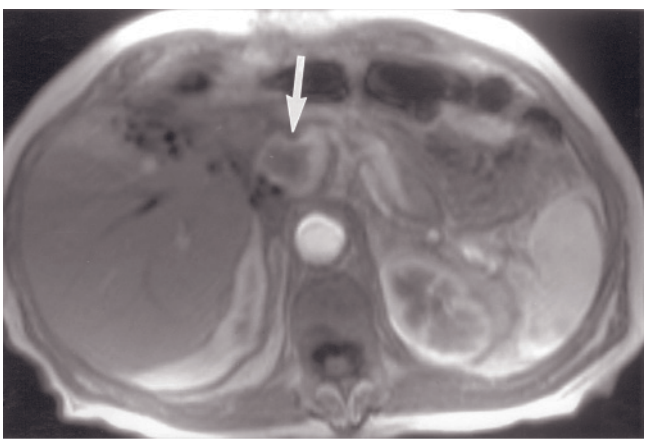

(*b*)

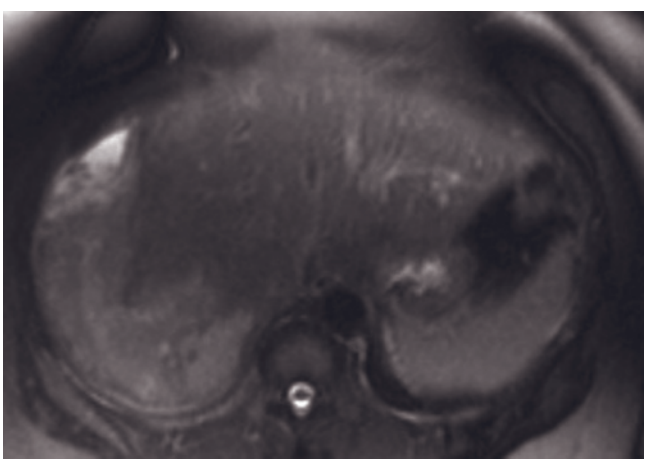

(*c*)

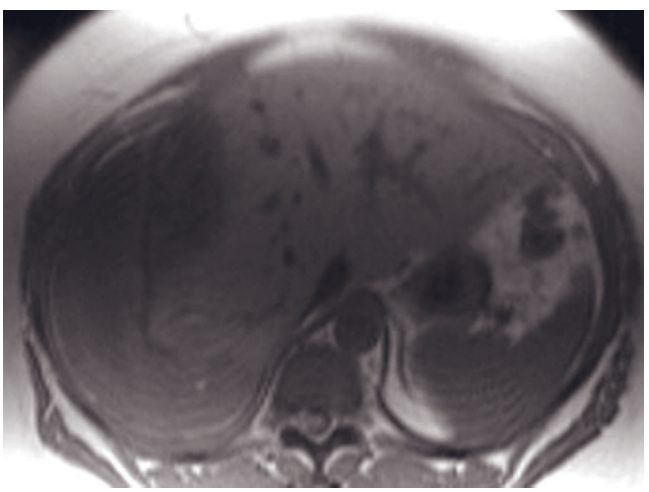

(*d*)

FIG. 2.178 Hematoma in recipient. Coronal SGE (*a*) and transverse immediate postgadolinium SGE (*b*) images in a patient who is the recipient of a right hepatic lobe transplant. There is a perihepatic fluid collection (arrows, *a, b*) that demonstrates a high-signal peripheral rim on noncontrast T1-weighted images (*a*), consistent with hematoma.

T2-weighted SS-ETSE (*c*), SGE (*d*), and 90-s fat-suppressed (*e*) postgadolinium SGE images in a second patient after liver

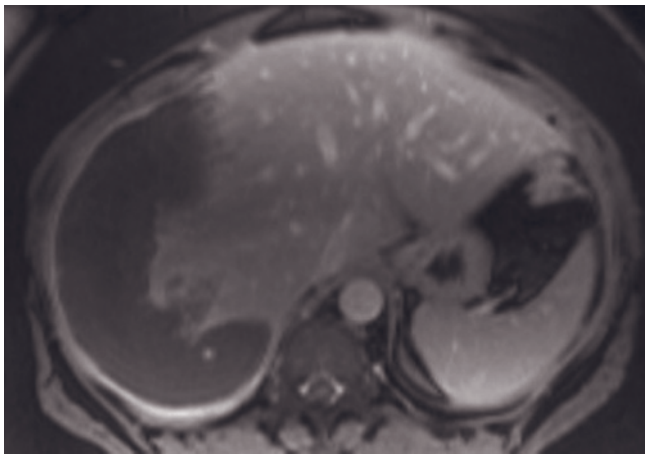

(*e*)

FIG. 2.178 (*Continued*) transplantation. There is a subcapsular collection characterized by heterogeneous mild/moderate high signal intensity on T2-weighted image (*c*), low signal intensity on T1-weighted image (*d*) and this capsular enhancement on late-phase image (*e*) consistent with a contained hemorrhage.

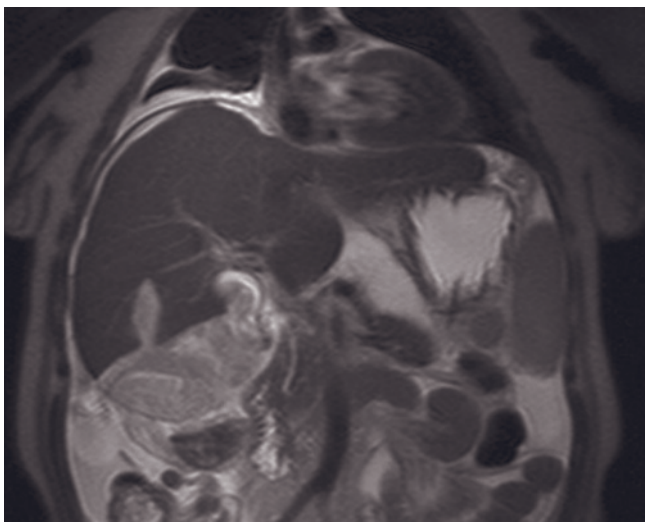

(*a*)

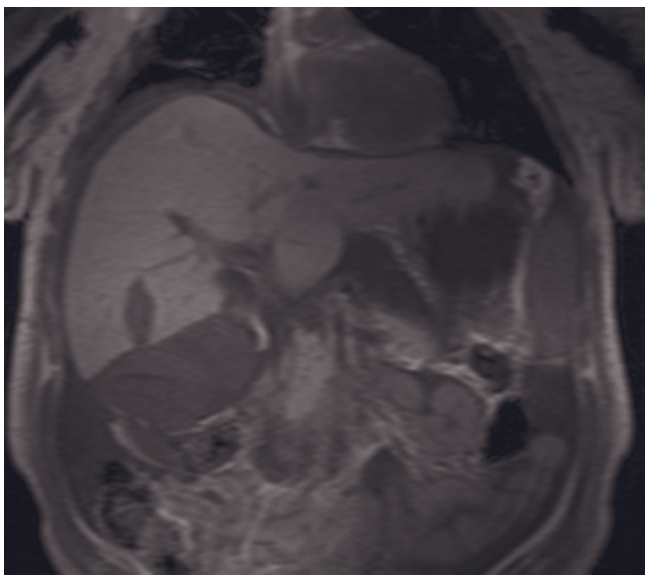

(*b*)

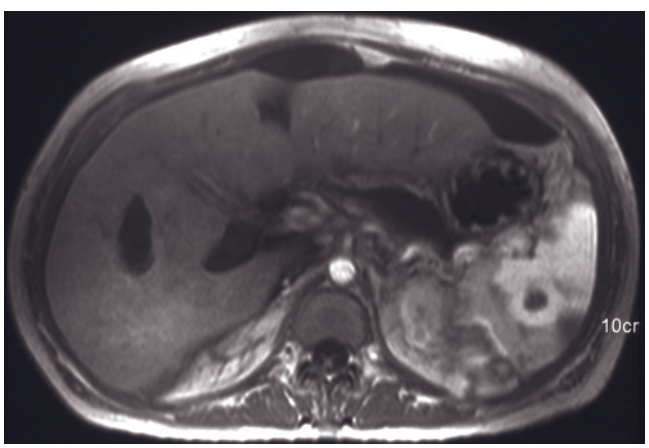

(*c*)

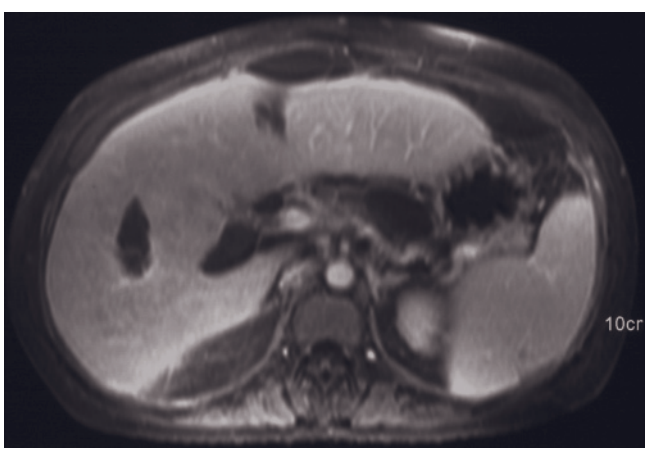

(*d*)

FIG. 2.179 Liver laceration and hematoma after liver transplant. Coronal T2-weighted SS-ETSE (*a*) and T1-weighted SGE (*b*) and transverse immediate (*c*) and 90-s fat-suppressed (*d*) postgadolinium SGE images. There is a linear laceration in the inferior portion of the liver associated with a hematoma.

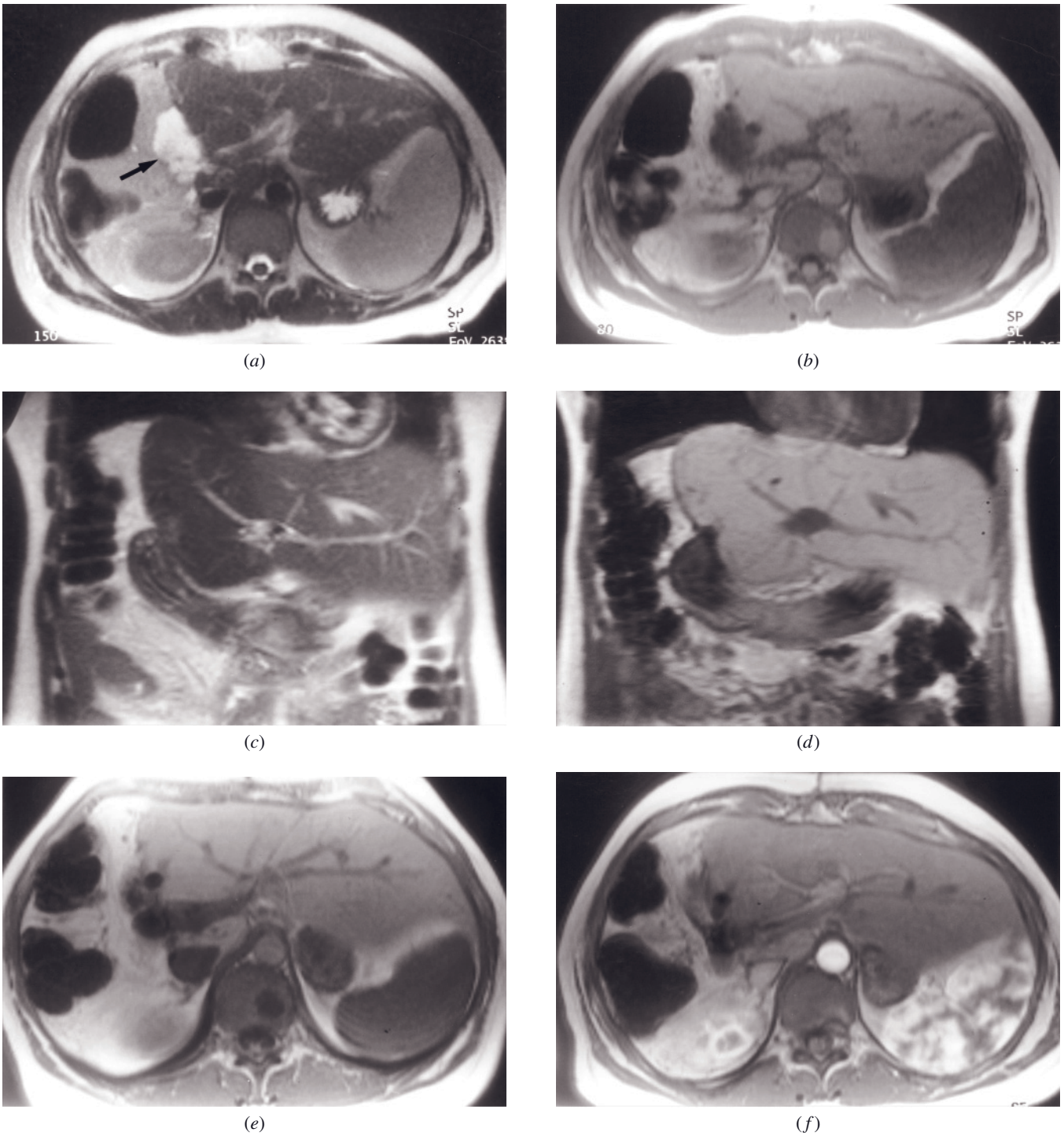

FIG. 2.180 Biloma after transplant. T2-weighted SS-ETSE (*a*) and SGE (*b*) images in a living-related right hemiliver donor after transplant. There is a fluid collection (arrow, *a*) along the resection margin of the liver that demonstrates high signal on T2-weighted (*a*) and low signal on T1-weighted (*b*) images, consistent with biloma.

Coronal T2-weighted SS-ETSE (*c*), coronal SGE (*d*), transverse SGE (*e*), and immediate (*f*) and 90-s fat-suppressed (*g*) post-gadolinium SGE images in the same patient 3 months after the prior exam. Note the resolution of the biloma.

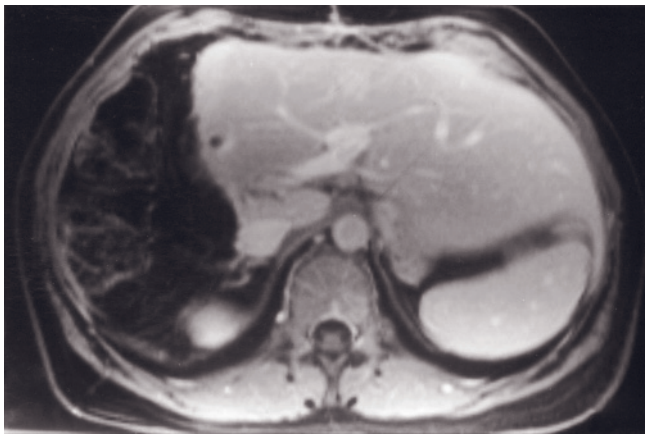

(*g*)

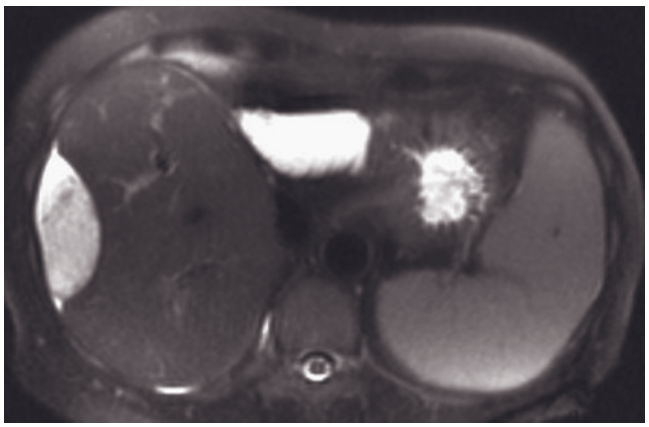

(*h*)

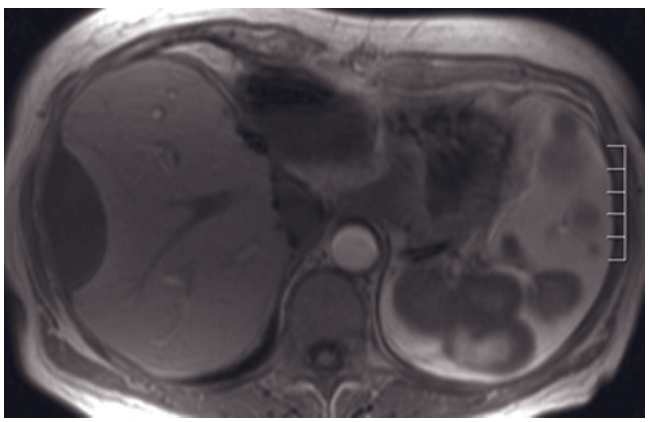

(*i*)

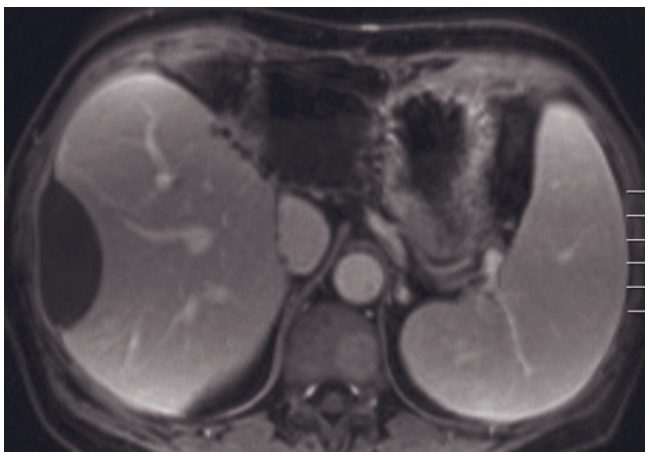

(*j*)

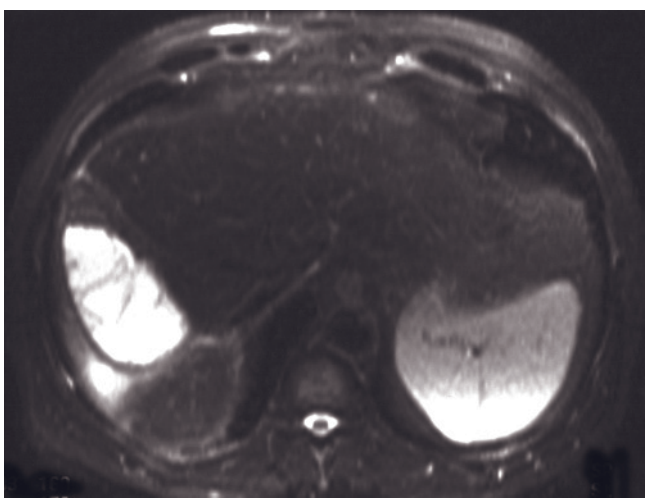

(*k*)

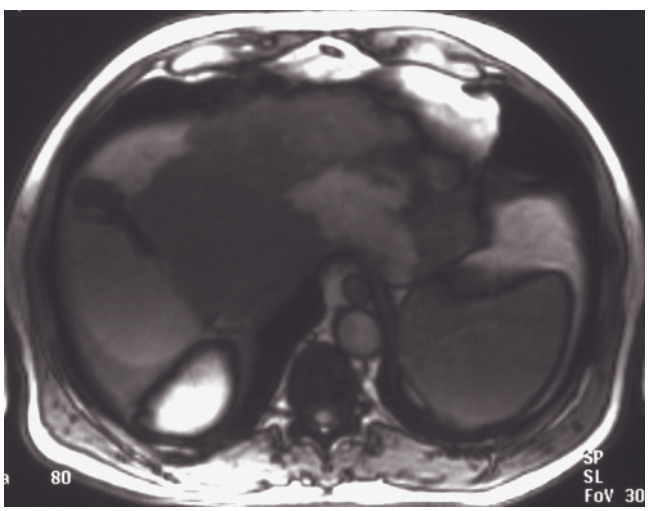

(*l*)

FIG. 2.180 (*Continued*) T2-weighted SS-ETSE (*h*), SGE (*i*), and 90-s fat-suppressed (*j*) postgadolinium SGE images in a liver recipient patient demonstrate an elongated subcapsular fluid collection consistent with a biloma.

T2-weighted SS-ETSE (*k*), out-of-phase SGE (*l*), and immediate (*m*) and 90-s fat-suppressed (*n*) postgadolinium SGE images in a liver recipient. A subcapsular biloma along the resection margin is present. Additionally, there are fatty spared regions shown on

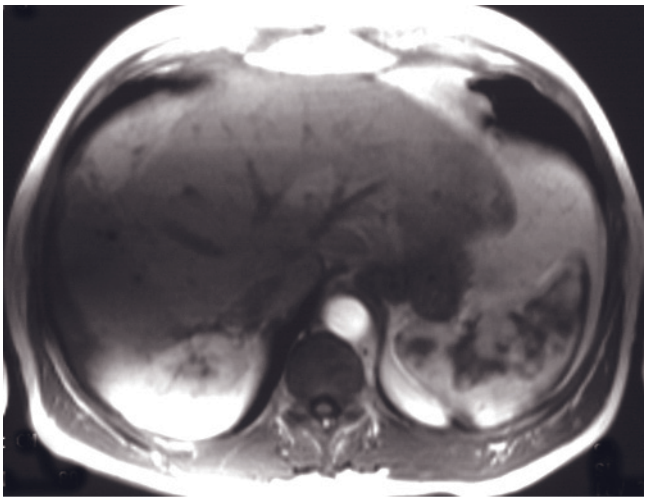

(*m*)

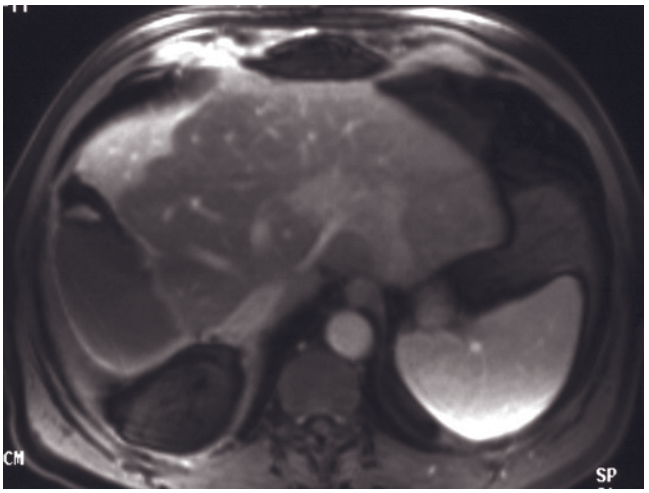

(*n*)

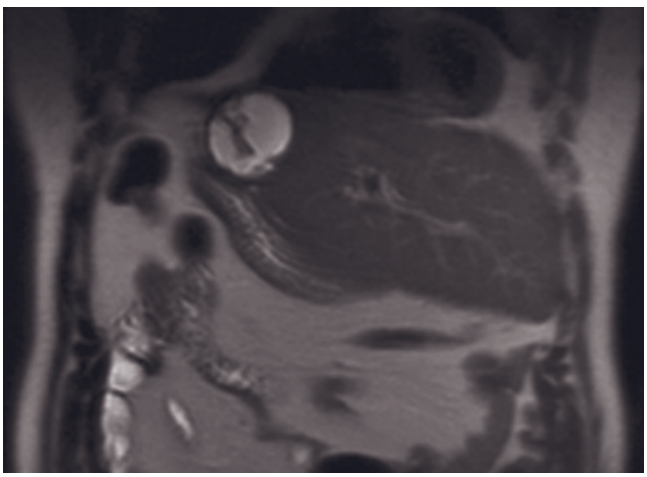

(*o*)

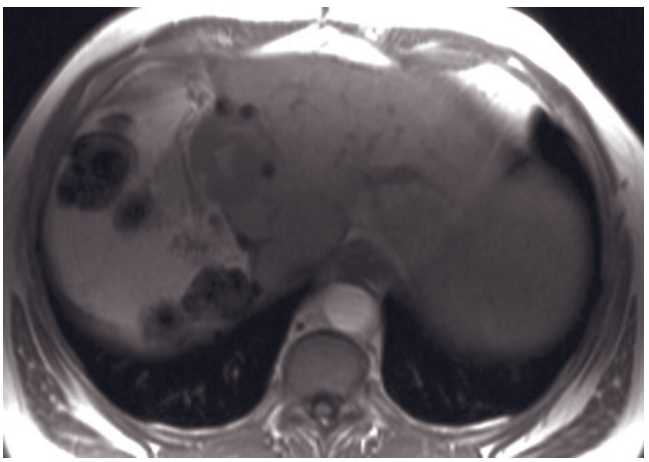

(*p*)

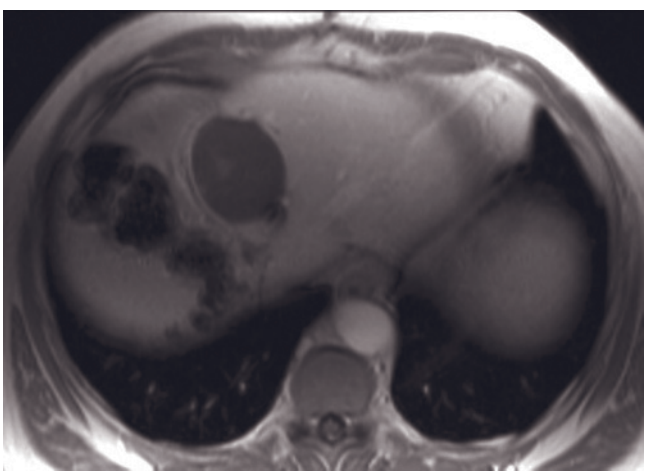

(*q*)

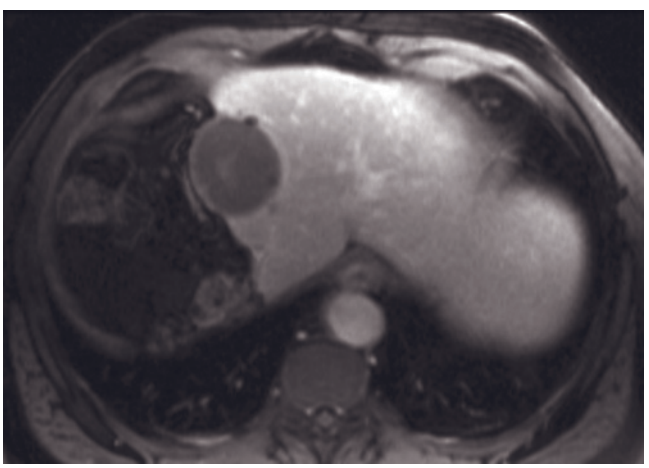

(*r*)

FIG. 2.180 (*Continued*) out-of-phase image that exhibit faint increased enhancement on early-phase image (*m*) and remain slightly higher signal on late-phase image (*n*). Enhancement differences likely reflect fat suppression effects of the fatty liver. Consideration must always be made of whether enhancement variations reflect true enhancement phenomena or reflect the use of concomitant fat suppression on some or all postcontrast sequences.

Coronal T2-weighted SS-ETSE (*o*), SGE (*p*), and immediate (*q*) and 90-s fat-suppressed (*r*) postgadolinium SGE images in a fourth patient demonstrate a biloma along the resection margin.

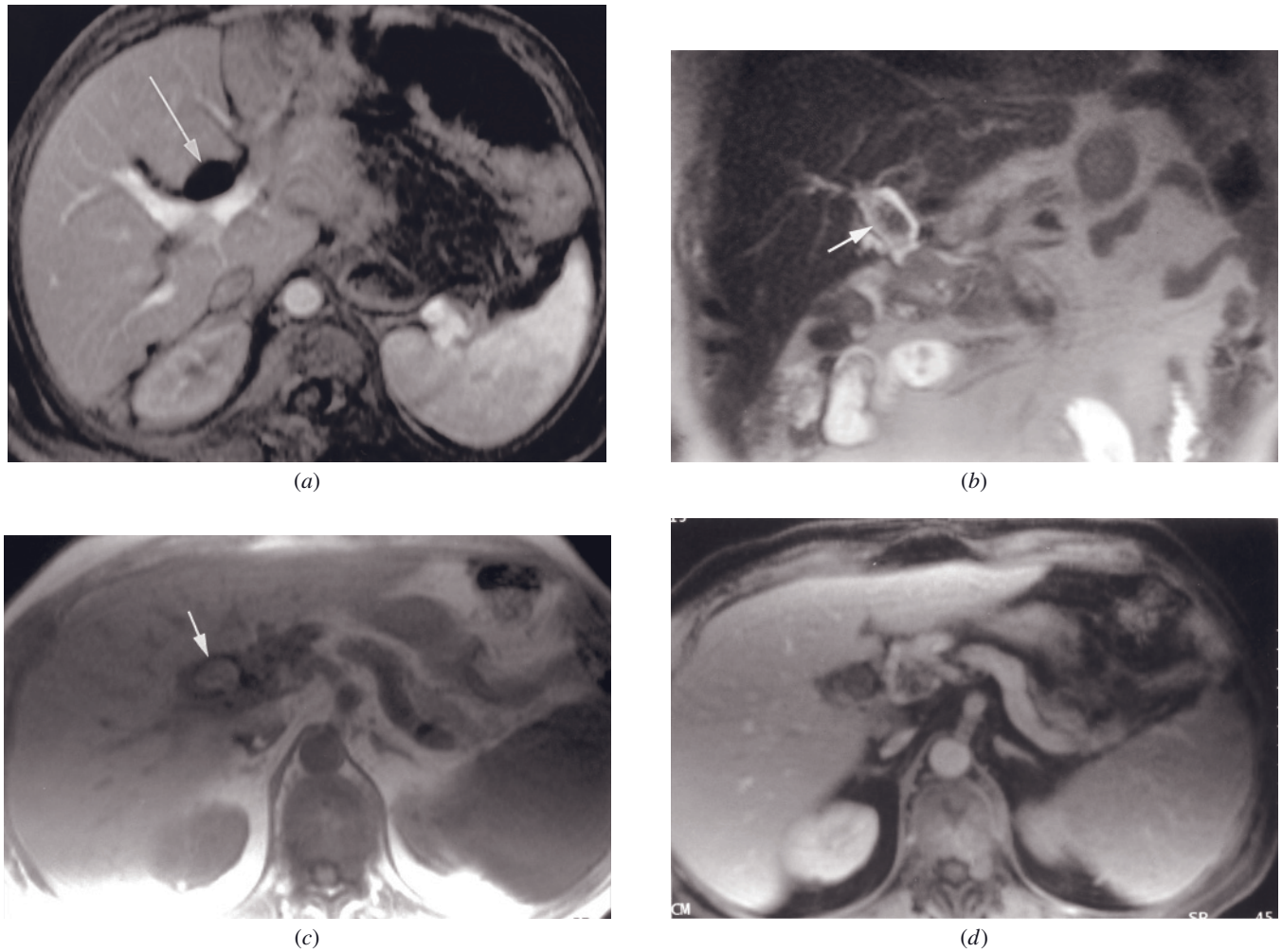

FIG. 2.181 Liver transplant, biliary duct stenosis. Transverse 90-s postgadolinium fat-suppressed SGE image (*a*). Dilatation of the common hepatic duct (arrow, *a*) is present, secondary to anastomotic stenosis.

Coronal T2-weighted SS-ETSE (*b*), SGE (*c*) and 90-s postgadolinium fat-suppressed SGE (*d*) images in a second patient. There is an anastomotic stricture associated with a filling defect within the common bile duct suggestive of sludge ball or stone (arrow, *b*, *c*). Note the mild intrahepatic biliary ductal dilatation (*b*). The findings were confirmed by ERCP.

images. Abnormal tissue is most substantial in the porta hepatis and extends along the branching portal tracts into the liver parenchyma (fig. 2.182) [281]. In many cases, periportal signal abnormalities may represent lymphocytic infiltration due to rejection; however, other causes such as dilated lymphatics due to impaired drainage after surgery must be considered [282]. Beyond the immediate transplant period, expansion of the periportal tissue in a masslike fashion may be a harbinger of posttransplant lymphoproliferative disorder (PTLD) (fig. 2.183) [283, 284]. PTLD occurs in transplant recipients whose immune systems are compromised. Most cases can be linked to infection with Epstein–Barr virus and may involve any organ in the body [283, 284]. Liver, small bowel, and kidney are the most common extranodal abdominal organs involved with PTLD [283]. PTLD is varied in presentation, ranging from polyclonal (nonmalignant) B cell proliferations to malignant lymphoma, usually B cell [285]. Inflammatory periportal tissue also may be observed in acute hepatitis, after biliary surgery, in various benign or malignant diseases, and in portal adenopathy [286].

Hepatocellular carcinoma may develop in the transplanted liver. This is an important complication in patients who were diagnosed with HCC before transplantation or in whom focal HCC was found incidentally in the pathologic evaluation of the recipient's resected liver (fig. 2.184) [276, 287].

MRI demonstrates a variety of morphologic abnormalities in transplanted livers and is able to identify various causes of graft failure (figs. 2.185–2.187). At present, however, no specific MRI findings have been

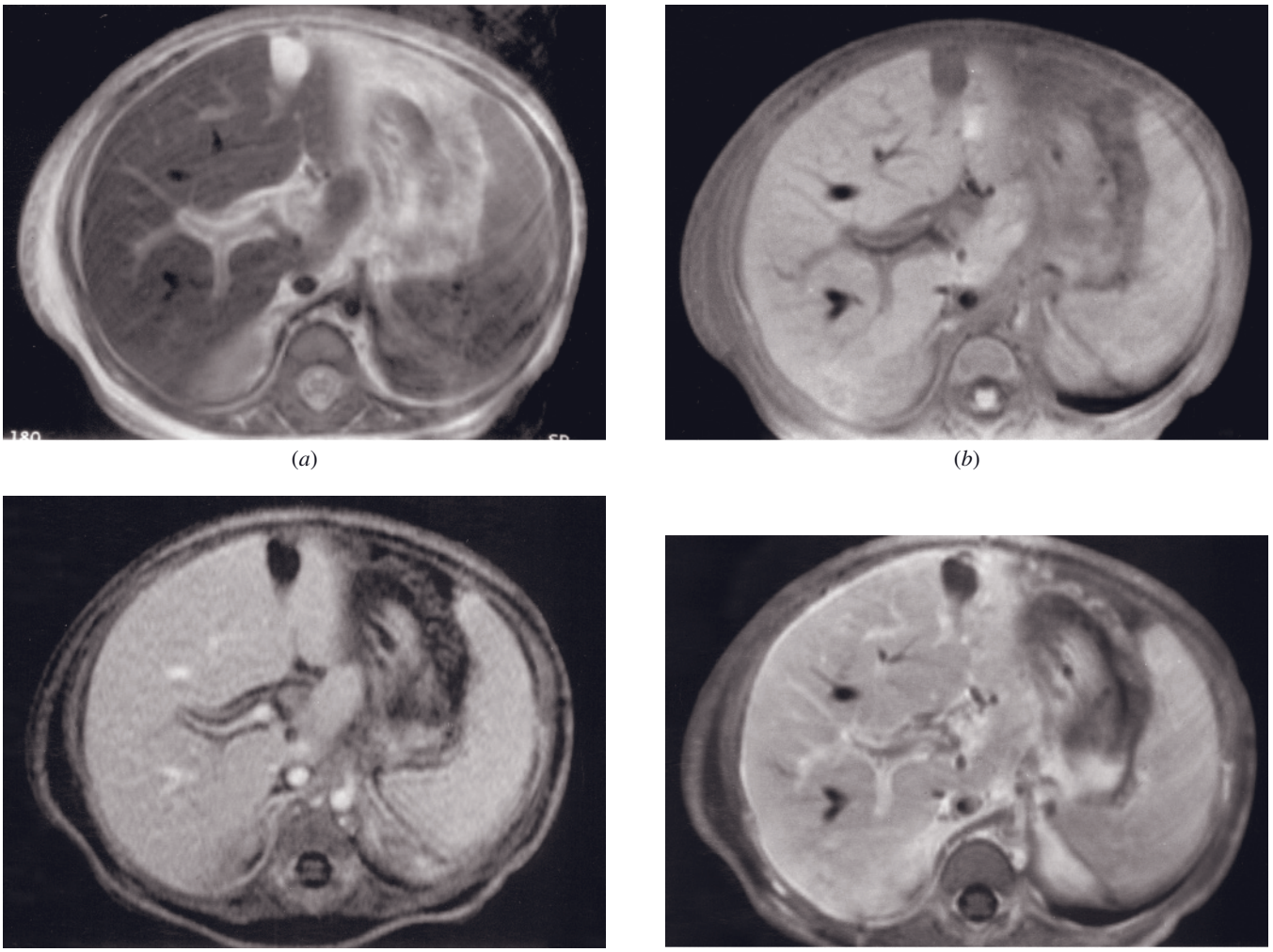

(*a*) (*b*) (*c*) (*d*)

FIG. 2.182 Periportal inflammation after liver transplant. T2-weighted SE (*a*), T1-weighted SE (*b*), immediate postgadolinium magnetization-prepared gradient-echo (*c*), and T1-weighted interstitial-phase postgadolinium fat-suppressed SE (*d*) images in a 17-month-old patient after liver transplant. There is a moderate amount of periportal inflammatory change, which appears high signal on T2 (*a*) and enhances on interstitial-phase postgadolinium fat-suppressed images (*c*), likely postsurgical changes.

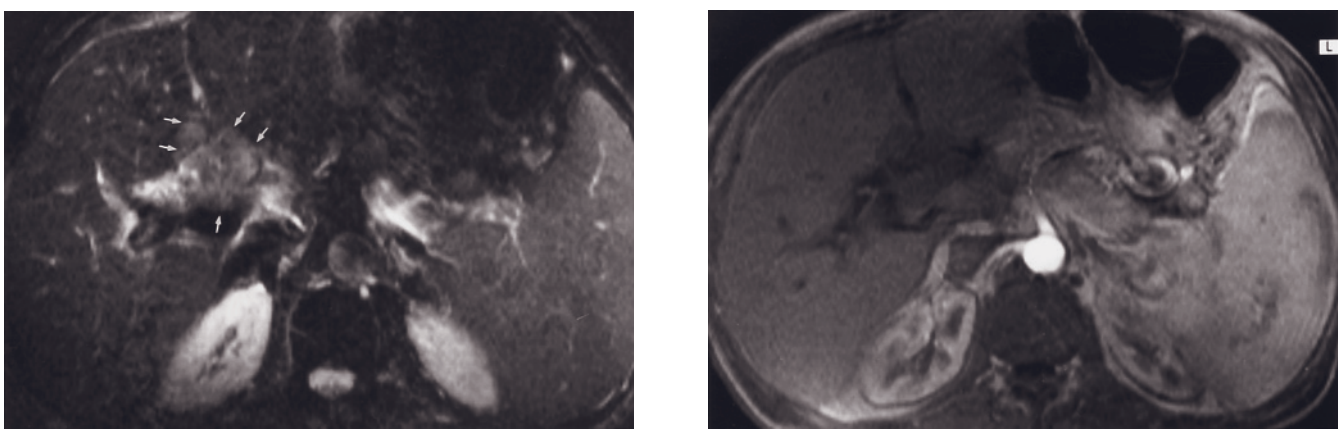

(*a*) (*b*)

FIG. 2.183 Lymphoproliferative disorder. T2-weighted fat-suppressed ETSE (*a*) and immediate postgadolinium SGE (*b*) images. A 3-cm mass is present in the porta hepatis that is moderate in signal on the T2-weighted image (arrows, *a*) and enhances minimally with gadolinium (*b*).

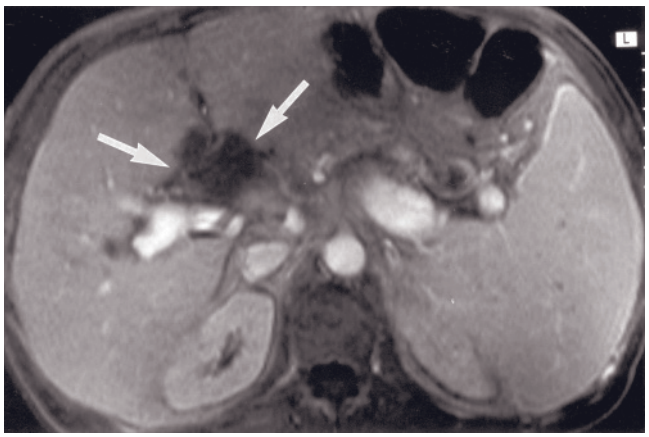

(*c*)

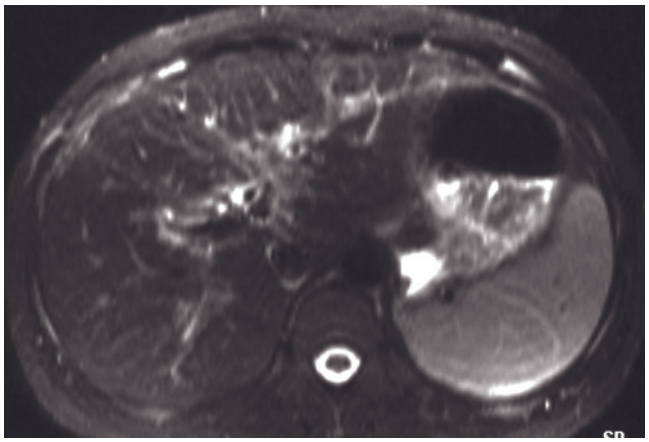

(*d*)

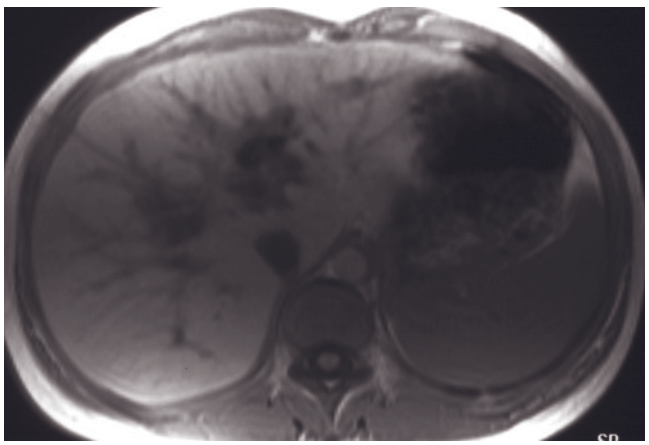

(*e*)

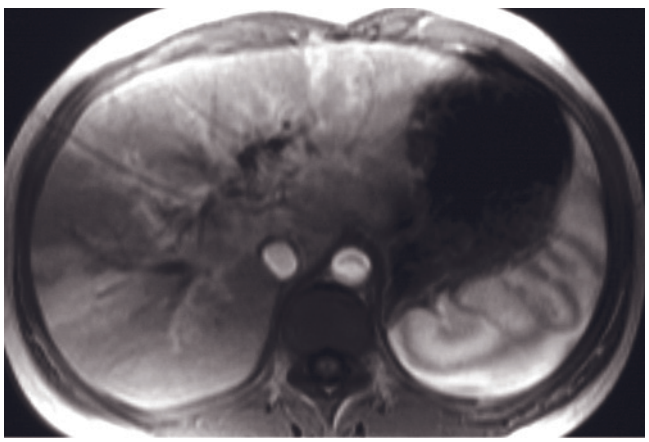

(*f*)

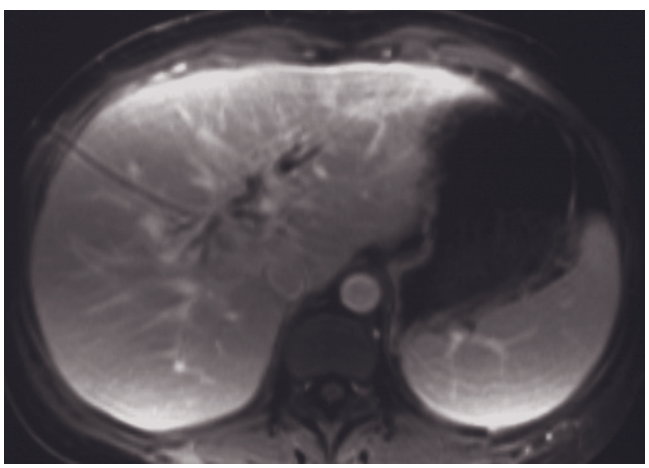

(*g*)

FIG. 2.183 (*Continued*) Interstitial-phase gadolinium-enhanced fat-suppressed SGE (*c*) image in a second patient with posttransplant lymphoproliferative disorder. A mass (arrows, *c*) in the porta hepatis is appreciated with negligible enhancement on the late postcontrast image (*c*).

T2-weighted fat-suppressed SS-ETSE (*d*), SGE (*e*), and immediate (*f*) and 90-s fat-suppressed (*g*) postgadolinium SGE images in a third patient. The central portion of the liver shows an abnormal area that is masslike and exhibits high signal intensity on T2-weighted images (*d*), low signal intensity on T1-weighted images (*e*), and moderate enhancement on early-phase images (*f*) and appears homogeneously enhanced on late-phase images (*g*). Histopathology was consistent with lymphoproliferative disorder. Air is present in the biliary tree secondary to the presence of a percutaneous biliary drain.

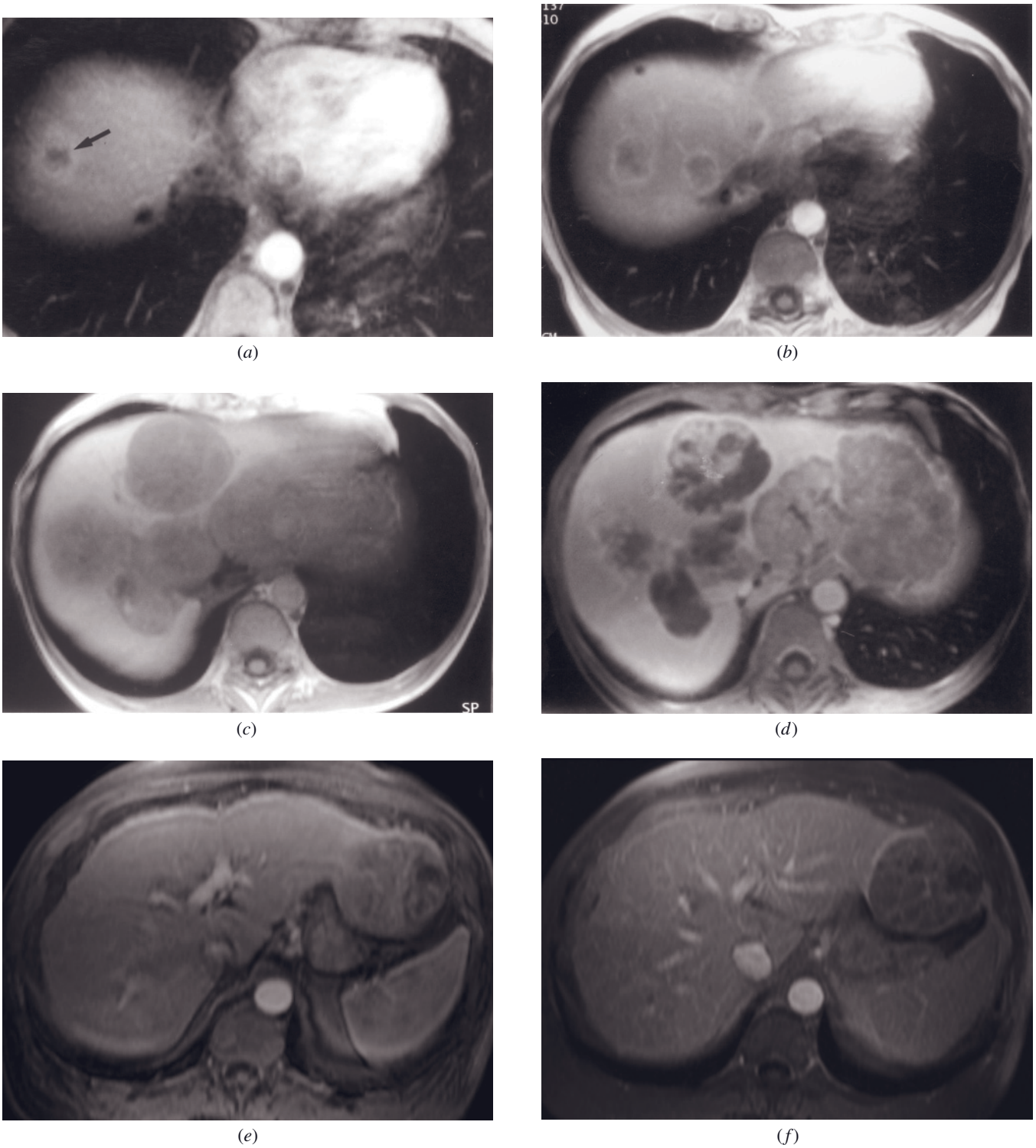

FIG. 2.184 Recurrent HCC in a liver transplant. Immediate postgadolinium SGE (*a*) image in a patient who has developed HCC within a transplanted liver. Multiple small masses involve the dome of the right lobe of the liver that demonstrate ring enhancement on the immediate postgadolinium image (arrow, *a*). Three months later the lesions have increased in size and number, as shown on the immediate postgadolinium SGE image (*b*). One year later, SGE (*c*), and 90-s postgadolinium fat-suppressed SGE (*d*) images demonstrate massive increase in size and number of HCCs. This represents metastases to a liver transplant in a patient who had HCC in her native liver.

T1-weighted fat-suppressed 3D-gradient echo images immediate (*e*), and 90-second (*f*) in a second with HCC imaged **at 3.0T** after liver transplantation. Metastatic foci of HCC are apparent.

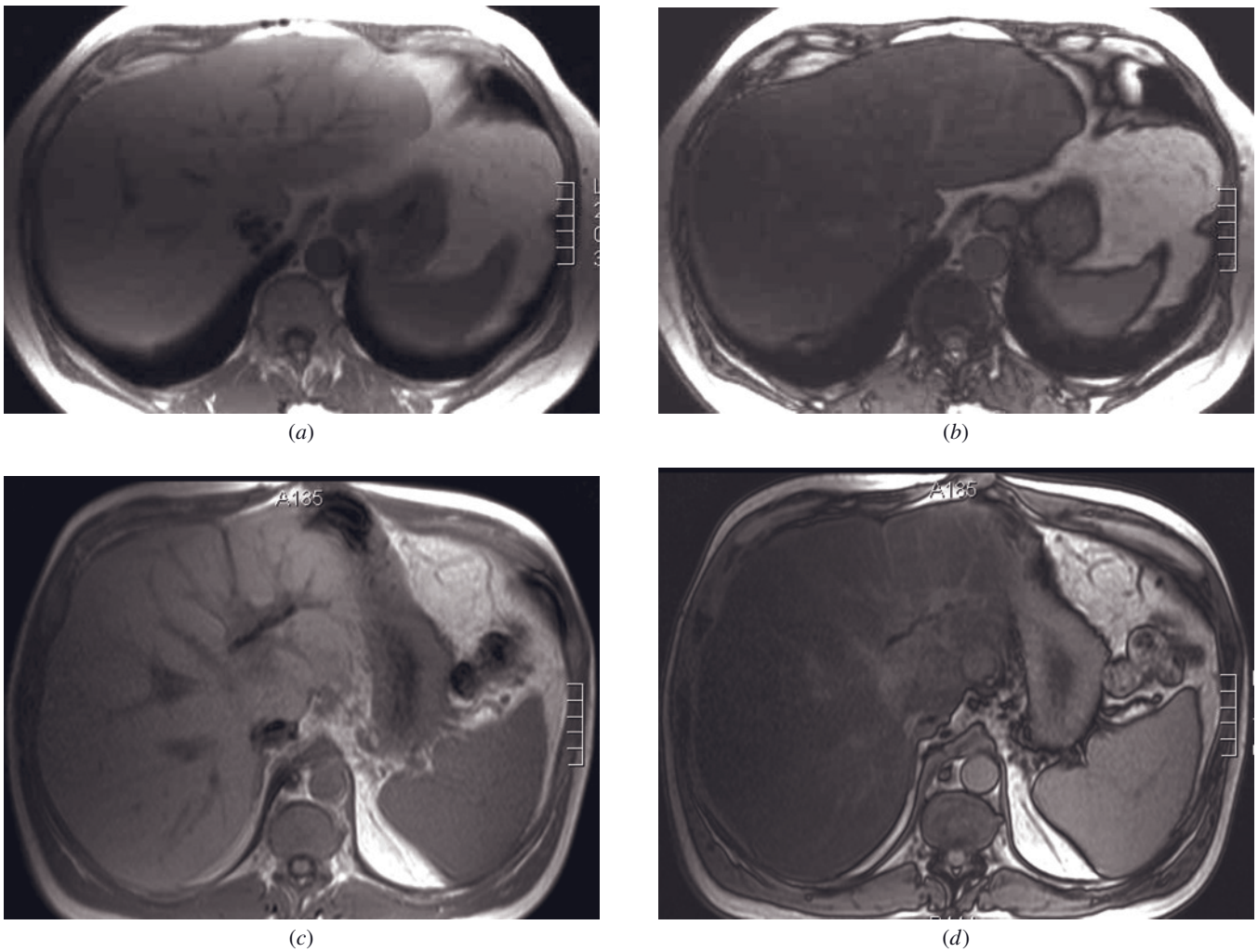

FIG. 2.185 Fatty liver after transplantation. SGE (*a*, *c*) and out-of-phase SGE (*b*, *d*) images in two different patients after liver transplantation that demonstrate signal loss from in-phase T1-weighted images (*a*, *c*) to out-of-phase images (*b*, *d*) compatible with fatty liver.

identified to establish or quantify transplant rejection or hepatocellular function. In the future, hepatocyte-specific contrast agents or MR spectroscopy may play a role in this determination.

DIFFUSE LIVER PARENCHYMAL DISEASE

Chronic Liver Diseases

Autoimmune Diseases

Autoimmune liver disorders are inflammatory liver diseases characterized histologically by a pronounced mononuclear cell infiltrate in the portal tracts and serologically by the presence of non-organ and liver-specific autoantibodies and increased levels of immunoglobulin G (IgG) in the absence of a known etiology [288]. Primary sclerosing cholangitis (PSC), autoimmune hepatitis (AIH), and primary biliary cirrhosis (PBC) are chronic liver diseases postulated to have an autoimmune basis for their pathogenesis [289].

Primary sclerosing cholangitis (PSC) is a chronic liver disease of unknown etiology. A number of factors have been proposed that might incite injury and cause recurrent damage to the bile ducts. These entities include bacteria, virus, toxins, vascular damage, or genetic abnormalities of immunoregulation. PSC is more common in males and has a high association with inflammatory bowel disease [290]. Also, patients with PSC have a higher risk of developing cholangiocarcinoma than the general population because of chronic biliary inflammatory changes [291].

The morphologic changes of PSC on pathologic evaluation consist of a lymphocytic infiltrate with fibrosing cholangitis of intra- and extrahepatic bile ducts and

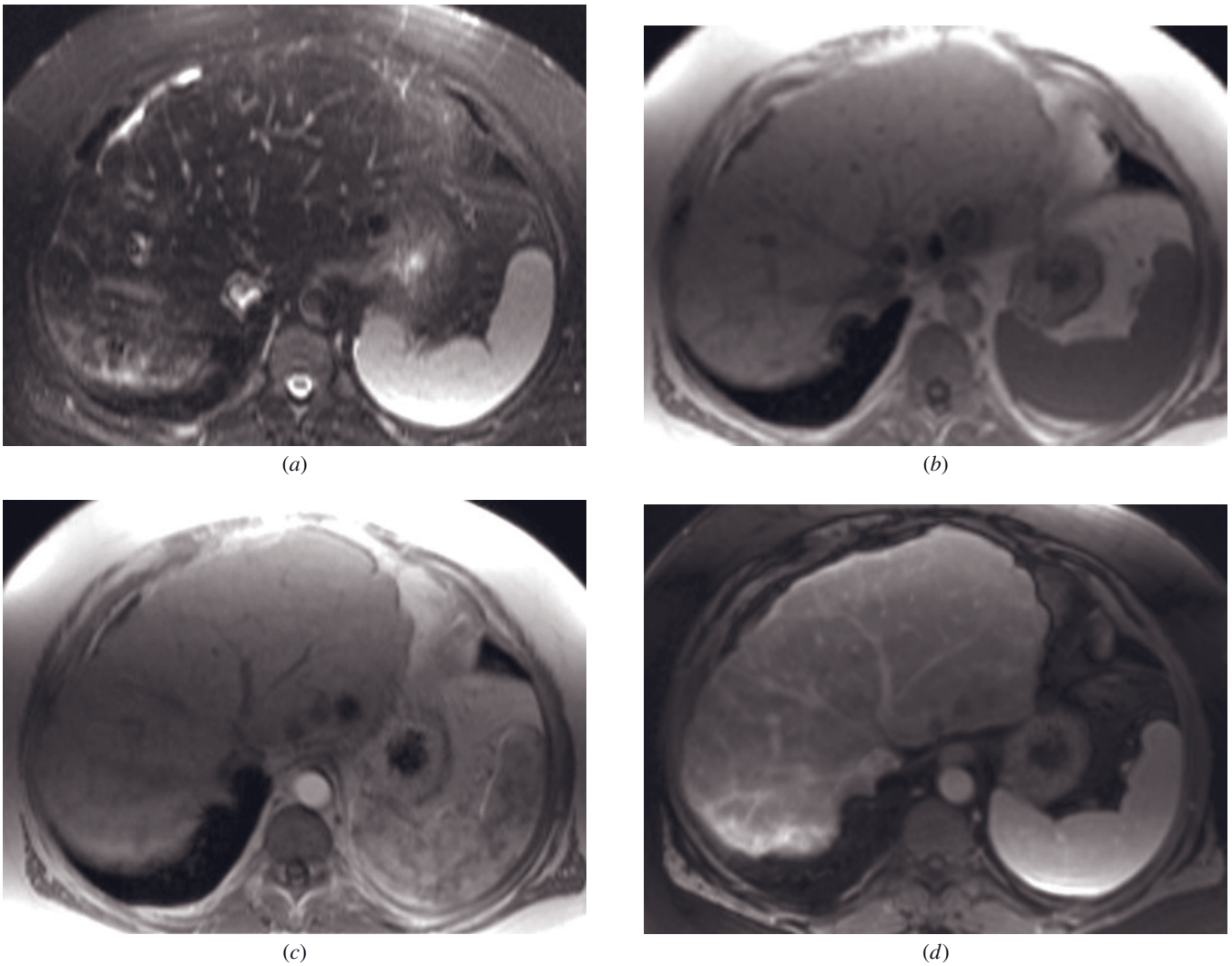

FIG. 2.186 Fibrosis after liver transplant. T2-weighted SS-ETSE (*a*), SGE (*b*), and immediate (*c*) and 90-s fat-suppressed (*d*) postgadolinium SGE images show strands of fibrosis in a posttransplant liver well shown on late-phase image (*d*).

progressive obliteration of their lumens. Between areas of scarring and progressive stricture, bile ducts become ectatic, presumably the result of downstream obstruction. Such a pattern of multifocal strictures and dilatations produces the well-recognized cholangiographic pattern of "beaded" bile ducts. The disease culminates in cirrhosis.

A prior study [292] described the MR findings of PSC and the association of imaging features with clinical severity by use of the Mayo End-Stage Liver Disease (MELD) and Child–Turcotte–Pugh scales. The association between macronodular morphology, biliary obstruction, and peripheral wedge-shaped atrophy was the most suggestive of PSC, and it was noticed in 23% (12/52) of patients. MR findings of liver cirrhosis were described in 87% of the patients. More than half of the patients had nodules ≥3 cm in the maximum diameter, and the number of nodules ranged from 1 to 5 in 57% of patients. The majority of nodules enhanced comparably to liver parenchyma. A distinctive feature is that up to 70% of these nodules were located in the central region of the liver. The compression of central ducts by large nodules causes peripheral biliary dilation, and this feature was shown in 29% of patients. The presence of intrahepatic biliary ductal dilatation was described in 85% of the patients, with segmental dilatation, a common finding. Peripheral wedge-shaped areas of parenchymal atrophy were noted in 46% of patients. On MRI, these areas were characterized as high signal on T2-weighted images and low signal on noncontrast T1-weighted images in up to 83%, with atrophic segments occasionally being high signal on T1-weighted images (figs. 2.188 and 2.189). After contrast, the wedge-shaped areas showed minimal enhancement (less than background

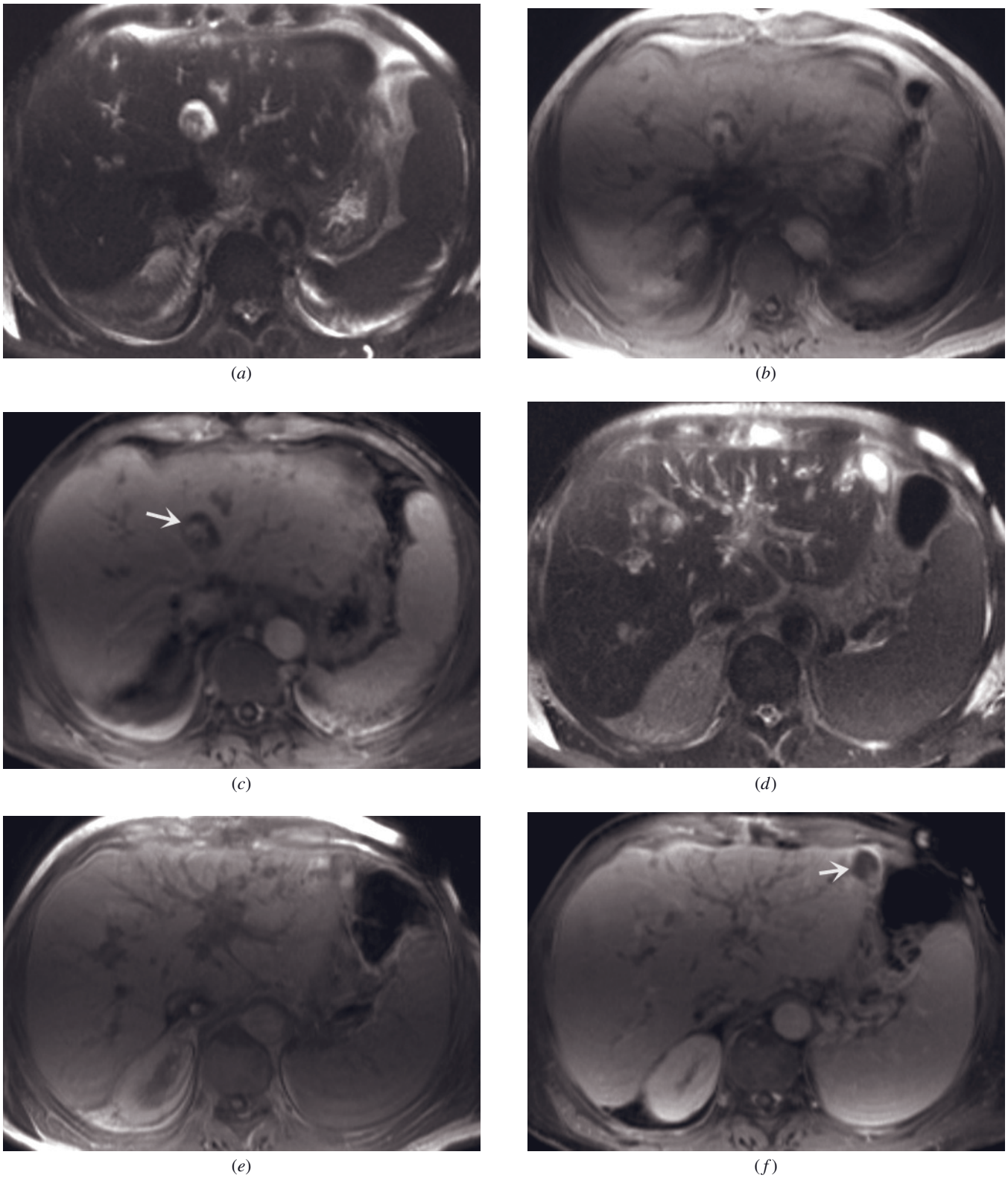

FIG. 2.187 Fungus infection after liver transplant. T2-weighted SS-ETSE (*a*, *d*), SGE (*b*, *e*), and 90-s fat-suppressed (*c*, *f*) postgadolinium SGE images in the same patient at two different tomographic levels. There are two cystic lesions (arrow, *c*, *f*) in the left hepatic lobe that demonstrate a small focus of internal debris. Note the presence of mild biliary dilatation and ascites.

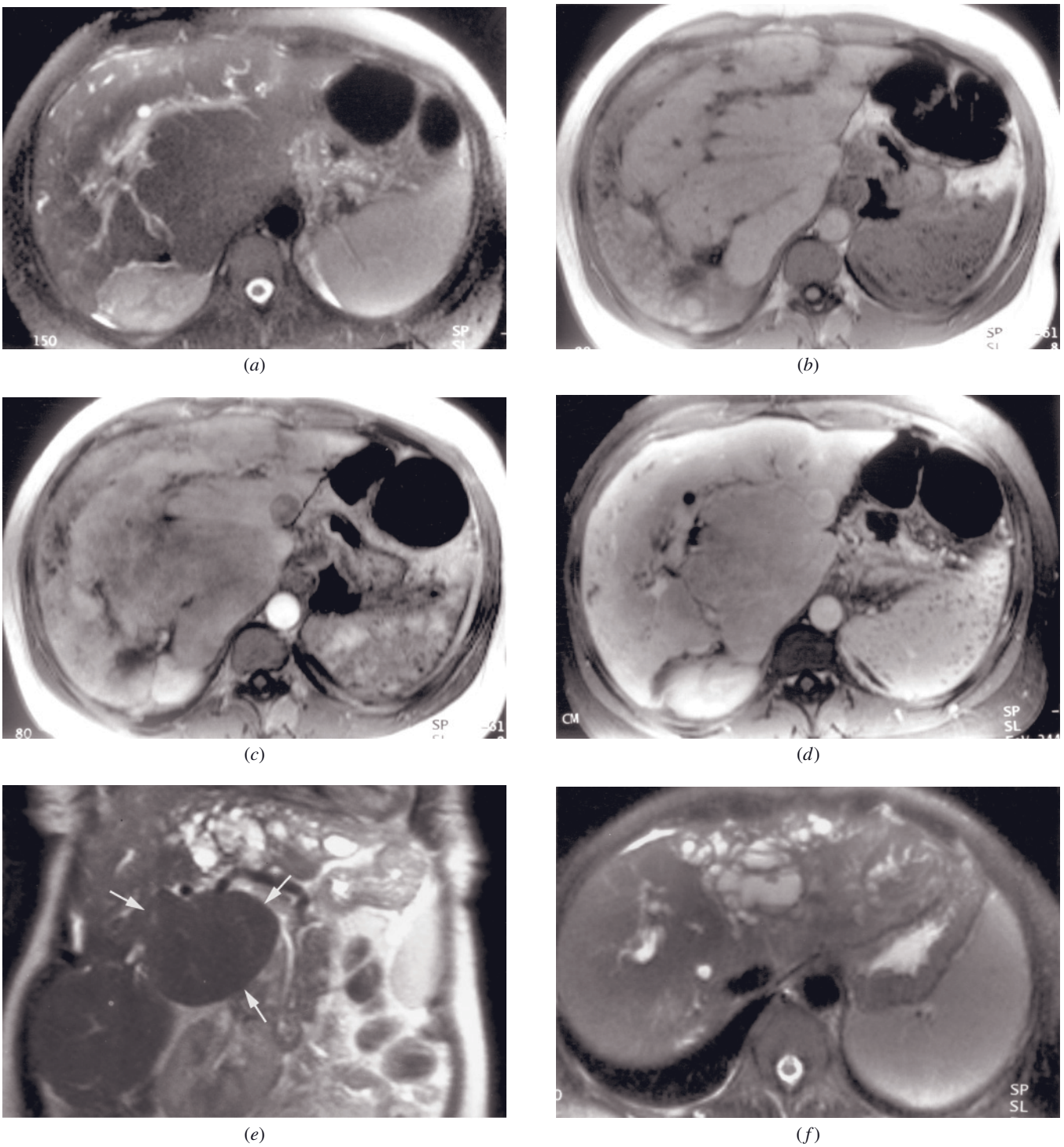

FIG. 2.188 Cirrhosis in primary sclerosing cholangitis. Echo-train STIR (*a*), SGE (*b*), and immediate (*c*) and 90-s fat-suppressed (*d*) postgadolinium SGE images. The liver shows distorted anatomy with heterogeneous signal. The caudate lobe is massively enlarged by large macroregenerative nodules that cause atrophy of the peripheral liver, resulting in signal changes of increased signal on T2 (*a*), decreased signal on T1 (*b*), and early negligible (*c*) and late progressive (*d*) enhancement. There is ductal dilatation in the peripheral liver, due to obstruction from the central hypertrophy. These findings are consistent with cirrhosis due to PSC.

Coronal T2-weighted SS-ETSE (*e*), T2-weighted fat-suppressed SS-ETSE (*f*), and 90-s fat-suppressed (*g*, *h*) postgadolinium SGE images in a second patient. Note the massive enlargement of the caudate lobe (arrows, *e*), which causes distal obstruction of the biliary tree.

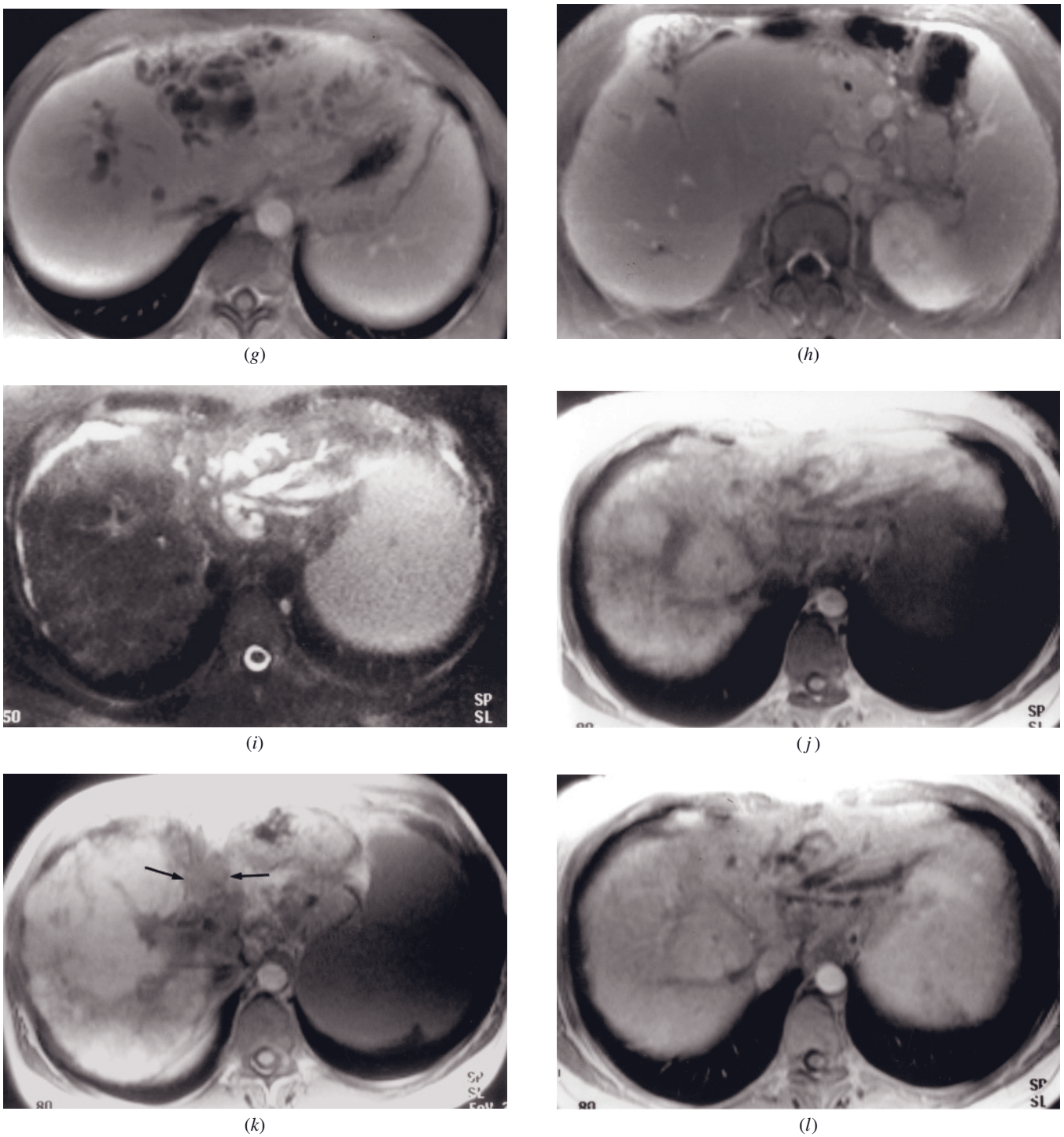

FIG. 2.188 (*Continued*) Echo-train STIR (*i*), SGE (*j*, *k*), and immediate (*l*) and 90-s fat-suppressed (*m*) postgadolinium SGE images in a third patient with PSC. The liver demonstrates a shrunken fibrotic appearance with multiple macroregenerative nodules, which are more widely distributed than in the first 2 patients. Severe lateral segment intrahepatic biliary ductal dilatation is present (*i*) from obstruction by dense fibrous tissue (arrows, *k*).

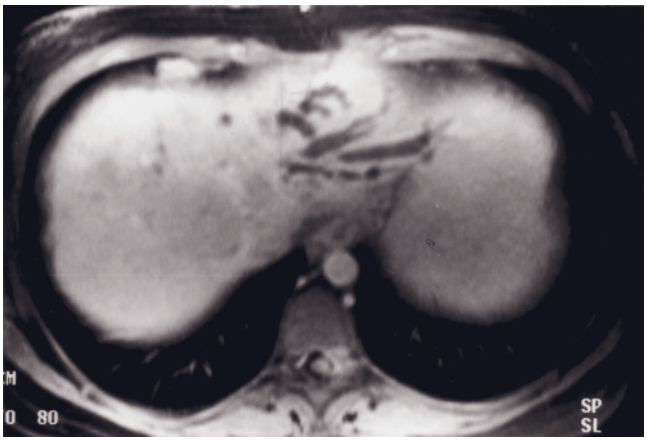

(*m*)

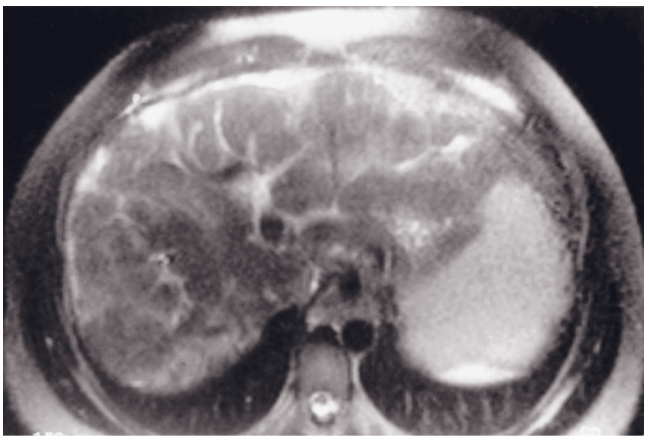

(*n*)

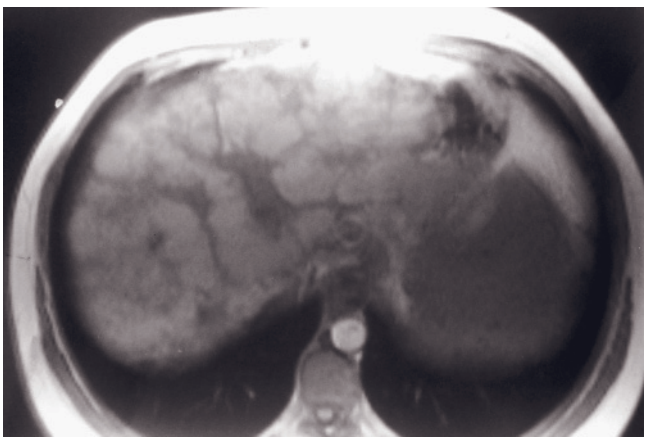

(*o*)

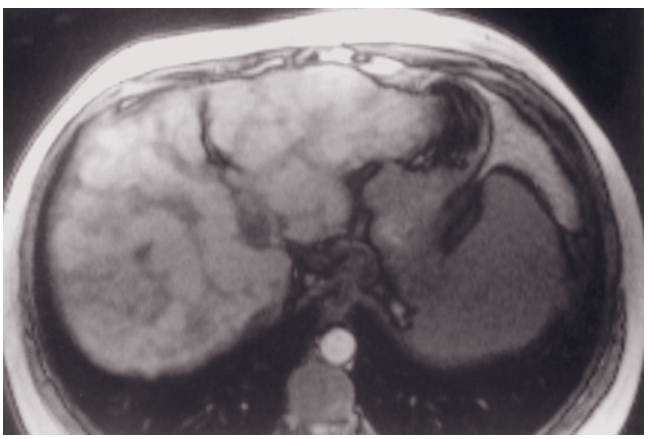

(*p*)

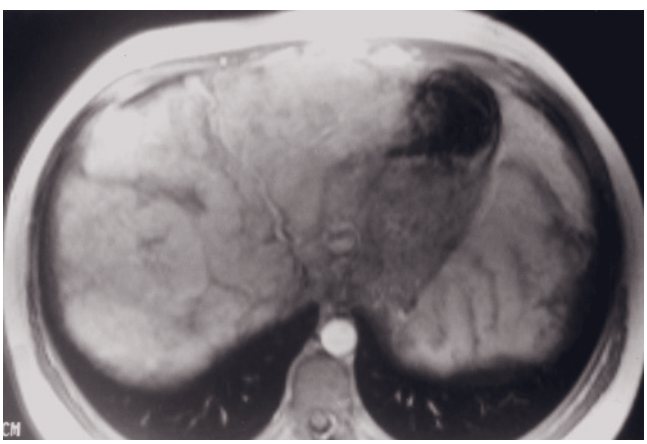

(*q*)

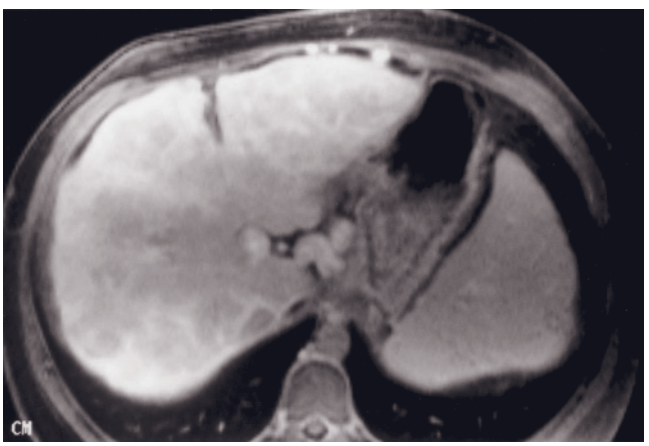

(*r*)

FIG. 2.188 (*Continued*) Echo-train STIR (*n*), SGE (*o*), out-of-phase SGE (*p*), and immediate (*q*) and 90-s fat-suppressed (*r*) post-gadolinium SGE images in a fourth patient with PSC. The liver is heterogeneous in signal on T2-weighted (*n*) and T1-weighted (*o*, *p*) images, with multiple macronodules and fibrotic bands present. This patient does not have the characteristic central macronodular pattern found in PSC.

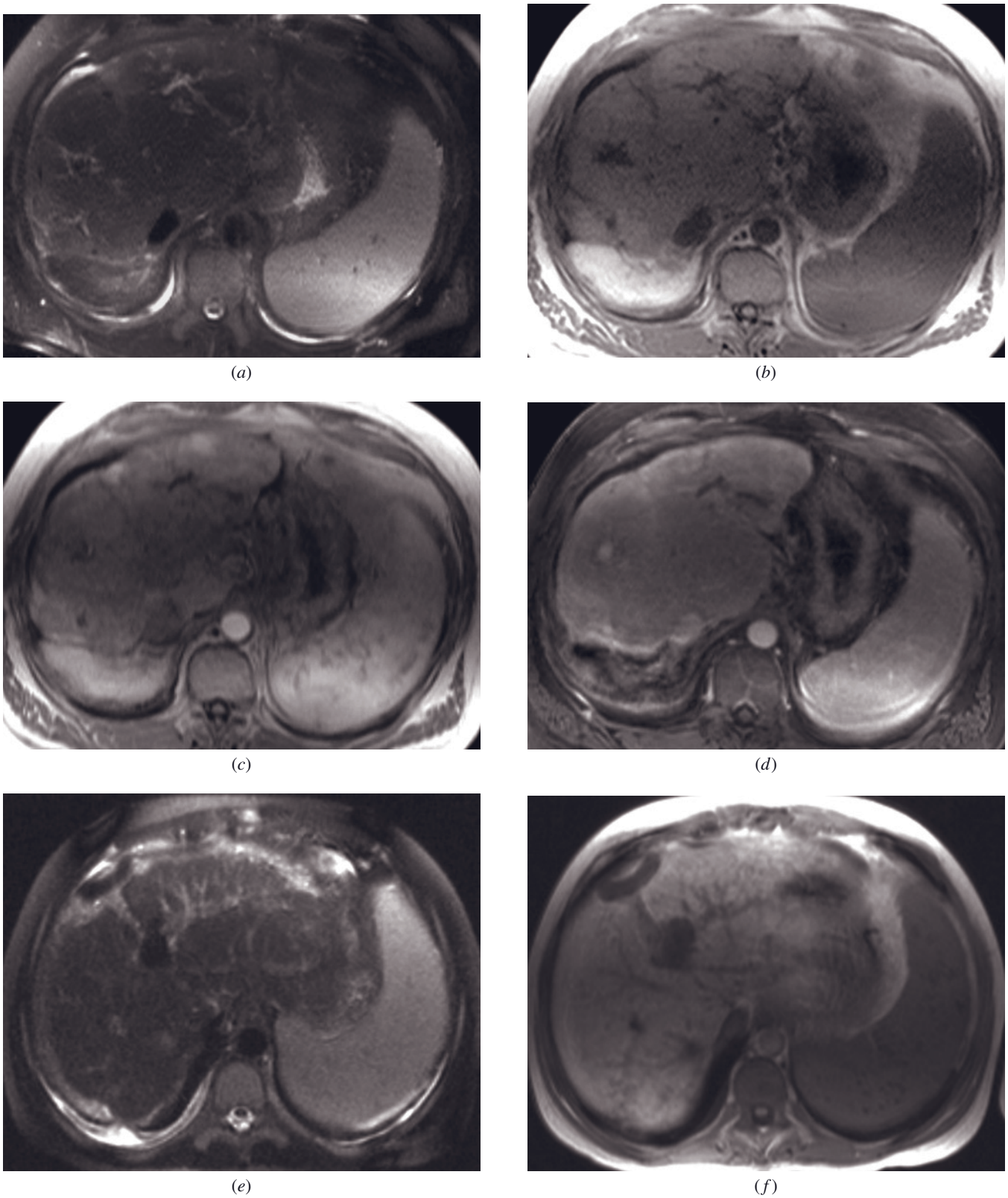

FIG. 2.189 Primary sclerosing cholangitis. T2-weighted fat-suppressed SS-ETSE (*a*), SGE (*b*), immediate (*c*) and 90-second fat-suppressed (*d*) postgadolinium SGE; T2-weighted fat-suppressed SS-ETSE (*e*), SGE (*f*), and immediate (*g*) and 90-second fat-suppressed (*h*) postgadolinium SGE images in two patients with PSC. T2-weighted fat suppressed SS-ETSE fat suppressed (*i*, *k*, *n*)

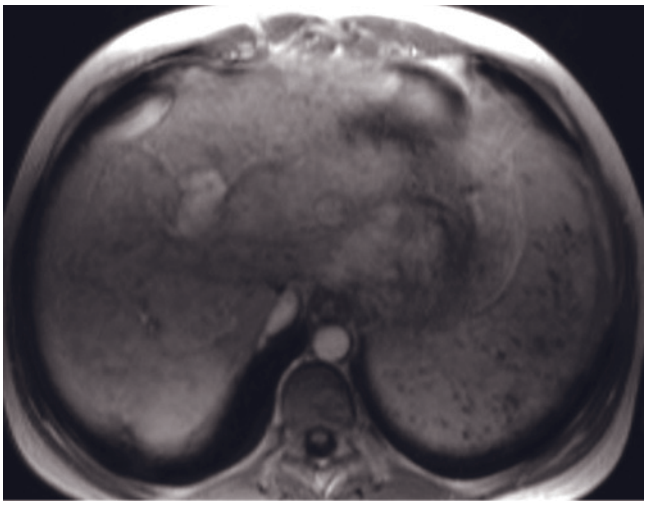

(*g*)

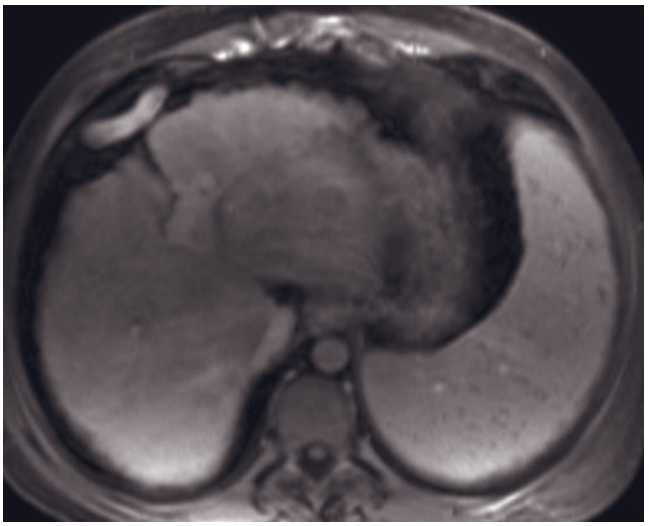

(*h*)

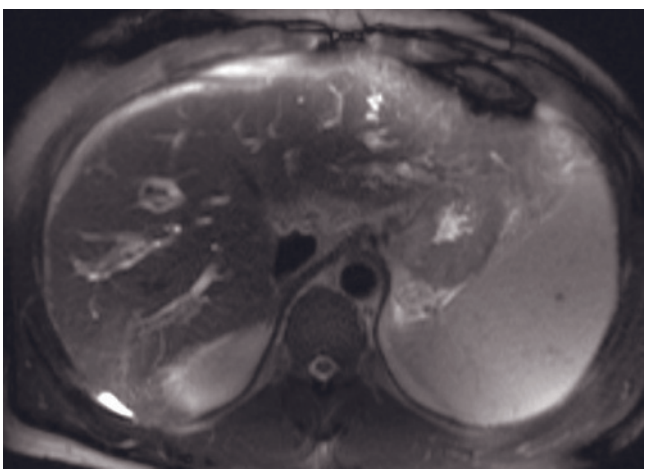

(*i*)

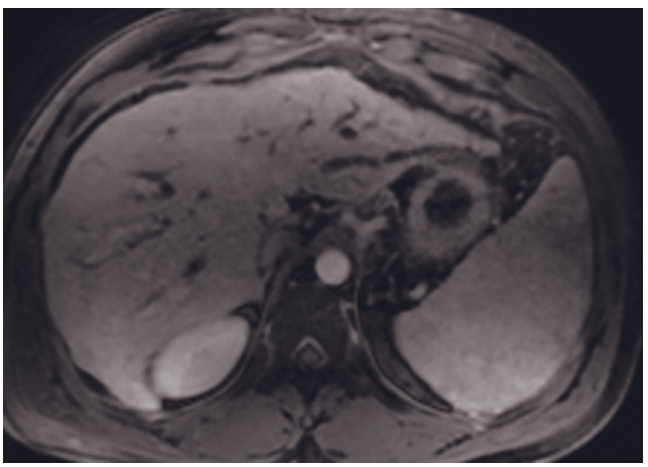

(*j*)

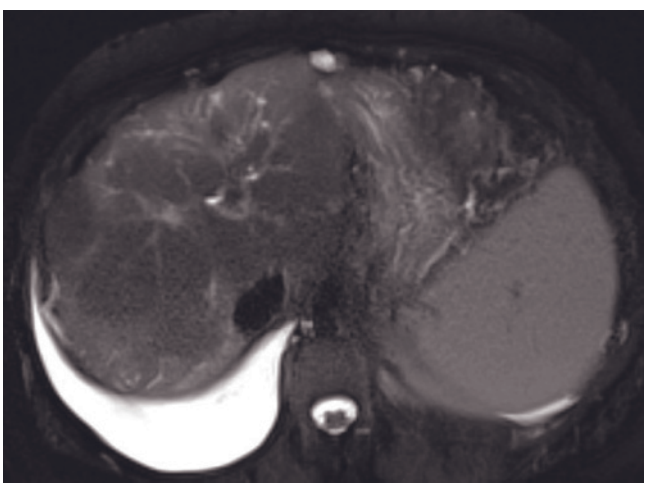

(*k*)

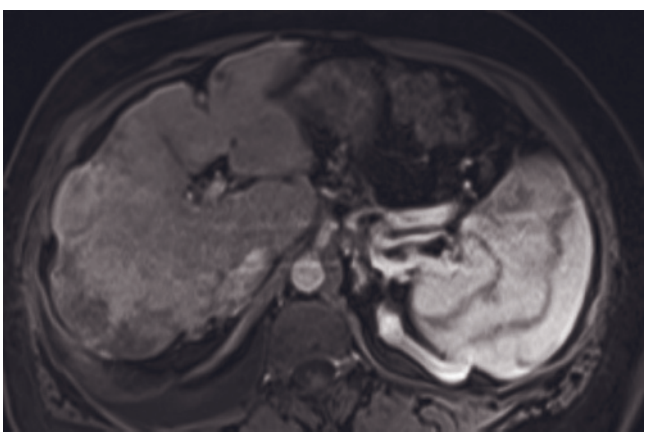

(*l*)

FIG. 2.189 (*Continued*) and T1-weighted fat-supressed 3D-vibe immediate post gadolinium (*l*, *o*) and 90-second post gadolinium (*j*, *m*, *p*) in three different patients imaged **at 3T**. Simlar findings of central regeneration are appreciated.

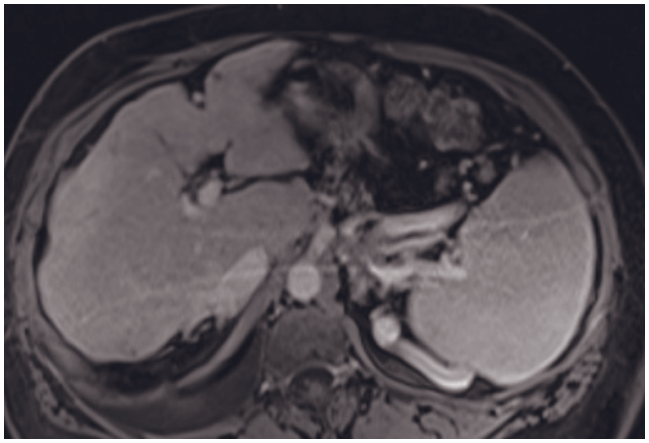

(*m*)

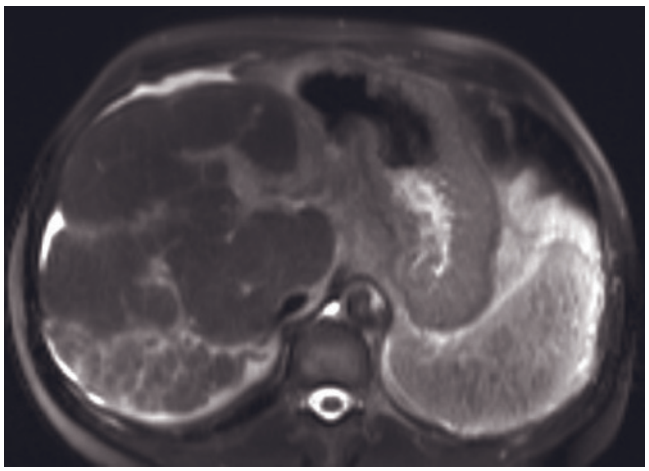

(*n*)

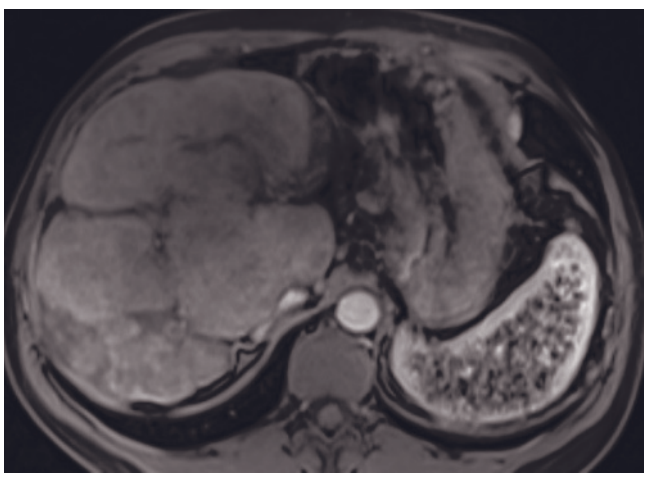

(*o*)

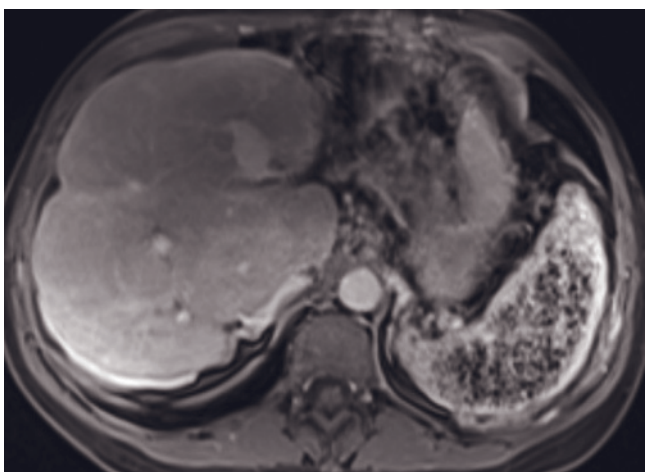

(*p*)

FIG. 2.189 (*Continued*)

parenchyma) on early-phase images that became more intense on late-phase images in more than half of these patients. The association between the severity of imaging findings and MELD and Child–Turcotte–Pugh were not statistically significant. This suggests that morphologic changes alone may not reflect the extent of hepatic compromise.

Changes of cirrhosis in patients with PSC are associated with extensive fibrotic changes, central macroregenerative nodules, and peripheral atrophy causing architectural distortion. Central macroregenerative nodules may result in true biliary ductal dilatation and peripheral liver atrophy distinct from the beaded biliary ductal changes of PSC. These patterns appear to be both relatively common and distinctive for PSC. Similar findings have been described by others [293–295].

Chronic Budd–Chiari syndrome may present some findings similar to those of PSC. Hypertrophy of the caudate lobe, presence of regenerative nodules and fibrosis are present in both entities. However, in PSC the regenerative nodules are preferably present in the central portion of the liver parenchyma, commonly causing dilation of bile ducts. A more complete description of Budd–Chiari is in the subsection on liver vascular diseases.

Autoimmune hepatitis (AIH) is a necro-inflammatory chronic liver disease that has an unknown etiology. AIH is characterized serologically by the presence of non-organ and liver-specific autoantibodies and increased levels of transaminases and immunoglobulin G [296]. Histologic features of AIH are not specific and instead are common to other forms of chronic active hepatitis. A dense periportal lymphoplasmacytic inflammatory infiltrate, fibrosis, and lobular necrosis are frequent findings [2]. An overlap between AIH and other chronic liver diseases is reported, most commonly with PSC [297, 298]. The distinction of AIH from other autoimmune liver diseases, namely, PSC and PBC, is particu-

larly important since therapeutic modalities may differ [298, 299].

A prior study [300] reported on the MR appearance of AIH. The great majority of patients were women, with incidence from age 20 and older. Almost all (93%) patients with AIH had a reticular and/or confluent fibrosis shown on MRI. Reticular and/or confluent fibrosis both appear as low signal on short-TE out-of-phase images and show negligible early enhancement with gadolinium and moderate/intense enhancement on delayed images. Four categories were described, based on the thickness of the reticular fibrotic strands and on the liver contour nodularity, as follows: 1) mild when fibrous tissue has a thickness <2 mm and does not cause liver nodularity; 2) moderate when fibrous tissue has a thickness between 2 and 5 mm and causes slight liver nodularity; 3) severe when fibrous tissue has a thickness >5 mm and causes gross liver nodularity; and 4) confluent fibrosis, which has a localized, masslike configuration. A moderate reticular fibrosis was predominantly observed (44% of patients; 14 of 32) followed by mild fibrosis (34% of patients; 11 of 32). Confluent fibrosis most commonly occurred in *segment* 8 of the liver and was noted along with reticular fibrosis in 18% of patients (6/32) (fig. 2.190). Biliary ductal dilatation was reported in 12.5% of patients with AIH. None of the patients in this study had HCC. AIH was therefore shown to have a prominent pattern of liver fibrosis in the setting of livers with relatively normal contours. At disease onset, AIH is characterized by substantial inflammatory cell infiltration, which should be observed as intense patchy enhancement on hepatic arterial dominant-phase images. All patients in this study were already on treatment for AIH, so the expected appearance of early

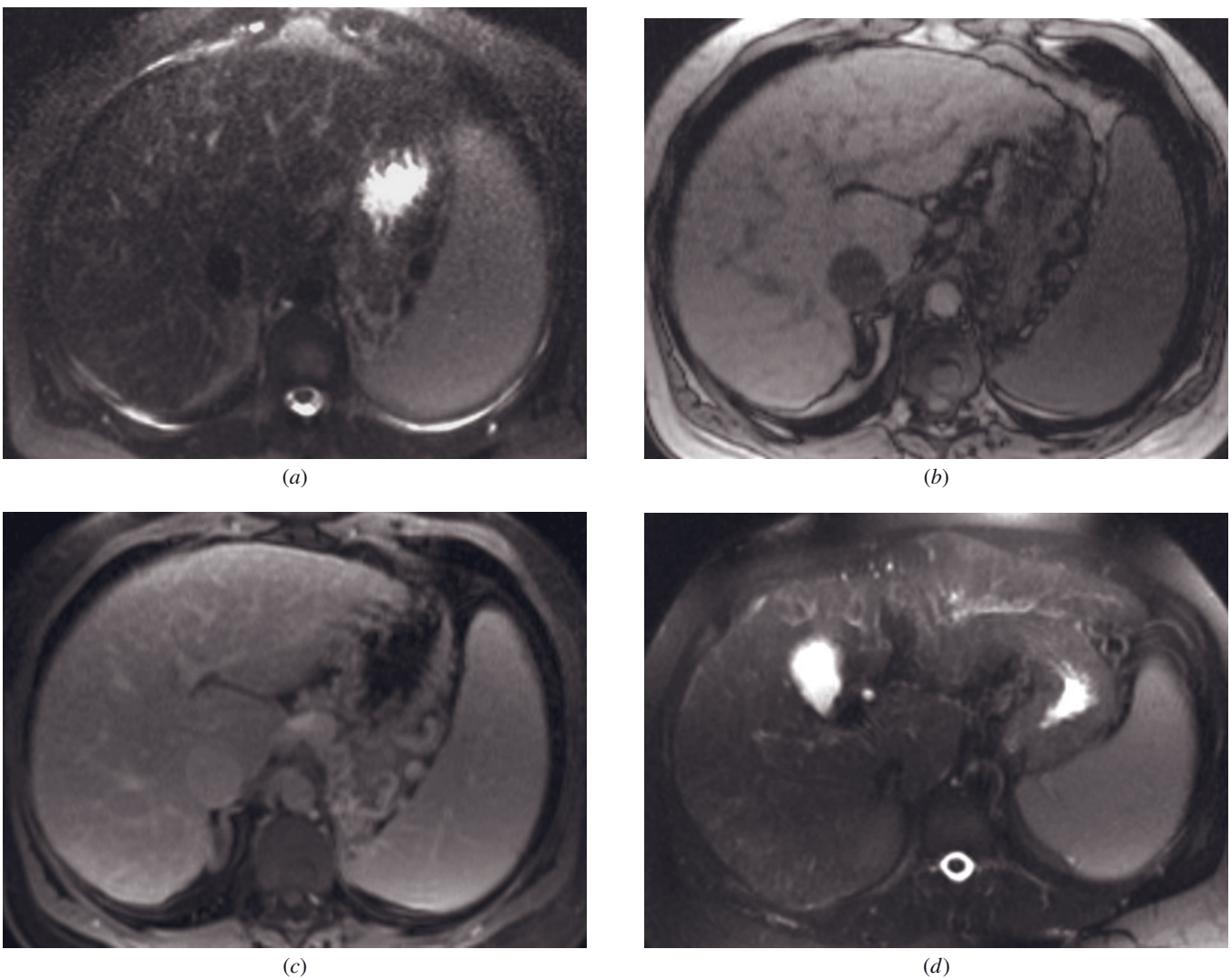

FIG. 2.190 Autoimmune hepatitis. T2-weighted SS-ETSE (*a*), out-of-phase SGE (*b*), and 90-s fat-suppressed postgadolinium SGE (*c*) images; T2-weighted SS-ETSE (*d*), out-of-phase SGE (*e*), and 90-s fat-suppressed postgadolinium SGE (*f*) images;

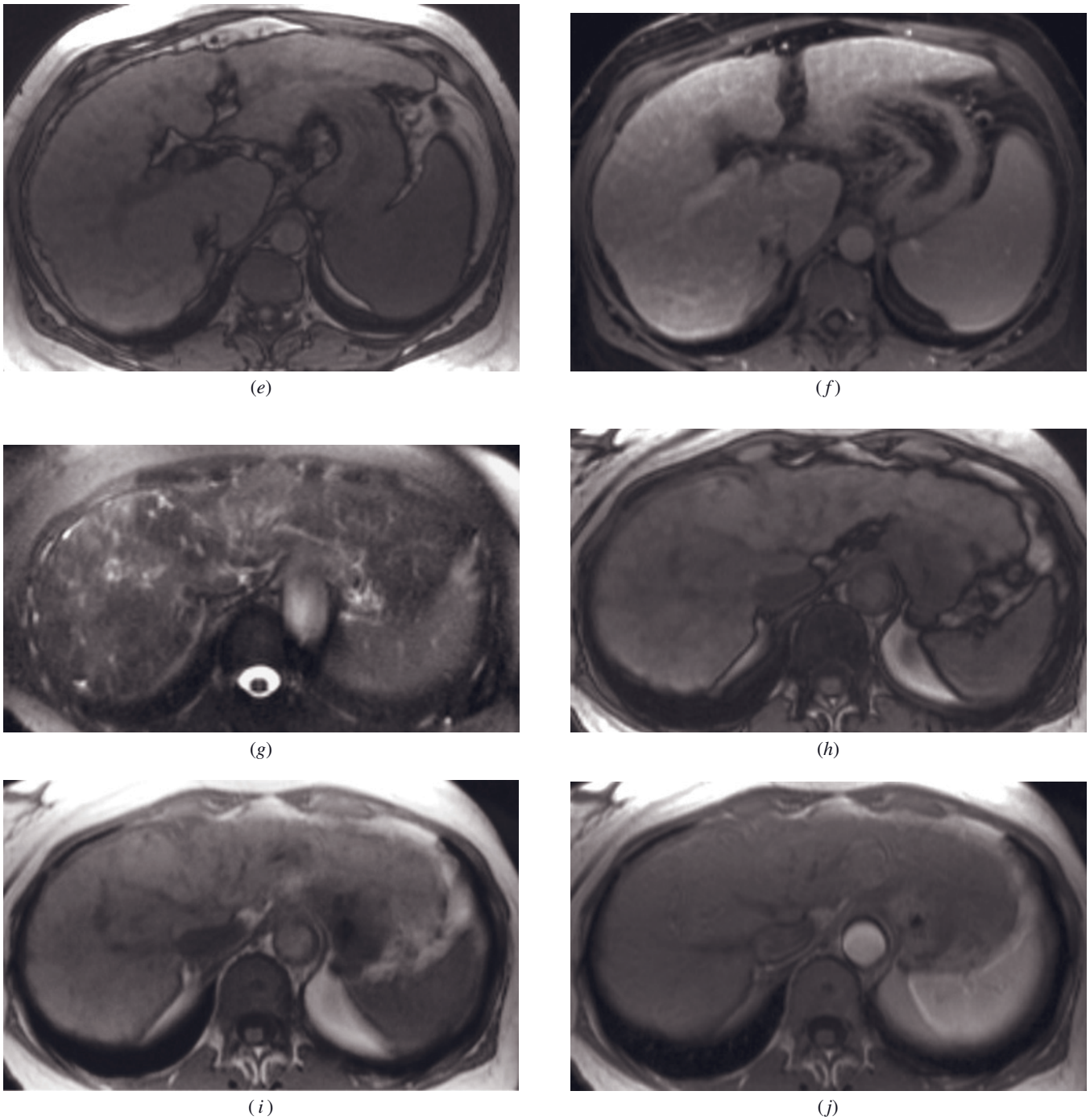

FIG. 2.190 (*Continued*) T2-weighted SS-ETSE (*g*), out-of-phase SGE (*h*), in-phase SGE (*i*), and immediate (*j*), 60-s (*k*) and 90-s (*l*) images in another patient demonstrate diffuse fibrosis that exhibits progressively intense enhancement over time. T2-weighted SS-ETSE fat-suppressed (*m*), SGE (*n*), and immediate (*o*) and 90-s fat-suppressed postgadolinium SGE (*p*) images in a patient with untreated AIH at presentation. Note the early patchy enhancement reflective of acute inflammatory disease. AIH is characterized by a prominent network of fibrosis even early in the course of disease (*d*, *f*). The hepatic changes are similar to PBC, and both AIH and PBC tend to have less architectural distortion than primary sclerosing cholangitis.

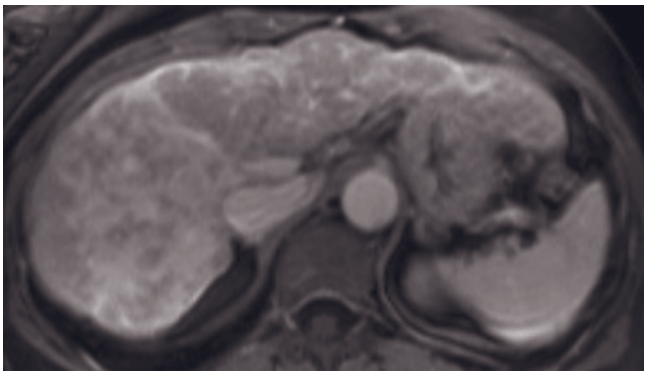

(*k*)

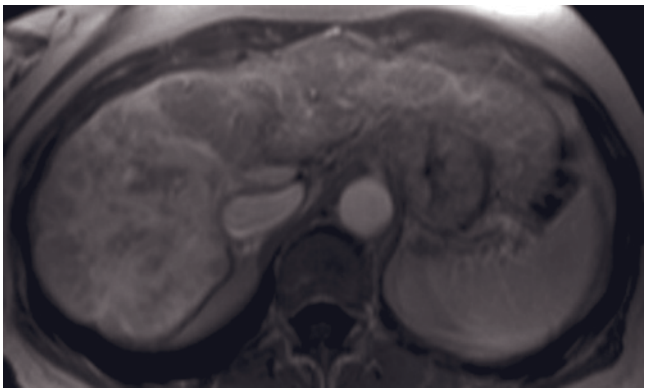

(*l*)

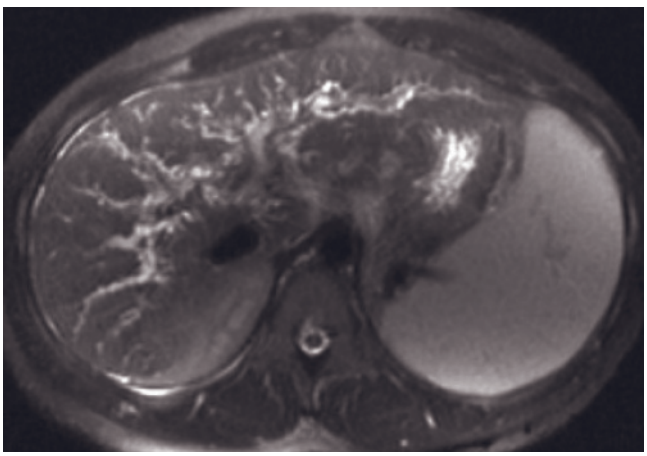

(*m*)

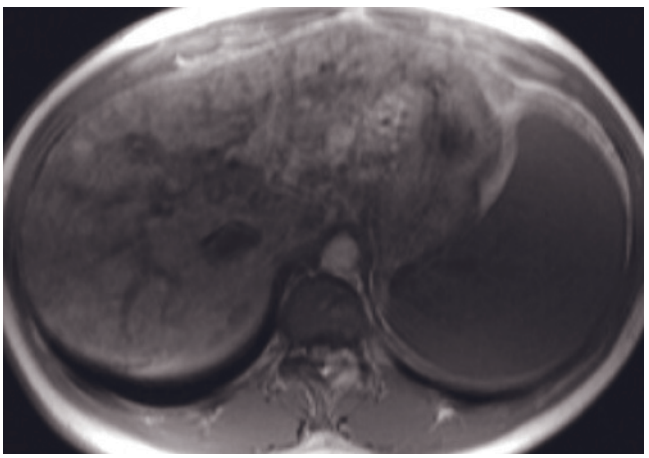

(*n*)

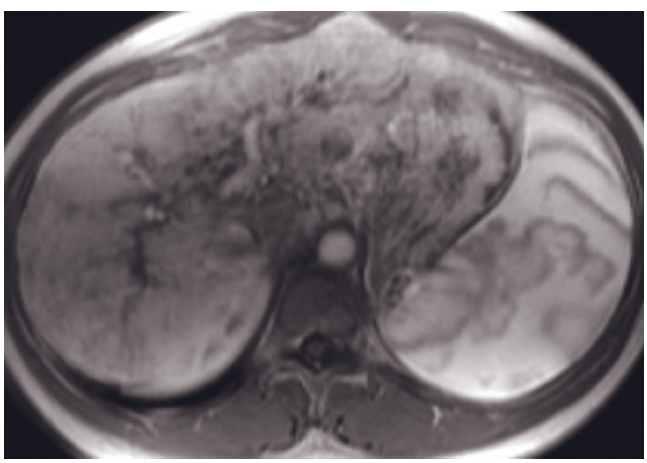

(*o*)

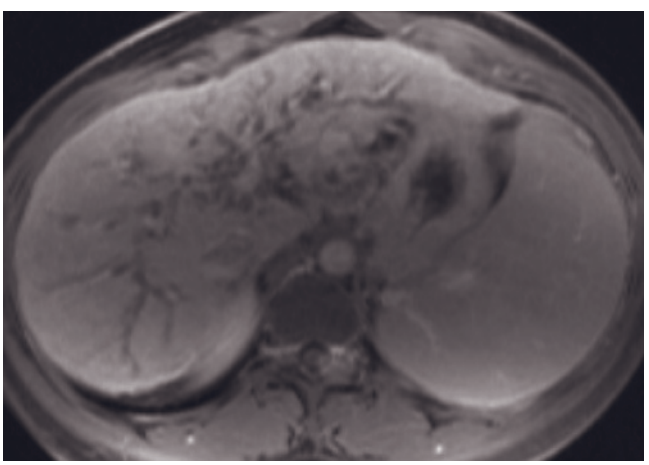

(*p*)

FIG. 2.190 (*Continued*)

intense patchy enhancement of untreated AIH was not observed in any of these patients. The correlation between imaging findings and MELD clinical score was not statistically significant. This again reflects that morphologic findings may not correlate with the severity of liver compromise.

Primary biliary cirrhosis (PBC) is a chronic progressive autoimmune liver disorder that causes the obliteration of the intrahepatic bile ducts, portal inflammation, fibrosis, and cirrhosis [301]. A few imaging studies describe the imaging appearance of PBC. A prior study [302] described the "periportal halo sign" in 43% (9/21)

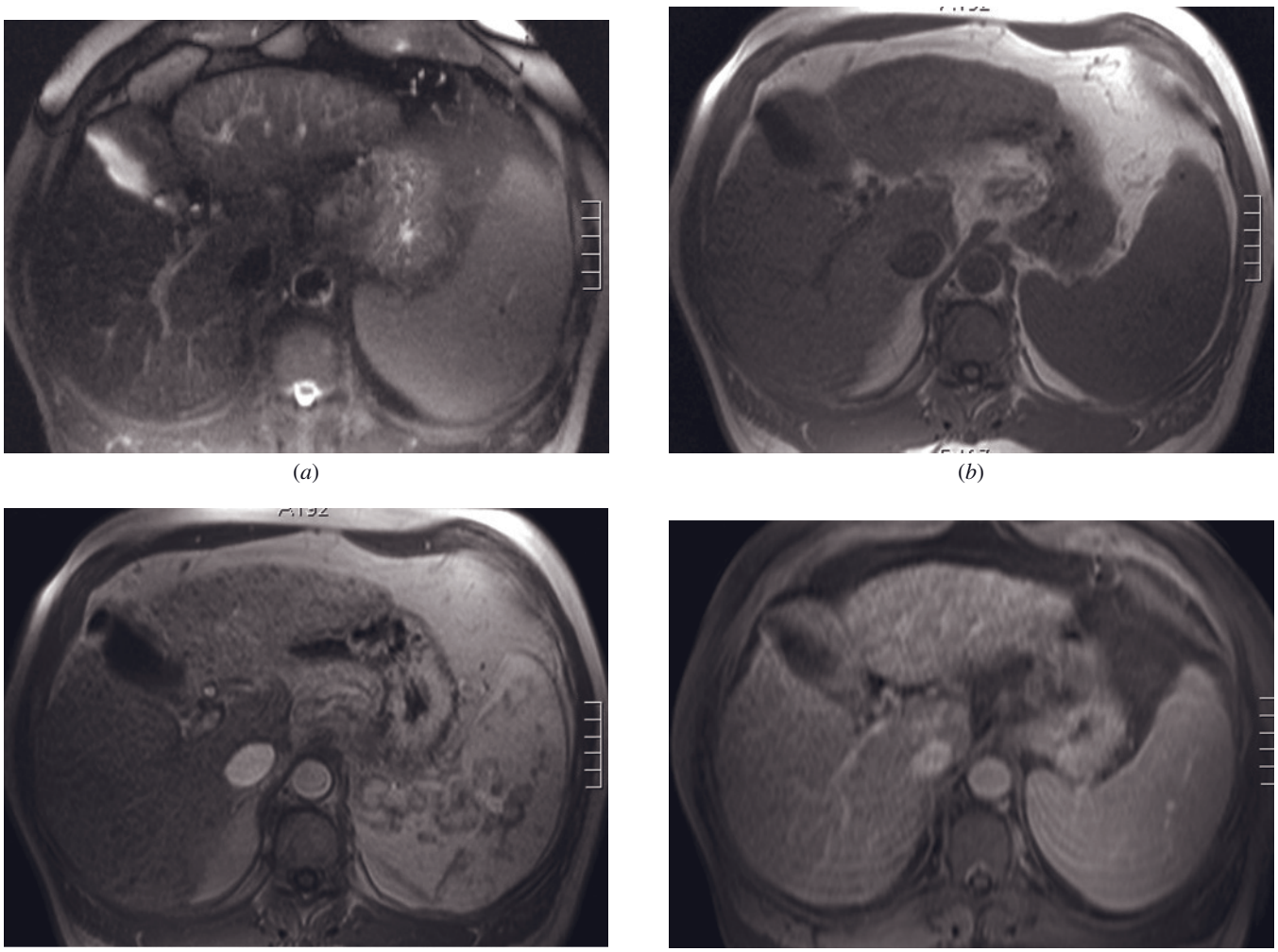

FIG. 2.191 Primary biliary cirrhosis (PBC). Fat-suppressed T2-weighted SS-ETSE (*a*), SGE (*b*), and immediate (*c*) and 90-s fat-suppressed (*d*) postgadolinium SGE images in a patient with PBC. The liver contains a fine network of fibrosis throughout, and has only mildly distorted morphology.

of patients with PBS, characterized by a hypointense rounded area surrounding the portal vein branches on both T2- and T1-weighted images. The authors attributed this finding to the presence of stellate, periportal hepatocellular parenchyma extension, surrounded by regenerative nodules. This finding was better appreciated on portal venous and interstitial phase. It may be that this appearance reflects a prominent pattern of fibrosis as also observed in AIH (fig. 2.191).

Overlap syndrome represents coexistence of more than one of the autoimmune conditions. MRI features can be helpful to determine the presence of the PSC overlap form. The presence of central regenerative nodules, peripheral atrophy, biliary duct beading, biliary dilation, in patients with laboratory evidence of AIH or PBC should raise suspicion for overlap syndrome (figs. 2.190 and 2.191) [301].

Genetic Diseases

Wilson Disease. Wilson disease is a rare autosomal recessive inherited disorder caused by copper overload in the liver and other organs [2]. The forms of liver disease associated with Wilson disease are highly variable and include fatty change, acute hepatitis, chronic active hepatitis, and cirrhosis [303]. Ultrasound, CT, and MR findings are nonspecific and reflect a full range of hepatic injury including fatty infiltration, acute hepatitis, chronic active hepatitis, and cirrhosis [303]. To date, no characteristic liver imaging finding has been established for Wilson disease (figs. 2.192 and 2.193).

α-1-Antitrypsin Deficiency. α-1-Antitrypsin deficiency is an autosomal recessive inherited disorder characterized by abnormally low serum levels of a major protease inhibitor. Hepatic syndromes are extremely

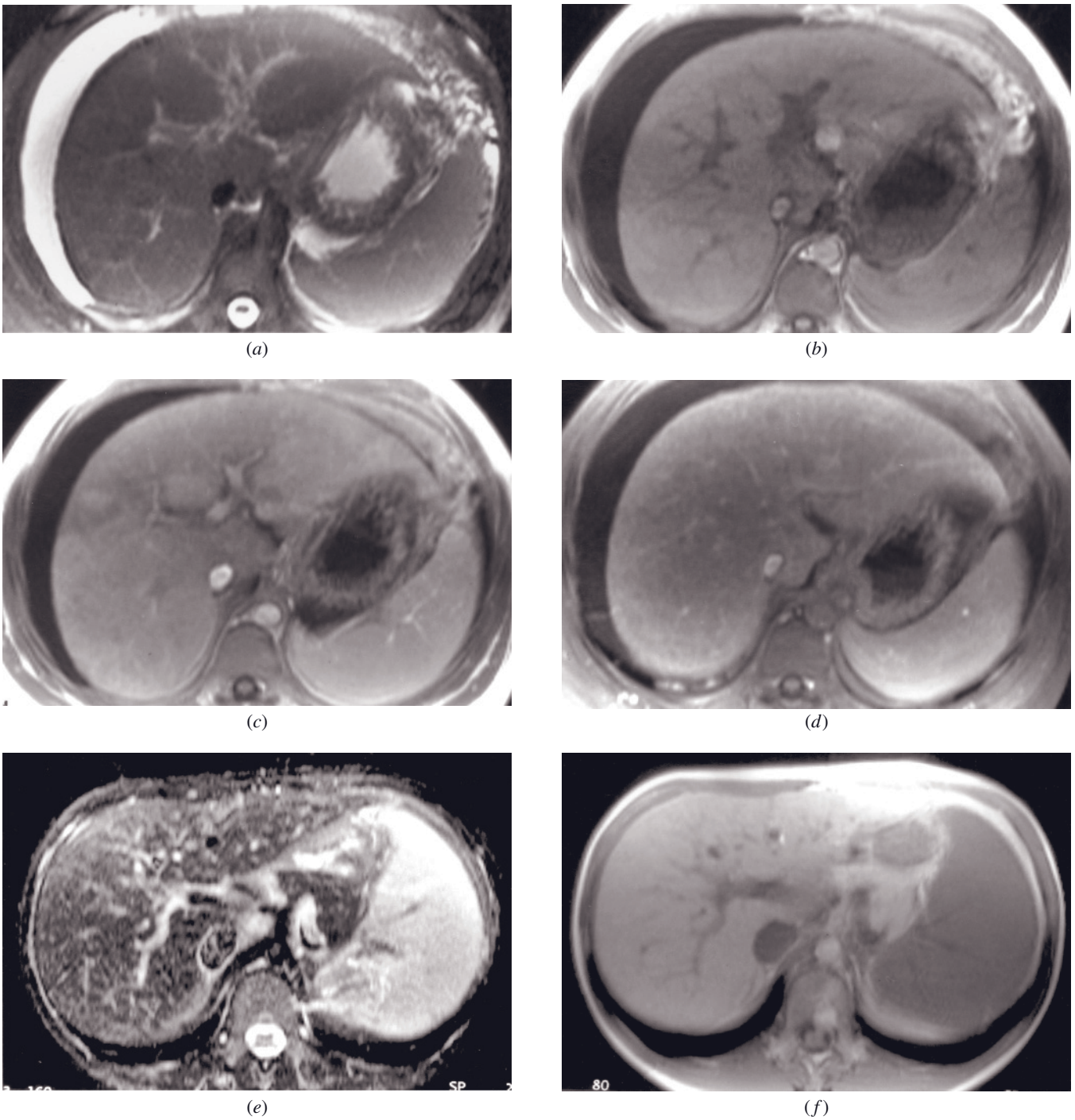

FIG. 2.192 Wilson disease. Echo-train STIR (*a*), SGE (*b*), and immediate (*c*) and 90-s fat-suppressed (*d*) postgadolinium SGE images in a patient with Wilson disease and acute presentation in fulminant liver failure. Early patchy enhancement (*c*) compatible with acute severe hepatitis and late linear stromal enhancement (*d*) are both present, consistent with acute on chronic hepatitis.

Echo-train STIR (*e*), SGE (*f*), out-of-phase SGE (*g*), and immediate (*h*) and 90-s fat-suppressed (*i*) postgadolinium SGE images in a second patient. There are multiple regenerative nodules throughout the liver parenchyma, which are best shown on the out-of-phase image (*g*) because of drop in signal of background fatty liver. Splenomegaly is also present.

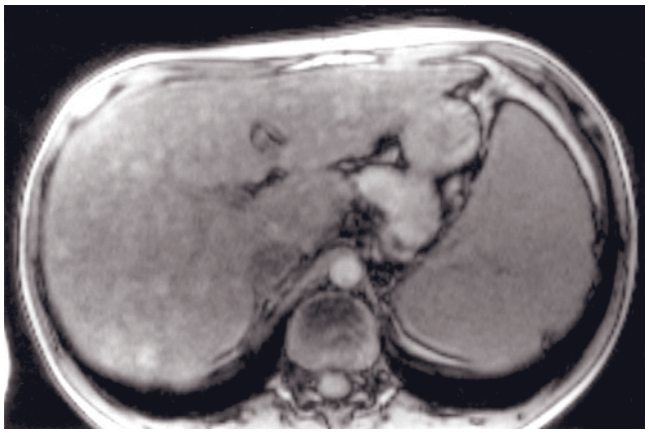

(*g*)

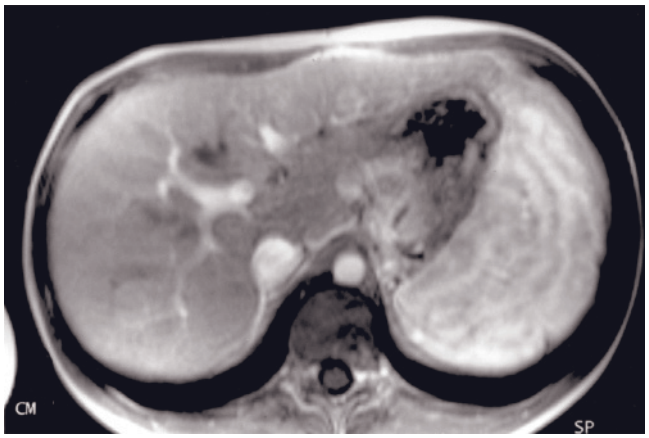

(*h*)

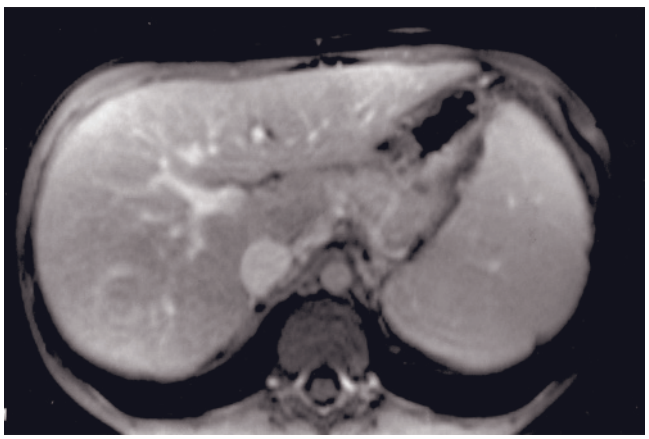

(*i*)

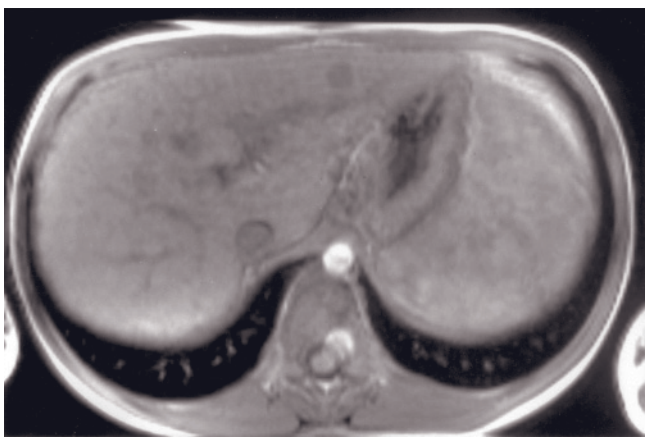

(*j*)

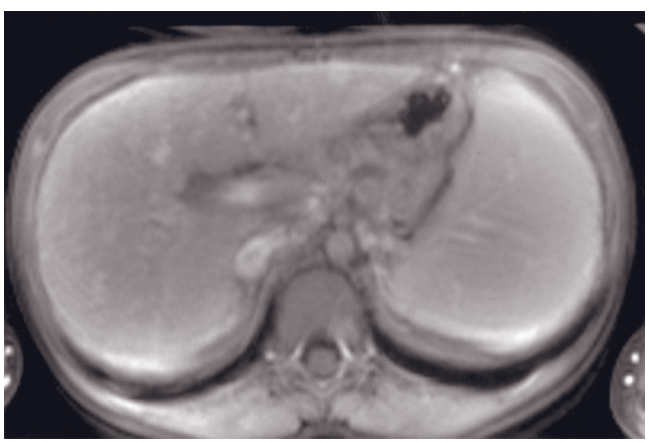

(*k*)

FIG. 2.192 (*Continued*) Immediate (*j*) and 90-s fat-suppressed (*k*) postgadolinium SGE images in a third patient with Wilson disease and changes of cirrhosis, including thin reticular fibrous stroma, perigastric varices, and splenomegaly.

The MR findings of Wilson disease do not at present appear to show characteristic features that distinguish it from other forms of chronic hepatic disease.

varied and range from neonatal hepatitis to childhood cirrhosis or cirrhosis late in life when liver fibrosis is advanced [2]. Although no distinctive features of cirrhosis are at present recognized for α-1-antitrypsin deficience. The coexistance of cirrhosis with pulmonary fibrosis should suggest the diagnosis.

Nonalcoholic Fatty Liver Disease. As obesity and type 2 diabetes increase to epidemic proportions, nonalcoholic fatty liver disease (NAFLD) has become the subject of intensified focus and diagnostic refinement. NAFLD has been recognized to be one of the most common causes of chronic liver disease in the U.S. [304]. Emerging evidence cites NAFLD as the most common cause of crytogenic cirrhosis [305]. Cirrhosis related to obesity and NAFLD are risk factors for HCC. The pathologic features of NAFLD are similar to alcohol-induced liver damage and traverse the spectrum of

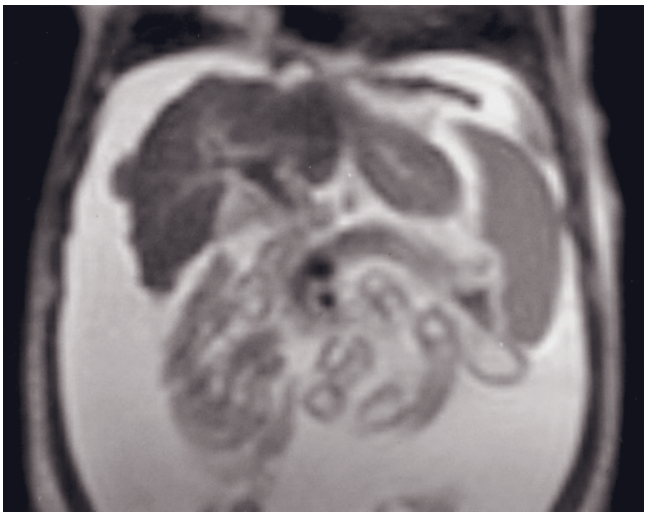

(*a*)

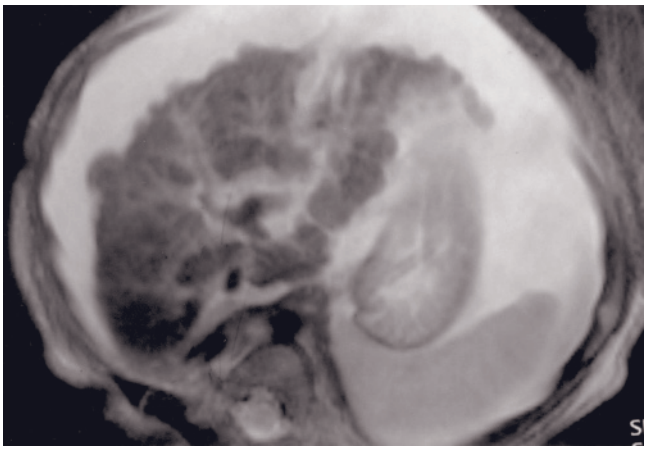

(*b*)

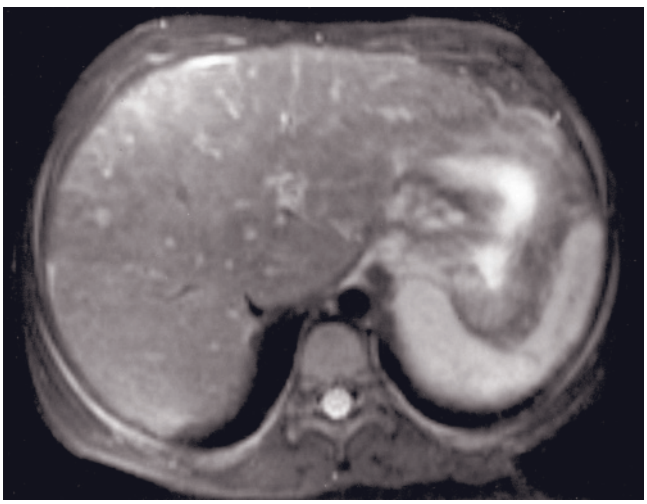

(*c*)

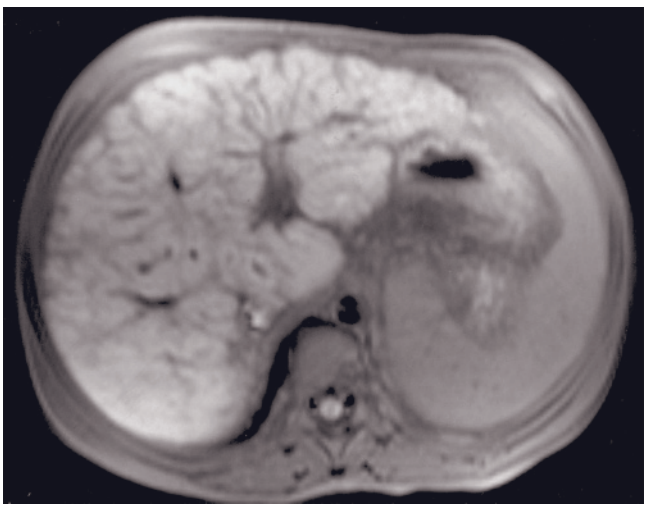

(*d*)

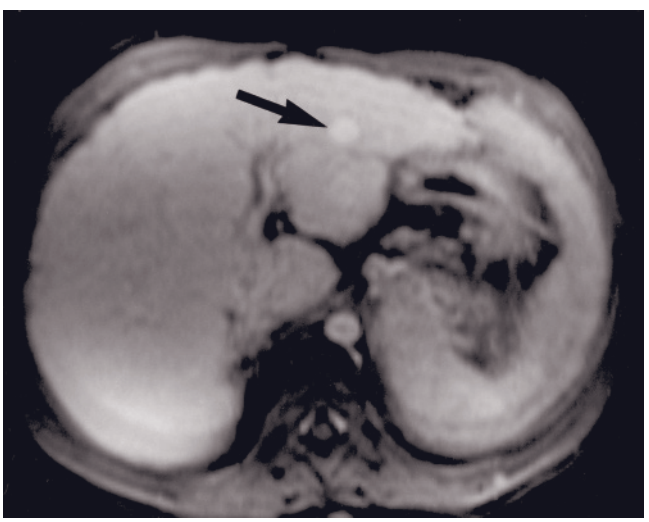

(*e*)

FIG. 2.193 Cirrhosis in pediatric patients. Coronal (*a*) and transverse (*b*) T2-weighted SS-ETSE images in a 1-month-old boy. The liver is small and markedly nodular in contour, consistent with cirrhosis. Note the massive ascites and periportal edema.

T2-weighted fat-suppressed SS-ETSE (*c*), T1-weighted fat-suppressed SE (*d*), and 90-s fat-suppressed (*e*) postgadolinium SGE images in a second patient, a 6-year-old who has a history of severe biliary fibrosis. The liver exhibits extensive fibrotic stroma, shown as low-signal linear structures on the T1-weighted fat-suppressed image (*d*). Mirror artifact of the aorta (arrow, *e*) in the left lobe should not be confused for a mass lesion.

changes, ranging from simple hepatic steatosis (fatty liver) at the most clinically benign, to cirrhosis at the opposite extreme. Nonalcoholic steatohepatitis (NASH) occupies a middle position in the range of NAFLD and represents an intermediate stage of fatty liver damage [306]. NASH is characterized by a constellation of histopathologic features including steatosis, hepatocyte degeneration, inflammation, and fibrosis. A recent study [307] demonstrates a significant correlation between histopathology grades of steatosis and degree of fibrosis in patients with underlying NASH and MRI findings, namely, steatosis and fibrosis. However, no significant correlation was demonstrated between MRI features and Mayo End-stage Liver Disease (MELD) score. It has been estimated that 10–30% of patients with NAFLD (steatosis or NASH) will develop cirrhosis during the ensuing decade [306]. The absence of steatosis in advanced cirrhosis as a result of NASH is well recognized, and this phenomenon is borne out in MR imaging (fig. 2.194).

From a clinical perspective, there are no laboratory tests that can reliably distinguish steatosis from steatohepatitis or cirrhosis [308]. Although the qualitative and quantitative measurement of hepatic steatosis is accurately assessed by chemical-shift MR imaging [309], there are to date no characteristic imaging findings that point to a specific assessment of NASH [310].

Viral Hepatitis. The term "viral hepatitis" is generally reserved for infection of the liver caused by a small group of hepatotropic viruses. Although agents such as Epstein–Barr virus and cytomegalovirus may produce liver lesions, these are usually a part of a systemic infection in which the liver is only one of several

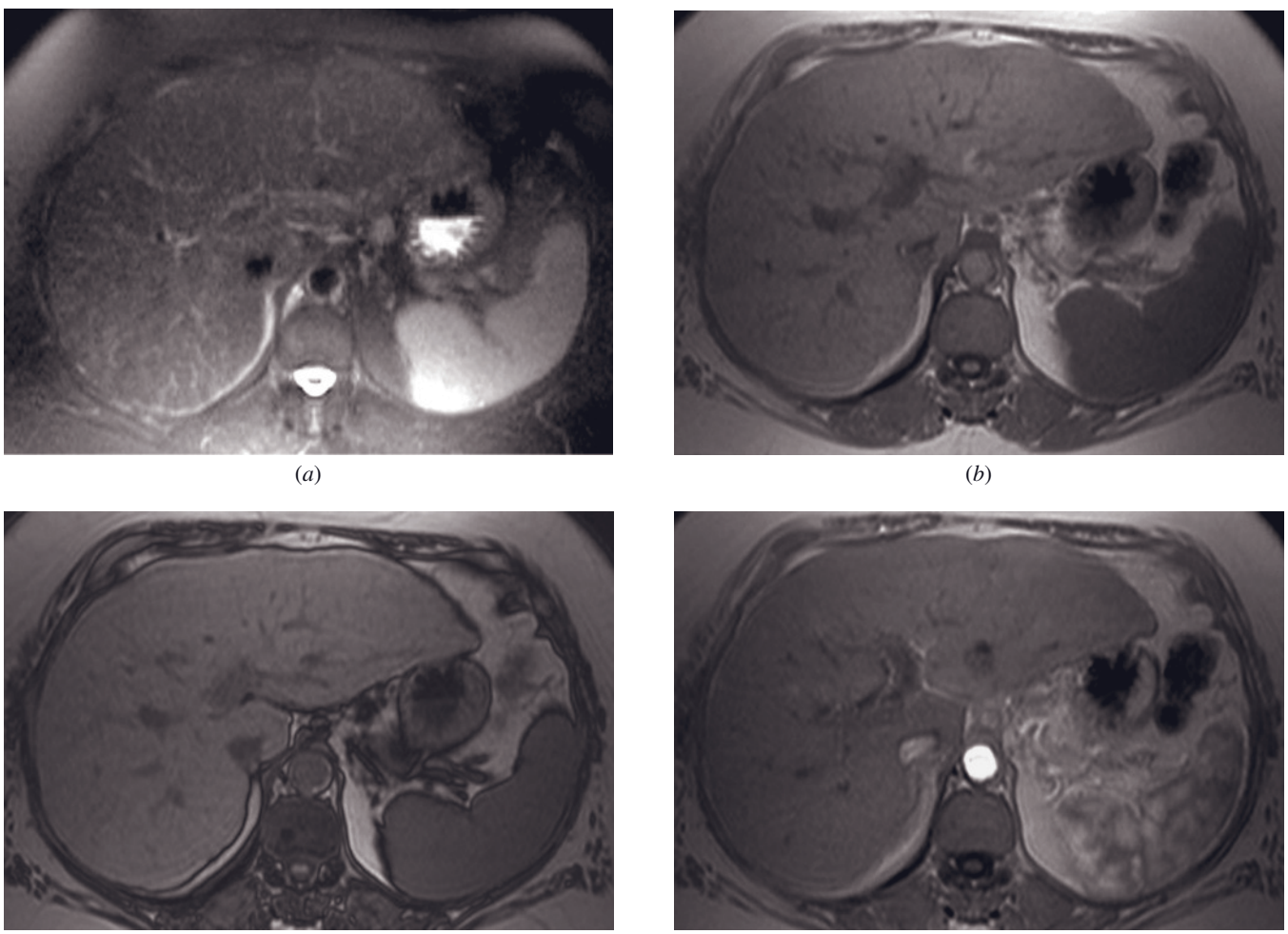

FIG. 2.194 Nonalcoholic steatohepatitis. T2-weighted SS-ETSE (*a*), SGE (*b*), out-of-phase SGE (*c*), and immediate (*d*) and 90-s fat-suppressed (*e*) postgadolinium SGE images. The liver is enlarged and shows a higher signal intensity than normal on T1-weighted image (*b*), which converges to the signal intensity of the spleen on out-of-phase image (*c*) suggestive of mild fatty infiltration. On early-phase image, (*d*) there are some patchy areas of enhancement that become homogeneous on late-phase image (*e*), reflecting acute on chronic inflammation. Histopathology was consistent with NASH.

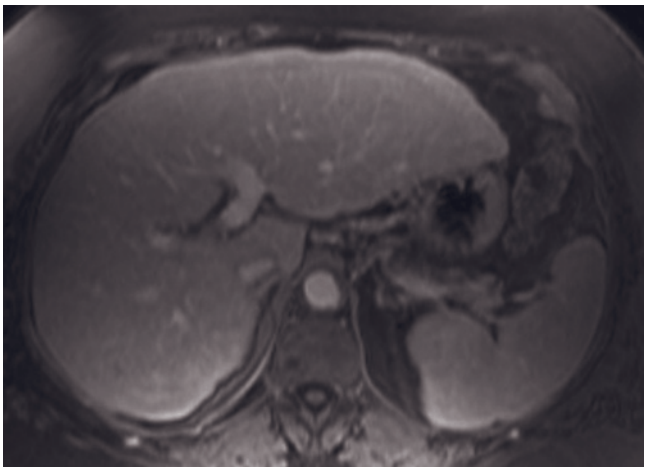

(*e*)

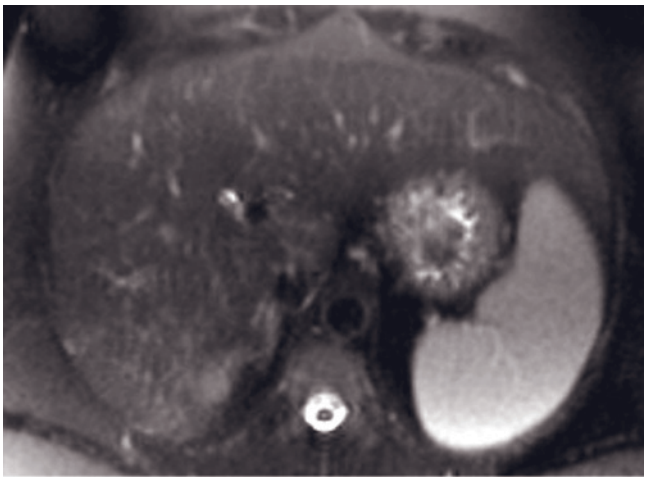

(*f*)

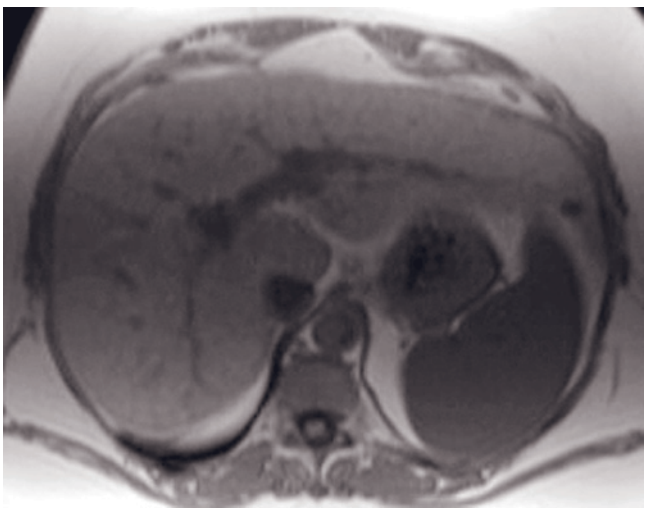

(*g*)

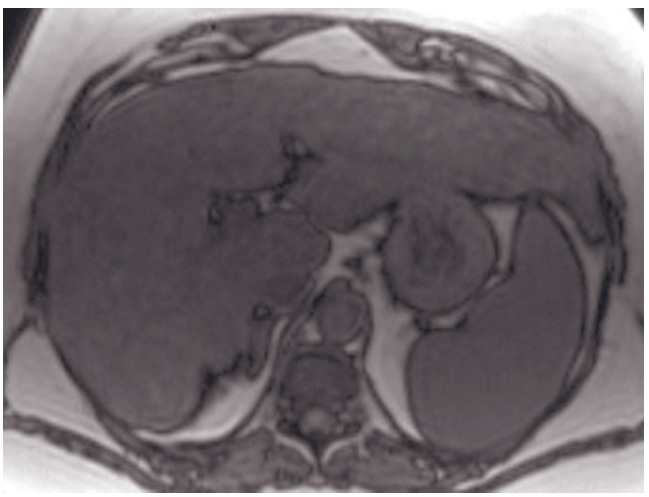

(*h*)

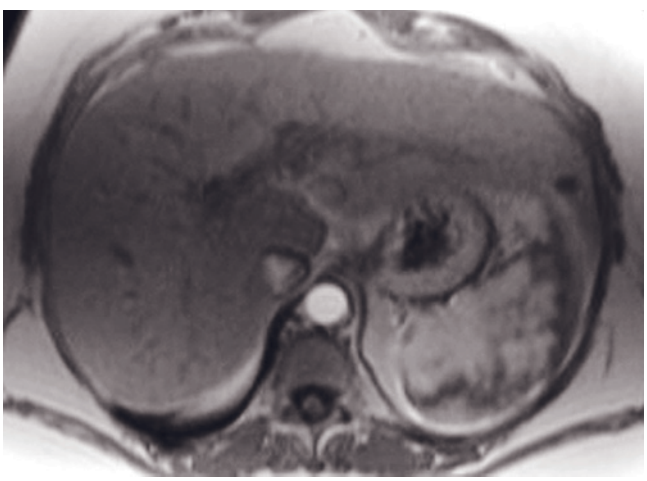

(*i*)

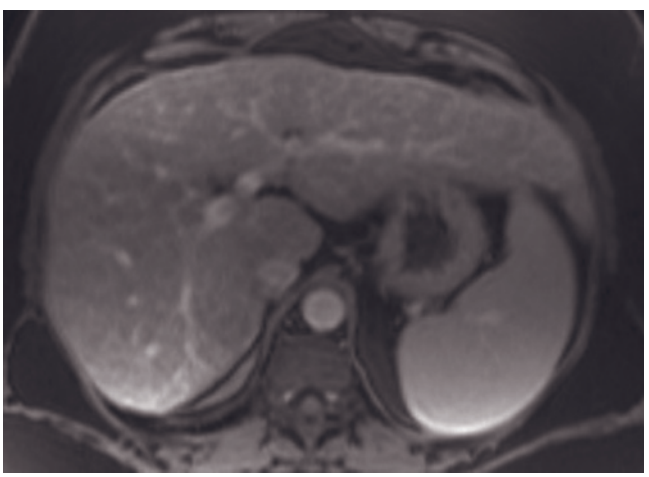

(*j*)

FIG. 2.194 (*Continued*) T2-weighted SS-ETSE (*f*), SGE (*g*), out-of-phase SGE (*h*), and immediate (*i*) and 90-s fat-suppressed (*j*) postgadolinium SGE images in a second patient, who exhibits findings of fatty liver comparing in-phase (*g*) and out-of-phase (*h*) images. Additionally, strands of fibrosis are present, well demonstrated as enhancing reticular structures on late-phase images (*j*). Histopathology was consistent with NASH.

organs or systems involved. Primary viral infection of the liver in the U.S. is caused most commonly by one of three hepatotropic viruses: hepatitis A (HAV), hepatitis B (HBV), and hepatitis C (HCV) [311].

Acute hepatitis is diagnosed by clinical and serologic studies. The major histologic findings in acute viral hepatitis are focal hepatocyte necrosis, inflammatory infiltrates, and evidence of hepatocyte regeneration [2, 3]. Imaging studies are generally not performed unless the clinical picture is complicated. Acute hepatitis may result in heterogeneous hepatic signal intensity, which is most apparent on T2-weighted images and immediate postgadolinium images. Periportal edema may be identified (fig. 2.195).

HBV is a double-stranded DNA virus from the hepadnavirus family that has several genotypes and serotypes capable of causing chronic disease. Two billion people worldwide, or one-third of the world's population, are infected with HBV. Of the 350 million individuals living with chronic HBV, 15-25% risk dying from HBV-related chronic liver disease, including chronic hepatitis, cirrhosis, and hepatocellular carcinoma. In the U.S., 1.25 million people have chronic HBV infection, resulting in more than 5000 deaths each year. Patients with HBV have an increased risk of developing HCC even in the precirrhotic hepatitis phase, when the underlying liver often looks morphologically normal by imaging studies (fig 2.196) [311].

HCV is an RNA virus from the flavivirus family with several known genotypes. The genetic heterogeneity of HCV has important implications for diagnosis, pathogenesis, and treatment. For example, the rapid mutation rate of HCV in opposition to the host immune response renders it a difficult virus to eliminate [311]. HCV infects up to 350 million people worldwide and is currently the leading indication for orthotopic liver transplantation in the U.S. [312]. While up to 50% of individuals clear HCV viremia after acute infection, most people develop persistent infection with chronic hepatitis (fig. 2.197) [312]. Serious sequelae include cirrhosis and hepatocellular carcinoma [313].

Chronic hepatitis may be defined as symptomatic, biochemical, or serologic evidence of continuing inflammation of the liver without improvement for at least 6 months. The microscopic changes of chronic viral hepatitis show chronic inflammation that often extends out from the portal tracts, spilling into the adjacent parenchyma with associated necrosis of hepatocytes. Progressive fibrosis may lead to fully developed cirrhosis [3, 314]. In patients with chronic viral hepatitis, imaging studies are more commonly obtained, usually to detect the presence of cirrhosis or HCC. Focal inflammatory changes or fibrosis may develop in chronic active hepatitis, resulting in diffuse or regional areas of high signal intensity on T2-weighted images and heterogeneous enhancement after contrast on gradient-echo images, most often appreciated as linear stromal enhancement on late fat-suppressed images (figs. 2.198 and 2.199) [315, 316]. On T2-weighted images, chronic active hepatitis often has periportal high signal intensity, corresponding to inflammation, enlarged lymph nodes, or both (fig. 2.200) [317]. This is a nonspecific finding observed in a number of hepatobiliary and pancreatic diseases [286]. A distinctive feature of HCV chronic liver disease, compared to other chronic diseases, including HBV, is prominent porta hepatis lymph nodes. Nodes measuring 2 cm and larger are common in HCV chronic liver disease.

Radiation-Induced Hepatitis

The liver may be included in radiation portals for a variety of malignancies, metastases in adjacent vertebra, or pancreatic ductal adenocarcinoma. Edema may develop within 6 months of radiation injury. Edema appears as increase signal intensity on T2-weighted images and decreased signal intensity on T1-weighted images (fig. 2.201) [318, 319]. Fat is usually decreased within the radiation portal in patients with fatty liver [320, 321]. This reflects decreased delivery of triglycerides due to diminished portal flow. Increased enhancement is apparent on delayed postgadolinium gradient-echo images in radiation-damaged liver. Increased enhancement is more conspicuous when fat suppression techniques are used (see fig. 2.201). This increased enhancement is related to leaky capillaries in early radiation injury and represents granulation tissue in late injury.

Cirrhosis

A concise definition of cirrhosis is "a diffuse process characterized by fibrosis and a conversion of normal architecture into structurally abnormal nodules" [322]. Cirrhosis is a stage in the evolution of many chronic liver diseases including viral infections, alcohol abuse, hemochromatosis, autoimmune disease, Wilson disease, and primary sclerosing cholangitis. The most common underlying causes in North America include viral hepatitis and alcohol abuse [323].

From a clinicopathologic perspective, cirrhosis is not a static phenomenon but a dynamic process that runs the gamut of inflammation, cell injury and death, fibrosis, and regeneration. Pathologic gross inspection of cirrhotic livers generally shows two types of patterns: 1) micronodular, in which parenchymal nodules are small (<3-mm diameter) and separated by thin fibrous septa, and 2), macronodular in which parenchymal nodules are large (>3 mm) and separated by fibrous septa, sometimes reaching proportions of large scars. Because of the underlying pathophysiology of the disease, the conversion from micro- to macronodular cirrhosis is considered to be a general phenomenon. The Copenhagen Study Group for Liver Disease studied 156 cirrhotic patients and observed a conversion ratio

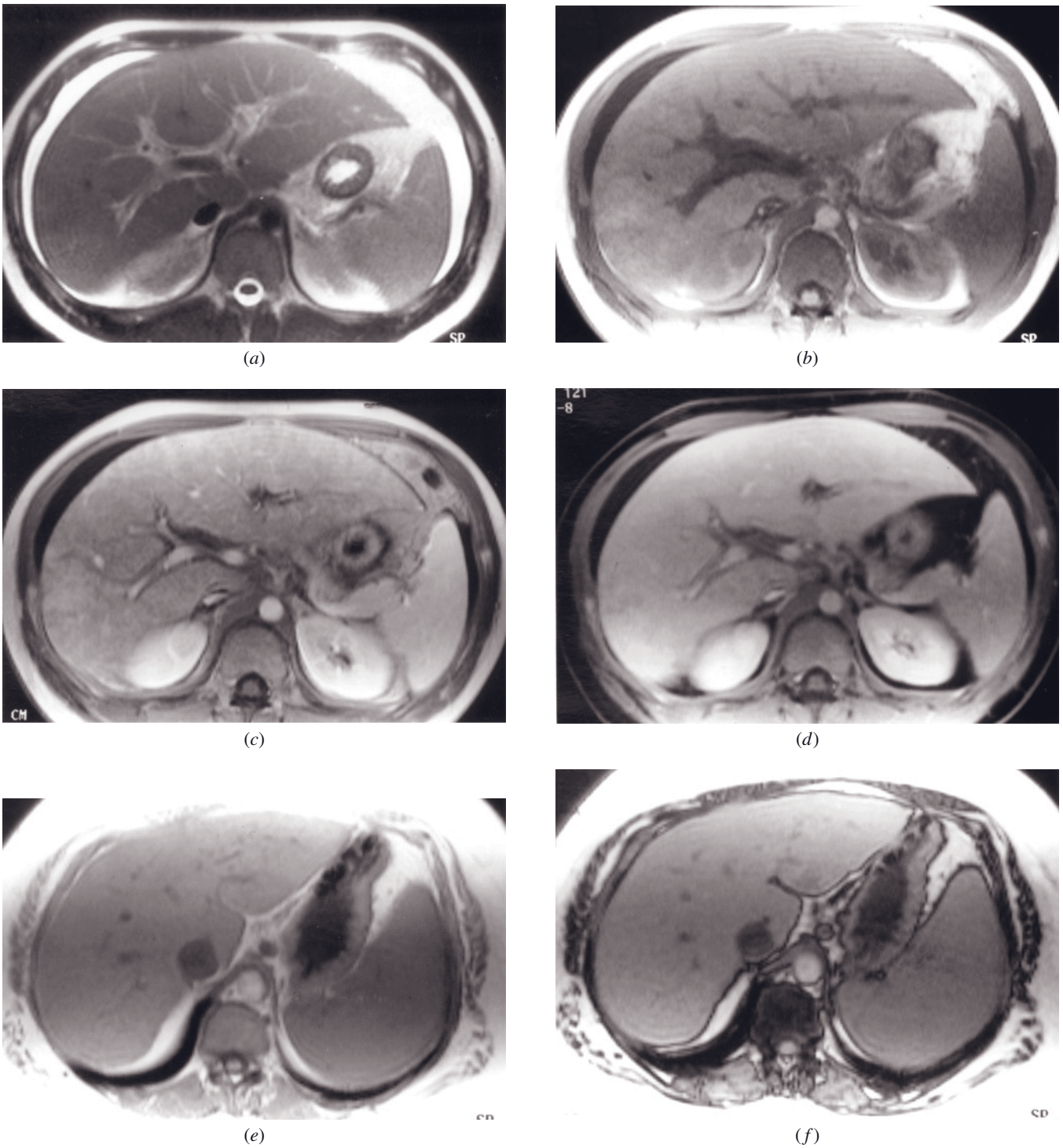

FIG. 2.195 Acute hepatitis. T2-weighted SS-ETSE (*a*), SGE (*b*), immediate (*c*) and 90-s fat-suppressed (*d*) postgadolinium SGE images in a patient with a history of leukemia. The liver is enlarged and demonstrates mild heterogeneous signal on both T2-weighted (*a*) and T1-weighted (*b*) images. On early-phase image (*c*), there is a transient heterogeneous intense patchy enhancement. The liver becomes more uniform in signal intensity on the late images (*d*). Periportal edema is present, which appears as high signal intensity on T2-weighted image (*a*) and does not enhance on postgadolinium images (*c*, *d*). Moderately large volume ascites is shown.

SGE (*e*), out-of-phase SGE (*f*), and immediate (*g*) and 90-s fat-suppressed (*h*) postgadolinium SGE images in a second patient. The liver is unremarkable in signal intensity on T1-weighted image (*e*), with signal intensity of liver and spleen becoming more comparable (converging) on the shorter TE out-of-phase sequence. This appearance of subtle loss of signal of the liver is consistent with mild fat infiltration. There are multiple patchy regions of enhancement after administration of contrast (*g*) throughout the liver consistent with acute on chronic hepatitis.

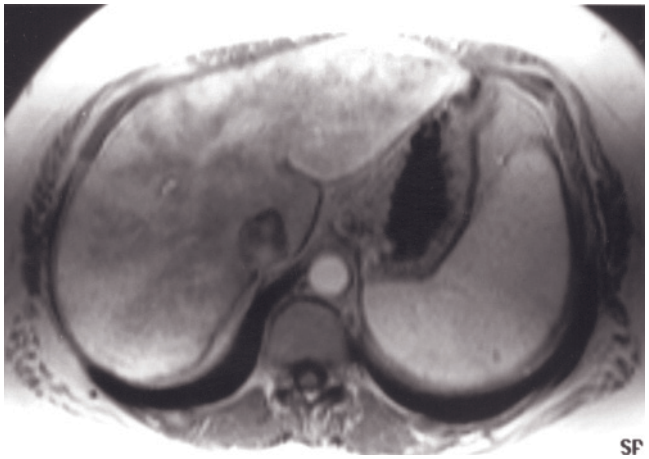

(*g*)

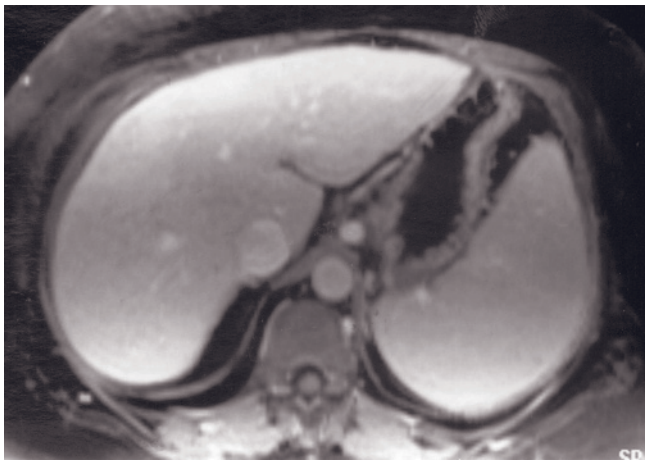

(*h*)

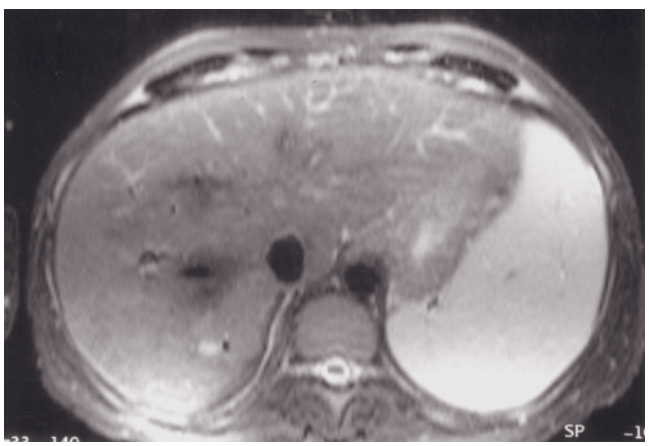

(*i*)

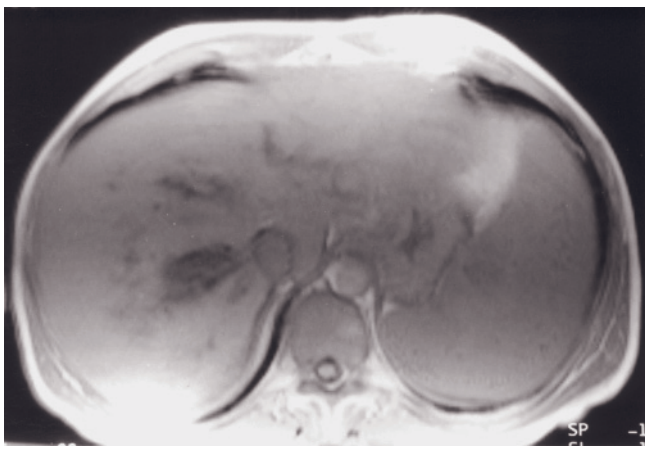

(*j*)

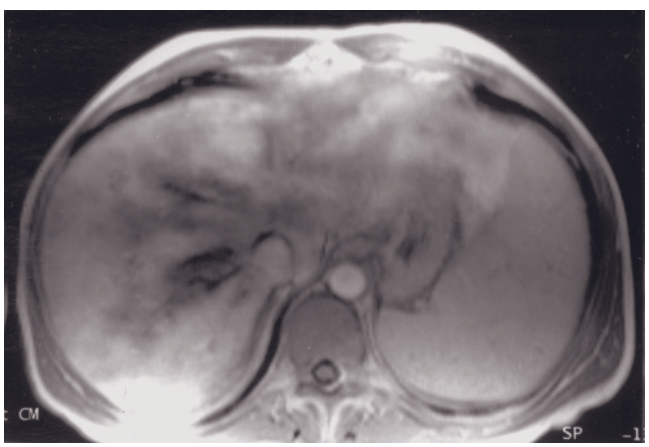

(*k*)

FIG. 2.195 (*Continued*) T2-weighted SS-ETSE (*i*), SGE (*j*), and immediate (*k*) and 90-s fat-suppressed (*l*) postgadolinium SGE images in a third patient. The liver demonstrates a markedly early heterogeneous enhancement pattern with low signal in a perihepatic vein distribution (*k*). Low signal intensity in perihepatic vein distribution is also appreciated on the T2-weighted image (*i*).

Coronal T2-weighted SS-ETSE (*m*), SGE (*n*), and immediate (*o*) and 90-s fat-suppressed (*p*) SGE images in a fourth patient. The liver is enlarged and exhibits heterogeneous enhancement on early-phase images (*o*) more evident in the liver periphery. On late-phase images (*p*) the liver demonstrates more homogeneous enhancement.

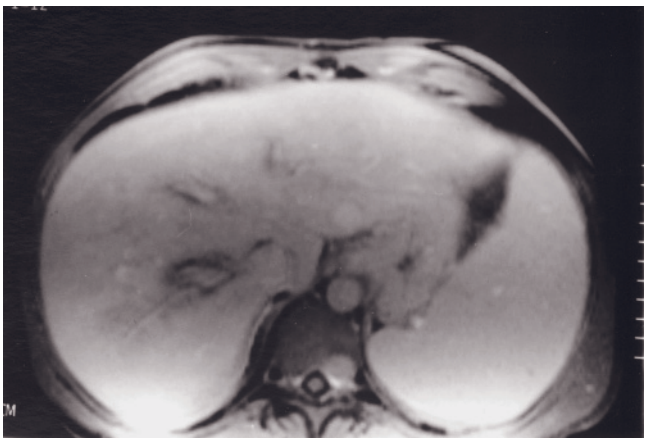

(*l*)

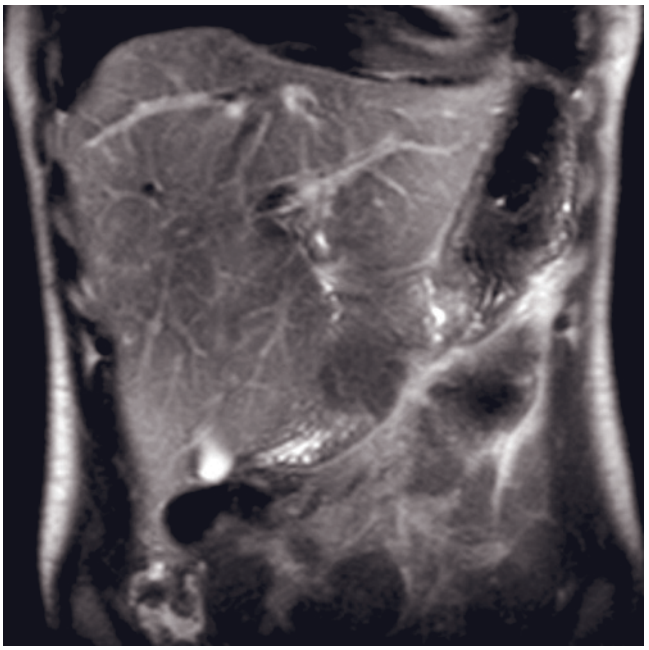

(*m*)

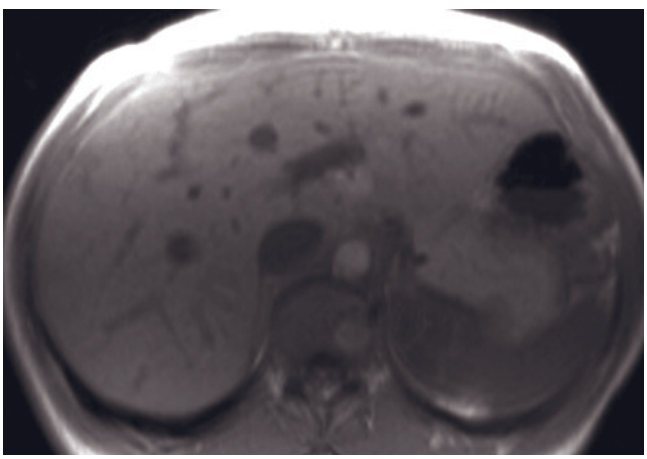

(*n*)

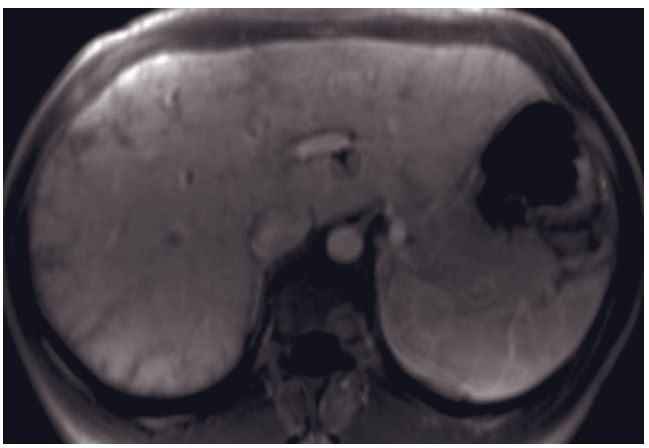

(*o*)

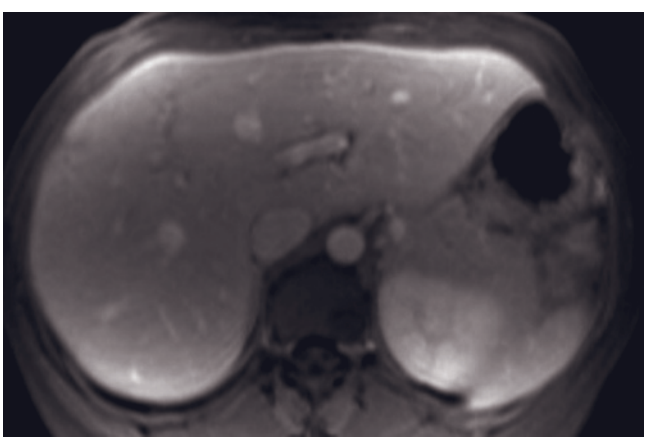

(*p*)

FIG. 2.195 (*Continued*)

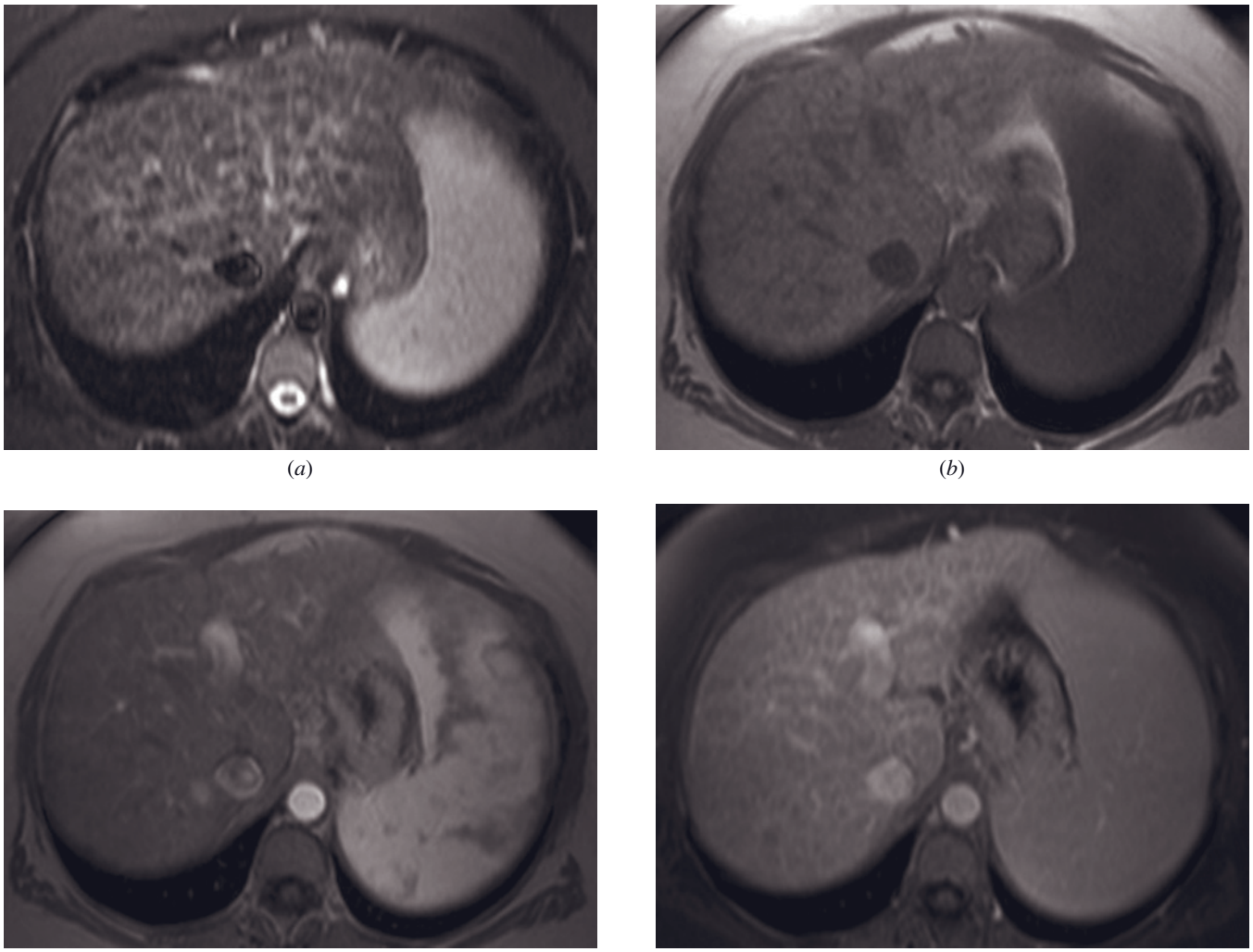

FIG. 2.196 Hepatitis B. T2-weighted fat-suppressed SS-ETSE (*a*), SGE (*b*), and immediate (*c*) and 90-s fat-suppressed (*d*) SGE images in a patient with hepatitis B. In this patient with longstanding disease, the liver is mildly reduced in size and has an irregular contour, with extensive fibrosis on late-phase images (*d*).

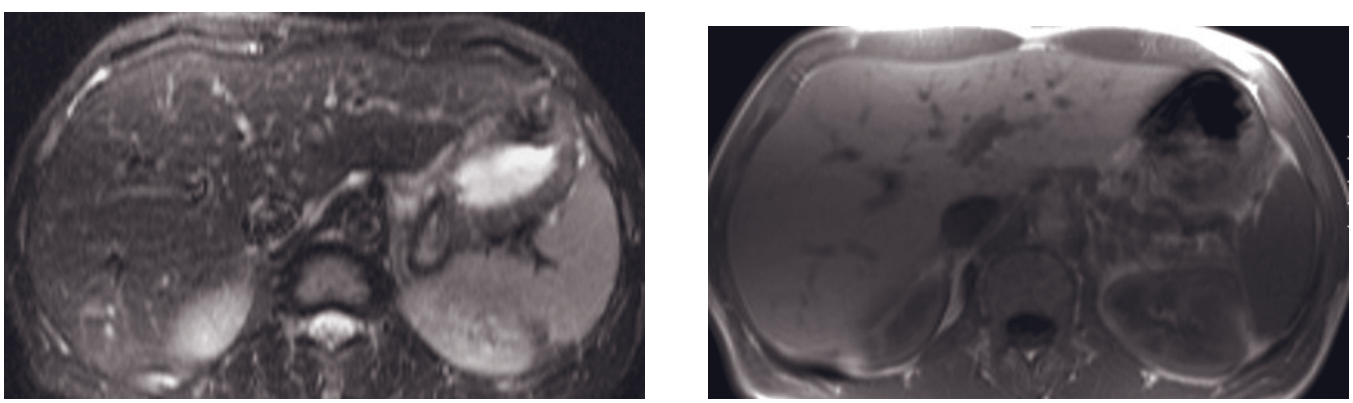

FIG. 2.197 Hepatitis C. T2-weighted SS-ETSE (*a*), SGE (*b*), and immediate (*c*) and 90-s fat-suppressed (*d*) images; T2-weighted

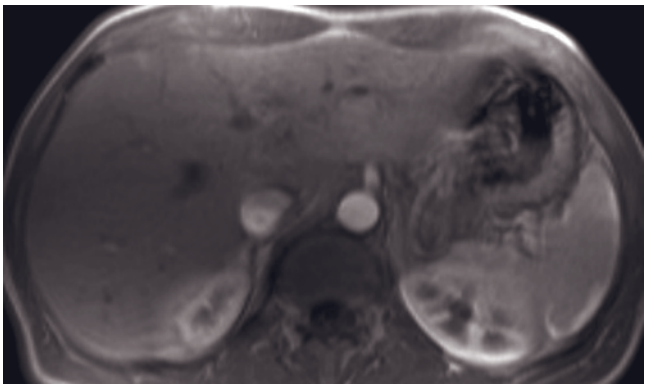

(*c*)

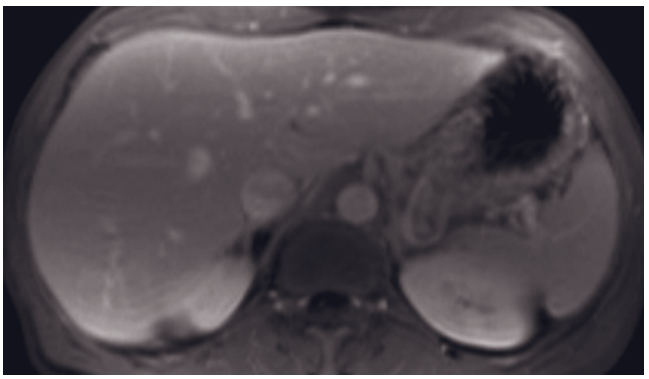

(*d*)

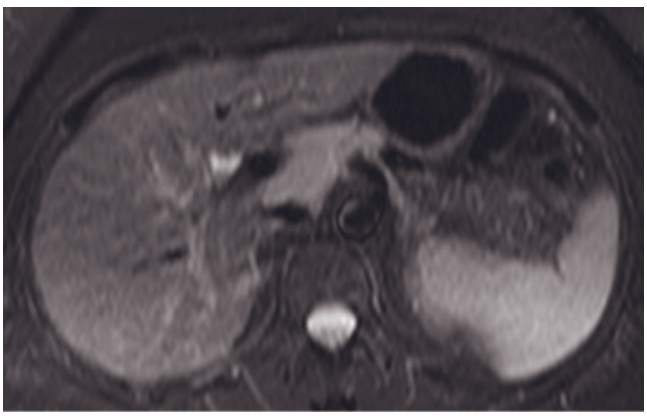

(*e*)

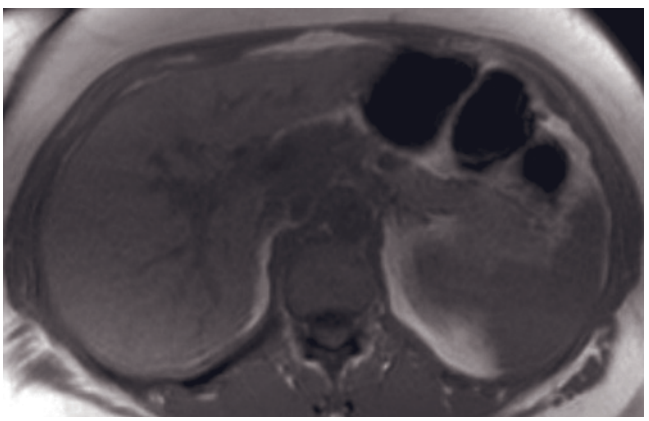

(*f*)

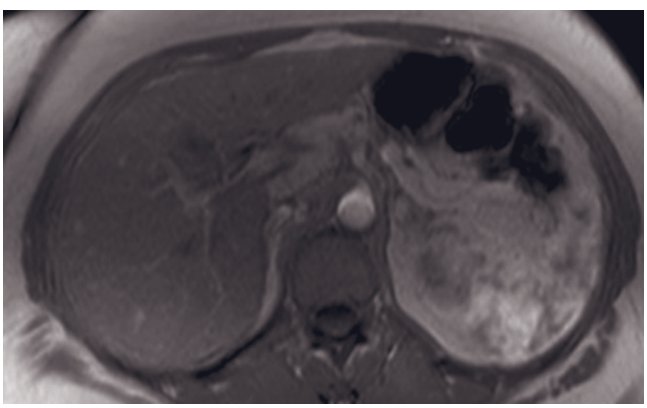

(*g*)

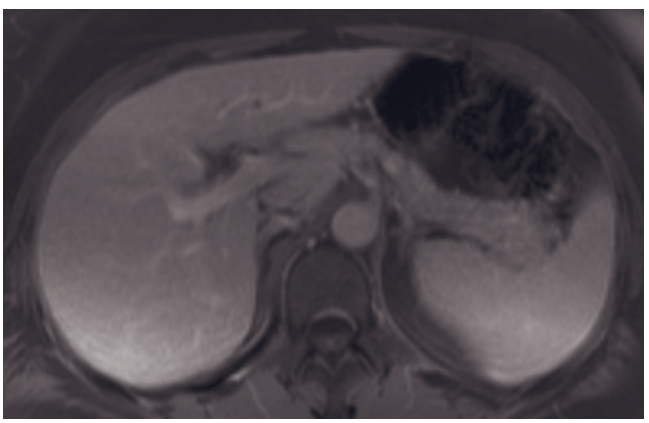

(*h*)

FIG. 2.197 (*Continued*) SS-ETSE (*e*), SGE (*f*), and immediate (*g*) and 90-s fat-suppressed (*h*) images; and T2-weighted SS-ETSE (*i*), out of phase SGE (*j*), and immediate (*k*) and 90-s fat-suppressed (*l*) images in three patients with hepatitis C in different stages. Prominent porta hepatis lymph nodes are usually present (*e*).

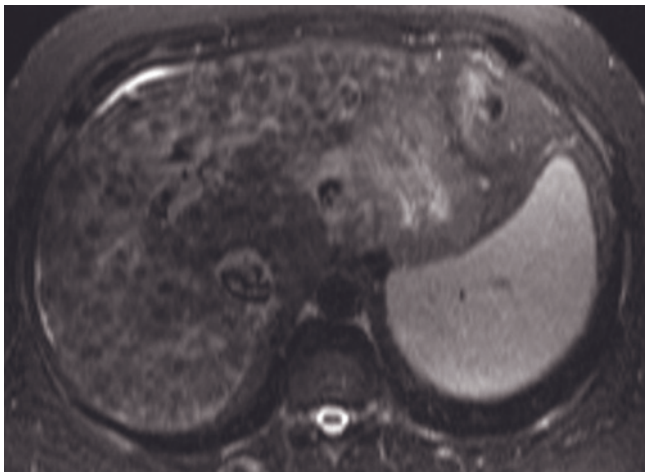

(*i*)

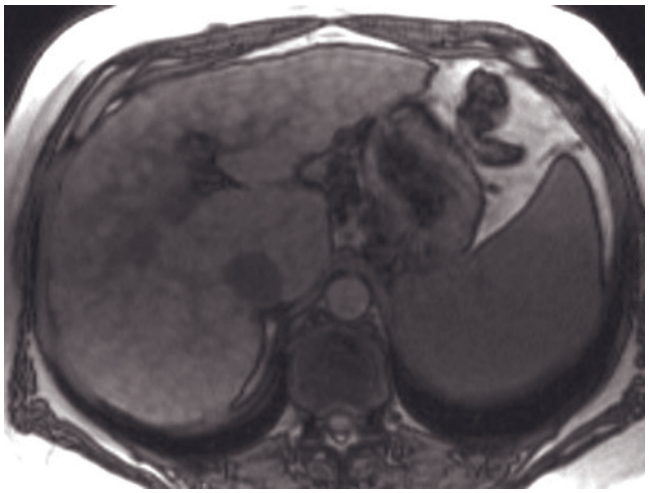

(*j*)

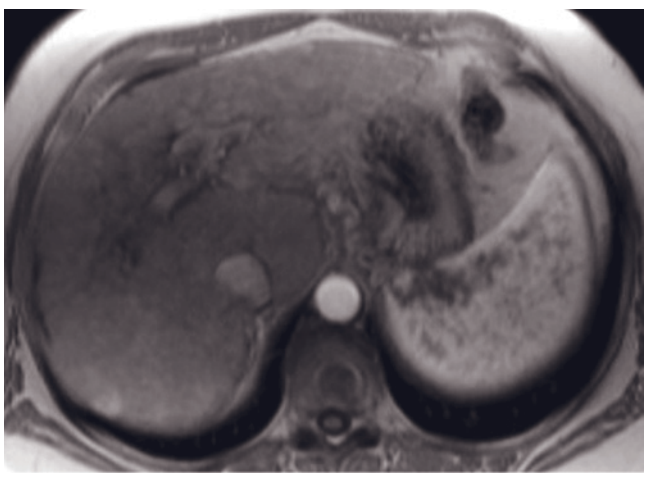

(*k*)

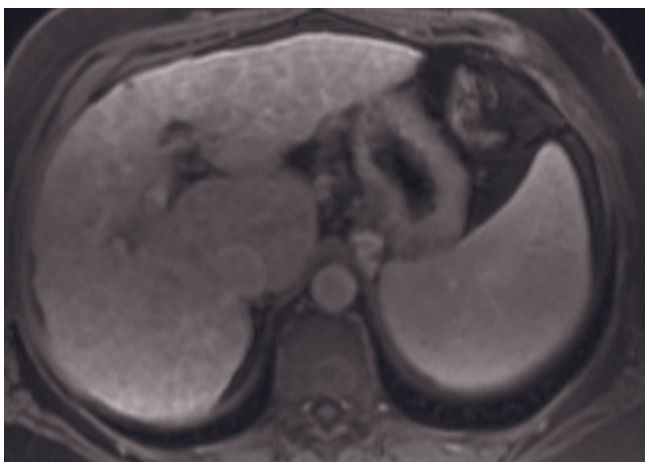

(*l*)

FIG. 2.197 (*Continued*)

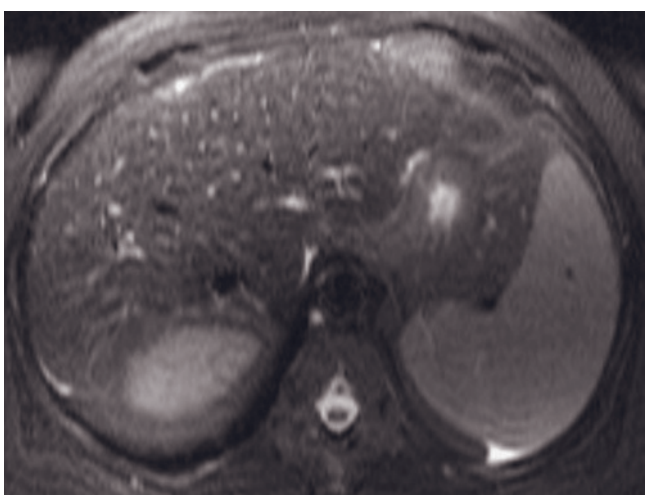

(*a*)

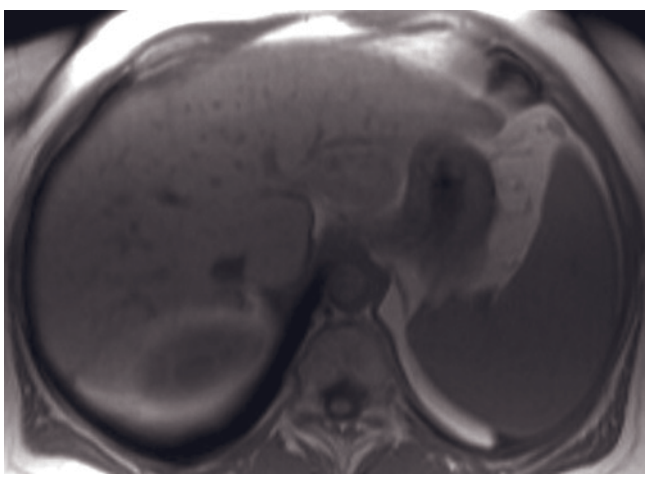

(*b*)

FIG. 2.198 Acute on chronic hepatitis. T2-weighted fat-suppressed SS-ETSE (*a*, *e*), SGE (*b*, *f*, *j*), and immediate (*c, g*, *i*, *k, m*, *n*), 45-s (*l*), and 90-s fat-suppressed (*d, h*) SGE images in five different patients. Although these patients demonstrate different stages

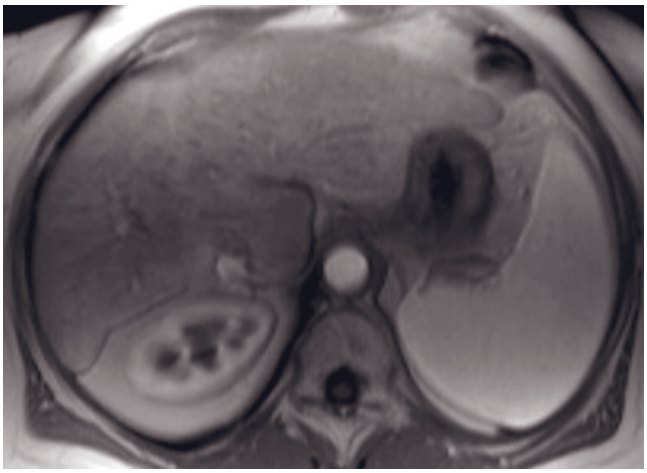

(*c*)

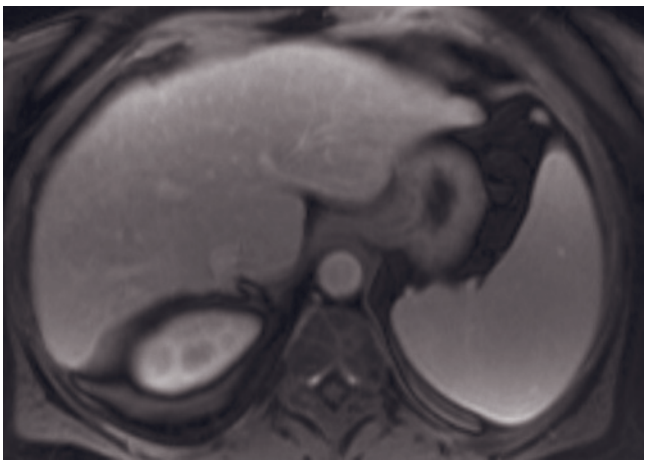

(*d*)

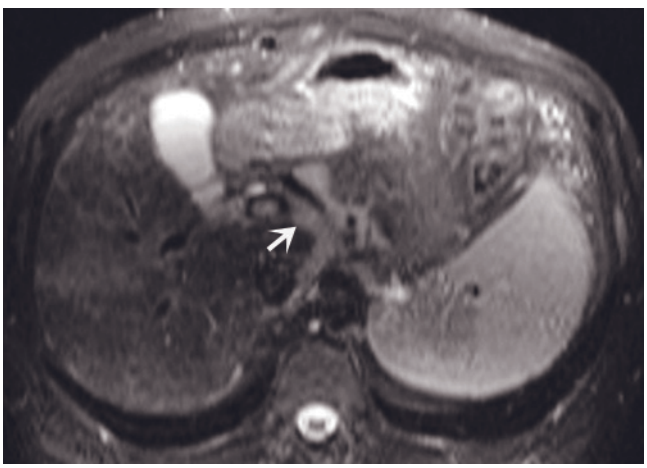

(*e*)

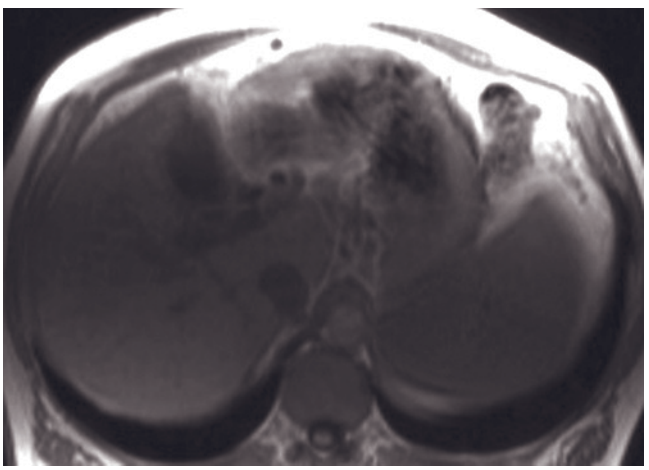

(*f*)

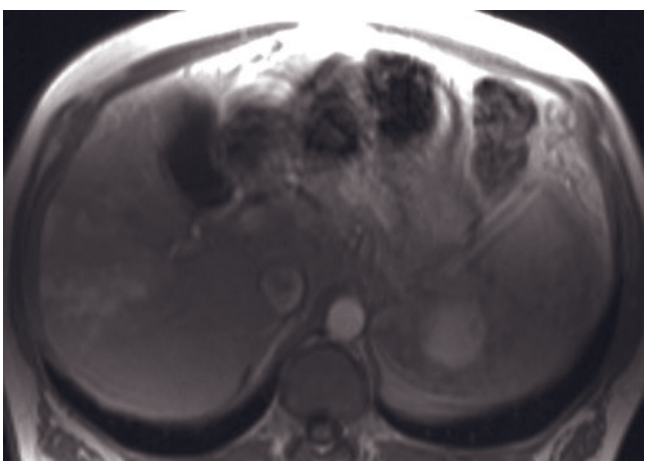

(*g*)

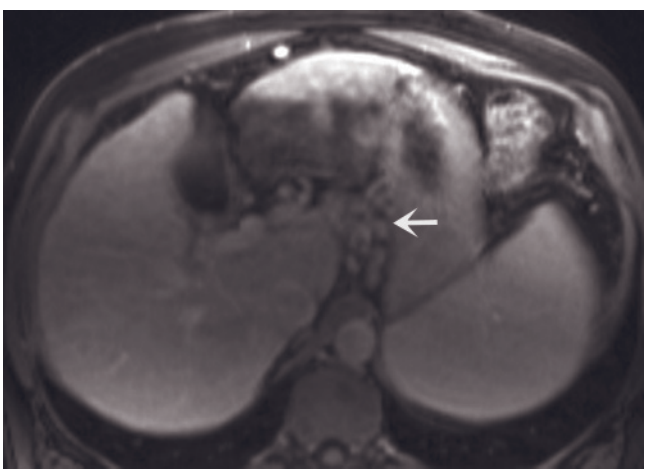

(*h*)

FIG. 2.198 (*Continued*) of chronic liver disease, all of them have a common finding, which is the heterogeneous enhancement on early-phase images (*c, g, k, m, n*) that becomes homogeneous on 45-s image (*l*) and remains homogeneous on late-phase images (*d*, *h*). This finding is compatible with acute on chronic hepatitis. Note that other signs of chronic liver disease are also appreciated in these patients such as lymphadenopathy (arrow, *e*), varices (arrow, *h*), ascites (*i*), and Gamna–Gandy bodies in the spleen (*m*).

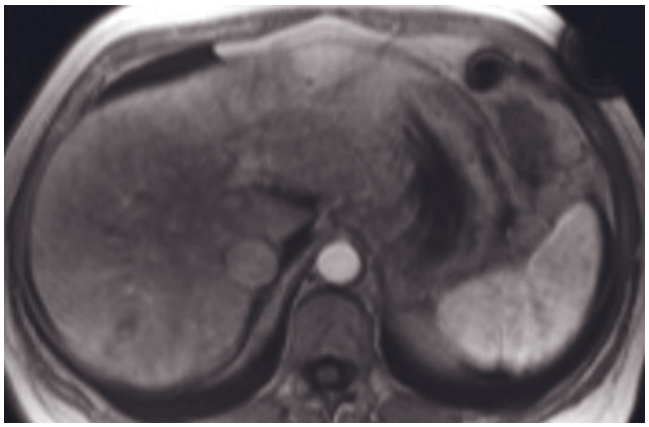

(*i*)

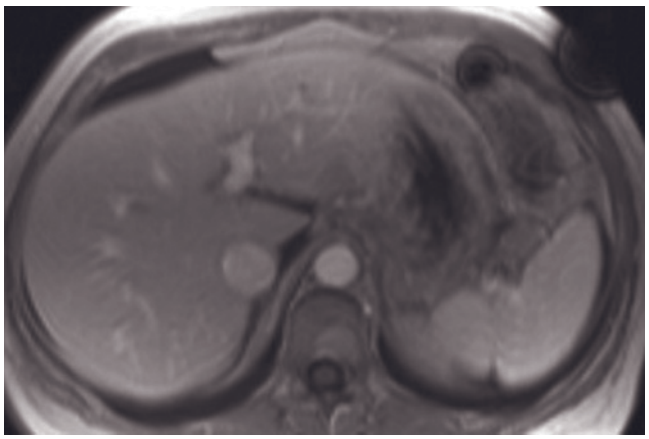

(*j*)

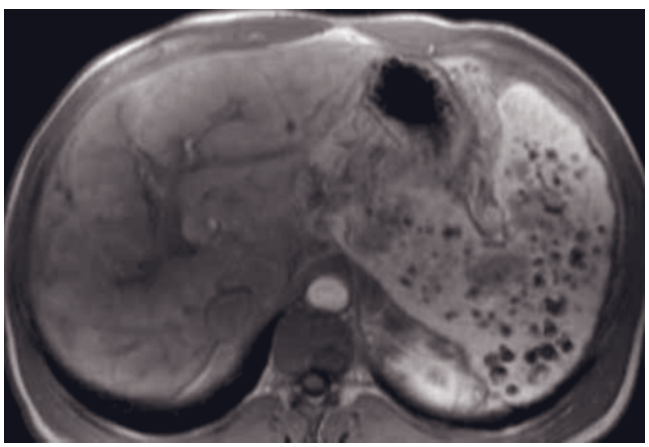

(*k*)

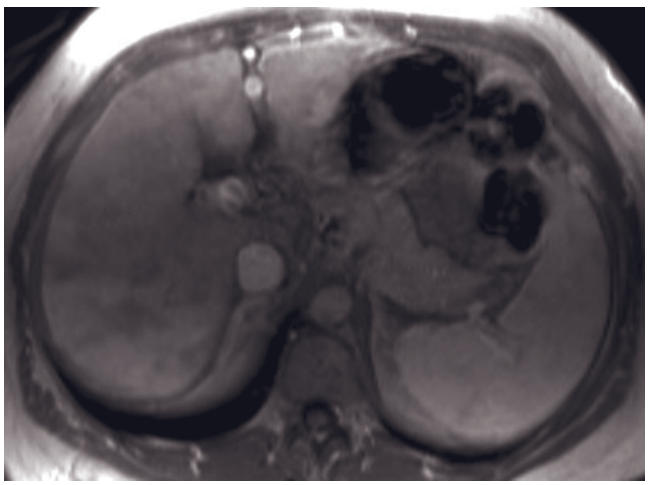

(*l*)

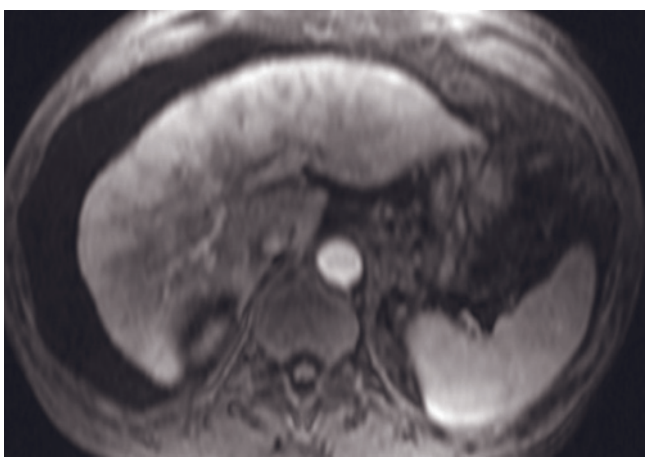

(*m*)

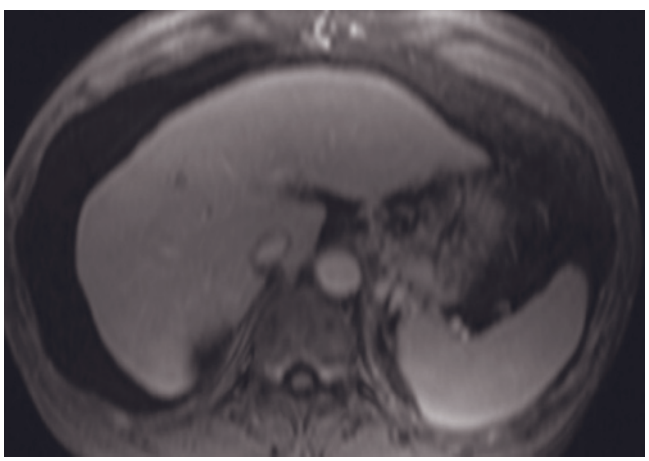

(*n*)

Fig. 2.198 (*Continued*) T1-weighted fat-suppressed 3D-gradient echo (*o*)- and 90-s (*p*)-immediate postgadolinium images show heterogeneous hepatic enhancement on early phase (*m*) that becomer homogeneous on late phase (*n*), features compatible with acute on chronic hepatitis.

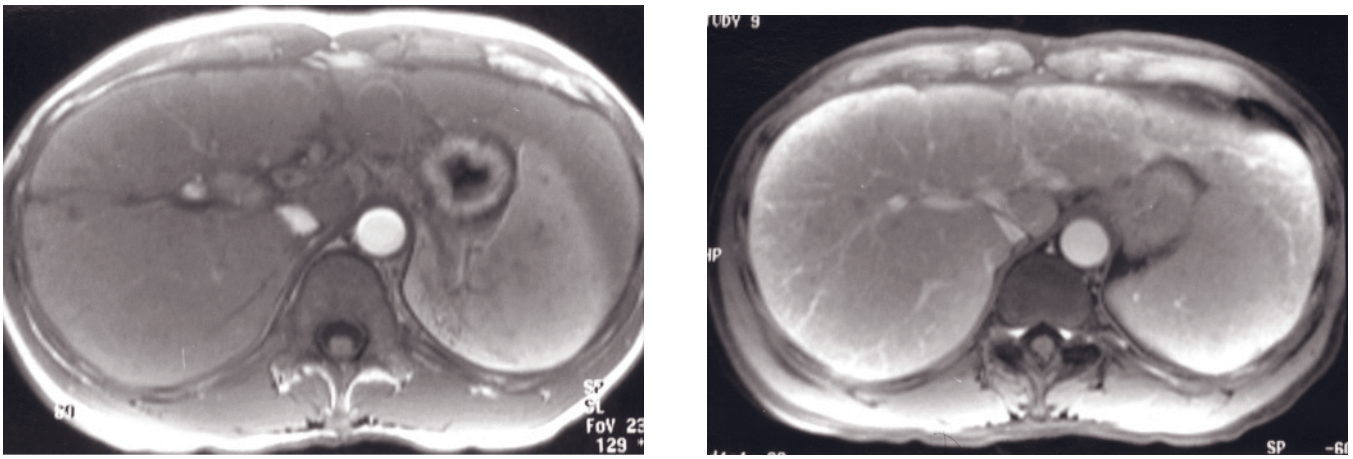

(*a*) (*b*)

FIG. 2.199 Chronic hepatitis. Immediate (*a*) and 90-s fat-suppressed (*b*) postgadolinium SGE images show delayed enhancement of liver fibrous tissue on late-phase image (*b*) consistent with fibrosis.

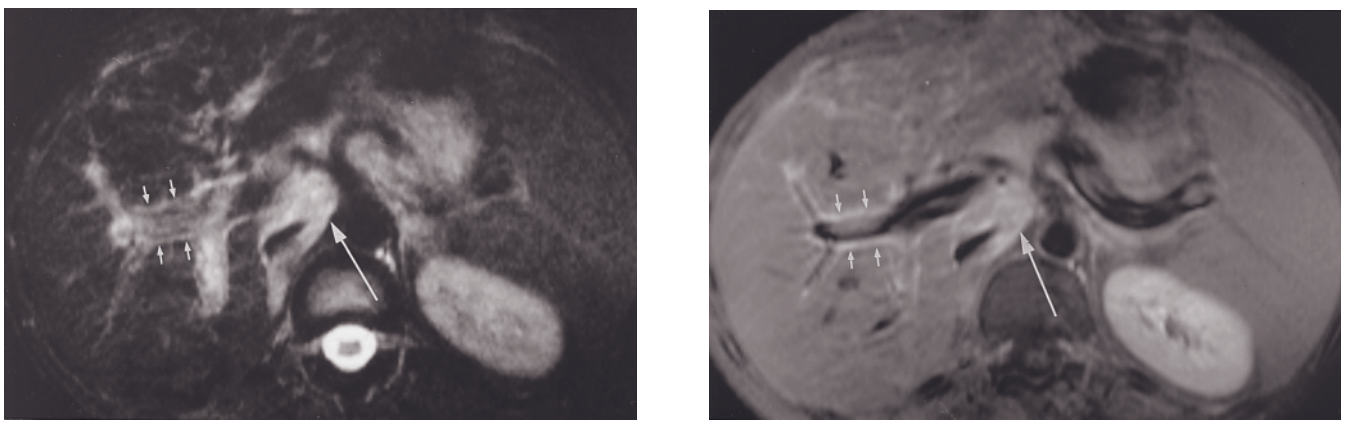

(*a*) (*b*)

FIG. 2.200 Viral hepatitis. T2-weighted fat-suppressed SE (*a*) and 90-s fat-suppressed postgadolinium SE (*b*) images in a patient with HIV infection and positive serology for hepatitis B and C. On the fat-suppressed T2-weighted sequence (*a*), porta hepatis and para-aortic lymph nodes (long arrow, *a*) are clearly shown as high-signal-intensity masses in lower-signal-intensity background. High signal within the liver in a periportal distribution is also present (small arrows, *a*). This periportal abnormality identified on the T2-weighted image is shown to be enhancing tissue (small arrows, *b*) on the gadolinium-enhanced T1-weighted fat-suppressed image (*b*). Gadolinium enhancement distinguishes periportal inflammatory or neoplastic tissue from edema, the latter would appear signal void after contrast. Enhancement of adenopathy (long arrow, *b*) is also appreciated.

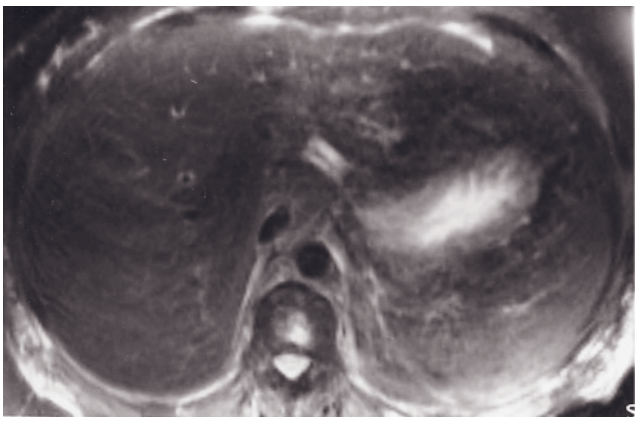

(*a*)

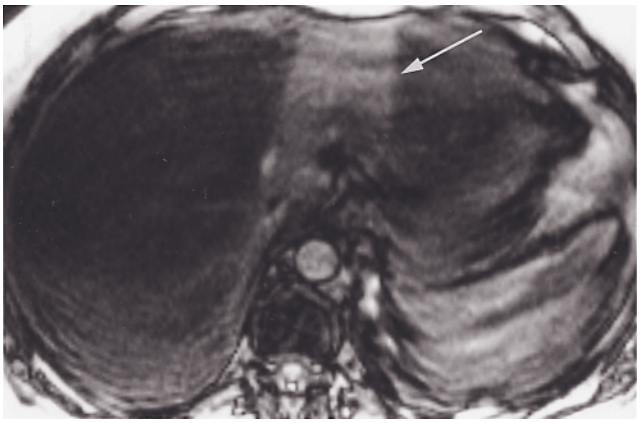

(*b*)

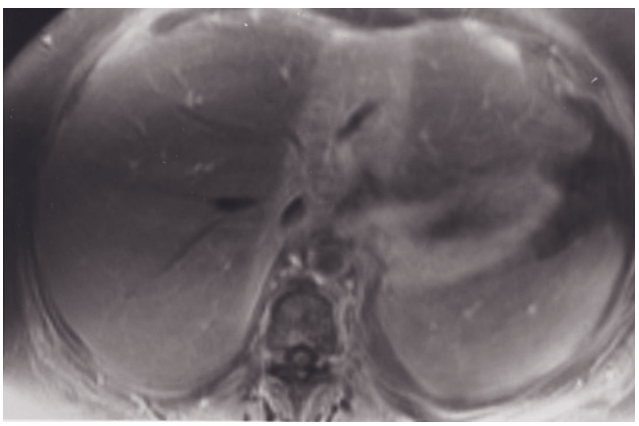

(*c*)

FIG. 2.201 Radiation injury. T2-weighted fat-suppressed SE (*a*), out-of-phase SGE (*b*), and 90-s fat-suppressed postgadolinium SE (*c*) images in a patient who had undergone radiation therapy for a vertebral body metastasis. The out-of-phase image (*b*) shows low-signal-intensity fatty replaced liver with a central, vertically oriented band of higher-signal-intensity nonfatty liver (arrow, *b*). Similar findings are apparent on the fat-suppressed T2-weighted image (*a*), with subtle higher signal intensity of the central band of nonfatty liver. The gadolinium-enhanced T1-weighted fat-suppressed image (*c*) demonstrates increased enhancement of the radiation-damaged liver, which may reflect radiation-induced vasculitis, in conjunction with lower signal of fatty liver due to fat-suppression effects.

of micronodular to macronodular cirrhosis of 90% in 10 years [314]. Cirrhotic nodules may be characterized based on histologic features into three majors categories, namely, 1) regenerative, representing a benign proliferation of hepatocytes surrounded by fibrous septa; 2) dysplastic, representing regenerative nodules with cellular atypia, an intermediate step in the pathogenesis of HCC; and 3) malignant or HCC [93].

By MR imaging, a variety of morphologic changes are common findings. Atrophy of the right lobe and the medial segment of the left lobe is common in cirrhotic livers. Relative sparing of the caudate lobe and lateral segment of the left lobe is often present. In fact, these segments may undergo hypertrophy. The combination of scarring, atrophy, and parenchymal regenerative activity may involve any segment of the liver and occasionally may result in a bizarre hepatic contour that can simulate tumor mass (fig. 2.202). Often the hypertrophic region of the liver possesses imaging and enhancement features comparable to those of normal liver, thus facilitating a correct diagnosis. Morphologic changes of the liver are seen less frequently in early compensated cirrhosis, impairing diagnosis by imaging. In cirrhotic livers, enlargement of the hilar periportal space was observed in 98% of patients who had atrophy of the medial segment of the left lobe, whereas this finding was seen in only 11% of patients with normal livers [324, 325]. Expansion of the major interlobar fissure may be seen in the late stage of disease, causing extrahepatic fat to fill the space between the left medial and lateral segments [326].

With advanced cirrhosis, morphologic liver changes become more evident. There may be marked atrophy of the right lobe and medial segment of the left lobe and hypertrophy of the caudate lobe and left lateral segment. The combination of these four findings is responsible for the enlargement of the pericholecystic space (gallbladder fossa), which is subsequently filled with fat, known as the "expanded gallbladder fossa sign." This imaging finding is highly suggestive of cirrhosis [324]. Moreover, with progression of the disease, the liver surface shows irregularities and the liver morphology exhibits distortion, both due to the presence of regenerative nodules and confluent or diffuse parenchymal fibrosis [300, 327].

The most consistent morphologic feature of cirrhosis is the demonstration of focal or diffuse fibrous tissue that appears on MRI as a reticular network of linear

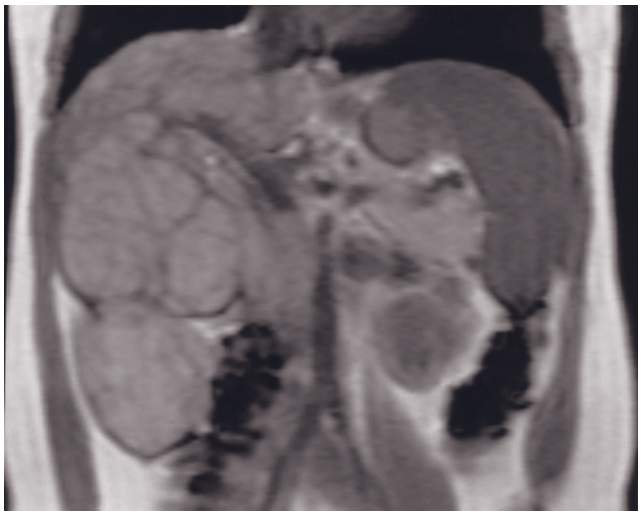

(*a*)

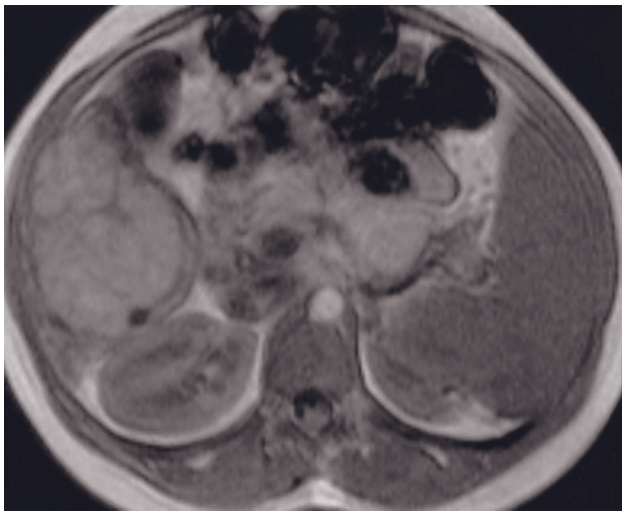

(*b*)

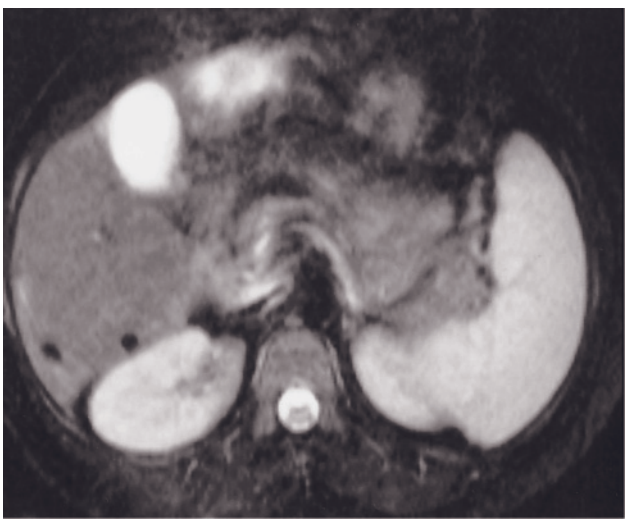

(*c*)

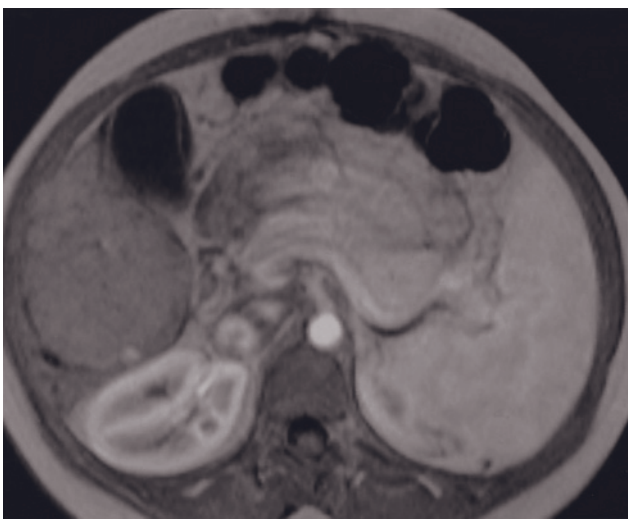

(*d*)

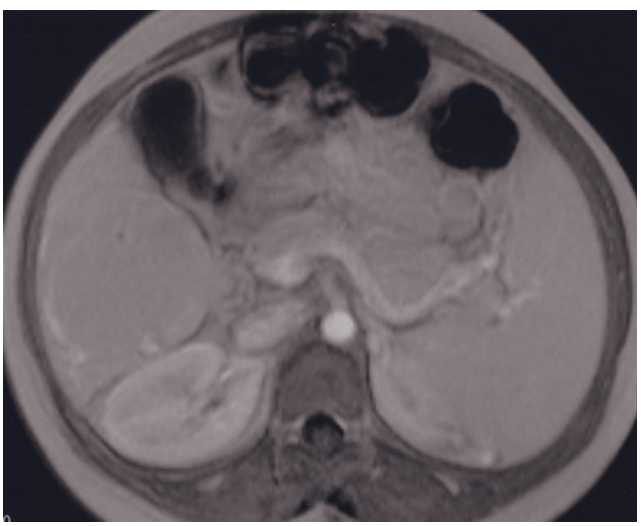

(*e*)

FIG. 2.202 Cirrhosis with macronodular regenerative nodule. Coronal SGE (*a*), SGE (*b*), T2-weighted fat-suppressed ETSE (*c*), and immediate (*d*) and 90-s (*e*) postgadolinium SGE images. Prominent linear bands that are low in signal intensity on T1-weighted images (*a*, *b*) are present throughout the liver, a finding consistent with scarring. The inferior portion of the right lobe has a bulbous contour that simulated a mass lesion on CT examination (not shown). The focal enlargement possesses the same signal intensity features as the remainder of the liver (*a*), which include fibrotic markings apparent on T1-weighted images (*a*, *b*), homogeneous intermediate signal intensity on T2-weighted images (*c*), early diminished enhancement of scar tissue (*d*), and more uniform enhancement on interstitial-phase images (*e*).

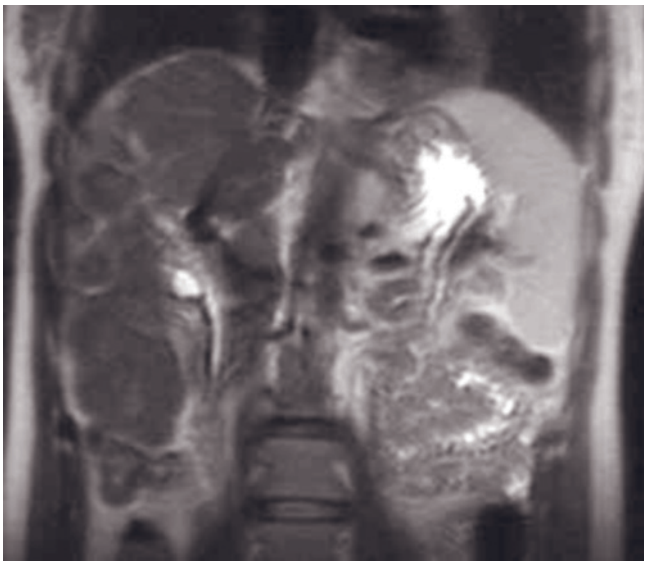

(*f*)

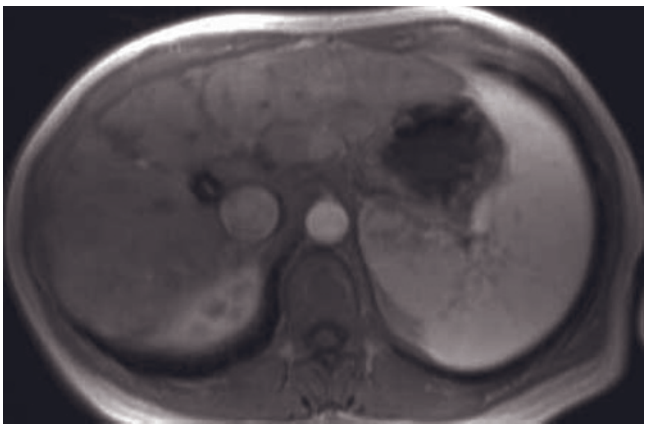

(*g*)

FIG. 2.202 (*Continued*) Coronal T2-weighted SS-ETSE (*f*) and transverse 45-s postgadolinium SGE (*g*) images in a second patient show similar findings.

stroma of varying thickness [328]. On T1-weighted images fibrous tissue is low signal; on T2-weighted images fibrous tissue varies from high signal to low signal, depending on chronicity, with acute fibrous tissue having a higher fluid content and therefore higher signal. On hepatic arterial dominant-phase images, fibrous tissue enhances negligibly and demonstrates late enhancement on hepatic venous phase images (fig. 2.203). Fibrous tissue is most consistently shown on short-TE T1-weighted gradient-echo images and well shown on TE = 2 ms out-of-phase imaging at 1.5 T, appearing as low-signal reticular tissue. Fibrosis is also well shown as late-enhancing stroma on 2-min postgadolinium fat-suppressed gradient-echo images (figs. 2.204 and 2.205) [329].

Many livers in the setting of chronic hepatitis or cirrhosis may contain regions that are high signal intensity on T2-weighted images and low signal intensity on T1-weighted images and enhance moderately intensely on arterial dominant-phase images, secondary to hepatocellular damage, inflammation, or arteriovenous shunts; which are most consistently, or only, shown on hepatic arterial dominant-phase images [330–332]. Acute on chronic liver inflammation is shown as regions of transient increased enhancement on immediate postgadolinium images [329, 332]. Many abnormal regions of enhancement are small with irregular or ill-defined margins. In these cases, distinction from tumor is not problematic. Occasionally, patchy areas of enhancement are large, and they generally fade to near isointensity by 1 min. Rarely, patchy areas of increased enhancement may show variable enhancement on later postcontrast images. Under these circumstances, distinction from diffuse HCC may be problematic. In the setting of diffuse HCC, an important distinguishing feature is the association with tumor thrombus. Bland thrombus is rare with acute on chronic hepatitis, and enhancing thrombus never occurs. Serum α-fetoprotein level may support the diagnosis, because serum α-fetoprotein is typically very elevated with diffuse HCC and only slightly elevated in patients with acute on chronic hepatitis [333].

Tiny peribiliary cysts may occur in cirrhotic livers. These cysts typically measure 5 mm or less in size [334–336].

In cirrhotic livers, parenchymal nodules are created by the regenerative activity of hepatocytes and the network of fibrosis. The formation of regenerative nodules (RNs) results in gross distortion of hepatic architecture. Micronodular cirrhosis, common in alcoholic liver disease and hemochromatosis, displays RNs ≤3 mm, sheathed by thin fibrous septa. In patients with virus-induced cirrhosis (mainly hepatitis B), the regenerative nodules are 3–15 mm with thick fibrous septa; this pattern is classified as macronodular cirrhosis. Although some diseases are classically associated with one pattern or another, most cirrhotic livers are mixed [337, 338]. MRI demonstrates RNs with greater conspicuity than any other imaging modality. The majority of RNs are isointense on T2- and T1-weighted images. Occasionally, RNs may appear low in signal intensity on T2-weighted images relative to high-signal-intensity inflammatory fibrous septa or damaged liver (figs. 2.206–2.208) [180, 181, 185]. Approximately 16 % (11/68)

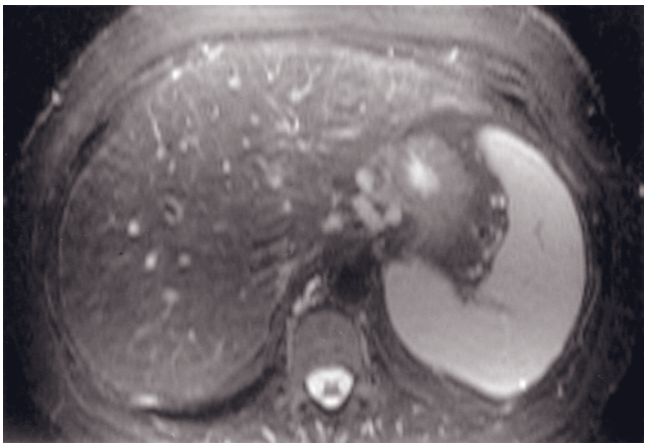

(*a*)

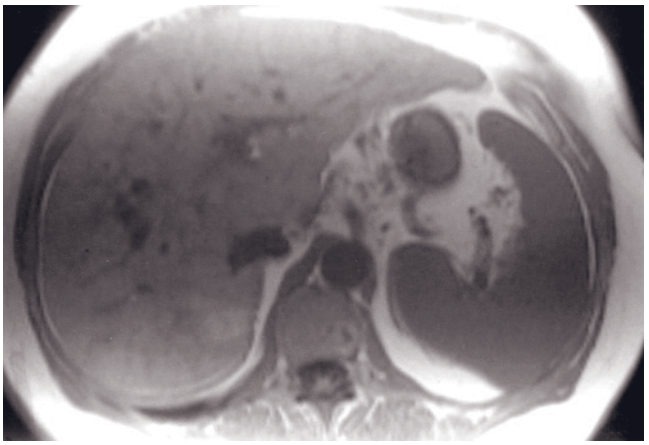

(*b*)

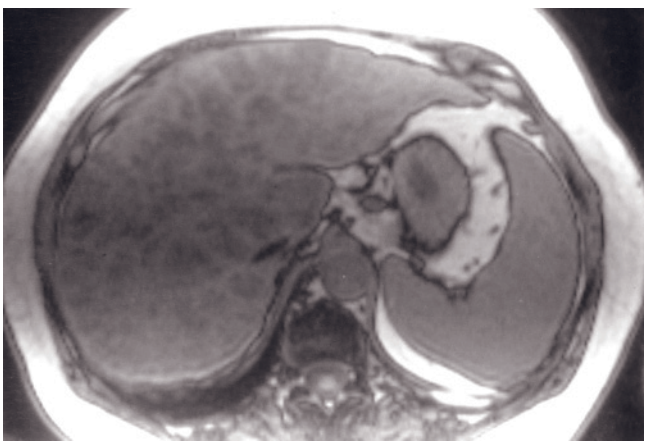

(*c*)

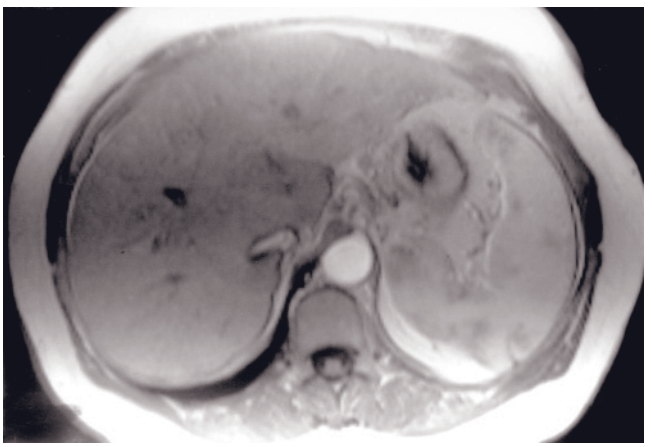

(*d*)

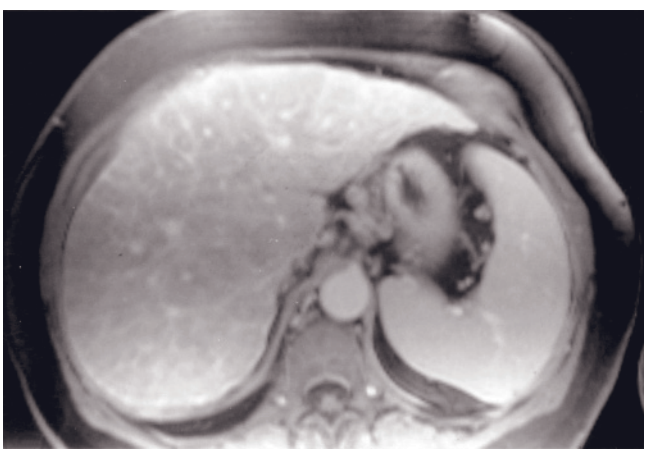

(*e*)

FIG. 2.203 Cirrhosis and fatty infiltration. Echo-train STIR (*a*), SGE (*b*), out-of-phase SGE (*c*), and immediate (*d*) and 90-s fat-suppressed (*e*) postgadolinium SGE images. The liver is mildly enlarged. Diffuse nodular fatty infiltration is appreciated, with foci of liver losing signal and intervening bands of fibrosis tissue retaining signal on out-of-phase images (*c*). Note that the fibrous tissue enhances on delayed images (*e*), creating a reticular appearance.

of RNs are hyperintense on T1-weighted images. The cause for this hyperintensity on T1 is unclear, unrelated to lipid, but possibly reflects high protein content. Because RNs have a portal venous blood supply with minimal contribution from hepatic arteries [339], RNs enhance minimally on hepatic arterial dominant-phase images.

Approximately 25% of RNs accumulate more iron than the surrounding hepatic parenchyma. This feature facilitates the identification of RNs as low signal on T2-weighted and T2*-weighted gradient-echo images and low signal on postgadolinium SGE images because surrounding hepatic parenchyma enhances to a greater degree than iron-containing nodules (fig. 2.209) [339,

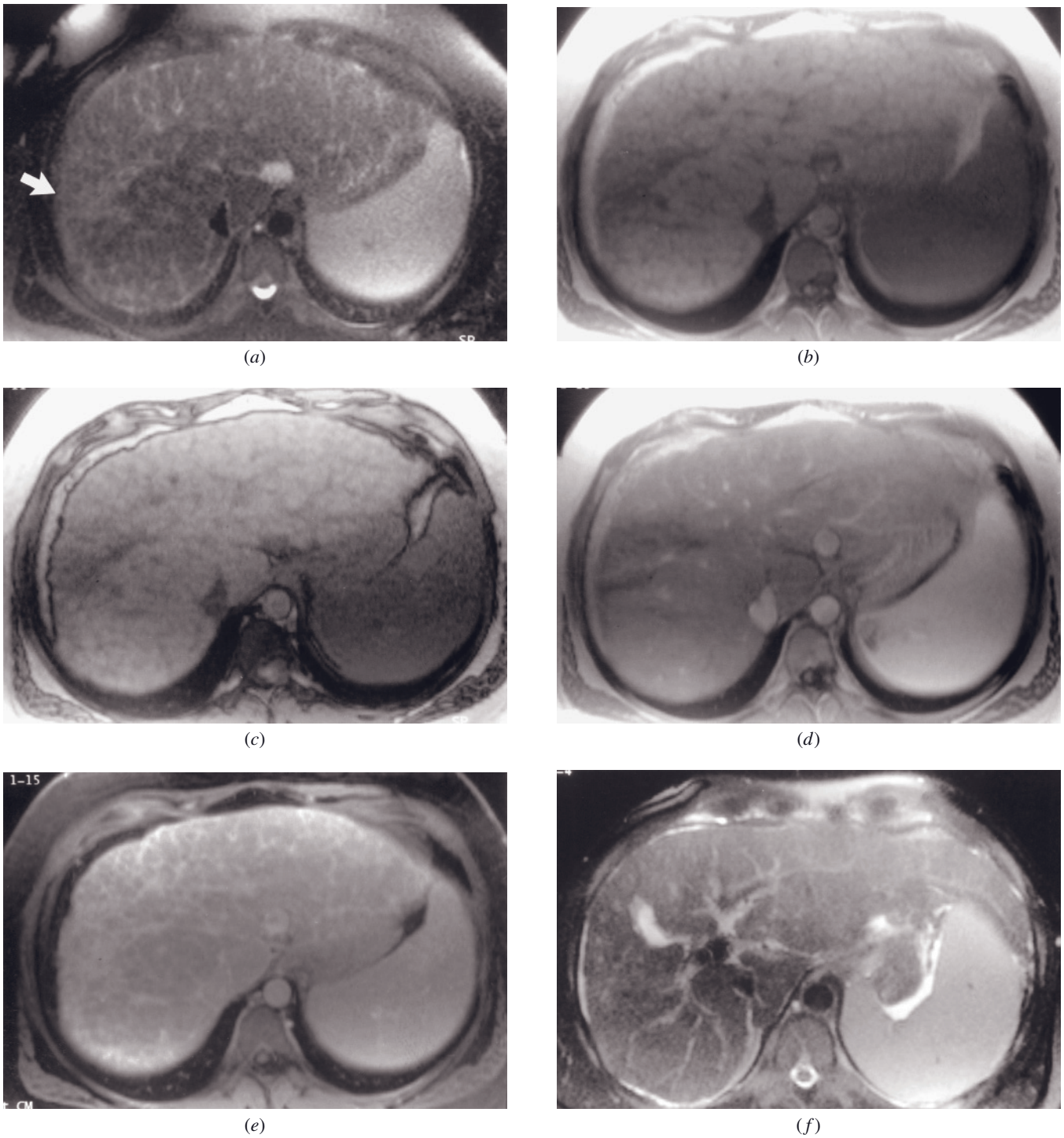

FIG. 2.204 Cirrhosis with confluent fibrosis. Echo-train STIR (*a*), SGE (*b*), out-of-phase SGE (*c*), and immediate (*d*) and 90-s fat-suppressed (*e*) postgadolinium SGE images. There is a linear pattern of fibrosis throughout the liver, with a focal region of confluent fibrosis (arrow, *a*) that is mildly high in signal on T2 (*a*) and mildly low in signal on T1-weighted image (*b*) and demonstrates negligible enhancement on early postcontrast image (*d*) and mild enhancement on late image (*e*). Note that the fine pattern of fibrosis present throughout the liver is particularly well shown on the short TE out-of-phase image (*c*) as low-signal linear structures (*c*) and on late postgadolinium as linear enhancing structures (*e*).

T2-weighted fat-suppressed SS-ETSE (*f*), SGE (*g*), out-of-phase SGE (*h*), and immediate (*i*) and 90-s fat-suppressed postgadolinium SGE (*j*) images in a second patient. The liver is small and nodular in contour and demonstrates a reticular heterogeneous

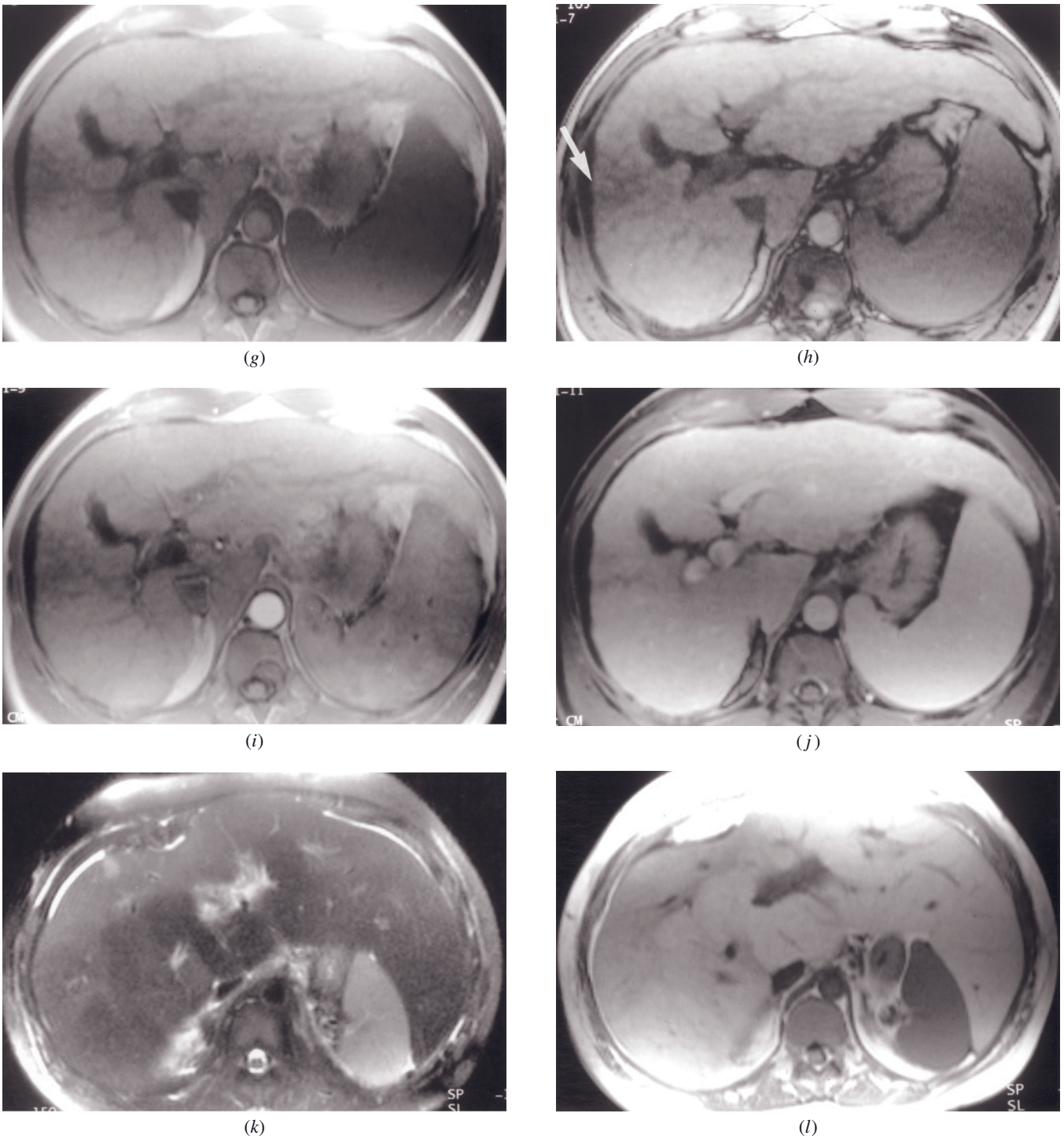

FIG. 2.204 (*Continued*) enhancement pattern consistent with cirrhosis. A confluent region of fibrosis is evident in segment 8 peripherally (arrow, *h*). No focal lesion is identified within the liver. Note the presence of splenomegaly.

T2-weighted fat-suppressed SS-ETSE (*k*), SGE (*l*), out-of-phase (*m*), and immediate (*n*) and 90-s fat-suppressed (*o*) postgadolinium SGE images in a third patient. The liver is enlarged, with the left lobe extending lateral to the spleen. On the out-of-phase image (*m*),

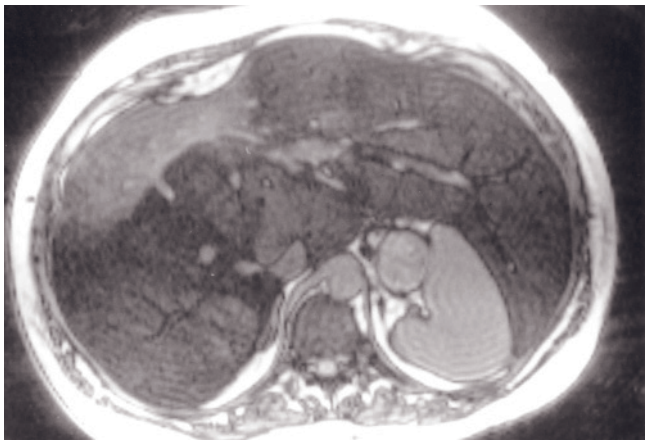

(*m*)

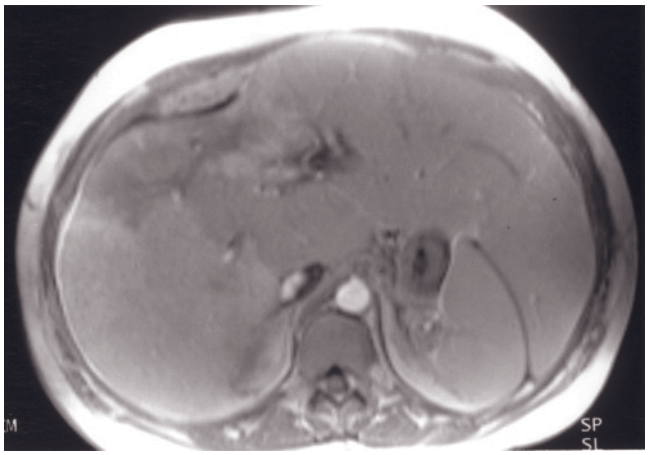

(*n*)

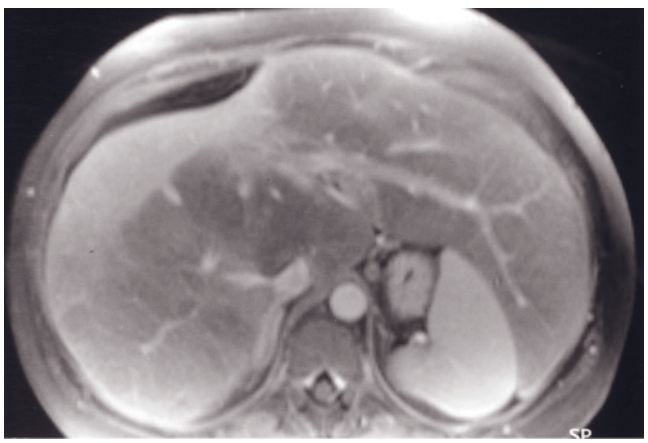

(*o*)

FIG. 2.204 (*Continued*) there is drop in signal of the hepatic parenchyma with focal sparing of the superficial parenchyma in segments 4 and 5. This is consistent with diffuse fatty infiltration of the liver, with lack of fatty infiltration in the region of fibrosis. Note the presence of atrophy in association with the fibrosis. The region of confluent fibrosis shows negligible early enhancement (*n*) with late increased enhancement (*o*).

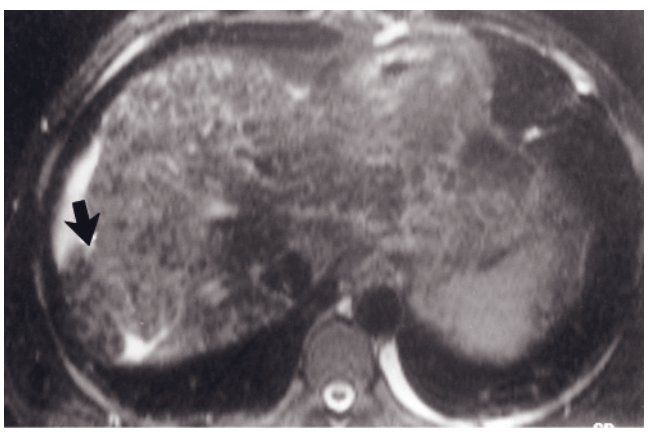

(*a*)

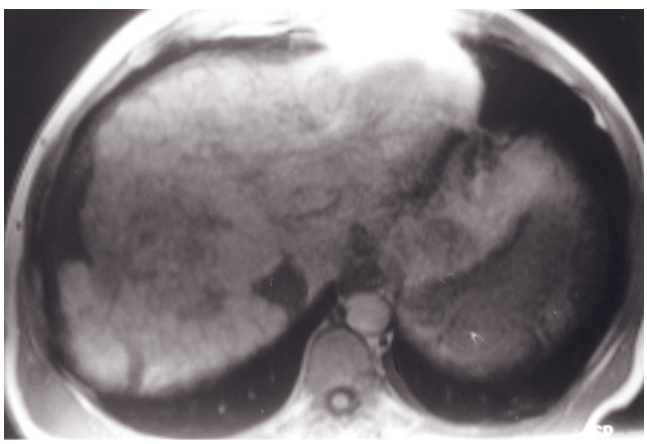

(*b*)

FIG. 2.205 Cirrhosis with extensive and confluent fibrosis. Echo-train STIR (*a*), SGE (*b*), and immediate (*c*), and 90-s fat-suppressed (*d*) postgadolinium SGE and echo-train STIR (*e*), SGE (*f*), out-of-phase SGE (*g*), and immediate (*h*), and 90-s fat-suppressed (*i*) postgadolinium SGE images in two different patients with cirrhosis. In both cases, the liver is diminutive in size and demonstrates

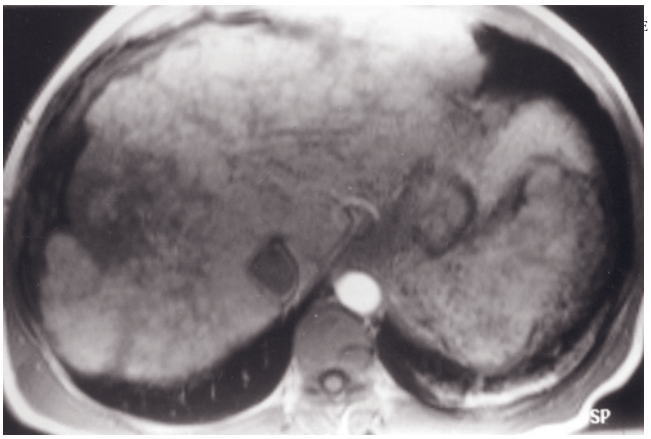

(*c*)

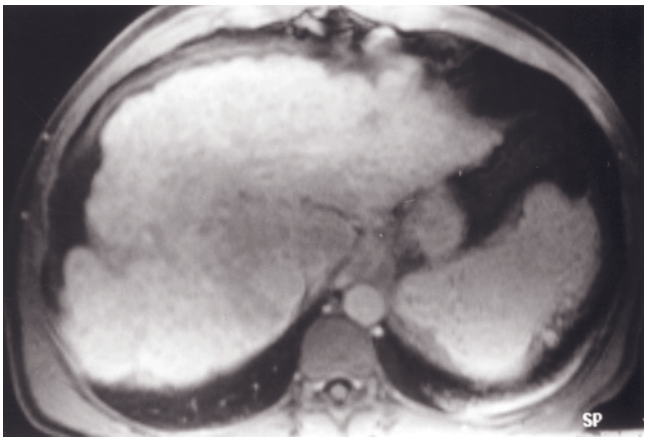

(*d*)

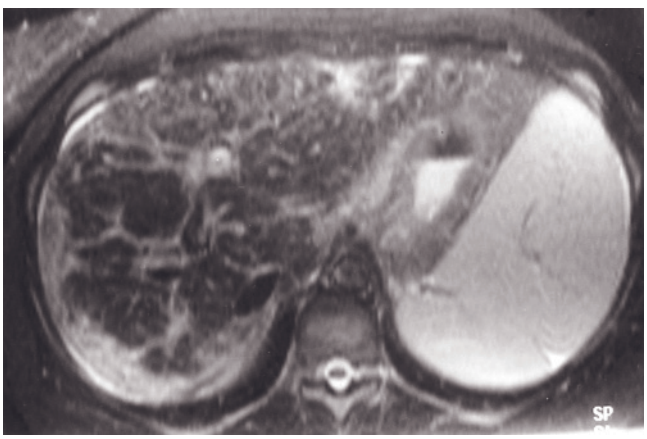

(*e*)

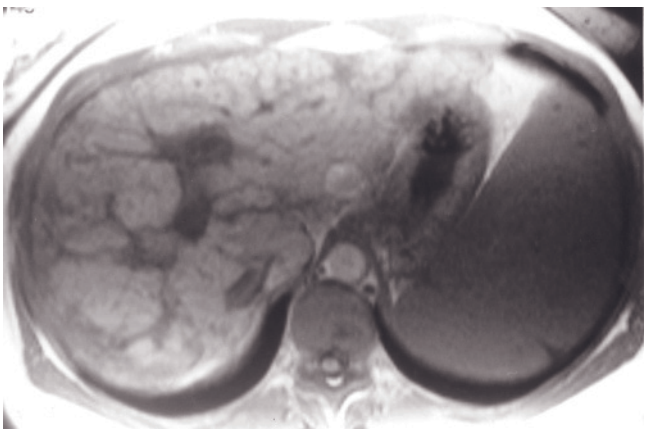

(*f*)

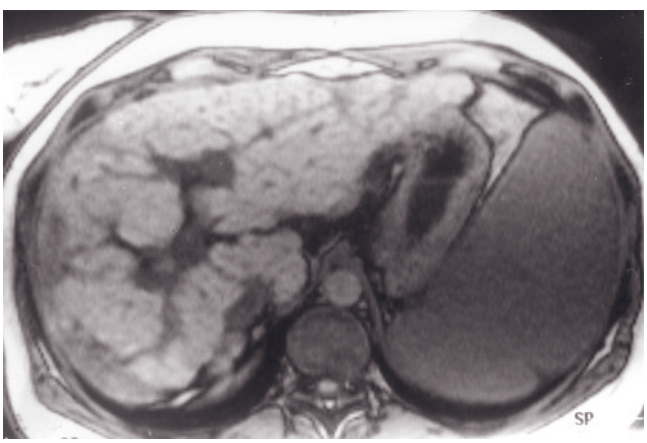

(*g*)

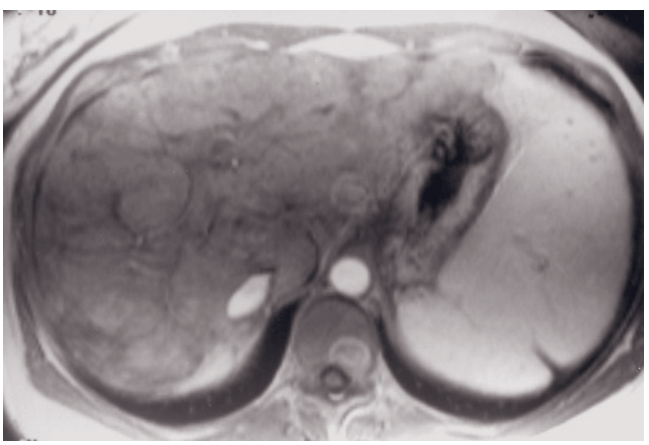

(*h*)

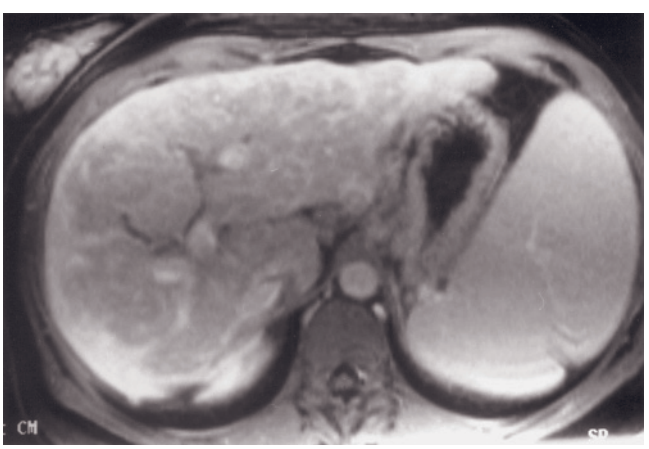

(*i*)

Fig. 2.205 (*Continued*) nodular and irregular contour with distorted anatomy. The hepatic parenchyma is heterogeneous in appearance with extensive linear fibrosis. The fibrous stroma is best shown on the short TE out-of-phase sequence (*g*) as low-signal reticular strands and on the late postgadolinium fat-suppressed SGE as enhancing tissue. Confluent areas of fibrosis are present in both patients. Parenchymal atrophy associated with the scarring results in an unusual-appearing exophytic region of hypertrophy in the first patient (arrow, *a*).

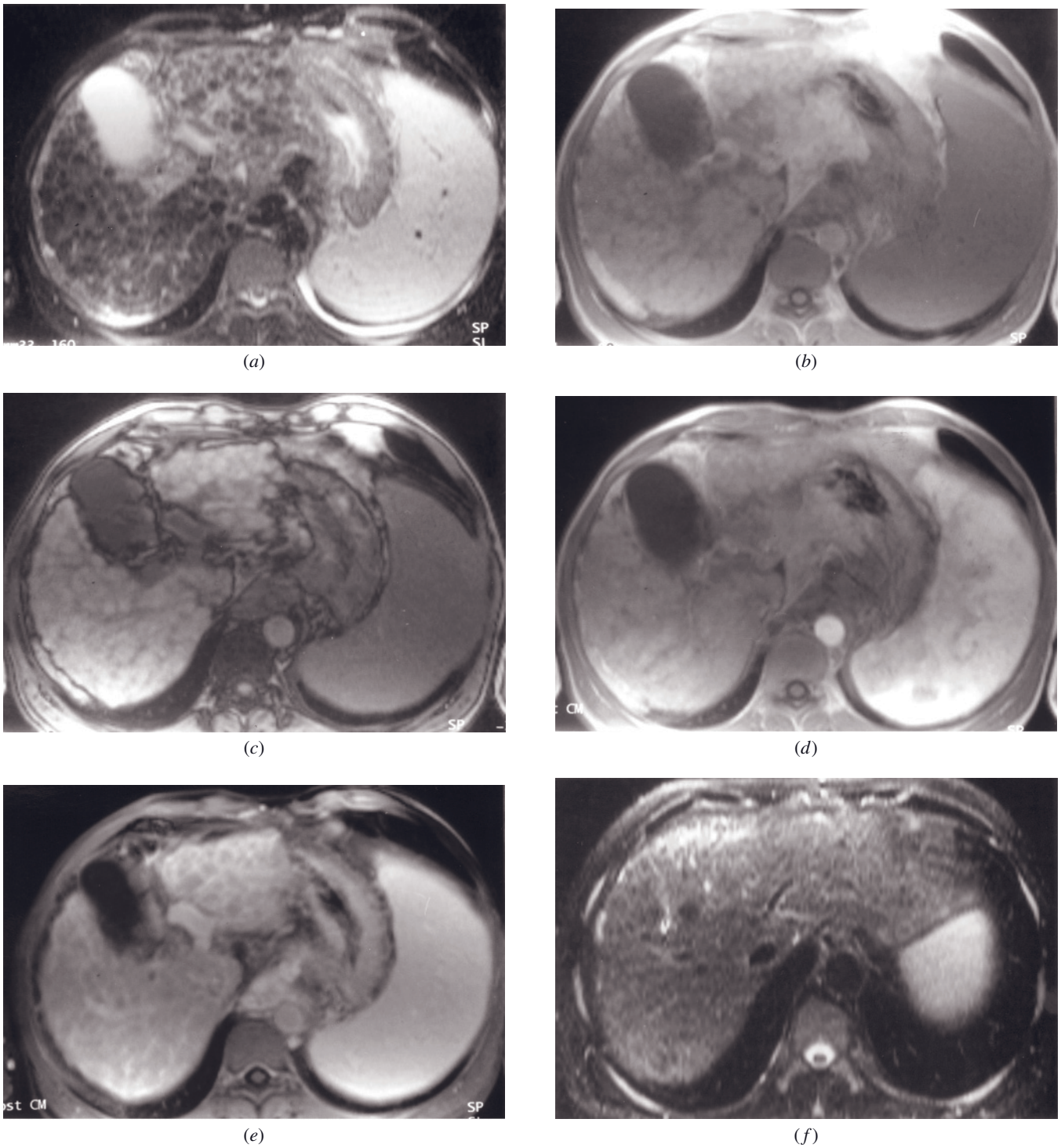

FIG. 2.206 Cirrhosis with regenerative nodules. Echo-train STIR (*a*), SGE (*b*), out-of-phase SGE (*c*), and immediate (*d*), and 90-s fat-suppressed (*e*) postgadolinium SGE images. The liver is small with an extensive nodular pattern. A reticular pattern of fibrosis is present, which is well shown on out-of-phase images (*c*) as low-signal-intensity linear tissue and demonstrates negligible enhancement on immediate postgadolinium images (*d*) with progressive enhancement on late images (*e*). Multiple regenerative nodules appear as rounded <1-cm masses well shown as high-signal lesions on out-of-phase images (*c*). Ascites, splenomegaly, and paraesophageal varices are present.

Echo-train STIR (*f*), SGE (*g*), out-of-phase SGE (*h*), and 45-s (*i*) and 90-s fat-suppressed (*j*) postgadolinium SGE images in a second patient. There are multiple scattered rounded foci throughout the liver that show decreased signal on T2 (*f*) and increased

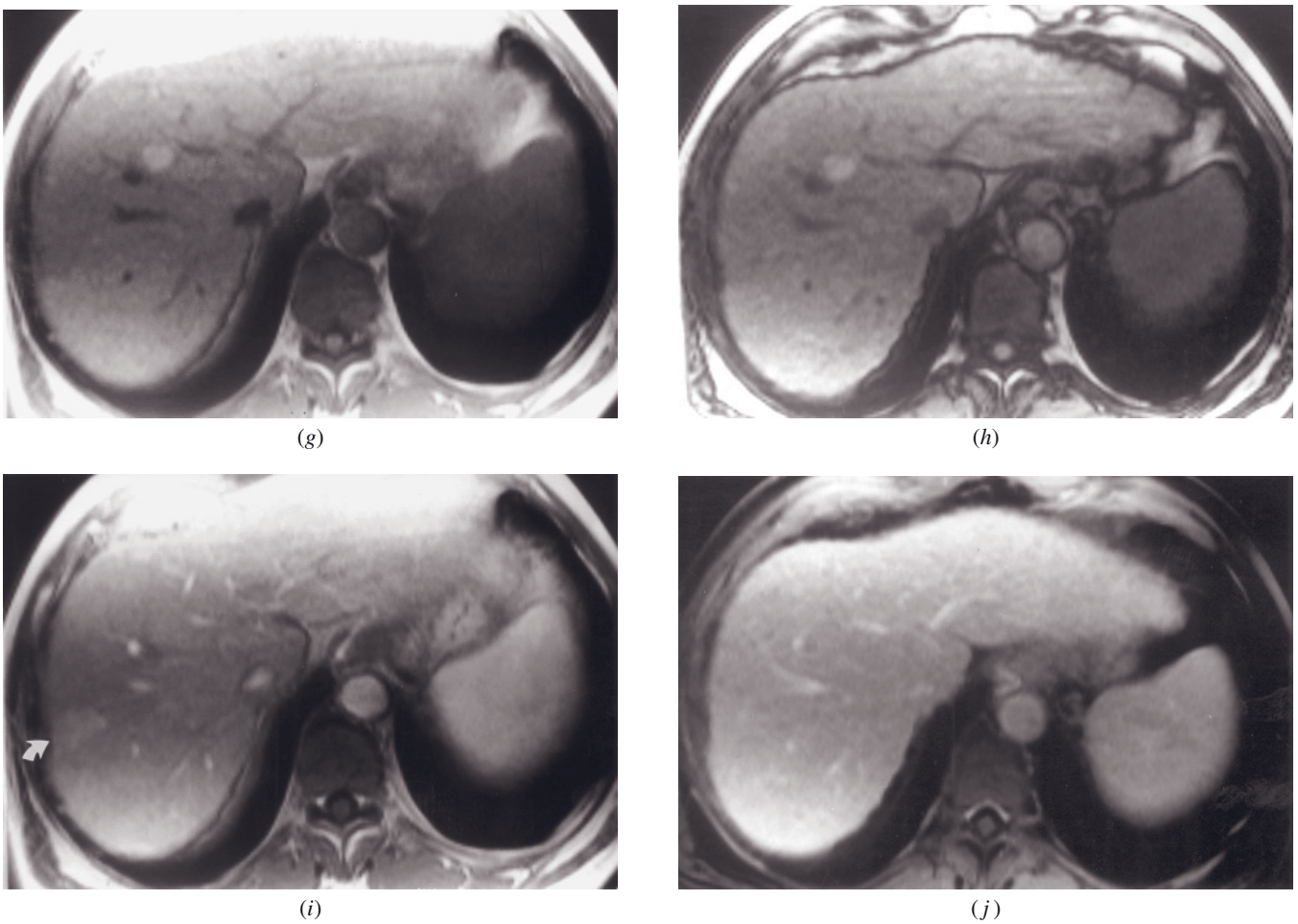

FIG. 2.206 (*Continued*) signal on noncontrast T1-weighted (*g*) and out-of-phase (*h*) images. Lesions are not apparent on early (*i*) or late (*j*) postgadolinium images, consistent with regenerative or mildly dysplastic nodules. Note also the fine reticular pattern on postgadolinium images (*i*, *j*) with progressive enhancement, consistent with fibrotic change associated with cirrhosis. A small transiently enhancing focus (curved arrow, *i*) is present in segment 8, which reflects a focal hyperperfusion abnormality.

340]. Although it is suggested that the presence of iron within RNs is a risk factor for HCC [341], this association is not yet well established.

Central large regenerative nodules may be most characteristic of cirrhosis due to PSC. In these cases, regions of atrophic, cirrhotic liver and obstructed bile ducts may be compressed at the periphery of massively expanded regenerative nodules.

The prevalence of RNs in Budd–Chiari syndrome is not known, but it is suggested that they may be observed in up to 25% of patients. In the setting of chronic Budd–Chiari syndrome, RNs may show atypical MR features, namely, high signal on T2- and T1-weighted images and moderate enhancement on arterial dominant phase. It is hypothesized that the hypervascularization of the RNs in this disorder reflects enlargement of hepatic arteries and an abnormality of portal flow [342–344].

Dysplastic nodules (DNs) are defined as neoplastic, clonal lesions that represent an intermediate step in the pathway of carcinogenesis of hepatocytes in cirrhotic livers [93, 338]. They are considered as premalignant nodules and are found in 15–25% of cirrhotic livers [345]. Studies have documented the development of HCC within a DN in as short as a 4-month period [346, 347]. On gross pathologic examination, DNs are usually larger than RNs, but the entities may be impossible to distinguish both pathologically and by MRI [165].

DNs are diagnosed histologically as low or high grade according to the current classification system for nodular hepatocellular lesions by the International Working Party [93]. Low- and high-grade DNs represent parts of a spectrum involving microscopic architectural changes and cytologic atypia [338].

On MR imaging, DNs are most commonly recognized as isointense or hypointense on T2-weighted

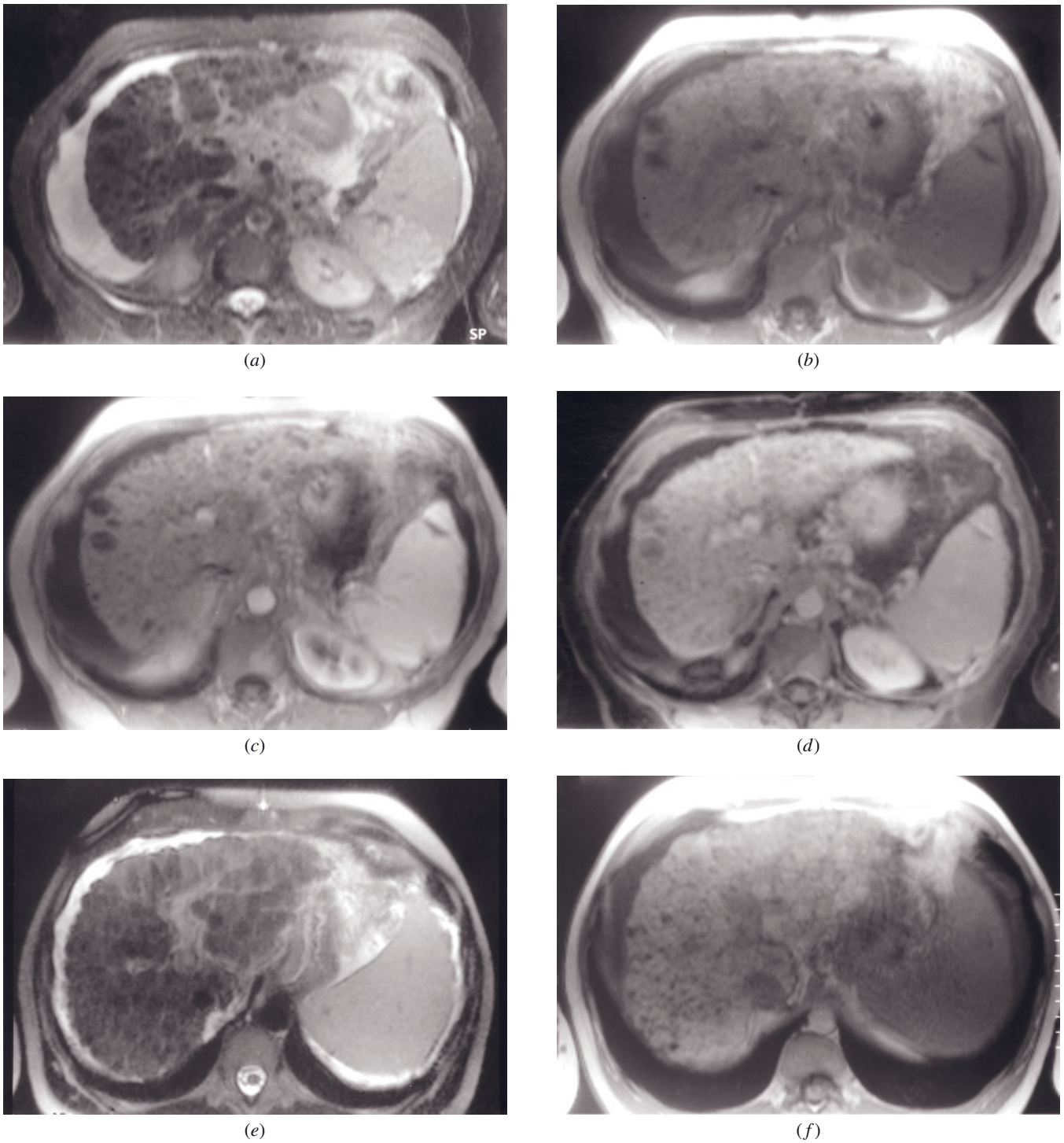

FIG. 2.207 Cirrhosis with regenerative nodules. Echo-train STIR (*a*), SGE (*b*), and immediate (*c*) and 90-s fat-suppressed (*d*) postgadolinium SGE and echo-train STIR (*e*), SGE (*f*), out-of-phase SGE (*g*), and immediate (*h*, *i*) and 90-s fat-suppressed (*j*) postgadolinium SGE images in two different patients. The livers are diminutive in size and show irregular nodular contours

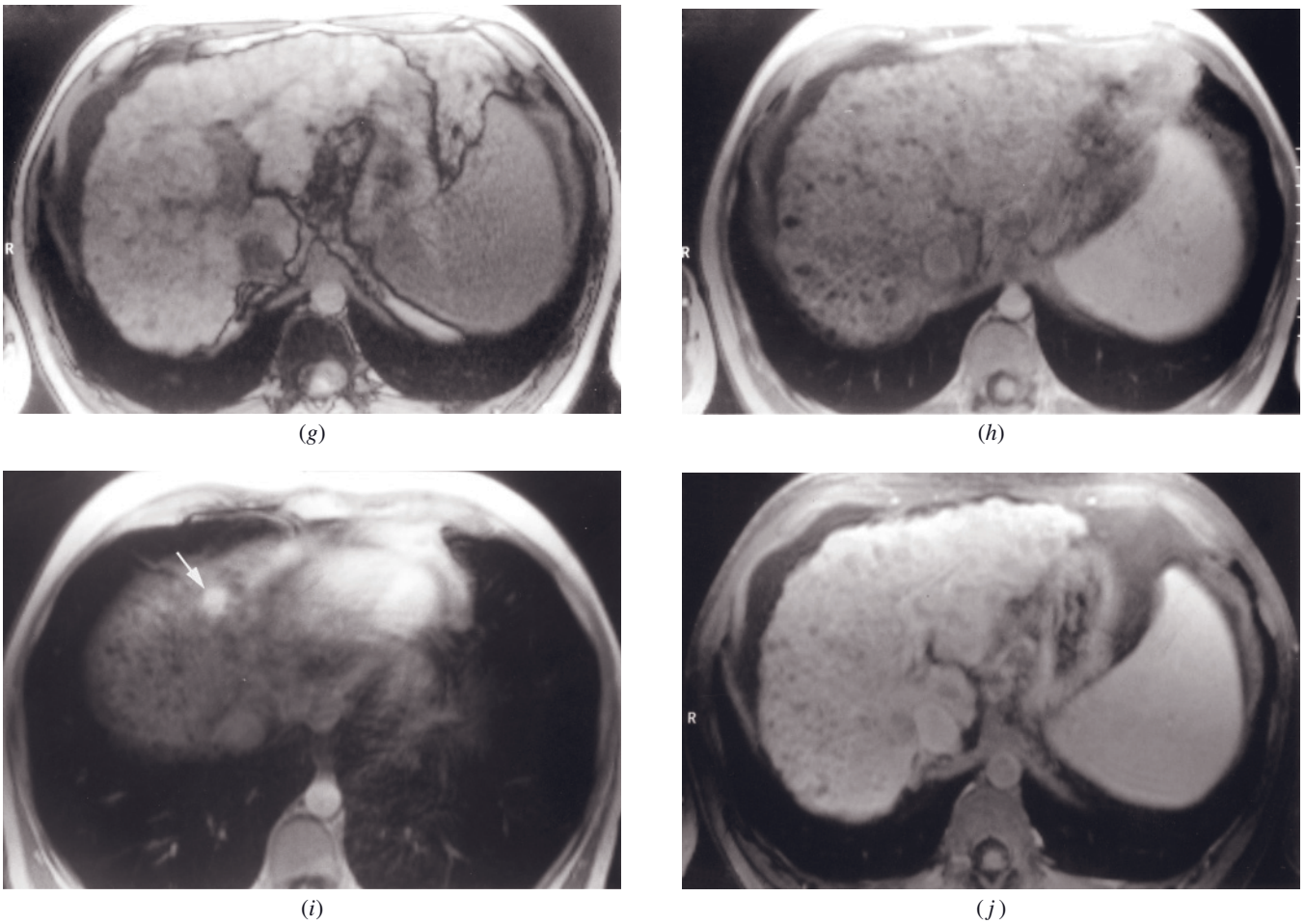

FIG. 2.207 (*Continued*) consistent with cirrhosis. Multiple varying-sized siderotic nodules are appreciated throughout the hepatic parenchyma that demonstrate low signal on both T2-weighted (*a*, *e*) and T1-weighted (*b*, *f*) images and negligible enhancement early (*h*) and late (*j*) after gadolinium administration, compatible with regenerative nodules. In the second patient, an intensely enhancing 1-cm nodule is also shown on early-phase image (arrow, *i*), which fades on late image (not shown) in the dome of the liver, consistent with a high grade dysplastic nodule.

images and hyperintense on T1-weighted images [185, 187, 348]. Like RNs, DNs may also contain iron, which then results in low signal intensity on both T2- and T1-weighted images. Unlike RNs, DNs have been found to contain isolated arteries unaccompanied by bile ducts [338]. Correlations exist between extent of enhancement on arterial dominant images and the grade of DNs. Increase in arterial blood supply and decrease of portal blood supply of hepatic nodules is closely related to the process of malignant transformation to HCC [349, 350]. On MR imaging, low-grade DNs show negligible enhancement or enhancement similar to the background parenchyma (i.e., isointense) on arterial dominant phase (figs. 2.210–2.212), and high-grade DNs may demonstrate enhancement ranging from mild to intense on arterial dominant-phase images (figs. 2.213 and 2.214). There is an overlap in the extent of vascularity and consequently of imaging findings between high-grade DNs and small HCCs [201, 349]. An ancillary feature of high-grade DNs is the tendency to fade toward background signal of the liver in the interstitial phase of enhancement, whereas small HCCs are more likely to exhibit lesion washout with late capsule enhancement. The signal intensity on T2-weighted images, the degree of lesional enhancement on interstitial-phase images, the interval growth, and the presence of large HCC may help in the distinction of high-grade DNs and small HCCs. Our current practice is to describe lesions that measure less than 1 cm with the imaging features of high DN as DN, recognizing the fact that many of these small lesions resolve on their own, likely reflecting a complex interplay between host and lesion pathophysiology.

Foci of small HCC that develop in a high-grade DN appear as a high-signal-intensity focus within a

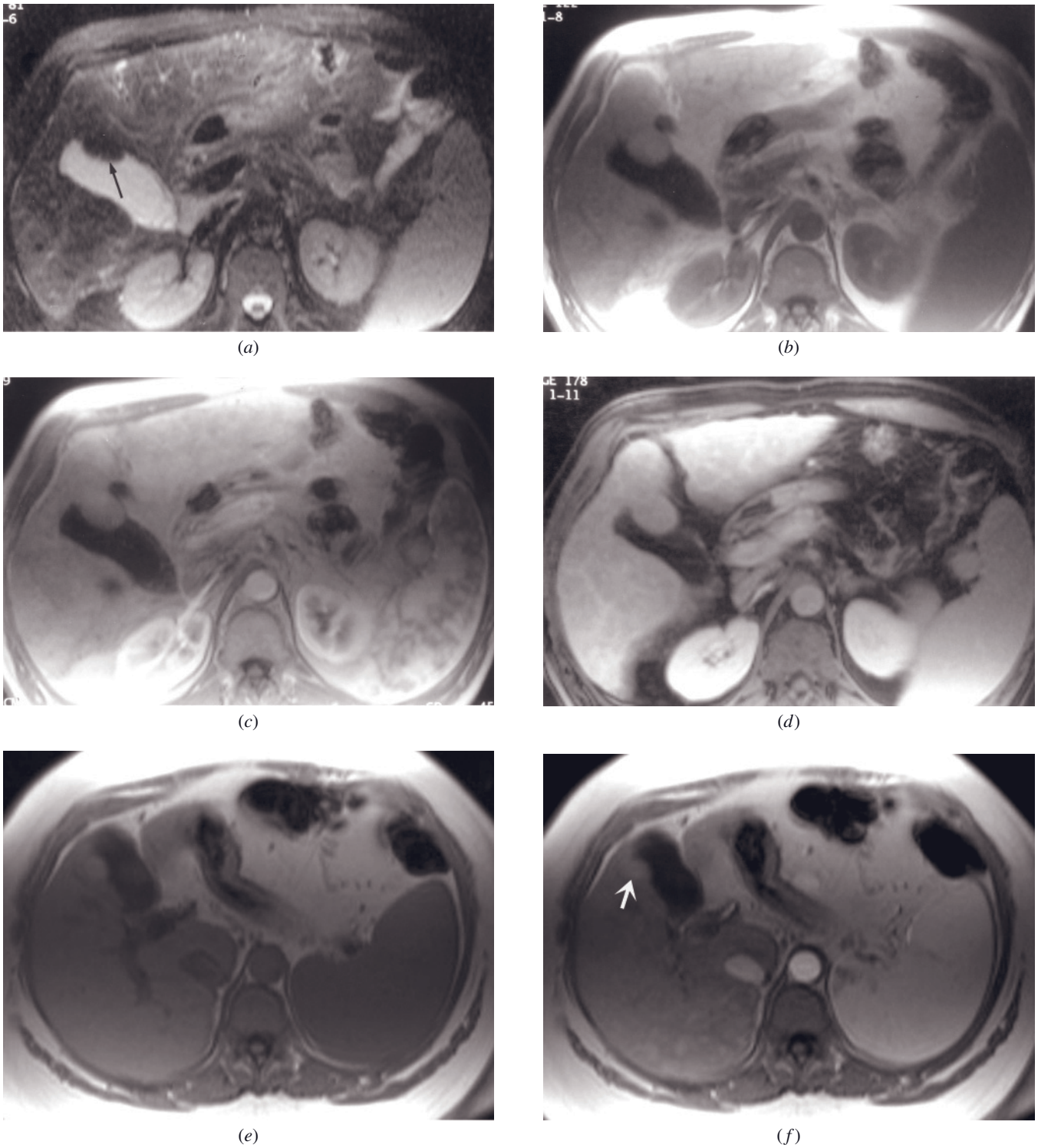

FIG. 2.208 Regenerative nodule extending into the gallbladder fossa. Echo-train STIR (*a*), SGE (*b*), and immediate (*c*) and 90-s fat-suppressed (*d*) postgadolinium SGE images. The liver demonstrates mild diffuse heterogeneous signal on all sequences. There is a hepatic nodule (arrow, *a*) that arises from the tip of segment 4 and indents the anterior wall of the gallbladder, which demonstrates near isointensity with liver on all sequences compatible with a regenerative nodule.

SGE (*e*) and immediate (*f*) images in a second patient that demonstrate a regenerative nodule compressing the posterior wall of the gallbladder (arrow, *f*). It is not uncommon that regenerative nodules bulge into the gallbladder fossa, presumably reflecting that this location experiences less tissue resistance facilitating growth of these nodules as they expand into the gallbladder fossa.

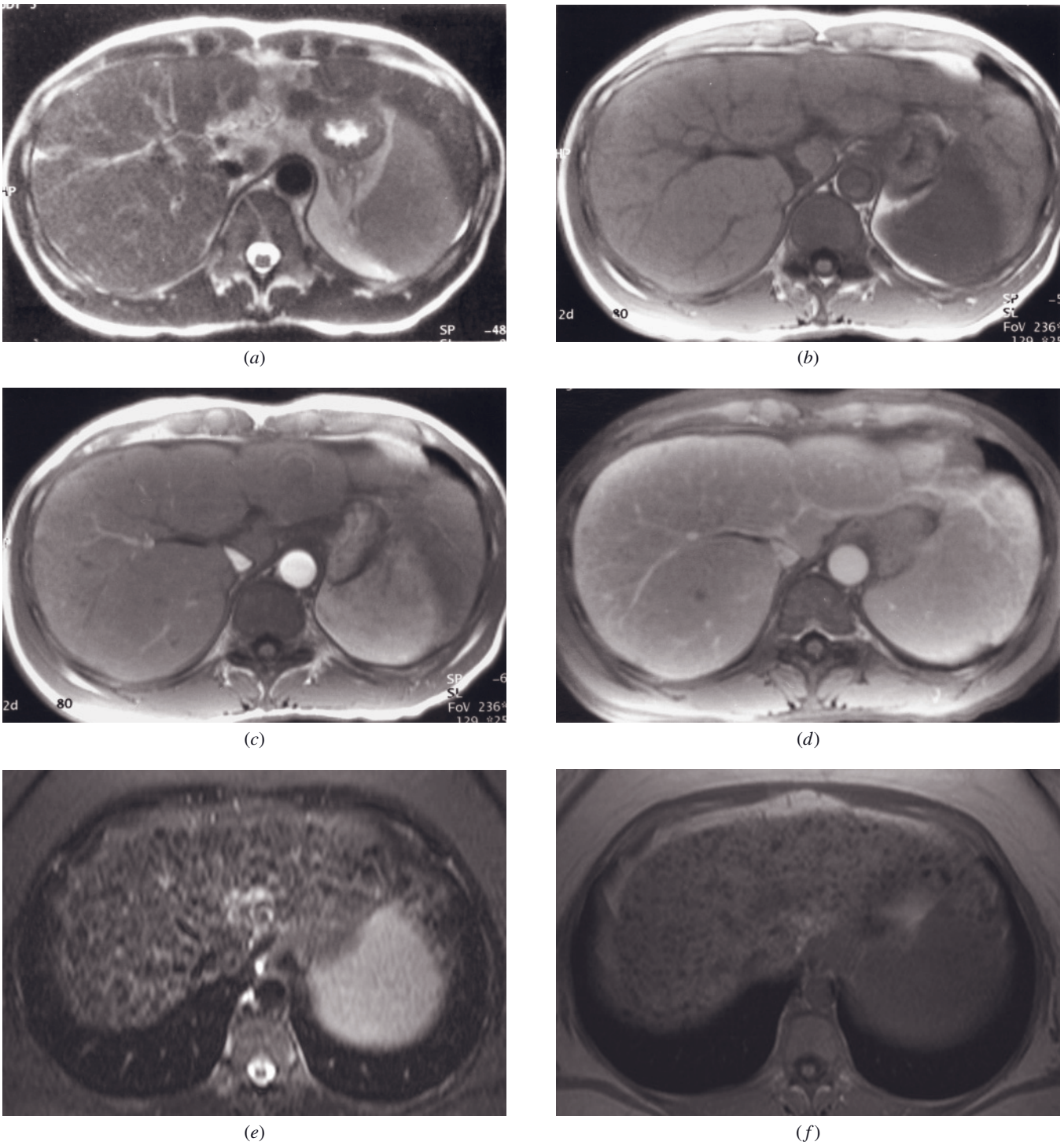

FIG. 2.209 Iron-containing regenerative nodules. T2-weighted ETSE (*a*), SGE (*b*), and immediate (*c*) and 90-s fat-suppressed (*d*) postgadolinium SGE images. There are multiple tiny lesions scattered throughout the liver that demonstrate mild hypointensity to background liver on T2-weighted (*a*) and T1-weighted (*b*) images and negligible enhancement after contrast administration (*c*), consistent with regenerative nodules. Lesions are best seen on the postgadolinium images. Note the fine reticular linear pattern of enhancement on the late image (*d*).

T2-weighted fat-suppressed SS-ETSE (*e*), SGE (*f*), out-of-phase SGE (*g*), and immediate (*h*) and 90-s fat-suppressed (*i*) postgadolinium SGE images (*j*) and SGE (*j*) and immediate (*k*) and 90-s fat-suppressed (*l*) postgadolinium SGE images in two different patients with regenerative nodules. Findings similar to those in the previous case are shown.

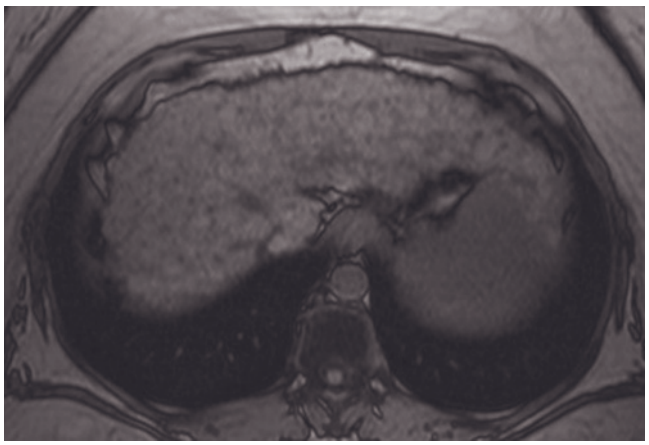

(*g*)

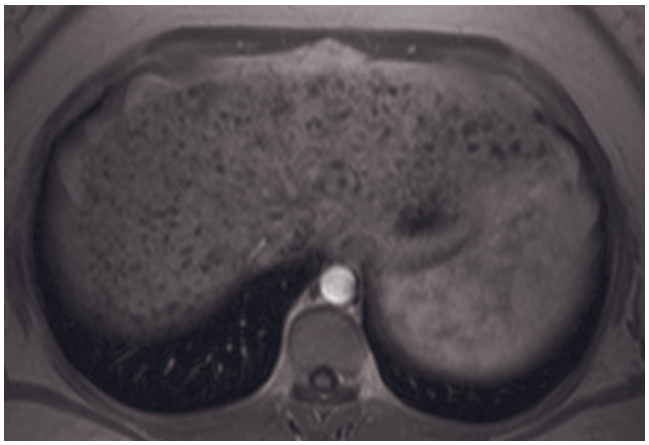

(*h*)

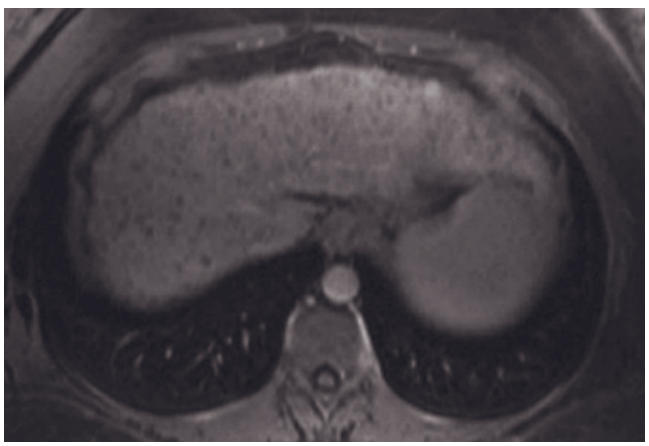

(*i*)

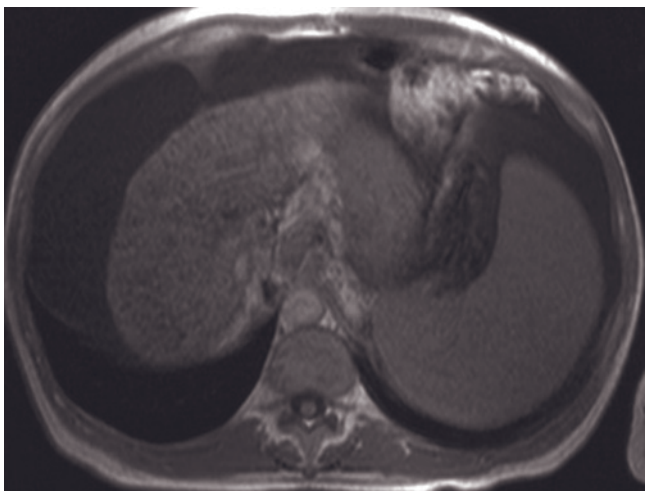

(*j*)

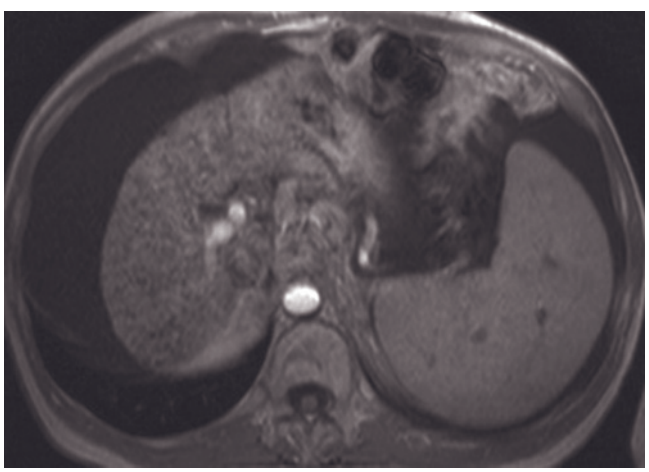

(*k*)

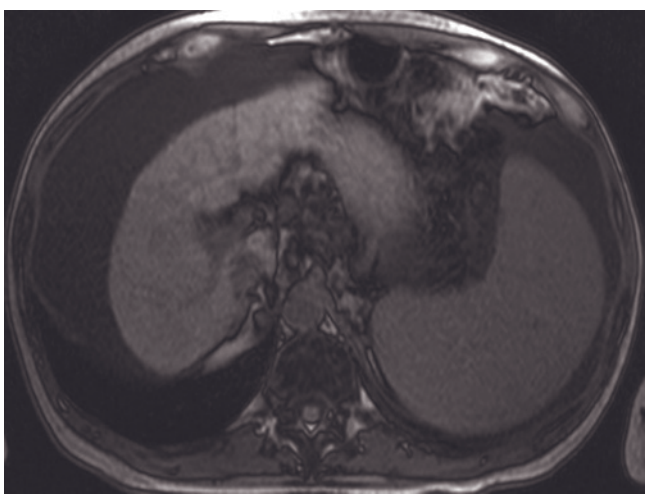

(*l*)

Fig. 2.209 (*Continued*)

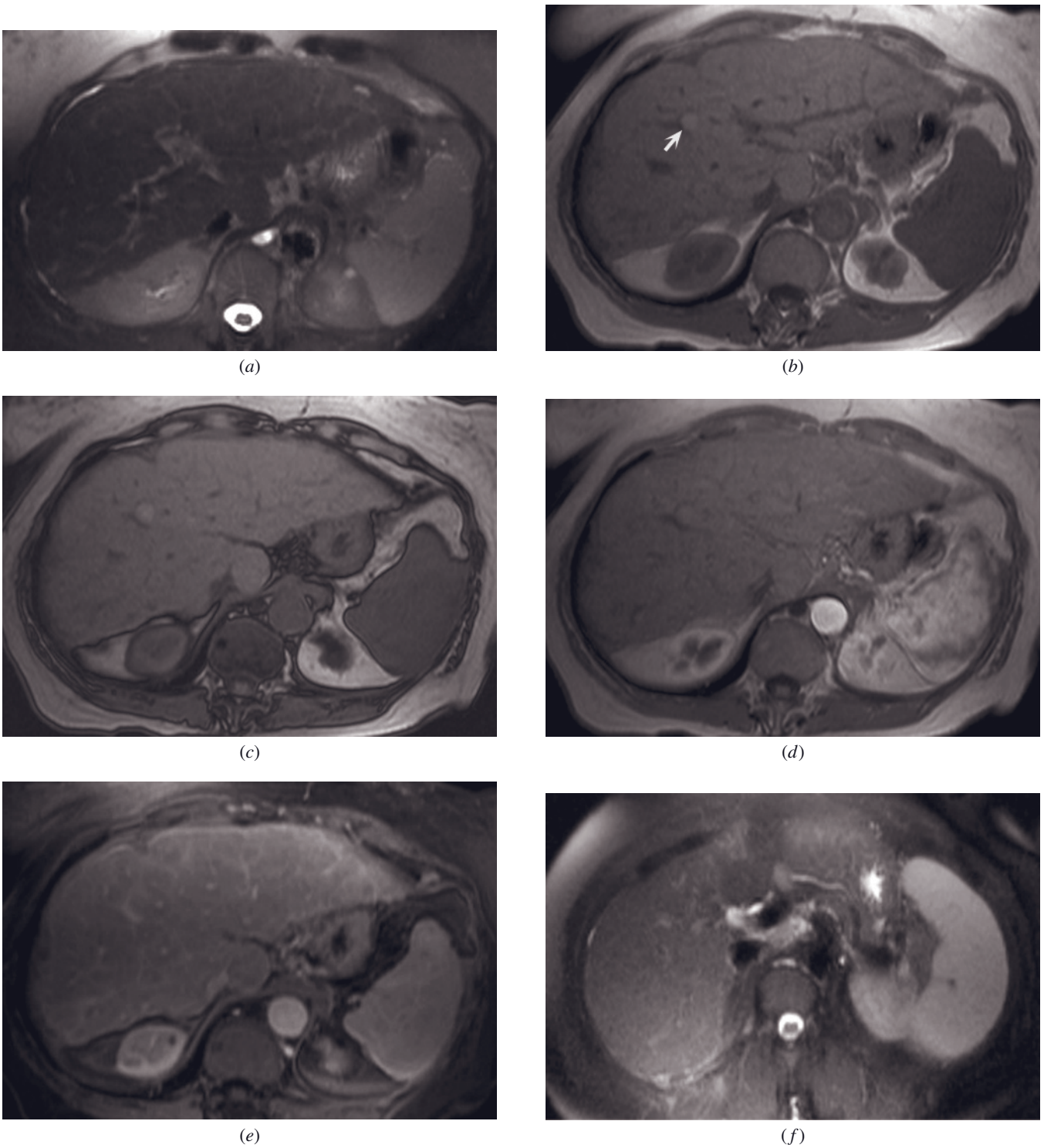

FIG. 2.210 Cirrhosis with low-grade dysplastic nodules. T2-weighted SS-ETSE (*a*), SGE (*b*), out-of-phase SGE (*c*), and immediate (*d*) and 90-s fat-suppressed (*e*) postgadolinium SGE images. There is a nodule in segment 8 of the liver that is isointense on T2 (*a*) and moderately high signal intensity on T1 (arrow, *b*), does not drop in signal intensity on out-of-phase image (*c*), and shows negligible enhancement on early-phase postgadolinium image (*d*) and remains isointense to the background parenchyma on late-phase image (*e*), consistent with a low-grade dysplastic nodule.

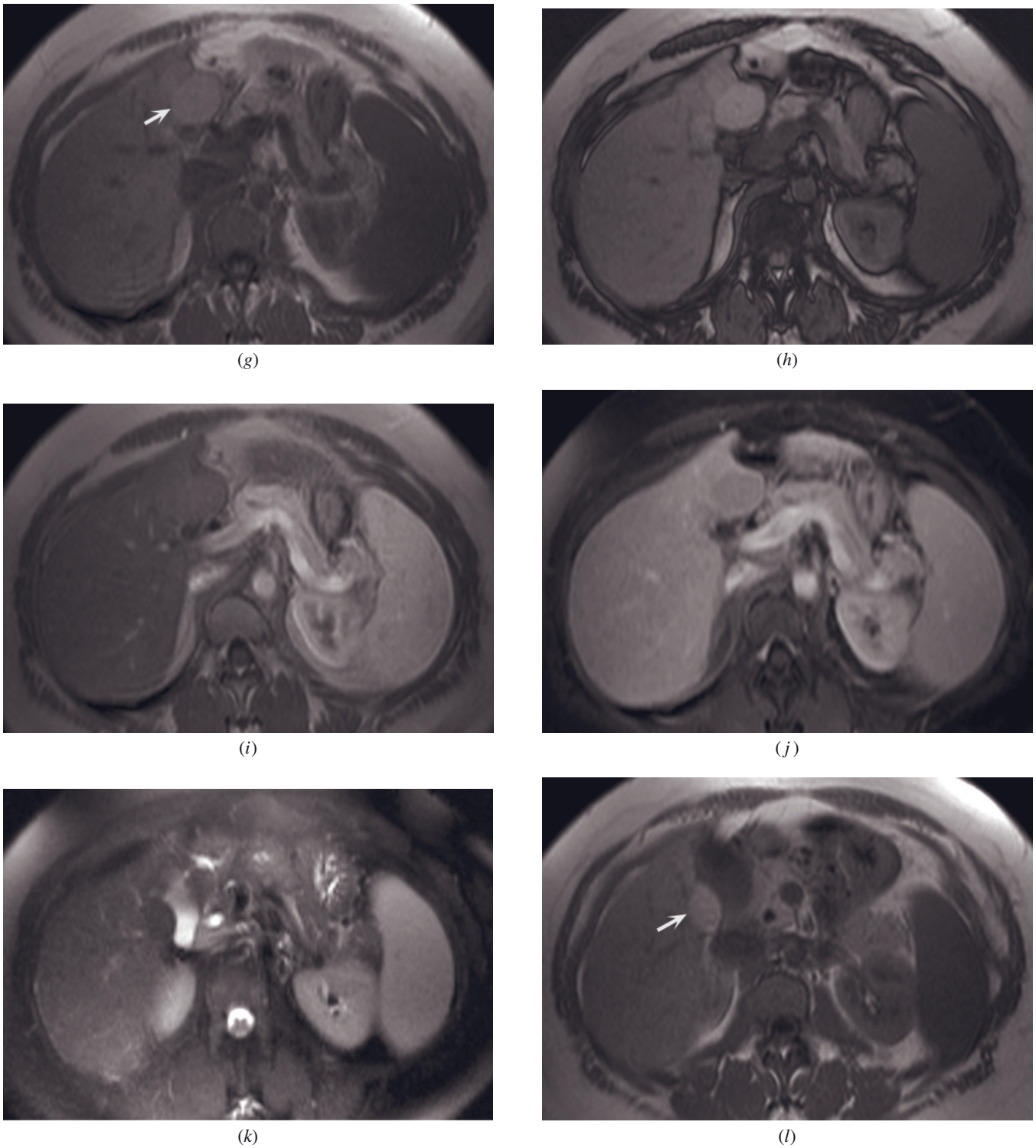

Fig. 2.210 (*Continued*) T2-weighted fat-suppressed SS-ETSE (*f*, *k*), SGE (*g*, *l*), out-of-phase SGE (*h*, *m*), and immediate (*i*, *n*) and 90-s fat-suppressed (*j*, *o*) postgadolinium SGE images in a second patient at two different tomographic levels. Nodules are present at both levels (arrow, *g, l*), demonstrating mildly decreased signal intensity on T2 (*f*, *k*), moderately high signal intensity on T1 (*g*, *l*), no signal drop on out-of-phase (*h*, *m*), and enhancement comparable to background parenchyma on early (*i*, *n*)- and late (*j*, *o*)-phase images.

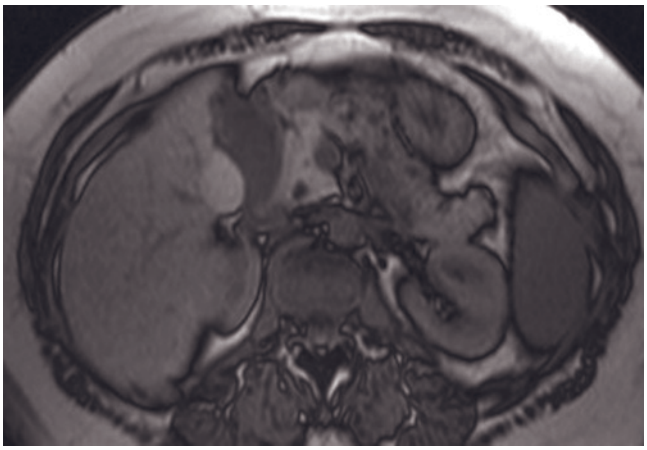

(*m*)

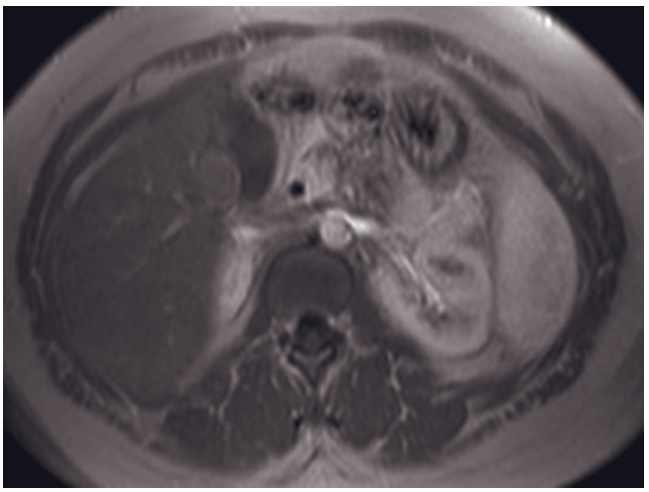

(*n*)

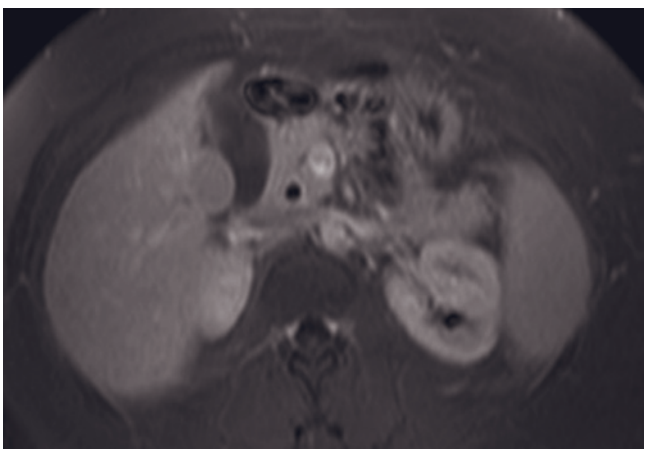

(*o*)

FIG. 2.210 (*Continued*)

low-signal-intensity nodule on T2-weighted images—a nodule within a nodule. This reflects the development of a high-T2-signal malignancy within a low-T2-signal dysplastic nodule. On T1-weighted images, the high-grade DN exhibits low signal and the foci of small HCC may appear isointense with the liver parenchyma. (fig. 2.215) [351–353].

Portal hypertension results from obstruction at presinusoidal (e.g., portal vein), sinusoidal (e.g., cirrhosis), postsinusoidal (e.g., hepatic vein), or multiple levels [354]. The most common cause of portal hypertension is cirrhosis. Portal hypertension causes or exacerbates complications of cirrhosis such as variceal bleeding, ascites, and splenomegaly. Portosystemic shunts may be identified with 2D time-of-flight techniques or gadolinium-enhanced SGE sequences. Gadolinium-enhanced 3D GE imaging, alone or with fat suppression, is a particularly effective technique. Direction of flow may be determined by using 2D phase-contrast techniques, or directional information may be derived by observing time-of-flight effects in the main portal vein and correlating it with time-of-flight effects in the aorta and inferior vena cava (IVC). The latter technique is best performed by acquiring superior and inferior multislice slabs, the bottom and top respectively, of the two slabs obtained at the level of the porta hepatis.

In the early stages of portal hypertension, the portal venous system dilates but flow is maintained. Later, substantial portosystemic shunting develops, reducing the volume of flow to the liver and decreasing the size of the portal vein. With advanced portal hypertension, portal flow may reverse and become hepatofugal. Thrombosis of the portal veins may develop, with development of collaterals referred to as cavernous transformation (figs. 2.216 and 2.217).

Mesenteric, omental, and retroperitoneal edema occur commonly in patients with cirrhosis, because of portal hypertension (figs. 2.218–2.220). The appearance

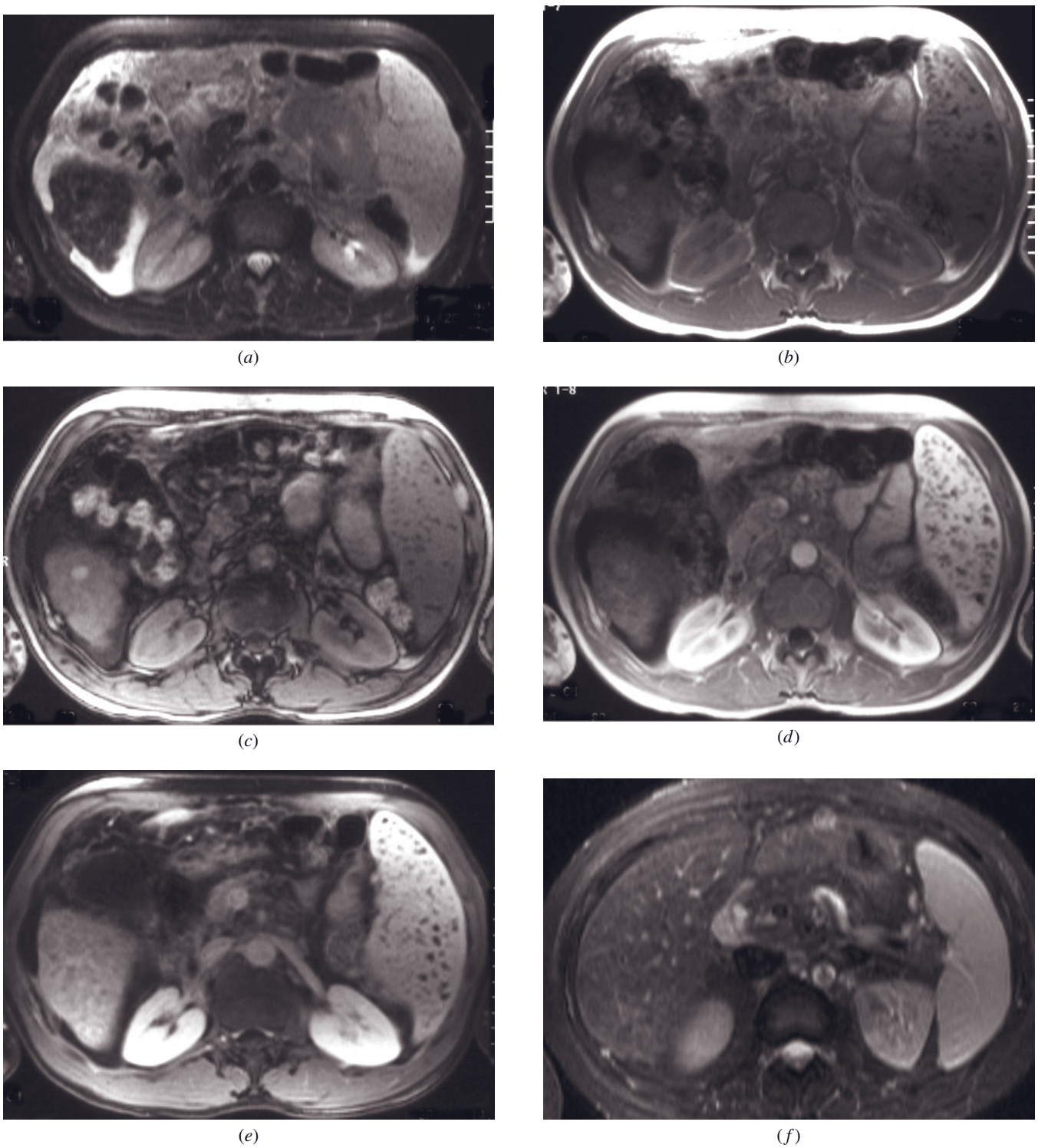

FIG. 2.211 Cirrhosis with low-grade dysplastic nodules. T2-weighted fat-suppressed SS-ETSE (*a*), SGE (*b*), out-of-phase SGE (*c*), and immediate (*d*) and 90-s fat-suppressed (*e*) postgadolinium SGE images. A nodule is present in segment 5 of the liver, which is low signal intensity on T2 (*a*) and high signal intensity on T1 (*b*), does not drop in signal intensity on out-of-phase image (*c*), and enhances to the same extent as background parenchyma on early (*d*)- and late (*e*)-phase images compatible with a low-grade dysplastic nodule.

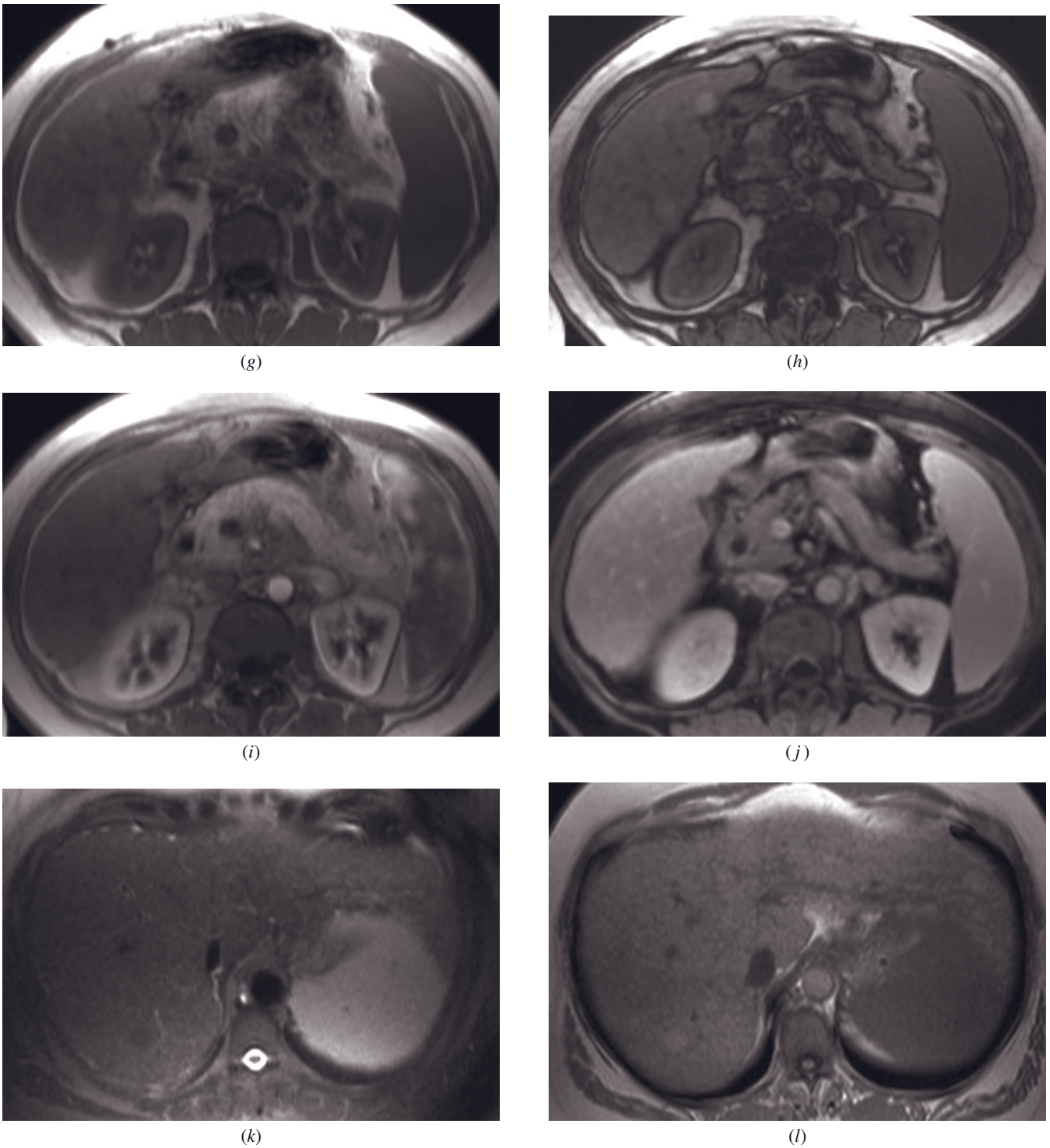

FIG. 2.211 (*Continued*) T2-weighted fat-suppressed SS-ETSE (*f*, *k*), SGE (*g*, *l*), out-of-phase SGE (*h*, *m*), and immediate (*i*, *n*) and 90-s fat-suppressed (*j*, *o*) postgadolinium SGE images in a second and third patient with low-grade dysplastic nodules. In both cases, the low-grade dysplastic nodules are most evident on T1 (*g, l*) and out-of-phase (*h*, *m*) images. On the other sequences, the low-grade dysplastic nodules have signal intensity similar to background parenchyma.

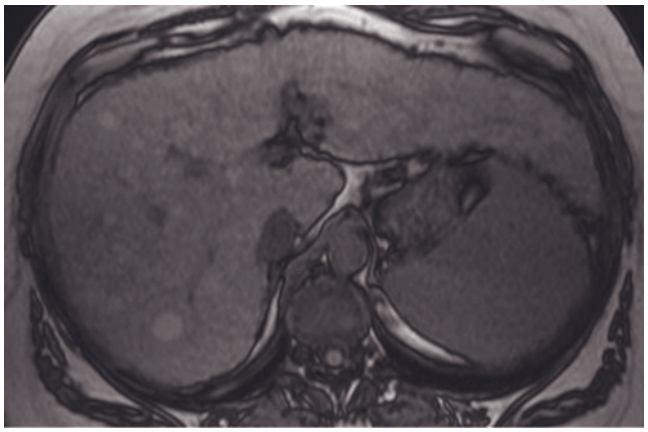

(*m*)

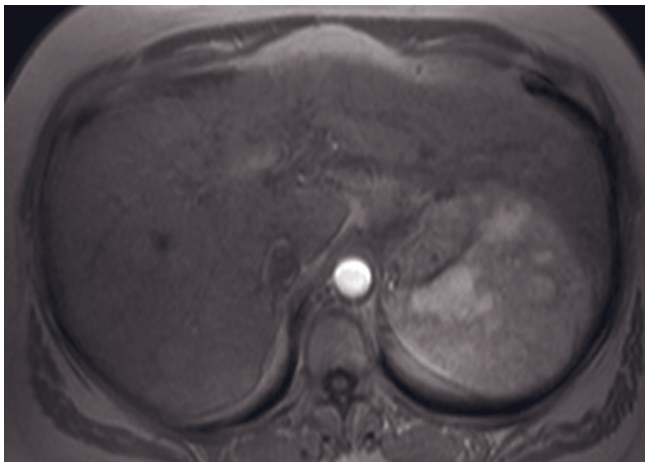

(*n*)

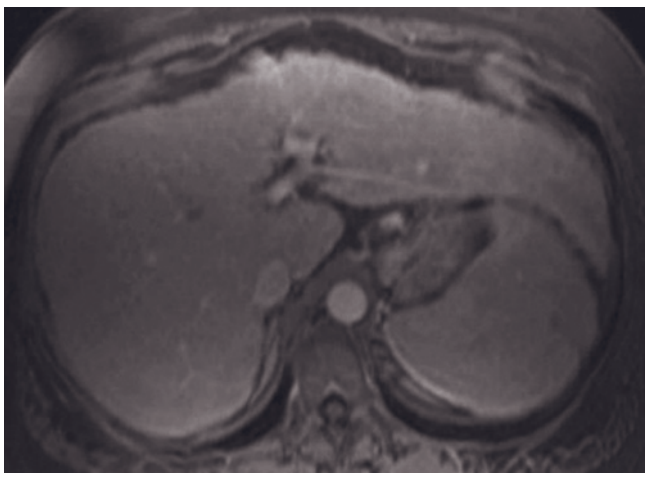

(*o*)

FIG. 2.211 (*Continued*)

of mesenteric edema varies from a mild infiltrative haze to a substantial masslike sheath that engulfs the mesenteric vessels [322, 355]. Gastrointestinal wall thickening is seen in as many as 25% of patients with end-stage cirrhosis, also secondary to portal hypertension. Many of these patients do not have specific bowel symptoms [322].

Portal varices arise from increased portal pressure, and portal blood is shunted into systemic veins, bypassing hepatic parenchyma. Nutrients absorbed from the gastrointestinal (GI) tract are metabolized less effectively, and hepatic function decreases. Toxic metabolites such as ammonia accumulate in the blood and result in clinical manifestations such as hepatic encephalopathy. Diminished portal flow to the liver parenchyma is a major factor in the production of liver atrophy and prevention of regeneration [356], and portosystemic shunting may play a role in the development of hepatic atrophy in advanced cirrhosis. Major sites of portosystemic collateralization include gastroesophageal junction, paraumbilical veins (figs. 2.221 and 2.222), retroperitoneal regions, perigastric, splenorenal, omentum, peritoneum, and hemorrhoidal veins [337]. Esophageal varices are a serious complication because they may rupture and produce life-threatening hemorrhage (fig. 2.223). Flow-sensitive gradient-echo or gadolinium-enhanced gradient-echo images effectively demonstrate varices as high-signal tubular structures (fig. 2.224) [357]. Varices are particularly conspicuous with fat suppression and gadolinium enhancement on gradient-echo images as the competing high signal intensity of fat is removed. Gadolinium-enhanced water excitation gradient echo is another approach to demonstrate varices, as the excitation pulse possesses time-of-flight effects that accentuate the high signal in vessels produced by gadolinium enhancement. These sequences are more sensitive than contrast angiography, endoscopy, or contrast-enhanced CT imaging for detecting varices [358].

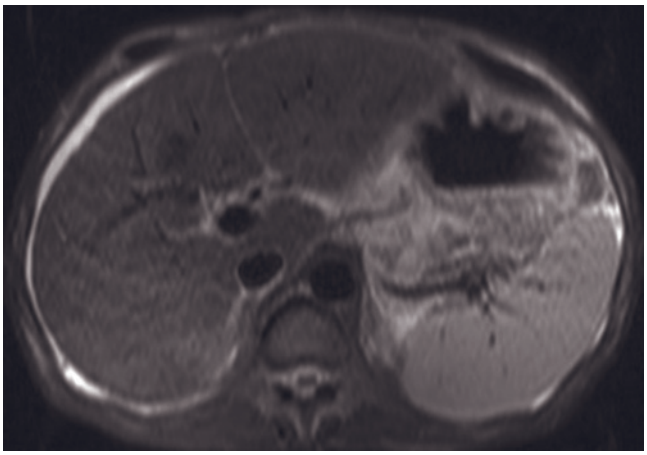

(*a*)

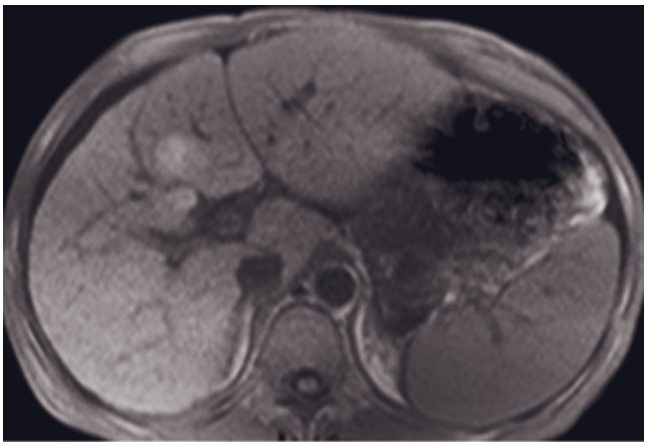

(*b*)

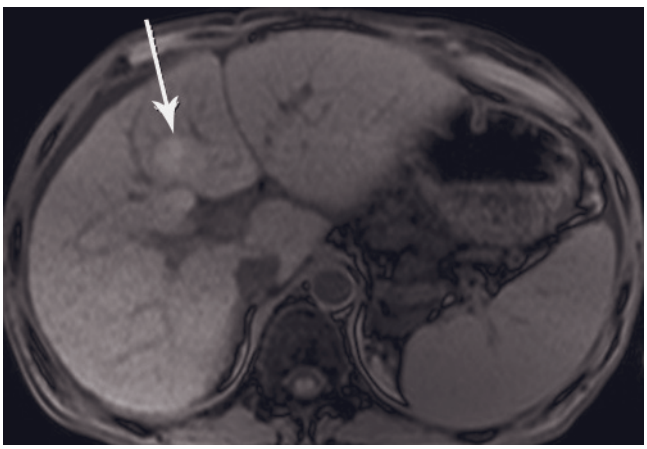

(*c*)

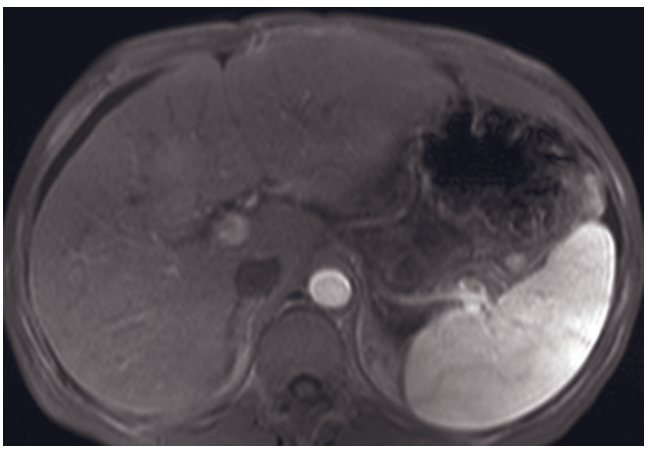

(*d*)

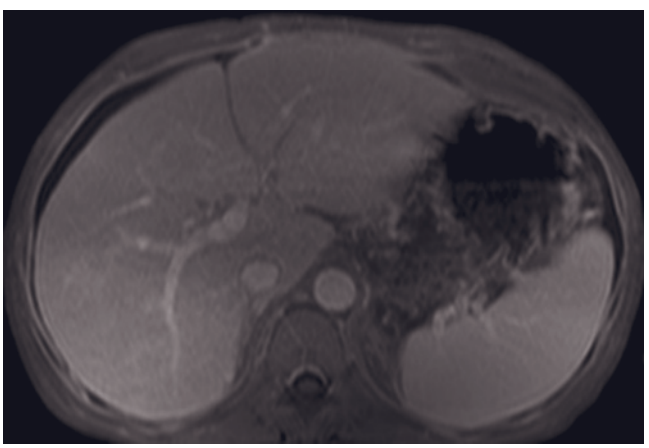

(*e*)

FIG. 2.212 Cirrhosis with low-grade dysplastic nodule. T2-weighted fat-suppressed SS-ETSE (*a*), SGE (*b*), out-of-phase SGE (*c*), and immediate (*d*) and 90-s fat-suppressed (*e*) postgadolinium SGE images. There is a nodule in the right hepatic lobe that shows low signal intensity on T2 (*a*) and high signal intensity on T1 (*b*), does not drop in signal intensity on out-of-phase image (arrow, *c*), and shows minimal enhancement on early-phase image (*d*) with isointensity with background parenchyma on late-phase image (*e*). Note also the presence of ascites.

Porta Hepatis Lymphadenopathy

Porta hepatis lymphadenopathy is a common finding in benign and malignant liver disease. Porta hepatis lymphadenopathy is almost invariably present in chronic liver disease [359]. The detection of malignant porta hepatis lymph nodes is crucial in decision making for management of patients with malignant disease. The most effective approach for the detection of lymph nodes is the combined use of a fat-suppressed T2-weighted sequence and interstitial-phase gadolinium-enhanced T1-weighted fat-suppressed imaging. On the T2 sequence, lymph

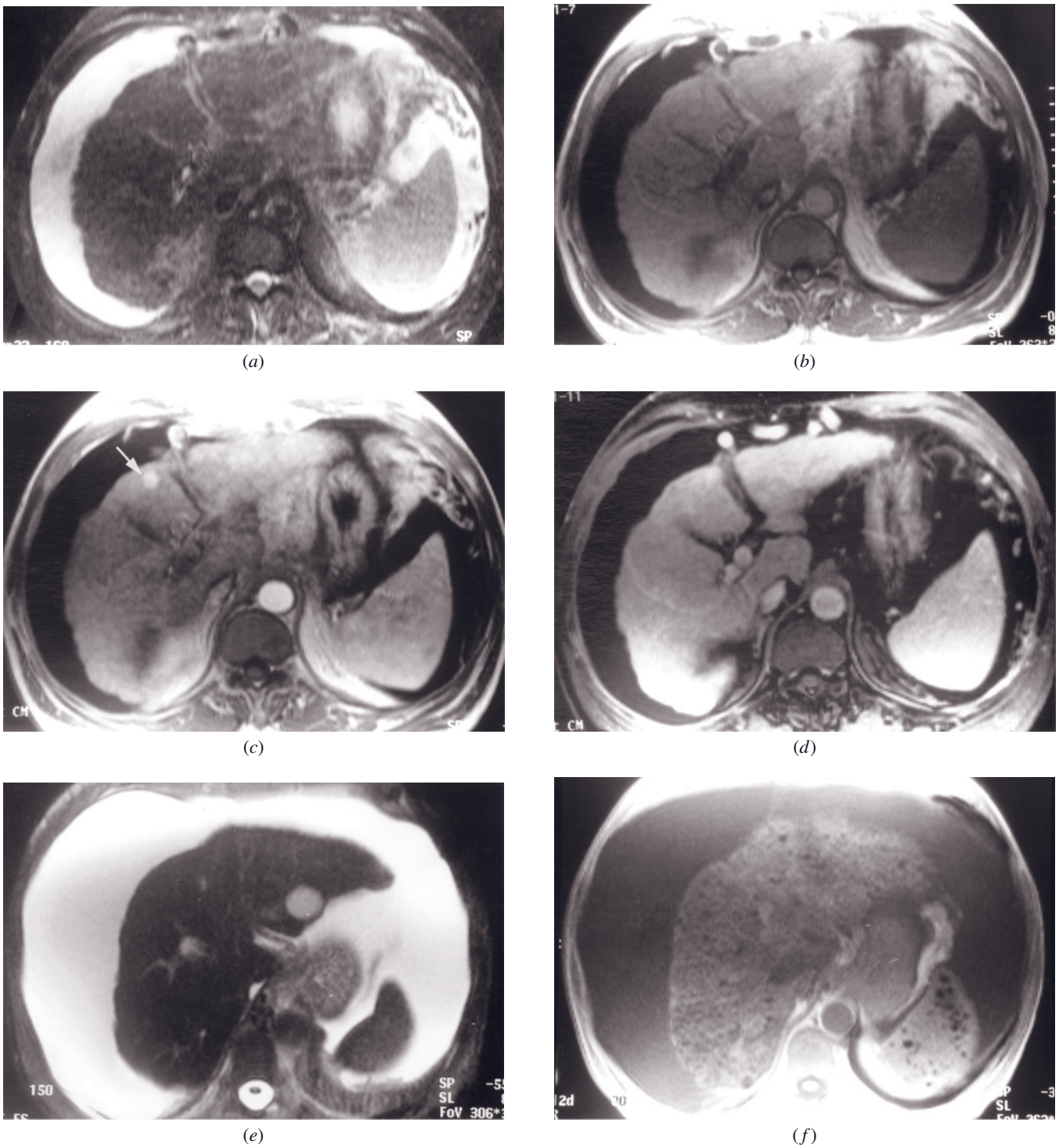

FIG. 2.213 Cirrhosis with high-grade dysplastic nodules. Echo-train STIR (*a*), SGE (*b*), and immediate (*c*) and 90-s fat-suppressed (*d*) postgadolinium SGE images. The liver is small and nodular, compatible with cirrhosis. There is a 1-cm lesion (arrow, *c*) in segment 4 that is not evident on T2 (*a*)- or T1 (*b*)-weighted images but displays intense enhancement on the immediate postgadolinium image (*c*) and fades to isointensity on the late image (*d*), consistent with a high-grade dysplastic nodule. Note also the presence of ascites and collateral vessels.

T2-weighted fat-suppressed SS-ETSE (*e*), SGE (*f*), and immediate (*g*, *h*) and 90-s fat-suppressed (*i*) postgadolinium SGE images in a second patient. The liver is very small, nodular, and irregular in contour, consistent with cirrhosis. Multiple nodules are identified in the liver that demonstrate isointense to mildly high signal intensity on T2 (*e*), low signal intensity on T1 (*f*), and intense enhancement immediately after administration of contrast (*g*, *h*), with persistent enhancement on late images (*i*), compatible with high-grade dysplastic nodules. Note the hemangiomas in the left lobe of the liver, Gamna–Gandy bodies in the spleen and large-volume ascites.

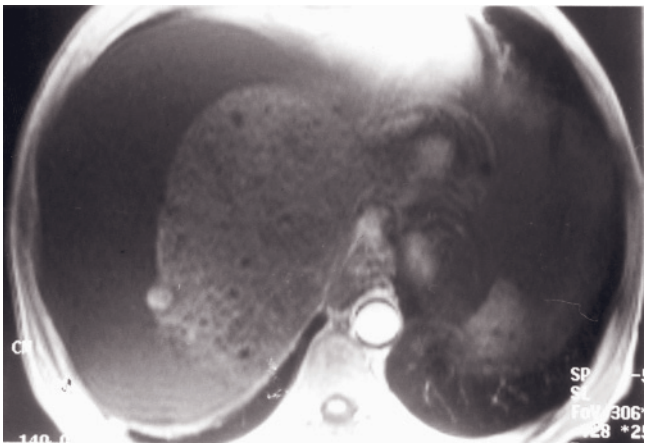

(*g*)

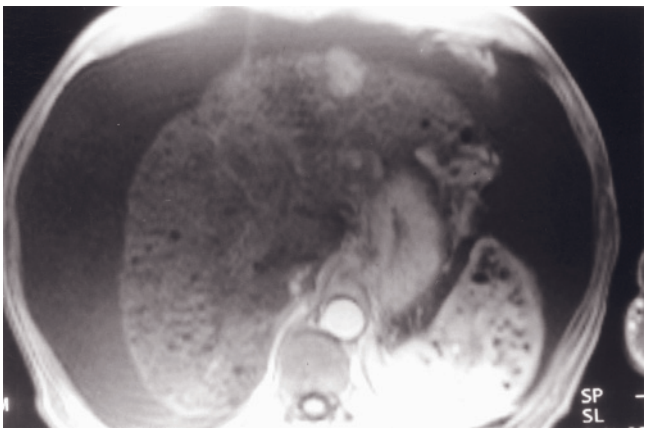

(*h*)

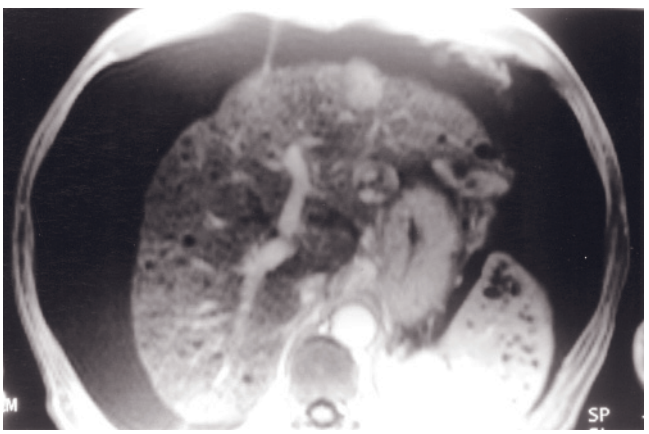

(*i*)

FIG. 2.213 (*Continued*)

nodes are moderately high signal and both liver and background fat are relatively low signal, rendering excellent conspicuity. Definition of the rounded contour of lymph nodes is optimal with the gadolinium-enhanced T1-weighted fat-suppressed technique and thereby distinguishes rounded lymph nodes from ill-defined inflammatory tissue, which is also high signal on T2 (fig. 2.225).

Iron Overload

Primary (Idiopathic Hemochromatosis)

Genetic Hemochromatosis. Genetic hemochromatosis (GH) is a common genetic disorder among the Caucasian population in the United States [360]. GH results from excessive gastrointestinal absorption and deposition of iron in tissues such as liver, heart, pancreas, anterior pituitary, joints. and skin. Early in the disease process, iron accumulation is restricted to the liver (fig. 2.226) [361]. Pathologic features of hemochromatosis in the liver include iron deposition as hemosiderin pigment granules in hepatocytes. Iron is a direct hepatotoxin. Fibrous septa develop slowly, leading to micronodular cirrhosis. Kupffer cell (RES) uptake of hemosiderin pigment is not marked. Over time, iron deposition progresses to involve other organs, primarily the pancreas and heart (fig. 2.227). Serologic abnormalities and mild symptoms may occur earlier in life, but the clinical signs and symptoms do not appear until the fifth or sixth decade of life [360]. Disease detection at an early stage, with institution of phlebotomy therapy, may result in a normal life expectancy [362]. Untreated, it results in end-organ damage, which may include cirrhosis and HCC; HCC often is the cause of death [360, 363, 364].

A diagnostic feature of idiopathic hemochromatosis is that signal intensity of the spleen is not substantially decreased on T2-weighted or T2*-weighted images. This finding is due to accumulation of iron within the parenchyma of the liver and pancreas and lack of selective uptake by the RES in the spleen. The presence of iron deposition in the pancreas correlates with irreversible changes of cirrhosis in the liver.

Some patients who present with HCC have previously unsuspected GH (fig. 2.228) [365]. Because tumor

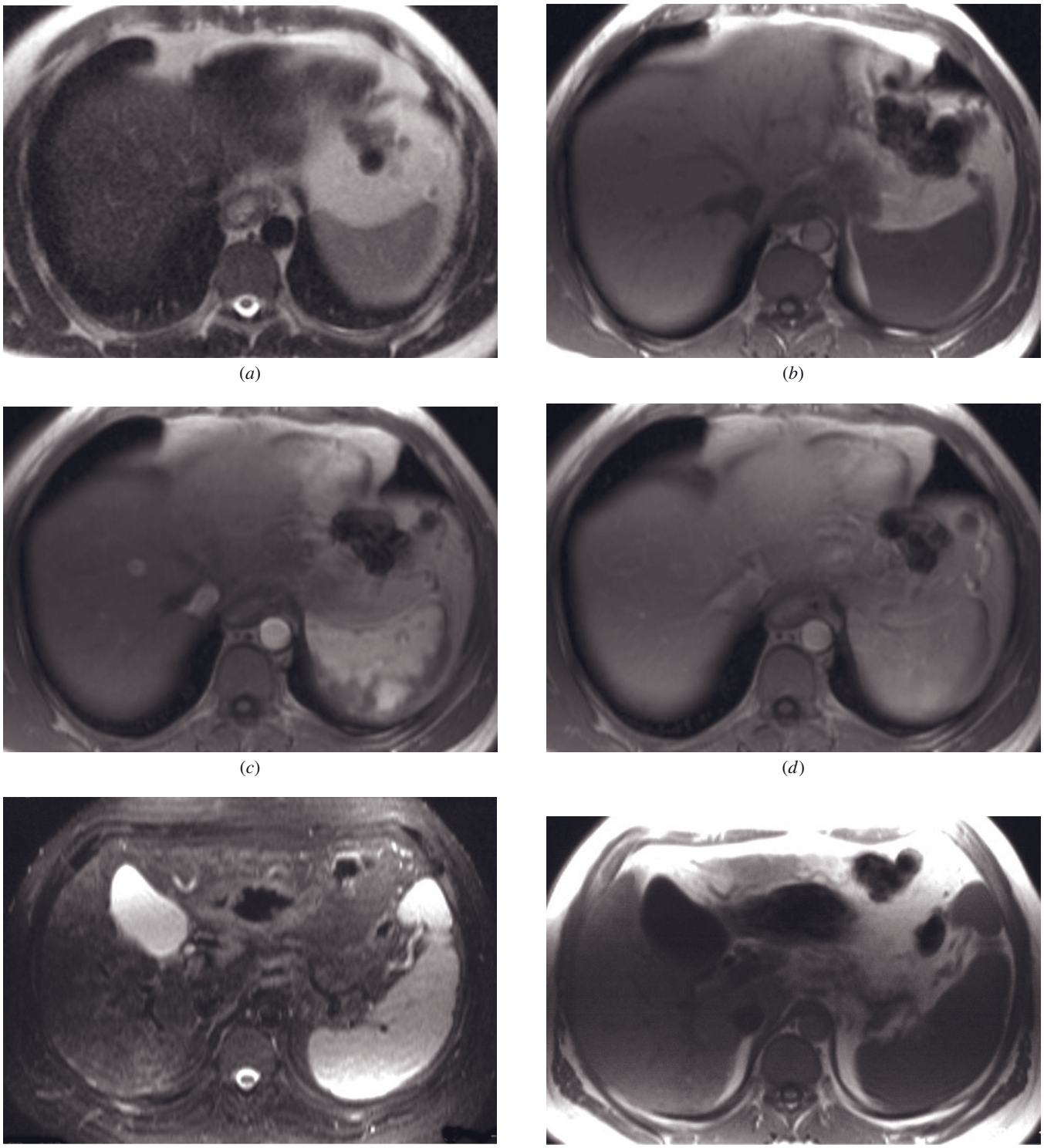

FIG. 2.214 Cirrhosis with high-grade dysplastic nodule. T2-weighted SS-ETSE (*a*), SGE (*b*), and immediate (*c*) and 45-s (*d*) postgadolinium SGE images in a cirrhotic patient. A high-grade dysplastic nodule is appreciated at the junction between segments 8 and 5, which demonstrates mildly high signal intensity on T2 (*a*), isointensity on T1 (*b*), and intense homogeneous enhancement on early-phase image (arrow, *c*) that fades on 45-s image (*d*).

T2-weighted fat-suppressed SS-ETSE (*e*), SGE (*f*), and immediate (*g*) and 90-s fat-suppressed (*h*) postgadolinium SGE images and

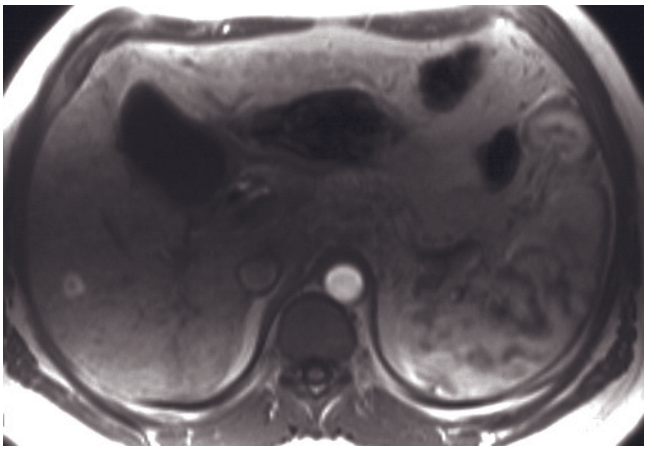

(*g*)

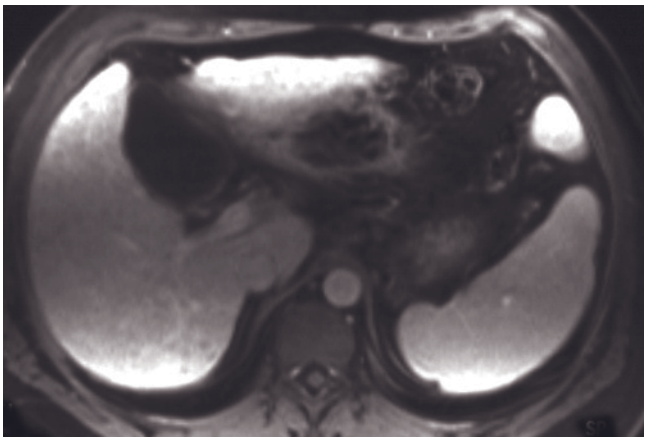

(*h*)

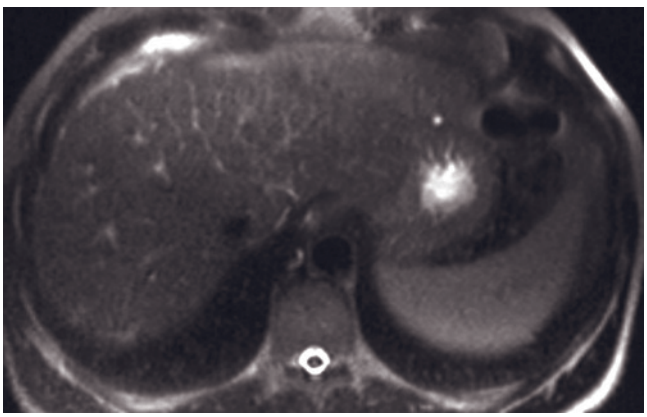

(*i*)

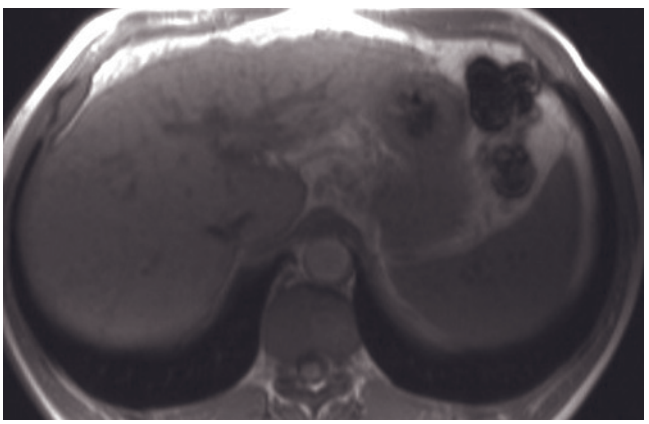

(*j*)

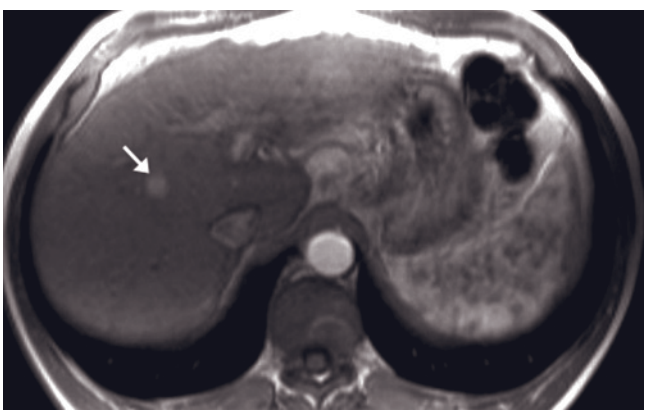

(*k*)

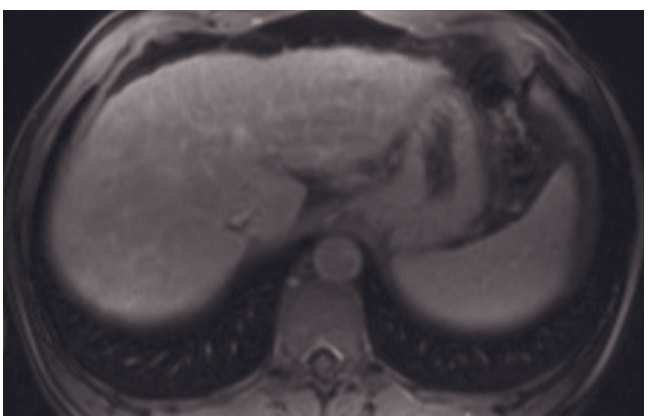

(*l*)

FIG. 2.214 (*Continued*) T2-weighted SS-ETSE (*i*), SGE (*j*), and immediate (*k*) and 90-s fat-suppressed (*l*) postgadolinium SGE images in a second and third cirrhotic patient with a high-grade dysplastic nodule. The nodule shows mildly high signal intensity on T2-weighted image (*e*), mildly low signal intensity on T1-weighted image (*f*), and intense enhancement on early-phase image (*g*) that fades on late-phase image (*h*). The same findings are observed in the third patient (arrow, *k*).

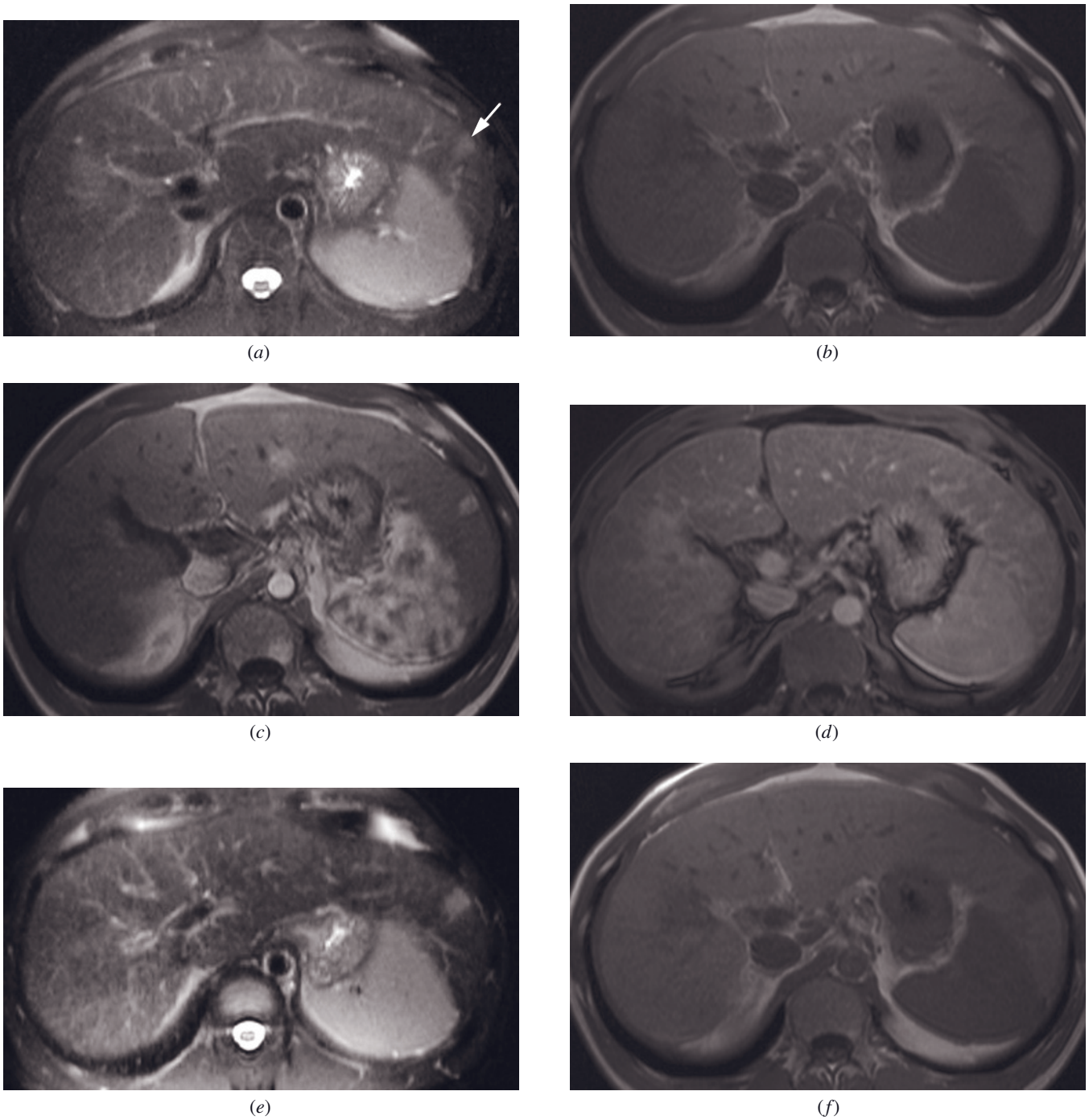

FIG. 2.215 Development of HCC from high-grade dysplastic nodule and nodule-in-nodule appearance of early HCC. Fat-suppressed T2-weighted SS-ETSE (*a*), SGE (*b*), and immediate (*c*) and 90-s fat-suppressed (*d*) postgadolinium SGE images. A lesion is seen in the left lobe that shows slightly high signal intensity on T2-weighted image (*a*) and slightly low signal intensity on T1-weighted image (*b*) and demonstrates moderate enhancement on early-phase image (*c*) that fades to background parenchyma on late-phase image (*d*), compatible with a high-grade dysplastic nodule. Fat-suppressed T2-weighted SS-ETSE (*e*), SGE (*f*), and

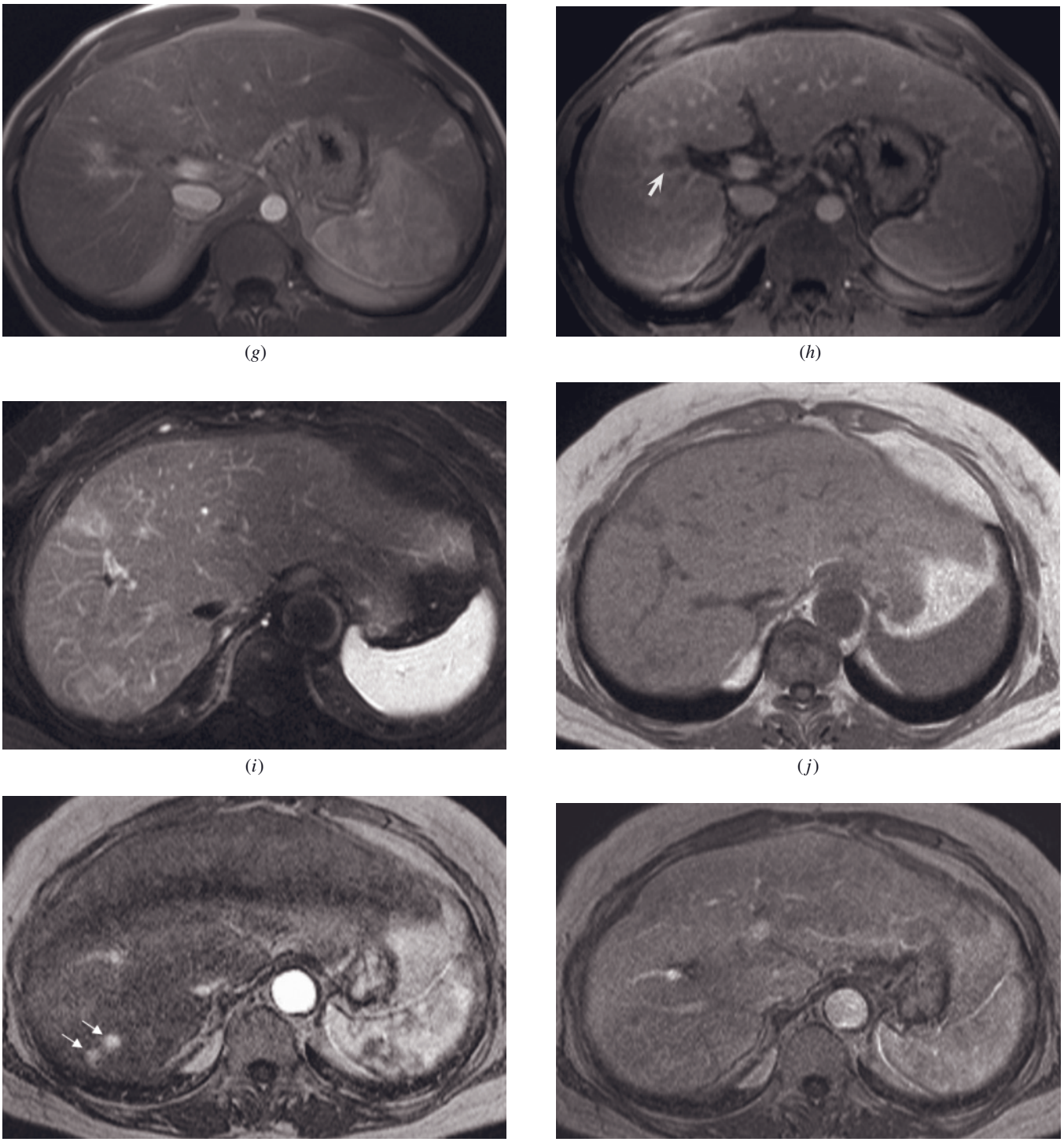

FIG. 2.215 (*Continued*) immediate (*g*) and 90-s fat-suppressed (*h*) postgadolinium SGE images in a 6-month follow-up examination show an intense enhancement on early-phase image (*g*) that washes out with capsule enhancement on late-phase image (arrow, *h*), consistent with HCC. T2-weighted fat-suppressed SE (*i*), T1-weighted SGE (*j*), and T1-weighted immediate (*k*) and 90-s post gadolinium (*l*) images in a second patient. T2-weighted (*i*) and T1-weighted (*j*) images show two areas in the right hepatic lobe that exhibit high and low signal intensity, respectively. After contrast, one of the areas demonstrates two foci (arrows, *k*) of intense enhancement that fades on late-phase images (*l*), consistent with small HCCs within a dysplastic nodule. (Courtesy of Masayuki Kanematsu, M.D., Gifu University, Japan.)

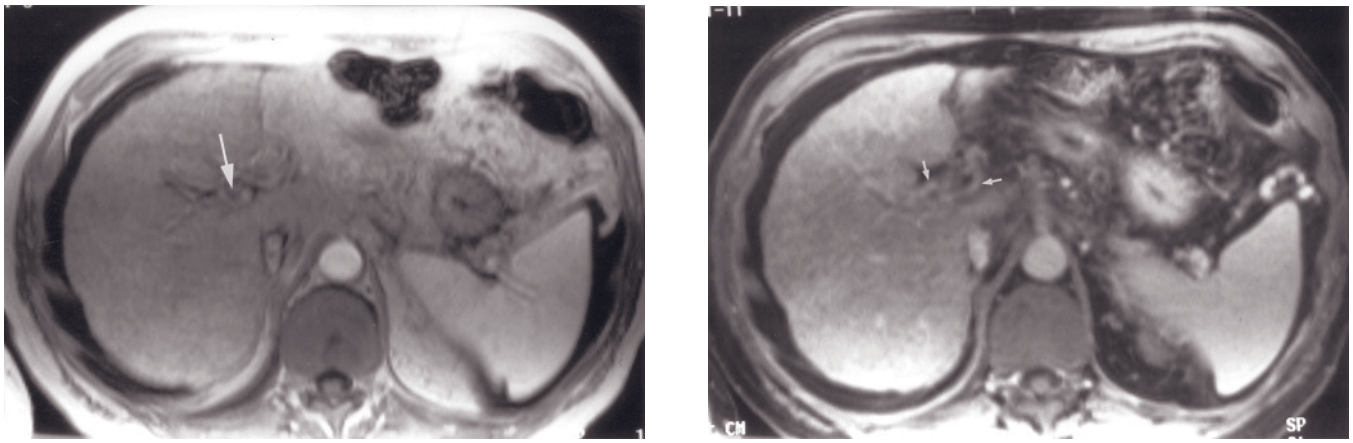

(*a*) (*b*)

FIG. 2.216 Cavernous transformation of the portal vein. Immediate (*a*) and 90-s fat-suppressed (*b*) postgadolinium SGE images in a patient who has a history of cirrhosis. Thrombus (arrow, *a*) is present in a diminutive portal vein, and multiple small serpiginous collateral vessels (arrows, *b*) are identified in the porta hepatis, consistent with cavernous transformation. Note also ascites and splenomegaly.

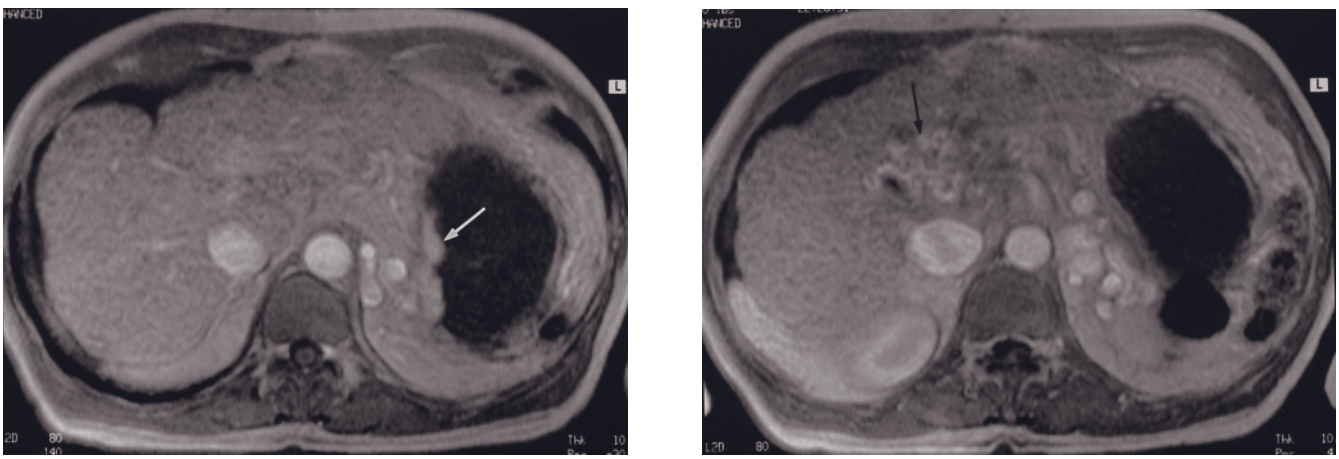

(*a*) (*b*)

FIG. 2.217 Gastric varices and cavernous transformation of the portal vein. Transverse 45-s postgadolinium SGE images (*a*, *b*) demonstrate a cirrhotic liver with irregular contour and multiple low-signal-intensity <5-mm regenerative nodules. Prominent varices are present along the lesser curvature, which are well shown on portal-phase postgadolinium images. Multiple small serpiginous enhancing structures are present in the porta hepatis (arrow, *b*) that reflect cavernous transformation of the portal vein. A prominent varix is present along the lesser curvature (arrow, *a*). Signal-void small-volume ascites is also present (*a*, *b*).

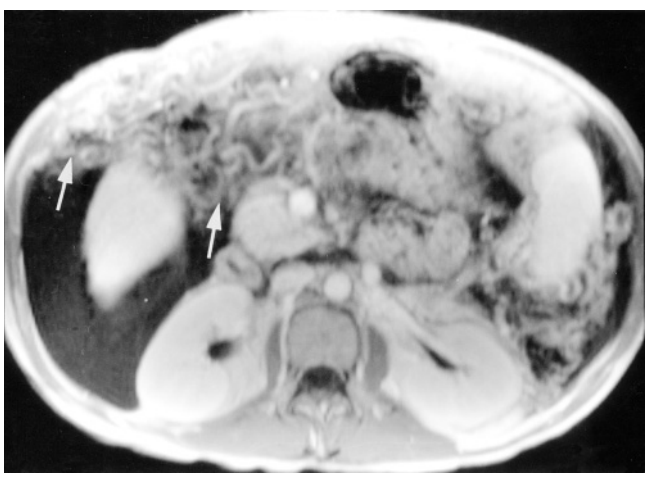

FIG. 2.218 Intraperitoneal and omental varices. Transverse 1-min postgadolinium SGE image demonstrates a tangle of small-caliber varices in the right intraperitoneal space with involvement of the omentum (arrows) and in a perisplenic location.

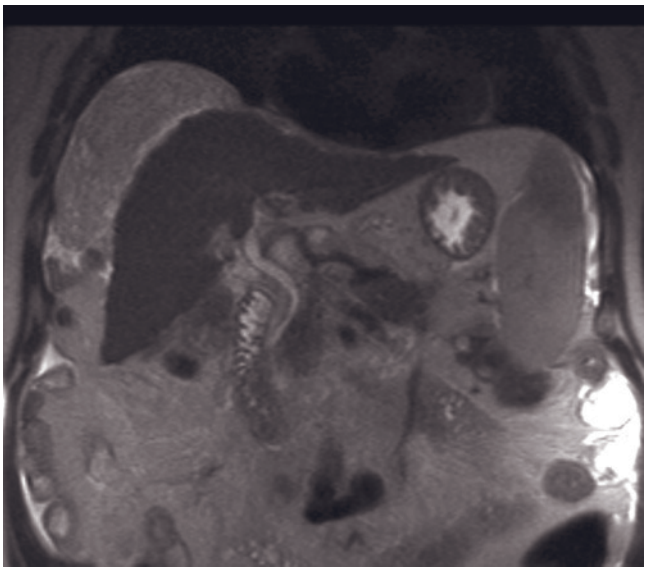

(*a*)

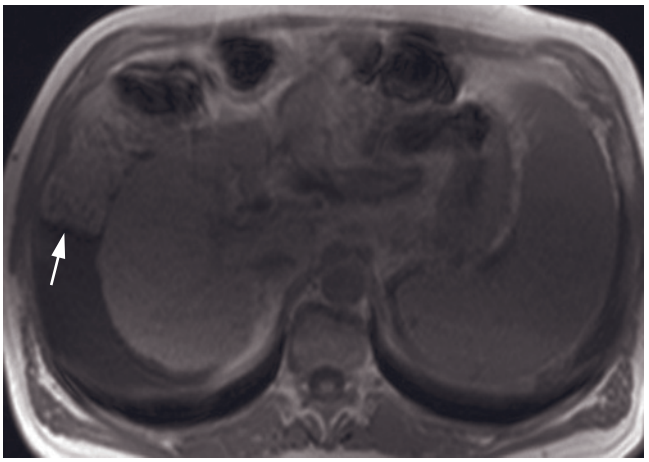

(*b*)

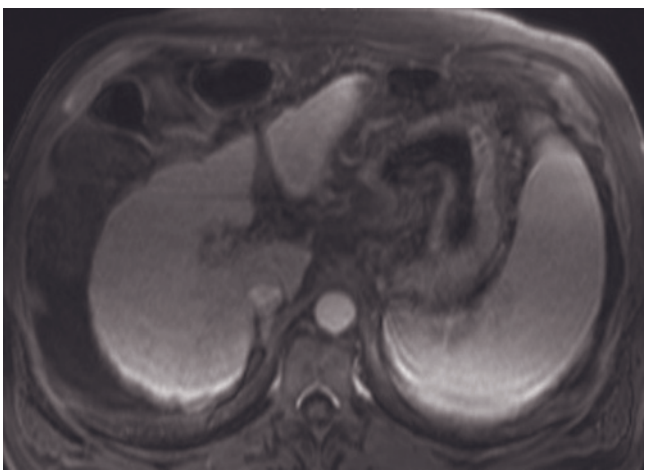

(*c*)

FIG. 2.219 Omental hypertrophy. Coronal T2-weighted SS-ETSE (*a*), transverse SGE (*b*) and 90-s fat-suppressed (*c*) postgadolinium SGE images in a cirrhotic patient that show substantial omental hypertrophy well shown on coronal image (arrows, *a*). Note that the majority of the omentum suppresses on the fat-suppressed image (*c*).

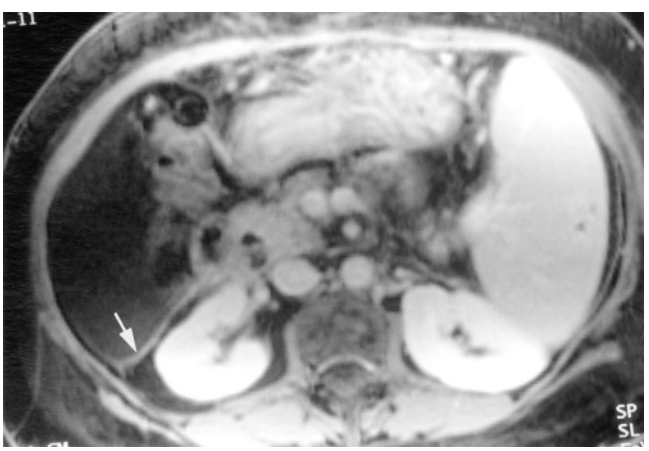

FIG. 2.220 Cirrhosis and peritoneal enhancement. Interstitial-phase gadolinium-enhanced fat-suppressed SGE image demonstrates mild linear peritoneal enhancement (arrow) consistent with microvarices in the peritoneal lining.

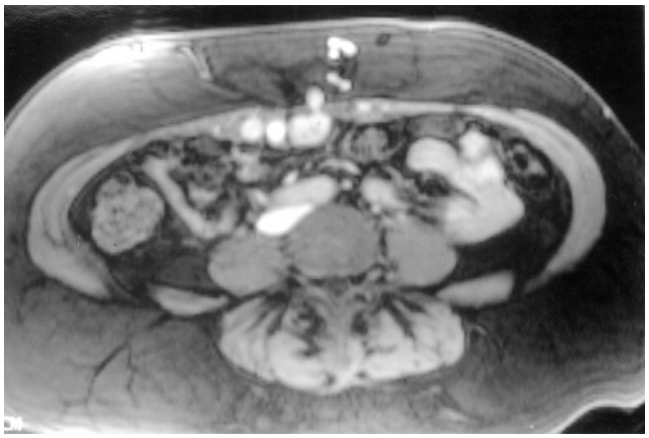

FIG. 2.221 Cirrhosis, paraumbilical varices (caput medusa). Transverse 90-s postgadolinium SGE image demonstrates large varices along the right paramedian peritoneum. Multiple subcutaneous paraumbilical varices are present, which are rendered very conspicuous because of removal of the competing high signal of fat.

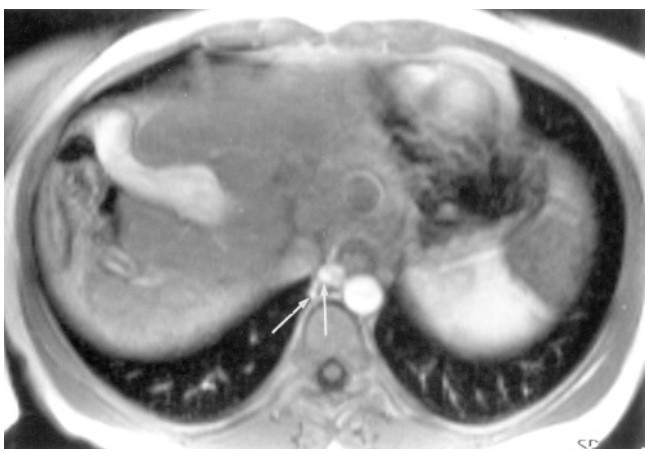

FIG. 2.222 Cirrhosis, varices, recanalized umbilical vein. Transverse 45-s postgadolinium SGE image demonstrates recanalization of a very large umbilical vein. Note that small paraesophageal varices (arrows) are also present.

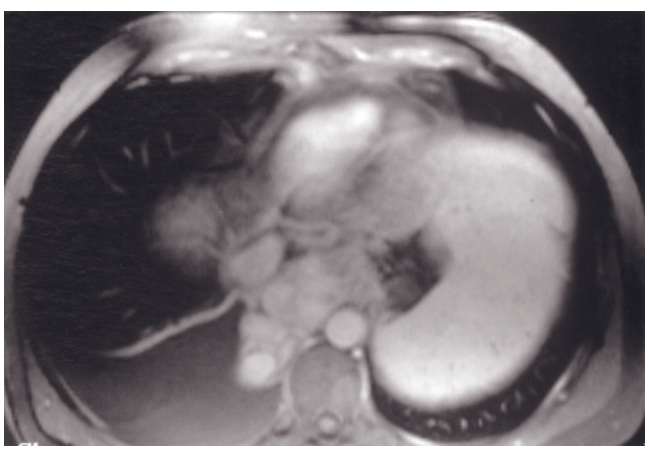

(*a*)

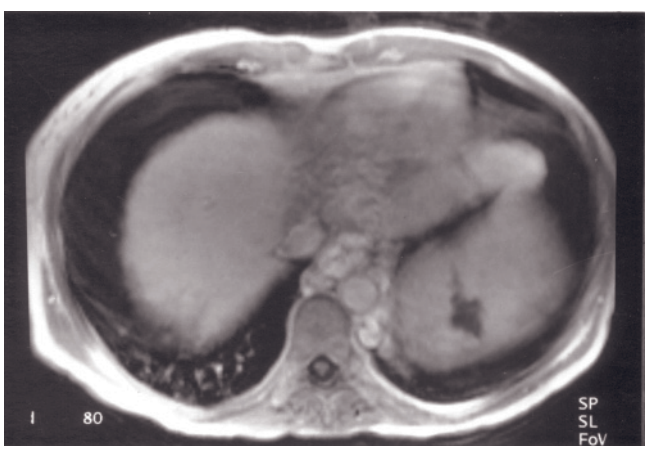

(*b*)

FIG. 2.223 Cirrhosis, paraesophageal varices. Transverse 45-s postgadolinium SGE images (*a*, *b*) in two patients demonstrate large paraesophageal varices.

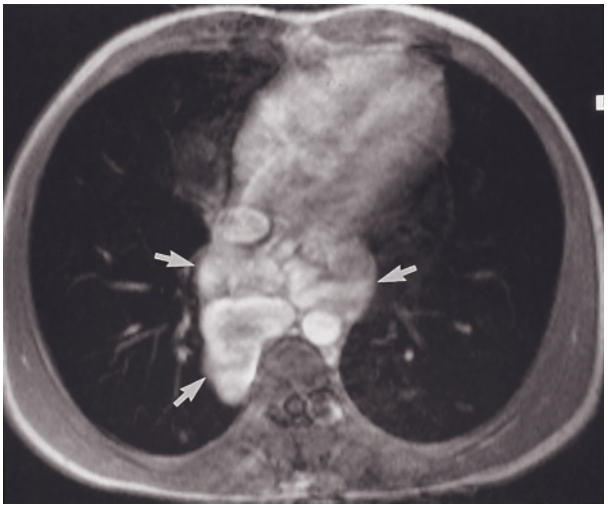

(*a*)

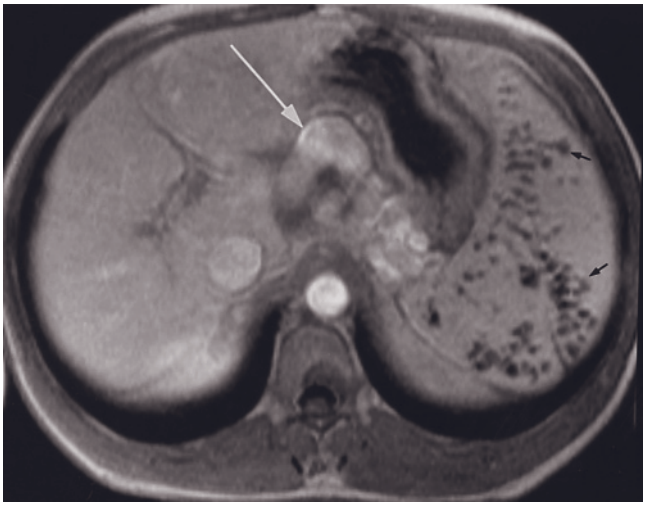

(*b*)

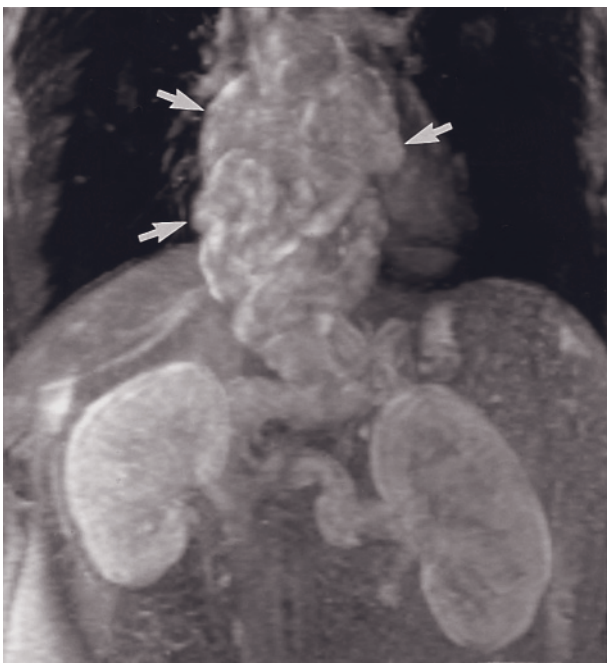

(*c*)

FIG. 2.224 Congenital hepatic fibrosis with massive varices. Transverse 45-s postgadolinium SGE (*a*, *b*) and maximum-intensity projection (MIP) reconstructed 90-s postgadolinium SGE (*c*) images. Massive esophageal varices (arrows, *a*) and large varices along the lesser curvature of the stomach are present (large arrow, *b*). The 3D reconstructed SGE images demonstrate the craniocaudal extent of esophageal varices (arrows, *c*). Gamna–Gandy bodies are present in the spleen (small arrows, *b*).

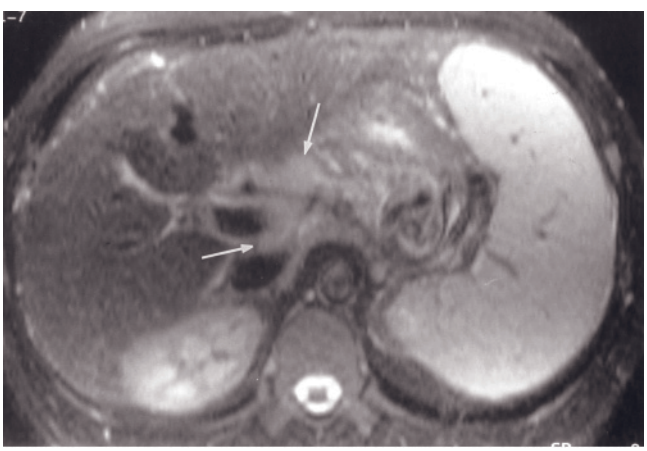

(*a*)

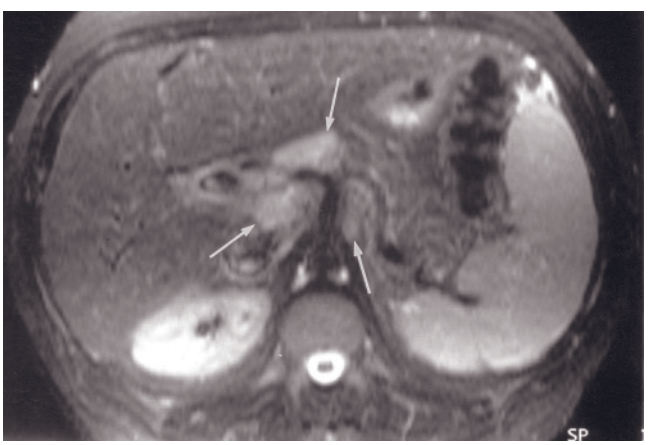

(*b*)

FIG. 2.225 Porta hepatis lymph nodes. Echo-train STIR (*a*, *b*) and 90-s fat-suppressed postgadolinium SGE (*c*, *d*) images;

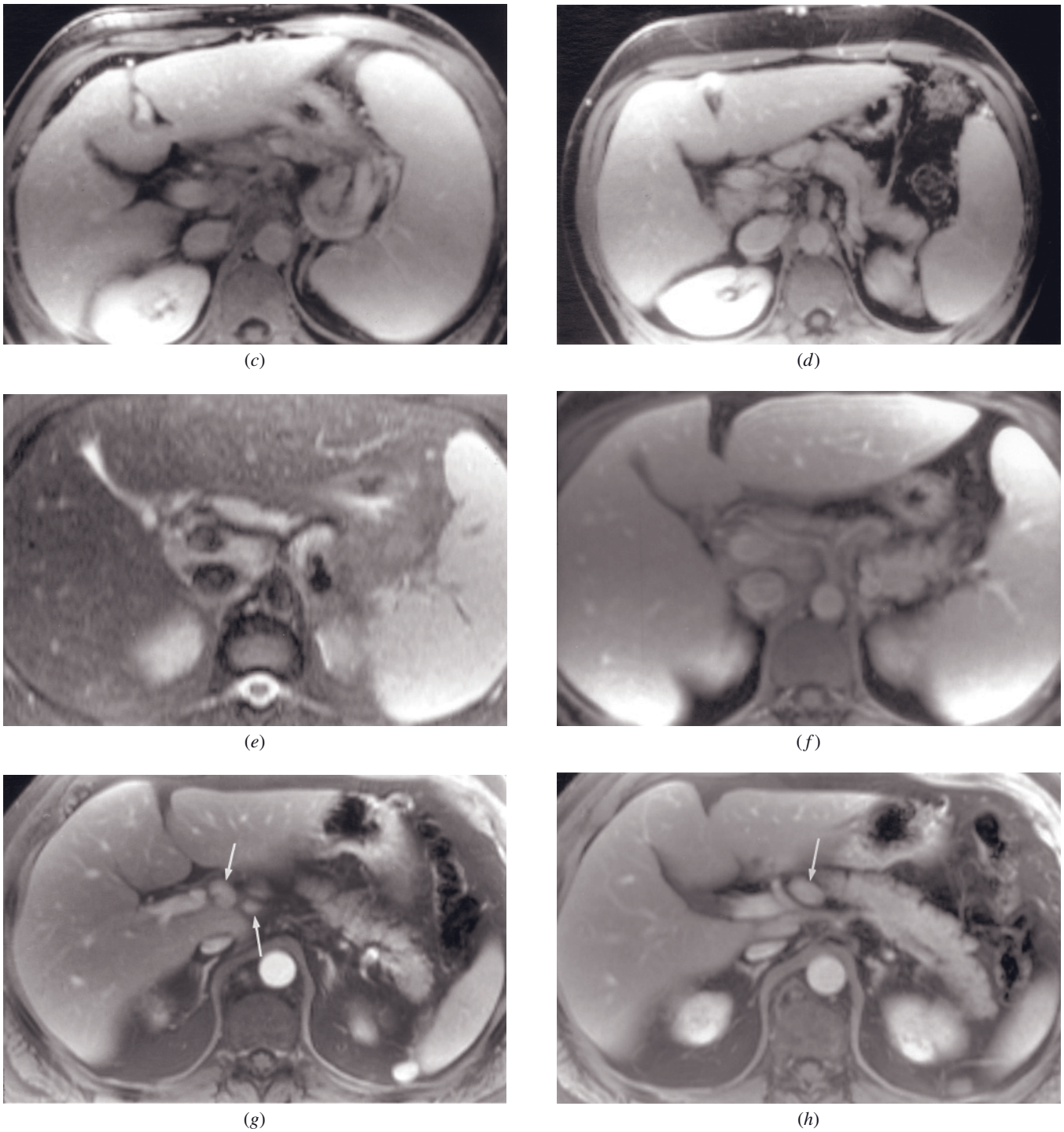

FIG. 2.225 (*Continued*) echo train-STIR (*e*) and 90-s fat-suppressed postgadolinium SGE (*f*) images; and 90-s fat-suppressed postgadolinium SGE images (*g*, *h*) in three patients with porta hepatis lymph nodes (arrows, *a, b*, *g, h*). The lymph nodes in the porta hepatis are best detected by the combination of identification of high-signal tissue on T2-weighted fat-suppressed images (*a*, *b*, *e*) and demonstration that the high-signal tissue has definable convex margins on interstitial-phase gadolinium-enhanced fat-suppressed SGE images (*c, d, f, g*, *h*). All of these patients have chronic hepatitis or cirrhosis. Enlarged porta hepatis lymph nodes are common in patients with chronic liver disease, especially secondary to hepatitis C infection.

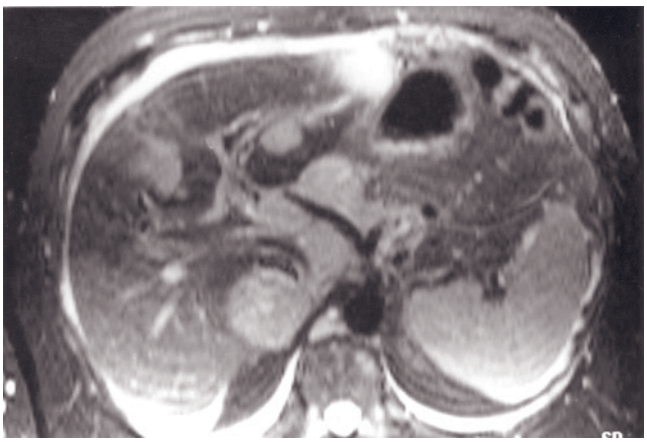

(*i*)

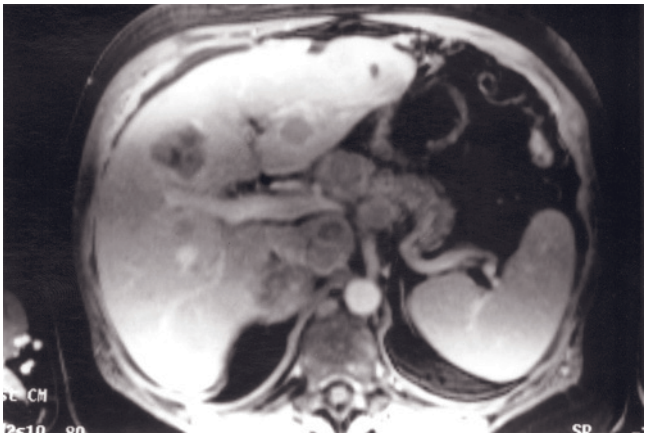

(*j*)

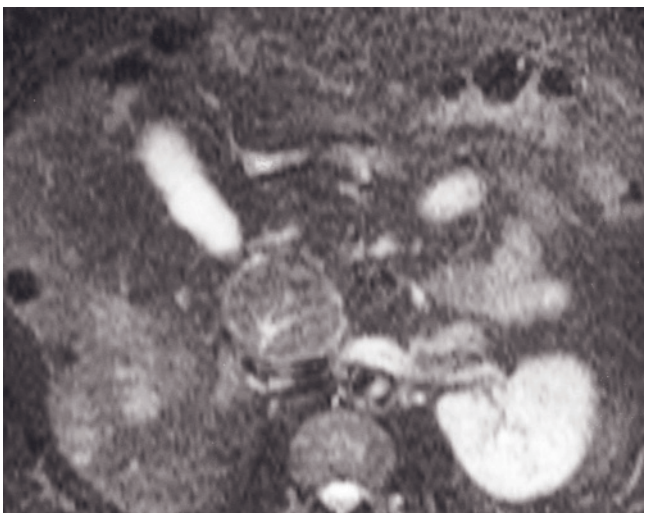

(*k*)

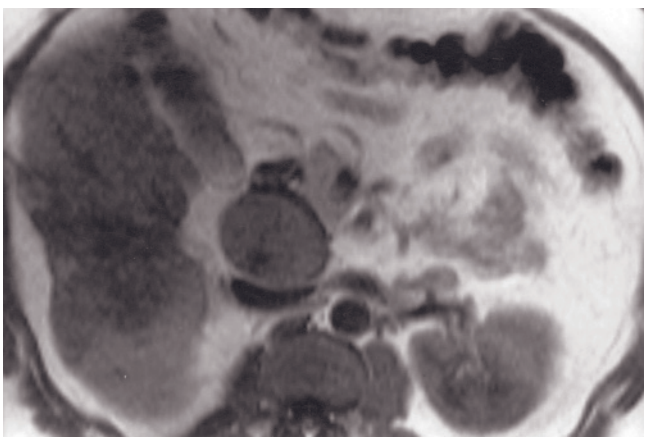

(*l*)

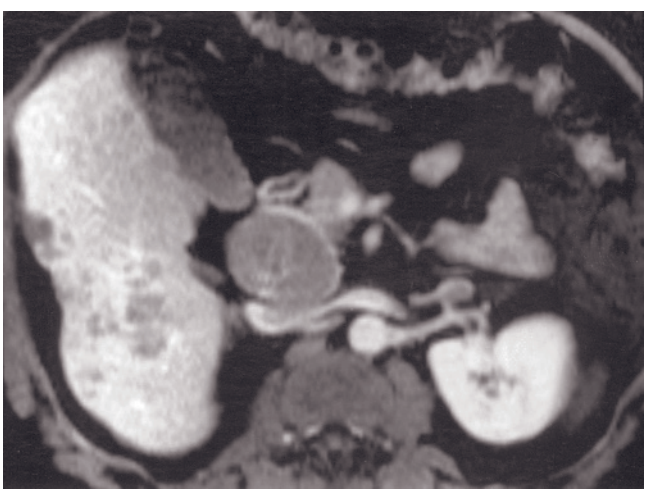

(*m*)

FIG. 2.225 (*Continued*) Echo-train STIR (*i*) and 90-s fat-suppressed postgadolinium SGE (*j*) images in a patient who has a history of squamous cell skin cancer. Multiple enlarged lymph nodes are present in the porta hepatis and celiac axis regions, consistent with malignant lymphadenopathy. Note also the presence of liver metastases. The combined use of fat-suppressed T2-weighed sequence and gadolinium-enhanced T1-weighted fat-suppressed images is the most consistent method to demonstrate porta hepatis lymphadenopathy.

Echo-train STIR (*k*), SGE (*l*), and 90-s fat-suppressed post-gadolinium SGE (*m*) images in a patient who has a history of HCC. There is a portal caval lymph node that demonstrates intermediate signal on T2 (*k*) and low signal on T1-weighted images (*l*) and moderate enhancement after administration of contrast (*m*). Malignant lymph nodes tend to have a rounded configuration, as in this case. Fat-suppressed T2-, non-fat-suppressed noncontrast T1-, and fat-suppressed gadolinium-enhanced T1-weighted sequences have good contrast between lymph nodes and background tissue.

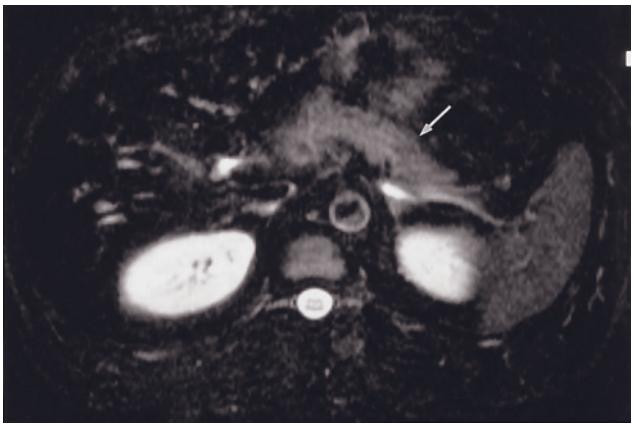

(*a*)

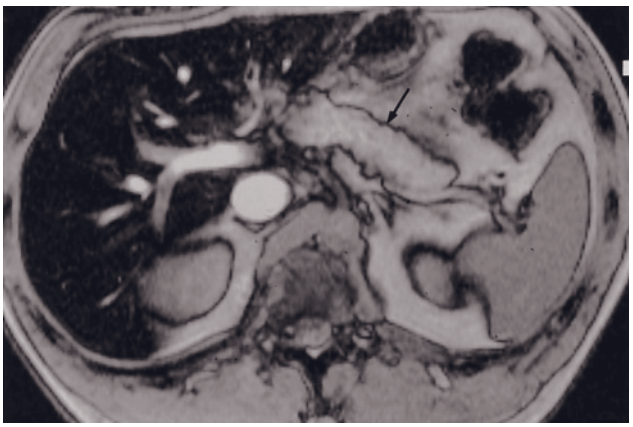

(*b*)

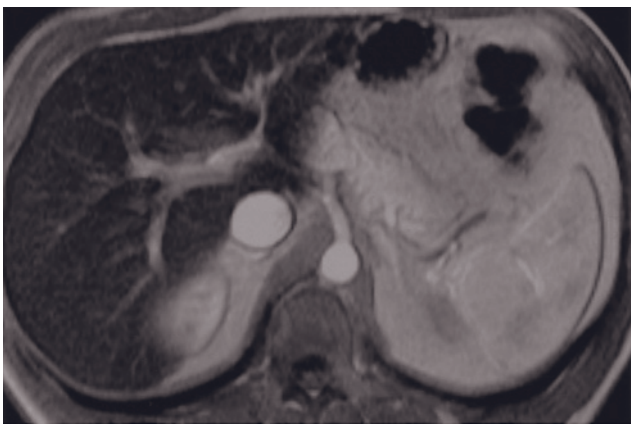

(*c*)

FIG. 2.226 Idiopathic hemochromatosis, early disease. T2-weighted fat-suppressed ETSE (*a*), out-of-phase SGE (*b*), and immediate postgadolinium SGE (*c*) images. The liver is low in signal intensity on noncontrast T2-weighted (*a*) and T1-weighted (*b*) images, consistent with substantial iron deposition. The spleen is relatively normal in signal intensity on these sequences, reflecting that iron is not in the RES but in the hepatocytes. The pancreas (arrow, *a*, *b*) is normal in signal intensity on noncontrast images and enhances normally with gadolinium. Iron deposition limited to the liver is consistent with early precirrhotic disease.

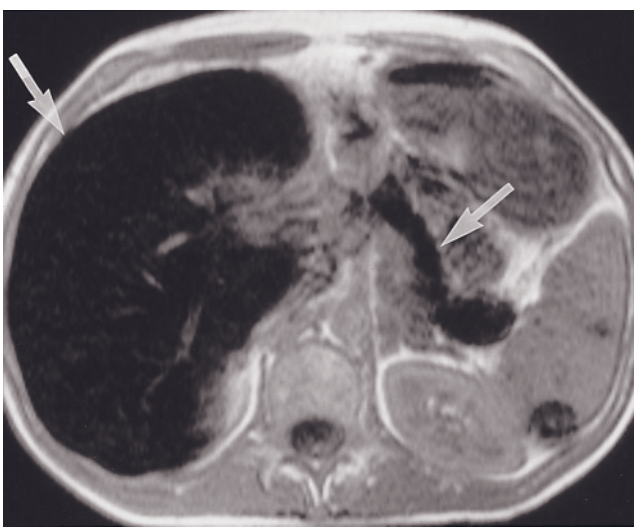

(*a*)

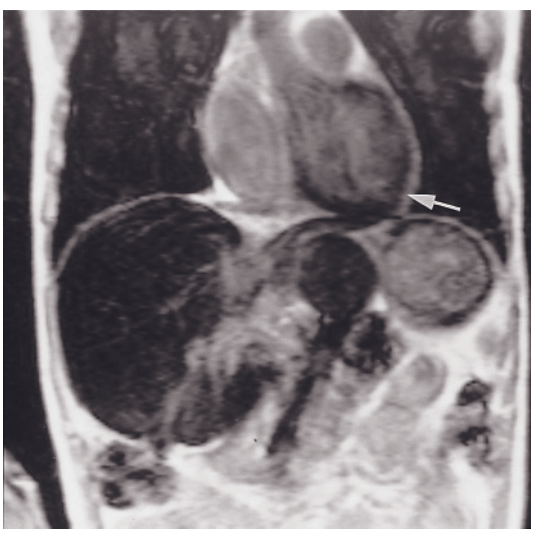

(*b*)

FIG. 2.227 Idiopathic hemochromatosis, advanced disease. Transverse (*a*) and coronal (*b*) SGE and coronal 45-s postgadolinium SGE (*c*) images. The precontrast T1-weighted image (*a*) demonstrates signal-void liver and pancreas (arrows, *a*). The coronal SGE image (*b*) also demonstrates low-signal-intensity left ventricular myocardium (arrow, *b*). On the 45-s postgadolinium image (*c*), multiple enhanced varices are shown (arrows, *c*), which reflects portal hypertension secondary to cirrhosis.

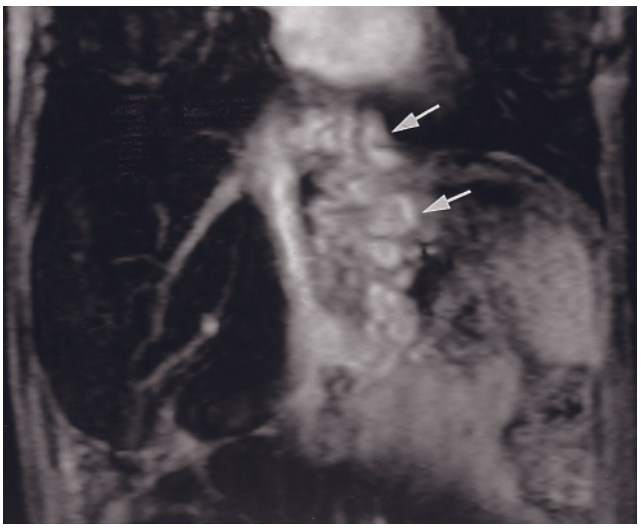

(*c*)

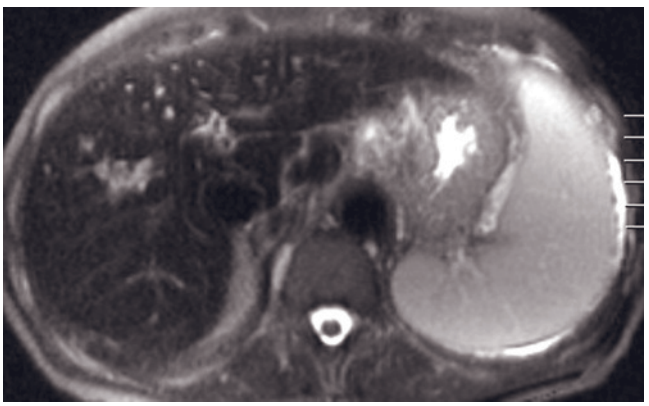

(*d*)

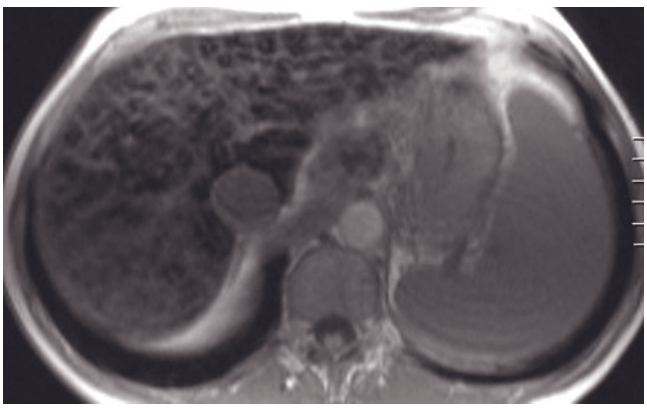

(*e*)

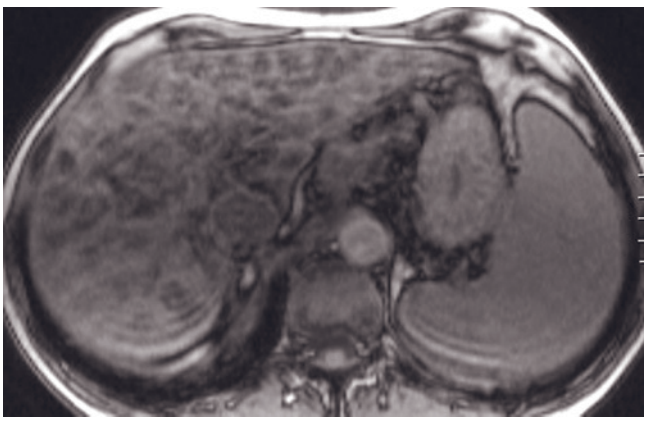

(*f*)

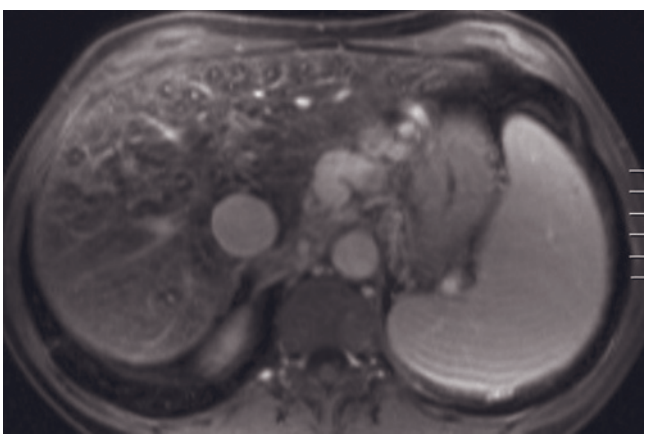

(*g*)

FIG. 2.227 (*Continued*) T2-weighted SS-ETSE (*d*), SGE (*e*), out-of-phase SGE (*f*), and 90-s fat-suppressed postgadolinium SGE (*g*) images in a second patient with idiopathic hemochromatosis and chronic liver disease. The liver is moderately lower in signal intensity on T2-weighted (*d*) and T1-weighted (*e*) images, consistent with iron deposition. Relative increase in signal intensity of the liver on out-of-phase images confirms that iron accounts for the low signal, as evidenced by lesser magnetic susceptibility effects on shorter TE sequences. Late-phase images (*g*) show enhancement of fibrous tissue consistent with a chronic liver disease.

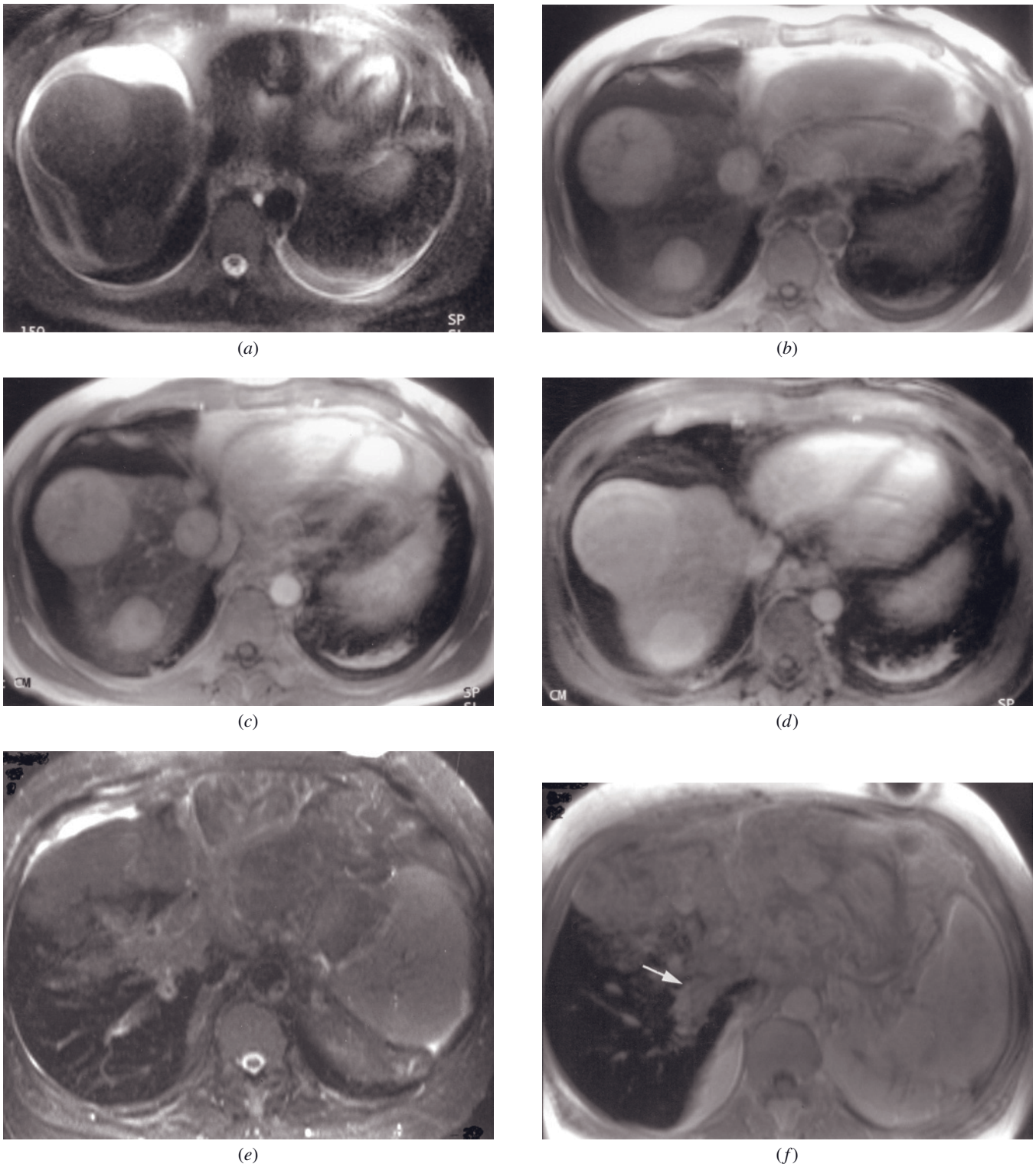

FIG. 2.228 Multifocal HCCs superimposed on idiopathic hemochromatosis. Fat-suppressed T2-weighted SS-ETSE (*a*), SGE (*b*), and immediate (*c*) and 90-s fat-suppressed (*d*) postgadolinium SGE images. There are three HCC nodules that show slight increased signal on T2-weighted (*a*) and T1-weighted (*b*) images and mildly increased enhancement immediately after gadolinium administration (*c*) and fade slightly over time (*d*). The liver is small and irregular in contour and demonstrates diffuse marked decreased signal intensity on T2-weighted (*a*) and T1-weighted (*b*) images, even after contrast, consistent with hepatocellular iron deposition in idiopathic hemochromatosis. Note also ascites.

Echo-train STIR (*e*) and immediate (*f*) and 90-s fat-suppressed (*g*) postgadolinium SGE images in a second patient with idiopathic

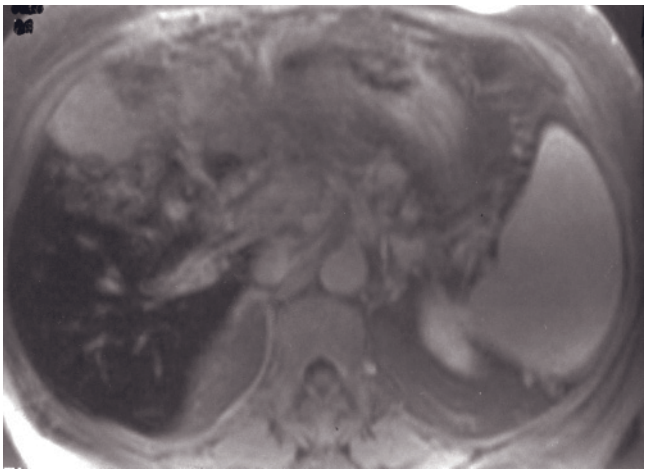

(*g*)

FIG. 2.228 (*Continued*) hemochromatosis. There is a very large HCC involving the entire left lobe and segments 5 and 8 of the right lobe that demonstrates heterogeneous and moderately increased signal on T2-weighted images and heterogeneous gadolinium enhancement. The entire portal venous system is expanded and enhances after gadolinium administration (arrow, *f*), consistent with tumor thrombus. Marked decreased signal intensity of liver parenchyma reflects the iron deposition in idiopathic hemochromatosis.

cells do not contain excess iron [366, 367] they are well shown as high-signal-intensity masses relative to iron-overloaded liver on T2-weighted images. In a patient with hemochromatosis, nonsiderotic nodules that are not hemangiomas or cysts are highly suspicious for HCC [364], because regenerative nodules in these patients contain iron. Dysplastic nodules in patients with increased hepatic iron may contain a different concentration of iron than surrounding hepatic parenchyma.

Secondary Hemochromatosis

Transfusional Iron Overload. Transfusional iron overload is the most common form of excess iron deposition in North America. Fibrosis is usually mild despite even heavy iron stores, and cirrhosis is rare. Iron deposition in the RES results in low signal intensity of the spleen, liver, and bone marrow on MR images, best shown on T2- or T2*-weighted images.

Iron overload from multiple transfusions may be distinguished from genetic hemochromatosis in that large amounts of iron accumulate primarily within the RES of the liver (Kupffer cells) and spleen (monocytes/macrophages) in transfusional overload, with relative sparing of the functional cells within the parenchyma. Evaluation by MRI of pancreatic and splenic signal intensity allows this distinction. Signal intensity of the spleen is usually normal with genetic hemochromatosis, whereas signal intensity of the pancreas is normal with most cases of transfusional overload. In massive iron overload (e.g., >100 units) direct tissue deposition may occur in other cells and tissues, notably the pancreas (fig. 2.229) [361, 365].

Regional variation in iron deposition in the liver parenchyma may occur, such as diffuse heterogeneous (fig. 2.230) or homogeneous iron deposition with focal sparing (fig. 2.231) and focal iron deposition. MR features are highly associated with the degree of iron overload in the liver [368–370]. In mild forms of transfusional overload, signal loss is appreciated only on T2- and T2*-weighted images, and signal intensity on T1-weighted images appears relatively normal (fig. 2.232). In moderate to severe forms of iron deposition, the T2-shortening effect of iron results in low signal on T1-weighted images as well (fig. 2.233). If liver and spleen are gray on in-phase SGE (TE = 4.2 ms), we consider iron deposition moderate, and if liver and spleen are near signal void, iron deposition is severe [361, 365].

Hemolytic Anemia. Hepatic signal intensity in patients with hemolytic anemia varies, based on the rate of reincorporation of iron into the bone marrow, the rate of absorption of oral iron, and the transfusional history. Patients with thalassemia vera have increased absorption of oral iron and, in the absence of blood transfusions, will develop erythrogenic hemochromatosis primarily affecting the liver [371]. The appearance is generally indistinguishable from idiopathic hemochromatosis (fig. 2.234). Patients with heterozygous forms of hemolytic anemias may not have low enough red blood cell counts or hemoglobin levels to necessitate transfusion, and may therefore develop this pattern of iron overload. The majority of patients with hemolytic anemias have received blood transfusions and therefore also develop coexisting transfusional iron overload (fig. 2.235).

Patients with sickle cell anemia have rapid turnover of hepatic iron and will have normal hepatic signal intensity unless they have undergone recent blood transfusions [371]. Renal cortical signal intensity may be decreased because of filtration and tubular absorption of free hemoglobin, the severity of which is not dependent on transfusional history (see chapter 9, *Kidneys*)

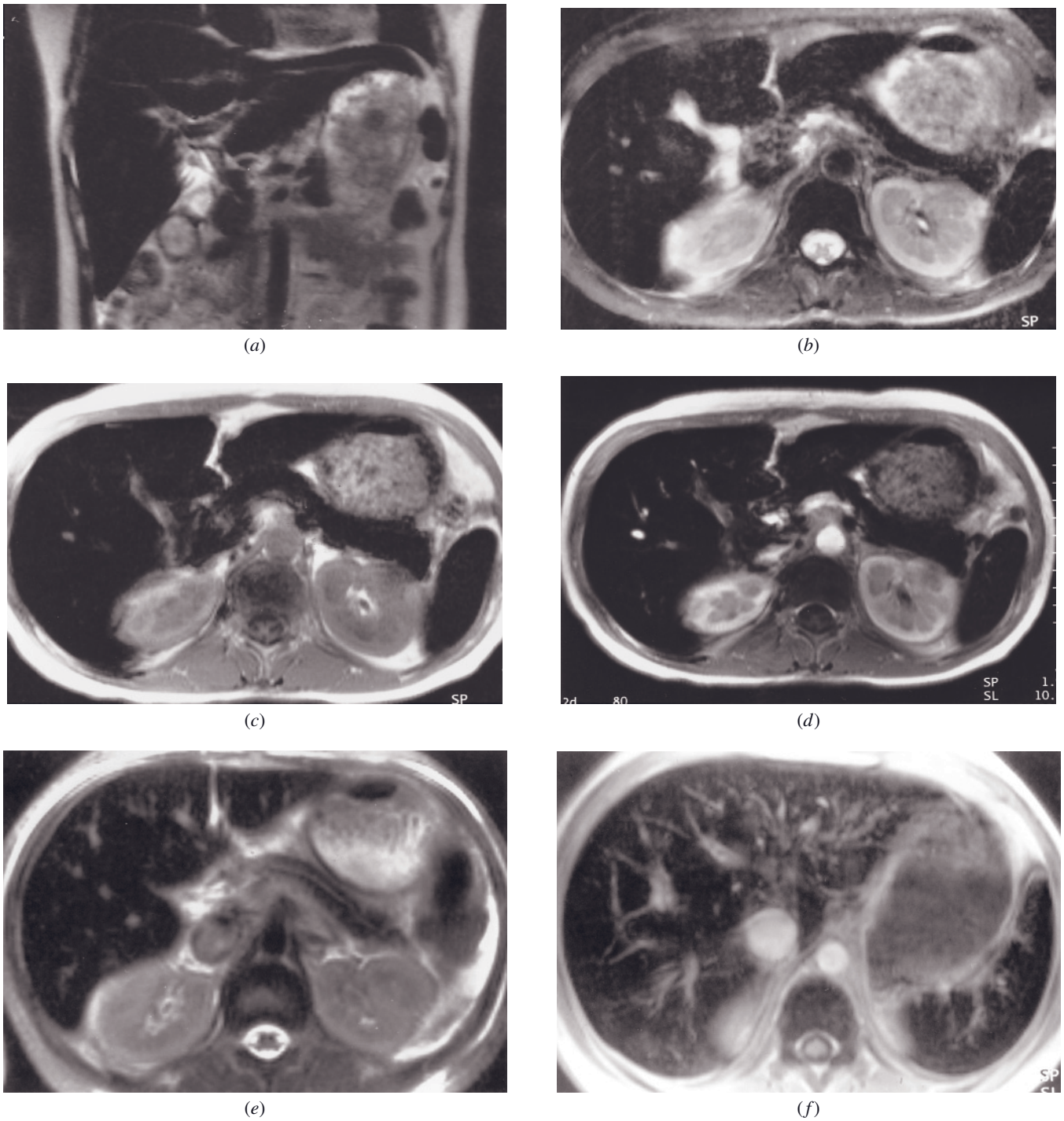

FIG. 2.229 Transfusional siderosis, massive. Coronal SS-ETSE (*a*), T2-weighted fat-suppressed ETSE (*b*), SGE (*c*), and immediate postgadolinium SGE (*d*) images. Massive iron deposition is present in the liver, spleen, and pancreas (*a–c*), demonstrated by signal-void liver, spleen, and pancreas. Magnetic susceptibility causes a "blooming" appearance surrounding the pancreas (*c*). These organs remain signal void after gadolinium administration (*d*).

T2-weighted SS-ETSE (*e*) and 1-min postgadolinium SGE (*f*) images in a second patient with massive iron deposition demonstrate dark liver, spleen, and pancreas on T2-weighted (*e*) and postgadolinium T1-weighted (*f*) images.

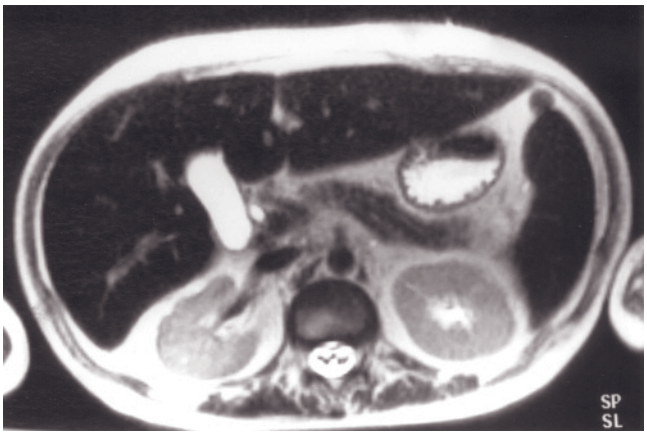

(*g*)

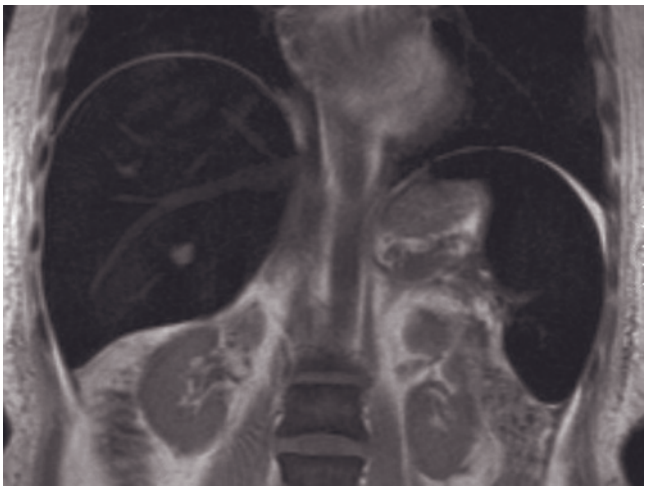

(*h*)

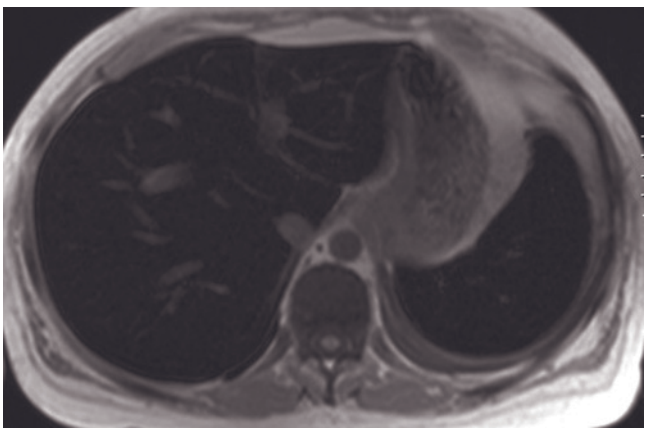

(*i*)

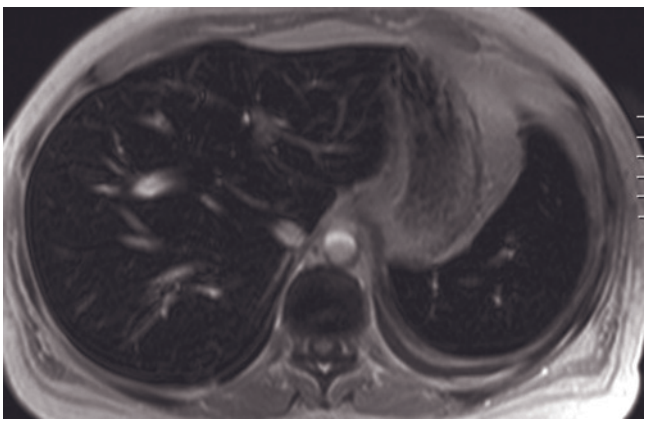

(*j*)

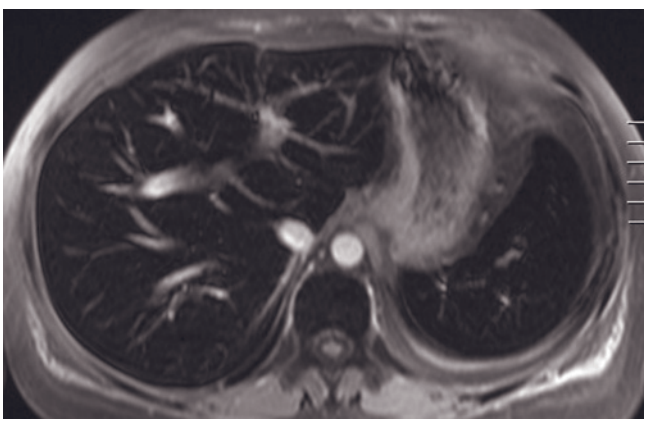

(*k*)

FIG. 2.229 (*Continued*) T2-weighted SS-ETSE image (*g*) in a third patient, who is 8 years old and has a history of lymphoma. There is decreased signal intensity of the liver, spleen, and pancreas on T2-weighted images. The decreased signal intensity in the pancreas reflects multiple blood transfusions.

Coronal T2-weighted SS-ETSE (*h*), SGE (*i*), and immediate (*j*) and 90-s fat-suppressed (*k*) postgadolinium SGE images in a fourth patient with massive iron deposition in the liver and spleen.

[361]. Iron overload in the liver and renal cortex is typically seen in patients with paroxysmal nocturnal hemoglobinuria [365].

Cirrhosis. Hepatocellular iron is commonly mildly increased in patients with cirrhosis, particularly those with cirrhosis secondary to ethanol abuse. Anemia, pancreatic insufficiency, and/ or decrease in the synthesis of transferrin probably all contribute to the excess iron deposition [372]. The degree of signal loss of the liver is not as great as that seen with idiopathic hemochromatosis or transfusional siderosis.

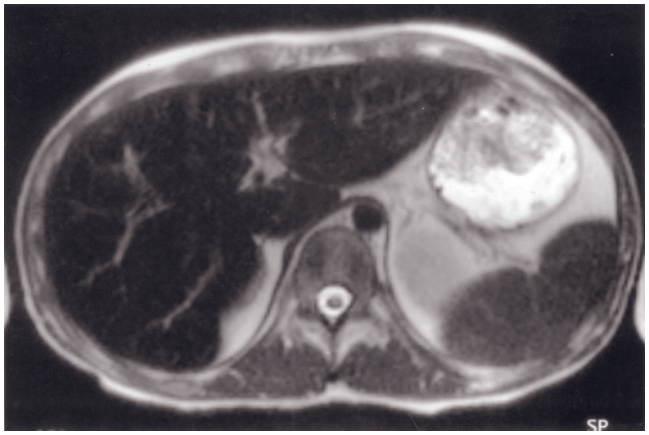

(*a*)

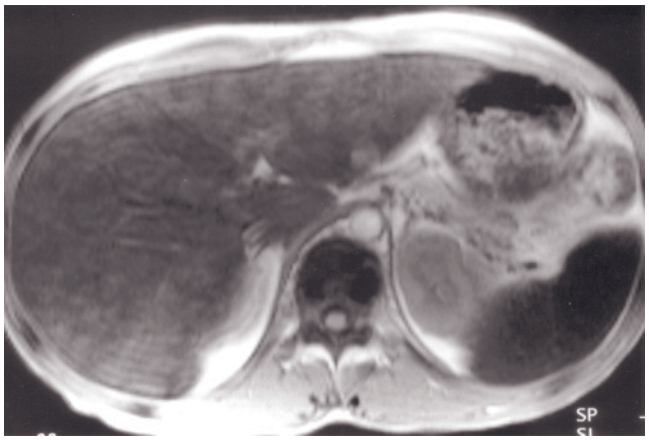

(*b*)

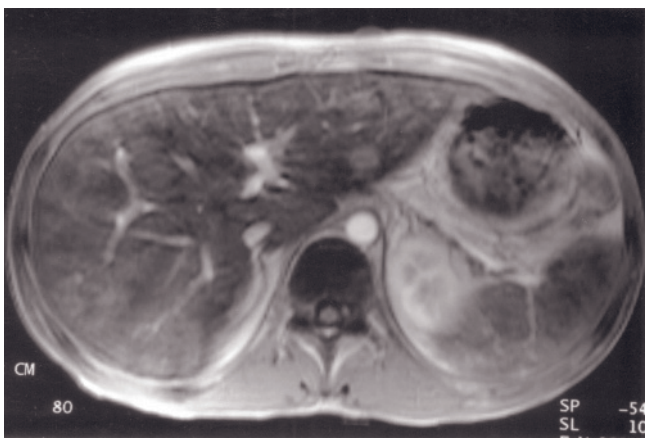

(*c*)

FIG. 2.230 Transfusional siderosis, heterogeneous iron deposition. T2-weighted SS-ETSE (*a*), SGE (*b*), and immediate postgadolinium SGE (*c*) images in a patient who has a history of acute leukemia. The liver and spleen are low signal intensity on T2-weighted (*a*) and T1-weighted (*b*) images, consistent with iron deposition. On pre- and postcontrast T1-weighted images, there is a heterogeneous appearance consistent with heterogeneous distribution of iron deposition, in the setting of transfusional siderosis.

Coexisting Fat and Iron Deposition

Fat and iron deposition may occur concurrently within the liver. Coexisting fat and iron deposition may be demonstrated by using several gradient-echo MR sequences with differing in-phase (TE = 4.2 ms) and out-of-phase (TE = 2.1 ms) echo times. In the presence of iron, signal intensity of the liver will decrease steadily as echo time increases because of T2* effects. At out-of-phase echo time both higher than and lower than the echo time for in-phase images, a disproportionate drop of liver signal intensity will occur relative to spleen because of fat-water phase cancellation. The combined observations that liver and spleen are nearly signal void on T2-weighted images, reflecting iron deposition, and that liver drops in signal intensity relative to spleen, comparing out-of- phase to in-phase SGE images, reflecting fat deposition, are also diagnostic for coexistent iron and fat deposition (fig. 2.236).

Fatty Liver

Fatty liver or steatosis is defined as accumulation of triglycerides within hepatocytes. It constitutes one of the most common abnormalities in liver surgical or autopsy specimens. The causes of hepatic steatosis include alcohol abuse, diabetes mellitus, obesity, malnutrition, and exposure to toxins [388]. Fatty degeneration may present as diffuse, uniform, or patchy and focal or with spared foci of normal liver. At times, focal fatty infiltration or geographic regions of normal liver within fatty liver (fat sparing) may mimic the appearance of mass lesions.

Fatty liver may interfere with the detection of focal liver masses on CT images or sonography [373]. However, out-of-phase gradient-echo (TE = 2.1 ms) imaging is a highly accurate MRI technique to examine for fatty liver and to distinguish focal fat from neoplastic masses (figs. 2.237 and 2.238) [374, 375]. Fat in substantial amount has high signal intensity on in-phase T1-weighted images because of its short T1. Comparing out-of-phase (TE = 2.1 ms) to in-phase (TE = 4.2 ms) gradient-echo images, the presence of fatty metamorphosis results in signal loss. This signal loss on out-of-phase images is progressively more evident in moderate and severe fatty infiltration [309]. The spleen is generally used as the organ of reference for signal loss. As fat content approaches 50% of the voxel element in the

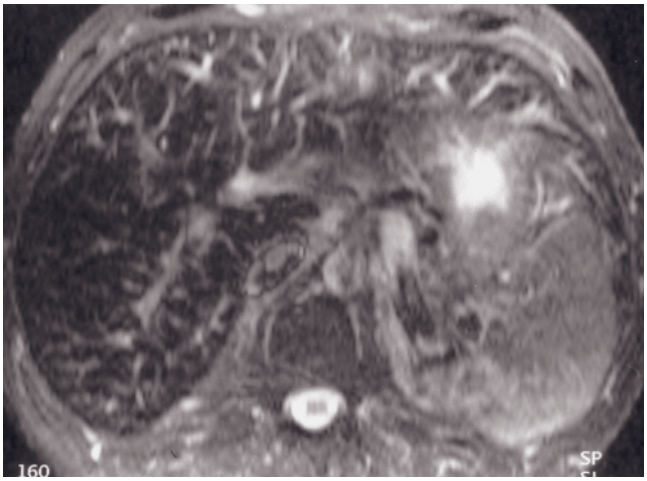

(*a*)

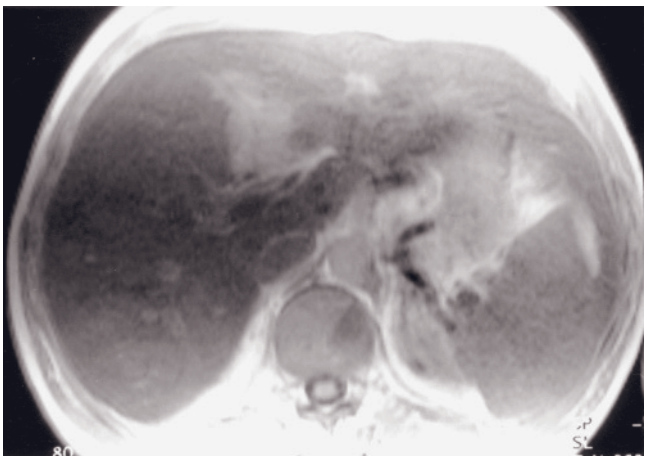

(*b*)

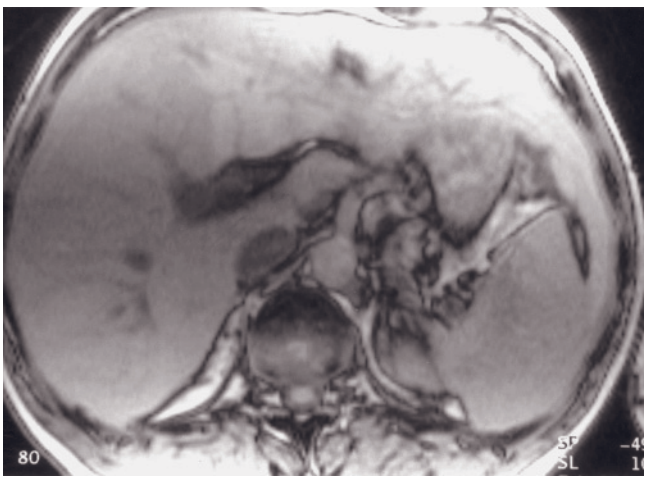

(*c*)

(*d*)

FIG. 2.231 Transfusional siderosis with focal sparing. Echo train-STIR (*a*), SGE (*b*), out-of-phase SGE (*c*), and immediate postgadolinium SGE (*d*) images. The liver is enlarged and demonstrates decreased signal reflecting iron deposition. There is a region in segment 4 with increased signal intensity on the T1-weighted image (*b*). On the short TE out-of-phase image (*c*), the susceptibility artifact from iron diminishes, resulting in a decrease in the signal intensity difference between iron-deposited and normal liver. This is virtually the opposite effect from that seen in focal normal liver in the setting of fat infiltration. Normal vessels are appreciated extending through the focal normal liver on the postgadolinium image (*d*).

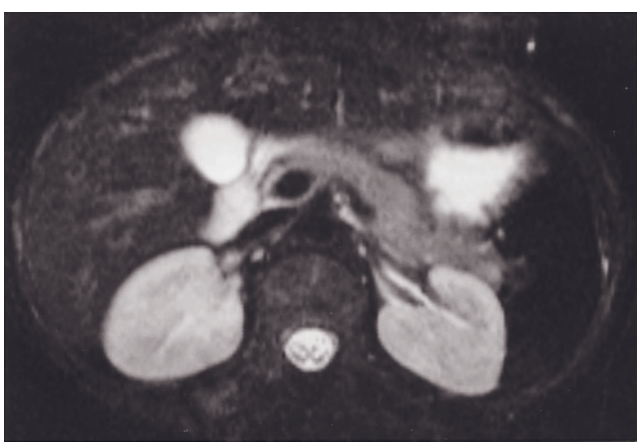

(*a*)

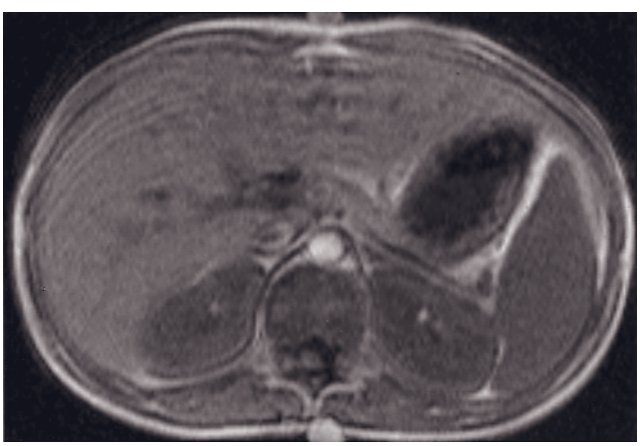

(*b*)

FIG. 2.232 Transfusional siderosis, mild. T2-weighted fat-suppressed ETSE (*a*) and SGE (*b*) images. On the T2-weighted image (*a*), the liver and spleen are low in signal intensity and the pancreas is normal in signal intensity. Signal intensity of the liver, spleen, and pancreas appear normal on the T1-weighted image (*b*). Iron deposition in the liver and spleen that results in signal loss appreciable only on T2-weighted images, and not on T1-weighted images, is compatible with mild transfusional siderosis.

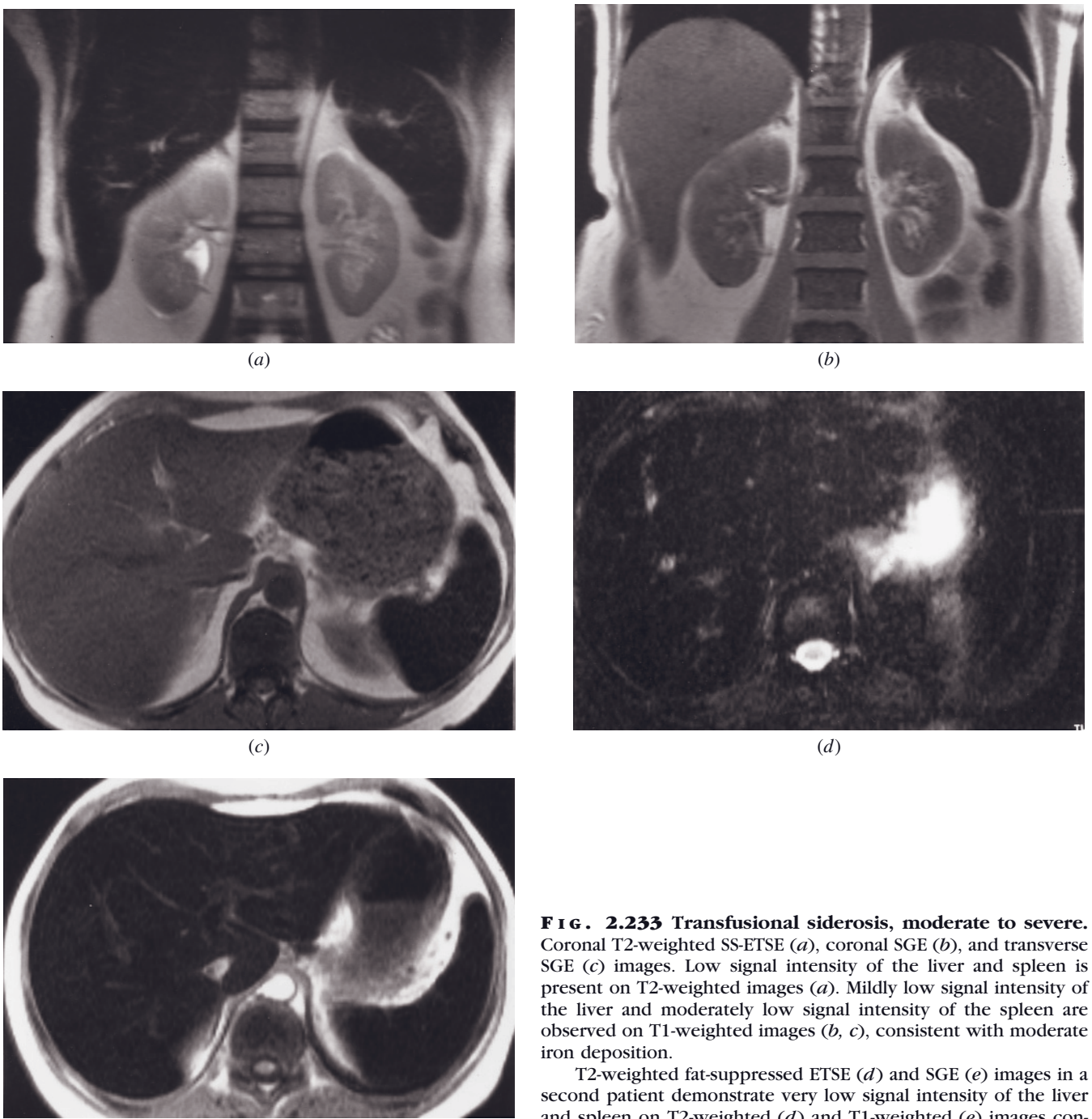

(*a*) (*b*) (*c*) (*d*) (*e*)

FIG. 2.233 Transfusional siderosis, moderate to severe. Coronal T2-weighted SS-ETSE (*a*), coronal SGE (*b*), and transverse SGE (*c*) images. Low signal intensity of the liver and spleen is present on T2-weighted images (*a*). Mildly low signal intensity of the liver and moderately low signal intensity of the spleen are observed on T1-weighted images (*b, c*), consistent with moderate iron deposition.

T2-weighted fat-suppressed ETSE (*d*) and SGE (*e*) images in a second patient demonstrate very low signal intensity of the liver and spleen on T2-weighted (*d*) and T1-weighted (*e*) images consistent with severe iron deposition.

liver, the liver appears blacker relative to the spleen on out-of-phase (TE = 2.1 ms) compared to in-phase (TE = 4.2 ms) sequence. For lesser amounts of fat (<15%) the signal of liver on out-of-phase sequence appears near equivalent to the signal of spleen.

Diffuse liver steatosis can be categorized by MRI based on the degree of fatty infiltration as follows: I, severe; II, moderate; III, mild; and IV, minimal. Severe steatosis demonstrates a very dramatic loss of signal on out-of-phase images compared to in-phase images; moderate steatosis shows that liver signal intensity drops below the signal of the spleen on out-of-phase images but not as intense as severe steatosis; mild steatosis exhibits equivalent signal intensity of liver and spleen on short TE out-of-phase images; and minimal steatosis is a subjective classification that we have begun

(*a*)

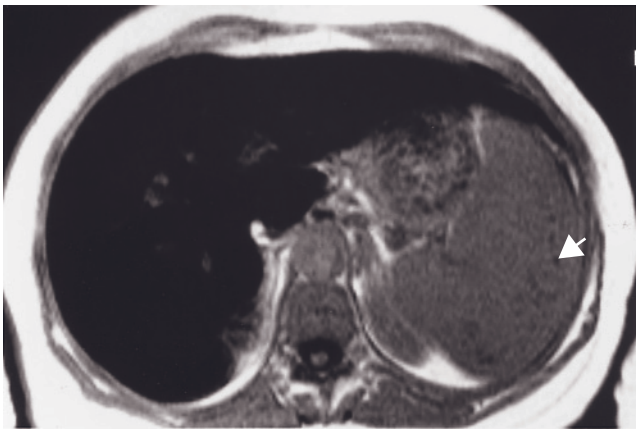

(*b*)

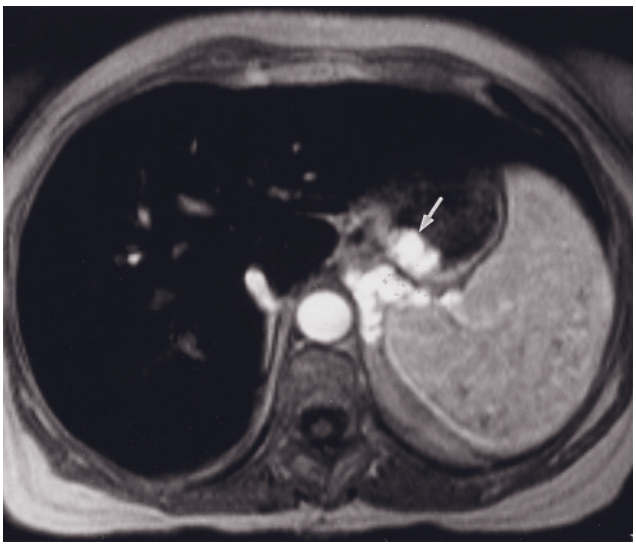

(*c*)

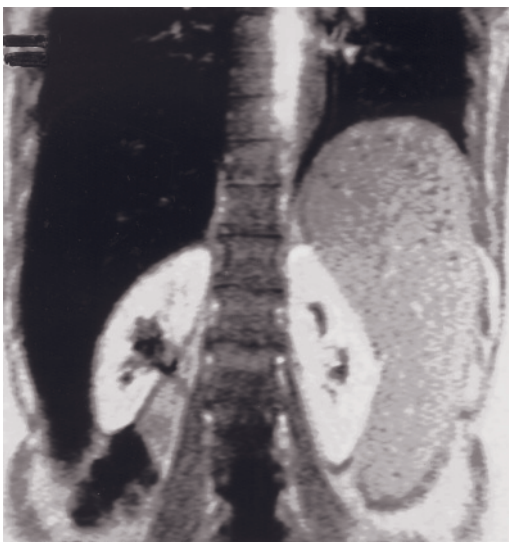

(*d*)

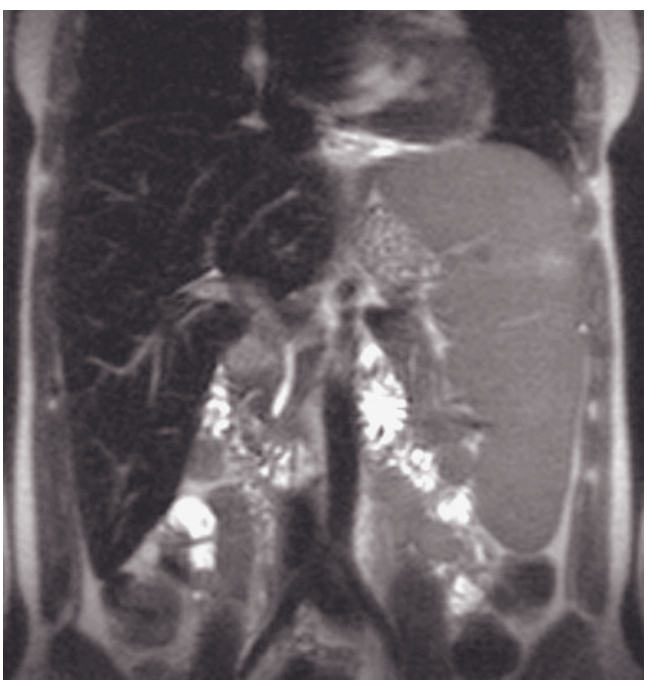

(*e*)

FIG. 2.234 Heterozygous thalassemia. T2-weighted fat-suppressed ETSE (*a*), SGE (*b*), and 45-s (*c*) and coronal 90-s (*d*) postgadolinium SGE images. The liver demonstrates severe iron deposition and is signal void on T2 (*a*)- and T1 (*b*)-weighted images. The spleen is greatly enlarged and shows negligible iron deposition but does contain Gamna–Gandy bodies (arrow, *b*). The pancreas is modestly low in signal intensity (arrow, *a*). Varices along the lesser curvature and within the gastric wall (arrow, *c*) are clearly shown on the 45-s postgadolinium images. Splenomegaly (*d*), Gamma–Gandy bodies, and varices are secondary to portal hypertension. The pattern of iron deposition reflects increased intestinal absorption without transfusional siderosis, which is a common appearance for heterozygous hemolytic anemias because these patients often do not require blood transfusions.

Coronal SS-ETSE (*e*), SGE (*f*), and immediate post gadolinium SGE (*g*) images in a second patient with history of heterozygous thalassemia. The liver is signal void on both T2-weighted (*a*) and

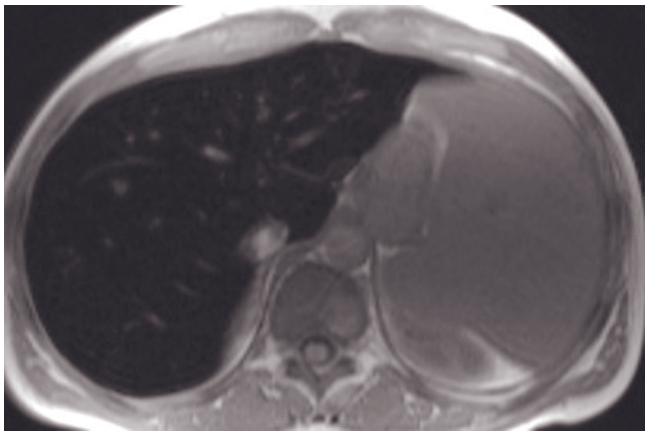

(*f*)

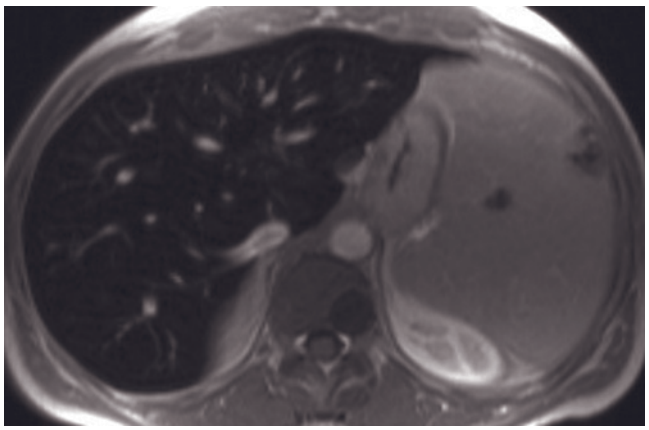

(*g*)

FIG. 2.234 (*Continued*) T1-weighted (*f*) images, reflecting iron deposition. The spleen is enlarged and normal in signal intensity, reflecting that the patient has not required blood transfusion. Note the presence of two lesions in the spleen consistent with hemangiomas.

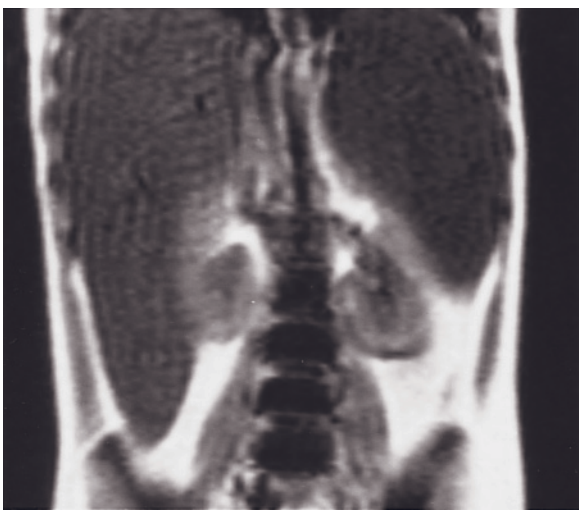

(*a*)

(*b*)

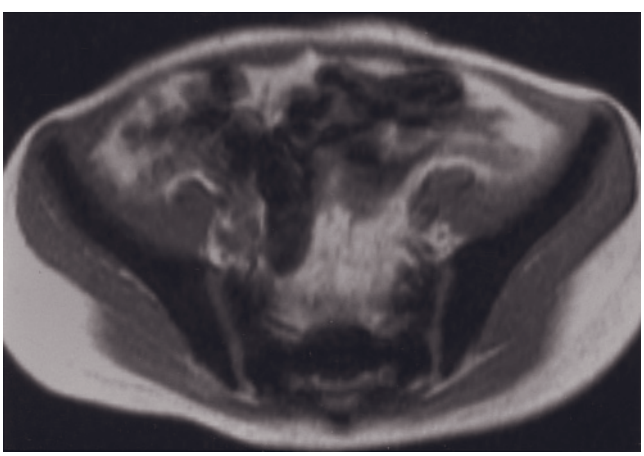

(*c*)

FIG. 2.235 **α-Thalassemia.** Coronal SGE (*a*) and T2-weighted fat-suppressed ETSE (*b*) images. Enlargement of the liver and spleen is apparent on T1-weighted image (*a*). These organs are also lower in signal intensity than psoas muscle on T1-weighted (*a*) and T2-weighted (*b*) images, consistent with severe iron deposition in the RES. Vertebral bodies are nearly signal void, which also reflects RES iron deposition. The pancreas is nearly signal void (arrow, *b*), reflecting coexistent iron deposition into tissues. SGE image (*c*) through the pelvis shows nearly signal-void pelvic bones secondary to iron deposition in the RES.

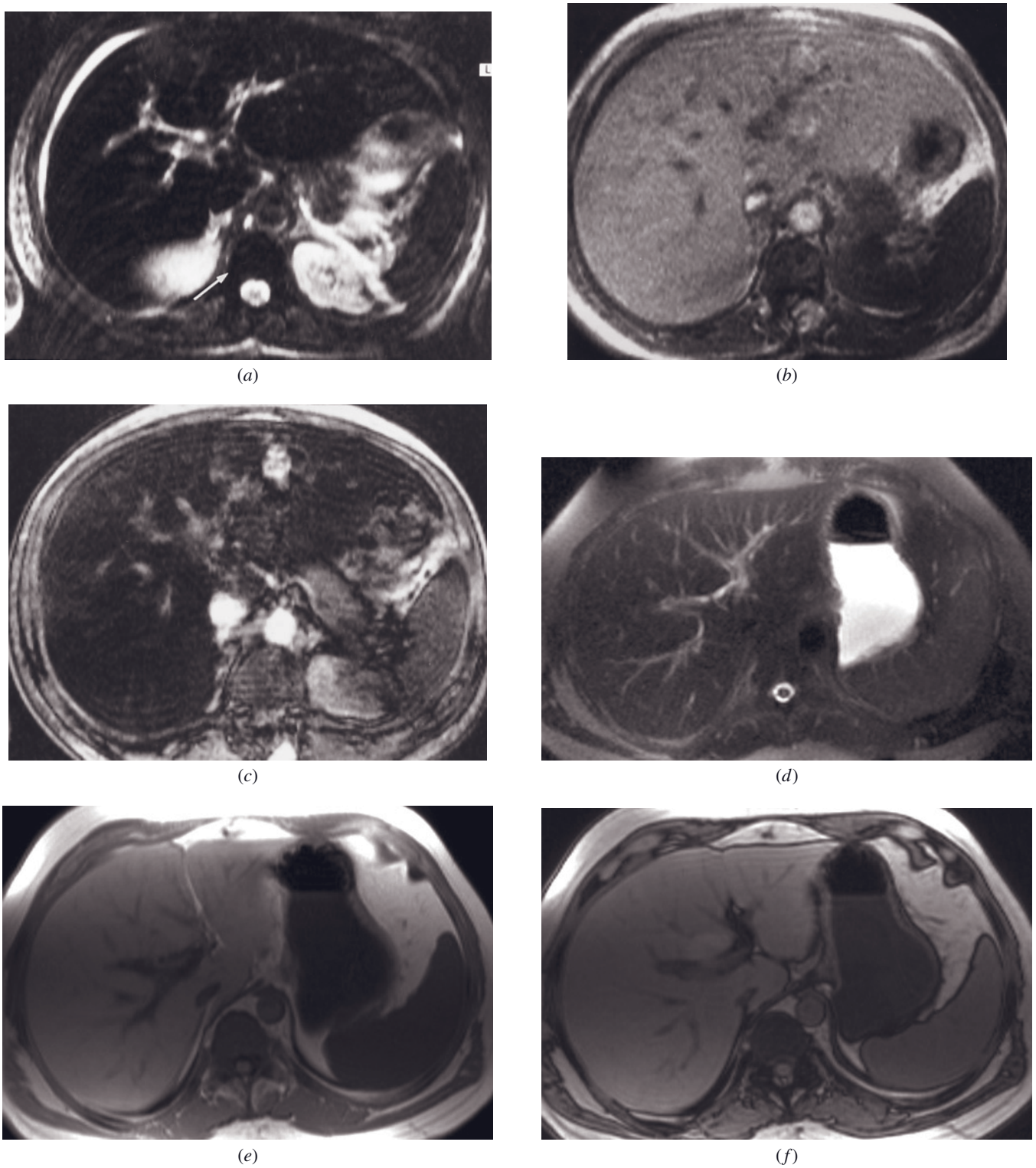

FIG. 2.236 Coexistent iron and fatty deposition. T2-weighted fat-suppressed SS-ETSE (*a*), SGE (*b*), and out-of-phase SGE (*c*) images. On T2-weighted images (*a*), the liver, spleen, and bone marrow (arrow, *a*) are nearly signal void, which is consistent with coexistent iron deposition. On T1-weighted images (*b*), liver and spleen have a normal signal intensity pattern, with the liver higher in signal intensity than the spleen. On the shorter echo-time out-of-phase image (*c*), the liver drops in signal intensity below that of spleen, which is consistent with fatty infiltration. Ascites is well shown as high-signal intensity fluid along the liver margin on the T2-weighted image (*a*).

Echo train STIR (*d*), in-phase SGE (*e*), and out-of-phase SGE (*f*) images in a second patient demonstrate iron deposition and mild fatty infiltration in the liver. Iron deposition is shown by the low signal on T2-weighted image (*d*), and fat is shown by the loss of liver-spleen contrast on the shorter-TE out-of-phase sequence (*f*). Iron alone would result in an increase in liver-spleen contrast on the shorter-TE sequence.

These cases illustrate the effect of iron on T2-weighted images. It is essential to be aware that T1-weighted gradient-echo sequences demonstrate both out-of-phase effects, which cycle with in-phase and out-of-phase times, and susceptibility effects, which increase with increase in TE.

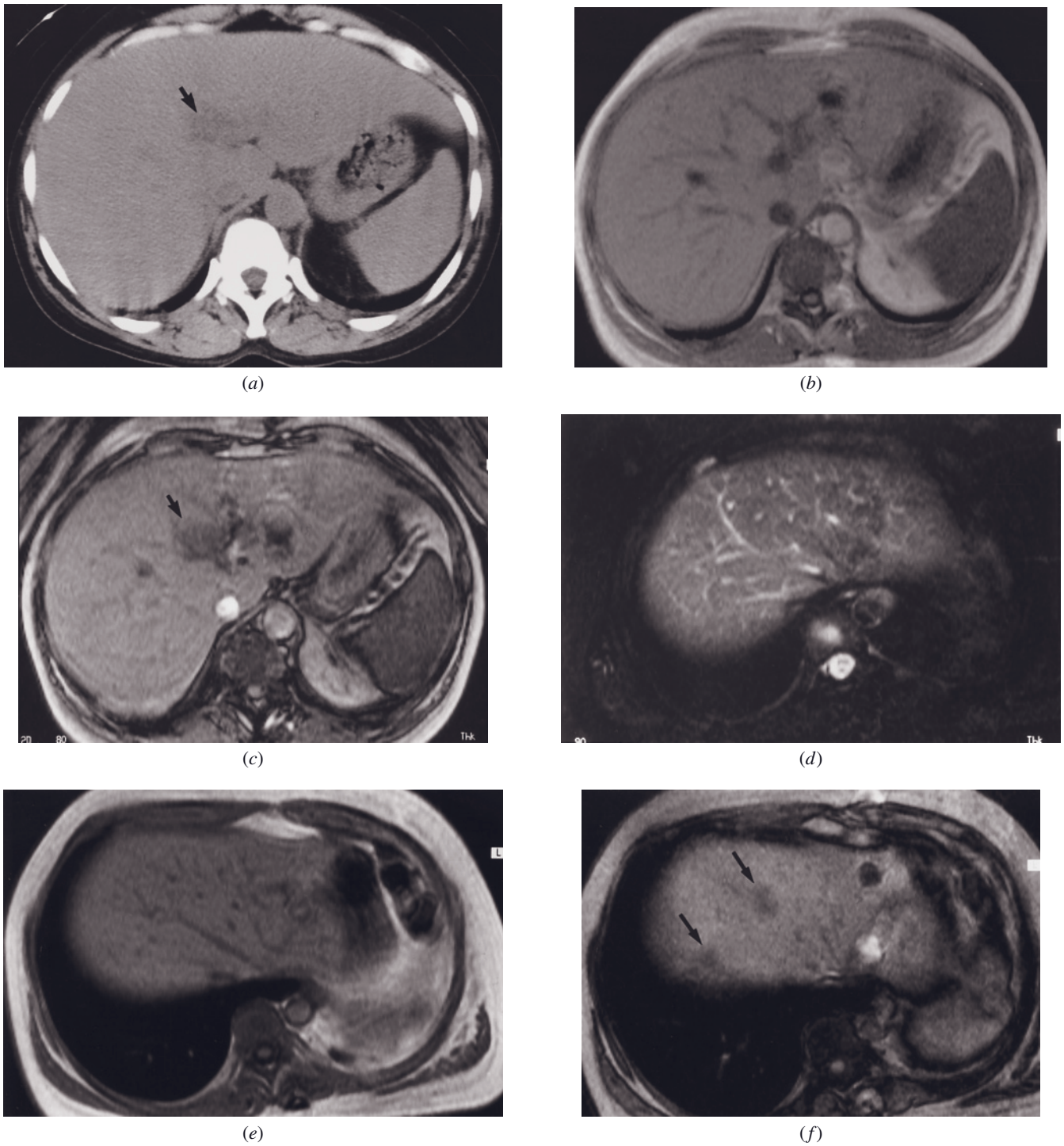

FIG. 2.237 Focal fatty liver. CT (*a*), SGE (*b*), and out-of-phase SGE (*c*) images. A CT image acquired in a patient with breast cancer demonstrates a low-density lesion in the medial segment (arrow, *a*). The in-phase T1-weighted image (*b*) shows no lesion in this location, whereas on the out-of-phase image (*c*), signal drop occurs in the central region of the medial segment (arrow, *c*), which is diagnostic for focal fatty infiltration when combined with the information that enhancement was isointense on the hepatic arterial dominant-phase images.

T2-weighted fat-suppressed ETSE (*d*), SGE (*e*), and out-of-phase SGE (*f*) images in a second patient. Previous ultrasound study in this young boy with acute myelogeneous leukemia demonstrated two liver lesions. No liver lesions are apparent on the in-phase T1-weighted image (*e*). On the out-of-phase image (*f*), two focal low-signal rounded masses are apparent (arrows, *f*). The T2-weighted image (*d*) does not reveal any lesion. No tumor blush was apparent on immediate postgadolinium images (not shown). The identification of lesions only on out-of-phase SGE images is diagnostic for fatty infiltration.

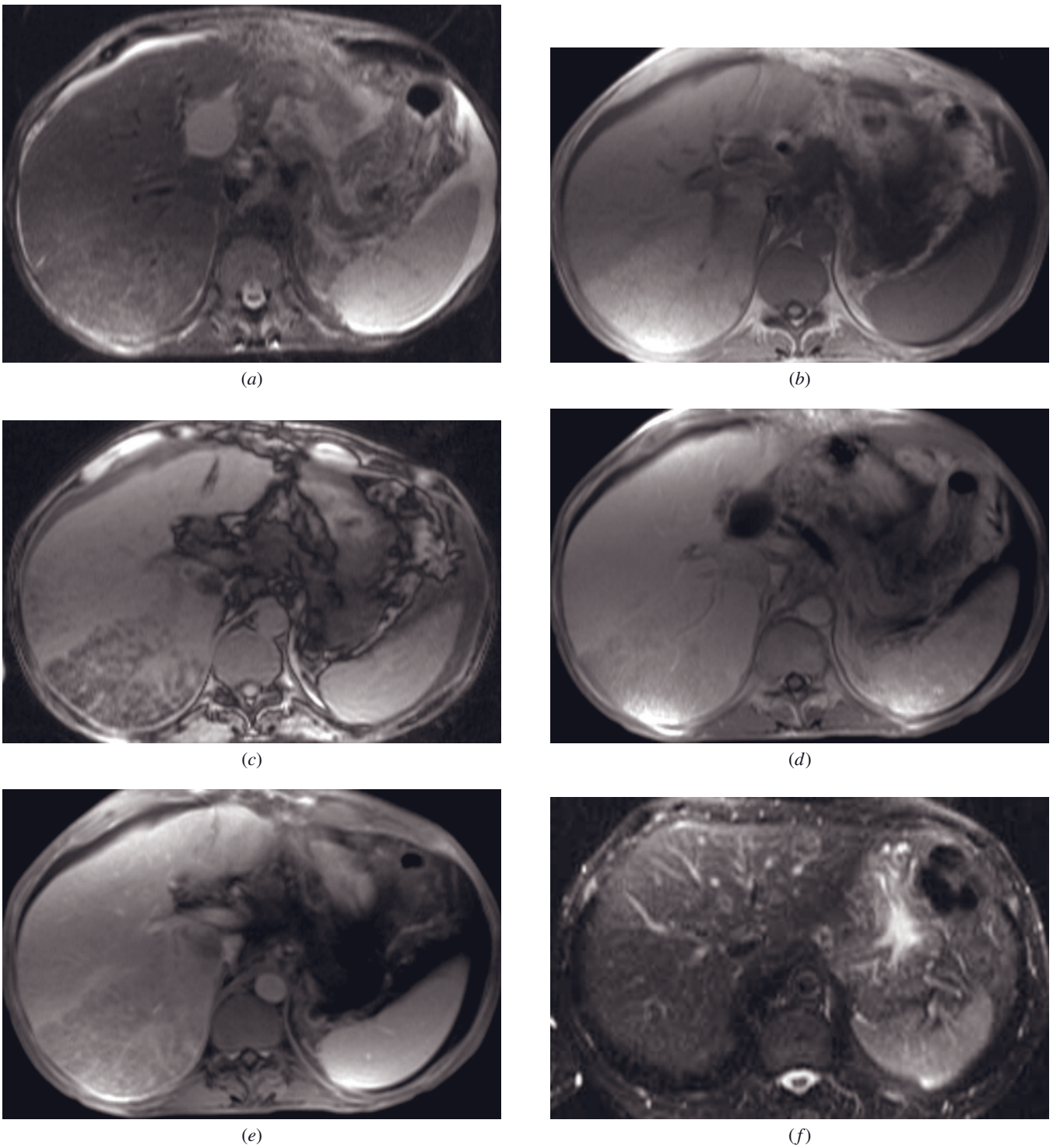

FIG. 2.238 Multiple small foci of fat. T2-weighted SS-ETSE (*a*), SGE (*b*), out-of-phase SGE (*c*), and 45-s (*d*) and 90-s fat-suppressed (*e*) post gadolinium SGE images. There are multiple small focal fat areas in the right hepatic parenchyma that drop in signal on out-of-phase images (*a*) compared with in-phase images (*b*). Although there is slight hepatic heterogeneity on other sequences, there is no evidence of abnormal enhancement of these foci alone, supporting that this appearance is that of multiple foci of fat deposition.

T2-weighted SS-ETSE (*f*), SGE (*g*), out-of-phase SGE (*h*), and immediate (*i*) and 90-s fat-suppressed (*j*) postgadolinium SGE images in a second patient that show multiple small foci of fat scattered throughout the hepatic parenchyma. The lesions lose signal on the out-of-phase images (*h*) and do not show differing enhancement from background liver.

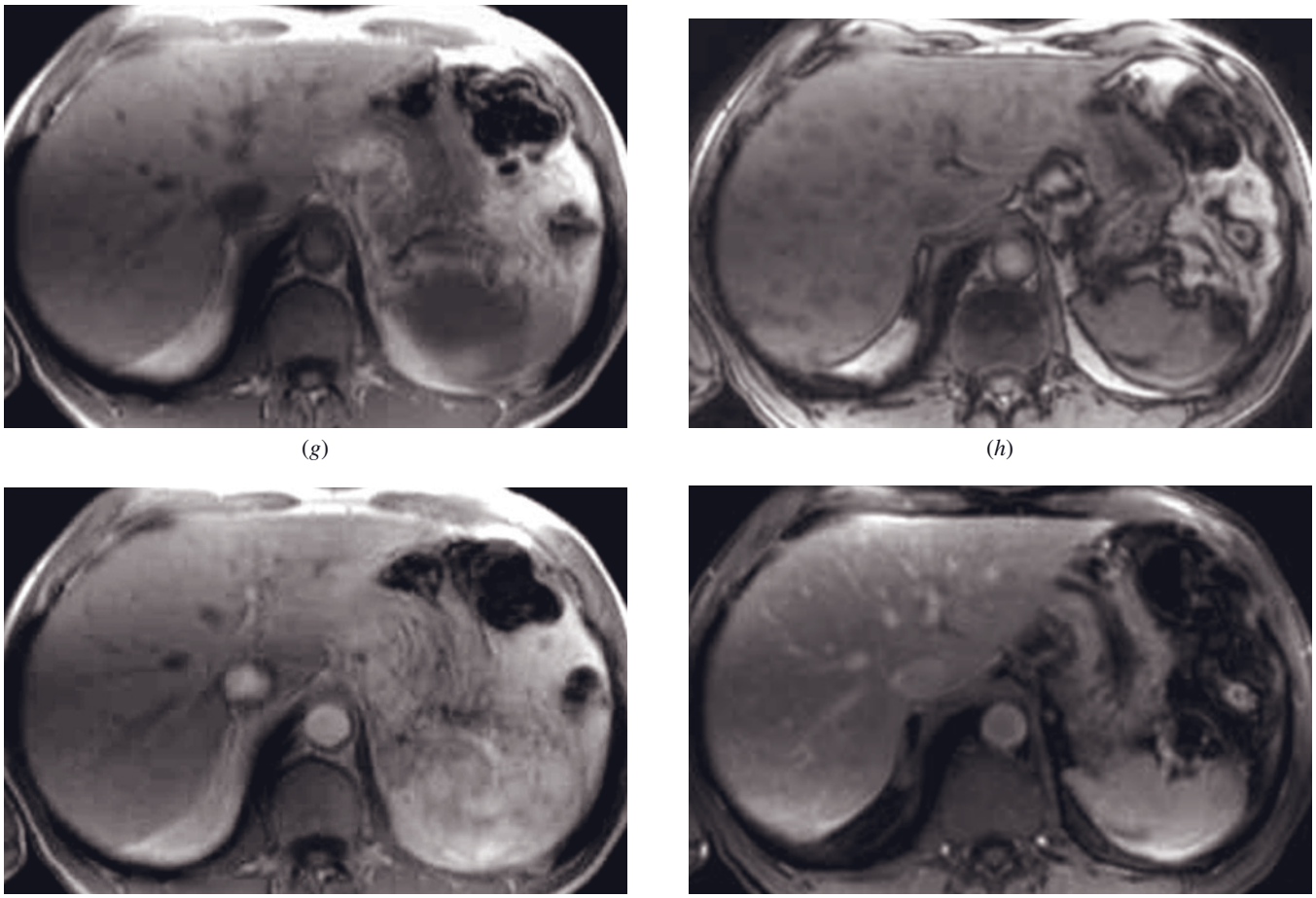

(*g*) (*h*)

(*i*) (*j*)

FIG. 2.238 (*Continued*)

to employ when the signal of liver and spleen converge on shorter TE out-of-phase compared to longer TE in-phase, that is, liver still brighter than spleen but the difference is less than on the in-phase sequence. At the present time, detection of minimal fat has not been substantiated (figs. 2.239–2.242).

FNH and metastases are the most common focal lesions associated with fatty liver. MRI is particularly effective in evaluating patients with fatty liver for the presence of focal lesions. Non-fat-suppressed T1-weighted images and fat-suppressed T2-weighted images maximize the contrast between the liver and lesions. On non-fat-suppressed T1-weighted images, the liver may be higher in signal intensity than normal liver, maximizing the contrast with low-signal-intensity masses, whereas on fat-suppressed T2-weighted images fatty liver is lower in signal intensity than normal liver, maximizing the contrast with moderately high-signal-intensity masses.

An area that is isointense or hyperintense to surrounding background parenchyma on in-phase images and loses signal homogeneously on out-of-phase images is highly diagnostic for focal fatty infiltration. The lack of surrounding mass effect, the presence of vessels, and the morphology of focal fat most often permit distinction from fat within tumors, such as HCC, adenoma, angiomyolipoma, or lipoma [309]. Focal fat usually has angular, wedge-shaped margins that are usually relatively well defined. Masses that contain fat usually have a rounded configuration. Common locations for focal fat are adjacent to the ligamentum teres, the central tip of segment 4, and, less commonly, along the gallbladder [376, 377]. Although the pathogenesis for focal fat is not well established, it is suggested that variations in blood supply may occur [378–380]. An important ancillary observation is that uncomplicated fatty deposition within the liver enhances with gadolinium usually indistinguishably from normal liver on all sequences. Almost invariably masses that contain fat enhance differently than background liver.

Hemorrhage, melanin, copper, and protein may be associated with nonfatty masses with high signal inten-

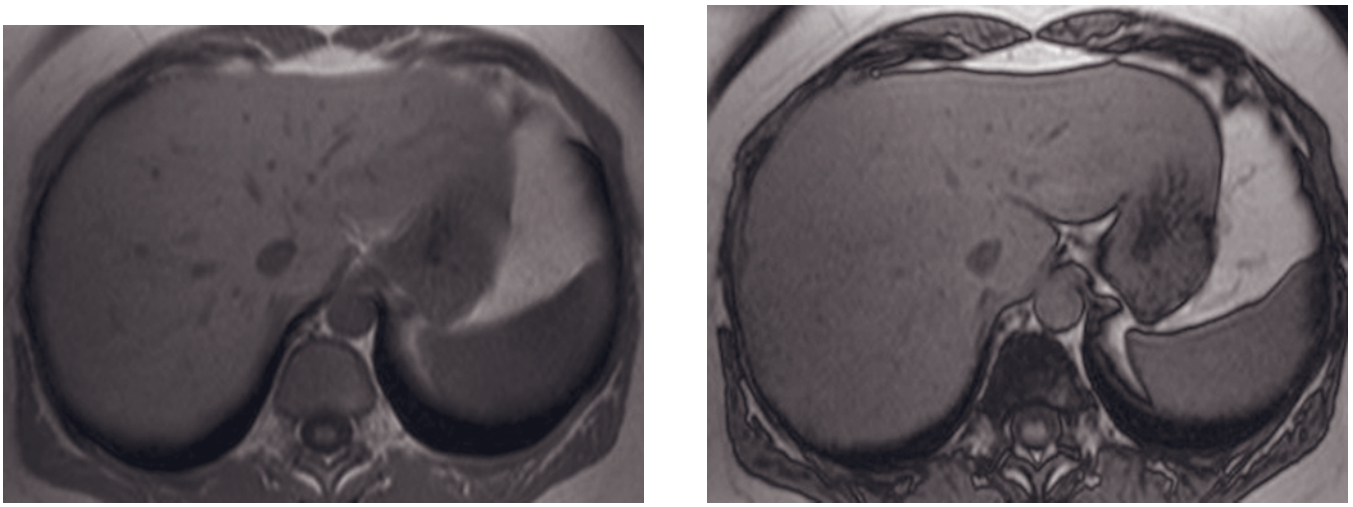

(*a*) (*b*)

FIG. 2.239 Minimal fatty infiltration. In-phase (*a*) and out-of-phase (*b*) SGE images. The liver appears unremarkable on the T1-weighted image (*a*). On out-of-phase image (*b*), the signal intensity of the liver converges toward the signal intensity of the spleen. Note that although the signal intensity of liver drops on out-of-phase image it remains higher than the signal intensity of the spleen, which may represent minimal fatty infiltration.

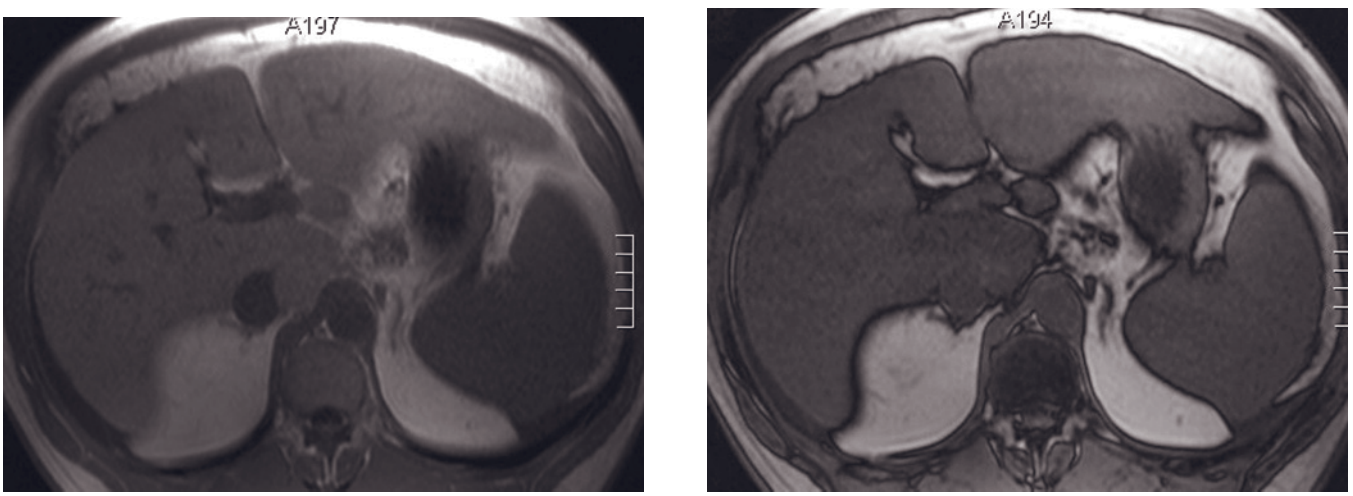

(*a*) (*b*)

FIG. 2.240 Mild fatty infiltration. In-phase (*a*) and out-of-phase (*b*) SGE images. The liver appears unremarkable on T1-weighted images (*a*) and exhibits a drop in signal intensity on out-of-phase image (*b*), with convergence of the signal intensity of the liver and spleen to comparable signal intensities. Note that the liver has not dropped lower in signal than the spleen, establishing that fatty infiltration is mild.

sity on T1-weighted images. Out-of-phase images distinguish between these tumors and lipid-containing masses or focal fatty infiltration. Although some well-differentiated HCCs contain lipid, most HCCs with high signal intensity on T1-weighted images do not. HCCs that contain lipid tend to be more well-defined masses than focal fatty infiltration. Moreover, HCCs are often encapsulated and are most commonly not homogeneously fatty. They usually contain some elements with high signal intensity on fat-suppressed T2-weighted images. Of all focal hepatic lesions, hepatic adenoma may most closely resemble focal fatty infiltration, as these tumors may have relatively uniform fat content. Demonstration of a capillary blush on arterial dominant images that fades on interstitial-phase postgadolinium images establishes the diagnosis of adenoma. Although angiomyolipoma and lipoma may be composed of fat, they do not drop in signal intensity on out-of-phase images; however, these lesions will demonstrate a phase-cancellation artifact along their margins with

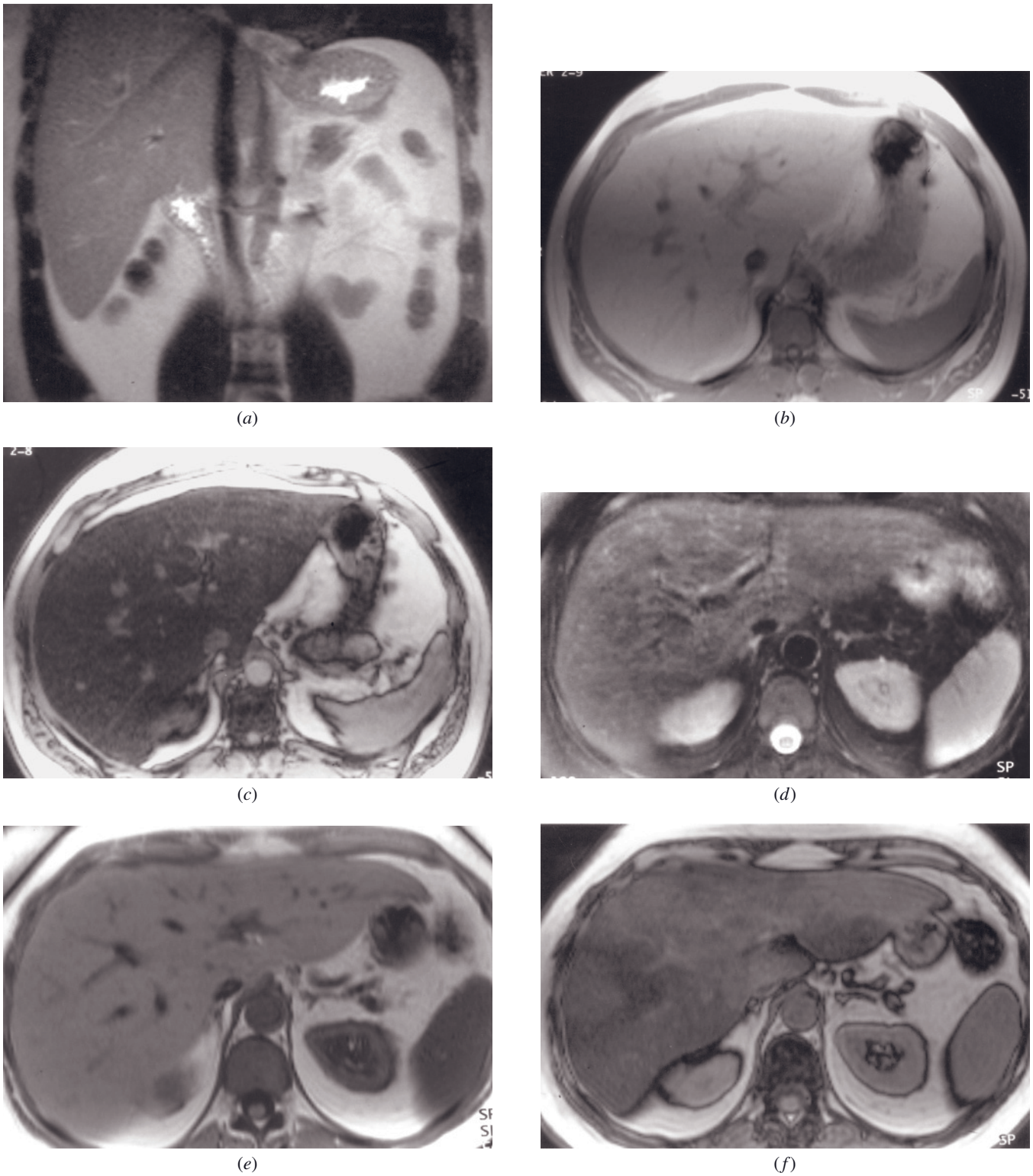

FIG. 2.241 Moderately severe diffuse fatty infiltration. Coronal T2-weighted SS-ETSE (*a*), SGE (*b*), and out-of-phase SGE (*c*) images. The liver is high in signal on T2-weighted image (*a*), which reflects the fact that fat, including fatty liver, is high signal on long echo-train sequences. A useful internal comparison is the psoas muscle: normal liver should be of comparable signal. Note in this patient that the liver is considerably higher in signal than psoas. In-phase (*b*) and out-of-phase (*c*) images confirm moderately severe fatty infiltration.

T2-weighted fat-suppressed ETSE (*d*), SGE (*e*), out-of-phase SGE (*f*), and immediate postgadolinium SGE (*g*) images in a second patient. The liver demonstrates moderately severe heterogeneous drop in signal intensity on out-of-phase image (*f*) with respect to in-phase (*e*) image, consistent with severe diffuse patchy fatty infiltration. Note that enhancement of fatty liver (*g*) is generally

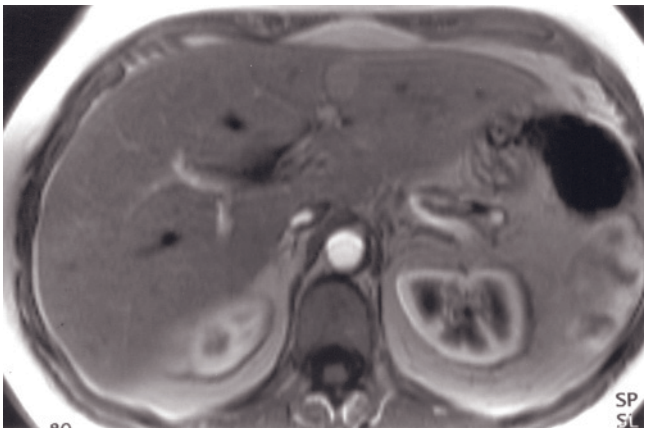

(*g*)

FIG. 2.241 (*Continued*) indistinguishable from normal when an in-phase echo time nonfat-suppressed sequence is used for gadolinium-enhanced imaging.

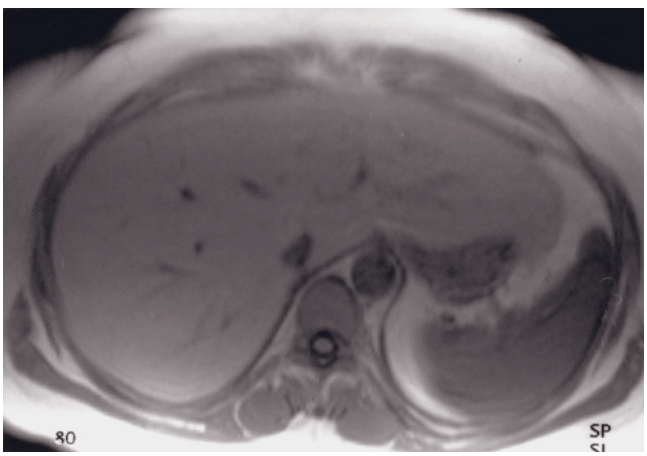

(*a*)

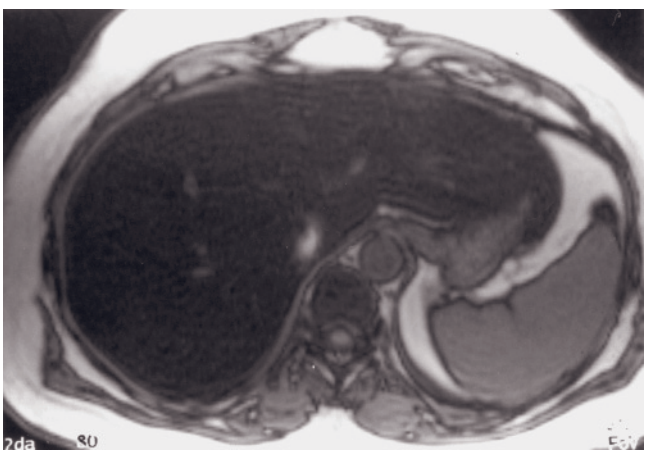

(*b*)

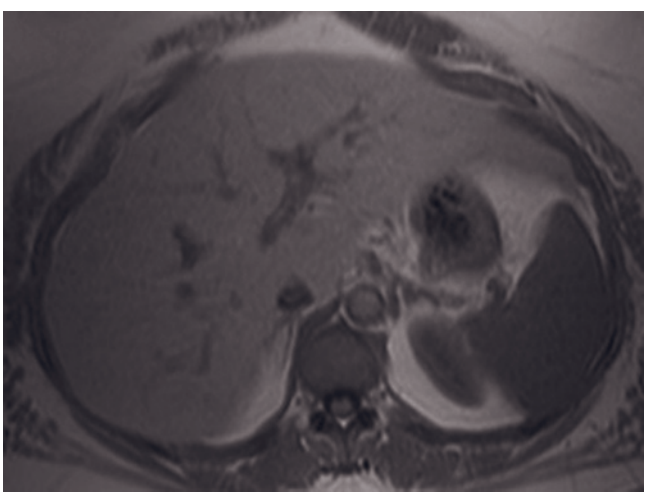

(*c*)

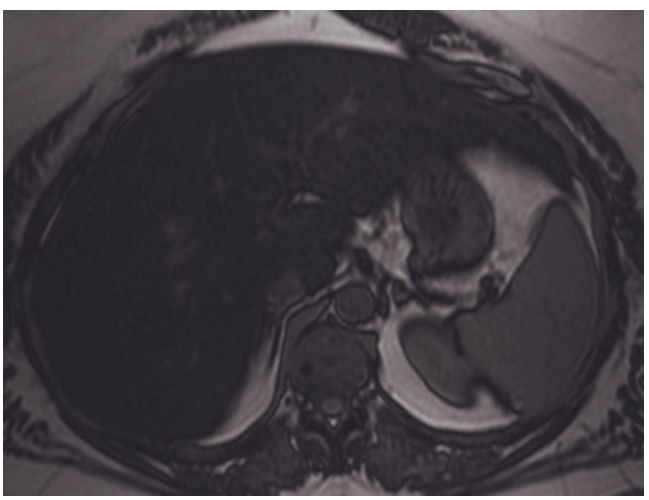

(*d*)

FIG. 2.242 Severe fatty infiltration. In-phase (*a*) and out-of-phase (*b*) SGE images and in-phase (*c*) and out-of-phase (*d*) SGE images in two different patients both with enlarged liver and marked fatty infiltration.

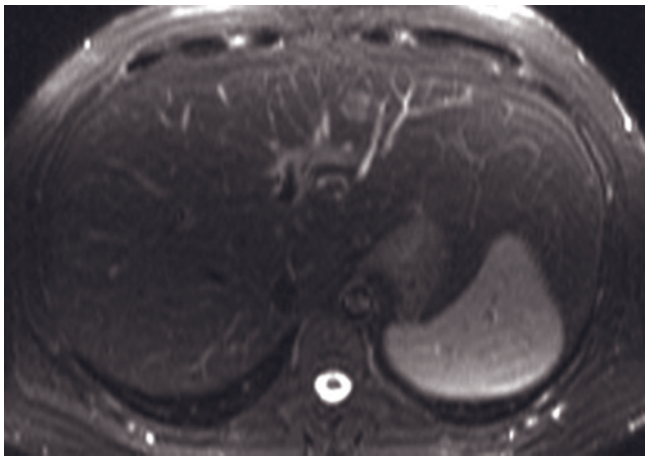

(*e*)

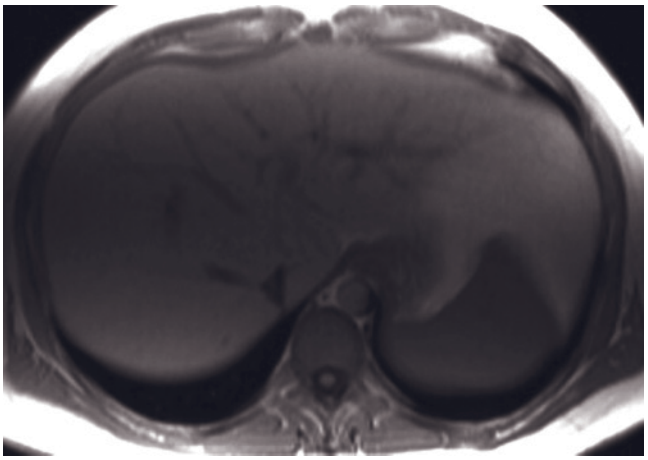

(*f*)

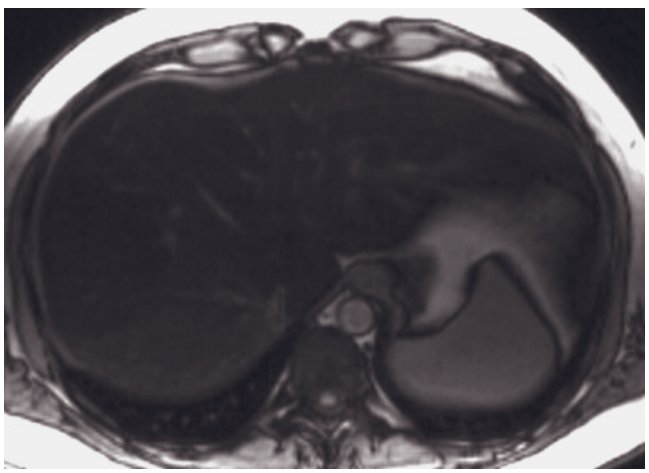

(*g*)

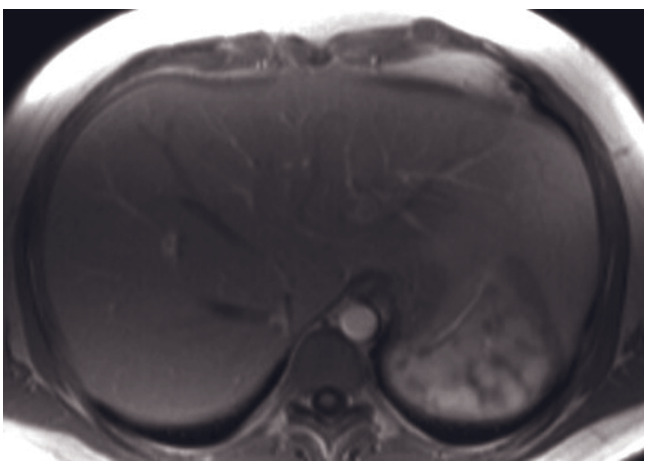

(*h*)

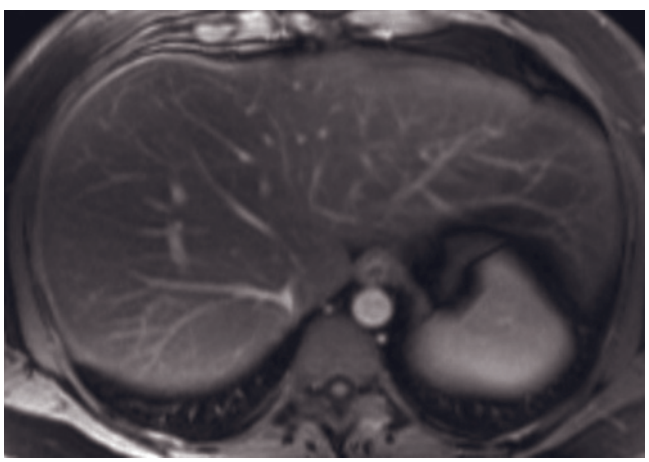

(*i*)

Fig. 2.242 (*Continued*) Echo-train STIR (*e*), SGE (*f*), out-of-phase SGE (*g*), and immediate (*h*) and 90-s fat-suppressed (*i*) postgadolinium SGE images in a third patient with severe fatty infiltration demonstrate similar findings.

liver. The extent of fat within those tumors is higher than in severe liver steatosis. Because of this difference, it is possible to distinguish between these tumors and fatty liver. Also, angiomyolipoma and lipoma visibly lose signal when fat-suppressed techniques are employed because of the very high fat content, which is most apparent with fatty liver.

Focal normal liver in the setting of diffuse fatty infiltration (focal sparing) appears as a focus of high signal intensity in a background of diminished-signal

liver on out-of-phase images (figs. 2.243 and 2.244). Arterioportal shunting, occlusion or compression of the portal vein, and decreased portal perfusion causing decreased delivery of lipid are the pathogenetic causes postulated for focal sparing [378–380]. The central tip of segment 4, surrounding gallbladder fossa and adjacent to falciform ligament, most commonly has anomalous vascular supply and, consequently, is more likely to have lesser fat deposition than the rest of the liver [376, 377]. Metastases in the setting of fatty liver may demonstrate peritumoral fat sparing due to vascular compression of this circumferential liver [309, 377, 381, 382].

Mucopolysaccharidoses

The mucopolysaccharidoses are a group of inherited disorders caused by incomplete degradation and storage of acid mucopolysaccharides (glycosaminoglycans). The clinical manifestations result from the accumulation of mucopolysaccharides in somatic and visceral tissues. Mucopolysaccharides are major components of the extracellular substance of connective tissue. Widespread accumulation of mucopolysaccharides along with involvement of many organ systems is observed in this condition. Hepatosplenomegaly, skeletal deformities,

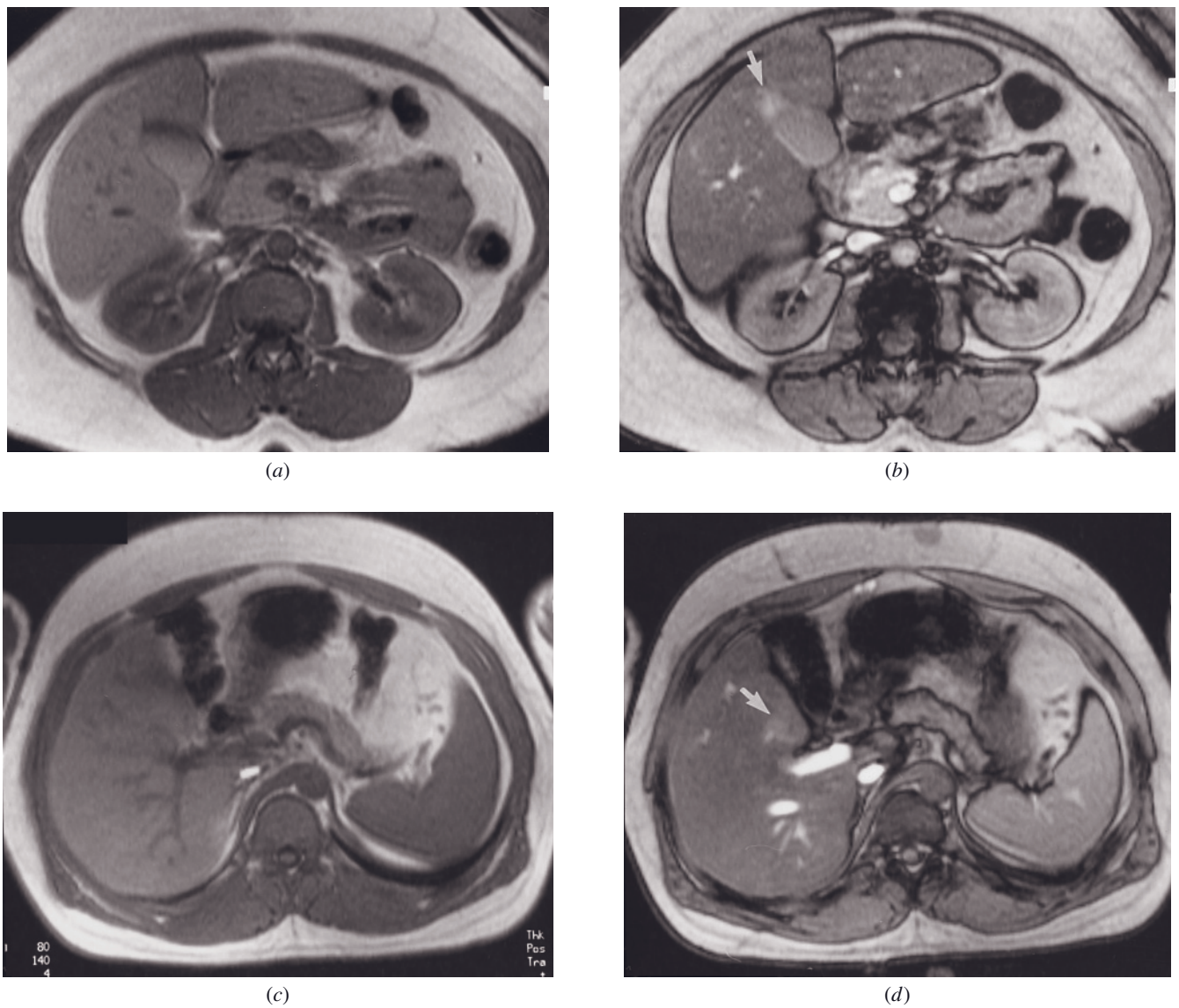

FIG. 2.243 Fatty infiltration with focal sparing. SGE (*a*) and out-of-phase SGE (*b*) images. Homogeneous signal of the liver is present on the T1-weighted image (*a*). On the out-of-phase image (*b*), the liver drops in signal, with a focus of higher signal adjacent to the gallbladder (arrow, *b*) representing focal normal liver.

SGE (*c*) and out-of-phase SGE (*d*) images in a second patient. The liver is normal in signal intensity on the in-phase image (*c*). On the out-of-phase image (*d*), the liver drops in signal intensity relative to the spleen, with focal sparing present in the tip of segment 4 (arrow, *d*).

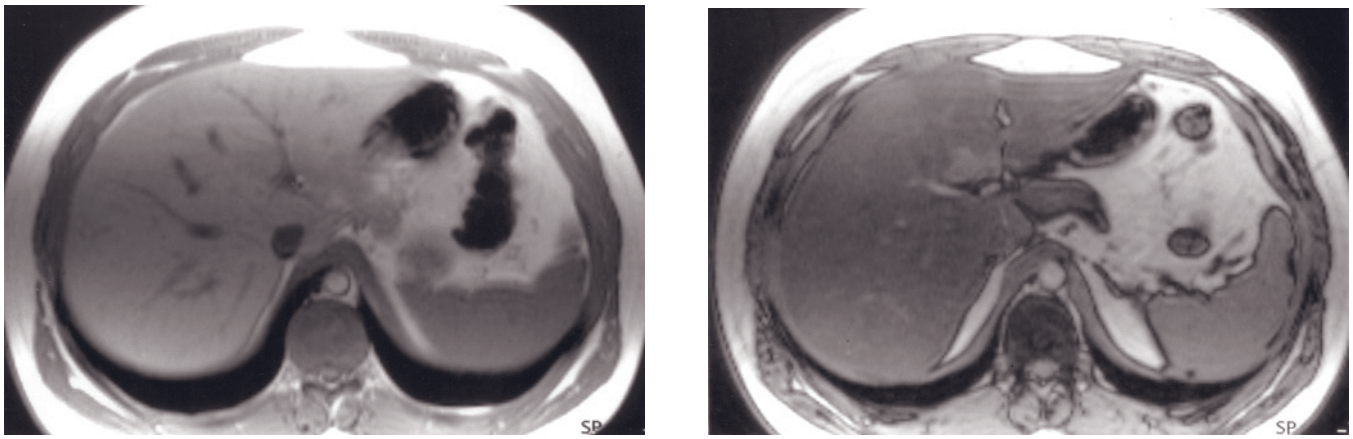

(*e*)

(*f*)

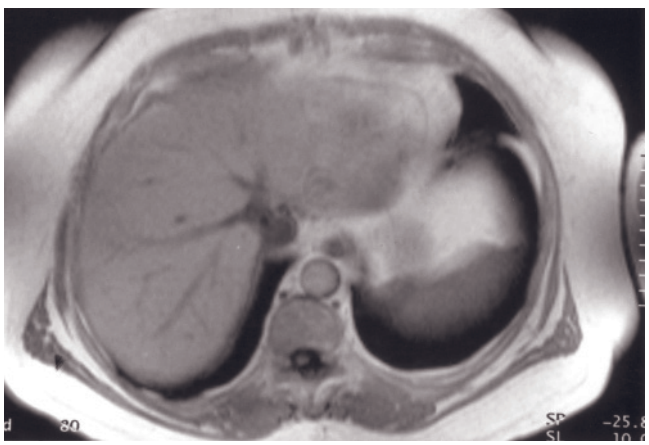

(*g*)

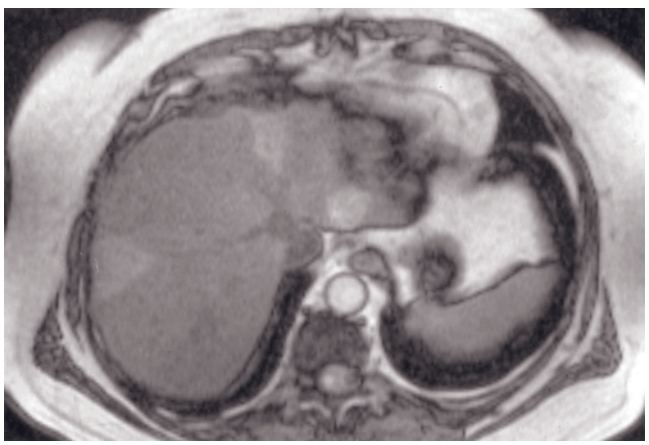

(*h*)

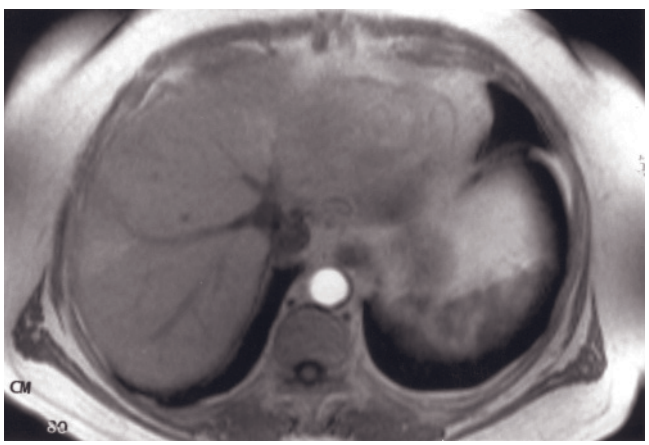

(*i*)

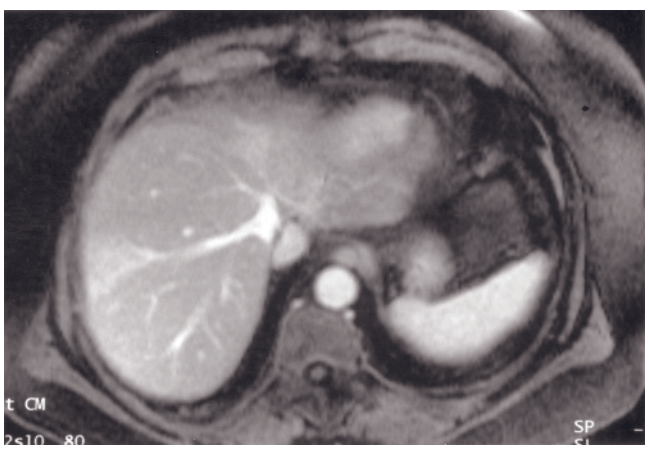

(*j*)

Fig. 2.243 (*Continued*) SGE (*e*) and out-of-phase SGE (*f*) images in a third patient. There is a mild fatty infiltration of the liver with focal sparing of the tip of segment 4 (*f*).

SGE (*g*), out-of-phase SGE (*h*), immediate postgadolinium SGE (*i*), and 90-s postgadolinium fat-suppressed SGE (*j*) images in a fourth patient. Wedge-shaped regions of focal normal liver in a fatty deposited liver are present. Note that on 90-s postgadolinium image (*j*) these same regions are identified as higher signal. This reflects a fat suppression effect of the fatty liver, rather than a gadolinium-enhanced effect of the regions of normal liver.

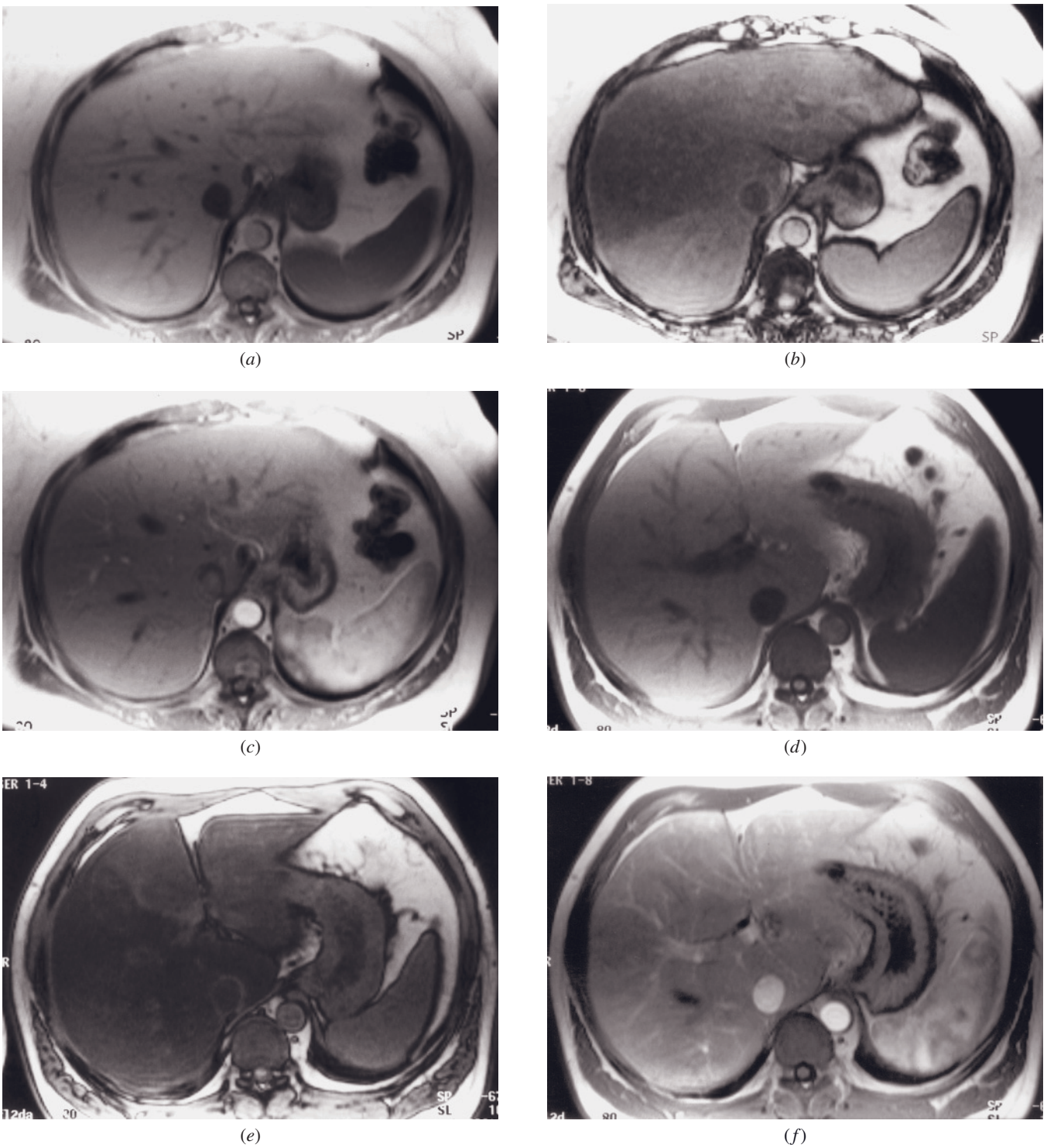

FIG. 2.244 Fatty infiltration with segmental variation in fat content. SGE (*a*), out-of-phase SGE (*b*), and immediate post-gadolinium SGE (*c*) images. On the out-of-phase (*b*) image, there is trisegmental signal loss with relative sparing of the posterior segment of the right lobe. Signal intensity on postgadolinium images (*c*) is unremarkable for the entire liver.

SGE (*d*), out-of-phase SGE (*e*), immediate post-gadolinium SGE (*f*), and 90-s postgadolinium fat-suppressed SGE (*g*) images in a second patient. There is slightly less fatty infiltration of the left lobe compared to the right, reflected by relatively lesser drop in signal on the out-of-phase image (*e*). After contrast, the liver enhances homogeneously.

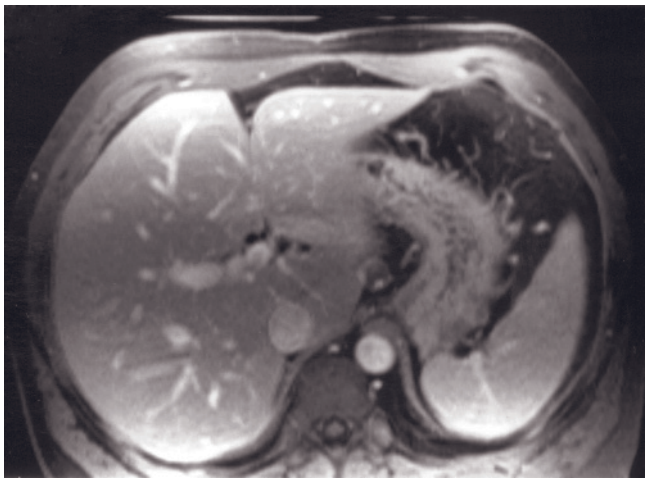

(*g*)

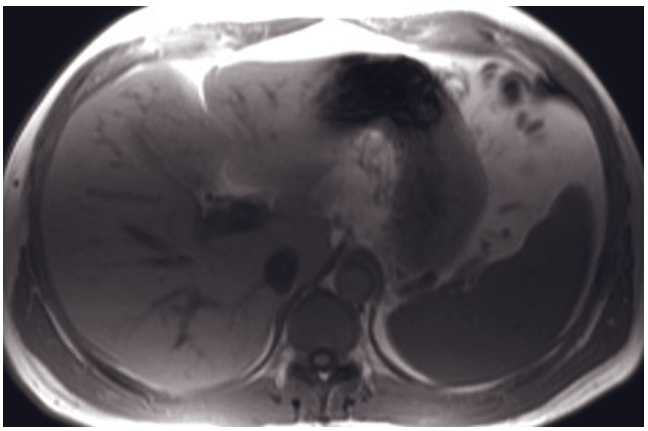

(*h*)

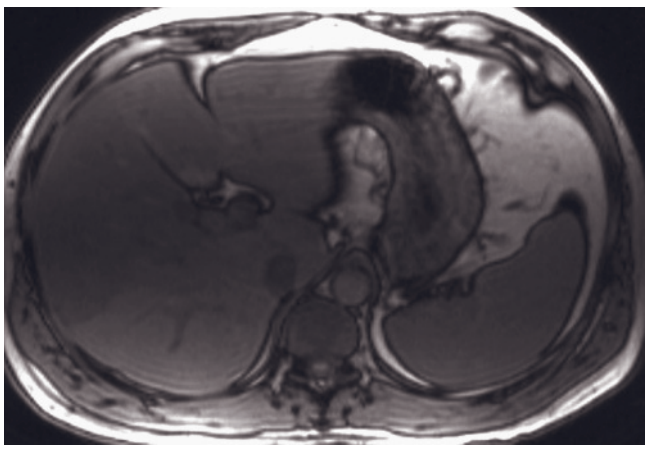

(*i*)

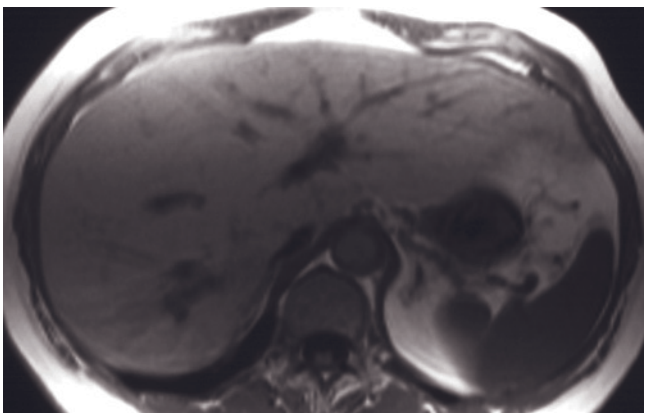

(*j*)

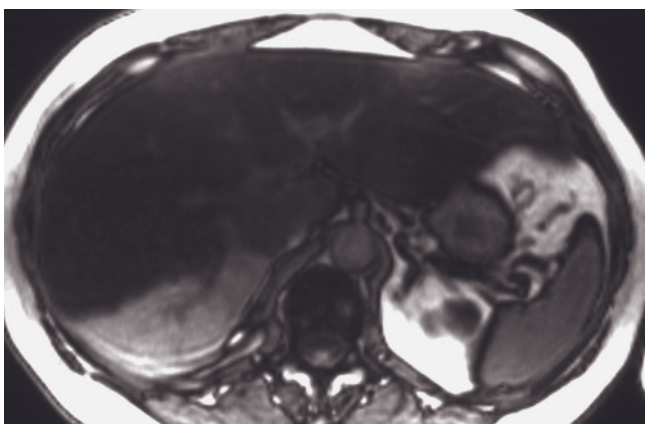

(*k*)

Fig. 2.244 (*Continued*) SGE (*h*) and out-of-phase SGE (*i*) images and SGE (*j*) and out-of-phase SGE (*k*) images in two different patients demonstrate segmental fat sparing in varying degrees.

valvular lesions, subendothelial deposits, particularly within the walls of coronary arteries, and CNS abnormalities are common. On MR images, hepatomegaly is commonly observed (fig. 2.245). Specific MR imaging features are yet to be elucidated. Pathologic macroscopic examination may show extensive fibrosis or cirrhosis [2]. A report involving postmortem examination of six cases of mucopolysaccharidoses revealed diffuse liver fibrosis in all cases [383]. Microscopic examination shows swollen hepatocyte and Kupffer cell cytoplasm, filled with abnormal storage material [2]. The degree of disability and overall prognosis in each of the muco-

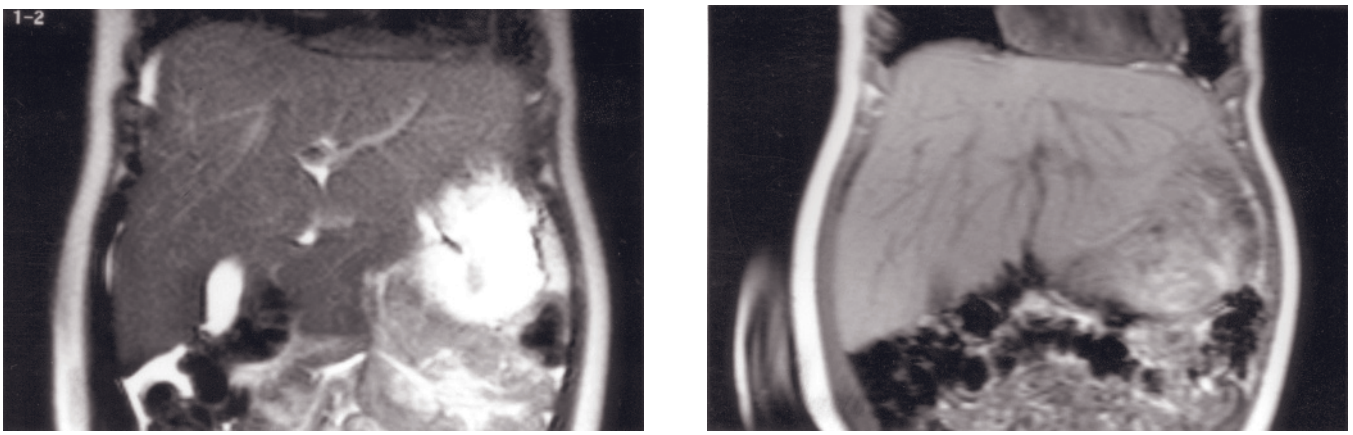

(*a*) (*b*)

FIG. 2.245 Storage disease. Coronal T2-weighted SS-ETSE (*a*) and SGE (*b*) images in a patient who has a history of mucopolysaccharidosis. Note enlargement of the liver well demonstrated on coronal images.

polysacharidoses are determined by the extent of physical and mental involvement [384].

Arteriovenous Fistulas

Abnormal arterial-venous communications or fistulas may occur in the liver secondary to injury, tumor, or congenital disease. Arteriovenous fistula is a well-known complication of percutaneous liver biopsy [385]. Clinically significant or symptomatic hepatic vascular fistulae are uncommon but are usually caused by trauma, including iatrogenic trauma [386]. Fistulas are well shown with gadolinium-enhanced techniques, either as a 2D or a 3D GRE or MRA technique. MRI features of posttraumatic arterial-vascular communications include dilation of afferent and efferent vessels, transient hepatic parenchymal blush in a watershed distribution, and early opacification of efferent vessels (fig. 2.246) [387]. A critical observation to establish the diagnosis is that the nidus of the shunt follows the enhancement characteristics of comparable intrahepatic vessels (i.e., they often retain contrast); whereas focal hepatic masses with the exception of hemangiomas, follow a different pattern, and often fade more quickly or washout.

Congenital vascular fistulas are rare. One of the more common conditions is hereditary hemorrhagic telangiectasia (Rendu–Osler–Weber syndrome). The disease is characterized by telangiectasias (skin, mucous membranes), arteriovenous fistulas in the liver (30% of cases) lungs. and CNS, and aneurysms [2, 3]. Visceral involvement has been documented in the GI tract, spleen, kidneys, and genital tract. On imaging, the liver may be filled with numerous variably sized abnormal arterial-venous communications. Lesions may appear as multiple well-defined enhancing masses that parallel the enhancement of vessels. A combination of vascularized lesions and thrombosed lesions may be observed, reflecting either the natural history of the condition or treatment approaches such as embolization (fig. 2.247).

Portal Venous Obstruction/Thrombosis

Thrombosis of the portal vein is generally associated with the presence of a hypercoaguable state, vascular injury, or stasis [2]. Obstruction of the portal vein may be insidious and well tolerated or may be an acute, potentially life-threatening event. Most cases fall between these two extremes. Blockage of the portal vein may be extrahepatic or intrahepatic. Common causes of extrahepatic portal vein obstruction include 1) massive hilar lymphadenopathy due to metastatic abdominal cancer; 2) phlebitis resulting from peritoneal sepsis (e.g., appendicitis); 3) propagation of splenic vein or superior mesenteric vein thrombosis secondary to pancreatitis; and 4) postsurgical thrombosis following abdominal procedures. Cirrhosis is the most common intrahepatic cause of portal venous obstruction. Intravascular invasion by primary or secondary malignancy in the liver may occur [388].

On imaging, portal vein thrombosis may be demonstrated by using black-blood techniques (e.g., spin-echo techniques with superior and inferior saturation pulses) and bright-blood techniques (e.g., time-of-flight gradient echo or gadolinium-enhanced gradient echo). A combination of both approaches is often useful to increase diagnostic confidence. Portal veins may be occluded by tumor thrombus, bland thrombus, or extrinsic compression. MRI usually is able to distinguish between these entities. Tumor and bland thrombus may

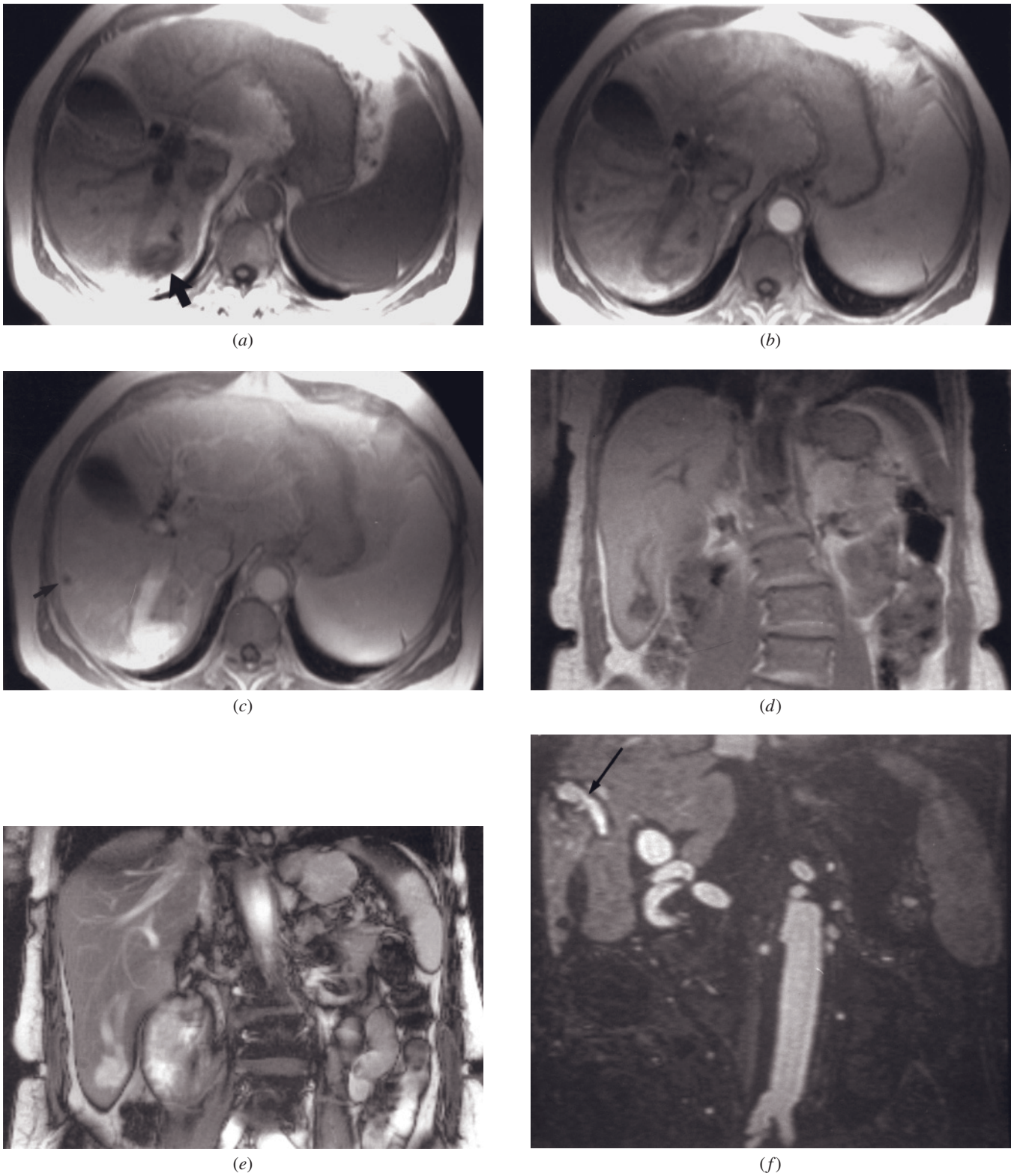

FIG. 2.246 Acquired arterio-venous malformation. SGE (*a*) and immediate (*b*) and 45-s postgadolinium SGE (*c*) images. There is a 2-cm rounded structure (arrow, *a*) in the posterior segment of the right lobe, with a prominent posterior branch of the right portal vein entering the lesion. After contrast administration, there is early minimal enhancement (*b*) and 45-s intense enhancement (*c*) of this lesion in continuity with the portal vein (*c*). Note also the tiny hepatic cyst or biliary hamartoma (arrow, *c*), nodular contour of the liver, and splenomegaly.

Coronal SGE (*d*) and gadolinium-enhanced refocused gradient-echo (*e*) images in a second patient. There is a lesion in the inferior aspect of the right lobe that demonstrates large paired vessels leading into and away from it. This lesion shows decreased signal on the precontrast image (*d*) and intense enhancement after gadolinium administration (*e*), consistent with arterio-venous malformation.

Coronal 3D gradient-echo 2-mm source image (*f*), MIP reconstruction of the 2-mm 3D gradient-echo sections (*g*), and transverse 90-s fat-suppressed SGE image (*h*) in a third patient. The 2D source image (*f*) demonstrates the connection between right hepatic

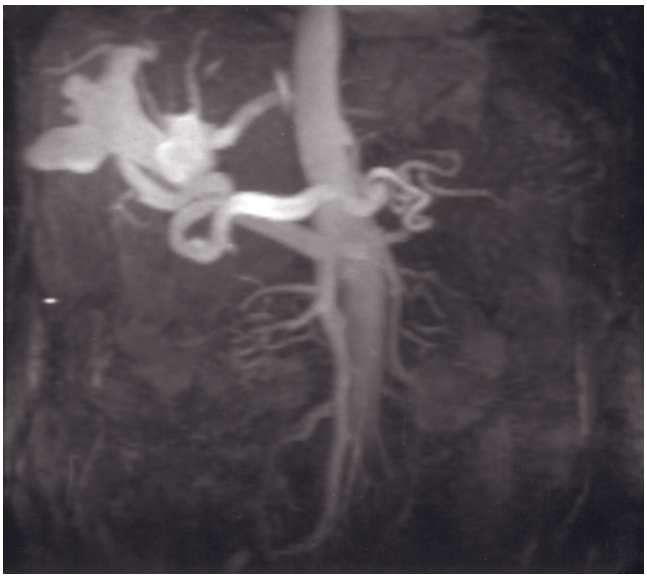

(*g*)

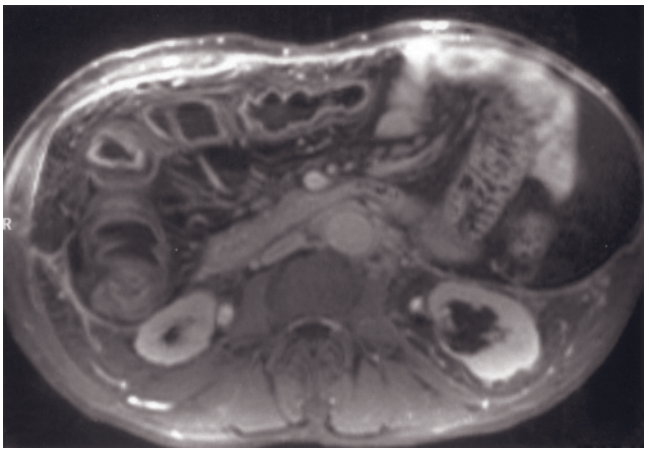

(*h*)

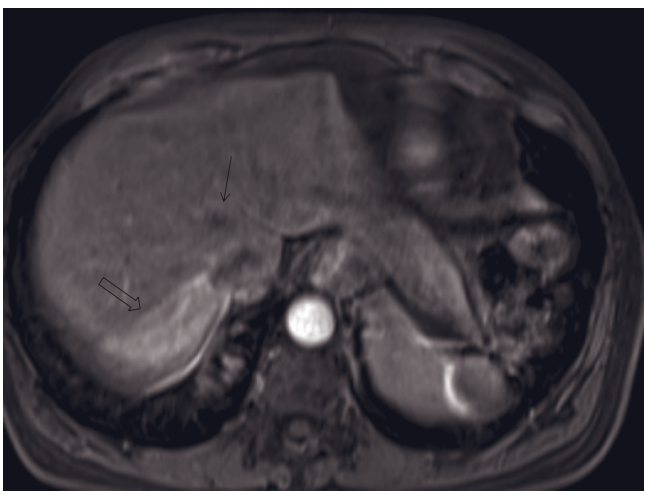

(*i*)

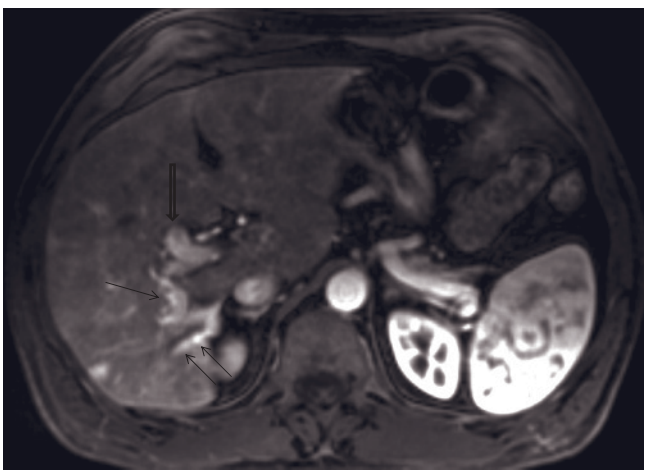

(*j*)

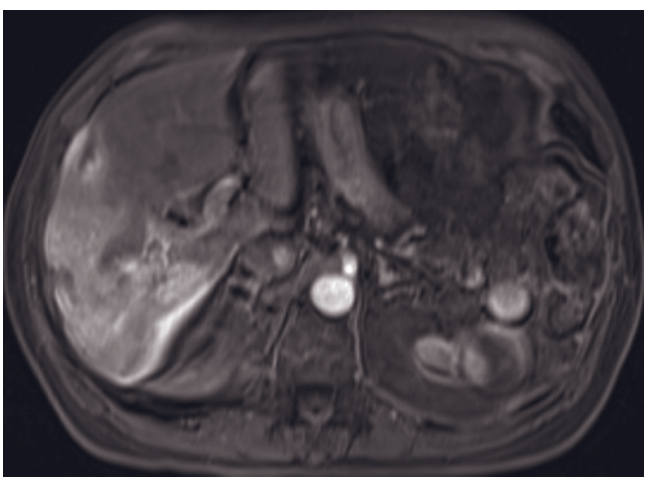

(*k*)

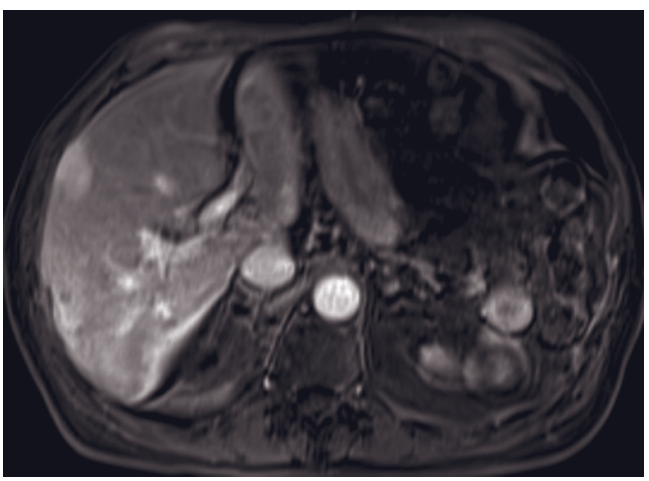

(*l*)

FIG. 2.246 (*Continued*) artery and right portal vein (arrow, *f*) and the MIP reconstruction image (*g*) displays the full length of the dilated right hepatic artery and portal vein. On the interstitial-phase gadolinium-enhanced fat-suppressed SGE image (*h*) there is submucosal edema of the colon with prominent serosal and mucosal enhancement reflecting congestion in the portal venous circulation secondary to the fistula.

T1-weighted fat-suppressed 3D gradient-echo immediate (*i*, *j*, *k*) and 45-s (*l*) postgadolinium images in a patient with posttraumatic vascular shunts. The superior tomographic section demonstrates early opacification of the right hepatic vein (thick arrow, *i*). Note that the middle hepatic vein (thin arrow, *i*) is not opacified. A tomographic section through the mid-liver shows dilatation of the right portal vein (thick arrow, *j*). The level of communication is also apparent (thin arrow, *j*).

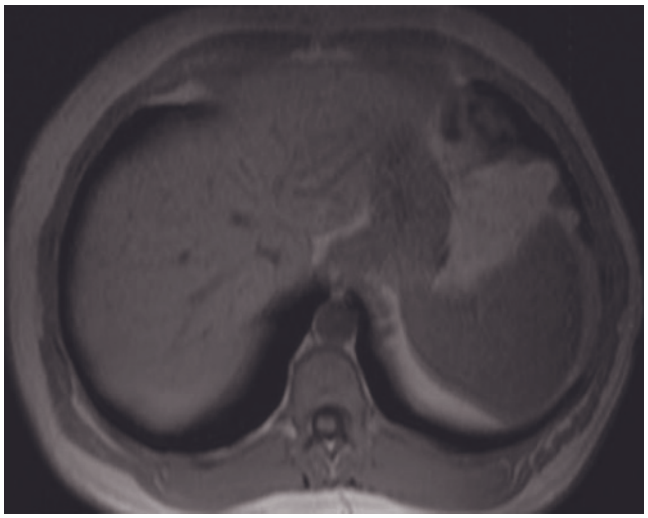

(*m*)

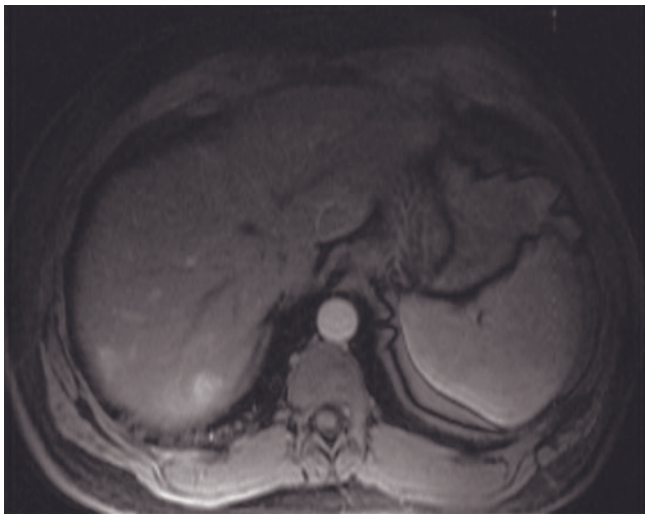

(*n*)

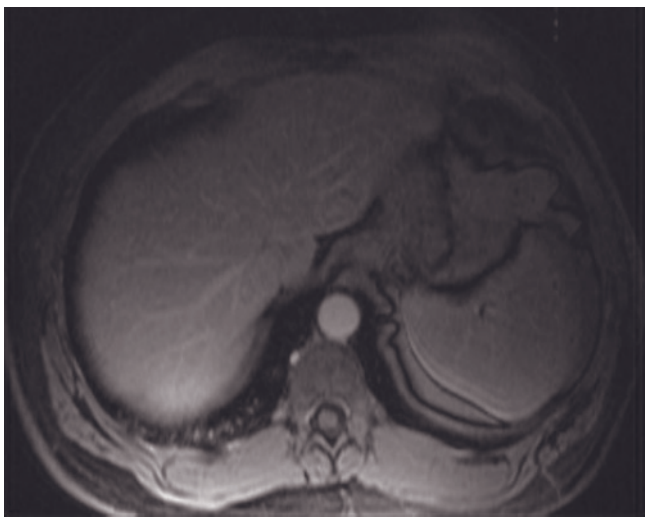

(*o*)

FIG. 2.246 (*Continued*) On the more inferior tomographic section (*k*), early intense geographic enhancement is noted in the right lobe. On the 45-s postgadolinium images (*l*), the region of increased enhancement has faded to background liver. The three features of traumatic arteriovenous shunts are: i) dilation of afferent vessel, ii) transient early increased parenchymal enhancement in a watershed distribution, and iii) early opacification of efferent vessel. The nidus of the malformation or shunt follows the opacification and enhancement pattern of comparable vessels, which distinguishes them from focal liver lesions. Note that on the late-phase images the transiently enhanced parenchyma tends to be isointense to background parenchyma.

T1-weighted fat-suppressed 3D gradient-echo (*m*), and immediate (*n*) and 90-s (*o*) fat-suppressed 3D gradient-echo image obtained **at 3T** demonstrating focal areas of intense enhancement on early phase (*n*) compatible with focal arteriovenous shunt. Note on the late phase (*o*) the shunt tends to be isointense as background parenchyma. This entity is distinguished from post-traumatic av shunt because there is no dilation of afferent or efferent vessels, or early appearance of contrast in draining veins.

be distinguished from each other by the observation that tumor thrombus is higher in signal intensity on T2-weighted images, has soft tissue signal intensity on time-of-flight gradient-echo images, and enhances with gadolinium (fig. 2.248). Bland thrombus is low in signal intensity on T2-weighted and time-of-flight gradient-echo images and does not enhance with gadolinium (figs. 2.249–2.251). Tumor thrombus is most often observed with hepatocellular carcinoma, most commonly in the diffuse type, although it may also occur with metastases. Bland thrombus may be observed in the setting of cirrhosis and various inflammatory/infectious processes involving organs in the portal circulation, with pancreatitis being the most common. Increased enhancement of the vein wall is appreciated in the setting of infected bland thrombus.

Extrinsic compression of portal veins is most commonly caused by malignant tumors, but may also occur with benign tumors such as hemangiomas. Cholangiocarcinoma, in particular, has a propensity to cause extrinsic compression and obstruction of portal veins. Lobar or segmental portal vein obstruction caused by tumor may result in discrete wedge-shaped regions of high signal intensity on T2-weighted images and enhancement on immediate postgadolinium gradient-echo images [374, 389–393]. Increased signal intensity on T2-weighted images may reflect some degree of hepatocellular injury. Decreased blood supply results in decreased size of hepatocytes, which increases the proportion of liver volume occupied by the vascular and interstitial spaces. Collateral periportal veins may maintain portal perfusion when the main portal vein

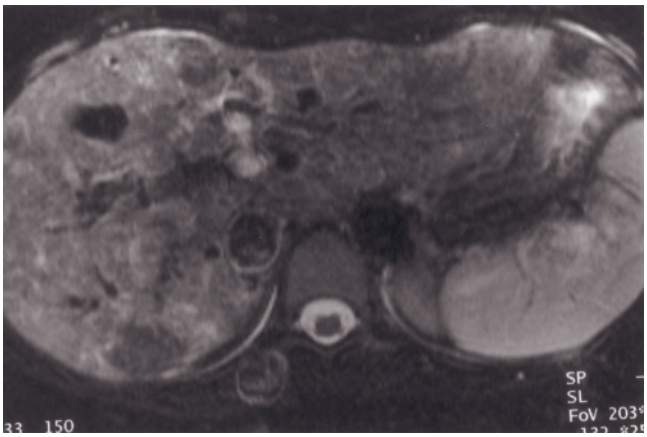

(*a*)

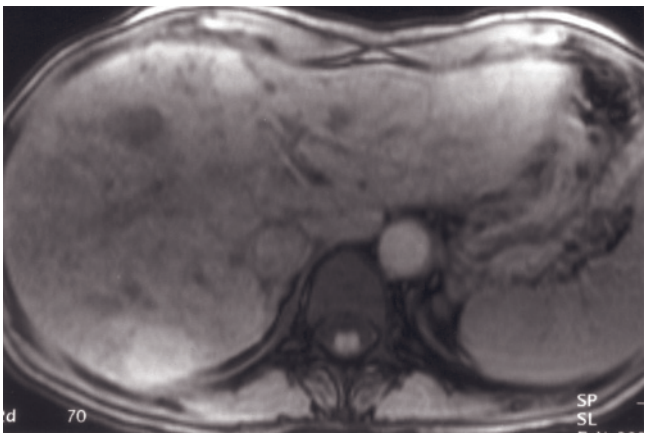

(*b*)

(*c*)

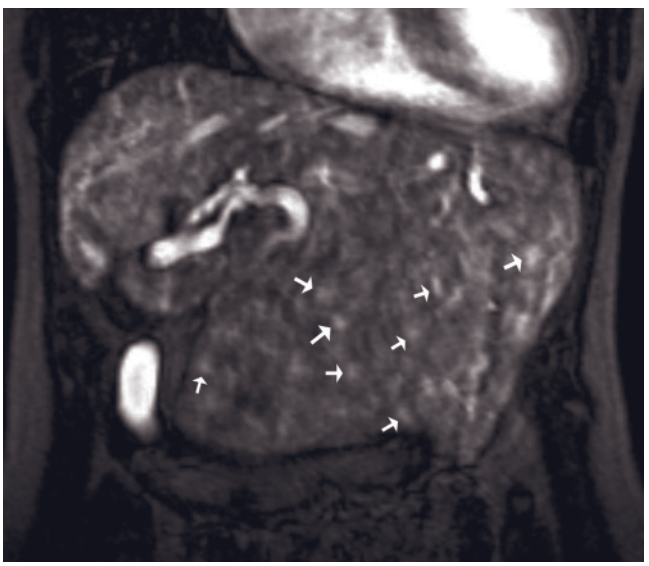

(*d*)

(*e*)

FIG. 2.247 Arterio-venous malformation in Rendu–Osler–Weber syndrome. T2-weighted fat-suppressed ETSE (*a*) and immediate postgadolinium SGE (*b*) images in a patient with Rendu–Osler–Weber Syndrome. There are multiple varying-sized liver lesions, many of which demonstrate intense enhancement on immediate postgadolinium images (*b*), representing arterio-venous malformation. Some lesions are low signal on T2 (*a*) and postgadolinium (*b*) images, consistent with hemorrhage and thrombosis.

Coronal source MRA images (*c*, *d*) from more posterior (*c*) and anterior (*d*) locations and MIP reconstructed image (*e*) of fat-suppressed gadolinium-enhanced 3D-MRA. Extensive small hyper-vascular arterio-venous malformations (small arrows, *c, d, e*) are present throughout the liver. Note massive dilatation of the hepatic artery (arrowhead, *c, e*) due to the tremendous blood flow to the liver (Courtesy of Bharat Aggarwal, M.D., Diwan Chand Satya Pal Aggarwal Imaging Research Center, New Delhi, India).

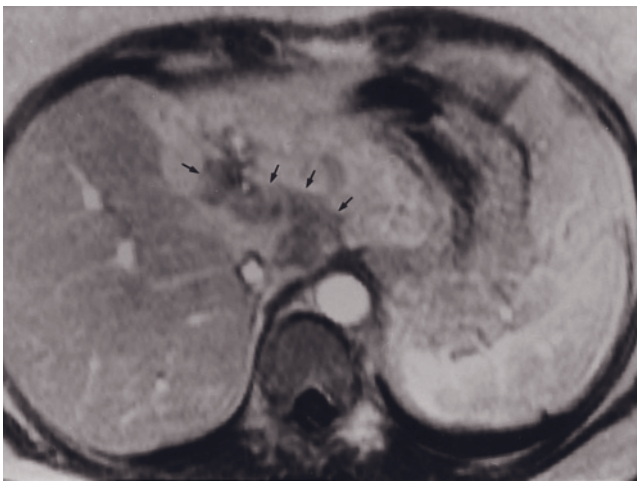

(*a*)

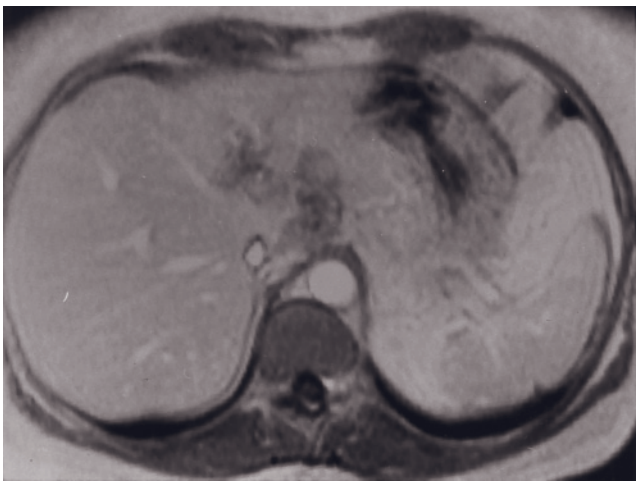

(*b*)

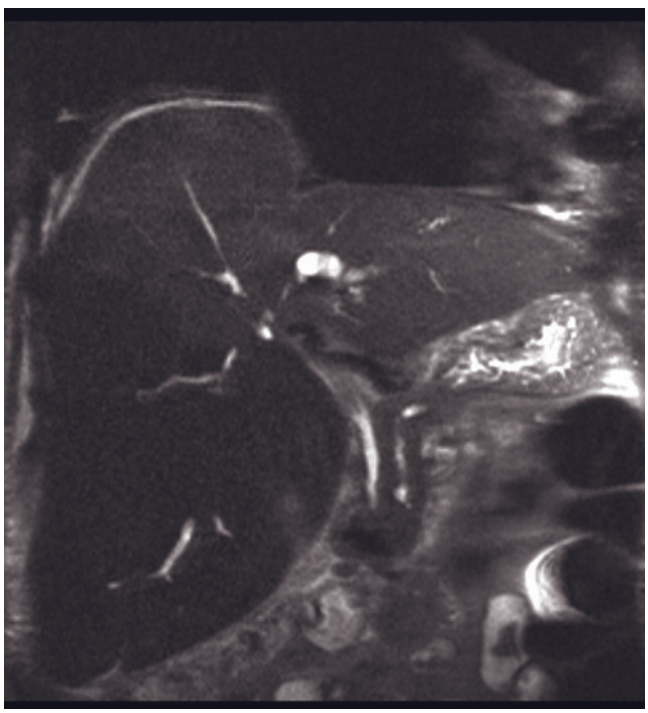

(*c*)

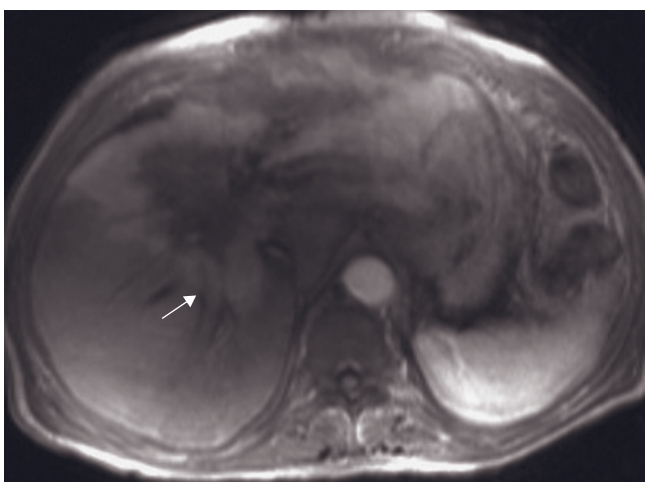

(*d*)

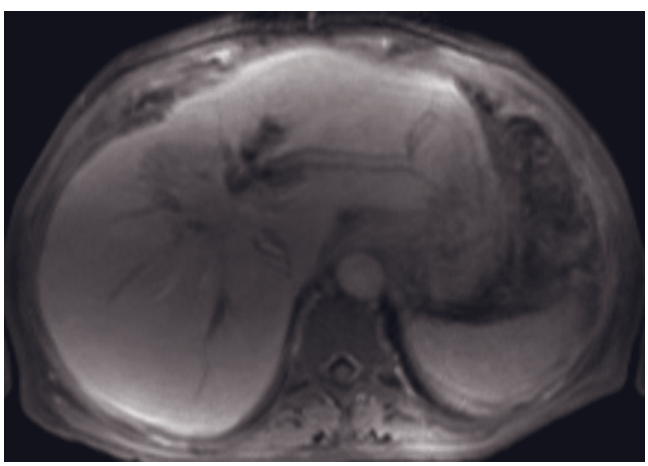

(*e*)

FIG. 2.248 Portal vein thrombosis, secondary to tumor. Immediate postgadolinium SGE (*a*) and 90-s postgadolinium SGE (*b*) images. A liver metastasis is present in the caudate lobe and the lateral segment associated with heterogeneously enhancing thrombus extending into the left portal vein (arrows, *a*). On the immediate postgadolinium image (*a*), there is increased enhancement of the left lobe, which fades by 90 s (*b*).

Coronal T2-weighted SS-ETSE (*c*) and immediate (*d*) and 90-s fat-suppressed (*e*) postgadolinium SGE images in a second patient who has HCC. There is a mass in the bifurcation of the portal vein that shows mild high signal intensity on T2-weighted images (*c*), low signal intensity on T1-weighted images (not shown), and negligible enhancement but with perilesional enhancement on early-phase image (*d*) and becomes homogeneously enhanced on late-phase image (*e*). Thrombus is present in the main portal vein extending from the main left branch, which demonstrates low signal intensity on T2-weighted images and enhances after contrast administration (arrow, *d*), compatible with tumor thrombus.

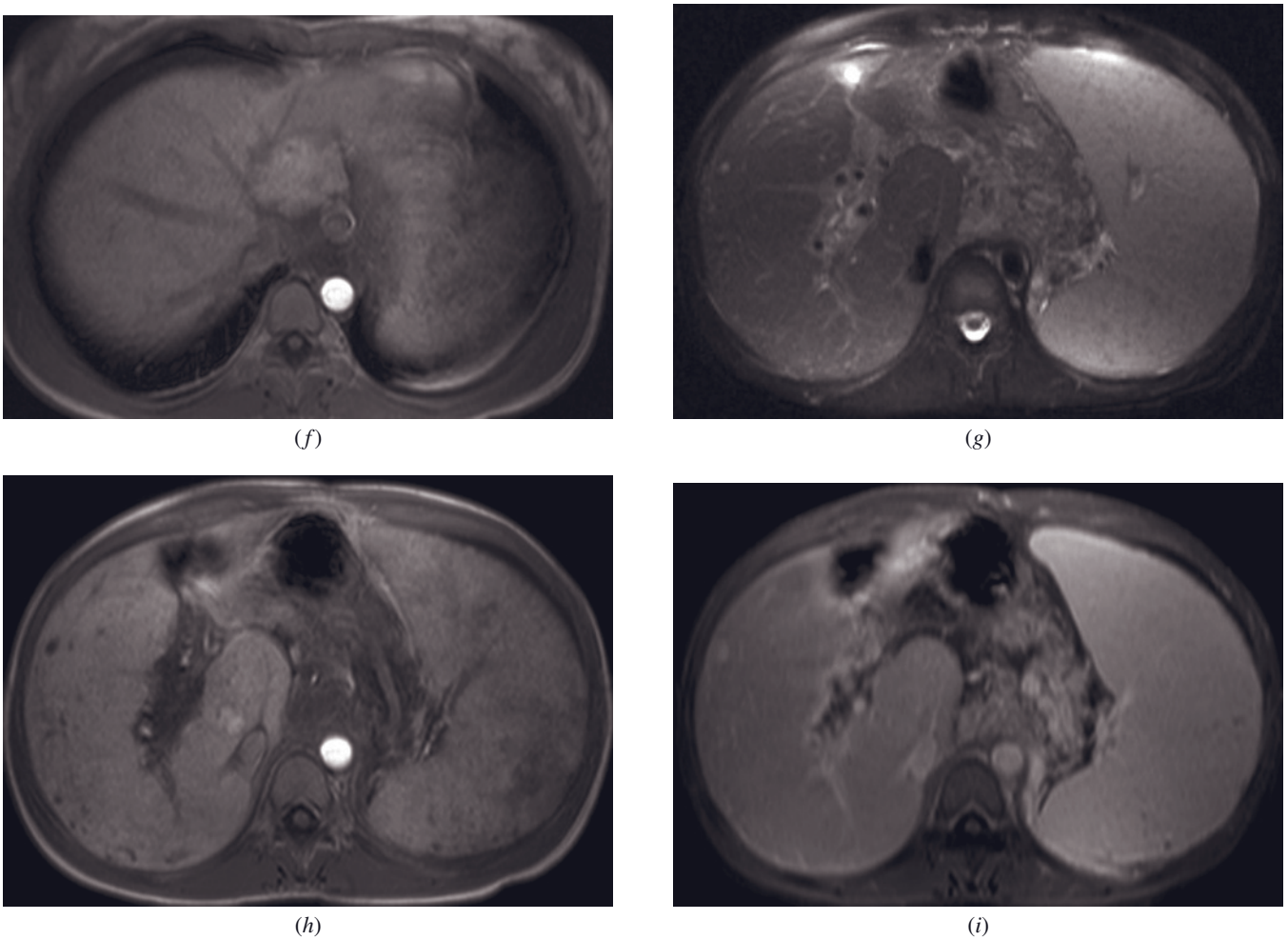

(*f*) (*g*)

(*h*) (*i*)

FIG. 2.248 (*Continued*) Immediate postgadolinium SGE (*f*, *h*), T2-weighted fat-suppressed SS-ETSE (*g*), and 90-s fat-suppressed postgadolinium SGE (*i*) images in a patient with a HCC. There is a mass in the left hepatic lobe that shows faint enhancement on early-phase postgadolinium image (*f*). The left, right, and main portal veins are expanded and appear low signal intensity on T2-weighted images (*g*) and early-phase images (*h*) with mild progressive enhancement on late-phase images (*i*) consistent with tumor thrombus.

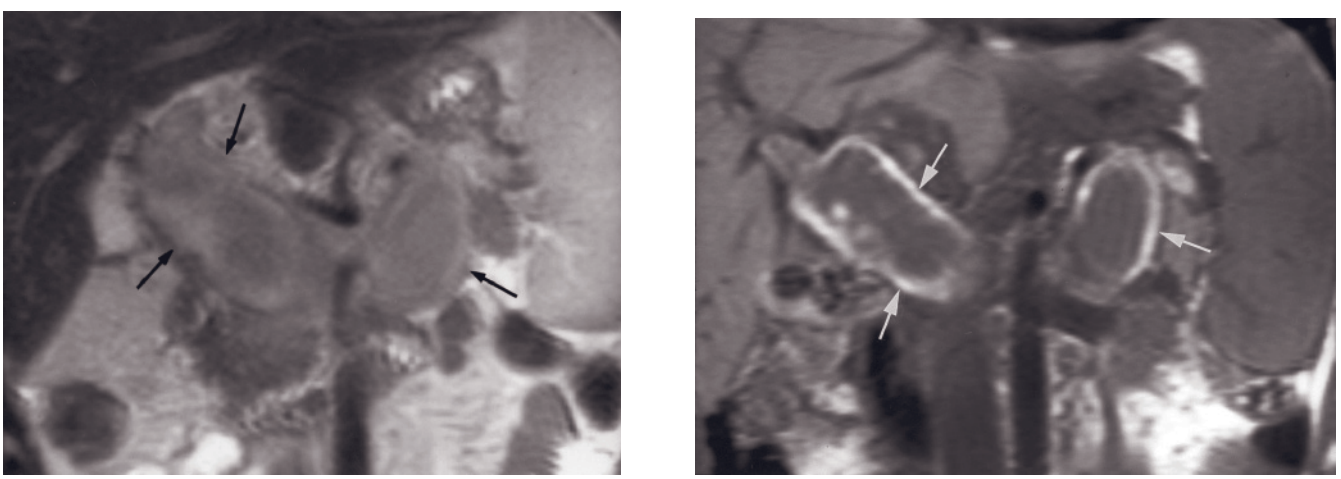

(*a*) (*b*)

FIG. 2.249 Portal and splenic vein thrombosis—subacute blood thrombus. Coronal T2-weighted SS-ETSE (*a*), coronal SGE (*b*), T2-weighted fat-suppressed SS-ETSE (*c*), SGE (*d*), fat-suppressed SGE (*e*), and 90-s fat-suppressed (*f, g, h*) postgadolinium SGE images in a 21-yr-old man who has a history of spontaneous retroperitoneal hematoma associated with portal and splenic vein thrombosis. There is marked dilatation of the splenic vein, portal vein, and proximal superior mesenteric vein, which contains

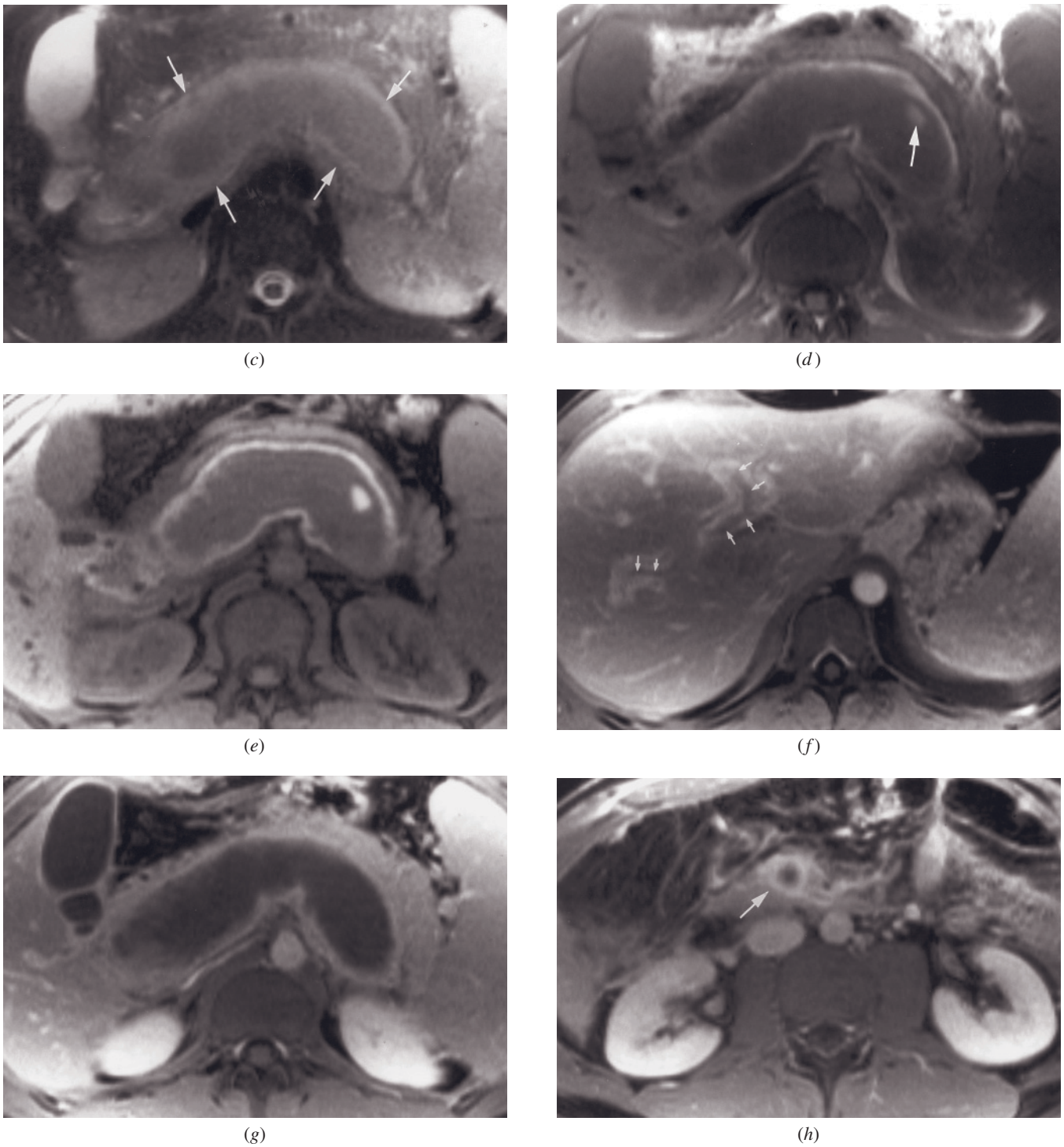

FIG. 2.249 (*Continued*) an expansile thrombus (arrows, *a–c*) extending throughout the venous system. The thrombus demonstrates an increased signal intensity rim on T1-weighted images (*b*, *d*, *e*) and a small focus of increased signal intensity (arrow, *d*) within the thrombus, consistent with blood products at different stages of breakdown. Fat-suppressed postgadolinium images (*f*, *g*) demonstrate no evidence of enhancement within the thrombus. Thrombus is present in normal-caliber intrahepatic portal vein branches (arrows, *f*). Substantially increased enhancement of tissues surrounding the thrombosed SMV (arrow, *h*) suggests an underlying inflammatory process.

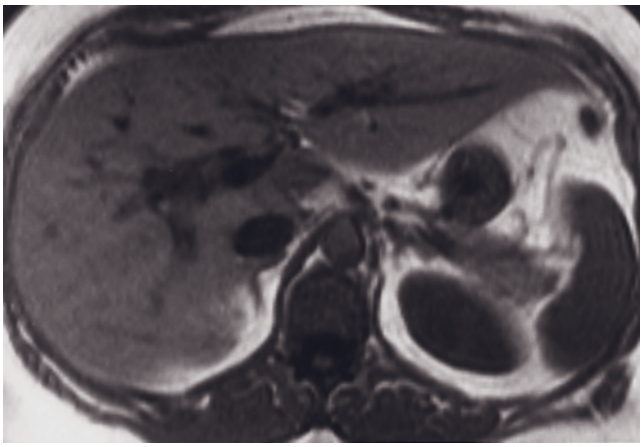

(*a*)

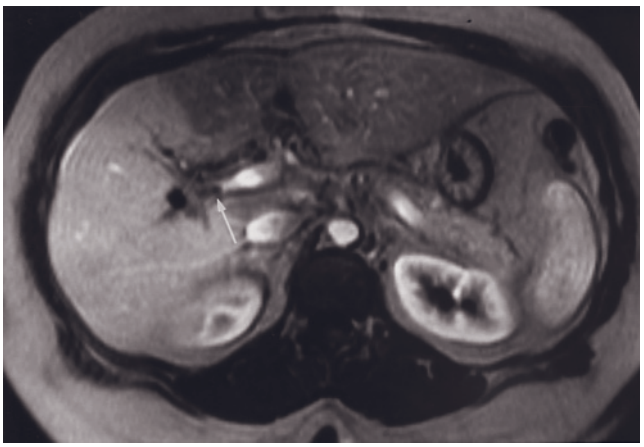

(*b*)

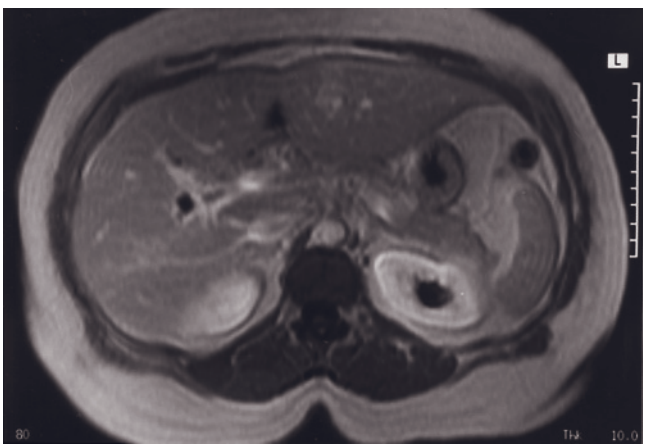

(*c*)

FIG. 2.250 Portal vein thrombosis—blood thrombus. SGE (*a*) and immediate (*b*) and 2-min (*c*) postgadolinium SGE images in a patient who has ascending cholangitis. The SGE image (*a*) demonstrates a liver with normal signal intensity. On the immediate postgadolinium image (*b*), increased enhancement of the right lobe of the liver is apparent, with signal-void thrombus (arrow, *b*) identified in continuity with the gadolinium-containing high-signal right portal vein. Liver parenchymal enhancement equilibrates by 2 min (*c*).

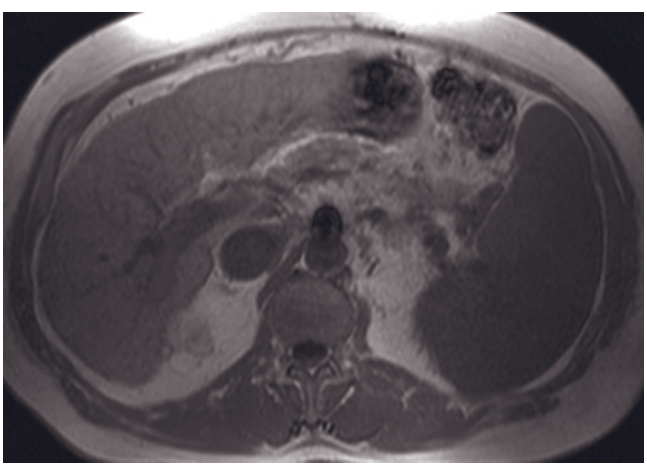

(*a*)

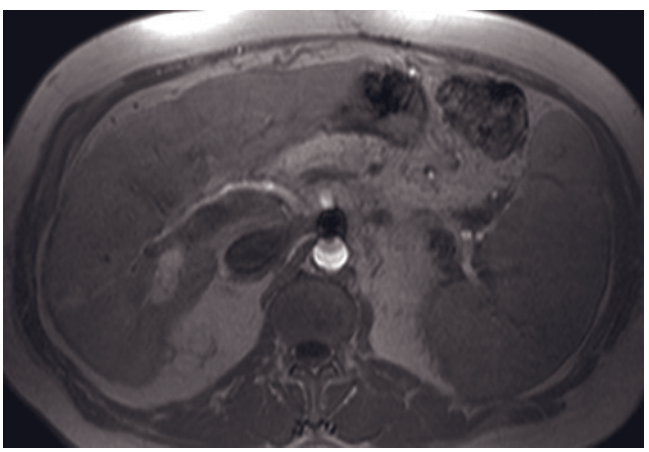

(*b*)

FIG. 2.251 Portal vein thrombosis—bland thrombus. SGE (*a*) and immediate (*b*) and 90-s fat-suppressed (*c*) postgadolinium SGE images. There is a bland thrombus in the right branch of the portal vein that is best visualized on the late-phase image as

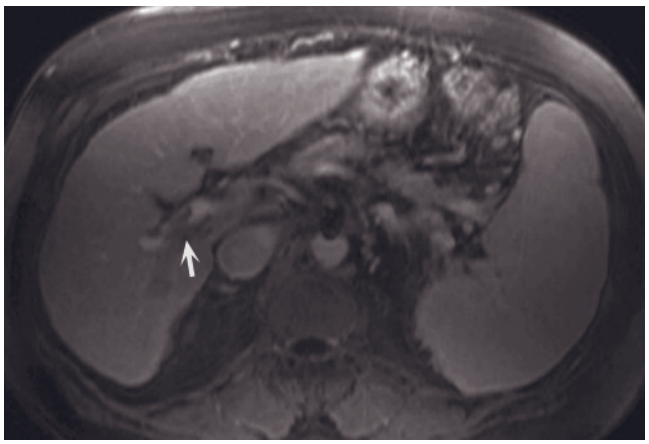

(*c*)

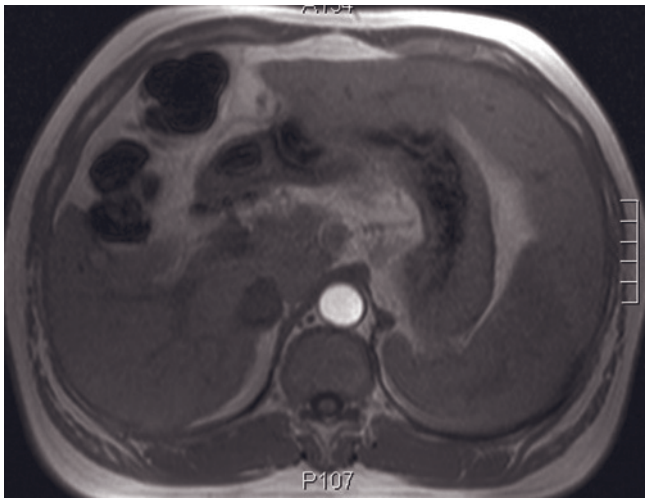

(*d*)

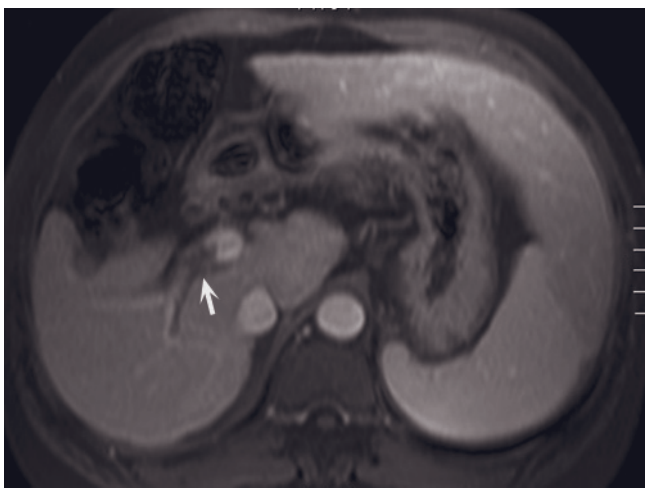

(*e*)

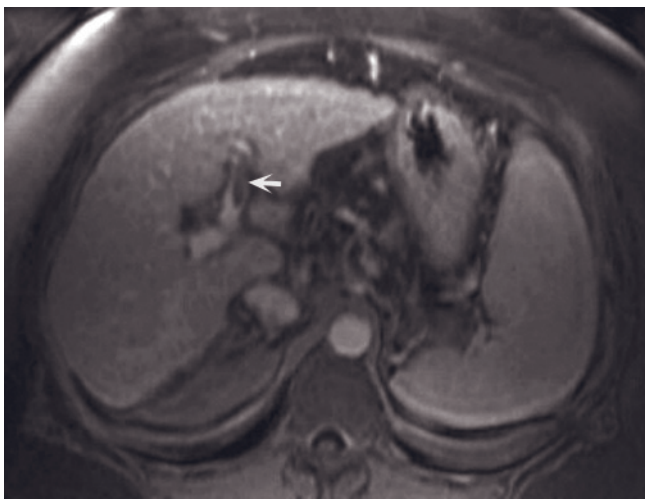

(*f*)

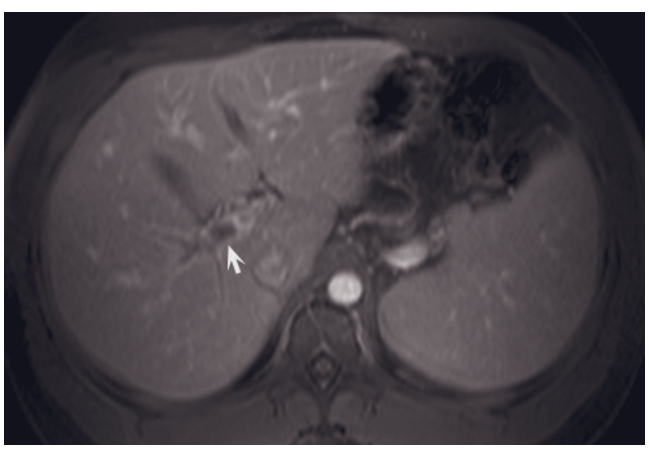

(*g*)

Fig. 2.251 (*Continued*) a nonenhanced tubular structure with adjacent enhanced portal vein (arrow, *c*). Note that the hepatic artery alone is enhanced on early-phase images, reflecting that image acquisition was slightly early.

Immediate (hepatic arterial phase) (*d*) and 90-s fat-suppressed (*e*, *f*) postgadolinium SGE images in a second and third patient with bland thrombus in the main branches of the portal vein (arrow, *e*, *f*).

Ninety-second fat-suppressed postgadolinium SGE image (*g*) in a fourth patient with bland thrombus within the right portal vein. Note enhancement along the outer margins of the thrombus consistent with flow around the thrombus (arrow, *g*).

is thrombosed. In time, this network of collateral venous channels dilates and the thrombosed portal vein retracts, producing cavernous transformation [394, 395]. Obstruction of segmental portal vein may also cause hepatic atrophy, with compensatory hypertrophy of other segments [374, 389].

After administration of intravenous gadolinium, transient increased enhancement of hepatic parenchyma may be apparent in areas with decreased portal perfusion during the hepatic arterial dominant phase of enhancement (see figs. 2.248 and 2.250) [396]. Exact correlation between perfusion defects on CTAP and regions of transient high signal intensity on immediate postgadolinium gradient-echo images has been reported in eight patients (fig. 2.252) [396]. These findings showed that regions with absent or diminished portal venous supply received increased hepatic arterial supply. This paradoxical increased enhancement of hepatic parenchyma distal to an obstructed portal vein branch largely reflects increased hepatic arterial supply due to an autoregulatory mechanism. Segments with obstructed portal venous supply and increased hepatic arterial supply will display early intense enhancement after contrast administration. Gadolinium delivered in the first pass is more concentrated in hepatic arteries than in portal veins and is delivered earlier by hepatic arteries than by portal veins. On later images, concentration of gadolinium in hepatic arteries and portal veins equilibrates, which explains the transient nature of the increased enhancement. In general, portal venous compromise appears as transient increased enhancement in a segmental distribution of involved liver.

Hepatic Venous Thrombosis

Budd–Chiari

Budd–Chiari syndrome is a disorder with numerous causes resulting from obstruction to hepatic venous outflow. Although originally described for acute, usually fatal, thrombotic occlusion of the major hepatic veins or inferior vena cava, the definition of Budd–Chiari syndrome has been broadened to include subacute and chronic occlusive syndromes.

Obstruction of venous outflow from the liver results in portal hypertension, ascites, and progressive hepatic failure. Budd–Chiari syndrome is more common in women, and an underlying thrombotic tendency is present in up to one-half of patients. Causes include polycythemia vera, pregnancy, postpartum state, and intraabdominal cancer, especially HCC [397]. Pathologically, acute changes after hepatic vein thrombosis show dilatation of veins and congestion of sinusoids. As disease advances, sinusoids become collagenized and hepatocytes become atrophic, with loss of parenchyma [2, 3].

Usually, hepatic venous outflow is not completely eliminated because a variety of accessory hepatic veins may drain above or below the site of obstruction. In some cases, obstruction may be segmental or subsegmental. Although the disease most commonly involves major hepatic veins, demonstration of patent central hepatic veins may be observed as small or intermediate-sized veins may be occluded in isolation [398]. In the chronic setting, regions with completely obstructed hepatic venous outflow will develop shunting of blood from hepatic arteries to portal veins, producing reversed portal venous flow [392, 399–401]. The involved liver parenchyma is thereby deprived of portal vein supply. Hepatic regeneration, hypertrophy, and atrophy depend in part on the degree of portal perfusion [356]. Budd–Chiari syndrome most often results in atrophy of peripheral liver, which experiences severe venous obstruction, and hypertrophy of the caudate lobe and central liver, which are relatively spared.

Absence of hepatic veins may be demonstrated by techniques in which flowing blood is signal void or by techniques in which flowing blood is high in signal intensity such as time-of-flight techniques or portal-phase gadolinium-enhanced gradient echo sequences. Generally, a combination of both approaches results in the highest diagnostic accuracy. However, the bright blood technique is the most accurate and usually suffices.

On immediate postgadolinium MR images, the peripheral atrophic liver in Budd–Chiari syndrome may enhance to a greater or lesser extent than normal or hypertrophied liver, which provides insight into the chronicity of the disease process. One study reported that dynamic enhancement patterns differed for acute, subacute, and chronic Budd-Chiari, with combinations of enhancement patterns present when acute is superimposed on subacute disease [402]. In acute-onset Budd–Chiari syndrome the peripheral liver enhances less than central liver, presumably because of acute increased tissue pressure with resultant diminished blood supply from both hepatic arterial and portal venous systems in the peripheral liver. This is associated with moderately high signal on T2-weighted images and low signal on T1-weighted images, reflecting associated edema. After contrast, the liver demonstrates a dramatic appearance of increased central enhancement compared to decreased enhancement of peripheral liver that persists on late images (figs. 2.253 and 2.254) [403].

In subacute Budd–Chiari syndrome, reversal of flow in portal veins and development of small intra- and extrahepatic venovenous collaterals occurs, features not present in other chronic liver diseases. Many of the collaterals are capsule based. Signal of the peripheral liver is mildly increased on T2-weighted images and mildly decreased on T1-weighted images, similar to

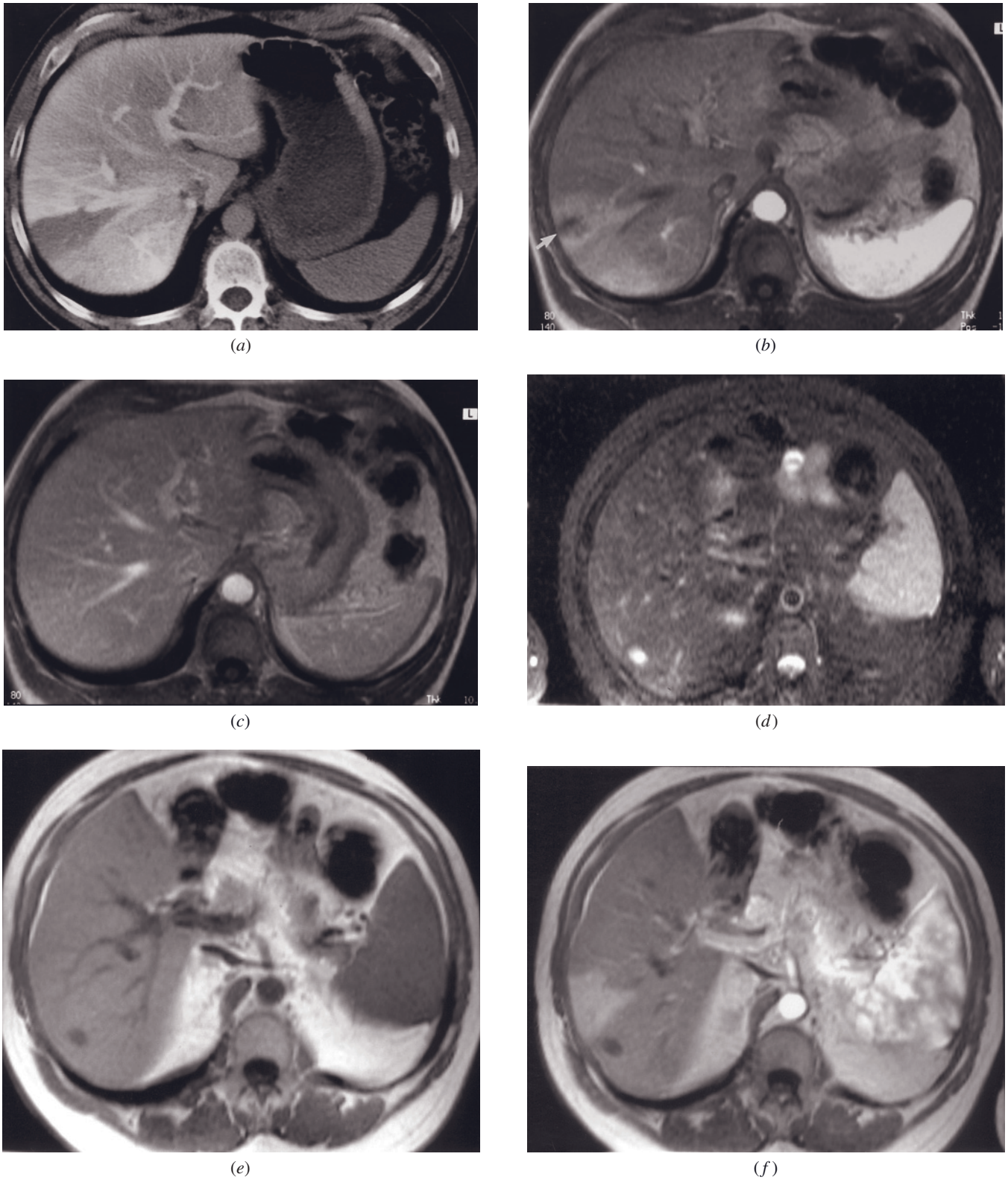

FIG. 2.252 Perfusional abnormality associated with liver metastases. Spiral CTAP (*a*) and immediate (*b*) and 90-s (*c*) postgadolinium SGE images. The CTAP image (*a*) demonstrates a wedge-shaped perfusion defect in the right lobe of the liver. On the immediate postgadolinium SGE image (*b*), wedge-shaped increased enhancement is present surrounding a peripheral 2-cm liver metastasis (arrow, *b*). By 90 s after gadolinium (*c*), both the perfusion defect and the metastases have equilibrated with liver. (Reproduced with permission from Semelka RC, Schlund JF, Molina PL, Willms AG, Kahlenberg M, Mauro MA, Weeks SM, Cance WG. Malignant liver lesions: comparison of spiral CT arterial portography and MR imaging for diagnostic accuracy, cost, and effect on patient management. *J Magn Reson Imaging* 1: 39–43, 1996).

Echo-train STIR (*d*), SGE (*e*), and immediate postgadolinium SGE (*f*) images in a second patient show a perfusional abnormality of transient increased enhancement seen on the immediate postgadolinium image (*f*) in a patient who has a history of colon cancer. Note the small cyst adjacent to the abnormal area. Perfusional abnormalities of transient increased enhancement are not uncommon in patients with colon cancer liver metastases. Many are related to metastases, but in some the cause is not clear, as in this case.

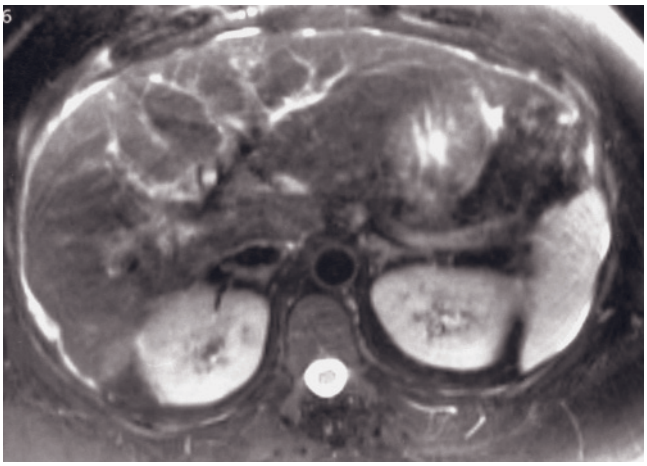

(*g*)

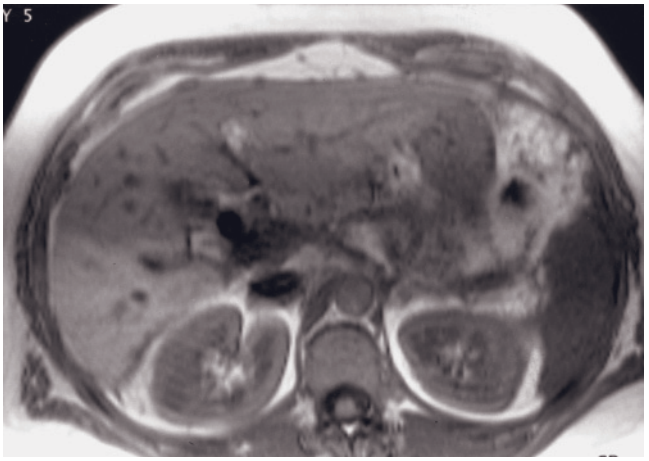

(*h*)

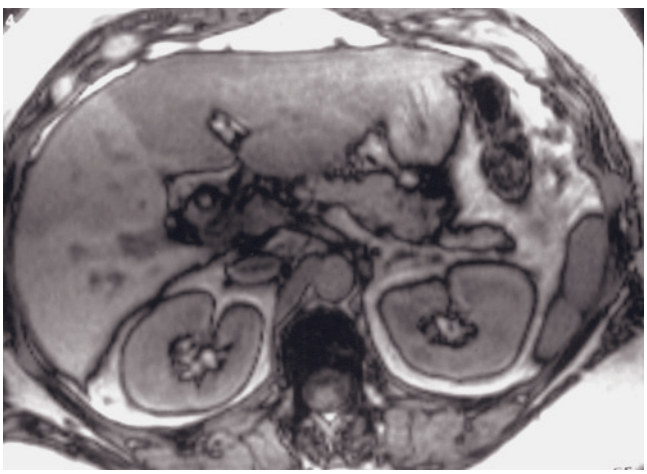

(*i*)

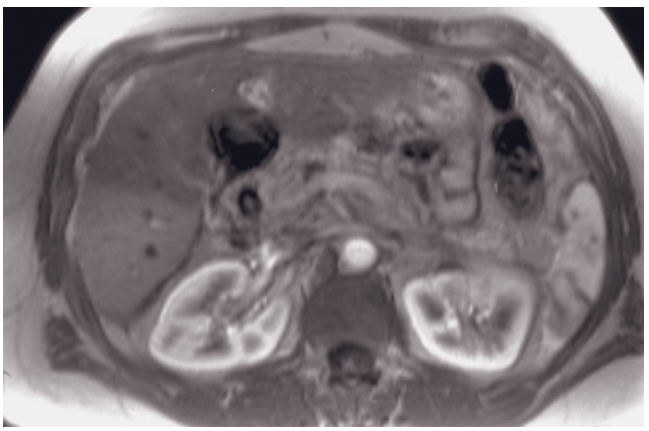

(*j*)

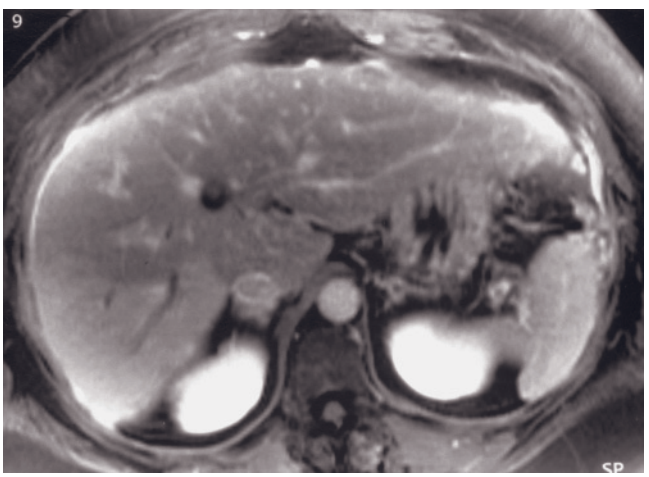

(*k*)

FIG. 2.252 (*Continued*) T2-weighted fat-suppressed ETSE (*g*), SGE (*h*), out-of-phase SGE (*i*), and immediate (*j*) and 90-s fat-suppressed (*k*) postgadolinium SGE images in a third patient with a history of colon cancer. There is a segmental signal intensity difference in liver, seen on T1-weighted images before and after gadolinium. Note also the thickening and enhancement of the liver capsule and peritoneum from peritoneal metastases, best seen on interstitial-phase fat-suppressed T1-weighted images (*k*).

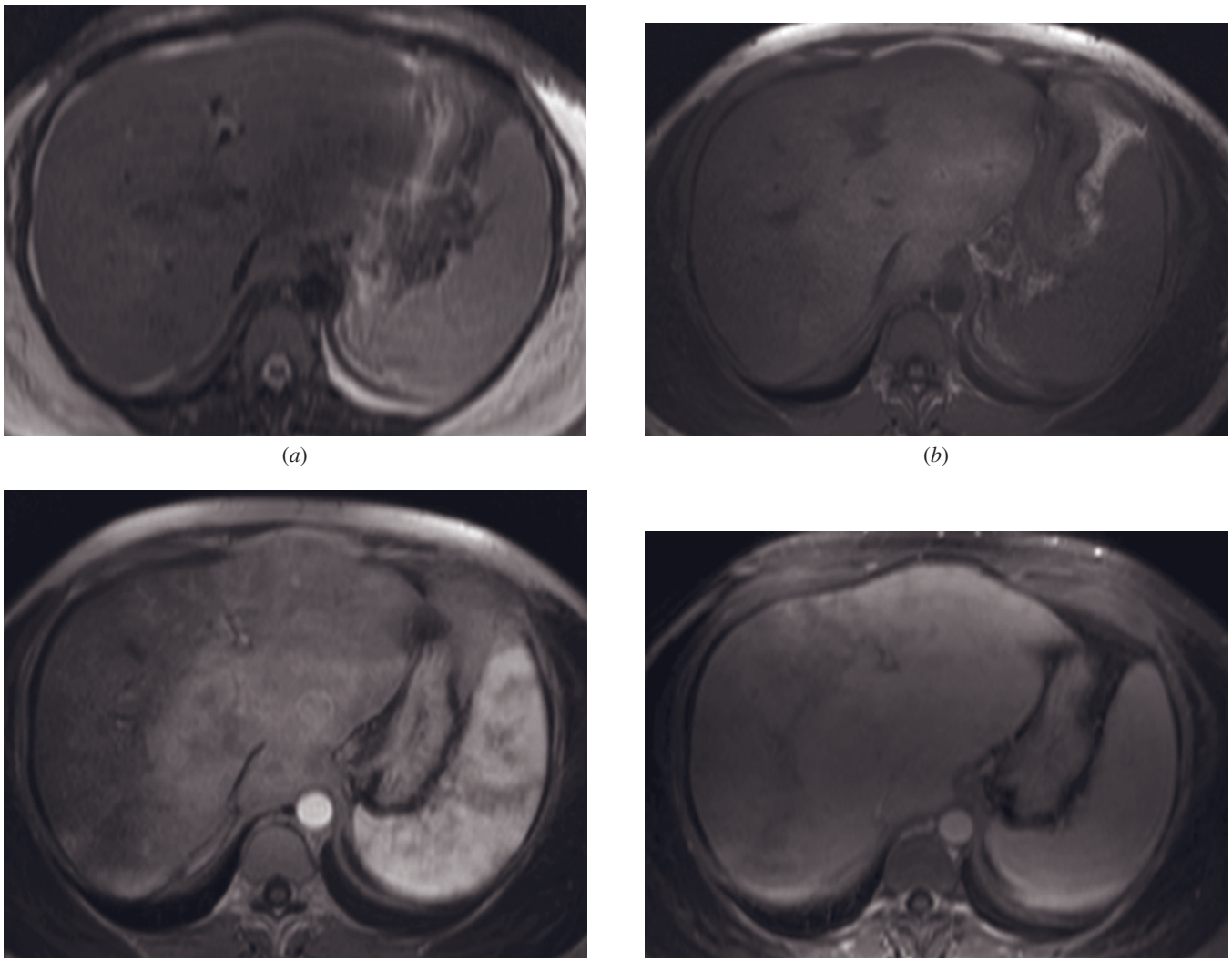

FIG. 2.253 Acute Budd–Chiari syndrome. T2-weighted ETSE (*a*), SGE (*b*), immediate (*c*), and 90-s postgadolinium SGE (*d*) images. The T2-weighted image (*a*) shows normal signal intensity of the caudate lobe and central liver and mild heterogeneous higher signal intensity of the peripheral liver. On the precontrast T1-weighted image (*b*), the caudate lobe and central portion of the liver are normal in signal intensity, whereas the peripheral liver is low in signal intensity. On the immediate postgadolinium image (*c*), the caudate lobe and central liver enhance heterogeneously and intensely, whereas peripheral liver shows lower enhancement. On late phase (*c*) liver appears more homogeneous than early phase but still shows increased enhancement in central areas.

acute Budd–Chiari syndrome. On dynamic gadolinium-enhanced MR images the enhancement of subacute disease differs substantially from the acute syndrome. Mildly increased and heterogeneous enhancement is apparent in the peripheral liver relative to central liver on hepatic arterial dominant-phase images that, over time, becomes more homogeneous with the remainder of the liver. Caudate lobe hypertrophy is mild to moderate, and collateral vessels are not prominent in the subacute setting (fig. 2.255).

In chronic Budd–Chiari syndrome, hepatic edema is not a prominent feature and fibrosis develops. Fibrosis results in decreased signal of peripheral liver on T2- and T1-weighted images. Enhancement differences between peripheral and central liver on serial postgadolinium images become more subtle. Venous thrombosis, appreciated in acute and subacute disease, is usually not observed in chronic disease. Massive caudate lobe hypertrophy, massive enlarged bridging intrahepatic collaterals, extrahepatic collaterals, and regenerative nodules are all features observed in chronic Budd–Chiari syndrome.

Curvilinear intrahepatic collaterals and capsule-based collaterals are characteristic of chronic Budd–Chiari syndrome (fig. 2.256). Varices are usually prominent in chronic Budd–Chiari syndrome and are well shown on

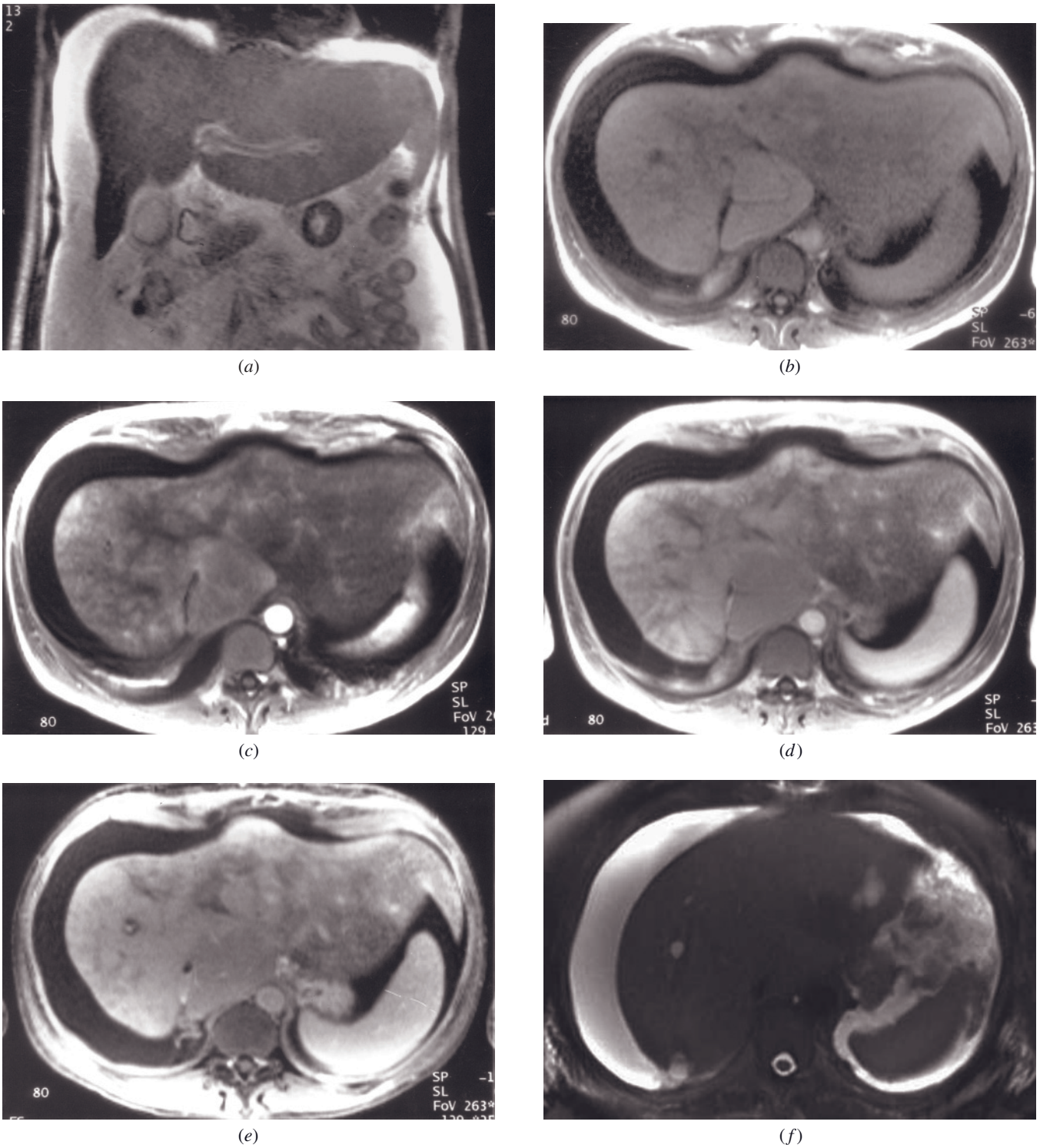

FIG. 2.254 Acute on subacute Budd–Chiari syndrome. Coronal T2-weighted SS-ETSE (*a*), transverse SGE (*b*), and immediate (*c*), 45-s (*d*), and 90-s fat-suppressed (*e*) postgadolinium SGE images. The coronal T2-weighted image (*a*) shows high signal of the lateral segment relative to the right lobe. On the T1-weighted image (*b*), moderately diminished signal is identified in the enlarged lateral segment of the left lobe, with mild diminished signal of the right lobe. The enlarged caudate lobe possesses more normal signal intensity. The immediate postgadolinium image (*c*) reveals markedly diminished enhancement of the lateral segment, consistent with acute changes of Budd–Chiari, and mildly heterogeneous and increase signal of the right lobe, consistent with subacute changes of Budd–Chiari. The caudate lobe has a mild heterogeneity with signal intensity intermediate between the acutely affected lateral segment and subacutely affected right lobe. Enhancement abnormalities diminish but persist on late postcontrast images (*e*).

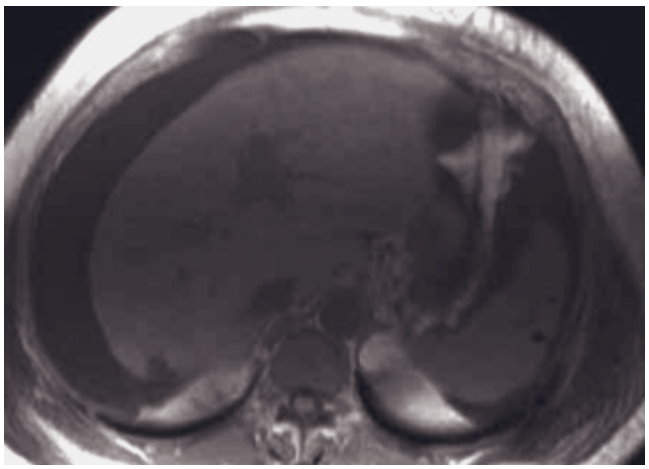

(*g*)

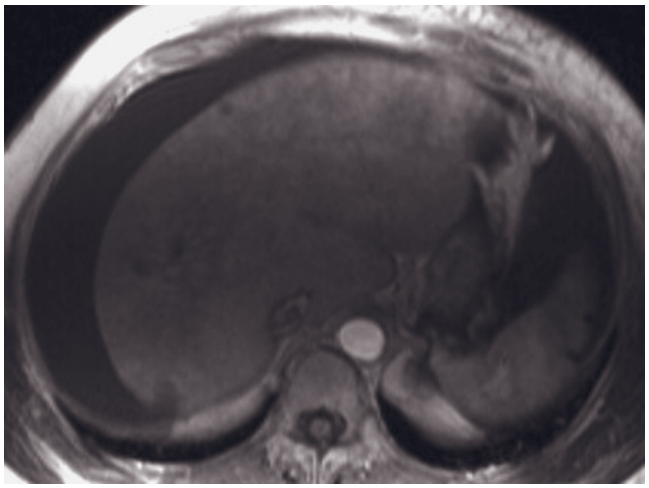

(*h*)

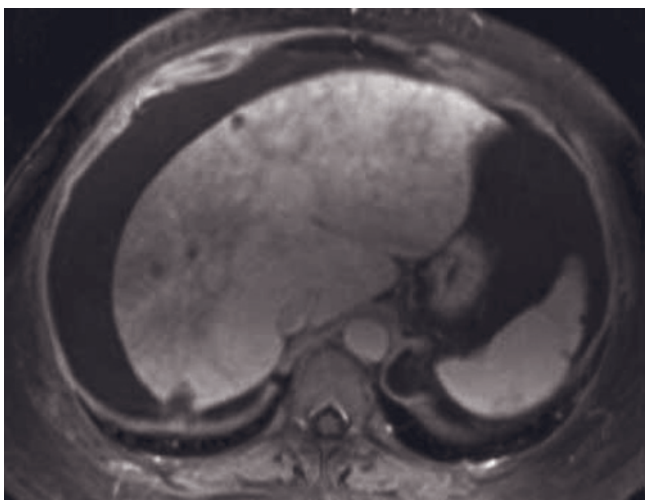

(*i*)

Fig. 2.254 (*Continued*) T2-weighted fat-suppressed SS-ETSE (*f*), SGE (*g*), and immediate (*h*) and 90-s fat-suppressed (*i*) postgadolinium SGE images in a second patient. T2-weighted (*f*) and T1-weighted (*g*) images of the liver demonstrate homogeneous signal intensity. On early-phase images (*h*), a patchy, diffuse faint liver enhancement is appreciated with no dominant segment. However, on late-phase image (*i*) the central portion of the liver becomes homogeneously enhanced while the periphery of the liver maintains the heterogeneous enhancement with a lower signal intensity than central liver.

interstitial-phase fat-suppressed images. Extensive portosystemic varices, as observed in other chronic liver diseases, are also present.

The development of nodular regenerative hyperplasia in the chronic setting is the result of hepatic ischemia caused by hepatic venous obstruction [404, 405]. The nodules are usually round, multiple, range from 0.5 to 4 cm, and cause distortion of the hepatic contour [406–408]. Most commonly, these nodules demonstrate isointensity or low signal intensity on T2-weighted images, and high signal intensity on T1-weighted images similar to macroregenerative nodules (see fig. 2.256). However, these nodules may be moderately hypervascular and tend to possess moderately intense enhancement on immediate postgadolinium gradient-echo images [343, 406, 407, 409]. The high signal intensity of the nodules on the precontrast T1-weighted images likely reflects the presence of protein.

Occasionally, large (>1 cm) regenerative nodules contain a central scar, resembling FNH. It has been postulated that the increased arterial hepatic perfusion in Budd–Chiari syndrome may be responsible for the development of this FNH-like lesion. The scar is characterized by high signal intensity on T2-weighted images, low signal intensity on T1-weighted images, and enhancement on late-phase images, as is typical for FNH [408, 410].

The relationship between Budd–Chiari syndrome and HCC is still controversial. Patients with the diagnosis of HCC may develop acute or subacute Budd–Chiari syndrome because of tumor invasion of major hepatic veins. The involvement of major hepatic veins by HCC has been reported in 6–23% of cases [411]. Few studies suggest that patients with chronic Budd–Chiari syndrome are at increased risk for the development of HCC [343], and there is little evidence to support

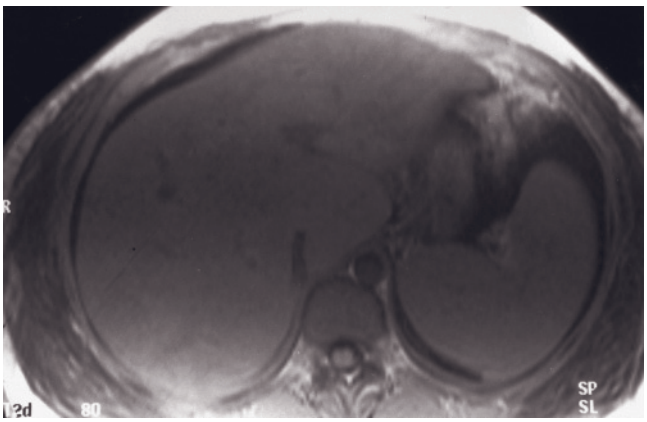

(*a*)

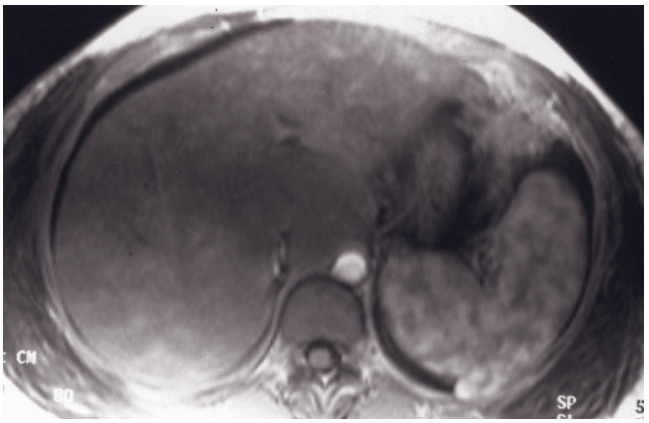

(*b*)

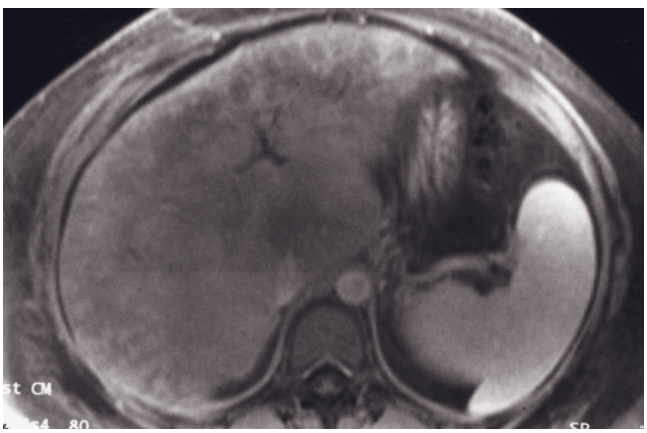

(*c*)

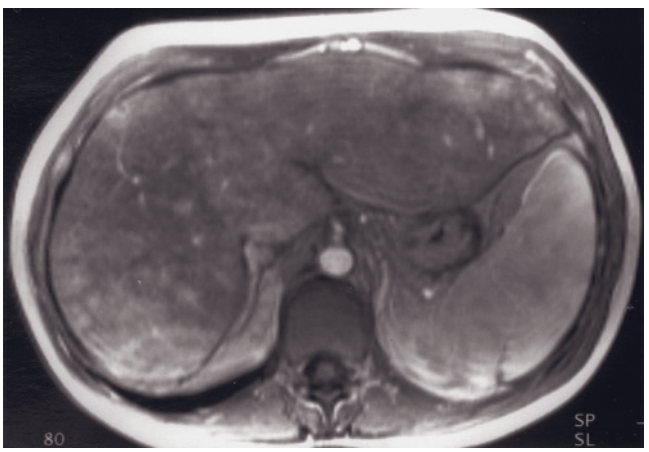

(*d*)

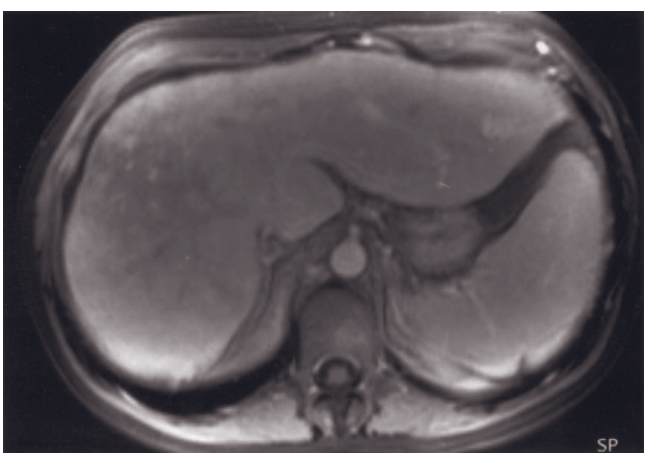

(*e*)

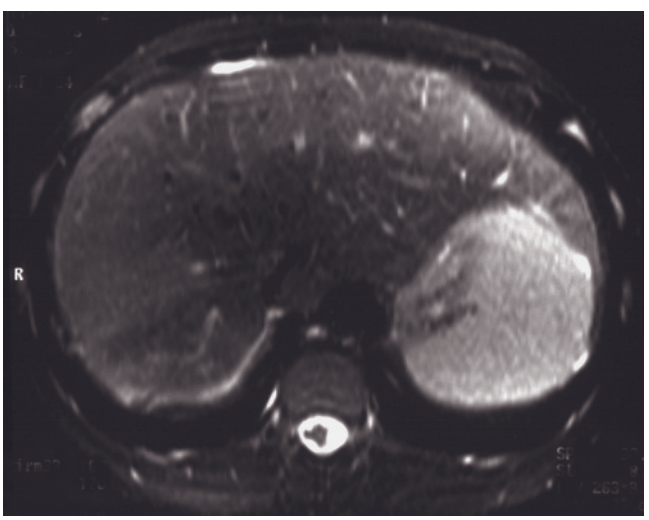

(*f*)

FIG. 2.255 Subacute Budd–Chiari syndrome. SGE (*a*) and immediate (*b*) and 90-s fat-suppressed (*c*) postgadolinium SGE images. Peripheral liver is diminished in signal on T1-weighted image (*a*) and demonstrates a diffuse, heterogeneous mildly increased enhancement on early-phase image (*b*) that persists on later image (*c*), consistent with hepatic vascular compensation to venous thrombosis as observed in subacute Budd–Chiari syndrome (Reproduced with permission from Noone TC, Semelka RC, Siegelman ES, Balci NC, Hussain SM, Kim PN, Mitchell DG. Budd-Chiari Syndrome: spectrum of appearances of acute, subacute, and chronic disease with magnetic resonance imaging. *J Magn Reson Imaging* 11: 44–50, 2000).

Immediate (*d*) and 90-s fat-suppressed (*e*) postgadolinium SGE images in a second patient. The liver is enlarged with an irregular contour. There is mild hypertrophy of the caudate lobe. After administration of contrast (*d*), the liver enhances in a diffusely heterogeneous pattern and becomes more homogeneous on the later image (*e*).

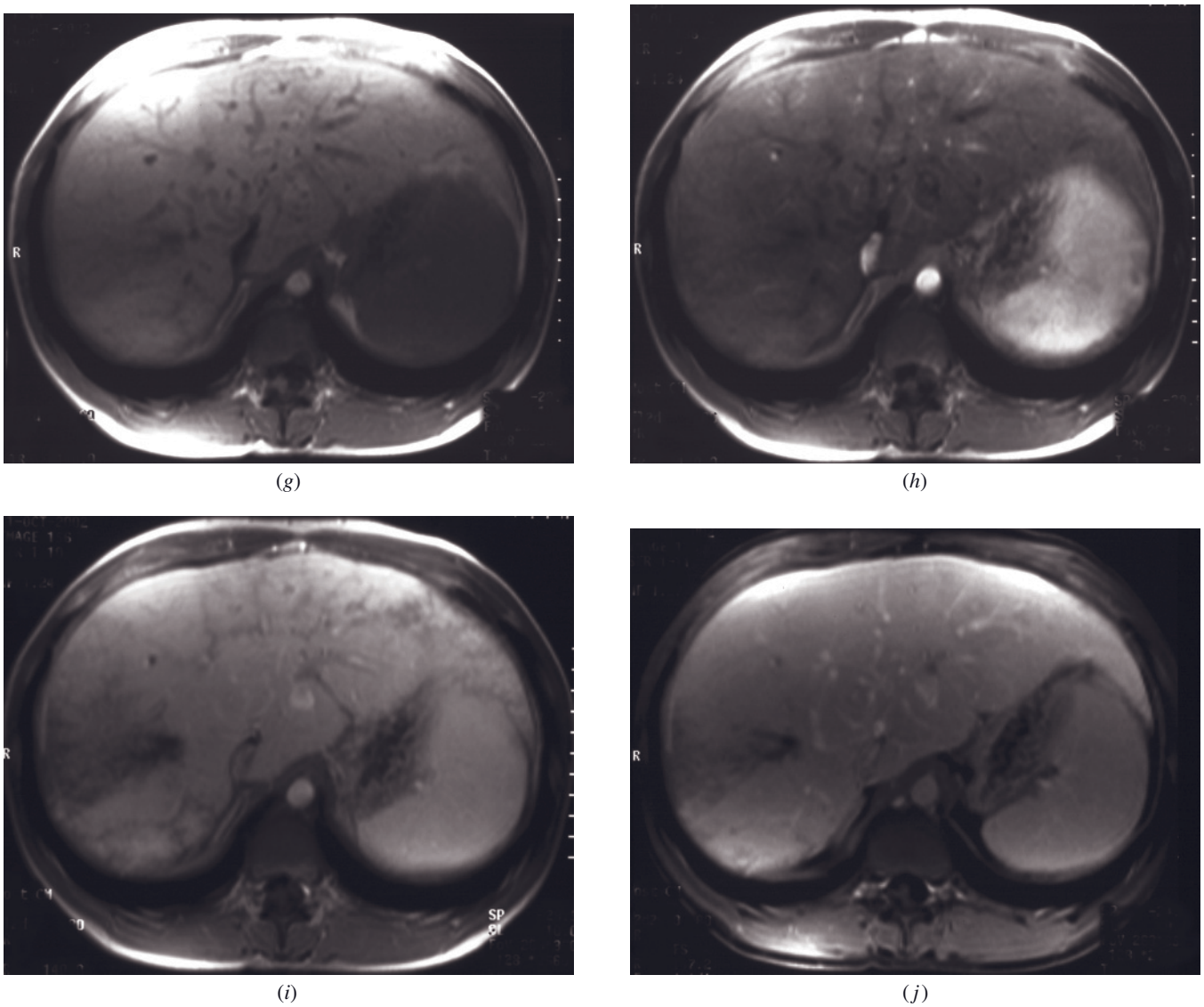

FIG. 2.255 (*Continued*) T2-weighted fat-suppressed SS-ETSE (*f*), SGE (*g*), and immediate (*h*), 45-s (*i*), and 90-s fat-suppressed (*j*) postgadolinium SGE images in a third patient. The liver is enlarged and shows mild hypertrophy of the caudate lobe. On T2-weighted image (*f*), a triangular shaped segmental area is seen in the right hepatic lobe that shows a higher signal intensity than the remainder of the hepatic parenchyma. On T1-weighted image (*g*), this segmental area demonstrates low signal intensity. On early-phase image (*h*), the liver exhibits a dominant peripheral patchy enhancement that becomes homogeneous on late-phase image (*j*). Note that the segmental area observed on precontrast images (*f*, *g*) shows faint enhancement on early-phase images (*h*) that washes out on 45-s (*i*) and late-phase (*j*) images, consistent with ischemic changes.

malignant transformation of the regenerative nodules [406, 407].

Hepatic Vein Thrombosis

Hepatic vein thrombosis affecting minor vessels may occur in the setting of malignant disease and is especially common in HCC. Tumor thrombosis demonstrates gadolinium enhancement, whereas bland thrombus does not enhance. As with the Budd–Chiari syndrome, the degree of enhancement of liver parenchyma that has thrombosed hepatic veins depends on the stage of the thrombosis. In acute thrombosis, involved parenchyma enhances less than surrounding liver in early-phase images [396]. In chronic thrombosis, enhancement is more variable and may be increased.

Hepatic Arterial Obstruction

Hepatic arterial obstruction is much less common than either portal vein or hepatic vein obstruction. Hepatic arterial obstruction is most commonly seen in the setting of liver transplantation. In patients without transplants,

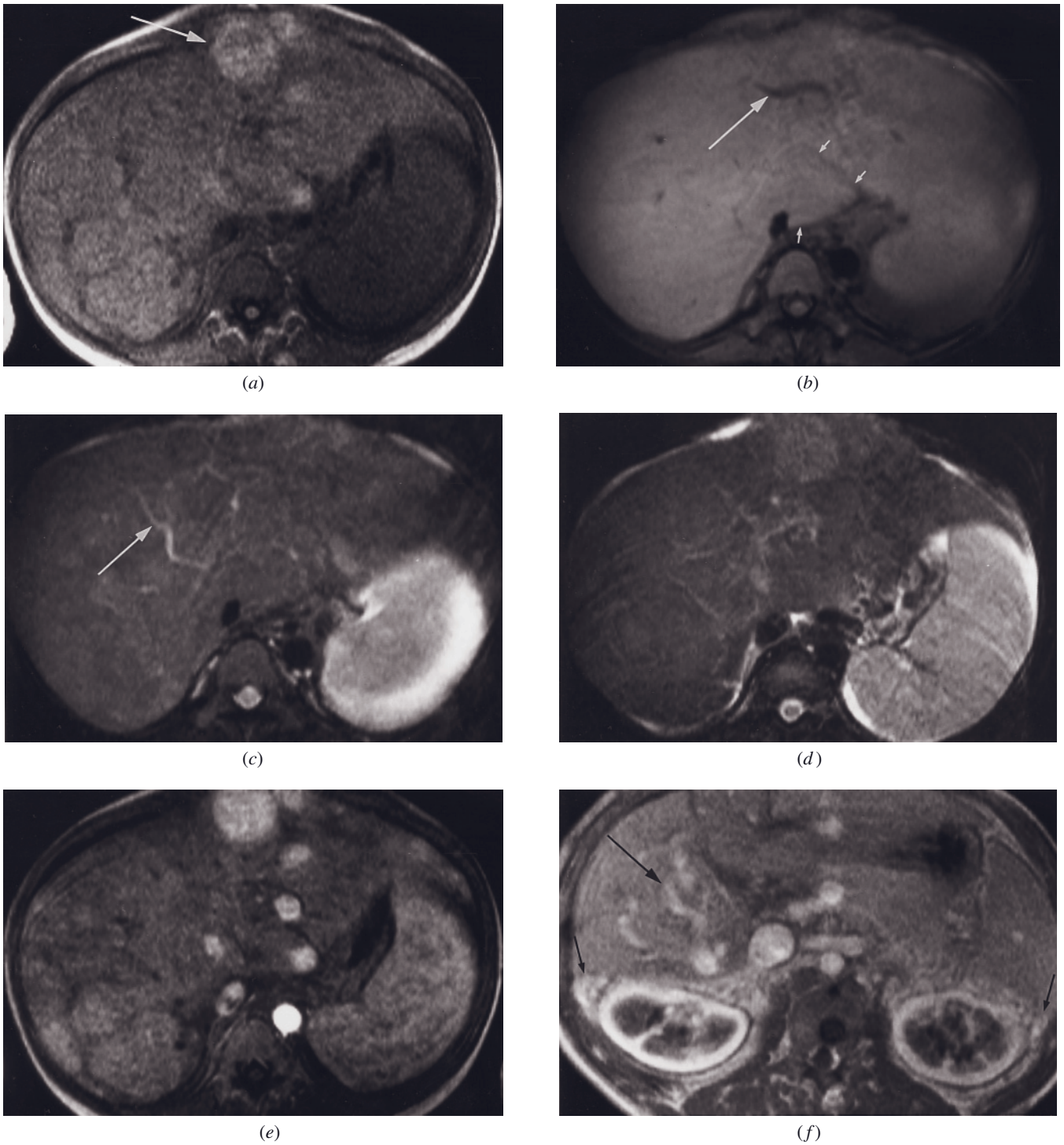

FIG. 2.256 Chronic Budd–Chiari syndrome. SGE (*a*), proton-density fat-suppressed spin-echo (*b*), T2-weighted fat-suppressed ETSE (*c*, *d*), and immediate postgadolinium SGE (*e*) images. On T1-weighted images (*a*), multiple well-defined high-signal-intensity mass lesions representing regenerative nodules are identified, the largest measuring 3.5 cm in diameter (arrow, *a*). The proton-density image at the expected level of the hepatic veins (*b*) demonstrates absence of hepatic veins, with intrahepatic curvilinear venous collaterals in their stead (arrow, *b*). Enlargement of the caudate lobe is shown (small arrows, *b*). The T2-weighted image (*c*) taken from a slightly higher tomographic section demonstrates curvilinear intrahepatic collaterals (arrow, *c*) with absence of hepatic veins. The immediate postgadolinium image (*e*) acquired at the same tomographic level as the precontrast images (*a*, *d*) shows enhancement of the regenerative nodules, with multiple enhancing nodules apparent that were not visualized on precontrast images. Slight heterogeneity of hepatic enhancement is present. The enhancement pattern is distinctly different from that of acute Budd–Chiari syndrome.

Immediate postgadolinium SGE image (*f*) in a second patient with chronic Budd–Chiari syndrome. Extensive abdominal collaterals are present (arrows, *f*), including curvilinear intrahepatic collaterals (long arrow, *f*).

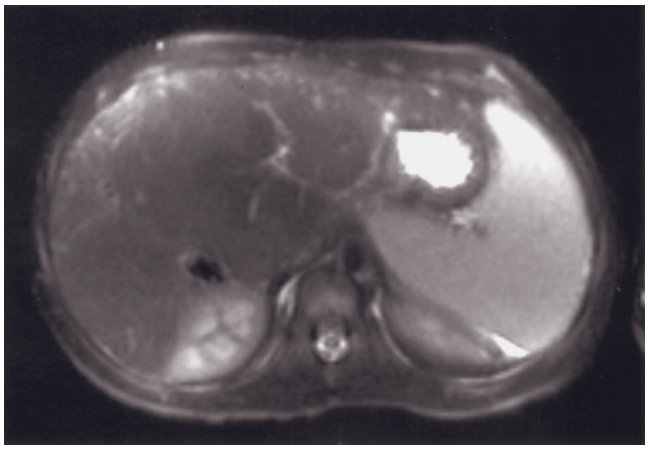

(*g*)

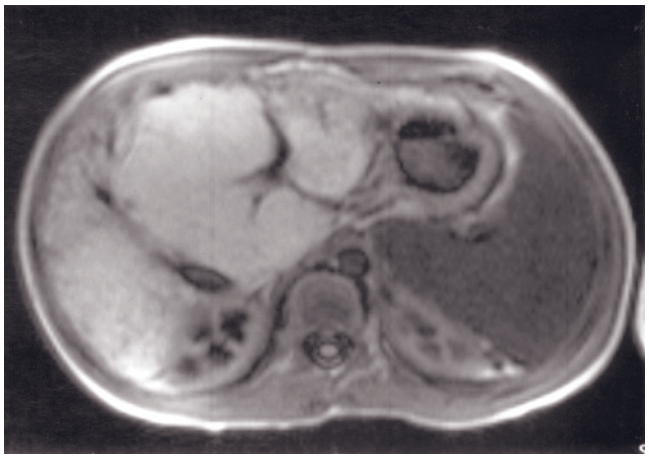

(*h*)

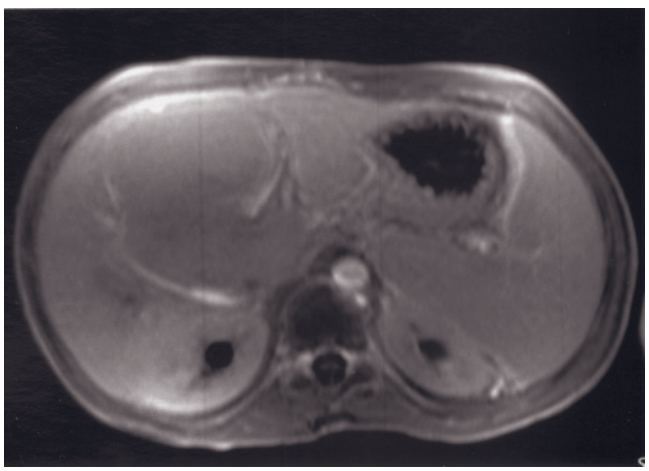

(*i*)

FIG. 2.256 (*Continued*) T2-weighted fat-suppressed SS-ETSE (*g*), magnetization-prepared gradient-echo (*h*), and immediate postgadolinium magnetization-prepared gradient-echo (*i*) images in an 8-year-old boy. Massive enlargement of the caudate lobe is present, with relative atrophy and peripheral nodularity of the peripheral liver consistent with chronic Budd–Chiari syndrome.

embolic occlusion is the most common cause of hepatic arterial compromise. Diminished enhancement of involved hepatic parenchyma is apparent on early post-contrast images (fig. 2.257). Hepatic arterial occlusion tends to be small, irregularly shaped, and not segmental in appearance. Larger occlusions result in peripheral wedge- or fan-shaped defects with an unusual serrated margin. An unusual feature is that T2- signal may be low, reflecting a lower fluid content.

Preeclampsia and Eclampsia

Hepatic disease is common in preeclampsia and may result in hemolytic anemia, elevated liver function tests, and low platelets (HELLP syndrome), which may cause peripheral vascular occlusions of the liver or hepatic hematoma [412]. Microscopically, sinusoids contain fibrin deposits with hemorrhage into the subendothelial space. Blood may dissect through portal connective tissue to form lakes of hemorrhage. MR images show peripheral wedge-shaped defects surrounded by regions of increased enhancement on postgadolinium images and heterogeneous high signal intensity on T2-weighted images from edema and, in more severe disease, infarction (figs. 2.258 and 2.259). This pattern reflects central infarction surrounded by a penumbra of ischemic hepatic parenchyma. Hematoma appears as a peripheral fluid collection with signal intensity depending on the age of the blood products, usually deoxyhemoglobin or intracellular methemoglobin reflecting the acute or subacute nature of the disease process.

Congestive Heart Failure

Patients with congestive heart failure may present with hepatomegaly and hepatic enzyme elevations. On early dynamic contrast-enhanced MR images, the liver may enhance in a mosaic fashion with a reticulated pattern of low-signal-intensity linear markings. By 1 min post-contrast, the liver becomes more homogeneous. The

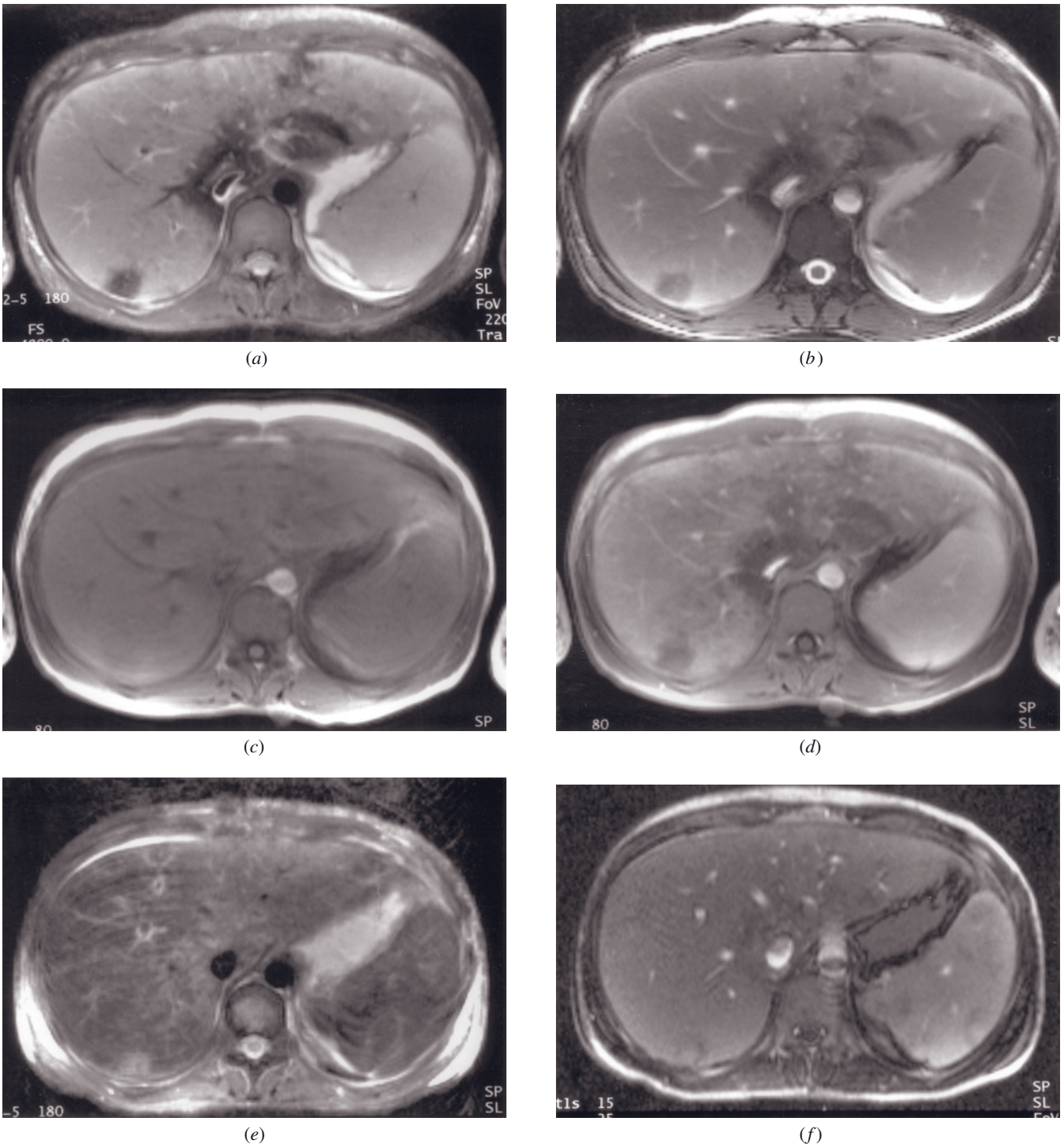

FIG. 2.257 Arterial ischemia. T2-weighted fat-suppressed ETSE (*a*), SS ETSE (*b*), SGE (*c*), and immediate (*d*) postgadolinium SGE images. The liver is enlarged with diffuse increased signal intensity on T2-weighted images (*a*), consistent with edema. There is a 2-cm focus in the right hepatic lobe and a irregular hepatic central region that demonstrate decreased signal intensity on both T2-weighted (*a*) and T1-weighted (*b*) images, most pronounced on T2, and negligible enhancement on early (*d*) postgadolinium images. These features are consistent with arterial ischemia.

T2-weighted fat-suppressed ETSE (*e*) and immediate postgadolinium magnetization-prepared gradient-echo (*f*) images in the same patient 15 days later show a slight increased signal intensity involving the focus in the right lobe and central liver on the T2-weighted image associated with diffuse low signal of the liver secondary to intervening blood transfusion. Note that the previously ischemic areas in the right lobe and central liver demonstrate enhancement on early-phase images (*f*). These findings are consistent with improved perfusion of ischemic regions, which matched the clinical picture.

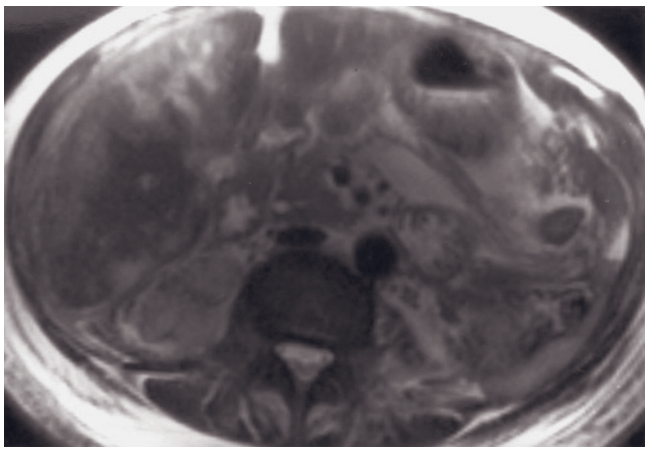

(*g*)

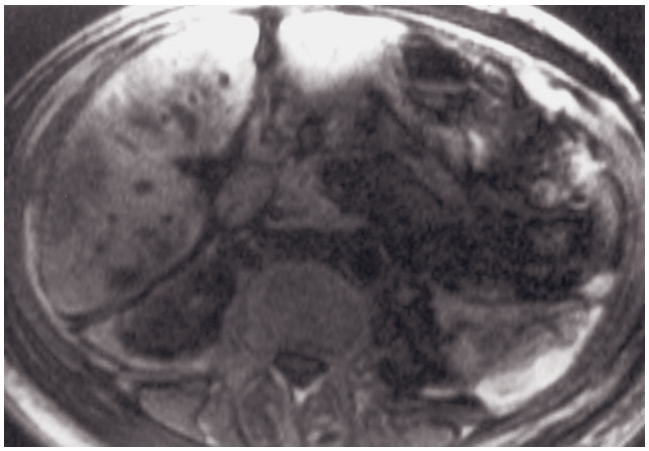

(*h*)

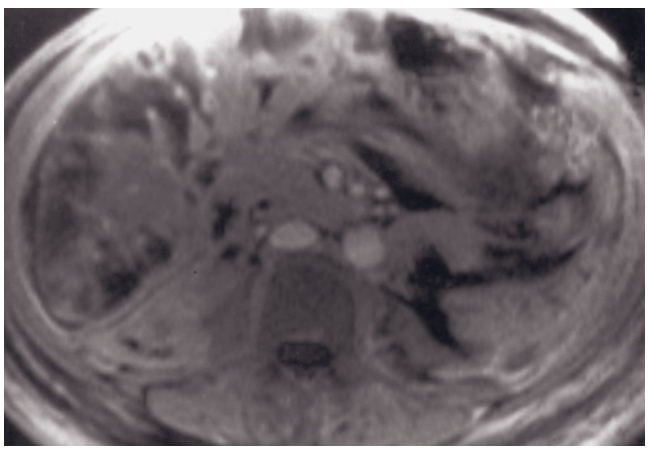

(*i*)

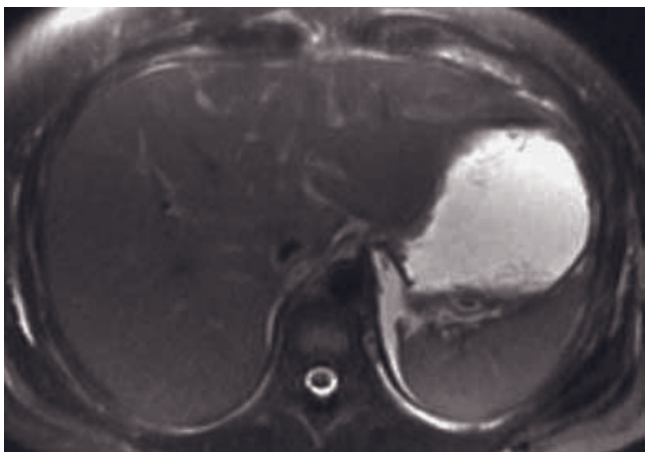

(*j*)

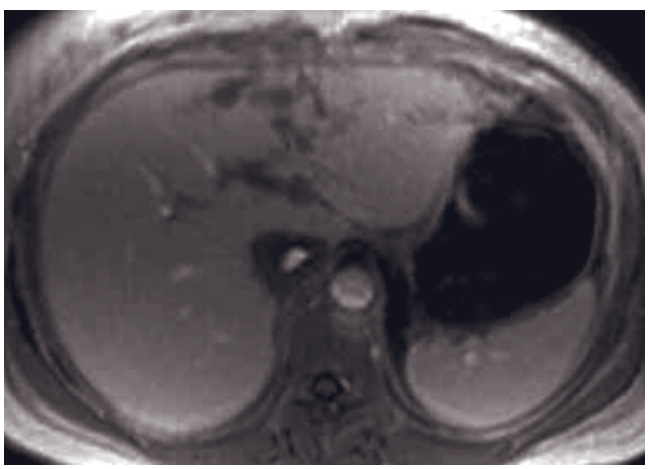

(*k*)

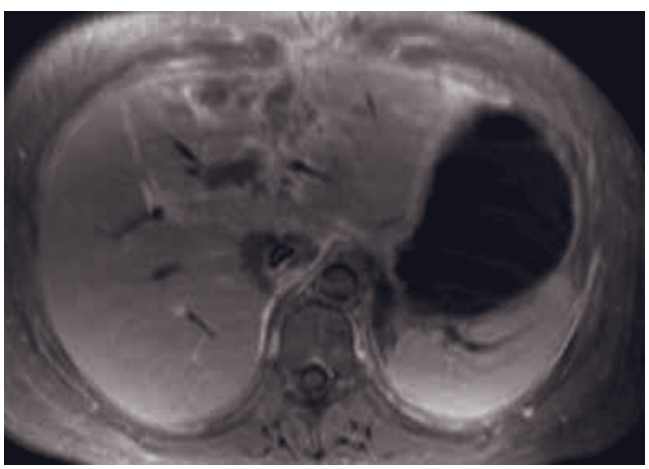

(*l*)

FIG. 2.257 (*Continued*) T2-weighted fat-suppressed SS-ETSE (*g*), SGE (*h*), and 90-s fat-suppressed postgadolinium SGE (*i*) images in a second patient demonstrate irregular peripheral regions in the right lobe inferiorly that are high signal on T2 (*g*) and low signal on T1 (*h*) and show negligible enhancement on late images (*i*), consistent with ischemic or infarcted regions caused by small branch arterial occlusion.

T2-weighted SS-ETSE (*j*) and 45-s (*k*) and 90-s fat-suppressed (*l*) postgadolinium SGE images in a third patient who is status post transplant. Irregular linear areas in the left hepatic lobe are present on early-phase images (*k*) that show peripheral enhancement on late-phase images (*l*) consistent with late enhancement of the ischemic rim. Air is present within bile ducts because of the presence of a biliary stent. Note the presence of air within vessels on the late-phase image (*l*).

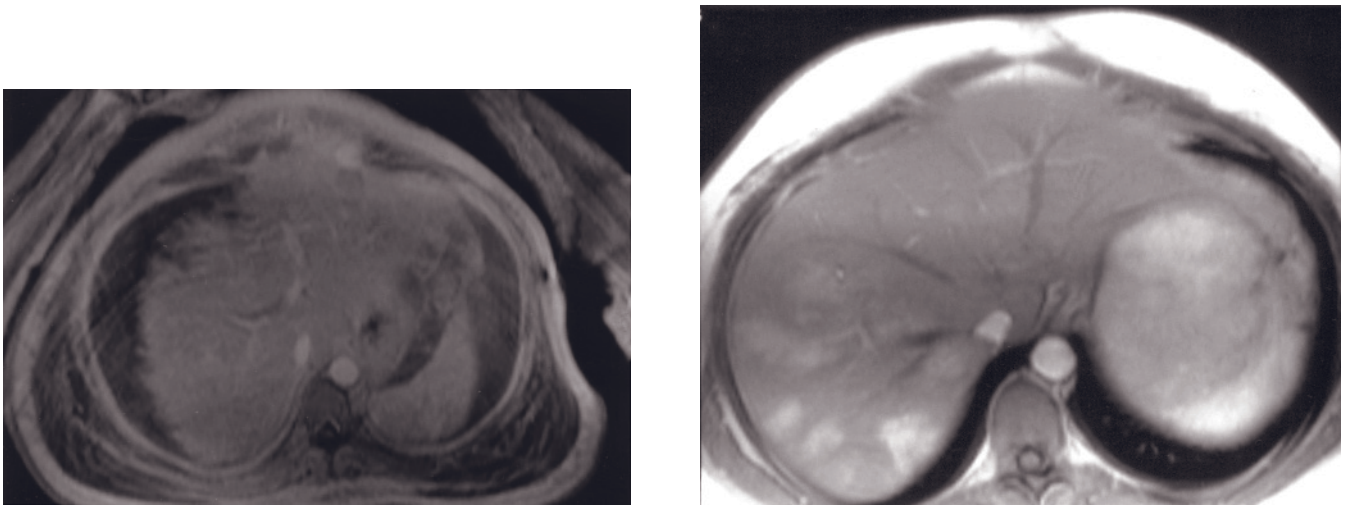

(*a*) (*b*)

FIG. 2.258 HELLP syndrome. Transverse 45-s postgadolinium SGE image (*a*) demonstrates an abnormal serrated margin of the liver and massive ascites. Liver changes reflect ischemic injury.

Immediate postgadolinium image (*b*) in a second patient with HELLP syndrome shows an early patchy enhancement of the liver.

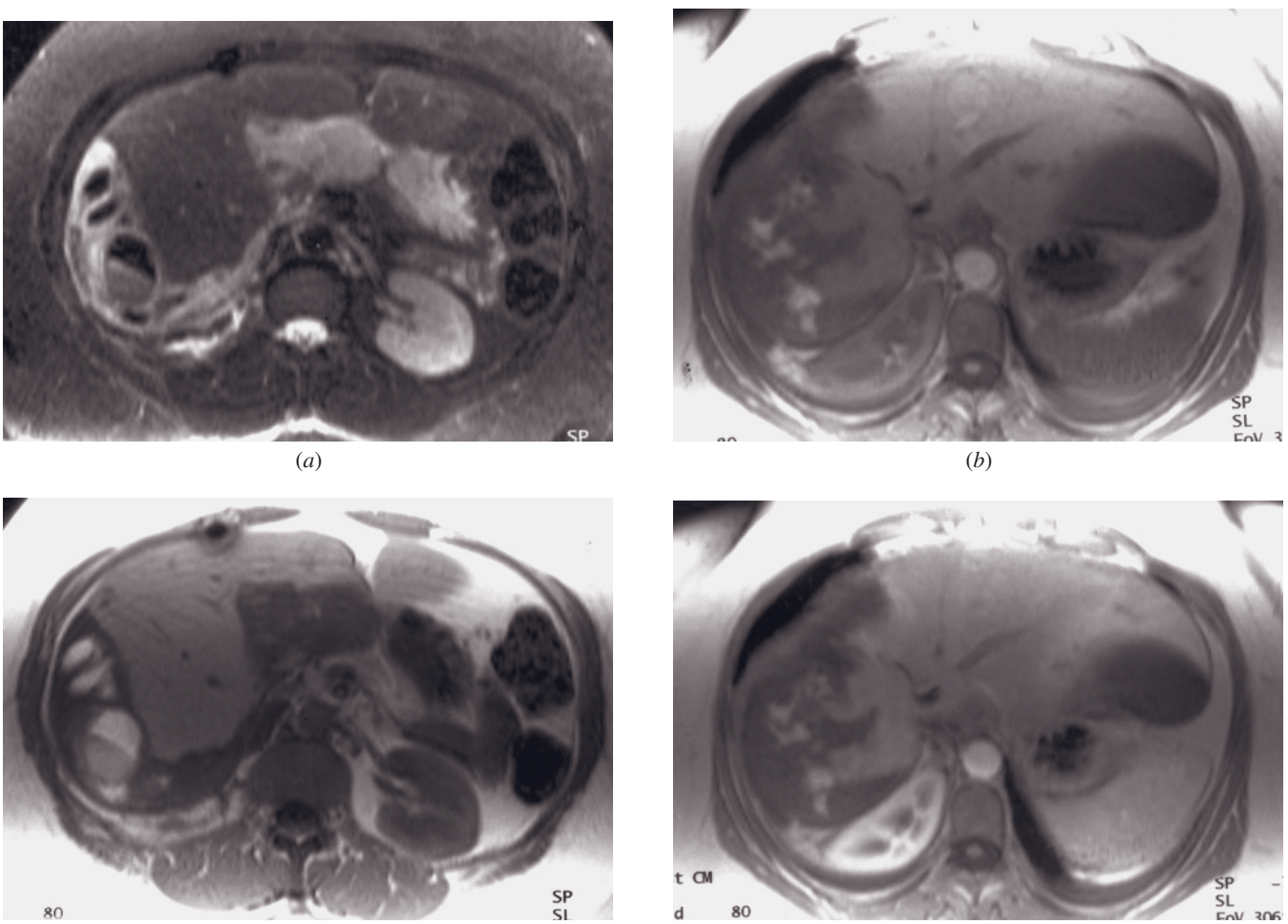

(*a*) (*b*)

(*c*) (*d*)

FIG. 2.259 Spontaneous intrahepatic hemorrhage. Echo train-STIR (*a*), SGE (*b, c*), immediate postgadolinium SGE (*d, e*),

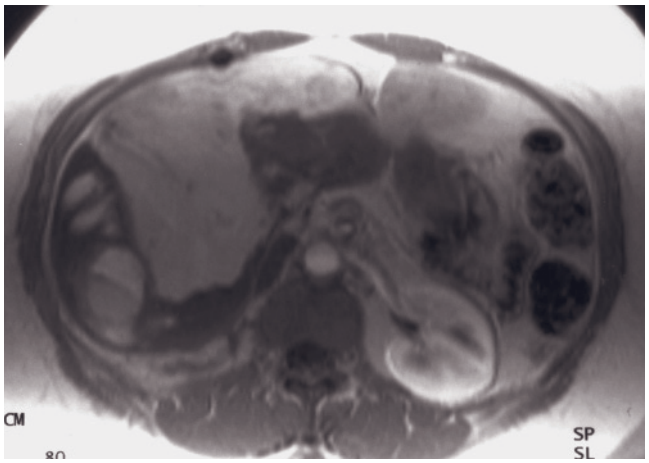

(*e*)

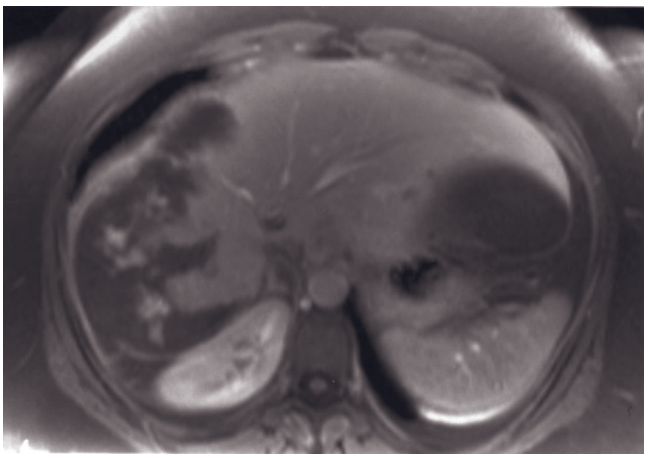

(*f*)

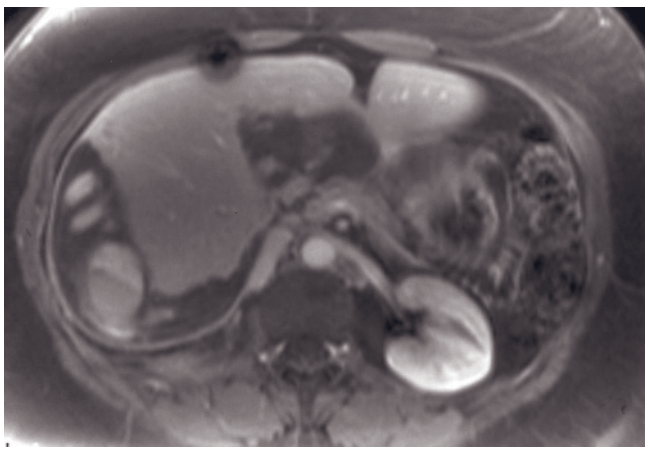

(*g*)

FIG. 2.259 (*Continued*) and 90-s postgadolinium fat-suppressed SGE (*f, g*) images in a 34-yr-old woman who has a history of spontaneous intrahepatic hematoma. There is a large complex subcapsular collection that demonstrates mixed signal intensity consistent with blood of different ages. Spontaneous intrahepatic hematoma occurs most commonly in patients who are on anticoagulant therapy. Hepatic adenomas are the most common cause in women of child-bearing age who are not on anticoagulation therapy and are taking birth control pills. Note the jagged peripheral margin of the liver (*b, d, f*), which is an appearance also observed in spontaneous hepatic hemorrhage in the HELLP syndrome.

suprahepatic IVC is frequently enlarged with enlargement of the hepatic veins. Contrast injected in a brachial vein may appear earlier in the hepatic veins and suprahepatic IVC than in the portal veins and infrahepatic IVC, reflecting reflux of contrast from the heart (fig. 2.260).

Portal Venous Air

Portal venous air, a serious condition associated with bowel ischemia, appears as signal-void foci within distal branches of the portal vein in the nondependent portion of the liver (typically the left lobe) on all imaging sequences. Magnetic susceptibility artifact may also be identified. Air is best demonstrated with a combination of high-resolution T2-weighted echo-train spin-echo and postgadolinium T1-weighted images in which air will be signal void on both sets of images. The air is most clearly shown on the postcontrast T1-weighted images (fig. 2.261). The T2-weighted images confirm the fact that the tubular structures that are dark on T1-weighted images are also dark on T2, reflecting signal-void air rather than high-signal fluid.

Air in the Biliary Tree

Air in the biliary tree is usually a relatively benign condition. Air in the biliary tree is less peripheral than air in the portal veins, and is more clearly observed as branching tubular structures conforming to the biliary tree. Air is most commonly observed in the left biliary ducts, reflecting the patient's supine position in the bore of the magnet. Air in the biliary tree is signal void on all MR sequences (fig. 2.262).

Diffuse Hyperperfusion Abnormality

This is a new term that reflects a descriptive, vascular dynamic process that affects the hepatic parenchyma. This entity is characterized by large regions of transient increased enhancement in the liver parenchyma in the hepatic arterial dominant phase that fades to isointensity

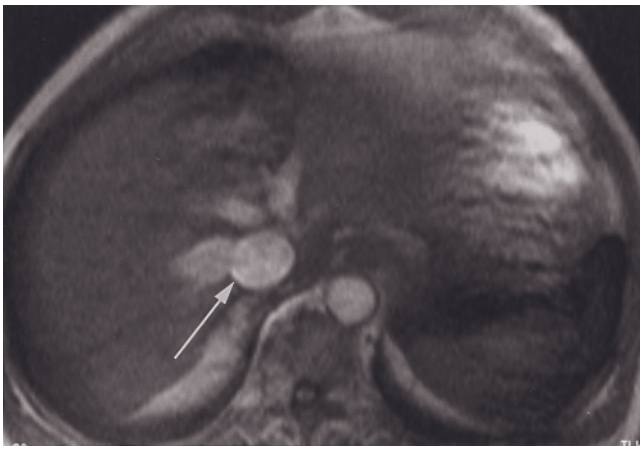

(*a*)

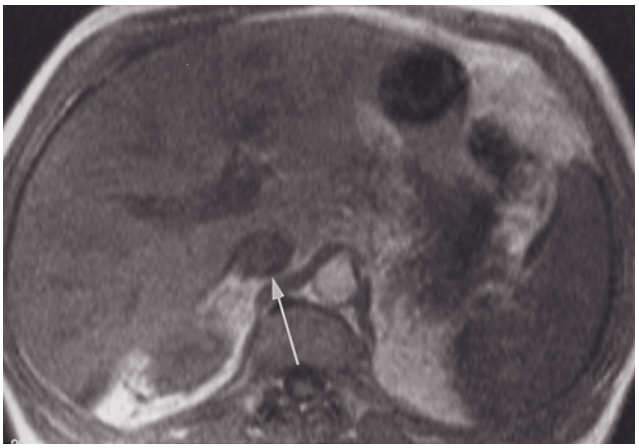

(*b*)

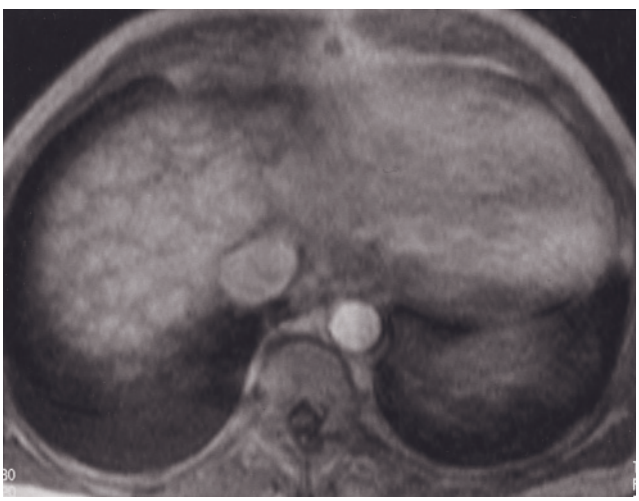

(*c*)

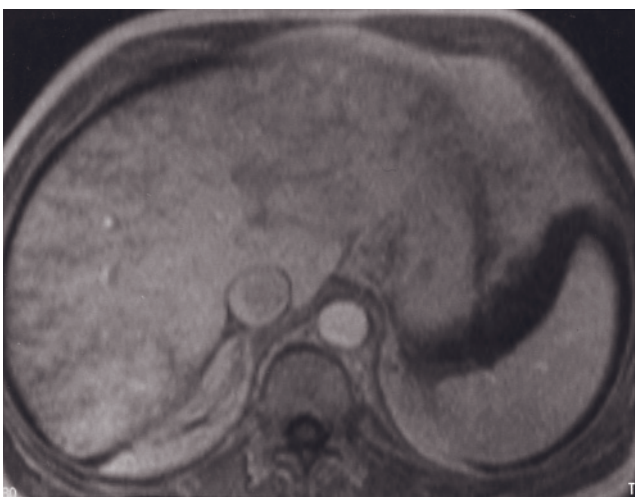

(*d*)

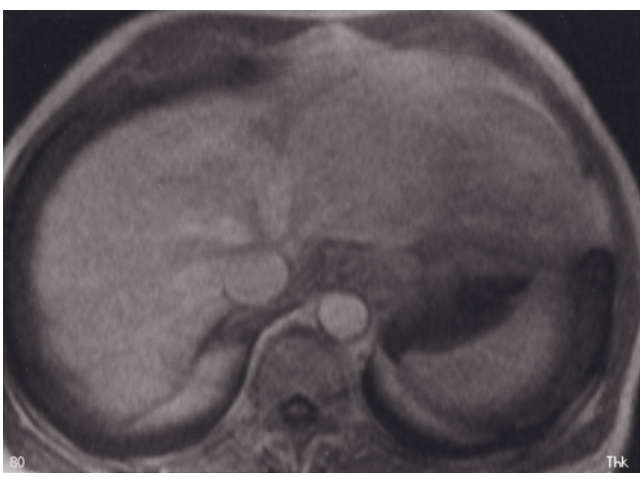

(*e*)

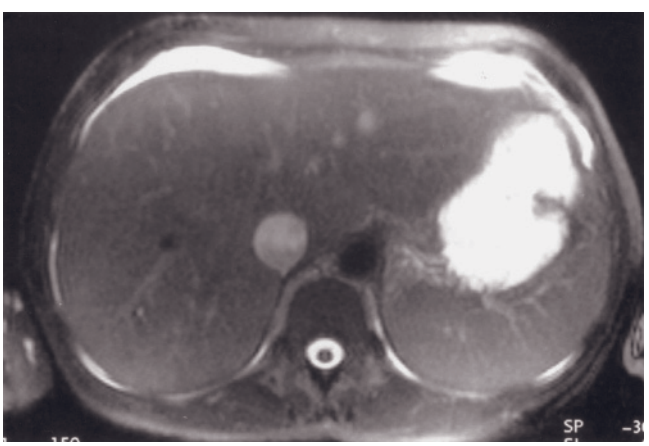

(*f*)

FIG. 2.260 Mosaic enhancement secondary to congestive heart failure. Immediate (*a, b*), 45-s postgadolinium (*c, d*), and 90-s postgadolinium SGE (*e*) images. The immediate postgadolinium images (*a, b*) demonstrate the presence of gadolinium in the superior IVC early in the arterial phase of enhancement with no enhancement of the abdominal organs, because of the low cardiac output state of the patient. Reflux of gadolinium into the dilated suprahepatic IVC and hepatic veins is present (arrow, *a*), with no contrast present in the infrahepatic IVC (arrow, *b*). On the 45-s postgadolinium images (*c, d*), a mosaic enhancement pattern is present throughout the liver, reflecting hepatic congestion. This mosaic enhancement resolves on the 90-s postgadolinium image (*e*).

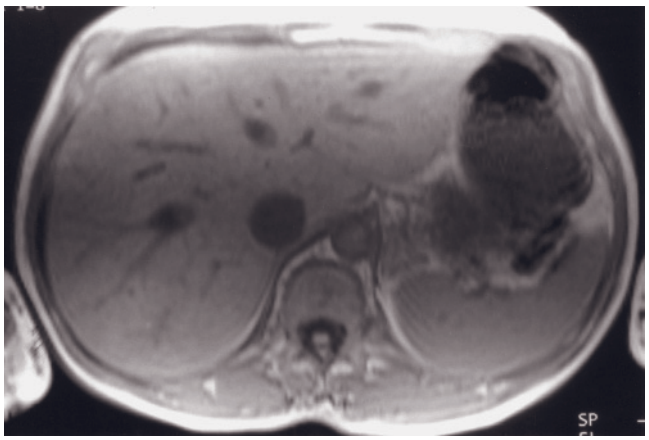

(*g*)

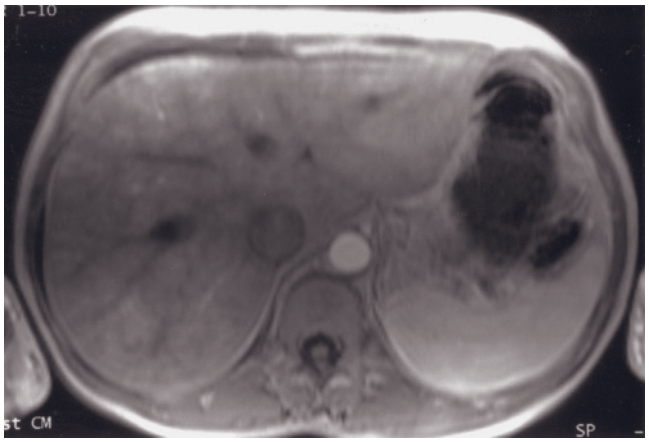

(*h*)

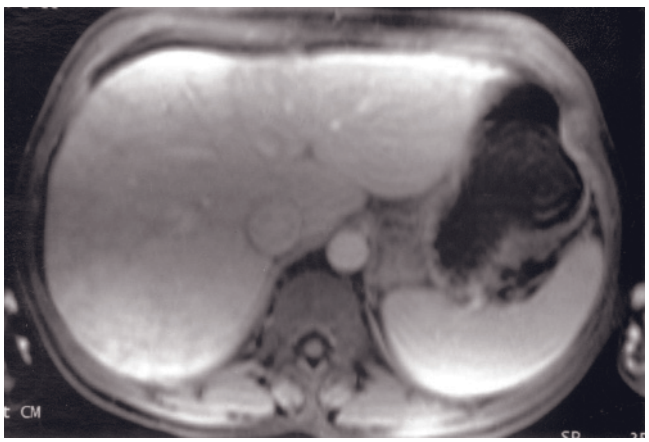

(*i*)

FIG. 2.260 (*Continued*) T2-weighted fat-suppressed SS-ETSE (*f*), SGE (*g*), immediate postgadolinium SGE (*h*), and 90-s postgadolinium fat-suppressed SGE (*i*) images in a patient with systemic amyloidosis and restrictive cardiomyopathy. The liver is enlarged with a mosaic enhancement pattern immediately after gadolinium administration (*h*) that diminishes on late images (*i*). Note the dilatation of inferior vena cava and small volume ascites.

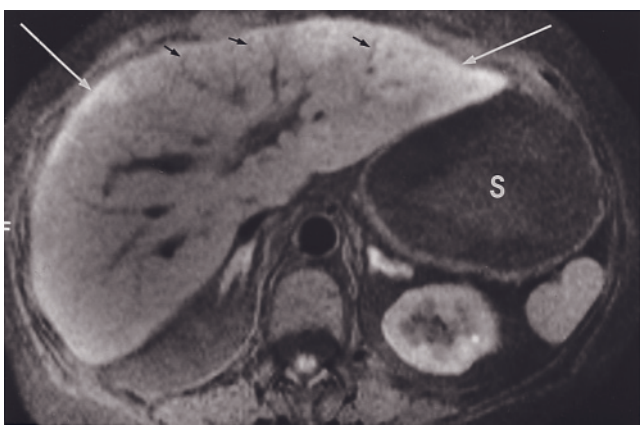

(*a*)

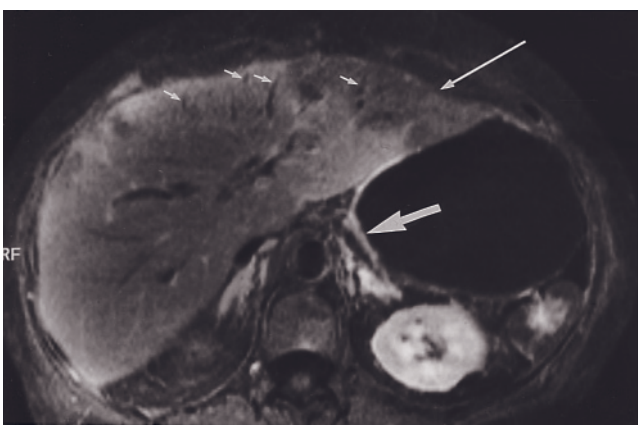

(*b*)

FIG. 2.261 Portal venous air. T1-weighted fat-suppressed SE (*a*) and 90-s postgadolinium fat-suppressed SE (*b*) images. On the precontrast T1-weighted fat-suppressed image (*a*), subtle, linear, signal-void, short, vertically oriented markings are present (small arrows, *a*). Regions of peripheral hepatic high signal intensity are present, reflecting hemorrhage (long arrows, *a*). The stomach (S) is dilated. On the gadolinium-enhanced T1-weighted fat-suppressed spin-echo image (*b*), the vertically oriented peripheral collections of portal venous air are more clearly defined (small arrows, *b*). Regions that were hyperintense on the precontrast image are shown to have diminished enhancement (long arrow, *b*). The dilated stomach shows increased mural enhancement (large arrow, *b*) consistent with ischemic changes. Portal venous air is signal void and poorly seen on T2-weighted images (not shown); fluid would be high in signal intensity and well shown on T2-weighted images.

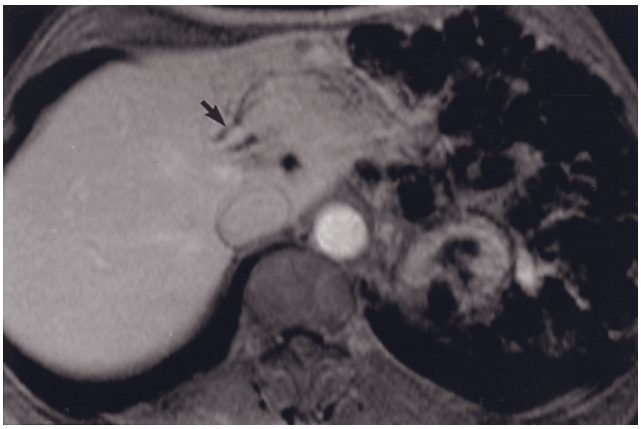

FIG. 2.262 Biliary tree air. Transverse 90-s postgadolinium SGE image in a patient with a choledochojejunostomy shows signal-void, tubular structures with an arborized pattern (arrow). This biliary tree air is more central in location than the portal venous air. The T2-weighted image (not shown) demonstrates signal-void, poorly shown bile ducts consistent with air-containing rather than fluid-containing ducts.

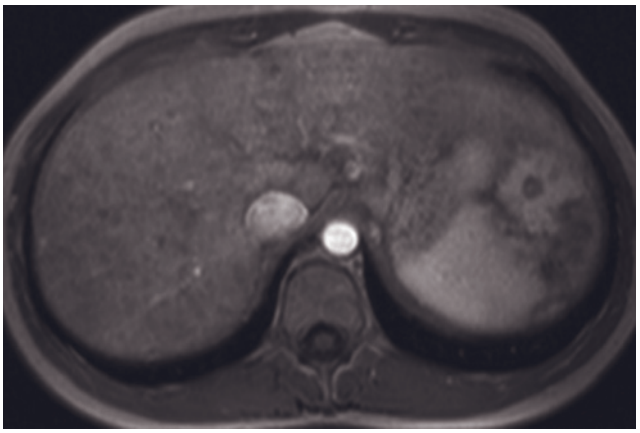

FIG. 2.263 Diffuse hyperperfusion abnormality. Immediate post-gadolinium 3D-gradient echo images demostrates diffuse heterogeneous increased enhancement, that rapidly fades to homogeneous signal on the early hepatic venous phase images (not shown). This appearance is most commonly seen in patients with acute on chronic hepatitis, but may result from a number of conditions. If no underlying explanation is present, then this enhancement is attributed to regional variations in the realtive contributions of hepatic arterial and portal venous supply to the liver. This circumstance may be incidental and not of clinical significance, and it may also be seen in combination with early homogeneous enhacement of the spleen.

rapidly, by the early hepatic venous phase. There are generally no associated signal intensity changes on noncontrast T1- or T2-weighted images. When findings of increased fluid content are apparent on noncontrast T1- or T2-weighted images (i.e., mild low signal on T1, mild high signal on T2) it implies that there is likely associated hepatocellular injury or edema. In its simplest form, diffuse hyperperfusion abnormality represents an imbalance between the normal vascular delivery patterns of blood flow to the liver by hepatic arteries and portal veins, where there is increased hepatic arterial supply. Perhaps the most common entity to result in this vascular phenomenon is acute on chronic hepatitis. A variety of processes, however, can result in this appearance. In patients with no apparent underlying hepatic disease or systemic process, it may reflect anomalous increased hepatic arterial supply (fig. 2.263). A variety of disease entities in addition to acute on chronic hepatitis (fig. 2.264) that can result in this feature are acute hepatitis, generalized systemic disease with generalized vascular effects, ascending cholangitis, drug toxicity, and acute liver transplant rejection, to name some of the more common. As mentioned above, as the disease process affecting the liver becomes more severe, signal intensity changes on T1- and T2-weighted images, and later postgadolinium images may become apparent (fig. 2.246).

Focal Hyperperfusion Abnormality

Focal hyperperfusion abnormalities (FHA) are small regions of transient increased enhancement on hepatic arterial dominant-phase images. These are generally not visible on noncontrast T1- and T2-weighted images. This entity is a new nomenclature for findings that have been previously termed transient hepatic arterial defects (THAD) or transient hepatic signal intensity differences (THID). Frequently these lesions correspond to vascular phenomenon such as arteriovenous shunting but likely can also result from a number of other vascular or inflammatory processes. The morphology of focal hyperperfusion abnormalities frequently allows differentiation from other entities such as dysplastic nodules. Nodules should have a round morphology, whereas FHA frequently appears more oblong or lozenge-shaped, with the more linear configuration rendering this entity more easy to correctly characterize (fig. 2.264).

Inflammatory Parenchymal Disease

Sarcoidosis

Sarcoidosis, a systemic inflammatory granulomatous disease of unknown etiology, is one of the most common causes of hepatic noncaseating granulomas. The liver follows lymph nodes and lung in the frequency of involvement, and the liver is involved histologically in 60–90% of patients [415]. The majority of patients show minimal evidence of clinical or biochemical hepatic

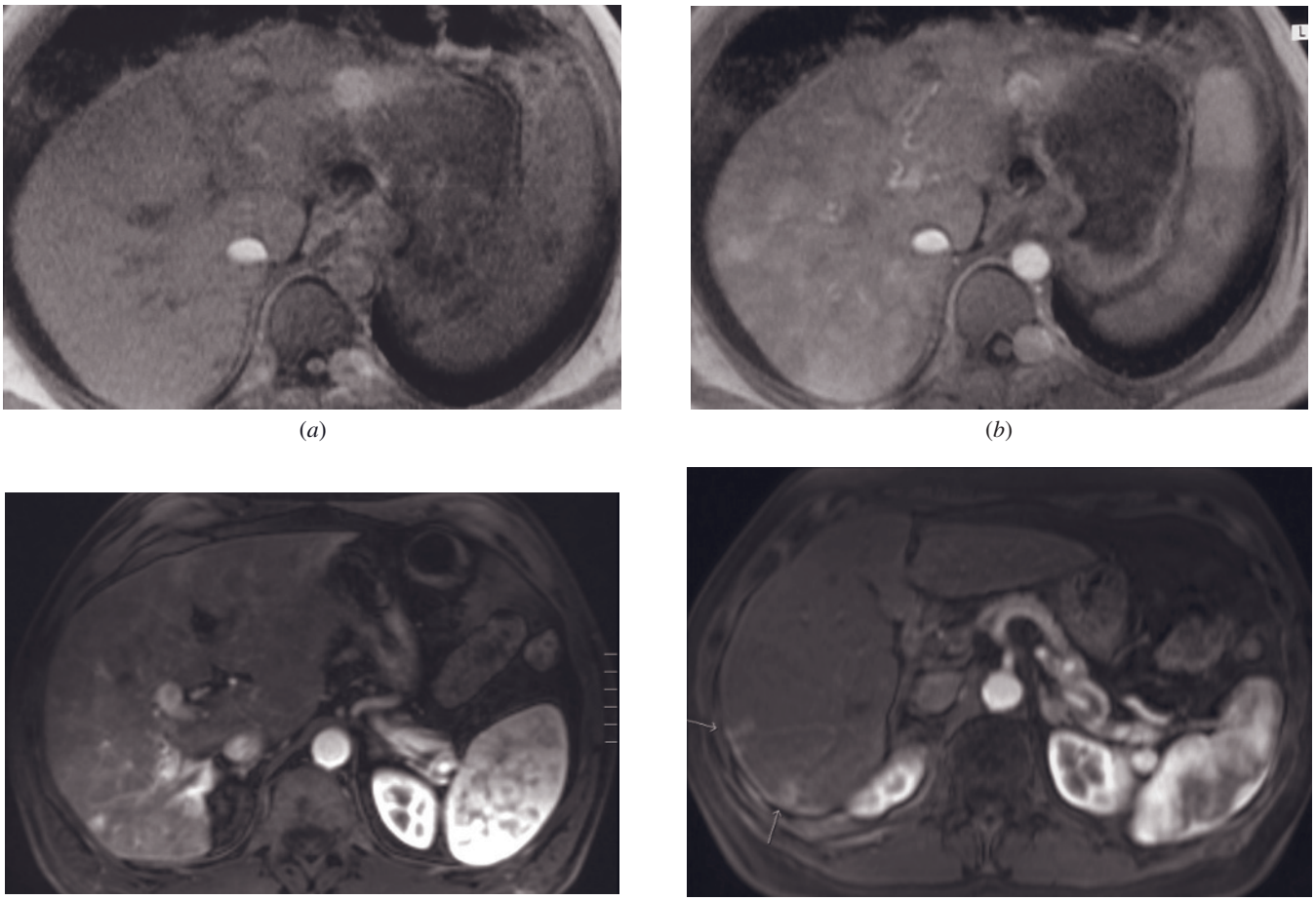

FIG. 2.264 Diffuse Hyperperfusion and Focal Hyperperfusion Abnormalities in the Cirrhotic Liver. SGE (*a*), immediate post-gadolinium SGE (*b*) in 1 patient, and immediate post-gadolinium 3D-gradient echo (*c*, *d*) images in two other patients with cirrhosis. Diffuse hyperperfusion abnormality may occur secondary to a number of vascular phenomena, but in the cirrhotic liver the most common cause is acute on chronic hepatitis. Note the patchy appearance of increased enhancement throughout the hepatic parenchyma, that is generally apparent only on immediate post-gadolinium images and may not be visible on precontrast or later postcontrast images. In two other patients, small, oval shaped foci of increased enhancement are appreciated on immediate post-gadolinium images (*c*, *d*, arrows on *d*), which were only apparent on immediate postcontrast images. These represent focal hyperperfusion abnormalities. This entity is also not uncommon in the cirrhotic liver, and the most common underlying mechanism is small intrahepatic arteriovenous shunts. Focal hyperperfusion abnormalities must be distinguished from hepatic nodules, and their non-spherical shape (often lozenge-shaped) and often ill-defined margins usually define their vascular nature.

dysfunction. Granulomas are characterized pathologically by compact aggregates of plump epithelioid cells, sometimes with multinucleated giant cells, surrounded by a cuff of lymphocytes and macrophages. Focal involvement of the liver and spleen in sarcoidosis with noncaseating granulomas is well demonstrated on MR images. Sarcoid granulomas are small (approximately 1 cm in diameter), rounded lesions low in signal intensity on T2- and T1-weighted images that enhance in a diminished, delayed fashion on gadolinium-enhanced gradient-echo images (fig. 2.265) [416, 417]. The diminished enhancement reflects the hypovascular nature of the granuloma. Occasionally, the spleen may be lower in signal intensity than liver on T2-weighted images [416]. Concomitant retroperitoneal lymph nodes are often present, exhibiting a distinctive, feathery, moderately high signal on T2-weighted images.

Inflammatory Myofibroblastic Tumor (Inflammatory Pseudotumor)

Inflammatory myofibroblastic tumor, formerly termed inflammatory pseudotumor, is an uncommon lesion that rarely presents in the liver [418]. Pathologic macroscopic evaluation may disclose a tumorlike, firm mass within the liver parenchyma or a soft tissue mass encasing the hilar area. Microscopic inspection shows a mixed inflammatory infiltrate consisting of plasma cells, macrophages, chronic inflammatory cells, and histiocytes. Special studies show polyclonality of the inflammatory infiltrate, pointing to the benign nature of the lesion

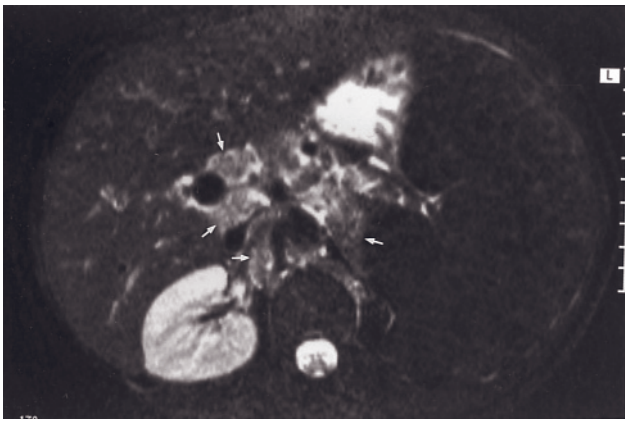

(*a*)

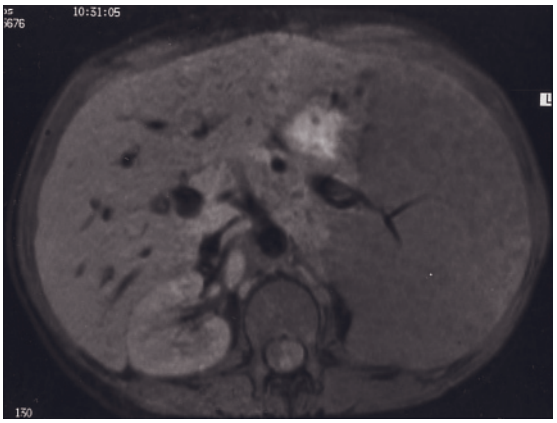

(*b*)

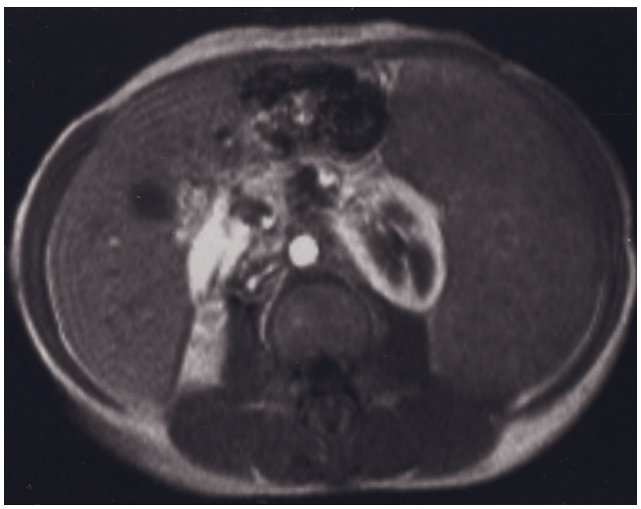

(*c*)

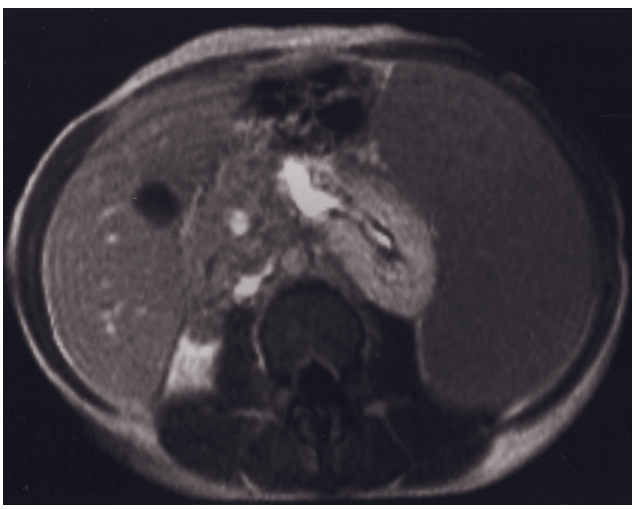

(*d*)

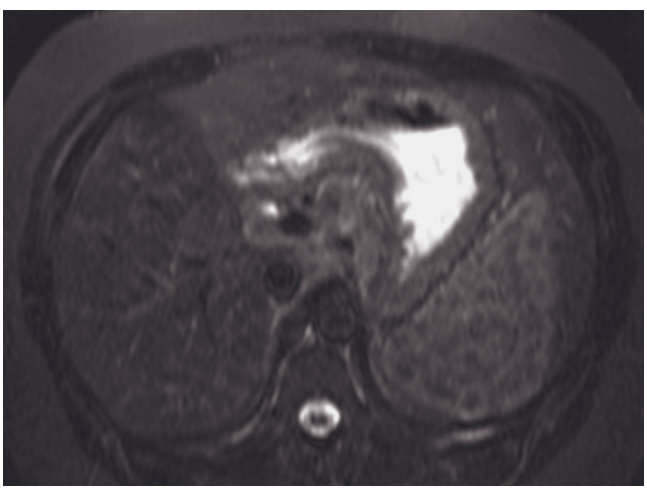

(*e*)

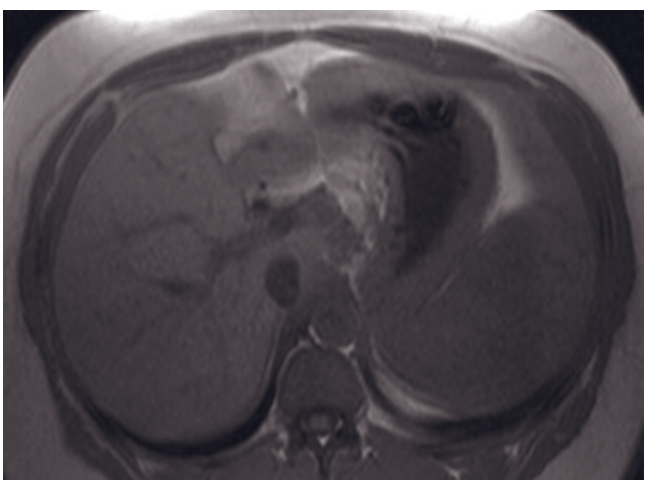

(*f*)

FIG. 2.265 Hepatosplenic sarcoidosis. T2-weighted fat-suppressed SE (*a*), T1-weighted fat-suppressed SE (*b*), and immediate (*c*) and 5-min (*d*) postgadolinium SGE images. The spleen is massively enlarged and contains multiple <1-cm nodules that are moderately low signal intensity on T2-weighted (*a*) and T1-weighted (*b*) images and demonstrate negligible enhancement on early-phase images (*c*) with gradual enhancement over time (*d*). Extensive retroperitoneal, celiac, and periportal lymphadenopathy is also present (*a*, *b*), which has a speckled appearance on the T2-weighted image (arrows, *a*). A speckled signal on T2 has been described for lymph nodes affected by sarcoidosis.

T2-weighted fat-suppressed SS-ETSE (*e*), SGE (*f*), and immediate (*g*) and 90-s fat-suppressed (*h*) postgadolinium SGE images in a second patient with sarcoidosis. The liver shows a patchy enhancement on early-phase image (*g*) that equilibrates on late-phase

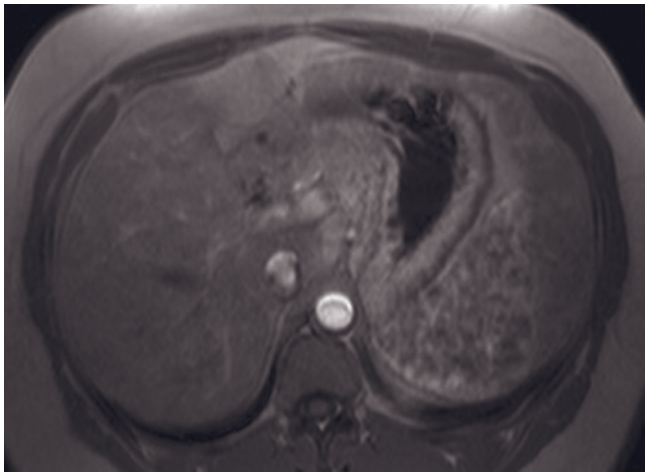

(*g*)

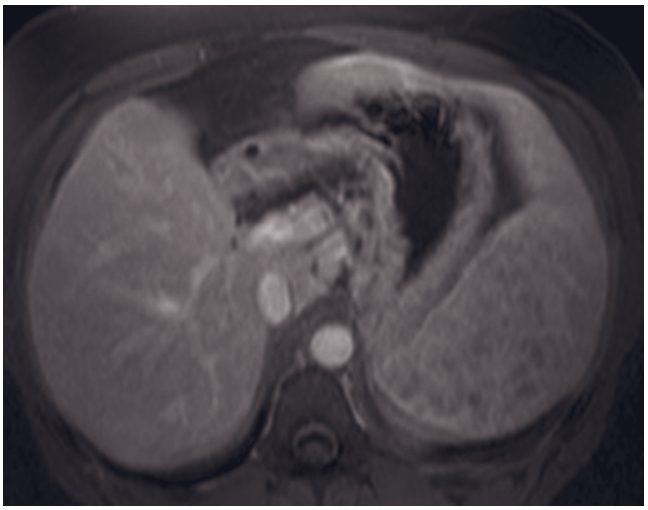

(*h*)

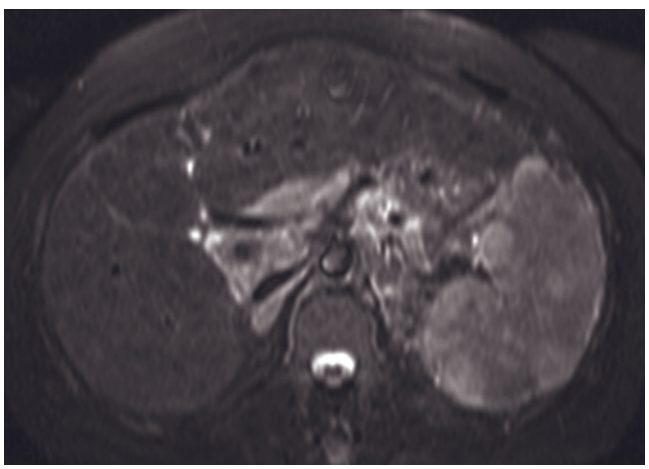

(*i*)

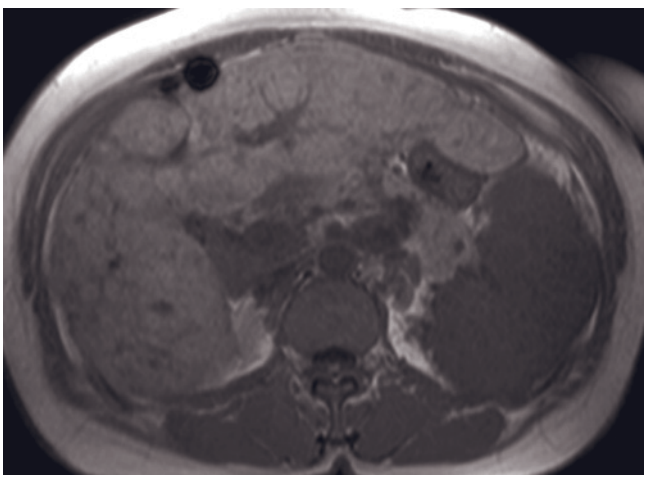

(*j*)

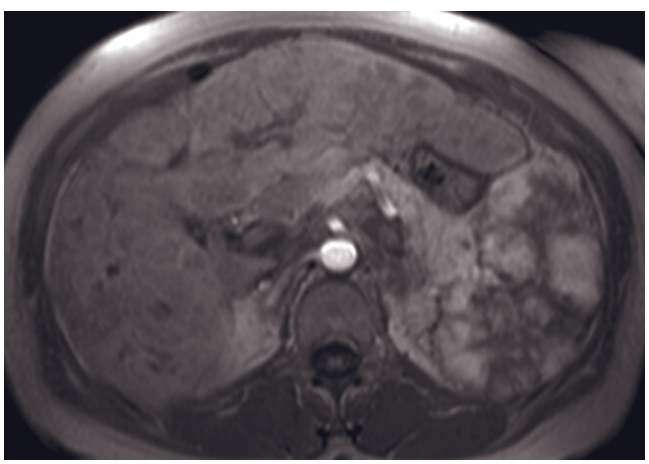

(*k*)

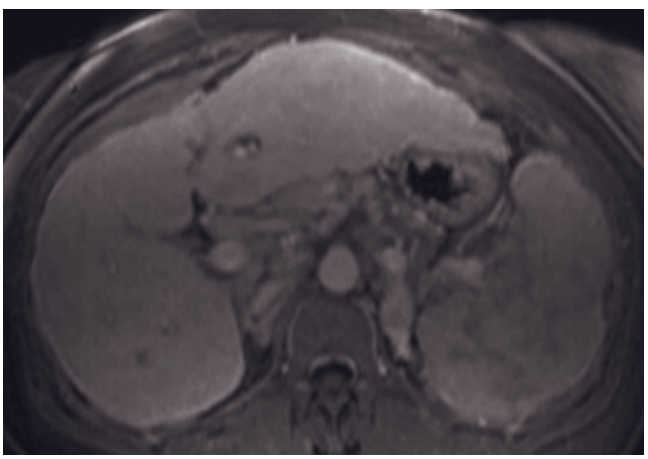

(*l*)

Fig. 2.265 (*Continued*) image (*h*), rendering the liver homogeneously enhanced. The spleen shows multiple small nodules that demonstrate low signal intensity on both T2-weighted (*e*) and T1-weighted (*f*) images, negligible enhancement on early-phase image (*g*), and progressive enhancement on late-phase image (*h*).

T2-weighted fat-suppressed SS-ETSE (*i*), SGE (*j*), and immediate (*k*) and 90-s fat-suppressed (*l*) postgadolinium SGE images in a third patient with sarcoidosis. Multiple nodules are seen in both liver and spleen. The liver nodules appear isointense on T2-weighted (*i*) and T1-weighted (*j*) images and enhance in a fashion similar to background parenchyma. Note that the hepatic architecture is distorted because of the nodules. The spleen nodules are high signal intensity on T2-weighted image (*i*), isointense on T1-weighted image (*j*), and intensely enhanced on early-phase image (*k*), fading on late-phase image (*l*). Lymphadenopathy is best seen on T2-weighted fat-suppressed image (*i*).

[419]. Prominent fibrosis is a characteristic feature. Areas of necrosis and obliteration of blood vessels may occasionally be noted.

Inflammatory myofibroblastic tumor may be associated with systemic symptoms, including fever, weight loss, malaise, and right upper quadrant pain [420]. Although the disease often responds to steroid administration and the prognosis is usually good, fatal outcome has been reported [421]. Inflammatory myofibroblastic tumors are not malignant neoplasms; however, if they occur at the hilum, effects of the lesion can be devastating. Hilar myofibroblastic tumor may encase the portal vein, hepatic artery, and bile duct [418]. Inflammatory infiltrate in the walls and lumen of the portal vein may cause an occlusive phlebitis that extends beyond margins of tumor [418].

On imaging, hepatic myofibroblastic tumor can present as an ill-defined, tumorlike lesion within the parenchyma or as a periportal soft tissue mass involving the hilum [422]. In the former pattern, lesions are usually solitary, but in 20% of cases they are multiple. Masses range from 1 to 20 cm but are generally less than 2 cm in diameter [420].

MRI features of inflammatory myofibroblastic tumor may vary according to the presence of necrosis and fibrosis within the lesion. Tumorlike lesions may demonstrate mild high signal on T2-weighted images, low signal or isointensity on T1-weighted images, and a moderate or intense enhancement on early-phase images that fades away on late-phase images. Soft tissue infiltration along the periportal region may possess MRI features similar to the tumorlike pattern on T2- and T1-weighted precontrast images but tends to demonstrate a lesser degree of enhancement on early-phase images, namely. mild or negligible enhancement (fig. 2.266) [422, 423]. The lesions may regress after treatment or spontaneously and then appear as areas of fibrosis, which in the chronic setting are mildly low signal on T2- and T1-weighted images and exhibit negligible enhancement. Similar to other causes of scarring, the margins of chronic inflammatory myofibroblastic tumors are irregular and angular [422].

Because inflammatory myofibroblastic tumor is a rare entity, lesions are often mistaken for hepatic malignancy. When a mass or tumorlike pattern is present, HCC and abscess should be considered in the differential diagnosis. In addition, the soft tissue infiltration pattern requires distinction from lymphoma and cholangiocarcinoma (see fig. 2.266) [422]. Final diagnosis is based on histologic analysis.

Infectious Parenchymal Disease

Abscesses

Pyogenic Abscess. Pyogenic abscesses are the most frequent form of focal hepatic infections resulting from an infectious process of bacterial origin. Pathologically, pyogenic liver abscesses may occur as solitary or multiple lesions ranging from millimeters to massive lesions. Microscopically, in early stages, lesions are ill defined with intense acute inflammation, purulent debris, and devastation of hepatic parenchyma and stroma. In later stages, the abscesses become circumscribed, surrounded by a shell of granulation tissue consisting of abundant, newly formed blood vessels, fibroblasts, and chronic inflammation. End stages show complete fibrous encapsulation.

Infectious agents reach the liver through hepatic artery, portal vein, biliary tract, and direct extension from contiguous organs [424]. Abscesses may occur in the context of recent surgery, Crohn disease, appendicitis, diverticulitis, and blunt or penetrating injuries [424, 425]. Portal vein thrombosis is frequently associated with bacterial abscesses. The infected bland thrombus is characterized by low signal intensity on T2- and T1-weighted images and time of flight gradient-echo images. The thrombus does not enhance after contrast; however, the vein wall shows a moderate/intense enhancement after contrast administration, best seen on late-phase fat-suppressed images caused by the inflammatory reaction (fig. 2.267).

Characteristic MRI findings of pyogenic abscesses are high signal intensity on T2-weighted images and low signal intensity on T1-weighted images and show moderate enhancement of stroma on immediate postgadolinium images with persistent enhancement on interstitial phase images and no enhancement of additional stroma or progressive fill in of the lesion over time [426]. Pyogenic abscesses also possess markedly thick walls and internal septations, which enhance moderately to intensely on early-phase images and demonstrate persistent enhancement on late-phase images that often appears more intensely enhanced (figs. 2.268–2.270) [424, 427]. Abscesses typically have a moderate perilesional enhancement with indistinct outer margins on immediate postgadolinium images because of a surrounding rim of granulation tissues and a hyperemic inflammatory response in adjacent liver (figs. 2.271 and 2.272) [426]. The perilesional enhancement rapidly diminishes, and is often nearly resolved by 1 min after injection. Layering of debris and gas within the abscess cavity, mainly after biliary drainage, is also commonly appreciated. Gas is identified as signal void on both T2- and T1-weighted images and debris as a low signal on T2- and high signal on T1-weighted images, since debris is usually composed of protein [426, 428].

The higher sensitivity of MRI to gadolinium chelates than of CT imaging to iodinated agents renders dynamic gadolinium-enhanced MRI a useful technique for patients in whom a distinction between simple cysts and multiple abscesses cannot be made on the basis of

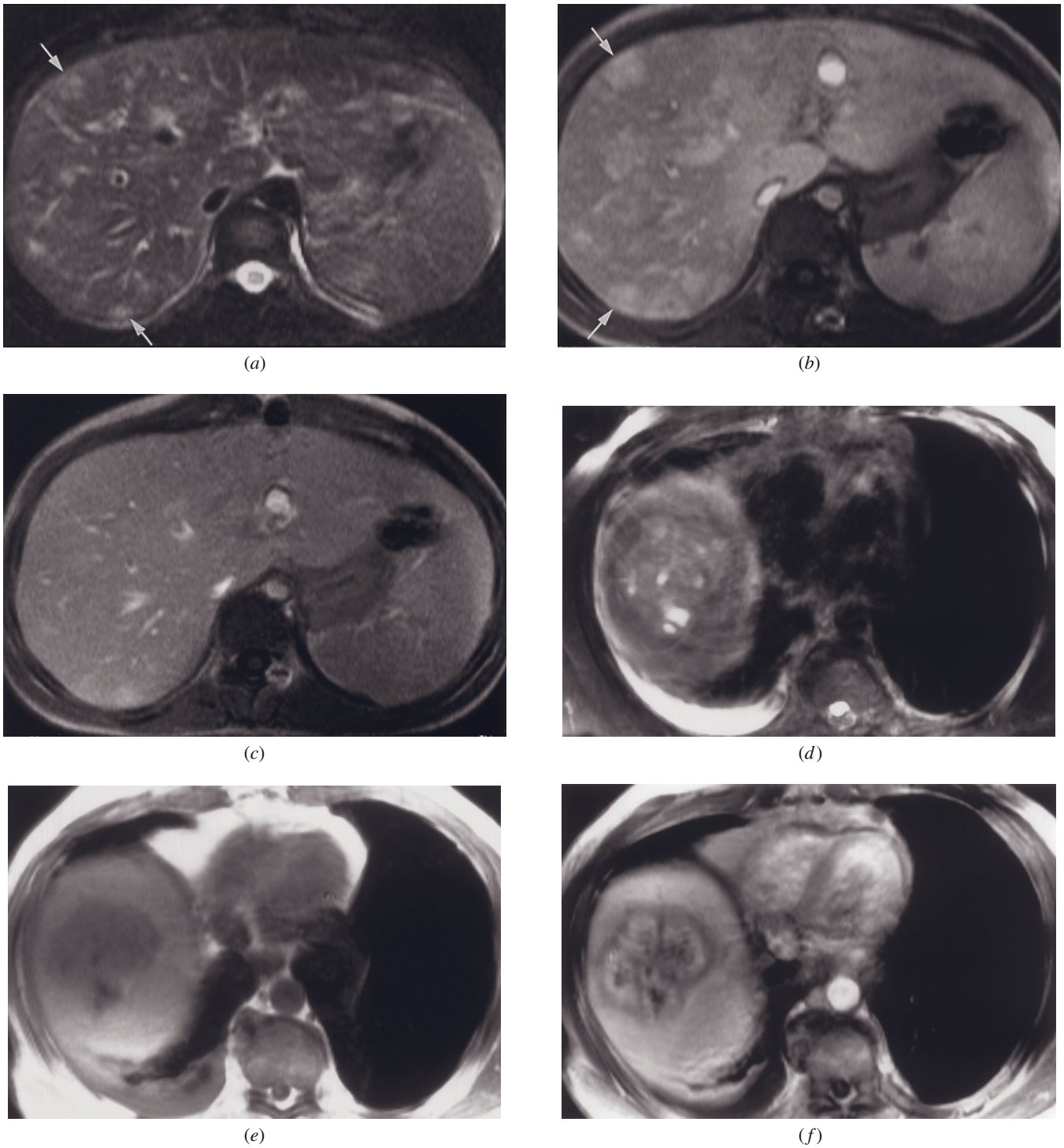

FIG. 2.266 Inflammatory myofibroblastic tumor (inflammatory pseudotumor). T2-weighted fat-suppressed SE (*a*) and immediate (*b*) and 90-s (*c*) postgadolinium SGE images. No definite lesions are apparent on the precontrast T1-weighted image (not shown). Occasional, mildly hyperintense ill-defined lesions are present on the T2-weighted image (arrows, *a*). Multiple small, irregular enhancing foci are demonstrated throughout the liver on early-phase image (arrows, *b*) that fade to isointensity on late-phase image (*c*).

T2-weighted fat-suppressed SS-ETSE (*d*), SGE (*e*), and immediate (*f*) and 90-s fat-suppressed (*g*) postgadolinium SGE images in a second patient. A 6-cm mass lesion is present in the dome of the liver, which is minimally high in signal intensity on T2-weighted image (*d*) and moderately low in signal intensity on T1-weighted image(*e*), enhances in an intense diffuse heterogeneous fashion on early-phase image (*f*), and fades on later images (*g*). The appearance resembles HCC; however, the liver is not cirrhotic. The patient also presented with fever and malaise, which are symptoms often observed with inflammatory pseudotumor.

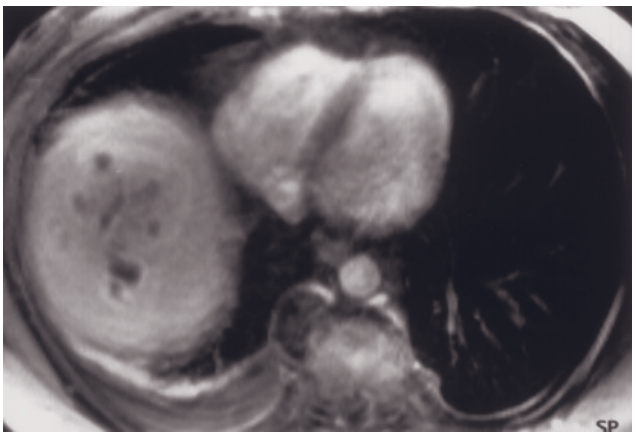

(*g*)

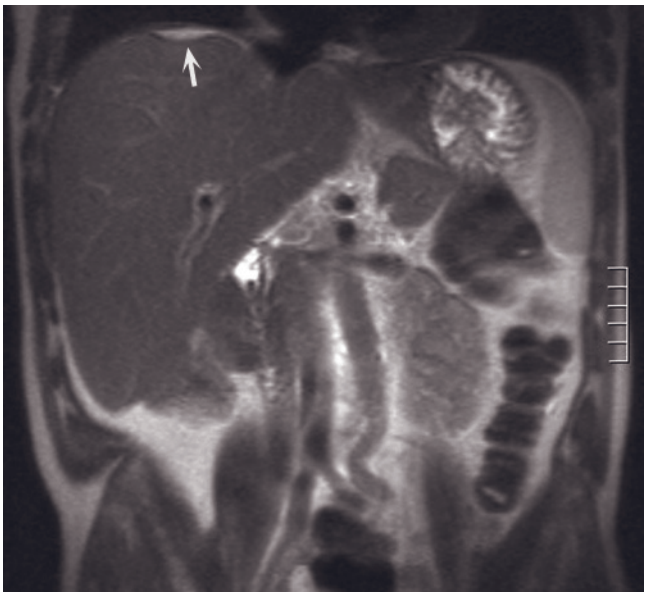

(*h*)

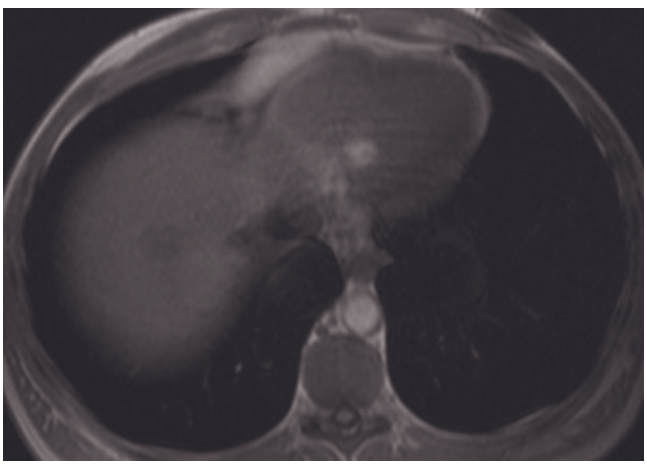

(*i*)

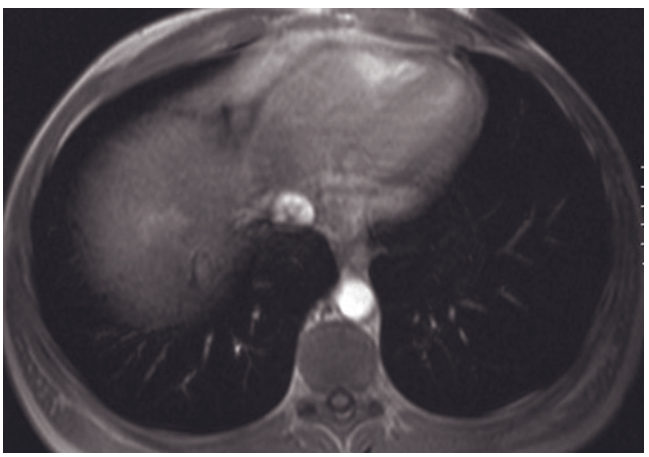

(*j*)

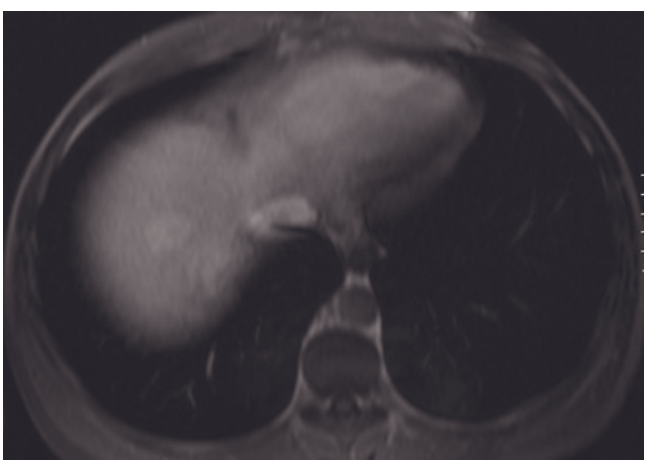

(*k*)

FIG. 2.266 (*Continued*) Coronal T2-weighted SS-ETSE (*h*), SGE (*i*), and immediate (*j*) and 90-s (*k*) postgadolinium SGE images in a third patient. There is a lesion in the dome of the liver that exhibits mildly low signal intensity on T1-weighted image (*i*) and mild enhancement on all phases after contrast (*j*, *k*). Also, note the liver retraction in the dome of the liver adjacent to the tumor, best seen on the coronal T2-weighted image (arrow, *h*). Inflammatory myofibroblastic tumor may range in appearance from a vascular active multifocal process to irregularly margined, poorly enhanced fibrosed lesions. Unlike in other conditions (e.g., metastases and abscesses) this range of appearance can occur with no history of treatment of the active disease.

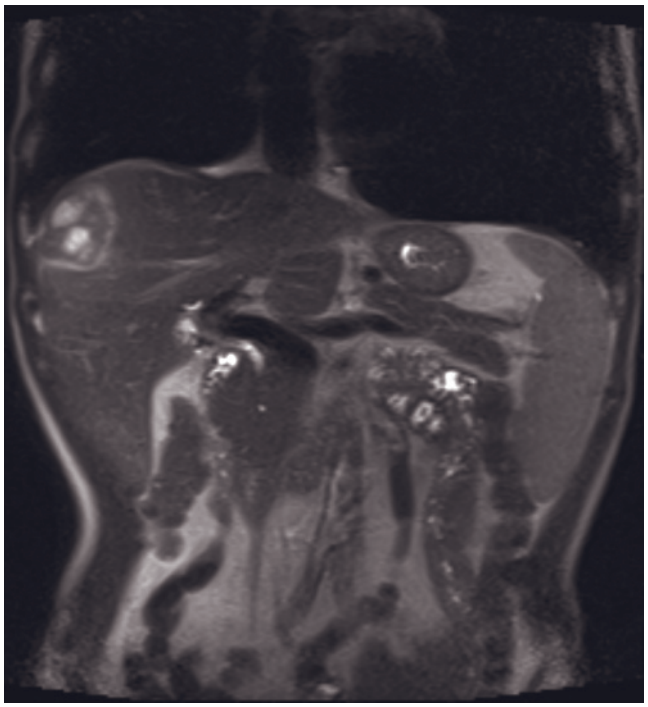

(*l*)

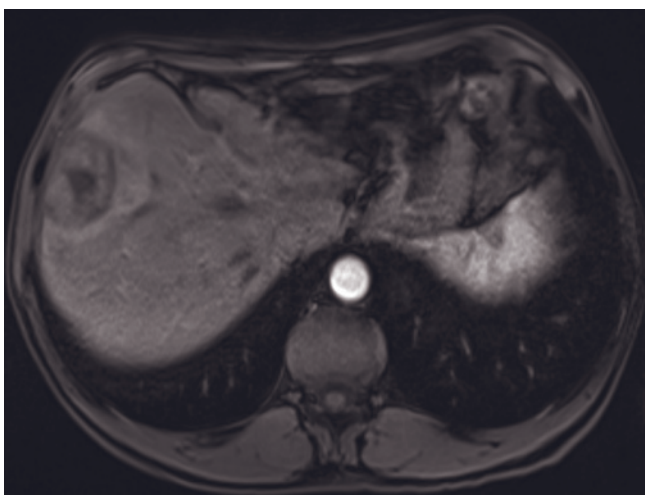

(*o*)

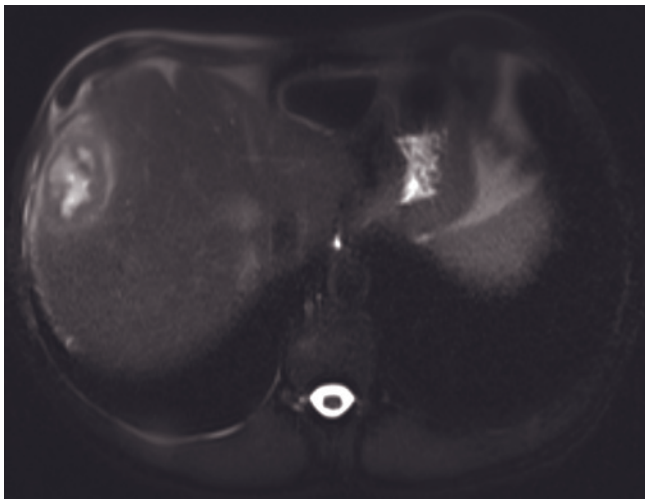

(*m*)

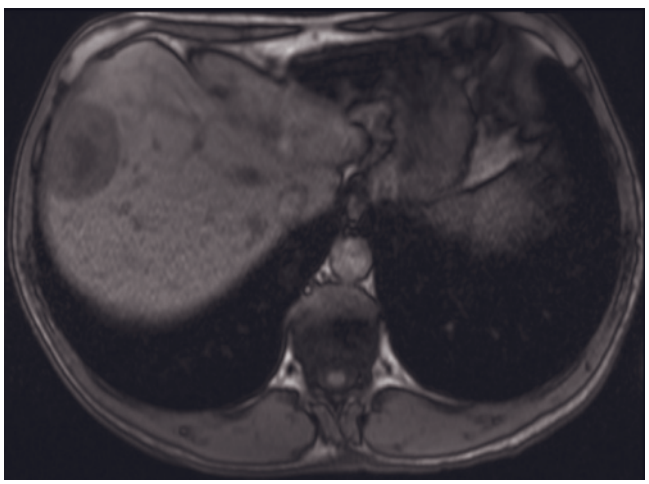

(*n*)

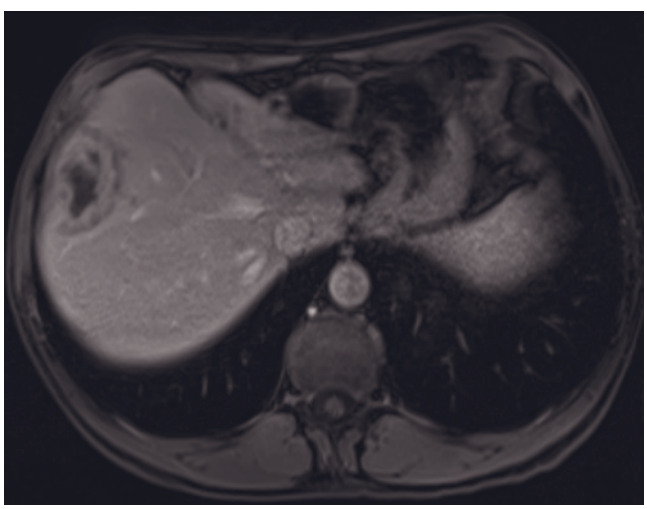

(*p*)

FIG. 2.266 (*Continued*) Coronal (*l*) and fat-suppressed transverse (*m*) T2-weighted SS-ETSE, out-of-phase SGE (*n*), and immediate (*o*) and 2 min (*p*) fat-suppressed 3D-gradient echo in another patient. An oval-shaped thick-walled lesion is present, which was histological diagnosed as an IMT. Following steroid therapy the lesion resolved.

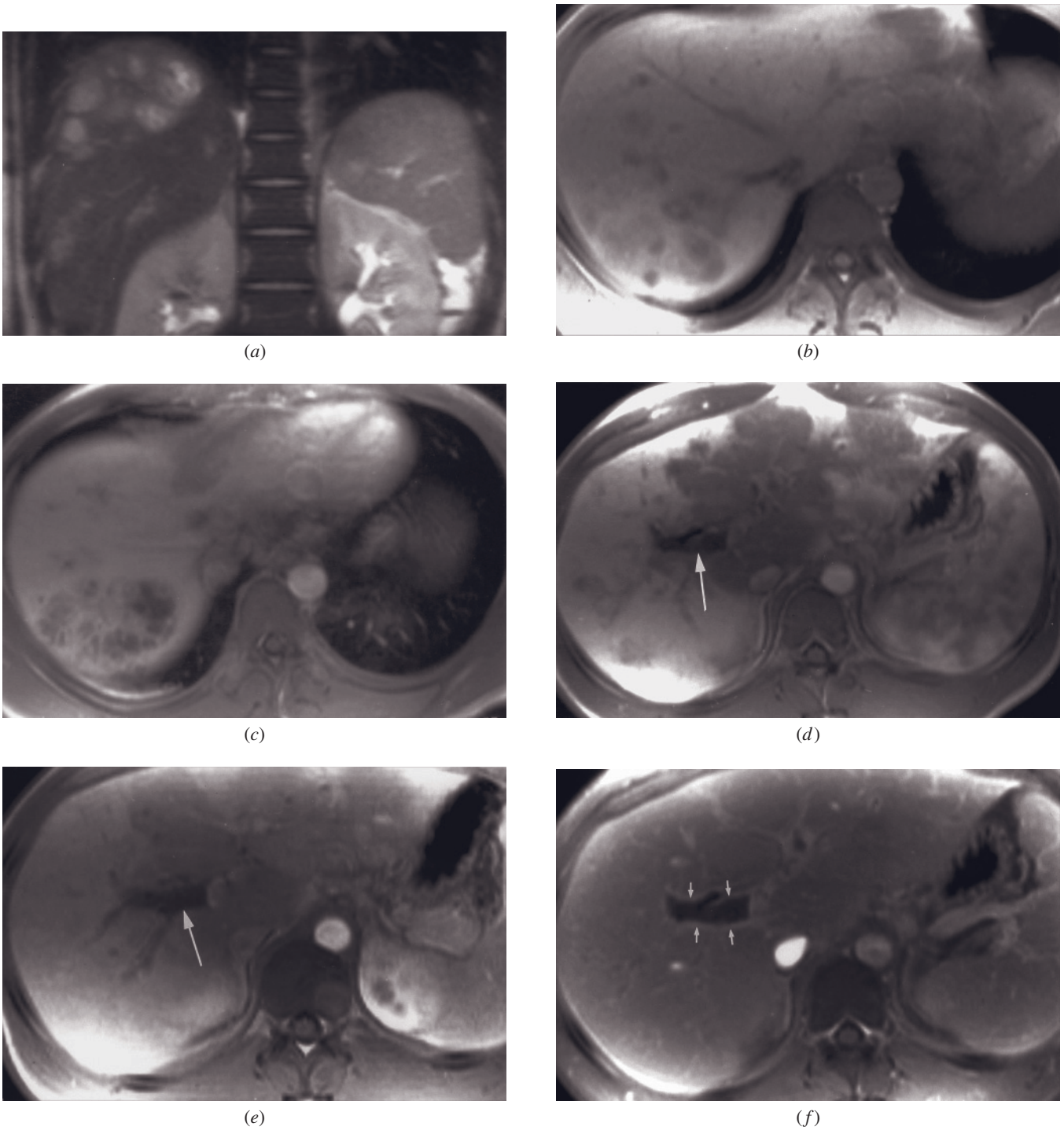

FIG. 2.267 Hepatic abscesses. Coronal T2-weighted SS-ETSE (*a*), transverse SGE (*b*), and immediate (*c*, *d*), 45-s (*e*), and 90-s fat-suppressed (*f*) postgadolinium SGE images of the abdomen and sagittal T2-weighted SS-ETSE (*g*) and 2.5-min fat-suppressed postgadolinium SGE (*h*) images of the pelvis in a patient with appendicitis and hepatic abscess. There are multiple lesions with a cluster appearance in the right hepatic lobe that demonstrate high signal intensity on T2-weighted image (*a*), low signal intensity on T1-weighted image (*b*), and enhancement of the abscess wall and septations with perilesional enhancement immediately after administration of contrast (*c*). Abnormal enhancement of the liver on the early-phase image (*d*) reflects the presence of portal vein thrombosis, with increased enhancement of the right lobe due to increased hepatic arterial supply. The portal vein is expanded with thrombus (arrow *d, e*) that is low signal on T1-weighted image and does not enhance after administration of contrast, consistent with a bland thrombus. The portal vein wall enhances (small arrows, *f*) on the late-phase images, reflecting that the thrombus is infected. Note on the sagittal images (*g*, *h*) that the appendix (arrows, *g, h*) is thick walled with increased enhancement, consistent with acute appendicitis.

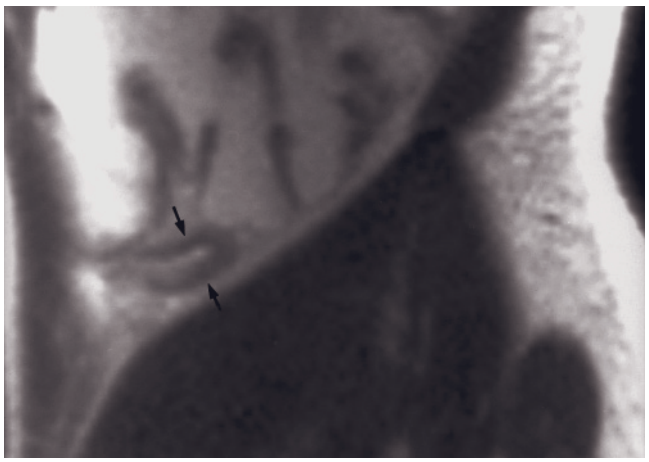

(*g*)

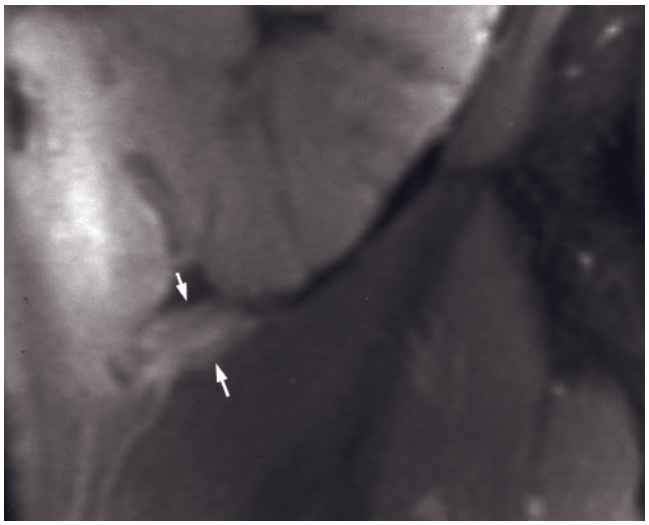

(*h*)

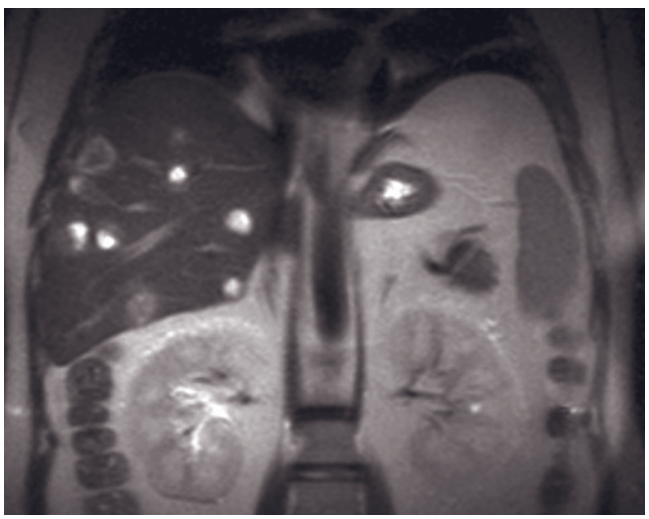

(*i*)

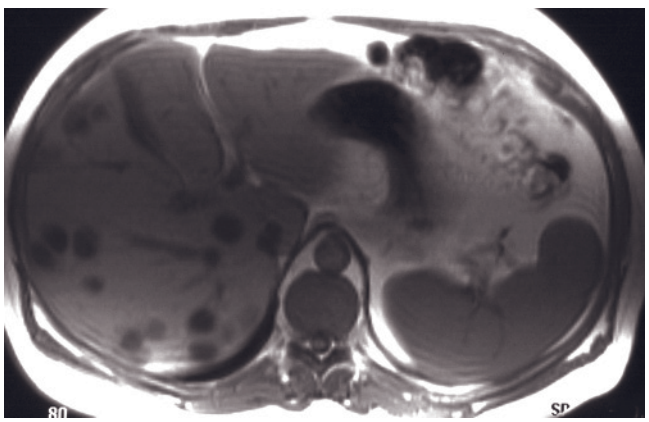

(*j*)

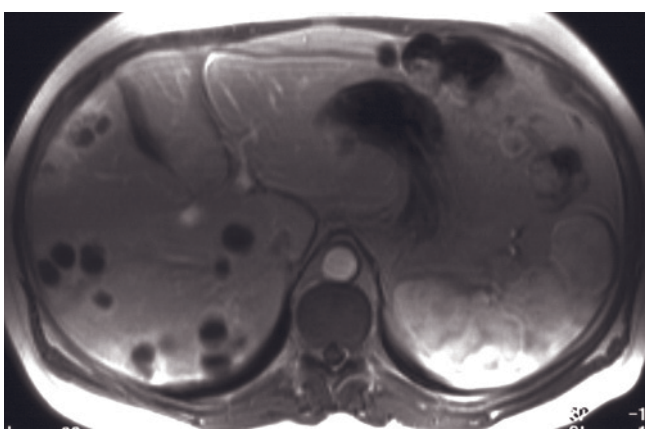

(*k*)

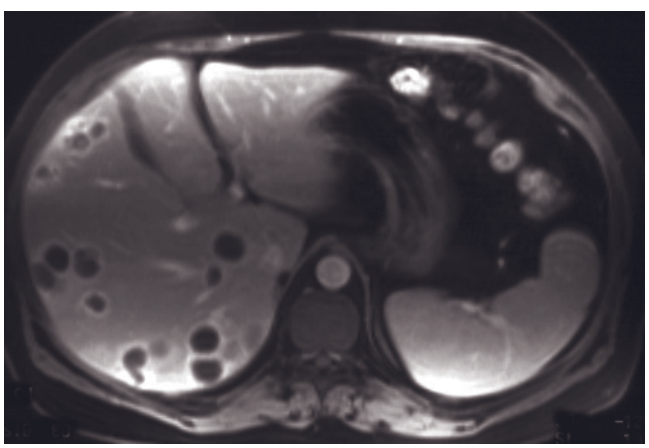

(*l*)

Fig. 2.267 (*Continued*) Coronal T2-weighted SS-ETSE (*i*), SGE (*j*), and immediate (*k*) and 90-s fat-suppressed (*l*) postgadolinium SGE images in a second patient, who has a history of Crohn disease. Multiple abscesses are seen in the right hepatic lobe and demonstrate high signal intensity on T2-weighted image (*i*), low signal intensity on T1-weighted image (*j*), and perilesional enhancement surrounding the whole lesion on early-phase image (*k*) with more intense abscess wall enhancement on late phase image (*l*).

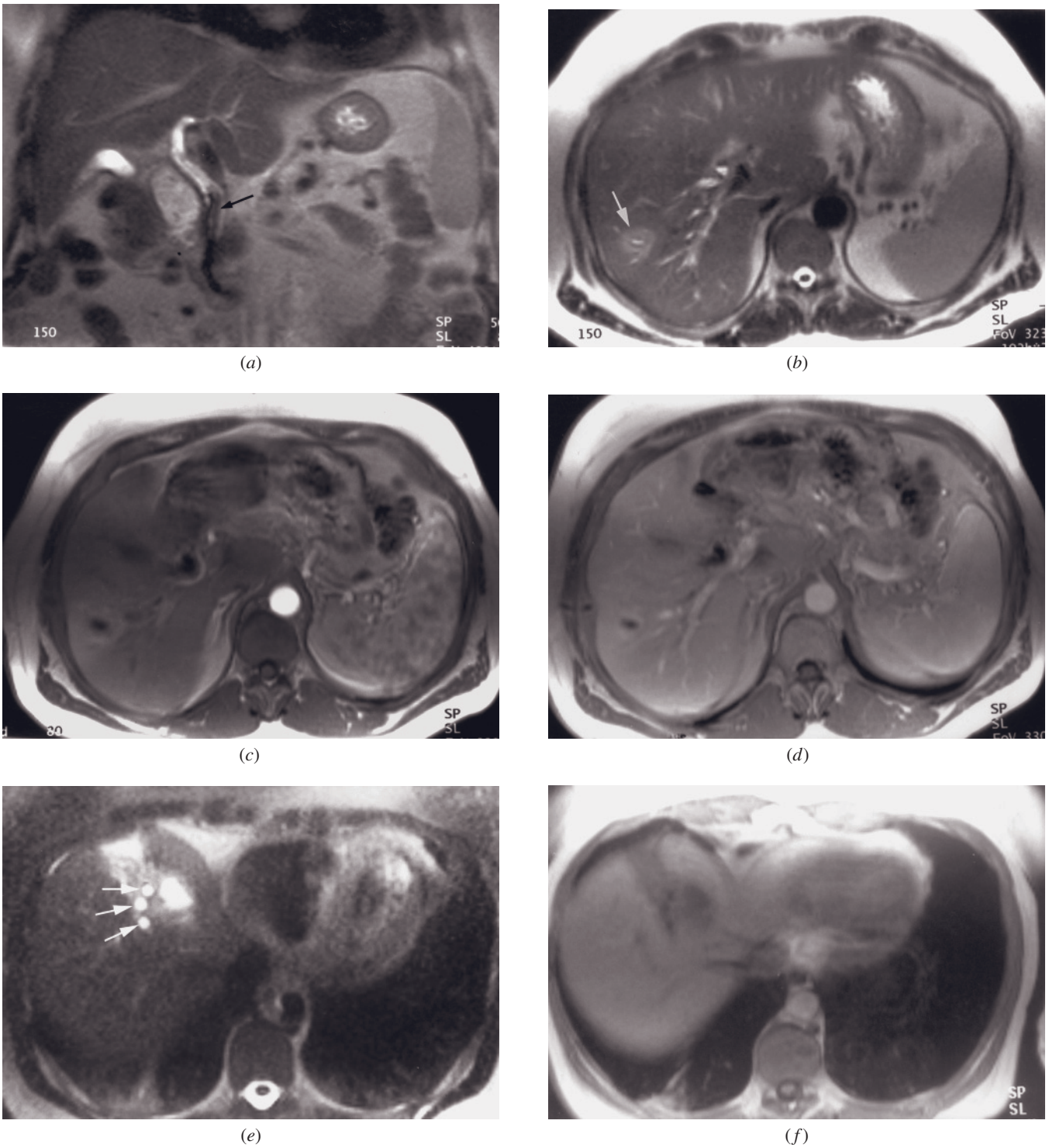

FIG. 2.268 Liver abscesses secondary to infective cholangitis. Coronal (*a*) and transverse (*b*) T2-weighted SS-ETSE and T1-weighted immediate (*c*) and 45-s (*d*) postgadolinium SGE images. There is a lesion in the right hepatic lobe (arrow, *b*) that demonstrates increased signal intensity on T2-weighted image (*b*) and decreased signal on T1-weighted image (not shown). After contrast, the lesion shows a circumferential ill-defined perilesional and capsular enhancement on immediate postgadolinium images (*c*), with fading of the perilesional enhancement but persistent capsular enhancement on 45-s image (*d*). There is no enhancement of internal stroma or fill-in of the lesion with time. Note the biliary stent (arrow, *a*) situated in the common bile duct (*a*).

T2-weighted SS-ETSE (*e*), SGE (*f*), immediate postgadolinium SGE (*g*), and 90-s postgadolinium fat-suppressed SGE (*h*) images in a second patient. There is an irregular region of increased signal on T2-weighted image (*e*) and decreased signal on T1-weighted

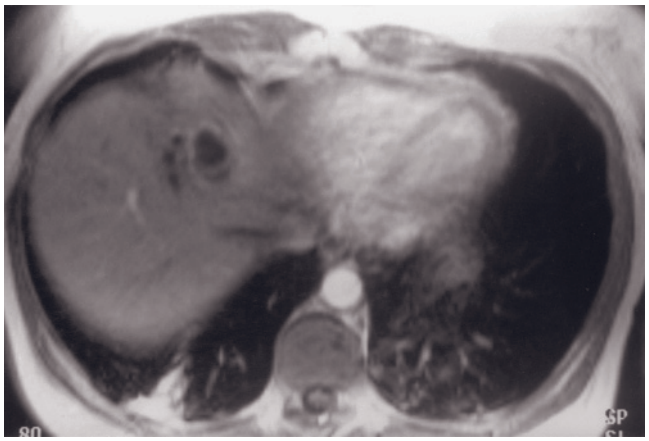

(*g*)

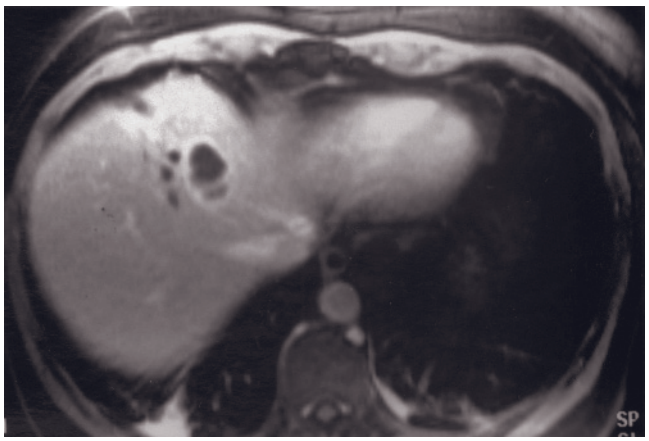

(*h*)

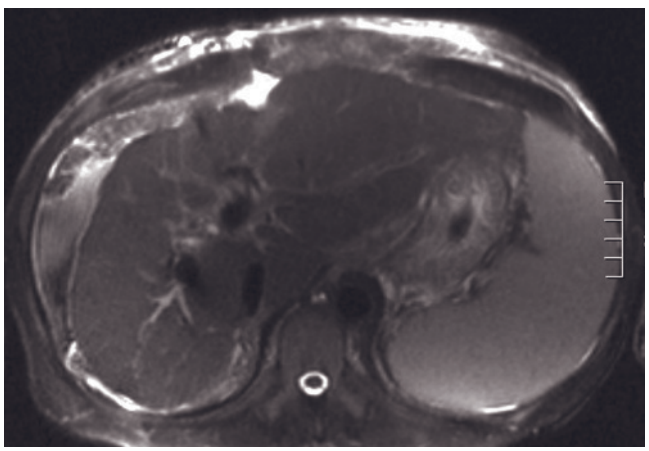

(*i*)

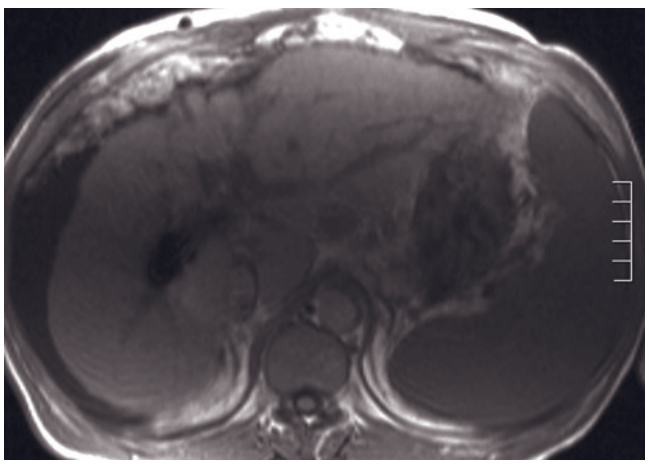

(*j*)

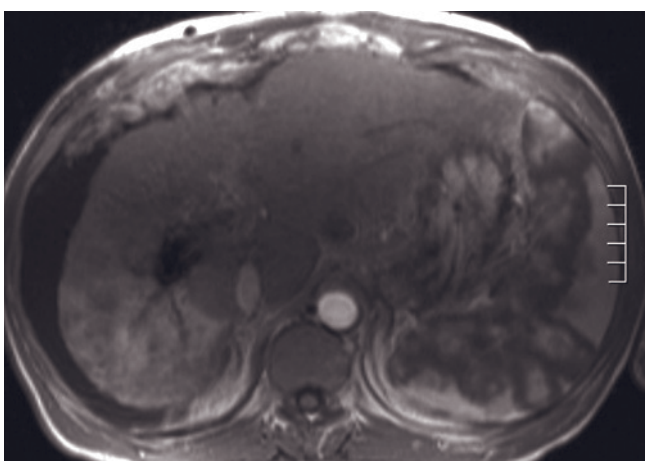

(*k*)

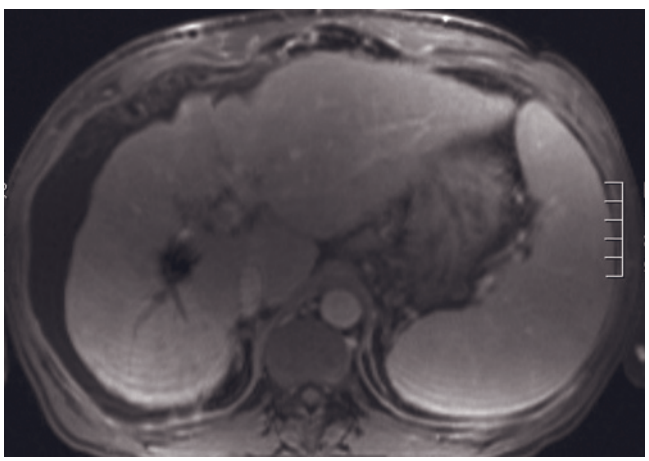

(*l*)

FIG. 2.268 (*Continued*) image (*f*) in the dome of the liver. Adjacent to this area, there are multiple rounded structures (arrows, *e*) that demonstrate increased signal on T2 (*e*) and decreased signal on T1 (*f*), which represent dilated ducts. After gadolinium administration (*g*, *h*), a cystic mass with a thickened, enhancing wall and internal septations is identified, consistent with an abscess secondary to segmental infective cholangitis.

Fat-suppressed T2-weighted SS-ETSE (*i*), SGE (*j*), and immediate (*k*) and 90-s fat-suppressed (*l*) postgadolinium SGE images in a third patient who has a previous history of cirrhosis and a current history of ascending cholangitis. The right hepatic liver enhances in a heterogeneous fashion on early-phase images (*k*) and becomes homogeneously enhanced on late-phase images (*l*).

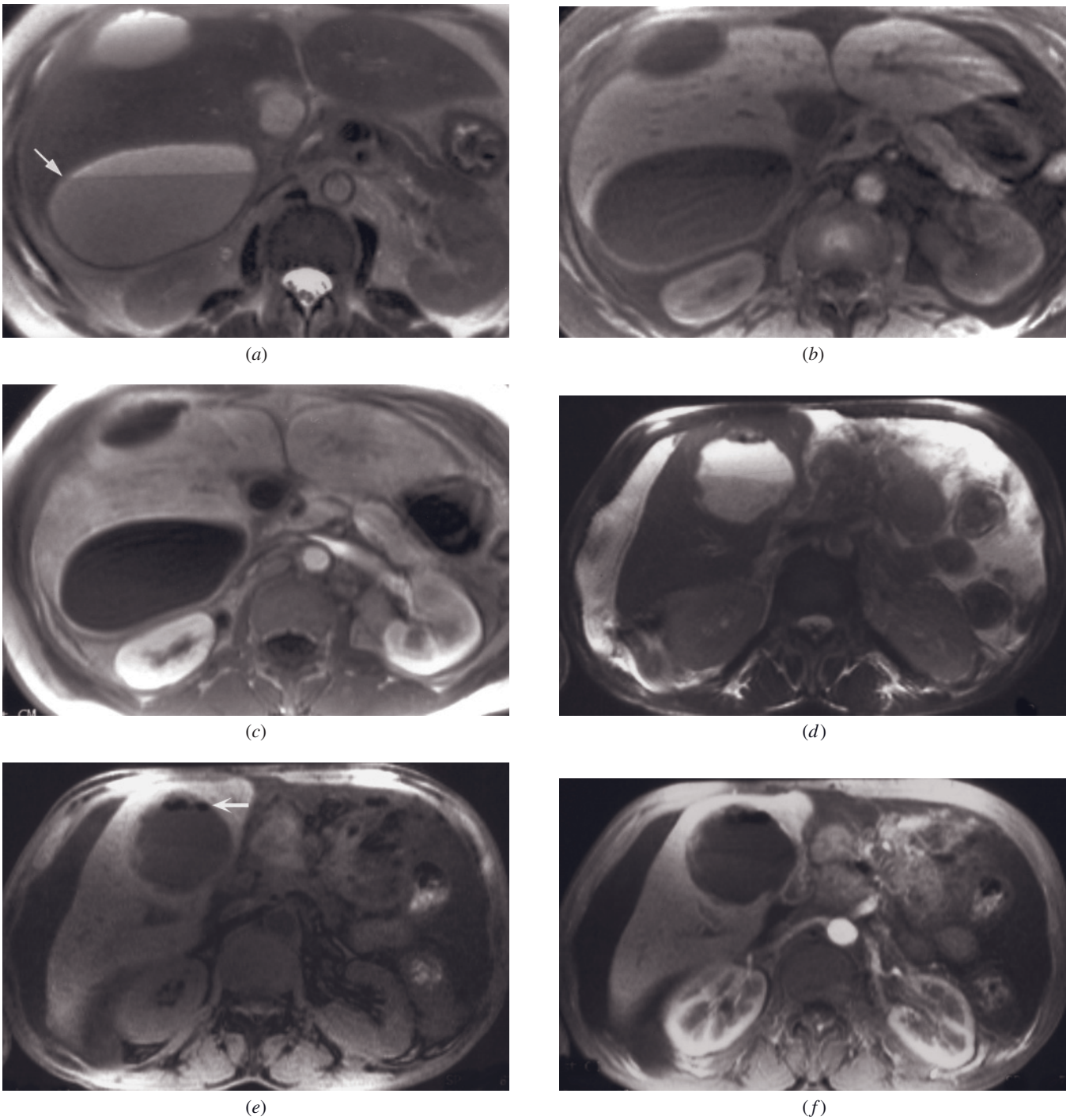

FIG. 2.269 Infected biloma. T2-weighted SS-ETSE (*a*), precontrast fat-suppressed SGE (*b*), and immediate postgadolinium SGE (*c*) images in a 79-year-old woman who has a history of trauma. Large subcapsular fluid collections are observed anterior and posterior to the right hepatic lobe. These collections demonstrate fluid-fluid levels (arrow, *a*) best shown on the breathing-independent single-shot T2-weighted image (*a*) and substantial wall enhancement (*c*) consistent with infection.

T2-weighted fat-suppressed SS-ETSE (*d*), T1-weighted fat-suppressed SGE (*e*), and immediate (*f*) and 90-s fat-suppressed (*g*) postgadolinium SGE images in a second patient, who has a history of trauma. Subcapsular infected biloma with fluid-fluid levels are present, one of which also contains air bubbles (arrow, *e*). Air bubbles appear as signal foci on all sequences.

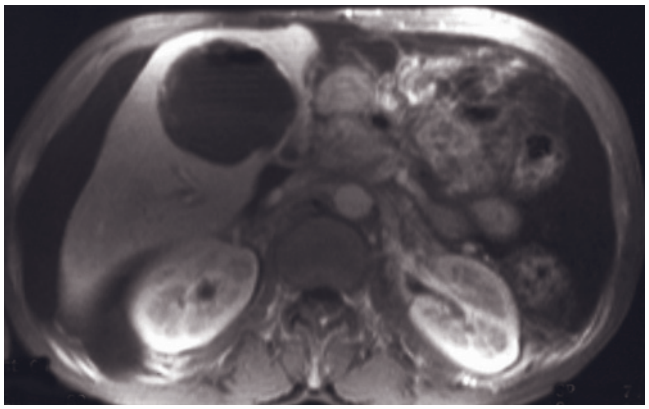

(*g*)

FIG. 2.269 (*Continued*)

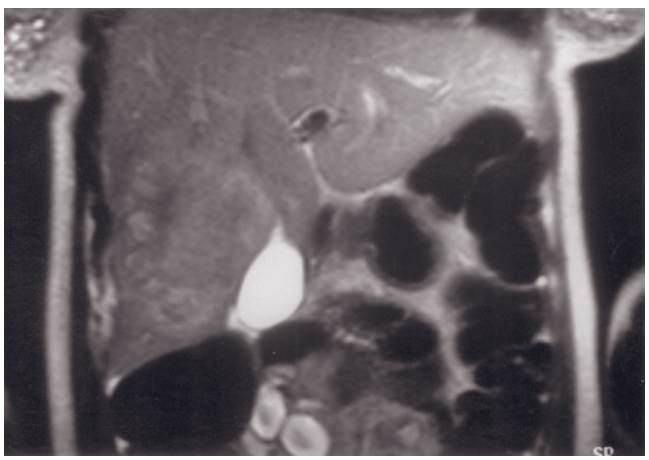

(*a*)

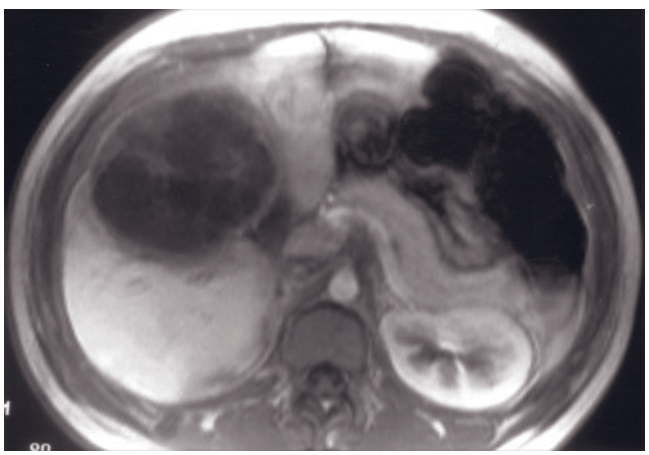

(*b*)

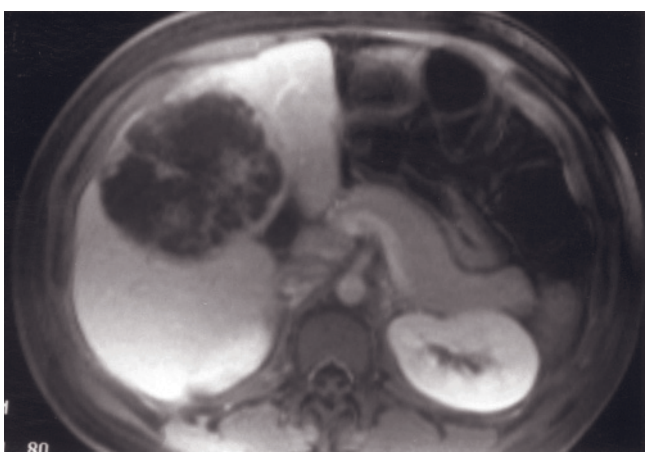

(*c*)

FIG. 2.270 Liver abscess—streptococcus. Coronal T2-weighted SS-ETSE (*a*) and immediate (*b*) and 90-s fat-suppressed (*c*) postgadolinium SGE images. A large mass is present in the right lobe of the liver, which is heterogeneous and mildly hyperintense on T2-weighted image (*a*). The mass contains multiple septations that exhibit minimal early enhancement (*b*), with increased intensity on the later image (*c*). No progressive lesion stromal enhancement is present.

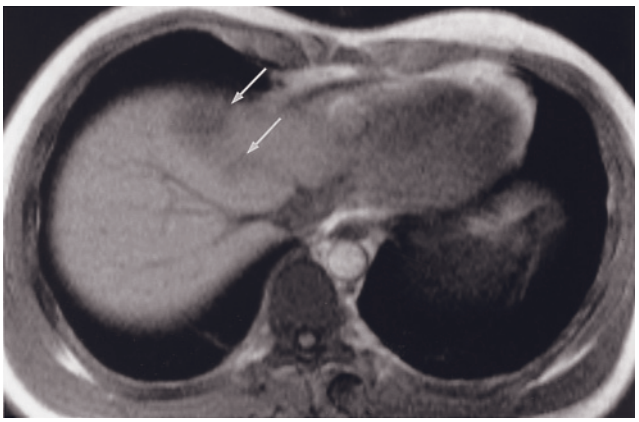

(*a*)

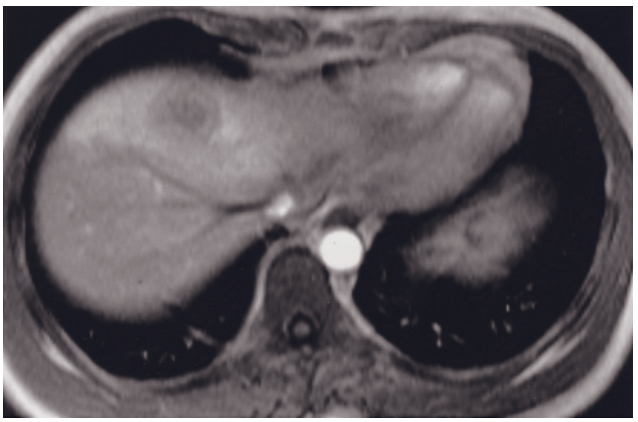

(*b*)

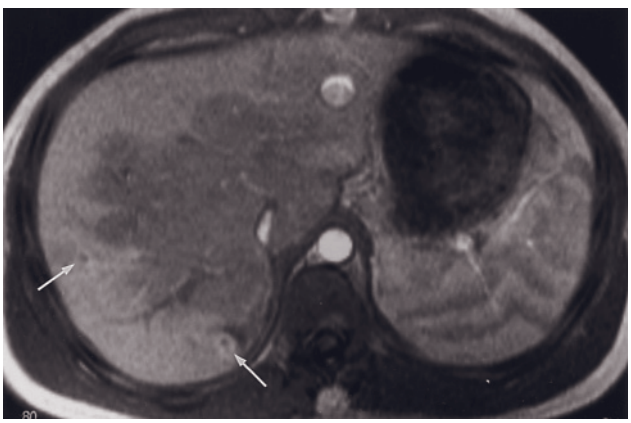

(*c*)

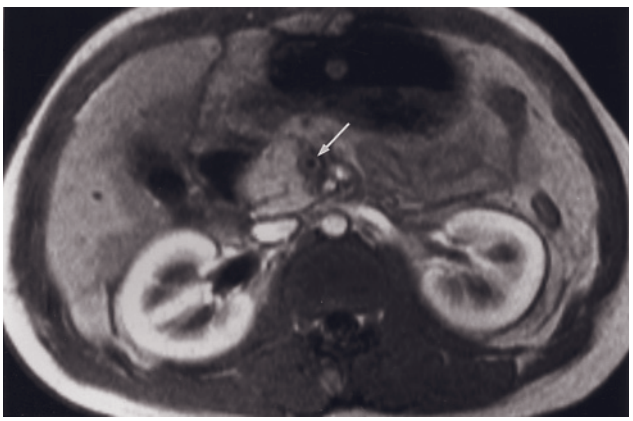

(*d*)

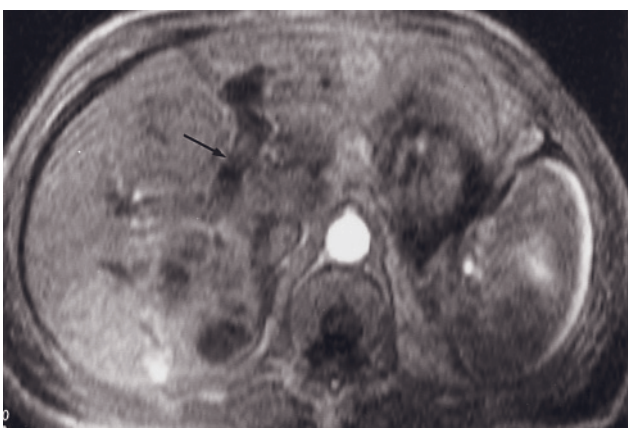

(*e*)

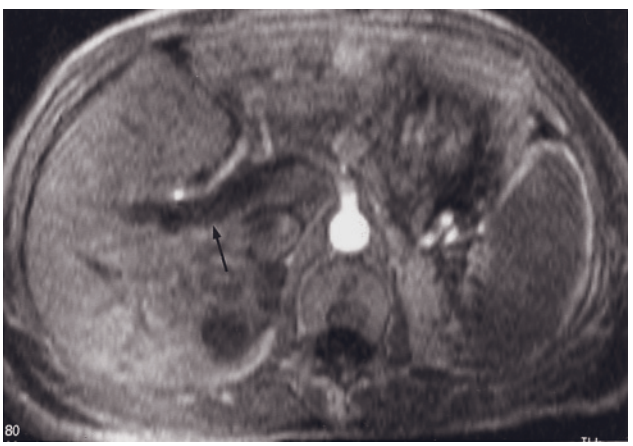

(*f*)

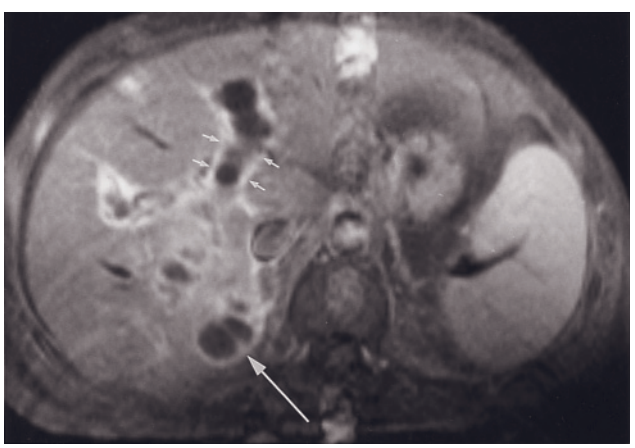

(*g*)

FIG. 2.271 Pyogenic abscesses. SGE (*a*) and immediate postgadolinium SGE (*b*) images in a patient with *Fusibacterium* liver abscesses. Two slightly ill-defined low-signal-intensity masses are present in the liver (arrows, *a*) on the precontrast T1-weighted image (*a*). Immediately after gadolinium administration (*b*), the lesions demonstrate substantial perilesional enhancement. The larger lesion demonstrates a thin outer low-signal rim surrounding an enhancing ring.

Immediate postgadolinium SGE images from cranial (*c*) and caudal (*d*) locations through the liver in a second patient. Abnormal diminished central enhancement is present in the liver (*c*) secondary to portal vein thrombosis. Small abscesses with enhancing rings (arrows, *c*) are shown in the right hepatic lobe. On the more inferior tomographic image (*d*), thrombus is identified in the SMV with enhancement of the vein wall (arrow, *d*), reflecting infection of the thrombus.

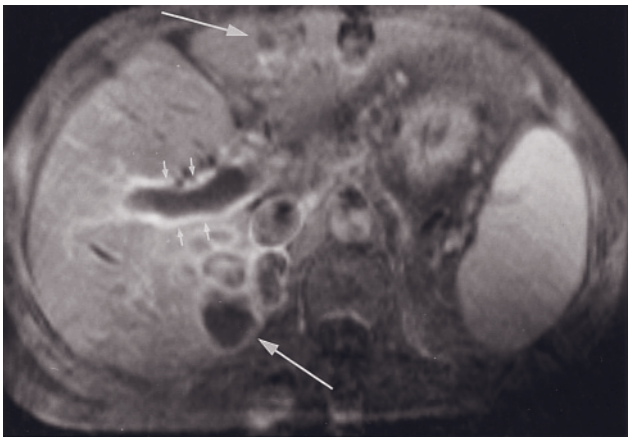

(*h*)

FIG. 2.271 (*Continued*) Immediate postgadolinium SGE images (*e*, *f*) and interstitial-phase gadolinium-enhanced T1-weighted fat-suppressed SE images (*g*, *h*) in a third patient obtained at the level of the left portal vein (*e*, *g*) and right portal vein (*f*, *h*). The left (arrow, *e*) and right (arrow, *f*) portal veins are expanded with low-signal thrombus on the immediate postgadolinium images. On the gadolinium-enhanced fat-suppressed images enhancement of the walls of the portal veins is present (small arrows, *g, h*), reflecting the infected nature of the thrombus. The abscesses in the right and left lobes of the liver are well seen on the interstitial-phase images as low-signal-intensity irregular-shaped cystic masses with enhancing rims (long arrows, *g, h*).

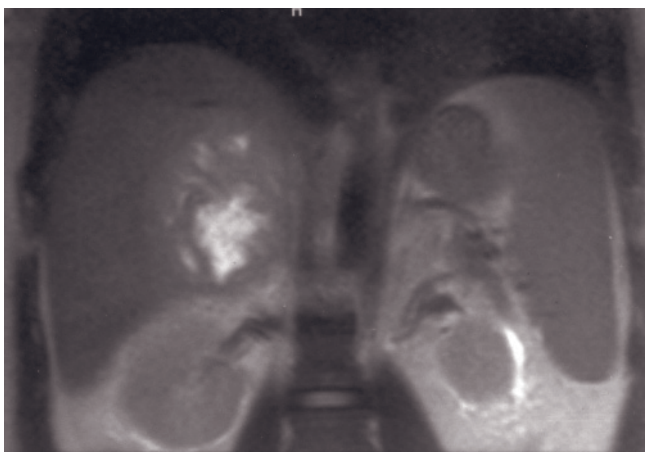

(*a*)

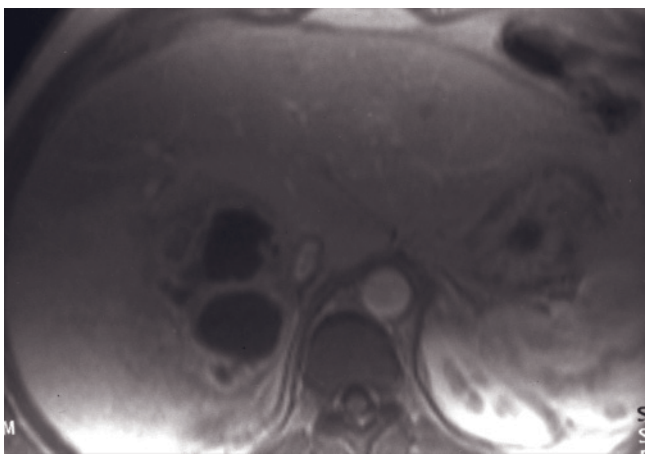

(*b*)

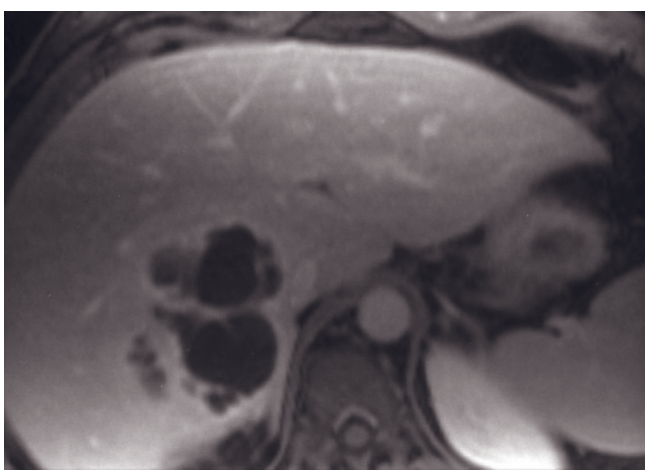

(*c*)

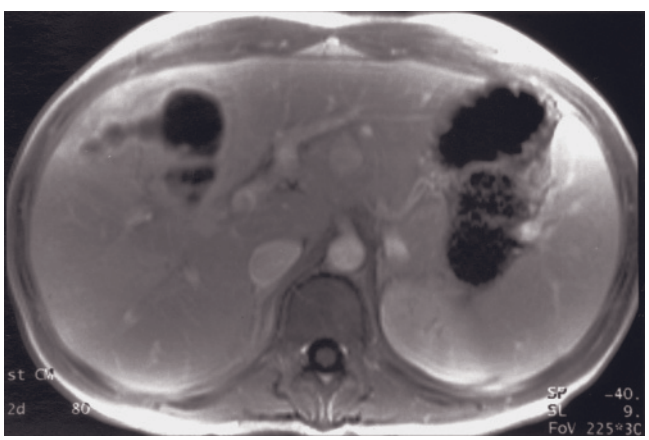

(*d*)

FIG. 2.272 Pyogenic liver abscesses. Coronal T2-weighted SS-ETSE (*a*) and immediate (*b*) and 90-s fat-suppressed (*c*) postgadolinium SGE images. A large septated lesion is present, which is heterogeneous and high signal intensity on T2-weighted image (*a*) and low signal intensity on T1-weighted images (*b*, *c*), with intense capsular and internal septa enhancement on early-phase image (*b*) that persists on the late image (*c*). A characteristic feature of abscesses is that the capsule and septa enhance on immediate postgadolinium images and persist in enhancement on 90-s image (*c*), with no progressive internal stromal enhancement. Enhancement of abscess walls frequently becomes more intense on later postcontrast images. Metastases, in distinction, tend to exhibit progressive stromal enhancement.

Transverse 45-s postgadolinium SGE (*d*) image in a second patient demonstrates a lesion with intense mural enhancement consistent with an abscess.

CT imaging. Metastases with large necrotic component may mimic the appearance of hepatic abscesses mainly because both may have prominent rim enhancement [426]. Abscesses exhibit moderately intense enhancement of stroma and internal septations on early-phase postgadolinium images, without progressive enhancement of stroma, whereas necrotic metastases generally show centripetal progression of stromal enhancement. Metastases may also mimic abscesses clinically if they become secondarily infected. The diagnosis of infected metastases should be considered when the lesion wall is thicker than 5 mm and has nodular irregular components and centripetal enhancement is evident.

Nonpyogenic Abscess: Amebic Abscess. Amebic liver abscesses are caused by a protozoan parasite, *Entamoeba histolytica*, and are not uncommon in developing tropical countries [424]. Amebic abscess may arise in patients who live in or have traveled to tropical climates. Amebic abscesses may develop secondary to small ischemic necrotic areas caused by obstruction of small venules by the trophosites and their by-products [424]. Presenting features include pain, fever, weight loss, nausea and vomiting, diarrhea, and anorexia [429]. Lesions are usually solitary, affect the right lobe more often than the left lobe [424, 428], and are prone to invade the diaphragm with development of pulmonary consolidation and empyema [430]. Lesions are encapsulated and thick walled (5–10 mm) and demonstrate substantial enhancement of the capsule on gadolinium-enhanced images, which permits differentiation from liver cysts (fig. 2.273).

Echinococcal Disease

Echinococcal disease is a worldwide zoonosis produced by two main types of larval forms of equinococcus tapeworms: *E. granulosus* and *E. alveolaris* [431]. *Echinococcus granulosus* is the causative organism for hydatid cysts and is the type of echinococcus indigenous in North America. Pathologically, the typical hydatid cyst is spherical with a fibrous rim. Surrounding liver reaction to the abscess is minimal, with small-volume granulation tissue. The typical imaging feature is in an intrahepatic encapsulated multicystic lesion with daughter cysts arranged peripherally within the larger

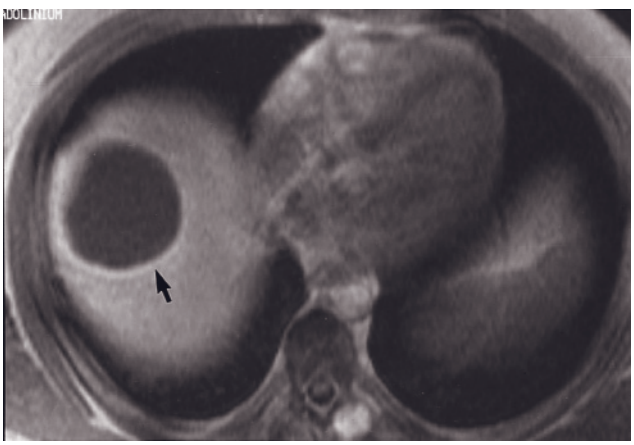

(*a*)

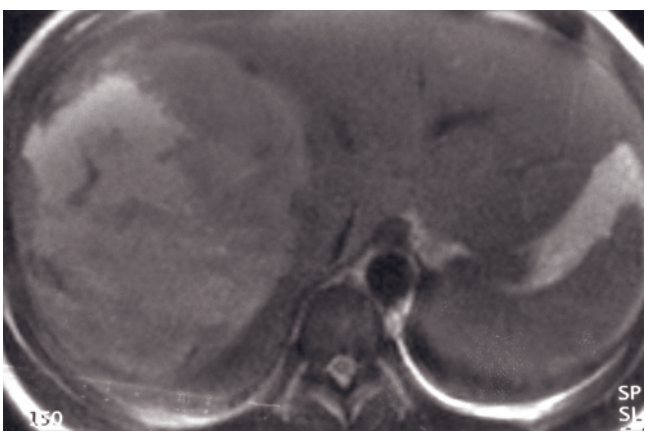

(*b*)

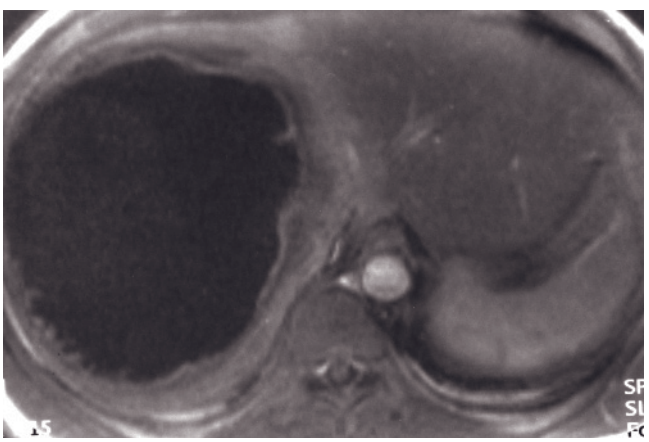

(*c*)

FIG. 2.273 Amebic abscess. Immediate postgadolinium SGE (*a*) image demonstrates a 7-cm cystic lesion located superiorly in the right lobe of the liver. The amebic abscess has a prominent enhancing wall (arrow, *a*) distinguishing it from a simple cyst.

T2-weighted SS-ETSE (*b*) and immediate postgadolinium magnetization-prepared gradient echo (*c*) images in a second patient. A large cystic lesion is seen in the right hepatic lobe, near the dome of the diaphragm, with a thick irregular wall and perilesional and capsular enhancement after gadolinium administration, consistent with abscess.

cyst. Satellite cysts located exterior to the fibrinous membrane of the main hepatic cyst are not uncommon and have been reported in 16% of hydatid cysts in a series of 185 patients [431]. Lesions are frequently complex, with mixed high signal intensity on T2-weighted images and mixed low signal intensity on T1-weighted images due to the presence of proteinaceous and cellular debris (fig. 2.274).The fibrous capsule and internal septations are well shown on T2-weighted images and gadolinium-enhanced T1-weighted images. SS-ETSE sequence is particularly effective at showing the architectural detail of cystic lesions. Calcification of the cyst wall and internal calcifications are frequently identified on CT images but may not be distinguishable from the fibrous tissue of the capsule on MR images. Superinfection and cyst rupture, after trauma or spontaneously, are the most frequent complications reported with hydatid cysts [428]. The rupture

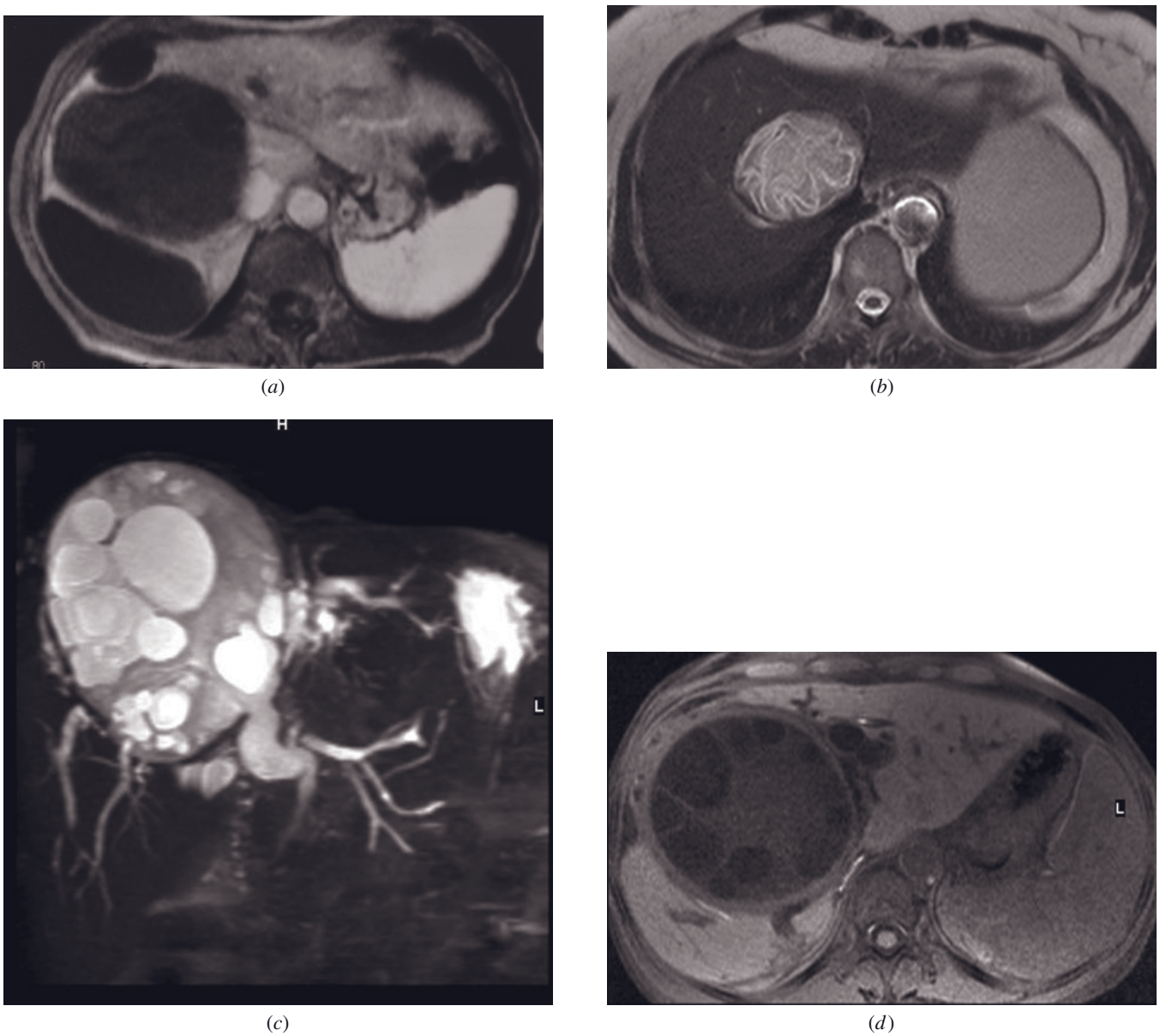

Fig. 2.274 Hydatid cyst. Immediate postgadolinium SGE image (*a*) exhibits a multicystic lesion in the right hepatic lobe with a dominant cyst centrally and daughter cysts peripherally. There is mild mural enhancement of the hydatid cyst wall.

T2-weighted SS-ETSE image (*b*) in a second patient infected by *E. granulosus*. Note the presence of a cystic lesion with additional small internal cystic lesions (courtesy of N. Cem Balci, M.D.).

Coronal T2-weighted SS-ETSE (*c*) and transverse SGE (*d*) in a third patient show multiple daughter cysts lining the wall of the dominant cystic lesion (courtesy of Bharat Aggarwal, M.D., Diwan Chand Satya Pal Aggarwal Imaging Research Center, New Delhi, India).

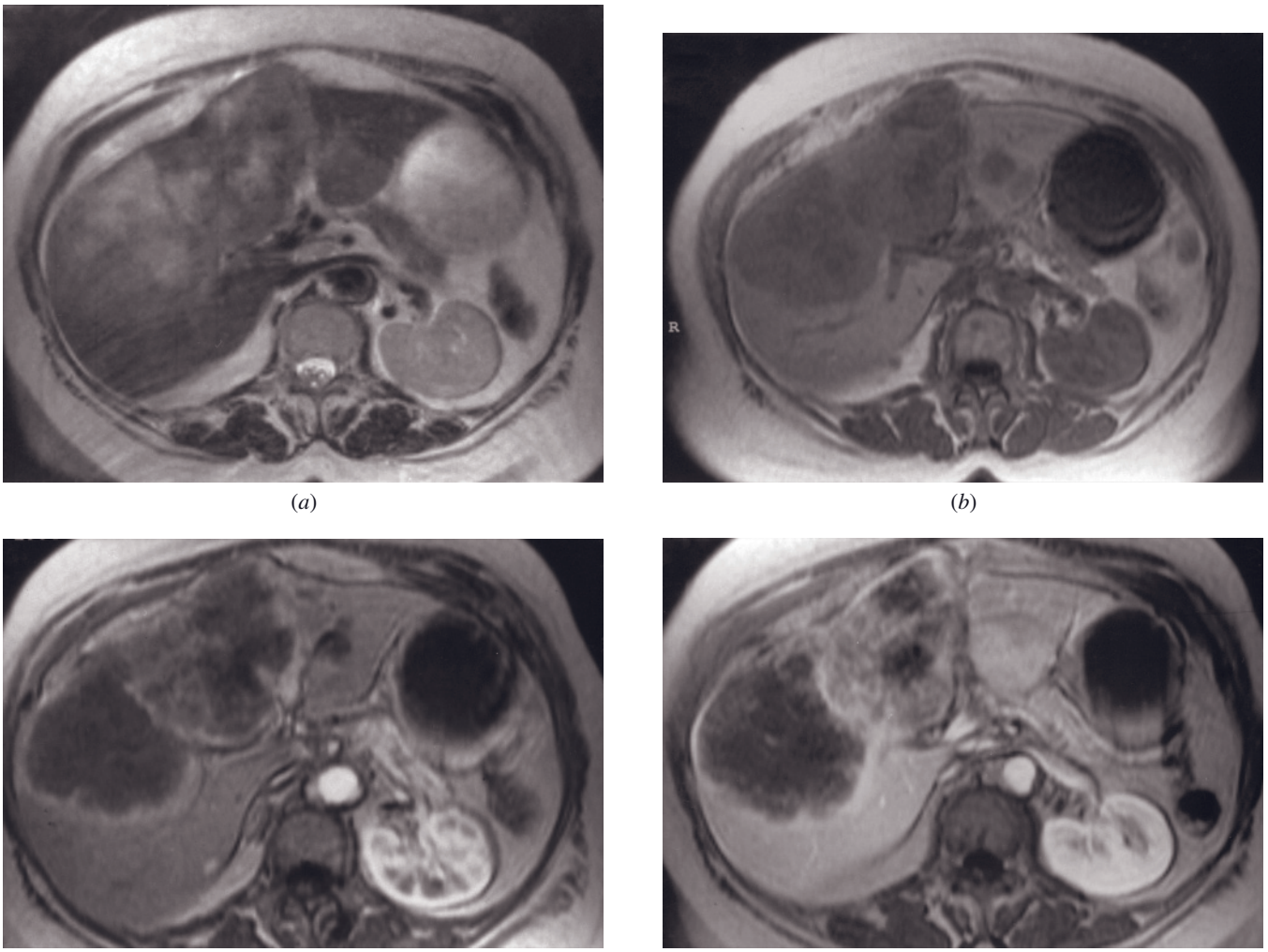

FIG. 2.275 Hepatic alveolar echinococcosis. T2-weighted ETSE (*a*), SGE (*b*), and immediate (*c*) and 90-s (*d*) postgadolinium SGE images. A large lesion with irregular margins is present in the liver that demonstrates mildly high signal on T2-weighted image (*a*) and low signal on T1-weighted image (*b*), and a peripheral rim of enhancement on early-phase image (*c*) that persists on late images (*d*). There is a substantial solid component within the large infective lesion. The lesions exhibits ill-defined margins. (Courtesy of N. Cem Balci, M.D.)

of a cyst may provoke an intense inflammatory and granulomatous reaction in surrounding tissue.

Echinococcus alveolaris is the causative organism for hepatic alveolar echinococcosis (HAE), a rare parasitic disease in which the fox is the main host of the adult parasite, with dogs and cats being less frequently cited hosts. Pathologically, HAE is characterized grossly by multilocular or confluent cystic, necrotic cavities. A fibrous rim is not present. Balci et al. [431] described the MR appearance of HAE in 13 patients. All lesions were large (mean 9.7 cm), solitary, with mixed cystic/solid components and irregular margins. By MRI, HAE demonstrated heterogeneous signal intensity on T2- and T1-weighted images and negligible lesional enhancement after contrast. A perilesional enhancement was reported in 5 cases (38%) (fig. 2.275).

Calcification is common in HAE and appears as clusters of microcalcifications or large calcified foci. HAE tends to involve extensive regions in the liver in an infiltrative pattern because it does not form membranes or capsules. HAE is more likely to involve the porta hepatitis, causing stenoses of portal veins, intrahepatic bile ducts, and hepatic veins, which commonly result in portal hypertension. The differential diagnosis of HAE includes various infiltrative lesions of the liver, such as HCCs and metastases. The typical pattern of enhancement of HCC and liver metastases, systemic features of infection, and geographic occurrence of the

disease may help in the differentiation. HAE can be differentiated from hydatid disease, because the latter process shows well-defined cyst walls and regular contours.

Mycobacterial Infection

Mycobacterium tuberculosis. Hepatic tuberculosis is the most frequent form of infectious hepatic granulomas [428]. The most common pathway for *Mycobacterium tuberculosis* bacilli to reach the liver is through the bloodstream [424]. Although abdominal tuberculosis preferentially affects lymph nodes and the ileocecal junction [424], the liver is also commonly involved. The incidence of hepatic tuberculosis is increasing, reflecting, in part, an increase in numbers of patients who are immunocompromised, such as patients with HIV infection.

Focal hepatic lesions are typically small and multiple with an appearance similar to that of fungal lesions (see next section). Infection has a propensity to involve the portal triads and spread in a superficial infiltrating fashion. This can be visualized as periportal high signal intensity on T2-weighted fat-suppressed images and moderate/intense enhancement on late-phase fat-suppressed postgadolinium images. Associated porta hepatis nodes are common.

Mycobacterium avium intracellulare (MAI). Nontuberculous mycobacterial hepatic infection is common and represents the most frequent hepatic infection in AIDS [432]. MAI infection is found in 50% of livers of patients dying with AIDS [433]. Microscopically, hepatic MAI lesions may show a spectrum of appearances ranging from loose aggregates of histiocytes to tight, well-formed granulomas. CT findings reported to be suggestive of disseminated MAI infection include enlarged mesenteric and/or retroperitoneal lymph nodes, hepatosplenomegaly, and diffuse jejunal wall thickening (fig. 2.276) [434]. Low-density centers of involved lymph nodes are considered a characteristic feature on CT images. Similar findings may be appreciated on MR images.

Fungal Infection

Hepatosplenic or visceral candidiasis is a form of invasive fungal infection that has emerged as a serious complication of the immunocompromised state, especially in AIDS patients, patients on medical therapy for acute myelogeneous leukemia (AML), and patients with bone marrow transplantation [435–437]. Prolonged duration of neutropenia is thought to be the most important risk factor for hepatosplenic candidiasis [437]. The most common infecting organism is *Candida albicans*, but other fungi may be found. Acute hepatosplenic candidiasis involves the liver and spleen, with renal involvement occurring in less than 50% of patients. Disseminated *C. albicans* infects the liver in a high proportion of cases, leading to development of multifocal microabscesses or granulomas. Although definitive diagnosis requires microbiologic or histologic evidence of infection, the absence of organisms on liver biopsy tissue or negative culture findings in the presence of clinical suspicion does not rule out the diagnosis. Moreover, patient survival depends on early diagnosis. Therefore, cross-sectional imaging is necessary for diagnosis [438]. Liver lesions are frequently smaller than 1 cm and subcapsular in location. The small size and peripheral nature of these lesions make them difficult to detect with CT imaging or standard spin-echo MR sequences. MRI employing T2-weighted fat suppression and dynamic gadolinium-enhanced gradient-echo images have been shown to be more sensitive for the detection of hepatosplenic candidiasis than contrast-enhanced CT imaging [438, 439].

T2-weighted fat-suppressed spin-echo sequences are effective at demonstrating these lesions, because of the high conspicuity of this sequence for small lesions and the absence of chemical shift artifact that may mask small peripheral lesions. STIR images also show these lesions well because of the fat-nulling effect of this sequence [440]. Patients with AML undergo multiple blood transfusions, so the liver and spleen are low in signal intensity on T2-weighted and T1-weighted images [440, 441].

Because acute lesions of fungal disease are abscesses, they are high in signal intensity on T2-weighted images. They also may be seen on gadolinium-enhanced T1-weighted images as signal-void foci with no appreciable abscess wall enhancement (figs. 2.277 and 2.278). It has been observed that patients with hepatosplenic candidiasis who are immunocompetent possess abscesses that demonstrate mural enhancement. The absence of abscess wall enhancement may reflect the patient's neutropenic state. Overall sensitivity of MRI is 100%, and specificity is 96% [438].

After institution of antifungal antibiotics, successful response may be demonstrated. Central high signal develops within lesions on T2-weighted and T1-weighted images that enhances with gadolinium, representing granuloma formation. In addition, a distinctive dark perilesional ring is observed on all sequences, representing collections of iron-laden macrophages throughout granulation tissue at the periphery of lesions (fig. 2.279) [442]. This represents the subacute treated phase, which may be consistent with a good prognostic finding, reflecting the patient's ability to mount an immune response.

MRI also demonstrates chronic healed lesions that have responded to antifungal therapy [439]. Chronic healed lesions are irregularly shaped, isointense and

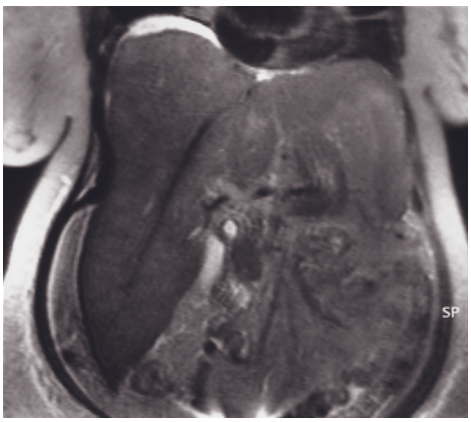

(*a*)

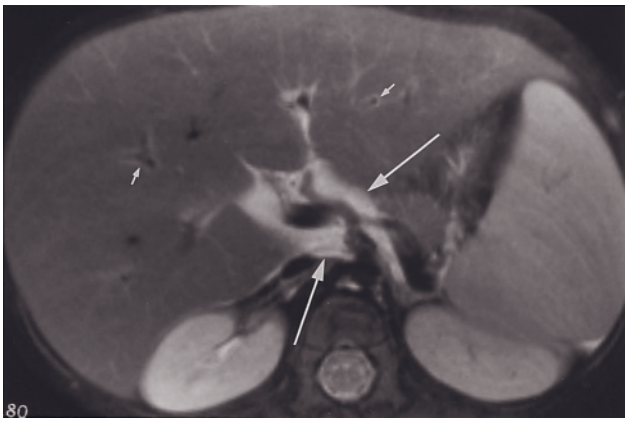

(*b*)

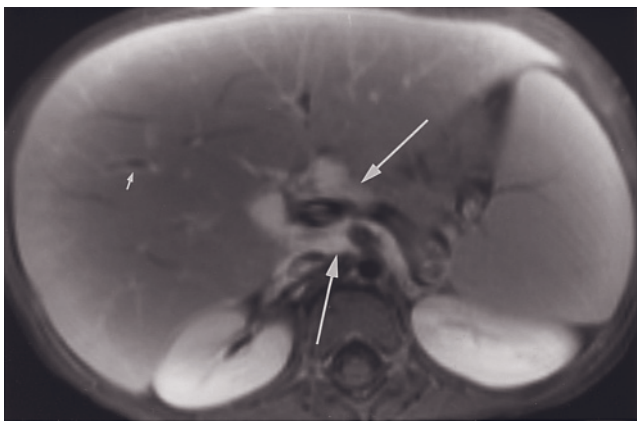

(*c*)

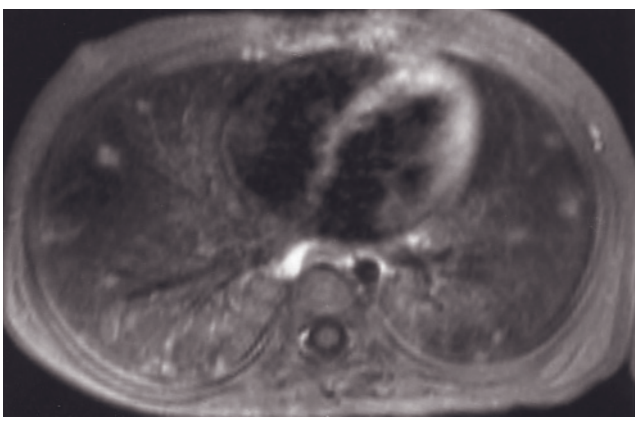

(*d*)

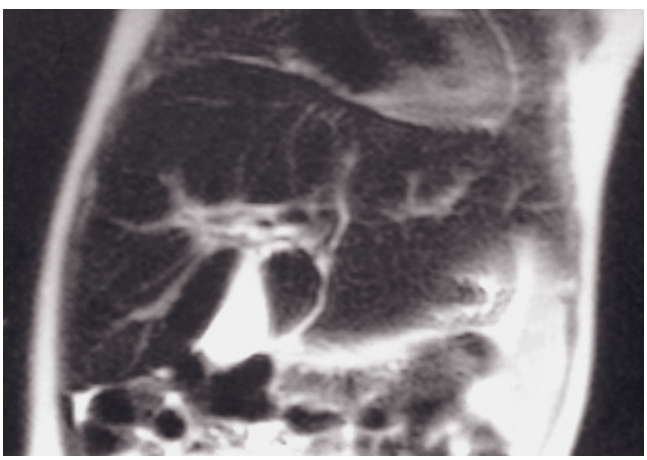

(*e*)

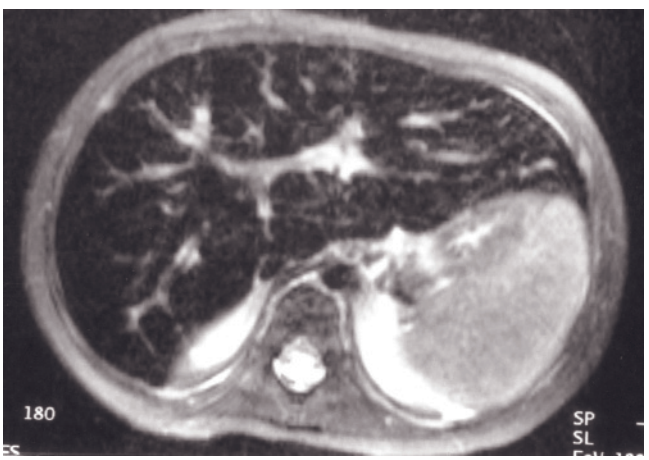

(*f*)

FIG. 2.276 ***Mycobacterium avium intracellulare*** **(MAI) hepatic infection.** Coronal T2-weighted SS-ETSE (*a*), transverse T2-weighted fat-suppressed ETSE (*b*), and interstitial-phase gadolinium-enhanced T1-weighted fat-suppressed SE (*c*) images. The coronal image (*a*) demonstrates hepatomegaly. On the fat-suppressed T2-weighted image (*b*), high-signal-intensity soft tissue is present in the porta hepatis (long arrows, *b*) that extends along periportal tracks (short arrows, *b*). After gadolinium administration (*c*), enhancing porta hepatis tissue is clearly shown on the fat-suppressed image (long arrows, *c*), and enhancement is also noted of the periportal tissue (short arrow, *c*). Periportal distribution is a common pattern of involvement with MAI. Gadolinium-enhanced, gated T2-weighted fat-suppressed SE image (*d*) of the lungs demonstrates a ground glass appearance with irregularly marginated 1-cm enhancing nodules consistent with MAI lung infection.

Coronal T2-weighted SS-ETSE (*e*), T2-weighted fat-suppressed SS-ETSE (*f*), immediate postgadolinium SGE (*g*), and 90-s post-gadolinium fat-suppressed SGE (*h*) images in a second patient, who has a history of hereditary blood dyscrasia and currently has MAI infection, demonstrate tissue in the porta hepatis and periportal tracks that is high signal on T2 (*e*, *f*) and enhances on late gadolinium-enhanced fat-suppressed T1-weighted images (arrows, *h*). Note also the iron deposition in the liver from transfusional siderosis.

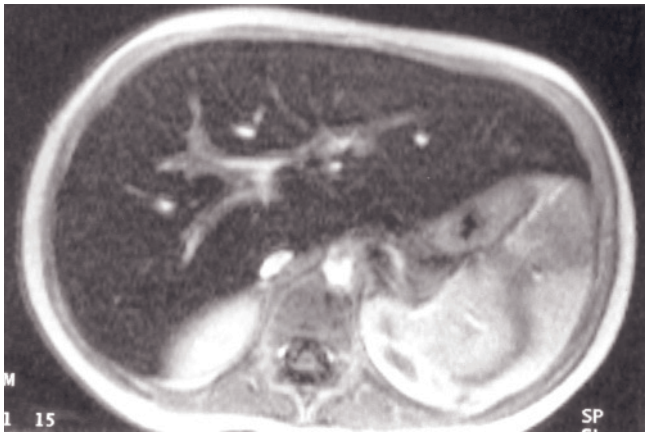

(*g*)

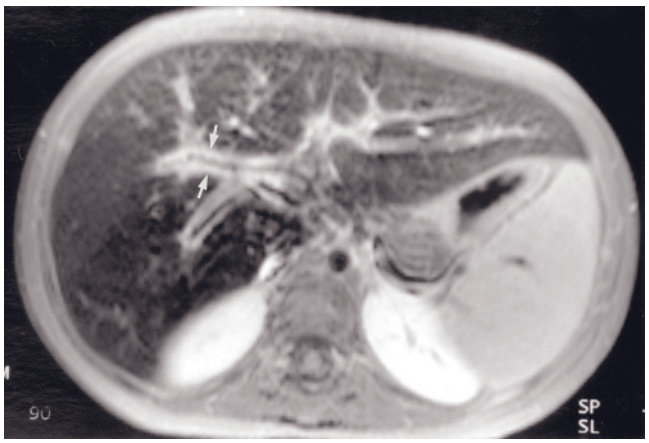

(*h*)

FIG. 2.276 (*Continued*)

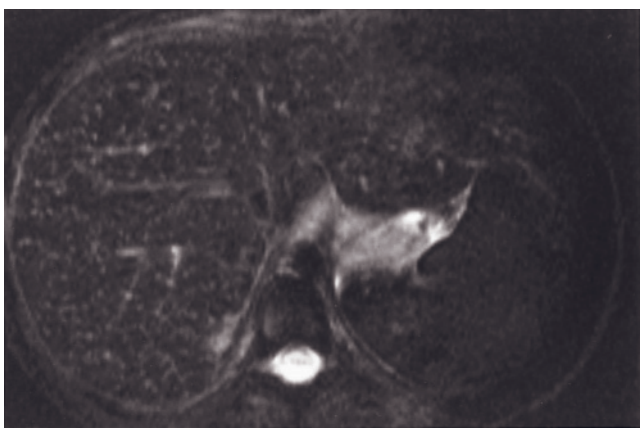

(*a*)

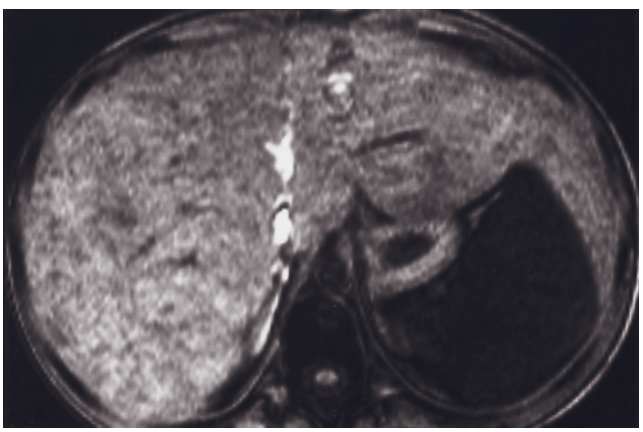

(*b*)

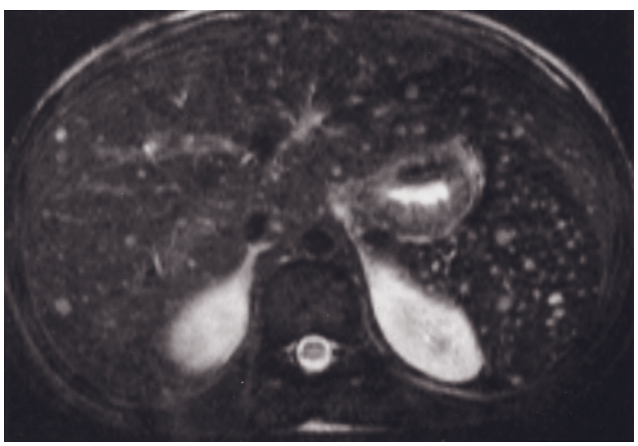

(*c*)

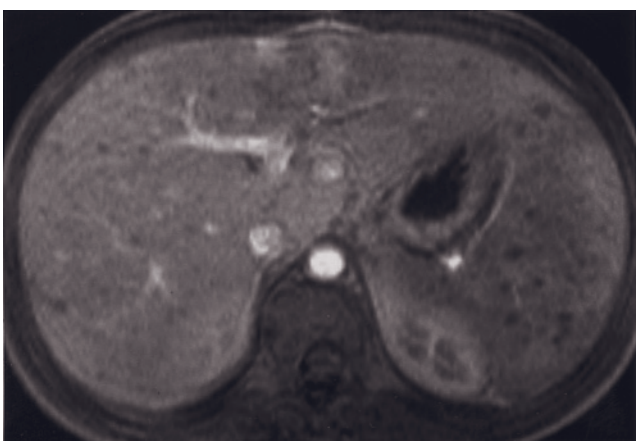

(*d*)

FIG. 2.277 Acute hepatosplenic candidiasis. T2-weighted fat-suppressed ETSE (*a*, *c*) and immediate postgadolinium SGE (*b*, *d*) images in two patients. On the T2-weighted images (*a*, *c*), multiple well-defined <1-cm high-signal-intensity foci are scattered throughout the hepatic parenchyma, with a smaller number of similar lesions apparent in the spleen. On the immediate postgadolinium image (*b*, *d*), the liver lesions are near signal void and do not show ring or perilesional enhancement.

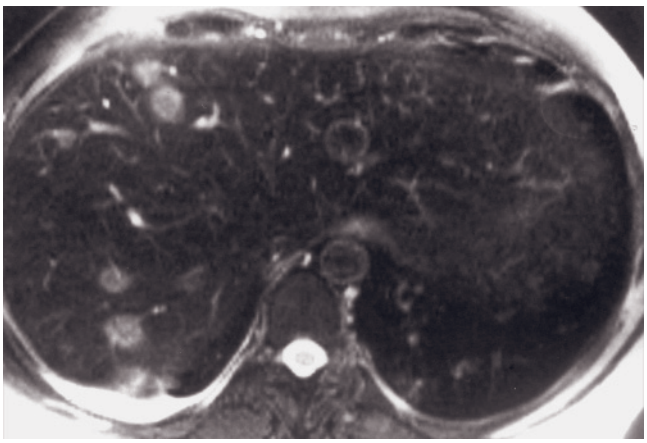

(*a*)

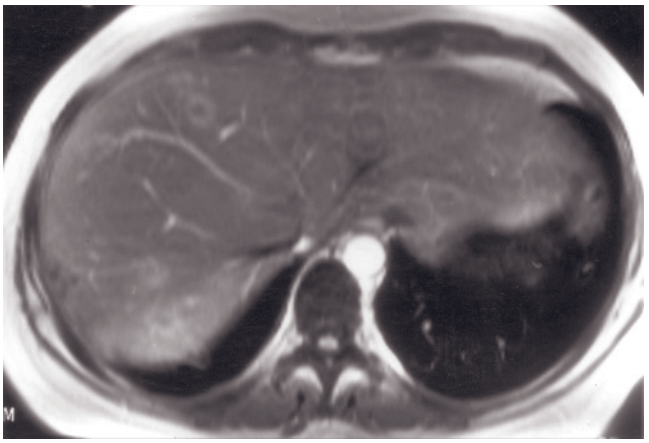

(*b*)

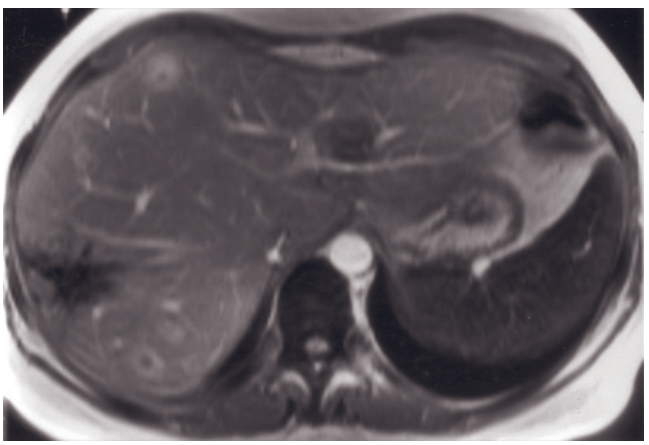

(*c*)

FIG. 2.278 Acute hepatosplenic candidiasis with ring enhancement. T2-weighted fat-suppressed SS-ETSE (*a*) and 45-s postgadolinium SGE (*b*, *c*) images. There are multiple small, rounded lesions scattered throughout the liver that show high signal intensity on T2 (*a*) and decreased signal intensity on T1-weighted images (not shown), with postgadolinium ring enhancement (*b*, *c*). Acute candidiasis was present at histopathology and microbiology. The presence of ring enhancement reflects that the patient is able to mount an immune response and therefore is not severely immunocompromised.

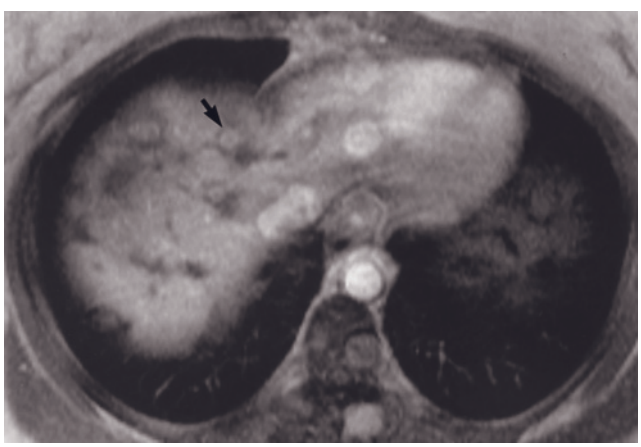

(*a*)

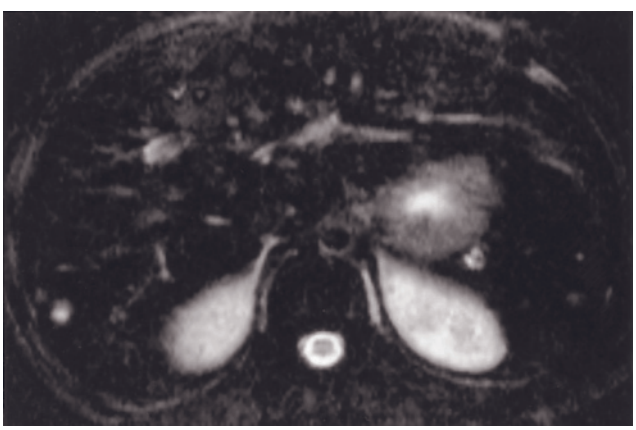

(*b*)

FIG. 2.279 Subacute hepatosplenic candidiasis. Immediate postgadolinium SGE image (*a*) demonstrates multiple lesions with a concentric ring pattern with an outer irregular signal-void rim, inner high-signal ring, and central low-signal dot (arrow, *a*).

T2-weighted fat-suppressed SE (*b*), SGE (*c*), and immediate postgadolinium SGE (*d*) images in a second patient. Multiple concentric ring lesions are evident that are best shown on precontrast and immediate postgadolinium SGE images (*c*, *d*). The outer

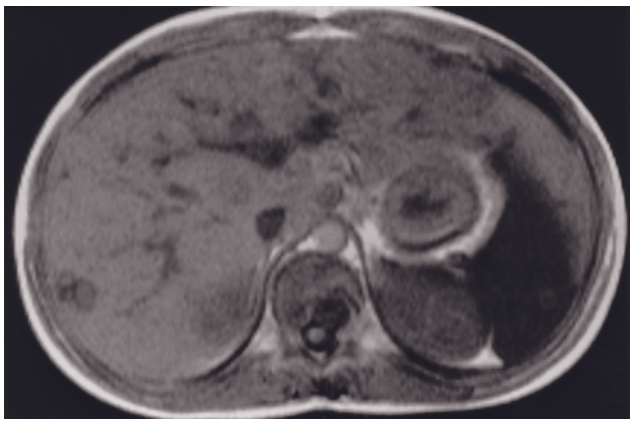

(*c*)

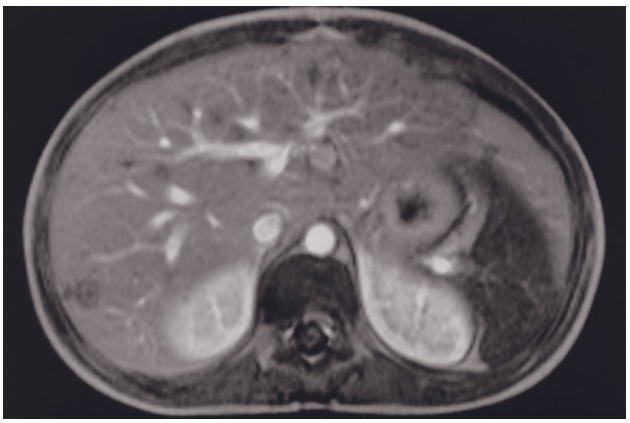

(*d*)

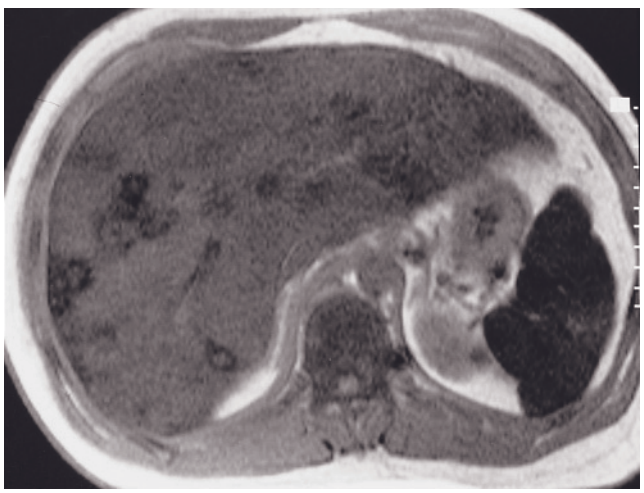

(*e*)

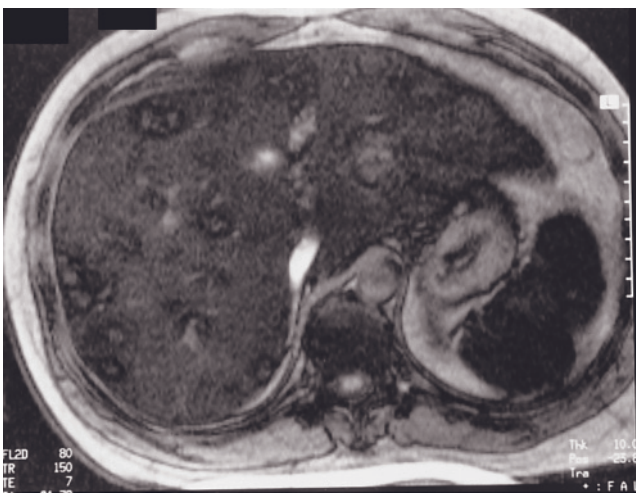

(*f*)

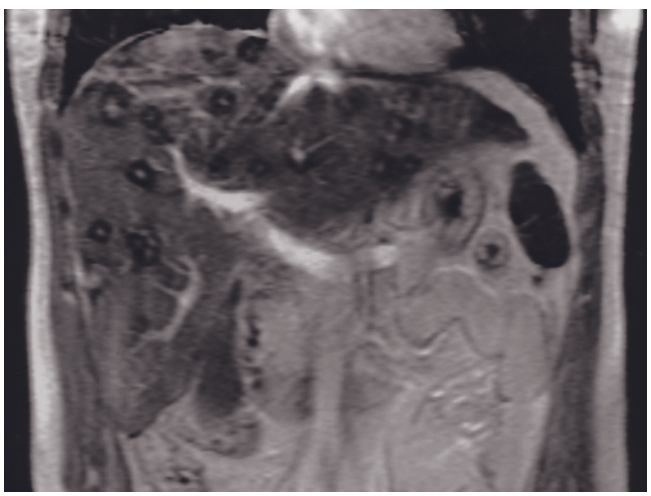

(*g*)

Fig. 2.279 (*Continued*) low-signal intensity ring is not appreciated on T2-weighted images (*b*) because the perilesional iron deposition blends in with the background RES iron deposition.

SGE (*e*), out-of-phase SGE (*f*), and coronal 45-s postgadolinium SGE (*g*) images in a third patient. Multiple concentric ring lesions are scattered throughout the liver on the SGE image (*e*). The outer signal-void ring becomes more prominent on the longer-TE out-of-phase image (*f*), because of a magnetic susceptibility artifact from iron. Lesion appearance is largely unchanged on the postgadolinium image (*g*).

poorly shown on T2-weighted images, and hypointense on T1-weighted images and demonstrate negligible enhancement after contrast (fig. 2.280). The lesions are most conspicuous as low-signal intensity defects with angular margins on immediate postgadolinium SGE images. Capsular retraction may also be observed adjacent to the lesions. This constellation of imaging features is consistent with chronic scar formation.

TRAUMA

Liver hematoma, liver laceration, perihepatic hematoma, and hemoperitoneum may be consequences of abdominal trauma and are all well demonstrated on MR images. Liver hematoma can exhibit any morphology; liver laceration is identified as a linear, intraparenchymal defect (figs. 2.281–2.283); perihepatic hematoma is characterized by a fluid collection between parenchyma and capsule (subcapsular); and hemoperitoneum is seen as free peritoneal fluid. MR features of these entities vary according to the paramagnetic effects of various products of hemoglobin such as oxygen saturation, iron, and protein content [443–448]. The sequence used and the magnetic field strength also play a role in MR findings [447, 449]. Five stages that reflect the age of hemorrhage are described, based on the breakdown products of hemoglobin and the resulting signal

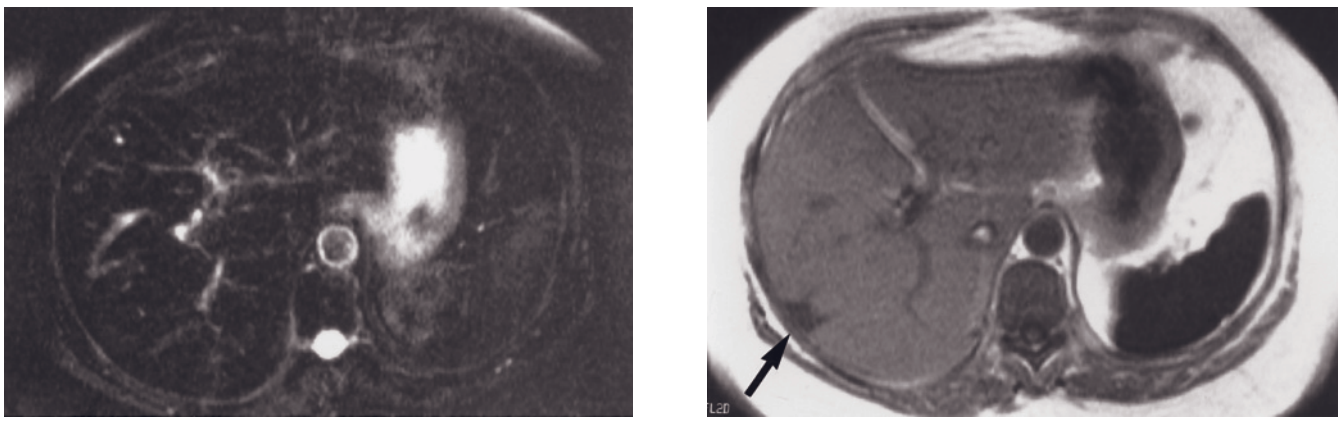

(*a*) (*b*)

FIG. 2.280 Chronic healed candidiasis. T2-weighted fat-suppressed SE (*a*) and SGE (*b*) images. On T2-weighted image (*a*) the area of fibrosis has signal intensity similar to background liver and is not definable. On T1-weighted image (arrow, *b*), an irregular, polygonal low-signal lesion is present in the right lobe of the liver.

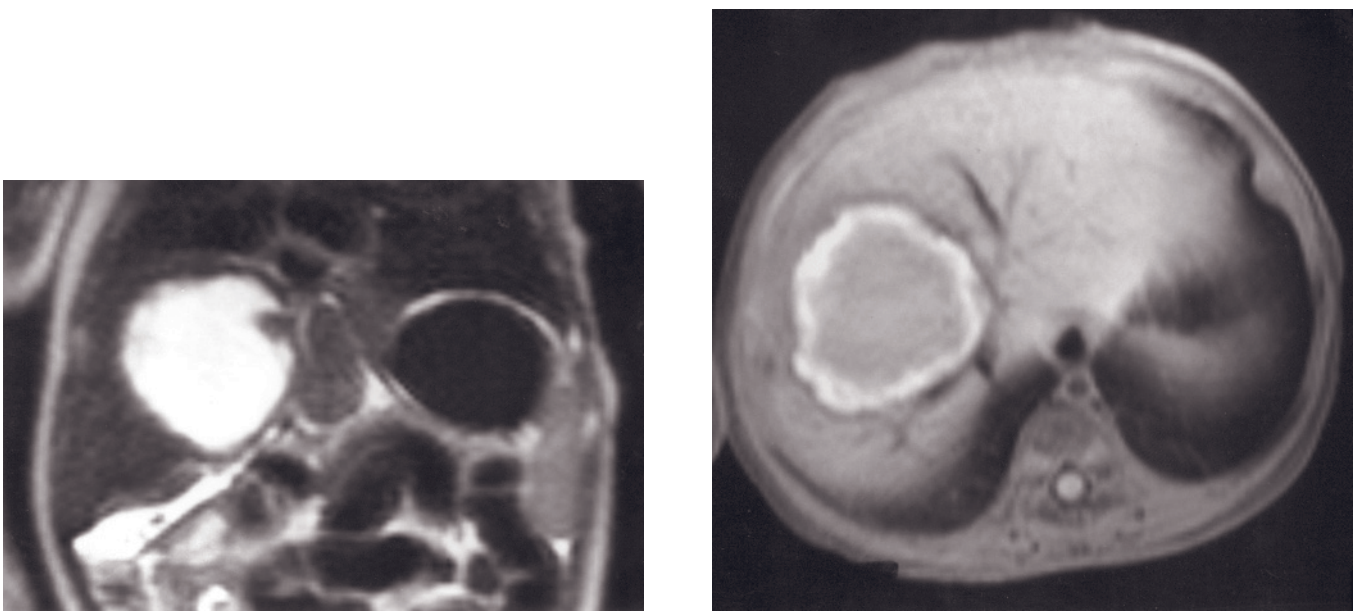

(*a*) (*b*)

FIG. 2.281 Liver hematoma. Coronal T2-weighted SS-ETSE (*a*) and T1-weighted fat-suppressed SE (*b*) images in an 8-week-old girl who has a history of malpositioned umbilical venous catheter and subsequent liver hematoma. There is a fluid collection in the right lobe of the liver that is hyperintense on T2-weighted images (*a*) and isointense centrally with a hyperintense peripheral ring on the fat-suppressed T1-weighted image (*b*), consistent with hematoma. The appearance on the T1-weighted image, with the high-signal peripheral ring, is diagnostic for a hematoma.

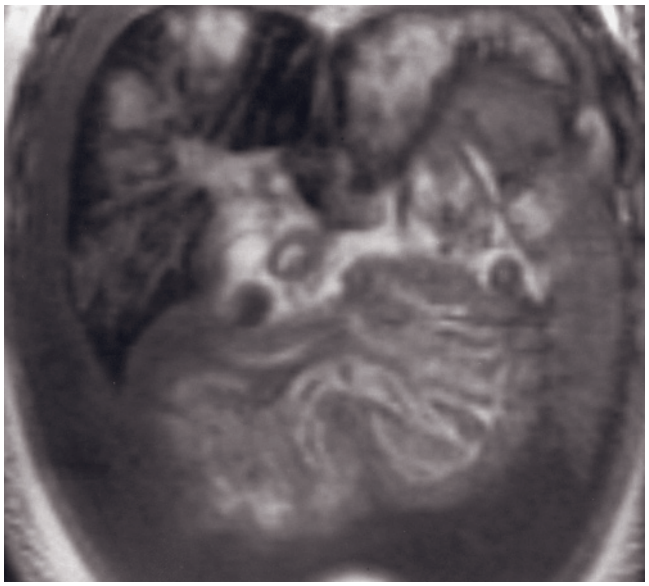

(*c*)

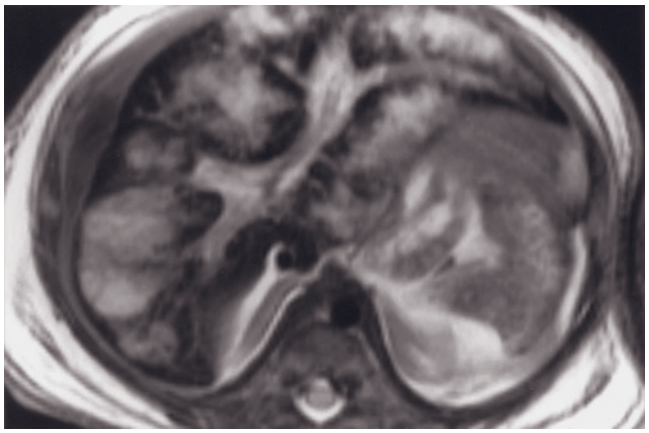

(*d*)

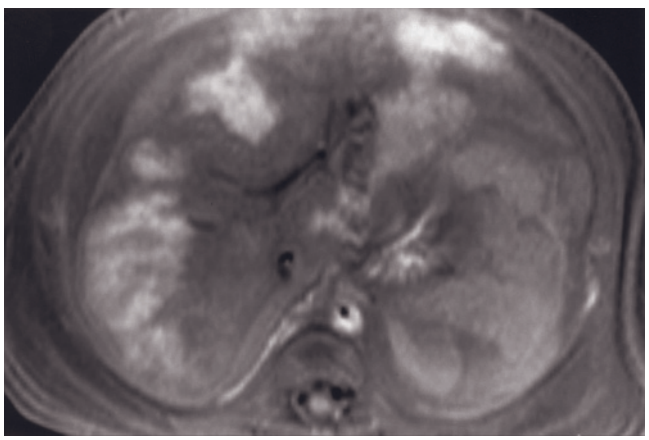

(*e*)

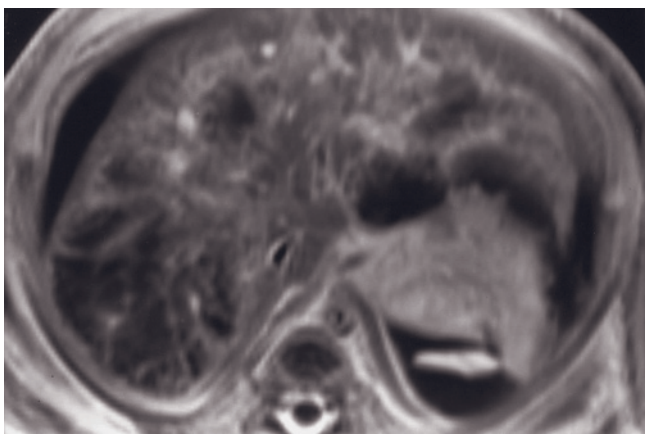

(*f*)

FIG. 2.281 (*Continued*) Coronal T2-weighted SS-ETSE (*c*), transverse T2-weighted fat-suppressed SS-ETSE (*d*), T1-weighted fat-suppressed SE (*e*), and T1-weighted interstitial phase fat-suppressed postgadolinium SE (*f*) images in a newborn patient with disseminated intravascular coagulation. There are abnormal patchy areas throughout the hepatic parenchyma that exhibit high signal intensity on T2-weighted images (*c*, *d*) and T1-weighted image (*e*) consistent with late subacute blood (extracellular methemoglobin). After contrast, these areas demonstrate negligible enhancement (*f*) compatible with ischemia.

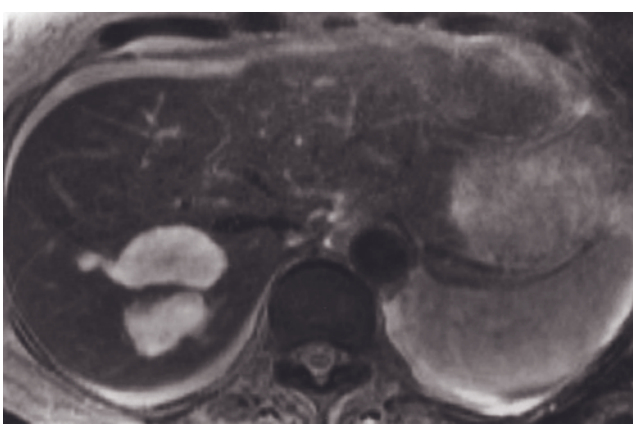

(*a*)

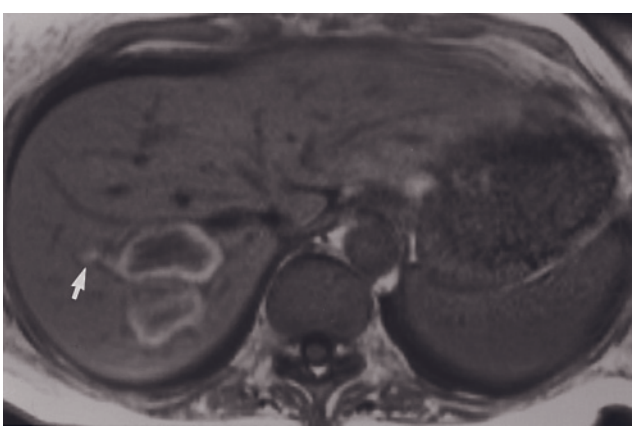

(*b*)

FIG. 2.282 Hepatic hemorrhage after trauma. T2-weighted fat-suppressed ETSE (*a*), SGE (*b*), and 45-s postgadolinium SGE (*c*) images. There are two hematomas in the liver parenchyma that demonstrate heterogeneous moderate high signal on T2-weighted

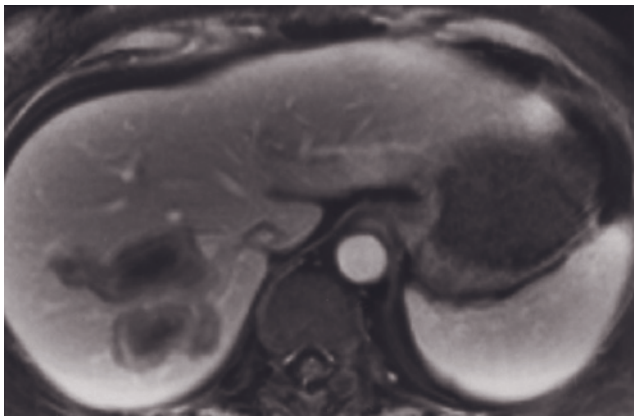

(*c*)

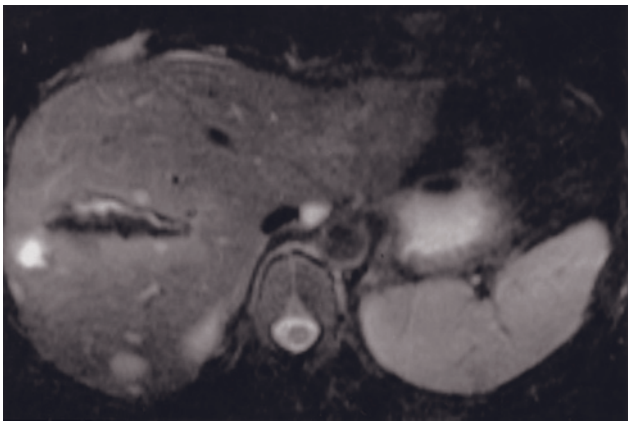

(*d*)

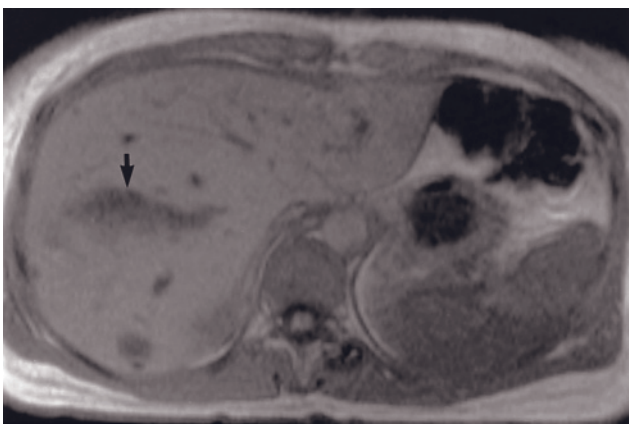

(*e*)

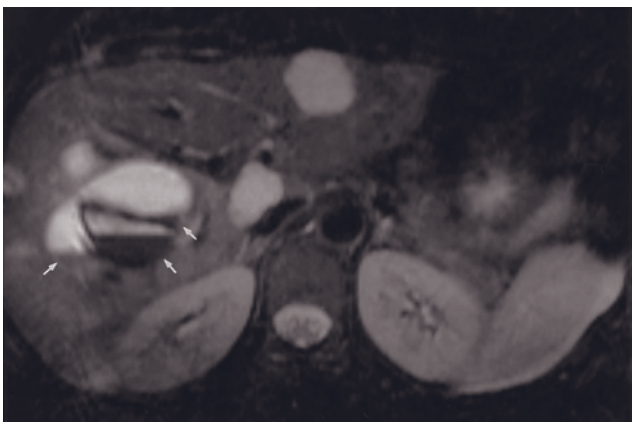

(*f*)

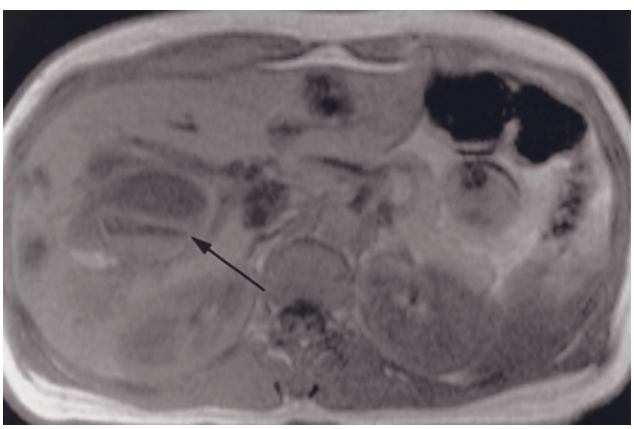

(*g*)

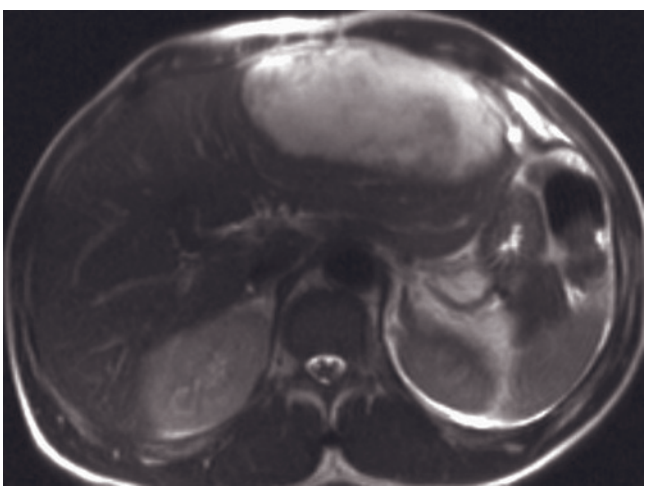

(*h*)

FIG. 2.282 (*Continued*) image (*a*) and central mild low signal and peripheral ring of high signal on T1-weighted precontrast image (*b*), which is diagnostic for subacute hematomas. These lesions do not enhance after gadolinium administration (*c*), but note that the methemoglobin ring remains hyperintense. A high-signal-intensity laceration tract is also noted (arrow, *b*).

T2-weighted fat-suppressed ETSE images (*d, f*) and T1-weighted noncontrast SGE (*e, g*) images acquired in a second patient from two tomographic levels (*d–g*). An acute liver laceration is present (arrow, *e*) through the right lobe of the liver, which contains fluid that is bright and dark (oxyhemoglobin) and dark and dark (deoxyhemoglobin) on T2- and T1-weighted images, respectively. Hemorrhage has extended into two liver cysts that contain a combination of hyperacute blood products including oxyhemoglobin (thin arrow, *g*) and deoxyhemoglobin (dark on T2- and isointense on T1-weighted images; short arrows, *f*).

T2-weighted SS-ETSE (*h*), SGE (*i*), and immediate postgadolinium SGE (*j*) images in a patient after liver trauma. A hematoma is seen in the left hepatic lobe that demonstrates high signal intensity on T2-weighted image (*h*) and low signal intensity on

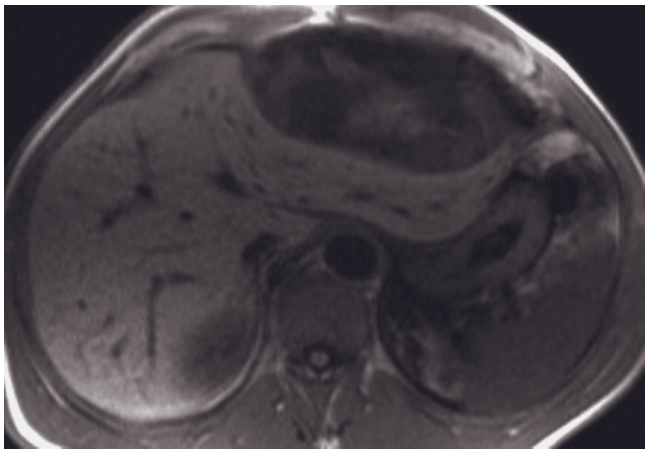

(*i*)

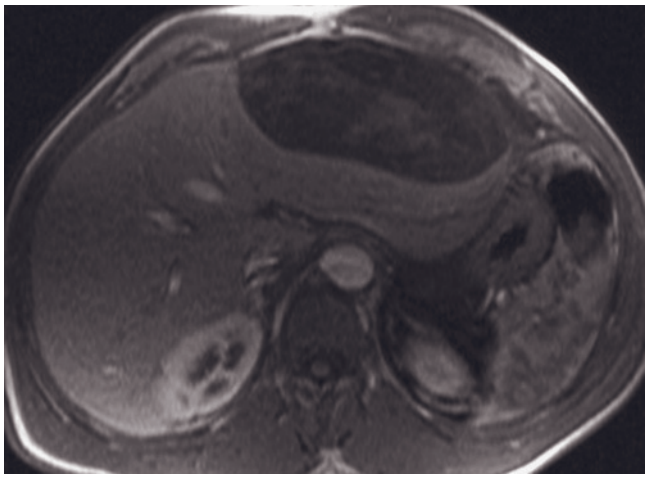

(*j*)

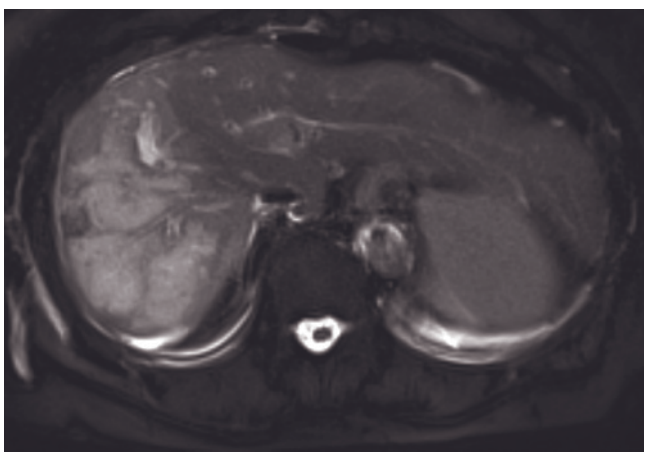

(*k*)

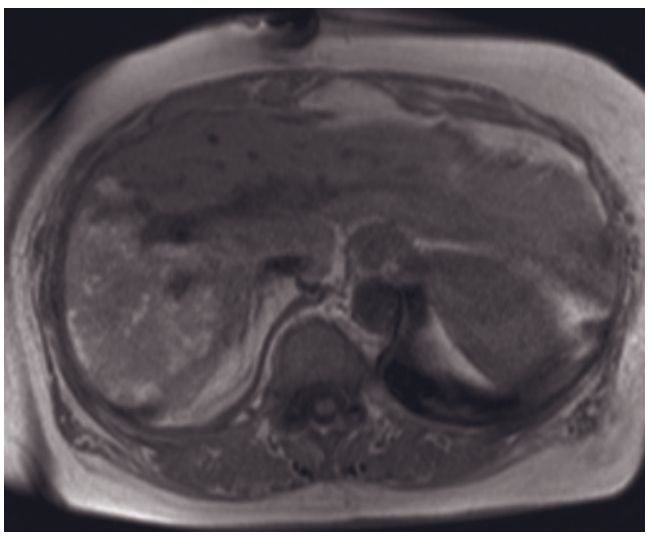

(*l*)

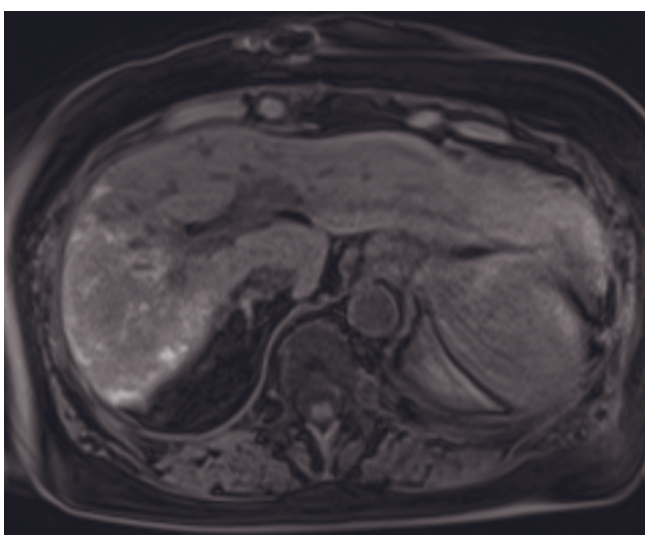

(*m*)

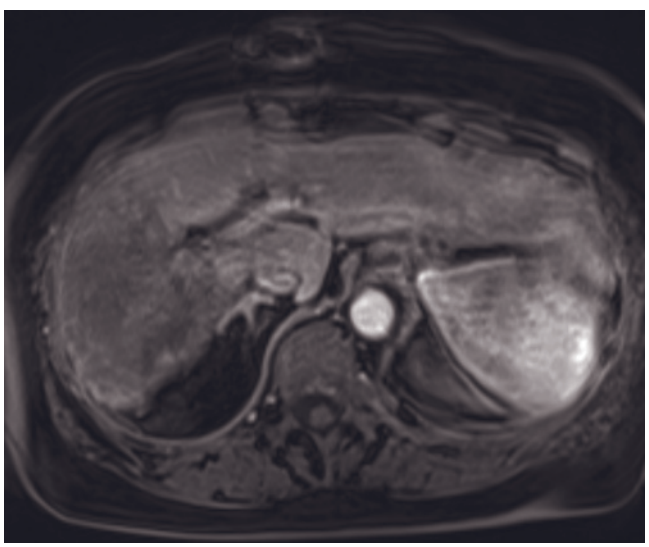

(*n*)

Fig. 2.282 (*Continued*) T1-weighted image with some areas of increased signal within the lesion (*i*). After administration of contrast (*j*), peripheral thin enhancement is appreciated surrounding the lesion. This lesion was compatible with hyperacute hematoma.

T2-weighted fat-suppressed ETSE (*k*), T1 in-phase (*l*), T1-fat-suppressed SGE (*m*), and 45-s postgadolinium fat suppressed SGE (*n*) images. There is area of heterogeneous persistent high signal intensity seen on the right lobe in all sequences, with no enhancement after contrast, compatible with subacute hematoma.

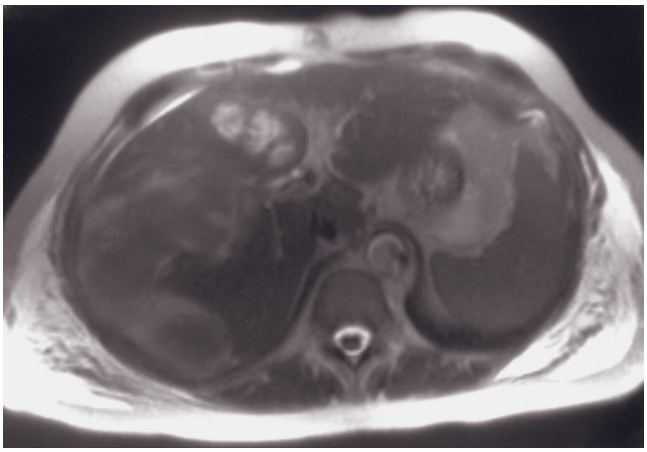

(*a*)

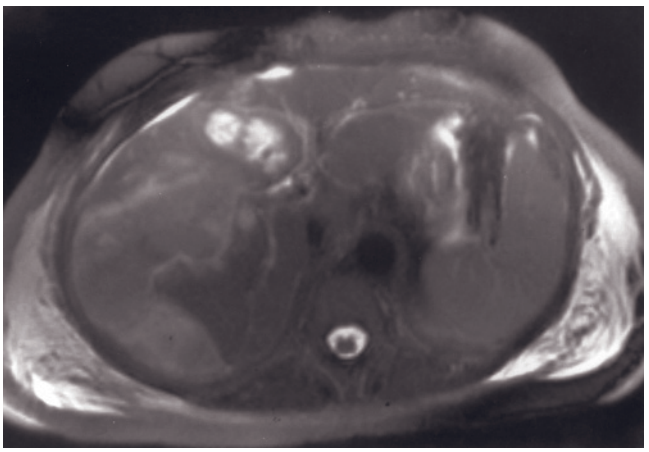

(*b*)

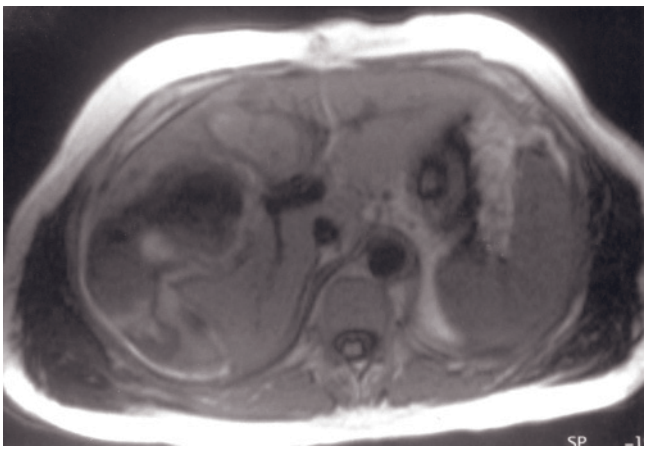

(*c*)

FIG. 2.283 Intrahepatic hemorrhage after surgery. T2-weighted SS-ETSE (*a*), T2-weighted fat-suppressed SS-ETSE (*b*), and single-shot magnetization-prepared gradient-echo (*c*) images in a patient after laparoscopic cholecystectomy who has a history of end-stage renal disease. There is a large area in the right hepatic lobe extending into the subcapsular space, which demonstrates heterogeneous increased signal intensity on both T2 (*a, b*)- and T1 (*c*)-weighted images consistent with late subacute hematoma. Note the peripheral rim of high signal on the T1-weighted image (*c*). Subcutaneous edema is more readily appreciated on the fat-suppressed T2-weighted image (*b*) than on the nonsuppressed image (*a*) because of removal of the competing high signal of fat on these long echo-train sequences.

Table 2.2 Stages of hemorrhage

STAGE	TIME AFTER TRAUMA	HEMOGLOBIN PRODUCTS	T2-W*	T1-W*
Hyperacute	4 to 6 hours	Oxyhemoglobin	High SI	Iso or low SI
Acute	7 to 72 hours	Deoxyhemoglobin	Very low SI	Iso or low SI
Early subacute	4 to 7 days	Intracellular methemoglobin	Very low SI	High SI or high signal in the periphery and isointensity on the central area
Late subacute	1 to 4 weeks	Extracellular methemoglobin	High SI	High SI
Chronic	months to years	Ferritin and hemosiderin	Low SI	Iso SI

*Signal intensity on T2- and T1-weighted images.

intensity on T2- and T1-weighted precontrast images, as follows: hyperacute, acute, early subacute, late subacute, and chronic. In the hyperacute stage, oxyhemoglobin is present, which does not have paramagnetic properties and appears as simple fluid on T2- or T1-weighted images. In the acute stage, deoxyhemoglobin produces a strong effect on T2-weighted images (near signal void), which is a very distinctive finding. In the early subacute stage, intracellular methemoglobin still has a strong effect on T2-weighted images (near signal void) but also has an effect on T1-weighed images (high signal intensity). In the late subacute stage, extracellular methemoglobin has a pronounced effect on T1-weighted images causing high signal intensity and appears high signal on T2-weighted images. In the chronic stage, hemorrhage is low signal intensity on T2-weighted and T1-weighted images due to hemosiderin and ferritin effects that usually accumulate peripherally located in the region of injury [444, 445, 450–452] (Table 2.2).

Active bleeding can be shown as progressive accumulation of high-signal gadolinium on serial postgadolinium images in a fluid-containing space [451].

REFERENCES

1. Couinaud C. *Le Foie; Etudes Anatomiques et Chirurgicales*. Paris, Masson, 1957.
2. MacSween RNM, Anthony PP, Scheuer PJ, Burt AD, Portamann BC, eds. *Pathology of the Liver*. 3th ed. London, Churchill Livingstone. 1994.
3. Ramalho M, Heredia V, Tsurusaki M, Altun E, Semelka RC. Qualitative and quantitative comparison of 3.0 T and 1.5 T MRI for the liver with chronic liver disease. *J Magn Reson Imaging* 29:869–879, 2009.
4. Goncalves Neto JA, Altun E, Elazzazi M, Chaney M, Vaidean G, Semelka RC. Enhancement of abdominal organs on hepatic arterial phaset: quantitative comparison between 1.5 T and 3.0 T MRI. *Magn Reson Imaging* 2009; Jul 2 (Epub ahead of print).
5. Semelka RC, Heimberger TK. Contrast agents for MR imaging of the liver. *Radiology* 218: 227–238, 2001.
6. Heredia V, Altun E, Ramalho M, Semelka RC. Magnetic resonance imaging of the liver: a review. *Exp Opin Med Diagnostics* 1: 1–11, 2007.
7. Goncalves Neto JA, Altun E, Vaidean G, et al. Early contrast enhancement of the liver: exact description of subphases using MRI. *Magn Reson Imaging* 27:976–987, 2009.
8. Whitney WS, Herfkens RJ, Jeffrey RB, McDonnell CH, Li KC, van Dalsem WJ, Low RN, Francis IR, Dabatin JF, Glazer GM. Dynamic breath-hold multiplanar spoiled gradient recolled MR imaging with gadolinium enhancement for differentiating hepatic hemangiomas from malignancies at 1.5T. *Radiology* 189: 863–870, 1993.
9. Lim KO, Stark DD, Leese PT, Pfefferbaum A, Rocklage SM, Quay SC. Hepatobiliary MR imaging: first human experience with MnDPDP. *Radiology* 178: 79–82, 1991.
10. Hamm B, Vogl TJ, Branding G, Schnell B, Taupitz M, Wolf KJ, Lissner J. Focal liver lesions: MR imaging with Mn-DPDP-initial clinical results in 40 patients. *Radiology* 182: 167–174, 1992.
11. Schuhmann-Giampieri G, Schmitt-Willich H, Press WR, Negishi C, Weinmann HJ, Speck U. Preclinical evaluation of Gd-EOB-DTPA as a contrast agent in MR imaging of the hepatobiliary system. *Radiology* 183: 59–64, 1992.
12. Kettritz U, Schlund JF, Wilbur K, Eisenberg LB, Semelka RA. Comparison of gadolinium chelates with Manganese-DPDP for liver lesion detection and characterization: preliminary results. *Magn Reson Imag* 14 (10): 1185–1190, 1996.
13. Martin DR, Semelka RC, Chung JJ, Balci NC, Wilber K. Sequential use of gadolinium chelate and mangafodipir trisodium for the assessment of focal liver lesions: initial observations. *Magn Reson Imaging* 18: 955–963, 2000.
14. Kim KW, Kim AY, Kim TK, Park SH, Kim HJ, Lee YK, Park MS, Ha HK, Kim PN, Kim JC, Lee MG. Small (< or = 2 cm) hepatic lesions in colorectal cancer patients: detection and characterization on mangafodipir trisodium-enhanced MRI. *AJR Am J Roentgenol* 182: 1233–1240, 2004.
15. Caudana R, Morana G, Pirovano GP, Nicoli N, Portuese A, Spinazzi A, Di Rito R, Pistolesi GF. Focal malignant hepatic lesions: MR imaging enhanced with gadolinium benzoxypropionictetra-acetate (BOPTA)- preliminary results of phase II clinical application. *Radiology* 199: 513–520, 1996.
16. Hamm B, Staks T, Muhler A, Bollow M, Taupitz M, Frenzel T, Wolf KJ, Weinmann HJ, Lange L. Phase I clinical evaluation of Gd-EOB-DTPA as a hepatobiliary MR contrast agent: safety, pharmacokinetics, and MR imaging. *Radiology* 195: 785–792, 1995.
17. Vogl TJ, Kummel S, Hammerstingl R, Schellenbeck M, Schumacher G, Balzer T, Schwarz W, Muller PK, Bechstein WO, Mack MG, Sollner O, Felix R. Liver tumors: comparison of MR imaging with Gd-EOB-DTPA and Gd-DTPA. *Radiology* 200: 59–67, 1996.
18. Reimer P, Rummeny EJ, Shamsi K, Balzer T, Daldrup HE, Tombach B, Hesse T, Berns T, Peters PE. Phase II clinical evaluation of Gd-EOB-DTPA: dose, safety aspects, and pulse sequence. *Radiology* 199: 177–183, 1996.
19. Reimer P, Rummeny EJ, Daldrup HE, Hesse T, Balzer T, Tombach B, Peters PE. Enhancement characteristics of liver metastases, hepatocellular carcinomas, and hemangiomas with Gd-EOB-DTPA: preliminary results with dynamic MR imaging. *Eur Radiol* 7: 275–280, 1997.
20. Petersein J, Spinazzi A, Giovagnoni A et al. Focal liver lesions: evaluation of the efficacy of gadobenate dimeglumine in MR imaging—a multicenter phase III clinical study. *Radiology* 215: 727–736, 2000.
21. Grazioli L, Morana G, Federle MP et al. Focal nodular hyperplasia: morphologic and functional information from MR imaging with gadobenate dimeglumine. *Radiology* 221: 731–739, 2001.
22. Hagspiel KD, Neidl KF, Eichenberger AC, Weder W, Marincek B. Detection of liver metastases: comparison of superparamagnetic iron oxide-enhanced and unenhanced MR imaging at 1.5T with dynamic CT, intraoperative US, and percutaneous US. *Radiology* 196: 471–478, 1995.
23. Ros PR, Freeny PC, Marms SE et al. Hepatic MR imaging with ferumoxides: a multicenter clinical trial of the safety and efficacy in the detection of focal hepatic lesions. *Radiology* 196: 481–488, 1995.
24. Yamamoto H, Yamashita Y, Yoshimatsu S, Baba Y, Hatanaka Y, Murakami R, Nishiharu T, Takahashi M, Higashida Y, Moribe N. Hepatocellular carcinoma in cirrhotic livers: detection with unenhanced and iron oxide-enhanced MR imaging. *Radiology* 195: 106–112, 1995.
25. Kumano S, Murakami T, Kim T, Hori M, Okada A, Sugiura T, Noguchi Y, Kawata S, Tomoda K, Nakamura H. Using superparamagnetic iron oxide-enhanced MRI to differentiate metastatic hepatic tumors and nonsolid benign lesions. *AJR Am J Roentgenol* 18: 1335–1339, 2003.
26. Montet X, Lazeyras F, Howarth N, Mentha G, Rubbia-Brandt L, Becker CD, Vallee JP, Terrier F. Specificity of SPIO particles for characterization of liver hemangiomas using MRI. *Abdom Imaging* 29: 60–70, 2004.
27. Mori K, Scheidler J, Helmberger T, Holzknecht N, Schauer R, Schirren CA, Bittmann I, Dugas M, Reiser M. Detection of malignant hepatic lesions before orthotopic liver transplantation: accuracy of ferumoxides-enhanced MR imaging. *AJR Am J Roentgenol* 179: 1045–1051, 2002.
28. Ward J, Guthrie JA, Wilson D, Arnold P, Lodge JP, Toogood GJ, Wyatt JI, Robinson PJ. Colorectal hepatic metastases: detection with SPIO-enhanced breath-hold MR imaging—comparison of optimized sequences. *Radiology* 228: 709–718, 2003.
29. Strotzer M, Gmeinwieser J, Schmidt J, Fellner C, Seitz J, Albrich H, Zirngibl H, Feuerbach S. Diagnosis of liver metastases from colorectal adenocarcinoma. Comparison of spiral-CTAP combined with intravenous contrast-enhanced spiral-CT and SPIO-enhanced MR combined with plain MR imaging. *Acta Radiol* 38: 986–992, 1997.
30. Vogl TJ, Schwarz W, Blume S, Pietsch M, Shamsi K, Franz M, Lobeck H, Balzer T, del Tredici K, Neuhaus P, Felix R, Hammerstingl RM. Preoperative evaluation of malignant liver tumors: comparison of unenhanced and SPIO (Resovist)-enhanced MR imaging with biphasic CTAP and intraoperative US. *Eur Radiol* 13: 262–272, 2003.
31. Ward J, Naik KS, Guthrie JA, Wilson D, Robinson PJ. Hepatic lesion detection: comparison of MR imaging after the administration of superparamagnetic iron oxide with dual-phase CT by using alternative-free response receiver operating characteristic analysis. *Radiology* 210: 459–466, 1999.

32. Reimer P, Jahnke N, Fiebich M, Schima W, Deckers F, Marx C, Holzknecht N, Saini S. Hepatic lesion detection and characterization: value of nonenhanced MR imaging, superparamagnetic iron oxide-enhanced MR imaging, and spiral CT-ROC analysis. *Radiology* 217: 152–158, 2000.
33. Hori M, Murakami T, Kim T, Tsuda K, Takahashi S, Okada A, Takamura M, Nakamura H. Detection of hypervascular hepatocellular carcinoma: comparison of SPIO-enhanced MRI with dynamic helical CT. *J Comput Assist Tomogr* 26: 701–710, 2002.
34. Kang BK, Lim JH, Kim SH, Choi D, Lim HK, Lee WJ, Lee SJ. Preoperative depiction of hepatocellular carcinoma: ferumoxides-enhanced MR imaging versus triple-phase helical CT. *Radiology* 226: 79–85, 2003.
35. Semelka RC, Lee JK, Worawattanakul S, Noone TC, Patt RH, Asher SM. Sequential use of ferumoxide particles and gadolinium chelate for the evaluation of focal liver lesions on MRI. *J Magn Reson Imaging* 8: 670–674, 1998.
36. Saini S, Edelman RR, Sharma P, Li W, Mayo-Smith W, Slater GJ, Eisenberg PJ, Hahn PF. Blood-pool MR contrast material for detection and characterization of focal hepatic lesions: initial clinical experience with ultrasmall superparamagnetic iron oxide (AMI-227). *AJR Am J Roentgenol* 164: 1147–1152, 1995.
37. Weissleder R, Lee AS, Fischman AJ, Reimer P, Shen T, Wilkinson R, Callahan RJ, Brady TJ. Polyclonal human immunoglobulin G labeled with polymeric iron oxide: antibody MR imaging. *Radiology* 181: 245–249, 1991.
38. Vogl TJ, Hammerstingl R, Schwarz W et al. Superparamagnetic iron oxide-enhanced versus gadolinium-enhanced MR imaging for differential diagnosis of focal liver lesions. *Radiology* 198: 881–887, 1996.
39. del Frate C, Bazzocchi M, Mortele KJ, Zuiani C, Londero V, Como G, Zanardi R, Ros PR. Detection of liver metastases: comparison of gadobenate dimeglumine-enhanced and ferumoxides-enhanced MR imaging examinations. *Radiology* 225: 766–772, 2002.
40. Kim SK, Kim SH, Lee WJ, Kim H, Seo JW, Choi D, Lim HK, Lee SJ, Lim JH. Preoperative detection of hepatocellular carcinoma: ferumoxides-enhanced versus mangafodipir trisodium-enhanced MR imaging. *AJR Am J Roentgenol* 179: 741–750, 2002.
41. Kim MJ, Kim JH, Chung JJ, Park MS, Lim JS, Oh YT. Focal hepatic lesions: detection and characterization with combination gadolinium- and superparamagnetic iron oxide-enhanced MR imaging. *Radiology* 2003 228: 719–726, 2003.
42. Kim YK, Kim CS, Lee YH, Kwak HS, Lee JM. Comparison of superparamagnetic iron oxide-enhanced and gadobenate dimeglumine-enhanced dynamic MRI for detection of small hepatocellular carcinomas. *AJR Am J Roentgenol* 182: 1217–1223, 2004.
43. Sherlock S and Dooley J. Anatomy and function. In: Sherlock S. and Dooley J. *Diseases of the Liver and Biliary System.* 10th ed. London, Blackwell Science. 1997. p. 4–5.
44. *Ackerman's Surgical Pathology.* 8th ed. St Louis, Mosby. 1995. p. 898–899.
45. Barnes PA, Thomas JL, Bernardino ME. Pitfalls in the diagnosis of hepatic cysts by computed tomography. *Radiology* 141: 129–133, 1981.
46. Semelka RC, Shoenut JP, Greenberg HM, Mickflickier AB. The liver. In: Semelka RC, Shoenut JP, eds. *MRI of the Abdomen with CT Correlation.* New York, Raven Press, 1993. p. 13–41.
47. Vilgrain V, Silbermann O, Benhamou JP, Nahum H. MR imaging in intracystic hemorrhage of simple hepatic cysts. *Abdom Imaging* 18: 164–167, 1993.
48. Kadoya M, Matsui O, Nakanuma Y, Yoshikawa J, Arai K, Takashima T, Amano M, Kimura M. Ciliated hepatic foregut cyst: radiologic features. *Radiology* 175: 475–477, 1990.
49. Shoenut JP, Semelka RC, Levi C, Greenberg H. Ciliated hepatic foregut cysts: US, CT, and contrast-enhanced MR imaging. *Abdom Imaging* 19: 150–152, 1994.
50. Mosetti MA, Leonardou P, Motohara T, Kanematsu M, Armao D, Semelka RC. Autosomal dominant polycystic kidney disease: MR imaging evaluation using current techniques. *J Magn Reson Imaging* 18(2): 210–215, 2003.
51. Itai Y, Ebihara R, Eguchi N, Saida Y, Kurosaki Y, Minami M, Araki T. Hepatobiliary cysts in patients with autosomal dominant polycystic kidney disease: prevalence and CT findings. *AJR Am J Roentgenol* 164: 339–342, 1995.
52. Semelka RC, Hussain SM, Marcos HB, Woosley JT. Biliary hamartomas: solitary and multiple lesions shown on current MR techniques including gadolinium enhancement. *J Magn Reson Imaging* 10: 196–201, 1999.
53. Powers C, Ros PR, Stoupis C, Johnson WK, Segel KH. Primary liver neoplasms: MR imaging with pathologic correlation. *Radiographics* 14: 459–482, 1994.
54. Choi BI, Lim JH, Han MC, Lee DH, Kim SH, Kim YI, Kim CW. Biliary cystadenoma and cystadenocarcinoma: CT and sonographic findings. *Radiology* 171: 57–61, 1989.
55. Kokubo T, Itai Y, Ohtomo K, Itoh K, Kawauchi N, Minami M. Mucin-hypersecreting intrahepatic biliary neoplasms. *Radiology* 168: 609–614, 1988.
56. Palacios E, Shannon M, Solomon C, Guzman M. Biliary cystadenoma: ultrasound, CT, and MRI. *Gastrointest Radiol* 15: 313–316, 1990.
57. Buetow PC, Buck JL, Pantongrag-Brown L, Ros PR, Devaney K, Goodman ZD, Cruess DF. Biliary cystadenoma and cystadenocarcinoma: clinical-imaging-pathologic correlation with emphasis on the importance of ovarian stroma. *Radiology* 196: 805–810, 1995.
58. Semelka RC. Metastatic liver tumor: circumferential versus wedge-shaped perilesional enhancement and quantitative image and pathologic correlation. *Radiology* 219: 298–300, 2001. (comment)
59. Aytaç S, Fitoz S, Akyar S, Atasoy Ç, Erekul S. Focal intrahepatic extramedullary hematopoiesis: color Doppler US and CT findings. *Abdom Imaging* 24: 366–368, 1999.
60. Navarro M, Crespo C, Perez L, Martinez C, Galant J, Gonzalez I. Massive intrahepatic extramedullary hematopoiesis in myelofibrosis. *Abdom Imaging* 25: 184–186, 2000.
61. Nonomura A, Mizukami Y, Cadoya M. Angiomyolipoma of the liver: a collective review. *J Gastroenterol.* 29(1): 95–105, 1994.
62. Worawattanakul S, Kelekis NL, Semelka RC, Woosley JT. Hepatic angiomyolipoma with minimal fat content: MR demonstration. *Magn Reson Imaging* 14: 687–689, 1996.
63. Morton KM, Bluemke DA, Hruban RH, Soyer P, Fishman EK. CT and MR imaging of benign hepatic and biliary tumors. *Radiographics* 19: 431–451, 1999.
64. Craig J, Peters R, Edmondson H. Tumors of the liver and intrahepatic bile ducts. In Hartman H, Sobin L. eds. *Atlas of Tumor Pathology.* 2nd ed. Washington, DC: Armed Forces Institute of Pathology, 1989.
65. Karhunen PJ. Benign hepatic tumours and tumour like conditions in men. *J Clin Pathol* 39: 183–188, 1986.
66. Mitsuodo K, Watanabe Y, Saga T et al. Nonenhanced hepatic cavernous hemangioma with multiple calcifications: CT and pathologic correlation. *Abdom Imaging* 20: 459–461, 1995.
67. Li KC, Glazer GM, Quint LE, Francis IR, Aisen AM, Ensminger WD, Bookstein FL. Distinction of hepatic cavernous hemangioma from hepatic metastases with MR imaging. *Radiology* 169: 409–415, 1988.
68. Lombardo DM, Baker ME, Spritzer CE, Blinder R, Meyers W, Herfkens RJ. Hepatic hemangiomas vs. metastases: MR differentiation at 1.5T. *AJR Am J Roentgenol* 155: 55–59, 1990.

69. Semelka RC, Shoenut JP, Kroeker MA, Greenberg HM, Simm FC, Minuk GY, Kroeker RM, Micflikier AB. Focal liver disease: comparison of dynamic contrast-enhanced CT and T2-weighted fat-suppressed, FLASH, and dynamic gadolinium-enhanced MR imaging at 1.5T. *Radiology* 184: 687–694, 1992.
70. Schmiedl U, Kolbel G, Hess CF, Klose U, Kurtz B. Dynamic sequential MR imaging of focal liver lesions: initial experience in 22 patients at 1.5T. *J Comput Assist Tomogr* 14: 600–607, 1990.
71. Quinn SF and Benjamin GG. Hepatic cavernous hemangiomas: simple diagnostic sign with dynamic bolus CT. *Radiology* 182: 545–548, 1992.
72. Low RN. MRI of the liver using gadolinium chelates. *Magn Reson Imaging Clin N Am.* 9(4): 717–743, 2001.
73. Semelka RC, Brown ED, Ascher SM, Patt RH, Bagley AS, Li W, Edelman RR, Shoenut JP, Brown JJ. Hepatic hemangiomas: a multi-institutional study of appearance on T2-weighted and serial gadolinium-enhanced gradient-echo MR images. *Radiology* 192: 401–406, 1994.
74. Choi BI, Han MC, Park JH, Kim SH, Han MH, Kim CW. Giant cavernous hemangioma of the liver: CT and MR imaging in 10 cases. *AJR Am J Roentgenol* 152: 1221–1226, 1989.
75. Danet IM, Semelka RC, Braga L, Armao D, Woosley JT. Giant hemangioma of the liver: MR imaging characteristics in 24 patients. *Magn Reson Imaging* 21: 95–101, 2003.
76. Semelka RC and Sofka CM. Hepatic hemangiomas. *Magn Reson Imaging Clin N Am* 5(2): 241–253, 1997.
77. Jeong MG, Yu JS, Kim KW. Hepatic cavernous hemangioma: Temporal peritumoral enhancement during multiphase dynamic MR imaging. *Radiology* 216: 692–697, 2000.
78. Wanless IR, Albrecht S, Bilbao J, Frei JV, Heathcote EJ, Roberts EA, Chiasson D. Multiple focal nodular hyperplasia of the liver associated with vascular malformations of various organs and neoplasia of the brain: a new syndrome. *Mod Pathol* 2: 456–462, 1989.
79. Noone TC, Semelka RC, Balci NC, Graham ML. Common occurrence of benign liver lesions in patients with newly diagnosed breast cancer investigated by MRI for suspected liver metastases. *J Magn Reson Imaging* 10: 165–169, 1999.
80. McFarland EG, Mayo-Smith WW, Saini S, Hahn PF, Goldberg MA, Lee MJ. Hepatic hemangiomas and malignant tumors: improved differentiation with heavily T2-weighted conventional spin-echo MR imaging. *Radiology* 193: 43–47, 1994.
81. Hamm B, Thoeni RF, Gould RG, Bernardino ME, Luning M, Saini S, Mahfouz AE, Taupitz M, Wolf KJ. Focal liver lesions: characterization with nonenhanced and dynamic contrast material-enhanced MR imaging. *Radiology* 190: 417–423, 1994.
82. Burdeny DA, Semelka RC, Kelekis NL, Kettritz U, Woosley JT, Cance WG, Lee JKT. Chemotherapy treated liver metastases mimicking hemangiomas on MR images. *Abdom Imag* 24: 378–382, 1999.
83. Dodd GD 3rd, Baron RL, Oliver JH 3rd, Federle MP. Spectrum of imaging findings of the liver in end-stage cirrhosis: Part II, focal abnormalities. *AJR Am J Roentgenol* 173: 1185–1192, 1999.
84. Mastropasqua M, Kanematsu M, Leonardou P, Braga L, Woosley JT, Semelka RC. Cavernous hemangiomas in patients with chronic liver disease: MR imaging findings. *Magn Reson Imaging* 22: 15–18, 2004.
85. Brancatelli G, Federle MP, Blachar A, Grazioli L. Hemangioma in the cirrhotic liver: diagnosis and natural history. *Radiology* 219(1): 69–74, 2001.
86. Siegel MJ. MR imaging of pediatric abdominal neoplasms. *Magn Reson Imaging Clin N Am* 8: 837–851, 2000.
87. Klatskin G, Conn HO. Neoplasms of the liver and intrahepatic bile ducts. *Histopathology of the Liver.* New York, Oxford University Press, 1993. chapter 25, p. 368–370.
88. Buetow PC, Rao P, Marshall H. Imaging of pediatric liver tumors. *Magn Reson Imaging Clin N Am* 5(2): 397–413, 1997.
89. Carneiro RC, Fordham LA, Semelka RC. MR imaging of the pediatric liver. *Magn Reson Imaging Clin N Am* 10(1): 137–164, 2002.
90. Gonzalez A, Canga F, Cardenas F, Castellano G, Garcia H, Cuenca B et al. An unusual case of hepatic adenoma in a male. *J Clin Gastroenterol* 19(2): 179–181, 1994.
91. Kerlin P, Davis GL, McGill DB, Weiland LH, Adson MA, Sheedy PFD. Hepatic adenoma and focal nodular hyperplasia: clinical, pathologic, and radiologic features. *Gastroenterology* 84: 994–1002, 1983.
92. Shortell CK and Schwartz SI. Hepatic adenoma and focal nodular hyperplasia. *Surg Gynecol Obstet* 173: 426–431, 1991.
93. International Working Party: Terminology of nodular hepatocellular lesions. International Working Party. *Hepatology* 22: 983–993, 1995.
94. Meissner K. Hemorrhage caused by ruptured liver cell adenoma following long-term oral contraceptives: a case report. *Hepatogastroenterology* 45(19): 224–225, 1998.
95. Foster JH, Berman MM. The malignant transformation of liver cell adenomas. *Arch Surg* 129(7): 712–717, 1994.
96. Paulson EK, McClellan JS, Washington K, Spritzer CE, Meyers WC, Baker ME. Hepatic adenoma: MR characteristics and correlation with pathologic findings. *AJR Am J Roentgenol* 163: 113–116, 1994.
97. Arrive L, Flejou JF, Vilgrain V, Belghiti J, Najmark D, Zins M, Menu Y, Tubiana JM, Nahum H. Hepatic adenoma: MR findings in 51 pathologically proved lesions. *Radiology* 193: 507–512, 1994.
98. Psatha EA, Semelka RC, Armao D, Woosley JT, Firat Z, Schneider G. Hepatocellular adenomas in men: MRI findings in four patients. *J Magn Reson Imaging* 22: 258–264, 2005.
99. Hamm B, Vogl TJ, Branding G, Schnell B, Taupitz M, Wolf KJ, Lissner J. Focal liver lesions: MR imaging with Mn-DPDP-initial clinical results in 40 patients. *Radiology* 182: 167–174, 1992.
100. Coffin CM, Diche T, Mahfouz A, Alexandre M, Caseiro-Alves F, Rahmouni A, Vasile N, Mathieu D. Benign and malignant hepatocellular tumors: evaluation of tumoral enhancement after mangafodipir trisodium injection on MR imaging. *Eur Radiol* 19(3): 444–449, 1999.
101. Flejou JF, Barge J, Menu Y et al. Liver adenomatosis: an entity distinct from liver adenoma? *Gastroenterology* 83: 1132–1138, 1985.
102. Grazioli L, Federle MP, Ichikawa T, Balzano E, Nalesnik M, Madariaga J. Liver adenomatosis: clinical, histopathologic, and imaging findings in 15 patients. *Radiology* 216: 395–402, 2000.
103. Bader TR, Braga L, Semelka RC. Exophytic benign tumors of the liver: appearance on MRI. *Magn Reson Imaging* 19: 623–628, 2001.
104. Balci NC, Sirvanci M, Duran C, Akinci A. Hepatic adenomatosis: MRI demonstration with the use of superparamagnetic iron oxide. *Clin Imaging* 26: 35–38, 2002.
105. DeLeve LD. Vascular liver diseases. *Curr Gastroenterol Rep* 5(1): 63–70, 2003.
106. Scheuer PJ, Schachter LA, Mathur S, Burroughs AK, Rolles K. Peliosis hepatitis after liver transplantation. *J Clin Pathol* 43(12): 1036–1037, 1990.
107. Verswijvel G, Janssens F, Colla P, Mampaey S, Verhelst H, Van Eycken P et al. Peliosis hepatis presenting as a multifocal hepatic pseudotumor: MR findings in two cases. *Eur Radiol* 13 *Suppl* 4: L40–L44, 2003.
108. Steinke K, Terraciano L, Wiesner W. Unusual cross-sectional imaging findings in hepatic peliosis. *Eur Radiol* 13(8): 1916–9, 2003.
109. Gouya H, Vignaux O, Legmann P, de Pigneux G, Bonnin A. Peliosis hepatis: triphasic helical CT and dynamic MRI findings. *Abdom Imaging* 26(5): 507–509, 2001.

110. Yekeler E, Dursun M, Tunaci A, Cevikbas U, Rozanes I. Diagnosing of peliosis hepatis by magnetic resonance imaging. *J Hepatol* 41(2): 351, 2004.
111. Ferrozzi F, Tognini G, Zuccoli G, Cademartiri F, Pavone P. Peliosis hepatis with pseudotumoral and hemorrhagic evolution: CT and MR findings. *Abdom Imaging* 26(2): 197–199, 2001.
112. Wanless IR, Mawdsley C, Adams R. On the pathogenesis of focal nodular hyperplasia of the liver. *Hepatology* 5(6): 1194–1200, 1985.
113. Mathieu D, Vilgrain V, Mahfouz AE, Anglade MC, Vullierme MP, Denys A. Benign liver tumor. *Magn Reson Imaging Clin N Am* 5(2): 255–288, 1997.
114. Mortelé KJ, Praet M, Vlierberghe HV, Kunnen M, Ros PR. CT and MR imaging findings in focal nodular hyperplasia of the liver: radiologic- Pathologic correlation. *AJR Am J Roentgenol* 175: 687–692, 2000.
115. Attal P, Vilgrain V, Brancatelli G, Paradis V, Terris B, Belghiti J, Taouli B, Menu Y. Telangiectatic focal nodular hyperplasia: US, CT, and MR imaging findings with histopathologic correlation in 13 cases. *Radiology* 228: 465–472, 2003.
116. Ferlicot S, Kobeiter H, Tran Van Nhieu J, Cherqui D, Dhumeaux D, Mathieu D, Zafrani ES. MRI of atypical focal nodular hyperplasia of the liver: *Radiology*-pathology correlation. *AJR Am J Roentgenol* 182: 1227–1231, 2004.
117. Lee MJ, Saini S, Hamm B, Taupitz M, Hahn PF, Seneterre E, Ferrucci JT. Focal nodular hyperplasia of the liver: MR findings in 35 proved cases. *AJR Am J Roentgenol* 156: 317–320, 1991.
118. Vilgrain V, Flejou JF, Arrive L, Belghiti J, Najmark D, Menu Y, Zins M, Vullierme MP, Nahum H. Focal nodular hyperplasia of the liver: MR imaging and pathologic correlation in 37 patients. *Radiology* 184: 699–703, 1992.
119. Schiebler ML, Kressel HY, Saul SH, Yeager BA, Axel L, Gefter WB. MR imaging of focal nodular hyperplasia of the liver. *J Comput Assist Tomogr* 11: 651–654, 1987.
120. Haggar AM, Bree RL. Hepatic focal nodular hyperplasia: MR imaging at 1.0 and 1.5T. *J Magn Reson Imaging* 2: 85–88, 1992.
121. Mahfouz AE, Hamm B, Taupitz M, Wolf KJ. Hypervascular liver lesions: differentiation of focal nodular hyperplasia from malignant tumors with dynamic gadolinium-enhanced MR imaging. *Radiology* 186: 133–138, 1993.
122. Eisenberg LB, Warshauer DM, Woosley JT, Cance WG, Bunzendahl H, Semelka RC. CT and MRI of hepatic focal nodular hyperplasia with peripheral steatosis. *J Comput Assist Tomogr* 19: 498–500, 1995.
123. Hamm B, Vogl TJ, Branding G, Schnell B, Taupitz M, Wolf KJ, Lissner J. Focal liver lesions: MR imaging with Mn-DPDP-initial clinical results in 40 patients. *Radiology* 182: 167–174, 1992.
124. Vogl TJ, Hamm B, Schnell B, McMahon C, Branding G, Lissner J, Wolf KJ. Mn-DPDP enhancement patterns of hepatocellular lesions on MR images. *J Magn Reson Imaging* 3: 51–58, 1993.
125. Grazioli L, Morana G, Federle MP et al. Focal nodular hyperplasia: morphologic and functional information from MR imaging with gadobenate dimeglumine. *Radiology* 221: 731–739, 2001.
126. Rummeny EJ, Wernecke K, Saini S, Vassallo P, Wiesmann W, Oestmann JW, Kivelitz D, Reers B, Reiser MF, Peters PE. Comparison between high-field-strength MR imaging and CT for screening of hepatic metastases: a receiver operating characteristic analysis. *Radiology* 182: 879–886, 1992.
127. Nelson RC, Chezmar JL, Sugarbaker PH, Murray DR, Bernardino ME. Preoperative localization of focal liver lesions to specific liver segments: utility of CT during arterial portography. *Radiology* 176: 89–94, 1990.
128. Sugarbaker PH and Kemeny N. Management of metastatic cancer to the liver. *Adv Surg* 22: 1–56, 1989.
129. Hughes KS, Rosenstein RB, Songhorabodi S, Adson MA, Ilstrup DM, Fortner JG, Maclean BJ, Foster JH, Daly JM, Fitzherbert D et al. Resection of the liver for colorectal carcinoma metastases: a multi-institutional study of long-term survivors. *Dis Colon Rectum* 31: 1–4, 1988.
130. Semelka RC, Hricak H, Bis KG, Werthmuller WC, Higgins CB. Liver lesion detection: comparison between excitation-spoiling fat suppression and regular spin-echo at 1.5T. *Abdom Imaging* 18: 56–60, 1993.
131. De Lange EE, Mugler JP III, Bosworth JE, DeAngelis GA, Gay SB, Hurt NS, Berr SS, Rosenblatt JM, Merickel LW, Harris EK. MR imaging of the liver: breath-hold T1-weighted MP-GRE compared with conventional T2-weighted SE imaging-lesion detection, localization, and characterization. *Radiology* 190: 727–736, 1994.
132. Larson RE, Semelka RC, Bagley AS, Molina PL, Brown ED, Lee JK. Hypervascular malignant liver lesions: comparison of various MR imaging pulse sequences and dynamic CT. *Radiology* 192: 393–399, 1994.
133. Semelka RC, Shoenut JP, Ascher SM, Kroeker MA, Greenberg HM, Yaffe CS, Micflikier AB. Solitary hepatic metastasis: comparison of dynamic contrast-enhanced CT and MR imaging with fat-suppressed T2-weighted, breath-hold T1-weighted FLASH, and dynamic gadolinium-enhanced FLASH sequences. *J Magn Reson Imaging* 4: 319–323, 1994.
134. Stark DD, Wittenberg J, Butch RJ, Ferrucci JT Jr. Hepatic metastases: randomized, controlled comparison of detection with MR imaging and CT. *Radiology* 165: 399–406, 1987.
135. Zeman RK, Dritschilo A, Silverman PM, Clark LR, Garra BS, Thomas DS, Ahlgren JD, Smith FP, Korec SM, Nauta RJ et al. Dynamic CT vs. 0.5T MR imaging in the detection of surgically proven hepatic metastases. *J Comput Assist Tomogr* 13: 637–644, 1989.
136. Balci NC, Semelka RC, Altun E. Fundamentals of MR imaging techniques applied to the abdomen and pelvis. *Applied Radiology* 35: 30–35, 2006.
137. Semelka RC, Worawattanakul S, Kelekis NL, John G, Woosley JT, Graham M, Cance WG. Liver lesion detection and characterization. Comparison of single-phase spiral CT and current MR techniques. *J Magn Reson Imaging* 7(6): 1040–1047, 1997.
138. Semelka RC, Martin DR, Balci Cem, Lance T. Focal liver lesions: comparison of dual phase CT and multisequence multiplanar MR imaging including dynamic gadolinium enhancement. *J Magn Reson Imaging* 13: 397–401, 2001.
139. Semelka RC, Unal B, Altun E. MRI and treatment response. *Imaging Economics* 2006 October Issue.
140. Semelka RC, Cance WG, Marcos HB, Mauro MA. Liver metastases: comparison of current MR techniques and spiral CT during arterial portography for detection in 20 surgically staged cases. *Radiology* 213: 86–91, 1999.
141. Danet IM, Semelka RC, Leonardou P, Braga L, Vaidean G, Woosley JT, Kanematsu M. Spectrum of MRI appearances of untreated metastases of the liver. *AJR Am J Roentgenol* 181(3): 809–817, 2003.
142. Braga L, Semelka RC, Pietrobon R, Martin D, de Barros N, Guller U. Does hypervascularity of liver metastases as detected on MRI predict disease progression in breast cancer patients? *AJR Am J Roentgenol* 182(5): 1207–1213, 2004
143. Larson RE, Semelka RC, Bagley AS, Molina PL, Brown ED, Lee JK. Hypervascular malignant liver lesions: comparison of various MR imaging pulse sequences and dynamic CT. *Radiology* 192: 393–399, 1994.
144. Semelka RC, Cumming MJ, Shoenut JP, Magro CM, Yaffe CS, Kroeker MA, Greenberg HM. Islet cell tumors: comparison of dynamic contrast-enhanced CT and MR imaging with dynamic gadolinium enhancement and fat suppression. *Radiology* 186: 799–802, 1993.

145. Mahfouz AE, Hamm B, Wolf KJ. Peripheral washout: a sign of malignancy on dynamic gadolinium-enhanced MR images of focal liver lesions. *Radiology* 190: 49–52, 1994.
146. Silva AC, Evans JM, McCullough AE, Jatoi MA, Vargas HE, Hara AK. MR imaging of hypervascular liver masses: a review of current techniques. *Radiographics* 29: 385–402, 2009.
147. Outwater E, Tomaszewski JE, Daly JM, Kressel HY. Hepatic colorectal metastases: correlation of MR imaging and pathologic appearance. *Radiology* 180(2): 327–32, 1991.
148. Muramatsu Y, Nawano S, Takayasu K, Moriyama N, Yamada T, Yamasaki S, Hirohashi S. Early hepatocellular carcinoma: MR imaging. *Radiology* 181: 209–213, 1991.
149. Gabata T, Matsui O, Kadoya M, Yoshikawa J, Ueda K, Kawamori Y et al. Delayed MR imaging of the liver: correlation of delayed enhancement of hepatic tumors and pathologic appearance. *Abdom Imaging* 23(3): 309–13, 1998.
150. Larson RE, Semelka RC. Magnetic resonance imaging of the liver. *Top Magn Reson Imaging* 7(2): 71–81, 1995.
151. Semelka RC, Hussain SM, Marcos HB, Woosley JT. Perilesional enhancement of hepatic metastases: correlation between MR imaging and histopathologic findings: initial observations. *Radiology* 215: 89–94, 2000.
152. Danet IM, Semelka RC, Nagase LL, Woosely JT, Leonardou P, Armao D. Liver metastases from pancreatic adenocarcinoma: MR imaging characteristics. *J Magn Reson Imaging*. 18(2): 181–188, 2003.
153. Terayama N, Matsui O, Ueda K, Kobayashi S, Sanada J, Gabata T, et al. Peritumoral rim enhancement of liver metastasis: hemodynamics observed on single-level dynamic CT during hepatic arteriography and histopathologic correlation. *J Comput Assist Tomogr* 26(6): 975–980, 2002.
154. Semelka RC, Bagley AS, Brown ED, Kroeker MA. Malignant lesions of the liver identified on T1- but not T2-weighted MR images at 1.5 T. *J Magn Reson Imaging* 4: 315–318, 1994.
155. Pedro MS, Semelka RC, Braga L. MR imaging of hepatic metastases. *Magn Reson Imaging Clin N Am*. 10(1): 15–29, 2002.
156. Outwater E, Tomaszewski JE, Daly JM, Kressel HY. Hepatic colorectal metastases: correlation of MR imaging and pathologic appearance. *Radiology* 180: 327–332, 1991.
157. Braga L, Semelka RC, Danet IM, Venkataraman S, Woosley JT. Liver metastases from unknown primary site: demonstration on MR images. *Magn Reson Imaging*. 21(8): 871–877, 2003.
158. Bader TR, Semelka RC, Chiu VC, Armao DM, Woosley JT. MRI of carcinoid tumors: spectrum of appearances in the gastrointestinal tract and liver. *J Magn Reson Imaging* 14(3): 261–269, 2001.
159. Soyer P, Riopel M, Bluemke DA, Scherrer A. Hepatic metastases from leiomyosarcoma: MR features with histopathologic correlation. *Abdom Imaging* 22(1): 67–71, 1997.
160. Jones EC, Chezmar JL, Nelson RC, Bernardino ME. The frequency and significance of small (less than or equal to 15 mm) hepatic lesions detected by CT. *AJR Am J Roentgenol* 158: 535–539, 1992.
161. Bruneton JN, Raffaelli C, Maestro C, Padovani B. Benign liver lesions: implications of detection in cancer patients. *Eur Radiol* 5: 387–390, 1995.
162. Mathieu D, Vilgrain V, Mahfouz AE, Anglade MC, Vullierme MP, Denys A. Benign liver tumor. *Magn Reson Imaging Clin N Am* 5(2): 255–288, 1997.
163. Trump DL, Fahnestock R, Cloutier CT, Dickman MD. Anaerobic liver abscess and intrahepatic metastases- a case report and review of the literature. *Cancer* 41(2): 682–686, 1978.
164. Eckel F, Lersch C, Huber W, Weiss W, Berger H, Schulte-Frohlinde E. Multimicrobial sepsis including clostridium perfringens after chemoembolization of a single liver metastases from common bile duct cancer. *Digestion* 62: 208–212, 2000.
165. Taouli B, Losada M, Holland A, Krinsky G. Magnetic resonance imaging of hepatocellular carcinoma. *Gastroenterology* 127(5 *Suppl* 1): S144–S152, 2004.
166. Fung J, Marsh W. The quandary over liver transplantation for hepatocellular carcinoma: the greater sin? *Liver Transpl* 8(9): 775–777, 2002.
167. El-Serag HB, Mason AC. Rising incidence of hepatocellular carcinoma in the United States. *N Engl J Med* 340(10): 745–750, 1999.
168. Yuen MF, Cheng CC, Lauder IJ, Lam SK, Ooi CG, Lai CL. Early detection of hepatocellular carcinoma increases the chance of treatment: Hong Kong experience. *Hepatology* 31(2): 330–335, 2000.
169. Hytiroglou P. Morphological changes of early human hepatocarcinogenesis. *Semin Liver Dis* 24(1): 65–75, 2004.
170. Ahn J, Flamm SL. Hepatocellular carcinoma. *Dis Mon* 50(10): 556–573, 2004.
171. Kerr M. Increase of liver cancer rate outpaces all other cancers. *Internal Medicine News*, 2005. p.72
172. Mastropasqua, M, Braga L, Kanematsu M, Vaidean G, Shrestha R, Polytimi L, Firat Z, Woosley JT, Semelka RC. Hepatic nodules in liver transplantation candidates: MR imaging and underlying hepatic disease. *Magn Reson Imaging* 23: 557–562, 2005.
173. Ahn J, Flamm SL. Hepatocellular carcinoma. *Dis Mon* 50(10): 556–573, 2004.
174. Miller WJ, Baron RL, Dodd GD III, Federle MP. Malignancies in patients with cirrhosis: CT sensitivity and specificity in 200 consecutive transplant patients. *Radiology* 193: 645–650, 1994.
175. Oi H, Murakami T, Kim T, Matsushita M, Kishimoto H, Nakamura H. Dynamic MR imaging and early-phase helical CT for detecting small intrahepatic metastases of hepatocellular carcinoma. *AJR Am J Roentgen* 166: 369–374, 1996.
176. Yamashita Y, Mitsuzaki K, Yi T, Ogata I, Nishiharu T, Urata J, Takahashi M. Small heptacellular carcinoma in patients with chronic liver damage: prospective comparison of detection with dynamic MR imaging and helical CT of the whole liver. *Radiology* 200: 79–84, 1996.
177. Yu JS, Kim KW, Lee JT, Yoo HS. MR imaging during arterial portography for assessment of hepatocellular carcinoma: comparison with CT during arterial portography. *AJR Am J Roentgenol* 170: 1501–1506, 1998.
178. Lim JH, Kim CK, Lee WJ, Park CK, Koh KC, Paik SW, Joh JW. Detection of hepatocellular carcinomas and dysplastic nodules in cirrhotic livers: accuracy of helical CT in transplant patients. *AJR Am J Roentgenol* 175(3): 693–698, 2000.
179. Valls C, Cos M, Figueras J, Andia E, Ramos E, Sanchez A, Serrano T, Torras J. Pretransplantation diagnosis and staging of hepatocellular carcinoma in patients with cirrhosis: value of dual-phase helical CT. *AJR Am J Roentgenol* 182(4): 1011–1007, 2004.
180. Ebara M, Watanabe S, Kita K, Yoshikawa M, Sugiura N, Ohto M, Kondo F, Kondo Y. MR imaging of small hepatocellular carcinoma: effect of intratumoral copper content on signal intensity. *Radiology* 180: 617–621, 1991.
181. Yamashita Y, Fan ZM, Yamamoto H, Matsukawa T, Yoshimatsu S, Miyazaki T, Sumi M, Harada M, Takahashi M. Spin-echo and dynamic gadolinium-enhanced FLASH MR imaging of hepatocellular carcinoma: correlation with histopathologic findings. *J Magn Reson Imaging* 4: 83–90, 1994.
182. Yasemin M K-B, Braga L, Birchard KR, Gerber D, Firat Z, Woosley JT, Shrestha R, Semelka R. Hepatocellular carcinoma missed on gadolinium enhanced MR imaging, discovered in liver explants: retrospective evaluation. *J Magn Reson Imaging* 23: 210–205, 2006.
183. Kelekis NL, Semelka RC, Worawattanakul S, de Lange EE, Ascher SM, Ahn IO, Reinhold C, Remer EM, Brown JJ, Bis KG, Woosley JT, Mitchell DG. Hepatocellular carcinoma in North America: a

multiinstitutional study of appearance on T1-weighted, T2-weighted, and serial gadolinium-enhanced gradient-echo images. *AJR Am J Roentgenol* 170: 1005–1013, 1998.
184. Hirai K, Aoki Y, Majima Y, Abe H, Nakashima O, Kojiro M, Tanikawa K. Magnetic resonance imaging of small hepatocellular carcinoma. *Am J Gastroenterol* 86: 205–209, 1991.
185. Kadoya M, Matsui O, Takashima T, Nonomura A. Hepatocellular carcinoma: correlation of MR imaging and histopathologic findings. *Radiology* 183: 819–825, 1992.
186. Muramatsu Y, Nawano S, Takayasu K, Moriyama N, Yamada T, Yamasaki S, Hirohashi S. Early hepatocellular carcinoma: MR imaging. *Radiology* 181: 209–213, 1991.
187. Earls JP, Theise ND, Weinreb JC, DeCorato DR, Krinsky GA, Rofsky NM, et al. Dysplastic nodules and hepatocellular carcinoma: thin-section MR imaging of explanted cirrhotic livers with pathologic correlation. *Radiology* 201(1): 207–214, 1996.
188. Ebara M, Fukuda H, Kojima Y, Morimoto N, Yoshikawa M, Sugiura N, Satoh T, Kondo F, Yukawa M, Matsumoto T, Saisho H. Small hepatocellular carcinoma: relationship of signal intensity to histopathologic findings and metal content of the tumor and surrounding hepatic parenchyma. *Radiology* 210(1): 81–88, 1999.
189. Kelekis NL, Semelka RC, Woosley JT. Malignant lesions of the liver with high signal intensity on T1-weighted MR images. *J Magn Reson Imaging* 6: 291–294, 1996.
190. Jeong YY, Mitchell DG, Kamishima T. Small (<20 mm) enhancing hepatic nodules seen on arterial phase MR imaging of the cirrhotic liver: clinical implications. *AJR Am J Roentgenol* 178(6): 1327–1334, 2002.
191. Shimizu A, Ito K, Koike S, Fujita T, Shimizu K, Matsunaga N. Cirrhosis or chronic hepatitis: evaluation of small (< or = 2-cm) early-enhancing hepatic lesions with serial contrast-enhanced dynamic MR imaging. *Radiology* 226(2): 550–555, 2003.
192. Peterson MS, Baron RL, Murakami T. Hepatic malignancies: usefulness of acquisition of multiple arterial and portal venous phase images at dynamic gadolinium-enhanced MR imaging. *Radiology* 201: 337–345, 1996.
193. Rummeny E, Weissleder R, Stark DD, Saini S, Compton CC, Bennett W, Hahn PF, Wittenberg J, Malt RA, Ferrucci JT. Primary liver tumors: diagnosis by MR imaging. *AJR Am J Roentgenol* 152: 63–72, 1989.
194. Matsui O, Kadoya M, Kameyama T, Yoshikawa J, Arai K, Gabata T, Takashima T, Nakanuma Y, Terada T, Ida M. Adenomatous hyperplastic nodules in the cirrhotic liver: differentiation from hepatocellular carcinoma with MR imaging. *Radiology* 173: 123–126, 1989.
195. Rosenthal RE, Davis PL. MR imaging of hepatocellular carcinoma at 1.5 tesla. *Gastrointest Radiol* 17: 49–52, 1992.
196. Itoh K, Nishimura K, Togashi K, Fujisawa I, Noma S, Minami S, Sagoh T, Nakano Y, Itoh H, Mori K et al. Hepatocellular carcinoma: MR imaging. *Radiology* 164: 21–25, 1987.
197. Mahfouz AE, Hamm B, Wolf KJ. Dynamic gadopentetate dimeglumine-enhanced MR imaging of hepatocellular carcinoma. *Eur Radiol* 3: 453–458, 1993.
198. Yoshida H, Itai Y, Ohtomo K, Kokubo T, Minami M, Yashiro N. Small hepatocellular carcinoma and cavernous hemangioma: differentiation with dynamic FLASH MR imaging with Gd-DTPA. *Radiology* 171: 339–342, 1989.
199. Yamamoto T, Ikebe T, Mikami S, Shuto T, Hirohashi K, Kinoshita H, Sakurai M. Immunohistochemistry and angiography in adenomatous hyperplasia and small hepatocellular carcinoma. *Pathol Int* 46: 364–371, 1996.
200. Yamamoto T, Hirohashi K, Kaneda K, Ikebe T, Mikami S, Uenishi T, Kanazawa A, Takemura S, Shuto T, Tanaka H, Kubo S, Sakurai M, Kinoshita H. Relationship of the microvascular type to the tumor size, arterialization and dedifferentiation of human hepatocellular carcinoma. *Jpn J Cancer Res* 92: 1207–1213, 2001.
201. Mikami S, Kubo S, Hirohashi K, Shuto T, Kinoshita H, Nakamura K, Yamada R. Computed tomography during arteriography and arterial portography in small hepatocellular carcinoma and dysplastic nodule: a prospective study. *Jpn J Cancer Res* 91: 859–863, 2000.
202. Kanematsu M, Semelka RC, Leonardou P, Mastropasqua M, Armao D, Vaidean G et al. Angiogenesis in hepatocellular nodules: correlation of MR imaging and vascular endothelial growth factor. *J Magn Reson Imaging* 2004;20(3): 426–434.
203. Hussain SM, Semelka RC, Mitchell DG. MR imaging of hepatocellular carcinoma. *Magn Reson Imaging Clin N Am* 10(1): 31–52, 2002.
204. Kadoya M, Matsui O, Takashima T, Nonomura A. Hepatocellular carcinoma: correlation of MR imaging and histopathologic findings. *Radiology* 183(3): 819–825, 1992.
205. Kierans AS, Leonardou P, Hayashi P, Elazazzi M, Shaikh F, Semelka RC. MR imaging findings of rapidly progressive hepatocellular carcinoma (submitted).
206. McKenzie CA, Lim D, Ransil BJ, Morrin M, Pedrosa I, Yeh EN, Sodickson DK, Rofsky NM. Shortening MR image acquisition for volumetric interpolated breath-hold examination with a recently developed parallel imaging reconstruction technique: clinical feasibility. *Radiology* 230: 589–594, 2004.
207. Kanematsu M, Semelka RC, Leonardou P, Mastropasqua M, Lee JK. Hepatocellular carcinoma of diffuse type: MR imaging findings and clinical manifestations. *Magn Reson Imaging* 18(2): 189–195, 2003.
208. Okuda K, Noguchi T, Kubo Y, Shimokawa Y, Kojiro M, Nakashima T. A clinical and pathological study of diffuse type hepatocellular carcinoma. *Liver* 1(4): 280–289, 1981.
209. Craig JR, Peters RL, Edmondson HA, Omata M. Fibrolamellar carcinoma of the liver: a tumor of adolescents and young adults with distinctive clinico-pathologic features. *Cancer* 46: 372–379, 1980.
210. Corrigan K and Semelka RC. Dynamic contrast-enhanced MR imaging of fibrolamellar hepatocellular carcinoma. *Abdom Imaging* 20: 122–125, 1995.
211. Ichikawa T, Federle MP, Grazioli L, Madariaga J, Nalesnik M, Marsh W. Fibrolamellar hepatocellular carcinoma: imaging and pathologic findings in 31 recent cases. *Radiology* 213(2): 352–361, 1999.
212. Scheimberg IB, Pollock DJ, Collins PW, Doran HM, Newland AC, van der Walt JD. Pathology of the liver in leukemia and lymphoma. A study of 110 autopsies. *Histopathology* 26: 311–322, 1995.
213. Kelekis NL, Semelka RC, Siegelman ES, Ascher SM, Outwater EK, Woosley TJ, Reinhold C, Mitchell DG. Focal hepatic lymphoma: MR demonstration using current techniques including gadolinium enhancement. *J Magn Reson Imaging* 15(6): 625–636, 1997.
214. Kelekis NL, Warshauer DM, Semelka RC, Sallah AS. Nodular liver involvement in light chains multiple myeloma: appearance on US and MRI. *Clin Imaging* 21: 207–209, 1997.
215. Anthony PP. Primary carcinoma of the liver: a study of 282 cases in Ugandan Africans. *J Pathol* 110(1):37–48, 1973.
216. Hamrick-Turner J, Abbitt PL, Ros PR. Intrahepatic cholangiocarcinoma: MR appearance. *AJR Am J Roentgenol* 158:77–79, 1992.
217. Low RN, Sigeti JS, Francis IR, Weinman D, Bower B, Shimakawa A, Foo TK. Evaluation of malignant biliary obstruction: efficacy of fast multiplanar spoiled gradient-recalled MR imaging vs. spin-echo MR imaging, CT, and cholangiography. *AJR Am J Roentgenol* 162:315–323, 1994.
218. Buetow PC, Buck JL, Ros PR, Goodman ZD. Malignant vascular tumors of the liver: radiologic-pathologic correlation. *Radiographics* 14:153–166, 1994.
219. Koyama T, Fletcher JG, Johnson CD, Kuo MS, Notohara K, Burgart LJ. Primary hepatic angiosarcoma: findings at CT and MR imaging. *Radiology* 222(3): 667–673, 2002.

220. Worawattanakul S, Semelka RC, Kelekis NL, Woosley JT. Angiosarcoma of the liver: MR imaging pre- and post-chemotherapy. *Magn Reson Imaging* 15(5): 613–617, 1997.
221. Leonardou P, Semelka RC, Kanematsu M, Braga L, Woosley JT. Primary malignant mesothelioma of the liver: MR imaging findings. *Magn Reson Imaging* 21(9): 1091–1093, 2003.
222. Moran CA, Ishak KG, Goodman ZD. Solitary fibrous tumor of the liver: a clinicopathologic and immunohistochemical study of nine cases. *Ann Diagn Pathol* 2(1): 19–24, 1998.
223. Dean PJ, Haggitt RC, O'Hara CJ. Malignant epithelioid hemangioendothelioma of the liver in young women. Relationship to oral contraceptive use. *Am J Surg Pathol* 9(10): 695–704, 1985.
224. Leonardou P, Semelka RC, Mastropasqua M, Kanematsu M, Woosley JT. Epithelioid hemangioendothelioma of the liver. MR imaging findings. *Magn Reson Imaging* 20(8): 631–633, 2002
225. Buetow PC, Rao P, Marshall H. Imaging of pediatric liver tumors. *Magn Reson Imaging Clin N Am* 5(2): 397–413, 1997.
226. Helmberger TK, Ros PR, Mergo PJ, Tomczak R, Reiser MF. Pediatric liver neoplasms: a radiologic-pathologic correlation. *Eur Radiol* 9(7): 1339–1347, 1999.
227. Ros PR, Olmsted WW, Dachman AH, Goodman ZD, Ishak KG, Hartman DS. Undifferentiated (embryonal) sarcoma of the liver: radiologic-pathologic correlation. *Radiology* 161(1): 141–145, 1986.
228. Buetow PC, Buck JL, Pantongrag-Brown L, Marshall WH, Ros PR, Levine MS, Goodman ZD. Undifferentiated (embryonal) sarcoma of the liver: pathologic basis of imaging findings in 28 cases. *Radiology* 203(3): 779–783, 1997.
229. Carneiro RC, Fordham LA, Semelka RC. MR imaging of the pediatric liver. *Magn Reson Imaging Clin N Am* 10(1): 137–164, 2002.
230. Psatha EA, Semelka RC, Fordham L, Firat Z, Woosley JT. Undifferentiated (embryonal) sarcoma of the liver (USL): MRI findings including dynamic gadolinium enhancement. *Magn Reson Imaging* 22(6): 897–900, 2004.
231. Arrive L, Hricak H, Goldberg HI, Thoeni RF, Margulis AR. MR appearance of the liver after partial hepatectomy. *AJR Am J Roentgenol* 152: 1215–1220, 1989.
232. Bartolozzi C, Lencioni R, Caramella D, Falaschi F, Cioni R, DiCoscio G. Hepatocellular carcinoma: CT and MR features after transcatheter arterial embolization and percutaneous ethanol injection. *Radiology* 191: 123–128, 1994.
233. Bartolozzi C, Lencioni R, Caramella D, Mazzeo S, Ciancia EM. Treatment of hepatocellular carcinoma with percutaneous ethanol injection: evaluation with contrast-enhanced MR imaging. *AJR Am J Roentgenol* 162: 827–831, 1994.
234. Giovagnoni A, Paci E, Terilli F, Cellerino R, Piga A. Quantitative MR imaging data in the evaluation of hepatic metastases during systemic chemotherapy. *J Magn Reson Imaging* 5: 27–32, 1995.
235. Lee MJ, Mueller PR, Dawson SL, Gazelle SG, Hahn PF, Goldberg MA, Boland GW. Percutaneous ethanol injection for the treatment of hepatic tumors: indications, mechanism of action, technique, and efficacy. *AJR Am J Roentgenol* 164: 215–220, 1995.
236. Nagel HS and Bernardino ME. Contrast-enhanced MR imaging of hepatic lesions treated with percutaneous ethanol ablation therapy. *Radiology* 189: 265–270, 1993.
237. Sironi S, De Cobelli F, Livraghi T, Villa G, Zanello A, Taccagni G, Del Maschio AL. Small hepatocellular carcinoma treated with percutaneous ethanol injection: unenhanced and gadolinium-enhanced MR imaging follow-up. *Radiology* 192: 407–412, 1994.
238. Shirkhoda A and Baird S. Morphologic changes of the liver following chemotherapy for metastatic breast carcinoma: CT findings. *Abdom Imaging* 19: 39–42, 1994.
239. Soyer P, Bluemke DA, Zeitoun G, Marmuse JP, Levesque MLC. Detection of recurrent hepatic metastases after partial hepatectomy: value of CT combined with arterial portography. *AJR Am J Roentgenol* 162: 1327–1330, 1994.
240. Young ST, Paulson EK, Washington K, Gulliver DJ, Vredenburgh JJ, Baker ME: CT of the liver in patients with metastatic breast carcinoma treated by chemotherapy: findings simulating cirrhosis. *AJR Am J Roentgenol* 163: 1385–1388, 1994.
241. Harned RK, II, Chezmar JL, Nelson RC. Recurrent tumor after resection of hepatic metastases from colorectal carcinoma: location and time of discovery as determined by CT. *AJR Am J Roentgenol* 163: 93–97, 1994.
242. Lang EK, Brown CL Jr. Colorectal metastases to the liver: selective chemoembolization. *Radiology* 189: 417–422, 1993.
243. Scwickert HC, Stiskal M, Roberts TPL, van Dijke CF, Mann J, Muehler A, Shames DM, Demsar F, Disston A, Brasch RC. Contrast-enhanced MR imaging assessment of tumor capillary permeability: effect of irradiation on delivery of chemotherapy. *Radiology* 198: 893–898, 1996.
244. Matsumoto R, Selig AM, Colucci VM, Jolesz FA. MR monitoring during cryotherapy in the liver: predictability of histologic outcome. *J Magn Reson Imaging* 3: 770–776, 1993.
245. Matsumoto R, Oshio K, Jolesz FA. Monitoring of laser and freezing-induced ablation in the liver with T1-weighted MR imaging. *J Magn Reson Imaging* 2: 555–562, 1992.
246. Vogl TJ, Muller PK, Hammerstingl R et al. Malignant liver tumors treated with MR imaging-guided laser-induced thermotherapy: technique and prospective results. *Radiology* 196: 257–265, 1995.
247. Kuszyk BS, Choti MA, Urban BA, Chambers TP, Bluemke DA, Sitzmann JV, Fishman EK. Hepatic tumors treated by cryosurgery: normal CT appearance. *AJR Am J Roentgenol* 166: 363–368, 1996.
248. McLoughlin RF, Saliken JF, McKinnon G, Wiseman D, Temple W. CT of the liver after cryotherapy of hepatic metastases: imaging findings. *AJR Am J Roentgenol* 165: 329–332, 1995.
249. Braga L, Guller U, Semelka, RC. Pre-, peri-, and post-treatment imaging of the liver. *Radiol Clin N Am* 43(5): 915–927, 2005.
250. Braga L, Semelka RC, Pedro MS, de Barros N. Post-treatment malignant liver lesions. MR imaging. *Magn Reson Imaging Clin N Am.* 10(1): 53–73, 2002.
251. Marn CS, Andrews JC, Francis IR, Hollett MD, Walker SC, Ensminger WD. Hepatic parenchymal changes after intraarterial Y-90 therapy: CT findings. *Radiology* 187: 125–128, 1993.
252. Bilimoria MM, Lauwers GY, Doherty DA, Nagorney DM, Belghiti J, Do KA et al. Underlying liver disease, not tumor factors, predicts long-term survival after resection of hepatocellular carcinoma. *Arch Surg* 136(5): 528–535, 2001.
253. Harmon KE, Ryan JA, Jr., Biehl TR, Lee FT. Benefits and safety of hepatic resection for colorectal metastases. *Am J Surg* 177(5): 402–404, 1999.
254. Holbrook RF, Koo K, Ryan JA. Resection of malignant primary liver tumors. *Am J Surg* 171(5): 453–455, 1996.
255. Goshima S, Kanematsu M, Matsuo M, Kondo H, Kako N, Yokoyama R et al. Malignant hepatic tumor detection with ferumoxide-enhanced magnetic resonance imaging: is chemical-shift-selective fat suppression necessary for fast spin-echo sequence? *J Magn Reson Imaging* 20(1): 75–82, 2004.
256. Haran EF, Maretzek AF, Goldberg I, Horowitz A, Degani H. Tamoxifen enhances cell death in implanted MCF7 breast cancer by inhibiting endothelium growth. *Cancer Res.* 54: 5511–5514, 1994.
257. Semelka RC, Worawattanakul S, Mauro M, Bernard SA, Cance WG. Malignant hepatic tumors: changes on MRI after hepatic arterial chemoembolization—preliminary findings. *J Magn Reson Imaging* 8(1): 48–56, 1998.
258. Kierans AS, Elazzazi M, Braga L, Leonardou P, Gerber D, Burke C, Qureshi W, Kanematsu M, Semelka RC. Thermo-ablative focal treatments for malignant liver lesions: 10-year experience of MRI appearances of treatment response. AJR, 2009 (in press).

259. Dromain C, de Baere T, Elias D, Kuoch V, Ducreux M, Boige V et al. Hepatic tumors treated with percutaneous radio-frequency ablation: CT and MR imaging follow-up. *Radiology* 223(1): 255–262, 2002.
260. Goldberg SN, Charboneau JW, Dodd GD 3rd, Dupuy DE, Gervais DA, Gillams AR et al. International Working Group on Image-Guided Tumor Ablation. Image-guided tumor ablation: proposal for standardization of terms and reporting criteria. *Radiology* 228(2): 335–345, 2003.
261. Choi D, Lim HK, Kim MJ, Lee SH, Kim SH, Lee WJ, et al. Recurrent hepatocellular carcinoma: percutaneous radiofrequency ablation after hepatectomy. *Radiology* 230(1): 135–141, 2004.
262. Limanond P, Zimmerman P, Raman SS, Kadell BM, Lu DS. Interpretation of CT and MRI after radiofrequency ablation of hepatic malignancies. *AJR Am J Roentgenol.* 181(6): 1635–1640, 2003.
263. Kuszyk BS, Boitnott JK, Choti MA, Bluemke DA, Sheth S, Magee CA, et al. Local tumor recurrence following hepatic cryoablation: radiologic-histopathologic correlation in a rabbit model. *Radiology* 217(2): 477–486, 2000.
264. Lim HK, Choi D, Lee WJ, Kim SH, Lee SJ, Jang HJ et al. Hepatocellular carcinoma treated with percutaneous radio-frequency ablation: evaluation with follow-up multiphase helical CT. *Radiology* 221(2): 447–454, 2001.
265. Goldberg SN, Gazelle GS, Compton CC, Mueller PR, Tanabe KK. Treatment of intrahepatic malignancy with radiofrequency ablation: radiologic-pathologic correlation. *Cancer* 88(11): 2452–2463, 2000.
266. Chopra S, Dodd GD 3rd, Chanin MP, Chintapalli KN. Radiofrequency ablation of hepatic tumors adjacent to the gallbladder: feasibility and safety. *AJR Am J Roentgenol* 180(3): 697–701, 2003.
267. Joseph FB, Baumgarten DA, Bernardino ME. Hepatocellular carcinoma: CT appearance after percutaneous ethanol ablation therapy. Work in progress. *Radiology* 186(2): 553–556, 1993.
268. Mitsuzaki K, Yamashita Y, Nishiharu T, Sumi S, Matsukawa T, Takahashi M, et al. CT appearance of hepatic tumors after microwave coagulation therapy. *AJR Am J Roentgenol* 171(5): 1397–1403, 1998.
269. Schlund JF, Semelka RC, Kettritz U, Weeks SM, Kahlenberg M, Cance WG. Correlation of perfusion abnormalities on CTAP and immediate postintravenous gadolinium-enhanced gradient echo MRI. *Abdom Imaging* 21(1): 49–52, 1996.
270. Centers for Disease Control, National Center of Health Statistics (NCHS) Vital Statistics System (1998).
271. Bassignani M, Fulcher AS, Szucs RA, Chong WK, Prasad UR, Marcos A. Use of imaging for living donor liver transplantation. *Radiographics* 21: 39–52, 2001.
272. Weisner R, Demetris A, Belle S et al. Acute hepatic allograft rejection: incidence risk factor and impact on outcome. *Hepatology* 28: 638–645,1998.
273. Demetris AJ, Lasky S, Van Thiel DH, Starzl TE, Dekker A. Pathology of hepatic transplantation: a review of 62 adult allograft recipients immunosuppressed with a cyclosporine/steroid regimen. *Am J Pathol* 118: 151–161, 1985.
274. Wozney P, Zajko AB, Bron KM, Point S, Starzl TE. Vascular complications after liver transplantation: a 5-year experience. *AJR Am J Roentgenol* 147: 657–663, 1986.
275. Glockner JF, Forauer AR, Solomon H, Varma CR, Perman WH. Three-dimensional gadolinium-enhanced MR angiography of vascular complications after liver transplantation. *AJR Am J Roentgenol* 174: 1447–1452, 2000.
276. Ito K, Siegelman ES, Stolpen AH, Mitchell DG. MR imaging of complications after liver transplantation. *AJR Am J Roentgenol* 175: 1145–1149, 2000.
277. Stange BJ, Glanemann M, Nuessler NC, Settmacher U, Steinmuller T, Neuhaus P. Hepatic artery thrombosis after adult liver transplantation. *Liver Transpl* 9(6): 612–620, 2003.
278. Stafford-Johnson DB, Hamilton BH, Dong Q, Cho KJ, Turcotte JG, Fontana RJ et al. Vascular complications of liver transplantation: evaluation with gadolinium-enhanced MR angiography. *Radiology* 207(1): 153–160, 1998.
279. Kim BS, Kim TK, Jung DJ, Kim JH, Bae IY, Sung KB, Kim PN, Ha HK, Lee SG, Lee MG. Vascular complications after living related liver transplantation: evaluation with gadolinium-enhanced three-dimensional MR angiography. *AJR Am J Roentgenol* 181: 467–474, 2003.
280. Zajko AB, Bennett MJ, Campbell WL, Koneru B. Mucocele of the cystic duct remnant in eight liver transplant recipients: findings at cholangiography, CT, and US. *Radiology* 177: 691–693, 1990.
281. Lang P, Schnarkowski P, Grampp S, van Dijke C, Gindele A, Steffen R, Neuhaus P, Felix R. Liver transplantation: significance of the periportal collar on MRI. *J Comput Assist Tomogr* 19: 580–585, 1995.
282. Marincek B, Barbier PA, Becker CD, Mettler D, Ruchti C. CT appearance of impaired lymphatic drainage in liver transplants. *AJR Am J Roentgenol* 147: 519–523, 1986.
283. Pickhardt PJ and Siegel MJ. Posttransplantation lymphoproliferative disorders of the abdomen: CT evaluation in 51 patients. *Radiology* 213: 73–78, 1999.
284. Strouse PJ, Platt JF, Francis IR, Bree RL. Tumorous intrahepatic lymphoproliferative disorder in transplanted livers. *AJR Am J Roentgenol* 167: 1159–1162, 1996.
285. Nalesnik MA. The diverse pathology of post-transplant lymphoproliferative disorders: the importance of a standardized approach. *Transpl Infect Dis* 3: 88–96, 2001
286. Matsui O, Kadoya M, Takashima T, Kameyama T, Yoshikawa J, Tamura S. Intrahepatic periportal abnormal intensity on MR images: an indication of various hepatobiliary diseases. *Radiology* 171: 335–338, 1989.
287. Ferris JV, Baron RL, Marsh JW Jr, Oliver JH 3rd, Carr BI, Dodd GD 3rd. Recurrent hepatocellular carcinoma after liver transplantation: spectrum of CT findings and recurrence patterns. *Radiology* 198: 233–238, 1996.
288. Mieli-Vergani G, Vergani D. Autoimmune liver disease. *Indian J Pediatr* 69(1): 93–98, 2002.
289. Feld JJ, Heathcote EJ. Epidemiology of autoimmune liver disease. *J Gastroenterol Hepatol* 18(10): 1118–1128, 2003.
290. Lee YM, Kaplan MM. Primary sclerosing cholangitis. *N Engl J Med* 332(14): 924–933, 1999.
291. Burak K, Angulo P, Pasha TM, Egan K, Petz J, Lindor KD. Incidence and risk factors for cholangiocarcinoma in primary sclerosing cholangitis. *Am J Gastroenterol* 99(3): 523–526, 2004.
292. Bader TR, Beavers KL, Semelka RC. MR imaging features of primary sclerosing cholangitis: patterns of cirrhosis in relationship to clinical severity of disease. *Radiology* 226(3): 675–685, 2003.
293. Dodd GD 3rd, Baron RL, Oliver JH 3rd, Federle MP. End-stage primary sclerosing cholangitis: CT findings of hepatic morphology in 36 patients. *Radiology* 211(2): 357–362, 1999.
294. Ito K, Mitchell DG, Outwater EK, Blasbalg R. Primary sclerosing cholangitis: MR imaging features. *AJR Am J Roentgenol* 172(6): 1527–1533, 1999.
295. Revelon G, Rashid A, Kawamoto S, Bluemke DA. Primary sclerosing cholangitis: MR imaging findings with pathologic correlation. *AJR Am J Roentgenol* 173(4): 1037–1042, 1999.
296. Vergani D, Alvarez F, Bianchi FB, Cancado EL, Mackay IR, Manns MP et al. Liver autoimmune serology: a consensus statement from the committee for autoimmune serology of the International Autoimmune Hepatitis Group. *J Hepatol* 41(4): 677–683, 2004.

297. Ben-Ari Z, Czaja AJ. Autoimmune hepatitis and its variant syndromes. *Gut* 49(4): 589–594, 2001.
298. Krawitt EL. Autoimmune hepatitis. *N Engl J Med* 354(1): 54–66, 2006.
299. Autoimmune Hepatitis Group Report: review of criteria for diagnosis of autoimmune hepatitis. *J Hepatol* 31(5): 929–938, 1999.
300. Bilaj F, Hyslop WB, Rivero H, Firat Z, Vaidean G, Shrestha R, Woosley JT, Semelka R. MRI findings in autoimmune hepatitis: correlation with clinical staging. *Radiology* 236(3): 896–902, 2005.
301. Hyslop WB, Kierans AS, Leonardou P, Fritchie K, Darling J, Elazzazi M, Semelka RC. Overlap syndrome of autoimmune chronic liver diseases: MR imaging findings. JMRI, 2007 (in press).
302. Wenzel JS, Donohoe A, Ford KL 3rd, Glastad K, Watkins D, Molmenti E. Primary biliary cirrhosis: MR imaging findings and description of MR imaging periportal halo sign. *AJR Am J Roentgenol* 176(4): 885–9, 2001.
303. Akhan O, Akpinar E, Oto A, Koroglu M, Ozmen MN, Akata D, et al. Unusual imaging findings in Wilson's disease. *Eur Radiol* 12 *Suppl* 3: S66–9, 2002.
304. Marrero JA, Fontana RJ, Su GL, Conjeevaram HS, Emick DM, Lok AS. NAFLD may be a common underlying liver disease in patients with hepatocellular carcinoma in the United States. *Hepatology* 36(6): 1349–54, 2002.
305. Ratziu V, Bonyhay L, Di Martino V, Charlotte F, Cavallaro L, Sayegh-Tainturier MH, et al. Survival, liver failure, and hepatocellular carcinoma in obesity-related cryptogenic cirrhosis. *Hepatology* 35(6): 1485–93, 2002.
306. Clark JM, Diehl AM. Nonalcoholic fatty liver disease: an underrecognized cause of cryptogenic cirrhosis. *JAMA* 289(22): 3000–4, 2003.
307. Elias J Jr, Altun E, Zacks S, Armao D, Woosley JT, Semelka RC. MRI findings in nonalcoholic steatohepatitis: Correlation with histopathology and clinical staging. *Magn Reson Imaging* 27: 976–987, 2009.
308. Clouston AD, Powell EE. Nonalcoholic fatty liver disease: is all the fat bad? *Intern Med J* 34(4): 187–91, 2004.
309. Venkataraman S, Braga L, Semelka RC. Imaging the fatty liver. *Magn Reson Imaging Clin N Am* 10(1): 93–103, 2002.
310. Saadeh S, Younossi ZM, Remer EM, Gramlich T, Ong JP, Hurley M, et al. The utility of radiological imaging in nonalcoholic fatty liver disease. *Gastroenterology* 123(3): 745–50, 2002.
311. Hochman JA, Balistreri WF. Chronic viral hepatitis: always be current! *Pediatr Rev* 24(12): 399–410, 2003.
312. Feld JJ, Liang TJ. HCV persistence: cure is still a four letter word. *Hepatology* 41: 23–5, 2005
313. Alter MJ, Kruszon-Moran D, Nainan OV, McQuillan GM, Gao F, Moyer LA, Kaslow RA, Margolis HS. The prevalence of hepatitis C virus infection in the United States, 1988 through 1994. *N Engl J Med.* 341(8): 556–62, 1999.
314. Fauerholdt L, Schlichting P, Christensen E, Poulsen H, Tygstrup N, Juhl E. Conversion of micronodular cirrhosis into macronodular cirrhosis. *Hepatology* 3: 928–931, 1983.
315. Itai Y, Ohtomo K, Kokubo T, Minami M, Yoshida H. CT and MR imaging of postnecrotic liver scars. *J Comput Assist Tomogr* 12: 971–975, 1988.
316. Stark DD, Goldberg HI, Moss AA, Bass NM: Chronic liver disease: Evaluation by magnetic resonance. *Radiology* 150: 149–151, 1984.
317. Zhang XM, Mitchell DG, Shi H, Holland GA, Parker L, Herrine SK, et al. Chronic hepatitis C activity: correlation with lymphadenopathy on MR imaging. *AJR Am J Roentgenol* 179(2): 417–22, 2002.
318. Unger EC, Lee JK, Weyman PJ. CT and MR imaging of radiation hepatitis. *J Comput Assist Tomogr* 11: 264–268, 1987.
319. Yankelevitz DF, Knapp PH, Henschke CI, Nisce L, Yi Y, Cahill P. MR appearance of radiation hepatitis. *Clin Imaging* 16: 89–92, 1992.
320. Cutillo DP, Swayne LC, Fasciano MG, Schwartz JR. Absence of fatty replacement in radiation damaged liver: CT demonstration. *J Comput Assist Tomogr* 13: 259–261, 1989.
321. Garra BS, Shawker TH, Chang R, Kaplan K, White RD. The ultrasound appearance of radiation-induced hepatic injury. Correlation with computed tomography and magnetic resonance imaging. *J Ultrasound Med* 7: 605–609, 1988.
322. Anthony PP, Ishak KG, Nayak NC, Poulsen HE, Scheuer PJ, Sobin LH. The morphology of cirrhosis. The morphology of cirrhosis. Recommendations on definition, nomenclature, and classification by a working group sponsored by the World Health Organization. *J Clin Pathol* 31: 395–414, 1978.
323. Gore RM. Diffuse liver disease. In: Gore RM, Levine NS, Laufer I, eds. *Textbook of Gastrointestinal Radiology.* Philadelphia, Saunders, 1994. p.1968–2017.
324. Ito K, Mitchell DG, Gabata T, Hussain SM. Expanded gallbladder fossa: simple MR imaging sign of cirrhosis. *Radiology* 211: 723–726, 1999.
325. Ito K, Mitchell DG, Gabata T. Enlargement of hilar periportal space: a sign of early cirrhosis at MR imaging. *J Magn Reson Imaging* 11(2): 136–40, 2000.
326. Lafortune M, Matricardi L, Denys A, Favret M, Dery R, Pomier-Layrargues G. Segment 4 (the quadrate lobe): a barometer of cirrhotic liver disease at US. *Radiology* 206(1): 157–60, 1998.
327. Ito K, Mitchell DG, Siegelman ES. Cirrhosis: MR imaging features. *Magn Reson Imaging Clin N Am* 10(1): 75–92, 2002.
328. Mitchell DG, Lovett KE, Hann HW, Ehrlich S, Palazzo J, Rubin R. Cirrhosis: Multiobserver analysis of hepatic MR imaging findings in a heterogeneous population. *J Magn Reson Imaging* 3: 313–321, 1993.
329. Semelka RC, Chung JJ, Hussain SM, Marcos HB, Woosley JT. Chronic hepatitis: correlation of early patchy and late linear enhancement patters on gadolinium-enhanced MR images with histopathology-initial experience. *J Magn Reson Imaging* 13: 385–391, 2001.
330. Marti-Bonmati L, Talens A, del Olmo J, de Val A, Serra MA, Rodrigo JM, Ferrandez A, Torres V, Rayon M, Vilar JS. Chronic hepatitis and cirrhosis: evaluation by means of MR imaging with histologic correlation. *Radiology* 188: 37–43, 1993.
331. Shimizu A, Ito K, Koike S, Fujita T, Shimizu K, Matsunaga N. Cirrhosis or chronic hepatitis: evaluation of small (< or = 2-cm) early-enhancing hepatic lesions with serial contrast-enhanced dynamic MR imaging. *Radiology* 226(2): 550–555, 2003.
332. Kanematsu M, Danet MI, Leonardou P, Mastropasqua M, Mosetti MA, Braga L, Woosley JT, Semelka RC. Early heterogeneous enhancement of the liver: magnetic resonance imaging findings and clinical significance. *J Magn Reson Imaging* 20(2): 242–249, 2004.
333. *Harrison's Principle of Internal Medicine.* 16th ed. / New York: McGraw-Hill.
334. Baron RL, Campbell WL, Dodd GD. Peribiliary cysts associated with severe liver disease: imaging-pathologic correlation. *AJR Am J Roentgenol* 162: 631–636, 1994.
335. Itai Y, Ebihara R, Tohno E, Tsunoda HS, Kurosaki Y, Saida Y, Doy M. Hepatic peribiliary cysts: multiple tiny cysts within the larger portal tract, hepatic hilum, or both. *Radiology* 191: 107–110, 1994.
336. Terayama N, Matsui O, Hoshiba K, Kadoya M, Yoshikawa J, Gabata T, Takashima T, Terada T, Nakanuma Y, Shinozaki K, et al. Peribiliary cysts in liver cirrhosis: US, CT, and MR findings. *J Comput Assist Tomogr* 19: 419–423, 1995.
337. Anthony PP, Ishak KG, Nayak NC, Poulsen HE, Scheuer PJ, Sobin LH. The morphology of cirrhosis. The morphology of cirrhosis. Recommendations on definition, nomenclature, and classification by a working group sponsored by the World Health Organization. *J Clin Pathol* 31: 395–414, 1978.

338. Hytiroglou P, Theise NH. Differential diagnosis of hepatocellular nodular lesions. *Semin Diag Pathol* 15: 285–299, 1998.
339. Ohtomo K, Itai Y, Ohtomo Y, Shiga J, Iio M. Regenerating nodules of liver cirrhosis: MR imaging with pathologic correlation. *AJR Am J Roentgenol* 154: 505–507, 1990.
340. Terada T, Nakanuma Y. Survey of iron-accumulative macroregenerative nodules in cirrhotic livers. *Hepatology* 10: 851–854, 1989.
341. Ito K, Mitchell DG, Gabata T, Hann HW, Kim PN, Fujita T, Awaya H, Honjo K, Matsunaga N. Hepatocellular carcinoma: association with increased iron deposition in the cirrhotic liver at MR imaging. *Radiology* 212(1): 235–240, 1999.
342. Soyer P, Lacheheb D, Caudron C, Levesque M. MRI of adenomatous hyperplastic nodules of the liver in Budd-Chiari syndrome. *J Comput Assist Tomogr* 17(1): 86–89, 1993.
343. Vilgrain V, Lewin M, Vons C, Denys A, Valla D, Flejou JF, Belghiti J, Menu Y. Hepatic nodules in Budd-Chiari syndrome: imaging features. *Radiology* 210(2): 443–450,1999.
344. Cazals-Hatem D, Vilgrain V, Genin P, Denninger MH, Durand F, Belghiti J, Valla D, Degott C. Arterial and portal circulation and parenchymal changes in Budd-Chiari syndrome: a study in 17 explanted livers. *Hepatology* 37(3): 510–519, 2003.
345. Theise ND, Schwartz M, Miller C, Thung SN. Macroregenerative nodules and hepatocellular carcinoma in forty-four sequential adult liver explants with cirrhosis. *Hepatology* 16(4): 949–955, 1992.
346. Sakamoto M, Hirohashi S, Shimosato Y. Early stages of multistep hepatocarcinogenesis: adenomatous hyperplasia and early hepatocellular carcinoma. *Hum Pathol* 22(2): 172–178, 1991.
347. Takayama T, Makuuchi M, Hirohashi S, Sakamoto M, Okazaki N, Takayasu K, Kosuge T, Motoo Y, Yamazaki S, Hasegawa H. Malignant transformation of adenomatous hyperplasia to hepatocellular carcinoma. *Lancet* 10;336(8724): 1150–1153, 1990.
348. Kadoya M, Matsui O, Takashima T, Nonomura A. Hepatocellular carcinoma: correlation of MR imaging and histopathologic findings. *Radiology* 183: 819–825, 1992.
349. Roncalli M, Roz E, Coggi G, Di Rocco MG, Bossi P, Minola E, et al. The vascular profile of regenerative and dysplastic nodules of the cirrhotic liver: implications for diagnosis and classification. *Hepatology* 30(5): 1174–8, 1999.
350. Ward J, Guthrie JA, Schott DJ, Atchley J, Wilson D, Davies MH, Wyatt JI, Robinson PJ. Hepatocellular carcinoma in the cirrhotic liver: double-contrast MR imaging for diagnosis. *Radiology* 216: 154–162, 2000.
351. Mitchell DG, Rubin R, Siegelman ES, Burk DL Jr, Rifkin MD. Hepatocellular carcinoma within siderotic regenerative nodules: appearance as a nodule within a nodule on MR images. *Radiology* 178(1): 101–103, 1991.
352. Muramatsu Y, Nawano S, Takayasu K, Moriyama N, Yamada T, Yamasaki S, Hirohashi S. Early hepatocellular carcinoma: MR imaging. *Radiology* 181(1): 209–213, 1991.
353. Sadek AG, Mitchell DG, Siegelman ES, Outwater EK, Matteucci T, Hann HW. Early hepatocellular carcinoma that develops within macroregenerative nodules: growth rate depicted at serial MR imaging. *Radiology* 195(3): 753–756, 1995.
354. Groszmann RJ, Atterbury CE. The pathophysiology of portal hypertension: a basis for classification. *Semin Liver Dis* 2: 177–186, 1982.
355. Chopra S, Dodd GD, Chintapalli KN, Esola CC, Ghiatas AA. Mesenteric, omental, and retroperitoneal edema in cirrhosis: frequency and spectrum of CT findings. *Radiology* 211: 737–742, 1999.
356. Starzl TE, Francavilla A, Halgrimson CG, Francavilla FR, Porter KA, Brown TH, Putnam CW. The origin, hormonal nature, and action of hepatotrophic substances in portal venous blood. *Surg Gynecol Obstet* 137: 179–199, 1973.
357. Matsuo M, Kanematsu M, Kim T, Hori M, Takamura M, Murakami T, Kondo H, Moriyama N, Nakamura H, Hoshi H. Esophageal varices: diagnosis with gadolinium-enhanced MR imaging of the liver for patients with chronic liver damage. *AJR Am J Roentgenol.* 180(2): 461–466, 2003.
358. Finn JP, Edelman RR, Jenkins RL, Lewis WD, Longmaid HE, Kane RA, Stokes KR, Mattle HP, Clouse ME. Liver transplantation: MR angiography with surgical validation. *Radiology* 179: 265–269, 1991.
359. Zhang XM, Mitchell DG, Shi H, Holland GA, Parker L, Herrine SK, Pasqualin D, Rubin R. Chronic hepatitis C activity: correlation with lymphadenopathy on MR imaging. *AJR Am J Roentgenol.* 179(2): 417–422, 2002.
360. Brandhagen DJ, Fairbanks VF, Batts KP, Thebodeau SN. Update on hereditary hemochromatosis and the HFE gene. *Mayo Clin Proc* 74: 917–9121, 1999.
361. Siegelman ES, Mitchell DG, Semelka RC. Abdominal iron deposition: metabolism, MR findings, and clinical importance. *Radiology* 199: 13–22, 1996.
362. Barton JC, McDonnell SM, Adams PC, Brissot P, Powell LW, Edwards CQ, Cook JD, Kowdley KV. Management of hemochromatosis. Hemochromatosis Management Working Group. *Ann Intern Med* 129: 932–939, 1998.
363. McLaren G, Muir W, Kellermeyer R. Iron overload disorders: natural history, pathogenesis, diagnosis and therapy. *Crit Rev Clin Lab Sci* 19: 205–226, 1984.
364. Guyader D, Gandon Y, Sapey T, Turlin B, Mendler MH, Brissot P, Deugnier Y. Magnetic resonance iron-free nodules in genetic hemochromatosis. *Am J Gastroenterol* 94: 1083–1086, 1999.
365. Siegelman ES, Mitchell DG, Rubin R, Hann HW, Kaplan KR, Steiner RM, Rao VM, Schuster SJ, Burk DL, Jr., Rifkin MD. Parenchymal versus reticuloendothelial iron overload in the liver: distinction with MR imaging. *Radiology* 179: 361–366, 1991.
366. Terada T, Kadoya M, Nakanuma Y, Matsui O. Iron-accumulating adenomatous hyperplastic nodule with malignant foci in the cirrhotic liver. Histopathologic, quantitative iron, and magnetic resonance imaging in vitro studies. *Cancer* 65: 1994–2000, 1990.
367. Terada T, Nakanuma Y. Iron-negative foci in siderotic macroregenerative nodules in human cirrhotic liver. A marker of incipient neoplastic lesions. *Arch Pathol Lab Med* 113: 916–920, 1989.
368. Ernst O, Sergent G, Bonvarlet P, Canva-Delcambre V, Paris JC, L'Hermine. Hepatic iron overload: diagnosis and quantification with MR imaging. *AJR Am J Roentgenol.* 168: 1205–8, 1997.
369. Bonkovsky HL, Rubin RB, Cable EE, Davidoff A, Rijcken TH, Stark DD. Hepatic iron concentration: noninvasive estimation by means of MR imaging techniques. *Radiology* 212: 227–34, 1999.
370. Alustiza JM, Artetxe J, Castiella A, Agirre C, Emparanza JI, Otazua P, Garcia-Bengoechea M, Barrio J, Mujica F, Recondo JA; Gipuzkoa Hepatic Iron Concentration by MRI Study Group. MR quantification of hepatic iron concentration. *Radiology* 230: 479–84, 2004.
371. Siegelman ES, Outwater E, Hanau CA, Ballas SK, Steiner RM, Rao VM, Mitchell DG. Abdominal iron distribution in sickle cell disease: MR findings in transfusion and nontransfusion dependent patients. *J Comput Assist Tomogr* 18: 63–67, 1994.
372. Pomerantz S and Siegelman ES. MR imaging of iron depositional disease. *Magn Reson Imaging Clin North Am* 10(1): 105–120, 2002.
373. Yates CK, Streight RA. Focal fatty infiltration of the liver simulating metastatic disease. *Radiology* 159: 83–84, 1986.
374. Mitchell DG. Focal manifestations of diffuse liver disease at MR imaging. *Radiology* 185: 1–11, 1992.
375. Mitchell DG, Kim I, Chang TS, Vinitski S, Consigny PM, Saponaro SA, Ehrlich SM, Rifkin MD, Rubin R. Fatty liver. Chemical shift phase-difference and suppression magnetic resonance imaging techniques in animals, phantoms, and humans. *Invest Radiol* 26: 1041–1052, 1991.

376. Matsui O, Kadoya M, Takahashi S, Yoshikawa J, Gabata T, Takashima T, Kitagawa K. Focal sparing of segment IV in fatty livers shown by sonography and CT: correlation with aberrant gastric venous drainage. *AJR Am J Roentgenol* 164: 1137–1140, 1995.
377. Itai Y. Focal sparing versus a hepatic tumor in fatty liver. *AJR Am J Roentgenol* 172: 242–243, 1999.
378. Arai K, Matsui O, Takashima T, Ida M, Nishida Y. Focal spared areas in fatty liver caused by regional decreased portal flow. *AJR Am J Roentgenol* 151: 300–302, 1988.
379. Arita T, Matsunaga N, Honma Y, Nishikawa E, Nagaoka S. Focally spared area of fatty liver caused by arterioportal shunt. *J Comput Assist Tomogr* 20: 360–362, 1996.
380. Kawamori Y, Matsui O, Takahashi S, Kadoya M, Takashima T, Miyayama S. Focal hepatic fatty infiltration in the posterior edge of the medial segment associated with aberrant gastric venous drainage: CT, US, and MR findings. *J Comput Assist Tomogr.* 20: 356–359, 1996.
381. Grossholz M, Terrier F, Rubbia L, Becker C, Stoupis C, Hadengue A, Mentha G. Focal sparing in the fatty liver as a sign of an adjacent space-occupying lesion. *AJR Am J Roentgenol* 17: 1391–1395, 1998.
382. Chung JJ, Kim MJ, Kim JH, Lee JT, Yoo HS. Fat sparing of surrounding liver from metastasis in patients with fatty liver: MR imaging with histopathologic correlation. *AJR Am J Roentgenol* 180: 1347–50, 2003.
383. Parfrey NA, Hutchins GN. Hepatic fibrosis in the mucopolysaccharises. *Am J Med* 81: 825–829, 1986.
384. Matalan, RH. Metabolic diseases. In: Behrman RE, Kligman RM, Nelson WE, Vaughan III VC, eds. *Textbook of Pediatrics.* 14 ed. Philadelphia, W.B. Saunders, 1992. p. 372–77.
385. Hurwitz LM, Thompson WM. Calcified hepatic arteriovenous fistula found after biopsy of the liver: unusual cause of calcification in the right upper quadrant. *AJR Am J Roentgenol* 79(5): 1293–5, 2002.
386. Sharlock S and Dooley J. *Diseases of the Liver and Biliary System.* p. 1086. 10 edition. Blackwell science. 1997.
387. Semelka RC, Lessa T, Shaikh F, Miller FH, Elazzazi M, Dyson M. MRI findings of intrahepatic vascular shunts. *J Magn Reson Imag* 29: 617–620, 2009.
388. Cotran RS, Cumar V, Robbins SL. *Pathologic Basis of Disease.* P. 872. 5th edition. W.B. Saunders Company Philadelphia, 1994.
389. Itai Y, Ohtomo K, Kokubo T, Okada Y, Yamauchi T, Yoshida H. Segmental intensity differences in the liver on MR images: a sign of intrahepatic portal flow stoppage. *Radiology* 167: 17–19, 1988.
390. Lorigan JG, Charnsangavej C, Carrasco CH, Richli WR, Wallace S. Atrophy with compensatory hypertrophy of the liver in hepatic neoplasms: Radiographic findings. *AJR Am J Roentgenol* 150: 1291–1295, 1988.
391. Carr DH, Hadjis NS, Banks LM, Hemingway AP, Blumgart LH. Computed tomography of hilar cholangiocarcinoma: a new sign. *AJR Am J Roentgenol* 145: 53–56, 1985.
392. Itai Y, Murata S, Kurosaki Y. Straight border sign of the liver: spectrum of CT appearances and causes. *Radiographics* 15: 1089–1102, 1995.
393. Schlund JF, Semelka RC, Kettritz U, Eisenberg LB, Lee JKT. Transient increased segmental hepatic enhancement distal to portal vein obstruction on dynamic gadolinium-enhanced gradient echo MR images. *J Magn Reson Imaging* 5: 375–377, 1995.
394. De Gaetano AM, Lafortune M, Patriquin H, De Franco A, Aubin B, Raradis K. Cavernous transformation of the portal vein: patterns of intrahepatic and splanchnic collateral circulation detected with Doppler sonography. *AJR Am J Roentgenol* 165: 1151–1156, 1995.
395. Nakao N, Miura K, Takahashi H, Miura T, Ashida H, Ishikawa Y, Utsunomiya J. Hepatic perfusion in cavernous transformation of the portal vein: evaluation by using CT angiography. *AJR Am J Roentgenol* 152: 985–986, 1989.
396. Schlund JF, Semelka RC, Kettritz U, Weeks SM, Kahlenberg M, Cance WG. Correlation of perfusion abnormalities on CTAP and immediate postintravenous gadolinium-enhanced gradient echo MRI. *Abdom Imaging* 21: 49–52, 1996.
397. Gilchrist AJ and Hayes PC. Vascular disorders of the liver. In: *Diseases of the Gastrointestinal Tract and Liver.* Shearman DJC, Finlayson NDC, Camilleri M. eds. 3 ed. New York, Churchill Livingstone, 1997. p. 1079–81.
398. Miller WJ, Federle MP, Straub WH, Davis PL. Budd-Chiari syndrome: imaging with pathologic correlation. *Abdom Imaging* 18: 329–335, 1993.
399. Mathieu D, Vasile N, Menu Y, Van Beers B, Lorphelin JM, Pringot J. Budd-Chiari syndrome: dynamic CT. *Radiology* 165: 409–413, 1987.
400. Murata S, Itai Y, Hisashi K, Nakajima K, et al. Effect of temporary occlusion of the hepatic vein on dual blood supply in the liver: evaluation with spiral CT. *Radiology* 195: 351–356, 1995.
401. Pollard JJ, Nebesar RA. Altered hemodynamics in the Budd-Chiari syndrome demonstrated by selective hepatic and selective splenic angiography. *Radiology* 89: 236–243, 1967.
402. Noone TC, Semelka RC, Siegelman ES, Balci NC, Hussain SM, et al. Budd-Chiari syndrome: spectrum of appearances of acute, subacute, and chronic disease with magnetic resonance imaging. *J Magn Reson Imaging* 11: 44–50, 2000.
403. Noone T, Semelka RC, Woosley JT, Pisano ED. Ultrasound and MR findings in acute Budd-Chiari syndrome with histopathologic correlation. *J Comput Assist Tomogr* 20: 819–822, 1996.
404. Castellano G, Canga F, Solis-Herruzo JA, Colina F, Martinez-Montiel MP, Morillas JD. Budd-Chiari syndrome associated with nodular regenerative hyperplasia of the liver. *J Clin Gastroenterol* 11: 698–702, 1989.
405. de Sousa JM, Portmann B, Williams R. Nodular regenerative hyperplasia of the liver and the Budd-Chiari syndrome. Case report, review of the literature and reappraisal of pathogenesis. *J Hepatol* 12: 28–35, 1991.
406. Brancatelli G, Federle MP, Grazioli L, Golfieri R, Lencioni R. Large regenerative nodules in Budd-Chiari syndrome and other vascular disorders of the liver: CT and MR imaging findings with clinicopathologic correlation. *AJR Am J Roentgenol.* 178: 877–83, 2002.
407. Brancatelli G, Federle MP, Grazioli L, Golfieri R, Lencioni R. Benign regenerative nodules in Budd-Chiari syndrome and other vascular disorders of the liver: radiologic-pathologic and clinical correlation. *Radiographics* 22: 847–62, 2002.
408. Maetani Y, Itoh K, Egawa H, Haga H, Sakurai T, Nishida N, Ametani F, Shibata T, Kubo T, Tanaka K, Konishi J. Benign hepatic nodules in Budd-Chiari syndrome: radiologic-pathologic correlation with emphasis on the central scar. *AJR Am J Roentgenol.* 178: 869–75, 2002.
409. Soyer P, Lacheheb D, Caudron C, Levesque M. MRI of adenomatous hyperplastic nodules of the liver in Budd-Chiari syndrome. *J Comput Assist Tomogr* 17: 86–89, 1993.
410. Cazals-Hatem D, Vilgrain V, Genin P, Denninger MH, Durand F, Belghiti J, Valla D, Degott C. Arterial and portal circulation and parenchymal changes in Budd-Chiari syndrome: a study in 17 explanted livers. *Hepatology* 37: 510–9, 2003.
411. Nakashima T, Okuda K, Kojiro M, et al. Pathology of hepatocellular carcinoma in Japan. 232 consecutive cases autopsied in 10 years. *Cancer* 51: 863–877, 1983.
412. Rooholamini SA, Au AH, Hansen GC, Kioumehr F, Dadsetan MR, Chow PP, Kurzel RB, Mikhail G. Imaging of pregnancy-related complications. *Radiographics* 13: 753–770, 1993.

413. Brown JJ, Borrello JA, Raza HS, Balfe DM, Baer AB, Pilgram TK, Atilla S. Dynamic contrast-enhanced MR imaging of the liver: parenchymal enhancement patterns. *Magn Reson Imaging* 13: 1–8, 1995.
414. Kanematsu M, Semelka RC, Matsuo M, Kondo H, Enya M, Goshima S, Moriyama N, Hoshi H. Gadolinium-enhanced MR imaging of the liver: optimizing imaging delay for hepatic arterial and portal venous phases–a prospective randomized study in patients with chronic liver damage. *Radiology* 225(2): 407–15, 2002.
415. Seeff LC, Seeff LB. Pulmonary disorders and the liver. In: *The Liver and Systemic Disease*. Gitlin N, ed. New York, Churchill Livingstone, New York, 1997. p. 29–31.
416. Kessler A, Mitchell DG, Israel HL, Goldberg BB. Hepatic and splenic sarcoidosis: Ultrasound and MR imaging. *Abdom Imaging* 18: 159–163, 1993.
417. Warshauer DM, Semelka RC, Ascher SM. Nodular sarcoidosis of the liver and spleen: appearance on MR images. *J Magn Reson Imaging* 4: 553–557, 1994.
418. Dasgupta D, Guthrie A, McClean P, Davison S, Luntley J, Rajwal S, et al. Liver transplantation for a hilar inflammatory myofibroblastic tumor. *Pediatr Transplant* 8(5): 517–21, 2004.
419. Horiuchi R, Uchida T, Kojima T, Shikata T. Inflammatory pseudotumor of the liver. Clinicopathologic study and review of the literature. *Cancer* 65(7): 1583–90, 1990.
420. Shek TW, Ng IO, Chan KW. Inflammatory pseudotumor of the liver. Report of four cases and review of the literature. *Am J Surg Pathol* 17: 231–238, 1993.
421. Horiuchi R, Uchida T, Kojima T, Shikata T. Inflammatory pseudotumor of the liver. Clinicopathologic study and review of the literature. *Cancer* 65: 1583–1590, 1990.
422. Venkataraman S, Semelka RC, Braga L, Woosley JT. Inflammatory myofibroblastic tumor of the hepato-biliary system: appearances on MRI. *Radiology* 227: 758–763, 2003.
423. Kelekis NL, Warshauer DM, Semelka RC, Eisenberg LB, Woosley JT. Inflammatory pseudotumor of the liver: appearance on contrast enhanced helical CT and dynamic MR images. *J Magn Reson Imaging* 5: 551–553, 1995.
424. Oto A, Akhan O, Ozmen M. Focal inflammatory diseases of the liver. *Eur J Radiol* 32: 61–75, 1999
425. Bertel CK, van Heerden JA, Sheedy PF. Treatment of pyogenic hepatic abscesses. Surgical vs. percutaneous drainage. *Arch Surg* 121: 554–558, 1986.
426. Balci NC, Semelka RC, Noone TC, Siegelman ES, Beeck BO, Brown JJ, Lee MG. Pyogenic hepatic abscesses: MRI findings on T1- and T2-weighted and serial gadolinium-enhanced gradient-echo images. *J Magn Reson Imaging* 9: 285–290, 1999.
427. Mendez RJ, Schiebler ML, Outwater EK, Kressel HY. Hepatic abscesses: MR imaging findings. *Radiology* 190: 431–436, 1994.
428. Balci NC and Sirvanci M. MR imaging of infective liver lesions. *Magn Reson Imaging*. 10 (1): 121–135, 2002.
429. Ralls PW, Henley DS, Colletti PM, Benson R, Raval JK, Radin DR, Boswell WD, Jr., Halls JM. Amebic liver abscess: MR imaging. *Radiology* 165: 801–804, 1987.
430. Balci NC, Tunaci A, Semelka RC, Tunaci M, Özden I, Rezanu IB. Hepatic alveolar echinococcosis: MRI findings. *Magn Reson Imaging* 18: 537–541, 2000.
431. Landay MJ, Setiawan H, Hirsch G, Christensen EE, Conrad MR. Hepatic and thoracic amaebiasis. *AJR Am J Roentgenol.* 135: 449–454, 1980.
432. Lebovics E, Thung SN, Schaffner F. The liver in the acquired immunodeficiency syndrome: a clinical and histologic study. *Hepatology* 5: 293–298, 1995
433. Schneiderman DJ, Arenson DM, Cello JP. Hepatic disease in patients with acquired immune deficiency syndrome (AIDS). *Hepatology* 7: 925–930,1987.
434. Pantongrag-Brown L, Krebs TL, Daly BD, et al. Frequency of abdominal CT findings in AIDS patients with *M. Avium* complex bacteraemia. *Clin Radiol.* 53: 816–819, 1998.
435. Shirkhoda A, Lopez-Berestein G, Holbert JM, Luna MA. Hepatosplenic fungal infection: CT and pathologic evaluation after treatment with liposomal amphotericin B. *Radiology* 159: 349–353, 1986.
436. Lewis JH, Patel HR, Zimmerman HJ. The spectrum of hepatic candidiasis. *Hepatology* 2: 479–487, 1982.
437. Sallah S, Semelka RC, Kelekis N, Worawattanakul S, Sallah W. Diagnosis and monitoring response of treatment of hepatosplenic candidiasis in patients with acute leukemia using magnetic resonance imaging. *Acta Haematol* 100: 77–81, 1998.
438. Semelka RC, Kelekis NL, Sallah S, Worawattanakul S, Ascher SM. Hepatosplenic fungal disease: diagnostic accuracy and spectrum of appearance on MR imaging. *AJR Am J Roentgenol.* 169(5): 1311–6, 1997.
439. Semelka RC, Shoenut JP, Greenberg HM, Bow EJ. Detection of acute and treated lesions of hepatosplenic candidiasis: comparison of dynamic contrast-enhanced CT and MR imaging. *J Magn Reson Imaging* 2: 341–345, 1992.
440. Cho JS, Kim EE, Varma DG, Wallace S. MR imaging of hepatosplenic candidiasis superimposed on hemochromatosis. *J Comput Assist Tomogr* 14: 774–776, 1990.
441. Lamminen AE, Anttila VJ, Bondestam S, Ruutu T, Ruutu PJ. Infectious liver foci in leukemia: comparison of short-inversion-time inversion-recovery, T1-weighted spin-echo, and dynamic gadolinium-enhanced MR imaging. *Radiology* 191: 539–543, 1994.
442. Kelekis NL, Semelka RC, Jeon HJ, Sallah AS, Shea TC, Woosley JT. Dark ring sign: finding in patients with fungal liver lesions and transfusional hemosiderosis undergoing treatment with antifungal antibiotics. *Magn Reson Imaging* 14: 615–618, 1996.
443. Grossman RI, Kemp SS, Ip CY, Fishman JE, Gomori JM, Joseph PM, Asakura T. Importance of oxygenation in the appearance of acute subarachnoid hemorrhage on high field magnetic resonance imaging. *Acta Radiol Suppl* 369: 56–58, 1986.
444. Gomori JM, Grossman RI, Yu-Ip C, Asakura T. NMR relaxation times of blood: dependence on field strength, oxidation state, and cell integrity. *J Comput Assist Tomogr* 11: 684–90, 1987.
445. Grossman RI, Gomori JM, Goldberg HI, Hackney DB, Atlas SW, Kemp SS, Zimmerman RA, Bilaniuk LT. MR imaging of hemorrhagic conditions of the head and neck. *Radiographics* 8: 441–454, 1988.
446. Hayman LA, Taber KH, Ford JJ, Saleem A, Gurgun M, Mohamed S, Bryan RN. Effect of clot formation and retraction on spin-echo MR images of blood: an in vitro study. *AJNR Am J Neuroradiol* 10: 1155–8, 1989.
447. Hayman LA, Taber KH, Ford JJ, Bryan RN. Mechanisms of MR signal alteration by acute intracerebral blood: old concepts and new theories. *AJNR Am J Neuroradiol* 12: 899–907, 1991.
448. Janick PA, Hackney DB, Grossman RI, Asakura T. MR imaging of various oxidation states of intracellular and extracellular hemoglobin. *AJNR Am J Neuroradiol* 12: 891–897, 1991.
449. Bradley WG Jr. MR appearance of hemorrhage in the brain. *Radiology* 189: 15–26, 1994.
450. Balci NC, Semelka RC, Noone TC, Ascher SM. Acute and subacute liver-related hemorrhage. MRI findings. *Magn Reson Imaging* 17(2): 207–211, 1999.
451. Hasegawa S, Eisenberg LB, Semelka RC. Active intrahepatic gadolinium extravasation following TIPS. *Magn Reson Imaging*. 16: 851–855, 1998.
452. Gomori JM, Grossman RI, Hackney DB, Goldberg HI, Zimmerman RA, Bilaniuk LT. Variable appearances of subacute intracranial hematomas on high-field spin-echo MR. *AJR Am J Roentgenol* 150: 171–8, 1988.

CHAPTER 3

GALLBLADDER AND BILIARY SYSTEM

ERSAN ALTUN, TILL BADER, JORGE ELIAS, JR., FAIQ SHAIKH, AND RICHARD C. SEMELKA

INTRODUCTION

Significant technical improvements of MRI hardware and software during recent years have led to the development of new and faster imaging sequences that are capable of demonstrating soft tissue well and visualizing the biliary and pancreatic ductal systems with excellent image quality, sharpness, and resolution previously only provided by endoscopic retrograde cholangiopancreatography (ERCP). In several studies, these MR techniques, termed magnetic resonance cholangiopancreatography (MRCP), have been shown to be comparable to ERCP in the diagnosis of choledocholithiasis, malignant obstruction of the biliary and pancreatic ducts, congenital anomalies, and chronic pancreatitis [1–8]. The advantages of MRCP over other imaging techniques include the following: 1) The examination is noninvasive and requires no anesthesia; 2) the examination is not operator dependent, and high-quality images can be obtained consistently; 3) no administration of intraductal or intravenous contrast agent is necessary; 4) no ionizing radiation is employed; 5) visualization of ducts proximal to an obstruction is superior to that achieved by ERCP; 6) MRCP can be successfully performed in the presence of biliary-enteric anastomoses (e.g., hepaticojejunostomy, choledochojejunostomy, Billroth II anastomosis); and 7) combination with conventional MR sequences is possible and helpful for the evaluation of duct wall and extraductal disease [9]. A significant advantage of ERCP is that it allows therapeutic interventions at the time of initial diagnosis. Although generally considered a safe procedure, ERCP is associated with morbidity and mortality rates of 8% and 1%, respectively [10]. In addition, unsuccessful cannulation of the common bile duct (CBD) or pancreatic duct occurs in 3–10% of cases [11, 12]. Therefore, in many institutions MRCP has become the primary imaging modality for diagnostic purposes in the biliary system, with ERCP reserved for therapeutic interventions (e.g., sphincterotomy, stone removal, dilatation of strictures, stent placement) [1, 13, 14]. Ultrasound, because of its lower costs, remains the modality of choice for the evaluation of cholecystolithiasis, which accounts for 90% of gallbladder diseases.

Abdominal-Pelvic MRI, Third Edition, edited by Richard C. Semelka. Copyright © 2010 John Wiley & Sons, Inc.

NORMAL ANATOMY

The intrahepatic bile ducts are a component of the intrahepatic portal triad. They follow the course of portal venous branches along their ventral aspect. Subsegmental branches join to form segmental branches that join to form the right and left hepatic biliary ducts, which join to form the common hepatic duct (CHD). The confluence of both hepatic ducts is usually at the level of the porta hepatis, but it can be substantially lower. The gallbladder is situated in the gallbladder fossa, located between the right and left lobes of the liver, between Couinaud segments four and five. Anatomically, the gallbladder is composed of the fundus, body, and neck. The gallbladder is usually oval in shape, measuring approximately 7–10 cm in length and 2–3.5 cm in width, which can vary substantially depending on dietary status. The wall thickness of a normal, well-filled gallbladder does not exceed 3 mm. The gallbladder is connected to the CHD via the cystic duct, which has a mucosal endoluminal fold (called the spiral fold or valve). The confluence of the cystic duct and the CHD is typically located superior to the head of the pancreas to form the common bile duct (CBD). The CBD enters the head of the pancreas and usually joins with the main pancreatic duct (Wirsung) just before it enters the duodenum through the sphincter of Oddi in the major papilla (papilla of Vater).

MRI TECHNIQUE

T2-Weighted Sequences/MRCP

Magnetic resonance cholangiopancreatography (MRCP) is based on the acquisition of heavily T2-weighted images to provide visualization of stationary or slow-moving fluids (e.g., bile) with high signal intensity. Because of the heavy T2 weighting of these sequences, the signal from the pancreatico-biliary system appears hyperintense, whereas the background tissue (e.g., hepatic and pancreatic tissue, peritoneal fat, fast-flowing blood) is either very low signal or signal void, resulting in excellent contrast and depiction of the pancreatico-biliary system. The use of phased-array surface coil imaging, small field of view, and fat suppression techniques has resulted in higher signal-to-noise and contrast-to-noise ratios, allowed the acquisition of thinner sections and measurement of T2 rather than T2* decay, decreased susceptibility artifacts, and diminished sensitivity to motion artifacts and slow blood flow [15–18].

Current MRCP techniques are based on echo-train spin-echo techniques that allow two-dimensional (2D) and three-dimensional (3D) approaches. Multiple 180° pulses with successive echoes (echo train) are acquired with a separate phase encoding gradient applied before each echo. Each of these detected echoes represents a different line within k-space. Ultrafast single-shot echo-train spin-echo techniques are capable of acquiring images in less than 1 s [19, 20]. After a single 90° excitation pulse, an extremely long echo train of 100–150 refocusing 180° pulses is obtained as a single-shot technique. After acquiring slightly more than half of k-space after the single 90° pulse, the remainder of k-space is filled by extrapolation, because of the intrinsic symmetry of k-space (half-Fourier technique). The extremely long echo train leads to diminution of echo signal intensity as the echo train progresses and, consequently, to decreased signal-to-noise and contrast-to-noise ratios. However, this effect is counteracted by the ultrashort acquisition time (less than 1 s), which "freezes" any physiological motion and avoids misregistration, and by the very low signal intensity from background tissue, which is an effect of the very long TE (600–1000 ms). Overall, this leads to a reduction of noise and an increase in contrast. The half-Fourier single-shot echo-train spin-echo sequences that are currently most widely used are half-Fourier RARE (rapid acquisition with relaxation enhancement) and HASTE (half-Fourier acquisition single-shot turbo spin echo) [21–23]. Acquisition of images with a very long TE renders very little signal from tissue with short TE such as fat and parenchymal organs, which makes the application of fat suppression techniques unnecessary. Fluids with relatively short TE, such as concentrated bile or mucinous fluid, however, will also give very little signal, which may hinder the depiction of small biliary ducts or mucinous lesions. An intermediate TE (80–100 ms) results in images in which all fluid, including concentrated bile and mucinous fluid, is bright and even small ducts are well depicted. The use of fat suppression to diminish the signal from surrounding tissue is advisable and makes maximum-intensity projection (MIP) post-processing possible. To suppress signal from intestinal fluid, oral application of iron- or manganese-containing contrast agents has been investigated. The diagnostic benefits, however, are questionable [24–26].

MRCP can be performed with thick-section and thin-section sequences. For thick-section images, a thick-collimation single section of 4- to 5-cm thickness is acquired in a right anterior oblique coronal plane, obtained in less than 2 s (figs. 3.1 and 3.2). Several slabs can be acquired in various rotations to view the ducts from different angles. The images resemble conventional ERCP images and are particularly useful to provide an overview of the pancreatico-biliary system and to visualize nondilated ducts. However, thick-section technique is not appropriate to investigate intraductal pathologies because visualization of small intraductal signal-void structures (e.g., calculi) is masked by partial

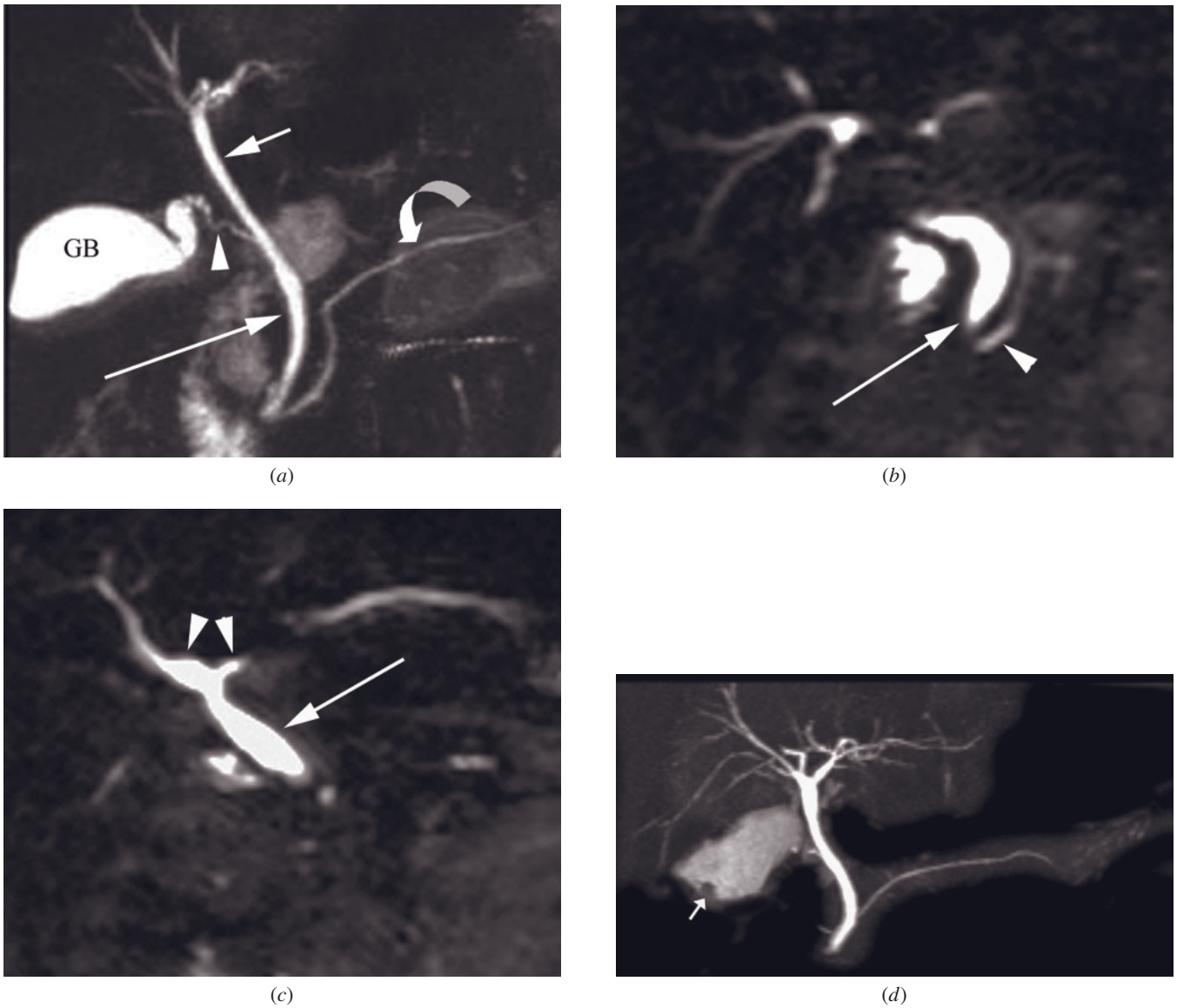

FIG. 3.1 Normal biliary system, MRCP. Thick-slab T2-weighted fat-suppressed single-shot echo-train spin-echo image (*a*) showing a good overview of the normal intra- and extrahepatic biliary system depicting the gallbladder (GB, *a*), the common bile duct (long arrow, *a*), the common hepatic duct (short arrow, *a*), the cystic duct (arrowhead, *a*), and the pancreatic duct (curved arrow, *a*). Thin-slab T2-weighted fat-suppressed single-shot echo-train spin-echo images (*b*, *c*) in a different patient demonstrate more detail and allow exact evaluation of the lumen and walls of the preampullary section of the common bile duct (long arrow, *b*), the pancreatic duct (short arrow, *b*), the common hepatic duct (long arrow, *c*), and the confluence of the right and left hepatic ducts (arrowheads, *c*). Navigator pulse triggered 30-MRCP in a third patient shows excellent depiction of biliary and pancreatic ducts. A gallstone is present in the gallbladder (arrow, *d*).

volume averaging with intraductal high signal from fluid (e.g., bile). Therefore, the additional acquisition of thin-section images with a thin-collimation multisection sequence is essential. Images in a right anterior oblique plane provide a cholangiographic display capturing the bifurcation of the CHD into right and left hepatic ducts (figs. 3.1 and 3.3). An additional acquisition in the axial plane provides a useful evaluation of the distal CBD and the pancreatic duct. Alternatively, thick-slab images in the coronal and axial planes can be used as localizers to focus the acquisition of thin-collimation images on the middle and distal CBD in the coronal plane. As another alternative, coronal thick-section images can be used to assess the range for axial thin-section images covering the entire biliary and pancreatic ductal system. On these images, a thin-section paracoronal series can be exactly targeted to depict the bifurcation of the CHD and the entire course of the CBD. Slice thickness of

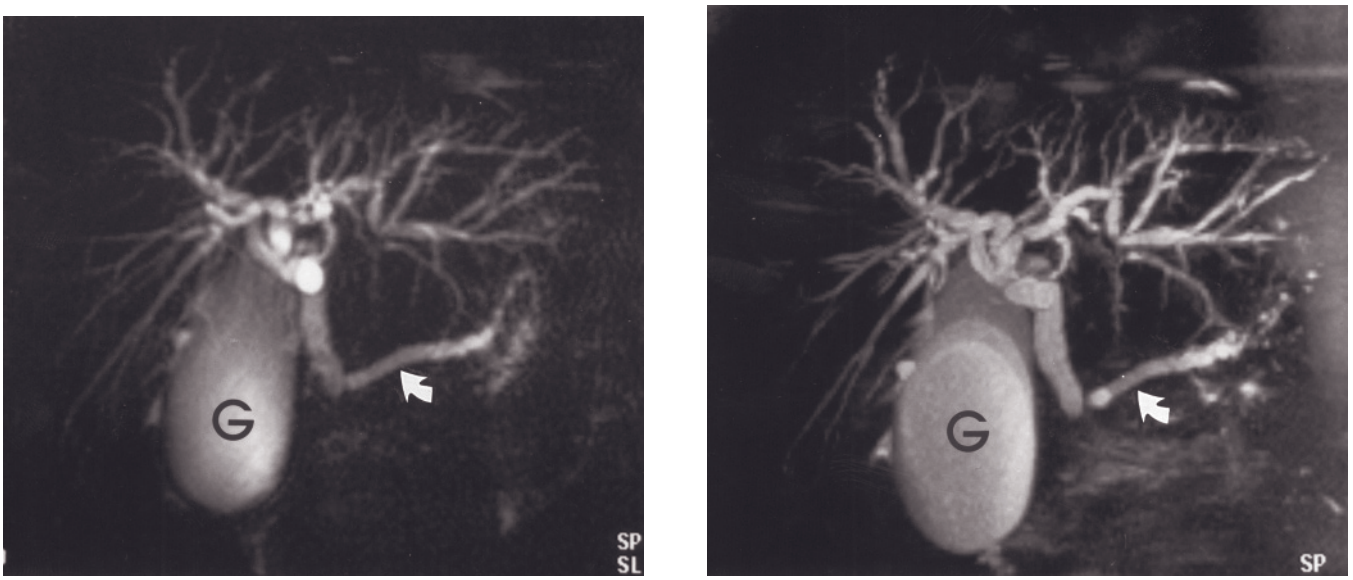

(*a*) (*b*)

Fig. 3.2 Thick-section MRCP versus 3D MIP reconstruction image. T2-weighted fat-suppressed thick-section MRCP single-shot echo-train spin-echo (*a*) and 3D MIP reconstruction image (*b*) from a series of thin-section single-shot echo-train spin-echo images. A pancreatic head carcinoma obstructs the preampullary CBD and pancreatic duct. The entire biliary tree and the pancreatic duct (curved arrow, *a*, *b*) are dilated. Note the finer resolution and detail of the 3D MIP image (*b*). G = gallbladder.

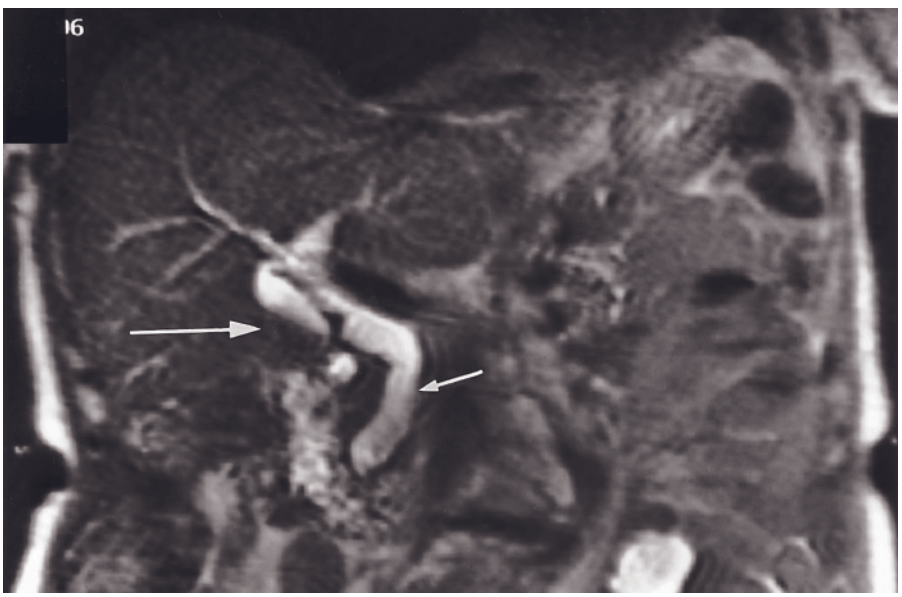

(*a*)

(*b*)

Fig. 3.3 Thin-section MRCP versus 3D MIP reconstruction image. MRCP 3D MIP reconstruction (*a*) and coronal T2-weighted fat-suppressed thin-section single-shot echo-train spin-echo (*b*) images. On the MIP image (*a*), severe dilation of the CBD (short arrow, *a*) is shown, but no CBD calculus is visualized. Multiple signal-void calculi are demonstrated in the gallbladder (long arrow, *a*). The coronal thin-section image (*b*) reveals a 5-mm preampullary CBD stone (arrow, *b*). Coronal T2-weighted thin-section echo-train

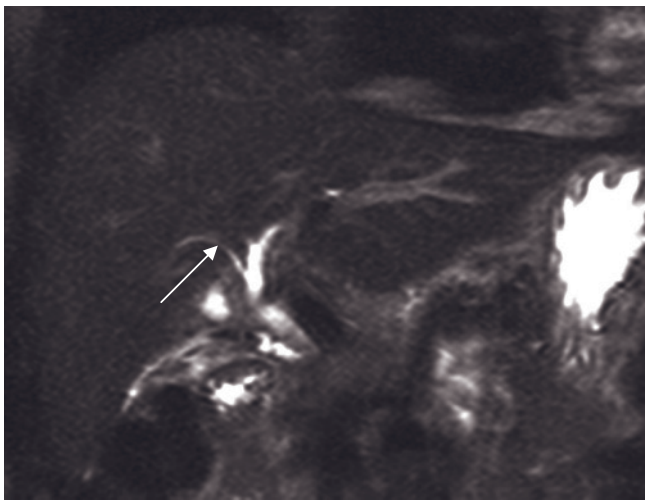

(*c*)

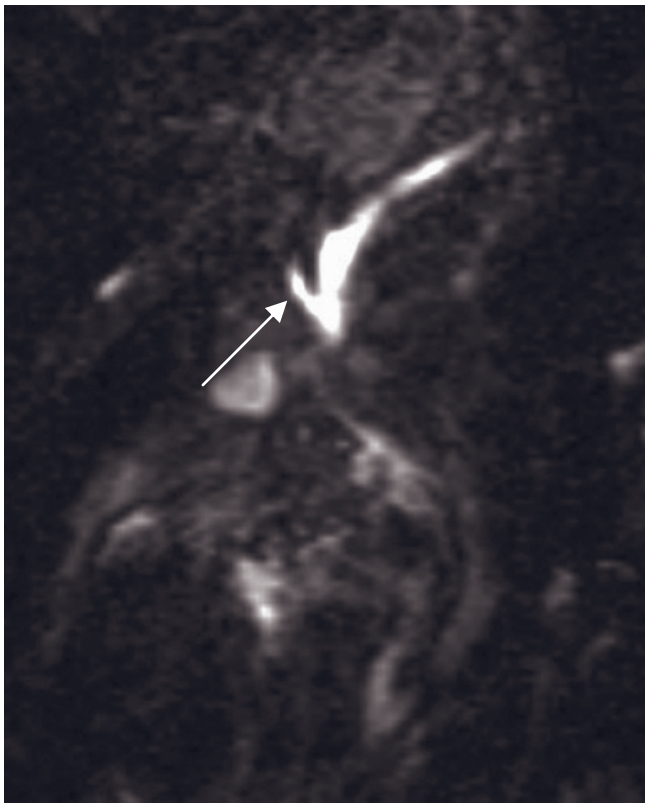

(*d*)

(*e*)

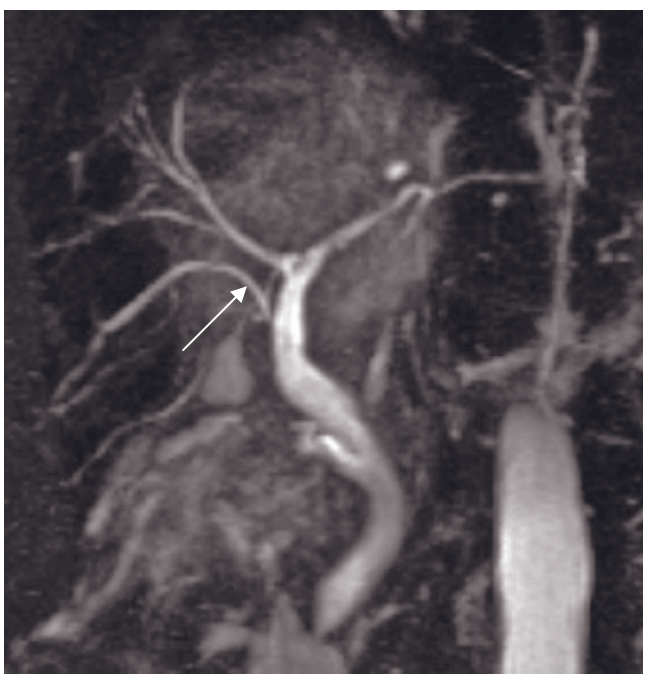

(*f*)

FIG. 3.3 (*Continued*) spin-echo (*c*), coronal thin-section fast spin-echo MRCP (*d*), thick-section fast spin-echo MRCP (*e*), and reconstructed 3D MIP MRCP (*f*) images demonstrate the right accessory bile duct in another patient.

1–3 mm provides sufficient signal to obtain good-quality images and is sufficiently thin to detect small calculi (see figs. 3.1 and 3.3). Thin-collimation images can be obtained as multiple single-section acquisitions with no gap in an interleaved fashion to avoid cross-talk.

Three-dimensional reconstruction can also be performed on the thin-collimation source images, using a maximum-intensity projection (MIP) algorithm that generates images that closely resemble conventional cholangiograms (see figs. 3.1 and 3.3). However, volume averaging effects degrade spatial and contrast resolution, which makes it necessary to use the thin-source images for the evaluation of pathology, in particular for the detection of small stones and subtle mural irregularity.

Single-shot echo-train spin-echo sequences, such as HASTE and RARE techniques, can be applied as breath-hold or breathing-independent sequences. The breathing-independent thick-section approach is the fastest technique and is especially useful in patients who are uncooperative or cannot hold their breath (e.g., infants, the very sick, and old patients). For thin-section acquisitions, misregistrations due to respiratory motion should be avoided and thus breath-hold sequences are generally preferable. A new non-breath-hold respiratory-triggered turbo spin echo (TSE) technique uses navigator pulses to register the movement of the diaphragm in order to compensate for respiratory motion [27, 28]. In this technique the high-resolution data set is acquired over several respiratory cycles. A series of navigator pulses are acquired in order to measure the diaphragm position and thus to detect when the patient has reached the relatively long quiet phase at end expiration. At that point, the sequence switches from navigation to imaging and acquires several lines of k-space using a TSE approach. The respiratory navigator then resumes in order to ensure that the next repetition is also acquired with the diaphragm in roughly the same position. With the use of a volumetric, heavily T2-weighted sequence (TE ~600 ms), 3D Turbo Spin-Echo images are acquired over a period of several minutes, which allows the reconstruction of 3D images and thin 2D images [27, 28].

T1-Weighted Sequences

T1-weighted sequences are useful for the evaluation of duct walls and parenchymal lesions. These can be acquired as T1-weighted gradient-echo sequences in a 2D or a 3D technique, obtained before and after gadolinium administration. Fat suppression techniques are essential as they improve the delineation of enhancing duct walls, inflammatory tissue, small lymph nodes, and tumor infiltration from surrounding fatty tissue [29]. The use of breath-hold T1-weighted gradient-echo sequences after gadolinium administration also provides information on the blood supply and interstitial space of diseased tissue that facilitates characterization.

In addition to standard nonspecific extracellular gadolinium chelates, T1-shortening intravenous contrast agents that are partly eliminated in bile have been used for the evaluation of the biliary system, including gadobenate dimeglumine (Multihance) and gadoxetic acid (Eovist) [30, 31]. Manganese-based contrast agent Mn-DPDP is also eliminated through the biliary route; however, it is not currently available in the USA. Owing to their lipophilic character, these contrast agents are taken up by hepatocytes and secreted into the biliary ductal system. Gadoxetic acid (Eovist) has a greater fractional elimination by the biliary system than gadobenate dimeglumine (Multihance), and as a result biliary elimination is visualized at 15 min with gadoxetic acid (Eovist) compared to 1 h with gadobenate dimeglumine (Multihance) [31]. On T1-weighted images, this leads to bright signal of contrasted bile in biliary ducts and gallbladder (fig. 3.4). Bright bile images can be generated with 2D or 3D T1-weighted gradient-echo techniques. However, in the presence of high-grade biliary obstruction the bile ducts distal to the obstruction may remain noncontrasted, and in patients with diminished hepatocyte function the biliary system may be poorly opacified. Laceration or injury to the biliary system may be revealed as high-signal fluid leaking beyond the biliary system.

NORMAL APPEARANCE AND VARIANTS

Gallbladder

On T2-weighted sequences, the walls of the gallbladder and bile ducts are of low signal intensity and normal bile shows high signal intensity (fig. 3.5). On T1-weighted images, the wall of the gallbladder is of intermediate signal intensity, comparable to adjacent soft tissue such as liver. Bile within the gallbladder may vary from very low to high signal intensity on T1-weighted images, because of variations in the concentration of water, cholesterol, and bile salts (see fig. 3.5) [32]. Nonconcentrated bile accumulates in the gallbladder and demonstrates low signal intensity on T1-weighted sequences, similar to water. With reabsorption of water and increased cholesterol and bile salt concentration, the T1 relaxation time decreases and the signal from concentrated bile becomes increasingly high with increased concentration (fig. 3.6) [32]. In the presence of concentrated bile (e.g., in prolonged fasting state), a layering effect is often appreciated, with the concentrated hyperintense bile in the dependent portion of the

(*a*)

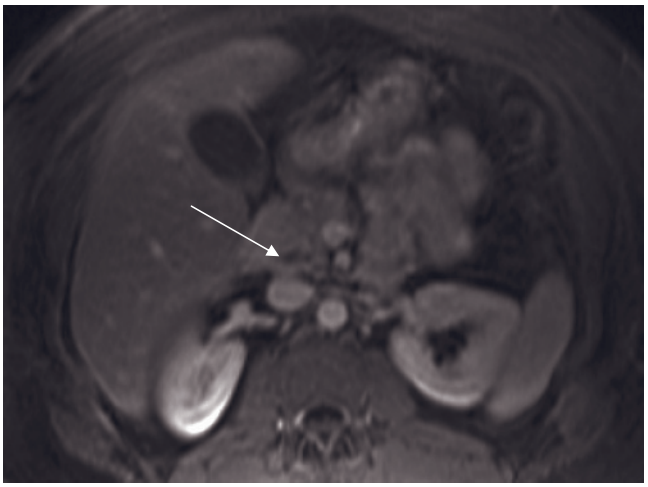

(*b*)

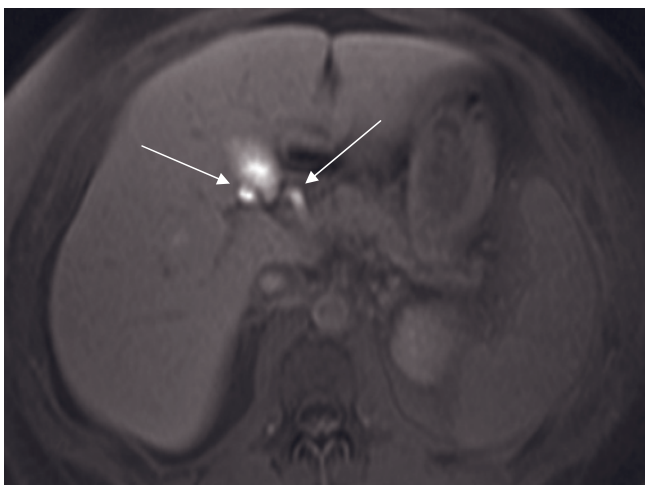

(*c*)

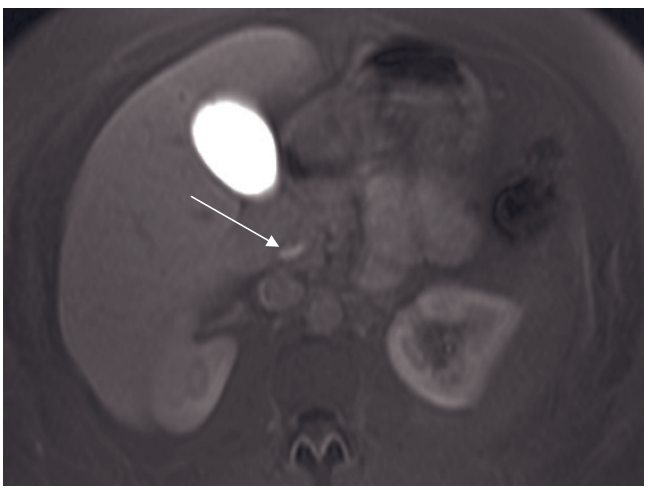

(*d*)

(*e*)

FIG. 3.4 Contrast-enhanced normal biliary tree. T1-weighted coronal Mn-DPDP-enhanced GE image (*a*) with fat suppression. The normal intrahepatic (small arrows) and extrahepatic (curved arrow) bile ducts demonstrate high signal intensity due to the T1 shortening of Mn-DPDP, which is excreted in the bile. Note also the enhancement of normal liver parenchyma. T1-weighted postgadolinium fat-suppressed 3D-GE images acquired after the administration of gadobenate dimeglumine (Multihance) (*b–d*) and gadoxetic acid (Eovist) (*e*). The common bile duct is seen as a hypointense structure on hepatic venous phase 3D-GE image (*b*) after the administration of gadobenate dimeglumine in another patient. The extrahepatic bile ducts (arrows, *c*), the common bile duct (arrow, *d*), and the gallbladder show contrast enhancement on 1-h delayed 3D-GE images (*c*, *d*) after the administration of gadobenate dimeglumine. The common bile duct (arrow, *e*) also shows enhancement on 15-min delayed coronal 3D-GE image (*e*) after the administration of gadoxetic acid in another patient. Gadobenate dimeglumine and gadoxetic acid have both extracellular and intracellular properties. They are hepatocyte-specific contrast agents (intracellular property) and are taken up by hepatocytes and excreted into the bile ducts. Therefore, they have dual elimination, including biliary and renal. They can be used as routine extracellular gadolinium agents for the acquisition of arterial, venous, and interstitial phase images. Delayed imaging also allows us to obtain additional morphologic and functional information for the liver and biliary system and their pathologies. Note that the liver is enhanced on delayed images (*c–e*). The enhancement of the liver is more with gadoxetic acid because of its higher biliary elimination (50%) compared to the biliary elimination of gadobenate dimeglumine (3%).

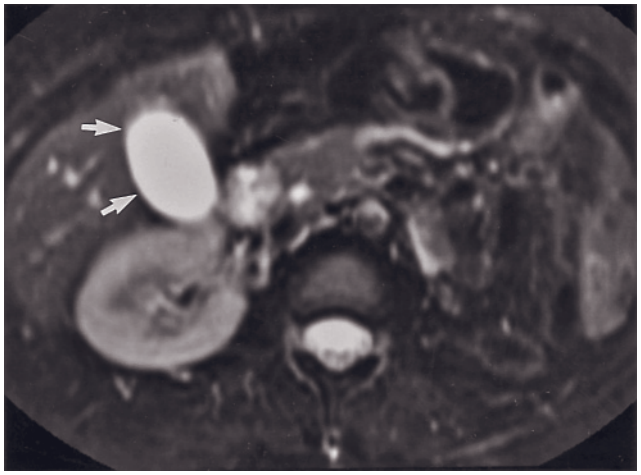

(*a*)

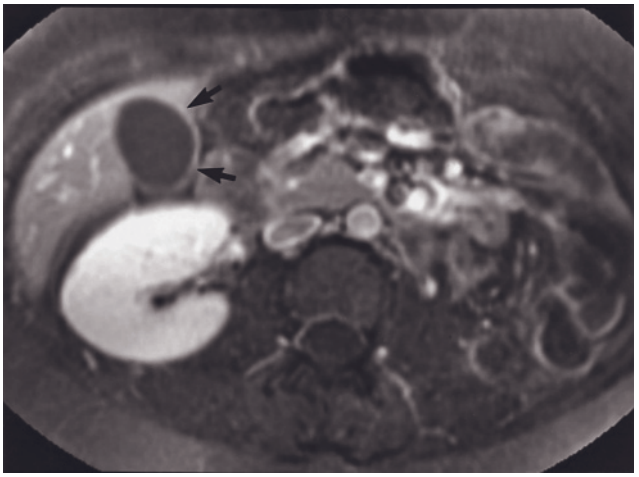

(*b*)

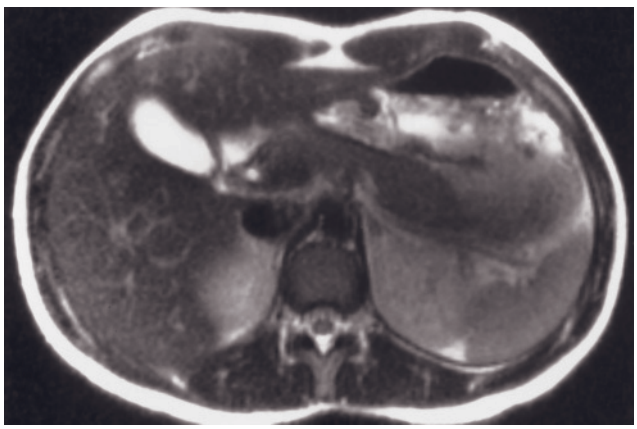

(*c*)

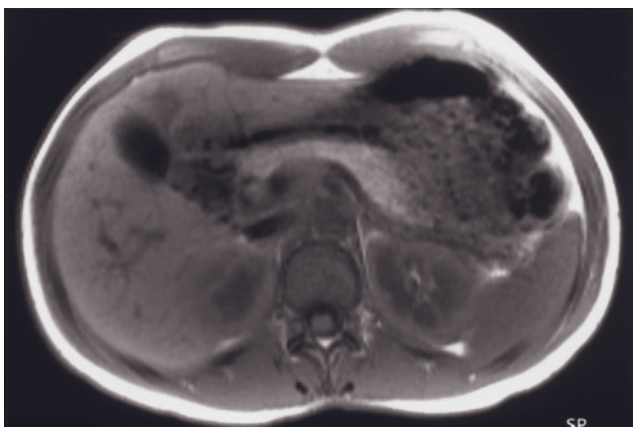

(*d*)

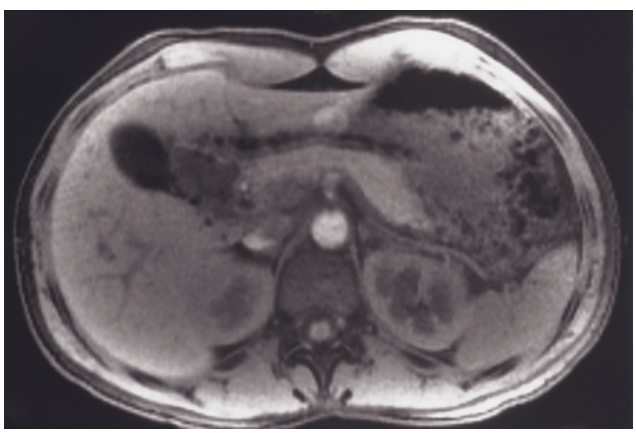

(*e*)

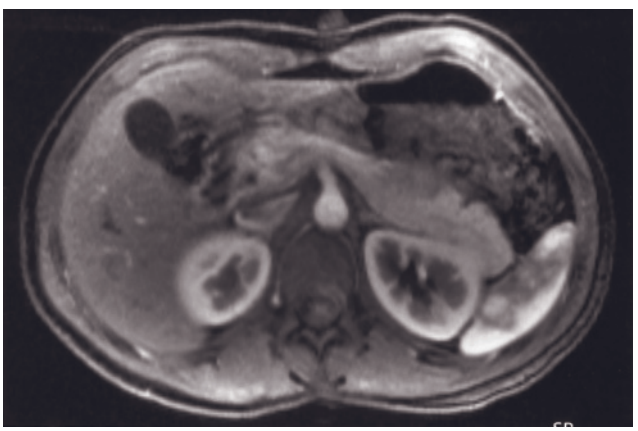

(*f*)

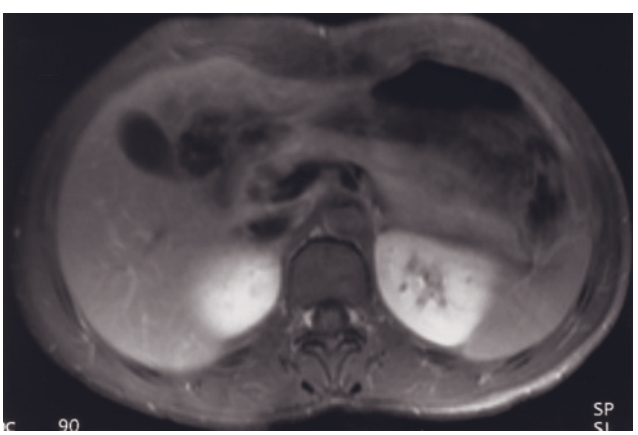

(*g*)

FIG. 3.5 Normal gallbladder. T2-weighted fat-suppressed spin-echo (*a*) and gadolinium-enhanced T1-weighted fat-suppressed spin-echo (*b*) images. On the T2-weighted image (*a*), the gallbladder content is high signal intensity and the gallbladder wall (arrows) is not well visualized. On the gadolinium-enhanced T1-weighted fat-suppressed spin-echo image (*b*), the gallbladder wall (arrows) is well shown as a thin enhancing structure. The gallbladder wall adjacent to the liver is not clearly defined because the enhancement of gallbladder wall and liver are similar.

T2-weighted simple shot echo-train spin-echo (*c*), T1-weighted GE (*d*), fat-suppressed GE (*e*), immediate postgadolinium fat-suppressed GE (*f*), and 2-min postgadolinium fat-suppressed spin-echo (*g*) images in a second patient with normal gallbladder. The bile is high in signal on the T2-weighted image (*c*) and low in signal on the T1-weighted images (*d–g*).The normal gallbladder wall is barely perceptible as a thin line, best shown on the immediate postgadolinium image (*f*).

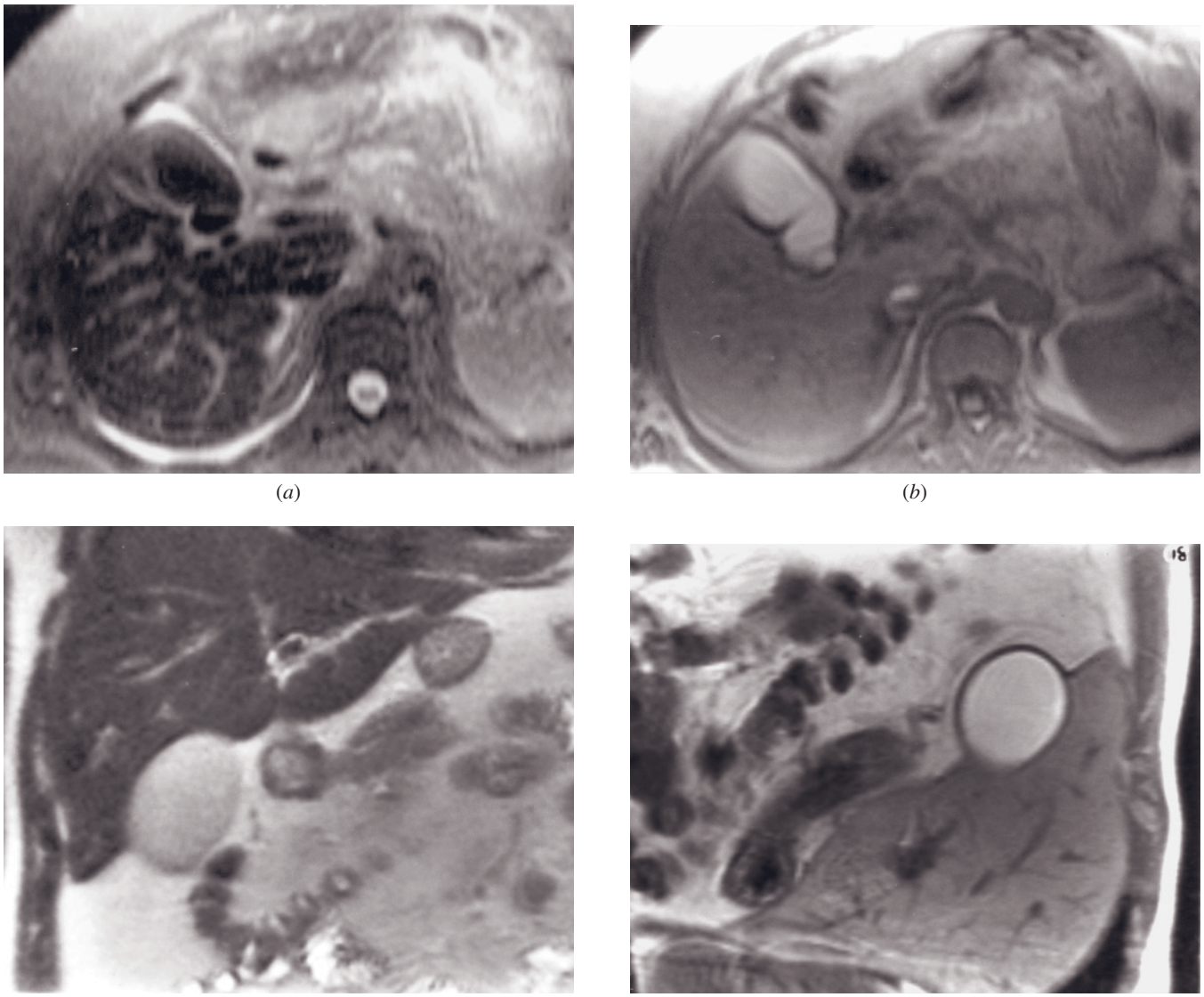

FIG. 3.6 Abnormal signal of bile. T2-weighted fat-suppressed spin-echo (*a*) and T1-weighted GE (*b*) images in a patient with primary biliary cirrhosis. The bile in the gallbladder is highly concentrated, resulting in low signal on the T2-weighted image (*a*) and high signal on the T1-weighted image (*b*). A small pleural effusion is present in the right posterior pleural recess showing high signal on the T2-weighted image (*a*).

Coronal T2-weighted single-shot echo-train spin-echo (*c*) and coronal T1-weighted GE (*d*) images in a second patient with concentrated bile in the gallbladder showing moderately high signal on the T2-weighted image (*c*) and high signal on the T1-weighted image (*d*). Note that on the T2-weighted image (*c*), both fluid and fat are higher signal than bile.

gallbladder fundus (fig. 3.7). After intravenous gadolinium administration, the normal gallbladder wall enhances homogeneously comparable to the enhancement of adjacent liver parenchyma (see fig. 3.5). Variations of the gallbladder include phrygian cap configuration, ectopic location (i.e., intrahepatic, retrohepatic, or beneath the left lobe), and septations. Septations are best visualized on single-shot T2-weighted sequences, in which they appear low signal in a background of high-signal fluid.

Bile Ducts

With MRCP sequences, the intrahepatic ducts can be visualized as an arborizing system of high signal intensity that can be followed into the outer third of the liver in over 90% of patients (see fig. 3.1) [33]. Anatomic variants, however, occur relatively frequently and are of clinical importance in laparoscopic cholecystectomy and in living donor liver transplantation because preoperatively unrecognized bile duct variations may result

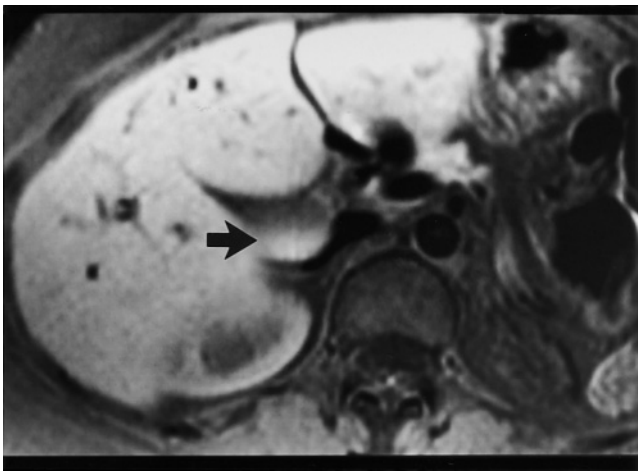

FIG. 3.7 Layering of gallbladder bile. T1-weighted fat-suppressed spin-echo image. Layering of the bile in the gallbladder is observed with the more concentrated, hyperintense bile (arrow) in the dependent portion of the gallbladder.

in complications [34]. The clinically most important variants are aberrant intrahepatic ducts that may join the common hepatic duct (CHD), common bile duct (CBD), cystic duct, gallbladder, or an anomalous right hepatic duct that joins the CBD, all of which place the patient at increased risk for bile duct injury at endoscopic cholecystectomy (fig 3.3) [35]. A right dorsocaudal intrahepatic branch draining into the left hepatic duct, known as crossover anomaly, is the most frequent bile duct variation. MRCP can play a valuable role in the preoperative evaluation of the biliary tree because of its excellent capability of noninvasively detecting aberrant or accessory ducts [6, 36].

The extrahepatic ducts (CHD, cystic duct, CBD) are consistently well evaluated (fig. 3.8). Occasionally, surgical clips, metallic stents, or pneumobilia may render segments of the ducts signal void. The cystic duct can be visualized in its full extent, including its insertion into the CBD (see fig. 3.1). A number of variations of its insertion are of clinical significance for laparoscopic cholecystectomy because they also have been shown to increase the risk of bile duct injury. Such variants include a low or medial duct insertion, insertion into the right hepatic duct, a long parallel course of the cystic and common hepatic ducts, and a short cystic duct [6, 37].

The CBD empties into the duodenum through the major papilla. This is a small mucosal protrusion into the duodenum resulting from the muscles that surround the distal CBD and ventral pancreatic duct. Its signal intensity is isointense to duodenal wall on T1- and T2-weighted images. Along the superior aspect of the major papilla is the superior papillary fold, which often forms a hood over the papilla that may be quite prominent. Inferior to the papilla is the longitudinal fold. The shape and size of the major papilla can vary, with reported average diameters of 15 × 7 mm (longitudinal × transverse) [38]. The minor papilla is the orifice of the dorsal pancreatic duct and is located proximal to the major papilla. With MRCP, the major papilla is visualized in 40% of cases [39]. The minor papilla is seen less frequently.

On T1-weighted sequences, the signal of bile in intrahepatic ducts is usually low because of its high water content. In the CBD, however, the signal can be variable, reflecting the concentration of bile, although concentrated bile is observed much less frequently in the CBD compared to the gallbladder. On postgadolinium fat-suppressed images acquired approximately 2 min after gadolinium administration, the bile duct walls are best depicted and show moderate enhancement that may be slightly higher than that of normal liver parenchyma.

Biliary Anastomoses

In the presence of end-to-end anastomosis (e.g., after orthotopic liver transplantation), Roux-en-Y, or other choledochoenteric anastomoses, ERCP is technically very difficult to perform or contraindicated. In such instances, MRCP is the imaging modality of choice and may be particularly useful to exclude strictures (e.g., at the anastomosis) and to demonstrate the morphology and diameter of the bile ducts distal and proximal to the anastomosis (fig. 3.9) [40]. The presence of a biliary-enteric anastomosis can be suspected when small bowel is noted tucked into the porta hepatis (see fig. 3.9).

DISEASES OF THE GALLBLADDER

Nonneoplastic Disease

Gallstone Disease

Predisposing factors for cholelithiasis can be summarized as "female, forty, fat, fair, fertile," preexisting cholestasis, inflammatory bowel disease, and metabolic disorders (e.g., diabetes mellitus, pancreatic disease, hypercholesterolemia, cystic fibrosis). The primary imaging modality for cholecystolithiasis is sonography. However, because of the high prevalence of this disease, gallstones frequently are encountered incidentally and familiarity with their MRI appearance is essential.

MRCP sequences are highly sensitive and accurate in depicting cholecystolithiasis and can outperform ultrasound and computed tomography [2]. Gallstones generally present as intraluminal, signal-void, round or faceted structures on both T1- and T2-weighted images (fig. 3.10). Occasionally, areas of high signal intensity will be present in gallstones on T1- and T2-weighted

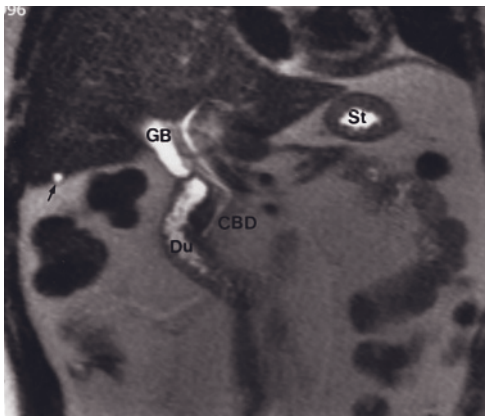

(*a*)

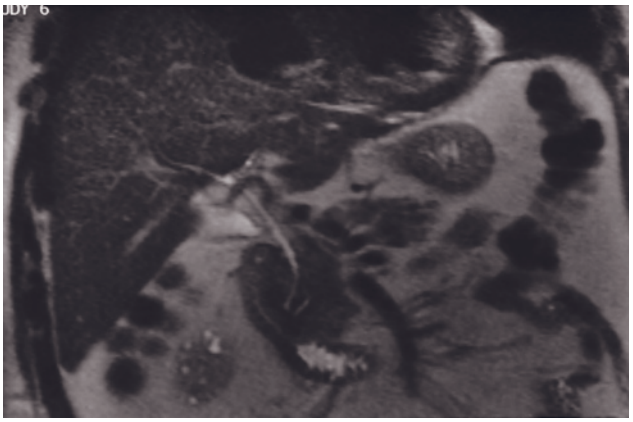

(*b*)

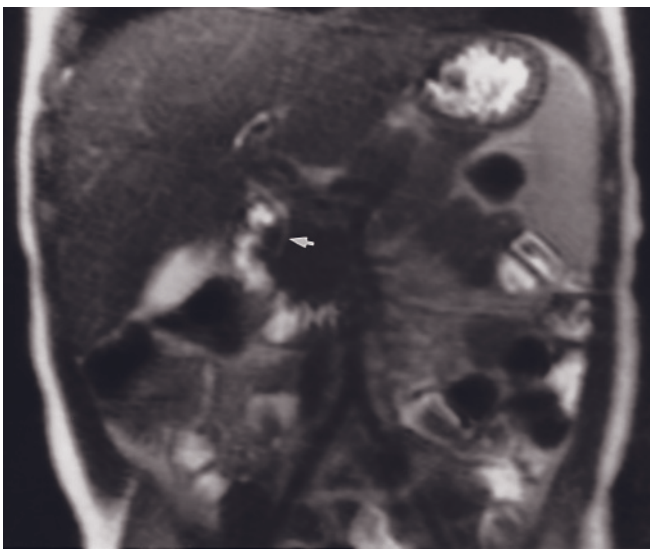

(*c*)

(*d*)

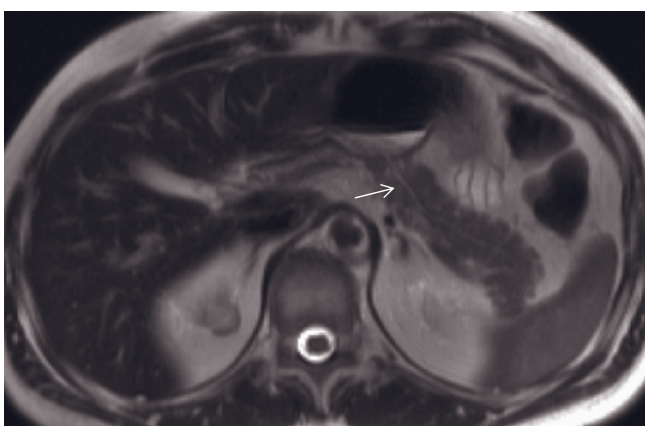

(*e*)

FIG. 3.8 Normal biliary tree. Coronal T2-weighted single-shot echo-train spin-echo images (*a*, *b*, *c*) in three patients. In the first patient (*a*), the biliary tree is visualized with high signal, allowing clear depiction of normal anatomy. The second part of the duodenum (Du) is outlined by a small amount of physiological fluid in this fasting patient (*a*) (CBD, common bile duct; GB, gallbladder; St, stomach). A small liver cyst (arrow, *a*) is present in the right lobe. In a second adult patient (*b*), the right and left hepatic, common hepatic, and common bile ducts are demonstrated. A short portion of the pancreatic duct is also seen. In a 1-yr-old child (*c*), the CBD (arrow) is well visualized despite the lack of patient cooperation. Coronal (*d*) and transverse (*e*) T2-weighted single-shot echo-train spin-echo images at 3.0 T demonstrate normal common bile duct (arrow, *d*) and pancreatic duct (arrow, *e*) in another patient. Note that valvula conniventes of the small intestine are seen very well, and there are biliary hamartomas in the liver.

sequences, or, less commonly, the stones will appear largely hyperintense on T1-weighted sequences (fig. 3.11) [41, 42]. The exact cause for the increased signal intensity has not yet been established. It has been shown, with spectroscopy and chemical analysis of gallstones, that it is not caused by high lipid content [42]. Therefore, the presence of protein macromolecules or dispersed calcium microparticles, which shorten T1

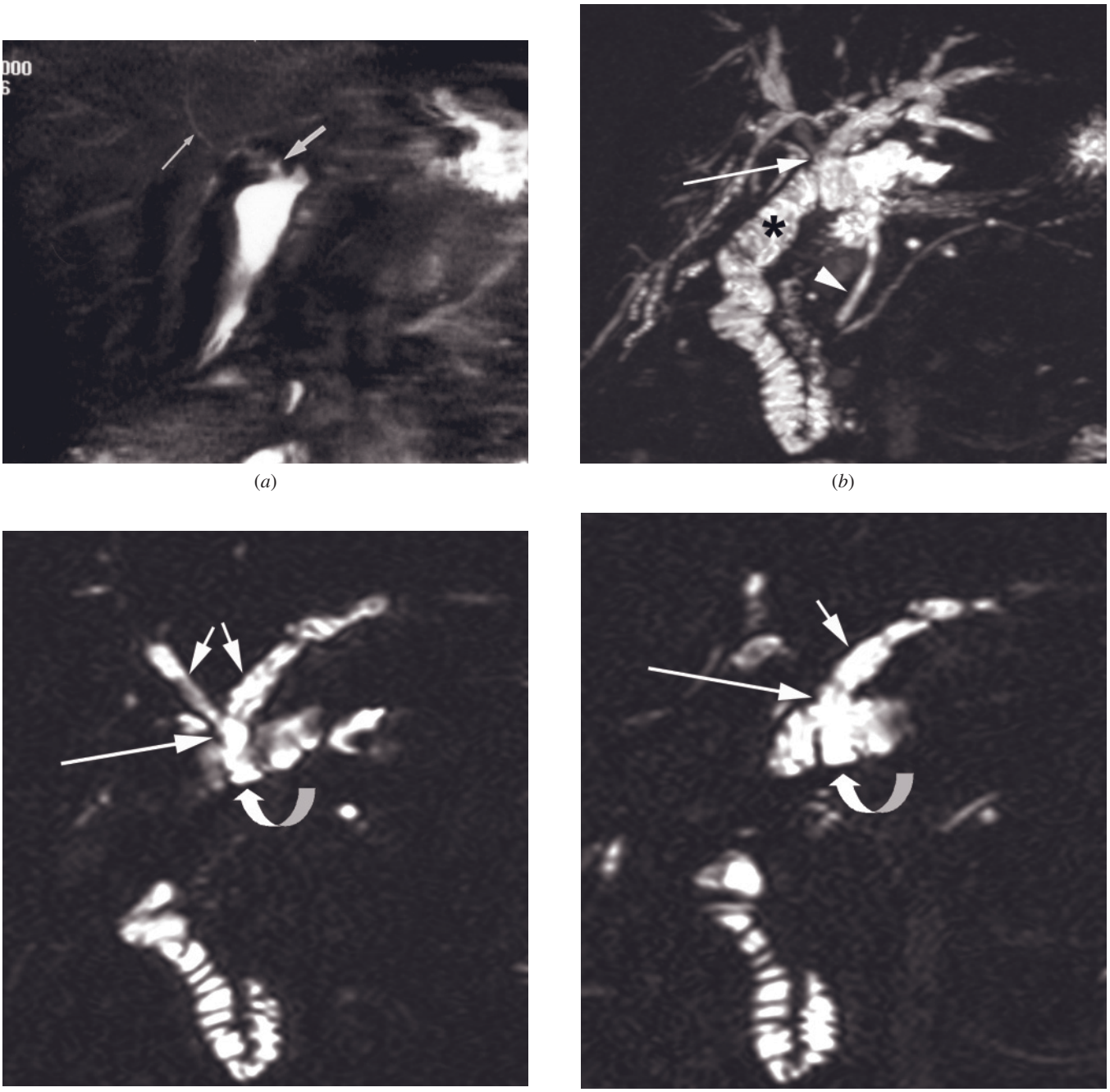

FIG. 3.9 Biliary anastomosis. Coronal T2-weighted fat-suppressed thin-section MRCP image (*a*) in a patient with hepatico-porto-enterostomy (after Kasai operation) showing the normal anastomosis between a bowel loop and the porta hepatis (arrow). Intrahepatic nondilated bile ducts are also well depicted (thin arrow). Paracoronal T2-weighted fat-suppressed thick-section MRCP image (*b*) and thin-section MRCP images (*c*, *d*) in a different patient with hepaticojejunostomy after liver transplantation. The thick-slab MRCP image (*b*) gives an excellent overview of the anatomic situation. The biliary anastomosis (long arrow, *b–d*) between the common hepatic duct and the jejunal bowel loop (asterisk, *b*; curved arrow, *c*, *d*) shows normal diameter and regular fluid signal. The intrahepatic bile ducts are mildly dilated, and the right and left hepatic ducts (short arrows, *c*, *d*) are well visualized. The remaining original common bile duct (arrowhead, *b*) and the adjacent pancreatic duct are also visualized. T2-weighted coronal

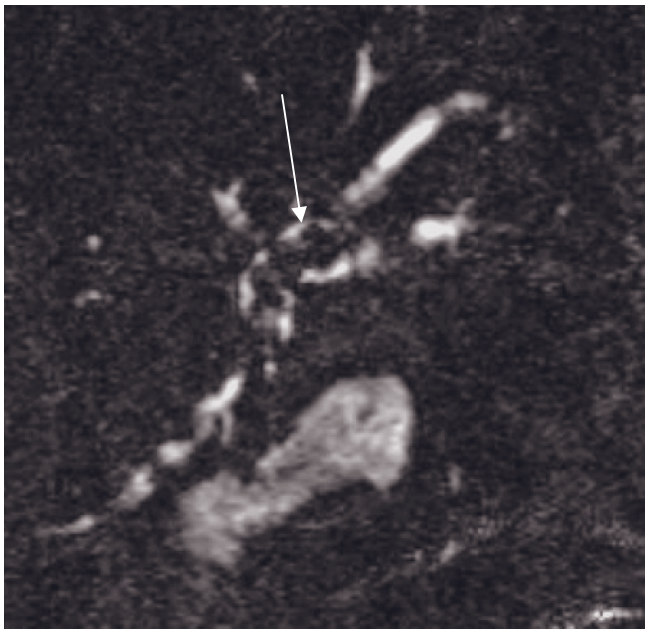

(*e*)

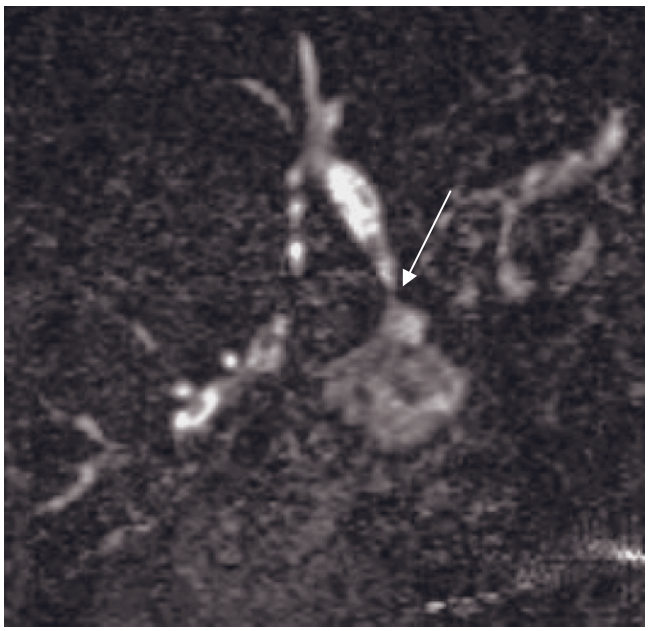

(*f*)

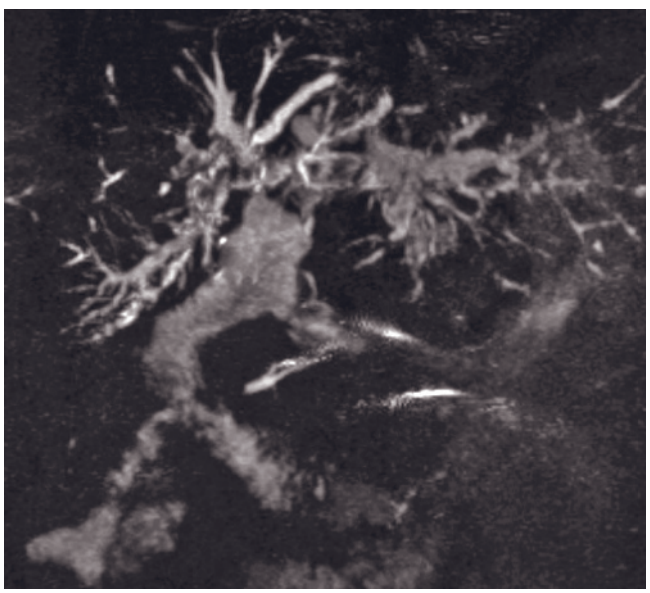

(*g*)

FIG. 3.9 (*Continued*) thin-section fast spin-echo MRCP (*e*, *f*) and reconstructed 3D MIP MRCP (*g*) images demonstrate the common bile duct-jejunum anastomosis in another patient. There is stenosis (arrow, *f*) in the region of anastomosis, and there are stones (arrows, *e*) proximally in the dilated bile ducts.

relaxation times, may be a reasonable explanation [43, 44]. Occasionally, the specific weight of a gallstone is lower than that of bile and the gallstone will float in the nondependent portion of the gallbladder (fig. 3.12). In this case, a gallstone can be differentiated from a gallbladder polyp by the lack of enhancement on T1-weighted postgadolinium images.

Acute Cholecystitis

Acute inflammation of the gallbladder is caused by obstruction of the cystic duct (e.g., by cystic duct stones) in 80–95% of patients. Morphologic criteria to establish the diagnosis have been described in the ultrasound literature. A combination of gallbladder wall thickening (>3 mm), three-layered appearance of the wall, hazy delineation of the gallbladder, localized pain (Murphy's sign), presence of gallstones, gallbladder hydrops, and fluid surrounding the gallbladder indicate a high probability of acute cholecystitis. In the presence of acalculous cholecystitis, or if many of these signs are absent, establishing the correct diagnosis with ultrasound is challenging and findings can be equivocal.

Acute cholecystitis results in increased blood flow and capillary leakage due to inflammatory changes,

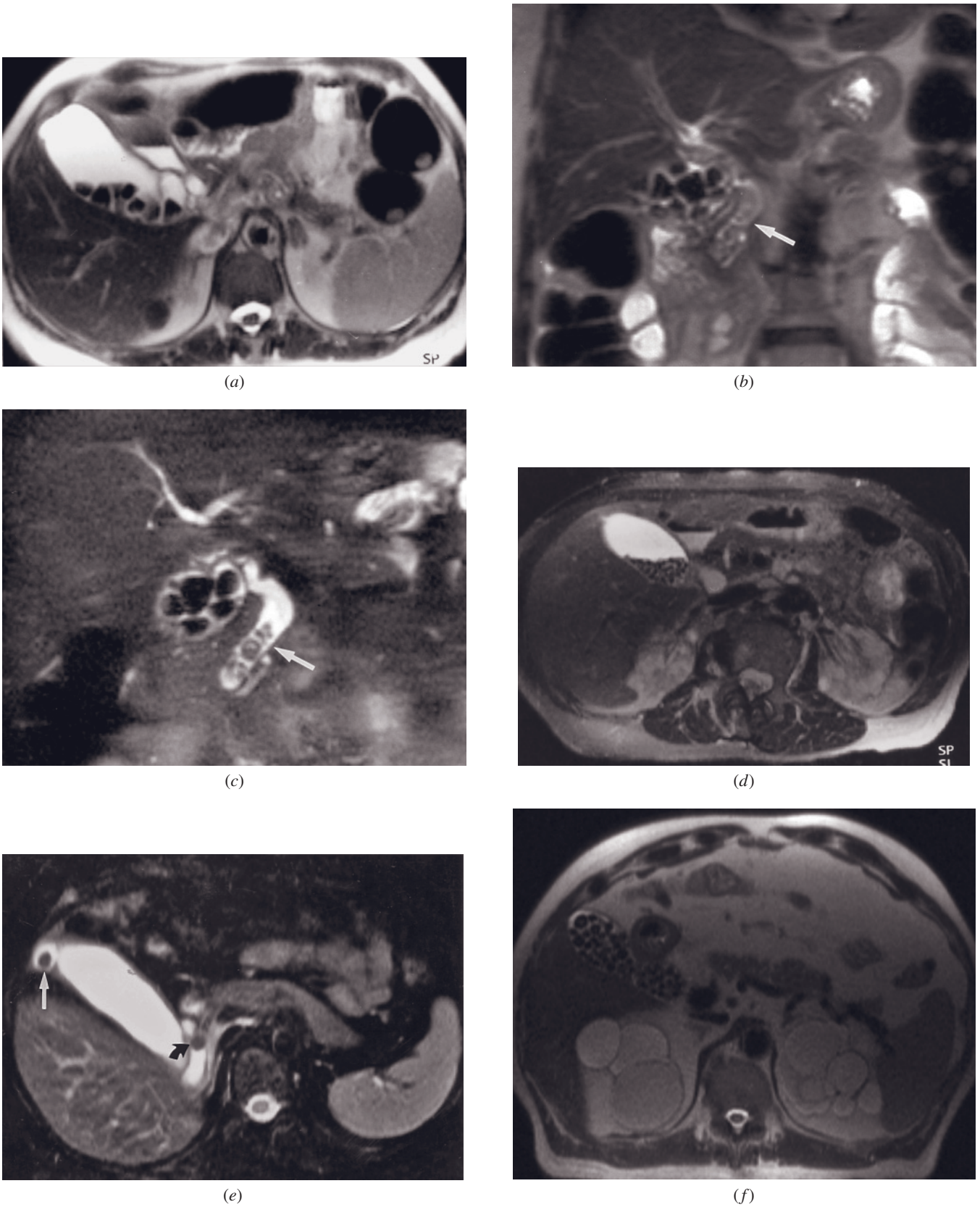

FIG. 3.10 Gallstone disease. T2-weighted 8-mm transverse (*a*) and coronal (*b*) single-shot echo-train spin-echo images and coronal thin-section MRCP single-shot echo-train spin-echo image with fat suppression (*c*). Multiple calculi are demonstrated as round or faceted signal-void structures in the gallbladder (*a*, *b*, *c*) and the CBD (arrows, *b* and *c*), outlined by high-signal bile. Note how much better the CBD stones are visualized on the thin-section MRCP image (*c*) compared to the standard 8-mm image (*b*).

Transverse T2-weighted single-shot echo-train spin-echo image (*d*) in a second patient showing multiple tiny signal-void calculi in the dependent portion of the gallbladder.

Transverse T2-weighted fat-suppressed spin-echo image (*e*) in a third patient showing stones in the phrygian cap of the gallbladder (straight arrow, *e*) and in the cystic duct (curved arrow, *e*). T2-weighted single-shot echo-train spin-echo (*f*), T1-weighted

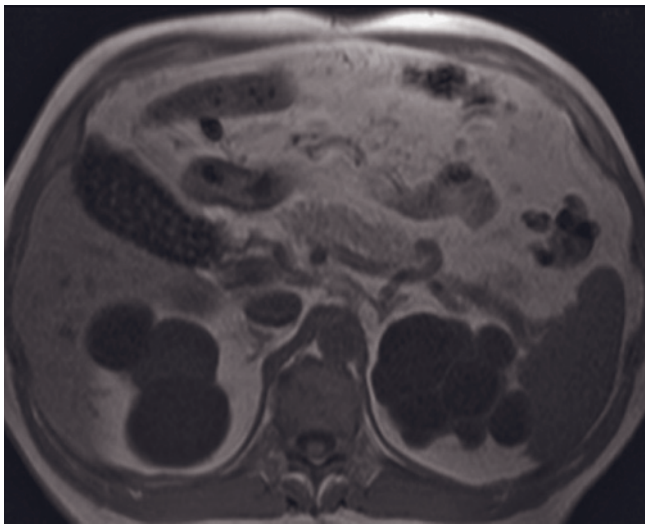

(*g*)

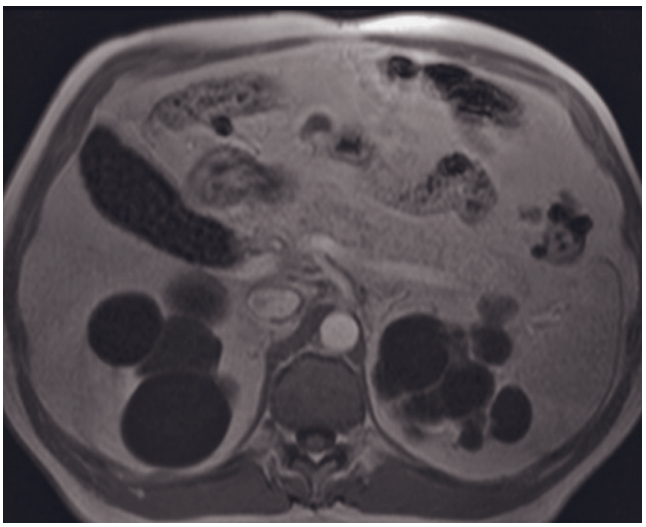

(*h*)

FIG. 3.10 (*Continued*) SGE (*g*), and T1-weighted postgadolinium interstitial phase SGE (*h*) images demonstrate multiple hypointense stones in the gallbladder in another patient. Note that there are multiple cysts in the kidneys and this finding is consistent with autosomal dominant polycystic kidney disease.

FIG. 3.11 Hyperintense gallstones. T1-weighted opposed-phase GE image showing several small gallstones (arrows) of uniform high signal intensity in the dependent portion of the gallbladder.

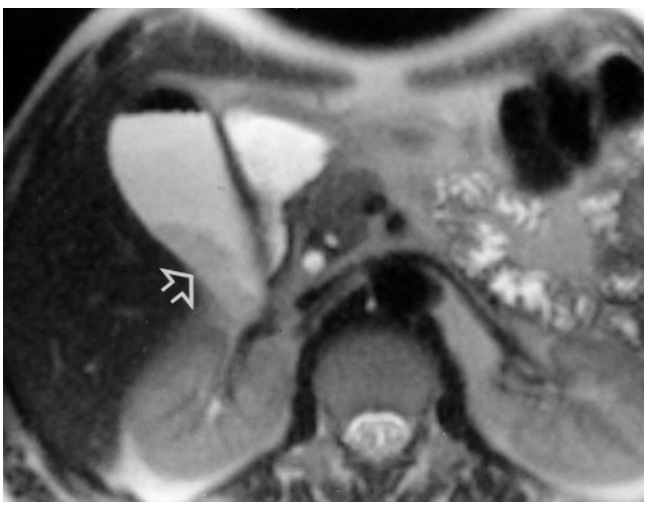

FIG. 3.12 Floating gallstones. Transverse T2-weighted single-shot echo-train spin-echo image demonstrating multiple small, signal-void calculi floating in the nondependent portion of the gallbladder. Concentrated bile (sludge), appears as moderately hypointense material in the dependent portion of the gallbladder (open arrow).

which is reflected on MRI by increased enhancement on postgadolinium images. The high sensitivity of MRI for gadolinium enhancement, especially with the use of fat suppression techniques, makes it an effective technique for the diagnosis of acute cholecystitis, demonstrating higher sensitivity and accuracy than ultrasound [45, 46]. The enhancement is most pronounced along the mucosal layer of the gallbladder wall on T1-weighted immediate postgadolinium images and progresses to involve the entire thickness of the wall on more delayed images (fig. 3.13). The percentage of contrast enhancement of the gallbladder wall has been shown to correlate well with the presence of acute cholecystitis and was more accurate than wall thickness in distinguishing acute from chronic cholecystitis and gallbladder malignancy [46, 47]. An important finding in acute

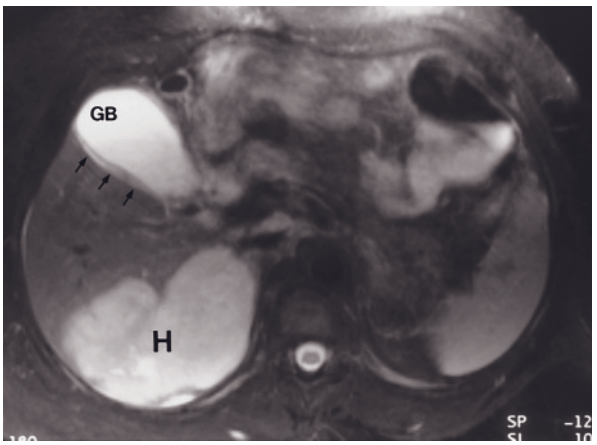

(*a*)

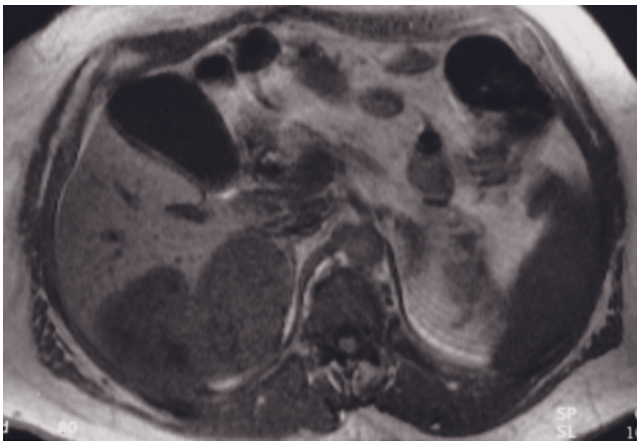

(*b*)

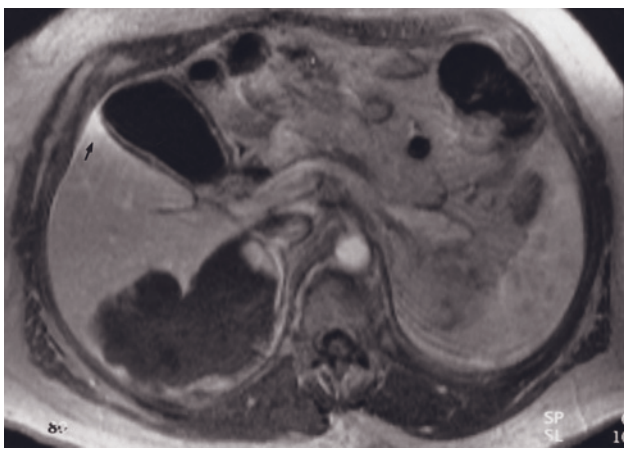

(*c*)

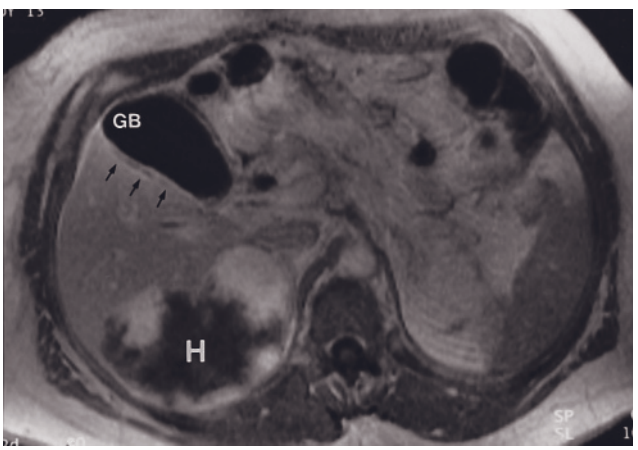

(*d*)

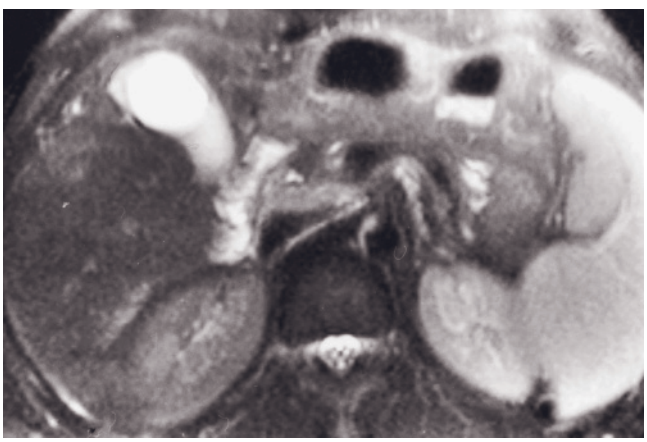

(*e*)

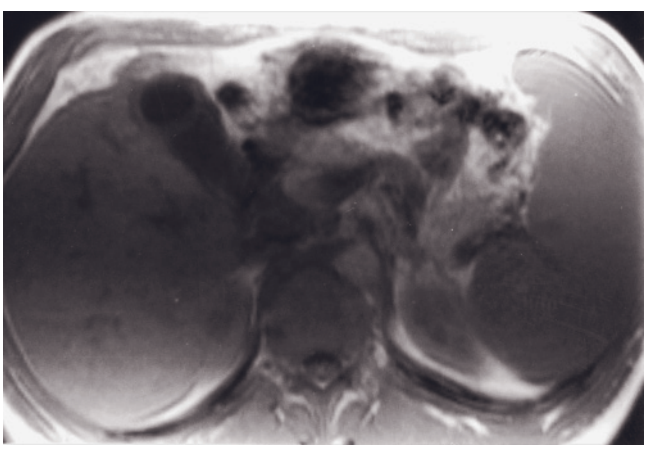

(*f*)

FIG. 3.13 Acute cholecystitis. Transverse T2-weighted fat-suppressed echo-train spin-echo (*a*),T1-weighted GE (*b*), immediate postgadolinium GE (*c*), and 90-s postgadolinium GE (*d*) images. The wall of the gallbladder (GB) is mildly thickened (4 mm) and shows increased signal intensity on the T2-weighted image (arrows, *a*). A giant hemangioma (H) is seen in *segment 6* of the liver. On the immediate postgadolinium image (*c*), increased enhancement of the gallbladder mucosa and transient increased enhancement of liver parenchyma adjacent to the gallbladder is apparent (arrow, *c*).On the 90-s postgadolinium image (*d*), increased enhancement of the entire gallbladder wall (arrows, *d*) is shown. Also note the peripheral nodular enhancement of the hemangioma (H).

T2-weighted fat-suppressed spin-echo (*e*), T1-weighted GE (*f*), immediate postgadolinium GE (*g*), and 2-min postgadolinium fat-suppressed GE (*h*) images in another patient. The gallbladder wall shows increased signal and wall thickening on the T2-weighted

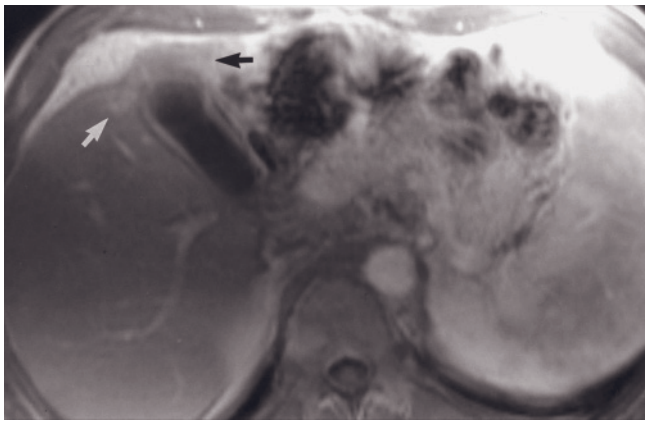

(*g*)

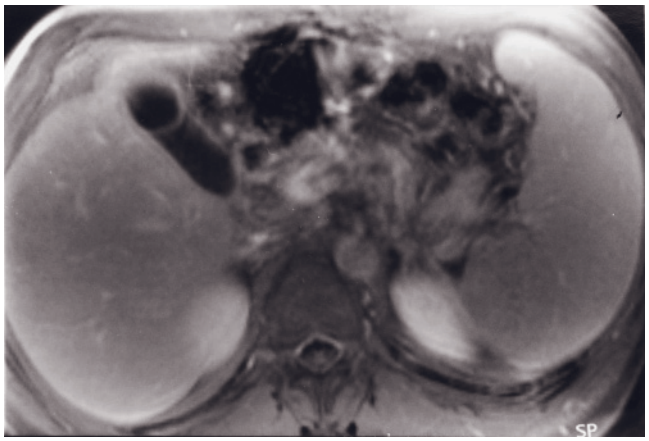

(*h*)

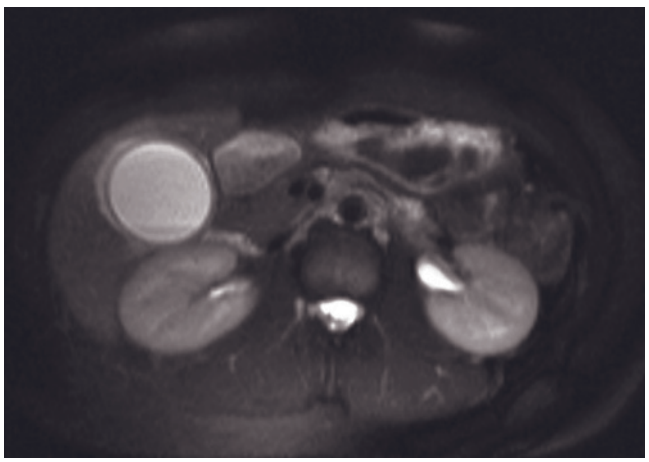

(*i*)

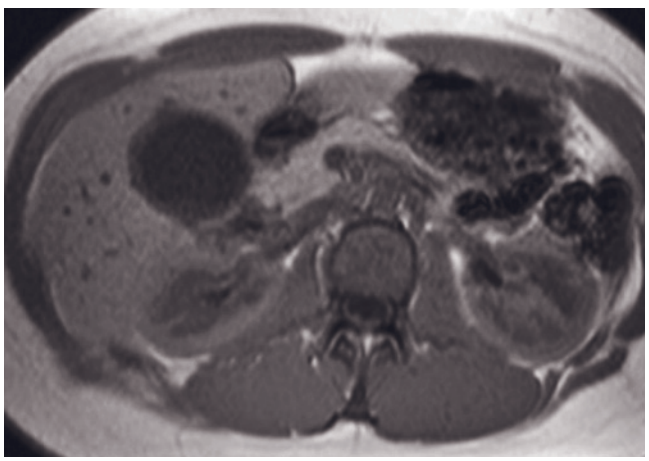

(*j*)

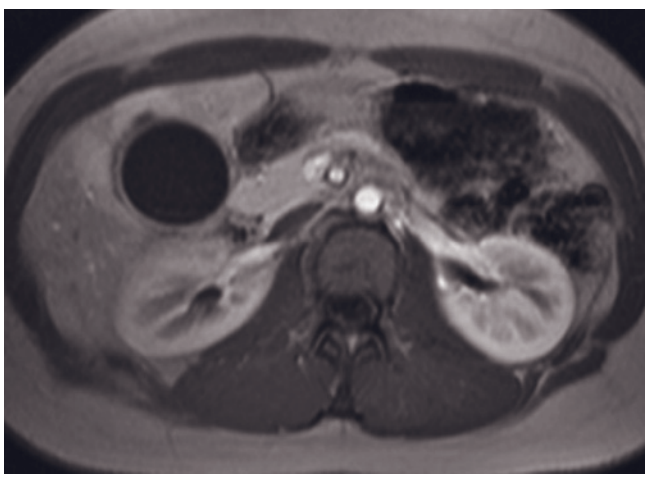

(*k*)

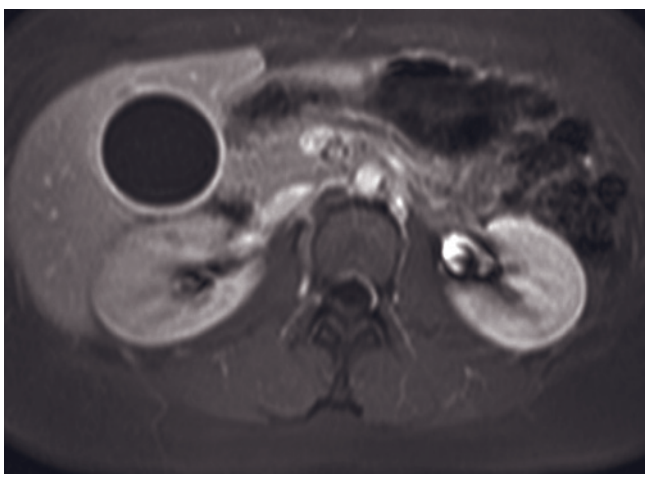

(*l*)

FIG. 3.13 (*Continued*) image (*e*). Increased enhancement of the gallbladder mucosa and transient increased enhancement of adjacent liver parenchyma (arrows, *g*) are seen on the immediate postgadolinium image (*g*). T2-weighted fat-suppressed single-shot echo-train spin-echo (*i*), T1-weighted SGE (*j*), T1-weighted postgadolinium hepatic arterial dominant phase SGE (*k*), and T1-weighted postgadolinium interstitial phase fat-suppressed SGE (*l*) images demonstrate acalculous cholecystitis in another patient. The gallbladder wall is thickened and shows hyperintense signal on T2-weighted image due to edema (*i*). There is transient increased pericholecystic hepatic parenchymal enhancement, which is a highly specific finding associated with acute inflammation, on the hepatic arterial dominant phase (*k*). The gallbladder wall shows intense enhancement on the interstitial phase (*l*). Note that

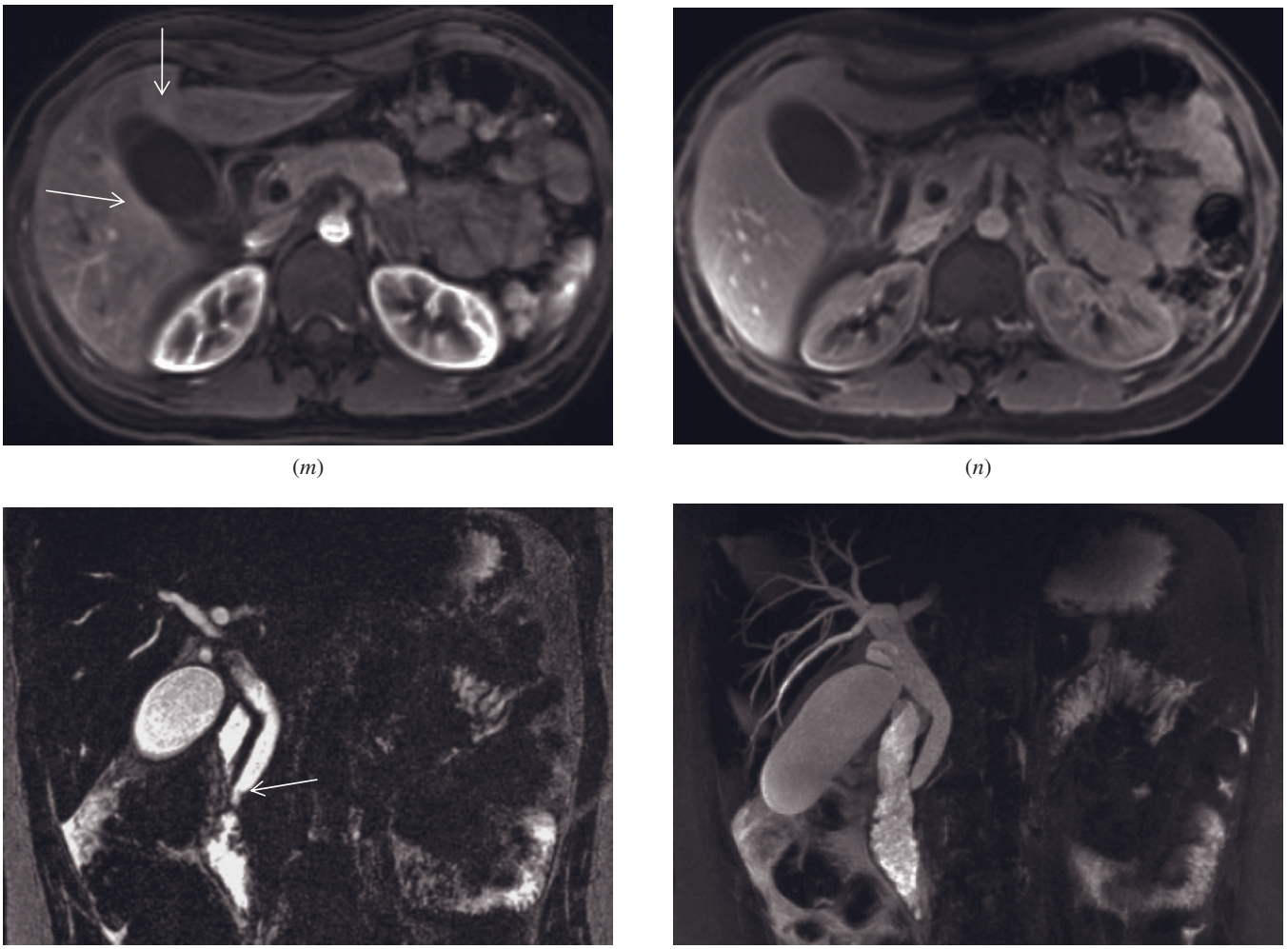

FIG. 3.13 (*Continued*) the bile shows layering on T2-weighted image (*i*) and the gallbladder is enlarged. T1-weighted postgadolinium fat-suppressed 3D-GE (*m*, *n*) and T2-weighted thin section fast spin echo MRCP (*o*) and reconstructed 3D MIP MRCP (*p*) images at 3.0 T demonstrate mild acalculous cholecystitis in another patient. There is transient increased pericholecystic hepatic parenchymal enhancement (arrows, *m*) on the hepatic arterial dominant phase (*m*), which fades to isointensity with the remaining liver parenchyma on the hepatic venous phase (*n*). The gallbladder wall shows prominent enhancement on the hepatic venous phase (*n*). MRCP images show the dilated biliary system due to ampullary stenosis secondary to passed stone. Fusiform ending of the common bile duct (arrow, *o*) suggests the presence of ampullary stenosis. Note that the gallbladder is enlarged.

cholecystitis is the transient increased enhancement of adjacent liver tissue on immediate postgadolinium images, which can be observed in approximately 70% of patients (figs. 3.13–3.15) [46, 47]. This reflects a hyperemic inflammatory response to the adjacent acute inflammation in the gallbladder wall. Thus findings that are indicative of acute cholecystitis on postgadolinium T1-weighted images include 1) increased wall enhancement, 2) transient increased enhancement of adjacent liver parenchyma on immediate postgadolinium images, and 3) increased thickness of the gallbladder wall [48]. Findings on T2-weighted images that are helpful to establish the diagnosis are 1) presence of gallstones, 2) presence of pericholecystic fluid, 3) presence of intramural edema or abscesses appearing as hyperintense foci in the gallbladder wall, and 4) increased wall thickness (see figs. 3.13–3.15) [47]. Periportal high signal intensity may be observed but is a nonspecific finding.

Acute acalculous cholecystitis comprises about 5–15% of all acute cholecystitis cases. It can be caused by depressed motility (e.g., in patients with severe trauma/surgery, burns, shock, anesthesia, diabetes mellitus), by decreased blood flow in the cystic artery due to extrinsic obstruction or embolization, or by bacterial infection (fig. 3.16). MR imaging may be especially useful for the diagnosis of acute acalculous cholecystitis in critically ill patients [46]. Complications of acute cholecystitis including abscess formation and

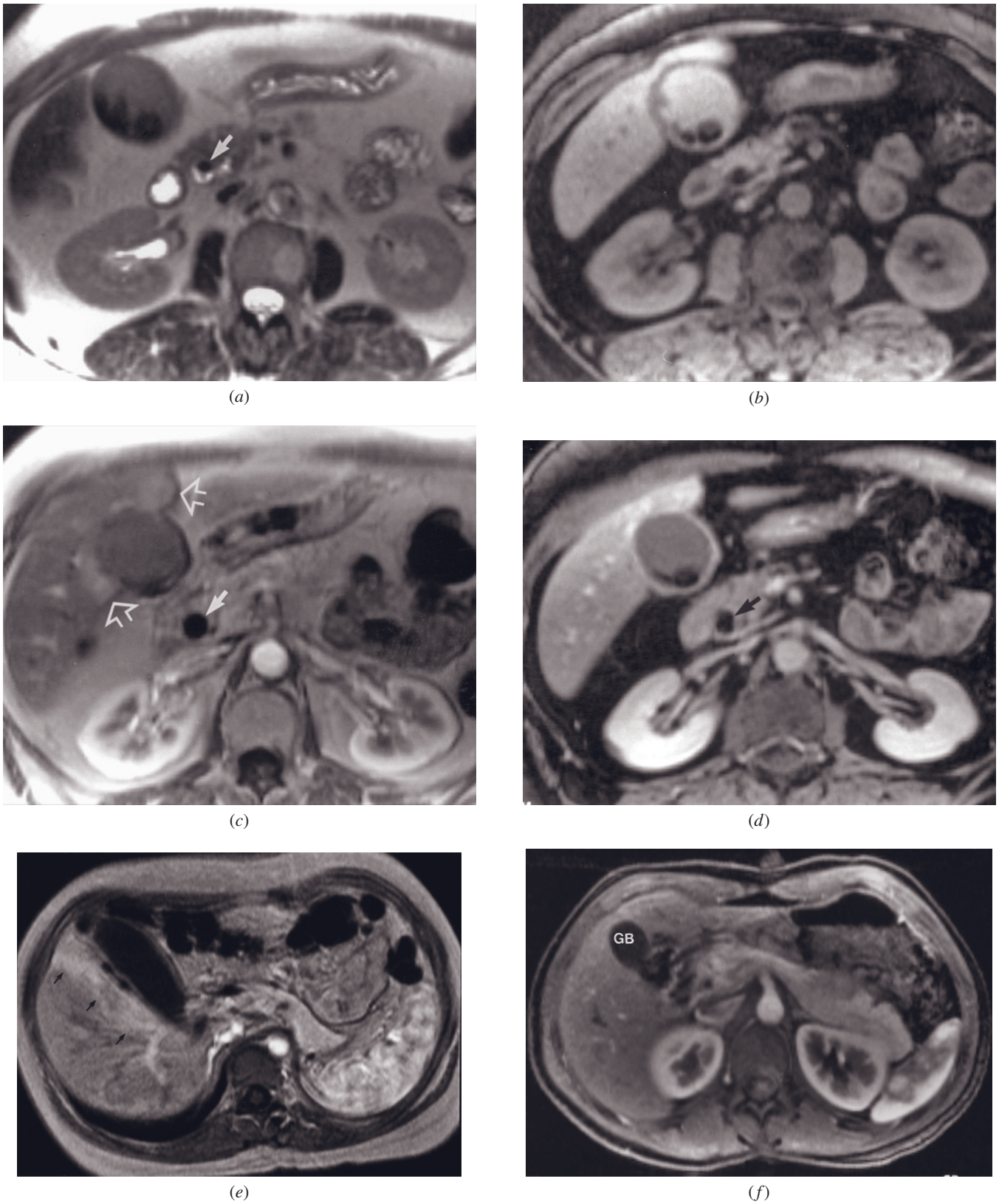

FIG. 3.14 Acute cholecystitis with gallstones. T2-weighted single-shot echo-train spin-echo (*a*),T1-weighted fat-suppressed GE (*b*), immediate postgadolinium GE (*c*), and 2-min postgadolinium fat-suppressed GE (*d*) images. The bile in the gallbladder is highly concentrated, showing low signal on the T2-weighted image (*a*) and high signal on the T1-weighted image (*b*).

Several low-signal gallstones are visualized in the gallbladder and the CBD (arrows, *a*, *c*, *d*). The gallbladder wall is thickened. On the immediate postgadolinium image (*c*), the adjacent liver parenchyma demonstrates transient increased enhancement (open arrows, *c*). Immediate postgadolinium GE image (*e*) in another patient demonstrating transient hyperemic enhancement of the liver (arrows, *e*) adjacent to the gallbladder. Immediate postgadolinium fat-suppressed GE image (*f*) in a normal subject for comparison,

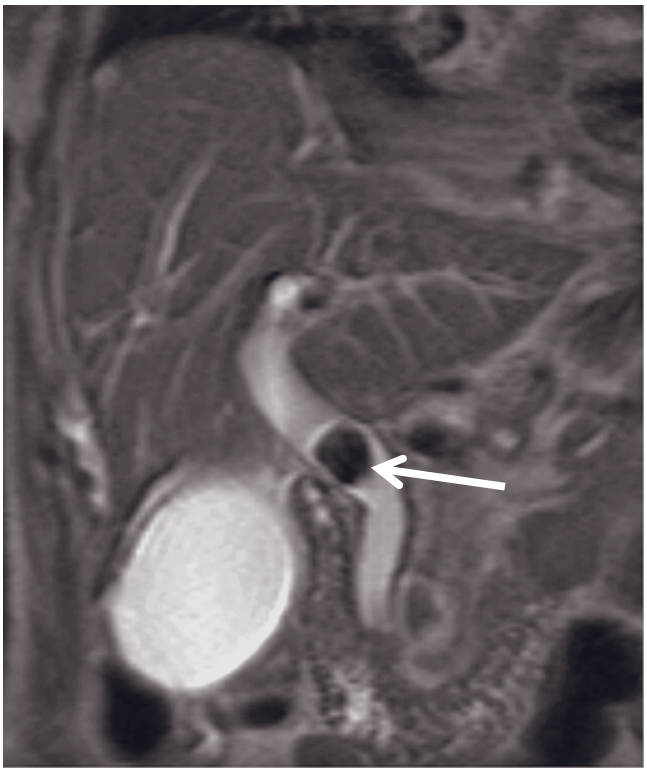

(*g*)

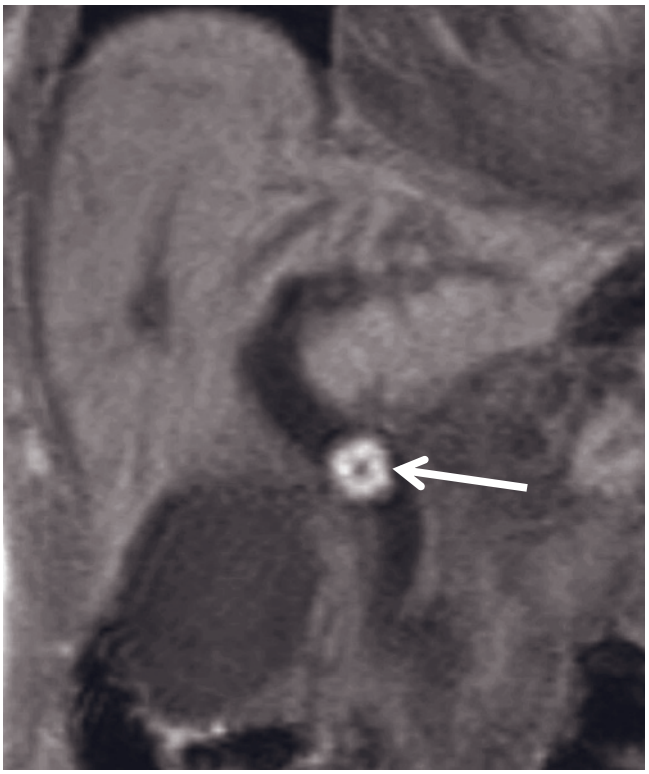

(*h*)

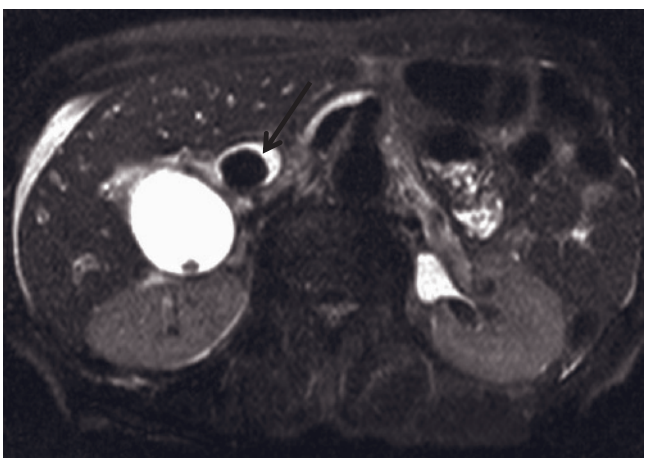

(*i*)

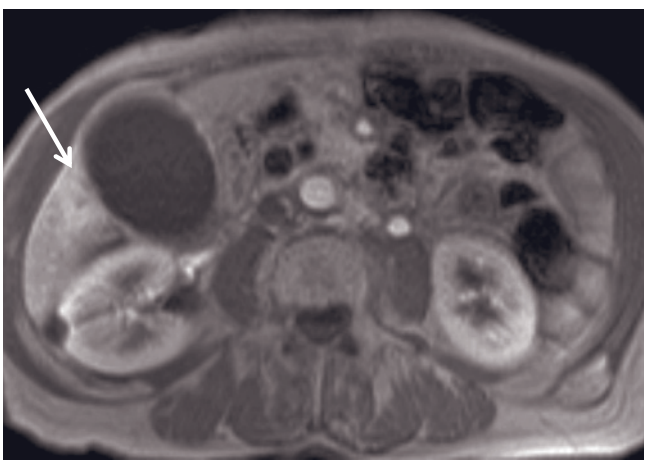

(*j*)

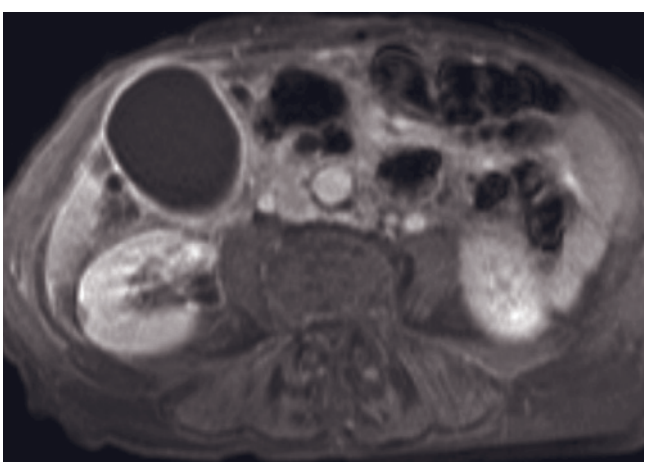

(*k*)

FIG. 3.14 (*Continued*) demonstrating homogeneous enhancement of the liver. GB, gallbladder. Coronal T2-weighted single-shot echo-train spin-echo (*g*), coronal T1-weighted SGE (*h*), transverse T2-weighted single-shot echo-train spin-echo (*i*), transverse T1-weighted postgadolinium hepatic arterial dominant phase SGE (*j*), and transverse T1-weighted postgadolinium fat-suppressed interstitial phase SGE (*k*) images demonstrate acute calculous cholecystitis in another patient. The common bile duct and the biliary system are dilated because of the presence of stone (arrows, *g–i*) in the common bile duct. Note that the stone is hyperintense on T1-weighted image (*h*) and there is another small stone in the gallbladder. The gallbladder is enlarged. The gallbladder wall is thickened and edematous. There is transient increased pericholecystic hepatic parenchymal enhancement (arrow, *j*) on the hepatic arterial dominant phase. The gallbladder wall shows prominent enhancement on the interstitial phase (*k*). Note the free fluid in the abdomen.

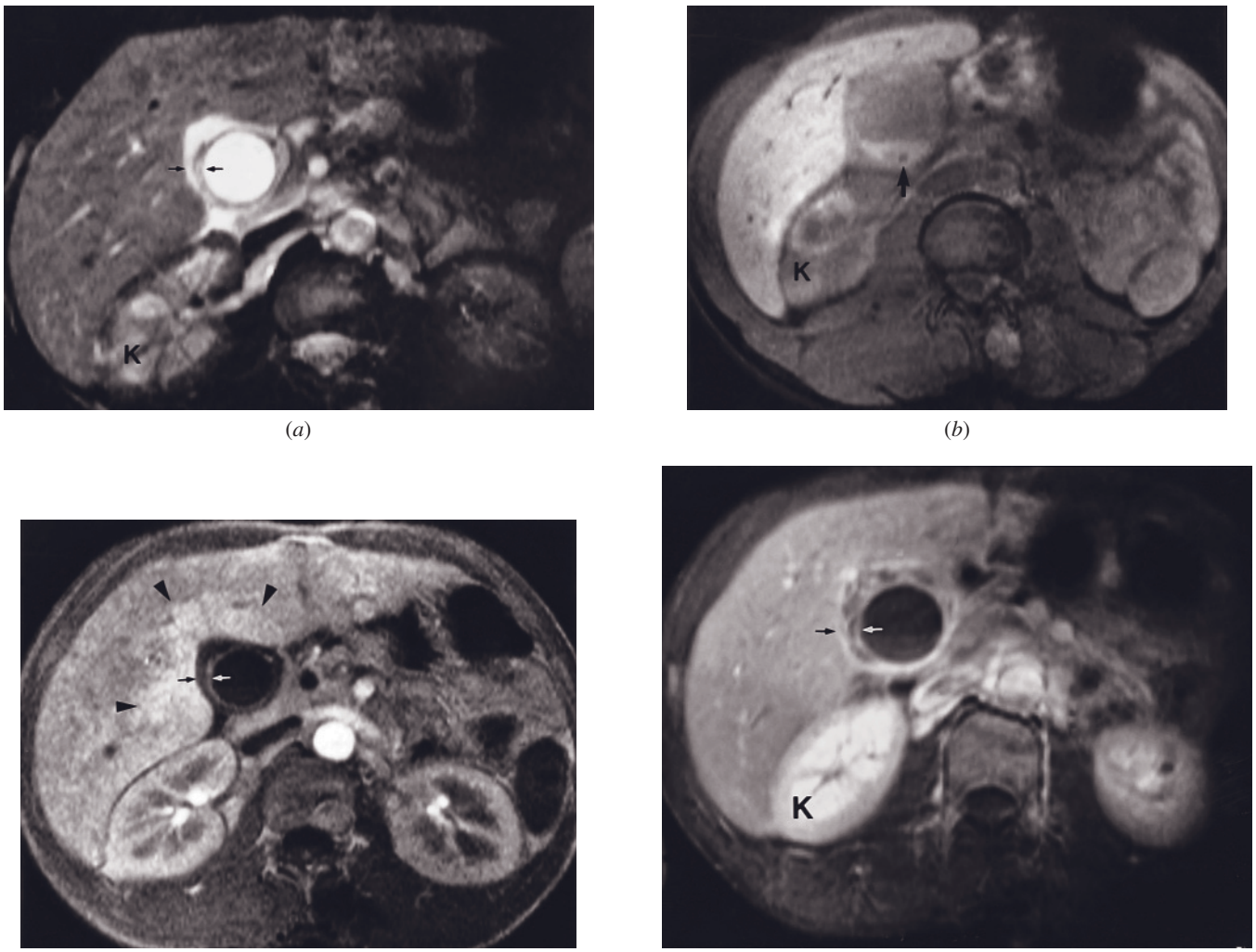

(*a*) (*b*) (*c*) (*d*)

FIG. 3.15 Acute on chronic cholecystitis. T2-weighted fat-suppressed echo-train spin-echo (*a*),T1-weighted fat-suppressed spin-echo (*b*), immediate postgadolinium GE (*c*), and 2-min postgadolinium fat-suppressed spin-echo (*d*) images. The gallbladder wall is thickened (arrows, *a*, *c*, *d*) with increased mural signal intensity on the T2-weighted image (*a*). On the T1-weighted image (*b*), layering of high-signal concentrated bile in the dependent portion and a small, hypointense, gallbladder stone (arrow, *b*) are shown.

On the immediate postgadolinium image (*c*), moderate enhancement of the gallbladder mucosa and transient increased enhancement of adjacent liver parenchyma (arrowheads, *c*) are consistent with acute cholecystitis. Delayed heterogeneous enhancement of the markedly thickened gallbladder wall, demonstrated on the 2-min postgadolinium image (*d*), is suggestive of chronic inflammatory changes. The low signal intensity of the renal cortex is due to iron deposition in this patient with sickle cell anemia. K, kidney.

perforation can also be evaluated with high accuracy with MRI.

Hemorrhagic Cholecystitis

Hemorrhagic cholecystitis is more prevalent in patients with acalculous cholecystitis than in patients with calculous cholecystitis. Blood breakdown products in the gallbladder wall and lumen can be clearly identified with precontrast MRI sequences. Because of the specific signal intensity characteristics of these blood breakdown products on T1- and T2-weighted sequences, the age of the hemorrhage may be determined (fig. 3.17). High signal on T1-weighted images is a distinctive feature of this condition, and MRI may be uniquely able to establish the diagnosis of hemorrhagic cholecystitis.

Chronic Cholecystitis

Chronic cholecystitis is more common than acute cholecystitis. However, the clinical findings of acute cholecystitis and chronic cholecystitis may overlap, and MR imaging may be used for the differentiation [46]. Because of the longstanding inflammatory process, a variable

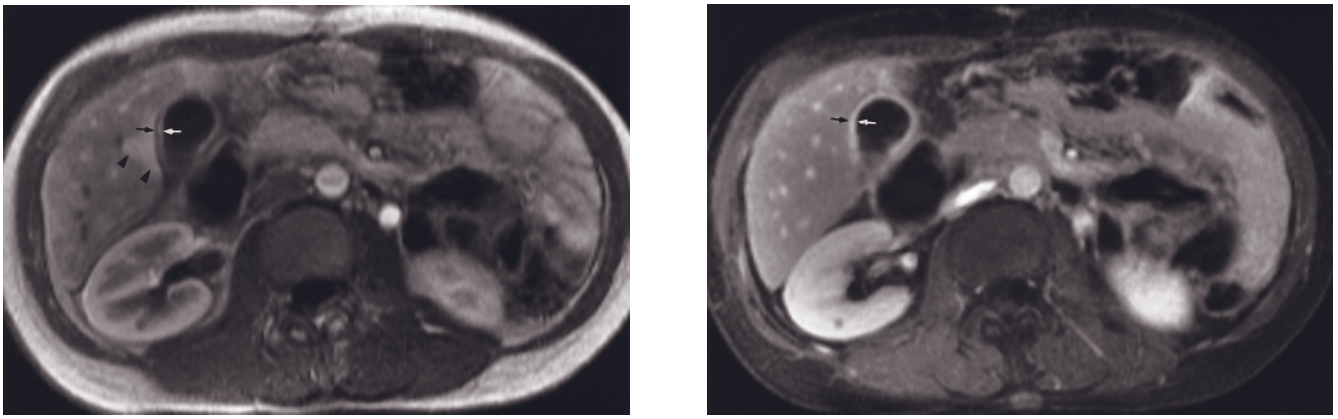

(*a*) (*b*)

Fig. 3.16 Chemoembolization-induced acute cholecystitis. Immediate (*a*) and 90-s (*b*) postgadolinium GE images. Transient pericholecystic enhancement of the liver parenchyma (arrowheads, *a*) is noted on the immediate postgadolinium image (*a*). Homogeneous enhancement is observed after 90 s (*b*). The thickened gallbladder wall (arrows, *a*, *b*) shows progressive enhancement from *a* to *b*.

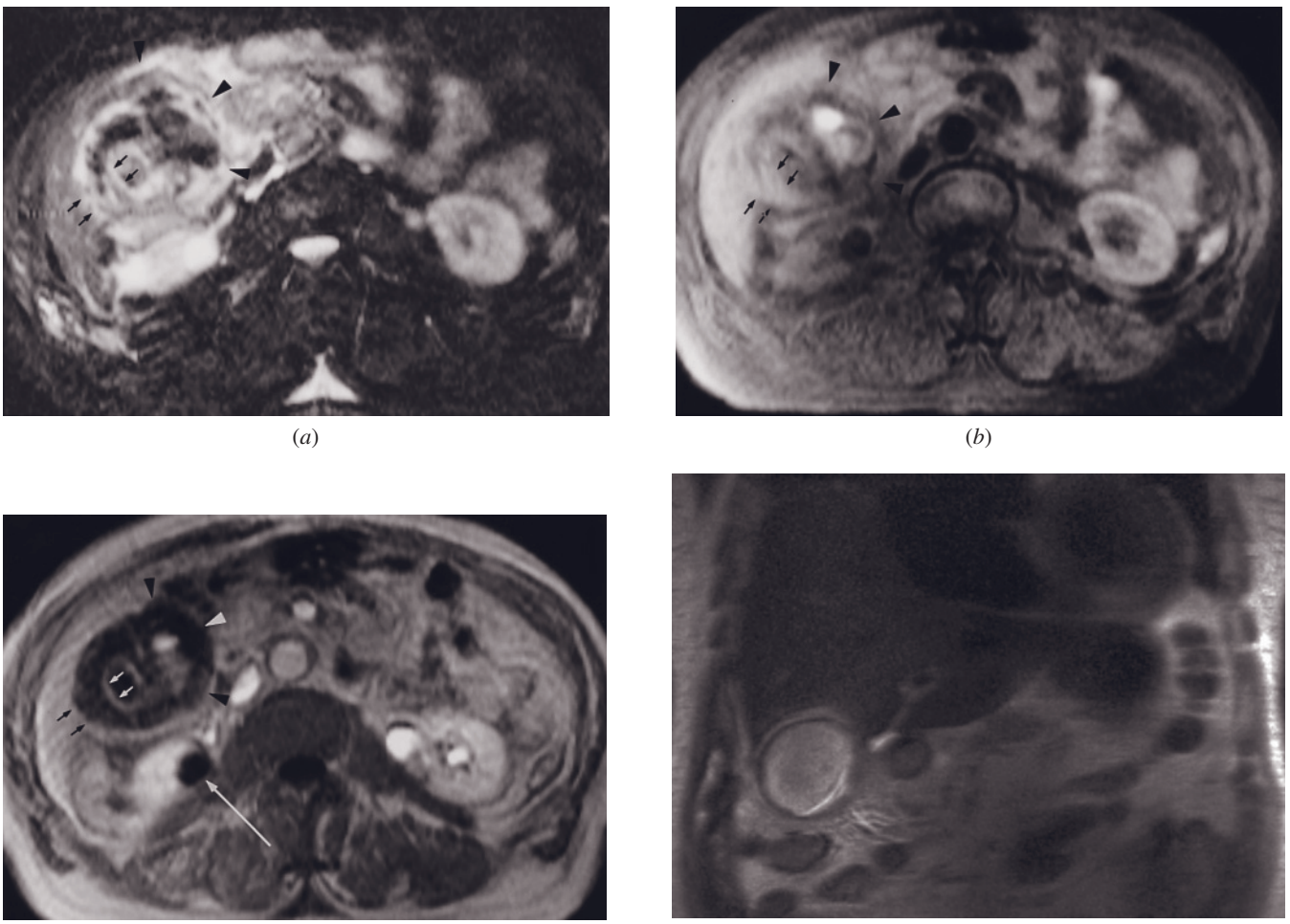

(*a*) (*b*)

(*c*) (*d*)

Fig. 3.17 Hemorrhagic cholecystitis. T2-weighted fat-suppressed echo-train spin-echo (*a*), T1-weighted fat-suppressed spin-echo (*b*), and immediate postgadolinium GE (*c*) images. On the T2-weighted image (*a*), the thickened gallbladder wall (small arrows, *a*) shows areas of high and low signal. A pericholecystic area of predominantly low signal (arrowheads, *a*) is located anteromedially. On the T1-weighted image (*b*), areas of high signal intensity consistent with hemorrhage are noted within the substantially thickened gallbladder wall (small arrows, *b*). The large complex anteromedial area (arrowheads, *b*) is predominantly of high signal, which in combination with the low signal on the T2-weighted image is consistent with intracellular methemoglobin in an area of hemorrhage. The delayed postgadolinium GE image (*c*) shows to better advantage the thick gallbladder wall (small arrows, *c*) and the hemorrhagic pericholecystic fluid collection (arrowheads, *c*). A calculus (long arrow, *c*) is incidentally shown in the right renal collecting system. Coronal T2-weighted single-shot echo-train spin-echo (*d*), transverse T1-weighted fat-suppressed 3D-GE (*e*),

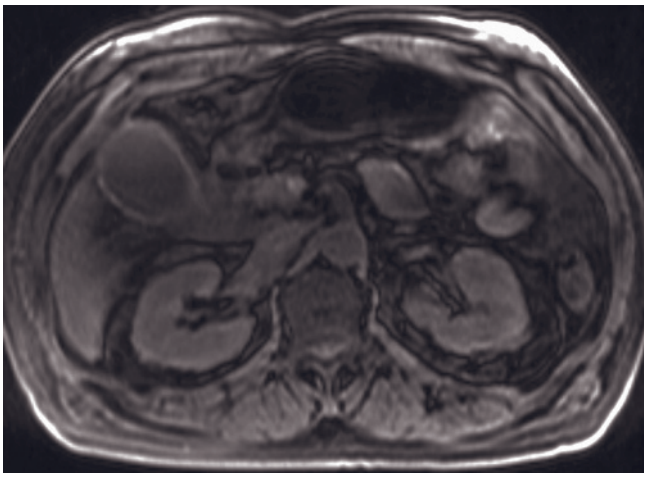

(*e*)

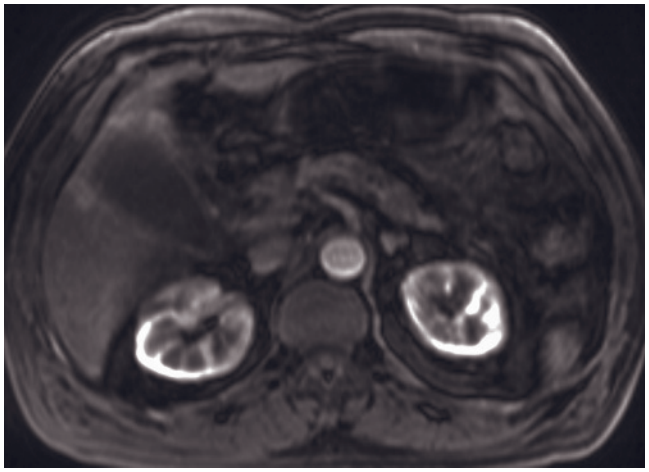

(*f*)

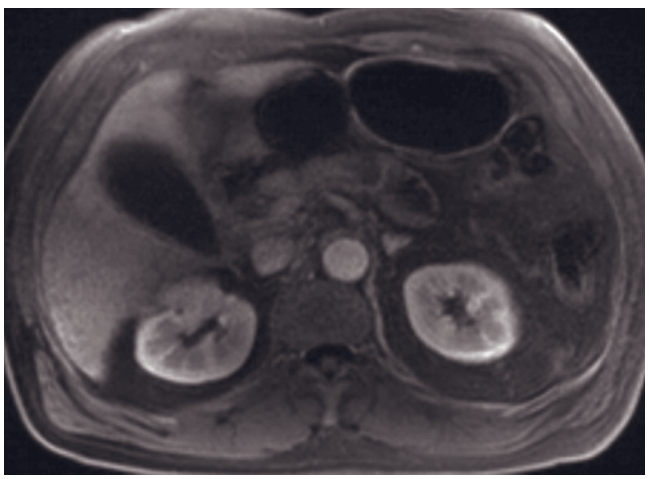

(*g*)

Fig. 3.17 (*Continued*) transverse T1-weighted postgadolinium arterial phase (*f*), and hepatic venous phase (*g*) fat-suppressed 3D-GE images at 3.0 T demonstrate acute hemorrhagic cholecystitis in another patient. The gallbladder is enlarged and its wall is thickened. The wall shows hypointense signal on T2-weighted image (*d*) and hyperintense signal on T1-weighted image (*e*), which is consistent with hemorrhage. There is transient increased pericholecystic hepatic parenchymal enhancement on the arterial phase (*f*), which fades to isointensity with the remaining liver parenchyma on the hepatic venous phase (*g*).

degree of fibrosis occurs, causing wall thickening and shrinkage of the gallbladder. In contrast to acute cholecystitis, mural gadolinium enhancement is mild and most prominent on delayed postgadolinium images. Pericholecystic enhancement is minimal or absent, because of the lesser severity of the inflammatory process (fig. 3.18). The adjacent liver parenchyma usually does not show increased enhancement [46, 49]. A recent report has shown that increased gallbladder wall enhancement and increased transient pericholecystic hepatic enhancement were the most significant differences between acute and chronic cholecystitis [46]. The wall of the gallbladder may calcify, resulting in porcelain gallbladder (fig. 3.19). On MR images, calcifications may appear as signal-void foci. Patients with porcelain gallbladder may be at increased risk for gallbladder carcinoma. Therefore, enhancing nodular tissue arising from the gallbladder wall, best shown on fat-suppressed late postgadolinium images, should raise suspicion of malignant disease in these patients. A uniform wall of less than 4 mm, however, excludes the presence of malignancy (see fig. 3.19).

Xanthogranulomatous Cholecystitis

Xanthogranulomatous cholecystitis (fibroxanthogranulomatous inflammation) is a rare, focal or diffuse, destructive inflammatory disease of the gallbladder that is assumed to be a variant of chronic cholecystitis. The pathogenesis is thought to be occlusion of mucosal outpouchings (Rokitansky–Aschoff sinuses) with subsequent rupture and intramural extravasation of inspissated bile and mucin that causes an inflammatory reaction with multiple intramural xanthogranulomatous nodules. The importance of this disease is that it mimics gallbladder carcinoma both clinically and radiologically [50]. The MRI findings are focal or diffuse gallbladder wall thickening with contrast enhancement. Small intramural abscesses may be demonstrated as foci of high signal on T2-weighted images and low signal on T1-weighted images [51].

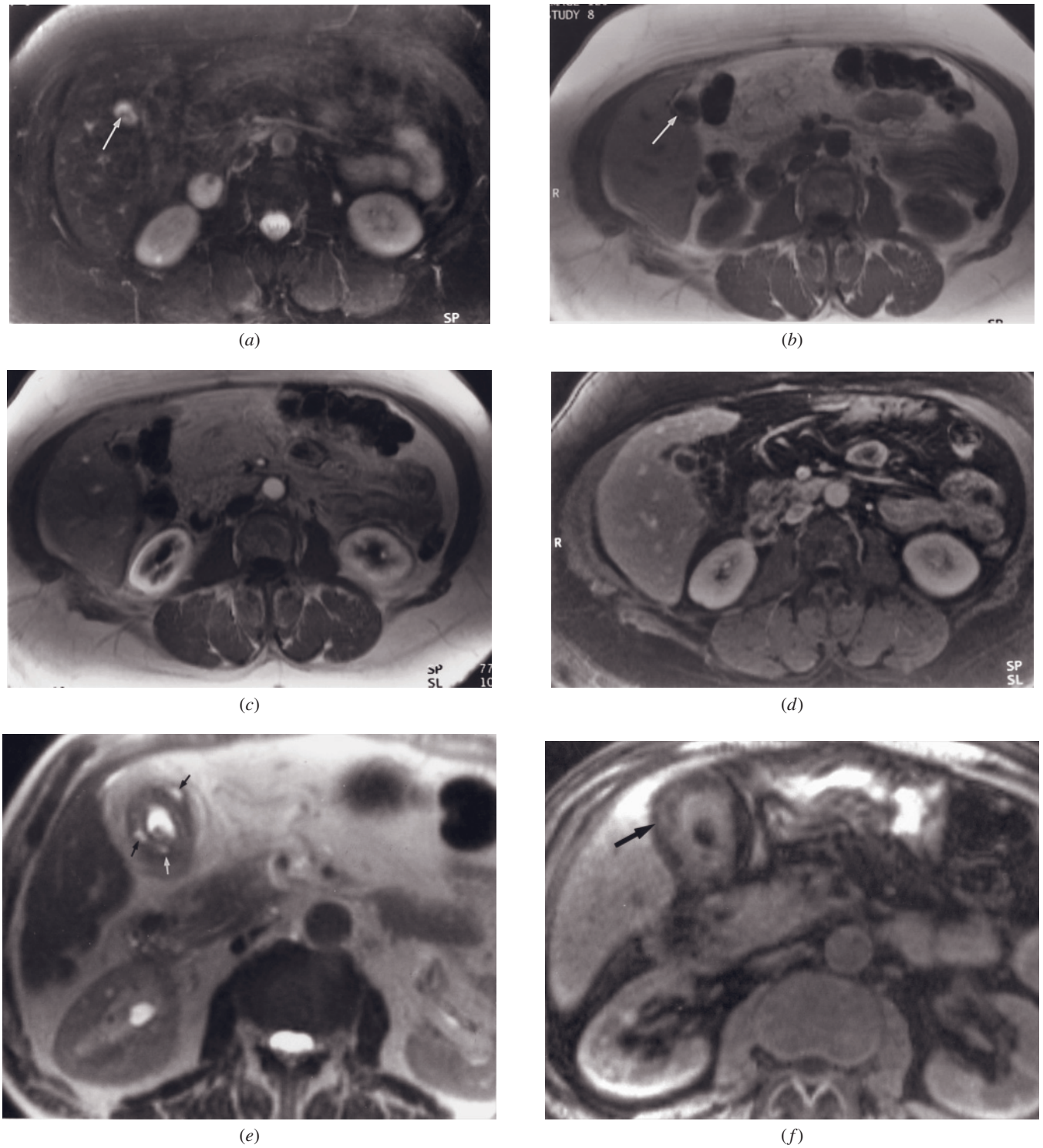

FIG. 3.18 Chronic cholecystitis. T2-weighted fat-suppressed spin-echo (*a*),T1-weighted GE (*b*), immediate postgadolinium GE (*c*), and 90-s postgadolinium fat-suppressed GE (*d*) images. On the T2-weighted image (*a*), the gallbladder is shrunken and irregular in shape, with poorly defined walls and a low-signal gallstone (arrow, *a*). On the precontrast T1-weighted image (*b*), the gallbladder wall is partly hyperintense (arrow, *b*). It enhances mildly on the immediate postgadolinium image (*c*), but no increased enhancement is noted in the adjacent liver parenchyma. On the 90-s postgadolinium fat-suppressed image (*d*), the gallbladder wall shows progressive enhancement.

T2-weighted single-shot echo-train spin-echo (*e*),T1-weighted fat-suppressed GE (*f*), and 2-min postgadolinium fat-suppressed GE (*g*) images in a second patient with chronic cholecystitis. The gallbladder is shrunken and irregular in shape and shows

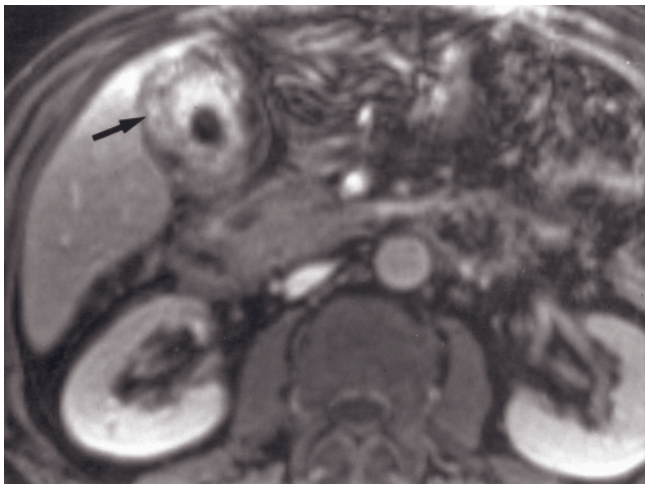

(*g*)

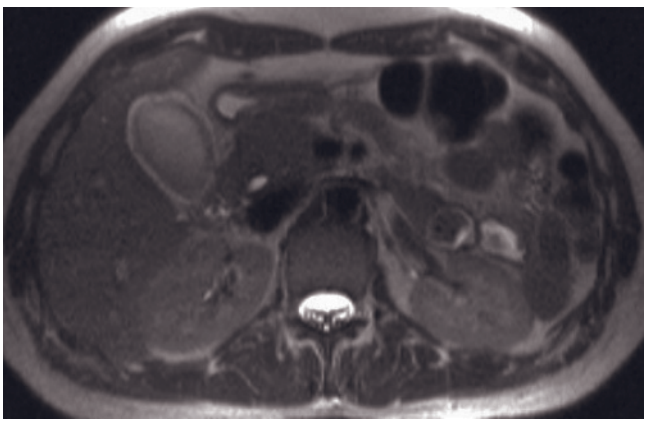

(*h*)

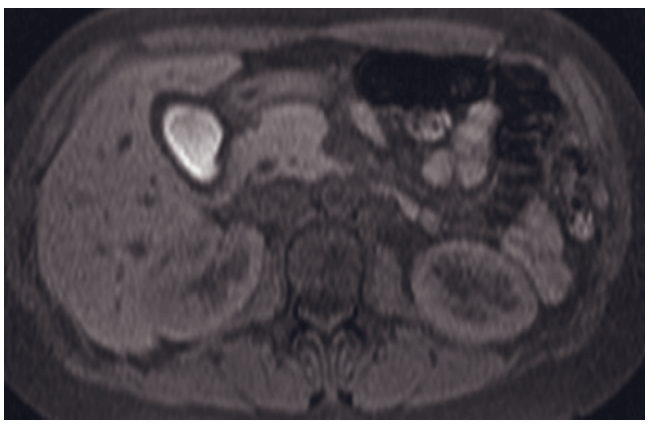

(*i*)

(*j*)

(*k*)

FIG. 3.18 (*Continued*) pronounced wall thickening. On the T2-weighted image (*e*), small hyperintense foci (short arrows, *e*) represent intramural fluid collections.

The gallbladder shows enhancement on the 2-min postgadolinium image (*g*). In the pericholecystic space, complex septations (arrows, *f*, *g*) demonstrating enhancement on the postgadolinium image (*g*) are suggestive of fibrous inflammatory tissue. Small low-signal calculi are seen in the gallbladder lumen (*e*–*g*). T2-weighted single-shot echo-train spin-echo (*h*), T1-weighted fat-suppressed SGE (*i*), T1-weighted fat-suppressed postgadolinium hepatic arterial dominant phase 3D-GE (*j*), and interstitial phase SGE (*k*) images demonstrate chronic cholecystitis in another patient. The gallbladder wall is thickened and shows hyperintense signal on T2-weighted image (*h*) due to edema. The gallbladder wall shows minimal enhancement on the hepatic arterial dominant phase (*j*) and moderate enhancement on the interstitial phase (*k*). The absence of associated transient increased pericholecystic hepatic parenchymal enhancement in combination with other findings suggest the presence of chronic cholecystitis. Note that the bile has high signal on T1-weighted image (*i*).

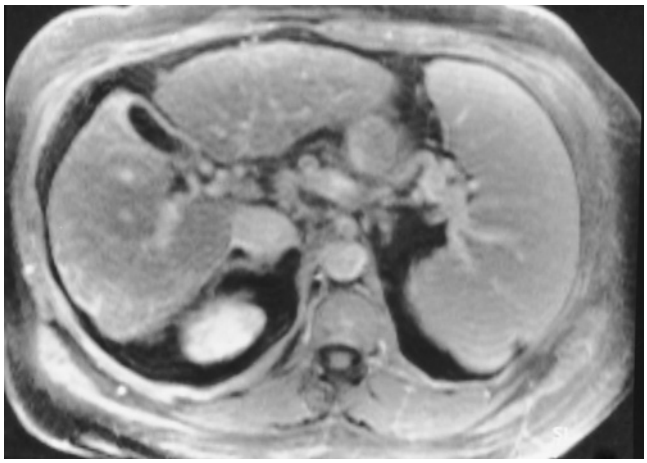

FIG. 3.19 Porcelain gallbladder. Diffuse calcification of the gallbladder wall was seen on a CT examination (not shown). The T1-weighted 2-min postgadolinium fat-suppressed GE image demonstrates uniform enhancement of a smooth 3-mm-thick gallbladder wall, which excludes superimposed malignancy.

Diffuse Gallbladder Wall Thickening

Diffuse gallbladder wall thickening may be present in a number of hepatic, biliary, and pancreatic diseases. Among nontumorous causes are hepatitis, liver cirrhosis, hypoalbuminemia, renal failure, systemic or hepatic venous hypertension, AIDS cholangiopathy, and graft-versus-host disease. Important features to discriminate these conditions from cholecystitis are minimal enhancement of the gallbladder wall and lack of increased enhancement of adjacent structures on postgadolinium images, in particular the lack of transient increased enhancement of adjacent liver parenchyma (fig. 3.20).

Neoplastic Disease

Gallbladder Polyps

Gallbladder polyps are often incidentally identified arising from the gallbladder wall and are either sessile or pedunculated. They comprise a wide spectrum of histologic types; however, the vast majority are benign. Nevertheless, gallbladder polyps pose a dilemma with respect to diagnosis of potential malignancy and determination of proper long-term management. The majority are cholesterol polyps that do not have malignant potential. Approximately 10% of gallbladder polyps, however, are adenomas, which are thought to have malignant potential [52]. However, this determination may be reliably established only by histology. Polyps are typically homogeneously low to intermediate in signal intensity on T1- and T2-weighted MR images. On T1-weighted postgadolinium images, they show moderate homogeneous enhancement that is most pronounced on delayed images (fig. 3.21). Polyps can be readily distinguished from calculi on the basis of gadolinium enhancement, or by location: While the polyp is located on the nondependent surface of the gallbladder wall, calculi generally layer on the dependent surface or float horizontally within the gallbladder. Polyp size may be used as an indicator for malignant potential: Polyps 1 cm or smaller have minimal risk for malignancy and can be managed by imaging follow-up [53]. Symptomatic lesions, irregular polyps, polyps larger than 1 cm, or interval increase in size are worrisome for malignancy, and cholecystectomy is indicated [54].

Gallbladder Adenomyomatosis

Adenomyomatosis is a relatively common disease with a reported incidence of up to 5% [55]. This disease entity is characterized by hyperplasia of epithelial and muscular elements with mucosal outpouching of epithelium-lined cystic spaces into a thickened muscularis layer. These changes can involve the entire gallbladder or may be focal. The mucosal outpouchings are termed Rokitansky–Aschoff sinuses, and they form small intramural diverticula that are pathognomonic. On MR images, these fluid-filled sinuses appear as small intramural foci of low signal intensity on T1-weighted images and high signal intensity on T2-weighted images [55–57]. After gadolinium administration, early mucosal enhancement and late homogeneous enhancement can be observed (fig. 3.22) [55]. Demonstration of Rokitansky–Aschoff sinuses with a breath-hold or breathing-independent T2-weighted sequence has been shown to be a useful imaging finding to differentiate adenomyomatosis from gallbladder carcinoma [55]. However, this differentiation may be difficult on the basis of imaging.

Gallbladder Carcinoma

Gallbladder carcinoma is the most common biliary malignancy and occurs predominantly in the sixth and seventh decades with a slight female predominance [58]. Porcelain gallbladder has been considered a predisposing factor for gallbladder carcinoma. A recent large series, however, has cast doubt on this supposition [59]: In a review of 10,741 cholecystectomies, 15 specimens were porcelain gallbladder, and none of these 15 had gallbladder carcinoma [59]. Other diseases that are associated with gallbladder carcinoma are cholecystolithiasis, inflammatory bowel disease (predominantly ulcerative colitis), and chronic cholecystitis. However, fewer than 1% of patients with gallstones develop gallbladder carcinoma, and the risk for carcinoma is minimal if the stones are small and asymptomatic. The risk of developing carcinoma is increased if the stones are large and symptomatic, warranting prophylactic cholecystectomy. The most common histologic type of gallbladder carcinoma is adenocarcinoma, with squamous

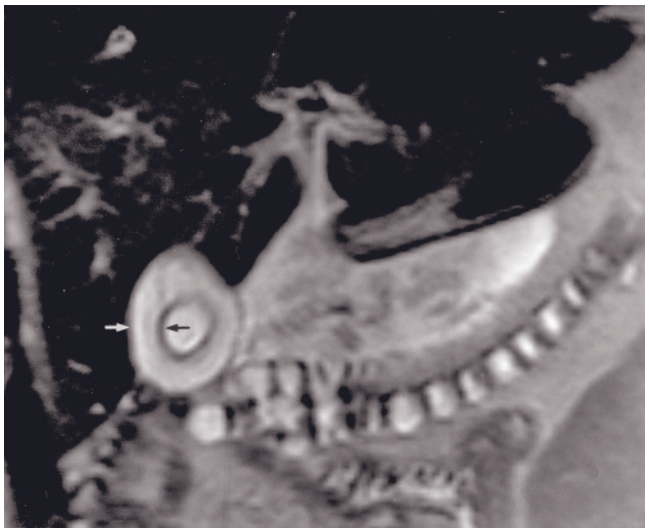

(*a*)

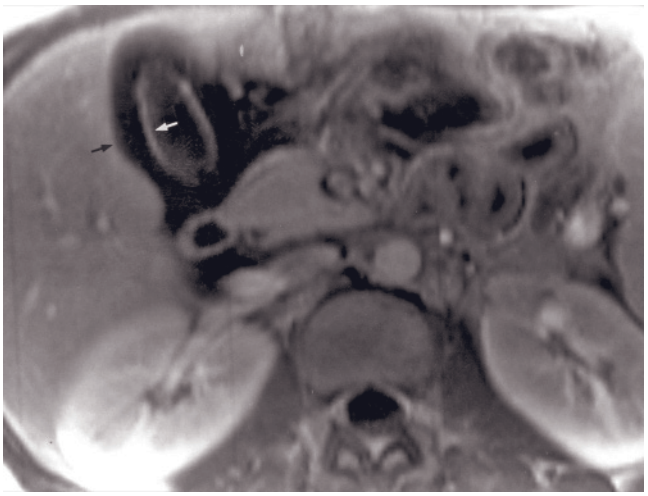

(*b*)

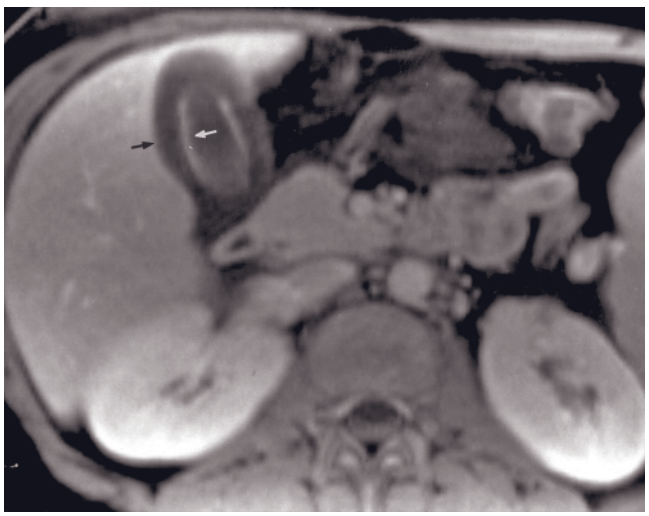

(*c*)

FIG. 3.20 Gallbladder wall edema. Coronal T2-weighted fat-suppressed single-shot echo-train spin-echo (*a*), T1-weighted immediate postgadolinium GE (*b*), and 2-min postgadolinium fat-suppressed GE (*c*) images. In this patient after bone marrow transplantation, the gallbladder wall is markedly edematous and thickened (arrows, *a–c*). Because of the high fluid content of the wall, the signal intensity is high on the T2-weighted image (*a*) and low on the T1-weighted images (*b*, *c*). The gallbladder mucosa shows moderate early and late enhancement (*b*, *c*). The adjacent liver parenchyma is normal.

cell tumor being far less common [60]. The 5-year survival rate is very poor (approximately 6%), reflecting that up to 75% of tumors are unresectable at initial presentation because of local invasion of adjacent organs.

Findings at MRI that are suggestive of gallbladder carcinoma are 1) a mass either protruding into the gallbladder lumen or replacing the lumen completely; 2) focal or diffuse thickening of the gallbladder wall greater than 1 cm; and 3) soft tissue (tumor) invasion of adjacent organs such as the liver, duodenum, and pancreas, which occurs frequently (fig. 3.23) [58, 61, 62]. On T1-weighted MR images, the tumor is hypo- or isointense compared to adjacent liver. On T2-weighted sequences, it is usually hyperintense relative to the liver and poorly delineated (see fig. 3.23) [62, 63]. The tumor usually enhances on T1-weighted immediate postgadolinium images in a heterogeneous fashion, which facilitates differentiation from chronic cholecystitis [64]. However, superimposed infection or perforation of gallbladder carcinoma may be indistinguishable from severe acute cholecystitis. Invasion of the tumor into adjacent organs and the presence of lymph node metastases are features of advanced disease and can be best visualized with a combination of a T2-weighted fat-suppressed sequence, T1-weighted immediate postgadolinium gradient echo, and 2-min postgadolinium fat-suppressed gradient-echo sequence (see fig. 3.23) [62]. Preservation of a fat plane between tumor and surrounding structures excludes invasion. Delayed fat-suppressed gadolinium-enhanced images are particularly useful to delineate tumor spread along bile ducts and into the mesenteric fatty tissue.

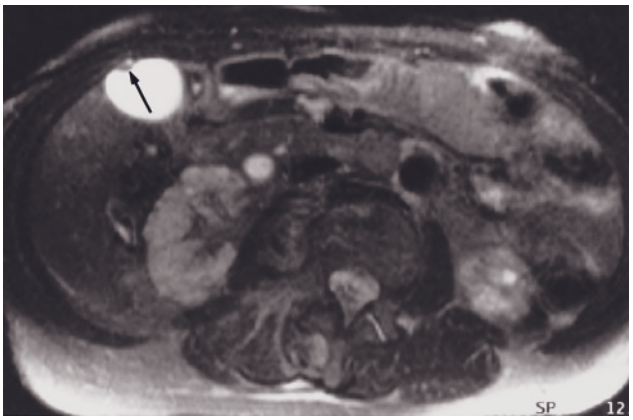

(*a*)

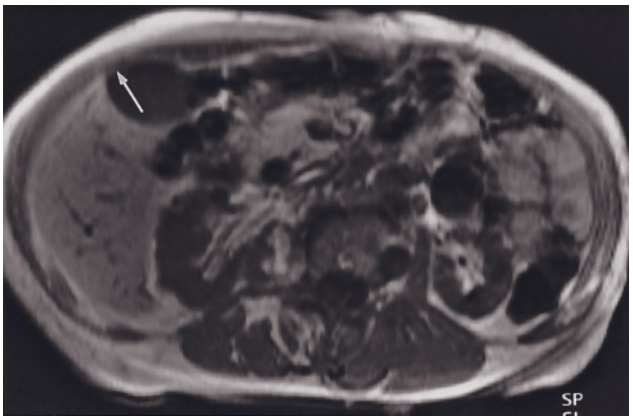

(*b*)

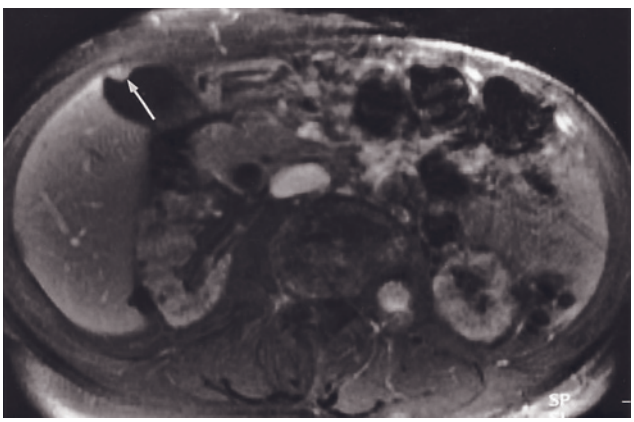

(*c*)

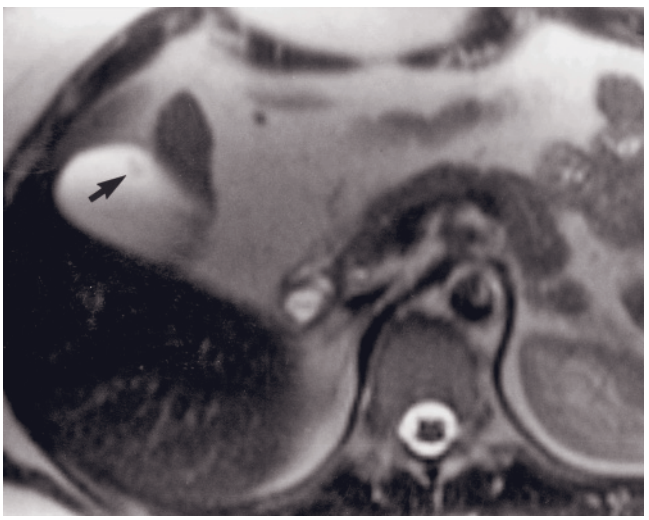

(*d*)

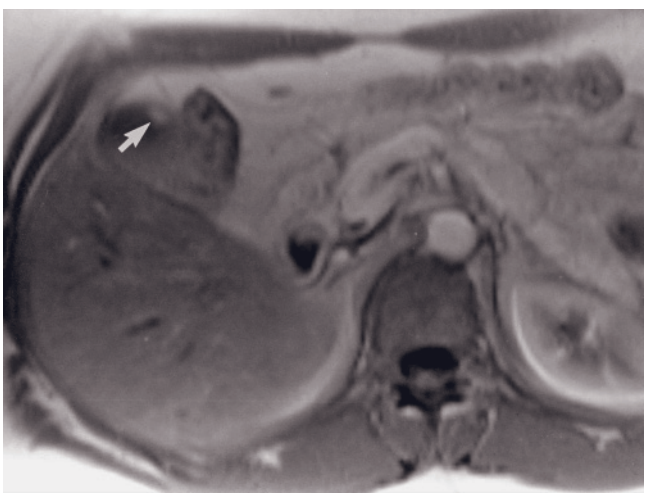

(*e*)

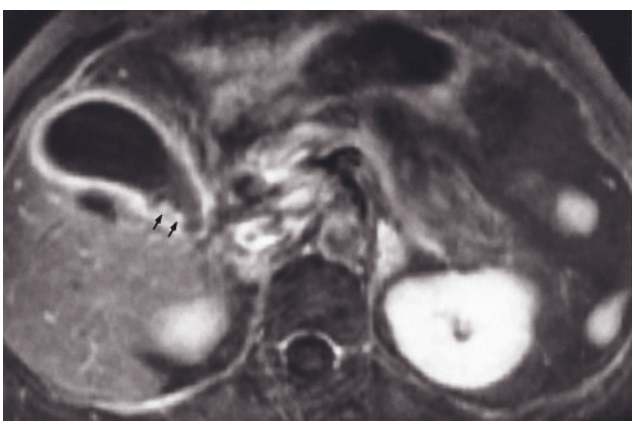

(*f*)

FIG. 3.21 Gallbladder polyps. T2-weighted fat-suppressed single-shot echo-train spin-echo (*a*),T1-weighted GE (*b*), and 2-min postgadolinium fat-suppressed GE (*c*) images. A 1-cm polyp (arrows, *a–c*) is shown on the nondependent surface of the gallbladder. The polyp is intermediate signal on the T2-weighted image (*a*), showing high contrast against bile. The polyp is low signal on the T1-weighted image (*b*) and can barely be seen. Intense uniform enhancement of the polyp is appreciated on the 2-min post-gadolinium image (*c*). Enhancement and nondependent location distinguish the polyp from a gallbladder calculus. T2-weighted single-shot echo-train spin-echo (*d*) and T1-weighted 60-s postgadolinium GE (*e*) images in a second patient.

A polyp (arrows, *d*, *e*) is demonstrated in the nondependent portion of the gallbladder, showing intermediate signal on the T2-weighted image (*d*) and enhancement on the postgadolinium image (*e*). Layering of concentrated bile in the dependent portion of the gallbladder is seen on both sequences (*d*, *e*).

Transverse interstitial phase gadolinium-enhanced fat-suppressed SE image (*f*) in a third patient, with coexistent acute acalculous cholecystitis, demonstrates two small enhancing polyps (arrows, *f*). Note the intense enhancement of the acutely inflamed and

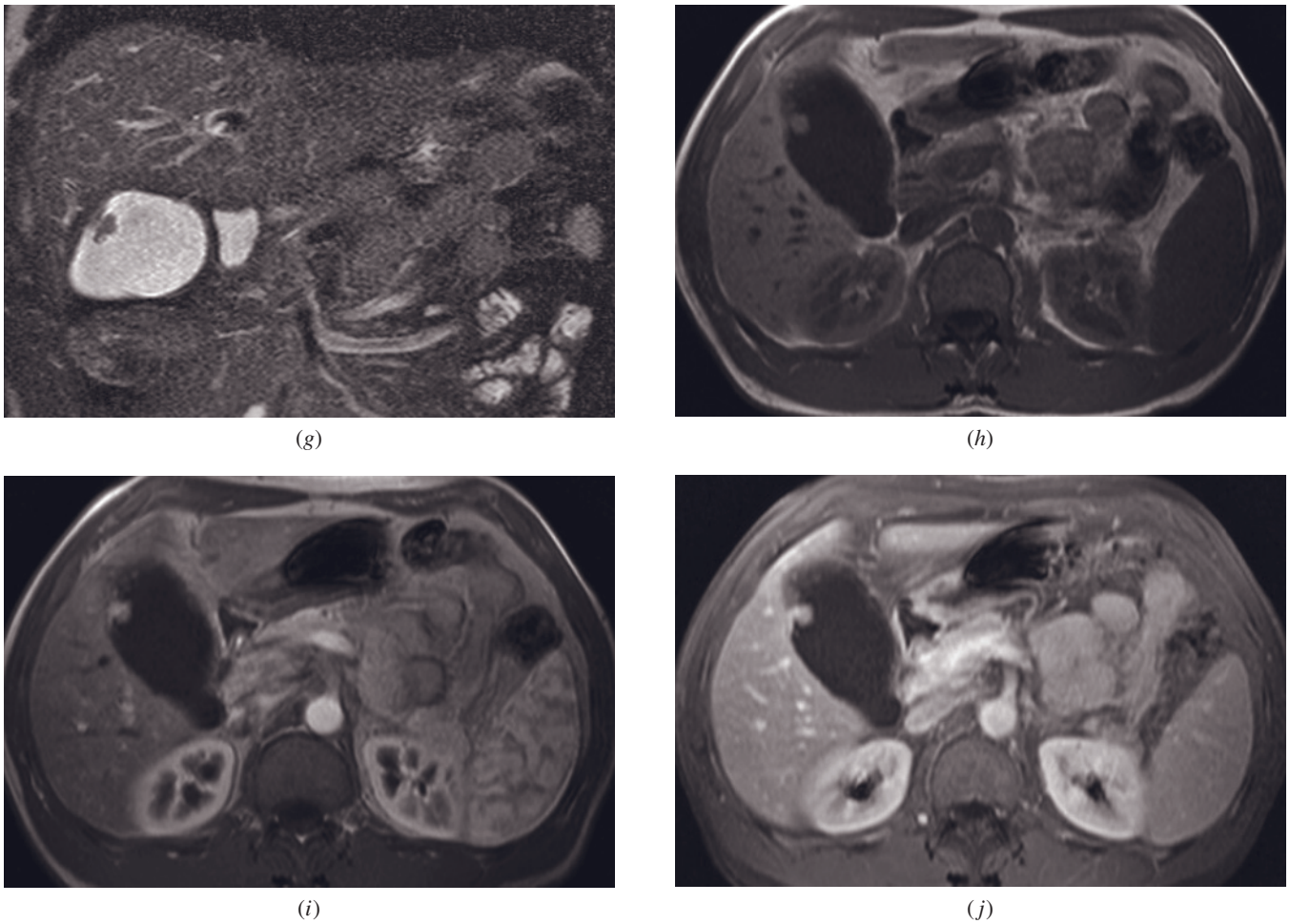

FIG. 3.21 (*Continued*) thickened gallbladder wall. Coronal T2-weighted echo train spin echo (*g*), transverse T1-weighted SGE (*h*), transverse T1-weighted postgadolinium hepatic arterial dominant phase SGE (*i*), and hepatic venous phase fat-suppressed SGE (*j*) images demonstrate the gallbladder wall polyp, which shows prominent enhancement on postgadolinium images in another patient. The size of the polyp is relatively large, and its contours are irregular. These findings suggest that the lesion has malignant features, and the histopathologic findings are consistent with adenocarcinoma not extending beyond the serosa.

Metastases to the Gallbladder

A number of malignant diseases can metastasize to the gallbladder. Among the most common primary malignancies are breast carcinoma, melanoma, and lymphoma. Breast cancer and melanoma more commonly show focal gallbladder involvement, whereas lymphoma more commonly presents with diffuse mural involvement and thickening (fig. 3.24).

DISEASES OF THE BILE DUCTS

One of the main indications for MRCP and/or conventional MRI of the biliary system is to reveal the cause for biliary obstruction and to characterize the lesion process as benign or malignant. MRCP has become the first-line imaging modality for the diagnostic evaluation of bile ducts including the obstruction. In patients in whom ERCP is difficult to perform or contraindicated (e.g., patients who have undergone liver transplantation or biliary-enteric anastomosis), MRCP is the primary modality to evaluate biliary obstruction [65]. Common causes for benign obstruction are gallstone disease or strictures as a sequel to inflammation or surgery [66]. Malignant causes are pancreatic head tumors, primary biliary tumors, ampullary tumors, and compression from adjacent malignancies. In all cases it is necessary to define the level, grade, and cause of the biliary obstruction. Therefore, demonstration of the lumen and the walls of the bile ducts, as well as the surrounding tissue, is required. This can be achieved with a combination of MRCP and conventional MRI sequences acquired before and after intravenous administration of gadolinium.

The normal maximal diameters of the CBD as visualized with MRCP (measured on coronal source images)

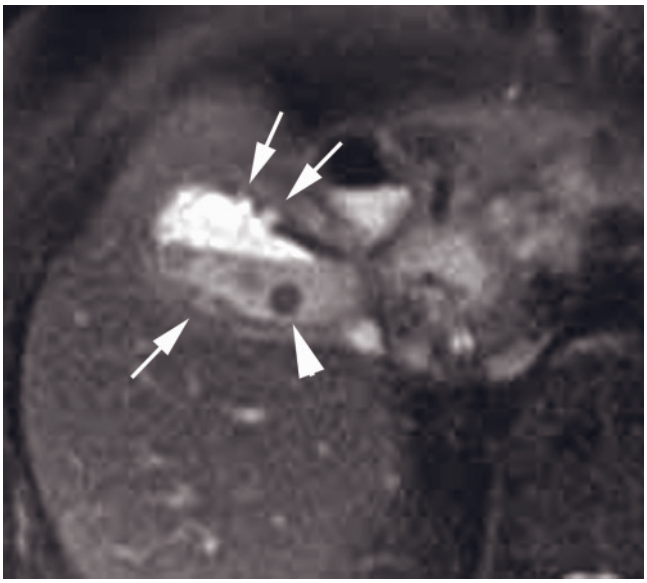

(*a*)

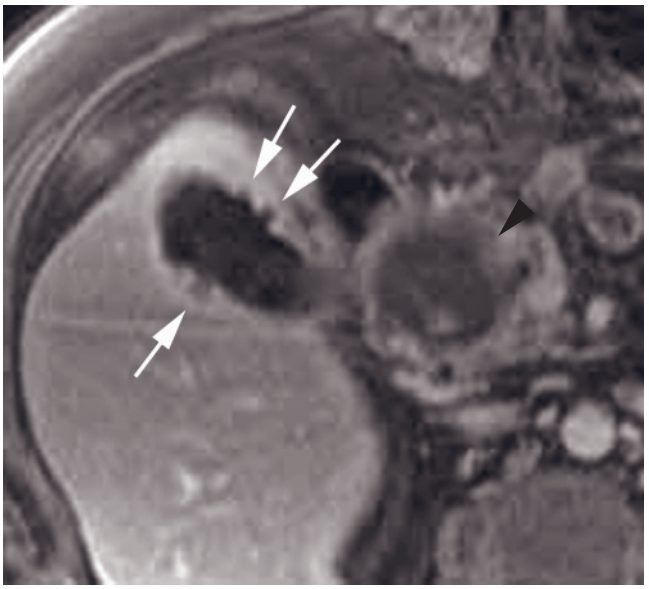

(*b*)

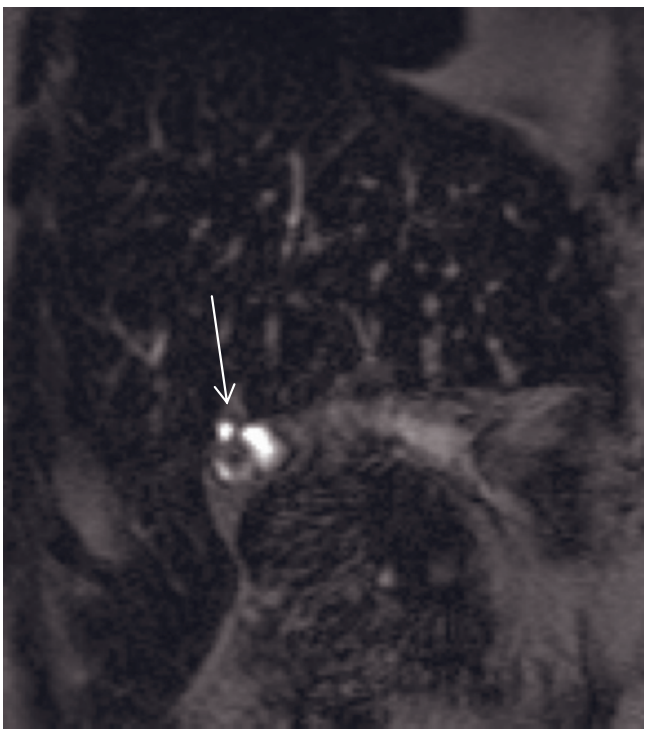

(*c*)

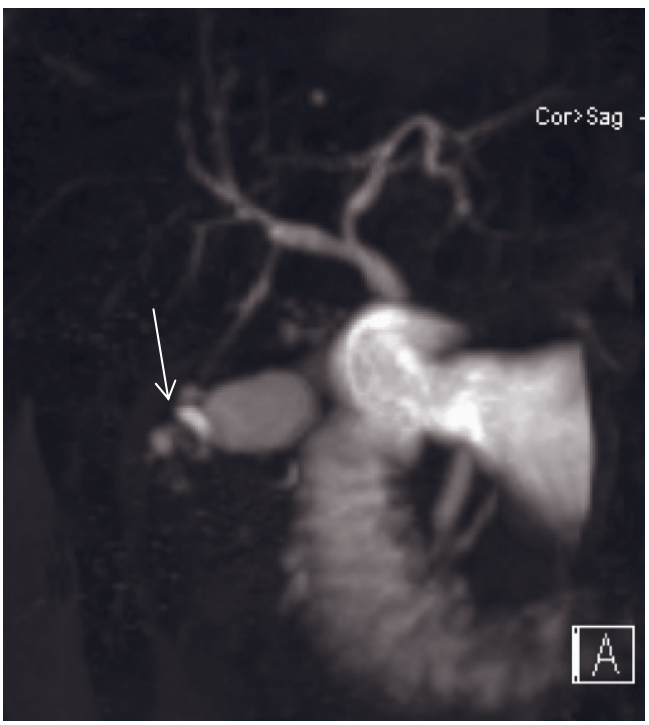

(*d*)

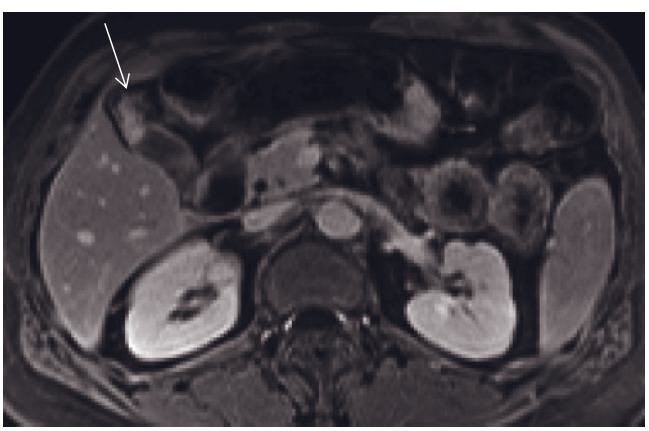

(*e*)

FIG. 3.22 Gallbladder adenomyomatosis. T2-weighted fat-suppressed single-shot echo-train spin-echo (*a*) and late postgadolinium T1-weighted GE (*b*) images. The gallbladder is shrunken and shows wall thickening. Layering of low-signal concentrated bile in the dependent portion is demonstrated on the T2-weighted image (*a*). Rokitansky–Aschoff sinuses (arrows, *a*, *b*) are visualized as high-signal foci in the gallbladder wall on the T2-weighted image (*a*) and as signal-void sinuses on the T1-weighted image (*b*). On the T2-weighted image (*a*), a small calculus (arrowhead, *a*) can be observed. A large adenocarcinoma in the pancreatic head (arrowhead, *b*) is better seen on the postgadolinium image (*b*).

Sagittal T2-weighted echo train spin echo (*c*), coronal reconstructed 3D MIP MRCP image (*d*), and transverse T1-weighted postgadolinium fat-suppressed 3D-GE image (*e*) demonstrate adenomyomatosis in another patient. Aschoff–Rokitansky sinuses (arrows, *c*, *d*) are seen as high signal intensity cystic spaces on T2-weighted image (*c*) and MRCP image (*d*). The gallbladder wall shows homogeneously enhancing thickening and unenhanced sinuses on postgadolinium image (*e*).

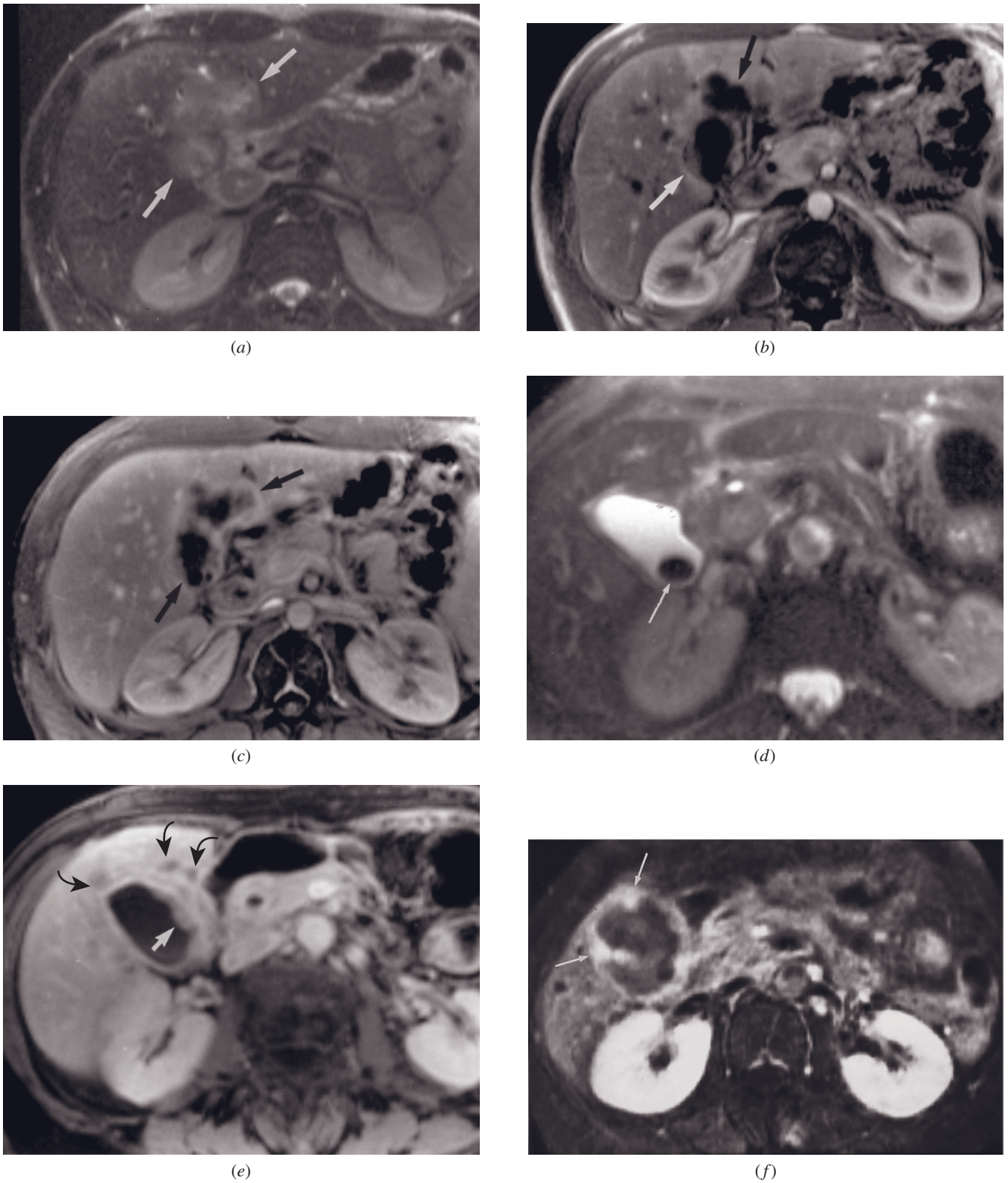

FIG. 3.23 Gallbladder carcinoma. T2-weighted fat-suppressed single-shot echo-train spin-echo (*a*), T1-weighted immediate postgadolinium GE (*b*), and 2-min postgadolinium fat-suppressed GE (*c*) images. The gallbladder (arrows, *a–c*) has a masslike appearance and shows an irregular and markedly thickened wall (arrows) that is moderately hyperintense on the T2-weighted image (*a*). Intense, slightly heterogeneous enhancement is demonstrated on the immediate and 2-min postgadolinium images (*b*, *c*), showing poor delineation from liver parenchyma.

T2-weighted fat-suppressed single-shot echo-train spin-echo (*d*) and T1-weighted 2-min postgadolinium fat-suppressed GE (*e*) images in a second patient with adenocarcinoma of the gallbladder. A signal-void stone is shown on the T2-weighted image (*d*). The gallbladder wall demonstrates partial irregular thickening (arrow, *e*), best visualized on the postgadolinium image (*e*). Small hypoenhancing areas in the adjacent liver parenchyma (curved arrows, *e*) are suggestive of metastases to the liver.

Transverse T1-weighted 2-min postgadolinium fat-suppressed GE image (*f*) in a third patient with gallbladder cancer demonstrates irregular nodular thickening of the gallbladder wall (arrows, *f*).

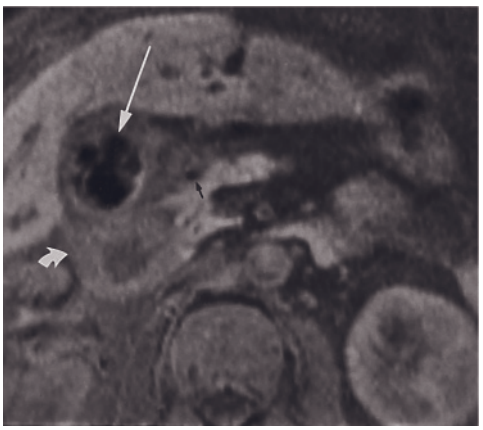

(*g*)

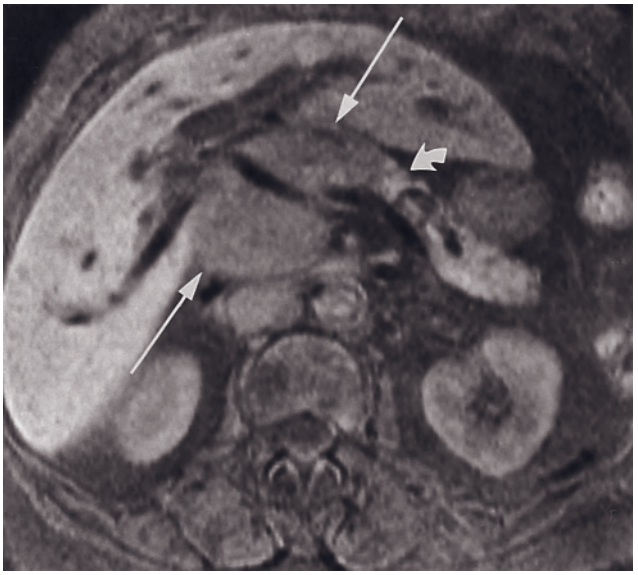

(*h*)

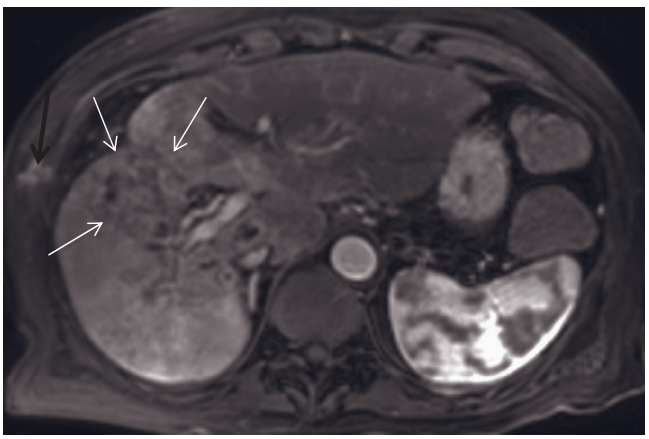

(*i*)

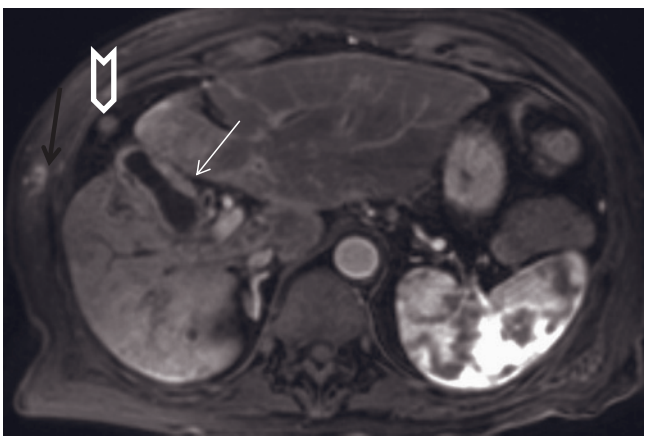

(*j*)

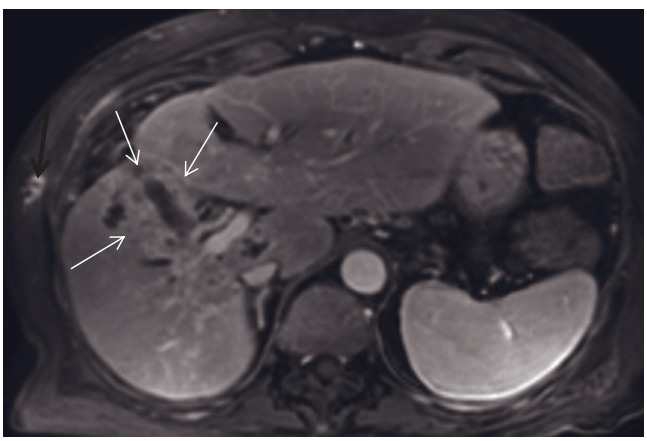

(*k*)

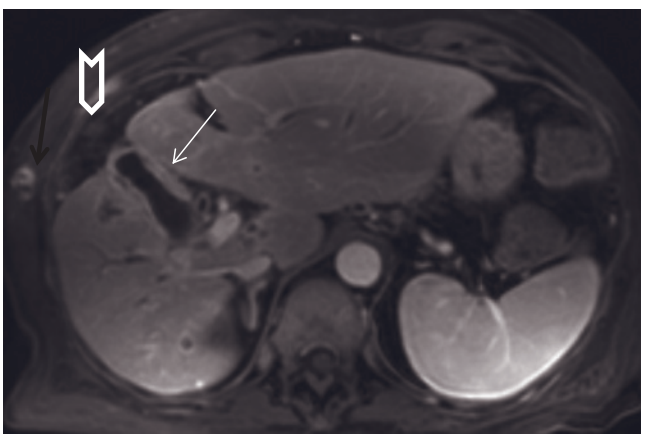

(*l*)

Fig. 3.23 (*Continued*) T1-weighted fat-suppressed spin-echo images (*g*, *h*) in a fourth patient demonstrating gallbladder cancer, which is intermediate in signal intensity and infiltrates along the duodenal wall (curved arrow, *g*) and head of the pancreas encasing the gastroduodenal artery (short arrow, *g*). Signal-void calculi are present within the gallbladder (long arrow, *g*). On a more superior image at the level of the porta hepatis (*h*), a large tumor (straight arrows, *h*) is demonstrated. Good contrast is observed between intermediate-signal tumor and high-signal pancreas (curved arrow, *h*).

T1-weighted postgadolinium hepatic arterial dominant phase (*i*, *j*) and hepatic venous phase (*k*, *l*) fat-suppressed 3D-GE images demonstrate gallbladder carcinoma in another patient. The gallbladder wall is irregularly thickened because of the tumor (white arrows, *j*, *l*). The adjacent liver parenchyma (white arrows, *i*, *k*) is heterogeneous because of tumor invasion. Multiple peripherally enhancing liver metastases are detected. Abdominal wall metastasis (black arrows, *i*–*l*) and peritoneal metastasis (open arrows, *j*, *l*) are also shown. There is increased differential enhancement in the right hepatic lobe on the hepatic arterial dominant phase (*i*, *j*) due to right portal vein thrombosis. Increased differential enhancement becomes isointense with the remaining liver parenchyma on the hepatic venous phase (*k*, *l*).

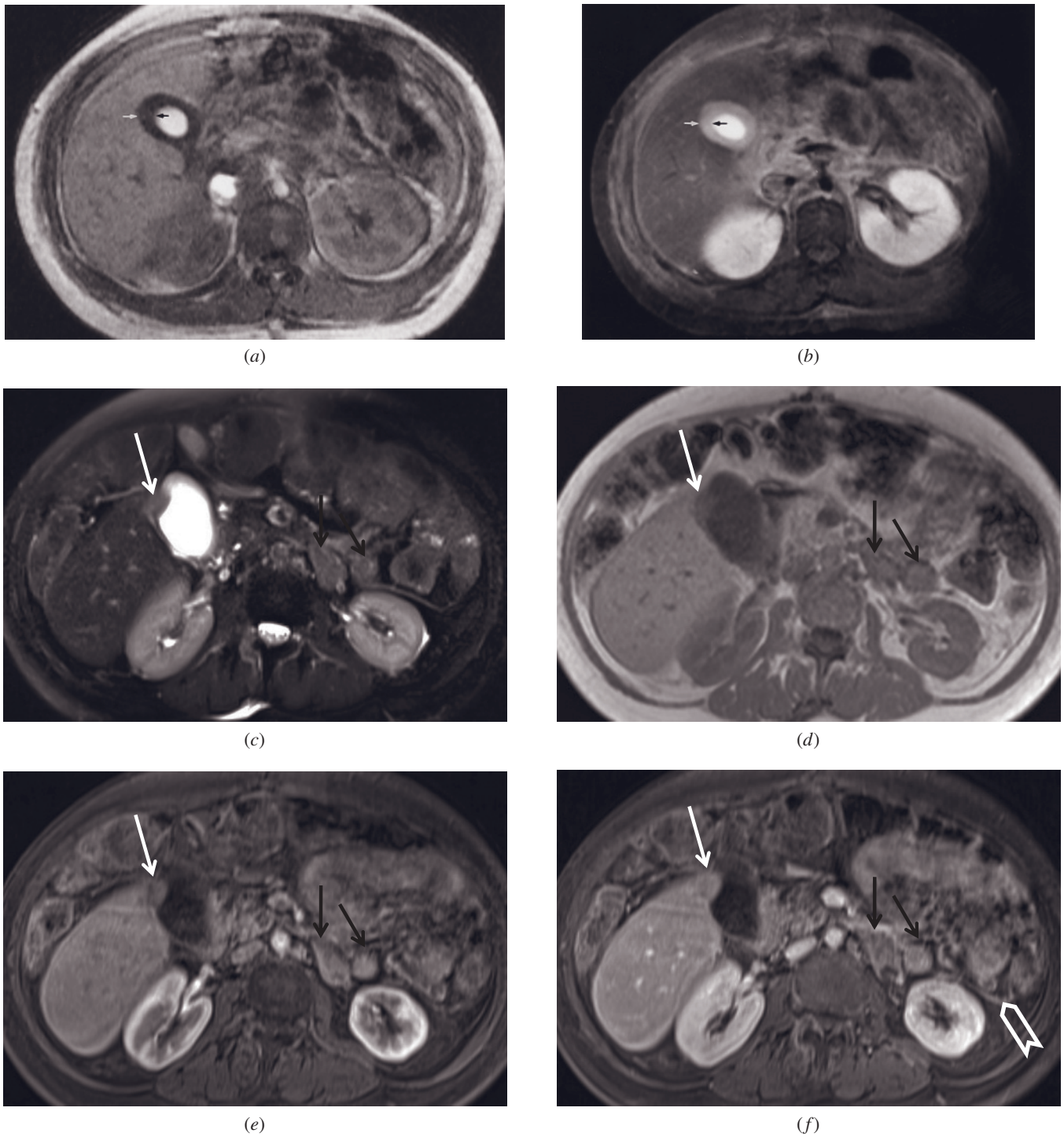

FIG. 3.24 Burkitt lymphoma of the gallbladder. T1-weighted GE (*a*) and 2-min postgadolinium fat-suppressed spin-echo (*b*) images. The gallbladder wall (arrows, *a*, *b*) is diffusely thickened because of infiltration by lymphoma. Note the uniform moderate enhancement of the wall after contrast administration (*b*), which is less than that observed for acute cholecystitis. **Gallbladder metastasis from ovarian cancer.** T2-weighted fat-suppressed single-shot echo-train spin-echo (*c*), T1-weighted SGE (*d*), and T1-weighted postgadolinium fat-suppressed hepatic arterial dominant phase (*e*) and interstitial phase (*f*) 3D-GE images demonstrate the gallbladder wall metastases (white arrows, *c–f*) from ovarian cancer. The tumor shows moderate enhancement on postgadolinium images (*e*, *f*). Note that there are lymph node (black arrows, *c–f*) and peritoneal (open arrow, *f*) metastases.

is considered 7 mm in patients with their gallbladder in place and 10 mm in patients after cholecystectomy. Duct diameter, however, increases slightly with increasing patient age. Normal intrahepatic bile ducts show smooth walls that taper slowly toward the periphery.

Benign Disease

Choledocholithiasis

Calculi in the biliary ducts, although less frequent than in the gallbladder, are the most common cause of extrahepatic obstructive jaundice. With the increase of laparoscopic cholecystectomy over recent years, the interest in preoperative diagnosis of choledocholithiasis has surged, because the presence of bile duct stones renders laparoscopic procedures extremely difficult. Ultrasound and CT imaging are not well suited for the diagnosis of choledocholithiasis because of their relatively low sensitivity and accuracy [67–70]. ERCP is still considered the gold standard technique for the evaluation of the biliary ductal system and allows therapeutic interventions such as sphincterotomy for the release of CBD stones. However, significant complications (e.g., pancreatitis) after sphincterotomy occur in 6–13% of patients, with an overall mortality rate up to 1.5% [71–73]. Even with diagnostic ERCP alone, the rate of major complications or death is 5–8% and the rate of failed ERCP is 5–20% [10, 74, 75].

MRCP is a noninvasive technique that is ideally suited for detecting bile duct stones because of the high contrast of calculi as intraluminal low-signal-intensity or signal-void structures against high-signal-intensity bile (fig. 3.25). A number of studies have shown that MRCP is superior to CT or ultrasound and comparable or superior to ERCP in detecting choledocholithiasis [2, 5, 21, 76, 77]. A study of 366 patients by Topal et al. [78]

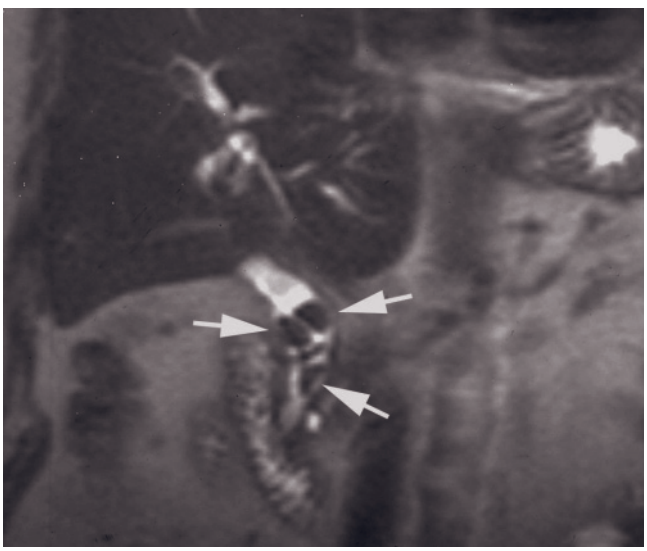

(*a*)

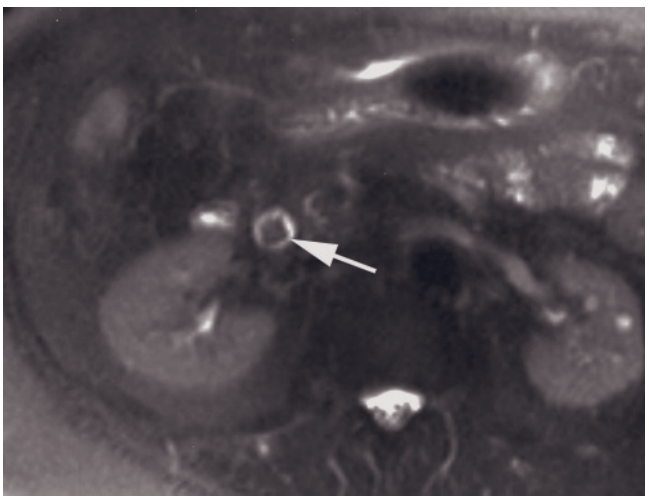

(*b*)

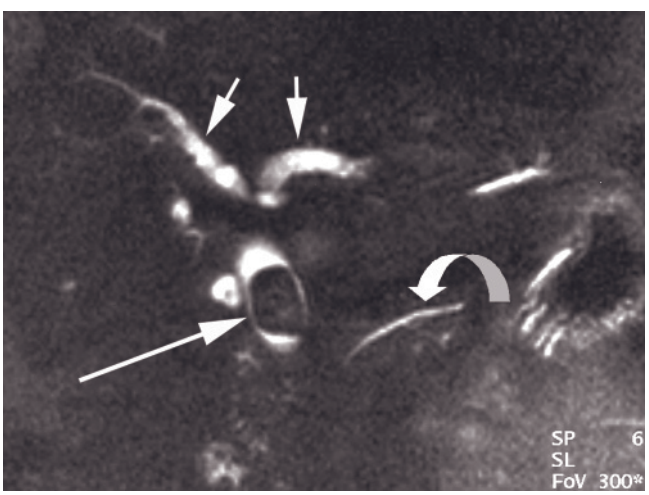

(*c*)

FIG. 3.25 Choledocholithiasis, MRCP. T2-weighted single-shot echo-train spin-echo images in the coronal (*a*) and transverse plane with fat suppression (*b*) and coronal thin-section MRCP single-shot echo-train spin-echo image with fat suppression (*c*). Multiple faceted low-signal calculi (arrows, *a*, *b*) are shown in the dilated CBD with good contrast against surrounding high-signal bile. On the thin-section MRCP image (*c*), the dilated intrahepatic ducts (short arrows, *c*) and a stone in the CHD (long arrow, *c*) are visualized more clearly. The normal pancreatic duct (curved arrow, *c*) is also well depicted.

came to the conclusion that in patients with a predicted probability of CBD stones of more than 5%, MRCP is recommended to confirm or rule out choledocholithiasis. For the detection of intrahepatic stones, MRCP proved to be even more effective than ERCP, with sensitivity and specificity of 97% and 93%, respectively, for MRCP versus 59% and 97%, respectively, for ERCP [79].

At MRI, ductal biliary stones typically have a rounded or oval-shaped configuration with a meniscus of fluid above their proximal edge (fig. 3.26). On thin-section source images, stones consistently appear as signal-void foci and can be detected as small as 2 mm in dilated and nondilated ducts [2]. On thick-section images, however, the detection rate of stones depends on their size. Large or medium-sized stones in normal-caliber ducts are readily detectable as signal-void structures, but small stones that are completely surrounded by fluid may escape detection because of volume averaging effects. Another potential missed diagnosis is an impacted stone in the ampulla, not surrounded by fluid, that may be misinterpreted as a stricture (fig. 3.27). Soto et al. [80] compared the performance of thick-slab, thin-slab, and 3D fast-SE MRCP sequences with ERCP for detecting choledocholithiasis in 49 patients. They found sensitivity and specificity rates exceeding 92% and 92%, respectively, for all sequences. There was 100% agreement between MRCP and ERCP in the detection of ductal dilatation.

Mirizzi's syndrome is a rare condition in which the stone in the cystic duct compresses the common bile duct and causes obstruction. This condition can also be successfully evaluated with MRCP (fig. 3.27).

Pitfalls of MRCP. A common pitfall in the diagnosis of choledocholithiasis is intraductal air bubbles (pneumobilia), which can be differentiated from stones by observing that air-filling defects lie on the nondependent portion of the bile duct against the wall or by recognition of an air-fluid level (fig. 3.28). Blood clots, however, may be indistinguishable from biliary stones (fig. 3.28). Other pitfalls that may mimic calculi include 1) tortuosity of the bile duct that results in the duct traveling in and out of the imaging plane; 2) insertion of the cystic duct into the CBD, which when observed en face on coronal images may appear as a round hypointense focus mimicking a stone; 3) flow artifacts in bile ducts (fig. 3.29); 4) metallic clips; and 5) external compression artifact from the right hepatic or gastroduodenal artery, which may result in a signal void focus (see fig. 3.29) [3, 81, 82]. Careful attention to the exact location of these defects (e.g., air in a nondependent location, continuation of the cystic duct or right hepatic or gastroduodenal arteries on adjacent images, clips in the gallbladder fossa) and interpretation of MRCP MIP reconstruction images in conjunction with thin-section source images most often permits correct exclusion of these entities as representing stones. Flow of bile that occurs intermittently during biliary contractions is fastest in the center of the ducts and can cause small flow-void artifacts, especially when the flow is perpendicular to the image plane. Acquiring thin-slab MRCP images in two perpendicular planes is most helpful to confirm or exclude the presence of a stone. The intraductal central location of this flow void is another hint to differentiate this artifact from stones because the latter tend to be located in the dependent portion of the ducts (see fig. 3.29).

Another pitfall is complete filling of the biliary system with debris, with the absence of visible high-signal bile within the biliary system. This may mask the fact that the bile ducts are dilated and debris-filled (fig. 3.29) [83].

Ampullary Stenosis

The clinical symptoms of ampullary stenosis include recurrent, intermittent upper abdominal pain, abnormal liver tests, and dilatation of the common bile duct.

Ampullary Fibrosis. The most common cause of benign ampullary stenosis is fibrosis, which occurs most frequently as a sequel to stone passage in the context of choledocholithiasis. The degree of biliary ductal dilatation is usually mild to moderate but can be severe. In the acute phase, swelling and edema of the ampulla may be present, shown as enlarged prominence of the ampulla and increased signal intensity on T2-weighted images. In the chronic stage, fibrosis of the ampulla appears as low signal intensity on T2-weighted images without enlargement of the ampulla. Rarely, these fibrotic changes are proliferative and lead to pronounced enlargement of the ampulla, which may give the impression of an obstructing tumor. T1-weighted immediate postgadolinium images are a useful tool to show normal enhancement of the periampullary pancreatic parenchyma to exclude pancreatic tumor (figs. 3.30 and 3.31). Nevertheless, endoscopic biopsy may sometimes be necessary to establish the correct diagnosis.

Papillary Dysfunction. Functional stenosis of the sphincter of Oddi includes spasm of the sphincter of Oddi and abnormalities of the sequencing or frequency rate of sphincteric contraction waves [84]. This results in delayed drainage of the CBD with clinical symptoms and radiologic signs of biliary obstruction at the level of the papilla. MRI can aid in establishing the diagnosis by ruling out morphologic causes for biliary ductal dilatation (fig. 3.32). To visualize the function of the sphincter of Oddi, serial thick-section MRCP single-shot echo-train spin-echo images ("functional MRCP") can help to show regular relaxation of the sphincter [84, 86].

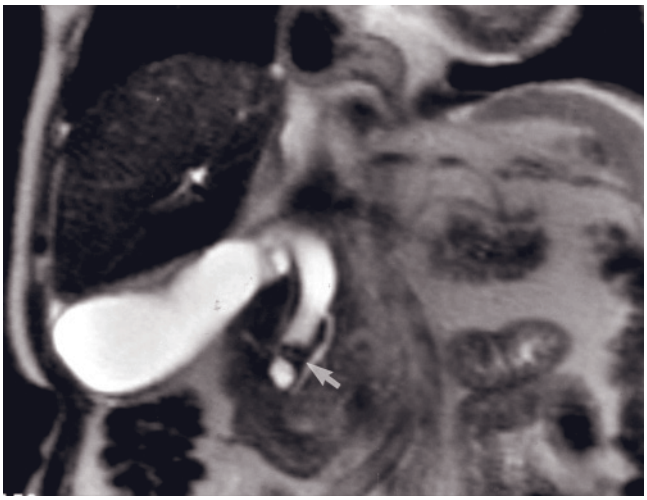

(*a*)

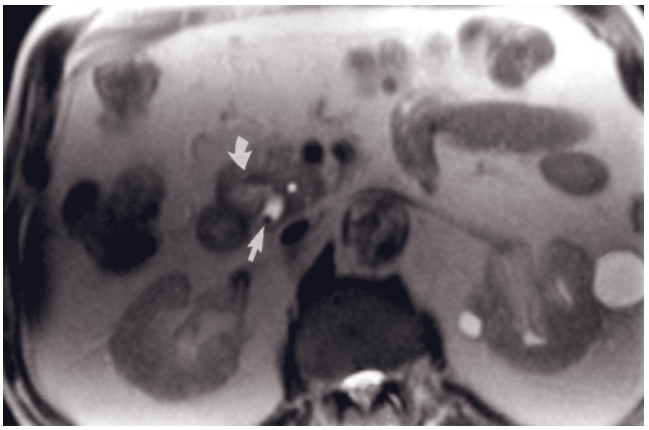

(*b*)

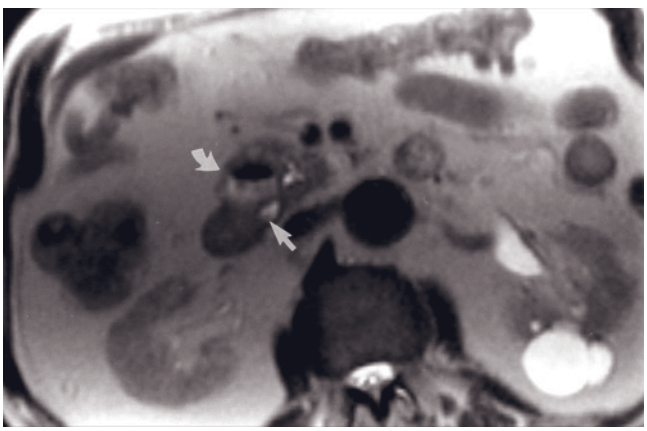

(*c*)

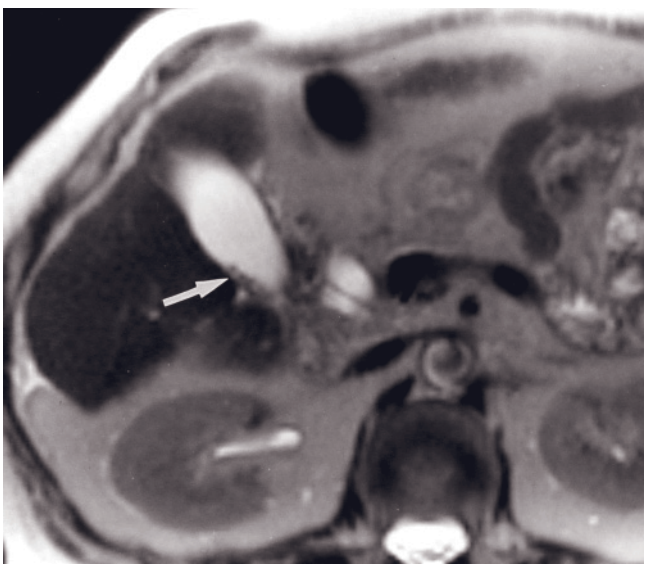

(*d*)

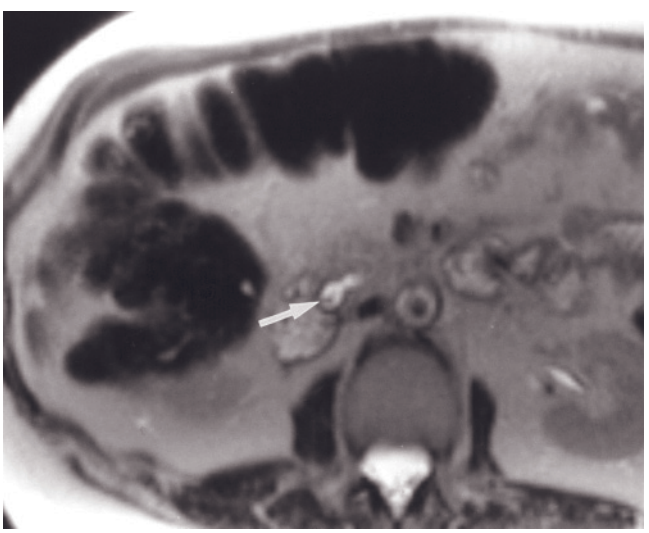

(*e*)

FIG. 3.26 Choledocholithiasis. Coronal T2-weighted single-shot echo-train spin-echo image (*a*). In the distal dilated CBD, a low-signal stone (arrow, *a*) is shown with a meniscus of high-signal bile above its proximal edge.

T2-weighted single-shot echo-train spin-echo images (*b*, *c*) in a second patient revealing a 2-mm low-signal choledocholith (arrow, *b*) in the mildly dilated distal CBD and another tiny calculus more caudally (*c*) in the preampullary CBD (arrow, *c*). A duodenal diverticulum (curved arrows, *b*, *c*) is shown with high-signal fluid content in the dependent and a signal-void air bubble in the nondependent portions. High-signal cortical renal cysts are present in the left kidney.

Transverse T2-weighted single-shot echo-train spin-echo images (*d*, *e*) in a third patient demonstrating several low-signal 2-mm calculi in the gallbladder (arrow, *d*) and in the preampullary CBD (arrow, *e*).

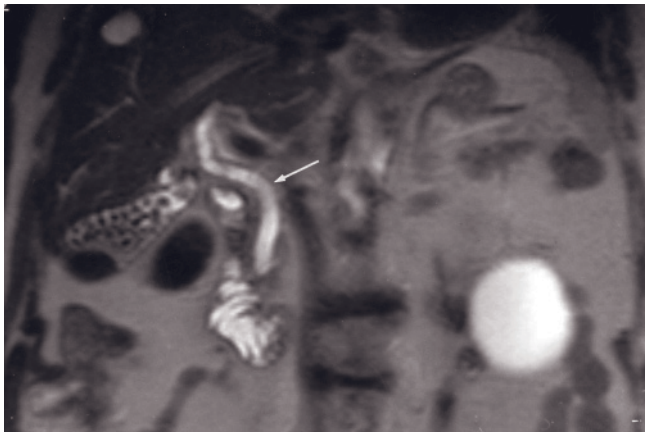

(*a*)

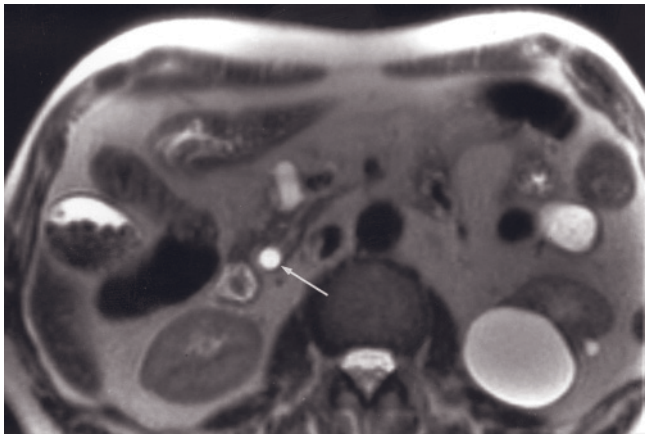

(*b*)

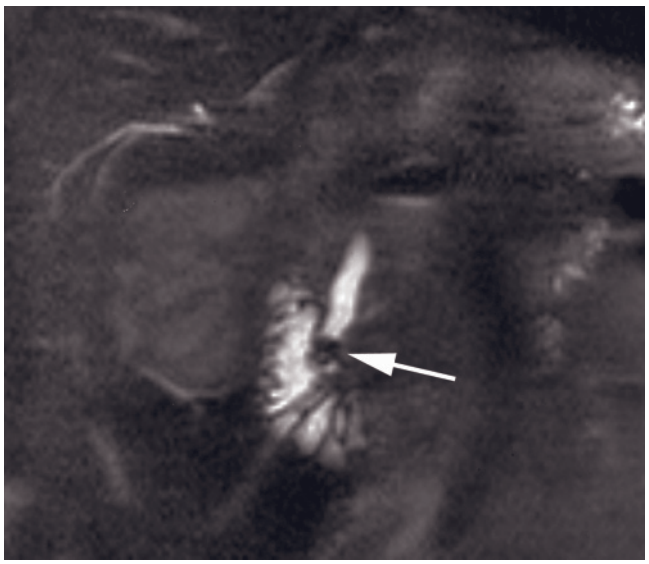

(*c*)

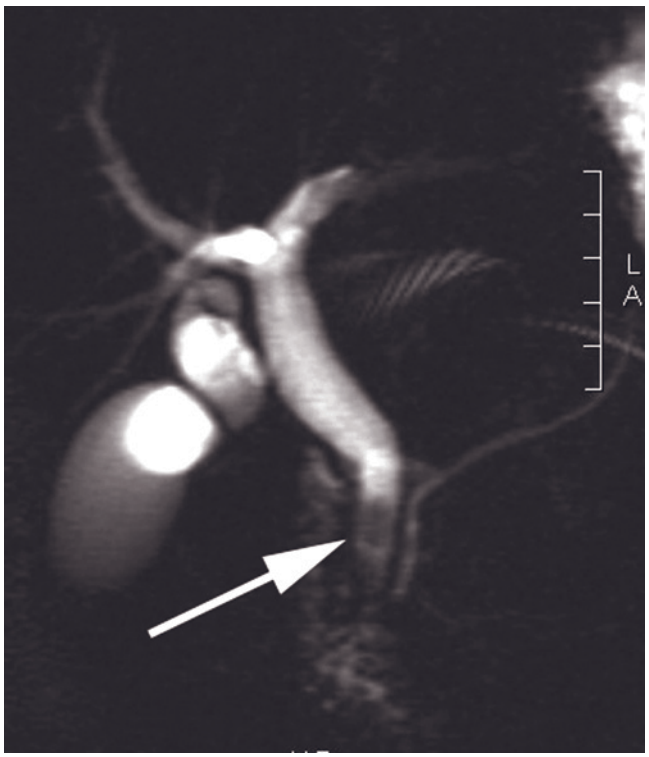

(*d*)

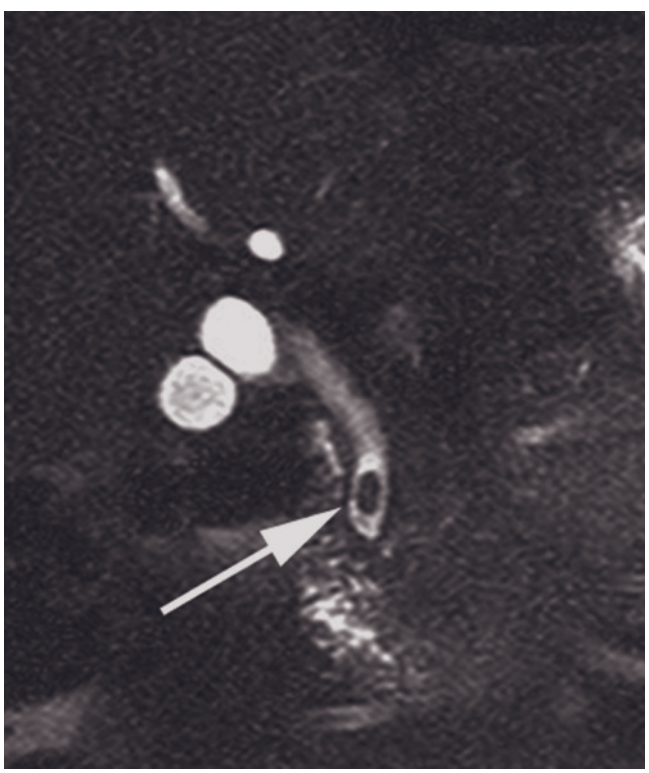

(*e*)

FIG. 3.27 Ampullary choledocholithiasis. Coronal (*a*) and transverse (*b*) T2-weighted single-shot echo-train spin-echo images and coronal thin-section MRCP single-shot echo-train spin-echo image with fat suppression (*c*). Multiple small low-signal calculi are demonstrated in the gallbladder (*a*, *b*). The CHD and CBD (arrows, *a*, *b*) are dilated but no intraductal stone is visualized on the 8-mm coronal and transverse images (*a*, *b*). The thin-section MRCP image (*c*) reveals a small choledocholith (arrow, *c*) that is lodged in the ampulla and obstructs the CBD. The duodenum is filled with fluid outlining its folds (*a*, *c*). High-signal cysts are incidentally revealed in the dome of the liver (*a*) and the left kidney (*a*, *b*). Paracoronal thick-section MRCP (*d*), thin-section MRCP (*e*), and axial T2-weighted single-shot echo-train spin-echo

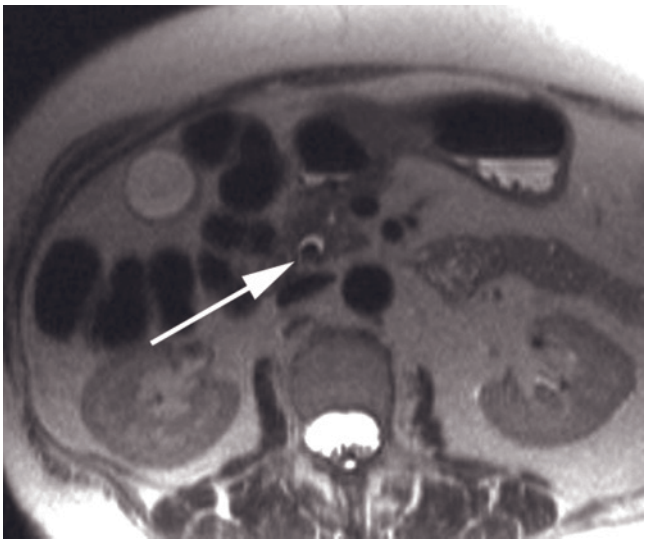

(*f*)

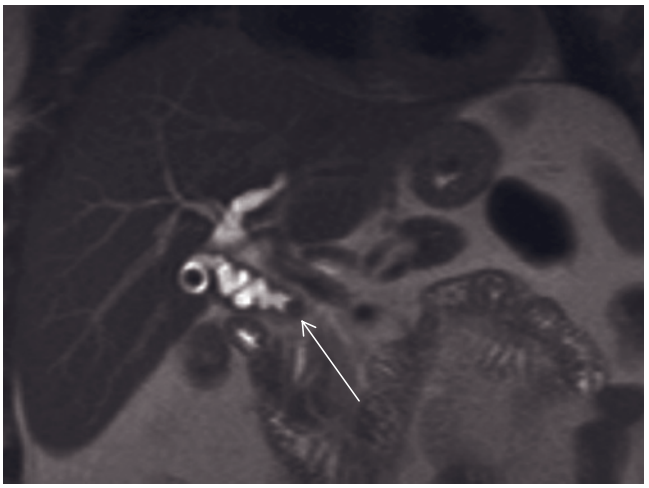

(*g*)

(*h*)

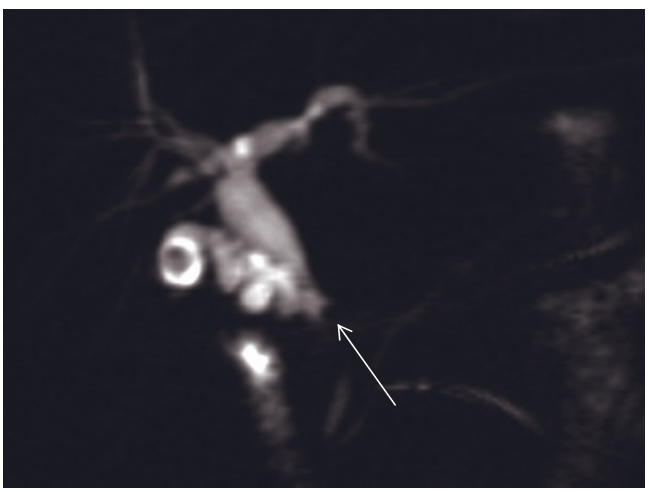

(*i*)

FIG. 3.27 (*Continued*) (*f*) images in a different patient. In the distal CBD, a low-signal stone (arrow, *d–f*) is shown with a meniscus of high-signal bile above its proximal edge. Note the dilatation of the proximal CBD. The paracoronal thin-section MRCP image (*e*) better visualizes the stone (arrow, *e*) and shows its preampullary position. The axial T2-weighted single-shot echo-train spin-echo image (*f*) shows the stone (arrow, *f*) in the dependent portion of the preampullary CBD and better demonstrates the adjacent organs.

Coronal T2-weighted single-shot echo-train spin-echo (*g*), coronal T2-weighted thin-section echo-train spin-echo (*h*), coronal thick-section fast spin-echo MRCP (*i*), and transverse T2-weighted fat-suppressed single-shot echo-train spin-echo (*j*) images demonstrate Mirizzi's syndrome in another patient with prior cholecystectomy. The common bile duct and proximal biliary ducts are dilated because of the compression of the common bile duct resulting from the presence of a stone (arrows, *g–j*) in the cystic duct. The cystic duct is also dilated, and there is another stone in the stump.

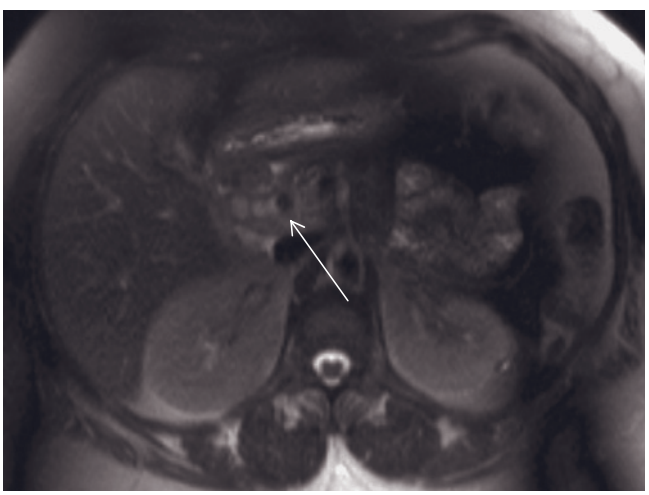

(*j*)

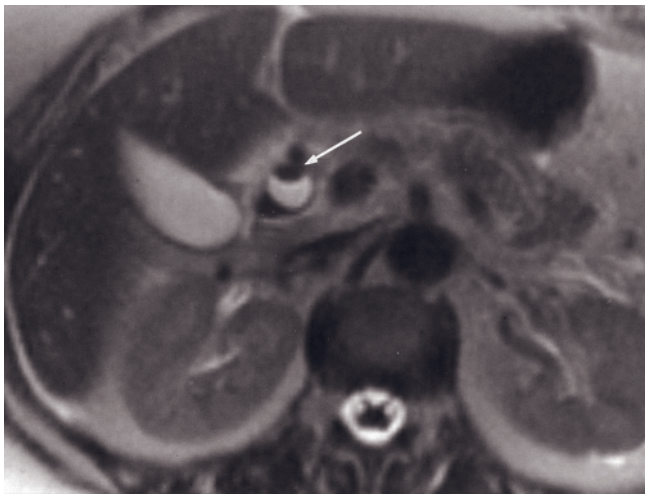

(*a*)

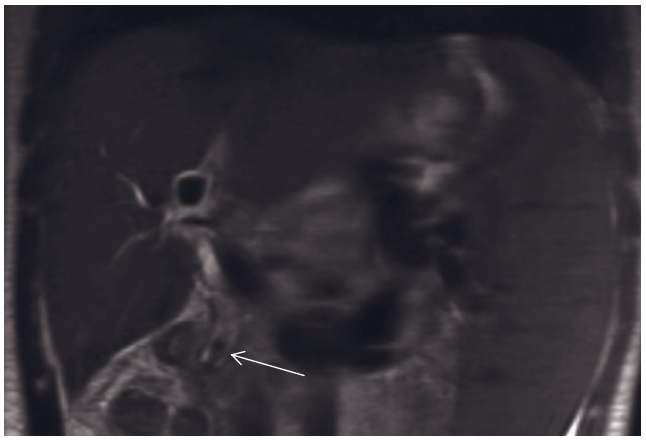

(*b*)

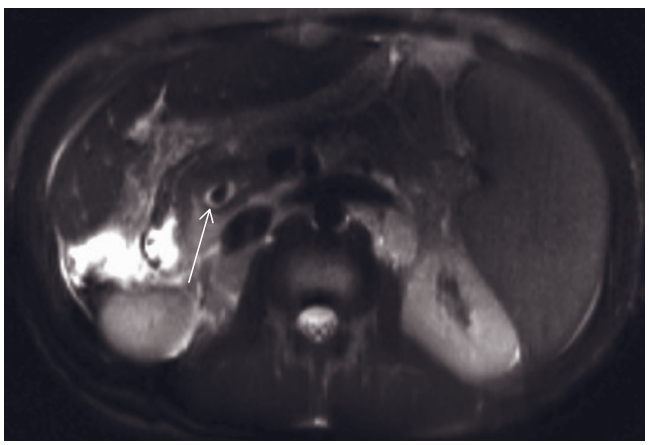

(*c*)

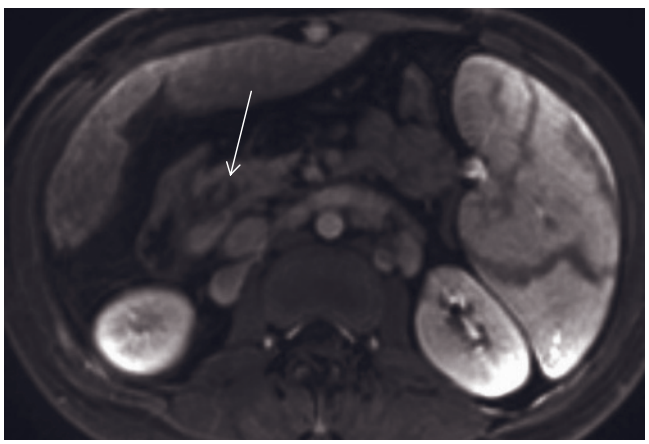

(*d*)

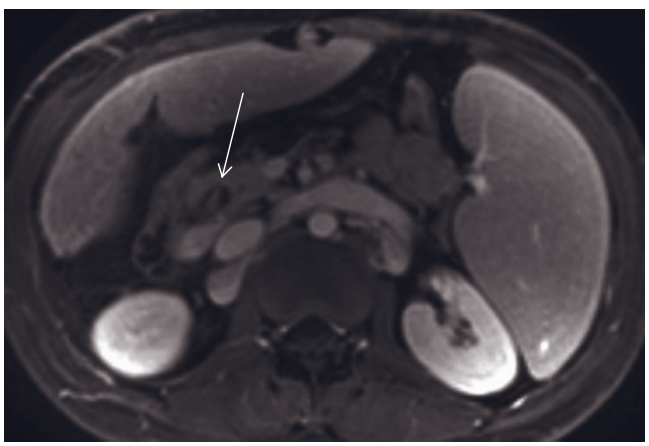

(*e*)

FIG. 3.28 Air in bile ducts. Transverse T2-weighted single-shot echo-train spin-echo image (*a*) in a patient after ERCP showing a signal-void air bubble (arrow) floating in the nondependent portion of the CBD. **Hemorrhage in bile ducts.** Coronal T2-weighted single-shot echo-train spin-echo (*b*), transverse T2-weighted single-shot echo-train spin-echo (*c*), and transverse fat-suppressed postgadolinium hepatic arterial dominant (*d*) and interstitial phase (e) images demonstrate the presence of blood in a patient who underwent prior ERCP in another patient. The common bile duct is dilated, and there is a distal intraluminal structure (arrows, *b*–*e*) which shows low signal on T2-weighted images (*b*, *c*) and intermediate signal on T1-weighted images (*d*, *e*). The findings are consistent with blood products. Note the portal hypertension findings.

MRCP performed after intravenous administration of 1 unit of secretin per kilogram of body weight ("pharmacodynamic MRCP") with images acquired every 30–60 s over a period of 10 min is under investigation for its role in papillary dysfunction [87, 88].

Sclerosing Cholangitis

Inflammation and obliterative fibrosis of intrahepatic and extrahepatic bile ducts characterize this disease entity. Progressive periductal fibrosis eventually leads to disappearance of small ducts and strictures of larger

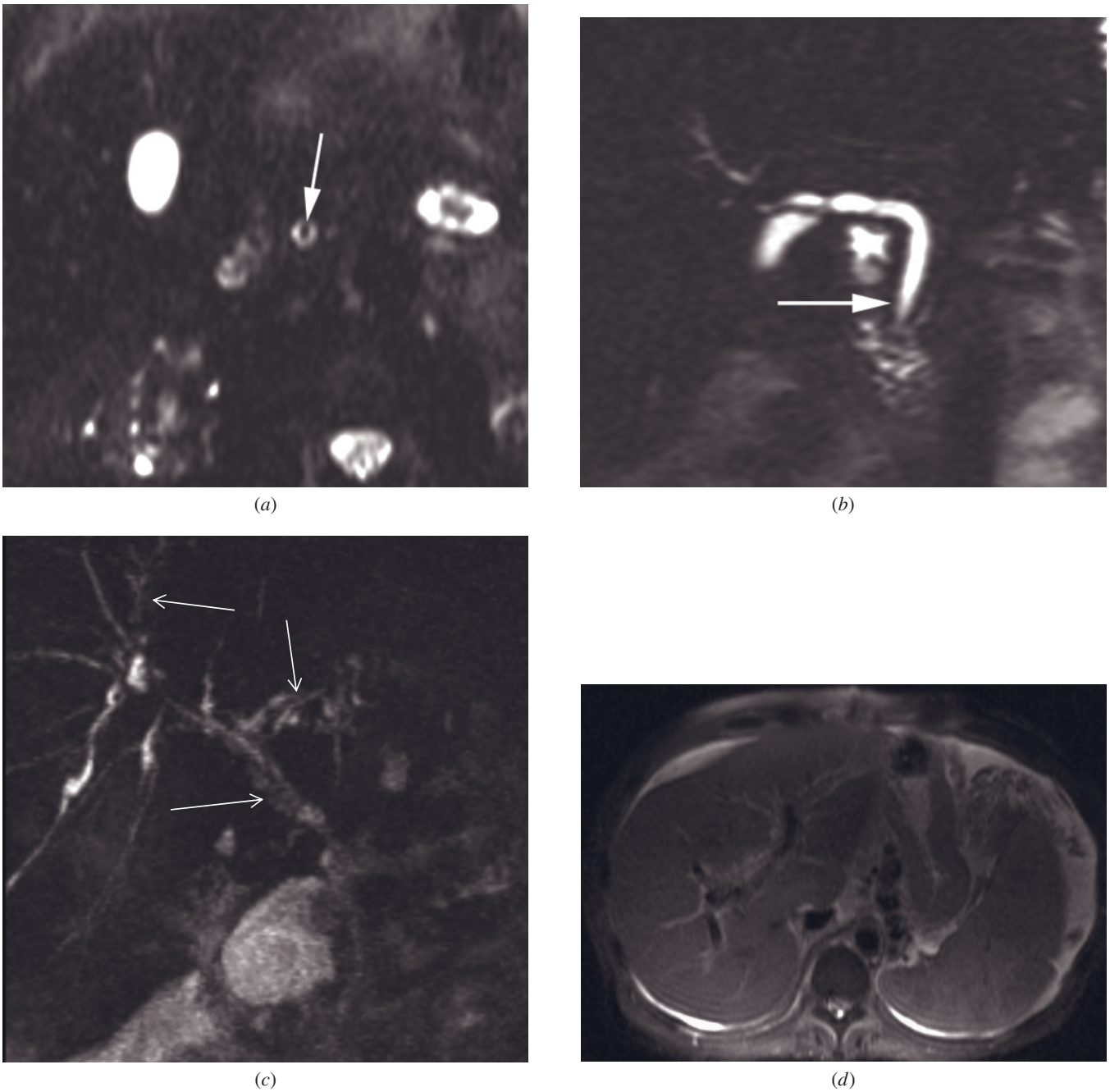

FIG. 3.29 Flow artifact mimicking a stone in an asymptomatic person. The axial thin-slab MRCP image (*a*) shows a small, signal-void round area (arrow, *a*) in the center of the preampullary common bile duct (CBD). The paracoronal thin-slab MRCP image (*b*) demonstrates a normal, fluid-filled CBD (arrow, *b*), excluding the presence of a stone. **Low signal of debris filled ducts masks dilated bile ducts.** Coronal thick-section fast spin-echo (*c*) and transverse T2-weighted fat-suppressed single-shot echo-train spin-echo (*d*) images demonstrate dilated and debris-filled bile ducts developing secondary to an obstruction in another patient who had prior liver transplantation. Dilated and debris-filled CBD and intrahepatic bile ducts show less signal (arrows, *c*). Note the portal hypertension findings and ascites on T2-weighted image (*d*).

ducts. The anatomic changes in the biliary tract and the hepatic histologic changes are nonspecific and can either be secondary to infection or hepatic arterial damage, or "primary" when immune factors are thought to underlie the disease [89].

Primary Sclerosing Cholangitis. Approximately 71% of patients with primary sclerosing cholangitis (PSC) also have inflammatory bowel disease [90]. Approximately 87% of these patients have ulcerative colitis, and 13% have Crohn disease [89]. PSC results in cholestasis with

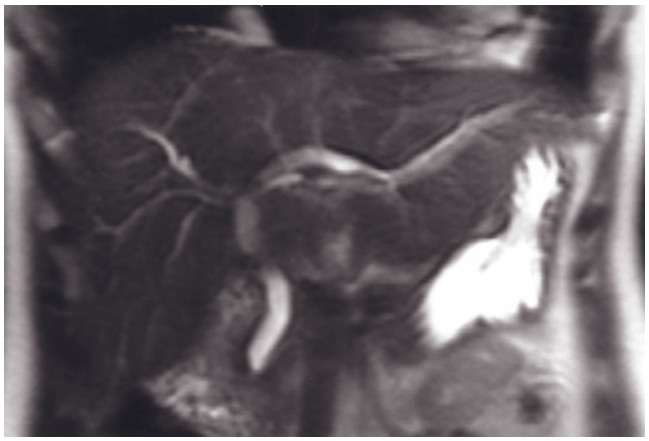

(*a*)

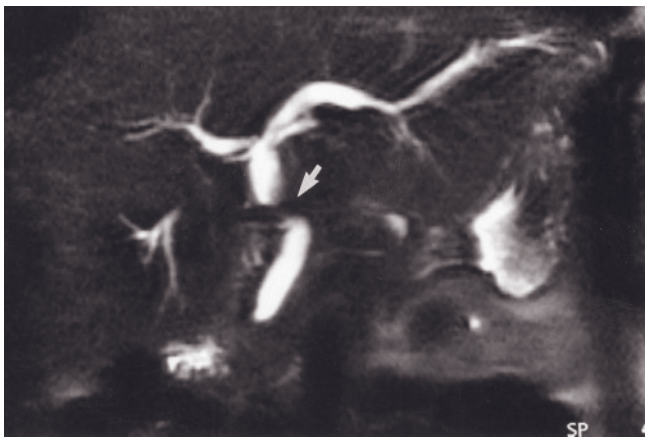

(*b*)

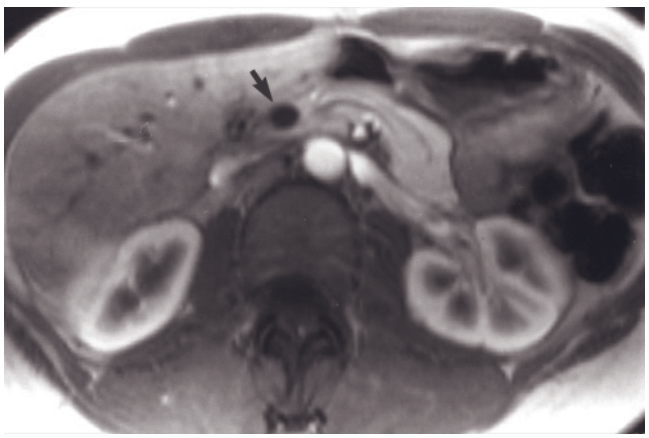

(*c*)

FIG. 3.30 Ampullary fibrosis, imaging artifacts. Coronal T2-weighted single-shot echo-train spin-echo image (*a*), thin-section MRCP single-shot echo-train spin-echo image with fat suppression (*b*), and transverse T1-weighted immediate postgadolinium GE image (*c*). The intrahepatic and extrahepatic bile ducts are dilated. The signal-void area in the proximal CBD (arrow, *b*) is caused by the crossing hepatic artery and does not represent an intraductal stone. The tubular nature of the vessel is better depicted on the MRCP image (*b*) than on the standard T2-weighted image (*a*). On the postgadolinium image (*c*), the pancreas is well delineated against the dilated CBD (arrow, *c*) and shows normal enhancement. The diagnosis of ampullary fibrosis was confirmed by ERCP.

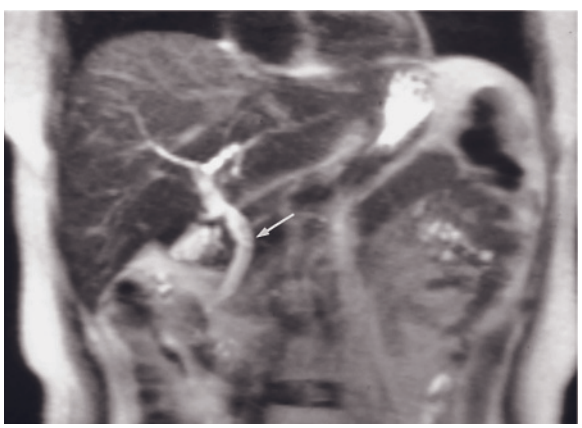

(*a*)

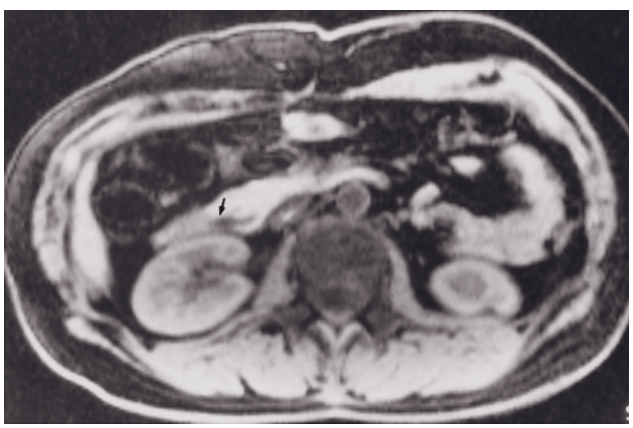

(*b*)

FIG. 3.31 Ampullary fibrosis. Coronal T2-weighted thin-section MRCP single-shot echo-train spin-echo image (*a*) shows the entire dilated CBD (arrow, *a*), excluding ductal calculi. Transverse T1-weighted fat-suppressed GE (*b*) and immediate postgadolinium

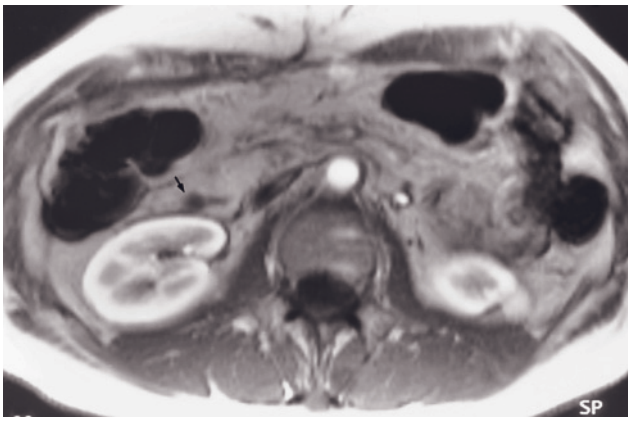

(*c*)

(*e*)

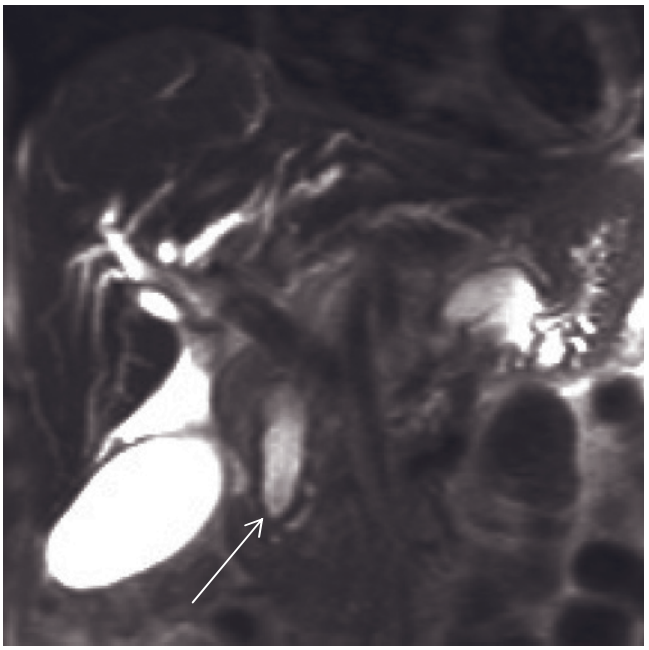

(*d*)

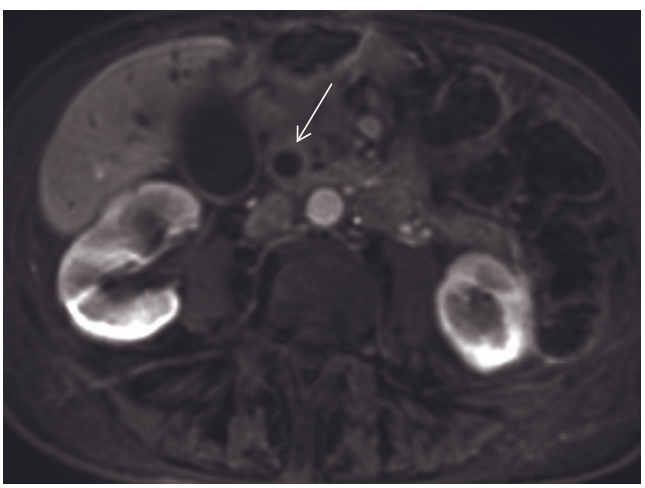

(*f*)

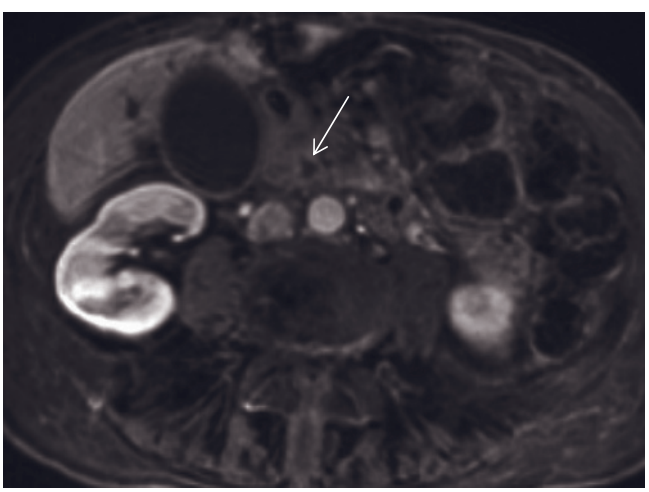

(*g*)

FIG. 3.31 (*Continued*) GE (*c*) images in a second patient with ampullary fibrosis. The pancreas and ampulla appear normal on the fat-suppressed GE image (*b*) at the level of the ampulla (arrow, *b*), with no evidence of a mass. This is confirmed on the immediate postgadolinium image (*c*), which shows homogeneous enhancement of the pancreas at the level of the ampulla (arrow, *c*), excluding tumor.

Coronal T2-weighted single-shot echo-train spin-echo (*d*), coronal reconstructed 3D MIP MRCP (*e*), and transverse postgadolinium hepatic arterial dominant phase fat-suppressed 3D-GE (*f*, *g*) images at 3.0 T demonstrate ampullary fibrosis in another patient. The biliary system is diffusely dilated. The common bile duct shows fusiform ending, and the distal common bile duct shows minimal enhancement and thickening (arrows, *d*–*g*). These findings suggest the presence of ampullary fibrosis.

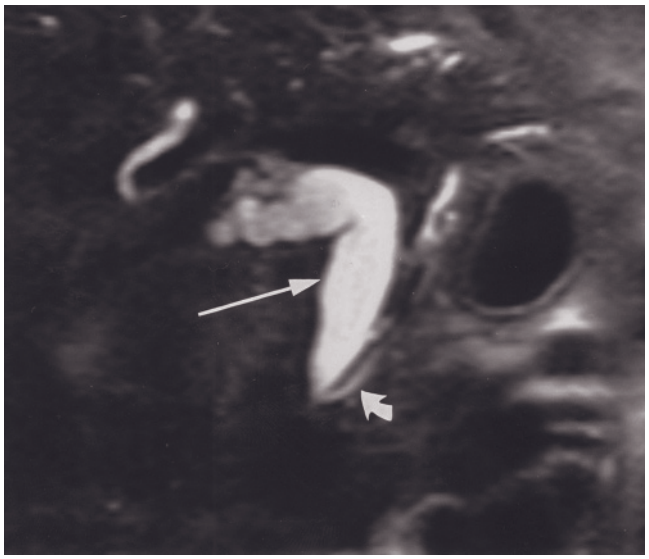

(*a*)

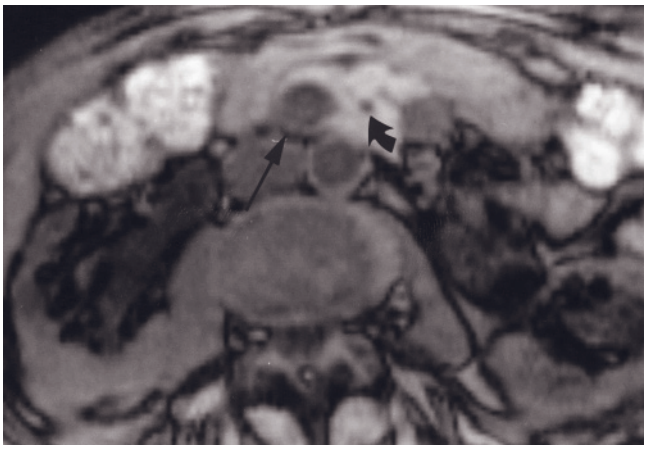

(*b*)

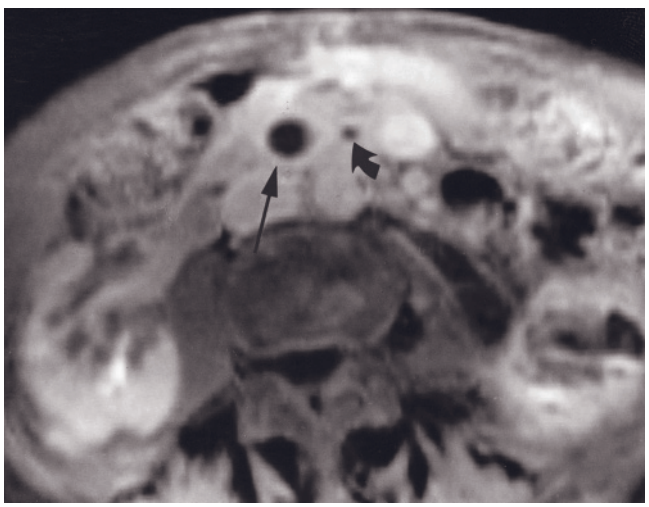

(*c*)

FIG. 3.32 Papillary dysfunction. Coronal T2-weighted thin-section MRCP single-shot echo-train spin-echo image with fat suppression (*a*) and transverse T1-weighted fat-suppressed GE (*b*) and 2-min postgadolinium fat-suppressed GE (*c*) images. The CBD (straight arrow, *a–c*) is severely dilated without evidence of an intraductal stone on the thin-section MRCP image (*a*). The pancreatic duct (curved arrow, *a–c*) is also mildly dilated. The pancreas and region of the ampulla show no evidence of a tumor on the precontrast (*b*) and postgadolinium (*c*) images. Papillary dysfunction was diagnosed on ERCP.

progression to secondary biliary cirrhosis and hepatic failure. Current hypotheses hold immune factors or toxic bacterial products that cross the inflamed colonic mucosa and enter the portal venous bloodstream accountable for PSC by inducing pericholangitic inflammation and fibrosis [90]. The diagnosis of PSC is made using cholangiographic findings supported by histologic results. Clinical features, such as ulcerative colitis or cholestasis, may be supportive but are not diagnostic.

The imaging appearance of PSC is characterized by multifocal, irregular strictures and dilatations of segments of the intra- and extrahepatic biliary tree. The strictures are usually short and annular, alternating with normal or slightly dilated segments, producing a beaded appearance (fig. 3.33). Because of fibrosis of higher-order intrahepatic bile ducts the biliary tree has the appearance of cut-off peripheral ducts, described as "pruning." The disease may involve intrahepatic ducts, extrahepatic ducts, or both, with the cystic duct usually spared. All of these findings are not pathognomonic for PSC and can be found in secondary forms as well. If the intrahepatic ducts are involved in isolation, differentiation must be made from primary biliary cirrhosis, which can be distinguished clinically from PSC. The conventional imaging modality to establish the diagnosis of PSC is ERCP. However, this method is associated with risks of pancreatitis and perforation and has been shown to result in progression of cholestasis in patients with PSC [74, 91]. MRCP has shown to be an adequate method for the diagnosis and follow-up of PSC [92, 93]. The imaging features that can be depicted in PSC are identical to the findings described for ERCP. In a comparative study with ERCP involving 150 patients, MRCP showed a sensitivity and specificity to depict PSC of

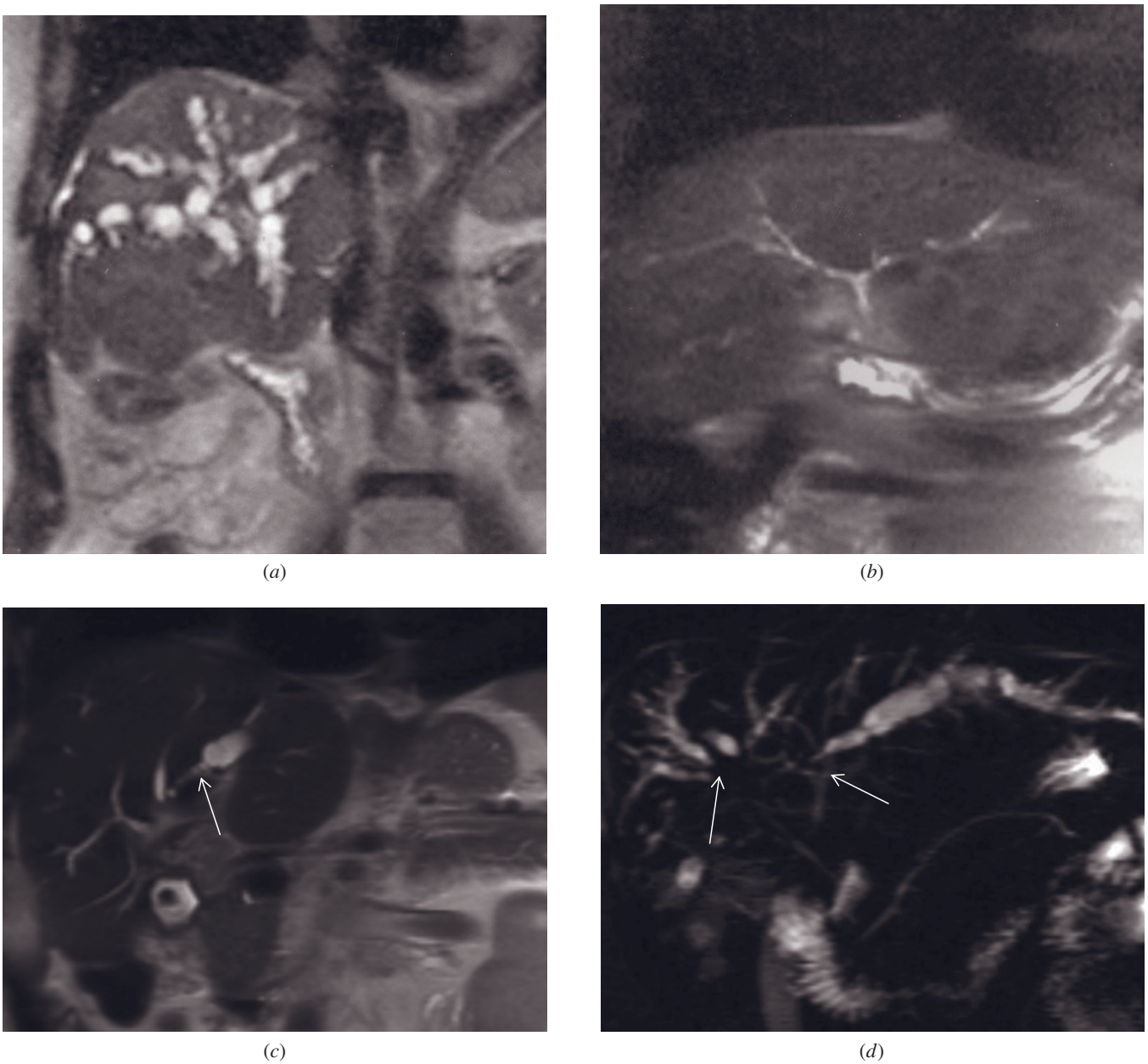

FIG. 3.33 Primary sclerosing cholangitis (PSC), beading. Coronal T2-weighted single-shot echo-train spin-echo images without (*a*) and with (*b*) fat suppression in two different patients (*a*, *b*, respectively).The high-signal intrahepatic bile ducts demonstrate beading caused by short strictures alternating with dilated (*a*) or normal-caliber (*b*) segments. Coronal T2-weighted single-shot echo-train spin-echo (*c*), coronal thick-section fast spin-echo MRCP (*d*), transverse T2-weighted single-shot echo-train spin-echo

88% and 99%, respectively, showing that its diagnostic accuracy is comparable to that of ERCP [93]. Factors that can lead to difficulties in interpreting the MR images and to false-positive and false-negative diagnoses are 1) the presence of liver cirrhosis and 2) PSC limited to the peripheral intrahepatic ducts. Cirrhosis may lead to distortion of the biliary tree that may mimic PSC even on ERCP images. If PSC is limited to the peripheral ductal system, the higher image resolution of ERCP makes this a more sensitive test compared to current MRCP sequences. However, a limitation of ERCP is that the presence of severe strictures may lead to inadequate opacification of proximal bile ducts and to false-negative diagnoses [93]. MRCP provides visualization of bile ducts proximal to even severe stenoses and demonstrates bile duct stones in these locations, where they often escape detection with ERCP. In fact, visualization of bile ducts is considered easier with MRCP in the presence of severe ductal obstruction, because of the expanded fluid-filled state of the obstructed ducts. In

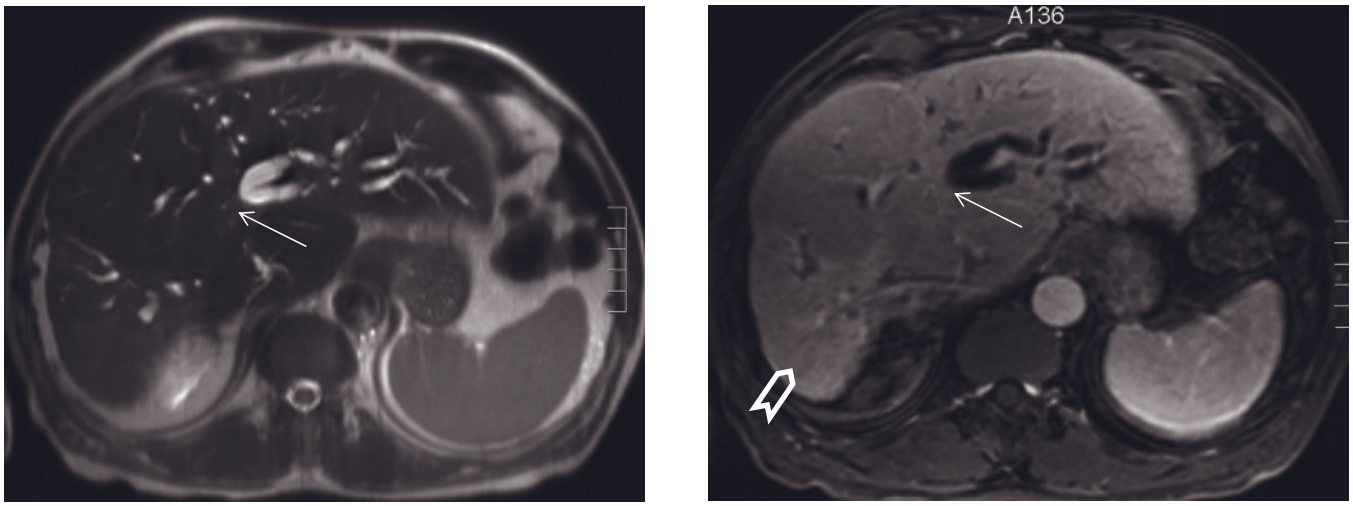

(*e*) (*f*)

FIG. 3.33 (*Continued*) (*e*), and transverse postgadolinium hepatic venous phase fat-suppressed 3D-GE (*f*) images at 3.0 T demonstrate PSC in another patient. Dilated intrahepatic bile ducts in combination with strictures and beading are detected (arrows, *c–f*). Pruning is seen both in the intrahepatic and extrahepatic bile ducts (*d*). Central regeneration and peripheral atrophy are also detected. Note that there is minimal inflammatory patchy enhancement (open arrow, *f*) in the right lobe posterior segment on postgadolinium image (*f*) and the liver is enlarged.

our experience, however, subtle changes of mild PSC can be difficult to detect with current MR techniques.

The use of conventional MR sequences and intravenous gadolinium provides information on the liver parenchyma and bile duct walls, which is valuable for a thorough evaluation [94, 95]. In a study of patients with PSC by Revelon et al. [96], peripheral, wedge-shaped zones of hyperintense signal on T2-weighted images were found in the liver in 72% of patients. These triangular areas ranged from 1 to 5 cm in diameter (fig. 3.34). Periportal edema or inflammation, seen as high signal intensity along the porta hepatis on T2-weighted images, was present in 40% of patients. A study by Ito et al. [97] evaluated the imaging features of PSC on dynamic gadolinium-enhanced MRI. Thickening of bile duct walls and wall enhancement were seen in 50% and 67% of patients, respectively (see fig. 3.34). On pre-gadolinium T1-weighted images, 23% of patients showed areas of increased signal intensity in the liver that did not represent focal fatty infiltration. On immediate post-gadolinium images, 56% of all patients showed areas of increased parenchymal enhancement that were patchy, peripheral, segmental, or a combination of these patterns. These regions remained mildly or markedly hyperintense on delayed-phase images in 90% of patients. Other findings occasionally associated with PSC are atrophy of liver segments, periportal lymphadenopathy, and findings attributable to liver cirrhosis and portal hypertension, such as hypertrophy of the caudate lobe, regenerative nodules, and abdominal varices. In our experience, cirrhosis secondary to PSC often results in large central regenerative nodules that may cause periportal obstruction of bile ducts and, eventually, segmental atrophy of peripheral liver (see fig. 3.34) [94].

PSC is associated with an increased malignant potential, and the most important and common malignant entity that may occur in these patients is cholangiocarcinoma. Cholangiocarcinoma is the second most common cause of death, after liver failure, in patients with PSC, occurring in up to 20% of patients [98]. The diagnosis of superimposed cholangiocarcinoma in patients with PSC is difficult because of the underlying morphologic bile duct changes. The MR appearance of cholangiocarcinoma is described below.

Infectious Cholangitis

Infectious, bacterial, or ascending cholangitis is a clinically defined syndrome caused by complete or partial biliary obstruction with associated ascending infection from the intestine. It encompasses a wide spectrum of clinical manifestations ranging from a mild form to a fulminating form that constitutes a life-threatening surgical emergency. Predisposing conditions are the presence of microorganisms in the bile and the presence of partial or complete biliary obstruction. The typical clinical symptoms that lead to the diagnosis of ascending cholangitis are jaundice, abdominal pain, and sepsis (chills and fever), referred to as Charcot's triad. This triad is present in approximately 70% of patients.

The distribution of inflammatory changes may be diffuse or segmental. The most consistent imaging finding in infectious cholangitis is generalized or segmental

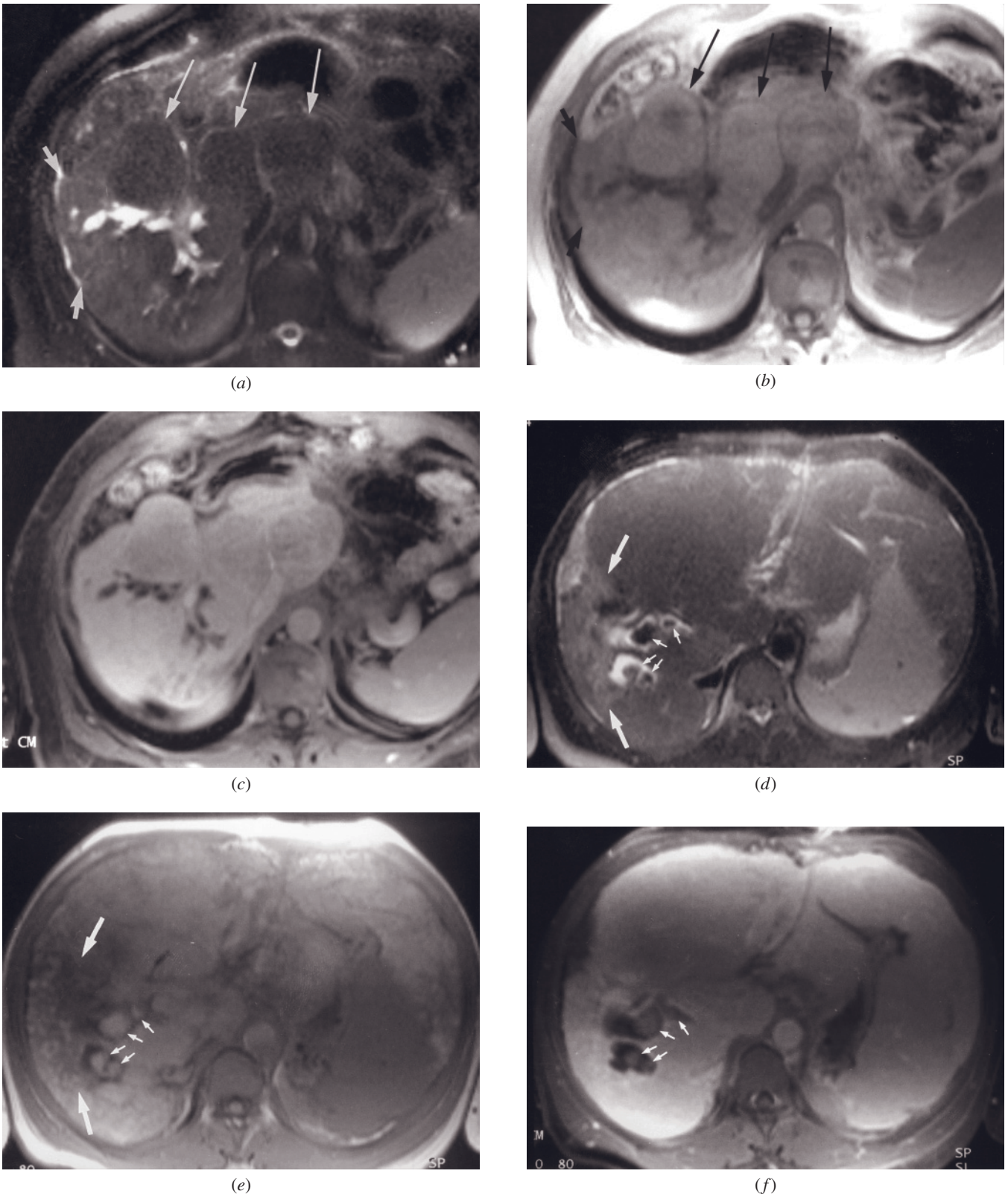

FIG. 3.34 Primary sclerosing cholangitis (PSC) with cirrhosis. T2-weighted fat-suppressed single-shot echo-train spin-echo (*a*), T1-weighted SGE (*b*), and 2-min postgadolinium fat-suppressed SGE (*c*) images. The intrahepatic bile ducts are dilated and demonstrate beading. The liver is nodular and cirrhotic in this patient with late-stage PSC. Three large macroregenerative nodules (long arrows, *a*, *b*) located in the central portion of the liver appear to obstruct the bile ducts centrally. The nodules are slightly hypoenhancing on the 2-min postgadolinium image (*c*). A subsegmental distal area of atrophic liver parenchyma (short arrows, *a*, *b*) appears slightly hyperintense on the T2-weighted image (*a*) and hypointense on the T1-weighted image (*b*). T2-weighted fat-suppressed single-shot echo-train spin-echo (*d*), T1-weighted SGE (*e*), and 2-min postgadolinium fat-suppressed SGE (*f*) images in a second patient. The liver shows multiple large macroregenerative nodules. The bile ducts in the right lobe of the liver are severely dilated and contain several calculi (arrows, *d–f*) that are high signal on the T1-weighted image (*e*). A wedge-shaped peripheral area of liver parenchyma (short arrows, *d–f*) is atrophic, showing high signal on the T2-weighted image (*d*) and low signal on the T1-weighted image (*e*) with late enhancement on the 2-min postgadolinium image (*f*). T1-weighted 2-min postgadolinium

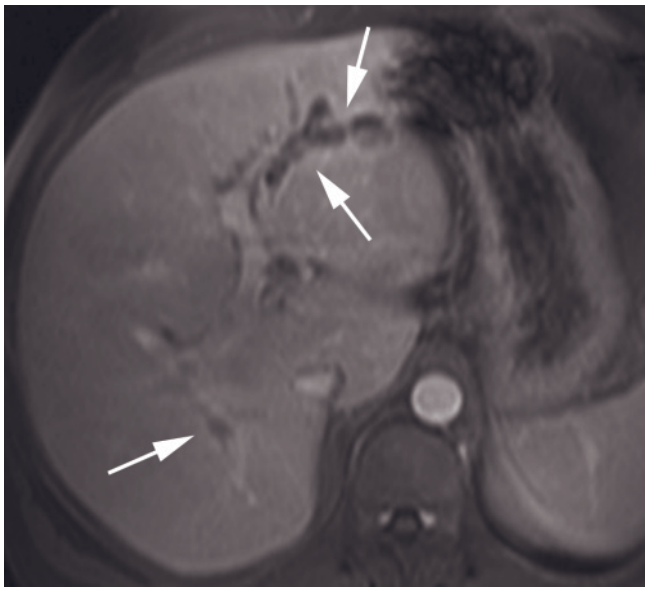

(*g*)

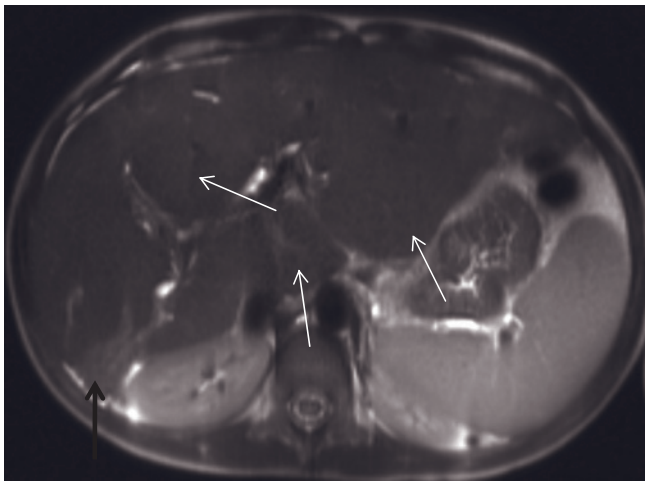

(*h*)

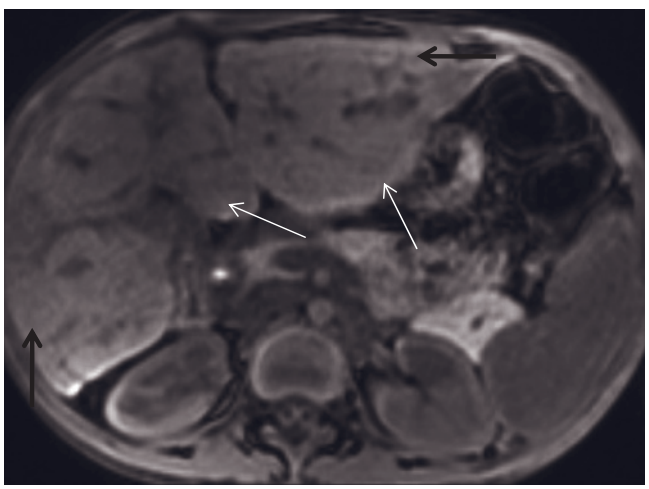

(*i*)

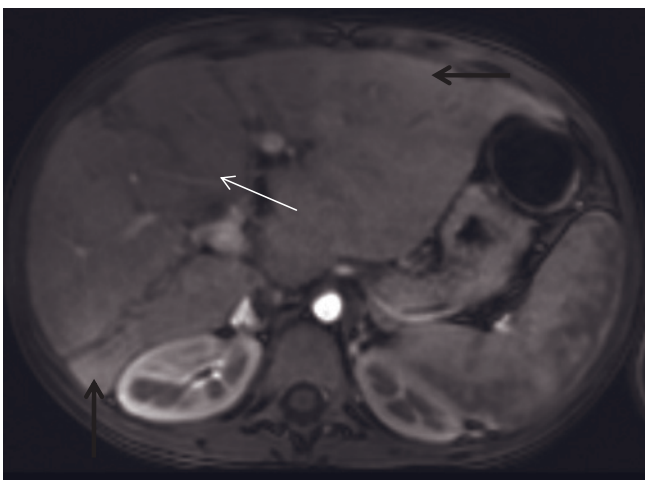

(*j*)

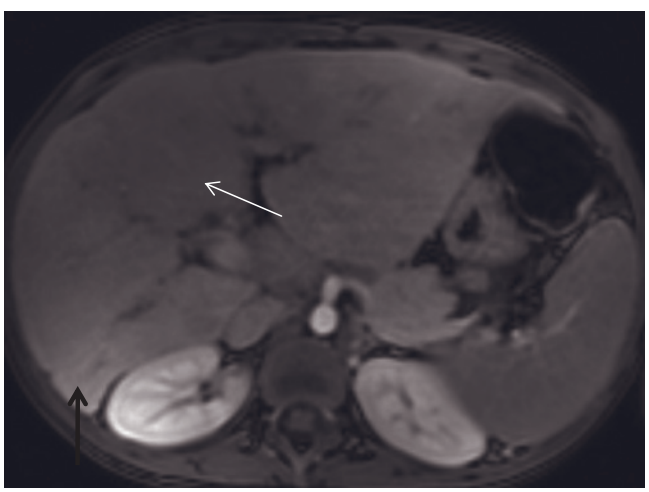

(*k*)

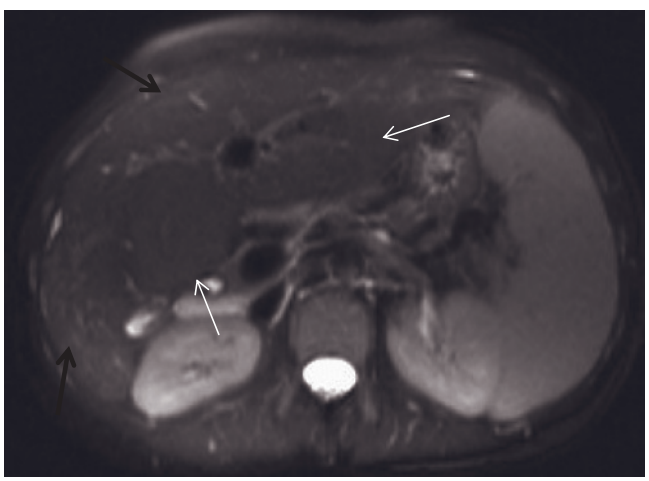

(*l*)

Fig. 3.34 (*Continued*) GE image with fat suppression (*g*) in a third patient demonstrating a beaded appearance of the intrahepatic bile ducts (arrows, *g*). The branches of the portal vein are enhanced, facilitating differentiation from low-signal dilated intrahepatic bile ducts. The walls of the bile ducts show increased enhancement. The liver demonstrates nodular enlargement of the left lobe and the caudal lobe.

T2-weighted single-shot echo-train spin-echo (*h*), T1-weighted fat-suppressed 3D-GE (*i*), and T1-weighted postgadolinium fat-suppressed hepatic arterial dominant phase (*j*) and interstitial phase (*k*) 3D-GE images at 3.0 T demonstrate PSC with cirrhosis in another patient. Central regeneration (white arrows, *h–k*) and peripheral atrophy (black arrows, *h–k*) are shown. Dilated bile ducts and periportal edema are also detected in combination with liver contour irregularity and hepatomegaly. T2-weighted fat-suppressed single-shot echo train spin echo (*l*), T1-weighted fat-suppressed 3D-GE (*m*), and T1-weighted postgadolinium fat-suppressed hepatic

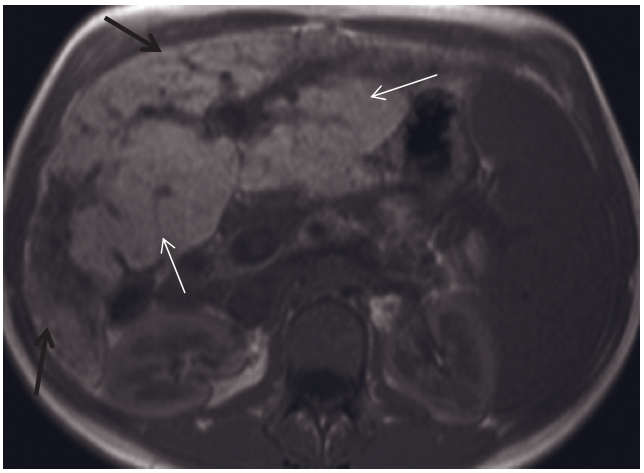

(*m*)

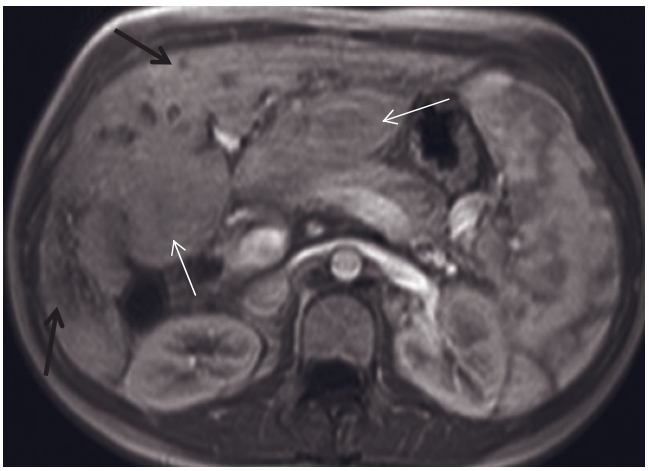

(*n*)

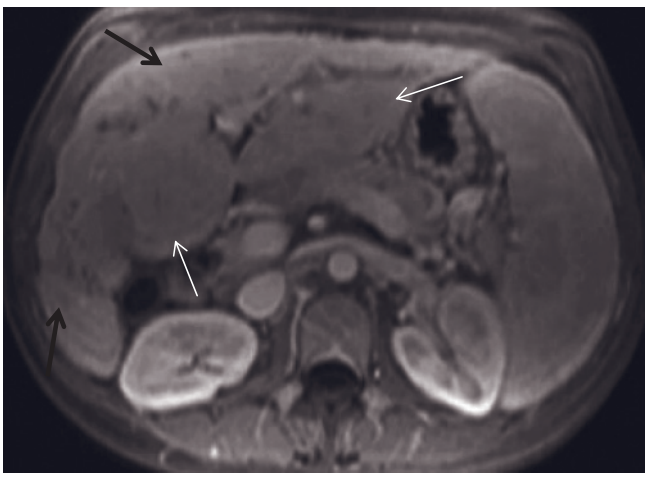

(*o*)

FIG. 3.34 (*Continued*) arterial dominant phase (*n*) and interstitial phase (*o*) 3D-GE images demonstrate PSC with severe cirrhosis and portal hypertension findings in another patient. Central regeneration (white arrows; *l–o*) and peripheral atrophy (black arrows; *l–o*) cause bizarre-shaped cirrhosis in patients with advanced PSC. Note that there are dilated bile ducts, periportal edema, and liver contour irregularity.

biliary dilatation that can be mild or severe but does not correlate well with the severity or stage of the disease [99]. Bile duct walls are commonly mild to moderately thickened and show increased enhancement, which can be best appreciated on T1-weighted fat-suppressed 2-min postgadolinium images (fig. 3.35). Imaging findings on T2-weighted images are streaky increased signal in the periportal area and wedge-shaped hyperintense regions in the liver parenchyma (see fig. 3.35) [100]. On pregadolinium T1-weighted images, these wedge-shaped regions in the liver are usually hypointense but may also show increased signal intensity. On immediate postgadolinium images, increased focal parenchymal enhancement can frequently be observed, consistent with inflammation (see fig. 3.35) [100]. The greater inflammatory nature of infectious cholangitis compared to PSC is reflected by the more common occurrence of regions of increased enhancement on immediate postgadolinium images in the former condition. Liver abscesses may complicate infectious cholangitis and are best visualized on T2-weighted and T1-weighted dynamic postgadolinium images. Thrombosis of the portal vein is not uncommonly associated with infectious cholangitis (fig. 3.36) and aids in the distinction from sclerosing cholangitis, in which this occurrence is uncommon.

A particular form of infectious cholangitis is recurrent pyogenic cholangitis (oriental cholangitis), which is caused by infestation of the biliary tract by *Clonorchis sinensis* or other parasites. This leads to inflammatory infiltration of bile ducts, proliferative fibrosis, periductal abscesses, and calculi (pigment stones). MR imaging findings are disproportionally severe dilatation of the extrahepatic bile ducts proximal and distal to calculi, stricture of bile ducts, thickening of duct walls, and hepatic abscesses [101] (fig. 3.37). Liver segments that contain biliary duct stones frequently undergo atrophy. Absence of a tumor mass helps to differentiate this condition from cholangiocarcinoma. However, cautious interpretation of findings is essential as these patients have an increased incidence of cholangiocarcinoma [101].

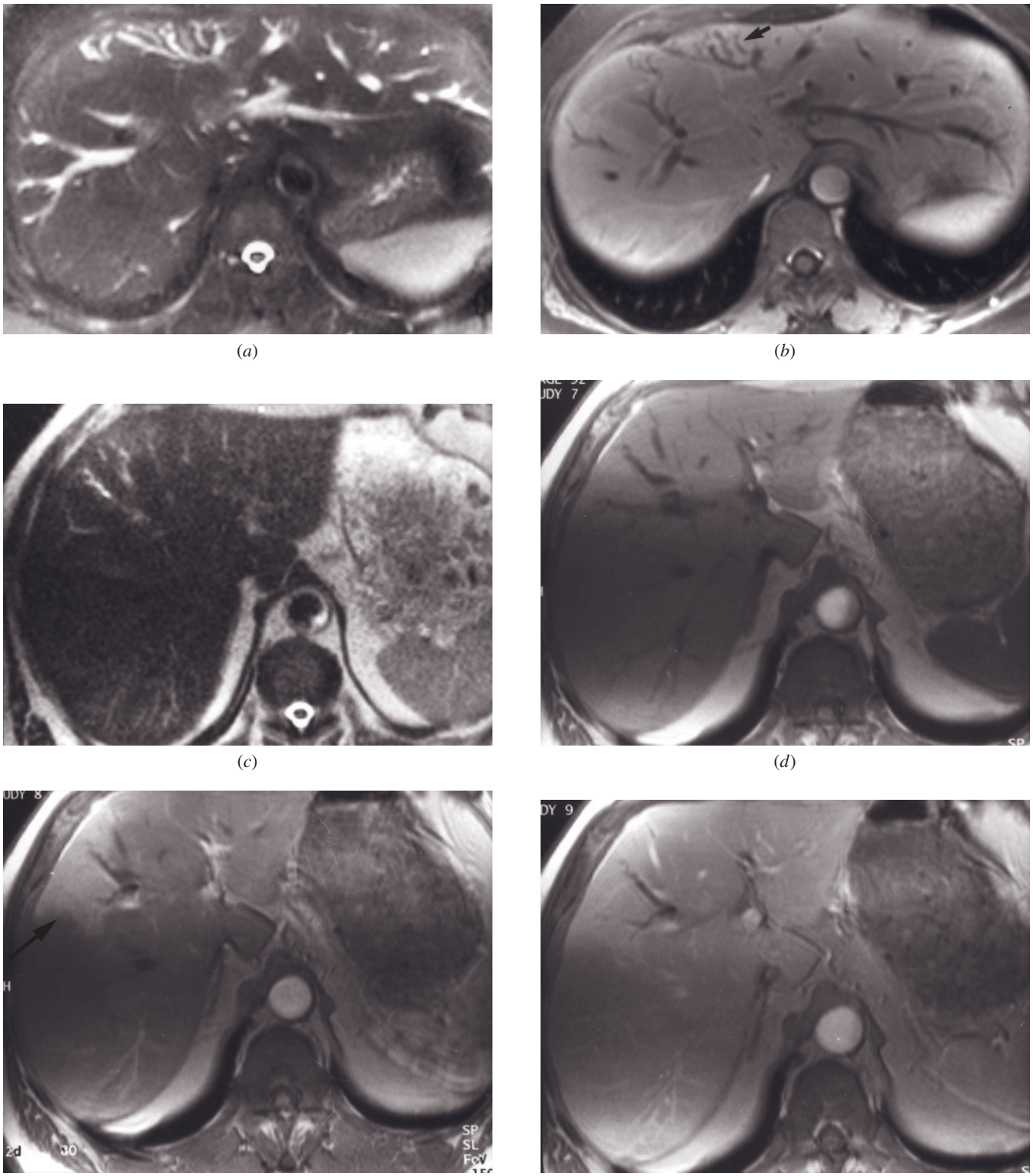

FIG. 3.35 Infectious cholangitis. T2-weighted fat-suppressed single-shot echo-train spin-echo (*a*) and T1-weighted 2-min postgadolinium fat-suppressed GE (*b*) images. The entire intrahepatic biliary tree is severely dilated, visualized as high signal on the T2-weighted image (*a*). On the T1-weighted image (*b*), the low-signal ducts are well differentiated from gadolinium-enhanced vessels. The walls of the bile ducts show increased enhancement that is most pronounced in *segment 4* of the liver (arrow, *b*).

T2-weighted single-shot echo-train spin-echo (*c*), T1-weighted GE (*d*), immediate postgadolinium GE (*e*), and 2-min postgadolinium fat-suppressed GE (*f*) images in a second patient. A peripheral wedge-shaped area of liver parenchyma between *segments 4* and *8* shows moderate biliary ductal dilatation. The liver parenchyma in this area demonstrates increased signal on both the T2 (*c*)- and T1 (*d*)-weighted images, consistent with inspissated bile. Increased enhancement of this area (arrow, *e*) is demonstrated on the postgadolinium images (*e*, *f*), reflecting local inflammation and hyperemia in the liver parenchyma. The bile duct walls show increased enhancement, best visualized on the 2-min postgadolinium image (*f*).

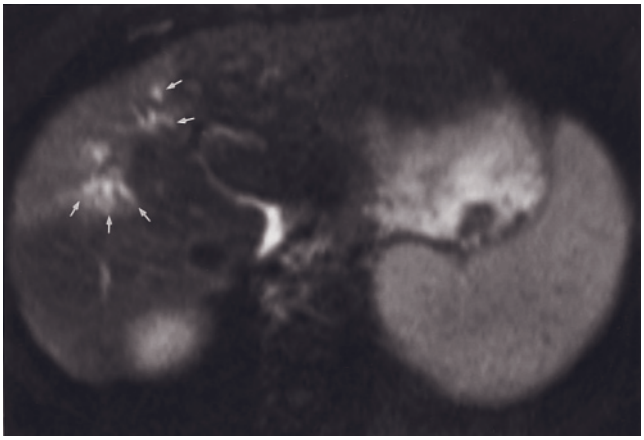

(*g*)

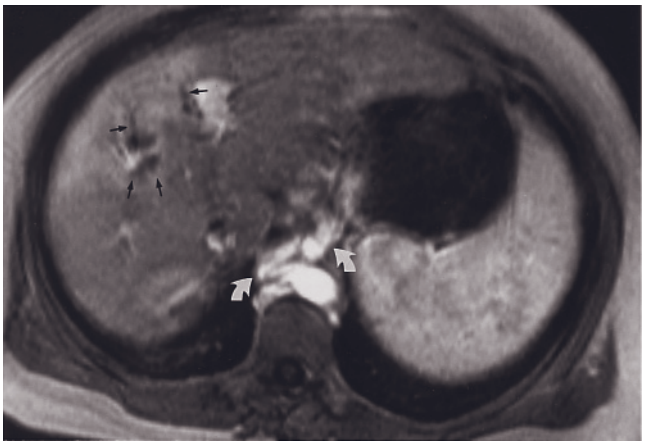

(*h*)

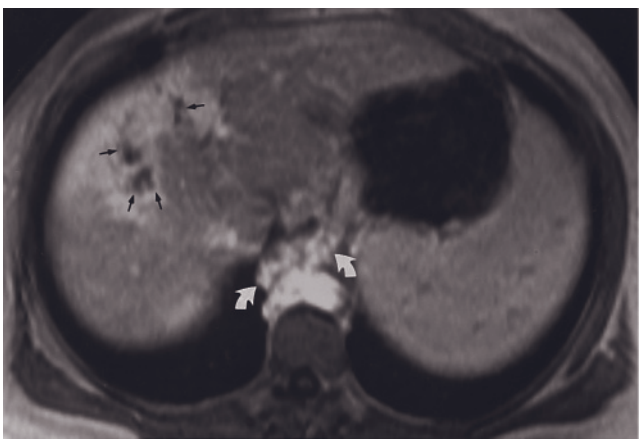

(*i*)

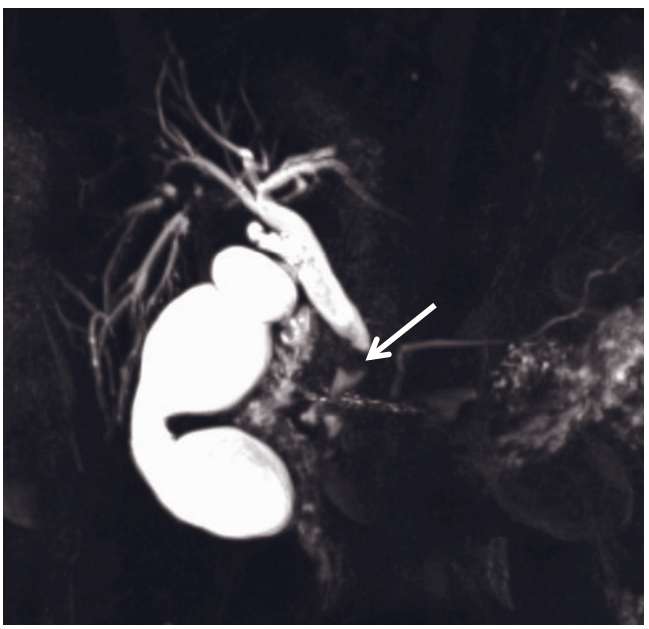

(*j*)

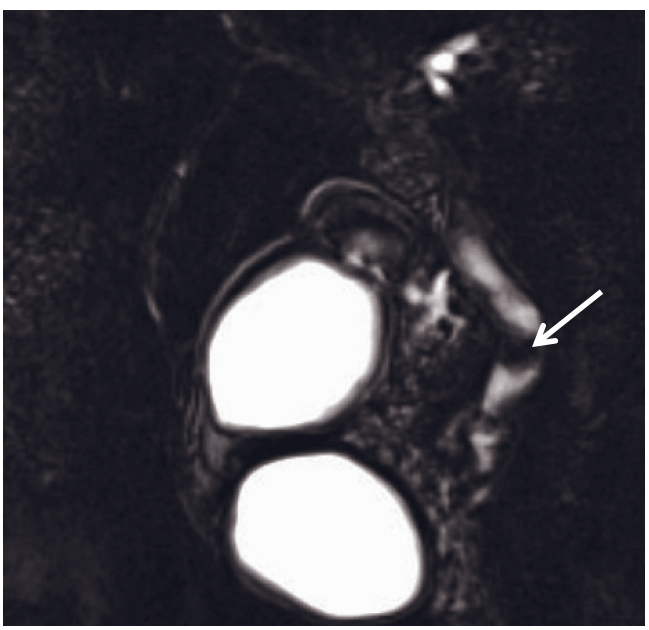

(*k*)

FIG. 3.35 (*Continued*) T2-weighted fat-suppressed spin-echo (*g*) and T1-weighted immediate (*h*) and 90-s (*i*) postgadolinium GE images in a third patient with liver cirrhosis and infectious cholangitis. A peripheral wedge-shaped area of liver parenchyma in the right lobe is hyperintense on the T2-weighted image (*g*) and demonstrates increased enhancement on the postgadolinium images (*h*, *i*), reflecting acute inflammation. The bile ducts (arrows, *g–i*) in this area are dilated and show increased mural enhancement, best demonstrated on the 90-s postgadolinium image (*i*). The spleen is enlarged, showing multiple small low-signal foci (Gamna–Gandy bodies) (*g–i*). Esophageal varices (curved arrows, *h*, *i*) are shown on the postgadolinium images (*h*, *i*).

Coronal T2-weighted thick-section fast spin-echo MRCP (*j*), coronal T2-weighted thin-section fast spin-echo MRCP (*k*),

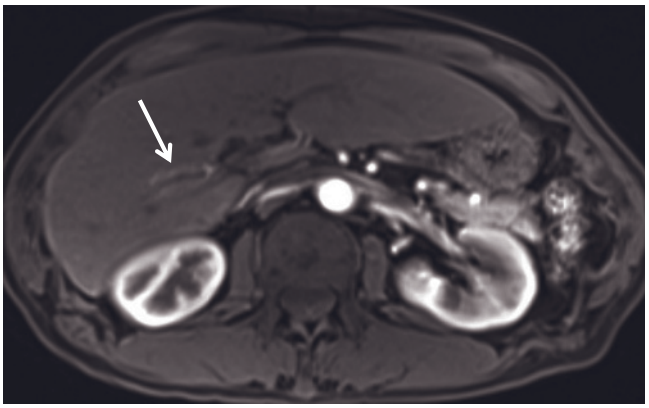

(*l*)

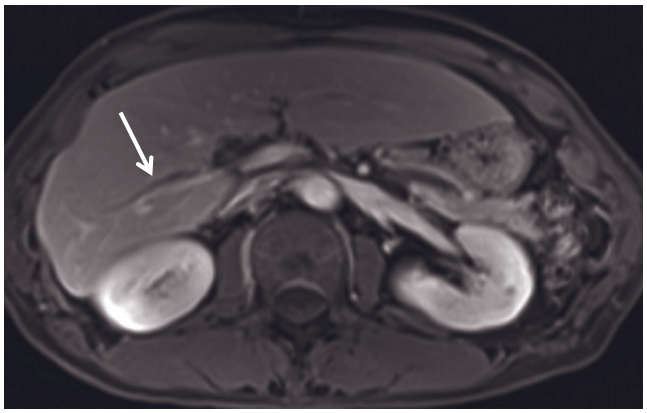

(*m*)

FIG. 3.35 (*Continued*) transverse T1-weighted postgadolinium fat-suppressed true late hepatic arterial phase (*l*), and hepatic venous phase (*m*) 3D-GE images demonstrate ascending cholangitis and choledocholithiasis in another patient. The common bile duct and intrahepatic bile ducts are dilated because of the stone (arrows, *j*, *k*) in the common bile duct. A dilated duct (arrows, *l*, *m*), which shows increased wall enhancement on postgadolinium images, is shown (*l*, *m*). These findings are suggestive of ascending cholangitis.

AIDS Cholangiopathy

In HIV-positive patients, involvement of the pancreaticobiliary tract may be an early feature of AIDS (acquired immunodeficiency syndrome) [102]. Inflammation and edema of the biliary mucosa resulting in mucosal thickening and irregularity is the hallmark of AIDS cholangiopathy. This may lead to strictures, dilatations, and pruning resembling sclerosing cholangitis [2, 102]. When the papilla of Vater is involved, ampullary stenosis with common bile duct dilatation may result. The gallbladder may also be involved and show acalculous cholecystitis with imaging features similar to acute cholecystitis. Furthermore, patients have a predisposition for superimposed infectious cholangitis, often by unusual pathogens (e.g., cytomegalovirus, cryptosporidium, mycobacteria, *Candida albicans*) [102].

Cystic Diseases of Bile Ducts

Congenital biliary cysts comprise choledochal cysts, diverticula originating from extrahepatic ducts, choledochocele, Caroli disease, and segmental cysts, depending on the location of the dilatation of the biliary tract. MRCP with 3D MIP reconstructions can display the anatomic extent and degree of these lesions, diagnose associated findings such as stone disease, and, in combination with gadolinium-enhanced T1-weighted images, evaluate for malignancy [103]. A classification system that groups all types of biliary cystic diseases together has been introduced by Todani et al. [104]: Type I, choledochal cyst; Type II, diverticulum of extrahepatic ducts; Type III, choledochocele; Type IV, multiple segmental cysts; and Type V, Caroli disease. It is, however, unclear whether they represent variations of the same disease or are separate entities with distinct etiologies. For clinical purposes, however, description of morphology and location is usually adequate.

Choledochal Cyst. The most common cystic dilatations are choledochal cysts (77–87%), which present before the age of 10 in approximately 50% of cases. Choledochal cysts are segmental aneurismal dilatations of the CBD alone or the CBD and CHD (fig. 3.38). The etiology is an anomalous junction of the CBD and the pancreatic duct, proximal to the major papilla, where there is no ductal sphincter. This allows a free reflux of pancreatic enzymes into the biliary system, weakening the walls of the bile ducts. Choledochal cysts are associated with an increased incidence of other biliary anomalies, gallstone disease, pancreatitis, and cholangiocarcinoma. Choledochal cysts may also be coexistent with intrahepatic bile duct cysts (multiple segmental cysts) (fig. 3.39). Cystic expansion of the common bile duct may also be short in length (see fig. 3.39); the etiology of these is at present uncertain.

Choledochocele. Choledochoceles are cystic dilatations of the distal CBD that herniate into the lumen of the duodenum and create a "cobra head" appearance on cholangiographic images (fig. 3.40).

Caroli Disease. Caroli disease is an uncommon form of congenital dilatations of intrahepatic bile ducts with normal extrahepatic ducts. Demonstration that these multiple cystic spaces communicate with the biliary tree is mandatory for the differentiation from cystic disease of the liver and abscesses. This can be

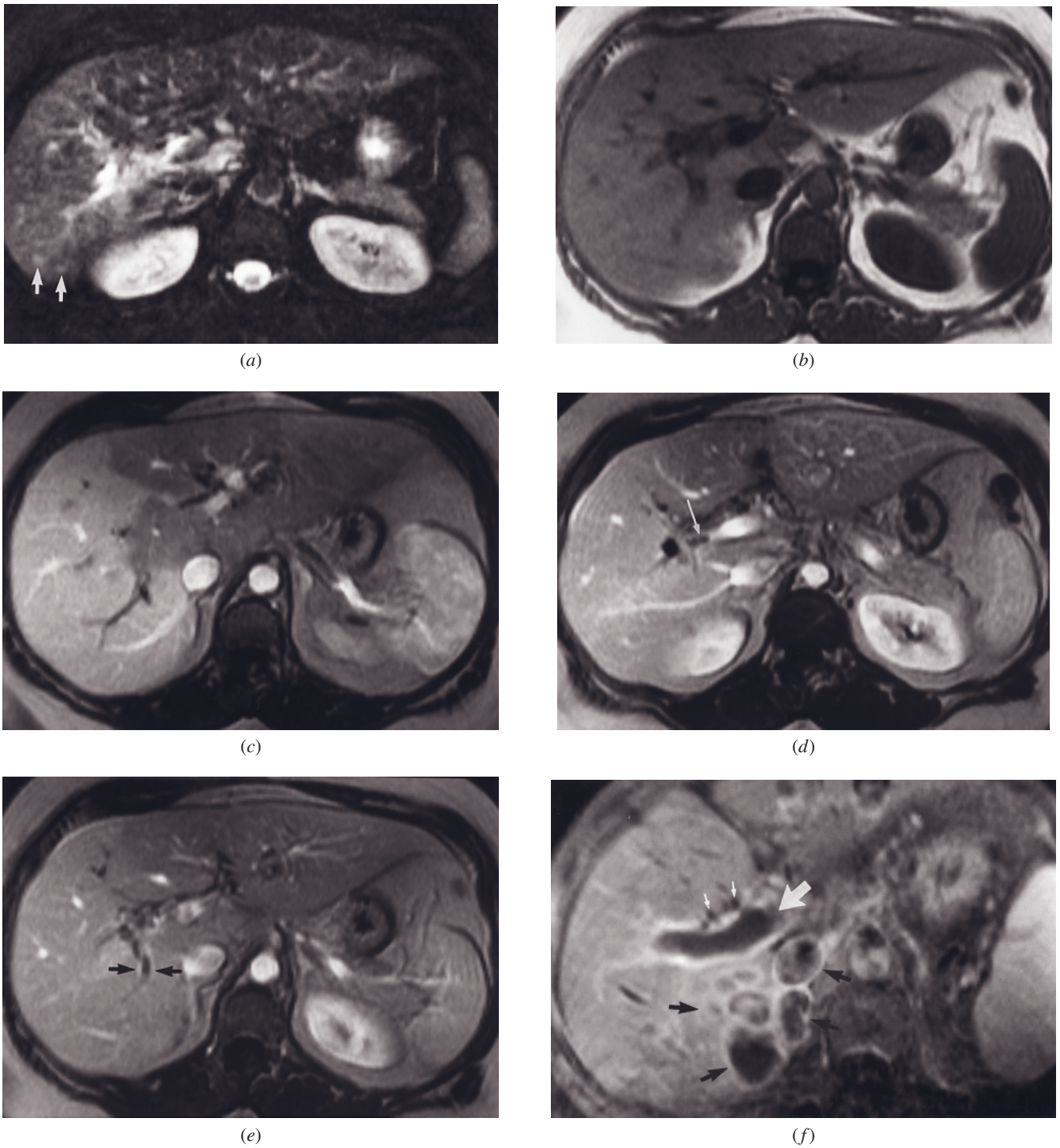

FIG. 3.36 Infectious cholangitis with portal vein thrombosis. T2-weighted fat-suppressed spin-echo (*a*),T1-weighted GE (*b*), immediate postgadolinium GE (*c*), and 1-min postgadolinium GE (*d*, *e*) images. The right lobe of the liver is hyperintense on both the T2 (*a*)- and T1 (*b*)-weighted images, consistent with edema and inspissated bile. On the T2-weighted image (*a*), small hyperintense areas (arrows, *a*) likely represent foci of infection. The liver parenchyma shows increased enhancement of the right lobe on the postgadolinium GE images (*c*, *d*) due to thrombosis of the right portal vein (arrow, *d*) and consequent arterial hyperperfusion. The thrombus (arrow, *d*) is best visualized as a near signal-void filling defect of the right portal vein on the 1-min postgadolinium image (*d*). Increased enhancement of bile duct walls is demonstrated on the 1-min postgadolinium GE images (arrows, *e*).

T1-weighted 2-min postgadolinium fat-suppressed GE image (*f*) in a second patient. The portal vein (large white arrow, *f*) is dilated and shows lack of central enhancement with increased enhancement of the vessel walls, consistent with thrombosis. Several liver abscesses (black arrows, *f*) are visualized as round hypointense lesions with enhancing rims. Several bile ducts (small white arrows, *f*) are moderately dilated.

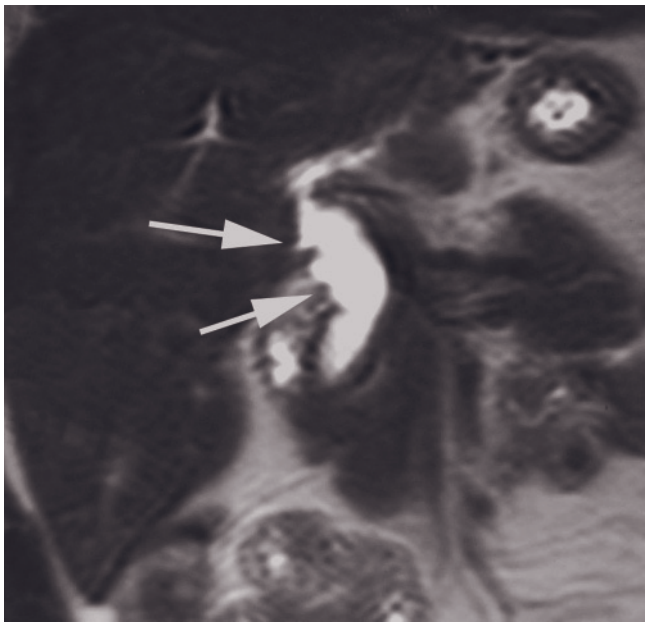

(*a*)

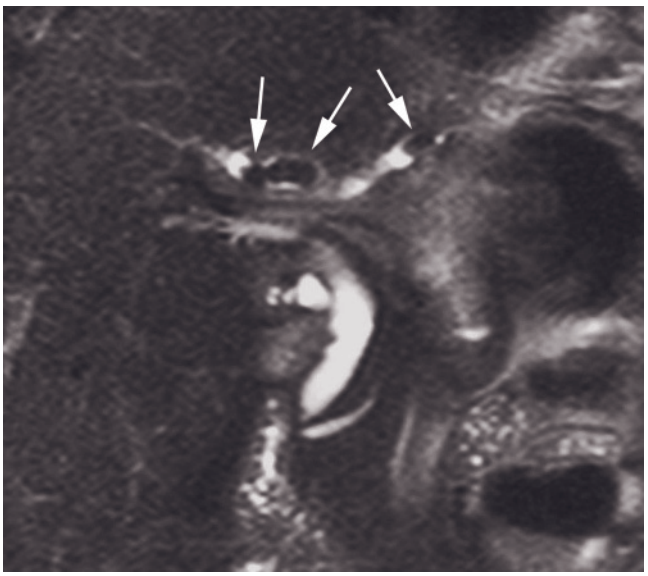

(*b*)

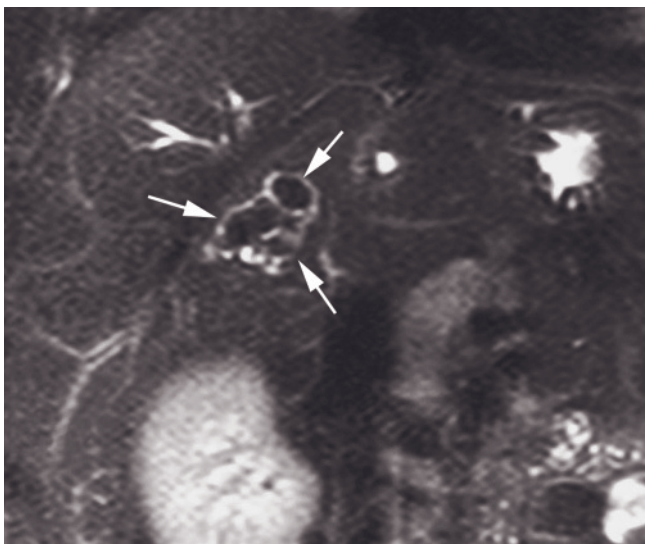

(*c*)

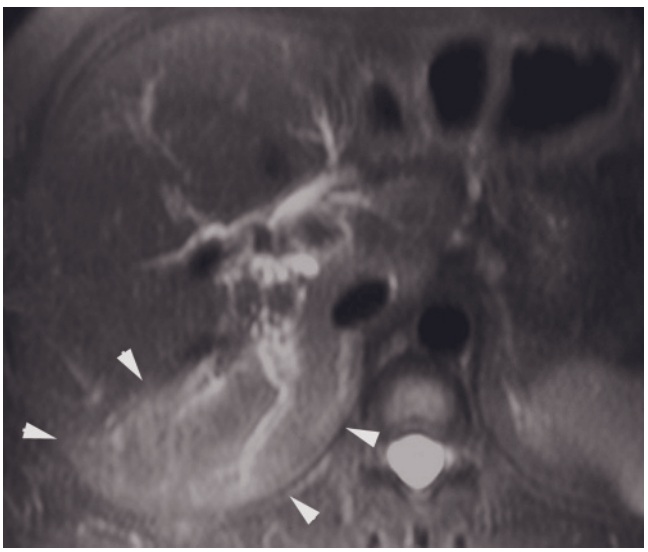

(*d*)

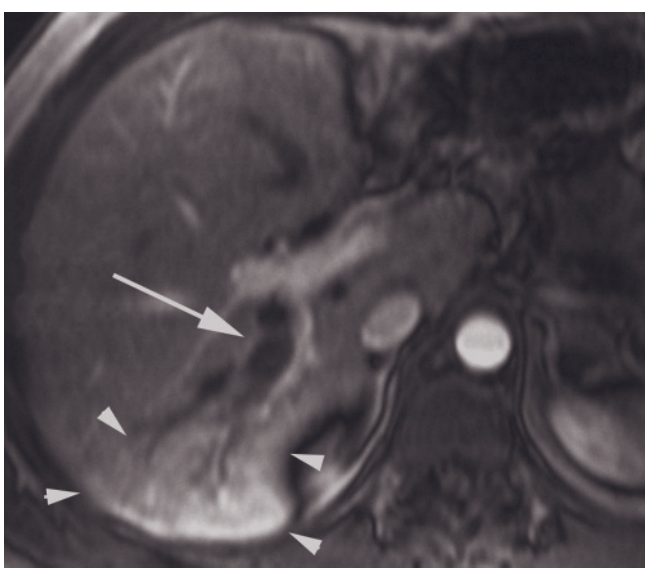

(*e*)

FIG. 3.37 Oriental cholangitis. Coronal T2-weighted single-shot echo-train spin-echo (*a*), thin-section MRCP in the coronal (*b*) and axial (*c*) planes, axial fat-suppressed T2-weighted TSE (*d*), and immediate postgadolinium GE (*e*) images. Disproportionate dilatation of the CBD (arrows, *a*) with slight wall irregularity is noted on the coronal T2-weighted image (*a*). Multiple intrahepatic bile duct stones (arrows, *b*, *c*) are best visualized on the thin-section MRCP images (*b*, *c*). Intrahepatic bile ducts show wall irregularities and strictures (arrow, *e*). The adjacent hepatic parenchyma (arrowheads, *d*, *e*) shows hyperintense signal on the T2-weighted image (*d*) and arterial hyperenhancement (*e*) indicative of inflammation.

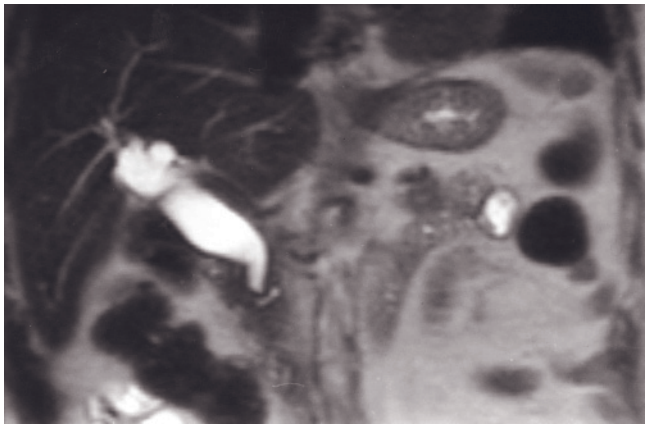

(*a*)

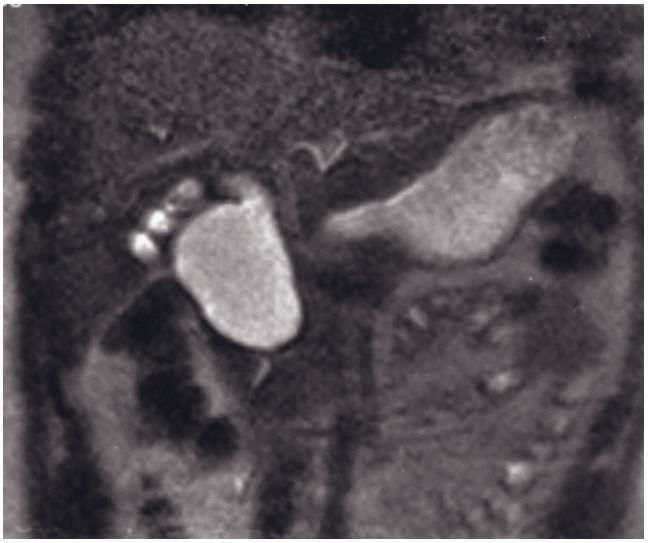

(*b*)

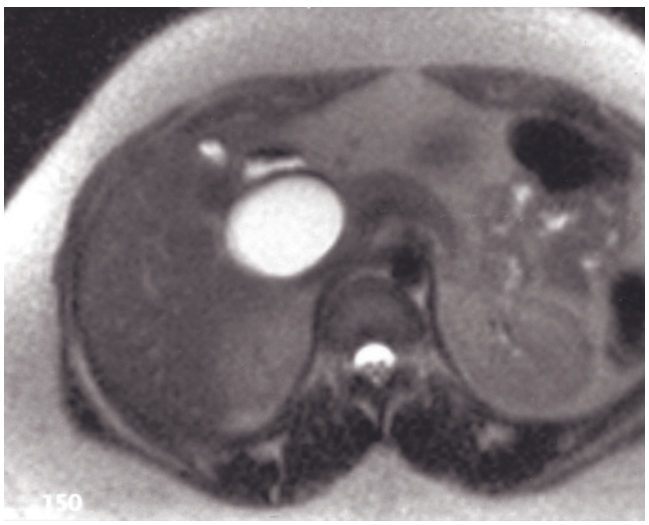

(*c*)

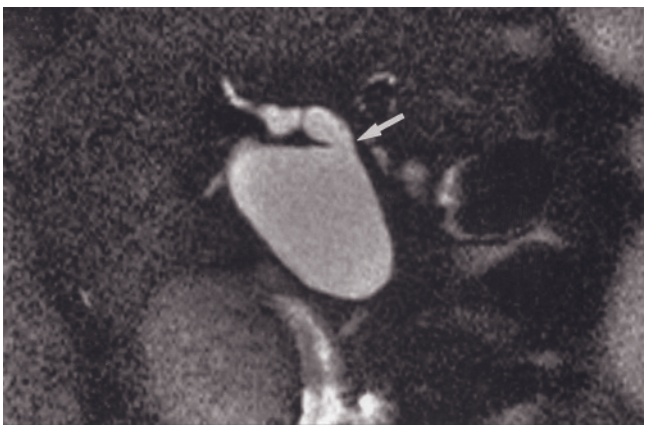

(*d*)

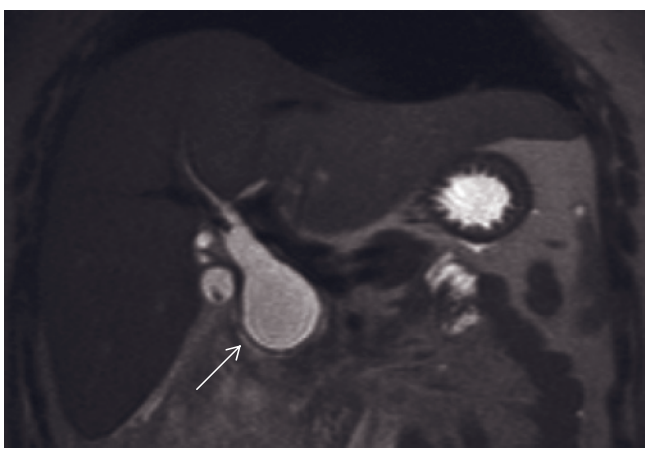

(*e*)

(*f*)

FIG. 3.38 Choledochal cyst. Coronal T2-weighted single-shot echo-train spin-echo image (*a*) showing a high-grade cylindrical dilatation of the CHD and CBD. The intrahepatic bile ducts are normal.

T2-weighted coronal (*b*) and transverse (*c*) single-shot echo-train spin-echo images and coronal thin-section MRCP single-shot echo-train spin-echo image with fat suppression (*d*) in a child demonstrating a saccular choledochal cyst arising from the CHD. The MRCP image (*d*) shows the origin of the choledochal cyst (arrow, *d*).

Coronal T2-weighted single-shot echo-train spin-echo (*e*), coronal thick-section fast spin-echo MRCP (*f*), transverse T1-weighted

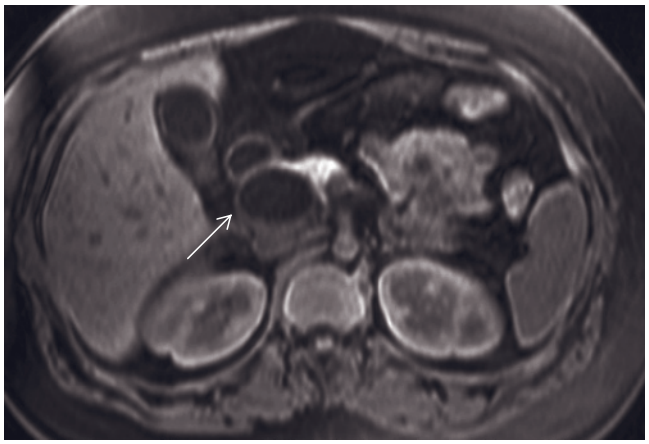

(*g*)

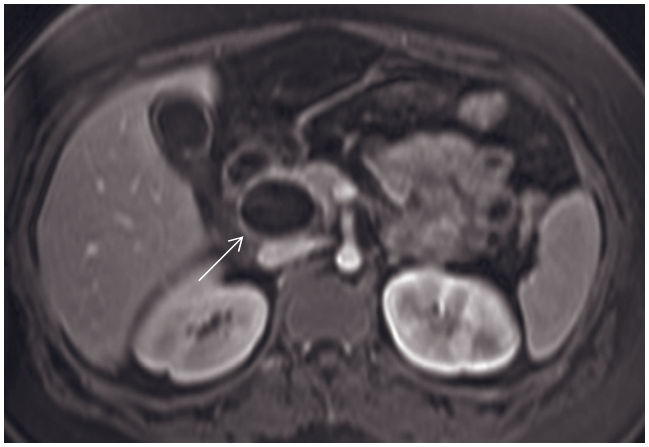

(*h*)

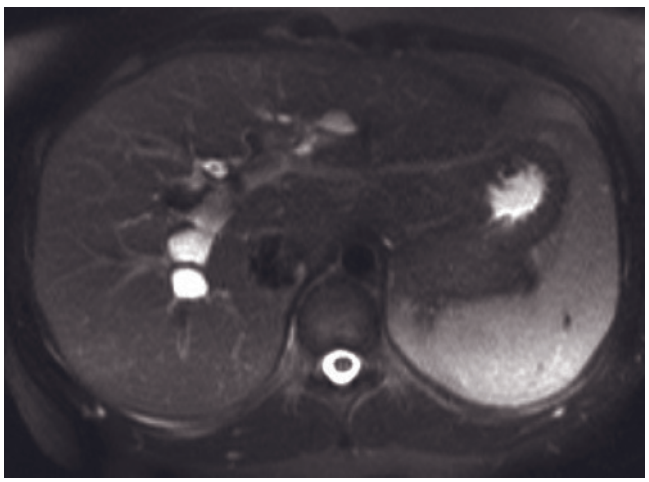

(*i*)

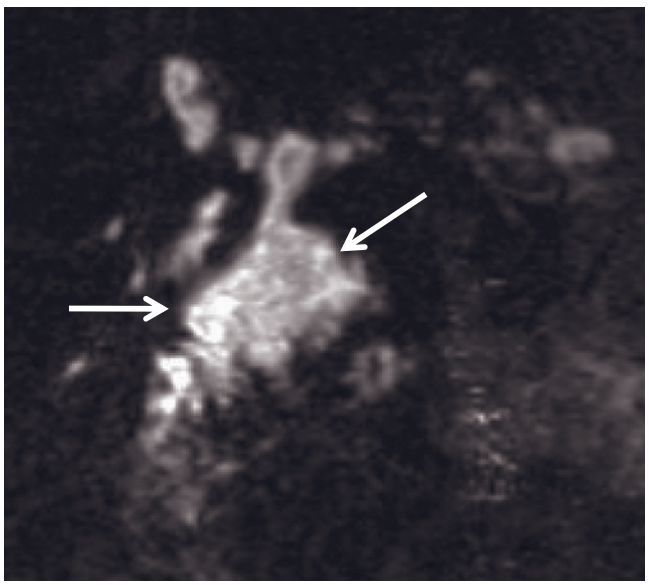

(*j*)

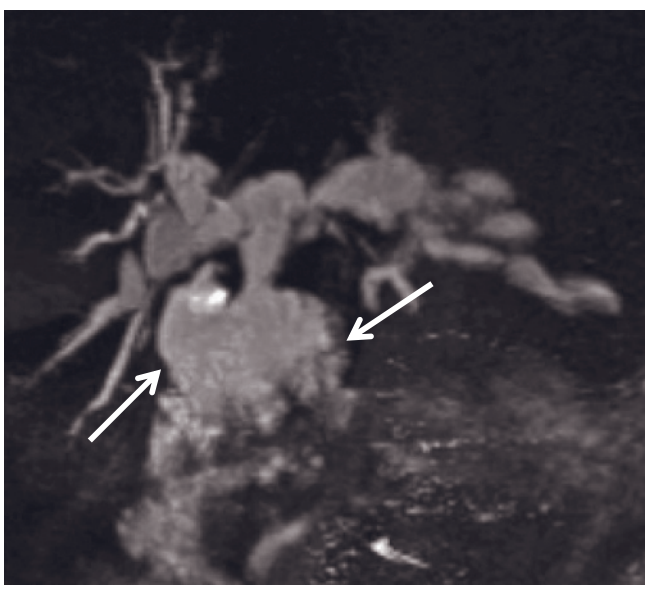

(*k*)

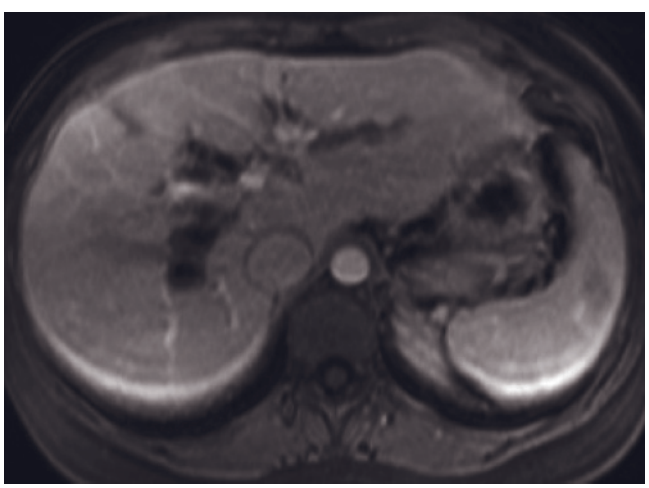

(*l*)

Fig. 3.38 (*Continued*) fat-suppressed 3D-GE (*g*), and transverse T1-weighted postgadolinium hepatic venous phase fat-suppressed 3D-GE (*h*) images demonstrate the choledochal cyst (arrows, *e–h*) in another patient. Transverse T2-weighted single-shot echo-train spin-echo (*i*), coronal thin-section fast spin-echo MRCP (*j*), coronal thick-section fast spin-echo MRCP (*k*), and transverse T1-weighted fat-suppressed postgadolinium hepatic venous phase 3D-GE (*l*) images demonstrate an irregular cyst (arrows, *j*, *k*) arising from the common bile duct in another patient. The proximal bile ducts are dilated. The histopathology of the large cystic lesion was consistent with cystadenoma.

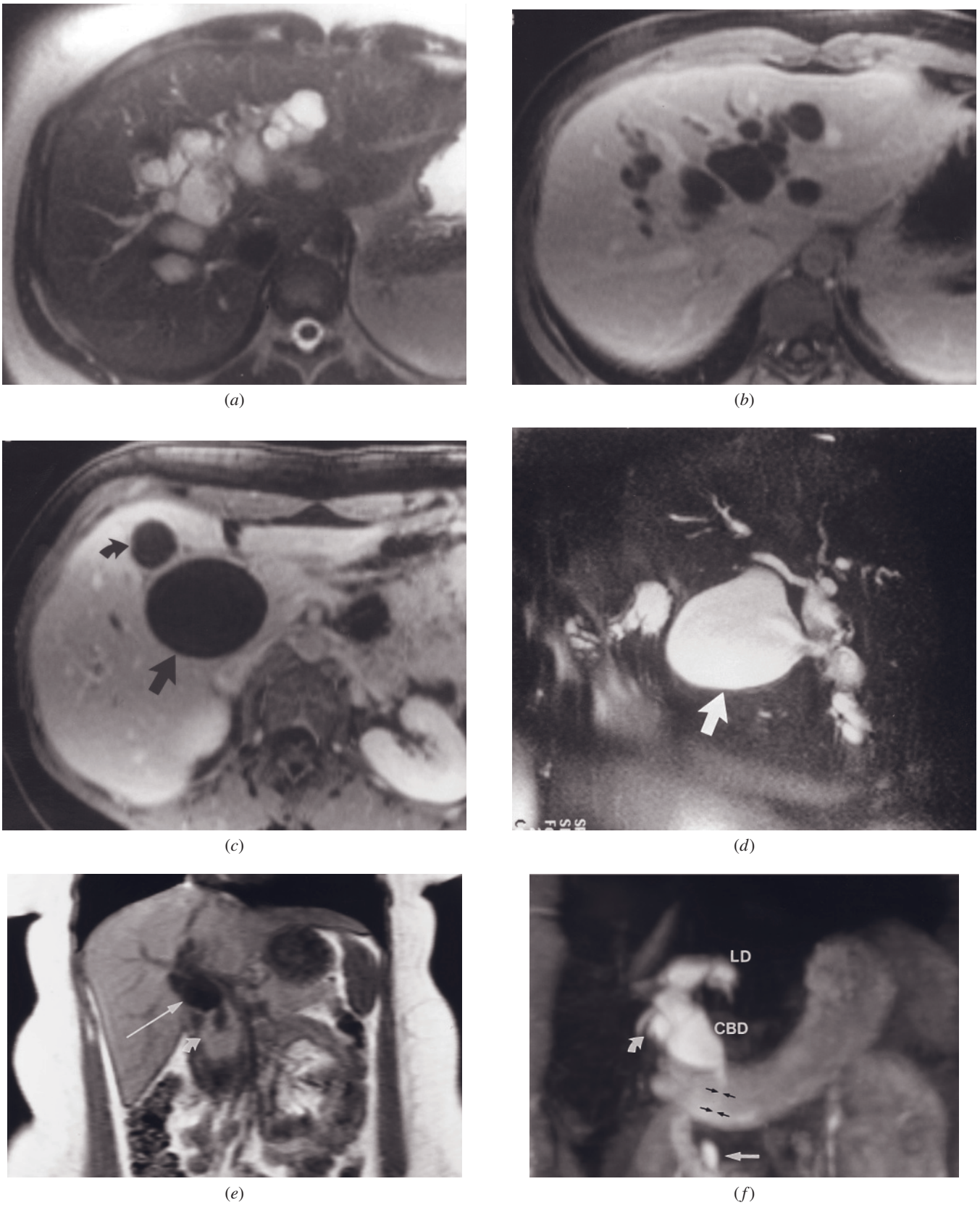

FIG. 3.39 Multiple bile duct cysts. T2-weighted single-shot echo-train spin-echo (*a*), T1-weighted 2-min postgadolinium fat-suppressed GE (*b*, *c*) images, and coronal T2-weighted thin-section MRCP single-shot echo-train spin-echo image with fat suppression (*d*). Multiple intrahepatic bile duct cysts are demonstrated showing high signal on the T2 (*a*)- and low signal on the T1 (*b*)-weighted images. A large choledochal cyst (straight arrow, *c*, *d*) is revealed abutting the gallbladder (curved arrow, *c*).The MRCP image (*d*) nicely demonstrates the intra- and extrahepatic extent of biliary cystic disease.

Coronal T1-weighted GE (*e*) and MRCP MIP reconstruction (*f*) images in a second patient. A cystic dilatation of the proximal CBD (long arrow, *e*) above the head of the pancreas (curved arrow, *e*) is appreciated on the GE image (*e*).The left hepatic duct (LD, *f*) shown with high signal on the MRCP MIP image (*f*) also demonstrates fusiform dilatations. Cystic dilatations are also visualized in the cystic duct at its insertion into the CHD (curved arrow, *f*) and of the preampullary CBD (straight arrow, *f*). The mid-CBD (small arrows, *f*) is of normal caliber.

(*a*)

(*b*)

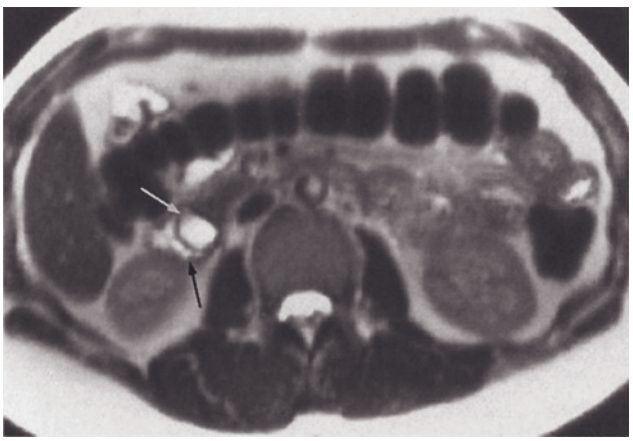

(*c*)

FIG. 3.40 Choledochocele. Coronal thin-section MRCP single-shot echo-train spin-echo image with fat suppression (*a*). The ampullary section of the CBD shows a small cystic dilatation (arrow, *a*) that protrudes into the lumen of the duodenum. The rest of the CBD is also dilated.

T2-weighted single-shot echo-train spin-echo images in the coronal plane with fat suppression (*b*) and the transverse plane without fat suppression (*c*) in a second patient. The CBD shows a cystic expansion (white arrows, *b*, *c*) of its ampullary section. The transverse image (*c*) demonstrates that the choledochocele (white arrows, *c*) bulges into the duodenum (black arrow, *c*), which contains high-signal intensity intraluminal fluid.

best demonstrated with thin-section T2- or T1-weighted images, on which Caroli disease presents with rounded cystic dilatations of equivalent signal intensity compared to bile (bright on T2- and low on T1-weighted images) communicating with bile ducts (fig. 3.41) [105].

Mass Lesions

Benign tumors that involve the biliary tract are relatively uncommon. Tumors can be solitary or multiple. Benign mass lesions can result in ductal obstruction and hepatic atrophy, resembling an imaging appearance comparable to malignant disease, as illustrated by a rare benign tumor, giant cell tumor of the bile duct (fig. 3.42).

Papillary Adenoma. Papillary adenomas of the biliary tract are rare benign epithelial tumors that have an increased risk for malignant transformation. Multiple small papillomas scattered throughout the biliary tree are characteristic of biliary papillomatosis. This condition is associated with an irregular pattern of intrahepatic bile duct dilatation due to obstruction by the papillomas. These small tumors are best visualized on 2-min postgadolinium fat-suppressed T1-weighted gradient-echo images as tiny enhancing mass lesions (fig. 3.43).

Ampullary Adenoma. Neoplasms that arise at the ampulla may have a benign histology. The most common benign ampullary tumor is an ampullary adenoma. The MRI appearance of this rare entity shows a well-defined mass, often polypoid, that shows no evidence of local invasion. Masses are generally small and enhance homogeneously (fig. 3.44).

Postsurgical Biliary Complications

Benign biliary strictures are a sequel of surgical injury (e.g., laparoscopic cholecystectomy, gastric and hepatic resection, biliary-enteric anastomosis, biliary reconstruction after liver transplantation) in 90–95% of cases [106, 107]. The remainder are secondary to penetrating or blunt trauma, inflammation associated with gallstone disease, chronic pancreatitis, ampullary fibrosis, toxic or ischemic lesions of the hepatic artery, or primary infection. The advent of minimally invasive therapeutic procedures, performed by interventional radiology or endoscopy, has greatly increased the need for preoperative diagnosis and

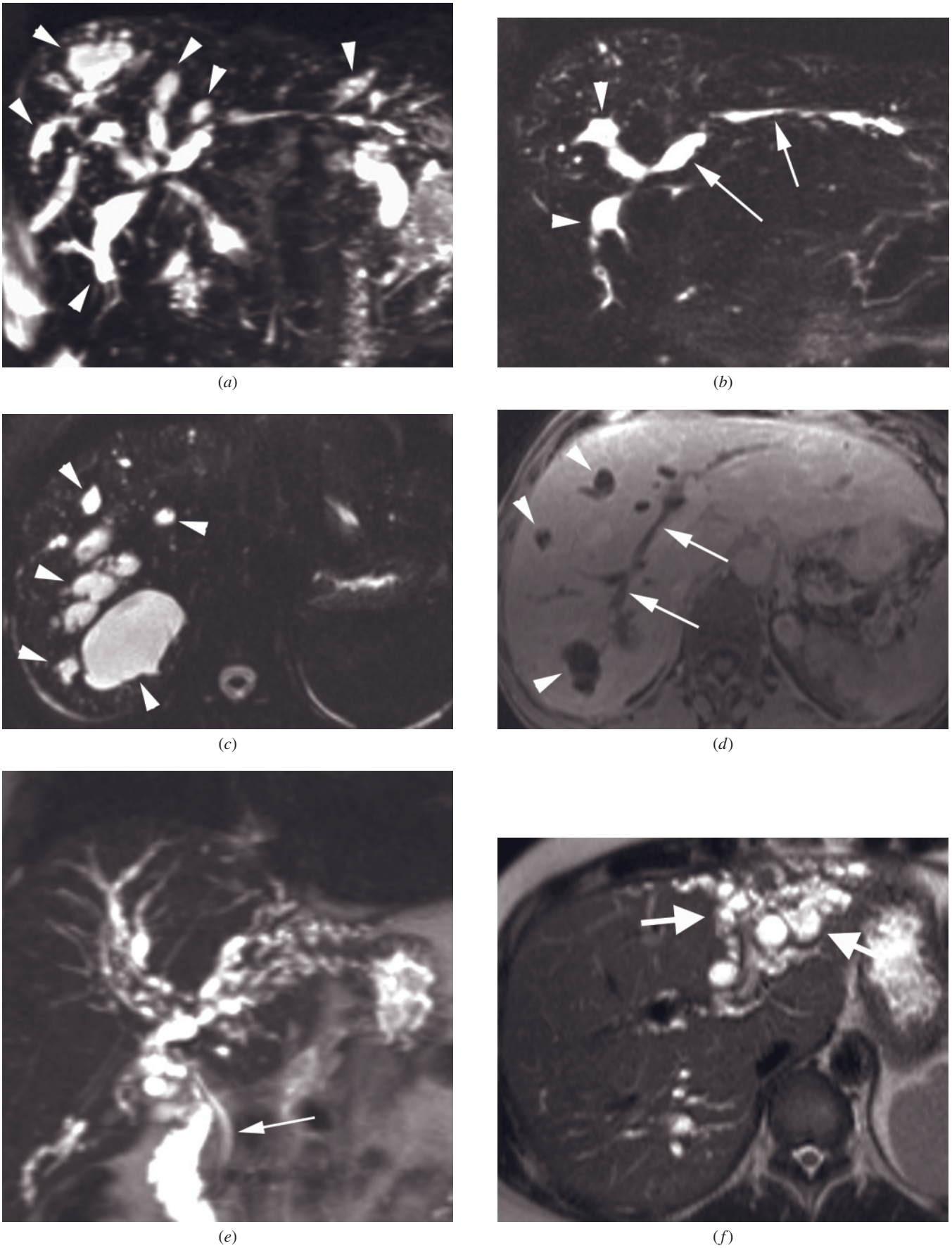

FIG. 3.41 Caroli disease. Paracoronal thick-section MRCP (*a*), paracoronal thin-section MRCP (*b*), axial fat-suppressed T2-weighted single-shot echo-train spin-echo (*c*), and axial 2-min postgadolinium GE (*d*) images. Cystic intrahepatic biliary dilatations (arrowheads, *a–d*) are present in the right and left lobes of the liver. Differentiation from liver cysts is made by demonstration of continuity with mildly dilated bile ducts (arrows, *b*, *d*). Differentiation of bile ducts from portal vein branches is facilitated on the postgadolinium image (*d*), where the latter demonstrate enhancement. MIP reconstruction MRCP (*e*), axial T2-weighted single-shot echo-train spin-echo (*f*), and axial 2-min postgadolinium GE (*g*) images of another patient with Caroli disease (Courtesy of

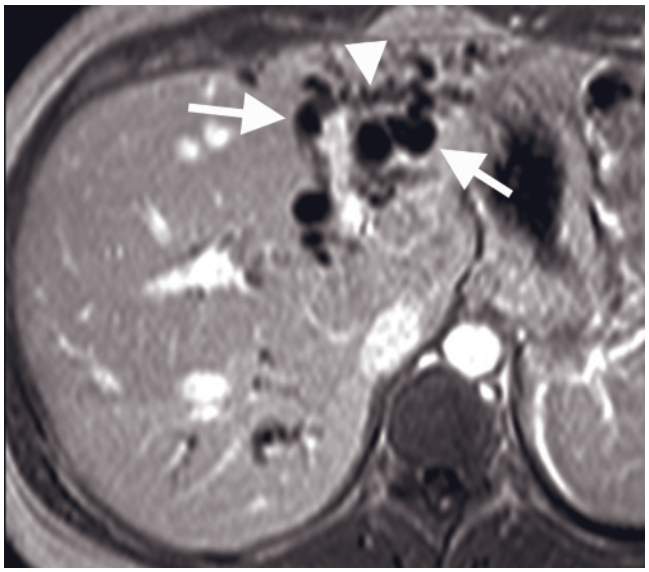

(*g*)

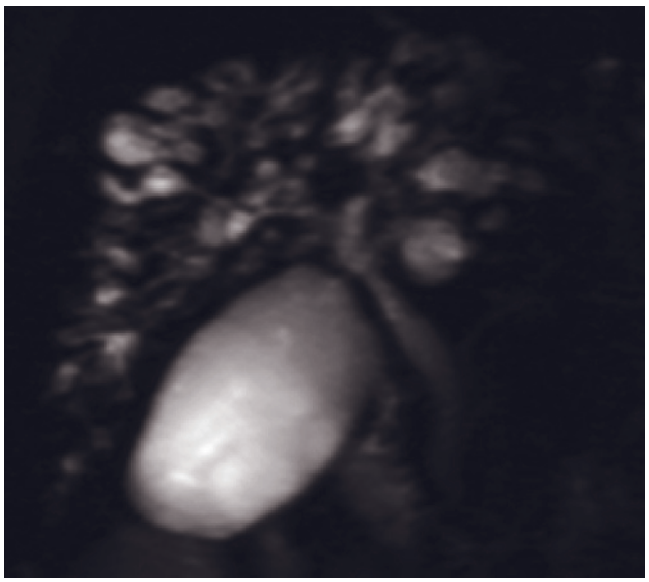

(*h*)

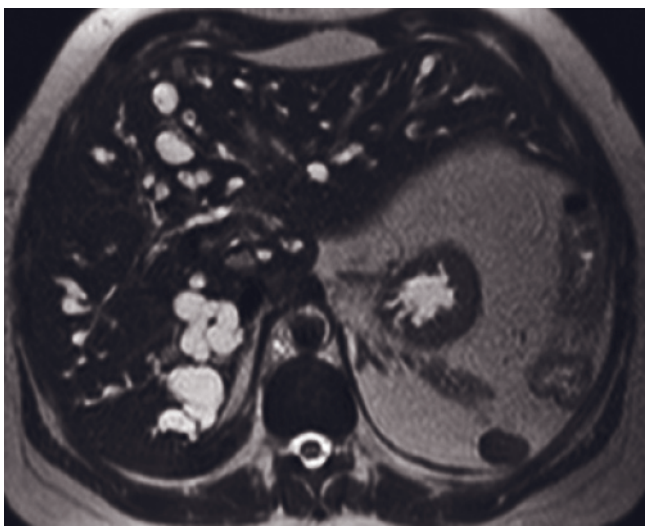

(*i*)

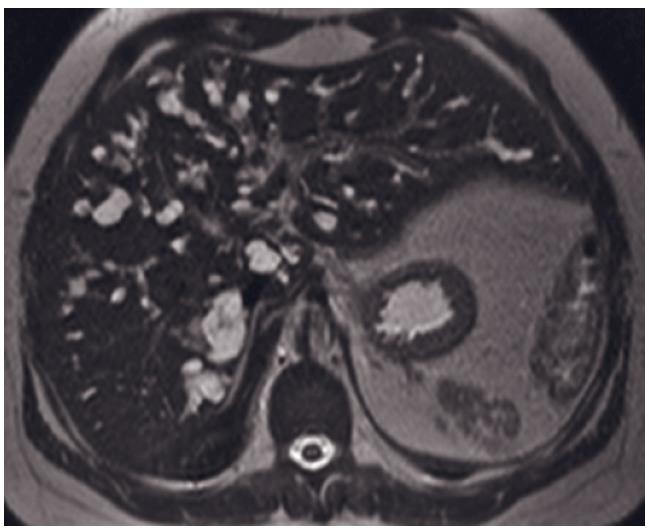

(*j*)

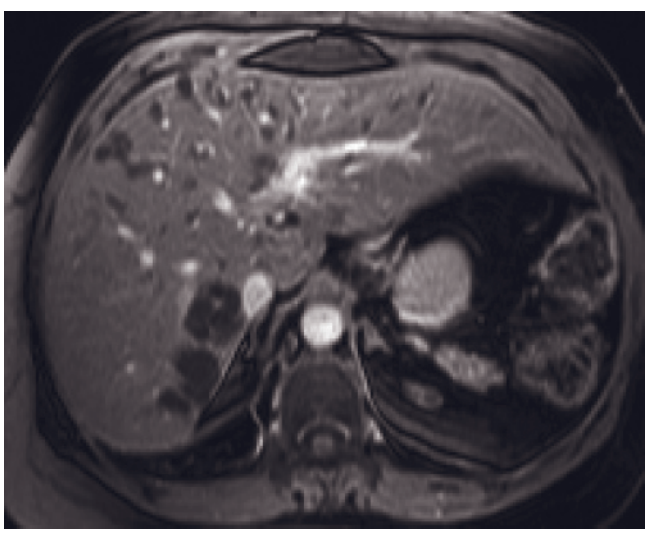

(*k*)

Fig. 3.41 (*Continued*) Shahid Hussain, M.D.). The common bile duct (arrow, *e*) is normal, but the intrahepatic biliary tree shows multiple cystic dilatations (arrows, *f*, *g*). Continuation of the cystic structures with bile ducts (arrowhead, *g*) is well visualized on the postgadolinium image (*g*).

Coronal thick-section fast spin-echo MRCP (*h*), transverse single-shot echo-train spin-echo (*i*, *j*), and transverse fat-suppressed postgadolinium hepatic venous phase 3D-GE (*k*) images demonstrate multiple cystic dilatations of intrahepatic bile ducts in another patient (Courtesy of Frank Miller, M.D.). There is no involvement in the extrahepatic ducts. No enhancement is detected in the cystic dilatations. Note that there is no spleen.

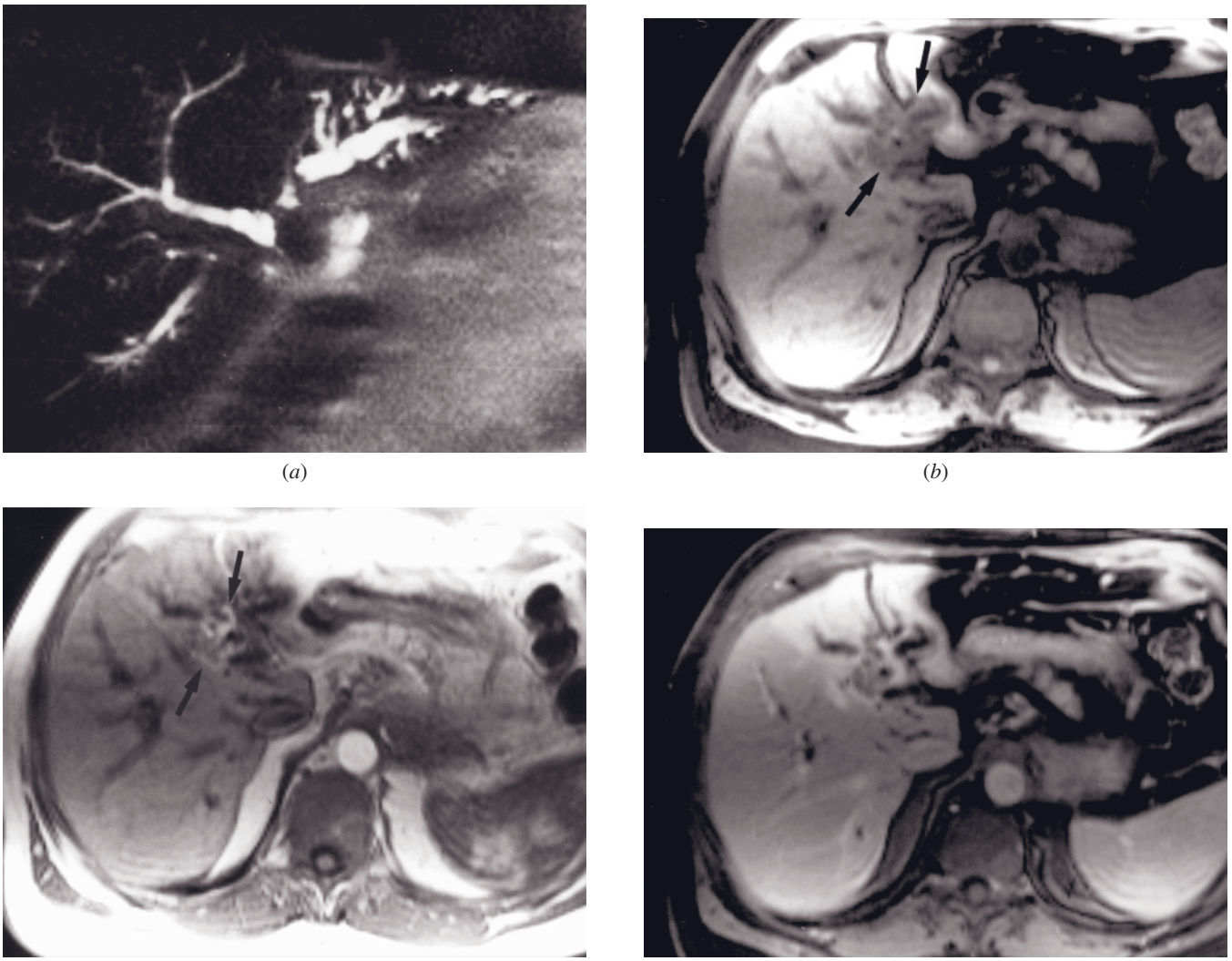

(*a*) (*b*) (*c*) (*d*)

FIG. 3.42 Giant cell tumor of the bile duct. Coronal thin-section MRCP single-shot echo-train spin-echo image with fat suppression (*a*), transverse T1-weighted fat-suppressed GE (*b*), immediate postgadolinium GE (*c*), and 2-min postgadolinium fat-suppressed GE (*d*) images. An obstruction at the confluence of the right and left main hepatic ducts is visualized on the MRCP image (*a*) with dilatation of the right and left intrahepatic biliary system. The tumor (arrows, *b*) appears moderately low signal intensity on the T1-weighted image (*b*). The tumor demonstrates increased enhancement (arrows, *c*) on the immediate postgadolinium image (*c*), with persistent enhancement on the 2-min postgadolinium image (*d*). The liver parenchyma distal to the tumor shows delayed increased enhancement (*d*). The tumor mimics the MRI appearance of Klatskin tumor but was diagnosed as giant cell tumor of the left hepatic duct at histopathology.

imaging in order to plan the optimal therapeutic approach. The major advantage of MRCP is the ability to visualize the biliary tree above and below a high-grade stricture or complete obstruction. The bile ducts distal to a stenosis, however, may be collapsed and nonvisualized on MIP-reconstruction images, leading to overestimation of the stricture. Thin-section source images must be used to evaluate the extent of high-grade stenoses, as even minimal amounts of fluid in collapsed ducts can be depicted on these images.

Other biliary complications of cholecystectomy are retained bile duct stones, biliary leak, and biliary fistula (fig. 3.45). In a study of such complications by Coakley et al. [108], two readers correctly categorized postsurgical complications in 88% and 76%, respectively. However, high-grade biliary stricture and transsection of bile ducts both presented as abrupt termination of a dilated duct, and, consequently, MRCP failed to distinguish between those entities but grouped them together as occlusion.

In patients with biliary-enteric anastomoses, ERCP can often not be performed. MRCP, however, is very effective in visualizing the anatomy of the anastomosis, strictures of the anastomosis or of intrahepatic ducts,

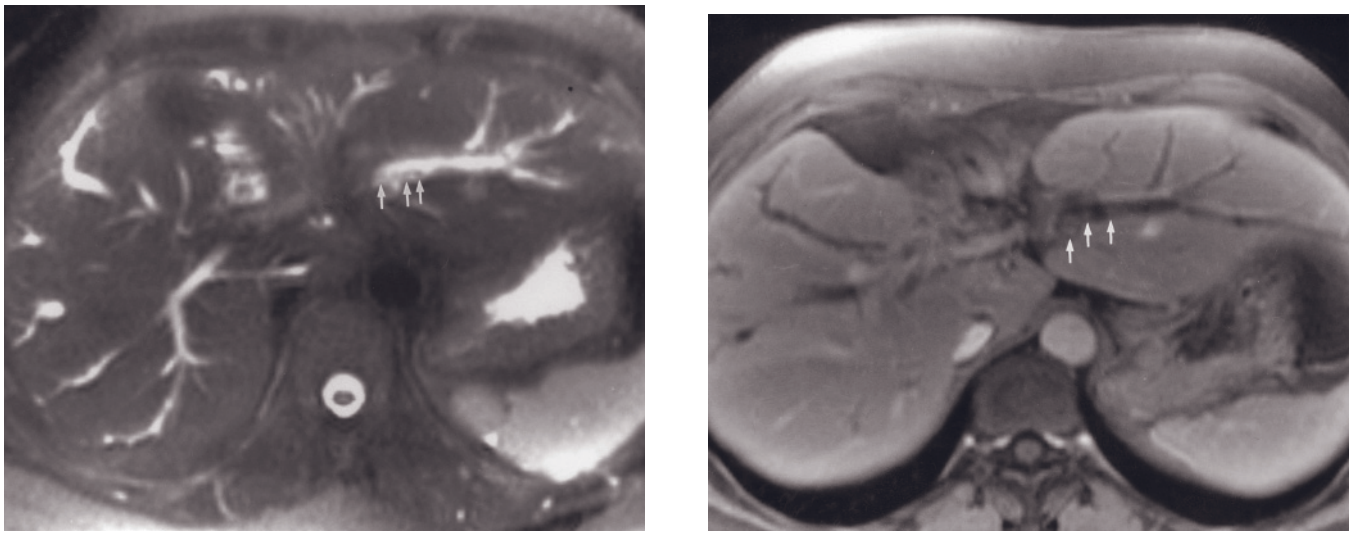

(*a*) (*b*)

FIG. 3.43 Biliary papillomatosis. T2-weighted single-shot echo-train spin-echo (*a*) and T1-weighted 2-min postgadolinium fat-suppressed GE (*b*) images. Several small, biliary intraductal, papillary tumors (arrows, *a*, *b*) are revealed showing enhancement on the postgadolinium image (*b*). The entire biliary tree is moderately dilated because of obstruction by papillomas in the CHD and CBD.

and biliary tract stones proximal to the anastomosis, in up to 100% of patients (see figs. 3.9, 3.43) [2, 109]. Close scrutiny of the thin-section source images is mandatory because the biliary-enteric anastomosis and stones can be obscured on thick-section and MIP-reconstruction images by the high signal intensity of surrounding bile and bowel fluid (fig. 3.46). Metallic surgical clips and pneumobilia can also produce artifacts that should not be mistaken as stones or strictures. Ischemic changes of the biliary system and obstruction secondary to a stricture following liver transplantation operations can also be well evaluated with MRI (fig. 3.46).

Malignant Disease

Cholangiocarcinoma

Cholangiocarcinomas are well-differentiated sclerosing adenocarcinomas in two-thirds of cases; the remainder are anaplastic, squamous cell, or cystadenocarcinomas. The most common predisposing diseases in Western countries are ulcerative colitis and sclerosing cholangitis. In Far Eastern countries, recurrent pyogenic cholangitis (caused by *Clonorchis sinensis* infestation) is the most common cause. Other predisposing factors are Caroli disease, choledochal cysts, α-1-antitrypsin deficiency, and autosomal dominant polycystic kidney disease. Cholangiocarcinoma is typically a malignancy of older patients (>50 yr). Patients usually present with jaundice and weight loss. Three types of cholangiocarcinomas can be differentiated based on anatomic distribution: the peripheral (or intrahepatic) type arising from peripheral bile ducts in the liver, the hilar type (Klatskin tumor) with its origin at the confluence of the right and left hepatic ducts, and the extrahepatic type arising from the main hepatic ducts, CHD or CBD [110, 111].

The peripheral type constitutes approximately 10% of all cholangiocarcinomas and is the second most common primary liver tumor after hepatocellular carcinoma (HCC). Peripheral cholangiocarcinomas usually present as masslike lesions that do not obstruct the central bile ducts [112]. Therefore, they can obtain a large size and show intrahepatic metastases before they cause clinical symptoms. Their typical MR imaging appearance is a mass lesion that is mildly heterogeneous with moderately low signal intensity on T1-weighted images and mildly to moderately hyperintense signal on T2-weighted images (fig. 3.47) [95]. On immediate postgadolinium images, they usually show mild to moderate enhancement that is usually diffuse heterogeneous in pattern. Progressive enhancement may be observed on late fat-suppressed images, reflecting a high content of fibrous tissue (see fig. 3.47). This feature, if present, may suggest this type of tumor and differentiate it from HCC, which typically shows intense, diffuse heterogeneous enhancement on immediate postgadolinium images and washout on delayed images [113]. Additional features that help differentiate cholangiocarcinomas from HCC are lack of vascular invasion and rare occurrence of cholangiocarcinoma in cirrhotic livers [113]. Peripheral cholangiocarcinoma is also described in Chapter 2, *Liver*.

Klatskin tumors are usually small-volume superficial spreading tumors that result in early biliary obstruction and dilatation of proximal ducts (fig. 3.48). These tumors

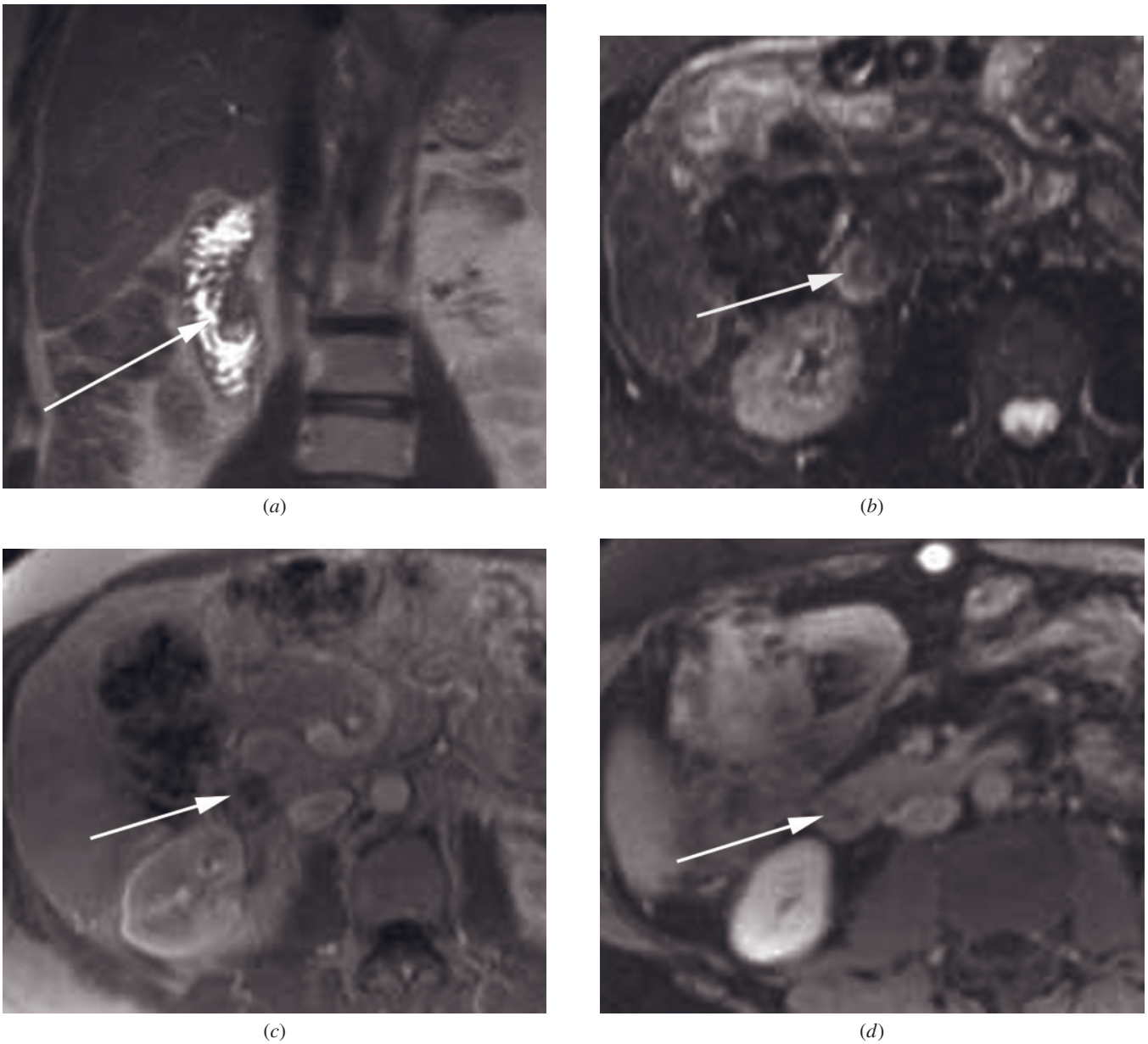

FIG. 3.44 Ampullary adenoma. Coronal T2-weighted echo-train spin-echo (*a*), axial STIR (*b*), axial immediate postgadolinium GE (*c*), and 2-min postgadolinium fat-suppressed GE (*d*) images. A prominent, masslike major papilla (arrows, *a–d*) is observed protruding into the duodenal lumen. Signal intensity and contrast enhancement are equivalent to a normal papilla. No sign of malignancy is observed.

may uncommonly present as masslike lesions similar to peripheral tumors. Most often, they show circumferential growth and spread along bile ducts with poor conspicuity on noncontrast MR images (fig. 3.49). Biliary dilatation can involve one or both lobes of the liver, depending on the location of the tumor. Lobar atrophy of the liver combined with marked biliary dilatation should raise suspicion of cholangiocarcinoma (fig. 3.50), but this feature is not pathognomonic [114].

Extrahepatic cholangiocarcinomas usually grow in a circumferential pattern similar to Klatskin tumors. They arise in the CBD and result in biliary obstruction in the vast majority of patients. The imaging features of Klatskin tumors and extrahepatic cholangiocarcinomas at MRCP are dilatation of the proximal biliary tree with stricture or abrupt termination at the tumor, typically showing a shoulder sign (fig. 3.51) [115]. Irregularity of the ductal wall is indicative of infiltration and raises a high suspicion of malignancy. Occasionally, tumors can show intraluminal papillary growth presenting as a filling defect on MRCP images. ERCP may on occasion poorly evaluate tumors because of incomplete biliary

FIG. 3.45 Biloma. T2-weighted fat-suppressed single-shot echo-train spin-echo (*a*) and T1-weighted 2-min postgadolinium fat-suppressed GE (*b*) images in a 44-yr-old woman with a history of open cholecystectomy and persistent right upper quadrant pain. A fluid collection (arrows, *a*, *b*) is depicted in the gallbladder bed, resembling a gallbladder. The fluid collection (biloma) has an enhancing wall (arrows, *b*) caused by an inflammatory reaction of the surrounding peritoneum. The common bile duct (arrowhead, *a*) shows inhomogeneous internal signal caused by a T-tube drain.

Coronal T2-weighted reconstructed 3D MIP MRCP image (*c*), transverse T1-weighted postgadolinium interstitial phase 3D-GE (*d*), and T1-weighted postgadolinium 1-h delayed fat-suppressed coronal and transverse 3D-GE (*e*, *f*) images acquired with gadobenate

opacification. An advantage of MRCP in combination with conventional MRI is that it can also visualize the biliary tree proximal to an occlusion, which often is not possible or advisable with ERCP, as well as detecting distant disease such as liver metastases or lymph node involvement.

On T1-weighted MR images with or without fat suppression, cholangiocarcinomas appear mildly to moderately hypointense but may also be isointense relative to liver parenchyma. On T2-weighted images, they are isointense or mildly hyperintense (see Figs. 3.47–3.49) [113]. Thickening of bile duct walls greater than 5 mm is highly suggestive of cholangiocarcinoma [95]. However, this measurement is not sensitive, as at least 50% of tumors show thinner wall diameters [113]. The finding of relatively minor increase of wall thickness (3–4 mm) in association with high-grade biliary obstruction is highly suggestive of cholangiocarcinoma in patients without a history of recent gallbladder surgery. On immediate postgadolinium images, cholangiocarcinomas

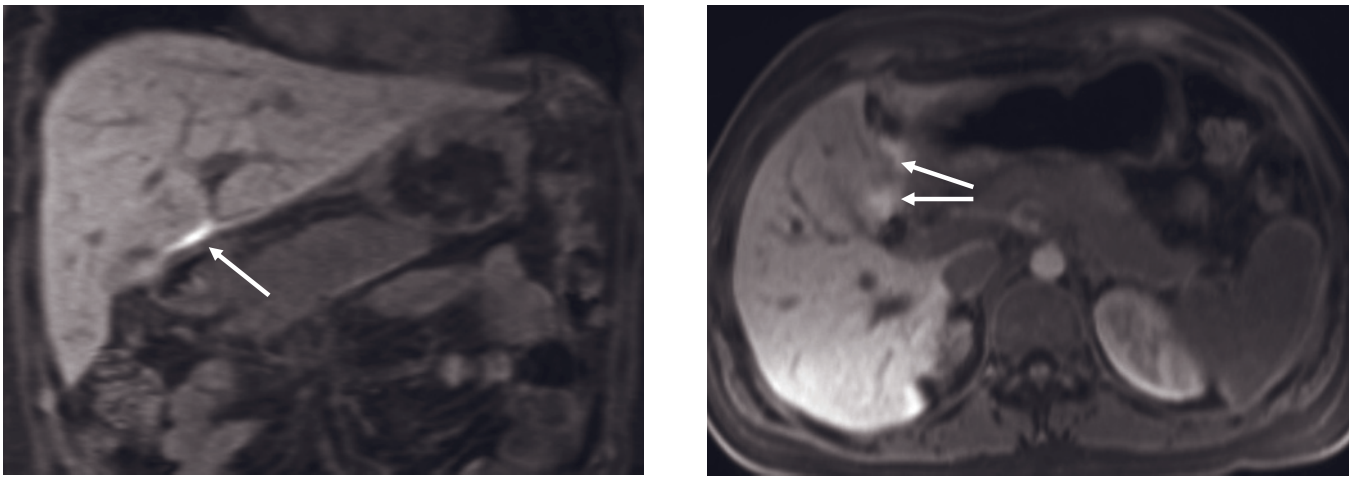

(*e*) (*f*)

FIG. 3.45 (*Continued*) dimeglumine (Multihance) demonstrate the bile leak (arrows, *e*, *f*) following the cholecystectomy operation in another patient. Free fluid (arrows, *c*) is detected along the inferior surface of the liver and gallbladder fossa. Because gadobenate dimeglumine is taken up by hepatocytes and excreted into the biliary ducts, intrabdominal bile leaks resulting from disruptions of the biliary system can be detected as high-signal intensity fluid (arrows, *e*, *f*) on delayed images. Note that high-signal-intensity intrabdominal bile cannot be detected on early postgadolinium image (*d*).

are usually hypovascular, showing minimal or moderate enhancement that intensifies on delayed images (see figs. 3.47–3.49) [113]. A combination of early and late fat-suppressed gadolinium-enhanced images is very helpful to identify these tumors. Fat suppression also reduces the signal of fatty tissue in the porta hepatis, which improves the conspicuity of cholangiocarcinomas and facilitates the evaluation of the extent of tumor and infiltration into adjacent tissues and organs.

Findings that indicate that a tumor is unresectable are vascular encasement and direct invasion of liver parenchyma. Large tumor size generally also confers inoperability (see fig. 3.50). Most cholangiocarcinomas are unresectable at the time of initial diagnosis and can be treated only with palliative biliary drainage. Biliary stent placement results in mild inflammation of bile duct walls, which appears as increased gadolinium enhancement with an appearance indistinguishable from superficial spread of cholangiocarcinoma (fig. 3.52). If feasible, it is preferable to image patients suspected of biliary tumor before stent placement to avoid the problem of incorrectly staging the tumor because of inflammatory changes secondary to the presence of the stent. Lymphadenopathy with portocaval and porta hepatis nodes is an associated finding in up to 73% of patients with cholangiocarcinoma (see fig. 3.50). This is best demonstrated with a combination of T2-weighted fat-suppressed and T1-weighted 2-min postgadolinium fat-suppressed images [113]. On these late postgadolinium images, fine tumor strands are frequently observed, and 5-mm or smaller lymph nodes are consistent with tumor extension if three or more of them are clustered in the region of the tumor. In advanced cholangiocarcinoma, intraperitoneal tumor spread may occasionally be found and is also best seen on late postgadolinium fat-suppressed images (fig. 3.53).

Periampullary and Ampullary Carcinoma

Carcinomas arising from the ampulla of Vater, periampullary duodenum, or distal CBD are grouped together and termed periampullary carcinomas. Their presentation is similar to that of pancreatic head ductal adenocarcinoma, including obstruction of both the CBD and pancreatic duct. The prognosis of periampullary carcinoma is significantly better than that of pancreatic carcinoma, with a 5-year survival rate up to 85% [116]. Periampullary carcinomas can cause ampullary obstruction and become clinically symptomatic even when they are only a few millimeters in size. Therefore, signs and symptoms of dilatation of the biliary tree and the pancreatic duct are observed relatively early in the course of these tumors, which likely accounts in part for their better prognosis. MRCP is very effective for the visualization of biliary and pancreatic ductal dilatation and the determination of the level of obstruction [117]. On T1-weighted fat-suppressed images, periampullary carcinomas typically appear as low-signal-intensity masses (fig. 3.54). Obstruction of the pancreatic duct eventually results in chronic pancreatitis. Chronic pancreatitis results in a reduced signal intensity of the pancreas on precontrast T1-weighted images, which diminishes the conspicuity of periampullary carcinomas on this

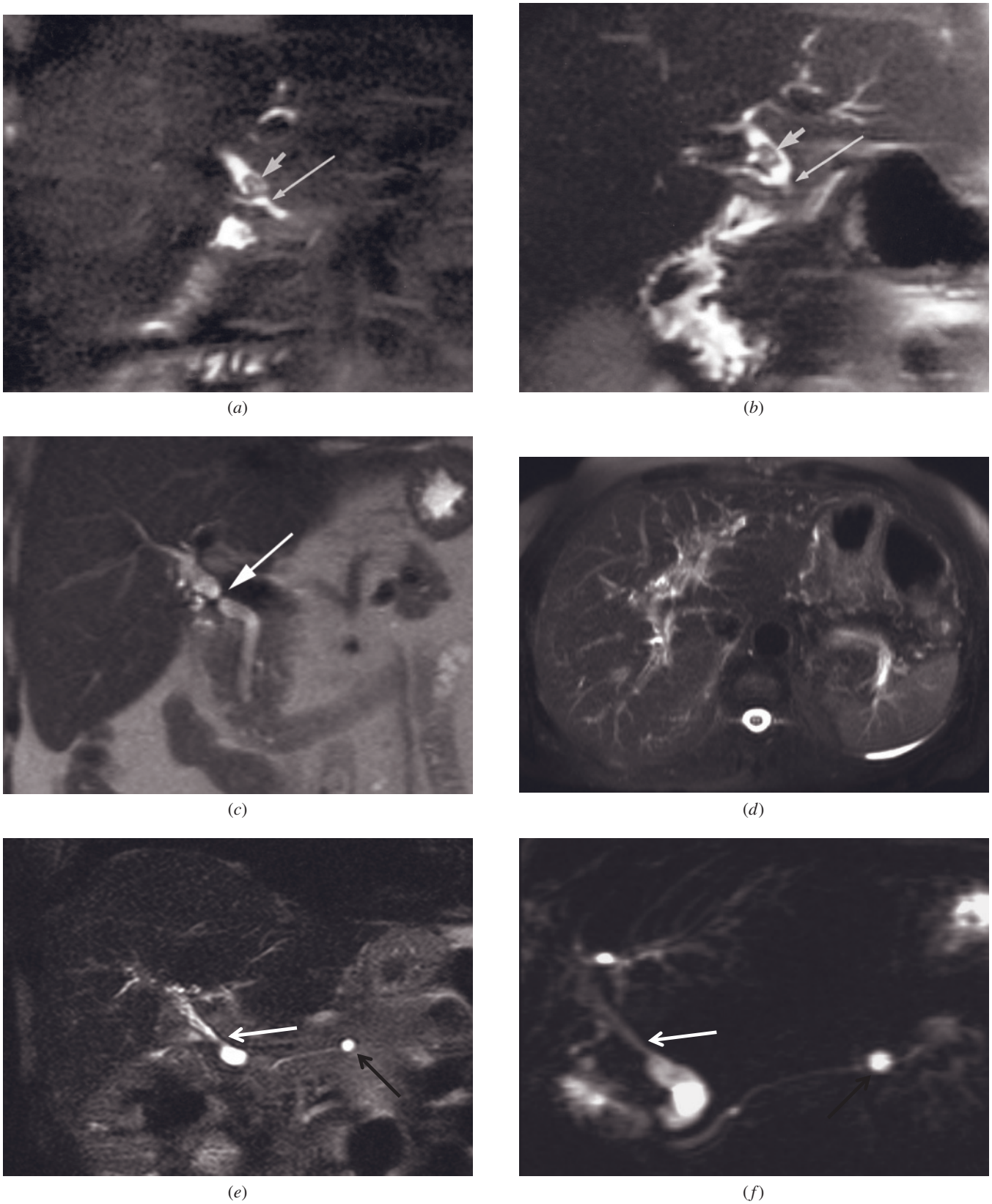

Fig. 3.46 MRCP after liver transplantation. Coronal thin-section MRCP single-shot echo-train spin-echo images with fat suppression (*a*, *b*). Slight narrowing of the anastomosis (long arrows, *a*, *b*) between the graft CBD and the host CBD is observed. A low-signal stone (short arrows, *a*, *b*) is visualized in the dilated graft CBD immediately proximal to the anastomosis. Coronal T2-weighted echo-train spin-echo image in another patient after liver transplantation (*c*). A circumscribed stricture (arrow, *c*) is observed at the anastomosis of the donor and recipient CBD. The proximal bile ducts are slightly dilated.

Transverse T2-weighted fat-suppressed single-shot echo-train spin-echo (*d*), coronal T2-weighted thin-section echo-train spin-echo (*e*), coronal thick-section fast spin-echo MRCP (*f*), and coronal reconstructed 3D MIP MRCP (*g*) images demonstrate ischemic

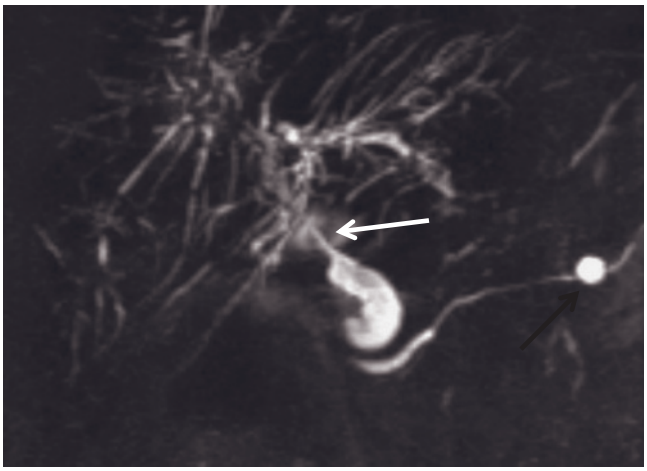

(*g*)

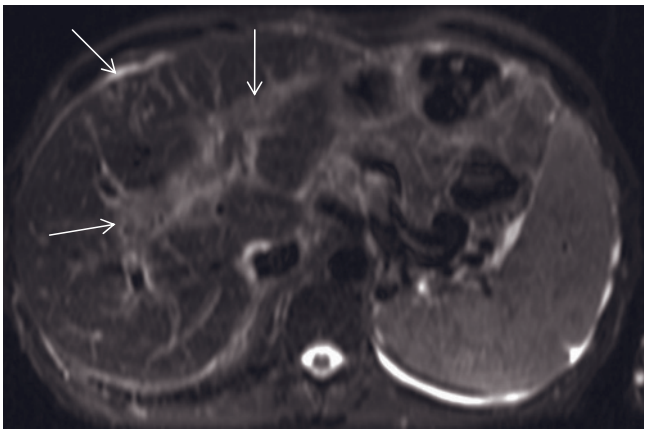

(*h*)

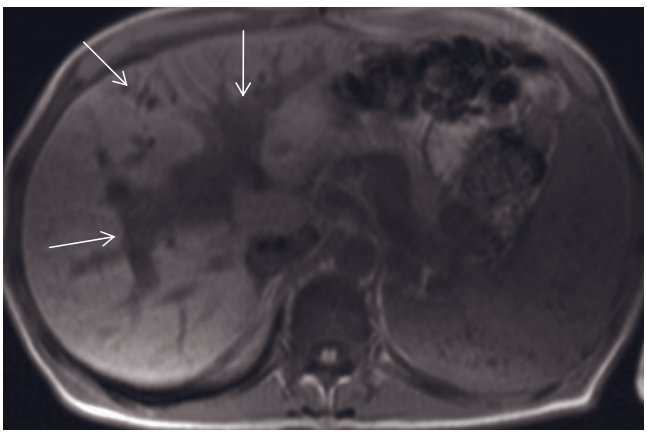

(*i*)

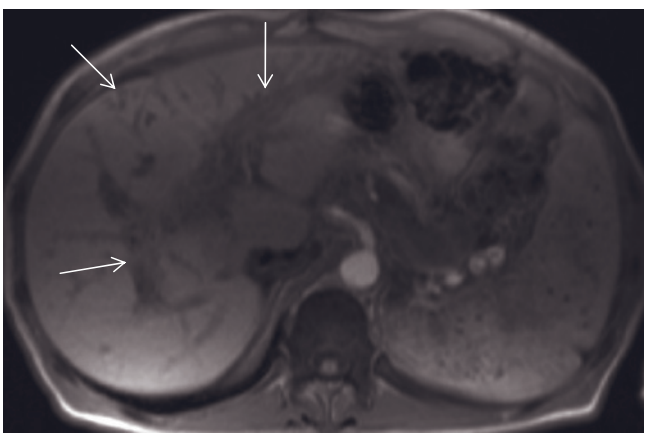

(*j*)

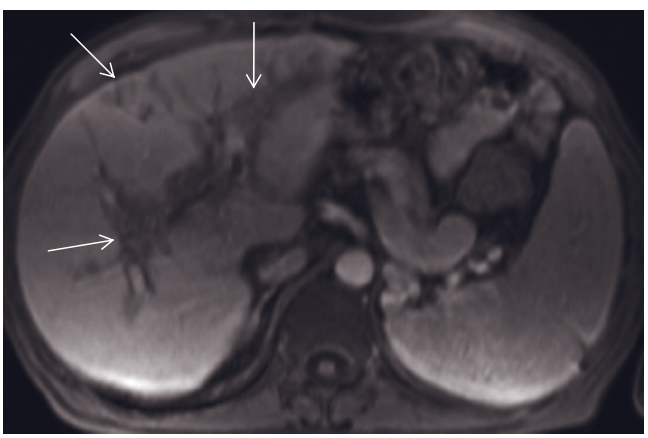

(*k*)

FIG. 3.46 (*Continued*) injury to the bile ducts in another patient who had prior liver transplantation. Central intrahepatic bile ducts are dilated. Ischemic injury causes stricture in the common bile duct (white arrows, *e*, *f*, *g*) and pruning in peripheral intrahepatic bile ducts (*f*, *g*). Note that there is a side branch IPMN (black arrows, *e*, *f*, *g*) and minimal free fluid in the abdomen.

T2-weighted fat-suppressed single-shot echo-train spin-echo (*h*), T1-weighted SGE (*i*), and T1-weighted postgadolinium late hepatic arterial phase SGE (*j*) and interstitial phase fat-suppressed 3D-GE (*k*) images demonstrate debris-filled dilated bile ducts in a patient who had liver transplantation. Debris-filled ducts (arrows, *h*–*k*) may have low or intermediate signal on T2-weighted images and this appearance of debris-filled dilated bile ducts and periportal edema mimics infiltrative lesions extending along the portal tracts such as posttransplant lymphoproliferative disorder. Debris filled bile ducts show mild enhancement, which suggests the presence of inflammation as well. Note the portal hypertension findings and ascites.

sequence. On immediate postgadolinium T1-weighted images, pancreatic parenchyma enhances greater than tumor, even in the presence of chronic pancreatitis. Periampullary carcinomas enhance minimally on early postgadolinium images because of their hypovascular character (figs. 3.54, 3.55) [118]. On 2-min postgadolinium fat-suppressed images, delayed enhancement is a typical finding [117]. A thin rim of enhancement is commonly observed along the periphery of these tumors and may also be a relatively specific finding (see

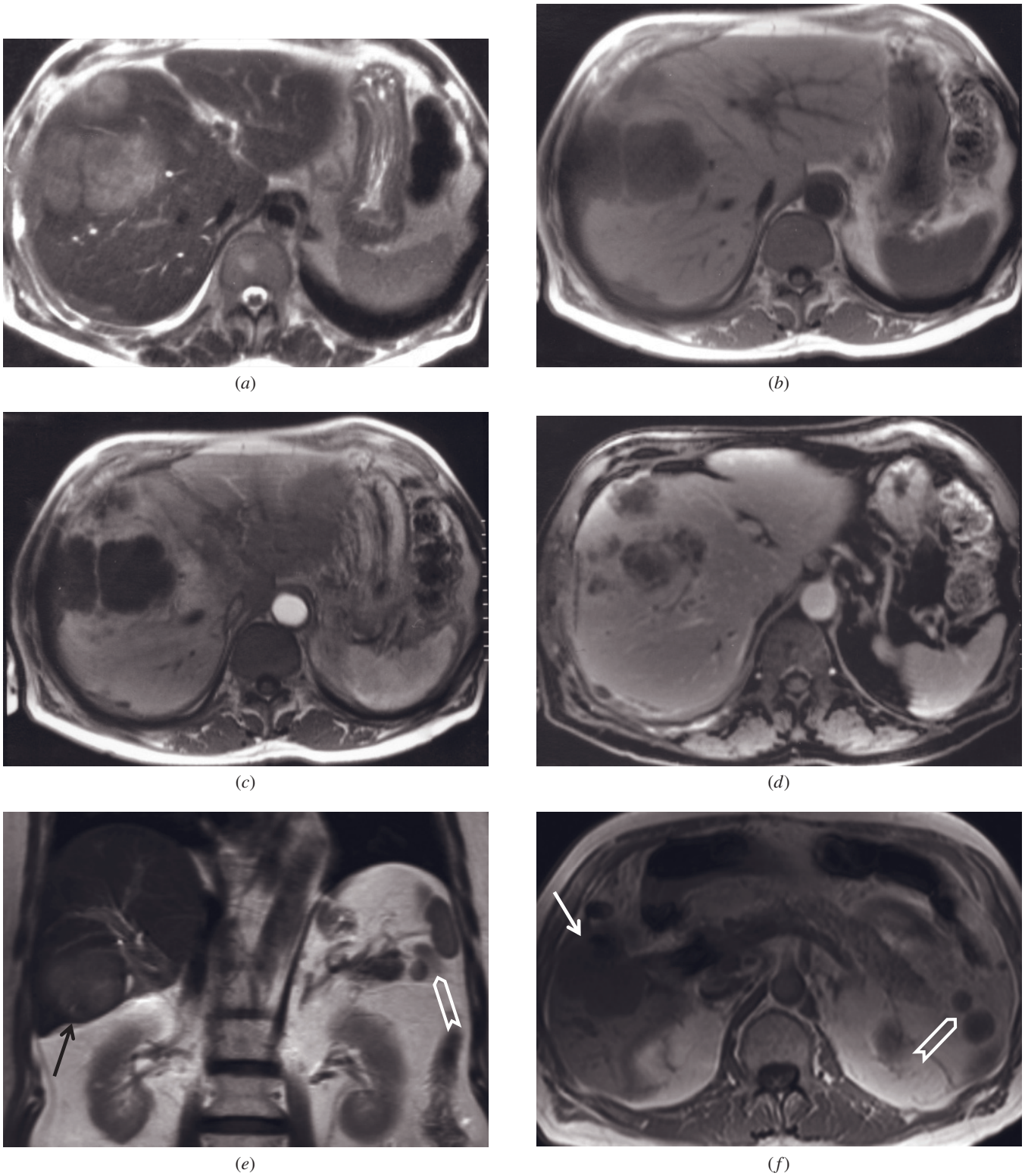

FIG. 3.47 Peripheral cholangiocarcinoma. T2-weighted single-shot echo-train spin-echo (*a*),T1-weighted GE (*b*), immediate postgadolinium GE (*c*), and 2-min postgadolinium fat-suppressed GE (*d*) images. A large tumor with intrahepatic metastases is observed in the right lobe of the liver. The signal is moderately hyperintense on the T2-weighted image (*a*) and hypointense on the T1-weighted image (*b*). On the immediate postgadolinium image (*c*), the tumors are hypoenhancing and demonstrate mild perilesional enhancement. Progressive heterogeneous enhancement of the tumors is observed on the 2-min postgadolinium image (*d*).

Coronal T2-weighted single-shot echo-train spin-echo (*e*), transverse T1-weighted SGE (*f*), transverse T1-weighted postgadolinium hepatic arterial dominant phase (*g*), and hepatic venous phase (*h*) fat-suppressed 3D-GE images at 3.0 T demonstrate a peripheral

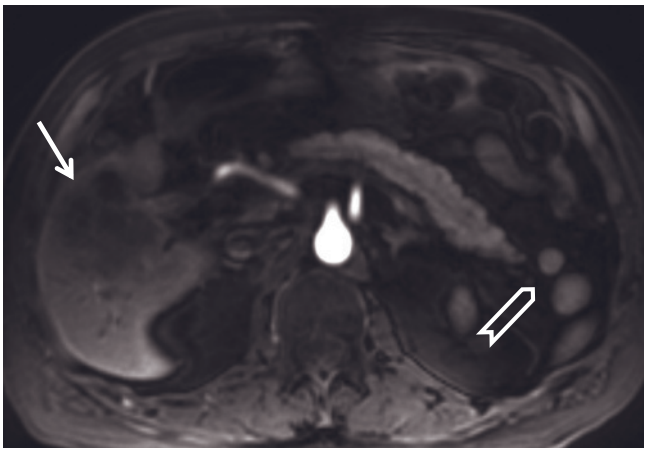

(*g*)

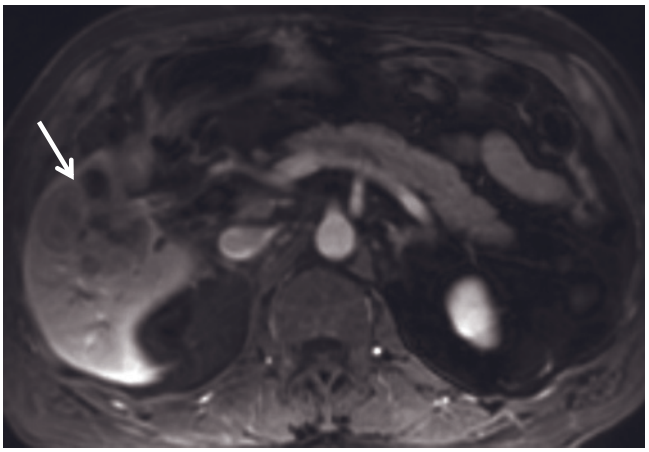

(*h*)

Fig. 3.47 (*Continued*) cholangiocarcinoma (solid arrows, *e–h*) in another patient with prior splenectomy and splenosis (open arrows, *e*, *f*, *g*). The tumor shows heterogeneous progressive enhancement on postgadolinium images and obstructs the peripheral biliary ducts.

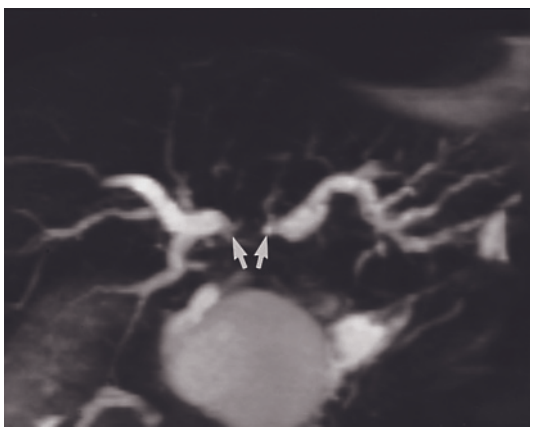

(*a*)

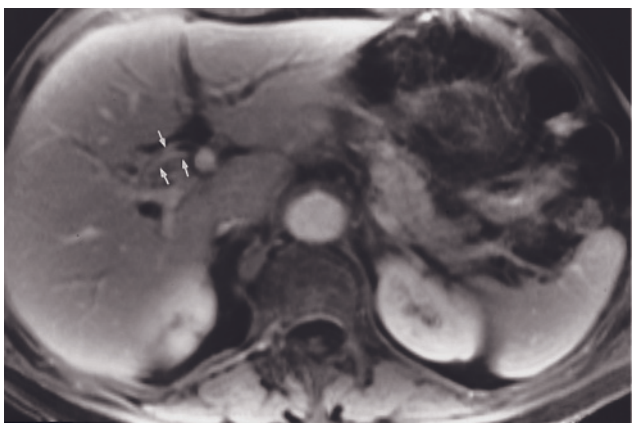

(*b*)

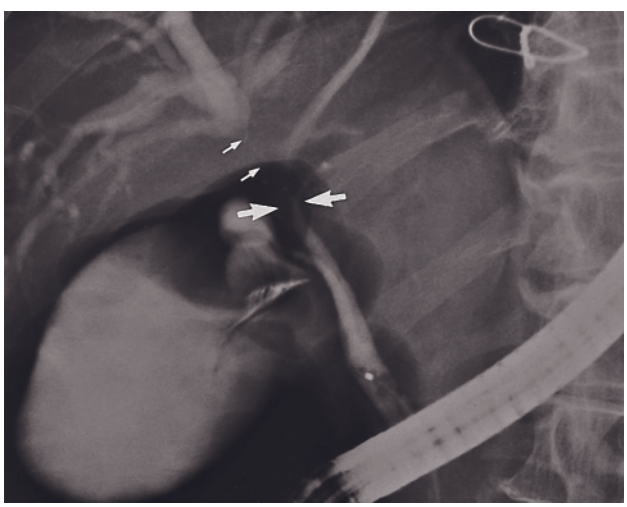

(*c*)

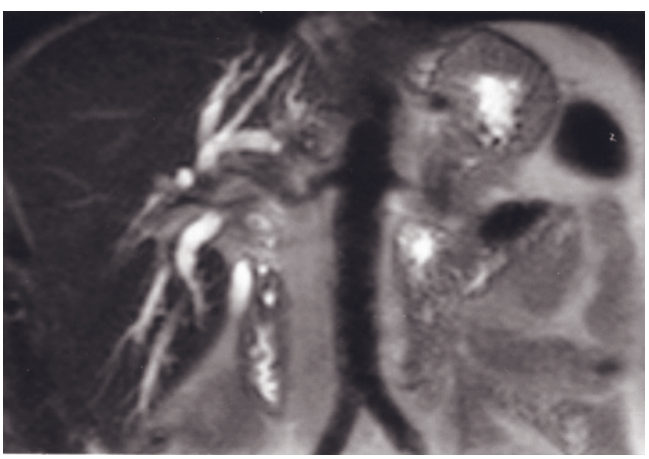

(*d*)

Fig. 3.48 Klatskin tumor. Coronal MRCP MIP reconstruction (*a*), transverse T1-weighted 2-min postgadolinium fat-suppressed GE (*b*), and ERCP (*c*) images. Obstruction of the right and left main hepatic ducts (arrows, *a*) at the level of the porta hepatis with dilatation of peripheral ducts is visualized on the MRCP image (*a*). A small enhancing tumor (small arrows, *b*), measuring 4 mm in diameter, extends from the CHD into the right main hepatic duct, as shown on the postgadolinium image (*b*). ERCP (*c*) also shows the obstruction (arrows, *c*) at the level of the porta hepatis and the extension of the tumor into the right main hepatic duct (small arrows, *c*). Note the poor visualization of the left biliary ductal system on the ERCP image (*c*) because of underfilling.

Coronal T2-weighted single-shot echo-train spin-echo (*d*), transverse T1-weighted fat-suppressed GE (*e*), and 2-min postgadolinium fat-suppressed GE (*f*) images in a second patient. Dilatation of the right and left intrahepatic biliary tree is observed on the

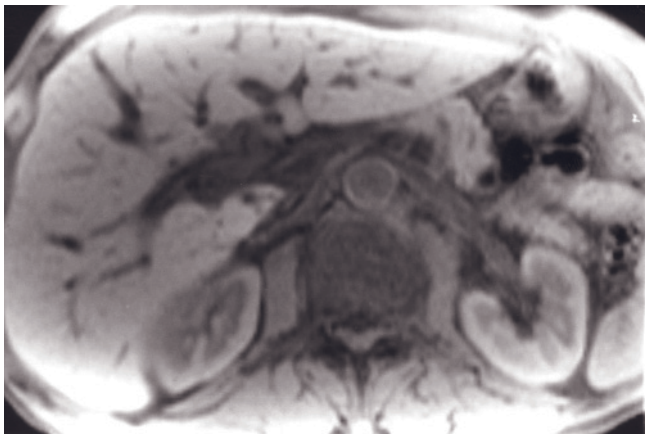

(*e*)

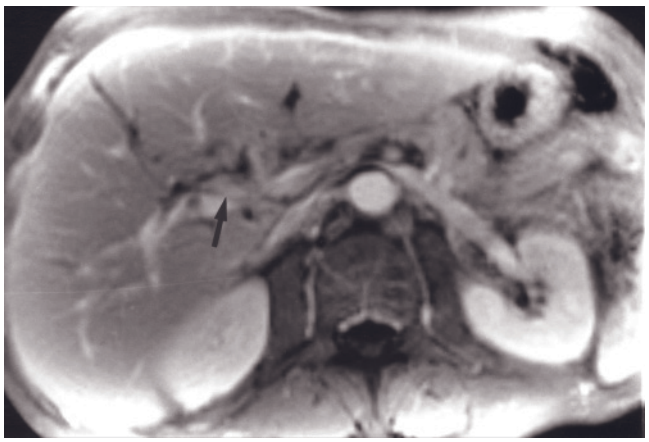

(*f*)

Fig. 3.48 (*Continued*) T2-weighted image (*d*).The tumor shows poor conspicuity on the precontrast GE image (*e*). On the 2-min postgadolinium image (*f*), the small Klatskin tumor (arrow, *f*) in the porta hepatis demonstrates enhancement and can be well differentiated from surrounding structures.

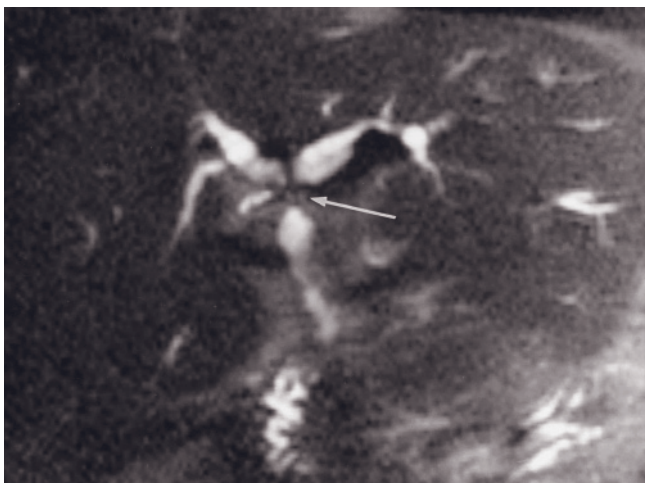

(*a*)

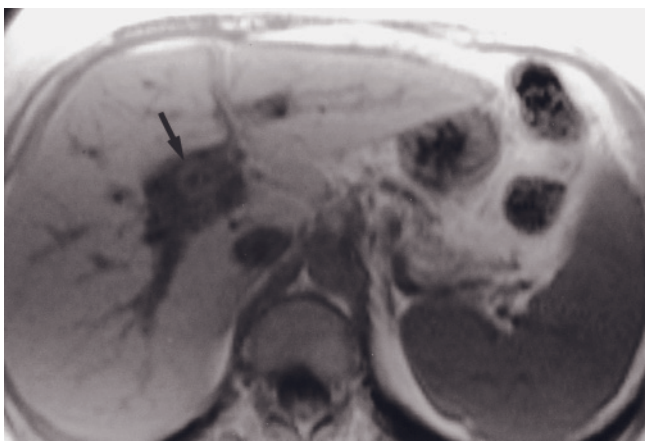

(*b*)

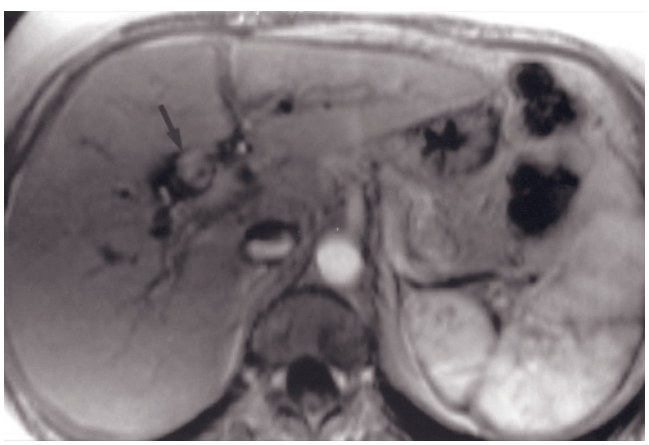

(*c*)

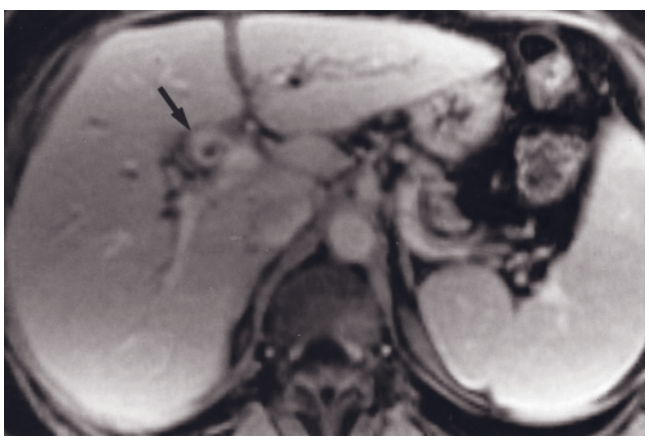

(*d*)

Fig. 3.49 Klatskin tumor, circumferential growth. Coronal T2-weighted thin-section MRCP single-shot echo-train spin-echo image with fat suppression (*a*) and transverse T1-weighted GE (*b*), immediate postgadolinium GE (*c*), and 2-min postgadolinium fat-suppressed GE (*d*) images. A short obstruction at the confluence of the right and left main hepatic ducts (arrow, *a*) is revealed on the MRCP image (*a*). It is difficult to delineate the tumor (arrow, *b*) from surrounding structures on the T1-weighted precontrast image (*b*). After gadolinium administration, the tumor shows moderately intense enhancement (arrows, *c*, *d*) on the immediate (*c*) and late (*d*) postgadolinium images. Note the circumferential growth and small volume of the Klatskin tumor, best visualized on the postgadolinium images (*c*, *d*).

(*e*)

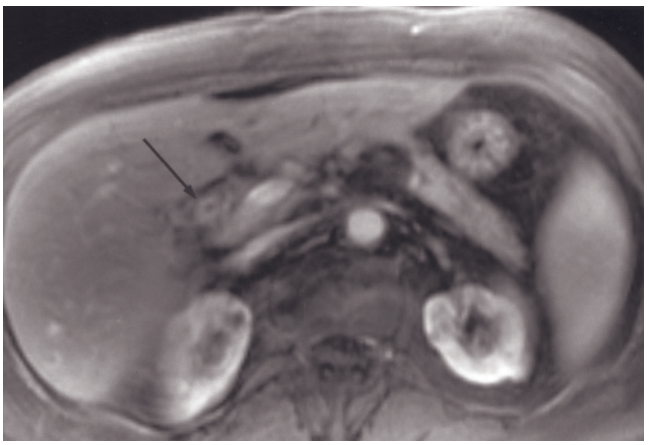

(*f*)

FIG. 3.49 (*Continued*) Coronal T2-weighted thin-section MRCP single-shot echo-train spin-echo image with fat suppression (*e*) and transverse T1-weighted 2-min postgadolinium fat-suppressed GE image (*f*) in a second patient. The Klatskin tumor obstructs the intrahepatic biliary system at the porta hepatis, demonstrated on the MRCP image (*e*). The tumor shows circumferential growth in the CHD (arrow, *f*) and increased enhancement on the late postgadolinium image (*f*).

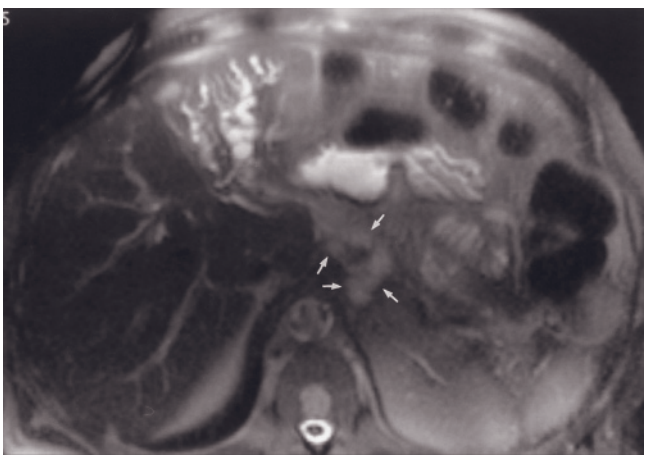

(*a*)

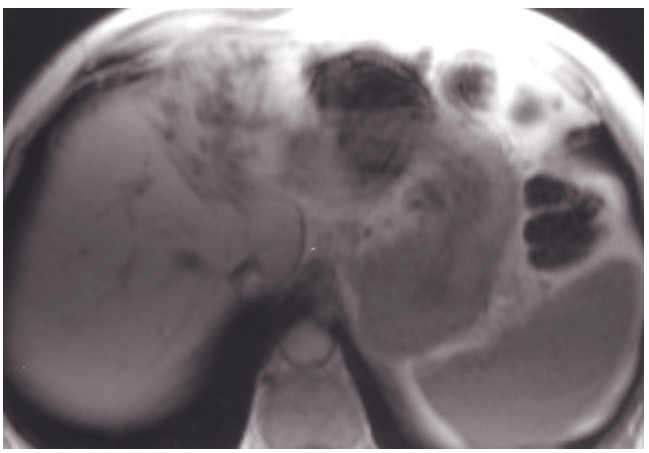

(*b*)

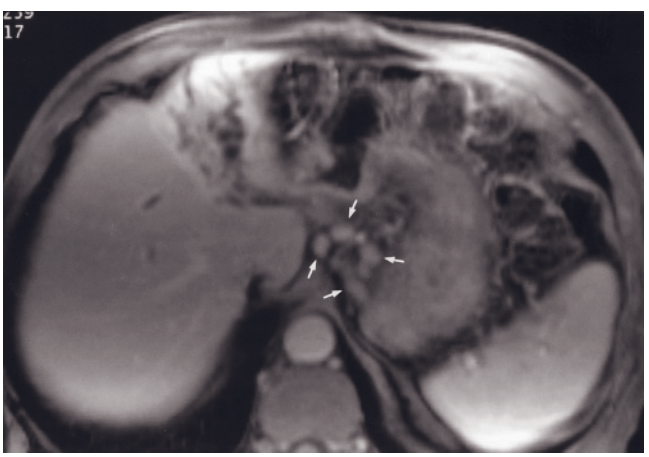

(*c*)

FIG. 3.50 Klatskin tumor, lobar atrophy. T2-weighted single-shot echo-train spin-echo (*a*),T1-weighted GE (*b*), and 2-min postgadolinium fat-suppressed GE (*c*) images. Severe biliary ductal dilatation in the left lobe of the liver is demonstrated on the T2-weighted image (*a*).The liver parenchyma of *segment 4* is atrophic and shows hyperintense signal on the T2-weighted image (*a*) and isointense signal on the T1-weighted image (*b*). Intense enhancement is demonstrated on the late postgadolinium image (*c*), consistent with fibrous changes due to atrophy. Lymph nodes (arrows, *a*, *c*) are visualized with high signal on the T2-weighted (*a*) and the fat-suppressed postgadolinium (*c*) images.

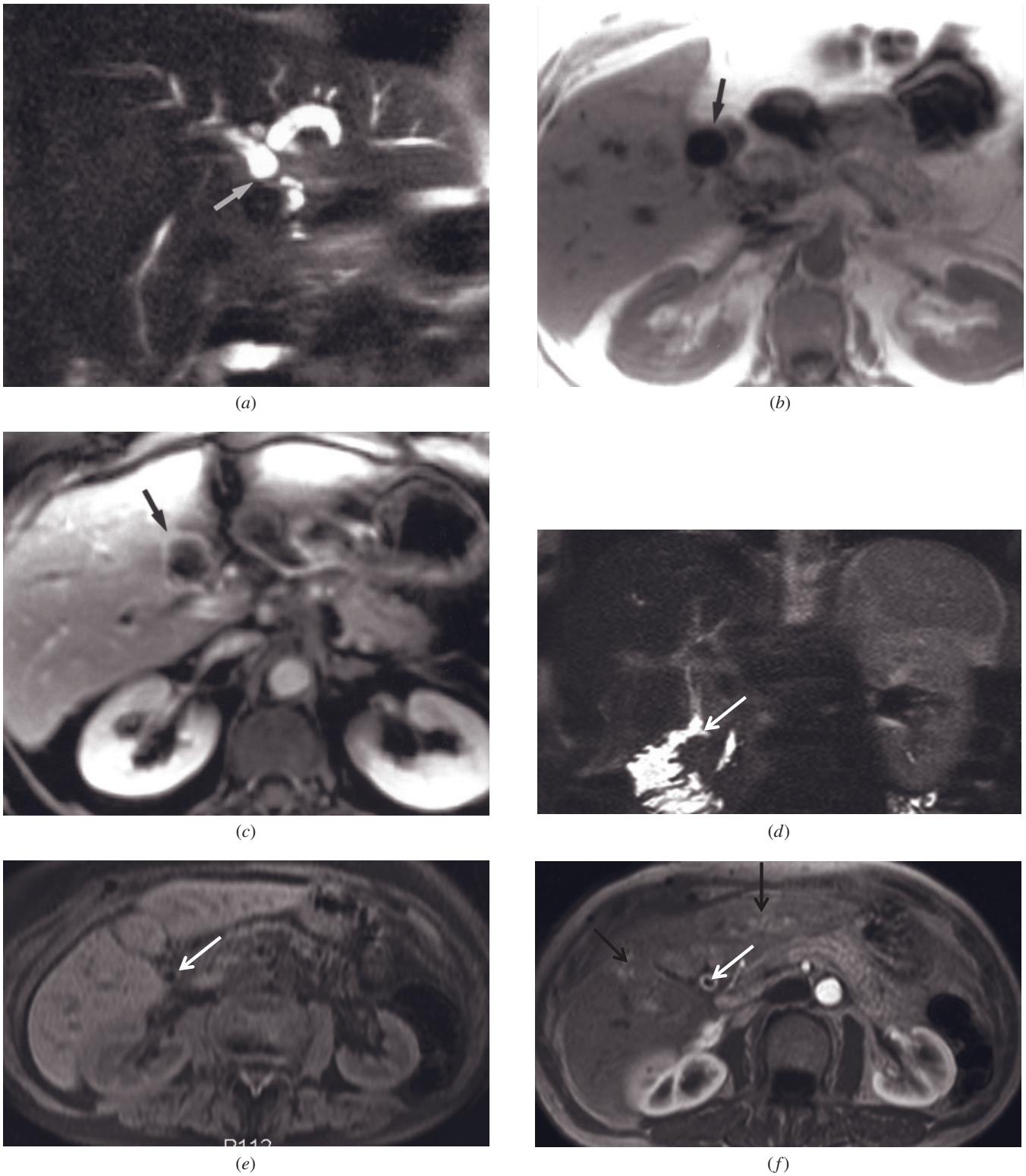

FIG. 3.51 Extrahepatic cholangiocarcinoma. Coronal T2-weighted thin-section MRCP single-shot echo-train spin-echo image with fat suppression (*a*) and transverse T1-weighted GE (*b*) and 2-minute postgadolinium fat-suppressed GE (*c*) images. Obstruction of the proximal CBD (arrow, *a*) is present, showing an abrupt cut-off ("shoulder sign") on the MRCP image (*a*). The intrahepatic biliary tree is markedly dilated (*a*). The extrahepatic cholangiocarcinoma shows circumferential growth along the dilated proximal CBD (arrows, *b*, *c*). On the late postgadolinium image (*c*), the tumor shows intense enhancement (arrow, *c*) and can be differentiated from adjacent liver parenchyma.

Coronal T2-weighted thin-section echo-train spin-echo (*d*), transverse T1-weighted fat-suppressed 3D-GE (*e*), transverse T1-weighted postgadolinium hepatic arterial dominant phase SGE (*f*), and hepatic venous phase fat-suppressed 3D-GE (*g*) images

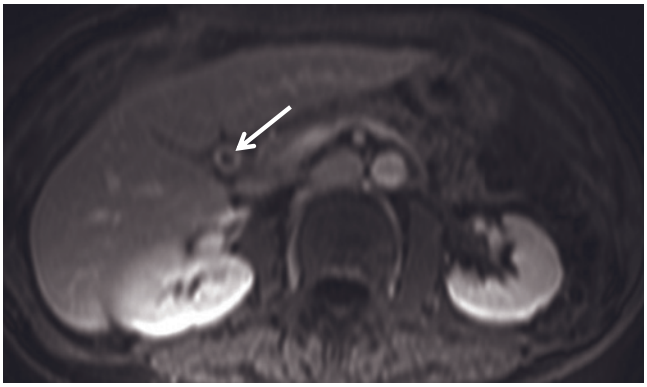

(*g*)

FIG. 3.51 (*Continued*) demonstrate distal common bile duct cholangiocarcinoma (arrows, *d–g*) in another patient. There is a stent in the common bile duct. There is an abrupt angulation and shoulder sign (arrow, *d*) between the common bile duct and duodenum. The common bile duct wall shows thickening and prominent enhancement (arrows, *e*, *f*, *g*), which may result from the involvement of the tumor and inflammation secondary to the stent placement and infectious cholangitis. Intrahepatic bile ducts show prominent enhancement suggestive of ascending cholangitis (black arrows, *f*).

FIG. 3.52 Klatskin tumor and biliary stent. Transverse 2-min postgadolinium fat-suppressed GE image. A biliary stent (white arrow) is present in this patient with Klatskin tumor of the right hepatic duct. The bile duct walls around the stent show intense enhancement that makes differentiation between reactive inflammation caused by the stent placement and tumor spread along the bile duct impossible. *Segment 8* of the liver (open arrow) shows biliary dilatation with increased enhancement of bile duct walls and increased parenchymal enhancement, which may reflect inflammatory changes.

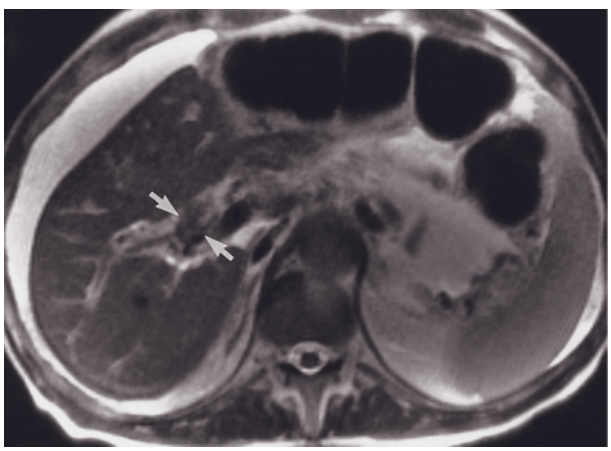

(*a*)

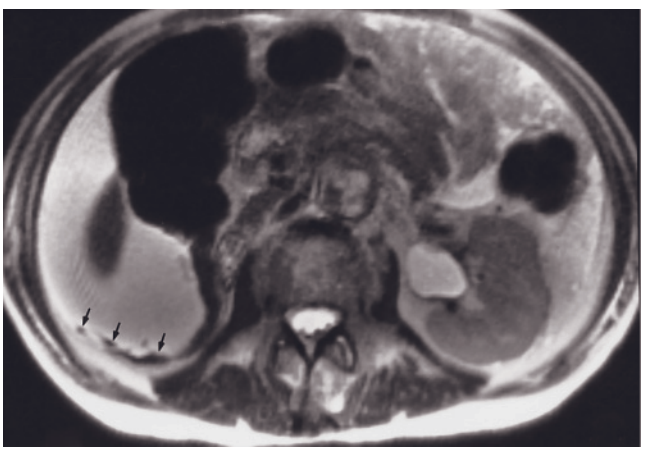

(*b*)

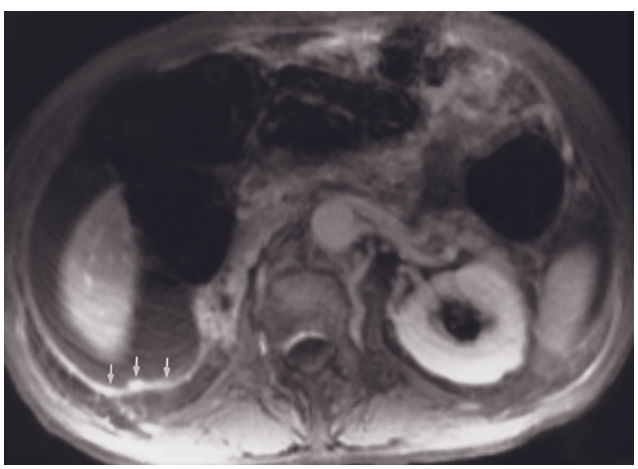

(*c*)

FIG. 3.53 Cholangiocarcinoma with peritoneal metastases. T2-weighted single-shot echo-train spin-echo (*a*, *b*) and 2-min postgadolinium fat-suppressed GE (*c*) images. In the porta hepatis (*a*), a tumor (arrows, *a*) is shown that is isointense compared to liver. Ascites surrounding the liver is demonstrated with high signal on the T2-weighted (*a*, *b*) and low signal on the T1-weighted (*c*) images. More caudally (*b*, *c*), nodular peritoneal implants (arrows, *b*, *c*) are visualized, demonstrating intense enhancement on the 2-min postgadolinium fat-suppressed image (*c*).

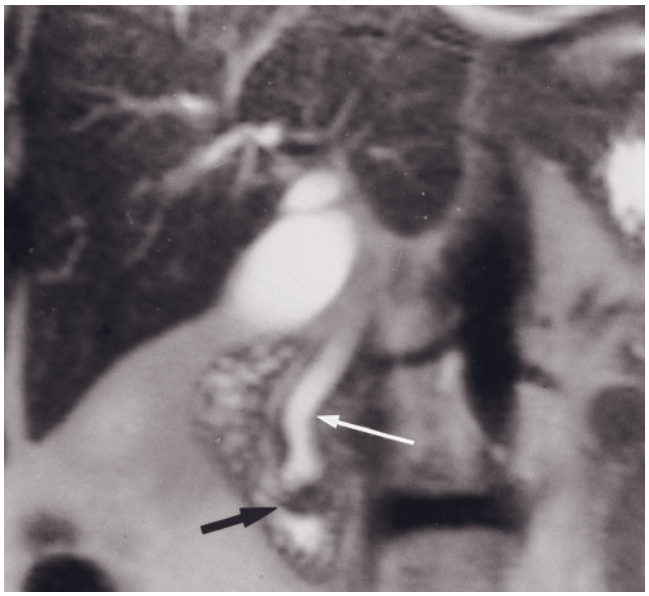

(*a*)

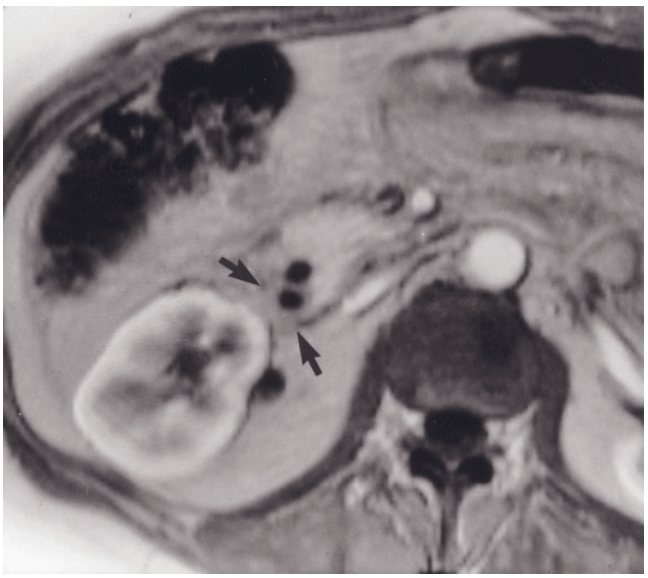

(*b*)

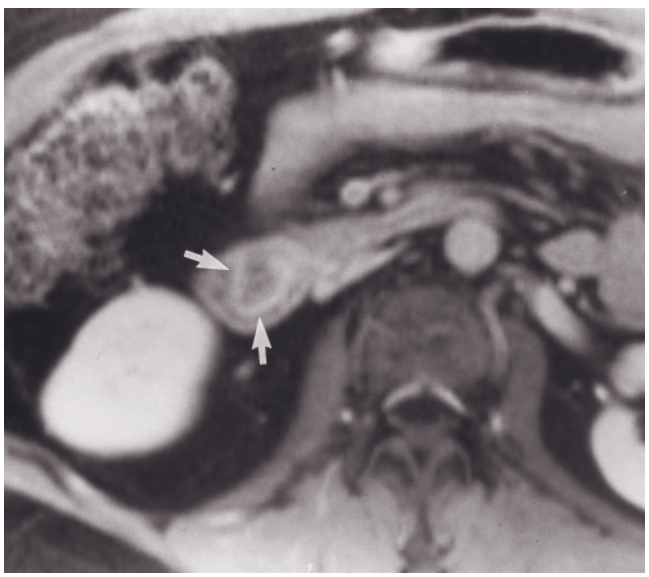

(*c*)

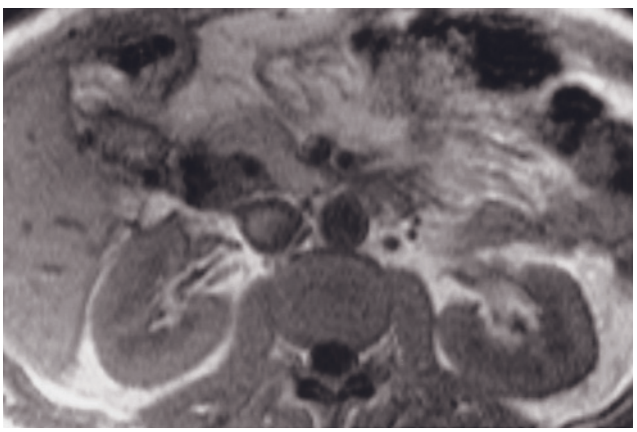

(*d*)

(*e*)

FIG. 3.54 Ampullary carcinoma. Coronal T2-weighted single-shot echo-train spin-echo (*a*), transverse T1-weighted immediate postgadolinium GE (*b*), and 2-min postgadolinium fat-suppressed GE (*c*) images. The ampullary carcinoma (black arrow, *a*) obstructs the CBD (white arrow, *a*), as visualized on the T2-weighted image (*a*). On the immediate postgadolinium image (*b*), the tumor (arrows, *b*) is hypoenhancing compared to normal pancreas and is well delineated. It surrounds the CBD completely and the pancreatic duct partially, which are both dilated and visualized as signal-void structures. Note the peripheral rim enhancement of the tumor (arrows, *c*) on the 2-min postgadolinium image (*c*) on a more inferior section where the tumor protrudes into the duodenum.

T1-weighted GE (*d*) and immediate postgadolinium GE (*e*) images in a second patient demonstrating a 2.5-cm ampullary carcinoma of low signal intensity that shows good contrast against high-signal pancreas on the precontrast image (*d*). The tumor is hypoenhancing compared to pancreatic parenchyma (*e*), surrounds the distal CBD (straight arrow, *e*), and protrudes into the duodenum (curved arrow, *e*).

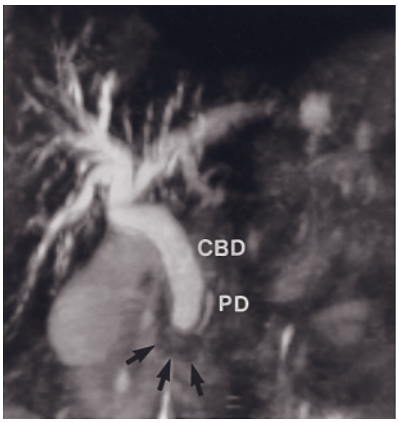

(*a*)

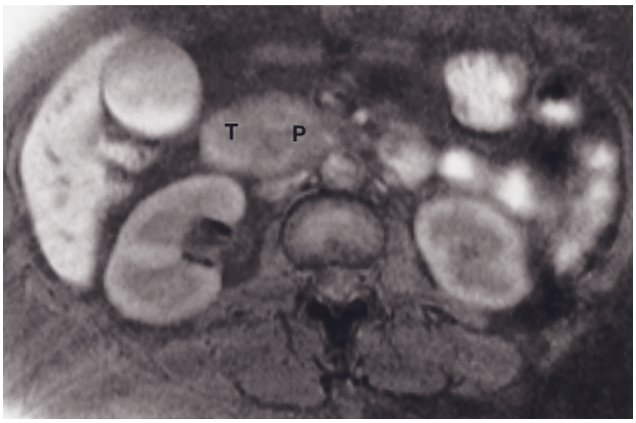

(*b*)

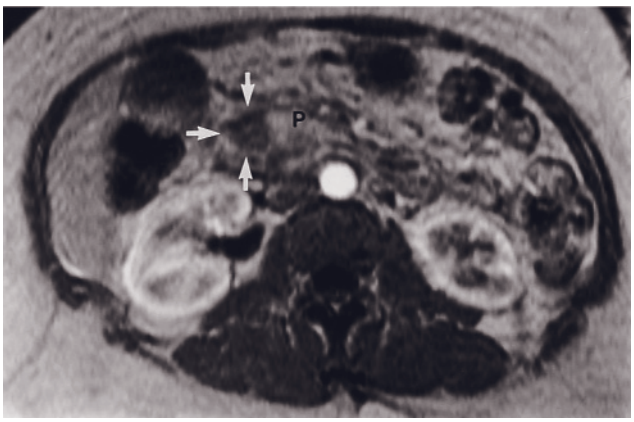

(*c*)

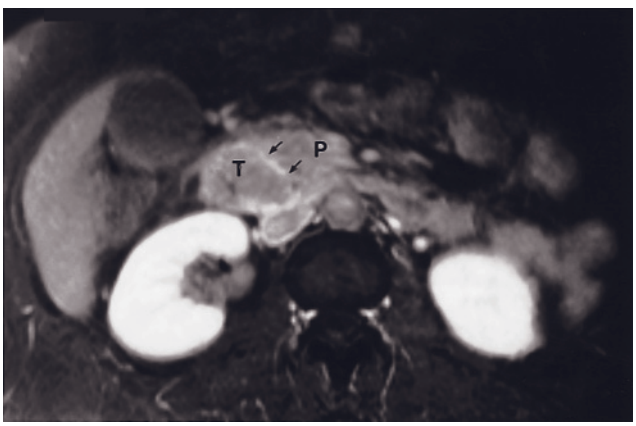

(*d*)

(*e*)

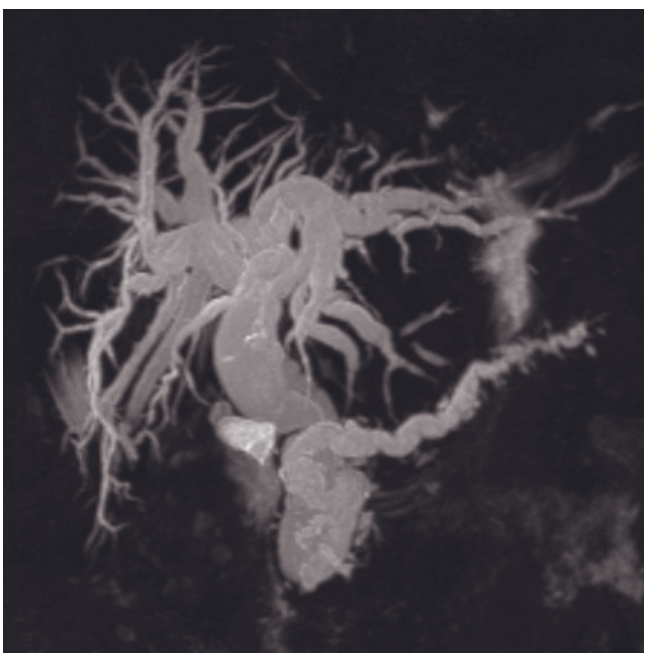

(*f*)

FIG. 3.55 Ampullary carcinoma. Coronal MRCP MIP reconstruction (*a*), T1-weighted fat-suppressed spin-echo (*b*), immediate postgadolinium GE (*c*), and 2-min postgadolinium fat-suppressed spin-echo (*d*) images. On the MRCP image (*a*), an obstructing mass (arrows, *a*) is visualized at the level of the ampulla resulting in severe dilatation of the intra- and extrahepatic biliary system and moderate dilatation of the pancreatic duct. On the precontrast T1-weighted image (*b*), the tumor (T, *b*) cannot be differentiated from the pancreas (P, *b*), which shows abnormal low signal intensity due to pancreatitis. On the immediate postgadolinium image (*c*), the tumor (arrows, *c*) is well visualized, demonstrating decreased enhancement compared to pancreas (P). Note a peripheral rim of enhancement (arrows, *d*) of the tumor on the 2-min postgadolinium image (*d*). CBD, common bile duct; GB, gallbladder; PD, pancreatic duct.

Small ampullary cancer shown on a combination of sequences in a second patient. Source MRCP (*e*), MIP reconstruction 3D-MRCP (*f*), immediate (*g*), and 90-s (*h*) fat-suppressed postgadolinium 3D gradient-echo images. Obstruction at the level of

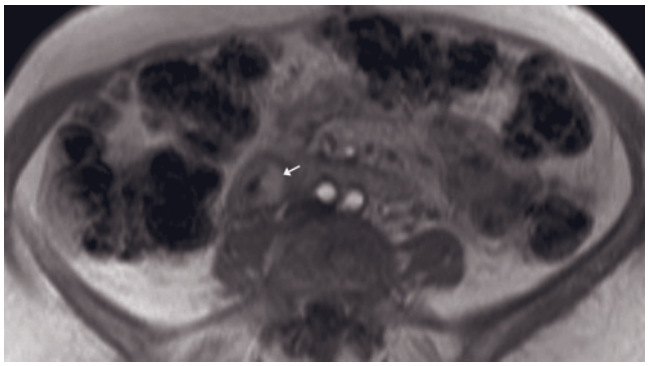

(*g*)

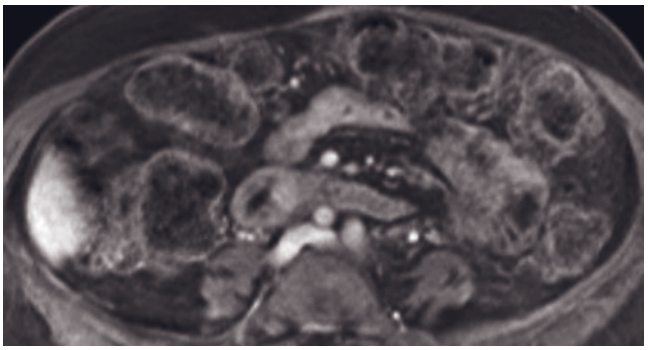

(*h*)

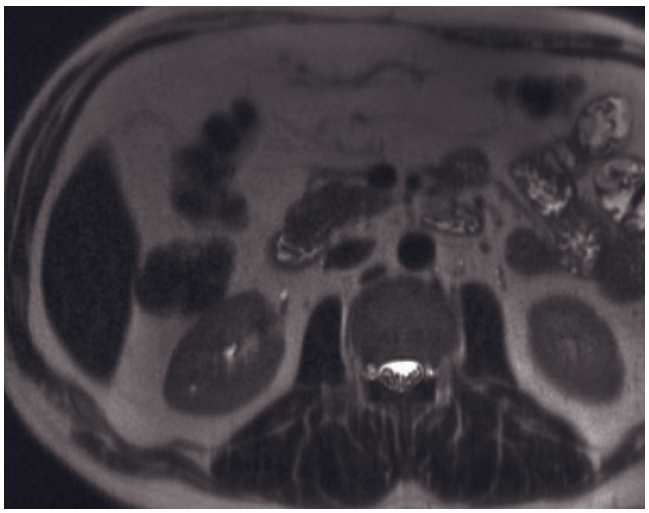

(*i*)

(*j*)

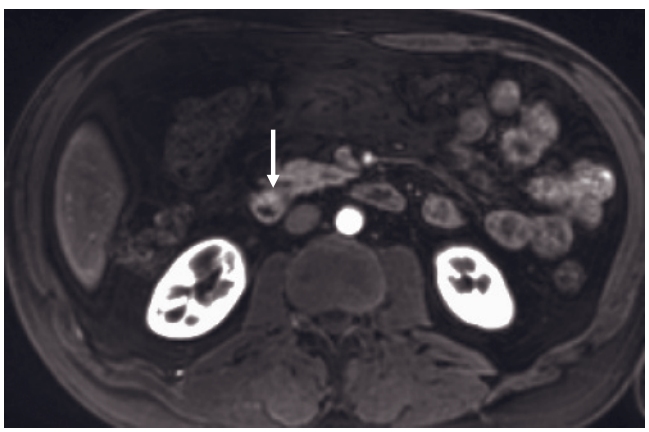

(*k*)

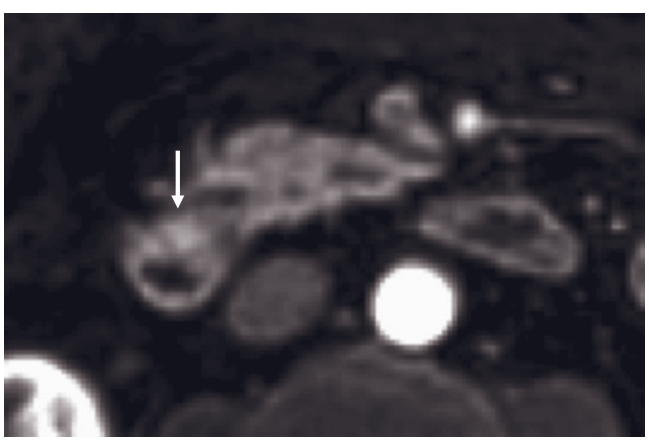

(*l*)

Fig. 3.55 (*Continued*) the ampulla is identified on MRCP images. A small mass is well shown at the ampulla (arrow, *g*) that was not shown at CT or at initial ERCP and biopsy. Ampullary adenocarcinoma was present in the post-Whipple procedure pathological specimen.

Transverse (*i*) T2-weighted single-shot echo-train spin-echo, coronal reconstructed 3D MIP MRCP image (*j*) and transverse T1-weighted postgadolinium hepatic arterial dominant phase fat-suppressed 3D-GE (*k*, *l*) images at 3.0 T demonstrate a small ampullary neuroendocrine carcinoma (arrow, *k*, *l*) in another patient. The enhancing tumor is under 1 cm in size, and it is detected on postgadolinium image because of higher spatial resolution at 3.0 T. Note that the findings are normal on T2-weighted images and there is no biliary obstruction.

(*a*)

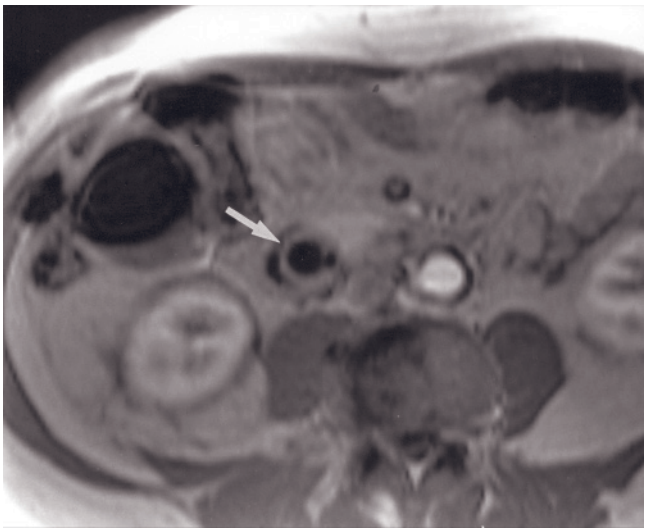

(*b*)

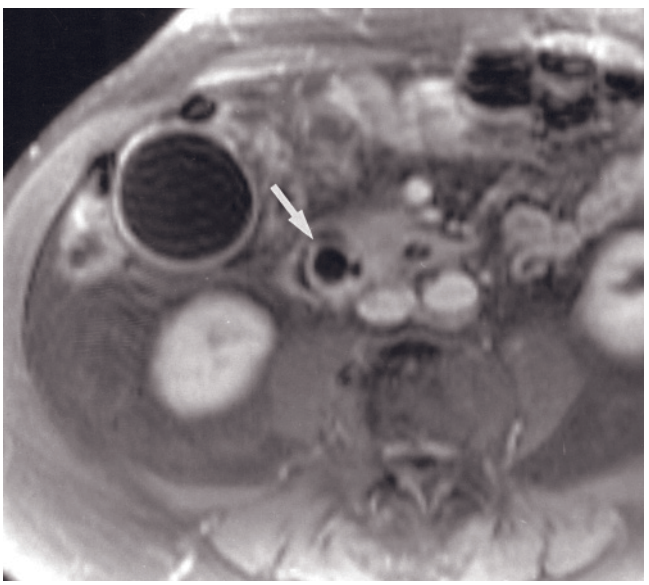

(*c*)

FIG. 3.56 Ampullary carcinoma superimposed on choledochocele. Coronal T2-weighted thin-section MRCP single-shot echo-train spin-echo image with fat suppression (*a*) and transverse immediate postgadolinium T1-weighted GE (*b*) and 2-min postgadolinium fat-suppressed GE (*c*) images in a patient with a choledochocele. The choledochocele (arrows, *a–c*) is visualized protruding into the duodenal lumen, and biliary obstruction with dilated intra- and extrahepatic ducts is observed on the MRCP image (*a*). The walls of the choledochocele are minimally thickened and show moderately intense enhancement on the 2-min postgadolinium image (*c*). On surgical resection, this was found to represent cholangiocarcinoma in the wall of the choledochocele. This patient had sudden development of jaundice and abdominal pain. Sudden development of these symptoms in the absence of stone disease should raise clinical suspicion of malignancy in patients with underlying cystic disease of the biliary tree.

figs. 3.54 and 3.55) [6]. Combining MRCP techniques with T1-weighted precontrast fat-suppressed and immediate and 2-min postgadolinium sequences is a very effective approach for the noninvasive evaluation of biliary obstructions [119]. Periampullary carcinomas may arise in the setting of choledochocele, fostered by long-standing chronic inflammation. A sudden change in clinical status or sudden development of jaundice may indicate the presence of cancer even if the tumor volume is small (fig. 3.56).

Metastases to the Bile Ducts and Ampulla

Metastases to the bile ducts or ampulla may occur in rare instances. Breast cancer, melanoma, and lymphoma are the most common malignancies involved. They result in biliary obstruction and resemble the appearance of primary tumors of the bile ducts and ampulla.

REFERENCES

1. Park MS, Kim TK, Kim KW et al. Differentiation of extrahepatic bile duct cholangiocarcinoma from benign stricture: findings at MRCP versus ERCP. *Radiology* 233(1): 234–240, 2004.
2. Fulcher AS, Turner MA, Capps GW et al. Half-Fourier RARE MR cholangiopancreatography: experience in 300 subjects. *Radiology* 207(1): 21–32, 1998.
3. Holzknecht N, Gauger J, Sackmann M et al. Breath-hold MR cholangiography with snapshot techniques: prospective com-

parison with endoscopic retrograde cholangiography. *Radiology* 206(3): 657–664, 1998.
4. Reinhold C, Taourel P, Bret PM et al. Choledocholithiasis: evaluation of MR cholangiography for diagnosis. *Radiology* 209(2): 435–442, 1998.
5. Guibaud L, Bret PM, Reinhold C et al. Bile duct obstruction and choledocholithiasis: diagnosis with MR cholangiography. *Radiology* 197(1): 109–115, 1995.
6. Taourel P, Bret PM, Reinhold C et al. Anatomic variants of the biliary tree: diagnosis with MR cholangiopancreatography. *Radiology* 199(2): 521–527, 1996.
7. Soto JA, Barish MA, Yucel EK et al. Pancreatic duct: MR cholangiopancreatography with a three-dimensional fast spin-echo technique. *Radiology* 196(2): 459–464, 1995.
8. Hirohashi S, Hirohashi R, Uchida H et al. Pancreatitis: evaluation with MR cholangiopancreatography in children. *Radiology* 203(2): 411–415, 1997.
9. Motohara T, Semelka RC, Bader TR. MR cholangiopancreatography. *Radiol Clin North Am* 41(1): 89–96, 2003.
10. Cohen SA, Siegel JH, Kasmin FE. Complications of diagnostic and therapeutic ERCP. *Abdom Imaging* 21(5): 385–394, 1996.
11. Rieger R, Wayand W. Yield of prospective, noninvasive evaluation of the common bile duct combined with selective ERCP/sphincterotomy in 1390 consecutive laparoscopic cholecystectomy patients. *Gastrointest Endosc* 42(1): 6–12, 1995.
12. Soto JA, Yucel EK, Barish MA et al. MR cholangiopancreatography after unsuccessful or incomplete ERCP. *Radiology* 199(1): 91–98, 1996.
13. Fulcher AS, Turner MA. MR cholangiopancreatography. *Radiol Clin North Am* 40(6): 1363–1376, 2002.
14. Park DH, Kim MH, Lee SS et al. Accuracy of magnetic resonance cholangiopancreatography for locating hepatolithiasis and detecting accompanying biliary strictures. *Endoscopy* 36(11): 987–992, 2004.
15. Ichikawa T, Nitatori T, Hachiya J et al. Breath-held MR cholangiopancreatography with half-averaged single shot hybrid rapid acquisition with relaxation enhancement sequence: comparison of fast GRE and SE sequences. *J Comput Assist Tomogr* 20(5): 798–802, 1996.
16. Hundt W, Petsch R, Scheidler J et al. Clinical evaluation of further-developed MRCP sequences in comparison with standard MRCP sequences. *Eur Radiol* 12(7): 1768–1777, 2002.
17. Takehara Y, Ichijo K, Tooyama N et al. Breath-hold MR cholangiopancreatography with a long-echo-train fast spin-echo sequence and a surface coil in chronic pancreatitis. *Radiology* 192(1): 73–78, 1994.
18. Reinhold C, Guibaud L, Genin G et al. MR cholangiopancreatography: comparison between two-dimensional fast spin-echo and three-dimensional gradient-echo pulse sequences. *J Magn Reson Imaging* 5(4): 379–384, 1995.
19. Hennig J, Nauerth A, Friedburg H. RARE imaging: a fast imaging method for clinical MR. *Magn Reson Med* 3(6): 823–833, 1986.
20. Augui J, Vignaux O, Argaud C et al. Liver: T2-weighted MR imaging with breath-hold fast-recovery optimized fast spin-echo compared with breath-hold half-Fourier and non-breath-hold respiratory-triggered fast spin-echo pulse sequences. *Radiology* 223(3): 853–859, 2002.
21. Regan F, Fradin J, Khazan R et al. Choledocholithiasis: evaluation with MR cholangiography. *AJR Am J Roentgenol* 167(6): 1441–1445, 1996.
22. Miyazaki T, Yamashita Y, Tsuchigame T et al. MR cholangiopancreatography using HASTE (half-Fourier acquisition single-shot turbo spin-echo) sequences. *AJR Am J Roentgenol* 166(6): 1297–1303, 1996.
23. Soto JA, Alvarez O, Munera F et al. Diagnosing bile duct stones: comparison of unenhanced helical CT, oral contrast-enhanced CT cholangiography, and MR cholangiography. *AJR Am J Roentgenol* 175(4): 1127–1134, 2000.
24. Riordan RD, Khonsari M, Jeffries J et al. Pineapple juice as a negative oral contrast agent in magnetic resonance cholangiopancreatography: a preliminary evaluation. *Br J Radiol* 77(924): 991–999, 2004.
25. Lorenzen M, Wedegartner U, Fiehler J et al. [Quality rating of MR-cholangiopancreatography with oral application of iron oxide particles]. *Rofo* 175(7): 936–941, 2003.
26. Sugita R, Nomiya T. Disappearance of the common bile duct signal caused by oral negative contrast agent on MR cholangiopancreatography. *J Comput Assist Tomogr* 26(3): 448–450, 2002.
27. Chavhan GB, Babyn PS, Manson D et al. Pediatric MR cholangiopancreatography: principles, technique, and clinical applications. *Radiographics* 28(7): 1951–1962, 2008.
28. Glockner JF. Hepatobiliary MRI: current concepts and controversies. *J Magn Reson Imaging* 25(4): 681–695, 2007.
29. Semelka RC, Shoenut JP, Greenberg HM et al. The liver. In: Semelka RC, Shoenut JP, editors. *MRI of the Abdomen with CT correlation*. New York: Raven Press, 1993, p. 13–41.
30. Hamm B, Staks T, Muhler A et al. Phase I clinical evaluation of Gd-EOB-DTPA as a hepatobiliary MR contrast agent: safety, pharmacokinetics, and MR imaging. *Radiology* 195(3): 785–792, 1995.
31. Dahlstrom N, Persson A, Albiin N et al. Contrast-enhanced magnetic resonance cholangiography with Gd-BOPTA and Gd-EOB-DTPA in healthy subjects. *Acta Radiol* 48(4): 362–368, 2007.
32. Demas BE, Hricak H, Moseley M et al. Gallbladder bile: an experimental study in dogs using MR imaging and proton MR spectroscopy. *Radiology* 157(2): 453–455, 1985.
33. Macaulay SE, Schulte SJ, Sekijima JH et al. Evaluation of a non-breath-hold MR cholangiography technique. *Radiology* 196(1): 227–232, 1995.
34. Limanond P, Raman SS, Ghobrial RM et al. The utility of MRCP in preoperative mapping of biliary anatomy in adult-to-adult living related liver transplant donors. *J Magn Reson Imaging* 19(2): 209–215, 2004.
35. Strasberg SM, Hertl M, Soper NJ. An analysis of the problem of biliary injury during laparoscopic cholecystectomy. *J Am Coll Surg* 180(1): 101–125, 1995.
36. Hirao K, Miyazaki A, Fujimoto T et al. Evaluation of aberrant bile ducts before laparoscopic cholecystectomy: helical CT cholangiography versus MR cholangiography. *AJR Am J Roentgenol* 175(3): 713–720, 2000.
37. Soper NJ, Brunt LM. The case for routine operative cholangiography during laparoscopic cholecystectomy. *Surg Clin North Am* 74(4): 953–959, 1994.
38. Sterling JA. The common channel for bile and pancreatic ducts. *Surg Gynecol Obstet* 98(4): 420–424, 1954.
39. David V, Reinhold C, Hochman M et al. Pitfalls in the interpretation of MR cholangiopancreatography. *AJR Am J Roentgenol* 170(4): 1055–1059, 1998.
40. Fulcher AS, Turner MA, Ham JM. Late biliary complications in right lobe living donor transplantation recipients: imaging findings and therapeutic interventions. *J Comput Assist Tomogr* 26(3): 422–427, 2002.
41. Moeser PM, Julian S, Karstaedt N et al. Unusual presentation of cholelithiasis on T1-weighted MR imaging. *J Comput Assist Tomogr* 12(1): 150–152, 1988.
42. Baron RL, Shuman WP, Lee SP et al. MR appearance of gallstones in vitro at 1.5T: correlation with chemical composition. *AJR Am J Roentgenol* 153(3): 497–502, 1989.
43. Dell LA, Brown MS, Orrison WW et al. Physiologic intracranial calcification with hyperintensity on MR imaging: case report and experimental model. *AJNR Am J Neuroradiol* 9(6): 1145–1148, 1988.

44. Bangert BA, Modic MT, Ross JS et al. Hyperintense disks on T1-weighted MR images: correlation with calcification. *Radiology* 195(2): 437–443, 1995.
45. Hakansson K, Leander P, Ekberg O et al. MR imaging in clinically suspected acute cholecystitis. A comparison with ultrasonography. *Acta Radiol* 41(4): 322–328, 2000.
46. Altun E, Semelka RC, Elias J, Jr. et al. Acute cholecystitis: MR findings and differentiation from chronic cholecystitis. *Radiology* 244(1): 174–183, 2007.
47. Loud PA, Semelka RC, Kettritz U et al. MRI of acute cholecystitis: comparison with the normal gallbladder and other entities. *Magn Reson Imaging* 14(4): 349–355, 1996.
48. Semelka RC, Shoenut JP, Micflikier AB et al. The gallbladder and biliary tree. In: Semelka RC, Shoenut JP, editors. *MRI of the Abdomen with CT correlation.* New York: Raven Press, 1993, pp. 43–52.
49. Kelekis NL, Semelka RC. MR imaging of the gallbladder. *Top Magn Reson Imaging* 8(5): 312–320, 1996.
50. Chun KA, Ha HK, Yu ES et al. Xanthogranulomatous cholecystitis: CT features with emphasis on differentiation from gallbladder carcinoma. *Radiology* 203(1): 93–97, 1997.
51. Furuta A, Ishibashi T, Takahashi S et al. MR imaging of xanthogranulomatous cholecystitis. *Radiat Med* 14(6): 315–319, 1996.
52. Roa I, Araya JC, Villaseca M et al. Preneoplastic lesions and gallbladder cancer: an estimate of the period required for progression. *Gastroenterology* 111(1): 232–236, 1996.
53. Chijiiwa K, Tanaka M. Polypoid lesion of the gallbladder: indications of carcinoma and outcome after surgery for malignant polypoid lesion. *Int Surg* 79(2): 106–109, 1994.
54. Kubota K, Bandai Y, Noie T et al. How should polypoid lesions of the gallbladder be treated in the era of laparoscopic cholecystectomy? *Surgery* 117(5): 481–487, 1995.
55. Yoshimitsu K, Honda H, Jimi M et al. MR diagnosis of adenomyomatosis of the gallbladder and differentiation from gallbladder carcinoma: importance of showing Rokitansky-Aschoff sinuses. *AJR Am J Roentgenol* 172(6): 1535–1540, 1999.
56. Haradome H, Ichikawa T, Sou H et al. The pearl necklace sign: an imaging sign of adenomyomatosis of the gallbladder at MR cholangiopancreatography. *Radiology* 227(1): 80–88, 2003.
57. Kim MJ, Oh YT, Park YN et al. Gallbladder adenomyomatosis: findings on MRI. *Abdom Imaging* 24(4): 410–413, 1999.
58. Rooholamini SA, Tehrani NS, Razavi MK et al. Imaging of gallbladder carcinoma. *Radiographics* 14(2): 291–306, 1994.
59. Towfigh S, McFadden DW, Cortina GR et al. Porcelain gallbladder is not associated with gallbladder carcinoma. *Am Surg* 67(1): 7–10, 2001.
60. Roa I, Araya JC, Villaseca M et al. Gallbladder cancer in a high risk area: morphological features and spread patterns. *Hepatogastroenterology* 46(27): 1540–1546, 1999.
61. Schwartz LH, Black J, Fong Y et al. Gallbladder carcinoma: findings at MR imaging with MR cholangiopancreatography. *J Comput Assist Tomogr* 26(3): 405–410, 2002.
62. Sagoh T, Itoh K, Togashi K et al. Gallbladder carcinoma: evaluation with MR imaging. *Radiology* 174(1): 131–136, 1990.
63. Rossmann MD, Friedman AC, Radecki PD et al. MR imaging of gallbladder carcinoma. *AJR Am J Roentgenol* 148(1): 143–144, 1987.
64. Demachi H, Matsui O, Hoshiba K et al. Dynamic MRI using a surface coil in chronic cholecystitis and gallbladder carcinoma: radiologic and histopathologic correlation. *J Comput Assist Tomogr* 21(4): 643–651, 1997.
65. Czako L, Takacs T, Morvay Z et al. Diagnostic role of secretin-enhanced MRCP in patients with unsuccessful ERCP. *World J Gastroenterol* 10(20): 3034–3038, 2004.
66. Khalid TR, Casillas VJ, Montalvo BM et al. Using MR cholangiopancreatography to evaluate iatrogenic bile duct injury. *AJR Am J Roentgenol* 177(6): 1347–1352, 2001.
67. Pasanen P, Partanen K, Pikkarainen P et al. Ultrasonography, CT, and ERCP in the diagnosis of choledochal stones. *Acta Radiol* 33(1): 53–56, 1992.
68. O'Connor HJ, Hamilton I, Ellis WR et al. Ultrasound detection of choledocholithiasis: prospective comparison with ERCP in the postcholecystectomy patient. *Gastrointest Radiol* 11(2): 161–164, 1986.
69. Cronan JJ. US diagnosis of choledocholithiasis: a reappraisal. *Radiology* 161(1): 133–134, 1986.
70. Stott MA, Farrands PA, Guyer PB et al. Ultrasound of the common bile duct in patients undergoing cholecystectomy. *J Clin Ultrasound* 19(2): 73–76, 1991.
71. Cotton PB, Lehman G, Vennes J et al. Endoscopic sphincterotomy complications and their management: an attempt at consensus. *Gastrointest Endosc* 37(3): 383–393, 1991.
72. Halme L, Doepel M, von Numers H et al. Complications of diagnostic and therapeutic ERCP. *Ann Chir Gynaecol* 88(2): 127–131, 1999.
73. Mehta SN, Pavone E, Barkun AN. Outpatient therapeutic ERCP: a series of 262 consecutive cases. *Gastrointest Endosc* 44(4): 443–449, 1996.
74. Duncan HD, Hodgkinson L, Deakin M et al. The safety of diagnostic and therapeutic ERCP as a daycase procedure with a selective admission policy. *Eur J Gastroenterol Hepatol* 9(9): 905–908, 1997.
75. Loperfido S, Angelini G, Benedetti G et al. Major early complications from diagnostic and therapeutic ERCP: a prospective multicenter study. *Gastrointest Endosc* 48(1): 1–10, 1998.
76. NIH. State-of-the-science statement on endoscopic retrograde cholangiopancreatography (ERCP) for diagnosis and therapy. *NIH Consens State Sci Statements* 19(1): 1–26, 2002.
77. Tang Y, Yamashita Y, Arakawa A et al. Pancreaticobiliary ductal system: value of half-Fourier rapid acquisition with relaxation enhancement MR cholangiopancreatography for postoperative evaluation. *Radiology* 215(1): 81–88, 2000.
78. Topal B, Van de Moortel M, Fieuws S et al. The value of magnetic resonance cholangiopancreatography in predicting common bile duct stones in patients with gallstone disease. *Br J Surg* 90(1): 42–47, 2003.
79. Kim TK, Kim BS, Kim JH et al. Diagnosis of intrahepatic stones: superiority of MR cholangiopancreatography over endoscopic retrograde cholangiopancreatography. *AJR Am J Roentgenol* 179(2): 429–434, 2002.
80. Soto JA, Barish MA, Alvarez O et al. Detection of choledocholithiasis with MR cholangiography: comparison of three-dimensional fast spin-echo and single- and multisection half-Fourier rapid acquisition with relaxation enhancement sequences. *Radiology* 215(3): 737–745, 2000.
81. Sugita R, Sugimura E, Itoh M et al. Pseudolesion of the bile duct caused by flow effect: a diagnostic pitfall of MR cholangiopancreatography. *AJR Am J Roentgenol* 180(2): 467–471, 2003.
82. Irie H, Honda H, Kuroiwa T et al. Pitfalls in MR cholangiopancreatographic interpretation. *Radiographics* 21(1): 23–37, 2001.
83. Shaikh F, Elazzazi M, Ryan A, Semelka RC. Debris-filled biliary system: a difficult diagnosis on MRI and MRCP. *Magn Reson Imaging* 2009, Submitted.
84. Takehara Y. Fast MR imaging for evaluating the pancreaticobiliary system. *Eur J Radiol* 29(3): 211–232, 1999.
85. Kim JH, Kim MJ, Park SI et al. Using kinematic MR cholangiopancreatography to evaluate biliary dilatation. *AJR Am J Roentgenol* 178(4): 909–914, 2002.
86. Mariani A, Curioni S, Zanello A et al. Secretin MRCP and endoscopic pancreatic manometry in the evaluation of sphincter of Oddi function: a comparative pilot study in patients with idiopathic recurrent pancreatitis. *Gastrointest Endosc* 58(6): 847–852, 2003.

87. Hosoki T, Hasuike Y, Takeda Y et al. Visualization of pancreaticobiliary reflux in anomalous pancreaticobiliary junction by secretin-stimulated dynamic magnetic resonance cholangiopancreatography. *Acta Radiol* 45(4): 375–382, 2004.
88. Matos C, Metens T, Deviere J et al. Pancreatic duct: morphologic and functional evaluation with dynamic MR pancreatography after secretin stimulation. *Radiology* 203(2): 435–441, 1997.
89. Sherlock S. Pathogenesis of sclerosing cholangitis: the role of nonimmune factors. *Semin Liver Dis* 11(1): 5–10, 1991.
90. Textor HJ, Flacke S, Pauleit D et al. Three-dimensional magnetic resonance cholangiopancreatography with respiratory triggering in the diagnosis of primary sclerosing cholangitis: comparison with endoscopic retrograde cholangiography. *Endoscopy* 34(12): 984–990, 2002.
91. Beuers U, Spengler U, Sackmann M et al. Deterioration of cholestasis after endoscopic retrograde cholangiography in advanced primary sclerosing cholangitis. *J Hepatol* 15(1-2): 140–143, 1992.
92. Ernst O, Asselah T, Sergent G et al. MR cholangiography in primary sclerosing cholangitis. *AJR Am J Roentgenol* 171(4): 1027–1030, 1998.
93. Fulcher AS, Turner MA, Franklin KJ et al. Primary sclerosing cholangitis: evaluation with MR cholangiography—a case-control study. *Radiology* 215(1): 71–80, 2000.
94. Bader TR, Beavers KL, Semelka RC. MR imaging features of primary sclerosing cholangitis: patterns of cirrhosis in relationship to clinical severity of disease. *Radiology* 226(3): 675–685, 2003.
95. Semelka RC, Shoenut JP, Kroeker MA et al. Bile duct disease: prospective comparison of ERCP, CT, and fat suppression MRI. *Gastrointest Radiol* 17(4): 347–352, 1992.
96. Revelon G, Rashid A, Kawamoto S et al. Primary sclerosing cholangitis: MR imaging findings with pathologic correlation. *AJR Am J Roentgenol* 173(4): 1037–1042, 1999.
97. Ito K, Mitchell DG, Outwater EK et al. Primary sclerosing cholangitis: MR imaging features. *AJR Am J Roentgenol* 172(6): 1527–1533, 1999.
98. LaRusso NF, Wiesner RH, Ludwig J et al. Current concepts. Primary sclerosing cholangitis. *N Engl J Med* 310(14): 899–903, 1984.
99. Balthazar EJ, Birnbaum BA, Naidich M. Acute cholangitis: CT evaluation. *J Comput Assist Tomogr* 17(2): 283–289, 1993.
100. Bader TR, Braga L, Beavers KL et al. MR imaging findings of infectious cholangitis. *Magn Reson Imaging* 19(6): 781–788, 2001.
101. Kim MJ, Cha SW, Mitchell DG et al. MR imaging findings in recurrent pyogenic cholangitis. *AJR Am J Roentgenol* 173(6): 1545–1549, 1999.
102. Miller FH, Gore RM, Nemcek AA, Jr. et al. Pancreaticobiliary manifestations of AIDS. *AJR Am J Roentgenol* 166(6): 1269–1274, 1996.
103. Matos C, Nicaise N, Deviere J et al. Choledochal cysts: comparison of findings at MR cholangiopancreatography and endoscopic retrograde cholangiopancreatography in eight patients. *Radiology* 209(2): 443–448, 1998.
104. Todani T, Watanabe Y, Narusue M et al. Congenital bile duct cysts: classification, operative procedures, and review of thirty-seven cases including cancer arising from choledochal cyst. *Am J Surg* 134(2): 263–269, 1977.
105. Pavone P, Laghi A, Catalano C et al. Caroli's disease: evaluation with MR cholangiopancreatography (MRCP). *Abdom Imaging* 21(2): 117–119, 1996.
106. Lillemoe KD, Pitt HA, Cameron JL. Current management of benign bile duct strictures. *Adv Surg* 25: 119–174, 1992.
107. Laghi A, Pavone P, Catalano C et al. MR cholangiography of late biliary complications after liver transplantation. *AJR Am J Roentgenol* 172(6): 1541–1546, 1999.
108. Coakley FV, Schwartz LH, Blumgart LH et al. Complex postcholecystectomy biliary disorders: preliminary experience with evaluation by means of breath-hold MR cholangiography. *Radiology* 209(1): 141–146, 1998.
109. Pavone P, Laghi A, Catalano C et al. MR cholangiography in the examination of patients with biliary-enteric anastomoses. *AJR Am J Roentgenol* 169(3): 807–811, 1997.
110. Soyer P, Bluemke DA, Reichle R et al. Imaging of intrahepatic cholangiocarcinoma. 1. Peripheral cholangiocarcinoma. *AJR Am J Roentgenol* 165(6): 1427–1431, 1995.
111. Soyer P, Bluemke DA, Reichle R et al. Imaging of intrahepatic cholangiocarcinoma. 2. Hilar cholangiocarcinoma. *AJR Am J Roentgenol* 165(6): 1433–1436, 1995.
112. Hamrick-Turner J, Abbitt PL, Ros PR. Intrahepatic cholangiocarcinoma: MR appearance. *AJR Am J Roentgenol* 158(1): 77–79, 1992.
113. Worawattanakul S, Semelka RC, Noone TC et al. Cholangiocarcinoma: spectrum of appearances on MR images using current techniques. *Magn Reson Imaging* 16(9): 993–1003, 1998.
114. Soyer P. Capsular retraction of the liver in malignant tumor of the biliary tract MRI findings. *Clin Imaging* 18(4): 255–257, 1994.
115. Fulcher AS, Turner MA. HASTE MR cholangiography in the evaluation of hilar cholangiocarcinoma. *AJR Am J Roentgenol* 169(6): 1501–1505, 1997.
116. Yamaguchi K, Enjoji M. Carcinoma of the ampulla of Vater. A clinicopathologic study and pathologic staging of 109 cases of carcinoma and 5 cases of adenoma. *Cancer* 59(3): 506–515, 1987.
117. Irie H, Honda H, Shinozaki K et al. MR imaging of ampullary carcinomas. *J Comput Assist Tomogr* 26(5): 711–717, 2002.
118. Semelka RC, Kelekis NL, John G et al. Ampullary carcinoma: demonstration by current MR techniques. *J Magn Reson Imaging* 7(1): 153–156, 1997.
119. Pavone P, Laghi A, Passariello R. MR cholangiopancreatography in malignant biliary obstruction. *Semin Ultrasound CT MR* 20(5): 317–323, 1999.

CHAPTER 4

PANCREAS

ERSAN ALTUN, JORGE ELIAS, JR., DIANE ARMAO, BUSAKORN VACHIRANUBHAP, AND RICHARD C. SEMELKA

> When health is absent, wisdom cannot reveal itself, art cannot manifest, strength cannot fight, wealth becomes useless, and intelligence cannot be applied.
>
> Herophilus, Greek anatomist, credited with the discovery of the pancreas, meaning "all flesh," in 336 B.C.

NORMAL ANATOMY

The pancreas is a soft, fleshy, lobulated gland retroperitoneally located against the posterior body wall. The anatomic divisions of the pancreas include the head, uncinate process, neck, body, and tail. The broad head is embraced by the curve of the duodenum. An extension of the head, the uncinate process hooks behind the superior mesenteric artery and vein. The border between the head and body is a slightly narrowed region, the neck. On the posterior aspect of the neck is a shallow groove marking the passage of the superior mesenteric vein and the beginning of the portal vein. The body is oriented in an oblique fashion extending to the right of midline, and the tail is located in the region of the splenic hilum. The anatomic relationship of the head of the pancreas includes the second portion of the duodenum laterally, the gastroduodenal artery anteriorly, the inferior vena cava posterolaterally, the third portion of the duodenum posteroinferiorly, and the superior mesenteric vessels medially.

The splenic vein lies along the posterior surface of the body and tail of the pancreas. This constant relationship is an important landmark for the identification of the pancreatic body. The left adrenal gland is seated posterior to the splenic vein. The tail of the pancreas often drapes over the left kidney and terminates in the splenic hilum. The tail may be folded anteriorly over the body of the pancreas. The stomach lies anterior to the pancreas and is separated from it by parietal peritoneum and the lesser sac. The transverse mesocolon forms the inferior boundary of the lesser sac and is formed by the fusion of leaves of the parietal peritoneum, which covers the anterior surface of the pancreas. The lesser sac and transverse mesocolon are common pathways for the tracking and accumulation of fluid in acute pancreatitis.

In elderly patients, fatty replacement of the pancreas occurs frequently as a normal degenerative process

Abdominal-Pelvic MRI, Third Edition, edited by Richard C. Semelka. Copyright © 2010 John Wiley & Sons, Inc.

and results in a feathery, lobulated appearance on imaging. The posterior aspect of the pancreas does not have a serosal covering, which accounts for the extensive dissemination of fluid in pancreatitis and the early spread of pancreatic ductal cancer into retroperitoneal fat.

The pancreatic duct measures 1–2 mm in diameter in normal subjects. Although considerable variation in the size of the head occurs, the normal pancreatic head is 2–2.5 cm in diameter, with the remainder of the gland approximately 1–2 cm thick. The main pancreatic duct extends from the tail of the pancreas through the head and empties via the sphincter of Oddi into the second part of the duodenum at the major papilla. The main duct is termed the duct of Wirsung. A smaller accessory duct, the duct of Santorini, is frequently present, extends from the body of the pancreas through the neck, and enters separately into the duodenum in a more proximal location at the minor papilla.

The pancreas is a mixed exocrine and endocrine gland. The main mass of pancreatic microstructure is exocrine in nature, composed of acinar cells, which store and release digestive enzymes. Embedded in acinar tissue are small, scattered islets of Langerhans composed of endocrine cells, which synthesize hormones. The major hormones released by the pancreas are insulin and glucagon.

MRI TECHNIQUE

New MRI techniques that limit artifacts in the abdomen have increased the role of MRI in detection and characterization of pancreatic disease. Breath-hold T1 weighted gradient-echo sequences obtained either as 2D or 3D gradient echo, fat suppression techniques, and dynamic administration of gadolinium chelate have resulted in image quality of the pancreas sufficient to detect and characterize focal pancreatic mass lesions smaller than 1 cm in diameter, and to evaluate diffuse pancreatic disease [1–4]. The use of high spatial resolution MR imaging at 3.0 T improves the detection of small focal lesions particularly.

MR cholangiopancreatography (MRCP) permits good demonstration of the biliary and pancreatic ducts to assess ductal obstruction, dilatation, and abnormal duct pathways [5–7]. The combination of tissue-imaging sequences and MRCP provides comprehensive information to evaluate the full range of pancreatic disease.

MRI of the pancreas is optimal at high field (1.5 T or 3.0 T) because of a good signal-to-noise (S/N) ratio, which facilitates breath-hold imaging, and increased fat-water frequency shift, which facilitates chemically selective excitation-spoiling fat suppression or water excitation. T1-weighted chemically selective fat suppression and T1-weighted breath-hold gradient echo are effective techniques for imaging pancreatic parenchyma. The highest image quality of the pancreas is achieved with imaging at 3.0 T [8]. The combination of higher signal to noise ratio, greater spectral separation, and increased sensitivity to gadolinium results in the acquisition of images with high quality, and high spatial and temporal resolution. Particularly, the image quality of postgadolinium sequences is superb at 3.0 T. This allows for improved detection and characterization of very small lesions [8]. The normal pancreas is high in signal intensity on T1-weighted fat-suppressed images because of the presence of aqueous protein in the acini of the pancreas [1]. Normal pancreas is well shown with this technique (fig. 4.1) [9, 10]. In elderly patients, the signal intensity of the pancreas may diminish and be lower than that of liver [2]. This may reflect changes of fibrosis secondary to the aging process.

Our standard MR protocol includes T1-weighted fat-suppressed gradient-echo and postgadolinium imaging in the capillary phase (immediate postcontrast, hepatic arterial dominant phase) and interstitial phase (1–10 min postcontrast) [4]. There may be advantages in performing postgadolinium gradient-echo imaging as a 3D gradient-echo technique for the following reasons: a) thinner sections can be obtained (3 mm vs. 5 mm for 2D-SGE) and b) the absence of mirror artifact from the aorta, which is problematic on 2D-SGE. T2-weighted echo-train spin-echo sequences such as T2-weighted half-Fourier acquisition snapshot turbo spin-echo (HASTE) provide a sharp anatomic display of the common bile duct (CBD) on coronal plane images and of the pancreatic duct on transverse plane images. MRCP images can be acquired oriented in the plane of the pancreatic duct, in an oblique coronal projection, to delineate longer segments of the pancreatic duct in continuity [11]. T2-weighted fat-suppressed images are useful for demonstrating liver metastases and islet cell tumors. T2-weighted images also provide information on the complexity of the fluid in pancreatic pseudocysts, which may reflect the presence of complications such as necrotic debris or infection. Regarding gadolinium enhancement, the pancreas demonstrates a uniform capillary blush on immediate postcontrast images, which renders it markedly higher in signal intensity than liver, neighboring bowel, and adjacent fat (fig. 4.2) [4]. By 1 min after contrast the pancreas shows approximately isointense signal with fat on non-fat-suppressed T1-weighted SGE, and moderately higher signal than background fat on fat-suppressed SGE or 3D-GE sequences (see fig. 4.1). Pancreatic head is readily distinguished from duodenum or adjacent bowel on immediate post-gadolinium images

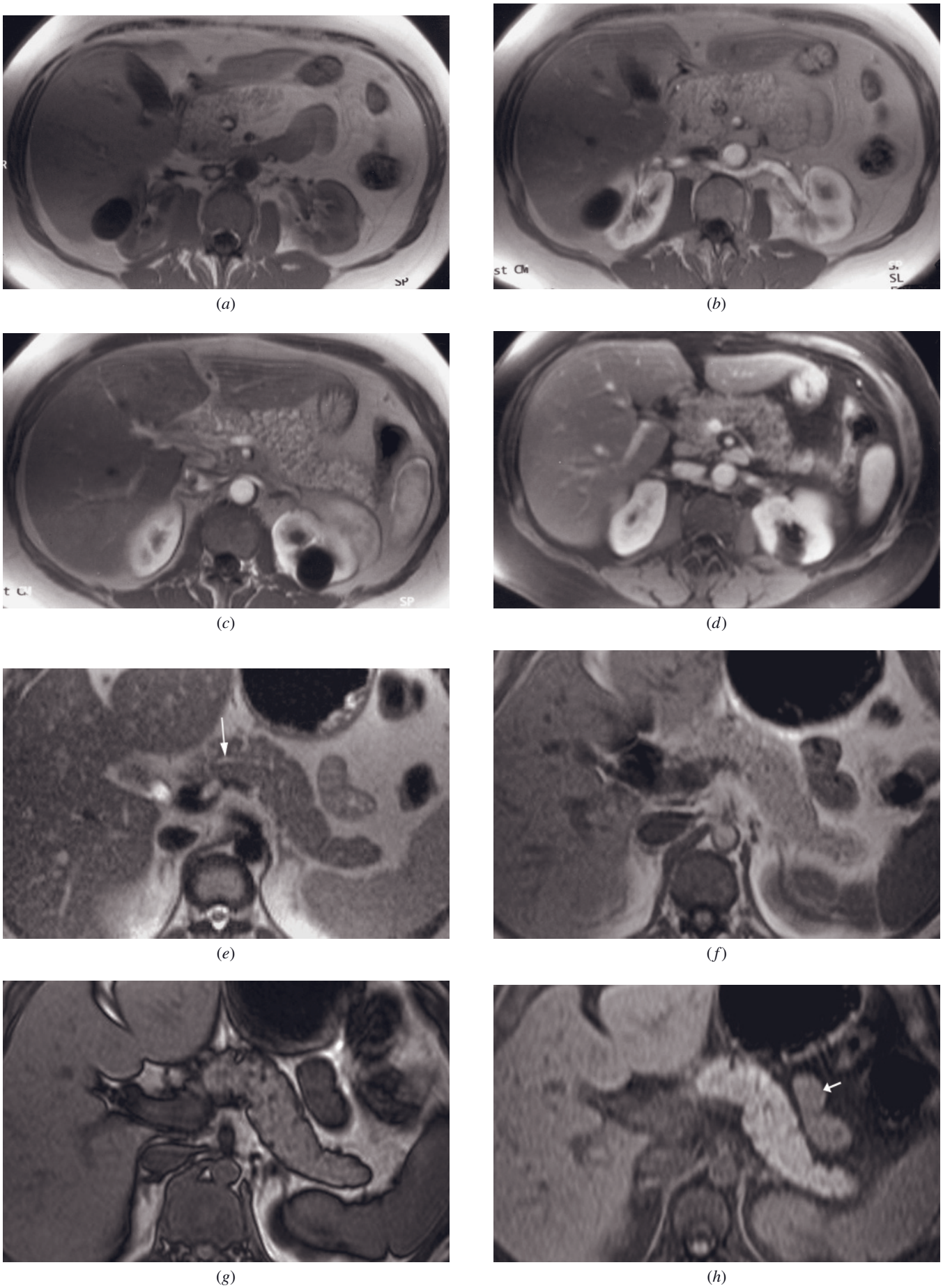

FIG. 4.1 Normal pancreas. T1-weighted SGE (*a*), immediate postgadolinium T1-weighted SGE (*b*, *c*), and 90-s postgadolinium fat-suppressed SGE (*d*) images. The pancreas has a marbled appearance, which is a normal finding associated with aging.

T2-weighted SS-ETSE (*e*), in-phase (*f*) and out-of-phase (*g*) T1-weighted gradient-echo, fat-suppressed T1-weighted gradient-echo (*h*),

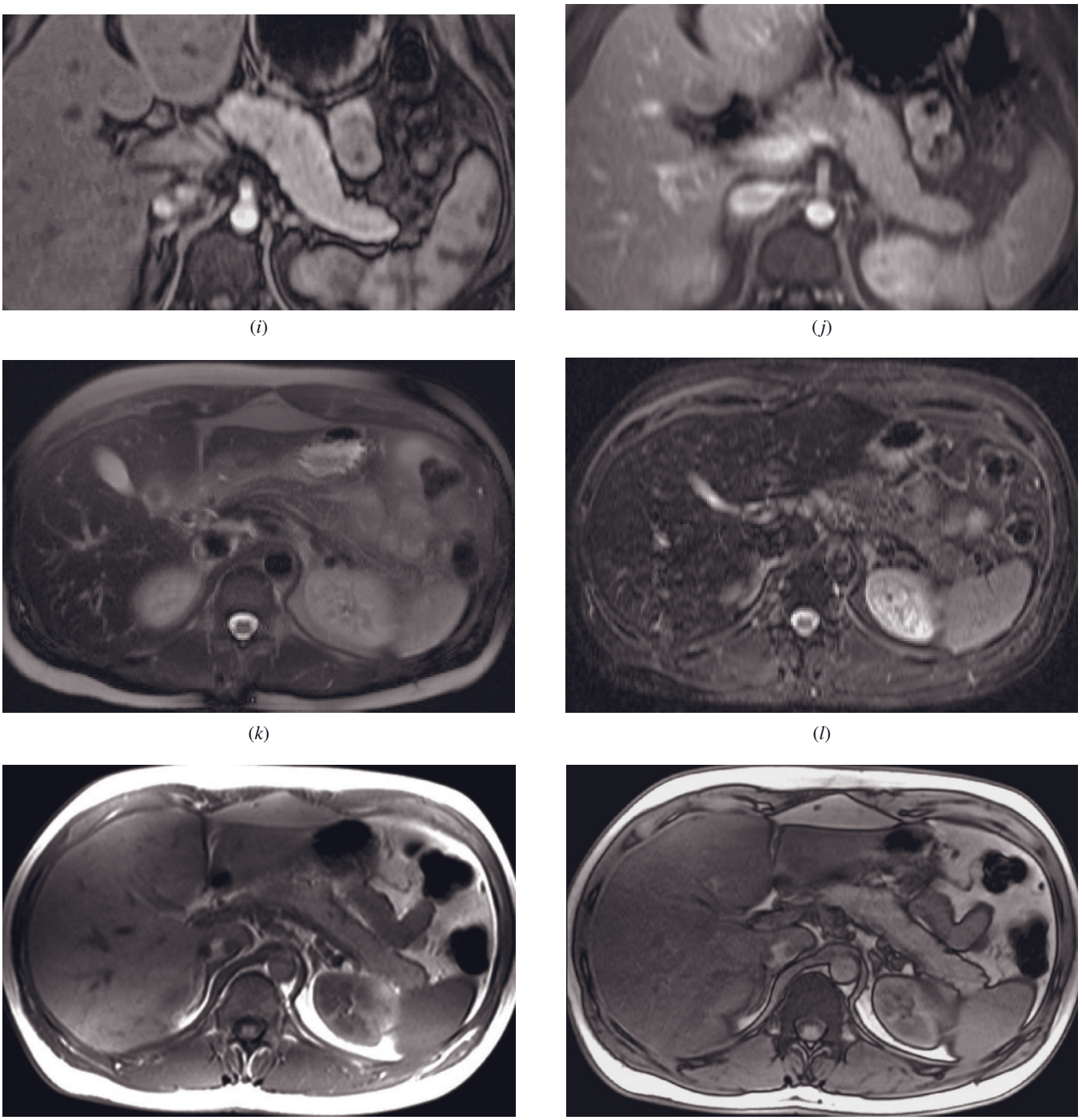

FIG. 4.1 (*Continued*) and immediate (*i*) and interstitial-phase (*j*) postgadolinium fat-suppressed T1-weighted gradient-echo images of pancreatic body and tail in a second patient. The normal pancreas is high in signal intensity on T1-weighted fat-suppressed image (*h*) because of the presence of aqueous protein in the acini of the pancreas. A uniform capillary blush is apparent on the immediate postgadolinium image (*i*). Small bowel is moderate in signal intensity on T1-weighted fat-suppressed image (arrow, *h*), which is clearly different from the homogeneous or marbled high signal intensity of the pancreas. The normal-caliber pancreatic duct is well shown (arrow, *e*) on T2-weighted image.

T2-weighted single-shot echo-train spin-echo (*k*), T2-weighted short-tau inversion recovery (*l*), T1-weighted in-phase (*m*) and out-of-phase (*n*) SGE, T1-weighted fat-suppressed SGE (*o*), and T1-weighted postgadolinium hepatic arterial dominant phase (*p*) and

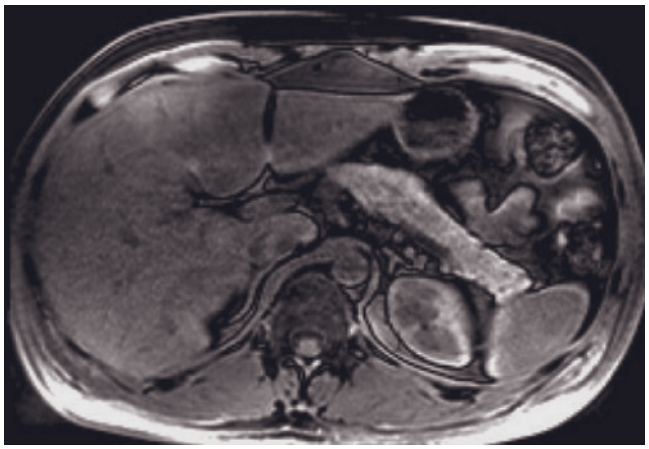

(*o*)

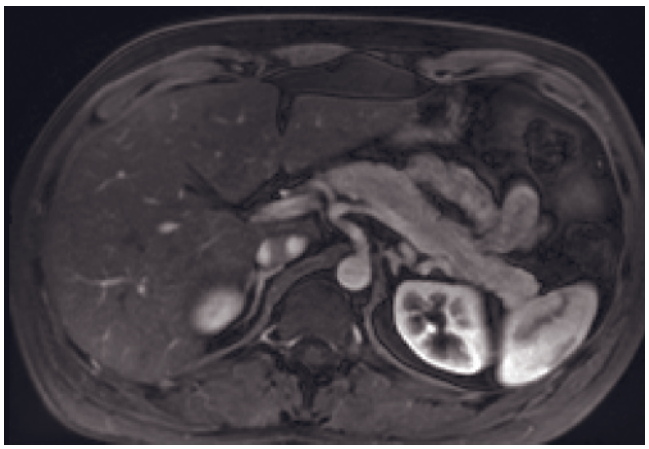

(*p*)

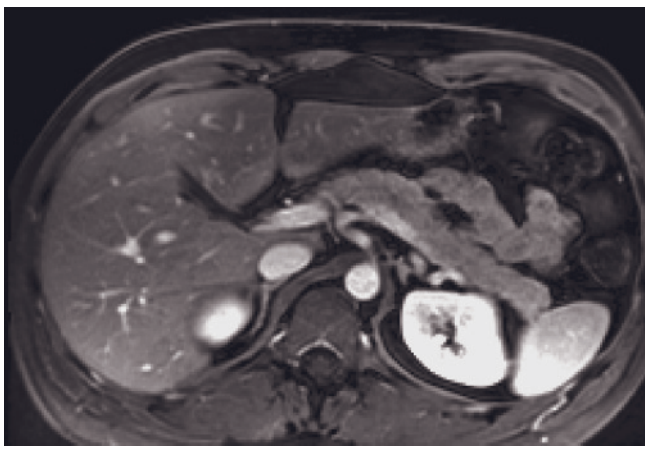

(*q*)

FIG. 4.1 (*Continued*) hepatic venous phase (*q*) fat-suppressed 3D-GE images at 3.0 T demonstrate the normal pancreas in a third patient. The normal pancreas again shows high signal intensity on T1-weighted precontrast images (*m–o*), particularly on the fat-suppressed SGE (*o*). Additionally, the normal pancreas shows capillary blush on the hepatic arterial dominant phase 3D-GE image (*p*). Note the superb image quality of 3.0 T images, especially postgadolinium 3D-GE images. The liver shows signal drop on out-of-phase image (*n*) compared to in-phase image (*m*) consistent with diffuse fat deposition.

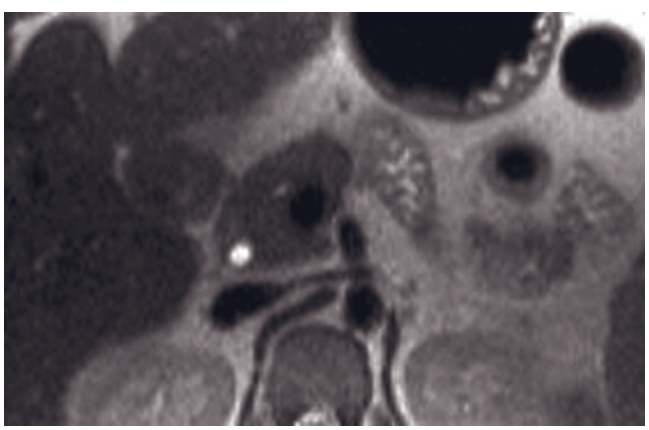

(*a*)

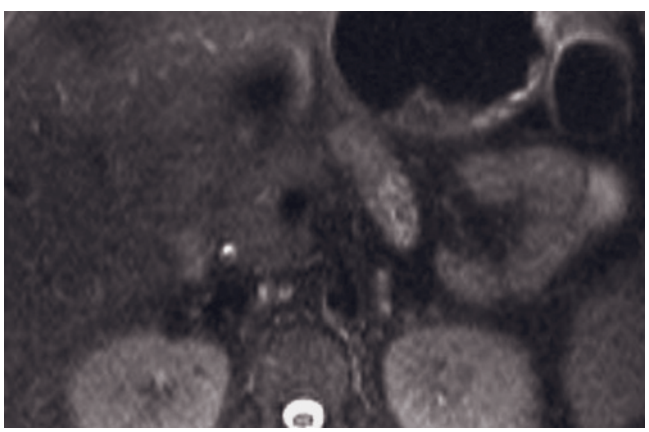

(*b*)

FIG. 4.2 Normal head of the pancreas. T2-weighted SS-ETSE (*a*), fat-suppressed T2-weighted SS-ETSE (*b*), fat-suppressed

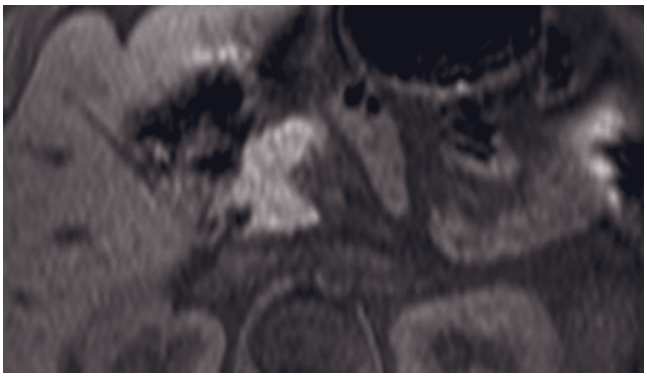

(*c*)

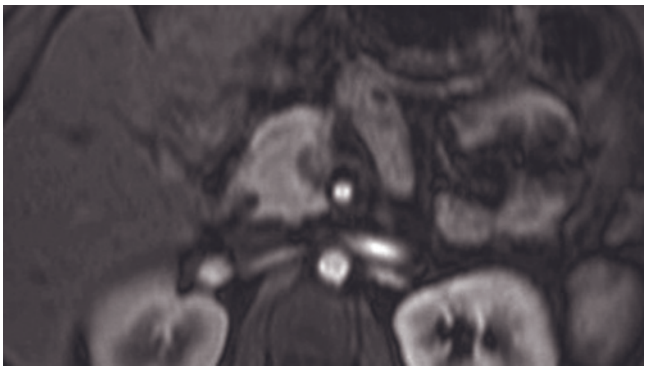

(*d*)

(*e*)

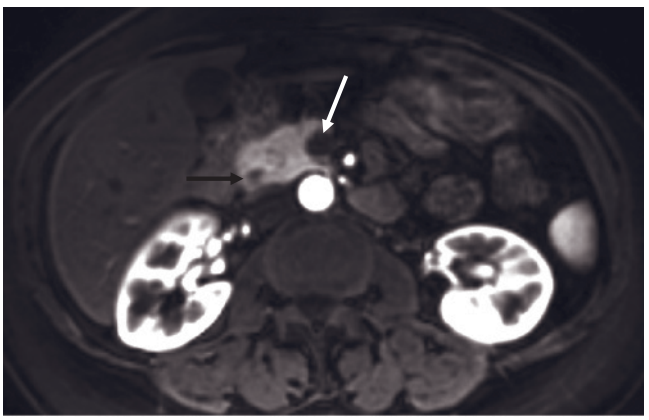

(*f*)

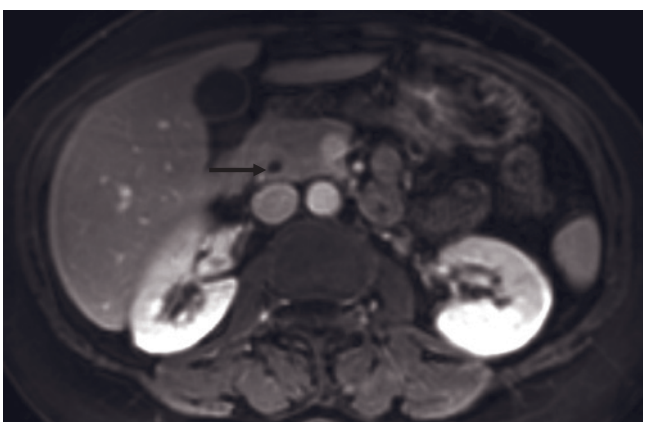

(*g*)

FIG. 4.2 (*Continued*) T1-weighted gradient-echo (*c*), and immediate (*d*) and interstitial-phase (*e*) postgadolinium fat-suppressed T1-weighted gradient-echo images of normal pancreatic head. The pancreatic head is low in signal intensity on T2-weighted SS-ETSE image (*a*) and easily delineated because of surrounding high-signal-intensity fat (*a*). Pancreatic head is high in signal intensity on fat-suppressed T1-weighted gradient-echo (*c*) image and enhances homogeneously and intensely on immediate postgadolinium image (*d*).

T1-weighted postgadolinium hepatic arterial dominant phase (*f*) and hepatic venous phase (*g*) fat-suppressed 3D-GE images at 3.0 T demonstrate the normal pancreatic head in a second patient. The pancreatic head shows capillary blush on the splenic vein on hepatic arterial dominant phase which is characterized by the presence of contrast in the portal and splenic vein but not in the superior mesenteric vein (white arrow, *f*). Additionally, the normal common bile duct (black arrow, *f*, *g*) is very well seen on both images.

because the pancreas enhances substantially greater than bowel (see fig. 4.1 and fig. 4.2). MRI combining T1, T2, early and late postgadolinium images, MRCP, and MRA generates comprehensive information on the pancreas [12].

Recognition of the characteristic high signal intensity of normal pancreas on precontrast T1-weighted fat-suppressed and immediate postgadolinium images is useful in circumstances of abnormalities of position. After left nephrectomy, the tail of the pancreas falls into the renal fossa, which can simulate recurrent disease on CT examination. Normal pancreas can be readily distinguished by its high signal intensity (fig. 4.3).

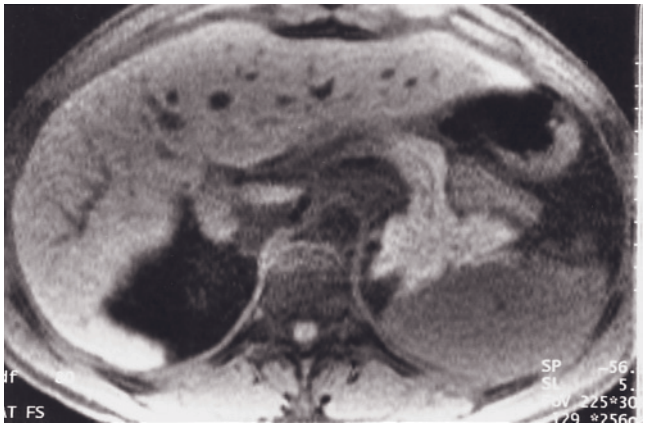

(*a*)

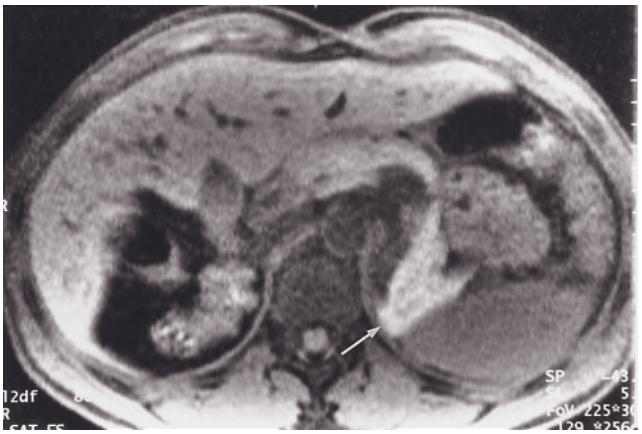

(*b*)

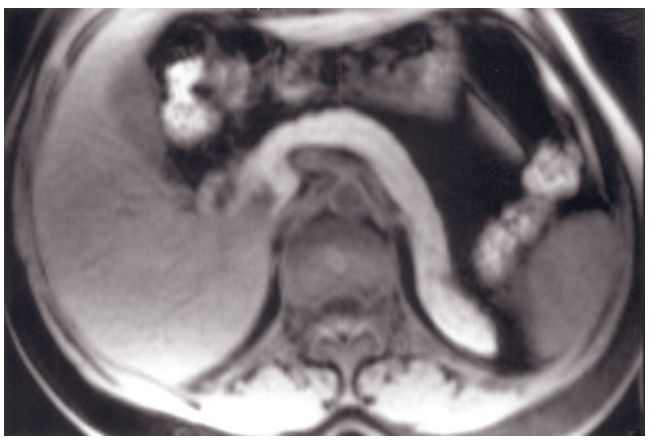

(*c*)

FIG. 4.3 Pancreatic tail seated in the left renal fossa after left nephrectomy. T1-weighted fat-suppressed SGE images (*a*, *b*) demonstrate normal high-signal-intensity pancreas situated in the left renal fossa (arrow, *b*).

T1-weighted fat-suppressed SGE image (*c*) in a second patient who underwent a bilateral nephrectomy shows the pancreatic tail seated posteriorly, filling the space in the renal fossa.

DEVELOPMENTAL ANOMALIES

Pancreas Divisum

Pancreas divisum is the most clinically important and common major anatomic variant. Although a misleading term, pancreas divisum is, by definition, a superficially normal-appearing pancreas in which no communication has developed between the duct of the dorsally derived pancreas and the duct of the embryonic ventral pancreas, which normally forms most of the main pancreatic duct [13]. The result of this congenital abnormality is that portions of the pancreas have separate ductal systems: A very short ventral duct of Wirsung drains only the lower portion of the head, whereas the dorsal duct of Santorini drains the tail, body, neck and upper aspect of the head. The incidence of this anomaly varies between 1.3 to 6.7% of the population [14]. One study described 108 patients who underwent both endoscopic retrograde cholangiopancreatography (ERCP) and MRCP and reported exact correlation between these modalities for the detection and exclusion of pancreas divisum [6]. On MRCP images, separate entries of the ducts of Santorini and Wirsung into the duodenum are consistently demonstrated because of the good conspicuity of the linear high-signal-intensity tubular structures (fig. 4.4). Variations in pancreas divisum are also shown, which include the dominant dorsal duct syndrome (see fig. 4.4).

Pancreas divisum has been reported to be a predisposing factor in recurrent pancreatitis [15, 16]. It is postulated that in some subjects the disproportion between the small caliber of the minor papilla and the large amount of secretion from the dorsal part of the gland leads to a relative outflow obstruction from the dorsal pancreas, resulting in pain or pancreatitis [17]. Compared with patients with pancreatitis and normal duct anatomy, the pancreas in pancreas divisum may appear normal in signal intensity on T1-weighted fat-suppressed images and immediate postgadolinium gradient echo-images because the attacks of recurrent pancreatitis tend to be less severe and changes of chronic pancreatitis may not develop.

Annular Pancreas

Annular pancreas is an uncommon congenital anomaly in which glandular pancreatic tissue, in continuity with

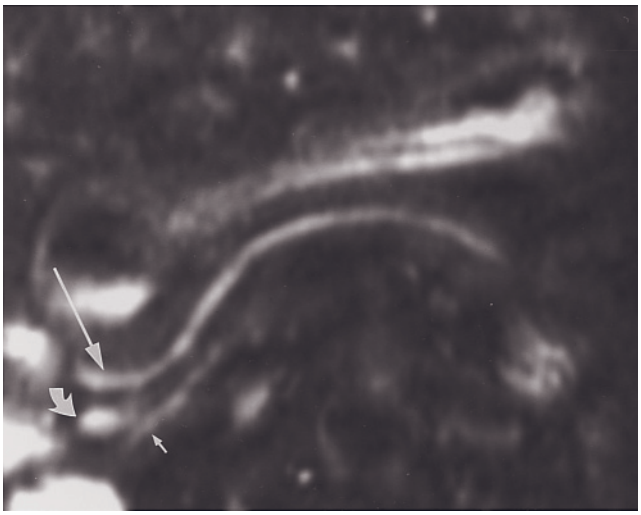

(*a*)

(*b*)

(*c*)

FIG. 4.4 Pancreas divisum. MRCP image (*a*) formatted in an oblique transverse plane demonstrates separate entry of the ducts of Santorini (long arrow, *a*) and Wirsung (short arrow, *a*) into the duodenum with no communication between the ductal systems. MRCP image (*b*) in a second patient with dominant dorsal duct syndrome shows a large duct of Santorini (long arrow, *b*) and a small communication with a diminutive duct of Wirsung (short arrow, *b*).The common bile duct (curved arrow, *a*, *b*) is identified between the ducts of Santorini and Wirsung. Oblique coronal MRCP (*c*) in a patient with normal ductal anatomy shows a small duct of Santorini (long arrow, *c*) and a larger duct of Wirsung (short arrow, *c*). The common bile duct (curved arrow, *c*) and gallbladder (open arrow, *c*) are also shown. MR pancreatography has the advantage of being a noninvasive diagnostic method for pancreas divisum. (Courtesy of Caroline Reinhold, M.D., Dept. of Radiology, McGill University.)

the head of the pancreas, encircles the duodenum. In most cases, the annular portion surrounds the second part of the duodenum. Patients may present with duodenal obstruction. On MR images, pancreatic tissue is identified encasing the duodenum. Noncontrast T1-weighted fat-suppressed and/or immediate post-gadolinium gradient-echo images are particularly effective at demonstrating this entity because of the high signal intensity of pancreatic tissue, which is readily distinguished from the lower signal intensity of adjacent tissue and duodenum (fig. 4.5) [18].

Congenital Absence of the Dorsal Pancreatic Anlage

Congenital absence of the dorsal pancreatic anlage is a very rare anomaly. This abnormality predisposes to recurrent attacks of pancreatitis with eventual exocrine and endocrine pancreatic failure [13]. The head of the pancreas terminates with a rounded contour (fig. 4.6), unlike surgical or posttraumatic absence of the distal pancreas, which has more squared-off or irregular terminations.

Uneven Fatty Infiltration of the Pancreas

Variation in fat content between the posterior head of pancreas and the anterior head through tail of pancreas may be observed. The underlying mechanism likely reflects the differing embryological origin of these portions of the pancreas. The importance of recognizing this condition is that it may simulate a mass lesion (fig. 4.6). MRI is superior to CT in correctly diagnosing this entity.

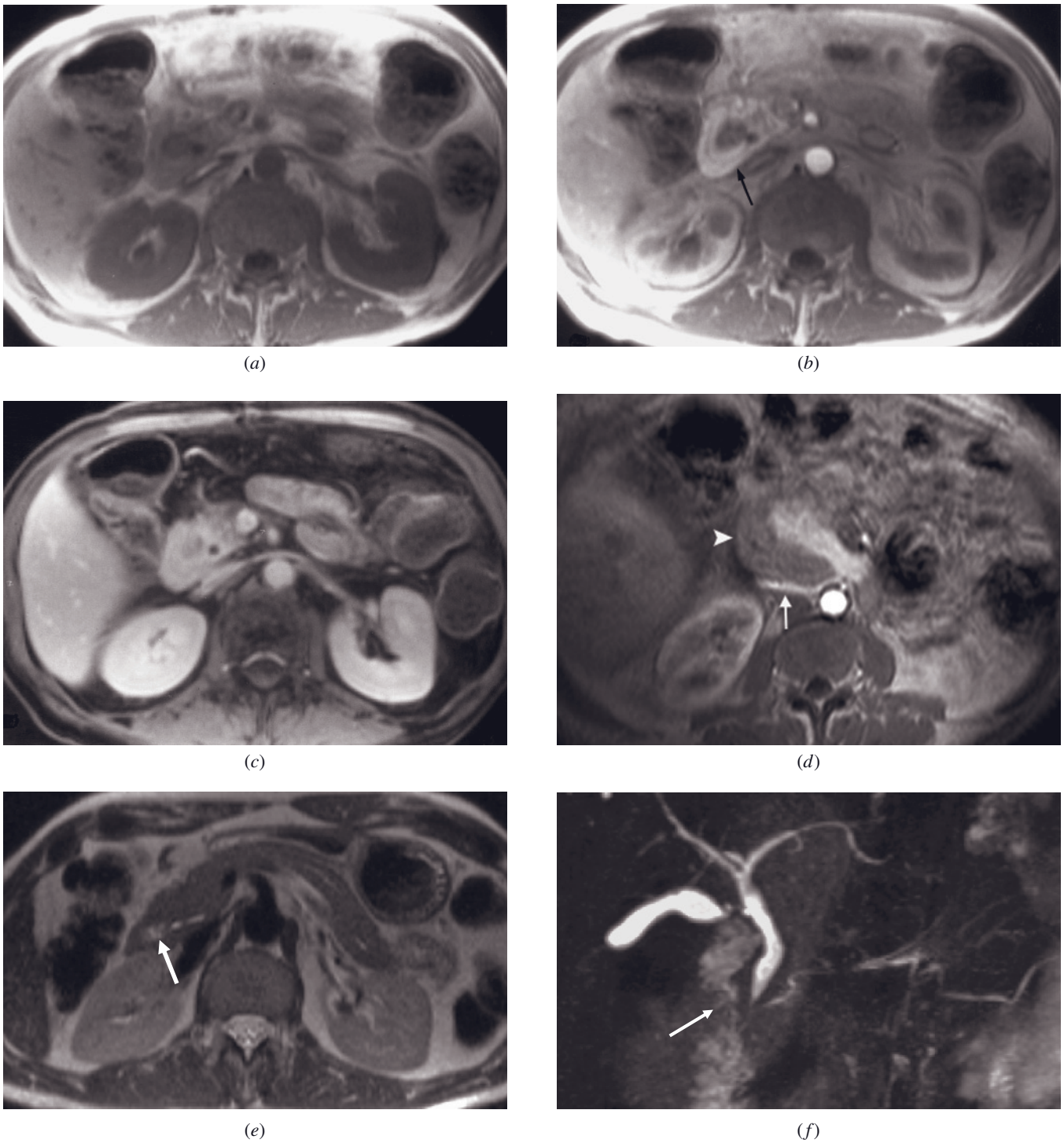

FIG. 4.5 Annular pancreas. T1-weighted SGE (*a*), immediate postgadolinium T1 SGE (*b*), and 90-s postgadolinium T1 fat-suppressed SGE (*c*) images. Normal pancreatic parenchyma (arrow, *b*) surrounds the second portion of the duodenum, diagnostic for annular pancreas. This is best shown on noncontrast T1-weighted fat-suppressed and immediate postgadolinium (*b*) images.

Immediate postgadolinium T1-weighted gradient-echo image (*d*) in a second patient demonstrates that the pancreatic head partially encircles the duodenum (arrowhead, *d*), suggestive of a variant of annular pancreas (arrow, *d*).

T2-weighted single-shot echo-train spin-echo (*e*), reconstructed MRCP image (*f*), T1-weighted fat-suppressed SGE (*g*), and T1-weighted postgadolinium hepatic arterial dominant phase SGE (*h*) images demonstrate an annular pancreas in another patient.

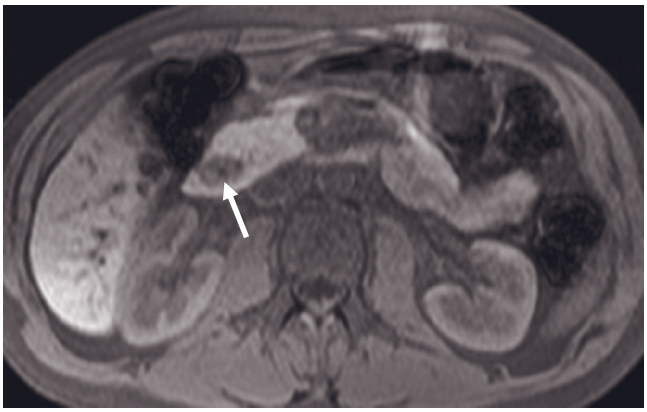

(*g*)

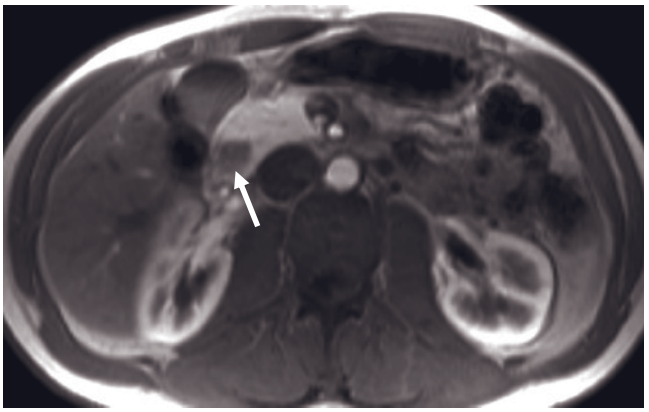

(*h*)

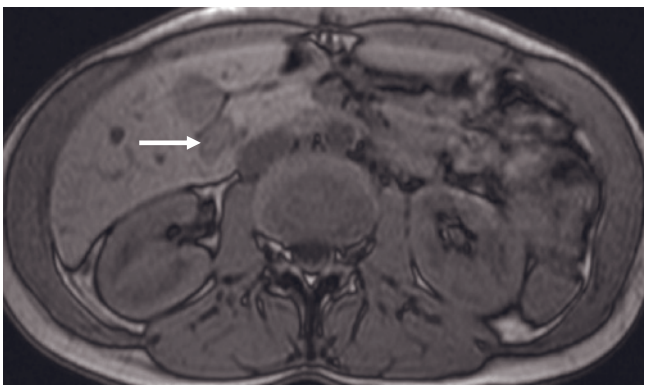

(*i*)

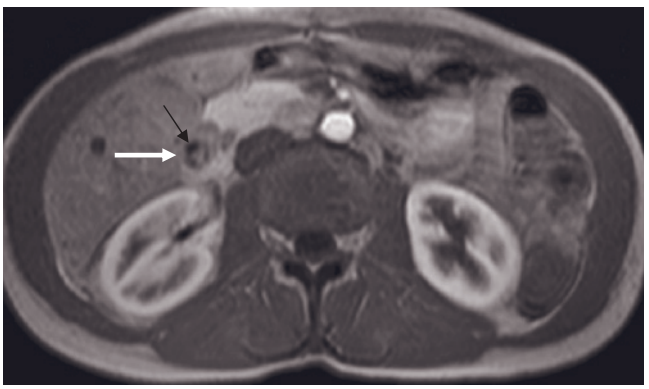

(*j*)

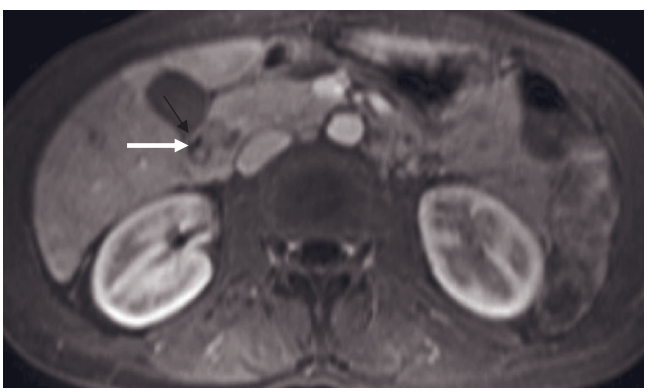

(*k*)

FIG. 4.5 (*Continued*) The pancreatic head completely encircles the second portion of the duodenum (arrows, *e–h*) and causes a narrowing (arrow, *f*) in this portion of the duodenum. Mucosal folds and air of the duodenum are also appreciated.

T1-weighted out-of-phase SGE (*i*), T1-weighted postgadolinium hepatic arterial dominant phase SGE (*j*), and hepatic venous phase fat-suppressed 3D-GE (*k*) images demonstrate an annular pancreas in another patient. The pancreatic head incompletely encircles the second portion of the duodenum (white arrows, *i–k*). Note the air in the second portion of the duodenum (black arrows, *j*, *k*).

Short Pancreas in the Polysplenia Syndrome

Polysplenia syndrome is a congenital syndrome characterized by multiple, misplaced small spleens characteristic in the right upper quadrant and isomerism (bilateral left-sidedness) [19]. In a study involving adults with polysplenia syndrome discovered incidentally, four of eight patients evaluated with CT showed a short pancreas. The short pancreas may also have an abnormal orientation (fig. 4.7). A possible explanation for the anomaly is disturbance in the blood supply to the pancreas-spleen region during embryonal life [20].

GENETIC DISEASE

Cystic Fibrosis

Cystic fibrosis is the most common lethal genetic disease affecting Caucasians, with an incidence of 1 in 2000 live births. It is an autosomal recessive multisystem disease with an abnormality of the long arm of chromosome 7, and homozygotes express the disease fully. The disease is characterized by a dysfunction of the secretory process of all exocrine glands and reduced mucociliar transport, which results in mucous plugging of the exocrine glands. The diagnosis is made during childhood when the

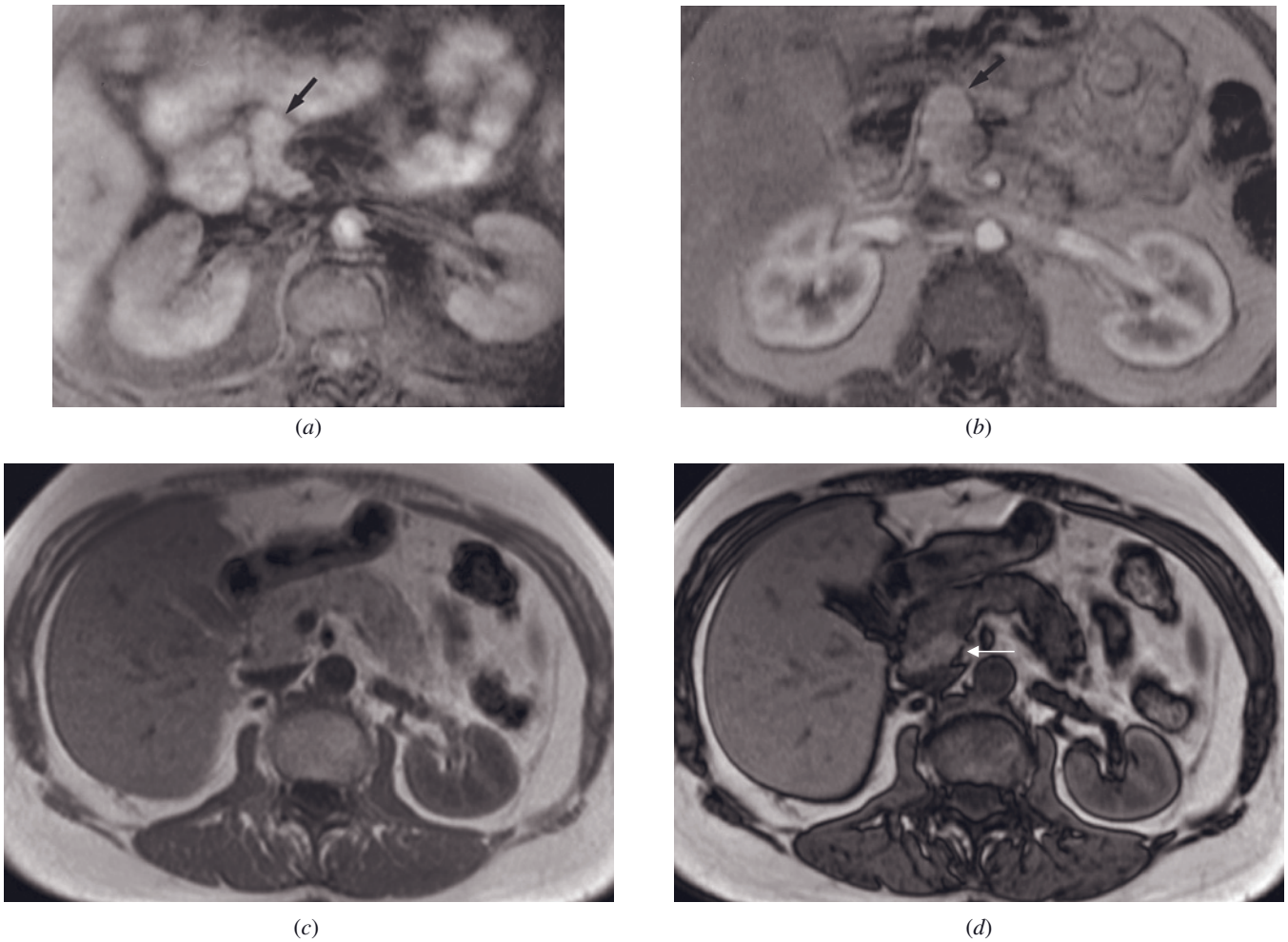

FIG. 4.6 Absence of the dorsal pancreas anlage. T1-weighted fat-suppressed spin-echo (*a*) and immediate postgadolinium T1-weighted SGE (*b*) images. A normal-appearing head of the pancreas is apparent. The pancreas terminates with a rounded contour (arrow, *a*, *b*) at the level of the pancreatic neck.

Uneven fatty infiltration of the pancreas. T1-weighted in-phase (*c*) and out-of-phase (*d*) SGE images demonstrate fatty infiltration of the pancreas with sparing of the posterior portion of the pancreatic head. The anterior portion of the pancreatic head and the pancreatic body shows signal drop on out-of-phase image (*d*), which is consistent with fatty infiltration. The posterior portion of the pancreatic head (arrow, d) does not show signal drop on out-of-phase image (*d*). This can be mistaken for a pancreatic head mass on CT, but the combination of standard and fat attenuated MR images clearly demonstrate that this appearance is due to varying fat content between anatomic regions of the pancreas.

patient has clinical manifestations of recurrent bronchopulmonary infections leading to chronic lung disease, malabsorption secondary to pancreatic insufficiency, and an increased sweat sodium concentration. MRI has proven to be an effective modality in demonstrating pancreas changes in patients with cystic fibrosis [21–23]. It is superior to ultrasound in showing fatty infiltration and avoids ionizing radiation used in computed tomography. The disadvantage of MRI is that it does not show small calcifications, which are encountered in a small percentage of patients with cystic fibrosis.

Pathologic examination of the pancreas in patients who have survived until early adulthood shows a spectrum of changes involving atrophy and fibrosis of the exocrine pancreas with varying degrees of fatty replacement. Three basic imaging patterns of pancreatic abnormalities have been described: pancreatic enlargement with complete fatty replacement with or without loss of the lobulated contour, atrophic pancreas with partial fatty replacement (fig. 4.8), and diffuse atrophy of the pancreas without fatty replacement [21–23]. Pancreatic enlargement with complete fatty replacement is the most common pattern observed in cystic fibrosis [23]. Fatty replacement is high in signal intensity on T1-weighted images and demonstrates loss of signal intensity on T1-weighted fat-suppressed images (see fig. 4.8). These findings correlate with the pathologic description of mature adipose tissue and isolated foci of Langerhans cell islets in the pancreas of patients with cystic fibrosis.

Another manifestation of cystic fibrosis is pancreatic cysts secondary to duct obstruction by secretion. Pancreatic cystosis is a rare manifestation characterized by large cysts. MRCP is valuable in demonstrating pancreatic duct abnormalities (narrowing, dilatation, stricture, beading).

Primary Hemochromatosis

Primary hemochromatosis is an autosomal recessive heritable disease in which there is excessive accumulation of body iron, most of which is deposited in the parenchyma of various organs. The liver, pancreas, and heart are primarily affected. Iron deposition results in a loss of signal intensity that is more pronounced on T2 or T2*-weighted sequences, but in severe deposition a loss of signal intensity is also apparent on T1-weighted images (fig. 4.9). Iron deposition in primary hemochromatosis is most substantial in the liver. Deposition of iron in the pancreas tends to occur late in the course of disease after liver damage is irreversible [24, 25].

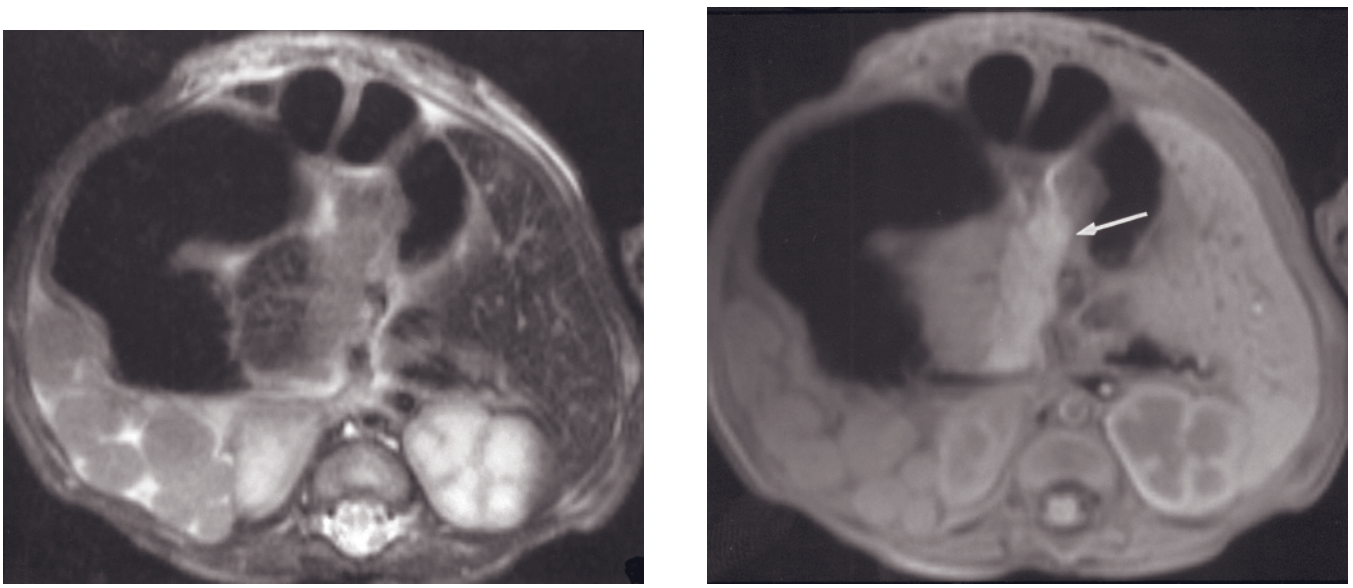

(*a*) (*b*)

FIG. 4.7 Short pancreas in the polysplenia syndrome. T2-weighted fat-suppressed SS-ETSE (*a*) and T1-weighted fat-suppressed spin-echo (*b*) images in a 9-wk-old boy with polysplenia syndrome. The pancreas has an abnormal anterior-posterior orientation and appears short (arrow, *b*), but the parenchyma signal intensity is normal. The most common pancreatic finding in polysplenia syndrome is short pancreas. Note situs inversus and multiple small spleens.

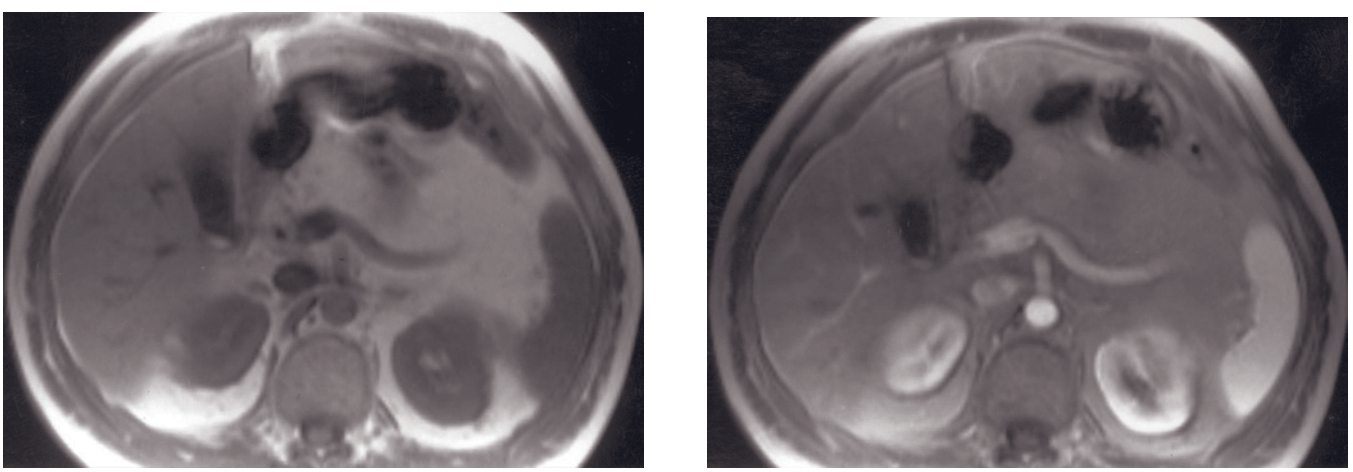

(*a*) (*b*)

FIG. 4.8 Cystic fibrosis. T1-weighted SGE (*a*), immediate postgadolinium T1-weighted SGE (*b*), and 90-s postgadolinium T1-weighted fat-suppressed SGE (*c*) images in a patient with cystic fibrosis. The pancreas is markedly enlarged and hyperintense on

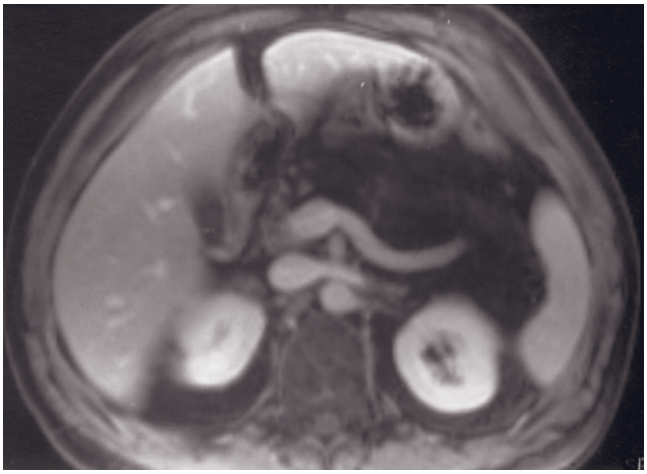

(*c*)

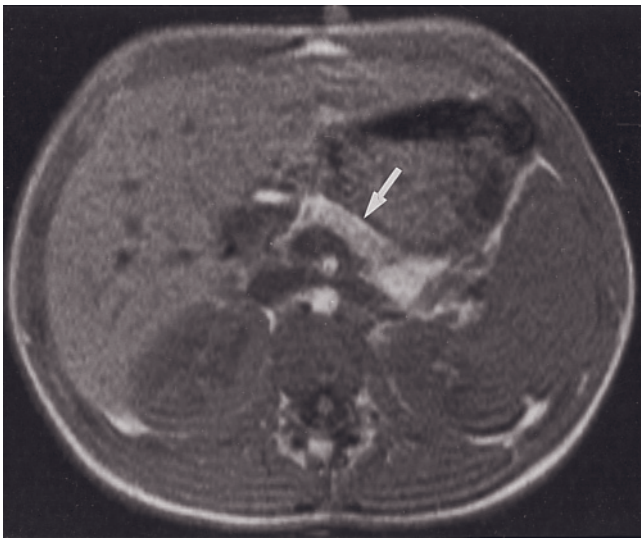

(*d*)

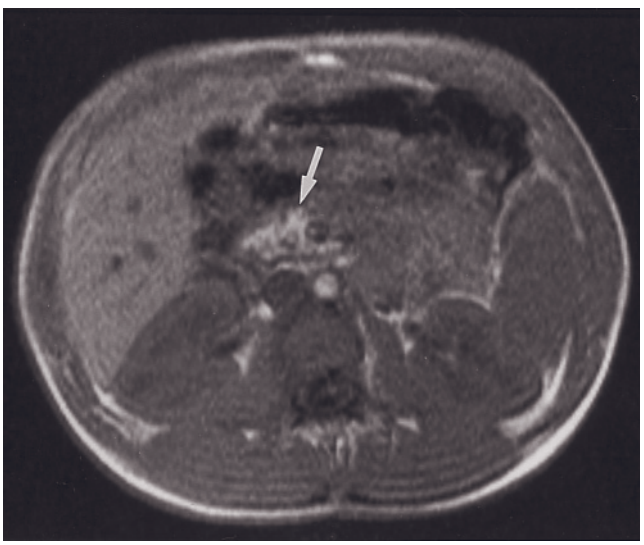

(*e*)

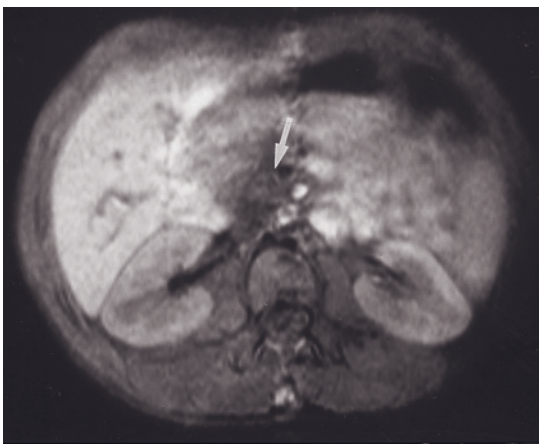

(*f*)

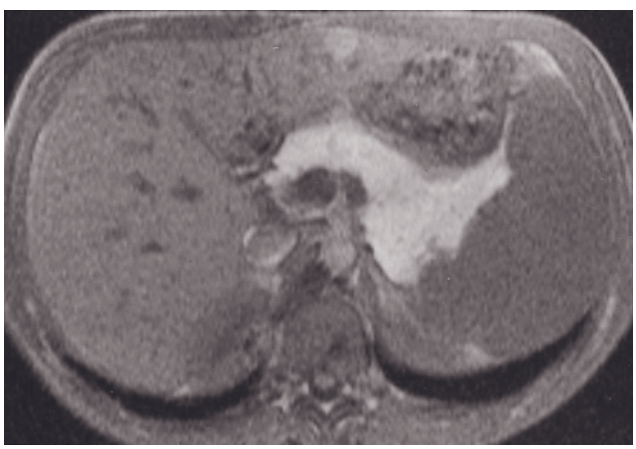

(*g*)

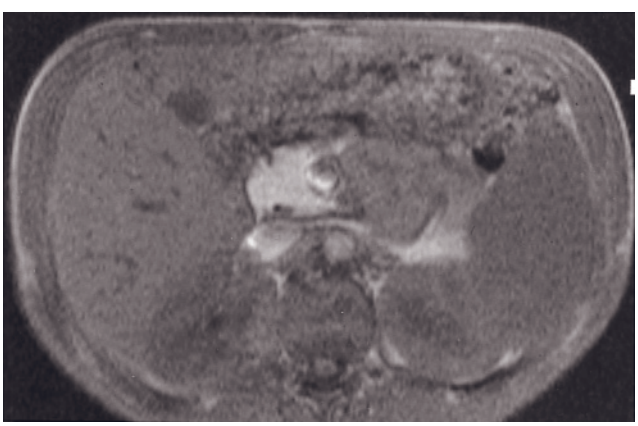

(*h*)

FIG. 4.8 (*Continued*) T1-weighted image and hypointense on fat-suppressed (*c*) images, consistent with fatty replacement of the pancreatic parenchyma by adipose tissue. The complete fatty replacement of the pancreas is the most common manifestation of cystic fibrosis. T1-weighted SGE (*d*, *e*) and T1-weighted fat-suppressed spin-echo (*f*) images in a second patient. The pancreas is atrophic and demonstrates fatty replacement. T1-weighted SGE (*g*, *h*), T1-weighted fat-suppressed spin-echo (*i*, *j*), and gated

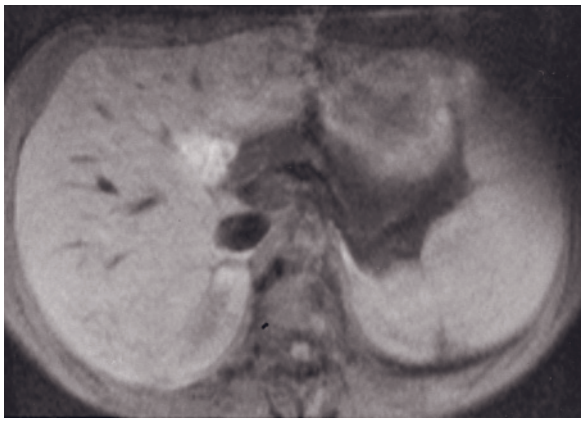

(*i*)

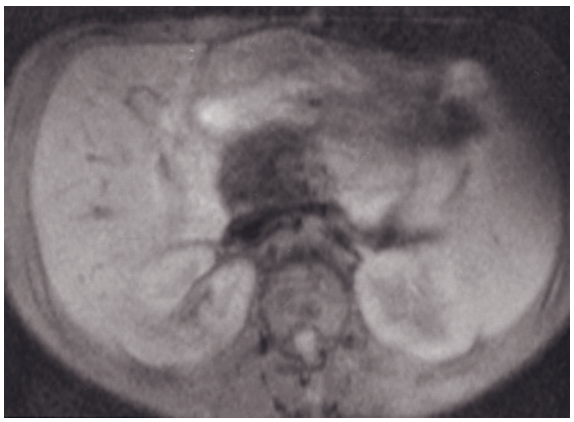

(*j*)

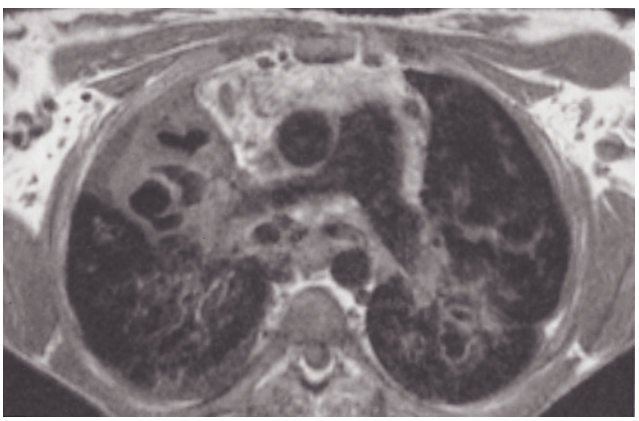

(*k*)

FIG. 4.8 (*Continued*) T1-SE (*k*) images in a third patient, who has an enlarged fatty replaced pancreas. Extensive pulmonary fibrosis is present (*k*).

(*a*)

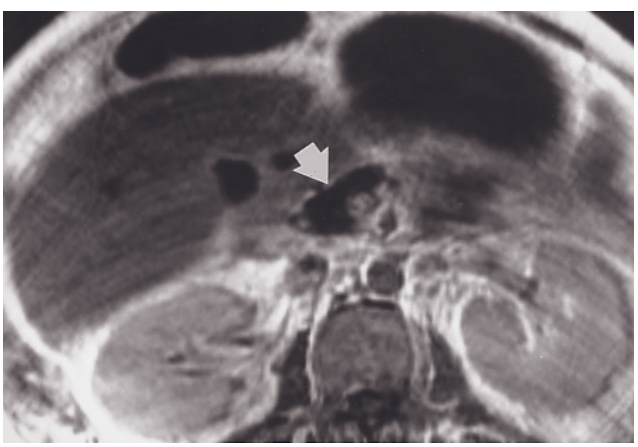

(*b*)

FIG. 4.9 Iron deposition in the pancreas from primary hemochromatosis. T1-weighted SGE (*a*, *b*) images. The pancreas (arrow, *a*, *b*) is signal void on T1-weighted images because of the susceptibility effect of iron. The liver is a transplanted liver and

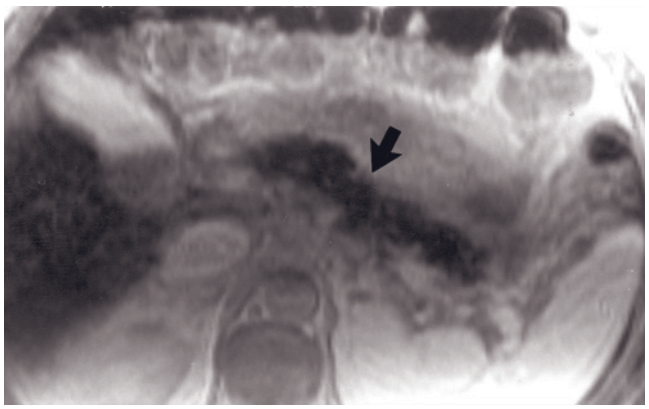

(*c*)

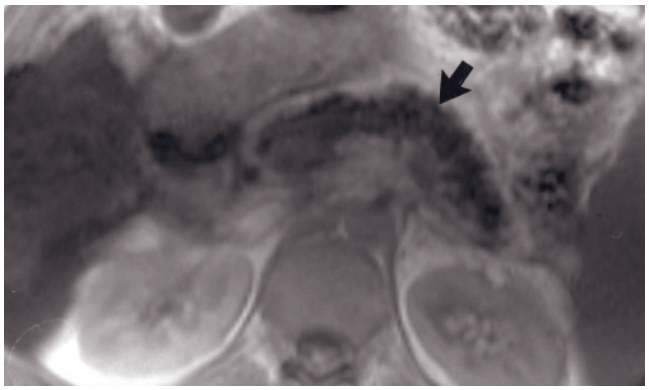

(*d*)

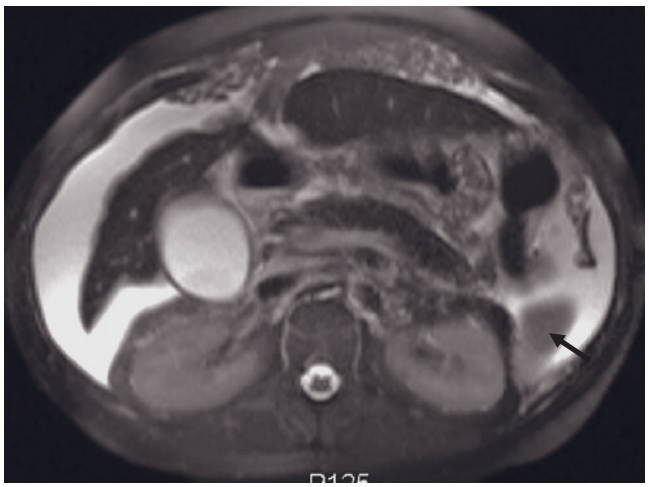

(*e*)

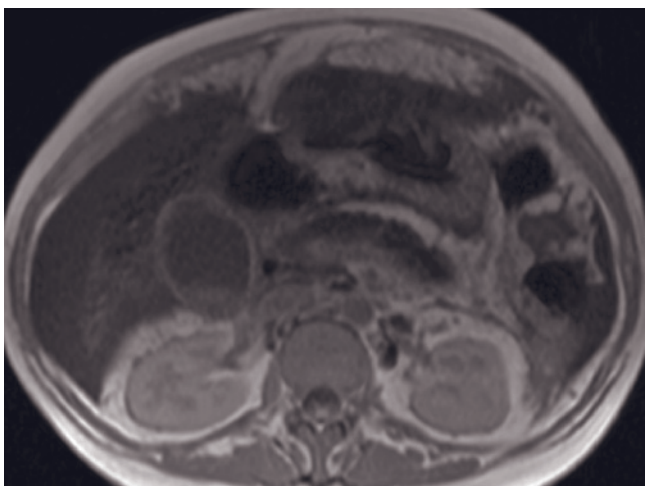

(*f*)

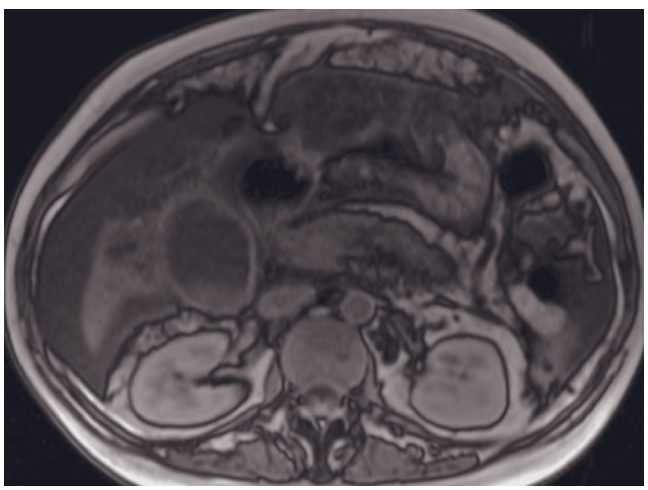

(*g*)

Fig. 4.9 (*Continued*) therefore has not sustained iron deposition. Transverse 1-min postgadolinium SGE image (*c*) in a second patient with primary hemochromatosis. Both the pancreas (arrow, *c*) and liver show decreased signal intensity. Gallstones are also present. T1-weighted SGE (*d*) image in a third patient with primary hemochromatosis shows a low-signal pancreas (arrow, *d*). T2-weighted single-shot echo-train spin-echo (*e*) and T1-weighted in-phase (*f*) and out-of-phase (*g*) SGE images demonstrate the deposition of iron in the liver and pancreas but not in the spleen in another patient. The diagnosis, therefore, is consistent with primary hemochromatosis. The liver and pancreas show decreased signal on T2-weighted and T1-weighted in-phase images. The liver and pancreas show signal increase on out-of-phase image compared to in-phase image because of shorter TE. The spleen (arrow, *e*) shows normal signal on all images. Note that the liver is cirrhotic, and there are ascites and omental hypertrophy.

von Hippel–Lindau Syndrome

Von Hippel–Lindau syndrome is an autosomal dominant condition with variable penetration. This condition is characterized by tumors in the cerebellum and retina. Patients may have cysts of the liver and kidney, with a strong propensity to develop renal cell carcinoma. Patients with von Hippel–Lindau syndrome may develop pancreatic cysts, islet cell tumors, or microcystic cystadenoma. In one series, cysts were the most common pancreatic lesions and were present in 19 of 52 patients in whom no other pancreatic lesions were present (fig. 4.10) [26].

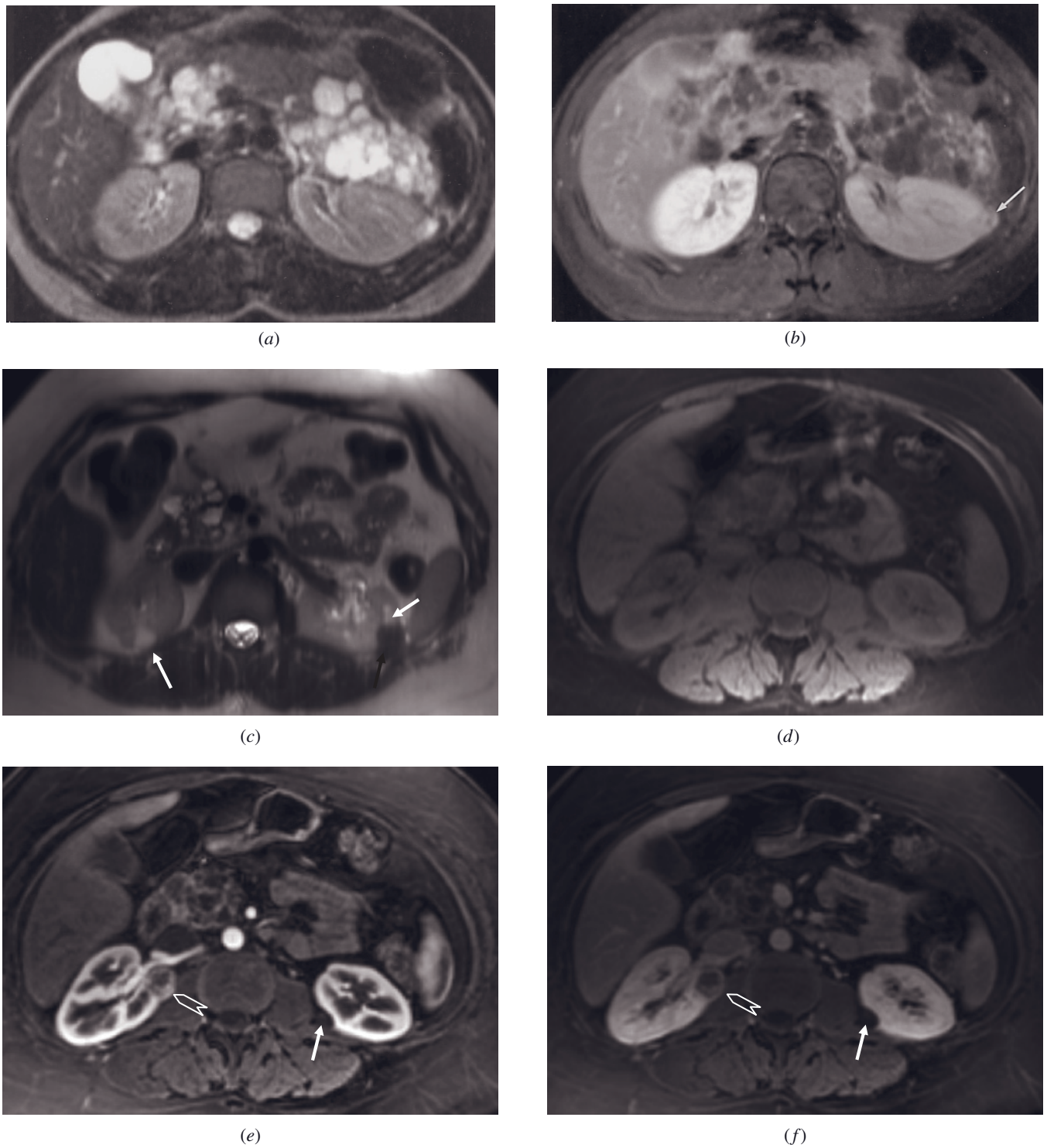

FIG. 4.10 Pancreatic cysts in von Hippel–Lindau disease. T2-weighted SS-ETSE (*a*) and gadolinium-enhanced T1-weighted fat-suppressed spin-echo (*b*) images. Multiple pancreatic cysts are scattered throughout the pancreas, which are high in signal intensity on T2-weighted images (*a*) and low in signal intensity on gadolinium-enhanced images (*b*). Thick septations are present between many of the clustered cysts. A small renal cancer is identified in the left kidney (arrow, *b*).

T2-weighted single-shot echo-train spin-echo (*c*), T1-weighted fat-suppressed SGE (*d*), T1-weighted postgadolinium true late hepatic arterial phase (*e*), and hepatic venous phase (*f*) fat-suppressed 3D-GE images at 3.0 T demonstrate multiple cysts located in the pancreatic head and bilateral kidneys in another patient with von Hippel–Lindau disease. Thick septations located between pancreatic cysts show enhancement. T2-weighted image shows simple cysts in both kidneys (white arrows, *c*) and a hemorrhagic cyst (black arrow, *c*) in the left kidney. Additionally, there is an enhancing lesion (open arrow, *e*, *f*) in the right kidney suggestive of renal cell carcinoma.

NEOPLASMS

Pancreatic mass lesions can be detected and successfully characterized with a pattern recognition approach using T1, T2, and immediate and late postgadolinium images. Table 4.1 summarizes a pattern recognition approach for the most common pancreatic tumors.

SOLID NEOPLASMS

Benign Solid Neoplasms

Lipoma

Lipoma is the most common benign solid tumor that affects the pancreas. Rounded morphology and larger

Table 4.1 Pattern Recognition: Focal Pancreatic Lesions

	T1	T2	EARLY Gd	LATE Gd	OTHER FEATURES
Ductal Adeno Ca (small)	ø	Δ	ø	ø–≠	Usually no background chronic pancreatitis, so tumor is well seen on precontrast T1.
Ductal Adeno Ca (large)	ø–Δ	Δ–≠	ø	ø	Usually background chronic pancreatitis; tumor is not well seen on precontrast T1. Focal mass with definable margins shown on early post Gd images is the most common imaging characteristic.
Islet Cell Tumors Insulinoma	ø	≠	≠, homogeneous and benign	Δ–≠	Tumors are usually <1 cm.
Gastrinoma	ø	≠	≠, ring	Δ–≠	Tumors are usually located in the region of the pancreatic head. Approximately 50% have metastases at initial diagnosis. Liver metastases tend to be uniform population of numerous smooth ring enhancing tumors shown on immediate postgadolinium images that exhibit peripheral washout on delayed images.
Somastostatinoma, Glucagonoma, Untyped	ø	≠	≠, diffuse heterogeneous	Δ heterogeneous	Tumors are usually large at initial diagnosis, with the majority having liver metastases. Liver metastases are numerous and vary in size with irregular ring enhancement.
VIPoma	ø	≠	≠	Δ	Primary tumor is usually small at initial diagnosis with few varying size liver metastases with irregular ring enhancement.
Serous Cystadenoma	ø	≠≠	Δ–≠	Δ	Small cysts best seen on single-shot T2 sequences. Septations usually thin and regular but may measure up to 4 mm in thickness with regular thickness. Septations may enhance moderately on immediate post-Gd images of larger tumors with thicker septations, and these tumors may possess a central scar that shows delayed enhancement.
Mucinous Cystadenoma	ø	≠≠	Δ–≠	Δ	Cysts >2 cm. Septations are uniform in thickness, and there is no evidence of irregular tumor tissue or nodule.
Macrocystic Cystadenocarcinoma	ø	≠	Δ–≠	Δ–≠	Cysts vary in signal and >2 cm, Septations are irregular in thickness with irregular-shaped tumor tissue and tumor nodule. Tumor may be very locally aggressive and may have liver metastases. Liver metastases may be high signal on T1 weighted images because of presence of mucin.

size distinguish this tumor from prominent fat within the interstices of the pancreas. The diagnosis is readily made with non-fat-suppressed and fat-attenuating techniques (fig. 4.11).

Malignant Solid Neoplasms

Adenocarcinoma

Adenocarcinoma of the pancreas refers to carcinoma arising in the exocrine portion of the gland. Pancreatic ductal adenocarcinoma accounts for 95% of malignant tumors of the pancreas. Pancreatic adenocarcinoma is the fourth most common cause of cancer death in the United States [27]. The lesion is more common in males and blacks [28]. The age range for tumor occurrence is the fourth through the eighth decade, with tumor incidence peaking in the eighth decade [29]. The tumor has a poor prognosis, with a 5-year survival of 5% [28].

Approximately 60–70% of pancreatic adenocarcinomas occur in the head (figs. 4.12–4.22), 15% in the body (figs. 4.23 and 4.24), 5% in the tail (fig. 4.25), and 10–20% with diffuse involvement (fig. 4.26) [30]. Tumors in the head of the pancreas are in a strategic position to encroach on the common bile duct, major papilla, and duodenum. They tend to present smaller in size than tumors in the body or tail because of the development of jaundice secondary to obstruction of the common bile duct. Painless jaundice is the classical presenting feature of carcinomas within the pancreatic head.

In general, the diagnosis of pancreatic adenocarcinoma is made when the tumor is relatively large (about 5 cm) and has extended beyond the pancreas (85% of cases). Carcinoma involving the body and tail of the pancreas grows insidiously and often has already metastasized widely at the time of diagnosis [31]. The most common sites of metastases, in order of decreasing frequency, are liver, regional lymph nodes, peritoneum, and lungs [30]. The rich lymphatic supply and lack of a capsule account for the early spread of cancer to regional lymph nodes. The nodal groups involved include parapancreatic, paraaortic, paracaval, paraportal, and celiac. Calcification is a rare constituent of the mass itself, although adenocarcinoma may occur in a pancreas containing calcification.

Pancreatic cancer arising in the head of the pancreas may cause obstruction of the CBD and pancreatic duct [32]. This appearance on MRCP studies results in the "double duct sign," which was originally described on ERCP (see fig. 4.15). A characteristic imaging appearance of pancreatic carcinoma consists of enlargement of the head of the pancreas with dilatation of the pancreatic and common bile duct and atrophy of the body and tail of the pancreas. However, enlargement of the head of the pancreas with obstruction of both ducts is not a feature unique to pancreatic cancer, as this same appearance may be appreciated, although less commonly, in patients with focal pancreatitis. One study evaluated the accuracy of MRI emphasizing T1-weighted 3D-GE sequences, for differentiating pancreatic carcinoma from chronic pancreatitis. The results showed a sensitivity of 93% and specificity of 75% [33]. The most discriminative finding for pancreatic carcinoma was relative demarcation of the mass compared to background pancreas in contrast to chronic pancreatitis on post-Gd 3D-GE sequences (fig. 4.15) [33]. Additional features included that chronic pancreatitis demonstrated progressively more intense enhancement on serial post gadolinium images than that of pancreatic cancer, and that destruction of pancreatic architecture was present with cancer and often absent with chronic pancreatitis [33].Other features that assist in the diagnosis of pancreatic cancer include the presence of lymphadenopathy, encasement of the celiac axis or superior mesenteric artery, and liver metastases (figs. 4.27 and 4.28) [30, 34]. On tomographic images, vascular encasement is observed as a loss of the fat plane around vessels [35]. Liver metastases are the only absolute indication of malignancy, as lymphadenopathy and vascular encasement may rarely occur in inflammatory disease. Because liver metastases are not common at initial presentation, the most useful imaging feature for the diagnosis of pancreatic cancer is the demonstration of a focal hypovascular mass within pancreatic parenchyma. Detection of carcinoma is best performed by immediate postgadolinium T1-weighted gradient-echo images (see fig. 4.12) [1, 4, 36–38]. Pancreatic tissue is well delineated from tumors, and tumor margins are clearly shown with this sequence in all regions of the pancreas. Small tumors or tumors of the pancreatic tail are also well demonstrated on noncontrast T1-weighted fat-suppressed images. Larger tumors in the pancreatic head are revealed less consistently with noncontrast T1weighted fat-suppressed images, as explained below. Conventional spin-echo images are generally limited in the detection of pancreatic cancer [39]. Tumors are usually minimally hypointense relative to pancreas on T2-weighted images and are therefore difficult to visualize. One study evaluated MRI, including noncontrast T1-weighted fat-suppressed spin echo and immediate postgadolinium gradient echo, for the detection or exclusion of pancreatic cancer in 16 patients with findings indeterminate for cancer on spiral CT imaging [37]. Immediate postgadolinium gradient echo was found to be the most sensitive approach to detect pancreatic cancer, particularly in the head of the pancreas. Both immediate postgadolinium gradient-echo and noncontrast T1-weighted fat-suppressed imaging performed well at excluding cancer, and both were significantly superior to spiral CT imaging (see figs. 4.13 and 4.17). These findings are similar to those reported by Gabata et al. [36], who

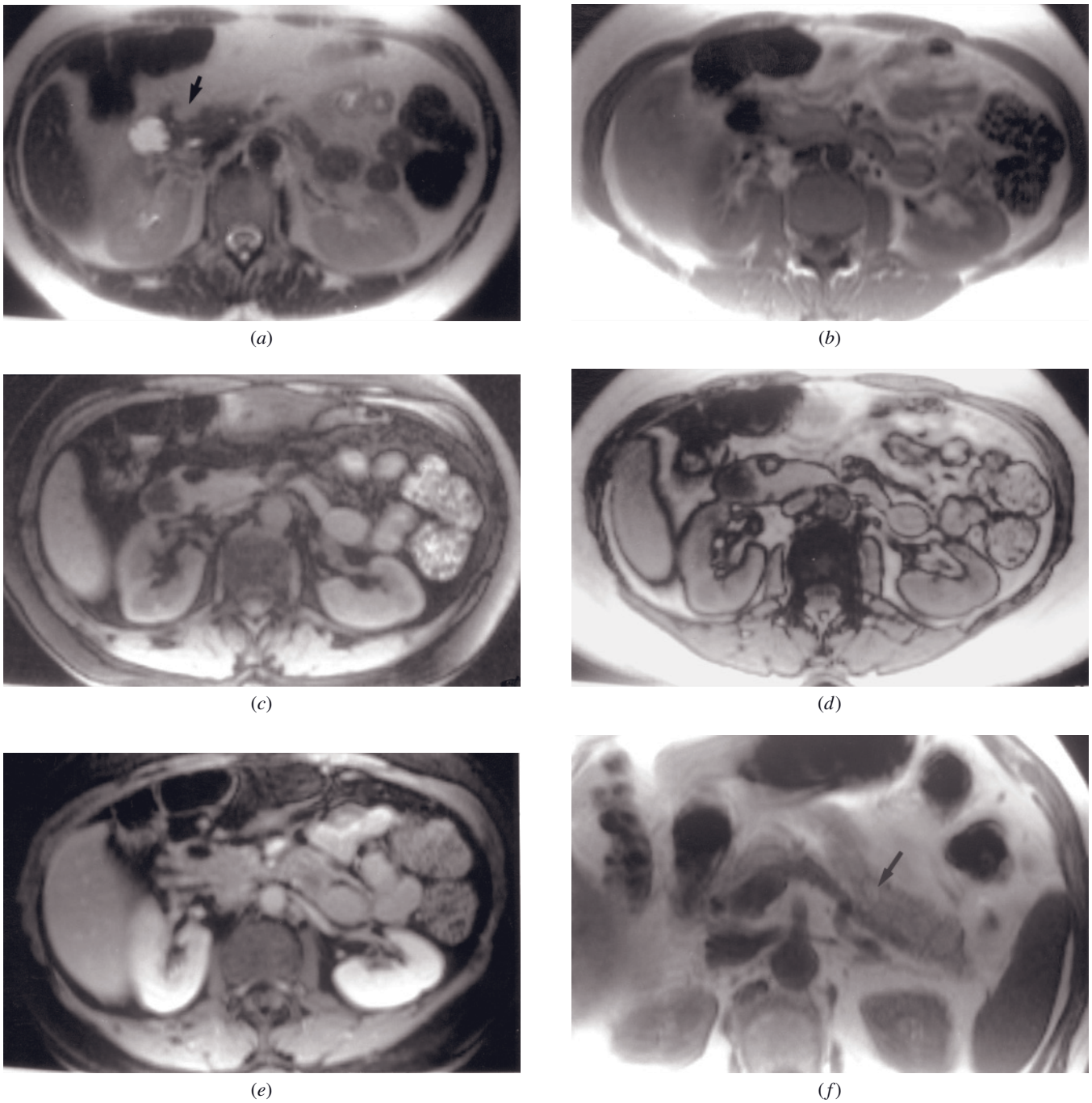

FIG. 4.11 Pancreatic lipoma. T2-weighted SS-ETSE (*a*), T1-weighted SGE (*b*), T1-weighted fat-suppressed SGE (*c*), T1-weighted out-of-phase SGE (*d*), and 90-s postgadolinium T1-weighted fat-suppressed SGE (*e*) images. There is a small lesion in the anterior aspect of the head of the pancreas (arrow, *a*), which appears isointense with adjacent intraperitoneal fat on T1 (*b*)- and T2 (*a*)-weighted images, with drop in signal intensity on fat-suppressed images (*c*, *e*). A phase-cancellation artifact surrounds the lesion on the T1 out-of-phase image (*d*).These findings are diagnostic for a pancreatic lipoma.

compared these MR techniques to dynamic contrast-enhanced CT imaging.

Because of their abundant fibrous stroma and relatively sparse vascularity, pancreatic cancers enhance to a lesser extent than surrounding normal pancreatic tissue on early postcontrast images [36]. It is therefore critical to exploit this difference in vascularity in contrast-enhanced studies by imaging in the dynamic capillary phase of enhancement (see figs. 4.12, 4.13, and 4.17) [36, 37]. Thin section thickness is also helpful, but

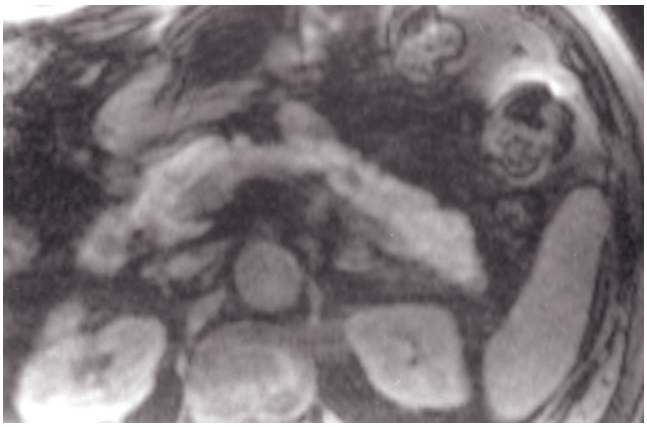

(*g*)

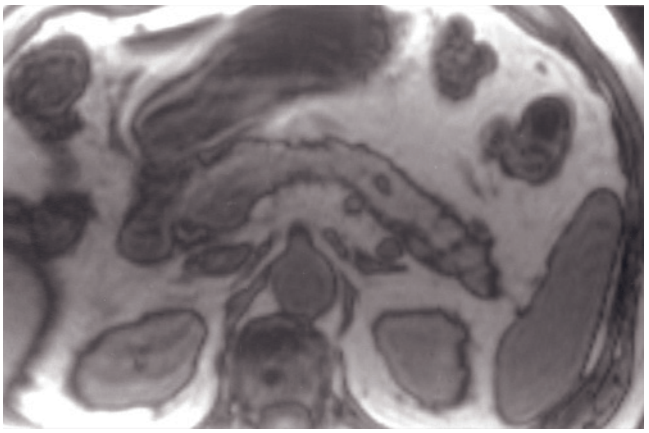

(*h*)

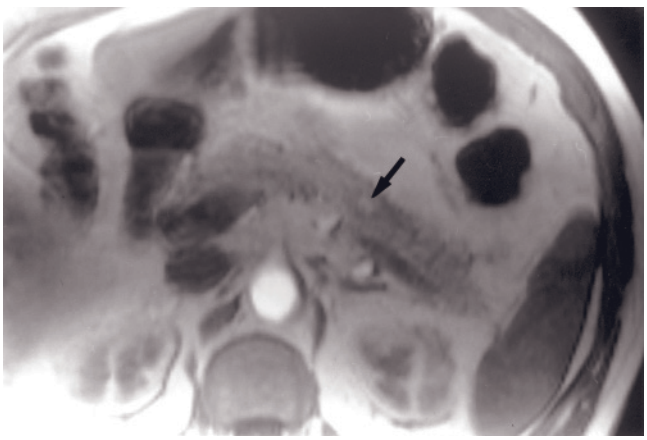

(*i*)

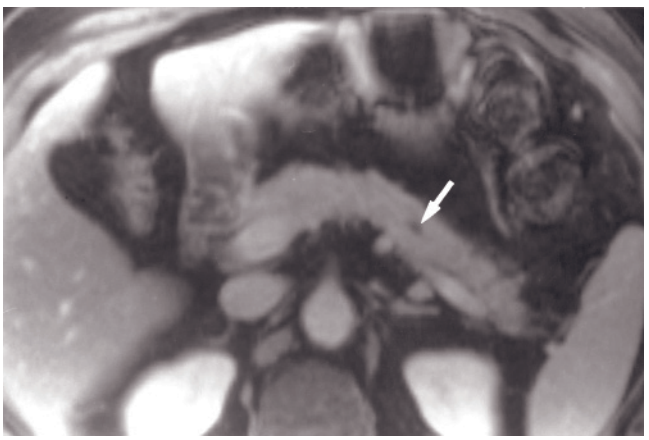

(*j*)

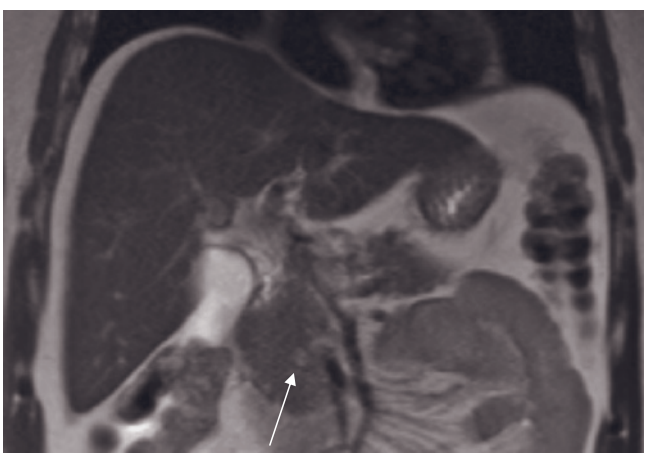

(*k*)

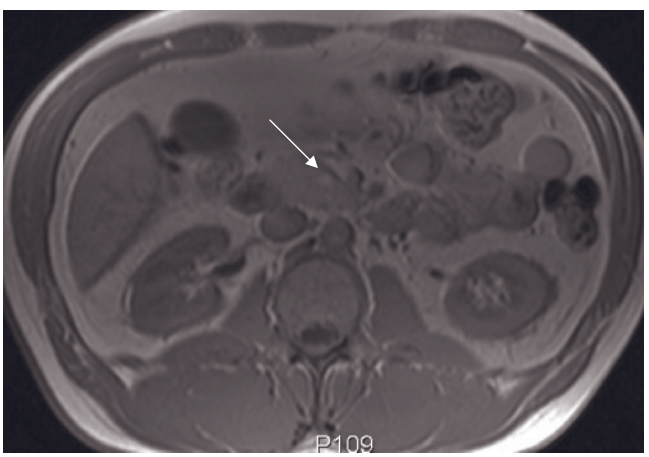

(*l*)

FIG. 4.11 (*Continued*) T1-weighted SGE (*f*), T1-weighted fat-suppressed SGE (*g*), T1-weighted out-of-phase SGE (*h*), immediate postgadolinium T1-weighted SGE (*i*), and 90-s postgadolinium fat-suppressed SGE (*j*) images in a second patient with a small lipoma (arrow, *f*) in the pancreatic body/tail. An important reason to correctly identify a lesion as a lipoma is not to misinterpret high signal on immediate postgadolinium nonsuppressed images as consistent with enhancement (arrow, *i*), nor to misinterpret low signal on interstitial-phase gadolinium-enhanced fat-suppressed images as consistent with washout (arrow, *j*).

Coronal T2-weighted single-shot echo-train spin-echo (*k*), transverse T1-weighted in-phase (*l*) and out-of-phase (*m*) SGE, and transverse T1-weighted postgadolinium hepatic arterial dominant phase (*n*) and hepatic venous phase (*o*) fat-suppressed 3D-GE

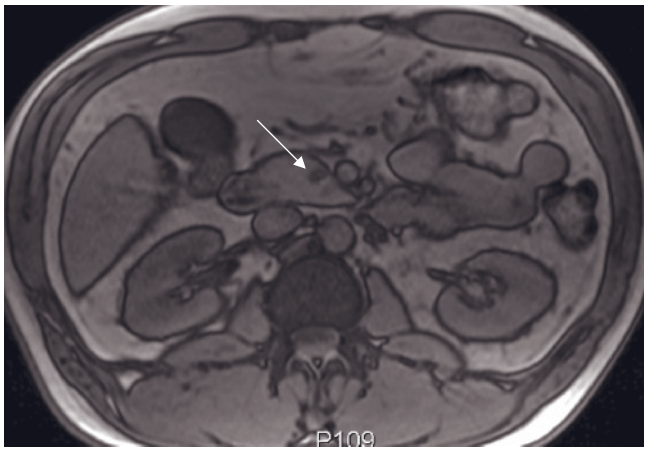

(*m*)

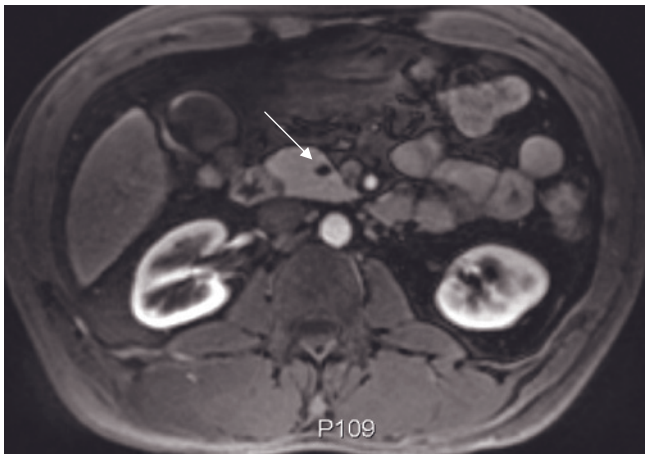

(*n*)

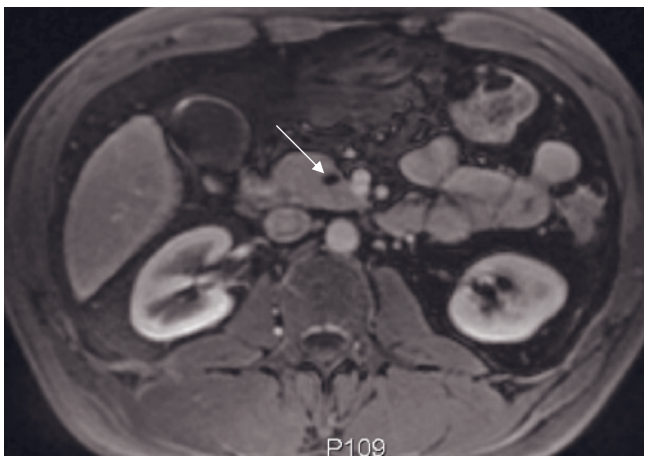

(*o*)

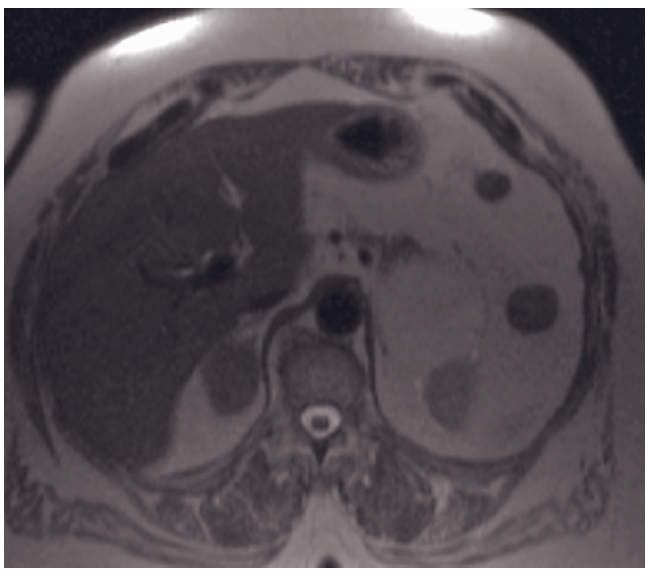

(*p*)

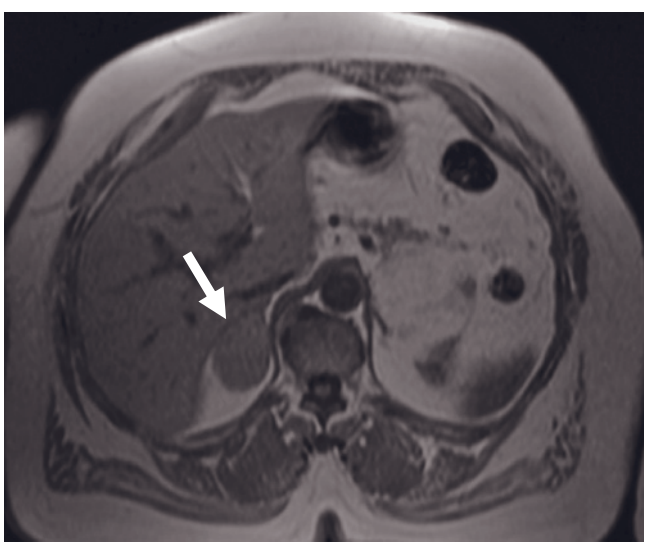

(*q*)

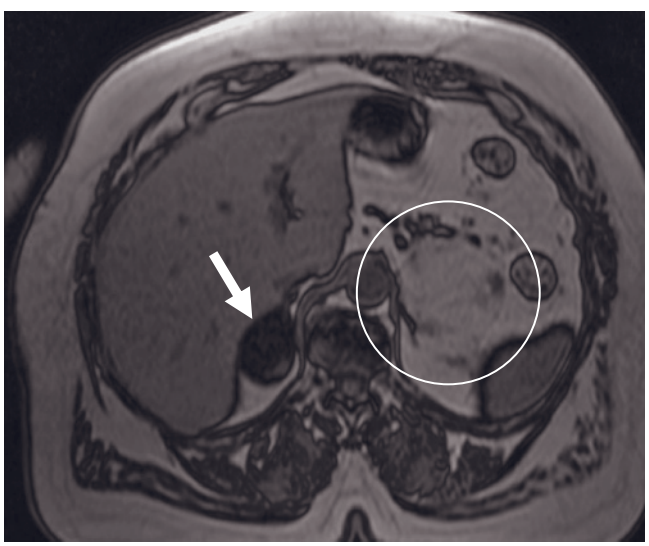

(*r*)

FIG. 4.11 (*Continued*) images at 3.0 T demonstrate a small pancreatic lipoma (arrows, *k–o*) in the pancreatic head of another patient, showing similar and characteristic findings.

T2-weighted single-shot echo-train spin-echo (*p*), T1-weighted in-phase (*q*) and out-of-phase (*r*) SGE, T1-weighted fat-suppressed SGE (*s*), and T1-weighted postgadolinium hepatic venous phase fat-suppressed 3D-GE (*t*) images demonstrate a large pancreatic lipoma

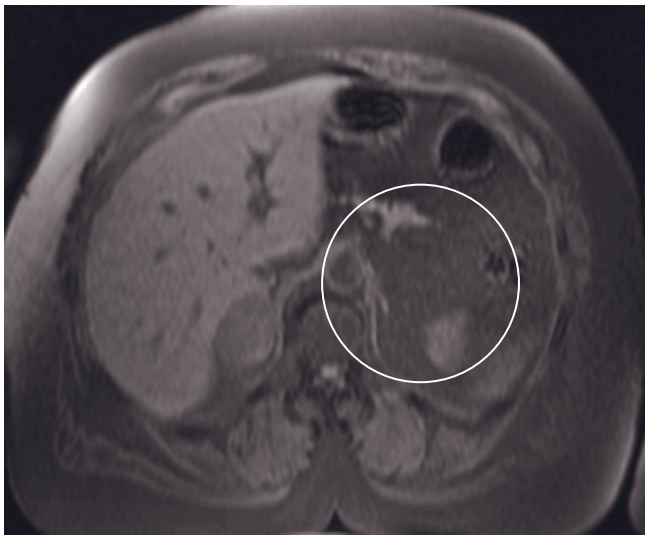

(*s*)

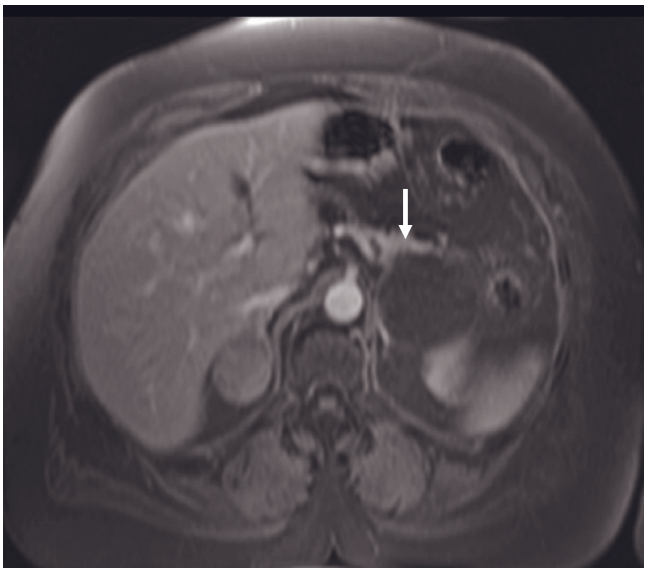

(*t*)

FIG. 4.11 (*Continued*) originating from the tail region and a right adrenal adenoma. The large pancreatic lipoma (circle, *r*, *s*) shows phase cancellation artifact on out-of-phase SGE image (*r*) and suppression on fat-suppressed SGE image (*s*). The pancreatic tail shows beaking (arrow, *t*) and the capsule of lipoma shows enhancement on postgadolinium image (*t*). The right adrenal adenoma (arrows, *q*, *r*) shows prominent signal drop on out-of-phase SGE (*r*) compared to in-phase SGE (*q*) and homogenous enhancement on post-gadolinium image (*t*). While the lipoma consisting of 100% fat demonstrates signal loss on fat-suppressed images, the adenoma shows signal loss on out-of-phase image due to its water and fat components.

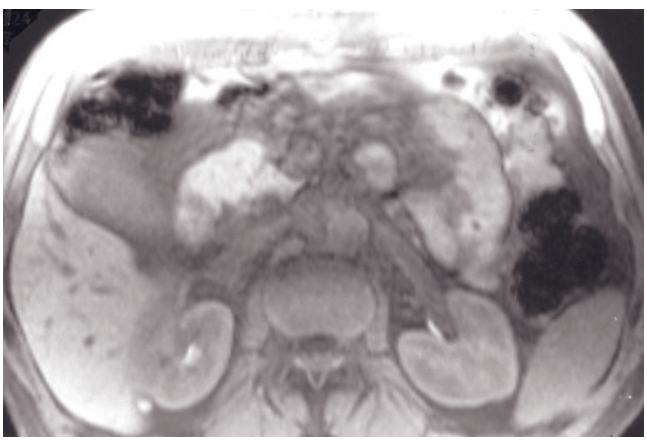

(*a*)

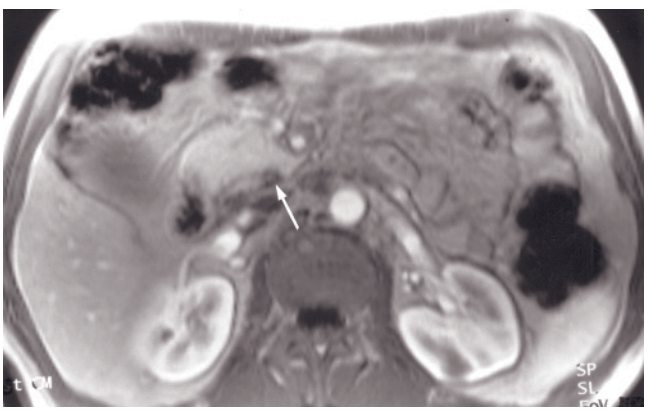

(*b*)

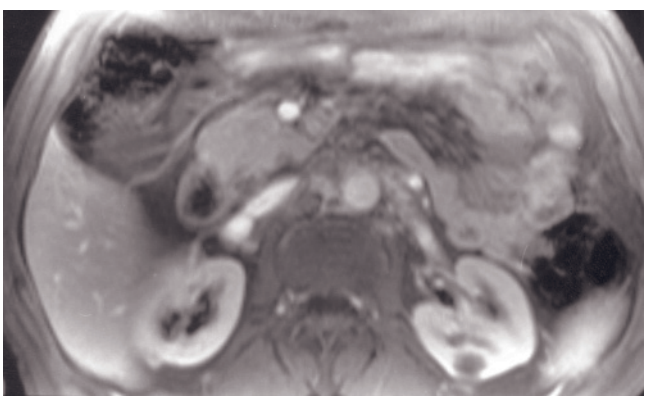

(*c*)

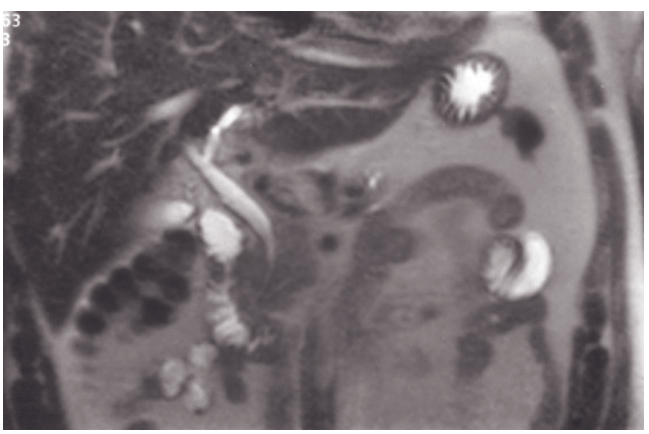

(*d*)

FIG. 4.12 Small pancreatic cancer arising in the head. T1-weighted fat-suppressed SGE (*a*), immediate postgadolinium T1-weighted SGE (*b*), and 90-s postgadolinium fat-suppressed SGE (*c*) images. A 6-mm tumor (arrow, *b*) is present in the uncinate process of the pancreas, which does not result in ductal obstruction because of its small size and location. Note that the mass is most clearly shown on the immediate postgadolinium image (*b*) as a small hypoenhancing lesion. Coronal (*d*) and transverse (*e*)

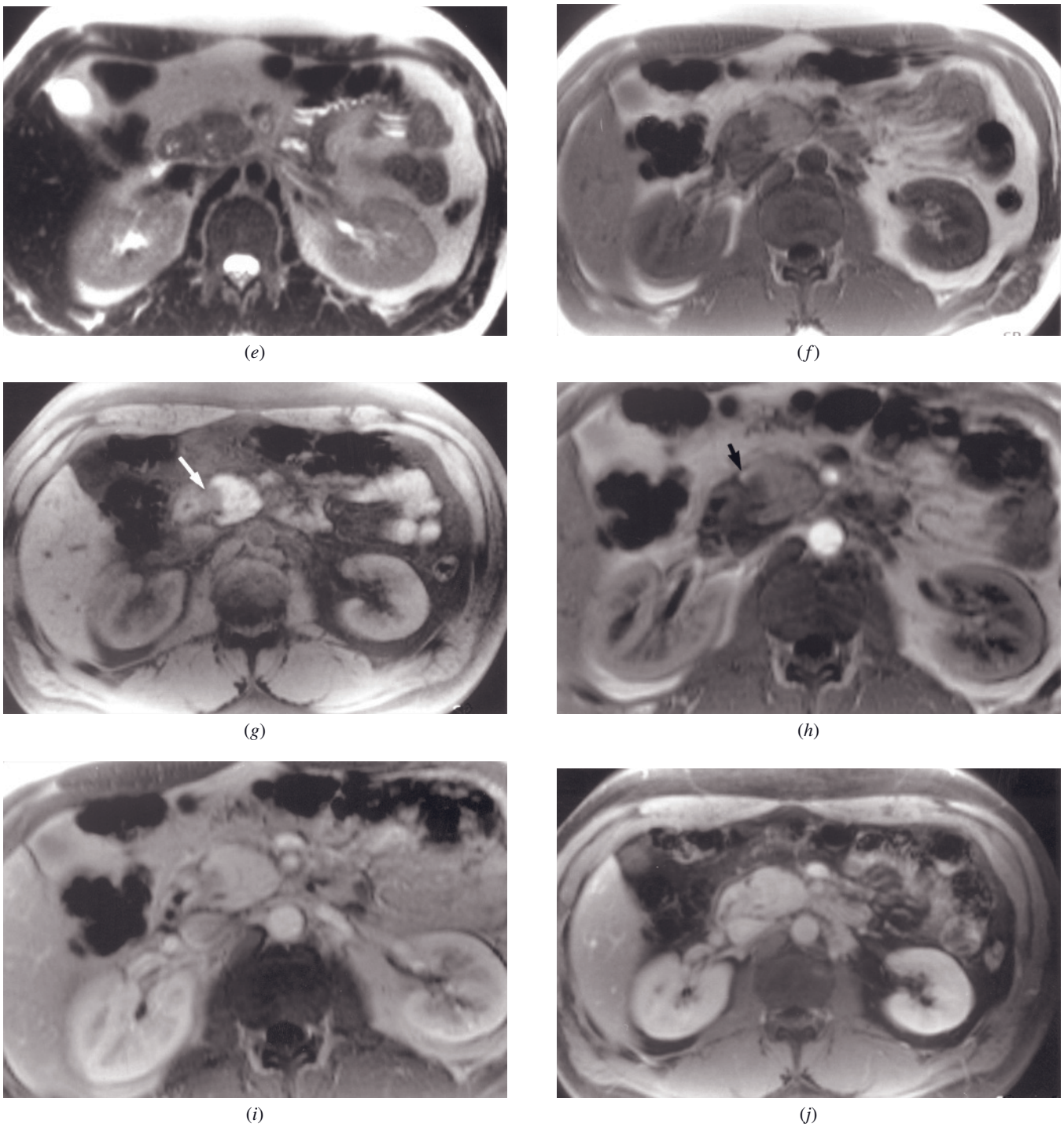

FIG. 4.12 (*Continued*) T2-weighted SS-ETSE, T1-weighted SGE (*f*), T1-weighted fat-suppressed SGE (*g*), and immediate (*h*) and 45-s (*i*) postgadolinium T1-weighted SGE and 90-s postgadolinium fat-suppressed SGE (*j*) images in a second patient with moderately differentiated adenocarcinoma. There is a 1.5-cm mass arising in the lateral aspect of the pancreatic head, which invades the duodenal wall and causes biliary ductal dilatation. On the T2-weighted images (*d*, *e*), CBD obstruction is well shown, but the tumor itself is almost imperceptible. The tumor (arrow, *g*) is most clearly appreciated on the noncontrast T1-weighted fat-suppressed SGE image (*g*) and the immediate postgadolinium SGE image (*h*). Progressive tumor enhancement and pancreatic parenchyma wash-out over time (*i*, *j*) diminishes the tumor-pancreas contrast, which is most problematic with small tumors. The gastroduodenal artery (arrow, *h*) is well shown on the immediate postgadolinium image as an enhancing structure. The tumor is shown to abut this vessel. Approximately one-quarter of all pancreas head cancers exhibit some degree of duodenal wall invasion.

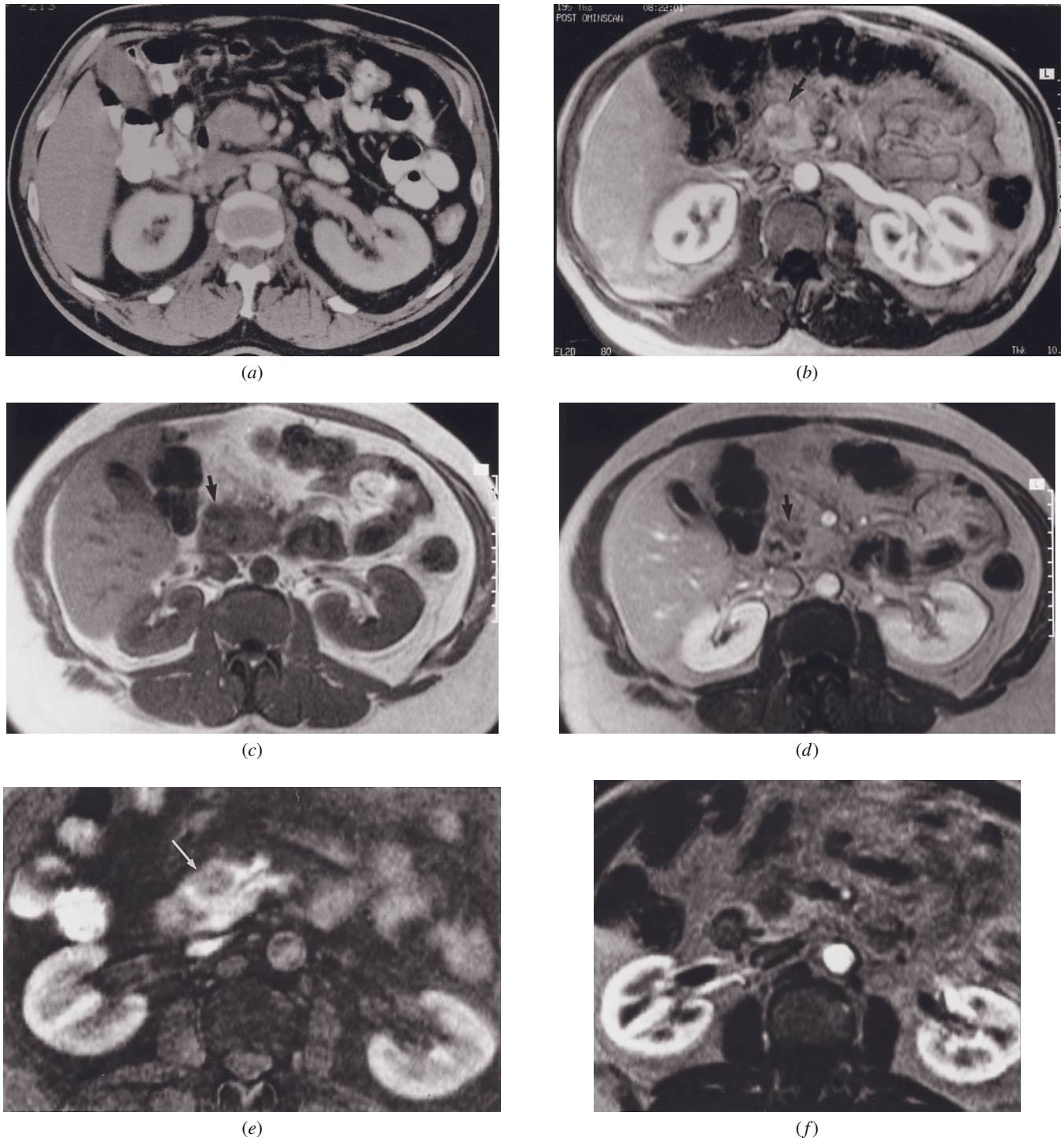

FIG. 4.13 Small pancreatic cancer arising in the head. Dynamic contrast-enhanced CT (*a*) and immediate postgadolinium T1-weighted SGE (*b*) images. The non-organ-deforming cancer is not apparent on the CT image (*a*). On the immediate postgadolinium image (*b*), a heterogeneous low-signal-intensity tumor (arrow, *b*) is identified in the head of the pancreas, clearly demarcated from uniform-enhancing pancreatic tissue.

T1-weighted SGE (*c*) and 45-s postgadolinium T1-weighted SGE (*d*) images in a second patient. A 2-cm pancreatic cancer is present that is minimally lower in signal intensity than pancreas on the precontrast image (*c*) and enhances substantially less than pancreas on the early postgadolinium image (arrow, *d*). T1-weighted fat-suppressed spin-echo (*e*), immediate postgadolinium T1-weighted SGE (*f*), and interstitial-phase gadolinium-enhanced T1-weighted fat-suppressed spin-echo (*g*) images in a third patient.

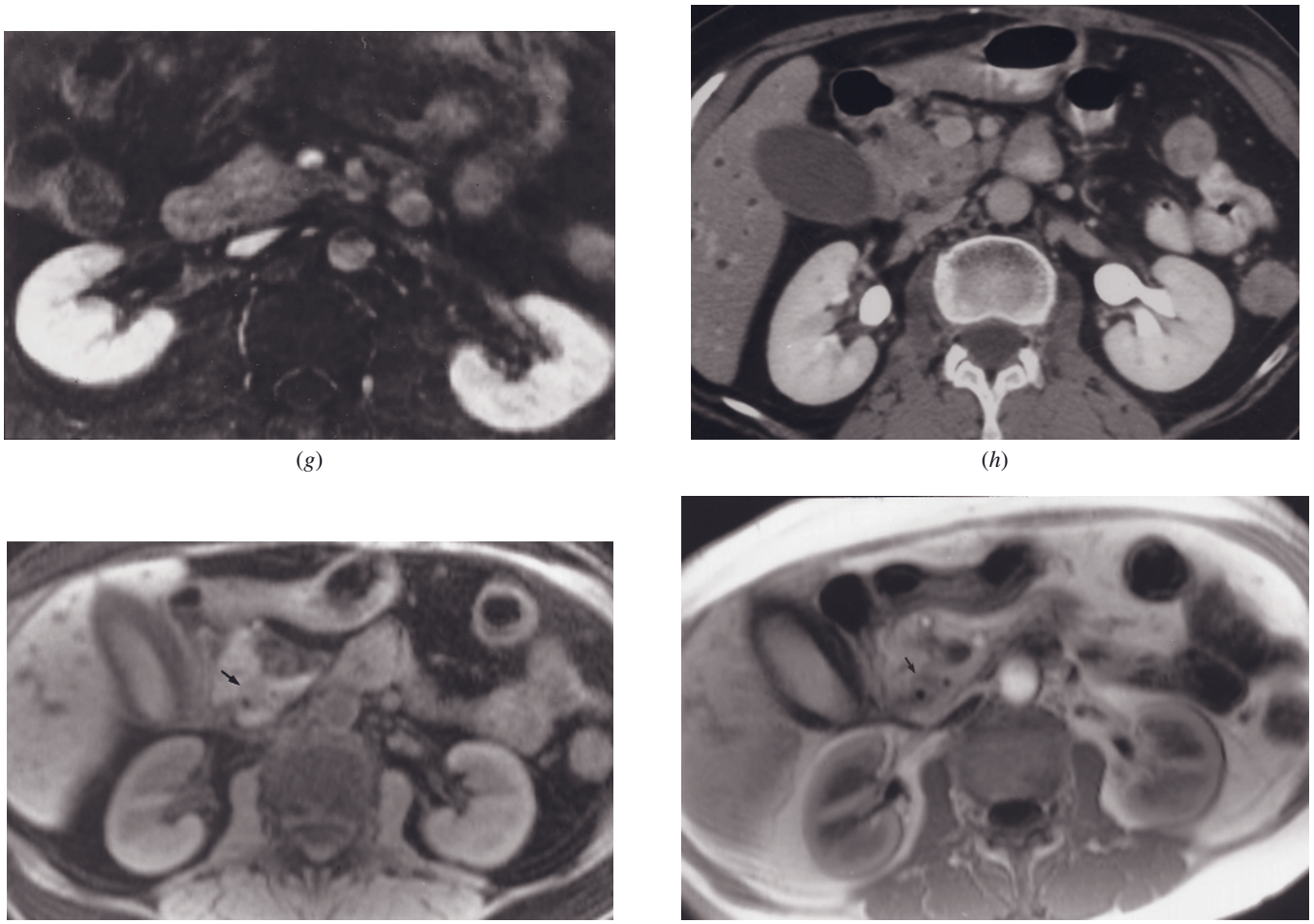

(*g*) (*h*)

(*i*) (*j*)

FIG. 4.13 (*Continued*) A small non-organ-deforming cancer is present in the head of the pancreas (arrow, *e*). The tumor does not obstruct the main pancreatic duct, so background pancreas remains high in signal intensity on T1-weighted fat-suppressed images (*e*). The immediate postgadolinium T1-weighted SGE image (*f*) demonstrates normal capillary enhancement of the pancreas with minimal enhancement of the cancer. The interstitial-phase gadolinium-enhanced T1-weighted fat-suppressed image (*g*) demonstrates minimally higher signal intensity of the tumor compared to the background pancreas, reflecting a greater accumulation of gadolinium by the tumor and obscuring the cancer.

Spiral CT (*h*),T1-weighted fat-suppressed SGE (*i*), and immediate postgadolinium T1-weighted SGE (*j*) images in a fourth patient. The pancreatic cancer is not visualized on the spiral CT image (*h*). On the T1-weighted fat-suppressed image, the tumor is low in signal intensity (arrow, *i*) relative to background pancreas. On the immediate postgadolinium image (*j*), the tumor (arrow, *j*) enhances less than background pancreas.

8-mm-thick sections may be sufficiently thin to detect even small (<1 cm) cancers because of the high contrast resolution on 2D-SGE images. An adequate signal-to-noise ratio may be achieved with section thickness of 5 mm by using a phased-array surface coil. On newer MR systems, 3D-GE is a good technique to detect small pancreatic cancers with 3 mm section thickness (see figs. 4.17 and 4.18). Although pancreatic cancers are lower in signal intensity than pancreas on immediate postgadolinium (capillary phase) images, the appearance of cancers on ≥1-min postgadolinium (interstitial phase) images is variable [36]. The enhancement of cancer relative to pancreas on interstitial phase images reflects the volume of extracellular space and venous drainage of cancers compared to pancreatic tissue. In general, large pancreatic tumors tend to remain low in signal intensity on later images (see figs. 4.23 and 4.25), whereas smaller tumors may range from hypointense to hyperintense.

Pancreatic cancers appear as low-signal-intensity masses on noncontrast T1-weighted fat-suppressed images and are clearly separated from normal pancreatic tissue, which is high in signal intensity [4, 36, 37]. Pancreatic tissue distal to pancreatic cancer is often lower in signal intensity than normal pancreatic tissue [36, 37]. This finding may be explained by

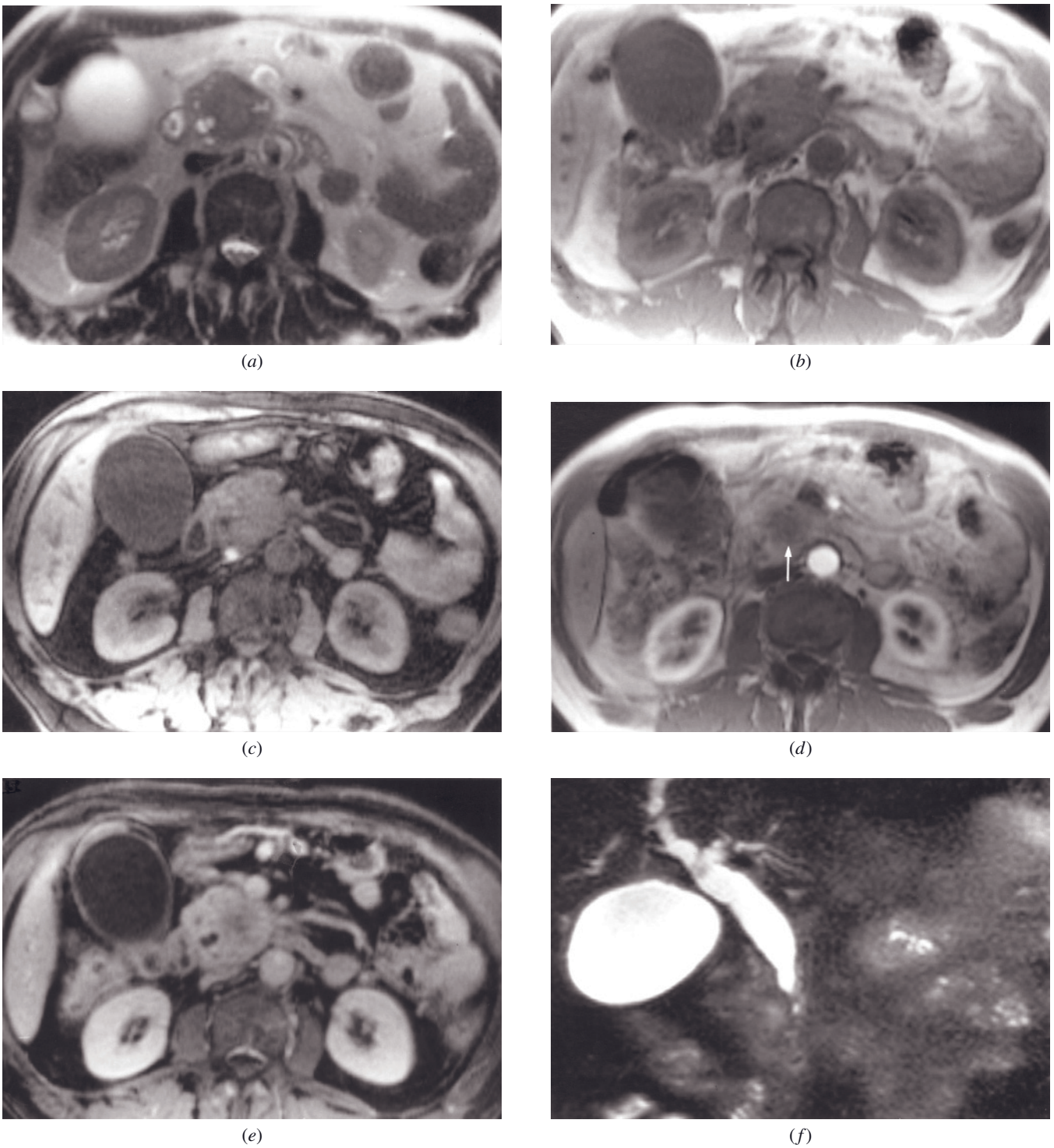

FIG. 4.14 Pancreatic cancer arising in the head. T2-weighted echo-train spin-echo (*a*), T1-weighted SGE (*b*), T1-weighted fat-suppressed SGE (*c*), immediate postgadolinium T1-weighted SGE (*d*), and 90-s postgadolinium fat-suppressed SGE (*e*) images. There is a 4-cm tumor arising in the pancreatic head, which appears hypointense on T1 (*b*, *c*)- and T2 (*a*)-weighted images. On immediate postgadolinium images (*c*), the tumor exhibits diminished enhancement compared to normal adjacent pancreatic parenchyma, with demarcation of the tumor edges (arrow, *d*) with background pancreas.

MRCP (*f*), immediate postgadolinium T1-weighted SGE (*g*), and 90-s postgadolinium fat-suppressed SGE (*h*) images in a second patient with poorly differentiated pancreatic adenocarcinoma. The pancreatic cancer appears as a hypoenhancing mass (arrow, *g*)

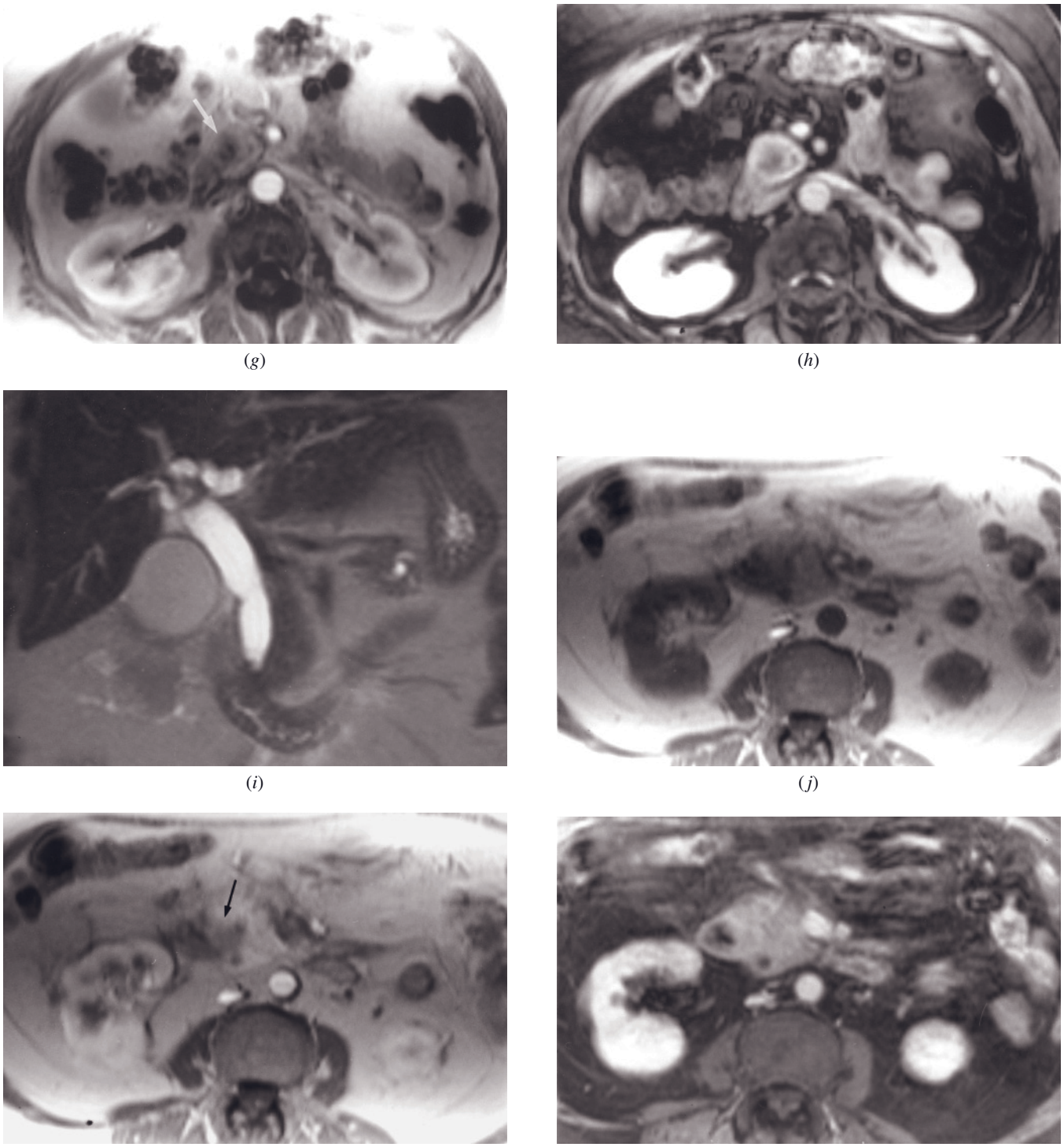

FIG. 4.14 (*Continued*) on the immediate postgadolinium image (*g*) with demarcated margins. Relationship to the superior mesenteric vessels, which are spared, is well shown on the interstitial phase gadolinium-enhanced fat-suppressed image (*h*). Coronal T2-weighted echo-train spin-echo (*i*),T1-weighted SGE (*j*), immediate postgadolinium T1-weighted SGE (*k*), and 90-s postgadolinium fat-suppressed SGE (*l*) images. A 2-cm moderately differentiated adenocarcinoma of the pancreatic head is present (arrow, *k*), which is most clearly depicted on the immediate postgadolinium image (*k*). On the interstitial-phase gadolinium-enhanced fat-suppressed image (*l*), the tumor has decreased in conspicuity because of progressive tumor enhancement and pancreatic parenchymal wash-out. Invasion of the medial duodenal wall is shown by contiguous extension of tumor to the wall.

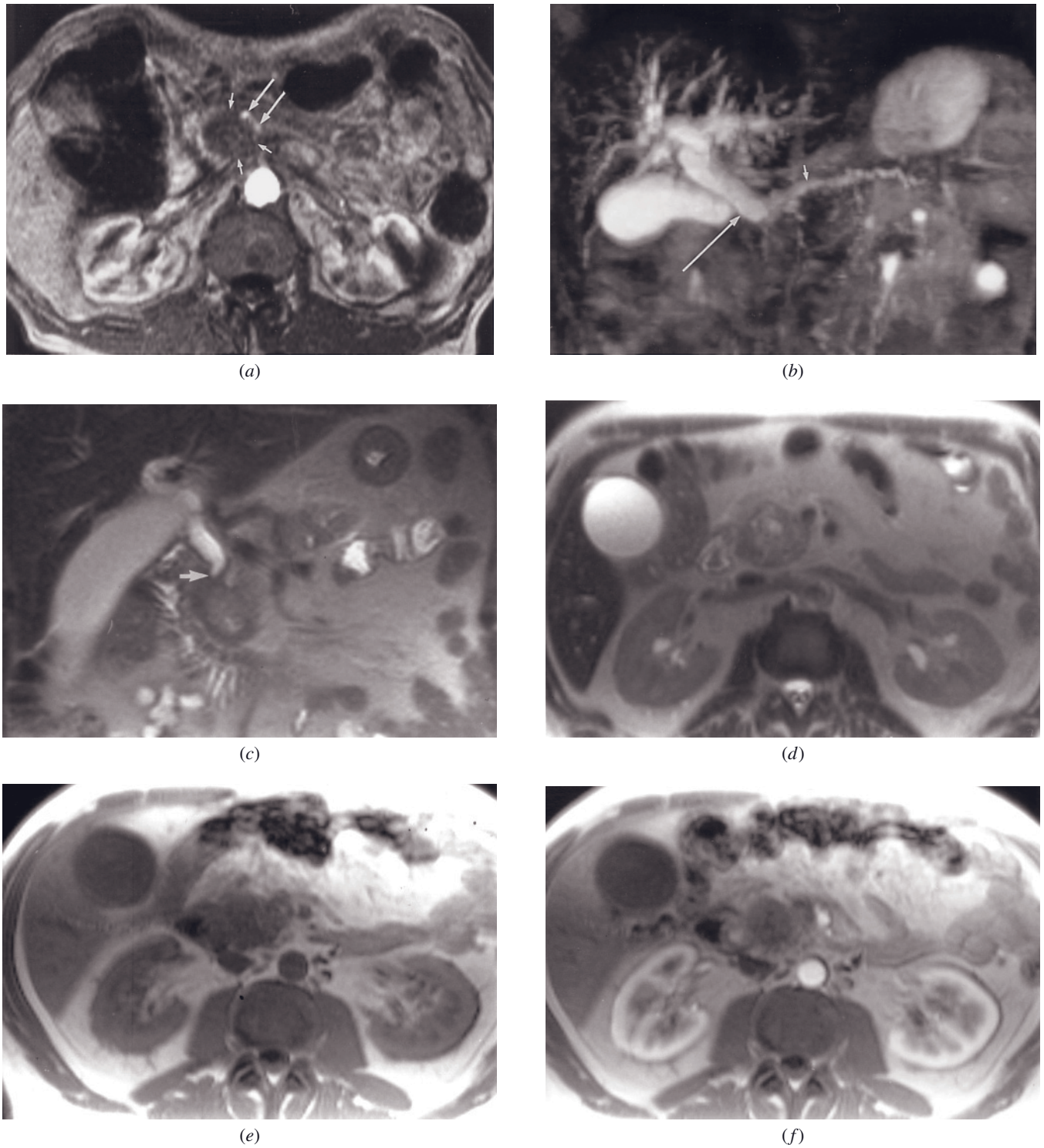

FIG. 4.15 Pancreatic cancer arising in the head with biliary tree dilatation. Immediate postgadolinium T1-weighted SGE (*a*) and non-breath-hold 3D MIP MRCP (*b*) images. A 3.5-cm cancer arises from the head of the pancreas. On the immediate post-contrast image (*a*), the tumor is well shown as a low-signal intensity mass (small arrows, *a*) that is closely applied to the superior mesenteric vein and superior mesenteric artery (long arrows, *a*). The MRCP image (*b*) demonstrates obstruction of the CBD (long arrow, *b*) and pancreatic duct (small arrow, *b*) creating the "double duct" sign.

Coronal (*c*) and transverse (*d*) T2-weighted SS-ETSE, T1-weighted SGE (*e*), immediate (*f*) and 45-s (*g*) postgadolinium T1-weighted SGE, and transverse (*h*) and coronal (*i*) interstitial-phase gadolinium-enhanced fat-suppressed SGE images in a second

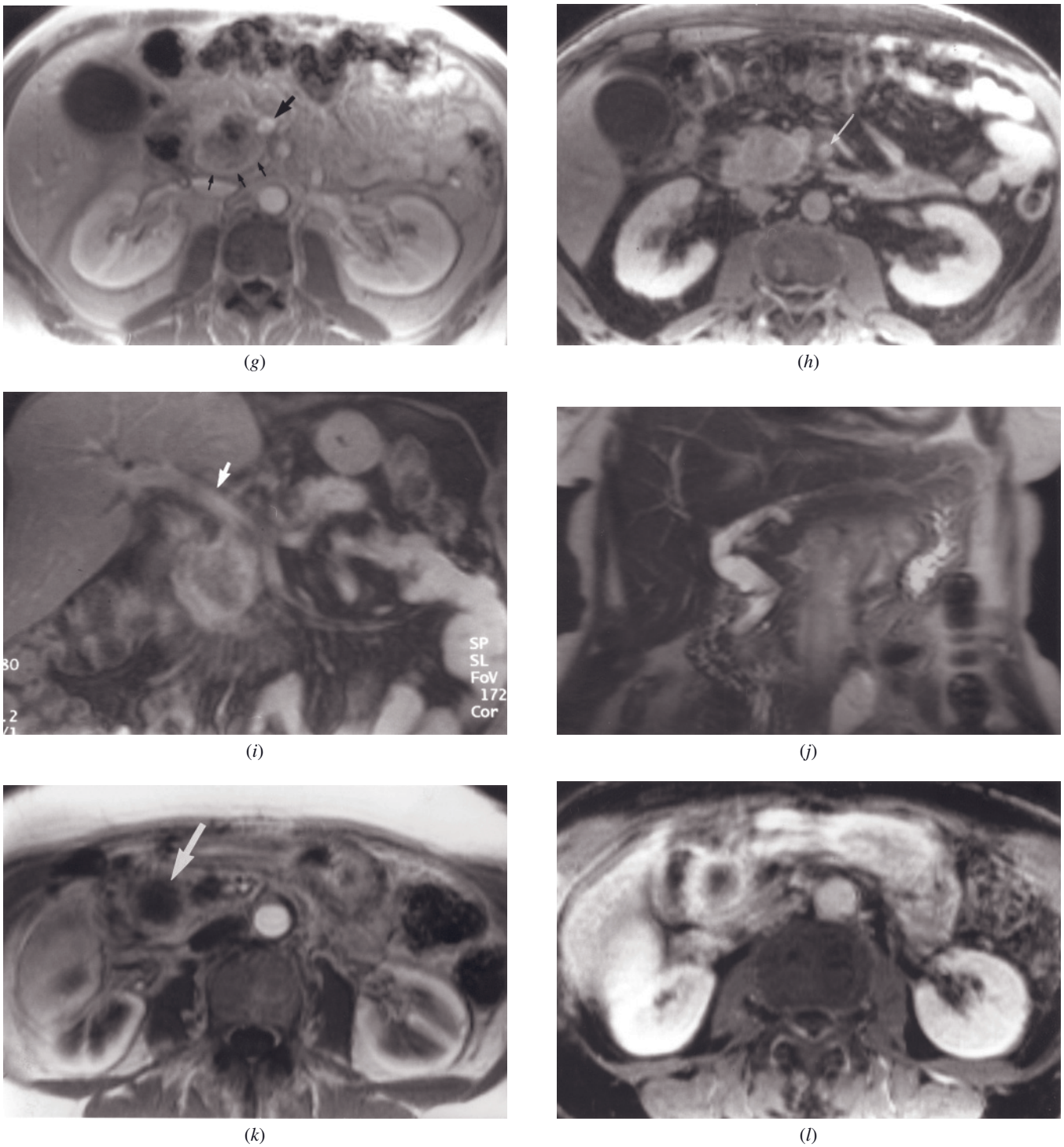

FIG. 4.15 (*Continued*) patient with a poorly differentiated pancreatic adenocarcinoma arising in the head. Obstruction of the CBD (arrow, *c*) by the pancreatic head cancer is clearly shown on the coronal image (*c*). The pancreatic mass is mildly heterogeneous and hyperintense on T2-weighted (*c*, *d*) images, with minimal enhancement on early postcontrast images (*f*) and progressive enhancement on later images (*h*). The tumor partially encases the superior mesenteric vein (arrow, *h*), and a definable margin with a thin rim of adjacent pancreas (small arrows, *g*) is appreciated. Duskiness of the fat around the superior mesenteric artery (arrow, *h*) is shown on the interstitial-phase gadolinium-enhanced fat-suppressed image (*h*). The coronal gadolinium-enhanced fat-suppressed image shows a patent portal vein (arrow, *i*) and its relationship with the cancer. Coronal T2-weighted SS-ETSE (*j*), immediate post-gadolinium T1-weighted SGE (*k*), and 90-s postgadolinium fat-suppressed SGE (*l*) images in a third patient with pancreatic cancer. Obstruction of the CBD is present. A hypoenhancing tumor (arrow, *k*) with definable margins with adjacent pancreas is clearly shown on the immediate postgadolinium image (*k*), which has central necrotic areas and causes biliary tree dilatation.

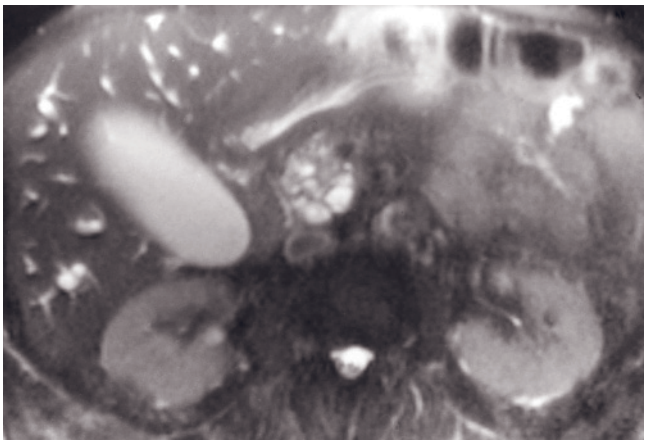

(*a*)

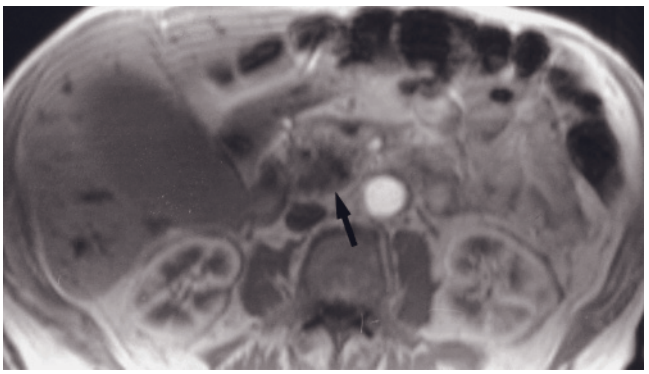

(*b*)

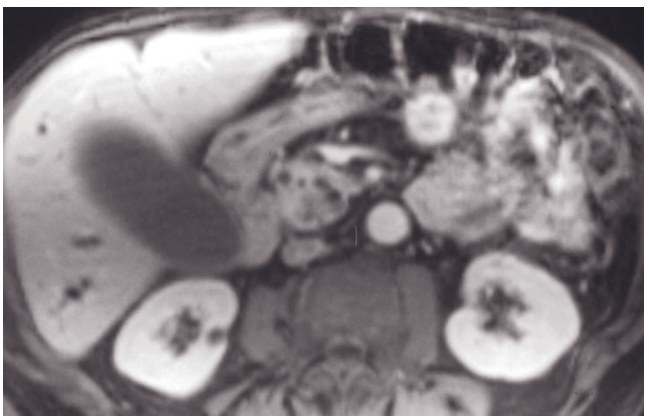

(*c*)

FIG. 4.16 Pancreatic head cancer with cystic components. T2-weighted SS-ETSE (*a*), immediate postgadolinium T1-weighted SGE (*b*), and 90-s postgadolinium fat-suppressed SGE (*c*) images. A 3-cm tumor arises from the posterior aspect of the pancreatic head (arrow, *b*), which is most clearly defined as a mass with demarcated borders on the immediate postgadolinium images (*b*). Extensive cystic changes are associated with the tumor, as shown on the T2-weighted image (*a*).

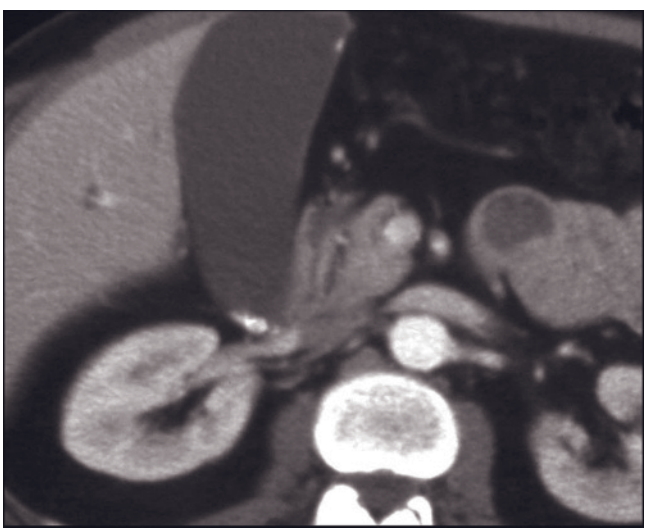

(*a*)

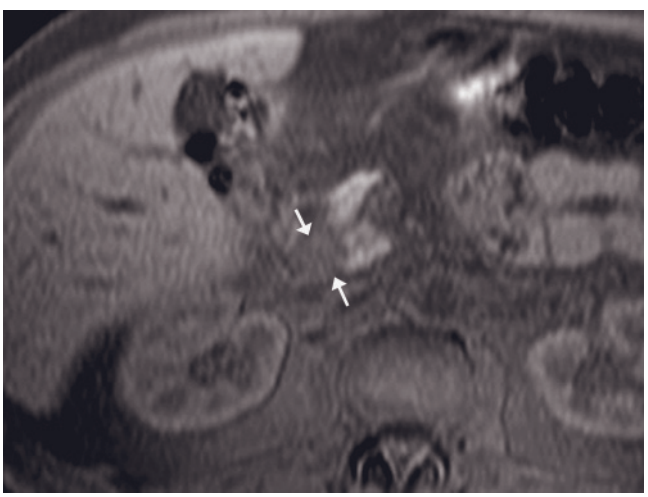

(*b*)

FIG. 4.17 Small pancreatic cancer arising in the head. Dynamic contrast-enhanced CT (*a*), fat-suppressed T1-weighted gradient-echo (*b*), immediate postgadolinium fat-suppressed T1-weighted 3D gradient-echo (*c*), and coronal reformat of

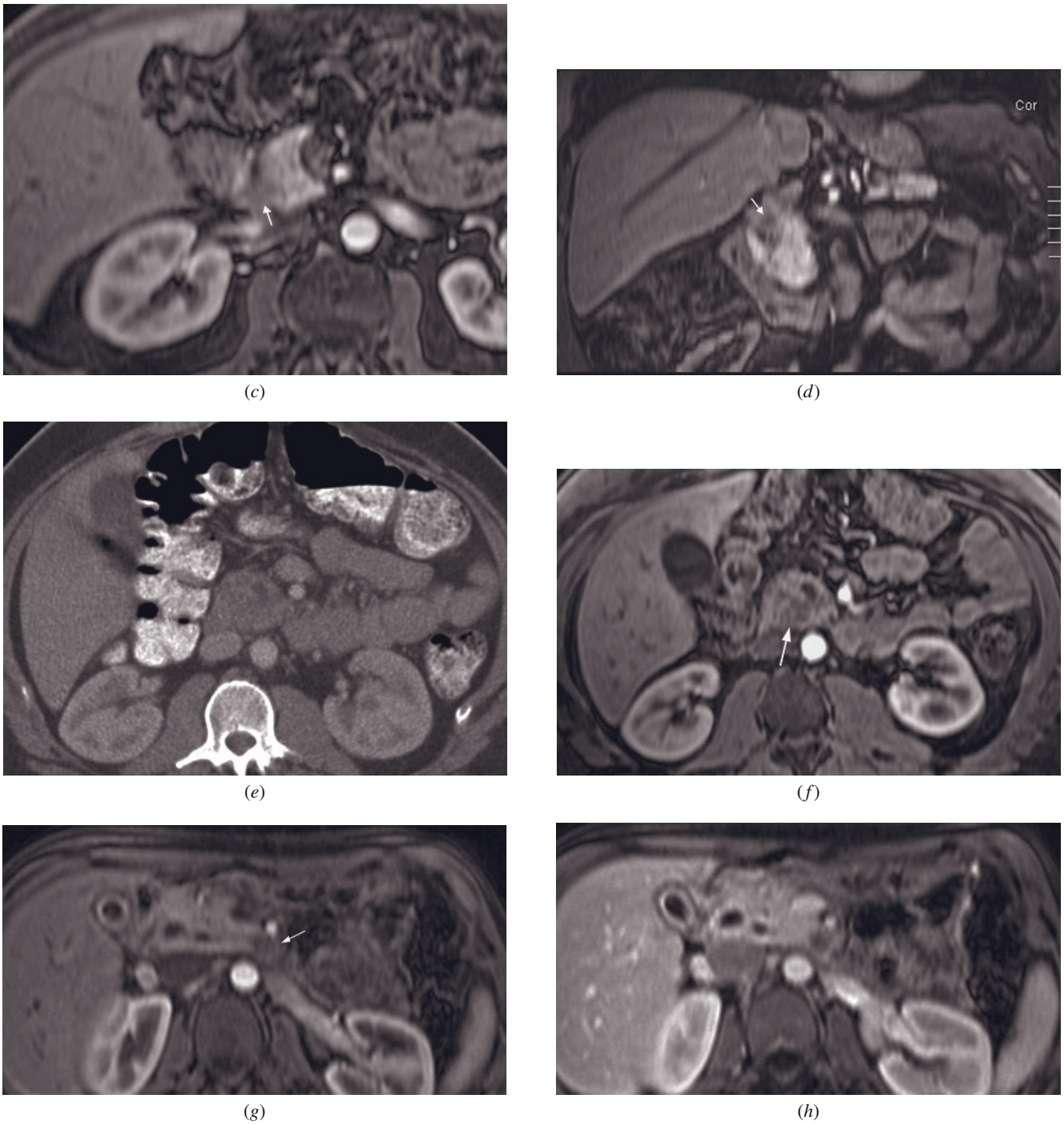

FIG. 4.17 (*Continued*) the immediate postgadolinium fat-suppressed T1-weighted 3D gradient-echo (*d*) images in a patient with small pancreatic cancer. A small cancer is present in the pancreatic head (arrows, *c*, *d*), which is most clearly defined as a mass with demarcated borders on fat-suppressed T1-weighted images (arrows, *b*). The small, non-organ-deforming tumor is not apparent on CT image. The tumor appears as a hypoenhancing mass (arrow, *c*) on the immediate postgadolinium image (*c*) with demarcated margins. Dynamic contrast-enhanced CT (*e*) and immediate postgadolinium fat-suppressed T1-weighted 3D gradient-echo (*f*) images in a second patient. A small cancer seen on the immediate postgadolinium image (arrow, *f*), is not appreciated on CT image.

Immediate and interstitial postgadolinium fat-suppressed T1-weighted gradient-echo images (*g*, *h*) in a third patient demonstrate a small hypoenhancing mass arising from the tip of the uncinate process. This mass is seen well only on the immediate postgadolinium 3D gradient-echo image (arrow, *g*).

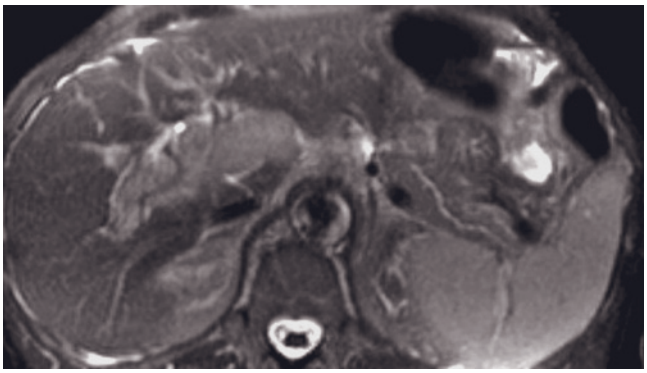

(*a*)

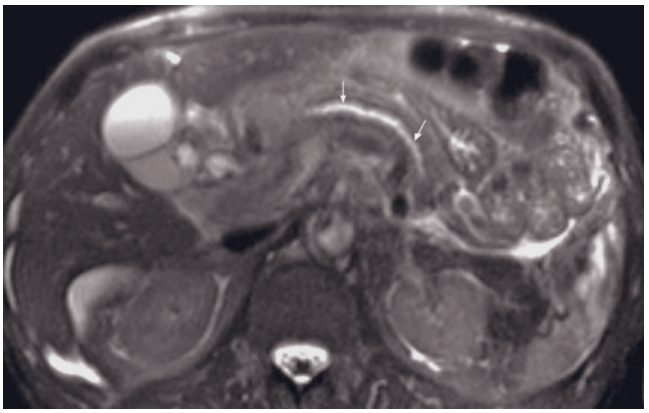

(*b*)

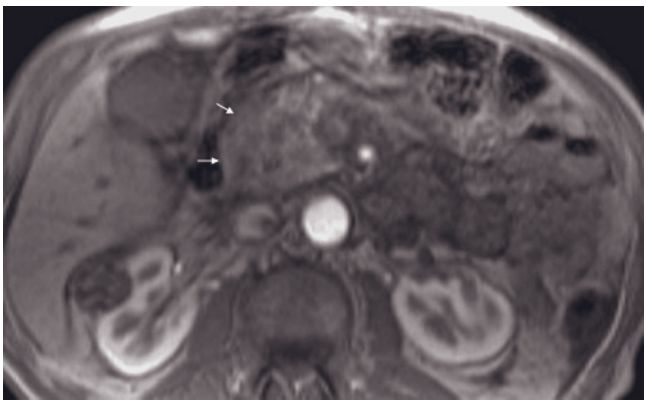

(*c*)

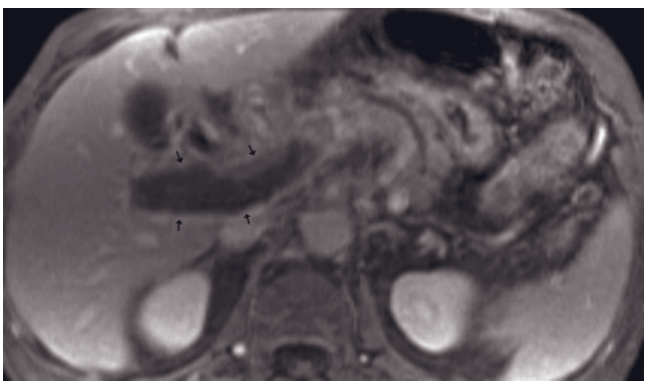

(*d*)

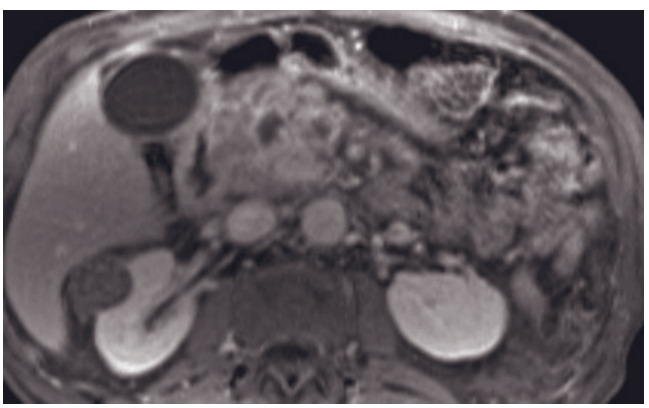

(*e*)

FIG. 4.18 Pancreatic head cancer with portal vein thrombosis. T2-weighted SS-ETSE (*a*, *b*) and immediate postgadolinium (*c*) and interstitial-phase postgadolinium fat-suppressed T1-weighted gradient echo (*d*, *e*) images. A large tumor is present in the head of the pancreas that results in obstruction of the pancreatic duct (arrows, *b*).The portal vein is thrombosed (arrows, *d*, *e*). The tumor enhances in a minimal heterogeneous fashion on the immediate postgadolinium image (arrows, *c*).

tumor-associated pancreatitis occurring distal to the tumor because of obstruction of the main pancreatic duct. With chronic inflammation of the pancreas, there is progressive fibrosis and glandular atrophy and the proteinaceous fluid of the gland diminishes [36, 40]. In these cases, depiction of cancer is poor on noncontrast T1-weighted fat-suppressed images [36, 37]. However, immediate postgadolinium gradient-echo images are able to define the size and extent of cancers that obstruct the pancreatic duct [36, 37]. Demonstration of a rim of increased enhancement representing surrounding pancreas is commonly observed in pancreatic cancer, particularly that arising in the head. This is an important imaging feature, which helps to establish the focal nature of the disease process (see fig. 4.15). These tumors appear as low-signal-intensity mass lesions in a background of slightly greater-enhancing chronically inflamed pancreas. Tumors are usually large when they cause changes of surrounding chronic pancreatitis, and in this setting diagnosis is not problematic. In carcino-

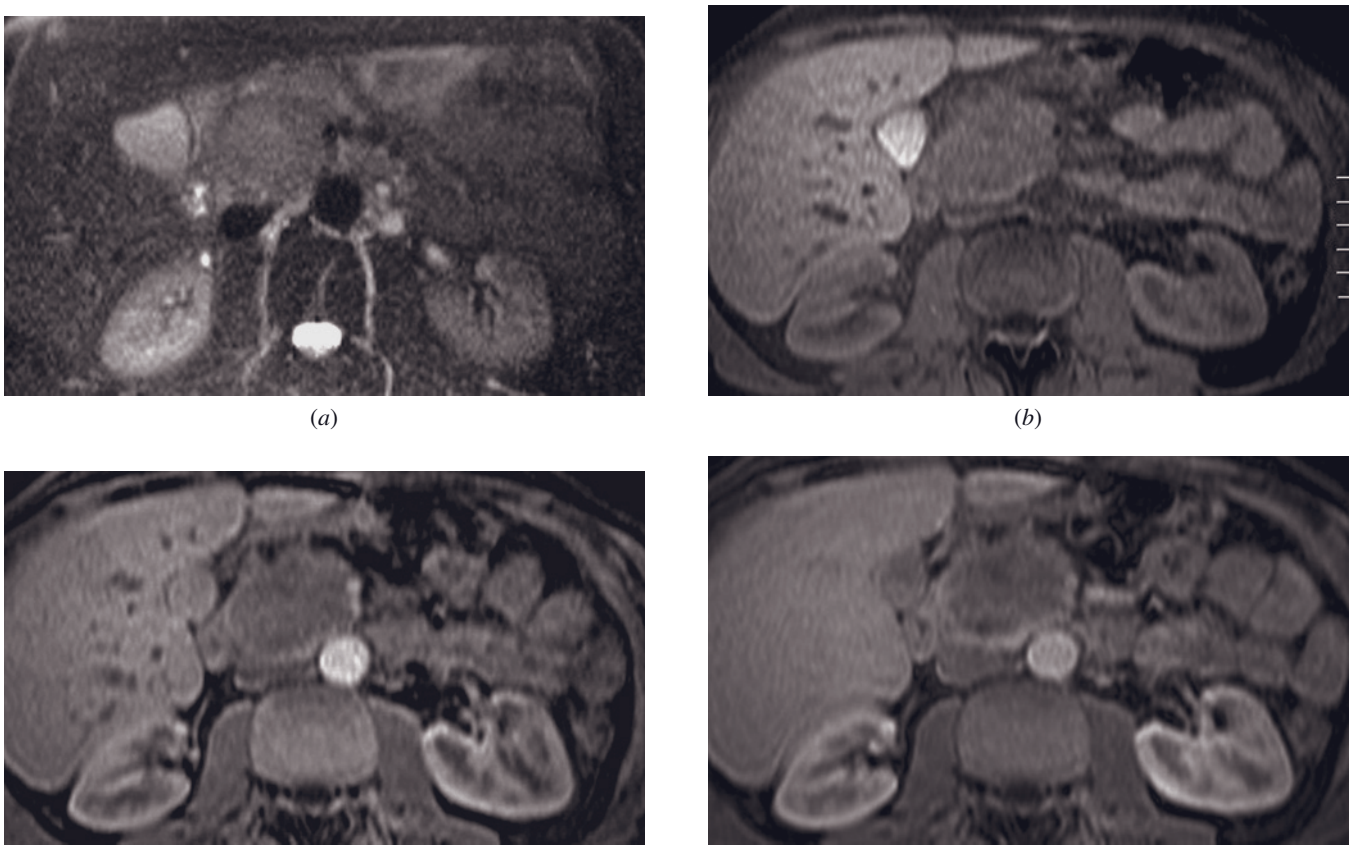

(*a*) (*b*)

(*c*) (*d*)

FIG. 4.19 Large pancreatic cancer arising in the head. Fat-suppressed T2-weighted SS-ETSE (*a*), fat-suppressed T1-weighted gradient-echo (*b*), and immediate (*c*) and interstitial-phase (*d*) postgadolinium fat-suppressed T1-weighted gradient-echo images in a patient with pancreatic cancer. A 5-cm mass is present in the pancreatic head. It is mildly hypointense relative to pancreas and demonstrates diminished enhancement on immediate and late postgadolinium T1-weighted images (*c*, *d*).

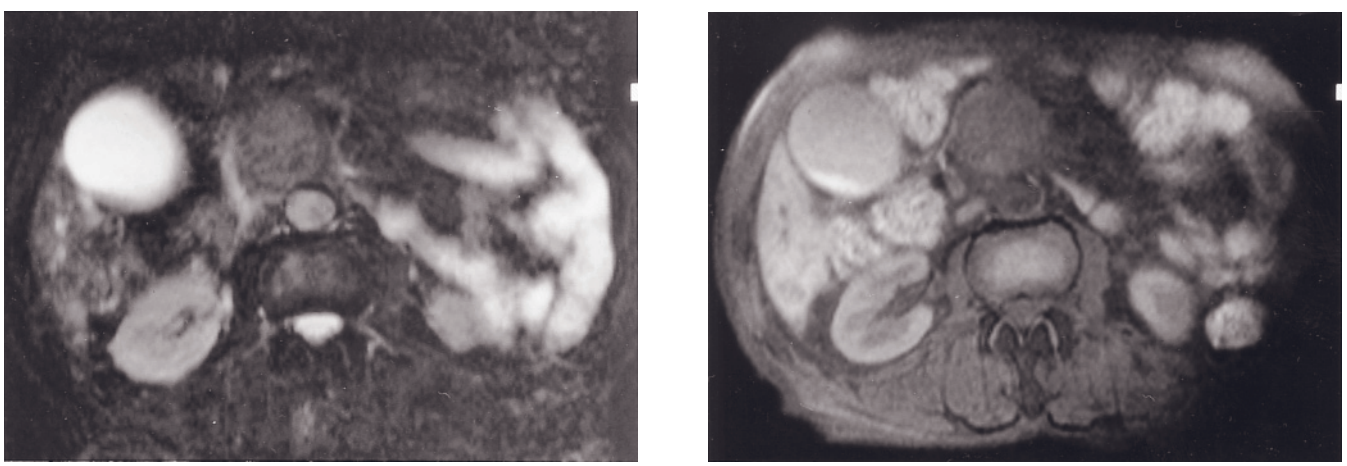

(*a*) (*b*)

FIG. 4.20 Large pancreatic cancer arising in the head. T2-weighted fat-suppressed SS-ETSE (*a*), T1-weighted fat-suppressed spin-echo (*b*), immediate postgadolinium T1-weighted SGE (*c*), and interstitial-phase gadolinium-enhanced T1-weighted

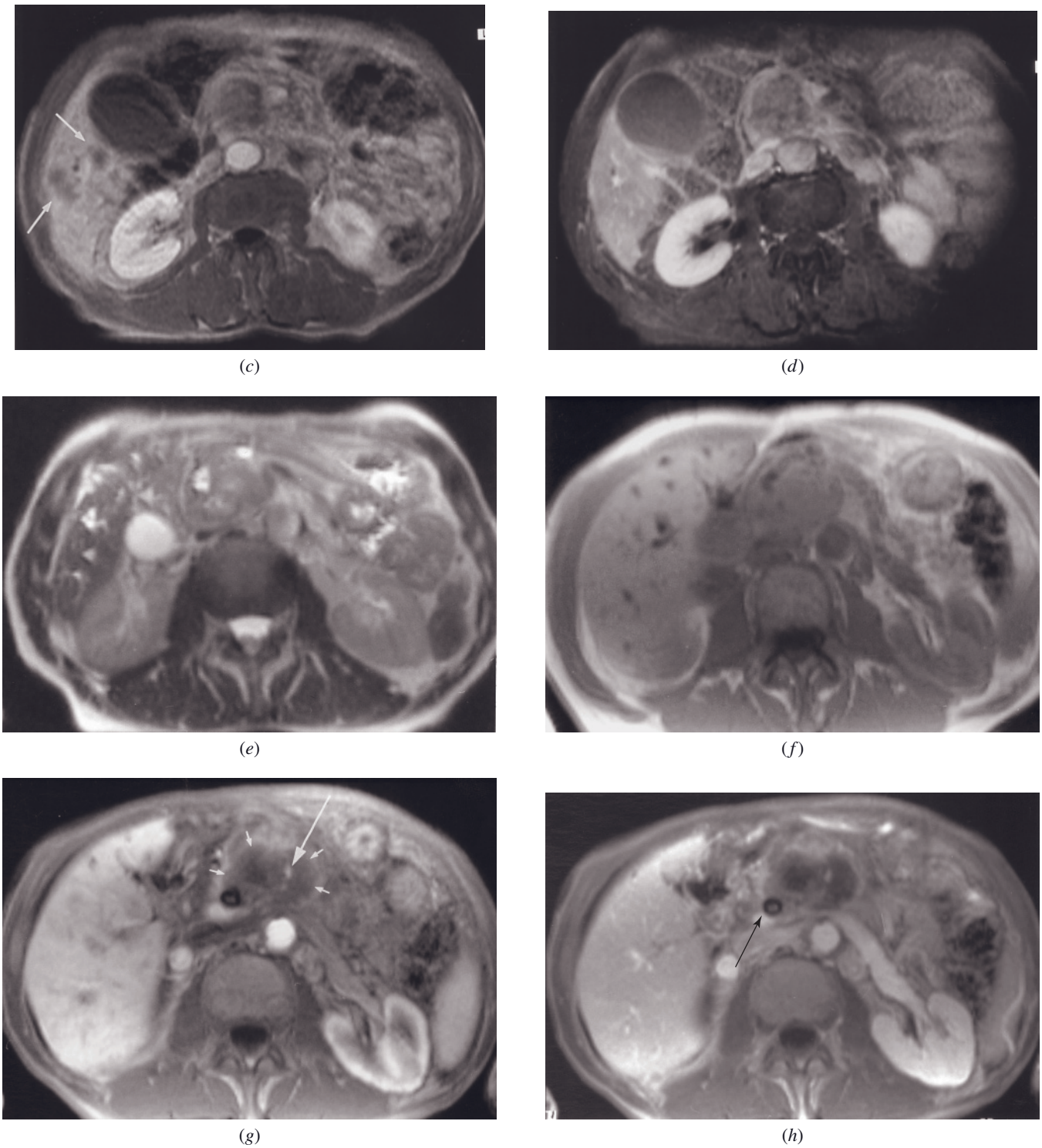

FIG. 4.20 (*Continued*) fat-suppressed spin-echo (*d*) images. A large 5-cm cancer is present in the head of the pancreas that is low in signal intensity on T1-weighted images (*b*) and low in signal intensity on T2-weighted images (*a*) and enhances minimally on early (*c*) and late (*d*) postgadolinium images. This represents the typical appearance of a large pancreatic ductal cancer. Liver metastases are present and are most clearly defined on immediate postgadolinium images as focal low-signal intensity masses with irregular rim enhancement (arrows, *c*). The liver is the most common site for metastatic lesions from primary pancreatic cancer.

T2-weighted SS-ETSE (*e*), T1-weighted SGE (*f*), immediate postgadolinium T1-weighted SGE (*g*), and 90-s postgadolinium fat-suppressed T1-weighted SGE (*h*) images in a second patient. There is a 5.5-cm adenocarcinoma (small arrows, *g*) arising in the pancreatic head, which encases the superior mesenteric artery (long arrow, *g*). The superior mesenteric vein is thrombosed and not visualized. There is a stent in the CBD that causes susceptibility artifact (arrow, *h*).

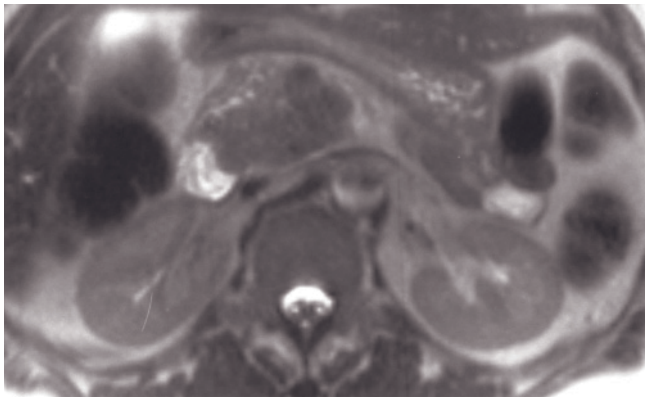

(*i*)

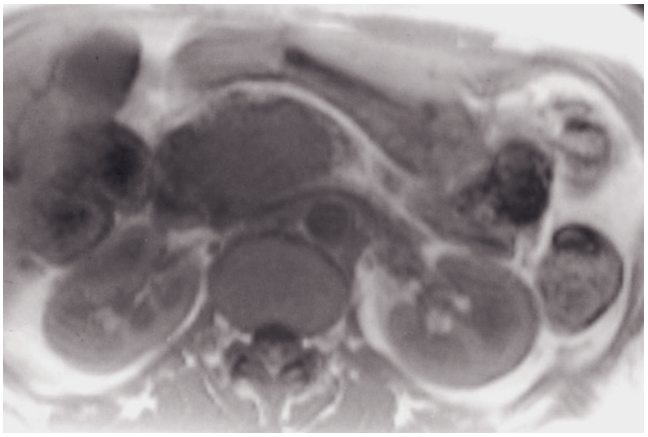

(*j*)

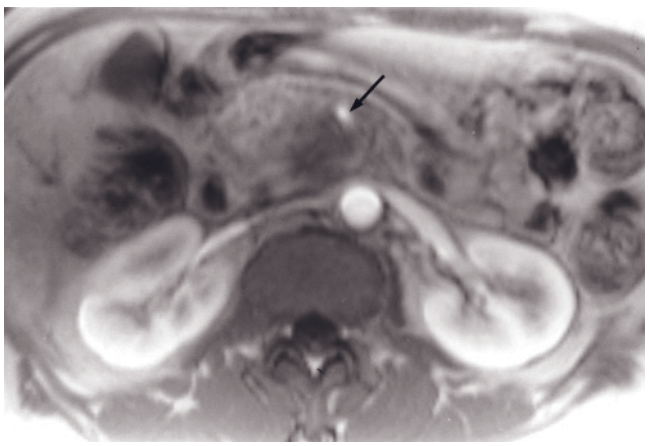

(*k*)

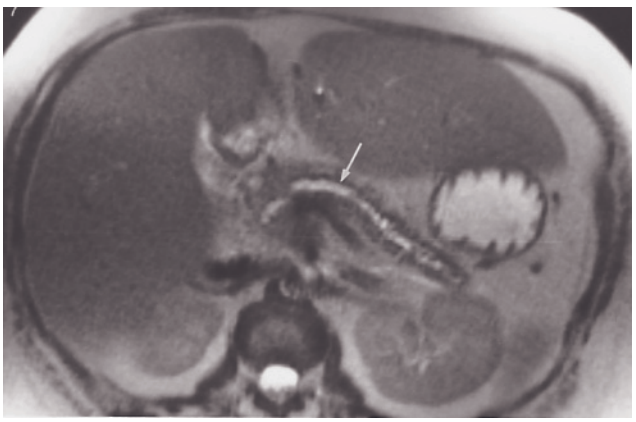

(*l*)

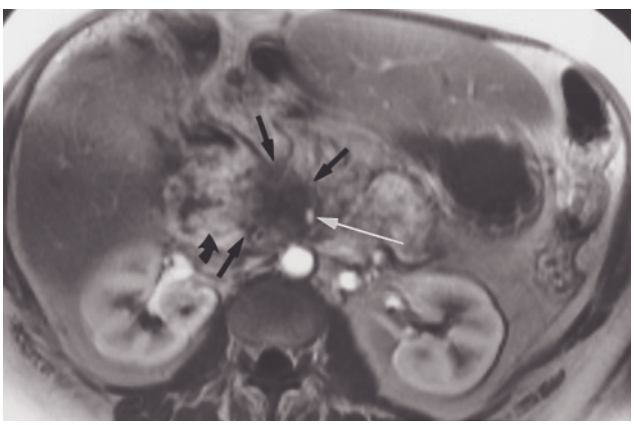

(*m*)

(*n*)

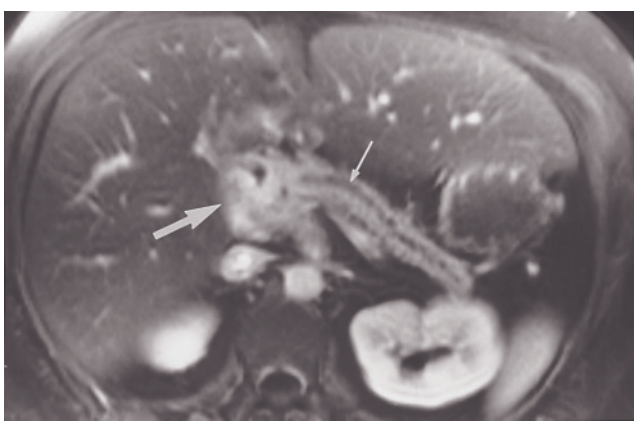

(*o*)

Fig. 4.20 (*Continued*) T2-weighted SS-ETSE (*i*), T1-weighted SGE (*j*), and immediate postgadolinium SGE (*k*) images in a third patient. A 6 × 5-cm cancer arises in the head and uncinate process of the pancreas, with an appearance comparable to the prior examples. Note encasement of the SMA (arrow, *k*).

T2-weighted single-shot SS-ETSE (*l*), immediate postgadolinium T1-weighted SGE (*m*), and 2-min postgadolinium fat-suppressed T1-weighted SGE (*n*, *o*) images in a fourth patient. A large 4-cm tumor is present in the head of the pancreas that results in obstruction of the pancreatic duct (arrow, *l*, *m*). The tumor is markedly low in signal intensity on the immediate postgadolinium image (short arrows, *m*), and encasement of the SMA is shown (thin arrow, *m*). Adjacent duodenum is thick walled, which is consistent with invasion (curved arrow, *m*). The tumor shows diminished central enhancement on the interstitial-phase fat-suppressed T1-weighted SGE image (arrows, *n*). Small periaortic lymph nodes are identified (long arrow, *n*). Tumor extension into the porta hepatis is present (large arrow, *o*).

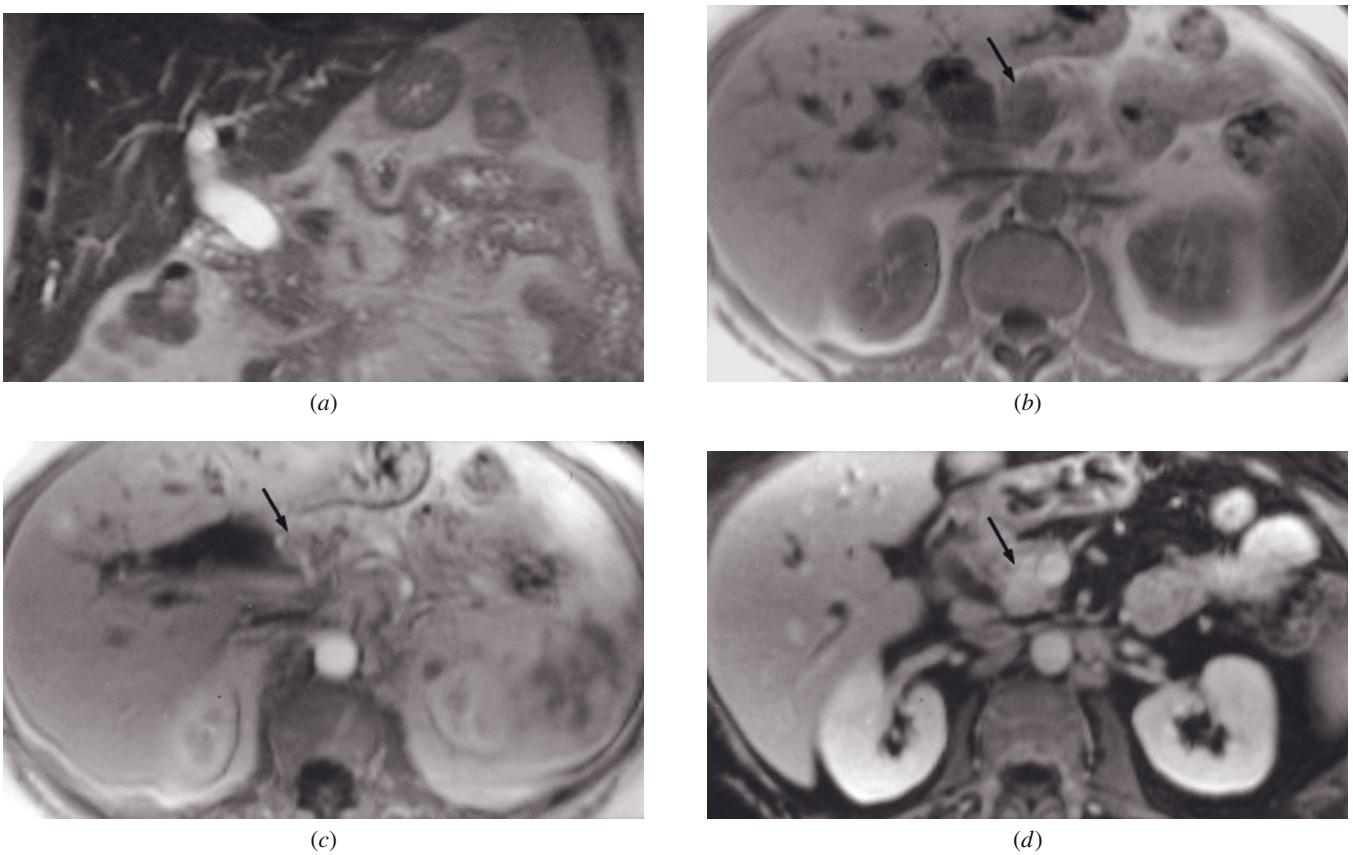

FIG. 4.21 Infiltrative pancreatic cancer arising in the upper head and neck. Coronal T2-weighted SS-ETSE (*a*), T1-weighted SGE (*b*), immediate postgadolinium T1-weighted SGE (*c*), and 90-s postgadolinium fat-suppressed SGE (*d*) images. A 3-cm poorly differentiated infiltrative adenocarcinoma is present in the pancreatic head, which causes high-grade obstruction of the CBD. The tumor is ill defined on all imaging sequences (arrow, *b*, *c*) and demonstrates late increased enhancement (arrow, *d*).These are features of an infiltrative desmoplastic neoplasm.

mas involving the tail, uninvolved pancreatic parenchyma proximal to the tumor usually is uninvolved and high in signal intensity on T1-weighted fat-suppressed images (see fig. 4.25). This differs from the circumstance of carcinoma within the pancreatic head and reflects the fact that chronic pancreatitis occurs distal to tumor that causes obstruction of the main pancreatic duct. An additional imaging feature, which assists in the distinction between carcinoma and chronic pancreatitis, is effacement of the fine, lobular contours of the gland by carcinoma. In contrast, in the setting of chronic pancreatitis, although there may be focal enlargement of the gland, the internal pancreatic architecture is generally preserved and retains the lobular, marbled or feathery appearance on MRI. On immediate postgadolinium images, pancreatic carcinoma has diminished signal intensity without well-defined internal structure, but with a mild heterogeneous morphology, whereas with chronic pancreatitis, although enhancement is diminished, the architectural pattern is often preserved.

In general, pancreatic carcinoma usually appears as a focal mass that is readily detected and characterized on immediate postgadolinium images. In these instances, the tumor is relatively well demarcated from adjacent uninvolved pancreas, which shows greater enhancement [41]. Pancreatic cancer may occasionally be poorly marginated [41]. In this setting, tumors will be ill defined without clear margination with adjacent pancreas and little or no definition of a mass [41]. These poorly-marginated tumors may have decreased enhancement on immediate postgadolinium images and may show slightly increased enhancement on 2-min postgadolinium fat suppressed gradient-echo images. This appearance is commonly observed in pancreatic cancer that has been treated with chemotherapy and radiation therapy (see below) but may also, uncommonly, be seen at initial presentation (see fig. 4.26). One study has showed that poorly-marginated appearance of pancreatic ductal carcinoma on MRI most commonly possessed moderate- to well-differentiated histopathology

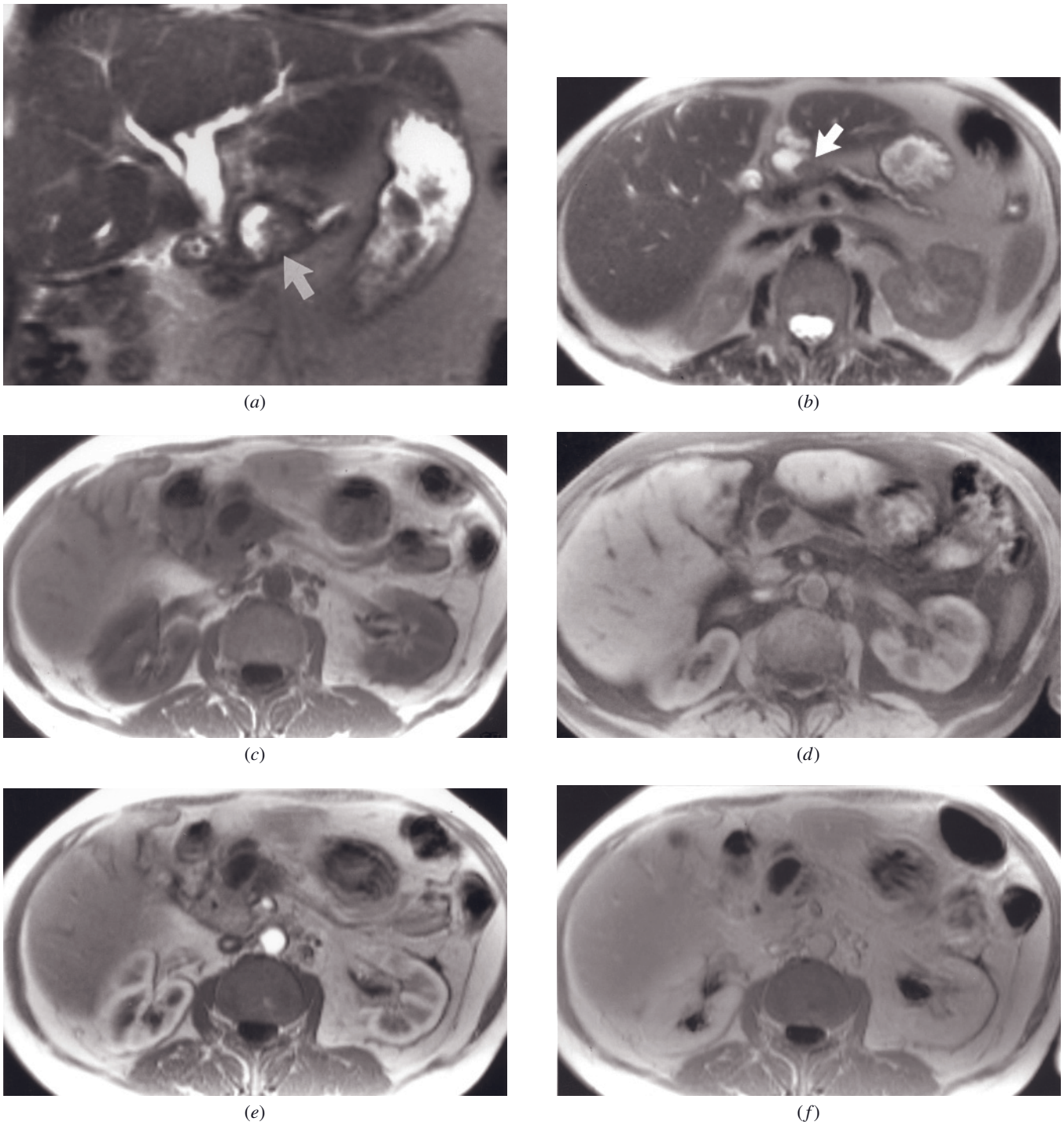

FIG. 4.22 Pancreatic cancer arising in the neck. Coronal (*a*) and transverse (*b*) T2-weighted SS-ETSE, T1-weighted SGE (*c*), T1-weighted fat-suppressed SGE (*d*), and immediate (*e*) and 45-s (*f*) postgadolinium T1-weighted SGE images in a patient with a pancreatic adenocarcinoma arising in the neck of the pancreas. There is a heterogeneous mass in the pancreatic neck (arrow, *a*, *b*), which contains a cystic component. The body and tail of the pancreas are atrophic with dilatation of the main pancreatic duct. The biliary tree is markedly dilated (*a*). Note diminished enhancement of the solid component of the mass (*e*, *f*).

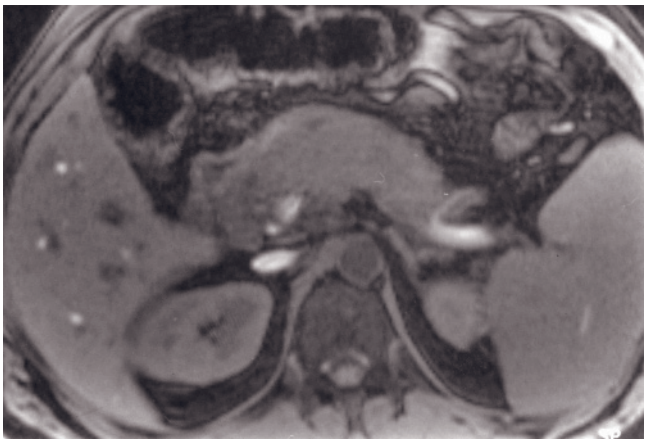

(*a*)

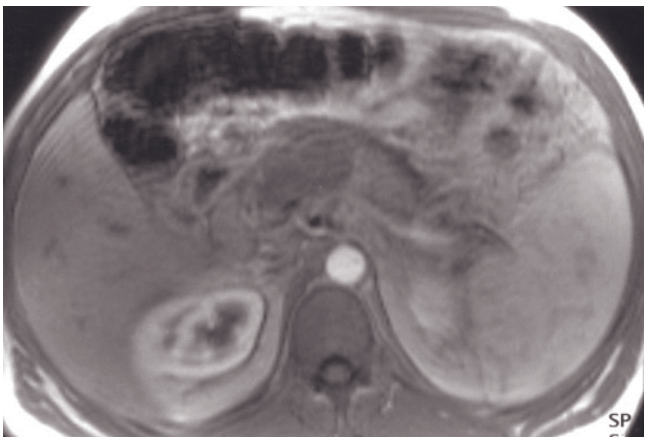

(*b*)

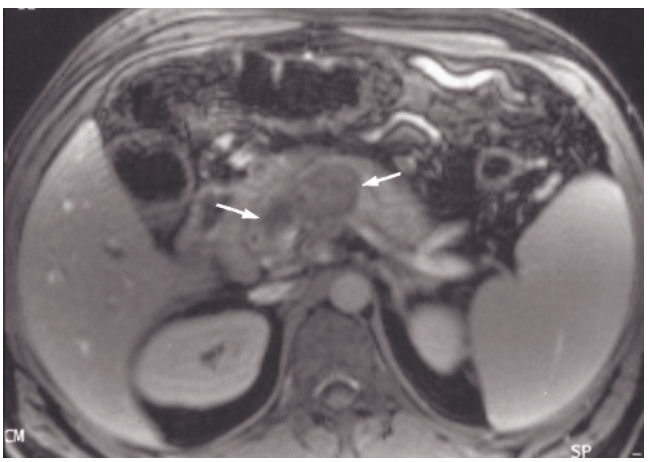

(*c*)

FIG. 4.23 Pancreatic cancer arising in the neck and body. T1-weighted fat-suppressed SGE (*a*), immediate postgadolinium T1-weighted SGE (*b*), and 90-s postgadolinium fat-suppressed SGE (*c*) images. On the noncontrast T1-weighted image, the body and tail of the pancreas are expanded, with no definition of a mass. The tumor (arrows, *c*) can be better delineated on gadolinium-enhanced images (*b*, *c*) because of lesser enhancement of the tumor in relation to the pancreatic parenchyma.

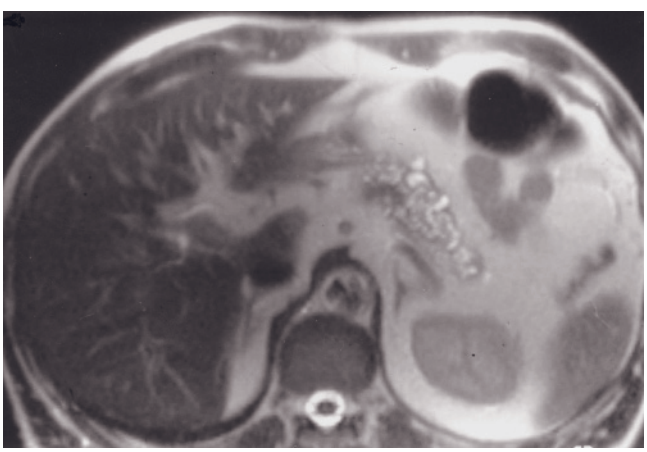

(*a*)

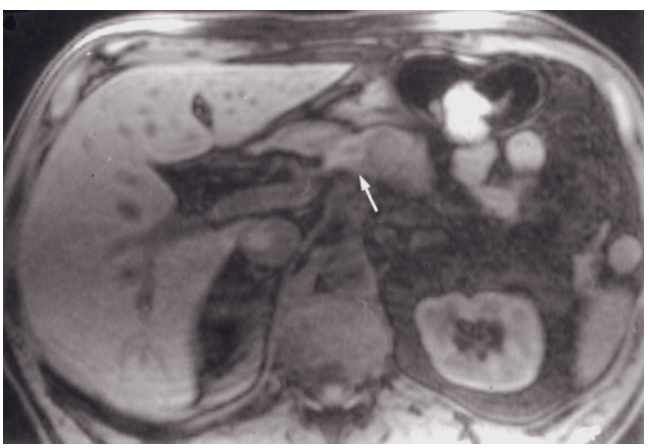

(*b*)

FIG. 4.24 Pancreatic cancer arising from the body. T2-weighted SS-ETSE (*a*), T1-weighted fat-suppressed SGE (*b*), immediate postgadolinium T1-weighted SGE (*c*), and 90-s postgadolinium fat-suppressed SGE (*d*) images. There is a 3-cm tumor arising in

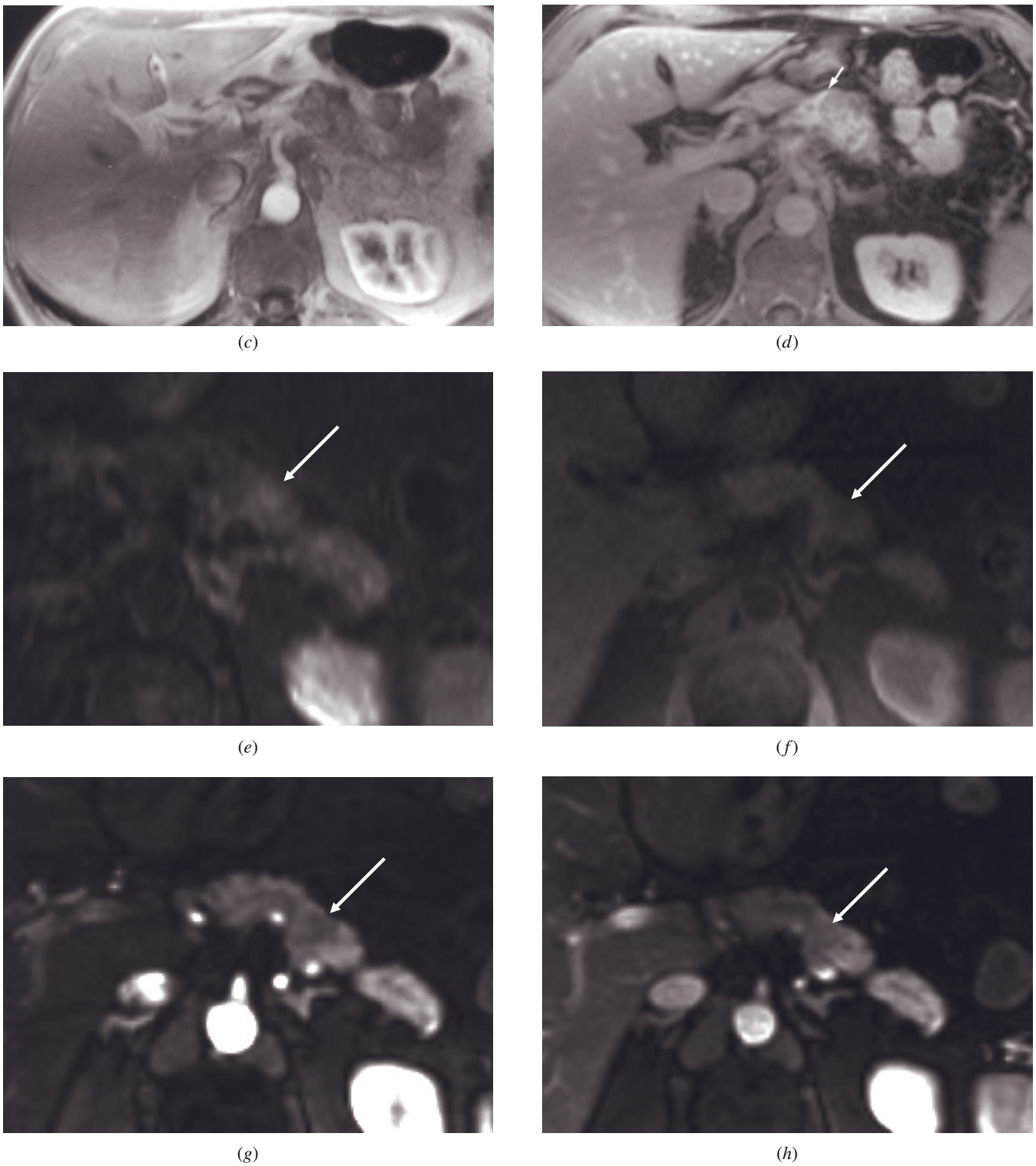

FIG. 4.24 (*Continued*) the midpancreatic body. A sharp transition is apparent between proximal normal pancreas and tumor (arrow, *b*), which causes distal chronic pancreatitis on T1-weighted fat-suppressed images (*b*) and postcontrast images (*c*, *d*). A claw sign is appreciated (arrow, *d*), reflecting that the mass arises from the pancreas. Dilated ectatic pancreatic duct side branches are present in the distal body and tail, which enhances less than the normal parenchyma.

T2-weighted short-tau inversion recovery (STIR) (*e*), T1-weighted fat-suppressed SGE (*f*), T1-weighted postgadolinium hepatic arterial dominant phase (*g*) and hepatic venous phase (*h*) fat-suppressed 3D-GE images at 3.0T demonstrate a very small lesion (arrows; *e–h*) showing mildly high signal on T2-weighted image (*e*), moderately low signal on T1-weighted SGE (*f*), and initial low signal with progressive enhancement on postgadolinium images (*g*, *h*) in another patient. The diagnosis was pancreatic adenocarcinoma histopathologically.

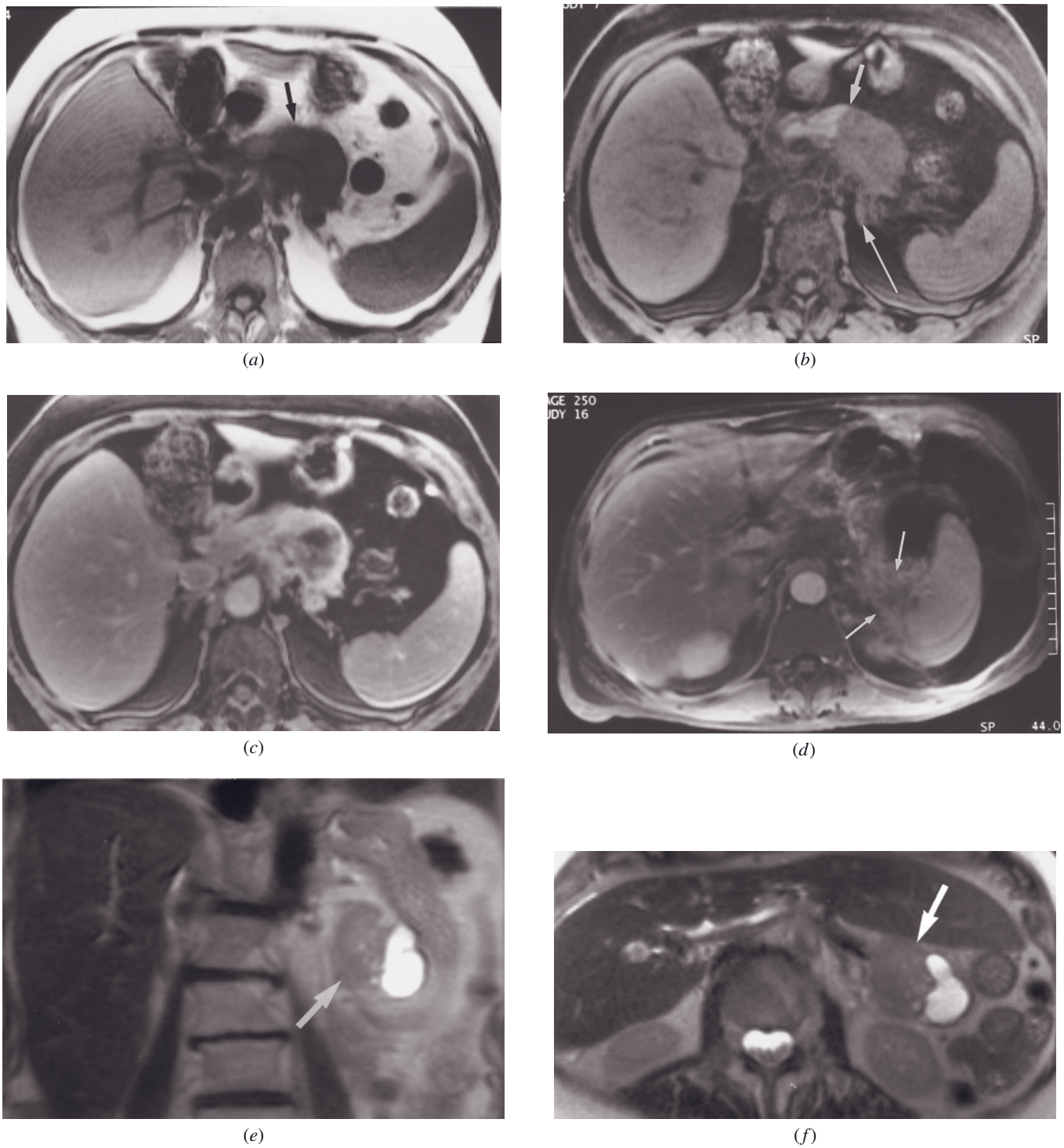

FIG. 4.25 Pancreatic cancer arising from the tail. T1-weighted SGE (*a*), fat-suppressed T1-weighted SGE (*b*), and interstitial-phase gadolinium-enhanced T1-weighted SGE (*c*) images. A large pancreatic tail cancer is present that has encased the splenic vein. The tumor is low in signal intensity on the T1-weighted image (arrow, *a*). Demarcation of tumor from uninvolved pancreas (short arrow, *b*) is clearly shown on the precontrast T1-weighted fat-suppressed image (*b*). The left adrenal is involved (long arrow, *b*). Heterogeneous enhancement with central low signal intensity is apparent on the interstitial-phase image (*c*).

Interstitial-phase gadolinium-enhanced T1-weighted SGE image (*d*) in a second patient demonstrates a pancreatic tail cancer (arrows, *d*) that invades the splenic hilum.

Coronal (*e*) and transverse (*f*) T2-weighted SS-ETSE, T1-weighted SGE (*g*), T1-weighted fat-suppressed SGE (*h*), immediate postgadolinium T1-weighted SGE (*i*), and 90-s postgadolinium fat-suppressed SGE (*j*) images in a third patient. A 5-cm cancer

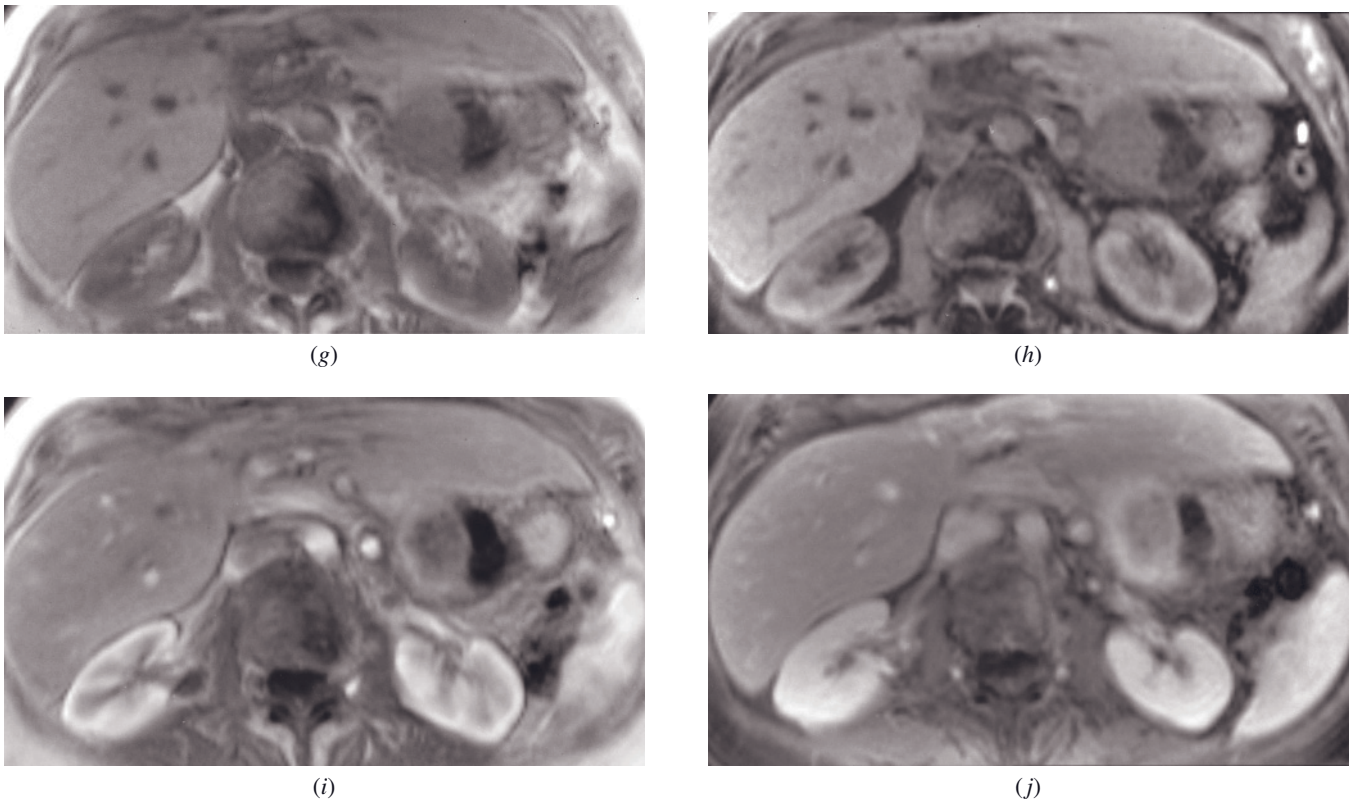

FIG. 4.25 (*Continued*) (arrow, *e*, *f*) arises from the tail of the pancreas and contains a cystic component. The tumor displaces the lesser gastric curvature laterally, best appreciated on the coronal image (*e*).

compared to focally-defined cancers which had more poorly differentiated histology [41]. Features that may aid in the distinction from chronic pancreatitis are the relatively short history of clinical findings (e.g., pain, jaundice), and the high-grade biliary and/or pancreatic ductal obstruction despite apparently small-volume disease.

Regarding tumor staging, local extension of cancer and lymphovascular involvement may be evaluated on nonsuppressed T1-weighted images [42, 43]. Low-signal-intensity tumor is well shown in a background of high-signal-intensity fat. Gadolinium-enhanced fat-suppressed gradient-echo images, acquired in the interstitial phase of enhancement (1–10 min postcontrast), demonstrate intermediate-signal-intensity tumor tissue extension into low-signal-intensity-suppressed fat (figs. 4.29 and 4.30). In comparison, noncontrast T1-weighted fat-suppressed images generally show minimal signal intensity difference between tumor, which is low in signal intensity, and suppressed background fat [36]. When tumor involves the body or tail of the pancreas, invasion of adjacent organs, such as the left adrenal gland, is well shown on a combination of sequences including nonsuppressed T1-weighted images and interstitial-phase gadolinium-enhanced fat-suppressed T1-weighted images (see figs. 4.29 and 4.30).

Vascular encasement by tumor is best shown with thin-section 3D gradient-echo images, which can be analyzed both as source images in the transverse plane and reformatted images in the coronal plane. Coronal plane reformatted images are of value to determine the relationship between tumor and the portal vein as it enters the porta hepatis and tumor and the superior mesenteric vein along the medial margin of the head of pancreas. Immediate postgadolinium gradient echo-images are useful for evaluating arterial patency and immediate and 45-s postgadolinium gradient-echo images for evaluating venous patency (see fig. 4.27).

When comparing approaches by CT and MRI, interstitial-phase gadolinium-enhanced fat-suppressed sequence is an effective technique to delineate peritoneal metastases and is superior to CT [44, 45]. MR does not perform well at local staging if this technique is not employed [46]. Peritoneal metastases appear moderately high signal in a dark background of suppressed fat and are very conspicuous even if peritoneal disease is of thin volume and relatively linear (fig. 4.31). Demonstration of focal thickening or nodules increases the likelihood

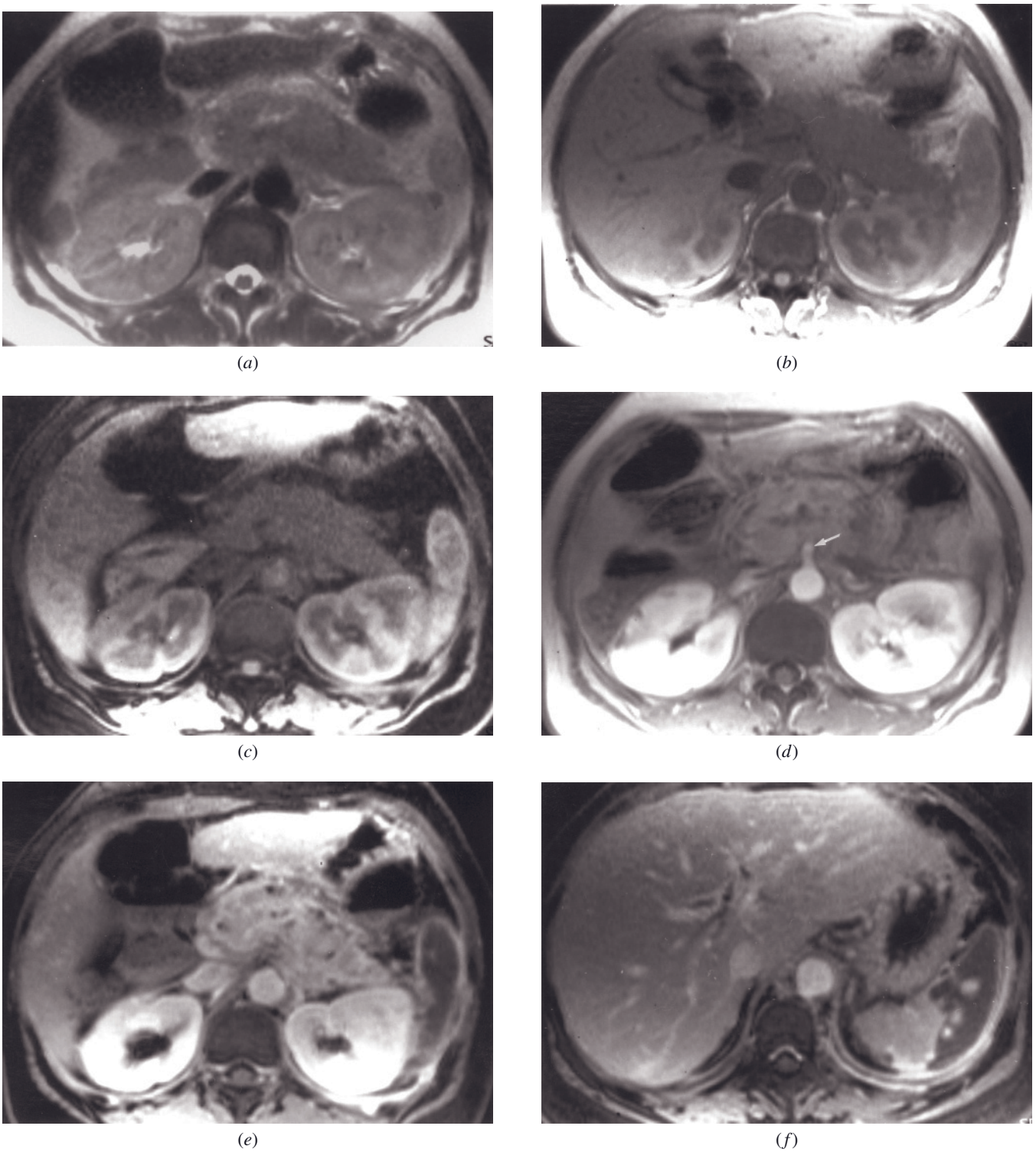

FIG. 4.26 Diffuse pancreatic adenocarcinoma. T2-weighted echo-train spin-echo (*a*), T1-weighted SGE (*b*), T1-weighted fat-suppressed SGE (*c*), immediate postgadolinium T1-weighted SGE (*d*), and 90-s postgadolinium fat-suppressed SGE (*e*, *f*) images. The pancreas is diffusely enlarged and hypointense on T2 (*a*) and T1 (*b*)-weighted images, with diminished and heterogeneous enhancement on early (*d*) and late (*e*) gadolinium-enhanced images. The tumor encases the superior mesenteric artery (arrow, *d*) and occludes the superior mesenteric vein and splenic vein. Extensive infarction of the spleen (*f*) reflects the vascular occlusion of splenic vessels.

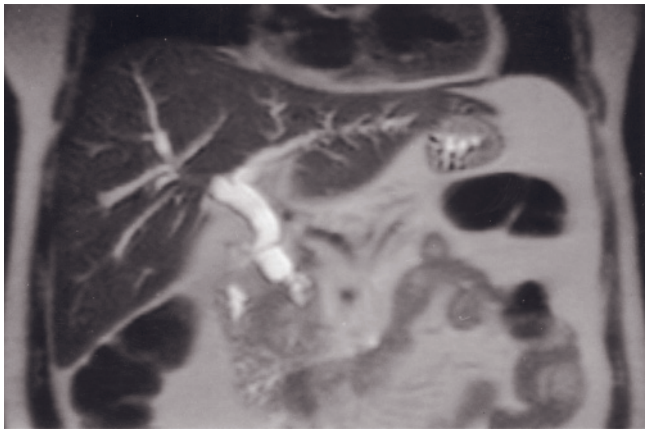

(*a*)

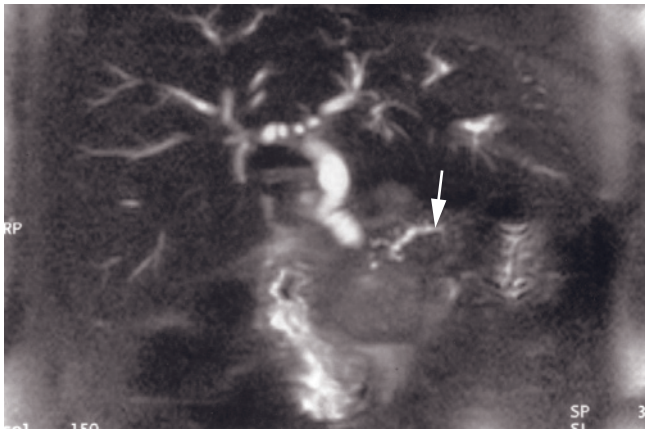

(*b*)

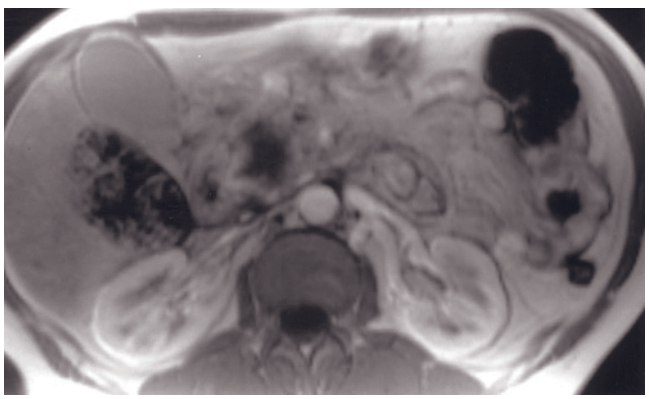

(*c*)

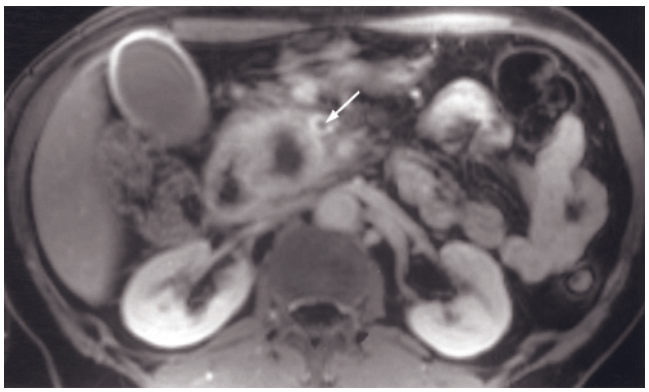

(*d*)

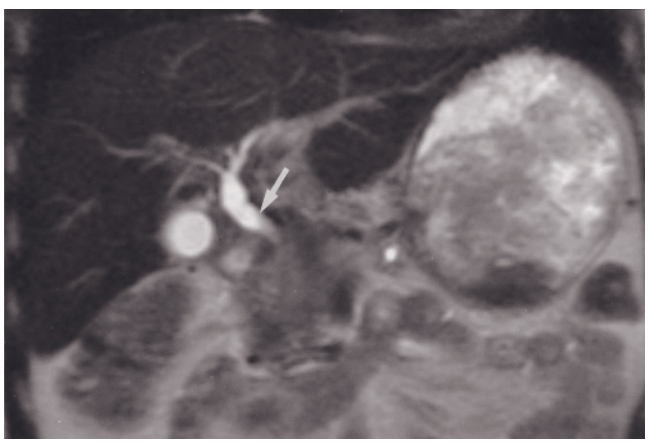

(*e*)

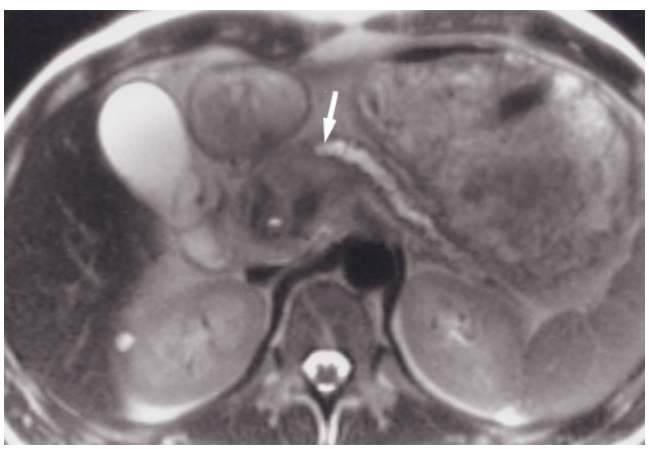

(*f*)

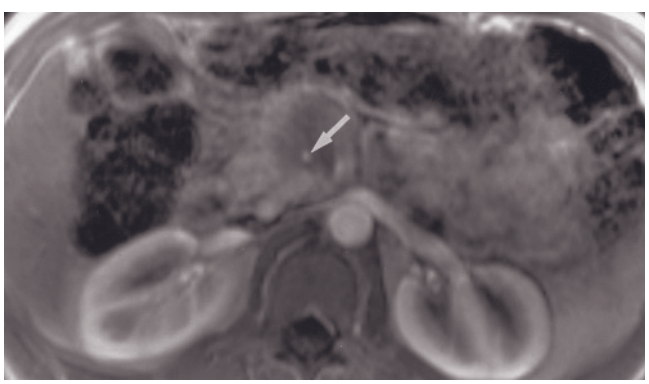

(*g*)

FIG. 4.27 Staging pancreatic cancer—vessel involvement. Coronal T2-weighted SS-ETSE (*a*), angled coronal MRCP (*b*), immediate postgadolinium T1-weighted SGE (*c*), and 90-s postgadolinium fat-suppressed SGE (*d*) images. A 5-cm tumor arises from the pancreatic head and obstructs the CBD and pancreatic duct (arrow, *b*), which is well shown on the MRCP image (*b*). The interstitial-phase gadolinium-enhanced image (*d*) shows a nonocclusive thrombus in the superior mesenteric vein (arrow, *d*) and tumor stranding around both superior mesenteric vessels.

Coronal (*e*) and transverse (*f*) T2-weighted SS-ETSE and immediate postgadolinium T1-weighted SGE (*g*) images in a second patient with pancreatic head adenocarcinoma. Note atrophy of the pancreatic body and tail with dilatation of main pancreatic duct. Ductal dilatations of the CBD (arrow, *e*) and pancreatic duct (arrow, *f*) are best shown on single shot T2-weighted images (including MRCP). The tumor is best shown on immediate postgadolinium images (*g*). Encased superior mesenteric artery is shown (arrow, *g*).

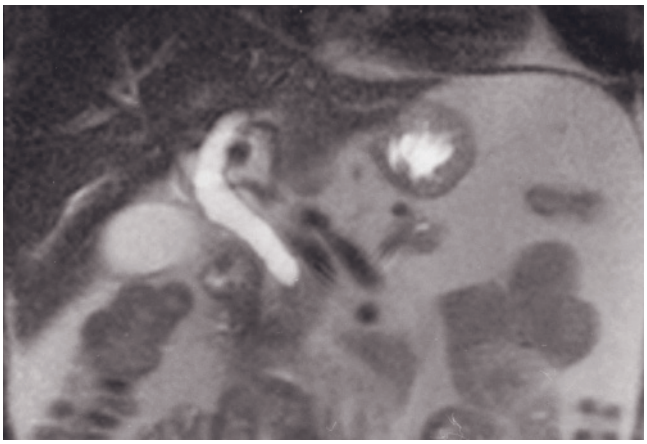

(*a*)

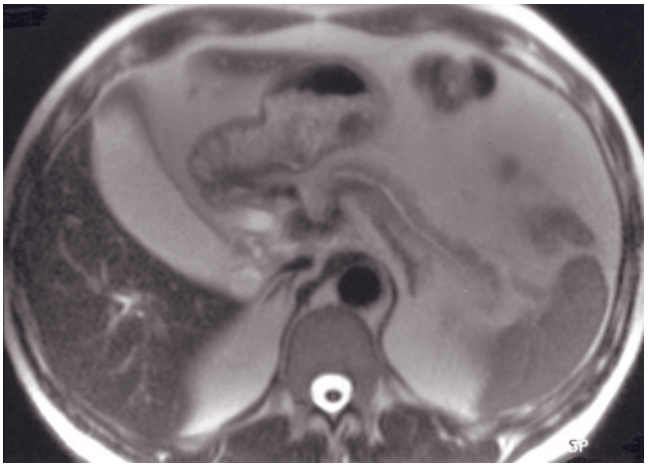

(*b*)

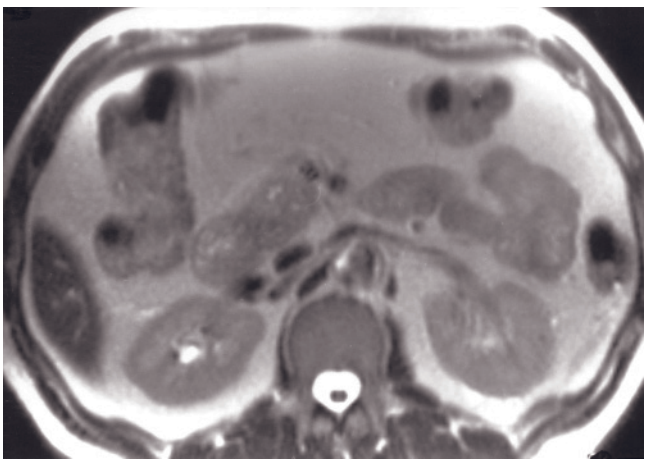

(*c*)

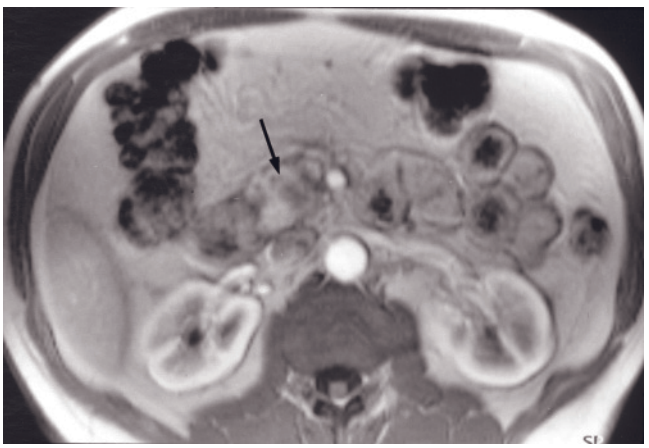

(*d*)

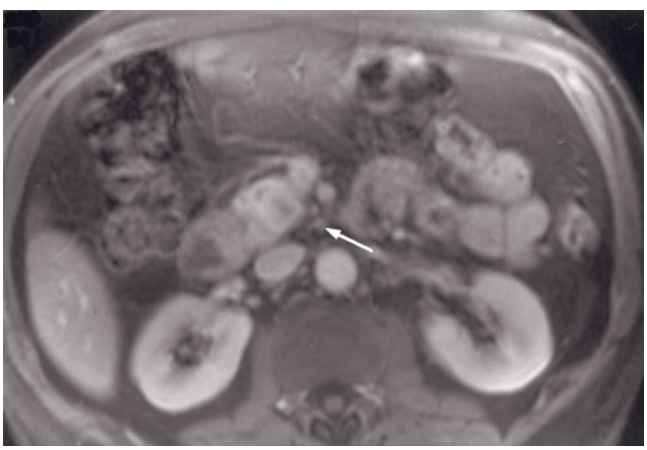

(*e*)

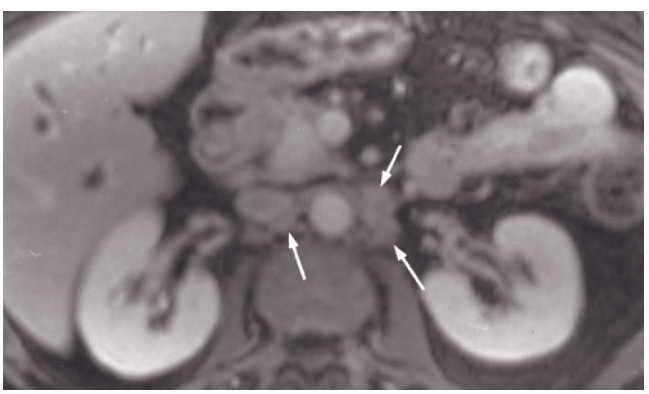

(*f*)

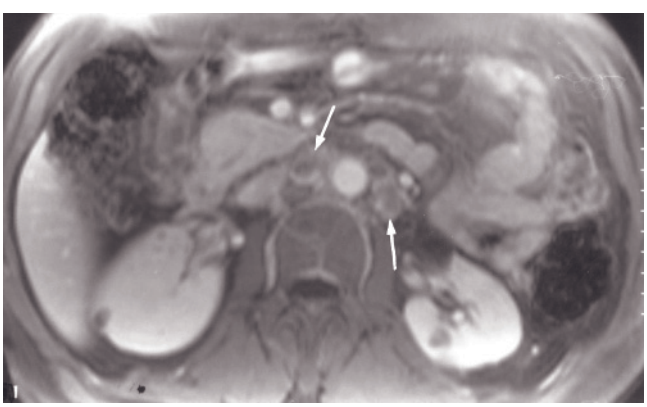

(*g*)

FIG. 4.28 Staging pancreatic cancer—lymph nodes. Coronal (*a*) and transverse (*b*, *c*) T2-weighted SS-ETSE, immediate postgadolinium T1-weighted SGE (*d*), and 90-s postgadolinium fat-suppressed SGE (*e*) images in a patient with pancreatic ductal adenocarcinoma (arrow, *d*) arising from the head. The CBD is markedly dilated (*a*), with mild dilatation of the pancreatic duct (*b*). Tumors are generally not well seen on T2 (*c*). Optimal tumor demonstration is on immediate postgadolinium images (*d*). Small regional nodes (arrow, *e*) are best seen on interstitial-phase gadolinium-enhanced fat-suppressed SGE images (*e*).

Interstitial-phase gadolinium-enhanced fat-suppressed SGE images (*f*, *g*) in two other patients demonstrate malignant retroperitoneal lymph nodes (arrows, *f*, *g*). In the latter patient (*g*), the lymph nodes have low-signal centers consistent with central necrosis.

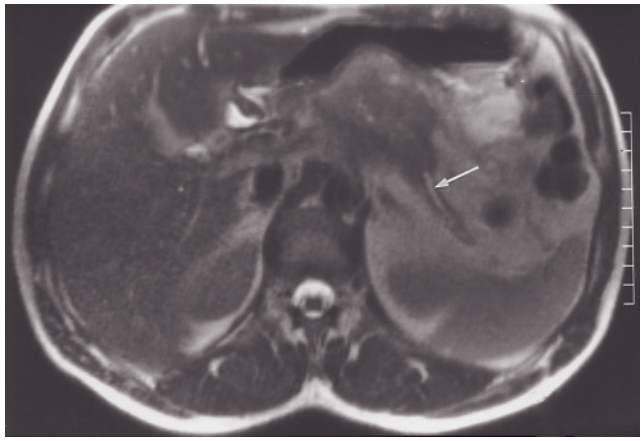

(*a*)

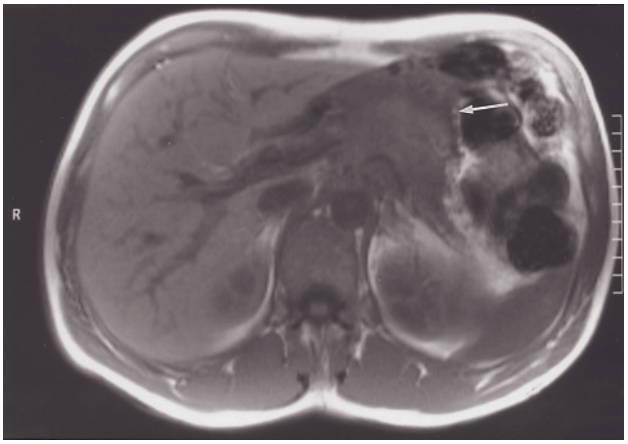

(*b*)

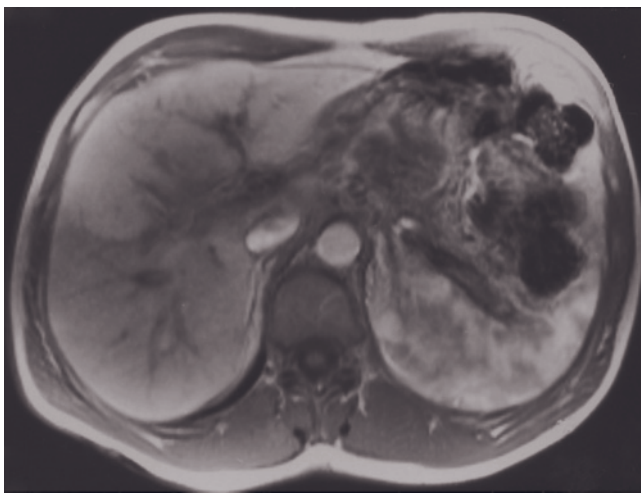

(*c*)

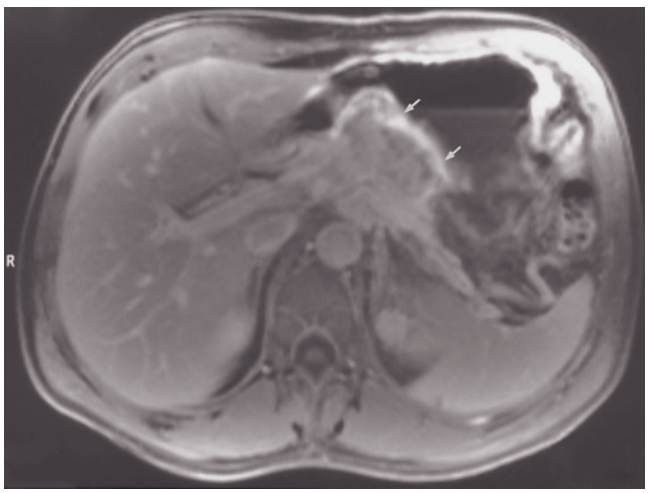

(*d*)

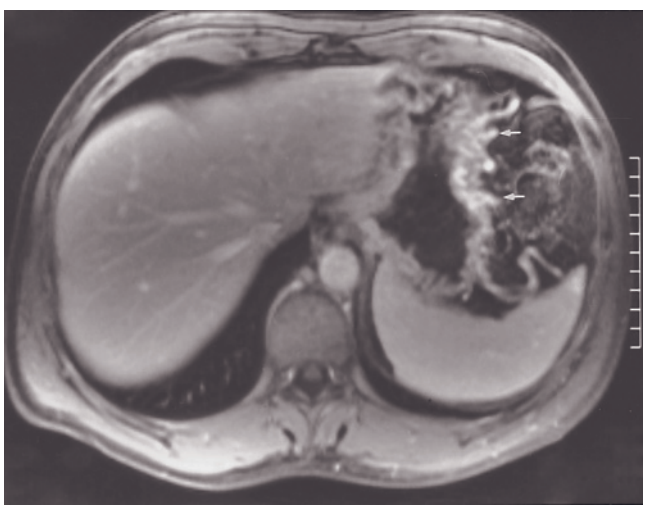

(*e*)

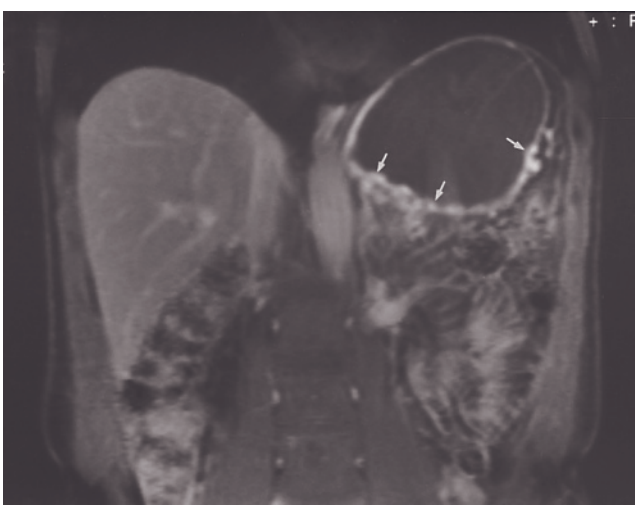

(*f*)

FIG. 4.29 Staging pancreatic cancer—stomach invasion and splenic vein thrombosis. T2-weighted SS-ETSE (*a*), T1-weighted SGE (*b*), immediate postgadolinium T1-weighted SGE (*c*), interstitial-phase gadolinium-enhanced T1-weighted fat-suppressed SGE (*d*, *e*), and coronal interstitial-phase gadolinium-enhanced T1-weighted fat-suppressed SGE (*f*) images. A large cancer is present arising from the body of the pancreas (arrow, *b*) that invades the posterior wall of the stomach. Atrophy of the pancreatic tail with ductal dilatation (arrow, *a*) is well shown on the single-shot T2-weighted image (*a*). Heterogeneous minimal enhancement of the tumor is present on the immediate postgadolinium T1-weighted SGE image (*c*). Improved demonstration of the stomach wall invasion was achieved by gastric distension with orally administered water on the interstitial-phase fat-suppressed T1-weighted SGE image (small arrows, *d*). Multiple varices along the greater curvature of the stomach are present due to thrombosis of the splenic vein. Varices are well shown on gadolinium-enhanced T1-weighted fat-suppressed SGE images as high-signal-intensity tubular structures (arrows, *e*, *f*).

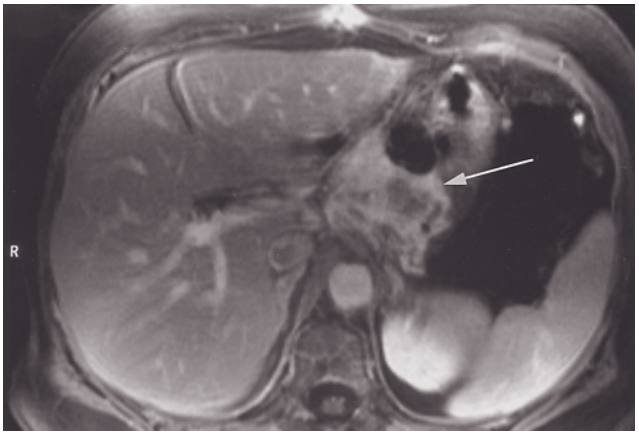

(*a*)

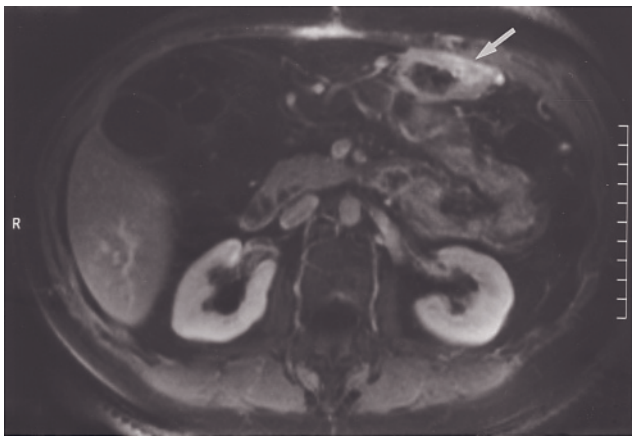

(*b*)

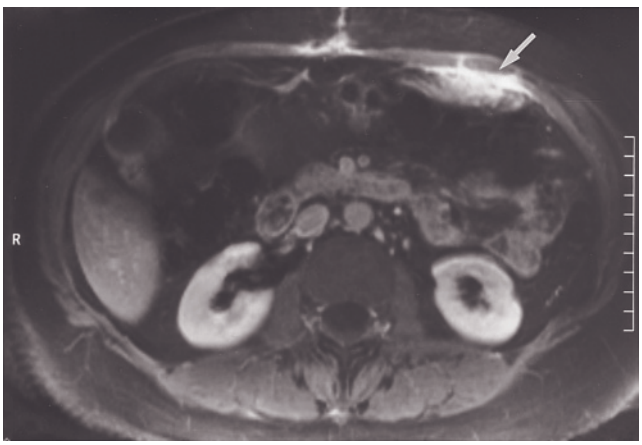

(*c*)

FIG. 4.30 Staging pancreatic cancer—extension along the transverse mesocolon. Interstitial-phase gadolinium-enhanced fat-suppressed T1-weighted SGE images (*a–c*). A large cancer arises from the body of the pancreas (arrow, *a*) that is adherent to the posterior wall of the stomach. Tumor extends inferiorly along the transverse mesocolon to involve the transverse colon (arrow, *b*), greater omentum, and adjacent peritoneum (arrow, *c*).

that peritoneal abnormalities represent a malignant process.

Lymph nodes are well shown on T2-weighted fat-suppressed images and interstitial-phase gadolinium-enhanced fat-suppressed T1-weighted images. Lymph nodes are moderately high in signal intensity in a background of low-signal-intensity suppressed fat with both of these techniques (figs. 4.28 and 4.32). T2-weighted fat-suppressed imaging is particularly useful for the demonstration of lymph nodes in close approximation to the liver because of the signal intensity difference between moderately high-signal-intensity nodes and moderately low-signal-intensity liver. Both lymph nodes and liver appear moderately enhanced on interstitial-phase gadolinium-enhanced fat-suppressed gradient-echo images, so lymph nodes are not as conspicuous in the region of the porta hepatis with this technique. To detect lymph nodes adjacent to liver it is useful to identify suspicious foci of high signal on the T2-weighted fat-suppressed images and confirm that they have the rounded morphology of lymph nodes on the gadolinium-enhanced fat-suppressed T1-weighted sequences. On nonsuppressed T1-weighted images, lymph nodes are conspicuous as low-signal-intensity focal masses in a background of high-signal-intensity fat [43], but this technique performs best in the detection of retroperitoneal nodes or mesenteric nodes in the setting of abundant fat in these locations. Coronal plane imaging provides good visualization of the locations.

Liver metastases from pancreatic cancers are generally irregular in shape, are low in signal intensity on conventional or fat-suppressed T1-weighted images and minimally hyperintense on T2-weighted images, and demonstrate irregular rim enhancement on immediate postcontrast gradient-echo images (figs. 4.32–4.34). The low-signal-intensity centers of metastatic lesions reflect the desmoplastic nature of the primary cancer [1]. The low fluid content and hypovascular nature of these metastases permit the distinction between these lesions from cysts and hemangiomas, respectively, even when lesions are 1 cm in diameter. Transient, ill-defined, increased perilesional enhancement in the hepatic parenchyma may be observed on immediate post-gadolinium images. A similar appearance is observed even more commonly for colon cancer metastases. Perilesional enhancement is more typically wedge-shaped

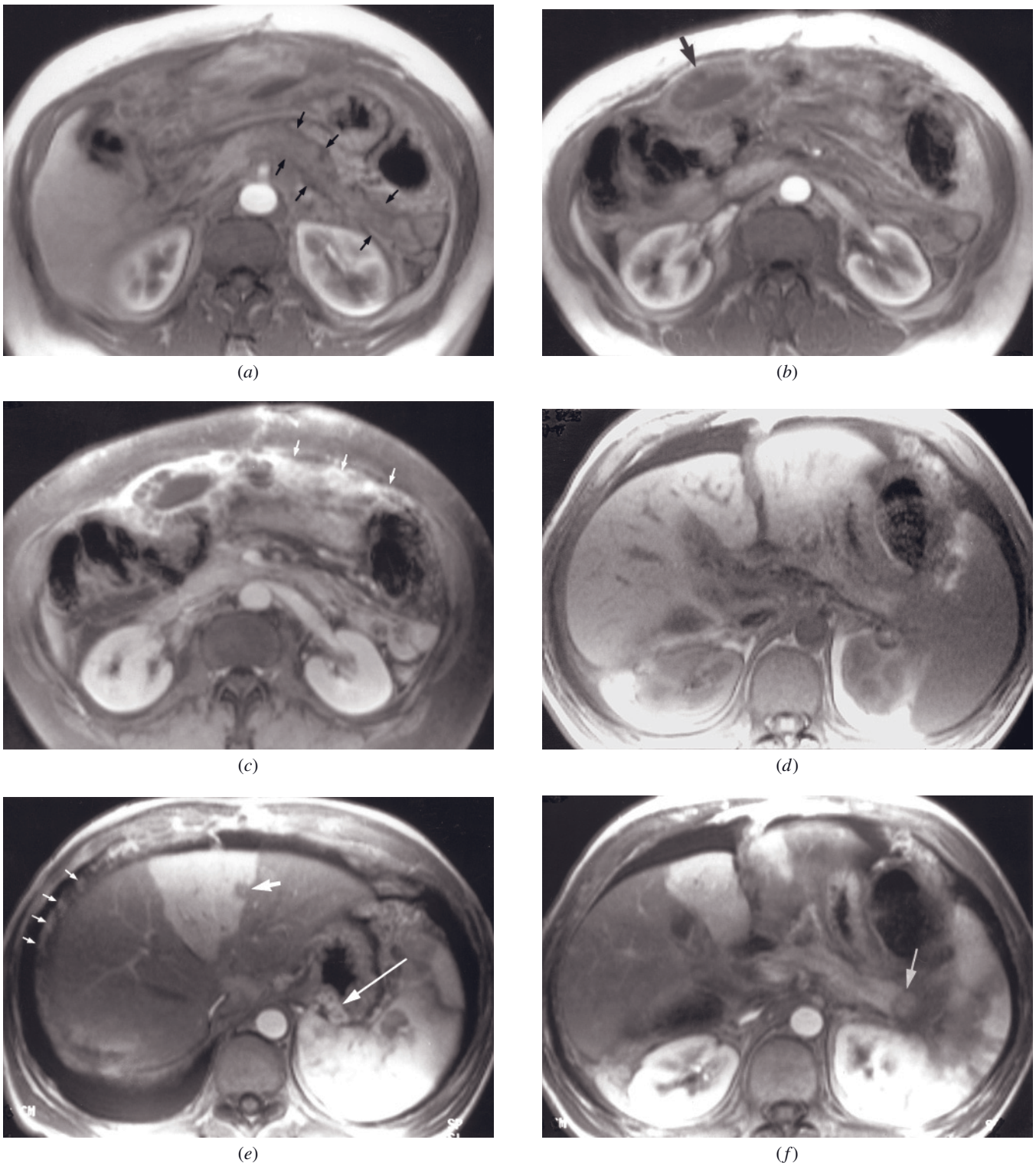

FIG. 4.31 Staging pancreatic cancer—peritoneal metastasis. Immediate postgadolinium SGE (*a*, *b*) and 90-s postgadolinium fat-suppressed SGE (*c*) images. There is normal enhancement of the pancreatic head and neck with an abrupt transition showing hypoenhancement of the body and tail of the pancreas (arrows, *a*). A focal mass is not present, and this is consistent with diffusely infiltrative pancreatic cancer. A large peritoneum-based mass (arrow, *b*) along the anterior abdominal wall is present, which has a multiloculated appearance with peripheral enhancement. There is adjacent peritoneal and omental (arrows, *c*) enhancement. These findings are consistent with diffusely infiltrative pancreatic adenocarcinoma with peritoneal metastasis.

T1-weighted SGE (*d*), immediate postgadolinium T1-weighted SGE (*e*, *f*), and 90-s postgadolinium fat-suppressed SGE (*g*) images at the level of the pancreatic body and tail in a second patient. A 2-cm cancer arises from the pancreatic tail (arrow, *f*), which is

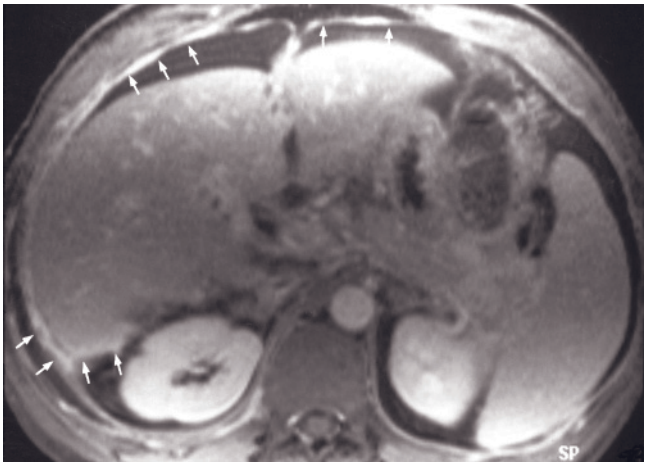

(*g*)

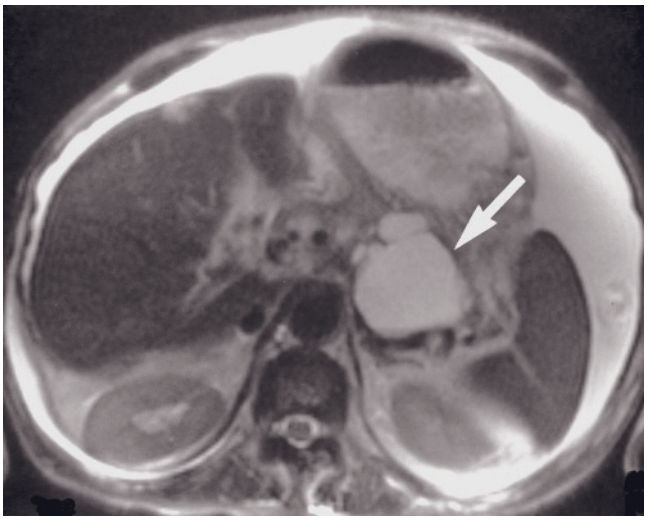

(*h*)

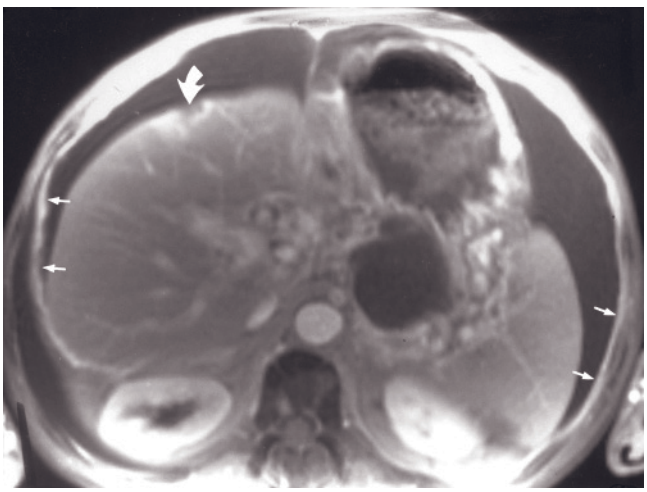

(*i*)

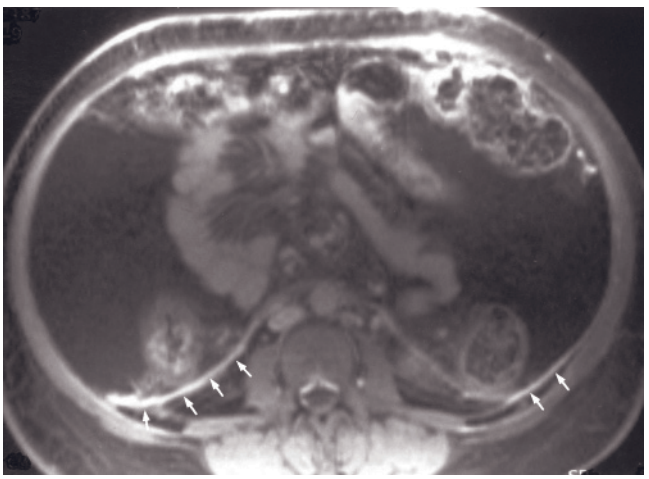

(*j*)

FIG. 4.31 (*Continued*) best shown on the immediate postgadolinium image (*f*). Wedge-shaped transient hyperenhancement of *segment 4* of the liver on the immediate postgadolinium images is present. Perilesional enhancement is commonly observed with pancreatic cancer liver metastases. A small defect is present in the hyperenhanced liver, which may represent a metastasis (small arrow, *e*). Diminished enhancement centrally in the spleen and a gastric wall varix (long arrow, *e*) reflect splenic vein thrombosis. Ascites and extensive peritoneal metastases are present (very small arrows, *e*, *g*), which are most conspicuous on interstitial-phase gadolinium-enhanced fat-suppressed SGE images (*g*).

T2-weighted fat suppressed SS-ETSE (*h*) and 90-s postgadolinium fat-suppressed T1-weighted SGE (*i*) images in a third patient who has pancreatic cancer with liver and peritoneal metastases. A 6-cm cystic mass is present in the lesser arc (arrow, *h*). Multiple varices are identified surrounding the cystic lesion (*i*). Ascites is appreciated on both T2 (*h*) and postgadolinium fat-suppressed T1-weighted (*i*) images. Extensive thickening and enhancement of the peritoneum (small arrows, *i*) is only appreciated on the fat-suppressed gadolinium-enhanced images (*i*). A 1.5-cm subcapsular metastasis is identified in *segment 4* (curved arrow, *i*).

Interstitial-phase gadolinium-enhanced fat-suppressed SGE image (*j*) in a fourth patient with pancreatic cancer, ascites, and peritoneal metastases (arrows, *j*).

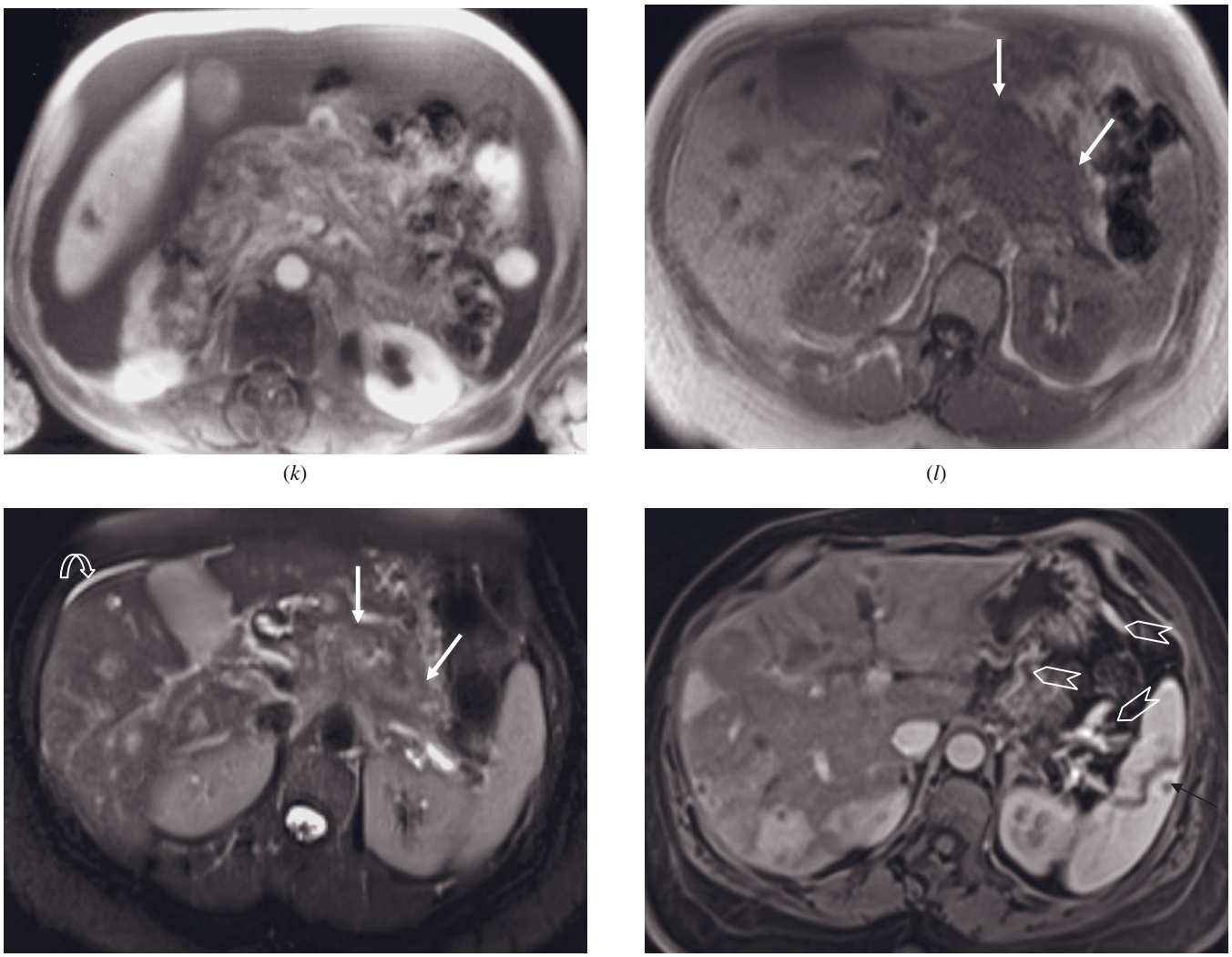

(*k*) (*l*)

(*m*) (*n*)

FIG. 4.31 (*Continued*) Interstitial-phase gadolinium-enhanced fat-suppressed SGE image (*k*) in a fifth patient demonstrates matting of bowel and mesentery due to tumor involvement.

T1-weighted SGE (*l*), T2-weighted single shot echo train spin echo (*m*), T1-weighted postgadolinium hepatic arterial dominant phase (*n*, *o*) fat-suppressed 3D-GE images demonstrate a large pancreatic adenocarcinoma (white arrows, *l*, *m*) located in the body in another patient. In the liver, there are multiple metastases showing peripheral enhancement (*n*). Those metastases located peripherally are also associated with wedge type of increased parenchymal enhancement. There is also a metastasis (black arrow, *n*) showing peripheral enhancement in the spleen. The peritoneal surfaces demonstrate plate-like enhancement consistent with peritoneal metastases. Splenic hilar and short gastric—left gastroepiploic varices (hollow arrows; *n*) are also detected due to splenic vein thrombosis. Note that there is free fluid peritoneal thickening (curved arrow, *m*) in the abdomen.

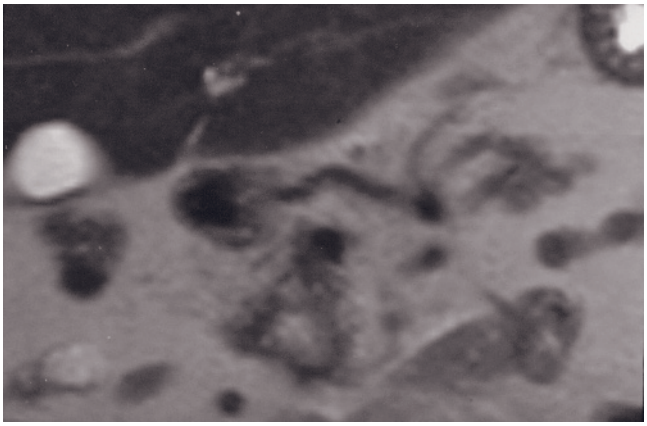

(*a*)

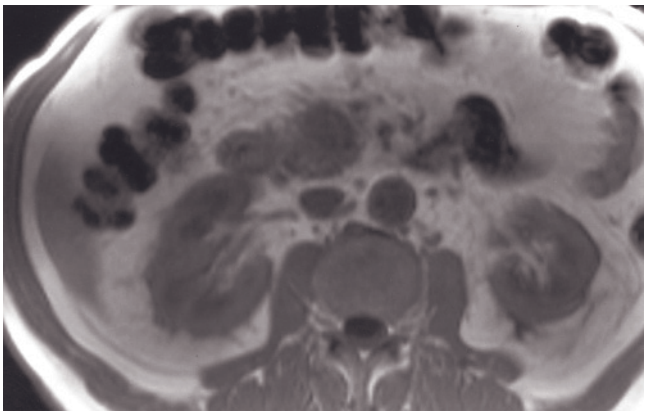

(*b*)

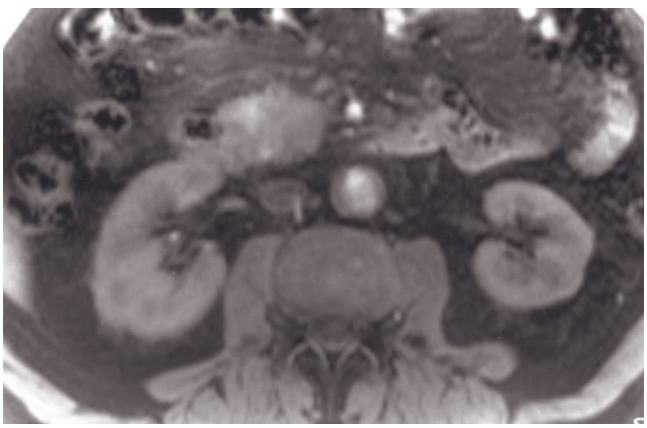

(*c*)

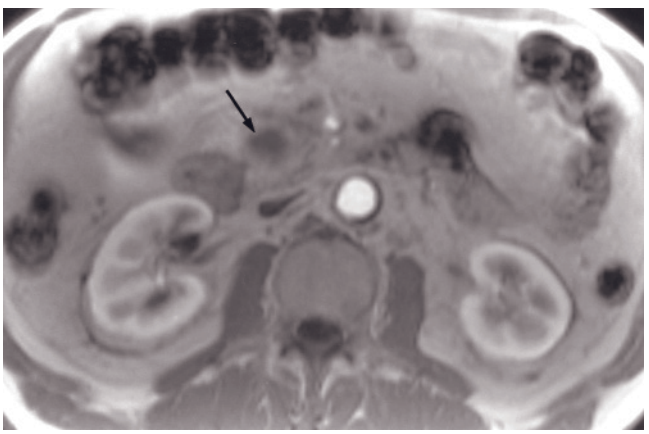

(*d*)

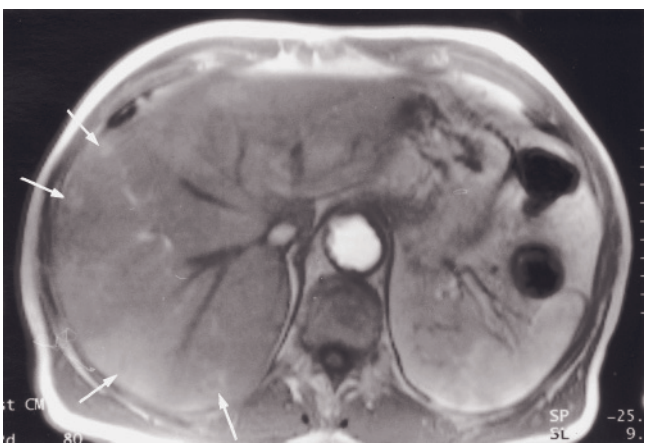

(*e*)

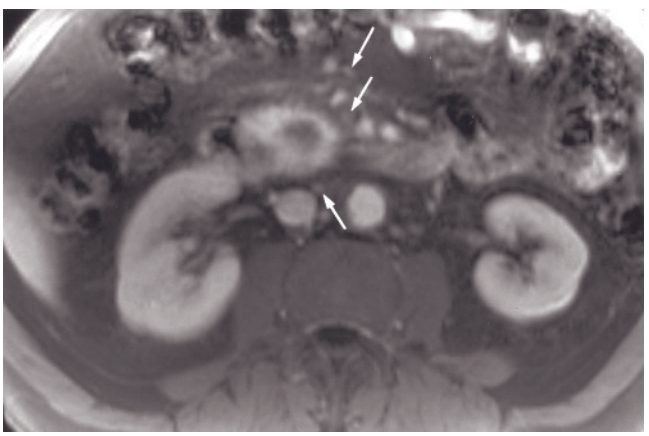

(*f*)

(*g*)

FIG. 4.32 Staging pancreatic cancer—lymphadenopathy and liver metastases. Coronal T2-weighted echo-train spin-echo (*a*), T1-weighted SGE (*b*), T1-weighted fat-suppressed SGE (*c*), immediate postgadolinium T1 SGE (*d*, *e*), and 90-s postgadolinium T1 weighted fat-suppressed SGE (*f*, *g*) images. There is a 3-cm pancreatic head cancer (arrow, *d*), which is clearly shown on the immediate postgadolinium image (*d*) as a hypoenhancing mass with demarcated borders and adjacent greater-enhancing pancreatic parenchyma. Both tumor and surrounding pancreas are low signal on the fat-suppressed image (*c*) because of changes of chronic pancreatitis in surrounding parenchyma. Liver metastases are present, which measure <1 cm and are predominantly situated in a subcapsular location. These small metastases are best shown on immediate postgadolinium images as uniformly hyperintense or ring enhancing lesions (arrows, *e*). The subcapsular location is quite typical for pancreatic cancer. Associated involved lymph nodes are best seen on interstitial-phase gadolinium-enhanced SGE images as small moderate-signal masses (arrows, *f*, *g*) in a background of suppressed fat. Pancreatic cancer has a propensity to involve nodes without resulting in increased size.

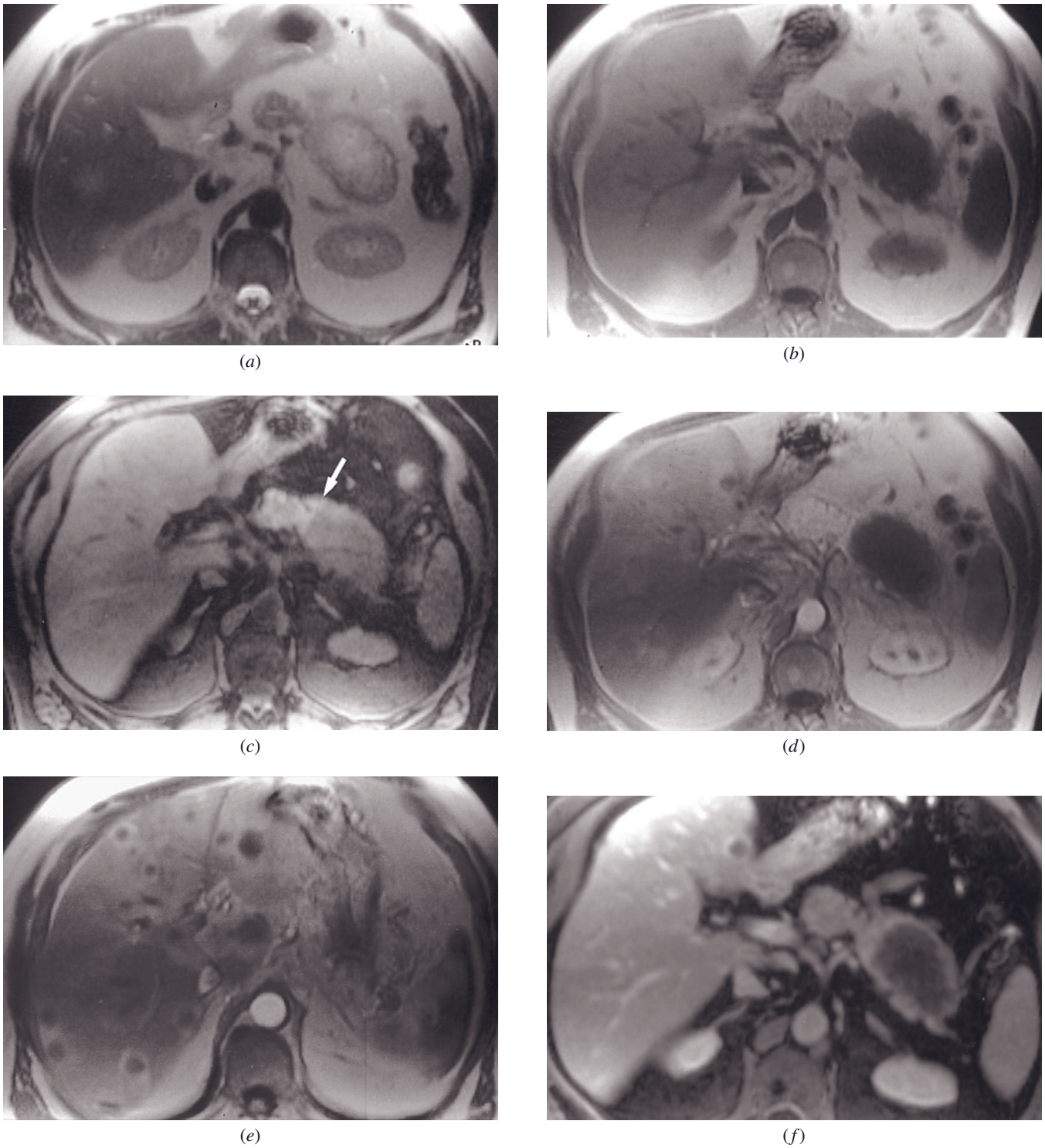

FIG. 4.33 Staging pancreatic cancer—liver metastases. T2-weighted SS-ETSE (*a*), T1-weighted SGE (*b*), T1-weighted fat-suppressed SGE (*c*), immediate postgadolinium T1-weighted SGE (*d*, *e*), and 90-s postgadolinium fat-suppressed SGE (*f*) images. A 4×5-cm tumor arises in the pancreatic tail. Note the shape demarcation of normal pancreas (arrow, *c*) proximal to the large pancreatic cancer. There are multiple liver metastases that are mildly hyperintense on T2 (*a*) and mildly low signal on T1, reflecting a low fluid content. Liver metastases are best seen as ring-enhancing lesions on immediate postgadolinium images (*d*, *e*) with ring-enhancing metastases involving both lobes. Pancreatic cancer most commonly metastasizes to the liver.

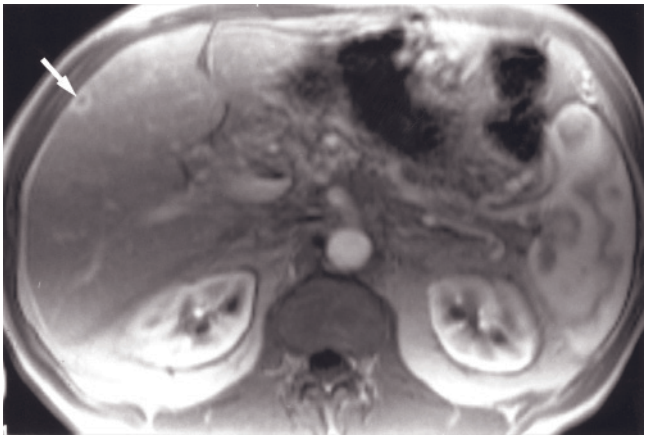

(*g*)

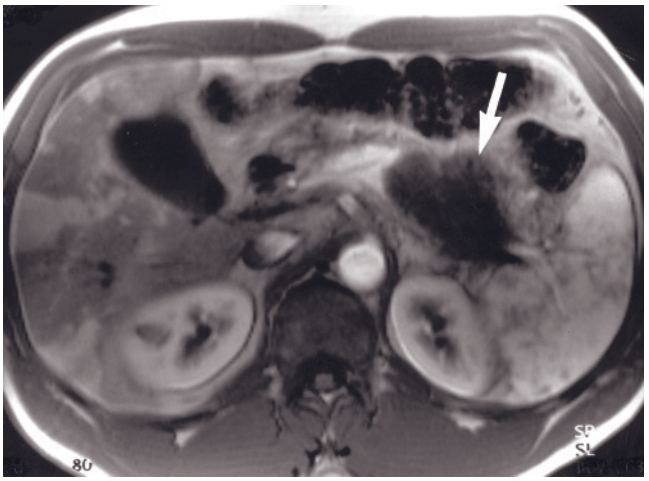

(*h*)

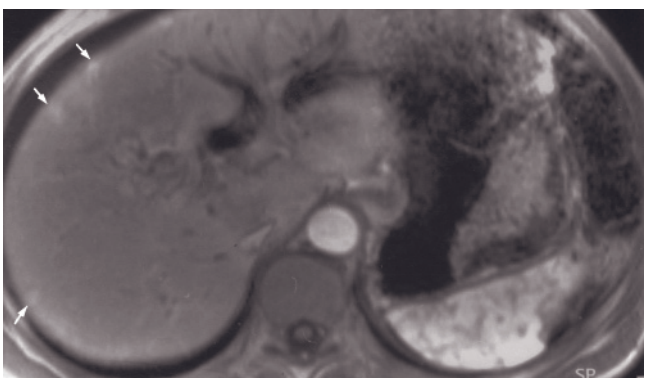

(*i*)

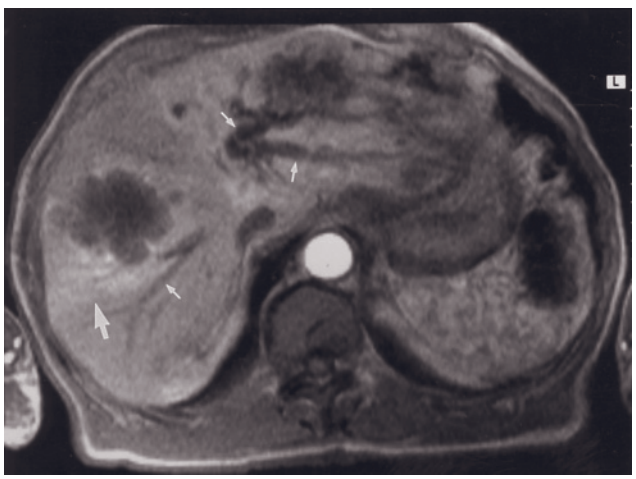

(*j*)

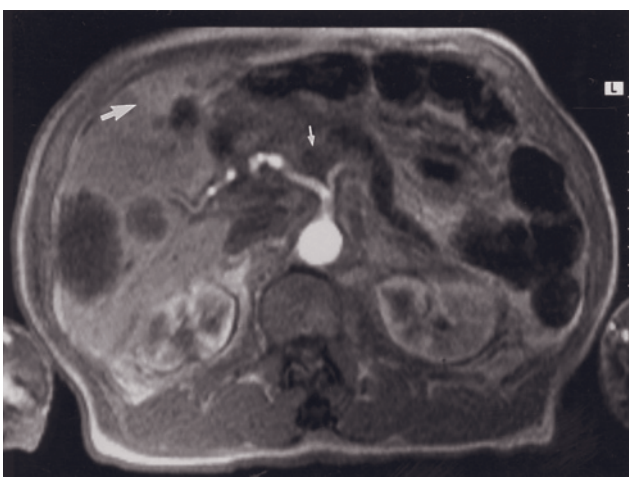

(*k*)

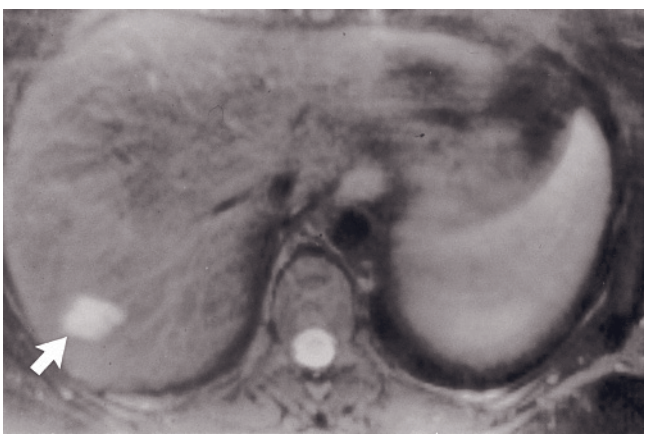

(*l*)

FIG. 4.33 (*Continued*) Immediate postgadolinium SGE image (*g*) in a second patient demonstrates a 1-cm ring-enhancing metastasis (arrow, *g*).

Immediate postgadolinium SGE image (*h*) in a third patient demonstrates a large hypovascular tumor arising from the tail of the tail of the pancreas (arrow, *h*). Note the beak sign with the proximal pancreatic parenchyma. Multiple hyperenhancing liver metastases are present, the majority <1 cm in size. Wedge-shaped areas of transient increased perilesional enhancement are appreciated surrounding several lesions. Perilesional enhancement is not uncommon in pancreatic ductal adenocarcinoma. The most commonly observed metastases with perilesional enhancement are colon adenocarcinoma.

Immediate postgadolinium T1-weighted SGE image (*i*) in a fourth patient. Multiple hyperenhancing <1-cm subcapsular liver metastases (arrows, *i*) are present that were not identifiable on other sequences.

Immediate postgadolinium T1-weighted SGE images (*j*, *k*) in a fifth patient. Multiple irregular hepatic metastases with rim enhancement are present. Ill-defined perilesional enhancement (arrow, *j*, *k*) is apparent surrounding several metastases. Substantial intrahepatic bile duct dilatation is also identified (small arrows, *j*) secondary to CBD obstruction by the pancreatic head cancer. Low-signal intensity tissue (small arrows, *k*) surrounds the celiac axis, a finding consistent with tumor involvement.

Breathing-averaged T2-weighted ETSE (*l*), immediate postgadolinium SGE (*m*), and 90-s postgadolinium T1-weighted

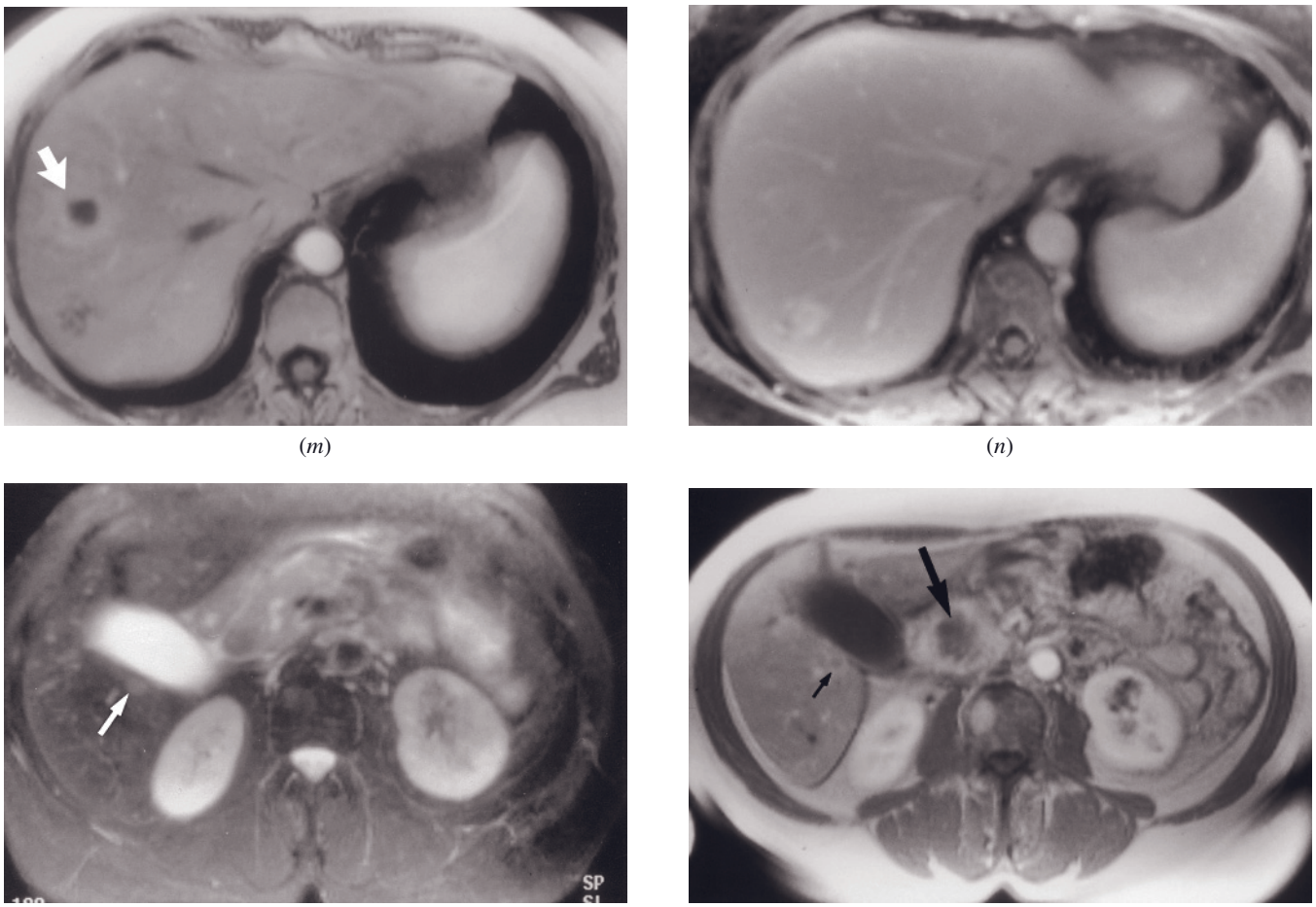

FIG. 4.33 (*Continued*) fat-suppressed SGE (*n*) images in a sixth patient who has liver metastases and a hemangioma. Hemangiomas and metastases can usually be readily distinguished. The hemangioma (arrow, *l*) is high signal on T2 (*l*) and demonstrates peripheral nodules on the immediate postgadolinium image (*m*) with relatively uniform hyperintense enhancement on delayed images (*n*). In contrast, the 3-cm metastasis is nearly invisible on T2 (*l*) and late postgadolinium images (*n*), with intense ring enhancement (arrow, *m*) on immediate post-gadolinium image (*m*). This constellation of findings is virtually pathognomonic on T2-weighted and postgadolinium images for a liver metastasis coexistent with a hemangioma.

Breathing averaged T2-weighted echo-train spin-echo (*o*) and immediate postgadolinium SGE (*p*) images in a seventh patient. The pancreatic tumor is not well seen on T2, but clearly shown as a hypoenhancing mass (arrow, *p*) on the immediate postgadolinium image (*p*). A <1-cm ring-enhancing lesion (small arrow, *p*) is apparent in a subcapsular location adjacent to the gallbladder in *segment V*. On the T2-weighted image (*o*) the lesion is only mildly hyperintense, consistent with minimal fluid content, characteristic of pancreatic ductal adenocarcinoma metastases.

with pancreatic cancer liver metastases than with colon cancer liver metastases and may have a dramatic appearance. Concomitant liver metastases in the setting of prominent wedge-shaped enhancement abnormalities are commonly small, hypervascular, and subcapsular in location. Small subcapsular hypervascular metastases are observed in over 80% of patients and may be the only pattern of liver mestastases in up to 20% of patients [47]. Optimal utilization of MRI in the investigation of pancreatic carcinoma occurs in the following circumstances: 1) detection of small, non-contour-deforming tumors (due to the high contrast resolution of pre-contrast T1-weighted fat-suppressed imaging and immediate postgadolinium gradient-echo images), 2) determination of tumor location for imaging-guided biopsy, 3) evaluation of vascular involvement by tumor, 4) determination and characterization of associated liver lesions, and 5) determination of the presence of lymph node and peritoneal metastases. MRI may be particularly valuable in patients who have an enlarged pancreatic head with no definition of a mass on CT images.

Surgery remains the main therapeutic treatment of patients with pancreatic cancer [28, 48]; therefore, earlier detection of potentially curable disease may result in

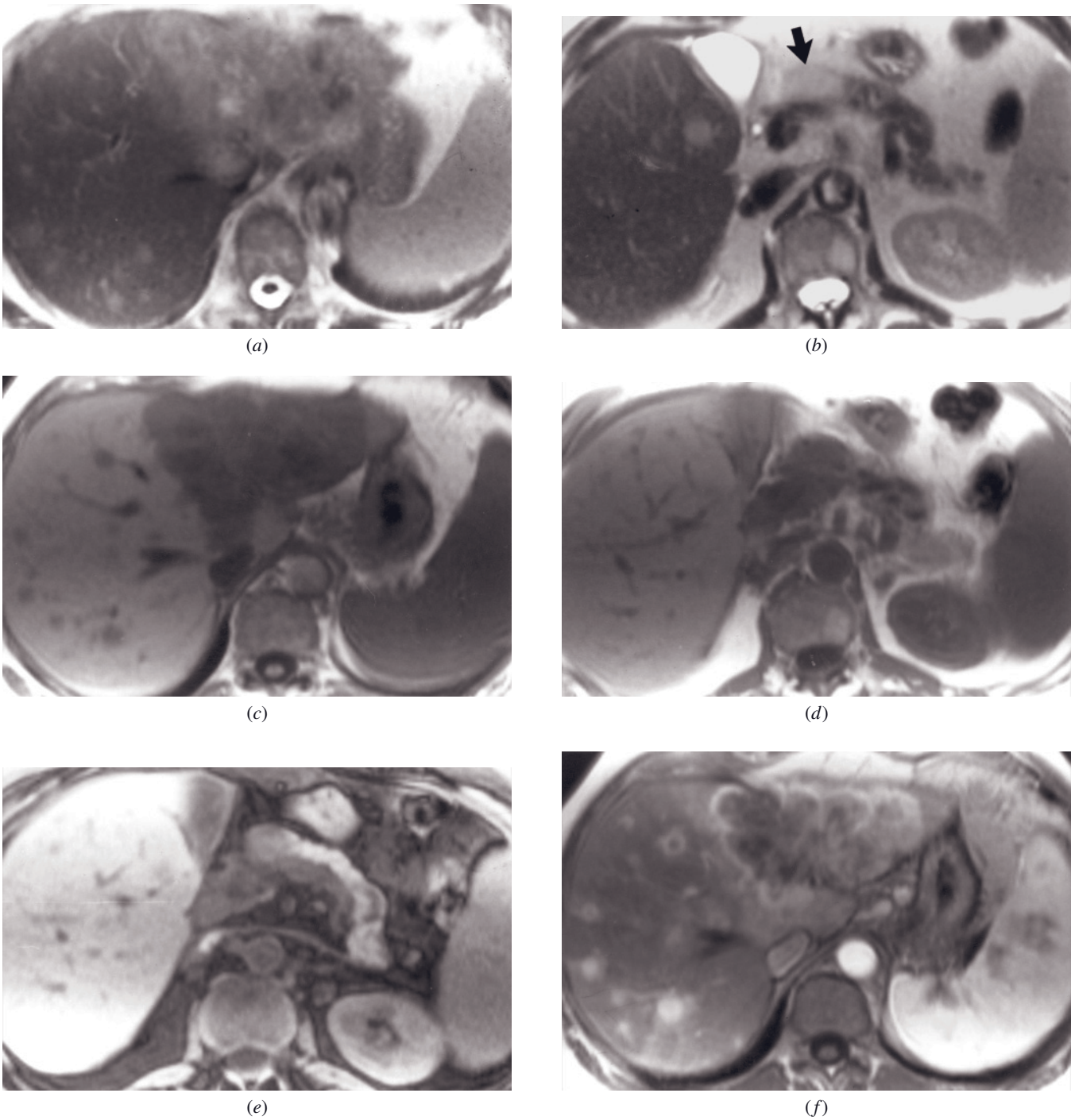

FIG. 4.34 Poorly differentiated carcinoma resembling islet cell tumor. T2-weighted SS-ETSE (*a*, *b*), T1-weighted SGE (*c*, *d*), T1-weighted fat-suppressed SGE (*e*), immediate postgadolinium T1-weighted SGE (*f*, *g*), and 90-s postgadolinium fat-suppressed

improved patient survival. Benassai et al. [48] recently reported on the factors associated with improvement in the 5-year actuarial survival for patients undergoing Whipple procedure (pancreaticoduodenectomy). Five-year survival was greater for node-negative than for node-positive patients (41.7% vs. 7.8%, $P < 0.001$) and for smaller (<3 cm) than for larger tumors (33.3% vs. 8.8%, $P < 0.006$). The five-year survival for patients with negative surgical margins was 23.3%, whereas no patients with positive surgical margins survived at 13 months ($P < 0.001$). Another recent report by Ariyama et al. [49] demonstrated a 5-year survival of 100% for

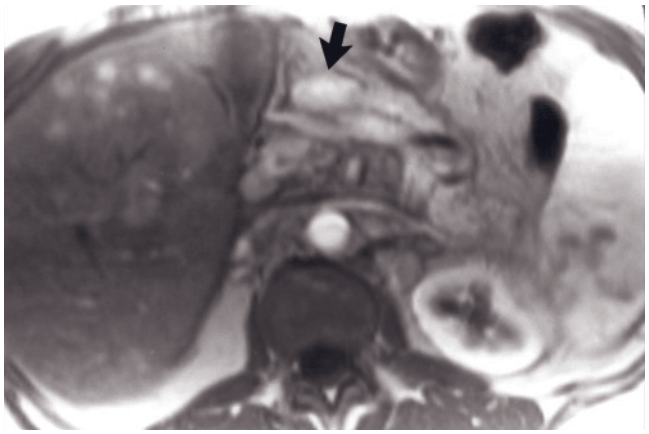

(*g*)

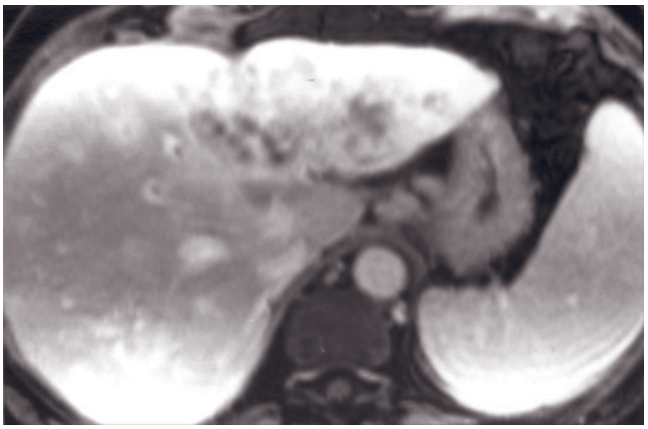

(*h*)

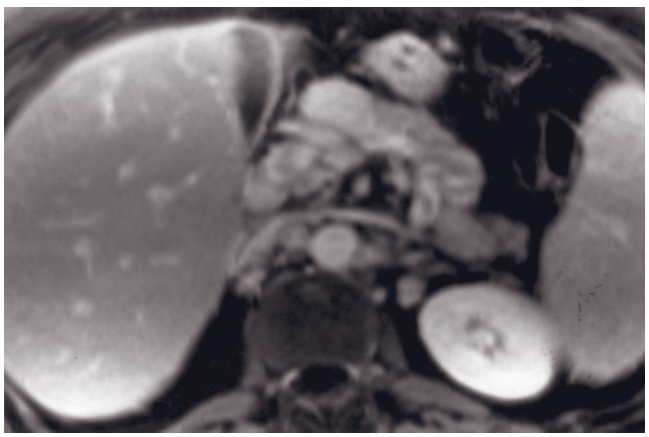

(*i*)

FIG. 4.34 (*Continued*) SGE (*h*, *i*) images. There is a 3-cm tumor (arrow, *b*) arising in the pancreatic neck, which is moderately hyperintense on T2 (*b*) and moderately hypointense on T1 (*d*, *e*), enhances in a uniform intense fashion immediately after gadolinium administration (arrow, *g*), and retains contrast on interstitial-phase images (*i*). There are multiple liver metastases that are moderately hyperintense on T2 (*a*) and moderately hypointense on T1 (*c*) and show uniform or ring enhancement on immediate postgadolinium images (*f*), mimicking an islet cell tumor.

patients with <1-cm tumors. It may be that MRI, particularly 3.0T MRI, is best suited to reliably detect these small tumors, and resultant small metastases and subtle vascular and adjacent organ-structure involvement as well.

Poorly Differentiated Carcinoma

Rarely malignant pancreatic cancers may not be classifiable because of too poorly differentiated or anaplastic cytology. These cancers may have an appearance similar to islet cell tumors, with tumors appearing high signal on T2-weighted images and extensive hypervascular liver metastases (see fig. 4.34). The spectrum of appearance for poorly differentiated carcinoma has not been elucidated.

Acinar Cell Carcinoma

Acinar cell carcinoma is a rare primary tumor of the exocrine gland of the pancreas, representing approximately 1% of pancreatic cancers. Tumors generally occur between the fifth and seventh decades. Tatli et al. [50] recently described the appearance of these tumors on CT and MR images. These cancers are generally exophytic, oval or round, well marginated, and hypovascular. Small tumors are generally solid, whereas larger tumors contain cystic areas representing regions of necrosis.

Chemotherapy/Radiation Therapy-Treated Pancreatic Ductal Adenocarcinoma

After chemotherapy and radiation therapy, morphologic and pathophysiologic changes occur in the tumor, in the pancreas, and in surrounding fatty tissues. In approximately 50% of cases decrease in size of tumor and surrounding fibrogenic response can be demonstrated on MR images that correlate with clinical response. However, in a sizable proportion of cases, the interface is indistinct between tumor margin and surrounding background pancreatic tissue. In these instances, evaluation of tumor dimensions is extremely difficult. In addition, in some cases, posttreatment images may show features consistent with acute on chronic pancreatitis. On imaging, both processes may demonstrate an increase in abnormal pancreatic tissue even though the tumor itself has decreased in size. Assessment of treatment response is challenging (fig. 4.35).

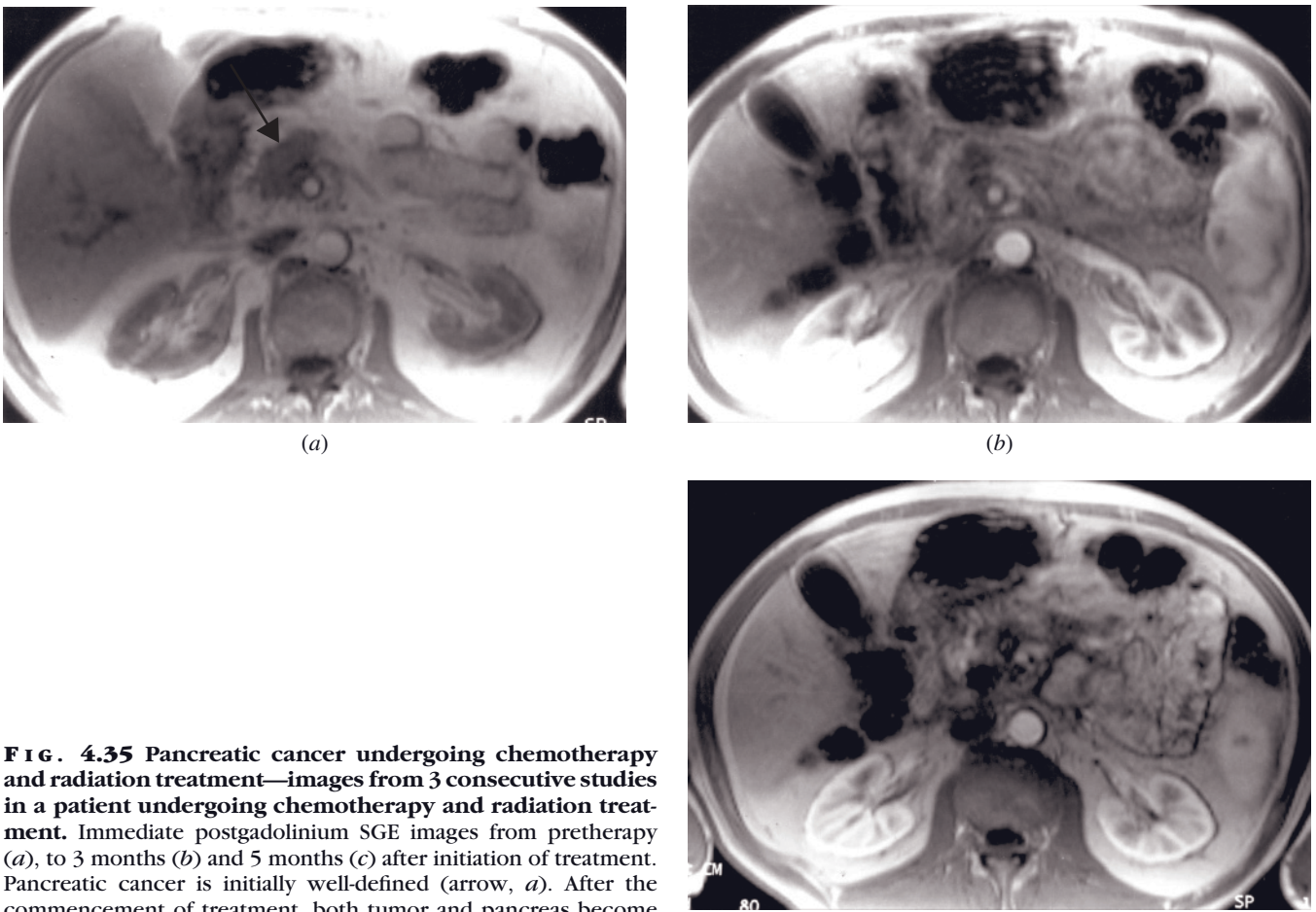

FIG. 4.35 Pancreatic cancer undergoing chemotherapy and radiation treatment—images from 3 consecutive studies in a patient undergoing chemotherapy and radiation treatment. Immediate postgadolinium SGE images from pretherapy (*a*), to 3 months (*b*) and 5 months (*c*) after initiation of treatment. Pancreatic cancer is initially well-defined (arrow, *a*). After the commencement of treatment, both tumor and pancreas become less defined (*b*, *c*).

Islet Cell Tumors

Islet cell tumors are a subgroup of gastrointestinal neuroendocrine tumors that occur within the endocrine pancreas. These tumors are rare in comparison with tumors arising from the exocrine portion. Islet cell tumors are uncommon, with a reported incidence of less than 1 per 100,000 [51]. Tumors may be nonfunctioning, or, more commonly, they may present with an endocrine abnormality resulting from the secretion of hormones [51]. Histopathologically, only a generic diagnosis of islet cell tumor can be made with routine staining methods. However, islet cell tumors are primarily identified by the peptide they contain, and the tumor itself is named after the hormone it secretes (e.g., an insulin-secreting tumor is termed an insulinoma). Only the results of special immunohistochemical techniques such as fluorescence-labeled antibody specific for a peptide, will permit the designation of a specific islet tumor such as insulinoma, gastrinoma, etc. A certain proportion of islet cell tumors will secrete no identifiable substance and remain uncategorized after special immunohistochemical procedures. The most common pancreatic islet cell tumors are insulinomas and gastrinomas [52], followed in frequency by nonfunctional or untyped tumors. In the authors' experience, the majority of clinically or immunohistochemically verified pancreatic neuroendocrine tumors are gastrinomas [53]. Hormonally functional tumors tend to present when they are small because of symptoms related to the hormones secreted by the tumors. Nonfunctional tumors account for at least 15–20% of islet cell tumors and tend to present with symptoms due to large tumor mass or metastatic disease [54]. Malignancy cannot be diagnosed on the basis of the histologic appearance of islet cell tumors. Instead, malignancy is determined by the presence of metastases or local invasion beyond the substance of the pancreas. Insulinomas are most commonly benign tumors, gastrinomas are malignant in approximately 60% of cases, and almost all other types, including nonfunctioning tumors, are malignant in the great majority of cases. The liver is the most common organ for metastatic spread. There is also a modest propensity for splenic metastases.

In the MRI investigation for islet cell tumors, precontrast T1-weighted fat-suppressed images, immediate

postgadolinium gradient-echo images, and T2-weighted fat-suppressed images or breath-hold T2-weighted images are useful [1, 55–58]. Because many MR techniques independently demonstrate islet cell tumors well, MR is particularly well suited for the investigation of these tumors. Tumors are low in signal intensity on T1-weighted fat-suppressed images, demonstrate homogeneous, ring, or diffuse heterogeneous enhancement on immediate postgadolinium gradient echo, and are high in signal intensity on T2-weighted fat-suppressed images (figs. 4.36–4.38) [53]. In rare instances, islet cell tumors may be very desmoplastic, appear low in signal intensity on T2-weighted images, and demonstrate negligible contrast enhancement (fig. 4.38). In these cases, the tumors may mimic the appearance of pancreatic ductal adenocarcinoma. Large noninsulinoma islet cell tumors not uncommonly contain regions of necrosis [59].

Features that distinguish the majority of islet-cell tumors from ductal adenocarcinomas include high signal intensity on T2-weighted images, increased homogeneous enhancement on immediate post-gadolinium images, and hypervascular liver metastases [57]. Because islet cell tumors rarely obstruct the pancreatic duct, T1-weighted fat-suppressed images most often show high signal intensity of background pancreas, rendering clear depiction of low-signal-intensity tumors in the majority of cases [56, 57]. Lack of pancreatic ductal obstruction and vascular encasement by tumor are features that differentiate islet cell tumor from pancreatic ductal adenocarcinoma. In contrast to the frequent occurrence of venous thrombosis in pancreatic ductal adenocarcinoma, thrombosis is rare in the setting of islet cell tumors. However, rarely, thromboses may occur and may represent tumor thrombosis (fig. 4.39) [60], unlike the circumstance in pancreatic ductal adenocarcinoma, where the thrombus is usually bland. Peritoneal metastasis and/or regional lymph node enlargement, characteristic features of pancreatic ductal adenocarcinoma, are generally not present in islet cell tumors.

Gastrinomas (G Cell Tumors). The Zollinger–Ellison syndrome is defined by the clinical triad of pancreatic islet cell gastrinoma, gastric hypersecretion, and recalcitrant peptic ulcer disease. Ulcers located in the postbulbar region of the duodenum or in the jejunum, particularly if multiple, suggest the diagnosis of a gastrinoma. Esophagitis is not infrequently observed in these patients.

Gastrinomas occur most frequently in the region of the head of the pancreas including pancreatic head, duodenum, stomach, and lymph nodes in a territory termed the gastrinoma triangle [34]. The anatomic boundaries of the triangle are the porta hepatis as the superior point of the triangle and the second and third parts of the duodenum forming the base. Although gastrinomas are usually solitary, multiple gastrinomas may occur, especially in the setting of multiple endocrine neoplasia syndrome, type 1. In this setting, patients have multiple pancreatic and duodenal islet cell tumors [46, 55, 61].

Gastrinomas are not as frequently hypervascular as insulinomas. Mean size at presentation is 4 cm [59]. CT imaging is able to detect gastrinomas reliably when the tumors measure more than 3 cm in diameter but performs less well in the detection of smaller tumors [62]. Conventional spin-echo MRI also has been limited in the detection of gastrinomas [63, 64]. However, MRI, using current techniques, is very effective at detecting tumors <1 cm in diameter. Gastrinomas are low in signal intensity on T1-weighted fat-suppressed images and high in signal intensity on T2-weighted fat-suppressed images, demonstrating peripheral ringlike enhancement on immediate postgadolinium gradient-echo images (fig. 4.40) [56]. These imaging features are observed in the primary lesion and in hepatic metastases. Central low signal intensity on postgadolinium images reflects central hypovascularity. Occasionally, lesions will be cystic. The enhancing rim of the primary tumor varies substantially in thickness, with the thickness of the rim reflecting the degree of hypervascularity of the tumor. If the enhancing rim is thin, it may appear nearly imperceptible because of similar enhancement of the surrounding pancreatic parenchyma. Gastrinomas may occur outside the pancreas, and fat-suppressed T2-weighted images are particularly effective at detecting these high-signal-intensity tumors in a background of suppressed fat (fig. 4.41). Multiple gastrinomas may be scattered throughout the pancreas and frequently are small. T2-weighted breathing-independent echo-train spin echo may be effective at demonstrating these tumors, because breathing-averaged T2-weighted sequences may result in blurring, which may mask the presence of small tumors (fig. 4.42).

Gastrointestinal imaging findings that may be observed in gastrinomas include enlargement of the rugal folds of gastric mucosa (hypertrophic gastropathy) and intense mucosal enhancement on early postgadolinium gradient-echo images (fig. 4.43), increased esophageal enhancement, and abnormal enhancement and/or thickness of proximal small bowel. These features are reflective of the inflammatory changes of peptic ulcer disease and gastric hyperplasia due to the effects of gastrin.

In general, islet cell tumor metastases to the liver are well shown on MR images. Gastrinoma metastases frequently are relatively uniform in size and shape [57]. These metastases are generally hypervascular and possess uniform intense rim enhancement on

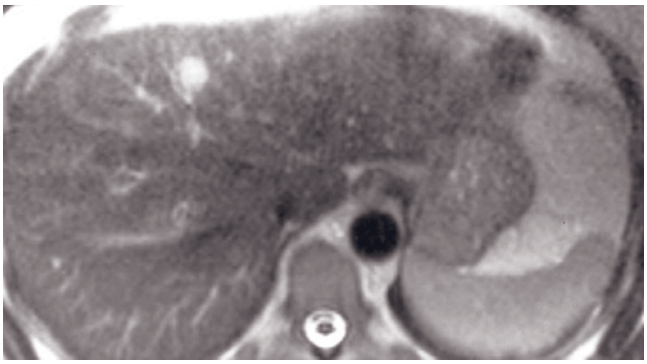

(*a*)

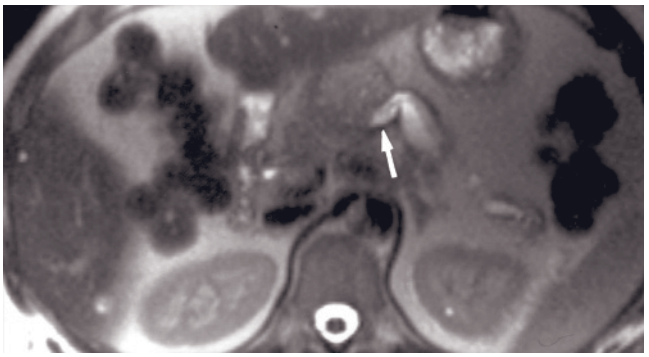

(*b*)

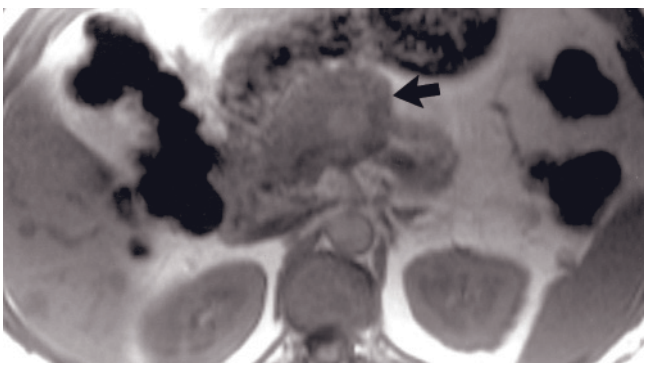

(*c*)

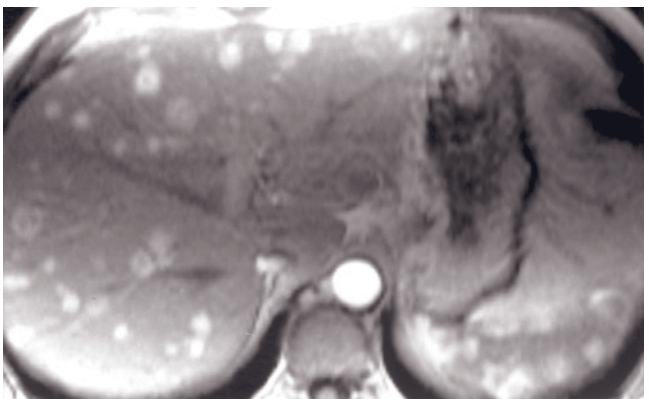

(*d*)

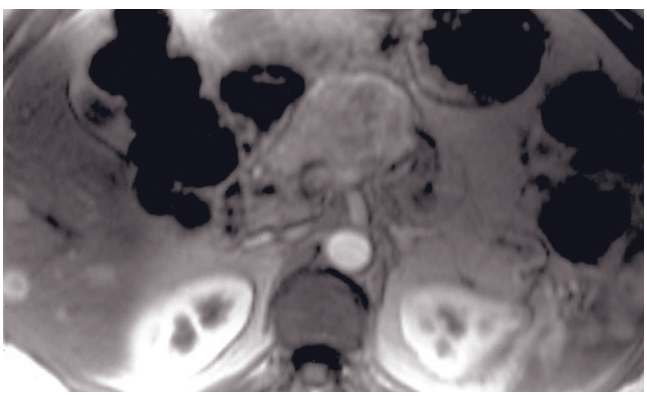

(e)

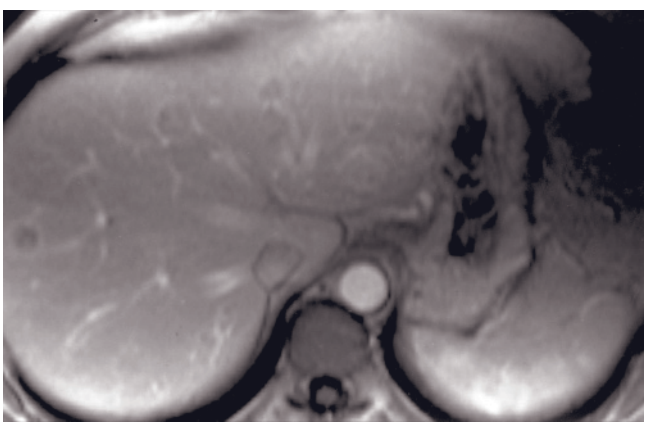

(*f*)

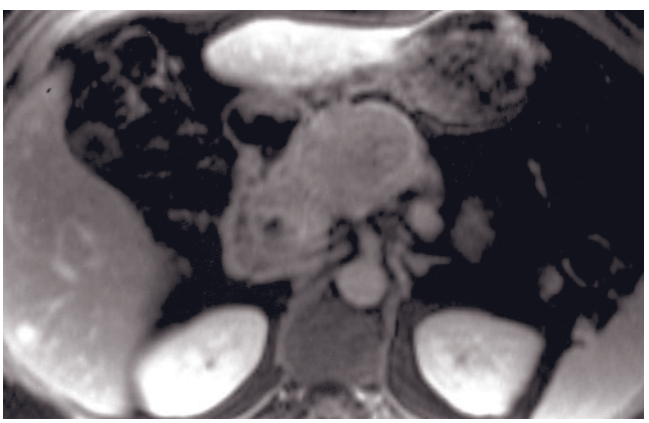

(*g*)

FIG. 4.36 Nonfunctioning islet cell tumor with pancreatic ductal obstruction. T2-weighted SS-ETSE (*a*, *b*), T1-weighted SGE (*c*), immediate (*d*, *e*) and 45-s (*f*) postgadolinium T1-weighted SGE, and 90-s postgadolinium fat-suppressed SGE (*g*) images. There is a 5-cm lobulated tumor (arrow, *c*) arising from the neck/proximal body of the pancreas. The tumor is mildly hyperintense on T2 (*b*) and mildly hypointense on T1 (*c*) and shows diffuse moderately intense enhancement on immediate postgadolinium SGE (*e*) with moderate washout on interstitial-phase images (*g*). The pancreatic duct (arrow, *b*) is obstructed by the tumor with associated distal atrophy of the pancreas. Multiple extensive liver metastases are present measuring up to 1.5 cm in diameter. These metastatic lesions are best seen as hyperintense uniform or ring-enhancing lesions on immediate postgadolinium images (*d*). Rapid washout of the metastasis occurs by 45 s after injection (*f*).

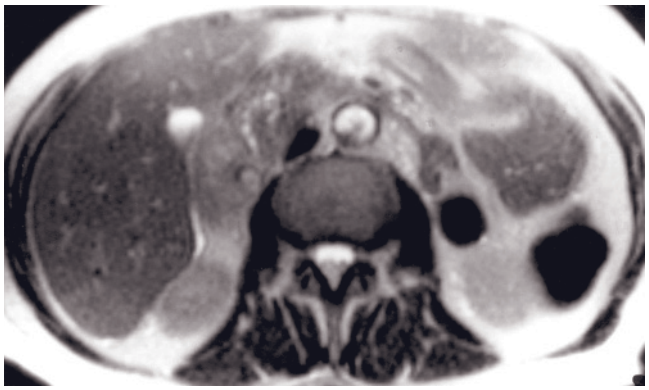

(*a*)

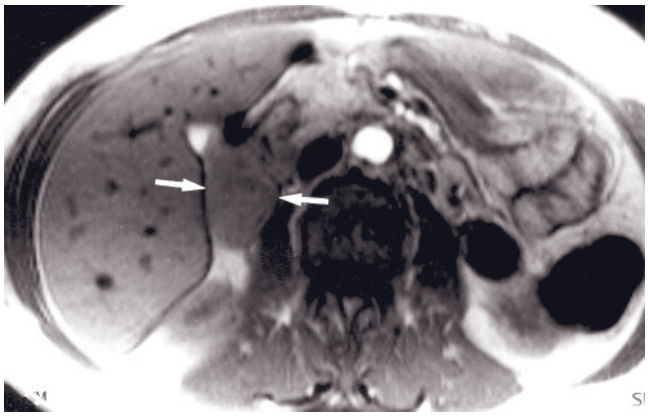

(*b*)

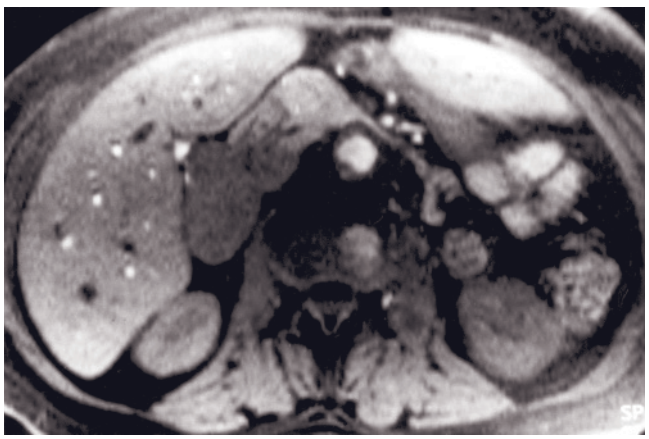

(*c*)

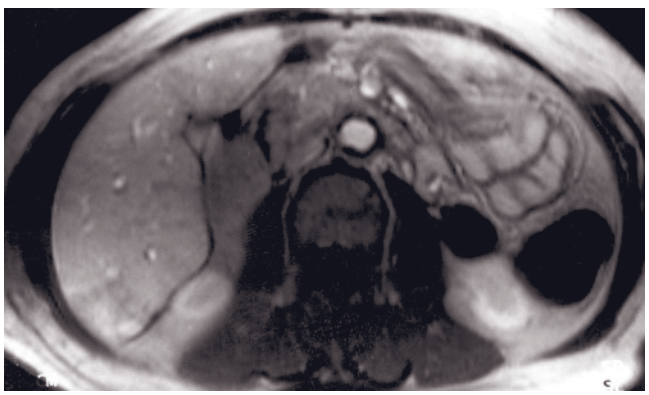

(*d*)

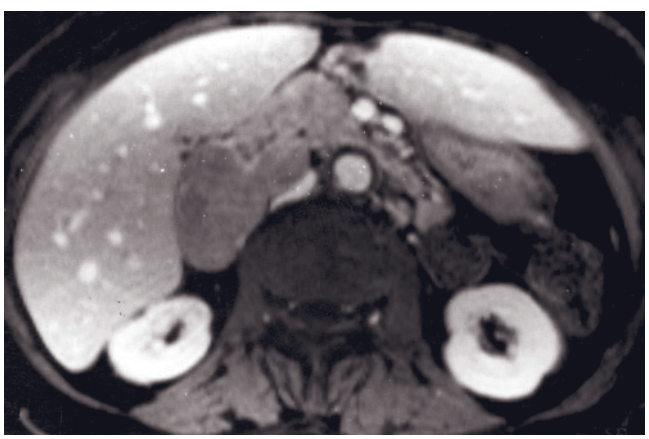

(*e*)

FIG. 4.37 Nonfunctioning well-differentiated neuroendocrine carcinoma. T2-weighted SS-ETSE (*a*), T1-weighted SGE (*b*), T1-weighted fat-suppressed SGE (*c*), immediate postgadolinium T1-weighted SGE (*d*), and 90-s postgadolinium fat-suppressed SGE (*e*) images. There is a exophytic mass (arrows, *b*) arising from the head of the pancreas, which is slightly hyperintense relative to the pancreas on T2 (*a*) and moderately hypointense on T1 (*b*, *c*) with mild early (*d*) and late (*e*) enhancement on gadolinium-enhanced images.

immediate postgadolinium gradient-echo images. Unlike pancreatic ductal cancer liver metastases, ill-defined perilesional enhancement is not observed with gastrinoma metastases, despite the substantial hepatic arterial blood supply of these tumors. Typically, lesions are very high in signal intensity on T2-weighted fat-suppressed images and have well-defined margins. This T2-weighted appearance may be confused with hemangiomas, which are also moderately high signal intensity and well defined. Islet cell tumor liver metastases are differentiated from hemangiomas by their enhancement patterns. Islet cell metastases have uniform ring enhancement on immediate postgadolinium images that fades with time [53], whereas hemangiomas have discontinuous peripheral nodular enhancement on immediate postgadolinium images with centripetal progression of enhancement.

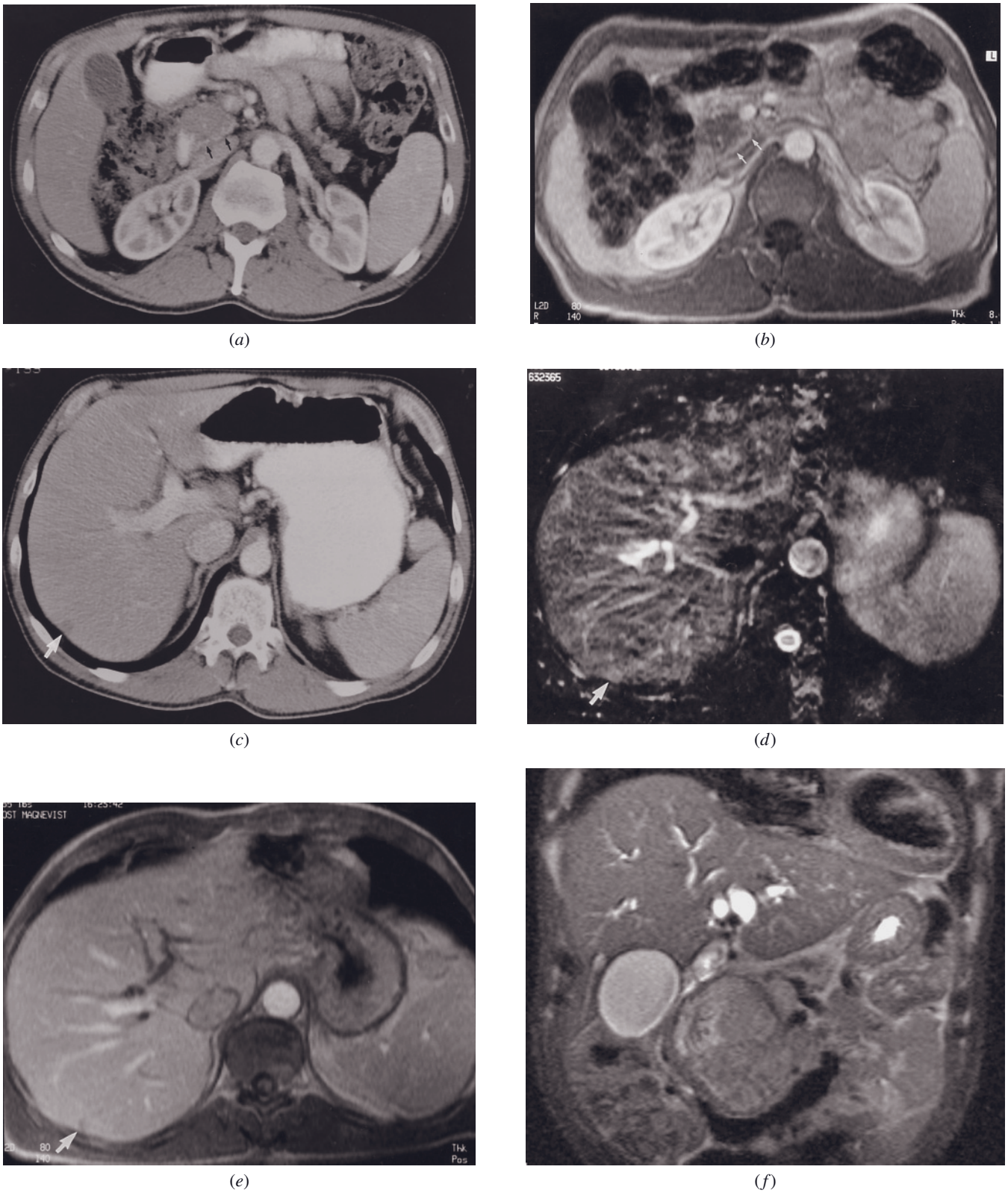

FIG. 4.38 Nonfunctioning islet cell tumor with liver metastases. Spiral CT (*a*) and immediate postgadolinium T1-weighted SGE (*b*) images. Low-attenuation/signal intensity tumor is well shown in the head of the pancreas on both spiral CT (*a*) and MR (*b*) images. A thin rim of greater-enhancing normal pancreas is noted posterior to the tumor (small arrows, *a*, *b*). On a higher tomographic section, an ill-defined low-density lesion is noted in the liver on spiral CT image (arrow, *c*) that was considered indeterminate. On the T2-weighted fat-suppressed spin-echo image (*d*), the liver lesion is noted to be low in signal intensity (arrow, *d*), which is not consistent with cyst or hemangioma and is compatible with a hypovascular metastasis. On the 45-s postgadolinium T1-weighted SGE image (*e*), the lesion enhances in a diminished fashion with faint peripheral rim enhancement (arrow, *e*) consistent with a hypovascular metastasis. A cyst would appear nearly signal void, which would be comparable in appearance to the dilated biliary ducts on the postgadolinium image (*e*).The hypovascular nature of this primary tumor is uncommon for islet cell tumors.

Fat-suppressed coronal T2-weighted SS-ETSE (*f*), fat-suppressed T1-weighted gradient-echo (*g*), and immediate (*h*, *i*, *j*) and interstitial-phase (*k*) postgadolinium fat-suppressed T1-weighted gradient-echo images in a second patient with islet cell tumor.

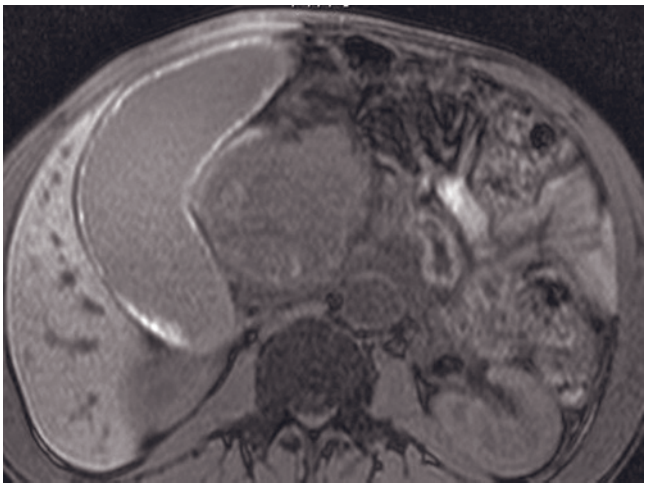

(*g*)

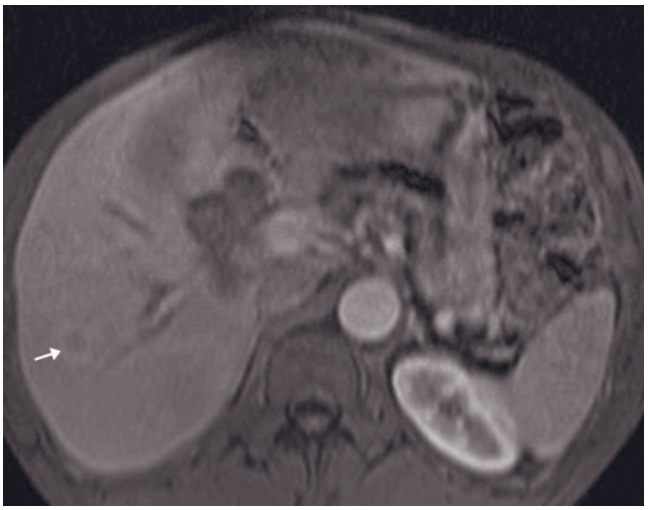

(*h*)

(*i*)

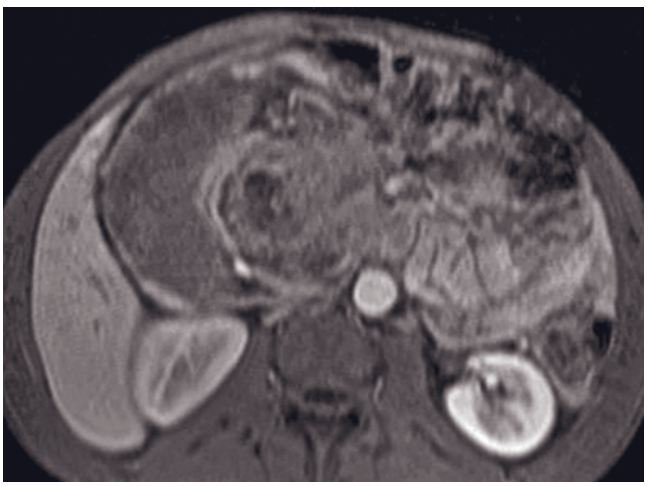

(*j*)

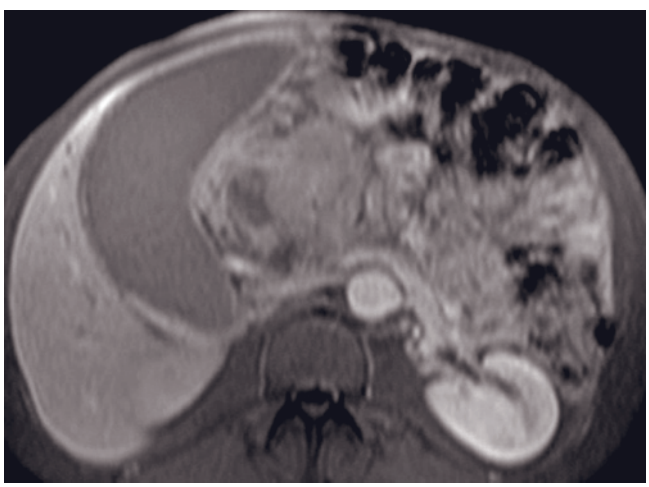

(*k*)

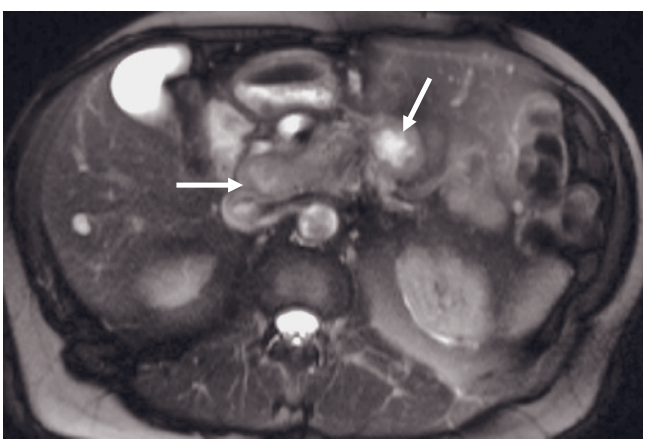

(*l*)

Fig. 4.38 (*Continued*) A 7-cm mass is present in the pancreatic head. The mass shows diminished and heterogeneous enhancement. Bile ducts are dilated secondary to compression by the mass. The gallbladder is markedly dilated. A ring enhancing lesion is seen in the liver on immediate postgadolinium T1-weighted image, consistent with a metastasis (arrow, *h*). The superior mesenteric artery is thrombosed (arrow, *i*).

T2-weighted fat-suppressed single-shot echo-train spin-echo (*l*) and T1-weighted postgadolinium hepatic arterial dominant phase (*m*) and hepatic venous phase (*n*) fat-suppressed 3D-GE images at 3.0 T demonstrate nonfunctioning islet cell tumors (white thick

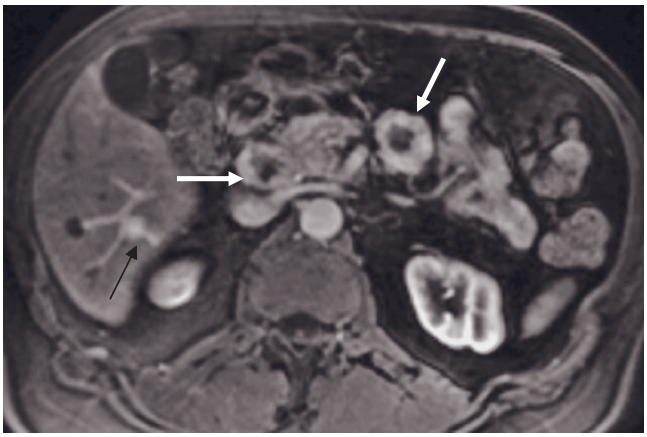

(*m*)

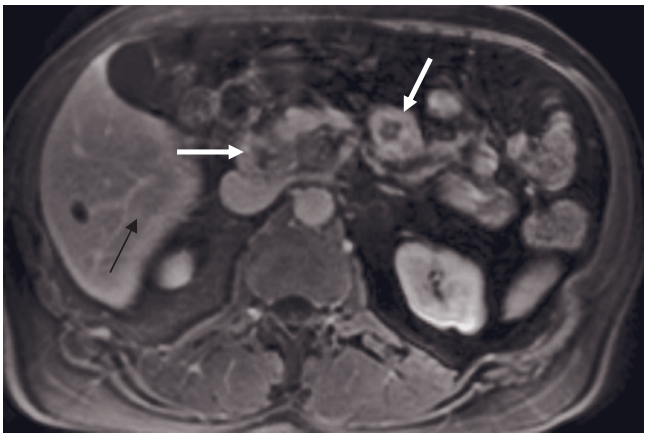

(*n*)

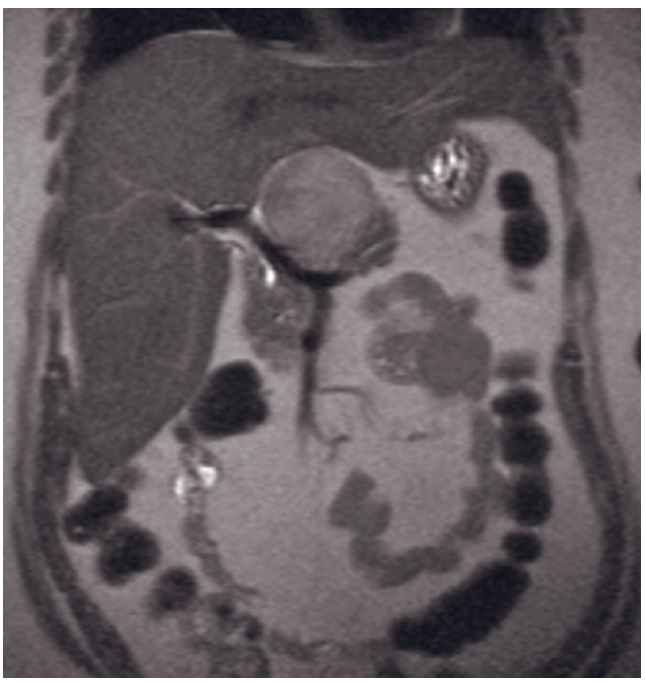

(*o*)

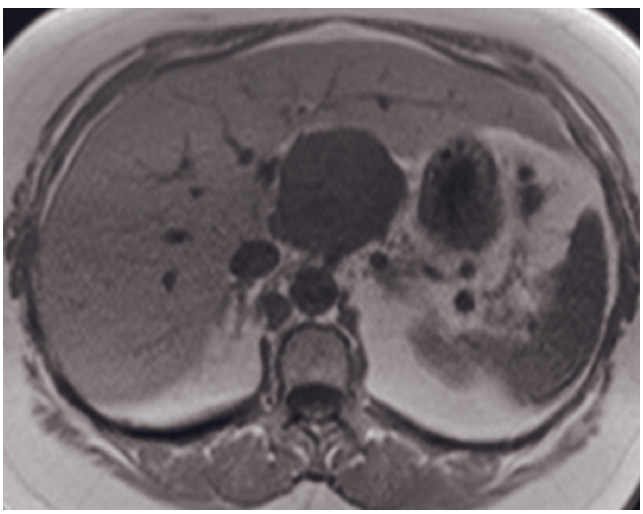

(*p*)

FIG. 4.38 (*Continued*) arrows, *l–n*) in another patient. The tumors (white thick arrows; *l–n*) are located in the pancreatic head and the pancreatic body. They contain central necrosis. There is also a hypervascular liver metastasis (black arrow, *m*, *n*) showing intense enhancement on the hepatic arterial dominant phase and fading on the hepatic venous phase. Note the liver cyst located in the right lobe of the liver.

Pancreatic schwannoma. Coronal T2-weighted fat-suppressed single-shot echo-train spin-echo (*o*), transverse T1-weighted SGE (*p*), and transverse T1-weighted postgadolinium hepatic arterial dominant phase (*q*) and hepatic venous phase (*r*) fat-suppressed 3D-GE images demonstrate a pancreatic schwannoma in another patient. The tumor is very well demarcated and shows markedly high signal on T2-weighted image like other neurogenic tumors. The tumor shows progressive heterogeneous enhancement on postgadolinium images. It is located adjacent to the portal vein and between the branches of celiac trunk. The tumor causes widening of the branches of celiac trunk.

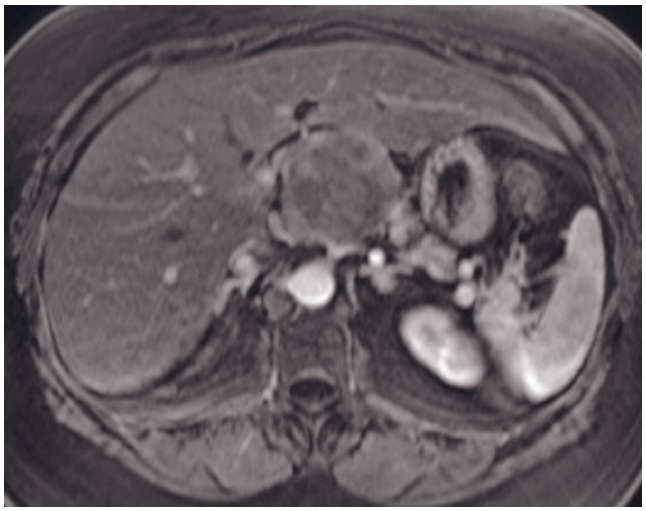

(*q*)

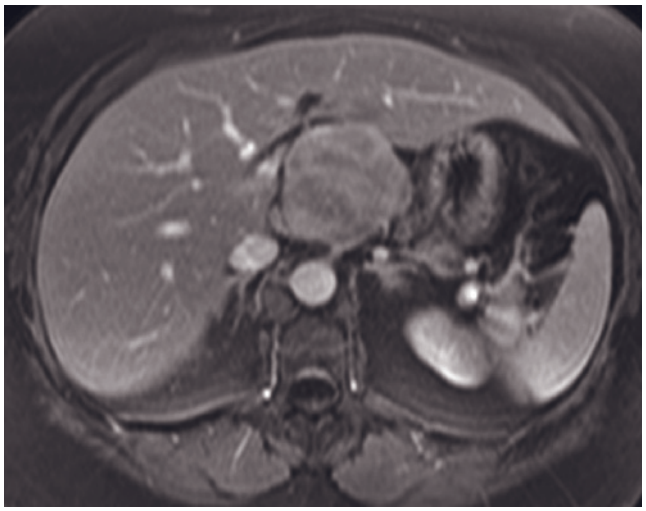

(*r*)

FIG. 4.38 (*Continued*)

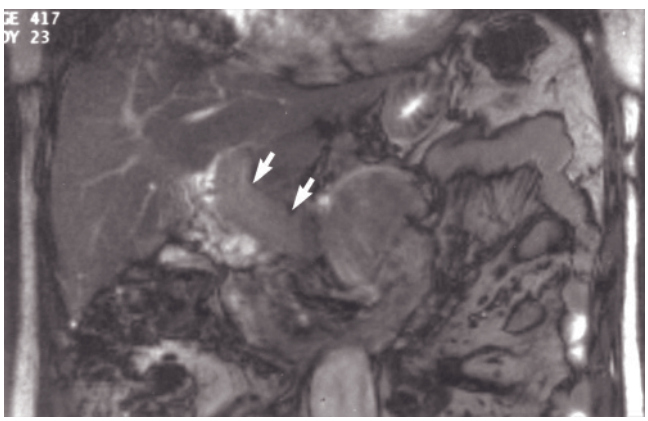

(*a*)

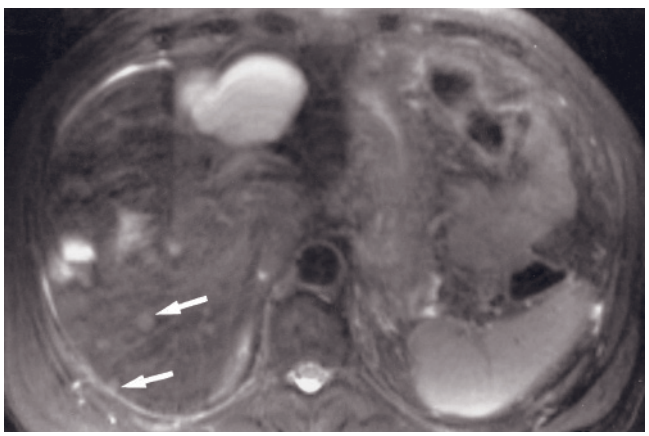

(*b*)

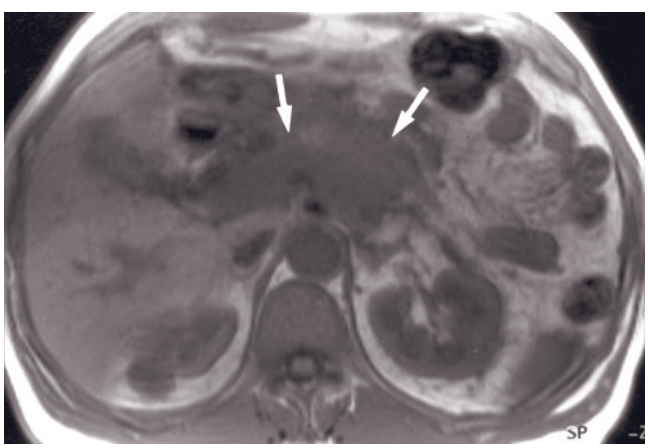

(*c*)

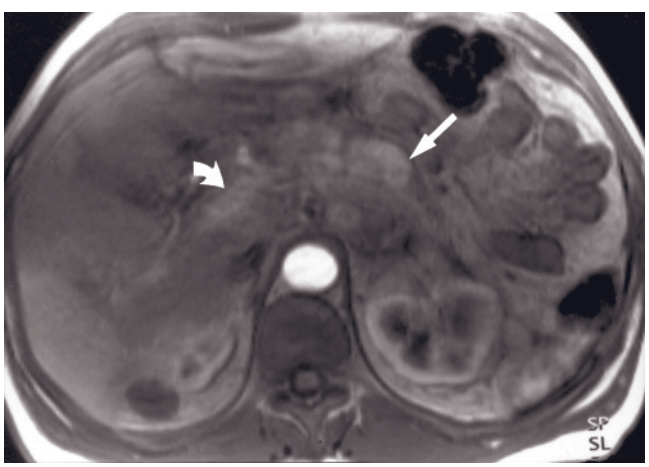

(*d*)

FIG. 4.39 Nonfunctioning islet cell tumor with tumor thrombus. Coronal gradient refocused flow-sensitive gradient-echo (*a*), T2-weighted fat-suppressed SS-ETSE (*b*), T1-weighted SGE (*c*), and immediate postgadolinium T1-weighted SGE (*d*) images in a second patient. A 8 × 5-cm mass arises in the pancreatic body (arrows, *c*). Expansible tumor thrombus (arrows, *a*) extending into the intrahepatic portal vein is appreciated on the coronal flow-sensitive gradient-echo image (*a*). Liver cysts and metastases are present, with the <1-cm liver metastases (arrows, *b*) best shown on the T2-weighted image (*b*).The primary tumor exhibits diffuse moderately intense heterogeneous enhancement (arrow, *d*), and enhancement of the tumor thrombus is also appreciated (curved arrow, *d*).

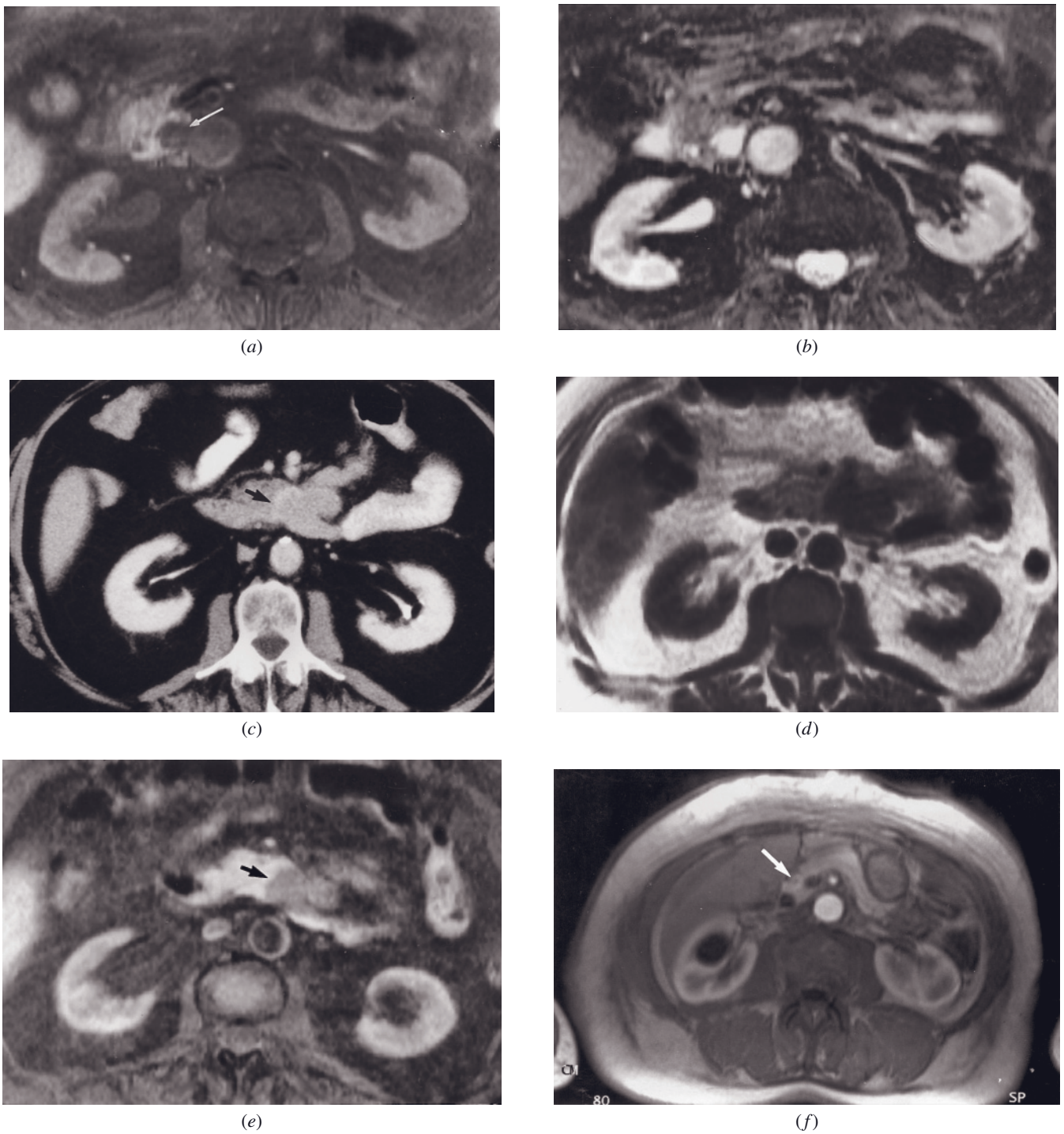

FIG. 4.40 Islet cell tumor—gastrinoma. T1-weighted fat-suppressed spin-echo (*a*) and T2-weighted fat-suppressed spin-echo (*b*) images. Islet cell tumors (arrow, *a*) are usually low in signal intensity in a background of high-signal intensity pancreas on T1-weighted fat-suppressed images (*a*) and high in signal intensity on T2-weighted images (*b*). The uncinate process is a common location for gastrinomas, because it is located in the "gastrinoma triangle."

Dynamic contrast-enhanced CT (*c*), T1-weighted SGE (*d*), and T1-weighted fat-suppressed spin-echo (*e*) images in a second patient. A 2-cm gastrinoma is present arising from the uncinate process of the pancreas (*c*–*e*).The tumor is most conspicuous on the T1-weighted fat-suppressed spin-echo image with a "beak" sign apparent (arrow, *e*) and was not identified on the CT examination prospectively. An enhancing rim (arrow, *c*) is apparent on the CT image.

Immediate postgadolinium SGE image (*f*) in a third patient demonstrates a 8-mm ring-enhancing tumor (arrow, *f*) in the neck of the pancreas diagnostic for a gastrinoma in the appropriate clinical setting. Gastrinomas most commonly possess uniform ring enhancement in both the primary tumor and liver metastases. This patient had two recent CT examinations that were both negative for gastrinoma.

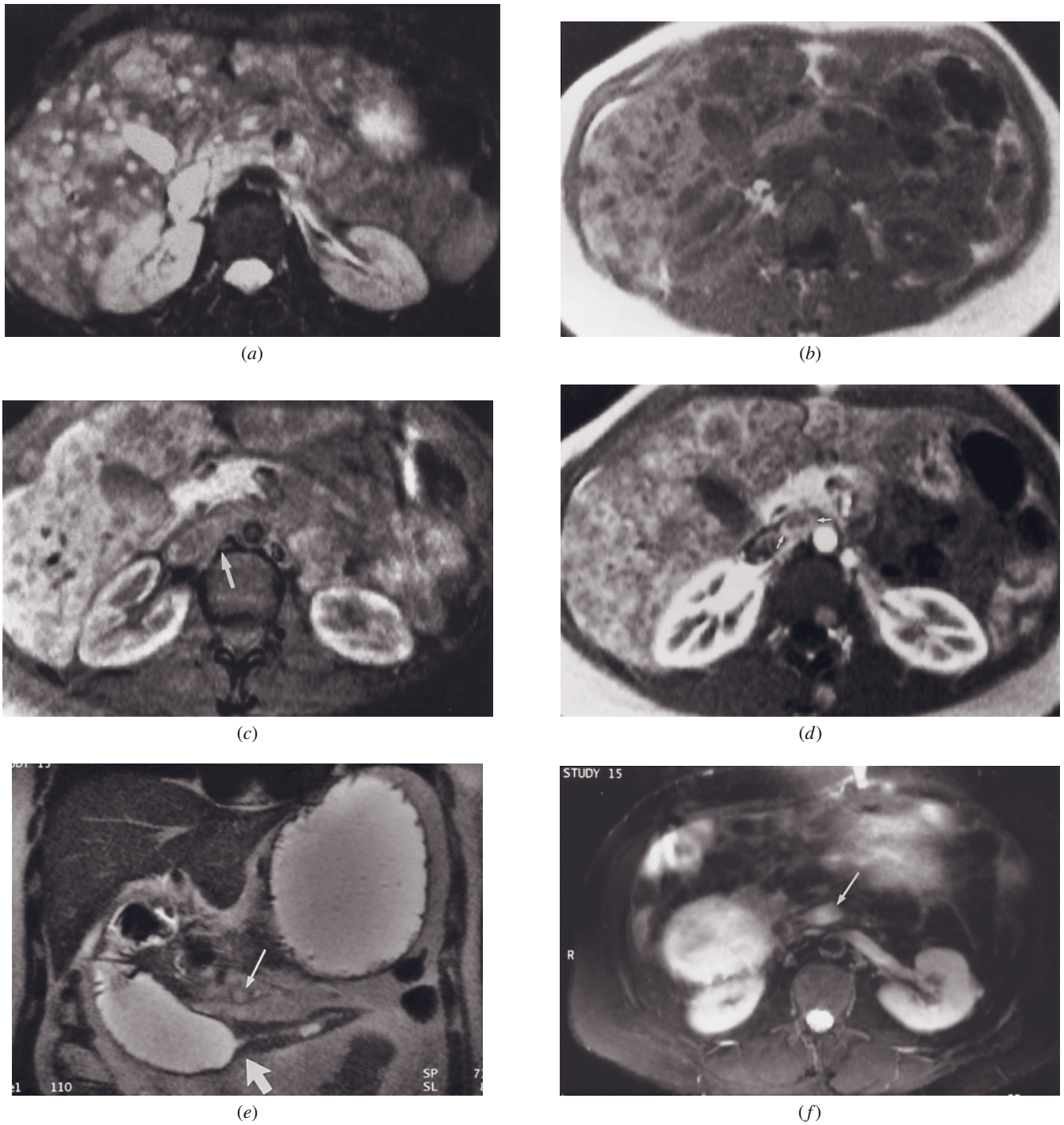

FIG. 4.41 Extrapancreatic gastrinoma. T2-weighted fat-suppressed spin-echo (*a*), T1-weighted SGE (*b*), T1-weighted fat-suppressed spin-echo (*c*), and immediate postgadolinium T1-weighted SGE (*d*) images. On the T2-weighted fat-suppressed image (*a*), multiple high-signal-intensity foci are present throughout the primary tumor, located posterior to the head of the pancreas with an appearance identical to the well-defined high-signal-intensity liver metastases. T1-weighted images (*b*, *c*) demonstrate the extrapancreatic gastrinoma multiple <1.5-cm liver metastases that possess similar low signal intensity. The primary tumor (arrow, *c*) is more clearly visible on the T1-weighted fat-suppressed image (*c*) because of the good signal difference between pancreas and tumor. On the immediate postgadolinium image (*d*), multiple ring-enhancing lesions are apparent in both the primary tumor (arrows, *d*) and the liver metastases.

Coronal SS-ETSE (*e*), fat-suppressed breathing-averaged ETSE (*f*), and 90-s postgadolinium fat-suppressed T1-weighted SGE (*g*) images in a second patient demonstrate a gastrinoma (arrows, *e–g*) superior to the fourth portion of the duodenum. The mass is

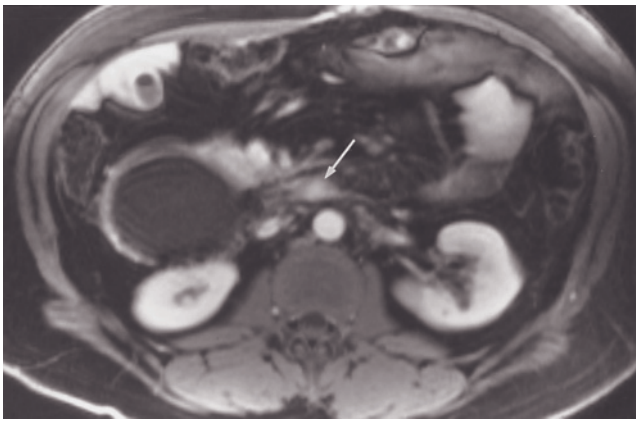

(*g*)

FIG. 4.41 (*Continued*) uniformly high in signal intensity on T2-weighted (*e*, *f*) and interstitial-phase gadolinium-enhanced T1-weighted (*g*) images. Stricturing of the fourth part of the duodenum (large arrow, *e*) reflects peptic ulcer disease in Zollinger–Ellison syndrome. Two prior CT imaging examinations were reported as negative.

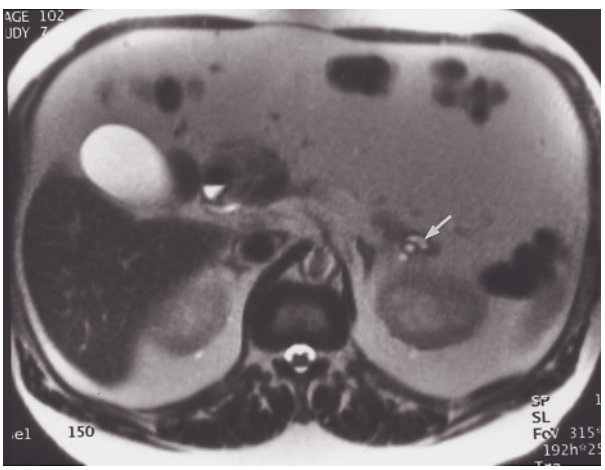

(*a*)

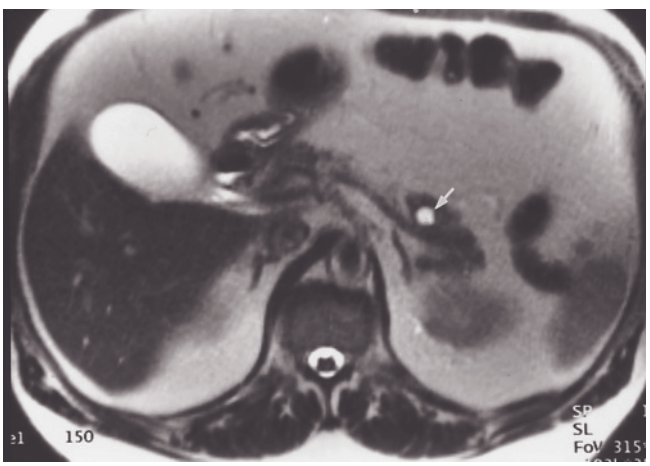

(*b*)

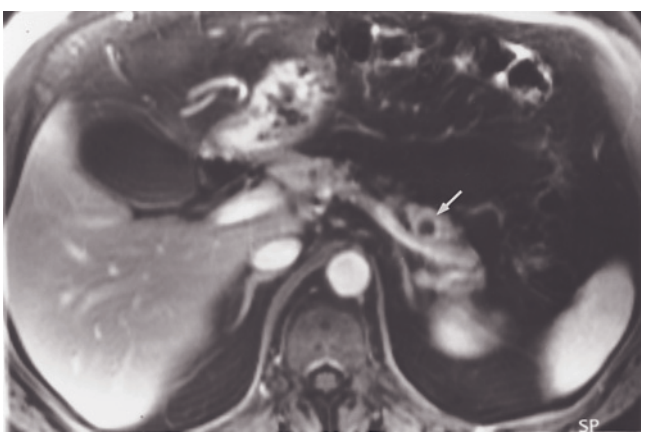

(*c*)

FIG. 4.42 Multiple gastrinomas. T2-weighted SS-ETSE (*a*, *b*) and interstitial-phase gadolinium-enhanced fat-suppressed T1-weighted SGE (*c*) images demonstrate multiple high-signal-intensity gastrinomas <1 cm in the tail of the pancreas. The absence of breathing artifact on the SS-ETSE images has resulted in good resolution of the small tumors (arrows, *a*, *b*). Ring enhancement is apparent on the largest 8-mm tumor (arrow, *c*).

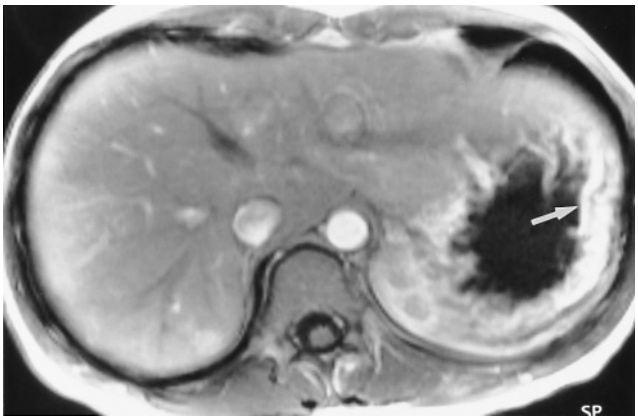

FIG. 4.43 Gastric wall hyperplasia. Immediate postgadolinium T1-weighted SGE image demonstrates intense enhancement of the prominent gastric rugal folds (arrow) in a patient with gastrinoma.

(For a discussion on hemangiomas, see Chapter 2, *Liver.*) These appearances are better shown on MR than CT images because of the higher sensitivity of MRI to contrast enhancement, faster delivery of a compact bolus of intravenous contrast, and greater imaging temporal resolution [53]. The peripheral enhancing rim may be thin or thick, resulting in differences in the degree of vascularity. Occasionally, thick rim enhancement may have a peripherally based spoke-wheel enhancement. Centripetal enhancement of gastrinoma metastases may occur on serial postgadolinium images. Peripheral washout is commonly observed for hypervascular gastrinoma metastases (fig. 4.44).

Insulinomas. Insulinomas are one of the most common islet cell tumors and are frequently functionally active. Tumors frequently come to clinical attention when they are small (<2 cm) because of the severity of the symptomatology [59]. Patients present with signs and symptoms of hypoglycemia. Insulinomas are usually richly vascular. Angiography has been reported as superior to CT imaging in detecting these tumors because of their small size and increased vascularity [65]. MRI may be superior to angiography for the detection of these tumors, reflecting the greater number of different types of data acquisition with MRI and the high sensitivity for contrast enhancement (figs. 4.45 and 4.46).

Insulinomas are low in signal intensity on T1-weighted images and high in signal intensity on T2-weighted images. They are well shown on T1-weighted fat-suppressed images (see fig. 4.45) [56]. Small insulinomas typically enhance homogeneously on immediate postgadolinium gradient-echo images (see fig. 4.45) [57]. Larger tumors, measuring more than 2 cm in diameter, often show ring enhancement. Liver metastases from insulinomas typically have peripheral ringlike enhancement, although small metastases tend to enhance homogeneously. Enhancement of small metastases frequently occurs transiently in the capillary phase of enhancement and fades on images acquired at 1 min after injection.

Glucagonoma, Somatostatinoma, VIPoma, and ACTHoma. These islet cell tumors are considerably rarer than insulinomas or gastrinomas. They are usually malignant, with liver metastases present at the time of diagnosis (figs. 4.47 and 4.48) [51, 58, 59, 66–69]. The primary pancreatic tumors of glucagonoma and somatostatinoma are large and heterogeneous on MR images [66–69]. They are usually moderately low in signal intensity on T1-weighted fat-suppressed images and moderately high in signal intensity on T2-weighted fat-suppressed images, enhancing heterogeneously on immediate postgadolinium images (see fig. 4.47) [58]. Liver metastases are generally heterogeneous in size and shape, unlike gastrinoma metastases, which are typically uniform (see fig. 4.47) [57]. Metastases possess irregular peripheral rims of intense enhancement on immediate post-gadolinium gradient-echo images (see fig. 4.47). Peripheral spoke-wheel enhancement may be observed in liver metastases on immediate postgadolinium images (fig. 4.49). Hypervascular liver metastases are best shown on immediate postgadolinium gradient-echo images, which are superior to spiral CT images for this determination [58]. Splenic metastases are not uncommon (see fig. 4.47).

ACTHomas may present with a large, heterogeneous enhancing primary tumor and small, hypervascular liver metastases. Their appearance may resemble glucagonomas and somatostatinoma masses.

VIPoma may have a characteristic appearance of a small primary tumor despite large and extensive liver metastases (fig. 4.49). Prior case reports have described ostensibly primary VIPoma of the liver without visualization of a pancreatic primary. The possibility exists that the primary pancreatic tumor may have been extremely small and escaped detection.

Islet Cell Tumors, Untyped or Uncategorized. Islet cell tumors do not receive a specific designation when special immunohistochemical stains or serum assays are negative. Tumors are generally large at presentation because they are clinically silent. The imaging appearance of these tumors resembles glucagonomas and somatostatinomas (see figs. 4.36–4.39). Liver metastases are generally present at the time of diagnosis. Pancreatic schwannomas (fig 4.38) may mimic the appearances of islet cell tumors as well as other pancreatic malignancies.

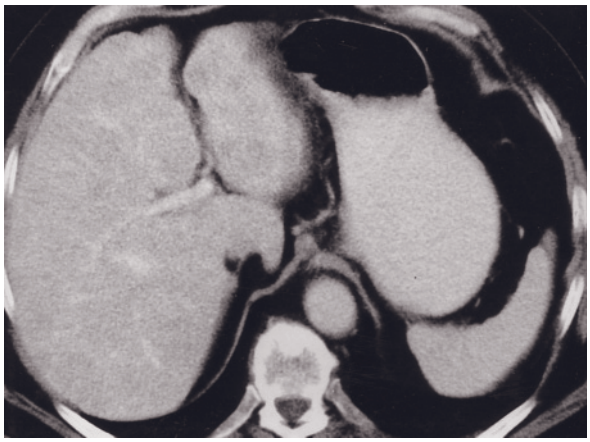

(*a*)

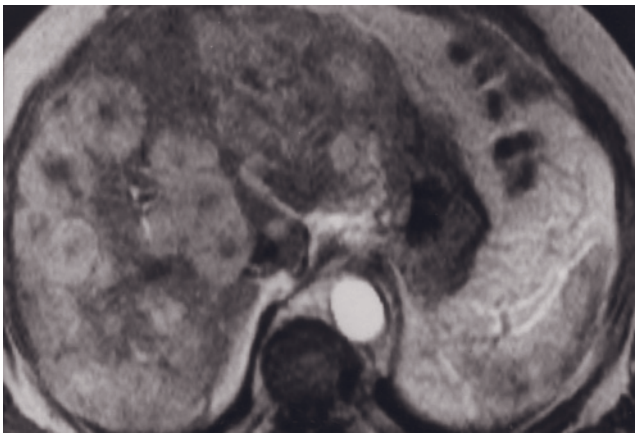

(*b*)

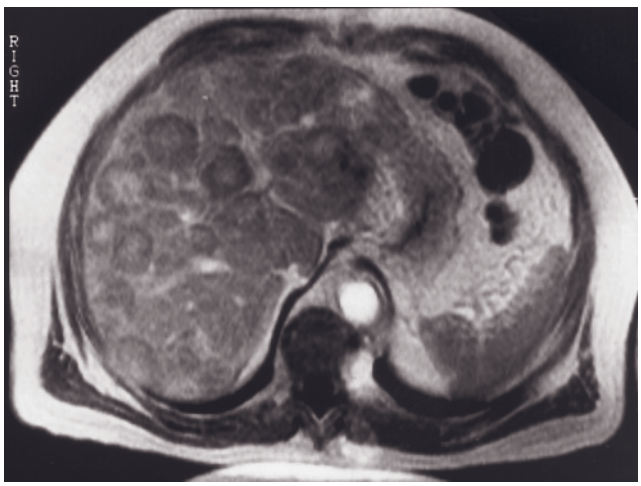

(*c*)

(*d*)

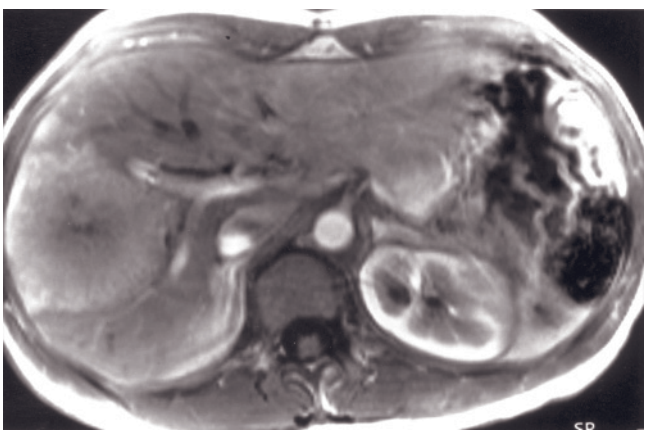

(*e*)

FIG. 4.44 Liver metastases from gastrinomas. Dynamic contrast-enhanced CT (*a*) and immediate (*b*) and 10-min (*c*) postgadolinium T1-weighted SGE images. Metastases are poorly visualized on the CT image (*a*). On the immediate postgadolinium T1-weighted SGE image (*b*), multiple metastases of similar size are identified with uniform intense rim enhancement. Peripheral washout is well shown on the 10-min postcontrast image (*c*).

Immediate postgadolinium SGE images (*d*) in a second patient show extensive <1.5-cm liver metastases throughout the liver with uniform ring enhancement.

Immediate postgadolinium SGE image (*e*) in a third patient show an unusual pattern for gastrinoma liver metastases with varying sized lesions with intense, almost uniform enhancement of a 5-cm metastasis. Often these large hypervascular islet cell metastases that enhance nearly uniformly on immediate postgadolinium images possess a radiating spoke-wheel pattern of bands of lesser-enhancing stroma.

Carcinoid Tumors

Rarely, carcinoid tumors may originate in the pancreas. Pancreatic carcinoids arise from the cells of the gastroenteropancreatic neuroendocrine system [53]. Carcinoid tumors are generally large at presentation, with coexistent liver metastases (fig. 4.50). Focal and diffuse involvements of the pancreas have been observed. Tumors are generally mildly hypointense on T1 and moderately hyperintense on T2 and show diffuse heterogeneous enhancement on immediate postgadolinium images (fig. 4.51) [53]. Enhancement of the primary tumor may be mild, despite extensive enhancement of

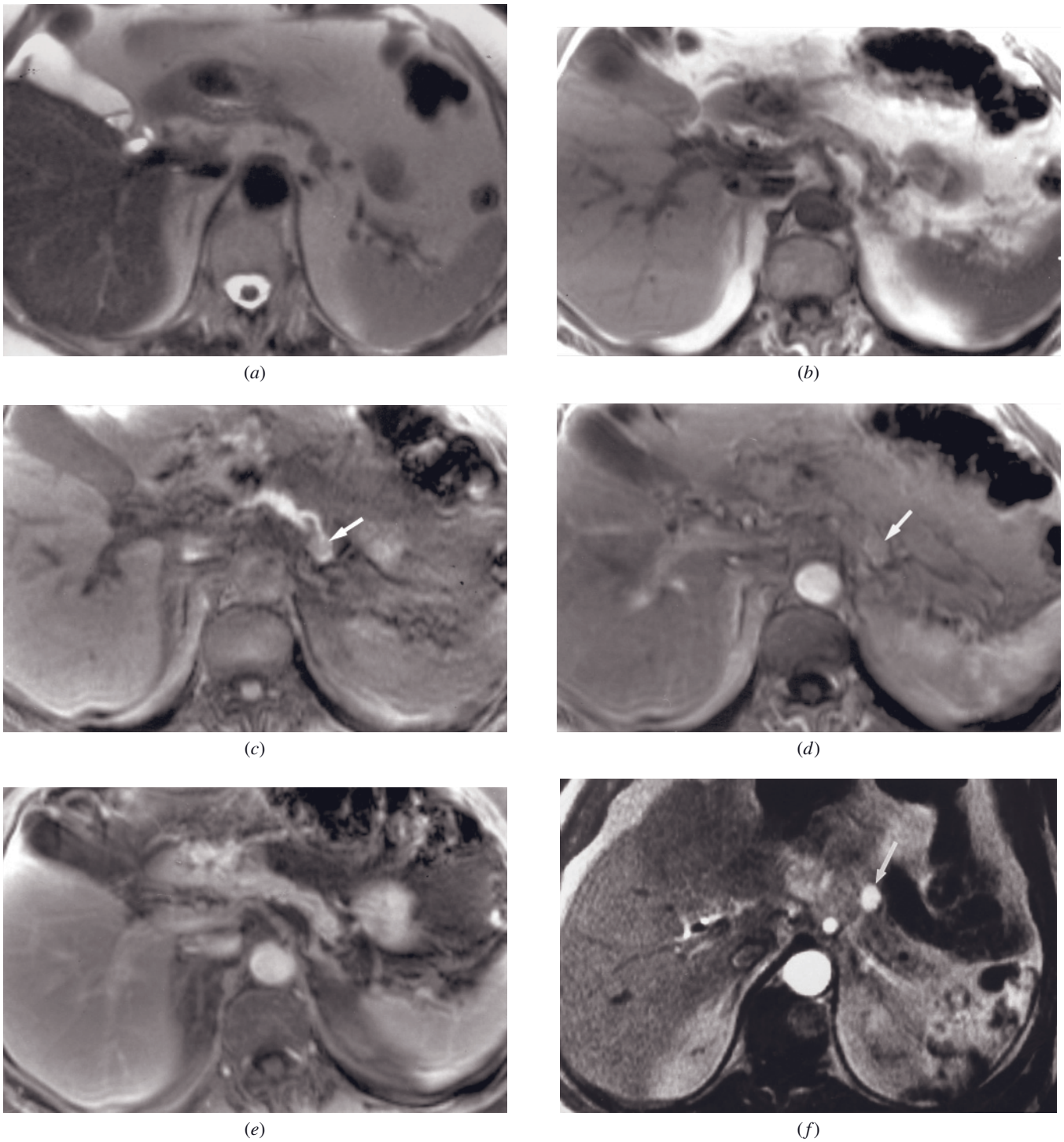

FIG. 4.45 Insulinoma. T2-weighted ETSE (*a*), T1-weighted SGE (*b*), T1-weighted fat-suppressed SGE (*c*), immediate postgadolinium T1-weighted SGE (*d*), and 90-s postgadolinium fat-suppressed SGE (*e*) images. A 1-cm tumor (arrow, *c*) arising in the superior aspect of the midbody of the pancreas is isointense on T2 (*a*) and T1 (*b*)-weighted images and low signal on T1-weighted fat-suppressed image (*c*) and enhances intensely and homogeneously (arrow, *d*) on the immediate postgadolinium image. The lesion fades to isointensity with background pancreas (*e*).

Immediate postgadolinium T1 SGE image (*f*) demonstrates a 1.2-cm uniformly enhancing insulinoma (arrow) arising from the body of the pancreas.

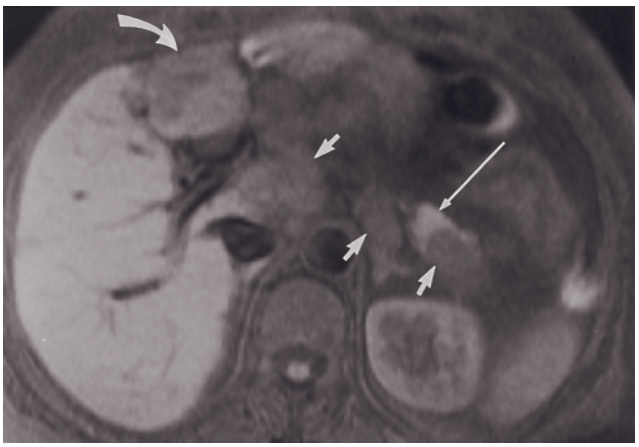

(*a*)

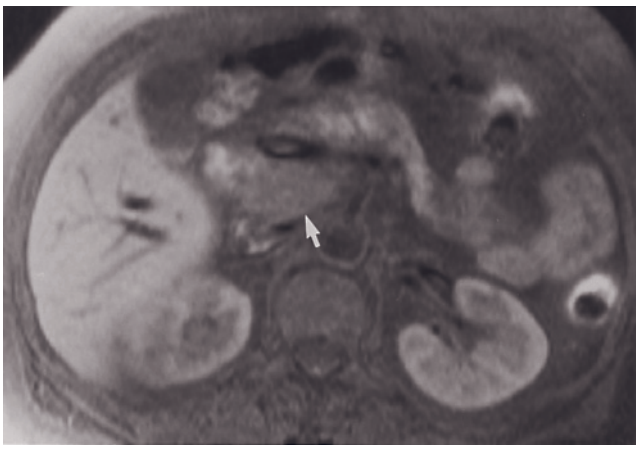

(*b*)

FIG. 4.46 Multiple malignant insulinomas. T1-weighted fat-suppressed spin-echo images (*a*, *b*). Multiple low-signal intensity insulinomas (arrows, *a*, *b*) ranging in diameter from 1 to 5 cm are present throughout the pancreas. Intervening pancreatic tissue is noted to be normal in signal intensity (long arrow, *a*). Liver metastases are also present (curved arrow, *a*). Multiple insulinomas are uncommon, occurring in <10% of all cases of B cell tumors.

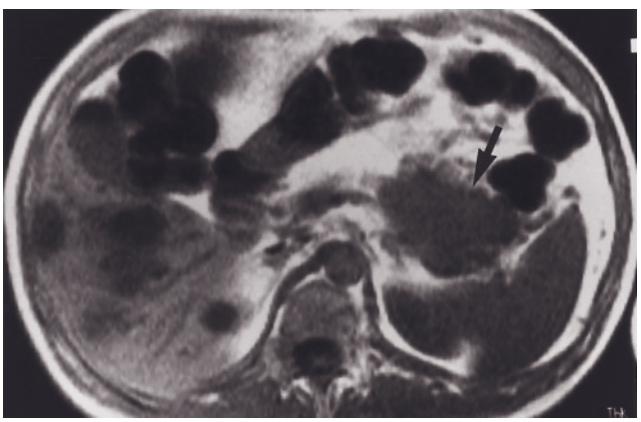

(*a*)

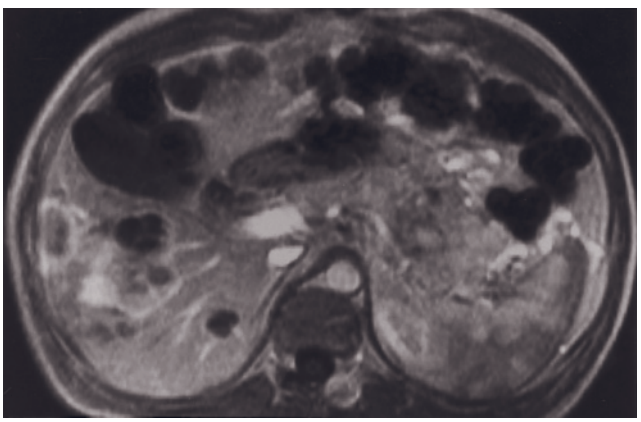

(*b*)

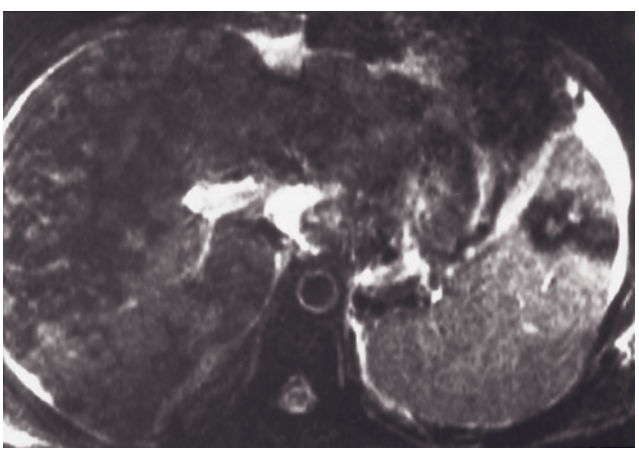

(*c*)

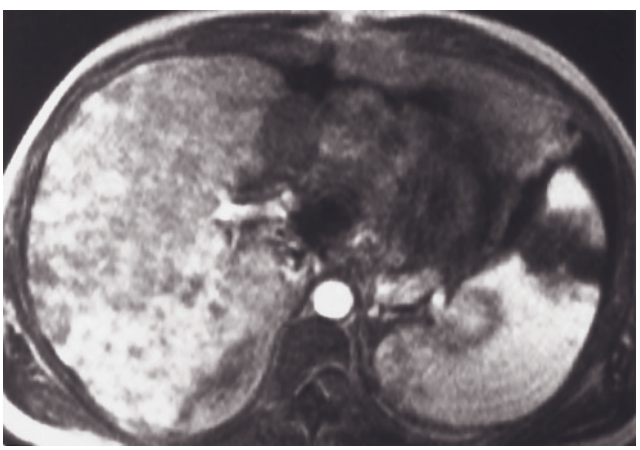

(*d*)

FIG. 4.47 Glucagonoma and somatostatinoma with liver and spleen metastases. T1-weighted SGE (*a*) and immediate postgadolinium T1-weighted SGE (*b*) images. A 6-cm tumor (arrow, *a*) arises from the tail of the pancreas (*a*). Multiple liver metastases are present, which are low in signal intensity on the precontrast T1-weighted image (*a*). On the immediate postgadolinium T1-weighted SGE image (*b*), the primary tumor enhances heterogeneously. Intense ring enhancement is present in many of the liver metastases, reflecting hypervascularity. Note that the liver metastases are variable in size and shape.

T2-weighted fat-suppressed SS-ETSE (*c*) and immediate postgadolinium T1-weighted SGE (*d*) images. On the T2-weighted image (*c*), multiple small, high-signal-intensity liver metastases and a large, low-signal-intensity splenic metastasis are present. On the immediate postgadolinium image (*d*), the liver metastases enhance intensely and the splenic metastasis is low in signal intensity.

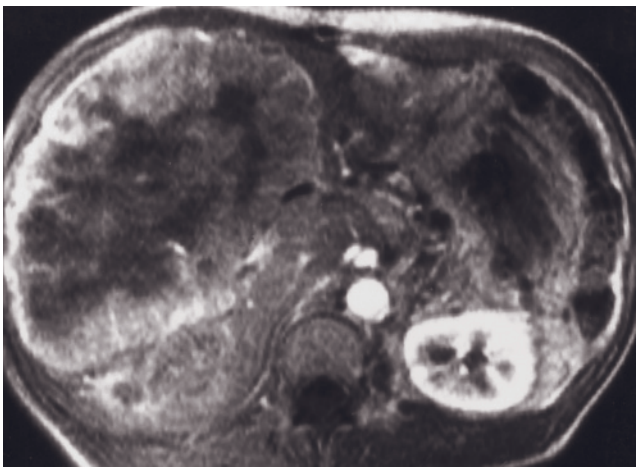

(*e*)

FIG. 4.47 (*Continued*) Immediate postgadolinium T1-weighted SGE image (*e*) in a second patient with somatostatinoma demonstrates a 14-cm liver metastasis with intense, irregular rim enhancement.

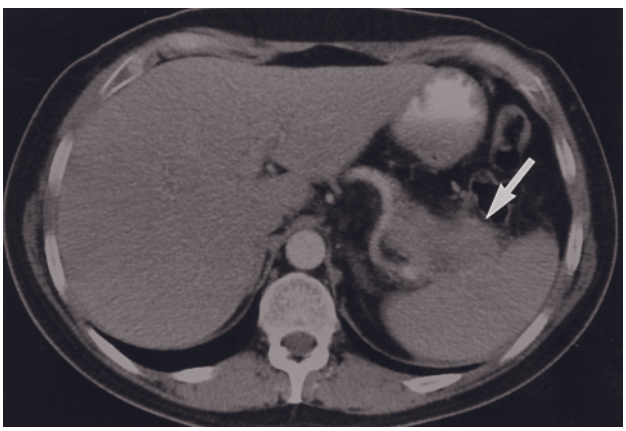

(*a*)

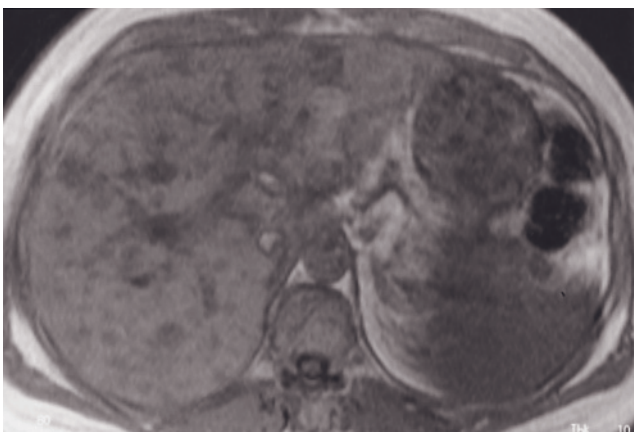

(*b*)

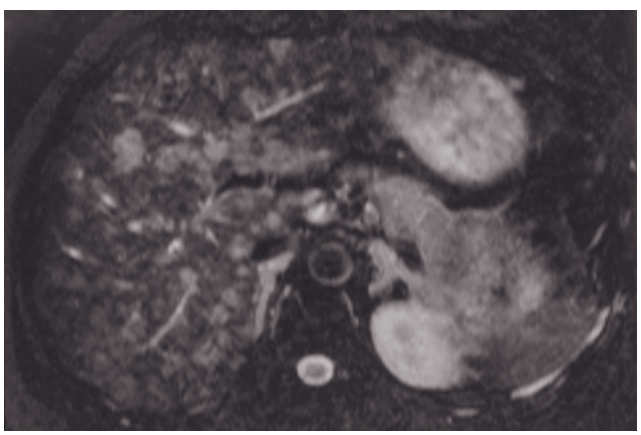

(*c*)

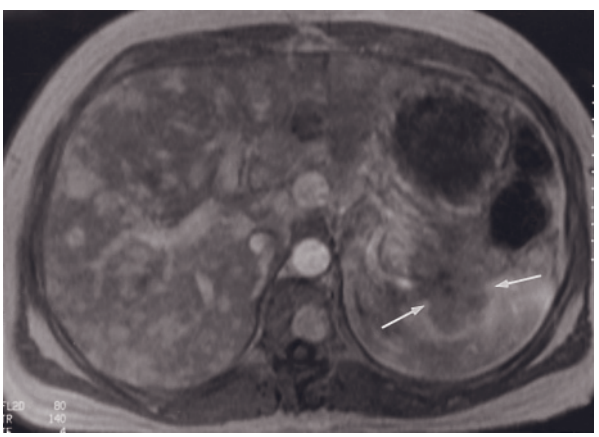

(*d*)

FIG. 4.48 ACTHoma. Spiral CT (*a*), T1-weighted SGE (*b*), T2-weighted fat-suppressed ETSE (*c*), and immediate postgadolinium T1-weighed SGE (*d*) images. A 4-cm ACTHoma is present in the tail of the pancreas (arrow, *a*). Direct extension of the primary tumor into the spleen is most clearly shown on the immediate postgadolinium T1-weighted SGE image (arrows, *d*). Multiple liver metastases are present, which are poorly seen on the spiral CT image (*a*) but are well shown on the MR images (*b–d*). Liver metastases are most conspicuous on the immediate postgadolinium T1-weighted SGE image (*d*). (Reproduced with permission from Kelekis NL, Semelka RC, Molina PL, Doerr ME: ACTH-secreting islet cell tumor: Appearances on dynamic gadolinium-enhanced MRI. *Magn Reson Imaging* 13: 641–644, 1995.)

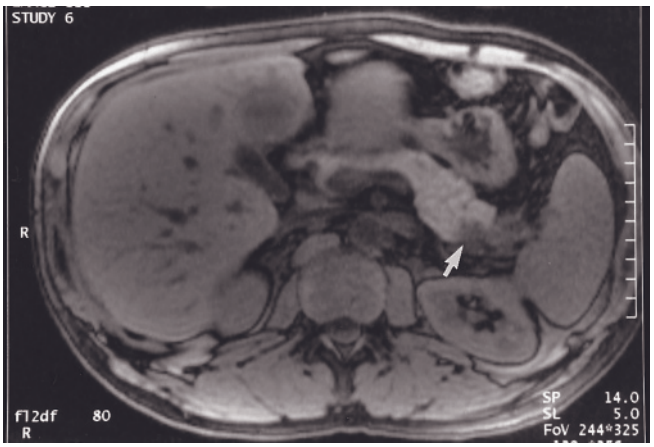

(*a*)

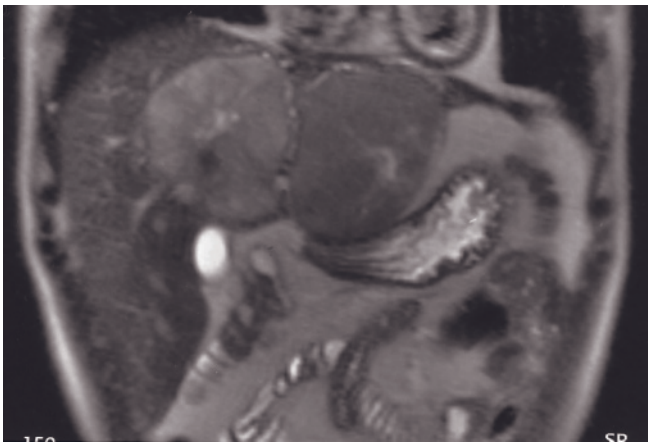

(*b*)

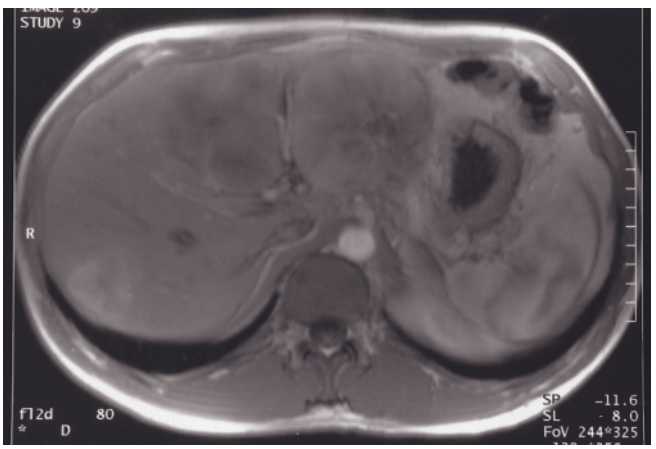

(*c*)

FIG. 4.49 VIPoma. T1-weighted fat-suppressed SGE (*a*), coronal T2-weighted SS-ETSE (*b*), and immediate postgadolinium T1-weighted SGE (*c*) images in a patient with VIPoma. A 1.5-cm tumor arises from the tail of the pancreas (arrow, *a*) that appears low in signal intensity on the T1-weighted image. Multiple metastases are present that are moderately low signal intensity on the T1-weighted image (*a*) and moderately high signal intensity on the T2-weighted image (*b*) and enhance in a moderately intense peripheral spoke-wheel type radial fashion on the immediate postgadolinium T1-weighted SGE image (*c*).

liver metastases. Liver metastases are variable in size and often exhibit intense enhancement, similar to islet cell tumor liver metastases.

CYSTIC NEOPLASMS

In general, this group of pancreatic tumors arises from the exocrine component of the gland and is much less common than solid exocrine carcinomas. Although secondary cystic change can be seen in most types of pancreatic neoplasms, cystic pancreatic neoplasms are characterized by their consistent, invariably present, cystic configuration.

Serous Cystadenoma

Serous cystadenoma is a benign neoplasm characterized by numerous tiny serous fluid-filled cysts [70]. Serous cystadenomas are usually microcystic and multilocular, and consist of multiple small cysts less than 1 cm in diameter (fig. 4.52). Uncommonly, serous cystadenomas may be macrocystic (cysts measuring from 1 to 8 cm) including multilocular, oligolocular or unilocular subtypes. This tumor frequently occurs in older patients and has an increased association with von Hippel–Lindau disease [70].

Microcystic serous cystadenoma is well demarcated and occasionally contains a central fibrotic scar. Tumors range in size from 1 to 12 cm, with an average diameter at presentation of 5 cm. The lesion may exhibit either a smooth or a nodular contour. On cut surface, small, closely packed cysts are filled with clear, watery (serous) fluid and separated by fine, fibrous septae, creating a honeycomb appearance. Calcifications may occasionally be present. On MR images, the tumors are well-defined and do not demonstrate invasion of fat or adjacent organs [71]. On T2-weighted images, the small cysts and intervening septations may be well shown as a cluster of small grapelike high-signal-intensity cysts. This appearance is more clearly shown on breath-hold or breathing-independent sequences such as single-shot echo-train spin echo, because the thin septations blur with longer-duration non-breath-hold sequence

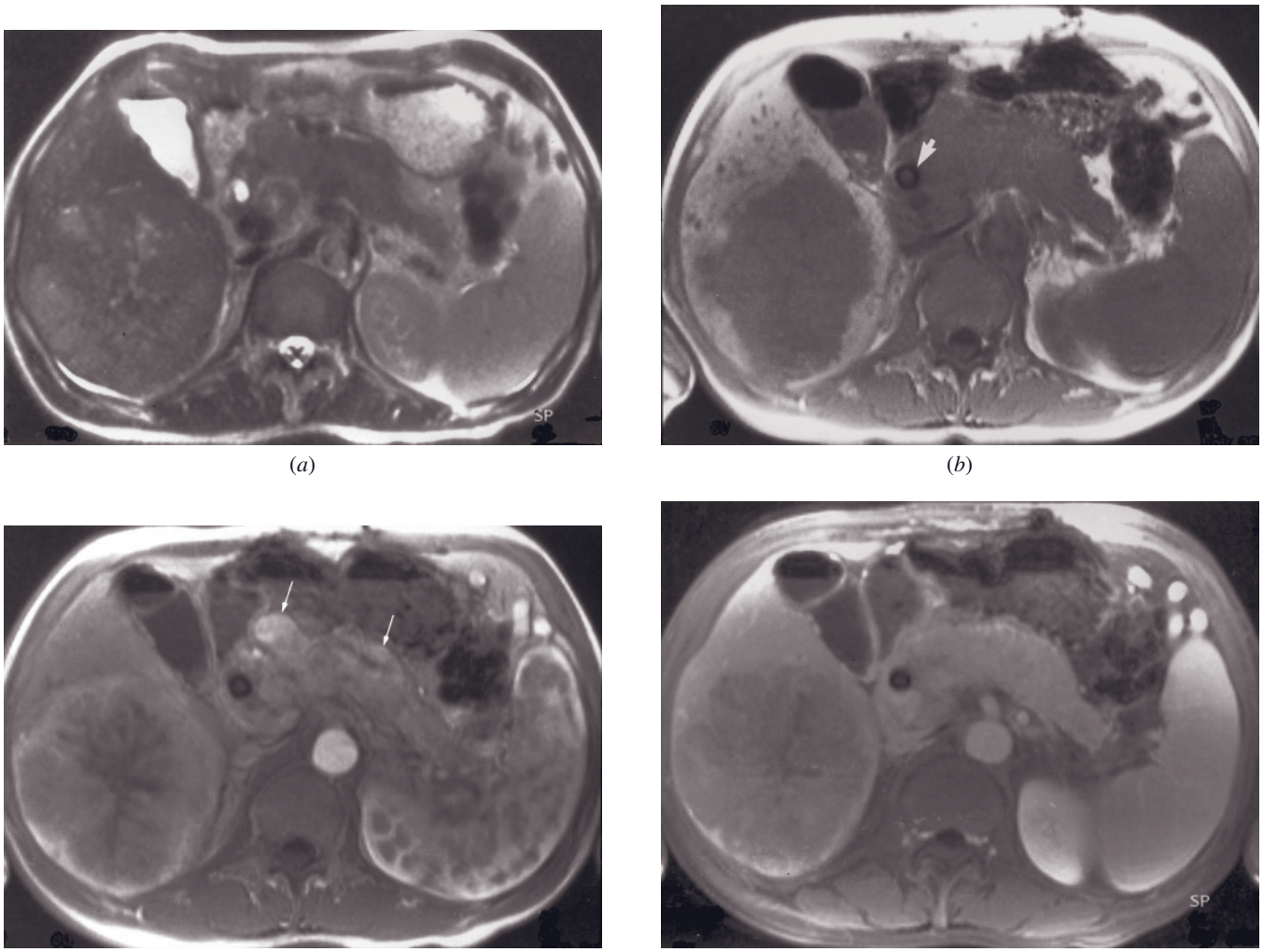

FIG. 4.50 Carcinoid tumor with liver metastases. T2-weighted echo-train spin-echo (*a*), T1-weighted SGE (*b*), immediate postgadolinium T1-weighted SGE (*c*), and 90-s postgadolinium fat-suppressed SGE (*d*) images in a patient with a carcinoid tumor with diffuse involvement of the pancreas and hypervascular liver metastasis. The pancreas is diffusely enlarged with irregular contour and enhances heterogeneously on the immediate postgadolinium image (arrows, *c*). The metastatic liver lesion shows a radial enhancement on gadolinium-enhanced images (*c*, *d*). Note a biliary stent in the CBD (arrow, *b*).

(fig. 4.52). Relatively thin uniform septations and absence of infiltration of adjacent organs and structures are features that distinguish serous cystadenoma from serous cystadenocarcinoma (see fig. 4.52). Tumor septations usually enhance minimally with gadolinium on early and late postcontrast images, although moderate enhancement on early postcontrast images may occur. Delayed enhancement of the central scar may occasionally be observed [1], and is more typical of large tumors. Delayed enhancement of the central scar on postgadolinium images is apparent in larger tumors, and this enhancement pattern is typical for fibrous tissue in general (see fig. 4.52). The central scar may represent compressed contiguous cyst walls of centrally located cysts.

Macrocystic serous cystadenomas (fig. 4.53) exhibit distinctly different macroscopic features from microcystic lesions and may pose diagnostic difficulties for both radiologist and pathologist. A computed tomography study evaluating these tumors misinterpreted all five cases as mucinous cystic neoplasms or pseudocysts. Microcystic and macrocystic serous tumors represent morphologic variants of the same benign pancreatic neoplasm [71, 72]. They are well demarcated tumors. They have high signal intensity on T2-weighted images and low signal on T1-weighted images. They may be multilocular, oligolocular or unilocular. The cyst wall and septations demonstrate progressive mild to moderate enhancement on postgadolinium T1-weighted images. The central scar is usually absent.

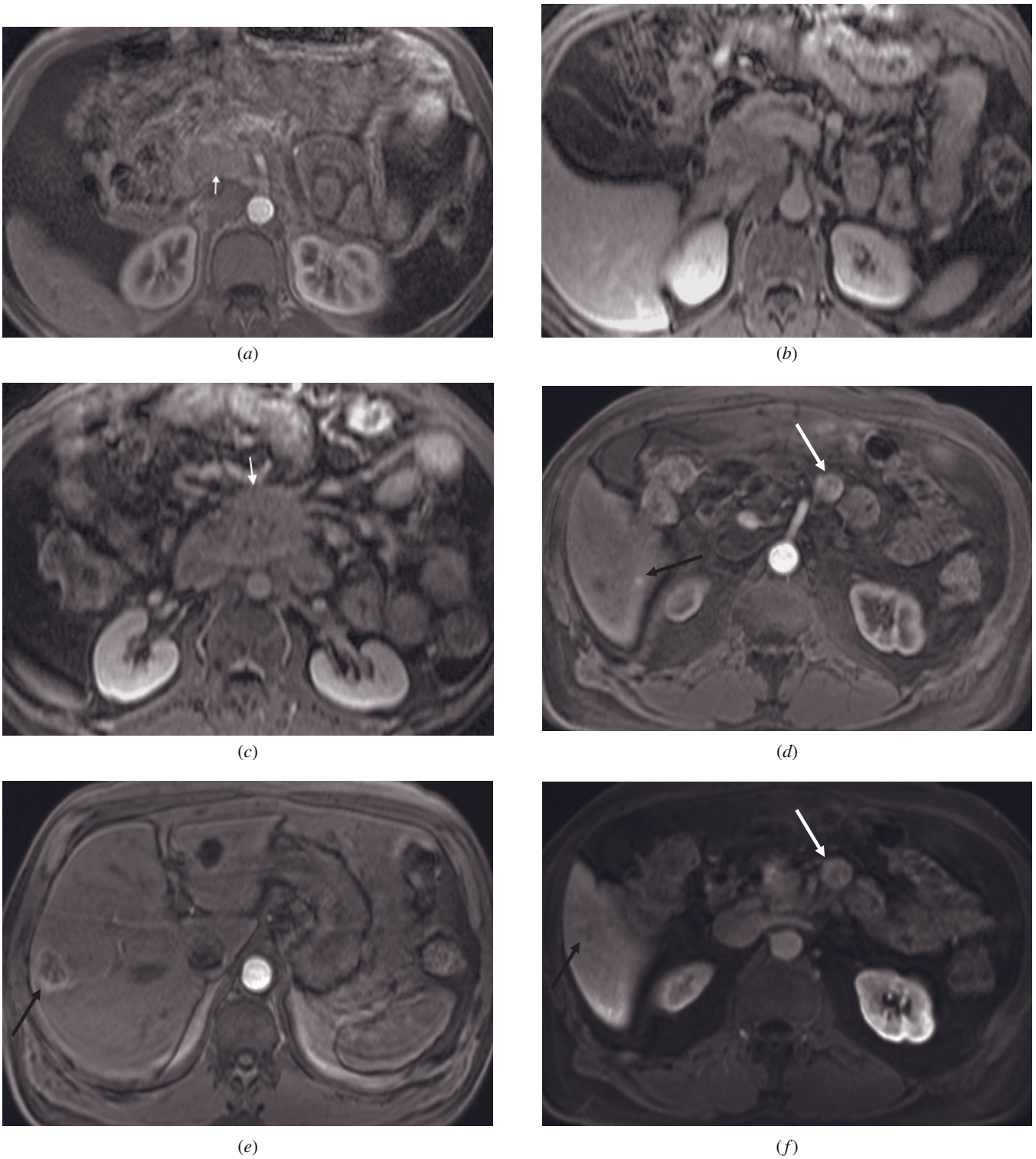

FIG. 4.51 Pancreatic carcinoid tumor. Immediate postgadolinium fat-suppressed T1-weighted gradient-echo (*a*) and 90-s postgadolinium fat-suppressed T1-weighted 3D gradient-echo (*b*, *c*) images from one patient show a large mass arising from the head of the pancreas (arrow, *a*). The mass enhances in a diminished fashion on immediate postgadolinium image (*a*), and "a" pancreatic tumor and a large mesenteric mass (arrow, *c*) are shown on interstitial-phase images. The presence of an associated large mesenteric mass is typical for carcinoid tumors. Lack of pancreatic duct dilation and atrophy of the body of the pancreas in the setting of a large pancreatic head mass are typical of a neuroendocrine tumor and not consistent with pancreatic ductal cancer.

T1-weighted postgadolinium late hepatic arterial phase fat-suppressed 3D-GE (*d*, *e*) and hepatic venous phase fat-suppressed 3D-GE (*f*) images at 3.0 T demonstrate a carcinoid tumor in another patient. The carcinoid tumor (white arrows, *d*, *f*), which shows intense heterogeneous enhancement, is located in the pancreatic body. There are also hypervascular metastases (black arrows, *d*–*f*) in the liver. Note that there is a liver cyst in the left lobe of the liver.

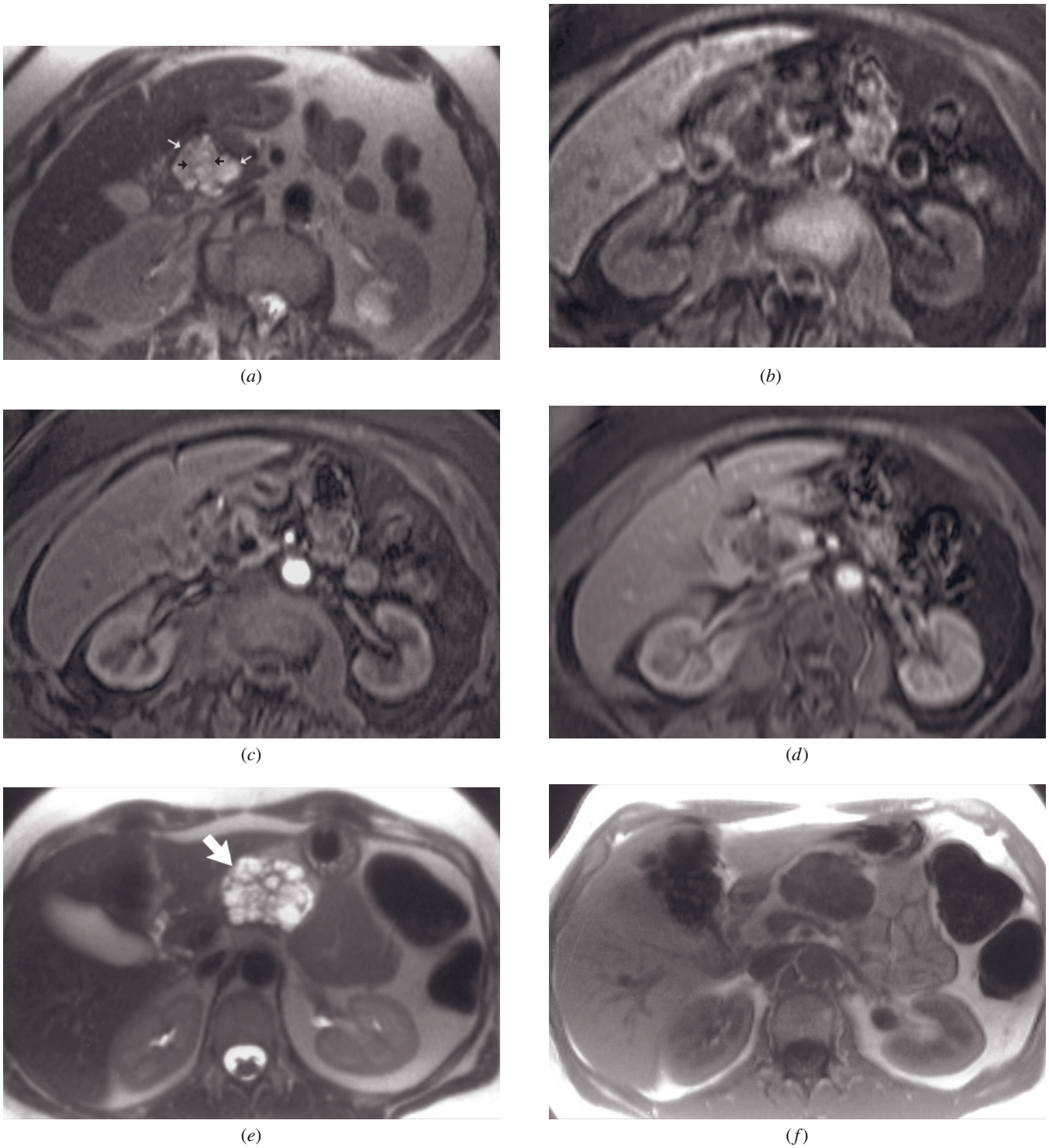

FIG. 4.52 Serous cystadenoma. T2-weighted SS-ETSE (*a*), fat-suppressed T1-weighted gradient-echo (*b*), and immediate (*c*) and interstitial-phase (*d*) postgadolinium fat-suppressed T1-weighted gradient-echo images demonstrate a cystic mass in the pancreatic head. The lesion is well defined and low in signal intensity in a background of high-signal-intensity pancreas. On the T2-weighted image (*a*), definition of fine septations (black arrows, *a*) within the cystic mass (white arrows, *a*) reveals that the cysts are <1 cm in diameter. The serous cystadenoma is high in signal intensity on T2-weighted images (*a*), reflecting their high fluid content.

T2-weighted SS-ETSE (*e*), T1-weighted SGE (*f*), T1-weighted fat-suppressed SGE (*g*), immediate postgadolinium T1-weighted SGE (*h*), and 90-s postgadolinium fat-suppressed SGE (*i*) images in a second patient. There is a 6-cm multicystic mass (arrows, *e*)

(*g*)

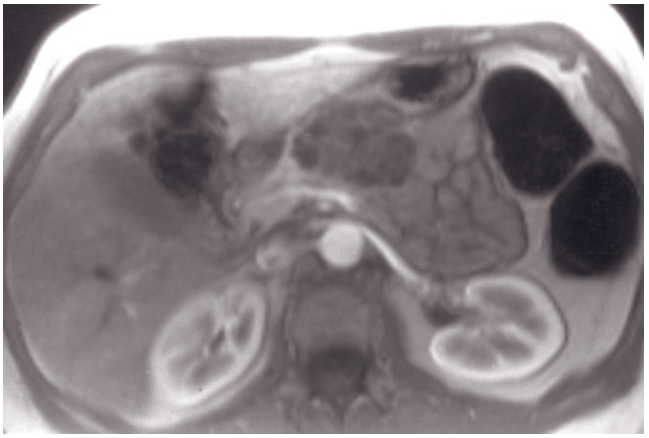

(*h*)

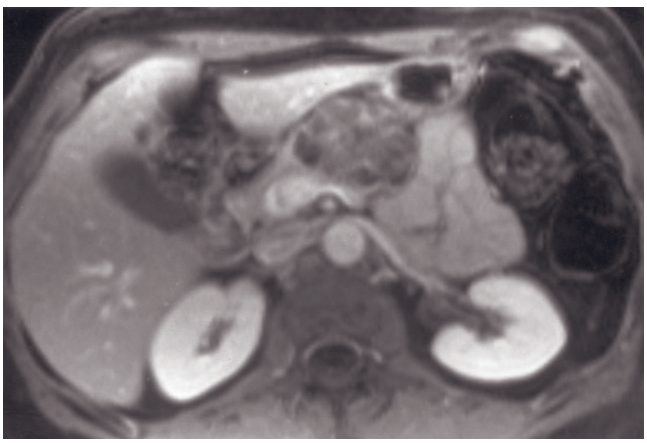

(*i*)

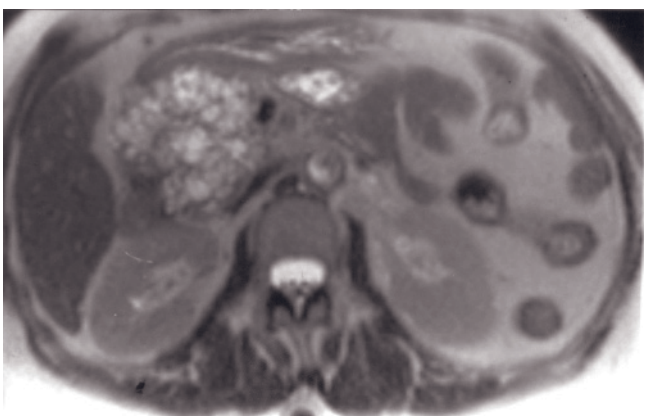

(*j*)

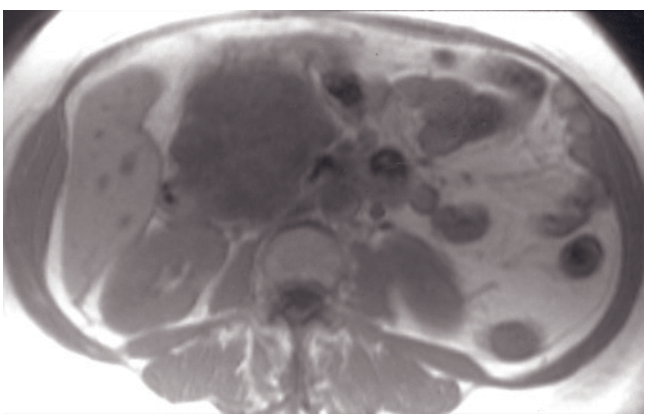

(*k*)

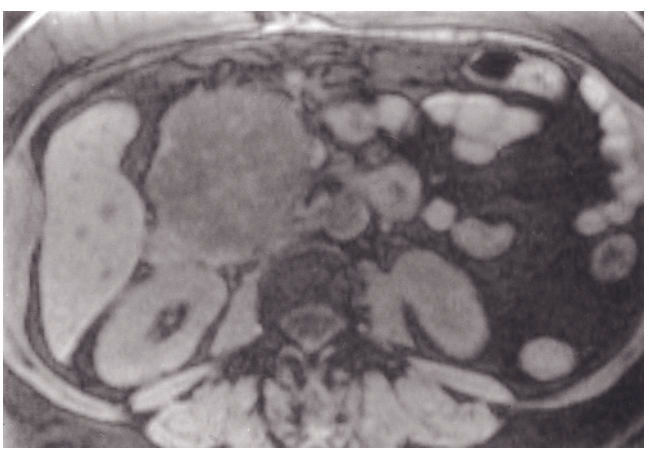

(*l*)

FIG. 4.52 (*Continued*) arising in the pancreatic body with thin septations creating <2-cm cysts. The single-shot T2-weighted sequence (*e*) performs very well at defining the septations in cystic masses. A "beak sign" is demonstrated in the pancreas (arrows, *g*), best shown on the noncontrast T1-weighted fat-suppressed (*g*) and immediate postgadolinium SGE (*h*) images, confirming that the mass originates from this organ. The septations enhance minimally on immediate postgadolinium images (*h*) with progressive enhancement on late images (*i*).

T2-weighted ETSE (*j*), T1-weighted SGE (*k*), T1-weighted fat-suppressed SGE (*l*), immediate postgadolinium T1-weighted SGE (*m*), and 90-s postgadolinium fat-suppressed SGE (*n*) images in a third patient. An 8-cm serous cystadenoma is present in the head

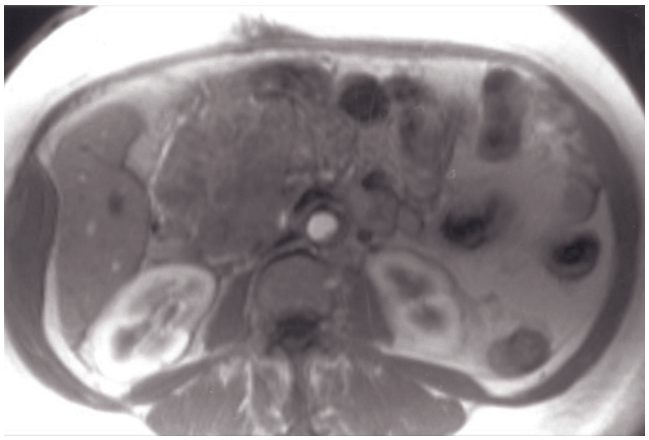

(*m*)

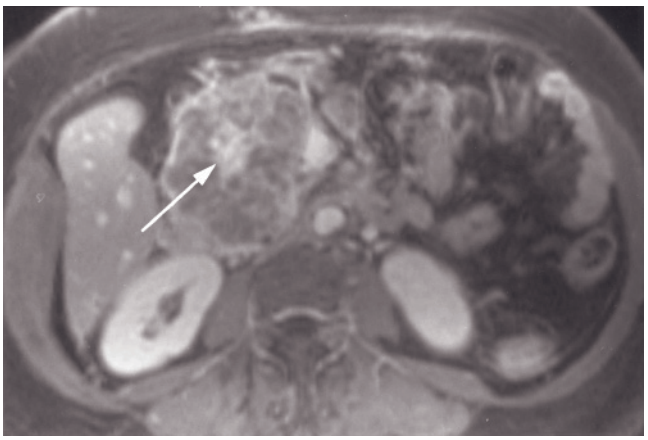

(*n*)

FIG. 4.52 (*Continued*) of the pancreas, best shown on the single-shot T2-weighted sequence. There is a central scar, typical for serous cystadenoma, which enhances on late images (arrow, *n*), consistent with fibrosis. Serous cystadenomas occur predominantly in women, as seen in these cases. The importance of the MR study is to differentiate this benign entity from mucinous cystadenomas that are potentially malignant.

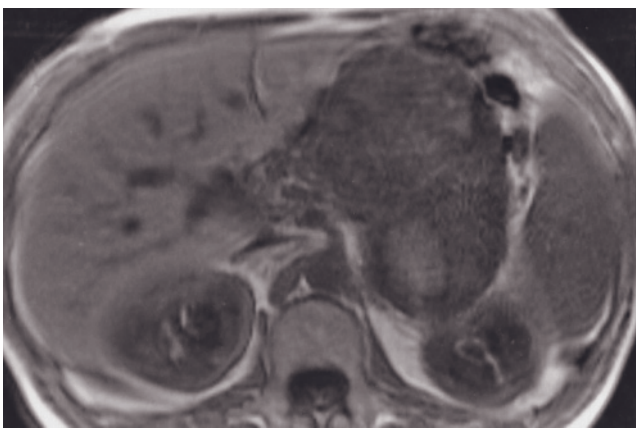

(*a*)

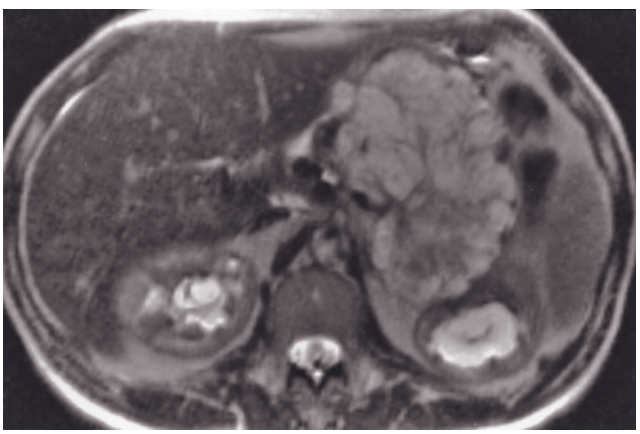

(*b*)

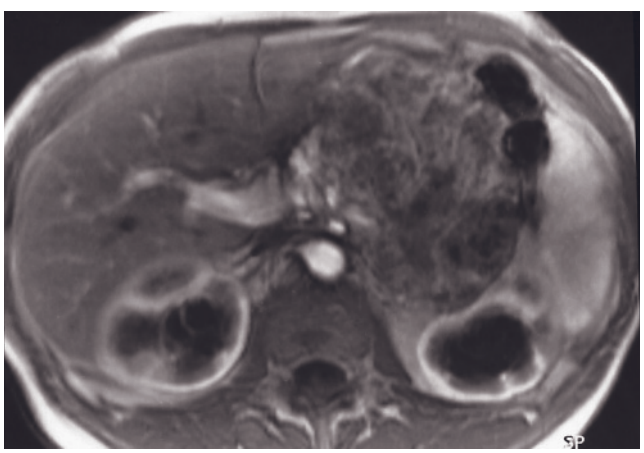

(*c*)

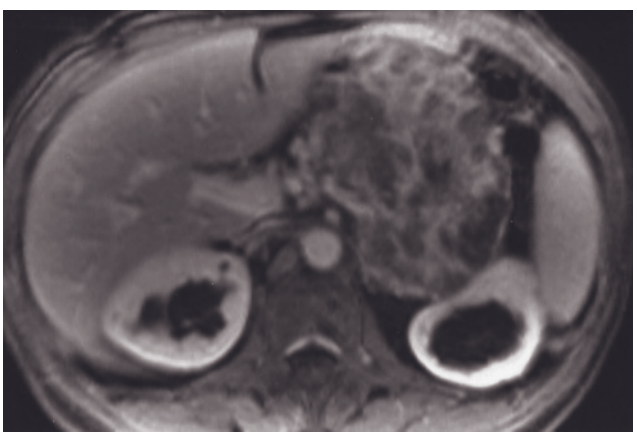

(*d*)

FIG. 4.53 Macrocystic serous cystadenoma. T1-weighted SGE (*a*), T2-weighted SS-ETSE (*b*), immediate postgadolinium T1-weighted SGE (*c*), and 90-s postgadolinium fat-suppressed SGE (*d*) images. A 10-cm mass arises from the tail of the pancreas. The tumor is mildly hypointense with regions of hyperintensity on precontrast T1-weighted images (*a*). Multiple septations are present throughout the mass, well shown on the breathing-independent T2-weighted image (*b*). Some of the cysts measure >2 cm. Moderately intense enhancement of the septations is present on immediate (*c*) and 90-s (*d*) postcontrast images.

Cystic pancreatic masses that contain cysts measuring less than 1 cm in diameter may represent microcystic cystadenoma or side branch type intraductal papillary mucinous tumor (IPMT), which can be difficult to distinguish. The presence of a central scar is a feature distinguishing serous cystadenoma from side branch IPMT, which does not exhibit this finding. Definition of communication with the pancreatic duct on MRCP images establishes the diagnosis of side branch IPMT.

Serous Cystadenocarcinoma

This malignant pancreatic tumor is extremely rare. Distinction from benign serous cystadenoma is difficult on histologic grounds alone and may only be established by the presence of metastatic disease or local invasion. The presence of thick septations and solid components are suggestive signs for serous cystadenocarcinoma.

Mucinous Cystadenoma / Cystadenocarcinoma

Mucinous cystic neoplasms of the pancreas are characterized by the formation of large unilocular or multilocular cysts filled with abundant, thick gelatinous mucin. Histopathologically these tumors are divided into benign (mucinous cystadenoma), borderline, and malignant (mucinous cystadenocarcinoma). However, at many institutions, all cases of mucinous cystic neoplasms are interpreted as mucinous cystadenocarcinomas of low-grade malignant potential to reinforce the need for complete surgical resection and close clinical follow up [70–75]. Mucinous cystic neoplasms occur more frequently in females (6 to 1), and approximately 50% occur in patients between the ages of 40 and 60 years [76]. These tumors usually are located in the body and tail of the pancreas. They may be large (mean diameter of 10 cm), often multiloculated, and encapsulated [74, 75]. Of these tumors, 10% may have scattered calcifications. There is a great propensity for invasion of local organs and tissues.

On gadolinium-enhanced T1-weighted fat-suppressed images, large, irregular cystic spaces separated by septa are demonstrated [1]. Cyst walls and septations are often thicker in mucinous cystadenocarcinomas than those of mucinous cystadenomas. Mucinous cystadenomas are well circumscribed, and they show no evidence of metastases or invasion of adjacent tissues (fig. 4.54). Mucinous cystadenomas described pathologically as having borderline malignant potential may be very large, but may not show imaging or gross evidence of metastases or local invasion (fig. 4.55). Histopathologically, these tumors show moderate epithelial dysplasia. Mucinous cystadenocarcinoma may be very locally aggressive malignancies with extensive invasion of adjacent tissues and organs (fig. 4.56). Absence of demonstration of tumor invasion into surrounding tissue does not, however, exclude malignancy. The presence of solid component is also suggestive of malignancy. The higher inherent soft-tissue contrast of MRI compared to CT imaging results in superior differentiation between microcystic and macrocystic cystadenomas because of sharp definition of cysts that permits evaluation of cyst size and margins [74]. Breathing-independent T2-weighted images are particularly effective at defining the cysts.

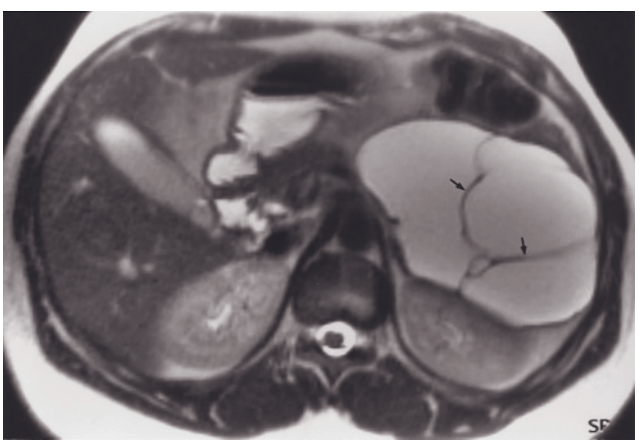

(*a*)

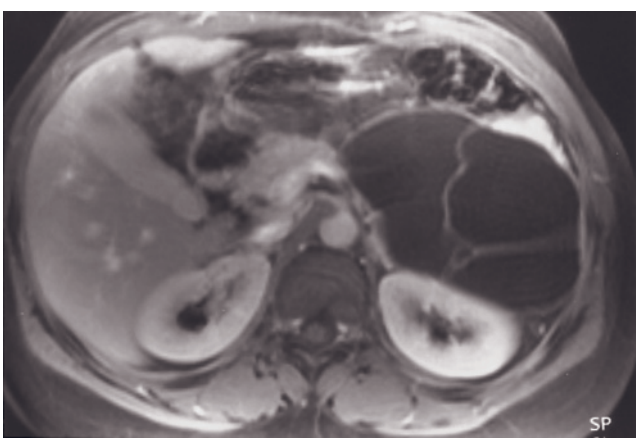

(*b*)

FIG. 4.54 Mucinous (macrocystic) cystadenoma. T2-weighted SS-ETSE (*a*) and 90-s postgadolinium fat-suppressed T1-weighed SGE (*b*) images. A well-defined cystic mass arises from the body and tail of the pancreas that is low in signal intensity on the T1-weighted image (not shown) and high in signal intensity on the T2-weighted image (*a*) and demonstrates enhancement of septations on the postgadolinium T1-weighted SGE image (*b*). No evidence of tumor nodules, invasion of adjacent tissue, or liver metastases is appreciated. The uniform thickness of the septations is clearly defined on the breathing-independent SS-ETSE image (arrows, *a*). Mucinous cystadenoma is potentially a low-grade malignant neoplasm.

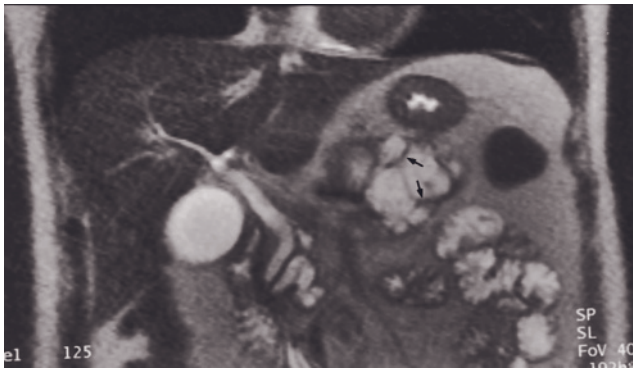

(*a*)

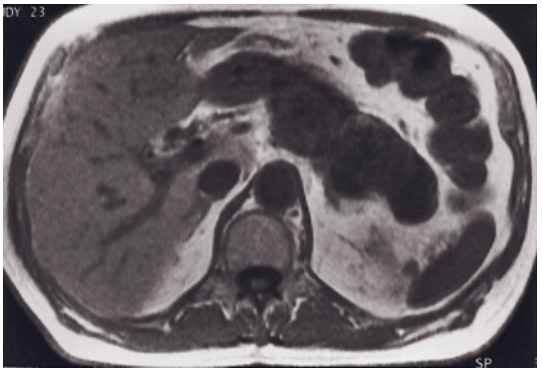

(*b*)

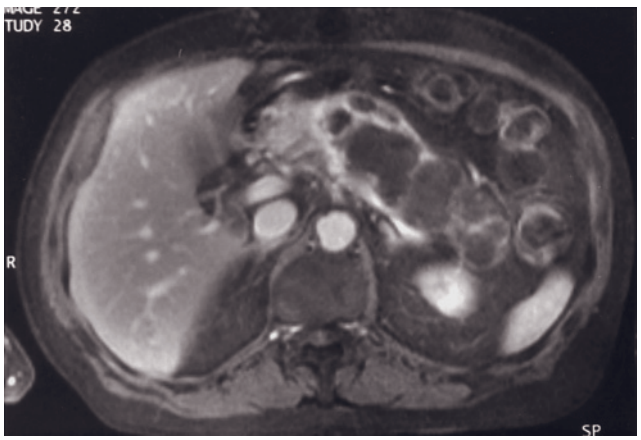

(*c*)

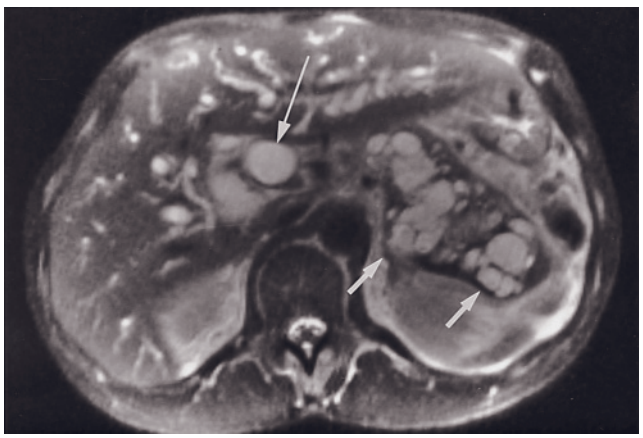

(*d*)

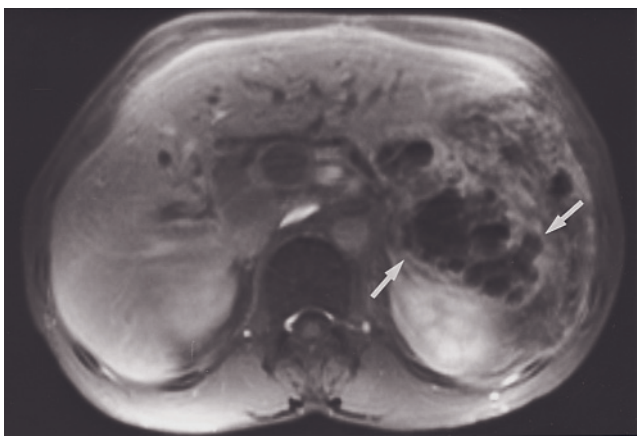

(*e*)

Fig. 4.55 Mucinous cystadenoma with carcinoma in situ. Coronal T2-weighted SS-ETSE (*a*), T1-weighted SGE (*b*), and 90-s postgadolinium fat-suppressed SGE (*c*) images. A multicystic mass involves the entire body and tail of the pancreas (*a–c*). Septations are well defined on the breathing-independent T2-weighted image (arrows, *a*). The moderate irregularity of the septations and the extent of tumor are features compatible with malignant changes.

T2-weighted SS-ETSE (*d*) and 90-s postgadolinium fat-suppressed T1-weighted SGE (*e*) images in a second patient demonstrate a mucinous cystadenocarcinoma in the body and tail (arrows, *d*, *e*). Dilatation of the CBD (long arrow, *d*) and intrahepatic biliary tree are also present.

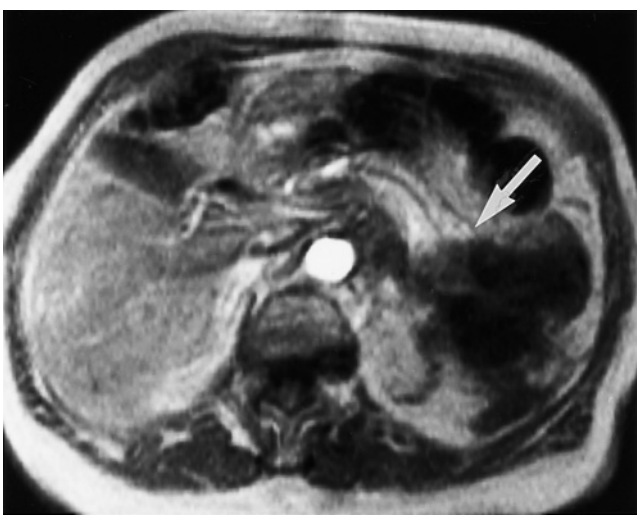

Fig. 4.56 Mucinous cystadenocarcinoma. Immediate postgadolinium T1-weighted SGE image demonstrates a tumor arising from the tail of the pancreas (arrow) that contains thick septations and multiple large cysts. The tumor is locally aggressive and invades into the splenic hilum (not shown).

Mucin produced by these tumors may result in high signal intensity on T1- and T2-weighted images of the primary tumor and liver metastases (figs. 4.57 and 4.58). Liver metastases are generally hypervascular and have intense ring enhancement on immediate gadolinium images. Metastases are commonly cystic and may contain mucin, which results in mixed low and high signal intensity on T1- and T2-weighted images (see fig. 4.58).

Intraductal Papillary Mucinous Neoplasms (Duct-Ectatic Mucin-Producing Tumor)

Intraductal papillary mucinous neoplasms (IPMN) arise in the pancreatic duct epithelium. The lesions can represent a spectrum of abnormalities from simple hyperplasia to dysplasia, papillary adenoma and carcinoma. This spectrum of abnormalities may coexist. In general hyperplasia, dysplasia and adenoma may undergo malignant transformation and transform into carcinoma; however, these carcinomas have low grade malignancies. Hyperplastic, dysplastic or malignant epithelial lining proliferates and forms papillary projections that protrude into and expand the main pancreatic duct or side branch ducts. Duct obstruction is secondary to tenacious plugs of mucin, elaborated by the epithelium, or ductal compression by cystic masses [77]. Intraductal papillary mucinous neoplasms may be classified into main duct and side branch duct types.

IPMN—Main Duct Type

These tumors are rare. Main pancreatic duct involvement presents as diffuse ductal dilatation, copious mucin production, and papillary growth. These tumors are rare and typically malignant [78]. Clinically these

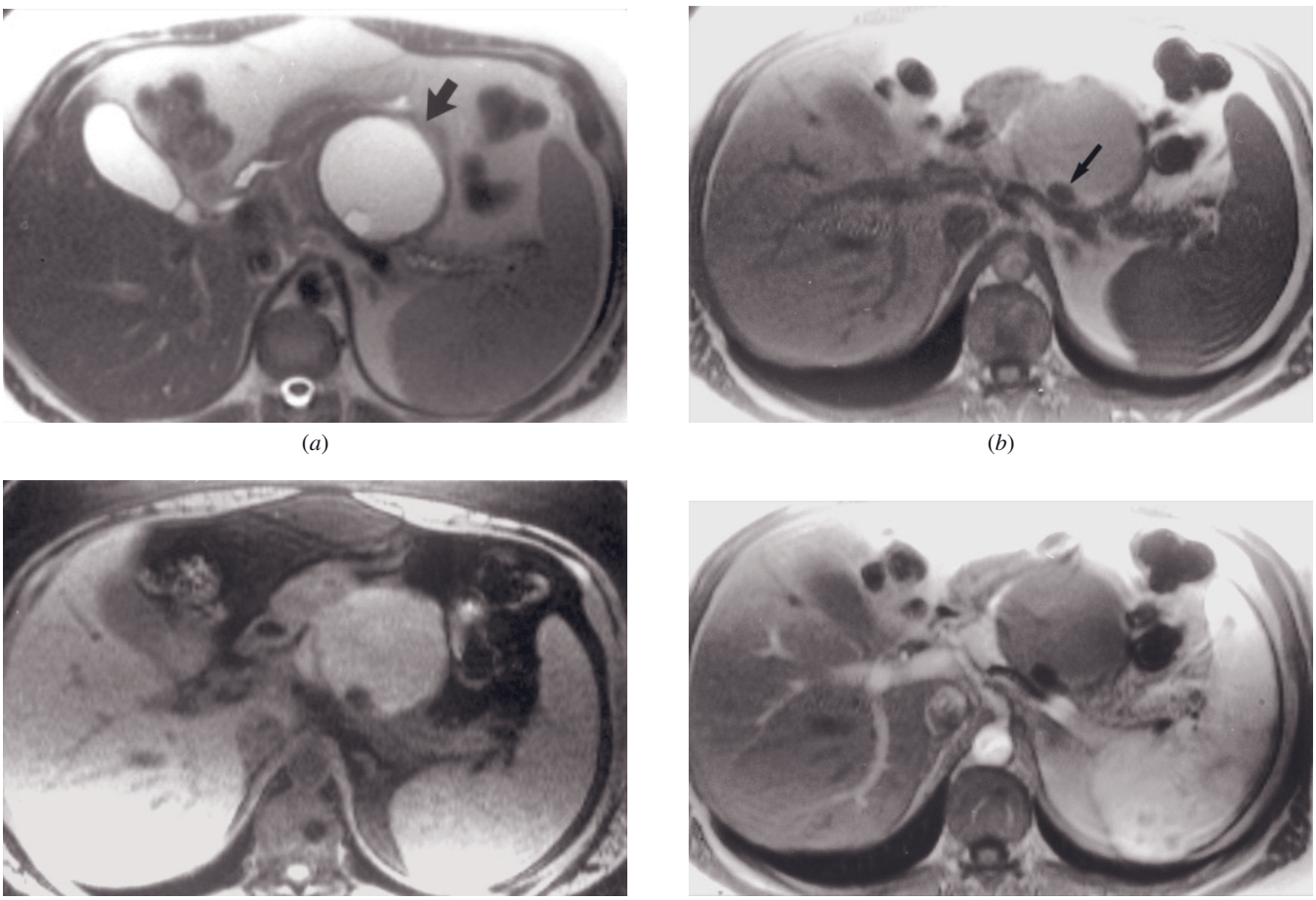

FIG. 4.57 Mucinous cystadenocarcinoma. T2-weighted ETSE (*a*), T1-weighted SGE (*b*), T1-weighted fat-suppressed SGE (*c*), immediate postgadolinium T1-weighted SGE (*d*), and 90-s postgadolinium fat-suppressed SGE (*e*) images. There is a large cystic

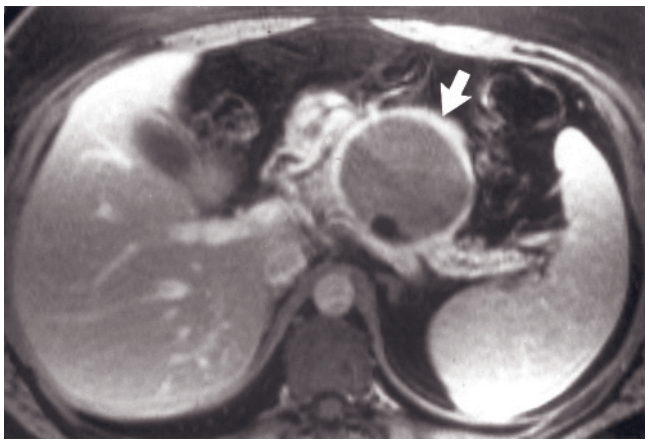

(*e*)

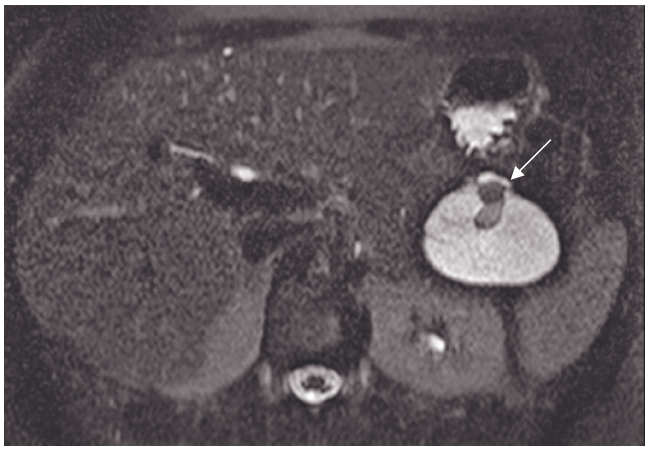

(*f*)

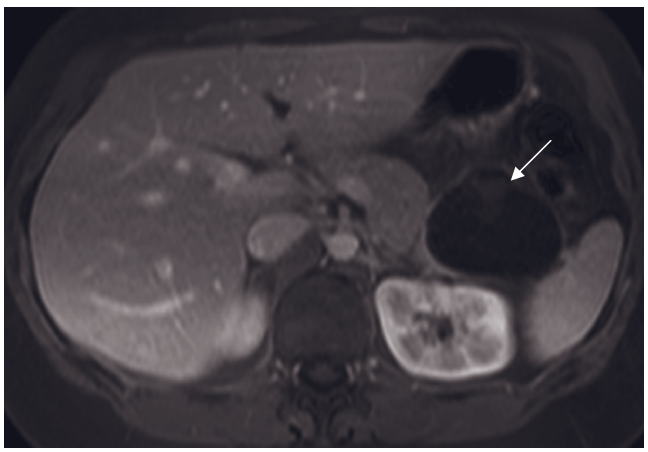

(*g*)

Fig. 4.57 (*Continued*) mass (arrow, *a*) arising from the pancreatic body, which has a thickened and slightly irregular wall, which demonstrates increased enhancement (arrow, *e*) on interstitial-phase gadolinium-enhanced fat-suppressed images. The cyst is high in signal on T1-weighted images (*b*, *c*), reflecting the presence of high protein content from mucin. The cyst contains a smaller cystic structure (arrow, *b*).

T2-weighted short-tau inversion recovery (STIR) (*f*) and hepatic venous phase fat-suppressed 3D-GE (*g*) images demonstrate mucinous cystadenocarcinoma in another patient. The lesion is a large cystic mass originating from the pancreatic tail. It has a complex structure containing thin septations and internal cystic structures (arrows, *f*, *g*). These internal cystic structures have low signal on T2-weighted image and intermediate signal on postgadolinium image because of their high protein content. While the internal cystic structures do not show appreciable enhancement, the wall of the large cyst shows enhancement.

tumors may result in large volumes of mucin production, which can be appreciated by direct inspection at ERCP investigation.

On MR images, a greatly expanded main pancreatic duct is demonstrated on T2-weighted images or MRCP images (fig. 4.59). Irregular-enhancing tissue along the ductal epithelium is appreciated on post-gadolinium images, confirming that underlying tumor is the cause of the ductal dilatation. Total resection is the treatment for this kind of tumor involving the whole main duct. Local resection may be sufficient for the treatment of tumors involving a segment of the main duct.

IPMN—Side-Branch Type

Intraductal papillary mucinous neoplasms involving predominantly side branch ducts appear as oval-shaped cystic masses in proximity to the main pancreatic duct. Septations are generally present, creating a cluster of grapes appearance. Side-branch type IPMN is usually a benign process that appears as a localized cystic parenchymal lesion. The majority of side-branch IPMN tumors are located in the head of the pancreas. Unlike the main branch type, side-branch IPMNs are not rare. MRCP images are able to show communication of the cystic tumor with the main pancreatic duct in the majority of cases (figs. 4.60 and 4.61) [73, 79–82]. Another feature distinguishing from microcystic cystadenoma is that central compacted septations are not present in IPMNs.

Side-branch IPMNs which are less than 2.5 cm in size are usually benign and grow very slowly. In our clinical experience, these kind of side-branch IPMNs also pursue a very nonaggressive, indolent course. Annual repeat MRI studies may be the best approach to following these patients, compared to more interventional forms of diagnosis and therapy, especially in elderly patients. Unless these lesions appear to contain soft tissue stromal elements, grow rapidly or more

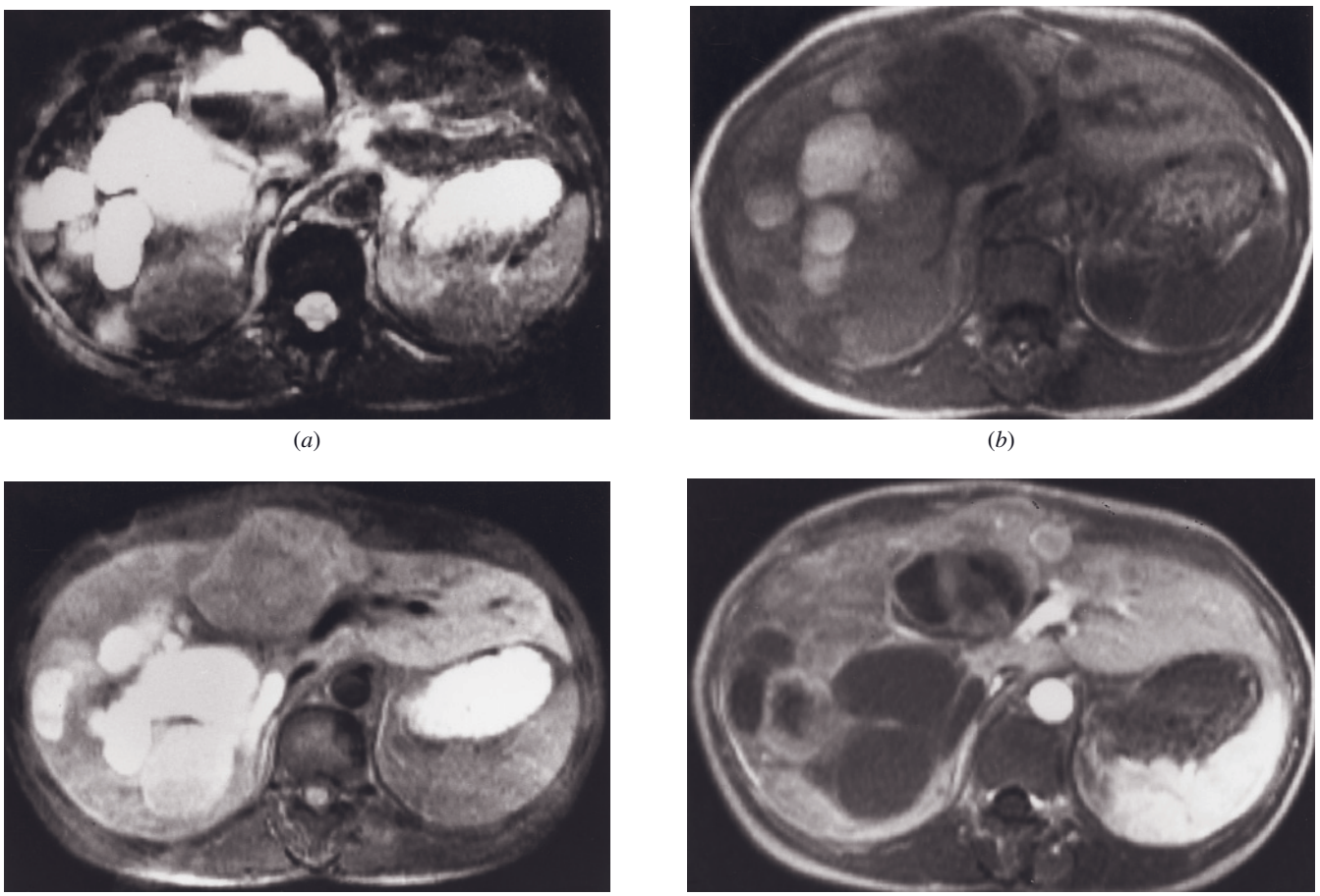

(*a*) (*b*) (*c*) (*d*)

FIG. 4.58 Mucinous cystadenocarcinoma liver metastases. T2-weighted fat-suppressed spin-echo (*a*), T1-weighted SGE (*b*), T1-weighted fat-suppressed spin-echo (*c*), and immediate postgadolinium T1-weighted SGE (*d*) images. Multiple metastases are present throughout the liver that are mixed low and high signal intensity on T1-weighted (*b*, *c*) and T2-weighted (*a*) images. This appearance is consistent with the presence of mucin in these tumors. On the immediate postgadolinium image (*d*), enhancement of the walls of the cysts is appreciated.

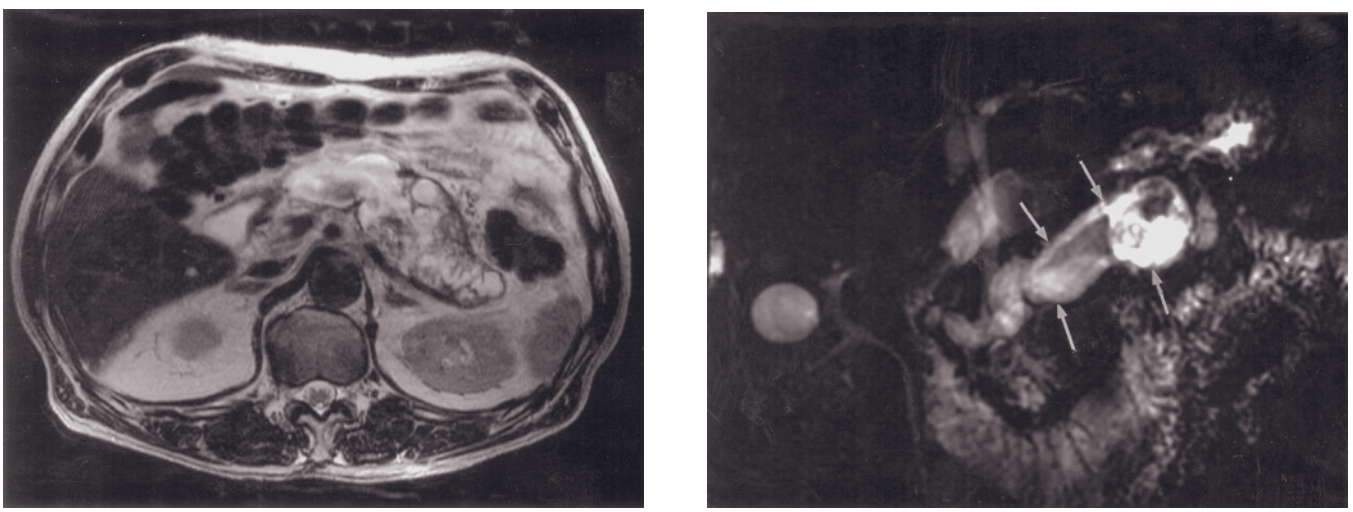

(a) (*b*)

FIG. 4.59 Intraductal papillary mucin secreting neoplasm—main duct type. T2-weighted echo-train spin-echo (*a*), thick-slab MRCP (*b*), immediate postgadolinium fat-suppressed SGE (*c*), and interstitial-phase gadolinium-enhanced fat-suppressed

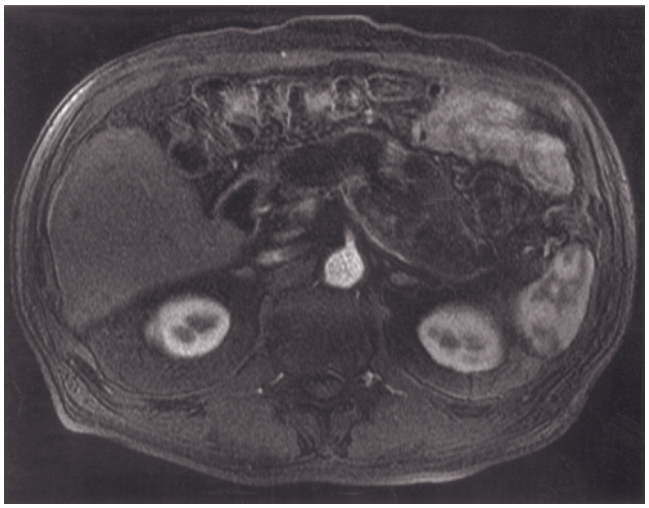

(*c*)

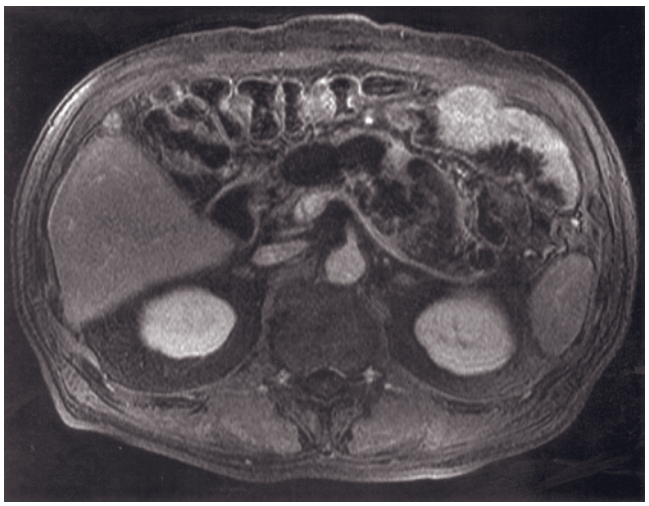

(*d*)

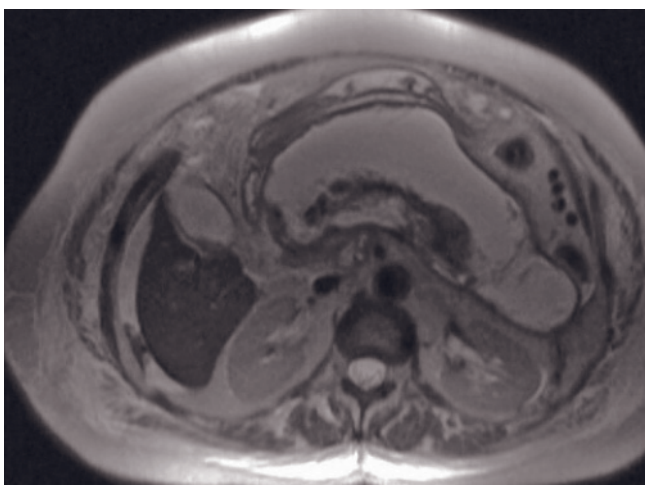

(*e*)

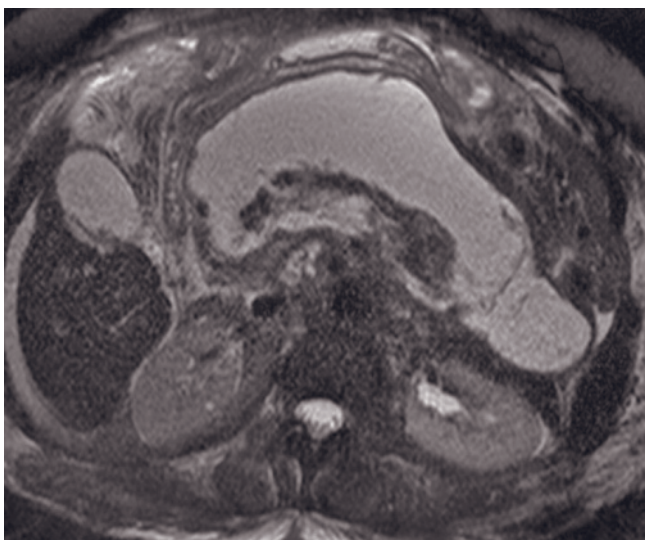

(*f*)

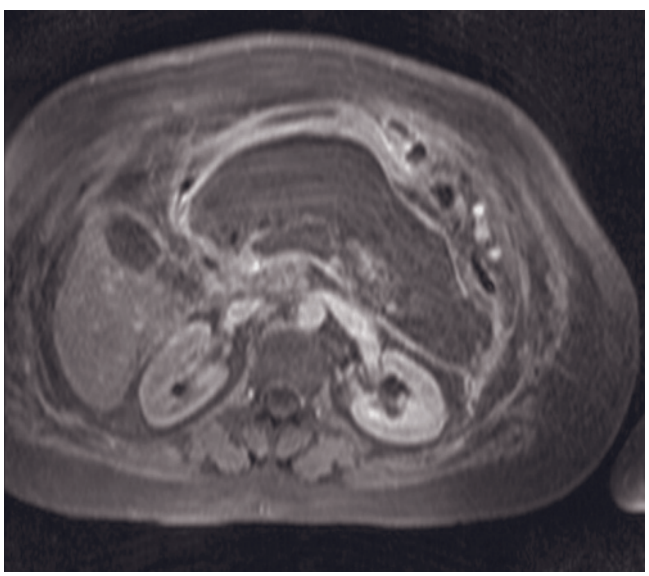

(*g*)

FIG. 4.59 (*Continued*) SGE (*d*) images. There is massive dilatation of the entire main pancreatic duct (arrows, *b*), which is well shown on the T2-weighted sequence (*a*) and MRCP (*b*). Enhancing tumor stroma is appreciated on the postcontrast images (*c*, *d*), with progressive enhancement on the later interstitial-phase images (*d*). (Courtesy of Masayuki Kanematsu, M.D., Gifu University School of Medicine, Japan.)

T2-weighted SS-ETSE (*e*), fat-suppressed T2-weighted SS-ETSE (*f*), and interstitial phase post-gadolinium fat-suppressed T1-weighted gradient echo (*g*) images in a second patient with main duct type intraductal papillary mucin secreting neoplasm demonstrate similar findings.

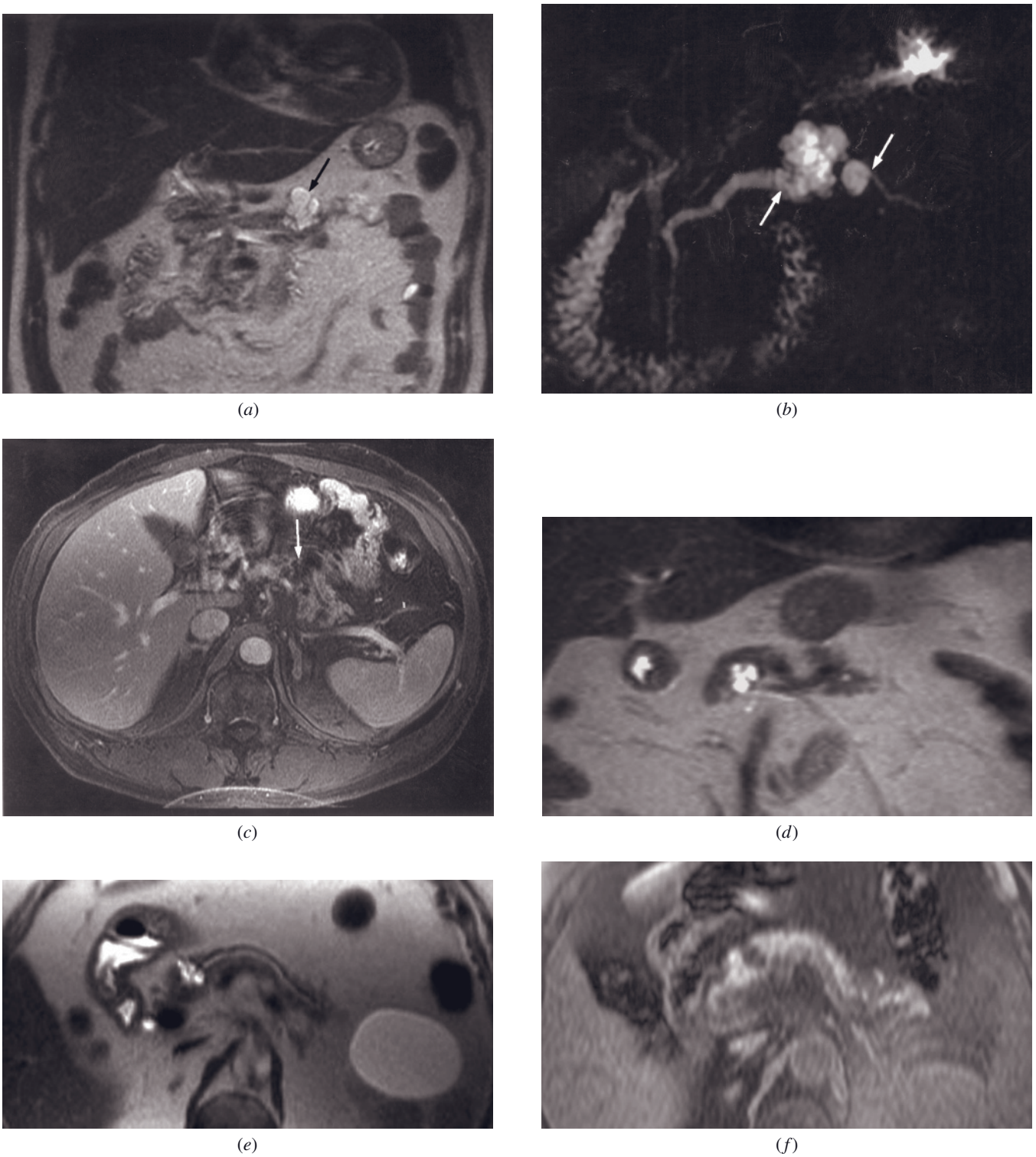

FIG. 4.60 Intraductal papillary mucin-secreting neoplasm—side-branch type. Coronal T2-weighted SS-ETSE (*a*), thick-section MRCP (*b*), and interstitial-phase gadolinium-enhanced fat-suppressed SGE (*c*) images in a patient with branch-type intraductal mucin-producing papillary neoplasm. There are clusters of multiple small cysts (arrow, *a*) in the pancreatic body, which exhibit communication with the main pancreatic duct. Communication with the main duct is well shown on the MRCP image. No apparent tumor stroma (arrow, *c*) is appreciated on postgadolinium images. Branch duct type tumor usually shows cystic parenchymal lesions and tends to be less aggressive than the main ductal type. (Courtesy of Masayuki Kanematsu, M.D., Gifu University School of Medicine, Japan.) Coronal (*d*) and axial (*e*) T2-weighted SS-ETSE, fat-suppressed T1-weighted gradient-echo (*f*), and

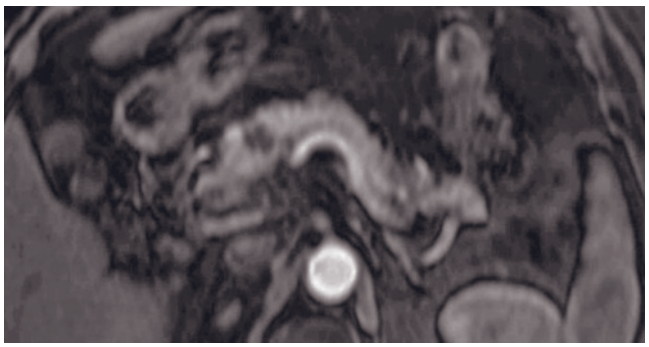

(*g*)

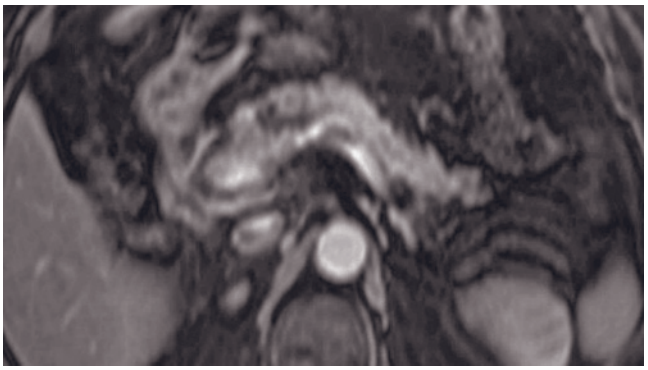

(*h*)

FIG. 4.60 (*Continued*) immediate (*g*) and interstitial-phase (*h*) postgadolinium fat-suppressed T1-weighted gradient-echo images in a second patient with side-branch IPMT demonstrate similar findings.

than 2.5 cm in size, resection may need to be contemplated.

Solid and Papillary Epithelial Neoplasm (Papillary Cystic Neoplasm)

These tumors are generally considered benign neoplasms, with occasional examples exhibiting low-grade malignant potential. Solid and papillary epithelial neoplasms occur most frequently in women between 20 and 30 years of age [83]. The gross appearance of tumors is an encapsulated mass, which on cut surface reveals areas of hemorrhage, necrosis, and cystic spaces. The capsule and inner portion of tumor may contain calcifications. MRI findings of solid and papillary epithelial neoplasms are virtually diagnostic in the appropriate clinical setting. The MR appearance is a large, well-encapsulated mass, which demonstrates focal signal-void calcification and regions of hemorrhagic degeneration (as evidenced by fluid-debris levels or signal intensities consistent with blood products). A mass with this appearance, discovered in a young female patient, is virtually diagnostic for this entity [84]. A report describing the MRI appearance of solid and papillary epithelial neoplasms found that all tumors were well-demarcated lesions that contained central high signal intensity on T1-weighted images [83]. This central high signal intensity corresponds to hemorrhagic necrosis. The presence of hemorrhage may be related to tumor size because smaller tumors may appear heterogeneous but may not be overtly hemorrhagic (fig. 4.62).

Lymphoma

Non-Hodgkin lymphoma may involve peripancreatic lymph nodes or may directly invade the pancreas [85]. Intermediate-signal-intensity peripancreatic lymph nodes are distinguished from high-signal-intensity normal pancreas on T1-weighted fat-suppressed images. Invasion of the pancreas is shown by loss of the normal high signal intensity of the pancreas on T1-weighted fat-suppressed images (fig. 4.63).

Burkitt lymphoma has a particular propensity to involve organs and structures within the abdominal cavity, including bowel, gallbladder, peritoneum, and pancreas (see fig. 4.63).

Metastases

Involvement of the pancreas by metastatic tumor may be the result of spread by direct extension or hematogenous metastases. Direct invasion by the extension of cancers arising in neighboring organs is common, particularly carcinoma of the stomach or transverse colon. Hematogenous metastases may occur with carcinomas of the lung, breast, and kidney and malignant melanoma. The MRI appearance of renal cell carcinoma metastases to the pancreas has been described as diffuse micronodular, multifocal, and solitary metastatic deposits [86]. Metastases are low in signal intensity on T1-weighted images and high in signal intensity on T2-weighted images. Small metastases (<1 cm in diameter) enhance uniformly on immediate postgadolinium gradient-echo images, and larger metastases enhance in a ring fashion (fig. 4.64). This appearance is analogous to the appearance of hypervascular metastases to the liver and reflects the pathophysiology of parasitization of host blood supply by metastatic disease. Renal cancer metastases resemble the appearance of islet cell tumors. Clinical history of renal cancer, even if remote, is essential to obtain in order to establish the correct diagnosis. Metastases from other primary tumors generally appear

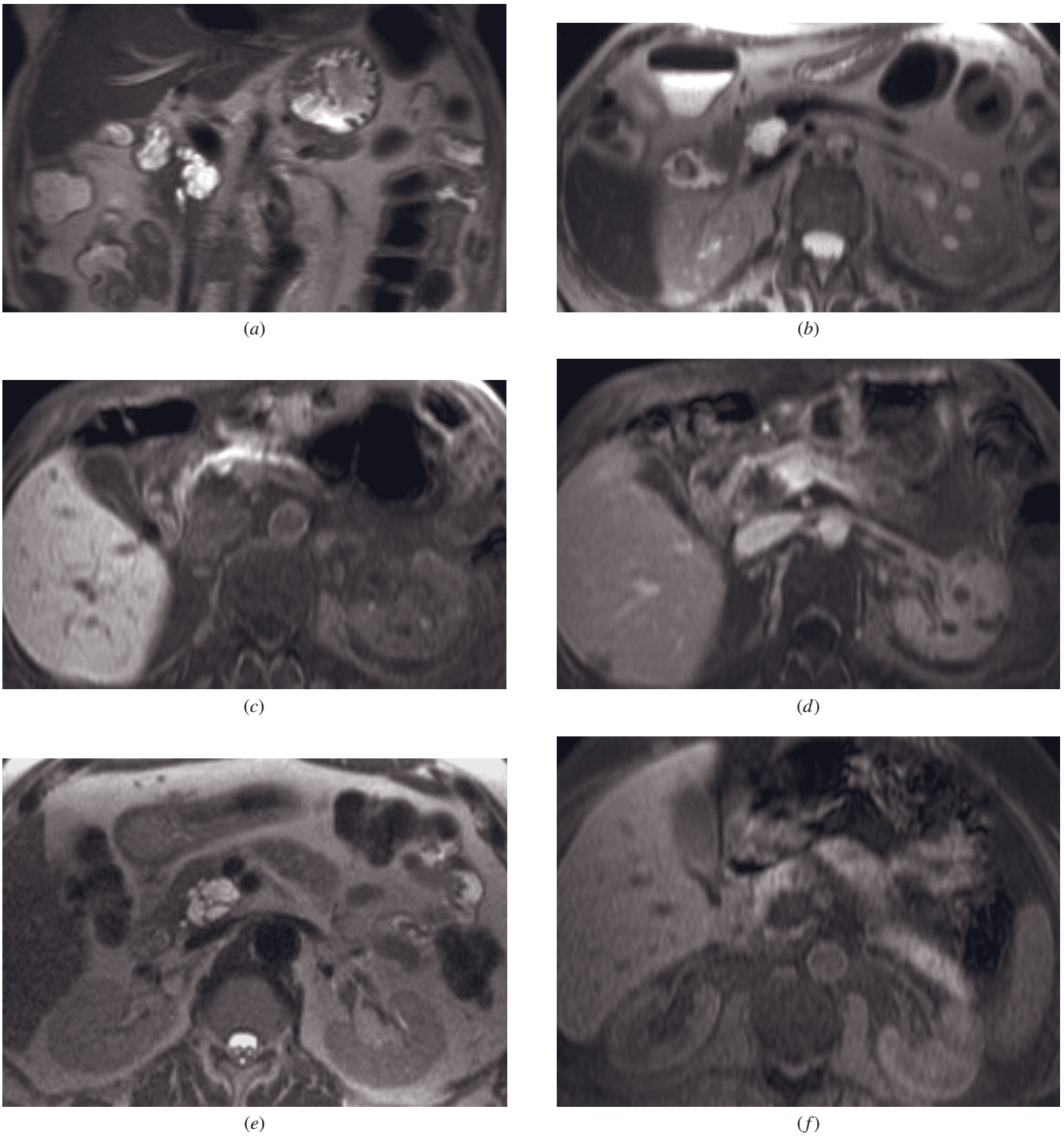

FIG. 4.61 Side-branch IPMN. Coronal (*a*) and axial (*b*) T2-weighted SS-ETSE, fat-suppressed T1-weighted gradient-echo (*c*) and immediate postgadolinium T1-weighted gradient-echo (*d*) images in a patient with side-branch IPMT demonstrate a 3-cm multilocular cystic mass in the pancreatic head. The lesion does not enhance after gadolinium administration (*d*).

T2-weighted SS-ETSE (*e*), fat suppressed T1-weighted gradient-echo (*f*), immediate postgadolinium fat-suppressed T1-weighted

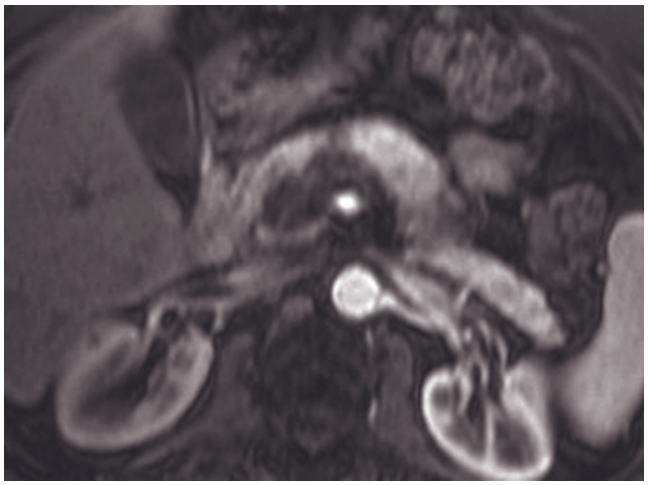

(*g*)

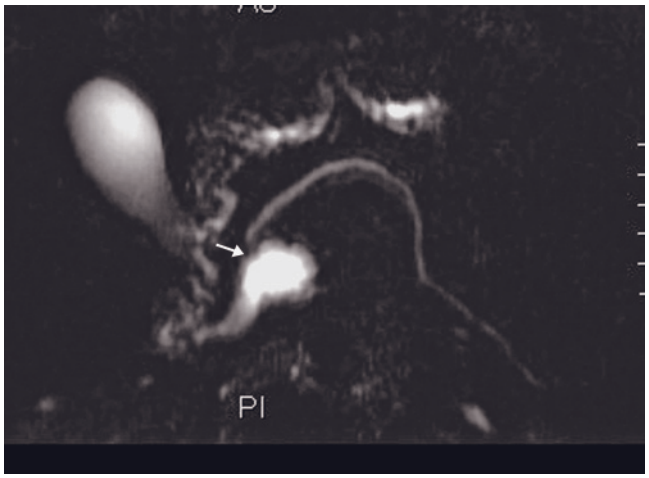

(*h*)

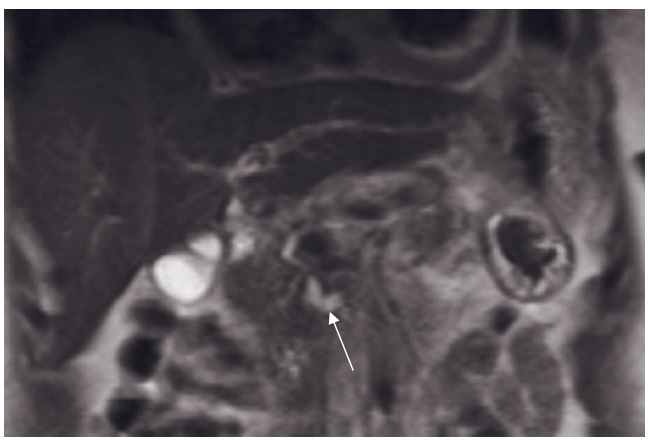

(*i*)

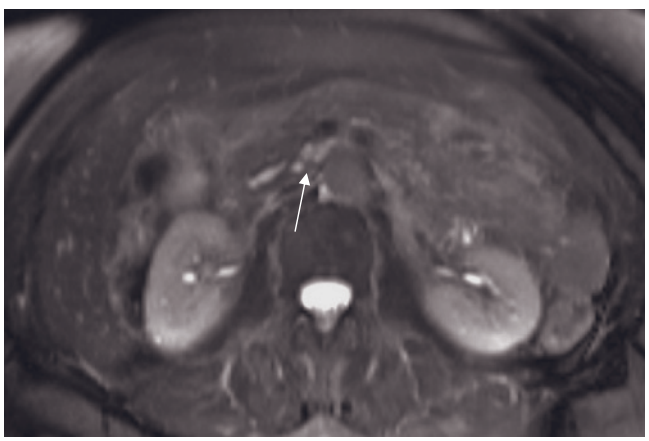

(*j*)

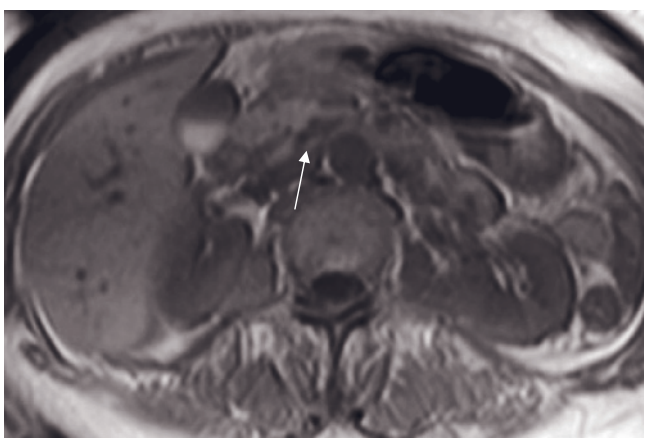

(*k*)

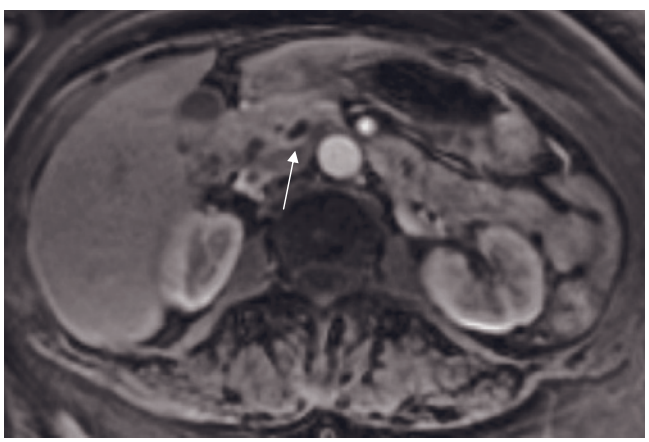

(*l*)

Fig. 4.61 (*Continued*) gradient-echo (*g*), and MRCP (*h*) images in a second patient with side-branch IPMT. There is a multicystic mass in the pancreatic head. Thin-section MRCP image shows that the cystic mass communicates with the main pancreatic duct (arrow, *h*), consistent with a side-branch IPMT. No enhancement of the cystic mass is appreciated on postgadolinium images (*g*).

Coronal T2-weighted single-shot echo-train spin-echo (*i*), transverse fat-suppressed single-shot echo-train spin-echo (*j*), transverse T1-weighted SGE (*k*), and transverse T1-weighted postgadolinium hepatic arterial dominant phase fat-suppressed 3D-GE (*l*) images at 3.0 T demonstrate a small septated cystic structure (arrows, *i–l*) in the pancreatic head in another patient. The diagnosis is consistent with side-branch IPMN.

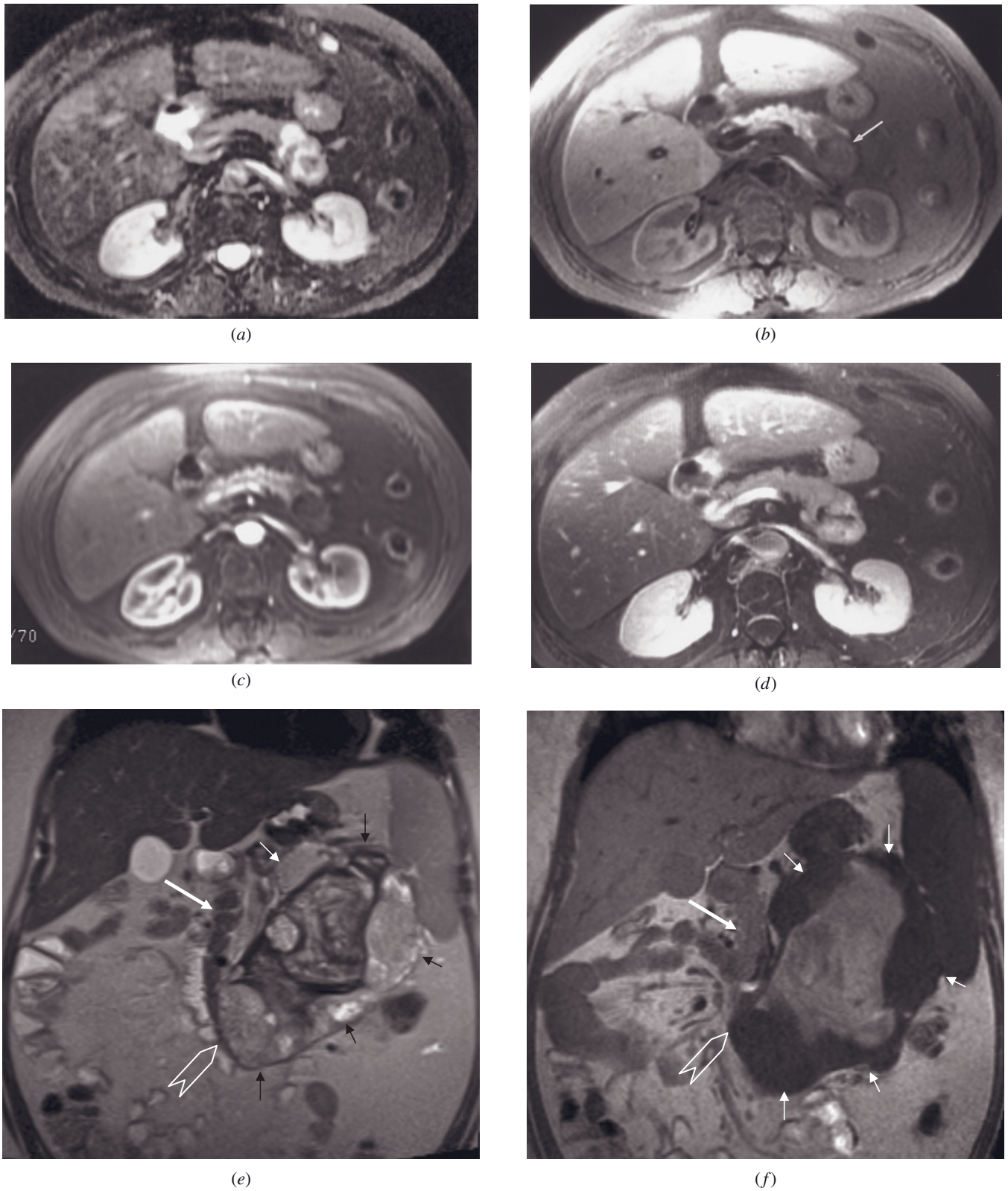

FIG. 4.62 Solid and papillary epithelial neoplasm. T2-weighted fat-suppressed spin-echo (*a*), T1-weighted fat-suppressed SGE (*b*), immediate postgadolinium T1-weighted fat-suppressed SGE (*c*), and 90-s postgadolinium fat-suppressed SGE (*d*) images. A 4-cm tumor mass arises from the tail of the pancreas that is low in signal intensity on the T1-weighted image (arrow, *b*) and heterogeneous on the T2-weighted image (*a*), enhances negligibly on the immediate postgadolinium T1-weighted SGE image (*c*), and shows heterogeneous enhancement on the interstitial-phase image (*d*).This rare low-grade malignant tumor is more frequent in young females and is typically located in the tail of the pancreas. MRI may be useful in these lesions by showing cystic degeneration and hemorrhagic necrosis, which are characteristic of this entity. (Courtesy of Caroline Reinhold, MD, Dept. of Radiology, McGill University.)

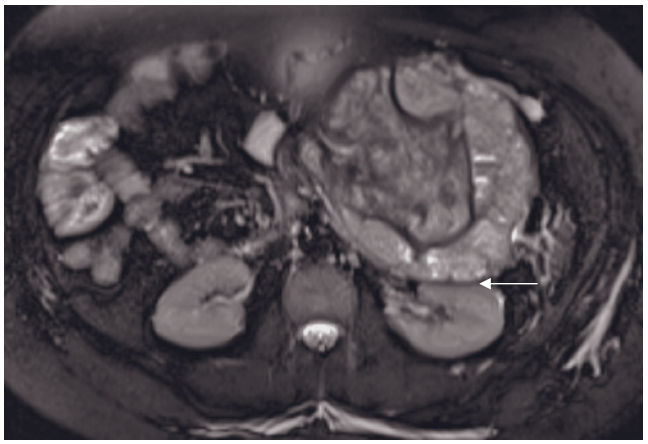

(*g*)

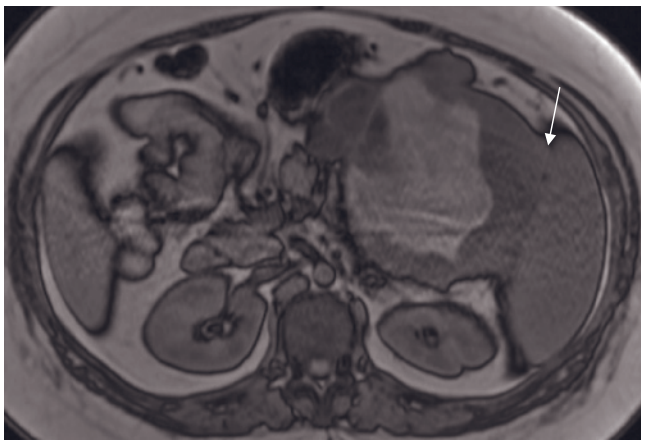

(*h*)

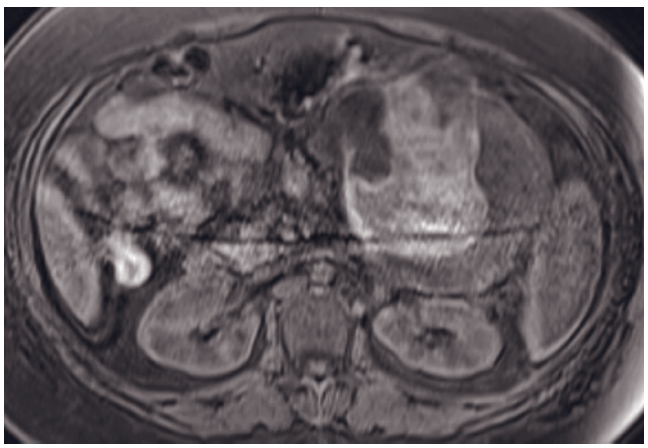

(*i*)

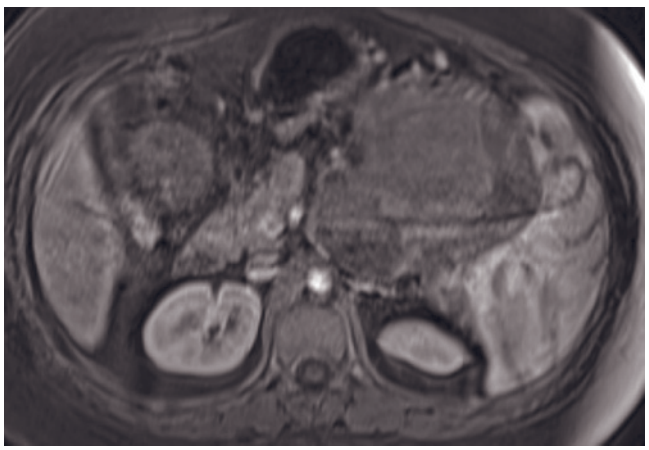

(*j*)

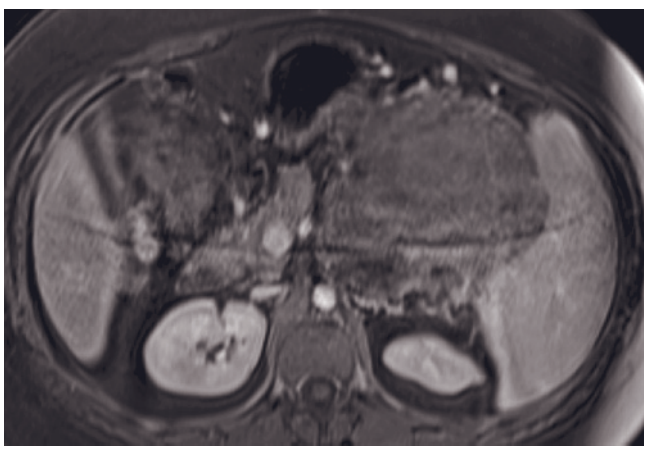

(*k*)

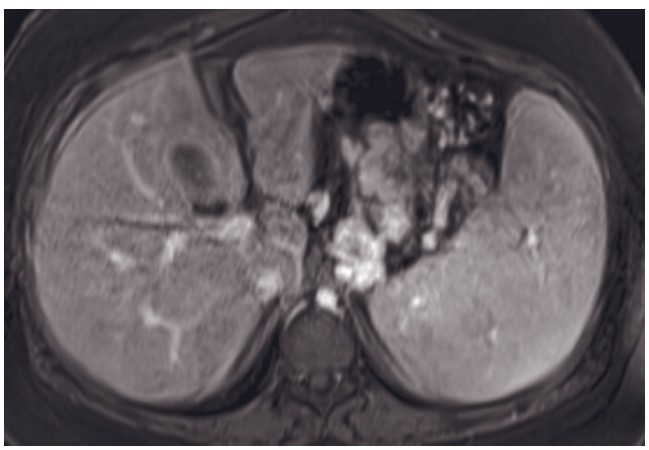

(*l*)

Fig. 4.62 (*Continued*) Coronal T2-weighted single-shot echo-train spin-echo (*e*), coronal T1-weighted SGE (*f*), transverse T2-weighted fat-suppressed single-shot echo-train spin-echo (*g*), transverse T1-weighted out-of-phase SGE (*h*), transverse fat-suppressed T1-weighted SGE (*i*), and transverse postgadolinium hepatic arterial dominant (*j*) and hepatic venous phase (*k*, *l*) fat-suppressed 3D-GE images in a young pregnant patient with solid and papillary tumor of the pancreas. The tumor (short arrows, *e*, *f*) is originating from the tail of the pancreas (open arrows, *e*, *f*) and depresses the whole pancreas (white long arrows, *e*, *f*) inferomedially. The tumor is well demarcated and compresses the left kidney (white arrow, *g*) and the spleen (white arrow, *h*). The tumor is very heterogeneous. It contains central hemorrhage which demonstrates high signal intensity on out-of-phase (*h*) and fat-suppressed (*i*) T1-weighted SGE images and heterogeneous low signal intensity on T2-weighted images (*e*, *g*). The tumor also contains cystic and necrotic regions, which show markedly high signal on T2-weighted images (*e*, *g*). The solid components of the tumor demonstrate intermediate to moderately high signal on T2-weighted images (*e*, *g*) and low signal on T1-weighted images (*f*, *h*, *i*). The tumor shows mild enhancement on postgadolinium images (*j*, *k*). Note that there are large varices in and around the stomach, and in the splenic hilum due to splenic vein thrombosis. There is an aliasing artifact at the center of transverse T1-weighted images due to the use of parallel imaging. Edema is also detected on the left and posterior body wall (*g*).

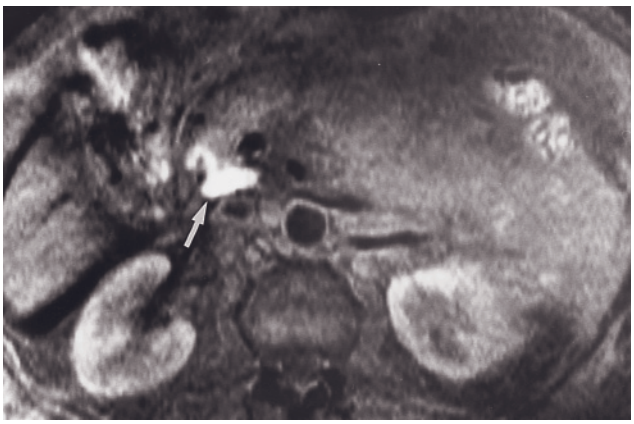

(*a*)

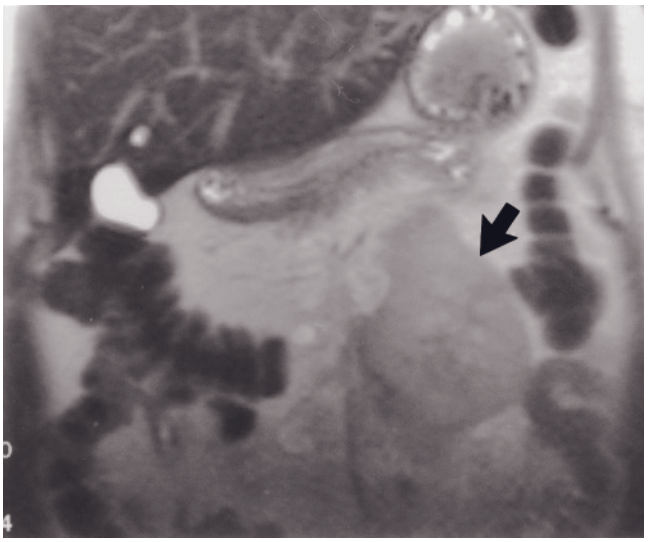

(*b*)

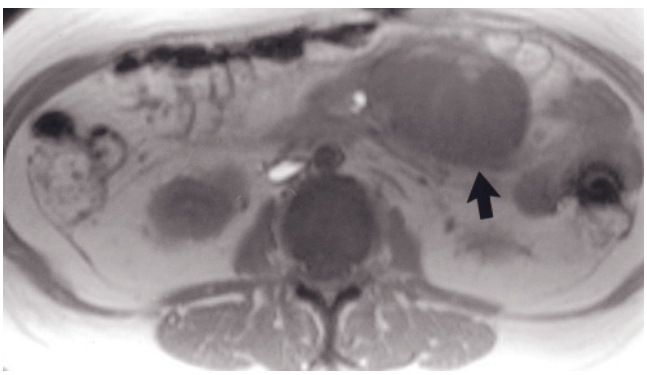

(*c*)

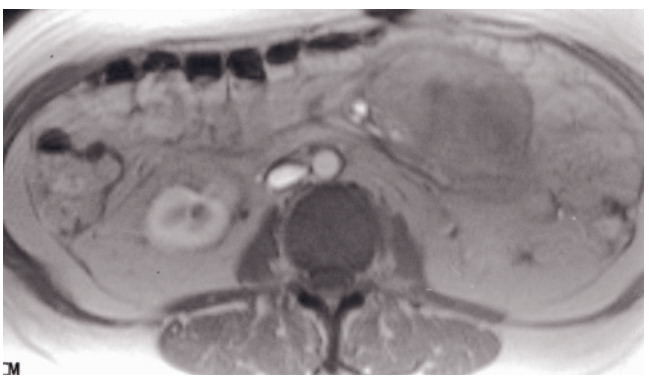

(*d*)

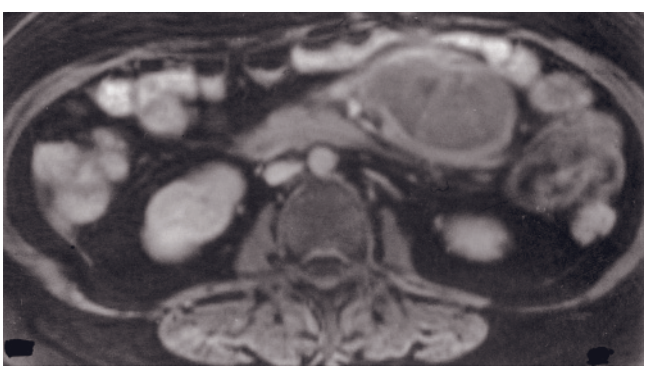

(*e*)

(*f*)

Fig. 4.63 Lymphoma. T1-weighted fat-suppressed spin-echo image (*a*) demonstrates replacement of the majority of the pancreas with intermediate-signal ill-defined lymphomatous tissue. The ventral portion of the pancreatic head is spared (arrow, *a*). (Reproduced with permission from Semelka RC, Shoenut JP, Kroeker MA, Micflikier AB. The Pancreas. In: Semelka RC, Shoenut JP. *MRI of the Abdomen with CT Correlation*. New York: Raven Press, p. 59–76, 1993.)

Coronal T2-weighted SS-ETSE (*b*), T1-weighted SGE (*c*), immediate postgadolinium T1-weighted SGE (*d*), and 90-s postgadolinium fat-suppressed SGE (*e*) images in a second patient, who has Burkitt lymphoma. A 10-cm mass (arrow, *b*, *c*) involves the pancreatic body and tail, which is mildly hypointense in signal intensity on both T1 (*c*)- and T2 (*b*)-weighted images and enhances minimally on early (*d*) and late (*e*) postgadolinium images.

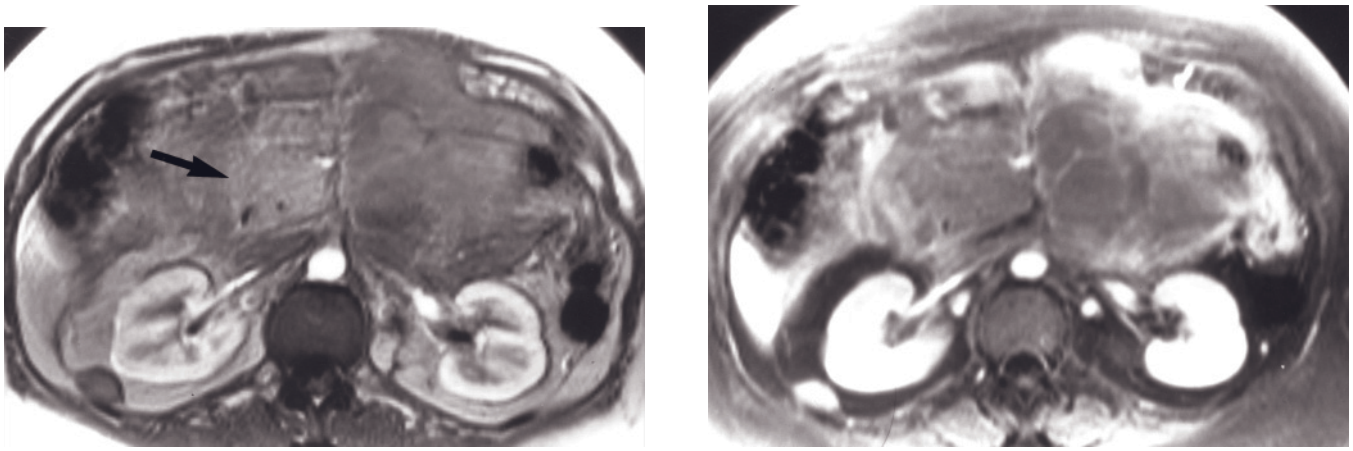

(*g*) (*h*)

FIG. 4.63 (*Continued*) Coronal T2-weighted SS-ETSE (*f*), immediate postgadolinium SGE (*g*), and 90-s postgadolinium fat-suppressed SGE (*h*) images in a third patient who has non-Hodgkin lymphoma. A large mass is present in the mesentery, which involves the pancreas as well. Mild enhancement of the mesenteric tumor and tumor involving the pancreatic head (arrow, *g*) is present on early (*g*) and late (*h*) postgadolinium images. As these cases illustrate, lymphoma typically exhibits mild enhancement on early and late postcontrast images.

as focal pancreatic masses that are mildly hypointense on T1-weighted images, moderately hypointense on T1-weighted fat-suppressed images, and mildly hyperintense on T2-weighted images. Metastases to the pancreas often enhance in a ring fashion (figs. 4.65 and 4.66), as observed with liver metastases, and their extent of enhancement generally varies with the angiogenic properties of the primary neoplasms. Ductal obstruction is uncommon, even with larger tumors, which is an important feature distinguishing from pancreatic ductal adenocarcinoma. The lack of ductal obstruction explains why metastases are generally well seen on noncontrast T1-weighted fat-suppressed images. Chronic pancreatitis that arises secondary to ductal obstruction is not present, and therefore background pancreas is moderately high signal intensity, creating sharp contrast with hypointense tumors.

Melanoma metastases may be high in signal intensity on T1-weighted images because of the paramagnetic properties of melanin pigment (fig. 4.67) [1]. Metastatic deposits tend to be focal, well-defined masses (figs. 4.68–4.70).

INFLAMMATORY DISEASE

Pancreatitis

Pancreatitis may occur secondary to chronic alcoholism, gallstones, hypercalcemia, hyperlipoproteinemia, blunt abdominal trauma, penetrating peptic ulcer disease, viral infections (most frequently Epstein–Barr), and certain drugs [87]. Pancreatitis can also be hereditary and predisposition may be inherited as an autosomal dominant trait [88].

Acute Pancreatitis

Acute pancreatitis is defined as an acute inflammatory condition typically presenting with abdominal pain and associated with elevations in pancreatic enzymes (particularly amylase and lipase). Acute pancreatitis arises in the majority of cases secondary to alcoholism or cholelithiasis [87]. Alcohol-related acute pancreatitis most frequently results in acute recurrent pancreatitis, whereas gallstone-related pancreatitis typically results in a single attack (fig. 4.71). The passage of biliary sludge may also cause acute pancreatitis [89]. At least 95% of patients with acute pancreatitis experience severe midepigastric pain that radiates to the back. Nausea and vomiting occur in 75–85% of patients, and fever occurs in approximately 50%.

Acute pancreatitis results from the exudation of fluid containing activated proteolytic enzymes into the interstitium of the pancreas and leakage of this fluid into surrounding tissue. Trypsin is suspected to be the primary enzyme involved in the coagulative necrosis. Pathologically, acute pancreatitis is characterized by a spectrum of morphologic features, which may be patchy or diffuse. In mild cases, edema predominates, producing so-called edematous or interstitial pancreatitis. There is scattered peripancreatic fat necrosis without parenchymatous or acinar necrosis. In severe cases, extensive

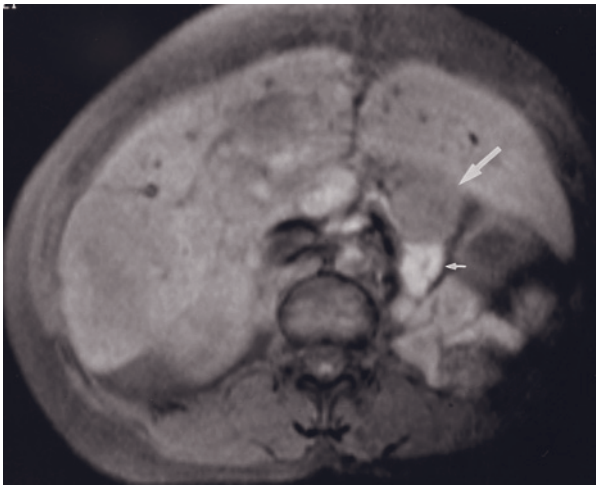

(*a*)

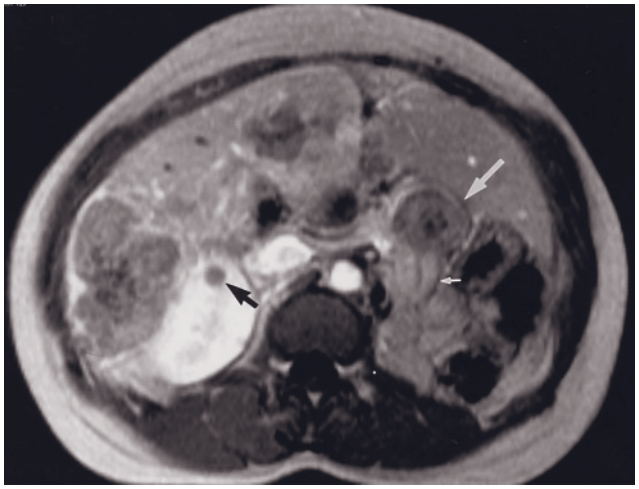

(*b*)

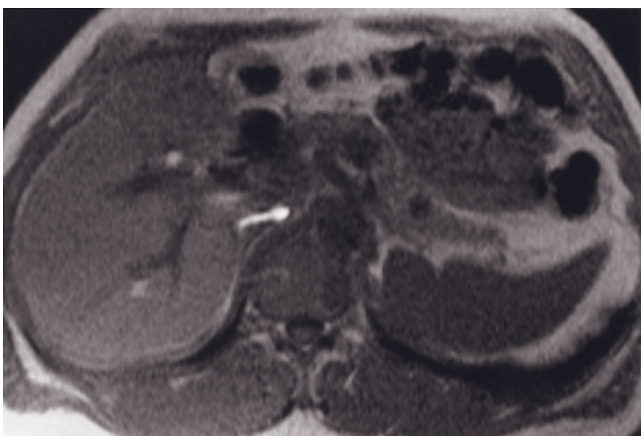

(*c*)

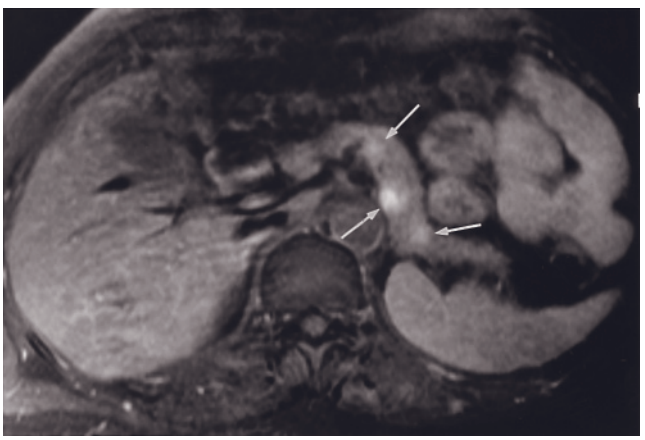

(*d*)

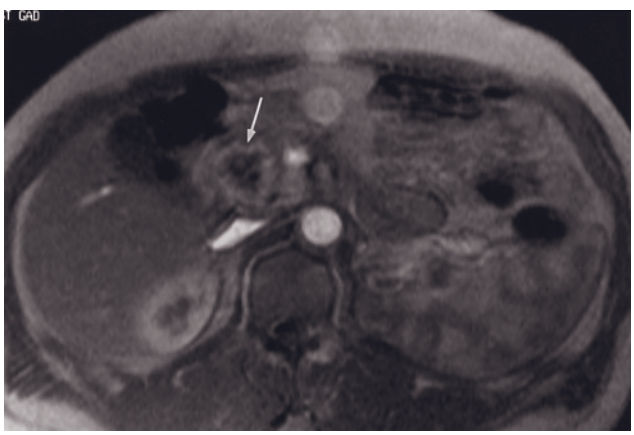

(*e*)

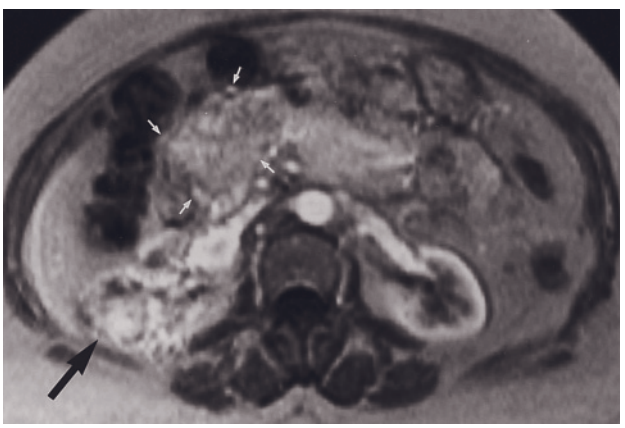

(*f*)

FIG. 4.64 Pancreatic metastases from renal cancer. T1-weighted fat-suppressed spin-echo (*a*) and immediate postgadolinium T1-weighted SGE (*b*) images demonstrate a 3-cm mass in the distal body of the pancreas (arrow, *a*, *b*).The uninvolved tail of the pancreas has a normal high signal intensity (small arrow, *a*, *b*). Multiple liver metastases are present that demonstrate predominant rim enhancement on the immediate postgadolinium image (*b*). Multiple renal cancers are present (black arrow, *b*, only one lesion shown).

T1-weighted SGE (*c*) and interstitial-phase gadolinium-enhanced T1-weighted fat-suppressed spin-echo (*d*) images of the body of the pancreas and immediate postgadolinium T1-weighted SGE image (*e*) in a second patient. Three metastases are present in the body of the pancreas (arrows, *d*) that are low in signal intensity on the precontrast T1-weighted SGE image (*c*) and enhance uniformly and with moderate intensity on the interstitial-phase gadolinium-enhanced image (*d*). A larger 3-cm metastasis is present in the head of the pancreas that demonstrates rim enhancement on the immediate postgadolinium image (arrow, *e*).

Immediate postgadolinium T1-weighted SGE image (*f*) in a third patient demonstrates multiple micronodular metastases to the pancreas <5 mm, which enhance uniformly and intensely on the immediate postgadolinium image (small arrows, *f*). The renal cancer is also shown (arrow, *f*). (Reproduced with permission from Kelekis NL, Semelka RC, Siegelman ES: MRI of pancreatic metastasis from renal cell cancer. *J Comput Assist Tomogr* 20: 249–253, 1996.) Renal cell cancer is among the most common metastatic lesions to the pancreas.

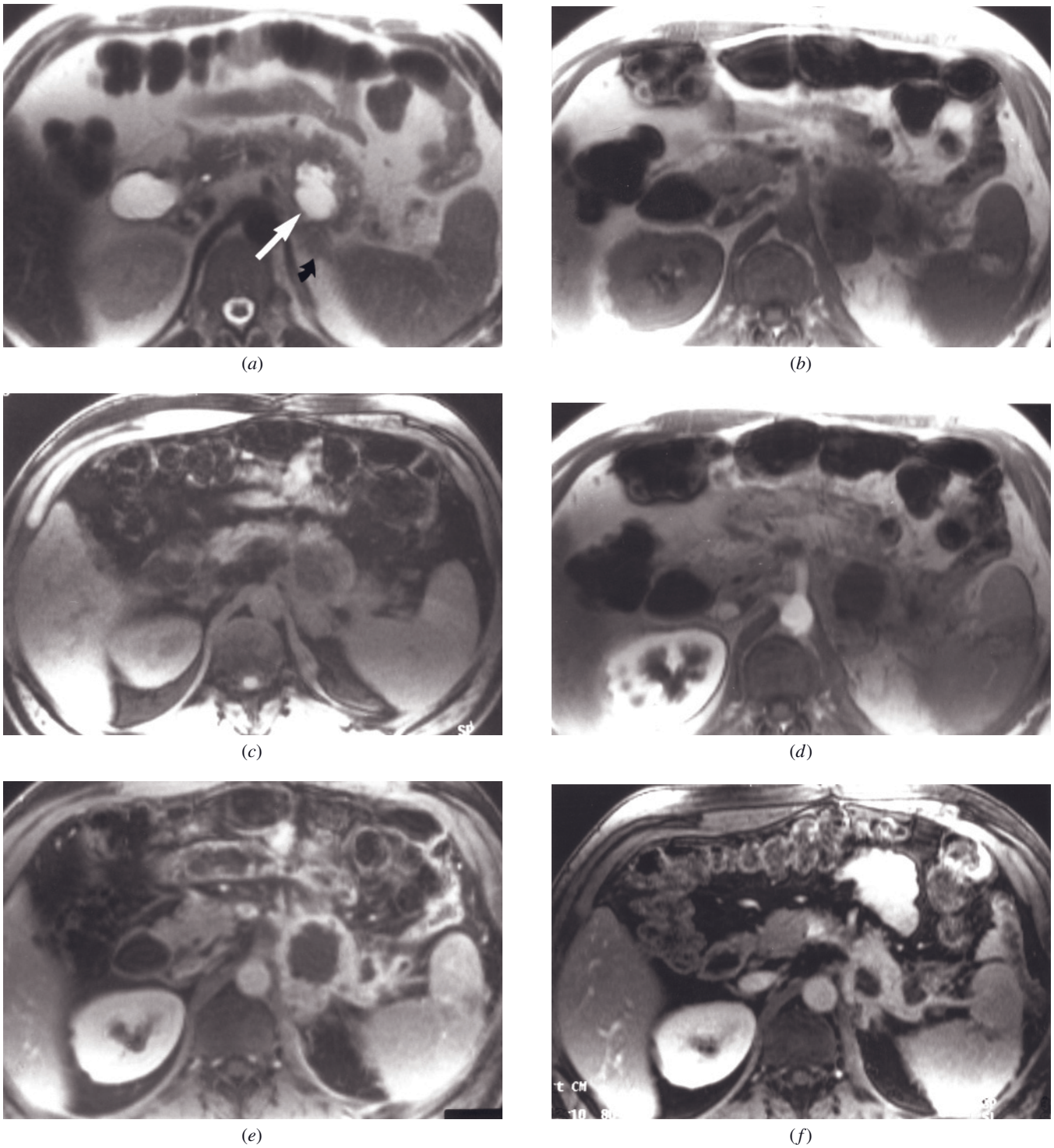

FIG. 4.65 Pancreatic metastasis from transitional cell cancer. T2-weighted ETSE (*a*), T1-weighted SGE (*b*), T1-weighted fat-suppressed SGE (*c*), immediate postgadolinium T1-weighted SGE (*d*), and 90-s postgadolinium fat-suppressed SGE (*e*) images in a patient with recurrent transitional cell cancer, originally from the left kidney. There is a cystic mass (arrow, *a*) that involves the pancreatic tail and the left adrenal gland (curved arrow, *a*). A thick enhancing rim is demonstrated on the interstitial-phase gadolinium-enhanced fat-suppressed image. Interstitial-phase gadolinium-enhanced fat-suppressed SGE image (*f*) obtained after a course of chemotherapy demonstrates substantial decrease in size of the cystic mass.

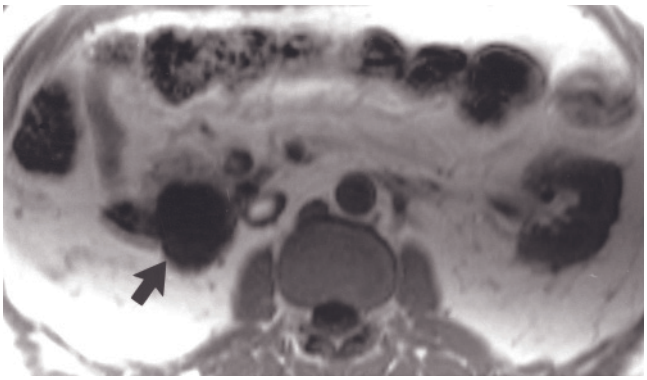

(*a*)

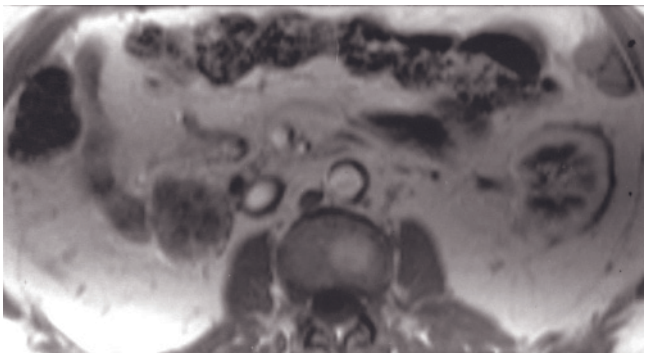

(*b*)

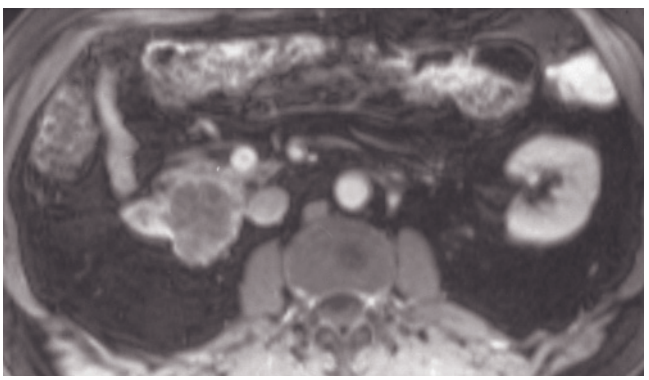

(*c*)

FIG. 4.66 Pancreatic metastasis from colon cancer. T1-weighted SGE (*a*), immediate postgadolinium T1-weighted SGE (*b*), and 90-s postgadolinium fat-suppressed SGE (*c*) images in a patient with colon cancer with liver metastases (not shown). There is a 3.5-cm lobulated mass (arrow, *a*) in the pancreatic head. The tumor appears hyperintense on T2 (not shown) and hypointense on T1-weighted image (*a*) and shows heterogeneous mild enhancement on early (*b*) and late (*c*) postgadolinium images.

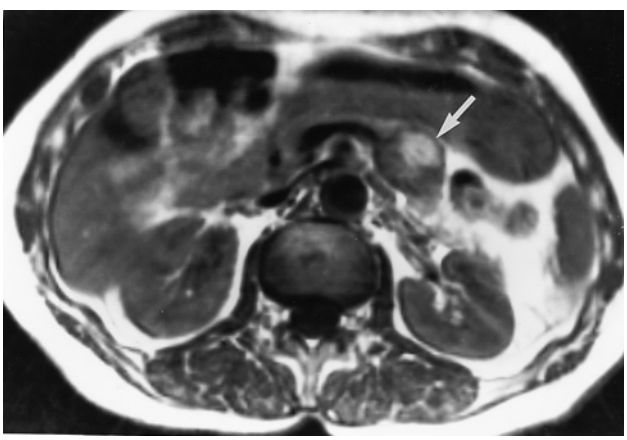

FIG. 4.67 Pancreatic metastasis from melanoma. T1-SGE image demonstrates a high-signal intensity mass in the tail of the pancreas (arrow). The high signal intensity of the mass is due to the paramagnetic effect of melanin. (Reproduced with permission from Semelka RC, Ascher SM: MRI of the pancreas—state of the art. *Radiology* 188: 593–602, 1993.)

pancreatic and peripancreatic fat necrosis, parenchymal necrosis, and hemorrhage occur. In its most devastating form, severe acute pancreatitis may produce an organ that resembles oily mud, where degenerative tissue, fat, and hemorrhage congeal [90].

The signal intensity features of the pancreas in uncomplicated mild acute pancreatitis resemble those of normal pancreatic tissue. The pancreas is high in signal intensity on precontrast T1-weighted fat-suppressed images and enhances in a normal uniform fashion on immediate postgadolinium images, reflecting a normal capillary blush (fig. 4.72). The acutely inflamed pancreas shows either focal or diffuse enlargement, which may be subtle. Peripancreatic fluid is well shown on noncontrast or immediate postgadolinium non-fat-suppressed gradient-echo images and appears as low-signal-intensity strands of fluid or fluid collections in a background of high-signal-intensity fat. T2-weighted single-shot echo-train spin-echo imaging employing fat suppression is the most sensitive technique for showing small-volume peripancreatic fluid, which appears as high signal in a background of intermediate- to low-signal pancreas and low-signal fat (see fig. 4.72). As a result, MRI is sensitive for the detection of subtle changes of acute pancreatitis, particularly minor peripancreatic inflammatory changes even in the setting of a morphologically normal pancreas. CT imaging examinations appear normal in 15–30% of patients with clinical features of acute pancreatitis [91]. The sensitivity of MRI exceeds that of CT imaging, suggesting a role for MRI in the evaluation of patients with suspected

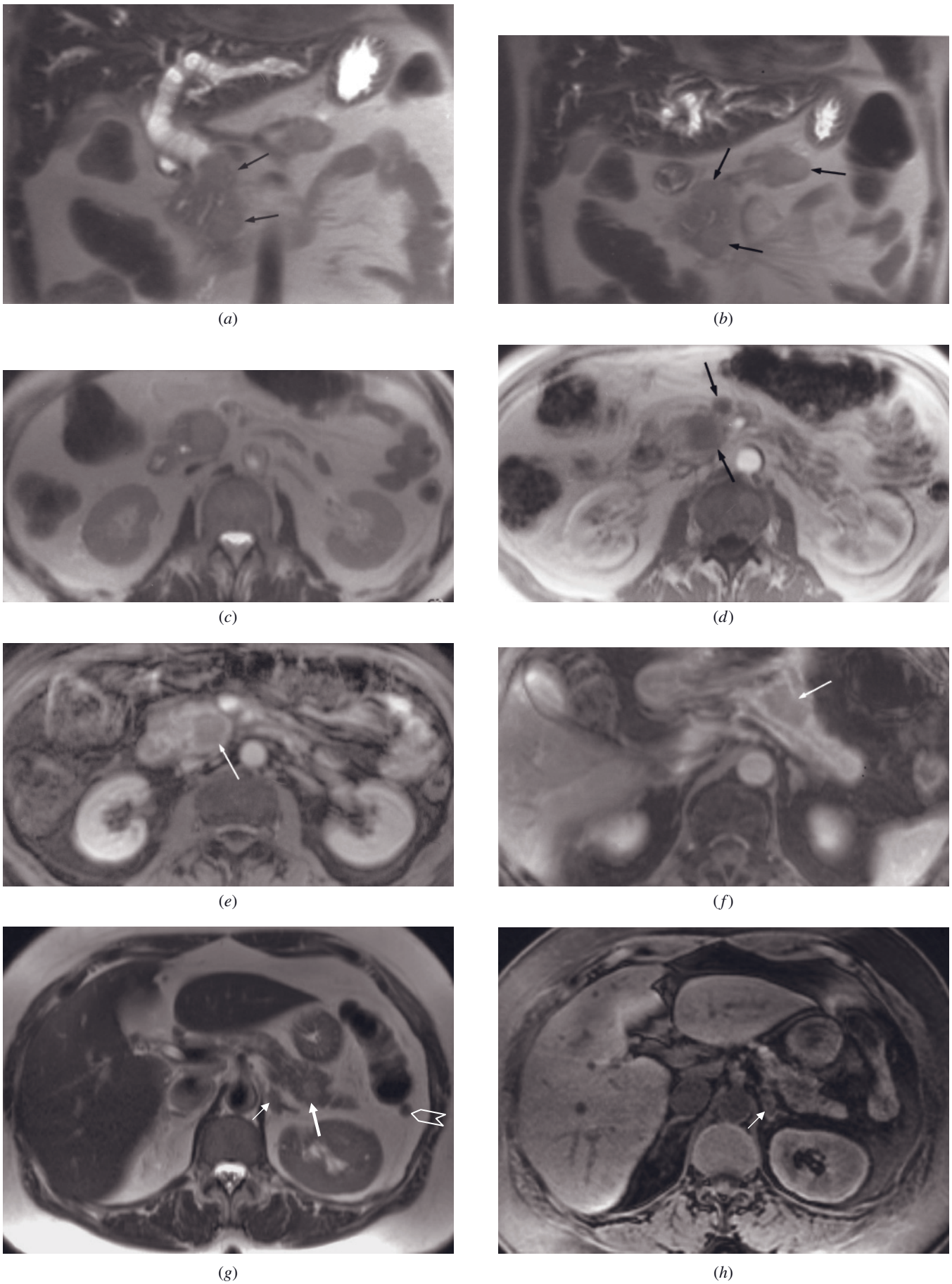

FIG. 4.68 Pancreatic metastasis from lung cancer. Coronal (*a*, *b*) and transverse (*c*) T2-weighted SS-ETSE, immediate postgadolinium T1-weighed SGE (*d*), and 90-s postgadolinium fat-suppressed SGE (*e*, *f*) images in a patient with small cell lung cancer. Multiple masses (arrows, *a*, *b*) are present throughout the pancreas that are mildly hyperintense on T2 (*a*–*c*) and enhance minimally on early (*d*) and late (*e*, *f*) postgadolinium images.

T2-weighted single-shot echo-train spin-echo (*g*), T1-weighted fat-suppressed SGE (*h*), T1-weighted postgadolinium hepatic

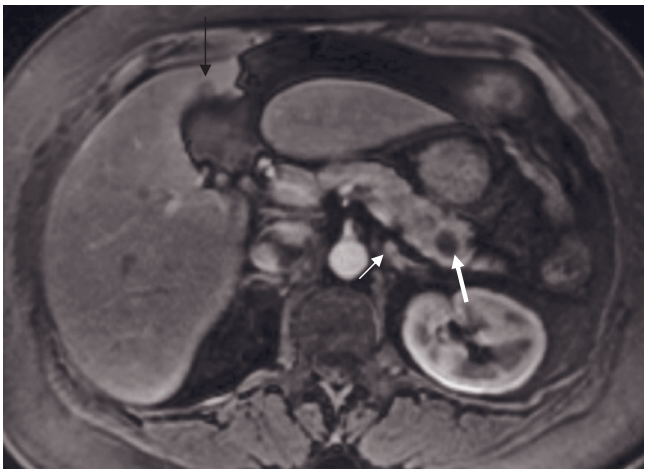

(*i*)

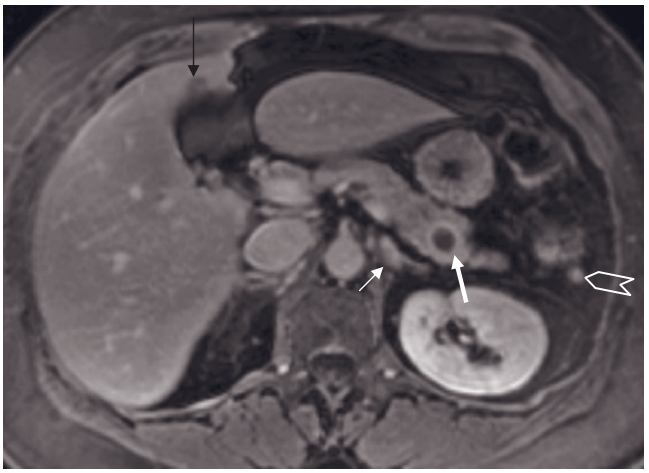

(*j*)

FIG. 4.68 (*Continued*) arterial dominant phase (*i*), and hepatic venous phase (*j*) fat-suppressed 3D-GE images at 3.0 T demonstrate a metastatic lesion (white long arrows, *g*, *i*, *j*) located in the pancreas in another patient with squamous cell lung cancer. The lesion shows peripheral enhancement on postgadolinium images. Note that there are also hypovascular liver metastasis (black arrow, *i*, *j*), peritoneal metastatic nodule (open arrow, *g*, *j*) and left adrenal corpus thickening (white short arrow, *g*–*j*). Lung cancer is among the most common primary tumors that metastasize to the pancreas.

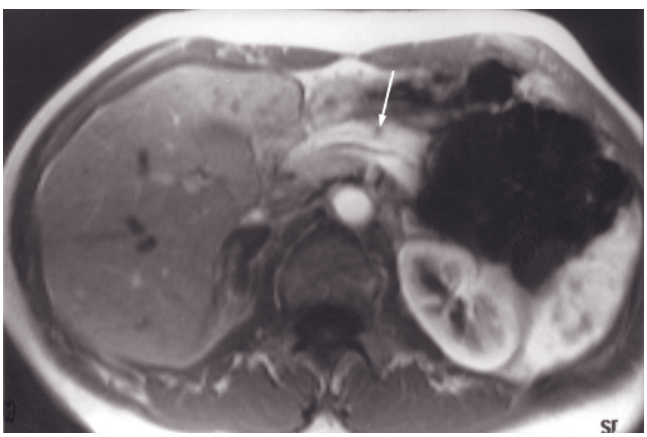

(*a*)

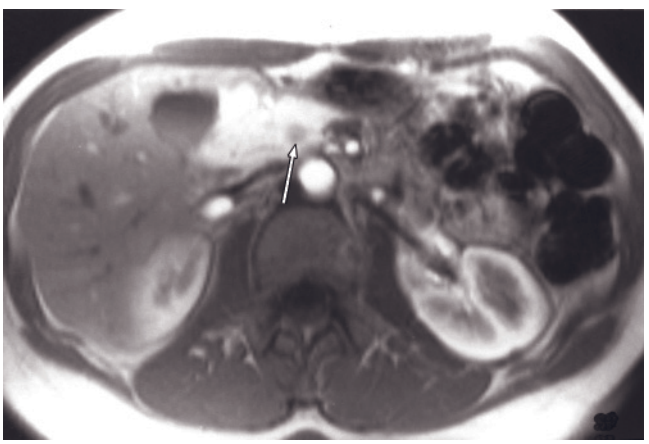

(*b*)

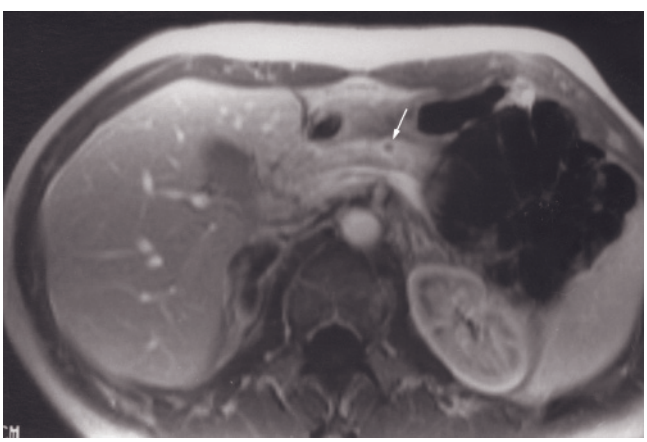

(*c*)

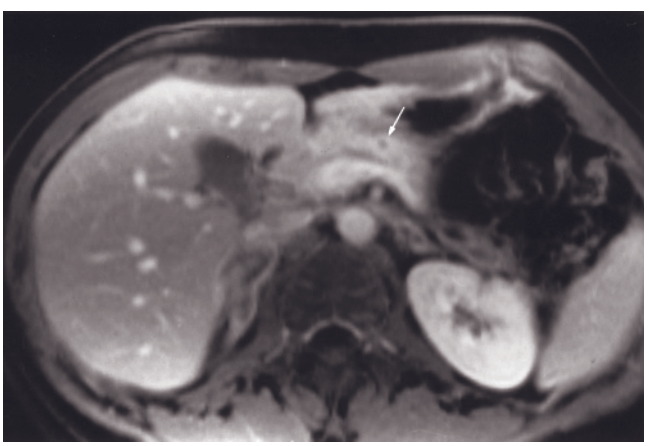

(*d*)

FIG. 4.69 Pancreatic metastasis from breast cancer. Immediate postgadolinium T1-weighted SGE (*a*, *b*), 45-s postgadolinium SGE (*c*), and interstitial-phase gadolinium-enhanced SGE (*d*) images demonstrate multiple <1-cm hypointense metastases (arrow, *a*, *b*) in the pancreatic head and body. Note ring enhancement of the metastases on the post contrast images (arrows, *c*, *d*).

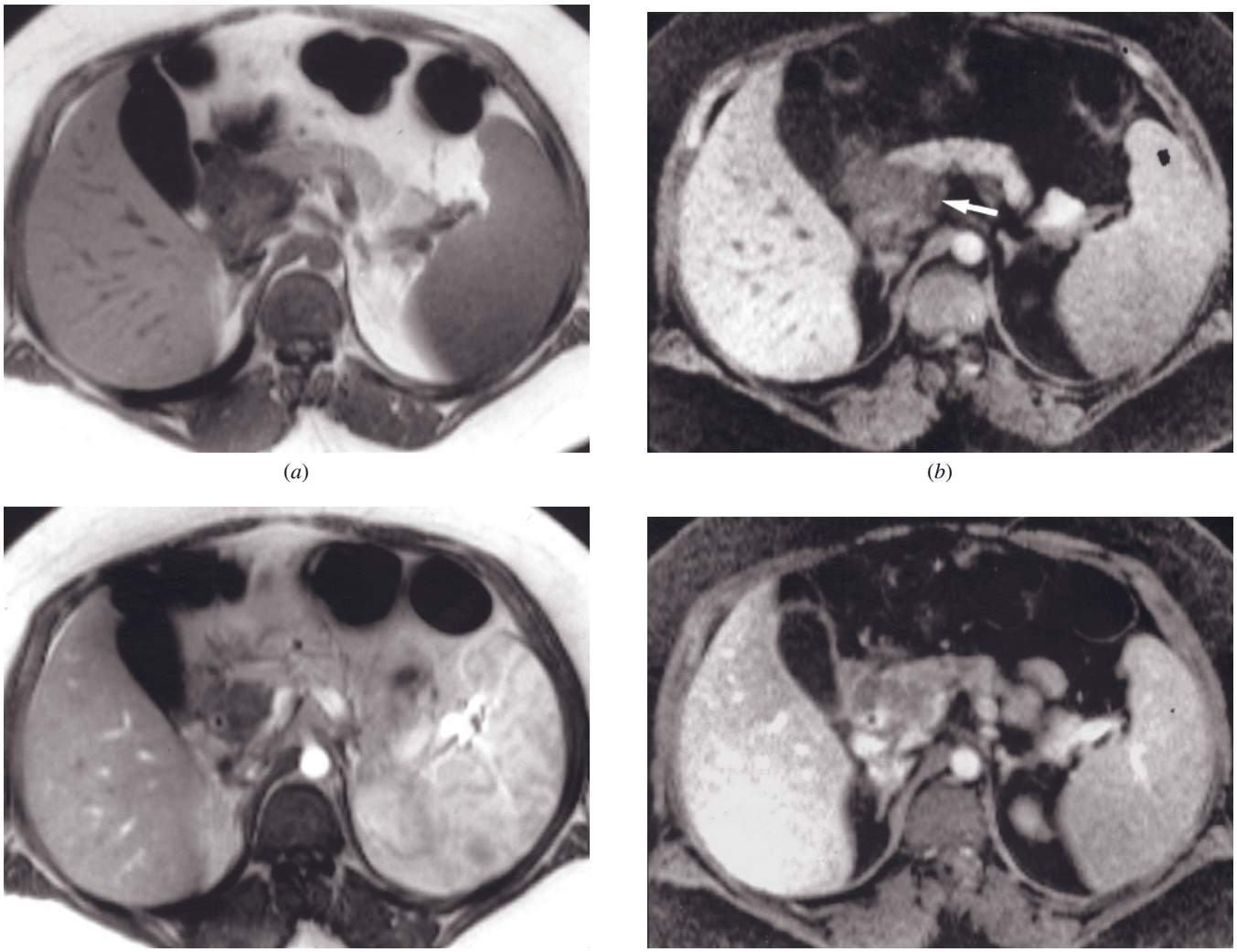

(*a*) (*b*) (*c*) (*d*)

FIG. 4.70 Pancreatic metastasis from Merkel cell cancer. T1-weighted SGE (*a*), T1-weighted fat-suppressed SGE (*b*), immediate postgadolinium T1-weighted SGE (*c*), and 90-s postgadolinium fat-suppressed SGE (*d*) images in a patient with pancreatic metastasis (arrow, *b*) from a primary neuroendocrine cancer of the skin (Merkel cell carcinoma). There is a well-defined 6-cm mass in the head of the pancreas that is hypointense on T1-weighted images (*a*, *b*) and enhances minimally on early (*c*) postcontrast images, with progressive enhancement on late images (*d*). Distant metastasis occurs in one-third of patients with Merkel cell cancers.

acute pancreatitis and negative CT imaging examination. As the extent of pancreatitis becomes more severe, the pancreas develops a heterogeneous appearance on pre-contrast T1-weighted fat-suppressed images and enhances in a more heterogeneous, diminished fashion on immediate postgadolinium images (figs. 4.73 and 4.74).

The percentage of pancreatic necrosis has been considered an important prognostic indicator in patients with acute pancreatitis [92, 93]. Dynamic gadolinium-enhanced gradient-echo images may be useful for this determination because MRI is very sensitive for the demonstration of the presence or absence of gadolinium enhancement. Saifuddin et al. [94] described comparable results for dynamic contrast-enhanced CT images and immediate postgadolinium gradient-echo images for determining the presence of pancreatic necrosis. Complications of acute pancreatitis such as hemorrhage, pseudocyst formation, or abscess are clearly shown on MRI (figs. 4.75–4.77). Hemorrhagic fluid collections are high in signal intensity on T1-weighted fat-suppressed images, and depiction of hemorrhage is superior on MR images compared to CT images. Martin et al. [95] demonstrated correlation between the extent of high signal on noncontrast T1-weighted fat-suppressed SGE and severity of acute

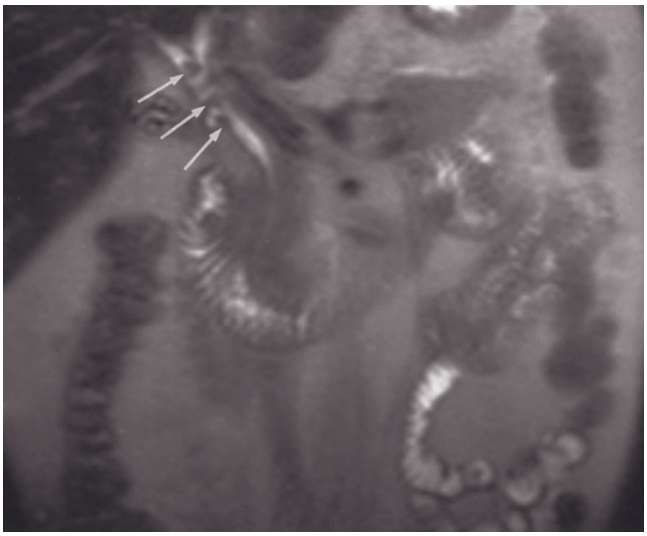

(*a*)

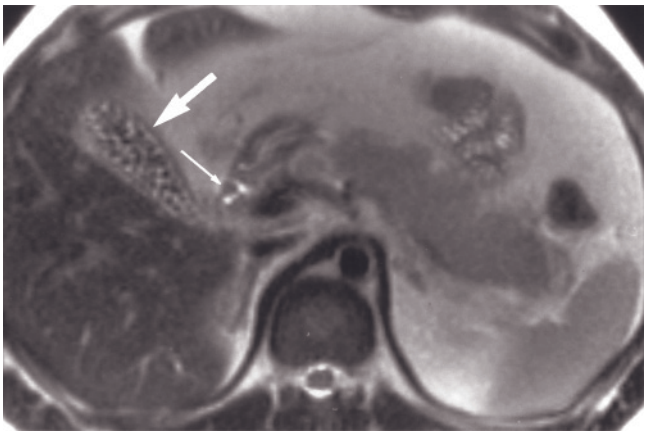

(*b*)

(*c*)

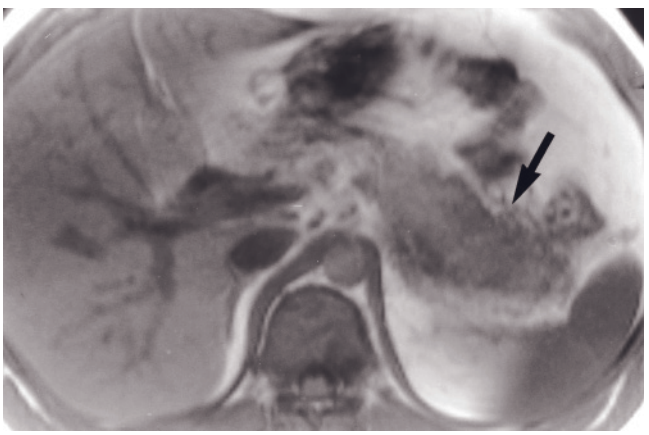

(*d*)

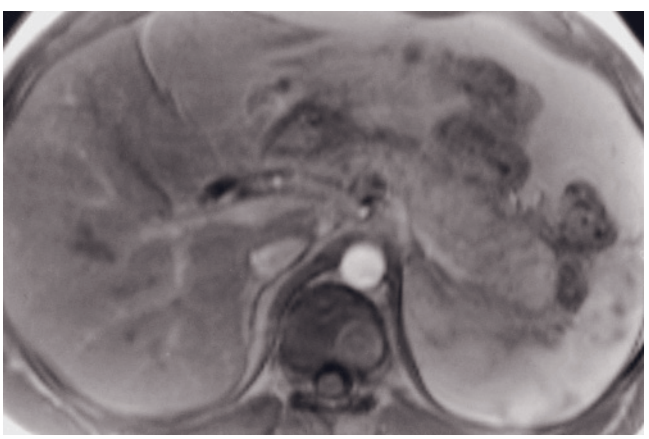

(*e*)

FIG. 4.71 Mild acute gallstone pancreatitis. Coronal (*a*) and transverse (*b*) T2-weighted ETSE, MRCP (*c*), T1-weighted SGE (*d*), and immediate postgadolinium T1-weighted SGE (*e*) images. Three stones are seen in the mildly dilated CHD and CBD (arrows, *a*, *b*, *c*), and multiple small stones are present in the gallbladder (large arrow, *b*). The pancreas is enlarged slightly and diffusely (arrow, *d*) with ill-defined margins and a minimal volume of surrounding fluid. Passage of calculi through the biliary tree is a common cause of single episodes of acute pancreatitis, which, as in this case, is generally of mild severity.

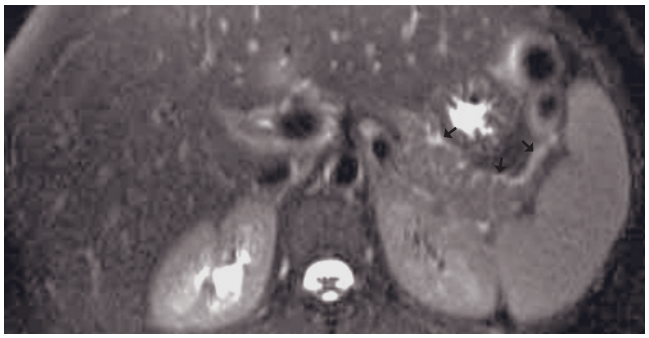

(*a*)

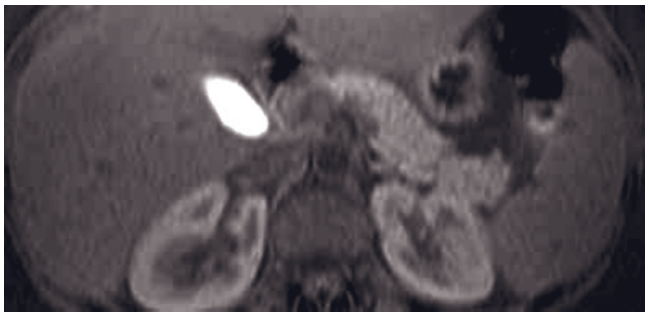

(*b*)

(*c*)

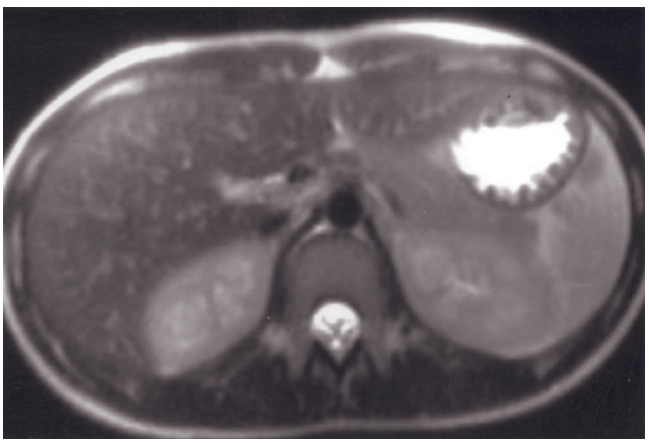

(*d*)

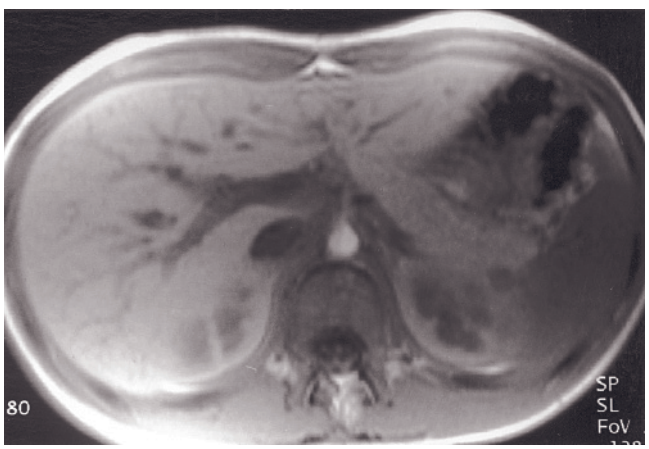

(*e*)

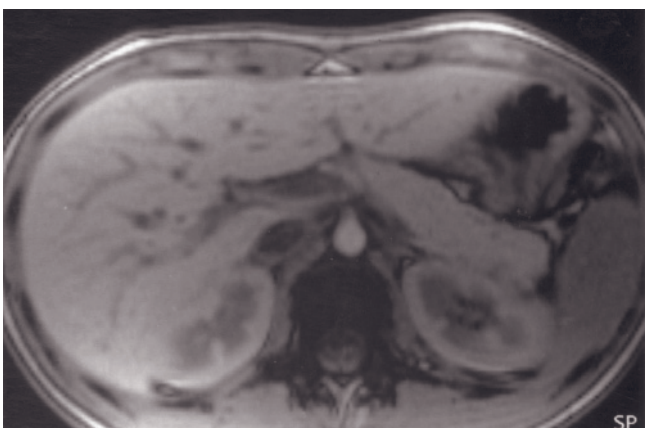

(*f*)

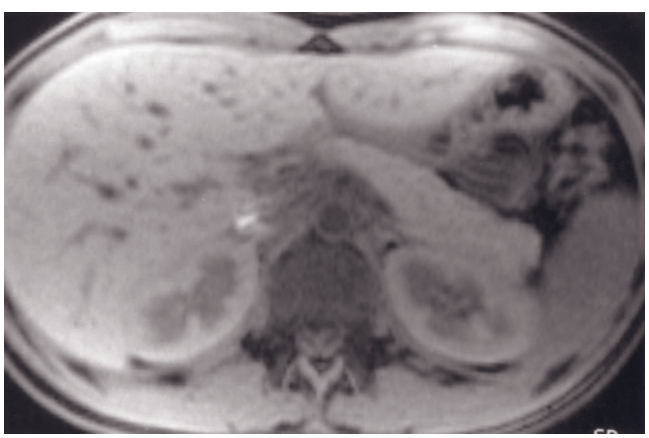

(*g*)

FIG. 4.72 Mild pancreatitis. Fat-suppressed T2-weighted SS-ETSE images (*a*), fat-suppressed T1 weighted gradient-echo (*b*), and immediate postgadolinium T1-weighted gradient-echo (*c*) images in a patient with mild acute pancreatitis demonstrate a thin layer of peripancreatic fluid that is best seen on fat-suppressed T2-weighted images (arrows, *a*). The signal intensity of the pancreas is normal on fat-suppressed T1-weighted (*b*) and immediate postgadolinium T1-weighted (*c*) images.

T2-weighted SS-ETSE (*d*), T1-weighted SGE (*e*), T1-weighted out-of-phase SGE (*f*), T1-weighted fat-suppressed SGE (*g*),

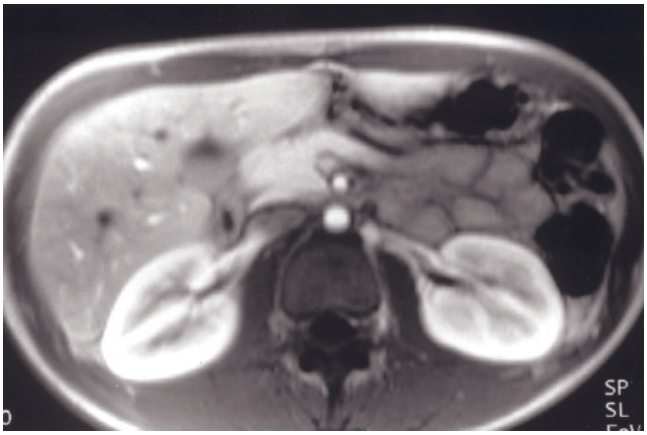

(*h*)

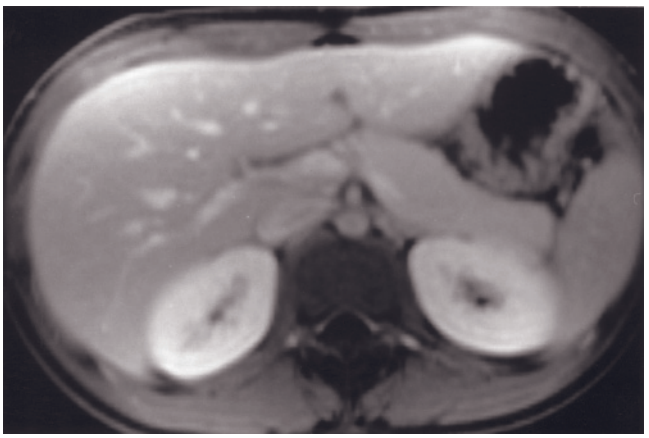

(*i*)

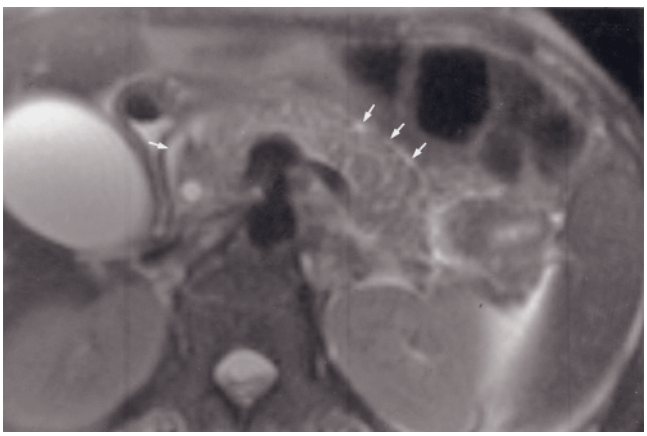

(*j*)

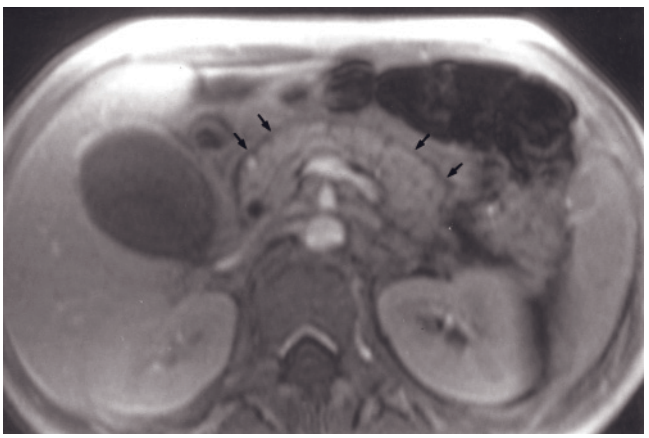

(*k*)

(*l*)

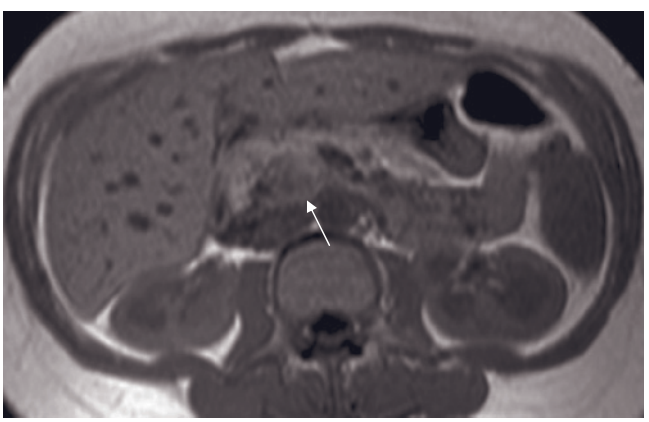

(*m*)

FIG. 4.72 (*Continued*) immediate postgadolinium SGE (*h*), and 90-s postgadolinium fat-suppressed SGE (*i*) images in a second patient.

The pancreas is minimally and diffusely enlarged with subtle loss of lobulated contour. The pancreas is normal in signal on noncontrast T1-weighted fat-suppressed images (*g*) and enhances normally on immediate postgadolinium images (*h*). The appearance is essentially that of normal pancreas, but clinical history and mildly elevated serum amylase were diagnostic for an episode of pancreatitis.

T2-weighted fat-suppressed SS-ETSE (*j*) and early postgadolinium single-shot magnetization-prepared gradient-echo (*k*) images in a third patient demonstrate mild diffuse enhancement of the pancreas and a thin film of peripancreatic fluid surrounding the pancreas (small arrows, *j*, *k*) and throughout the interstices of the marbled pancreatic parenchyma. Fat-suppressed breathing-independent single-shot T2-weighted sequences are very effective at showing small volumes of fluid, as surrounding fat and pancreas are both low signal and only fluid will be high signal (*j*). This case is also noteworthy in that image quality is reasonable despite the fact that the patient was very ill and a noncooperative MR imaging protocol was employed, which uses only breathing-independent single-shot images.

T2-weighted fat-suppressed single-shot echo-train spin-echo (*l*), T1-weighted SGE (*m*), T1-weighted postgadolinium hepatic arterial dominant phase SGE (*n*), and T1-weighted interstitial phase fat-suppressed 3D-GE (*o*) images demonstrate mild focal

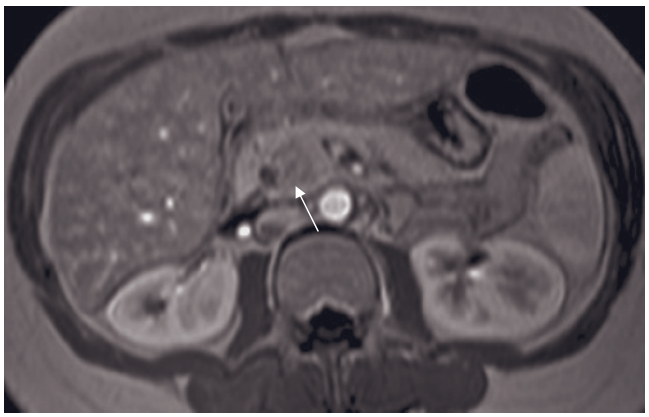

(*n*)

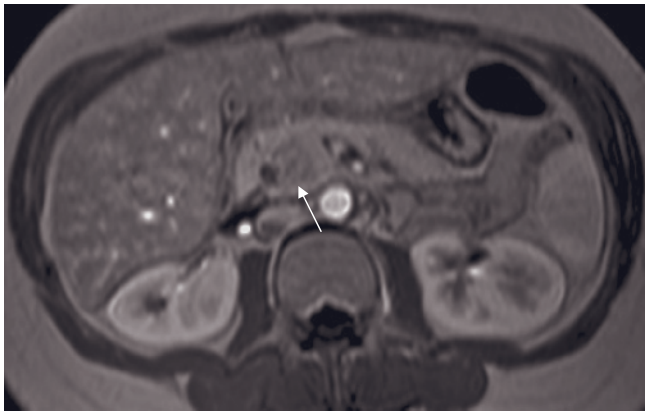

(*o*)

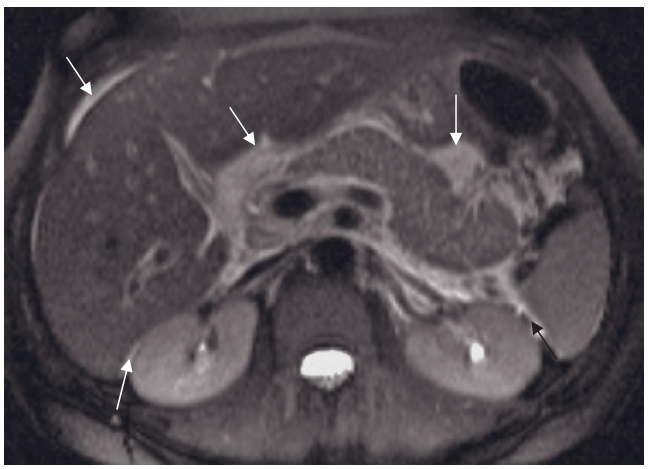

(*p*)

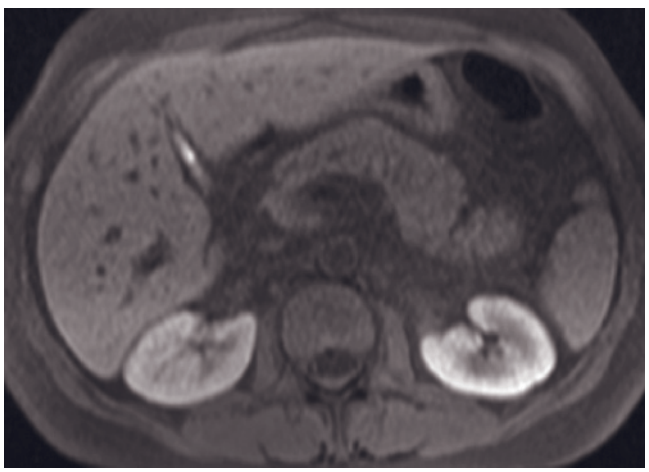

(*q*)

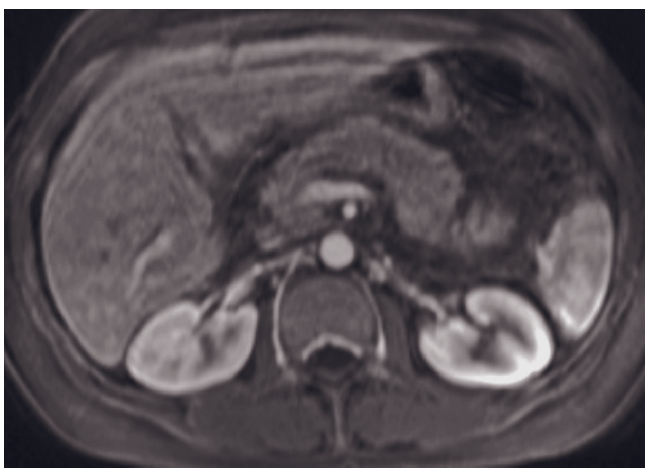

(*r*)

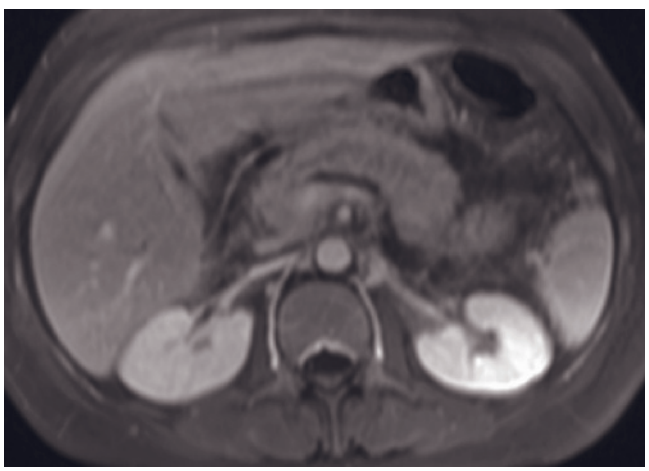

(*s*)

Fig. 4.72 (*Continued*) pancreatitis located in the pancreatic head in another patient. Focal pancreatitis (arrows, *l*, *m*) shows high signal on T2-weighted image (*l*) and low signal on T1-weighted SGE image (*m*). The pancreatic head is enlarged. There is minimal free fluid (open arrows, *l*) adjacent to the pancreatic head. The lesion (arrows, *n*, *o*) shows progressive enhancement on postgadolinium images (*n*, *o*). Additionally, the liver shows heterogeneous transient enhancement on the hepatic arterial dominant phase image due to associated inflammation. The remaining pancreatic parenchyma shows normal signal and enhancement pattern. The lesion can be differentiated from malignancies because it does not cause common bile duct compression although it encircles the common bile duct.

T2-weighted fat-suppressed single-shot echo-train spin-echo (*p*), T1-weighted fat-suppressed SGE (*q*), T1-weighted hepatic arterial dominant phase (*r*), and hepatic venous phase (*s*) fat-suppressed 3D-GE images in the same patient with focal pancreatitis show the progression of the disease to severe pancreatitis. The pancreas is enlarged, and there is abundant free fluid (arrows, *p*) in the peripancreatic region extending into bilateral anterior pararenal space, perihepatic space, and lesser sac. The signal of pancreas is less than normal on T1-weighted SGE image (*q*). The enhancement of the pancreas is less than normal on postgadolinium images (*r*, *s*).

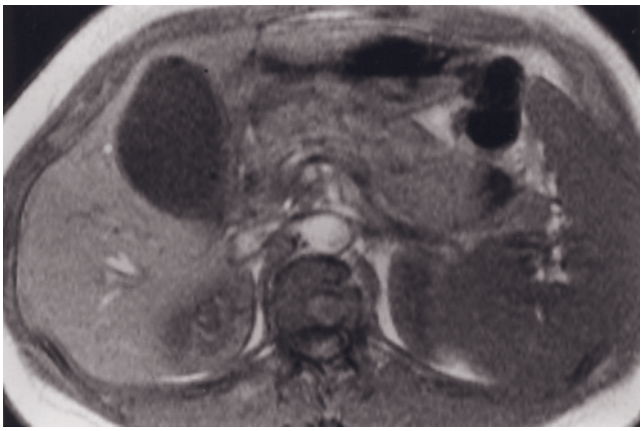

(*a*)

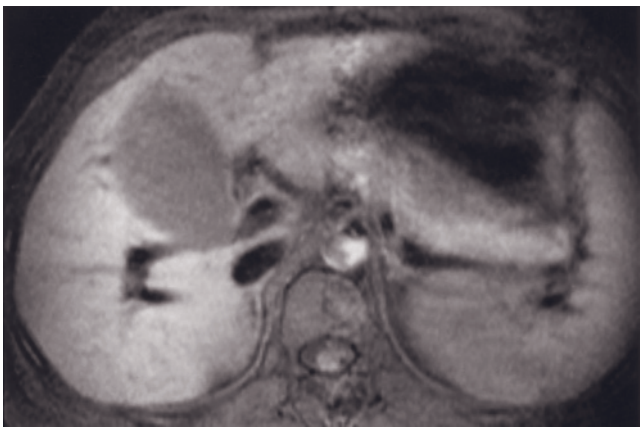

(*b*)

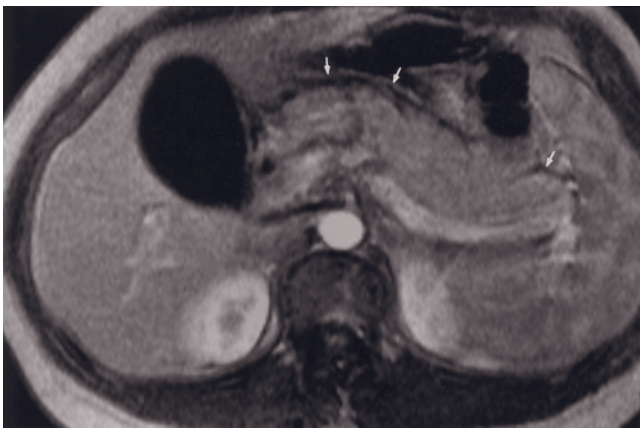

(*c*)

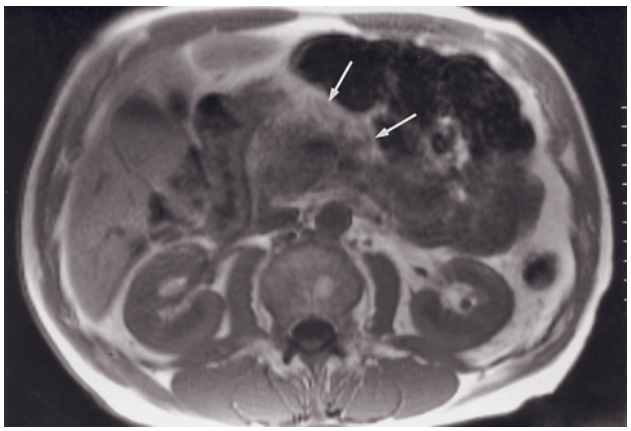

(*d*)

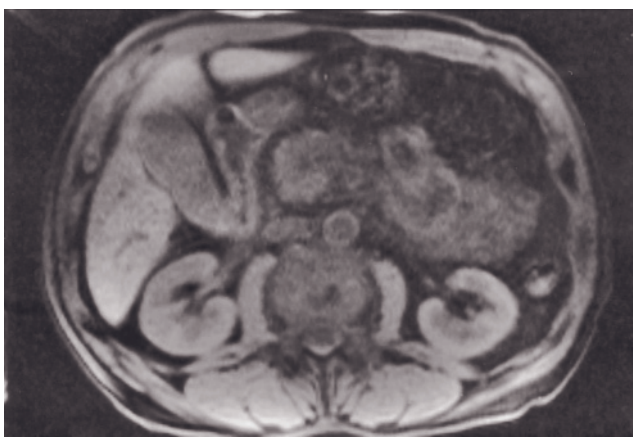

(*e*)

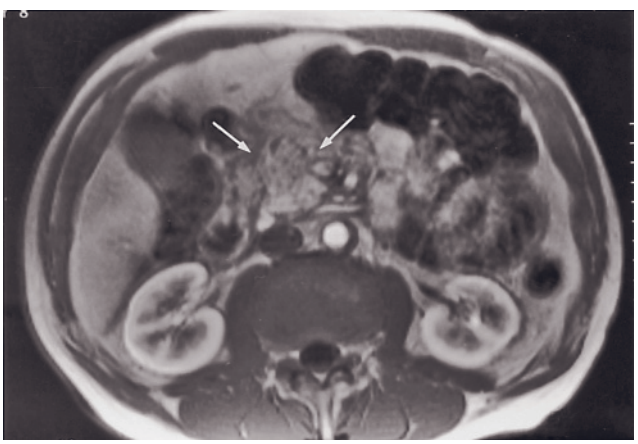

(*f*)

FIG. 4.73 Moderately severe acute pancreatitis. T1-weighted SGE (*a*), T1-weighted fat-suppressed spin-echo (*b*), and immediate postgadolinium T1-weighted SGE (*c*) images. The pancreas is diffusely enlarged (*a–c*). The signal intensity of the pancreas is heterogeneous on the T1-weighted fat-suppressed image (*b*), which suggests a decrease in the proteinaceous fluid content within the acini of the pancreas. Signal-void fluid is shown surrounding the body and tail of the pancreas on the immediate postgadolinium image (arrows, *c*).The intensity of pancreatic enhancement is less than normal for pancreas on the capillary-phase image (*c*).

T1-weighted SGE (*d*), T1-weighted fat-suppressed SGE (*e*), and immediate postgadolinium T1-weighted SGE (*f*) images in a second patient. Peripancreatic fluid is well shown as low-signal intensity stranding in the high-signal intensity fat on the T1-weighted SGE image (arrows, *d*).The anterior portion of the head of the pancreas is lower in signal intensity on the precontrast fat-suppressed image (*e*) and enhances less (arrows, *f*) on immediate postgadolinium images (*f*), reflecting more severe changes of pancreatitis. Relative sparing of either anterior or posterior portions of the head of the pancreas is not uncommon because of separate pancreatic ductal systems. Despite the focal nature of the diminished enhancement of the dorsal head of the pancreas, there is lobular architecture similar to that of the ventral pancreatic head. A pancreatic neoplasm would not exhibit lobular architecture.

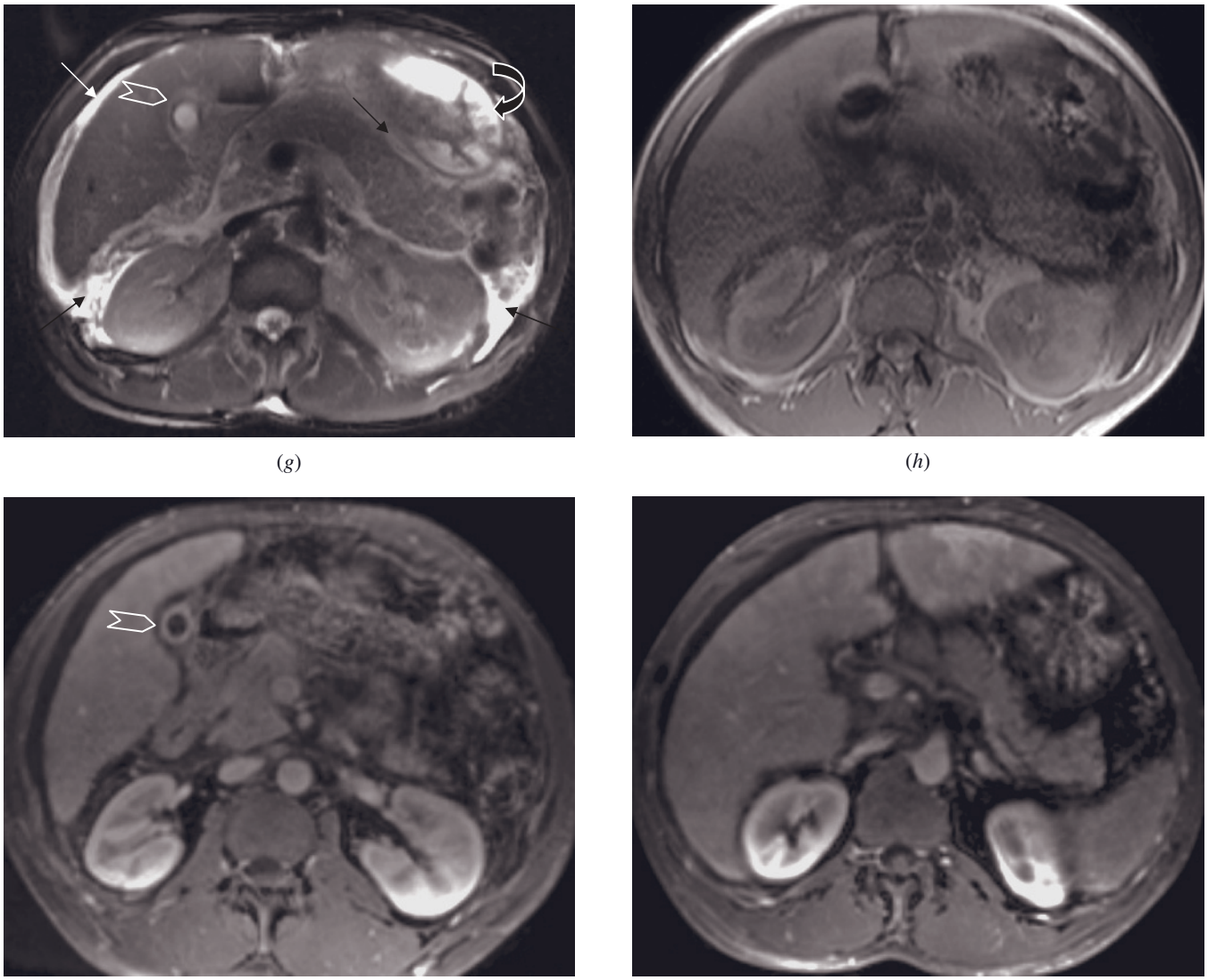

FIG. 4.73 (*Continued*) **Severe acute pancreatitis.** T2-weighted fat-suppressed single-shot echo-train spin-echo (*g*), T1-weighted fat-suppressed SGE (*h*), and T1-weighted hepatic arterial dominant phase fat-suppressed 3D-GE (*i*, *j*) images at 3.0 T demonstrate severe pancreatitis in another patient. The pancreas is diffusely enlarged and there is abundant free fluid (arrows, *g*) in the perihepatic space, bilateral anterior pararenal spaces, lesser sac, and left paracolic gutter. The pancreas shows diminished signal on T1-weighted SGE image (*h*). The enhancement of the pancreas is less than normal on postgadolinium images. The gallbladder wall (open arrow, *g*) is also thickened and edematous. The gallbladder wall, particularly the mucosa, (open arrow, *i*) shows intense enhancement on postgadolinium image (*i*). The stomach wall (curved arrow, *g*) is also thickened and edematous. There are regions of heterogeneous enhancement in the liver as well. Associated cholecystitis, gastritis, and inflammation in the liver are not uncommon in the presence of pancreatitis.

pancreatitis, where high signal correlated with hemorrhagic changes. Simple pseudocysts are low in signal intensity or signal void in a background of normal-signal-intensity pancreatic tissue on both noncontrast non-fat-suppressed gradient-echo and T1-weighted fat-suppressed gradient echo images (figs. 4.77–4.80). Extrapancreatic pseudocysts are well shown on breath-hold gradient-echo images because of high contrast with high-signal-intensity fat. Image acquisition in multiple planes permits determination of pseudocyst location in relation to various organs and structures (see fig. 4.79). Pseudocyst walls enhance minimally on early postgadolinium images and show progressively intense enhancement on 5-min postcontrast images, consistent

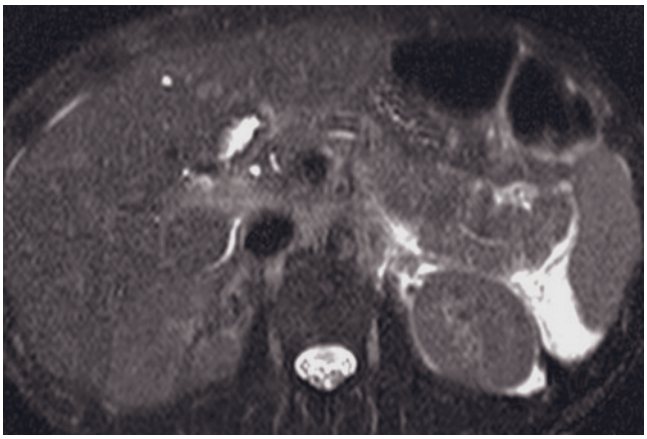

(*a*)

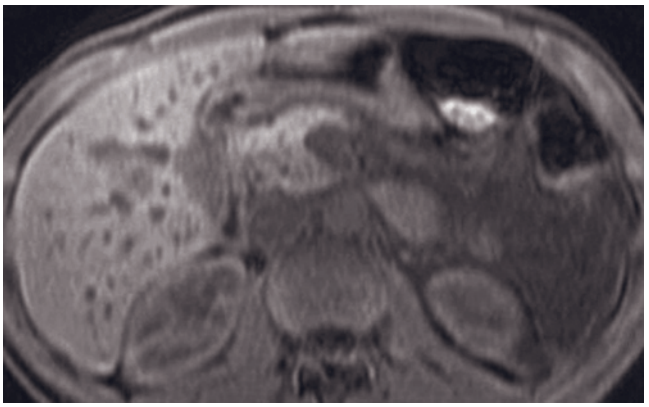

(*b*)

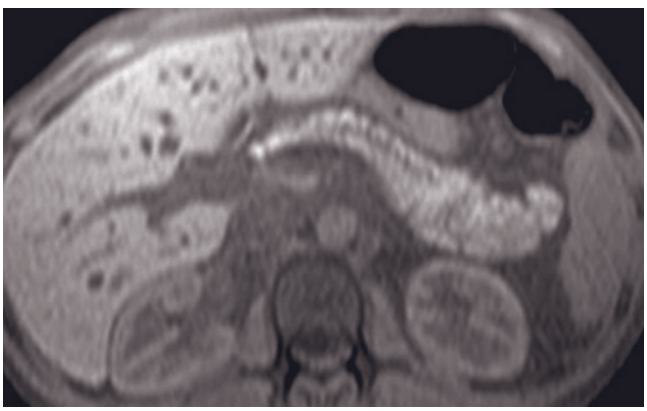

(*c*)

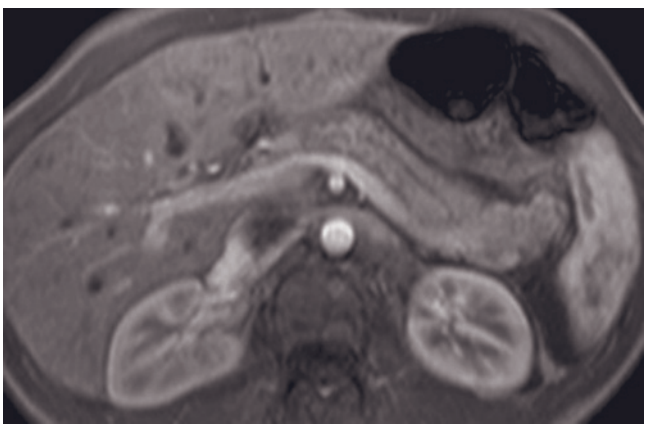

(*d*)

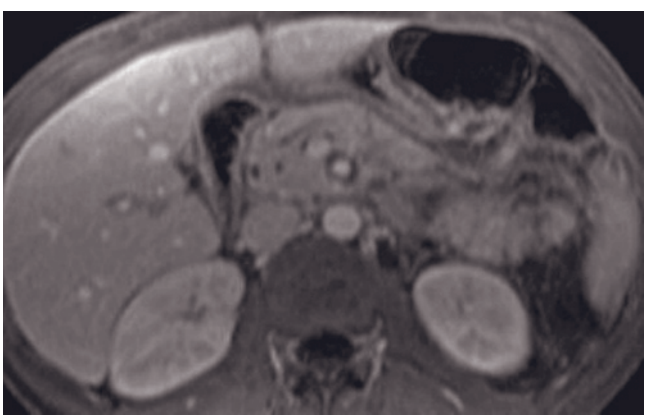

(*e*)

FIG. 4.74 Moderate pancreatitis with more severe involvement of the pancreatic head. Fat-suppressed T2-weighted SSETSE (*a*), fat-suppressed T1-weighted gradient-echo (*b*, *c*), and immediate (*d*) and interstitial-phase (*e*) postgadolinium fat-suppressed T1-weighted gradient-echo images in a patient with acute pancreatitis. The pancreas is mildly enlarged and demonstrates heterogeneous signal, which is slightly decreased on T1-weighted images (*b*, *c*) and increased on T2-weighted images (*a*). There is a sharp delineation in signal differences between the pancreatic body and head. The appearance suggests more severe pancreatitis in the pancreatic head.

with the appearance of fibrous tissue. Simple pseudocysts are relatively homogeneous and high in signal intensity on T2-weighted images. Pseudocysts complicated by necrotic debris, hemorrhage, or infection are heterogeneous in signal intensity on T2-weighted images [94]. Proteinaceous fluid tends to layer in a gradation of concentration with low-signal-intensity concentrated proteinaceous material in the dependent portion of the cyst. Necrotic material may appear as irregularly shaped regions of low signal intensity in the pseudocyst (see fig. 4.80) [96]. This information may provide both therapeutic and prognostic information because pseudocysts that contain necrotic material may not respond to simple percutaneous drainage

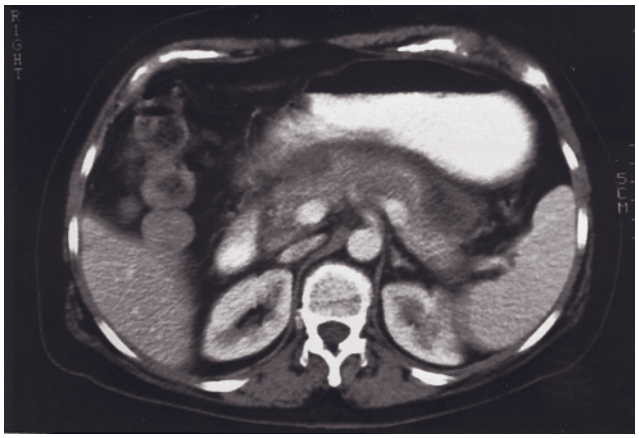

(*a*)

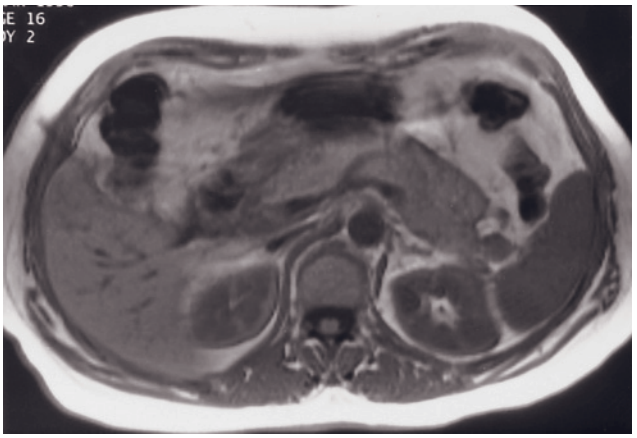

(*b*)

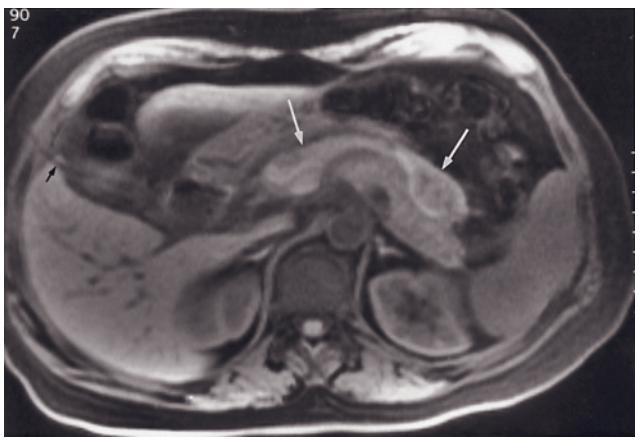

(*c*)

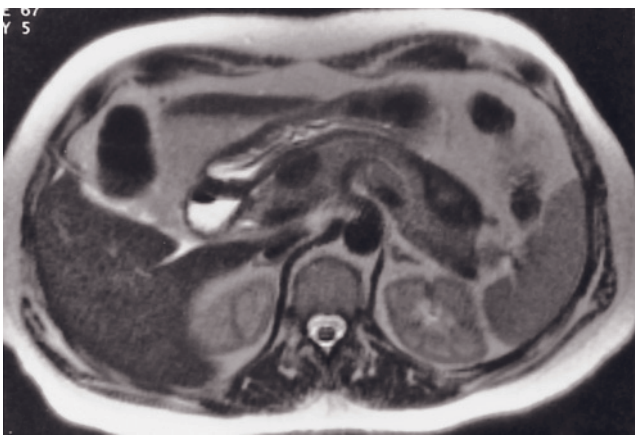

(*d*)

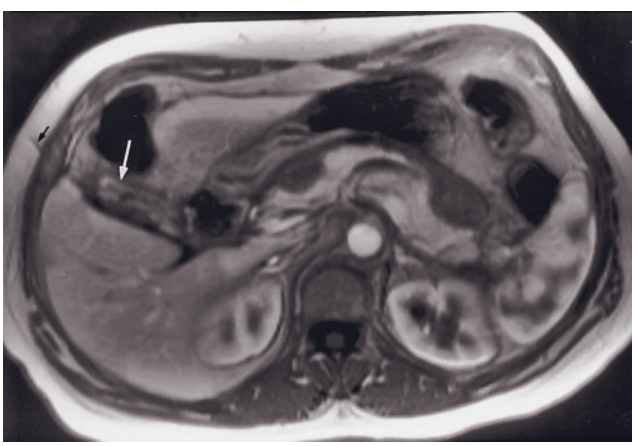

(*e*)

FIG. 4.75 Hemorrhagic pancreatitis. Contrast-enhanced spiral CT (*a*), T1-weighted SGE (*b*), T1-weighted fat-suppressed SGE (*c*), T2-weighted SS-ETSE (*d*), and immediate postgadolinium T1-weighted SGE (*e*) images. The CT image demonstrates an enlarged pancreas with free fluid along its anterior margin, findings consistent with acute pancreatitis. On the T1-weighted SGE image (*b*), the fluid collections are noted to be hyperintense, which is accentuated on the fat-suppressed image (arrows, *c*).

The fluid is low in signal on the T2-weighted image (*d*) and therefore possesses the signal characteristics of intracellular methemoglobin in acute blood. The pancreas enhances relatively uniformly on the immediate postgadolinium image, reflecting the absence of pancreatic necrosis (*e*). A collapsed acutely inflamed gallbladder (arrow, *e*) is present, in which a cholecystostomy catheter was placed (small arrow, *c*, *e*).

and thus require open debridement. Breathing-independent T2-weighted sequences such as single-shot echo-train spin echo may be useful to evaluate these pseudocyst collections, not only because they are the most effective at demonstrating the complexity of fluid but also because many of these patients are very debilitated and unable to cooperate with breath-holding instructions.

Chronic Pancreatitis

Chronic pancreatitis is defined pathologically by continuous or relapsing inflammation of the organ leading to irreversible morphologic injury and typically leading to impairment of function. Chronic pancreatitis is acquired either as a disease process distinct from acute pancreatitis or as a complication of repeated attacks of acute pancreatitis. There is a strong association between

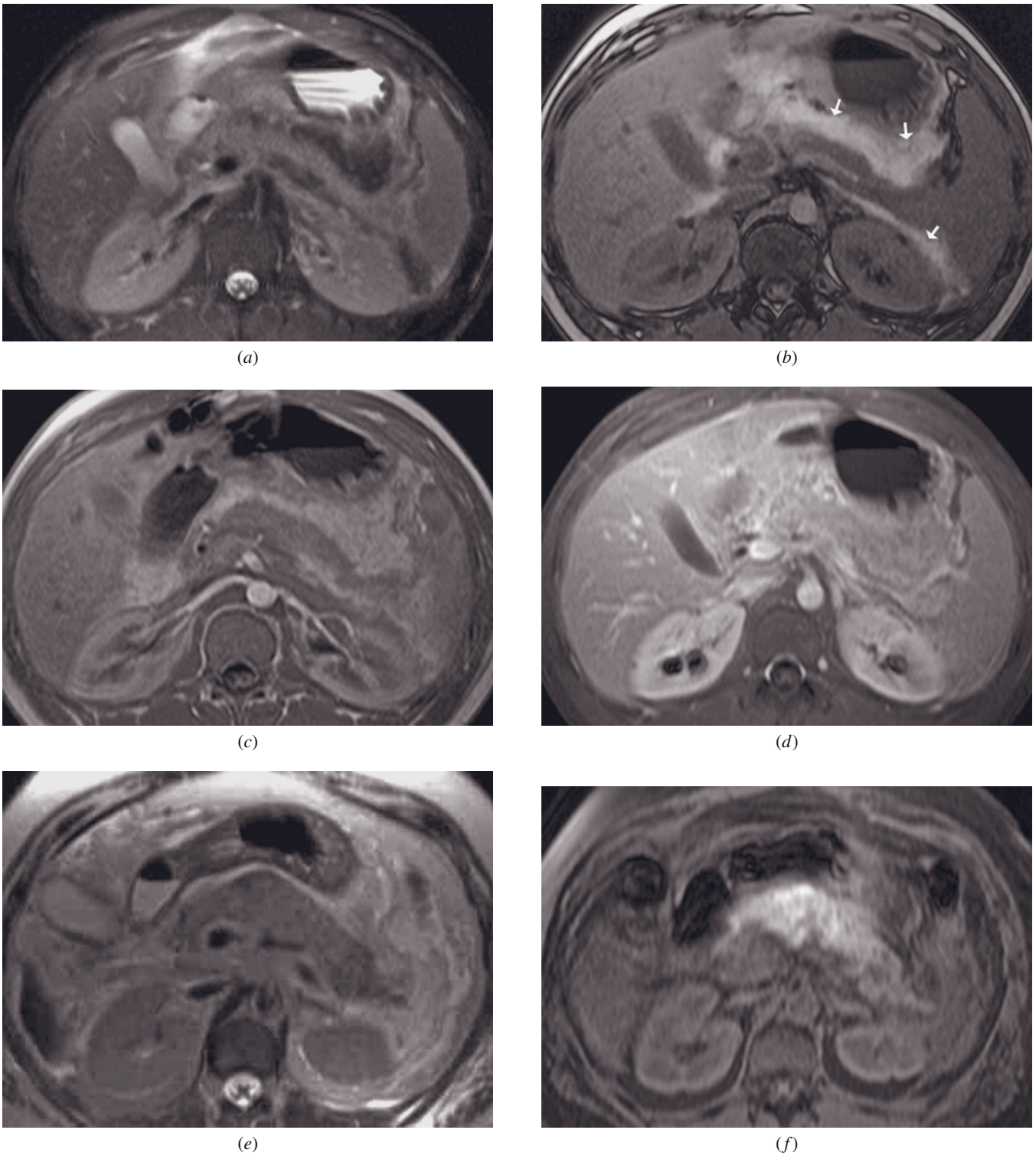

FIG. 4.76 Hemorrhagic pancreatitis. Axial fat-suppressed T2-weighted SS-ETSE (*a*), T1-weighted gradient-echo (*b*), immediate postgadolinium T1-weighted gradient-echo (*c*), and interstitial-phase postgadolinium T1-weighted gradient-echo (*d*) images in a patient with acute pancreatitis. The pancreas demonstrates diffuse hypoenhancement on immediate postgadolinium images, reflecting severe disease. The fluid surrounding the pancreas is hyperintense on T1 (arrows, *b*) and hypointense on T2-weighted images. This appearance is consistent with intracellular methemoglobin seen in subacute hemorrhage. T2-weighted SS-ETSE (*e*), fat-suppressed T1-weighted gradient-echo (*f*), and immediate postgadolinium fat-suppressed T1-weighted gradient-echo (*g*) images

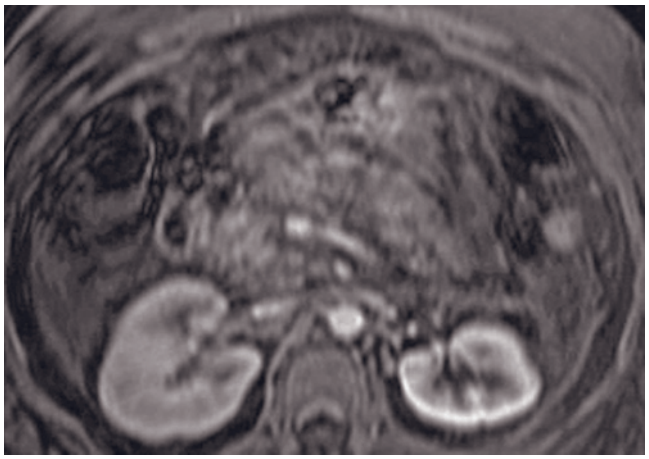

(*g*)

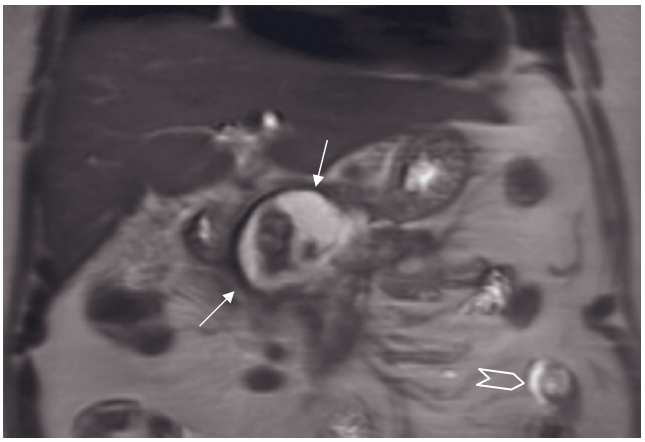

(*h*)

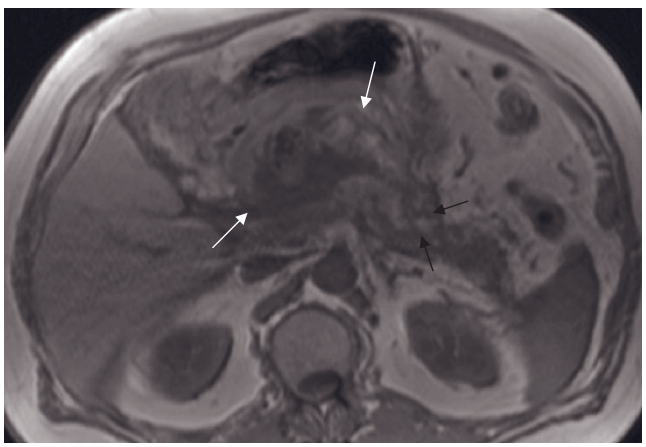

(*i*)

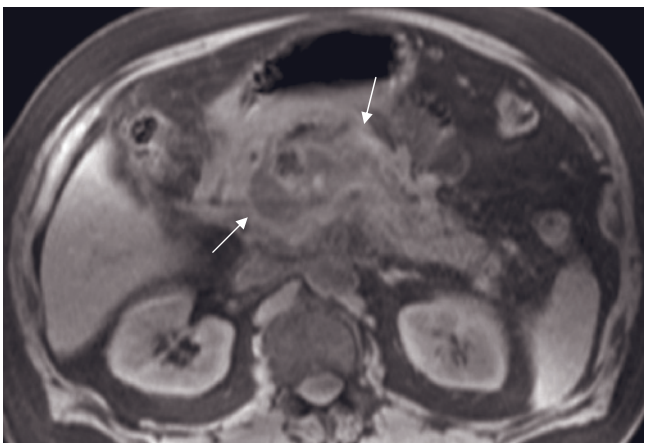

(*j*)

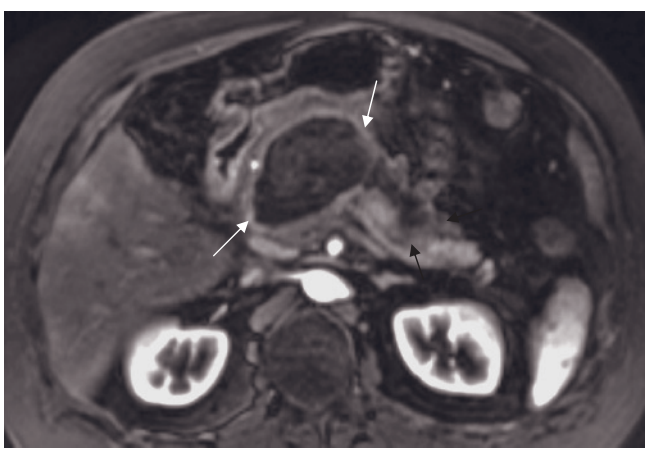

(*k*)

Fig. 4.76 (*Continued*) in a second patient with hemorrhagic pancreatitis. The pancreas is enlarged (*e*) and shows very high signal intensity on fat-suppressed T1-weighted images (*g*) and low signal on T2-weighted images (*e*), consistent with subacute hemorrhage. The patchy enhancement of the pancreas on immediate postgadolinium images reflects foci of pancreatic necrosis (*g*).

Coronal T2-weighted single-shot echo-train spin-echo (*h*), T1-weighted SGE (*i*), T1-weighted fat-suppressed SGE (*j*), and T1-weighted postgadolinium hepatic arterial dominant phase fat-suppressed 3D-GE (*k*) images at 3.0T demonstrate hemorrhagic necrotizing pancreatitis in another patient. A large pseudocyst (white arrows, *h–k*) containing blood product is located in the pancreatic head and body region. The blood products show low signal on T2-weighted image (*h*) but high signal on T1-weighted precontrast images (*i*, *j*). There is mild free fluid (open arrow, *h*) in the abdomen. Peripancreatic tissue is low in signal intensity on precontrast images. There are foci of blood products (black arrows, *i*) and necrosis (black arrows, *k*) in the pancreatic parenchyma. Note that there is associated gastric mucosal inflammation and hepatic inflammation, which are characterized by increased enhancement.

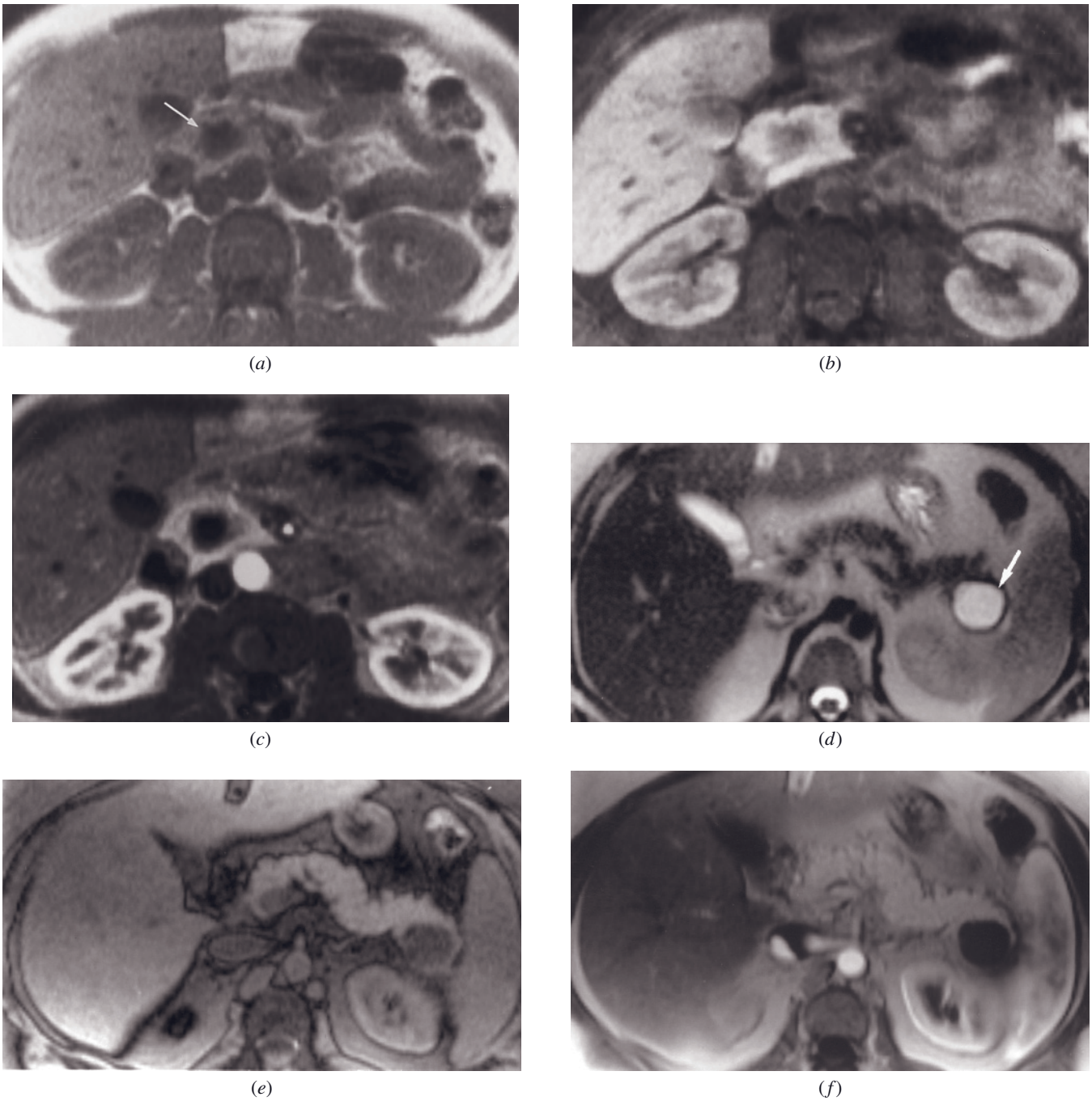

FIG. 4.77 Pseudocyst in acute pancreatitis. T1-weighted SGE (*a*), T1-weighted fat-suppressed spin-echo (*b*), and immediate postgadolinium T1-weighted SGE (*c*) images. A low-signal intensity pseudocyst (arrow, *a*) is present in the head of the pancreas (*a–c*). The pancreas has normal high signal intensity on the T1-weighted fat-suppressed image (*b*), and there is normal uniform enhancement of the pancreas on the immediate postgadolinium image (*c*). These imaging features are consistent with a pseudocyst in the setting of acute pancreatitis because the background pancreas has normal signal intensity features. The lesion did not change in size and shape on delayed images, excluding a poorly vascularized tumor.

T2-weighted SS-ETSE (*d*), T1-weighted fat-suppressed SGE (*e*), immediate postgadolinium T1-weighted SGE (*f*), and 90-s postgadolinium fat-suppressed SGE (*g*) images in a second patient. A 3-cm pseudocyst (arrow, *d*) is in the pancreatic tail. The pancreas

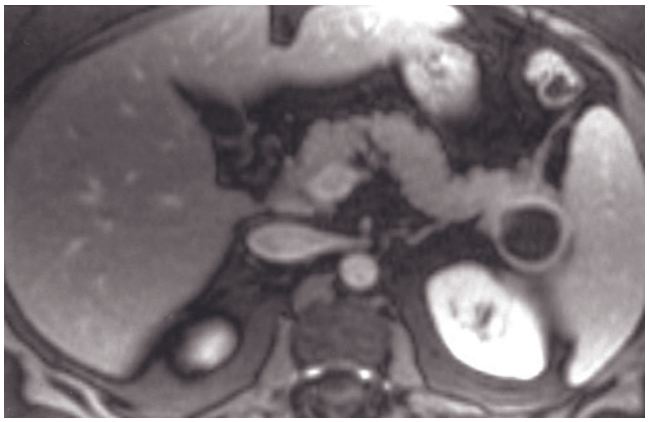

(*g*)

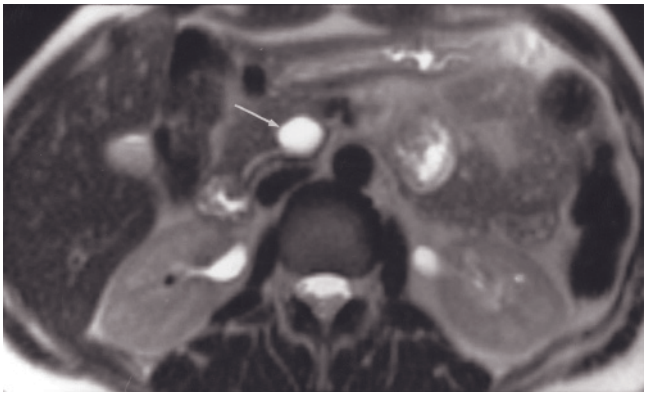

(*h*)

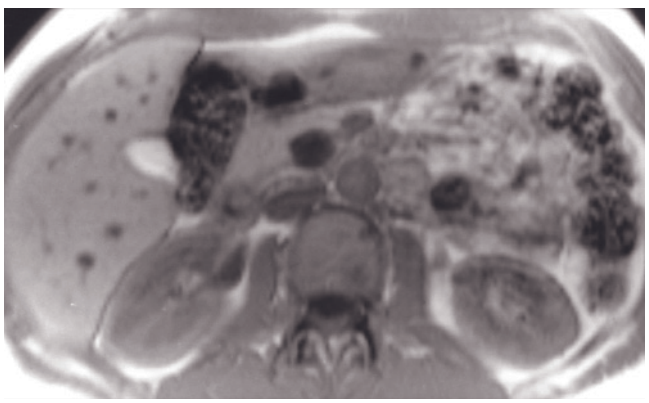

(*i*)

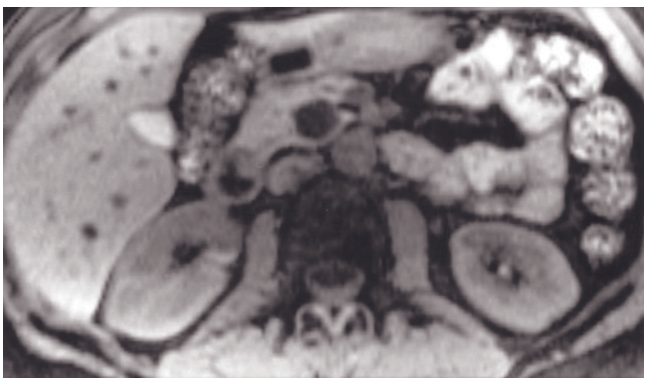

(*j*)

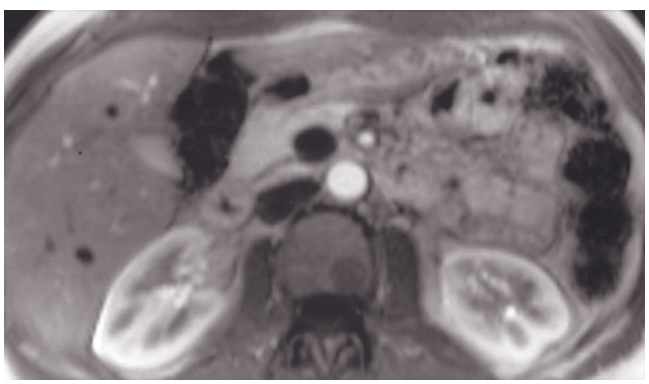

(*k*)

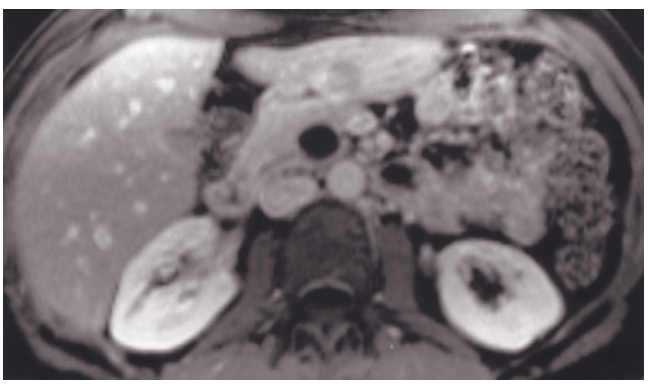

(*l*)

Fig. 4.77 (*Continued*) is normal in signal on noncontrast T1-weighted fat-suppressed images (*e*) and enhances normally on early (*f*) and late (*g*) images, consistent with no substantial parenchymal disease. There is progressive enhancement of the wall of the pseudocyst (*g*), which is typical for fibrous tissue. The pancreas, spleen, and liver are mildly hypointense on T2-weighted images (*d*) secondary to iron deposition from multiple blood transfusions.

T2-weighted SS-ETSE (*h*), T1-weighted SGE (*i*), T1-weighted fat-suppressed SGE (*j*), immediate postgadolinium T1-weighted SGE (*k*), and 90-s postgadolinium fat-suppressed SGE (*l*) images demonstrate a 2-cm pseudocyst (arrow, *h*) in the uncinate process of the pancreas. The normal signal intensity of the pancreas, especially on noncontrast T1-weighted fat-suppressed (*j*) and immediate postgadolinium SGE (*k*) images, shows that background pancreas is not substantially diseased.

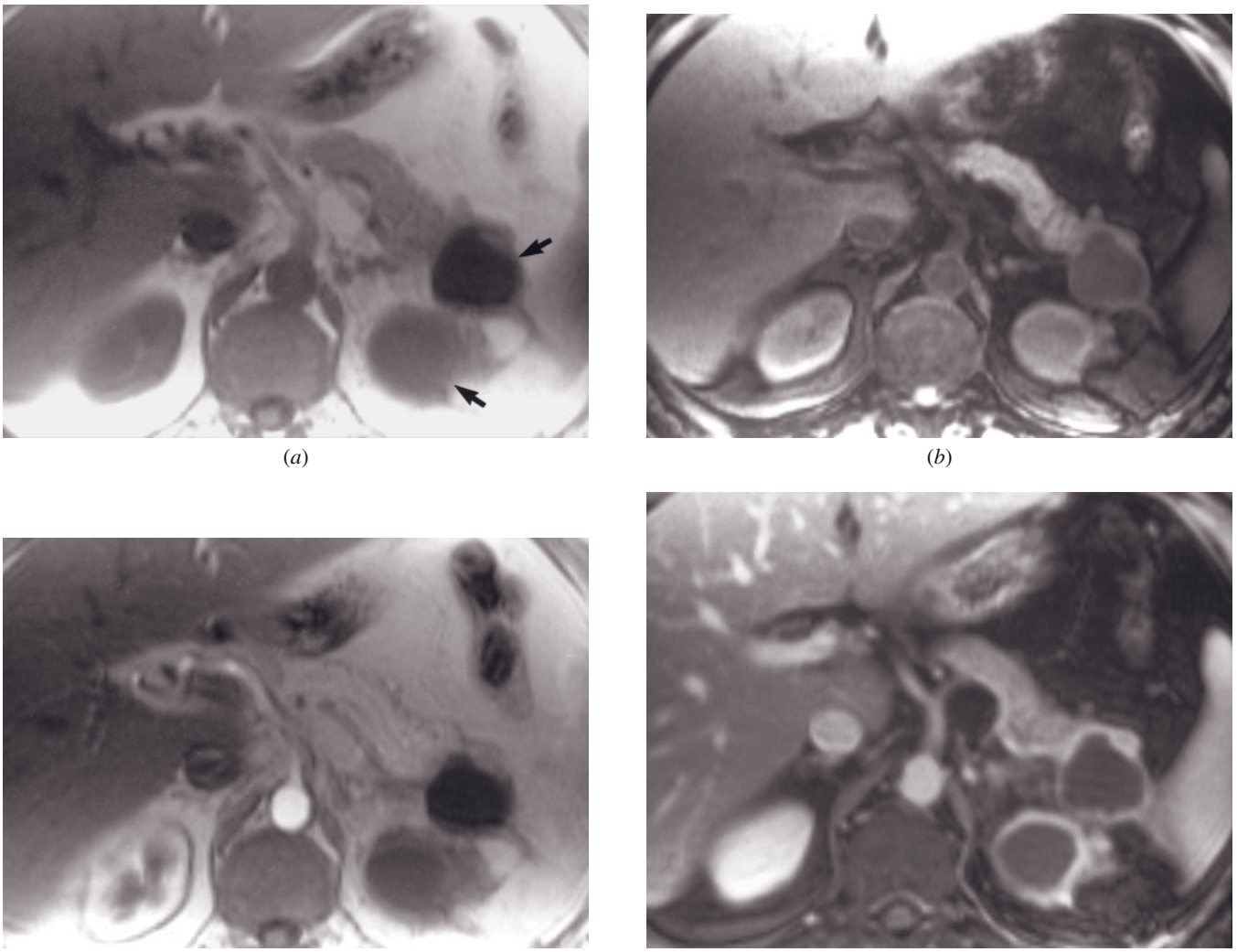

(*a*) (*b*) (*c*) (*d*)

FIG. 4.78 Pancreatic pseudocysts. T1-weighted SGE (*a*), T1-weighted fat-suppressed SGE (*b*), immediate postgadolinium T1-weighted SGE (*c*), and 90-s postgadolinium T1-weighted fat-suppressed SGE (*d*) images. There is a pseudocyst in the tail of the pancreas and a second one adjacent in the upper pole of the left kidney (arrows, *a*). Late enhancement of the pseudocyst walls is appreciated (*d*).

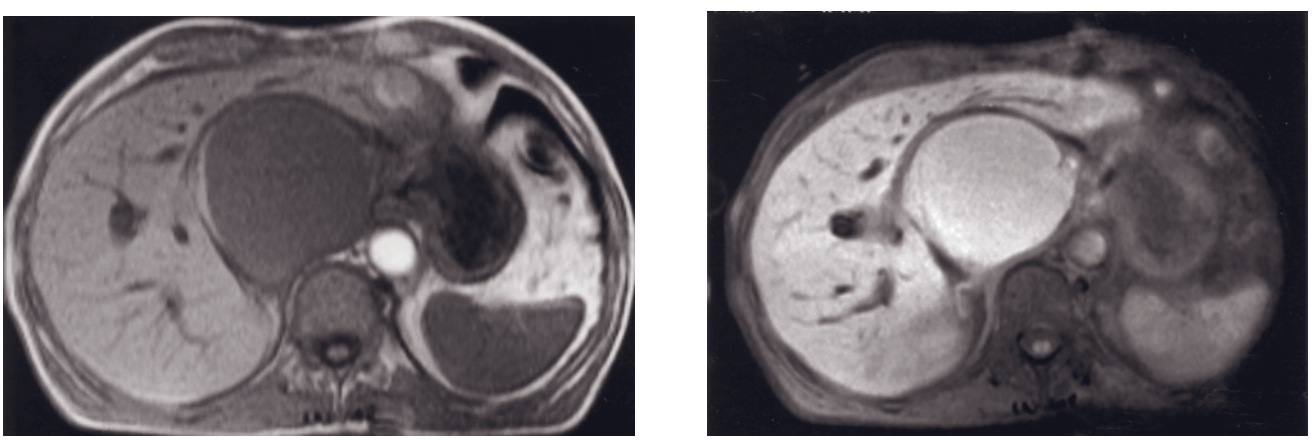

(*a*) (*b*)

FIG. 4.79 Pseudocysts—large. T1-weighted SGE (*a*), T1-weighted fat-suppressed spin-echo (*b*), T2-weighted fat-suppressed

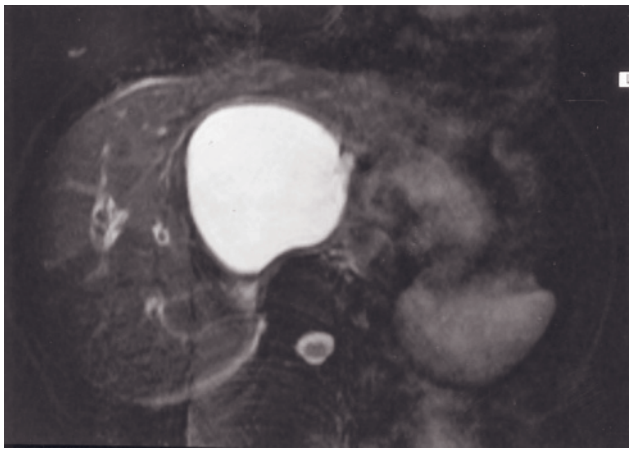

(*c*)

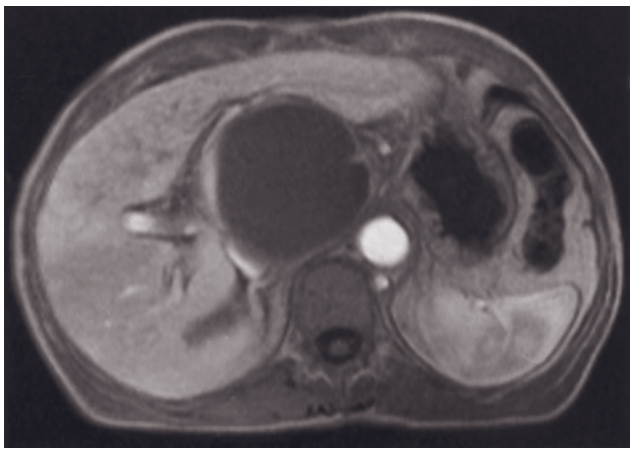

(*d*)

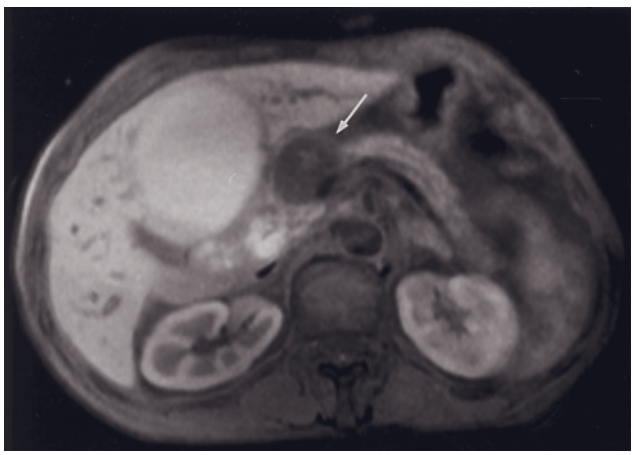

(*e*)

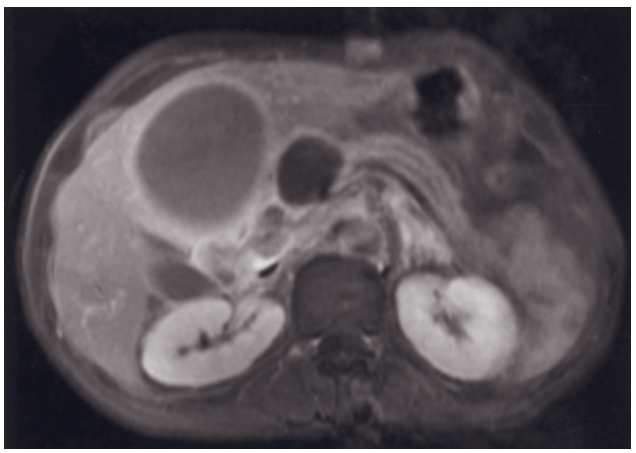

(*f*)

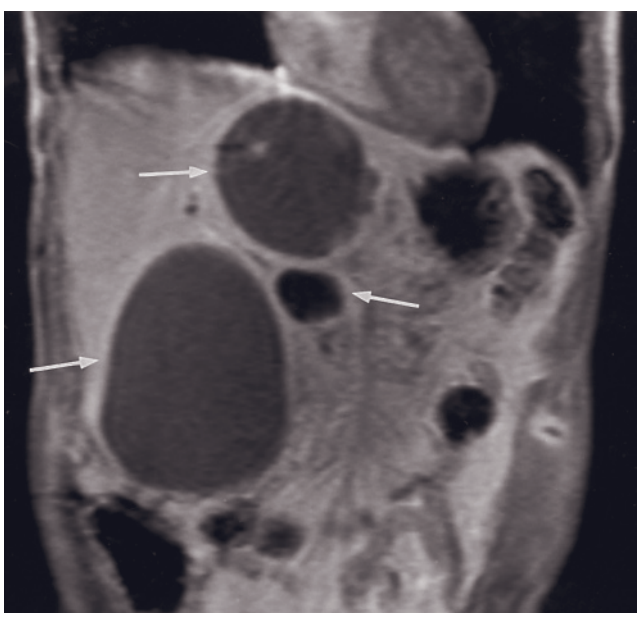

(*g*)

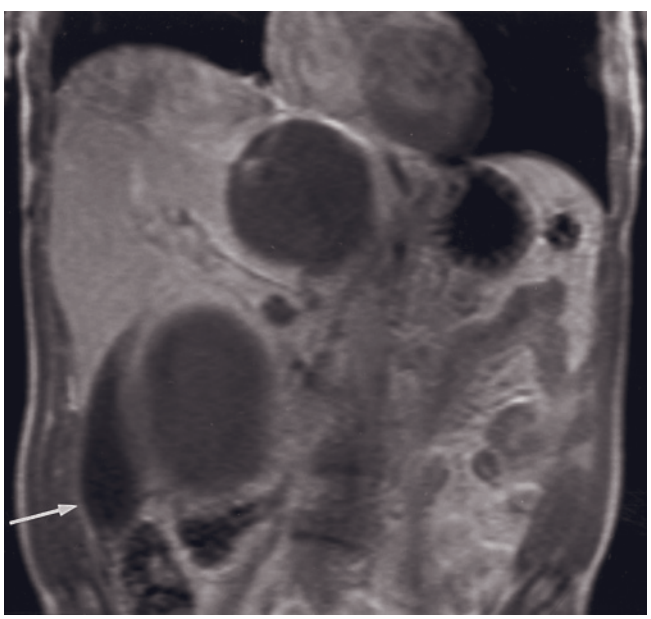

(*h*)

FIG. 4.79 (*Continued*) SSETSE (*c*), and immediate postgadolinium T1-weighted SGE (*d*) images obtained superior to the pancreas, T1-weighted fat-suppressed spin-echo (*e*) and gadolinium-enhanced T1-weighted fat-suppressed spin-echo (*f*) images at the level of the body of the pancreas, coronal gadolinium-enhanced T1-weighted SGE images from midhepatic (*g*) and more anterior (*h*) locations, and sagittal-plane (*i*) T1-weighted SGE images.

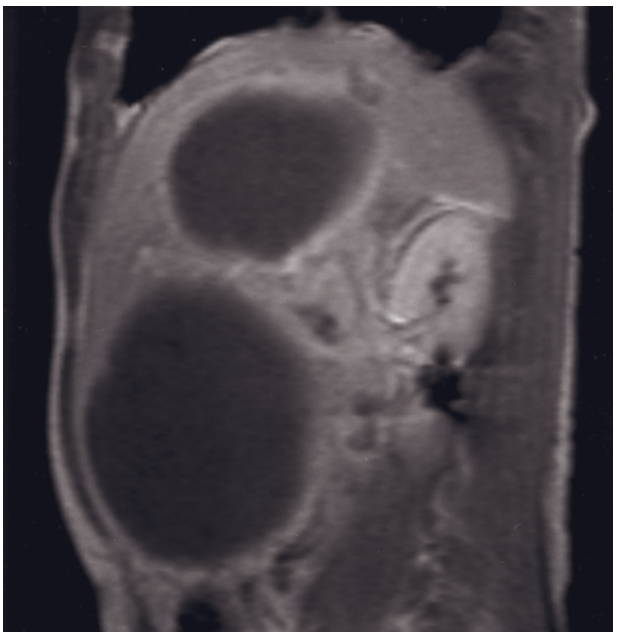

(*i*)

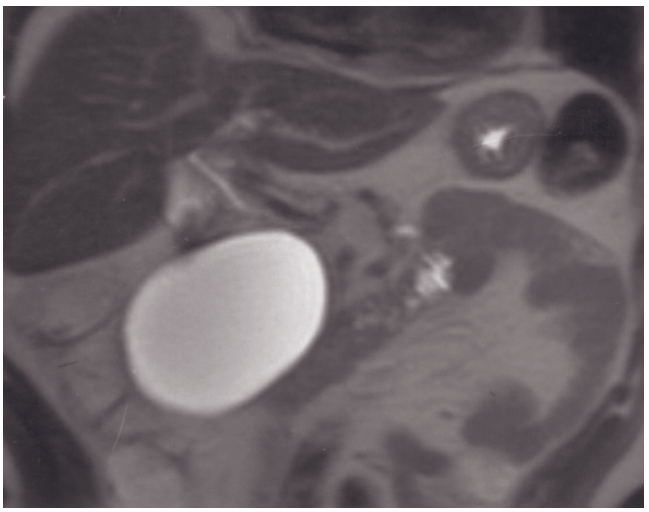

(*j*)

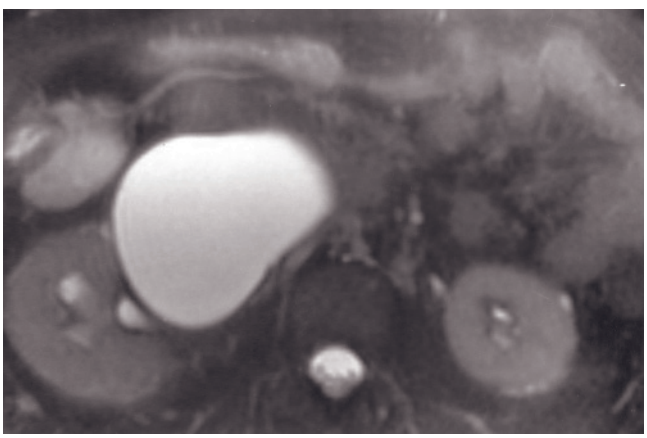

(*k*)

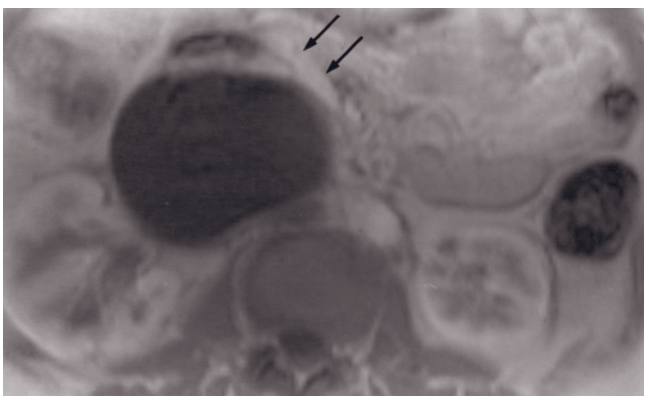

(*l*)

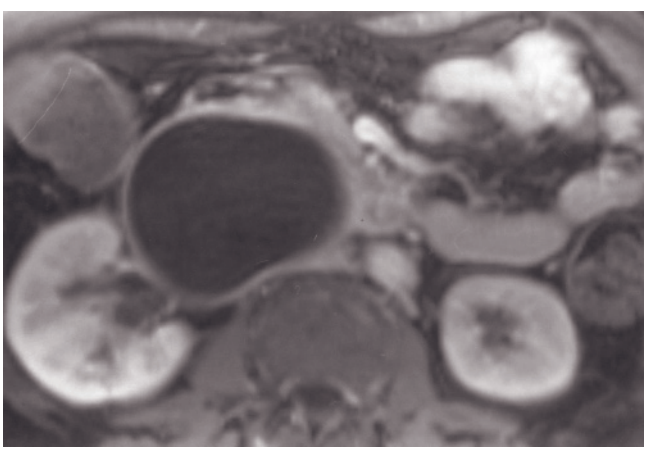

(*m*)

Fig. 4.79 (*Continued*) An 8-cm pseudocyst is present in the region of the porta hepatis that is mildly high in signal intensity on T1-weighted images (*a*, *b*) and high in signal intensity on the T2-weighted image (*c*). The mild, high signal intensity on T1-weighted images is more conspicuous with fat suppression (*b*) and consistent with dilute blood or protein. The homogeneous signal intensity on T2-weighted images suggests that the fluid, although proteinaceous, is not complicated by infection or cellular debris. A 3-cm pseudocyst (arrow, *e*) is identified within the body of the pancreas (*e*, *f*).

Fluid in the pseudocyst is low in signal intensity on the precontrast T1-weighted image (*e*). Capsular enhancement of the pseudocysts is shown on the fat-suppressed gadolinium-enhanced image (*f*). Coronal plane gadolinium-enhanced T1-weighted SGE images (*g*, *h*) demonstrate the relationship of the pseudocysts to surrounding structures. Three pseudocysts (arrows, *g*) are shown in the coronal plane (*g*). Gallbladder (arrow, *h*) is displaced laterally by the large pseudocyst in the porta hepatis. The sagittal plane image (*i*) demonstrates the anteroposterior orientation of the pseudocysts to other structures.

Coronal SS-ETSE (*j*), transverse fat-suppressed SS-ETSE (*k*), immediate postgadolinium T1-weighted SGE (*l*), and 90-s postgadolinium fat-suppressed SGE (*m*) images in a second patient. A large, 8 × 7 cm, pancreatic pseudocyst is situated between the right kidney and second portion of the duodenum. The pancreatic head is displaced anteriorly (arrows, *l*).

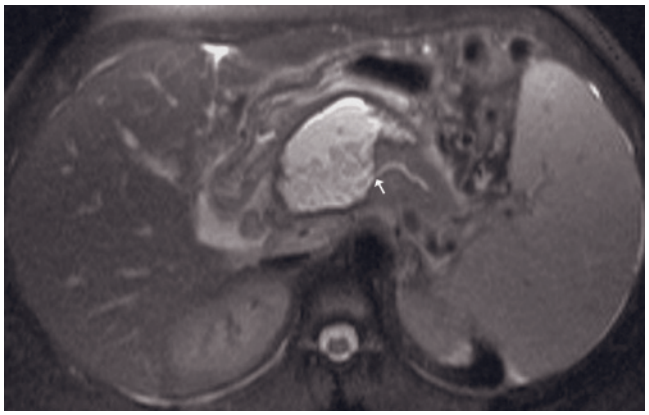

(*a*)

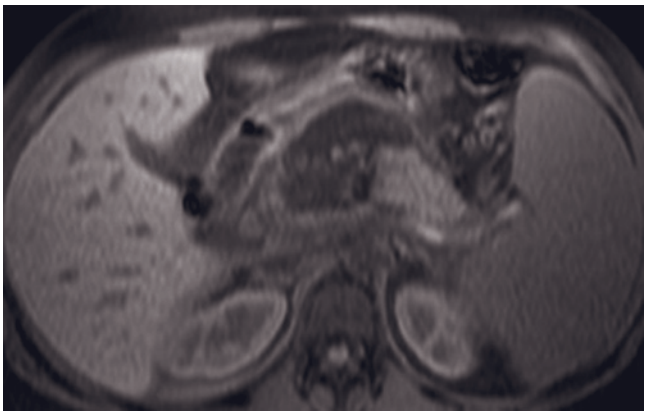

(*b*)

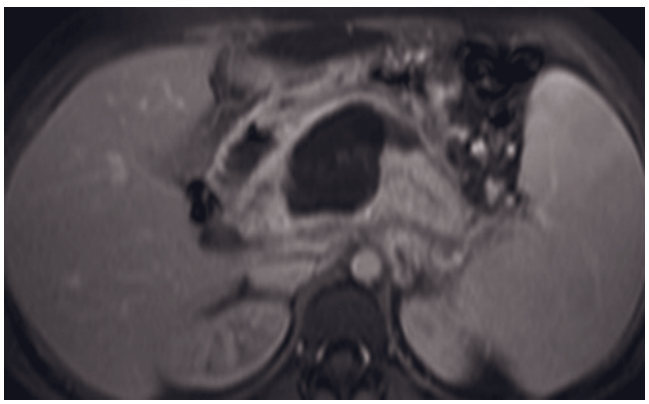

(*c*)

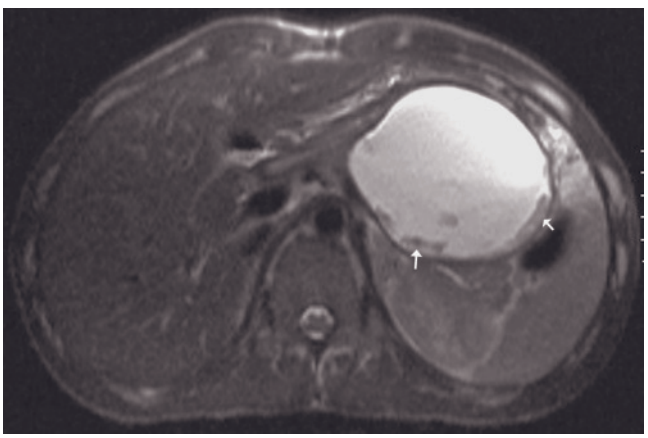

(*d*)

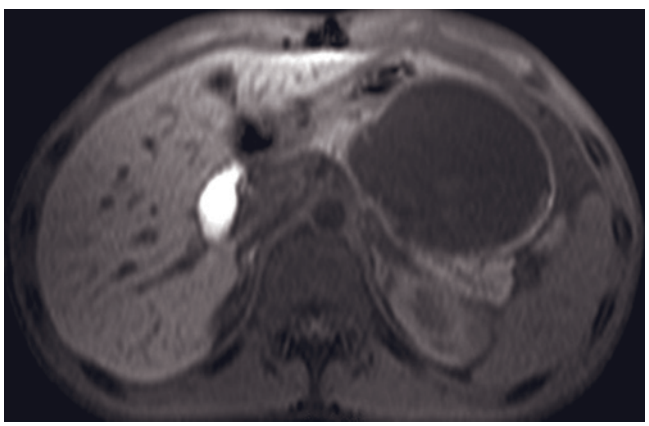

(*e*)

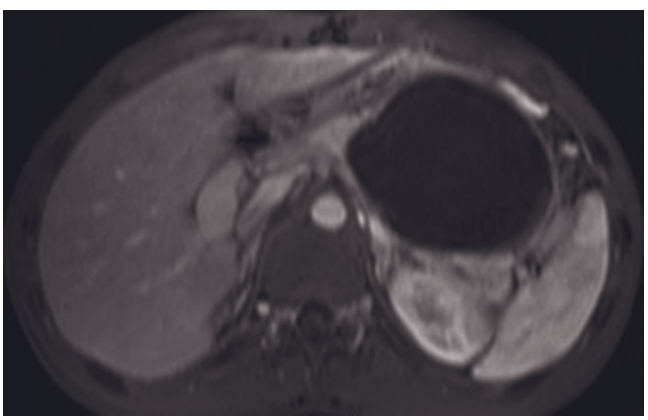

(*f*)

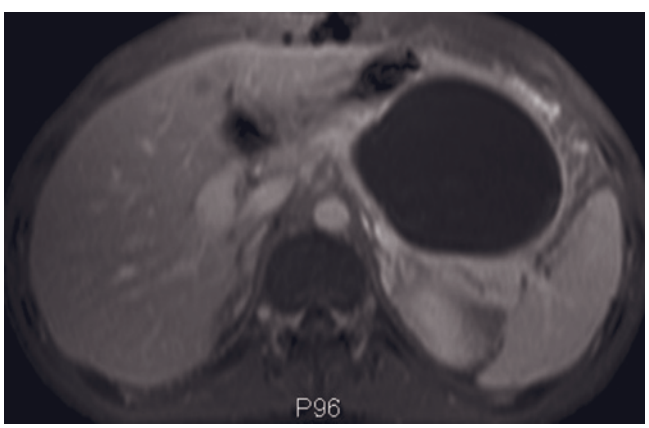

(*g*)

FIG. 4.80 Large pseudocyst. Fat-suppressed T2-weighted SS-ETSE (*a*), fat-suppressed T1-weighted gradient-echo (*b*), and interstitial-phase postgadolinium fat-suppressed T1-weighted gradient-echo (*c*) images. A large pseudocyst is present in the pancreatic head and neck. The continuity of the cyst with the main pancreatic duct is best seen on the T2-weighted image (arrow, *a*). The heterogeneous signal intensity on the T2-weighted images suggests that the fluid is complicated by infection or cellular debris. Fat-suppressed T2-weighted SS-ETSE (*d*), fat-suppressed T1-weighted gradient-echo (*e*), and immediate (*f*) and interstitial-phase (*g*) postgadolinium fat-suppressed T1-weighted gradient-echo images in a second patient with pancreatic pseudocyst. A large pseudocyst is present in the pancreatic tail. Debris within the pseudocyst is best seen on the T2-weighted image (arrows, *d*).

alcoholism and the development of chronic pancreatitis [97, 98]. Obstruction of the pancreatic duct from various causes, including pancreatic ductal cancer, results in chronic pancreatitis [98]. Acute pancreatitis secondary to gallstone disease rarely results in chronic pancreatitis.

Chronic pancreatitis is associated with decreased endocrine as well as exocrine function [97, 98]. Patients with chronic pancreatitis have an increased risk of developing pancreatic cancer [99].

An analysis of patients with chronic pancreatitis imaged on dynamic contrast-enhanced CT images showed the following features: 66% had dilatation of the main pancreatic duct, 54% had parenchymal atrophy, 50% had pancreatic calcifications, 34% had pseudocysts, 32% had focal pancreatic enlargement, 29% had biliary ductal dilatation, and 16% had densities in peripancreatic fat or fascia. No abnormalities were present in 7% of patients [100]. Calcification, which is the pathognomonic feature of chronic pancreatitis on CT images, is a late occurrence following development of fibrosis and is observed in only half of these patients. CT imaging is not sensitive at detecting the early changes of fibrosis in chronic pancreatitis. Focal chronic pancreatitis may be difficult to distinguish from adenocarcinoma in the head of the pancreas because both entities may cause focal enlargement (fig. 4.81), obstruction of the common bile duct (figs. 4.82 and 4.83) and pancreatic duct, atrophy of the tail of the pancreas, and obliteration of the fat plane around the superior mesenteric artery (SMA) [101–103].

MRI may perform better than CT imaging at detecting changes of chronic pancreatitis in that MRI detects not only morphologic findings but also the presence of fibrosis. Fibrosis is shown by diminished signal intensity on T1-weighted fat-suppressed images and diminished heterogeneous enhancement on immediate postgadolinium gradient-echo images [104]. Low signal intensity on T1-weighted fat-suppressed images reflects loss of the aqueous protein in the acini of the pancreas. Diminished enhancement on capillary-phase images reflects disruption of the normal capillary bed and increased chronic inflammation and fibrous tissue (fig. 4.84). Most cases of chronic pancreatitis show progressive parenchymal enhancement on 5-min postcontrast images, reflecting the pattern of enhancement of fibrous tissue. A study that described MRI findings in 13 patients with chronic calcifying pancreatitis and 9 patients with acute recurrent pancreatitis demonstrated differences between these groups on T1-weighted fat-suppressed images and immediate postgadolinium gradient-echo images [104]. All patients with pancreatic calcifications on CT examination had a diminished-signal-intensity pancreas on T1-weighted fat-suppressed images and an abnormally low percentage of contrast enhancement on immediate postgadolinium gradient-echo images (fig. 4.85). Patients with acute recurrent pancreatitis had signal intensity features of the pancreas comparable to normal pancreas. Secretin-enhanced MRCP has been used for the evaluation of patients with pancreatic pathologies including chronic pancreatitis. Secretin induces pancreatic duct secretion. Therefore, it has been reported that it improves the visualization of pancreatic ductal system and associated pathologies. Secretin-MRCP has been reported to show early ductal changes (dilatations-strictures) associated with chronic pancreatitis (fig. 4.85). Secretin-MRCP has also been reported to evaluate and grade pancreatic exocrine

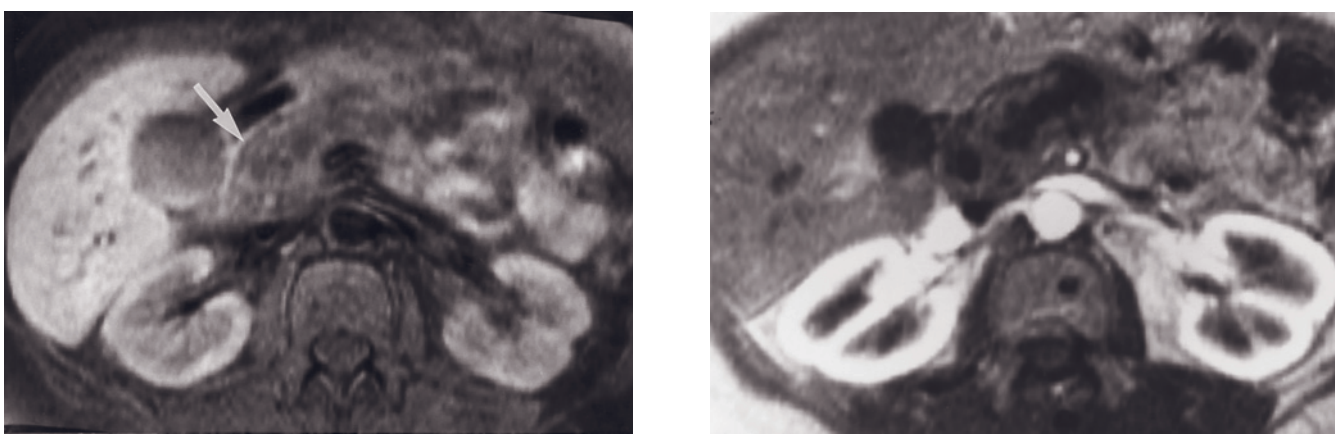

(*a*) (*b*)

FIG. 4.81 Chronic pancreatitis with focal enlargement of the head of the pancreas. T1-weighted fat-suppressed spin-echo (*a*), immediate postgadolinium T1-weighted SGE (*b*), and gadolinium-enhanced T1-weighted fat-suppressed spin-echo (*c*) images. The head of the pancreas is enlarged (arrow, *a*).The pancreas is diffusely low in signal intensity on the precontrast T1-weighted fat-suppressed image (*a*). The pancreas shows diffuse diminished enhancement on the immediate postgadolinium image (*b*).

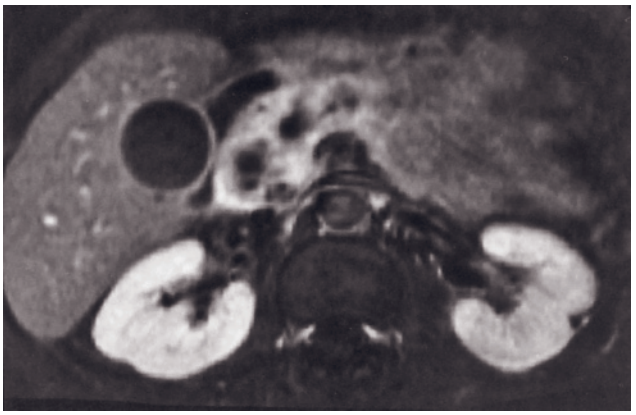

(*c*)

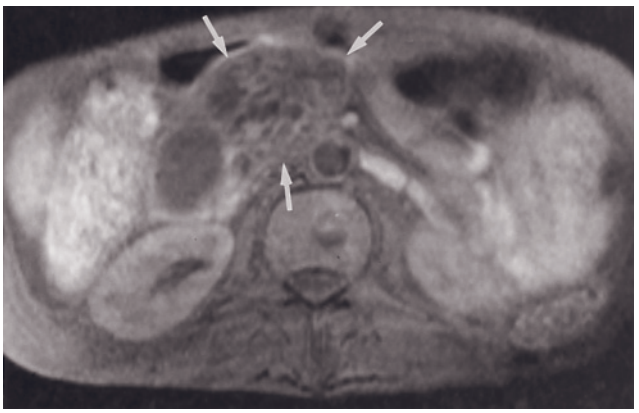

(*d*)

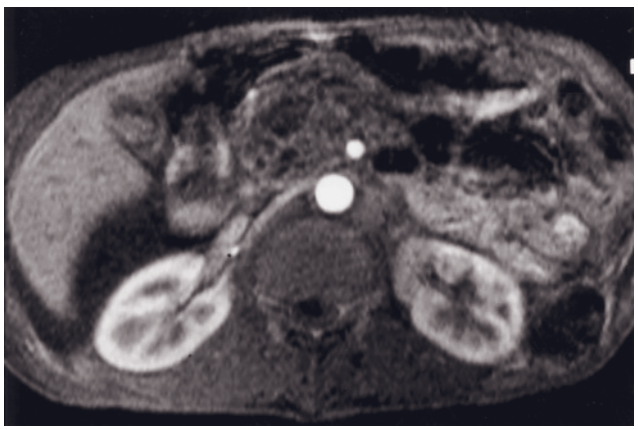

(*e*)

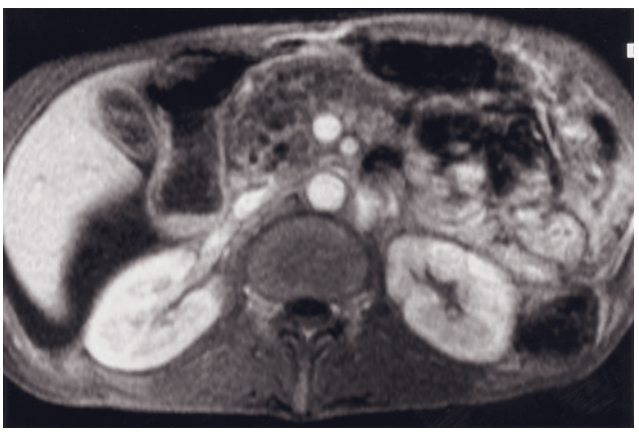

(*f*)

(*g*)

Fig. 4.81 (*Continued*) The lack of definition of a focal mass lesion on the immediate postgadolinium image is the most important observation that excludes tumor. On the interstitial-phase gadolinium-enhanced image (*c*), signal-void foci are identified that represent cysts, pseudocysts, dilated pancreatic duct, and calcifications. T1-weighted fat-suppressed spin-echo (*d*) and immediate (*e*) and 90-s (*f*) postgadolinium T1-weighted SGE images in a second patient demonstrate enlargement of the pancreatic head (arrows, *d*).The head enhances in a diminished fashion on immediate (*e*) and 90-s (*f*) postgadolinium images with no definition of a mass lesion and preservation of a marbled texture. Multiple small signal-void foci represent calcifications. The 90-s postgadolinium image (*g*) demonstrates that signal-void foci are also present throughout the body and tail.

function noninvasively (fig. 4.85). Following secretin stimulation, good duodenal filling should be present in the presence of normal exocrine function. Despite its use in routine clinical practice for the last 10 years, the role of secretin-MRCP for the assessment of pancreatic duct pathologies has not been well established yet.

Focal enlargement of the head of the pancreas with chronic pancreatitis may be difficult to distinguish from cancer on CT images [33]. MR images permit distinction between these two entities with greater reliability [33]. Both chronic pancreatitis and carcinoma show similar signal intensity changes of the enlarged region of pancreas on noncontrast T1-weighted fat-suppressed and T2-weighted images: generally mildly hypointense on T1-weighted images and heterogenous and mildly hyperintense on T2-weighted images. On immediate postgadolinium images, focal pancreatitis shows heterogeneous enhancement with the presence of signal-void

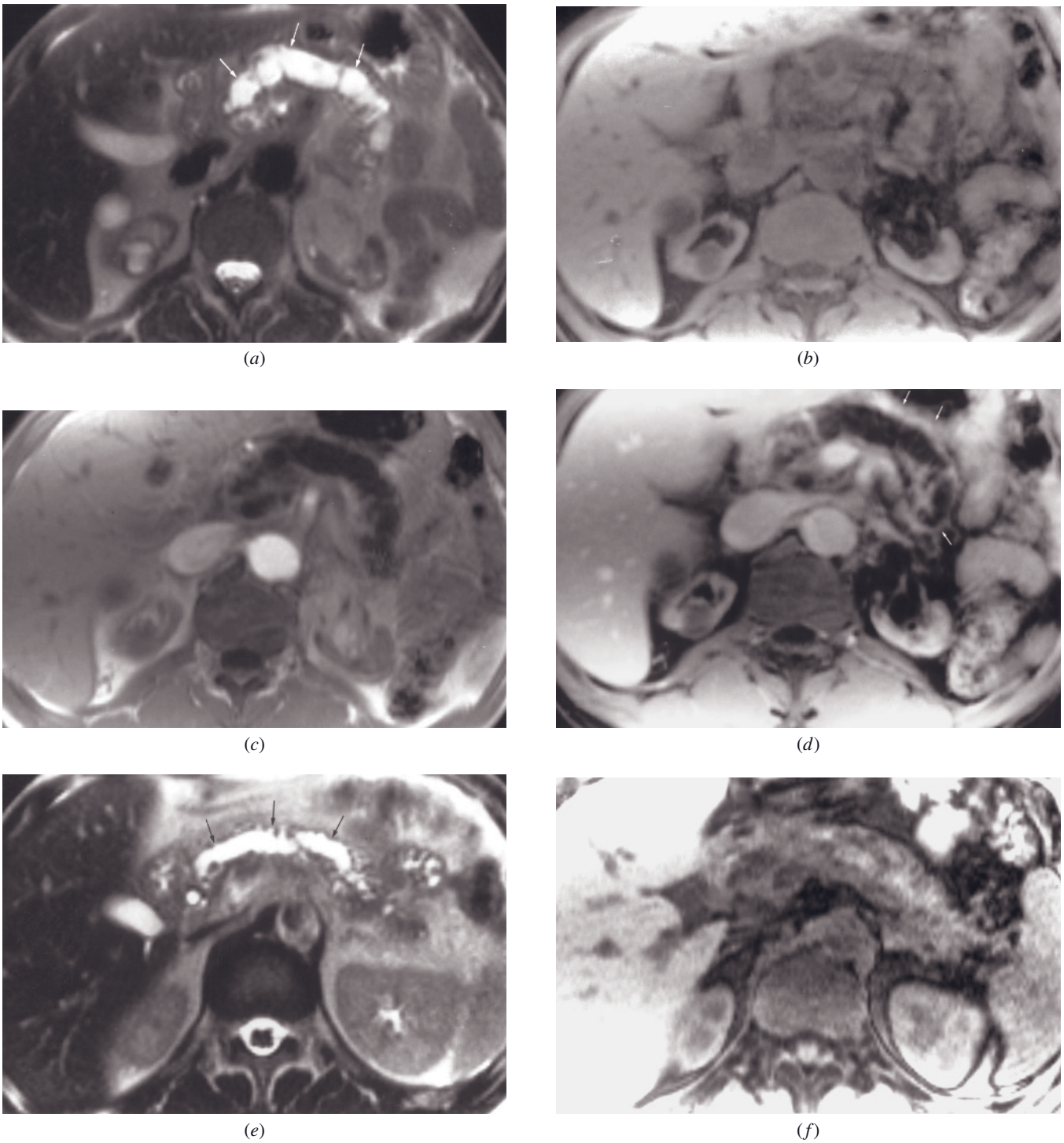

FIG. 4.82 Chronic pancreatitis with moderate to severe pancreatic duct dilatation. T2-weighted SS-ETSE (*a*), T1-weighted fat-suppressed SGE (*b*), immediate postgadolinium T1-weighted SGE (*c*), and 90-s postgadolinium fat-suppressed SGE (*d*) images in a patient with hereditary pancreatitis and recurrent bouts of pancreatitis. The pancreatic ductal is very dilated (arrows, *a*). The pancreatic parenchyma is atrophic and is low signal on noncontrast T1-weighted fat-suppressed SGE (*b*). The thin rim of atrophic pancreas enhances minimally on immediate postgadolinium image (*c*) and shows late enhancement (arrows, *d*) consistent with changes of fibrosis. The pancreas is atrophic for the patient's age (18 years old), and it shows heterogeneous signal intensity on T1-weighted images (*b*) with diminished enhancement on postgadolinium images (*d*). The pancreatic duct is severely dilated.

T2-weighted SS-ETSE (*e*), T1-weighted fat-suppressed SGE (*f*), immediate postgadolinium T1-weighted SGE (*g*), and 90-s postgadolinium fat-suppressed SGE (*h*) images on a second patient demonstrate similar findings. Note moderately severe dilatation of the pancreatic duct (arrows, *e*) and late enhancement of atrophic pancreatic parenchyma (arrows, *h*).

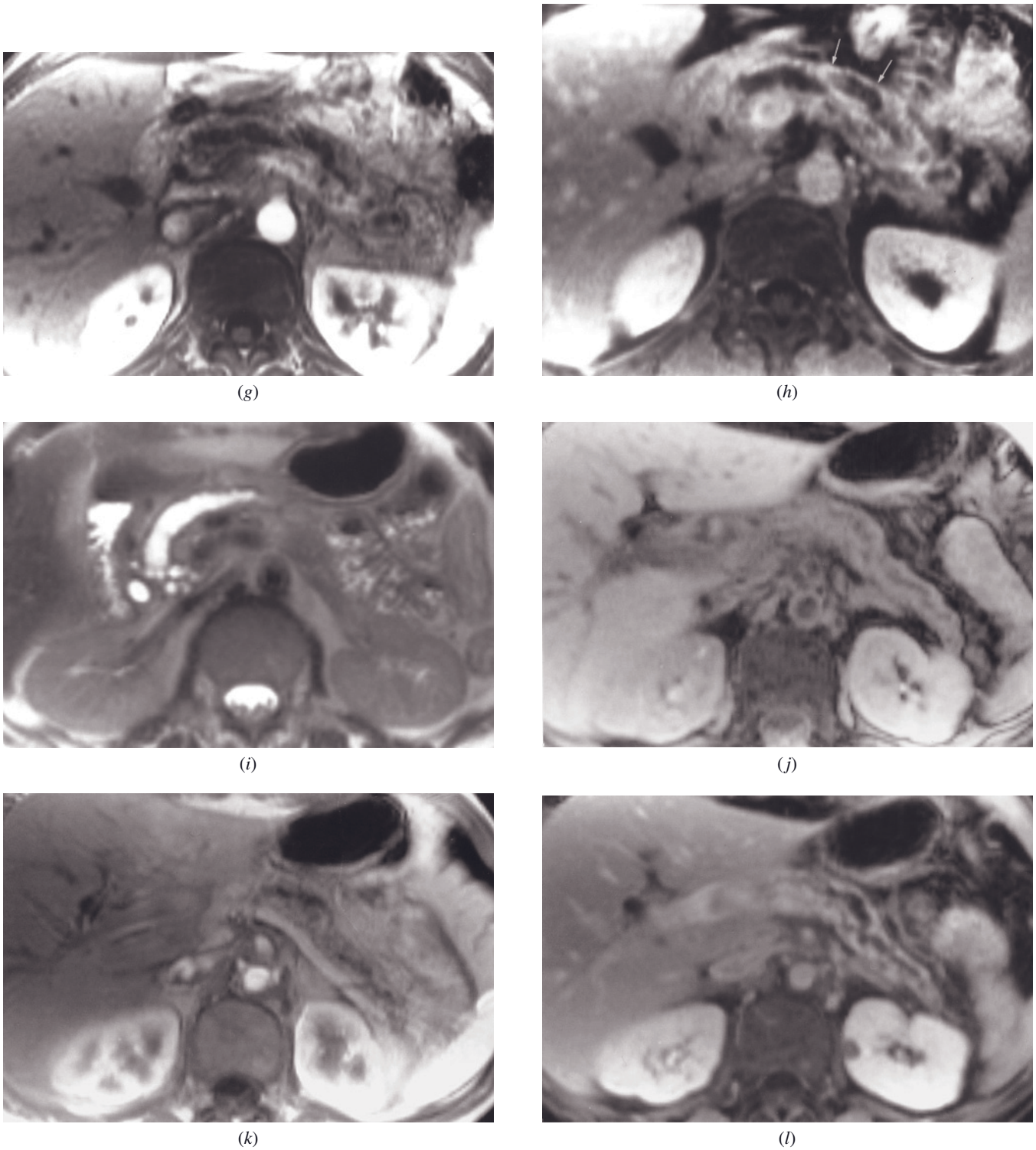

FIG. 4.82 (*Continued*) T2-weighted SS-ETSE (*i*), T1-weighted fat-suppressed SGE (*j*), immediate postgadolinium fat-suppressed SGE (*k*), and 90-s post-gadolinium fat-suppressed SGE (*l*) images in a third patient show the same findings of moderately severe pancreatic ductal dilatation with parenchymal signal intensity changes of chronic pancreatitis.

(*a*)

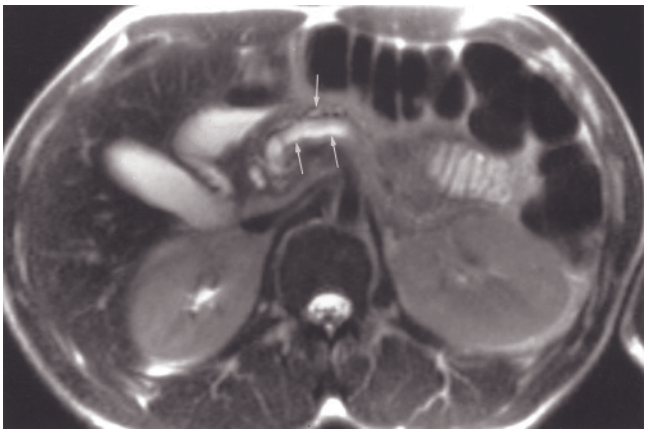

(*b*)

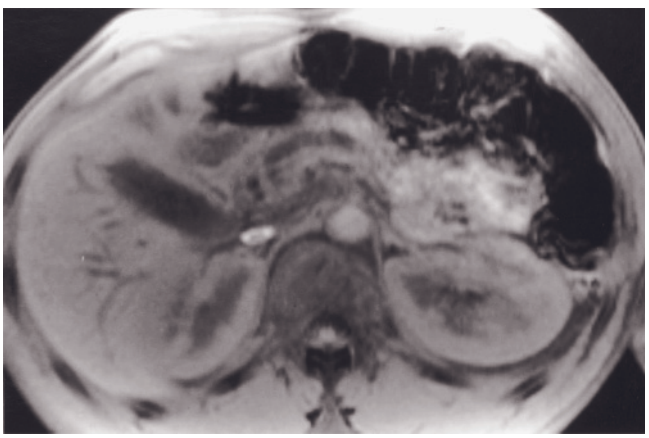

(*c*)

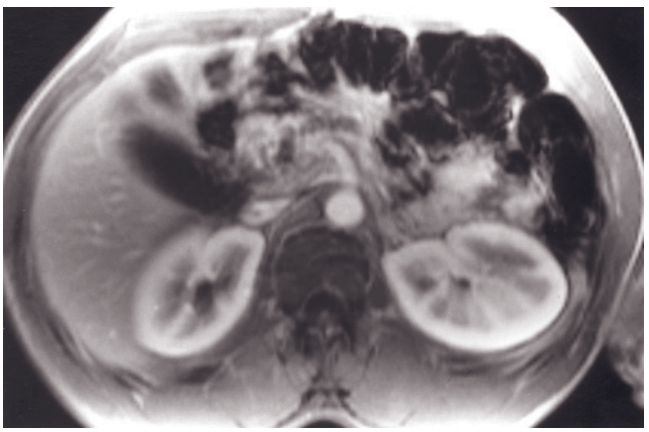

(*d*)

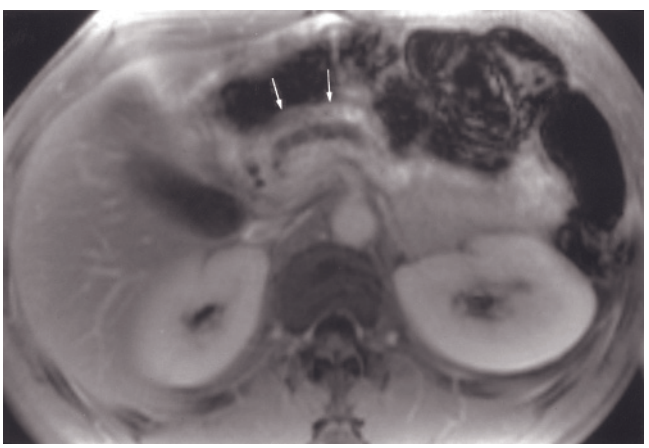

(*e*)

FIG. 4.83 Chronic pancreatitis with main pancreatic and side branch ductal dilatation. Coronal MRCP (*a*) and transverse T2-weighted SS-ETSE (*b*), T1-weighted fat-suppressed SGE (*c*), immediate postgadolinium T1-weighted SGE (*d*), and 90-s postgadolinium fat-suppressed SGE (*e*) images. The main pancreatic duct and its side branches are markedly dilated, which is best seen on MRCP and single-shot T2-weighted images (arrows, *a*, *b*). Parenchymal changes of chronic pancreatitis are present including low signal on noncontrast T1-weighted fat-suppressed images (*c*) and minimal heterogeneous early enhancement (*d*) with late progressive parenchymal enhancement (arrows, *e*). The presence of dilated ectatic side branches is a feature more consistent with chronic pancreatitis than pancreatic ductal adenocarcinoma, with the latter entity more typically causing dilatation of the main pancreatic duct without side branch ectasia.

cysts and calcifications, without evidence of a marginated definable, minimally enhancing mass lesion. Demonstration of a definable, circumscribed mass lesion is most often diagnostic for tumor. In chronic pancreatitis, the focally enlarged portion of the pancreas usually shows preservation of a glandular, feathery, or marbled texture similar to that of the remaining pancreas [33]. In contrast, in pancreatic cancer, the focally enlarged portion of the pancreas loses its usual anatomic detail. Tumor disrupts the underlying architecture and generally exhibits irregular, heterogeneous, diminished enhancement. Diffuse low signal intensity of the entire pancreas, similar to and including the area of focal enlargement, on T1-weighted fat-suppressed and

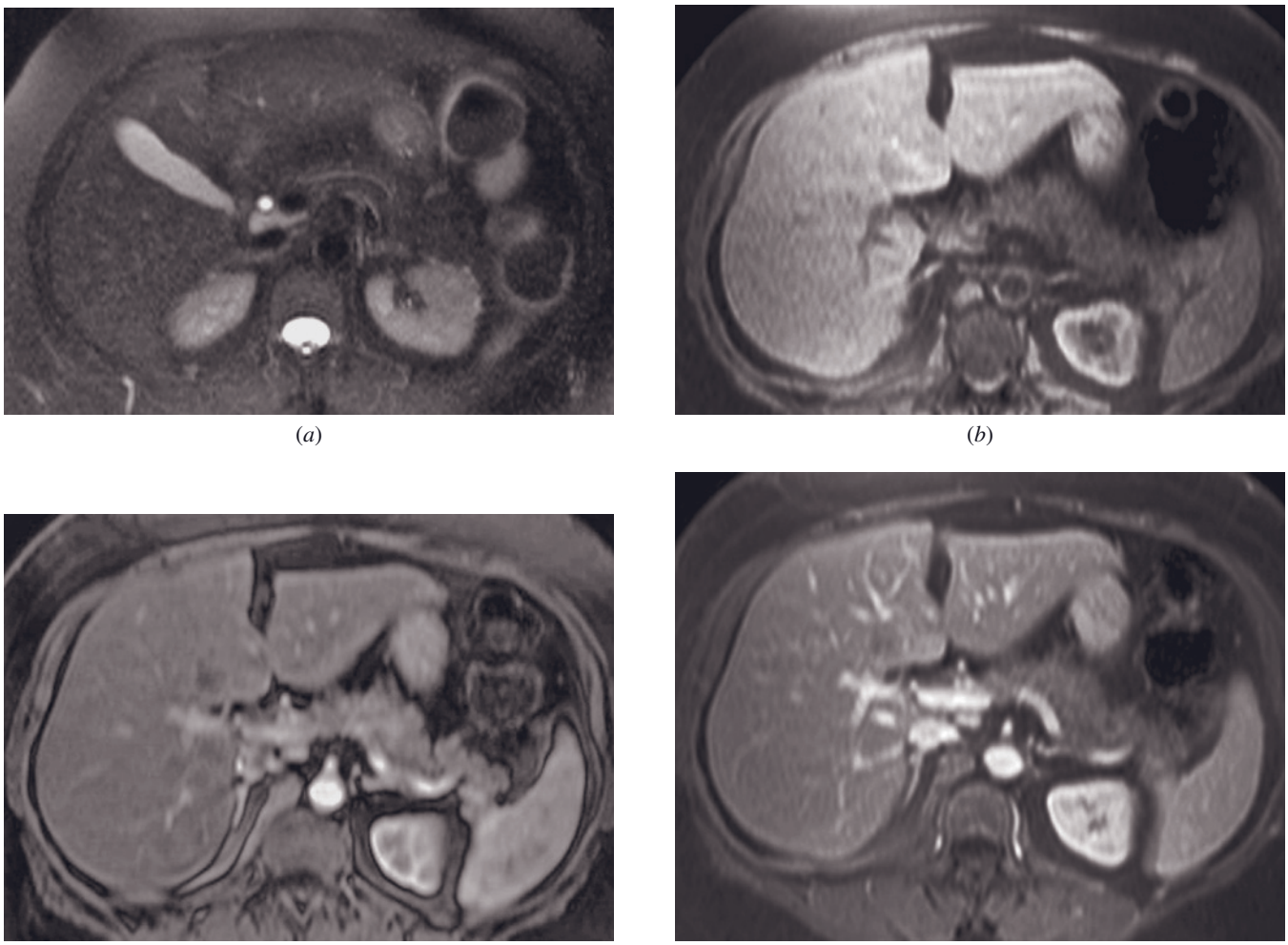

(*a*) (*b*)

(*c*) (*d*)

FIG. 4.84 Early chronic pancreatitis. Fat-suppressed T2-weighted SS-ETSE (*a*), fat-suppressed T1-weighted gradient-echo (*b*), and immediate (*c*) and interstitial-phase (*d*) postgadolinium fat-suppressed T1-weighted gradient-echo images in a patient with early chronic pancreatitis demonstrate mildly diminished signal intensity on fat-suppressed and immediate postgadolinium T1-weighted images. Low signal intensity on T1-weighted fat-suppressed image (*b*) reflects loss of aqueous protein in the acini of the pancreas. Diminished enhancement on capillary-phase image (*c*) reflects disruption of the normal capillary bed due to chronic inflammation and fibrous tissue.

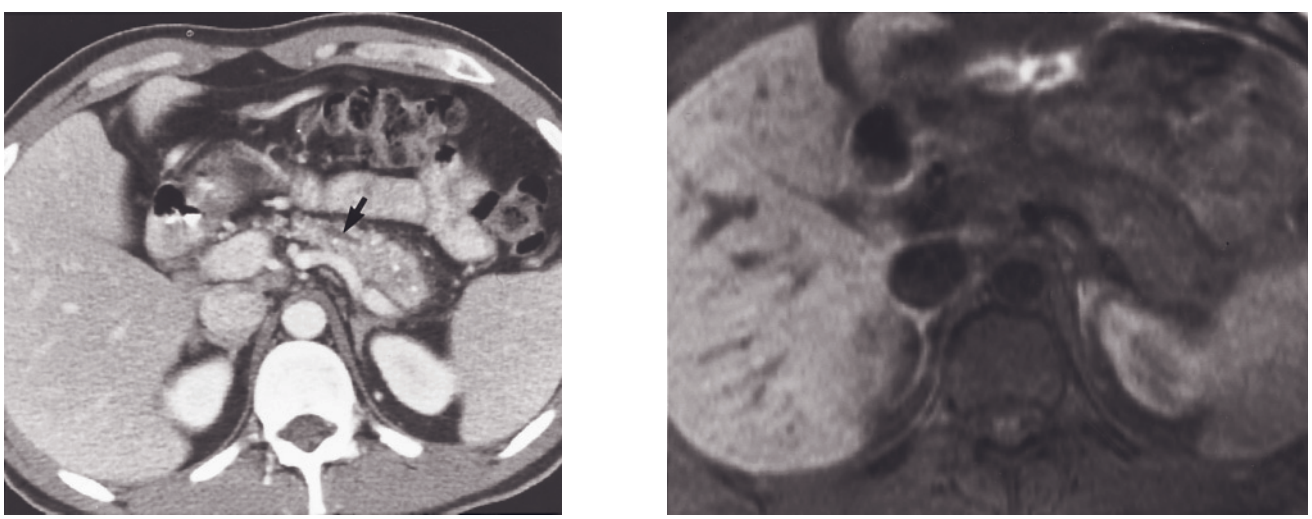

(*a*) (*b*)

FIG. 4.85 Chronic pancreatitis. Contrast-enhanced CT (*a*) T1-weighted fat-suppressed spin-echo (*b*), and immediate postgadolinium

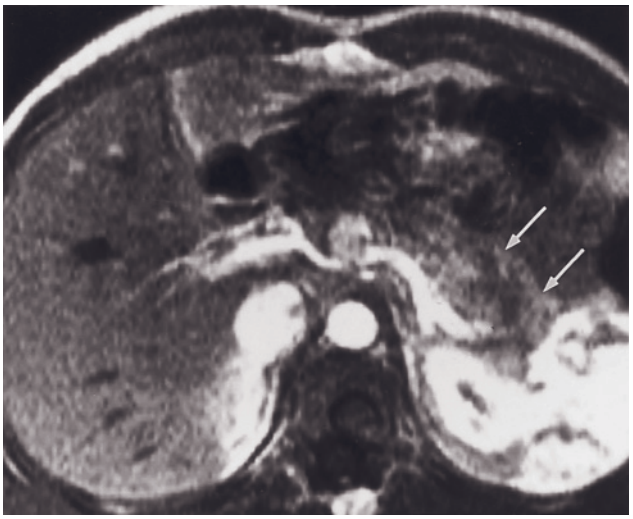

(*c*)

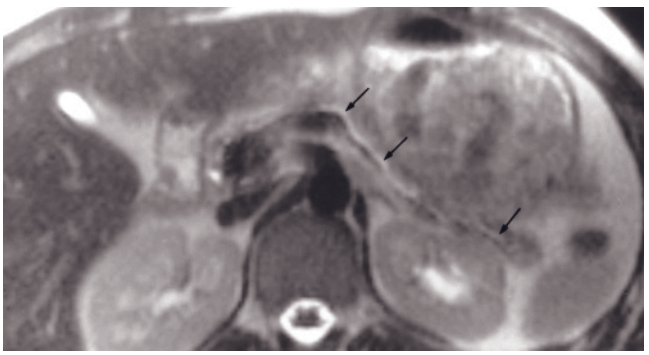

(*d*)

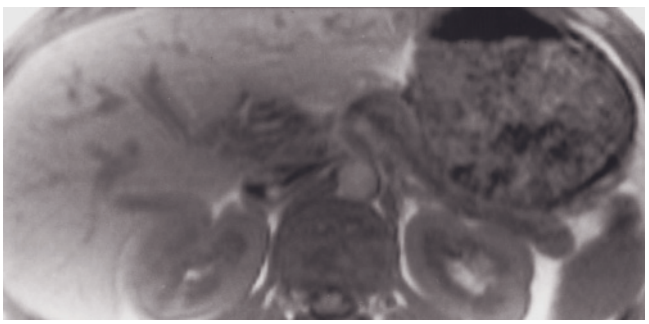

(*e*)

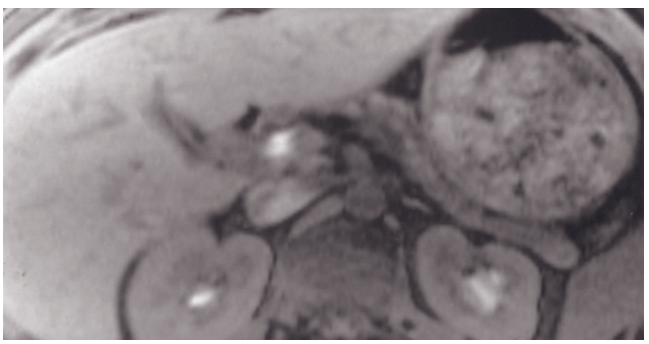

(*f*)

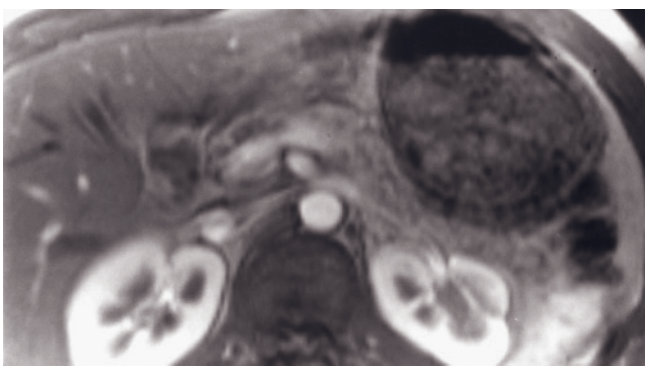

(*g*)

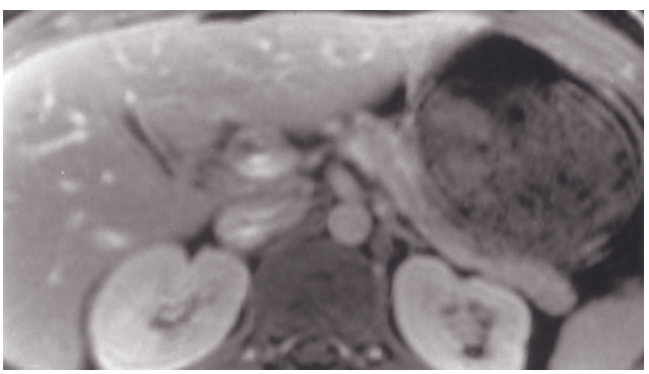

(*h*)

FIG. 4.85 (*Continued*) T1-weighted SGE (*c*) images. The CT image demonstrates pancreatic calcifications, which is diagnostic for chronic pancreatitis. Mild pancreatic ductal dilatation (arrow, *a*) and mild pancreatic enlargement are also present. The pancreas is low in signal intensity on the T1-weighted fat-suppressed image, which is consistent with loss of aqueous protein in the acini. The immediate postgadolinium T1-weighted SGE image demonstrates heterogeneous diminished enhancement of the pancreas (arrows, *c*), reflecting replacement of the normal capillary bed with lesser vascularized fibrotic tissue. (Reproduced with permission from Semelka RC, Kroeker MA, Shoenut JP, Kroeker R, Yaffe CS, Micflikier AB: Pancreatic disease: Prospective comparison of CT, ERCP, and 1.5 T MR imaging with dynamic gadolinium enhancement and fat suppression. *Radiology* 181: 785–791, 1991.)

T2-weighted SS-ETSE (*d*),T1-weighted SGE (*e*), noncontrast T1-weighted fat-suppressed SGE (*f*), immediate postgadolinium T1-weighted SGE (*g*), and 90-s postgadolinium fat-suppressed SGE (*h*) images in a second patient. Moderate dilatation of the pancreatic duct is present (arrows, *d*). There is moderate atrophy of the pancreatic parenchyma, which is low signal on T1-weighted fat-suppressed SGE (*f*) and demonstrates minimal enhancement on immediate postgadolinium images (*g*) with progressive enhancement on 90-s postcontrast images (*h*). These are classic features for chronic pancreatitis.

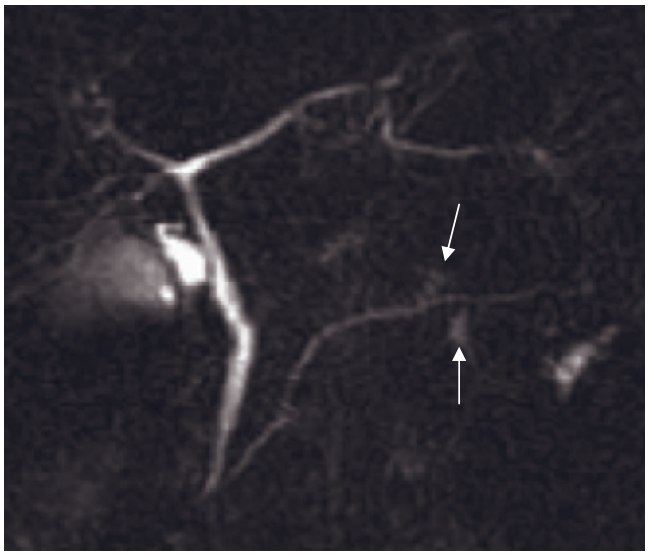

(*i*)

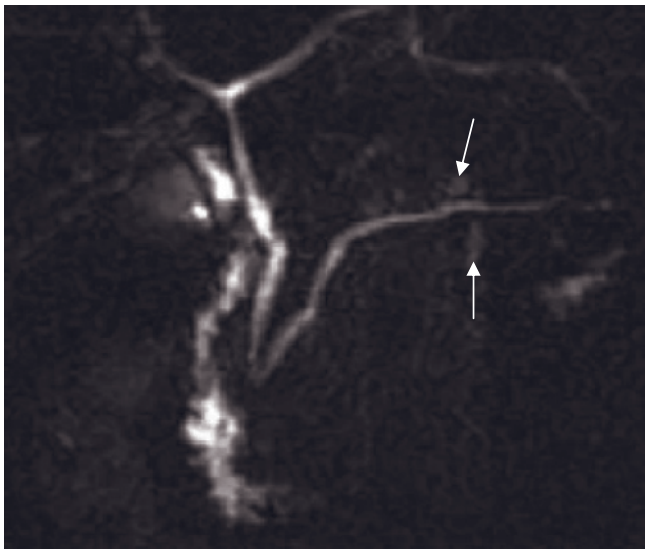

(*j*)

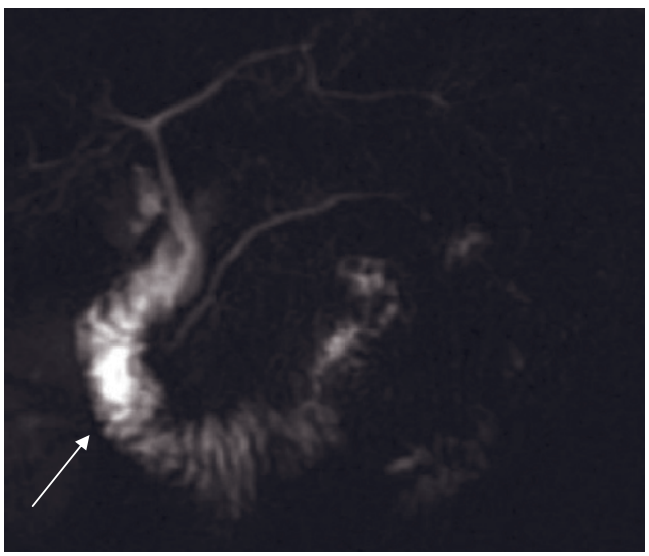

(*k*)

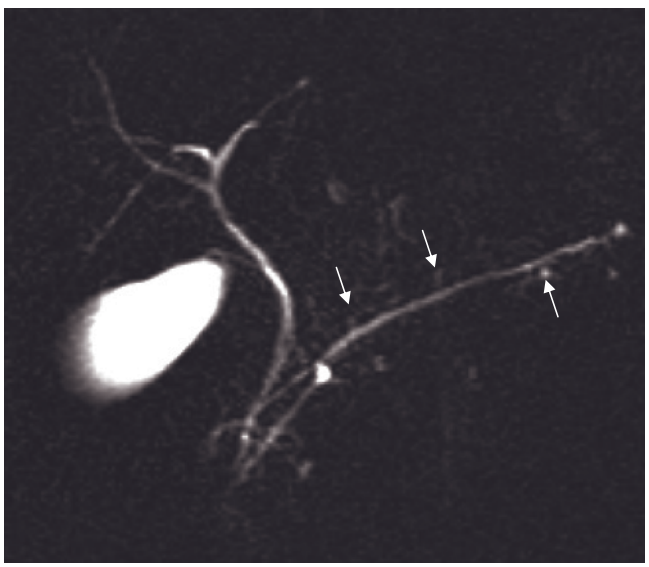

(*l*)

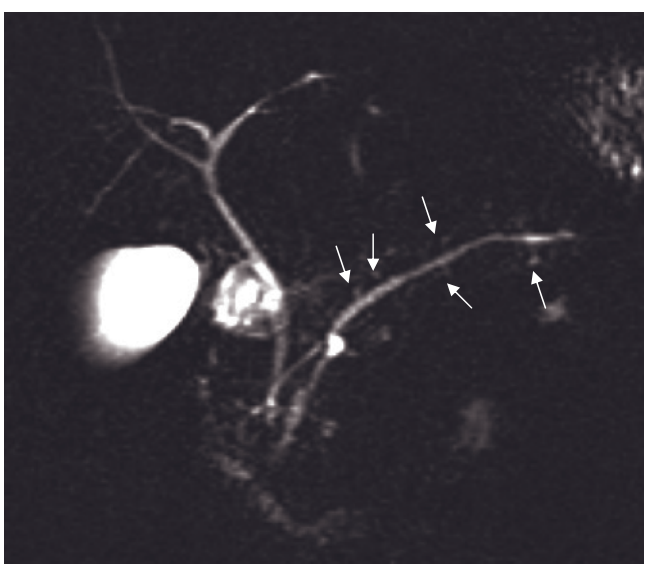

(*m*)

Fig. 4.85 (*Continued*) **Chronic pancreatitis—Secretin MRCP.** Presecretin (*i*) and postsecretin MRCP (*j*, *k*) images in a patient with mild chronic pancreatitis. Side branch dilatations (arrows, *i*) are detected on MRCP image (*i*) acquired before secretin administration. After secretin administration, the pancreatic duct and side branch dilatations (arrows, *j*) are seen better. On MRCP image (*k*) acquired at 10 min after the administration of secretin, there is good duodenal filling (arrow, *k*) suggesting normal exocrine function of the pancreas. Presecretin (*l*) and postsecretin MRCP (*m*) images in a patient with mild chronic pancreatitis. Side branch dilatations (arrows, *l*) are detected on MRCP image (*l*) acquired before secretin administration. After secretin administration, more side branch dilatations (arrows, *m*) are detected on MRCP image (*m*) acquired at 10 min. However, duodenal filling is less than normal and consistent with decreased estimated pancreatic exocrine function.

immediate postgadolinium SGE images is typical for chronic pancreatitis (fig. 4.86). In the setting of pancreatic cancer, the enhancement of the tumor is less than adjacent pancreatic parenchyma. Rarely, chronic pancreatitis may involve only the focally enlarged portion of the pancreas, with the reminder of the pancreas having no inflammatory changes. In these cases, the focus of chronic pancreatitis can simulate the appearance of pancreatic ductal adenocarcinoma. The inflammatory process may also be sufficiently destructive that underlying stromal pattern is lost. In these rare cases, diagnosis can only be established by surgical resection and histopathologic examination confirming the absence of malignancy.

Recurrent bouts of acute pancreatitis superimposed on the chronic disease typify the usual clinical course of these patients. Acute on chronic pancreatitis is well shown on MR images (figs. 4.87–4.89). Pancreatic pseudocysts observed in patients with chronic pancreatitis often arise as a sequel of episodes of acute inflammation [98]. Small pseudocysts and cysts are well shown on gadolinium-enhanced T1-weighted fat-suppressed images as nearly signal-void oval structures (fig. 4.90). Pseudocysts are generally high in signal intensity on T2-weighted images, but signal intensity varies considerably depending on the presence of blood, protein, infection, and debris (fig. 4.91). Pseudocyst walls generally show minimal early postgadolinium enhancement and progressive enhancement on 5-min postgadolinium images.

Autoimmune Pancreatitis

Most patients presenting with chronic pancreatitis will have alcohol-related disease. In approximately 30% of patients, the nature and course of chronic pancreatitis are unclear, and these cases may be labeled idiopathic.

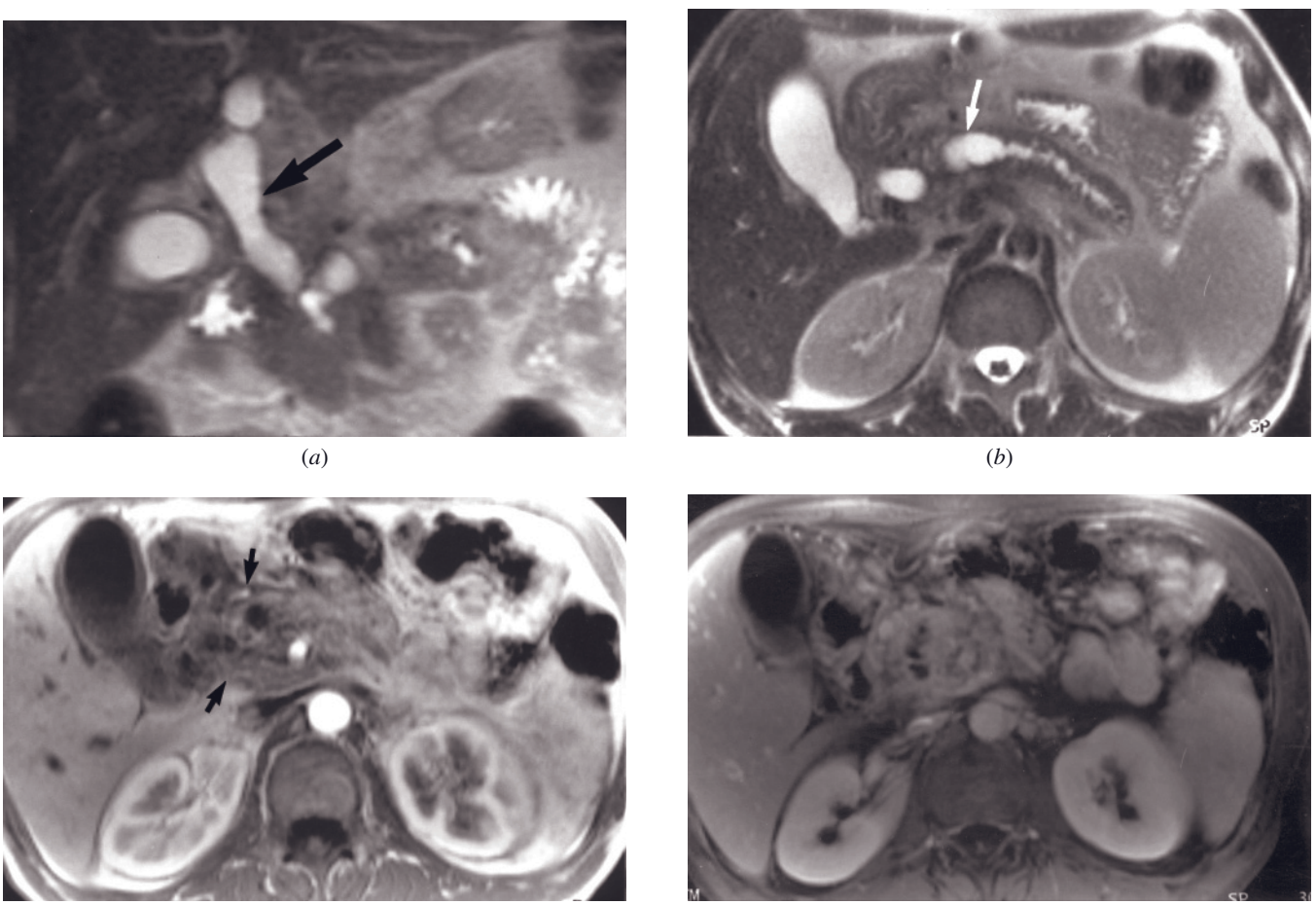

FIG. 4.86 Chronic pancreatitis simulating pancreatic cancer. Coronal (*a*) and transverse (*b*) T2-weighted SS-ETSE, immediate postgadolinium T1-weighted SGE (*c*), and 90-s postgadolinium fat-suppressed SGE (*d*) images. The CBD (arrow, *a*) and pancreatic (arrow, *b*) ducts are severely dilated, with atrophy of the pancreatic body (*b*) creating the double duct sign. On early (*c*) and late (*d*) postgadolinium images, no demarcated pancreatic mass is observed in the head of the pancreas. Instead, the enlarged pancreas shows a marbled texture (arrows, *c*) comparable in appearance to the remainder of the pancreas.

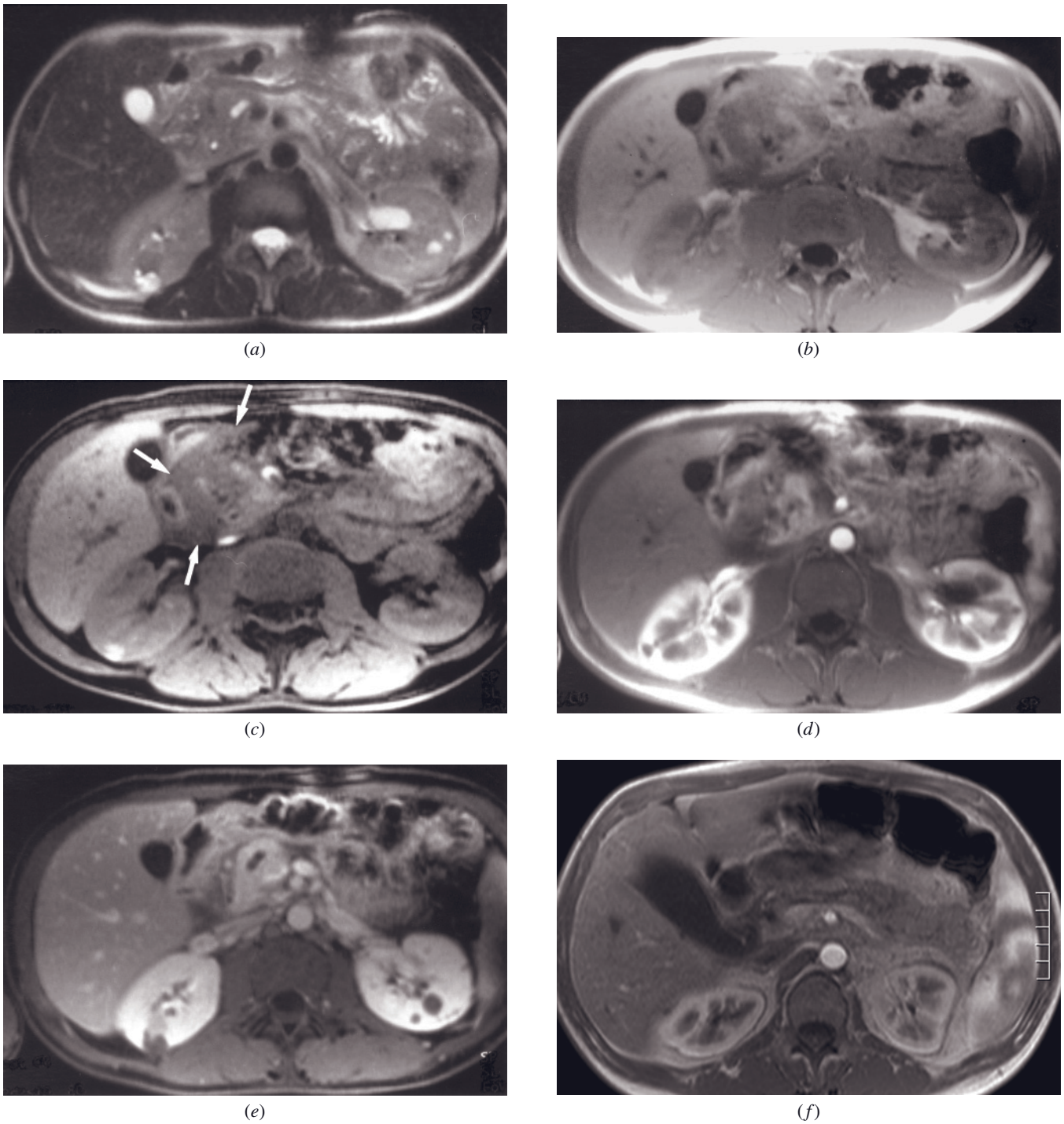

FIG. 4.87 Acute on chronic pancreatitis. T2-weighted SS-ETSE (*a*), T1-weighted SGE (*b*), T1-weighted fat-suppressed SGE (*c*), immediate postgadolinium T1-weighted SGE (*d*), and 90-s postgadolinium fat-suppressed SGE (*e*) images. Complex fluid surrounds the pancreas, predominantly located between the head and the second portion of duodenum (arrows, *c*). The pancreatic head is enlarged and shows decreased signal on noncontrast T1-weighted fat-suppressed SGE (*c*) and heterogeneous and reduced enhancement on immediate postgadolinium images (*d*), which is characteristic of chronic pancreatitis.

Immediate postgadolinium T1-weighted gradient-echo (*f*), interstitial-phase postgadolinium fat-suppressed T1-weighted gradient-echo (*g*), and MRCP (*h*) images in a patient with acute on chronic pancreatitis. The enhancement of the pancreas is

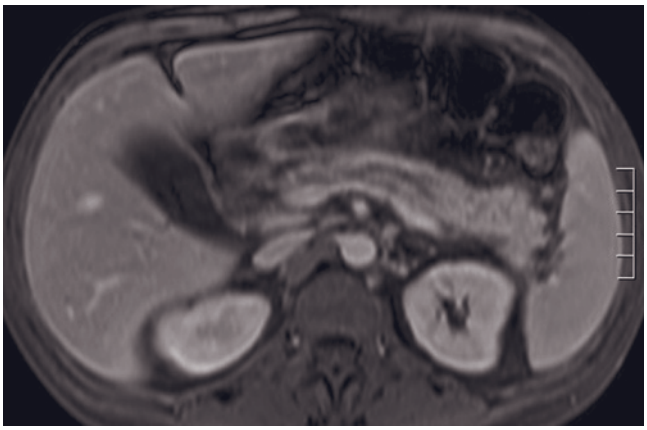

(*g*)

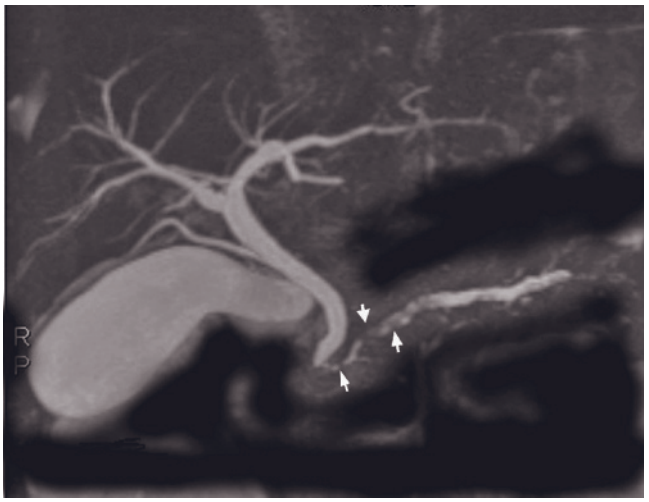

(*h*)

FIG. 4.87 (*Continued*) decreased on immediate postgadolinium image (*f*). The main pancreatic duct is mildly dilated and irregular (arrows, *h*).

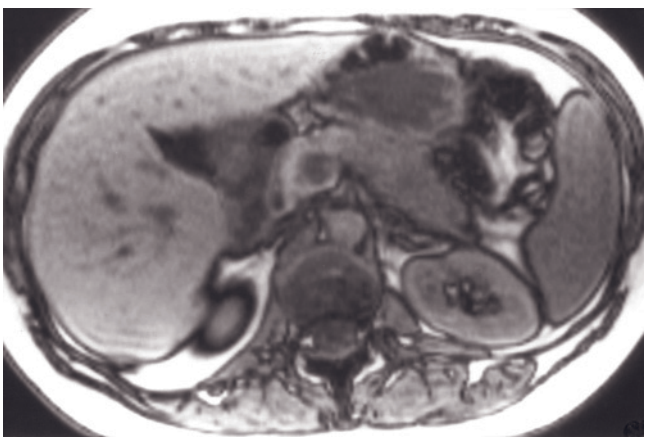

(*a*)

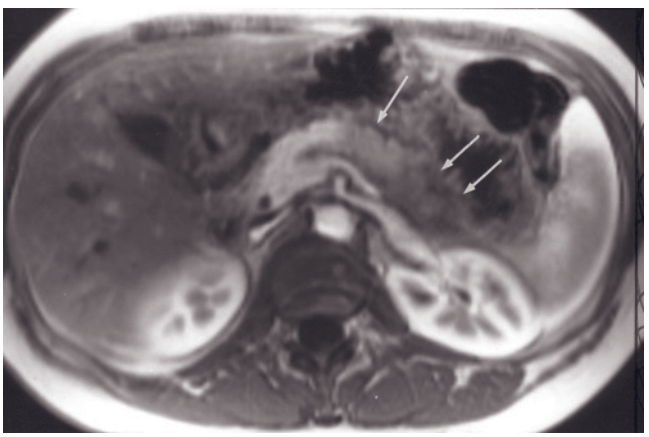

(*b*)

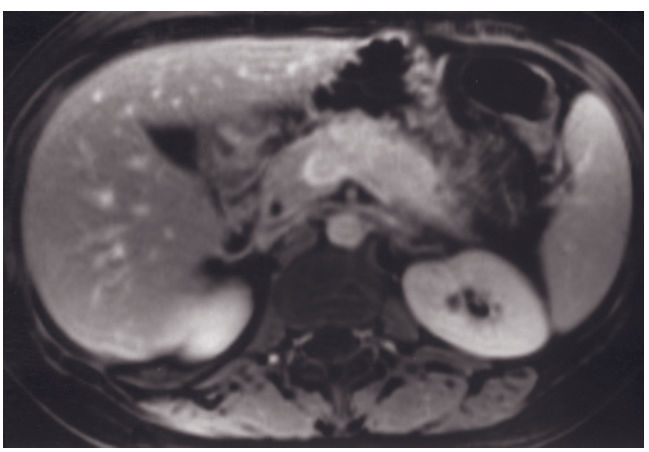

(*c*)

FIG. 4.88 Distal acute on chronic pancreatitis. T1-weighted out-of-phase SGE (*a*), immediate postgadolinium T1-weighted SGE (*b*), and 90-s postgadolinium fat-suppressed SGE (*c*) images. The distal portion of the body and tail of the pancreas is mildly enlarged with ill-defined borders. Enhancement is minimal of the distal pancreas on immediate postgadolinium image (arrows, *b*) and shows delayed increased enhancement (*c*). This enhancement pattern is typical for fibrous tissue as observed in chronic pancreatitis. A thin layer of fluid around the pancreas, appreciated on the immediate postgadolinium image (*b*), is consistent with acute inflammation.

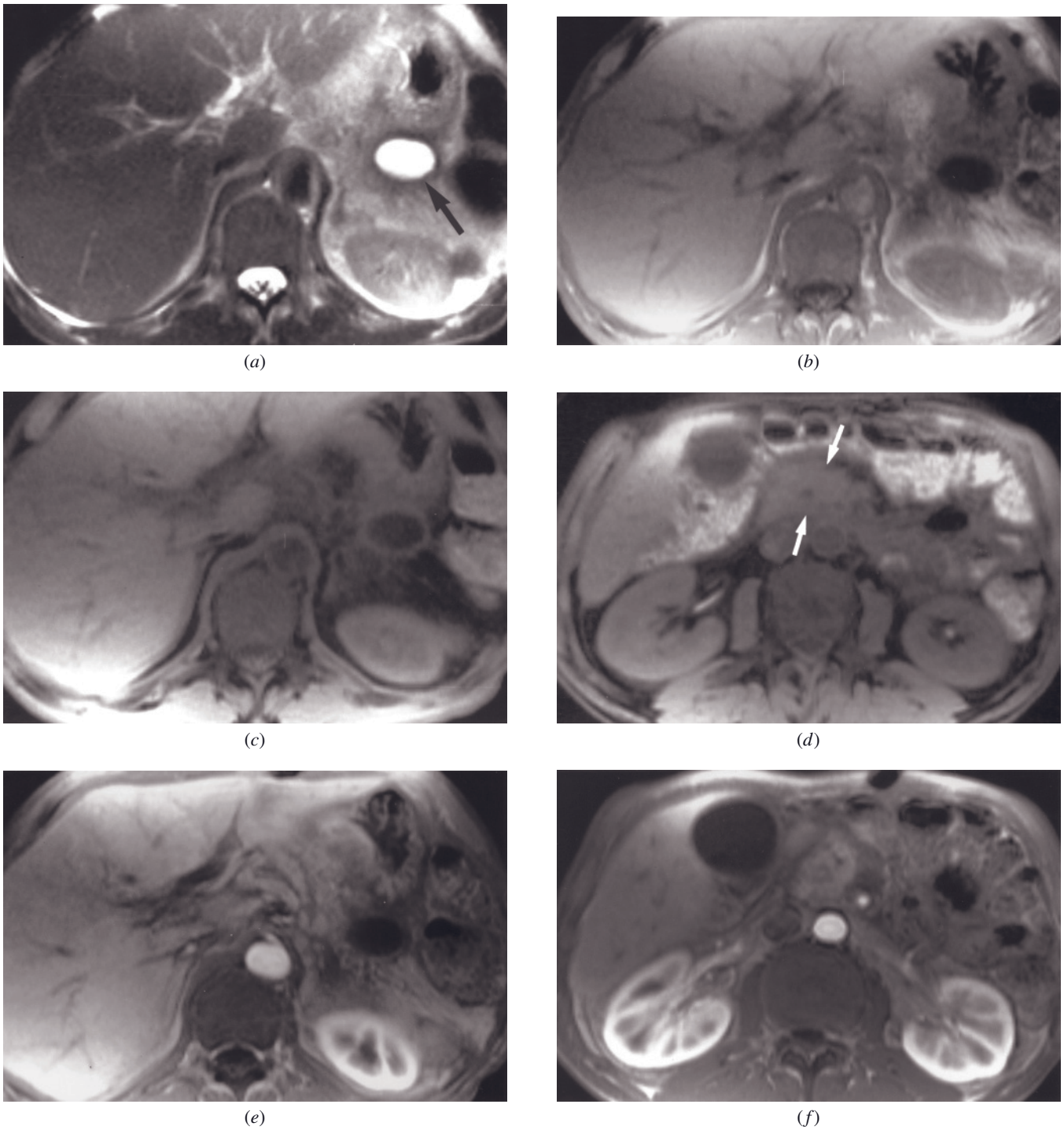

FIG. 4.89 Acute on chronic pancreatitis with pseudocyst formation. T2-weighted SS-ETSE (*a*), T1-weighted SGE (*b*), T1-weighted fat-suppressed SGE (*c*, *d*), immediate postgadolinium T1-weighted SGE (*e*, *f*), and 90-s postgadolinium fat-suppressed

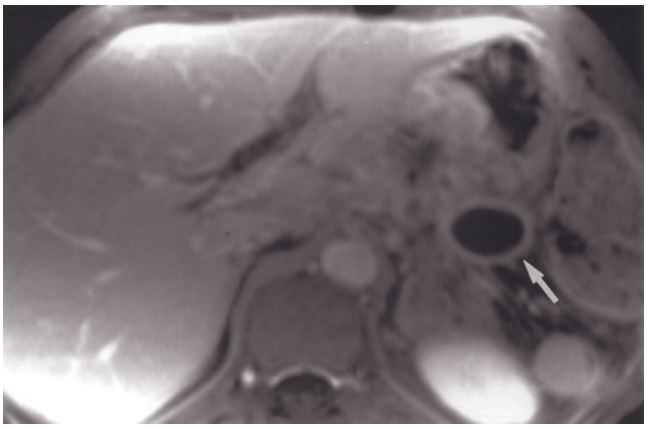

(*g*)

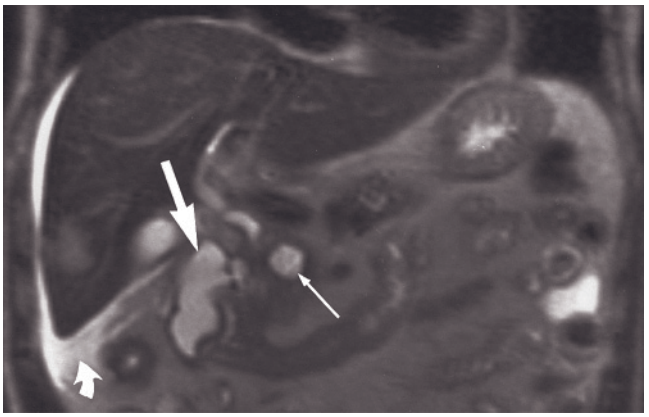

(*h*)

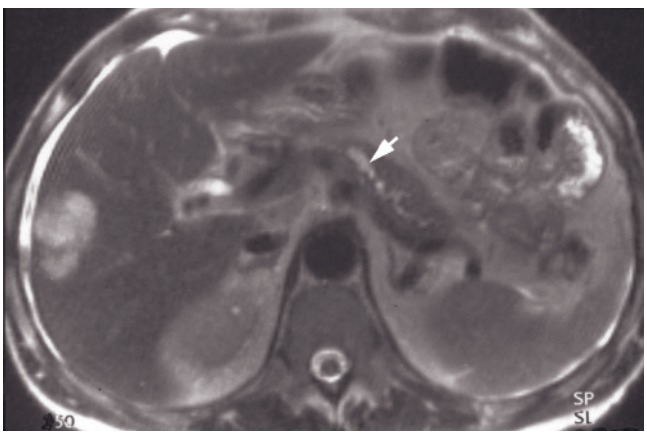

(*i*)

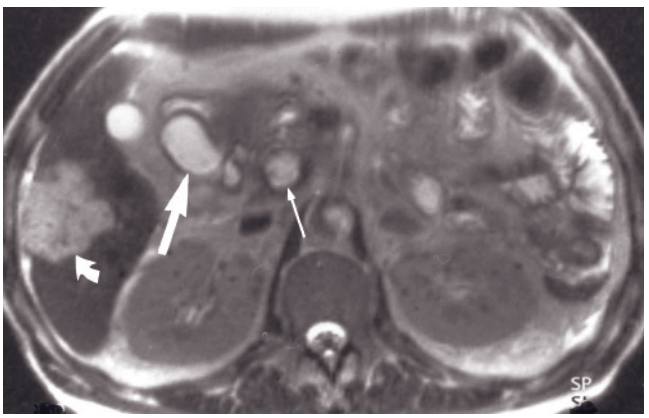

(*j*)

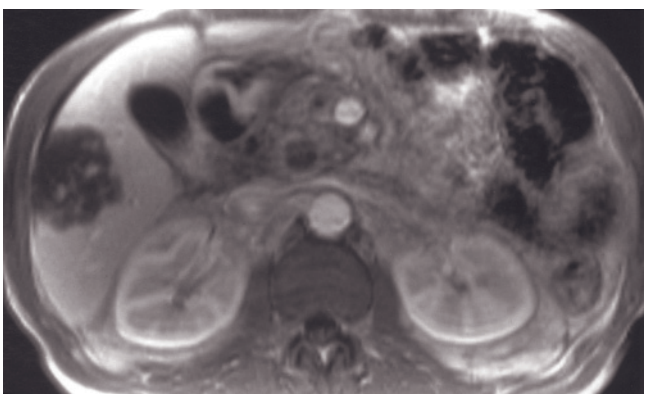

(*k*)

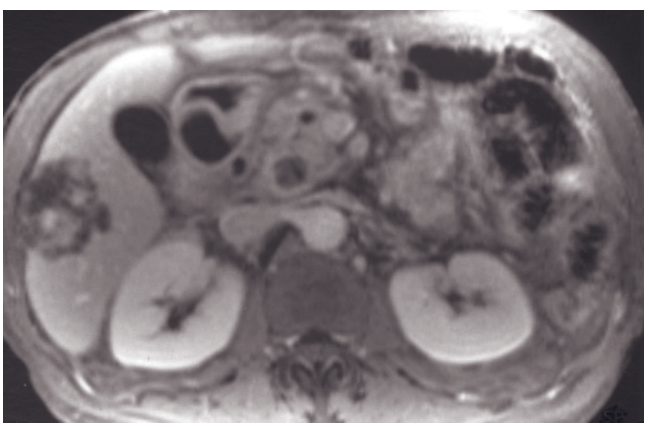

(*l*)

FIG. 4.89 (*Continued*) SGE (*g*) images. There is a pseudocyst (arrow, *a*) in the pancreatic tail, which has a thickened wall that exhibits progressive late enhancement (arrow, *g*). The pancreatic head and neck region (arrows, *d*) are enlarged (*d*, *f*) and exhibit low-signal on noncontrast fat-suppressed images (*d*) and diminished heterogeneous enhancement on immediate postgadolinium SGE images (*f*) consistent with focal acute on diffuse chronic pancreatitis. Note that renal corticomedullary difference is diminished on the noncontrast T1-weighted fat-suppressed image consistent with decreased renal function (*d*).

Coronal (*h*) and transverse (*i*, *j*) T2-weighted SS-ETSE, immediate postgadolinium T1-weighted SGE (*k*), and 90-s postgadolinium fat-suppressed SGE (*l*) images in a second patient. There is mild pancreatic duct dilatation and irregularity (arrow, *i*), which is commonly observed in chronic pancreatitis (*i*). A 2-cm pseudocyst is present in the posterior aspect of the pancreatic head (small arrow, *h*, *j*) and an irregular 4-cm pseudocyst (large arrow, *h*, *j*) adjacent to the second portion of the duodenum. A small volume of ascites is present (curved arrow, *h*). Note an incidental hemangioma in the liver that is high signal on T2 (curved arrow, *j*) demonstrating peripheral nodular enhancement with enlargement and coalescence of the nodules (*k*, *l*).

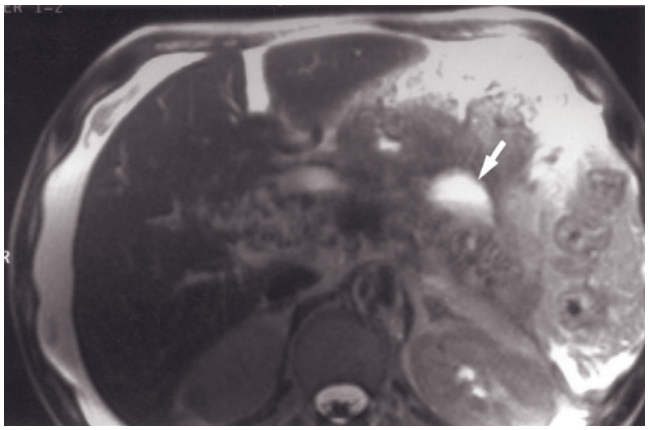

(*m*)

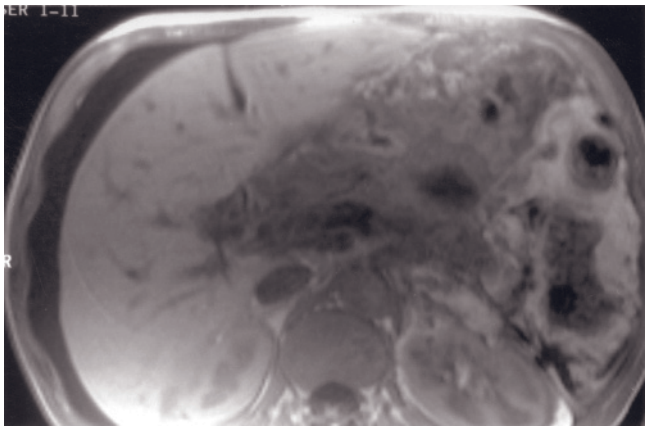

(*n*)

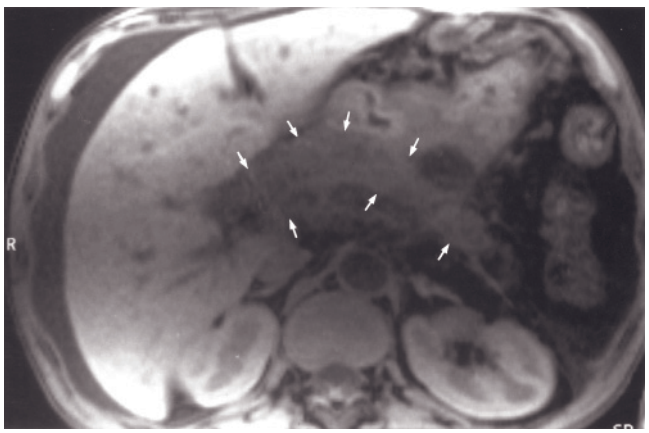

(*o*)

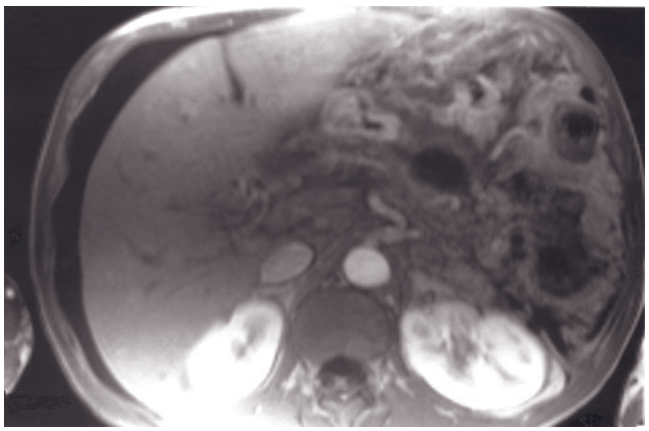

(*p*)

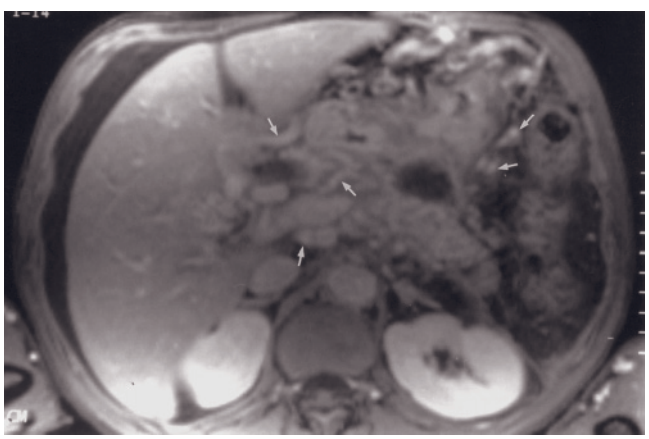

(*q*)

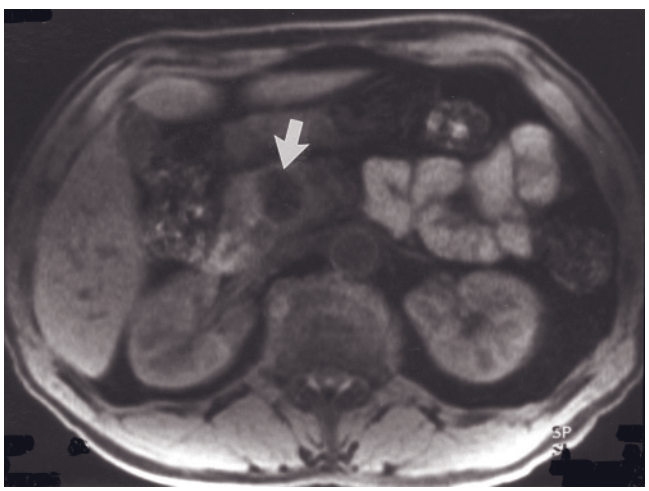

(*r*)

Fig. 4.89 (*Continued*) T2-weighted echo-train spin-echo (*m*), T1-weighted SGE (*n*), T1-weighted fat-suppressed SGE (*o*), immediate postgadolinium T1 SGE (*p*), and 90-s postgadolinium T1-weighted fat-suppressed SGE (*q*) images in a third patient. The pancreas is enlarged and ill-defined with blurring of the adjacent fat. The pancreas is low signal (arrows, *o*) on noncontrast T1-weighted fat-suppressed images (*o*) and on immediate postgadolinium SGE images (*q*) consistent with chronic pancreatitis. The pancreatic parenchyma shows progressive enhancement on late gadolinium-enhanced images (*q*), which is also a feature of chronic pancreatitis. There is a thick-walled pseudocyst anterior to the distal body of the pancreas, which contains a fluid-fluid level (arrow, *m*) on T2 (*m*). Multiple varices (small arrows, *q*) observed on the interstitial-phase gadolinium-enhanced image (*q*) reflect thrombosis of the splenic vein from longstanding severe chronic pancreatitis. T1-weighted fat-suppressed SGE (*r*), immediate postgadolinium

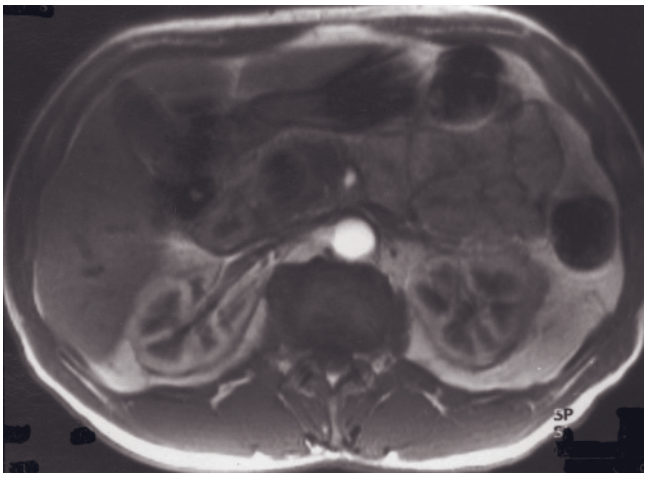

(*s*)

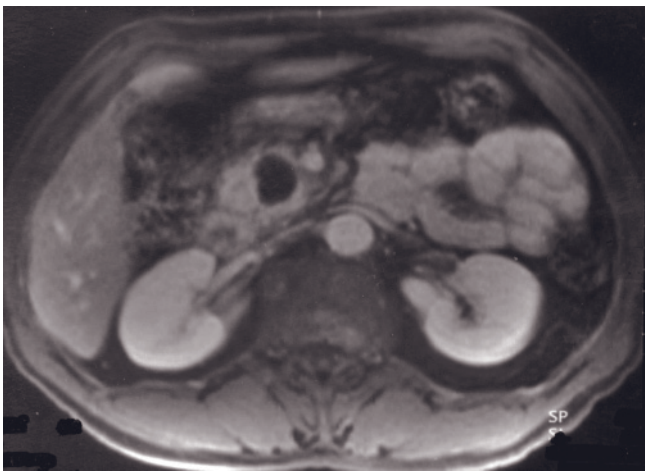

(*t*)

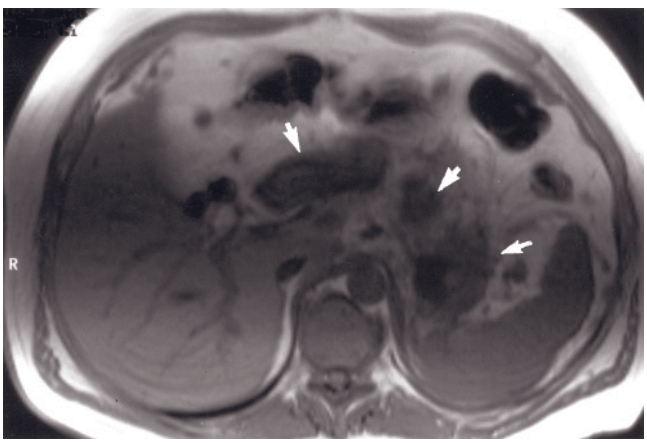

(*u*)

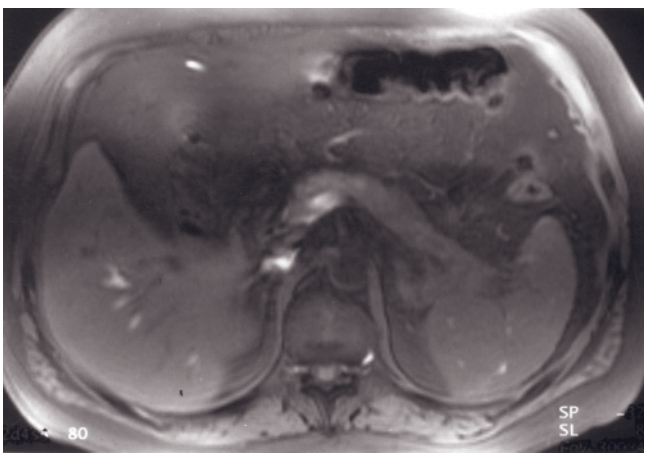

(*v*)

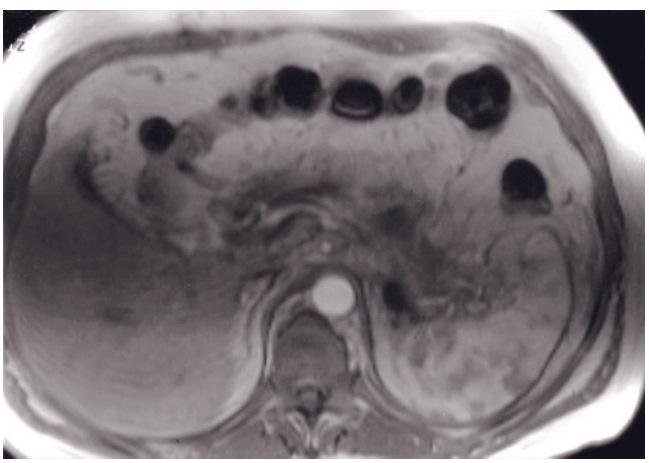

(*w*)

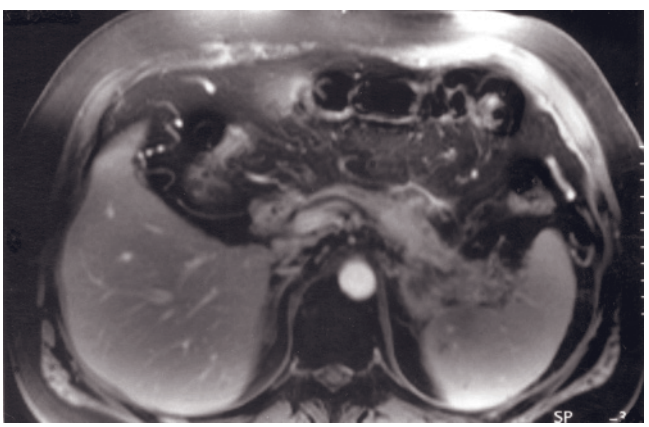

(*x*)

FIG. 4.89 (*Continued*) T1-weighted SGE (*s*), and 90-s postgadolinium fat-suppressed SGE (*t*) images in a fourth patient. A pseudocyst is present in the head of the pancreas (arrow, *r*). Note the decreased signal on the noncontrast T1-weighted fat-suppressed SGE image (*r*), and minimal heterogeneous enhancement on the immediate postgadolinium SGE image (*s*) with progressive enhancement on the parenchyma (*t*), which are imaging features of chronic pancreatitis. Compare this appearance to the pseudocyst in the pancreatic head of patients with acute pancreatitis (fig. 4.77).

T1-weighted SGE (*u*), T1-weighted fat-suppressed SGE (*v*), immediate postgadolinium SGE (*w*), and 90-s postgadolinium fat-suppressed SGE (*x*) images in a fifth patient. Multiple pseudocysts (arrows, *u*) and peripancreatic fluid strands from acute inflammation present superimposed on chronic pancreatitis. The peripancreatic fluid strands are more clearly shown on the non-fat-suppressed images (*u*, *w*) than on the fat-suppressed images (*v*, *x*), because of the excellent contrast between low-signal fluid and high-signal background fat. Background chronic pancreatitis is shown as low signal of a small pancreas on noncontrast T1-weighted fat-suppressed image (*v*) and minimal early enhancement of the pancreas (*w*) with progressive enhancement on late images (*x*).

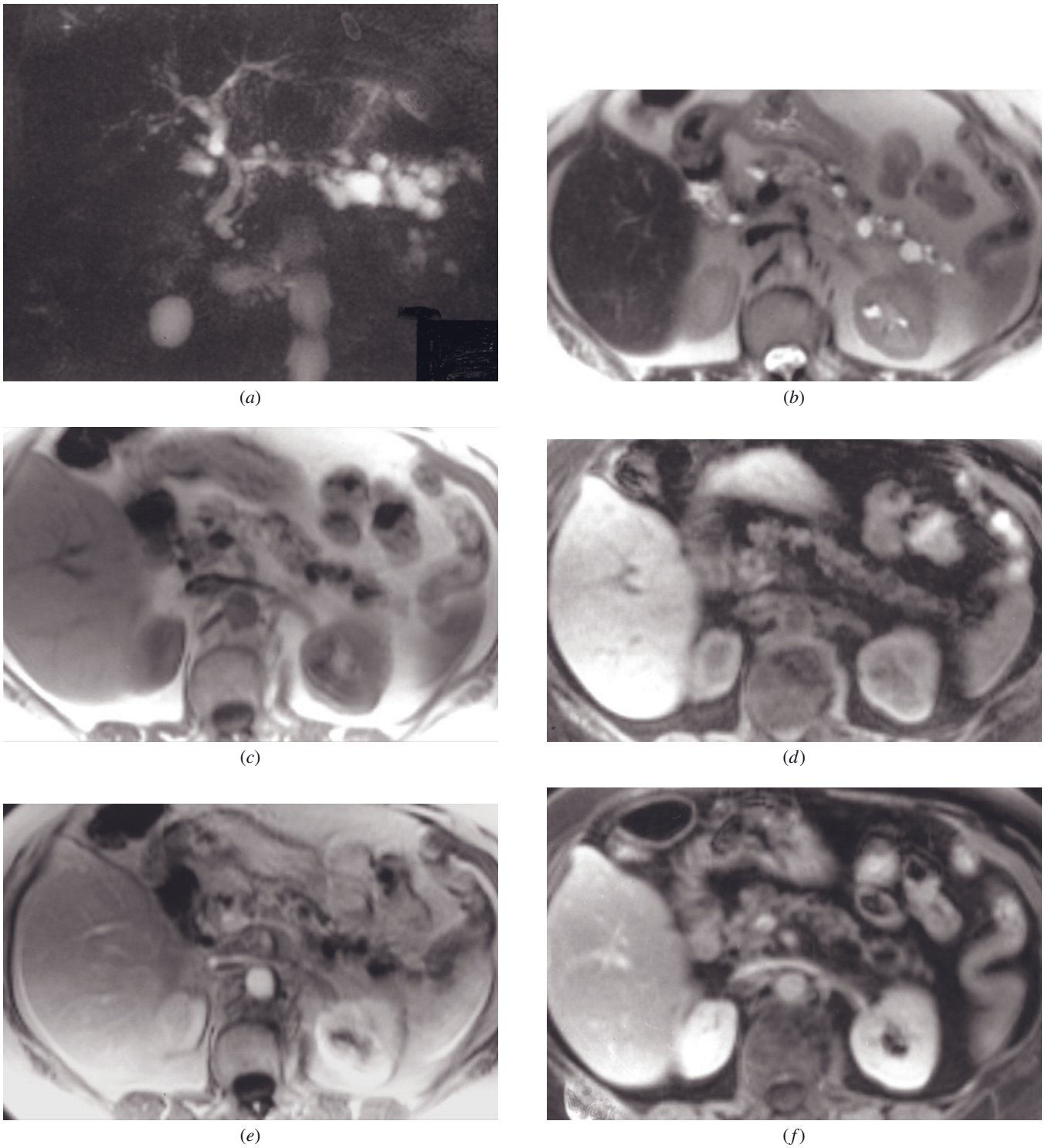

FIG. 4.90 Chronic pancreatitis with multiple small pseudocysts. MRCP (*a*), T2-weighted SS-ETSE (*b*), T1-weighted SGE (*c*), T1-weighted fat-suppressed SGE (*d*), immediate postgadolinium T1-weighted SGE (*e*), and 90-s postgadolinium fat-suppressed SGE (*f*) images. Multiple small pseudocysts are present throughout the atrophic background pancreatic parenchyma and appear hyperintense on T2-weighted images (*a*, *b*) and hypointense on T1-weighted images (*c*, *d*) and show lack of enhancement on early (*e*) and late (*f*) postgadolinium images, consistent with pseudocysts.

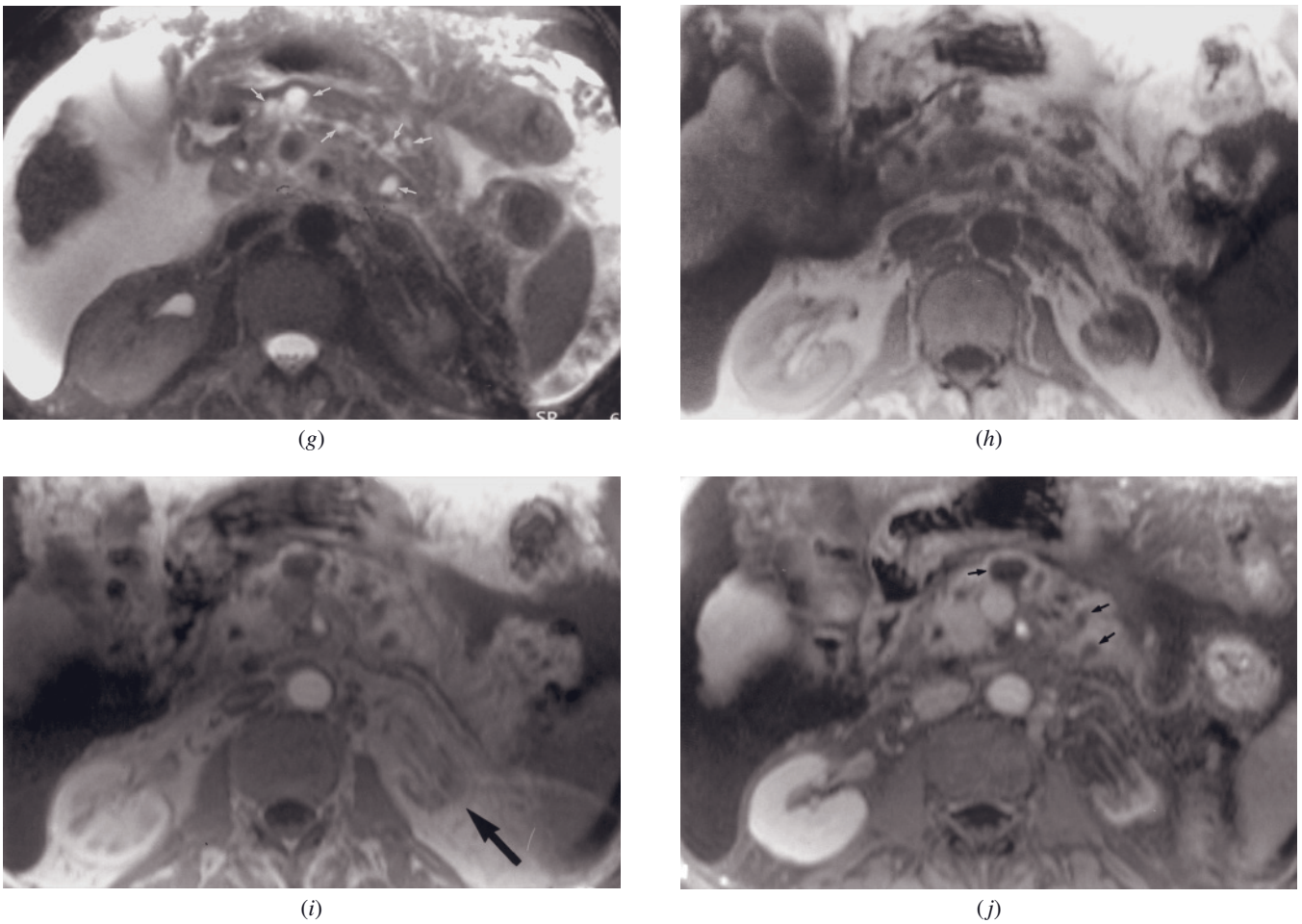

FIG. 4.90 (*Continued*) T2-weighted SS-ETSE (*g*), T1-weighted SGE (*h*), immediate postgadolinium T1-weighted SGE (*i*), and 90-s postgadolinium fat-suppressed SGE (*j*) images in a second patient with alcoholic pancreatitis. There are numerous cysts (arrows, *g*, *j*) scattered throughout the pancreas, and the pancreatic parenchyma enhances poorly on postgadolinium images. There is a large volume of ascites secondary to liver cirrhosis. Note also ischemic nephropathy of the left kidney (arrow, *i*) from main renal artery disease.

A subgroup of these cases has been associated with autoimmune disorders such as Sjögren syndrome, primary biliary cirrhosis, and primary sclerosing cholangitis [105, 106]. Histopathologic examination in cases of chronic nonalcoholic pancreatitis, including associated autoimmune disorders, shows periductal chronic inflammation and fibrosis. This process may result in obstruction or destruction of ducts [107]. Recent studies underscore the importance of diagnosing cases of suspected autoimmune-related chronic pancreatitis because these disorders may have a salutary response to steroid therapy [108]. Recent studies have described the MR appearance of autoimmune chronic pancreatitis as characterized by enlarged pancreas with moderately decreased signal intensity on T1-weighted images, moderately high signal intensity on T2-weighted images, and delayed enhancement of the pancreatic parenchyma after gadolinium administration (fig. 4.92). Additional findings that may be observed in autoimmune pancreatitis include 1) capsulelike rim surrounding the diseased parenchyma that is hypointense on T2-weighted images and demonstrates delayed enhancement after gadolinium administration [105], 2) absence of parenchymal atrophy, 3) ductal dilatation proximal to the site of stenosis, 4) absence of extra-pancreatic fluid, and 5) clear demarcation of the lesion [106].

Inflammatory Conditions and Infections of the Pancreas

A variety of bacterial, granulomatous, viral, and parasitic diseases may rarely affect the pancreas. Inflammatory diseases may appear as ill-defined focal masses that show irregular infiltration of pancreatic tissue (fig. 4.93). Differentiation between malignant and inflammatory

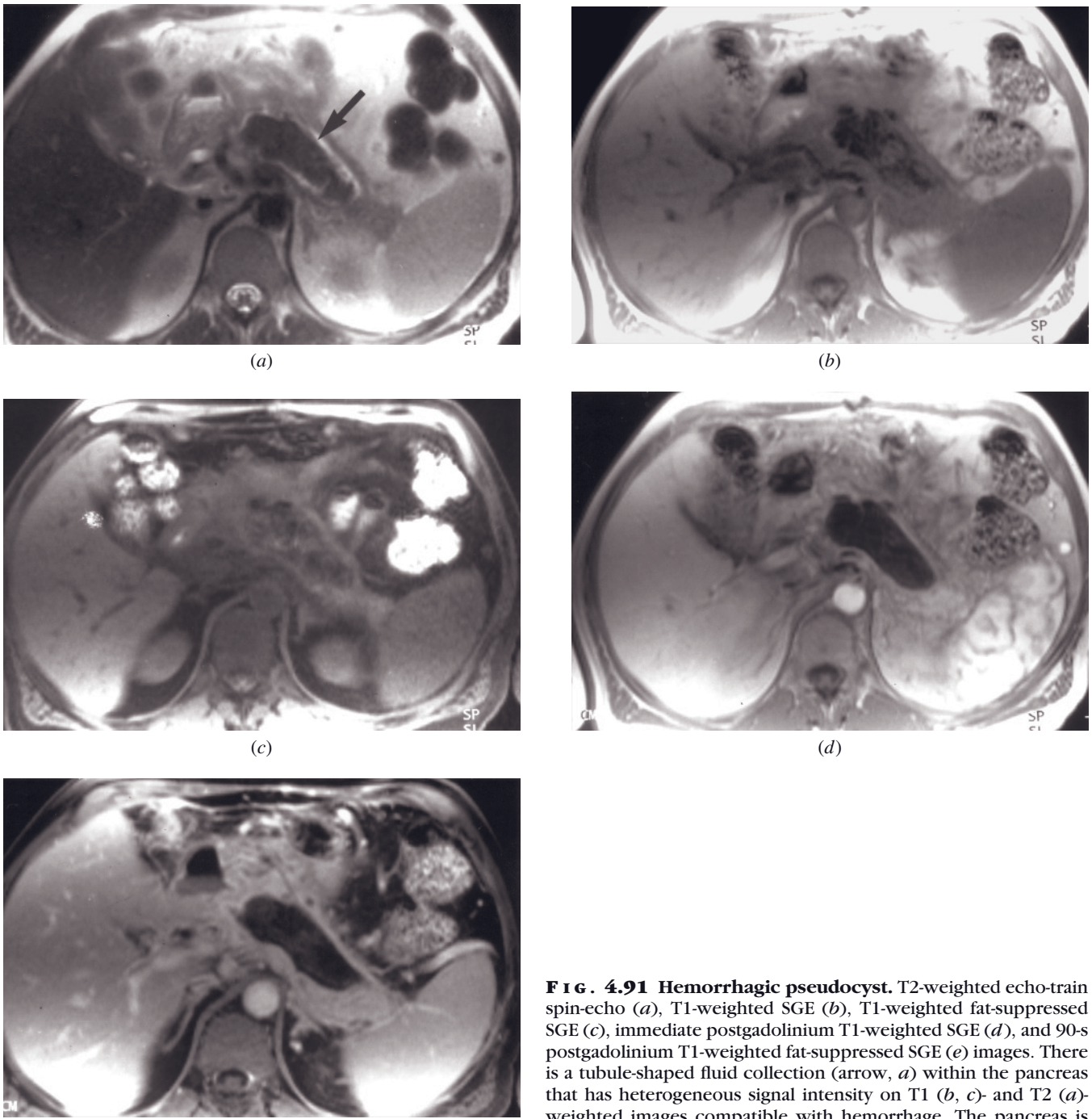

FIG. 4.91 Hemorrhagic pseudocyst. T2-weighted echo-train spin-echo (*a*), T1-weighted SGE (*b*), T1-weighted fat-suppressed SGE (*c*), immediate postgadolinium T1-weighted SGE (*d*), and 90-s postgadolinium T1-weighted fat-suppressed SGE (*e*) images. There is a tubule-shaped fluid collection (arrow, *a*) within the pancreas that has heterogeneous signal intensity on T1 (*b*, *c*)- and T2 (*a*)-weighted images compatible with hemorrhage. The pancreas is enlarged and has a blurred contour.

diseases may not, however, be reliably made on imaging studies. Pancreatitis may also arise as a reaction to drugs (fig. 4.94) or toxins.

TRAUMA

Traumatic injury of the pancreas may result in a spectrum of abnormalities from mild contusion to laceration and transection. Stenosis of the pancreatic duct with distal ductal dilatation may be observed as a sequel of trauma (fig. 4.95). A combination of tissue imaging sequences and MR pancreatography can facilitate this diagnosis by the demonstration of ductal dilatation and changes of chronic pancreatitis of the pancreas distal to the stenosis (fig. 4.96). This condition is not rare, and this entity should be entertained when a sharp transition is observed in the midbody of the pancreas, overlying

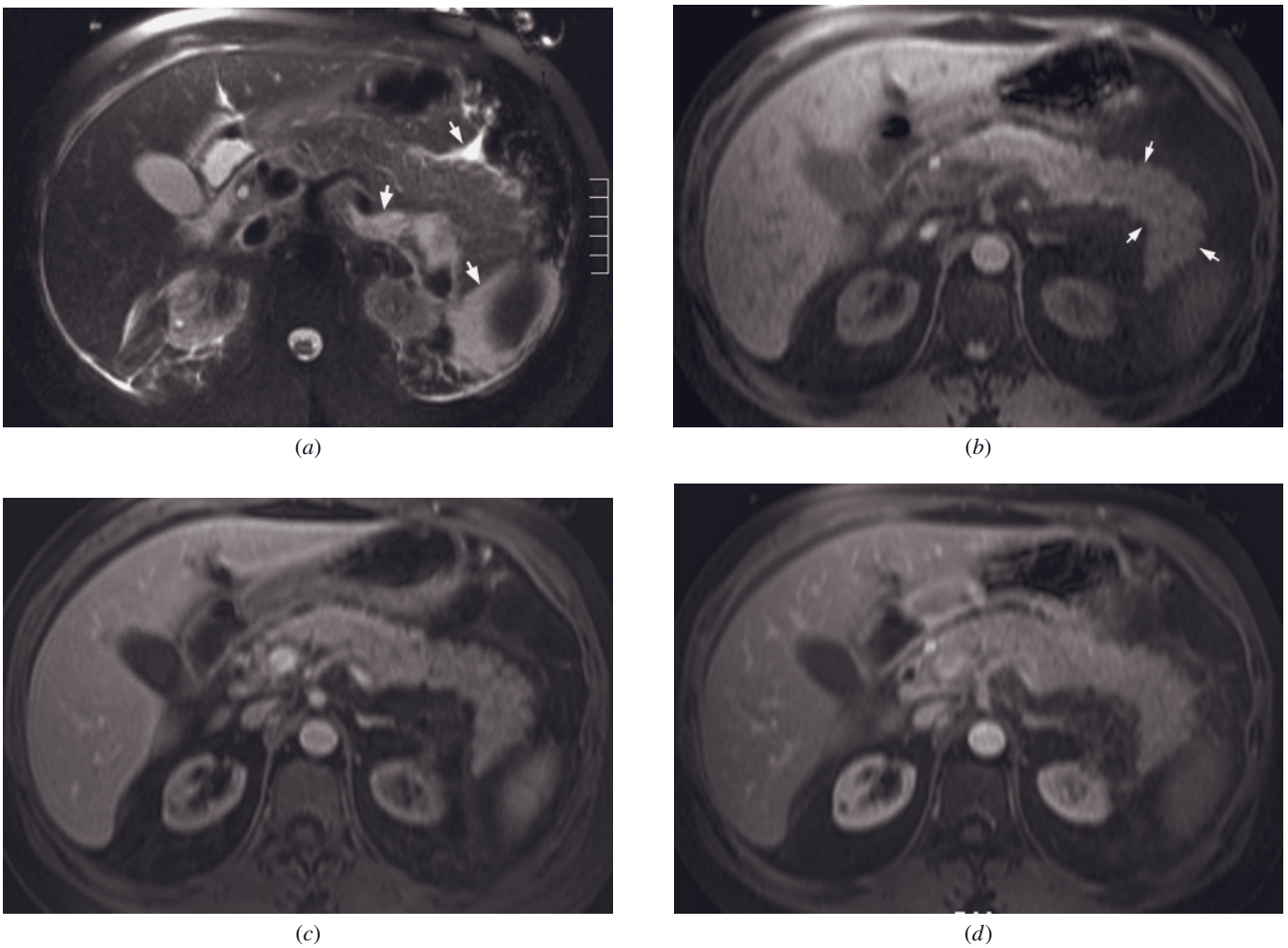

(*a*) (*b*) (*c*) (*d*)

FIG. 4.92 Autoimmune pancreatitis. Fat-suppressed T2-weighted SS-ETSE (*a*), fat-suppressed T1-weighted gradient-echo (*b*), and immediate (*c*) and interstitial-phase (*d*) postgadolinium fat-suppressed T1-weighted images in a patient with autoimmune pancreatitis demonstrate a thin layer of peripancreatic and perisplenic fluid that is best seen on fat-suppressed T2-weighted images (arrows, *a*). The distal body and tail of the pancreas show decreased signal intensity compared to the remainder of the pancreas on fat-suppressed T1-weighted gradient-echo images (arrows, *b*). On immediate postgadolinium image the enhancement of the distal pancreas is less than the proximal portion (*c*). On interstitial-phase image distal pancreas becomes isointense with the rest of the pancreas (*d*).

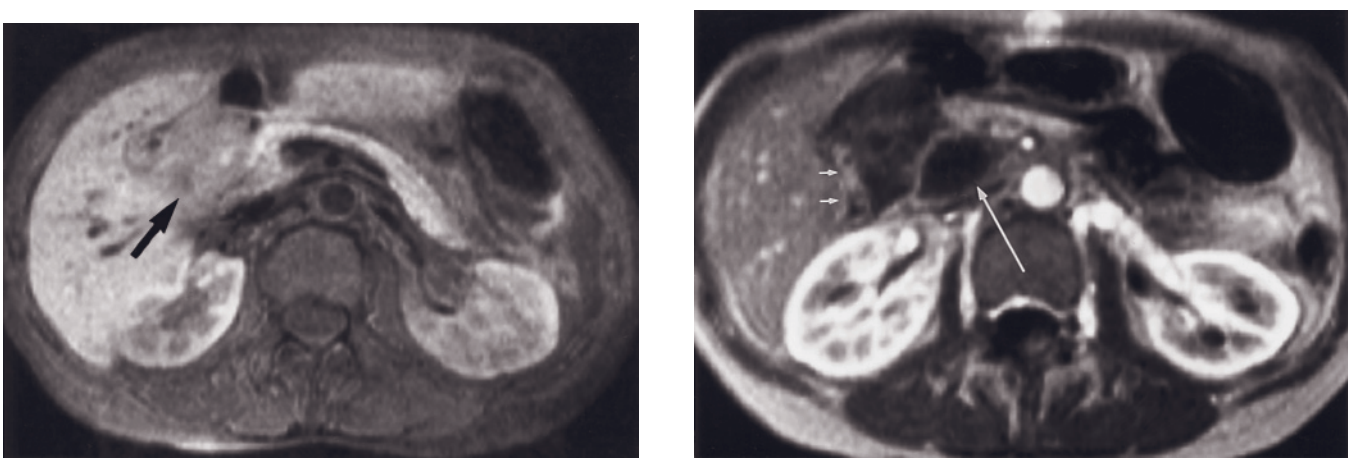

(*a*) (*b*)

FIG. 4.93 Necrotizing granulomatous pancreatitis. T1-weighted fat-suppressed spin-echo (*a*), immediate postgadolinium T1-weighted SGE (*b*), and gadolinium-enhanced T1-weighted fat-suppressed spin-echo (*c*) images. A heterogeneous low-signal

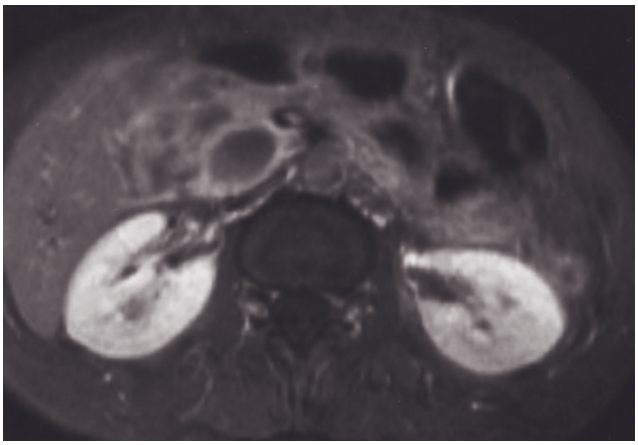

(*c*)

FIG. 4.93 (*Continued*) intensity mass is present, arising from the lateral aspect of the head of the pancreas (arrow, *a*). The remainder of the pancreas is normal and moderately high in signal intensity on T1-weighted fat-suppressed spin-echo images (*a*). The lesion enhances in a heterogeneous minimal fashion on immediate postgadolinium T1-weighted SGE images (*b*). The duodenum (small arrows, *b*) is displaced laterally by the mass. The mass contains a cystic component (thin arrow, *b*). Heterogeneous enhancement of the mass is also present on the interstitial-phase gadolinium-enhanced T1-weighted fat-suppressed image (*c*).

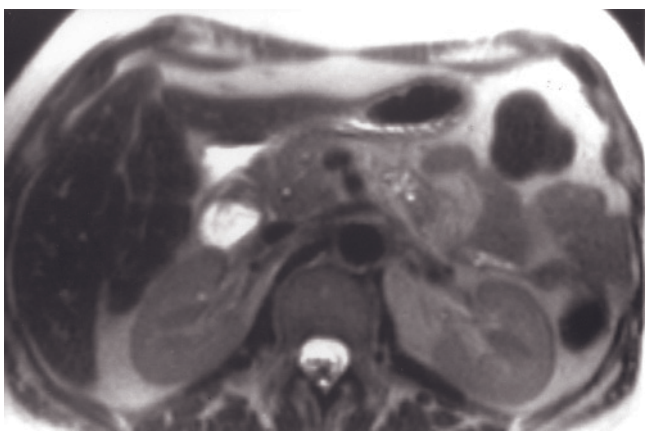

(*a*)

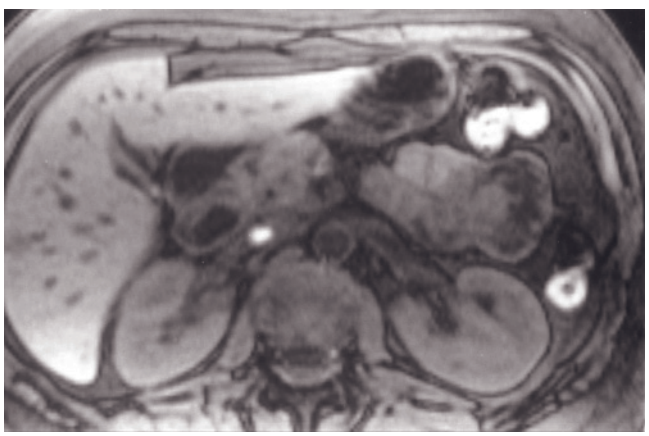

(*b*)

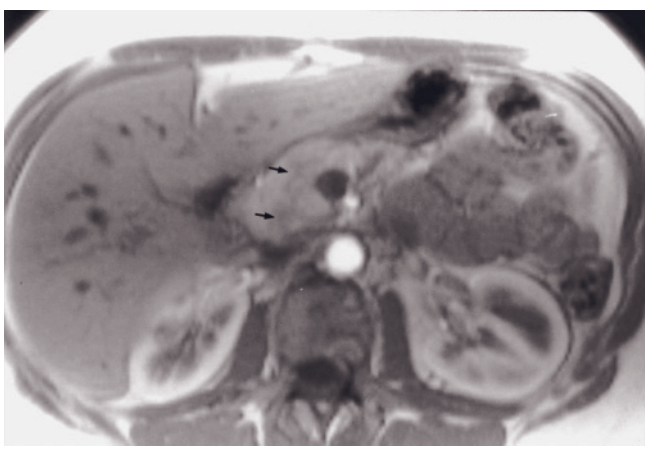

(*c*)

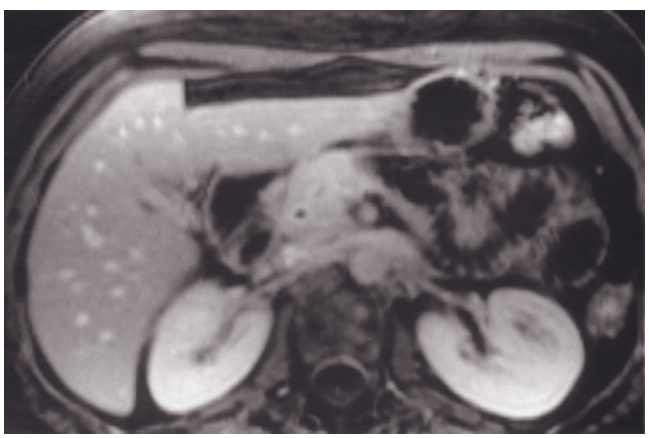

(*d*)

FIG. 4.94 Chemotherapy-induced pancreatitis. T2-weighted ETSE (*a*), T1-weighted fat-suppressed SGE (*b*), immediate postgadolinium T1-weighted SGE (*c*), and 90-s postgadolinium fat-suppressed SGE (*d*) images. In this patient undergoing chemotherapy for breast cancer, there is a heterogeneous low-signal region in the head of the pancreas on the noncontrast T1-weighted fat-suppressed image (*b*) that also shows heterogeneous decreased enhancement (arrows, *c*) on the immediate postgadolinium SGE image (*c*) consistent with pancreatitis secondary to chemotherapy toxicity.

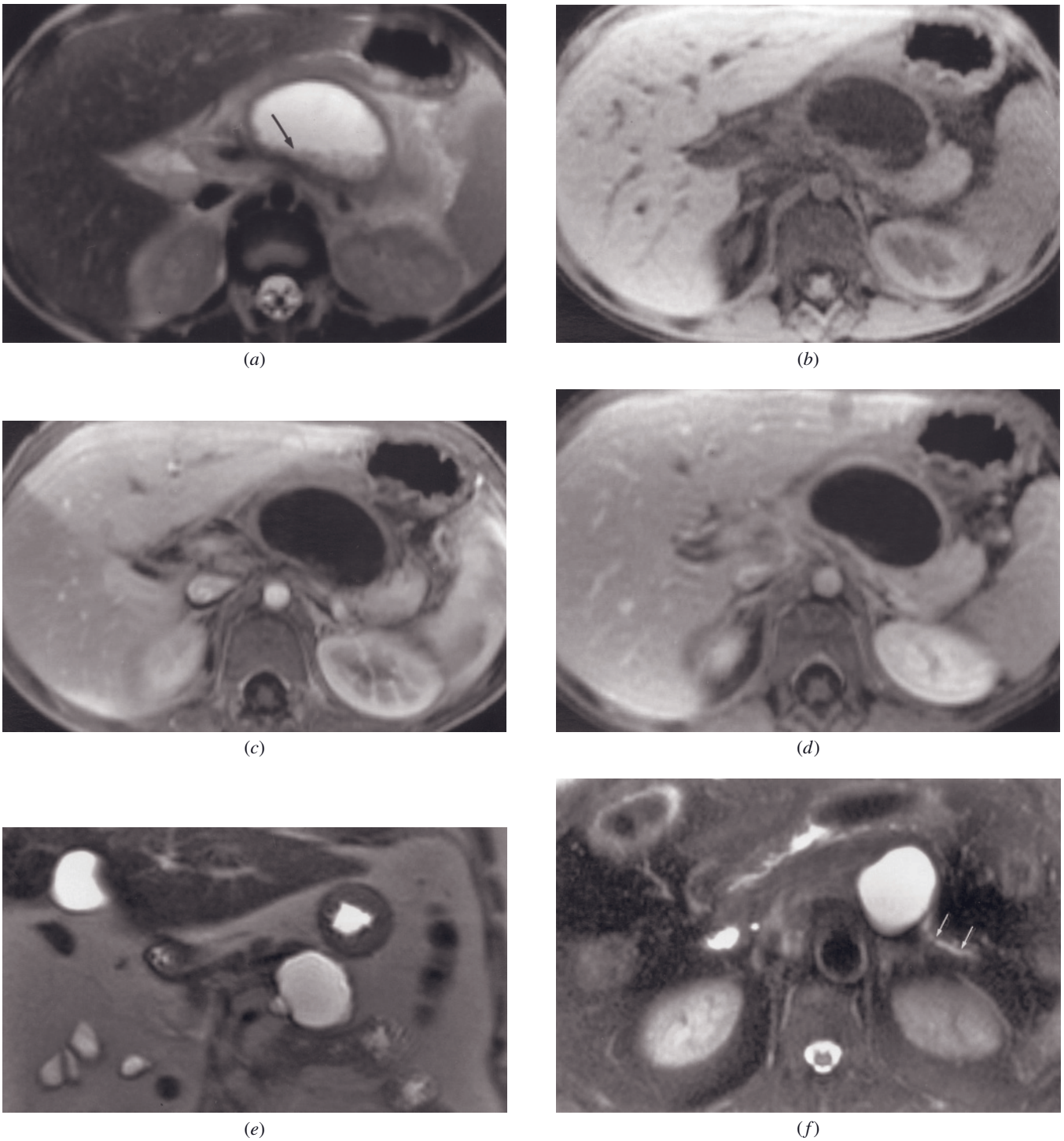

FIG. 4.95 Traumatic pseudocyst. T2-weighted SS-ETSE (*a*), T1-weighted fat-suppressed SGE (*b*), immediate postgadolinium T1-weighted SGE (*c*), and 90-s postgadolinium fat-suppressed SGE (*d*) images in a patient with a history of recent abdominal trauma. There is a pseudocyst in the anterior aspect of the pancreatic body/tail, which contains layering protein/hemoglobin in the dependent portion of the cyst, best appreciated on the T2-weighted image (arrow, *a*). Note transient increased enhancement of the left lobe of the liver on the immediate postgadolinium image (*c*), which reflects compromise of the left portal vein.

Coronal (*e*) and transverse (*f*) T2-weighted SS-ETSE, T1-weighted SGE (*g*), T1-weighted fat-suppressed SGE (*h*), immediate postgadolinium SGE (*i*), and 90-s postgadolinium SGE (*j*) images in a second patient. There is a 4-cm pseudocyst transversing

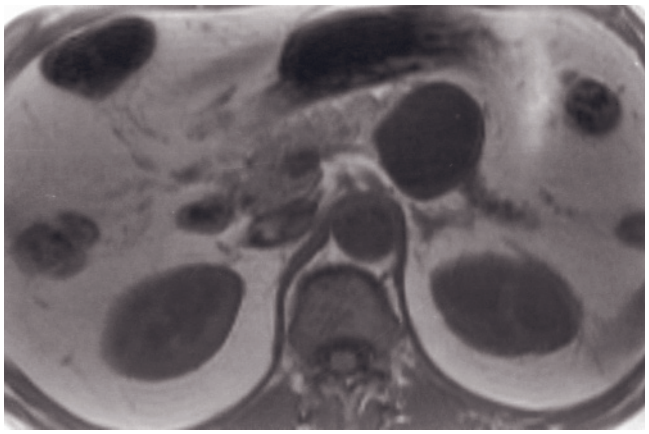

(*g*)

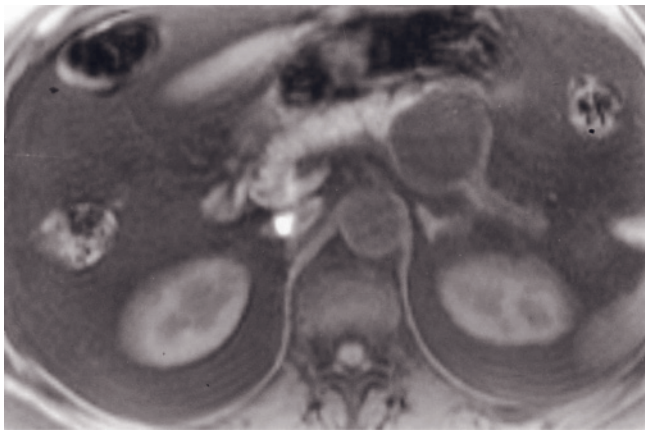

(*h*)

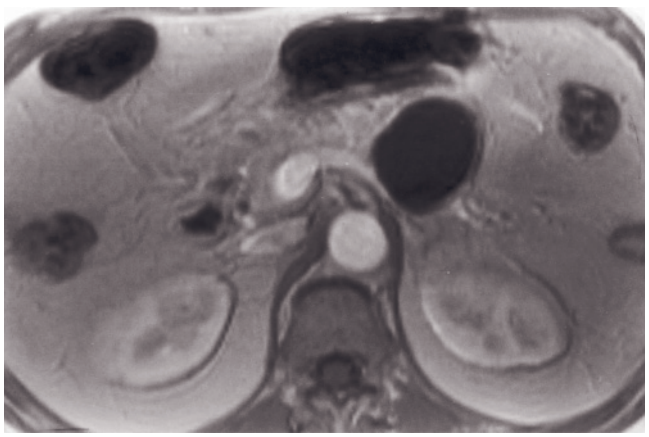

(*i*)

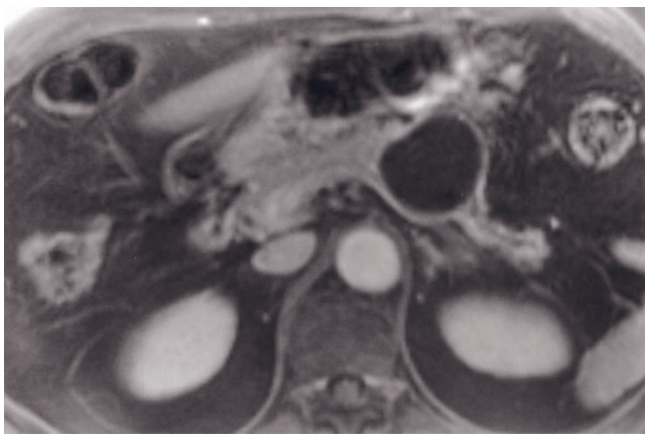

(*j*)

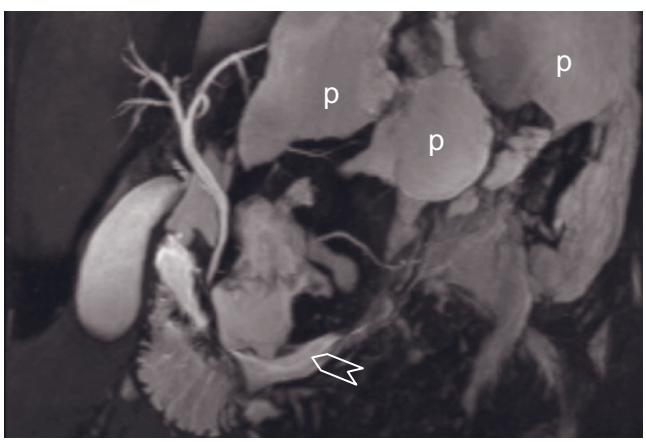

(*k*)

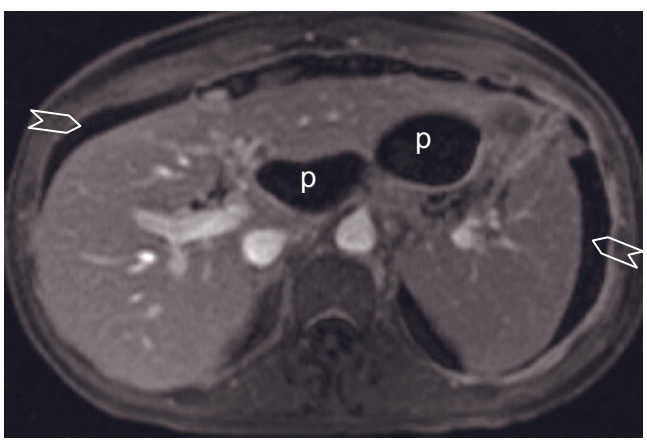

(*l*)

Fig. 4.95 (*Continued*) the pancreas at the junction of the body and tail. The pancreas proximal to the traumatic pseudocyst appears normal. Distal to the pseudocyst, the tail shows ductal dilatation (arrows, *f*) and atrophy consistent with changes of long-term ductal obstruction and resultant chronic pancreatitis, in this patient with a remote history of abdominal trauma. Reconstructed MRCP (*k*), T1-weighted postgadolinium interstitial phase water excitation magnetization prepared rapid gradient echo images (*l–n*) demonstrate traumatic transections located in the pancreatic neck (white arrows, *m*, *n*) and left lobe of the liver (black arrows, *m*, *n*).

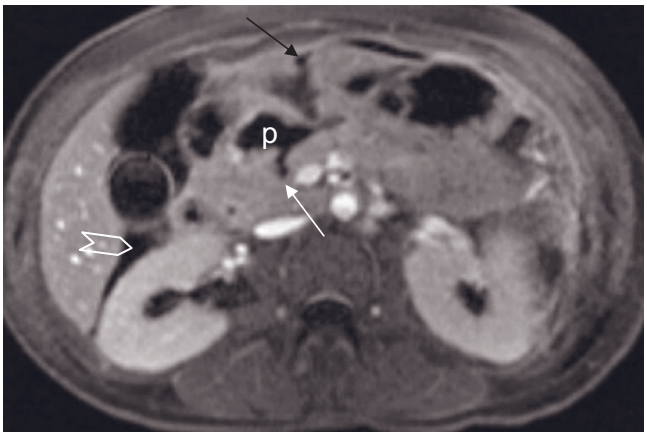

(*m*)

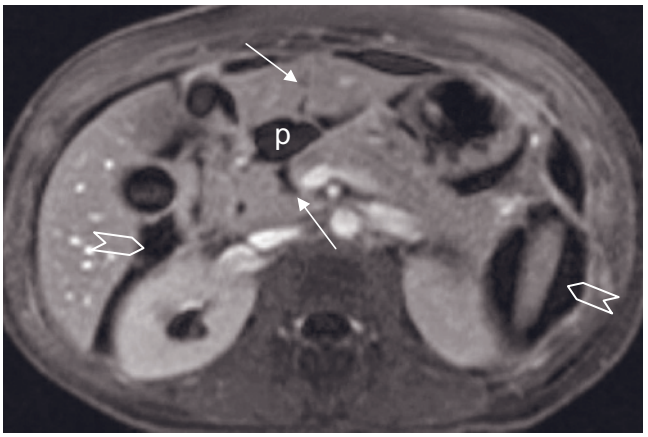

(*n*)

FIG. 4.95 (*Continued*) There are multiple pseudocysts (p, *k*; *l–n*) and free fluid (open arrow; *k–n*) in the abdomen. The peritoneal surfaces also show enhancement due to inflammation.

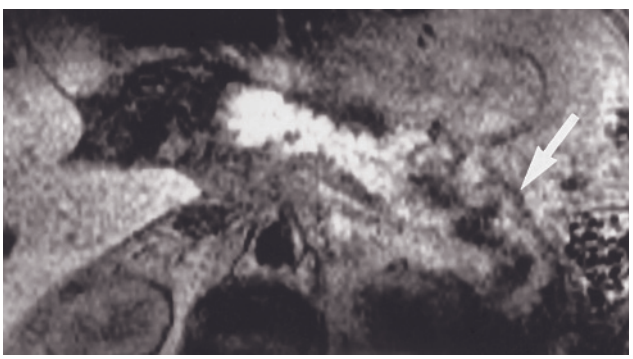

(*a*)

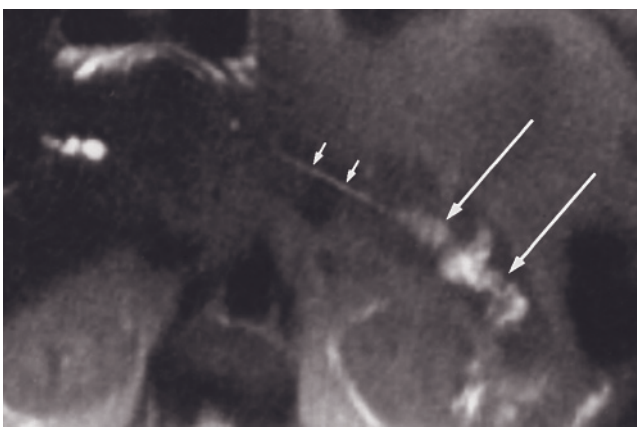

(*b*)

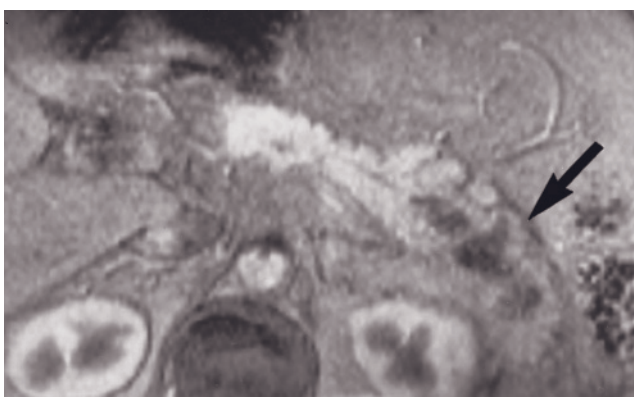

(*c*)

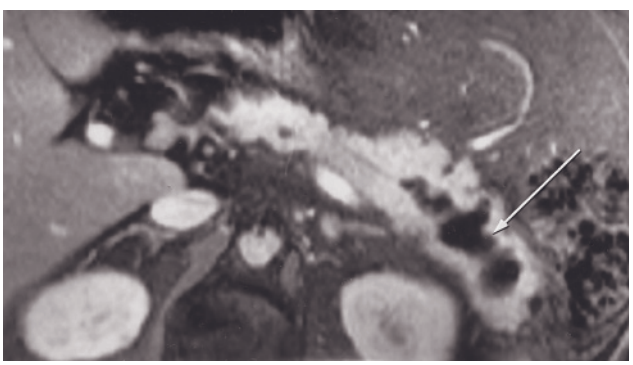

(*d*)

FIG. 4.96 Posttraumatic stenosis of the pancreatic duct. Fat-suppressed T1-weighted SGE (*a*), T2-weighted SS-ETSE (*b*), and immediate (*c*) and 90-s (*d*) postgadolinium fat-suppressed T1 SGE images in a patient who had undergone abdominal trauma 6 years earlier. A transition is noted in the body of the pancreas between normal-appearing proximal pancreas and abnormal-appearing distal pancreas containing an irregularly dilated pancreatic duct. On the precontrast, fat-suppressed image (*a*), the distal pancreas (arrow, *a*) is noted to be low in signal intensity, consistent with changes of chronic pancreatitis. On the SS-ETSE image (*b*) a transition is well shown between normal-caliber pancreatic duct (small arrows, *b*) and abnormally expanded distal pancreatic duct (long arrows, *b*). The distal pancreas is noted to enhance minimally on the immediate postgadolinium image (arrow, *c*). Enhancement of the pancreas is more uniform on the interstitial phase image (*d*), with clear definition of the irregularly dilated pancreatic duct (long arrow, *d*). (Courtesy of Susan M. Ascher, M.D., Dept. of Radiology, Georgetown University Medical Center.)

the vertebral column, with normal pancreatic head and midbody and distal atrophy and ductal dilatation. History of trauma, typically motor vehicle accident, even if remote, should be sought.

PANCREATIC TRANSPLANTS

Dynamic gadolinium-enhanced MRI has been used to assess rejection of pancreatic transplants (fig. 4.97) [109–112]. Enhancement in six normal grafts was 98 ± 23% within the first minute compared to 42 ± 20% in six dysfunctional grafts [109]. Inflammation and infection including abscesses can also be well demonstrated with MRI (fig. 4.97). MR angiography also has been used to detect acute vascular compromise, with high sensitivity and specificity (fig. 4.98) [110, 111]. Complications such as venous thrombosis are well shown on gadolinium-enhanced gradient echo, especially 3D-GE imaging, because of the high spatial resolution [112].

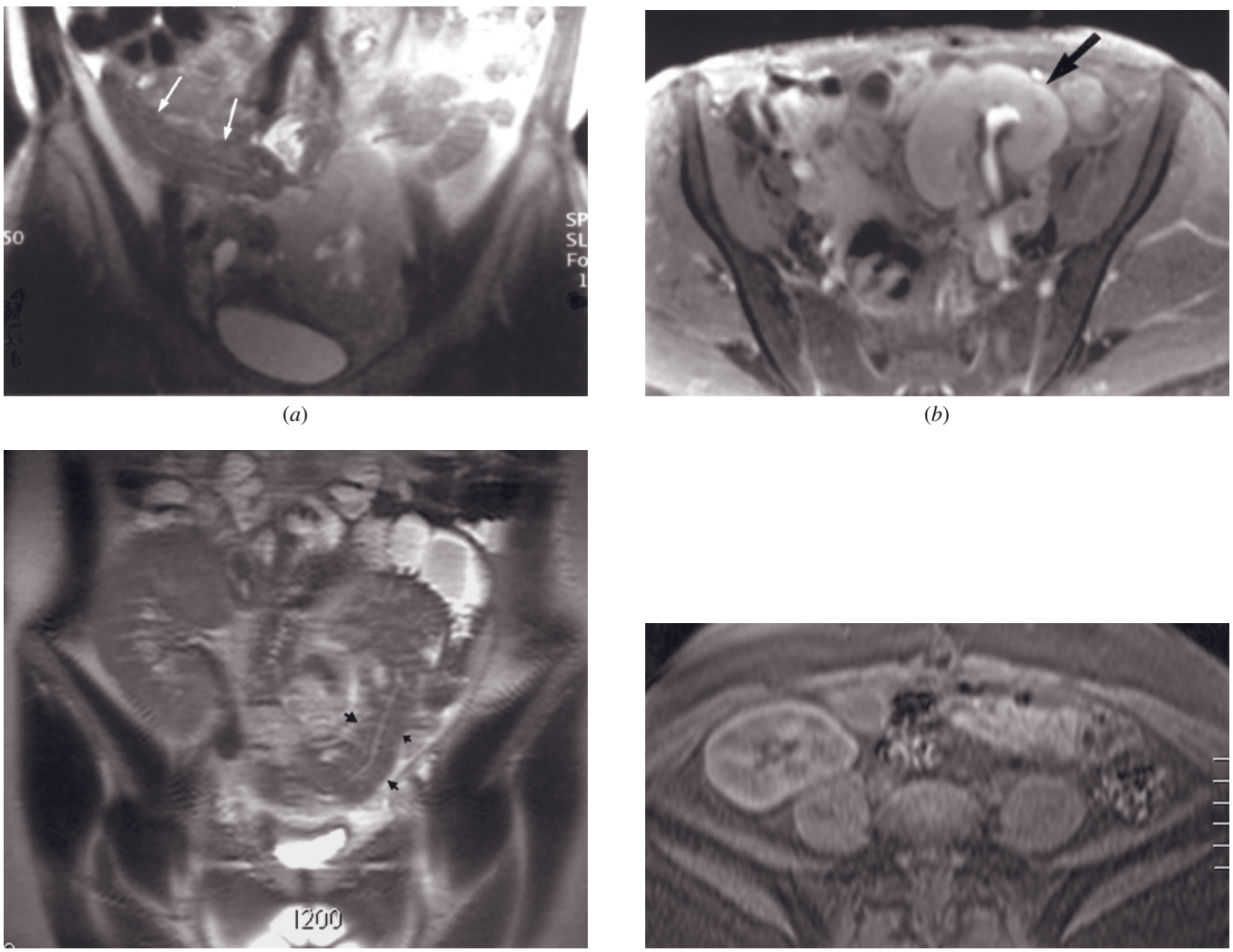

FIG. 4.97 Normal pancreatic transplant. Coronal T2-weighted ETSE (*a*) and 90-s postgadolinium fat-suppressed SGE (*b*) images in a patient status post-pancreas and renal transplant. The transplanted pancreas is normal in signal intensity and is located in the right lower quadrant (arrows, *a*).The transplanted kidney is in the left lower quadrant (arrow, *b*).

Transplanted pancreas and kidney. Coronal T2-weighted SS-ETSE (*c*), fat-suppressed T1-weighted gradient-echo (*d*), immediate postgadolinium fat-suppressed T1-weighted gradient-echo (*e*) and interstitial-phase postgadolinium T1-weighted

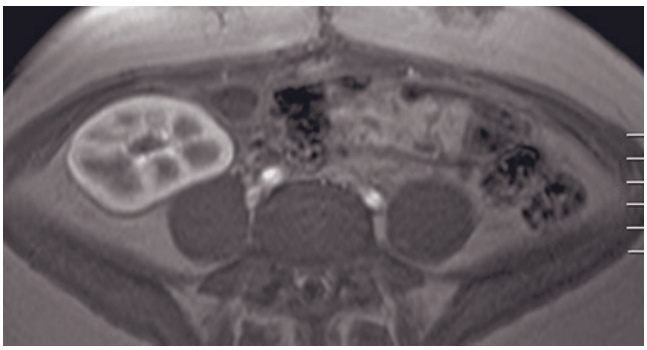

(*e*)

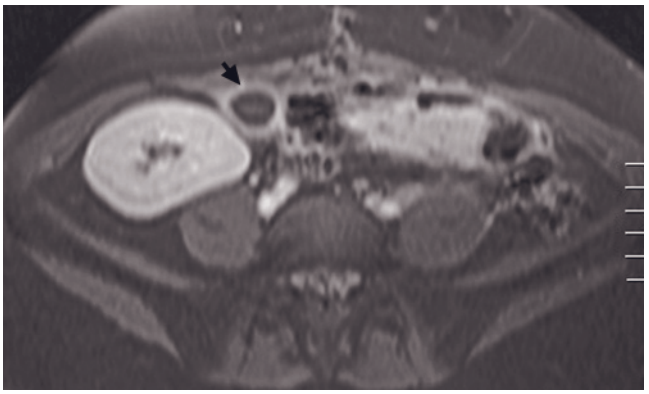

(*f*)

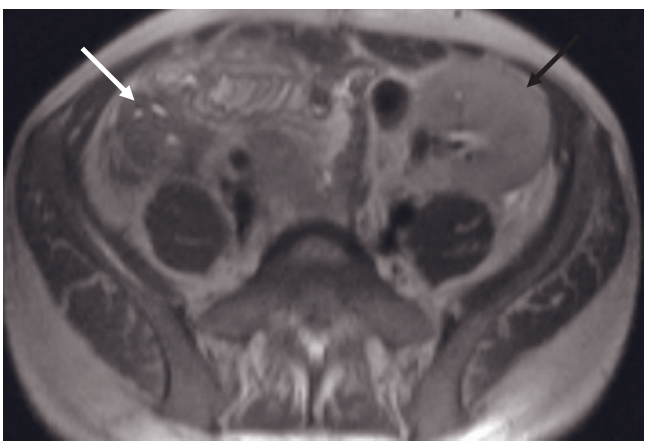

(*g*)

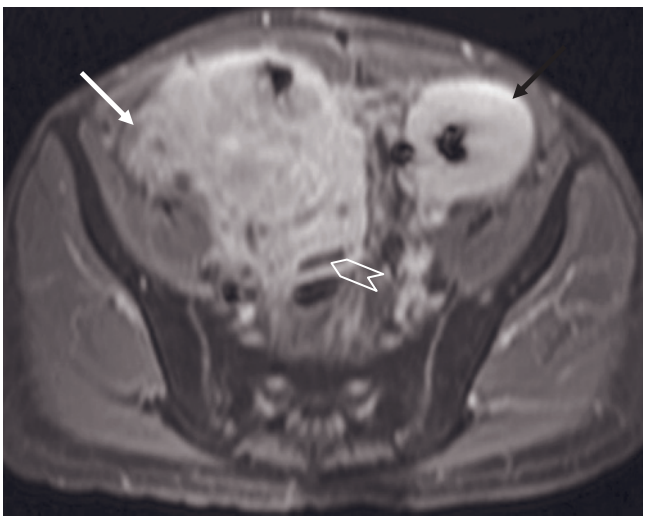

(*h*)

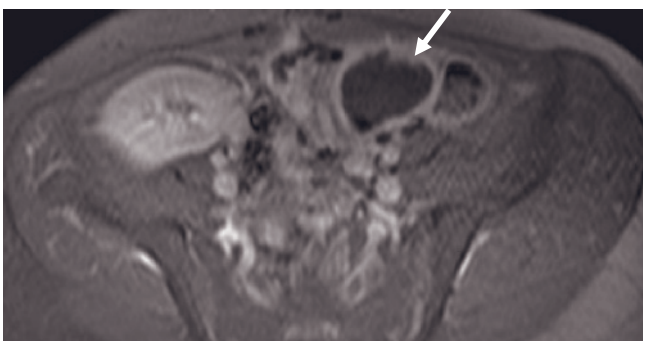

(*i*)

FIG. 4.97 (*Continued*) gradient-echo (*f*, *g*) images in a second patient status postpancreas and renal transplant. The transplanted pancreas (arrows, *c*) is normal in signal intensity on all sequences. There is a small abscess medial to the transplanted kidney (arrow, *f*). T2-weighted single shot echo train spin echo (*g*) and T1-weighted postgadolinium fat-suppressed interstitial phase 3D-GE (*h*) images in a patient with severe pancreatic transplant inflammation. The pancreatic transplant (white arrows, *g*, *h*) is seen in the right lower quadrant. The renal transplant (black arrows, *g*, *h*) is seen in the left lower quadrant. There is severe inflammation involving the pancreatic transplant and adjacent bowel loops in the right lower quadrant, which is characterized by intense enhancement. A small abscess (open arrow, *h*) is also detected adjacent to the transplant and bowel loops. The renal transplant (black arrow, *g*) is edematous and enlarged. T1-weighted postgadolinium fat-suppressed interstitial phase 3D-GE (*i*) image in another patient with an abscess adjacent to a pancreatic transplant. A large abscess (arrow, *i*) containing free air is detected in the left lower quadrant adjacent to the pancreatic transplant tissue.

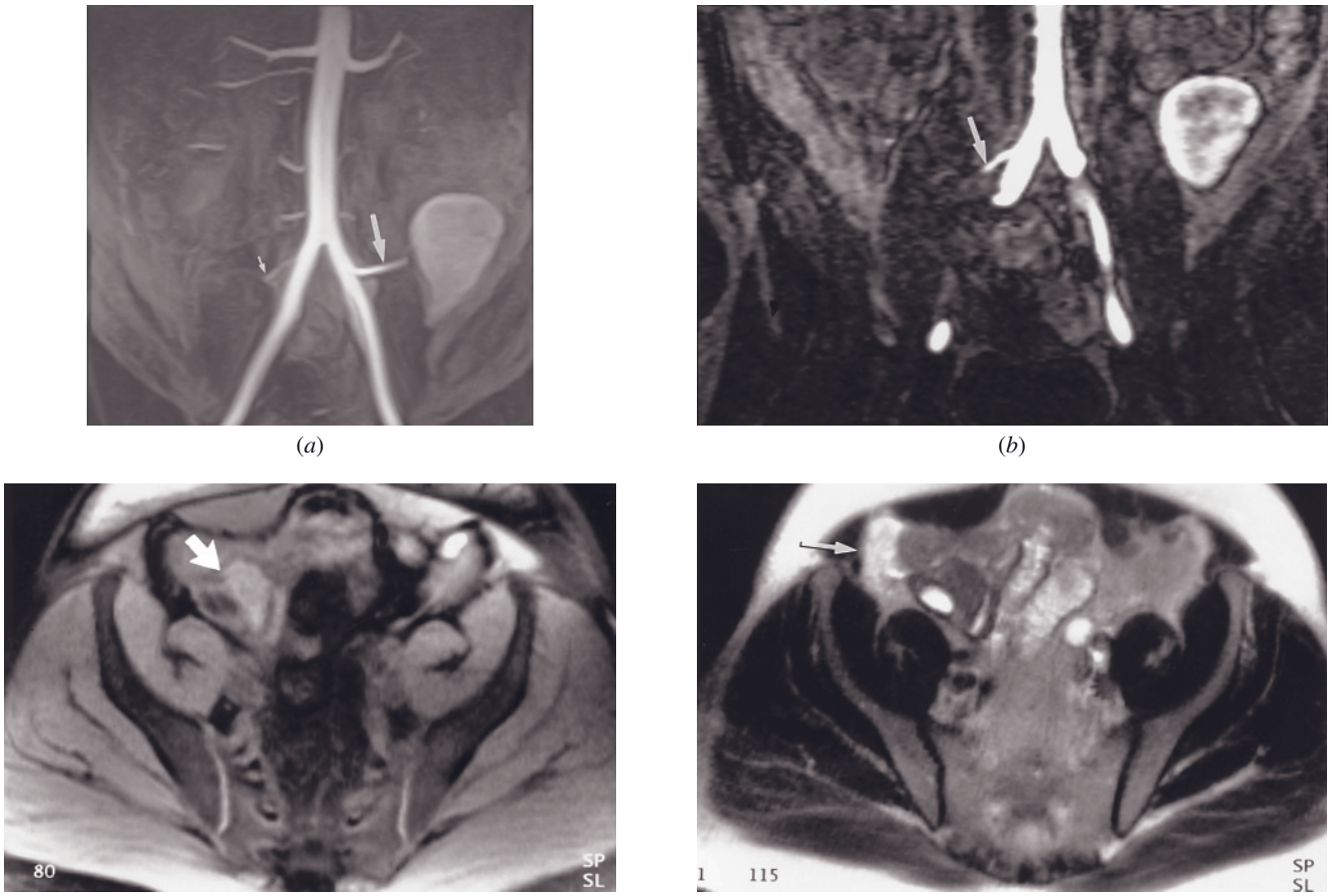

FIG. 4.98 Pancreatic transplant with arterial thrombosis. Coronal MIP reconstructed MR angiography (MRA) (*a*), gadolinium-enhanced 2-mm 3D gradient-echo source (*b*), T1-weighted fat-suppressed SGE (*c*), and T2-weighted SS-ETSE (*d*) images. The MIP reconstructed MRA image demonstrates a normal artery (arrow, *a*) feeding the renal transplant in the left pelvis and an occluded artery (small arrow, *a*) feeding the pancreas transplant in the right pelvis. To establish the diagnosis of occlusion, examination of the source images is essential; occlusion is confirmed on the source image (arrow, *b*) as abrupt termination of the contrast-enhanced vascular lumen. The transplant is identified in the right side of the pelvis on T1-weighted (arrow, *c*) and T2-weighted (*d*) images. Inflammatory fluid (arrow, *d*) is noted adjacent to the pancreas transplant.

REFERENCES

1. Semelka RC, Ascher SM. MR imaging of the pancreas-state of the art. *Radiology* 188(3): 593–602, 1993.
2. Winston CB, Mitchell DG, Outwater EK et al. Pancreatic signal intensity on T1-weighted fat saturation MR images: clinical correlation. *J Magn Reson Imaging* 5(3): 267–271, 1995.
3. Mitchell DG, Vinitski S, Saponaro S et al. Liver and pancreas: improved spin-echo T1 contrast by shorter echo time and fat suppression at 1.5T. *Radiology* 178(1): 67–71, 1991.
4. Semelka RC, Kroeker MA, Shoenut JP et al. Pancreatic disease: prospective comparison of CT, ERCP, and 1.5-T MR imaging with dynamic gadolinium enhancement and fat suppression. *Radiology* 181(3): 785–791, 1991.
5. Takehara Y, Ichijo K, Tooyama N et al. Breath-hold MR cholangiopancreatography with a long-echo-train fast spin-echo sequence and a surface coil in chronic pancreatitis. *Radiology* 192(1): 73–78, 1994.
6. Bret PM, Reinhold C, Taourel P et al. Pancreas divisum: evaluation with MR cholangiopancreatography. *Radiology* 199(1): 99–103, 1996.
7. Soto JA, Barish MA, Yucel EK et al. Pancreatic duct: MR cholangiopancreatography with a three-dimensional fast spin-echo technique. *Radiology* 196(2): 459–464, 1995.
8. Zapparoli M, Semelka RC, Altun E et al. 3.0-T MRI evaluation of patients with chronic liver diseases: initial observations. *Magn Reson Imaging* 26(5): 650–660, 2008.
9. Semelka RC, Simm FC, Recht MP et al. MR imaging of the pancreas at high field strength: comparison of six sequences. *J Comput Assist Tomogr* 15(6): 966–971, 1991.
10. Mitchell DG, Winston CB, Outwater EK et al. Delineation of pancreas with MR imaging: multiobserver comparison of five pulse sequences. *J Magn Reson Imaging* 5(2): 193–199, 1995.
11. Fulcher AS, Turner MA. MR pancreatography: a useful tool for evaluating pancreatic disorders. *Radiographics* 19(1): 5–24; discussion 41–24; quiz 148–149, 1999.

12. Catalano C, Pavone P, Laghi A et al. Pancreatic adenocarcinoma: combination of MR imaging, MR angiography and MR cholangiopancreatography for the diagnosis and assessment of resectability. *Eur Radiol* 8(3): 428–434, 1998.
13. Cruikshank AH, Benbow EW. *Pathology of the Pancreas*. In. 2nd ed. London: Springer; 1995. p. 30.
14. Delhaye M, Engelholm L, Cremer M. Pancreas divisum: congenital anatomic variant or anomaly? Contribution of endoscopic retrograde dorsal pancreatography. *Gastroenterology* 89(5): 951–958, 1985.
15. Delhaye M, Cremer M. Clinical significance of pancreas divisum. *Acta Gastroenterol Belg* 55(3): 306–313, 1992.
16. Rosai J. In: *Ackerman's Surgical Pathology*. 8th ed. St. Louis, MO: Mosby; 1996. p. 1004.
17. Quest L, Lombard M. Pancreas divisum: opinio divisa. *Gut* 47(3): 317–319, 2000.
18. Desai MB, Mitchell DG, Munoz SJ. Asymptomatic annular pancreas: detection by magnetic resonance imaging. *Magn Reson Imaging* 12(4): 683–685, 1994.
19. Applegate KE, Goske MJ, Pierce G et al. Situs revisited: imaging of the heterotaxy syndrome. *Radiographics* 19(4): 837–852; discussion 853–834, 1999.
20. Gayer G, Apter S, Jonas T et al. Polysplenia syndrome detected in adulthood: report of eight cases and review of the literature. *Abdom Imaging* 24(2): 178–184, 1999.
21. Tham RT, Heyerman HG, Falke TH et al. Cystic fibrosis: MR imaging of the pancreas. *Radiology* 179(1): 183–186, 1991.
22. Ferrozzi F, Bova D, Campodonico F et al. Cystic fibrosis: MR assessment of pancreatic damage. *Radiology* 198(3): 875–879, 1996.
23. King LJ, Scurr ED, Murugan N et al. Hepatobiliary and pancreatic manifestations of cystic fibrosis: MR imaging appearances. *Radiographics* 20(3): 767–777, 2000.
24. Siegelman ES, Mitchell DG, Outwater E et al. Idiopathic hemochromatosis: MR imaging findings in cirrhotic and precirrhotic patients. *Radiology* 188(3): 637–641, 1993.
25. Siegelman ES, Mitchell DG, Semelka RC. Abdominal iron deposition: metabolism, MR findings, and clinical importance. *Radiology* 199(1): 13–22, 1996.
26. Hough DM, Stephens DH, Johnson CD et al. Pancreatic lesions in von Hippel-Lindau disease: prevalence, clinical significance, and CT findings. *AJR Am J Roentgenol* 162(5): 1091–1094, 1994.
27. Boring CC, Squires TS, Tong T. Cancer statistics, 1991. *CA Cancer J Clin* 41(1): 19–36, 1991.
28. Warshaw AL, Fernandez-del Castillo C. Pancreatic carcinoma. *N Engl J Med* 326(7): 455–465, 1992.
29. Moossa AR. Pancreatic cancer: approach to diagnosis, selection for surgery and choice of operation. *Cancer* 50(11 Suppl):2689–2698, 1982.
30. Clark LR, Jaffe MH, Choyke PL et al. Pancreatic imaging. *Radiol Clin North Am* 23(3): 489–501, 1985.
31. Rosai J. In: *Ackerman's Surgical Pathology*. 8th ed. St. Louis, MO: Mosby; 1996. p. 976.
32. Baron RL, Stanley RJ, Lee JK et al. Computed tomographic features of biliary obstruction. *AJR Am J Roentgenol* 140(6): 1173–1178, 1983.
33. Kim JK, Altun E, Elias J, Jr. et al. Focal pancreatic mass: distinction of pancreatic cancer from chronic pancreatitis using gadolinium-enhanced 3D-gradient-echo MRI. *J Magn Reson Imaging* 26(2): 313–322, 2007.
34. Wittenberg J, Simeone JF, Ferrucci JT, Jr. et al. Non-focal enlargement in pancreatic carcinoma. *Radiology* 144(1): 131–135, 1982.
35. Megibow AJ, Bosniak MA, Ambos MA et al. Thickening of the celiac axis and/or superior mesenteric artery: a sign of pancreatic carcinoma on computed tomography. *Radiology* 141(2): 449–453, 1981.
36. Gabata T, Matsui O, Kadoya M et al. Small pancreatic adenocarcinomas: efficacy of MR imaging with fat suppression and gadolinium enhancement. *Radiology* 193(3): 683–688, 1994.
37. Semelka RC, Kelekis NL, Molina PL et al. Pancreatic masses with inconclusive findings on spiral CT: is there a role for MRI? *J Magn Reson Imaging* 6(4): 585–588, 1996.
38. Birchard KR, Semelka RC, Hyslop WB et al. Suspected Pancreatic Cancer: Evaluation by Dynamic Gadolinium-Enhanced 3D Gradient-Echo MRI. *AJR Am J Roentgenol* 185(3): 700–703, 2005.
39. Steiner E, Stark DD, Hahn PF et al. Imaging of pancreatic neoplasms: comparison of MR and CT. *AJR Am J Roentgenol* 152(3): 487–491, 1989.
40. Sarles H, Sahel J. Pathology of chronic calcifying pancreatitis. *Am J Gastroenterol* 66(2): 117–139, 1976.
41. Elias J, Jr., Semelka RC, Altun E et al. Pancreatic cancer: correlation of MR findings, clinical features, and tumor grade. *J Magn Reson Imaging* 26(6): 1556–1563, 2007.
42. Vellet AD, Romano W, Bach DB et al. Adenocarcinoma of the pancreatic ducts: comparative evaluation with CT and MR imaging at 1.5T. *Radiology* 183(1): 87–95, 1992.
43. Pavone P, Laghi A, Passariello R. MR cholangiopancreatography in malignant biliary obstruction. *Semin Ultrasound CT MR* 20(5): 317–323, 1999.
44. Low RN, Semelka RC, Worawattanakul S et al. Extrahepatic abdominal imaging in patients with malignancy: comparison of MR imaging and helical CT in 164 patients. *J Magn Reson Imaging* 12(2): 269–277, 2000.
45. Low RN, Semelka RC, Worawattanakul S et al. Extrahepatic abdominal imaging in patients with malignancy: comparison of MR imaging and helical CT, with subsequent surgical correlation. *Radiology* 210(3): 625–632, 1999.
46. Nishiharu T, Yamashita Y, Abe Y et al. Local extension of pancreatic carcinoma: assessment with thin-section helical CT versus with breath-hold fast MR imaging–ROC analysis. *Radiology* 212(2): 445–452, 1999.
47. Danet IM, Semelka RC, Nagase LL et al. Liver metastases from pancreatic adenocarcinoma: MR imaging characteristics. *J Magn Reson Imaging* 18(2): 181–188, 2003.
48. Benassai G, Mastrorilli M, Quarto G et al. Factors influencing survival after resection for ductal adenocarcinoma of the head of the pancreas. *J Surg Oncol* 73(4): 212–218, 2000.
49. Ariyama J, Suyama M, Satoh K et al. Imaging of small pancreatic ductal adenocarcinoma. *Pancreas* 16(3): 396–401, 1998.
50. Tatli S, Mortele KJ, Levy AD et al. CT and MRI features of pure acinar cell carcinoma of the pancreas in adults. *AJR Am J Roentgenol* 184(2): 511–519, 2005.
51. Mozell E, Stenzel P, Woltering EA et al. Functional endocrine tumors of the pancreas: clinical presentation, diagnosis, and treatment. *Curr Probl Surg* 27(6): 301–386, 1990.
52. Beger HG, Warshaw AL, Carr-Locke D et al. The Pancreas. In. 1st ed. London: Blakwell Science; 1998. p. 1183.
53. Semelka RC, Custodio CM, Cem Balci N et al. Neuroendocrine tumors of the pancreas: spectrum of appearances on MRI. *J Magn Reson Imaging* 11(2): 141–148, 2000.
54. Thompson NW, Eckhauser FE, Vinik AI et al. Cystic neuroendocrine neoplasms of the pancreas and liver. *Ann Surg* 199(2): 158–164, 1984.
55. Mitchell DG, Cruvella M, Eschelman DJ et al. MRI of pancreatic gastrinomas. *J Comput Assist Tomogr* 16(4): 583–585, 1992.
56. Kraus BB, Ros PR. Insulinoma: diagnosis with fat-suppressed MR imaging. *AJR Am J Roentgenol* 162(1): 69–70, 1994.
57. Semelka RC, Cumming MJ, Shoenut JP et al. Islet cell tumors: comparison of dynamic contrast-enhanced CT and MR imaging with dynamic gadolinium enhancement and fat suppression. *Radiology* 186(3): 799–802, 1993.

58. Kelekis NL, Semelka RC, Molina PL et al. ACTH-secreting islet cell tumor: appearances on dynamic gadolinium-enhanced MRI. *Magn Reson Imaging* 13(4): 641–644, 1995.
59. Buetow PC, Parrino TV, Buck JL et al. Islet cell tumors of the pancreas: pathologic-imaging correlation among size, necrosis and cysts, calcification, malignant behavior, and functional status. *AJR Am J Roentgenol* 165(5): 1175–1179, 1995.
60. Smith TM, Semelka RC, Noone TC et al. Islet cell tumor of the pancreas associated with tumor thrombus in the portal vein. *Magn Reson Imaging* 17(7): 1093–1096, 1999.
61. Pipeleers-Marichal M, Donow C, Heitz PU et al. Pathologic aspects of gastrinomas in patients with Zollinger-Ellison syndrome with and without multiple endocrine neoplasia type I. *World J Surg* 17(4): 481–488, 1993.
62. Wank SA, Doppman JL, Miller DL et al. Prospective study of the ability of computed axial tomography to localize gastrinomas in patients with Zollinger-Ellison syndrome. *Gastroenterology* 92(4): 905–912, 1987.
63. Frucht H, Doppman JL, Norton JA et al. Gastrinomas: comparison of MR imaging with CT, angiography, and US. *Radiology* 171(3): 713–717, 1989.
64. Muller MF, Meyenberger C, Bertschinger P et al. Pancreatic tumors: evaluation with endoscopic US, CT, and MR imaging. *Radiology* 190(3): 745–751, 1994.
65. Galiber AK, Reading CC, Charboneau JW et al. Localization of pancreatic insulinoma: comparison of pre- and intraoperative US with CT and angiography. *Radiology* 166(2): 405–408, 1988.
66. Tjon ATRT, Jansen JB, Falke TH et al. MR, CT, and ultrasound findings of metastatic vipoma in pancreas. *J Comput Assist Tomogr* 13(1): 142–144, 1989.
67. Carlson B, Johnson CD, Stephens DH et al. MRI of pancreatic islet cell carcinoma. *J Comput Assist Tomogr* 17(5): 735–740, 1993.
68. Tjon ATRT, Jansen JB, Falke TH et al. Imaging features of somatostatinoma: MR, CT, US, and angiography. *J Comput Assist Tomogr* 18(3): 427–431, 1994.
69. Doppman JL, Nieman LK, Cutler GB, Jr. et al. Adrenocorticotropic hormone–secreting islet cell tumors: are they always malignant? *Radiology* 190(1): 59–64, 1994.
70. Ros PR, Hamrick-Turner JE, Chiechi MV et al. Cystic masses of the pancreas. *Radiographics* 12(4): 673–686, 1992.
71. Lewandrowski K, Warshaw A, Compton C. Macrocystic serous cystadenoma of the pancreas: a morphologic variant differing from microcystic adenoma. *Hum Pathol* 23(8): 871–875, 1992.
72. Khurana B, Mortele KJ, Glickman J et al. Macrocystic serous adenoma of the pancreas: radiologic-pathologic correlation. *AJR Am J Roentgenol* 181(1): 119–123, 2003.
73. Buetow PC, Rao P, Thompson LD. From the Archives of the AFIP. Mucinous cystic neoplasms of the pancreas: radiologic-pathologic correlation. *Radiographics* 18(2): 433–449, 1998.
74. Minami M, Itai Y, Ohtomo K et al. Cystic neoplasms of the pancreas: comparison of MR imaging with CT. *Radiology* 171(1): 53–56, 1989.
75. Friedman AC, Lichtenstein JE, Dachman AH. Cystic neoplasms of the pancreas. Radiological-pathological correlation. *Radiology* 149(1): 45–50, 1983.
76. Compagno J, Oertel JE. Mucinous cystic neoplasms of the pancreas with overt and latent malignancy (cystadenocarcinoma and cystadenoma). A clinicopathologic study of 41 cases. *Am J Clin Pathol* 69(6): 573–580, 1978.
77. Silas AM, Morrin MM, Raptopoulos V et al. Intraductal papillary mucinous tumors of the pancreas. *AJR Am J Roentgenol* 176(1): 179–185, 2001.
78. Traverso LW, Peralta EA, Ryan JA, Jr. et al. Intraductal neoplasms of the pancreas. *Am J Surg* 175(5): 426–432, 1998.
79. Procacci C, Megibow AJ, Carbognin G et al. Intraductal papillary mucinous tumor of the pancreas: a pictorial essay. *Radiographics* 19(6): 1447–1463, 1999.
80. Koito K, Namieno T, Ichimura T et al. Mucin-producing pancreatic tumors: comparison of MR cholangiopancreatography with endoscopic retrograde cholangiopancreatography. *Radiology* 208(1): 231–237, 1998.
81. Onaya H, Itai Y, Niitsu M et al. Ductectatic mucinous cystic neoplasms of the pancreas: evaluation with MR cholangiopancreatography. *AJR Am J Roentgenol* 171(1): 171–177, 1998.
82. Irie H, Honda H, Aibe H et al. MR cholangiopancreatographic differentiation of benign and malignant intraductal mucin-producing tumors of the pancreas. *AJR Am J Roentgenol* 174(5): 1403–1408, 2000.
83. Ohtomo K, Furui S, Onoue M et al. Solid and papillary epithelial neoplasm of the pancreas: MR imaging and pathologic correlation. *Radiology* 184(2): 567–570, 1992.
84. Thompson LD, Becker RC, Przygodzki RM et al. Mucinous cystic neoplasm (mucinous cystadenocarcinoma of low-grade malignant potential) of the pancreas: a clinicopathologic study of 130 cases. *Am J Surg Pathol* 23(1): 1–16, 1999.
85. Zeman RK, Schiebler M, Clark LR et al. The clinical and imaging spectrum of pancreaticoduodenal lymph node enlargement. *AJR Am J Roentgenol* 144(6): 1223–1227, 1985.
86. Kelekis NL, Semelka RC, Siegelman ES. MRI of pancreatic metastases from renal cancer. *J Comput Assist Tomogr* 20(2): 249–253, 1996.
87. Steinberg W, Tenner S. Acute pancreatitis. *N Engl J Med* 330(17):1198–1210, 1994.
88. Kattwinkel J, Lapey A, Di Sant'Agnese PA et al. Hereditary pancreatitis: three new kindreds and a critical review of the literature. *Pediatrics* 51(1): 55–69, 1973.
89. Lee SP, Nicholls JF, Park HZ. Biliary sludge as a cause of acute pancreatitis. *N Engl J Med* 326(9): 589–593, 1992.
90. Shearman DJC, Finlayson N, Camilleri M et al. In: *Diseases of the Gastrointestinal Tract and Liver*. 3rd ed. New York: Churchill Livingstone; 1997. p. 1253.
91. Balthazar EJ. CT diagnosis and staging of acute pancreatitis. *Radiol Clin North Am* 27(1): 19–37, 1989.
92. Balthazar EJ, Robinson DL, Megibow AJ et al. Acute pancreatitis: value of CT in establishing prognosis. *Radiology* 174(2): 331–336, 1990.
93. Johnson CD, Stephens DH, Sarr MG. CT of acute pancreatitis: correlation between lack of contrast enhancement and pancreatic necrosis. *AJR Am J Roentgenol* 156(1): 93–95, 1991.
94. Saifuddin A, Ward J, Ridgway J et al. Comparison of MR and CT scanning in severe acute pancreatitis: initial experiences. *Clin Radiol* 48(2): 111–116, 1993.
95. Martin DR, Karabulut N, Yang M et al. High signal peripancreatic fat on fat-suppressed spoiled gradient echo imaging in acute pancreatitis: preliminary evaluation of the prognostic significance. *J Magn Reson Imaging* 18(1): 49–58, 2003.
96. Morgan DE, Baron TH, Smith JK et al. Pancreatic fluid collections prior to intervention: evaluation with MR imaging compared with CT and US. *Radiology* 203(3): 773–778, 1997.
97. Bank S. Chronic pancreatitis: clinical features and medical management. *Am J Gastroenterol* 81(3): 153–167, 1986.
98. Steer ML, Waxman I, Freedman S. Chronic pancreatitis. *N Engl J Med* 332(22):1482–1490, 1995.
99. Lowenfels AB, Maisonneuve P, Cavallini G et al. Pancreatitis and the risk of pancreatic cancer. International Pancreatitis Study Group. *N Engl J Med* 328(20):1433–1437, 1993.
100. Luetmer PH, Stephens DH, Ward EM. Chronic pancreatitis: reassessment with current CT. *Radiology* 171(2): 353–357, 1989.

101. Aranha GV, Prinz RA, Freeark RJ et al. The spectrum of biliary tract obstruction from chronic pancreatitis. *Arch Surg* 119(5): 595–600, 1984.
102. Lammer J, Herlinger H, Zalaudek G et al. Pseudotumorous pancreatitis. *Gastrointest Radiol* 10(1): 59–67, 1985.
103. Sostre CF, Flournoy JG, Bova JG et al. Pancreatic phlegmon. Clinical features and course. *Dig Dis Sci* 30(10):918–927, 1985.
104. Semelka RC, Shoenut JP, Kroeker MA et al. Chronic pancreatitis: MR imaging features before and after administration of gadopentetate dimeglumine. *J Magn Reson Imaging* 3(1): 79–82, 1993.
105. Irie H, Honda H, Baba S et al. Autoimmune pancreatitis: CT and MR characteristics. *AJR Am J Roentgenol* 170(5): 1323–1327, 1998.
106. Van Hoe L, Gryspeerdt S, Ectors N et al. Nonalcoholic duct-destructive chronic pancreatitis: imaging findings. *AJR Am J Roentgenol* 170(3): 643–647, 1998.
107. Ectors N, Maillet B, Aerts R et al. Non-alcoholic duct destructive chronic pancreatitis. *Gut* 41(2): 263–268, 1997.
108. Ito T, Nakano I, Koyanagi S et al. Autoimmune pancreatitis as a new clinical entity. Three cases of autoimmune pancreatitis with effective steroid therapy. *Dig Dis Sci* 42(7): 1458–1468, 1997.
109. Fernandez MP, Bernardino ME, Neylan JF et al. Diagnosis of pancreatic transplant dysfunction: value of gadopentetate dimeglumine-enhanced MR imaging. *AJR Am J Roentgenol* 156(6): 1171–1176, 1991.
110. Krebs TL, Daly B, Wong JJ et al. Vascular complications of pancreatic transplantation: MR evaluation. *Radiology* 196(3): 793–798, 1995.
111. Krebs TL, Daly B, Wong-You-Cheong JJ et al. Acute pancreatic transplant rejection: evaluation with dynamic contrast-enhanced MR imaging compared with histopathologic analysis. *Radiology* 210(2): 437–442, 1999.
112. Eubank WB, Schmiedl UP, Levy AE et al. Venous thrombosis and occlusion after pancreas transplantation: evaluation with breath-hold gadolinium-enhanced three-dimensional MR imaging. *AJR Am J Roentgenol* 175(2): 381–385, 2000.

CHAPTER 5

SPLEEN

ERSAN ALTUN, JORGE ELIAS, JR., YOUNG HOON KIM, AND RICHARD C. SEMELKA

To cure the mind's wrong bias, spleen,
some recommend the bowling green,
some, hilly walks;
all exercise
The Spleen (1737) Matthew Green

Throughout the ages, the human spleen has received attention from poets as the producer of melancholy and ill temper. Long conceived as the seat of negative temper, it was Galen (131–201 A.D.) who believed that the spleen, with its spongy consistency, extracted "melancholy" from the blood or liver before excreting the "humor" via splenogastric veins into stomach. Though couched in the language of antiquity, Galen's theory was a prescient one and prefigured the modern-day, well-established functions of the organ as a specialized filter of blood and in immune surveillance.

NORMAL ANATOMY

The spleen consists of a large encapsulated mass of vascular and lymphoid tissue and is situated posteriorly in the left upper quadrant of the abdomen. It is typically crescent shaped, with a convex lateral border conforming to the abdominal wall and left hemidiaphragm and a concave medial border conforming to the stomach and left kidney. The splenic hilum is directed anteromedially, and the splenic artery and vein enter the spleen at this location. The splenic vein follows a relatively straight course along the posterior surface of the body and tail of the pancreas. The splenic artery is slightly superior to the vein and is often tortuous. The spleen is suspended by diaphragmatic attachments and by the splenorenal, gastrosplenic, and splenocolic ligaments. Veins within these ligamentous structures commonly dilate in the presence of portal hypertension. Isolated dilatation of short gastric veins and left gastro-omental veins along the greater curvature of the stomach may be seen in the presence of splenic vein thrombosis.

The freshly cut surface of an unfixed spleen is a reflection of its underlying microscopic architecture, as one can observe glistening maroon parenchyma, or red pulp, flecked with gray-white nodules, the white pulp. Microscopically, the red pulp consists of numerous, thin-walled vascular sinusoids separated by the splenic cords (Billroth cords). The sinusoids are lined by fenestrated

Abdominal-Pelvic MRI, Third Edition, edited by Richard C. Semelka. Copyright © 2010 John Wiley & Sons, Inc.

endothelium providing easy passage of cells between sinusoidal lumens and surrounding cords. The splenic cords are spongelike and consist of a labyrinth of macrophages loosely connected by long dendritic process, reticular cells, and reticular fibers. This framework provides a physical and functional filter through which systemic circulatory blood can slowly seep. The white pulp consists of lymphoid follicles containing a central arteriole surrounded by the periarteriolar lymphoid sheath (PALS). The lymphoid cells forming PALS are predominantly T cells, whereas lymphoid follicles consist mainly of B cells. In neonates, the spleen is predominantly composed of red pulp. With age and progressive antigenic stimulation, the volume of white pulp gradually increases to occupy approximately 20% of the splenic parenchyma in the adult.

The white pulp is intimately associated with the arterial tree, whereas the red pulp is associated with the venous system draining the spleen. Splenic microcirculation has long been a subject of controversy because of the complexity of vascular channels and conflicting experimental evidence. Two basic pathways exist for splenic circulation. The closed circulation, which accounts for most of the splenic blood flow and corresponds to the functionally rapid component of the circulation, allows blood to pass from arterioles and capillaries directly into venous sinuses. The open circulation, which corresponds to the functionally slow component, permits blood to percolate through the reticular tissue of the splenic cords before filtering through minute slits in the walls of venous sinuses.

MRI TECHNIQUE

The standard MRI protocol includes precontrast breath-hold T1-weighted spoiled gradient-echo (SGE) sequences including in-phase and out-of-phase SGE sequences, precontrast fat-suppressed three-dimensional gradient echo (3D-GE), T2-weighted sequences including short-tau inversion recovery (STIR), non-fat-suppressed and fat-suppressed single-shot echo-train spin echo (although usually fat-suppressed single-shot echo-train spin echo is sufficient), and immediate and delayed postgadolinium SGE with the delayed images often acquired with fat suppression or immediate and delayed postgadolinium fat-suppressed 3D-GE sequences. The choice between SGE and 3D-GE sequences depends on the type of scanners.

NORMAL

Normal splenic parenchyma is invariably low in signal intensity on T1-weighted images and usually high in signal intensity on T2-weighted images (fig. 5.1).

Signal intensity on T2-weighted images of the spleen may vary and not uncommonly is relatively low. This is usually secondary to prior blood transfusions, which result in iron deposition in the reticuloendothelial system (RES) of the spleen (fig. 5.2). The signal intensity of most forms of benign and malignant disease processes parallels the pattern of low signal intensity on T1-weighted images and high signal intensity on T2-weighted images. As a result, noncontrast MR images are limited in the detection of splenic disease. Differences in blood supply of spleen and diseased tissue permit detection of abnormalities on immediate postgadolinium images.

Immediate postgadolinium breath-hold T1-weighted SGE or 3D-GE sequences demonstrate the different circulations in the normal spleen as regions of transient higher and lower contrast enhancement, usually in an arciform or serpiginous pattern [1–4]. This appears as an alternating pattern of high-signal (closed circulation) and low-signal (open circulation) stroma. Variations of this pattern occur, such as central low and peripheral high signal intensity. This variegated pattern becomes homogeneous and high in signal intensity within 1 min after contrast.

Three variations in splenic enhancement patterns have been described in spleen not infiltrated by disease on immediate postgadolinium image [4]. The most common (79% of patients) is serpiginous enhancement, termed arciform. This pattern has been observed in all normal spleens in nondiseased patients and in some spleens of patients with inflammatory or neoplastic disease (fig. 5.3). The second most common pattern (16% of patients) is homogeneous high-signal-intensity enhancement (fig. 5.4). This has been observed in patients with inflammatory or neoplastic diseases, hepatic focal fatty infiltration, or hepatic enzyme abnormalities. A nonspecific immune response may be responsible for this pattern of enhancement. This appearance may represent the conversion of a mixture of slow and fast channels to only fast channels, reflecting a mechanism to increase transit of immune system cells. The third pattern is uniform low signal intensity (5% of patients) (fig. 5.5). This was found in all patients who had undergone multiple recent blood transfusions. The T2-shortening effects from hemosiderin deposition in the RES supersede the T1-shortening effects of gadolinium [5, 6].

Superparamagnetic iron oxide particles are selectively taken up by the RES and have been used to evaluate the spleen. These particles diminish the signal intensity of the normal spleen on T2-weighted sequences, whereas tumors remain unchanged in signal characteristics [7–9]. Superparamagnetic iron oxide crystals embedded in a starch matrix [magnetic starch microspheres (MSM), Nycomed Imaging, Oslo, Norway] have

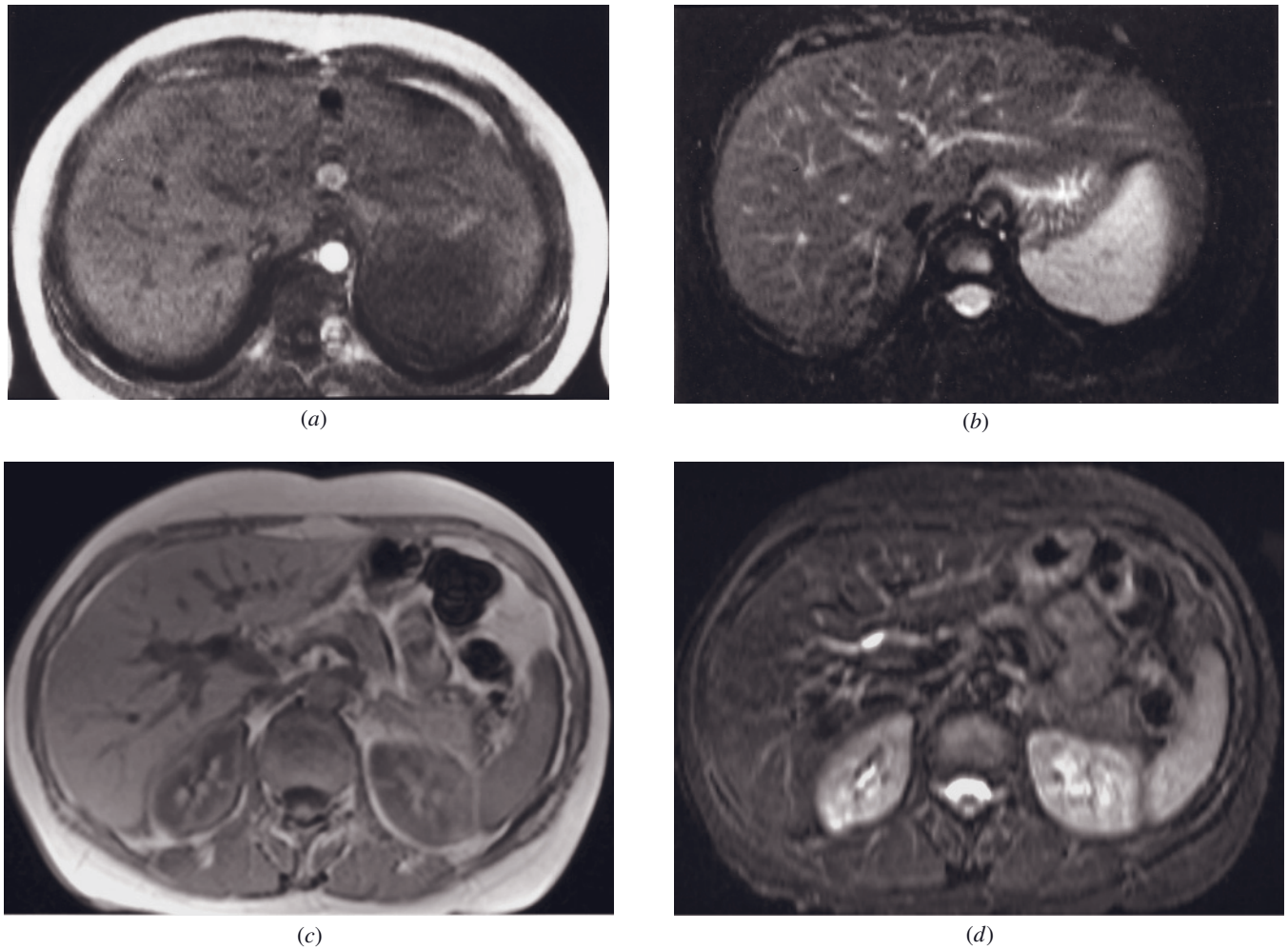

FIG. 5.1 Normal spleen. T1-weighted SGE (*a*) and T2-weighted fat-suppressed spin-echo (*b*) images. Normal spleen is low in signal intensity on T1-weighted image (*a*) and high in signal intensity on T2-weighted image (*b*). Liver is higher in signal intensity on T1-weighted images and lower in signal intensity on T2-weighted images than spleen, which results in a clear distinction between the elongated lateral segment of the liver and the adjacent spleen in this patient. T1-weighted SGE (*c*) and T2-weighted short-tau inversion recovery (STIR) (*d*) images at 3.0 T in a second patient with normal findings demonstrate similar signal characteristics for the spleen and liver compared to 1.5 T.

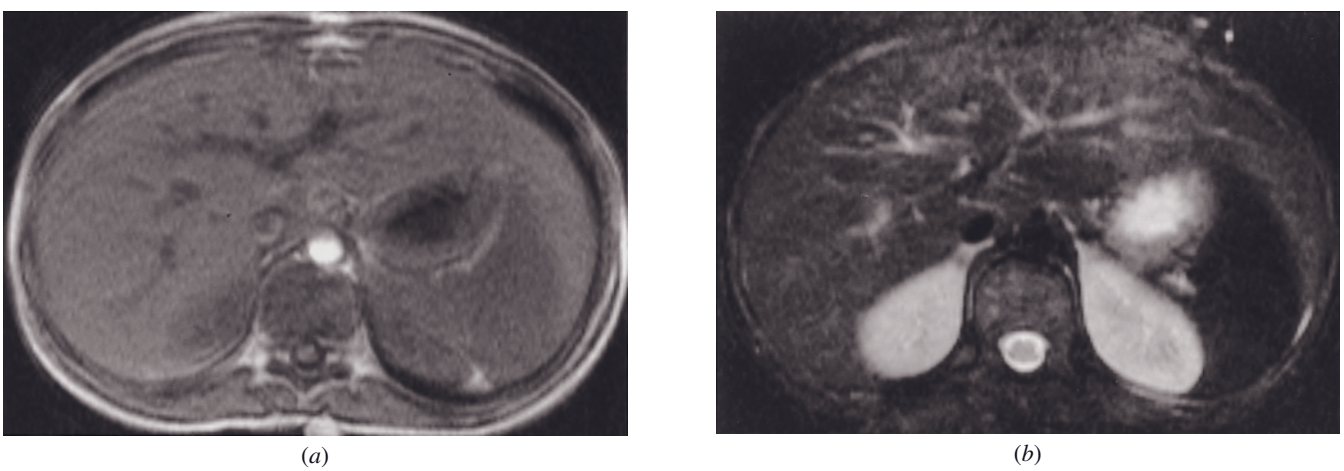

FIG. 5.2 Iron deposition in the spleen. T1-weighted SGE (*a*) and T2-weighted fat-suppressed spin-echo (*b*) images. Signal intensity of the spleen is only slightly lower than normal on the T1-weighted image (*a*), which is consistent with mild iron deposition in the RES. Signal intensity of the spleen is noted to be nearly signal void on the T2-weighted image (*b*), with low signal intensity also noted of liver and bone marrow due to iron deposition in the RES in these organs.

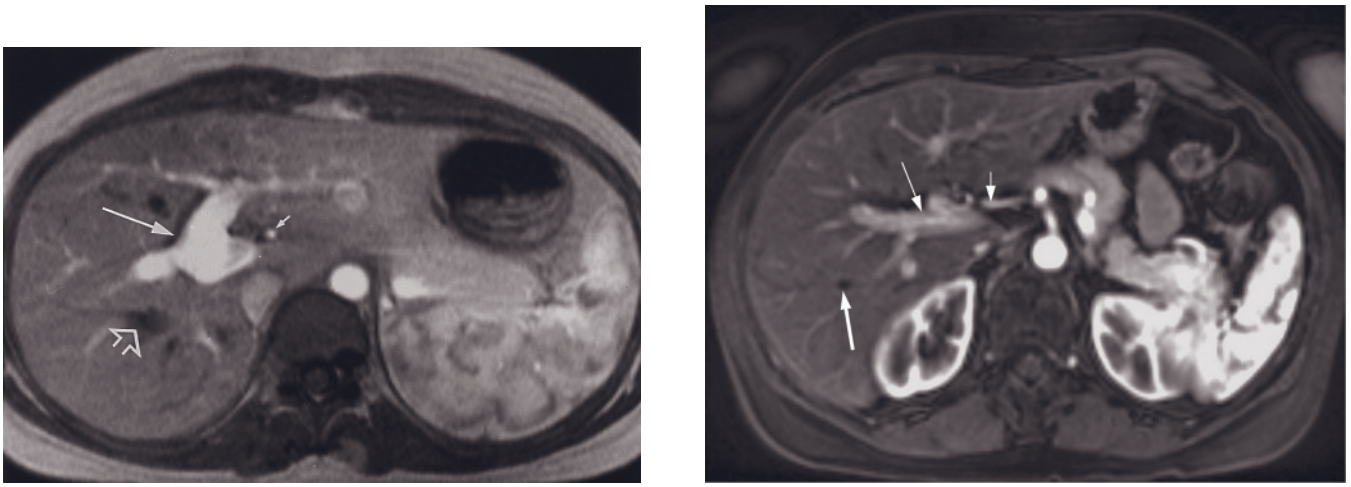

(*a*) (*b*)

FIG. 5.3 Arciform enhancement in the normal spleen. Postgadolinium T1-weighted SGE image (*a*) acquired at 1.5 T on the hepatic arterial dominant phase shows the serpiginous, tubular bands of low signal intensity throughout the splenic parenchyma. Contrast identified in portal vein (long arrow, *a*) and hepatic arteries (short arrow, *a*) and lack of contrast in hepatic veins (open arrow, *a*) define the capillary or hepatic arterial dominant phase of enhancement. Postgadolinium fat-suppressed T1-weighted 3D-GE image (*b*) acquired at 3.0 T on the hepatic arterial dominant phase, which is again characterized by the presence of contrast in the hepatic artery (short thin arrow, *b*) and portal vein (long thin arrow, *b*) and by the absence of contrast in the hepatic veins (thick arrow, *b*), demonstrates arciform enhancement pattern of the normal spleen.

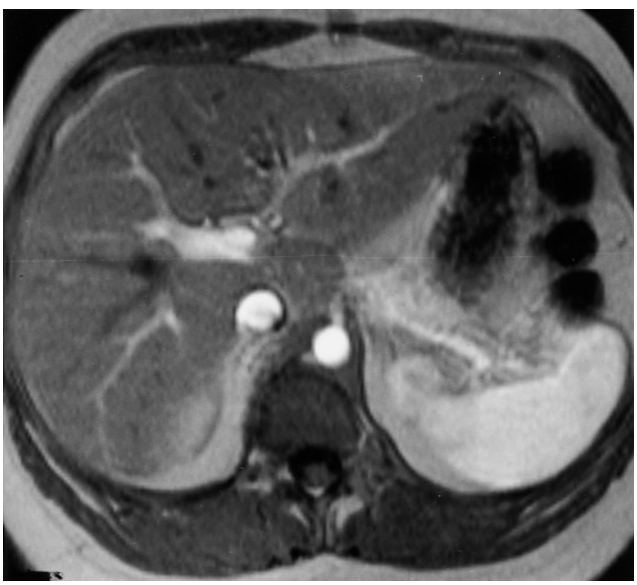

FIG. 5.4 Homogeneous intense splenic enhancement. The spleen is noted to enhance intensely and uniformly in the capillary phase of enhancement. Contrast in hepatic arteries and portal veins and lack of contrast in hepatic veins demonstrate that the image was acquired in the capillary phase of enhancement.

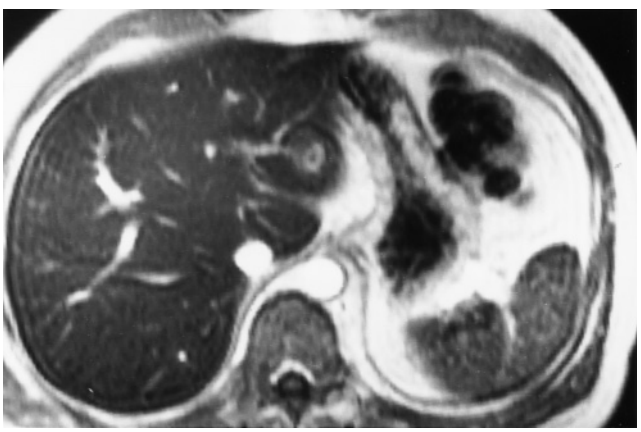

FIG. 5.5 Homogeneous low-signal-intensity splenic enhancement. The spleen is low in signal intensity on immediate postgadolinium images because of the predominant T2-shortening effects of iron in the spleen.

been studied in animal models and have been shown to increase conspicuity of both focal and diffuse splenic lesions [9]. Normal spleen diminishes in signal on T2-weighted or T2*-weighted images, whereas focal or diffuse disease retains signal, which renders disease conspicuous by being relatively high in signal intensity.

In the neonate and until the infant is approximately 8 months old, the spleen signal intensity is isointense to the liver on T1-weighted images and varies from iso- to hypointense relative to the liver on T2-weighted images (fig. 5.6). As the RES matures, the spleen displays a hypointense signal relative to the liver on T1-weighted images, with a gradual increase in the spleen signal relative to the liver on T2-weighted images, approaching the normal appearance of the adult spleen [10].

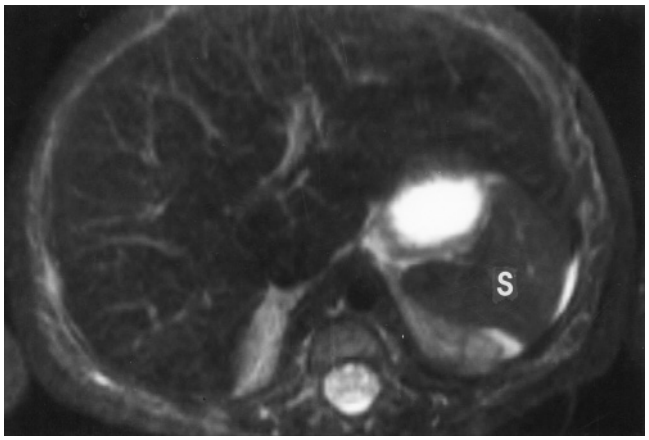

FIG. 5.6 Normal spleen in a 1-month-old patient. T2-weighted fat-suppressed spin-echo image. Normal spleen (S) is low signal intensity, comparable to liver on T2-weighted image.

Normal Variants and Congenital Disease

Accessory Spleens and Wandering Spleen

Accessory spleens, or "spleniculi," are congenital ectopic foci of splenic tissue that fail to fuse with the spleen. This anatomic variant is found in about 10–30% of non-selected autopsy cases. Because of its congenital origin, the accessory spleens are located within the embryological dorsal mesentery of stomach and pancreas. The majority of spleniculi are located in close proximity to the splenic hilum. One in six accessory spleens is located in or adjacent to the tail of the pancreas, which may resemble the appearance of an islet cell tumor (fig. 5.7) [11]. Most intrapancreatic accessory spleens are well marginated and have rounded morphology similar to other pancreatic lesions, especially like pancreatic neuroendocrine tumors [11]. Superparamagnetic iron oxide (SPIO) particles can be used for the differentiation of intrapancreatic accessory spleens from these tumors. Intrapancreatic accessory spleens take up SPIO and show decreased signal on postcontrast T2-weighted images (fig 5.7), but the tumors do not take up the agent [11]. Other accessory spleen locations include the suspensory ligament of spleen, left kidney, left testis, or elsewhere in retroperitoneum (fig. 5.8*a–c*). Their size varies from microscopic deposits to nodules with a diameter ranging from a few millimeters to 3 cm. After splenectomy they may enlarge considerably in size [12]. The diagnosis of accessory spleen should be considered when a mass has pre- and postcontrast imaging characteristic similar to those of spleen. They are clinically important insofar as they must be differentiated from other mass lesions. Spleniculi may also be confidently characterized in the patient who has undergone repeated blood transfusions because they will be nearly signal void on T2- or T2*-weighted sequences because of iron deposition within the RES of the splenules [13].

Wandering spleen is a condition in which the spleen is free to move if the ligamentous attachments of the spleen are lax or absent [10]. The spleen is not located in the left upper quadrant and may be found in the center of the abdomen or pelvis (fig. 5.8*d–g*). This condition is usually seen in patients with deficient musculature of the anterior abdominal wall such as prune-belly syndrome [10]. The splenic hilum is usually located anteriorly. Patients with wandering spleen may present with acute abdominal symptoms due to torsion about an elongated pedicle [14]. Splenic ischemia, infarction, and twisted elongated pedicle can be detected with MRI, particularly on postgadolinium images [14]. Edema may be seen as increased signal in the splenic parenchyma on T2-weighted images, and decreased enhancement or the lack of enhancement in the splenic parenchyma may be seen on postgadolinium images.

Asplenia

Asplenia syndrome, right isomerism (situs ambiguous with asplenia, bilateral right-sidedness), or Ivemark syndrome is a congenital syndrome characterized by absence of the spleen associated with thoracoabdominal abnormalities (fig. 5.9). The majority of patients die in infancy, with few surviving longer than 1 year. The mortality in the first year of life approaches 80% because of complex and severe cardiovascular anomalies and a compromised immune system. In cardiac MRI studies in which cardiovascular anomalies raise the possibility of asplenia, a limited abdominal MRI should be performed at the same time to evaluate abdominal situs ambiguous and associated abnormalities, abdominal vessels, and the presence of the spleen, because asplenic patients are at risk of sepsis [15–17]. Associated abnormalities include the liver located in the midline, ipsilateral inferior vena cava and aorta, dextrocardia or levocardia, and variable forms of intestinal malrotation.

Polysplenia

Polysplenia syndrome is a congenital syndrome characterized by multiple small splenic masses and left isomerism (situs ambiguous with polysplenia, bilateral left-sidedness). The splenic masses vary from 2 to 16 in number and are distributed along the greater curvature of the stomach (fig. 5.10). Other associated abnormalities include cardiopulmonary anomalies, malrotation of the intestinal tract, absence of the hepatic segment of the inferior vena cava with azygous or hemiazygous continuation, duplicated inferior vena cava, midline or left-sided liver, right-sided aorta, and a short pancreas. Polysplenia has also been associated with cystic kidney

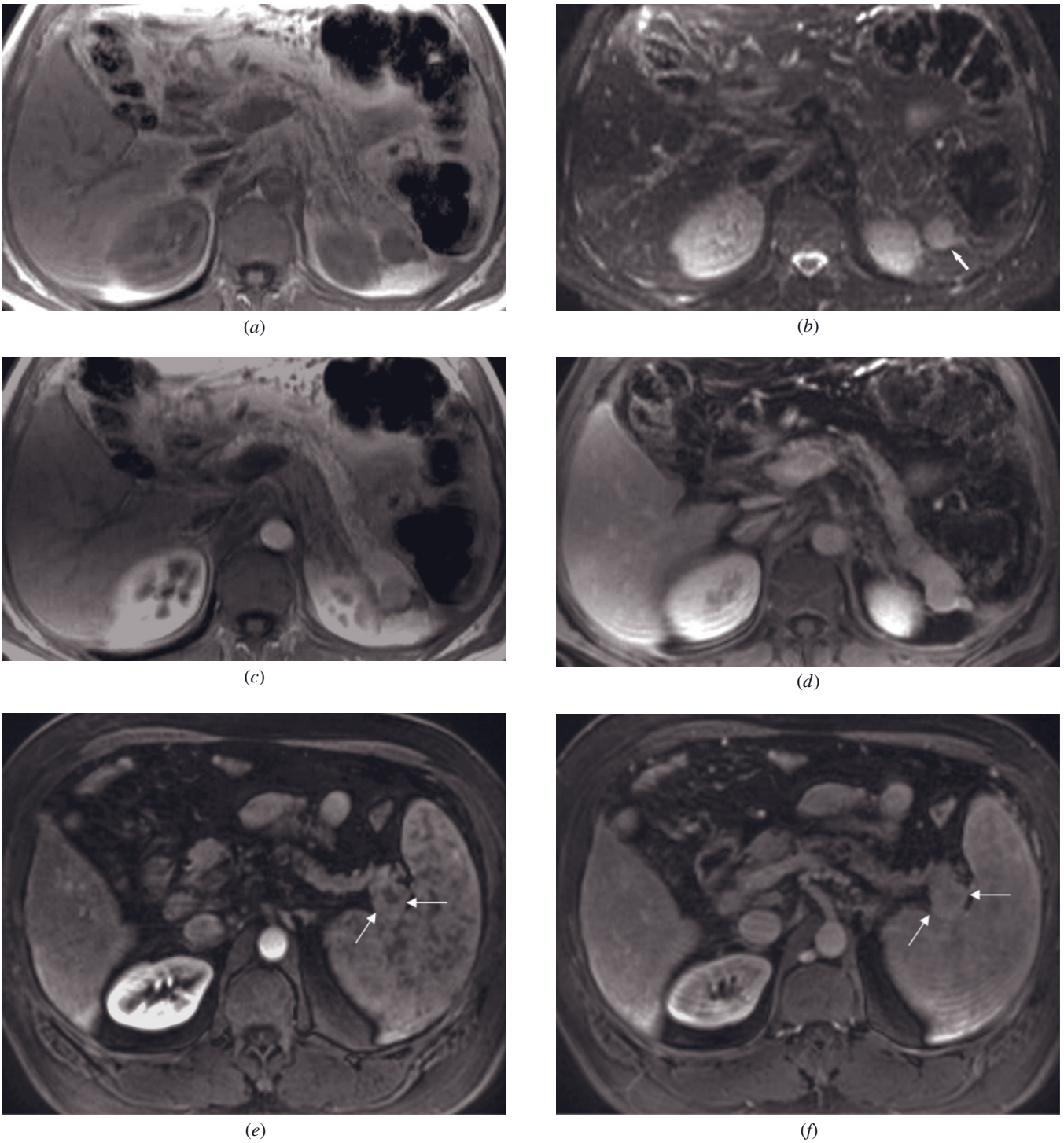

FIG. 5.7 Accessory spleen in pancreas. T1-weighted SGE (*a*), T2-weighted fat-suppressed echo-train single-shot (*b*), immediate postgadolinium T1-weighted SGE (*c*), and delayed T1-weighted fat-suppressed SGE (*d*) images. T1-weighted SGE demonstrates a mass in the pancreatic tail that is homogeneously hypointense compared to background pancreas (*a*). T2-weighted fat-suppressed image shows a round mass in the tail of the pancreas that demonstrates moderate homogeneous hyperintensity (arrow, *b*). Immediate postgadolinium-enhanced T1-weighted SGE demonstrates homogeneous enhancement of the mass (*c*). Ninety-second gadolinium-enhanced T1-weighted fat-saturated SGE demonstrates lower enhancement of the mass compared with surrounding pancreatic tissue (*d*). Immediate (*e*) and 45-s (*f*) postgadolinium T1-weighted fat-suppressed 3D-GE images, precontrast T2-weighted single-shot echo-train spin-echo (*g*), and post-superparamagnetic iron oxide (SPIO) T2-weighted single-shot echo-train spin-echo (*h*) images in a second patient with intrapancreatic accessory spleen. The lesion (arrows) is located in the pancreatic tail and demonstrates enhancement pattern similar to the spleen, which is seen as a serpiginous enhancement pattern on immediate and 45-s 3D-GE images (*e, f*). The lesion (arrows), which shows similar signal intensity to the spleen on precontrast T2-weighted image (*g*),

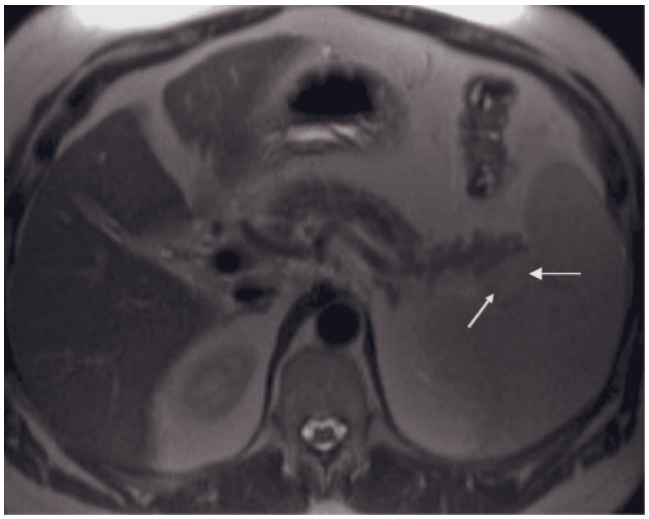

(*g*)

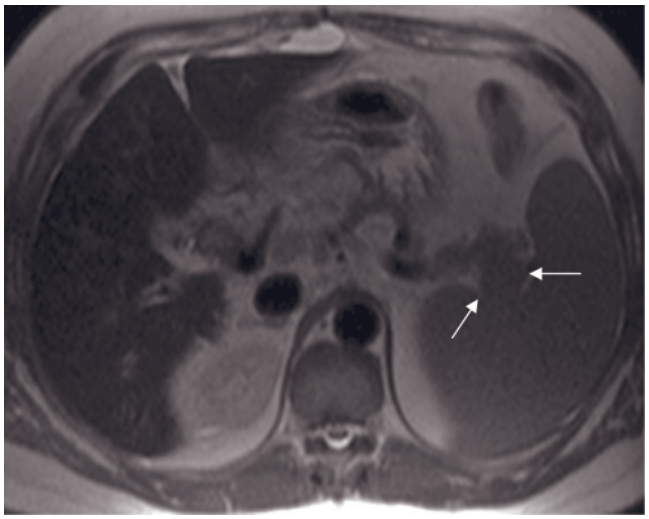

(*h*)

FIG. 5.7 (*Continued*) demonstrates signal drop on post-SPIO T2-weighted image (*h*) similar to the spleen, due to the presence of RES cells.

diseases. In comparison with asplenia, polysplenia has a lower mortality, and serious cardiac malformations are less common. MRI can demonstrate the situs ambiguous, abdominal vessels, and the number of spleens together with such complications as splenic hemorrhages or infarcts [16, 17].

Gaucher Disease

Gaucher disease is an autosomal recessive lysosomal multisystem hereditary disease caused by deficient glucocerebrosidase activity. Glucocerebroside, a glycolipid, accumulates in the mononuclear phagocytic cells of organs [18]. The abdominal manifestations of Gaucher disease in a population of 46 patients have been described with conventional spin-echo technique [18]. All patients had hepatosplenomegaly. Splenic nodules of variable signal intensity were present in 14 patients (30%). Fifteen patients (33%) had splenic infarcts with or without associated subcapsular fluid collections, and four patients (9%) had both infarcts and nodules. Focal areas of abnormal signal intensity were noted in the livers of nine patients (20%).

Sickle Cell Disease

The manifestations of sickle cell anemia vary and depend on whether the patient is homozygous or heterozygous for the hemoglobinopathy. The spleen shows low signal because of iron deposition from blood transfusions. In patients with homozygous disease, the spleen is nearly and diffusely signal void because of the sequela of iron deposition coupled with microscopic perivascular and parenchymal calcifications [19] (fig. 5.11*a*). Regions of scarring and infarcts are also common (fig. 5.11*b–d*).

MASS LESIONS

The appearance of common splenic lesions on T1-weighted, T2-weighted, and early and late postgadolinium images is presented in Table 5.1.

Benign Masses

Cysts

Cysts are the most common of the benign splenic lesions. Three types of nonneoplastic cysts exist: posttraumatic or pseudocyst, epidermoid cysts, and hydatid cysts [20]. Most splenic cysts are posttraumatic in origin. They are not lined by epithelium and thus are pseudocysts. Epidermoid cysts are true cysts discovered in childhood or early adulthood that may have trabeculations or septations in their walls with occasional peripheral calcification [20, 21] (fig. 5.12). Hydatids, or echinococcal cysts, are rare. They are characterized by extensive wall calcification. The MRI features of cysts include sharp lesion margination, low signal intensity on T1-weighted images, and very high signal intensity on T2-weighted images. Cysts complicated by proteinaceous fluid or hemorrhage may have regions of high signal intensity on T1-weighted images, regions of mixed signal intensity on T2-weighted images, or both. Cysts do not enhance on postgadolinium images. Pseudocysts may be complicated by hemorrhage, particularly early in their evolution, and thus may contain

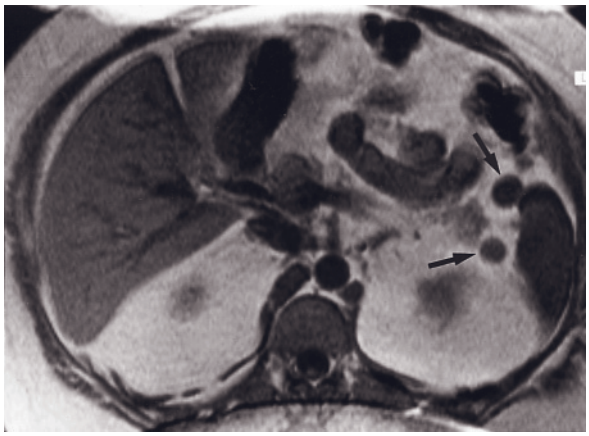

(*a*)

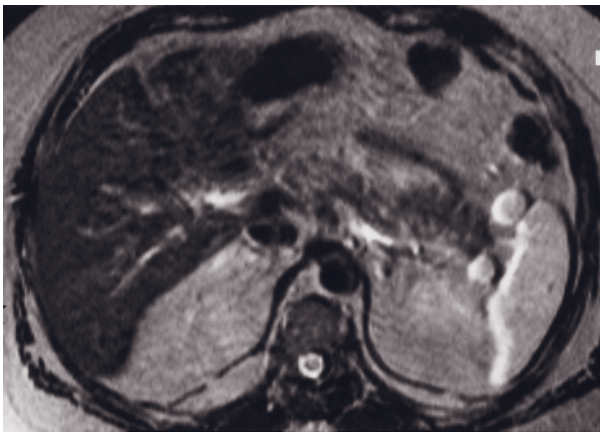

(*b*)

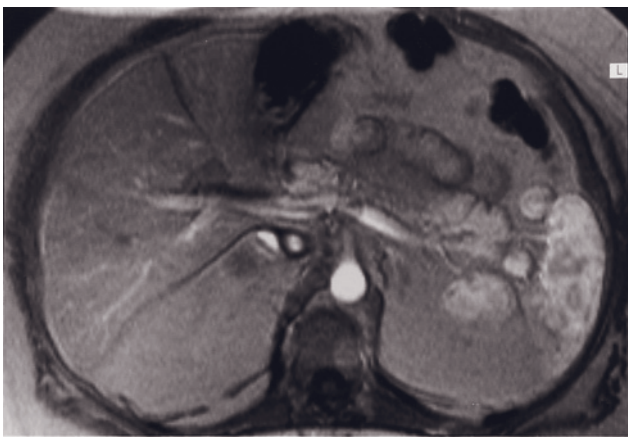

(*c*)

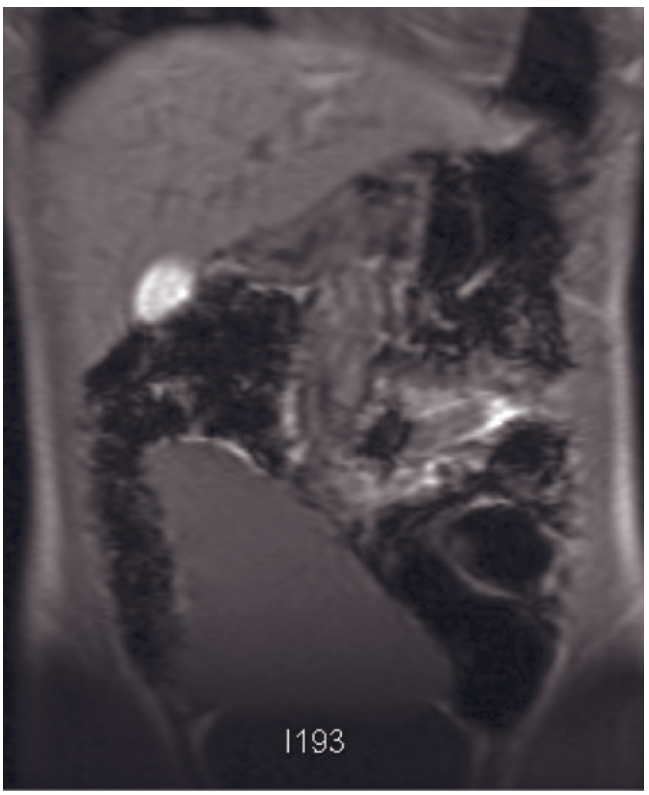

(*d*)

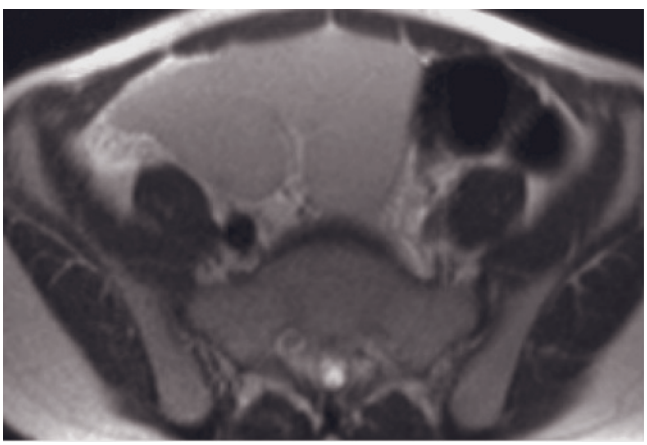

(*e*)

FIG. 5.8 Splenules and wandering spleen. T1-weighted SGE (*a*), T2-weighted spin-echo (*b*), and immediate postgadolinium SGE (*c*) images. Two splenules are identified (arrows, *a*) that parallel the signal intensity of the spleen. They are low in signal intensity on T1-weighted images (*a*) and high in signal intensity on T2-weighted images (*b*) and enhance intensely on immediate postgadolinium image (*c*).The splenules show heterogeneous enhancement on immediate postcontrast images, which suggests that they have architecture similar to that of the spleen. T1-weighted coronal SGE (*d*), T2-weighted single-shot echo-train spin-echo (*e*),

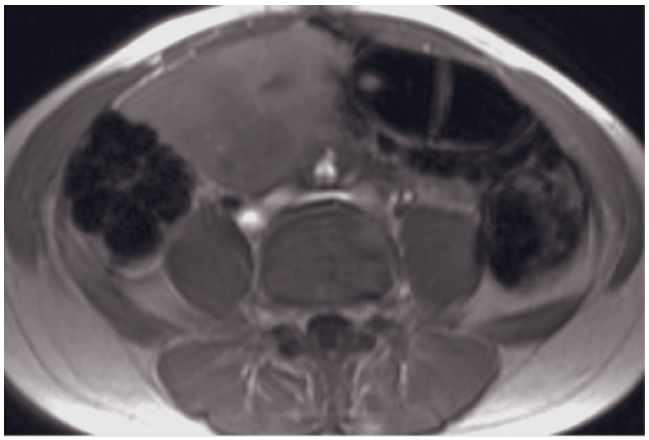

(*f*)

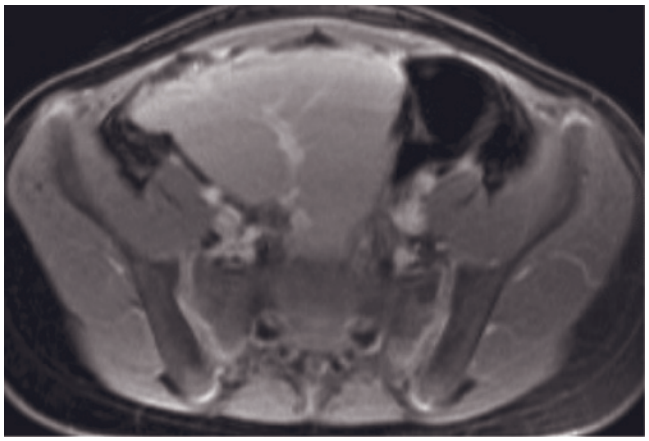

(*g*)

FIG. 5.8 (*Continued*) immediate postgadolinium T1-weighted SGE (*f*), and delayed postgadolinium fat-suppressed T1-weighted SGE (*g*) images demonstrate the wandering spleen located in the pelvis in another patient.

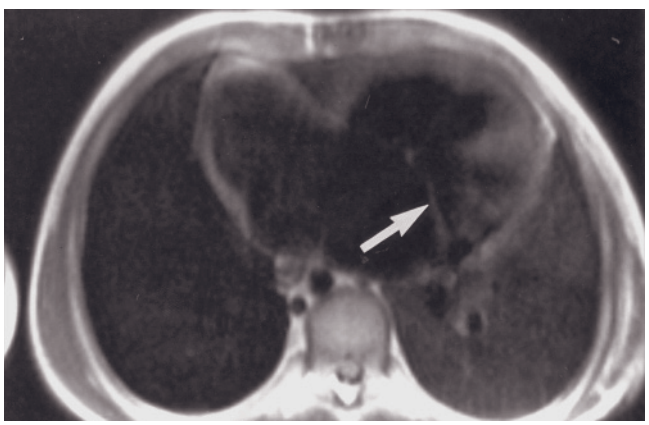

(*a*)

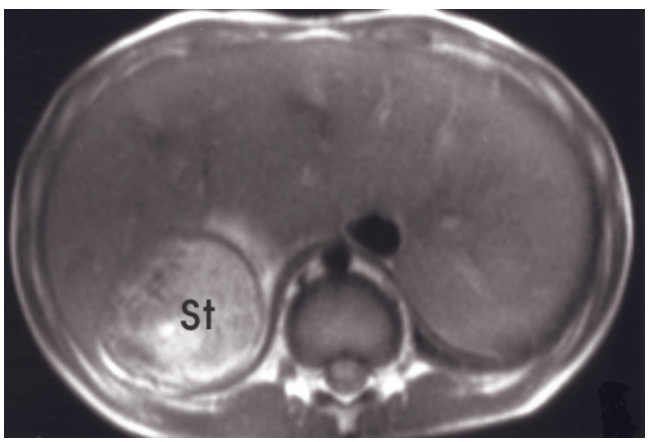

(*b*)

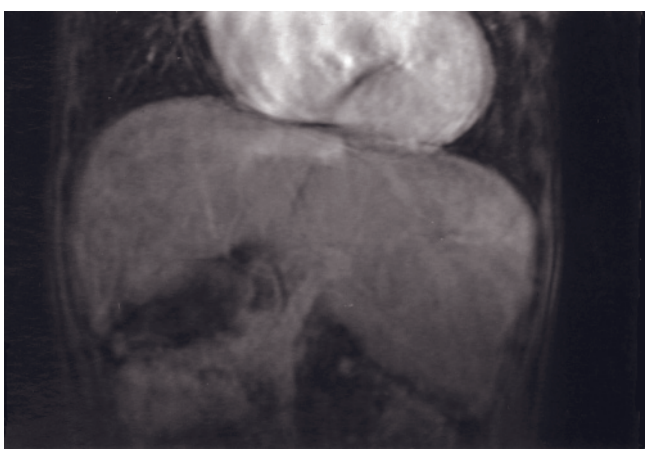

(*c*)

FIG. 5.9 Asplenia. T2 black blood single-shot echo-train spin-echo (*a*, *b*) at the level of the heart (*a*) and liver (*b*) and coronal source MRA (*c*) images. Eight-month-old patient with endocardial cushion defect, common AV valve (arrow, *a*), and situs ambiguous, with the stomach (St, *b*) on the right side. No spleen is present.

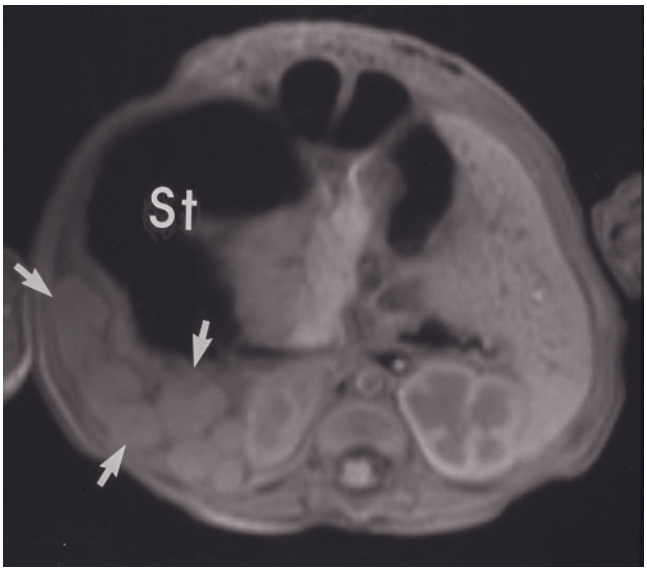

(*a*)

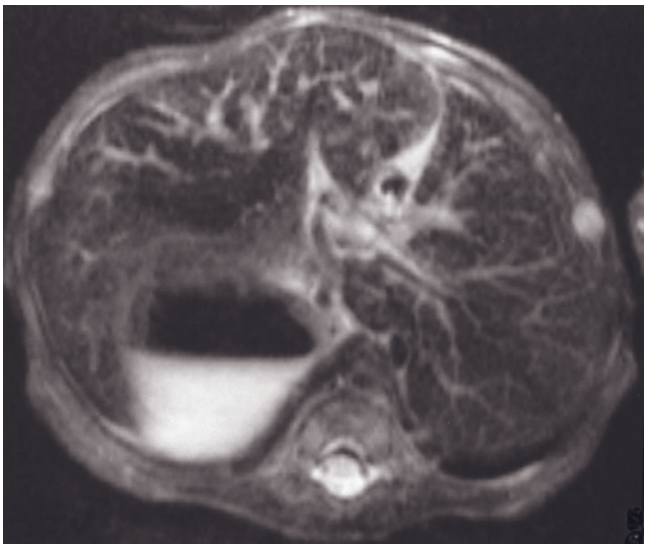

(*b*)

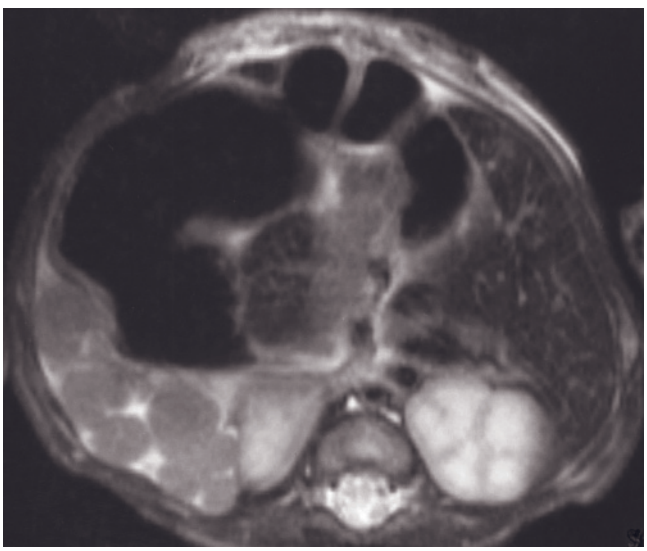

(*c*)

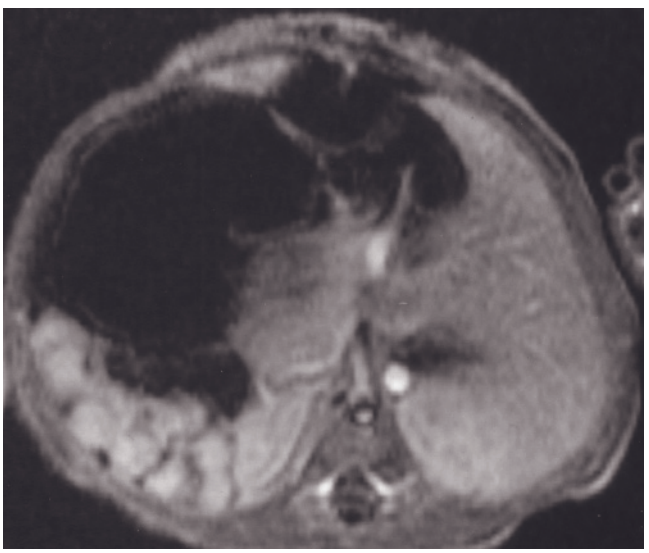

(*d*)

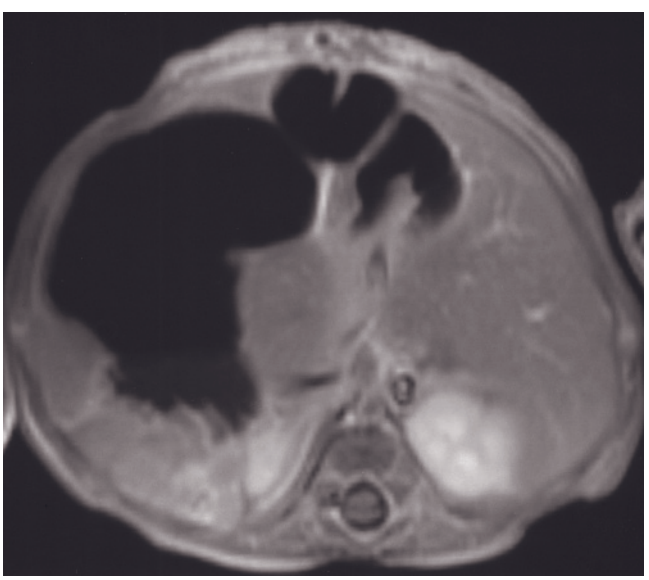

(*e*)

FIG. 5.10 Polysplenia. T1-weighted fat-suppressed SE (*a*), T2-weighted fat-suppressed SE at the level of the upper (*b*) and lower (*c*) liver, immediate postgadolinium T1-weighted snap-shot gradient-echo (*d*), and 2-min postgadolinium T1-weighted fat-suppressed spin-echo (*e*) images. Situs ambiguous is present in this 3-month-old patient (*a*, *b*), with the liver in the left upper abdomen and the stomach (St, *a*) in the right upper abdomen. Multiple small spleens are noted along the greater curvature of the stomach (arrows, *a*), which are moderately low signal on T1 (*a*) and moderately high signal on T2 (*c*) and demonstrate early intense enhancement (*d*) with fading on delayed postgadolinium images (*e*), consistent with the MR imaging appearance of multiple spleens.

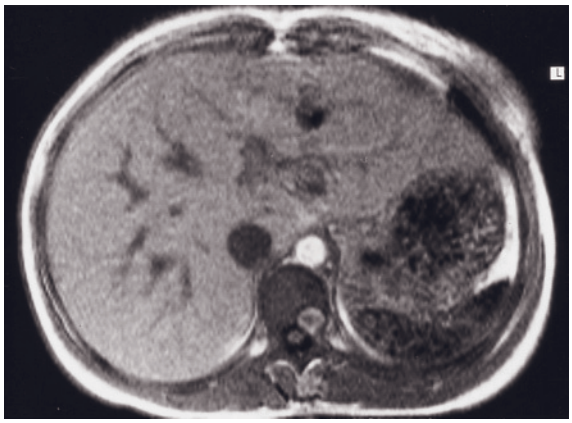

(*a*)

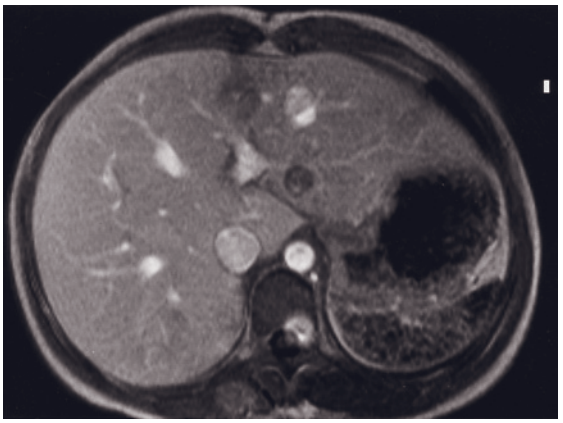

(*b*)

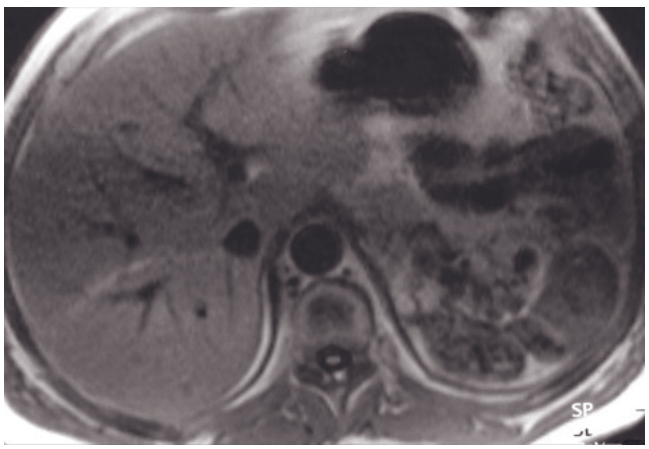

(*c*)

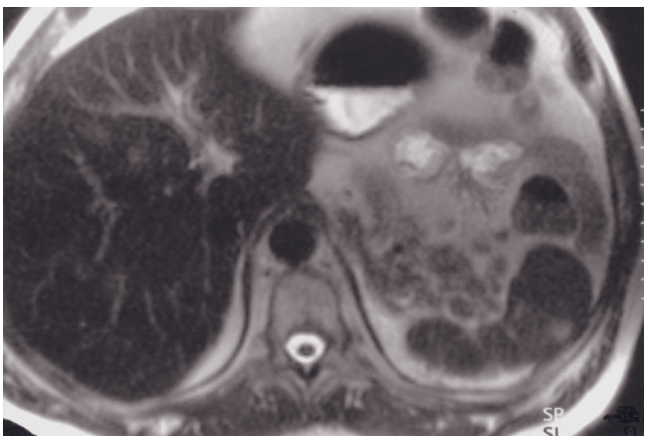

(*d*)

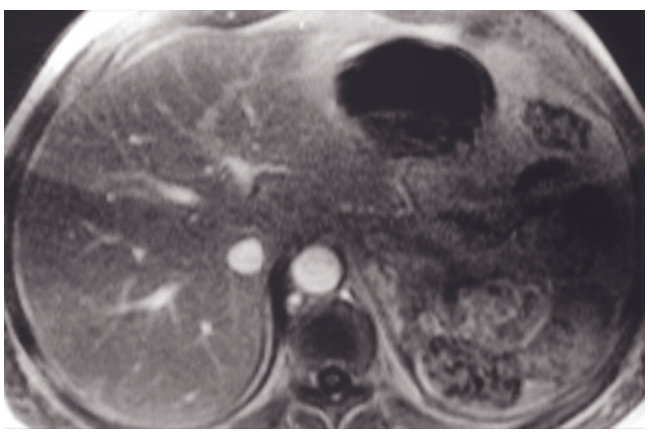

(*e*)

Fig. 5.11 Sickle cell disease. T1-weighted SGE (*a*) and hepatic venous phase postgadolinium T1-weighted SGE (*b*) images. The spleen is noted to be small and low in signal intensity on all MR images (*a*, *b*). On the precontrast T1-weighted SGE image (*a*), multiple 1-cm signal-void foci are noted in the small, low-signal-intensity spleen. These foci are better demarcated after contrast administration (*b*) because of enhancement, although minimal, of surrounding splenic parenchyma. T1-weighted SGE (*c*), T2-weighted echo-train spin-echo (*d*), and hepatic venous phase postgadolinium T1-weighted SGE (*e*) images in a second patient. The spleen is small and irregular with extensive low-signal iron deposition, regions of scarring, and infarction.

foci of high signal intensity on precontrast T1-weighted images (fig. 5.13).

Hemangiomas

Hemangiomas are the most common of the benign splenic neoplasms [22, 23]. Lesions may be single or multiple. Splenic hemangiomas are mildly low to isointense on T1-weighted images and mildly to moderately hyperintense on T2-weighted images, similar to hepatic hemangiomas. Hemangiomas are minimally hypointense to isointense with background spleen on T1-weighted images, because of the relatively low signal intensity of spleen on these images, and minimally hyperintense relative to spleen on T2-weighted images, because of the moderately high signal intensity of spleen on T2-weighted images. Three patterns of contrast

Table 5.1 Pattern Recognition of the Most Common Splenic Lesions

	T1	T2	Early Gd	Late Gd	Other Features
Cyst	↓–Ø	↑↑	None	None	Well-defined
Hamartoma	Ø	Ø–↑	Heterogeneous intense	Homogeneous enhancement, isointense to the spleen	Usually >4 cm and arise from the medial surface of the spleen
Hemangioma	↓–Ø	↑	Peripheral nodules or homogeneous	Centripetal enhancement; retain contrast	Usually <2 cm Lesion more commonly enhances homogeneously on immediate post-Gd images compared to liver hemangiomas, reflecting their small size Peripheral nodules are not as clearly defined as liver hemangiomas
Metastases	↓–Ø	Ø–↑	Focal lesions with minimal enhancement	Isointense or hypointense	Metastases commonly become isointense by 1 min post-Gd
Lymphoma —focal	↓–Ø	↓–↑	Focal lesions with minimal enhancement	Isointense or hypointense	Other sites of nodal disease Lymphomatous lesions commonly become isointense by 1 min post-Gd
Lymphoma —diffuse	↓–Ø	↓–↑	Irregular regions with minimal enhancement	Isointense or hypointense	Other sites of nodal disease Lymphomatous lesions commonly become isointense by 1 min post-Gd

Keys: ↓↓: moderately to markedly decreased; ↓: mildly decreased; Ø: isointense; ↑: mildly increased; ↑↑: moderately to markedly increased.

FIG. 5.12 Epidermoid cyst. Immediate postgadolinium T1-weighted SGE image demonstrates a signal-void cystic lesion with peripheral septations.

enhancement are observed: 1) immediate homogeneous enhancement with persistent enhancement on delayed images, 2) peripheral enhancement with progression to uniform enhancement on delayed images (fig. 5.14), and 3) peripheral enhancement with centripetal progression but persistent lack of enhancement of central scar. These patterns are similar to those observed for hepatic hemangiomas. However, unlike hepatic hemangiomas, splenic hemangiomas generally do not demonstrate well-defined nodules on early postgadolinium images. This may, in part, reflect the blood supply from the background organ. Uniform high signal on immediate postgadolinium SGE images is a common appearance for small (<1.5 cm) hemangiomas, as it is with hepatic hemangiomas. Rarely, hemangiomas with a very large central scar can appear hypointense on T2-weighted images, reflecting the lower fluid content of the central scar (fig. 5.15). These may be termed sclerosing hemangiomas.

Littoral Cell Angioma

Littoral cell angioma (LCA) is a vascular lesion that was first described in 1991 as a benign vascular tumor arising from littoral cells, which line the splenic sinus of the red pulp [24]. LCA is composed of multiple blood-filled vascular channels. Macroscopically, the spleen is enlarged, and these tumors are usually multiple and nodular, with their size ranging from 0.2 to 9 cm. They are well defined and compress the adjacent splenic tissue. Patients with LCA commonly present with signs of hypersplenism (anemia, thrombocytopenia). LCA are thought to be benign tumors, but the malignant potential of LCA has not yet been ascertained. MRI shows the tumor to be multiple with regular well-defined margins and mildly low signal to isointensity on T1-weighted SGE images, low to moderately high signal intensity on T2-weighted images, mild heterogeneous enhancement on arterial dominant phase, and homogenous enhancement on delayed phase [25, 26] (fig. 5.16). Homogenous delayed enhancement and absence of underlying disease such as lymphoma, metastatic diseases, sarcoidosis, or tuberculosis help to establish the correct diagnosis.

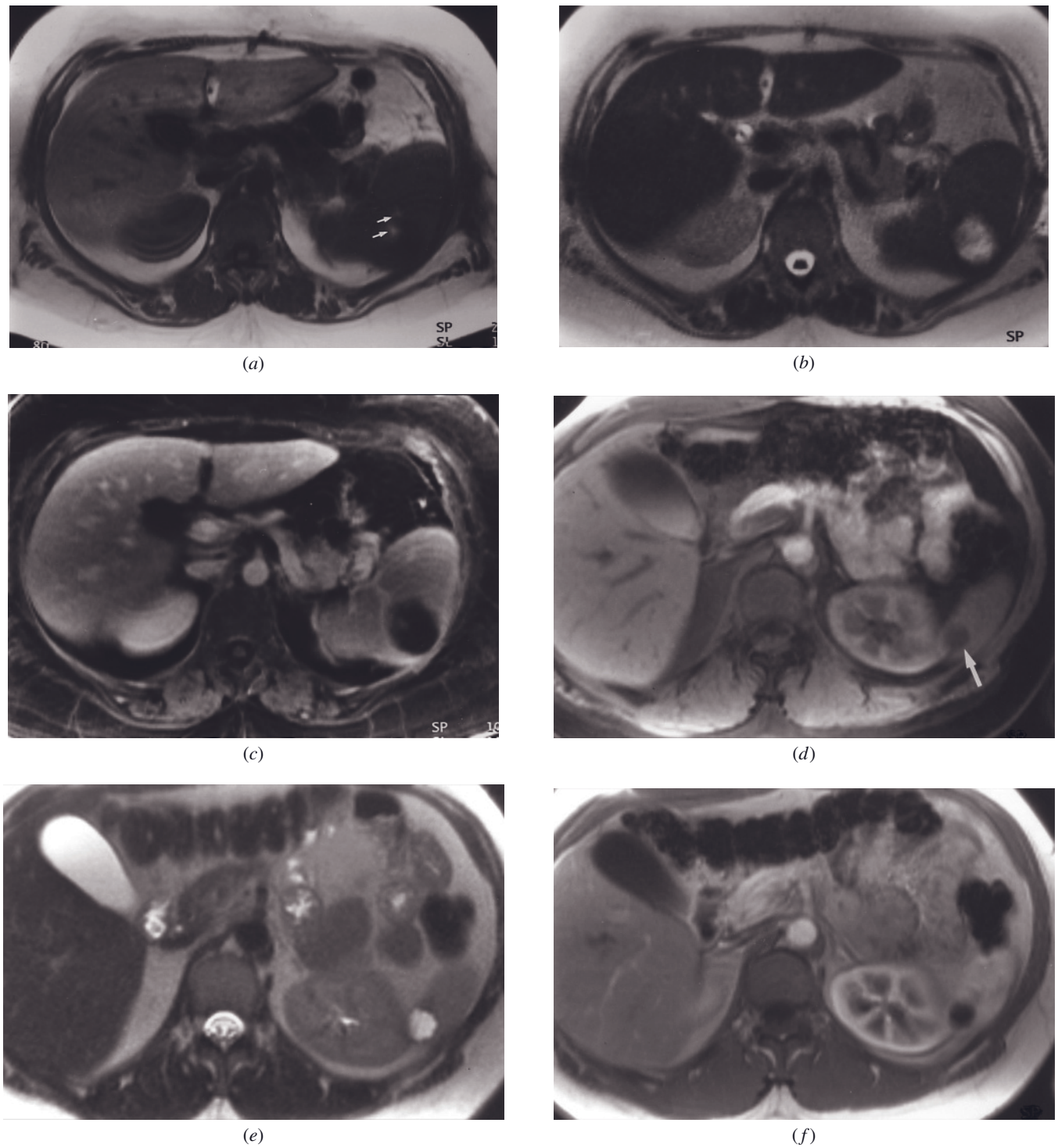

(*a*) (*b*) (*c*) (*d*) (*e*) (*f*)

FIG. 5.13 Pseudocyst. T1-weighted SGE (*a*), T2-weighted single-shot echo-train spin-echo (*b*), and 90-s gadolinium-enhanced fat-suppressed SGE (*c*) images. High-signal-intensity foci are identified in the cyst on the precontrast SGE image (arrows, *a*), a finding consistent with hemorrhage. Slight heterogeneity of the cyst on the T2-weighted image (*b*) also reflects the presence of blood degradation products. The cyst is sharply demarcated after gadolinium administration (*c*).The foci of blood remain high in signal intensity on postgadolinium images. T1-weighted fat-suppressed SGE (*d*), T2-weighted single-shot echo-train spin-echo (*e*), immediate postgadolinium T1-weighted SGE (*f*), and 90-s gadolinium-enhanced T1-weighted fat-suppressed SGE (*g*) images in

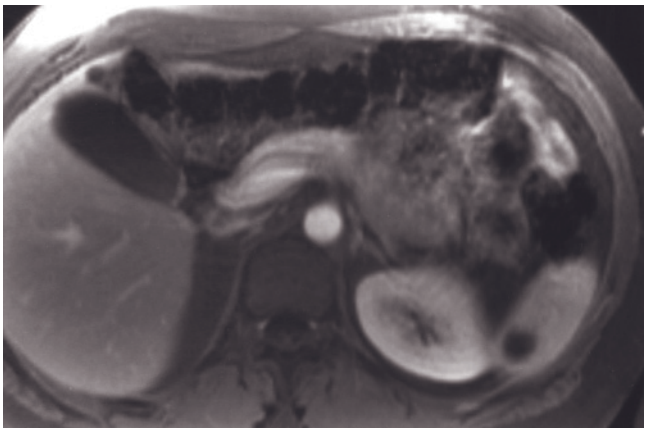

(*g*)

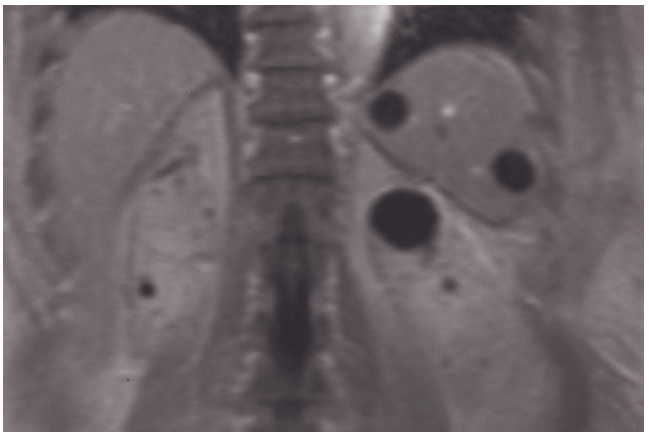

(*h*)

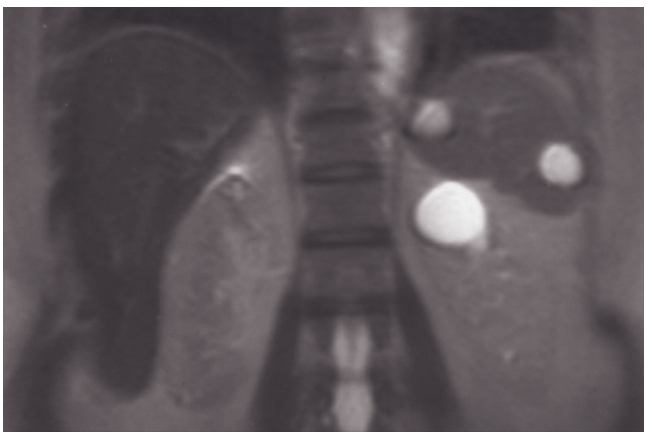

(*i*)

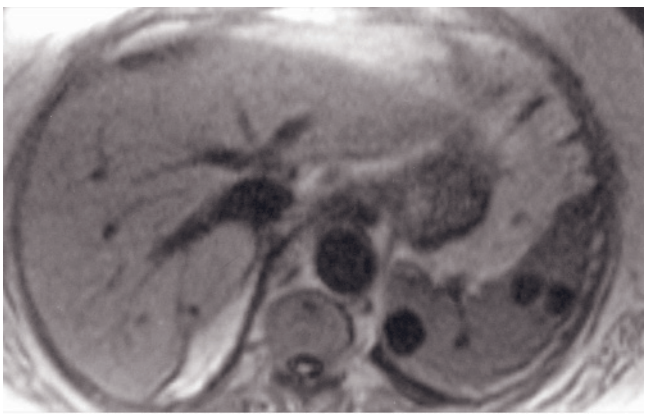

(*j*)

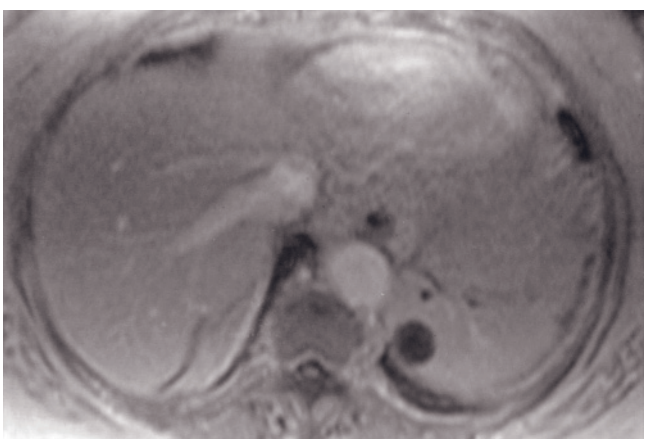

(*k*)

FIG. 5.13 (*Continued*) a second patient. The pseudocyst is low signal on T1 (arrow, *d*) and high signal on T2 (*e*) and does not enhance on early (*f*) or late (*g*) postgadolinium images. Coronal T1-weighted single-shot magnetization-prepared gradient-echo (*h*), coronal T2-weighted echo-train spin-echo (*i*), T1-weighted single-shot magnetization-prepared gradient-echo (*j*), and 45-s postgadolinium single-shot magnetization-prepared gradient-echo (*k*) images in a third patient with multiple splenic cysts. Renal cysts are also present.

Hamartomas

Hamartomas are rare and composed of structurally disorganized mature splenic red pulp elements. The lesions tend to be single, spherical, and predominantly solid. They are most likely to occur in the midportion of the spleen, arising from the anterior or posterior aspect of the convex surface. These tumors are mildly low to isointense on T1-weighted images and moderately high in signal intensity on T2-weighted images [23, 27, 28]. They frequently are moderately heterogeneous, in part because of the presence of cystic spaces of varying size. If the composition of fibrous tissue is substantial, hamartomas may have regions of low signal intensity on T2-weighted images [27]. They enhance on immediate

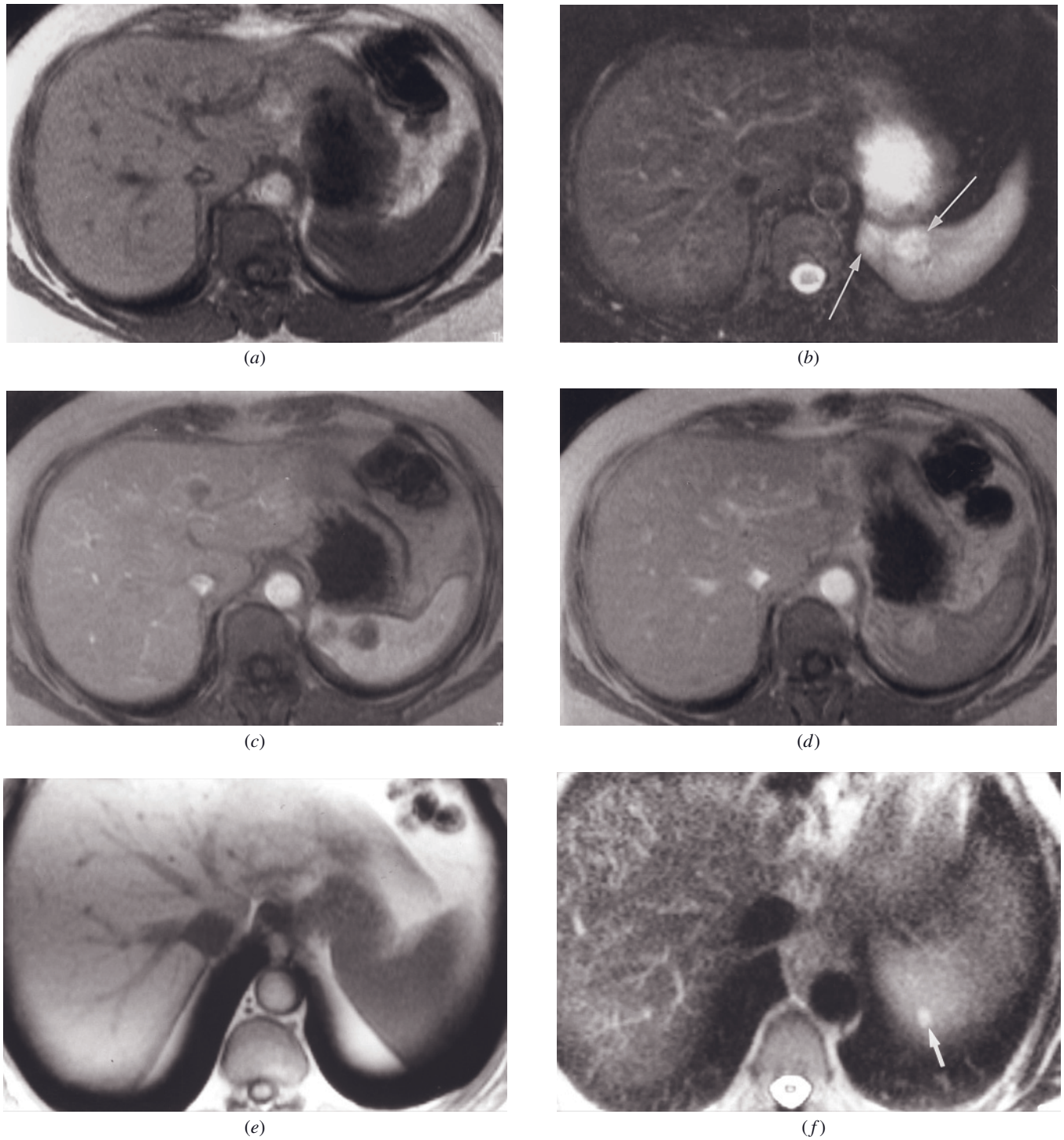

FIG. 5.14 Hemangiomas. T1-weighted SGE (*a*), T2-weighted fat-suppressed spin-echo (*b*), and 45-s (*c*) and 10-min (*d*) postgadolinium SGE images. Two small, <1.5 cm, hemangiomas are present that are minimally hypointense on T1-weighted images (*a*) and moderately hyperintense on T2-weighted images (arrows, *b*). Peripheral nodules are present on early postgadolinium images (*c*), and enhancement progresses to uniform high signal intensity by 10 min (*d*). T1-weighted SGE (*e*), T2 fat-suppressed spin-echo (*f*), immediate postgadolinium T1 SGE (*g*), and 90-s postgadolinium T1-fat-suppressed SGE (*h*) images in a second patient.

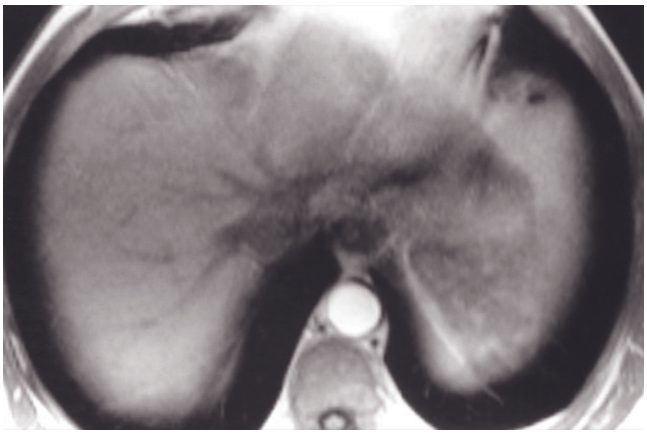

(*g*)

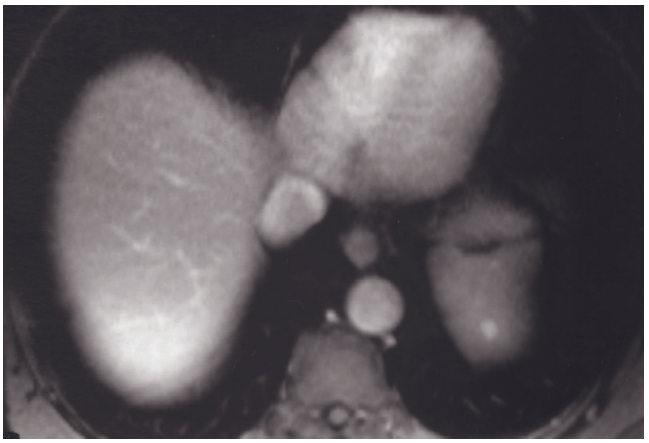

(*h*)

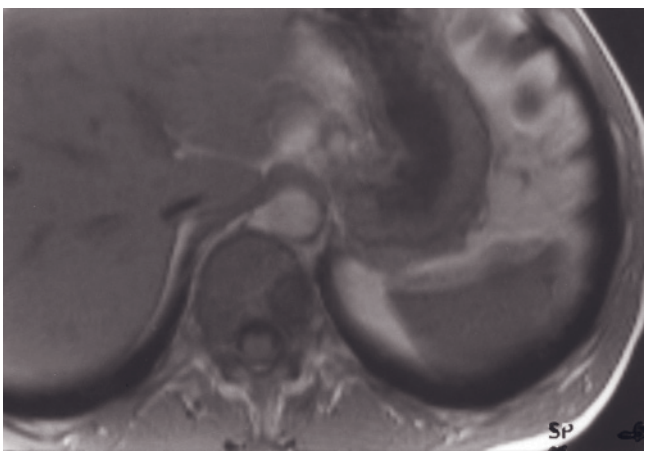

(*i*)

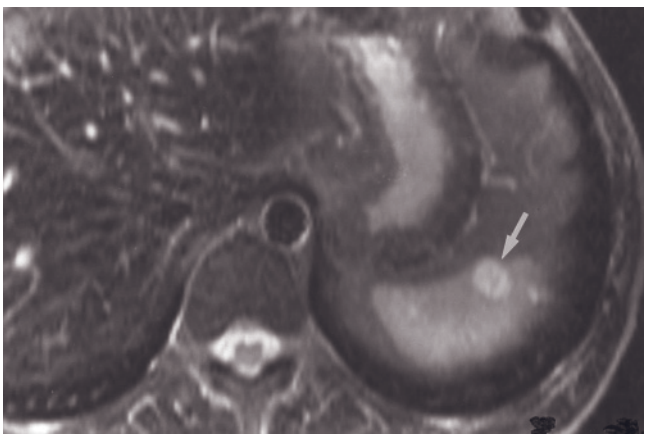

(*j*)

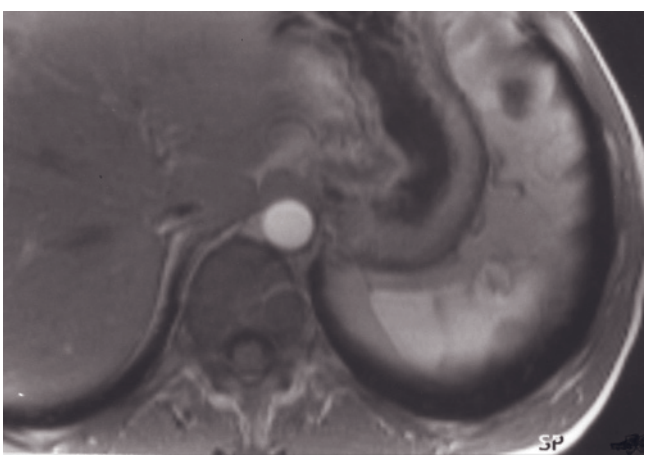

(*k*)

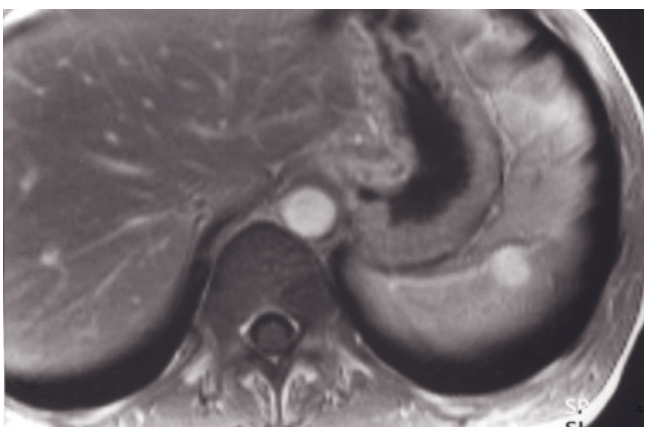

(*l*)

FIG. 5.14 (*Continued*) The small hemangioma in the superior aspect of the spleen is isointense on T1 and moderately hyperintense on T2 (arrow, *f*) and shows early uniform enhancement (*g*) that persists on the late postgadolinium image (*h*). The hemangioma is better demonstrated on the later postgadolinium image as background splenic enhancement has diminished and is uniform. Early uniform enhancement is common in <1.5-cm hemangiomas.

T1-weighted SGE (*i*), T2-weighted fat-suppressed spin-echo (*j*), immediate postgadolinium T1-weighted SGE (*k*), and 90-s gadolinium-enhanced T1-weighted SGE (*l*) images in a third patient. The lesion is isointense on T1(*i*) and moderately hyperintense on the T2-weighted image (arrow, *j*). Note centripetal (*k*, *l*) progressive enhancement of the hemangioma resembling the pattern of a hepatic hemangioma.

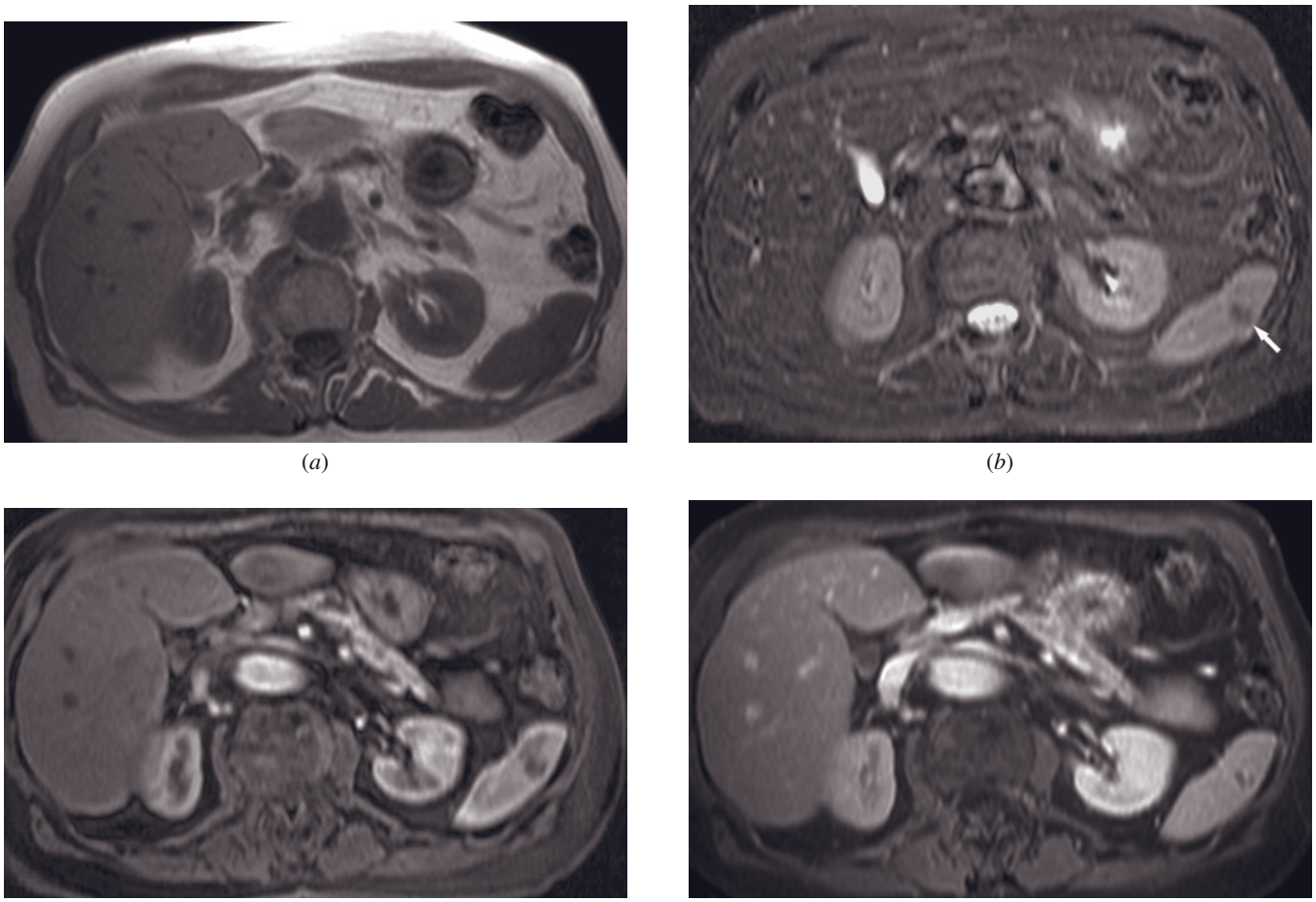

FIG. 5.15 Sclerosing hemangioma. T1-weighted SGE (*a*), T2-weighted fat-suppressed single-shot echo-train spin-echo (*b*), and immediate and 90-s postgadolinium T1-weighted fat-suppressed 3D GRE (*c*, *d*) images demonstrate a 1-cm hemangioma that is isointense with spleen on the T1-weighted image (*a*) and markedly hypointense on the T2-weighted image (arrow, *b*). Peripheral nodule of enhancement is present on the early postgadolinium image (*c*), with moderate progressive enhancement on the delayed postgadolinium image (*d*). The combination of hypointensity on T2-weighted image with only moderate progression of nodular enhancement on postcontrast T1-weighted image is consistent with a sclerosing hemangioma.

postgadolinium SGE images in an intense diffuse heterogeneous fashion [23, 27, 28] (fig. 5.17). Diffuse enhancement on immediate postgadolinium images is generally observed in tumors that are native to the organ in which they occur. Lesion size and enhancement pattern may mimic a more aggressive lesion. Lesions may also resemble normal splenic parenchyma (fig. 5.17). Enhancement becomes homogeneous on more delayed images, with signal intensity slightly greater than in background spleen. The early diffuse heterogeneous enhancement permits distinction from hemangioma [23].

Lymphangiomas

Lymphangiomas are composed of collections of small and cystically dilated lymphatic channels. Splenic lymphangiomatosis is rare and usually appears as a subcapsular multiloculated mass with increased signal intensity on T2-weighted images and enhancing septa on late-phase gadolinium-enhanced imaging [29].

Malignant Masses

Lymphoma and Other Hematologic Malignancies

Hodgkin and non-Hodgkin lymphomas often involve the spleen [30–32]. Lymphomatous deposits in the spleen frequently parallel the signal intensity of splenic parenchyma on T1- and T2-weighted images. Therefore, conventional unenhanced spin-echo MRI has had only limited success in imaging lymphomatous involvement of the spleen [31]. Immediate postgadolinium SGE images, however, surpass CT images for the evaluation of lymphoma [4]. This is explained by the higher sensitivity of MRI for gadolinium and its ability to acquire

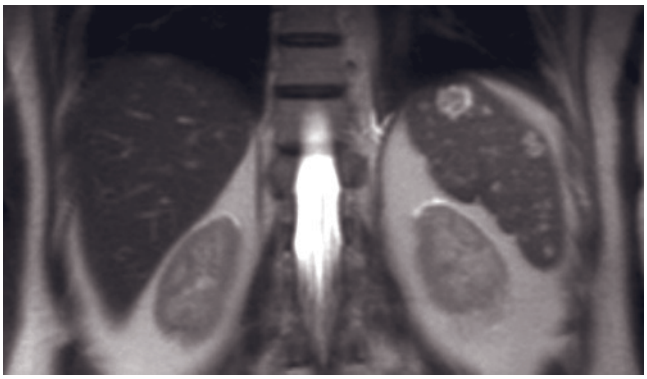

(*a*)

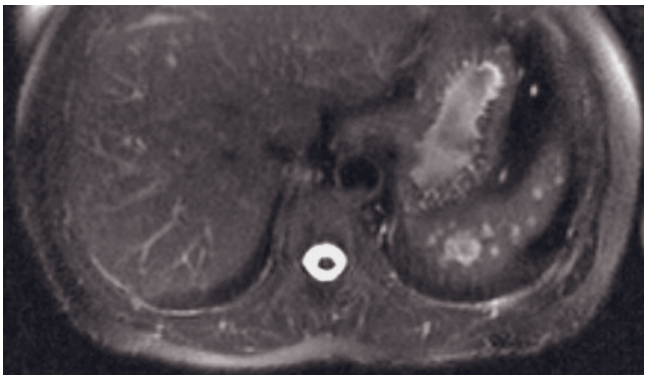

(*b*)

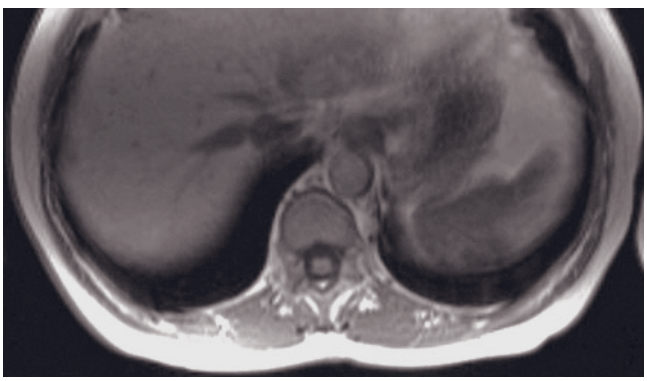

(*c*)

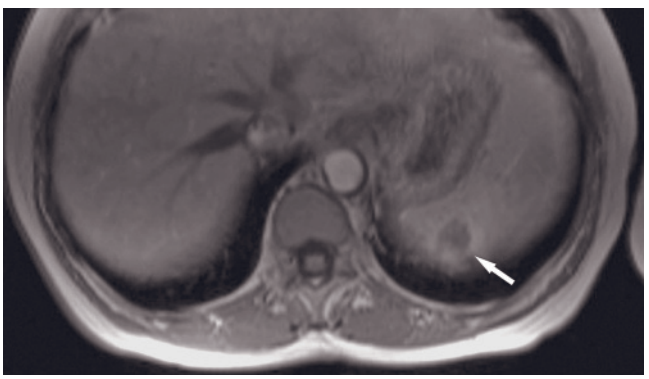

(*d*)

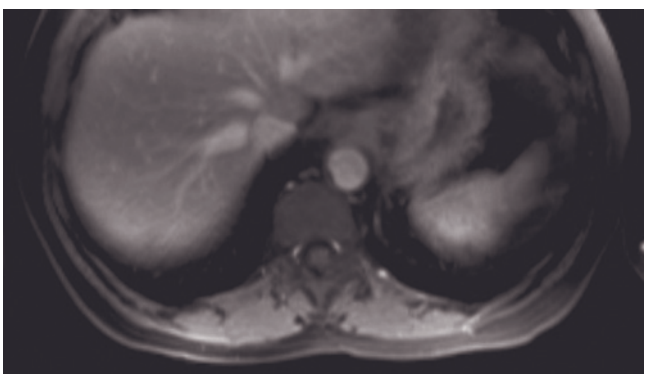

(*e*)

FIG. 5.16 Littoral cell angioma. Coronal T2-weighted echo-train spin-echo (*a*), T2-weighted fat-suppressed echo-train spin-echo (*b*), T1-weighted SGE (*c*), immediate T1-weighted SGE (*d*), and delayed postgadolinium fat-suppressed SGE (*e*) images. There are multiple splenic lesions that are moderately high in signal intensity on T2-weighted coronal image (*a*), high in signal intensity on T2-weighted fat-suppressed image (*b*), and isointense on T1-weighted image (*c*) and enhance heterogeneously on immediate postgadolinium images (arrow, *d*) and progress to isointensity in late images (*e*).

images of the entire spleen in a rapid fashion after a compact bolus of contrast.

Splenic involvement may have various appearances on immediate postgadolinium images. Diffuse involvement may appear as large, irregularly enhancing regions of high and low signal intensity (fig. 5.18), in contrast to the uniform bands that characterize normal arciform enhancement. Multifocal disease is also common, appearing as focal low-signal-intensity mass lesions scattered throughout the spleen [4]. Focal lesions may occur in a background of arciform-enhancing spleen or in a background of uniformly enhancing spleen. Focal involvement appears as spherical lesions, in distinction to the wavy tubular pattern of arciform enhancement of uninvolved spleen. Focal lymphomatous deposits may be low in signal intensity compared to background spleen on T2-weighted images (fig. 5.19), which is a feature distinguishing lymphomas from metastases, which are rarely low in signal intensity and usually isointense to hyperintense. Although splenomegaly is most often present, lymphoma may involve normal-sized spleens (fig. 5.20). Lymphoma also may appear as a large mass involving spleen and contiguous organs such as stomach, adrenal, or kidney. Bulky lymphadenopathy is frequently, but not invariably, present. It is critical to acquire SGE images within the first 30 s after

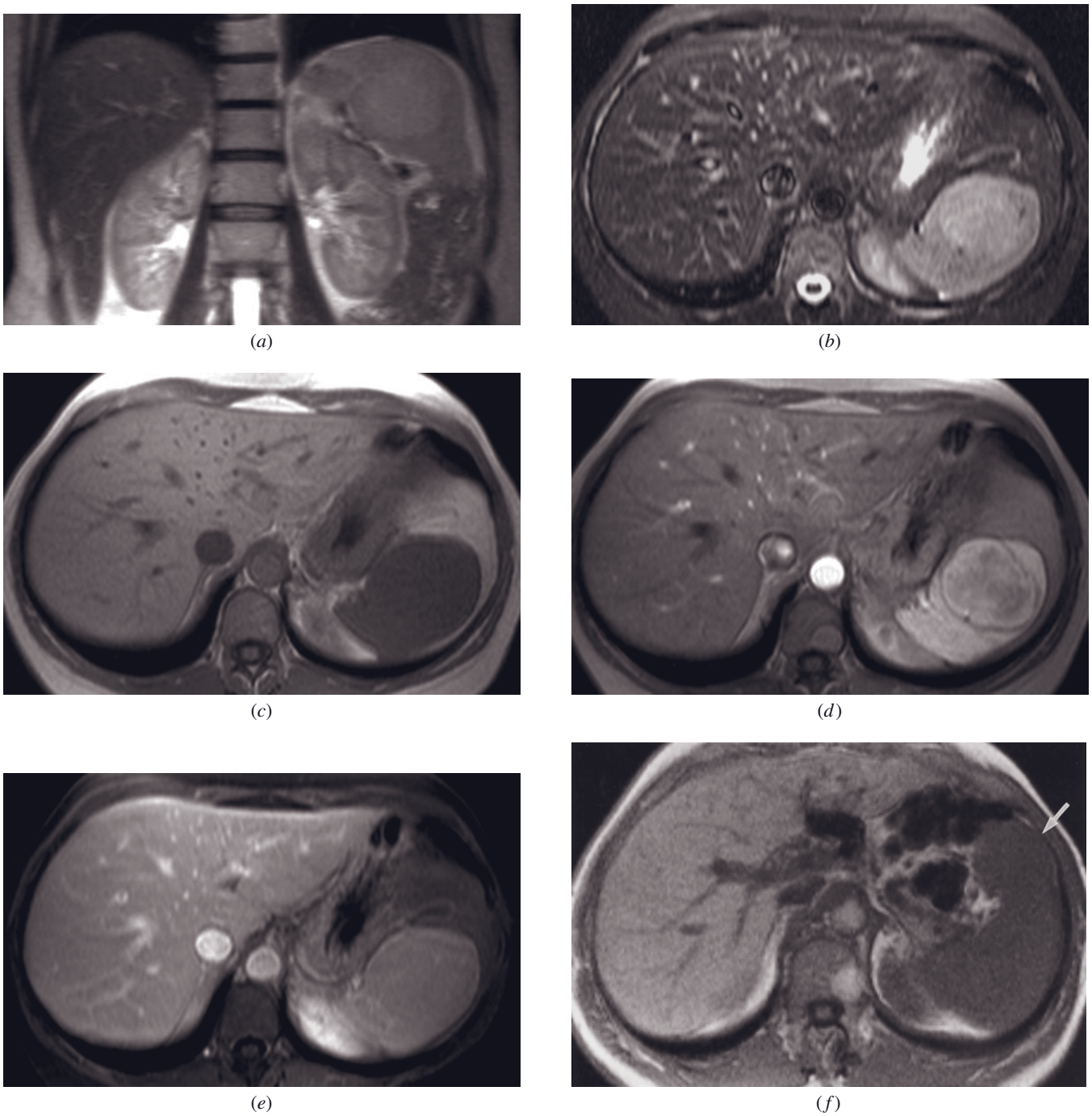

FIG. 5.17 Hamartoma. Coronal T2-weighted single-shot echo-train spin-echo (*a*), T2-weighted fat-suppressed single-shot echo-train spin-echo (*b*), T1-weighted SGE (*c*), immediate postgadolinium T1-weighted SGE (*d*), and late postgadolinium T1-weighted fat-suppressed spin-echo (*e*) images demonstrate a lesion in the spleen that is moderately high in signal intensity on T2-weighted images (*a*, *b*) and isointense on T1-weighted image (*c*). The lesion enhances heterogeneously on immediate postgadolinium SGE image (*d*). On delayed image (*e*) enhancement becomes more homogeneous and is greater than that of background spleen. T1-weighted SGE (*f*), T2-weighted fat-suppressed spin-echo (*g*), and immediate (*h*), 90-s (*i*), and 10-min (*j*) postgadolinium images

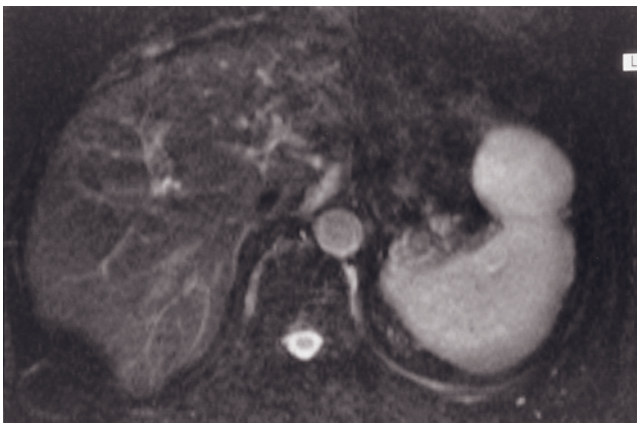

(*g*)

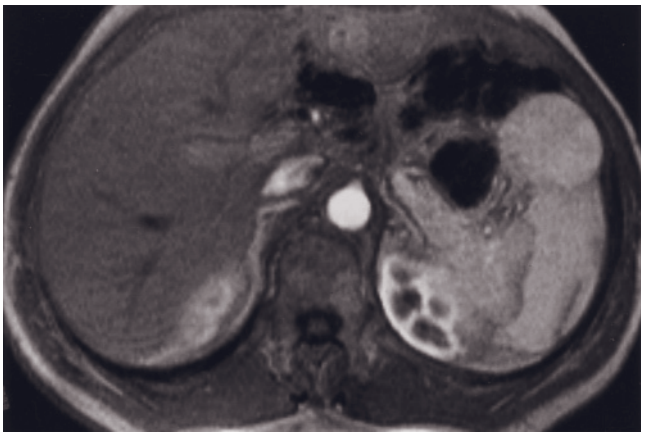

(*h*)

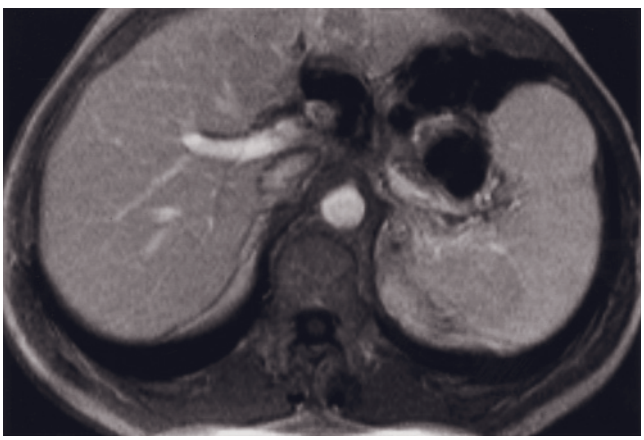

(*i*)

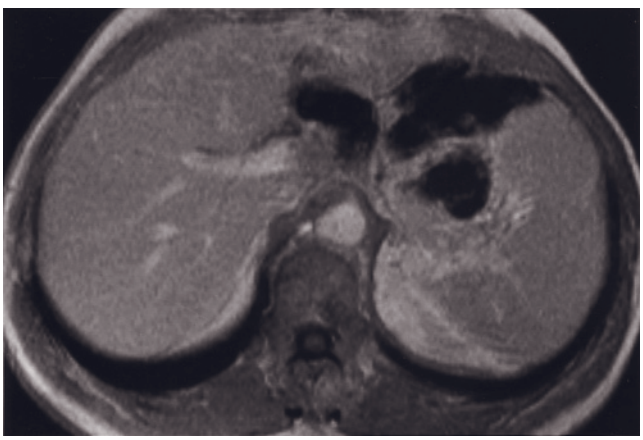

(*j*)

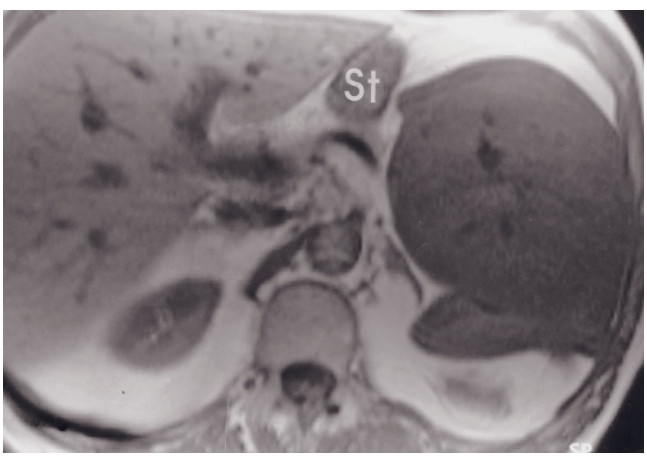

(*k*)

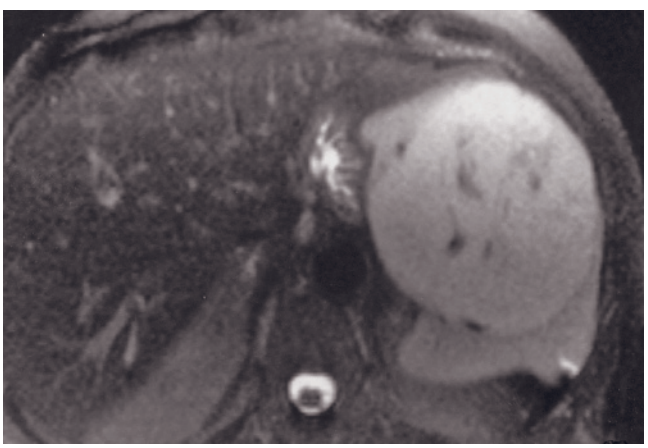

(*l*)

FIG. 5.17 (*Continued*) in a second patient. A 4-cm hamartoma arises from the anterior aspect of the midportion of the spleen (arrow, *f*). The signal intensity of the hamartoma is very similar to that of background spleen on all imaging sequences. A cleavage plane from spleen is noted on the T2-weighted image (*g*). On the immediate postgadolinium image (*h*), the tumor has intense, uniform enhancement, which is different from the arciform enhancement of the normal splenic parenchyma.

T1-weighted SGE (*k*),T2-weighted fat-suppressed echo-train spin-echo (*l*), immediate postgadolinium T1-weighted SGE (*m*), and 90-s gadolinium-enhanced T1-weighted fat-suppressed SGE (*n*) images in a third patient. A large hamartoma in the anterior

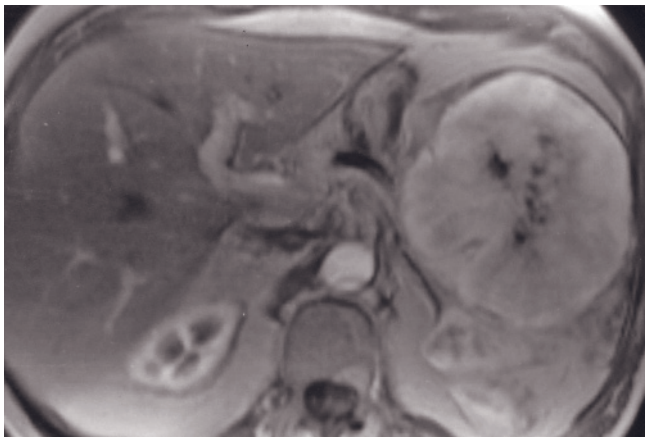

(*m*)

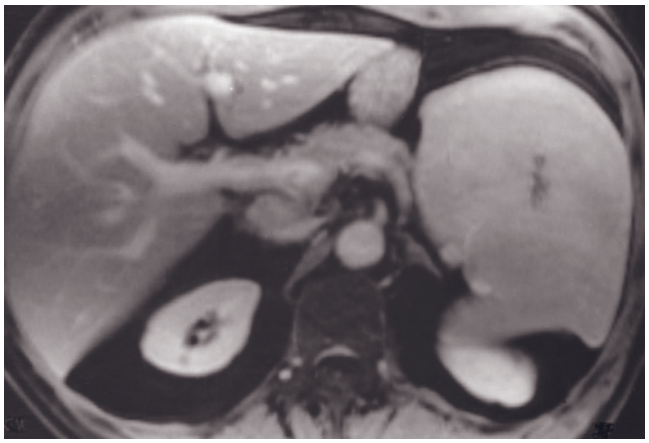

(*n*)

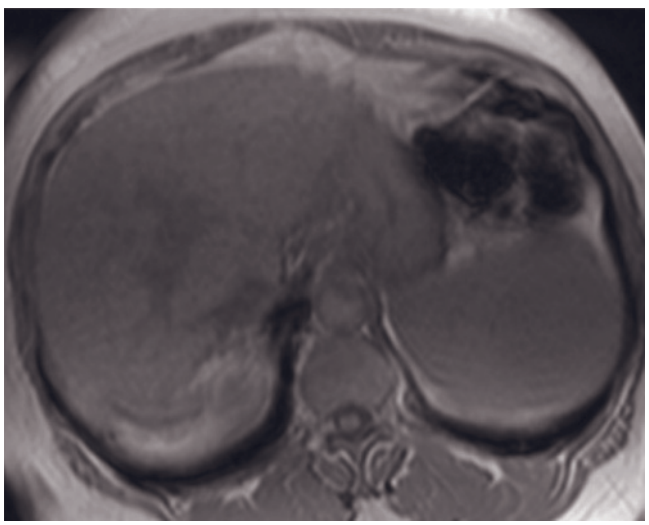

(*o*)

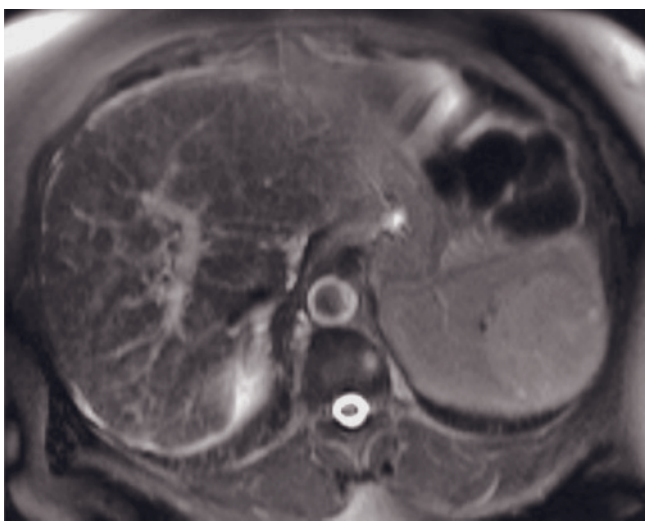

(*p*)

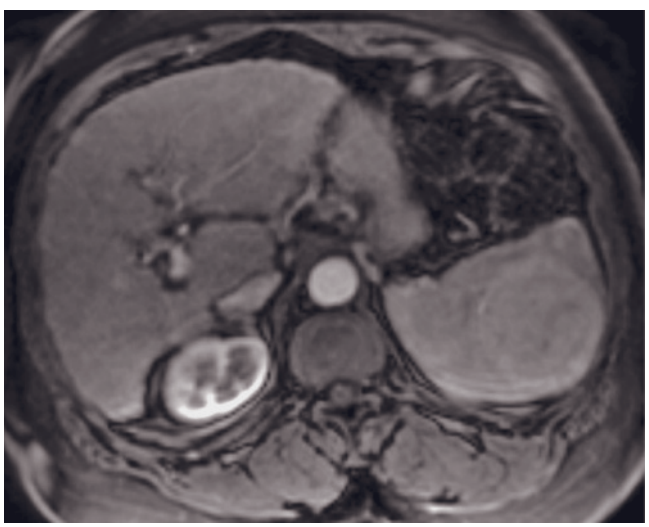

(*q*)

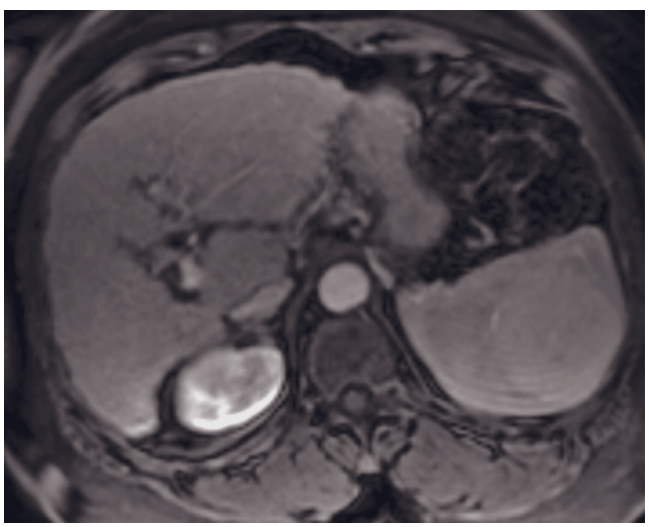

(*r*)

FIG. 5.17 (*Continued*) aspect of the spleen displaces the stomach (St, *k*) medially. The mass is near-isointense to the spleen on all sequences. It shows intense heterogeneous enhancement on the immediate postgadolinium image, similar to the intensity of spleen but with a different pattern. T1-weighted SGE (*o*), T2-weighted fat-suppressed single-shot echo-train spin-echo (*p*), and immediate (*q*) and delayed (*r*) postgadolinium T1-weighted fat-suppressed 3D-GE images at 3.0 T show splenic hamartoma demonstrating similar findings in another patient with cirrhosis and portal hypertension.

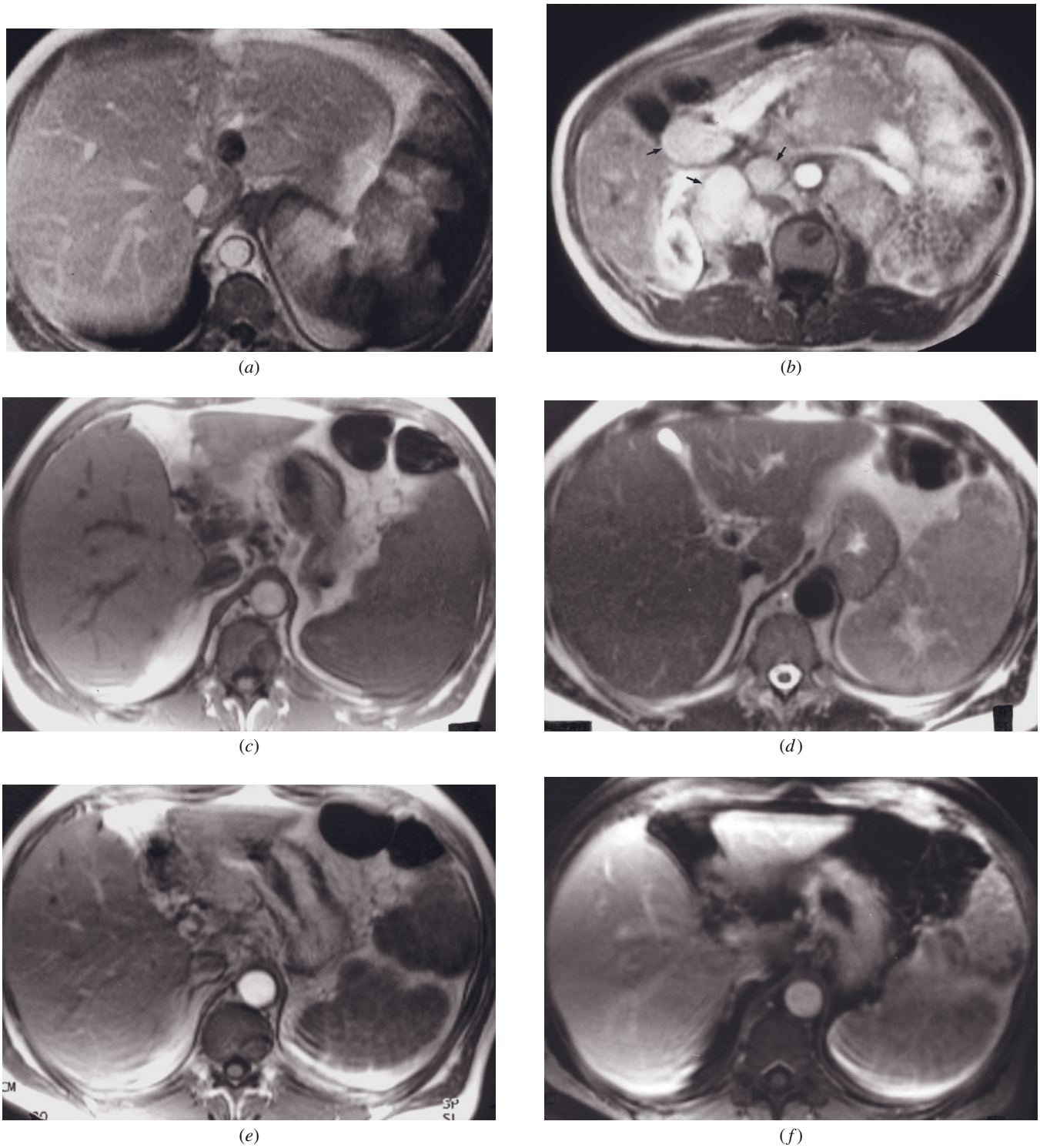

FIG. 5.18 Diffuse infiltration with lymphoma. Immediate postgadolinium T1-weighted SGE image (*a*) demonstrates irregular regions of high and low signal intensity in the spleen in this patient with non-Hodgkin lymphoma. Irregular enhancement is observed in the setting of diffuse infiltration. Immediate postgadolinium SGE image (*b*) in a second patient with non-Hodgkin lymphoma demonstrates irregular enhancement of the spleen consistent with diffuse infiltration. Enhancing lymph nodes (arrows, *b*) are also noted. T1-weighted SGE (*c*), T2-weighted echo-train spin-echo (*d*), immediate postgadolinium T1-weighted SGE (*e*), and 90-s postgadolinium T1-weighted fat-suppressed SGE (*f*) images in a third patient with B cell lymphoma infiltrating the spleen. The spleen is homogeneous in signal intensity on T1 (*c*) and is heterogeneous on the T2-weighted image (*d*). Diffuse heterogeneous enhancement with large irregular foci of decreased enhancement is appreciated on the immediate postgadolinium image (*e*) that persists on the late image (*f*).

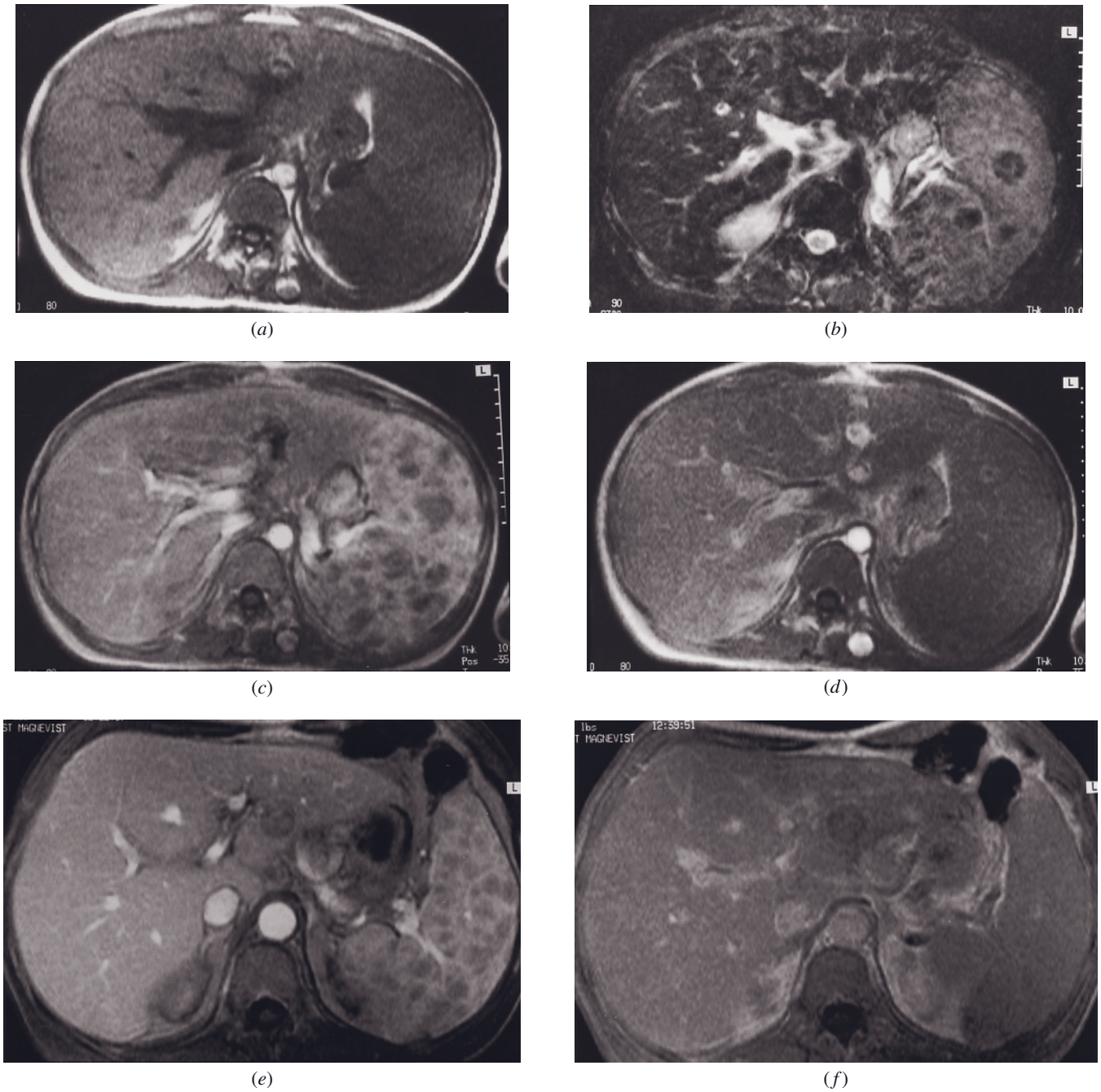

FIG. 5.19 Non-Hodgkin lymphoma with multifocal splenic involvement. T1-weighted SGE (*a*), T2-weighted fat-suppressed spin-echo (*b*), and immediate (*c*) and 2-min (*d*) postgadolinium SGE images. Splenomegaly is present. Lesions are not apparent on the precontrast SGE image. Several low-signal-intensity focal mass lesions are identified on T2-weighted images, an appearance that is not uncommon for lymphoma but rare for other malignant tumors. Multiple focal masses are most clearly demonstrated on immediate postgadolinium images (*c*). Lymphomatous foci become isointense with background spleen by 2 min after contrast (*d*). Immediate (*e*) and 90-s (*f*) postgadolinium SGE images in a second patient. Multiple low-signal-intensity masses are identified on the immediate postgadolinium image (*e*). Lesions become isointense with background spleen by 90 s.

contrast administration because foci of lymphoma equilibrate early, becoming isointense with normal splenic tissue within 2 min and frequently earlier [2, 4]. A rare appearance is that of a solitary mass involving the spleen, which may also show relatively internal diffuse and mildly heterogeneous enhancement on immediate postgadolinium SGE images (fig. 5.21). This appearance may mimic that of splenic hamartomas. The presence of symptoms and signs of systemic disease may suggest the diagnosis of lymphoma.

Superparamagnetic particles also improve the accuracy of diagnosing splenic lymphoma [9, 10]. These particles are selectively taken up by the RES cells and cause a decrease in signal intensity. By contrast, malignant cells do not take up superparamagnetic particles. Therefore, splenic lymphoma remains hyperintense compared to the normal spleen, improving tumor-spleen contrast [9, 10].

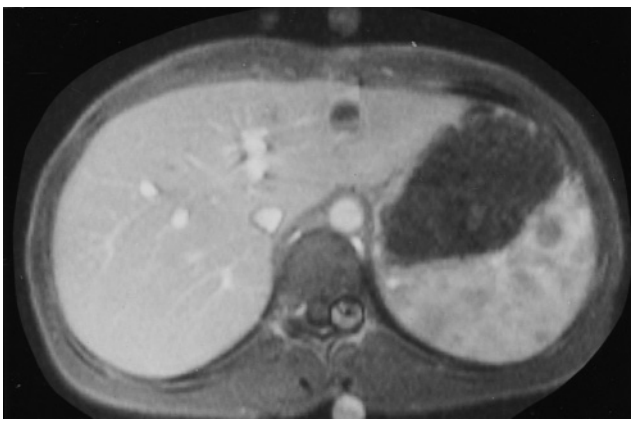

FIG. 5.20 Hodgkin lymphoma. Immediate postgadolinium image demonstrates multiple low-signal-intensity masses within a normal-sized spleen. Rounded lesions are present in a background of arciform-enhancing spleen.

Chronic lymphocytic leukemia frequently involves the spleen and may result in massive splenomegaly. Focal deposits are more infiltrative and less well-defined than lymphoma. Deposits are well shown after gadolinium administration and appear as irregular hypointense masses on early postcontrast images (fig. 5.22). Malignancies related to leukemia, such as angioimmunoblastic lymphadenopathy with dysproteinemia, have a similar appearance, with irregular regions of low signal intensity within the spleen on immediate postgadolinium images (fig. 5.23). Lymphadenopathy is frequently present.

Chemotherapy-treated lymphomatous deposits in the spleen can appear as fibrotic nodules that are low signal intensity on T1-weighted and T2-weighted images and demonstrate negligible enhancement on early and late postgadolinium images (fig. 5.24). These imaging features may be correlated clinically with a favorable response to therapy.

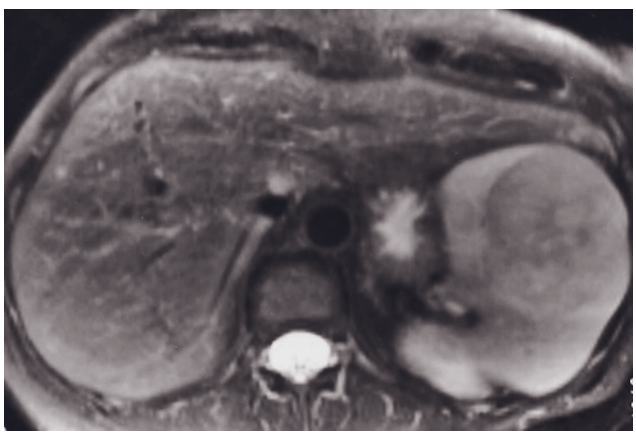

(*a*)

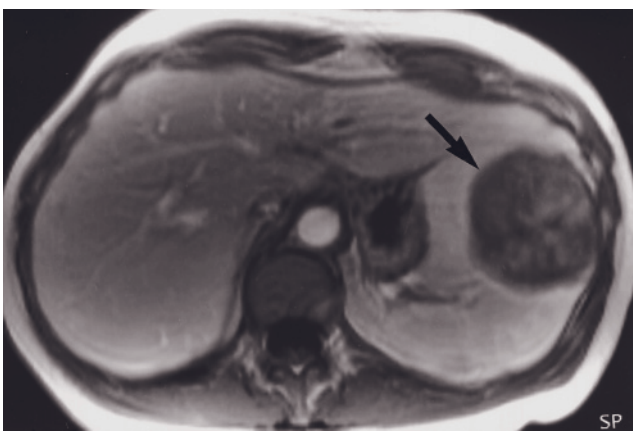

(*b*)

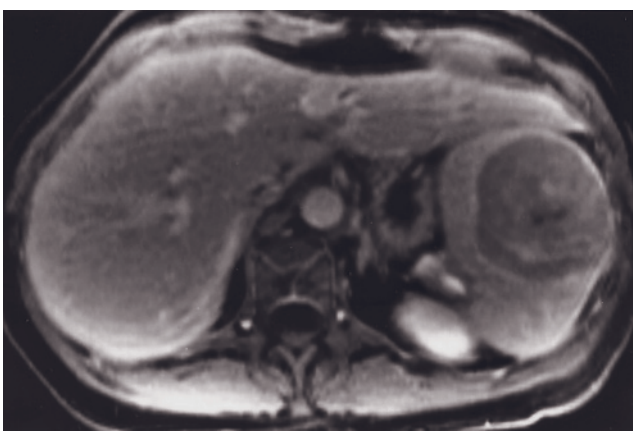

(*c*)

FIG. 5.21 Splenic lymphoma presenting as a solitary mass. T2-weighted fat-suppressed echo-train spin-echo (*a*), immediate postgadolinium T1-weighted SGE (*b*), and 90-s postgadolinium fat-suppressed SGE (*c*) images. A 6-cm solitary mass arises from the spleen that is mildly heterogeneous and hyperintense on the T2-weighted image (*a*). The mass enhances moderately in a diffuse heterogeneous fashion on the immediate postgadolinium image (arrow, *b*), with slightly increased signal intensity by 90 s after contrast (*c*). The appearance resembles a hamartoma, with diffuse heterogeneous enhancement. Substantially less enhancement is present of this lymphomatous mass than is typically seen with a hamartoma. The patient presented with systemic symptoms, which is a picture in keeping with lymphoma and not hamartoma. The patient did not have retroperitoneal adenopathy, which is another uncommon feature of splenic lymphoma.

Metastases

Although tumors may invade the spleen from contiguous viscera, true tumor metastasis to the spleen is rare, usually occurring only in the setting of disseminated disease in the terminal stage. Breast cancer, lung cancer, and melanoma are the most common primary tumors [33]. The most generally accepted theory to account for the relative scarcity of splenic metastasis is based on the absence of afferent lymphatic channels within the spleen [34]. Metastases tend to be in the form of nodules or aggregates of tumor, and they are particularly prone to disrupt the normal splenic architecture. Splenic metastases often are occult on conventional spin-echo imaging [32]. One notable exception is melanoma, because its paramagnetic properties may result in a mixed population of high- and low-signal-intensity lesions on both T1- and T2-weighted images. Lesion detection is improved by acquiring immediate postgadolinium SGE images [3] (fig. 5.25). Metastases are lower in signal intensity than normal splenic tissue on these images. Images must be acquired within the first 30 s after gadolinium administration because metastases rapidly equilibrate with splenic parenchyma. Image acquisition with superparamagnetic iron oxide particles renders metastases higher in signal intensity than normal spleen [7, 9]. An attractive feature of iron oxide particles is that the imaging window is longer (60 min) than for gadolinium (<1 min) [7, 9].

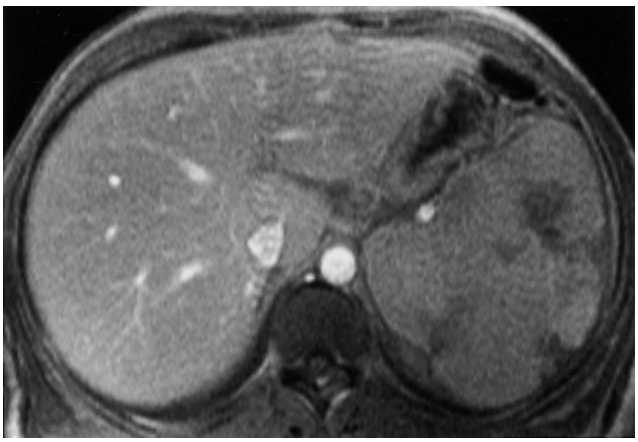

FIG. 5.22 Chronic lymphocytic leukemia. The spleen is noted to be massively enlarged and contains irregularly marginated focal low-signal-intensity masses on the 45-s postgadolinium T1-weighted SGE image.

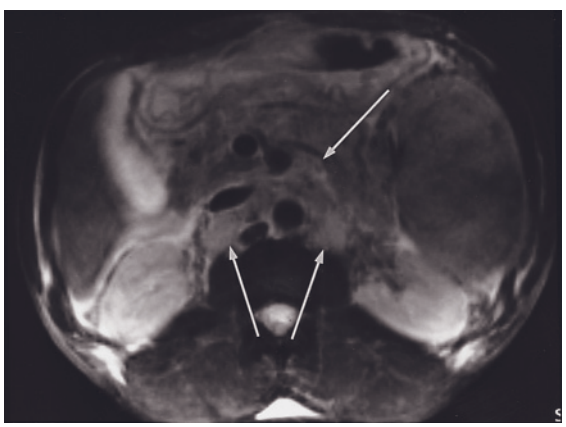

(*a*)

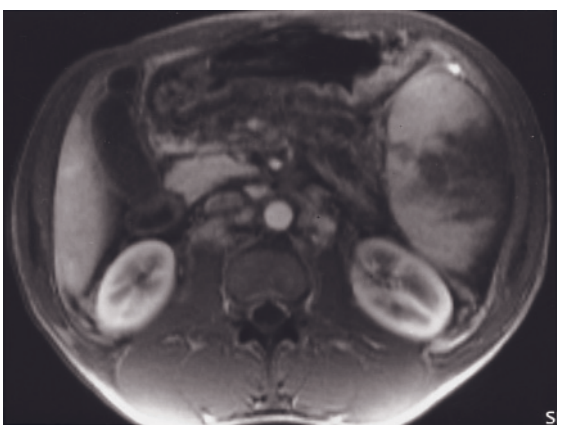

(*b*)

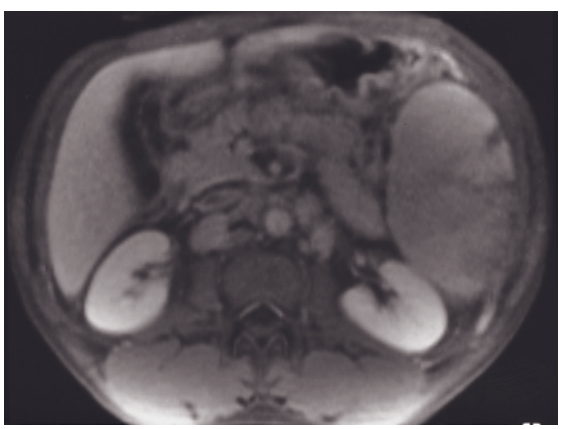

(*c*)

FIG. 5.23 Angioimmunoblastic lymphadenopathy with dysproteinemia. T2-weighted fat-suppressed spin-echo (*a*), immediate postgadolinium T1-weighted SGE (*b*), and 90-s postgadolinium fat-suppressed SGE (*c*) images. The spleen is noted to be markedly enlarged. Lymphadenopathy is moderately high in signal intensity on T2-weighted images and is rendered conspicuous because of the suppression of fat signal intensity (arrows, *a*). Mild enhancement of lymph nodes is noted on immediate postgadolinium SGE (*b*). Lymph nodes enhance more intensely in the interstitial phase and are more clearly defined by the suppression of fat signal intensity (*c*). Splenic involvement is demonstrated by irregular, poorly marginated, large regions of diminished enhancement on the immediate postgadolinium image (*b*). Enhancement of the spleen is more uniform by 90 s after contrast (*c*), and signal intensity is mildly heterogeneous on the T2-weighted image.

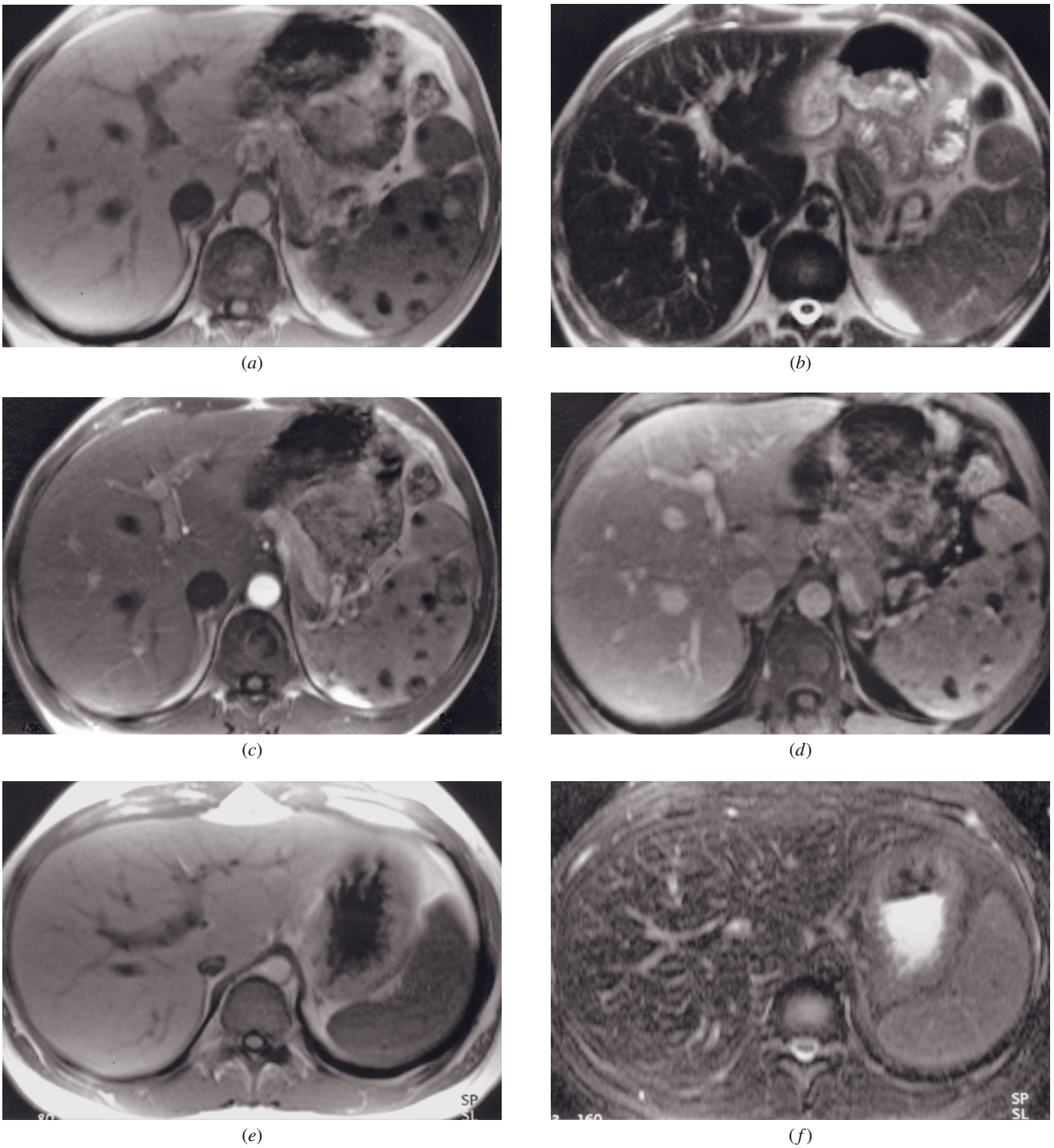

FIG. 5.24 Chemotherapy-treated splenic lymphoma. T1-weighted SGE (*a*), T2-weighted single-shot echo-train spin-echo (*b*), immediate postgadolinium T1-weighted SGE (*c*), and 90-s postgadolinium T1-weighted fat-suppressed SGE (*d*) images. Foci of treated lymphoma are hypointense on T1 (*a*) and hypo- to isointense on T2 (*b*) and demonstrate negligible enhancement on early (*c*) and late (*d*) postgadolinium images. The low signal on T2 reflects a diminished fluid content, and fibrous changes result in the diminished enhancement. T1-weighted SGE (*e*), breath-hold STIR (*f*), immediate postgadolinium SGE (*g*), and 90-s postgadolinium

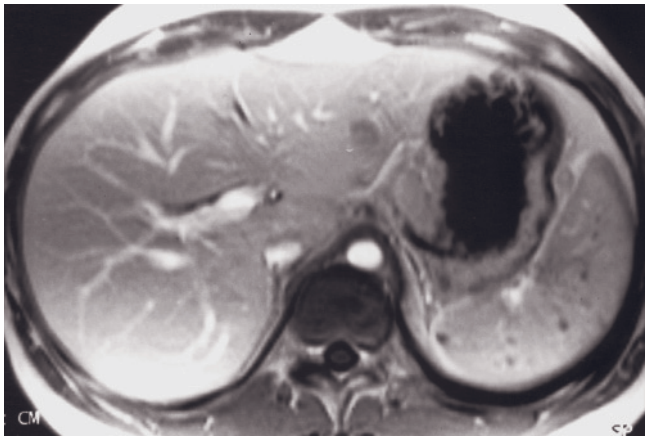

(*g*)

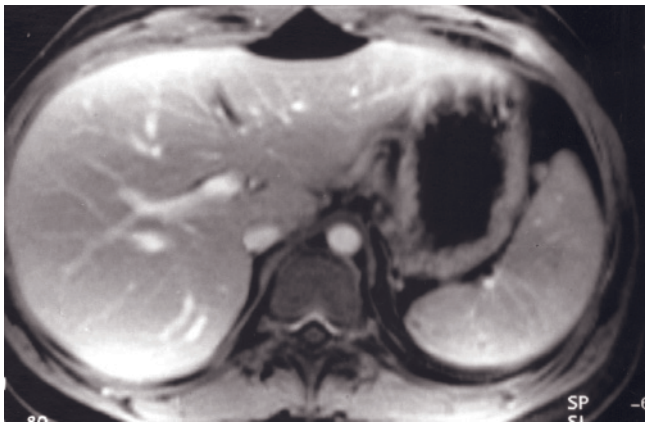

(*h*)

FIG. 5.24 (*Continued*) SGE (*b*) images in a second patient with Hodgkin lymphoma receiving chemotherapy. There are multiple small hypointense lesions on T1 (*e*)- and T2 (*f*)-weighted images, which shows peripheral or diffuse enhancement after contrast administration (*g*, *h*) reflecting the different stages of the fibrotic process. These lesions remained stable in appearance in follow-up MRI exams (not shown).

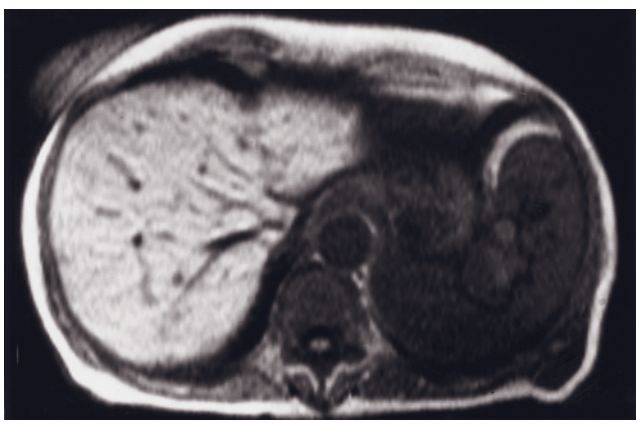

(*a*)

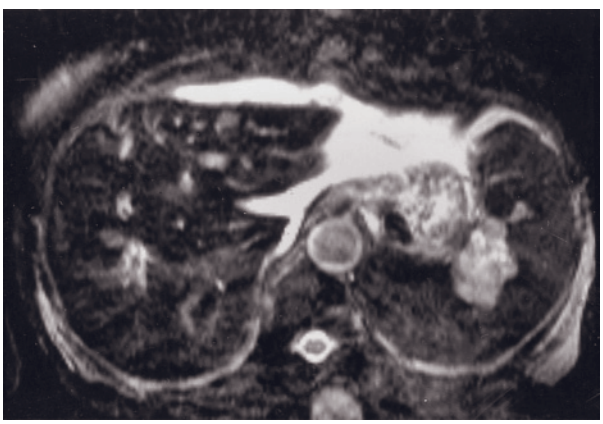

(*b*)

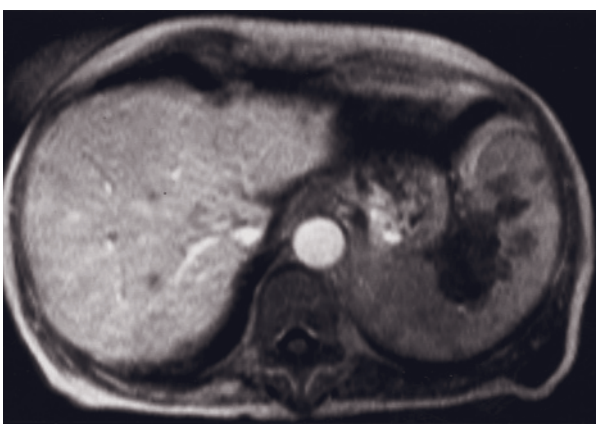

(*c*)

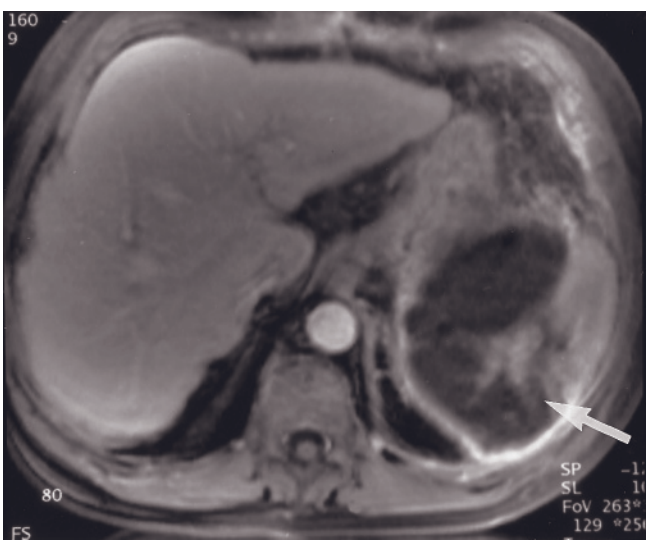

(*d*)

FIG. 5.25 Splenic metastases. T1-weighted SGE (*a*), T2-weighted fat-suppressed spin-echo (*b*), and immediate postgadolinium T1-weighted SGE (*c*) images in a woman with endometrial cancer. Metastases are noted throughout the spleen that are mixed hypointense and isointense on the T1-weighted image (*a*), mixed isointense and hyperintense on the T2-weighted image (*b*), and low in signal intensity on the immediate postgadolinium image (*c*). Note that metastases are best shown on the immediate postgadolinium image. The largest metastasis is distinctly demonstrated on the T2-weighted image (*b*). The smaller lesions are poorly shown, despite the presence of iron deposition. Ascites is also present and is low in signal intensity on pre- and postcontrast T1-weighted images and high in signal intensity on the T2-weighted image. Transverse 90-s postgadolinium fat-suppressed SGE image (*d*) in a second patient demonstrates an expansive destructive lesion (arrow, *d*) in the posterior aspect of the spleen associated

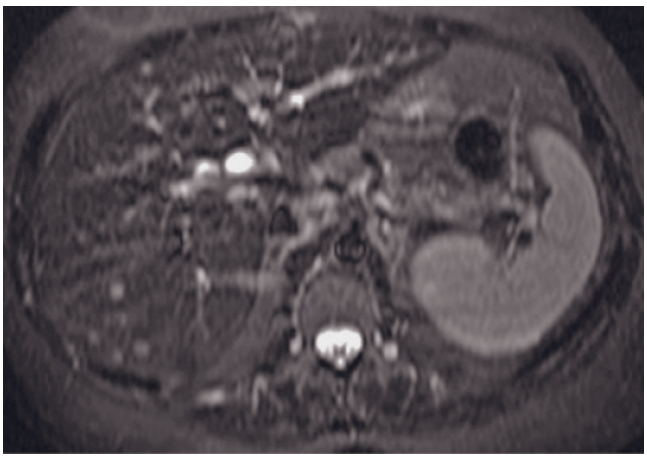

(*e*)

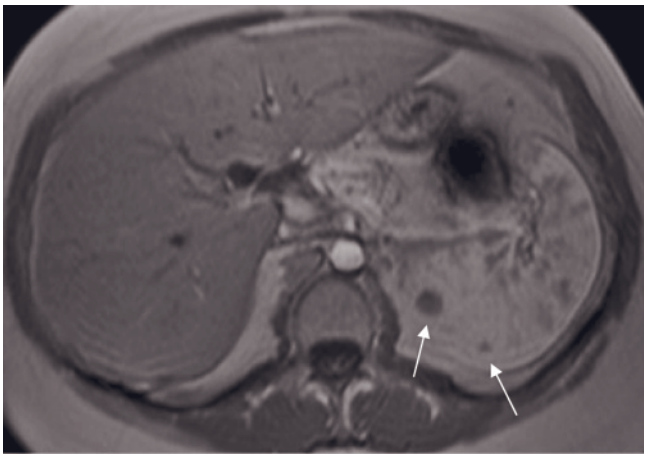

(*f*)

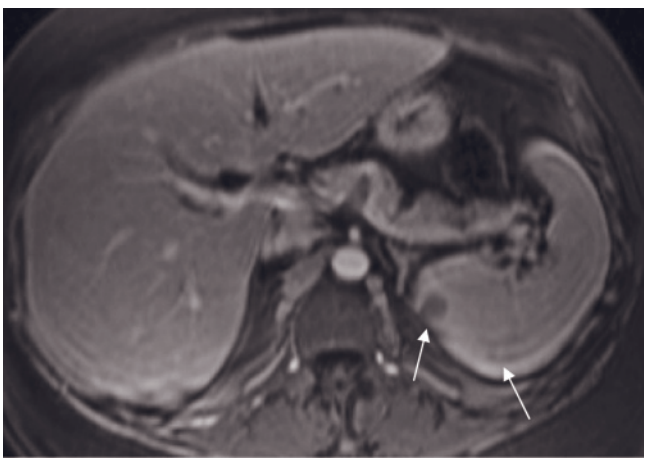

(*g*)

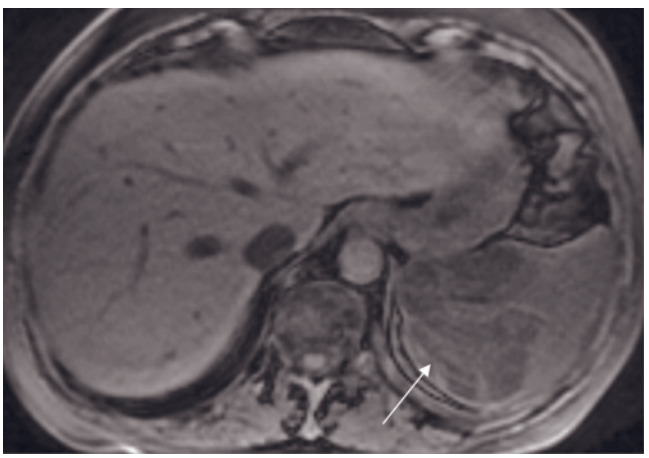

(*h*)

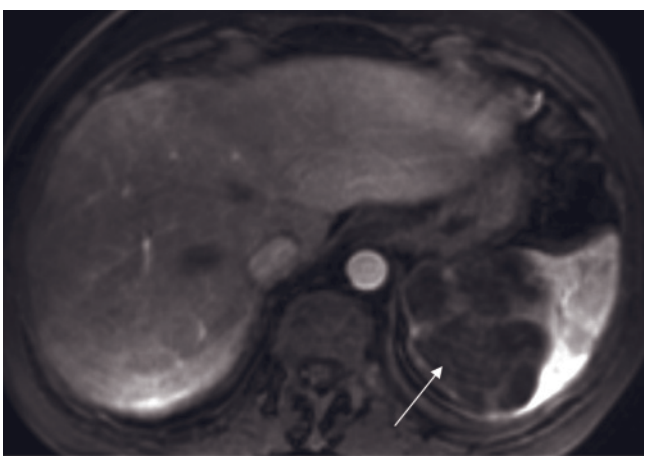

(*i*)

FIG. 5.25 (*Continued*) with a large subcapsular fluid collection. T2-weighted short-tau inversion recovery (STIR) (*e*), T1-weighted immediate postgadolinium SGE (*f*), and T1-weighted delayed postgadolinium fat-suppressed 3D-GE (*g*) images in another patient with spleen and liver metastases from lung cancer. The metastases show mildly high signal on STIR image. Splenic metastases (arrows, *f, g*) which are hypovascular demonstrate peripheral enhancement on postgadolinium images. T1-weighted fat-suppressed 3D-GE (*h*) and T1-weighted immediate postgadolinium fat-suppressed 3D-GE (*i*) images at 3.0 T in another patient with ovarian cancer. There is a large metastasis (arrows, *h, i*) located in the spleen demonstrating heterogeneous enhancement on immediate postgadolinium 3D-GE image (*i*).

Direct Tumor Invasion

Direct tumor invasion is most commonly observed with pancreatic cancers including ductal adenocarcinoma, islet cell tumor, and macrocystic cystadenocarcinoma (fig. 5.26). Direct extension from tumors of gastric, colonic, renal, and adrenal origins, in decreasing order of frequency, is also observed. Lymphoma has a particular propensity to involve the spleen in continuity with other organs.

Angiosarcoma

Angiosarcoma is rare but represents the most common primary nonlymphoid malignant tumor of the spleen. Tumors may be single or multiple and demonstrate an

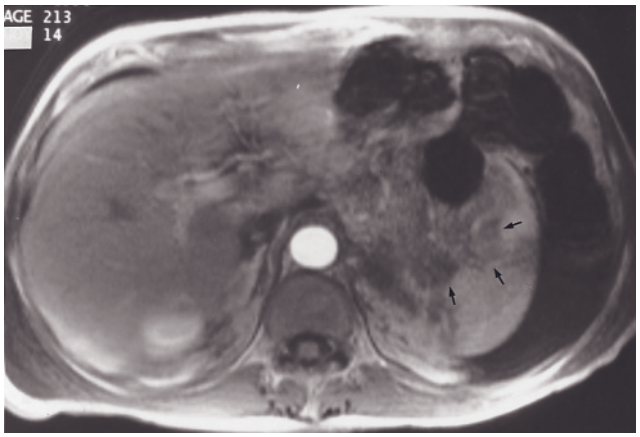

(*a*)

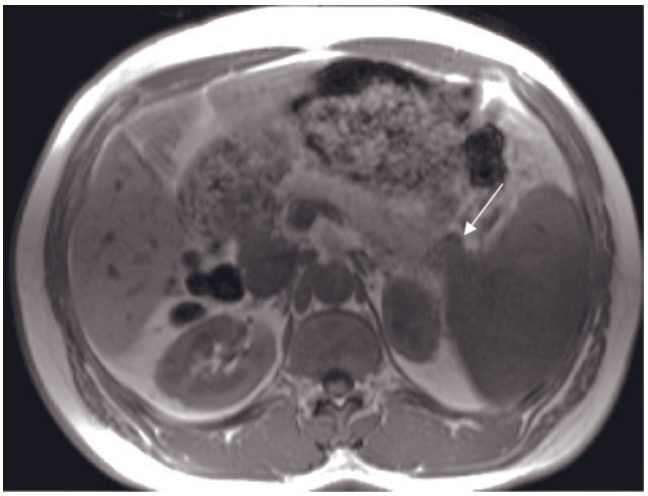

(*b*)

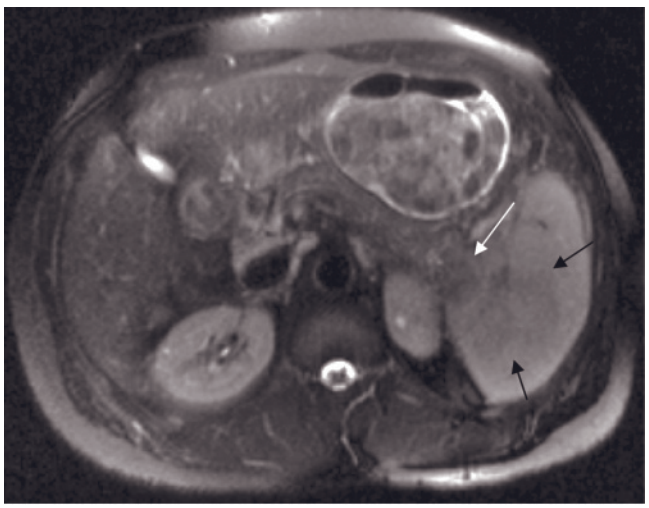

(*c*)

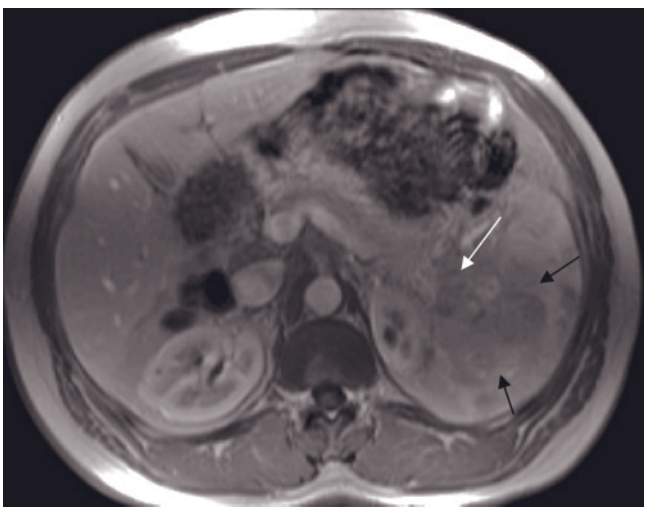

(*d*)

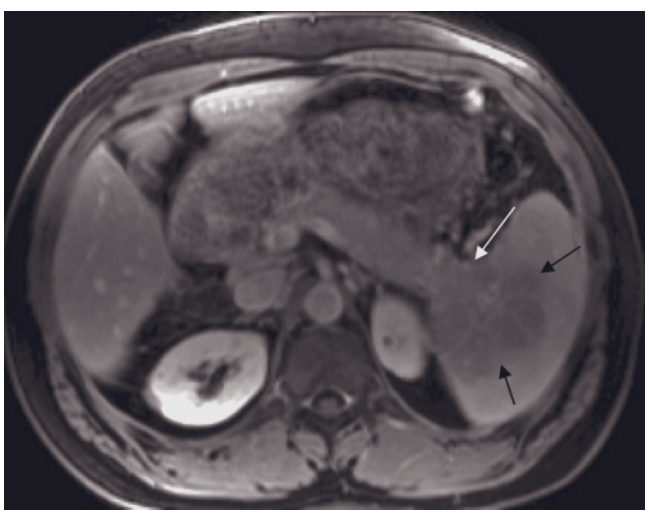

(*e*)

FIG. 5.26 Direct tumor invasion. Immediate postgadolinium T1-weighted SGE (*a*) image demonstrates invasion of the splenic hilum by a large infiltrative pancreatic ductal adenocarcinoma (arrows, *a*). T1-weighted SGE (*b*), T2-weighted fat-suppressed single-shot echo-train spin-echo (*c*), T1-weighted postgadolinium 45-s SGE (*d*) and 90-s fat-suppressed 3D-GE (*e*) images in another patient with pancreatic neuroendocrine tumor. The tumor (white arrows, *b–e*) is located in the pancreatic tail and invades the spleen (black arrows, *c–e*).

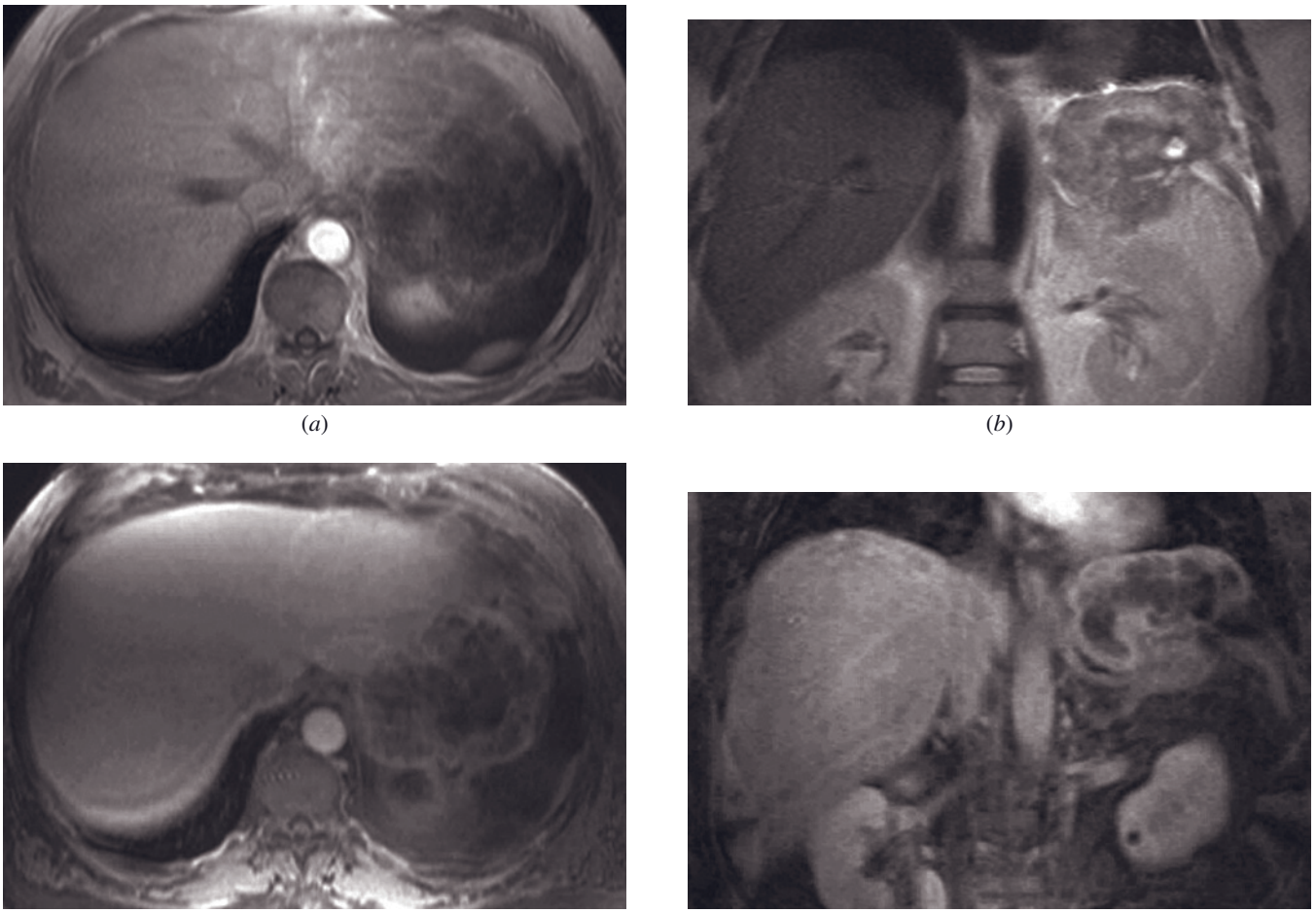

(*a*) (*b*) (*c*) (*d*)

FIG. 5.27 Angiosarcoma of the spleen. T1-weighted SGE (*a*), coronal T2-weighted single-shot echo-train spin-echo (*b*), immediate postgadolinium T1-weighted fat-suppressed 3D GRE (*c*), and delayed postgadolinium coronal T1-weighted fat-suppressed 3D GRE (*d*) images demonstrate a large splenic mass that is hypointense on T1-weighted image (*a*) and mildly high in signal intensity on T2-weighted image (*b*). The mass enhances heterogeneously on immediate postgadolinium images (*c*), and enhancement progresses on delayed images (*d*).

aggressive growth pattern [35, 36]. Rupture is not uncommon, and hemorrhage is a frequent finding. Angiosarcomas commonly demonstrate a variety of signal intensities on T1-weighted images because of the varying ages of blood products [37]. Tumors are usually highly vascular and enhance intensely with gadolinium [37] (fig. 5.27).

MISCELLANEOUS

Splenomegaly and Vascular Pathologies

Splenomegaly may be observed in a number of disease states including venous congestion (portal hypertension), leukemia, lymphoma, metastases, and various infections. In North America, the most common cause of splenomegaly is secondary to portal hypertension. On immediate postgadolinium images, demonstration of arciform or uniform high-signal-intensity enhancement is consistent with portal hypertension and excludes the presence of malignant disease (fig. 5.28).

Perisplenic varices and splenorenal shunts are also seen commonly in patients with portal hypertension in combination with splenomegaly (fig. 5.28).

Splenic vein thrombosis can be bland or malignant. Bland splenic vein thrombosis is commonly seen in patients with portal hypertension (for an in-depth discussion, see Chapter 2, *Liver*, and fig. 2.249). Malignant splenic vein thrombosis is usually seen in patients with pancreatic adenocarcinoma (for an in-depth discussion, see Chapter 4, *Pancreas*, and fig. 4.29).

Splenic artery aneurysms are the most common visceral artery aneurysms [38]. The prevalence of splenic artery aneurysm has been reported as 0.04–0.10% at autopsy [38]. Most aneursyms are small (usually less

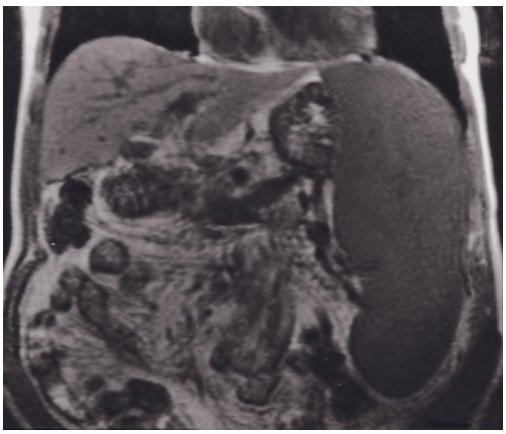

(*a*)

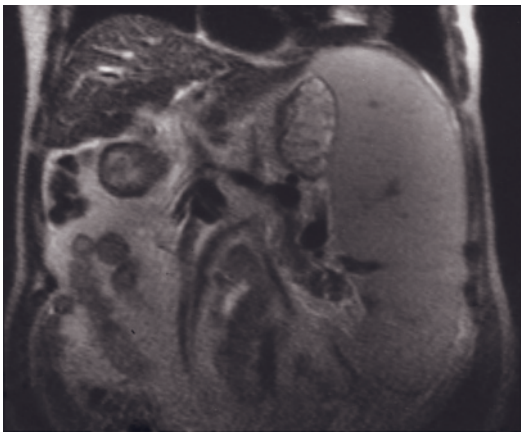

(*b*)

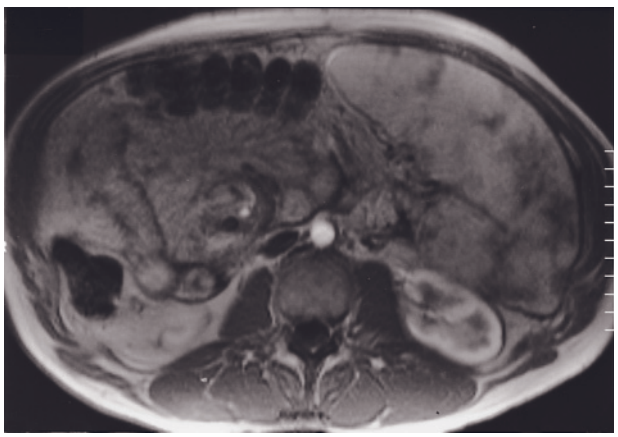

(*c*)

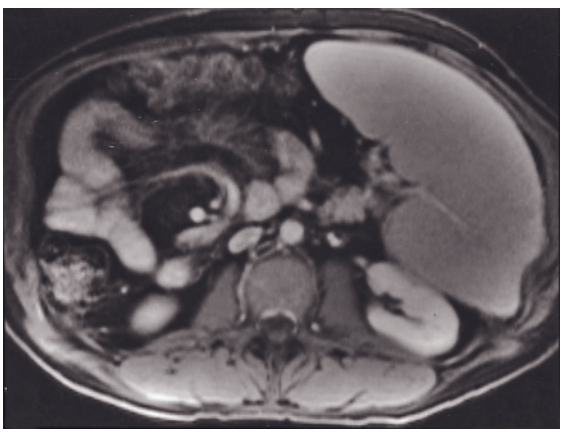

(*d*)

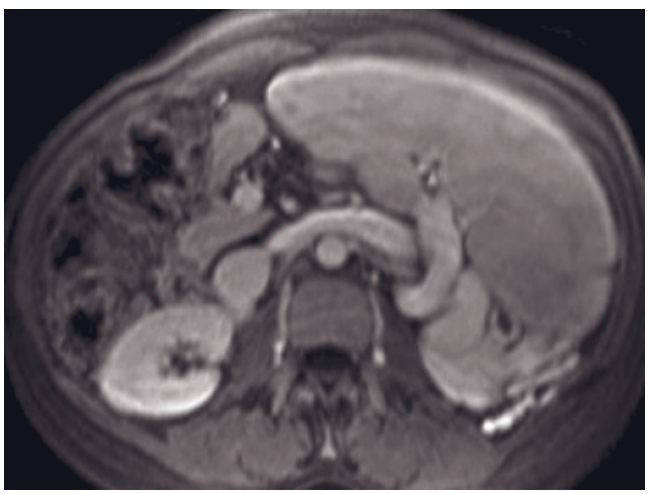

(*e*)

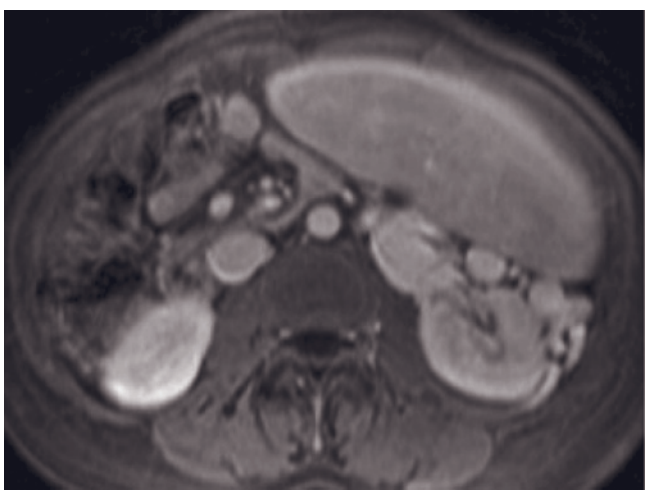

(*f*)

FIG. 5.28 Splenomegaly secondary to portal hypertension, splenorenal shunt, and splenic artery aneurysm. Coronal T1-weighted SGE (*a*), coronal T2-weighted echo-train spin-echo (*b*), immediate postgadolinium T1-weighted SGE (*c*), and 90-s postgadolinium fat-suppressed SGE (*d*) images. Massive splenomegaly is demonstrated on all MR images. No focal lesions are present on precontrast T1 (*a*) or T2-weighted (*b*) images. The presence of arciform enhancement on the immediate postgadolinium SGE image (*c*) excludes the presence of malignant disease. At 90 s, the spleen becomes homogeneous in signal (*d*). T1-weighted delayed postgadolinium 3D-GE images (*e, f*) demonstrate splenomegaly, splenorenal shunt, and portosystemic collaterals in another patient with portal hypertension. Axial T1-weighted 45-s postgadolinium fat-suppressed 3D-GE images (*g, h*) and coronal reformatted 3D-GE

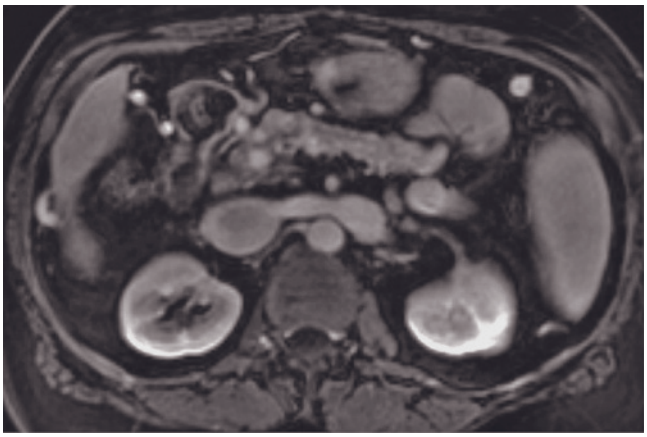

(*g*)

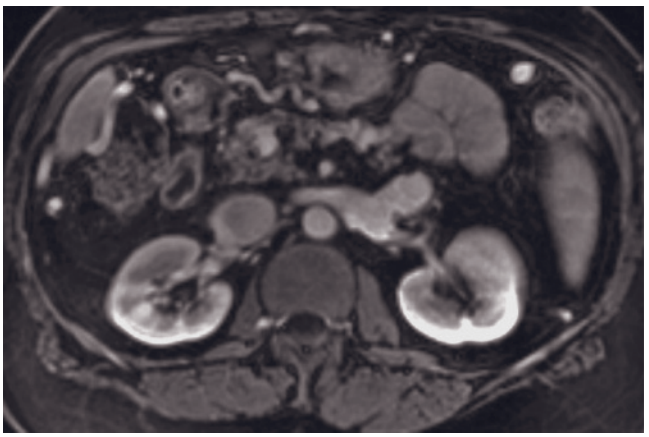

(*h*)

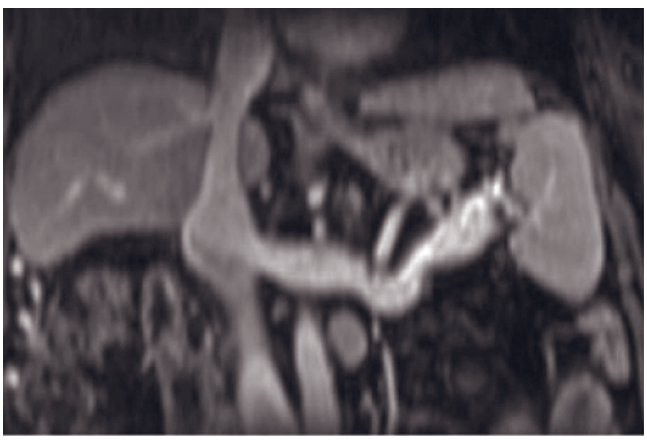

(*i*)

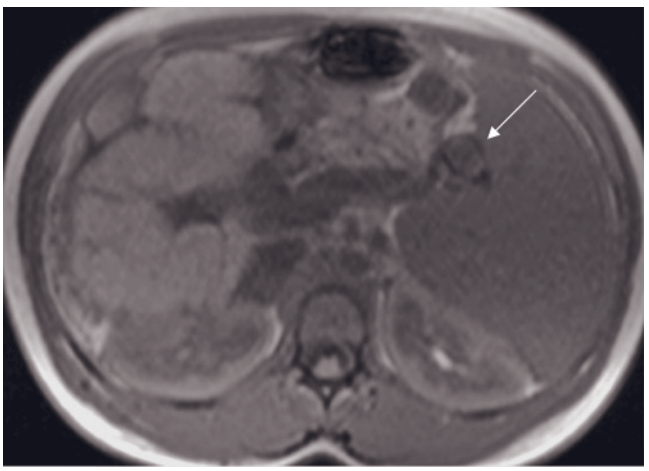

(*j*)

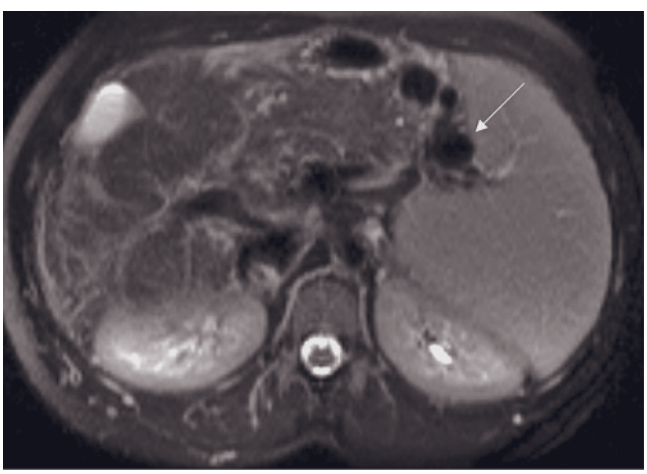

(*k*)

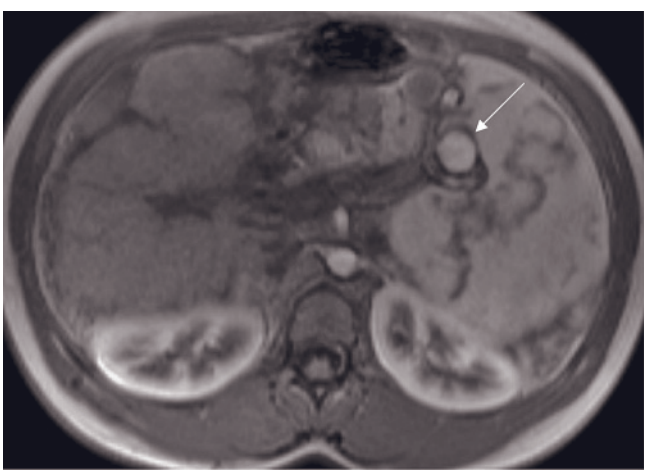

(*l*)

FIG. 5.28 (*Continued*) image (*i*) at 3.0 T demonstrate the splenorenal shunt in another patient with portal hypertension. T1-weighted SGE (*j*), T2-weighted fat-suppressed single-shot echo-train spin-echo (*k*), T1-weighted immediate postgadolinium SGE (*l*),

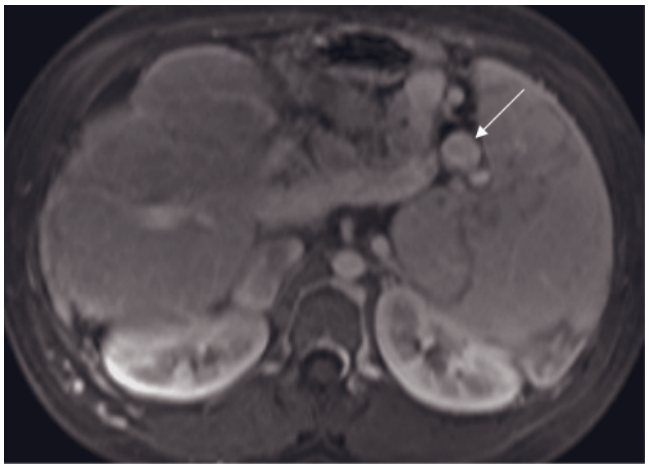

(*m*)

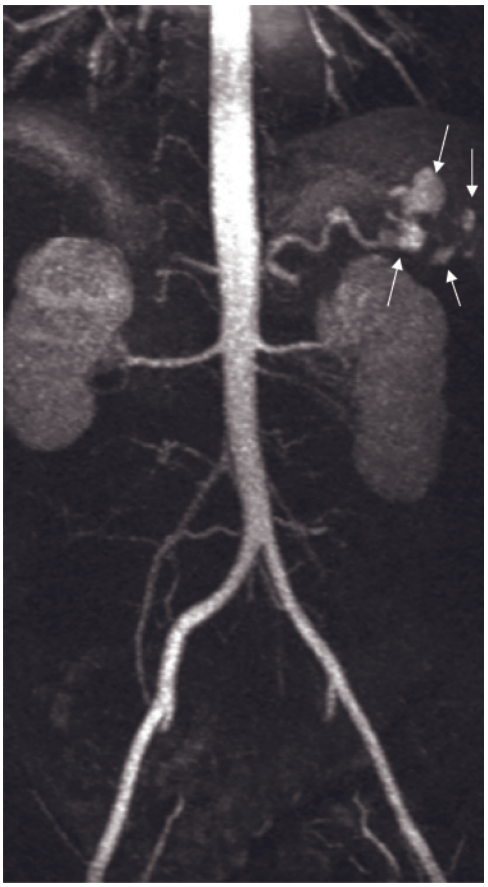

(*n*)

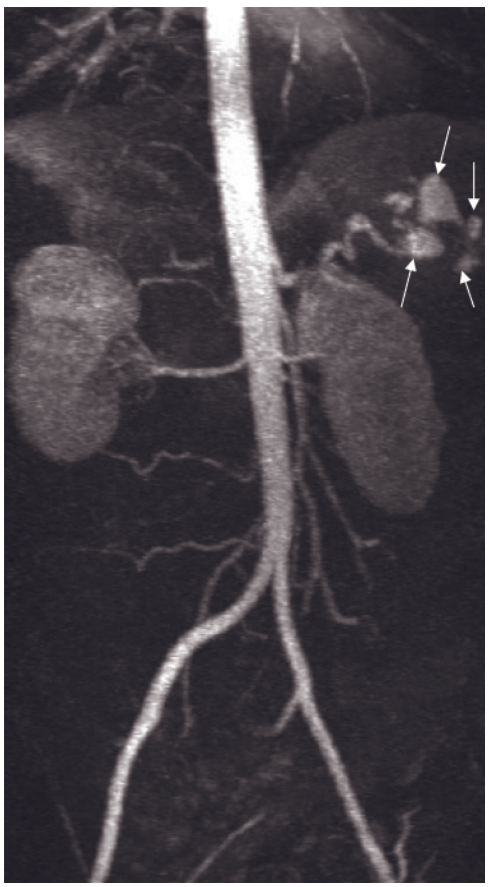

(*o*)

Fig. 5.28 (*Continued*) and 45-s fat-suppressed 3D-GE (*m*) images in another patient with primary sclerosing cholangitis, splenomegaly, and portal hypertension demonstrate splenic artery aneurysm (arrows). The aneurysm is signal void on T2-weighted image (*k*) and enhances earlier on the arterial phase image (*l*). Reconstructed 3D-MR angiography images (*n, o*) demonstrate distal splenic artery aneurysms in another patient (arrows).

than 2 cm) and saccular. They are located in the middle or distal segment of the splenic artery. They can be multiple in 20% of cases and substantially more common in patients with portal hypertension and cirrhosis (fig. 5.28). Splenic artery pseudoaneurysms may also be seen secondary to digestion of the arterial wall by proteolytic pancreatic enzymes in patients with pancreatitis. Splenic artery aneurysms are usually detected incidentally. Their rupture is rare; however, it may be associated with high mortality rate [38].

Infection

Viral infection may result in splenomegaly. The three most common viruses to involve the spleen are Epstein–Barr, varicella, and cytomegalovirus. Nonviral infectious

agents that involve the spleen in patients with normal immune status cause histoplasmosis, tuberculosis, and echinococcosis [39]. These infectious agents are observed in immunocompromised patients with an even greater frequency (fig. 5.29). In the immunocompromised patient, the most common hepatosplenic infection is fungal infection with *Candida albicans* and *Cryptococcus* [40, 41]. Patients with acute myelogenous leukemia are at particular risk for developing fungal infections. Multiorgan involvement is common. The gastrointestinal tract is almost invariably involved, and although esophageal disease is well shown on MR images, involvement of the intestines is frequently not visible. Esophageal candidiasis is common and rarely associated with hepatosplenic candidiasis, whereas small intestine candidiasis is more frequently associated with this infection. Lesions are most commonly observed in the spleen and liver, whereas renal disease is somewhat uncommon. MR images can demonstrate lesions in the acute phase, subacute treated phase, and chronic healed phase [40, 42]. Lesions in each of these phases have distinctive MRI appearances. These varying appearances are more distinct for liver lesions. (For an in-depth discussion, see Chapter 2, *Liver.*) Acute lesions are generally more apparent in the spleen than in the liver, whereas the reverse is true for subacute-treated and chronic-healed lesions. In the acute phase, hepatosplenic candidiasis results in small (<1 cm), well-defined abscesses in the spleen and liver. They are well shown on T2-weighted fat-suppressed images as high signal-intensity rounded foci (fig. 5.30). Lesions also may be visible postgadolinium images, but they usually are not visualized on precontrast SGE images.

MRI has been shown to be superior to contrast-enhanced CT imaging for the detection of fungal microabscesses [40]. MRI should be used routinely in the investigation of hepatosplenic candidiasis because patient survival depends on swift pharmacologic intervention with antifungal agents.

Bacterial and fungal abscesses are rare in the spleen. Abscesses appear slightly hypo- to isointense on T1-weighted images and heterogeneous and mildly to moderately hyperintense on T2-weighted images. These lesions show intense mural enhancement on early gadolinium-enhanced images. This pattern persists on later postgadolinium images, accompanied by the pres-

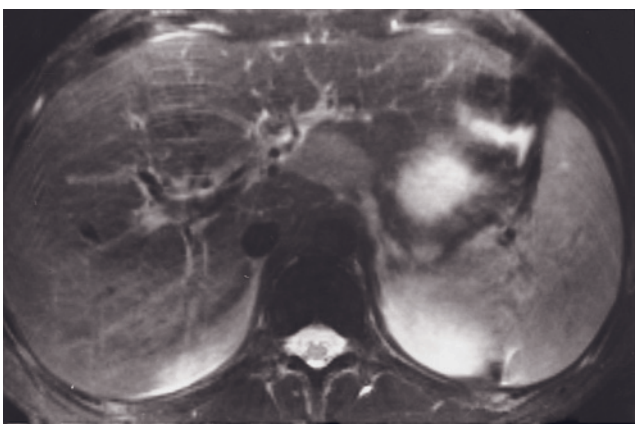

(*a*)

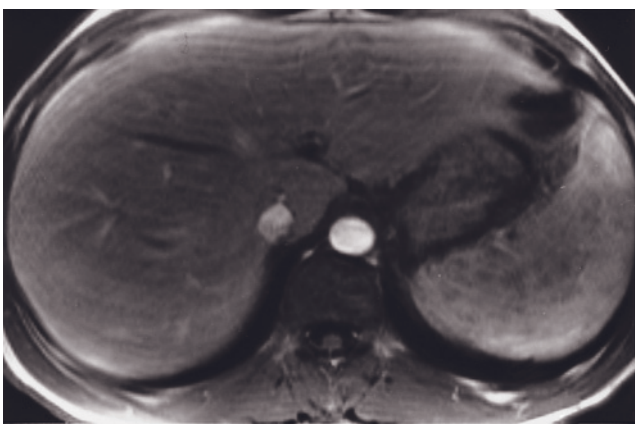

(*b*)

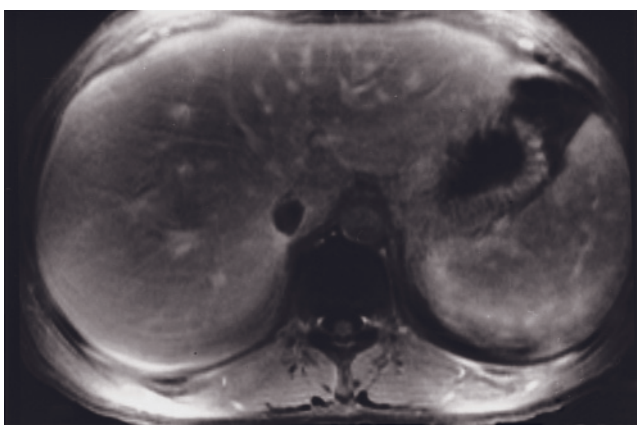

(*c*)

FIG. 5.29 Hepatosplenorenal histoplasmosis. T2-weighted fat-suppressed echo-train spin-echo (*a*), immediate postgadolinium T1-weighted SGE (*b*), and 90-s postgadolinium fat-suppressed SGE (*c*) images in a patient with human immunodeficiency virus (HIV) infection. Multiple lesions <1 cm are demonstrated in the liver, spleen, and kidneys. Lesions are poorly visualized on T2-weighted images and appear as small minimally hyperintense lesions (*a*). On immediate postgadolinium image, lesions appear low in signal intensity (*b*). By 90 s after gadolinium, lesions enhance more than background tissue.

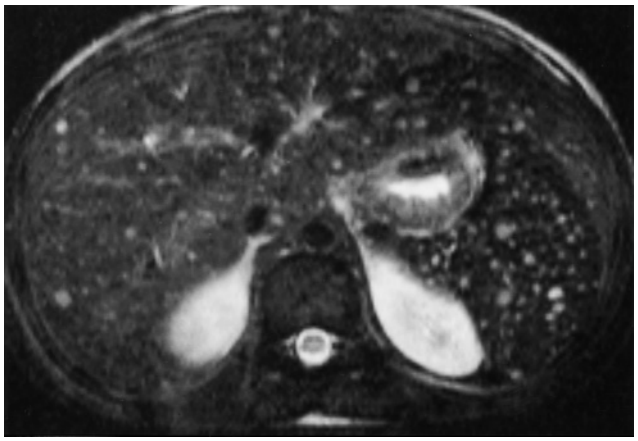

FIG. 5.30 Hepatosplenic candidiasis. T2-weighted fat-suppressed echo-train spin-echo image demonstrates multiple, well-defined, high-signal-intensity candidiasis abscesses <1 cm in the liver and spleen.

ence of periabscess increased enhancement of surrounding tissue on immediate postgadolinium images (fig. 5.31).

Sarcoidosis

Lesions of sarcoidosis are small (<1 cm) and hypovascular. Because of their hypovascularity, the lesions are low in signal intensity on T1- and T2-weighted images and enhance on gadolinium-enhanced images in a minimal and delayed fashion [43] (fig. 5.32). Low signal intensity on T2-weighted images is a feature that distinguishes these lesions from acute infective lesions.

Gamna–Gandy Bodies

Foci of iron deposition occur commonly in patients with cirrhosis and portal hypertension due to microhemorrhages in the splenic parenchyma. On occasion, such foci are observed in patients receiving blood transfusions [44, 45]. Lesions vary in size but are generally smaller than 1 cm. Lesions appear signal void on all pulse sequences [44, 45] (fig. 5.33). Susceptibility artifact is demonstrated on gradient-echo images as blooming artifact, and this artifact is pathognomonic for this entity. An imaging feature that is helpful to distinguish Gamna–Gandy bodies from fibrotic nodules is that Gamna–Gandy bodies appear smaller on shorter TE sequences because of a diminution of susceptibility artifact (e.g., smaller on TE = 2 ms sequence compared to TE = 4 ms sequence at 1.5 T) whereas the size of fibrotic nodules is unchanged on shorter TE sequences.

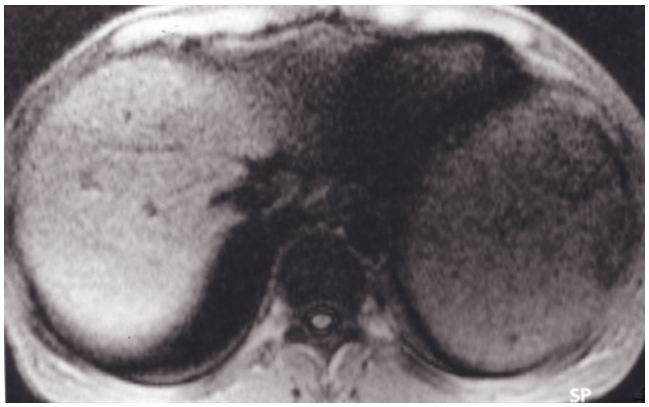

(*a*)

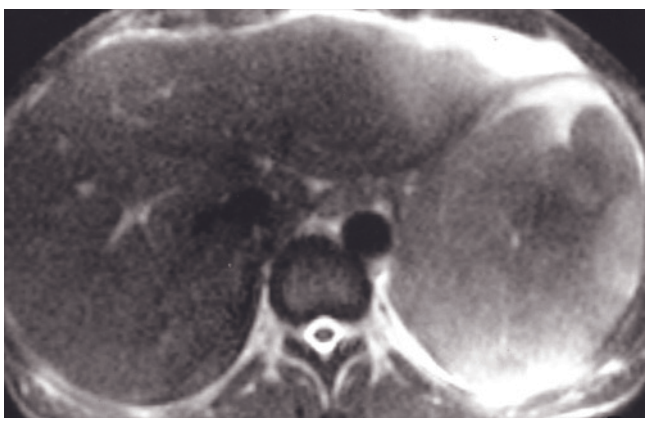

(*b*)

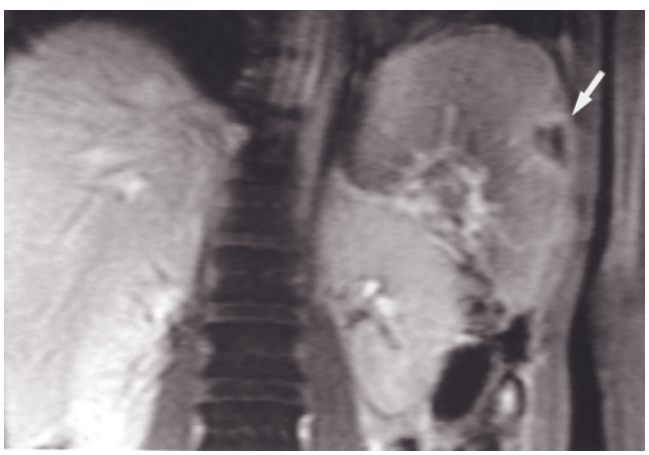

(*c*)

FIG. 5.31 Cryptococcal abscess. T1-weighted magnetization-prepared gradient-echo (*a*), T2 fat-suppressed single-shot echo-train spin-echo (*b*), and coronal 3-min postgadolinium T1-weighted magnetization-prepared gradient-echo (*c*) images in an immunocompromised patient with HIV and generalized cryptococcal infection. The abscess appears mildly hypointense on T1 (*a*) and mildly hyperintense on T2 (*b*), with subtle signal difference compared to spleen. Lack of enhancement and peripheral ring enhancement (arrow, *c*) present on the postgadolinium image (*c*) are features of bacterial and some fungal abscesses.

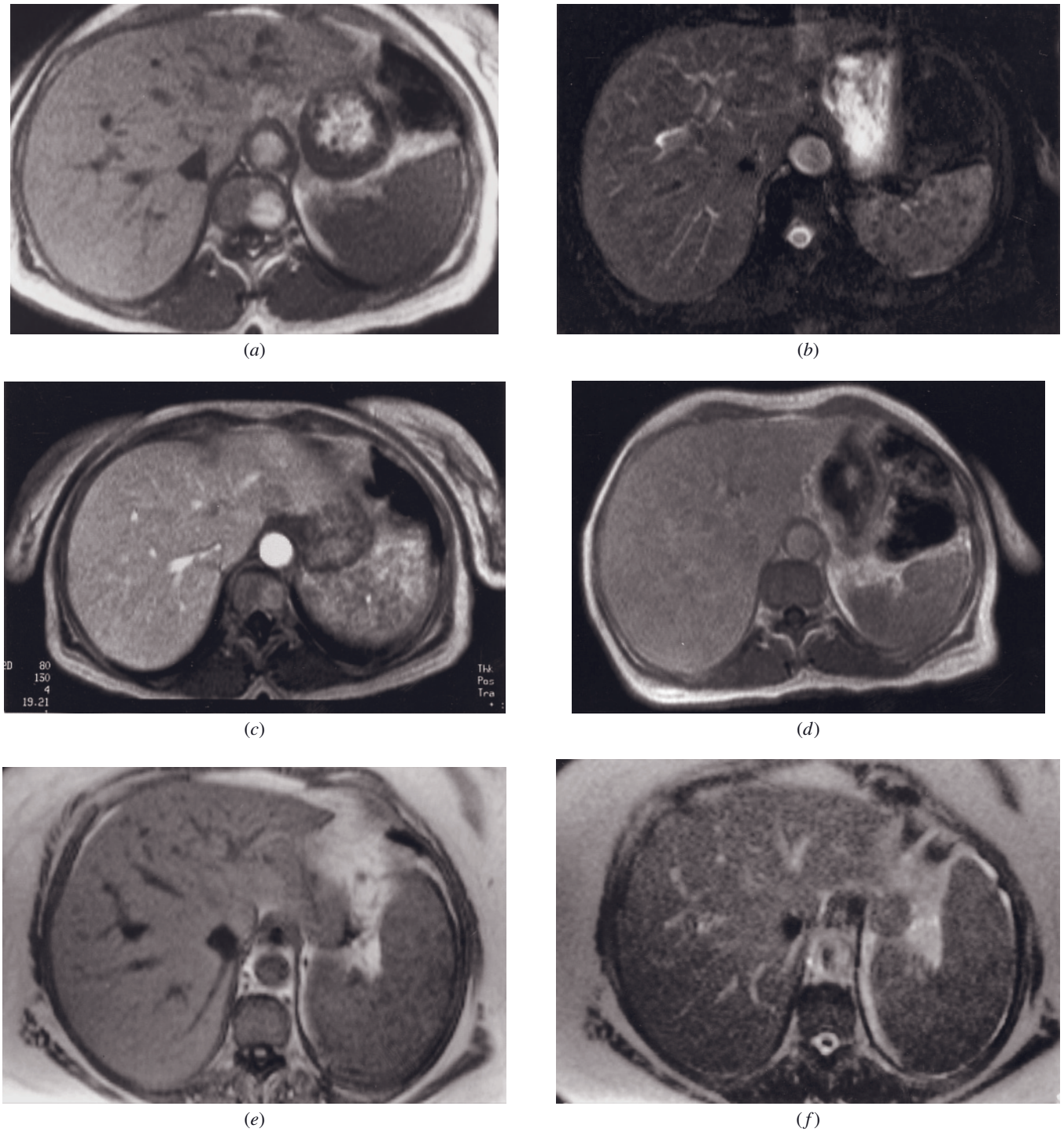

FIG. 5.32 Sarcoidosis. T1-weighted SGE (*a*), T2-weighted fat-suppressed spin-echo (*b*), and immediate (*c*) and 10-min (*d*) postgadolinium T1-weighted SGE images. Multiple sarcoidosis granulomas, smaller than 1 cm, are present in the spleen. Lesions are mildly hypointense to isointense on T1-weighted images (*a*), moderately hypointense on T2-weighted images (*b*), and hypointense on immediate postgadolinium images (*c*), gradually enhancing to near isointensity on delayed postgadolinium images (*d*). Hypointensity on T2-weighted images distinguishes these lesions from those of infectious etiologies. (Reproduced with permission from Warshauer DM, Semelka RC, Ascher SM: Nodular sarcoidosis of the liver and spleen: appearance on MR images. *J Magn Reson Imaging* 4: 553–557, 1994.) T1-weighted SGE (*e*), T2-weighted single-shot echo-train spin-echo (*f*), immediate postgadolinium

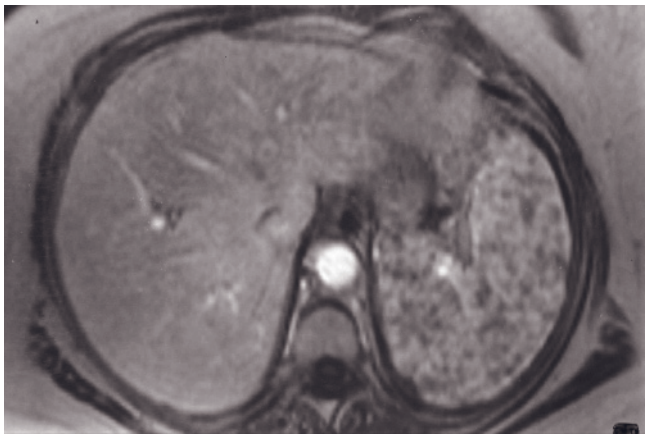

(*g*)

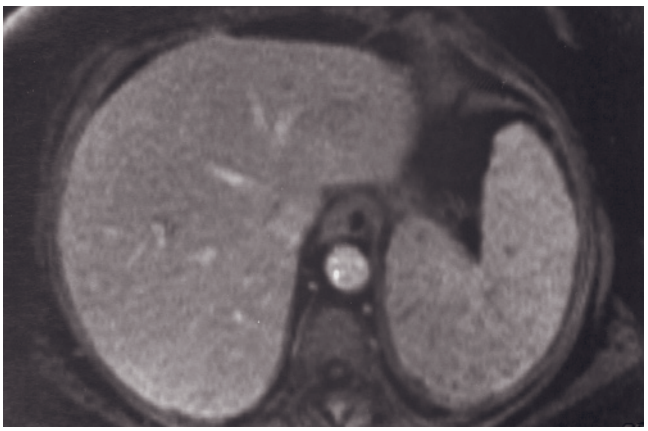

(*h*)

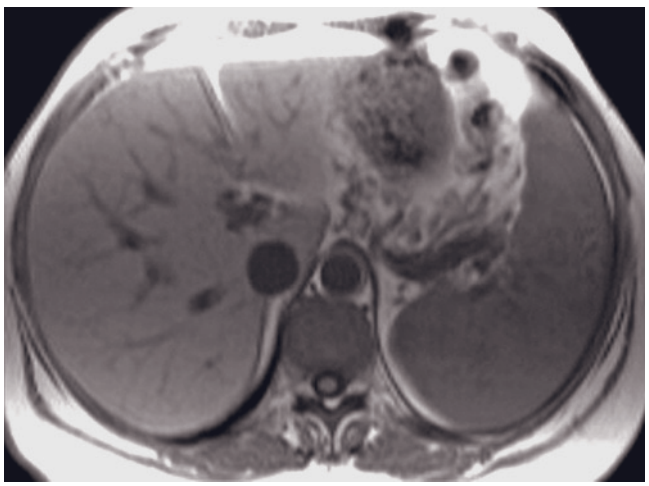

(*i*)

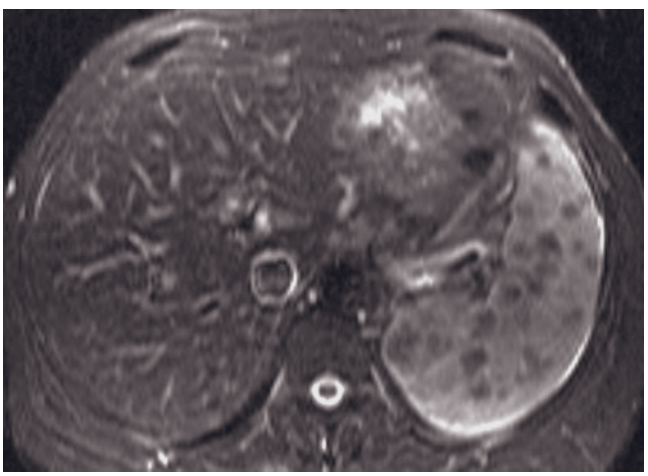

(*j*)

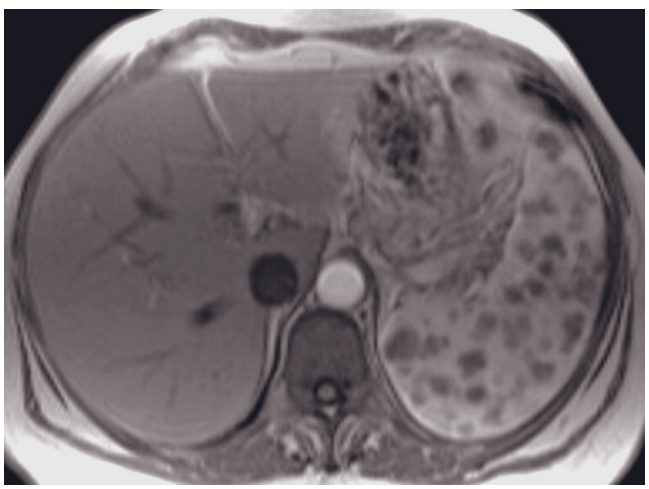

(*k*)

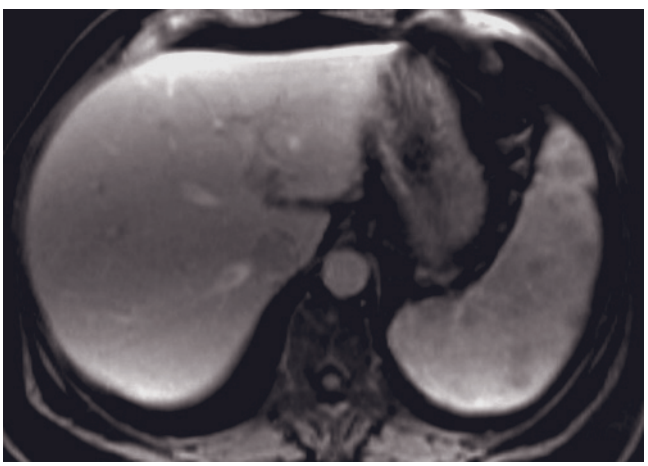

(*l*)

FIG. 5.32 (*Continued*) T1 single-shot magnetization-prepared gradient-echo (*g*), and 90-s postgadolinium T1-weighted fat-suppressed spin-echo (*h*) images in a second patient. The imaging features are comparable to those for the above-described patient. T1-weighted SGE (*i*), T2-weighted fat suppressed single-shot echo-train spin-echo (*j*), immediate postgadolinium T1-weighted SGE (*k*), and 90-s postgadolinium T1-weighted fat-suppressed SGE (*l*) images in a third patient demonstrate similar findings.

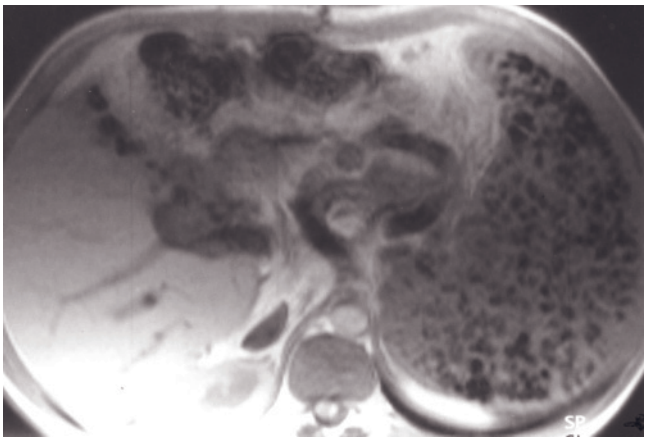

(*a*)

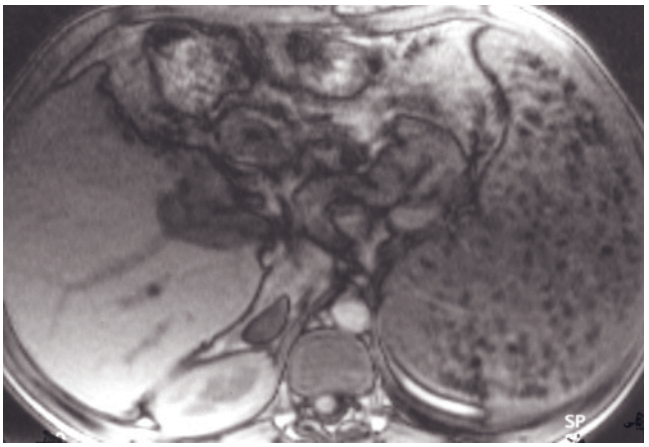

(*b*)

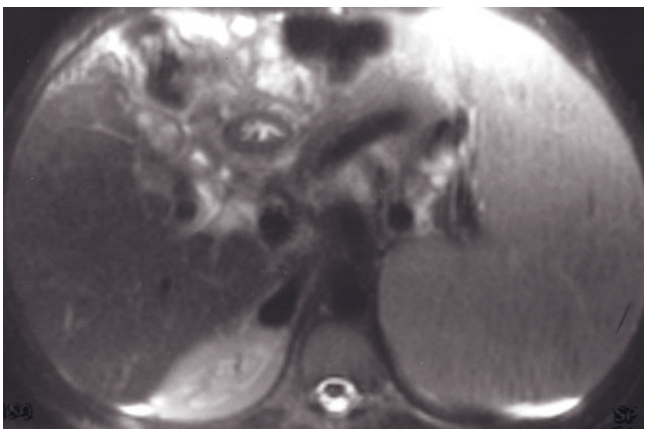

(*c*)

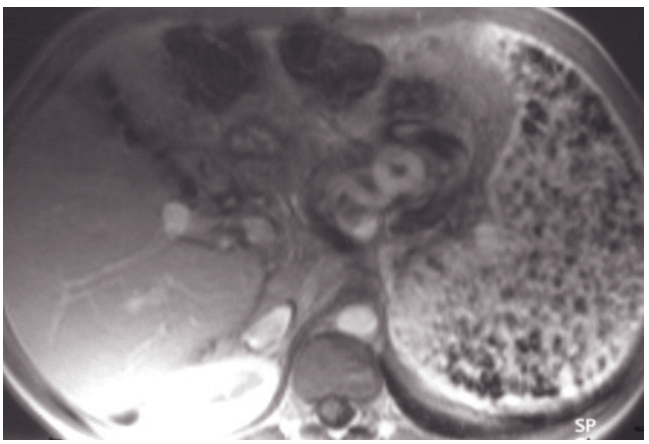

(*d*)

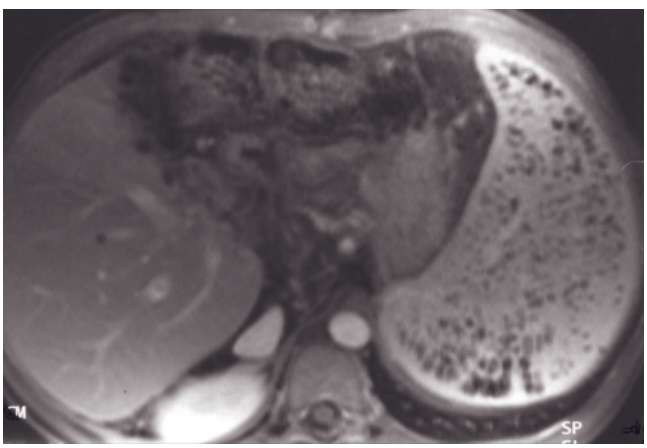

(*e*)

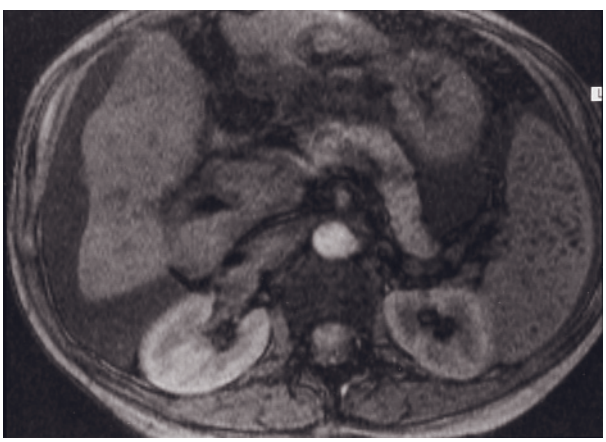

(*f*)

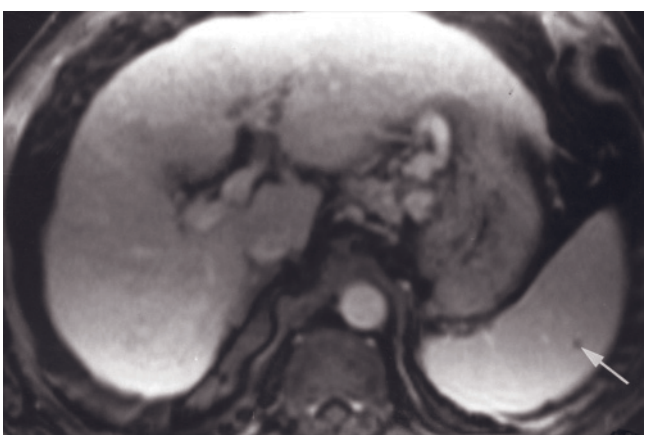

(*g*)

Fig. 5.33 Gamna–Gandy bodies of the spleen. T1-weighted SGE (*a*), T1-weighted out-of-phase SGE (*b*), T2-weighted fat-suppressed single-shot echo-train spin-echo (*c*), immediate postgadolinium T1-weighted SGE (*d*), and 90-s postgadolinium T1-weighted fat-suppressed SGE (*e*) images. Gamna–Gandy bodies are typically multiple and <1 cm in diameter. Gamna–Gandy bodies are near signal void on all imaging sequences, reflecting the magnetic susceptibility effects of iron. A helpful diagnostic feature of the magnetic susceptibility effects of iron, which aids in distinction from low-fluid-content granulomas, is that the foci of susceptibility artifact appear smaller on the out-of-phase (*b*) compared to the in-phase (*a*) images. T1-SGE image (*f*) in a second patient with cirrhosis demonstrates multiple <5-mm Gamna–Gandy bodies. Ninety-second postgadolinium fat-suppressed SGE image (*g*) in a third patient shows a solitary Gamna–Gandy body (arrow, *g*). Note large varices along the lesser curve of the stomach, accentuated with the use of fat suppression.

Trauma

The spleen is the most commonly ruptured abdominal organ in the setting of trauma. Injury to the spleen may take several forms: subcapsular hematoma, contusion, laceration, and devascularization/infarct. Subcapsular or intraparenchymal hematoma secondary to contusion or laceration demonstrates a time course of changes in signal intensity due to the paramagnetic properties of the degradation products of hemoglobin (fig. 5.34). Subacute hemorrhage is particularly conspicuous because of its distinctive high signal intensity on T1- and T2-weighted images (fig. 5.35). Traumatic injury of the spleen, especially devascularization, is well shown on immediate postgadolinium SGE images. Areas of devascularization are nearly signal void compared to the high signal intensity of vascularized tissue.

Subcapsular Fluid Collections

Multiple causes for subcapsular fluid collections exist, the most common being sequelae to trauma. Enhancement of the capsule and surface of the spleen may be observed on postgadolinium images, which confirms the location of these fluid collections (fig. 5.36).

Splenosis

Splenosis is the term used for ectopic tissue resulting from splenic injury. The most common appearance of splenosis on magnetic resonance imaging is solid, well-circumscribed nodules in the abdominal cavity, with signal intensity similar to that of the normal spleen (fig. 5.37).

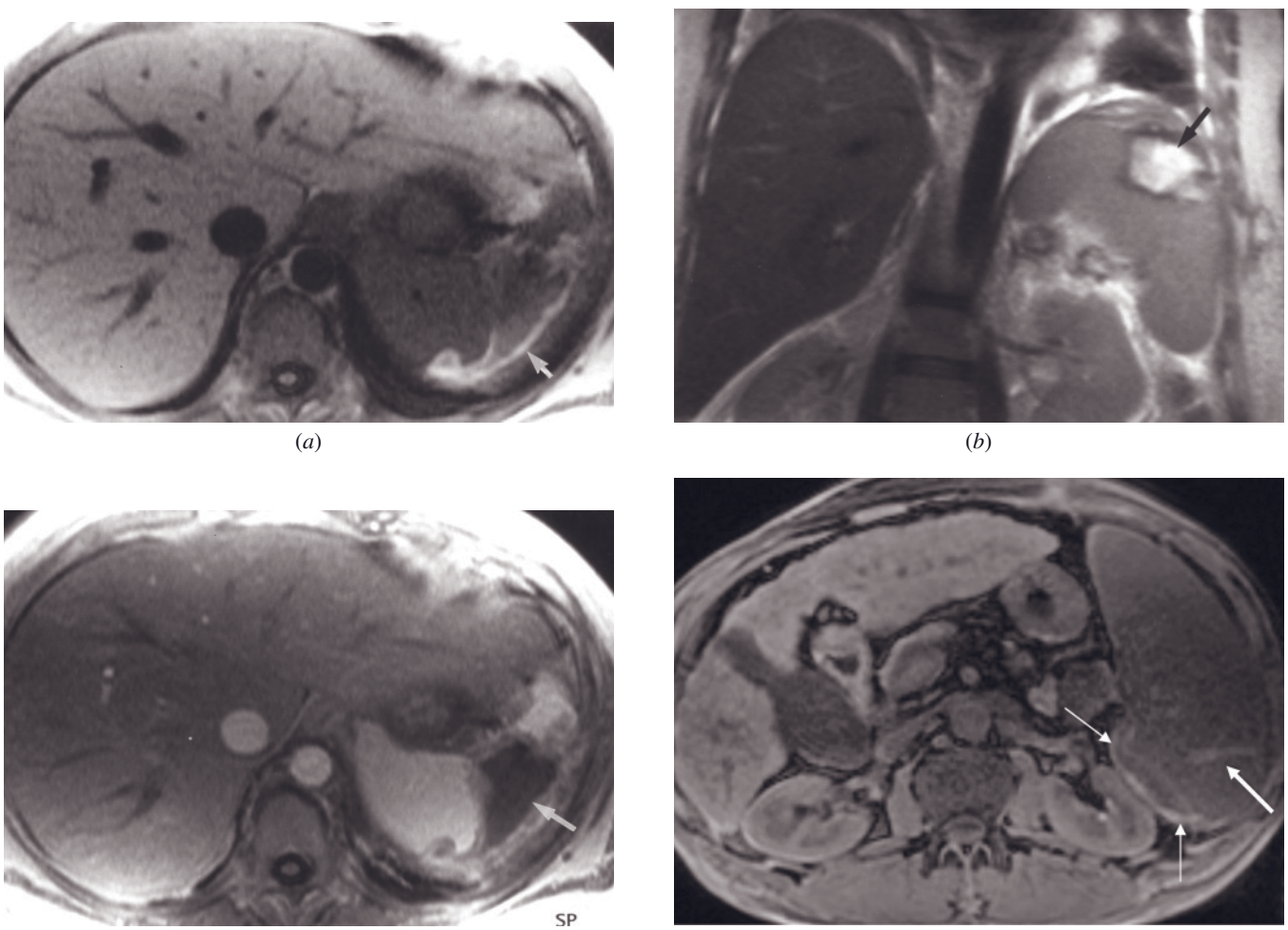

FIG. 5.34 Splenic laceration with subcapsular hematoma. T1-weighted single-shot magnetization-prepared gradient-echo (*a*), coronal T2-weighted single-shot echo-train spin-echo (*b*), and immediate postgadolinium single-shot magnetization-prepared gradient-echo (*c*) images. Subcapsular blood (arrow, *a*) is appreciated as high-signal fluid on the precontrast T1-weighted image (*a*).The laceration is isointense on T1 (*a*) and high signal on T2 (arrow, *b*) and demonstrates lack of enhancement (arrow, *c*) on the postgadolinium image (*c*). T1-weighted fat-suppressed 3D-GE (*d*), T2-weighted short-tau inversion recovery (STIR) (*e*), and

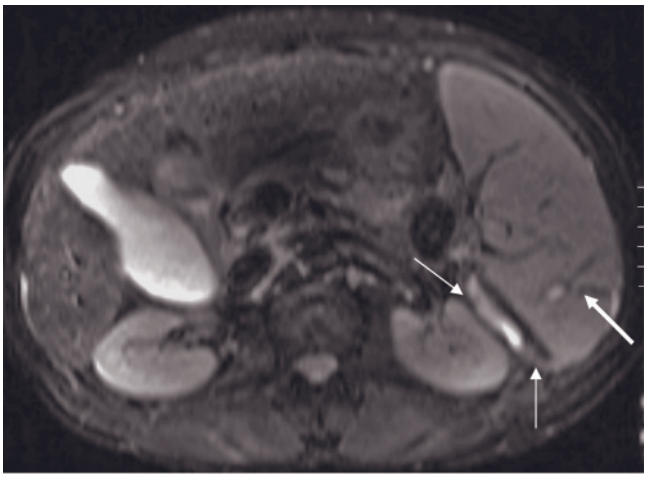

(*e*)

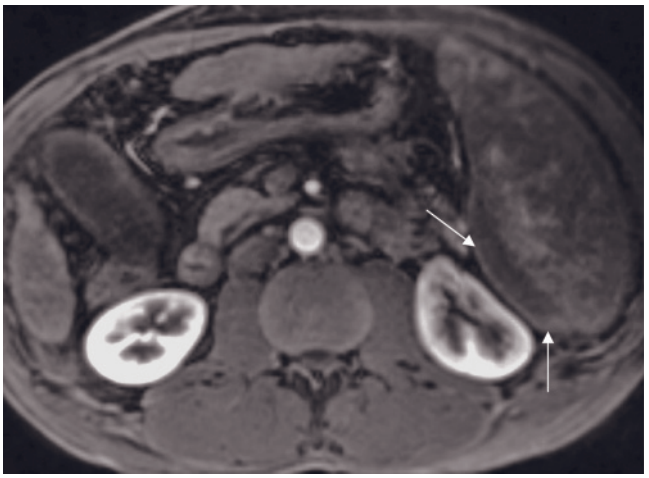

(*f*)

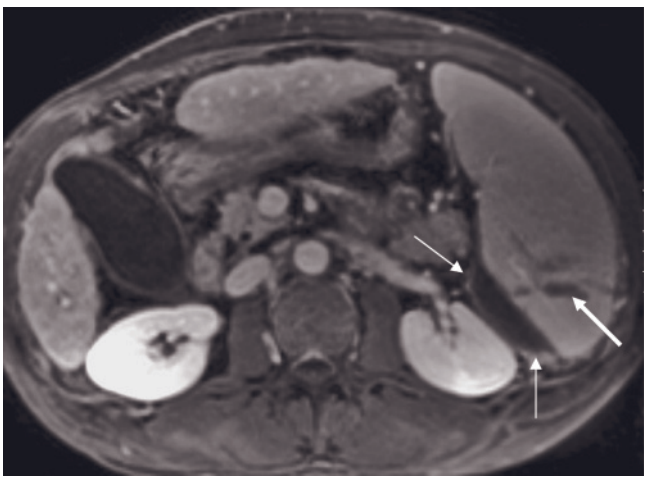

(*g*)

FIG. 5.34 (*Continued*) T1-weighted fat-suppressed immediate (*f*) and 90-s (*g*) postgadolinium 3D-GE images at 3.0 T in another patient with cirrhosis, splenomegaly, splenic laceration, and subcapsular hematoma (thin arrows, *d–g*). The subcapsular hematoma is in a subacute stage, and it has high peripheral signal intensity on T1- and T2-weighted images. The lacerations (thick arrows, *d, e, g*) also show high signal on T1-weighted and mixed signal on T2-weighted images, consistent with subacute blood products.

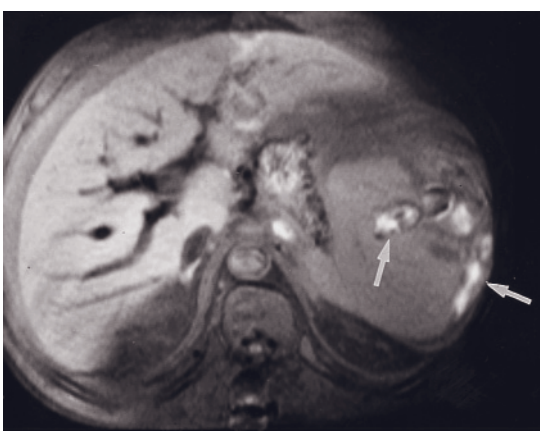

(*a*)

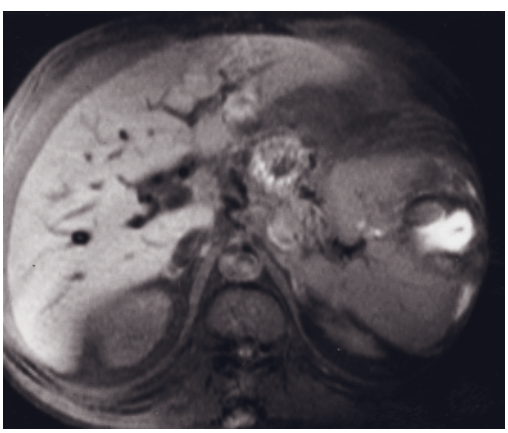

(*b*)

FIG. 5.35 Splenic laceration. T1-weighted fat-suppressed spin-echo images from adjacent cranial (*a*) and caudal (*b*) transverse sections. Mixed, predominantly high-signal-intensity fluid is present in an intraparenchymal and subcapsular location (arrows, *a*) in the spleen, which represents subacute blood.

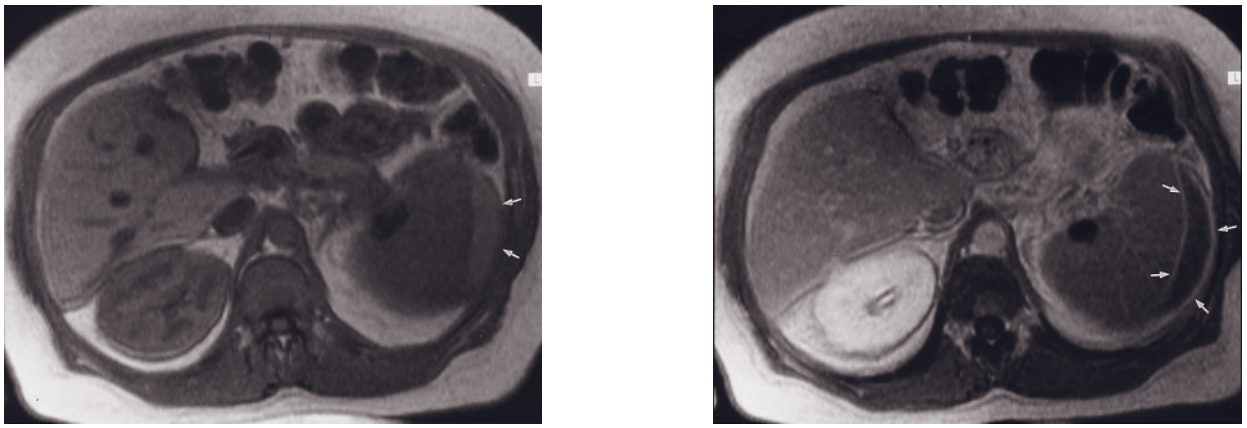

(*a*) (*b*)

FIG. 5.36 Subcapsular fluid collection secondary to pancreatitis. T1-weighted SGE (*a*) and 90-s postgadolinium SGE (*b*) images. A subcapsular fluid collection is present that is slightly high in signal intensity on the T1-weighted image, a finding consistent with the presence of blood or protein (arrows, *a*). Enhancement of the capsule and surface of the spleen on the postgadolinium image (arrows, *b*) confirms the subcapsular location of the fluid collection.

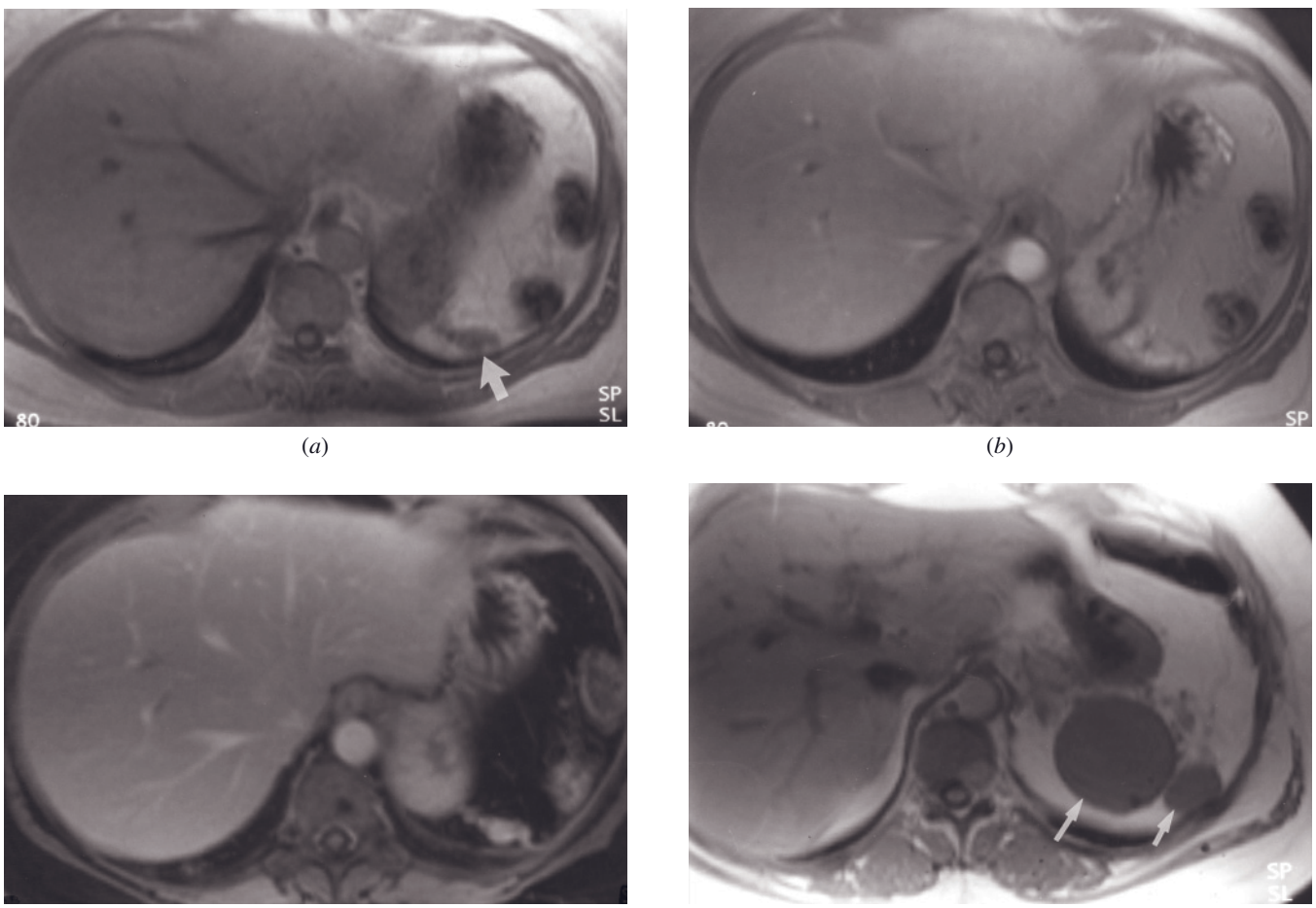

(*a*) (*b*)

(*c*) (*d*)

FIG. 5.37 Splenosis. T1-weighted SGE (*a*), immediate postgadolinium T1-weighted SGE (*b*), and 90-s postgadolinium T1-weighted fat-suppressed SGE (*c*) images. A small, elongated mass is present in the left upper abdominal quadrant in a patient with prior splenectomy. The mass is slightly hypointense to the liver on the T1-weighted image (arrow, *a*), with intense enhancement on the immediate postgadolinium image (*b*) and persistent enhancement on the delayed postgadolinium image (*c*). T1-weighted SGE (*d*), coronal T2-weighted echo-train spin-echo (*e*), breath-hold STIR (*f*), immediate postgadolinium T1-weighted SGE (*g*), and

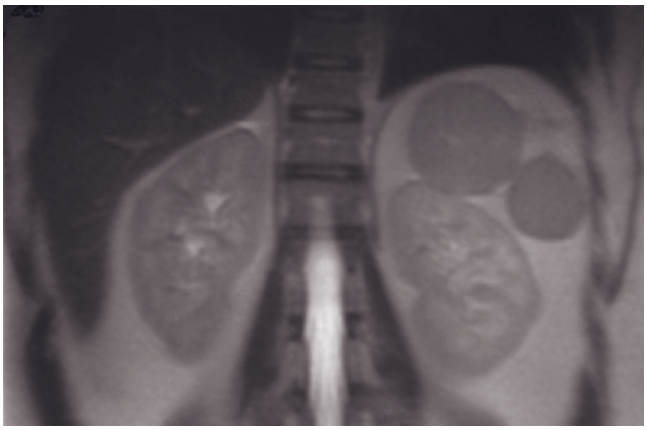

(*e*)

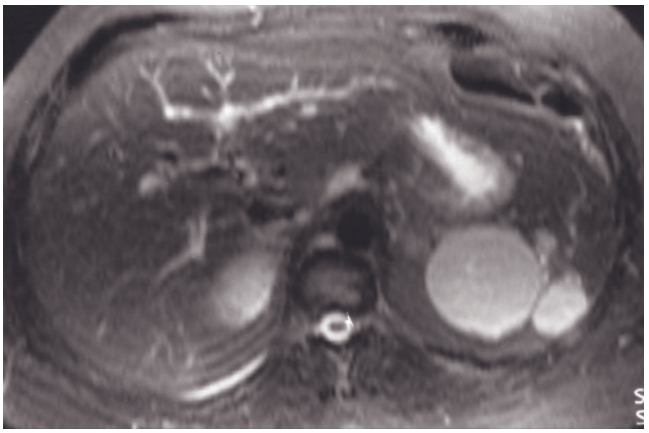

(*f*)

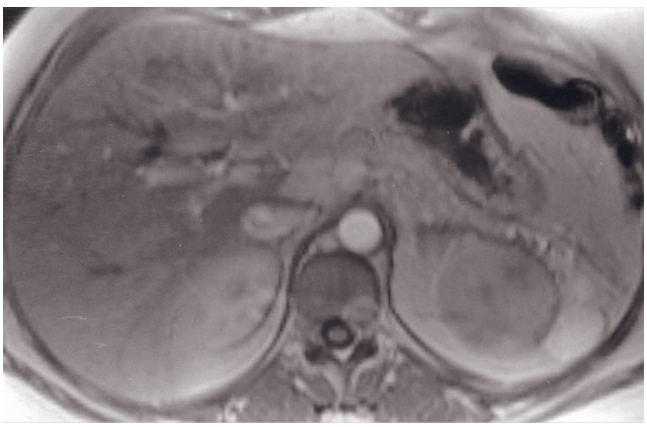

(*g*)

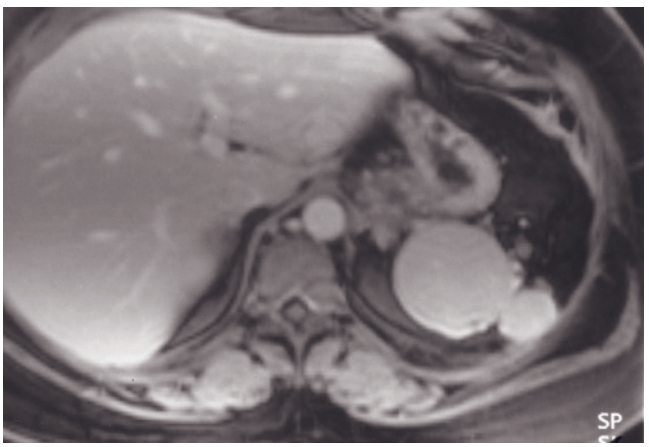

(*h*)

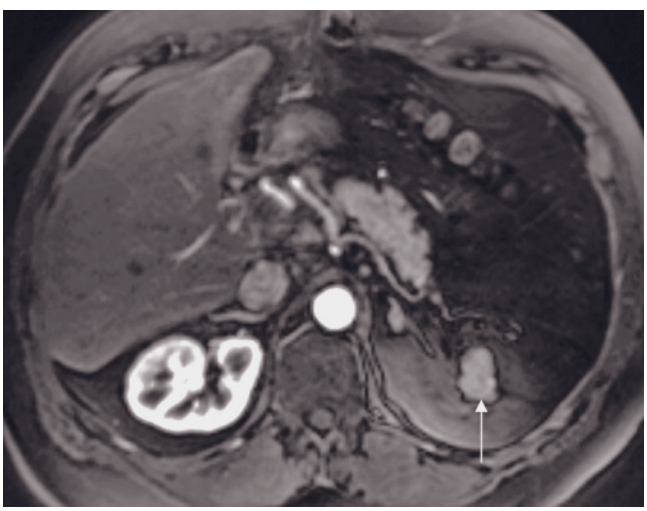

(*i*)

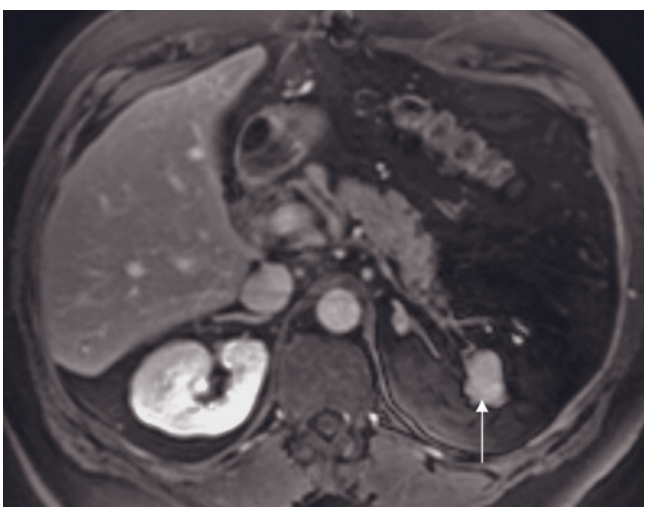

(*j*)

FIG. 5.37 (*Continued*) 90-s postgadolinium T1-weighted fat-suppressed SGE (*h*) images in a second patient with prior splenectomy. Two splenules are present in the left upper abdomen (arrows, *d*). The masses have an appearance similar to normal spleen, with mild hypointensity on T1 (*d*), moderate hyperintensity on T2 (*e*), and early heterogeneous enhancement (*g*), which becomes more homogeneous on delayed images (*h*). Note that the enhancement of the larger mass is less than that of the smaller mass, presumably reflecting a smaller feeding arterial supply. T1-weighted fat-suppressed immediate (*i*) and delayed (*j*) postgadolinium 3D-GE images at 3.0 T show an enhancing mass (arrows) consistent with splenosis in another patient with prior splenectomy. The mass shows serpiginous enhancement pattern on immediate postgadolinium 3D-GE image (*i*) and homogenous enhancement on postgadolinium delayed 3D-GE image (*j*). T1-weighted fat-suppressed immediate postgadolinium 3D-GE images (*k, l, m*) show

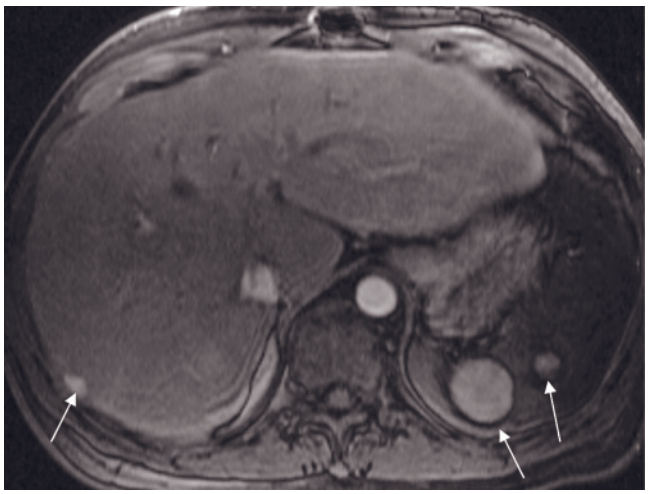

(*k*)

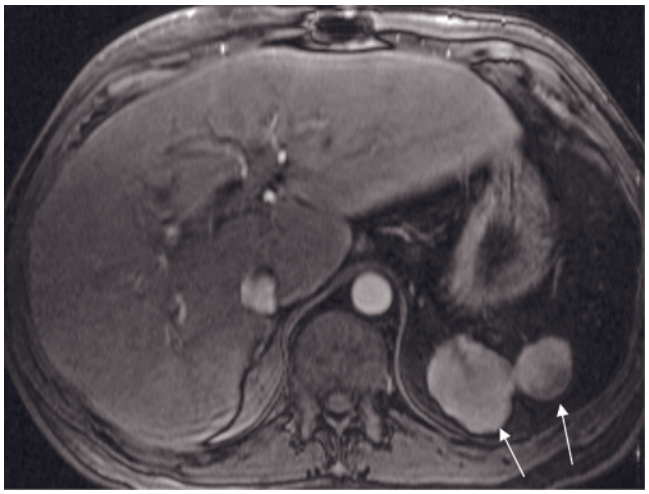

(*l*)

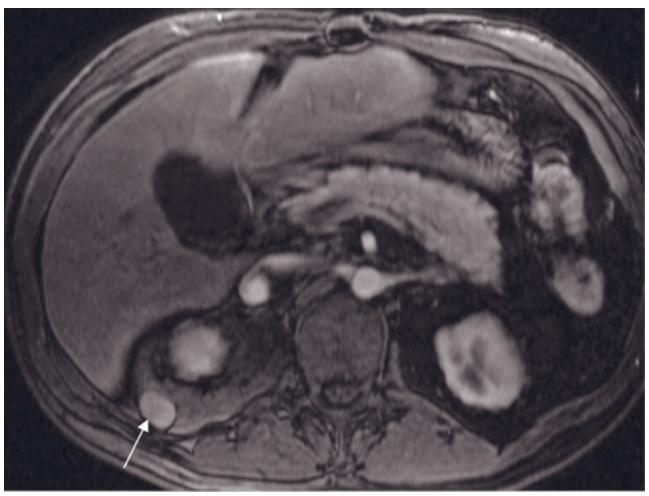

(*m*)

FIG. 5.37 (*Continued*) enhancing masses (arrows), which are located in the liver capsule and the retroperitoneum at both sides, in another patient with prior splenectomy. The bigger lesions demonstrate serpiginous enhancement pattern, and the lesions are consistent with splenosis.

Infarcts

Splenic infarcts are a common occurrence in the setting of obstruction of the splenic artery or one of its branches. The most common cause is cardiac emboli, but local thrombosis, vasculitis, and splenic torsion are also described. Infarcts appear as peripheral wedge-shaped, round, or linear defects that are most clearly defined on 1- to 5-min postgadolinium images as low-signal-intensity wedge-shaped regions (fig. 5.38).

The splenic capsule is commonly observed as a thin peripheral, enhancing linear structure. Massive splenic infarcts may appear as diffuse low signal intensity on T1-weighted images and inhomogeneous high signal on T2-weighted images. Lack of enhancement on early and late postgadolinium images of wedge-shaped regions is the most diagnostic feature (fig. 5.39).

CONCLUSION

MRI is a valuable tool in the evaluation of the spleen and surpasses CT imaging in many clinical settings. One of the major indications for MRI is the investigation of hepatosplenic candidiasis. Other circumstances in which MRI may be of value include the detection of malignant lesions (metastases or lymphoma) and infections, and the characterization of lesions such as hemangiomas or hamartomas. MRI is useful in the further investigation of patients with a CT diagnosis of splenomegaly to determine whether underlying tumor infiltration is present. Superparamagnetic iron oxide particles can be used as a problem-solving approach in selected cases for definitive splenic lesion characterization when not achieved by standard dynamic gadolinium-enhanced MRI.

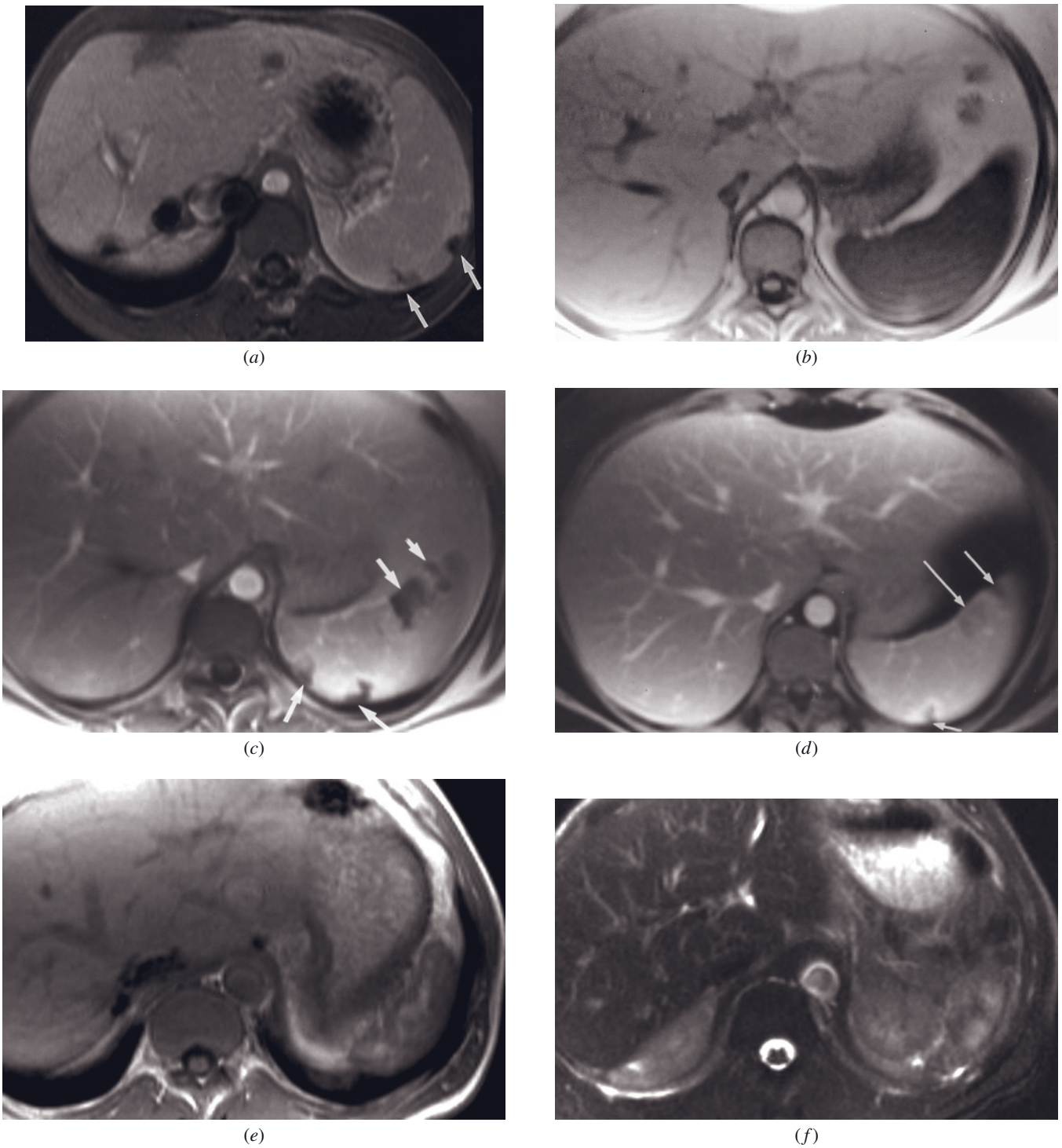

FIG. 5.38 Splenic infarct. One-minute postgadolinium T1-weighted SGE image (*a*). Peripheral wedge-shaped defects are noted in the spleen (arrows, *a*) secondary to infarcts. T1-weighted SGE (*b*), immediate postgadolinium T1-weighted SGE (*c*), and 90-s postgadolinium T1-weighted fat-suppressed SGE (*d*) images in a second patient. An ill-defined posterior subcapsular hyperintensity is present on the T1-weighted image (*b*). Infarct regions are best seen on postgadolinium images (*c*, *d*) and appear as well-defined wedge-shaped defects (arrows, *c*, *d*). Peripheral linear enhancement of the capsule may also be appreciated. Note that some of the regions that have no enhancement on the immediate postgadolinium images show delayed enhancement. These are consistent with areas of ischemia. T1-weighted SGE (*e*), T2-weighted fat-suppressed single-shot echo-train spin-echo (*f*), immediate T1-weighted

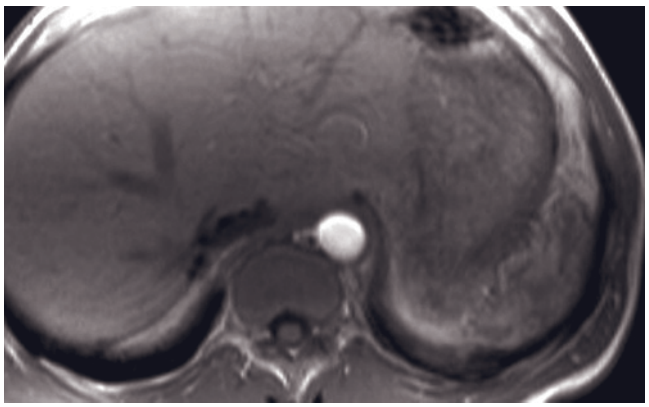

(*g*)

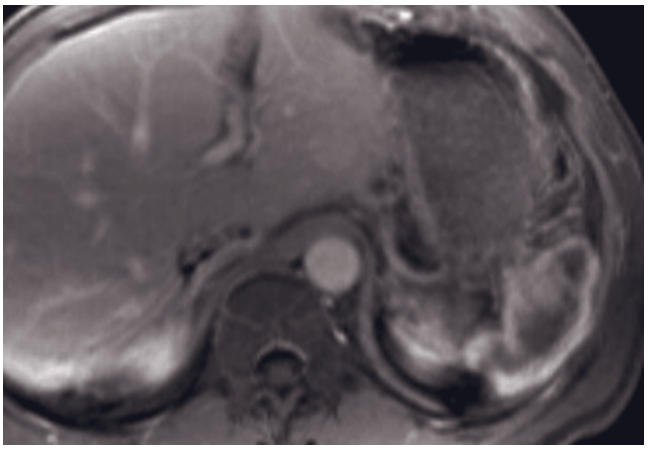

(*h*)

FIG. 5.38 (*Continued*) SGE (*g*), and 90-s T1-weighted fat-suppressed SGE (*h*) images in a third patient demonstrate similar findings.

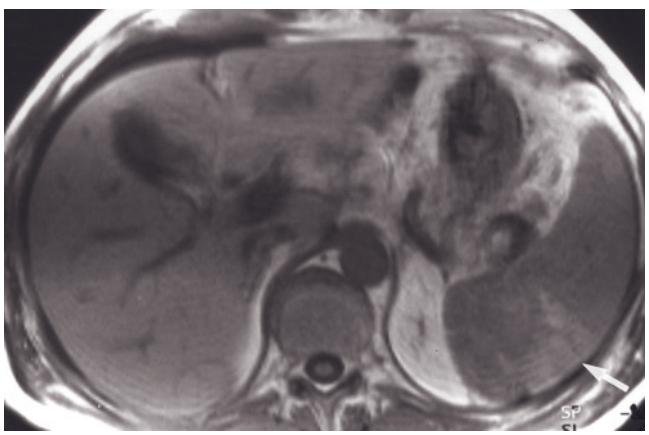

(*a*)

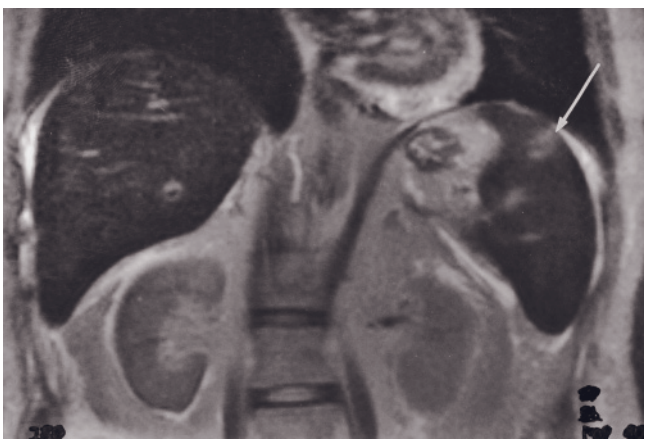

(*b*)

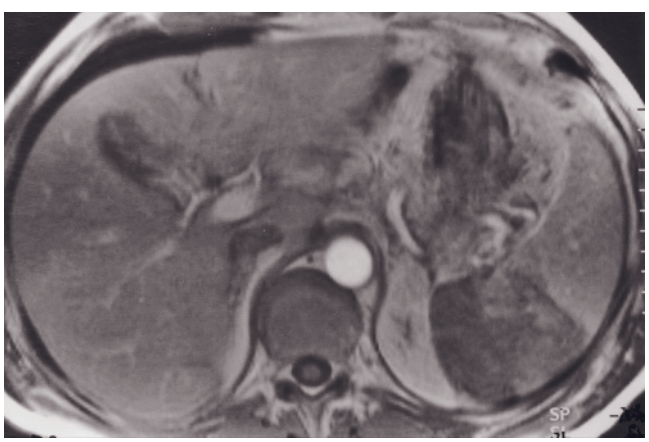

(*c*)

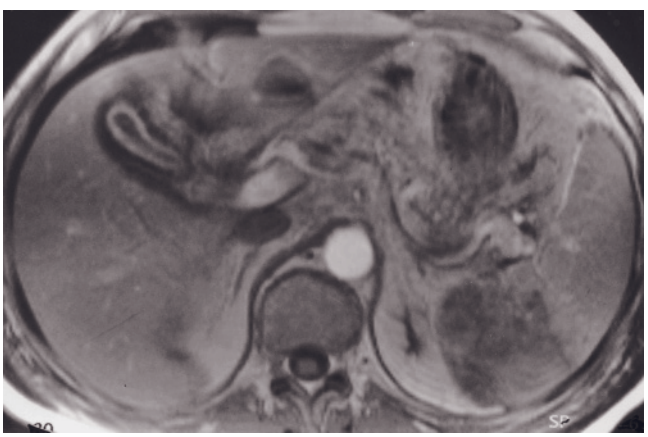

(*d*)

FIG. 5.39 Extensive posterior splenic infarct. T1-weighted SGE (*a*), coronal T2-weighted single-shot echo-train spin-echo (*b*), immediate (*c*) and 45-s (*d*) postgadolinium T1-weighted SGE, and 90-s postgadolinium T1-weighted fat-suppressed SGE (*e*) images. The splenic infarcts appear heterogeneous and mildly high signal on T1-weighted (arrow, *a*) and heterogeneous and moderately high signal on T2-weighted (arrow, *b*) images. On the immediate (*c*), 45-s (*d*), and 90-s (*e*) postgadolinium images there is

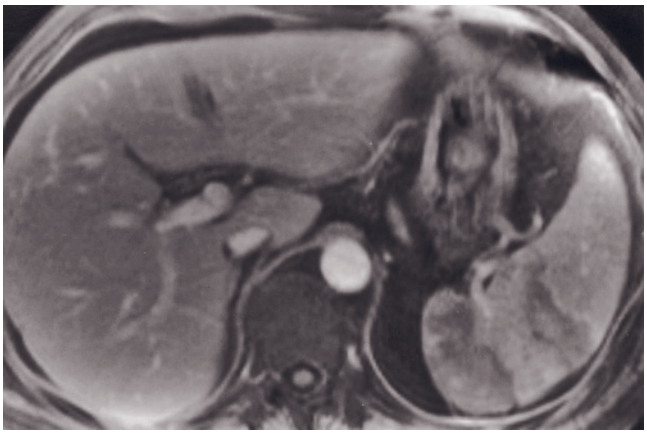

(*e*)

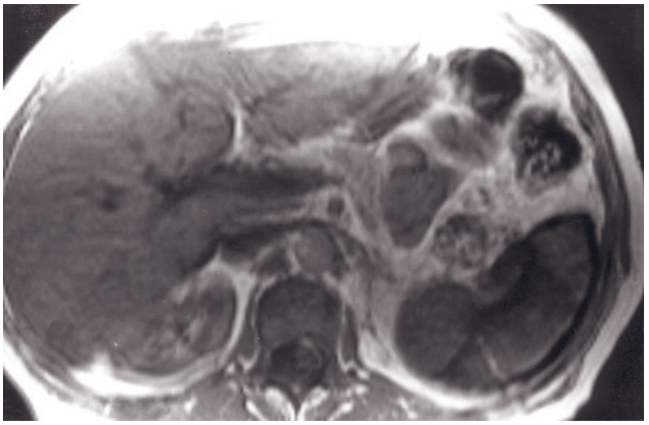

(*f*)

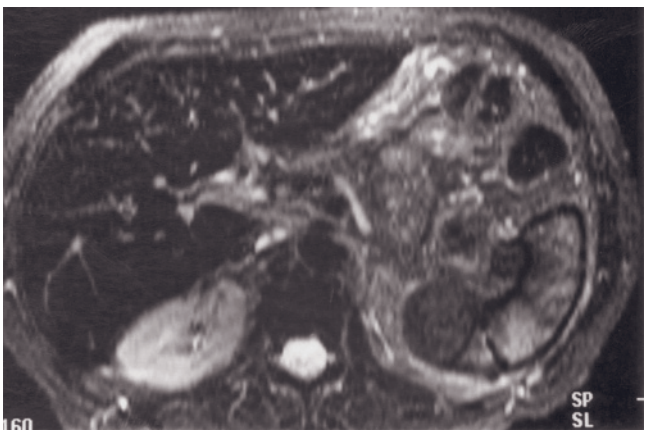

(*g*)

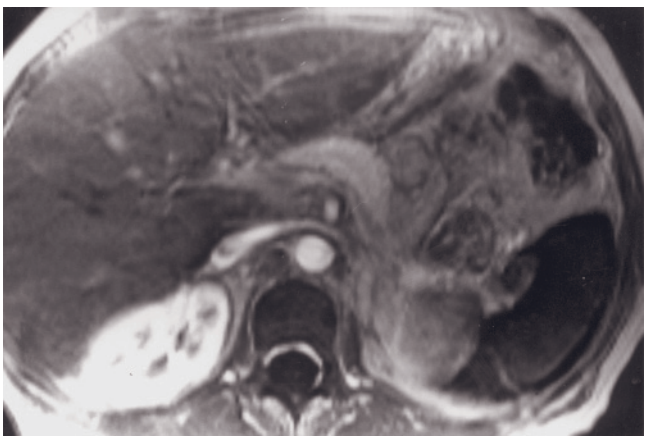

(*h*)

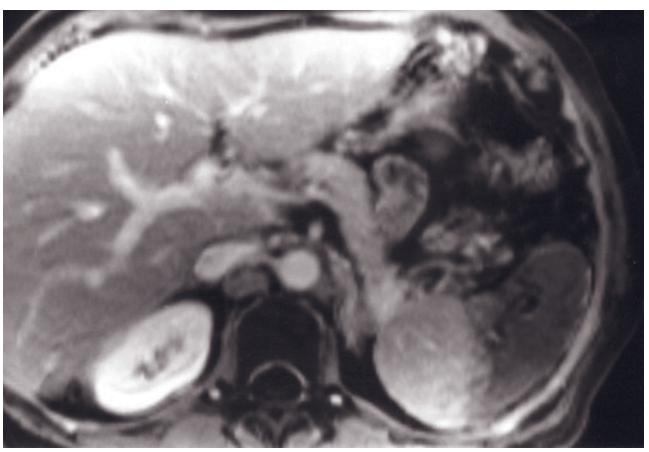

(*i*)

FIG. 5.39 (*Continued*) heterogeneous lack of enhancement of the regions of infarction. T1-weighted SGE (*f*), breath-hold STIR (*g*), immediate postgadolinium SGE (*h*), and 90-s postgadolinium fat-suppressed SGE (*i*) images in a second patient presenting splenic infarcts. The large anterior splenic infarct is heterogeneous on T1 (*f*)- and T2 (*g*)-weighted images. Lack of enhancement on early (*h*) and late (*i*) postcontrast images most clearly demonstrates that this region has undergone infarction. Lack of enhancement is more apparent on the later postcontrast image.

REFERENCES

1. Mirowitz SA, Brown JJ, Lee JK et al. Dynamic gadolinium-enhanced MR imaging of the spleen: normal enhancement patterns and evaluation of splenic lesions. *Radiology* 179(3): 681–686, 1991.
2. Mirowitz SA, Lee JK, Gutierrez E et al. Dynamic gadolinium-enhanced rapid acquisition spin-echo MR imaging of the liver. *Radiology* 179(2): 371–376, 1991.
3. Semelka RC, Shoenut JP, Lawrence PH et al. Spleen: dynamic enhancement patterns on gradient-echo MR images enhanced with gadopentetate dimeglumine. *Radiology* 185(2): 479–482, 1992.
4. Hamed MM, Hamm B, Ibrahim ME et al. Dynamic MR imaging of the abdomen with gadopentetate dimeglumine: normal enhancement patterns of the liver, spleen, stomach, and pancreas. *AJR Am J Roentgenol* 158(2): 303–307, 1992.
5. Siegelman ES, Mitchell DG, Rubin R et al. Parenchymal versus reticuloendothelial iron overload in the liver: distinction with MR imaging. *Radiology* 179(2): 361–366, 1991.

6. Siegelman ES, Mitchell DG, Semelka RC. Abdominal iron deposition: metabolism, MR findings, and clinical importance. *Radiology* 199(1): 13–22, 1996.
7. Weissleder R, Hahn PF, Stark DD et al. Superparamagnetic iron oxide: enhanced detection of focal splenic tumors with MR imaging. *Radiology* 169(2): 399–403, 1988.
8. Weissleder R, Elizondo G, Stark DD et al. The diagnosis of splenic lymphoma by MR imaging: value of superparamagnetic iron oxide. *AJR Am J Roentgenol* 152(1): 175–180, 1989.
9. Kreft BP, Tanimoto A, Leffler S et al. Contrast-enhanced MR imaging of diffuse and focal splenic disease with use of magnetic starch microspheres. *J Magn Reson Imaging* 4(3): 373–379, 1994.
10. Paterson A, Frush DP, Donnelly LF et al. A pattern-oriented approach to splenic imaging in infants and children. *Radiographics* 19(6): 1465–1485, 1999.
11. Heredia V, Altun E, Bilaj F et al. Gadolinium- and superparamagnetic-iron-oxide-enhanced MR findings of intrapancreatic accessory spleen in five patients. *Magn Reson Imaging* 26(9): 1273–1278, 2008.
12. Beahrs JR, Stephens DH. Enlarged accessory spleens: CT appearance in postsplenectomy patients. *AJR Am J Roentgenol* 135(3): 483–486, 1980.
13. Storm BL, Abbitt PL, Allen DA et al. Splenosis: superparamagnetic iron oxide-enhanced MR imaging. *AJR Am J Roentgenol* 159(2): 333–335, 1992.
14. Deux JF, Salomon L, Barrier A et al. Acute torsion of wandering spleen: MRI findings. *AJR Am J Roentgenol* 182(6): 1607–1608, 2004.
15. Applegate KE, Goske MJ, Pierce G et al. Situs revisited: imaging of the heterotaxy syndrome. *Radiographics* 19(4): 837–852; discussion 853–834, 1999.
16. Franco V, Aragona F. Association of specific syndromes with renal cystic disease. *Hum Pathol* 20(5): 496, 1989.
17. Fulcher AS, Turner MA. Abdominal manifestations of situs anomalies in adults. *Radiographics* 22(6): 1439–1456, 2002.
18. Hill SC, Damaska BM, Ling A et al. Gaucher disease: abdominal MR imaging findings in 46 patients. *Radiology* 184(2): 561–566, 1992.
19. Adler DD, Glazer GM, Aisen AM. MRI of the spleen: normal appearance and findings in sickle-cell anemia. *AJR Am J Roentgenol* 147(4): 843–845, 1986.
20. Urrutia M, Mergo PJ, Ros LH et al. Cystic masses of the spleen: radiologic-pathologic correlation. *Radiographics* 16(1): 107–129, 1996.
21. Shirkhoda A, Freeman J, Armin AR et al. Imaging features of splenic epidermoid cyst with pathologic correlation. *Abdom Imaging* 20(5): 449–451, 1995.
22. Disler DG, Chew FS. Splenic hemangioma. *AJR Am J Roentgenol* 157(1): 44, 1991.
23. Ramani M, Reinhold C, Semelka RC et al. Splenic hemangiomas and hamartomas: MR imaging characteristics of 28 lesions. *Radiology* 202(1): 166–172, 1997.
24. Levy AD, Abbott RM, Abbondanzo SL. Littoral cell angioma of the spleen: CT features with clinicopathologic comparison. *Radiology* 230(2): 485–490, 2004.
25. Oliver-Goldaracena JM, Blanco A, Miralles M et al. Littoral cell angioma of the spleen: US and MR imaging findings. *Abdom Imaging* 23(6): 636–639, 1998.
26. Bhatt S, Huang J, Dogra V. Littoral cell angioma of the spleen. *AJR Am J Roentgenol* 188(5): 1365–1366, 2007.
27. Ohtomo K, Fukuda H, Mori K et al. CT and MR appearances of splenic hamartoma. *J Comput Assist Tomogr* 16(3): 425–428, 1992.
28. Abbott RM, Levy AD, Aguilera NS et al. From the archives of the AFIP: primary vascular neoplasms of the spleen: radiologic-pathologic correlation. *Radiographics* 24(4): 1137–1163, 2004.
29. Ito K, Mitchell DG, Honjo K et al. MR imaging of acquired abnormalities of the spleen. *AJR Am J Roentgenol* 168(3): 697–702, 1997.
30. Bragg DG, Colby TV, Ward JH. New concepts in the non-Hodgkin lymphomas: radiologic implications. *Radiology* 159(2): 291–304, 1986.
31. Castellino RA. Hodgkin disease: practical concepts for the diagnostic radiologist. *Radiology* 159(2): 305–310, 1986.
32. Hahn PF, Weissleder R, Stark DD et al. MR imaging of focal splenic tumors. *AJR Am J Roentgenol* 150(4): 823–827, 1988.
33. Klein B, Stein M, Kuten A et al. Splenomegaly and solitary spleen metastasis in solid tumors. *Cancer* 60(1): 100–102, 1987.
34. Drinkr CK, Yoffey JM. *Lymphatics, Lymph and Lymphoid Tissue*. Cambridge, MA: Harvard University Press, 1941.
35. Thompson WM, Levy AD, Aguilera NS et al. Angiosarcoma of the spleen: imaging characteristics in 12 patients. *Radiology* 235(1): 106–115, 2005.
36. Vrachliotis TG, Bennett WF, Vaswani KK et al. Primary angiosarcoma of the spleen—CT, MR, and sonographic characteristics: report of two cases. *Abdom Imaging* 25(3): 283–285, 2000.
37. Rabushka LS, Kawashima A, Fishman EK. Imaging of the spleen: CT with supplemental MR examination. *Radiographics* 14(2): 307–332, 1994.
38. Madoff DC, Denys A, Wallace MJ et al. Splenic arterial interventions: anatomy, indications, technical considerations, and potential complications. *Radiographics* 25 Suppl 1: S191–S211, 2005.
39. Fan ZM, Zeng QY, Huo JW et al. Macronodular multi-organs tuberculoma: CT and MR appearances. *J Gastroenterol* 33(2): 285–288, 1998.
40. Semelka RC, Shoenut JP, Greenberg HM et al. Detection of acute and treated lesions of hepatosplenic candidiasis: comparison of dynamic contrast-enhanced CT and MR imaging. *J Magn Reson Imaging* 2(3): 341–345, 1992.
41. Cho JS, Kim EE, Varma DG et al. MR imaging of hepatosplenic candidiasis superimposed on hemochromatosis. *J Comput Assist Tomogr* 14(5): 774–776, 1990.
42. Kelekis NL, Semelka RC, Jeon HJ et al. Dark ring sign: finding in patients with fungal liver lesions and transfusional hemosiderosis undergoing treatment with antifungal antibiotics. *Magn Reson Imaging* 14(6): 615–618, 1996.
43. Warshauer DM, Semelka RC, Ascher SM. Nodular sarcoidosis of the liver and spleen: appearance on MR images. *J Magn Reson Imaging* 4(4): 553–557, 1994.
44. Sagoh T, Itoh K, Togashi K et al. Gamna-Gandy bodies of the spleen: evaluation with MR imaging. *Radiology* 172(3): 685–687, 1989.
45. Minami M, Itai Y, Ohtomo K et al. Siderotic nodules in the spleen: MR imaging of portal hypertension. *Radiology* 172(3): 681–684, 1989.

CHAPTER 6

GASTROINTESTINAL TRACT

DIEGO R. MARTIN, ERSAN ALTUN, JORGE ELIAS, JR., MOHAMED ELAZZAZI, MIGUEL RAMALHO, CHANG-HEE LEE, AND RICHARD C. SEMELKA

Single-shot echo-train T2-weighted sequences and T1-weighted SGE or 3D GE sequences, combined with intravenous gadolinium enhancement and fat suppression, have resulted in consistent image quality of the gastrointestinal tract. These techniques arrest bowel motion, remove competing high signal of intra-abdominal fat, expand the dynamic range of abdominal tissue signal intensities, decrease susceptibility artifacts, and distinguish between intraluminal bowel contents and bowel wall [1]. The addition of oral or rectal contrast agents may further improve the contrast between lumen and bowel wall to improve the conspicuity of disease. Direct multiplanar imaging has achieved an important role in distinguishing the bowel, which shows a tubular configuration in at least one of two planes, from masses, which do not. Current applications of gastrointestinal MRI include 1) distinguishing type and severity of inflammatory bowel disease (IBD) [1–6]; 2) identifying enteric abscesses and fistulae [7, 8]; 3) preoperative staging of malignant neoplasms, especially rectal carcinoma [5, 9, 10]; and 4) differentiating postoperative and radiation therapy changes from recurrent carcinoma [11–16]. The potential for using MR imaging for screening to detect colonic polyps and early malignancy has also been proposed.

Most recently, reliable 3D-GE T1-weighted sequences (3D VIBE, T1 FAME, 3D THRIVE) have become widely available, permitting volumetric acquisition before and after contrast [17]. Also, newly available True-FISP (FIESTA, BFFE) sequences obtained in the 2D form can be very helpful in delineation of bowel wall pathology, mesentery, and overall bowel anatomy, particularly when combined with a water-based intraluminal distending agent [17]. 3.0 T MR imaging also allows the acquisition of higher-resolution, thinner slices with higher temporal resolution. Therefore, 3.0 T MRI may detect smaller lesions and subtle abnormalities of the GI tract compared to 1.5 T MRI.

THE ESOPHAGUS

Normal Anatomy

The organization of tissues within the esophageal wall follows the general scheme of the entire digestive tract;

Abdominal-Pelvic MRI, Third Edition, edited by Richard C. Semelka. Copyright © 2010 John Wiley & Sons, Inc.

namely (from lumen outward) the mucosa with an epithelial lining, submucosa, muscularis externa (propria) with an inner circular and an outer longitudinal muscle layer, and, below the level of the diaphragm, mesothelium-lined serosa instead of adventitia. Except for the portion of the esophagus in the peritoneal cavity, the rest is covered by a layer of loose connective tissue, or adventitia, that blends into surrounding tissue. The lack of a serosal surface explains the rapid spread of esophageal cancer into adjacent mediastinal fat. The esophagus lies posterior to the trachea in the neck. As it enters the thoracic inlet, the esophagus courses toward the left to reside in the posterior mediastinum.

The esophagus then enters the abdomen via the diaphragmatic esophageal hiatus and lies immediately anterior to the aorta. The normal esophageal wall thickness is 3 mm. On cross-sectional images the esophagus tends to be collapsed, although a small amount of air in the lumen is not abnormal.

MRI Technique

Techniques that have been used for MRI of the esophagus include fat saturation, gadolinium enhancement, and cardiac gating (fig. 6.1). The difficulty with T1-weighted ECG-gated fat-suppressed spin-echo imaging is that the sequence is lengthy and the image quality is inconsistent because of the combination of phase artifacts from breathing, patient motion, and cardiac pulsation. The esophagus, therefore, of all bowel segments, suffers the most from image artifacts and uniquely experiences artifacts from cardiac pulsation resulting in severe artifacts on SGE sequences, which form an important component of imaging protocols of other bowel segments. Currently, imaging of the mediastinum and esophagus has been significantly improved with the use of a gadolinium-enhanced 3D GE technique that is acquired during a short breath hold, results in minimized artifacts from motion, and allows excellent depiction of the esophageal wall and mediastinum (fig. 6.2). The 3D GE T1 sequence uses a much shorter TR and TE than utilized with standard fast spin-echo techniques, with the additional benefit of reducing paramagnetic artifacts that arise in the region of gas-soft tissue interfaces, as can be encountered with air within the esophageal lumen or from lung. T1-weighted imaging can be supplemented by T2-weighted imaging using the single-shot echo-train (SSET) technique, acquired during a breath hold. T2-weighted imaging can be used to detect the presence of fluid within cystic masses or collections within the mediastinum around the esophagus. SSET sequences are acquired as a series of individual slices and are very resistant to deterioration from motion. If necessary, this sequence can be combined with respiratory triggering while the patient breathes freely, with only a minor time penalty and total acquisition times for the chest typically remaining under 45–60 s in duration. Two-dimensional steady-state precession-balanced echo, or true-FISP type, techniques yield images that have both T1- and T2-weighted properties but may be used as a substitute for or in conjunction with SSET images. The images can appear to have good edge sharpness, partly due to these sequences having an out of- phase TE yielding a thin black signal cancellation border at the esophageal border with adjacent mediastinal fat, particularly if combined with cardiac triggering. However, the role for routine evaluation of the esophagus is not established.

Congenital Lesions

Duplication Cysts

Gastrointestinal duplication cysts may occur throughout the alimentary tube. The cysts occur in or adjacent to the wall of a portion of the gastrointestinal tract, and, although they are lined by epithelium, it may not be of the same histologic type as that of the involved segment. Duplication cysts usually are discovered in childhood or infancy secondary to mass effect, hemorrhage, and/or infection resulting from intestinal stasis combined with bowel communication [18]. Patients may also present later in life with peptic ulcers or pancreatitis if the cysts contain gastric or pancreatic epithelium, respectively. In the esophagus, they tend to be small, ovoid, fluid-filled structures in the lower one-third of the esophagus located posteriorly in a periesophageal location or within the esophageal wall. Cysts have variable signal intensity on T1-weighted images, depending on the concentration of mucin or protein within the cyst. Duplication cysts are generally high in signal intensity on T2-weighted images (fig. 6.2) [19]. The cyst wall typically is thin and may enhance after intravenous gadolinium administration, whereas the fluid-filled lumen does not enhance and may appear near signal void on fat-suppressed gadolinium-enhanced delayed-phase images. Relatively intense cyst wall enhancement may reflect the presence of gastric mucosa or inflammatory changes.

Mass Lesions

Benign Masses

Leiomyomas. Leiomyomas are the most common benign tumors of the esophagus. These tumors are composed of smooth muscle and arise from the muscularis externa. They most frequently occur in the distal esophagus and may be single or multiple [20, 21]. Esophageal leiomyomas appear as small, oval masses that may be pedunculated on MRI images. They are often close to isointensity with surrounding bowel wall on T1- and

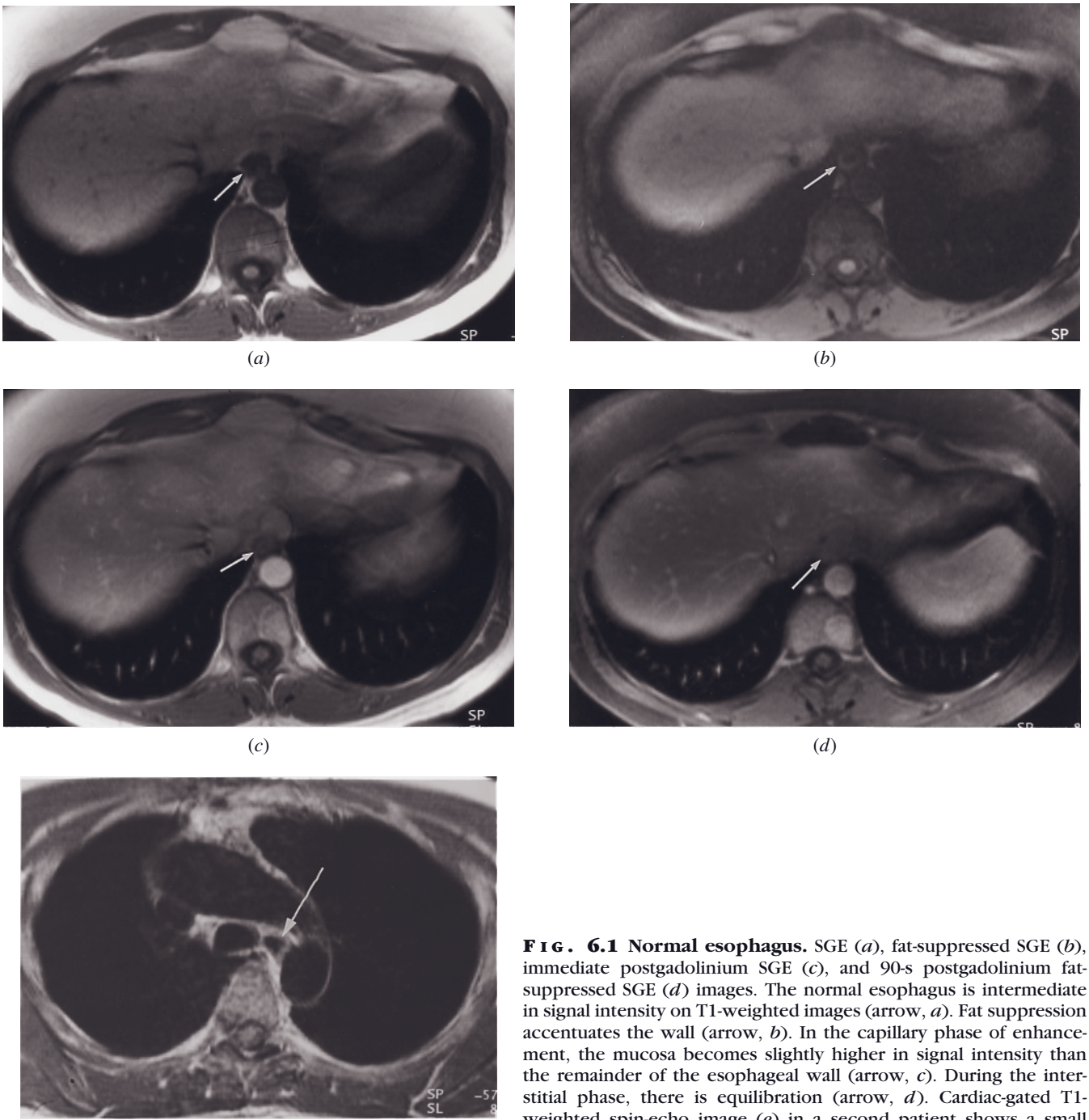

FIG. 6.1 Normal esophagus. SGE (*a*), fat-suppressed SGE (*b*), immediate postgadolinium SGE (*c*), and 90-s postgadolinium fat-suppressed SGE (*d*) images. The normal esophagus is intermediate in signal intensity on T1-weighted images (arrow, *a*). Fat suppression accentuates the wall (arrow, *b*). In the capillary phase of enhancement, the mucosa becomes slightly higher in signal intensity than the remainder of the esophageal wall (arrow, *c*). During the interstitial phase, there is equilibration (arrow, *d*). Cardiac-gated T1-weighted spin-echo image (*e*) in a second patient shows a small amount of air in the lumen of a normal esophagus (arrow, *e*).

T2-weighted images; however, with gadolinium, leiomyomas will enhance in a uniform fashion and to a greater degree than adjacent bowel wall in the interstitial phase of enhancement (fig. 6.3). Leiomyomas belong to the gastrointestinal stromal tumor (GIST) classification.

Varices. Varices, or tortuous, dilated submucosal veins, develop in the setting of portal hypertension or splenic vein thrombosis. They occur along the lower esophagus, the stomach, and other locations with portosystemic communications. Varices are best demonstrated on fat-suppressed 3D T1-weighted gadolinium-enhanced delayed-phase imaging (fig. 6.4) but may be demonstrated on SGE postgadolinium images or as signal-void tubular structures on spin-echo images. True-FISP imaging may display varices as tubular

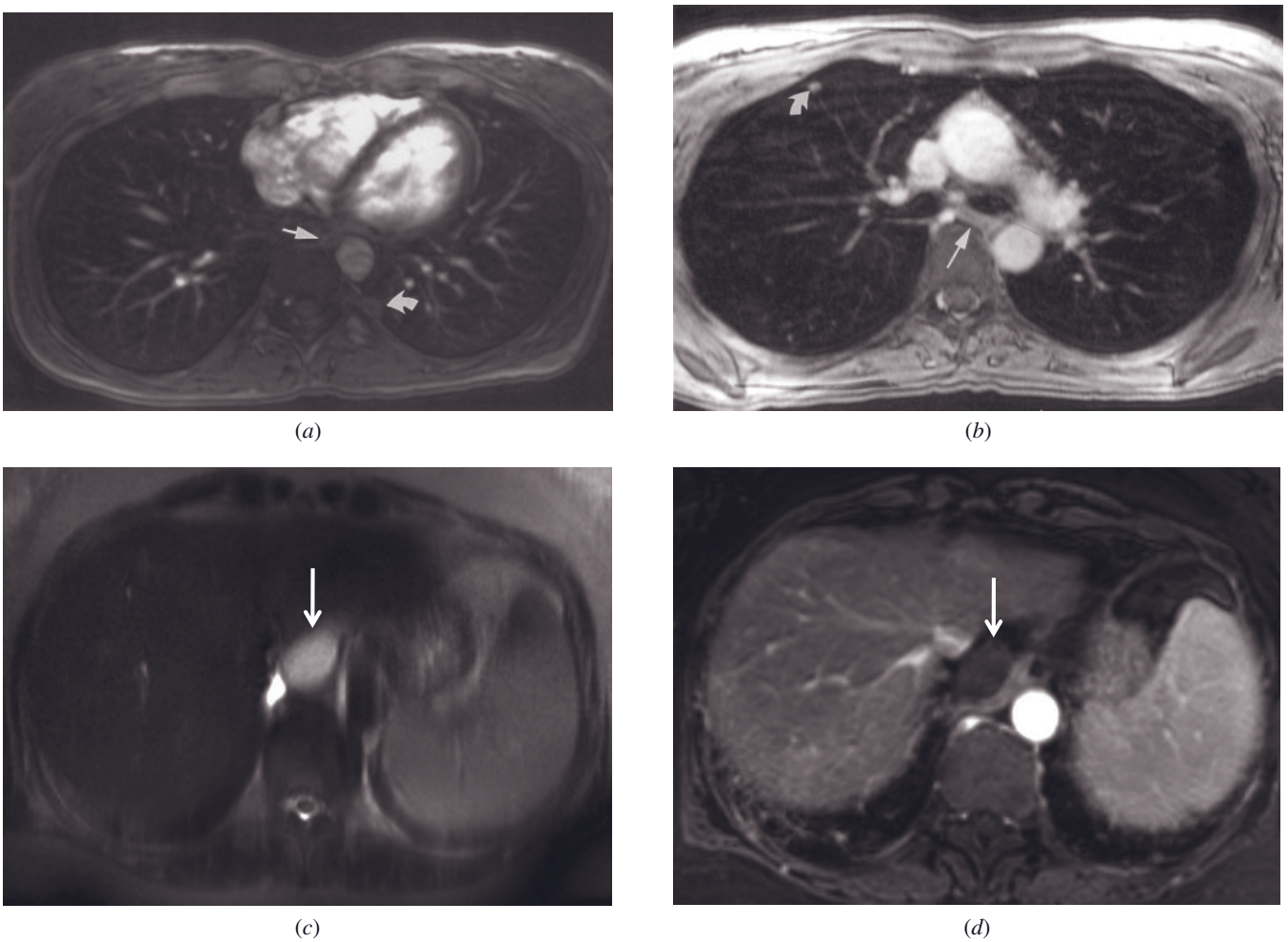

FIG. 6.2 Normal esophagus. Transverse gadolinium-enhanced 3D gradient-echo (*a* and *b*) images in two patients. On gadolinium-enhanced 3D images, the esophagus is well shown (short arrows, *a*, *b*) and is free of cardiac motion artifact. Note also a subtle pleura-based density along the posterior left hemithorax (curved arrow, *a*) and pulmonary metastasis (curved arrow, *b*). **Duplication cyst.** T2-weighted single-shot echo-train spin-echo (*c*) and T1-weighted postgadolinium hepatic venous phase fat-suppressed 3D-GE (*d*) images at 3.0 T demonstrate a paraesophageal cyst (arrows, *c*, *d*), which shows high signal on T2-weighted image (*c*) and no appreciable enhancement on postgadolinium image (*d*).

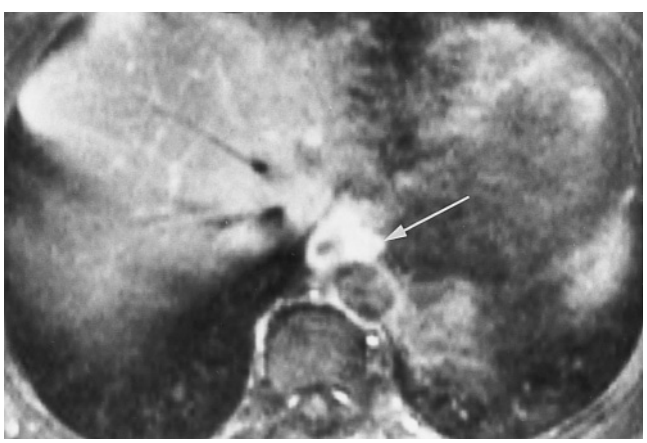

FIG. 6.3 Esophageal leiomyoma. Gadolinium-enhanced T1-weighted fat-suppressed spin-echo image shows a 2-cm leiomyoma (arrow) arising from the lateral aspect of the distal esophagus. Leiomyomas are the most common benign tumors of the esophagus. (Reprinted with permission from Shoenut JP, Semelka RC, Silverman R, Yaffe CS, Mickflikier AB: The gastrointestinal tract. In Semelka RC, Shoenut JP (eds.), *MRI of the Abdomen with CT Correlation*. New York: Raven Press, 1993, pp. 119–143.)

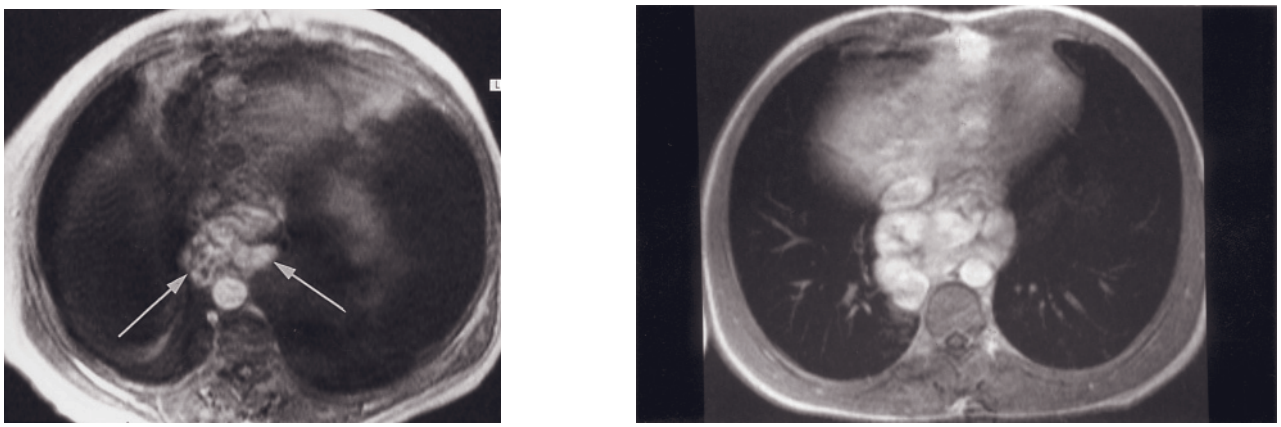

(*a*) (*b*)

FIG. 6.4 Esophageal varices. Transverse 45-s postgadolinium SGE image (*a*) in a patient with portal hypertension. Enhancing serpiginous tubular structures (arrows) in the lower esophagus represent varices. Transverse gadolinium-enhanced T1-weighted SGE image (*b*) in a second patient with congenital hepatic fibrosis demonstrates massive esophageal varices.

structures with high internal signal from blood and can be used in situations where gadolinium enhancement may not be possible, such as inadequate venous access or end-stage renal disease.

Malignant Masses

Before 1975, squamous cell carcinoma accounted for 95% of all cases of esophagus cancer. Since that time there has been a marked increase in the incidence of adenocarcinomas among esophagus cancers. At the present time, the overall relative incidence between squamous cell carcinoma and adenocarcinoma is about equal in the United States [22].

The etiology of squamous cell carcinoma is unknown, but there is an association with alcohol consumption and tobacco use [23]. It occurs more commonly in males (3 to 1) and African Americans [24]. Primary adenocarcinoma of the esophagus may arise de novo in Barrett esophagus, or it may arise in the stomach and cross the gastroesophageal junction to involve the distal esophagus and simulate achalasia [25]. It is more common in Caucasian males. Tumors that commonly metastasize to the esophagus include breast and lung carcinoma and melanoma. Gadolinium-enhanced fat-suppressed SGE and 3D-GE techniques delineate primary tumors of the distal esophagus, whereas SGE with cardiac gating or 3D-GE with or without cardiac gating is useful to image midesophageal cancers posterior to the heart (fig. 6.5) [26]. Squamous cell cancers (see fig. 6.5) and adenocarcinomas (fig. 6.6) appear similar on MR images. Predisposing factors such as Barrett esophagus or tumor location, with more proximal tumors mostly represented by squamous cell origin, may aid in making this distinction. The success of MRI in staging esophageal cancer has been inconsistent, reflecting the variable image quality of breathing-averaged, cardiac-gated sequences [27, 28]. At present, there is no reported series describing the use of gadolinium-enhanced 3D GE in the evaluation of esophageal cancers. This may prove to be the most consistent MR technique to investigate these tumors. The combined use of fat suppression and intravenous gadolinium may facilitate identification of mediastinal involvement. The presence of multiple (more than 5) paraesophageal normal-sized lymph nodes is worrisome for tumor involvement; however, accurate determination awaits the use of contrast agents that can define the presence of tumor in normal-sized lymph nodes. A comprehensive exam for staging patients with esophageal carcinoma should include a metastatic survey of the liver.

Metastases to the esophagus may appear indistinguishable from a primary esophageal tumor, and clinical history helps to establish the diagnosis (fig. 6.7).

Inflammatory and Infectious Disorders

Reflux Esophagitis

Gastroesophageal reflux is defined as the retrograde flow of gastric and sometimes duodenal contents into the esophagus. In general, reflux esophagitis refers to esophageal inflammation resulting from gastroesophageal reflux. Reflux esophagitis may result from several disease entities and/or their treatments: hiatal hernia, achalasia, and scleroderma. Gastroesophageal reflux is common in the setting of hiatal hernia. (For a more complete discussion of hiatal hernia see Chapter 7, *Peritoneal Cavity.*) Achalasia is a primary esophageal disorder that results in failure of relaxation of the lower esophageal sphincter (LES) coupled with nonperistaltic

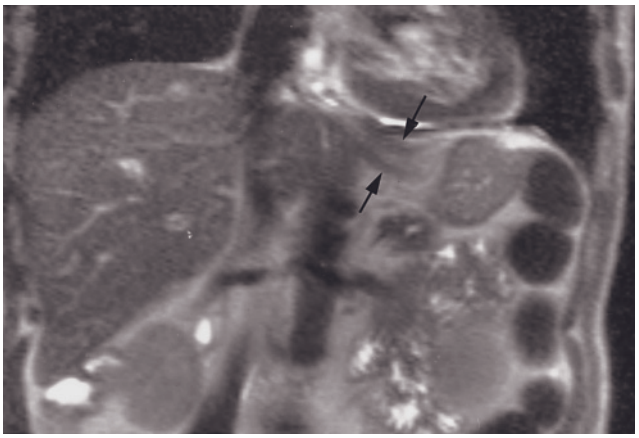

(*a*)

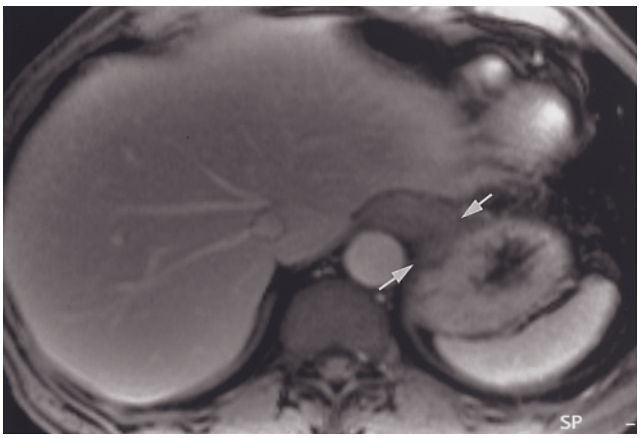

(*b*)

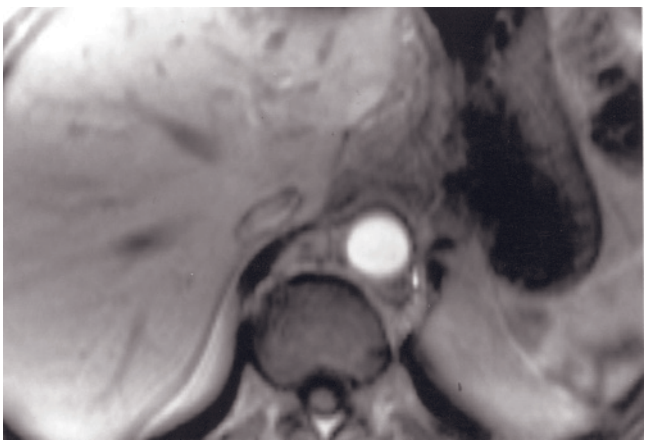

(*c*)

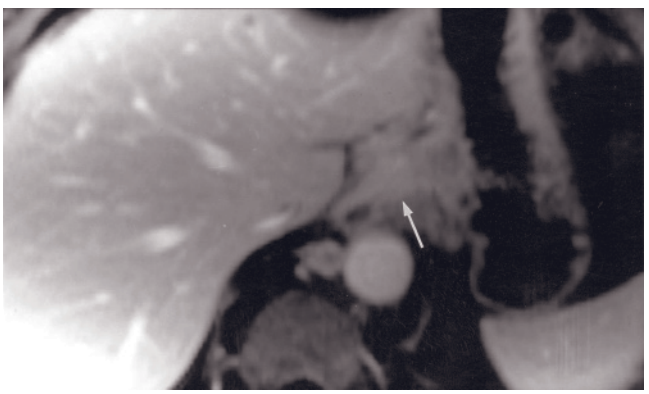

(*d*)

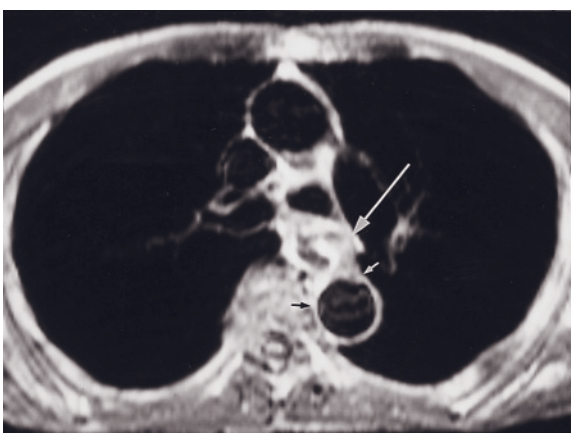

(*e*)

FIG. 6.5 Esophageal squamous cell carcinoma. Coronal SS-ETSE (*a*) and 45-s postgadolinium fat-suppressed SGE (*b*) images. Increased thickness of the distal esophagus is present on the precontrast image (arrows, *a*).The squamous cell carcinoma of the distal esophagus is clearly defined, and tumor is shown to extend to the gastroesophageal junction (arrows, *b*). Lack of extension into the stomach is well shown by demonstration of normal-enhancing higher-signal gastric mucosa. Transverse immediate postgadolinium T1-weighted SGE (*c*) and interstitial-phase gadolinium-enhanced fat-suppressed SGE (*d*) images in a second patient demonstrate a mass lesion centered in the region of the gastroesophageal junction (arrow, *d*), consistent with distal esophageal squamous cell carcinoma. Gadolinium-enhanced gated T1-weighted spin-echo image (*e*) in a third patient with squamous cell carcinoma of the midesophagus. A 2-cm cancer (arrow, *e*) is present that shows heterogeneous extension into the aortic wall (small arrows, *e*).

esophageal contractions. Balloon dilation of the LES is the mainstay of treatment and may lead to reflux esophagitis. Scleroderma involvement of the esophagus results in a patulous gastroesophageal junction with substantial reflux of gastric contents. In all of these conditions, MRI demonstrates a thickened esophageal wall, and, after the administration of gadolinium, the inflamed and possibly fibrosed wall shows marked enhancement on delayed images (fig. 6.8).

Radiation Esophagitis

Patients undergoing radiation therapy to the thorax are at risk of developing radiation damage to the esophagus. In the early period, 4–6 weeks after treatment,

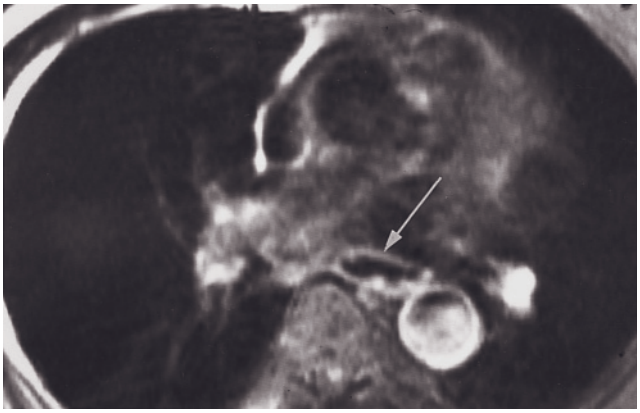

(*a*)

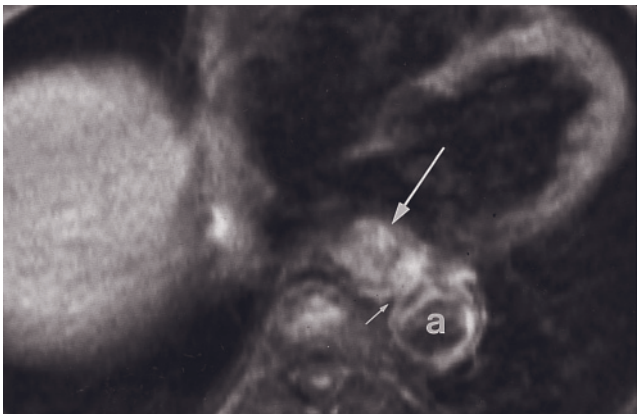

(*b*)

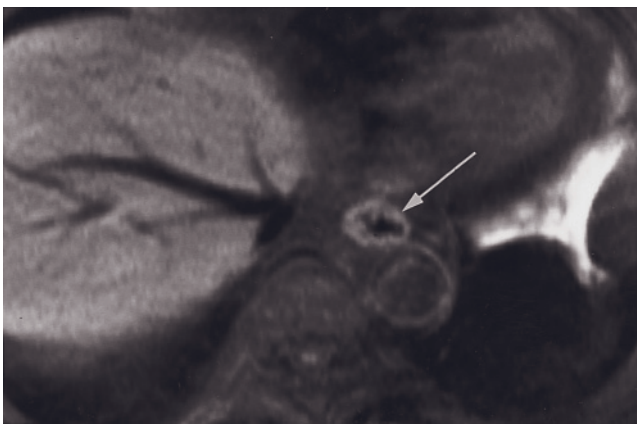

(*c*)

FIG. 6.6 Esophageal adenocarcinoma. Gadolinium-enhanced T1-weighted fat-suppressed (*a*, *b*) and T1-weighted fat-suppressed (*c*) spin-echo images in a patient with esophageal adenocarcinoma. Above the tumor at the level of the midthorax, the esophagus has a normal-appearing thin wall (arrow, *a*). More inferiorly at the level of the mitral valve, a 2.5-cm tumor (long arrow, *b*) is identified in the esophagus. Note that the interface of the tumor with the descending aorta (a, *b*) is less than 90° (short arrow, *b*). Below the tumor the esophagus once again has a normal thin wall (arrow, *c*). (Reprinted with permission from Shoenut JP, Semelka RC, Silverman R, Yaffe CS, Mickflikier AB: The gastrointestinal tract. In Semelka RC, Shoenut JP (eds.), *MRI of the Abdomen with CT Correlation*. New York: Raven Press, 1993.)

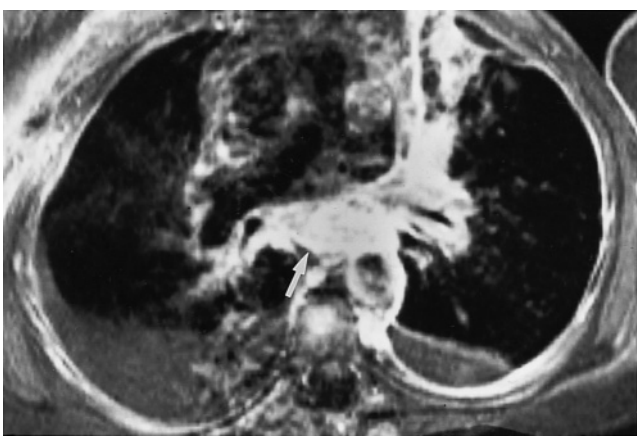

FIG. 6.7 Esophageal metastases. Gadolinium-enhanced T1-weighted fat-suppressed image in a woman with metastatic breast carcinoma. Enhancing tumor (arrow) encases the esophagus, extends along the left hilum and left mediastinum, and invades the chest wall. (Reprinted with permission from Shoenut JP, Semelka RC, Silverman R,Yaffe CS, Mickflikier AB: The gastrointestinal tract. In Semelka RC, Shoenut JP (eds.), *MRI of the Abdomen with CT Correlation*. New York: Raven Press, 1993, pp. 119–143.)

mucosal edema may be seen. Approximately 6–8 months after treatment, strictures may begin to develop.

Corrosive Esophagitis

Ingestion of caustic material such as strong alkaline or acidic agents or very hot liquids may cause esophagitis. Damage to tissue is most severe after ingestion of strongly alkaline agents. These substances cause a liquefactive necrosis that penetrates the entire esophageal wall rapidly. Acute changes include edema and ulceration. Stricture formation occurs later, and there is a strong association between corrosive stricture and the development of carcinoma.

Infectious Disease

Esophageal infection by *Candida albicans*, cytomegalovirus (CMV), and herpes simplex virus (HSV) is commonly observed in association with immunocompromised conditions. *Candida albicans* may be found in the esophagus of normal patients but is frequently pathological in patients who have bone marrow transplantation, chemotherapy, acquired immunodeficiency

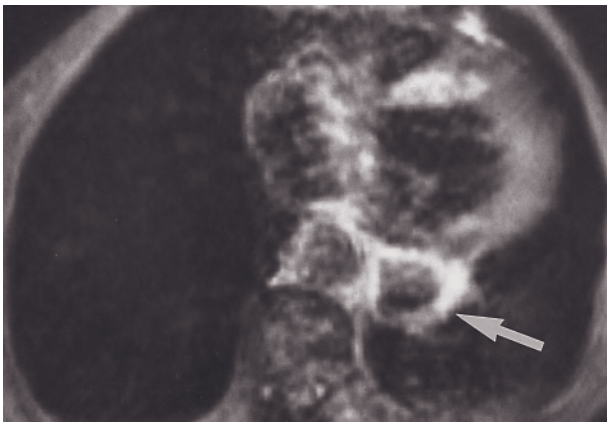

(*a*)

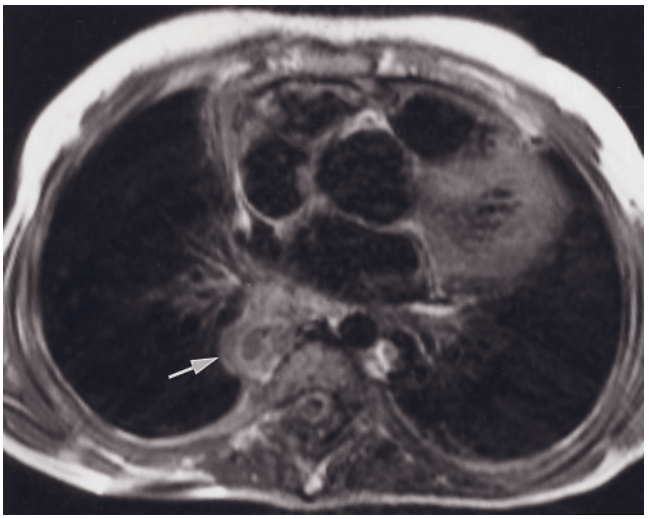

(*b*)

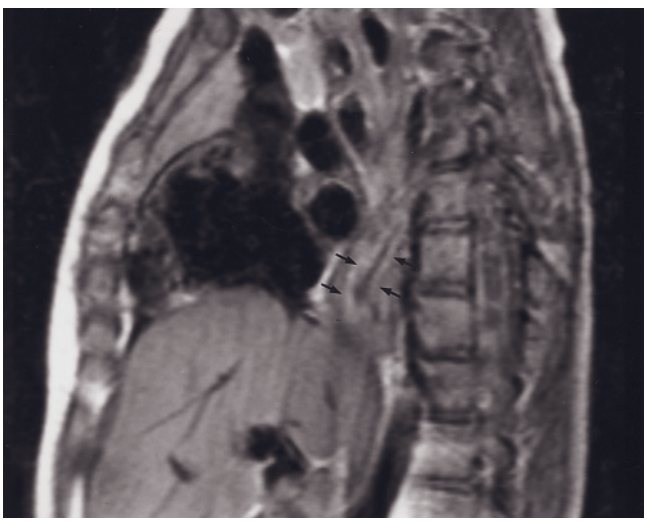

(*c*)

FIG. 6.8 Reflux esophagitis. Gadolinium-enhanced T1-weighted fat-suppressed spin-echo (*a*), gadolinium-enhanced gated transverse (*b*), and sagittal (*c*) T1-weighted spin-echo images in two patients [(*a*) and (*b*, *c*)] with reflux esophagitis. In a patient with achalasia (*a*), balloon dilation for achalasia predisposes to reflux esophagitis. The esophagus appears dilated, and the wall is thickened with increased mural enhancement. The esophagus in a second patient with reflux esophagitis due to hiatal hernia shows increased thickness of the esophageal wall (arrow, *b*) and increased signal intensity of the mucosa. The superior extent of inflamed mucosa (small arrows) is well shown on the sagittal image (*c*).

syndrome (AIDS), administration of exogenous steroids, or blood dyscrasias. Infection is diffuse, with white-colored plaques coating the mucosa. The mucosa becomes friable, and ulceration results. MRI demonstrates a high-signal-intensity thickened esophageal wall on T2-weighted images. Hyperemia and capillary leakage account for the marked enhancement after intravenous gadolinium injection (fig. 6.9).

Achalasia

The underlying defect in achalasia results from altered nervous control of esophageal coordinated contraction and relaxation with development of an inability to relax the circular muscle at the gastroesophageal junction that interferes with the passage of esophageal contents into the stomach. There is associated impaired primary peristaltic contraction of the esophagus, and the esophagus typically becomes markedly dilated, with development of beaklike narrowing at the closed gastroesophageal junction (fig. 6.10). Treatment involves balloon dilation, but this often results in only transient improvement, or distal esophagomyotomy. MR imaging provides an alternative to standard fluoroscopic techniques and provides the advantage of allowing visualization of the soft tissues in and adjacent to the wall of the distal esophagus and cardia of the stomach. Primary achalasia may develop from causes including infection, such as Chagas disease, but may also occur secondary to neoplasm. When considering the diagnosis of achalasia, cross-sectional imaging should be performed in every case to exclude the possibility of a secondary etiology.

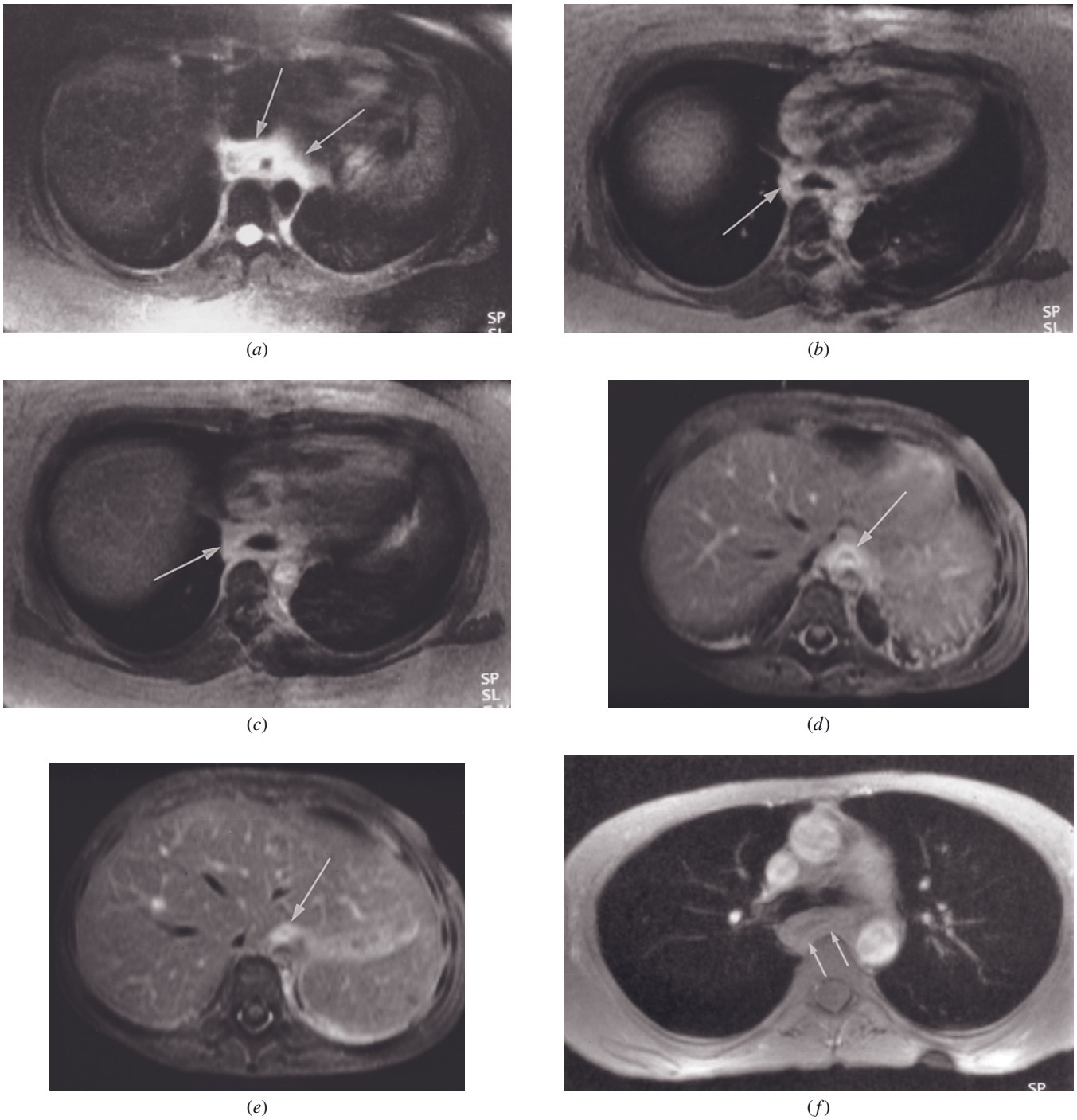

(*a*) (*b*) (*c*) (*d*) (*e*) (*f*)

FIG. 6.9 Esophagitis. T2-weighted fat-suppressed echo-train spin-echo (*a*) and contiguous 45-s postgadolinium SGE (*b*, *c*) images in a patient with AIDS and esophageal candidiasis. The high signal intensity on the T2-weighted images reflects both the fungal plaques that coat the esophagus and the underlying inflamed wall (arrows, *a*). After contrast, the thickened esophageal wall enhances (arrows, *b*, *c*). Gadolinium-enhanced T1-weighted fat-suppressed spin-echo images (*d*, *e*) in a second immunocompromised patient with acute myelogenous leukemia on chemotherapy. Capillary leakage associated with inflammation leads to marked mucosal enhancement (arrows, *d*, *e*) in this patient with *Candida albicans* esophageal invasion. Transverse gadolinium-enhanced SGE (*f*) image in a third patient who has AIDS and dysphagia shows diffuse esophageal wall thickening (arrows, *f*) consistent with inflammatory changes.

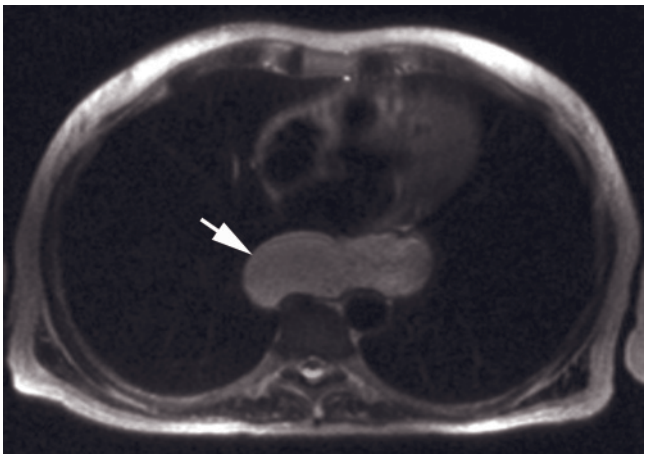

(*a*)

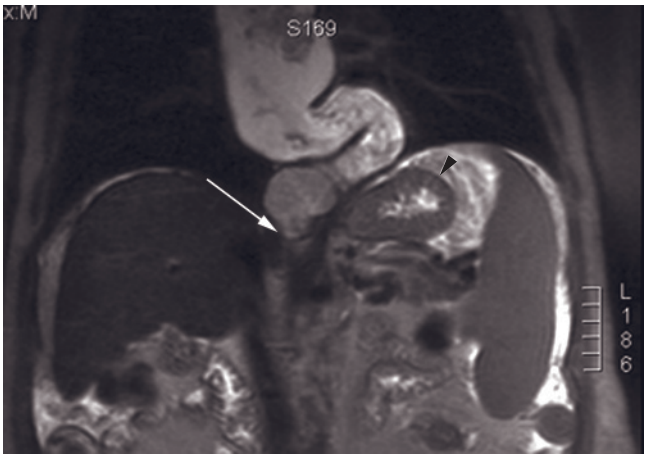

(*b*)

(*c*)

FIG. 6.10 Achalasia. Axial (*a*) and coronal (*b*) T2-weighted single-shot spin-echo and coronal T1-weighted gradient-echo (*c*) images show marked dilatation of the fluid-filled esophagus (arrow, *a*) with abrupt tapered narrowing at the gastroesophageal junction (arrows, *b, c*). The fundal portion of the stomach is normal (arrowheads, *b, c*), with no evidence of mass demonstrated.

THE STOMACH

Normal Anatomy

The stomach serves as a reservoir for ingested food and continues the process of mechanical and chemical breakdown. Although the stomach is typically J-shaped and resides in the posterior aspect of the left upper quadrant, its position varies with degree of distension and body habitus. Gross inspection shows four anatomic regions: cardia, fundus, body, and antrum. The antrum ends at the pylorus, from the Greek *pyl ros*, or gatekeeper, a narrow channel that connects the stomach to the duodenum. The stomach's curved morphology also gives rise to a greater (caudal) and a lesser (cephalic) curvature in addition to anterior and posterior walls. Four distinct layers comprise the stomach wall: mucosa, submucosa, muscularis, and serosa. Subdivisions exist within each layer. The mucosa is composed of distinct populations of endocrine and exocrine cells. The muscularis externa has three different muscle groups: inner oblique, middle circular, and outer longitudinal.

MRI Technique

Imaging the stomach achieves best results with distension and hypotonia. MRI examinations of the stomach may benefit from administration of water in an approximate volume of 1 liter and intravenous glucagon, with 0.5 mg administered intravenously immediately before the start of the examination and 0.5 mg before the administration of gadolinium [29].

A recommended imaging protocol includes: 1) T1-weighted fat-suppressed SGE or 3D-GE imaging before and after intravenous gadolinium, 2) unenhanced T1-weighted SGE imaging, and 3) T2-weighted non-fat-suppressed and fat-suppressed single-shot echo-train spin-echo [e.g., half-Fourier single-shot turbo spin-echo (HASTE)] imaging (fig. 6.11). Gastric mucosa enhances more intensely than other bowel mucosa after intravenous gadolinium [30]. This observation may be helpful

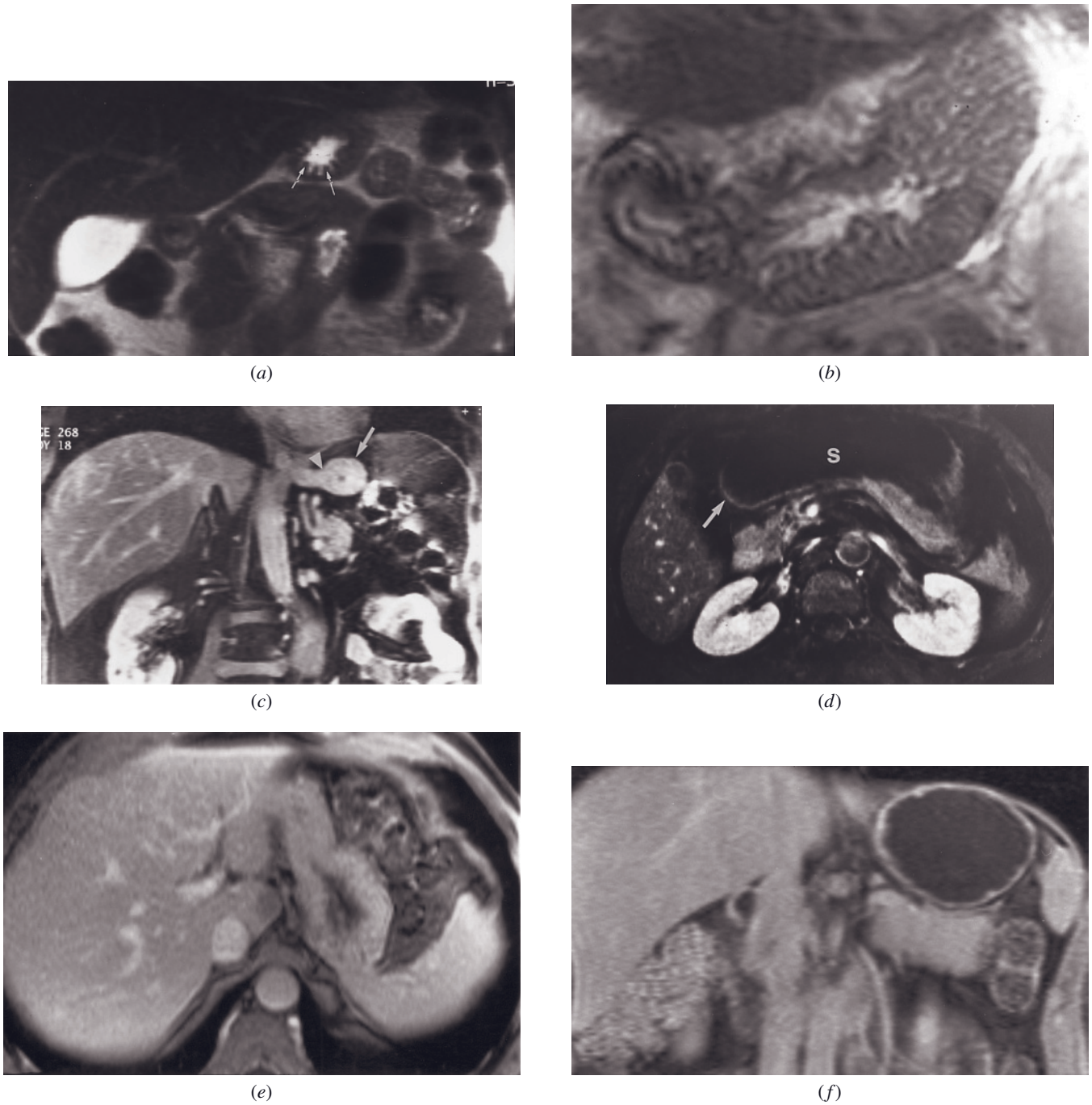

FIG. 6.11 Normal stomach. Coronal T2-weighted SS-ETSE (*a*, *b*) and coronal (*c*) and transverse (*d*) interstitial-phase gadolinium-enhanced fat-suppressed SGE images in four patients with a normal stomach. T2-weighted SS-ETSE is well-suited for imaging the rugal folds (arrows, *a*, *b*). After intravenous contrast the stomach wall shows marked enhancement (arrows, *c*, *d*). The normal gastroesophageal junction (arrowhead, *c*) is frequently well-defined by imaging in transverse and coronal planes. Optimal stomach (s, *d*) distension was obtained after ingestion of a negative oral contrast agent. Transverse gadolinium-enhanced fat-suppressed SGE (*e*) and coronal gadolinium-enhanced fat-suppressed SGE (*f*) images in a another patient before and after water ingestion. Optimal gastric distension can also be achieved with water.

for the detection of a gastric mucosa-lined duplication cyst or Meckel diverticulum.

Congenital Lesions

Congenital lesions, except for hypertrophic pyloric stenosis, are rare in the stomach.

Gastric Duplication Cysts

Gastric duplication cysts account for less than 4% of duplications of the gastrointestinal tract. They occur along the greater curvature and are more common in females. Occasionally, gastric duplication cysts calcify, and in 15% the cysts communicate with the gastric lumen. Although gastric duplication cysts are uncommon, they are important to recognize because 35% of these patients will have other congenital anomalies [31].

Congenital Heterotopias

Congenital heterotopias result from cellular entrapment during the morphogenic movements throughout embryogenesis. Pancreatic rests occur throughout the alimentary tract but are most common along the greater curvature or posterior antral wall of the stomach. Heterotopic pancreas usually appears as a solitary, submucosal globoid mass with a central nipplelike structure representing ductal openings into the gastric lumen [32].

Congenital Diverticula

Congenital diverticula may also be demonstrated in the stomach (fig. 6.12) [29]. Gastric diverticula are rare, and more than 75% of them occur in a juxtacardiac position high on the posterior wall of the stomach, approximately 2 cm below the gastroesophageal junction and 3 cm from the lesser curvature of the stomach [33]. Congenital diverticula are characterized as solitary, well-defined, oval or pear-shaped pouches that communicate with the gastric lumen via a narrow or broad-based opening [34]. The clinical presentation depends on location, size, type of mucosa of the diverticulum, and presence or absence of communication with the stomach.

Mass Lesions

Benign Masses

Polyps. Gastric polyps may be hyperplastic, adenomatous, or hamartomatous. They may be isolated findings or associated with a polyposis syndrome. Eighty to ninety percent of gastric polyps are hyperplastic and benign, whereas approximately 10% are adenomatous. Hyperplastic polyps are nonneoplastic lesions that result from an exaggerated regenerative response to injury, namely ulcers, gastroenterostomy stomas, or a background of chronic gastritis. In contrast to hyperplastic polyps, adenomatous polyps are true neoplasms, morphologically similar to those seen in the colon. Microscopic features show close-packed glandular structures lined by neoplastic cells with cytologic atypia. Approximately one-third of adenomatous polyps contain a focus of adenocarcinoma [35]. Malignant potential is related to size, with up to 46% of adenomas larger than 2 cm containing carcinoma [36]. Both hyperplastic and adenomatous polyps are found in patients with chronic atrophic gastritis and Gardner and familial polyposis syndromes, conditions associated with an increased incidence of malignancy. (For a more complete discussion on polyposis syndromes, see the section on the large intestine in this chapter.) Although most polyps are asymptomatic, anemia related to chronic blood loss, iron deficiency, or malabsorption of vitamin B12 may be present. Hamartomatous gastric polyps are lesions produced by excessive, disorganized overgrowth of mature normal cells and tissues indigenous to the stomach. Hamartomatous polyps may be an isolated finding or can occur in patients with Peutz–Jeghers syndrome. Although both isolated hamartomatous polyps and those associated with Peutz–Jeghers syndrome are benign lesions, patients with Peutz–Jeghers syndrome have an increased risk of developing carcinomas of the gastrointestinal tract, pancreas, breast, lung, ovary, and uterus.

Benign polyps are generally isointense with the gastric wall on unenhanced MR images. Adequate distension of the stomach is mandatory to distinguish a polyp from a prominent rugal fold. Benign polyp enhancement is usually isointense to slightly hyperintense compared to normal gastric mucosa on early postgadolinium images and mildly hyperintense on 2-min postgadolinium images, reflecting retention of contrast in the interstitial space (fig. 6.13). In polyps complicated by invasive adenocarcinoma, more heterogeneous gadolinium enhancement and disruption of the underlying gastric wall may be observed.

Leiomyomas. Leiomyomas are the most common benign nonepithelial tumors of the stomach. They arise from the smooth muscle of the gastric wall. They may grow inward toward the lumen and mimic a polyp or extend to the serosa and present as an exophytic mass. When large, the overlying gastric mucosa may ulcerate, leading to gastrointestinal bleeding.

Neurogenic Tumors and Lipomas. Other mesenchymal gastric wall elements may give rise to benign neoplasms: neurogenic tumors (fig. 6.13), lipomas (fig. 6.13), fibromas, and hemangiomas. Except for lipomas, these mesenchymal tumors are indistinguishable from each other on MRI. Similar to fatty lesions elsewhere in

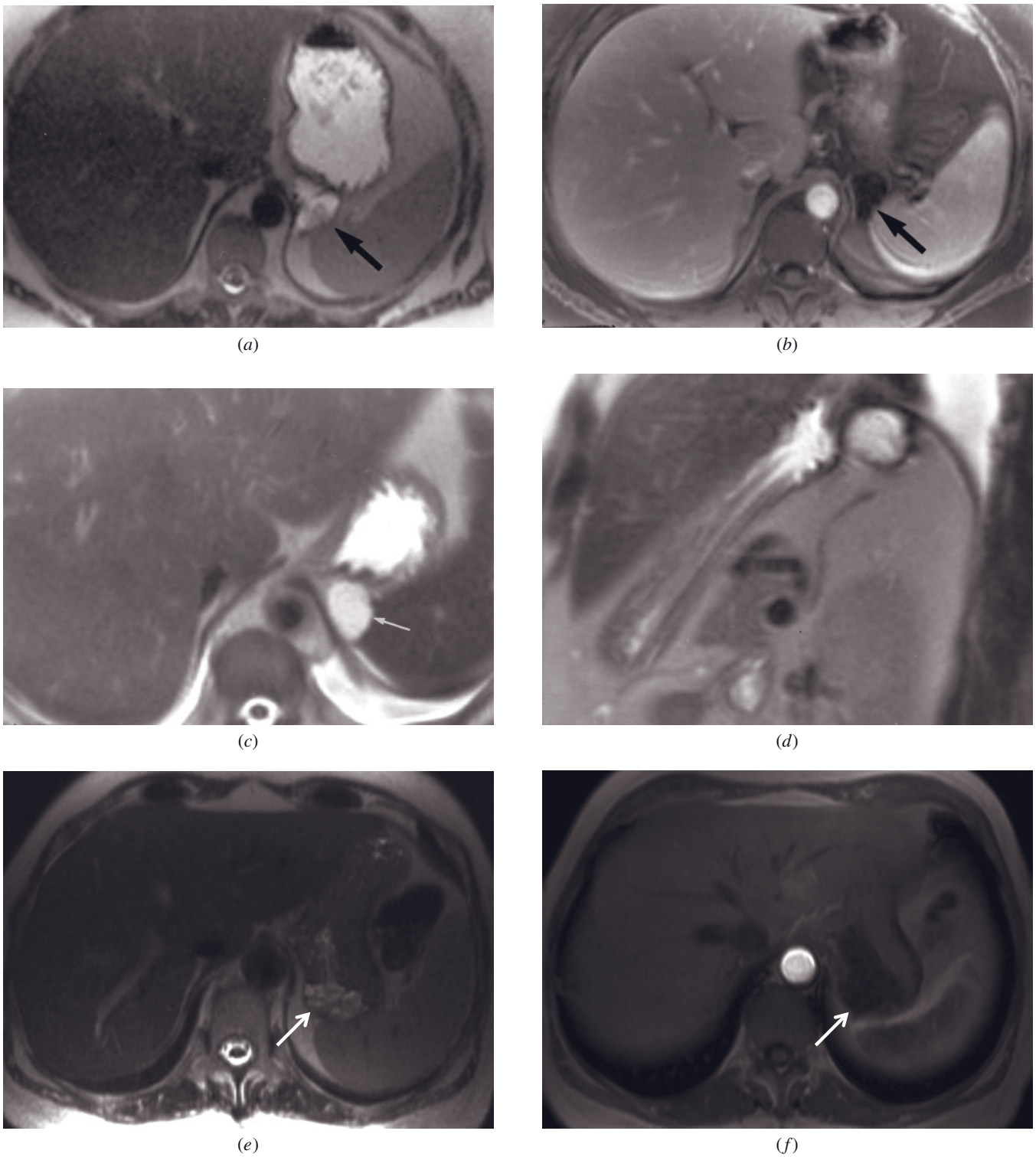

FIG. 6.12 Gastric diverticulum. Transverse T2-weighted SS-ETSE (*a*) and 90-s postgadolinium fat-suppressed SGE (*b*) images. A small cystic thin-walled mass (arrow, *a*) is shown, which is high signal intensity and intimately related to the posterior aspect of the cardiac portion of the stomach. On the 90-s postgadolinium image (*b*), the diverticulum appears signal void with a thin enhancing wall (arrow, *b*). (Reprinted with permission from Marcos HB, Semelka RC: Stomach diseases: MR evaluation using combined T2-weighted single-shot echo train spin-echo and gadolinium-enhanced spoiled gradient-echo sequences. *J Magn Reson Imaging* 10: 950–960, 1999.) Transverse (*c*) and coronal (*d*) T2-weighted SS-ETSE in a second patient. A small posterior gastric diverticulum (arrow, *c*) is seen in the fundus of the stomach. T2-weighted single-shot echo-train spin-echo (*e*), T1-weighted postgadolinium early arterial-phase SGE (*f*) and T1-weighted postgadolinium fat-suppressed interstitial- phase 3D-GE (*g*) images demonstrate a broad-based gastric diverticulum (arrows, *e–g*) in the posterior aspect of the cardia portion of the stomach in another patient. The diverticulum shows high signal on T2-weighted image (*f*), and thin enhancing wall is appreciated on the interstitial phase (*g*).

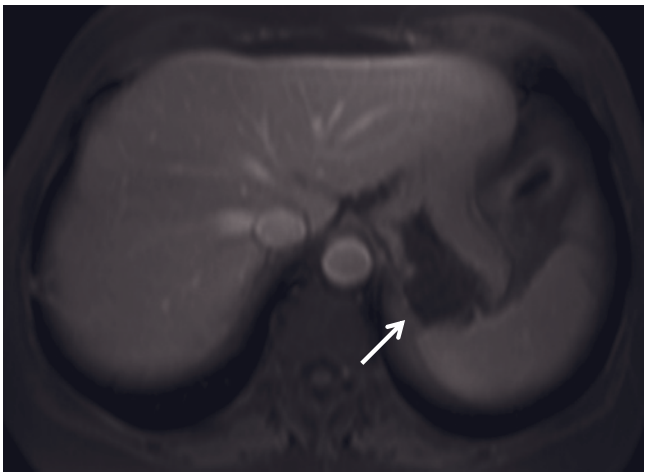

(*g*)

FIG. 6.12 (*Continued*)

the body, lipomas will be high in signal intensity on T1-weighted images and decreased in signal intensity on fat-suppressed images.

Varices. Portal hypertension and splenic vein thrombosis lead to gastric varices. Varices restricted to the short gastric veins along the greater curvature of the stomach should raise the suspicion of splenic vein thrombosis (fig. 6.14).

Bezoar. The word bezoar derives from the Arabic *bazahr* or *badzeahr*, meaning antidote. Bezoars were valued for their medicinal qualities and were thought to be imbued with magical powers and to be effective antidotes for poisoning [37].

The term bezoar is used to refer to an intragastric mass composed of accumulated ingested material. It may be composed of hair (trichobezoar), fruit or vegetable products (phytobezoar), or concretions such as resins, asphalt, or other material. Factors that predispose to bezoar development include psychiatric illness, lack of teeth, previous vagotomy or gastric surgery, and diseases such as diabetes and muscular dystrophies. Altered gastric motility or anatomy that causes retention of material in the stomach underlies most of the risk factors (fig. 6.15).

Malignant Masses

Carcinoma is the most important and the most common tumor of the stomach. Most gastric carcinomas are adenocarcinomas [38].

Adenocarcinoma. The incidence of gastric adenocarcinoma is on the decline. At present, 22,800 Americans are diagnosed with gastric cancer each year [39]. Males are affected twice as often as females. Predisposing conditions include atrophic gastritis, pernicious anemia, adenomatous polyps, dietary nitrates, and Japanese heritage [40, 41]. The tumors show a predilection for the lesser curvature of the antropyloric region. Grossly, adenocarcinomas of the stomach can be divided generally into three forms: 1) exophytic or polypoid, projecting into the lumen; 2) ulcerated, with a shallow or deeply erosive crater; and 3) diffusely infiltrative. The last-named form of adenocarcinoma creates a rigid, thickened "leather" stomach wall termed linitis plastica carcinoma. Gastric cancer may spread hematogenously to the liver and lung, contiguously to adjacent organs, lymphatically to regional and remote lymph nodes, and/or intraperitoneally to the abdominal lining, mesentery, and serosa. The overall prognosis is poor. A TNM system is used for staging (Table 6.1).

Early in the disease, symptoms are vague and include dyspepsia, anorexia, and weight loss. Later, vomiting and hematemesis may occur in association with a palpable epigastric mass and anemia.

The goals of MRI in patients with gastric cancer are to demonstrate the primary tumor, assess the depth of invasion, and detect extragastric disease. Adequate distension is necessary for surveying the gastric wall. On T1-weighted sequences, gastric adenocarcinoma is isointense to normal stomach and may be apparent as focal wall thickening. On T2-weighted images, tumors usually are slightly higher in signal intensity than adjacent normal stomach [42].

An important observation on gadolinium-enhancement MRI images is that collapsed normal gastric wall enhances identically to the remainder of the wall on early and late postgadolinium images (fig. 6.16), whereas tumors show more heterogeneous enhancement that may be decreased or increased relative to the gastric wall on early, late, or both sets of images [29].

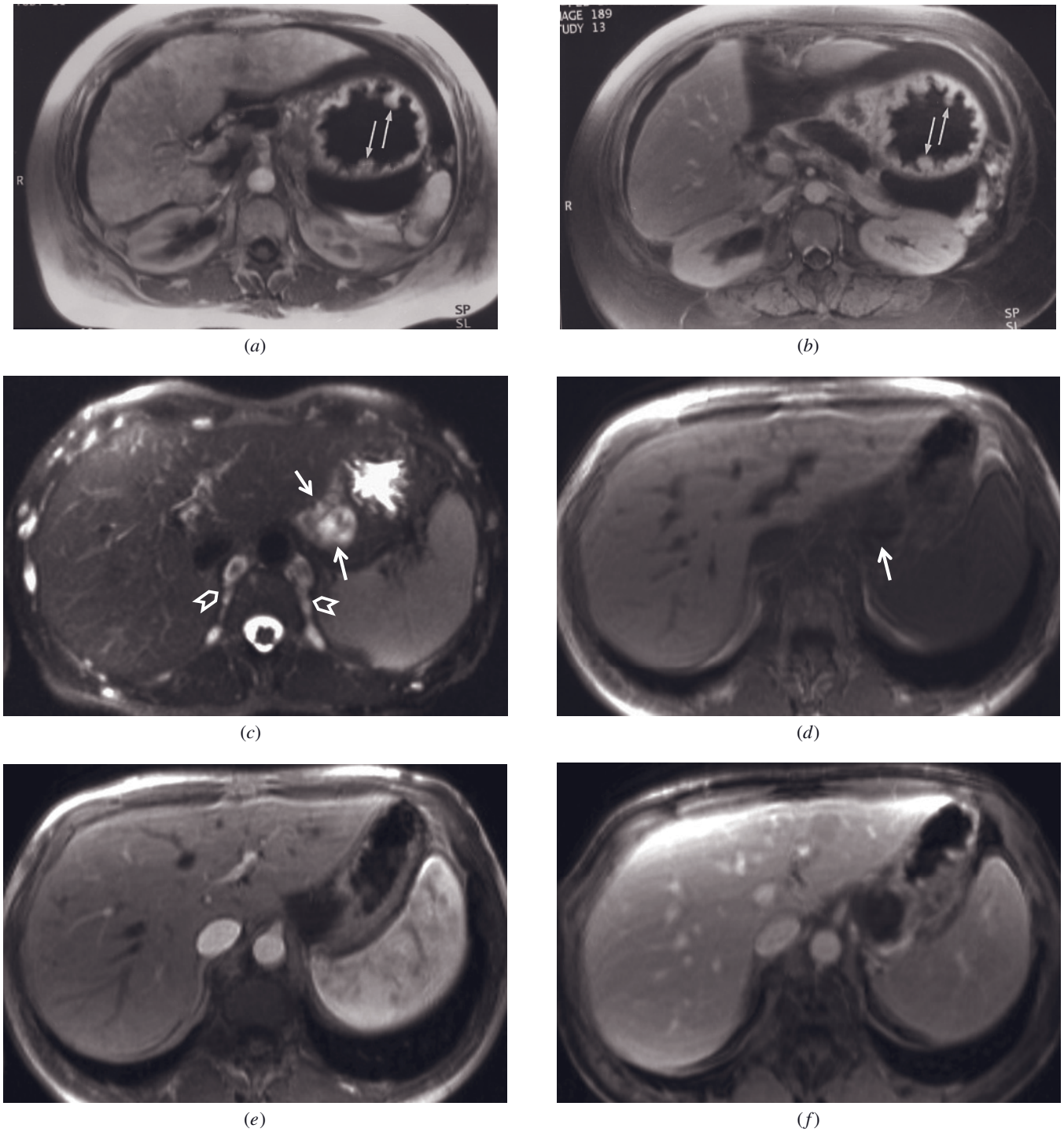

FIG. 6.13 Gastric polyps. Immediate postgadolinium SGE (*a*) and 90-s postgadolinium fat-suppressed SGE (*b*) images in a patient with Gardner syndrome demonstrate multiple enhancing gastric polyps (arrows, *a*, *b*). The polyps possess intense enhancement. **Gastric neurofibromas.** T2-weighted single-shot echo-train spin-echo (*c*), T1-weighted SGE (*d*), T1-weighted postgadolinium hepatic arterial dominant-phase SGE (*e*), and T1-weighted postgadolinium fat-suppressed hepatic venous-phase SGE (*f*) images demonstrate neurofibromas (arrows, *c*, *d*) located in the cardia portion of the stomach. The lesions show heterogeneous high signal on T2-weighted image (*c*) and low signal on T1-weighted image (*d*). The lesions show negligible enhancement on postgadolinium images (*e*, *f*). Note that paravertebral neurofibromas (open arrows, *c*) are present. **Gastric schwannoma.** Coronal T2-weighted

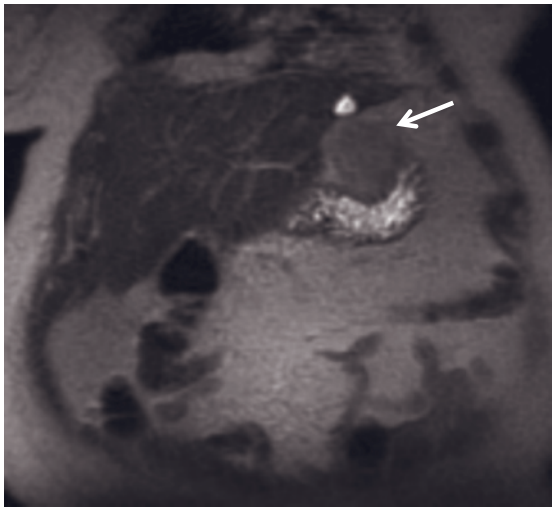

(*g*)

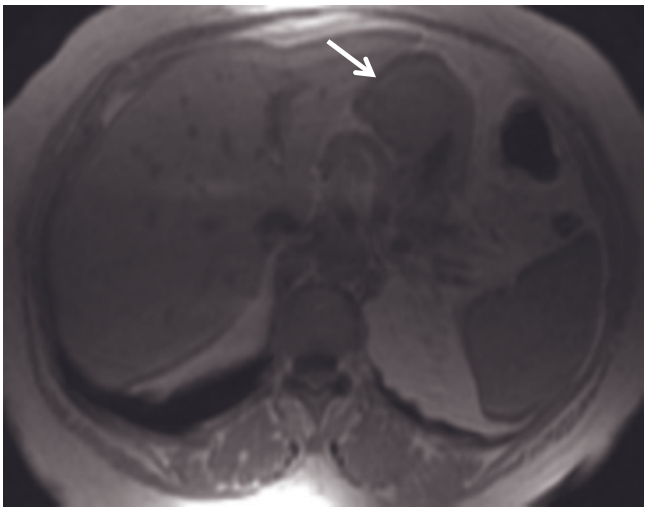

(*h*)

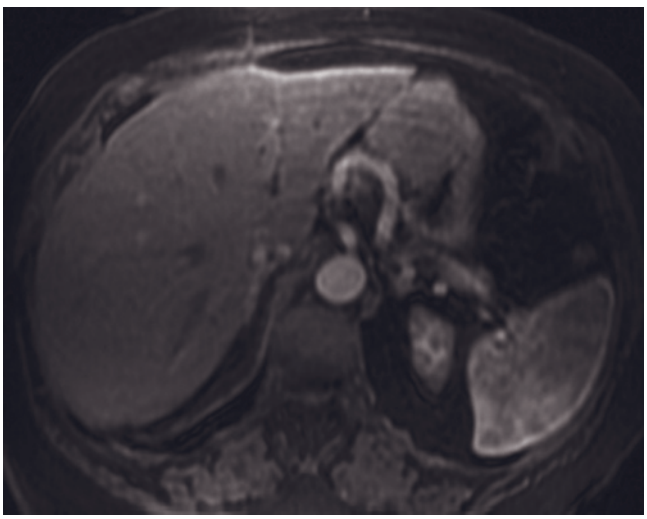

(*i*)

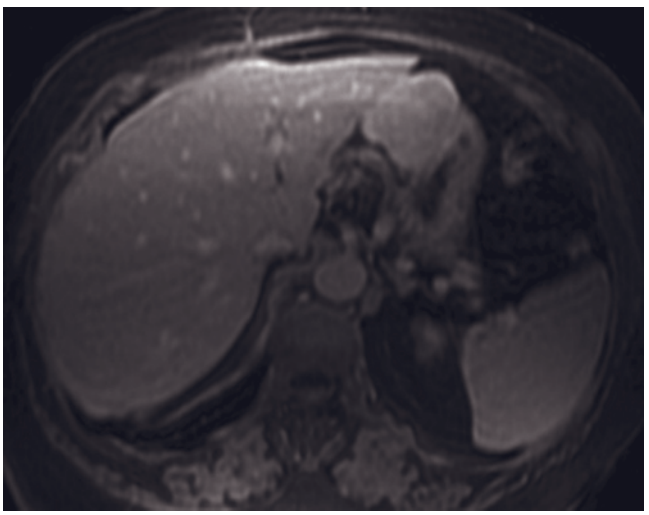

(*j*)

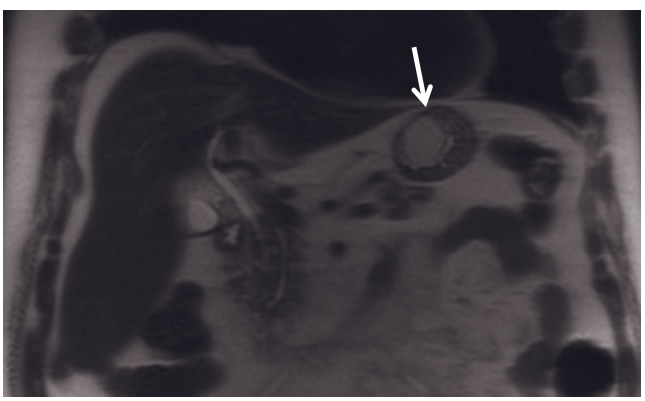

(*k*)

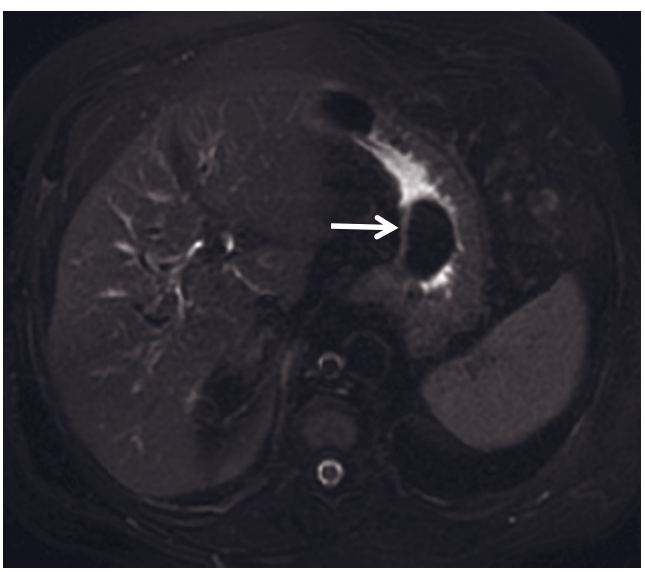

(*l*)

Fig. 6.13 (*Continued*) single-shot echo-train spin-echo (*g*), transverse T1-weighted SGE (*h*), transverse T1-weighted postgadolinium fat-suppressed hepatic arterial dominant-phase (*i*), and hepatic venous-phase (*j*) 3D-GE images demonstrate a gastric schwannoma (arrows, *g*, *h*) located in the lesser curvature. Exophytic lesion shows intermediate signal on precontrast sequences and homogeneous enhancement on postgadolinium images. Note that there is a cyst in the left liver lobe. **Gastric lipoma.** Coronal

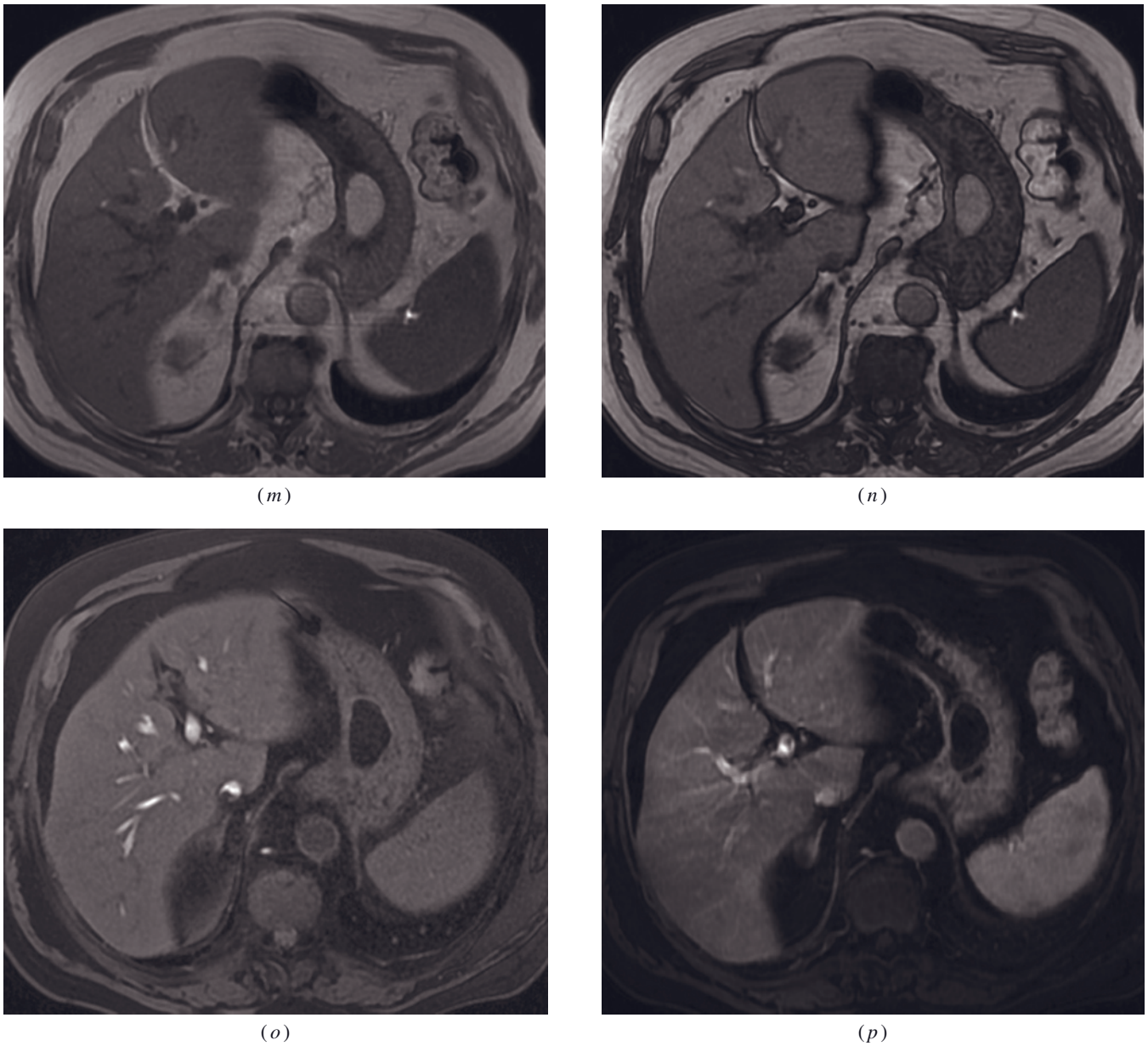

Fig. 6.13 (*Continued*) T2-weighted single-shot echo-train spin-echo (*k*), transverse T2-weighted fat-suppressed single-shot echo-train spin-echo (*l*), transverse T1-weighted in-phase (*m*) and out-of-phase (*n*) SGE, transverse T1-weighted fat-suppressed 3D-GE (*o*), and transverse T1-weighted postgadolinium hepatic venous-phase 3D-GE (*p*) images demonstrate a lipoma in the stomach lumen. The lesion shows high signal on precontrast non-fat-suppressed images (*k*, *m*, *n*). The lesion shows low signal on fat-suppressed images (*l*, *o*). Note that phase-cancellation artifact is present around the lipoma on out-of-phase image (*n*). The capsule of lipoma shows enhancement, and no enhancement is detected in the lipoma (*p*).

Tumors that originate in the cardia (fig. 6.17), body (fig. 6.18), antrum (fig. 6.19), and pylorus (fig. 6.20) are all well shown. Diffusely infiltrative carcinoma (linitis plastica carcinoma) tends to be lower in signal intensity than normal adjacent stomach on T2-weighted images because of its desmoplastic nature. Linitis plastic carcinoma enhances only modestly after intravenous contrast (fig. 6.21). In contradistinction, the other morphologic types of gastric carcinoma enhance more intensely with intravenous gadolinium. Gadolinium-enhanced fat-suppressed SGE or 3D-GE imaging aids in identification of transmural spread including peritoneal disease (fig. 6.22) and tumor involvement of lymph nodes. In vitro work with resected gastric cancer specimens at high field strength has demonstrated mucosal, submucosal, and muscle invasion [42].

Metastases enhance conspicuously against a background of low-signal-intensity fat. Detection of hepatic

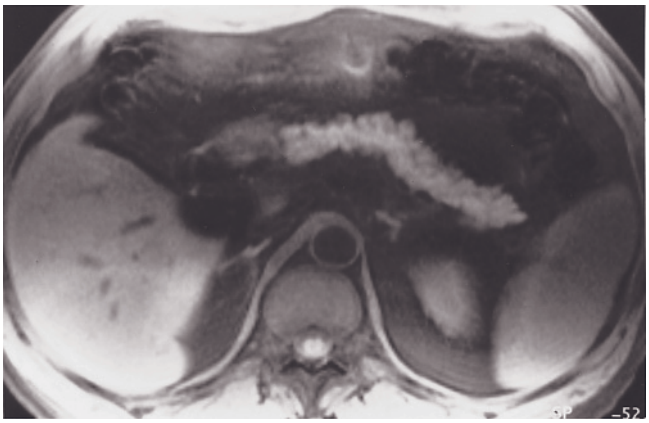

(*a*)

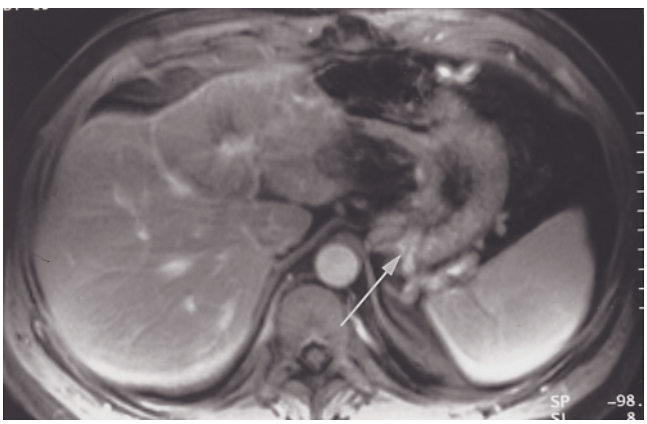

(*b*)

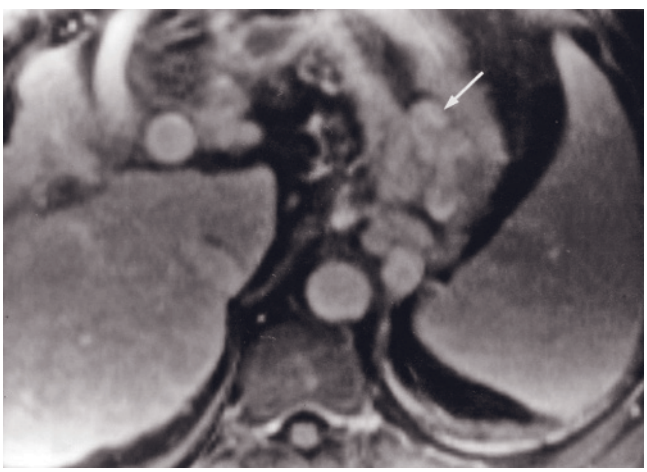

(*c*)

FIG. 6.14 Gastric varices. Fat-suppressed SGE (*a*) and 90-s postgadolinium fat-suppressed SGE (*b*) images. No splenic vein is identified posterior to the pancreas (*a*). After intravenous gadolinium administration (*b*), gastric varices enhance. These veins are part of the portosystemic circulation that are recruited to provide alternative venous channels in the presence of splenic vein thrombosis. A prominent varix is identified in the gastric wall (arrow, *b*). Transverse interstitial-phase gadolinium-enhanced fat-suppressed SGE image (*c*) in a second patient with hepatic cirrhosis. Large-caliber varices (arrow, *c*) are seen within the posterior wall stomach, immediately distal to the GE junction.

FIG. 6.15 Gastric bezoar. Transverse interstitial-phase gadolinium-enhanced fat-suppressed SGE image. The stomach is distended and filled with debris, which demonstrates a rounded configuration that represents a bezoar.

Table 6.1 TNM Staging for Cancer of the Stomach

T—Primary tumor

Tx Primary tumor cannot be assessed

T0 No evidence of primary tumor

Tis Pre-invasive carcinoma (carcinoma in situ)

T1 Tumor limited to the mucosa, or mucosa and submucosa regardless of extent and location

T2 Tumor with deep infiltration occupying not more than one-half of one region

T3 Tumor with deep infiltration occupying more than one-half but not more than one region

T4 Tumor with deep infiltration occupying more than one-half but not more than one region or extending to neighboring structures

N—Regional lymph nodes

Nx Regional lymph nodes cannot be assessed

N0 No evidence of regional lymph node metastasis

N1 Metastasis in lymph node(s) within 3 cm of the primary tumor along the greater or lesser curvatures

N2 Evidence of lymph node metastasis more than 3 cm from the primary tumor including those along the left gastric, splenic, celiac, and common hepatic arteries

N3 Evidence of involvement of the para-aortic and hepatoduodenal lymph nodes and/or other intra-abdominal lymph nodes

M—Metastases

Mx Distant metastases cannot be assessed

M0 No distant metastases

M1 Distant metastases

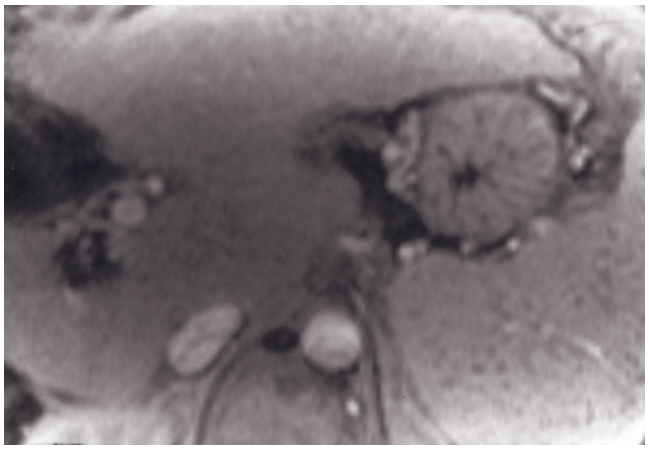

(*a*)

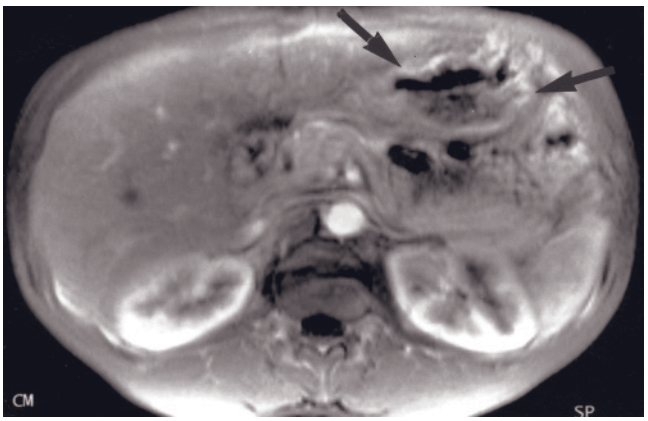

(*b*)

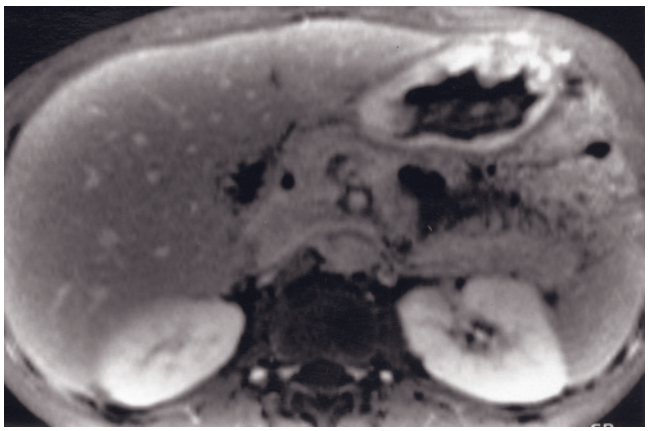

(*c*)

FIG. 6.16 Comparison between normal collapsed gastric wall and tumor. Transverse interstitial-phase gadolinium-enhanced fat-suppressed SGE image (*a*) in a normal patient. Note that the stomach is collapsed and the gastric wall enhancement is homogeneous. Note the symmetric radial fold pattern of the gastric rugae in the collapsed stomach. Transverse immediate postgadolinium (*b*) and interstitial-phase gadolinium-enhanced fat-suppressed SGE (*c*) images in a second patient with gastric cancer show diffuse gastric wall thickening and heterogeneous enhancement of the gastric wall. (Reprinted with permission from Marcos HB, Semelka RC: Stomach diseases: MR evaluation using combined T2-weighted single-shot echo train spin-echo and gadolinium-enhanced spoiled gradient-echo sequences. *J Magn Reson Imaging* 10: 950–960, 1999.)

involvement is facilitated by T2-weighted fat-suppressed sequences and dynamic gadolinium-enhanced SGE or 3D-GE techniques. This combined approach is superior to conventional CT imaging [43].

Marcos and Semelka reported on the detection and staging of gastric carcinoma [29]. In five of eight patients, focal, asymmetric gastric wall thickening or mass, consistent with gastric adenocarcinoma, was well demonstrated on MR evaluation. Failure of detection was related to small tumor size (<1–2 cm), lack of gastric distension, tumor enhancement similar to stomach wall, and tumoral isointensity on T2-weighted images. Staging accuracy was good, reflecting the adequate display of tumor and tumor extent on gadolinium-enhanced fat-suppressed SGE or 3D-GE images.

Gastrointestinal Stromal Tumors (GISTs). Gastrointestinal mesenchymal neoplasms can be divided into two broad categories, those that represent clear-cut diagnostic entities (such as leiomyomas and lipomas) and those that are difficult to classify into any specific cell lineage, that is, ultrastructural or immunohistochemical studies are not able to determine the histogenesis of the neoplastic cell population. The latter group of tumors falls into the category of gastrointestinal stromal tumors (GISTs). Although rare, GISTs most commonly occur in the stomach. All symptomatic GISTs are potentially malignant. These tumors are divided pathologically into lesions of 1) uncertain malignant potential, 2) low-grade malignant GIST, and 3) high-grade GIST. Grossly, these tumors differ from adenocarcinoma and lymphoma in that they often have a large exophytic component. Liquefactive necrosis and intratumoral hemorrhage are common. Spread is via direct extension and hematogenous metastases. High-grade GISTs are heterogeneous and high in signal on T2-weighted and gadolinium-enhanced fat-suppressed SGE or 3D-GE images because of their increased vascularity (figs. 6.23–6.26). During the capillary phase of imaging, they show marked enhancement that persists throughout the interstitial phase. Hasegawa et al. [44] reported that high-grade tumors have ill-defined tissue planes with adjacent tissues and organs, reflecting invasion, whereas low-grade tumors have well-defined planes, reflecting less

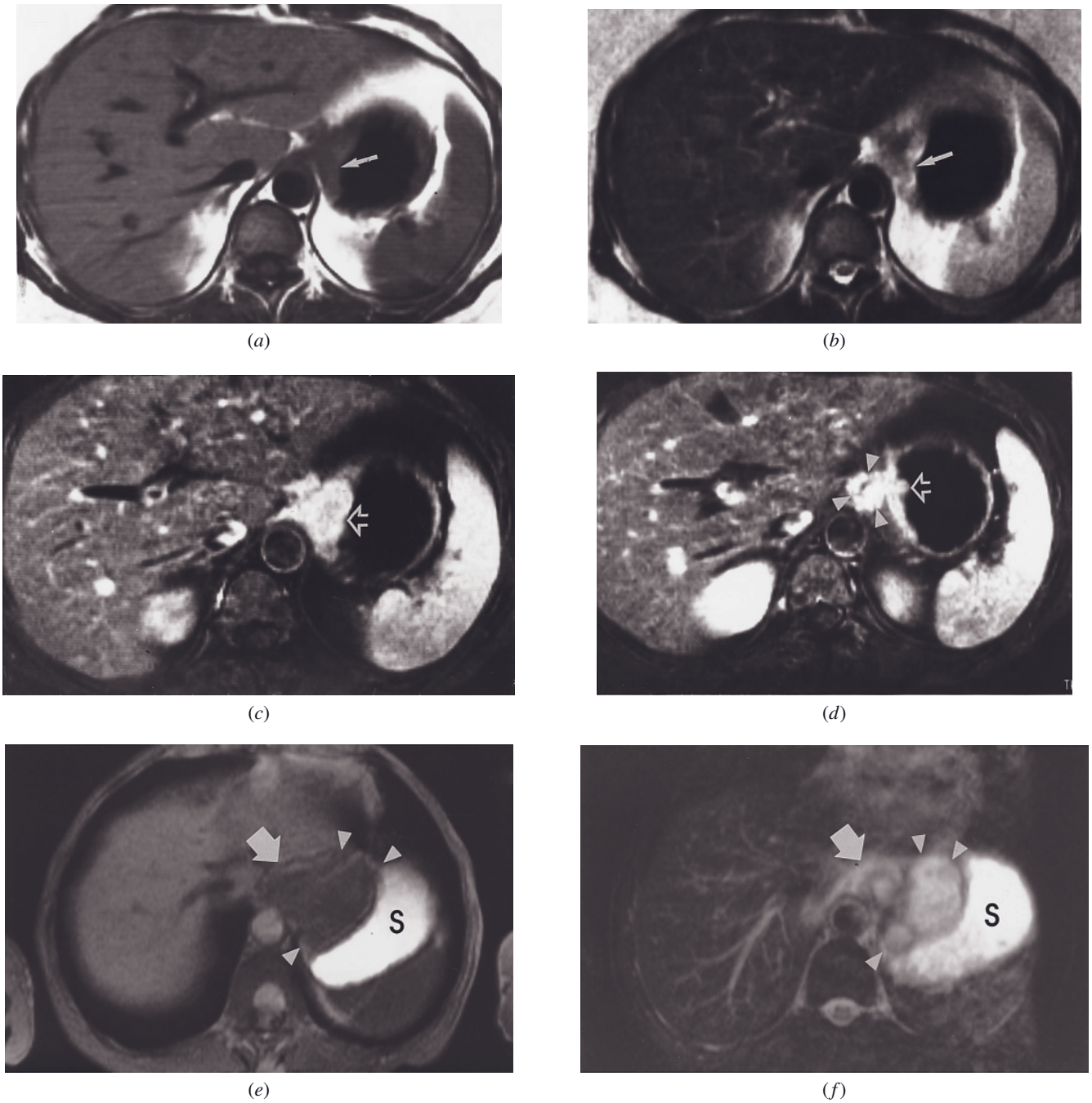

FIG. 6.17 Gastric adenocarcinoma, cardia. T1-weighted (*a*), T2-weighted (*b*), and gadolinium-enhanced T1-weighted fat-suppressed spin-echo (*c*, *d*) images in a patient with gastric cancer. The stomach has been distended with negative oral contrast agent. The gastric adenocarcinoma causes wall thickening medially, which is intermediate in signal intensity on the T1-weighted image (arrow, *a*) and heterogeneous and slightly hyperintense on the T2-weighted image (arrow, *b*). After intravenous gadolinium administration, the tumor (open arrows, *c*, *d*) enhances more than the normal stomach. The distal esophagus is also abnormally thickened with increased enhancement (arrowheads, *d*), which is consistent with spread across the gastroesophageal junction. SGE (*e*), T2-weighted fat-suppressed echo-train spin-echo (*f*), and immediate postgadolinium SGE (*g*) images in a second patient. The stomach (S, *e–g*) has been distended with a positive oral contrast agent. A large tumor in the cardia of the stomach (arrowheads, *e–g*) causes mass effect on the lumen. The cancer is low in signal intensity on the T1-weighted image (*e*) and heterogeneous and high in signal intensity on the T2-weighted image (*f*) and enhances heterogeneously after intravenous contrast (*g*). Note that

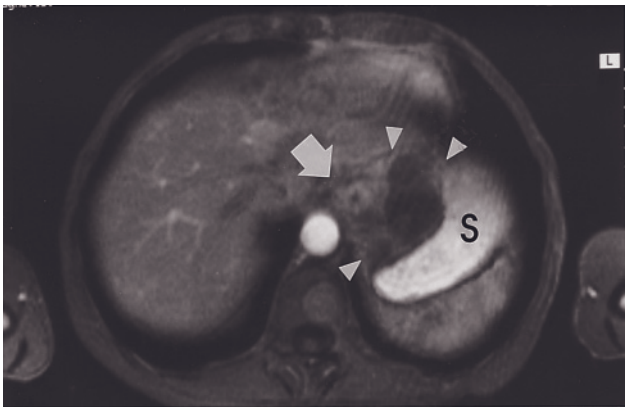

(*g*)

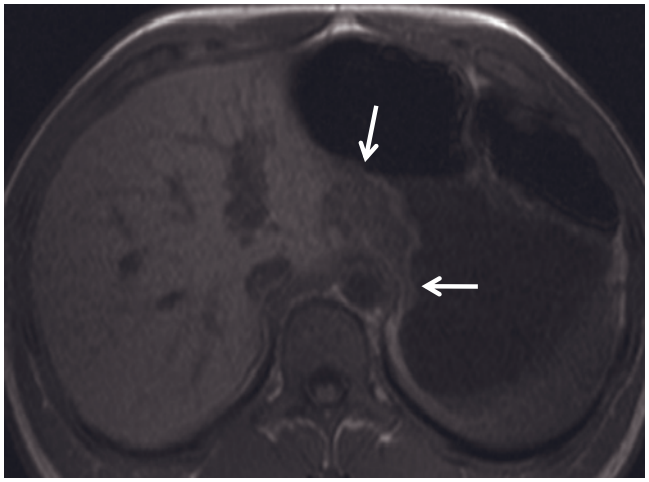

(*h*)

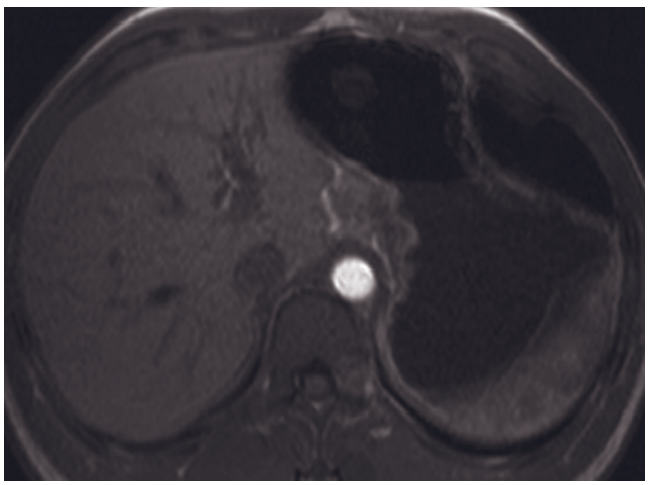

(*i*)

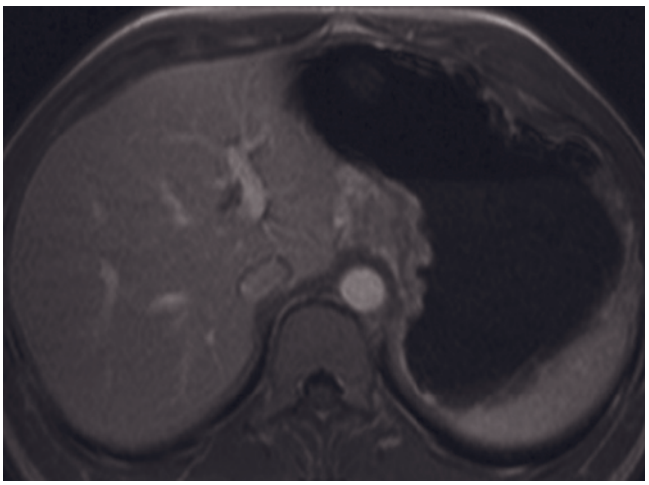

(*j*)

FIG. 6.17 (*Continued*) the tumor also involves the distal esophagus (large arrow, *e–g*). T1-weighted SGE (*h*), T1-weighted hepatic arterial phase (*i*), and hepatic venous phase (*j*) SGE images demonstrate ulcerated gastric adenocarcinoma (arrow, *h*) located in the cardia of the stomach in another patient. The tumor shows progressive enhancement on postgadolinium images.

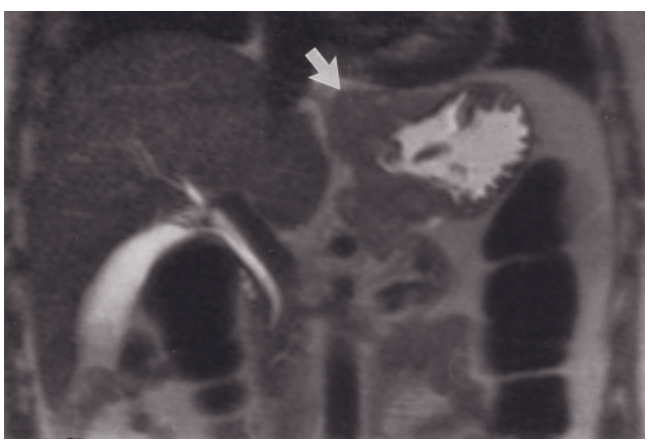

(*a*)

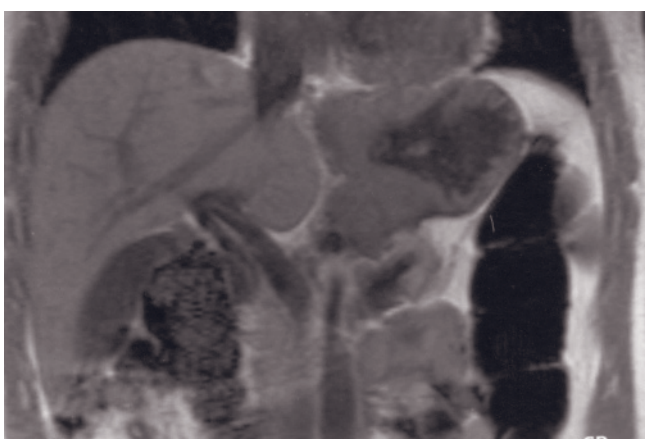

(*b*)

FIG. 6.18 Gastric adenocarcinoma, body. Coronal T2-weighted SS-ETSE (*a*), coronal precontrast SGE (*b*), transverse immediate postgadolinium SGE (*c*), and transverse 2-min postgadolinium fat-suppressed SGE (*d*) images. A circumferential low-signal-intensity mass is demonstrated in the body of the stomach. The high-signal-intensity fluid contents of the stomach permit good delineation of the low-signal-intensity mass on the T2-weighted SS-ETSE image (arrow, *a*). The mass is isointense to the stomach wall on the precontrast T1-weighted image (*b*). On the immediate postgadolinium image, the tumor (arrows, *c*) shows mild

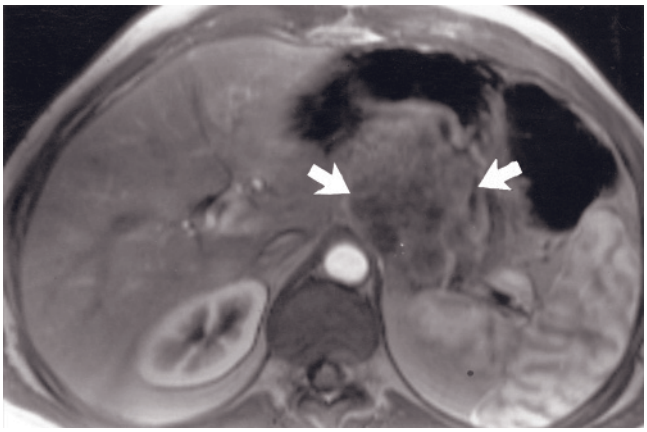

(*c*)

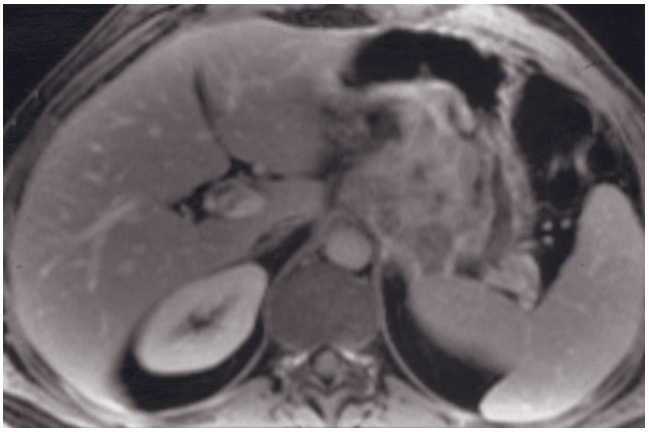

(*d*)

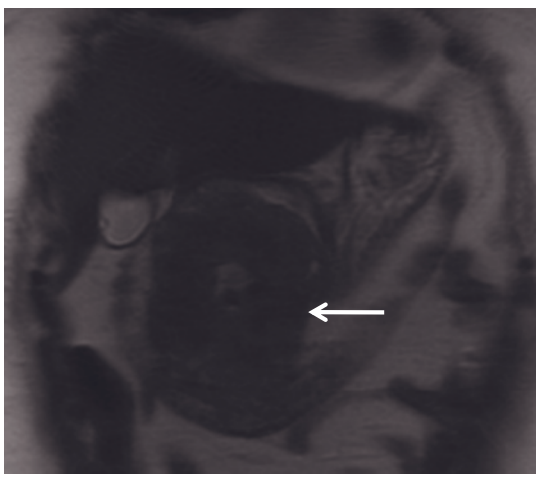

(*e*)

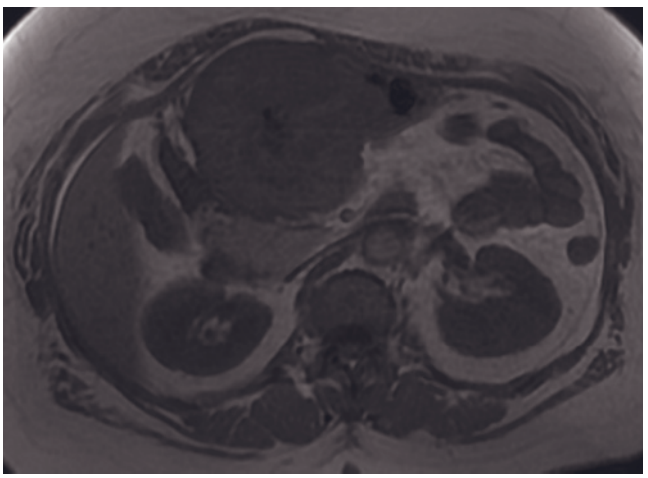

(*f*)

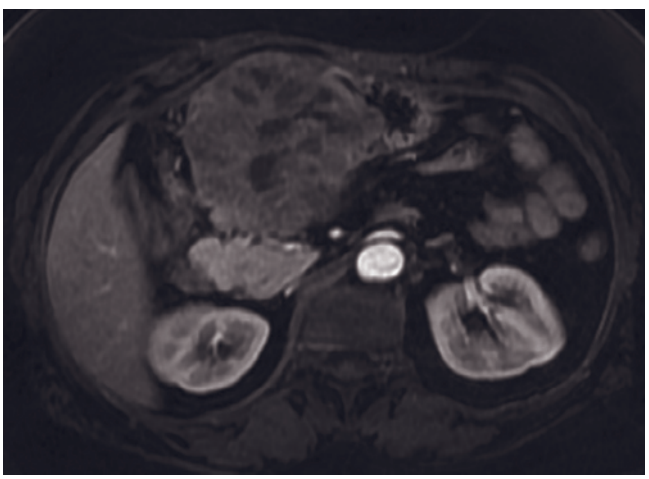

(*g*)

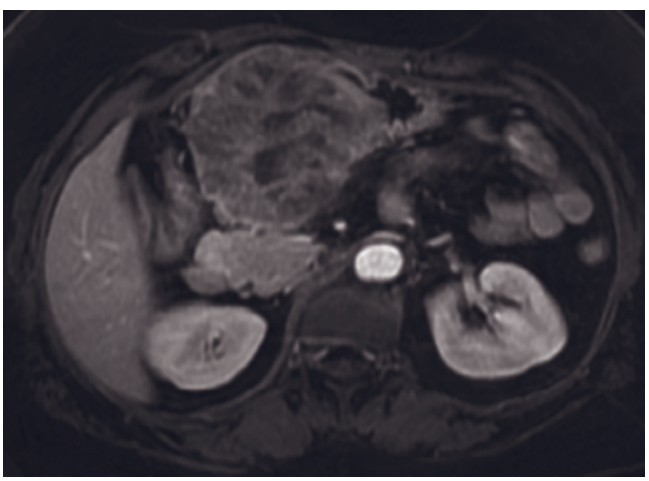

(*h*)

FIG. 6.18 (*Continued*) heterogeneous enhancement. On 2-min postgadolinium image (*d*), the tumor continues to enhance but to a lesser extent and heterogeneously compared to the remainder of the gastric wall. Note the intense enhancement of the normal renal cortex, which is greater than the enhancement of gastric wall or tumor. (Reprinted with permission from Marcos HB, Semelka RC: Stomach diseases: MR evaluation using combined T2-weighted single-shot echo train spin-echo and gadolinium-enhanced spoiled gradient-echo sequences. *J Magn Reson Imaging* 10: 950–960, 1999.) Coronal T2-weighted single shot echo train spin echo (*e*), transverse T1-weighted SGE (*f*), transverse postgadolinium fat-suppressed hepatic arterial dominant phase (*g*) and hepatic venous phase (*h*) 3D-GE images demonstrate a large adenocarcinoma (arrow, *e*) located in the body of the stomach in another patient. The exophytic tumor shows continuity with the stomach wall, and it displaces the transverse colon along its interface with transverse colon. The tumor is also adjacent to the pancreatic head, which is located posteriorly. The tumor demonstrates low signal on pre-contrast images (*e*, *f*). Progressive heterogeneous enhancement of the tumor is detected on postgadolinium images (*g*, *h*). Central necrosis is also present. Note that the tumor mimics gastrointestinal stromal tumor.

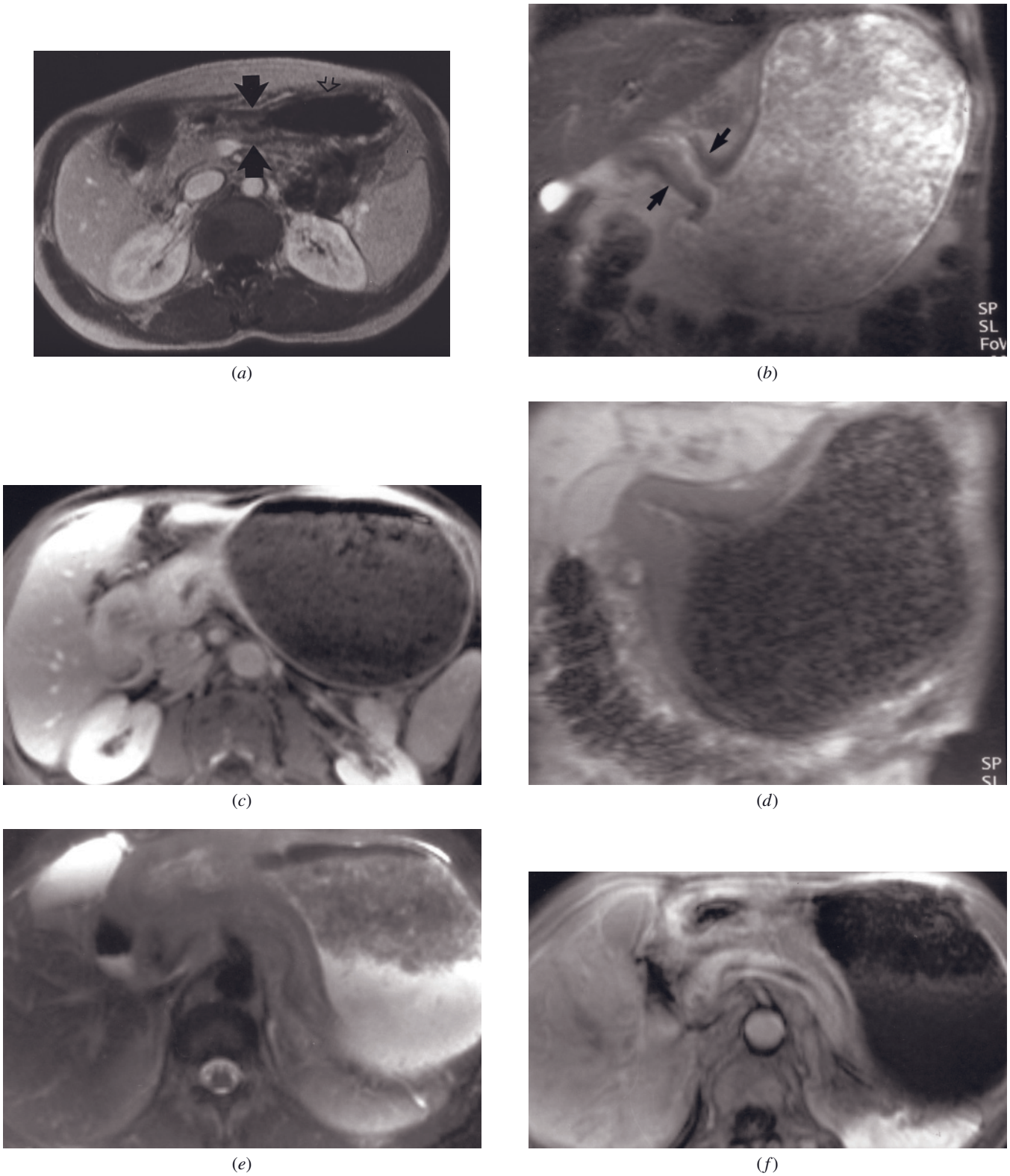

FIG. 6.19 Gastric adenocarcinoma, antrum. Transverse 45-s postgadolinium SGE image (*a*) demonstrates thickening and increased enhancement of the antrum secondary to gastric carcinoma (solid arrows, *a*). The remaining normal stomach has a thin wall (open arrow, *a*). Coronal SS-ETSE (*b*) and transverse interstitial-phase gadolinium-enhanced SGE (*c*) images in a second patient with antral tumor demonstrate a large, distended, debris-filled stomach secondary to gastric outlet obstruction. Note the substantial thickening and increased enhancement with gadolinium (*c*) of the antrum (arrows, *b*). Coronal (*d*) and transverse (*e*) T2-weighted SS-ETSE and transverse interstitial-phase gadolinium-enhanced fat-suppressed SGE (*f*) images in a third patient also show circumferential thickening and increased enhancement of the gastric antrum, with marked distension of the stomach.

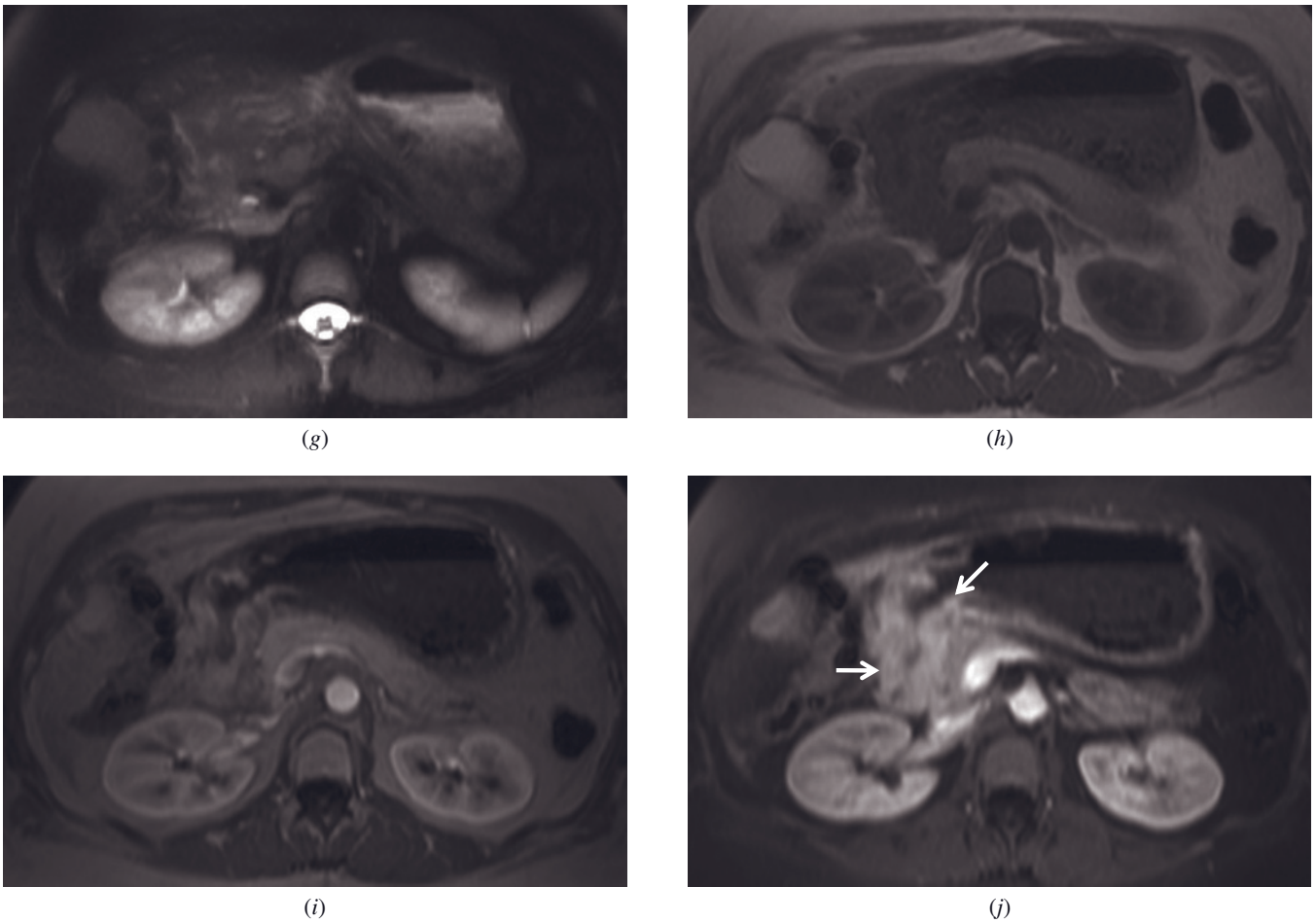

FIG. 6.19 (*Continued*) T2-weighted single-shot echo-train spin-echo (*g*), T1-weighted SGE (*h*), T1-weighted postgadolinium hepatic arterial dominant-phase SGE (*i*), and T1-weighted postgadolinium hepatic venous phase fat-suppressed 3D-GE (*j*) images demonstrate gastric adenocarcinoma (arrows, *j*) in the antrum in another patient. The wall of the antrum is thickened and shows intense enhancement due to tumoral involvement. The tumor extends into the duodenal wall. Note that the stomach is moderately dilated because of outlet obstruction.

aggressive tumor behavior. The necrotic portions of the tumor remain signal void on postcontrast images. Dynamic gadolinium-enhanced T1-weighted imaging also detects hepatic metastases. The hypervascular lesions show early ring or uniform enhancement, which rapidly becomes isointense with normal hepatic parenchyma. Low-grade tumors enhance to a lesser extent than higher-grade tumors (fig. 6.27). GIST of the stomach may be submucosal, intramural, or subserosal; subserosal lesions may be predominantly exophytic, and their origin from the gastric wall may not be apparent on radiologic evaluation [45]. In the Hasegawa series, the gastric origin of the tumor was uncertain in three of nine cases because of the large exophytic component, relatively small gastric pedicle, and absence of mucosal invasion. It is therefore prudent to consider the possibility of GIST for any large tumor with central necrosis and hemorrhage that may appear radiologically to only abut the stomach.

Kaposi Sarcoma. Kaposi sarcoma most commonly occurs in immunocompromised patients, usually AIDS patients or recipients of organ transplantation. Grossly, the lesions of gastrointestinal tract Kaposi sarcoma consist of solitary, but frequently multiple, submucosal nodules. Microscopically, tumor is characterized by proliferation of spindle cells admixed with numerous vascular channels and red blood cell extravasation. Although approximately 50% of patients with AIDS-related Kaposi sarcoma will have gastrointestinal lesions at autopsy, most patients are asymptomatic. In rare instances, gastrointestinal Kaposi sarcoma may cause obstruction, intussusception, or hemorrhage. The stomach is the most common site of gut involvement,

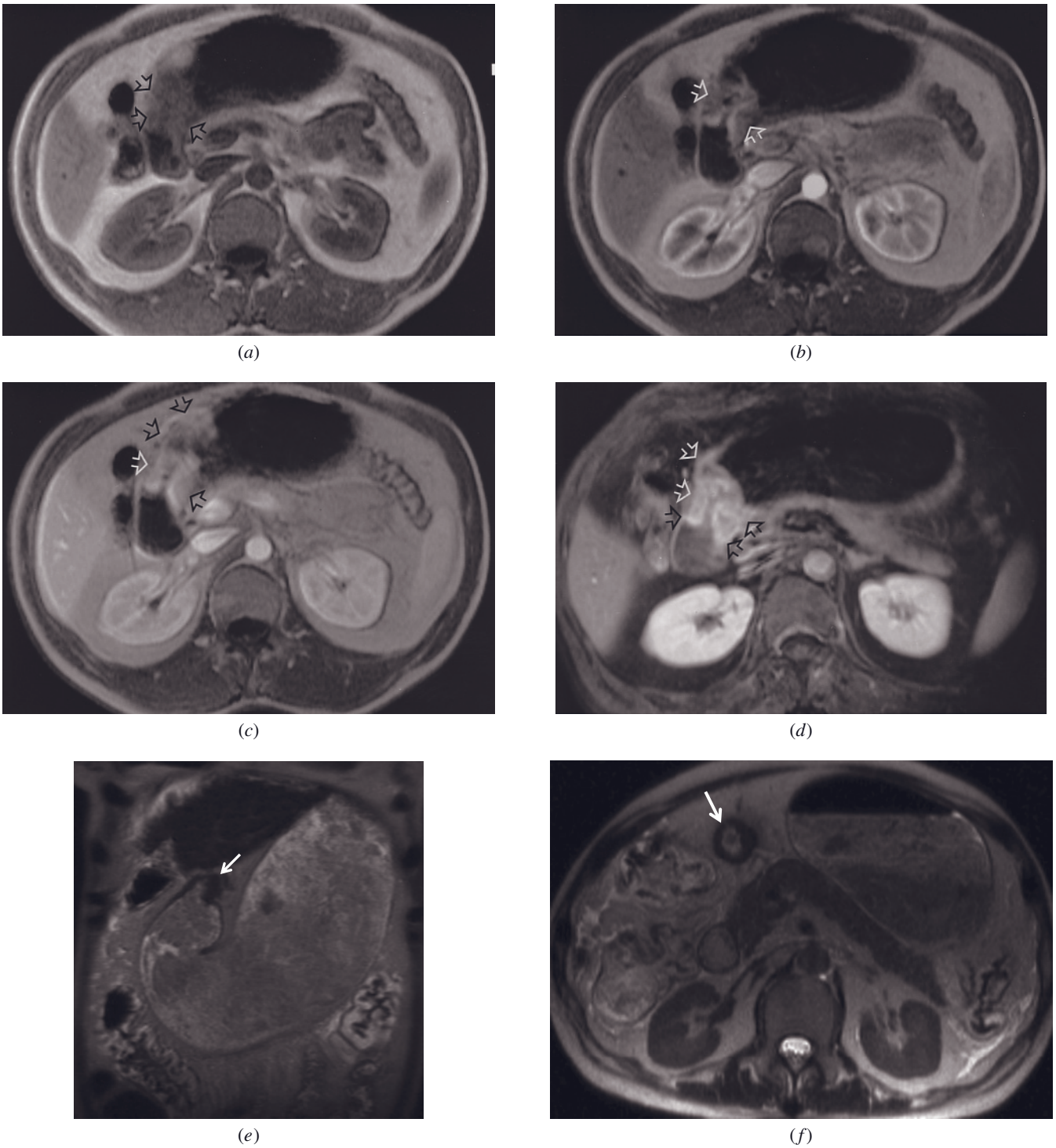

FIG. 6.20 Gastric adenocarcinoma, pylorus. SGE (*a*), 1-s (*b*) and 45-s (*c*) postgadolinium SGE, and interstitial-phase gadolinium-enhanced T1-weighted fat-suppressed spin-echo (*d*) images. A circumferential pyloric channel adenocarcinoma with duodenal extension (arrows, *a–d*) is present. The tumor enhances heterogeneously (*b*) and increases in signal intensity on the 3-min interstitial-phase image (*d*). This reflects accumulation of contrast in the interstitial space of the tumor. Coronal (*e*) and transverse (*f*) T2-weighted single-shot echo-train spin-echo images demonstrate gastric adenocarcinoma of the pylorus in another patient. The wall of the pylorus is thickened (arrows; *e*, *f*) because of tumoral involvement. Note that the stomach is dilated because of outlet obstruction and there is small amount of free fluid in the abdomen.

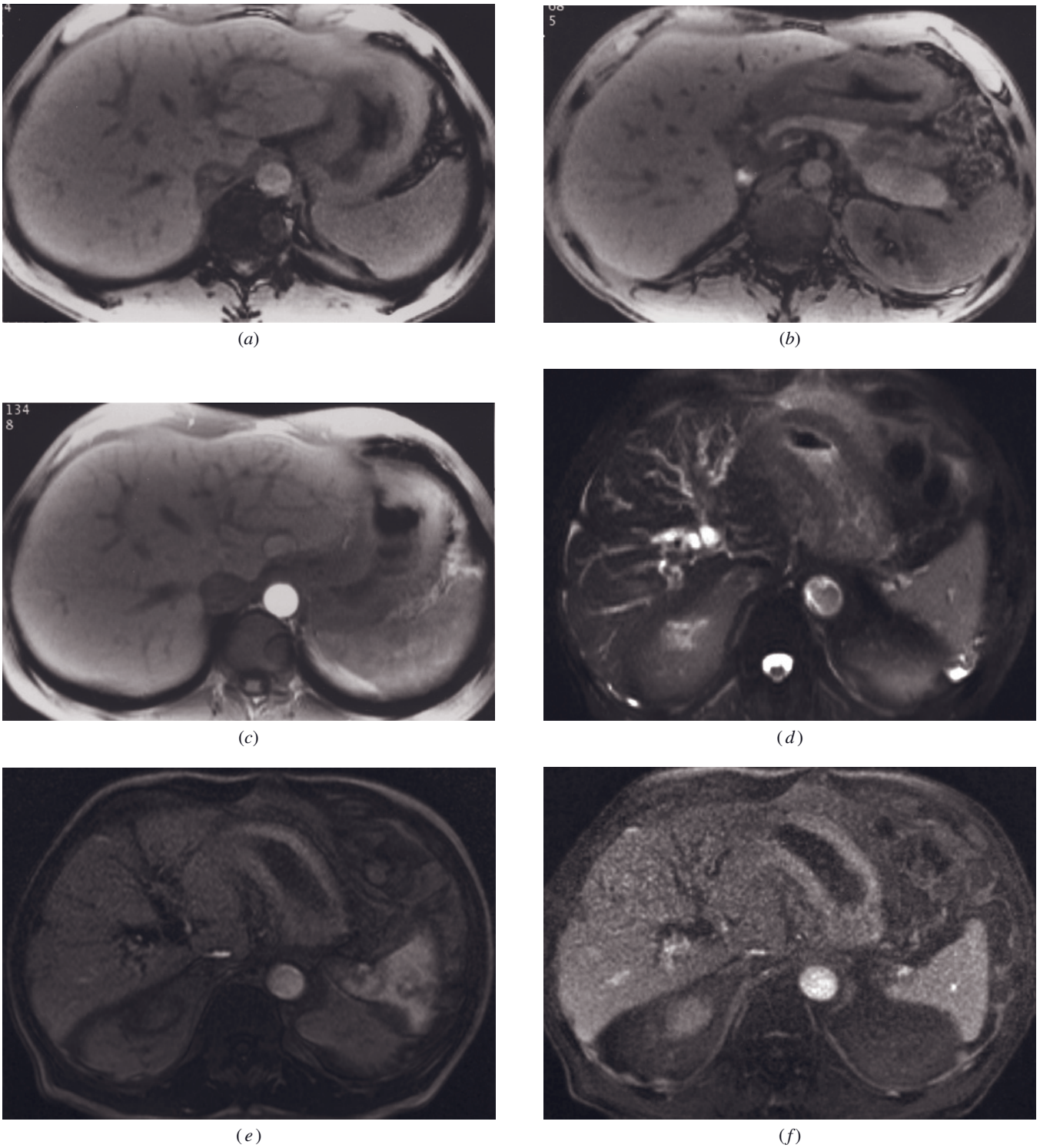

FIG. 6.21 Gastric adenocarcinoma, linitis plastica. Fat-suppressed SGE (*a*, *b*) and immediate postgadolinium SGE (*c*) images. Diffuse relatively homogeneous gastric wall thickening is present (*a*, *b*). Minimal enhancement is appreciated on the immediate postgadolinium SGE image (*c*). Transverse T2-weighted single-shot echo-train spin-echo (*d*) and T1-weighted postgadolinium magnetization-prepared gradient-echo (MPRAGE) transverse (*e*, *f*) and coronal (*g*) images demonstrate linitis plastica in

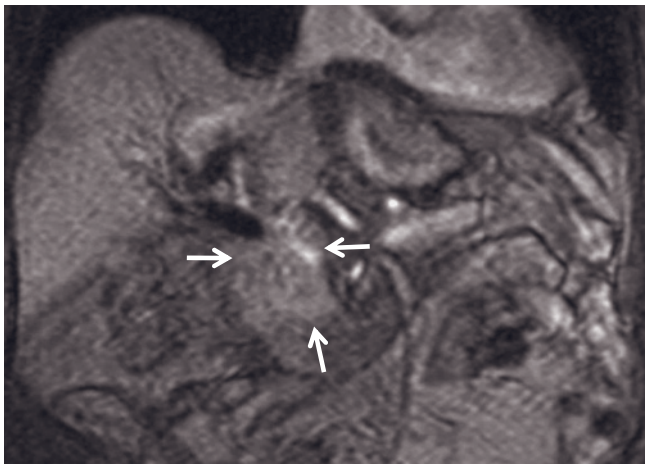

(*g*)

FIG. 6.21 (*Continued*) another patient. The gastric wall is diffusely thickened and shows diffuse enhancement. Note that the bile ducts are dilated because of the tumor (arrows, *g*) invasion.

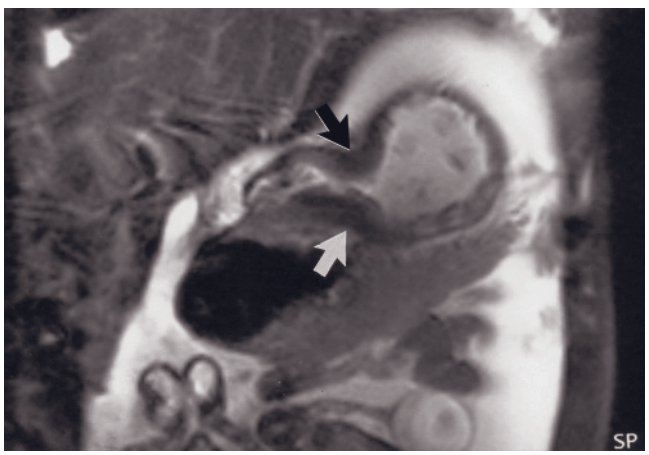

(*a*)

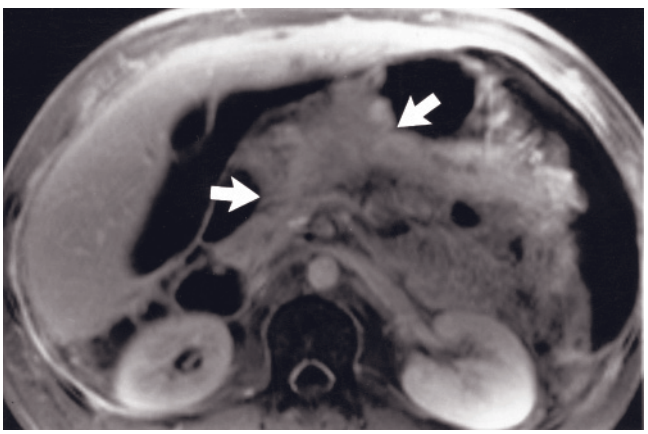

(*b*)

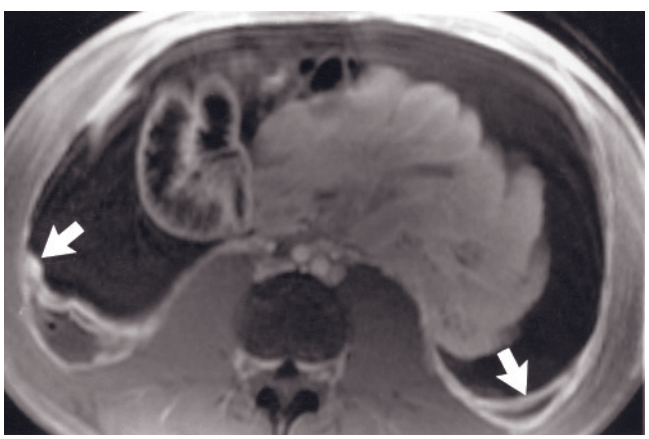

(*c*)

FIG. 6.22 Gastric adenocarcinoma with extensive carcinomatosis. Coronal T2-weighted SS-ETSE (*a*) image and transverse 2-min postgadolinium fat-suppressed SGE images at more superior (*b*) and inferior (*c*) tomographic levels. Diffuse thickening of a low-signal-intensity gastric wall is appreciated (arrows, *a*). Ascites is shown as high-signal-intensity intraperitoneal fluid on the T2-weighted image (*a*). The gastric tumor (arrows, *b*) is mildly enhanced on the 2-min postgadolinium image (*b*) compared to gastric wall. At a lower tomographic level (*c*), intense peritoneal enhancement (arrows, *c*) with nodules is shown, representing peritoneal metastases. (Reprinted with permission from Marcos HB, Semelka RC: Stomach diseases: MR evaluation using combined T2-weighted single-shot echo train spin-echo and gadolinium-enhanced spoiled gradient-echo sequences. *J Magn Reson Imaging* 10: 950–960, 1999.)

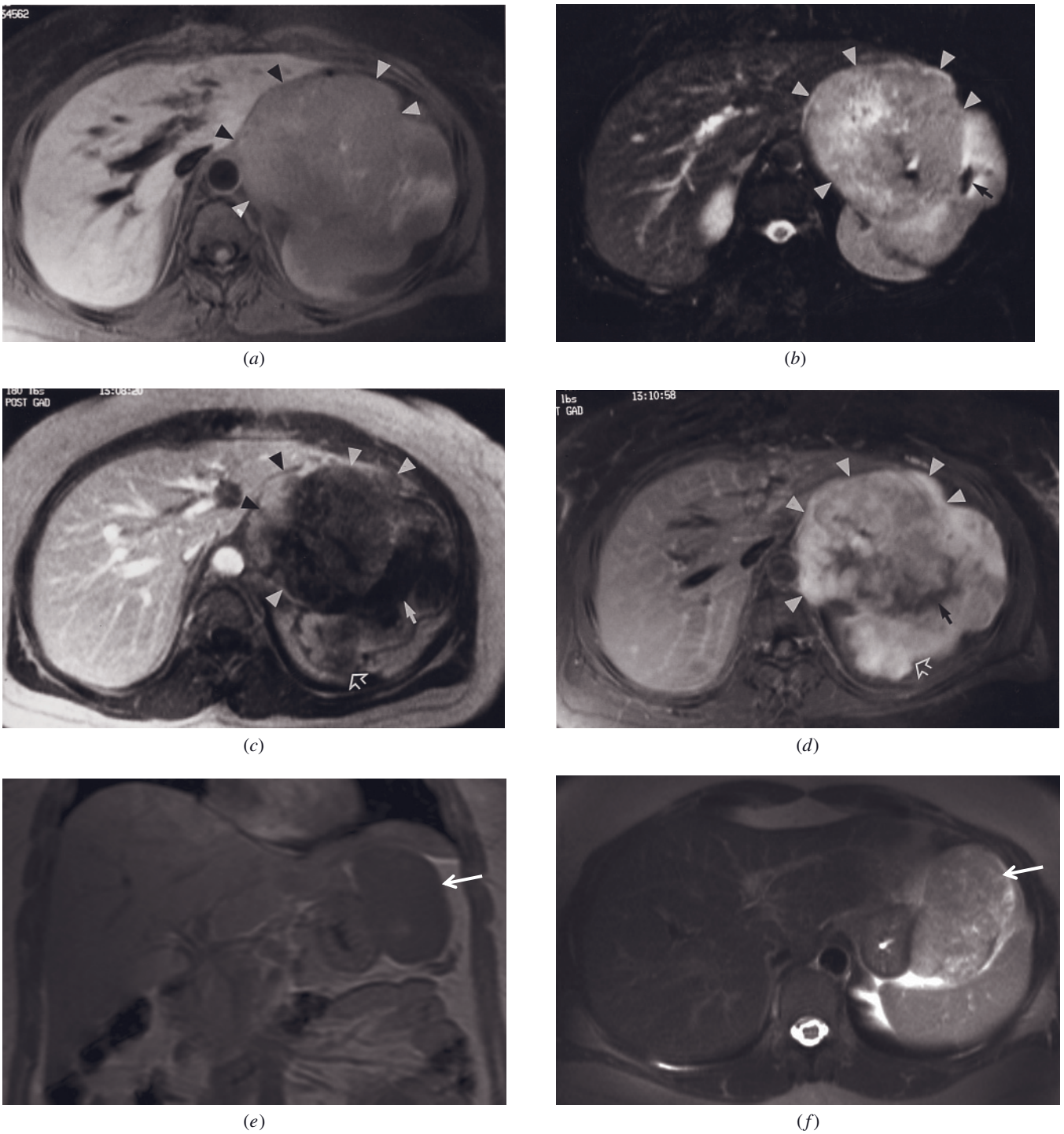

FIG. 6.23 Gastrointestinal stromal tumor (GIST). T1-weighted fat-suppressed spin-echo (*a*), T2-weighted fat-suppressed spin-echo (*b*), 45-s postgadolinium SGE (*c*), and gadolinium-enhanced fat-suppressed spin-echo (*d*) images. A large exophytic GIST arises from the lesser curvature (arrowheads, *a–d*) and is contiguous with the spleen. The tumor is heterogeneous and high in signal intensity on the T2-weighted image (*b*) and enhances intensely (*c*, *d*). Enhancing tumor extends adjacent to the spleen (open arrow, *c*, *d*). Signal-void areas within the tumor are consistent with necrosis. Air within the gastric lumen is also signal void (solid arrow, *b–d*). Coronal T1-weighted SGE (*e*), transverse T2-weighted single-shot echo-train spin-echo (*f*), and transverse T1-weighted postgadolinium hepatic venous phase fat-suppressed 3D-GE (*g*) images at 3.0 T demonstrate an exophytic GIST (arrows, *e–g*) arising from the greater curvature of the stomach in another patient. The tumor shows low signal on T1-weighted image (*e*), mildly high signal on T2-weighted image (*f*), and mild enhancement on postgadolinium image (*g*). CT (*h*), T2-weighted fat-suppressed

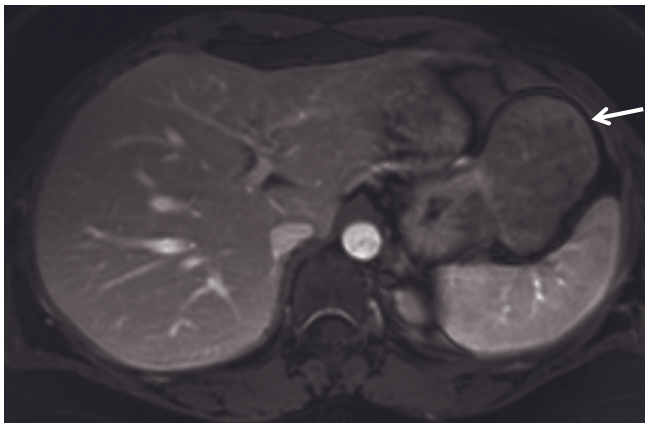

(*g*)

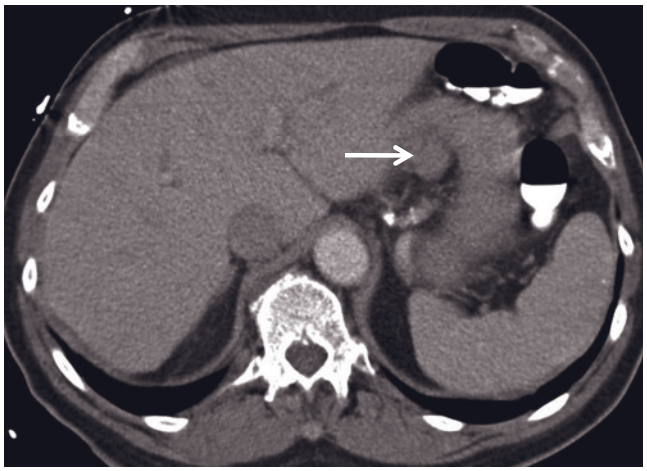

(*h*)

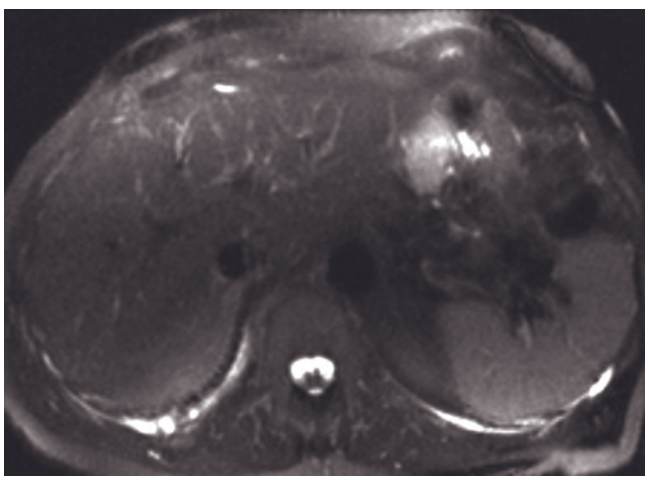

(*i*)

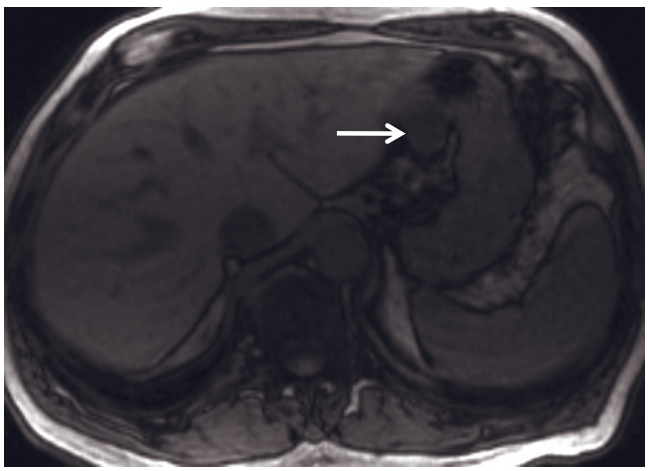

(*j*)

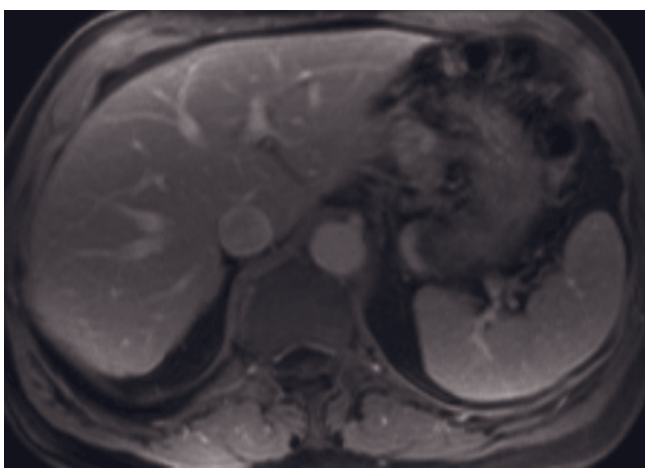

(*k*)

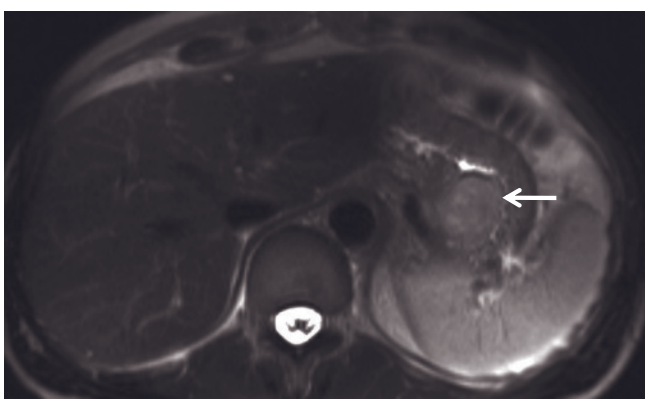

(*l*)

Fig. 6.23 (*Continued*) single-shot echo-train spin-echo (*i*), T1-weighted out-of-phase SGE (*j*), and T1-weighted postgadolinium hepatic venous phase fat-suppressed 3D-GE (*k*) images demonstrate subserosal GIST (arrows, *h*, *j*) arising from the lesser curvature in another patient. The tumor shows high signal on T2-weighted image (*i*), low signal on T1-weighted image (*j*), and prominent enhancement on postgadolinium image (*k*). T2-weighted single-shot echo-train spin-echo (*l*), T1-weighted SGE (*m*), T1-weighted

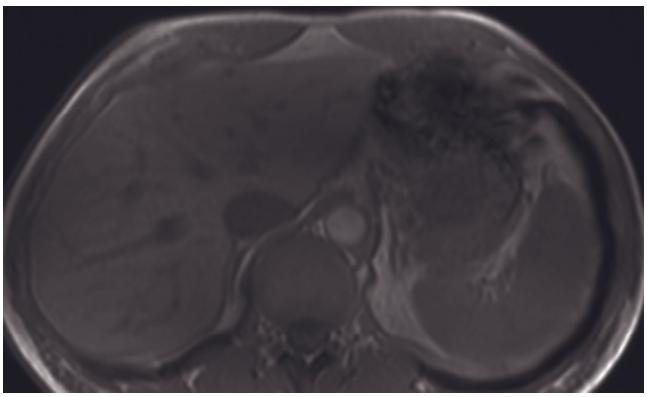

(*m*)

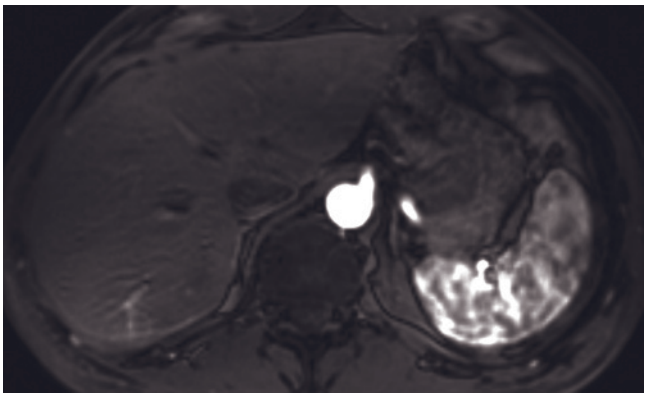

(*n*)

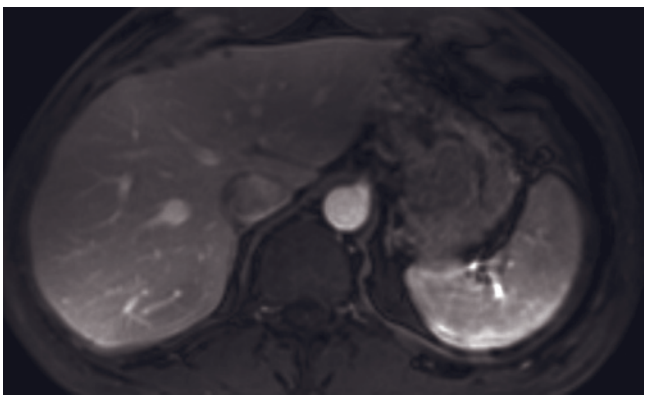

(*o*)

FIG. 6.23 (*Continued*) postgadolinium fat-suppressed hepatic arterial dominant phase (*n*), and hepatic venous phase (*o*) 3D-GE images at 3.0 T demonstrate submucosal GIST (arrow, *l*) protruding into the lumen of the stomach in another patient. The tumor shows high signal on T2-weighted image (*l*), low signal on T1-weighted image (*m*), and mild enhancement on postgadolinium images (*n*).

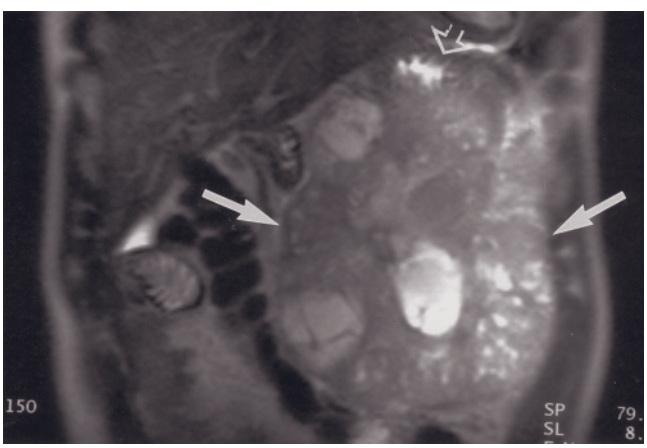

(*a*)

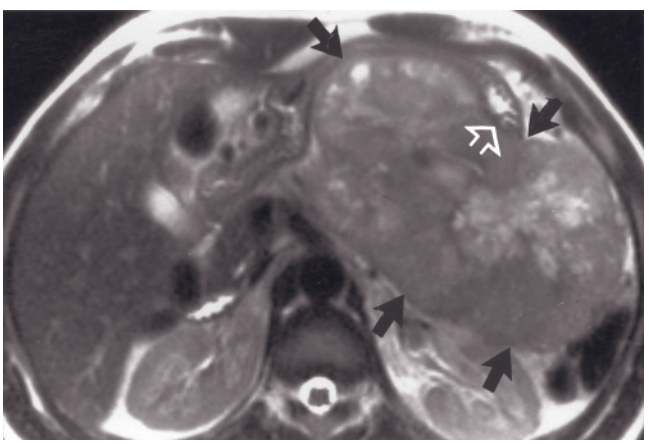

(*b*)

FIG. 6.24 Gastrointestinal stromal tumor (GIST). Coronal (*a*) and transverse (*b*) T2-weighted SS-ETSE, immediate postgadolinium SGE (*c*), and 90-s postgadolinium fat-suppressed SGE (*d*) images. A large multilobulated tumor (arrows, *a*, *b*) measuring 18 × 16 × 13 cm is shown arising from the gastric wall (open arrow, *a*, *b*). Multiple internal foci of high signal intensity are seen, representing areas of hemorrhage and necrosis. On the immediate postgadolinium image (*c*), the tumor enhances heterogeneously

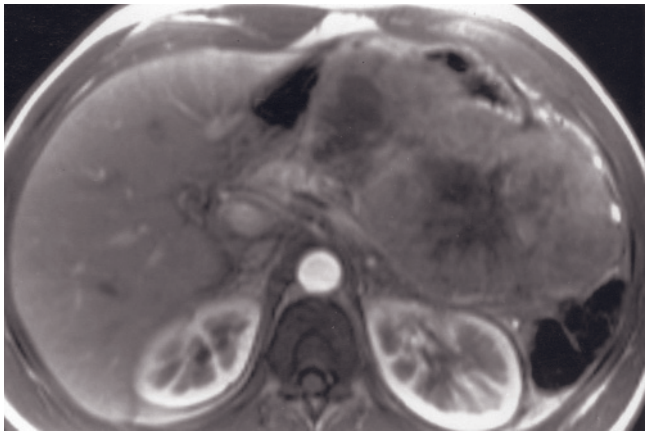

(*c*)

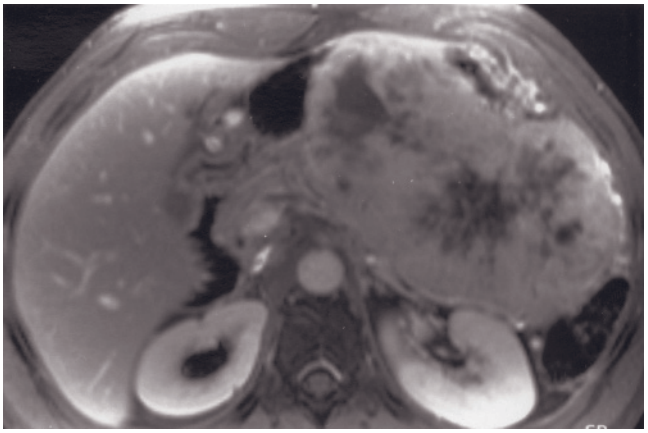

(*d*)

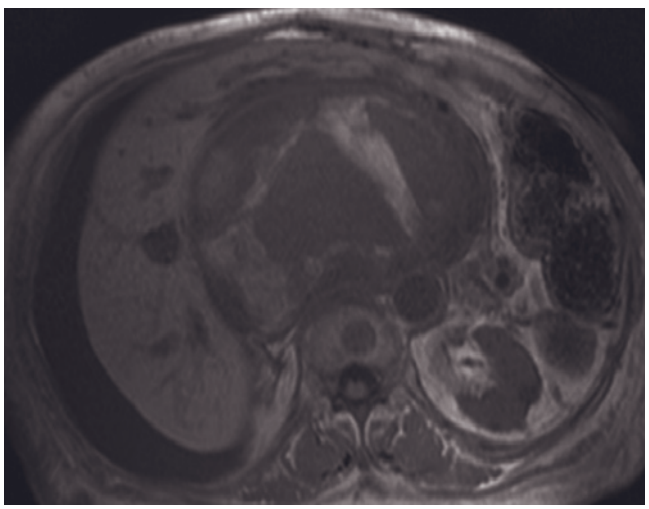

(*e*)

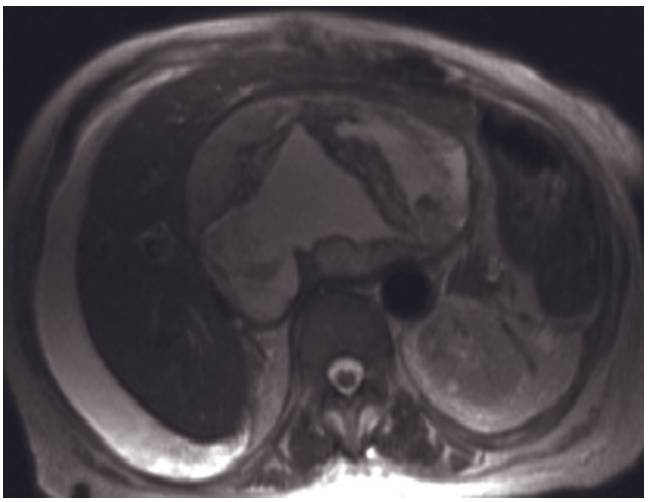

(*f*)

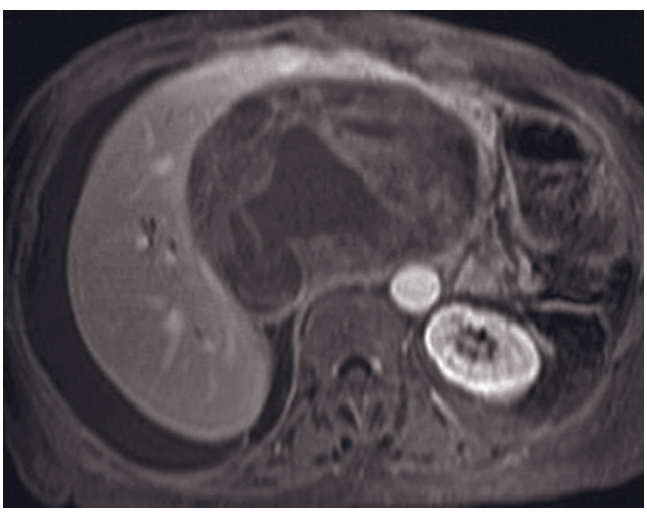

(*g*)

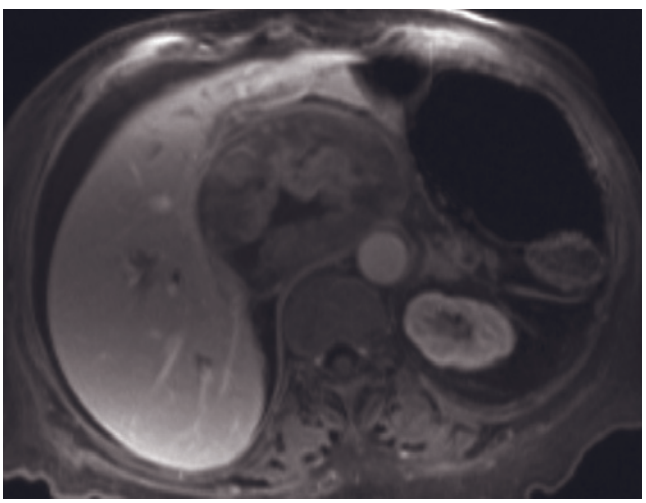

(*h*)

FIG. 6.24 (*Continued*) and is mildly hyperintense. On the 90-s fat-suppressed SGE image (*d*), increased heterogeneous enhancement of the mass is shown, which contains nonenhancing areas of necrosis and hemorrhage. (Reprinted with permission from Marcos HB, Semelka RC: Stomach diseases: MR evaluation using combined T2-weighted single-shot echo train spin-echo and gadolinium-enhanced spoiled gradient-echo sequences. *J Magn Reson Imaging* 10: 950–960, 1999.) T1-weighted SGE (*e*), T2-weighted single-shot echo-train spin-echo (*f*) and T1-weighted postgadolinium fat-suppressed interstitial-phase 3D-GE (*g*) images demonstrate a GIST arising from the stomach in another patient. The tumor is very heterogeneous and contains hemorrhagic and necrotic foci. Hemorrhagic foci show high signal on T1-weighted image (*e*) and heterogeneously low signal on T2-weighted image (*f*). Necrotic foci show low signal on T1-weighted image (*e*) and high signal on T2-weighted image (*f*). The tumor shows heterogeneous enhancement on postgadolinium image (*g*). Note that there is peritoneal enhancement and ascites, which are consistent with metastatic peritoneal disease. The tumor displaces the IVC and aorta laterally and the liver anteriorly. After chemotherapy, the tumor shows decrease in size (*h*).

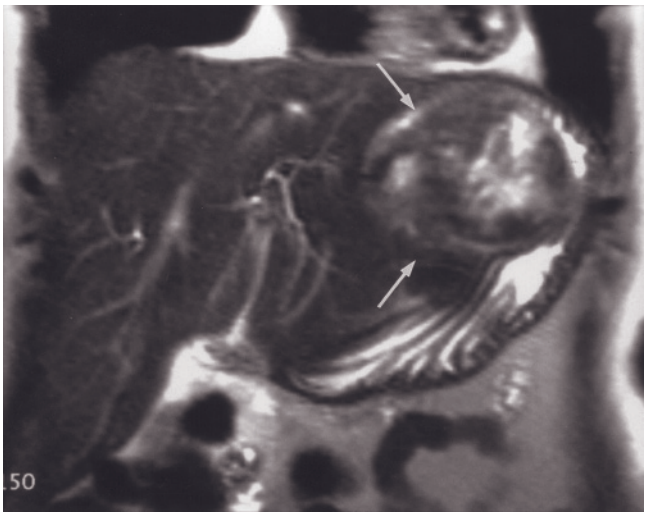

(*a*)

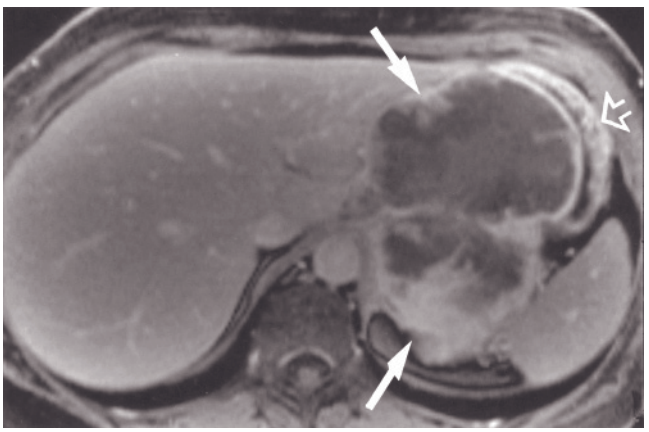

(*b*)

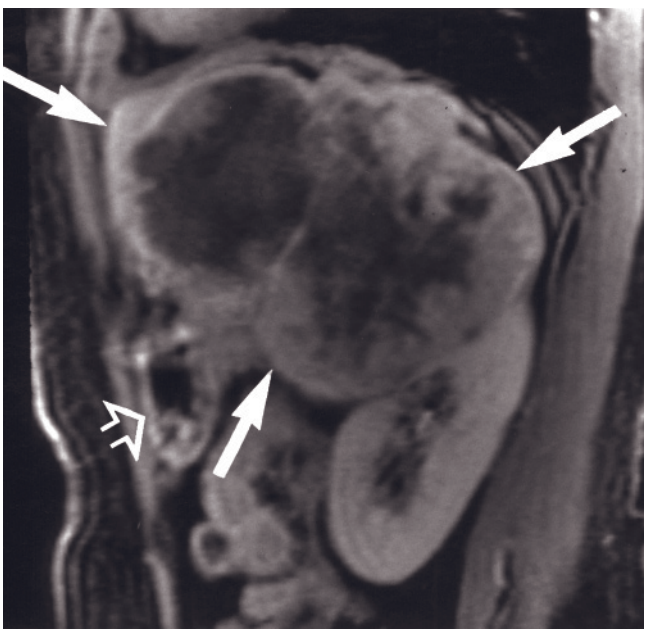

(*c*)

FIG. 6.25 High-grade GIST. Coronal T2-weighted SS-ETSE (*a*) and transverse (*b*) and sagittal (*c*) 2- to 3-min gadolinium-enhanced fat-suppressed SGE images. A large, heterogeneous tumor (arrows, *a–c*) arises from the gastric fundus and body. The lesion has ill-defined margins that correspond to high-grade cellular features seen at histopathologic examination. The stomach (open arrow, *b*, *c*) is compressed and deviated by the mass.

but lesions may occur throughout the gastrointestinal tract. Kaposi sarcoma should be considered in an AIDS patient who has gastrointestinal lesions in concert with bulky retroperitoneal lymphadenopathy, hepatic and splenic lesions, and infiltration of the psoas or abdominal wall [46].

Lymphoma. Primary gastric lymphoma is rare. Hodgkin lymphomas and non-Hodgkin lymphomas (NHL) are more commonly observed in the context of disseminated disease. Approximately 50% of gastrointestinal NHL arise in the stomach, 40% in the small intestine, and 10% in the colon [47]. Infiltration of the gastric wall by tumor cells results in diffuse mural thickening [48, 49]. Non-Hodgkin lymphoma often preserves gastric distensibility, whereas Hodgkin lymphoma mimics the diffusely infiltrating form of primary gastric adenocarcinoma (linitis plastica): a desmoplastic reaction predominates, leading to a noncompliant aperistaltic viscus. Diffuse gastric wall thickening is best seen on single-shot echo-train spin-echo and gadolinium-enhanced fat-suppressed SGE or 3D-GE images (fig. 6.28). Involved regional lymph nodes also can be identified with these techniques.

Carcinoid. These tumors were first described by Obendorfer in 1907 as *karzinoide* (resembling carcinoma) because, despite their malignant potential, they

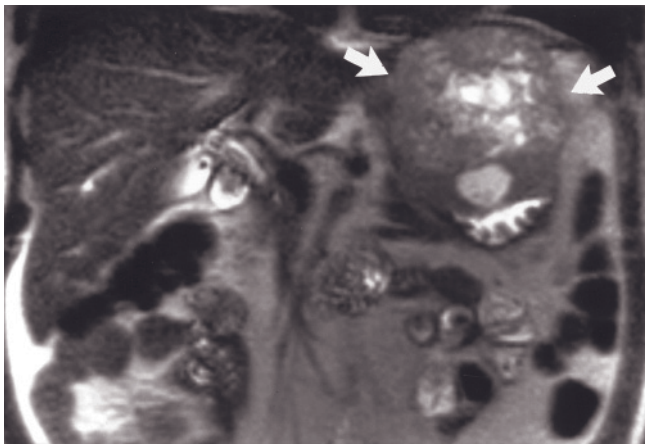

(*a*)

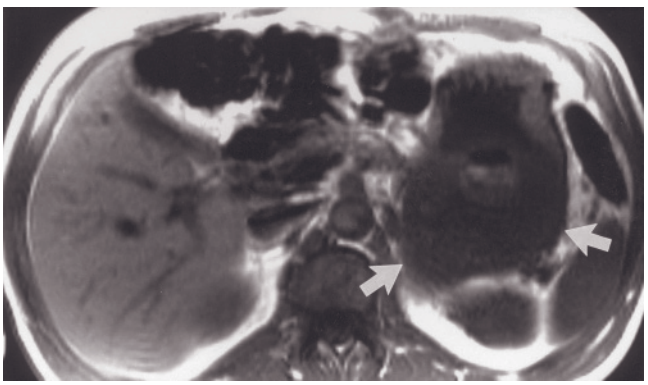

(*b*)

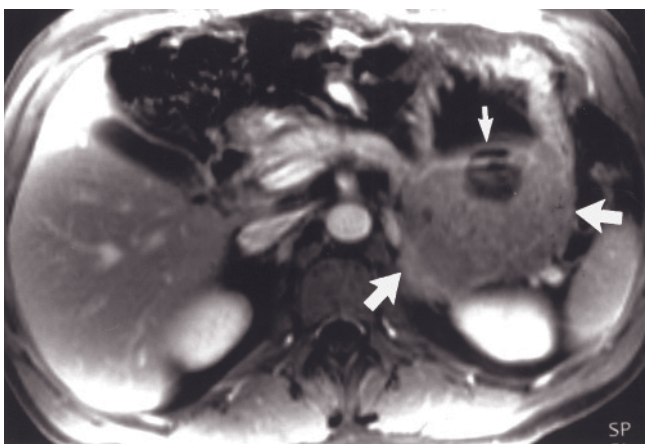

(*c*)

FIG. 6.26 Intermediate- to high-grade GIST. Coronal T2-weighted SS-ETSE (*a*), SGE (*b*), and 90-s gadolinium-enhanced fat-suppressed SGE (*c*) images. A large mass is seen (arrows, *a–c*) arising from the posterosuperior aspect of the gastric fundus. The tumor has heterogeneous signal intensity, contains hemorrhagic foci, and demonstrates moderate signal intensity. The mass has a long interface with the left hemidiaphragm and surrounding organs, but there is no evidence of deep invasion. A dominant necrotic focus is evident that represents an ulcer crater (small arrow, *c*).

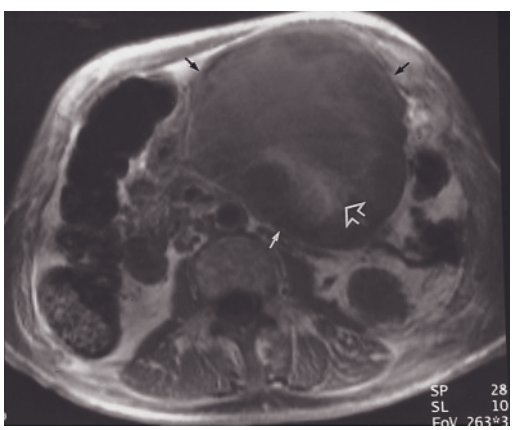

(*a*)

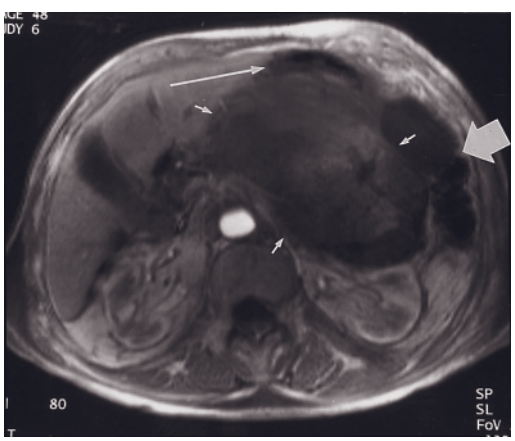

(*b*)

FIG. 6.27 Gastrointestinal stromal tumor (GIST), low grade. Transverse SGE (*a*), immediate postgadolinium SGE (*b*), and 90-s postgadolinium fat-suppressed SGE (*c*, *d*) images in a low-grade GIST (short arrows, *a–d*). On the precontrast image, high signal within the tumor represents hemorrhage (open arrow, *a*). Low-grade GISTs enhance minimally after intravenous contrast. The tumor causes mass effect on the remaining stomach (long arrows, *b*, *c*) and the adjacent colon (large arrows, *b*, *c*).

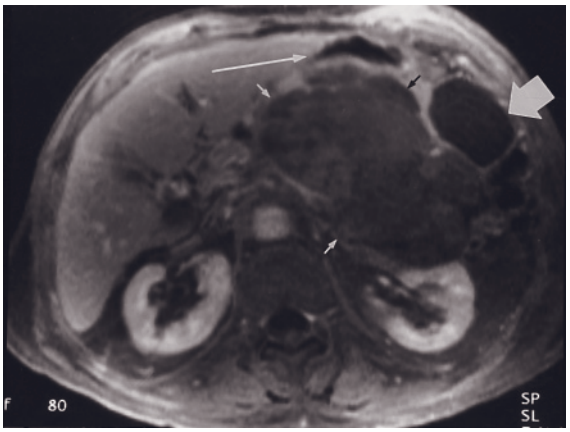

(*c*)

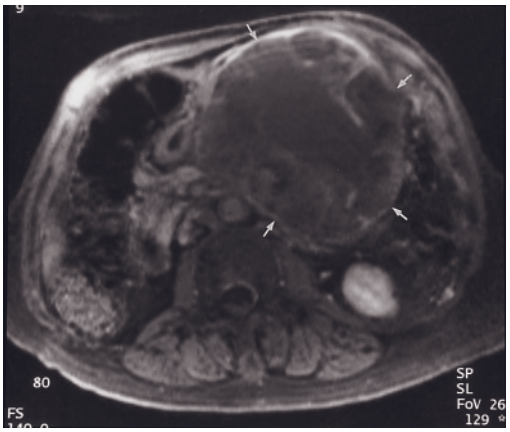

(*d*)

FIG. 6.27 (*Continued*)

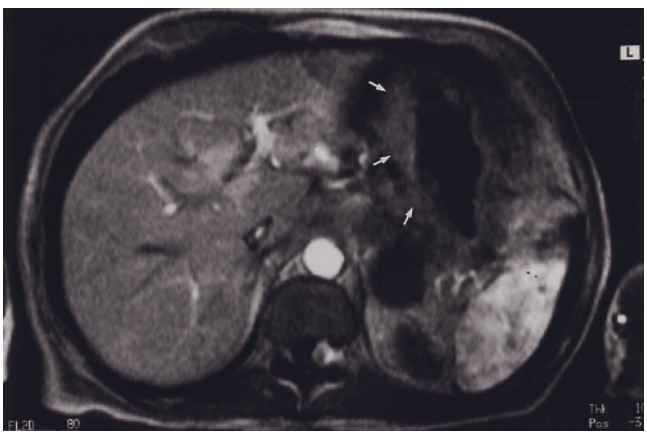

(*a*)

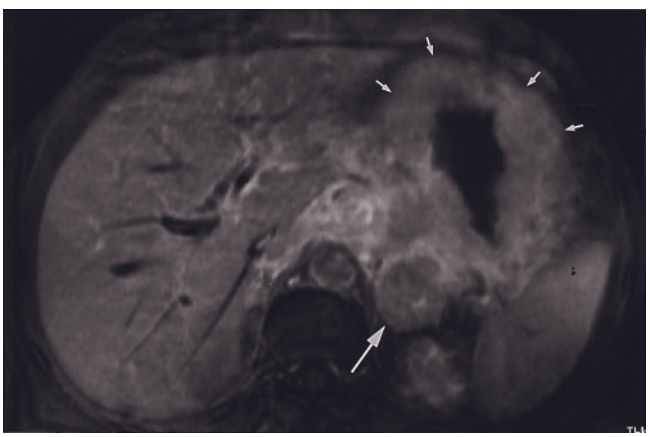

(*b*)

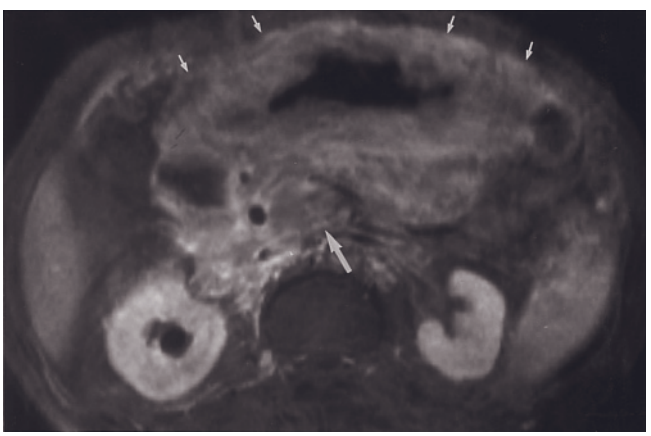

(*c*)

FIG. 6.28 Non-Hodgkin lymphoma of the stomach. Immediate postgadolinium SGE (*a*) and gadolinium-enhanced T1-weighted fat-suppressed spin-echo (*b*, *c*) images. There is diffuse circumferential lymphomatous infiltration of the stomach wall (short arrows, *a*–*c*). Lymphoma extends to the left adrenal gland (long arrow, *b*). At a lower tomographic section, prominent retroperitoneal lymphadenopathy is present (arrow, *c*), which is commonly observed in the setting of gastric lymphoma.

exhibited slow growth patterns and were slow to metastasize. Carcinoids are best characterized as well-differentiated neuroendocrine neoplasms that occur most commonly in the appendix and small intestine (see discussion under small intestine). Gastric carcinoids are divided into two basic clinicopathologic categories, depending on whether they arise in the presence or absence of chronic atrophic gastritis [50].

Gastrin is secreted in a normal physiologic state by G cells in the gastric antrum. Secretion rates are normally controlled by gastric acid levels (mainly hydrochloric acid secretion by parietal cells in the fundus). When hydrochloric acid levels decrease, as occurs in the setting of chronic atrophic gastritis, increased secretion by G cells causes hypergastrinemia. Gastrin acts as a trophic factor to neuroendocrine-like cells in the fundic mucosa, resulting in hyperplasia progressing to carcinoid tumors. These tumors arise in situations of hypergastrinemia in conditions such as chronic autoimmune atrophic gastritis (pernicious anemia), chronic atrophic gastritis associated with *Helicobacter pylori* infection, and prolonged iatrogenic acid suppression with proton pump inhibitors (such as omeprazole) [51]. Hypergastrinemia may also occur in patients with Zollinger–Ellison syndrome and multiple endocrine neoplasia (MEN) type I. Gastric carcinoid tumors associated with chronic atrophic gastritis tend to occur in the fundus and are multiple, limited to the mucosa and submucosa. Lesions are rarely malignant and regress when gastrin levels are decreased, usually after antrectomy (gastrin-producing cells reside predominantly in the antrum). This situation is in sharp contrast to gastric carcinoid tumors that arise sporadically in a normogastrinemic state. Sporadic gastric carcinoid tumors arise anywhere in the stomach and may be small (<2-cm diameter) submucosal nodules or large tumors that invade deeply and promote prominent fibrosis in surrounding tissues. Sporadic gastric carcinoids should be regarded as malignant neoplasms and should be completely surgically resected.

On MR images, carcinoid tumors are near-isointense on T1 and mildly hyperintense and heterogeneous on T2 and often show increased enhancement on early and later postgadolinium images (fig. 6.29).

Metastases. Metastatic involvement of the stomach is uncommon. Gastric metastatic lesions are generally

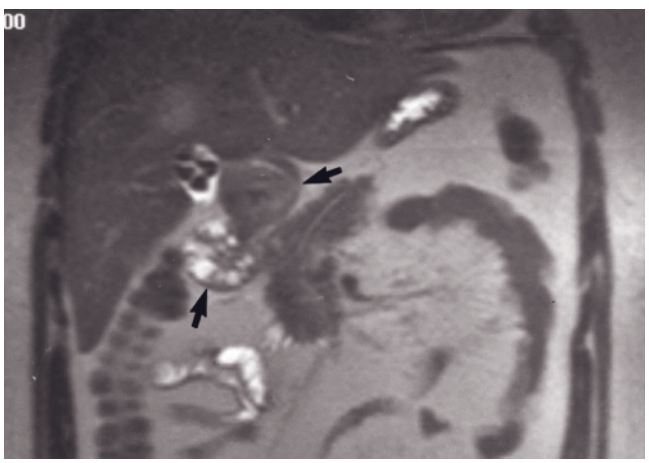

(*a*)

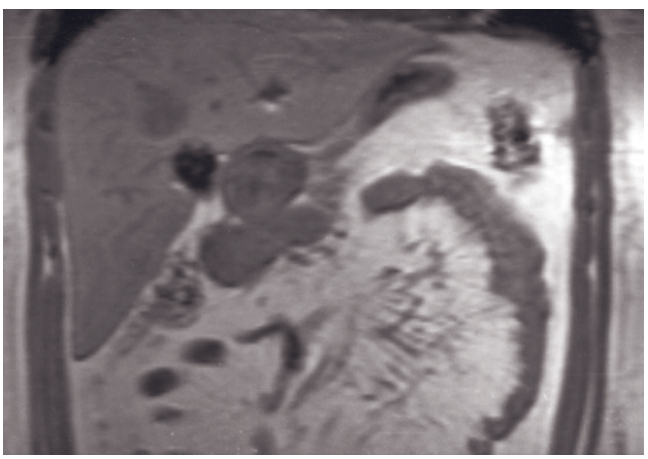

(*b*)

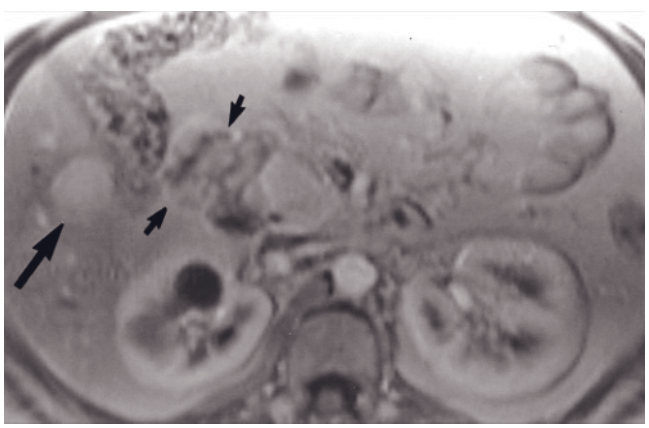

(*c*)

FIG. 6.29 Gastric carcinoid. Coronal T2-weighted SS-ETSE (*a*), coronal SGE (*b*), and transverse immediate postgadolinium SGE (*c*) images. This primary carcinoid tumor of the stomach appears as a mass in the wall of the antrum that invades the duodenum and pancreas. The tumor is mixed solid with cystic spaces (arrows, *a*) on T2 and isointense on T1 (*b*) and enhances heterogeneously after contrast administration (arrows, *c*). There are also hepatic metastases that are moderately hyperintense on T2-weighted image and hypointense on precontrast SGE image (*b*) and show homogeneous early enhancement (large arrow, *c*). A simple cyst is also seen in the right kidney.

submucosal. Tumors of neighboring organs, such as esophagus, pancreas, and transverse colon, may involve the stomach by direct extension. Specifically, colon carcinoma arising in the transverse colon invades the stomach via the gastrocolic ligament, whereas pancreatic carcinoma invades the posterior wall of the gastric body and antrum via the transverse mesocolon. Carcinomas of lung and breast and melanoma are the most common primary malignancies that result in hematogenous gastric metastases (fig. 6.30). Breast cancer metastases are noteworthy in that submucosal involvement with diffuse thickening of gastric wall may be indistinguishable from diffusely infiltrative gastric adenocarcinoma (linitis plastica) (fig. 6.30).

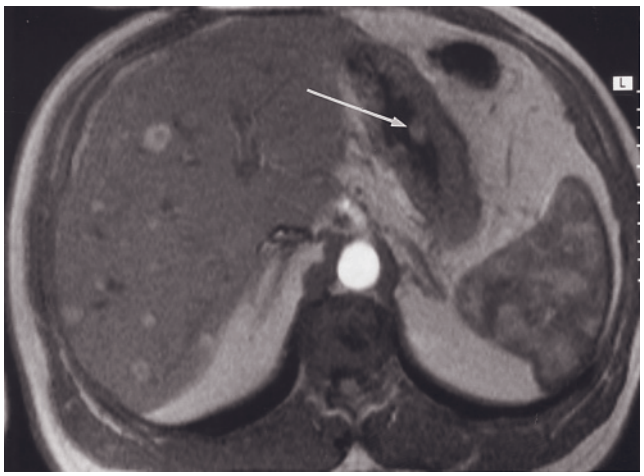

(*a*)

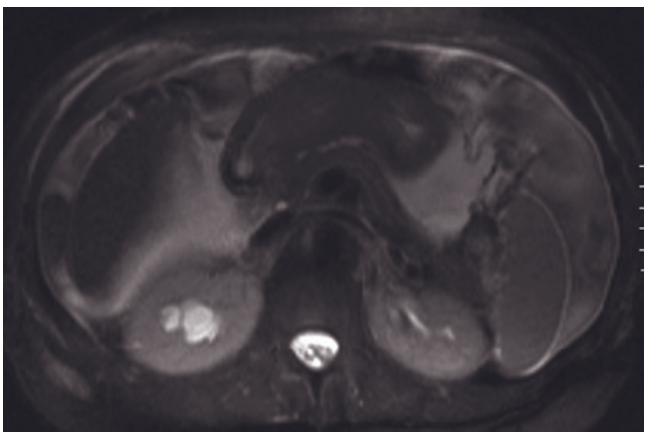

(*b*)

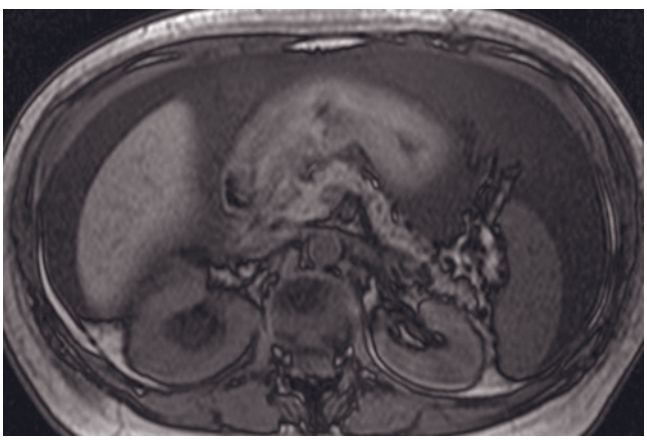

(*c*)

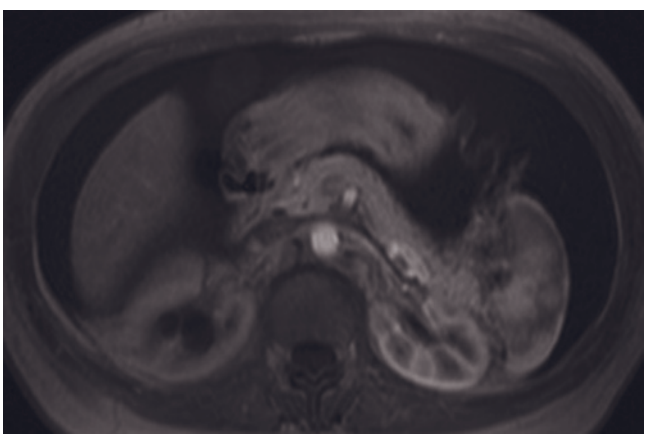

(*d*)

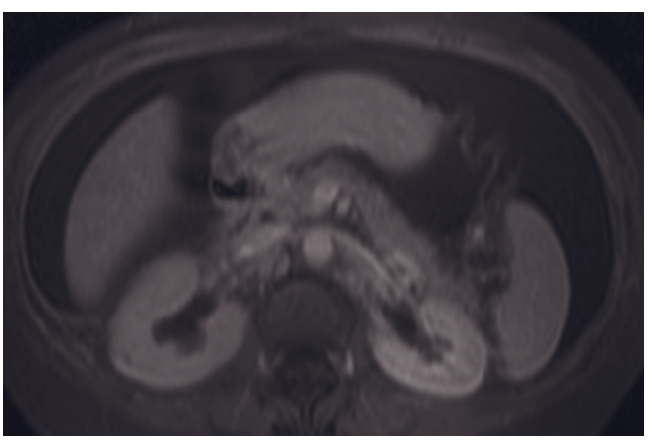

(*e*)

FIG. 6.30 Melanoma metastasis to the stomach. Immediate postgadolinium SGE image (*a*) in a patient with metastatic melanoma. Malignant melanoma metastasizes hematogenously, and in this patient multiple liver metastases and a gastric metastasis (long arrow, *a*) are identified. The metastases are high in signal on this T1-weighted image because of the paramagnetic properties of melanin. **Breast cancer metastases to the stomach and peritoneum.** T2-weighted single-shot echo-train spin-echo (*b*), T1-weighted out-of-phase SGE (*c*), T1-weighted postgadolinium hepatic arterial dominant-phase SGE (*d*), and T1-weighted postgadolinium interstitial-phase fat-suppressed 3D-GE (*e*) images demonstrate hematogenous metastases in the stomach and peritoneum from breast cancer in another patient. The gastric wall is diffusely thickened and shows diffuse prominent enhancement due to metastatic involvement. Note that there is peritoneal enhancement and ascites, which are consistent with metastatic peritoneal disease. Parapelvic cysts are present in the right kidney.

Inflammatory and Infectious Disorders

Gastric Ulceration and Gastritis

Ulcers are defined pathologically as localized, destructive lesions involving full-thickness mucosa. Ulcer craters may extend into submucosa or deeper aspects of the gut wall. The two most important factors involved in the etiology of chronic peptic ulcer disease are the amount of gastric acid and the mucosal resistance. An almost invariable feature of gastric ulcer disease is evidence of diffuse inflammation of surrounding mucosa, indicative of chronic antral gastritis that is mainly caused by *H. pylori* infection. In some cases, gastritis may result from repeated exposure to toxic substances including alcohol, drugs, and bile salts. Approximately 10% of patients have ulcers in both the antrum and the duodenum [52].

Benign gastric ulcers most commonly occur along the lesser curvature in the region of the border zone between the corpus and antral mucosa.

Marcos and Semelka reported on the MR appearance of gastric ulcers [29]. Gastric inflammatory disease in general results in increased mural enhancement on both early and late gadolinium images (fig. 6.31). Ulcer craters may be demonstrated on both single-shot echo-train spin-echo and gadolinium-enhanced fat-suppressed SGE or 3D-GE images (fig. 6.31).

Gastritis is defined as inflammation of the gastric mucosa. Inflammation may be acute, consisting predominantly of neutrophils, or chronic, with a preponderance of lymphocytes or plasma cells.

Acute gastritis is usually transient in nature and may be associated with a variety of factors including heavy use of drugs, especially NSAIDs, excessive alcohol consumption, smoking, and severe stress (e.g., trauma, burns, surgery). Severe acute gastritis is often characterized pathologically by the presence of erosions and hemorrhage. The term "erosion" denotes the loss of superficial epithelium, in contrast to ulcers, which involve the full-thickness mucosa. Gastritis causes mural edema, which is seen as high signal intensity in the submucosa (fig. 6.31). Gastritis also results in increased mural enhancement on both early and late gadolinium images (fig. 6.31).

Chronic gastritis is characterized by the presence of chronic inflammation leading to mucosal atrophy and abnormal changes in the epithelium (fig. 6.32). Erosions generally do not occur in this setting. The major etiologies of chronic gastritis include immunologic (pernicious anemia), chronic infection, especially with *Helicobacter pylori*, and toxic, as in alcohol consumption and cigarette smoking.

Both acute and chronic gastritis may occur in patients receiving high-dose radiation therapy. A chronic ulcer may develop months to several years after radiation exposure. Gastric inflammation, fibrosis, and stricture formation may lead to outlet obstruction (fig. 6.33) [53].

Gastric Wall Edema

Mural edema without substantial inflammatory changes is shown by the combination of mural high signal on single-shot T2-weighted images in combination with the lack of substantial enhancement on postgadolinium fat-suppressed T1-weighted gradient-echo images. A useful internal standard is to compare the extent of enhancement of the gastric wall with nearby renal cortex. The wall should not enhance more than renal cortex to establish the diagnosis of gastric wall edema. A variety of disease processes may result in gastric wall edema, including food allergies (fig. 6.33).

Hypertrophic Rugal Folds

Localized or diffuse thickening and gross enlargement of rugal folds ("cerebriform") may result from discrete hyperplasia of one of the epithelial mucosal components, inflammatory diseases, or tumors, most notably lymphoma or carcinoma. Causes of diffuse mucosal hypertrophy include hyperplasia of the parietal cells in Zollinger–Ellison syndrome (fig. 6.34) or of surface foveolar mucous cells in Menetrier disease. Types of specific inflammatory conditions that may cause rugal enlargement, often localized to the antrum, include infections such as tuberculosis and syphilis, chronic granulomatous diseases, and sarcoidosis [54].

The use of the single-shot echo-train spin-echo technique coupled with adequate distension permits detection of rugal thickening. The hyperemia and capillary leakage that accompany inflammation are highlighted on T1-weighted fat-suppressed SGE or 3D-GE images. The inflamed tissue demonstrates early marked enhancement, which persists as the contrast pools in the interstitium. The inflammatory nature of some of these gastric diseases is best shown on gadolinium-enhanced images.

The Postoperative Stomach

A spectrum of surgical procedures involves the stomach. These procedures may be categorized as drainage with or without partial gastric resection, antireflux operations, gastroplasty, resection, band surgery (fig. 6.35), and feeding gastrostomy (fig. 6.35). Familiarity with the exact surgical procedure performed aids radiologic investigation. The single-shot T2-weighted technique allows visualization of the anatomic changes following surgery, such as bowel anastomoses (fig. 6.35). Evaluation of inflammatory changes is accomplished with gadolinium-enhanced images.

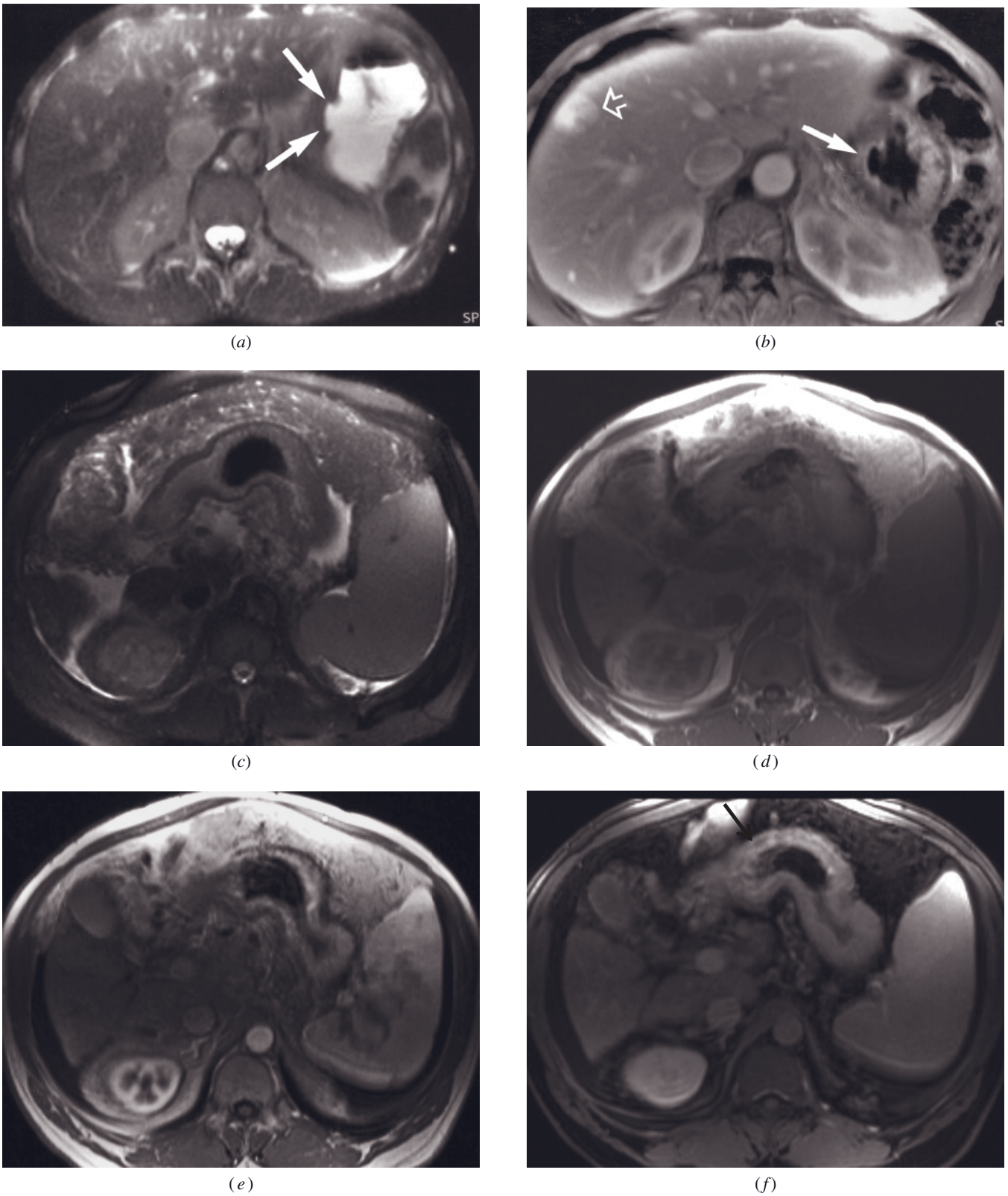

FIG. 6.31 Gastric ulcer. Transverse T2-weighted SS-ETSE (*a*) and transverse 1-min postgadolinium SGE (*b*) images. The high signal intensity of gastric contents (orally administered water) delineates the ulcer crater (arrows, *a*) on the mucosal surface of the lesser curvature. On the 1-min postgadolinium SGE image (*b*), the ulcer shows mildly increased enhancement (arrow). A 2-cm hemangioma is incidentally noted as an intensely enhancing mass lesion in the liver on the 1-min postgadolinium image (open arrow, *b*). (Reprinted with permission from Marcos HB, Semelka RC: Stomach diseases: MR evaluation using combined T2-weighted single-shot echo train spin-echo and gadolinium-enhanced spoiled gradient-echo sequences. *J Magn Reson Imaging* 10: 950–960, 1999.) **Gastritis.** T2-weighted single-shot echo-train spin-echo (*c*), T1-weighted SGE (*d*), T1-weighted postgadolinium hepatic arterial dominant-phase SGE (*e*), and T1-weighted postgadolinium hepatic venous phase fat-suppressed 3D-GE (*f*) images demonstrate diffuse gastritis in another patient. The gastric wall is diffusely thickened, but the rugal folds are regularly seen. The gastric wall shows diffuse prominent enhancement on postgadolinium images (*e*, *f*). Bilaminar enhancement of the gastric wall (arrow, *f*), which is due to the presence of edema, is seen on the hepatic venous phase (*f*). Note that portal hypertension findings including splenomegaly, ascites, and varices are present.

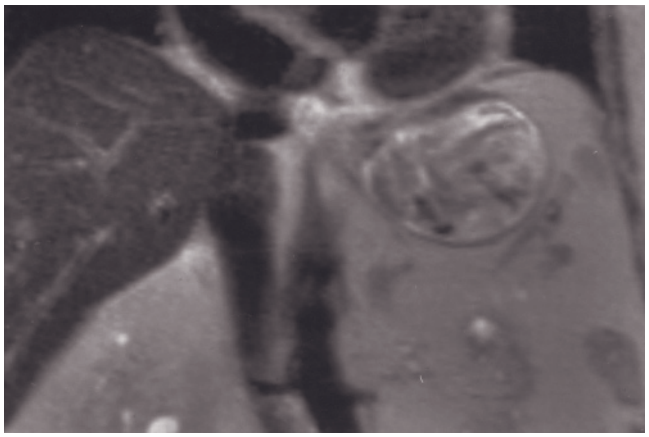

(*a*)

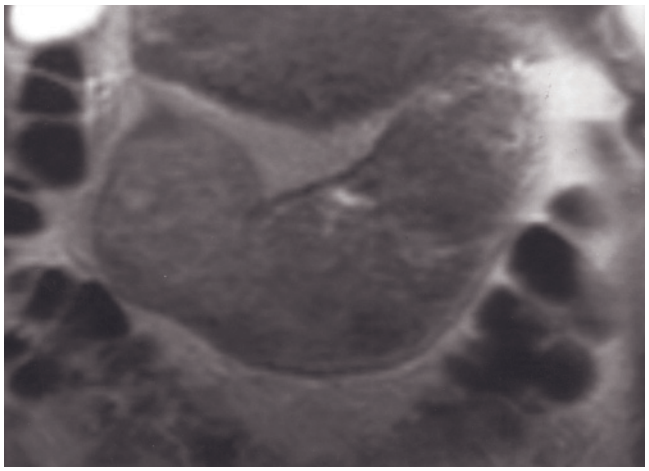

(*b*)

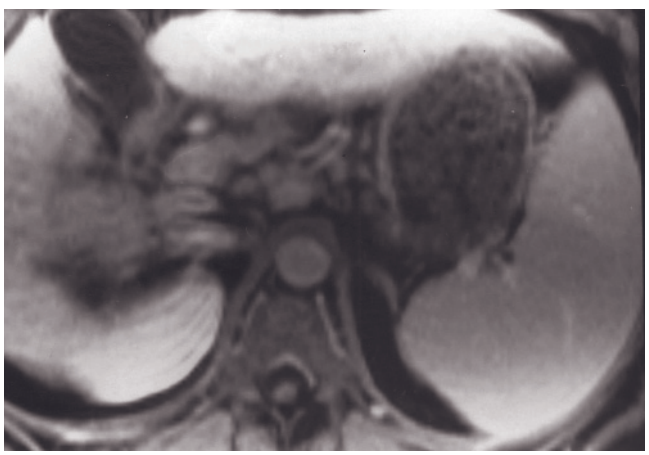

(*c*)

FIG. 6.32 Atrophic gastritis. Coronal T2-weighted SS-ETSE image (*a*).The gastric wall is noted to be thin and featureless, consistent with atrophy of the gastric rugae. Coronal T2-weighted SSETSE image (*b*) and transverse interstitial-phase fat-suppressed postgadolinium SGE image (*c*) in a second patient show similar features of gastric wall atrophy.

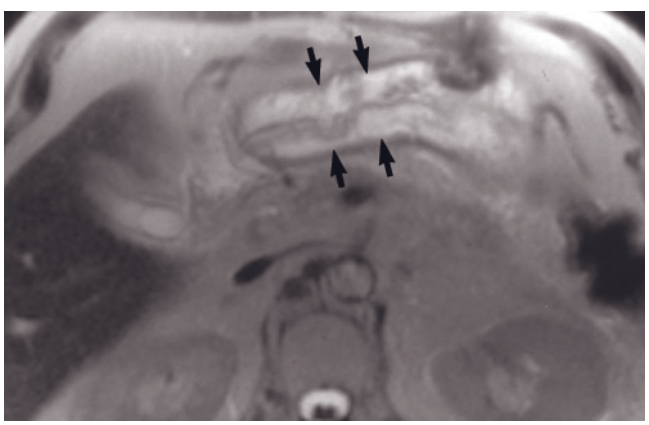

(*a*)

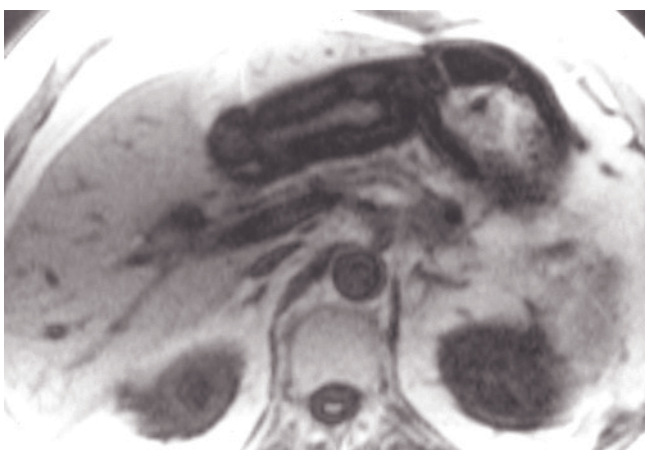

(*b*)

FIG. 6.33 Radiation gastritis. Transverse T2-weighted SSETSE (*a*), SGE (*b*), and 90-s postgadolinium fat-suppressed SGE (*c*) images in a patient after radiation therapy for pancreatic cancer. There is marked wall thickening of the stomach with submucosal edema. Note the high signal of the thickened submucosa on the T2-weighted image (arrows, *a*), reflecting edema. After contrast administration, mucosal enhancement is noted. **Gastric wall edema secondary to food allergy.** Coronal T2-weighted single-shot

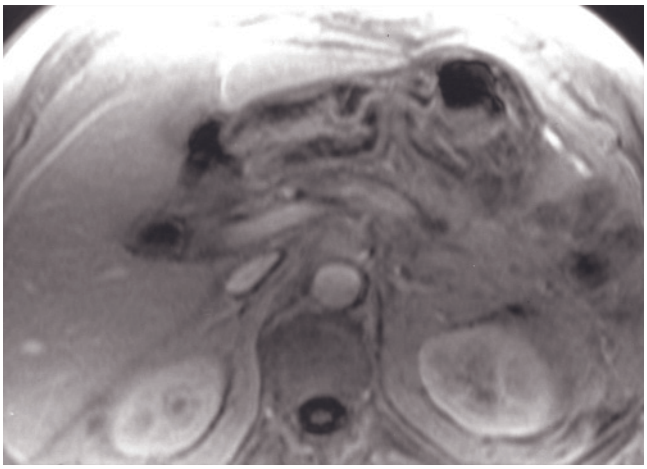

(*c*)

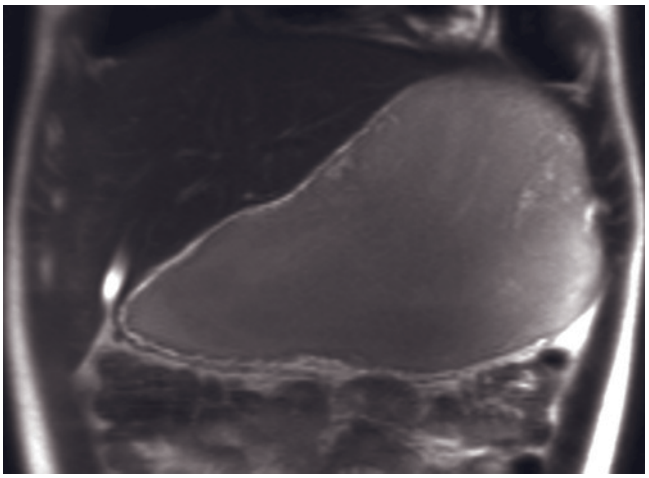

(*d*)

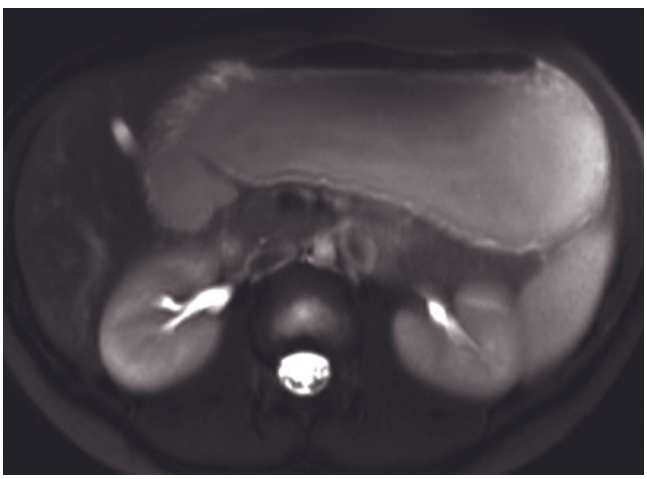

(*e*)

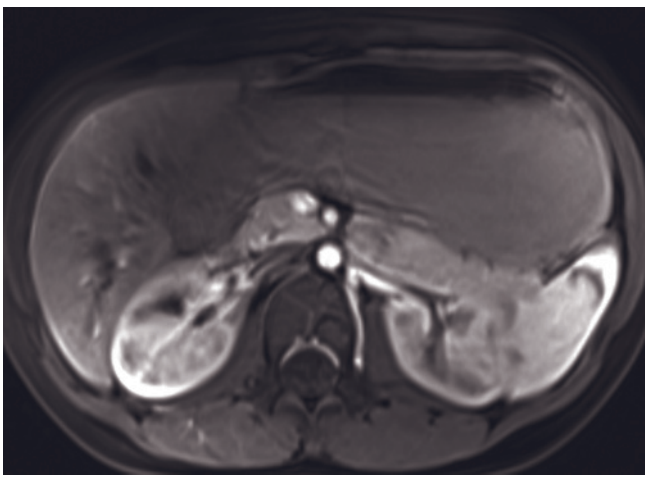

(*f*)

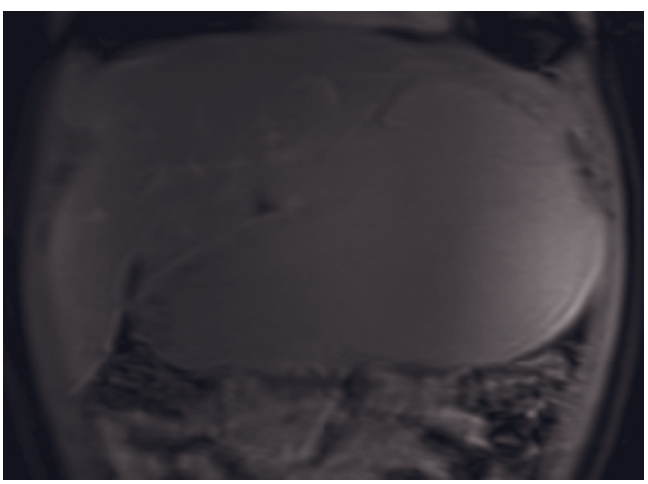

(*g*)

FIG. 6.33 (*Continued*) echo-train spin-echo (*d*), transverse fat-suppressed single-shot echo-train spin-echo (*e*), transverse T1-weighted postgadolinium hepatic arterial dominant-phase fat-suppressed 3D-GE (*f*), and coronal T1-weighted postgadolinium hepatic venous phase fat-suppressed 3D-GE (*g*) images demonstrate edema in the submucosal space, observed as a thin line of high signal on T2-weighted images (*d*, *e*), in another patient with food allergy. The gastric wall shows high signal intensity due to edema but no abnormal enhancement. The stomach is distended due to oral administration of one L of water to achieve adequate visualization of the gastric wall.

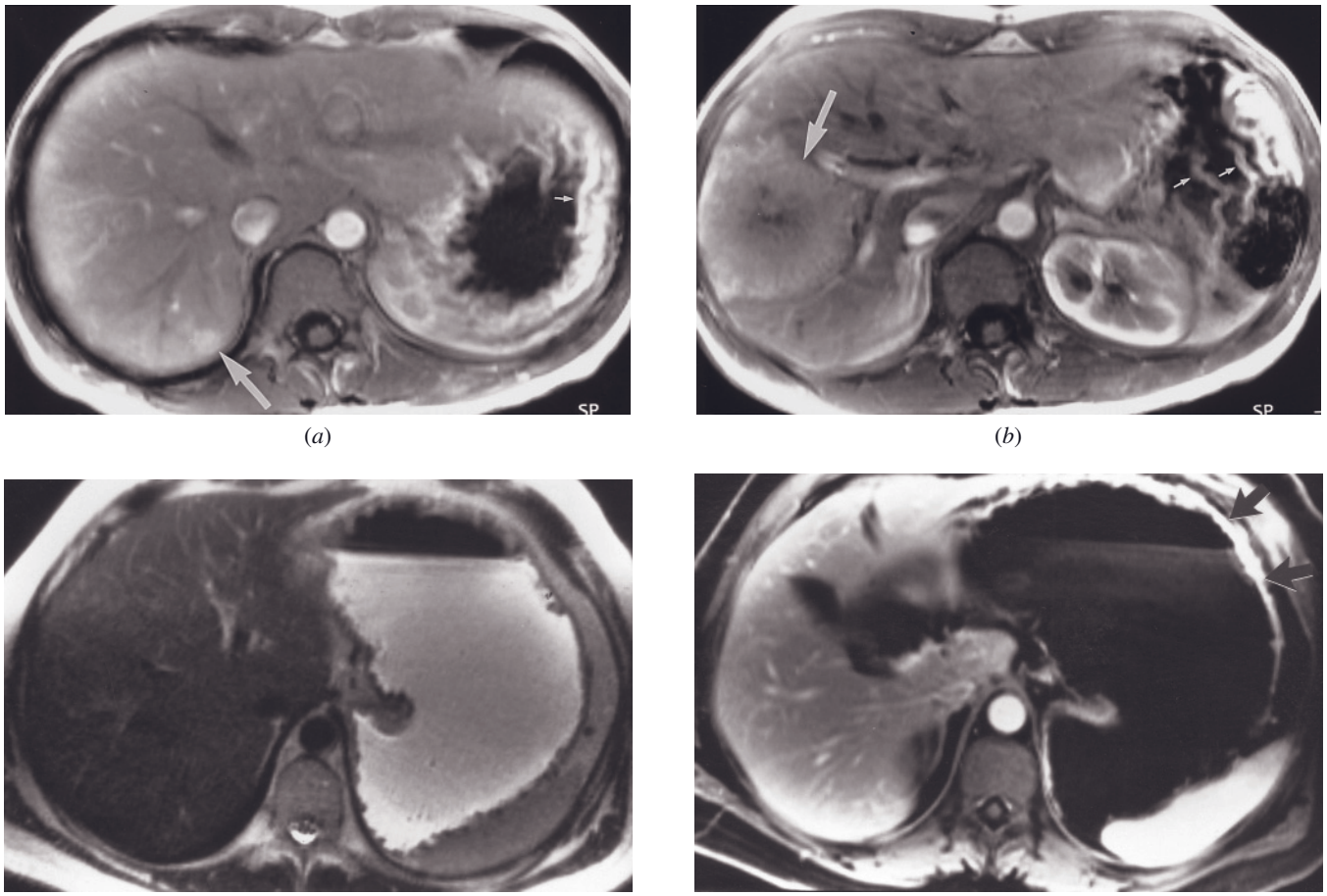

FIG. 6.34 Zollinger–Ellison syndrome. Immediate postgadolinium SGE images (*a*, *b*). Intense enhancement and increased thickness of gastric rugae are appreciated (small arrows, *a*, *b*). Hypervascular liver metastases are also present (large arrow, *a*, *b*). Transverse T2-weighted SS-ETSE (*c*) and transverse 90-s fat-suppressed postgadolinium SGE (*d*) images in a second patient. There is a marked distension of the stomach and duodenum, and the anterior gastric wall is thickened. On the 90-s postgadolinium fat-suppressed SGE image (*d*), the gastric wall shows intense enhancement (arrows, *d*). (Reprinted with permission from Marcos HB, Semelka RC: Stomach diseases: MR evaluation using combined T2-weighted single-shot echo train spin-echo and gadolinium-enhanced spoiled gradient-echo sequences. *J Magn Reson Imaging* 10: 950–960, 1999.)

THE SMALL INTESTINE

Normal Anatomy

The small bowel measures approximately 20–22 feet from the ligament of Treitz to the ileocecal valve. On gross inspection, the lining of the small intestine shows a series of permanent circular folds, plicae circulares. Each fold is covered by mucosa and contains a core of submucosa. The mucosal surface covered by villi, and the plicae circulares, increase the surface area and act as partial barriers that attenuate the forward flow of intraluminal contents, thus increasing the time of contact with absorptive surfaces. The duodenum is in continuation with the pylorus. It extends in a C shape to curve around the pancreatic head to end at the duodenal-jejunal flexure in the left upper quadrant. The duodenum is divided into four parts: bulb, descending, horizontal, and ascending segments. The bulb is the only intraperitoneal portion of the duodenum and is the most mobile. The second portion is in close proximity to the head of the pancreas, and both the pancreatic and common bile ducts converge to enter the posteromedial aspect forming the ampulla. The mesenteric small intestine begins at the jejunum. The jejunum occupies the superior and left abdomen, and the ileum occupies the inferior and right abdomen. Their mesenteric attachment gives rise to two distinct borders, the concave or mesenteric border and the convex or antimesenteric border. The ileum has a narrower lumen and, migrating from jejunum to distal ileum, has progressively fewer mucosal folds and a greater number of

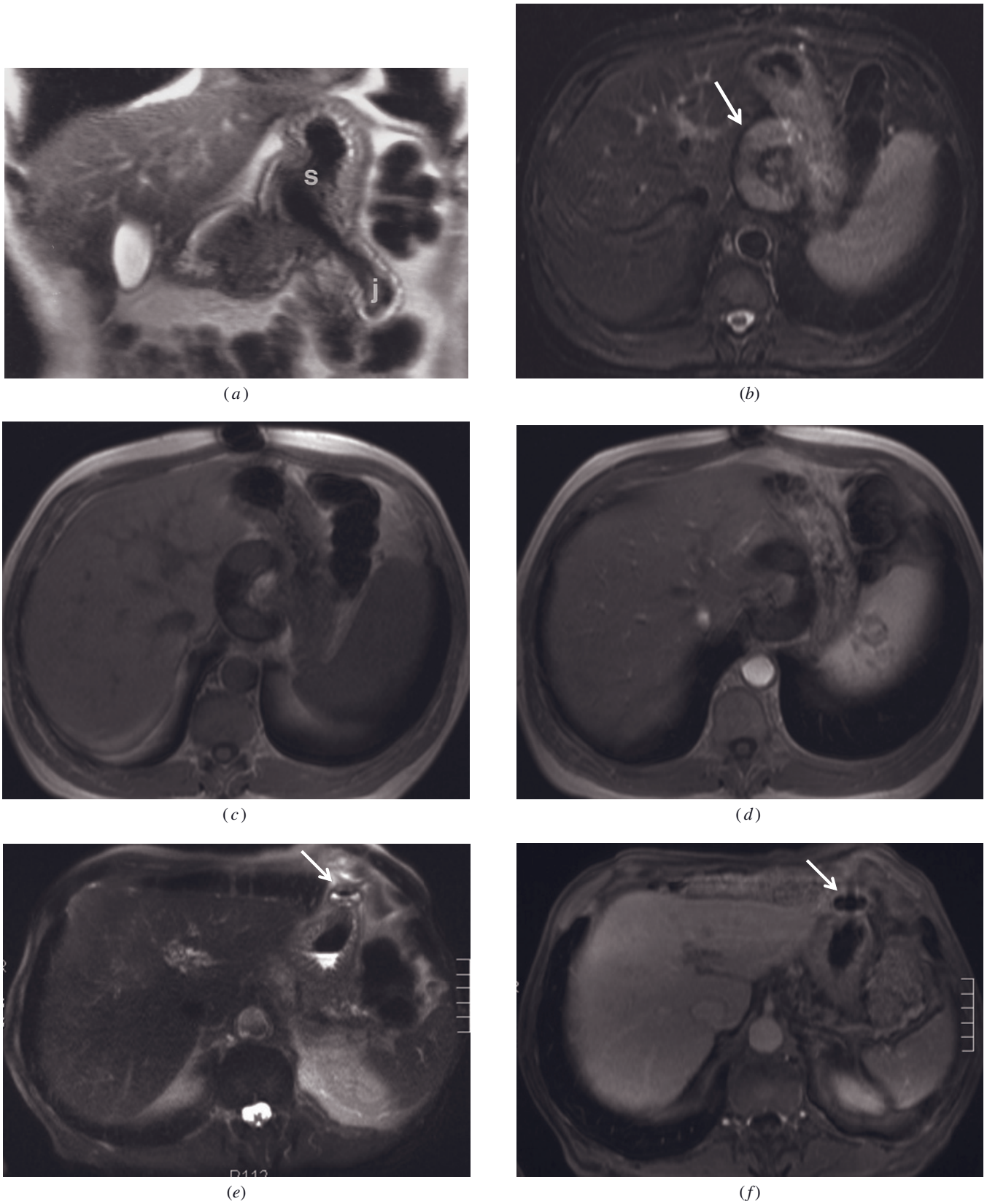

FIG. 6.35 Gastrojejunostomy. Coronal T2-weighted SSETSE image (*a*) shows the side-to-end anastomosis of the stomach (s) to the jejunum (j) in this patient status post gastrointestinal bypass surgery. **Gastric band.** T2-weighted short-tau inversion recovery (*b*), T1-weighted SGE (*c*), and T1-weighted postgadolinium hepatic arterial dominant phase SGE (*d*) images show gastric band (arrow, *b*) secondary to the operation. **Percutaneous gastrostomy tube.** T2-weighted single-shot echo-train spin-echo (*e*) and T1-weighted hepatic venous phase fat-suppressed 3D-GE (*f*) images demonstrate that the percutaneous gastrostomy tube is not located in the gastric lumen.

mesenteric arcades. Normal bowel wall thickness should not exceed 3–4 mm.

MRI Technique

Previously, MRI had a limited role in assessing the small bowel because of poor intrinsic contrast resolution and motion artifacts caused by peristalsis. The combination of single-shot echo-train spin-echo images that are less sensitive to motion deterioration and pre- and postgadolinium fat-suppressed breath-hold SGE or 3D-GE images is an effective approach for imaging the bowel (fig. 6.36). As a routine, patients should fast for at least 5 hours before the exam to decrease bowel motion and peristalsis with the resulting blurring artifact. Ingested water coupled with the single-shot echo-train spin-echo technique provides high-quality images of the small bowel (see fig. 6.36). Images of the upper and midabdomen should be obtained in the axial and coronal planes to distinguish bowel, which will show tubular-shaped configuration in at least one plane, from masses, which will not. Unenhanced SGE images with and without fat suppression followed by gadolinium-enhanced T1-weighted fat-suppressed SGE or 3D-GE images are necessary for a comprehensive exam. Normal bowel has a feathery appearance on unenhanced images because of the plicae circulares and after intravenous gadolinium enhances in a moderate and uniform fashion [55] (see fig. 6.36). Small bowel enhances less than the gastric wall (see fig. 6.36) and pancreas. Use of 3D-GE fat-suppressed gadolinium-enhanced images provide an optimal technique for T1-weighted imaging. The shorter TR and TE result in decreased image deterioration from paramagnetic effects from intraluminal gas, and the short TR allows faster imaging, resulting in more coverage with higher resolution during a shorter breath hold period than can be achieved with SGE technique. Combined with parallel processing, such as sensitivity-enhanced (SENSE) methods, rapid breath-hold examination of the abdomen and pelvis has become more feasible. In addition, development of coil and software-hardware schemes, including multistep table technology, has facilitated optimization of the signal-to-noise ratio of the images through utilization of surface coils that can cover larger fields of view and allow evaluation of the abdomen and pelvis without having to pause the examination to readjust coils or reacquire preparation scans. The lesser enhancement of small bowel compared to pancreas generally allows clear distinction between these two organs on immediate postgadolinium images. The administration of intravenous gadolinium in combination with fat-suppressed 3D-GE T1-weighted sequences permits evaluation of the bowel wall and assessment of mesenteric and retroperitoneal lymphadenopathy, peritoneal disease, and accompanying fistula, if present. The use of true-FISP sequence is also helpful for the evaluation of small bowel and mesentery.

MR Small Bowel Follow-Through and Enteroclysis

Recent studies have described small bowel follow-through and small bowel enema performed as MR

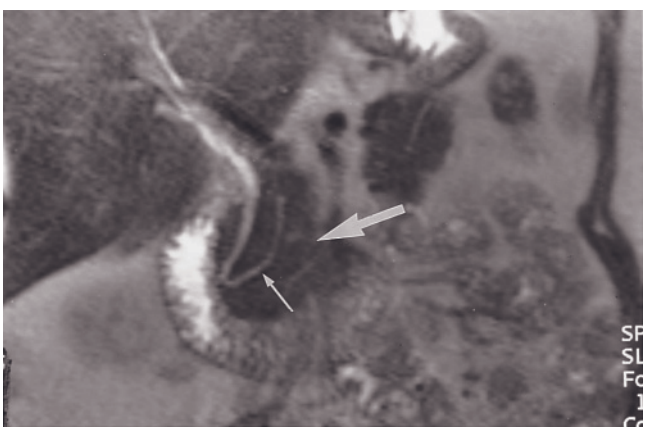

(*a*)

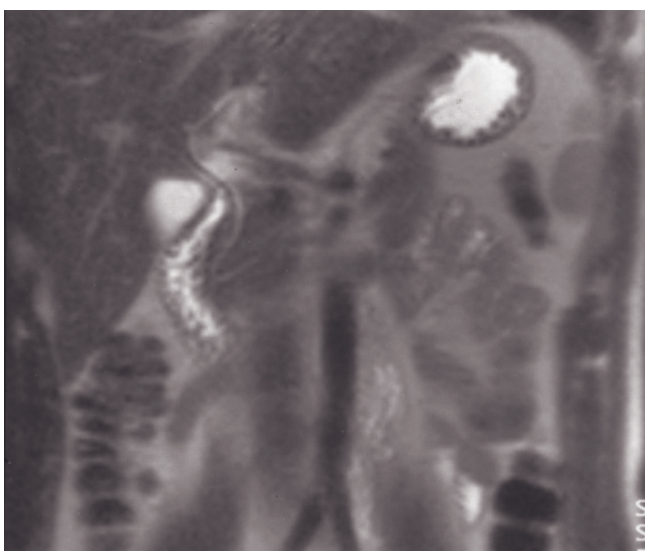

(*b*)

FIG. 6.36 Normal bowel. Coronal T2-weighted SS-ETSE images (*a–e*) in five patients. The valvulae conniventes of the C loop of the duodenum (*a–c*) and of multiple loops of jejunum and ileum are well shown as low-signal-intensity bands on the T2-weighted images (arrows, *e*) and stand out in relief against the high-signal-intensity intraluminal contents and moderately high-signal-intensity fat. Normal head of pancreas (large arrow, *a*), and pancreatic duct (thin arrow, *a*) are demonstrated. Fat-suppressed SGE (*f*) and

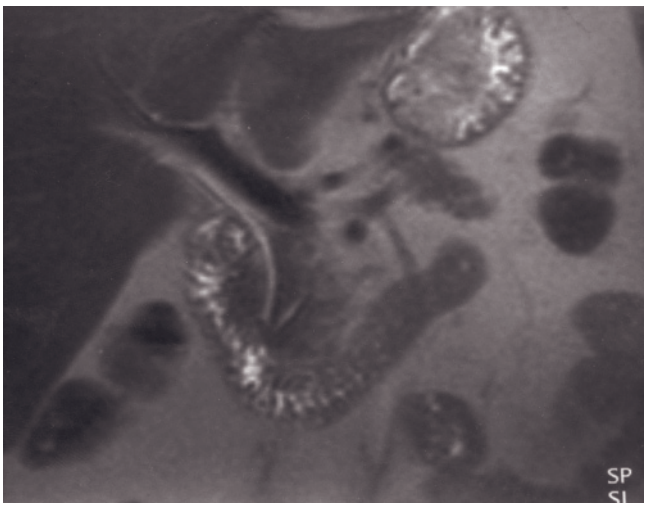

(*c*)

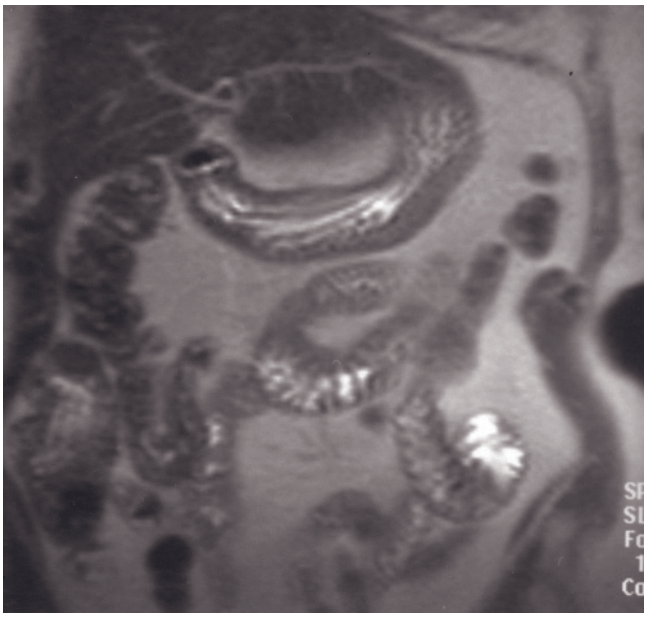

(*d*)

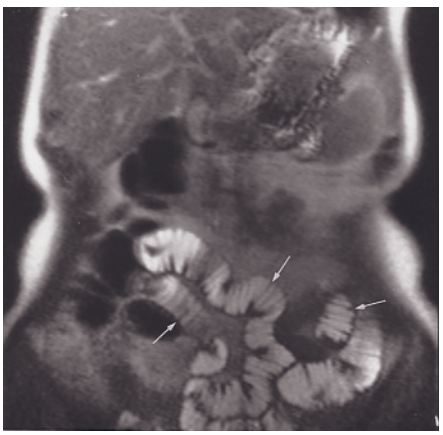

(*e*)

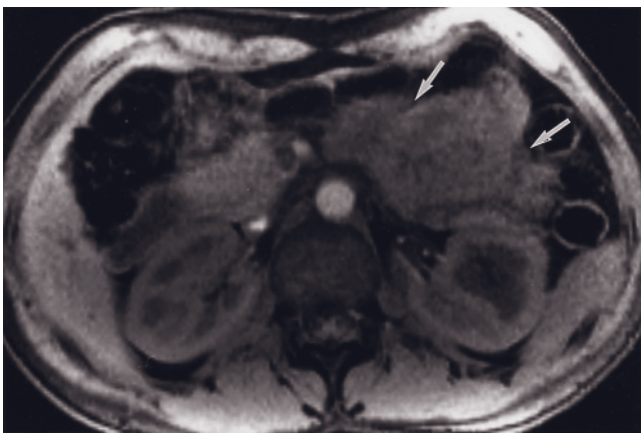

(*f*)

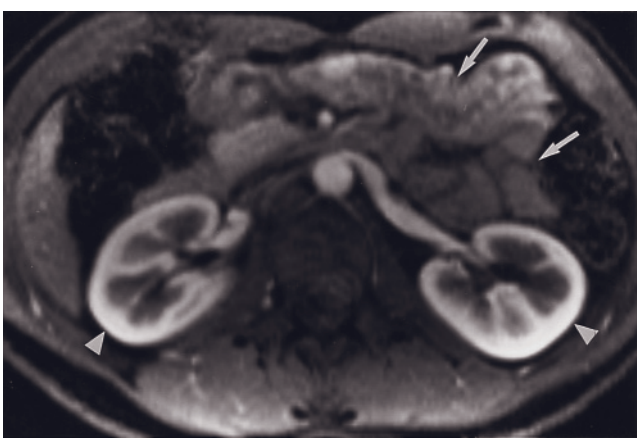

(*g*)

FIG. 6.36 (*Continued*) immediate postgadolinium T1-weighted fat-suppressed SGE (*g*) images in another patient with normal small bowel. On the precontrast fat-suppressed SGE image (*f*), the normal small bowel has a feathery appearance (arrows, *f*). Immediately after intravenous contrast the walls of the small intestine (arrows, *g*) show modest enhancement. In contradistinction, the renal cortex shows marked enhancement (arrowheads, *g*). The renal cortex can be used as an internal standard to judge the severity of inflammatory bowel disease because severe disease enhances comparably to renal cortex.

studies. The technique involves administering a large volume of fluid by mouth or enteric tube and acquiring thick-section (5–8 cm) single-shot echo-train spin-echo images with strong T2 weighting, to obtain images that resemble fluoroscopic small bowel images (fig. 6.37). Although both bright and dark lumen contrast agents have been proposed, water-based methods may be relatively easy to implement and may provide excellent signal characteristics, resulting in bright lumen on T2-weighted and dark lumen on T1-weighted images. In addition, to slow absorption of the water, which normally would occur rapidly in the jejunum, osmotic and viscosity agents may be added.

The use of a naso-jejunal tube for administration of intraluminal contrast may provide superior small bowel distension; oral administration may provide sufficient advantage for visualization of disease, particularly for demonstration of inflammatory bowel disease and related complications. Furthermore, enteroclysis requires fluoroscopic assistance and is an invasive procedure for which patient compliance may be less favorable compared to an MR small bowel follow-through technique. The addition of 2.5% mannitol, a nondigested carbohydrate, provides an osmotic load that slows water absorption. The further addition of a viscosity agent has been shown to further improve small bowel distension. This approach may be preferable to methylcellulose and water, as used for conventional fluoroscopic small bowel examinations, as the degree of reflux emesis is felt to be a drawback particular to methylcellulose. Between 1000 and 1200 ml of the water-based contrast can be given to the patient for oral ingestion 20 to 30 minutes before the examination and 20 mg of metoclopromide or 100 mg of erythromycin given intravenously to promote gastric emptying. Metoclopromide is well tolerated, whereas erythromycin can generate nausea, although generally well-tolerated at the low dose used here.

Initial images can be obtained with both single-shot T2 and true-FISP, both acquired with breath hold or respiratory gated and both providing high contrast and resistant to deterioration from bowel motion. These images can give information regarding the degree and location of optimal small bowel distension. Fat-suppressed single-shot T2 technique may yield key images for visualization of edema and abnormal fluid collections outside of the bowel. In addition, a coronal MRCP heavily T2-weighted single-shot slab technique can be used to produce a single slice within 2 to 5 s,

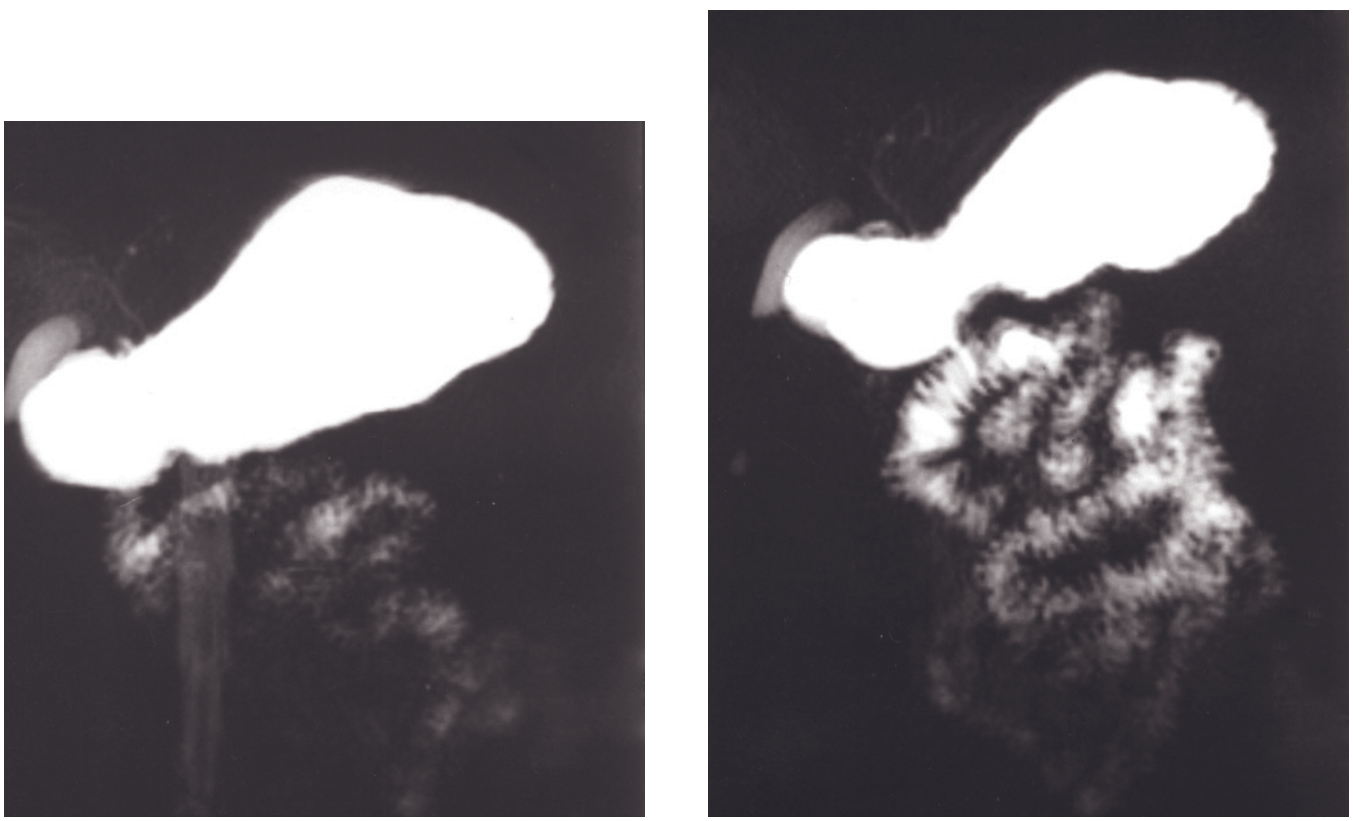

(*a*) (*b*)

FIG. 6.37 Small bowel follow-through. SS-ETSE images with strong T2-weighting.Thick-slab (6 cm) images obtained 5 (*a*) and 20 (*b*) min after ingestion of a large volume of water resemble fluoroscopic small bowel images.

resulting in an image that is similar to a small bowel fluoroscopic view. However, without concerns for radiation dose, these slab images can be obtained serially over time to monitor progression of the oral contrast and these images then can scrolled together into a single series of images that, when viewed one after the other, may generate information regarding bowel motion and reveal subtle areas of abnormalities such as fixed narrowing from adhesion or hernia. Once the distal ileum is distended, gadolinium-enhanced 3D-GE T1-weighted images are acquired in both the coronal and axial planes. A 20-s delay image set through the liver and upper abdomen can be obtained and then followed by 70- and 90-s acquisitions in the coronal and axial planes through the abdomen and pelvis. This provides comprehensive examination of the abdominal solid organs. Just before gadolinium administration, 1 mg of glucagon or 20 mg of Buscopan may be injected intravenously to produce bowel paralysis and improve image quality. This will also slow progression of the oral contrast. Advantages and specific applications for disease visualization are discussed in the corresponding sections that follow.

Congenital Lesions

Rotational Abnormalities

Intestinal malrotations or nonrotations result from disordered or interrupted embryonic intestinal counterclockwise rotations around the axis of the superior mesenteric artery. In rotational abnormalities, the normal rotations and fixations are either incomplete or occur out of sequence [56]. The most common form, nonrotation, is readily apparent on tomographic images, demonstrated by the lack of normal passage of the third and fourth parts of the duodenum from right to left of midline. The other types of malrotation occur less frequently and include incomplete rotation, reversed rotation, and anomalous fixation or fusion of the mesenteries. Marcos et al. [57] have shown that rotational abnormalities can be well visualized on snap-shot echo-train spin-echo images (fig. 6.38).

Diverticulum

A diverticulum is defined as a mucosal outpouching emanating from the alimentary tract that communicates with the gut lumen. Congenital diverticula usually contain all three layers with a complete muscularis externa in the outpouching; in contrast, acquired diverticula lack a muscularis externa. Diverticula of the jejunum and ileum involve the mesenteric side of the bowel. In the small intestine muscular wall, points at which mesenteric vessels and nerves enter provide potential sites of weakness where mucosa may herniated into the mesentery.

Small bowel diverticula occur most commonly in the duodenum. Multiple small bowel diverticula may be associated with intestinal bacterial overgrowth and resultant metabolic complications. Diverticula may be demonstrated on MR images as air or air fluid-containing structures that arise from the bowel (fig. 6.39). Change in size of the diverticulum may be observed between sequences in an MRI examination, reflecting contraction and expansion. Single-shot echo-train spin echo is effective at demonstrating this entity. The absence of appreciable susceptibility artifact from air in the diverticula with this technique allows clear delineation of diverticula and their origin from bowel [57].

Meckel Diverticulum

Meckel diverticulum is a remnant of the omphalomesenteric duct (vitelline duct). Normally, this duct is obliterated by the fifth week of gestation. Meckel diverticulum is common, with a prevalence of about 2% in the general population. It occurs within 25 cm of the ileocecal valve along the antimesenteric border. Most patients with Meckel diverticulum are asymptomatic. If the diverticulum contains acid-secreting epithelium of gastric mucosa, ulceration and bleeding may result. Intussusception and inflammation may also occur, irrespective of the type of mucosa present. The mainstay of diagnosis has been ^{99m}Tc-pertechnetate scintigraphy and enteroclysis. MRI, like scintigraphy, exploits the presence of gastric mucosa in making the diagnosis. Because gastric mucosa enhances more than any other segment of bowel, a gastric-lined Meckel diverticulum will demonstrate marked enhancement on immediate (capillary phase) and interstitial-phase postgadolinium images (fig. 6.40) [58, 59].

Atresia and Stenosis

Intestinal atresia results in complete absence of a portion of bowel or closure by an occluding mucosal diaphragm, whereas congenital stenosis implies a narrowing of an intestinal segment by fibrosis or stricture. Both may cause intestinal obstruction. Duodenal atresia represents the most common gastrointestinal atresia; jejunal and ileal atresia are rare and occur with equal frequency.

Approximately 25% of cases will have associated congenital anomalies including malrotation of the gut and Meckel diverticulum. Although the precise etiology of congenital atresia and stenosis is not known, lesions appear to arise from developmental failure, intrauterine vascular accidents, or intussusceptions occurring after the intestine has developed. Barium studies are the most common means of diagnosis, although T2-weighted single-shot echo-train spin-echo images can highlight the atretic/stenotic segment and proximal dilatation (fig. 6.41).

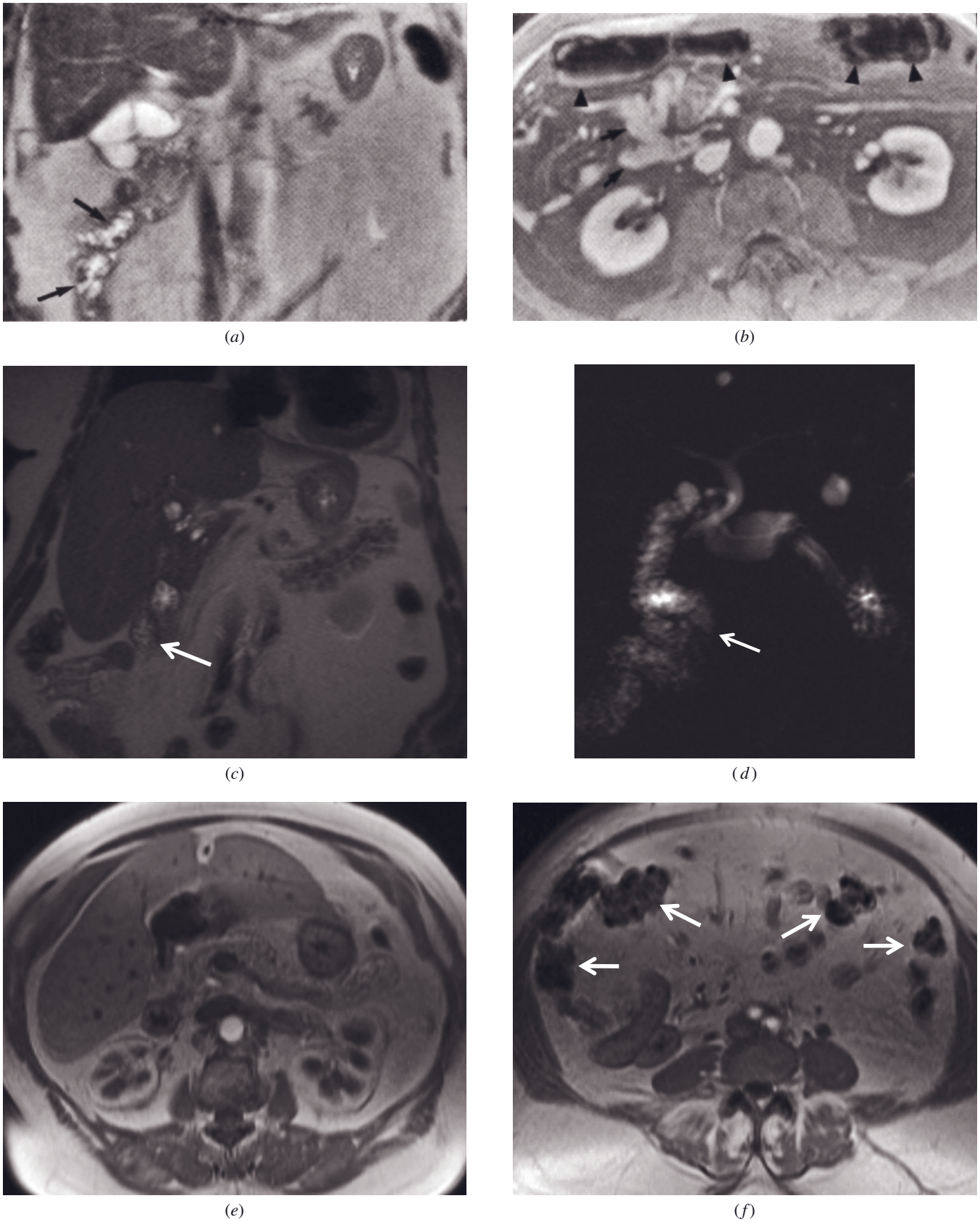

Fig. 6.38 Malrotation. Coronal T2-weighted SS-ETSE (*a*) and transverse 90-s postgadolinium fat-suppressed SGE (*b*) images. Coronal T2 image (*a*) demonstrates that small bowel is predominantly located in the right side of the abdomen (arrows). The 90-s postgadolinium fat-suppressed SGE image (*b*) demonstrates that the third and fourth portions of the duodenum are located to the right of midline (arrows, *b*). Note that the large bowel is in a normal location (arrowheads). (Reprinted with permission from Marcos HB, Semelka RC, Noone TC, Woosley JT, Lee JKT: MRI of normal and abnormal duodenum using half-Fourier single-shot RARE and gadolinium-enhanced spoiled gradient-echo sequences. *Magn Reson Imaging* 17: 869–880, 1999.) Coronal T2-weighted single-shot echo-train spin-echo (*c*), coronal fast spin-echo thick-section MRCP (*d*), and transverse T1-weighted postgadolinium arterial-phase SGE (*e*, *f*) images demonstrate malrotation of the small bowel in another patient. The duodenum does not form its normal C loop, and the 4th part of duodenum and jejunal loops are located at the right side of the abdomen (arrows, *c*, *d*). These findings are consistent with malrotation. Note that the colon is located in its normal position (arrows, *f*).

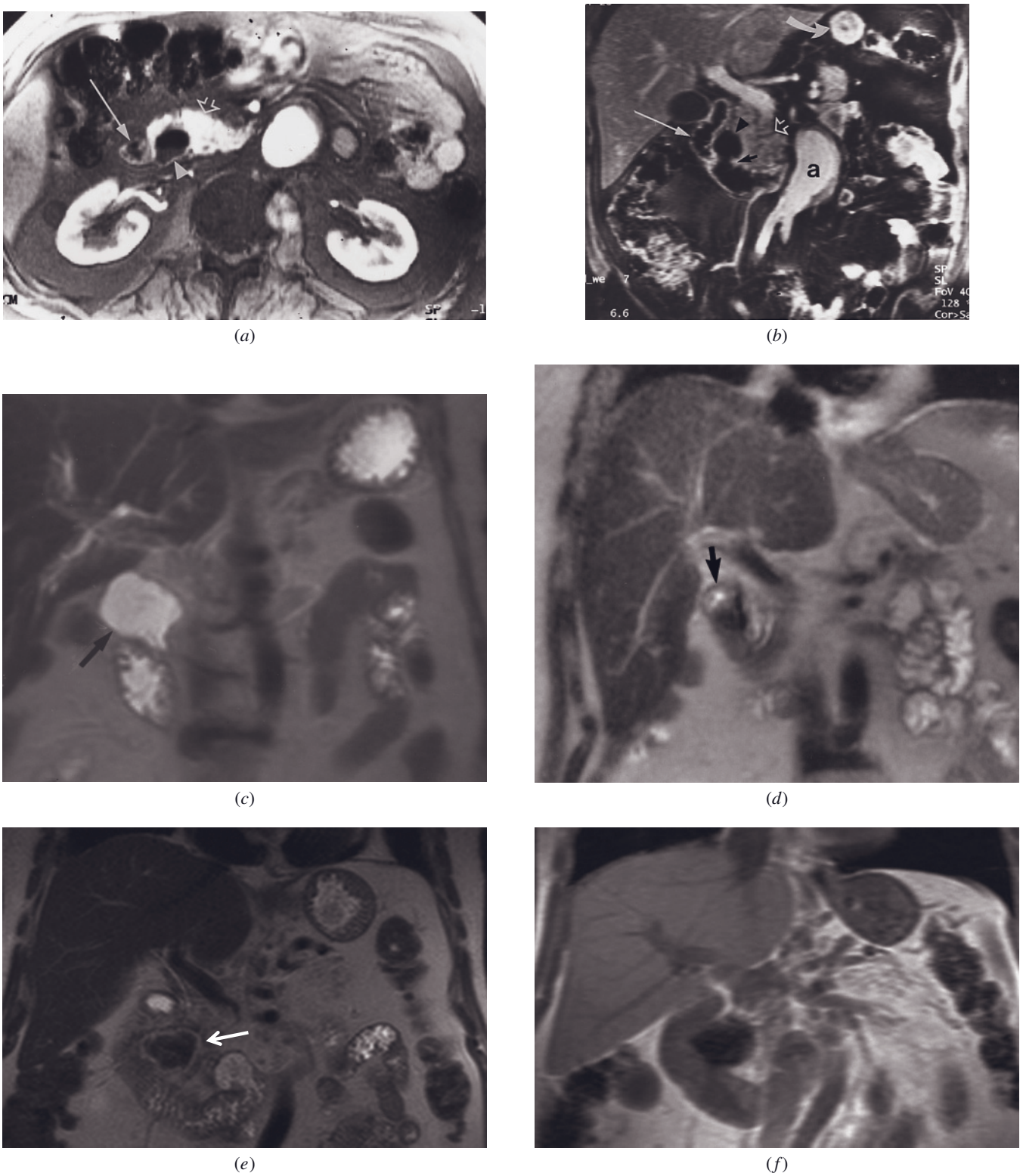

FIG. 6.39 Duodenal diverticulum. Transverse immediate (*a*) and coronal 90-s (*b*) postgadolinium fat-suppressed SGE images. An air- and fluid-containing diverticulum (arrowheads, *a*, *b*) is interposed between the duodenum (long arrows, *a*, *b*) and the head of the pancreas (open arrows, *a*, *b*). On the coronal image, a neck (short arrow, *b*) connecting the diverticulum to the duodenum is well shown, which confirms that the lesion represents a diverticulum and not a cystic mass in the head of the pancreas. Duodenal diverticula are common and usually incidental findings. The normal gastric wall (curved arrow, *b*) enhances more intensely than normal small bowel. An abdominal aortic aneurysm (a, *b*) is also present. Coronal T2-weighted SS-ETSE images (*c*, *d*) in two other patients demonstrate fluid-containing duodenal diverticula (arrow, *c*, *d*). Coronal T2-weighted single shot-echo-train spin-echo (*e*), coronal T1-weighted SGE (*f*), transverse T1-weighted SGE (*g*), and transverse T1-weighted postgadolinium hepatic venous phase

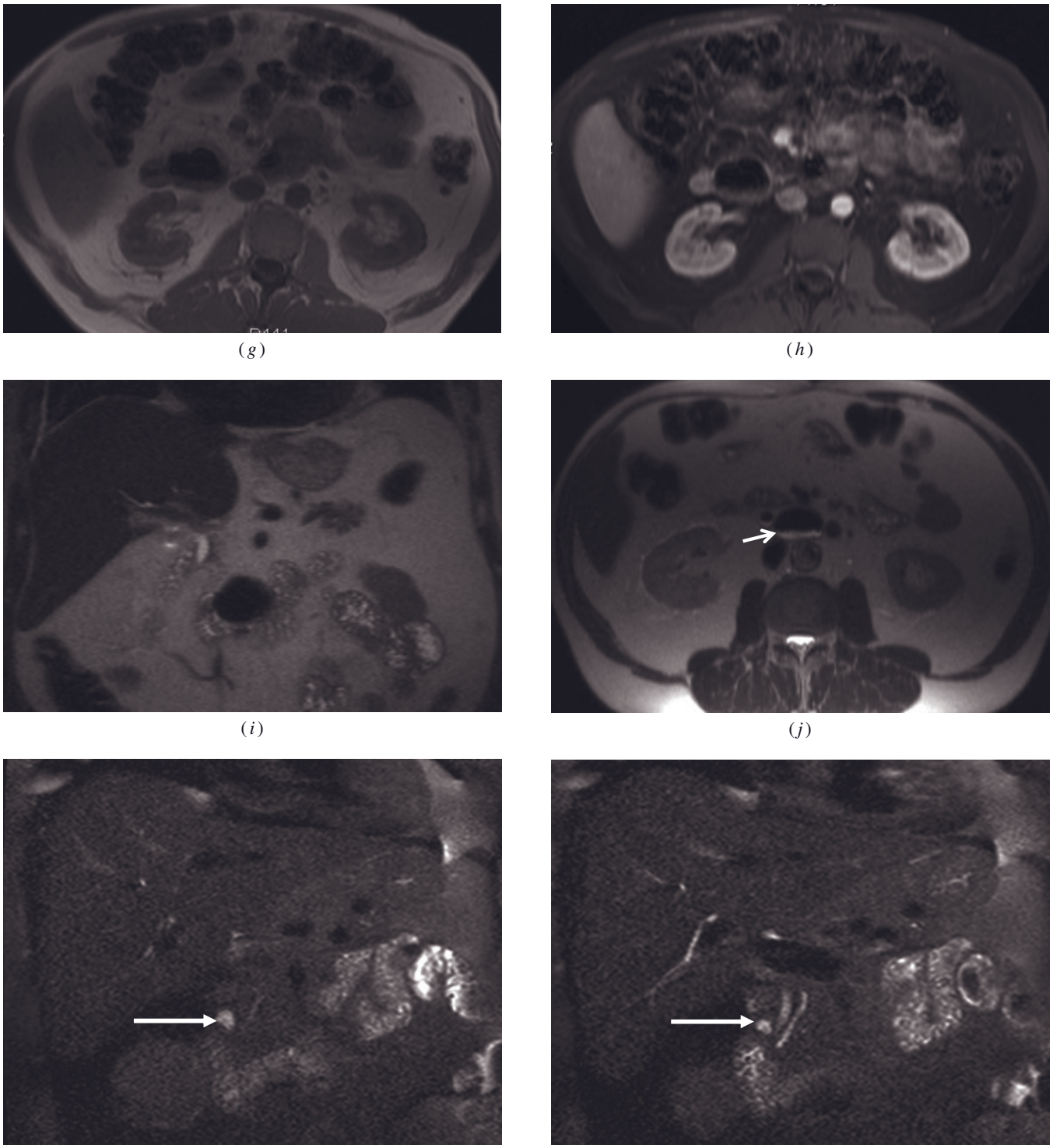

FIG. 6.39 (*Continued*) fat-suppressed SGE (*h*) images demonstrate a duodenal diverticulum (arrow, *e*) in another patient. The duodenal diverticulum is located at the medial side of the second portion of the duodenum. It contains air and therefore shows low signal on both on T2-weighted and T1-weighted images. The duodenal wall shows regular enhancement on postgadolinium image (*h*). Note that an air-fluid level is seen in the diverticulum on postgadolinium image (*h*). Coronal (*i*) and transverse (*j*) T2-weighted single-shot echo-train spin-echo images demonstrate a duodenal diverticulum in another patient. The diverticulum is located in the 3rd to 4th portion of the duodenum. Note that an air-fluid level (arrow, *j*) is seen on transverse image (*j*). Coronal T2-weighted thin-section single-shot echo-train spin-echo MRCP (*k*, *l*) and reconstructed 3D MIP MRCP (*m*) images demonstrate a small duodenal diverticulum (arrows, *k–m*) located at the medial aspect of the 2nd portion of the duodenum adjacent to the major papilla in another patient. The diverticulum does not have any connection with the common bile duct and shows high signal because of its fluid content.

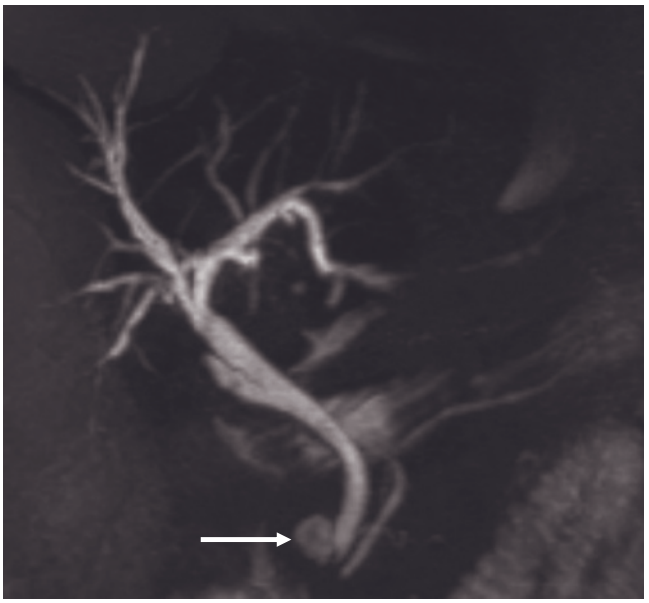

FIG. 6.39 (*Continued*) (*m*)

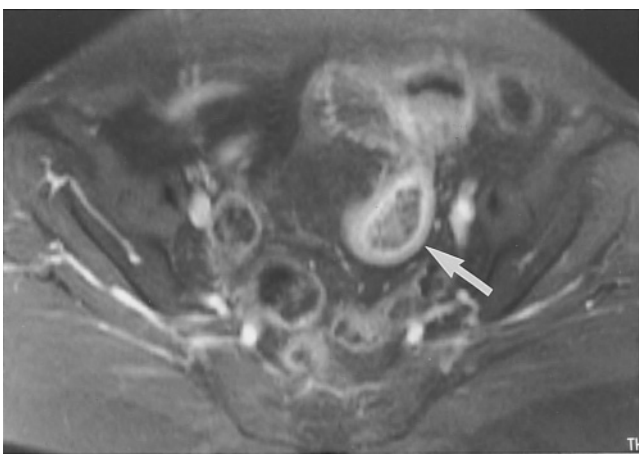

FIG. 6.40 Meckel diverticulum. Gadolinium-enhanced T1-weighted fat-suppressed spin-echo image in a patient with lower gastrointestinal bleeding. A teardrop-shaped Meckel diverticulum (arrow) extends from a loop of mildly dilated ileum. The inner wall of the diverticulum enhances to a greater extent than adjacent small bowel and colon. This allows detection of the diverticulum, and the degree of enhancement is consistent with the presence of gastric mucosa.

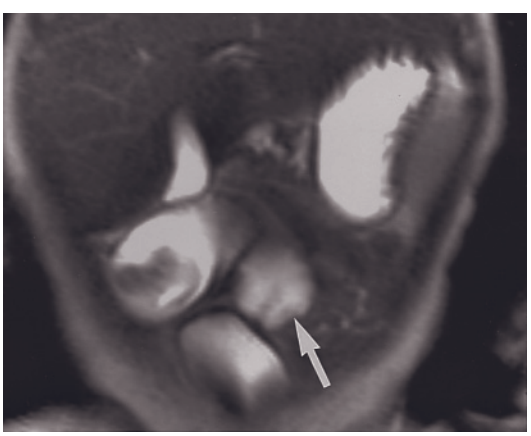

(*a*)

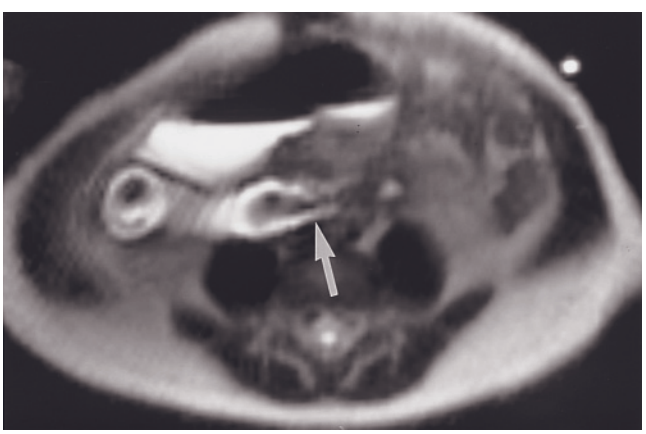

(*b*)

FIG. 6.41 Congenital stenosis, duodenum. Coronal (*a*) and transverse (*b*) T2-weighted SS-ETSE images. The coronal image demonstrates dilatation of the third part of the duodenum (arrow, *a*). The duodenum is noted to narrow (arrow, *b*) at the crossing of the superior mesenteric artery on the transverse image (*b*).

Choledochocele

Choledochocele is a congenital anomaly characterized by cystic dilatation of the distal common bile duct in the region of the papilla. Clinically, it may be associated with abdominal pain, bleeding, jaundice, and pancreatitis. The diverticulum can contain calculi. On imaging examinations, these may appear as polypoid masses indistinguishable from papillary edema or carcinoma. When large enough, they can protrude into the duodenum and even occlude it. MR cholangiopancreatography (MRCP) (see Chapter 3, *Gallbladder and Biliary System*) and single-shot echo-train spin-echo images facilitate establishing the correct diagnosis (fig. 6.42).

Mass Lesions

Benign and malignant small intestinal tumors are uncommon. Adenomas, leiomyomas, and lipomas constitute the three most common primary benign small intestinal tumors [60]. In general, benign tumors occur less commonly in the duodenum and increase in frequency toward the ileum.

Benign Masses

Polyps. The term "polyp" is a clinical term for any tumorous mass that projects above the surrounding normal mucosa. Hamartomatous, hyperplastic, and inflammatory polyps are benign, nonneoplastic lesions; adenomatous polyps (fig. 6.43) are true neoplastic tumors containing dysplastic epithelium and are precursors of carcinoma.

Polyps are infrequently symptomatic and are usually incidental findings at autopsy. Clinically evident polyps present with pain, obstruction, or bleeding. Polyps are the most common lead points for intussusceptions in adults. Except in hereditary polyposis syndrome, adenomatous polyps of the small intestine are rare, with <0.05% of all intestinal adenomas arising in the small intestine [61]. Overall, the frequency of cancer in adenomas ranges from 45% to 63% [62]. Multiple adenomas predominate in the setting of Gardner and familial polyposis syndromes. Small bowel hamartomas occur commonly in Peutz–Jeghers syndrome and rarely in juvenile polyposis syndromes.

Similar to polyps elsewhere in the gastrointestinal tract, small bowel polyps appear as enhancing masses on gadolinium-enhanced fat-suppressed SGE or 3D-GE images (fig. 6.44). On single-shot echo-train spin-echo images, polyps appear as rounded low-signal-intensity masses. Polyps are termed pedunculated when they are anchored by a slender stalk and sessile when they are attached by a broad base. Although it may not be possible to exclude a focus of carcinoma within the polyp, extraserosal extension of a polyp is compatible with malignant degeneration.

Neurofibromas. Primary neurogenic tumors of the gastrointestinal tract are rare. Pathologically, neurofibromas consist of neoplastic cells arising from the nerve sheath.

Gastrointestinal involvement in neurofibromatosis type 1, or Von Recklinghausen disease, is well recognized, and solitary or multiple gastrointestinal tumors have been reported in 11–25% of patients with this disease [63, 64].

Neurofibromatosis type 1 predisposes individuals to an increased risk of a variety of gastrointestinal lesions, including neurofibromas, schwanomas, smooth muscle tumors, and neuroendocrine tumors of the duodenum and ampullary region [63].

The detection of these tumors by MRI depends essentially on their size [65]. They appear as intraluminal masses that enhance to the same extent as bowel wall (fig. 6.45).

Leiomyomas. Leiomyomas are common tumors of the small bowel, but the majority are subcentimetric and not visible on imaging studies. The frequency of small bowel leiomyoma is comparable to that of adenoma. Leiomyomas are smooth muscle proliferations that usually originate in the submucosa or muscularis externa. Depending on their location, they may protrude into the lumen or produce a mass effect on adjacent bowel. In general, leiomyomas are usually solitary lesions. As leiomyomas enlarge, they may undergo central necrosis and bleeding. Features of small bowel leiomyoma include the following: They are mural-based and do not encroach substantially on the lumen, they are well-defined and oval, enhancement is relatively uniform, and they exhibit delayed relatively increased enhancement at 2–5 min after contrast (fig. 6.46).

Lipomas. Lipomas are mature adipose tissue proliferations that arise in the submucosa and occur predominantly in the duodenum and ileum. Similar to leiomyomas, they may ulcerate and bleed. Lipomas are high in signal intensity on T1-weighted images and have signal intensity comparable to intra-abdominal fat on T2-weighted images. On T1-weighted fat-suppressed images these lesions show a characteristic loss of signal intensity.

Varices. Duodenal varices may be seen in isolation or in conjunction with portal vein obstruction. SGE or fat-suppressed SGE gadolinium-enhanced images obtained during the venous phase or further delayed phase demonstrate varices as thin tubular structures within the bowel wall (fig. 6.47). 3D-GE T1-weighted gadolinium-enhanced fat suppressed technique provides optimal visualization; however, varices can also be visualized with a steady-state precession true-FISP sequence.

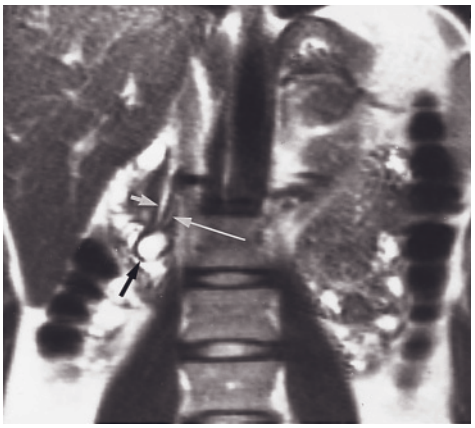

(*a*)

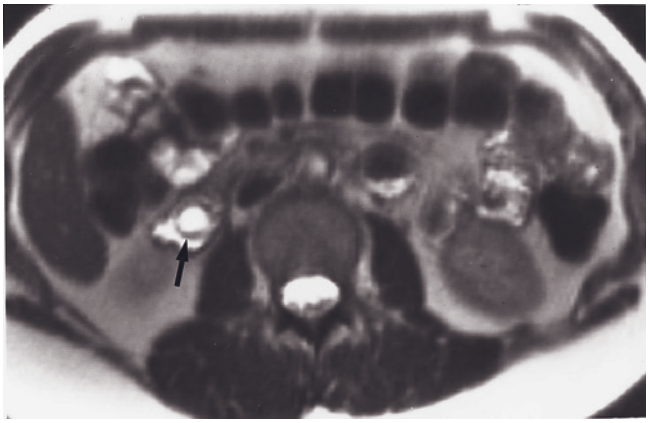

(*b*)

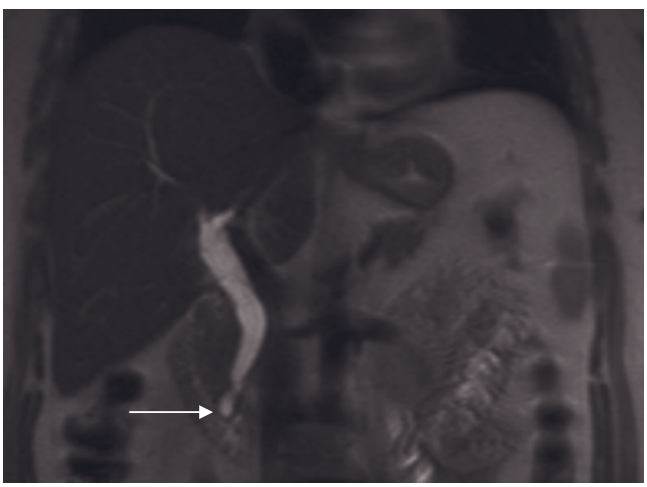

(*c*)

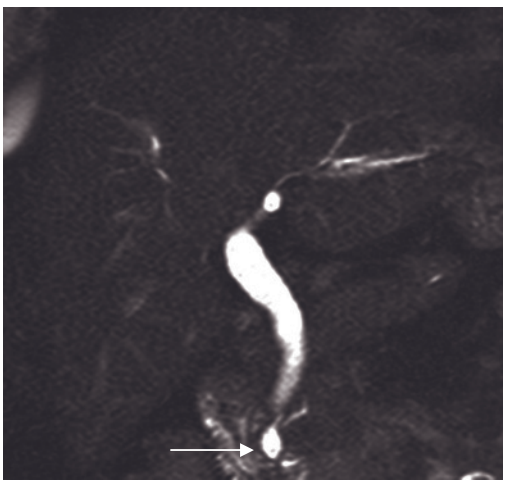

(*d*)

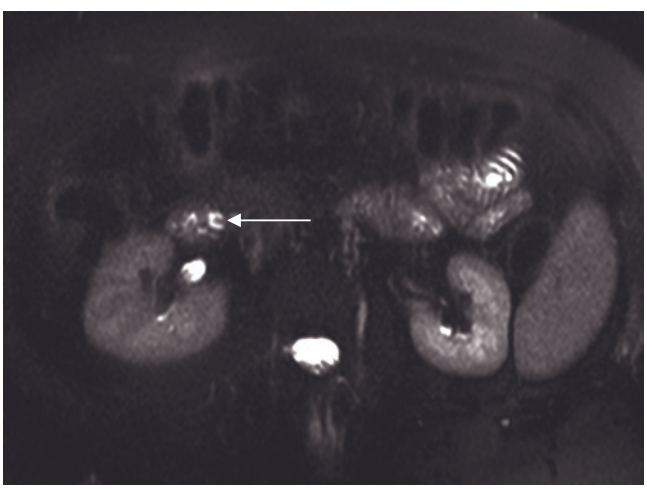

(*e*)

(*f*)

FIG. 6.42 Choledochocele. Coronal (*a*) and transverse (*b*) T2-weighted SS-ETSE images in a patient with recurrent bouts of pancreatitis. A high-signal-intensity choledochocele (black arrow, *a*, *b*) protrudes into the duodenum. The HASTE image clearly defines the cystic nature of the lesion, which excludes an ampullary tumor, and demonstrates the relationship to the common bile duct (small arrow, *a*) and the pancreatic duct (long arrow, *a*). Coronal T2-weighted single-shot echo-train spin-echo (*c*), coronal (*d*) and transverse (*e*) thin-section T2-weighted single-shot echo-train spin-echo MRCP, and reconstructed 3D MIP MRCP (*f*) images demonstrate the protrusion of choledochocele (arrows, *c*–*f*) into the duodenum in another patient.

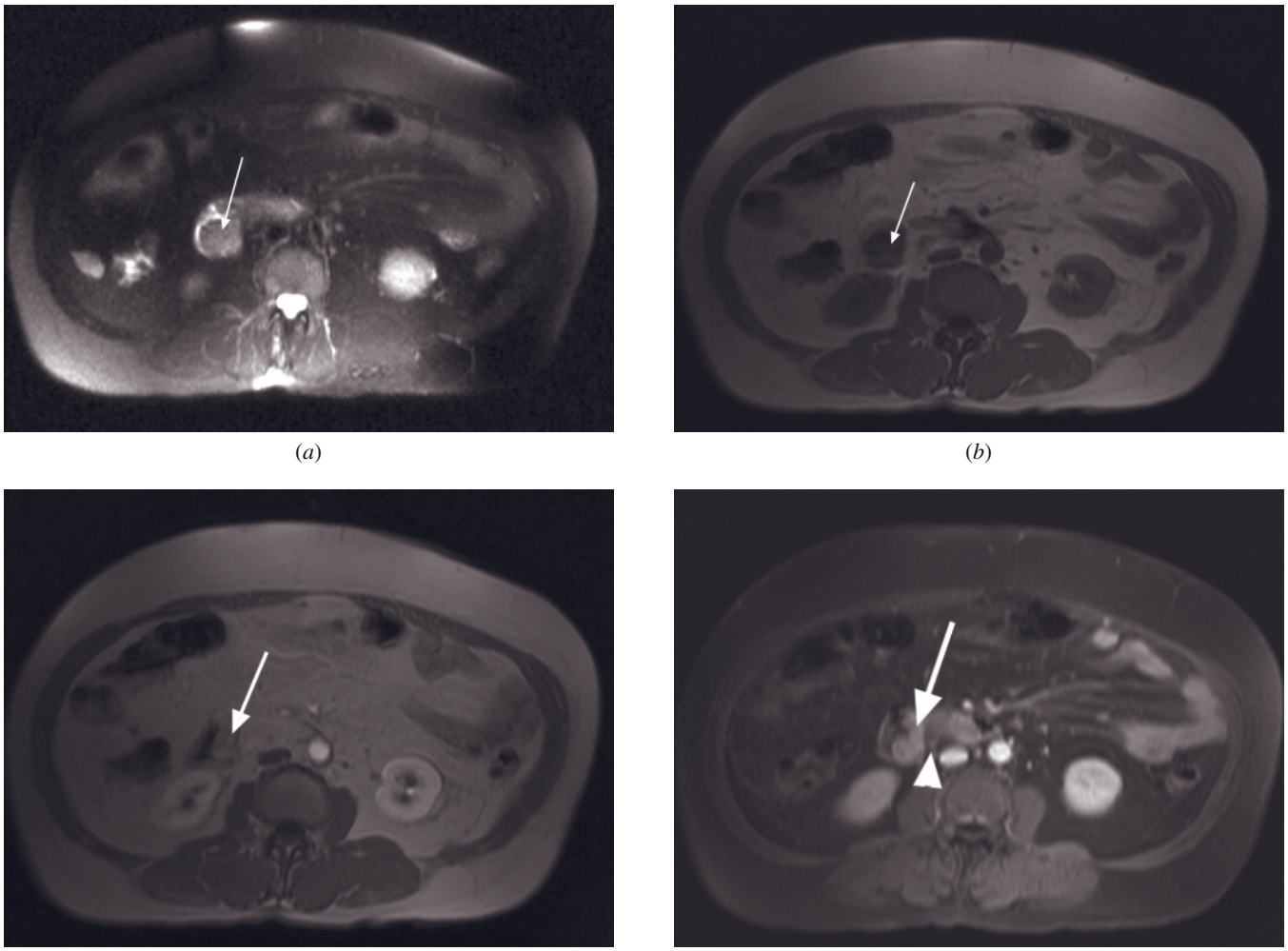

(*a*) (*b*) (*c*) (*d*)

FIG. 6.43 Duodenal adenoma. Axial T2 (*a*),T1 gradient-echo (*b*), and early (*c*) and late (*d*) gadolinium-enhanced T1 images show a discrete mass and thickening of the medial wall of the second part of the duodenum. The pancreas can be clearly seen separate from this mass (arrowhead, *d*).

Malignant Masses

Adenocarcinomas. Small bowel tumors account for only 1% of all gastrointestinal malignancies, and one-half are adenocarcinomas [27]. The most common site for small bowel adenocarcinoma is the duodenum. This tumor frequently occurs in close proximity to the ampulla and as a result may cause obstructive jaundice [66]. Other symptoms, regardless of location, include intestinal obstruction, chronic blood loss, or both. Patients usually are asymptomatic early in the course of their disease; as a result, presentation is often late with advanced disease [27]. The combined use of T2-weighted single-shot echo-train spin-echo and gadolinium-enhanced fat-suppressed SGE or 3D-GE imaging has resulted in reproducibly high image quality for the evaluation of small bowel neoplasms [67]. Duodenal neoplasms are particularly well shown because of the relatively fixed position of the duodenum in the anterior pararenal space. The most consistent MR imaging feature that permits their detection is that tumors enhance heterogeneously on interstitial-phase gadolinium-enhanced images (fig. 6.48). T2-weighted single-shot echo-train spin-echo images provide information about the tumor itself and can be performed as an MRCP study to evaluate the biliary tree. Immediate postgadolinium SGE or 3D-GE images may be used to survey the liver for metastatic disease, whereas 2-min postgadolinium fat-suppressed SGE or 3D-GE images may be obtained to determine the presence of lymphadenopathy and intraperitoneal spread.

Gastrointestinal Stromal Tumor (GIST). Although the stomach is the principal site for approximately two-thirds of all gut stromal tumors (see

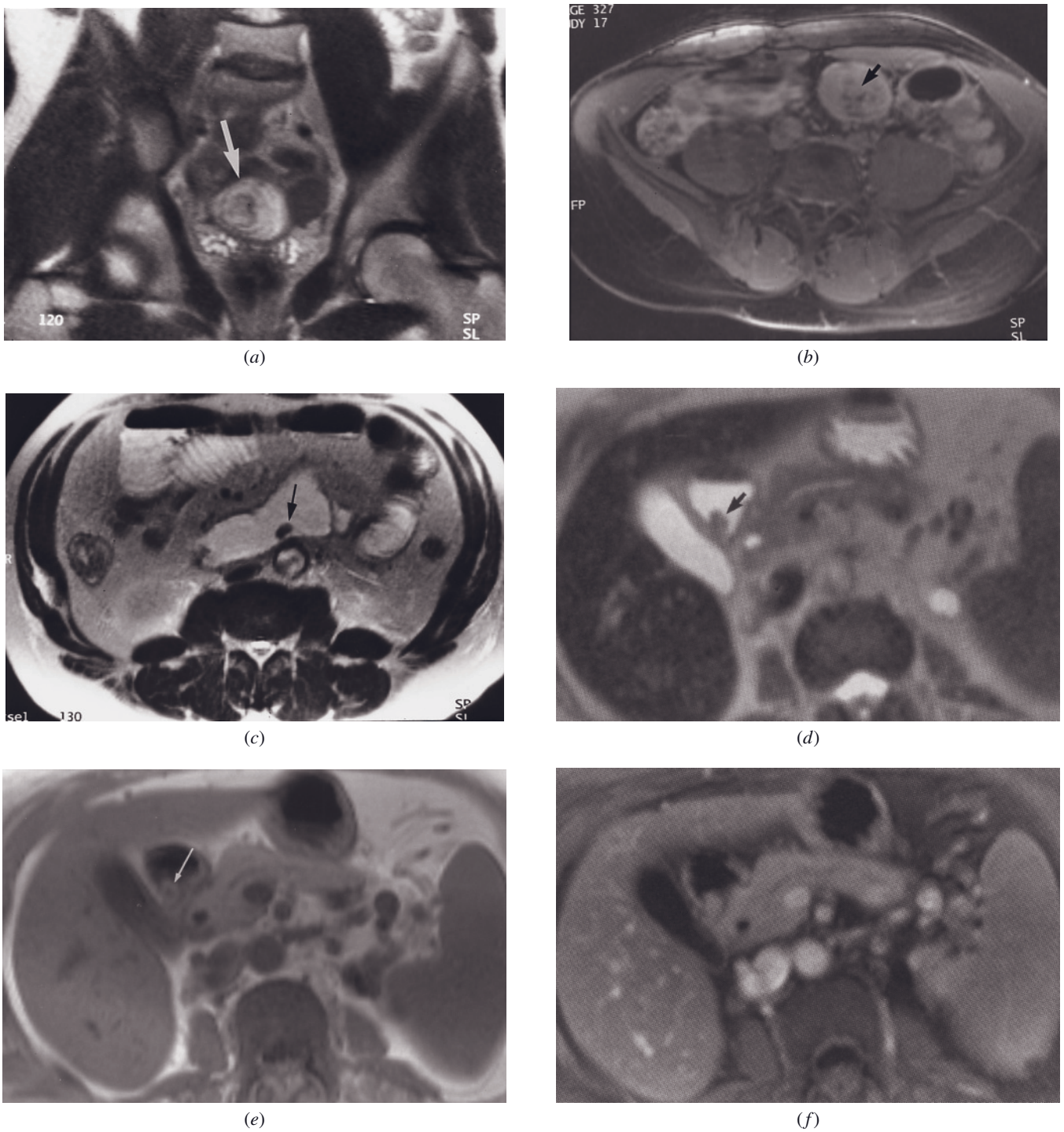

FIG. 6.44 Small bowel polyps. T2-weighted SS-ETSE (*a*) and gadolinium-enhanced fat-suppressed SGE (*b*) images of a hamartoma in Peutz–Jeghers syndrome. A bowel-within-bowel appearance (arrow, *a*) is identified on the T2-weighted image (*a*) in the proximal jejunum because of intussusception. The intussusception is caused by a hamartomatous polyp that has acted as a lead point. The hamartoma is shown as a 1-cm uniformly enhancing mass (arrow) on the gadolinium-enhanced fat-suppressed SGE image (*b*). T2-weighted image (*c*) in a second patient demonstrates a 1-cm polyp (arrow) within a slightly dilated loop of duodenum. T2-weighted SS-ETSE (*d*), SGE (*e*), and 90-s postgadolinium fat-suppressed SGE (*f*) images in a third patient. T2 image shows a low-signal-intensity mass (arrow, *d*) measuring 1.5 cm located in the descending portion of the duodenum. Note that the high signal intensity of intraluminal fluid within the duodenum clearly delineates the polyp, which appears moderately low in signal intensity. Comparing precontrast (*e*) and postgadolinium (*f*) images, enhancement of the polyp is demonstrated, showing it to remain comparable in signal to the duodenal wall, reflecting the tissue nature of the polyp. (Reprinted with permission from Marcos HB, Semelka RC, Noone TC, Woosley JT, Lee JKT: MRI of normal and abnormal duodenum using half-Fourier single-shot RARE and gadolinium-enhanced spoiled gradient-echo sequences. *Magn Reson Imaging* 17: 869–880, 1999.)

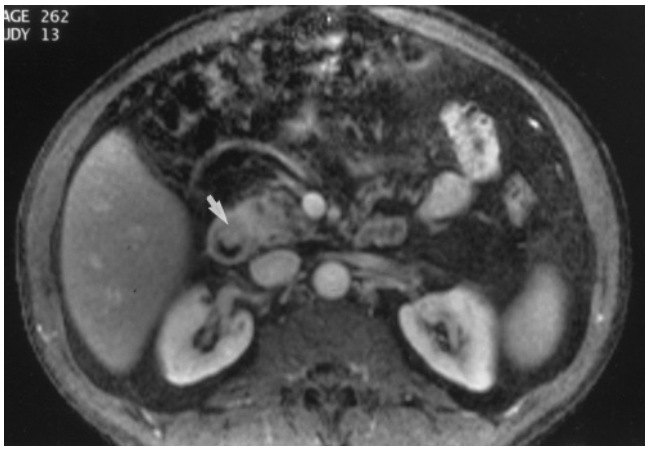

FIG. 6.45 Neurofibroma of duodenum. Transverse 90-s postgadolinium fat-suppressed SGE image in a patient with type 1 neurofibromatosis. A 1-cm intraluminal mass (arrow) arises in the second part of the duodenum. This mass enhances to the same extent as the duodenal wall, reflecting the tissue composition of the neurofibroma. The patient expired, and at autopsy multiple cutaneous and gastrointestinal neurofibromas were found. (Reprinted with permission from Semelka RC, Marcos HB: Polyposis syndromes of the gastrointestinal tract. *J Magn Reson Imaging* 11: 51–55, 2000.)

description above), the small intestine accounts for about 25% of these tumors. As in the stomach, these may be large and ulcerating. Gadolinium-enhanced SGE/3D-GE or fat-suppressed SGE/3D-GE images demonstrate heterogeneous and substantial enhancement of the primary tumor (fig. 6.49). Local or intraperitoneal recurrence may occur after surgical resection (fig. 6.50) and is relatively common, and fat-suppressed gadolinium-enhanced SGE or 3D-GE images are optimal in order to develop maximized contrast between the enhancing tumor and the surrounding retroperitoneal or mesenteric fat. MRI using immediate postgadolinium SGE or 3D-GE is particularly effective at detecting liver metastases because these tend to be hypervascular and often are small.

Lymphoma. Throughout the small intestine and colon are nodules of lymphoid tissue within the mucosa and submucosa. Primary gastrointestinal non-Hodgkin lymphomas are most commonly of the B cell type and appear to arise from B cells of mucosa-associated lymphoid tissue (MALT) (fig. 6.51). In the small intestine, the terminal ileum is the most common site affected (fig. 6.52), which may reflect the relatively greater amount of lymphoid tissue present in this segment compared to the duodenum and jejunum [68]. Gastrointestinal lymphomas comprise 1–2% of all gastrointestinal malignancies and can assume different gross appearances: 1) diffusely infiltrating lesions that often produce full-thickness mural thickening with effacement of overlying mucosal folds, 2) polypoid lesions that protrude into the lumen, and 3) large, exophytic, fungating masses that are prone to ulceration and fistula formation. The small intestine is involved in up to 50% of patients with widespread primary nodal non-Hodgkin lymphoma. The MRI features of small intestine lymphoma include moderately enhancing thickened loops of bowel and large tumor masses that invade the bowel but usually do not result in obstruction (fig. 6.53). In the setting of diffusely infiltrating lesions, the bowel may appear dilated, possibly because of interference with the normal innervation and regulation of smooth muscle bowel wall contraction. The presence of bowel wall mass and dilation without proximal bowel obstruction is suggestive of lymphoma. The presence of splenic lesions or diffuse splenomegaly and mesenteric and retroperitoneal lymphadenopathy supports the diagnosis.

Carcinoid. Carcinoids are the most common primary neoplasm of the small bowel. Tumors are well-differentiated neuroendocrine neoplasms that occur primarily in the distal ileum, in which location they are almost always malignant. Men and women are affected with equal frequency. Most patients present with tumor-related symptoms of bleeding and bowel obstruction or intussusception. Particular to ileal carcinoids are regional mesenteric metastases and vascular sclerosis. The primary tumor may be quite small, with the accompanying lymphadenopathy and desmoplastic reaction in the root of the mesentery presenting as the only visible manifestation of disease. However, when large enough, the primary tumor causes asymmetric bowel wall thickening and enhances heterogeneously, usually moderate in intensity after intravenous gadolinium (figs. 6.54 and 6.55). The characteristic desmoplastic changes in the mesentery and retroperitoneum that occur in response to the secretion of serotonin and tryptophan are low in signal on both T1- and T2-weighted images and show negligible enhancement after contrast. Liver metastases are responsible for the "carcinoid syndrome," which is characterized by vasomotor instability, intestinal hypermotility, and bronchoconstriction [69]. Liver metastases are often hypervascular and high in signal intensity on T2-weighted images, possessing intense ring or uniform enhancement on immediate postgadolinium SGE or 3D-GE images. In the recent series by Bader et al. [70], 98% of liver metastases were hypervascular. Occasionally, carcinoid liver metastases are hypovascular and appear nearly isointense with liver on T2-weighted images and demonstrate faint ring enhancement on immediate postgadolinium SGE or 3D-GE images.

Metastases. Tumors arising in the mesentery, pancreas, stomach, or colon may involve the small intestine

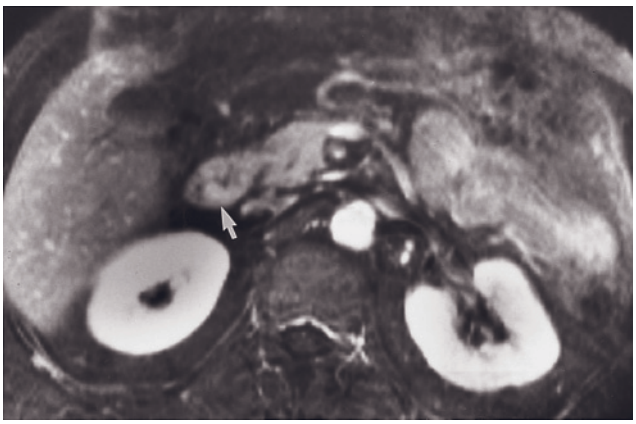

(*a*)

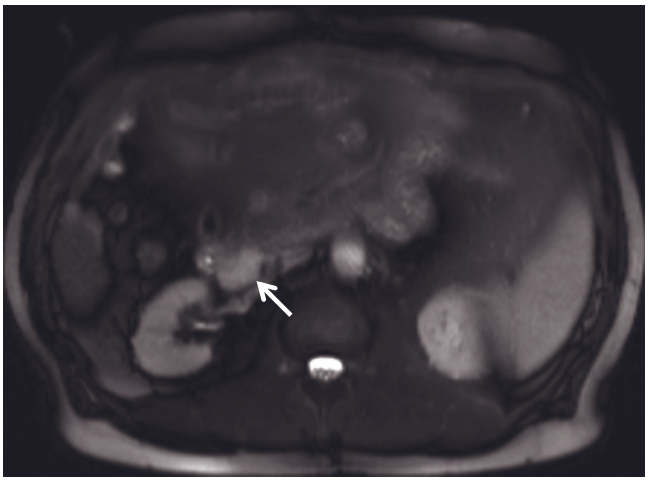

(*b*)

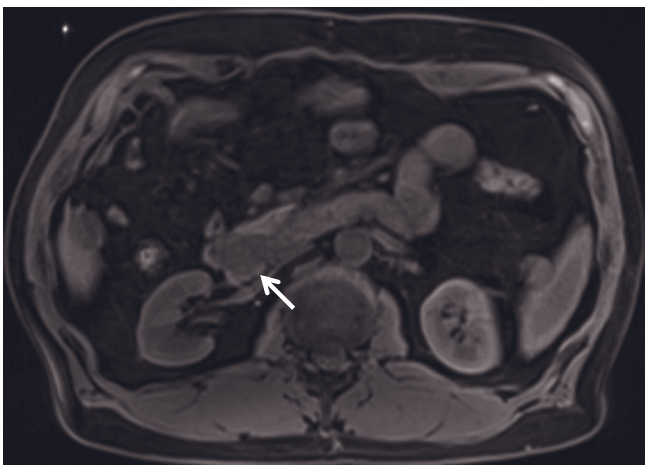

(*c*)

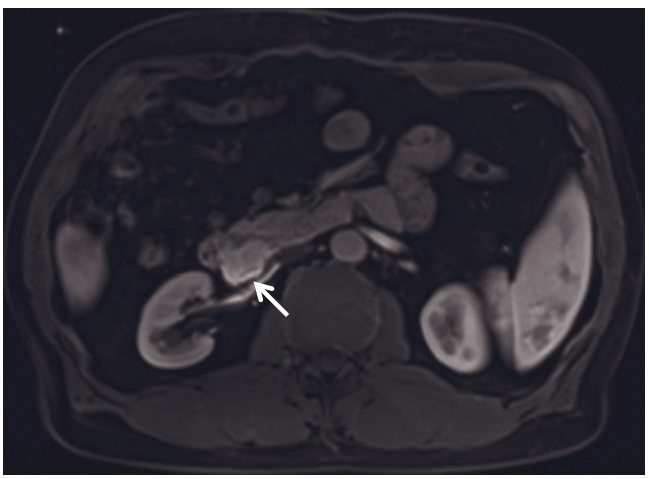

(*d*)

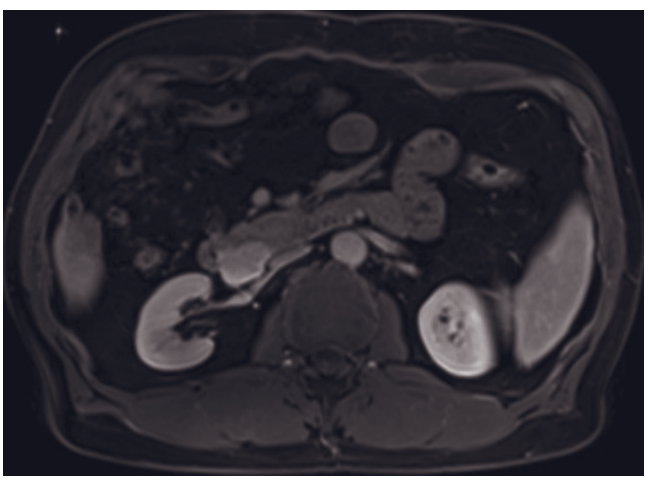

(*e*)

FIG. 6.46 Duodenal leiomyoma. Gadolinium-enhanced T1-weighted fat-suppressed spin-echo image (*a*) shows a uniformly enhancing mass (arrow) protruding into the duodenum. When intraluminal, leiomyomas are indistinguishable from polyps. (Reprinted with permission from Shoenut JP, Semelka RC, Silverman R,Yaffe CS, Mickflikier AB: The gastrointestinal tract. In Semelka RC, Shoenut JP (eds.), *MRI of the Abdomen with CT Correlation.* New York: Raven Press, 1993, p. 119–143.) T2 single-shot echo-train spin-echo (*b*), T1-weighted fat-suppressed 3D-GE (*c*), and T1-weighted postgadolinium hepatic arterial dominant-phase (*d*) and interstitial-phase (*e*) fat-suppressed 3D-GE images at 3.0 T demonstrate a duodenal leiomyoma in another patient. A 2-cm well-defined mass (arrows, *b–d*) is evident in the posterior wall of the third part of the duodenum. The mass is homogeneous and mildly high signal on T2 (*b*) and mildly low signal on T1 (*c*) and exhibits mild homogeneous early enhancement (*c*), with progressive enhancement on the interstitial phase (*d*). The uniform moderately intense enhancement of the leiomyoma on the interstitial phase is a typical feature for this entity. Note that the tumor does not prominently extend into the lumen.

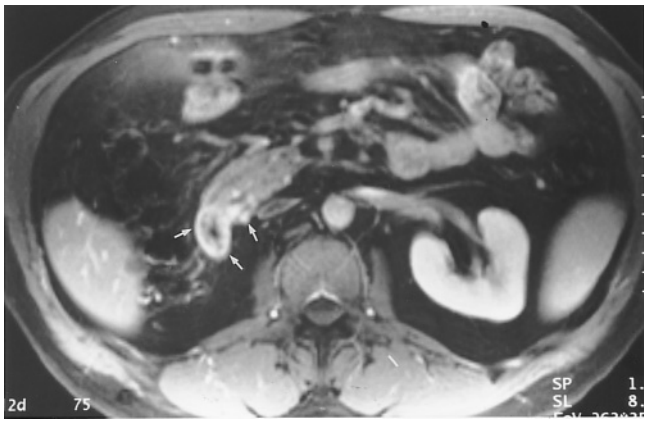

FIG. 6.47 Periduodenal and duodenal varices. Transverse 90-s postgadolinium fat-suppressed SGE image in a patient with splenic vein thrombosis. Periduodenal and duodenal varices are clearly shown as thin enhancing tubular structures adjacent to and within the wall of the duodenum. Venous blood is rerouted to periduodenal and duodenal varices as one of the collateral pathways in the setting of splenic vein thrombosis.

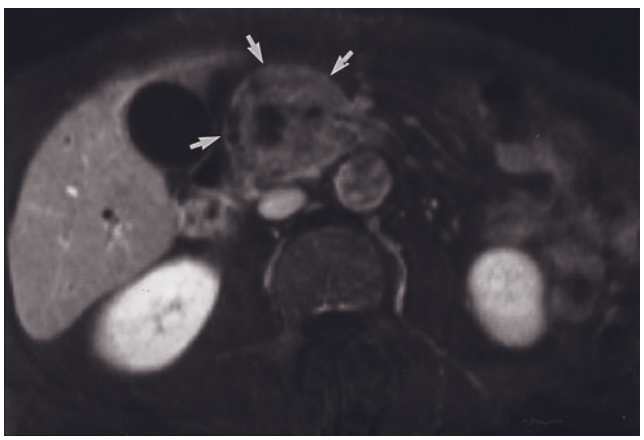

(*a*)

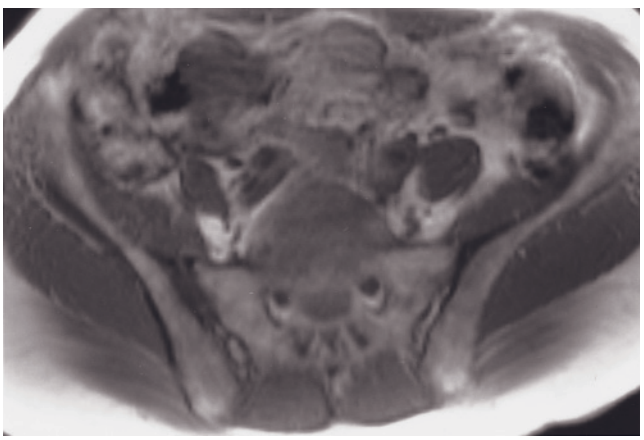

(*b*)

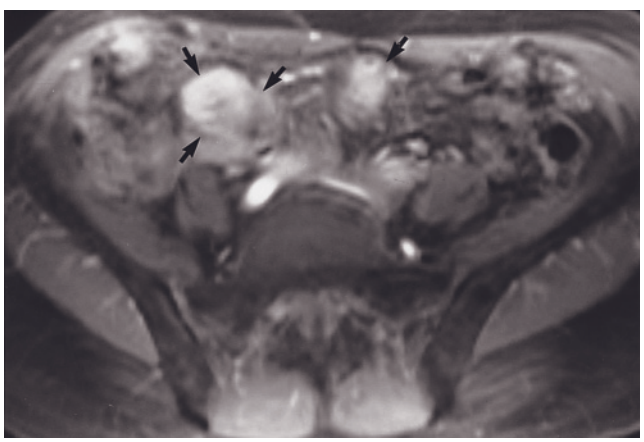

(*c*)

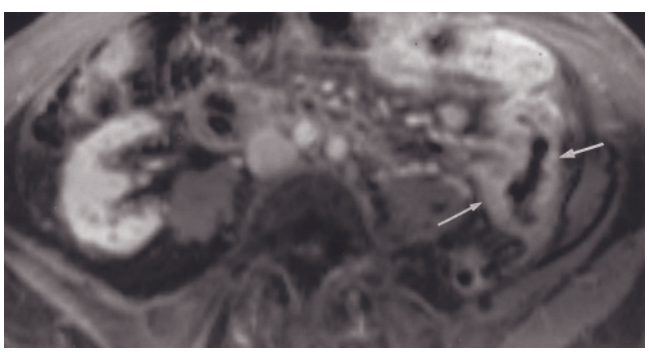

(*d*)

FIG. 6.48 Small bowel adenocarcinoma. Gadolinium-enhanced T1-weighted fat-suppressed spin-echo (*a*), SGE (*b*), and postgadolinium T1-weighted fat-suppressed spin-echo (*c*) images in two patients with small bowel adenocarcinoma. In the first patient (*a*), the size and extent of a large duodenal tumor (arrows) is well shown on the gadolinium-enhanced fat-suppressed image. In the second patient (*b*, *c*), the neoplasm is difficult to identify on the precontrast SGE image (*b*) because it is isointense with background bowel. On the gadolinium-enhanced fat-suppressed SGE image (*c*), the distal jejunal tumors are conspicuous (*c*) because they are higher in signal intensity and heterogeneous compared to background bowel. Transverse 90-s postgadolinium fat-suppressed SGE image (*d*) in another patient with adenocarcinoma of the jejunum. Irregular thickening and enhancement of a segment of proximal jejunum is apparent (arrows, *d*). Coronal (*e*) and transverse (*f*) T2-weighted single-shot echo-train spin-echo and transverse

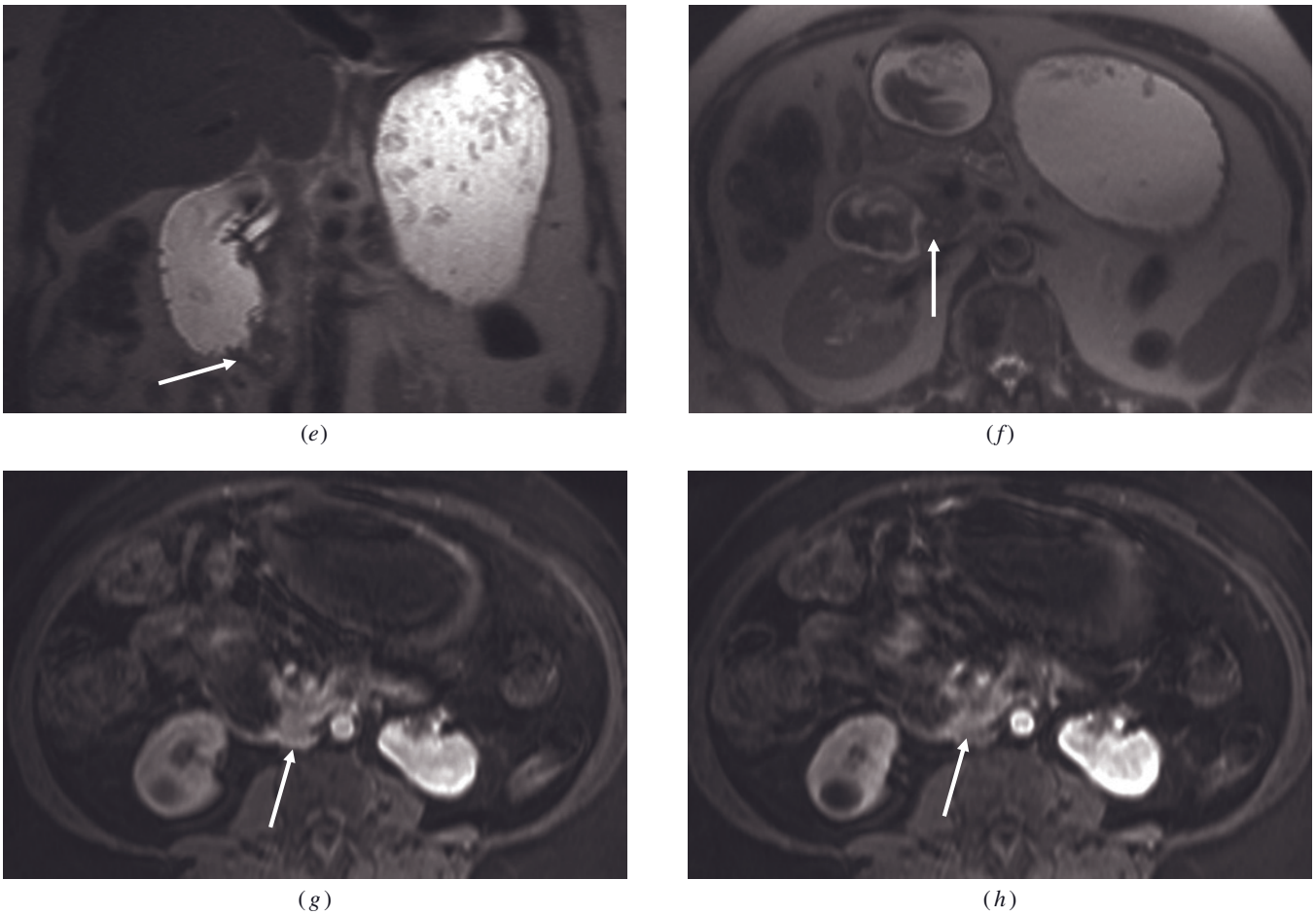

FIG. 6.48 (*Continued*) T1-weighted postgadolinium interstitial-phase fat-suppressed 3D-GE (*g*, *h*) images demonstrate a duodenal adenocarcinoma (arrows, *e–h*) in another patient. The wall of the third portion of the duodenum is diffusely thickened because of adenocarcinoma. The tumor shows intense enhancement and causes obstruction. The stomach and proximal portions of the duodenum is dilated because of the obstruction.

through contiguous extension (fig. 6.56). Metastases to small intestine from melanoma and carcinomas of the lung, testes, adrenal, ovary, stomach, large intestine, uterus, cervix, liver, and kidney have been reported. Of these malignancies, ovarian tumors are the most common cause of disseminated serosal implants in females and colon adenocarcinoma in males (fig. 6.57).

On gadolinium-enhanced fat-suppressed SGE or 3D-GE images, metastases are moderately high in signal intensity in contrast to the low signal intensity of intra-abdominal fat. Malignant peritoneal tissue enhances moderately to substantially on interstitial-phase gadolinium-enhanced images and appears as nodular or irregularly thickened peritoneal or serosal tissue (fig. 6.58). Gadolinium-enhanced fat-suppressed imaging has been shown to be more sensitive than CT imaging in detecting small tumor nodules [71, 72]. Metastatic spread of carcinomas from distal sites such as breast and lung occur, and lesions often lodge on the antimesenteric border of the small bowel. These lesions may be visualized as intramural masses (fig. 6.59). Metastatic tumor may create large submucosal masses and serve as lead points for intussusception, or mechanical obstruction. The use of water-based oral contrast and a MR small bowel follow-through technique may be valuable in exacerbating and demonstrating metastatic disease and obstruction of different degrees (see fig. 6.57).

Inflammatory, Infectious, and Diffuse Disorders

Inflammatory Bowel Disease

Crohn disease and ulcerative colitis are the most common forms of inflammatory bowel disease (IBD). MRI findings correlate well with clinical evaluation, endoscopy, and histologic findings. It is a robust tech-

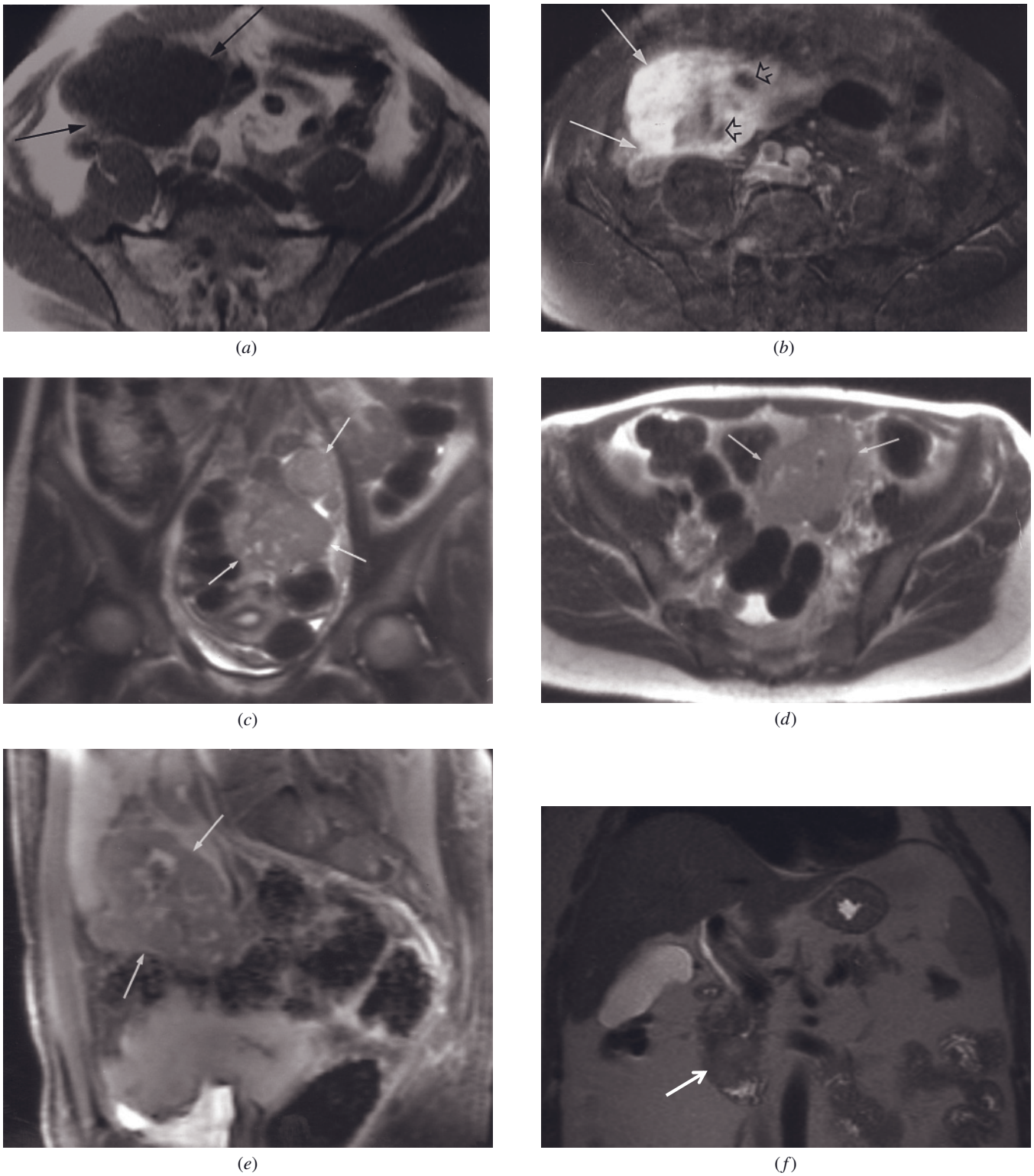

FIG. 6.49 Gastrointestinal stromal tumor (GIST). SGE (*a*) and gadolinium-enhanced T1-weighted fat-suppressed spin-echo (*b*) images. A large exophytic mass (arrows, *a*) arises from the ileum. Lack of proximal bowel obstruction is consistent with its eccentric origin. The tumor's large size coupled with intense enhancement (arrows, *b*) and regions of necrosis (open arrows, *b*) are typical features of GIST. Coronal (*c*) and transverse (*d*) T2-weighted SS-ETSE and sagittal interstitial-phase gadolinium-enhanced fat-suppressed SGE (*e*) images in a second patient with small bowel GIST also show large heterogeneous lobulated masses (arrows, *c–e*) in the pelvis. Coronal T2-weighted single-shot echo-train spin-echo (*f*), transverse T2-weighted fat-suppressed single-shot

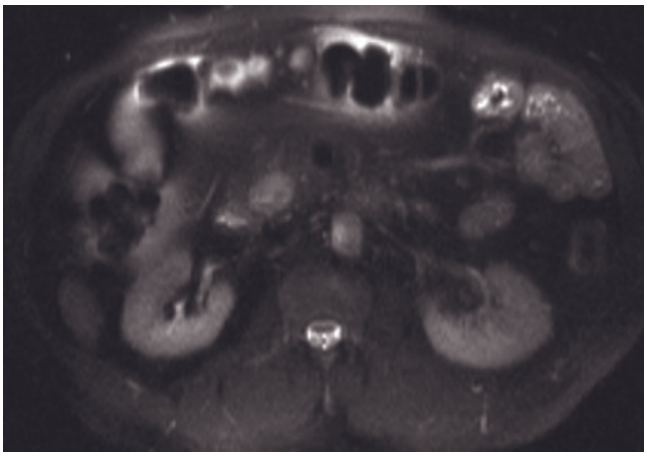

(*g*)

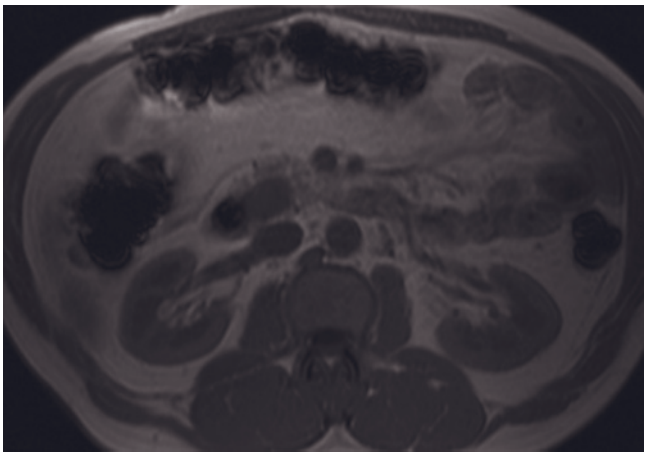

(*h*)

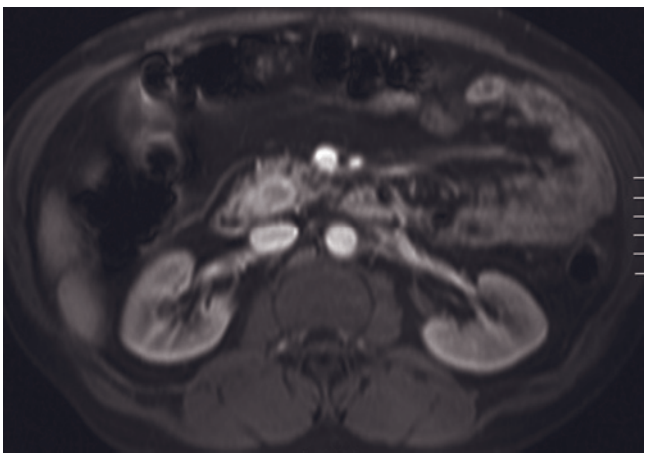

(*i*)

FIG. 6.49 (*Continued*) echo-train spin-echo (*g*), transverse T1-weighted SGE (*h*), and transverse T1-weighted postgadolinium fat-suppressed SGE (*i*) images demonstrate a GIST (arrow, *f*) arising from the second portion of the duodenum in another patient. The tumor shows mildly high signal on T2-weighted images (*f*, *g*), low signal on T1-weighted SGE (*h*), and intense enhancement on postgadolinium image (*i*). The tumor does not cause luminal obstruction and shows homogeneous internal structure due to its small size.

nique capable of diagnosing type, evaluating severity, and monitoring response to treatment in patients with IBD [1–4]. Conventional fluoroscopic and CT methods of examination of the small bowel may be able to detect disease but have been found to be nonspecific in regard to determining activity of disease. Capsule endoscopy utilizes a miniaturized camera that is ingested and that records the images taken as it passes through the small bowel. This represents another technique sensitive for early mucosal changes. The combination of capsule endoscopy and MR small bowel examination may provide a comprehensive and noninvasive safe approach for detection and characterization of the spectrum of changes associated with IBD, from early to progressed disease.

Crohn Disease. In North America, Crohn disease is the most common inflammatory condition to affect the small bowel. The incidence is greatest in the second and third decades of life, and Crohn disease is most prevalent in urban-dwelling women. There is evidence for familial associations in Crohn disease, and there is a higher incidence in Ashkenazi Jews. Although the precise etiology of this disease is not fully understood, there is clearly a combination of genetic, immunologic, and infectious factors [73]. Crohn disease usually presents in young adults but can occur in any age group including children and the elderly. Symptoms include watery diarrhea, crampy abdominal pain, weight loss, and fever. Patients with longstanding Crohn disease have a well-documented increased incidence of cancer (approximately 3% of patients) of the gastrointestinal tract, usually involving the colon or ileum.

Although any part of the gastrointestinal tract, from the mouth to the anus, may become involved with Crohn disease, it most commonly involves the terminal ileum, frequently in association with disease in the right colon. Involvement of the terminal ileum occurs in approximately 70% of patients, with combined terminal ileal and cecal disease present in 40% of the total and isolated terminal ileal involvement in the remaining 30%. Five percent of patients will manifest Crohn disease

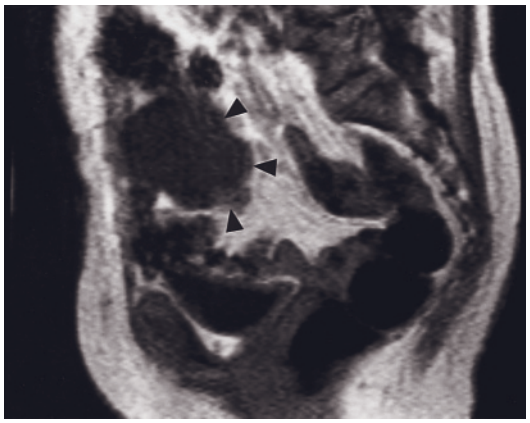

(*a*)

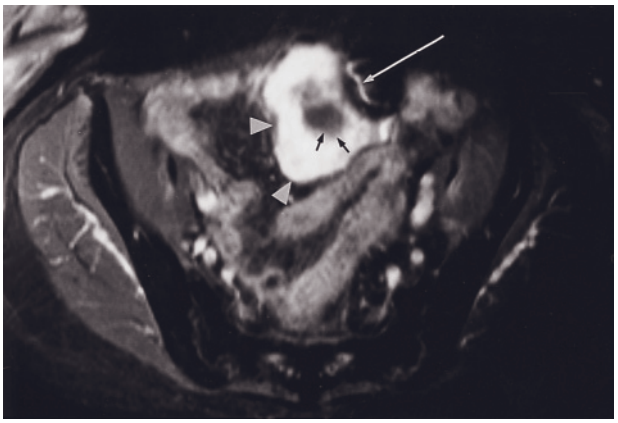

(*b*)

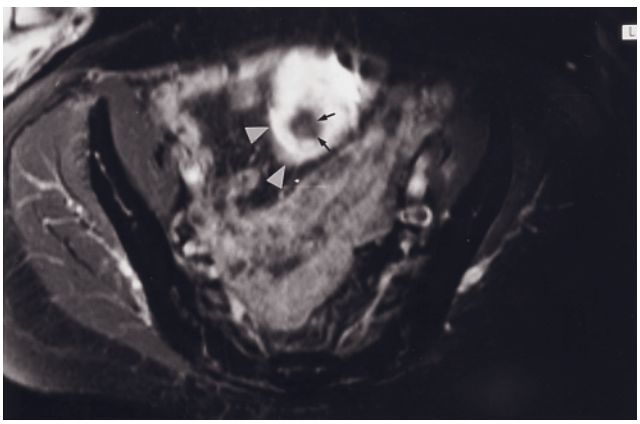

(*c*)

FIG. 6.50 Recurrent gastrointestinal stromal tumor (GIST). Sagittal SGE (*a*) and gadolinium-enhanced T1-weighted fat-suppressed spin-echo (*b*, *c*) images in a patient with previous surgical resection for GIST. Recurrent GIST exhibits features similar to those of the primary tumor: large size, exophytic growth, hypervascularity, and central necrosis. The eccentric location of the tumor (arrowheads, *a*–*c*) is seen on all imaging planes. Marked enhancement after intravenous contrast reflects hypervascularity. Necrosis often accompanies these large tumors (short arrows, *b*, *c*). Note the susceptibility artifact (long arrow, *b*) associated with surgical clips from prior resection.

in the duodenum or jejunum. Twenty to thirty percent will have isolated colon involvement [74]. Crohn disease is characterized pathologically by sharply defined areas showing transmural involvement by chronic inflammation, fibrosis, and noncaseating granulomas. Sometimes several well-demarcated lesions are separated by normal bowel, producing what are termed "skip lesions." This particular pattern is not found in ulcerative colitis, which produces instead a confluent or continuous region of inflammation that begins in the rectum and progresses contiguously to involve more proximal large bowel to different degrees. Other features typical of Crohn disease include prominent lymph follicles, lymphangiectasia, and submucosal edema. Grossly, at the beginning stages of Crohn disease, the mucosa may show only small, hyperemic ("aphtoid") ulcerations. In time, the ulcers extend transmurally, often beyond the intestinal serosa to become sinus tracts or fistulae. With the evolution of the disease, the bowel wall becomes thickened and inflexible, secondary to fibrosis. In addition, strictures, abscesses, and lymphoid hyperplasia may complicate the disease. The mesenteric changes include inflammatory stranding, a reflection of dilated vasa rectae and sinus tracts, reactive lymphadenopathy, and mesenteric fat that becomes stranded and retracted because of development of fibrotic bands, resulting in the descriptive term "creeping" fat. Current therapeutic strategy is based on medical therapy, using a combination of steroid and antibiotics for suppressing acute exacerbations and long-term therapy utilizing immunosuppressants such as 6-mercaptopurine. Surgery is reserved for complicated cases, but anastomotic recurrence is common. Surgery is felt to represent a therapeutic intervention of last resort. Typically, disease will first appear in the second or third decade and subside by the midadult years, allowing eventual weaning from immunosuppressant therapy.

Changes of Crohn disease are well shown on MRI. Severe disease is characterized by wall thickness greater than 1 cm, length of involvement greater than 15 cm, and mural enhancement greater than 100% (fig. 6.60). Mild disease results in subtle findings that may only be appreciated on gadolinium-enhanced fat-suppressed images (fig. 6.61). Multiplanar imaging provides comprehensive information on disease extent and complications. T2-weighted single-shot echo-train spin-echo and

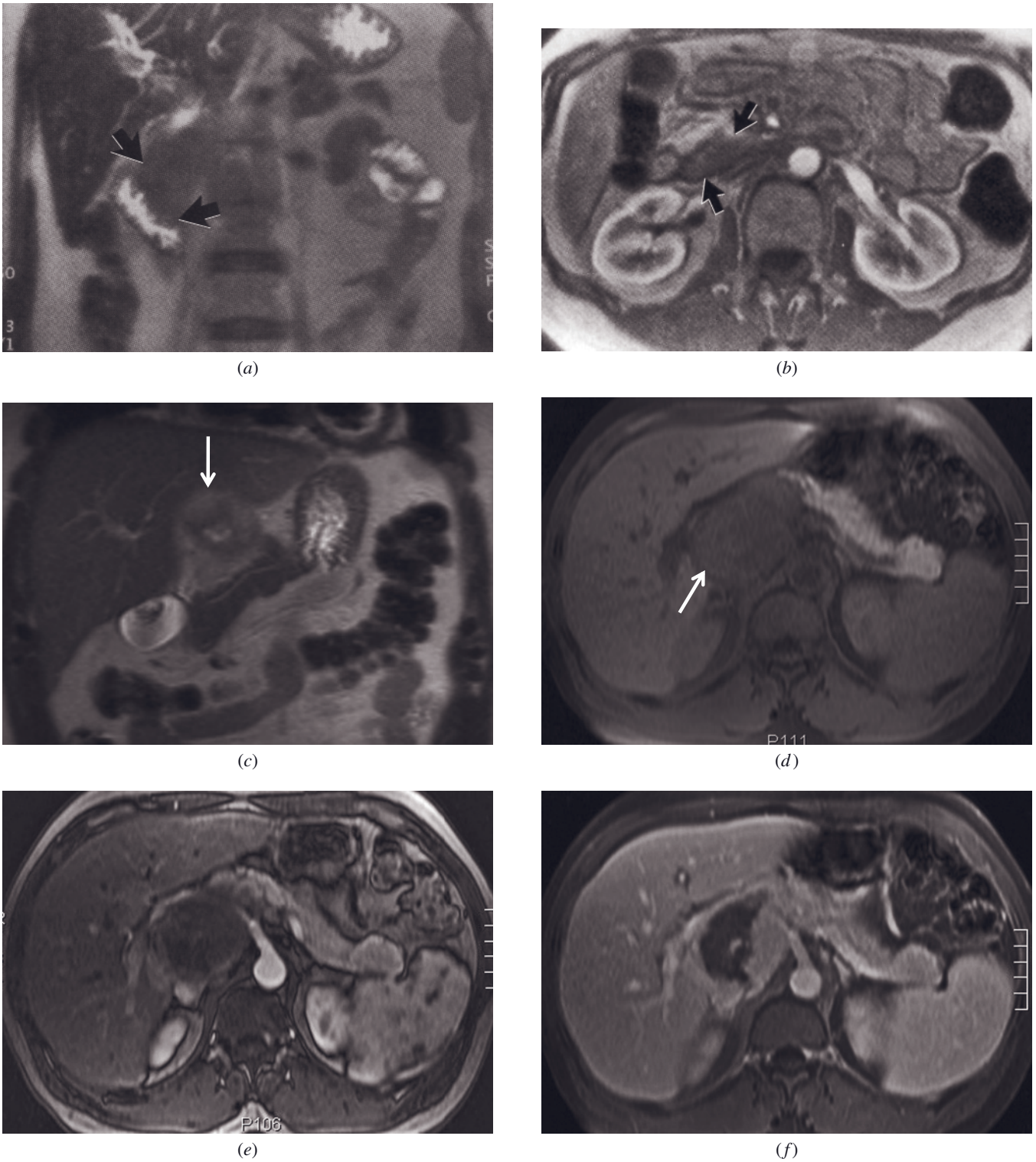

FIG. 6.51 Duodenal MALToma. Coronal T2-weighted SS-ETSE (*a*) and immediate postgadolinium fat-suppressed SGE (*b*) images. T2-weighted image demonstrates irregular thickening of the superior aspect of the duodenal wall caused by a paraduodenal mass (arrows, *a*). Postgadolinium image (*b*) shows a mass that is interposed between the third portion of the duodenum and the head of the pancreas. This mass shows mild heterogeneous enhancement compared to duodenal wall and pancreas, which permits a good distinction between mass and pancreas. Low-grade lymphoma (MALToma type) was proven by endoscopic biopsy. (Reprinted with permission from Marcos HB, Semelka RC, Noone TC, Woosley JT, Lee JKT: MRI of normal and abnormal duodenum using half-Fourier single-shot RARE and gadolinium-enhanced spoiled gradient-echo sequences. *Magn Reson Imaging* 17: 869–880, 1999.) Coronal T2-weighted single-shot echo-train spin-echo (*c*), T1-weighted fat-suppressed SGE (*d*), and T1-weighted postgadolinium hepatic arterial dominant-phase (*e*) and fat-suppressed interstitial-phase (*f*) 3D-GE images demonstrate a large mass originating from the duodenum in another patient. The tumor shows mildly high signal on T2-weighted image (*c*), low signal on T1-weighted image (*d*), and progressive enhancement on postgadolinium images (*e*, *f*). Central necrotic region is detected in the tumor. No biliary or proximal gastrointestinal dilatation is detected. The tumor is located adjacent to the pancreatic head and displaces the IVC posterolaterally and the portal vein anteriorly. The diagnosis is MALToma histopathologically.

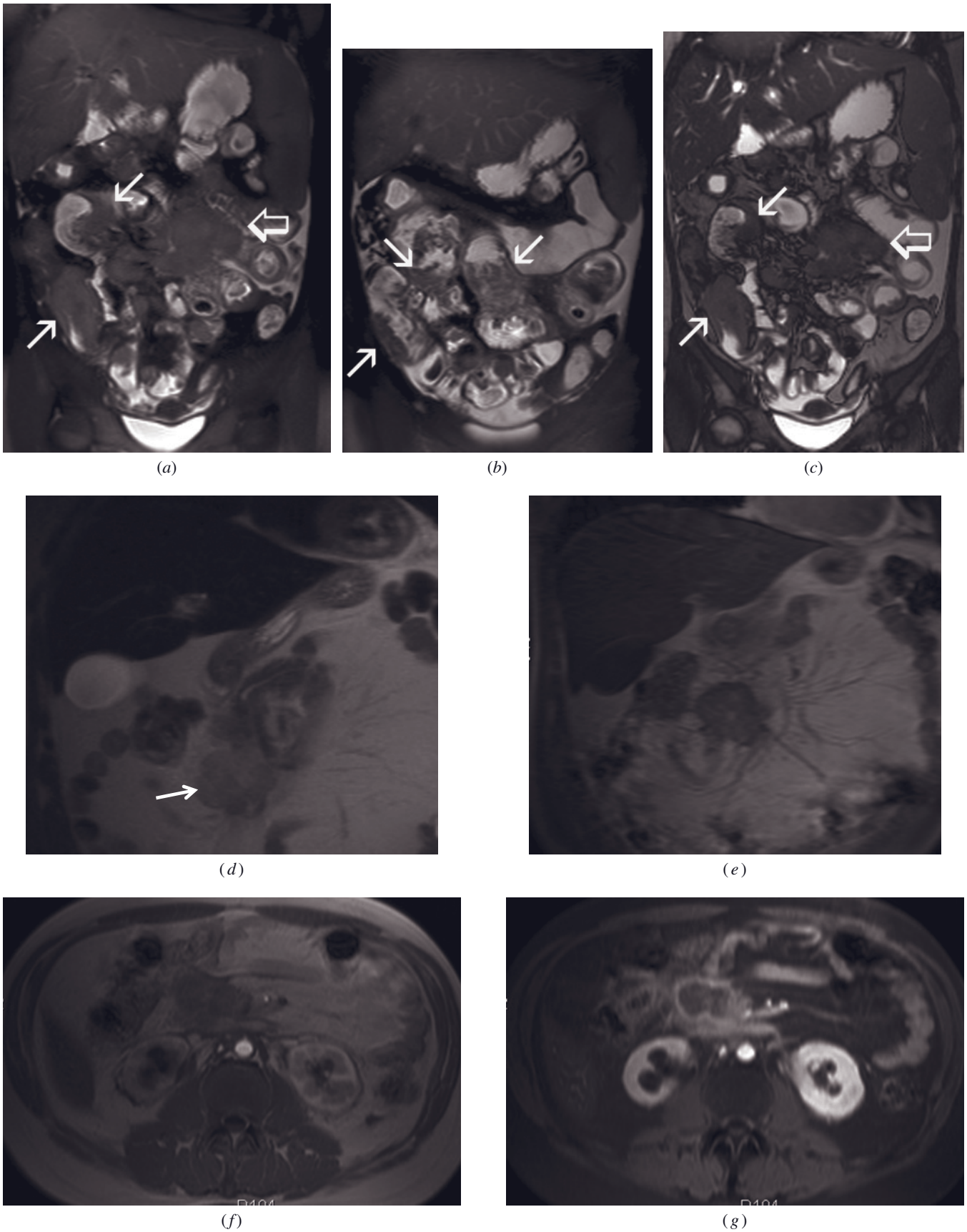

Fig. 6.52 Small bowel lymphoma. A 58-year-old female patient with non-Hodgkin lymphoma of the abdomen. Coronal single-shot echo-train T2 (*a* and *b*) and coronal true-FISP (*c*) images show large mesenteric lymph nodes (open arrows). Lymphoma infiltration of the bowel wall is seen as diffuse wall thickening (arrows, a–*c*). Coronal T2-weighted single-shot echo-train spin-echo (*d*), coronal T1-weighted SGE (*e*), transverse T1-weighted postgadolinium arterial-phase SGE (*f*), and transverse T1-weighted post-gadolinium interstitial-phase fat-suppressed 3D-GE (*g*) images demonstrate duodenal lymphoma (arrow, *d*) in another patient. The exophytic tumor is located in the third portion of the duodenum. The tumor shows high signal on T2-weighted image and low signal on T1-weighted image. The enhancement is progressive and predominantly peripheral. Note that there is no proximal luminal obstruction. The liver shows low signal on precontrast images because of iron deposition.

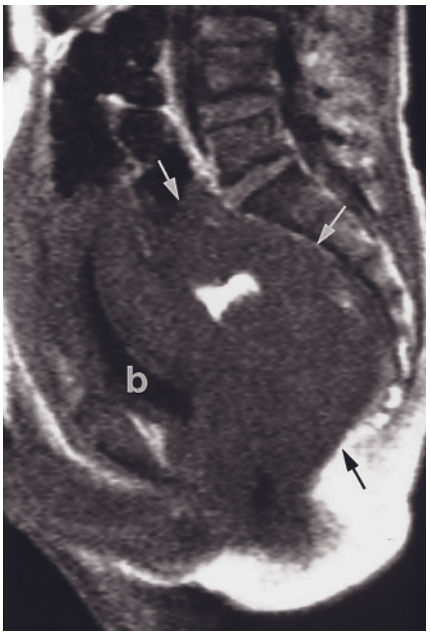

(*a*)

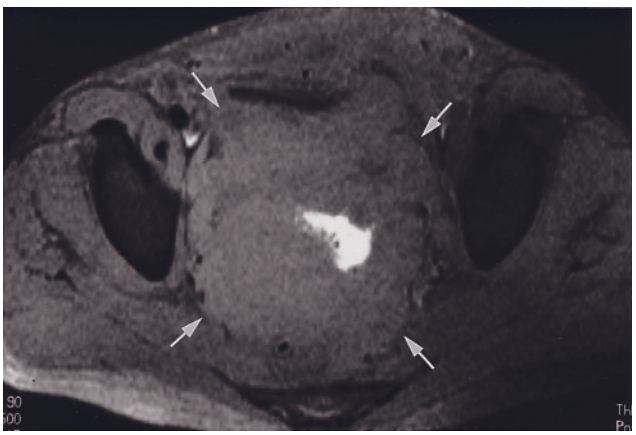

(*b*)

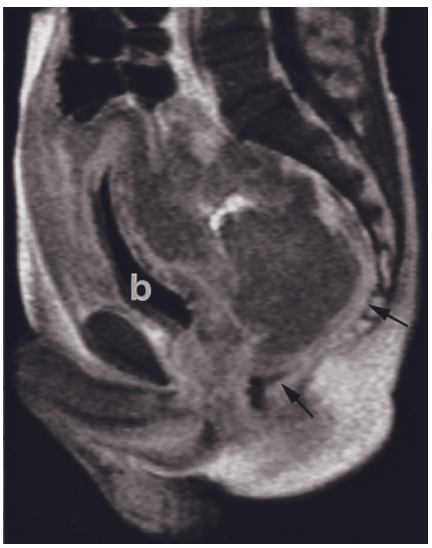

(*c*)

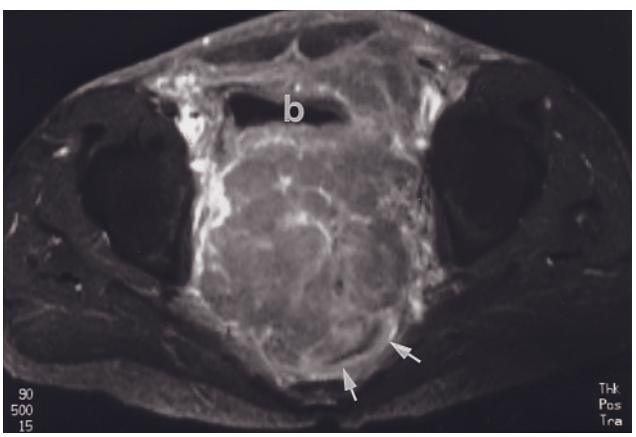

(*d*)

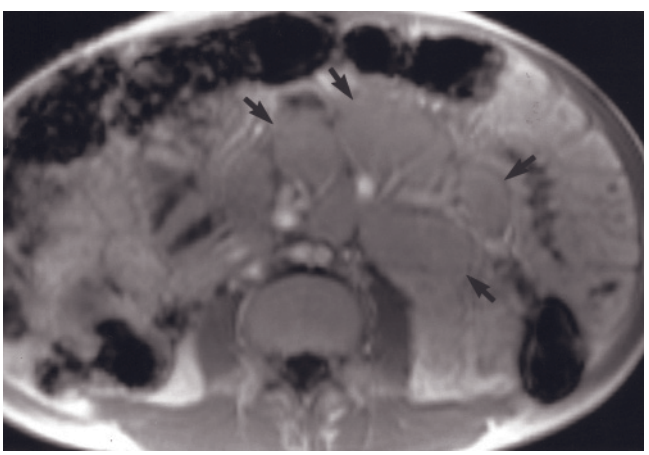

(*e*)

FIG. 6.53 Small intestine lymphoma. Sagittal SGE (*a*), T1-weighted fat-suppressed spin-echo (*b*), sagittal 45-s postgadolinium SGE (*c*), and gadolinium-enhanced T1-weighted fat-suppressed spin-echo (*d*) images in a patient with diffuse lymphomatous infiltration of the distal jejunum and ileum. A large pelvic mass (arrows, *a*, *b*) is seen on precontrast images. After intravenous gadolinium, minimal enhancement of the mass is present on early postgadolinium images (*c*), and heterogeneous slightly greater enhancement is present on the interstitial-phase image (*d*). Minimal enhancement on early postgadolinium images with slight increase and minimal heterogeneous enhancement on more delayed images is common for lymphoma in general. The relationship of the mass to adjacent structures can be assessed by imaging in multiple planes. The rectum (arrows, *c*, *d*) is displaced and compressed by the tumor. Despite extensive disease, there is no proximal small bowel obstruction, a characteristic finding with small intestine lymphoma. High signal intensity within the pelvic mass is consistent with hemorrhage. Bladder = b (*a*, *c*, *d*).

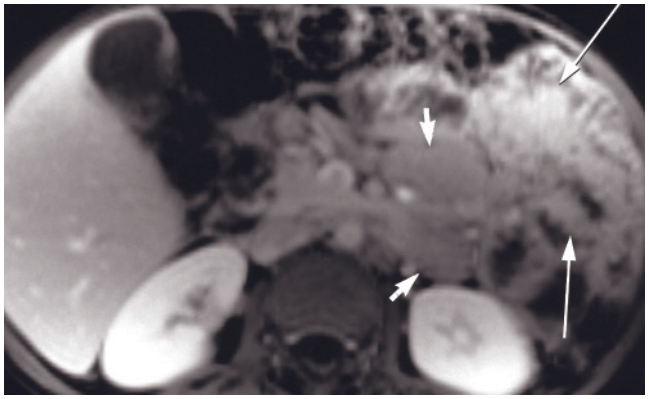

(*f*)

FIG. 6.53 (*Continued*) Transverse gadolinium-enhanced SGE (*e*) and interstitial-phase gadolinium-enhanced fat-suppressed SGE (*f*) images in a second patient with non-Hodgkin lymphoma. Bulky mesenteric lymphadenopathy (small arrows, *e*, *f*) is observed as well as thickening of small bowel loops (long arrows, *f*).

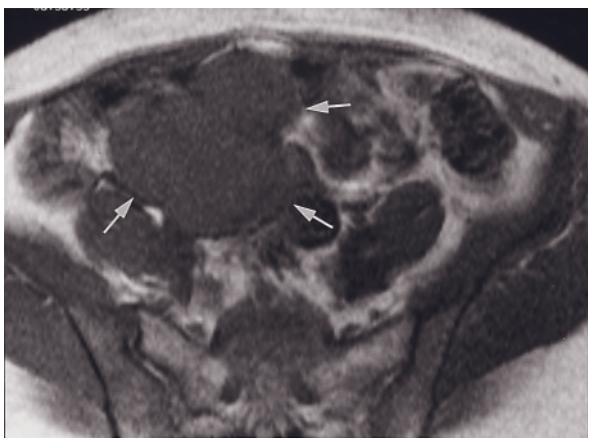

(*a*)

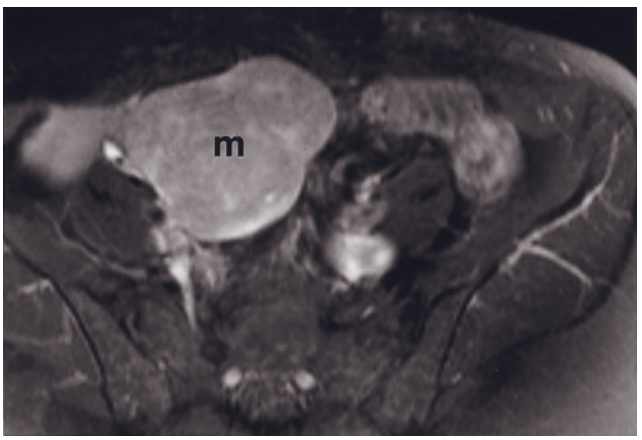

(*b*)

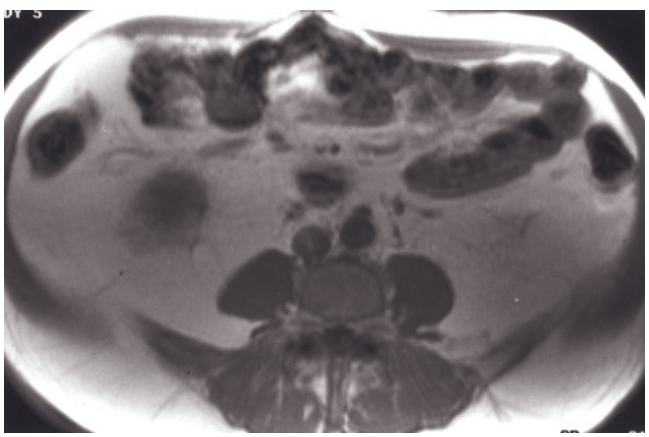

(*c*)

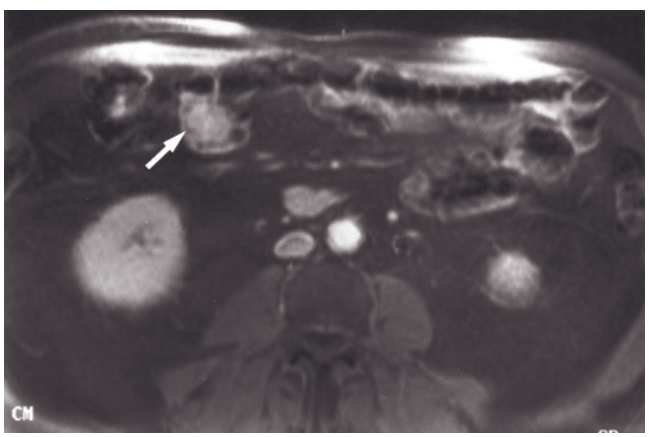

(*d*)

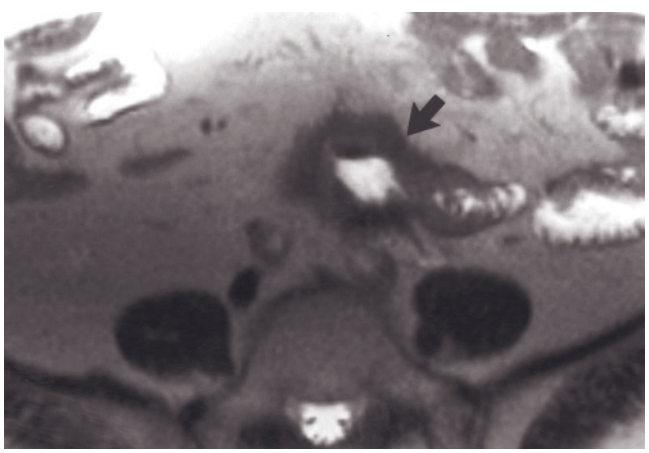

(*e*)

FIG. 6.54 Ileal carcinoid. SGE (*a*) and gadolinium-enhanced T1-weighted fat-suppressed spin-echo (*b*) images. The carcinoid tumor (arrows, *a*) causes asymmetric bowel wall thickening, is isointense with bowel on the T1-weighted image (*a*), and enhances heterogeneously and moderately intensely on gadolinium-enhanced interstitial-phase images (*b*). Transverse SGE (*c*) and interstitial-phase gadolinium-enhanced fat-suppressed SGE (*d*) images in a second patient with ileal carcinoid demonstrate a nodular mass originating from the bowel loop that is isointense on the transverse precontrast T1-weighted image and enhances moderately and heterogeneously on the delayed image (arrow, *d*). Transverse T2-weighted SS-ETSE (*e*) in a third patient shows irregular circumferential thickening small bowel consistent with carcinoid tumor.

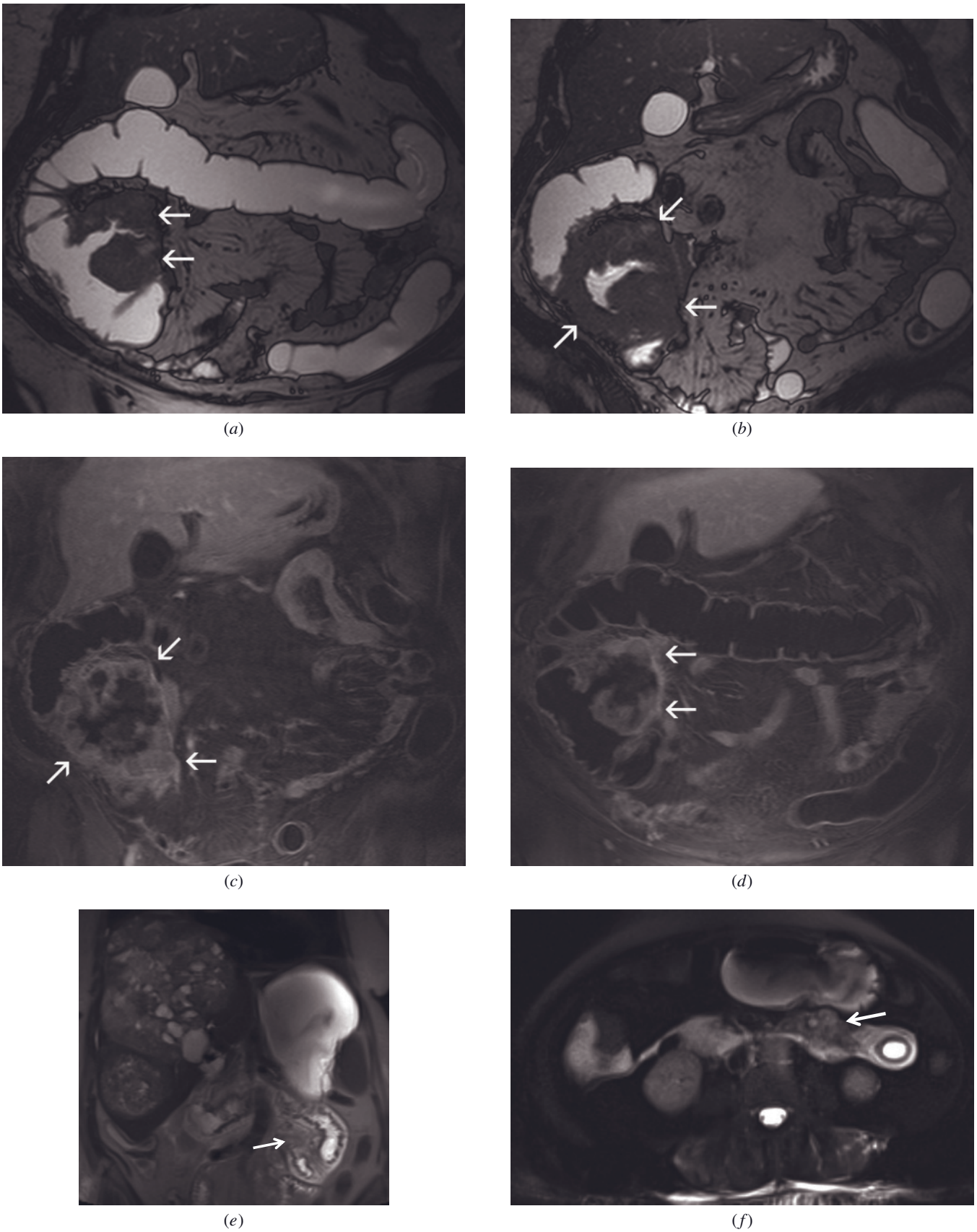

Fig. 6.55 Carcinoid involving the terminal ileum. A 56-year-old man has a large carcinoid tumor demonstrated on coronal true-FISP images (arrows, *a, b*). Central tumor necrosis is best shown on the coronal interstitial-phase gadolinium-enhanced T1-weighted fat-suppressed 3D-GE sequence (arrows, *c*, *d*). **Jejunal neuroendocrine tumor.** Coronal T2-weighted single-shot echo-train spin-echo (*e*), transverse T2-weighted fat-suppressed single-shot echo-train spin-echo (*f*), transverse T1-weighted fat-suppressed

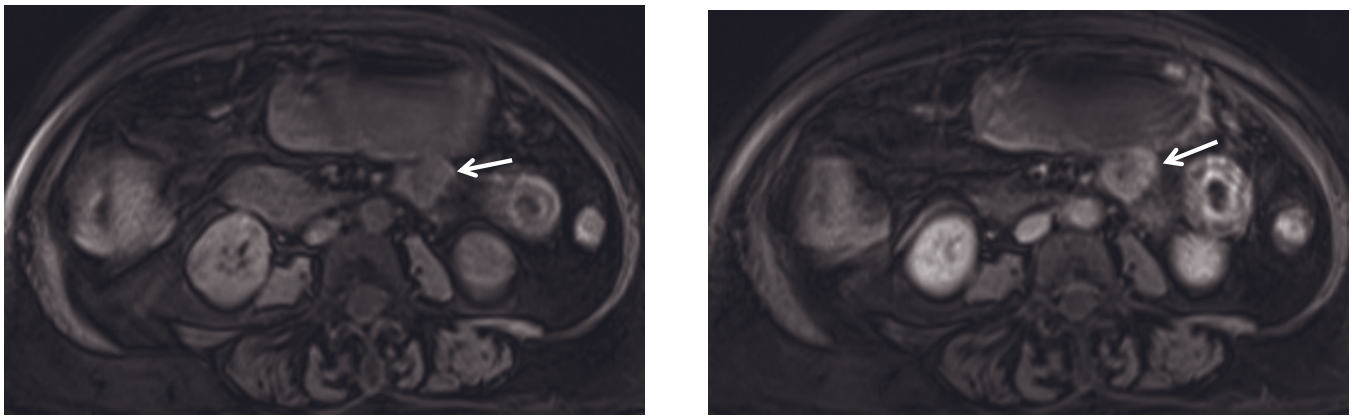

(*g*) (*h*)

FIG. 6.55 (*Continued*) 3D-GE (*g*), and T1-weighted postgadolinium interstitial phase fat-suppressed 3D-GE (*h*) images demonstrate a small neuroendocrine tumor (arrows, *e–h*) located in the mesentery adjacent to the jejunum. The tumor shows heterogeneous signal on T2-weighted images (*e*, *f*) and enhances moderately on the interstitial phase (*h*). Multiple liver metastases and ascites are detected. Note that the wall of the jejunal segment adjacent to the tumor shows edema and moderate enhancement.

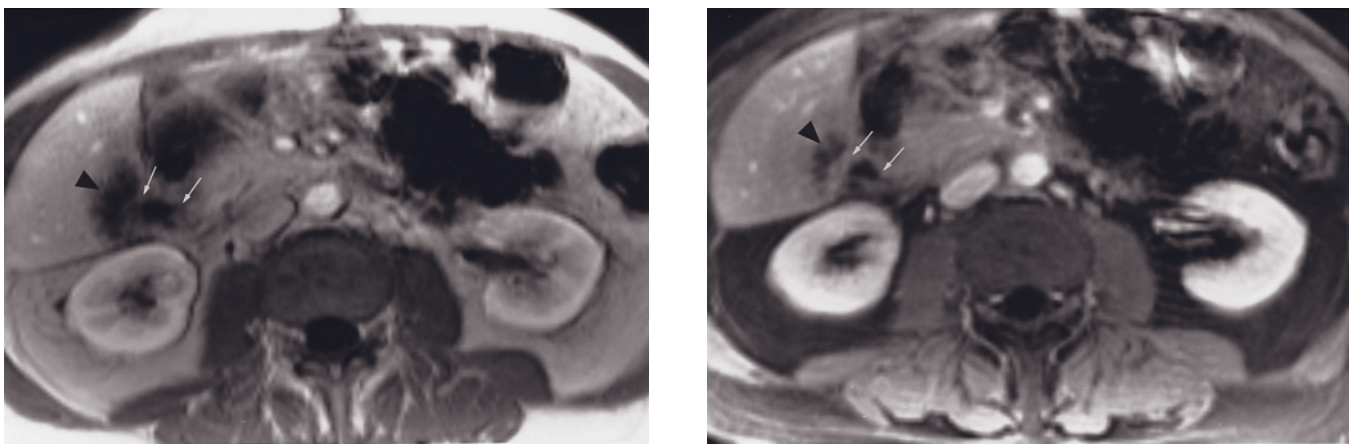

(*a*) (*b*)

FIG. 6.56 Colon cancer liver metastasis with invasion of the duodenum. Immediate postgadolinium SGE (*a*) and 90-s postgadolinium fat-suppressed SGE (*b*) images in a patient with colon cancer metastasis to liver and duodenum. A peripheral hepatic metastasis (arrowhead, *a*, *b*) transgresses the liver capsule to directly invade the adjacent duodenum (arrows, *a*, *b*).

gadolinium-enhanced T1-weighted fat-suppressed SGE or 3D-GE images demonstrate characteristic findings: transmural involvement, skip lesions, and mesenteric inflammatory changes (figs. 6.62–6.64).

Marcos and Semelka evaluated the capability of single-shot echo-train spin-echo and gadolinium-enhanced T1 SGE images for evaluating bowel changes and complications of Crohn disease [75]. The results of this study showed that single-shot echo-train spin-echo image is a very effective technique to demonstrate dilated obstructed bowel, whereas gadolinium-enhanced fat-suppressed SGE is useful in demonstrating inflammatory changes in bowel. Both techniques were effective in showing wall thickening and abscess formation.

Good correlation has been reported between MRI findings and disease activity [2, 4, 5], where demonstration of edema on T2 fat-suppressed images is associated with disease activity (fig. 6.65). These results are in contrast to barium or CT studies, which have limited correlation with symptomatology or response to therapy. It is challenging to discriminate between edema and fibrosis on CT imaging, and it may be largely for this reason that CT findings have not correlated well with disease activity.

Moreover, the potential harm of radiation exposure from serial barium examinations in pregnant women and patients of reproductive age is not inconsequential [74]. MRI may be the modality of choice for evaluation

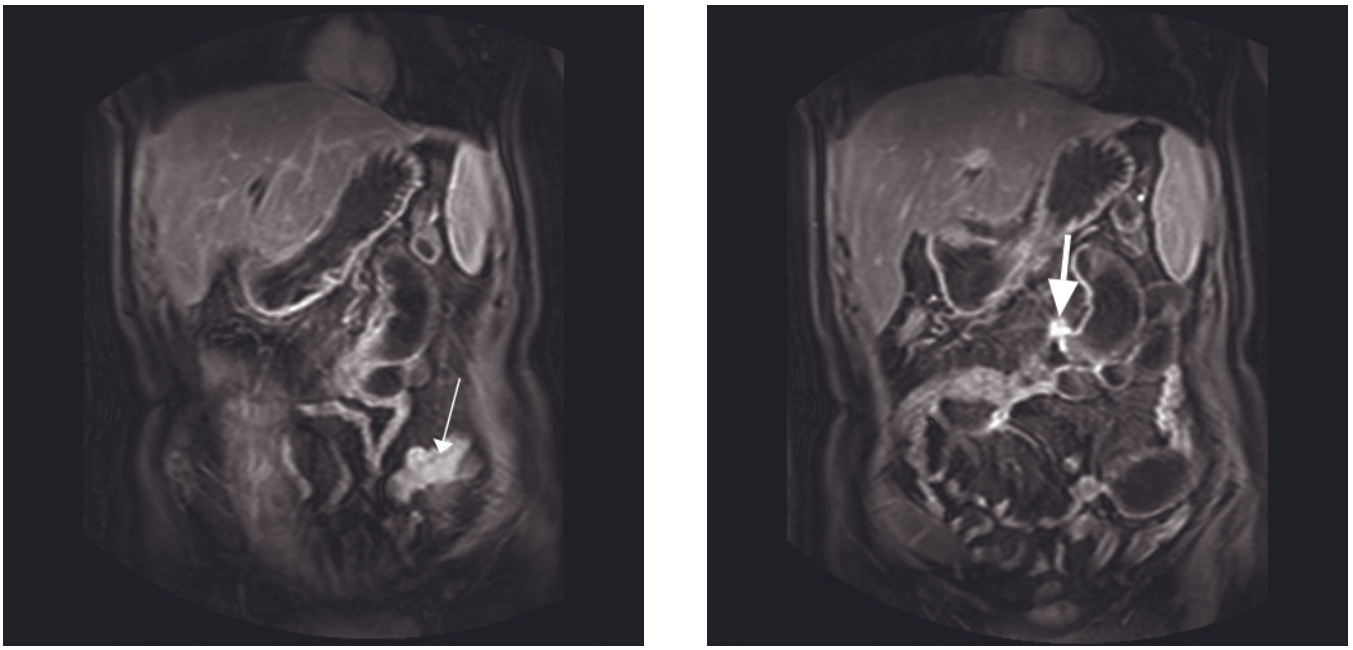

(*a*) (*b*)

FIG. 6.57 Serosal metastases with small bowel obstruction. Multiple serosal metastases from large bowel adenocarcinoma resulted in mesenteric metastases and multiple partial small bowel obstructions. Metastases can be identified on gadolinium-enhanced T1 coronal 3D gradient-echo images as abnormal enhancement adjacent to distal (arrow, *a*) and proximal (arrow, *b*) small bowel associated with focal narrowing and proximal dilation of the involved bowel segment. The patient was given oral water-based contrast mixed with mannitol and locust bean gum to achieve better small bowel distension and to increase the conspicuity of partially obstructing lesions.

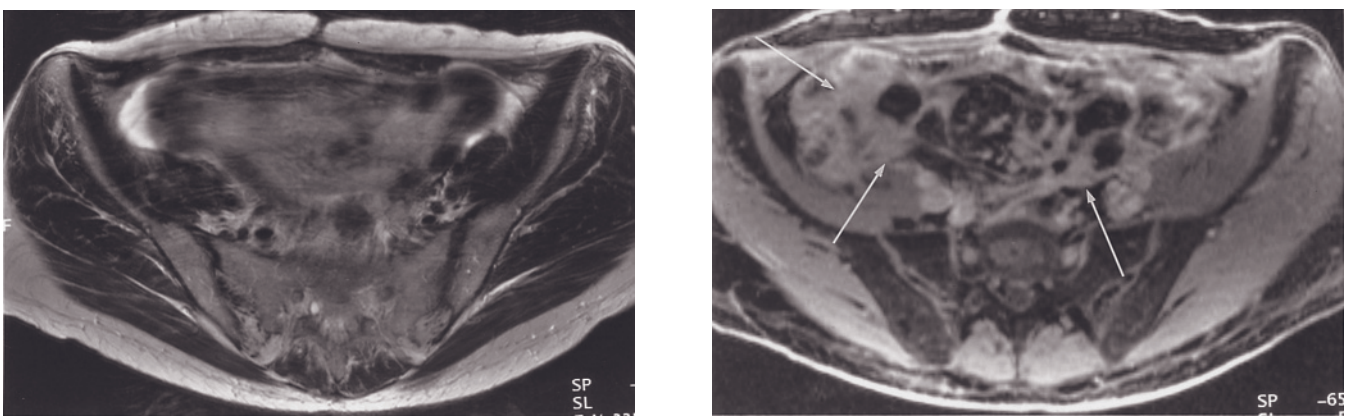

(*a*) (*b*)

FIG. 6.58 Ovarian carcinoma metastases to the peritoneal and serosal surfaces. Transverse 512-resolution T2-weighted echo-train spin-echo (*a*) and 90-s postgadolinium fat-suppressed SGE (*b*) images highlight the improvement in disease detection afforded by breath-hold gadolinium-enhanced fat-suppressed SGE. On the high-resolution T2-weighted image, bowel motion degrades image quality; no metastatic disease can be identified. On the gadolinium-enhanced fat-suppressed SGE image, the acquisition during suspended respiration avoids breathing artifact and minimizes bowel motion. Enhancement of irregularly thickened tissue along the peritoneum and serosal surface of bowel (arrows, *b*) is consistent with widespread metastatic disease.

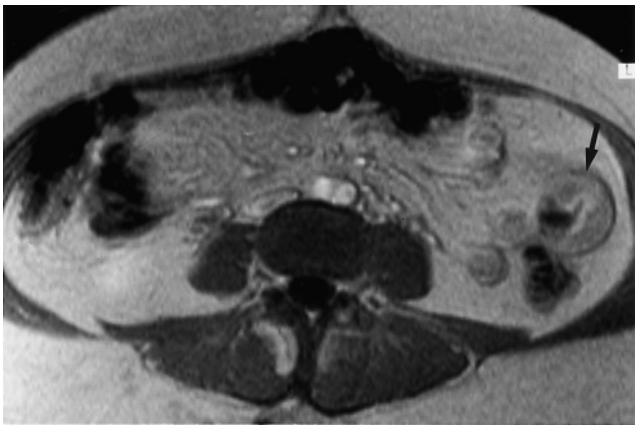

FIG. 6.59 Hematogenous metastases. Transverse 45-s post-gadolinium SGE image demonstrates an eccentric mural tumor in the midjejunum (arrow).This tumor was a hematogenous metastasis from uterine leiomyosarcoma.

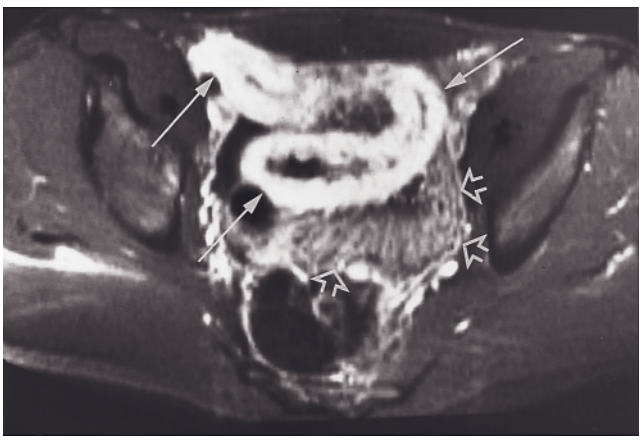

(*a*)

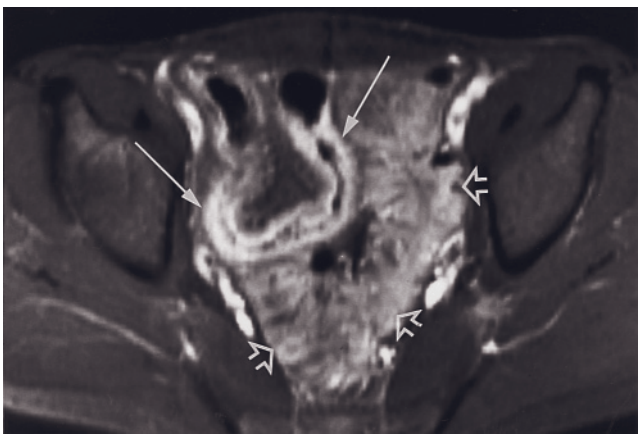

(*b*)

(*c*)

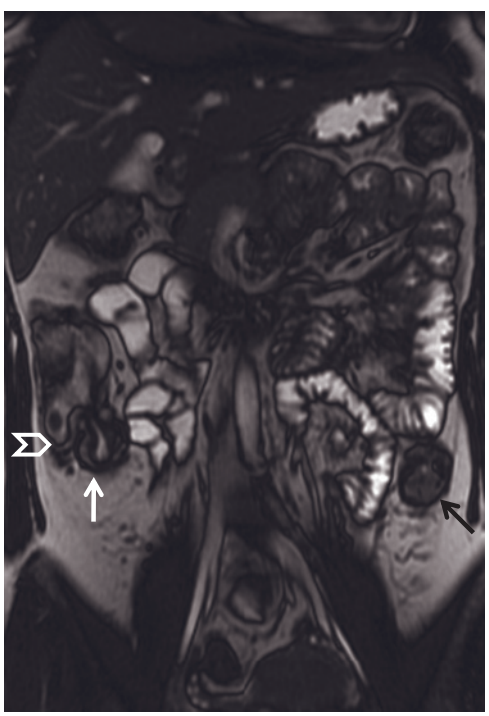

(*d*)

FIG. 6.60 Severe Crohn disease. Gadolinium-enhanced T1-weighted fat-suppressed spin-echo images (*a–c*) in three patients with severe Crohn disease. A thickened loop of substantially enhancing ileum (arrows, *a*) with associated mesenteric inflammation (open arrows, *a*) are characteristic findings for Crohn disease. In the second patient (*b*), similar findings of a thickened, intensely enhancing loop of ileum (arrows) with associated mesenteric inflammation (open arrows) are identified. In the third patient (*c*), multiple thickened loops of intensely enhancing ileum are present (arrows). Coronal T2-weighted true-FISP (*d*, *e*) and coronal T1-weighted

(*e*)

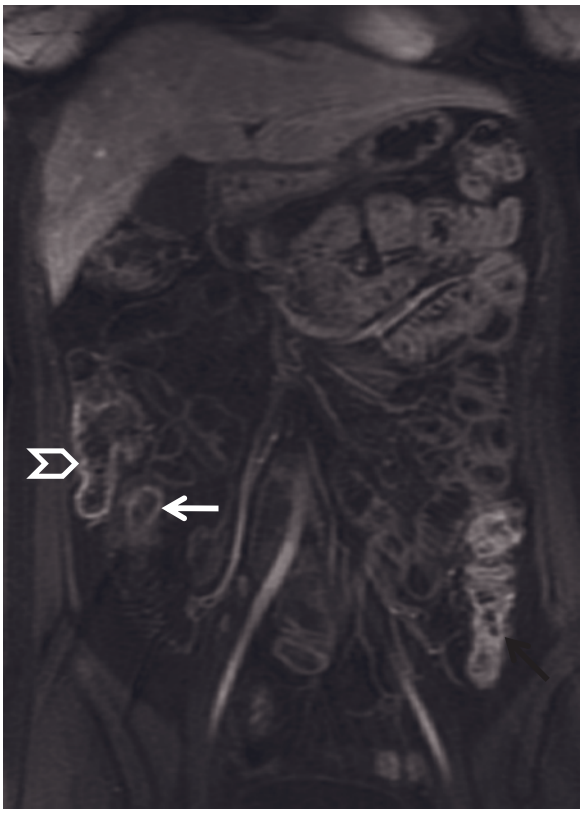

(*f*)

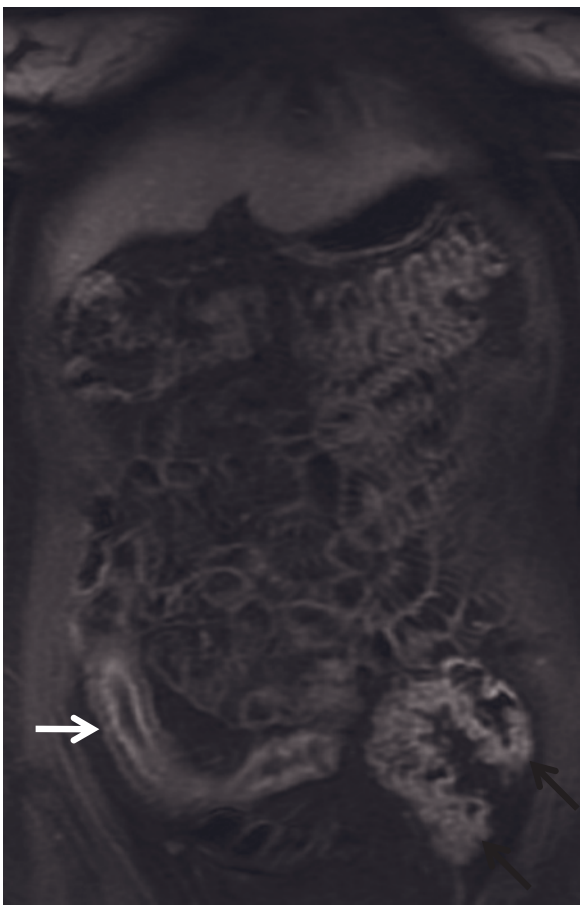

(*g*)

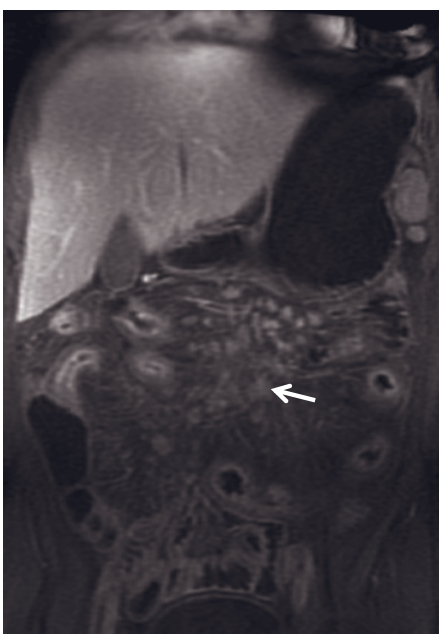

(*h*)

Fig. 6.60 (*Continued*) postgadolinium fat-suppressed interstitial-phase 3D-GE (*f*, *g*) images demonstrate severe Crohn disease in another patient. The walls of terminal ileum (white arrows, *d*–*g*), cecum (open arrows, *d*, *f*), descending colon (black arrows, *d*, *f*), and sigmoid colon (black arrows, *e*, *g*) show thickening and edema (white arrows, *d*, *e*). Edema is seen as high signal in the wall. Associated mild mesenteric inflammation and fibrofatty proliferation are detected. The wall of terminal ileum shows trilaminar enhancement (white arrow, *g*) pattern due to the presence of submucosal edema, which is seen as low signal intensity. The walls of the cecum and colon show diffuse enhancement (open and black arrows, *f*, *g*). Coronal T1-weighted postgadolinium interstitial phase fat-suppressed 3D-GE image (*h*) in another patient with severe Crohn disease demonstrates multiple enlarged and enhancing mesenteric lymph nodes (arrow, *h*). Note that the walls ileal and colonic segments show diffuse and mucosal increased enhancement, respectively.

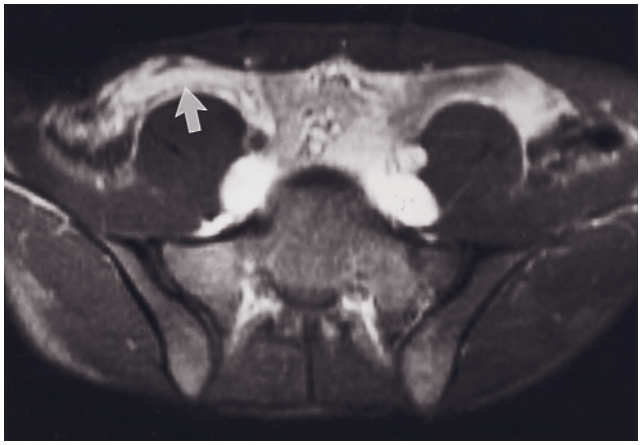

(*a*)

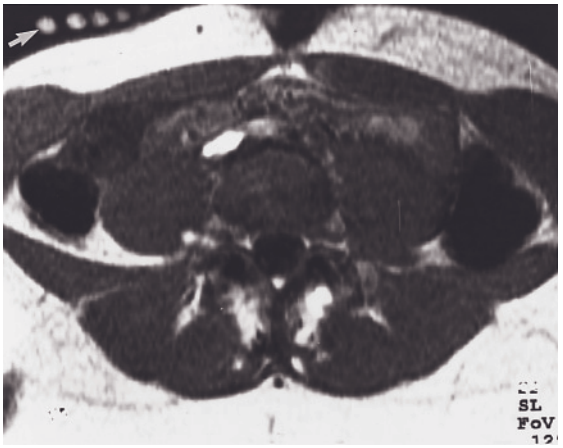

(*b*)

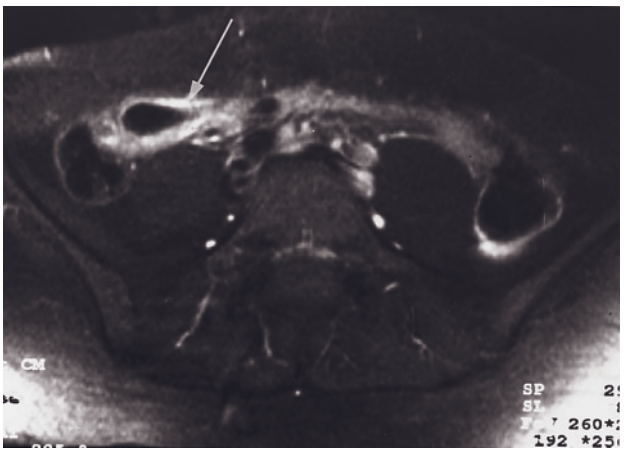

(*c*)

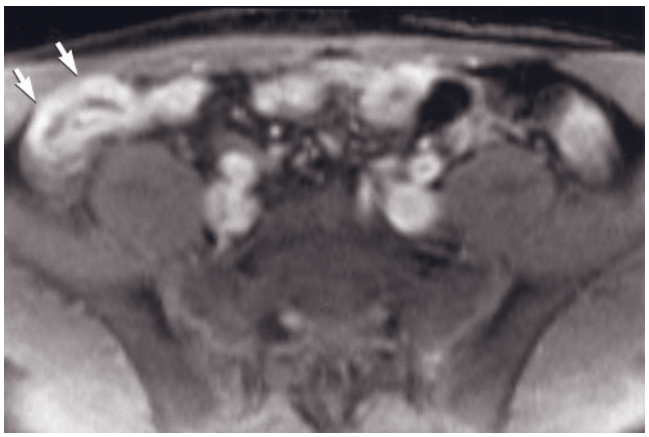

(*d*)

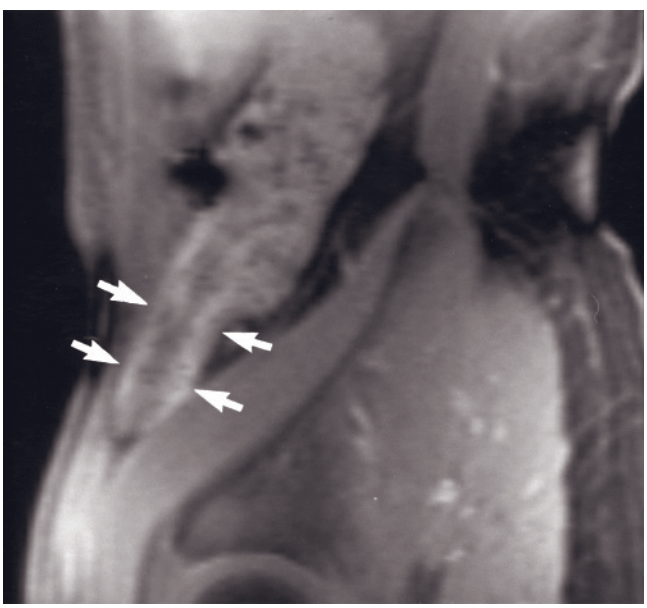

(*e*)

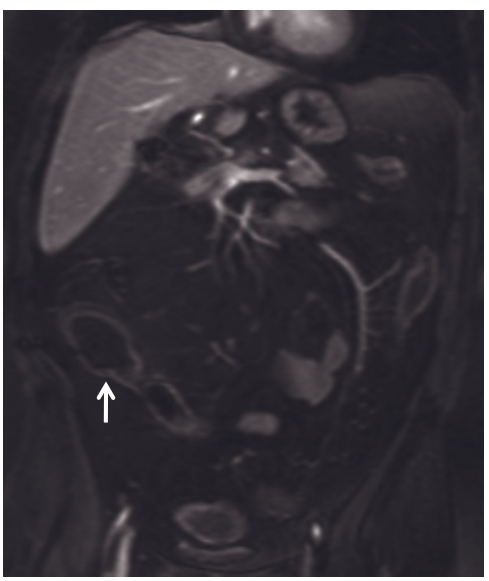

(*f*)

Fig. 6.61 Mild to moderate Crohn disease. Transverse gadolinium-enhanced T1-weighted fat-suppressed image (*a*) demonstrates moderate inflammatory disease of the terminal ileum (arrow, *a*), that has a wall thickness of 5 mm,<10 cm of diseased bowel, and moderate wall enhancement. SGE (*b*) and gadolinium-enhanced T1-weighted fat-suppressed spin-echo (*c*) images in a second patient with mild Crohn disease. The unenhanced image (*b*) appears unremarkable. On the gadolinium-enhanced image, transmural enhancement is apparent with wall thickness of 5 mm, length of involved segment of <10 cm, and moderate mural enhancement. This constellation of imaging findings is consistent with mild disease. Assessment of severity of disease must be determined on the nondependent bowel wall (arrow, *c*) after intravenous contrast administration. Lipid beads (small arrow, *b*) demarcate the area of patient tenderness. Transverse (*d*) and sagittal (*e*) interstitial-phase gadolinium-enhanced fat-suppressed SGE images in a third patient show segmental wall thickening and abnormal enhancement of the distal ileum (arrows, *d*, *e*). Coronal (*f*) and transverse (*g*) T1-weighted postgadolinium interstitial phase fat-suppressed 3D-GE images at 3.0 T demonstrate mild Crohn disease in another patient.

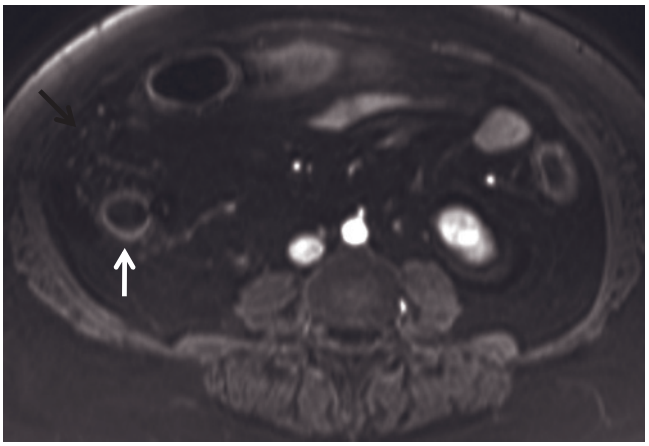

(*g*)

FIG. 6.61 (*Continued*) The wall of terminal ileum (white arrows, *f*, *g*) is thickened and shows diffuse increased enhancement. Adjacent mesenteric inflammation (black arrow, *g*) and inflamed lymph nodes (black arrow, *g*) are detected. Note that fatty proliferation is seen around the terminal ileum.

of Crohn disease in patients with contraindication to barium examinations or CT imaging (fig. 6.66).

The MRI criteria of mild, moderate, and severe disease have been described and are a function of wall thickness, length of diseased segment, and percentage of mural contrast enhancement (Table 6.2). The extent of mural enhancement may also be determined by comparison of bowel enhancement on gadolinium-enhanced fat-suppressed SGE or 3D-GE with that of the renal parenchyma [75]. Bowel should not enhance to the same degree as renal cortex on either early capillary-phase images or >1-min interstitial-phase images. Enhancement equivalent to or greater than renal cortex is abnormal and most often reflects the presence of inflammatory change.

MRI assessment is made on gadolinium-enhanced T1-weighted fat-suppressed images using the nondependent bowel surface. It is critical that the time point for determining percentage of enhancement is standardized. This establishes reproducible measures of disease activity between studies in the same patient. We have used a time point of 2.5 min after injection. Immediate postgadolinium images reflect significant perivascular inflammation and increased capillary blood flow. Commonly, the inner half of the bowel wall enhances most intensely in this phase of enhancement in severely inflamed bowel. Later interstitial-phase images demonstrate more uniform enhancement in diseased bowel, reflecting capillary leakage and decreased venous removal in transmurally inflamed bowel. A pilot study found good correlation between clinical indices to measure Crohn activity [Crohn Disease Activity Index (CDAI) and the modified Index of the International Organization for the Study of Inflammatory Bowel Disease (IOIBD)] and an MRI determinant, the MRI product [wall thickness × length of diseased segment × percentage mural enhancement (MRP)] (fig. 6.67) [4].

This work suggests that MRI may be the best modality for evaluating the severity of Crohn disease. It may provide complementary or confirmatory information to clinical assessment. MRI also may have a role in the evaluation of acute exacerbations of Crohn disease. Specifically, in patients with longstanding disease, marked enhancement of the mucosa with substantially thickened wall and minimal enhancement of the outer layer is suggestive of acute on chronic involvement and may have a role in the evaluation of acute exacerbations of Crohn disease (see fig. 6.67). In patients with nonactive chronic disease, there may remain persistent thickening and abnormal enhancement seen on delayed postgadolinium images. Acute disease results in edema that may be best visualized on fat-suppressed single-shot T2-weighted images. It has been suggested that more detailed evaluation of the bowel wall in patients with longstanding disease may reveal marked enhancement of the mucosa with a thickened and minimally enhancing outer layer, suggestive of acute on chronic involvement (fig. 6.68).

Crohn disease may also result in large patulous segments of small bowel that may contain debris due to the presence of chronic distal small bowel obstruction. Patients may be symptomatic from the effects of bacterial overgrowth. On MR images, greatly dilated segments of bowel are shown that contain substantial debris. Single-shot echo-train spin echo is very effective in delineating the extent of dilatation and gadolinium-enhanced fat-suppressed SGE or 3D-GE technique for showing the inflammation (fig. 6.69), and MR small bowel follow-through technique may also help in this evaluation.

Ulcerative Colitis. Ulcerative colitis is a recurrent acute and chronic ulcero-inflammatory disorder of unknown etiology that affects the large bowel and is discussed in the section on the large intestine. Small

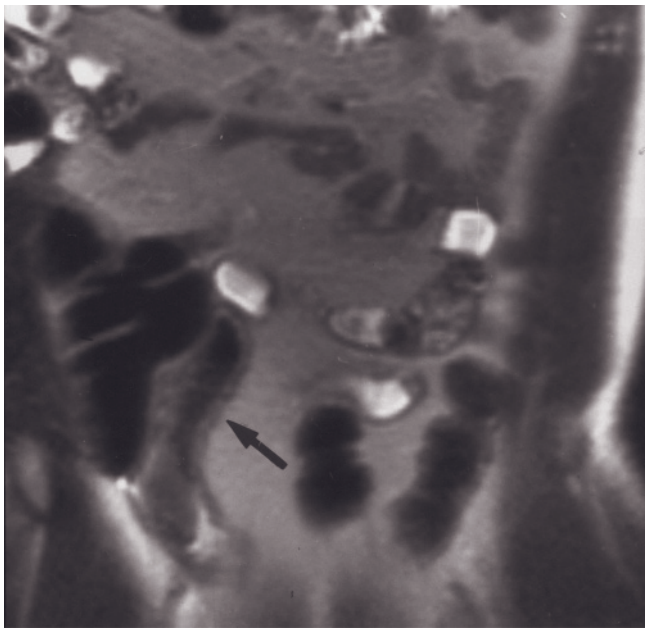

(*a*)

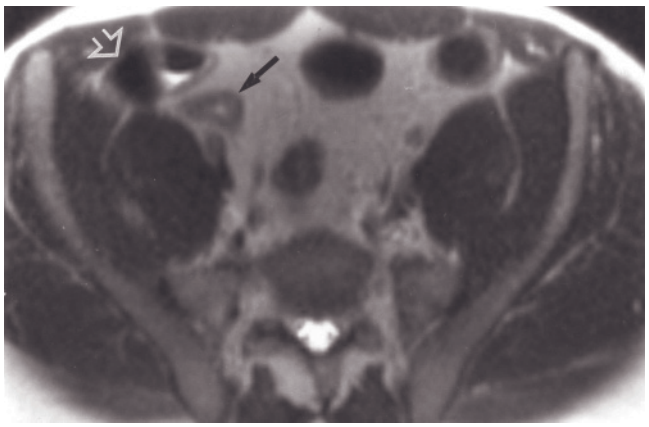

(*b*)

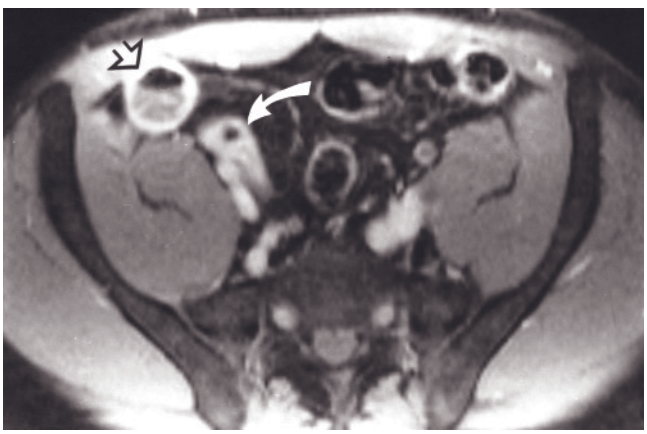

(*c*)

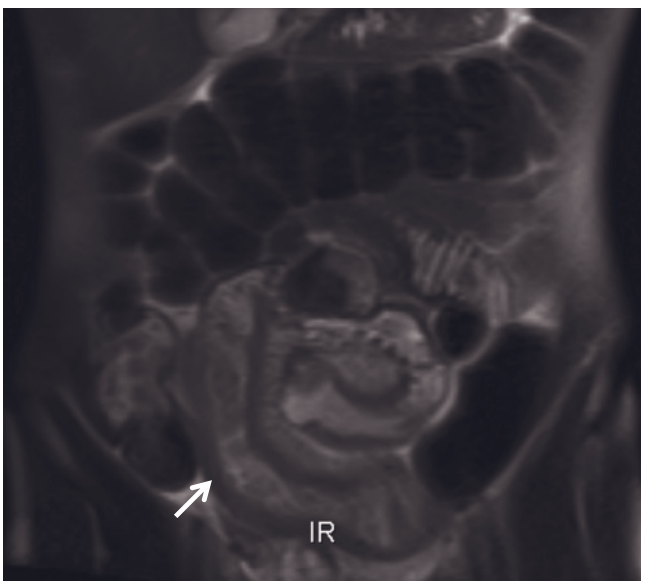

(*d*)

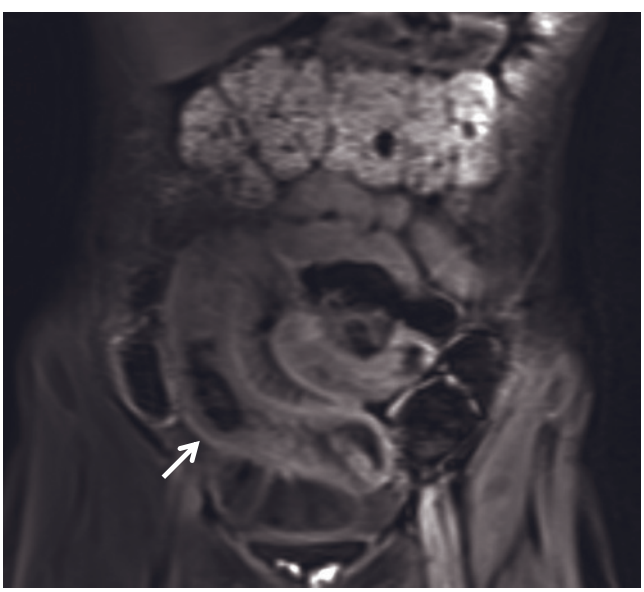

(*e*)

FIG. 6.62 Moderate Crohn disease. Coronal (*a*) and transverse (*b*) T2-weighted SS-ETSE and 2-min fat-suppressed SGE (*c*) images. The distal terminal ileum (arrow, *a*, *b*) shows increased wall thickness, whereas the ascending colon (open arrow, *b*) demonstrates normal wall thickness. On the 2-min fat-suppressed SGE image (*c*), moderate enhancement of the thickened distal terminal ileum (curved arrow) and ascending colon (open arrow) are present, reflecting moderate severity of the disease. Note that the ascending colon has a normal wall thickness associated with moderately increased enhancement due to Crohn involvement. (Reprinted with permission from Marcos HB, Semelka RC: Evaluation of Crohn's disease using half-Fourier RARE and gadolinium-enhanced SGE sequences: initial results. *Magn Reson Imaging* 18: 263–268, 2000.) Coronal T2-weighted single-shot echo-train spin-echo (*d*) and coronal T1-weighted postgadolinium fat-suppressed interstitial-phase 3D-GE (*e*) images at 3.0 T demonstrate moderate Crohn disease in another patient. The walls of involved ileal segments (arrows, *d*, *e*) are thickened and show increased enhancement. Note that inflammatory stranding is evident in the mesentery.

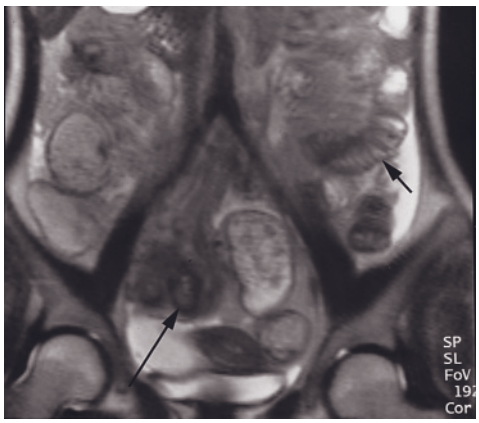

(*a*)

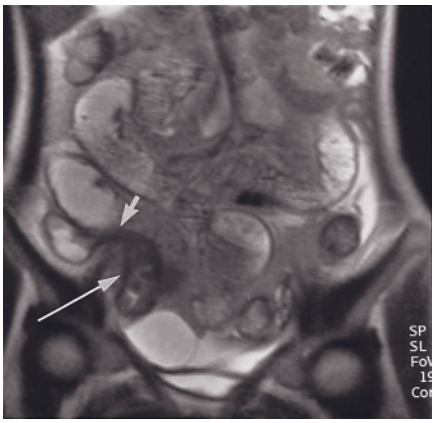

(*b*)

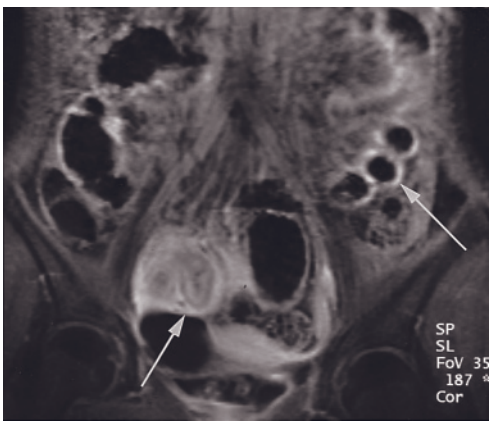

(*c*)

(*d*)

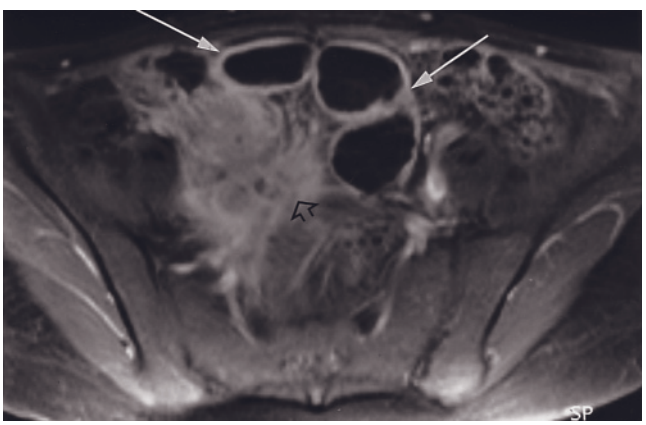

(*e*)

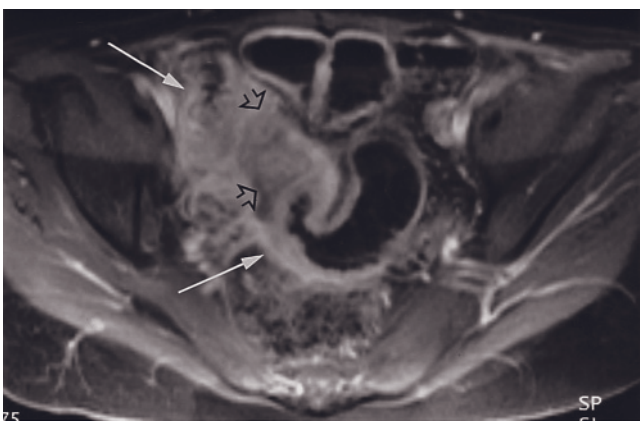

(*f*)

FIG. 6.63 Severe Crohn disease. Coronal SS-ETSE (*a*, *b*) and coronal (*c*, *d*) and transverse (*e*, *f*) 2- to 3-min postgadolinium fat-suppressed SGE images in a patient with severe disease. Coronal T2-weighted images from midabdominal plane (*a*) and 2 cm more anterior (*b*) demonstrate thickened loops of distal small bowel (long arrows, *a*, *b*). The terminal ileum is well shown at its entry into the cecum (small arrow, *b*). Coronal gadolinium-enhanced fat-suppressed SGE images acquired from similar tomographic sections, respectively, demonstrate substantial enhancement of the thickened loops of bowel and surrounding tissues. An enhancing fistulous tract (arrow, *d*) is apparent close to the ileocecal valve. Transverse gadolinium-enhanced images demonstrate intense enhancement of multiple loops of bowel, including loops with wall thickness of 4 mm (arrows, *e*). On the more inferior tomographic section narrowing of distal ileum is apparent (long arrows, *f*), which accounts for the mild dilation of more proximal loops (arrows, *e*). Inflammatory mesenteric changes are evident (open arrows, *e*, *f*). Normal-appearing proximal jejunum (small arrow, *a*) is appreciated on the T2-weighted image.

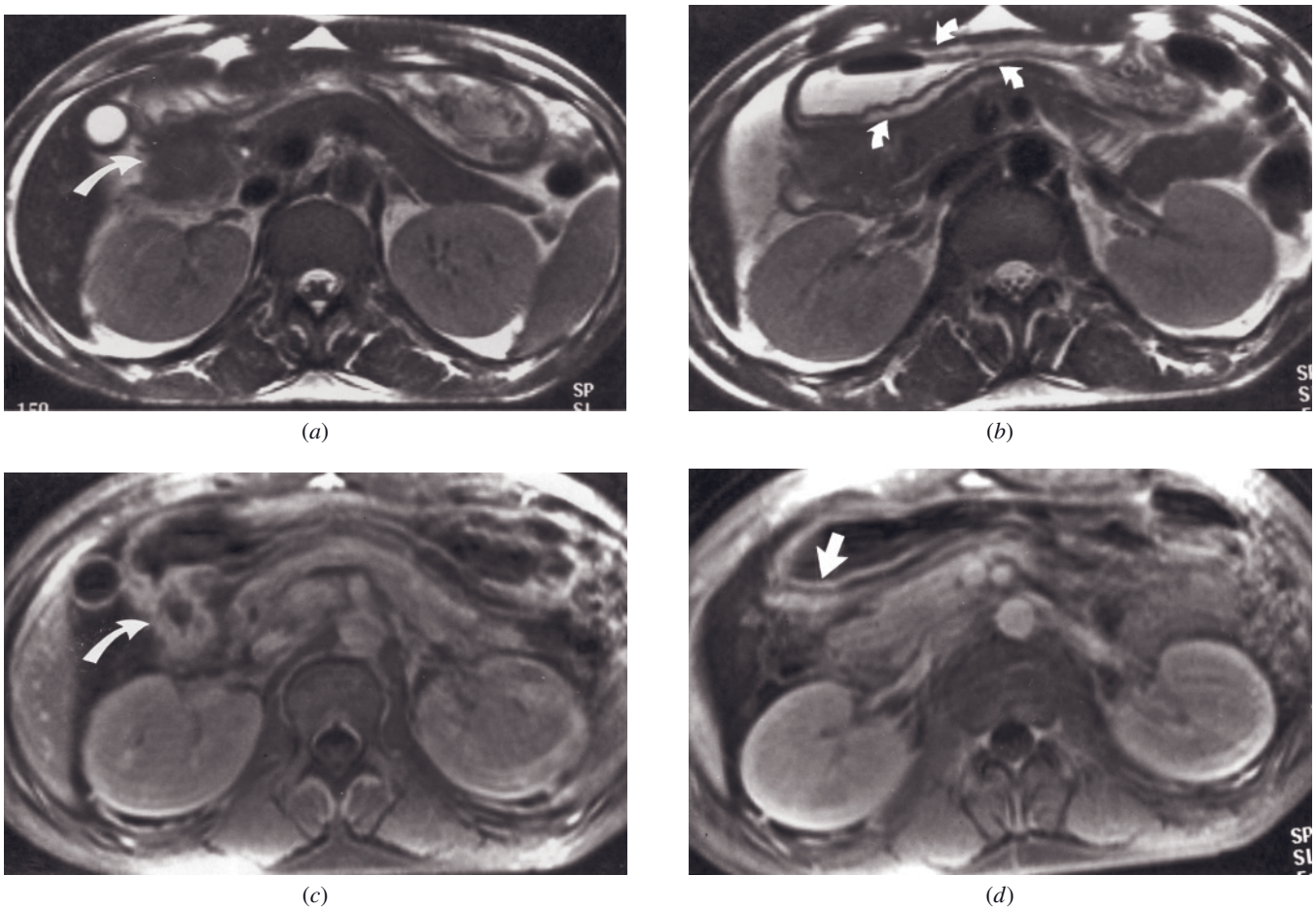

FIG. 6.64 Duodenal Crohn disease and gastric outlet obstruction. Transverse T2-weighted SS-ETSE (*a*, *b*) and 2-min post-gadolinium fat-suppressed (*c*, *d*) images. The stomach and proximal duodenum are dilated a with transition point in the second portion of the duodenum. The duodenum at the level of obstruction shows increased wall thickness on the T2-weighted image (curved arrow, *a*). High signal intensity of the submucosa of the antrum and first portion of the duodenum is identified (curved arrows, *b*). The thickened portion of the duodenum demonstrates moderately increased mural enhancement (curved arrow, *c*), with mucosa and serosa layers of the antrum and proximal duodenum demonstrating enhancement reflecting moderate chronic inflammatory changes (arrow, *d*). Low signal intensity of the submucosa on the postgadolinium T1-weighted images (*c*, *d*) represents submucosal edema and corresponds to high signal intensity on the T2-weighted image. (Reprinted with permission from Marcos HB, Semelka RC: Evaluation of Crohn's disease using half-Fourier RARE and gadolinium-enhanced SGE sequences: initial results. *Magn Reson Imaging* 18: 263–268, 2000.)

bowel involvement ("backwash ileitis") is the sequel of pancolonic disease. Free reflux of colon contents into the ileum via a patulous, incompetent ileocecal valve is believed to be responsible [74]. The lumen of the ileum is moderately dilated, and on MRI the diseased ileal wall is abnormal, showing mild dilatation and moderately increased enhancement with gadolinium, reflective of diffuse inflammation, erosion, and ulcerations (fig. 6.70).

Gluten-Sensitive Enteropathy (Celiac Disease, Celiac Sprue)

Gluten-sensitive enteropathy (GSE) is an immunologically mediated gastrointestinal disease that produces a malabsorption syndrome. GSE likely results from a specific immunologic hyperactivity to a constituent of dietary gluten. The diagnosis is made through jejunal biopsy and is based on the presence of mucosal atrophy with blunting or complete loss of the villi and inflammation within the mucosa of the small intestine. T2-weighted single-shot echo-train spin-echo technique may demonstrate an abnormal mucosal fold pattern of the small bowel, associated with an increase of intraluminal fluid (figs. 6.71 and 6.72) [57]. One recent study showed that MRI is able to demonstrate intra- and extraintestinal features that may lead to the diagnosis of celiac disease in adults [76]. The authors have studied 31 patients with celiac disease and have found that MRI

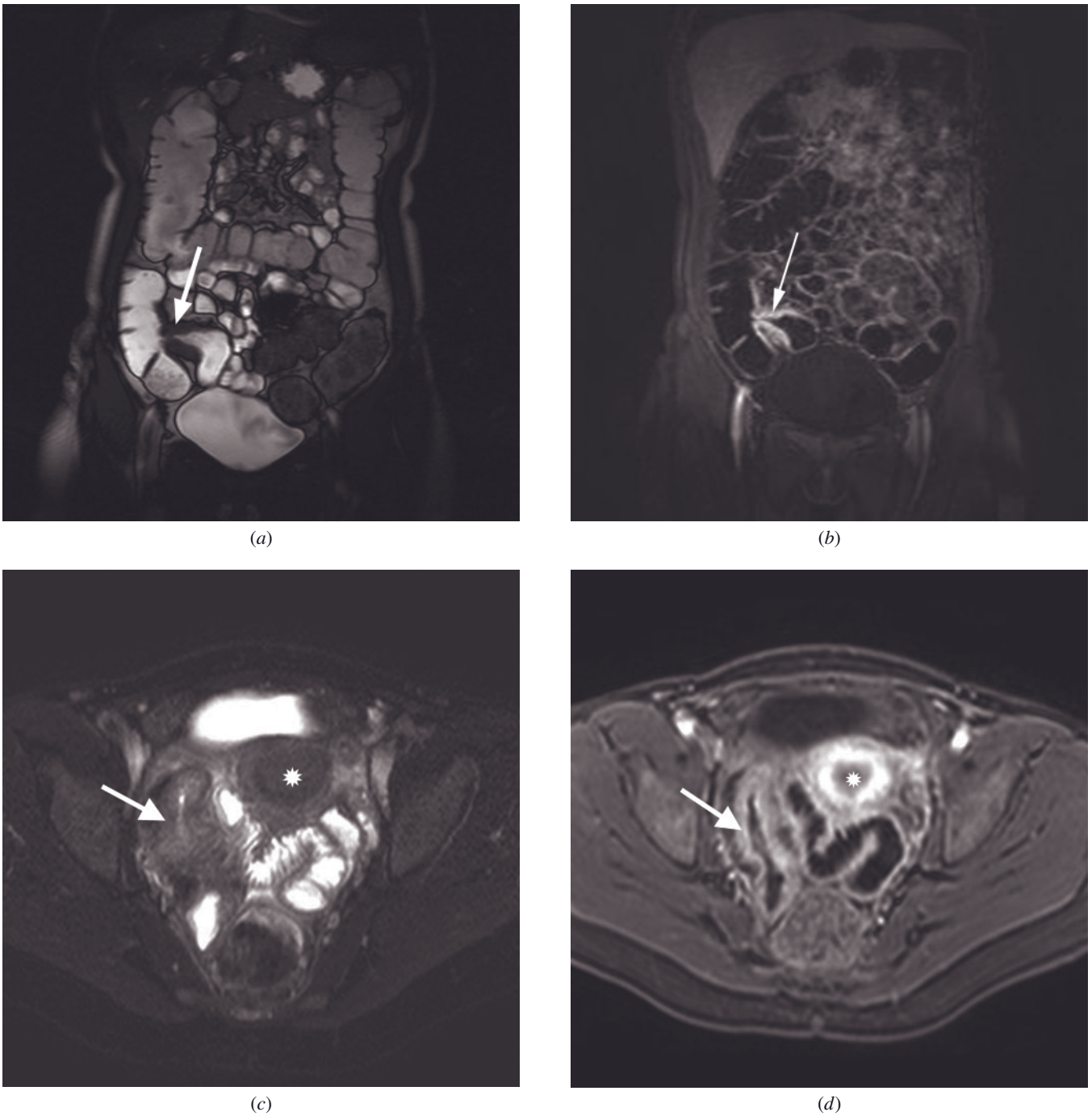

FIG. 6.65 Crohn disease. Images were obtained over a period of 2 years and show different degrees of disease activity, with examples of images obtained during quiescent nonactive disease (*a*, *b*), 2 years later on acute presentation with active disease (*c*, *d*), 1 month later while on immunosuppressant and oral antibiotic therapy (*e*, *f*), and 3 months after therapy with resolution of acute imaging findings and complications (*g–j*).The terminal ileum (TI) is concentrically thickened (*a*) and demonstrates dark signal intensity on coronal T2-weighted imaging (WI) (arrow, *a*), indicating no evidence of edema and consistent with quiescent Crohn disease, whereas coronal gadolinium-enhanced delayed-phase T1-weighted imaging (arrow, *b*) demonstrates that the abnormally thickened tissue enhances. This combination of features is consistent with fibrosis and chronic disease. Two years later, active Crohn disease has developed and is demonstrated by a long segment of distal ileum (*c, d*) that has abnormal wall thickening with high signal on T2-weighted imaging (arrow, *c*) associated with abnormal enhancement (arrow, *d*) in keeping with active inflammation. The uterus is noted within the image as a normal structure (asterisks, *c, d*). One month after immunosuppressive,

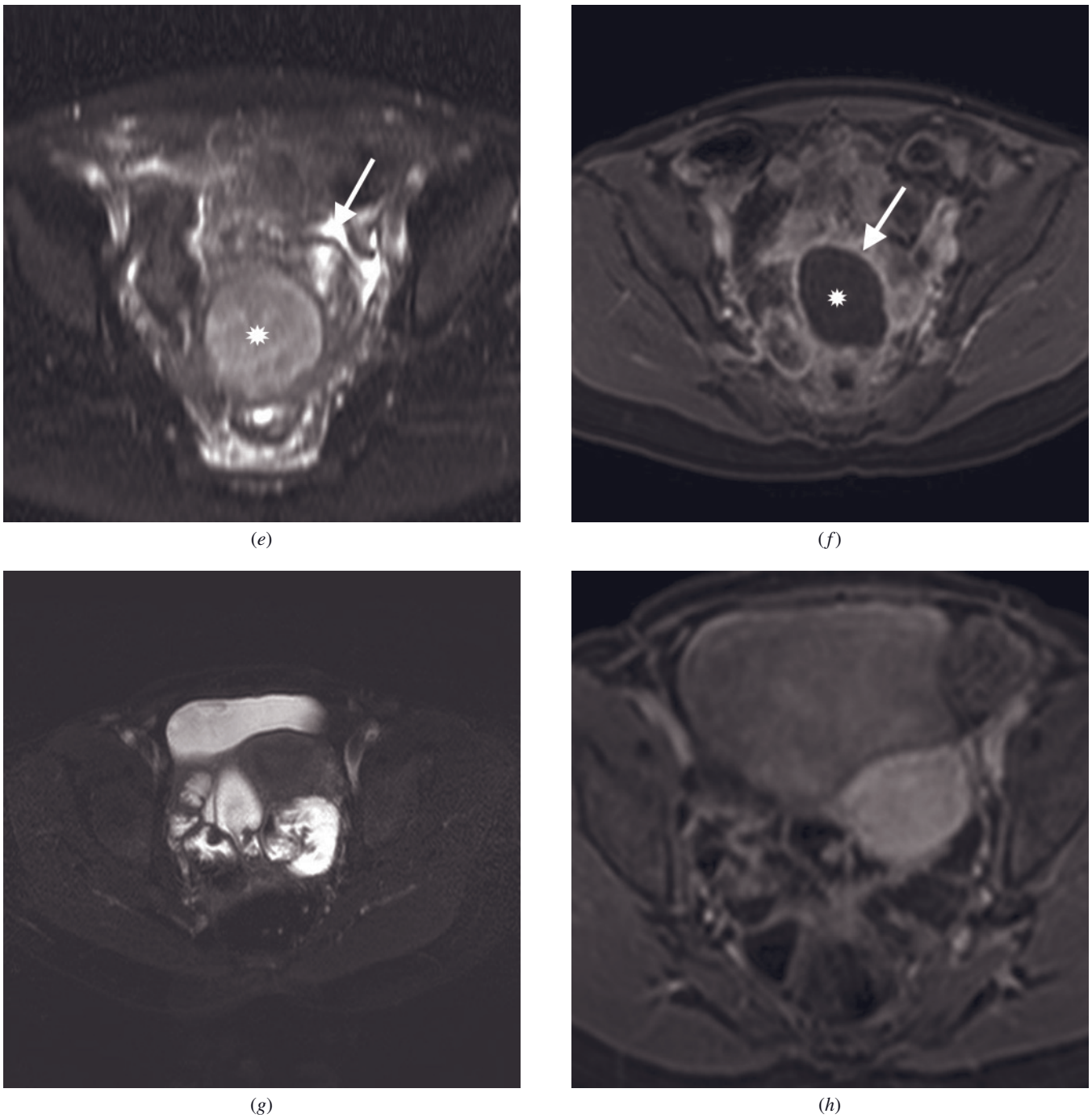

FIG. 6.65 (*Continued*) anti-inflammatory, and oral antibiotic therapy the patient presented with mild pelvic discomfort and pressure symptoms with imaging demonstrating development of a central pelvic abscess situated in the cul de sac on T2-weighted imaging (star, *e*) and delayed gadolinium-enhanced T1-weighted imaging (asterisk, *f*), with a thickened enhancing abscess wall (arrow, *f*). There remains marked diffuse mesenteric edema and fluid (arrow, *e*). Two months after acute presentation, the abscess has been percutaneously drained with complete resolution of the abscess, inflammation, and pelvic edema on T2-weighted imaging (*g*) and gadolinium enhanced T1-weighted imaging (*h*). The TI has returned to nearly the same appearance as 2 years previously

(*i*)

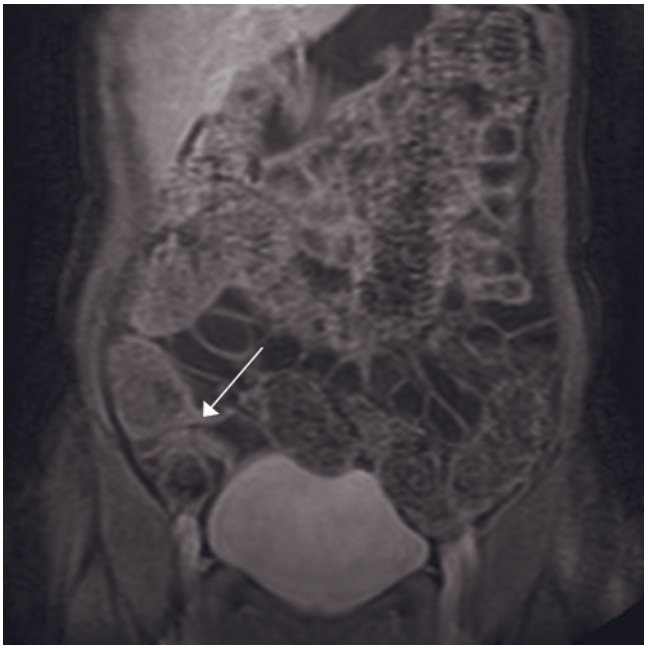

(*j*)

FIG. 6.65 (*Continued*) on coronal T2 (*i*)- and gadolinium-enhanced T1 (*j*)-weighted images, consistent with persistent fibrosis and return to quiescent disease.

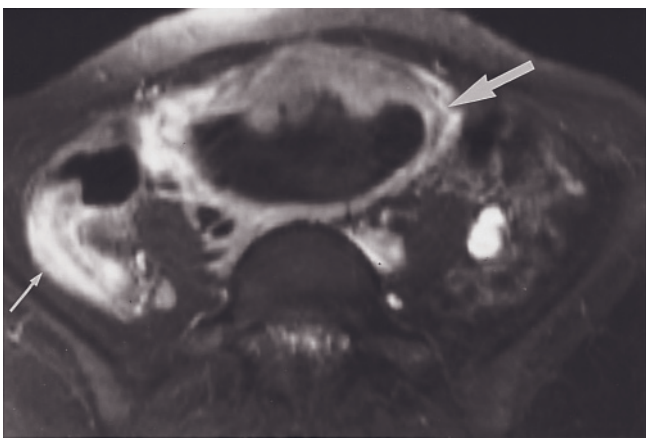

(*a*)

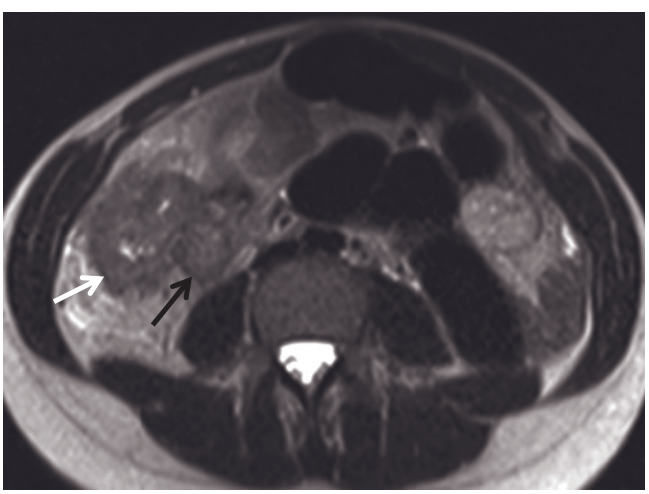

(*c*)

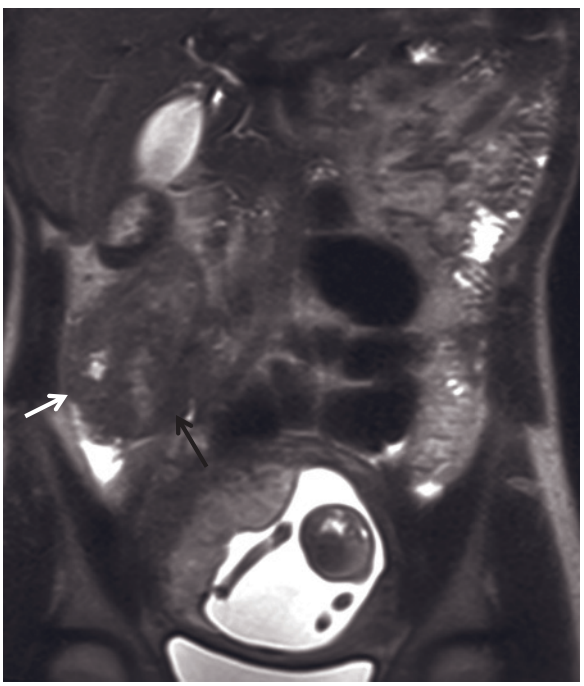

(*b*)

FIG. 6.66 Crohn disease in pregnancy. Gadolinium-enhanced T1-weighted fat-suppressed spin-echo image (*a*) in a patient in the second trimester of pregnancy. Thickened and intensely enhancing distal ileum is present (arrow, *a*). The pregnant uterus is also well shown (large arrow, *a*). Coronal (*b*) and transverse (*c*) T2-weighted single-shot echo-train spin-echo images demonstrate Crohn disease in a pregnant patient. No postgadolinium imaging was performed because of the pregnancy. Diffuse wall thickening is present in the cecum (white arrows, *b*, *c*) and terminal ileum (black arrows, *b*, *c*). Inflammatory stranding is detected in the fat tissue around the terminal ileum and cecum. Note that minimal free fluid is also present around the terminal ileum and cecum.

Table 6.2 Crohn Disease Severity Criteria

Severity	Contrast Enhancement (%)	Wall Thickness (mm)	Length of Diseased Segment (cm)
Mild*	<50	<5	<5
Moderate	50–100	5–20	Variable
Severe	>100	>10	>5**

*Bowel-wall thickening must be at least 4 mm, and one of the other 2 criteria must be satisfied.
**Typically >10 cm of affected bowel.
Reprinted with permission from Ascher SM, Semelka RC: MRI of the gastrointestinal tract. In Higgins CB, Hricak H, Helms CA (eds.). *Magnetic Resonance Imaging of the Body.* New York: Raven Press, p. 677–700, 1997.

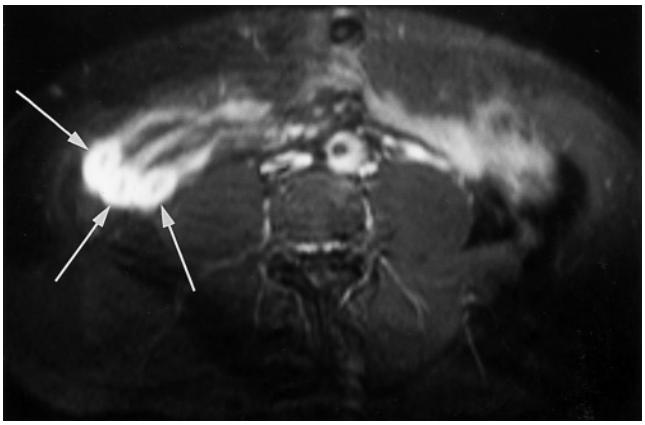

FIG. 6.67 Crohn disease activity assessment. Gadolinium-enhanced T1-weighted fat-suppressed spin-echo image in a patient with active Crohn disease. There is good correlation between clinical indices [CDAI, 185 (active disease 1150); modified IOIBD index, 8 (scale 1–10)] and MRI findings (arrows) of thickened wall, length of diseased segment, and percentage of mural enhancement (MRP, 4,664). (Reprinted with permission from Kettritz U, Isaacs K, Warshauer DM, Semelka RC: Crohn's disease: pilot study comparing MRI of the abdomen with clinical evaluation. *J Clin Gastroenterol* 21: 249–253, 1995.)

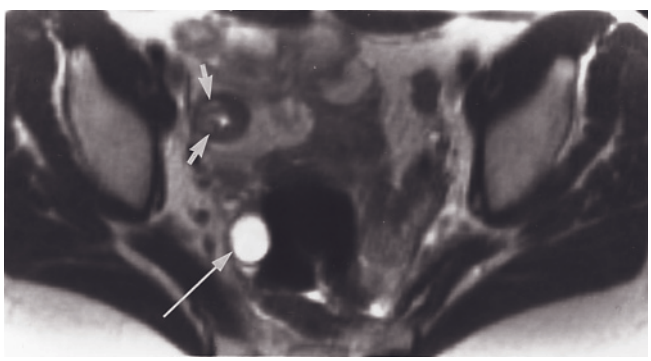

(*a*)

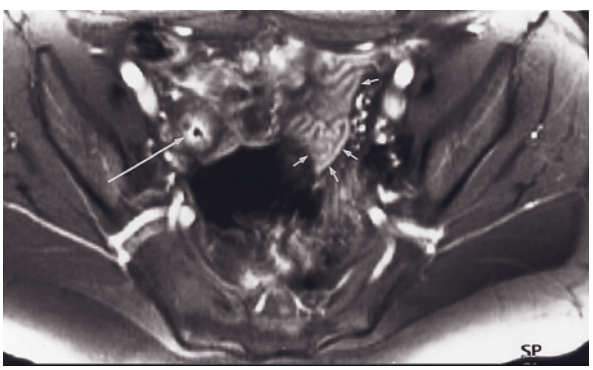

(*b*)

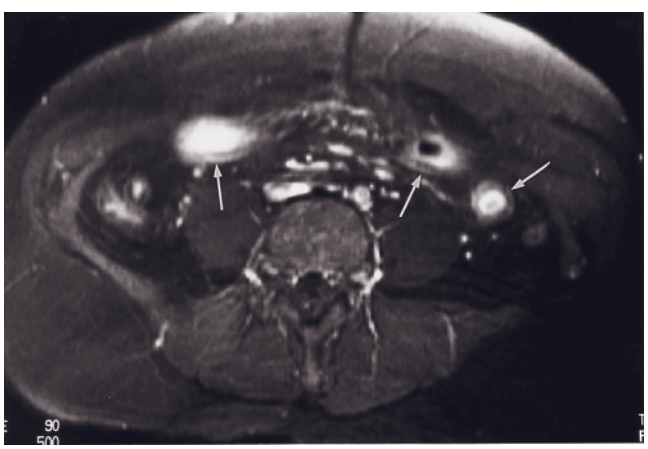

(*c*)

FIG. 6.68 Acute on chronic Crohn disease. T2-weighted SS-ETSE (*a*) and gadolinium-enhanced T1-weighted fat-suppressed spin-echo (*b*) images in a patient with longstanding disease. Increased thickness of distal ileum is present, which demonstrates increased signal intensity in the inner aspect of the wall (arrow, *a*). Acute exacerbation is characterized by intense mucosal enhancement (long arrow, *b*), with minimal enhancement of the outer wall in substantially thickened bowel. Accompanying hyperemia of the mesentery reflects the active inflammatory process (short arrows, *b*). Incidental note is made of a right adnexal cyst (long arrow, *a*) and free fluid in the pelvis. Gadolinium-enhanced T1-weighted fat-suppressed spin-echo image (*c*) in a second patient with a long history of Crohn disease. Thickened loops of small bowel with intense enhancement of the inner wall are apparent (arrows, *c*). The appearance is that of acute mucosal exacerbation

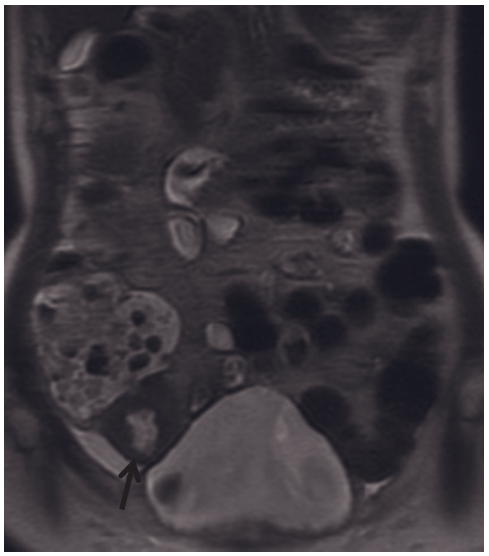

(*d*)

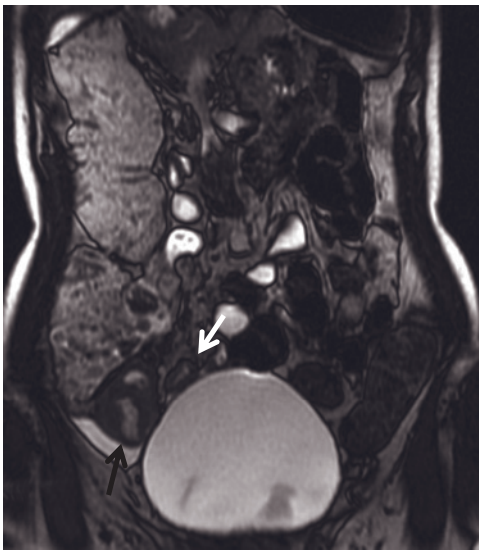

(*e*)

(*f*)

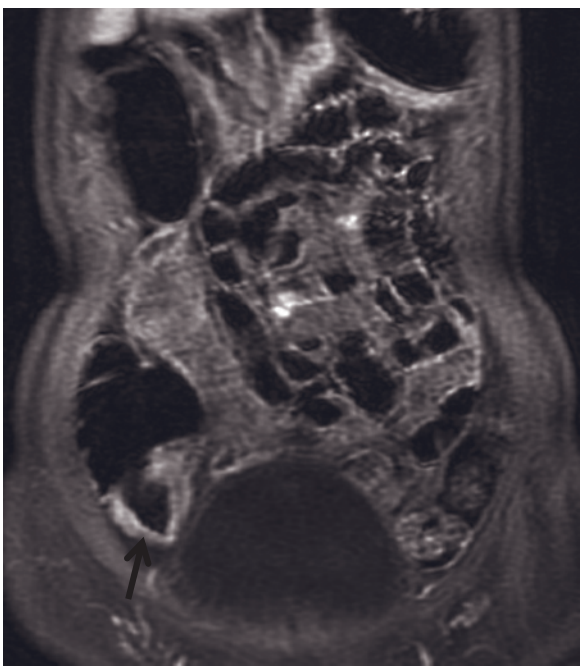

(*g*)

FIG. 6.68 (*Continued*) superimposed on a chronically thickened wall. Coronal T2-weighted single-shot echo-train spin-echo (*d*), coronal T2-weighted true-FISP (*e*), and coronal T1-weighted fat-suppressed postgadolinium interstitial-phase 3D-GE (*f*, *g*) images demonstrate acute on chronic Crohn disease in another patient. The cecum (black arrows, *d*–*g*) is retracted because of fibrosis, and its thickened wall shows progressive enhancement due to fibrosis and inflammation. The wall of the terminal ileum is also thickened and shows increased enhancement (white arrows, *e*, *f*). Free fluid is also detected in the right lower quadrant. The presence of retracted fibrotic cecum, and thickened and enhancing terminal ileum in combination with free fluid suggests the diagnosis of acute on chronic Crohn disease.

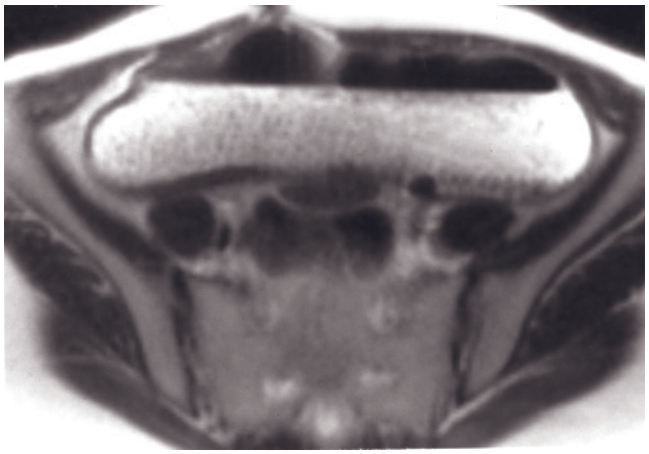

(*a*)

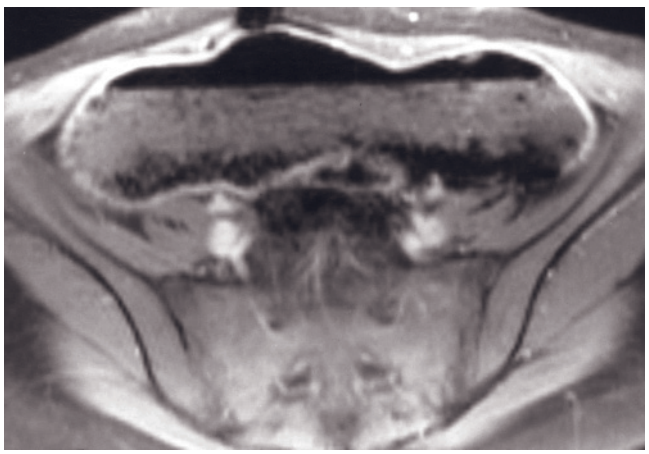

(*c*)

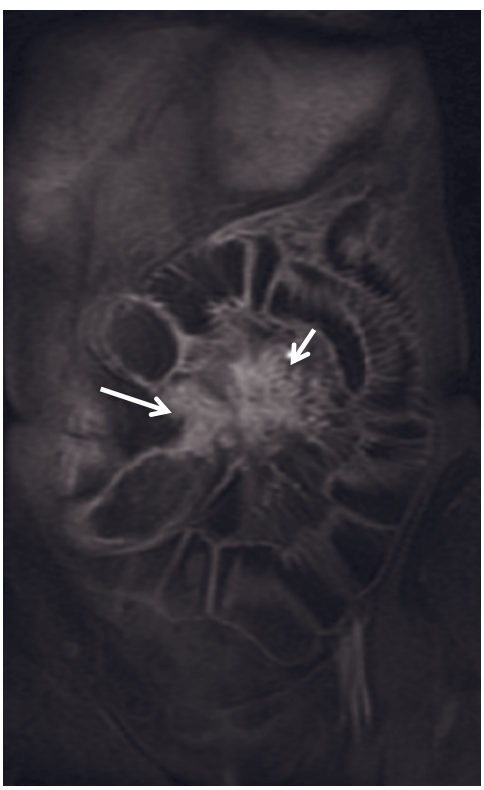

(*e*)

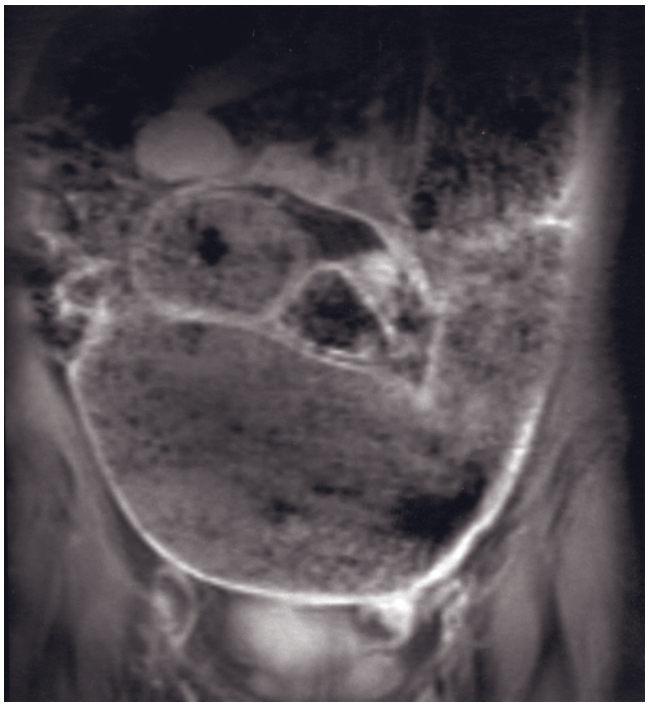

(*b*)

(*d*)

FIG. 6.69 Crohn disease with dilated stagnant bowel loop. Transverse T2-weighted SS-ETSE (*a*) and coronal (*b*) and transverse (*c*) gadolinium-enhanced interstitial-phase fat-suppressed SGE images. An enlarged loop of distal small bowel is present that contains substantial debris. Enlarged stagnant loops of small bowel are a complication of long-standing distal small bowel obstruction as observed in Crohn disease. Coronal T2-weighted true-FISP (*d*) and coronal T1-weighted postgadolinium fat-suppressed 3D-GE (*e*) images demonstrate stenotic small bowel segment (white arrows, *d*, *e*) and prestenotic dilated bowel segments in another patient with Crohn disease. The wall of stenotic bowel segment is thickened and shows increased enhancement on postgadolinium image (*e*). Note that there is associated enhancing mesenteric inflammation (short arrow, *e*).

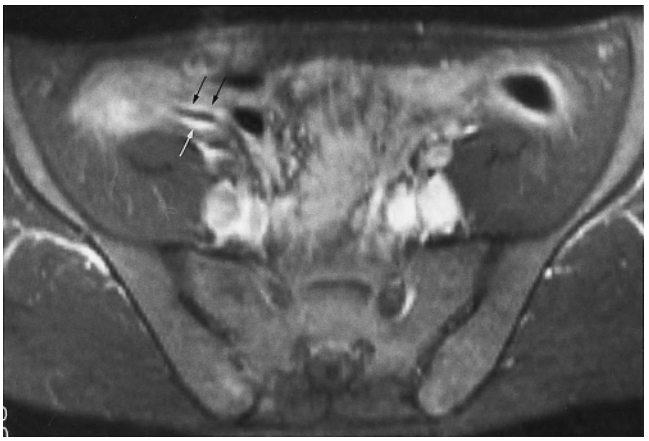

FIG. 6.70 Backwash ileitis. Gadolinium-enhanced T1-weighted fat-suppressed spin-echo image in a patient with ulcerative colitis. Pancolonic involvement with ulcerative colitis results in a patulous ileocecal valve. Reflux of colon contents into the ileum causes inflammatory changes (arrows). (Reprinted with permission from Shoenut JP, Semelka RC, Silverman R,Yaffe CS, Mickflikier AB: The gastrointestinal tract. In Semelka RC, Shoenut JP (eds.), *MRI of the Abdomen with CT Correlation.* New York: Raven Press, 1993, pp. 119–143.)

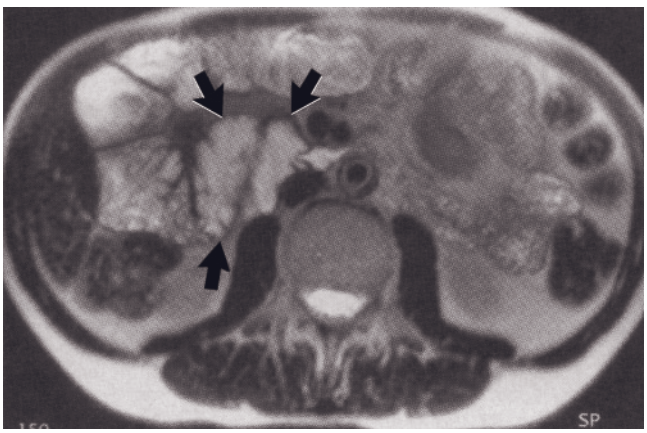

(*a*)

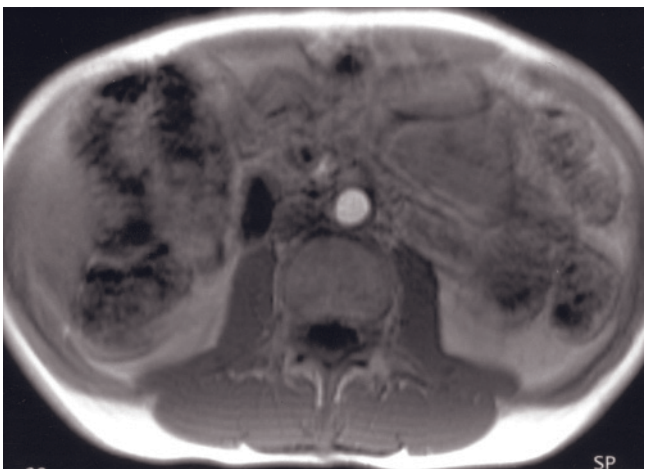

(*b*)

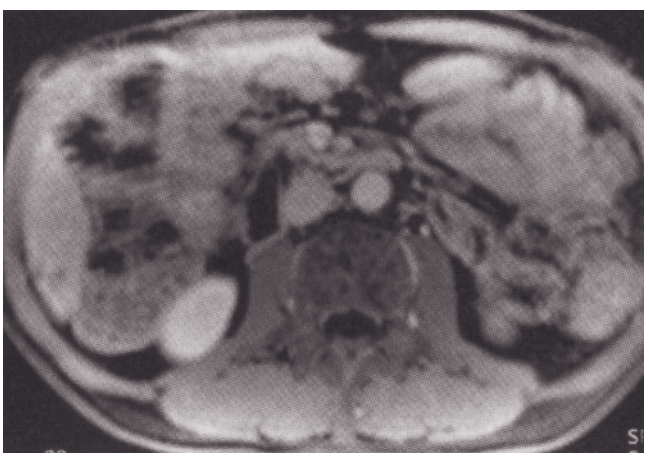

(*c*)

FIG. 6.71 Gluten-sensitive enteropathy. T2-weighted SSETSE (*a*), immediate postgadolinium SGE (*b*), and 90-s postgadolinium fat-suppressed SGE (*c*) images. T2-weighted image demonstrates an abnormally prominent mucosal pattern in the duodenum associated with an increase in intraluminal fluid (arrows, *a*). The duodenal mucosa enhances normally, which reflects a lack of vascular changes related to the disease process. Upper gastrointestinal endoscopy with biopsy was performed, and histopathologic examination established the diagnosis of gluten-sensitive enteropathy. (Reprinted with permission from Marcos HB, Semelka RC, Noone TC, Woosley JT, Lee JKT: MRI of normal and abnormal duodenum using half-Fourier single-shot RARE and gadolinium-enhanced spoiled gradient-echo sequences. *Magn Reson Imaging* 17: 869–880, 1999.)

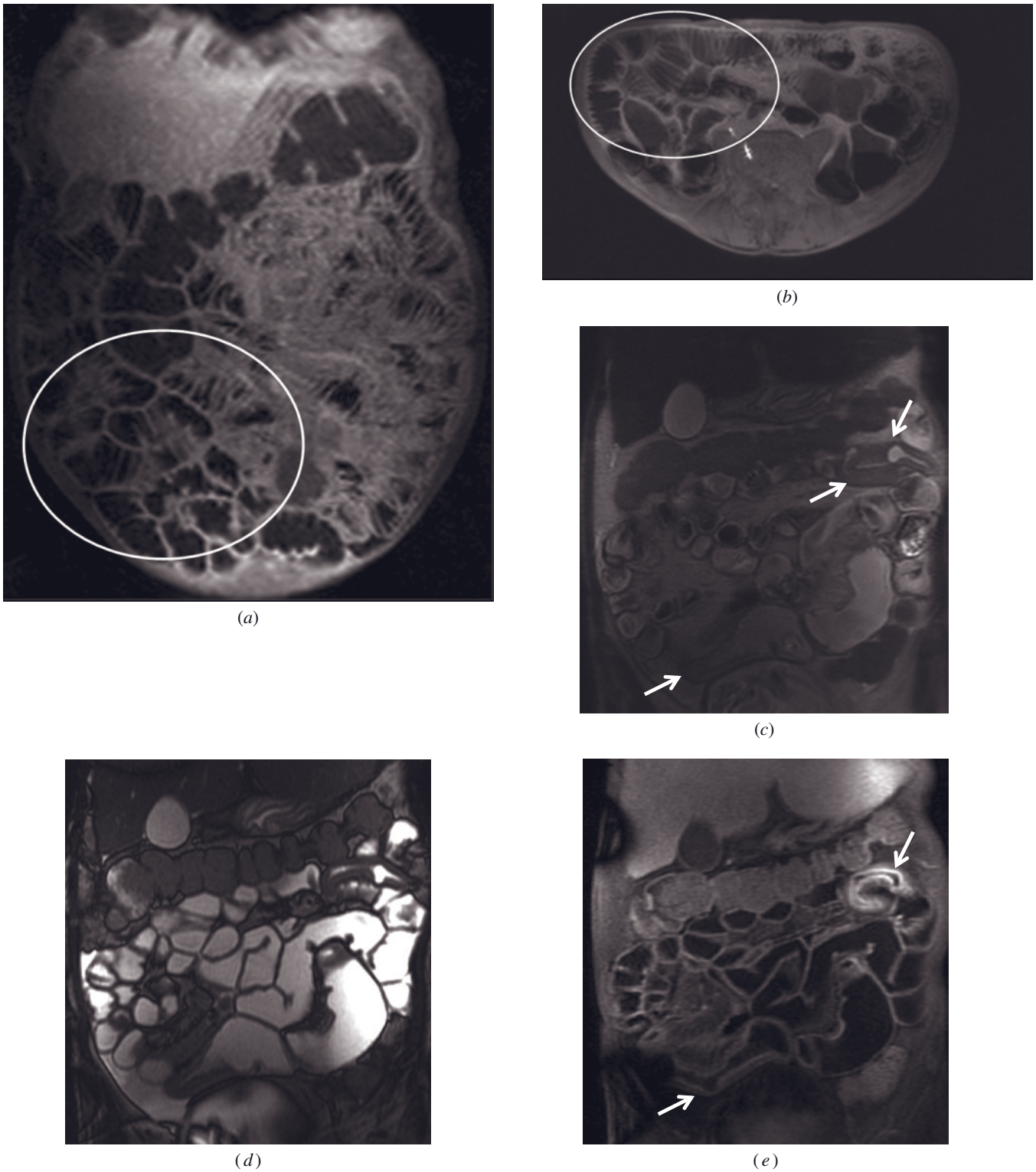

FIG. 6.72 Gluten-sensitive enteropathy. Coronal (*a*) and axial (*b*) interstial-phase gadolinium-enhanced T1-weighted fat-suppressed 3D-GE images in a 61-year-old man demonstrate abnormal ileal fold pattern (small bowel loops shown within circle, *a* and *b*) with increased number and irregularity of folds mimicking the appearance normally associated with the jejunum. Coronal T2-weighted single-shot echo-train spin-echo (*c*), coronal T2-weighted true-FISP (*d*), and coronal T1-weighted postgadolinium interstitial phase fat-suppressed 3D-GE (*e*,*f*) images demonstrate refractory gluten-sensitive enteropathy (RGSE) in another patient. Valvula conniventes of the jejunum are lost due to RGSE. Segmental wall thickening (arrows, *c*) and associated increased enhancement (arrows, *e*) are detected in the jejunum and ileum, suggesting jejunoileitis. Submucosal edema is detected in these segments.

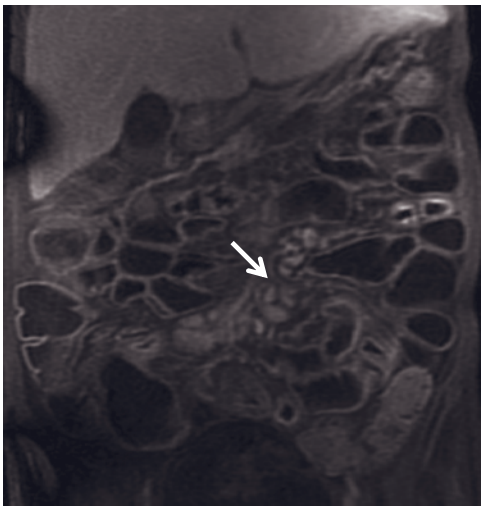

(*f*)

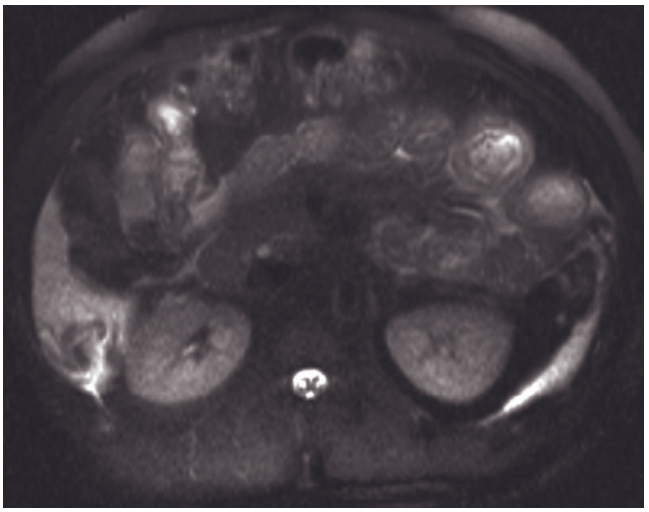

(*g*)

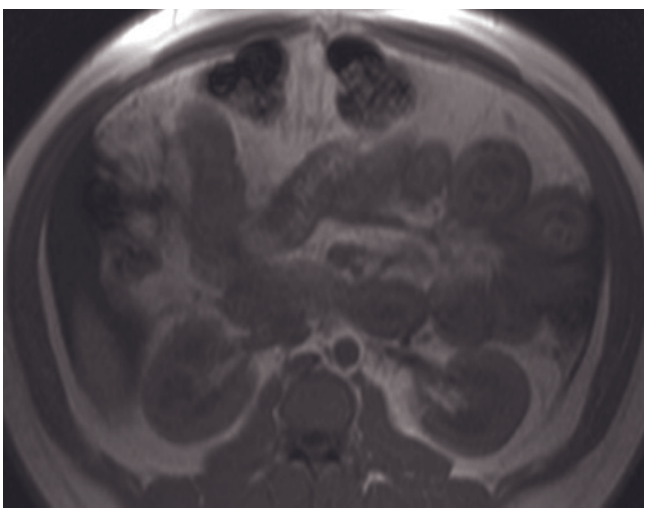

(*h*)

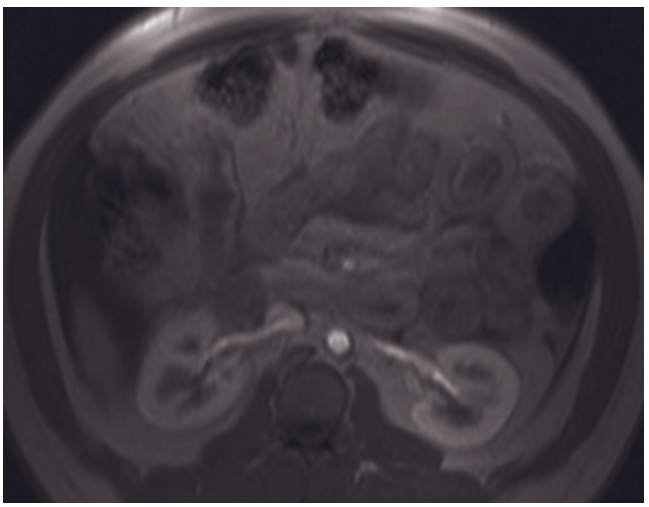

(*i*)

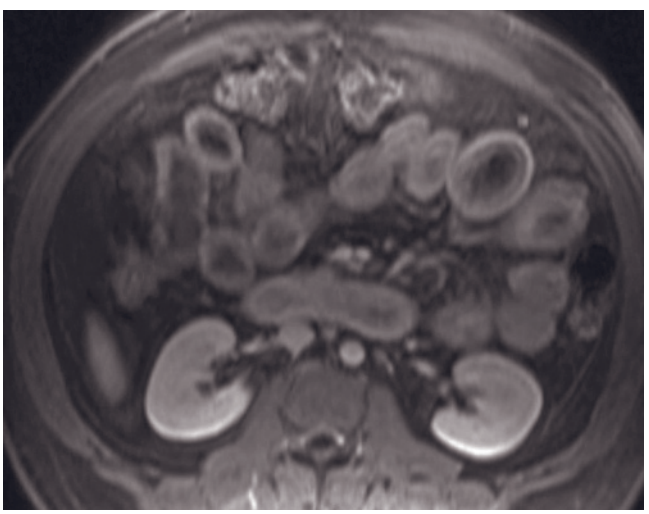

(*j*)

FIG. 6.72 (*Continued*) Note that enlarged and enhanced mesenteric lymph nodes (arrow, *f*) are also present. **Eosinophilic gastroenteritis.** T2-weighted short-tau inversion recovery (STIR) (*g*), T1-weighted SGE (*h*), T1-weighted postgadolinium arterial phase SGE (*i*), and T1-weighted postgadolinium fat-suppressed 3D-GE (*j*) images demonstrate eosinophilic gastroenteritis in another patient. The walls of small bowel segments are thickened because of edema, which shows high signal intensity on T2-weighted image (*g*). The bowel segments are moderately dilated, and their walls show progressive increased enhancement. Note that free fluid is also present in the abdomen.

showed bowel dilatation in 61.3% (n = 19), increased number of ileal folds in 48.4% (n = 15), reversed fold pattern abnormality in 38.7% (n = 12), increased wall thickness in 16.1% (n = 5), duodenal stenosis in 6.5% (n = 2), intussusception in 12.9% (n = 4), mesenteric lymphadenopathy in 41.9% (n = 13), mesenteric vascular changes in 22.6% (n = 7), ascites in 6.5% (n=2), and no abnormalities in 12.9% (n = 4) [76]. The overall specificity and accuracy were 100%, and sensitivity was 79% and 75% for increased number of ileal folders and reversed fold pattern abnormality, respectively [76]. MRI can detect the complications of GSE including jejunoileitis and lymphoma.

Eosinophilic Gastroenteritis

Eosinophilic gastroenteritis is a rare disease affecting both children and adults. It is characterized by the presence of GI symptoms, eosinophilic infiltration in the GI tract, the absence of an identified cause of eosinophilia, and the exclusion of eosinophilic involvement in organs other than the GI tract. Atopy or food allergy history may be present. MR imaging features are nonspecific and include gastric or bowel dilatation, thickened or flattened valvula conniventes, gastric and bowel wall thickening, strictures, ulcerations, enlarged lymph nodes, and ascites. Edema in the bowel wall submucosa can be seen as high-signal-intensity changes on T2-weighted images. Thickened bowel wall shows increased enhancement on postgadolinium images.

Scleroderma

Scleroderma, or progressive systemic sclerosis, is a connective tissue disease that often involves the gastrointestinal tract. There is a patchy destruction of the muscularis propria in the small intestine, mainly involving the duodenum and jejunum. There is also degeneration of both circular and longitudinal muscle layers and replacement by collagen tissue [77]. Dilatation is the most common finding in imaging studies (fig. 6.73), and

(*a*)

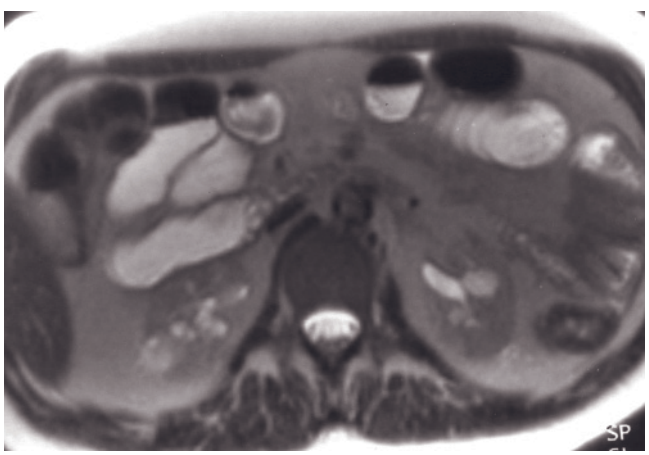

(*c*)

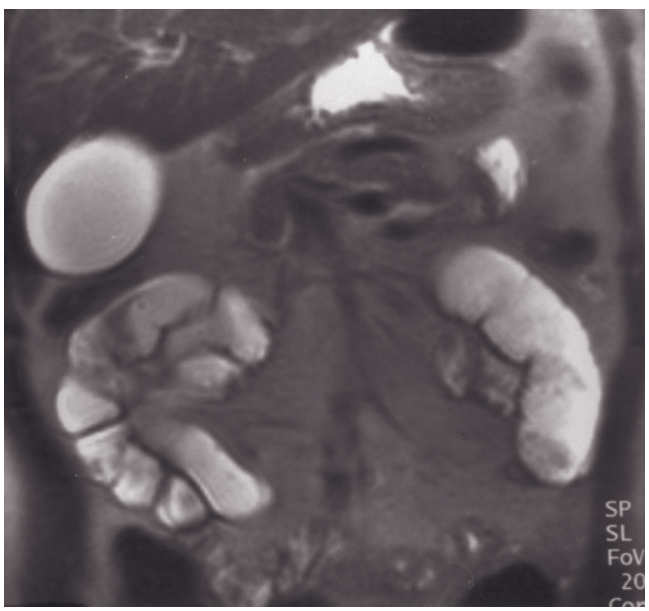

(*b*)

FIG. 6.73 Scleroderma. Coronal (*a*, *b*) and transverse (*c*) T2-weighted SS-ETSE images show dilatation of the duodenum and multiple small bowel loops without evidence of obstruction.

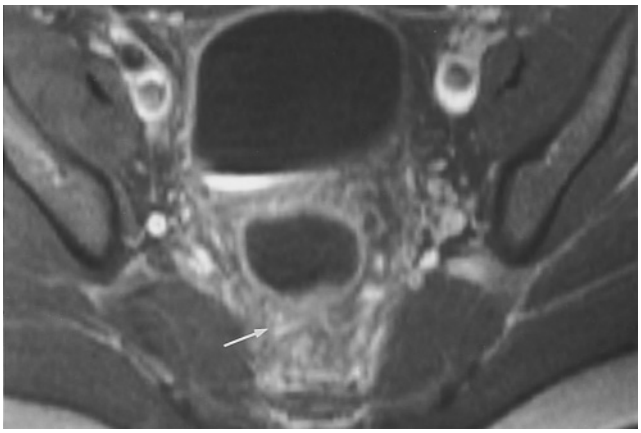

FIG. 6.74 Pouchitis. Gadolinium-enhanced T1-weighted fat-suppressed spin-echo image demonstrates slight thickening of the pouch with stranding in the surrounding fat (arrow).

sacculation with formation of pseudodiverticula also may develop.

Pouchitis

A continent ileostomy ("pouch") is often fashioned for patients after total colectomy. The creation of an ileal pouch changes the usual function of this part of the small intestine from absorption to fecal storage. With fecal storage, stasis and bacterial overgrowth may occur. The most common long-term complication of an ileal reservoir is inflammation known as "pouchitis." This condition is more common in patients with Crohn disease [78], MRI features of which include an enhancing and thickened pouch wall and inflammatory stranding of the "peripouch" fat (fig. 6.74).

Fistula

A fistula is defined as an abnormal passage or communication, generally between two internal organs or leading from an organ to the surface of the body. In the setting of small bowel pathology, fistulas result from compromise in the integrity of the visceral wall and may be sequelae of infection, inflammation, neoplasia, radiation therapy, and ischemia (embolic, thrombotic, or vasoconstrictive). MRI's good contrast and spatial resolution, in conjunction with direct image acquisition in any plane, makes it a very effective modality in the workup of fistulas. The appearance of a fistula will depend on its contents, the degree of inflammation, and the type of sequence employed. Fluid-filled tracts are high in signal intensity on T2-weighted sequences, whereas gas-filled tracts are signal void. Fat suppression combined with intravenous gadolinium highlights the enhancing fistulous tracts amid the surrounding low-signal intensity intra-abdominal fat. Focal discontinuity of the involved organ at the site of tract penetration is diagnostic (fig. 6.75) [7, 8].

Infectious Enteritis

Active inflammation may be caused by a variety of bacterial, protozoal, fungal, or viral pathogens. *Yersinia enterocolitica* infection may cause acute gastroenteritis, terminal ileitis, mesenteric lymphadenitis, and colitis [79]. *Yersinia* ileitis and *Yersinia* enterocolitis may mimic appendicitis and Crohn disease, respectively. *Campylobacter jejuni* may produce diarrhea, severe gastroenteritis, or colitis [80]. *Giardia lamblia* and *Strongyloides stercoralis* are protozoa that typically involve proximal small bowel. The increasing population of immunocompromised patients has led to an increase in occurrence of infectious granulomatous disease of the bowel. Tuberculosis mycobacteria infection involves the terminal ileum. Patients may be symptomatic from the acute inflammatory response, late fibrotic stenosis, or both. *Mycobacterium avium-intracellulare* favors the colon and is frequently accompanied by bulky retroperitoneal lymphadenopathy. Cytomegalovirus and *Cryptosporidium parvum* are infections common in AIDS patients. In all of these inflammatory conditions, the MRI findings may be nonspecific, demonstrating bowel wall thickening, increased secretions, and mesenteric edema. Gadolinium-enhanced fat-suppressed SGE or 3D-GE imaging demonstrates bowel wall thickening and increased enhancement (fig. 6.76) and detects the presence of abscesses by the identification of encapsulated fluid collections that possess an enhancing rim. Clinical history, coupled with the segment of bowel affected, may suggest the correct diagnosis. For example, in an AIDS patient, small bowel wall thickening and submucosal hemorrhage may be seen in cytomegalovirus infection, whereas focal thickening of the bowel wall and mildly dilated, fluid-filled segments may suggest *Cryptosporidium* infection [46].

Pancreatitis

Small bowel changes also may occur adjacent to an active inflammatory process. Specifically, in patients with pancreatitis, small bowel wall thickening and focal ileus are seen on gadolinium-enhanced SGE or 3D-GE images (fig. 6.77). An MRI colon cutoff sign also may be demonstrated.

Drug Toxicity

Inflammatory changes of small bowel may result from a number of etiologies. Chemotherapy toxicity is one example. Diffuse and circumferential wall thickening with increased enhancement are observed (fig. 6.78).

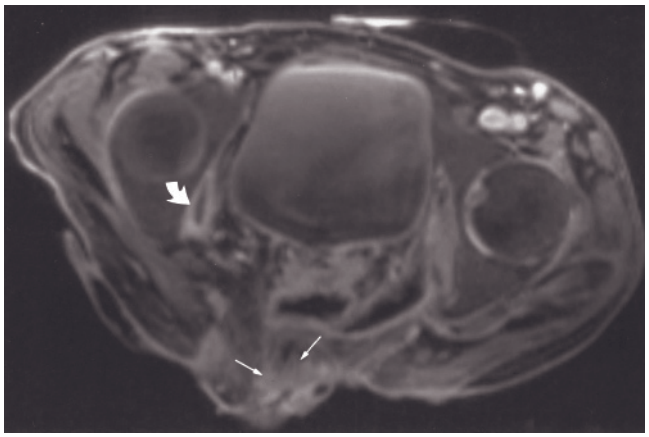

(*a*)

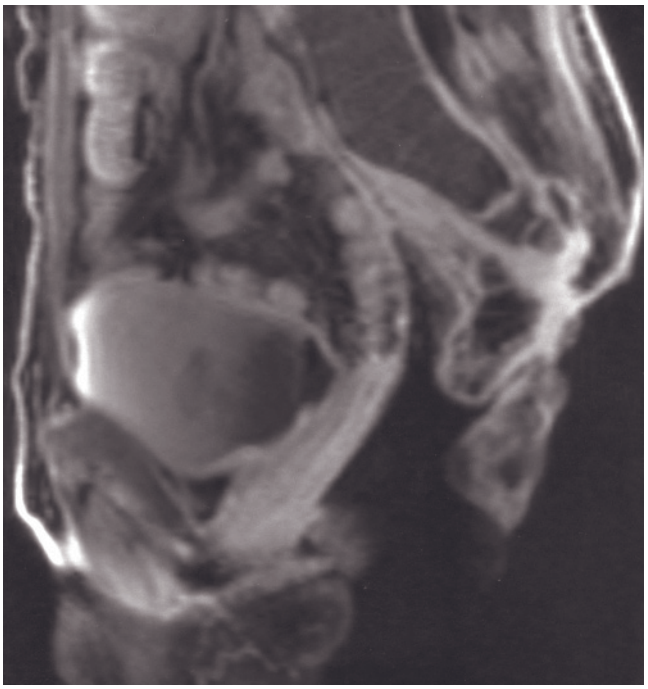

(*b*)

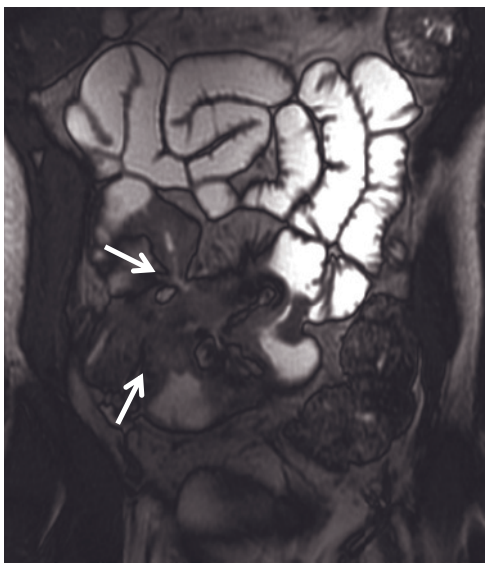

(*c*)

(*d*)

(*e*)

FIG. 6.75 Pelvic fistulas in a patient with Crohn disease. Transverse (*a*) and sagittal (*b*) interstitial-phase gadolinium-enhanced fat-suppressed SGE images. There is a large decubitus ulcer associated with destruction of the coccyx and lower part of the sacrum. Extensive pelvic cutaneous fistulas appear as enhancing track walls (arrows, *a*). An abscess of the obturator internus muscle is present (curved arrow, *a*). **Entero-enteric fistulas in patients with Crohn disease.** Coronal T2-weighted true-FISP (*c*), single-shot echo-train spin-echo (*d*), and coronal T1-weighted postgadolinium interstitial-phase fat-suppressed 3D-GE (*e*) images demonstrate several entero-enteric fistulas in another patient with Crohn disease. Several small bowel segments with thickened and abnormally enhancing walls form fistulas (arrows, *c–e*) with each other. Note the associated

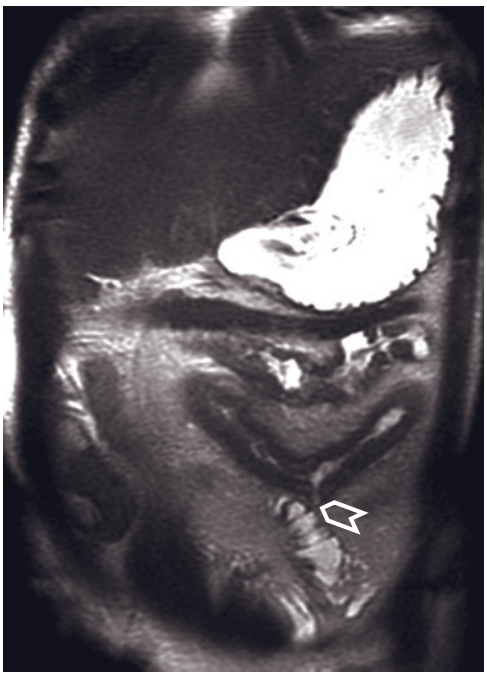

(*f*)

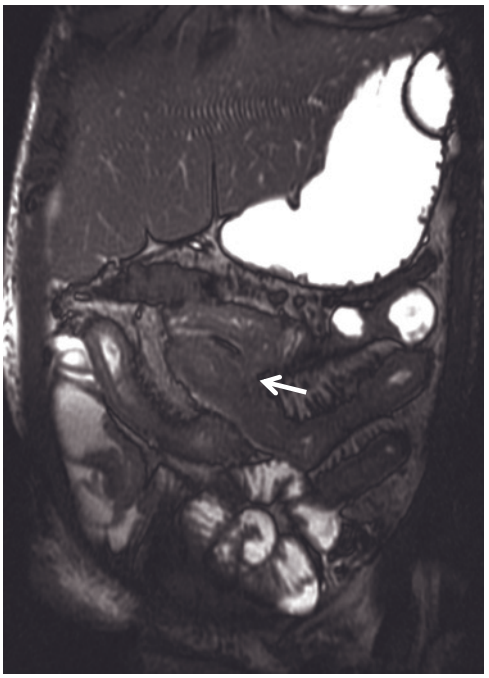

(*g*)

(*h*)

FIG. 6.75 (*Continued*) mesenteric inflammation adjacent to the fistulas. Coronal T2-weighted single-shot echo-train spin-echo (*f*), coronal T2-weighted true-FISP (*g*), and coronal T1-weighted postgadolinium fat-suppressed interstitial phase 3D-GE (*h*) images demonstrate an entero-enteric fistula (white arrow, *g*, *h*) and an ulcer (open arrow, *f*, *h*) in another patient with Crohn disease. The walls of small bowel segments are thickened and show increased enhancement. A fistula (white arrows, *g*, *h*) is present between two jejunal segments. Note that there is stranding in the mesenteric fat adjacent to the involved segments, which is best seen on true-FISP (*g*) and postgadolinium (*h*) images. An ulcer (open arrow, *f*, *h*) that is detected in the inferior border of a jejunal segment shows high signal on T2-weighted image (*f*) and increased enhancement on postgadolinium image (*h*) within the wall. **Entero-vesical fistula in**

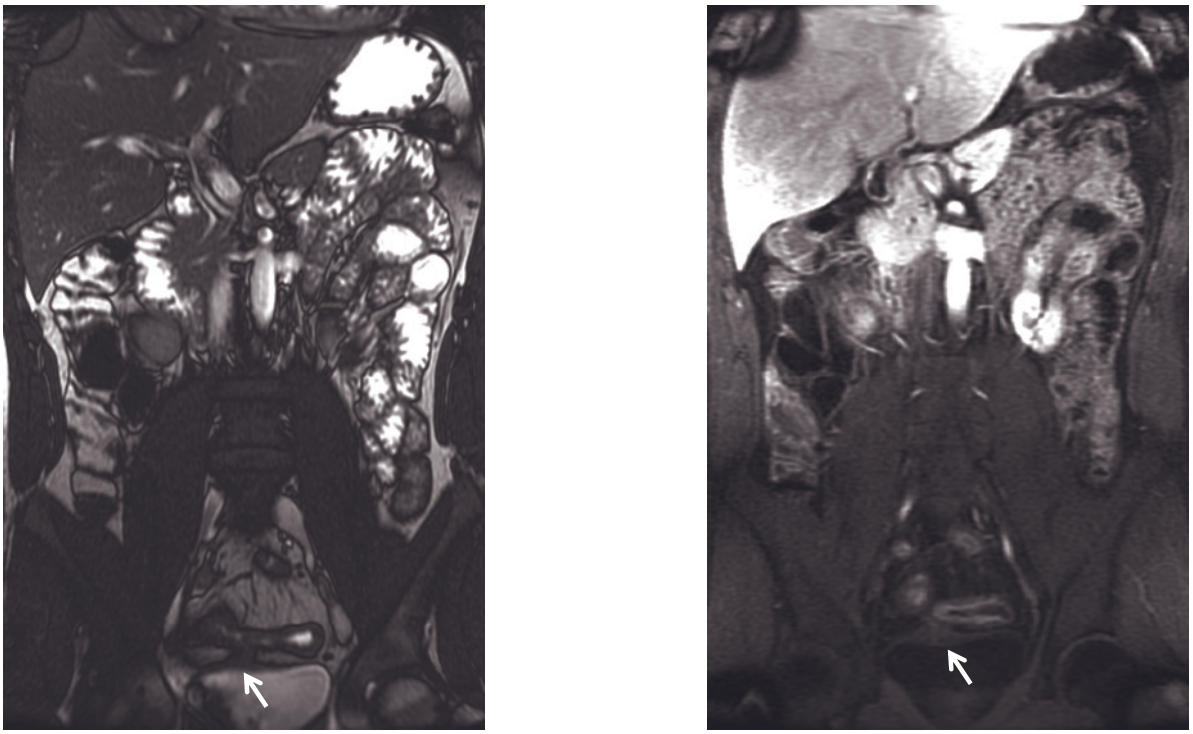

(*i*) (*j*)

FIG. 6.75 (*Continued*) **a patient with Crohn disease.** Coronal T2-weighted true-FISP (*i*) and coronal T1-weighted post-gadolinium interstitial-phase fat-suppressed 3D-GE (*j*) images demonstrate a fistula (arrow, *i*, *j*) between an ileal segment and the dome of the bladder. Note that the wall of the ileal segment is thickened and shows increased enhancement.

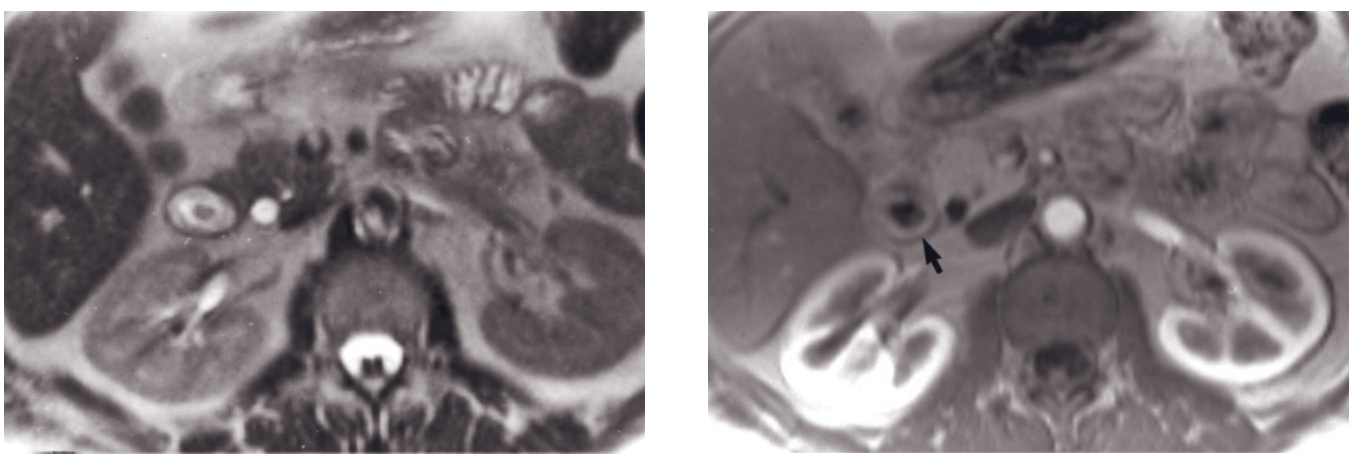

(*a*) (*b*)

FIG. 6.76 Duodenitis. Transverse T2-weighted SS-ETSE (*a*), immediate postgadolinium SGE (*b*), and interstitial-phase gadolinium-enhanced fat-suppressed SGE (*c*) images. Diffuse wall thickening and enhancement (arrow, *b*) involving the second part of

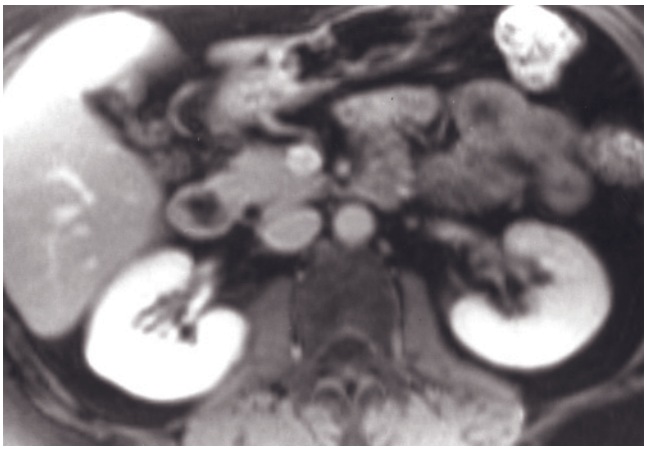

(*c*)

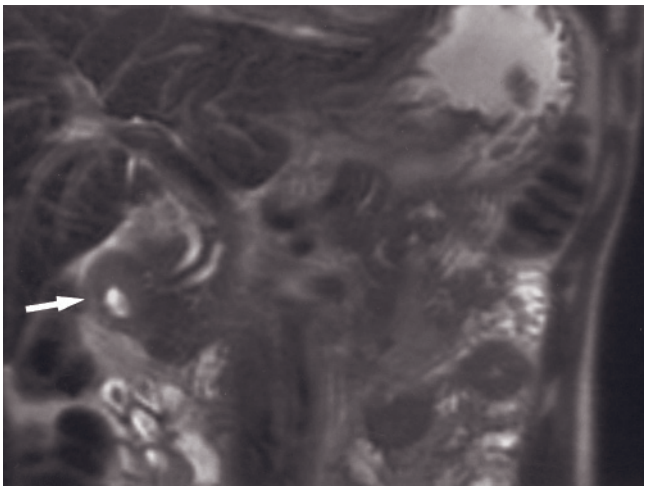

(*d*)

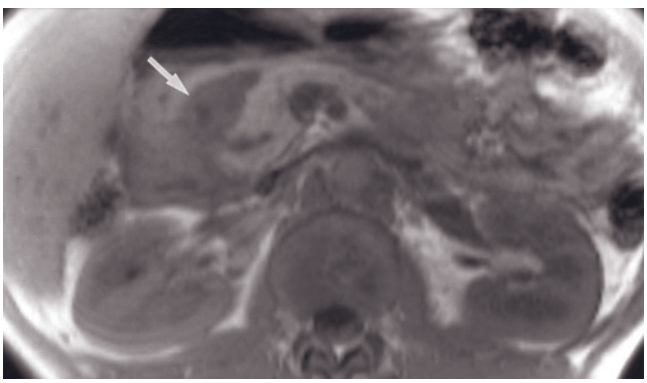

(*e*)

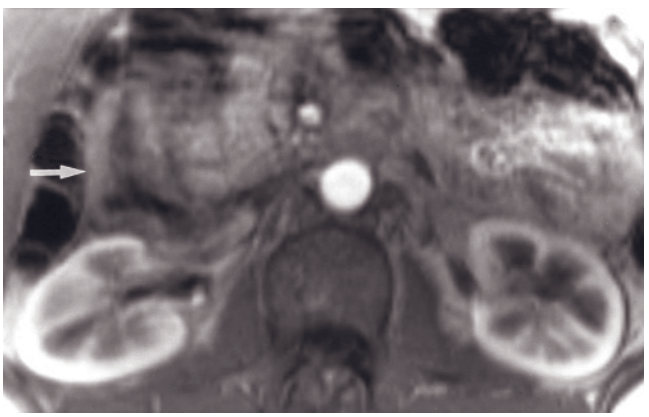

(*f*)

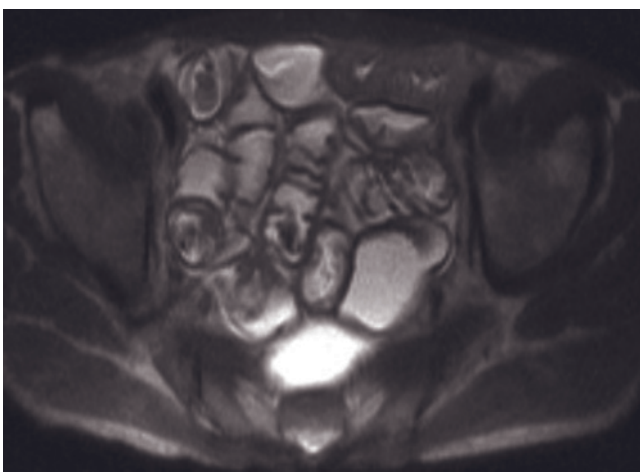

(*g*)

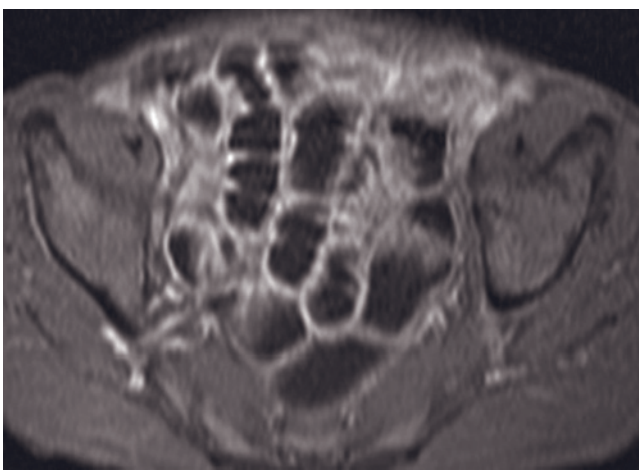

(*h*)

FIG. 6.76 (*Continued*) the duodenum are observed in a patient with infectious enteritis. Coronal T2-weighted SS-ETSE (*d*), transverse SGE (*e*), and immediate postgadolinium T1-weighted SGE (*f*) images in a second patient with eosinophilic enteritis. There is thickening of the first and second portions of the duodenum (arrows, *d–f*) with duodenal dilatation. **Infectious enteritis.** T2-weighted single-shot echo-train spin-echo (*g*) and T1-weighted postgadolinium interstitial-phase fat-suppressed 3D-GE (*h*) images demonstrate dilated small bowel loops with intensely enhancing thickened walls in another patient with AIDS.

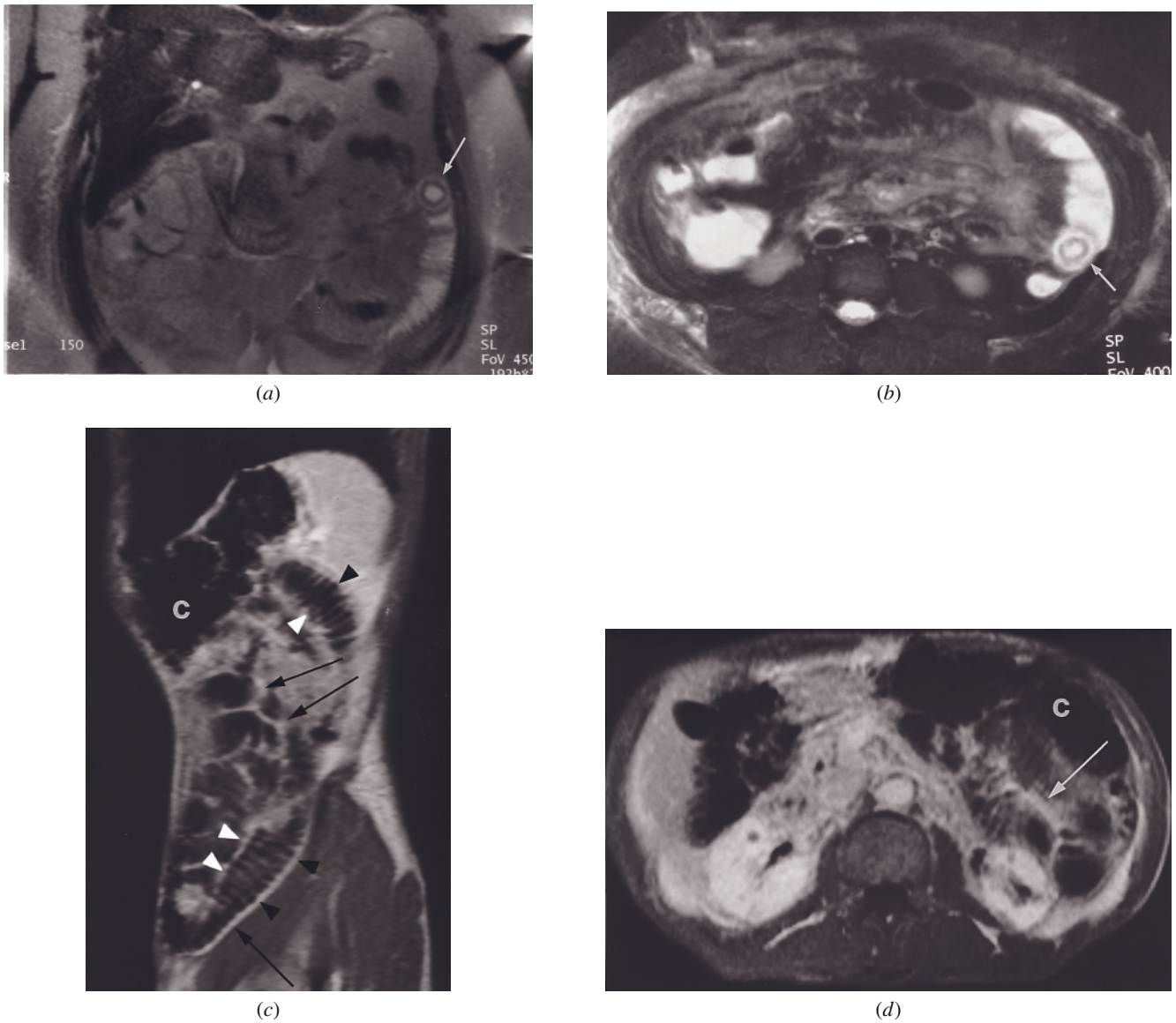

FIG. 6.77 Small intestine inflammation secondary to pancreatitis. Coronal T2-weighted SS-ETSE (*a*) and T2-weighted fat-suppressed echo-train spin-echo (*b*) images demonstrate circumferential high signal intensity of the wall of the jejunum (arrow, *a*, *b*) secondary to edema caused by inflammatory changes induced by pancreatitis. The outer wall is high in signal intensity, whereas the inner wall is low in signal intensity, reflecting the extrinsic nature of the bowel inflammation. Sagittal (*c*) and transverse (*d*) interstitial-phase gadolinium-enhanced SGE images in a second patient demonstrate dilatation (arrowheads, *c*) of small bowel with increased wall enhancement (arrows, *c*, *d*).The transverse colon (c, *c*, *d*) shows a transition from normal caliber to narrowed, which is the transverse colon cutoff sign of pancreatitis.

Radiation Enteritis

In the gastrointestinal tract, the small intestine is the region most sensitive to radiation injury. Radiation therapy for malignant disease may cause an enteritis with tumor doses greater than 45 Gy. The majority of cases are secondary to treatment for female genital tract malignancy. The distal jejunum and ileum are the most common sites affected. Acute injury to the small intestine occurs within hours to days after radiation therapy. Although some damage to the intestinal wall is a regular occurrence, lesions are variable in severity. Microscopic inspection may show sloughed villi with mucosal hemorrhage, edema, focal necrosis, and inflammation. Early postradiotherapy complications include ulceration, necrosis, bleeding, perforation, and abscess formation. The development of chronic radiation enteritis is variable, developing months to years after the radiation event. Chronic radiation enteritis is a progressive disease resulting from underlying vascular damage. Vascular injury includes fibrosis and hyalinization of blood vessel

walls leading to obliterative endarteritis within the intestinal wall and mesentery. Progression of the vascular pathology causes ischemia. Normal tissue is replaced by parenchymal atrophy and progressive fibrosis. Complications of chronic radiation enteritis include strictures, fistulas, bowel fixation, and angulation. Varying degrees of small bowel obstruction may result. Gadolinium-enhanced fat-suppressed SGE or 3D-GE imaging is the most effective technique for detecting the diffuse early ischemic and inflammatory changes of radiation enteritis as well as the more focal late fibrotic sequelae. Changes caused by radiation effect are reflected in diffuse symmetric bowel wall thickening and enhancement of multiple loops of small bowel in the same region of the abdomen. Radiation effect can be readily distinguished from recurrent tumor, which demonstrates irregular, nodular bowel wall thickening (fig. 6.79).

Ischemia and Hemorrhage

Ischemia and hemorrhage may occur in tandem or as isolated events. Ischemia, regardless of etiology, leads to wall edema secondary to capillary leakage (fig. 6.80). If prolonged, infarction can result. The MRI findings parallel the severity of blood flow compromise. Early changes include mural thickening and increased enhancement on late postcontrast images (fig. 6.81). Increased enhancement on immediate postgadolinium images reflects leaky capillaries. Necrotic bowel manifests MRI findings consistent with hemorrhage, and in severe cases portal venous gas may be observed (see fig. 6.81). Vascular compromise or thrombosis may be well shown on early (>1 min) postgadolinium images (fig. 6.82) and MRA images (see fig. 6.81). Bowel wall hemorrhage from trauma or ischemia may be diagnosed by high signal intensity within the submucosa on both T1- and T2-weighted sequences due to the presence of extracellular methemoglobin [81]. Noncontrast T1-weighted fat-suppressed images are the most sensitive for the detection of subacute blood (fig. 6.83). One study evaluated the MR appearance of small bowel wall hemorrhage and showed that MR findings was able to distinguish mural-based hematoma from contained perimural small bowel hematoma (fig. 6.83) [81]. The most effective MR feature to make this distinction was demonstration of the lack of involvement of the wall with single-shot T2-weighted images (fig. 6.83) [81].

Hypoproteinemia

Hypoproteinemia may arise from a number of causes, the most common of which are cirrhosis and malnourishment. In the setting of cirrhosis, hypoproteinemia has been postulated as the primary cause of intestinal wall edema of the large and small bowel. It is generally thought that edema is diffuse and results from changes in oncotic pressure [82]. Generalized bowel wall thickening is present, which is best appreciated in the jejunum. Unlike inflammatory conditions, enhancement on gadolinium-enhanced images is negligible (fig. 6.84).

Intussusception

Intussusception is a form of intestinal obstruction characterized by the telescoping of one intestinal segment into another. Predisposing factors include masses and motility disorders [83]. Transient asymptomatic intussusceptions are not uncommon imaging findings, but multiple nonobstructing intussusceptions suggest an underlying bowel disorder such as sprue. The invaginating bowel segment is referred to as the intussusceptum, and the bowel segment into which the prolapse has occurred is referred to as the intussuscipiens. Intussusception is clearly demonstrated on T2-weighted single-shot echo-train spin-echo images because of the sharp anatomic detail of this sequence. In the setting of intussusception, fluid in dilated bowel provides excellent intrinsic contrast for the bowel-within-bowel appearance (fig. 6.85). The use of T2-weighted single-shot echo train spin echo sequences is very helpful in pregnant patients (fig. 6.85) since postgadolinium imaging should be avoided in pregnant patients unless maternal and fetal survival depend on it.

Hernia

Small bowel mechanical obstruction is most commonly related to adhesions (fig. 6.85) or hernias. Small bowel hernias may be classified as internal, as may form from a loop of small bowel passing through an abnormal defect or tear within the mesentery, or as external, as may form from a small bowel loop passing into an inguinal defect (fig. 6.86). Distension of the small bowel with an oral contrast agent may provide additional sensitivity by making even a partially obstructed small bowel segment more conspicuous. A water-based agent can serve well for this purpose by producing high signal (bright lumen) on T2-weighted and low signal (dark lumen) on T1-weighted images (see fig. 6.86) [84–86].

Graft-Versus-Host Disease

Graft-versus-host disease (GVHD) is an immunologic disorder that occurs in any situation in which immunologically competent donor cells are transplanted into an immunologically incompetent recipient. GVHD most commonly follows bone marrow or organ transplantation. The acute form involves the gastric antrum, small bowel, and colon and occurs within days (7–100) in recipients. Histologically, acute GVHD shows loss of normal intestinal mucosal architecture with ulceration, mucosal denudation, and submucosal edema. On MR

(*a*)

(*b*)

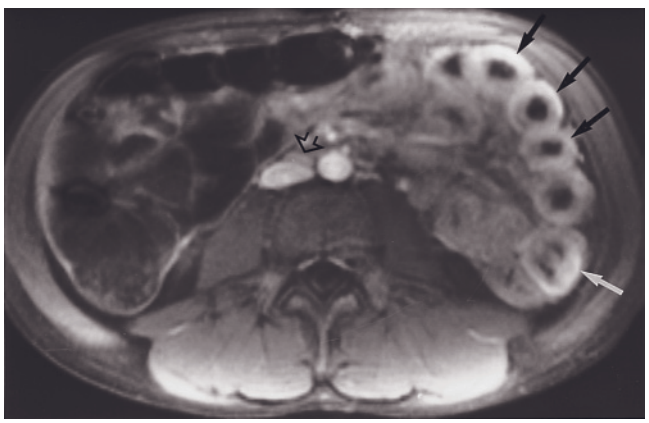

(*c*)

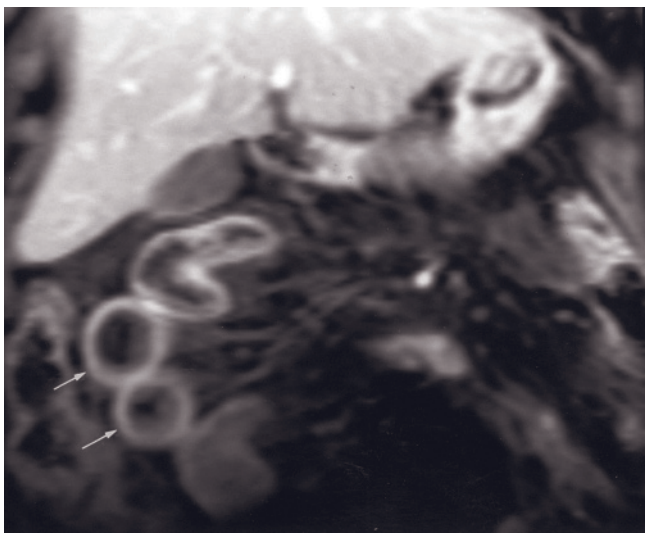

(*d*)

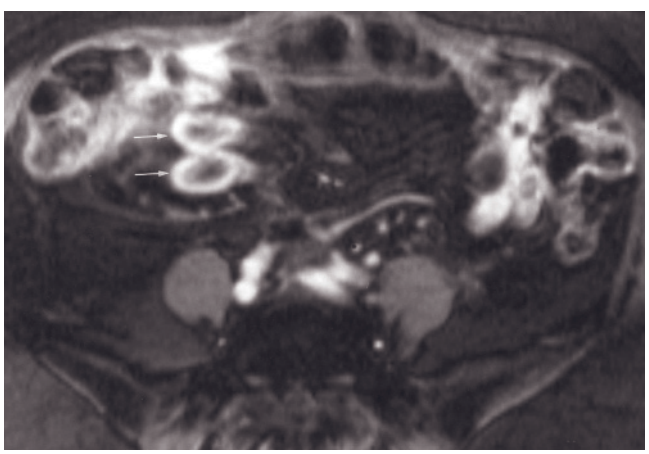

(*e*)

FIG. 6.78 Chemotherapy toxicity enteritis. Coronal T2-weighted SS-ETSE (*a*), immediate postgadolinium SGE (*b*), and 90-s postgadolinium fat-suppressed SGE (*c*) images in a patient with chemotherapy toxicity enteritis. Many etiologic agents may cause inflammation of the small bowel. The findings are nonspecific and include diffuse circumferential wall thickening (short arrows, *a*), marked bowel wall enhancement (arrows, *b*, *c*), mesenteric infiltration and hyperemia (open arrow, *b*), and lymphadenopathy (open arrow, *c*). Note the normal common bile duct on the T2-weighted image (long arrow, *a*). Coronal (*d*) and transverse (*e*) interstitial-phase gadolinium-enhanced fat-suppressed SGE images in a second patient, who underwent chemotherapy for ovarian cancer. There is abnormal enhancement of multiple loops of small bowel (arrows, *d*, *e*) consistent with chemotherapy toxicity enteritis.

images there is diffuse bowel wall thickening with increased enhancement of the inner wall layers (fig. 6.87). The chronic form of GVHD may follow the acute form or occur insidiously and is usually associated with esophageal involvement. Microscopic examination of the esophagus shows a sloughed and hyperemic mucosa. This desquamative esophagitis may lead to webs and strictures.

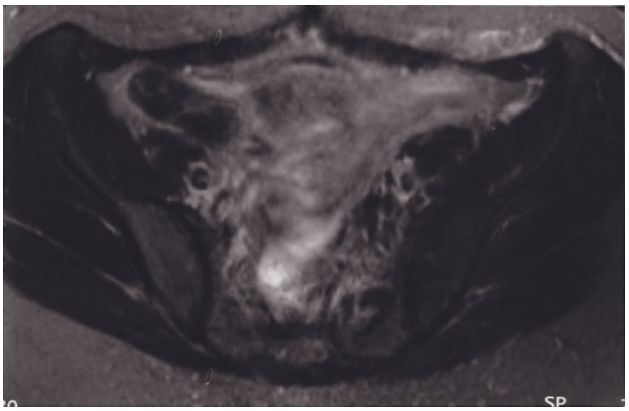

(*a*)

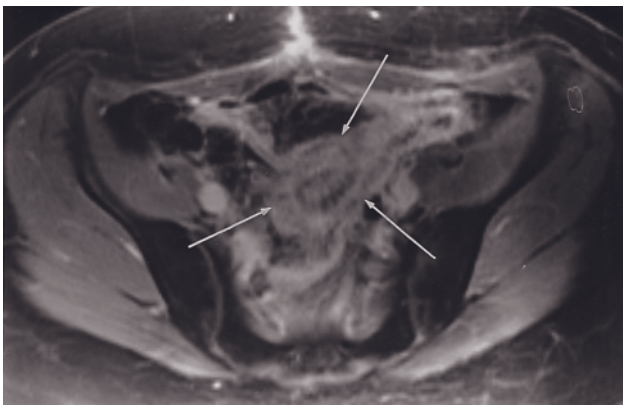

(*b*)

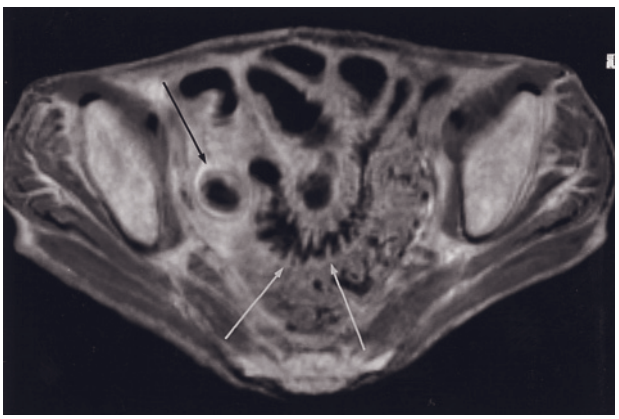

(*c*)

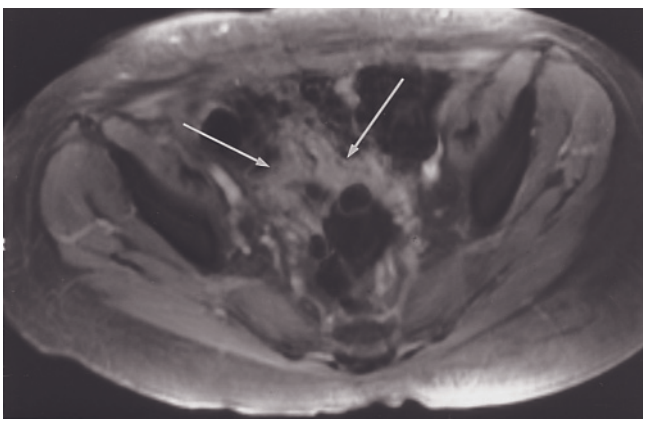

(*d*)

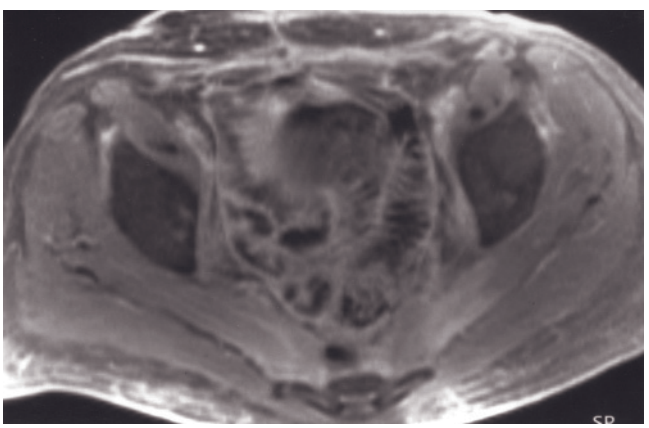

(*e*)

FIG. 6.79 Small intestine radiation enteritis versus metastatic disease. Transverse 512-resolution T2-weighted echo-train spin-echo (*a*), 90-s postgadolinium fat-suppressed SGE (*b*), and 90-s postgadolinium SGE (*c*) images in two patients [(*a*, *b*) and (*c*)] with radiation enteritis. In the first patient, the T2-weighted echo-train spin-echo image (*a*) is degraded by blurring artifact secondary to peristalsis. Breath-hold technique coupled with gadolinium-enhanced fat-suppressed imaging at the same level highlights postradiation therapy changes of the small bowel: diffuse, symmetric wall thickening with increased enhancement (arrows, *b*). Similar changes are noted in the second patient after radiation therapy (arrows, *c*). Transverse 90-s postgadolinium fat-suppressed SGE image (*d*) in a third patient, who has recurrent ovarian cancer, demonstrates irregular focal thickening of small bowel. Note the difference between the symmetric and uniform bowel thickening associated with radiation changes (*b*, *c*) and the more focal and asymmetric changes produced by metastatic disease to the small bowel (arrows, *d*). Transverse gadolinium-enhanced interstitial-phase fat-suppressed SGE (*e*) image in a fourth patient, after radiation therapy for colon cancer, shows circumferential small bowel thickening.

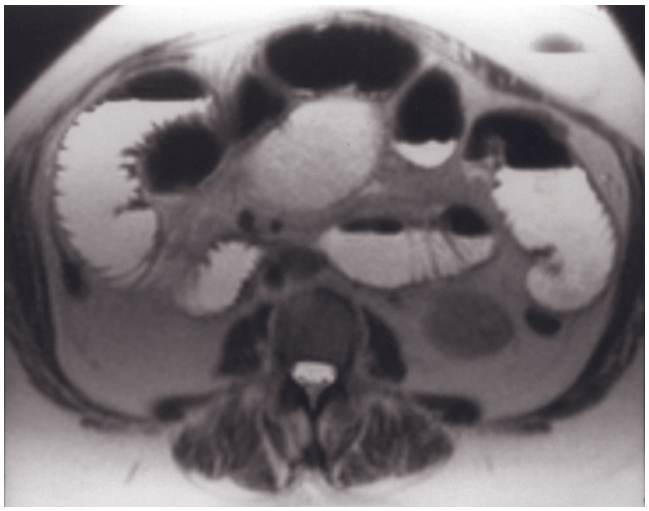

(*a*)

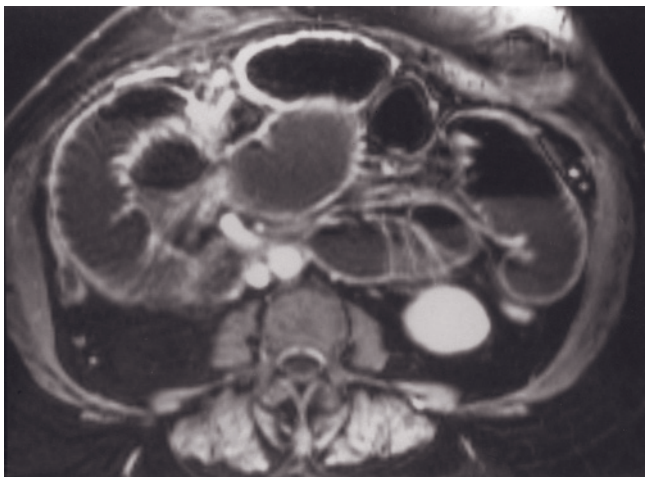

(*b*)

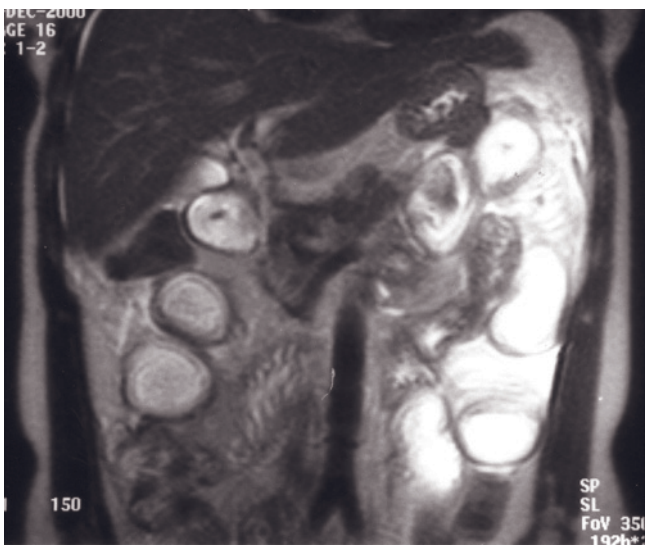

(*c*)

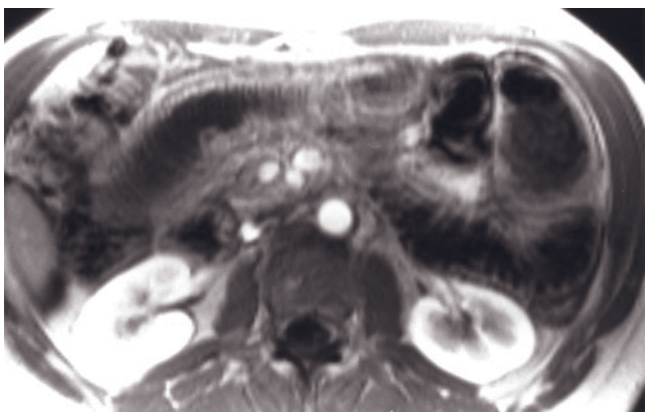

(*d*)

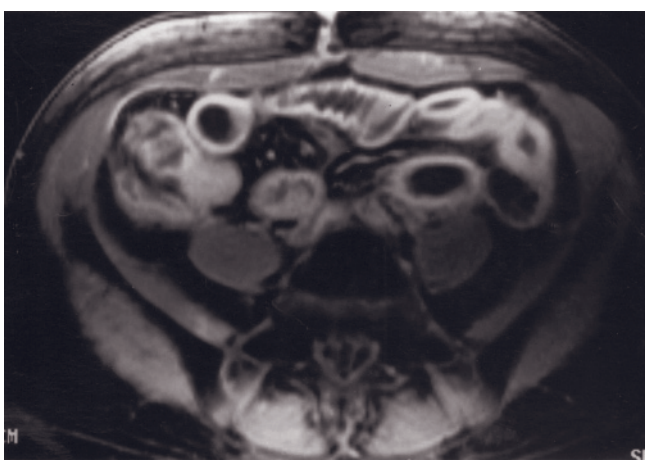

(*e*)

FIG. 6.80 Small bowel ischemia. T2-weighted SS-ETSE (*a*) and interstitial-phase gadolinium-enhanced fat-suppressed SGE (*b*) images in a patient with incarcerated hernia. Multiple dilated enhancing loops of small bowel with increased mural enhancement are observed. Air-fluid levels are identified on T2-weighted image (*a*). Coronal T2-weighted SS-ETSE (*c*), immediate postgadolinium T1-weighted SGE (*d*), and interstitial-phase gadolinium-enhanced fat-suppressed SGE (*e*) images in a second patient, who underwent radiotherapy for cervix cancer. Small bowel dilatation with increased thickness and enhancement is present. Operative findings were consistent with multiple adhesions and bowel ischemia. Coronal T2-weighted SS-ETSE (*f*) image in a third patient shows diffuse, markedly dilated small bowel loops.

(*f*)

FIG. 6.80 (*Continued*)

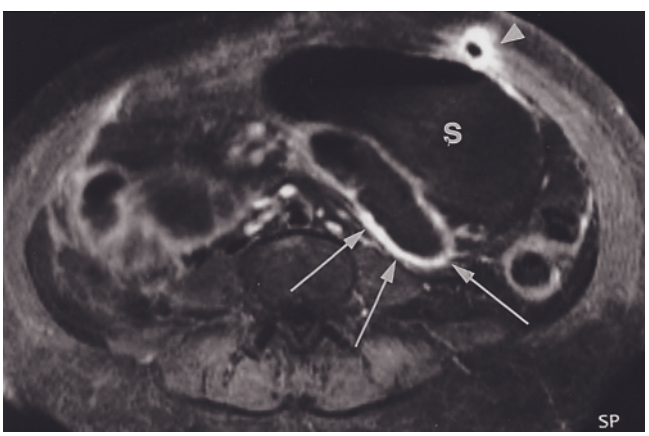

(*a*)

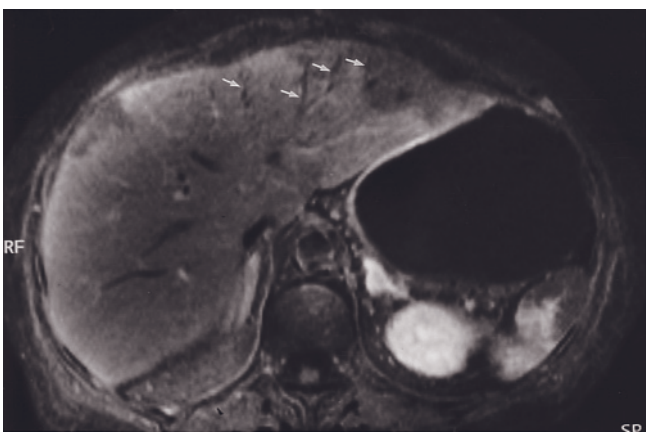

(*b*)

FIG. 6.81 Small bowel ischemia. Gadolinium-enhanced T1-weighted fat-suppressed spin-echo images (*a*, *b*).The patient had undergone previous small bowel resection. Increased enhancement of a loop of proximal small bowel (arrows, *a*) is present. The stomach (s, *a*) also contains regions of increased mural enhancement. Increased enhancement results from leaky capillaries in ischemic bowel disease. Portal venous gas (small arrows, *b*) is an ominous finding suggesting bowel necrosis. Susceptibility artifact (arrowhead, *a*) is noted within the anterior abdominal wall. Coronal T2-weighted single-shot echo-train spin-echo (*c*) and

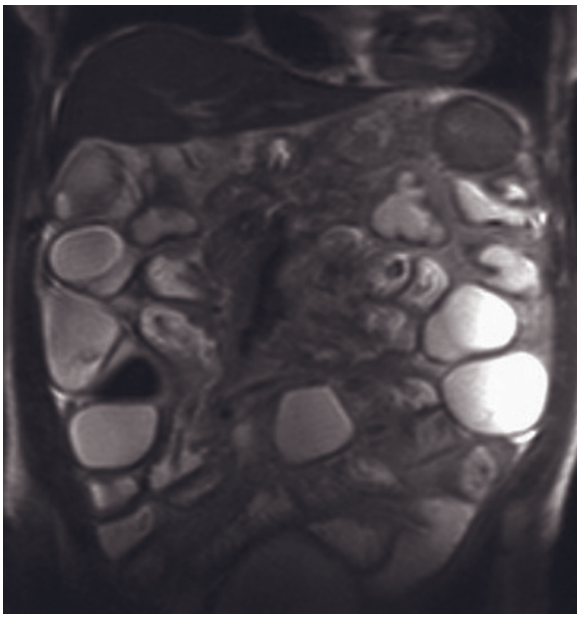

(*c*)

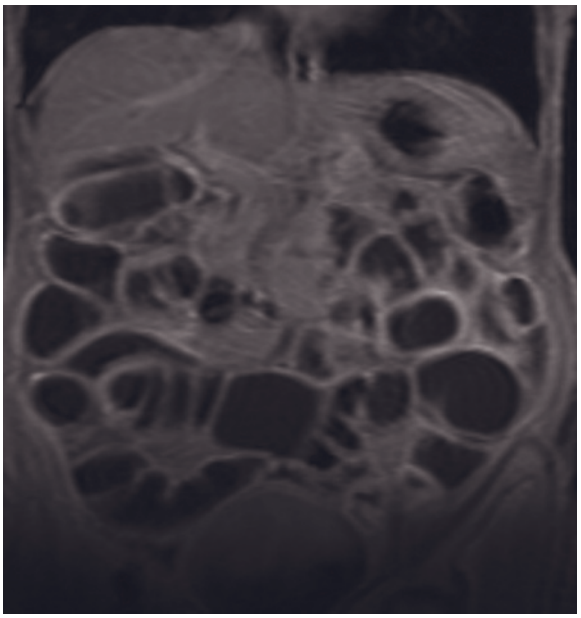

(*d*)

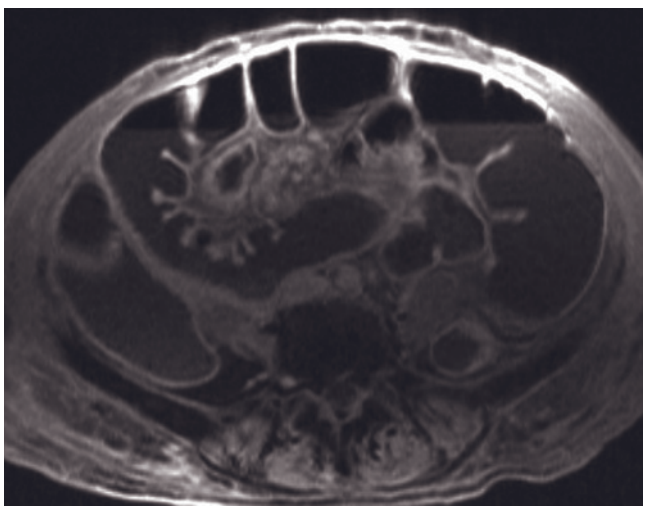

(*e*)

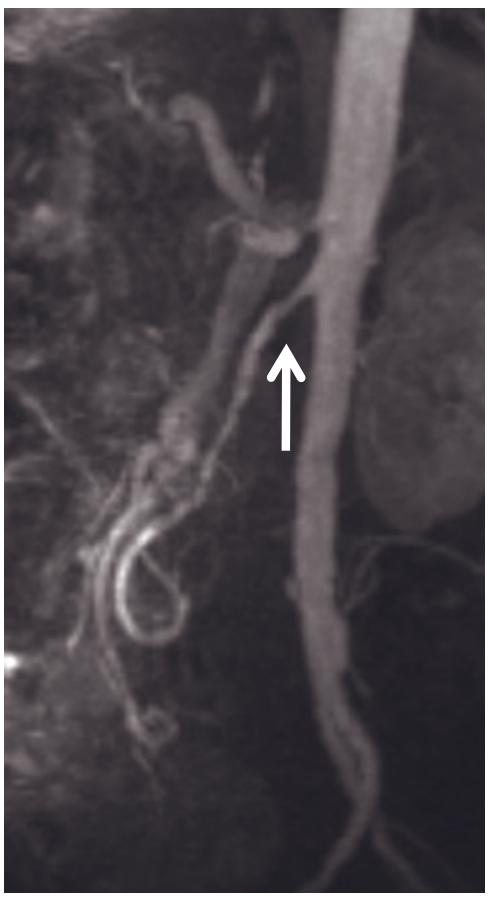

(*f*)

FIG. 6.81 (*Continued*) coronal (*d*) and transverse (*e*) T1-weighted postgadolinium interstitial-phase fat-suppressed SGE images demonstrate small and large bowel ischemia and dilatation secondary to shock in another patient. The walls of the bowel are thickened and show increased enhancement on the interstitial phase. Sagittal reconstructed 3D MIP MRA (*f*) image also shows additional superior mesenteric artery stenosis (arrow) and similar findings of the celiac trunk. Note that free fluid is present in the abdomen.

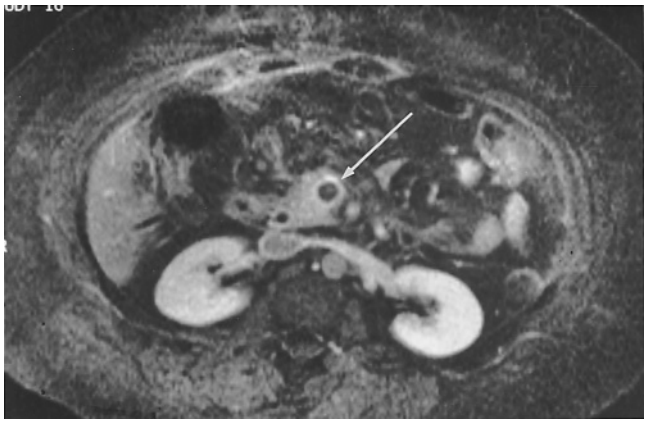

FIG. 6.82 Superior mesenteric vein (SMV) thrombosis. Transverse 90-s postgadolinium fat-suppressed SGE image demonstrates signal-void thrombus in the SMV with increased enhancement of the SMV wall (arrow), which was caused by infection associated with thrombosis.

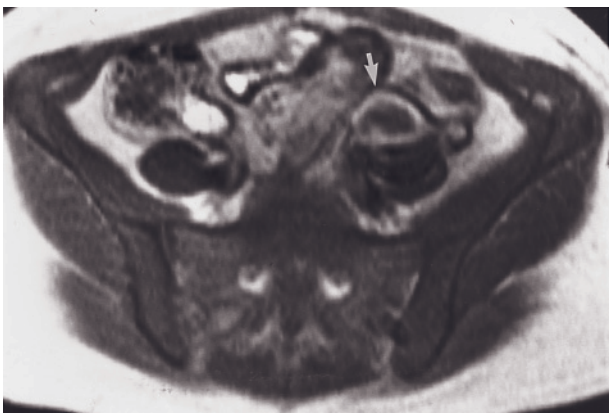

(*a*)

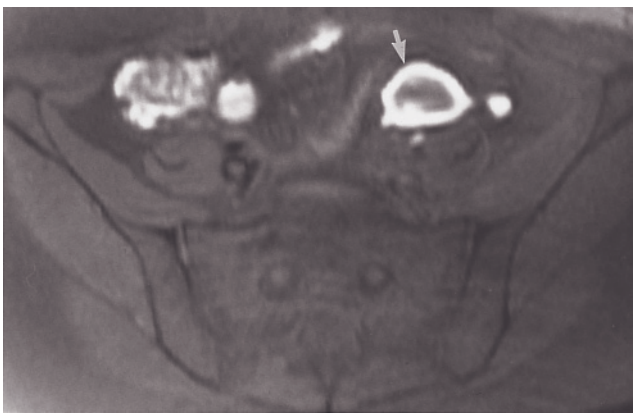

(*b*)

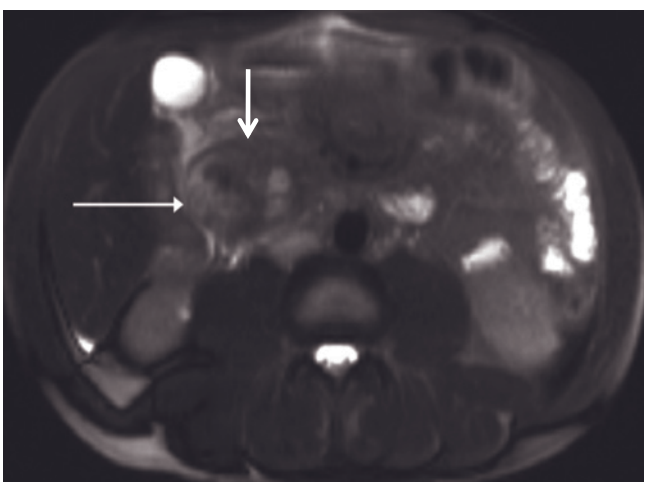

(*c*)

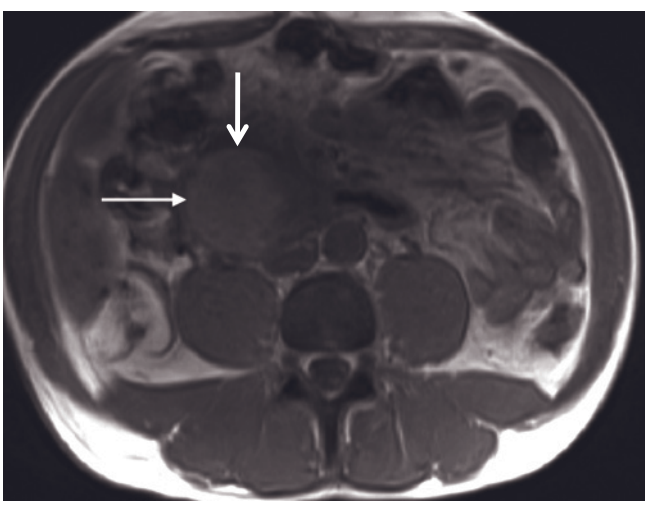

(*d*)

FIG. 6.83 Submucosal hemorrhage. SGE (*a*) and T1-weighted fat-suppressed spin-echo (*b*) images in a woman status post hysterectomy who had undergone vigorous intraoperative bowel retraction. Increased signal intensity in the bowel wall on the SGE image (arrow, *a*) becomes more conspicuous after fat suppression (arrow, *b*). **Duodenal hematoma.** Transverse T2-weighted single-shot echo-train spin-echo (*c*), transverse T1-weighted SGE (*d*), and coronal T1-weighted postgadolinium interstitial-phase fat-suppressed 3D-GE (*e*) images demonstrate an intramural duodenal hematoma (arrows, *c–e*) in another patient. An eccentrically

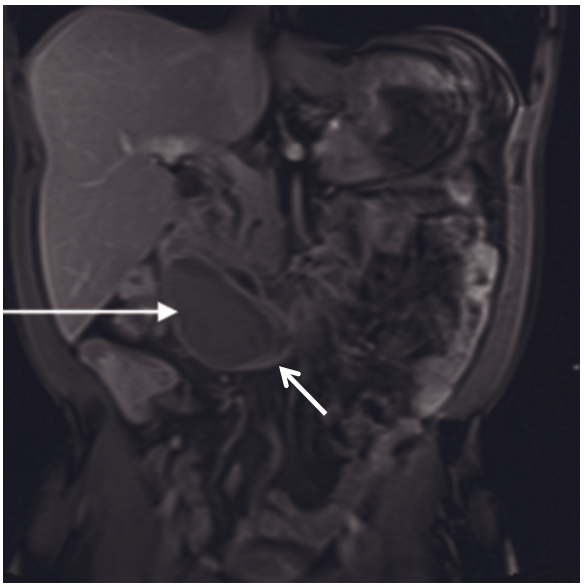

(*e*)

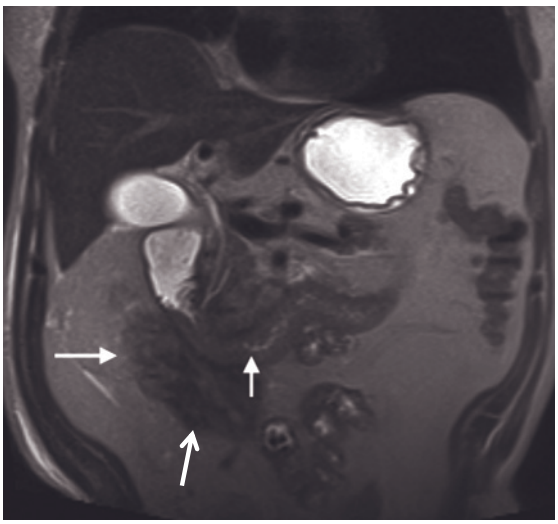

(*f*)

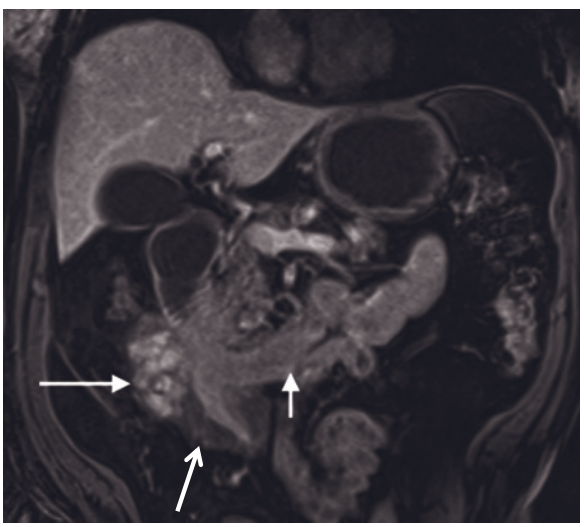

(*g*)

FIG. 6.83 (*Continued*) located duodenal mass shows heterogeneously high signal on T2-weighted image (*c*) and intermediate signal on T1-weighted image (*d*). No enhancement is detected in the lesion on postgadolinium image (*e*). Note that minimal perihepatic free fluid is detected. Coronal T2-weighted single-shot echo-train spin-echo (*f*) and coronal T1-weighted fat-suppressed interstitial-phase 3D-GE (*g*) images demonstrate periduodenal hematoma in another patient. Periduodenal hematoma (long arrows, *f*, *g*) is present in the mesentery along the 2nd and 3rd portions of the duodenum. The hematoma shows intermediate signal on T2-weighted image (*f*) and high signal on T1-weighted precontrast image (not shown). The hematoma does not show any enhancement on postgadolinium image (*g*). Note that the duodenal wall (short arrow, *f*, *g*) is intact.

THE LARGE INTESTINE

Normal Anatomy

The large bowel measures approximately 4.5 ft in length and is divided into the appendix, cecum, ascending colon, transverse colon, descending colon, sigmoid colon, rectum, and anal canal. Its main functions include absorption of water and electrolytes, storage of fecal matter, and mucus secretion.

The cecum lies below the level of the ileocecal valve. Although the cecum is in the right iliac fossa, it possesses a mesentery and sometimes is freely mobile. This mobility predisposes the cecum to volvulus formation. The ascending and descending colon are retroperitoneal and located in the anterior pararenal space. The transverse colon is located anteriorly in the peritoneal cavity suspended by the transverse mesocolon, which originates from the peritoneal covering of the anterior surface of the pancreas. The gastrocolic ligament connects the superior surface of the transverse colon to the greater curvature of the stomach. The sigmoid colon is intraperitoneal and suspended by a mesentery, whereas the rectum is retroperitoneal and relatively fixed. The frontal and lateral surfaces of the rectum are covered with peritoneum, which is then reflected anteriorly, forming the rectovaginal recess in females and the rectovesical recess in males. Below the coccyx, the rectum traverses the levator ani muscles to become the anal canal.

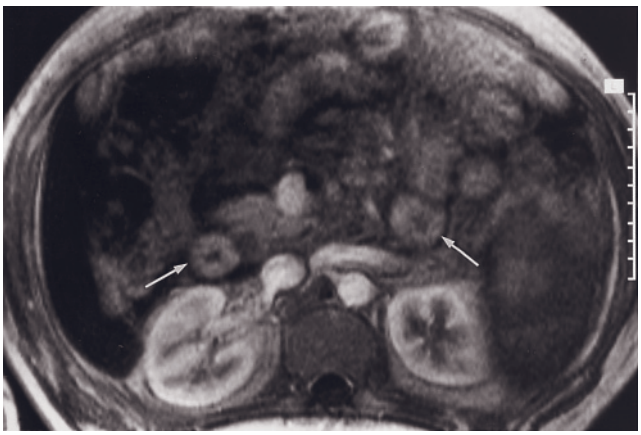

(*a*)

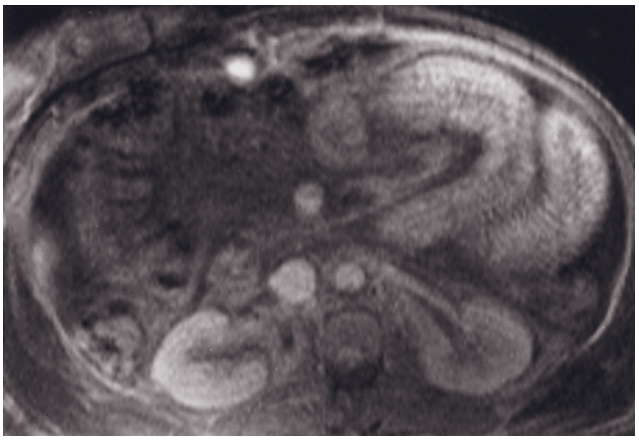

(*b*)

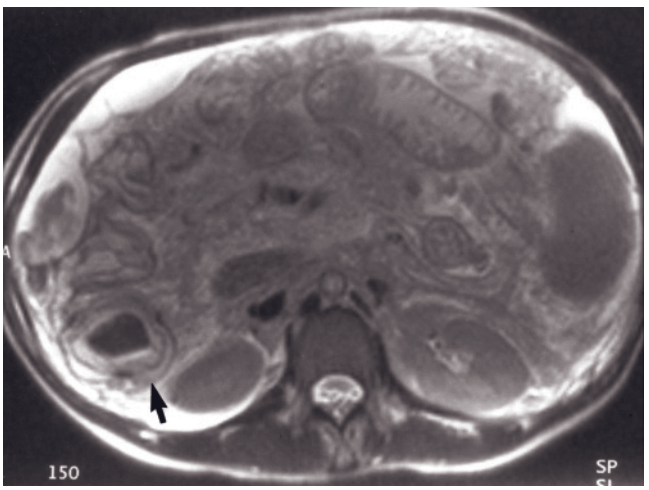

(*c*)

FIG. 6.84 Small bowel edema in cirrhosis. Immediate post-gadolinium SGE (*a*), 90-s postgadolinium SGE (*b*), and T2-weighted single-shot echo-train spin-echo (*c*) images in three different patients with cirrhosis. Ascites and diffuse thickening of multiple loops of small bowel (arrows, *a*) are present. Third-spacing of fluid secondary to hypoproteinemia accounts for the bowel wall thickening. High-signal submucosal edema is well shown on the single-shot T2-weighted image (arrow, *c*)

Colonic microstructure consists of four layers: mucosa, submucosa, muscularis externa, and serosa. The bowel wall is usually less than 4 mm thick. The muscularis consists of an inner circular and an outer longitudinal layer. Thickened muscular bundles of the outer muscle layer form the taeniae coli. Because the taeniae are shorter in length than the colonic wall itself, taeniae coli gather the wall into sacculations or haustra. Colonic luminal diameter is greatest in the cecum and gradually decreases distally to the level of the rectal ampulla, where the caliber again increases.

MRI Technique

The technique and considerations for studying the large bowel parallel those for the small bowel. Fasting at least 4–6 h before imaging is recommended to reduce peristalsis. Blurring artifact from bowel motion decreases image quality of long-acquisition-time T2-weighted conventional and fast spin-echo techniques. T2-weighted single-shot echo-train spin-echo and True-FISP techniques overcome this limitation and should be performed in the axial and coronal planes for imaging colonic disease, with the sagittal plane reserved for imaging the rectum. Gadolinium-enhanced fat-suppressed SGE or 3D-GE imaging is an important sequence for imaging the colon, as with all other segments of intra-abdominal bowel. Normal colon is thin walled, has haustrations, and enhances minimally with gadolinium (fig. 6.88).

The rectum deserves special mention. Unlike the remaining large intestine, the relatively fixed position of the rectum benefits from high-resolution (512 matrix) T2-weighted echo-train spin-echo imaging. This technique is particularly useful for the evaluation of rectal carcinoma, assessing the extent of bowel wall involvement by tumor, determining the relationship of tumors to adjacent structures, and distinguishing tumor recurrence from fibrosis. Endorectal MRI also may be used to study the rectum. The endoluminal surface coil optimizes

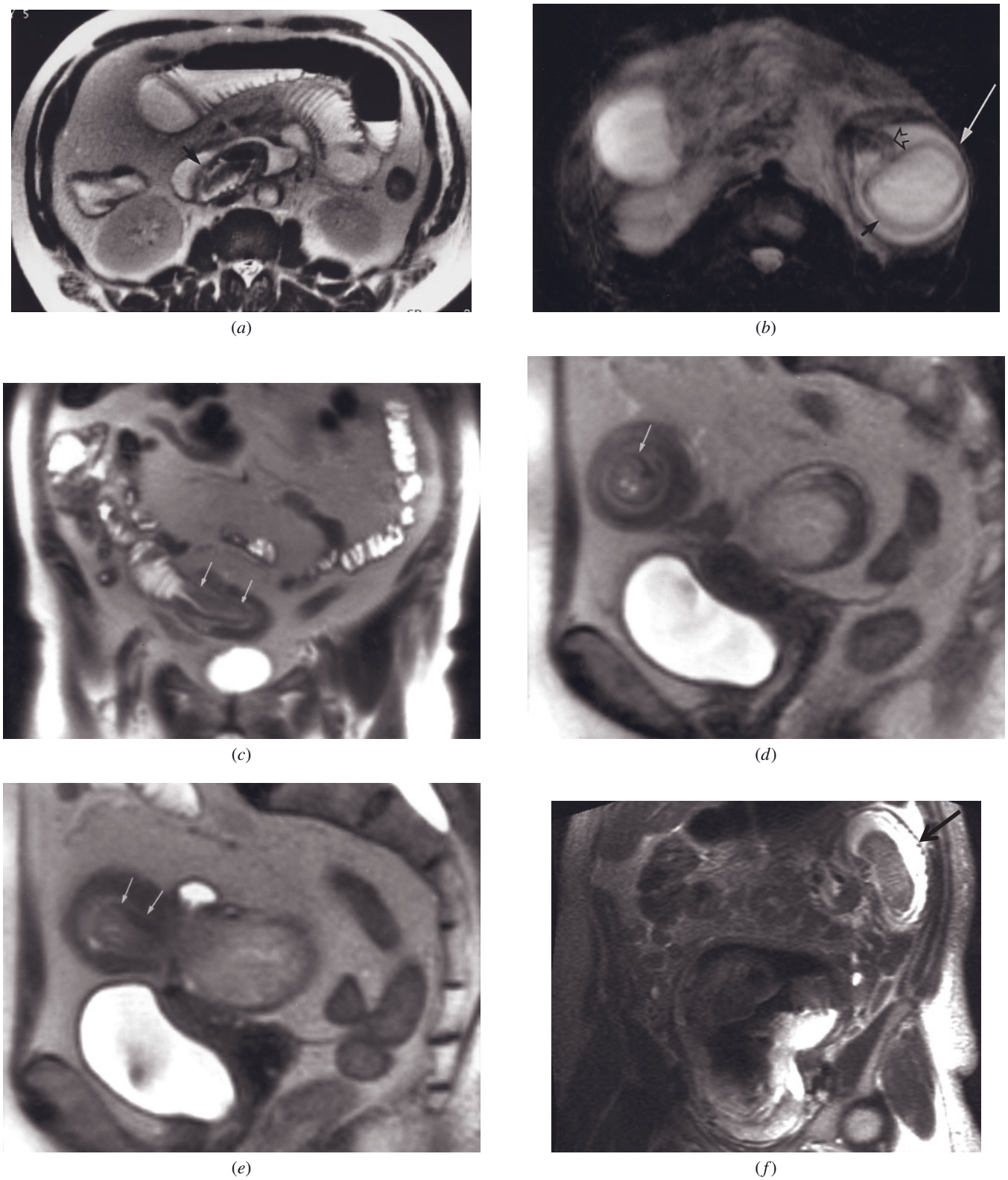

FIG. 6.85 Small bowel intussusception. T2-weighted SS-ETSE (*a*) and T2-weighted fat-suppressed echo-train spin-echo (*b*) images in two patients. In the first patient, the T2-weighted image (*a*) provides clear definition of the bowel-within-bowel appearance (arrow) of intussusception. In the second patient (*b*), respiratory and bowel motion degrades the majority of the peritoneal cavity. However, the dilated, relatively fixed, hypotonic loop of the intussuscipiens (long arrow, *b*) is relatively well shown. The intussusceptum (short arrow, *b*) is clearly shown, and its mesentery (open arrow, *b*) is also appreciated. In this second patient adequate visualization of the intussusception occurred in this non-breath-hold study because of the hypotonicity of the involved bowel segments. Coronal (*c*) and sagittal (*d*, *e*) T2-weighted SSETSE images in a third patient. The bowel-within-bowel appearance (arrows, *a–c*) is clearly demonstrated. (Courtesy of N. Cem Balci, Florence Nightingale Hospital, Istanbul, Turkey). **Intussusceptions**

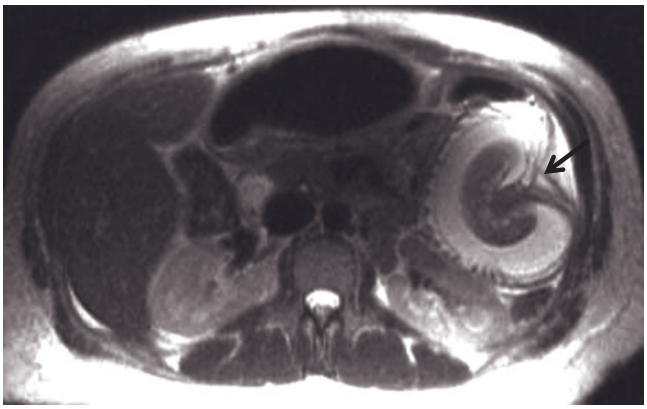

(*g*)

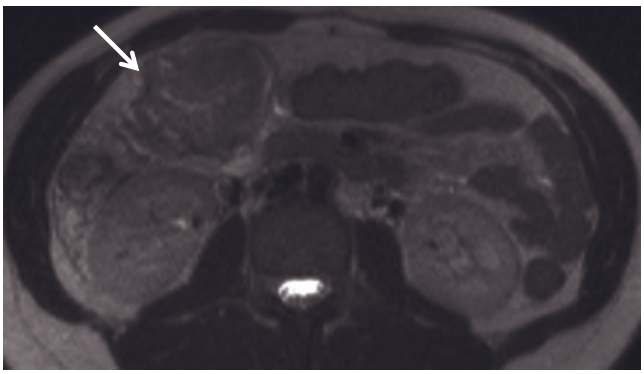

(*i*)

(*k*)

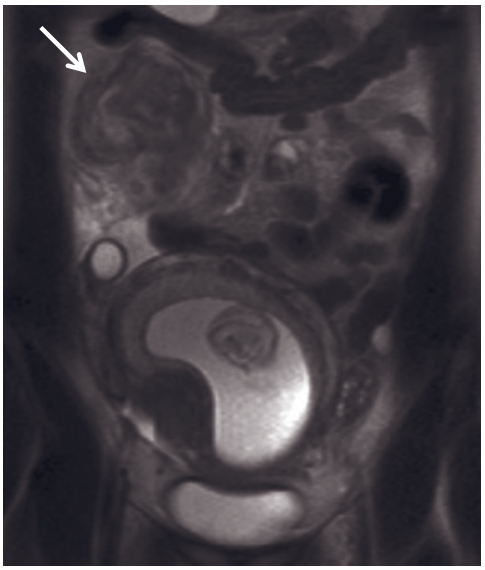

(*h*)

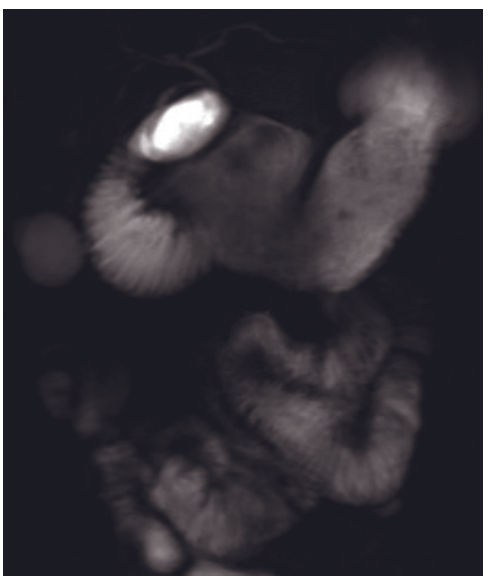

(*j*)

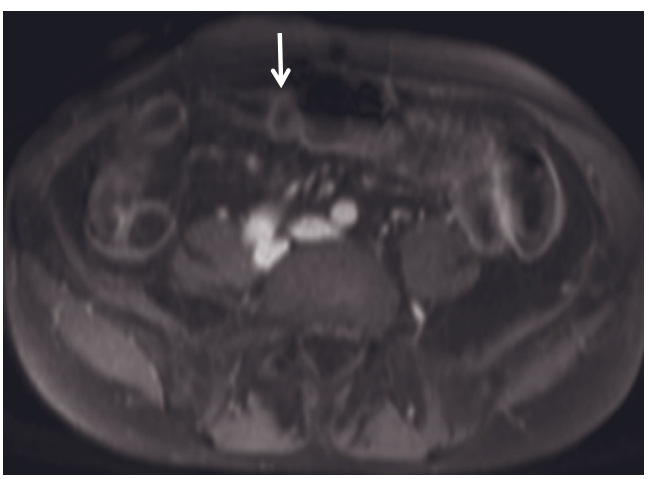

(*l*)

FIG. 6.85 (*Continued*) **in pregnant patients.** Coronal (*f*) and transverse (*g*) T2-weighted single-shot echo-train spin-echo and coronal (*h*) and transverse (*i*) single-shot echo-train spin-echo images demonstrate intussusceptions in two pregnant patients. Bowel-within-bowel appearance (black arrow, *f*, *g*) is detected in the left upper quadrant in a patient with jejuno-jejunal intussusception. Note the pregnancy and free fluid in this patient. Bowel-within-bowel appearance is detected in the right upper quadrant in another patient with colo-colic intussusception. Inflammatory stranding is present around the intussusception. Note the pregnancy and free fluid in this patient. **Small bowel obstruction secondary to adhesion.** T2-weighted thick-section fast spin-echo MRCP (*j*), T1-weighted SGE (*k*), and T1-weighted post-gadolinium fat-suppressed interstitial-phase 3D-GE (*l*) images demonstrate small bowel obstruction secondary to adhesions. Small bowel dilatation in combination with small bowel wall thickening and increased mural enhancement are detected. The transition point (arrows, *k*, *l*) between dilated small bowel segments and normal caliber small bowel segment is shown.

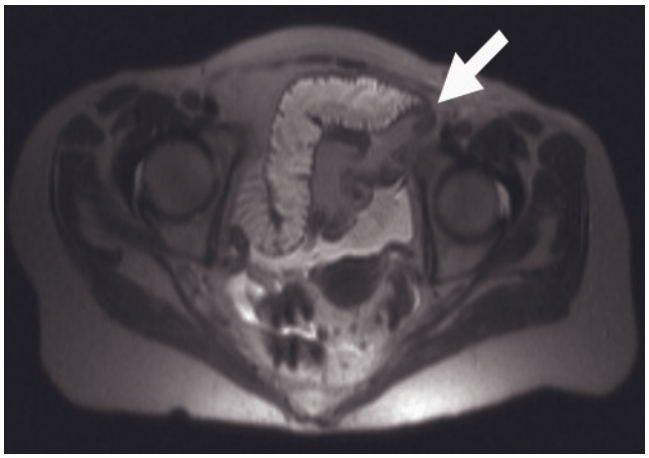

(*a*)

(*b*)

FIG. 6.86 Small bowel inguinal hernia. Axial single-shot T2 (*a*) and sagittal gadolinium-enhanced delayed-phase gradient-echo fat-suppressed T1 (*b*) images show an inguinal hernia (arrows) with mild dilatation of the small bowel proximal to the involved segment.

spatial resolution and demonstrates the rectal wall layers, anal sphincter complex, and disease processes [9, 10, 87, 88]. The use of intraluminal contrast to distend the colon may improve detection of mucosal abnormalities [89]. The layers of the rectal wall can be visualized on gadolinium-enhanced T1-weighted fat-suppressed images, high-resolution T2-weighted images, and endorectal coil T2-weighted images (see fig. 6.88). The transition between the rectum and the anal canal can be determined by the observation that the rectum contains intraluminal air and the anal canal is collapsed (fig. 6.89). Phased array torso coil imaging is generally used for imaging the rectum due to ease of use and patient acceptive. High-resolution (512 matrix) T2-weighted image combined with gadolinium-enhanced thin section 3D gradient echo is generally recommended.

MR colonography is a relatively recent technique that involves distending the colon with fluid and obtaining coronal thick-slab (5–8 cm) T2-weighted single-shot echo-train spin echo to generate images that resemble fluoroscopic barium enemas [90–92]. Water serves well as an intraluminal contrast agent.

Congenital Anomalies

Malrotation

Nonrotation, the most common rotational abnormality, is discussed above. In this condition the large bowel will occupy the left side of the abdomen (fig. 6.89).

Duplication

Colonic duplications represent a congenital longitudinal division of the developing gut. Grossly, two intestinal lumens are identified. The abnormalities may be limited to a single segment of large bowel, or they can involve the entire colon (fig. 6.90). Symptoms will depend on whether or not there is communication of the duplication with the remainder of the colon. Patients with right colon duplication are at risk for intussusception.

Anorectal Anomalies

Most cases of anorectal anomalies occur in association with other congenital malformations. MRI has been successful in evaluating these patients because it directly demonstrates the rectal pouch and sphincter muscles in

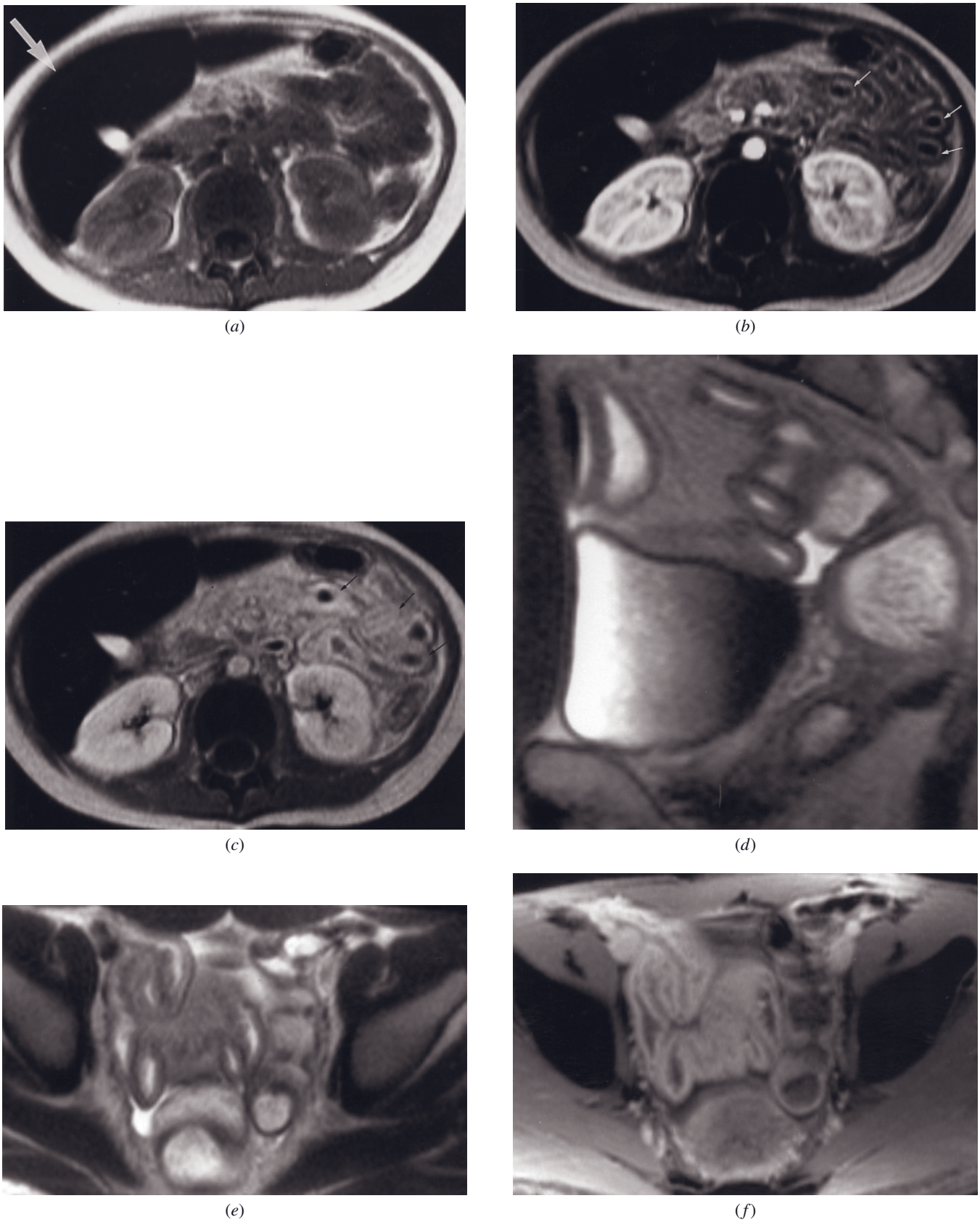

FIG. 6.87 Graft-versus-host disease. SGE (*a*) and immediate (*b*) and 90-s (*c*) postgadolinium SGE images in a patient after bone marrow transplant. Unenhanced images suggest thickening of multiple loops of small bowel. Immediately after intravenous contrast, intense mucosal enhancement of multiple loops of small bowel (arrows, *b*) is appreciated. On the interstitial-phase image (*c*), enhancement has spread to involve the majority of the wall (arrows). This enhancement pattern reflects hyperemia and capillary leakage, respectively. The decreased signal intensity of the liver (arrow, *a*) is consistent with iron overload secondary to multiple blood transfusions. (Reprinted with permission from Ascher SM, Semelka RC: MRI of the gastrointestinal tract. In Higgins CB, Hricak H, Helms CA (eds.), *Magnetic Resonance Imaging of the Body*. New York: Raven Press, 1997, p. 677–700.) Sagittal (*d*) and transverse (*e*) T2-weighted SS-ETSE and transverse interstitial-phase gadolinium-enhanced fat-suppressed SGE (*f*) images in a second

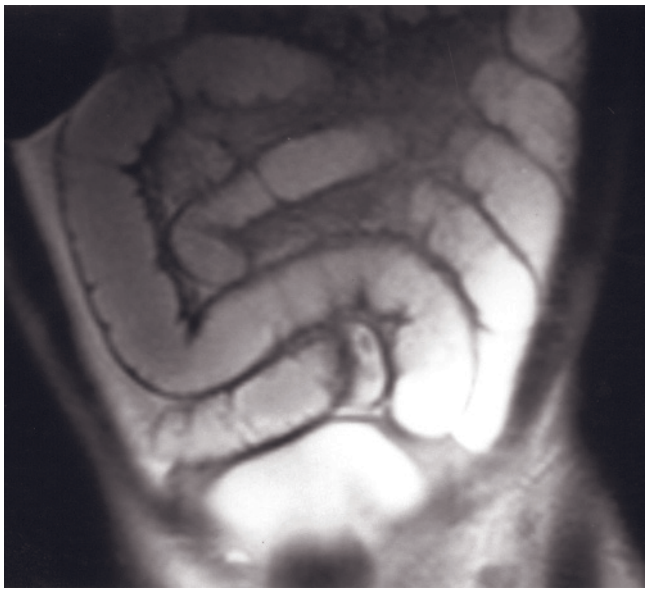

(*g*)

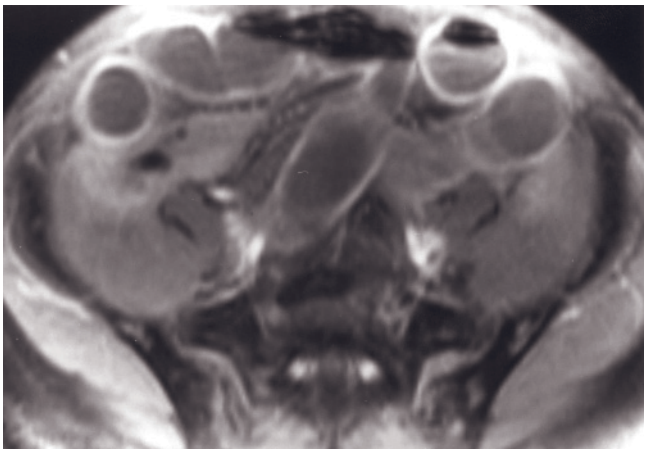

(*h*)

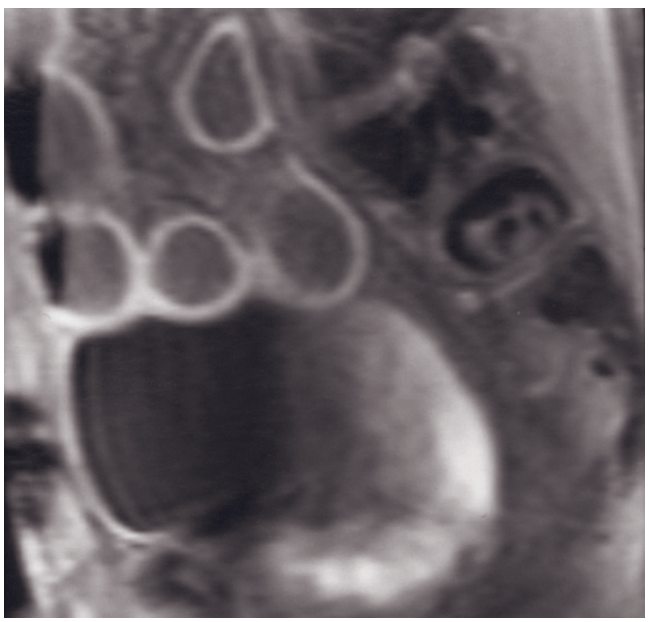

(*i*)

FIG. 6.87 (*Continued*) patient after bone marrow transplant. There is marked and diffuse wall thickening and increased mural enhancement of multiple bowel loops. Coronal T2-weighted SS-ETSE (g) and transverse (*h*) and sagittal (*i*) interstitial-phase gadolinium-enhanced fat-suppressed SGE images in a third patient after bone marrow transplant for ALL. There are dilated, fluid-filled small bowel loops associated with diffuse enhancement of the bowel wall.

multiple planes. This permits exact determination of the location and developmental status of the sphincter muscles as well as identification of associated anomalies of the kidneys and spine. MRI is also valuable for postoperative assessment of the neorectum and sphincteric muscles (figs. 6.91 and 6.92) [93].

Mass Lesions

Benign Masses

Polyps and Polyposis Syndromes. Adenomas are the most common form of colorectal polyp. Colonic adenomatous polyps are the most common large bowel neoplasm. All adenomatous polyps arise as the result of epithelial proliferative dysplasia or deranged development (fig. 6.93). In this regard, adenomas are precursor lesions for colorectal adenocarcinoma. Three basic patterns of adenomatous polyps are discerned pathologically: tubular, tubulovillous, and villous. Villous adenomas are characterized by a neoplastic growth composed of fine fingerlets or villi that project from the muscularis mucosae to the outer tip of the adenoma and show a propensity for the rectum and rectosigmoid area. Villous architecture tends to be found more frequently in larger adenomas and is associated with a higher risk of malignancy (fig. 6.94) [94]. Multiple colonic adenomas are seen in association with familial adenomatous polyposis or Gardner syndrome, whereas

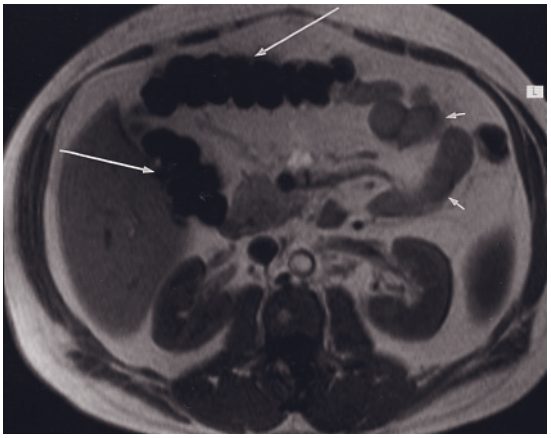

(*a*)

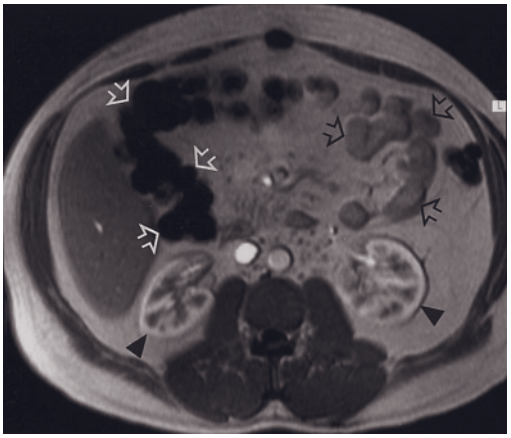

(*b*)

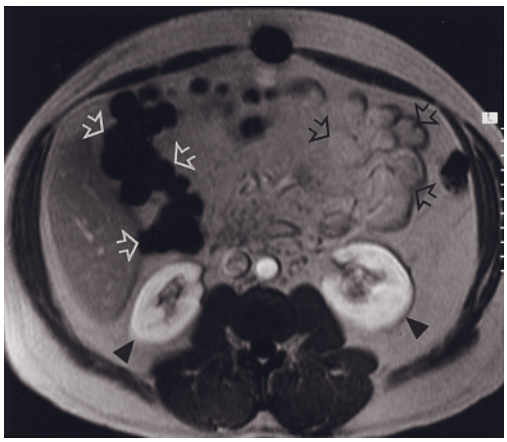

(*c*)

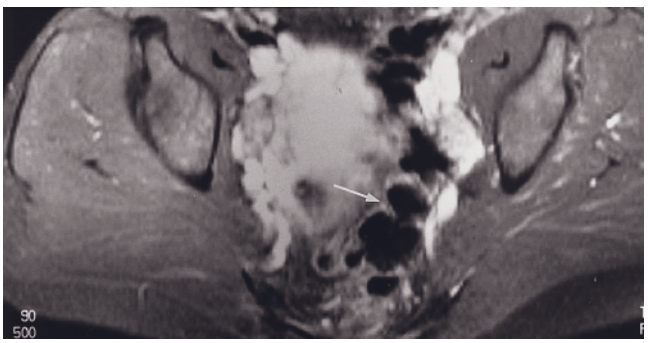

(*d*)

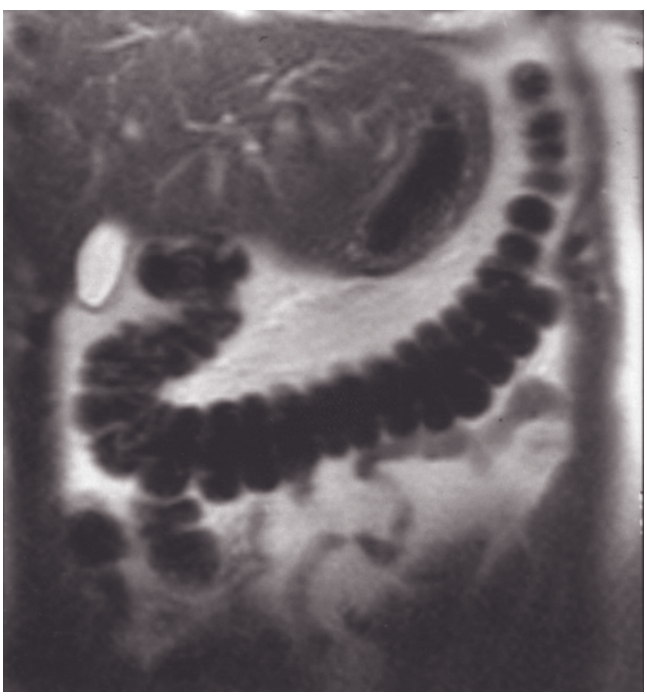

(*e*)

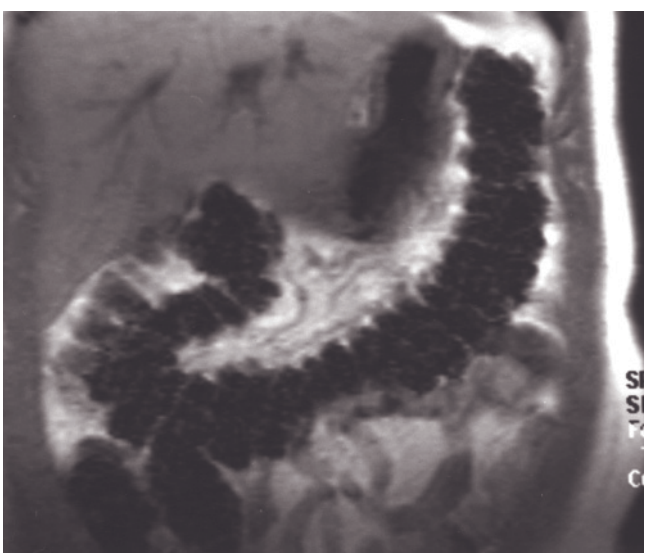

(*f*)

FIG. 6.88 Normal large bowel. SGE (*a*) and immediate (*b*) and 90-s (*c*) postgadolinium SGE images. Air-filled colon (long arrows) and normal small bowel (short arrows) are seen on the precontrast T1-weighted image (*a*). After intravenous gadolinium administration the walls of the large and small bowel (open arrows, *b*, *c*) enhance less than adjacent renal parenchyma (arrowheads, *b*, *c*) on capillary-phase (*b*) and interstitial-phase (*c*) images. Gadolinium-enhanced T1-weighted fat-suppressed spin-echo image (*d*) in another subject demonstrates a normal-appearing sigmoid colon that shows minimal mural enhancement, thin wall, and haustrations (arrow). Coronal T2-weighted SS-ETSE (*e*) and coronal SGE (*f*) images in a third patient demonstrate normal transverse colon with multiple haustrations.

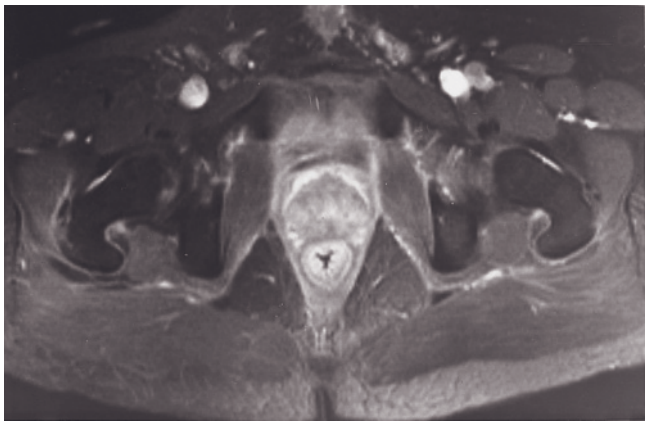

(*a*)

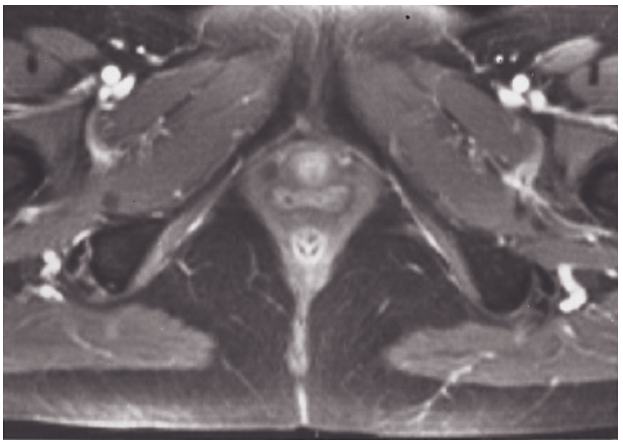

(*b*)

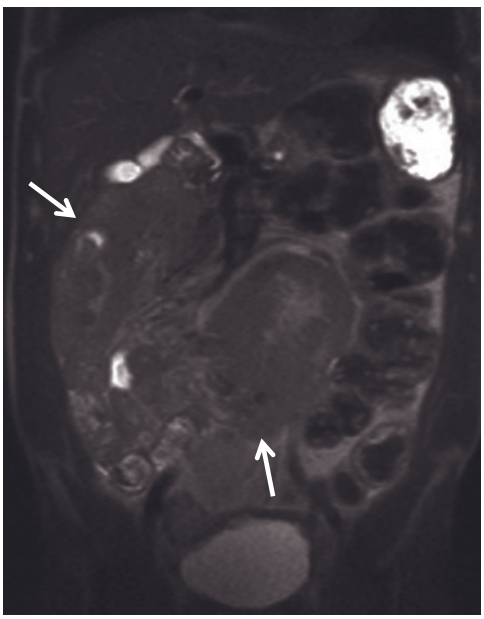

(*c*)

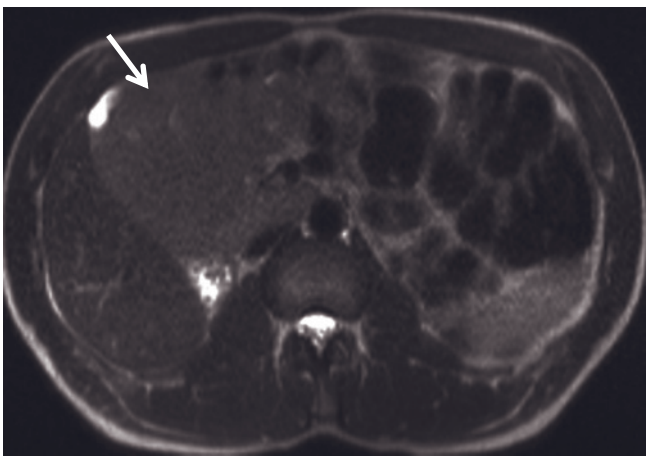

(*d*)

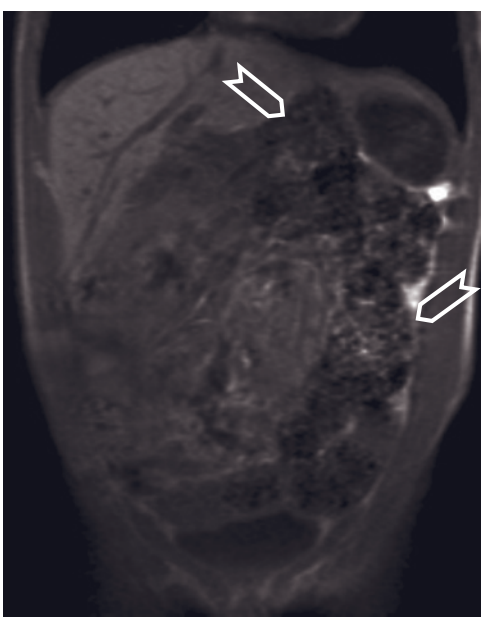

(*e*)

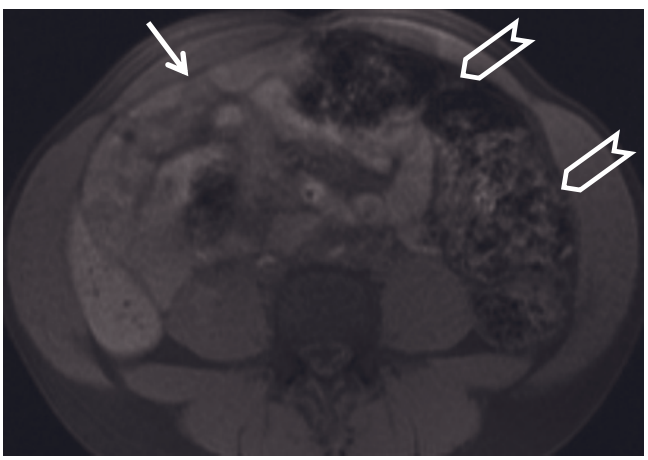

(*f*)

Fig. 6.89 Normal rectum and anal canal. Gadolinium-enhanced T1-weighted fat-suppressed spin-echo image (*a*) in a man highlights the different layers of the rectum (from inner layer to outer layer): high-signal-intensity mucosa, low-signal-intensity muscularis mucosa and lamina propria, high-signal-intensity submucosa, and low-signal-intensity muscularis propria. The rectum contains air within the lumen. Gadolinium-enhanced T1-weighted fat-suppressed spin-echo image (*b*) in a woman demonstrates the same enhancement features of the anal canal. Note that the anal canal is collapsed and does not contain air. **Malrotation.** Coronal (*c*) and transverse (*d*) T2-weighted single-shot echo-train spin-echo and coronal (*e*) and transverse (*f*) T1-weighted SGE images demonstrate malrotation of the small and large bowel. While the small bowel (arrows, *c*, *d*, *f*) is located at the midline and right side of the abdomen, the large bowel (including the cecum) (open arrows, *e*, *f*) is located at the midline and the left side of the abdomen.

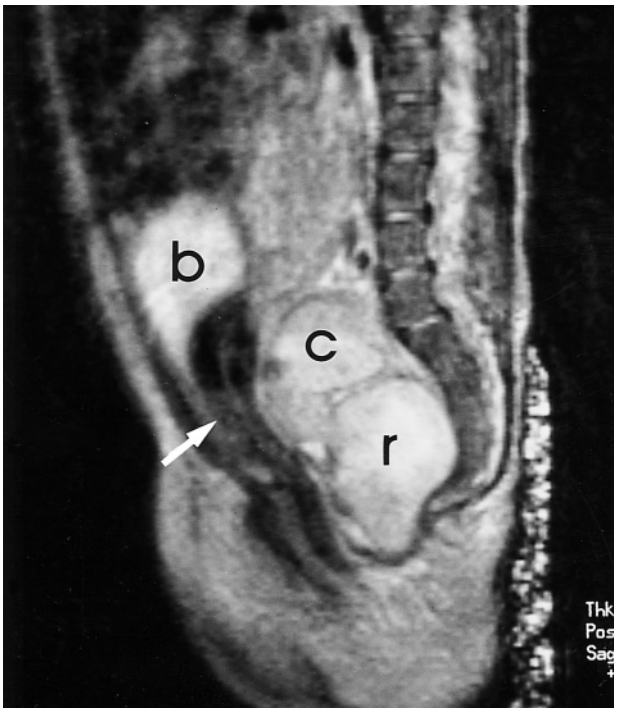

FIG. 6.90 Colonic duplication. T2-weighted spin-echo image in a patient with colonic duplication. The uterus (arrow) and bladder (b) are anteriorly displaced by two fluid-filled viscous structures that represent the rectum (r) and the duplication cyst (c).

multiple colonic hamartomas may be seen in Peutz–Jeghers syndrome or juvenile polyposis syndromes.

A number of polyposis syndromes have been described. The most common are familial adenomatous polyposis, Gardner and Peutz–Jeghers syndromes, and the juvenile polyposis syndromes. Familial adenomatous polyposis syndrome is an autosomal dominant disorder characterized by numerous adenomas affecting primarily the colon and the rectum. Familial adenomatous polyposis represents a prototype of a hereditary precancerous syndrome because the risk of malignant transformation to colorectal carcinoma approaches 100%. Patients with familial adenomatous polyposis syndrome have an increased risk of developing periampullary duodenal carcinoma. Gardner syndrome is an autosomal dominant condition with diffuse adenomatous polyps, bony abnormalities (osteomas), and soft tissue tumors. Presently regarded as a variation of familial adenomatous polyposis syndrome, Gardner syndrome confers the same risk of progression to colon adenocarcinoma. Peutz–Jeghers syndrome is an autosomal dominant disorder characterized clinically by skin and mucosal pigmented macules and gastrointestinal hamartomas. The hamartomas favor the small bowel in 95% of cases, with colonic and stomach involvement in up to 25%. Although the hamartomatous polyps themselves do not have malignant potential, patients with this syndrome have an increased incidence of both benign and malignant tumors arising in many organs. Up to 3% of patients with Peutz–Jeghers syndrome will develop adenocarcinoma of the stomach or duodenum, and 5% of women will have ovarian cysts or tumors. There are three distinct syndromes associated with juvenile polyps of the alimentary tract: juvenile polyposis, gastrointestinal juvenile polyposis, and the Cronkhite–Canada syndromes. Hamartomas are common to all three syndromes [95, 96].

Gadolinium-enhanced fat-suppressed SGE or 3D-GE images can demonstrate polyps, whether they occur in isolation or in association with a polyposis syndrome. Semelka and Marcos reported on the MR appearance of polyposis syndromes [65]. In that series, polyps were well seen with a combination of gadolinium-enhanced fat-suppressed SGE images and T2-weighted single-shot echo-train spin-echo images. The importance of demonstrating polyp enhancement by comparing precontrast and postcontrast fat-suppressed SGE images was emphasized, because this observation permitted distinction between polyps and colon contents. Polyps smaller than 1 cm in familial polyposis syndrome were not commonly observed. The most common appearance is an enhancing sessile or pedunculated mass arising from the bowel wall and protruding into the lumen (figs. 6.95 and 6.96). If frondlike polyp morphology or enhancement is observed, the possibility of a villous adenoma should be raised. Similarly, extension beyond the bowel wall signifies malignant degeneration.

Lipomas. Lipomas are the second most common benign neoplasm of the large bowel. They usually originate in the submucosa. Most are asymptomatic, although changes in bowel habits, bleeding, or both have been reported in patients with large lesions. The most common locations for colonic lipomas are the cecum, ascending colon, and sigmoid colon. The MRI appearance of lipomas with T1-weighted and fat-suppressed T1-weighted sequences are pathognomonic: high in signal intensity on T1-weighted images and diminished in signal intensity on fat-suppressed T1-weighted images (fig. 6.97) [97]. Additional use of out-of-phase SGE may demonstrate fat-water black ring phase cancellation surrounding the polyp (fig. 6.98). Lipomas may also act as lead point for intussusceptions (fig. 6.99).

Other Mesenchymal Neoplasms. Leiomyomas, hemangiomas (fig. 6.100), and neurofibromas are all rare.

Mucocele. A mucocele is defined as a dilatation of the appendiceal lumen resulting from mucus accumulation associated with luminal obstruction. Mucoceles are frequently asymptomatic unless they become secondarily infected or rupture. Pathologically, it is important to distinguish between nonneoplastic lesions (retention) and neoplastic mucoceles. Nonneoplastic

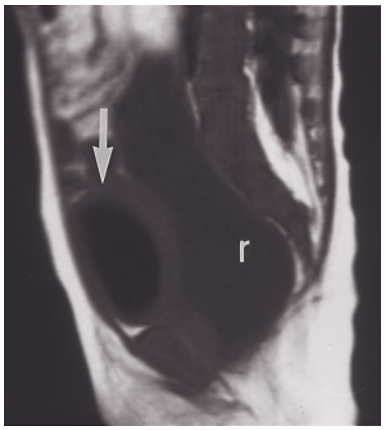

(*a*)

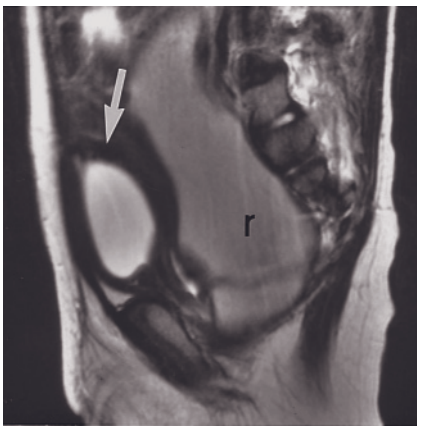

(*b*)

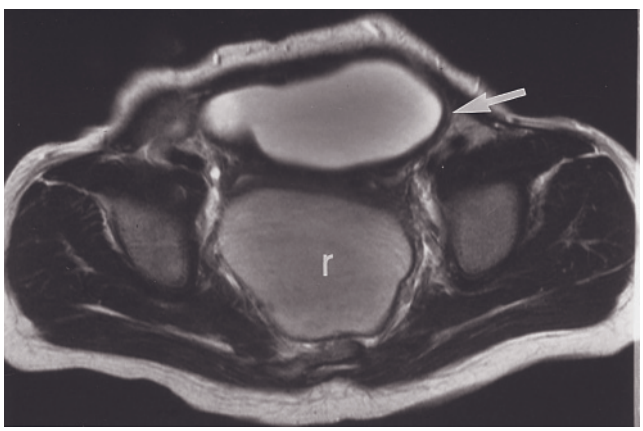

(*c*)

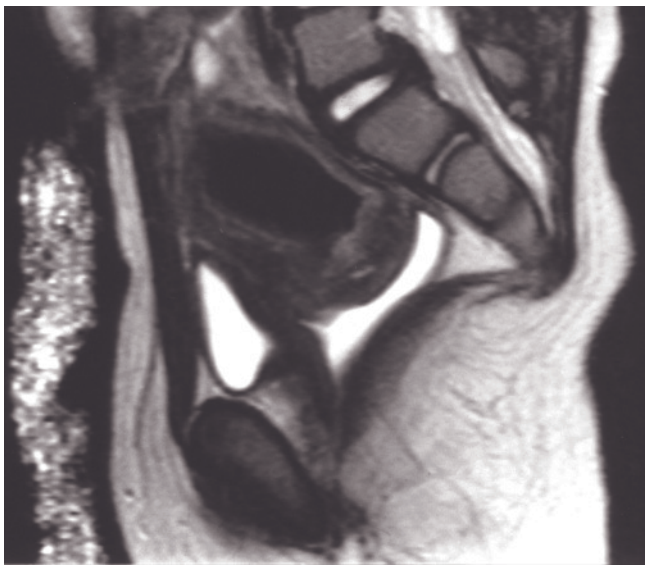

(*d*)

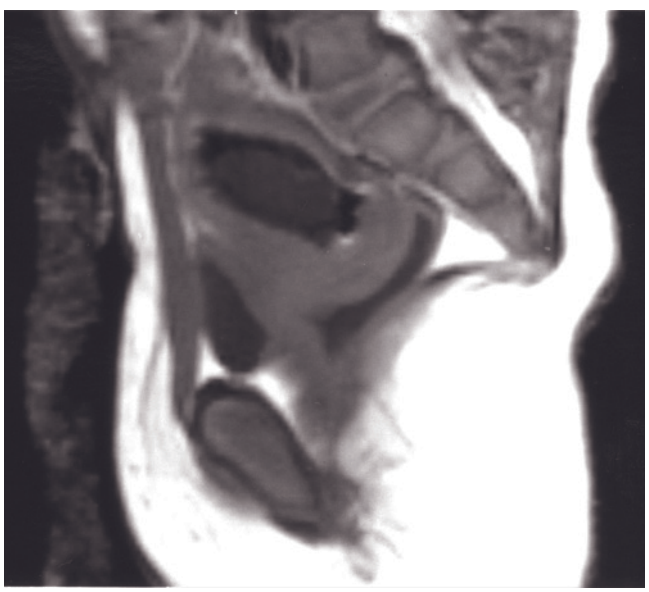

(*e*)

FIG. 6.91 Surgical repair of persistent cloaca. Sagittal T1-weighted spin-echo (*a*), sagittal T2-weighted echo-train spin-echo (*b*), and transverse T2-weighted echo-train spin-echo (*c*) images. A capacious neorectum (r, *a–c*) is present. The bladder (large arrow, *a–c*) is thick-walled and anteriorly displaced. Absence of the vagina is noted. Sagittal T2-weighted SS-ETSE (*d*) and T1-weighted SGE (*e*) images in a second patient with cloacal anomaly who had undergone multiple surgeries. The levator ani complex is diminutive in size, and distal sacral segments are absent. There is a fluid-filled structure situated posterior to the uterus that represents the anal canal and rectum.

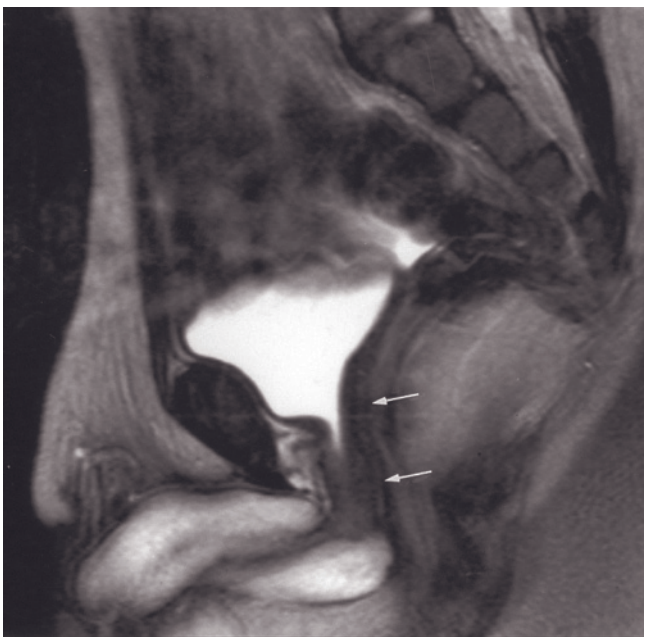

(*a*)

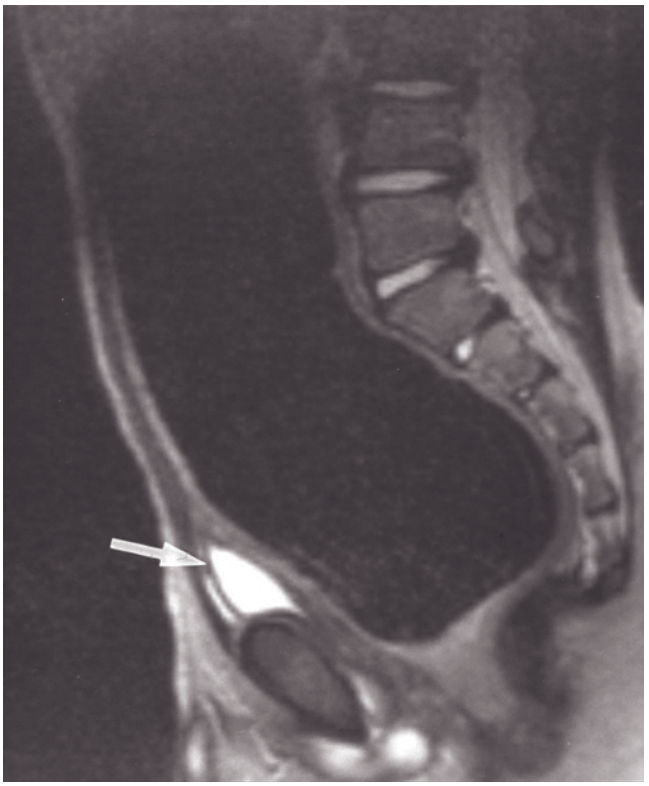

(*b*)

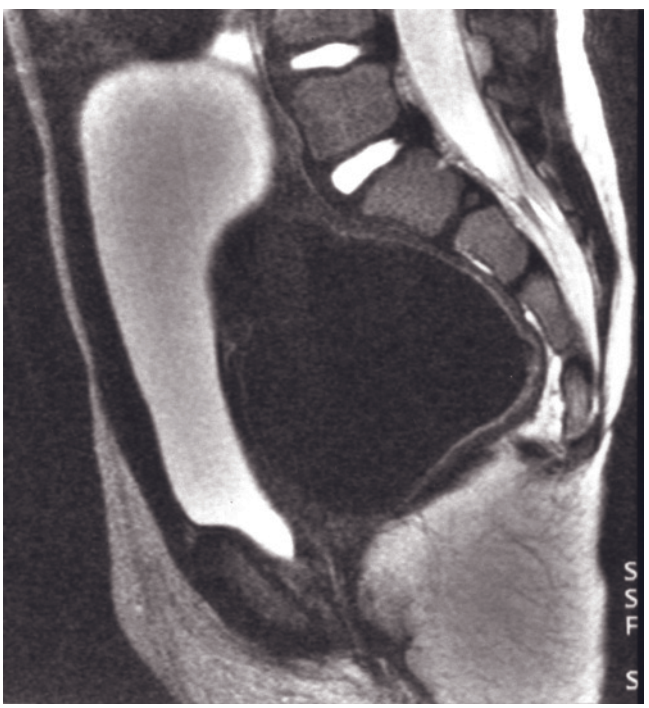

(*c*)

FIG. 6.92 Reconstructed imperforate anus. Sagittal T2-weighted SS-ETSE (*a*) image in a 1-year old boy shows that the anal canal is situated in an anterior location, just posterior to the prostate. The levator ani muscle is intact. Sagittal T2-weighted echo-train spin-echo images in a second (*b*) and a third (*c*) patient demonstrate a markedly dilated air-filled rectum, compressing and displacing the bladder anterosuperiorly (arrow, *b*).

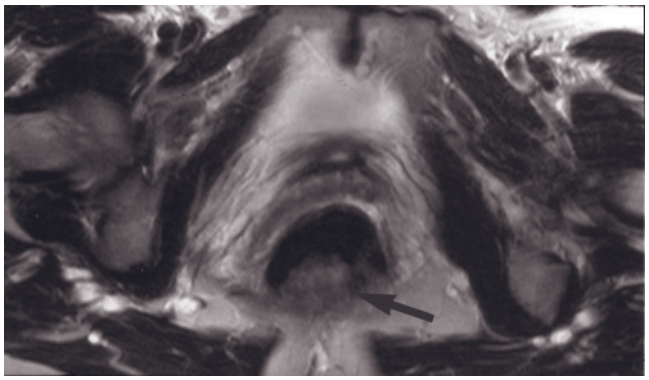

(*a*)

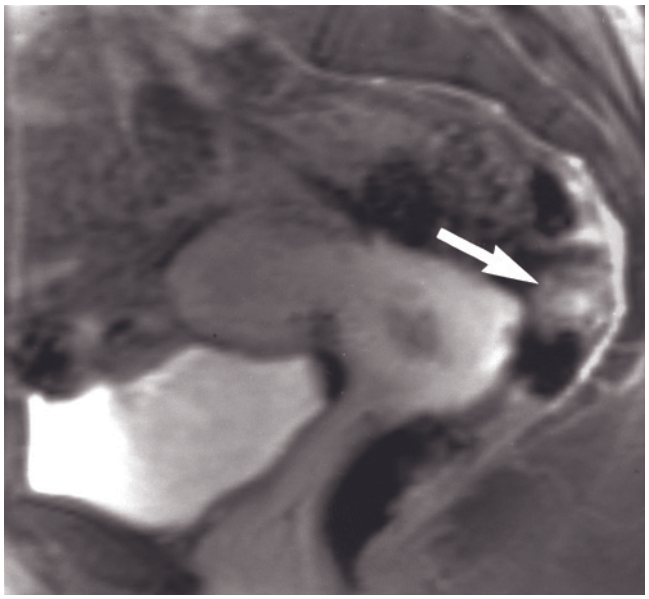

(*b*)

Fig. 6.93 Adenomatous polyp of rectum. Transverse T2-weighted echo-train spin-echo (*a*) and sagittal interstitial-phase gadolinium-enhanced fat-suppressed SGE (*b*) images. There is a 1.6-cm polypoid mass (arrows, *a*, *b*) arising from the posterior wall of the rectum, without evidence of extension beyond the rectal wall.

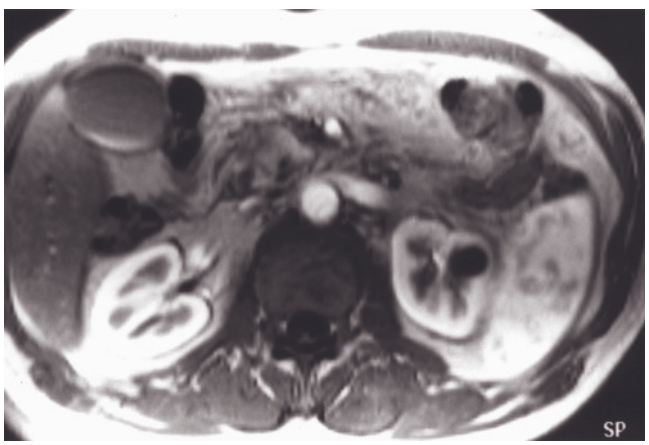

(*a*)

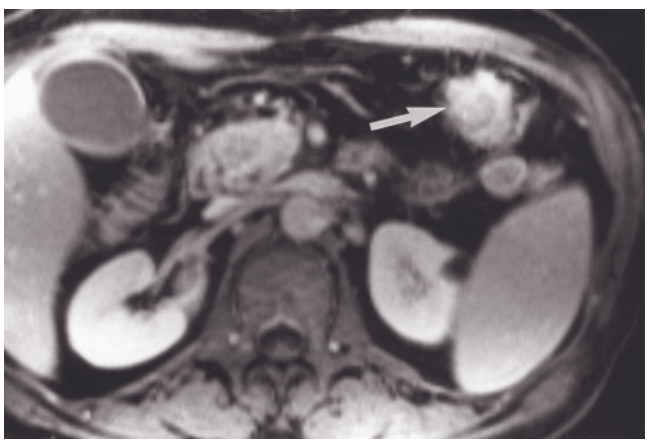

(*b*)

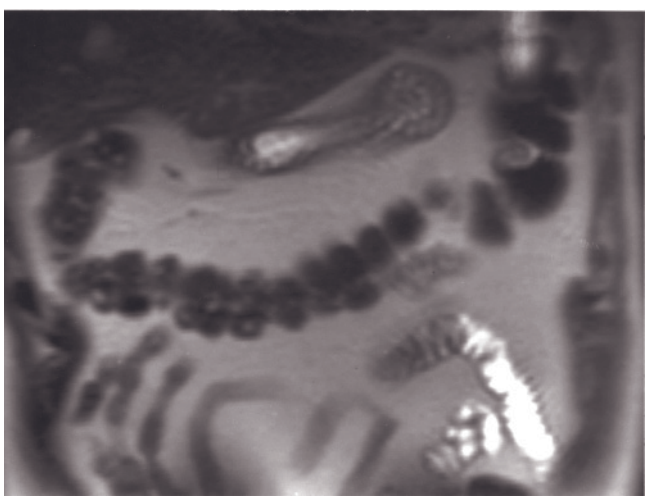

(*c*)

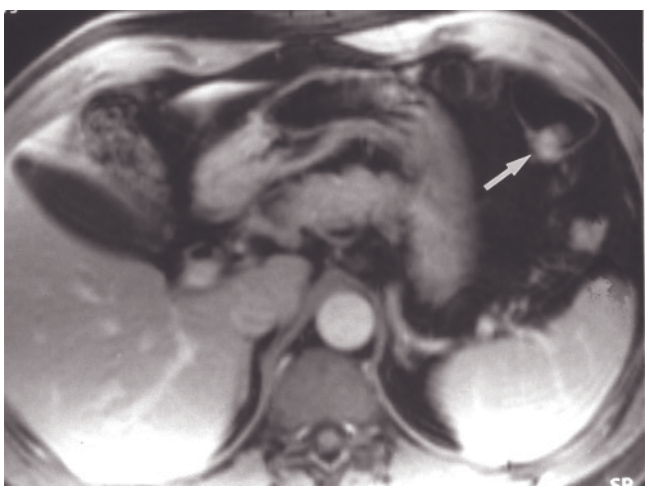

(*d*)

Fig. 6.94 Villous adenoma. Immediate postgadolinium SGE (*a*) and interstitial-phase gadolinium-enhanced fat-suppressed SGE (*b*) images. A polypoid mass is seen within the distal transverse colon. The mass enhances minimally on immediate postgadolinium images (*a*) and in a moderately intense fashion with mild heterogeneity on 2-min postgadolinium image (arrow, *b*). Coronal T2-weighted SS-ETSE (*c*) and transverse interstitial-phase gadolinium-enhanced fat-suppressed SGE (*d*) images in a second patient with villous adenoma of transverse colon (arrow, *d*) demonstrate an appearance similar to the previous patient. Most tumors show moderately intense enhancement with mild heterogeneity on 2-min postgadolinium interstitial-phase images, reflecting a larger and more irregular interstitial space than adjacent normal bowel. Sagittal (*e*) and coronal (*f*) single shot echo train spin echo and transverse (*g*) high resolution fast spin echo T2-weighted images and transverse (*h*, *i*) and sagittal (*j*) T1-weighted fat-suppressed postdgadolinium interstitial phase 3D-GE images at 3.0 T demonstrate a villous adenoma (white thick arrows; *e-g*) located in

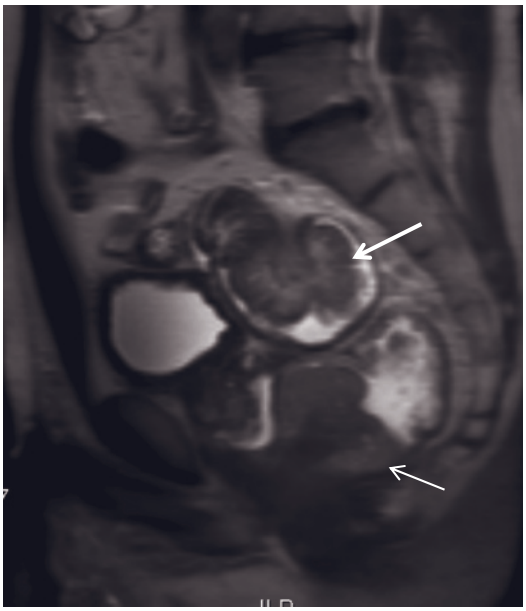

(*e*)

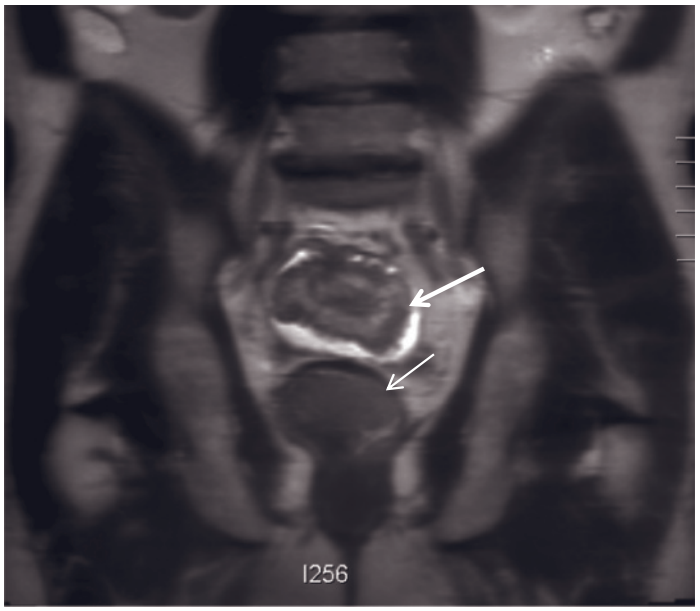

(*f*)

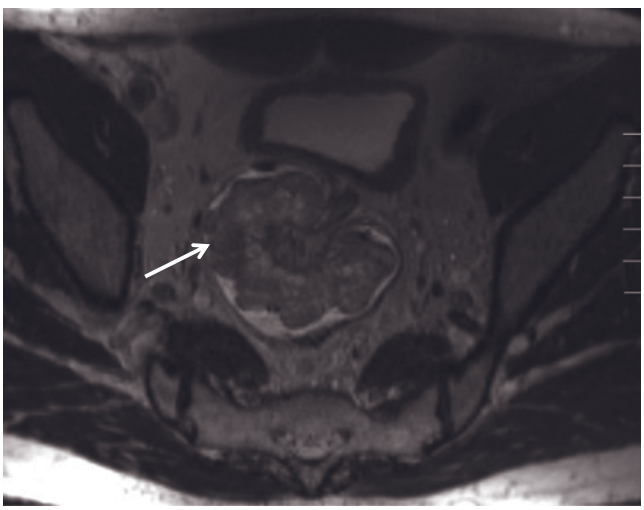

(*g*)

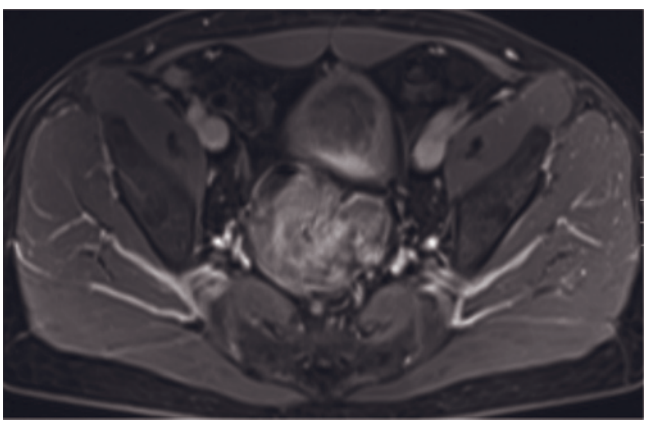

(*h*)

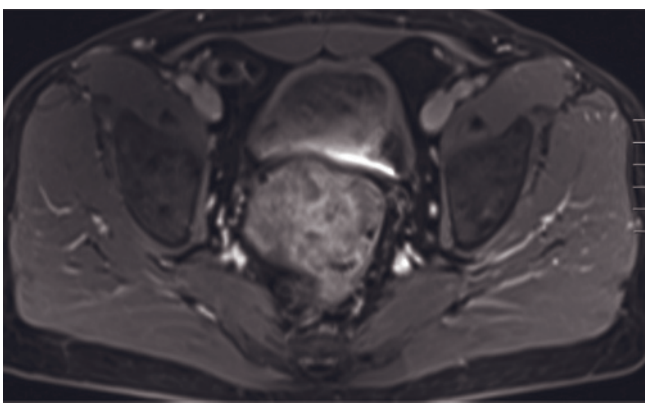

(*i*)

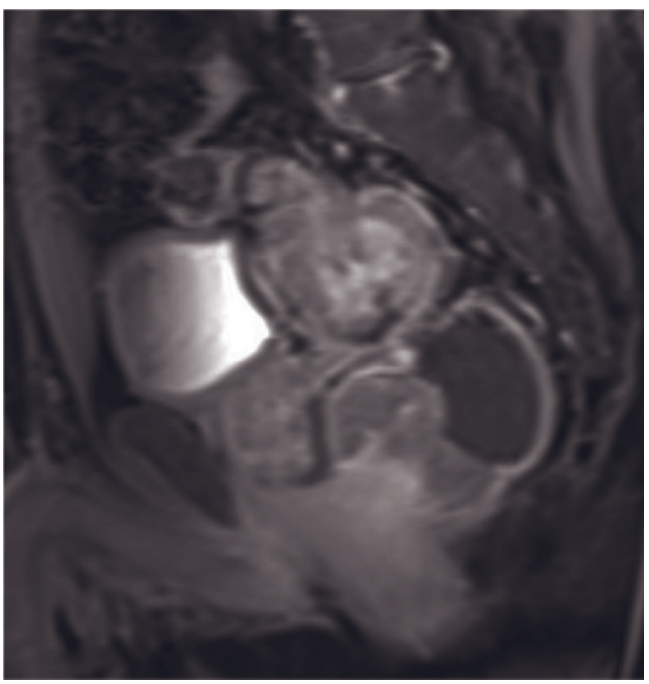

(*j*)

Fig. 6.94 (*Continued*) the rectosigmoidal junction and an adenocarcinoma (white thin arrow, *g*) located in the anorectal junction in another patient. The villous adenoma is seen as a pedunculated, broad based polipoid lesion and extends into the lumen obliterating the lumen partially. The rectosigmoid wall is intact. Both the villous adenoma and adenocarcinoma show heterogeneous and prominent enhancement. Note the presence of a few perirectal lymph nodes located in the perirectal soft tissues.

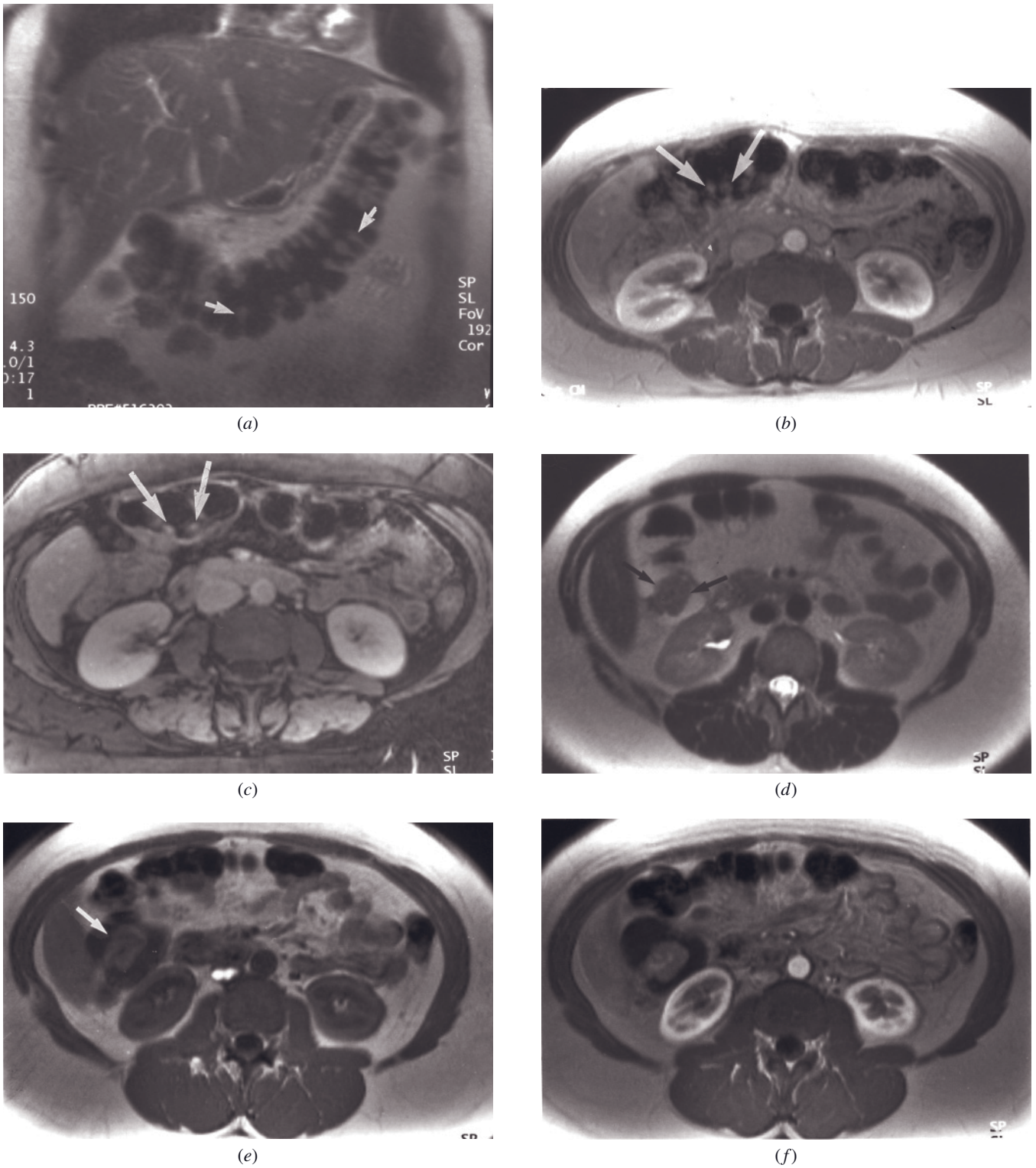

FIG. 6.95 Familial adenomatous polyposis syndrome. Coronal T2-weighted SS-ETSE (*a*), immediate postgadolinium SGE (*b*), and interstitial-phase gadolinium-enhanced fat-suppressed SGE (*c*) images. Numerous polyps are seen measuring less than 1 cm in diameter in the transverse colon (arrows, *a*). The signal void of the air in the colon provides good contrast from the soft tissue polyps on the T2-weighted image (*a*). The polyps are mildly enhanced (arrows) on the immediate postgadolinium image (*b*). Polyps demonstrate persistent enhancement on interstitial-phase images (arrows, *c*). This patient underwent total colectomy, which demonstrated numerous adenomatous polyps. Transverse T2-weighted SS-ETSE (*d*), SGE (*e*), and immediate postgadolinium SGE (*f*) images in another patient with familial polyposis syndrome. A 2.5-cm polyp is present that arises in the ascending colon. The high signal intensity of the fluid contents of the colon permits good delineation of the low signal intensity of the polyp on the SS-ETSE image (arrows, *d*).The polyp is isointense to the bowel wall on the precontrast T1-weighted image (arrow, *e*). On the early postgadolinium image, the polyp shows mild heterogeneous enhancement comparable to the bowel wall. Note the intense enhancement of the normal renal cortex, which is greater than the enhancement of the bowel wall or the polyp. This patient underwent sigmoidoscopy with biopsy followed by total colectomy (Reprinted with permission from Semelka RC, Marcos HB: Polyposis syndromes of the gastrointestinal tract. *J Magn Reson Imaging* 11: 51–55, 2000.). Coronal SS-ETSE (*g*, *h*) images in a third patient with

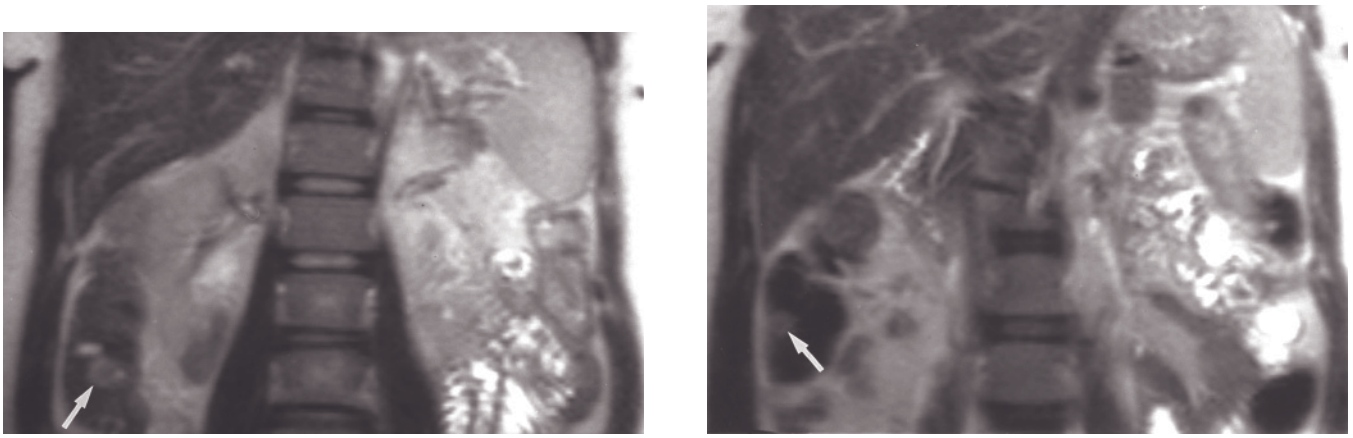

(*g*) (*h*)

FIG. 6.95 (*Continued*) familial adenomatous polyposis demonstrate polypoid lesions in the ascending colon (arrows, *g*, *h*).

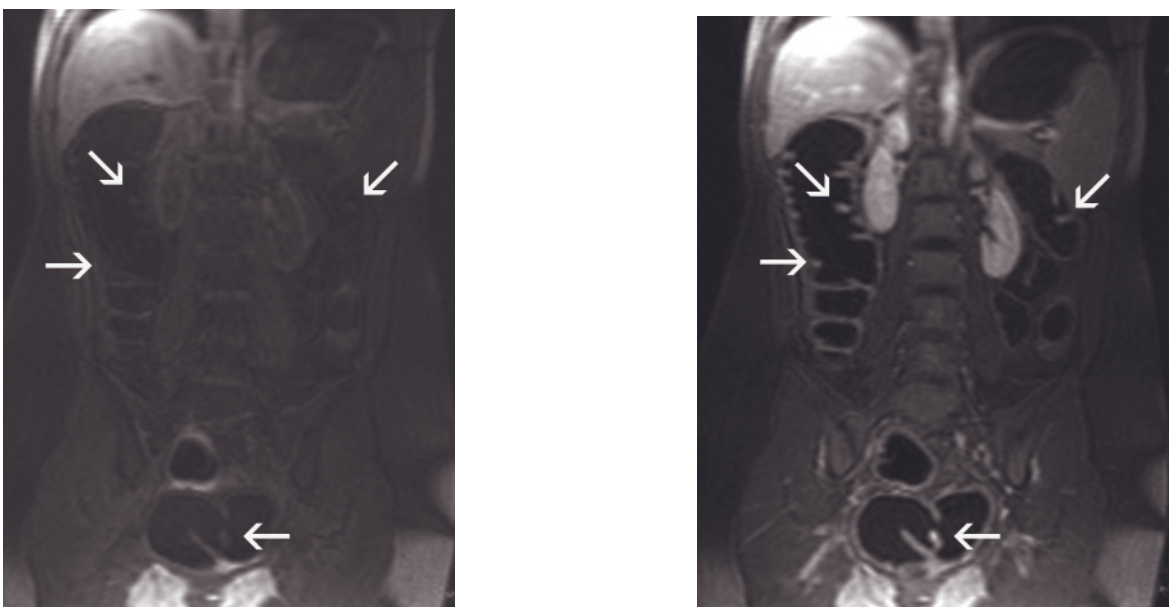

(*a*) (*b*)

FIG. 6.96 Polyposis coli. With dark-lumen water enema contrast MR colonography, multiple colonic polyps can be detected in this 12-year-old female patient with polyposis coli. These lesions show an avid contrast enhancement comparing precontrast (arrows, *a*) and postcontrast (arrows, *b*) T1-weighted sequences.

lesions show an inflamed mucosa or hyperplastic epithelium. Neoplastic mucoceles are best classified as mucinous cystoadenoma or mucinous cystadenocarcinoma. In mucinous cystoadenocarcinoma, spread of malignant cells beyond the appendix in the form of peritoneal implants is frequently present. Pseudomyxoma peritonei, with the findings of adenocarcinomatous cells, distinguishes this malignant process from simple mucinous spillage, which may occur with rupture of a retention mucocele or cystadenoma. Because of the possibility of an underlying malignancy and the risk of rupture, mucoceles should be prophylactically removed.

T2-weighted single-shot echo-train spin-echo images show a high-signal-intensity tubular structure in the region of the appendix. Mucoceles have a higher signal intensity than simple fluid on T1-weighted sequences owing to their protein content. In uncomplicated cases, the wall of the mucocele is thin and enhances minimally after intravenous gadolinium administration (fig. 6.101).

Varices. Rectal varices develop in patients with portal hypertension. The incidence of hemorrhoids is not increased in these patients [98].

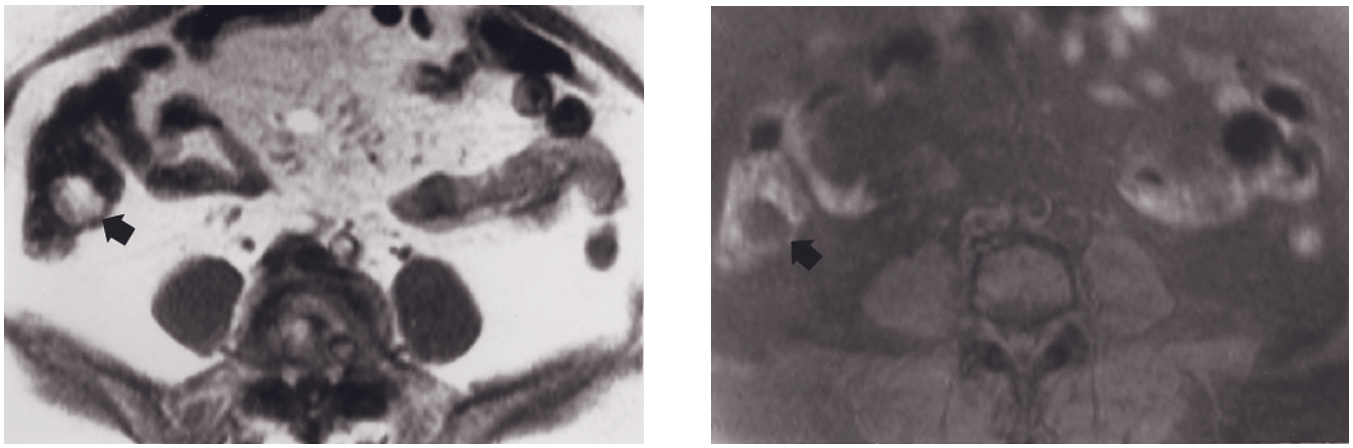

(*a*) (*b*)

FIG. 6.97 Cecal lipoma. SGE (*a*) and T1-weighted fat-suppressed spin-echo (*b*) images. A mass in the cecum is high in signal intensity on the T1-weighted image (arrow, *a*) and diminishes in signal intensity on the fat-suppressed image (arrow, *b*). These imaging characteristics are pathognomonic for a fat-containing tumor. The cecum is a common location for large bowel lipomas. (Reprinted with permission from Shoenut JP, Semelka RC, Silverman R,Yaffe CS, Mickflikier AB: Magnetic resonance imaging evaluation of the local extent of colorectal mass lesions. *J Clin Gastroenterol* 17: 248–253, 1993.)

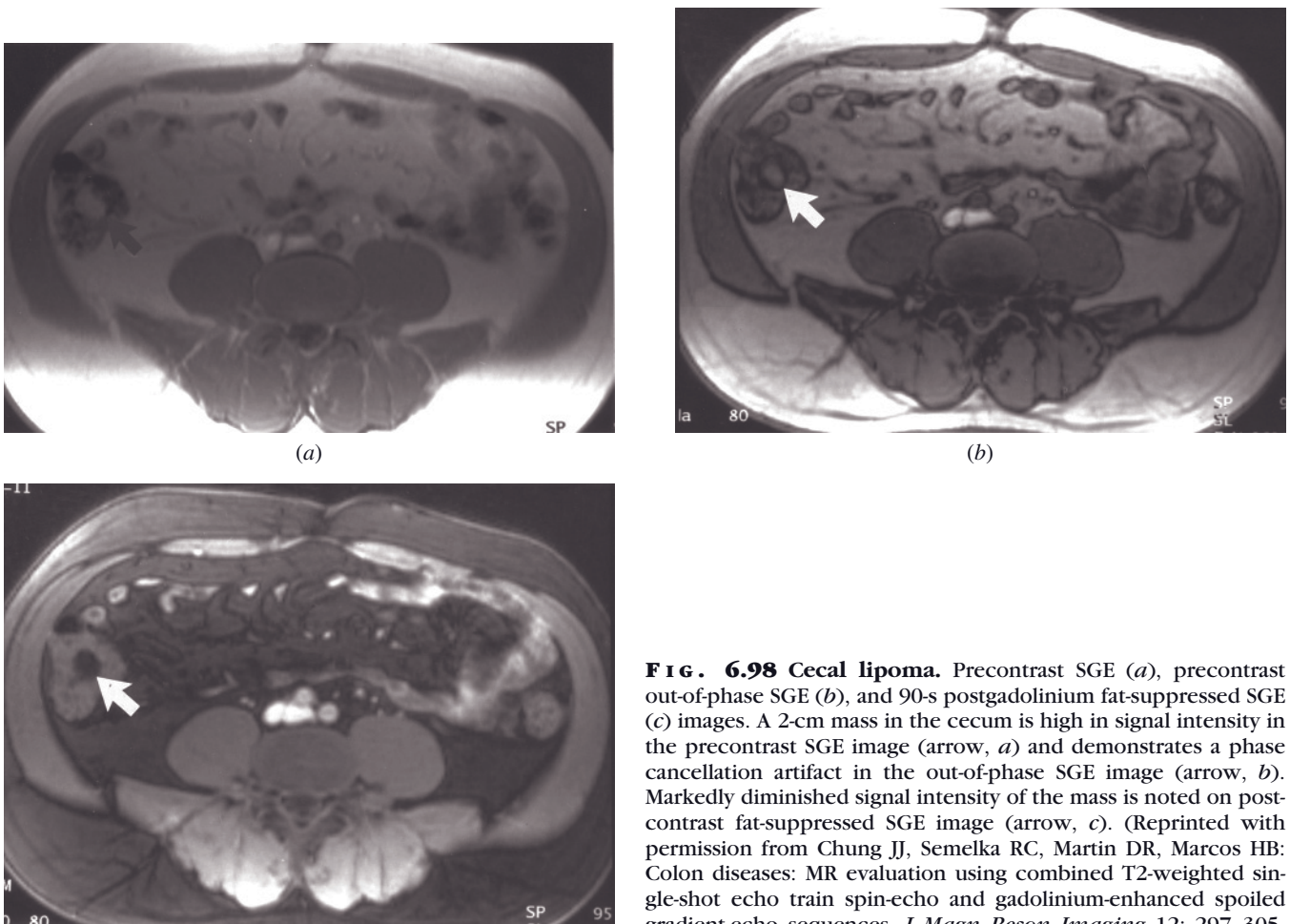

(*a*) (*b*)

(*c*)

FIG. 6.98 Cecal lipoma. Precontrast SGE (*a*), precontrast out-of-phase SGE (*b*), and 90-s postgadolinium fat-suppressed SGE (*c*) images. A 2-cm mass in the cecum is high in signal intensity in the precontrast SGE image (arrow, *a*) and demonstrates a phase cancellation artifact in the out-of-phase SGE image (arrow, *b*). Markedly diminished signal intensity of the mass is noted on postcontrast fat-suppressed SGE image (arrow, *c*). (Reprinted with permission from Chung JJ, Semelka RC, Martin DR, Marcos HB: Colon diseases: MR evaluation using combined T2-weighted single-shot echo train spin-echo and gadolinium-enhanced spoiled gradient-echo sequences. *J Magn Reson Imaging* 12: 297–305, 2000.)

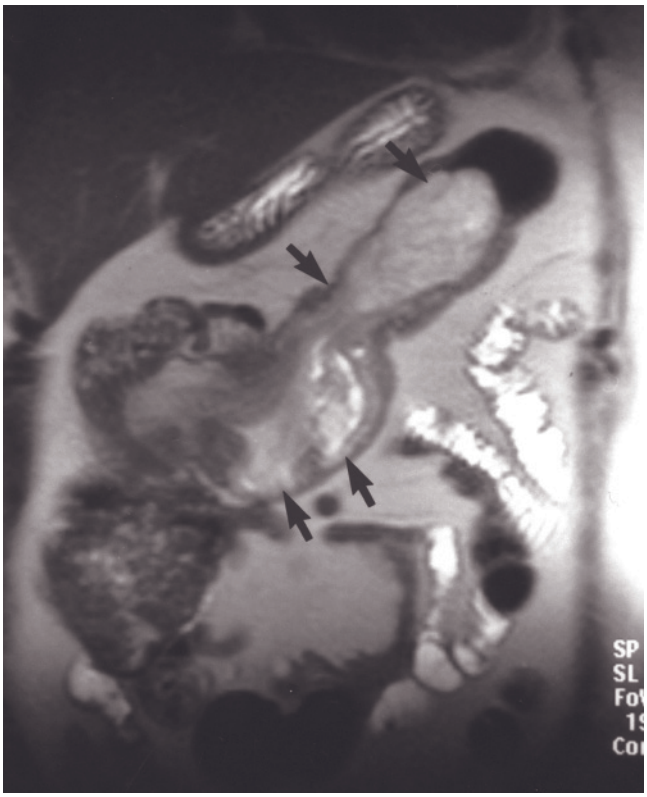

(*a*)

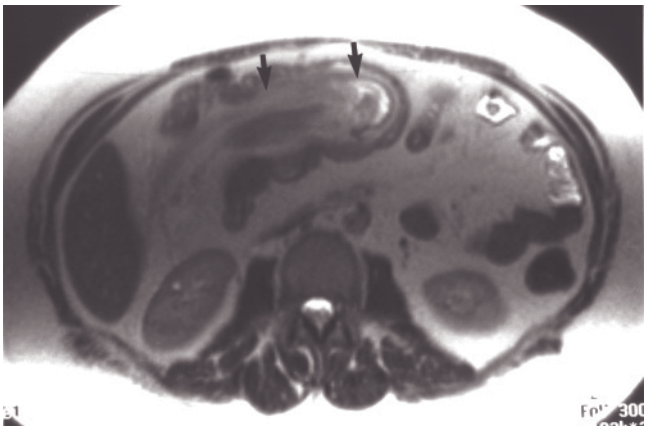

(*b*)

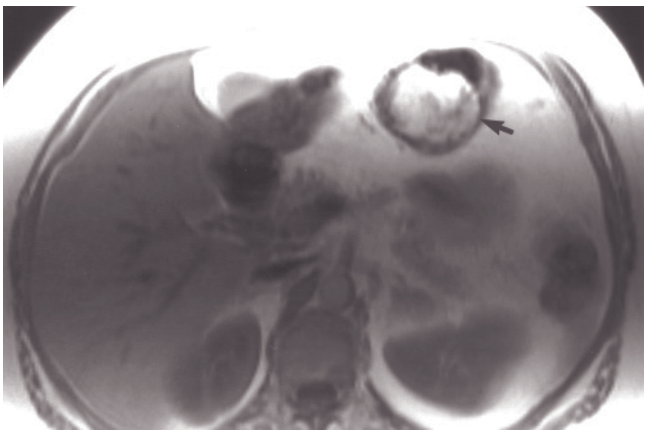

(*c*)

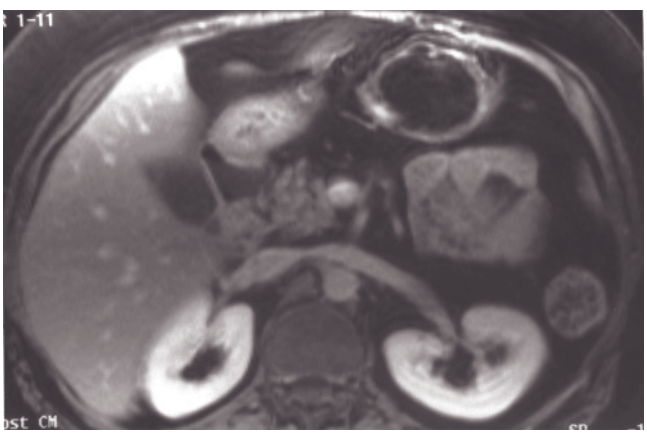

(*d*)

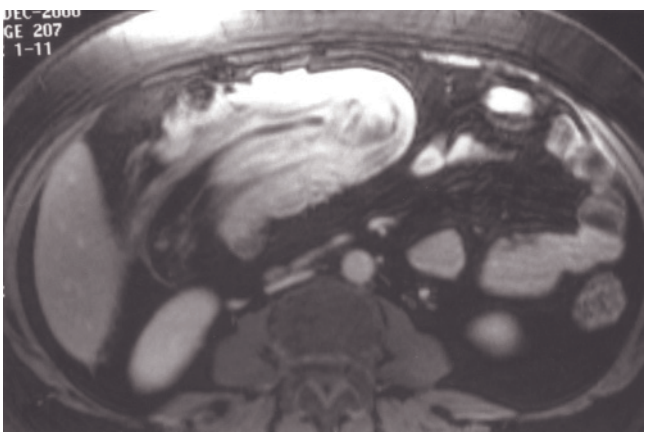

(*e*)

FIG. 6.99 Colonic lipoma as a lead point for intussusception. Coronal (*a*) and transverse (*b*) SS-ETSE, precontrast SGE (*c*), and 90-s postgadolinium fat-suppressed SGE (*d*, *e*) images. There is a lipoma situated within the lumen of the mid-transverse colon (arrow, *c*) at the end of a colo-colonic intussusception (arrows, *a*, *b*), which arose from the mid-ascending colon.

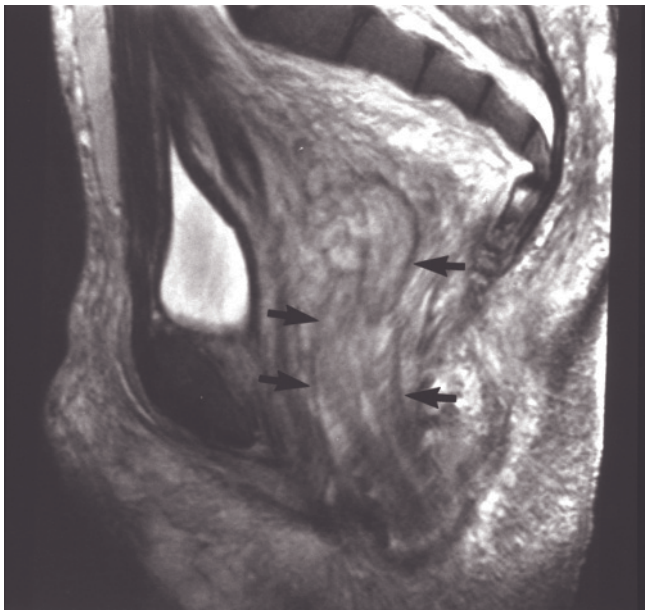

(*a*)

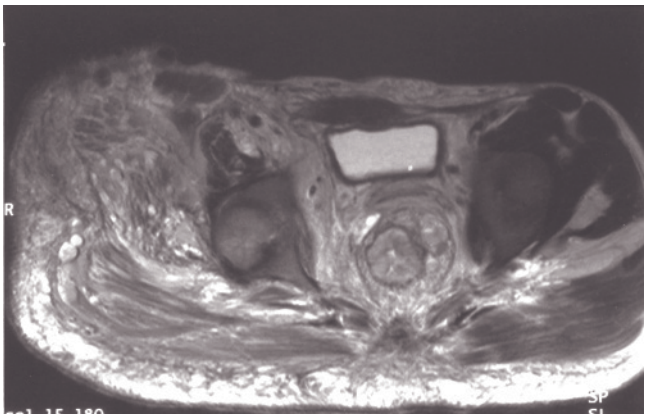

(*b*)

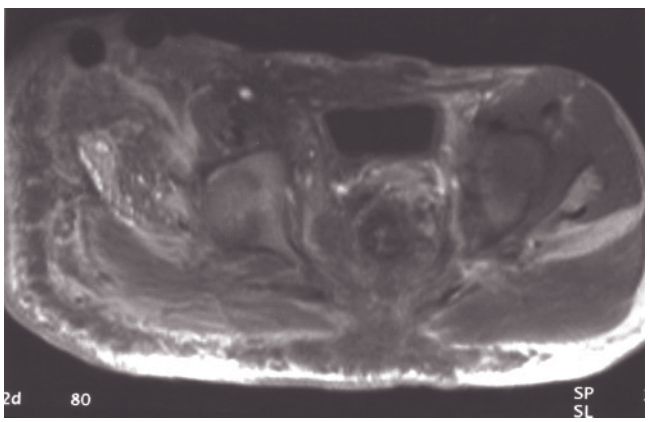

(*c*)

FIG. 6.100 Hemangiomatous infiltration in Klippel–Trenaunay syndrome. Sagittal (*a*) and transverse (*b*) T2-weighted ETSE and transverse SGE (*c*) images in a patient with Kippel–Trenaunay syndrome. The intrapelvic fat is extensively infiltrated with hemangiomatous tissue. The wall of the rectum and anal canal are noted to be expanded (arrows, *a*) because of hemangiomatous infiltration. Note also the extensive infiltrative hemangiomas involving the soft tissues of the pelvis and right gluteal region, which is expanded.

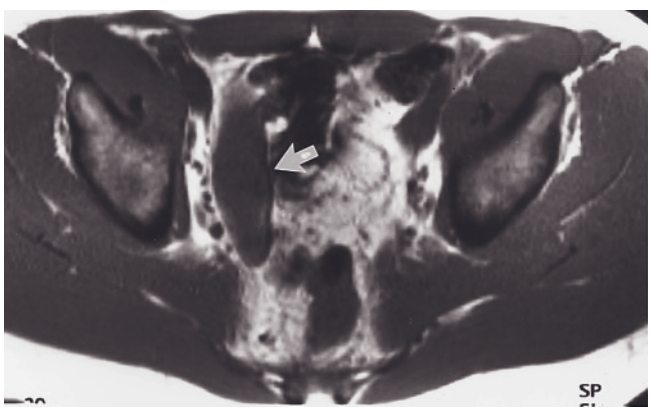

(*a*)

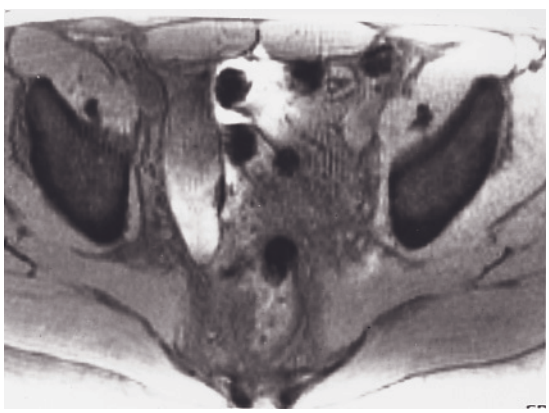

(*b*)

FIG. 6.101 Mucocele of the appendix. SGE (*a*), fat-suppressed SGE (*b*), SS-ETSE (*c*), sagittal SS-ETSE (*d*), and immediate postgadolinium fat-suppressed SGE (*e*) images. An oblong-shaped mucocele of the appendix is present (arrow, *a*) that contains high-signal-intensity material in the dependent portion of the cyst on the T1-weighted image (*a*), which is accentuated with the application of fat suppression (*b*). The mucocele is high in signal intensity on the T2-weighted image, with slight heterogeneity in

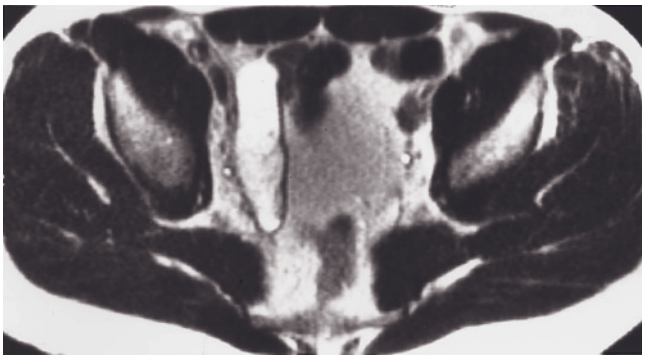

(*c*)

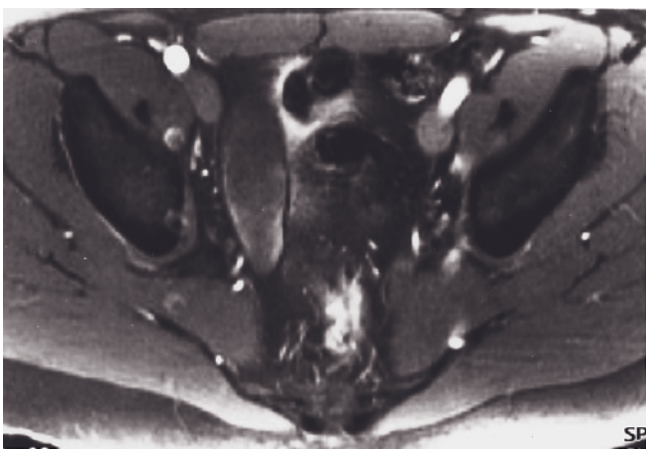

(*e*)

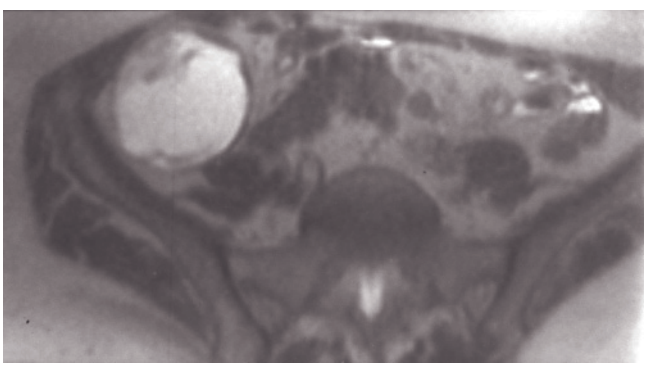

(*g*)

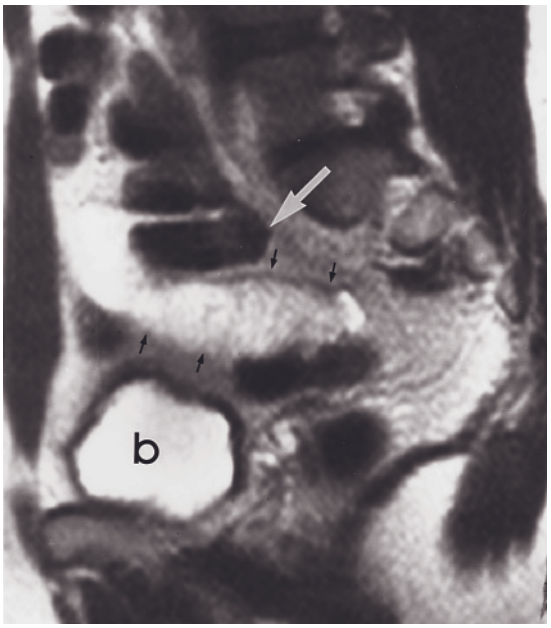

(*d*)

(*f*)

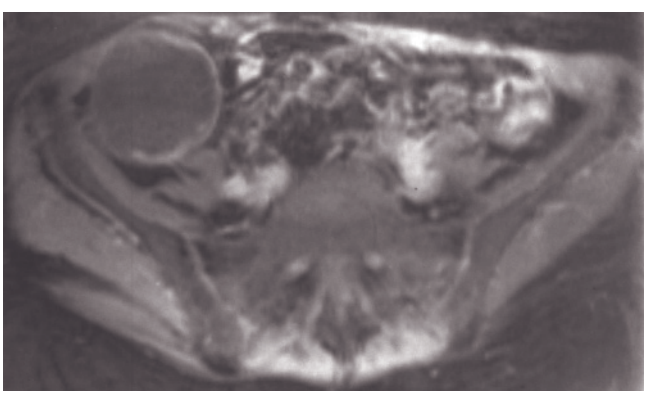

(*h*)

FIG. 6.101 (*Continued*) the dependent portion (*c*). The sagittal-plane image (*d*) shows the orientation of the mucocele (small arrows, *d*) to the base of the cecum (arrow, *d*) and the relationship to the bladder (b, *d*). No appreciable enhancement of the mucocele wall is noted on the postgadolinium image (*e*), which excludes the diagnosis of abscess. Sagittal (*f*) and transverse (*g*) SS-ETSE and interstitial-phase gadolinium-enhanced SGE (*h*) images in a second patient show a large cystic mass in the lower right quadrant of the abdomen extending into the pelvic inlet. Note the presence of septations and a thin rim of enhancement.

Malignant Masses

Adenocarcinoma. Adenocarcinoma of the colon is the most common gastrointestinal tract malignancy and the second most common visceral cancer in North America. The estimated incidence in the United States is 138,000 new cases per year, and the 5-year survival is 50–60% [39]. The incidence of adenocarcinoma of the colon increases with advancing age. Sporadic cancers are increased in first-degree family relatives of patients with known colorectal carcinoma. Other conditions that predispose to the development of colon cancer include familial adenomatous polyposis, Gardner syndrome, Lynch syndrome, ulcerative colitis, Crohn colitis, and previous ureterosigmoidostomies. Cancers occur most often in the rectosigmoid colon, but right-sided cancers are reported to occur in increasing frequency [99]. Tumors may be polypoid, circumferential ("apple core"), or plaquelike. Symptoms reflect tumor location and morphology, with most patients reporting a combination of change in bowel habits, bleeding, pain, and weight loss. A TNM system is used for staging (Table 6.3).

Good correlation is observed between gadolinium-enhanced fat-suppressed MRI techniques and surgical specimens for tumor size, bowel wall involvement, peritumoral extension, and lymph node detection [5]. Malignant lymph nodes are usually not enlarged in gastrointestinal adenocarcinoma. However, the presence of more than five lymph nodes that measure smaller than 1 cm in a regional distribution related to the tumor correlates well with tumor involvement. All segments of the colon and the appendix are well shown on MR images. The combination of T2-weighted single-shot echo-train spin-echo and gadolinium-enhanced fat-suppressed SGE or 3D-GE images results in the most reproducible image quality for the colon above the rectum (figs. 6.102–6.109). Rectal and colon cancers

Table 6.3 TNM Staging for Cancer of the Colon

T—Primary Tumor
Tx Primary tumor cannot be assessed
T0 No evidence of primary tumor
Tis Pre-invasive carcinoma (carcinoma in situ)
T1 Tumor limited to the mucosa or mucosa and submucosa
T2 Tumor with extension to muscle or muscle and serosa
T3 Tumor with extension beyond the colon to immediately contiguous structures
T3a Tumor without fistula formation
T3b Tumor with fistula formation
T4 Tumor with deep infiltration occupying more than one-half but not more than one region or extending to neighboring structures
N—Regional lymph nodes
Nx Regional lymph nodes cannot be assessed
N0 No evidence of regional lymph node metastasis
N1 Evidence of regional lymph node involvement
N2, N3 Not applicable
N4 Evidence of involvement of juxta-regional lymph nodes
M—Metastases
Mx Distant metastases cannot be assessed
M0 No distant metastases
M1 Distant metastases

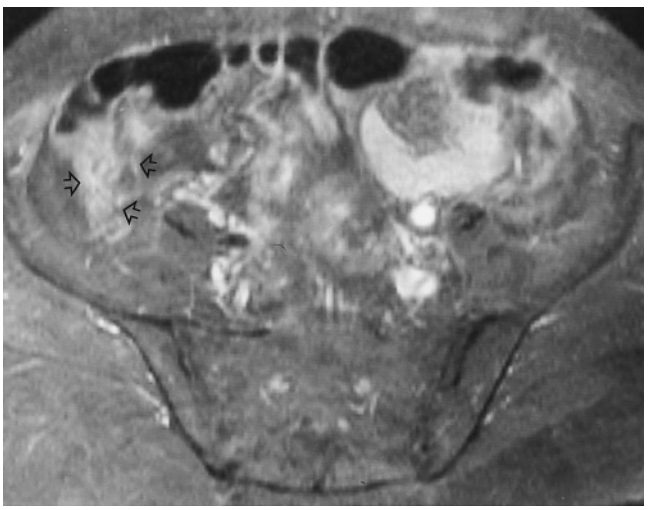

FIG. 6.102 Appendiceal adenocarcinoma. Gadolinium-enhanced T1-weighted fat-suppressed spin-echo image demonstrates heterogeneous enhancing infiltrative tumor arising from the appendix (open arrows).

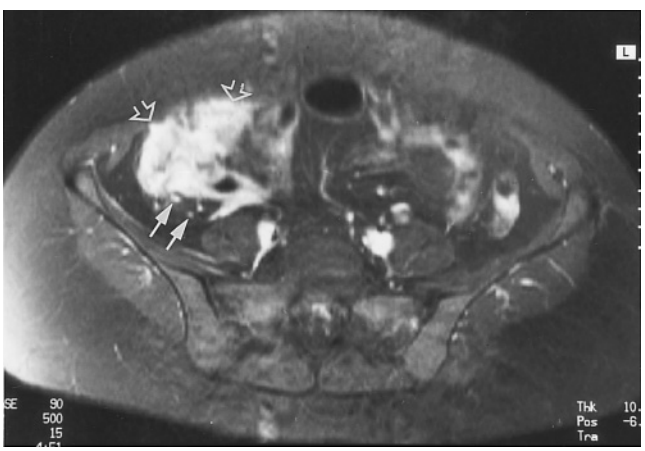

FIG. 6.103 Colonic adenocarcinoma, cecum. Gadolinium-enhanced T1-weighted fat-suppressed spin-echo image demonstrates a large heterogeneous intensely enhancing cecal carcinoma (open arrows) that extends to the anterior peritoneal wall. Multiple enhancing lymph nodes smaller than 5 mm are identified (arrows), which are malignant.

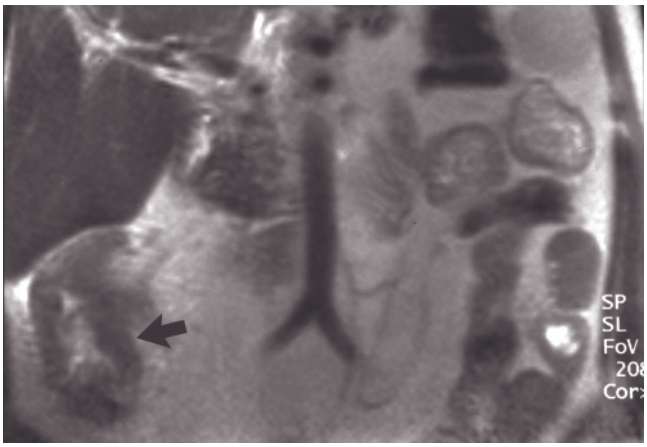

(*a*)

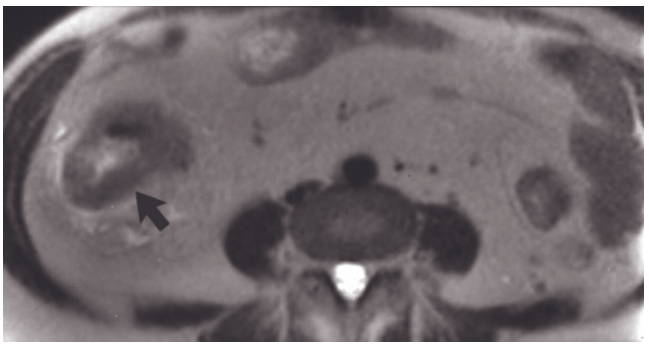

(*b*)

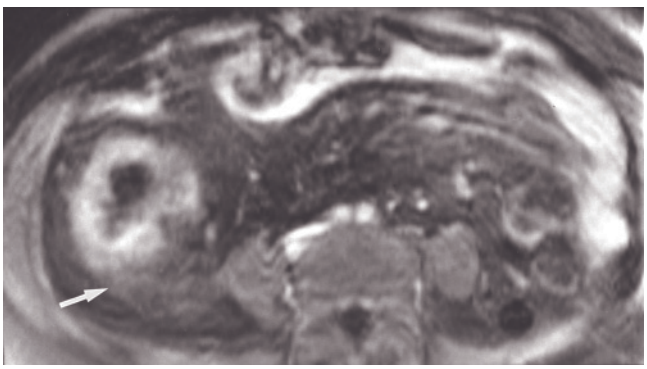

(*c*)

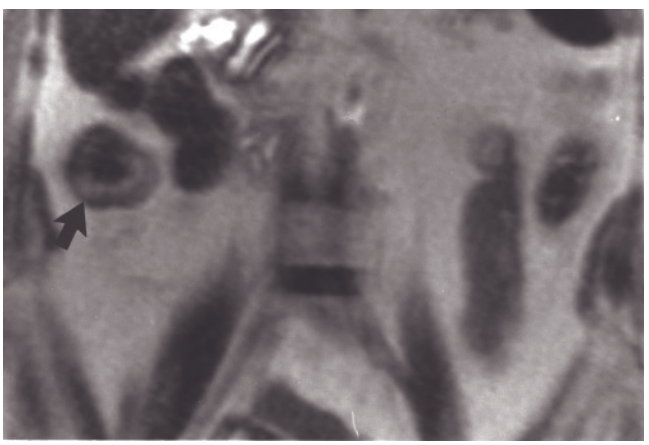

(*d*)

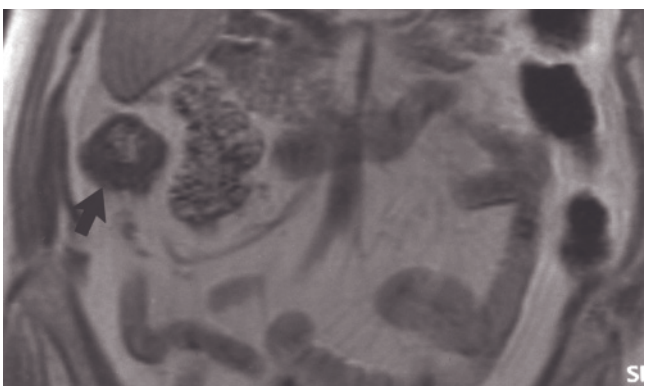

(*e*)

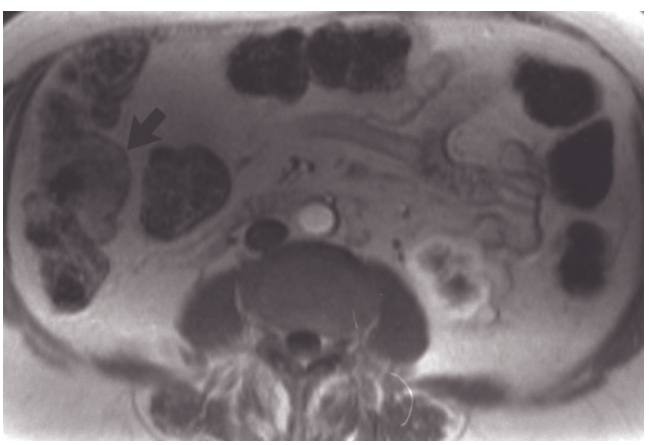

(*f*)

FIG. 6.104 Colon adenocarcinoma, ascending colon. Coronal (*a*) and transverse (*b*) SS-ETSE and 90-s postgadolinium fat-suppressed SGE (*c*) images. Irregularly thickened bowel wall with intermediate signal intensity representing cancer is noted in the ascending colon (arrows, *a*, *b*). The cancer enhances in a moderate and slightly heterogeneous fashion. Pericolonic fat infiltration is demonstrated in the ascending colon on postcontrast fat-suppressed SGE image as enhancing strands of tissue (arrow, *c*). Coronal SS-ETSE (*d*), coronal precontrast SGE (*e*), and transverse immediate postcontrast SGE (*f*) images in a second patient also demonstrate an irregular thickening of the ascending colon wall (arrow, *d*–*f*). There is no evidence of pericolonic fat infiltration with sharp external margins to the tumor.

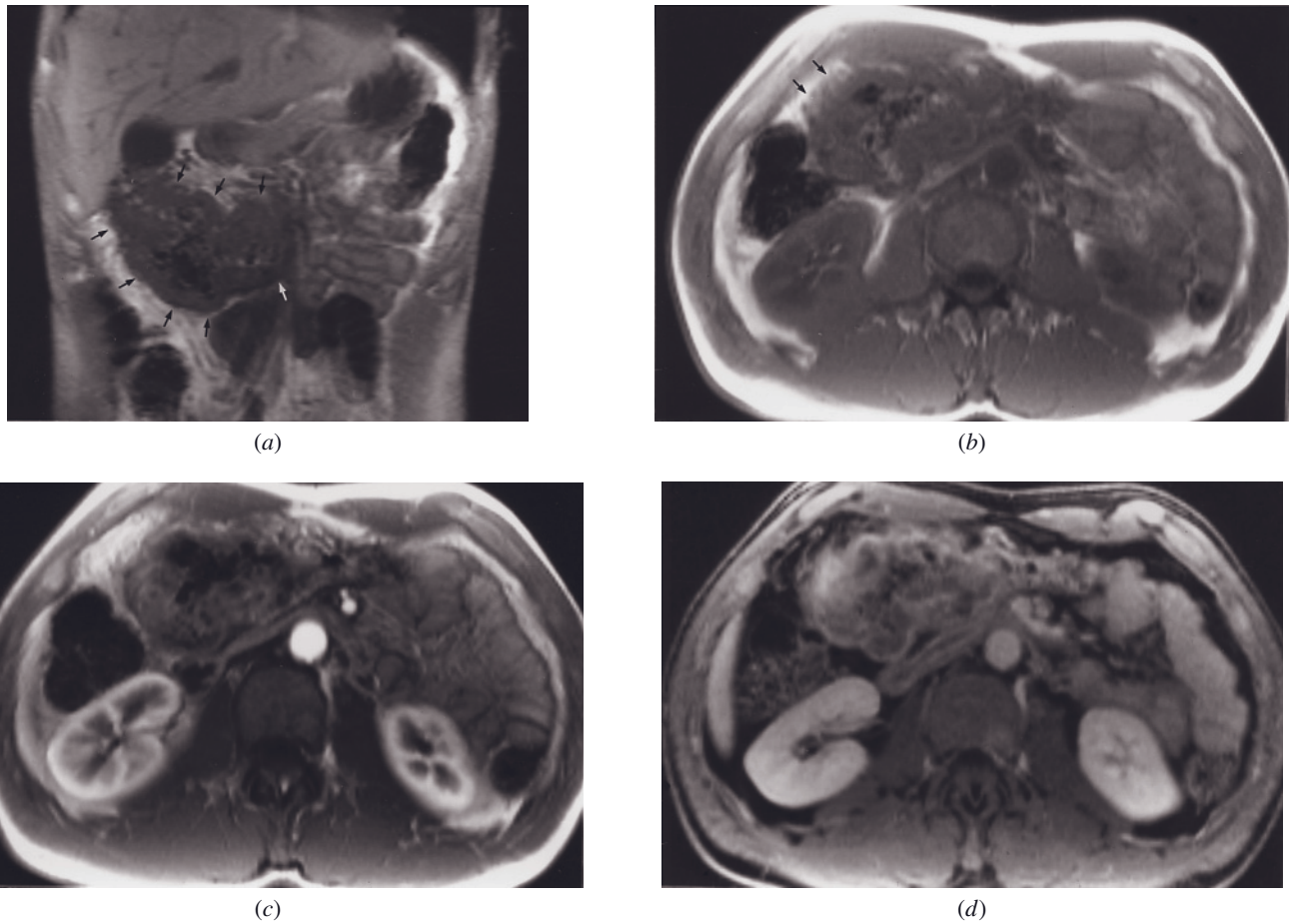

FIG. 6.105 Colon adenocarcinoma, transverse colon. Coronal SGE (*a*), SGE (*b*), immediate postgadolinium SGE (*c*), and 90-s postgadolinium fat-suppressed SGE (*d*) images. A large cancer arises from the transverse colon (small arrows, *a*). The outer margin of the tumor is indistinct (small arrows, *b*), a finding consistent with lymphovascular extension. The tumor is heterogeneous and moderate in signal intensity on capillary-phase (*c*) and interstitial-phase (*d*) images.

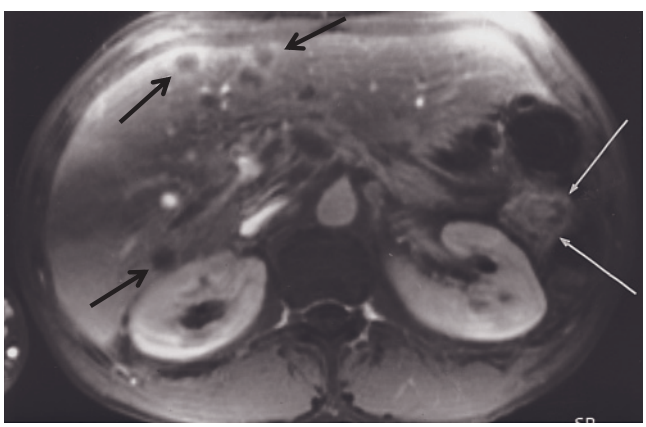

FIG. 6.106 Colon adenocarcinoma, proximal descending colon. Transverse 90-s postgadolinium SGE image demonstrates a heterogeneously enhancing tumor (white arrows) in the proximal descending colon with prominent enhancing strands in the surrounding mesentery consistent with lymphovascular extension. Multiple ring-enhancing liver metastases are apparent (black arrows).

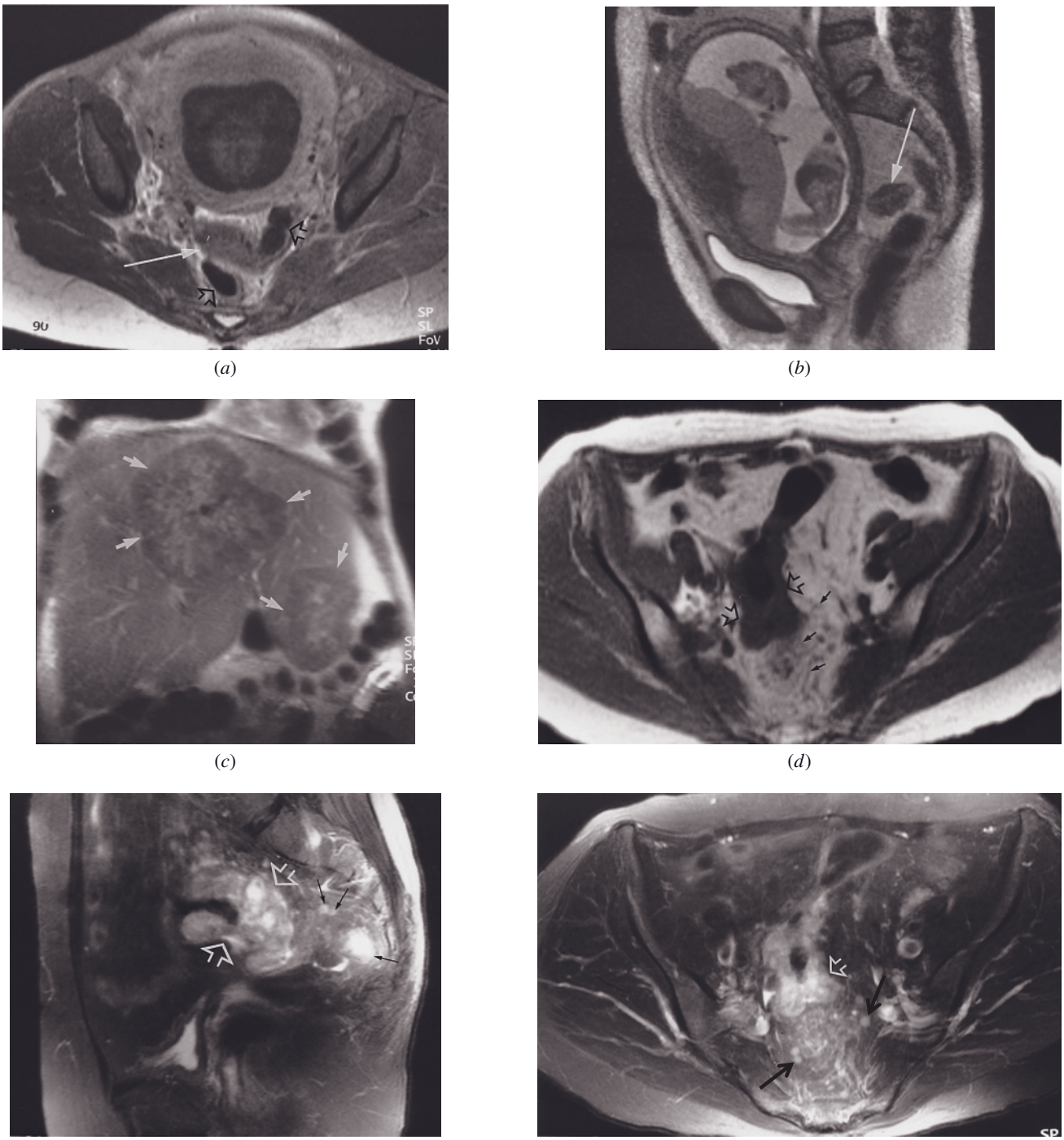

FIG. 6.107 Sigmoid adenocarcinoma. SGE (*a*) and sagittal (*b*) and coronal (*c*) SS-ETSE images in a pregnant patient with colon cancer. The SGE image shows air-filled colon (open arrows, *a*) proximal and distal to the 4-cm sigmoid cancer (arrow, *a*). The SS-ETSE images show the primary tumor (arrow, *b*) and the liver metastases (arrows, *c*). The gravid uterus is well imaged with the single-shot T2-weighted breathing-independent technique (*b*). SGE (*d*), sagittal T2-weighted fat-suppressed spin-echo (*e*), and gadolinium-enhanced T1-weighted fat-suppressed spin-echo (*f*) images in a second patient with advanced sigmoid adenocarcinoma. The precontrast image demonstrates abnormal thickening of the sigmoid colon (open arrows, *d*) with low-signal-intensity strands infiltrating the pericolonic fat (small arrows, *d*). The primary tumor (open arrows, *e*, *f*) and pericolonic extension are well shown as high-signal-intensity structures in a low-signal-intensity background on both fat-suppressed T2-weighted (*e*) and gadolinium-enhanced T1-weighted fat-suppressed (*f*) images. Multiple small regional malignant lymph nodes are identified (black arrows, *e*, *f*).

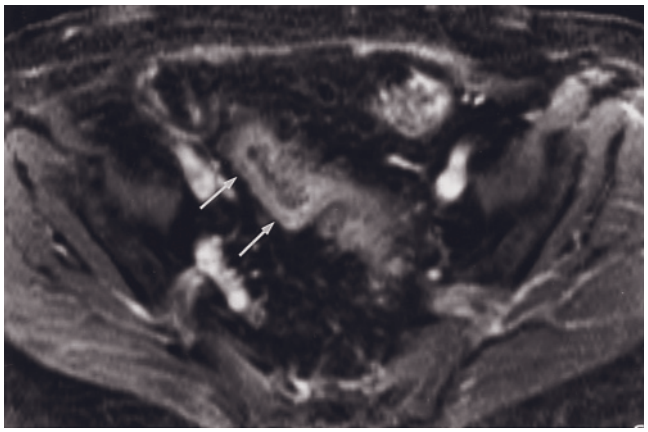

(*g*)

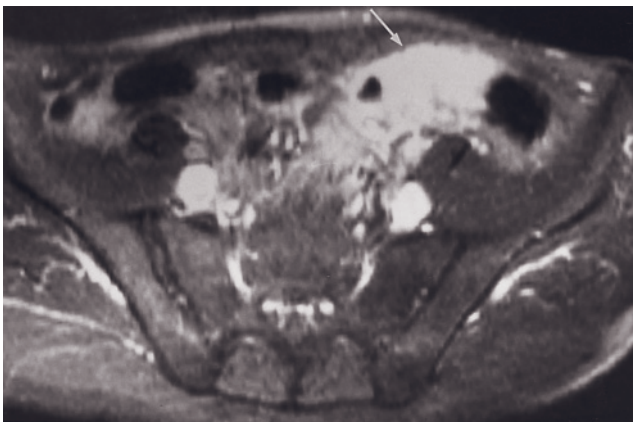

(*h*)

FIG. 6.107 (*Continued*) Transverse 90-s postgadolinium SGE image (*g*) in a third patient demonstrates a circumferential 4-cm sigmoid colon cancer (arrows, *g*) that does not show lymphovascular extension. Gadolinium-enhanced T1-weighted fat-suppressed spin-echo image (*h*) in a fourth patient demonstrates an intensely enhancing sigmoid colon cancer (arrow) involving the anterior peritoneum.

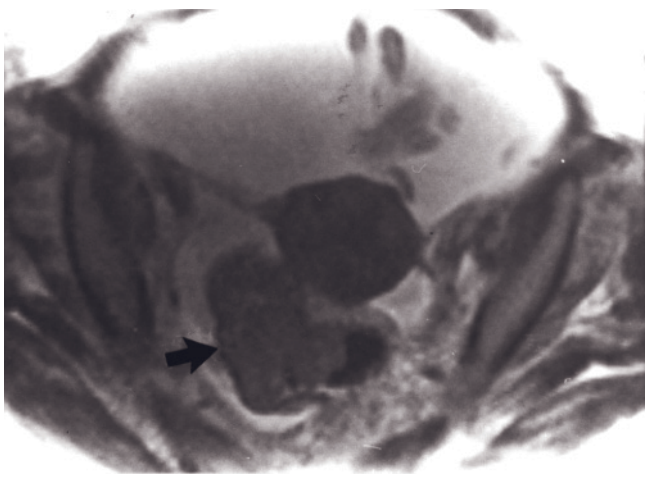

(*a*)

(*b*)

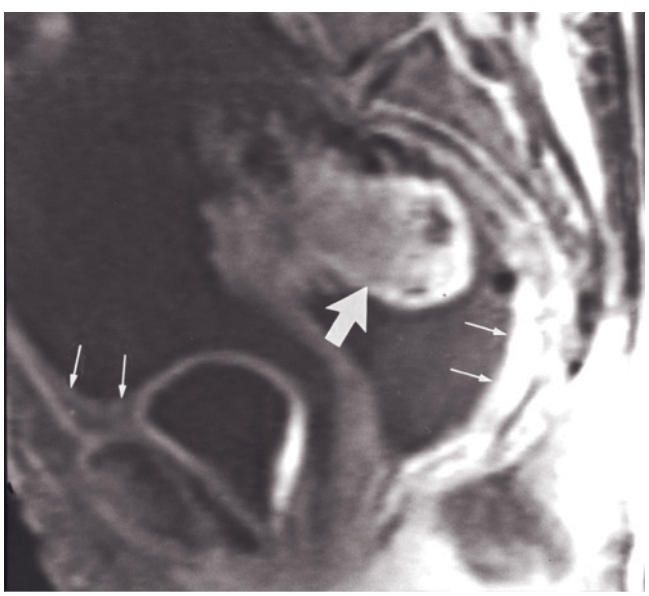

(*c*)

FIG. 6.108 Sigmoid adenocarcinoma with peritoneal metastases. Transverse SS-ETSE (*a*) and transverse (*b*) and sagittal (*c*) 2- to 3-min postgadolinium fat-suppressed SGE images. There is a soft tissue enhancing mass in the sigmoid colon representing tumor (arrow, *a–c*). Note the increased peritoneal enhancement and thickening (small arrows, *c*) and large volume of ascites, consistent with peritoneal disease.

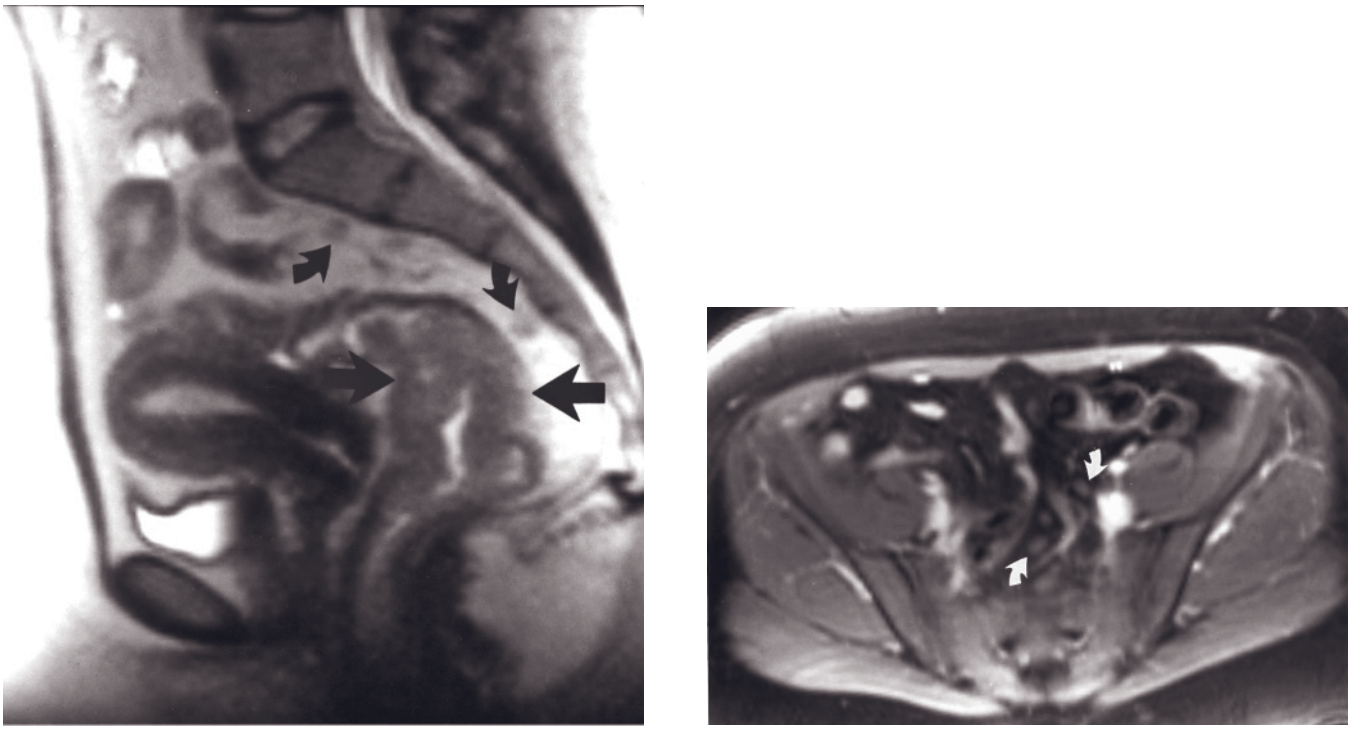

(*a*) (*b*)

FIG. 6.109 Rectosigmoid colon adenocarcinoma. Sagittal SS-ETSE (*a*) and 90-s postgadolinium fat-suppressed SGE (*b*) images. Markedly thickened tumor mass (large arrows, *a*) is noted in the rectosigmoid region on the SS-ETSE image. Multiple regional lymph nodes less than 1 cm in diameter are well demonstrated in the pelvis (curved arrows, *a*, *b*). Small nodes are best shown on gadolinium-enhanced fat-suppressed SGE images. (Reprinted with permission from Chung JJ, Semelka RC, Martin DR, Marcos HB: Colon diseases: MR evaluation using combined T2-weighted single-shot echo train spin-echo and gadolinium-enhanced spoiled gradient-echo sequences. *J Magn Reson Imaging* 12: 297–305, 2000.)

benefit from the combined use of gadolinium-enhanced fat-suppressed SGE or 3D-GE and high-resolution T2-weighted echo-train spin-echo images (fig. 6.110). MR colonography employing a bowel cleansing preparation and administration of rectal water enema has been shown effective in demonstrating small polyps (figs. 6.96 and 6.111) and tumors (figs. 6.112, 6.113) [90–92].

Gadolinium-enhanced fat-suppressed GE imaging is valuable in demonstrating perirectal tumor extension, regional lymph nodes, and seeding of peritoneum by tumor. This reflects the high-contrast resolution of this technique for detecting enhancing diseased tissue (figs. 6.114, 6.115). Thin-section 3D-GE may be of particular value to assess tumor extension to the perirectal fascia, the presence of which will affect surgical technique and patient prognosis. Image acquisition of T2-weighted echo-train spin echo or single-shot echo-train spin echo after the administration of gadolinium is commonly done when abdomen and pelvis studies are combined in one examination. As an additional benefit to a shortened MR examination, dependent, concentrated gadolinium in the bladder, which is low in signal intensity, may increase the conspicuity of high-signal-intensity rectal tumor invasion of the bladder wall (see fig. 6.114).

MRI has established an important role in the evaluation of rectal cancer based on the combination of overall topographic display and appreciation of soft tissue contrast resolution [100–102]. One of the strengths of MRI is to evaluate the integrity of the mesorectum, which may be observed as a thin linear structure that envelops the immediate perirectal fat [101, 102]. The ability to routinely visualize this thin structure, which is low signal on T2-weighted images and exhibits enhancement on postgadolinium fat-suppressed images, allows for improved staging of rectal cancer and guidance of appropriate therapy. A large multicentric European prospective observational study showed a MRI specificity of 92% (327/354, 90% to 95%) in predicting curative resection of rectal cancer [103].

When feasible, surface torso coils (e.g., phased-array torso coil) should be employed to ensure better definition of perirectal tumor extension [104]. Phased-array torso coils also provide good overall topographic display that improves detection of features such as regional lymph nodes.

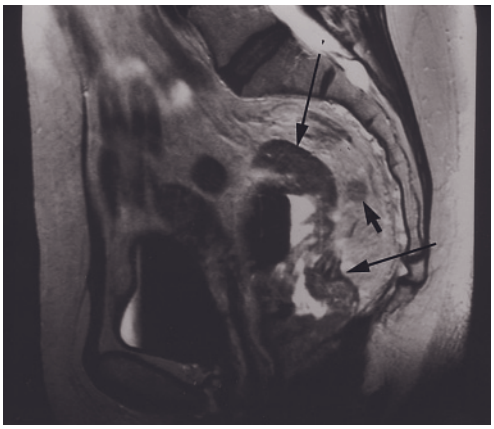

(*a*)

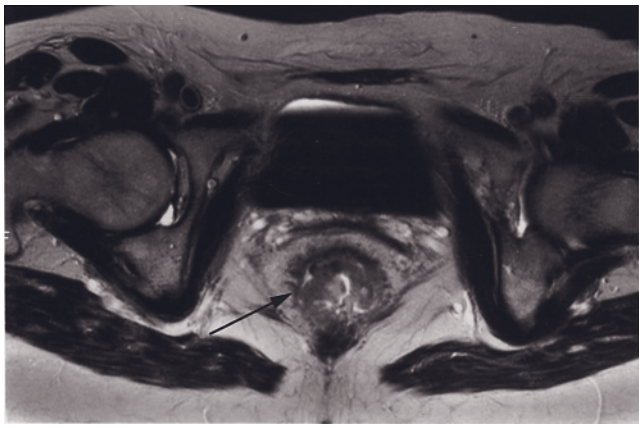

(*b*)

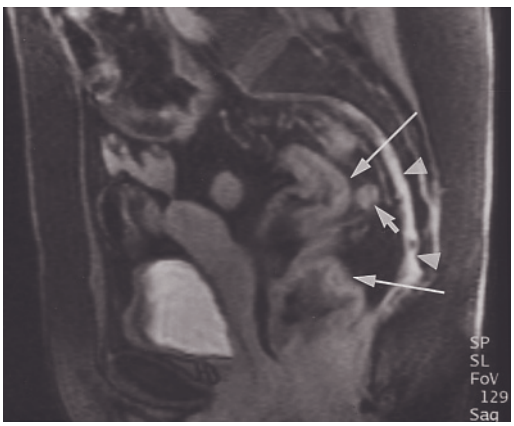

(*c*)

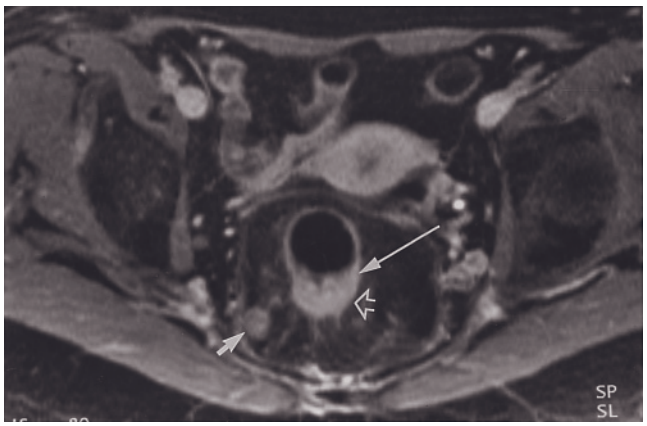

(*d*)

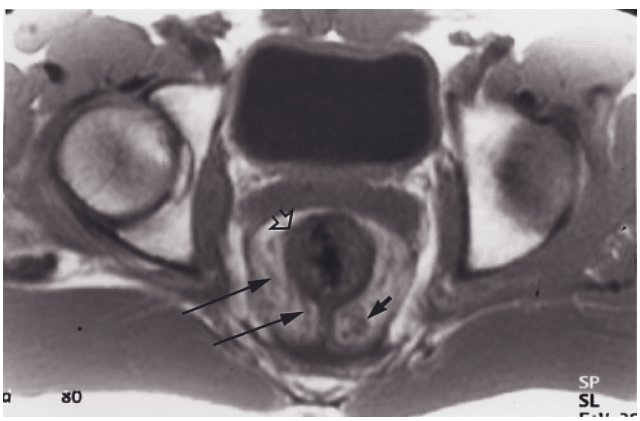

(*e*)

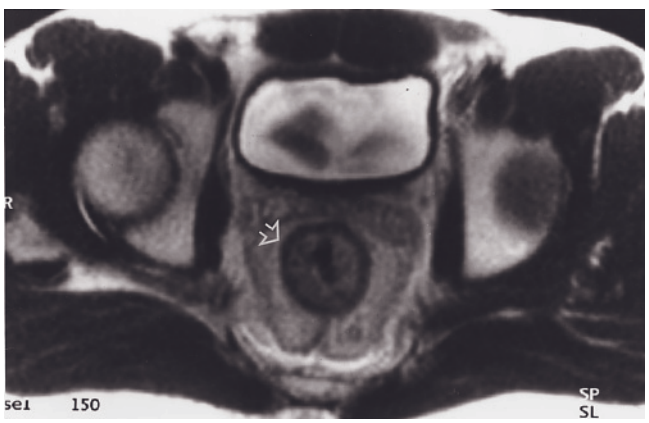

(*f*)

FIG. 6.110 Rectal adenocarcinoma. Sagittal and transverse postgadolinium high-resolution T2-weighted echo-train spin-echo (*a*, *b*) and sagittal and transverse postgadolinium fat-suppressed SGE (*c*, *d*) images in a patient with advanced colon cancer. A large rectal cancer is present (long arrows, *a*, *c*). The craniocaudal extent of tumor is well shown on sagittal images (*a*, *c*). The tumor extends inferiorly in the rectum (arrow, *b*) to the anal verge. Lymphovascular extension with involved lymph nodes (small arrows, *a*, *c*, *d*) is present. At the superior margin, the tumor is mainly posterior in location (open arrow, *d*). The transition from normal colon to tumor (long arrow, *d*) is clearly shown. Presacral spread of tumor is shown as enhancing tissue on the sagittal gadolinium-enhanced fat-suppressed image (arrowheads, *c*). SGE (*e*), SS-ETSE (*f*), and postgadolinium fat-suppressed SGE (*g*) images in a second patient with rectal adenocarcinoma and similar imaging findings. The rectal tumor (open arrows, *e*, *f*, *g*), lymphovascular extension (long arrows, *e*, *g*), and perirectal lymph nodes (short arrows, *e*, *g*) are well shown. Sagittal and transverse postgadolinium

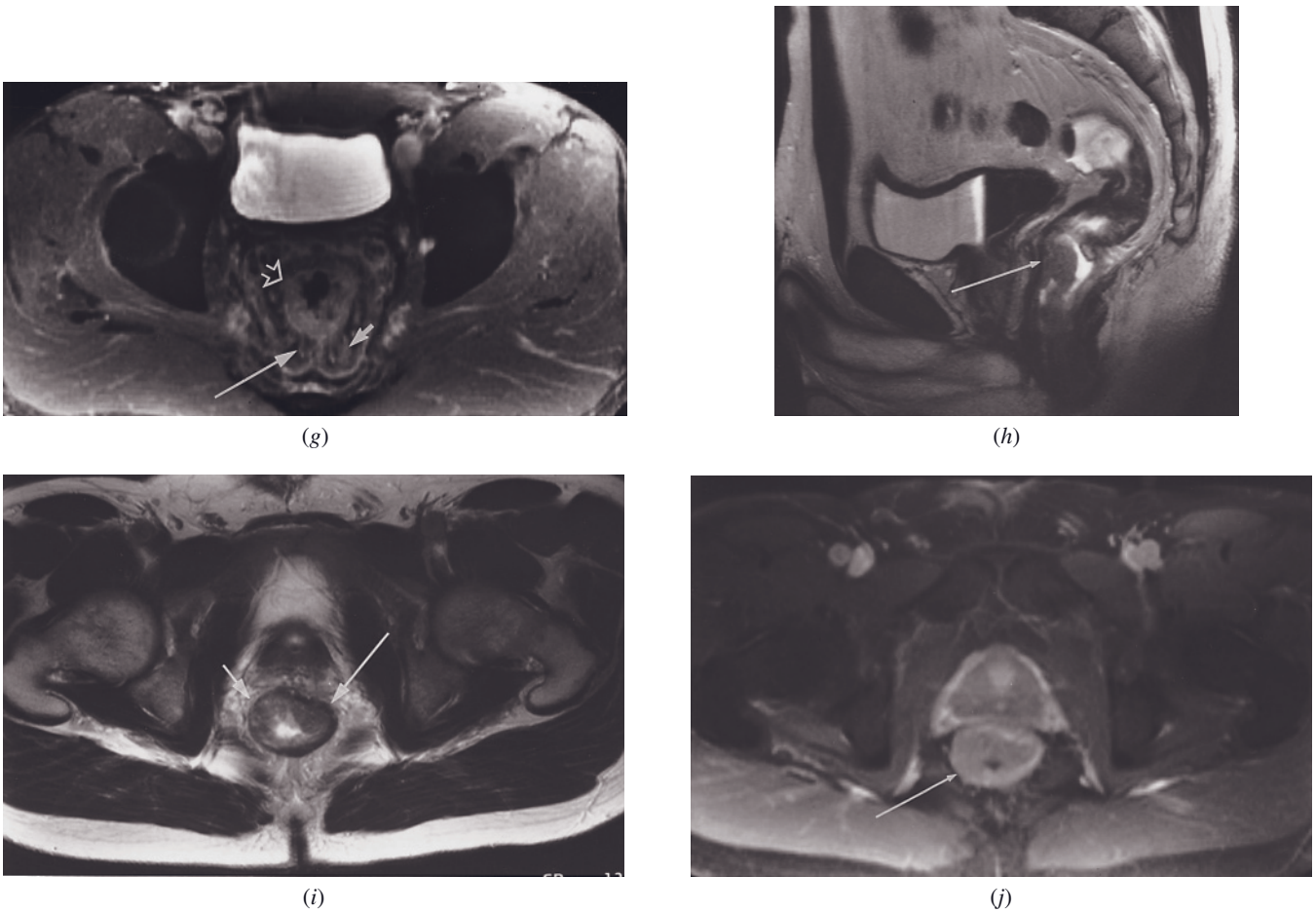

FIG. 6.110 (*Continued*) 512-resolution T2-weighted echo-train spin-echo (*h*, *i*) and interstitial-phase gadolinium-enhanced fat-suppressed SGE (*j*) images in a third patient. Asymmetric tumor involvement of the rectal wall is apparent on the 512-resolution T2-weighted images (long arrows, *h*, *i*). Tumor penetrates the full thickness of the right aspect of the rectum (short arrow, *i*). This is shown by interruption of the muscular wall that appears low signal intensity on the T2-weighted image (long arrow, *i*). On the gadolinium-enhanced fat-suppressed SGE image, lower-signal-intensity tumor (arrow, *j*) penetrates the full thickness of the higher-signal-intensity wall. Postgadolinium T2-weighted imaging is a novel technique for assessing possible bladder invasion. Enhancing tumor is conspicuous against the low signal intensity produced by concentrated gadolinium excreted into the bladder. In this case, the bladder is spared.

Endorectal coil imaging permits differentiation of the anatomic layers of the rectal wall on T2-weighted fat-suppressed images [10]. Local staging of rectal carcinoma also benefits from endorectal coil imaging (fig. 6.116) [9, 10].

Recurrence rates for rectosigmoid carcinoma, which are reported to range from 8% to 50%, are a function of the stage of the primary tumor at initial presentation [12]. Tumors tend to recur locally, and curative surgery is feasible. The sagittal imaging plane facilitates MRI detection of recurrent rectal carcinoma. Using T1-weighted, T2-weighted, and gadolinium-enhanced T1-weighted sequences, one study reported a 93.3% accuracy in detecting recurrent disease [12]. Others have shown that MRI is superior to conventional CT imaging and is more specific than transrectal ultrasound for identifying recurrent tumor [11, 13–15]. Specifically, MRI correctly diagnosed recurrent rectal carcinoma in 83.2% of patients versus transrectal ultrasound, which diagnosed recurrence in only 41.6% [16].

Recurrent tumor tends to be low in signal intensity on T1-weighted images and enhances moderately after intravenous gadolinium (figs. 6.117–6.119) [6, 11, 105]. On T2-weighted images, recurrent tumor usually is moderately high in signal intensity. This may be difficult to appreciate on echo-train spin-echo sequences because the surrounding fat is also moderately high in signal intensity on these sequences (see fig. 6.118). Caution must be exercised in interpreting images in patients with possible recurrent disease on echo-train spin-echo sequences: Tumor appears lower in signal intensity compared to its appearance on conventional

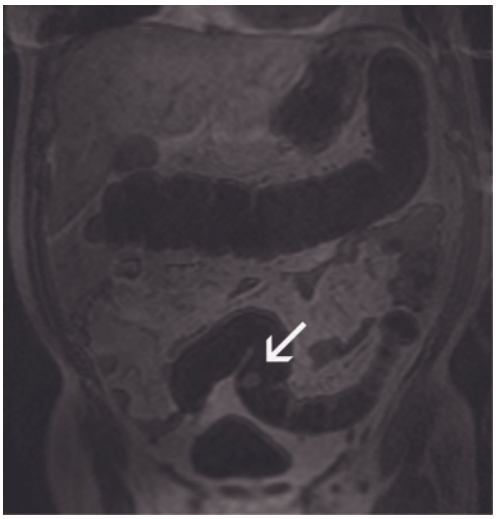

(*a*)

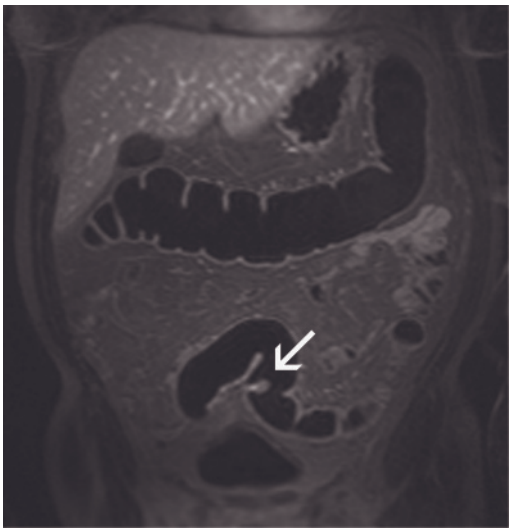

(*b*)

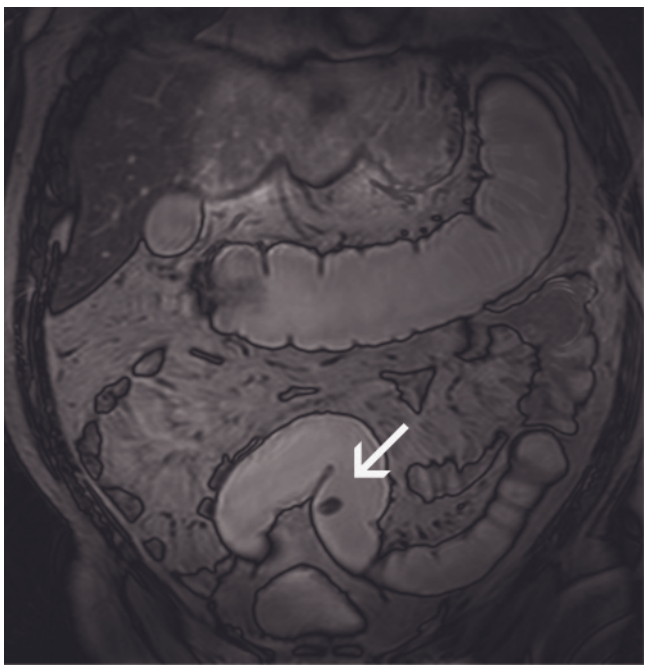

(*c*)

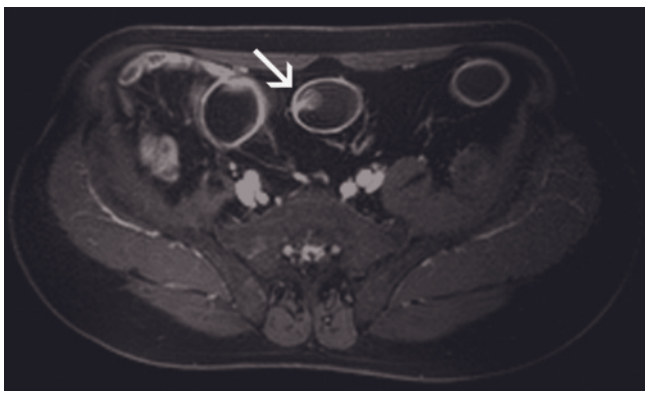

(*d*)

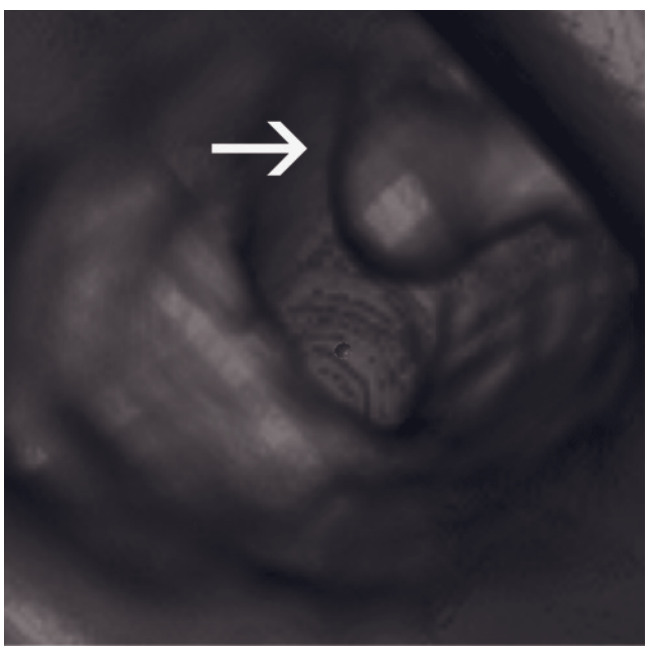

(*e*)

FIG. 6.111 Polyp demonstrated on screening MR colonography. A 48-year-old male patient undergoing a MR colonography for screening purposes using dark lumen water enema contrast. The patient underwent a bowel cleansing procedure 1 day before the imaging study. A 13-mm-sized pedunculated polyp is visualized on the coronal T1-weighted 3D-GE sequences by comparing the precontrast (arrow, *a*) and postcontrast (arrow, *b*) images to demonstrate contrast enhancement. This helps discriminate an enhancing polyp from potentially confounding remnant stool. The polyp can also be demonstrated on coronal true-FISP (arrow, *c*), on interstitial-phase T1-weighted fat suppressed 3D-GE (arrow, *d*), as well as on a virtual endoscopic reconstruction (arrow, *e*).

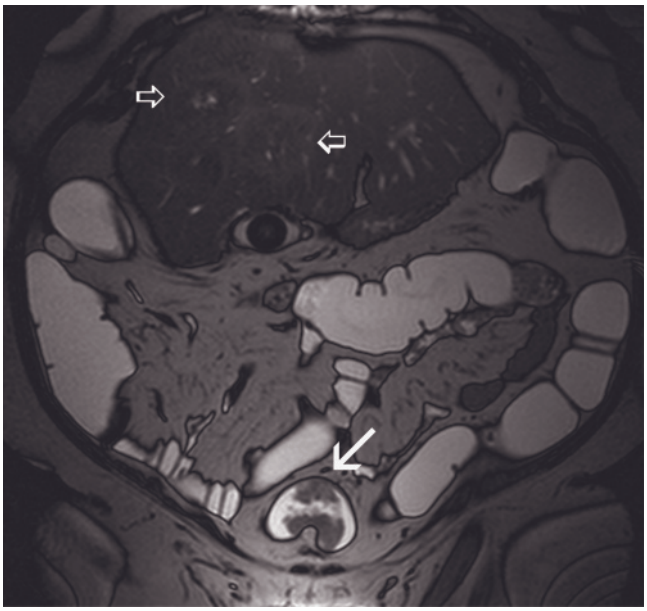

(*a*)

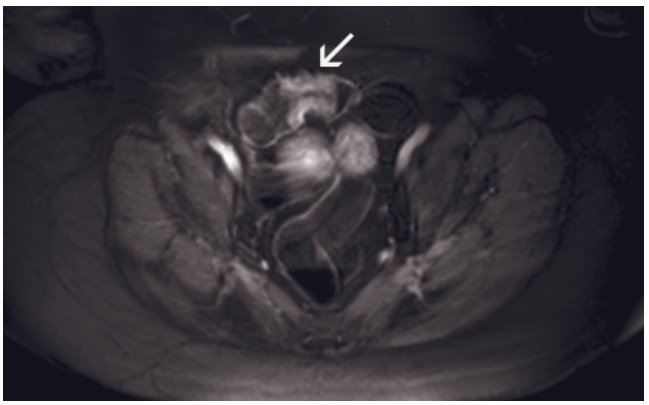

(*b*)

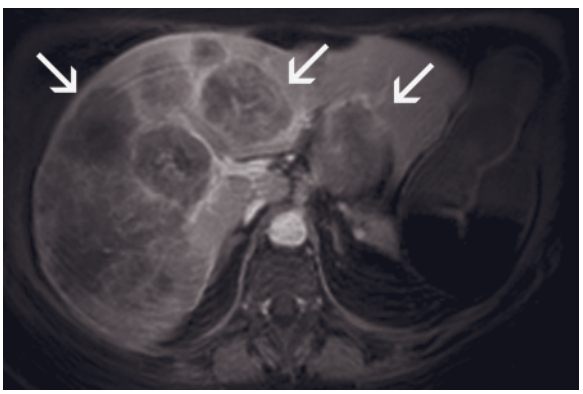

(*c*)

FIG. 6.112 Adenocarcinoma of the sigmoid colon. A 58-year-old male patient with colon adenocarcinoma arising from the sigmoid colon showing an apple core lesion growth pattern. The adenocarcinoma can be easily depicted on the coronal true-FISP image (arrow, *a*) as well as on the transverse gadolinium-enhanced T1-weighted fat-suppressed 3D-GE image (arrow, *b*). Simultaneous display of the parenchymal abdominal organs show multiple hepatic metastases, which can be accurately detected and characterized on gadolinium-enhanced T1-weighted fat-suppressed 3D-GE image (arrows, *c*), whereas the diagnosis is difficult to make on true-FISP images (open arrows, *a*).

spin-echo sequences. This reflects the relatively high signal intensity of fat on echo-train spin-echo sequences.

Demonstration of sacral invasion is well shown on T2-weighted fat-suppressed echo-train spin-echo and gadolinium-enhanced T1-weighted fat-suppressed images. Marrow is low in signal intensity on both of these sequences, particularly in the setting of postradiation fatty replacement, which is often present in these patients, and tumor extension is conspicuous because of its high signal intensity (figs. 6.120, 6.121). In the assessment of sacral involvement, imaging in the sagittal plane is essential for visualizing invasion of the cortex of the sacrum. In selected cases, oblique coronal images (following the angulation of the sacrum) are helpful (see fig. 6.120). Recurrent tumor often has a nodular configuration. Recurrent rectosigmoid cancer and post-treatment (surgical and/or radiation) fibrosis frequently coexist (figs. 6.121, 6.122).

Postradiation fibrosis in patients more than 1 year after therapy often demonstrates low signal intensity in the surgical bed on T1- and T2-weighted images and may show negligible enhancement after intravenous gadolinium administration (fig. 6.123) [6, 11, 106]. Enhancement of fibrosis with gadolinium, particularly on fat-suppressed images, often persists for 1.5–2 years after therapy, which is longer than the period of time that fibrosis is high in signal intensity on T2-weighted images. Morphologically, fibrosis often has a plaquelike appearance. Unfortunately, the imaging features of postradiation changes, especially in patients receiving doses in excess of 45 Gy, may not always follow a predictable time course, and overlap in signal behavior between recurrent tumor and posttreatment fibrosis exists [105]. On echo-train spin-echo images, the high signal intensity of fat admixed with fibrous tissue may simulate recurrence (fig. 6.124). Although the T2-weighted signal intensity of fibrosis usually decreases 1

(*a*)

(*b*)

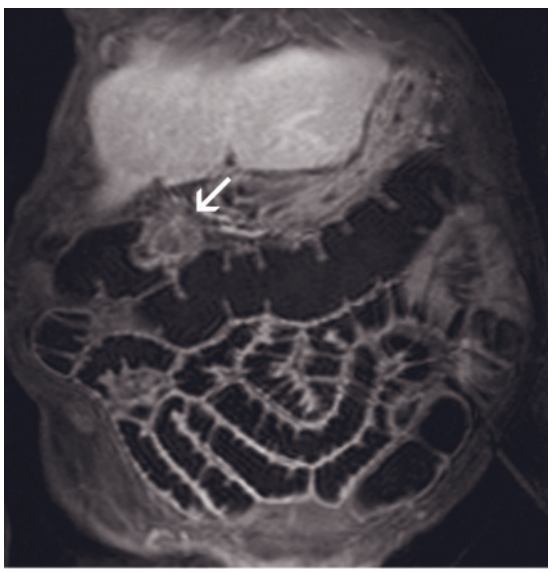

(*c*)

Fig. 6.113 Multifocal adenocarcinoma and polyp. A 61-year-old female patient is examined with dark-lumen water enema contrast MR colonography in conjunction with contrast-enhanced T1-weighted imaging after a bowel cleansing preparation. A stenotic tumor in the sigmoid colon is conspicuous and demonstrated as an enhancing mass (arrow, *a*). In addition, a pedunculated polyp is noted in the descending colon (arrow, *b*) and a metachronous second focus of adenocarcinoma is identified near the hepatic flexure (arrow, *c*). In this patient, a conventional colonoscopy only demonstrated the distal sigmoid lesion, but because of the stenotic nature of this mass, the scope could not be passed and the more proximal lesions were not observed.

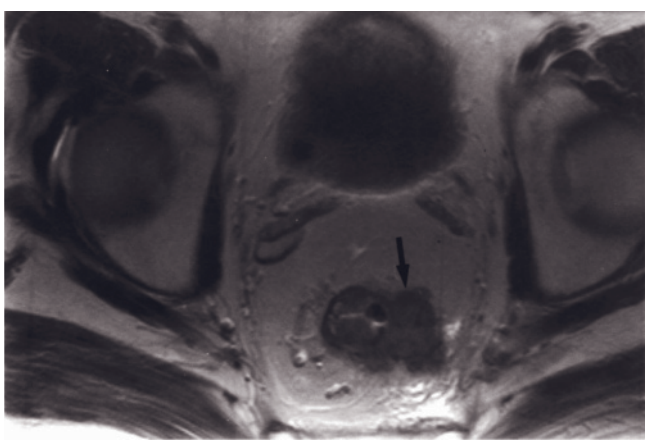

(*a*)

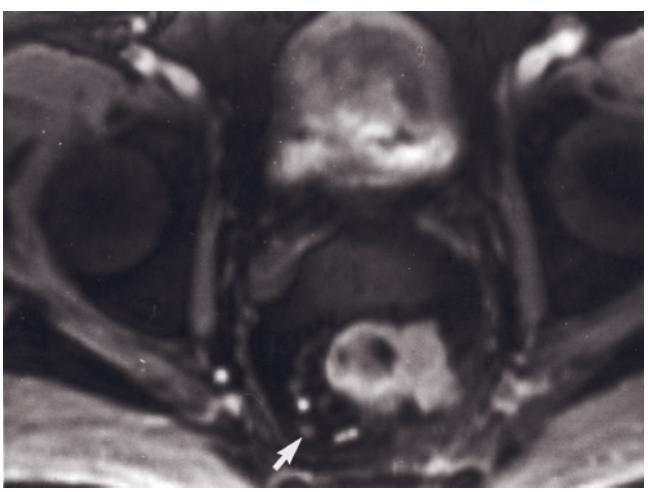

(*b*)

Fig. 6.114 Rectal cancer. Transverse T2-weighted ETSE (*a*) and interstitial-phase gadolinium-enhanced SGE (*b*) images. There is a soft tissue mass involving the wall of the rectosigmoid with gross tumor extension through the left aspect of the wall (arrow, *a*). Small regional lymph nodes are also identified (arrow, *b*). Sagittal postgadolinium SS-ETSE (*c*) and interstitial-phase

(*c*)

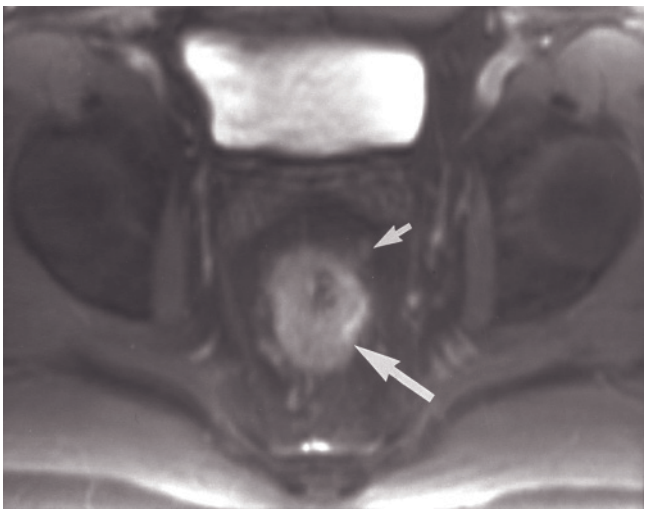

(*d*)

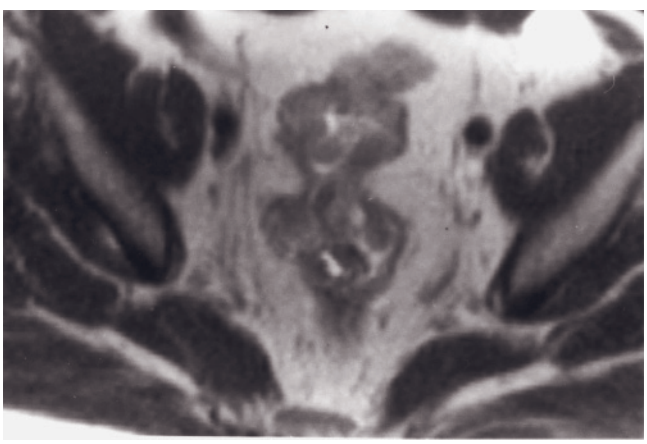

(*e*)

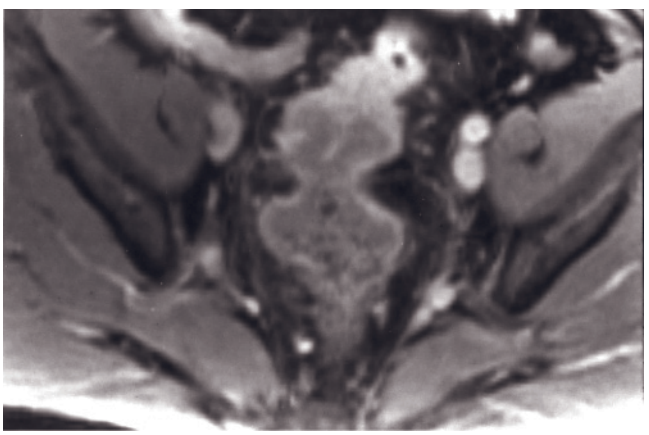

(*f*)

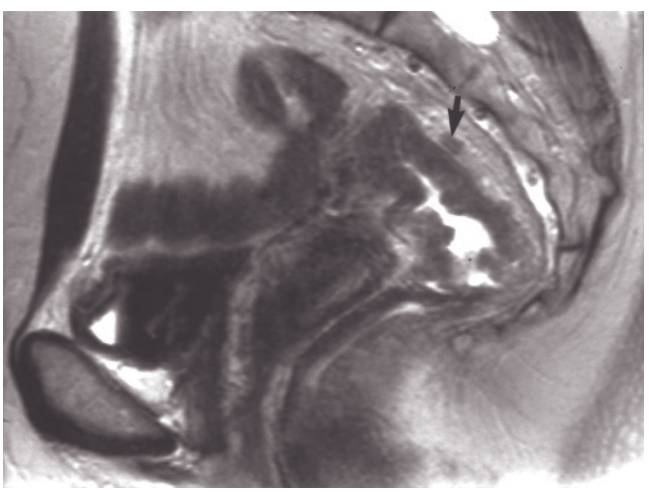

(*g*)

FIG. 6.114 (*Continued*) gadolinium-enhanced SGE (*d*) images in a second patient demonstrate circumferential thickening of the rectum with infiltration of perirectal fat (large arrow, *d*). Small regional nodes are present (small arrow, *d*). Transverse SS-ETSE (*e*) and interstitial-phase gadolinium-enhanced SGE (*f*) images in a third patient also show diffuse thickening of the rectal wall associated with stranding of perirectal fat and small perirectal nodes. Sagittal T2-weighted ETSE (*g*) image in a fourth patient demonstrates similar features. Small regional nodes are present (arrow, *g*).

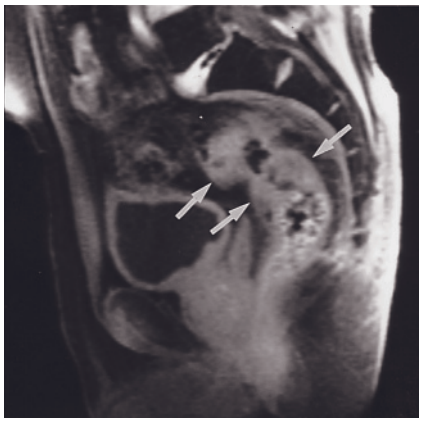

(*a*)

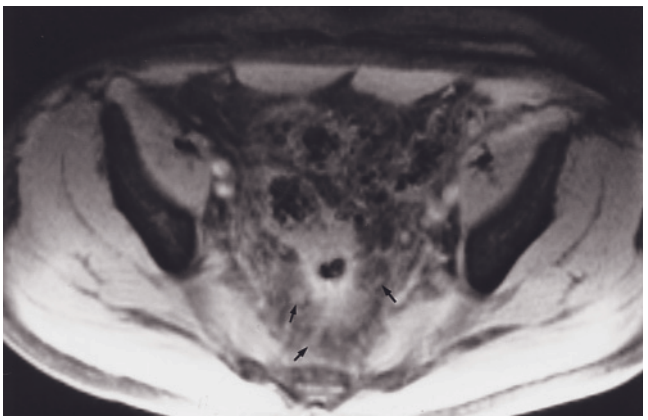

(*b*)

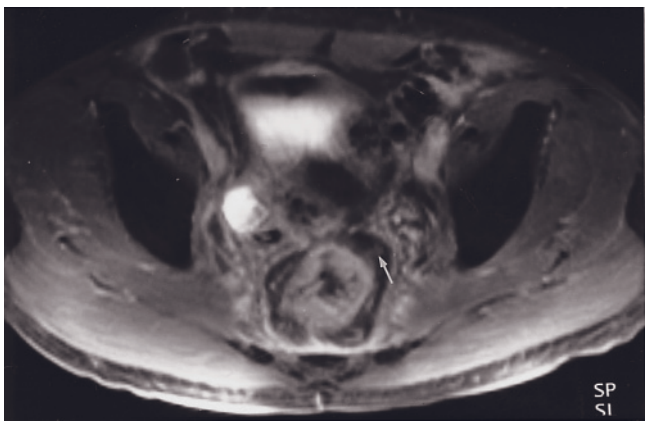

(*c*)

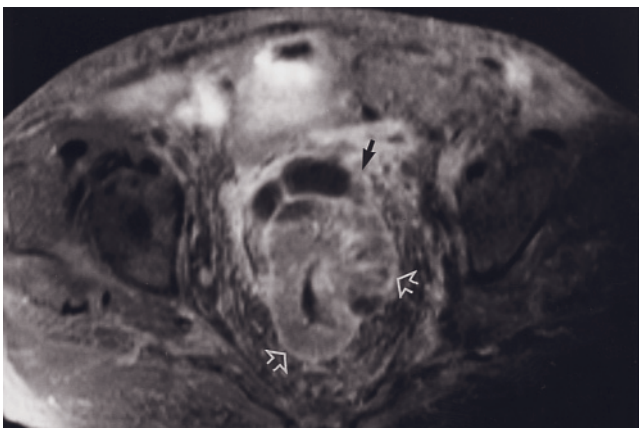

(*d*)

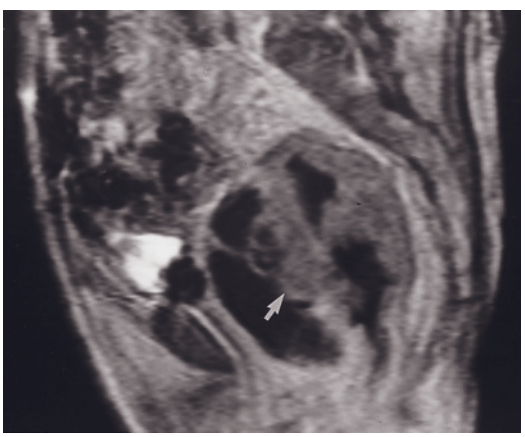

(*e*)

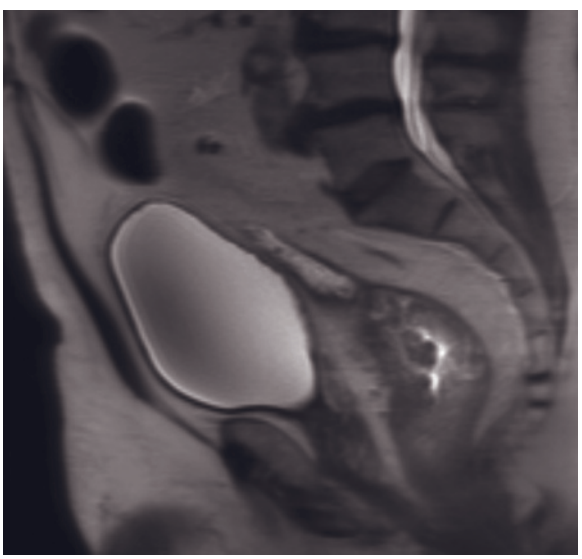

(*f*)

FIG. 6.115 Rectal adenocarcinoma. Sagittal (*a*) and transverse (*b*, *c*) interstitial-phase gadolinium-enhanced fat-suppressed SGE images demonstrate a large rectal adenocarcinoma (arrows, *a*) with prominent lymphovascular extension and multiple small malignant lymph nodes (arrows, *b*, *c*). The sagittal imaging plane (*a*) highlights the inferior and superior extent of the tumor. Transverse gadolinium-enhanced fat-suppressed SGE (*d*) and sagittal postgadolinium SGE (*e*) images in a second patient demonstrate a large rectal cancer (open arrows, *d*) that has prominent lymphovascular invasion. Invasion of adjacent small bowel (arrow, *d*, *e*) is shown. Sagittal T2-weighted single-shot echo-train spin-echo (*f*), transverse T2-weighted high-resolution fast spin-echo (*g*), and transverse T1-weighted postgadolinium interstitial-phase fat-suppressed 3D-GE (*h*, *i*) images at 3.0 T demonstrate rectal adenocarcinoma in another patient. The rectal wall is diffusely thickened (arrow, *h*) and shows intense enhancement (arrow, *h*) due to

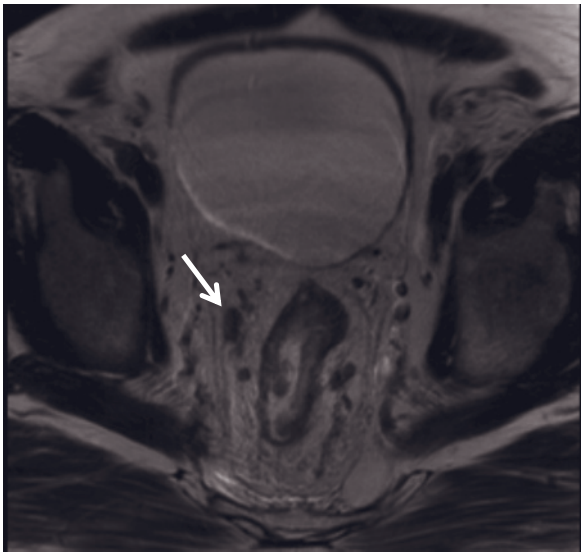

(*g*)

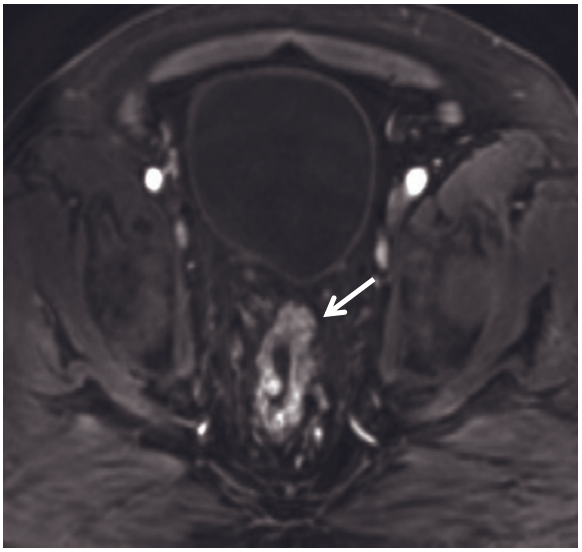

(*h*)

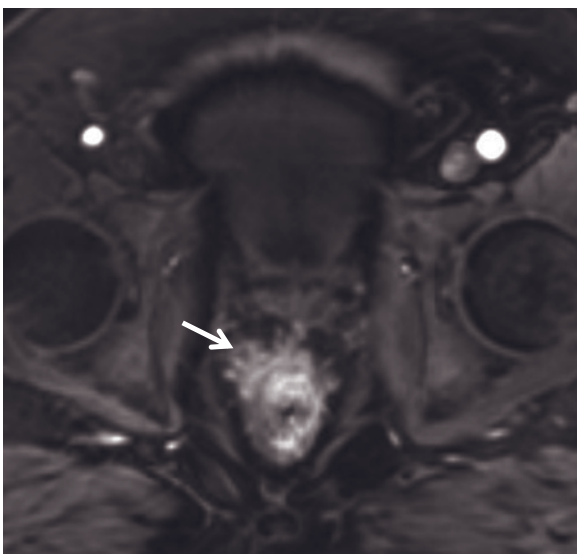

(*i*)

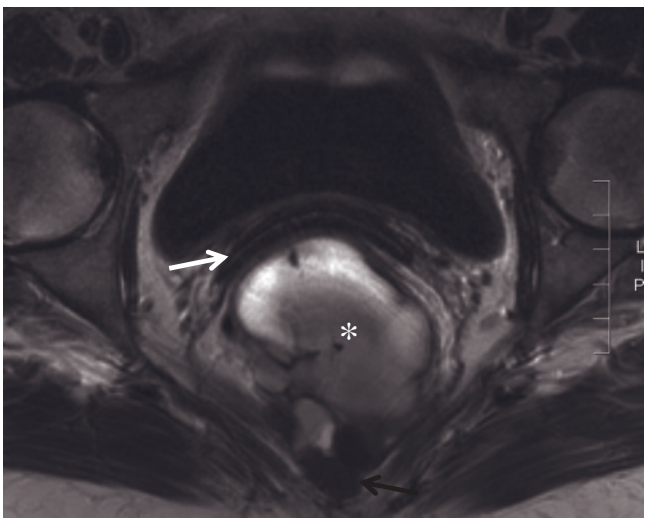

(*j*)

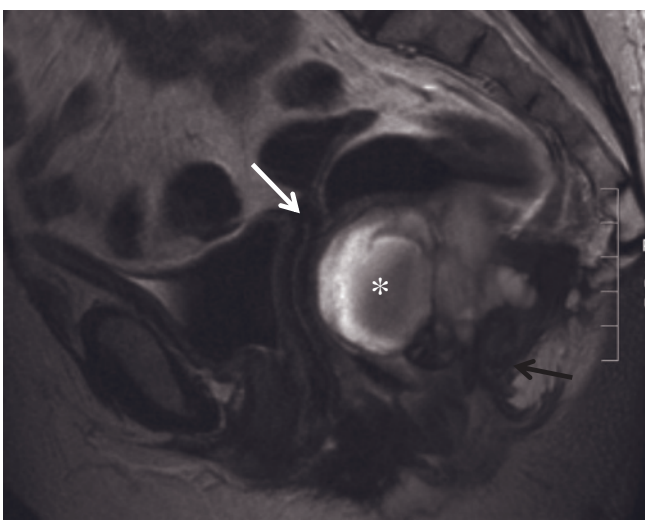

(*k*)

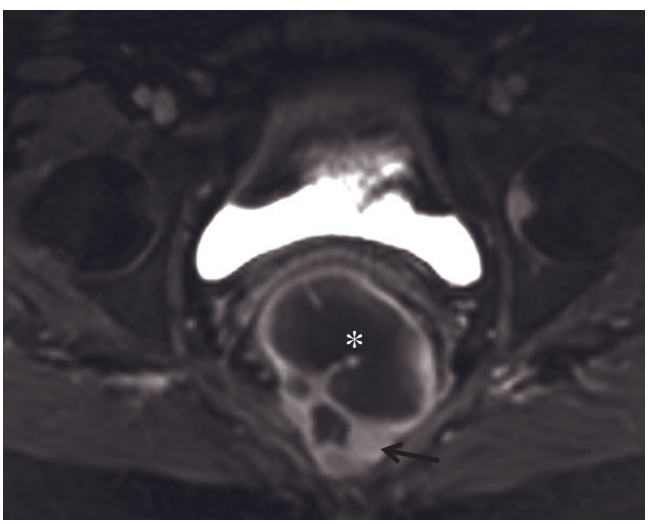

(*l*)

Fig. 6.115 (*Continued*) tumoral involvement. Note that there are spiculations (arrow, *i*) extending from the rectal wall to surrounding perirectal soft tissue, suggesting the presence of serosal invasion. Perirectal lymph nodes (arrow, *g*) are also detected. Transverse (*j*) and sagittal (*k*) T2-weighted high-resolution fast spin-echo and transverse T1-weighted postgadolinium interstitial-phase fat-suppressed 3D-GE (*l*) images at 3.0 T demonstrate a complex structure containing cystic (*, *j–l*) and solid (black arrows, *j–l*) components in another patient with rectal adenocarcinoma. High-resolution imaging is helpful for the staging. The vagina (arrows, *j*, *k*) is displaced anteriorly without any invasion. The wall and the solid component of the tumor show intense enhancement.

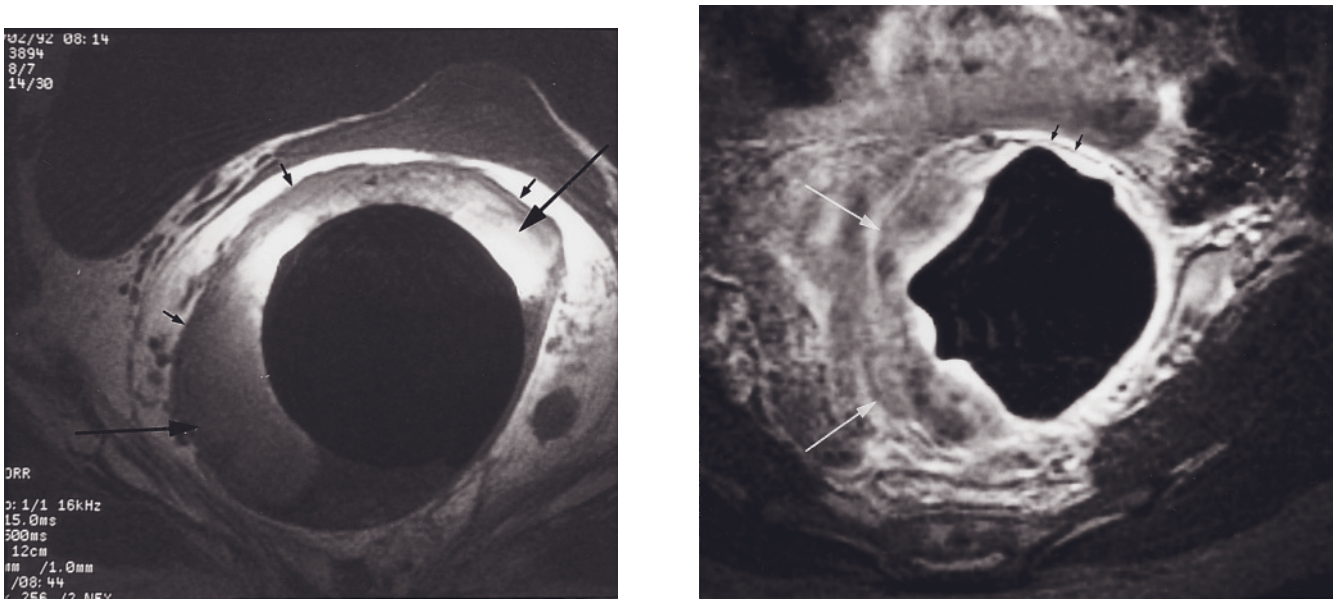

(*a*) (*b*)

FIG. 6.116 Endorectal coil imaging of rectal cancer. Gadolinium-enhanced T1-weighted image (*a*) demonstrates a T2 rectal cancer (long arrows). Preservation of low-signal-intensity muscular wall (short arrows, *a*) along the outer margin of the tumor confirms lack of full-thickness involvement. Gadolinium-enhanced T1-weighted fat-suppressed spin-echo image (*b*) in a second patient with T3 rectal cancer. Heterogeneous moderate enhancing tumor (long arrows, *b*) is noted to extend beyond the confines of muscularis propria (short arrows, *b*). [Courtesy of Rahel A. Kubik Huch.]

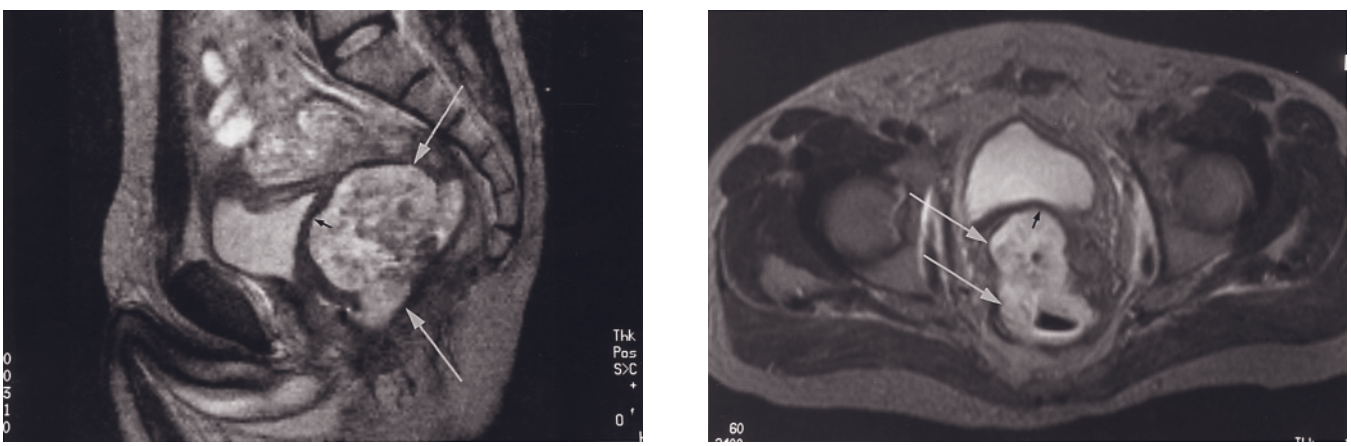

(*a*) (*b*)

FIG. 6.117 Recurrent rectal adenocarcinoma. Sagittal and transverse T2-weighted echo-train spin-echo (*a*, *b*) and interstitial-phase gadolinium-enhanced T1-weighted fat-suppressed spin-echo (*c*) images. A large heterogeneous mass occupies the rectal fossa, a finding consistent with recurrence. Recurrent tumors are usually moderately high in signal intensity on T2-weighted images (long arrows, *a*, *b*) and enhance moderately after intravenous contrast (long arrows, *c*). Central necrosis is well shown on the gadolinium-enhanced T1-weighted fat-suppressed image. The tumor is contiguous with the bladder wall (short arrow, *a–c*), but the low signal intensity of the bladder wall on the T2-weighted images shows that the bladder wall is not invaded. Sagittal and

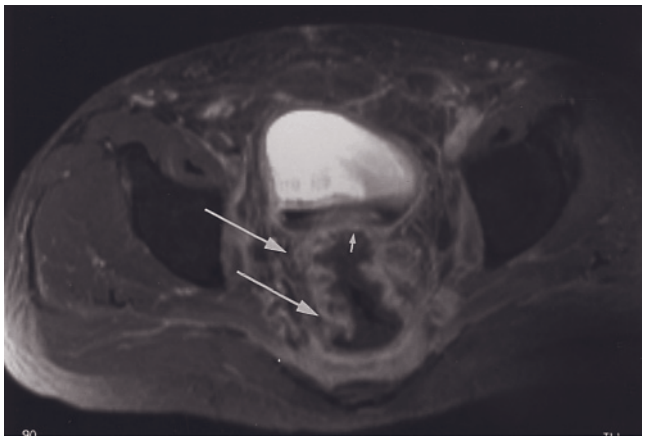

(*c*)

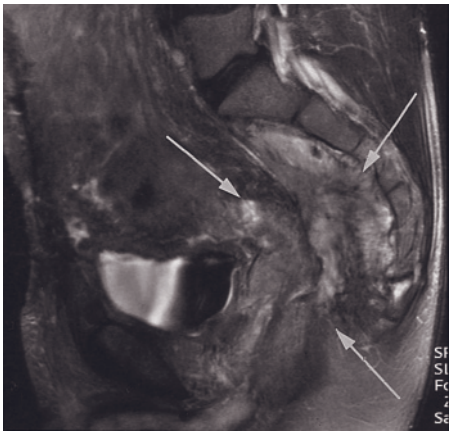

(*d*)

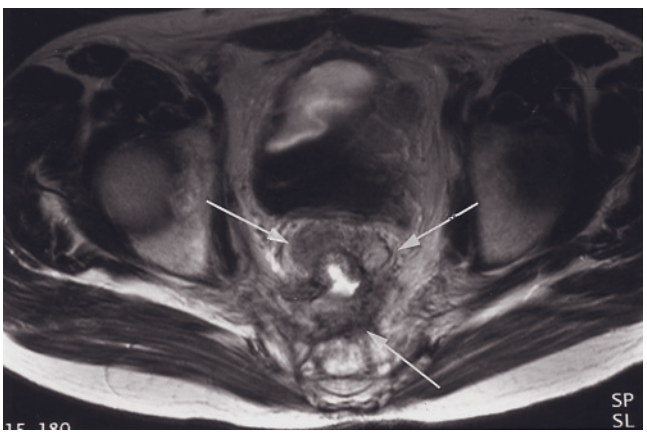

(*e*)

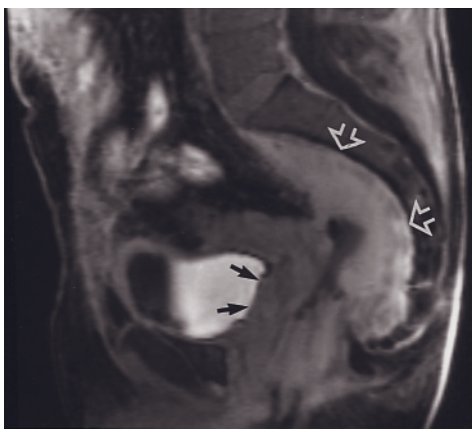

(*f*)

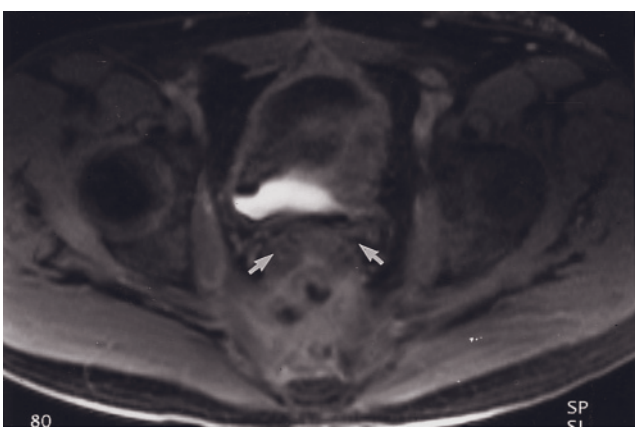

(*g*)

FIG. 6.117 (*Continued*) transverse postgadolinium 512-resolution T2-weighted echo-train spin-echo (*d*, *e*) and sagittal and transverse interstitial-phase gadolinium-enhanced fat-suppressed SGE (*f*, *g*) images in a second patient with recurrent rectal tumor. The 512-resolution T2-weighted images show a large heterogeneous tumor in the rectal bed (arrows, *d*, *e*). Low-signal-intensity urine reflects concentrated gadolinium dependently. The gadolinium-enhanced fat-suppressed SGE images (*f*, *g*) demonstrate extensive recurrent disease involving the rectal fossa, rectovesical space (arrows, *f*, *g*), presacral space (open arrows, *f*), and sciatic foramina.

year after radiation, granulation tissue may show persistent high signal intensity up to 3 years after therapy, particularly if intervening inflammation or infection has developed. Persistent increased signal intensity is most pronounced on gadolinium-enhanced T1-weighted fat-suppressed images. Finally, recurrent tumor may mimic radiation fibrosis when desmoplastic features predominate [6, 11]. Clinical history will often aid radiologic diagnosis: elevation of CEA levels, onset of presacral pain, or both, are harbingers of tumor recurrence irrespective of imaging features.

Evidence of distant metastases in the setting of recurrent disease is also well shown with MRI. Liver metastases are optimally shown on MRI, and peritoneal disease and lymphadenopathy are also revealed (see fig. 6.119).

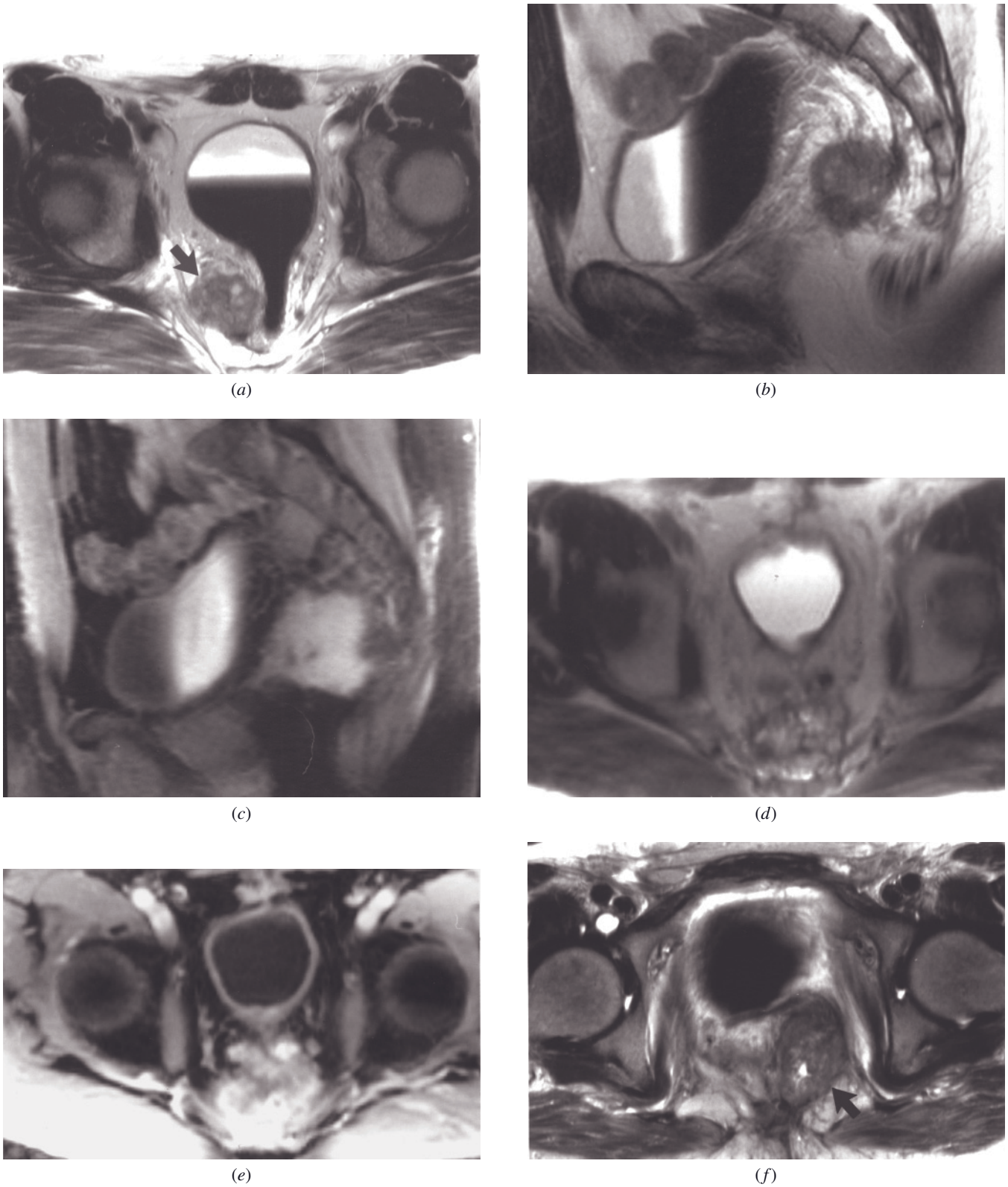

FIG. 6.118 Recurrent rectal cancer. Transverse (*a*) and sagittal (*b*) T2-weighted postcontrast SS-ETSE and sagittal interstitial-phase gadolinium-enhanced SGE (*c*) images in a patient after abdominoperineal resection (APR) for rectal cancer. There is a 4-cm mass in the right presacral space that is mildly heterogeneous on T2 (arrow, *a*) and heterogeneously enhancing consistent with tumor recurrence. Note the abnormal posterior position of the bladder after APR surgery. T2-weighted SS-ETSE (*d*) and interstitial-phase gadolinium-enhanced SGE (*e*) images in a second patient demonstrate an irregular presacral mass, which enhances heterogeneously after gadolinium administration. T2-weighted ETSE (*f*) image in a third patient with tumor recurrence also shows a mass (arrow, *f*) in the presacral space.

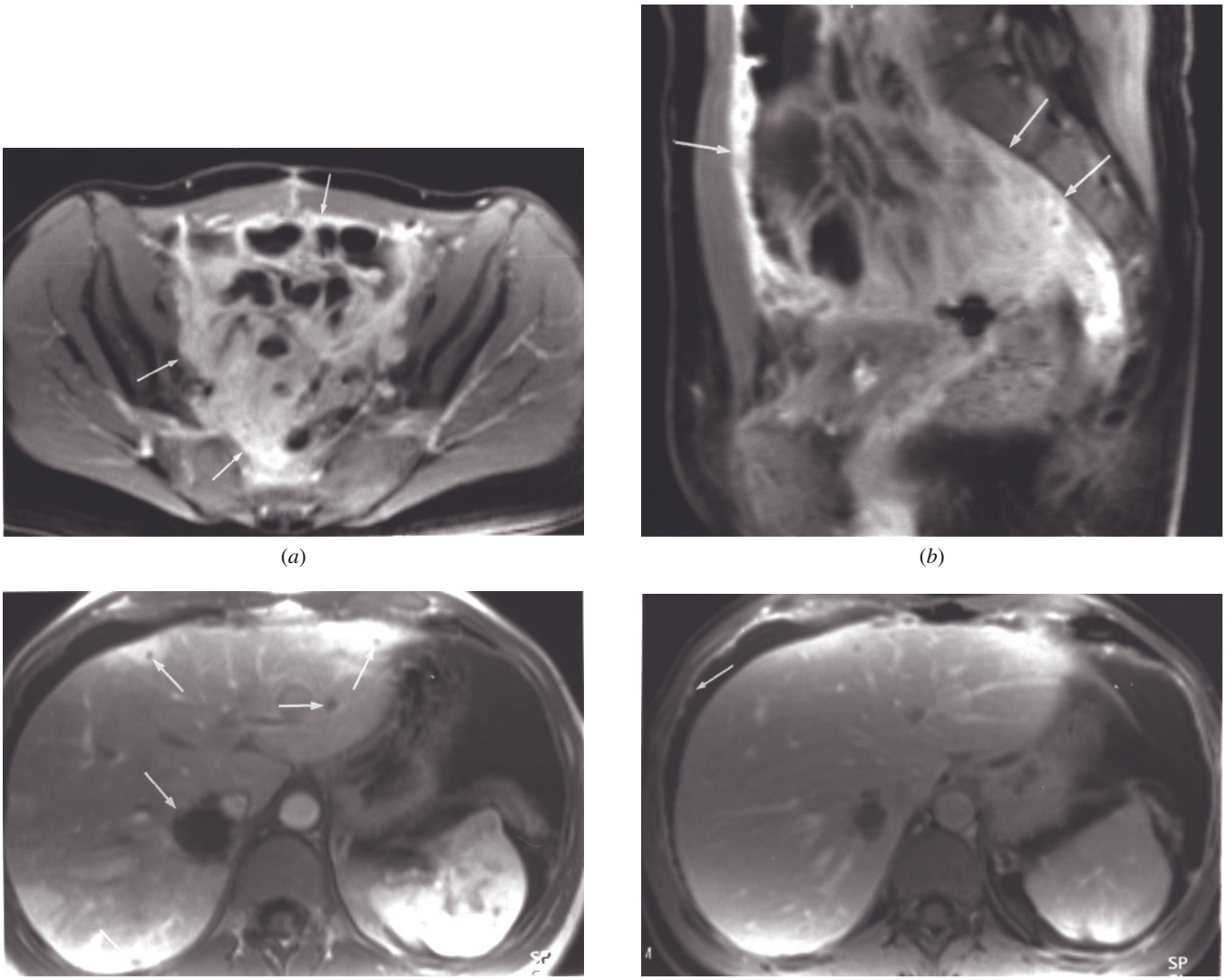

FIG. 6.119 Colon cancer with peritoneal disease and hepatic metastases. Transverse (*a*) and sagittal (*b*) T2-weighted SSETSE, transverse immediate postgadolinium SGE (*c*), and 90-s postgadolinium fat-suppressed SGE (*d*) images demonstrate a large recurrent rectal carcinoma in the presacral space, with extensive local infiltration in the pelvis (arrows, *a*, *b*). Immediate postgadolinium image demonstrates the presence of hepatic metastases (arrows, *c*). The peritoneal involvement in the upper abdomen is well shown on interstitial-phase postcontrast image (arrow, *d*).

Squamous Cell Carcinoma. Squamous cell cancer occurs in the anal canal, and its imaging characteristics resemble those of adenocarcinoma. Evaluation of local and distant spread is aided by gadolinium-enhanced fat-suppressed SGE or 3D-GE images (fig. 6.125).

GIST. Less than 10% of GISTs are seen in the colon and rectum (fig. 6.125). MR imaging findings are similar to the findings of gastric or small bowel GISTs.

Lymphoma. Primary non-Hodgkin lymphoma accounts for approximately 0.5% of all colorectal malignancies. Primary lymphoma is most often seen in patients with human immunodeficiency virus (HIV) infection or chronic ulcerative colitis [107, 108]. The cecum is the most common site of involvement, followed by the rectosigmoid colon. Secondary involvement of the colon by lymphoma occurs in the setting of widespread disease, especially in the elderly population. The MRI appearance includes isolated or multiple enhancing masses. Alternatively, diffuse nodularity with wall thickening may be seen after intravenous gadolinium administration (fig. 6.126) [48, 49]. Coexistent lymphadenopathy and splenic lesions may aid in the diagnosis.

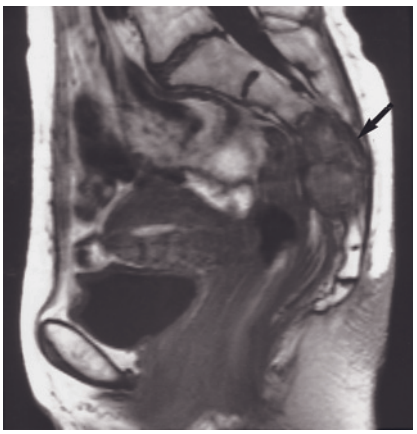

(*a*)

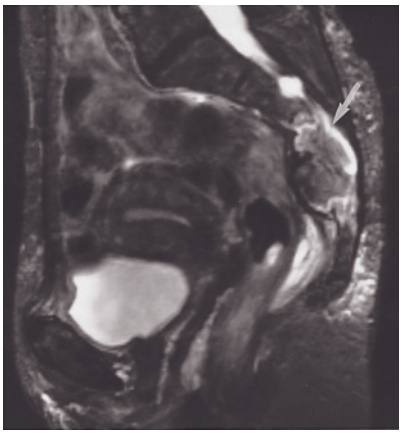

(*b*)

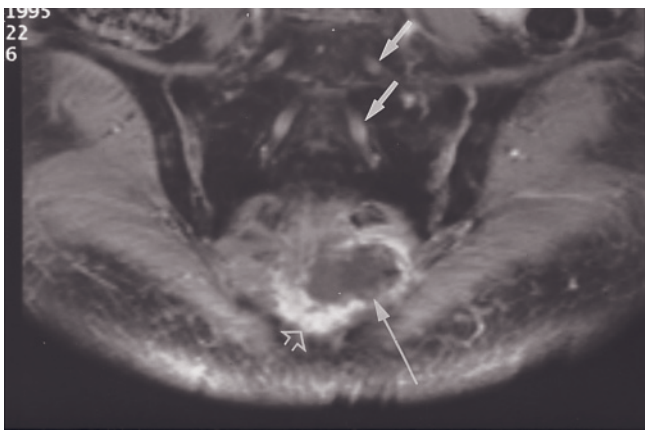

(*c*)

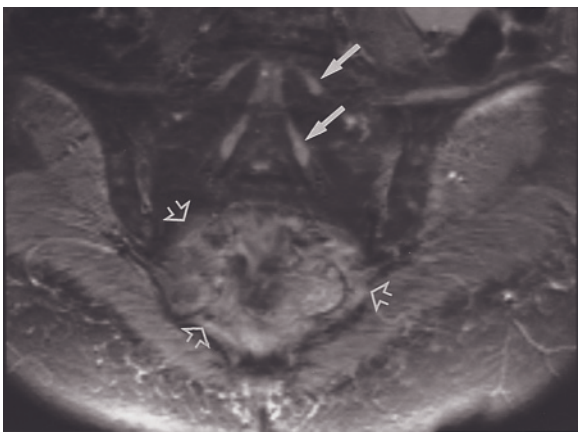

(*d*)

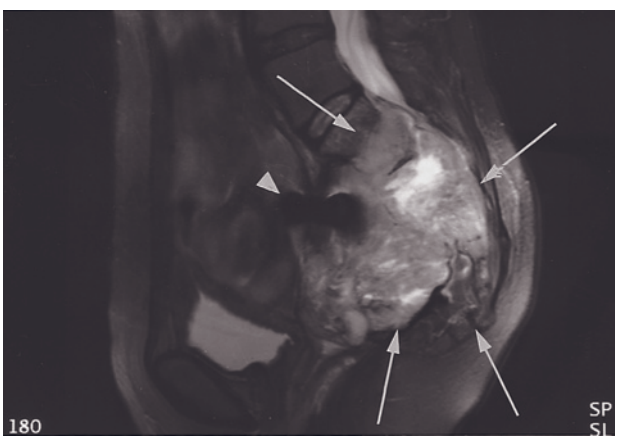

(*e*)

FIG. 6.120 Recurrent rectal adenocarcinoma invading sacrum. Sagittal T1-weighted SGE (*a*), sagittal 512-resolution T2-weighted fat-suppressed echo-train spin-echo (*b*), and oblique coronal postgadolinium fat-suppressed SGE (*c*, *d*) images. A large recurrent tumor mass invades the sacrum and is intermediate in signal intensity on the T1-weighted image (arrow, *a*) and heterogeneously high in signal intensity on the T2-weighted image (arrow, *b*). After contrast the tumor enhances heterogeneously (open arrows, *c*, *d*) and contains an area of central necrosis (long arrow, *c*). S1 and S2 sacral segments are not involved, and uninvolved S1 and S2 nerve roots are shown (short arrows, *c*, *d*). Sparing of the upper two sacral segments is a finding on which surgeons used to base surgical resection. At surgery, the upper margin of the tumor involved S3, sparing the S2 sacral segment. Sagittal 512-resolution T2-weighted echo-train spin-echo image (*e*) in a second patient demonstrates sacral invasion by a large recurrent rectal adenocarcinoma (arrows). This tumor involves the entire sacrum and precludes a surgical resection attempt. Surgical clip from prior resection produces a signal-void susceptibility artifact (arrowhead, *e*).

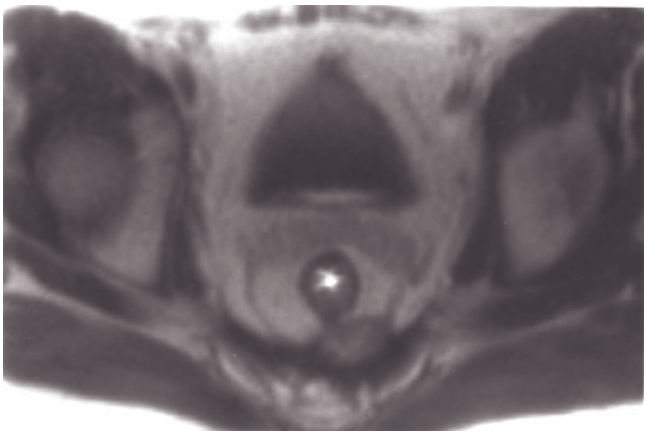

(*a*)

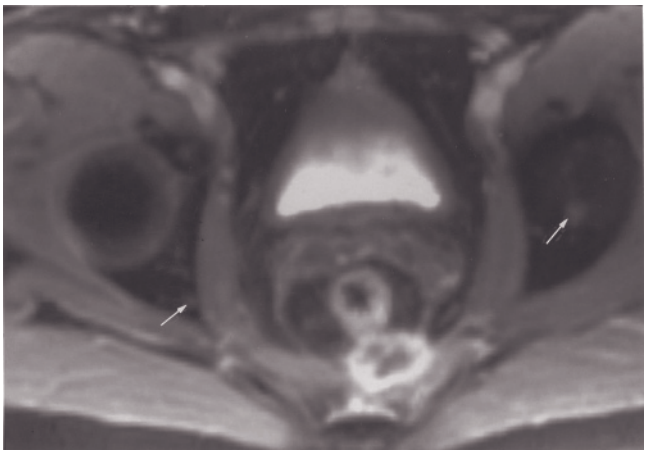

(*b*)

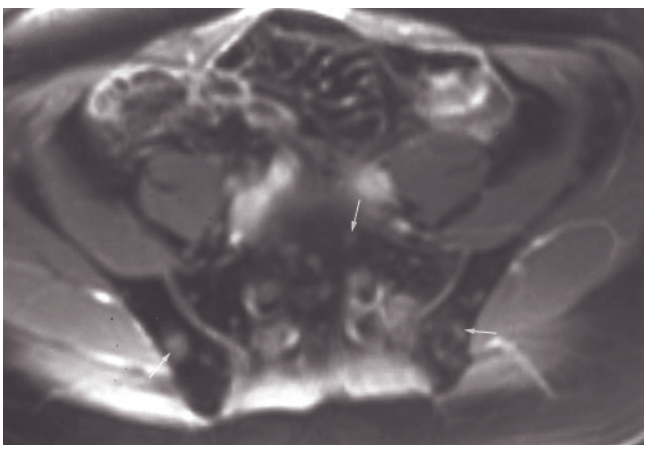

(*c*)

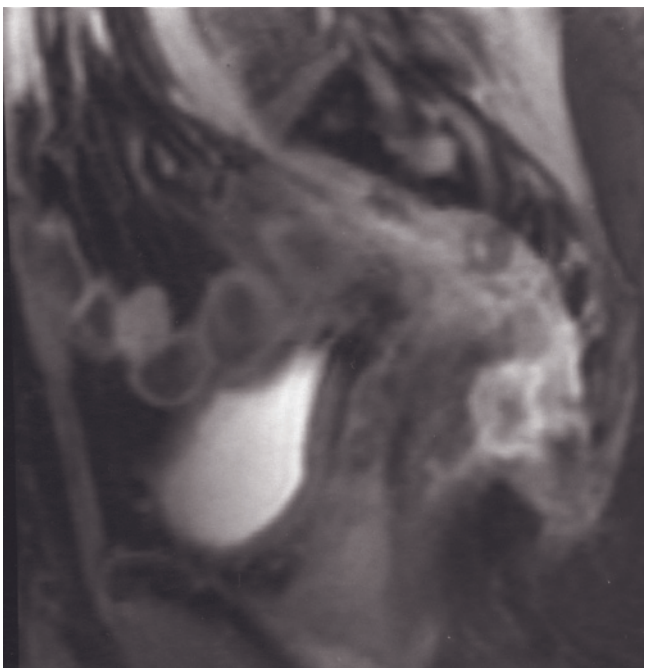

(*d*)

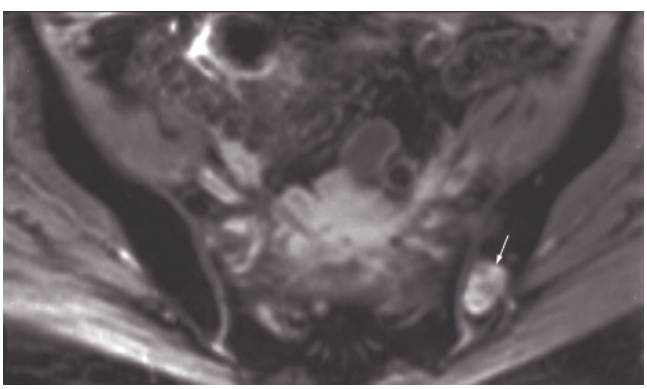

(*e*)

FIG. 6.121 Recurrent rectal carcinoma with bone metastases. T2-weighted SS-ETSE (*a*) and transverse (*b*, *c*) and sagittal (*d*) interstitial-phase gadolinium-enhanced SGE images. A soft tissue mass is present in the left presacral region. The tumor demonstrates peripheral enhancement. Additionally, there are multiple enhancing lesions within the bone marrow of the sacrum and pelvis (arrows, *b*–*d*), consistent with metastases. Transverse (*e*) and sagittal (*f*) interstitial-phase gadolinium-enhanced SGE images in a second patient show presacral abnormalities consistent with tumor recurrence associated with radiation changes. Note the presence of metastatic lesions (arrows, *e*, *f*) within the sacrum and left iliacus.

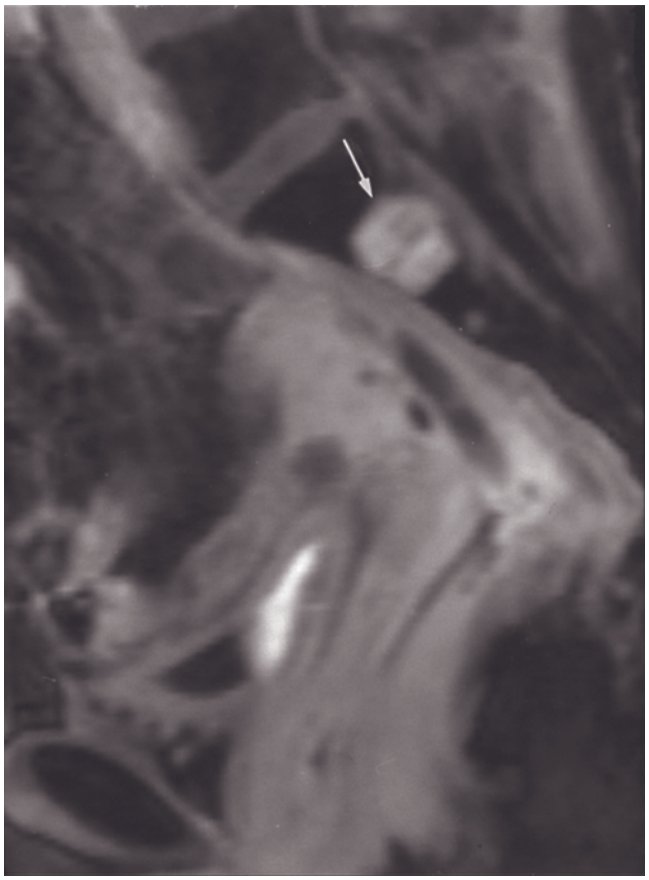

(*f*)

FIG. 6.121 (*Continued*)

(*a*)

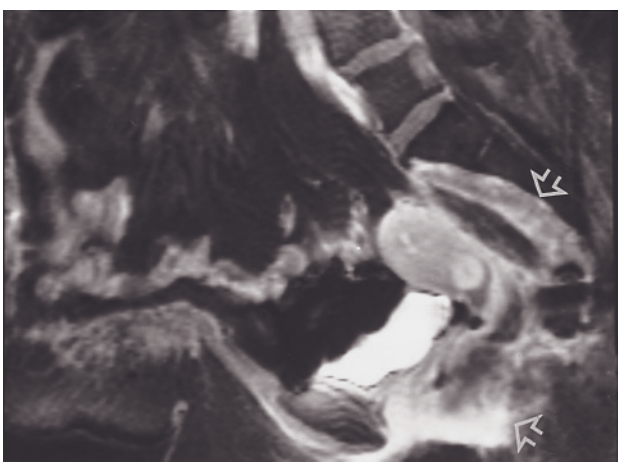

(*b*)

FIG. 6.122 Recurrent rectal adenocarcinoma and postradiation therapy changes. Sagittal postgadolinium 512-resolution T2-weighted fat-suppressed echo-train spin-echo (*a*) and sagittal interstitial-phase gadolinium-enhanced fat-suppressed SGE (*b*) images in a woman status post radiotherapy for rectal adenocarcinoma. Recurrent tumor is high in signal intensity on the T2-weighted fat-suppressed image and enhances after gadolinium administration (open arrows, *a*, *b*). Cervical stenosis (arrow, *a*) secondary to radiation therapy causes widening of the proximal endocervical and endometrial canal.

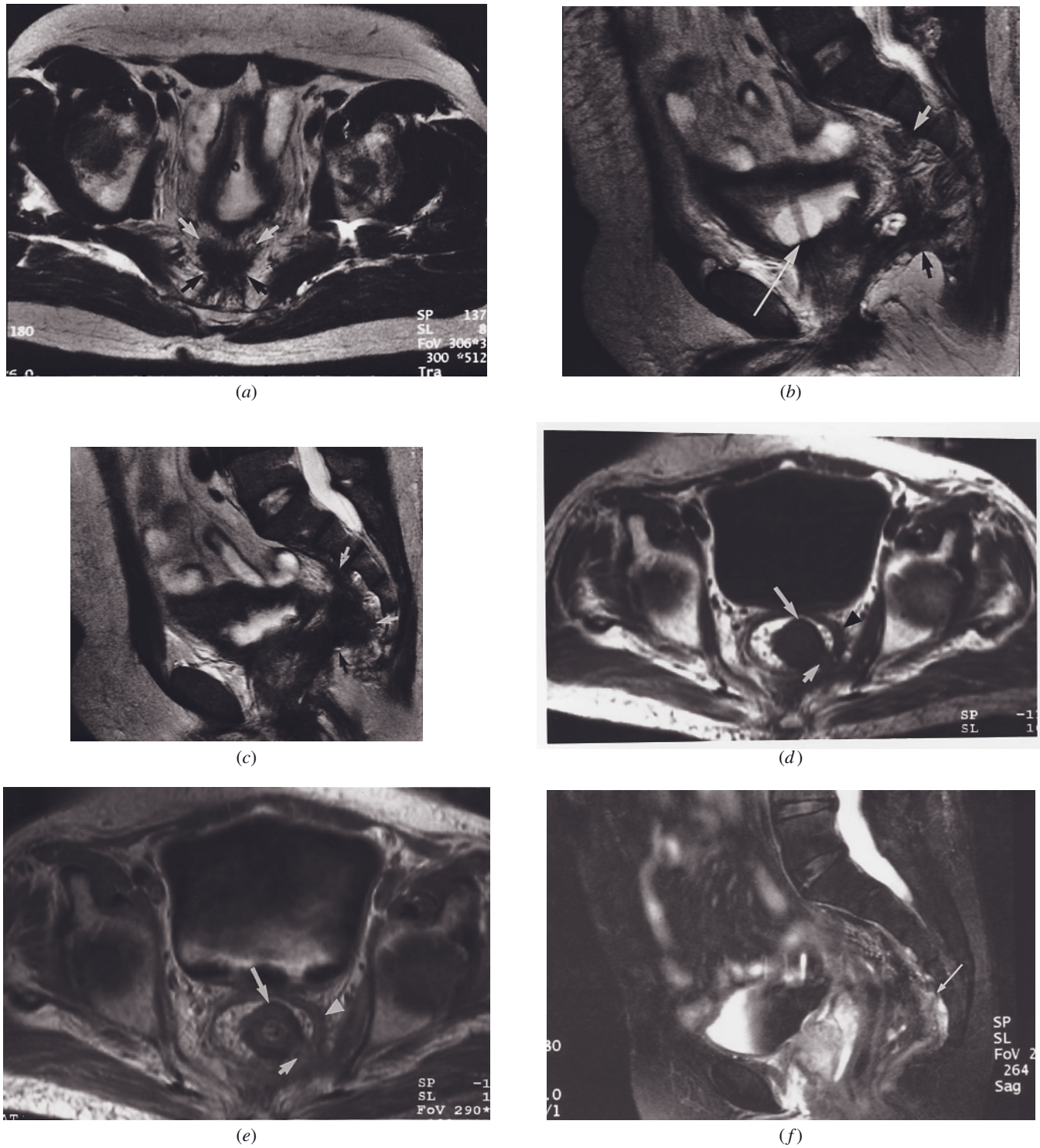

FIG. 6.123 Posttreatment fibrosis. Transverse (*a*) and sagittal (*b*, *c*) 512-resolution T2-weighted echo-train spin-echo images demonstrate low signal intensity in the surgical bed (arrows, *a*–*c*) consistent with fibrosis. Fibrosis has a plaquelike morphology, whereas recurrence tends to be more nodular. A Foley catheter is in place (long arrow, *b*). SGE (*d*) and 4-min postgadolinium SGE (*e*) images in a second patient show thickening of the rectal wall (long arrows, *d*, *e*) and perirectal tissue (arrowheads, *d*, *e*). Prominent perirectal strands are also present (short arrows, *d*, *e*). Negligible enhancement is consistent with perirectal fibrosis. The perirectal halo of fibrotic tissue is a common finding after radiation therapy for rectal cancer. Sagittal (*f*) and transverse (*g*) 512-resolution T2-weighted fat-suppressed echo-train spin-echo images and interstitial-phase gadolinium-enhanced fat-suppressed SGE image (*h*) in a third patient demonstrate platelike tissue in the presacral space that is low in signal intensity on T2-weighted images (arrows, *f*, *g*) and does not enhance substantially after gadolinium administration (arrow, *h*). Normal seminal vesicles have a cluster-of-grapes appearance (large arrow, *g*) on T2-weighted images, which permits distinction from recurrent tumor.

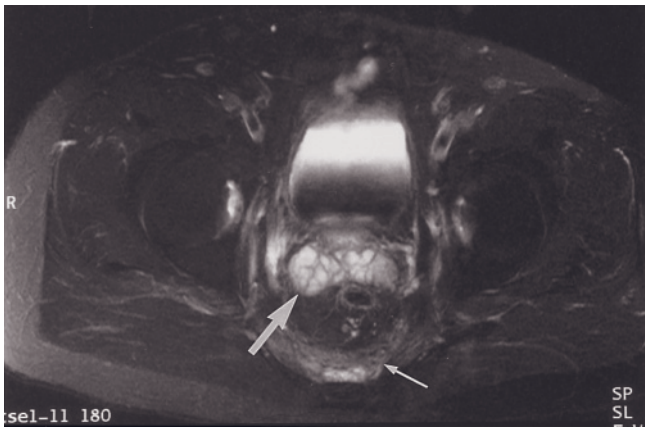

(*g*)

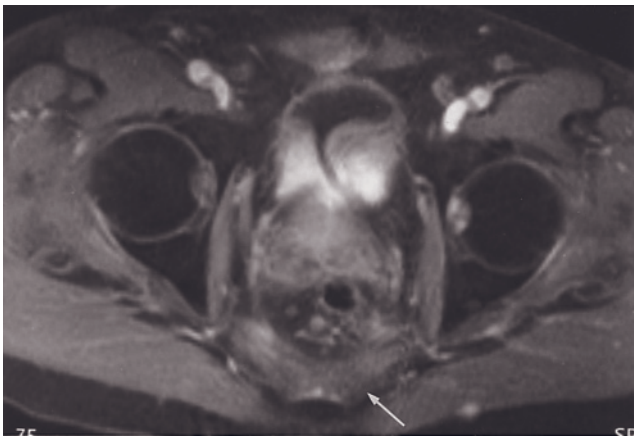

(*h*)

FIG. 6.123 (*Continued*)

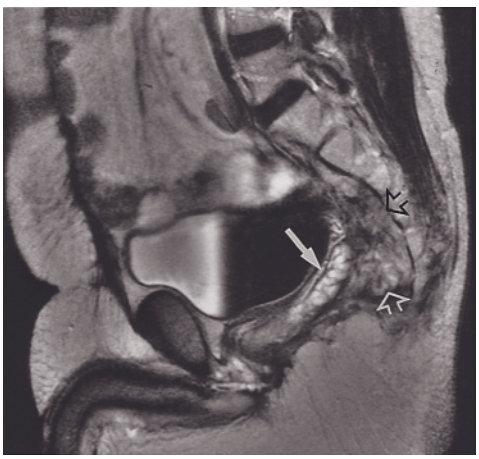

(*a*)

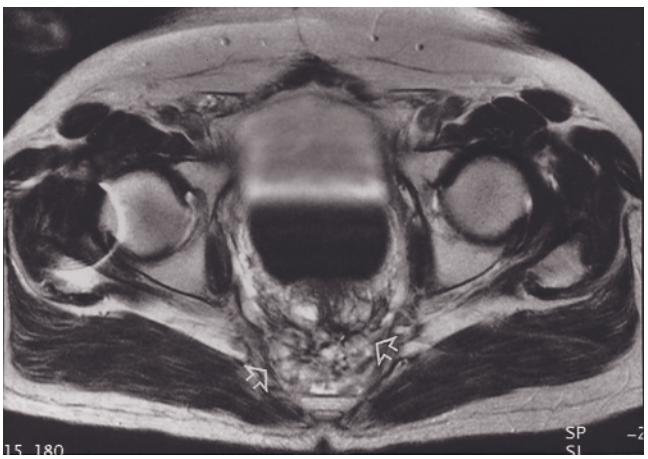

(*b*)

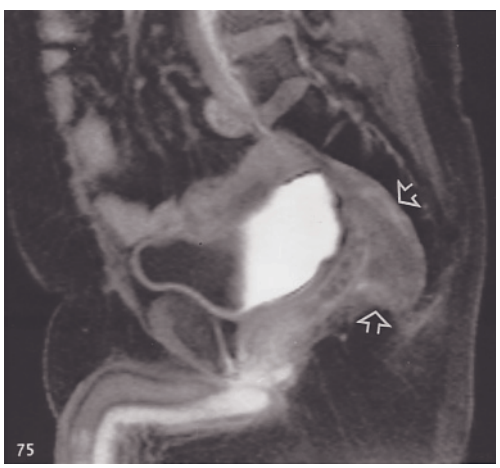

(*c*)

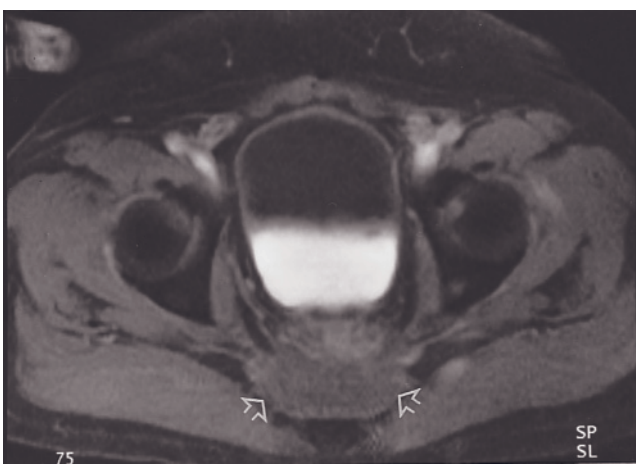

(*d*)

FIG. 6.124 Radiation fibrosis simulating recurrence. Sagittal (*a*) and transverse (*b*) postgadolinium 512-resolution T2-weighted echo-train spin-echo and sagittal (*c*) and transverse (*d*) interstitial-phase gadolinium-enhanced fat-suppressed SGE images in a patient 1.5 years after treatment for rectal cancer. Heterogeneous, bulky high-signal-intensity tissue occupies the rectal fossa (open arrows, *a*, *b*), on the T2-weighted echo-train spin-echo images, worrisome for recurrent disease. Other diagnostic possibilities include granulation tissue associated with radiation, inflammation, or infection. The heterogeneity is misleading because it reflects low-signal-intensity fibrotic tissue interspersed with high-signal-intensity fat. The high signal of fat is a consequence of the echo-train spin-echo technique. Minimal enhancement on the gadolinium-enhanced fat-suppressed SGE is consistent with fibrosis (open arrows, *c*, *d*). The seminal vesicles are distinguished from tissue in the rectal bed by the normal high signal intensity and grapelike morphology on the T2-weighted image (arrow, *a*).

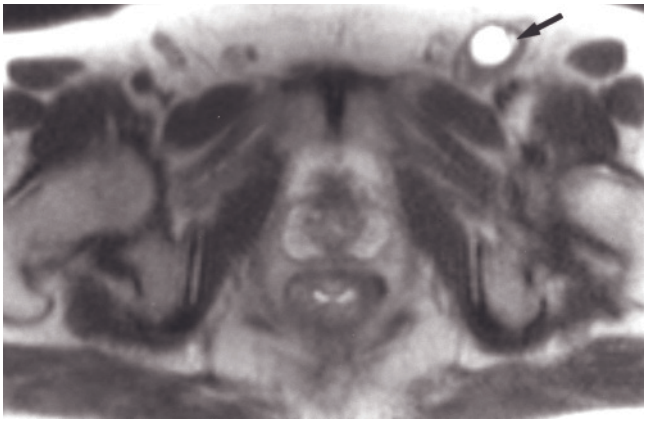

(*a*)

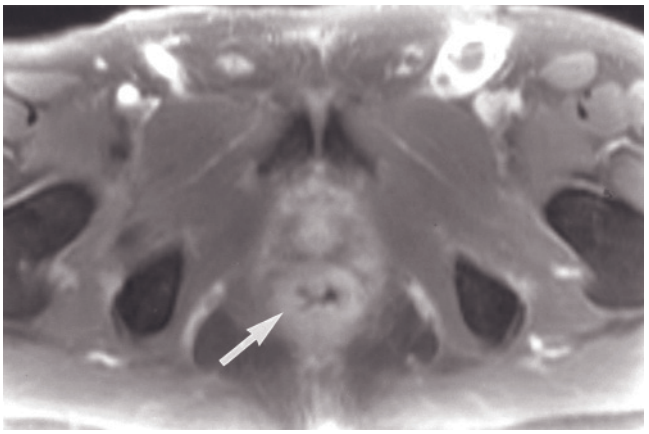

(*b*)

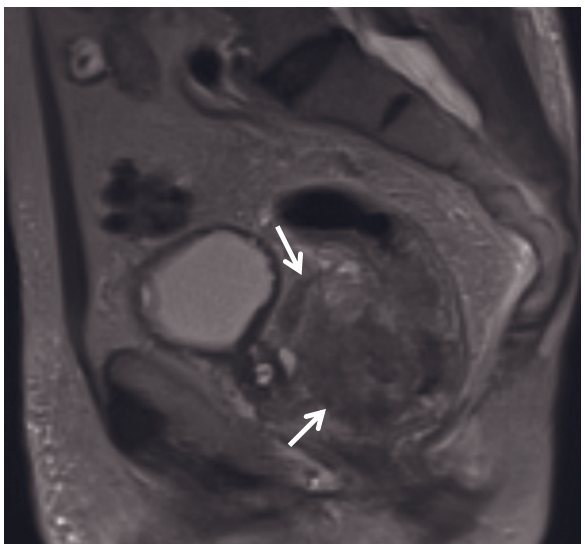

(*c*)

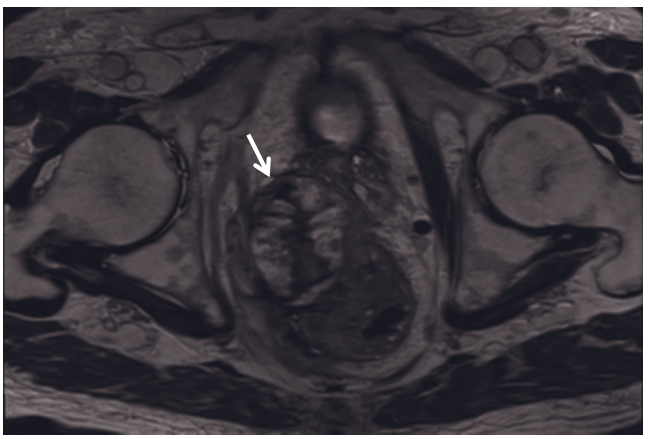

(*d*)

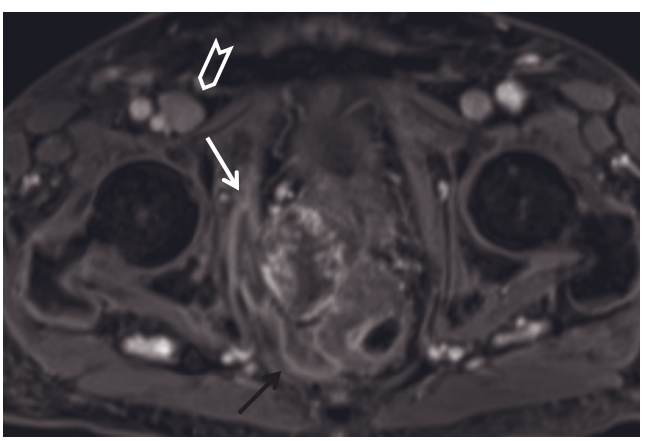

(*e*)

FIG. 6.125 Squamous cell carcinoma of anal canal. T2-weighted SS-ETSE (*a*) and interstitial-phase gadolinium-enhanced SGE (*b*) images. There is a diffuse wall thickening of the anal canal associated with stranding in the perianal fat, consistent with cancer (arrow, *b*). Note the necrotic left inguinal lymph node, which contains central high signal on T2 (arrow, *a*) and is centrally low signal with intense peripheral enhancement on postgadolinium fat-suppressed T1-weighted image. **Rectal GIST.** Sagittal T2-weighted single-shot echo-train spin-echo (*c*), transverse T2-weighted high-resolution fast spin-echo (*d*), and transverse T1-weighted postgadolinium fat-suppressed interstitial phase 3D-GE (*e*) images demonstrate a rectal GIST in another patient. The tumor is located eccentrically and arises from the anterolateral aspect of the rectum. The tumor shows heterogeneous high signal on T2-weighted image and contains central necrosis. It invades the right internal obturator muscle (white arrow, *e*) laterally and perirectal soft tissue (black arrow, *e*) posteriorly. The rectal wall is also thickened, suggesting the tumoral involvement posteriorly. Note that an enlarged right inguinal lymph node (open arrow, *e*) is present.

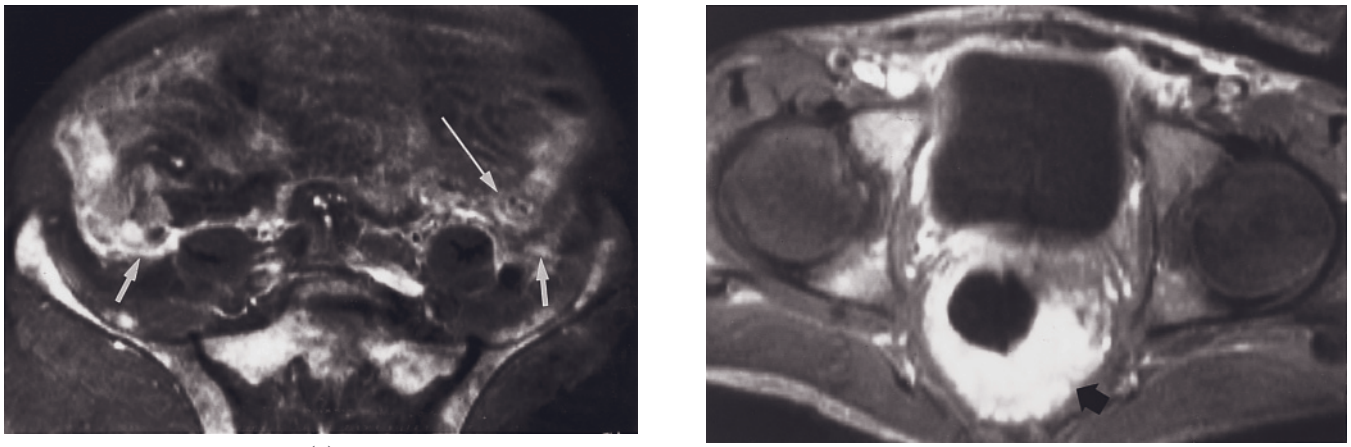

(*a*) (*b*)

FIG. 6.126 Colonic lymphoma. Gadolinium-enhanced T1-weighted fat-suppressed spin-echo images (*a*, *b*) in two patients with lymphoma. In the first patient with Burkitt lymphoma (*a*), there is enhancing soft tissue in both paracolic gutters (arrows), thickening of the descending colon (long arrow), and ill-defined stranding in the mesentery. Note the diffuse enhancing bone marrow involvement. The second patient (*b*) has HIV infection and a primary rectal lymphoma (arrow). HIV patients are at risk for developing primary large bowel lymphoma. (Reprinted with permission from Shoenut JP, Semelka RC, Silverman R, Yaffe CS, Mickflikier AB: The gastrointestinal tract. In Semelka RC, Shoenut JP (eds.), *MRI of the Abdomen with CT Correlation*. New York: Raven Press, 1993, pp. 119–143.)

Carcinoid Tumors. The rectum is a common location for carcinoid tumor (fig. 6.127). A retrospective report of 170 carcinoid tumors found that 94 (55%) were primary rectal lesions. Larger tumors were associated with metastatic disease and poor survival [109]. The imaging features of carcinoid tumors have been discussed elsewhere. As with other rectal diseases, direct sagittal-plane imaging is useful. Liver metastases are best studied with dynamic gadolinium-enhanced SGE or 3D-GE technique.

Melanoma. Primary colonic melanoma is rare and carries a poor prognosis [110]. Owing to the paramagnetic effects of melanin, the lesion can have characteristic high signal intensity on T1-weighted images (fig. 6.128). Tumors may demonstrate ring enhancement after gadolinium administration.

Metastases. The large intestine may be the site of metastasis from a number of tumors including lung and breast carcinoma. The most common mode of secondary colonic involvement is peritoneal seeding [111]. Ovarian carcinoma commonly extends along peritoneal surfaces to involve the large bowel. Prostate or cervical carcinoma may affect the rectum by direct extension. Colorectal involvement is well shown on gadolinium-enhanced fat-suppressed T1-weighted images [71] (fig. 6.129).

Inflammatory and Infectious Disorders

Ulcerative Colitis

Ulcerative colitis is a chronic ulcero-inflammatory disease limited to the large bowel. It has a predictable distribution: disease begins in the rectum and extends proximally in a continuous fashion to involve part or all of the colon. "Skip" lesions, such as occur in Crohn disease, are absent. The incidence of ulcerative colitis is greatest in the second through fourth decades of life. There is a Caucasian, Jewish, and female predominance, and a positive family history is reported in up to 25% of cases [112]. The cause is unknown, but, similar to Crohn disease, a multifactorial etiology has been postulated. Ulcerative colitis is variable in presentation, but symptoms tend to be indolent with intermittent diarrhea and rectal bleeding. Patients with ulcerative colitis are at risk for developing toxic megacolon, which may be the presenting feature. Chronic ulcerative colitis is associated with an increased risk of colon cancer.

In contrast to Crohn disease, which affects full-thickness bowel wall, ulcerative colitis is a mucosal disease. In active ulcerative colitis, there are multifocal full-thickness ulcerations of the mucosa. Adjacent to these sites, edematous, inflammatory tags of mucosa may bulge upward toward the lumen as "pseudopolyps." In longstanding ulcerative colitis, intestinal shortening with loss of haustral folds may occur. This abnormality is ascribed to muscular abnormalities and is most marked in the distal colon and rectum.

The MRI appearance of ulcerative colitis reflects the underlying physiology: 1) rectal involvement progressing in a retrograde fashion to involve a variable amount of colon and 2) submucosal sparing (fig. 6.130). The latter is especially well seen on gadolinium-enhanced fat-suppressed SGE or 3D-GE images showing marked mucosal enhancement and negligible submucosal

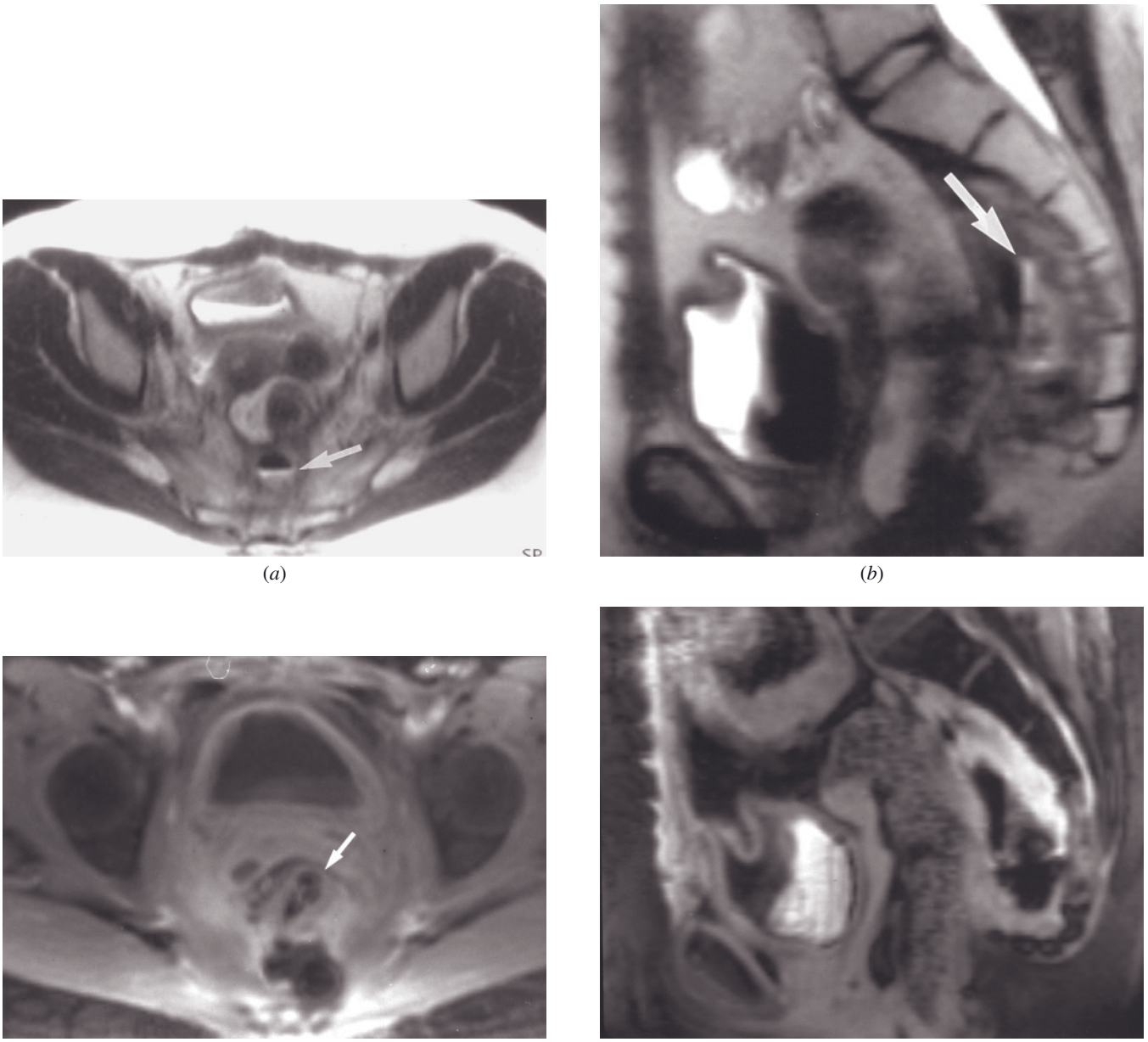

FIG. 6.127 Rectal carcinoid recurrence associated with abscess. Transverse (*a*) and sagittal (*b*) postgadolinium T2-weighted SS-ETSE and transverse (*c*) and sagittal (*d*) interstitial-phase gadolinium-enhanced T1-weighted SGE fat-suppressed images. There is thickening and enhancement of the rectal wall (arrow, *c*) associated with soft tissue stranding within the pelvis. An air-fluid level is present in the presacral space (arrow, *a*, *b*), consistent with a small abscess.

enhancement. Comparable to other inflammatory processes, the vasa rectae are prominent. The appearance of submucosal sparing is particularly pronounced in longstanding disease because of the combination of submucosal edema and lymphangiectasia [1–3, 6].

Toxic megacolon is characterized by total or segmental colonic dilatation with loss of its contractile ability. Toxic megacolon usually affects patients with universal colonic involvement ("pancolitis") and, unlike acute exacerbation and chronic indolent ulcerative colitis, is a transmural process. The entire bowel wall enhances after intravenous contrast administration (fig. 6.131). Patients are prostrate with debilitating bloody diarrhea, fever, leukocytosis, and abdominal pain.

Inflammatory bowel disease may be exacerbated during pregnancy. These patients are particularly well suited for MR examination because of the relative safety of the procedure (fig. 6.132).

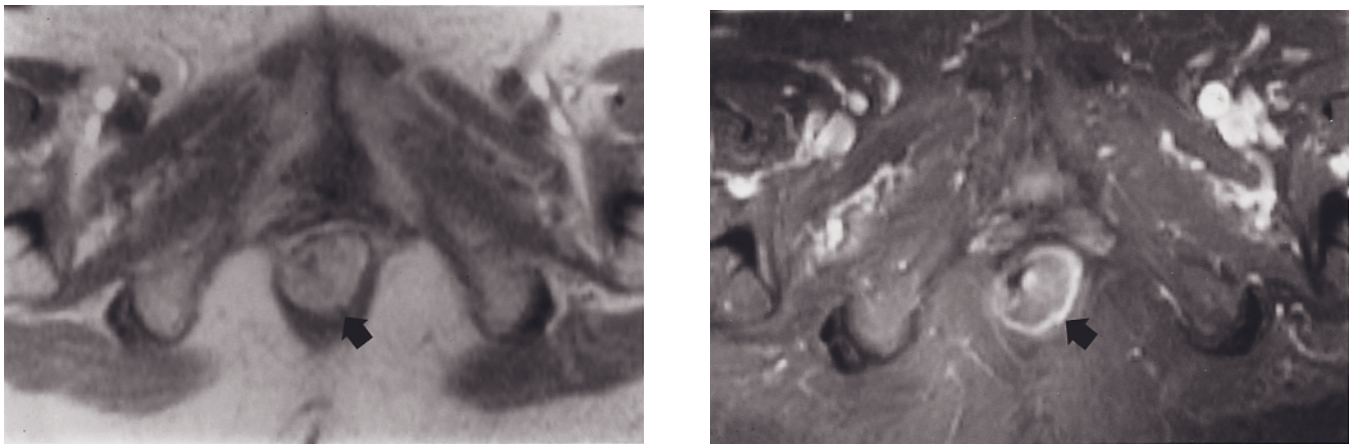

(*a*) (*b*)

FIG. 6.128 Anorectal malignant melanoma. SGE (*a*) and gadolinium-enhanced T1-weighted fat-suppressed spin-echo (*b*) images in a patient with melanoma. Melanoma may be bright on T1-weighted sequences (arrow, *a*) owing to the paramagnetic properties of melanin. Rim enhancement is apparent after contrast and allows accurate determination of mural extent (arrow, *b*) (Reprinted with permission from Shoenut JP, Semelka RC, Silverman R, Yaffe CS, Mickflikier AB: The gastrointestinal tract. In Semelka RC, Shoenut JP (eds.), *MRI of the Abdomen with CT Correlation.* New York: Raven Press, 1993, pp. 119–143.)

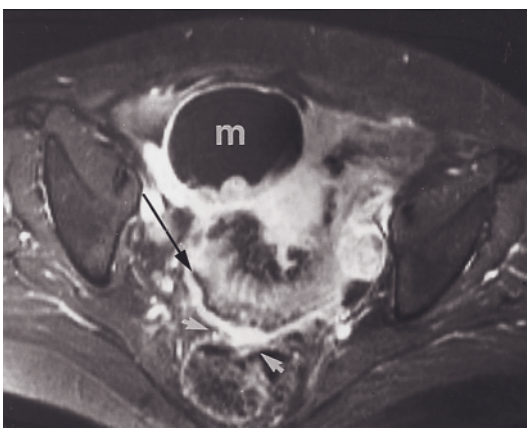

FIG. 6.129 Ovarian carcinoma metastatic to colon. Gadolinium-enhanced T1-weighted fat-suppressed spin-echo image in a patient with metastatic ovarian carcinoma. A complex cystic mass (m) encases the sigmoid colon (long arrow) and invades the rectum (short arrows). Tumor extension is clearly defined as enhancing tissue in a background of suppressed fat. (Reprinted with permission from Shoenut JP, Semelka RC, Silverman R, Yaffe CS, Mickflikier AB: The gastrointestinal tract. In Semelka RC, Shoenut JP (eds.), *MRI of the Abdomen with CT Correlation.* New York: Raven Press, 1993, p. 119–143.)

Crohn Colitis

Isolated colon involvement is noted in approximately one-fourth of cases. When Crohn colitis is limited to the anorectal region, differentiation from ulcerative colitis may be difficult [74]. In rare instances, Crohn colitis also may present with toxic megacolon (fig. 6.133). Crohn colitis is distinguished from ulcerative colitis by the following features: 1) persistence of colonic redundancy and haustrations in pancolonic disease and 2) transmural enhancement, which at times may show the most intense enhancement in the submucosal layer, a layer that is spared in ulcerative colitis (fig. 6.134). As with ulcerative colitis, submucosal edema may also be present (fig. 6.135).

Diverticulitis

Diverticula occur throughout the colon and tend to be most numerous in the sigmoid colon (fig. 6.136). Inflamed diverticula favor the left colon, whereas hemorrhagic diverticula tend to occur in the right colon. Several studies have shown cross-sectional imaging to be equivalent to, and in some cases superior to, barium enema in the evaluation of diverticulitis (fig. 6.137) [113, 114]. Bowel wall thickening and diverticular abscesses are well seen with a combination of gadolinium-enhanced fat-suppressed T1-weighted SGE or 3D-GE images and T2-weighted single-shot echo-train spin echo images (figs. 6.138 and 6.139) [115]. Similarly, sinus tracts and fistulas can be identified with this technique. On unenhanced T1-weighted SGE images, inflammatory changes appear as low-signal-intensity curvilinear strands located within the high signal intensity of the pericolonic fat. Sinus tracts, fistulas, and abscess walls enhance and are well shown in a background of suppressed fat on gadolinium-enhanced fat-suppressed SGE or 3D-GE images. It may be difficult to distinguish a perforated colon cancer from diverticulitis, and the two may coexist (fig. 6.140).

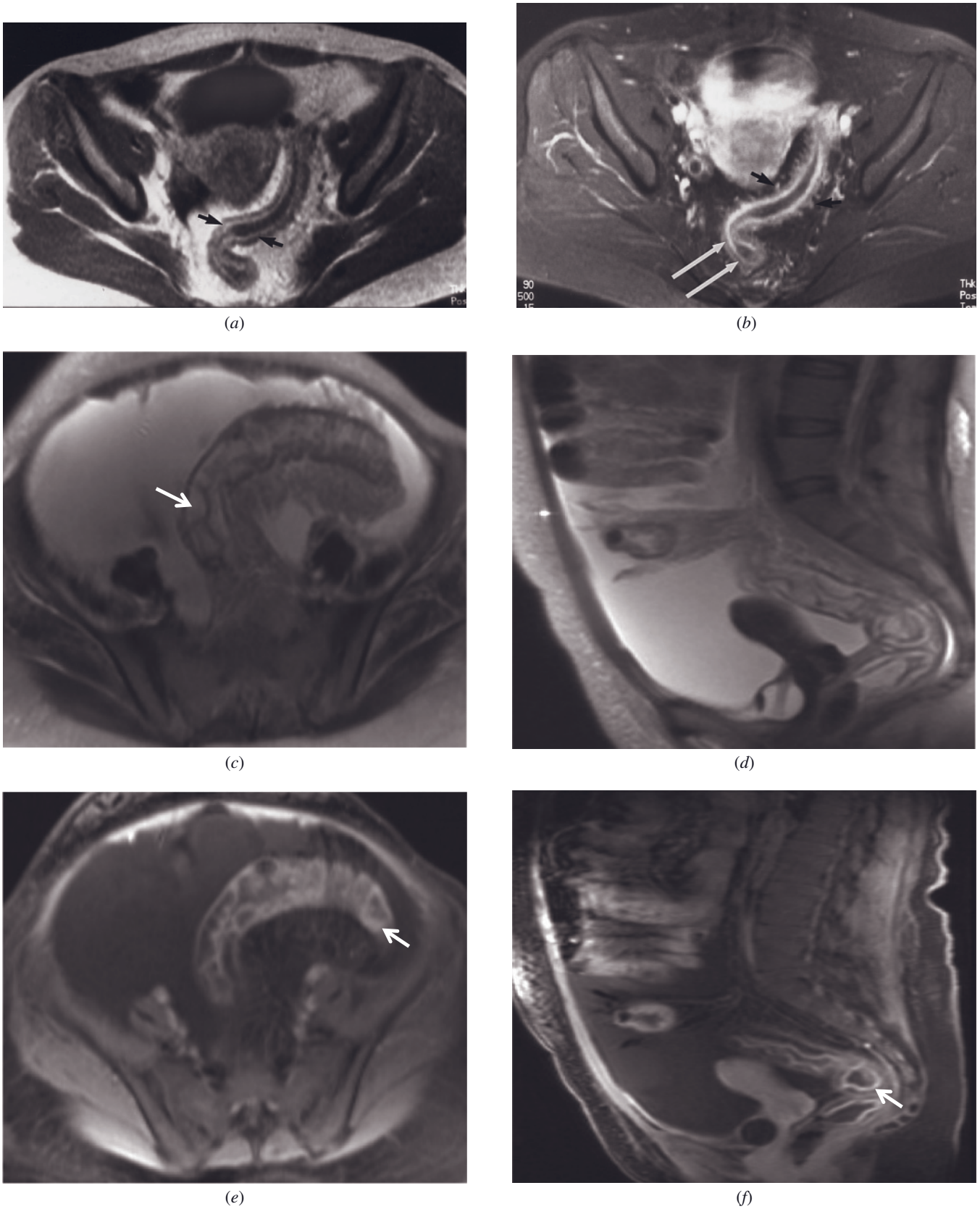

FIG. 6.130 Ulcerative colitis. Immediate postgadolinium SGE (*a*) and gadolinium-enhanced T1-weighted fat-suppressed spin-echo (*b*) images in a patient with ulcerative colitis. Increased enhancement on the immediate postgadolinium image (*a*) reflects increased capillary blood flow observed in severe disease. On the interstitial-phase image (*b*), there is marked mucosal enhancement with prominent vasa rectae (short arrows) and submucosal sparing (long arrows). Transverse (*c*) and sagittal (*d*) T2-weighted single-shot echo-train spin-echo, and transverse (*e*) and sagittal (*f*) postgadolinium fat-suppressed T1-weighted SGE images demonstrate ulcerative colitis and ascites in another patient. Submucosal edema (arrow, *c*) is detected in the sigmoid colon on T2-weighted images (*c*, *d*). Prominent mucosal enhancement (arrows, *e*, *f*) is detected on postgadolinium images (*e*, *f*). Note that no haustra is detected in the sigmoid colon.

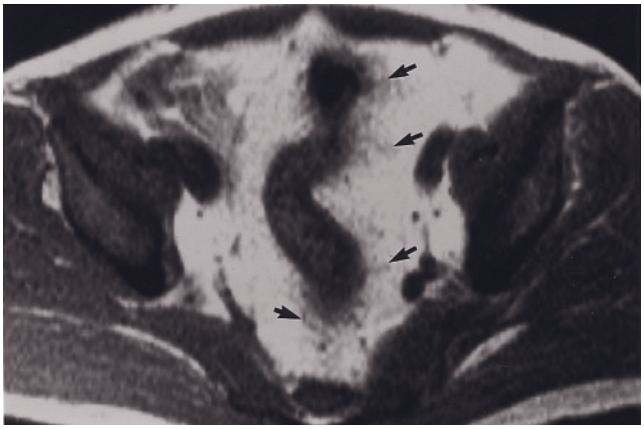

(*a*)

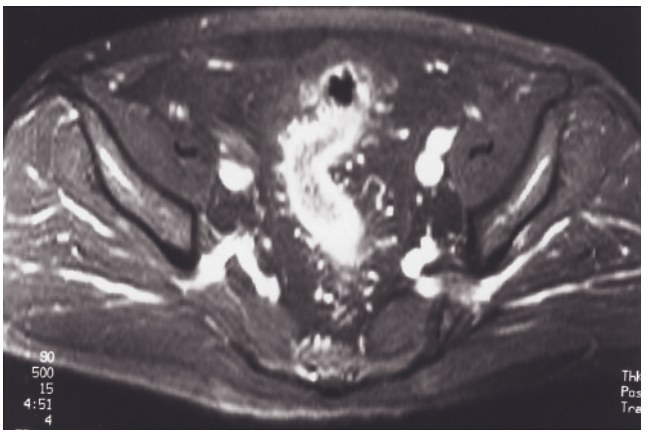

(*b*)

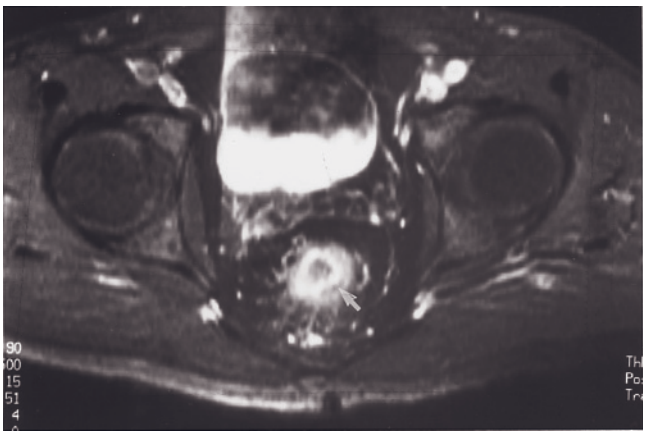

(*c*)

FIG. 6.131 Ulcerative colitis, toxic colon. SGE (*a*) and gadolinium-enhanced T1-weighted fat-suppressed spin-echo (*b*, *c*) images. The precontrast image shows irregular low-signal-intensity strands (arrows, *a*) related to a thick-walled sigmoid colon. After contrast there is marked mural enhancement. Enhancement of the pericolonic strands reflects prominent vasa rectae. Submucosal sparing is apparent (arrow, *c*), which is a feature of ulcerative colitis. Note the very intense enhancement of the colon wall, which appears to involve full thickness in the sigmoid colon. This is consistent with the patient's presentation of toxic colon.

(*a*)

(*b*)

FIG. 6.132 Ulcerative colitis with acute exacerbation in pregnancy. Coronal (*a*) and sagittal (*b*) T2-weighted SS-ETSE images in a pregnant patient with history of ulcerative colitis. Diffuse irregular circumferential wall thickening of the descending (arrow, *b*) and sigmoid colon is present. Note the fetus (arrow, *a*) in the gestational sac.

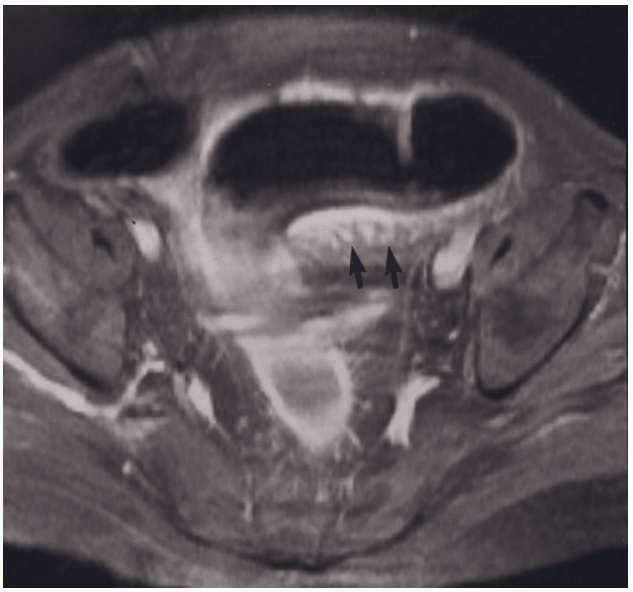

FIG. 6.133 Crohn disease presenting as toxic megacolon. Gadolinium-enhanced T1-weighted fat-suppressed spin-echo image in a patient with toxic megacolon. Dilatation and full-thickness involvement characterize toxic megacolon, a complication of inflammatory bowel disease (IBD). Note the prominent vasa rectae (arrows), a common finding in the setting of bowel inflammation. (Reprinted with permission from Shoenut JP, Semelka RC, Silverman R,Yaffe CS, Mickflikier AB: Magnetic resonance imaging in inflammatory bowel disease. *J Clin Gastroenterol* 17: 73–78, 1993.)

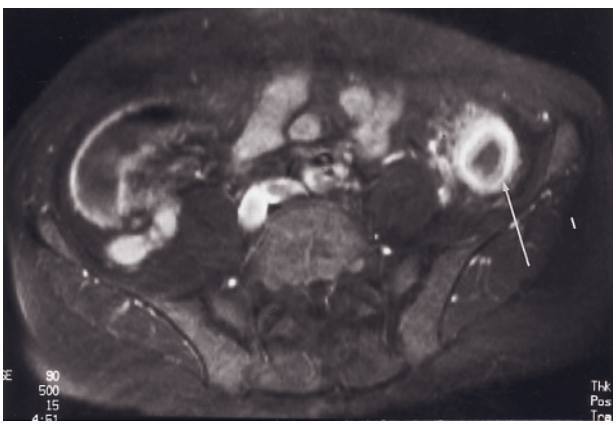

(*a*)

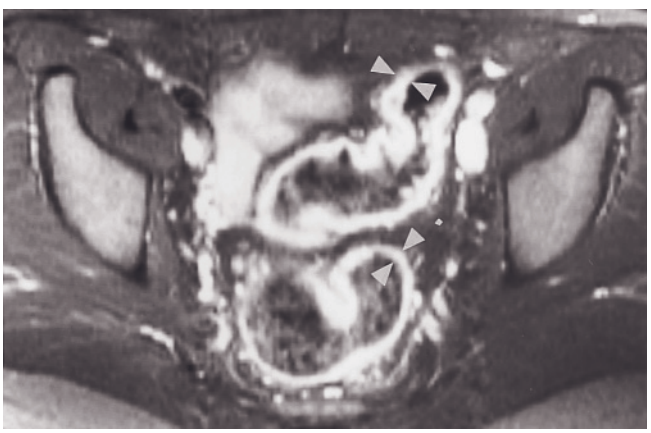

(*b*)

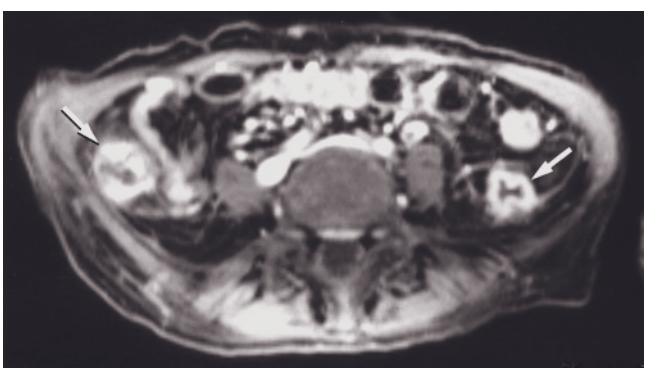

(*c*)

FIG. 6.134 Crohn colitis. Gadolinium-enhanced T1-weighted fat-suppressed spin-echo image (*a*) demonstrates transmural enhancement with greater enhancement of the submucosa (arrow) than the other bowel wall layers, which is diagnostic of Crohn disease and excludes the diagnosis of ulcerative colitis. In a second patient with Crohn colitis, gadolinium-enhanced T1-weighted fat-suppressed spin-echo image (*b*) shows full-thickness enhancement of the sigmoid colon (arrowheads). The distribution of colon involvement is compatible with ulcerative colitis. However, the colon has remained redundant with persistence of haustrations despite severe disease. These findings combined with transmural enhancement are consistent with Crohn colitis. Note the enhancing pericolonic inflammation in both patients. (Reprinted with permission from Shoenut JP, Semelka RC, Magro CM, Silverman R, Yaffe CS, Mickflikier AB: Comparison of magnetic resonance imaging and endoscopy in distinguishing the type and severity of inflammatory bowel diseases. *J Clin Gastroenterol* 19: 31–35, 1994) Interstitial-phase gadolinium-enhanced T1-weighted SGE (*c*) image in a third patient with Crohn colitis shows thickening and enhancement of the ascending and descending colon (arrows).

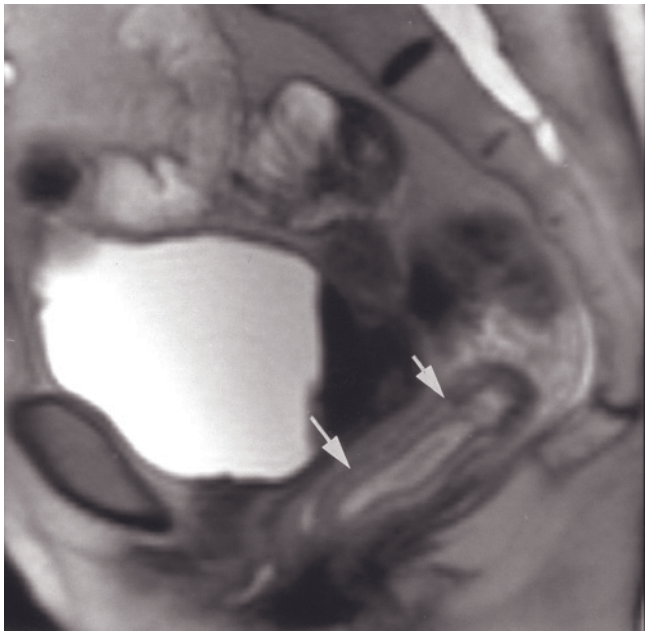

(*a*)

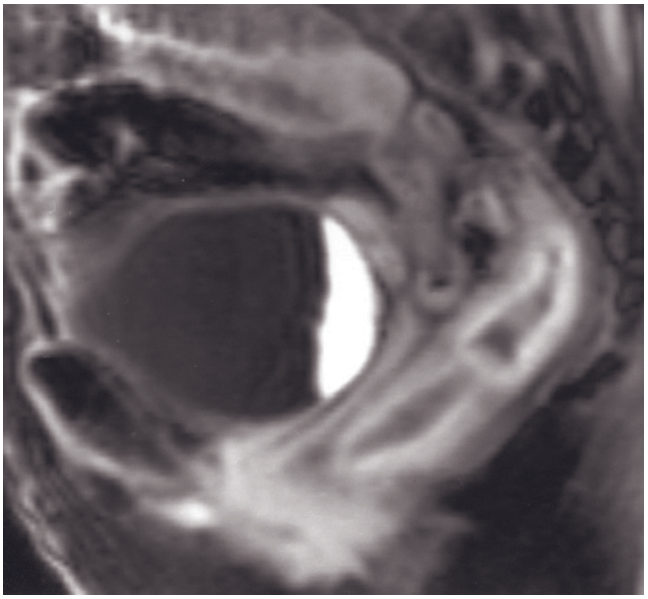

(*b*)

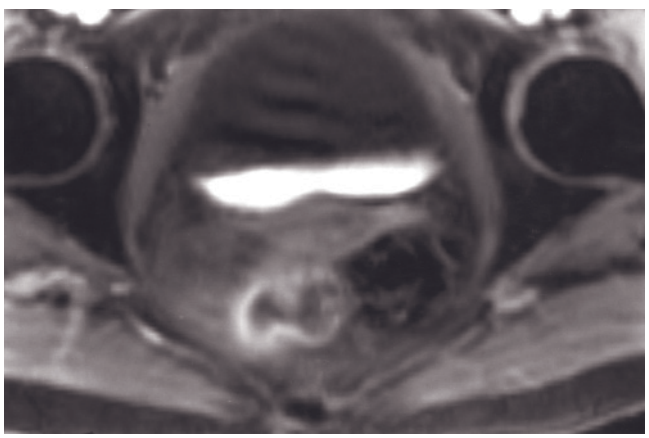

(*c*)

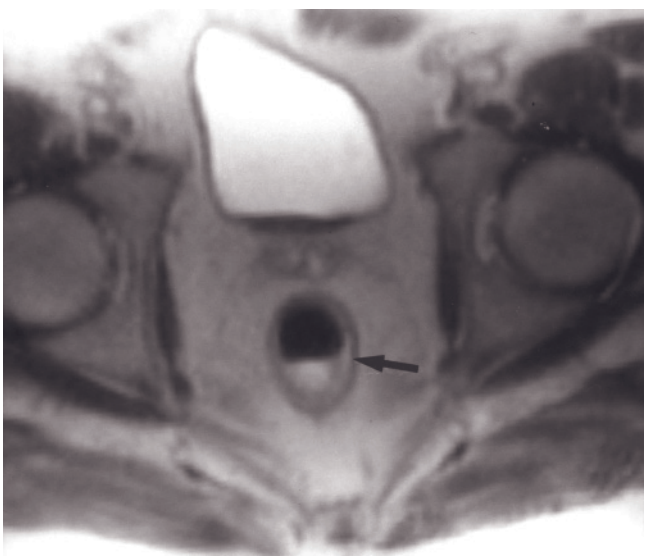

(*d*)

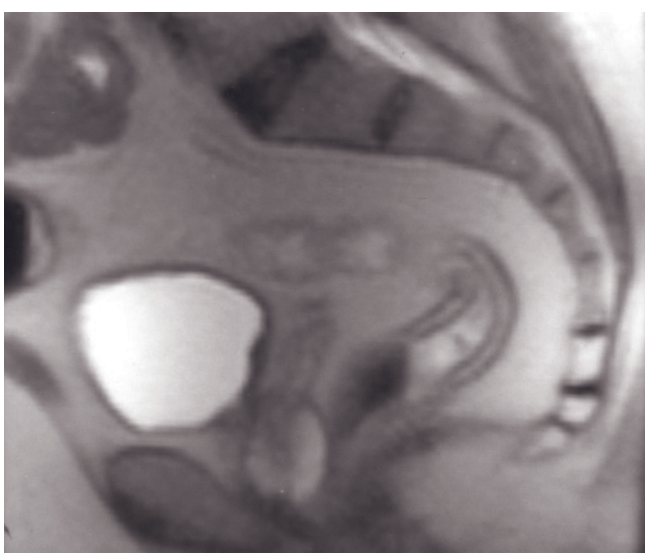

(*e*)

Fig. 6.135 Crohn proctitis. Sagittal T2-weighted postgadolinium SS-ETSE (*a*) and sagittal (*b*) and transverse (*c*) interstitial-phase gadolinium-enhanced SGE images. Prominent enhancement and thickening of the rectal wall are observed. Submucosal edema is appreciated as a high-signal stripe on the T2-weighted image (arrows, *a*). There is also diffuse perirectal soft tissue enhancement consistent with perirectal inflammatory changes. Transverse (*d*) and sagittal (*e*) T2-weighted SS-ETSE images in a second patient demonstrate thickening of the rectum associated with submucosal edema (arrow, *d*). Sagittal T2-weighted high-resolution

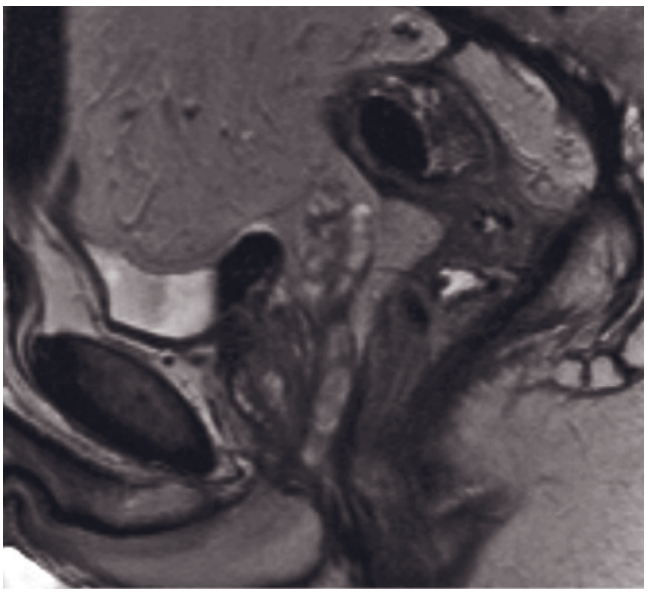

(*f*)

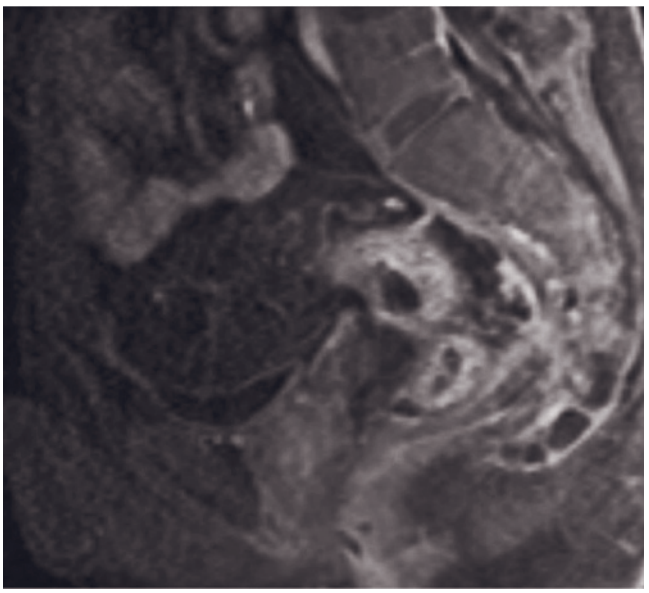

(*g*)

FIG. 6.135 (*Continued*) fast spin-echo (*f*) and sagittal T1-weighted postgadolinium fat-suppressed interstitial phase 3D-GE (*g*) images demonstrate rectal wall thickening and prominent rectal wall enhancement in another patient with Crohn proctitis. Note that perirectal tissue shows increased enhancement due to inflammation.

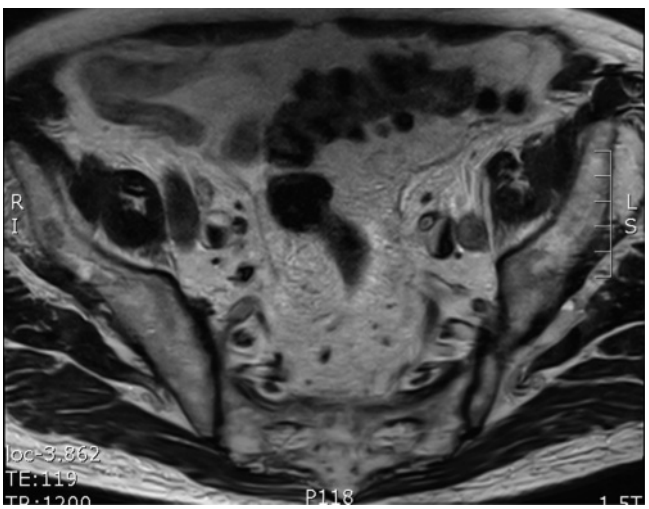

FIG. 6.136 Diverticulosis. Transverse T2-weighted 3D SPACE image demonstrates multiple signal void sacculations arising from the sigmoid colon consistent with diverticulosis. Diverticula are common and often incidental findings. Complications of diverticula include diverticulitis and frank abscess.

Appendicitis

Diagnostic imaging in cases of appendicitis is typically reserved for unusual presentations. Although CT imaging and ultrasound have surpassed barium enema in the workup of appendicitis [116, 117], MRI has several features that make it an attractive alternative. Specifically, MRI has high contrast resolution for inflammatory processes and does not involve ionizing radiation. The latter feature is not inconsequential, because appendicitis is most common in children and young adults of reproductive age. MRI is especially useful to accurately show abdominal and pelvic disease in pregnant patients, including appendicitis and appendiceal abscess [118]. On gadolinium-enhanced T1-weighted fat-suppressed images, the inflamed appendix and surrounding tissues show marked enhancement (fig. 6.141). Inflammatory stranding in the surrounding fat is well visualized on unenhanced T1-weighted SGE images. In cases complicated by a periappendiceal abscess, the abscess wall shows enhancement with intravenous contrast administration, whereas the cavity remains signal void (fig. 6.142). Acute appendicitis can be diagnosed based on the findings of noncontrast sequences, particularly T2-weighted sequences in pregnant patients (see fig. 6.141).

Abscess

Abscess formation may be a complication of gastrointestinal or biliary surgery, diverticulitis, appendicitis, or inflammatory bowel disease (IBD). CT imaging and ultrasound are the mainstays of diagnosis and have the added advantage of ease of percutaneous drainage capabilities. For MRI to compete effectively with these modalities, automatic table motion, MRI-compatible needle and drainage equipment, and ultrafast imaging techniques must be in common usage.

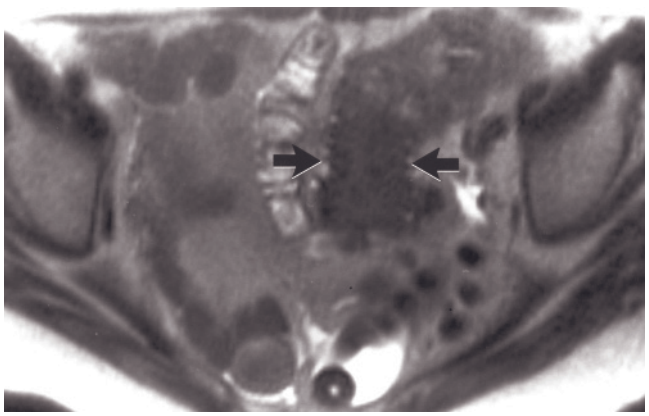

(*a*)

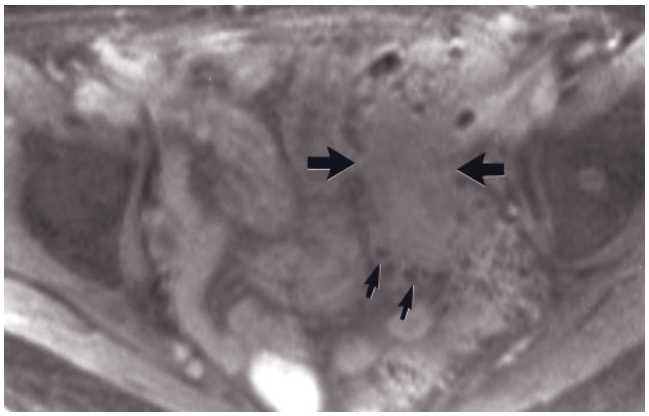

(*b*)

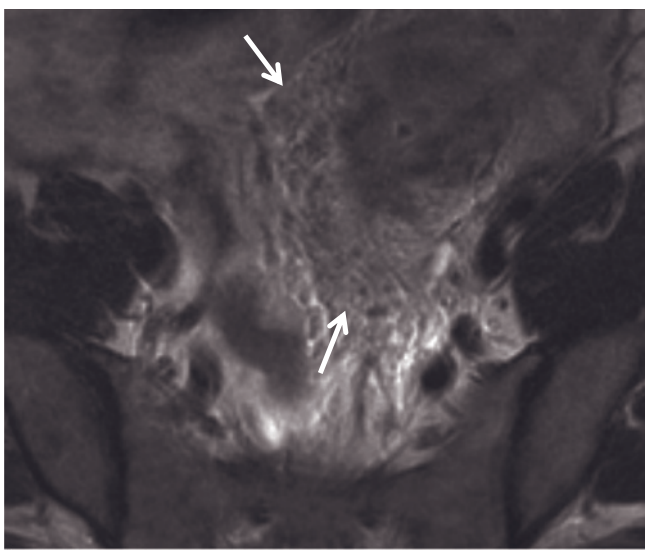

(*c*)

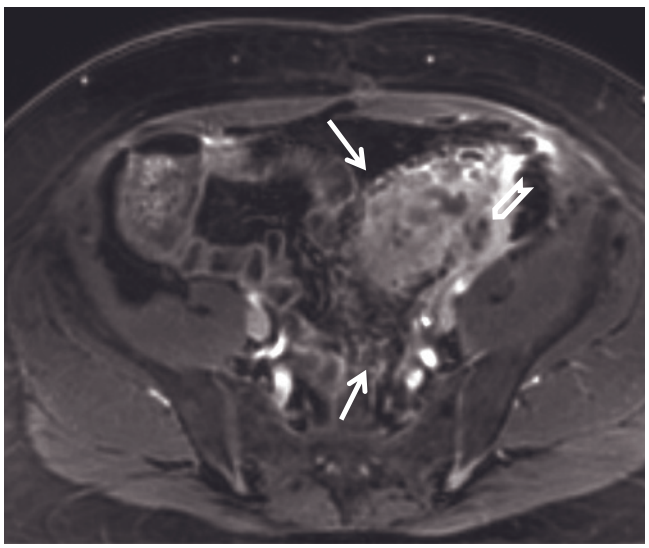

(*d*)

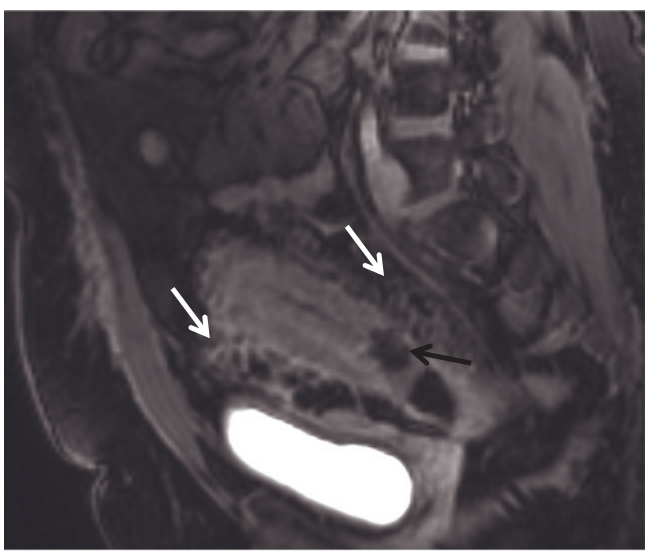

(*e*)

Fig. 6.137 Diverticulitis. T2-weighted SS-ETSE (*a*) and 90-s postgadolinium fat-suppressed SGE (*b*) images. Marked concentric wall thickening of an 8-cm segment of sigmoid colon is noted on the T2-weighted SS-ETSE image (arrows, *a*). The thickness of the colon wall measures up to 1 cm. Moderate contrast enhancement and marked wall thickening in the sigmoid colon (large arrows, *b*) are shown, with small diverticula (small arrows, *b*) on the postcontrast fat-suppressed SGE image. (Reprinted with permission from Chung JJ, Semelka RC, Martin DR, Marcos HB: Colon diseases: MR evaluation using combined T2-weighted single-shot echo train spin-echo and gadolinium-enhanced spoiled gradient-echo sequences. *J Magn Reson Imaging* 12: 297–305, 2000.) Transverse T2-weighted high-resolution fast spin-echo (*c*) and transverse (*d*) and sagittal (*e*) T1-weighted postgadolinium interstitial-phase fat-suppressed 3D-GE images demonstrate diverticulitis in another patient. The wall of the sigmoid colon is thickened and shows intense enhancement. Multiple diverticula (open arrow, *d*) are detected in the sigmoid colon. Associated inflammatory stranding (white arrows, *c–e*) in the mesocolon is detected. Note that small abscesses (black arrow, *e*) are also present.

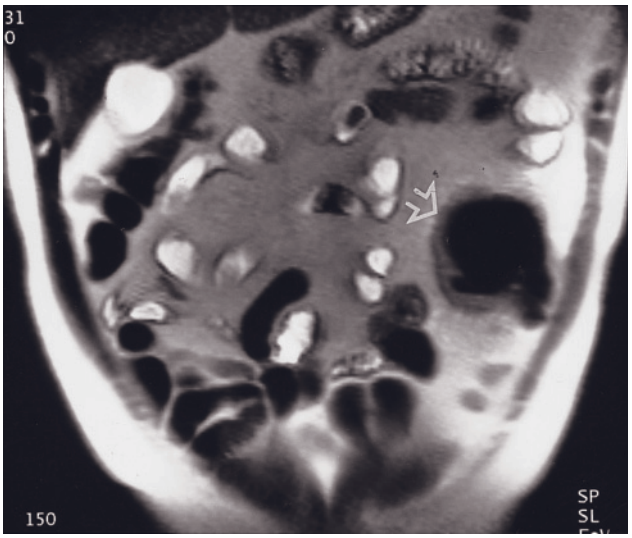

(*a*)

(*b*)

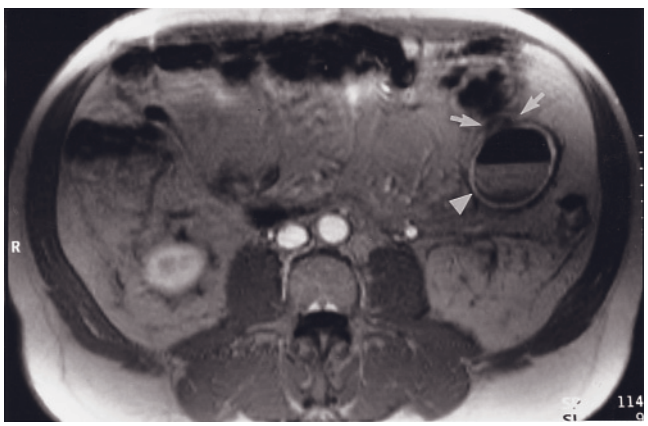

(*c*)

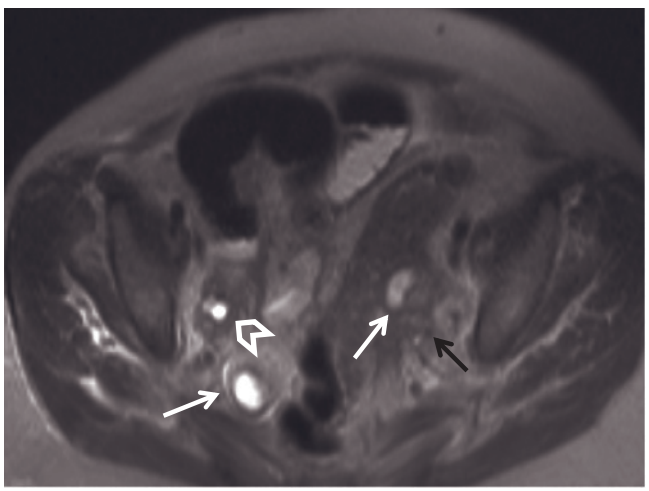

(*d*)

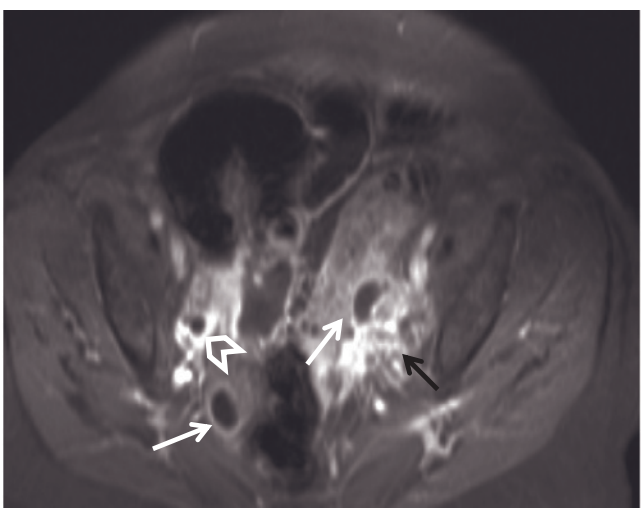

(*e*)

FIG. 6.138 Diverticular abscess. Coronal (*a*) and sagittal (*b*) SS-ETSE and immediate postgadolinium SGE (*c*) images. An air and fluid-containing collection (open arrow, *a*, *b*) originates from the descending colon (solid arrows, *b*, *c*), a finding consistent with a diverticular abscess. On the immediate postgadolinium image, the inner wall of the abscess (arrowhead, *c*) enhances. An air-fluid level is apparent on the transverse image (*c*). T2-weighted single-shot echo-train spin-echo (*d*) and T1-weighted postgadolinium fat-suppressed interstitial-phase 3D-GE (*e*) images demonstrate abscesses (white arrows, *d*, *e*) in another patient with diverticulitis. The abscesses show peripheral enhancement. The wall of the sigmoid colon is thickened, and there is adjacent inflammation, which is seen as enhancing inflammatory tissue (black arrows, *d*, *e*) along the sigmoid colon. Note that there is another focus of inflammatory tissue (open arrows; *d*, *e*) on the right side of the pelvis. T2-weighted single-shot echo-train spin-echo (*f*) and

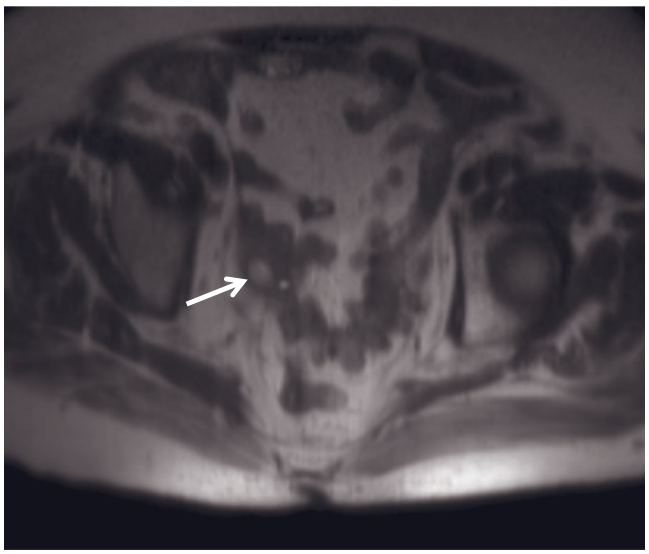

(*f*)

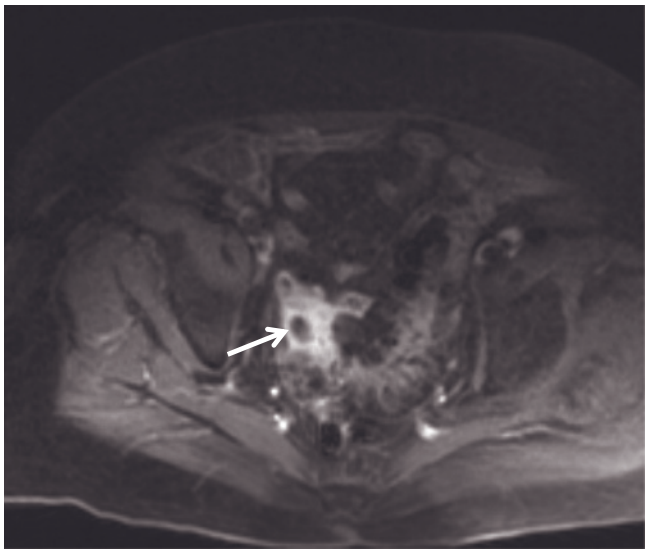

(*g*)

FIG. 6.138 (*Continued*) T1-weighted postgadolinium fat-suppressed interstitial phase 3D-GE (*g*) images demonstrate an abscess (white arrows, *f*, *g*) in another patient with diverticulitis. The abscess shows intense peripheral enhancement. Multiple sigmoid diverticula and associated mesenteric inflammation are present.

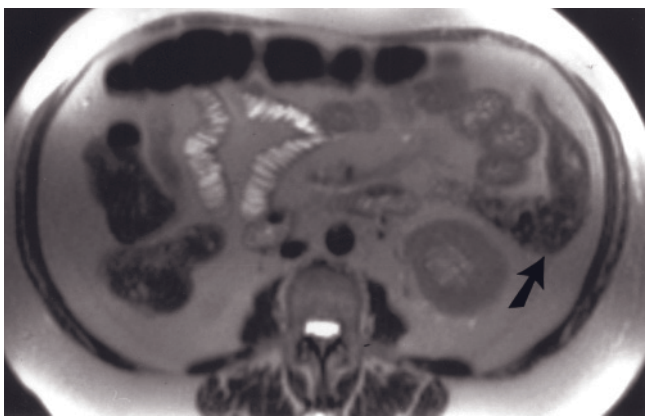

(*a*)

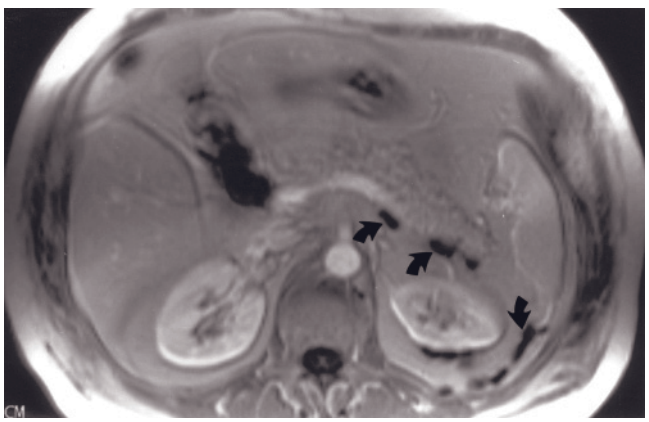

(*b*)

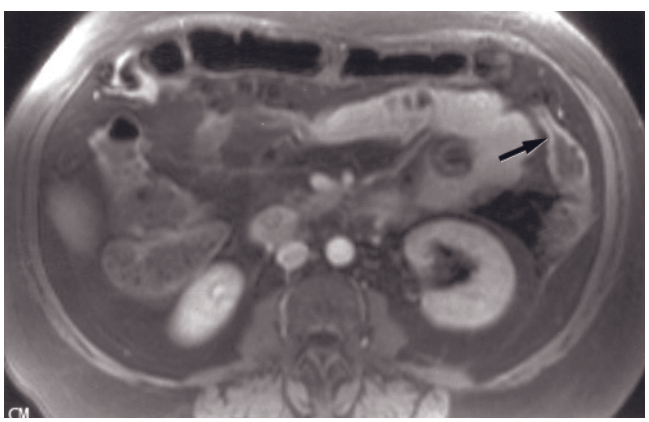

(*c*)

FIG. 6.139 Diverticulitis with pericolonic abscess. T2-weighted SS-ETSE (*a*), immediate postgadolinium SGE (*b*), and 90-s postgadolinium fat-suppressed SGE (*c*) images. An irregularly shaped gas collection is noted in the left anterior pararenal space, posterior to the descending colon, on the T2-weighted image (arrow, *a*). This appears to be in direct communication with a thickened segment of descending colon with an irregular focus of mural discontinuity. Multiple small gas pockets in the left retroperitoneal space are also apparent on the immediate postcontrast SGE image (curved arrows, *b*). The involved descending colon shows marked contrast enhancement (arrow, *c*) with an adjacent gas-containing abscess in the pericolonic fat on the 90-s postgadolinium fat-suppressed SGE image. (Reprinted with permission from Chung JJ, Semelka RC, Martin DR, Marcos HB: Colon diseases: MR evaluation using combined T2-weighted single-shot echo train spin-echo and gadolinium-enhanced spoiled gradient-echo sequences. *J Magn Reson Imaging* 12: 297–305, 2000.)

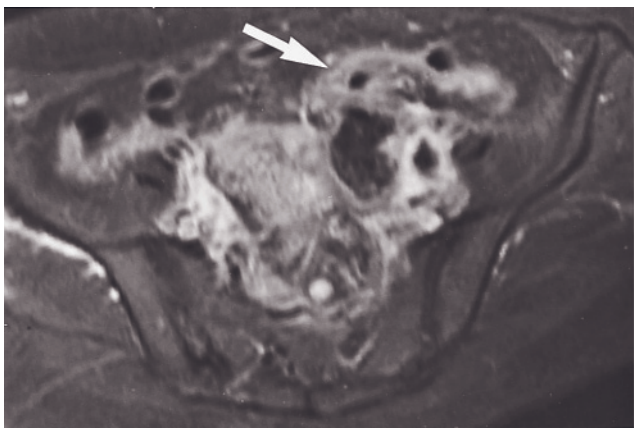

(*a*)

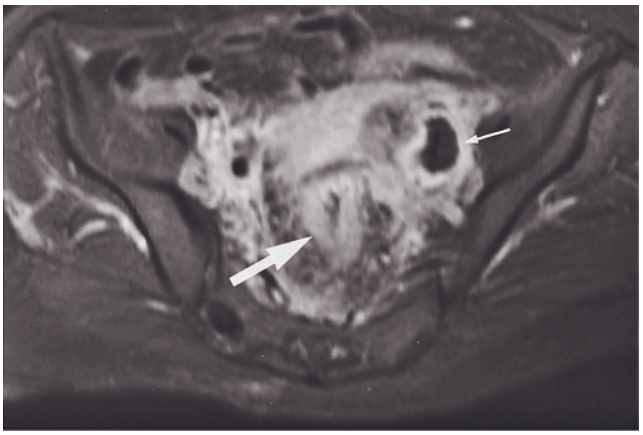

(*b*)

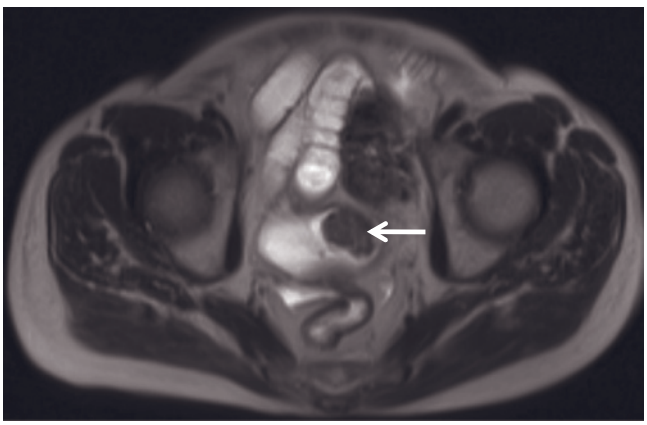

(*c*)

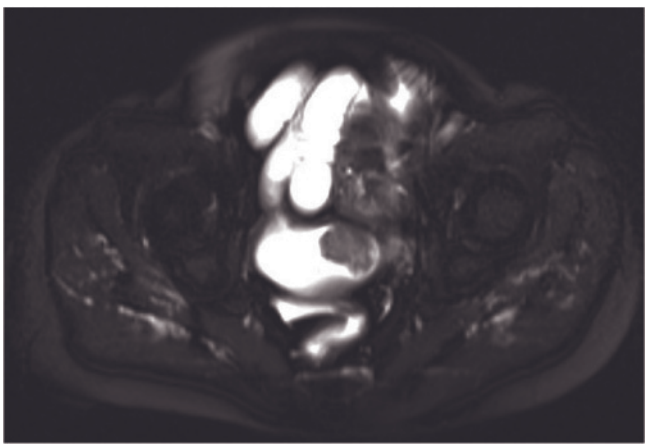

(*d*)

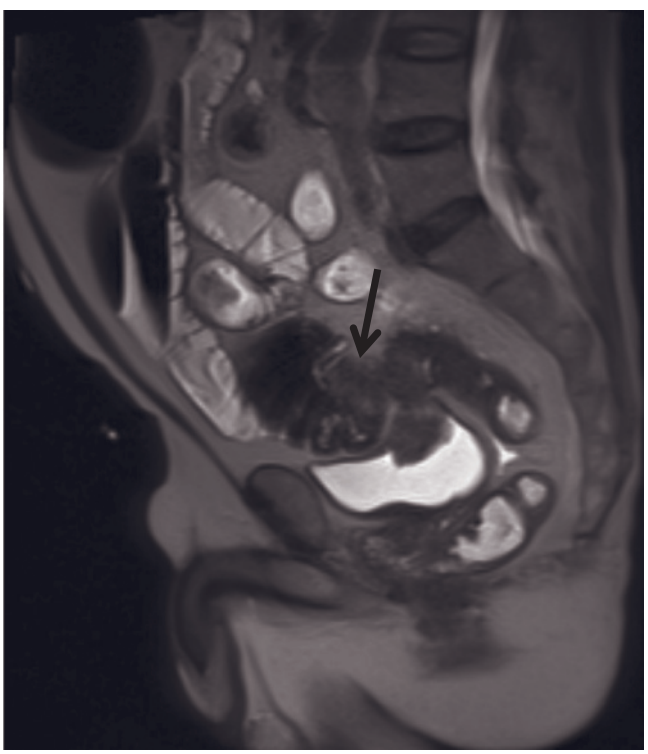

(*e*)

FIG. 6.140 Colon cancer with coexistent diverticulitis. Gadolinium-enhanced T1-weighted fat-suppressed spin-echo images (*a*, *b*) demonstrate a heterogeneously enhancing thickened segment of sigmoid colon (large arrows, *a*, *b*) with an adjoining abscess (thin arrow, *b*), features that were considered compatible with diverticulitis. Colon cancer was found in conjunction with diverticulitis at surgery. **Diverticulitis mimicking colon cancer invading the bladder.** Transverse non-fat-suppressed (*c*) and fat-suppressed (*d*) T2-weighted single-shot echo-train spin-echo, sagittal T2-weighted single shot echo train spin echo (*e*) and transverse T1-weighted SGE (*f*) images demonstrate a mass arising from the sigmoid colon (black arrow, *e*) and invading the bladder (white arrow, *c*) in another patient with diverticulitis. The wall of the sigmoid colon (black arrow, *f*) is

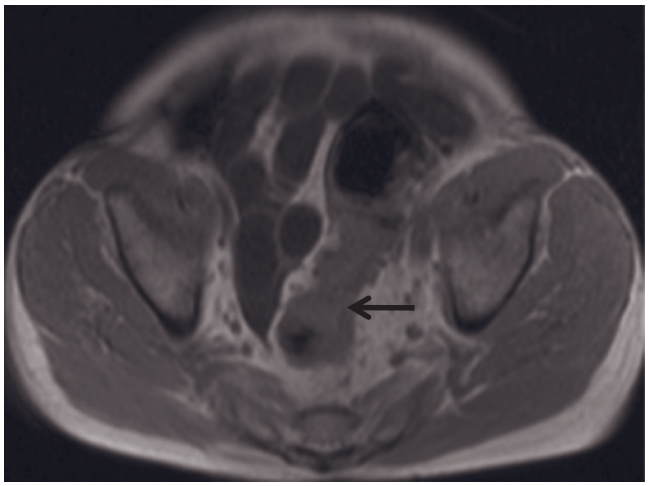

(*f*)

FIG. 6.140 (*Continued*) thickened on noncontrast T1-weighted image. The mass was diagnosed as colon cancer invading the bladder based on MR findings, and also on the basis of colonoscopy. Colectomy was performed, and the diagnosis was inflammatory tissue secondary to diverticulitis histopathologically. The inability to perform postgadolinium imaging in this patient because of end-stage renal disease hindered demonstrating post-contrast findings of diverticulitis and may have masked the correct diagnosis. It should be emphasized that diverticulitis can both mask and mimic colon cancer.

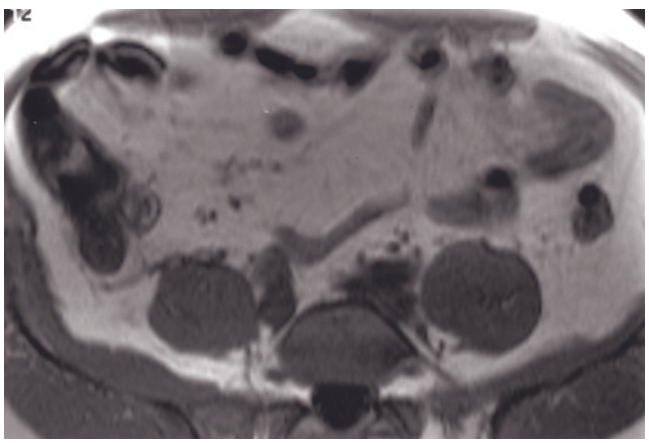

(*a*)

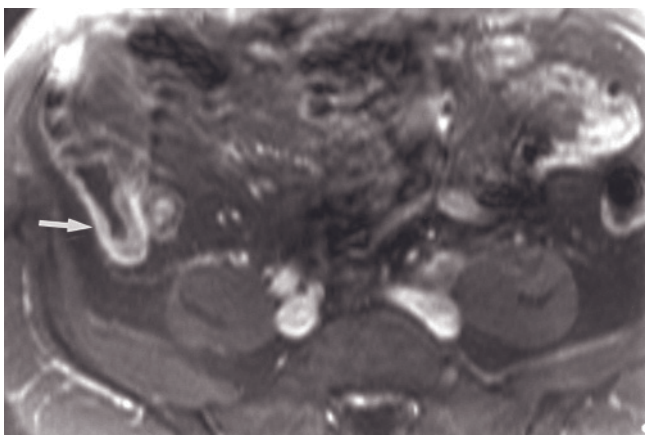

(*b*)

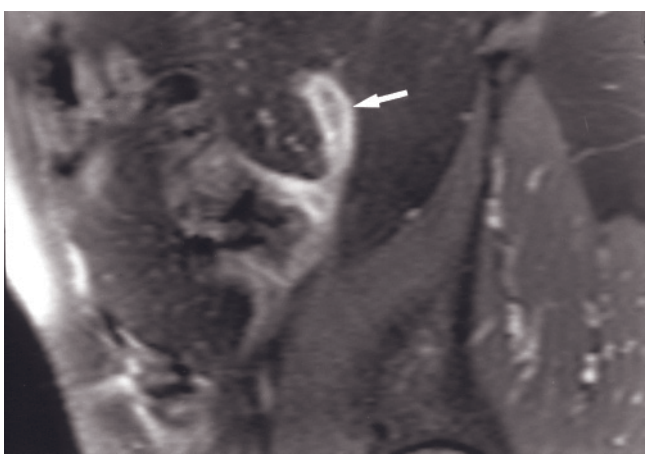

(*c*)

FIG. 6.141 Acute appendicitis. SGE (*a*) and transverse (*b*) and sagittal (*c*) interstitial-phase gadolinium-enhanced fat-suppressed SGE images demonstrate a small-caliber tubular structure in the lower right quadrant with intense mural enhancement. The findings are consistent with acute appendicitis. The direct multiplanar imaging permits display of a low segment of the inflamed retrocecal abscess on the sagittal projection (*c*).

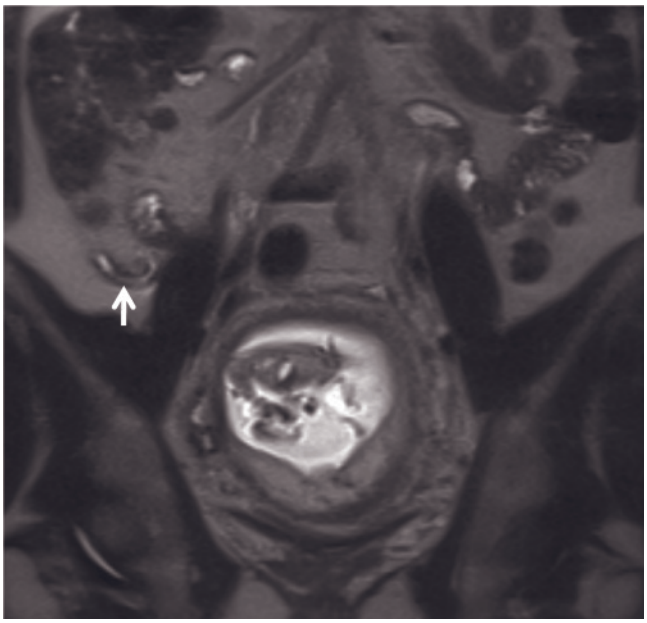

(*d*)

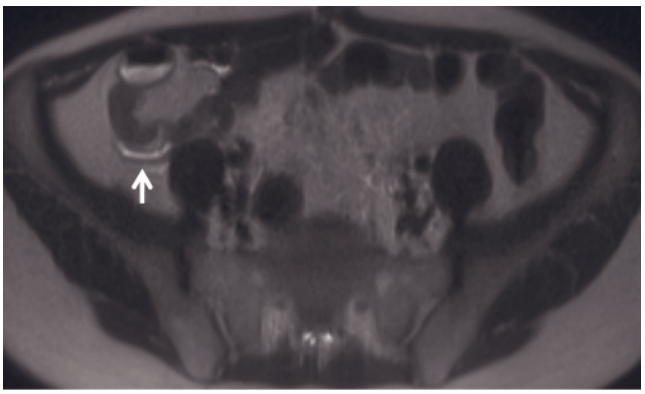

(*e*)

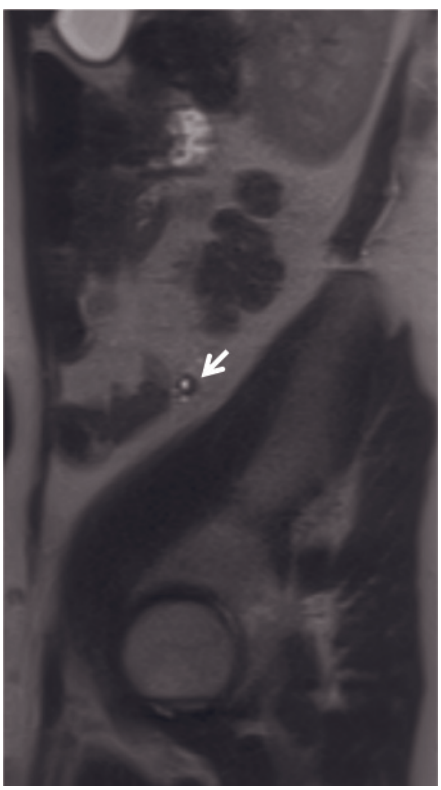

(*f*)

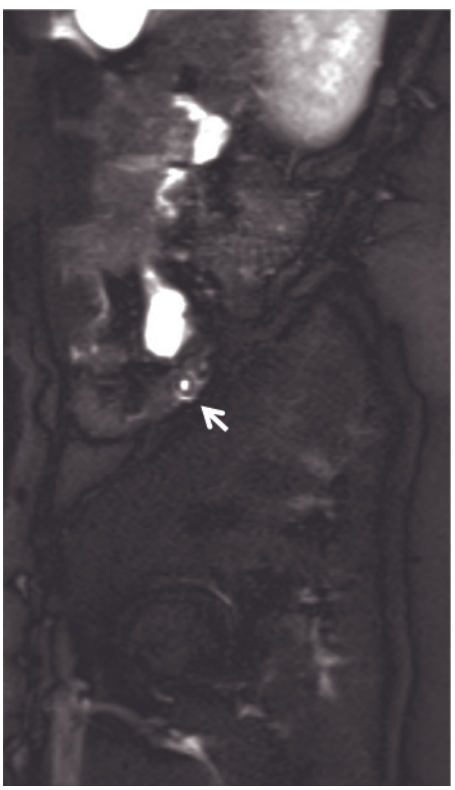

(*g*)

FIG. 6.141 (*Continued*) **Acute appendicitis in pregnant patients.** T2-weighted single-shot echo-train spin-echo non-fat-suppressed coronal (*d*), transverse (*e*), and sagittal (*f*) and fat-suppressed sagittal (*g*) images demonstrate mild acute appendicitis in a pregnant patient. The appendix is mildly dilated, and its wall is mildly thickened. Note that there is minimal free fluid around the appendix. Acute appendicitis can be diagnosed based on the findings of noncontrast sequences, particularly T2-weighted sequences. Postgadolinium imaging should not be performed routinely and should be avoided unless maternal and/or fetal survival depends on it. For further descriptions, see Chapter 16.

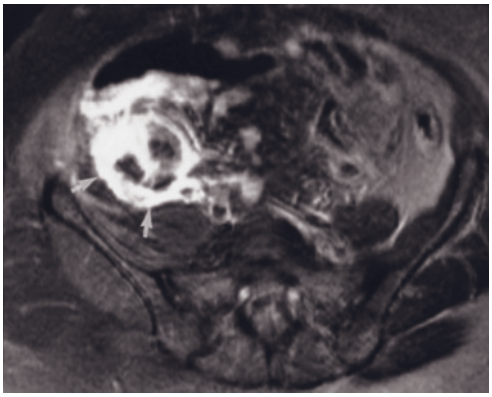

(*a*)

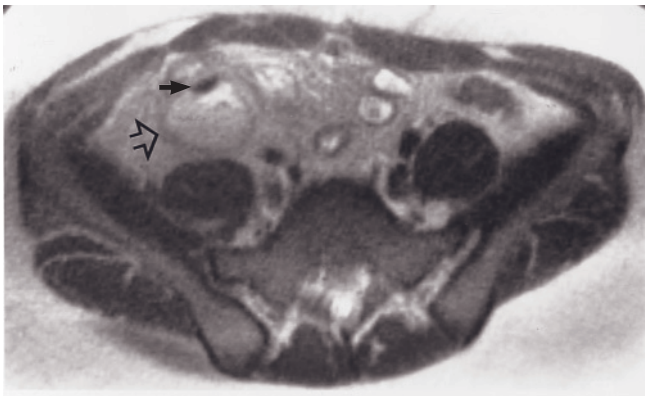

(*b*)

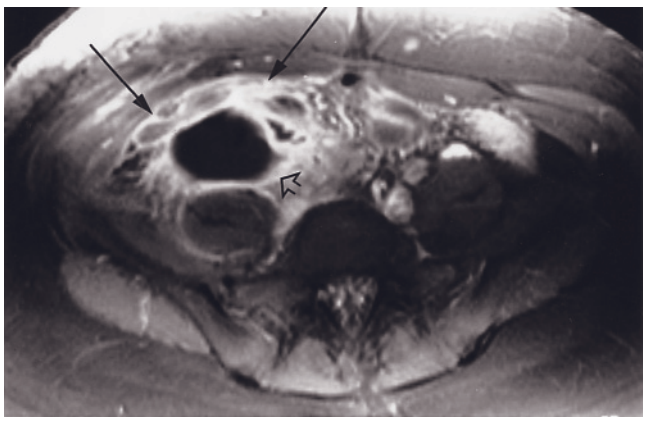

(*c*)

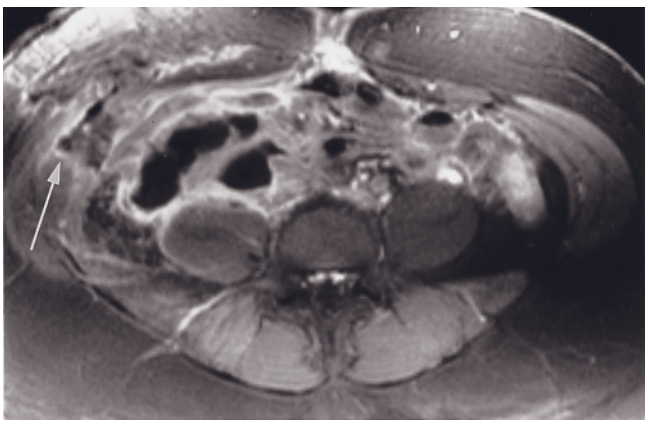

(*d*)

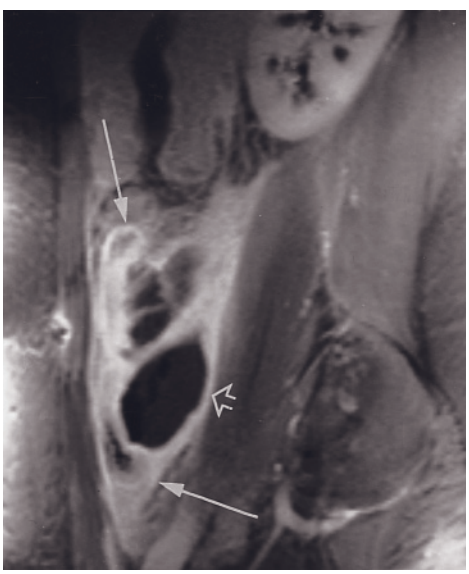

(*e*)

Fig. 6.142 Appendiceal abscess. Gadolinium-enhanced T1-weighted fat-suppressed spin-echo image (*a*) demonstrates a low-signal-intensity appendiceal abscess with a prominent enhancing rim (arrow). SS-ETSE (*b*) and transverse (*c*, *d*) and sagittal (*e*) postgadolinium fat-suppressed SGE images in a second patient. A large multiloculated appendiceal abscess is present (open arrow, *b*, *c*, *e*). Air within the abscess is signal void (arrow, *b*) on the T2-weighted image. After gadolinium administration (*c*, *d*, *e*) the abscess rim enhances (open arrow, *c*, *e*), and extensive enhancement of periabscess tissue is present (long arrows, *c*, *d*, *e*).

Noone et al. [119] reported a high diagnostic accuracy of MRI in evaluating suspected acute intraperitoneal abscess. In that series, abscesses were visualized as well-defined fluid collections with peripheral rim enhancement on gadolinium-enhanced T1-weighted fat-suppressed images.

The presence of signal-void air within the collection confirms the diagnosis (fig. 6.143) [120]. The role of oral or rectal contrast in distinguishing bowel from abscess is not firmly established. Most abscesses can be confidently differentiated from bowel with gadolinium-enhanced T1-weighted fat-suppressed SGE or 3D-GE

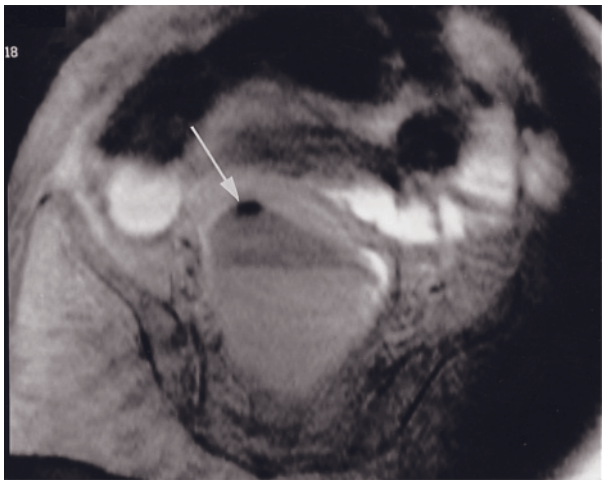

(*a*)

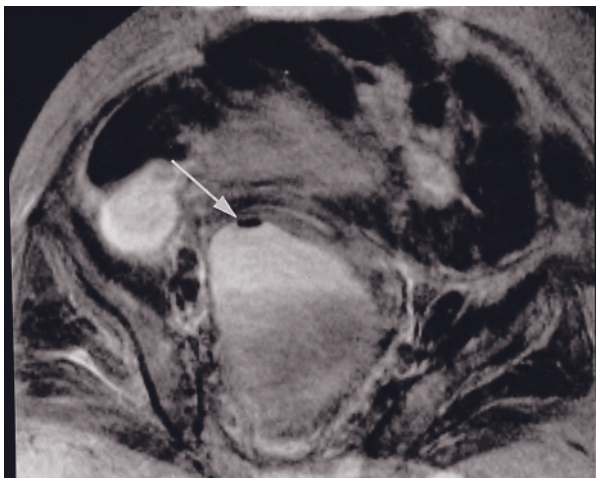

(*b*)

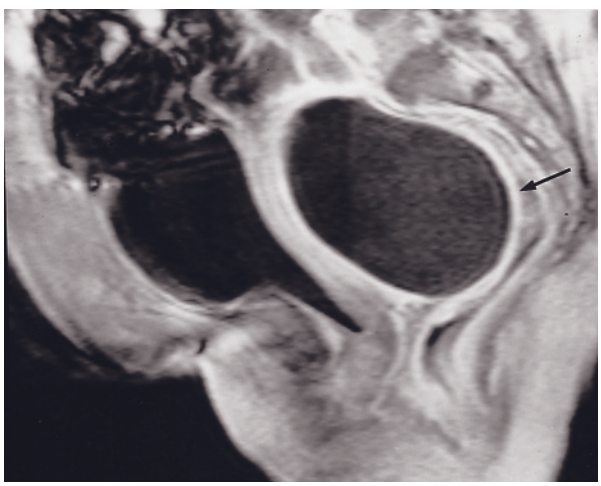

(*c*)

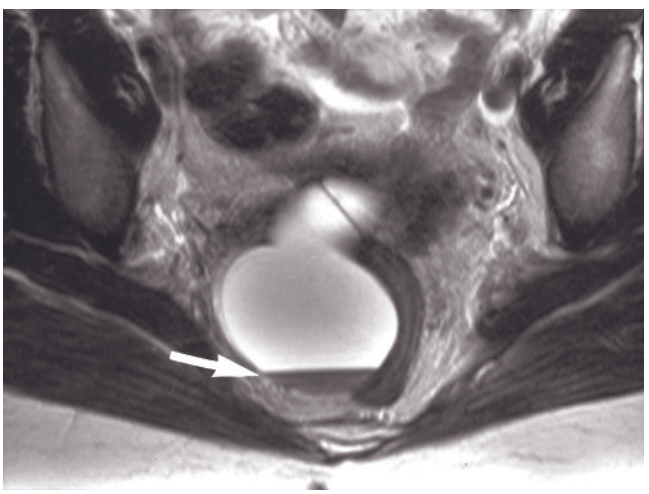

(*d*)

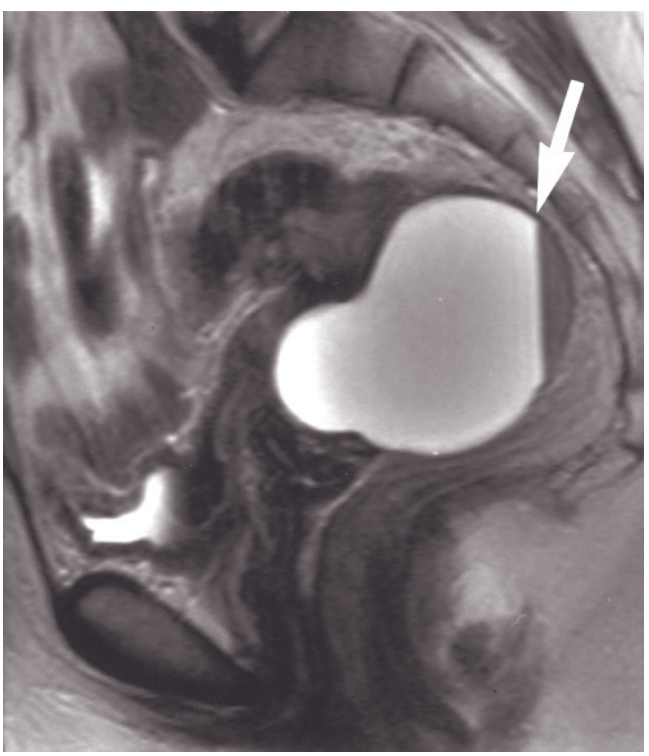

(*e*)

FIG. 6.143 Pouch of Douglas abscess. T1-weighted fat-suppressed spin-echo (*a*), T2-weighted echo-train spin-echo (*b*), and sagittal 45-s postgadolinium SGE (*c*) images. An 8-cm pouch of Douglas abscess is present that contains a focus of air that is signal void on T1-weighted (*a*) and T2-weighted (*b*) images (arrow, *a*, *b*). The abscess has a thick, enhancing rim (arrow) on the early postgadolinium image (*c*) with increased enhancement of surrounding tissue. Note the layering of debris on all MR images (*a*–*c*). Transverse (*d*) and sagittal (*e*) T2-weighted SS-ETSE and transverse (*f*) and sagittal (*g*) interstitial-phase gadolinium-enhanced fat-suppressed images in a second patient. There is a cystic mass situated in a right perirectal location that exhibits layering of low-signal material (arrows, *d*, *e*) on T2-weighted images. Moderately intense enhancement is observed of the

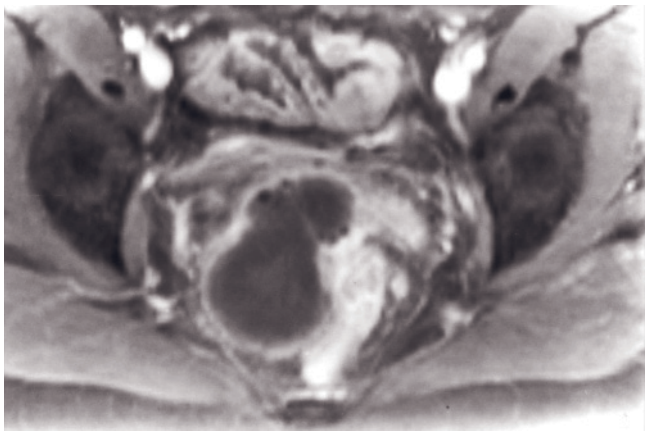

(*f*)

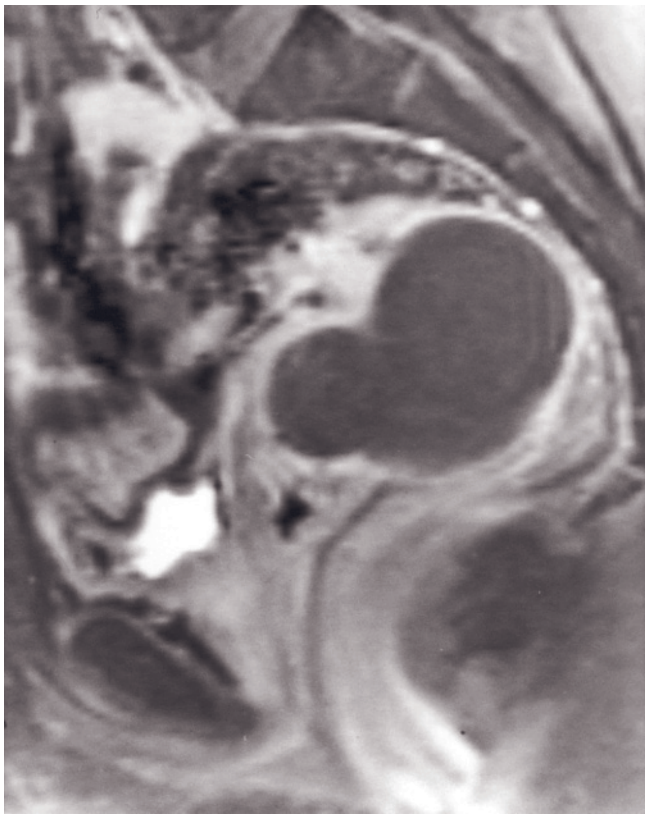

(*g*)

FIG. 6.143 (*Continued*) abscess wall (*f*). The abscess displaces the rectal-sigmoid region to the left. Layering of low-signal material on T2-weighted images is a relatively specific feature of abscesses.

and T2-weighted single-shot echo-train spin-echo images acquired in two planes. This approach demonstrates the oval shape of abscesses and permits their distinction from adjacent tubular bowel. Enhancement of periabscess tissues on gadolinium-enhanced T1-weighted fat-suppressed SGE or 3D-GE images confirms the inflammatory nature of the fluid collections (fig. 6.144). The layering effect of low-signal-intensity material in the dependent portion of the abscess on T2-weighted images is an important ancillary feature observed in the majority of abscesses [120]. The absence of motion artifact on T2-weighted single-shot echo-train spin echo facilitates identification of the dependent low-signal material in abscesses. The low signal reflects the high protein content of products of infection.

In patients with a contraindication to iodinated intravenous contrast secondary to allergy, MRI should be considered for the evaluation of abscess. MRI is particularly advantageous over CT in patients in whom high-density barium is present in bowel, because the barium creates severe artifacts on CT and may, if anything, improve the image quality in MRI. MRI also may be effective as a method to follow therapeutic interventions (fig. 6.145).

Colonic Fistulas

MRI is an effective imaging modality for evaluating colonic fistulas [7, 8, 121–123]. In particular, the multiplanar imaging capability of MRI has been shown to be useful for surgical planning for perirectal/perianal fistulas. The relationship of fistulas to the levator ani muscle is well shown on a combination of transverse, coronal, and sagittal plane images. T1-weighted images, T2-weighted images, and gadolinium-enhanced T1-weighted fat-suppressed images all provide good contrast between fistulas and surrounding tissues (fig. 6.146).

Infectious Colitis

Pseudomembranous colitis is defined as an acute colitis characterized pathologically by the formation of an adherent inflammatory "membrane" (pseudomembrane) overlying areas of mucosal damage. This disease occurs in the setting of broad-spectrum antibiotic use. The infectious organism most frequently implicated is *Clostridium difficile* [124]. The severity of the disease varies from mild to life-threatening. MRI shows thickening of the affected large bowel with marked enhancement (figs. 6.147 and 6.148).

In the past, neutropenic enterocolitis (typhlitis) was a disease affecting predominantly children treated for leukemia. The disorder also affects healthier neutropenic patients with solid tumors and other conditions. The cecum and ascending colon are the segments most commonly affected (fig. 6.149). MRI findings are nonspecific in patients with infectious colitis and generally demonstrate increased wall thickness and enhancement. Other infectious agents and infections that target the colon include *Shigella*, *Salmonella*, *Escherichia coli*, amebiasis, and cholera.

Patients with AIDS are prone to *Mycobacterium avium-intracellulare* colitis. *Mycobacterium avium-intracellulare* also affects the large bowel and produces

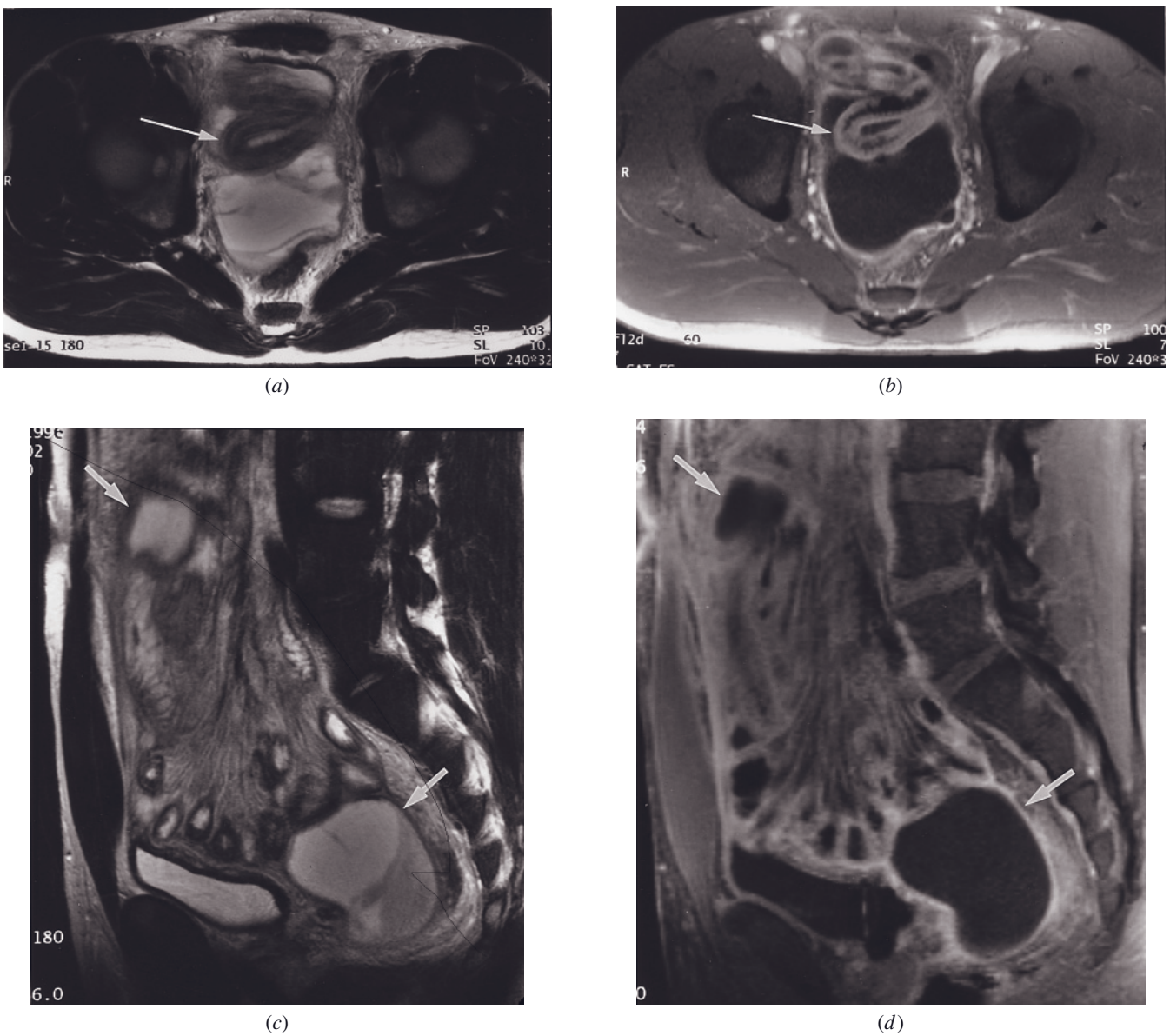

FIG. 6.144 Midabdominal and pelvic abscesses. Transverse 512-resolution echo-train spin-echo (*a*) and gadolinium-enhanced fat-suppressed SGE (*b*) images through the pelvis and sagittal 512-resolution echo-train spin-echo (*c*) and sagittal gadolinium-enhanced fat-suppressed SGE (*d*) images through the pelvis and midabdomen. An 8-cm, irregular, oval-shaped abscess is present in the recto-vesicle space that demonstrates dependent layering of low-signal-intensity debris on the T2-weighted image (*a*) and substantial enhancement of the abscess wall (*b*). Inflammatory thickening of a loop of ileum (arrow, *a*) abutting the abscess is identified. Enhancement of the serosal surface of the bowel is appreciated (arrow, *b*). The sagittal plane images demonstrate the pelvic and midabdominal abscesses (arrows, *c*, *d*). Layering of low-signal-intensity material in the dependent portion of the pelvic abscess is shown on the T2-weighted image (*c*). Enhancement of the abscess wall and increased enhancement of multiple loops of small bowel are noted on the gadolinium-enhanced fat-suppressed SGE image (*d*). Transverse 512-resolution T2-weighted echo-train

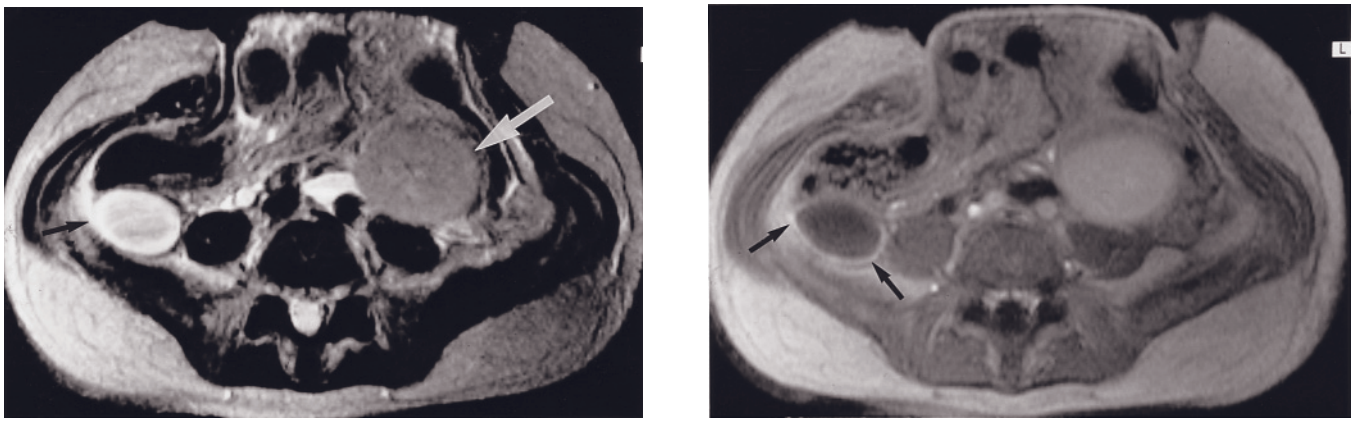

(*e*) (*f*)

FIG. 6.144 (*Continued*) spin-echo (*e*) and immediate postgadolinium SGE (*f*) images in a second patient. This patient with chronic renal failure had undergone multiple abdominal surgical procedures for bowel ischemia and has a large anterior abdominal wall dehiscence with exposed peritoneal lining. A retrocecal abscess collection is present (black arrows, *e*, *f*) that is high in signal intensity on the T2-weighted image and demonstrates ring enhancement on the immediate postgadolinium image. A chronically failed renal transplant is also identifiable (large arrow, *e*).

(*a*) (*b*)

FIG. 6.145 Pelvic abscess, before and after catheter drainage. Sagittal 512-resolution T2-weighted echo-train spin-echo (*a*) and sagittal (*b*) and transverse (*c*) interstitial-phase gadolinium-enhanced fat-suppressed SGE images. The sagittal images demonstrate a 5-cm abscess in the pouch of Douglas (long arrow, *a*, *b*) and a smaller midabdominal abscess (short arrow, *a*, *b*). On the T2-weighted image, heterogeneous low signal is present in the dependent portion, which is a common finding in abscesses. On the postgadolinium images, substantial enhancement of the abscess wall and the adjacent rectum (open arrow, *b*) is present. Multiple Nabothian cysts are present in the cervix (small arrow, *a*, *b*). The transverse gadolinium-enhanced fat-suppressed image through

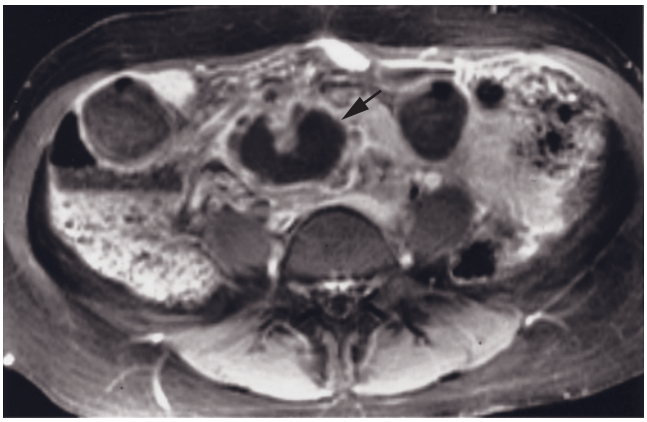

(*c*)

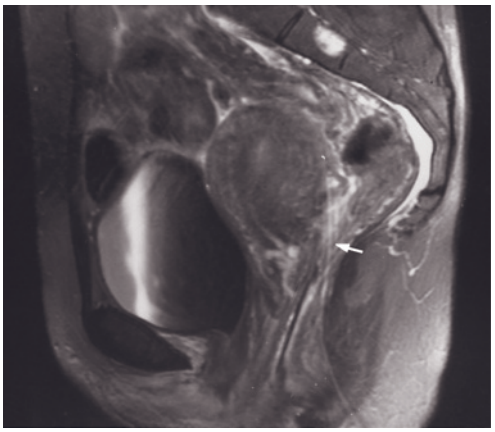

(*d*)

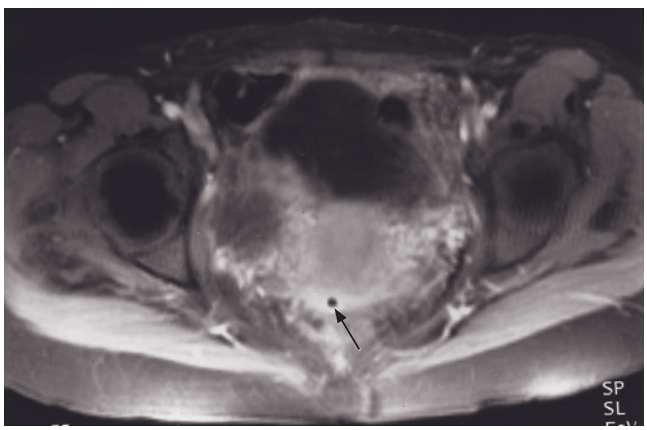

(*e*)

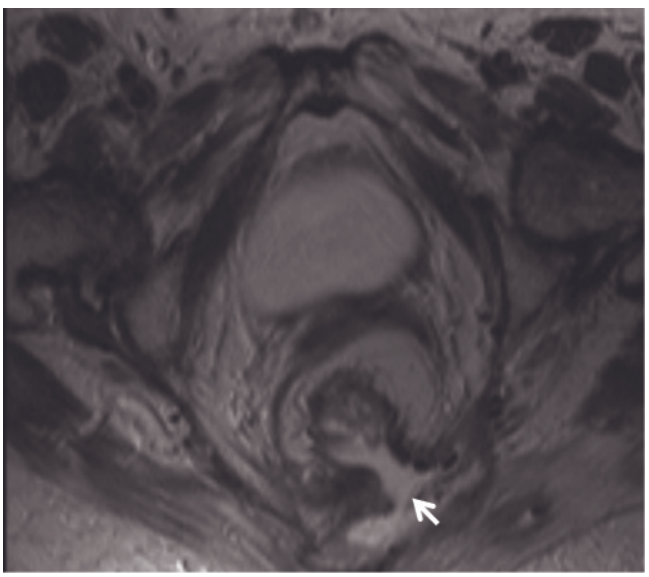

(*f*)

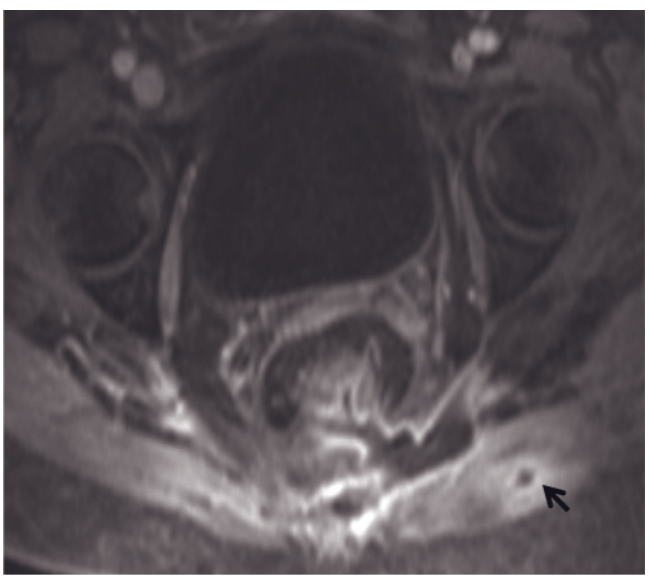

(*g*)

FIG. 6.145 (*Continued*) the midabdomen demonstrates a 4-cm abscess (arrow, *c*) with enhancement of the abscess wall and the periabscess tissue. Sagittal 512-resolution T2-weighted echo-train spin-echo (*d*) and transverse interstitial-phase gadolinium-enhanced fat-suppressed SGE (*e*) images obtained 1 week after transrectal placement of a drainage catheter demonstrate substantial resolution of the pelvic abscess. The drainage catheter is identified as a signal-void tube (arrow, *d*, *e*). The degree of inflammatory reaction has also substantially diminished, but persistent enhancing tissue around the catheter is visualized (*e*). **Rectal perforation and abscess formation.** T2-weighted high-resolution fast spin-echo (*f*) and T1-weighted postgadolinium fat-suppressed interstitial-phase 3D-GE (*g*) images demonstrate that the rectum integrity is lost (white arrow, *f*) on the posterior aspect and there is an associated abscess formation that shows intense peripheral enhancement in continuity with the rectal wall. The abscess extends into the gluteus muscles. Note that there is another small abscess (black arrow, *g*) in the left gluteus muscle.

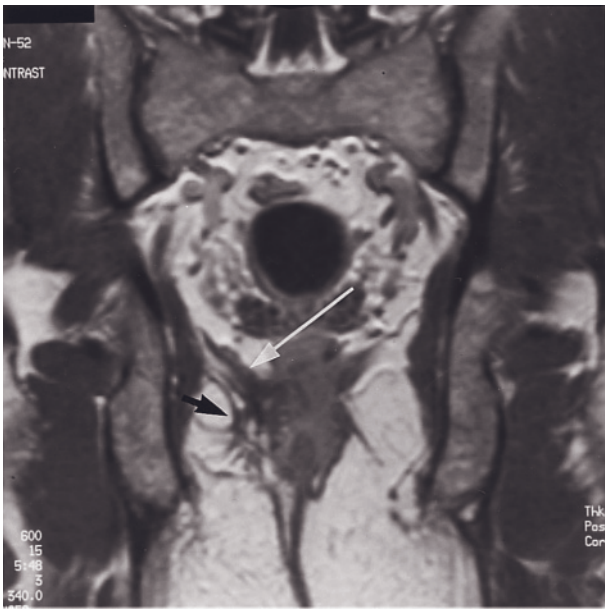

(*a*)

(*b*)

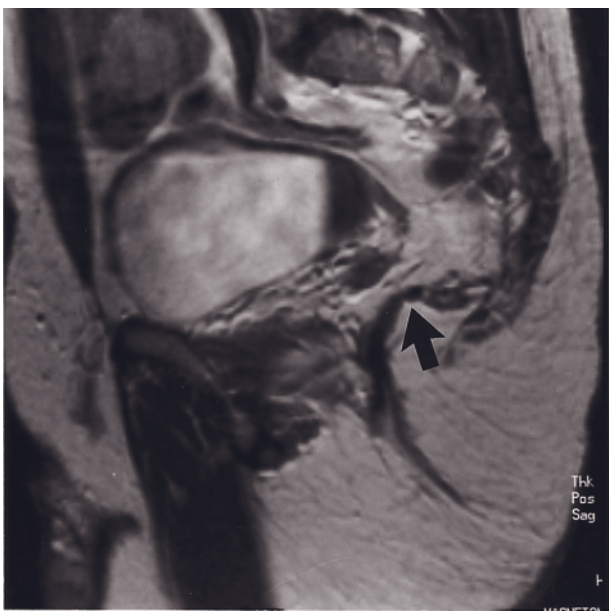

(*c*)

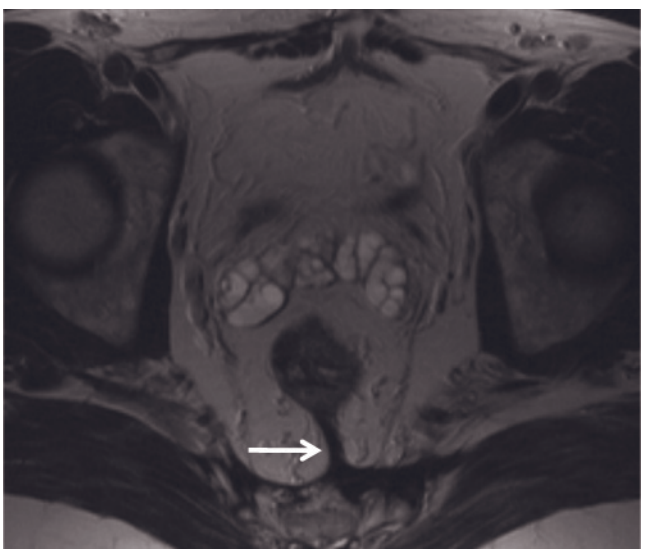

(*d*)

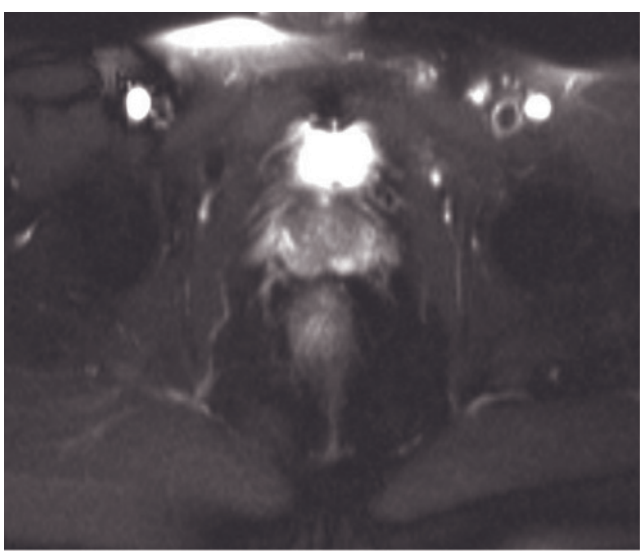

(*e*)

Fig. 6.146 Perianal fistula. Coronal T1-weighted spin-echo (*a*), sagittal T2-weighted spin-echo (*b*), and gadolinium-enhanced T1-weighted spin-echo (*c*) images. A complex fistula (arrow, *a*) is present in a right perianal location that extends to the levator ani muscle (long arrow, *a*). The fistula is low in signal on T1-weighted (arrow, *a*), T2-weighted (arrow, *b*), and postgadolinium (arrow, *c*) images, reflecting its the chronic fibrotic nature. T2-weighted high-resolution fast spin-echo (*d*), T2-weighted fat-suppressed single-shot echo-train spin-echo (*e*), and T1-weighted postgadolinium

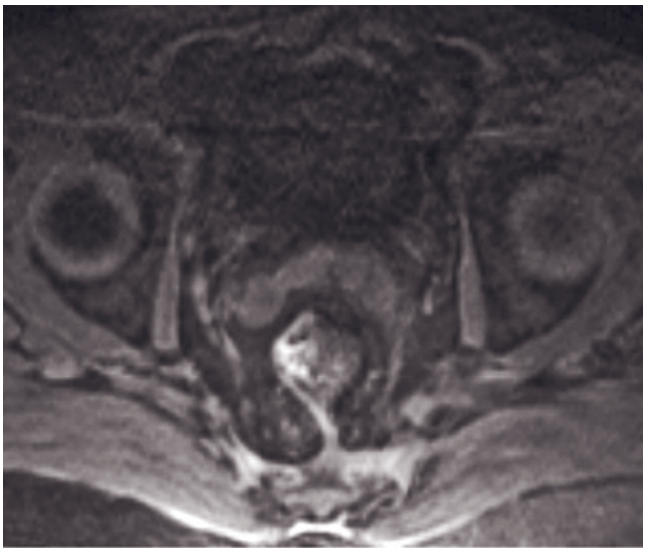

(*f*)

FIG. 6.146 (*Continued*) interstitial-phase fat-suppressed 3D-GE (*f*) images demonstrate a pelvic fistula (arrow, *d*) extending from the rectum to the presacral soft tissue in another patient with Crohn proctitis. The fistulous tract shows enhancement on post-gadolinium image (*f*).

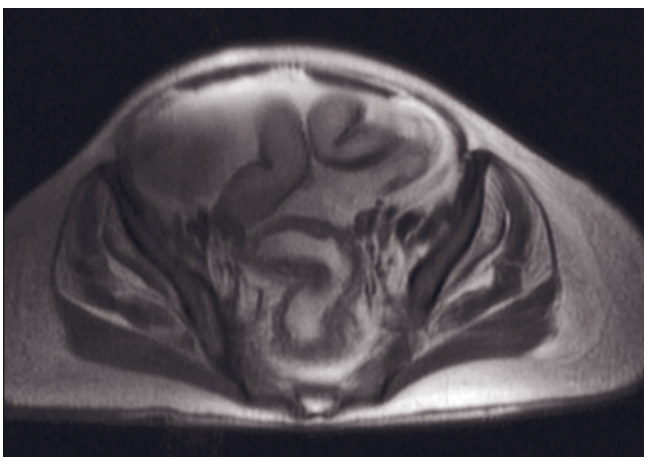

(*a*)

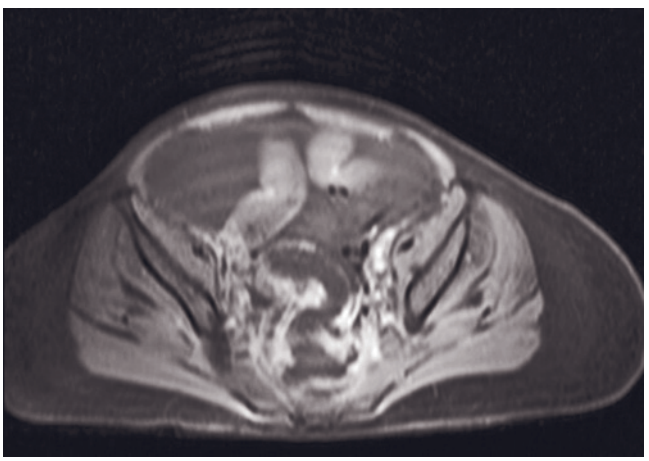

(*b*)

FIG. 6.147 ***Clostridium difficile*** **colitis.** T2-weighted single-shot ETSE (*a*) and T1-weighted fat-suppressed gadolinium-enhanced interstitial-phase T1 (*b*) images through the pelvis show marked diffuse wall thickening and edema of the sigmoid colon and proximal rectum. A moderate amount of free fluid is noted within the peritoneum.

wall thickening (fig. 6.150) [46]. Cytomegalovirus colitis (fig. 6.150) may also be seen in these patients. Bowel wall thickening secondary to submucosal hemorrhage is the most characteristic finding. Patients with AIDS frequently develop proctitis. Opportunistic infection leads to rectal wall thickening and stranding in the perirectal space. Occasionally, frank perirectal abscesses occur. Gadolinium-enhanced T1-weighted fat-suppressed SGE and 3D-GE images demonstrate bowel wall thickening with increased enhancement and abscess formation. Unenhanced SGE imaging is effective for showing perirectal stranding, which appears low in signal intensity in a background of high-signal-intensity fat.

Radiation Enteritis

The rectum is the segment of large bowel most susceptible to radiation enteritis. This finding may be attributed to the large radiation doses used to treat tumors arising in the pelvic area and the relatively fixed position of the rectosigmoid colon. Pathologic changes of acute radiation injury include prominent submucosal edema, ulceration, inflammatory polyps, and ischemic changes. Chronic radiation injury may show the histologic features of mucosal atrophy, vascular occlusion, and fibrosis. Late effects of radiation damage are evidenced pathologically by mucosal, submucosal, and muscular fibrosis with stricture formation [125]. In one study, the T1- and T2-weighted MRI features of the rectum in 42

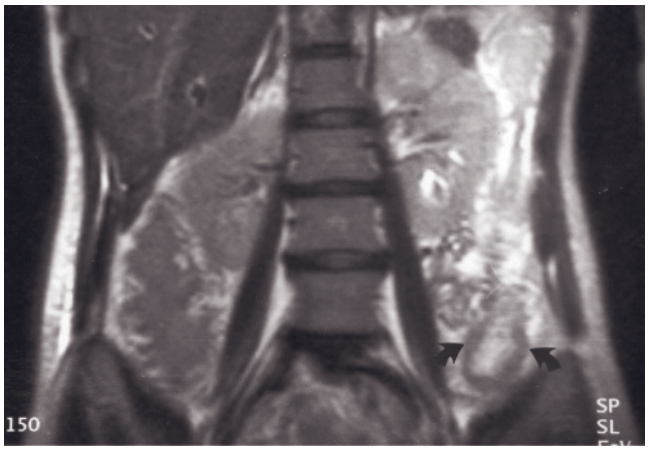

(*a*)

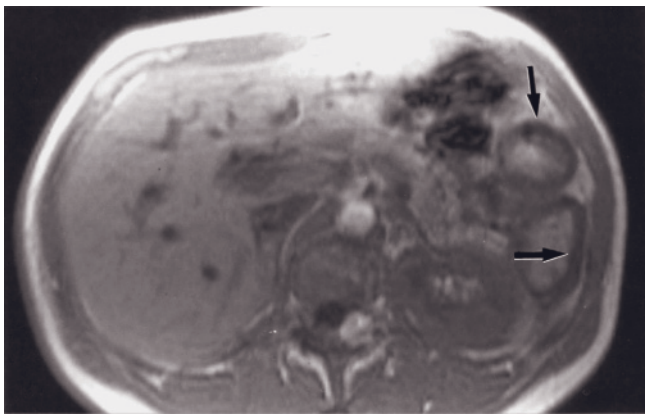

(*b*)

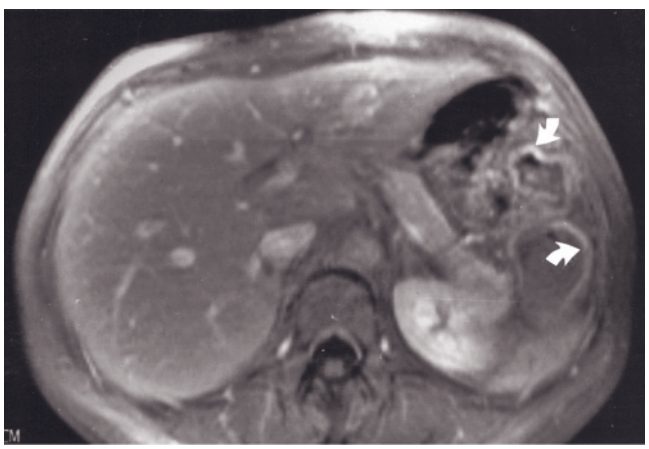

(*c*)

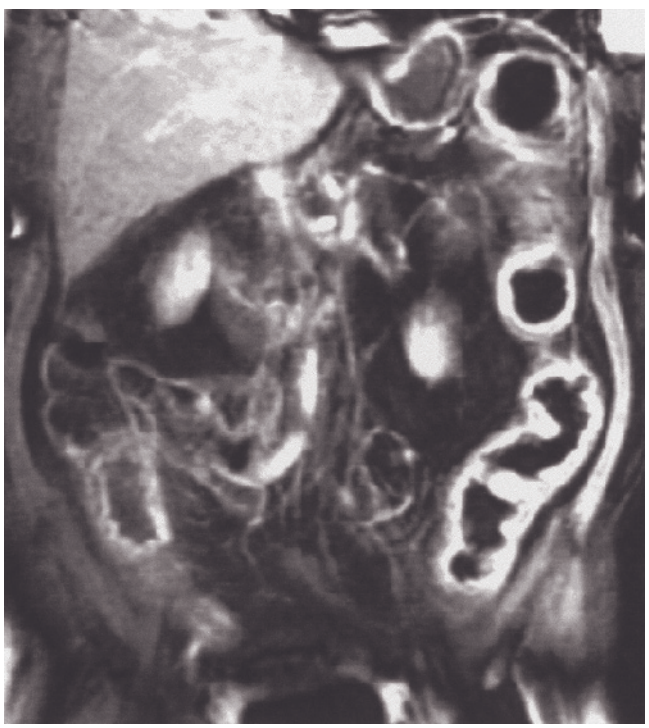

(*d*)

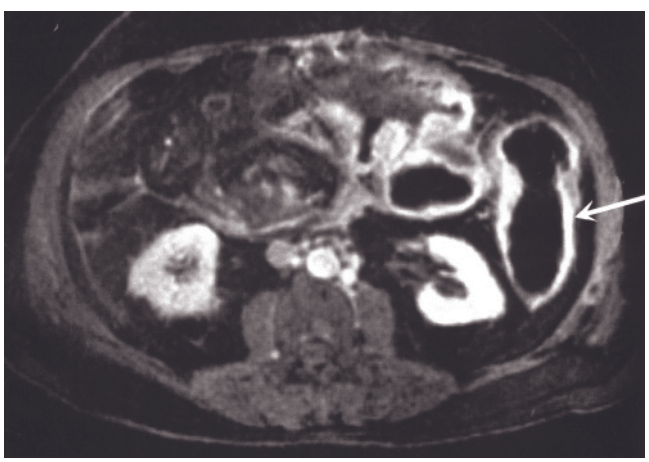

(*e*)

FIG. 6.148 Pseudomembranous colitis. T2-weighted SS-ETSE (*a*), precontrast SGE (*b*), and 90-s postgadolinium fat-suppressed SGE (*c*) images. Diffuse bowel wall thickening is noted in the descending colon on the coronal T2-weighted image (curved arrows, *a*). Circumferential bowel wall thickening is seen in the splenic flexure of the large bowel on the precontrast SGE image (arrows, *b*). Moderately increased enhancement and wall thickening of the splenic flexure is noted on the postcontrast fat-suppressed SGE image (curved arrows, *c*). (Reprinted with permission from Chung JJ, Semelka RC, Martin DR, Marcos HB: Colon diseases: MR evaluation using combined T2-weighted single-shot echo train spin-echo and gadolinium-enhanced spoiled gradient-echo sequences. *J Magn Reson Imaging* 12: 297–305, 2000.) Coronal (*d*) and transverse (*e*) interstitial-phase gadolinium-enhanced fat-suppressed SGE images in a second patient demonstrate diffuse thickening of the descending colon (arrow, *e*) with intense mural enhancement. (Courtesy of Russel Low, M.D., Sharp Clinic, San Diego.)

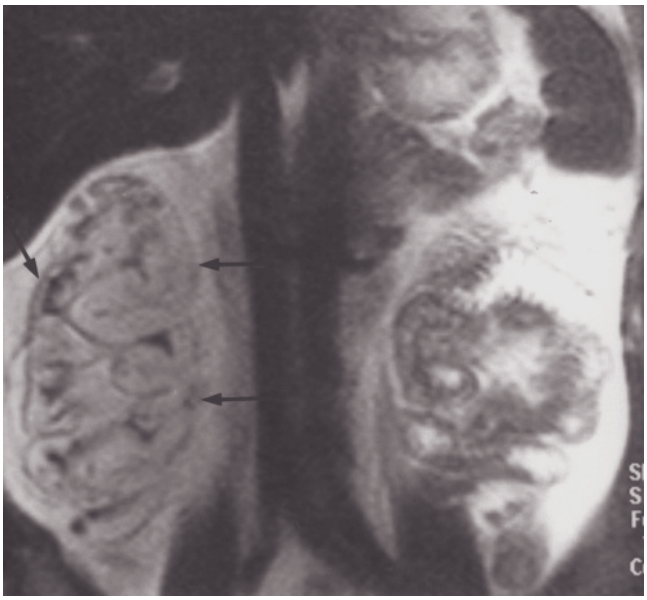

(*a*)

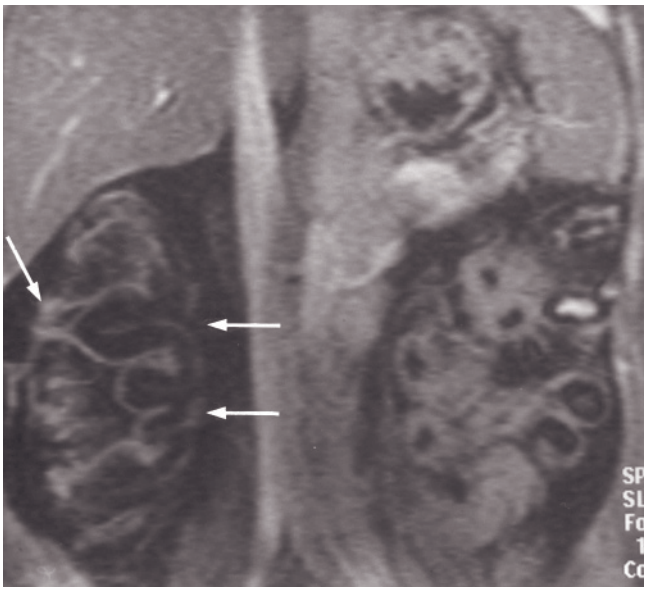

(*b*)

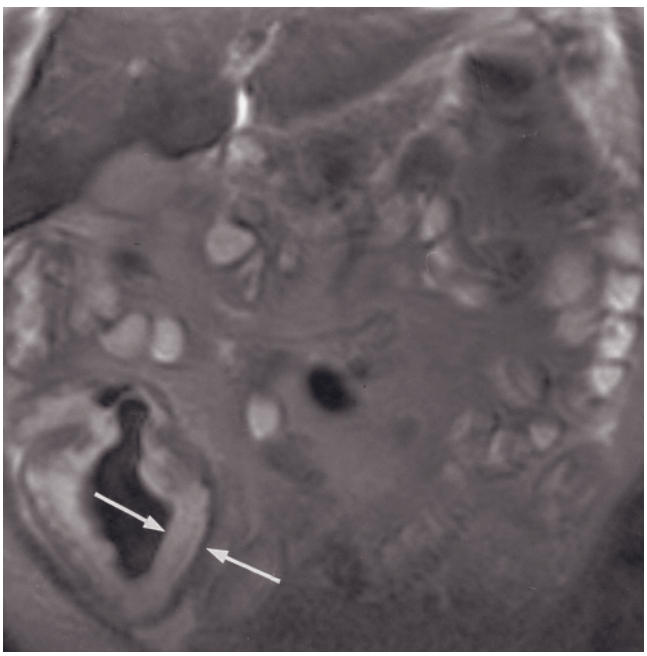

(*c*)

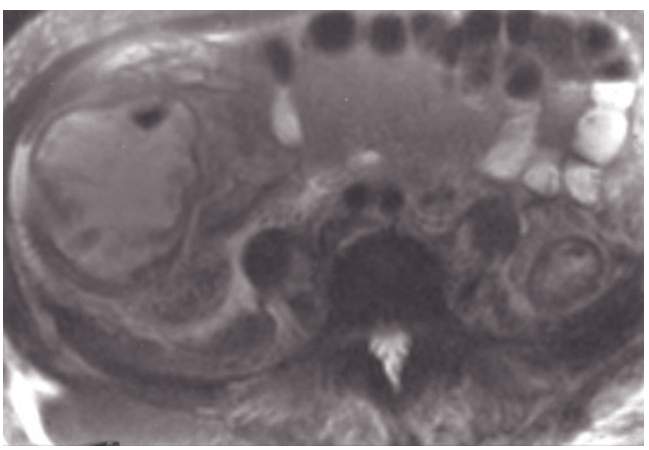

(*d*)

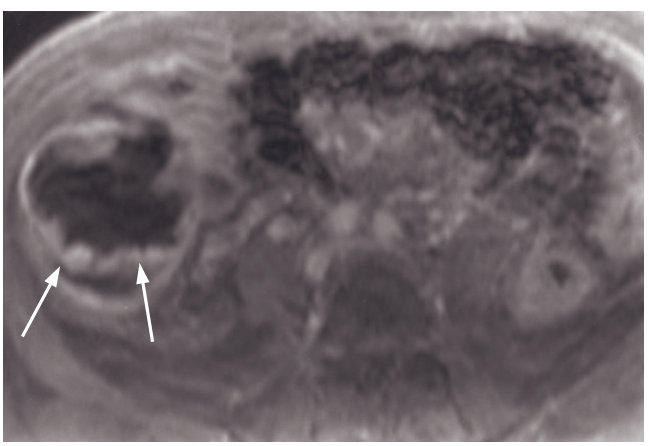

(*e*)

FIG. 6.149 Neutropenic colitis (typhlitis). Coronal T2-weighted SS-ETSE (*a*) and coronal interstitial-phase gadolinium-enhanced SGE (*b*) images in a patient with acute myelogenous leukemia history. There is marked thickening of the ascending colon (arrows, *a*, *b*) consistent with neutropenic colitis. Small bowel thickening and ascites are also present. Coronal (*c*) and transverse (*d*) T2-weighted SS-ETSE and transverse interstitial-phase gadolinium-enhanced SGE (*e*) images in a second patient after chemotherapy. The cecum shows dilatation with marked thickening and enhancement of the wall (arrows, *c*, *e*).

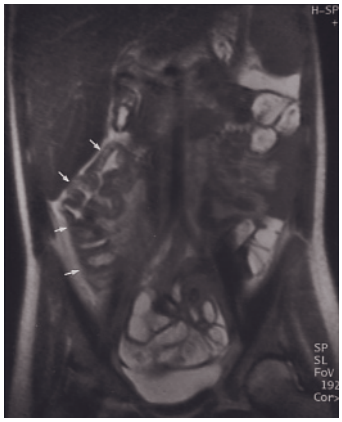

(*a*)

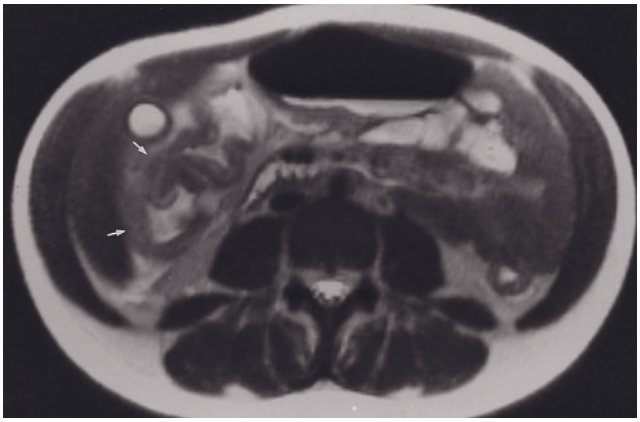

(*b*)

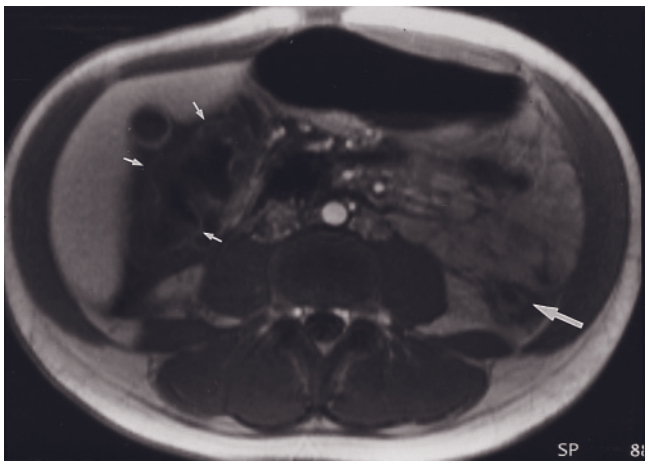

(*c*)

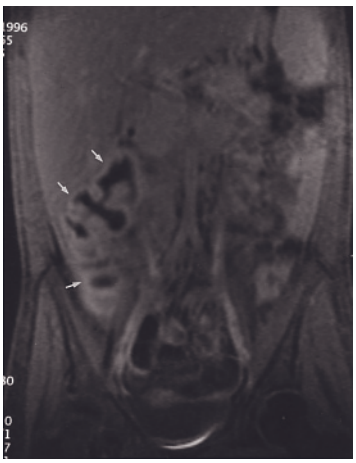

(*d*)

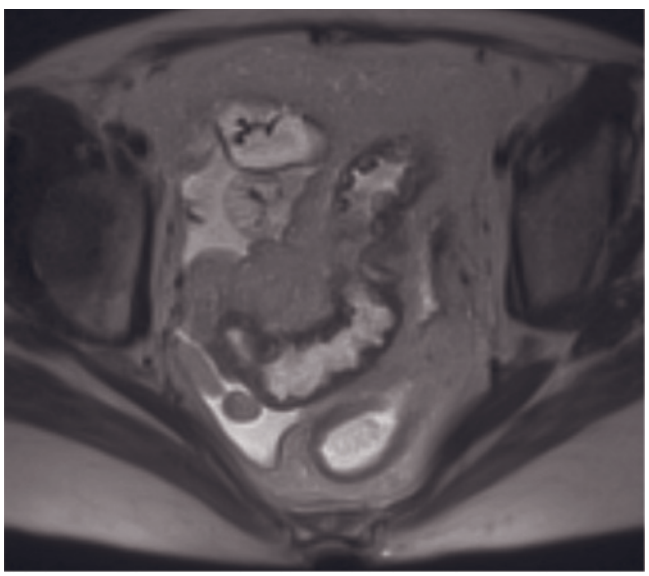

(*e*)

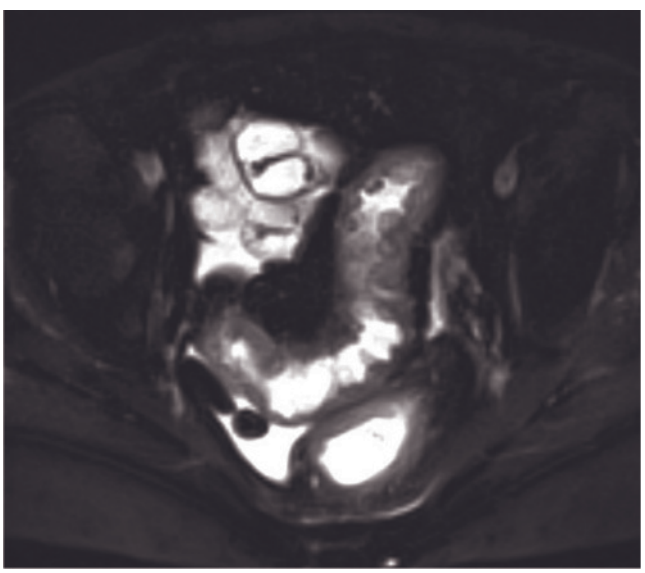

(*f*)

Fig. 6.150 ***Mycobacterium avium-intracellulare (MAI) colitis.*** Coronal (*a*) and transverse (*b*) SS-ETSE, immediate postgadolinium SGE (*c*), and coronal 90-s postgadolinium fat-suppressed SGE (*d*) images in a patient with *Mycobacterium avium-intracellulare* colitis. SS-ETSE images (*a*, *b*) demonstrate marked wall thickening of the ascending colon (small arrows, *a*, *b*) with relative sparing of the descending colon. The mucosal surface enhances on the immediate postgadolinium image (small arrows, *c*), with negligible enhancement of the thickened outer wall. Less severe involvement of the descending colon is also seen (arrow, *c*). Enhancement of the wall increases and becomes more uniform (small arrows, *d*) on interstitial-phase images, reflecting capillary leakage. ***Cytomegalovirus colitis.*** Transverse T2-weighted non-fat-suppressed (*e*) and fat-suppressed (*f*) single-shot echo-train spin-echo, T1-weighted SGE (*g*), and T1-weighted postgadolinium fat-suppressed interstitial-phase 3D-GE (*h*) images demonstrate cytomegalovirus colitis in another patient. The sigmoid colon and rectum walls are edematous and thickened, and show intense enhancement. Note that mesenteric inflammation and free fluid are also present.

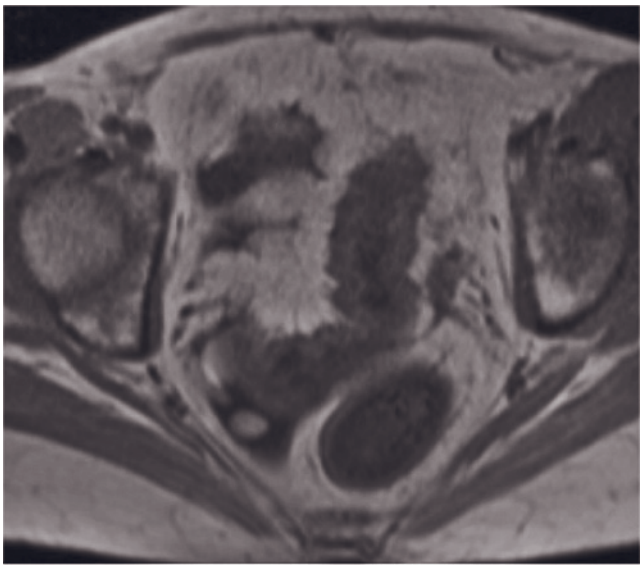

(*g*)

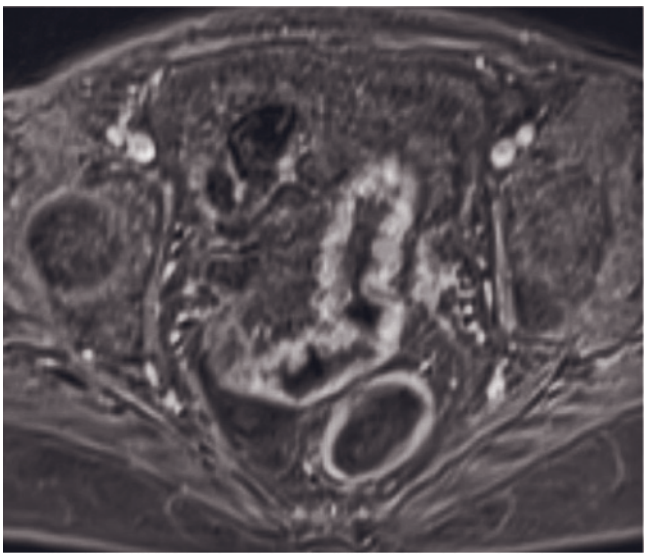

(*h*)

FIG. 6.150 (*Continued*)

patients status post radiation therapy were graded with respect to wall thickness and signal intensity of the muscular layers and submucosa. A spectrum of tissue changes were seen in the rectum regardless of the time from initiation of therapy. MRI had excellent sensitivity for depicting abnormalities, but specificity was limited [106]. The results of this study emphasize the need for detailed clinical history to ensure optimal MRI. The routine use of gadolinium-enhanced T1-weighted fat-suppressed imaging is effective for evaluating postradiation changes because of the high sensitivity of this technique for inflammatory changes. High-resolution T2-weighted images demonstrate the findings of submucosal edema in acute radiation proctocolitis well (figs. 6.151 and 6.152).

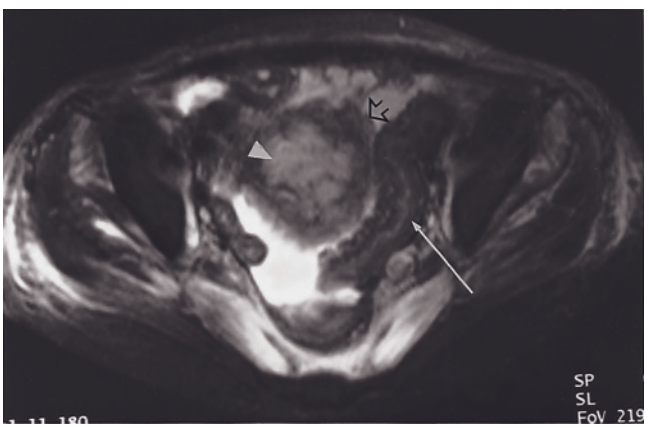

FIG. 6.151 Radiation enteritis. Transverse 512-resolution T2-weighted echo-train spin-echo image in a patient after radiation therapy. The sigmoid colon is thick-walled with marked submucosal edema (long arrow). The circumferential and symmetric nature of the bowel wall changes are suggestive of radiation enteritis. Note the thick-walled bladder (open arrow) and its heterogeneous contents (arrowhead), findings consistent with hemorrhagic cystitis, another sequela of radiation therapy. Free pelvic fluid is also present.

Rectal Surgery

A number of surgical procedures are performed for rectal cancer and other disease processes. Abdominoperineal resection (APR) is performed for tumors that are distal in the rectum, in which a tumor-free distal margin may not be achievable. After APR, more anteriorly positioned pelvic structures reposition more posteriorly, including the bladder, the prostate and seminal vesicles, and the uterus. The pelvis is often packed with omental fat to prevent small bowel from filling the potential space when postoperative radiation therapy is contemplated (fig. 6.153).

Intraluminal Contrast Agents

The goals of intraluminal contrast agent use are twofold: 1) reliable differentiation of bowel from adjacent structures and 2) better delineation of pathologic processes involving the bowel wall. Oral contrast agents fall into two major categories, positive (signal intensity increasing) and negative (signal intensity decreasing) agents. Positive agents shorten T1-relaxation time, whereas negative agents either shorten T2-relaxation time or rely on immobile protons to decrease intraluminal signal intensity. Biphasic intraluminal agents are formulated to produce high signal intensity on T1-weighted images and low signal intensity on T2-weighted images [126].

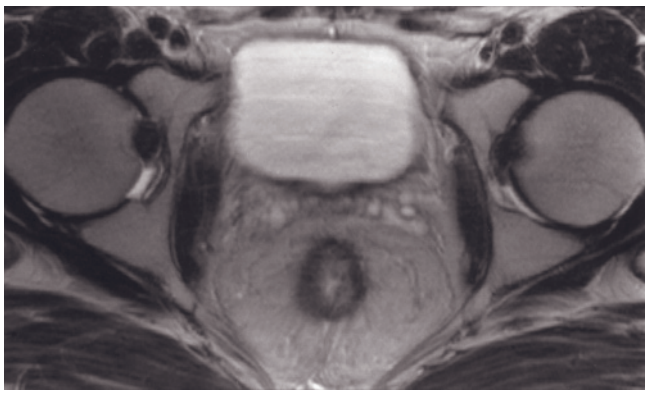

(*a*)

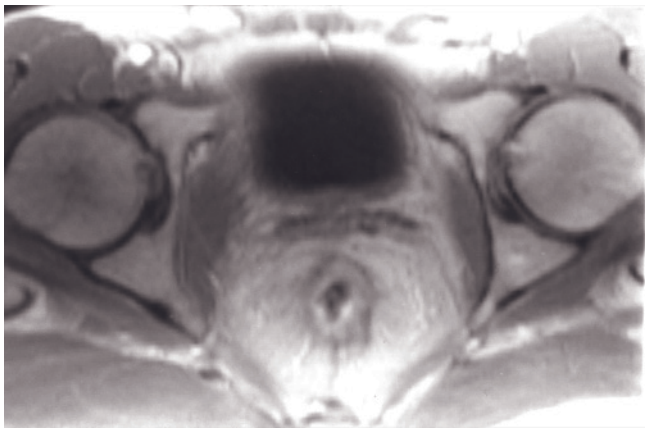

(*b*)

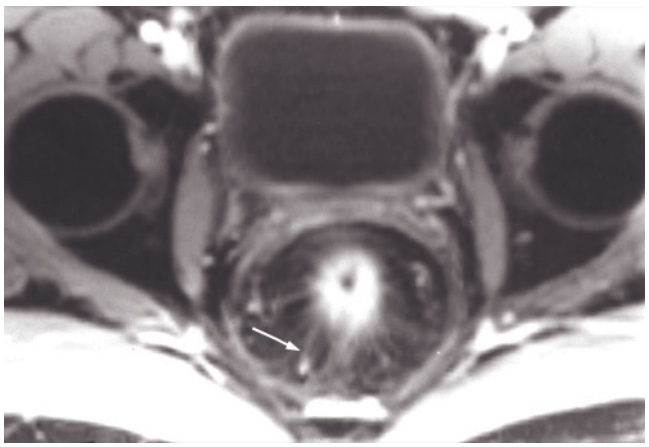

(*c*)

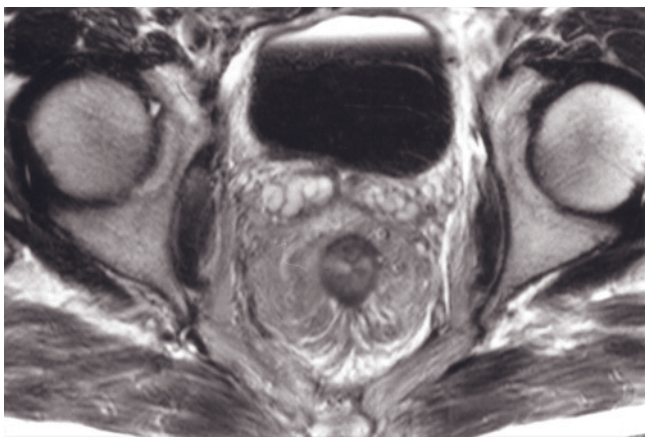

(*d*)

(*e*)

FIG. 6.152 Radiation proctitis. Transverse T2-weighted ETSE (*a*), immediate postgadolinium SGE (*b*), and interstitial-phase gadolinium-enhanced SGE (*c*) images. The rectal wall is thickened with multiple radiating soft tissue strands (arrow, *c*) in the perirectal fat. There is intense enhancement of the rectum consistent with radiation-induced inflammation. Abundant perirectal fat is also appreciated. These findings are consistent with postradiation changes. Transverse (*d*) and sagittal (*e*) T2-weighted ETSE and transverse (*f*) and sagittal (*g*) interstitial-phase gadolinium-enhanced SGE images in a second patient after radiation therapy show substantial thickening of the rectal wall with extensive linear strands in the enlarged perirectal fat.

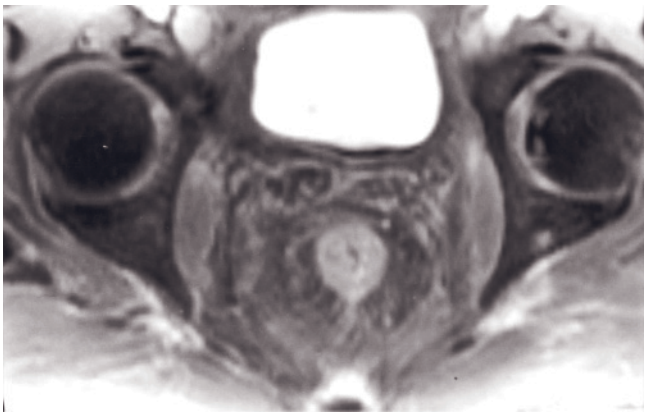

(*f*)

(*g*)

FIG. 6.152 (*Continued*)

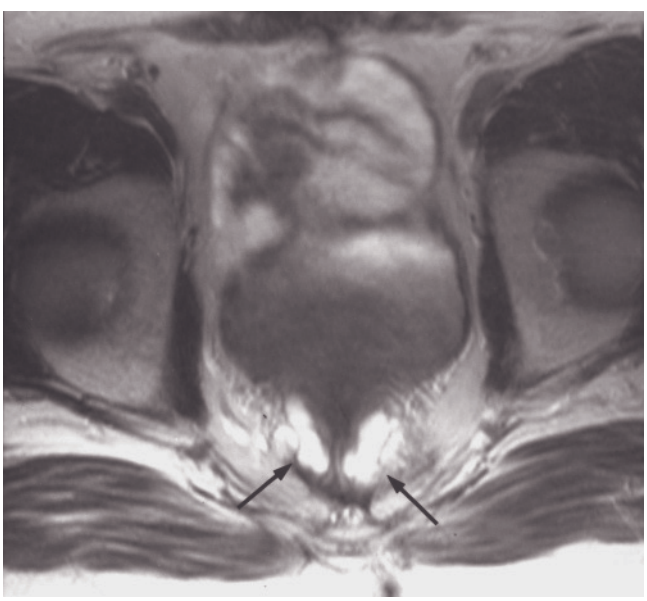

(*a*)

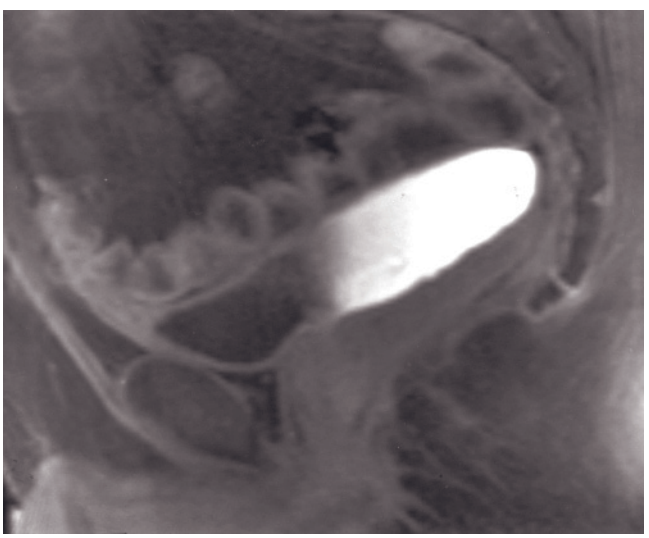

(*b*)

FIG. 6.153 Abdominoperineal resection (APR). Axial T2-weighted ETSE (*a*) and sagittal interstitial-phase gadolinium-enhanced fat-suppressed SGE (*b*) images. The bladder and the seminal vesicles (arrows, *a*) are located posteriorly in the pelvis.

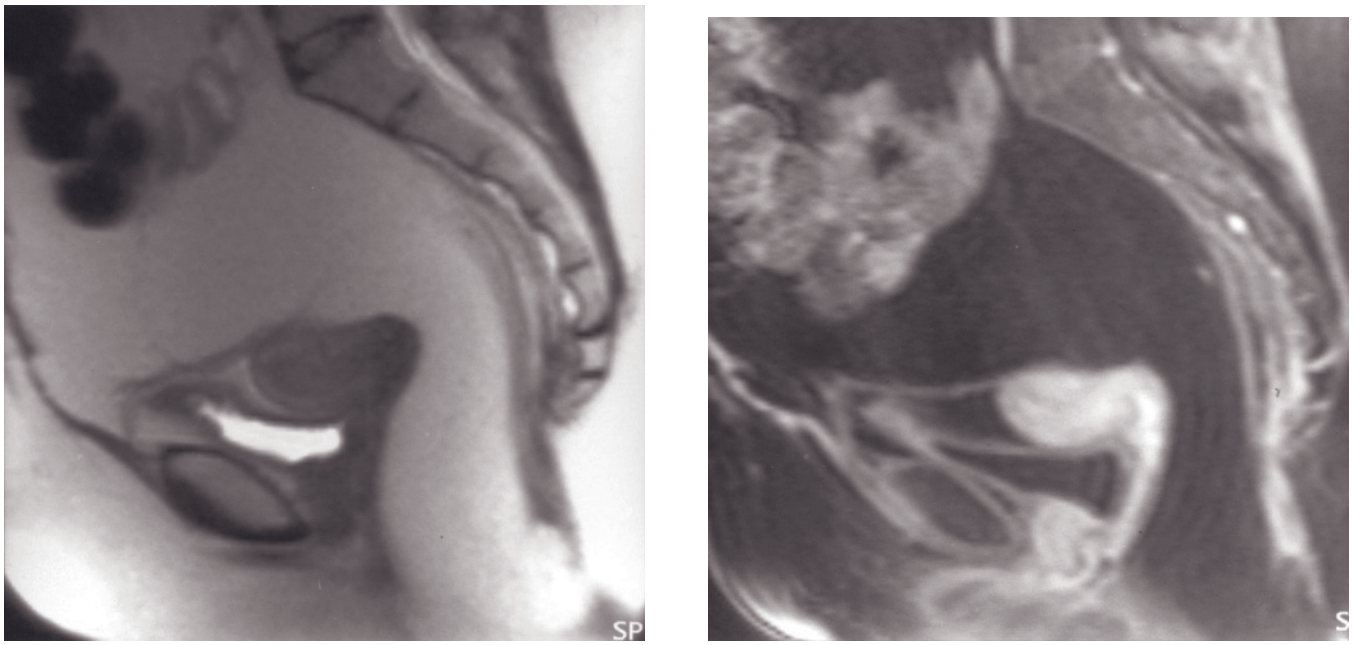

(*c*) (*d*)

FIG. 6.153 (*Continued*) Sagittal T2-weighted SS-ETSE (*c*) and sagittal interstitial-phase gadolinium-enhanced fat-suppressed SGE (*d*) images in a second patient show increase of pelvic fat consistent with omental packing.

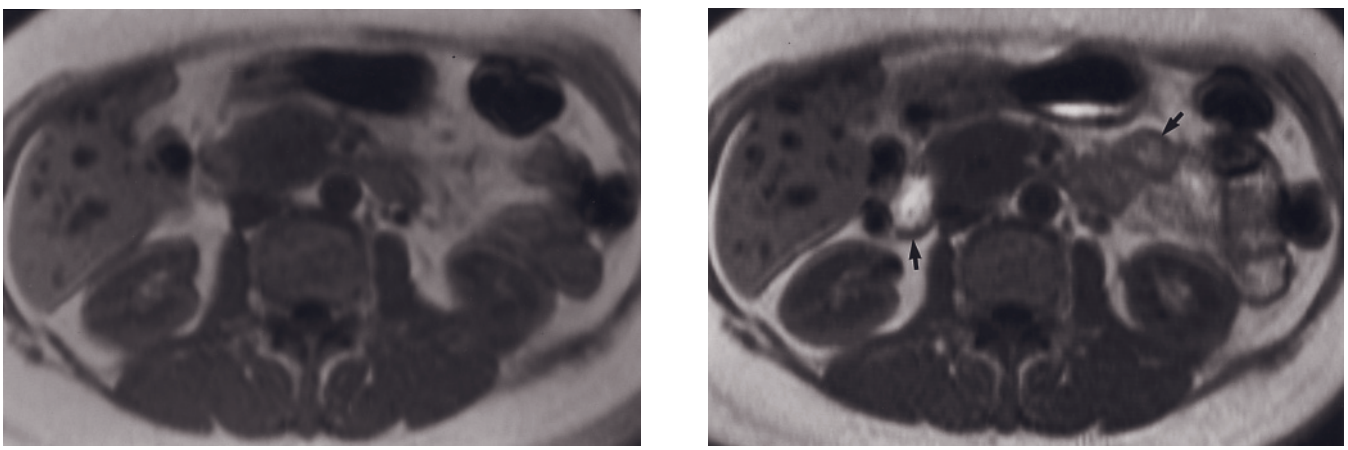

(*a*) (*b*)

FIG. 6.154 Positive oral contrast agent. SGE images before (*a*) and after (*b*) ingestion of ferric ammonium citrate (FAC). Oral contrast causes high signal intensity within the bowel (arrows, *b*). The bowel loops are readily distinguished from the adjacent pancreas after oral contrast administration. Note that FAC not only results in signal intensity change of the bowel lumen but distends it as well.

Positive Intraluminal Contrast Agents

Manganese-containing agents, ferric ammonium citrate, and gadolinium-containing agents have been employed as positive intraluminal agents (fig. 6.154). They are all paramagnetic [127–129]. To date, none of these agents is in routine use. Positive intraluminal agents may be useful to distinguish bowel (which would be rendered as high signal) from encapsulated fluid collections such as abscesses (which would remain low signal). Opacification of fistulous tract could also be demonstrated with these agents. On the other hand, positive intraluminal agents may mask the enhancement of inflammatory bowel wall or bowel masses.

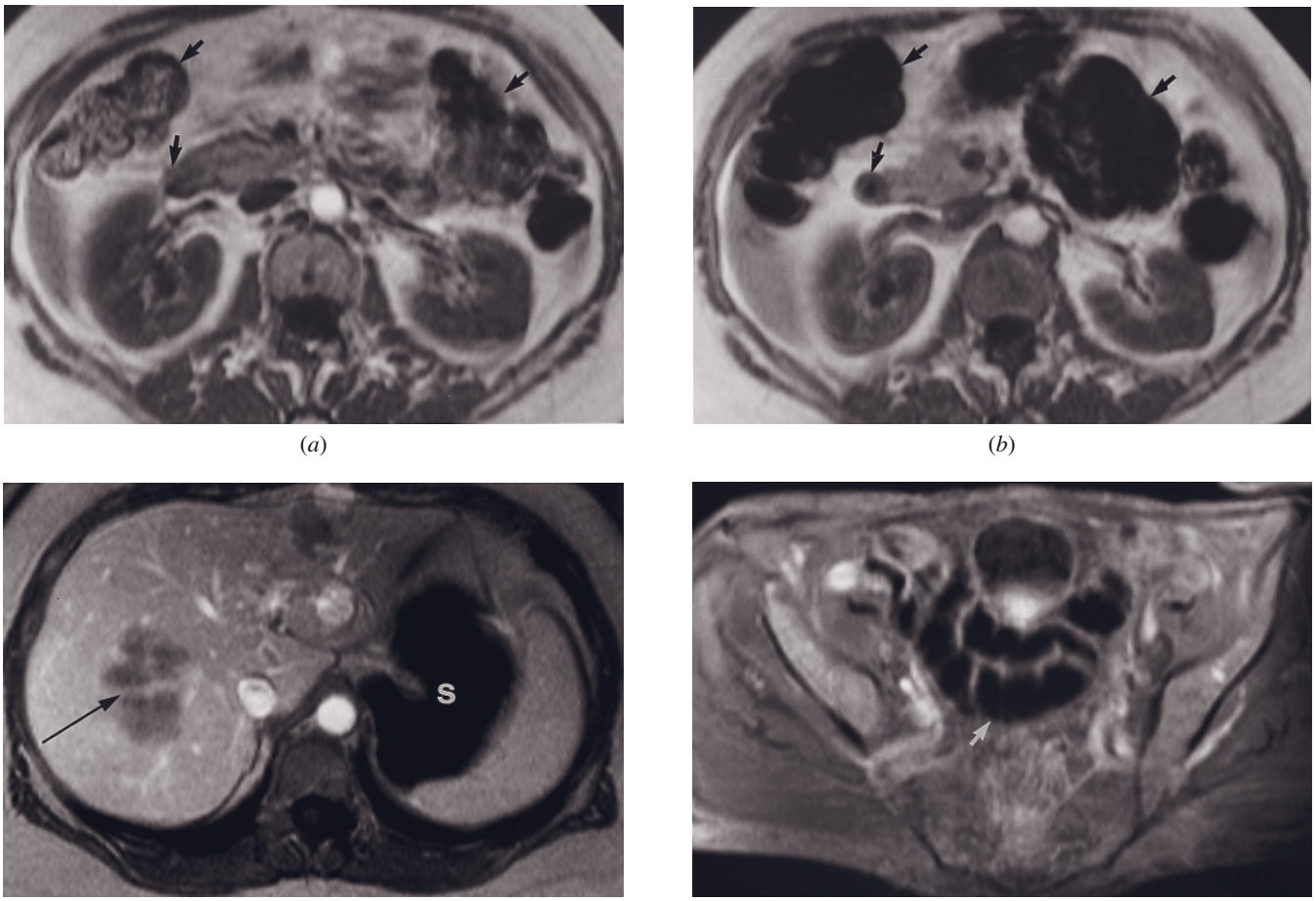

FIG. 6.155 Negative oral contrast agent. SGE images before (*a*) and after (*b*) perfluorooctylbromide (PFOB) ingestion, intravenous gadolinium-enhanced SGE image after PFOB ingestion (*c*), and gadolinium-enhanced T1-weighted fat-suppressed spin-echo image after PFOB ingestion (*d*) in three patients. In the first patient (*a*, *b*), bowel contents are heterogeneous before PFOB intake (arrows, *a*), but after ingestion of PFOB they become nearly signal void (arrows, *b*). PFOB is signal void in the stomach (s, *c*) of a woman with hepatic metastases (arrow, *c*) from cervical carcinoma. In a third patient (*d*), distal small bowel is signal void (arrow, *d*) after PFOB administration. Oral agents distend the bowel, which may aid detection of mucosal abnormalities.

Negative Intraluminal Contrast Agents

Intraluminal contrast agents may result in darkening of the bowel lumen because of lack of mobile protons (perfluorooctylbromide) (fig. 6.155) [130] or superparamagnetic susceptibility effects (oral magnetic particles) (fig. 6.156) [131]. Because of high cost, perfluorooctylbromide is not available at present. A drawback of oral magnetic particles is occasional disturbing susceptibility artifact on T1-weighted SGE images, particularly in the region of the pancreas. Dilute barium results in a high fluid content of bowel and therefore low signal intensity on T1-weighted images and has achieved routine clinical use by some investigators [126]. Water functions well as a low-signal agent on T1-weighted images in the stomach (by oral administration) and colon (by rectal administration) (figs. 6.111–6.113) and has been proposed for screening examinations [90].

FUTURE DIRECTIONS

Future directions include the use of oral contrast agents described above, new intravenous agents, and new imaging techniques. Regarding intravenous agents, iron oxide particle agents have been used for MR lymphography in pilot studies [132]. These agents are taken up by normal lymphoid tissue and hyperplastic lymph nodes, which decrease uniformly in signal intensity on T2-weighted images, whereas nodes involved with malignant disease retain signal intensity. This agent may increase the specificity of detecting malignancy involvement in normal-sized (<1 cm) lymph nodes. Normal-sized malignant lymph nodes are a common occurrence with gastrointestinal malignancies; therefore, improved specificity is of particular value for these tumors. Future imaging directions include real-time,

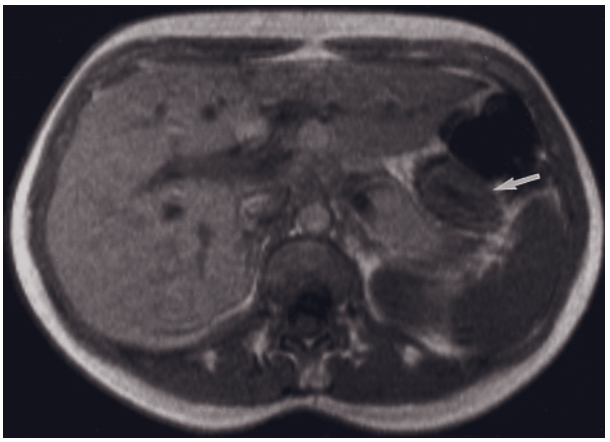

(*a*)

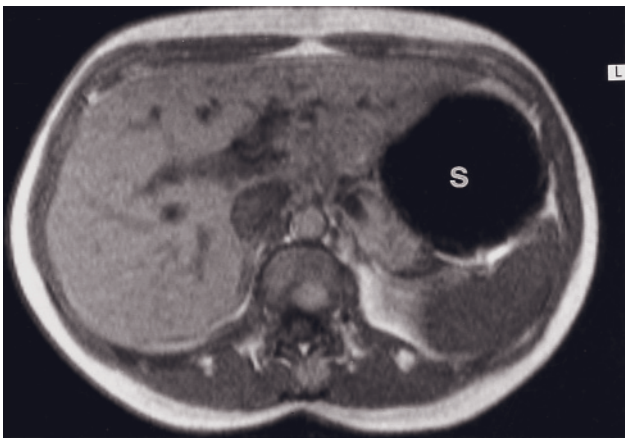

(*b*)

(*c*)

FIG. 6.156 Negative oral contrast agent. SGE before (*a*) and after (*b*, *c*) oral magnetic particle (OMP) ingestion. Before OMP ingestion, the stomach is collapsed, with apparent wall thickening. Once distended with oral contrast, the stomach wall is barely perceptible. Similarly, the small and large bowel are distended and marked by OMP (arrows, *c*). Susceptibility artifact is visualized in many of the loops of bowel (*c*).

dynamic alimentary track imaging (MRI upper GI), 3D intraluminal display (MRI endoscopy, colonography), and therapeutic interventions (e.g., abscess drainage).

REFERENCES

1. Semelka RC, Shoenut JP, Silverman R et al. Bowel disease: prospective comparison of CT and 1.5-T pre- and postcontrast MR imaging with T1-weighted fat-suppressed and breath-hold FLASH sequences. *J Magn Reson Imaging* 1(6): 625–632, 1991.
2. Shoenut JP, Semelka RC, Silverman R et al. Magnetic resonance imaging in inflammatory bowel disease. *J Clin Gastroenterol* 17(1): 73–78, 1993.
3. Shoenut JP, Semelka RC, Magro CM et al. Comparison of magnetic resonance imaging and endoscopy in distinguishing the type and severity of inflammatory bowel disease. *J Clin Gastroenterol* 19(1): 31–35, 1994.
4. Kettritz U, Isaacs K, Warshauer DM et al. Crohn's disease. Pilot study comparing MRI of the abdomen with clinical evaluation. *J Clin Gastroenterol* 21(3): 249–253, 1995.
5. Shoenut JP, Semelka RC, Silverman R et al. Magnetic resonance imaging evaluation of the local extent of colorectal mass lesions. *J Clin Gastroenterol* 17(3): 248–253, 1993.
6. Shoenut JP, Semelka RC, Silverman R et al. The gastrointestinal tract. In: Semelka RC, Shoenut JP, editors. *MRI of the Abdomen with CT Correlation.* New York: Raven Press; 1993. p. 119–143.
7. Outwater E, Schiebler ML. Pelvic fistulas: findings on MR images. *AJR Am J Roentgenol* 160(2): 327–330, 1993.
8. Semelka RC, Hricak H, Kim B et al. Pelvic fistulas: appearances on MR images. *Abdom Imaging* 22(1): 91–95, 1997.
9. Chan TW, Kressel HY, Milestone B et al. Rectal carcinoma: staging at MR imaging with endorectal surface coil. Work in progress. *Radiology* 181(2): 461–467, 1991.
10. Schnall MD, Furth EE, Rosato EF et al. Rectal tumor stage: correlation of endorectal MR imaging and pathologic findings. *Radiology* 190(3): 709–714, 1994.
11. de Lange EE, Fechner RE, Wanebo HJ. Suspected recurrent rectosigmoid carcinoma after abdominoperineal resection: MR imaging and histopathologic findings. *Radiology* 170(2): 323–328, 1989.
12. Balzarini L, Ceglia E, D'Ippolito G et al. Local recurrence of rectosigmoid cancer: what about the choice of MRI for diagnosis? *Gastrointest Radiol* 15(4): 338–342, 1990.
13. Gomberg JS, Friedman AC, Radecki PD et al. MRI differentiation of recurrent colorectal carcinoma from postoperative fibrosis. *Gastrointest Radiol* 11(4): 361–363, 1986.
14. Krestin GP, Steinbrich W, Friedmann G. [Diagnosis of recurrent rectal cancer: Comparison of CT and MR]. *Rofo* 148(1): 28–33, 1988.

15. Pema PJ, Bennett WF, Bova JG et al. CT vs MRI in diagnosis of recurrent rectosigmoid carcinoma. *J Comput Assist Tomogr* 18(2): 256–261, 1994.
16. Waizer A, Powsner E, Russo I et al. Prospective comparative study of magnetic resonance imaging versus transrectal ultrasound for preoperative staging and follow-up of rectal cancer. Preliminary report. *Dis Colon Rectum* 34(12): 1068–1072, 1991.
17. Martin DR, Danrad R, Herrmann K et al. Magnetic resonance imaging of the gastrointestinal tract. *Top Magn Reson Imaging* 16(1): 77–98, 2005.
18. Macpherson RI. Gastrointestinal tract duplications: clinical, pathologic, etiologic, and radiologic considerations. *Radiographics* 13(5): 1063–1080, 1993.
19. Rafal RB, Markisz JA. Magnetic resonance imaging of an esophageal duplication cyst. *Am J Gastroenterol* 86(12): 1809–1811, 1991.
20. Mutrie CJ, Donahue DM, Wain JC et al. Esophageal leiomyoma: a 40-year experience. *Ann Thorac Surg* 79(4): 1122–1125, 2005.
21. Taylor FH, Christenson W, Zollinger RW 2nd et al. Multiple leiomyomas of the esophagus. *Ann Thorac Surg* 60(1): 182–183, 1995.
22. Blot WJ, Devesa SS, Fraumeni JF Jr. Continuing climb in rates of esophageal adenocarcinoma: an update. *JAMA* 270(11): 1320, 1993.
23. Bujanda L. The effects of alcohol consumption upon the gastrointestinal tract. *Am J Gastroenterol* 95(12): 3374–3382, 2000.
24. Maram ES, Kurland LT, Ludwig J et al. Esophageal carcinoma in Olmsted County, Minnesota, 1935–1971. *Mayo Clin Proc* 52(1): 24–27, 1977.
25. Adler DG, Romero Y. Primary esophageal motility disorders. *Mayo Clin Proc* 76(2): 195–200, 2001.
26. Takashima S, Takeuchi N, Shiozaki H et al. Carcinoma of the esophagus: CT vs MR imaging in determining resectability. *AJR Am J Roentgenol* 156(2): 297–302, 1991.
27. Trenkner SW, Halvorsen RA Jr., Thompson WM. Neoplasms of the upper gastrointestinal tract. *Radiol Clin North Am* 32(1): 15–24, 1994.
28. Halvorsen RA Jr., Thompson WM. Primary neoplasms of the hollow organs of the gastrointestinal tract. Staging and follow-up. *Cancer* 67(4 Suppl): 1181–1188, 1991.
29. Marcos HB, Semelka RC. Stomach diseases: MR evaluation using combined T2-weighted single-shot echo train spin-echo and gadolinium-enhanced spoiled gradient-echo sequences. *J Magn Reson Imaging* 10(6): 950–960, 1999.
30. Hamed MM, Hamm B, Ibrahim ME et al. Dynamic MR imaging of the abdomen with gadopentetate dimeglumine: normal enhancement patterns of the liver, spleen, stomach, and pancreas. *AJR Am J Roentgenol* 158(2): 303–307, 1992.
31. Scholz FJ, Vincent ME. The stomach. In: Putnam CE, Ravin CE (eds.), *Textbook of Diagnostic Imaging*. Philadelphia: Saunders, 1988. p. 778–807.
32. Hsia CY, Wu CW, Lui WY. Heterotopic pancreas: a difficult diagnosis. *J Clin Gastroenterol* 28(2): 144–147, 1999.
33. Ciftci AO, Tanyel FC, Hicsonmez A. Gastric diverticulum: an uncommon cause of abdominal pain in a 12 year old. *J Pediatr Surg* 33(3): 529–531, 1998.
34. Velanovich V. Gastric diverticulum. Endoscopic and radiologic appearance. *Surg Endosc* 8(11): 1338–1339, 1994.
35. Nakamura T, Nakano G. Histopathological classification and malignant change in gastric polyps. *J Clin Pathol* 38(7): 754–764, 1985.
36. Eisenberg RL. Single filling defects in the colon. In: Eisenberg RL, editor. *Gastrointestinal Radiology*. Philadelphia: Lippincott; 1983. p. 681–710.
37. Fenoglio-Preiser CM, Noffsinger AE, Stemmermann GN et al. Gastrointestinal Pathology. *Gastrointestinal Pathology*. Philadelphia: Lippincott; 1999, p. 232.
38. Ming SC, Goldman H. *Pathology of the Gastrointestinal Tract*. Philadelphia: Lippincott, 1998.
39. Wingo PA, Tong T, Bolden S. Cancer statistics, 1995. *CA Cancer J Clin* 45(1): 8–30, 1995.
40. Lambert R, Guilloux A, Oshima A et al. Incidence and mortality from stomach cancer in Japan, Slovenia and the USA. *Int J Cancer* 97(6): 811–818, 2002.
41. Parkin DM. International variation. *Oncogene* 23(38): 6329–6340, 2004.
42. Auh YH, Lim TH, Lee DH et al. In vitro MR imaging of the resected stomach with a 4.7-T superconducting magnet. *Radiology* 191(1): 129–134, 1994.
43. Semelka RC, Shoenut JP, Kroeker MA et al. Focal liver disease: comparison of dynamic contrast-enhanced CT and T2-weighted fat-suppressed, FLASH, and dynamic gadolinium-enhanced MR imaging at 1.5 T. *Radiology* 184(3): 687–694, 1992.
44. Hasegawa S, Semelka RC, Noone TC et al. Gastric stromal sarcomas: correlation of MR imaging and histopathologic findings in nine patients. *Radiology* 208(3): 591–595, 1998.
45. Chadrasoma P. *Gastrointestinal Pathology*. Stamford: Appleton & Lange, 1999, p. 371.
46. Jeffrey RB Jr. Abdominal imaging in the immunocompromised patient. *Radiol Clin North Am* 30(3): 579–596, 1992.
47. Liang R, Todd D, Chan TK et al. Prognostic factors for primary gastrointestinal lymphoma. *Hematol Oncol* 13(3): 153–163, 1995.
48. Chou CK, Chen LT, Sheu RS et al. MRI manifestations of gastrointestinal lymphoma. *Abdom Imaging* 19(6): 495–500, 1994.
49. Chou CK, Chen LT, Sheu RS et al. MRI manifestations of gastrointestinal wall thickening. *Abdom Imaging* 19(5): 389–394, 1994.
50. Modlin IM, Lye KD, Kidd M. Carcinoid tumors of the stomach. *Surg Oncol* 12(2): 153–172, 2003.
51. Chadrasoma P. *Gastrointestinal Pathology*. Stamford: Appleton & Lange, 1999, p. 110.
52. Ming SC, Goldman H. *Pathology of the Gastrointestinal tract*. Philadelphia: Lippincott, 1998, p. 563.
53. Yamada T, Alpers DH. *Textbook of Gastroenterology*. Philadelphia: Lippincott, 1991, p. 1302–1305.
54. Ming SC, Goldman H. *Pathology of the Gastrointestinal tract*. Philadelphia: Lippincott, 1998, p. 583.
55. Lee JK, Marcos HB, Semelka RC. MR imaging of the small bowel using the HASTE sequence. *AJR Am J Roentgenol* 170(6): 1457–1463, 1998.
56. Torres AM, Ziegler MM. Malrotation of the intestine. *World J Surg* 17(3): 326–331, 1993.
57. Marcos HB, Semelka RC, Noone TC et al. MRI of normal and abnormal duodenum using half-Fourier single-shot RARE and gadolinium-enhanced spoiled gradient echo sequences. *Magn Reson Imaging* 17(6): 869–880, 1999.
58. Levy AD, Hobbs CM. From the archives of the AFIP. Meckel diverticulum: radiologic features with pathologic correlation. *Radiographics* 24(2): 565–587, 2004.
59. Chew FS, Zambuto DA. Meckel's diverticulum. *AJR Am J Roentgenol* 159(5): 982, 1992.
60. Gill SS, Heuman DM, Mihas AA. Small intestinal neoplasms. *J Clin Gastroenterol* 33(4): 267–282, 2001.
61. Perzin KH, Bridge MF. Adenomas of the small intestine: a clinicopathologic review of 51 cases and a study of their relationship to carcinoma. *Cancer* 48(3): 799–819, 1981.
62. Chappuis CW, Divincenti FC, Cohn I, Jr. Villous tumors of the duodenum. *Ann Surg* 209(5): 593–598; discussion 598–599, 1989.
63. Shekitka KM, Sobin LH. Ganglioneuromas of the gastrointestinal tract. Relation to Von Recklinghausen disease and other multiple tumor syndromes. *Am J Surg Pathol* 18(3): 250–257, 1994.
64. Losty P, Hu C, Quinn F et al. Gastrointestinal manifestations of neurofibromatosis in childhood. *Eur J Pediatr Surg* 3(1): 57–58, 1993.

65. Semelka RC, Marcos HB. Polyposis syndromes of the gastrointestinal tract: MR findings. *J Magn Reson Imaging* 11(1): 51–55, 2000.
66. Teplick SK. The duodenum. In: Putnam CE, Ravin CE, editors. *Textbook of Diagnostic Imaging*. Philadelphia: Saunders, 1988, p. 808.
67. Semelka RC, John G, Kelekis NL et al. Small bowel neoplastic disease: demonstration by MRI. *J Magn Reson Imaging* 6(6): 855–860, 1996.
68. Al-Mondhiry H. Primary lymphomas of the small intestine: east-west contrast. *Am J Hematol* 22(1): 89–105, 1986.
69. Rubesin SE, Gilchrist AM, Bronner M et al. Non-Hodgkin lymphoma of the small intestine. *Radiographics* 10(6): 985–998, 1990.
70. Bader TR, Semelka RC, Chiu VC et al. MRI of carcinoid tumors: spectrum of appearances in the gastrointestinal tract and liver. *J Magn Reson Imaging* 14(3): 261–269, 2001.
71. Semelka RC, Lawrence PH, Shoenut JP et al. Primary ovarian cancer: prospective comparison of contrast-enhanced CT and pre-and postcontrast, fat-suppressed MR imaging, with histologic correlation. *J Magn Reson Imaging* 3(1): 99–106, 1993.
72. Low RN, Barone RM, Lacey C et al. Peritoneal tumor: MR imaging with dilute oral barium and intravenous gadolinium-containing contrast agents compared with unenhanced MR imaging and CT. *Radiology* 204(2): 513–520, 1997.
73. Brahme F, Lindstrom C, Wenckert A. Crohn's disease in a defined population. An epidemiological study of incidence, prevalence, mortality, and secular trends in the city of Malmo, Sweden. *Gastroenterology* 69(2): 342–351, 1975.
74. Goldberg HI, Caruthers SB Jr., Nelson JA et al. Radiographic findings of the National Cooperative Crohn's Disease Study. *Gastroenterology* 77(4 Pt 2): 925–937, 1979.
75. Marcos HB, Semelka RC. Evaluation of Crohn's disease using half-Fourier RARE and gadolinium-enhanced SGE sequences: initial results. *Magn Reson Imaging* 18(3): 263–268, 2000.
76. Tomei E, Semelka RC, Braga L et al. Adult celiac disease: what is the role of MRI? *J Magn Reson Imaging* 24(3): 625–629, 2006.
77. Feeny PC, Stevenson GW. *Margulis*. 5th ed. St Louis: Mosby, 1994, pp. 678–679.
78. Deutsch AA, McLeod RS, Cullen J et al. Results of the pelvic-pouch procedure in patients with Crohn's disease. *Dis Colon Rectum* 34(6): 475–477, 1991.
79. Gutmann LT. *Yersinia enterocolitica* and *Yersinia pseudotuberculosis*. In: Gorbach SI, editor. *Infectious Diarrheia*. Boston: Blackwell Scientific, 1986, p. 65.
80. Lambert ME, Schofield PF, Ironside AG et al. Campylobacter colitis. *Br Med J* 1(6167): 857–859, 1979.
81. Leonardou P, Kierans AS, Elazazzi M, et al. MR imaging findings of small bowel hemorrhage: two cases of mural involvement and one of perimural. *J Magn Reson Imaging* 29(5):1185–1189, 2009.
82. Guingrich JA, Kuhlman JE. Colonic wall thickening in patients with cirrhosis: CT findings and clinical implications. *AJR Am J Roentgenol* 172(4): 919–924, 1999.
83. Warshauer DM, Lee JK. Adult intussusception detected at CT or MR imaging: clinical-imaging correlation. *Radiology* 212(3): 853–860, 1999.
84. Ajaj W, Goehde SC, Schneemann H et al. Dose optimization of mannitol solution for small bowel distension in MRI. *J Magn Reson Imaging* 20(4): 648–653, 2004.
85. Prassopoulos P, Papanikolaou N, Grammatikakis J et al. MR enteroclysis imaging of Crohn disease. *Radiographics* 21 Spec No: S161–172, 2001.
86. Laghi A, Carbone I, Catalano C et al. Polyethylene glycol solution as an oral contrast agent for MR imaging of the small bowel. *AJR Am J Roentgenol* 177(6): 1333–1334, 2001.
87. Hussain SM, Stoker J, Lameris JS. Anal sphincter complex: endoanal MR imaging of normal anatomy. *Radiology* 197(3): 671–677, 1995.
88. Hussain SM, Stoker J, Zwamborn AW et al. Endoanal MRI of the anal sphincter complex: correlation with cross-sectional anatomy and histology. *J Anat* 189 (Pt 3): 677–682, 1996.
89. Okizuka H, Sugimura K, Ishida T. Preoperative local staging of rectal carcinoma with MR imaging and a rectal balloon. *J Magn Reson Imaging* 3(2): 329–335, 1993.
90. Ajaj W, Pelster G, Treichel U et al. Dark lumen magnetic resonance colonography: comparison with conventional colonoscopy for the detection of colorectal pathology. *Gut* 52(12): 1738–1743, 2003.
91. Ajaj W, Lauenstein TC, Pelster G et al. MR colonography: how does air compare to water for colonic distention? *J Magn Reson Imaging* 19(2): 216–221, 2004.
92. Martin DR, Yang M, Thomasson D et al. MR colonography: development of optimized method with ex vivo and in vivo systems. *Radiology* 225(2): 597–602, 2002.
93. Sato Y, Pringle KC, Bergman RA et al. Congenital anorectal anomalies: MR imaging. *Radiology* 168(1): 157–162, 1988.
94. Chadrasoma P. *Gastrointestinal Pathology*. Stamford: Appleton & Lange, 1999, p.319.
95. Chadrasoma P. *Gastrointestinal Pathology*. Stamford: Appleton & Lange, 1999, p. 333.
96. Eisenberg RL. Multiple filling defects in the colon. In: Eisenberg RL, (ed). *Gastrointestinal Radiology*. Philadelphia: Lippincott, 1983. p. 711–739.
97. Younathan CM, Ros PR, Burton SS. MR imaging of colonic lipoma. *J Comput Assist Tomogr* 15(3): 492–494, 1991.
98. Bernstein WC. What are hemorrhoids and what is their relationship to the portal venous system? *Dis Colon Rectum* 26(12): 829–834, 1983.
99. Kee F, Wilson RH, Gilliland R et al. Changing site distribution of colorectal cancer. *Bmj* 305(6846): 158, 1992.
100. Shihab OC, Moran BJ, Heald RJ et al. MRI staging of low rectal cancer. *Eur Radiol* 19(3): 643–650, 2009.
101. Brown G, Radcliffe AG, Newcombe RG et al. Preoperative assessment of prognostic factors in rectal cancer using high-resolution magnetic resonance imaging. *Br J Surg* 90(3): 355–364, 2003.
102. Videhult P, Smedh K, Lundin P et al. Magnetic resonance imaging for preoperative staging of rectal cancer in clinical practice: high accuracy in predicting circumferential margin with clinical benefit. *Colorectal Dis* 9(5): 412–419, 2007.
103. MERCURY Study Group. Diagnostic accuracy of preoperative magnetic resonance imaging in predicting curative resection of rectal cancer: prospective observational study. *BMJ* 333(7572): 779, 2006.
104. de Lange EE, Fechner RE, Edge SB et al. Preoperative staging of rectal carcinoma with MR imaging: surgical and histopathologic correlation. *Radiology* 176(3): 623–628, 1990.
105. Ito K, Kato T, Tadokoro M et al. Recurrent rectal cancer and scar: differentiation with PET and MR imaging. *Radiology* 182(2): 549–552, 1992.
106. Sugimura K, Carrington BM, Quivey JM et al. Postirradiation changes in the pelvis: assessment with MR imaging. *Radiology* 175(3): 805–813, 1990.
107. Bartolo D, Goepel JR, Parsons MA. Rectal malignant lymphoma in chronic ulcerative colitis. *Gut* 23(2): 164–168, 1982.
108. Dragosics B, Bauer P, Radaszkiewicz T. Primary gastrointestinal non-Hodgkin"s lymphomas. A retrospective clinicopathologic study of 150 cases. *Cancer* 55(5): 1060–1073, 1985.
109. Jetmore AB, Ray JE, Gathright JB, Jr. et al. Rectal carcinoids: the most frequent carcinoid tumor. *Dis Colon Rectum* 35(8): 717–725, 1992.
110. Pack GT, Oropeza R. A comparative study of melanoma and epidermoid carcinoma of the anal canal: a review of 20

melanomas and 29 epidermoid carcinomas (1930 to 1965). *Dis Colon Rectum* 10(3): 161–176, 1967.
111. Fenoglio-Preiser CM, Noffsinger AE, Stemmermann GN et al. *Gastrointestinal Pathology.* Philadelphia: Lippincott, 1999, p. 1050.
112. Acheson ED. The distribution of ulcerative colitis and regional enteritis in United States veterans with particular reference to the Jewish religion. *Gut* 1: 291–293, 1960.
113. Hulnick DH, Megibow AJ, Balthazar EJ et al. Computed tomography in the evaluation of diverticulitis. *Radiology* 152(2): 491–495, 1984.
114. Cho KC, Morehouse HT, Alterman DD et al. Sigmoid diverticulitis: diagnostic role of CT—comparison with barium enema studies. *Radiology* 176(1): 111–115, 1990.
115. Chung JJ, Semelka RC, Martin DR et al. Colon diseases: MR evaluation using combined T2-weighted single-shot echo train spin-echo and gadolinium-enhanced spoiled gradient-echo sequences. *J Magn Reson Imaging* 12(2): 297–305, 2000.
116. Balthazar EJ, Megibow AJ, Siegel SE et al. Appendicitis: prospective evaluation with high-resolution CT. *Radiology* 180(1): 21–24, 1991.
117. Keyzer C, Zalcman M, De Maertelaer V et al. Comparison of US and unenhanced multi-detector row CT in patients suspected of having acute appendicitis. *Radiology* 236(2): 527–534, 2005.
118. Birchard KR, Brown MA, Hyslop WB et al. MRI of acute abdominal and pelvic pain in pregnant patients. *AJR Am J Roentgenol* 184(2): 452–458, 2005.
119. Noone TC, Semelka RC, Worawattanakul S et al. Intraperitoneal abscesses: diagnostic accuracy of and appearances at MR imaging. *Radiology* 208(2): 525–528, 1998.
120. Semelka RC, John G, Kelekis NL et al. Bowel-related abscesses: MR demonstration preliminary results. *Magn Reson Imaging* 16(8): 855–861, 1998.
121. Lunniss PJ, Armstrong P, Barker PG et al. Magnetic resonance imaging of anal fistulae. *Lancet* 340(8816): 394–396, 1992.
122. Barker PG, Lunniss PJ, Armstrong P et al. Magnetic resonance imaging of fistula-in-ano: technique, interpretation and accuracy. *Clin Radiol* 49(1): 7–13, 1994.
123. Myhr GE, Myrvold HE, Nilsen G et al. Perianal fistulas: use of MR imaging for diagnosis. *Radiology* 191(2): 545–549, 1994.
124. Larson HE, Price AB, Honour P et al. Clostridium difficile and the aetiology of pseudomembranous colitis. *Lancet* 1(8073): 1063–1066, 1978.
125. Fenoglio-Preiser CM, Noffsinger AE, Stemmermann GN et al. *Gastrointestinal Pathology.* Philadelphia: Lippincott; 1999. p. 819.
126. Pels Rijcken TH, Davis MA, Ros PR. Intraluminal contrast agents for MR imaging of the abdomen and pelvis. *J Magn Reson Imaging* 4(3): 291–300, 1994.
127. Bernardino ME, Weinreb JC, Mitchell DG et al. Safety and optimum concentration of a manganese chloride-based oral MR contrast agent. *J Magn Reson Imaging* 4(6): 872–876, 1994.
128. Wesbey GE, Brasch RC, Goldberg HI et al. Dilute oral iron solutions as gastrointestinal contrast agents for magnetic resonance imaging; initial clinical experience. *Magn Reson Imaging* 3(1): 57–64, 1985.
129. Kaminsky S, Laniado M, Gogoll M et al. Gadopentetate dimeglumine as a bowel contrast agent: safety and efficacy. *Radiology* 178(2): 503–508, 1991.
130. Brown JJ, Duncan JR, Heiken JP et al. Perfluoroctylbromide as a gastrointestinal contrast agent for MR imaging: use with and without glucagon. *Radiology* 181(2): 455–460, 1991.
131. Rubin DL, Muller HH, Sidhu MK et al. Liquid oral magnetic particles as a gastrointestinal contrast agent for MR imaging: efficacy in vivo. *J Magn Reson Imaging* 3(1): 113–118, 1993.
132. Hovels AM, Heesakkers RA, Adang EM et al. Cost-analysis of staging methods for lymph nodes in patients with prostate cancer: MRI with a lymph node-specific contrast agent compared to pelvic lymph node dissection or CT. *Eur Radiol* 14(9): 1707–1712, 2004.

INDEX

For each index term, the volume number(s) for the page entries is given (*V1*, *V2*).

Abdominal cysts, fetal assessment, *V2*: 1617, 1619
Abdominal fibromatosis, in pregnancy, maternal imaging, *V2*: 1569–1570, 1575
Abdominal imaging:
  abdominal wall hernia, *V2*: 904, 908–909
  abscess, *V2*: 951, 955–959
  aortic aneurysm, *V2*: 1200–1207
  fetal assessment:
    anomalies, *V2*: 1612–1617
    neoplasms, *V2*: 1617–1620
    normal development, *V2*: 1583–1585
  MR strategies for, *V1*: 20–24
    3T general abdomen, *V1*: 23–24
Abdominal-pelvic imaging, protocol for, *V1*: 20, 22
Abdominal wall:
  endometriosis, *V2*: 1504–1507, 1513
  fetal assessment, congenital defects, *V2*: 1615–1617
  MR imaging techniques:
    benign neoplasms, *V2*: 1274, 1281–1283
    hernias, hematomas, and other lesions, *V2*: 904, 908–909, 1274, 1290–1293
    malignant neoplasms, *V2*: 1274, 1284–1290
  in pregnancy, maternal imaging, *V2*: 1570, 1574–1575
Abdominoperineal resection, postsurgical infection, *V1*: 892, 894–895
Ablative therapies, liver metastases, *V1*: 278–287
Abscess(es):
  appendiceal, *V1*: 874, 881
    in pregnancy, maternal imaging, *V2*: 1561–1564
  breast, *V2*: 1712
  enteric, gastrointestinal tract imaging, *V1*: 725
  infectious colitis, *V1*: 888
  intraabdominal, *V1*: 874, 884–885
  kidney, *V2*: 1142, 1144, 1149–1152
    renal transplants, *V2*: 1177, 1180–1181
  large intestine, *V1*: 874, 876–877, 881–886
    pericolonic abscess, diverticulitis, *V1*: 874, 877
  liver:
    amebic (nonpyogenic), *V1*: 430
    metastases, secondary infection, *V1*: 180, 188, 191–192
    pyogenic, *V1*: 418, 422–432
  ovarian abscess, *V2*: 1514, 1516–1517
  pancreas, pancreatic transplants, *V1*: 671–673
  pelvic, *V1*: 874, 884–886
  peritoneal, *V2*: 949, 951, 954–959
  Pouch of Douglas, *V1*: 874, 882–883
  prostate gland, *V2*: 1373–1374
  psoas muscle, *V2*: 1273–1274, 1276–1279
  rectal carcinoids, *V1*: 867–868
  spleen infection, *V1*: 710–711
  testicular, *V2*: 1397–1398
Accessory spleens, MR imaging, *V1*: 681–685
Achalasia, MR imaging, *V1*: 729–730, 732, 734
Acinar cell carcinoma, MR imaging, *V1*: 589
Acquired cystic disease of dialysis, *V2*: 1049, 1052, 1061–1062
Acquired immunodeficiency syndrome (AIDS). *See also* Human immunodeficiency virus (HIV)
  cholangiopathy, *V1*: 505
  esophageal infection, *V1*: 732–733
  infectious colitis, *V1*: 884, 888–892
  infectious enteritis, *V1*: 810, 813–814
  Kaposi sarcoma, *V1*: 748, 756
  mycobacterium avium intracellulare, *V1*: 433–435
ACTHoma, MR imaging, *V1*: 601, 605
Acute cholecystitis, magnetic resonance cholangiopancreatography, *V1*: 468–475
  chemoembolization-induced, *V1*: 468, 476
Acute hepatitis, *V1*: 321–329
Acute mastitis, inflammatory breast carcinoma, differential diagnosis, *V2*: 1739
Acute myelogenous leukemia, spleen infection, *V1*: 710–711
Acute pancreatitis:
  alcohol-related, *V1*: 625
  gallstone-related, *V1*: 625, 632
  MR imaging, *V1*: 625, 628, 631, 636–647
Acute pyelonephritis, *V2*: 1142, 1147–1149
  renal transplants, *V2*: 1177, 1179–1180
Acute tubular necrosis, *V2*: 1120, 1122
Addison disease, adrenal glands, *V2*: 1020
Adenocarcinoma:
  appendiceal, *V1*: 843
  bladder, *V2*: 1316, 1319–1320
  endometroid, *V2*: 1474, 1478
  esophagus, *V1*: 729–731
  fallopian tubes, *V2*: 1551
  female urethra, *V2*: 1403–1404
  gastric, *V1*: 738, 741, 743–751
  large intestine (*See also* Rectal cancer; specific cancers, e.g., Colon cancer)
    imaging studies, *V1*: 843–865
    mucocele, *V1*: 838, 841–842
  liver metastases, imaging studies, *V1*: 151, 153, 157–158
    undifferentiated tumors, *V1*: 162, 164, 177–179
  ovarian malignancies, undifferentiated neoplasms, *V2*: 1533, 1541
  pancreas, *V1*: 552–553, 556–589
  prostate cancer, *V2*: 1352, 1356–1373
  renal metastases, *V2*: 1112, 1115
  small bowel, *V1*: 777, 781–782
  uterus, *V2*: 1488–1491
  vaginal malignancies, *V2*: 1416, 1420–1426
Adenofibromas, benign ovarian neoplasm, *V2*: 1520, 1522–1523
Adenoma malignum, cervix, *V2*: 1489–1491
Adenomatoid tumor, testes, *V2*: 1386, 1388, 1390
Adenomatosis, liver, *V1*: 114–118
Adenomatous polyps:
  gastric polyps, *V1*: 736, 739–741
  rectum, *V1*: 829, 832, 835
  small intestine, *V1*: 775, 777–778
Adenomyomatosis:
  benign prostatic hyperplasia, *V2*: 1349
  endometrial carcinoma, *V2*: 1474–1475
  gallbladder neoplasms, *V1*: 480, 484

Abdominal-Pelvic MRI, Third Edition, edited by Richard C. Semelka. Copyright © 2010 John Wiley & Sons, Inc.

Adenomyosis, uterine, *V2*: 1456, 1466–1470
Adenosclerosis, benign breast lesions, *V2*: 1714, 1716
Adhesions, peritoneal, ovarian cysts, *V2*: 1504, 1508
Adiabatic pulses, fat-suppressed echo-train spin-echo sequences, *V1*: 9–10
Adnexa:
  fallopian tubes:
    carcinoma, *V2*: 1550–1552
    metastases to, *V2*: 1551–1553
    normal anatomy, *V2*: 1500, 1503
  metastases to, endometrial carcinoma, *V2*: 1474, 1476–1477
  MR imaging techniques, *V2*: 1499–1500
  ovary:
    benign neoplasms, *V2*: 1518–1531
      epithelial origin, *V2*: 1518–1523
      germ cell origin, *V2*: 1520–1521, 1526–1529
      sex cord-stromal origin, *V2*: 1525–1526, 1530–1531
    congenital anomalies, *V2*: 1503
    cysts, *V2*: 1500, 1502–1503
      functional cysts, *V2*: 1500, 1502, 1504–1506
      paraovarian/peritoneal cysts, *V2*: 1504, 1508
      theca-lutein cysts, *V2*: 1504, 1507–1508
    ectopic pregnancy, *V2*: 1517
    endometriosis, *V2*: 1504–1513
    hydrosalpinx, *V2*: 1517
    malignant neoplasms, *V2*: 1518
      carcinosarcoma, *V2*: 1545, 1548
      clear cell carcinoma, *V2*: 1533, 1538–1540
      epithelial origin, *V2*: 1531–1533
      germ cell origin, *V2*: 1533–1534, 1540–1544
      lymphoma, *V2*: 1545, 1548–1549
      mucinous tumors, *V2*: 1533, 1536–1538
      primary ovarian carcinoma, *V2*: 1526–1527, 1531
      serous tumors, *V2*: 1533–1536
      sex cord-stromal origin, *V2*: 1540, 1542, 1545–1547
    metastases to, *V2*: 1546–1547, 1549–1550
    normal anatomy, *V2*: 1500–1501
    ovarian torsion, *V2*: 1509–1510, 1514–1516
    pelvic inflammatory disease/tubo-ovarian abscess, *V2*: 1514, 1516–1517
    pelvic varices, *V2*: 1517–1518
    polycystic ovaries, *V2*: 1507, 1509, 1514
    transposed ovary, *V2*: 1500–1502
  pediatric imaging, *V2*: 1650
  in pregnancy, maternal imaging, masses, differential diagnosis, *V2*: 1567, 1569–1570
Adrenal cortex. *See* Adrenal glands, benign and malignant cortical lesions
  carcinoma, *V2*: 998, 1002–1006
Adrenal glands:
  Addison disease, *V2*: 1020
  benign cortical lesions:
    adenomas, *V2*: 969, 971–985
      bilateral, *V2*: 971, 974–976, 981, 984
      capillary blush, *V2*: 971–973, 978–979
      Dixon technique, *V2*: 971, 979
      hyperfunctioning adenomas, *V2*: 971
      minor hemorrhage, *V2*: 971, 982–984
      out-of-phase imaging, *V2*: 971, 983
      signal drop, *V2*: 971, 974, 982–983
    aldosteronomas, *V2*: 977, 986–987
    cysts and pseudocysts, *V2*: 980–981, 984, 991–993
    hemangioma, *V2*: 993–994
    hyperplasia, *V2*: 969–970, 977, 986–987
    myelolipoma, *V2*: 977–980, 988–990
  hemorrhage, *V2*: 1019–1020
  inflammatory disease, *V2*: 1019
  lesion classification and pattern recognition, *V2*: 969
  malignant cortical lesions:
    adrenal cortical carcinoma, *V2*: 998, 1002–1006
    metastastes, *V2*: 994–1002
  medullary masses:
    ganglioma, *V2*: 1006, 1013, 1017
    ganglioneuroblastoma to, *V2*: 1006, 1013, 1017–1018
    lymphoma, *V2*: 1017, 1019
    neuroblastoma, *V2*: 1006, 1012–1017
    pheochromocytoma, *V2*: 998, 1005–1111
    schwannoma, *V2*: 1006
  metastases (*See also* specific types of cancer)
    adenomas, differential diagnosis, *V2*: 964–968, 971
    hepatocellular carcinoma, *V1*: 192, 199
    imaging techniques, *V2*: 994–1002
  MR imaging techniques, *V2*: 963–968
  normal anatomy, *V2*: 963–968
  pediatric imaging, *V2*: 1650
Adrenal insufficiency, Addison disease, *V2*: 1020
Aggressive fibromatosis, *V2*: 912–914
Aicardi syndrome, fetal assessment, *V2*: 1588–1592
Air bubble artifacts:
  bile duct imaging, *V1*: 489, 493–494
  peritoneum, postsurgical air and fluid, *V2*: 936, 940
Aldosteronomas, *V2*: 977, 986–987
Allergy, gastric wall edema, *V1*: 761, 764
Alobar holoprosencephaly, fetal assessment, *V2*: 1588–1592
α1-Antitrypsin deficiency, imaging studies, *V1*: 315, 317
α-fetoprotein (AFP), hepatocellular carcinoma, venous thrombosis, *V1*: 235
Ambiguous genitalia, *V2*: 1415–1416
Amebic abscess, hepatic, *V1*: 430
American College of Radiology (ACR), breast MRI interpretation guidelines, *V2*: 1696–1700
American Joint Committee staging:
  breast cancer, *V2*: 1723–1725
  prostate cancer, *V2*: 1358, 1368
  testicular cancer, *V2*: 1392–1396
Amniotic band syndrome, fetal assessment, *V2*: 1621
Amniotic fluid, MR imaging and, *V2*: 1622–1623
Ampullary adenoma, MR imaging, *V1*: 511, 516
Ampullary carcinoma, bile duct imaging, *V1*: 518, 520, 527–530
Ampullary fibrosis, MRCP imaging, *V1*: 489, 495–496
Ampullary stenosis (bile duct):
  gadolinium-based contrast agent imaging, *V2*: 1771–1773
  MRCP imaging, *V1*: 489
Amyloid, urethra diffuse disease, *V2*: 1377–1380
Amyloidosis, seminal vesicles, *V2*: 1382, 1385
Anal canal:
  anorectal anomalies, *V1*: 827, 831, 833–834
  anorectal melanoma, *V1*: 867, 869
  cloacal repair, *V1*: 827, 833
  normal anatomy, *V1*: 824, 827, 831
  perianal fistula, *V1*: 883, 887–888
  squamous cell carcinoma, *V1*: 860, 866
Androgen exposure, female pseudohermaphroditism, *V2*: 1415–1416
Anesthesia, pediatric MRI, *V2*: 1638–1639, 1645
Aneurysms:
  abdominal aortic, *V2*: 1200–1207
  magnetic resonance angiography, *V2*: 1673, 1684
  renal artery disease, *V2*: 1133, 1135–1136
  renal vein, *V2*: 1138
  splenic artery aneurysm, *V1*: 706–709
Angioimmunoblastic lymphadenopathy, splenic involvement, *V1*: 700–702
Angiomas, spleen, *V1*: 688, 694
Angiomyolipomas:
  fatty liver differential diagnosis, *V1*: 383
  kidney, *V2*: 1063–1068
  liver lesions, *V1*: 67, 70, 80–81
  tuberous sclerosis and, *V2*: 1066, 1069–1071
Angiomyxoma, vulvar malignancies, *V2*: 1421
Angiosarcoma:
  breast cancer, *V2*: 1740–1741
  inferior vena cava, *V2*: 1237–1241
  liver metastases, *V1*: 240, 242, 249
  spleen, *V1*: 704, 706
Angiotropic intravascular lymphoma, liver metastases, *V1*: 238, 242
Anhydramnios, renal agenesis, *V2*: 1613

Annular pancreas, MR imaging, *V1*: 541–544
Anterior urethra, normal anatomy, *V2*: 1375–1376
Antiphospholipase deficiency, renal artery, *V2*: 1137
Aorta:
magnetic resonance angiography, *V2*: 1673, 1679–1684
normal anatomy:
MIP reconstruction, *V2*: 1198–1200
phase mapping, *V2*: 1194
retroperitoneal imaging, *V2*: 1200–1227
aortic aneurysm, *V2*: 1200–1207
aortic dissection, *V2*: 1201, 1208–1212
aortoiliac atherosclerotic disease/thrombosis, *V2*: 1204, 1207, 1214–1223
penetrating ulcers/intramural dissecting hematoma, *V2*: 1201, 1204, 1213
postoperative graft evaluation, *V2*: 1207, 1214, 1216, 1224–1227
Aortic atheroemboli, renal artery disease, *V2*: 1137, 1143
"Aortic cobwebs," aortic dissection, *V2*: 1201, 1208–1212
Aortic dissection:
magnetic resonance angiography, *V2*: 1673, 1684
renal artery disease, *V2*: 1133, 1135
Aortobifemoral graft:
infection, *V2*: 1214, 1216, 1226
postsurgical evaluation, *V2*: 1207, 1214, 1216, 1224–1225
Aortoiliac atherosclerotic disease/thrombosis, retroperitoneal imaging, *V2*: 1204, 1207, 1214–1223
"Aphtoid" ulcerations, Crohn disease, *V1*: 785
Apparent diffusion coefficient (ADC), breast imaging, *V2*: 1696
Appendicitis:
diagnostic imaging, *V1*: 874, 879–881
infectious enteritis, differential diagnosis, *V1*: 810, 813–814
in pregnancy, maternal imaging, *V2*: 1561–1564
Appendix:
abscess, peritoneal inflammation, *V2*: 951, 956
adenocarcinoma, *V1*: 843
carcinoma, peritoneal metastases, *V2*: 918, 923–924, 926
mucocele, *V1*: 832, 841–842
Aqueductal stenosis, fetal assessment, *V2*: 1585–1592
Arachnoid cysts, fetal assessment, *V2*: 1594–1595
Arciform enhancement, spleen, *V1*: 678–681
Arcuate uterus, *V2*: 1441, 1444, 1448
Arterial-phase bolus-track liver examination (ABLE) technique, hepatic arterial dominant phase (HADP) contrast agent, *V2*: 1774–1777
Arterial thrombosis, pancreatic transplants, *V1*: 671, 673
Arteriovenous fistulas, liver imaging, *V1*: 388–392
Arteriovenous malformations, abdominal wall, *V2*: 1274
Ascending colon:
adenocarcinoma, *V1*: 843–844
lipoma, *V1*: 832
Ascites:
intraperitoneal, *V2*: 936, 940–942
benign, *V2*: 936, 942
high-protein-content, *V2*: 936, 941
MRI signal intensity and, *V1*: 1–2
ovarian:
malignant epithelial tumors, *V2*: 1532–1533
theca-lutein ovarian cysts, *V2*: 1504, 1507–1508
Ashkenazi Jews, Crohn disease in, *V1*: 784
Asplenia syndrome, MR imaging, *V1*: 681, 685
Atherosclerotic disease:
abdominal aortic aneurysm, *V2*: 1201–1207
aortoiliac atherosclerotic disease/thrombosis, *V2*: 1204, 1207, 1214–1223
magnetic resonance angiography, *V2*: 1673, 1679–1684
penetrating aortic ulcers, *V2*: 1201, 1204, 1213
renal arterial disease, *V2*: 1128–1129, 1131–1144
Atresia, intestinal, *V1*: 770, 774
Atypical ductal hyperplasia (ADH), benign breast lesions, *V2*: 1715
Autoimmune diseases, chronic liver disease, *V1*: 303–304, 306–315
autoimmune hepatitis, *V1*: 311–314
primary biliary cirrhosis, *V1*: 314–315
primary sclerosing cholangitis, *V1*: 303–304, 306–311
Autoimmune pancreatitis, MR imaging, *V1*: 656, 664, 666
Autosomal dominant polycystic kidney disease (ADPKD):
hepatic cysts, *V1*: 67, 71–72
renal cell carcinoma, *V2*: 1098, 1101
renal cysts, *V2*: 1044, 1047, 1051–1056
Autosomal recessive polycystic kidney disease (ARPKD):
cystic lesions, *V2*: 1047, 1056–1058
fetal assessment, *V2*: 1614–1616

B1 inhomogeneities, 3T MR imaging, *V1*: 33
Background enhancement, breast MRI, *V2*: 1698–1700
"Backwash ileitis," *V1*: 799, 806
Bacterioides spp., tubo-ovarian abscess, *V2*: 1514, 1516–1517
Balloon dilation, achalasia, *V1*: 729–730, 732, 734
Barium studies:
Crohn disease, *V1*: 791
intestinal atresia and stenosis, *V1*: 770, 774
large intestine imaging, negative oral contrast agents, *V1*: 896–897
Bartholin glands:
carcinoma, *V2*: 1421
cysts, *V2*: 1416–1418
Basal cell carcinoma, vulvar malignancies, *V2*: 1421
"Beading," primary sclerosing cholangitis, MRCP imaging, *V1*: 497–499
Beckwith-Wiedemann syndrome, Wilms tumor and, *V2*: 1103–1106
Behçet disease, urethrovaginal fistulas, *V2*: 1408
"Bell clapper" deformity, testicular torsion, *V2*: 1396–1397
Bence Jones proteinuria, renal tubular blockage, *V2*: 1120, 1123–1124
Benign prostatic hyperplasia (BPH), *V2*: 1349–1354
prostate adenocarcinoma, differential diagnosis, *V2*: 1352, 1356–1358
Bezoar, gastric imaging, *V1*: 738, 742
Bicornuate uterus, *V2*: 1441, 1444, 1446
Bile, intraperitoneal, *V2*: 942, 945–946
Bile duct:
abnormal bile signal, *V1*: 460, 463
biliary cystadenoma/cystadenocarcinoma, liver lesions, *V1*: 67, 77–78
cystic disease, *V1*: 489, 493–494, 505, 508–511
diseases:
benign disease:
AIDS-related cholangiopathy, *V1*: 505
ampullary adenoma, *V1*: 511, 516
ampullary fibrosis, *V1*: 489, 495–496
ampullary stenosis, *V1*: 489
Caroli disease, *V1*: 505, 511–513
cholecdocholithiasis, *V1*: 488–492
choledochal cyst, *V1*: 505, 508–510
choledochocele, *V1*: 505, 511
cysts, *V1*: 489, 493–494, 505
infectious cholangitis, *V1*: 499, 502–507
mass lesions, *V1*: 511, 514–520
papillary adenoma, *V1*: 511, 515
papillary dysfunction, *V1*: 489, 493, 497
postsurgical complications, *V1*: 511, 514–515, 517–520
primary sclerosing cholangitis, *V1*: 494, 497–502
sclerosing cholangitis, *V1*: 493–494
imaging studies, *V1*: 483–488
pitfalls, *V1*: 489, 493–494
malignant disease:
carcinoma, intrahepatic/peripheral metastases, *V1*: 238–240, 242, 247–249
cholangiocarcinoma, *V1*: 515–518, 521–526
metastases to, *V1*: 530

Bile duct: (*Continued*)
periampullary/ampullary carcinoma, *V1*: 518, 520, 527–530
gadolinium-based contrast agent imaging, *V2*: 1768, 1770–1773
giant cell tumor, *V1*: 511, 514
magnetic resonance cholangiopancreatography, *V1*: 457, 463–464
normal anatomy, *V1*: 456–460
obstruction:
hepatic transplantation, *V1*: 292, 299
hepatocellular carcinoma, *V1*: 202, 224
pancreatic cancer, obstruction of, *V1*: 552, 562–564
T1-weighted magnetic resonance cholangiopancreatography, *V1*: 460–461
Bilharziosis, bladder calculi, *V2*: 1305
Biliary anastomoses, coronal imaging, *V1*: 464, 466–467
Biliary hamartoma, liver lesions, *V1*: 67, 73–77
colon cancer metastasis, *V1*: 67, 76–77
multiple, *V1*: 67, 74–75
solitary, *V1*: 67, 73
Biliary papillomatosis, MR images, *V1*: 514–515
Biliary system (tree):
air in, liver imaging, *V1*: 411, 413–414
gadolinium-based contrast agents, *V2*: 1771
magnetic resonance cholangiopancreatography, *V1*: 456–457
pancreatic adenocarcinoma, *V1*: 562–563, 566
pediatric imaging, *V2*: 1649
postsurgical complication, *V1*: 511, 514–515, 517–520
stricture, hepatic transplantation, *V1*: 292, 299
Billroth cords, splenic anatomy, *V1*: 677–678
Bilomas:
bile duct imaging, *V1*: 511, 517–518
hepatic transplantation, *V1*: 292, 296–298
infected, pyogenic hepatic abscess, *V1*: 418, 426–427
intraperitoneal, *V2*: 942, 944–945
Black-blood techniques:
aortic imaging, *V2*: 1200
abdominal aortic aneurysm, *V2*: 1201–1207
inferior vena cava, *V2*: 1216, 1223, 1229
congenital anomalies, *V2*: 1223, 1228–1230
portal venous thrombosis, *V1*: 388
vessel imaging, *V2*: 1194–1200
Bladder. *See also* Exstrophic bladder
benign masses:
calcifications, *V2*: 1304–1306
hemangiomas, *V2*: 1304
inflammatory myofibroblastic tumor, *V2*: 1304
leiomyoma, *V2*: 1300, 1302–1303
neurogenic tumors, *V2*: 1304–1305
papilloma, *V2*: 1300–1301
pheochromocytoma, *V2*: 1303
benign prostatic hyperplasia and, *V2*: 1349, 1351–1352
congenital disease, *V2*: 1298–1301
cystitis, *V2*: 1326–1328
cystitis cystica, *V2*: 1326, 1329–1330
cystitis glandularis, *V2*: 1326
edema, *V2*: 1324
endometriosis, *V2*: 1326
fistulas, *V2*: 1326, 1331–1335
cervical cancer metastases, *V2*: 1486, 1489
granulomatous disease, *V2*: 1326
hemorrhagic cystitis, *V2*: 1326, 1329
hypertrophy, *V2*: 1324–1325
malignant masses (*See* Bladder cancer)
metastases to:
cervical cancer, *V2*: 1486, 1488–1489, 1492–1495
vaginal carcinoma, *V2*: 1416, 1423
MR imaging techniques, *V2*: 1297–1298
artifacts, *V2*: 1298–1299
normal anatomy, *V2*: 1297–1298
pediatric imaging, *V2*: 1650
pelvic lipomatosis, *V2*: 1326, 1329–1330
postoperative evaluation, *V2*: 1331, 1335
radiation changes, *V2*: 1331, 1337
reconstruction, *V2*: 1331, 1335–1336
Bladder cancer:
adenocarcinoma, *V2*: 1316, 1319–1320
differential diagnosis, *V2*: 1298–1299
incidence and epidemiology, *V2*: 1305–1306
lymphoma and chloroma, *V2*: 1316, 1321
metastases, *V2*: 1320–1324
nonepithelial neoplasms, *V2*: 1316
primary urothelial neoplasm:
carcinosarcoma, *V2*: 1316
squamous cell carcinoma, *V2*: 1316–1318
transitional cell carcinoma, *V2*: 1306–1316
prostate cancer metastases, *V2*: 1358–1373
urachal carcinoma, *V2*: 1316
Blake pouch cyst, fetal assessment, *V2*: 1591
Bland thrombus, portal venous thrombosis, *V1*: 391, 396–397
Blood imaging, intraperitoneal, *V2*: 936, 943–944. *See also* Black-blood techniques; Bright-blood techniques
Blood pool agents, gadolinium-based, *V2*: 1768, 1772–1774
Blood thrombus, portal venous thrombosis, *V1*: 391, 396
Bochdalek hernia, *V2*: 904–905
Bolus-chase technique, vessel imaging, *V2*: 1195–1200
Bone metastases:
adrenal gland neuroblastoma, *V2*: 1013–1017
bladder cancer, transitional cell carcinoma, *V2*: 1307–1316
body wall tumors, *V2*: 1274, 1288–1290
gadolinium-enhanced T1-weighted images, *V1*: 13
prostate cancer, *V2*: 1358, 1367–1373
rectal adenocarcinoma, *V1*: 852, 861–863
Bourneville disease, renal cysts, *V2*: 1066, 1069–1071
Bowel imaging, fetal assessment, normal development, *V2*: 1583–1585
Bowel obstruction, in pregnancy, maternal imaging, *V2*: 1564
Bowel peristalsis:
abdominal-pelvic MRI artifacts, fast scanning, *V1*: 1–2
adnexal imaging artifacts, *V2*: 1499
Brain imaging:
fetal assessment:
neoplasms, *V2*: 1598
normal anatomy, *V2*: 1578–1583
whole body imaging, *V1*: 36, 40–42
BRCA1/BRCA2 gene, breast cancer, *V2*: 1722–1723
Breast:
benign lesions:
abscess, *V2*: 1712
cysts, *V2*: 1700–1703
fibroadenoma, *V2*: 1702–1706
hamartoma (fibroadenolipoma), *V2*: 1709, 1711
multiple papillomatosis, *V2*: 1709–1711
papilloma, *V2*: 1707–1709
phyllodes tumor, *V2*: 1706–1707
benign mesenchyma tumors, *V2*: 1739–1741
biopsy, MRI guidance and intervention, *V2*: 1760–1762
biopsy, MRI-guided interventions, *V2*: 1760–1762
fat necrosis in, *V2*: 1746, 1749–1752
implants, *V2*: 1754–1759
cancer and, *V2*: 1759
categories, *V2*: 1754–1755
failure, *V2*: 1687–1689, 1755–1757
fat necrosis, *V2*: 1746, 1749–1752
imaging techniques, *V2*: 1757–1759
postoperative MRI, *V2*: 1744–1749
lymph nodes, *V2*: 1712–1714
metastases to, *V2*: 1743–1744
MR imaging techniques:
artifacts, *V2*: 1695
coil systems, *V2*: 1693
congenital anomalies, *V2*: 1700–1701
contrast agents, *V2*: 1694
fat suppression, *V2*: 1695
gradient system, *V2*: 1693
imaging plane, *V2*: 1693–1694
imaging protocol, *V2*: 1694–1695
indications for imaging, *V2*: 1691
interpretation guidelines, *V2*: 1696–1700
magnetic field strength, *V2*: 1692–1693
morphological/kinetic diagnostic features, *V2*: 1697
normal anatomy, *V2*: 1687–1691

patient preparation and positioning, *V2*: 1694
region of interest, *V2*: 1691
reporting system and assessment categories, *V2*: 1697–1698
silicone implant rupture, *V2*: 1687–1689
specificity improvement, *V2*: 1695–1696
nonmass lesions
ductal carcinoma in situ, *V2*: 1715, 1718–1721
fibrocystic changes and sclerosing adenosis, *V2*: 1712, 1714–1716
lobular carcinoma in situ, *V2*: 1721–1722
radial scar, *V2*: 1714–1715, 1717
posttherapeutic MRI, *V2*: 1744–1749
Breast cancer:
angiosarcoma, *V2*: 1740–1742
bile duct/ampulla metastases, *V1*: 520
breast implants and, *V2*: 1759
classification and staging, *V2*: 1723–1725
colloid carcinoma, *V2*: 1732, 1734
dermatofibrosarcoma protuberans, *V2*: 1739, 1741
gallbladder metastases, *V1*: 483, 487
implants, detection in, *V2*: 1759
incidence and prevalence, *V2*: 1722–1723
inflammatory carcinoma, *V2*: 1737, 1739
intraductal papilloma, *V2*: 1736, 1738
invasive diagnostic features, MR imaging, *V2*: 1723
invasive ductal carcinoma, *V2*: 1725–1731, 1736
invasive lobular carcinoma, *V2*: 1727, 1731–1733
liver metastases:
benign lesions, differential diagnosis, *V1*: 177, 190
hemangiomas and, *V1*: 90
infiltrative pattern, *V1*: 162, 172
miliary pattern, *V1*: 173–175
post-radiation recurrence, *V1*: 257, 262–263
pre- and post-chemotherapy, *V1*: 257, 266–268
primary site studies, *V1*: 162, 171–175
ring enhancement imaging, *V1*: 162, 171
lymphoma, *V2*: 1741–1743
medullary carcinoma, *V2*: 1732–1733
mesenchymal tumors, *V2*: 1739–1741
metastases, *V2*: 1743–1744
invasive lobular carcinoma, *V2*: 1727, 1731–1733
MR imaging techniques, *V2*: 1688–1691
neoadjuvant chemotherapy monitoring, *V2*: 1749, 1753–1754
Paget disease, *V2*: 1737–1738
pancreatic metastases, *V1*: 619, 625, 630
papillary carcinoma, *V2*: 1733, 1737
postoperative residual carcinoma, *V2*: 1744–1749
radiation-induced carcinoma, *V2*: 1743
small intestine metastases, *V1*: 782, 792
splenic metastases, *V1*: 701, 703–706
stomach metastases, *V1*: 760
subcutaneous body wall metastases, *V2*: 1274, 1284
tubular carcinoma, *V2*: 1733–1736
Breast-conserving therapy (BCT):
fat necrosis, *V2*: 1746, 1749–1752
posttreatment MRI, *V2*: 1744–1749
Breast feeding, gadolinium-based contrast agents and, *V2*: 1786
Breast Image Reporting and Data System (BI-RADS®):
breast cancer imaging, *V2*: 1723
breast cysts, *V2*: 1701–1703
breast MRI interpretation guidelines, *V2*: 1696–1700
fibroadenomas, *V2*: 1706
lesion management protocols, *V2*: 1698–1700
reporting system and assessment categories, *V2*: 1697–1700
Breath-hold imaging:
1.5T *vs.* 3T imaging motion sensitivity, *V1*: 35
adrenal glands, *V2*: 964–968
aortic dissection, *V2*: 1201, 1208–1212
gradient echo sequences, motion artifact reduction, *V1*: 2–3
inferior vena cava, *V2*: 1216, 1223, 1229
kidneys, multicystic dysplastic kidney, *V2*: 1048–1049, 1058
noncooperative patients, *V1*: 25
pancreas, *V1*: 536
acute pancreatitis, *V1*: 625, 628, 634–647
islet-cell tumors, *V1*: 591–598
mucinous cystadenoma/cystadenocarcinoma, *V1*: 612–616
serous cystadenoma, *V1*: 606–607, 609–612
pediatric MRI, *V2*: 1637, 1639, 1642–1643
older children, *V2*: 1645–1646
peritoneal inflammation, abscess, *V2*: 951, 954–959
peritoneal metastases, intraperitoneal seeding, *V2*: 918–924
peritoneum, ascites, *V2*: 936, 940–942
renal cell carcinoma, *V2*: 1073–1095
retroperitoneal imaging, *V2*: 1194
small intestine, *V1*: 767–770
spleen, *V1*: 678–681
spoiled gradient echo sequences, *V1*: 3
T1-weighted magnetic resonance cholangiopancreatography, *V1*: 460–461
uterus and cervix, *V2*: 1434
Breathing-averaged protocol, pediatric MRI, *V2*: 1637–1638, 1640
Brenner tumors, benign ovarian neoplasms, *V2*: 1518, 1520–1523
"Bridging vascular sign," ovarian leiomyomas, *V2*: 1525–1526
Bright-blood techniques:
aortic imaging, *V2*: 1200
abdominal aortic aneurysm, *V2*: 1201–1207
inferior vena cava, *V2*: 1216, 1223, 1229
congenital anomalies, *V2*: 1223, 1229–1230
malignancies *vs.* thrombus, differential diagnosis, *V2*: 1240–1241
portal venous thrombosis, *V1*: 388
pulmonary emboli, *V2*: 1673, 1675–1677
vessel imaging, *V2*: 1194–1200
Broad ligament:
leiomyoma of, *V2*: 1449, 1453–1454
paraovarian cysts, *V2*: 1504, 1508
Bronchial stenosis, fetal assessment, *V2*: 1611–1612
Bronchogenic cysts, fetal assessment, *V2*: 1612
Bronchopulmonary sequestration, fetal assessment, *V2*: 1606, 1611–1612
Buck fascia fibrosis, *V2*: 1380–1381
Budd-Chiari syndrome:
acute-onset, *V1*: 398, 401
chronic, *V1*: 401, 406–407
cirrhosis, regenerative nodules, *V1*: 340
hepatic venous thrombosis, *V1*: 398, 401–405
primary sclerosing cholangitis, differential diagnosis, *V1*: 311
subacute, *V1*: 398, 402–405
Burkitt lymphoma:
gallbladder metastases, *V1*: 483, 487
pancreas, *V1*: 619, 624–625
pediatric patient imaging, *V2*: 1648–1649
retroperitoneal malignant masses, *V2*: 1253, 1257
Buttram-Gibbons classification system:
Müllerian duct anomalies, *V2*: 1440–1448
müllerian duct defects, *V2*: 1503

Cadaveric liver assessment, hepatic transplantation protocol, *V1*: 287, 292
Calcifications:
bladder calculi, *V2*: 1304–1306
breast, *V2*: 1688, 1690
breast implants, *V2*: 1759
prostate gland, *V2*: 1371, 1373
renal cysts, *V2*: 1042, 1048
seminal vesicles, *V2*: 1382, 1385
Calculi:
bladder, *V2*: 1304–1306
renal, *V2*: 1159, 1166–1169
Calyceal diverticulum, *V2*: 1164, 1172
Campylobacter jejuni, infectious enteritis, differential diagnosis, *V1*: 810, 813–814
Candida albicans:
esophageal infection, *V1*: 731–734
hepatic parenchyma fungal infection, *V1*: 433, 435–438
spleen infection, *V1*: 710–711

Candidiasis:
hepatic parenchyma, *V1*: 433, 435–438
renal, *V2*: 1155
Capillary phase enhancement:
adrenal glands, *V2*: 964–968
adrenal adenoma, *V2*: 971–973, 975, 978–979
gadolinium-enhanced images, *V1*: 2
T1-weighted sequences, *V1*: 10–13
hepatic arterial dominant phase imaging, gadolinium-based contrast agent, *V2*: 1775–1777
kidneys:
adenoma, *V2*: 1068
oncocytomas, *V2*: 1068, 1072
pancreatic imaging, *V1*: 536
acute pancreatitis, *V1*: 628, 636–647
chronic pancreatitis, *V1*: 648–665
pancreatic adenocarcinoma, *V1*: 553, 557–559, 564–565
spoiled gradient echo sequences, *V1*: 3–4
"Carcinoid syndrome," small intestine carcinoids, *V1*: 779, 790–791
Carcinoid tumors:
ileal, *V1*: 779, 789
kidney, *V2*: 1109–1110
liver metastases, *V1*: 164, 183–185
transcatheter arterial chemoembolization, *V1*: 270, 273
pancreas, *V1*: 602, 607–608
peritoneal metastases, *V2*: 936, 939–940
rectum, *V1*: 867–868
small intestine, *V1*: 779, 790–791
stomach, *V1*: 756, 759
terminal ileum, *V1*: 779, 790–791
Carcinosarcoma:
bladder, *V2*: 1316
endometriosis, *V2*: 1504, 1513
ovarian, *V2*: 1545, 1548
uterine, *V2*: 1475, 1479–1481
Cardiac gating:
esophageal imaging, *V1*: 726–727
vessel imaging, *V2*: 1194–1200
Cardiac motion artifacts, breast MRI, *V2*: 1695
Caroli disease, bile duct cysts, *V1*: 505, 511–513
Caruncle, female urethra, *V2*: 1407
Castleman disease, retroperitoneal benign lymphadenopathy, *V2*: 1249–1250
Catheterization:
bladder imaging, *V2*: 1298–1299
intraperitoneal, *V2*: 945
Cauliflower-type imaging, liver metastases, *V1*: 161–162, 168–170
Cavernous hemangioma, *V2*: 1416, 1420
Cavum septum pellucidum, absence, fetal assessment, *V2*: 1594
Cecum:
adenocarcinoma, *V1*: 843
lipoma, *V1*: 832, 839
lymphoma, *V1*: 860, 867
Celiac disease/sprue, small intestine, *V1*: 799, 807–809
Central nervous system, fetal imaging:
anomalies, *V2*: 1584–1585
normal anatomy, *V2*: 1578–1583
ventriculomegaly, *V2*: 1585–1592
Cerebellar vermis, fetal assessment, MRI, *V2*: 1578–1583
Cerebral ischemia, fetal assessment, *V2*: 1596–1601
Cervical cancer:
adenocarcinoma, undifferentiated carcinoma/sarcoma, *V2*: 1488–1491
adenoma malignum, *V2*: 1489–1491
bladder metastases, *V2*: 1320–1324
carcinoma, *V2*: 1482–1489
recurrence and posttreatment change, *V2*: 1492–1495
endometrial carcinoma, *V2*: 1472–1481
FIGO staging, *V2*: 1482–1488
in pregnancy, maternal imaging, *V2*: 1569, 1572
recurrent carcinoma and posttreatment change, *V2*: 1492–1494
retroperitoneal fibrosis, *V2*: 1249, 1252–1253
urethral metastases, *V2*: 1405
Cervical incompetence, *V2*: 1629–1631
Cervix:
benign disease, nabothian cysts, *V2*: 1467–1468, 1471
congenital anomalies, *V2*: 1441, 1444, 1447–1449
diethylstilbestrol exposure, *V2*: 1448
endometriosis, in pregnancy, *V2*: 1569, 1573–1574
fibroids, in pregnancy, maternal imaging, *V2*: 1569, 1573
metastases to, *V2*: 1492
MR imaging techniques, *V2*: 1433–1434
normal anatomy, *V2*: 1434–1437, 1436–1437
pediatric imaging, *V2*: 1650
in pregnancy:
cervical incompetence, *V2*: 1629–1631
endometriosis, *V2*: 1569, 1573–1574
stenosis, endometriosis and, *V2*: 1506, 1510
Cesarean scar pregnancy, *V2*: 1577–1580
Cesarean section:
placental imaging and, *V2*: 1623, 1625–1627
postpartum uterus imaging, *V2*: 1575–1580
Chagas disease, achalasia, *V1*: 732, 734
Charcot's triad, infectious cholangitis, *V1*: 499
Chemical shift imaging:
3T MR imaging, *V1*: 31–32
bladder artifacts, *V2*: 1298–1299
breast MRI, *V2*: 1695
gradient echo sequences, *V1*: 3
Chemoembolization:
acute cholecystitis, *V1*: 468, 476
transcatheter arterial chemoembolization, liver metastases, *V1*: 268, 270–278
Chemotherapy:
breast cancer, neoadjuvant, posttreatment MRI, *V2*: 1744–1753
liver metastases, *V1*: 257, 264–270
gadolinium-enhanced T1-weighted images, hepatic arterial dominant (capillary) phase, *V1*: 11–13
hemangiomas, differential diagnosis, *V1*: 101, 177, 190
pancreatic cancer, *V1*: 589–590
pancreatitis from, *V1*: 666–667
peritonitis and, *V2*: 949, 953
small intestine, toxicity enteritis, *V1*: 810, 817
spleen lymphomas, *V1*: 700, 702–703
tubulointerstitial kidney disease, *V2*: 1120–1121
Chest-abdominal-pelvic imaging:
protocol for, *V1*: 20, 23
whole body imaging, *V1*: 36, 39–40
Chest imaging. *See also* Lung cancer; Pulmonary disease
future research issues, *V2*: 1684–1685
hilar and mediastinal lymphadenopathy, *V2*: 1666–1667
mass lesions, *V2*: 1666, 1673–1674
mestastases to, *V2*: 1654, 1659–1660, 1662–1665, 1673–1674
MR imaging techniques, *V2*: 1653–1654
normal chest, *V2*: 1655–1657
pleural disease, *V2*: 1666, 1671–1672
protocol for, *V1*: 20, 22
pulmonary infiltrates, *V2*: 1666, 1668–1671
pulmonary MRA:
pulmonary emboli, *V2*: 1673, 1675–1677
vascular abnormalities, *V2*: 1673, 1678–1684
screening applications, *V2*: 1684
Chiari II malformation, fetal assessment, ventriculomegaly, *V2*: 1585–1592
Child-Turcotte-Pugh scale, primary sclerosing cholangitis, *V1*: 304, 311
Chlamydia trachomatis, tubo-ovarian abscess, *V2*: 1514, 1516–1517
Chloroma:
bladder, *V2*: 1316, 1321
kidney, *V2*: 1109, 1111
Cholangiocarcinoma:
bile duct imaging, *V1*: 515–518, 521–526
diffuse hepatocellular carcinoma, differential diagnosis, *V1*: 235
extrahepatic, *V1*: 516–518, 525–527
liver metastases, *V1*: 238–240, 242, 247–249
oriental cholangitis, differential diagnosis, *V1*: 502, 507
peritoneal metastases, *V2*: 918, 923–925

portal venous compression, *V1*: 391
primary sclerosing cholangitis, *V1*: 499
Cholangiopathy, AIDS-related, *V1*: 505
Cholangitis, infectious:
hepatic abscess, *V1*: 418, 424–425
MRCP imaging, *V1*: 499, 502–507
Cholecystectomy, bile duct complications, *V1*: 511, 514–515
Cholecystitis:
acute cholecystitis, *V1*: 468–475
chemoembolization-induced, *V1*: 468, 476
acute on chronic cholecystitis, *V1*: 468, 475
chronic, *V1*: 475, 477–478
hemorrhagic, *V1*: 475–477
xanthogranulomatous, *V1*: 477
Cholecystolithiasis, sonographic imaging, *V1*: 464
Choledochal cysts, MR imaging, *V1*: 505, 508–510
Choledochocele:
ampullary carcinoma and, *V1*: 520, 530
MR imaging, *V1*: 505, 511
small intestine, *V1*: 775–776
Choledocholithiasis:
magnetic resonance cholangiopancreatography, *V1*: 488–492
in pregnancy, maternal imaging, *V2*: 1564
Cholestasis, primary sclerosing cholangitis, MRCP imaging, *V1*: 494, 497–502
Choline levels:
breast NMR spectroscopy, *V2*: 1696
prostate cancer, adenocarcinoma, *V2*: 1352, 1356–1373
Chordoma, abdominal wall metastases, *V2*: 1274, 1289–1290
Choroid plexus papillomas, fetal assessment, *V2*: 1598–1599
Chronic cholecystitis, magnetic resonance cholangiopancreatography, *V1*: 475, 477–479
Chronic liver disease:
autoimmune diseases, *V1*: 303–304, 306–315
autoimmune hepatitis, *V1*: 311–314
primary biliary cirrhosis, *V1*: 314–315
primary sclerosing cholangitis, *V1*: 303–304, 306–311
genetic diseases, *V1*: 315–317
α1-antitrypsin deficiency, *V1*: 315, 317
Wilson disease, *V1*: 315–318
hemangiomas, *V1*: 101, 103–106
hepatitis:
acute on chronic, *V1*: 321, 327
chronic, *V1*: 321
hepatocellular carcinoma, incidence and prevalence, *V1*: 190, 192
nonalcoholic fatty liver disease, *V1*: 317, 319–320
radiation-induced hepatitis, *V1*: 321, 331
viral hepatitis, *V1*: 319, 321–330
Chronic lymphocytic leukemia (CLL), splenomegaly, *V1*: 700–701
Chronic membranous glomerulonephritis, *V2*: 1117, 1119
Chronic pancreatitis, *V1*: 640, 648–665
acute on chronic pancreatitis, *V1*: 656, 657–663
pancreatic adenocarcinoma:
differential diagnosis, *V1*: 575
risk for, *V1*: 552, 562–564
pancreatic adenocarcinoma imaging, differential diagnosis, *V1*: 575
Chronic prostatis, *V2*: 1373
Chronic pyelonephritis, *V2*: 1126, 1128, 1130
Chronic renal failure:
glomerular disease, *V2*: 1117–1120
renal cell carcinoma, *V2*: 1098–1101
Ciliated foregut hepatic cysts, *V1*: 60, 66–70
Circulating fibrocyte hypothesis, nephrogenic systemic fibrosis, *V2*: 1783
Cirrhosis:
autosomal dominant polycystic kidney disease, hepatic cysts, *V1*: 67, 72
biliary:
primary sclerosing cholangitis, *V1*: 304, 306–309, 311, 314–315, 497–502
regenerative nodules, *V1*: 333–334, 339–345
diffuse hyperperfusion and focal hyperperfusion abnormalities in, *V1*: 411, 414–415
dysplastic nodules, *V1*: 340, 342, 346–354
fatty infiltration, *V1*: 333–334
hemangiomas and, *V1*: 101, 103–106
hepatocellular carcinoma incidence and prevalence, *V1*: 188–189, 192
iron-containing nodules, *V1*: 334, 340, 344–346
iron overload, *V1*: 370
liver metastases, differential diagnosis, *V1*: 257, 270
macronodular regenerative nodules, *V1*: 331–333, 339–340
MR imaging studies, *V1*: 331–362
nonalcoholic fatty liver disease, *V1*: 317, 319–320
omental metastases, differential diagnosis, *V2*: 923–924
pathophysiology, *V1*: 321, 331
in pediatric patients, *V1*: 317–318
pediatric patients, imaging protocols, *V2*: 1637, 1642
portal hypertension, *V1*: 348, 351, 359–362
primary biliary cirrhosis, *V1*: 314–315
small intestine, hypoproteinemia, *V1*: 816, 824
subcutaneous varices, *V2*: 1274, 1290–1291
Cisterna chyli dilation, *V2*: 1237
Citrate levels, prostate cancer, *V2*: 1352
Clear cell carcinoma:
endometriosis, *V2*: 1504, 1513
malignant ovarian neoplasms, *V2*: 1533, 1538–1540
vaginal malignancies, *V2*: 1416, 1420–1421
Cleft palate, fetal assessment, *V2*: 1595–1596
head and neck imaging, *V2*: 1601–1607
Cloaca, persistent:
fetal assessment, *V2*: 1614
surgical repair, *V1*: 827, 833
vaginal agenesis/partial agenesis, *V2*: 1410–1411
Cloacogenic carcinoma, liver metastases, *V1*: 128, 137
Clostridium difficile, pseudomembranous colitis, *V1*: 883–884, 892
Clubfoot, fetal assessment, *V2*: 1622
Cocoon formation, intraperitoneal, *V2*: 945, 947
Coil systems, breast MRI, *V2*: 1693
Collagen injections, pelvic floor relaxation, *V2*: 1408–1410
Colloid carcinoma, breast cancer, *V2*: 1732, 1734
Colon cancer. *See also* Ascending colon; Proximal descending colon; Rectosigmoid colon; Sigmoid colon; Transverse colon
adenocarcinoma, *V1*: 843–865
cecum, *V1*: 843
multifocal adenocarcinoma, *V1*: 848, 853
diverticulitis, differential diagnosis, *V1*: 869, 878–879
duodenal metastases, *V1*: 779, 782, 791
imaging protocol for, *V1*: 16, 19–20
liver metastases:
biliary hamartoma, *V1*: 67, 76–77
low-fluid-content metastases, *V1*: 149, 154–155
MR imaging:
contrast agents, *V1*: 52–58
primary site studies, *V1*: 161, 165–171
post-chemotherapy, *V1*: 257, 269
post-resection recurrence, *V1*: 256, 261–262
lymphoma, *V1*: 860, 867
melamona, *V1*: 867, 869
pancreatic metastases, *V1*: 619, 625, 628
peritoneal metastases, *V2*: 918, 923–924, 926
polyps, MR colonography screening, *V1*: 848, 851
squamous cell carcinoma, *V1*: 860, 866
stomach metastases, *V1*: 760
ulcerative colitis and, *V1*: 867
Colonic duplication, *V1*: 827, 832
Colonic fistulae, *V1*: 883, 887–888
Colonic lipoma, *V1*: 832, 840
Colorectal adenocarcinoma, adenomatous polyps, *V1*: 829
Colostomy, peristomal hernia, *V2*: 904, 909

Combined extracellular-intracellular gadolinium-based contrast agents, *V2*: 1768
Common bile duct (CBD). *See* Bile duct
Common hepatic duct (CHD), normal anatomy, *V1*: 456
Computed tomography (CT):
acute pancreatitis, *V1*: 628, 631
adrenal gland imaging:
metastases, *V2*: 998–1002
MR imaging *vs.*, *V2*: 971
bladder cancer, transitional cell carcinoma, *V2*: 1308–1316
chronic pancreatitis imaging, *V1*: 648–665
Crohn disease, *V1*: 791
iodine-based contrast agents, *V2*: 1767
kidneys:
chronic renal failure, *V2*: 1098
MRI *vs.*:
Bosniak classification allteration, *V2*: 1037
calcified renal cysts, *V2*: 1042
liver imaging:
focal nodular hyperplasia, MR imaging *vs.*, *V1*: 121, 129
hepatic transplantation protocol, *V1*: 292
hepatocellular carcinoma, *V1*: 192
MRI *vs.*, *V1*: 192, 203–205
metastases:
computed tomography arterial portography *vs.* MRI, *V1*: 143, 145–147
spiral CT *vs.* MRI, *V1*: 128, 141–144
mycobacterium avium intracellulare, *V1*: 433–435
pancreatic cancer:
adenocarcinoma, *V1*: 552, 558–559
gastrinomas, *V1*: 591
macrocystic serous cystadenoma, *V1*: 607, 611–612
peritoneal metastases, *V1*: 575, 581–583
renal cell carcinoma, MR imaging *vs.*, *V2*: 1098–1099, 1102
whole body imaging, *V1*: 41–42
Computed tomography arterial portography (CTAP), liver imaging:
hemangiomas, *V1*: 88, 100
metastases imaging, MRI *vs.*, *V1*: 143, 145–147
coexistent cysts, *V1*: 190
portal venous thrombosis, *V1*: 397, 399–400
Computed tomography pulmonary angiography (CTPA), *V2*: 1673
Computer-aided diagnosis, breast cancer, *V2*: 1691
Concurrent disease, imaging protocol for, *V1*: 16, 19–20
Congenital adrenal hyperplasia, female pseudohermaphroditism, *V2*: 1415–1416
Congenital heterotopias, stomach, *V1*: 736
Congestive heart failure, liver imaging, *V1*: 407, 411–413
Conjoined twins, imaging studies, *V2*: 1623–1624
Connective tissue disease, cortical necrosis, renal artery, *V2*: 1137, 1142
Conn syndrome, adrenal gland adenomas and hyperplasia, *V2*: 977, 986–987
Contrast agents:
amniotic fluid as, *V2*: 1583–1585
bladder imaging, *V2*: 1298–1299
breast MRI, *V2*: 1694
categorization, *V2*: 1767–1779
contrast-induced nephropathy risk *vs.* nephrogenic system fibrosis risk assessment, *V2*: 1784–1786
gadolinium-based, *V2*: 1767–1777
classification, *V2*: 1768–1774
complications, *V2*: 1779–1786
early hepatic venous phase, *V2*: 1776
enhancement phases, *V2*: 1774
hepatic arterial dominant phase, *V2*: 1774–1777
hepatocyte phase, *V2*: 1777
interstitial phase, *V2*: 1776
gastrointestinal tract imaging, *V1*: 725
intraluminal, large intestine imaging, *V1*: 892, 895–897
iron-based, *V2*: 1777–1779
liver imaging, *V1*: 50–58
manganese-based, *V2*: 1778–1779
pediatric imaging, *V2*: 1647
Contrast-induced nephropathy (CIN):
nephrogenic systemic fibrosis risk *vs.*, *V2*: 1784–1786
risk factors, *V2*: 1767
Core needle biopsy:
breast lesion underestimation, *V2*: 1722
intraductal papilloma, *V2*: 1707, 1709
multiple papillomatosis, *V2*: 1707–1710
radial scar, *V2*: 1714
Coronal plane imaging:
biliary anastomosis, *V1*: 464, 466–467
breast MRI, *V2*: 1693–1694
female urethra, normal anatomy, *V2*: 1401–1403
hepatic transplantation, *V1*: 287, 289
liver:
hepatic cysts, *V1*: 60, 63–64
hypovascular cystic metastases, *V1*: 152
metastases, *V1*: 128, 137–138, 143, 148
Reidel lobe, *V1*: 58–59
viral hepatitis, *V1*: 321, 323–324
magnetic resonance cholangiopancreatography, *V1*: 456, 459
biliary anastomoses, *V1*: 464, 466–467
normal biliary tree, *V1*: 464–465
renal cell carcinoma, stage 3a, *V2*: 1076–1077, 1079–1081
vagina, *V2*: 1409–1410
Corpus callosum, fetal assessment, MRI, *V2*: 1578–1583
agenesis, *V2*: 1585–1592
Corpus cavernosa:
diffuse disease, *V2*: 1377–1380
inflammatory disease, *V2*: 1380–1381
normal anatomy, *V2*: 1375–1376
Corpus luteal cysts, *V2*: 1500, 1503, 1504
in pregnancy, maternal imaging, *V2*: 1569
Corpus spongiosum:
diffuse disease, *V2*: 1377–1380
normal anatomy, *V2*: 1375–1376
Corrosive esophagitis, *V1*: 731
Cortical development malformation, fetal assessment, *V2*: 1595–1596
Cortical necrosis, renal artery disease, *V2*: 1137, 1142
Corticomedullary differentiation (CMD):
acute tubular necrosis, *V2*: 1120, 1122
crossed fused ectopia, *V2*: 1032, 1034
renal artery disease, *V2*: 1133
renal function, *V2*: 1112, 1116–1117
renal parenchymal disease, *V2*: 1112–1124
obstruction, *V2*: 1121, 1125–1126, 1128–1129
renal transplants, *V2*: 1178–1184
Cost issues, whole body MR imaging, *V1*: 41–42
Cranio-caudal view, breast MRI, *V2*: 1693–1694
"Creeping" fat, Crohn disease, *V1*: 785
Crohn collitis, *V1*: 869, 872–874
Crohn disease:
acute on chronic, *V1*: 796, 803–804
Crohn colitis, large intestine, *V1*: 869, 872–874
dilated stagnant bowel loop, *V1*: 796, 805
entero-vesical fistulae, *V1*: 810, 813
infectious enteritis, differential diagnosis, *V1*: 810, 813–814
mild to moderate, *V1*: 795–796
moderate, *V1*: 797
pelvic fistulae, *V1*: 810–812
in pregnancy, *V1*: 796, 802
primary sclerosing cholangitis, MRCP imaging, *V1*: 494, 497–502
severe, *V1*: 793–794, 798–799
severity criteria, *V1*: 796, 802
small intestine, *V1*: 784–785, 791, 793–805
ulcerative colitis, differential diagnosis, *V1*: 785, 867–869, 870–874
urethrovaginal fistulas, *V2*: 1408
Crohn Disease Activity Index (CDAI), *V1*: 796
Cronkhite-Canada syndrome, colonic hamartomas, *V1*: 832
Crossed fused kidney ectopia, *V2*: 1032, 1034–1035
Cryotherapy:
liver metastases, *V1*: 278, 286–287
prostate cancer, *V2*: 1368–1373
Cryptococcal abscess, spleen, *V1*: 710–711
Cryptococcus, spleen infection, *V1*: 710–711

Cryptorchidism, *V2*: 1386–1388
fetal assessment, *V2*: 1613–1614
Cryptosporidium parvum, infectious enteritis, *V1*: 810, 813–814
Cushing syndrome, adrenal glands:
adenomas, *V2*: 971, 982–983
cortical hyperplasia, *V2*: 969–971
Cystadenofibroma, ovarian tumors:
benign neoplasm, *V2*: 1520–1523
borderline malignancy, *V2*: 1531–1532
Cystectomy, bladder reconstruction, *V2*: 1331, 1336
Cystic adenomatoid malformation (CCAM), fetal assessment, *V2*: 1604–1606, 1610–1612
Cystic ectasia, benign prostatic hyperplasia, *V2*: 1349–1354
Cystic fibrosis, pancreatic imaging, *V1*: 544–548
Cystic hygromas, fetal assessment, *V2*: 1598, 1603
Cystic nephroma, *V2*: 1060, 1063–1064
Cystic teratoma, benign ovarian neoplasms, *V2*: 1520–1521, 1523–1528
Cystitis, bladder, *V2*: 1326–1328
hemorrhagic, *V2*: 1326, 1329
Cystitis cystica, bladder, *V2*: 1326, 1329–1330
Cystitis glandularis:
adenocarcinoma, *V2*: 1316, 1319–1320
bladder, *V2*: 1326
Cystoceles, female urethra, *V2*: 1408–1410
Cysts. *See also* Pseudocysts
abdominal/pelvic, fetal assessment, *V2*: 1617, 1619
adrenal glands, *V2*: 980–981, 984, 991–993
pheochromocytoma, *V2*: 1005–1111
arachnoid, fetal assessment, *V2*: 1594–1595
bile duct, *V1*: 489, 493–494, 505, 508–513
choledochal cyst, *V1*: 505, 508–510
Blake pouch cyst, fetal assessment, *V2*: 1591
body wall, *V2*: 1274, 1280–1283
breast, *V2*: 1700–1703
cervix, nabothian cysts, *V2*: 1467–1468, 1471
choledochal cysts, MR imaging, *V1*: 505, 508–510
dacryocystocele, fetal assessment, *V2*: 1604, 1607
esophagus, duplication cysts, *V1*: 726, 728
fetal assessment:
arachnoid cysts, *V2*: 1594–1595
dacryocystocele, *V2*: 1604, 1607
thoracic, *V2*: 1612
ventriculomegaly, *V2*: 1590–1592
gastric duplication cysts, *V1*: 736
hepatic:
autosomal dominant polycystic kidney disease, *V1*: 67, 71–72
ciliated foregut, *V1*: 60, 66–70
ciliated foregut cysts, *V1*: 60, 66–70
coexistent metastases, *V1*: 165, 190
hemorrhagic cyst, *V1*: 60, 65
hydatid cyst, echinococcal disease, *V1*: 430–431
multilocular cyst, *V1*: 60, 65–66
solitary (nonparasitic), *V1*: 60–66
unilocular cyst, *V1*: 60–61
hydatid cyst:
liver imaging, *V1*: 430–431
spleen, *V1*: 683, 687–690
mesenteric cysts, *V2*: 907, 910
ovarian, *V2*: 1500, 1502–1503
dermoid cyst, *V2*: 1520–1521, 1526–1529
endometriotic cyst, *V2*: 1520, 1522–1523
functional cysts, *V2*: 1502, 1504–1506
paraovarian/peritoneal cysts, *V2*: 1504, 1508
in pregnancy, differential diagnosis, *V2*: 1567, 1569–1570
theca-lutein cysts, *V2*: 1504, 1507–1508
prostate, *V2*: 1344, 1347–1349
renal, *V2*: 1035, 1037–1064
acquired dialysis-related cystic disease, *V2*: 1049, 1052, 1061–1062
angiomyolipoma, *V2*: 1063–1068
autosomal dominant polycystic kidney disease, *V2*: 1044, 1047, 1052–1056
autosomal recessive polycystic kidney disease, *V2*: 1047, 1056–1058
calcified cysts, *V2*: 1042, 1048
complex cysts, *V2*: 1037, 1040–1041
fetal assessment, *V2*: 1614–1616
hemhorragic/proteinaceous cysts, *V2*: 1037, 1042–1047
medullary cystic disease, *V2*: 1049, 1059–1060
medullary sponge kidney, *V2*: 1049, 1060
multicystic dysplastic kidney, *V2*: 1047–1049, 1058
multilocular cystic nephroma, *V2*: 1060, 1063–1064
perinephric pseudocysts (parapelvic cysts), *V2*: 1042, 1044, 1050
septated cysts, *V2*: 1042, 1047
simple renal cysts, *V2*: 1035, 1037
thickened wall and infiltration, *V2*: 1043, 1049
tuberous sclerosis, *V2*: 1066, 1069–1071
von Hippel-Lindau disease, *V2*: 1066, 1068, 1072
seminal vesicles, *V2*: 1382, 1384
spleen:
epidermoid cysts, *V1*: 683, 688
hydatid cyst, *V1*: 683, 687–690
testes, scrotum and epididymis, *V2*: 1386, 1389
thoracic, fetal assessment, *V2*: 1612
urachal, *V2*: 1300–1301
vaginal:
Bartholin glands cyst, *V2*: 1416–1418
cavernous hemangioma, *V2*: 1416, 1420
Gartner duct cysts, *V2*: 1416, 1418–1419
Cytomegalovirus:
esophageal infection, *V1*: 731–734
infectious colitis, *V1*: 888
splenomegaly and, *V1*: 709–711

Dacryocystocele, fetal assessment, *V2*: 1604, 1607
Dandy-Walker complex, fetal assessment:
posterior fossa anomalies, *V2*: 1591, 1593–1597
ventriculomegaly, *V2*: 1585–1592
Denys-Drash syndrome, Wilms tumor and, *V2*: 1103–1106
Dermatofibrsarcoma protuberans, breast cancer, *V2*: 1739–1741
Dermoid cyst:
benign ovarian neoplasms, *V2*: 1520–1521, 1526–1529
pediatric patient, imaging protocol, *V2*: 1637, 1643
Desmoid tumor, *V2*: 912–914
Gardner syndrome, *V2*: 1274, 1280–1283
Diabetes mellitus, seminal vesicle calcification, *V2*: 1382, 1385
Dialysis, acquired cystic disease, *V2*: 1049, 1052, 1061–1062
Diaphragm:
fetal assessment:
anomalies, *V2*: 1604, 1612
hernia, *V2*: 1604–1605, 1608–1609
hernias in, *V2*: 904–909
Didelphys uterine anomaly, *V2*: 1441, 1444–1446
vaginal duplication, *V2*: 1412, 1414–1415
Diethylstilbestrol (DES) exposure:
ovarian anomalies, *V2*: 1503
uterine anomalies, *V2*: 1448
vaginal malignancies, *V2*: 1416, 1420–1426
Diffuse hyperperfusion abnormality, liver imaging, *V1*: 389–391, 411, 414–415
Diffuse infiltrative gastric adenocarcinoma, *V1*: 738, 741
Diffuse infiltrative hepatocellular carcinoma, *V1*: 212, 227, 234–238
Diffuse pancreatic adenocarcinoma, *V1*: 570, 576
Diffusion-weighted imaging (DWI), breast, *V2*: 1696
Diffusion-weighted single-shot echo planar imaging:
fetal assessment, *V2*: 1561
non-fat-suppressed *vs.* fat-suppressed images, *V1*: 35–37
Dilated stagnant bowel loop, Crohn disease, *V1*: 796, 805
Direct tumor invasion:
renal cell carcinoma metastases, *V2*: 1082, 1084–1085
splenic metastases, *V1*: 704–705

Disease-based strategies:
MR imaging sequences, *V1*: 14–24
screening applications, *V2*: 1684
whole body imaging, *V1*: 41–42
Disease conspicuity, abdominal-pelvic MRI, signal intensity differences and, *V1*: 1–2
Distal esophagomyotomy, achalasia, *V1*: 732, 734
Distribution of area enhancement, breast cancer imaging, *V2*: 1723
Diverticula, congenital:
bladder, *V2*: 1299–1301
female urethra, *V2*: 1405–1407
small intestine:
duodenal, *V1*: 770, 772–774
Meckel diverticulum, *V1*: 770, 774
stomach, *V1*: 736–738
Diverticular abscess, *V1*: 874, 876–877
Diverticulitis, *V1*: 869, 874–879
pericolonic abscess, *V1*: 874, 877
Diverticulosis, *V1*: 869, 874
Dixon breath-hold imaging technique, adrenal glands:
adenoma, *V2*: 971, 979
normal anatomy, *V2*: 964–968
Donor assessment, hepatic transplantation protocol, *V1*: 287–291
Dotarem gadolinium-based contrast agent, *V2*: 1768
"Double duct sign," pancreatic cancer, bile duct obstruction, *V1*: 552, 562–564
Double-echo out-of-phase imaging, adrenal glands, *V2*: 963–968
Double surface coils, bladder imaging, *V2*: 1298–1299
Drug toxicity, small intestine, *V1*: 810, 817
Ductal carcinoma in situ (DCIS):
benign masses, *V2*: 1715, 1717–1721
breast cancer, risk and prevalence, *V2*: 1723
diagnostic criteria, *V2*: 1699–1700
intraductal papilloma, differential diagnosis, *V2*: 1707–1709
Ductal intraepithelial neoplasia (DIN):
ductal carcinoma in situ, benign lesions, *V2*: 1715, 1718–1721
fibroadenomas, *V2*: 1702–1706
Duct-ectatic mucin-producing tumor, MR imaging, *V1*: 614–621
Duke colon cancer classification, fallopian tube carcinoma, *V2*: 1551, 1554
Duodenum:
adenocarcinoma, *V1*: 777, 781–782
Peutz-Jeghers syndrome, *V1*: 832
colon cancer metastases, *V1*: 779, 782, 791
Crohn disease in, *V1*: 785, 799
diverticulum, *V1*: 770, 772–774
hematoma, *V1*: 816, 823
inflammatory disease (duodenitis), *V1*: 810, 813–814
leiomyoma, *V1*: 775, 780
MALToma, *V1*: 779, 786
neurofibroma, *V1*: 775, 779
varices, *V1*: 775, 781
Duplication anomalies:
cervix, *V2*: 1441, 1444, 1447–1449
colonic duplication, *V1*: 827, 832
enteric duplication cyst, fetal assessment, *V2*: 1617, 1619
esophageal, *V1*: 726, 728
female urethra, *V2*: 1403
gastric duplication cysts, *V1*: 736
kidney, *V2*: 1613
vagina, *V2*: 1412, 1414–1415
Dynamic contrast-enhanced breast MRI, *V2*: 1695–1696
Dysgerminomas, ovarian malignancies, *V2*: 1533
Dysplastic nodules (DNs):
cirrhosis, *V1*: 340, 342, 346–354
hepatocellular carcinoma, *V1*: 189, 198, 202, 212, 357–358
Dysproteinemia, angioimmunoblastic lymphadenopathy, splenic involvement, *V1*: 700–702

Early hepatic arterial dominant phase (EHADP) imaging, gadolinium-based contrast agent, *V2*: 1774–1777
Echinococcal disease, liver imaging, *V1*: 430–433
Echo time (TE):
3T MR imaging, *V1*: 32–36
adrenal gland imaging, *V2*: 963–968
kidney imaging, paroxysmal nocturnal hemoglobinuria, *V2*: 1121, 1127
magnetic resonance cholangiopancreatography, *V1*: 456
small intestine imaging, *V1*: 767–770
whole body imaging, *V1*: 40–42
Echo-train short-tau inversion recovery (Echo-train-STIR) imaging, liver imaging:
focal nodular hyperplasia, *V1*: 121–127
hemangiomas, *V1*: 88, 97–99
hepatic cysts, *V1*: 60, 63
hepatocellular carcinoma, *V1*: 192, 195–197
metastases characterization, *V1*: 128, 140–141
primary sclerosing cholangitis, *V1*: 304, 306–308
Echo-train spin-echo (ETSE) sequences:
abdominal-pelvic imaging, *V1*: 6–10
fat-suppressed echo-train spin-echo sequences, *V1*: 7–10
single-shot echo-train spin-echo sequences, *V1*: 7–8
adnexa, *V2*: 1499–1500
aortic dissection, *V2*: 1201, 1208–1212
bladder, *V2*: 1298
chest imaging, *V2*: 1653–1654
colon cancer, *V1*: 848, 854–857
Gaucher disease, *V1*: 683
imaging parameters, *V1*: 23–24
kidney imaging, *V2*: 1029–1031
lung cancer, pulmonary nodules, *V2*: 1654, 1657, 1662–1665
magnetic resonance cholangiopancreatography, *V1*: 456–461
male pelvis, *V2*: 1343–1344
noncooperative patients, *V1*: 25
pediatric patients, *V2*: 1644
peritoneal inflammation, abscess, *V2*: 951, 954–959
placental imaging, *V2*: 1625–1627
rectal adenocarcinoma, *V1*: 848–850, 852, 857–860
fibrosis, *V1*: 852, 861–865
rectum, *V1*: 824, 827
retroperitoneum imaging, *V2*: 1194
benign lymphadenopathy, *V2*: 1247–1250
malignant metastatic lymphadenopathy, *V2*: 1258–1263
primary neoplasms, *V2*: 1266, 1271
uterine-cervical MRI, *V2*: 1434
Eclampsia, liver imaging, *V1*: 407, 410–411
Ectopic kidney, *V2*: 1032–1033
fetal assessment, *V2*: 1613
Ectopic pregnancy:
cesarean scar pregnancy, *V2*: 1577–1580
sites for, *V2*: 1517
theca-lutein ovarian cysts, *V2*: 1504, 1507–1508
Edema:
bladder, *V2*: 1324
ovarian torsion, *V2*: 1514–1516
Edge artifact, breast MRI, *V2*: 1695
Ejaculatory duct, cysts, *V2*: 1344, 1347–1349
Embryonal carcinoma, testes lesions, *V2*: 1390–1396
Embryonal rhabdomyosarcoma, retroperitoneal imaging, *V2*: 1266, 1272
Encephalocele, fetal assessment, *V2*: 1594–1595, 1597
Endarteritis, small intestine, radiation enteritis, *V1*: 816, 818
Endodermal sinus tumors, ovarian malignancies, *V2*: 1533–1534, 1542–1544
Endoluminal aortic graft placement, *V2*: 1214, 1216, 1224–1227
Endoluminal coil imaging, uterus, *V2*: 1433
Endometrial cancer:
adrenal metastases, *V2*: 994–995, 998–999
carcinoma, *V2*: 1468, 1470–1481
endometriosis, *V2*: 1504, 1513
fallopian tube metastases, *V1*: 155, 1551
hemorrhagic ovarian cyst, *V2*: 1500, 1503
polycystic ovarian syndrome, *V2*: 1509, 1514
liver metastases, imaging studies, *V1*: 149, 151

Endometrial hyperplasia, *V2*: 1448–1450
malignant ovarian neoplasms and, *V2*: 1542, 1545–1547
Endometrial polyps, *V2*: 1448–1450
malignant ovarian neoplasms and, *V2*: 1542, 1545–1547
Endometrioid tumors:
benign ovarian neoplasm, *V2*: 1520–1523
malignant ovarian neoplasms, *V2*: 1533, 1538
Endometrioma:
overian benign neoplasms, *V2*: 1504–1505, 1509, 1512–1513
pregnancy-related, *V2*: 1504, 1513, 1569, 1574–1575
Endometriosis, *V2*: 911
abdominal wall, *V2*: 1504–1507, 1513
bladder involvement, *V2*: 1326
body wall masses, *V2*: 1274, 1282
ovarian benign disease, *V2*: 1504–1507, 1510–1513
in pregnancy, cervical, *V2*: 1569, 1573–1574
Endometritis, postpartum uterus, *V2*: 1578–1580
Endometrium, vaginal agenesis/partial agenesis, *V2*: 1410–1413
Endorectal coil MRI:
bladder, *V2*: 1298–1299
coil imaging, rectal adenocarcinoma, *V1*: 850, 857
female urethra, normal anatomy, *V2*: 1401–1403
male pelvis, *V2*: 1343–1344
rectum, *V1*: 824, 827
vagina, *V2*: 1410
Endoscopic retrograde cholangiopancreatography (ERCP):
biliary anastomoses, *V1*: 464, 466–467
choledocholithiasis, MRCP *vs.*, *V1*: 488–489
intraductal papillary mucinous neoplasms, *V1*: 615
MR imaging *vs.*, *V1*: 455
pancreas divisum, *V1*: 541
pancreatic adenocarcinoma, bile duct obstruction, *V1*: 552, 562–564
primary sclerosing cholangitis, *V1*: 497–502
T2-weighted MRCP, *V1*: 456–457
Endothelial cysts, adrenal glands, *V2*: 981, 984, 991–993
Endovaginal coil imaging:
female urethra:
diverticulum, *V2*: 1405, 1407
normal anatomy, *V2*: 1401–1403
uterus, *V2*: 1433
vagina, *V2*: 1410
Endovascular graft, postsurgical evaluation, *V2*: 1214, 1216, 1226
End-stage kidney disease, hypertension, *V2*: 1146–1147
Entamoeba histolytica, hepatic abscess, *V1*: 430
Enteric abscesses, gastrointestinal tract imaging, *V1*: 725
Enteric duplication cyst, fetal assessment, *V2*: 1617, 1619
Enteric fistulae, gastrointestinal tract imaging, *V1*: 725
Enteritis:
radiation-induced, large intestine, *V1*: 888, 892–894
small intestine:
infectious, *V1*: 810, 813–814
radiation enteritis, *V1*: 815–816, 818
Enterobacter spp., prostate infection, *V2*: 1373–1374
Enteroceles, female urethra, *V2*: 1408–1410
Enterocystoplasty, bladder reconstruction, *V2*: 1331, 1335
Entero-vesical fistulae, Crohn disease, *V1*: 810, 813
Eosinophilic gastroenteritis, small intestine, *V1*: 809
Eovist gadolinium-based contrast agent, *V2*: 1768, 1771–1772
Epidermoid cysts, spleen, *V1*: 683, 688
Epididymis:
congenital anomalies, *V2*: 1386
cystic lesions, *V2*: 1386, 1389
infectious disease, *V2*: 1397–1398
MR imaging, *V2*: 1385
normal anatomy, *V2*: 1383–1384
Epignathi, fetal assessment, *V2*: 1599
Epispadias, *V2*: 1376
Epithelial ovarian neoplasms:
benign tumors, *V2*: 1518–1523
malignant tumors, *V2*: 1531–1533
primary peritoneal carcinoma, differential diagnosis, *V2*: 912, 917
Epithelioid hemangioendothelioma (EHE), liver metastases, *V1*: 251–253
Epstein-Barr virus, splenomegaly and, *V1*: 709–711
Epulis, congenital, fetal assessment, *V2*: 1601, 1605
Erectile dysfunction, congenital anomalies and, *V2*: 1376
Erythropoietin levels, nephrogenic systemic fibrosis and, *V2*: 1782–1783
Escherichia coli, prostate infection, *V2*: 1373–1374
Esophageal varices:
cirrhosis, portal hypertension, *V1*: 351, 361
MR imaging, *V1*: 727
Esophagitis:
radiation-induced, *V1*: 730–731
reflux, *V1*: 729–730, 732
Esophagus. *See also* Lower esophageal sphincter
benign masses, leiomyomas, *V1*: 726–728
duplication cysts, *V1*: 726, 728
infectious disease, *V1*: 731–734
inflammatory disease:
corrosive esophagitis, *V1*: 731
radiation esophagitis, *V1*: 730–731
reflux esophagitis, *V1*: 729–730, 732
malignant masses, *V1*: 729–731
metastases to:
achalasia, *V1*: 732, 734
esophageal cancer, differential diagnosis, *V1*: 729, 731
MR imaging, *V1*: 726
normal anatomy, *V1*: 725–726
Estrogen receptors, invasive ductal carcinoma, *V2*: 1723–1727
Ewing sarcoma, pelvic metastases, *V2*: 1274, 1288
Examination duration, MR imaging strategies and, *V1*: 14–24
Exophytic focal nodular hyperplasia (FNH), MR imaging, *V1*: 121, 133–134
Exophytic gastric adenocarcinoma, *V1*: 738
Exstrophic bladder, *V2*: 1299
adenocarcinoma, *V2*: 1316, 1319–1320
fetal assessment, *V2*: 1617–1618
Extracellular contrast agents, gadolinium-based, *V2*: 1768–1774
Extrahepatic ducts, variations, *V1*: 460, 464
Extramedullary hematopoiesis (EH):
kidney myelofibrosis, *V2*: 1068, 1073
liver MR imaging, *V1*: 67, 79–80
retroperitoneal masses, *V2*: 1249, 1251
Extrarenal pelvis, *V2*: 1164, 1170
Extremeties, fetal MRI, *V2*: 1620–1622
Ex utero intrapartum treatment (EXIT), fetal head and neck anomalies, MRI, *V2*: 1598–1699, 1601–1607

Fallopian tubes:
carcinoma, *V2*: 1550–1552
endometriosis, *V2*: 1505
hydrosalpinx, *V2*: 1517
metastases to, *V2*: 1551–1553
normal anatomy, *V2*: 1500, 1503
paraovarian cysts of Morgagni, *V2*: 1504, 1508
tubo-ovarian abscess, *V2*: 1514, 1516–1517
Familial adenomatous polyposis syndrome, *V1*: 829, 832, 837–838
Fast spin-echo sequences, *V1*: 6
breast, silicone implants, *V2*: 1688–1689, 1757–1759
vaginal metastases, *V2*: 1421–1426
Fat detection:
adrenal gland myelolipoma, *V2*: 979–980, 988–990
adrenal gland pheochromocytoma, *V2*: 1005–1111
echo-train spin-echo sequences, *V1*: 6–7
gradient echo sequences, *V1*: 3
hepatocellular carcinoma, *V1*: 192, 209–212
liver imaging:
angiomyolipomas, *V1*: 67, 70, 80–81
hepatocellular adenoma, *V1*: 107, 109–114
iron deposition coexistence, *V1*: 371, 376

Fat detection: (*Continued*)
out-of-phase (opposed-phase) spoiled gradient echo sequences, *V1*: 4–5
ovaries, benign germ cell tumors, *V2*: 1520–1521, 1526–1529
pancreas, uneven fatty infiltration, *V1*: 542, 545
Fat necrosis (FN), breast-conserving therapy, *V2*: 1746, 1749–1752
Fat-suppressed (FS) echo-train spin-echo sequences:
abdominal-pelvic imaging, *V1*: 7–10
adrenal gland imaging, *V2*: 963–968
neuroblastoma, *V2*: 1013–1017
breast MRI, *V2*: 1695
chronic pancreatitis, *V1*: 649, 652, 653–654
esophageal imaging, *V1*: 726–727
gastrointestinal tract, *V1*: 725
hepatic transplantation, ischemic changes, *V1*: 287, 290–292
liver imaging, *V1*: 46–48
angiomyolipomas, *V1*: 67, 70, 80–81
computed tomography *vs.*, *V1*: 128, 141–144
hepatocellular carcinoma, diffuse infiltrative, *V1*: 212, 227, 234–238
hypovascular metastases, *V1*: 149, 155–157
metastases, *V1*: 128, 138–139
mycobacterium avium intracellulare, *V1*: 433–435
primary sclerosing cholangitis, *V1*: 304, 309–311
viral hepatitis, *V1*: 321, 323–325
pediatric patients, *V2*: 1637
renal function, *V2*: 1112, 1116–1117
renal function assessment, *V2*: 1112, 1116–1117
retroperitoneum:
benign lymphadenopathy, *V2*: 1247–1250
lymphoma, *V2*: 1253–1257
malignant metastatic lymphadenopathy, *V2*: 1258–1263
Fat-suppressed gradient echo sequences:
adnexa, *V2*: 1499–1500
adrenal glands, *V2*: 963–968
adrenal cortical carcinoma, *V2*: 998, 1002–1006
metastases, *V2*: 995–1002
aortic graft evaluation, *V2*: 1214, 1216, 1224–1227
aortoiliac atherosclerotic disease/thrombosis, *V2*: 1204, 1207, 1214–1223
basic principles, *V1*: 4
bile duct, papillary adenoma, *V1*: 511, 515
bladder, *V2*: 1298
fistulas, *V2*: 1331–1335
transitional cell carcinoma, *V2*: 1307–1316
breast MRI, *V2*: 1695
cavernous hemangioma, *V2*: 1416, 1420
cirrhosis, portal hypertension, *V1*: 348, 351, 359–362
colon cancer, *V1*: 843–865
esophageal imaging, esophageal varices, *V1*: 727, 729
esophagus, malignant masses, *V1*: 729–731
kidneys:
angiomyolipomas, *V2*: 1063–1068
renal function assessment, *V2*: 1112, 1116–1117
large intestine:
lipomas, *V1*: 832, 839–840
ulcerative colitis, *V1*: 867–868, 870–871
liver imaging:
hepatic cysts, *V1*: 60–62, 64
metastases detection and characterization, *V1*: 128, 137–143
magnetic resonance cholangiopancreatography, *V1*: 460–461
ovaries:
endometriomas, *V2*: 1506, 1509–1512
pelvic inflammatory disease, *V2*: 1514, 1516–1517
pancreas, *V1*: 536–541
acute pancreatitis, *V1*: 628, 636–647
annular pancreas, *V1*: 542–544
chronic pancreatitis, *V1*: 648–665
cystic fibrosis, *V1*: 545–548
islet-cell tumors, *V1*: 590–598
pancreatic adenocarcinoma, *V1*: 552, 555–556, 570, 577–578
peritoneal inflammation:
abscess, *V2*: 949, 951, 954–959
pancreatitis, *V2*: 940–942, 946, 949
peritoneal metastases, *V2*: 923–924
pleural disease imaging, *V2*: 1666, 1671–1672
rectum, techniques, *V1*: 827, 831
renal function, *V2*: 1112, 1116–1117
retroperitoneum, *V2*: 1193–1194
scrotal hernia, *V2*: 1390
small intestine, *V1*: 775, 781
adenocarcinoma, *V1*: 777, 781–782
Crohn disease, *V1*: 785, 791, 793–805
gastrointestinal stromal tumor, *V1*: 779, 783–785
infectious enteritis, *V1*: 810, 813–814
ischemia and hemorrhage, *V1*: 816, 819–823
polyps, *V1*: 775, 777–778
radiation enteritis, *V1*: 816, 818
stomach, *V1*: 734
gastric adenocarcinoma, *V1*: 743
gastrointestinal stromal tumors, *V1*: 743, 748, 752–758
vessel imaging, inferior vena cava thrombus, *V2*: 1229–1237
Fat suppression effects:
3T MR imaging, ETSE *vs.* SGE sequences, *V1*: 33
magnetic resonance imaging variables, *V1*: 13–15
single-shot echo-train spin-echo *vs.* single-shot echo planar imaging, *V1*: 33–34
Fatty liver:
focal nodular hyperplasia and, *V1*: 379
hepatocellular carcinoma and, *V1*: 380
imaging studies, *V1*: 371, 373, 377–387
adenomatosis, *V1*: 114–115
fat-suppressed echo-train spin-echo sequences, *V1*: 7–10
focal imaging, *V1*: 371, 377
focal nodular hyperplasia, MRI *vs.* CT, *V1*: 121, 129
focal sparing, *V1*: 377, 384–385
hemangiomas, *V1*: 106
hepatic transplantation, *V1*: 299, 303
metastases, *V1*: 128, 140–142
adenoma, *V1*: 128, 142
mild infiltration, *V1*: 377, 380
minimal infiltration, *V1*: 377, 380
moderately severe diffuse infiltration, *V1*: 377, 381–382
multiple small foci, *V1*: 371, 378–379
nonalcoholic fatty liver disease, *V1*: 317, 319–320
segmental variation, *V1*: 377, 386–387
severe infiltration, *V1*: 377, 382–383
pediatric patients, *V2*: 1644
Feridex, iron-based contrast agent, *V2*: 1778–1779
Ferric ammonium citrate, positive intraluminal contrast agents, large intestine imaging, *V1*: 895
Ferumoxide contrast agents, *V2*: 1778–1779
Ferumoxtran contrast agents, *V2*: 1778–1779
Fetal assessment:
anomalies:
abdominal/pelvic cysts, *V2*: 1617–1620
abdominal wall defects, *V2*: 1615–1617
central nervous system, *V2*: 1584–1585
congenital hemangioma, *V2*: 1604, 1607
cortical development anomalies, *V2*: 1595–1596
cystic renal disease, *V2*: 1614–1616
destructive lesions, *V2*: 1596–1601
developmental, *V2*: 1594–1595
gastrointestinal system, *V2*: 1614–1615
head and neck, *V2*: 1598–1599, 1601–1607
hernia, *V2*: 1604–1605, 1608–1609
hydronephrosis, *V2*: 1613–1614
kidneys, *V2*: 1612–1613
persistent cloaca, *V2*: 1614
posterior fossa, *V2*: 1591, 1593–1597
pulmonary maformations, *V2*: 1605–1606, 1610–1612
renal agenesis, *V2*: 1613
renal ectopia and fusion abnormalities, *V2*: 1613
thoracic cysts, *V2*: 1612
thorax, *V2*: 1604, 1612
ventriculomegaly, *V2*: 1585–1592

extremities, *V2*: 1620–1622
fetal weight and amniotic fluid, *V2*: 1622–1623
MR imaging techniques, *V2*: 1561, 1578
multiple gestation, *V2*: 1623–1624
neoplasms:
abdominal, *V2*: 1617–1620
brain, *V2*: 1598–1599, 1600–1607
thoracic, *V2*: 1612
normal anatomy:
abdomen and pelvis, *V2*: 1583–1585
central nervous system, *V2*: 1578–1583
head and neck, *V2*: 1583
thorax, *V2*: 1583
placental imaging, fetal demise, *V2*: 1623, 1625–1627
safety and procedures, *V2*: 1559–1561
Fetal demise, invasive placenta, *V2*: 1625, 1627
Fetal weight, MR imaging and, *V2*: 1622–1623
Fibroadenolipoma, *V2*: 1709, 1711
Fibroadenoma (FA), breast, *V2*: 1702–1706
Fibrocystic breast changes (FCC), *V2*: 1712, 1714–1716
Fibroids, uterine, *V2*: 1456, 1462–1464. *See also* Leiomyomas
in pregnancy, maternal imaging, *V2*: 1567
Fibrolamellar carcinoma, imaging studies, *V1*: 238–239
Fibromas:
benign ovarian neoplasms, *V2*: 1525–1526, 1529–1530
malignant ovarian neoplasms, *V2*: 1540, 1542, 1545–1547
Fibromatosis, aggressive, *V2*: 912–914
Fibromuscular dysplasia, renal arteries and, *V2*: 1133, 1137
Fibrosarcoma, abdominal wall metastases, *V2*: 1274, 1287
Fibrosis:
bladder, transitional cell carcinoma recurrence, differential diagnosis, *V2*: 1308, 1316
chronic pancreatitis, *V1*: 648–665
cirrhosis and, *V1*: 333, 335–338
varices, *V1*: 351, 362
Crohn disease, *V1*: 785
liver:
autoimmune hepatitis and, *V1*: 312–314
chronic hepatitis, *V1*: 321, 330
diffuse hepatocellular carcinoma, differential diagnosis, *V1*: 235
fetal assessment, renal cysts, *V2*: 1614–1616
hepatic transplantation, *V1*: 299, 304
hepatocellular adenoma, *V1*: 113
ovarian, endometriosis, *V2*: 1506–1507, 1509–1512
penis and urethra inflammatory disease, *V2*: 1380–1381
primary sclerosing cholangitis, *V1*: 497–502
rectosigmoid colon adenocarcinoma, *V1*: 852, 858, 861–865
retroperitoneum:
benign masses, *V2*: 1240, 1242–1244
lymphoma, *V2*: 1253–1257
malignant masses, *V2*: 1249, 1252–1253
Fibrothecoma:
benign ovarian neoplasms, *V2*: 1525–1526
malignant ovarian neoplasms, *V2*: 1540, 1542, 1545–1547
Fibrous histiocytoma:
abdominal wall metastases, *V2*: 1274, 1286
inferior vena cava, *V2*: 1240–1241
Fibrous stromal tumors, benign ovarian neoplasms, *V2*: 1518–1523
Field-focusing effect, 3T MR imaging, *V1*: 33
Field of view (FOV):
breast MRI, *V2*: 1692–1693
parallel MR imaging, *V1*: 29–31
three-dimensional gradient echo sequences, *V1*: 3
uterine-cervical MRI, *V2*: 1434
whole body imaging, *V1*: 36, 38
FIGO (International Federation of Gynecology and Obstetrics) classification:
cervical cancer, *V2*: 1482–1488
endometrial carcinoma, *V2*: 1470, 1472–1474
fallopian tube carcinoma, *V2*: 1551
ovarian cancer, epithelial tumors, *V2*: 1532–1533
vaginal malignancies, *V2*: 1416, 1420–1426
Fistulae:
arteriovenous fistulas, liver imaging, *V1*: 388–392
bladder, *V2*: 1326, 1331–1335
cervical cancer metastases, *V2*: 1486, 1489
colonic fistulae, *V1*: 883, 887–888
Crohn disease:
entero-vesical, *V1*: 810, 813
pelvic, *V1*: 810–812
enteric, gastrointestinal tract imaging, *V1*: 725
female urethra, *V2*: 1407–1408
peritoneal, pelvic abscess and, *V2*: 951, 959
small intestine, *V1*: 810–813
vaginal, *V2*: 1421, 1426, 1429–1430
Floating gallstones, T2-weighted imaging, *V1*: 464, 469
Focal hyperperfusion abnormality (FHA), liver imaging, *V1*: 414–415
Focal nodular hyperplasia (FNH):
Budd-Chiari syndrome, *V1*: 403, 406–407
fatty liver and, *V1*: 379
hemangiomas and, *V1*: 90
hepatocellular adenoma, differential diagnosis, *V1*: 113
hepatocyte-specific contrast agents, imaging studies, *V2*: 1768, 1770–1771
hypervascular liver metastases, differential diagnosis, *V1*: 177, 180
liver metastases, differential diagnosis, *V1*: 177, 180
MR imaging, *V1*: 119, 121–136
contrast agents, *V1*: 54, 55–58
exophytic FNH, *V1*: 121, 133–134
fatty infiltration, *V1*: 121, 130–132
in fatty liver, CT comparison, *V1*: 121, 129
large-sized FNH, *V1*: 121, 127
medium-sized FNH, *V1*: 121, 123–126
Foldover artifacts, parallel MR imaging, *V1*: 29–30
Follow-through MR imaging, small intestine:
Crohn disease, *V1*: 796
enteroclysis, *V1*: 767–770
Foregut hepatic cysts, *V1*: 60, 66–70
Foreign bodies, intraperitoneal, *V2*: 945–947
Frequency-selective fat-suppression methods, gradient echo sequences *vs.*, *V1*: 3
Fungal infection:
hepatic parenchyma, *V1*: 433, 435–438
hepatic transplantation, *V1*: 299, 305
renal candidiasis, *V2*: 1155
spleen, *V1*: 710–711

Gadofosveset trisodium (Vasovist), vessel imaging, *V2*: 1198–1200
Gadolinium-based contrast agents (GBCAs), *V2*: 1767–1777
breast feeding and, *V2*: 1786
chronic toxicity, *V2*: 1876
classification, *V2*: 1768–1774
complications, *V2*: 1779–1786
early hepatic venous phase, *V2*: 1776
enhancement phases, *V2*: 1768, 1770, 1774
hepatic arterial dominant phase, *V2*: 1774–1777
hepatocyte phase, *V2*: 1768, 1770, 1777
interstitial phase, *V2*: 1776
nephrogenic systemic fibrosis, *V2*: 1780–1786
pharmacokinetics, *V2*: 1781–1782
toxicity studies, *V2*: 1779–1786
Gadolinium-enhanced imaging. *See also* MultiHance contrast agent (Gd-BOPTA); Primivist (Gd-EOB-DTPA)-enhanced imaging
acute cholecystitis, *V1*: 468, 470–475
adnexa, *V2*: 1499–1500
adrenal glands, *V2*: 963–968
metastases, *V2*: 995–1002
aorta, *V2*: 1200–1227
aortic dissection, *V2*: 1201, 1208–1212
aortic graft evaluation, *V2*: 1214, 1216, 1224–1227
aortoiliac atherosclerotic disease/thrombosis, *V2*: 1204, 1207, 1214–1223

Gadolinium-enhanced imaging (*Continued*)
appendicitis diagnostic imaging, *V1*: 874, 879–881
bile duct, cholangiocarcinoma, *V1*: 517–518, 521–526
bladder, *V2*: 1298
congenital anomalies, *V2*: 1299–1301
cystitis, *V2*: 1326–1328
fistulas, *V2*: 1331–1335
neurofibromas, *V2*: 1304–1305
papilloma, *V2*: 1300–1301
radiation changes, *V2*: 1337
squamous cell carcinoma, *V2*: 1316–1319
transitional cell carcinoma, *V2*: 1307–1316
breast, *V2*: 1688, 1690–1691
breast cancer, *V2*: 1723
chest imaging, *V2*: 1654
hilar and mediastinal lymphadenopathy, *V2*: 1666–1667
pulmonary emboli, *V2*: 1673, 1675–1677
cirrhosis, portal hypertension, *V1*: 348, 351, 359–362
colon cancer, *V1*: 843–865
lymphoma, *V1*: 860, 867
melanoma, *V1*: 867, 869
perirectal/peritoneal metastases, *V1*: 848, 854–857
contrast agents, *V2*: 1767–1777
disease detection and characterization, *V1*: 2
esophageal imaging, *V1*: 726–727
esophageal varices, *V1*: 727, 729
leiomyomas, *V1*: 726–728
malignant masses, *V1*: 729–731
reflux esophagitis, *V1*: 730, 732
fat effects and, *V1*: 13–15
fat-suppressed gradient echo sequences, *V1*: 4
female urethral diverticulum, *V2*: 1405–1407
gallbladder:
acute cholecystitis, *V1*: 472–475
adenomyomatosis, *V1*: 480, 484
carcinoma, *V1*: 481, 485–486
neoplastic polyps, *V1*: 480, 482–483
gastrointestinal tract, *V1*: 725
hepatic abscess, pyogenic, *V1*: 418, 422–432
hepatic transplantation, ischemic changes, *V1*: 287, 290–292
hepatocyte targeting, contrast agents, *V1*: 50–58
kidneys, *V2*: 1029–1031
fibromuscular dysplasia, *V2*: 1133, 1136–1137
hemodialysis effects, *V2*: 1102
hypertrophic kidney, *V2*: 1032, 1037
iron deposition, *V2*: 1121, 1125–1127
lymphoma, *V2*: 1106–1110
myelofibrosis, *V2*: 1073
pelvic kidney, *V2*: 1032
perinephric pseudocyst, *V2*: 1042, 1044, 1050
persistent fetal lobulation, *V2*: 1031
prominent columns of Bertin, *V2*: 1031
renal artery disease, *V2*: 1129, 1131–1144
renal collecting system dilation, *V2*: 1164, 1172
renal filling defects, *V2*: 1159, 1166–1169
renal function, *V2*: 1173–1177
transplants, *V2*: 1177–1184
trauma, *V2*: 1172–1174
Wilms tumor, *V2*: 1103–1106
large intestine:
abscesses, *V1*: 881–886
colonic adenomatous polyps, *V1*: 832, 835–838
colonic fistulae, *V1*: 883, 887–888
diverticulitis, *V1*: 869, 874–879
infectious colitis, *V1*: 888
mucocele, *V1*: 838, 841–842
positive intraluminal contrast agents, *V1*: 895
rectosigmoid carcinoma, *V1*: 850, 857–860
rectosigmoid colon adenocarcinoma, *V1*: 852, 863–865
techniques, *V1*: 824
ulcerative colitis, *V1*: 867–868, 870–871
liver, *V1*: 46, 49–50
arteriovenous fistulas, *V1*: 388–392
autoimmune hepatitis, *V1*: 312–314
bile duct carcinoma, intrahepatic/peripheral metastases, *V1*: 239–240, 242, 247–249
Budd-Chiari syndrome, hepatic venous thrombosis, *V1*: 398, 401–405
contrast agents, *V1*: 54, 55–58
hepatic cysts, solitary (nonparasitic) cysts, *V1*: 60, 64
metastases detection and characterization, *V1*: 128, 137–143
mycobacterium avium intracellulare, *V1*: 433–435
porta hepatis lymphadenopathy, *V1*: 352, 354, 359, 362–365
pyogenic abscess, *V1*: 418, 422–432
transcatheter arterial embolization, *V1*: 268, 270–278
undifferentiated sarcoma, *V1*: 251, 256
magnetization-prepared rapid-acquisition gradient echo sequences, *V1*: 5–6
male pelvis, *V2*: 1343–1344
ovaries:
endometrial implants, *V2*: 1506
endometrioma, *V2*: 1504–1505, 1509, 1513
germ cell tumors, *V2*: 1521
Krukenberg tumor, ovarian metastases, *V2*: 1547, 1550
mucinous cystadenocarcinoma, *V2*: 1533, 1536–1537
pelvic inflammatory disease, *V2*: 1514, 1516–1517
primary ovarian carcinoma, *V2*: 1531
sex cord-stromal tumors, *V2*: 1525–1526, 1529–1531
pancreas, *V1*: 536–541
acute pancreatitis, *V1*: 631
annular pancreas, *V1*: 542–544
autoimmune pancreatitis, *V1*: 664, 666
chronic pancreatitis, *V1*: 648–665
insulinomas, *V1*: 601, 603
mucinous cystadenoma/cystadenocarcinoma, *V1*: 612–616
pancreatic adenocarcinoma, *V1*: 552, 558–559, 562–564
pancreatic transplants, *V1*: 671–673
pediatric patients, *V2*: 1647
pelvic varices, *V2*: 1518
penis and urethra:
inflammatory disease, *V2*: 1380–1381
normal anatomy, *V2*: 1375–1376
peritoneal inflammation:
abscess, *V2*: 949, 951, 954–959
pancreatitis, *V2*: 940–942, 946, 949
peritoneal metastases, intraperitoneal seeding, *V2*: 918–924
portal venous thrombosis, *V1*: 393–398
in pregnancy, *V2*: 1560–1561
placental imaging, *V2*: 1625–1627
postpartum uterus, *V2*: 1578–1580
primary sclerosing cholangitis, MRCP imaging and, *V1*: 499–502
prostate cancer, adenocarcinoma, *V2*: 1357–1373
rectum:
adenocarcinoma, *V1*: 848–850, 858
rectal carcinoid tumors, *V1*: 867–868
techniques, *V1*: 827, 831
renal cell carcinoma, *V2*: 1099, 1102
staging, *V2*: 1073, 1077, 1079–1082, 1084–1087
retroperitoneum, *V2*: 1193–1194
benign lymphadenopathy, *V2*: 1247–1250
small intestine, *V1*: 767–770
adenocarcinoma, *V1*: 777, 781–782
carcinoid tumors, *V1*: 779, 790–791
Crohn disease, *V1*: 785, 791, 793–805
gastrointestinal stromal tumor, *V1*: 779, 783–785
infectious enteritis, *V1*: 810, 813–814
metastases to, *V1*: 782, 791–792
pancreatitis, *V1*: 810, 815
polyps, *V1*: 775, 777–778
radiation enteritis, *V1*: 816, 818
spleen, lymphomas, *V1*: 693–694, 699–703
stomach, *V1*: 734
gastric adenocarcinoma, *V1*: 738, 741, 743–751
gastrointestinal stromal tumors, *V1*: 743, 748, 752–758
postoperative evaluation, *V1*: 761, 766

T1-weighted magnetic resonance cholangiopancreatography, *V1*: 460–461
T1-weighted sequences, *V1*: 10–13
hepatic arterial dominant (capillary) phase, *V1*: 10–13
hepatic venous (interstitial) phase, *V1*: 11
portal venous/early hepatic venous phase, *V1*: 11
testes, scrotum and epididymis, *V2*: 1385
benign neoplasms, *V2*: 1388, 1390
infectious disease, *V2*: 1397–1398
three-dimensional gradient echo sequences, *V1*: 4
uterus:
endometrial hyperplasia/polyps, *V2*: 1449–1450
leiomyomas, *V2*: 1449, 1455–1457
vaginal malignancies, *V2*: 1416, 1420–1426
vessel imaging, *V2*: 1195–1200
inferior vena cava thrombus, *V2*: 1229–1237
signal intensity, *V1*: 14
whole body imaging, *V1*: 39–42
Gadovist gadolinium-based contrast agent, *V2*: 1768
Galactocele, breast cancer, *V2*: 1739–1740
Galactography, intraductal papilloma, differential diagnosis, *V2*: 1707–1709
Gallbladder:
bile layering, *V1*: 460, 464
cirrhosis regenerative nodules, *V1*: 334, 343
diffuse wall thickening, *V1*: 480–481
fetal assessment, normal development, *V2*: 1584–1585
gallstone disease:
acute cholecystitis with, *V1*: 468, 473–475
floating gallstones, *V1*: 464, 469
hyperintense gallstones, *V1*: 464, 469
neoplastic disease:
adenomyomatosis, *V1*: 480, 484
gallbladder carcinoma, *V1*: 480–481, 485–486
gallbladder polyps, *V1*: 480, 482–483
metastases to, *V1*: 483, 487
nonneoplastic disease:
acute cholecystitis, magnetic resonance cholangiopancreatography, *V1*: 468–475
chemoembolization-induced, *V1*: 468, 476
acute on chronic cholecystitis, *V1*: 468, 475
chronic cholecystitis, *V1*: 475, 477–478
gallstone disease, *V1*: 464–465, 467–469
hemorrhagic cholecystitis, *V1*: 475–477
xanthogranulomatous cholecystitis, *V1*: 477
normal anatomy, *V1*: 456
variants, *V1*: 460, 462–464
pediatric imaging, *V2*: 1649
porcelain gallbladder, *V1*: 477, 480
T1-weighted magnetic resonance cholangiopancreatography, *V1*: 460–461
Gallstones, acute pancreatitis and, *V1*: 625, 632
Gamna-Gandy bodies:
cirrhosis and, *V1*: 353
heterozygous thalassemia, *V1*: 374
spleen, *V1*: 711, 714
Ganglioma, adrenal glands, *V2*: 1006, 1012–1017
Ganglioneuroblastoma:
adrenal glands, *V2*: 1006, 1013, 1015–1017
retroperitoneum, *V2*: 1266
Ganglioneuromas, bladder lesions, *V2*: 1304–1305
Gardner syndrome:
colonic adenomatous polyps, *V1*: 829, 832
desmoid tumor, *V2*: 1274, 1280–1283
Gartner duct cyst, *V2*: 1416, 1418–1419
Gas bubbles, liver imaging, post-ablative therapies, *V1*: 286–287
Gastric adenocarcinoma, *V1*: 738, 741, 743–751
antrum, *V1*: 741, 747–748
body, *V1*: 741, 745–746
cardia, *V1*: 741, 744–745
colon cancer, differential diagnosis, *V1*: 843
extensive carcinomatosis, *V1*: 738, 751
pylorus, *V1*: 741, 749
TNM staging, *V1*: 738, 741–742
Gastric banding, *V1*: 761, 766
Gastric bowel imaging, protocol for, *V1*: 20, 22
Gastric diverticulum, imaging studies, *V1*: 736–738
Gastric duplication cysts, imaging studies, *V1*: 736
Gastric neurofibromas, *V1*: 739
Gastric outlet, Crohn disease obstruction, *V1*: 785, 799
Gastric polyps, imaging studies, *V1*: 736, 739–741
Gastric schwannoma, *V1*: 736, 740
Gastric ulceration, *V1*: 761–764
Gastric varices:
cirrhosis, *V1*: 348, 351, 359
MR imaging, *V1*: 738, 742
Gastric wall edema, *V1*: 761, 764
Gastric wall hyperplasia, MR imaging, *V1*: 601
Gastrinomas:
extrapancreatic, *V1*: 591, 593, 599–600
liver metastases, *V1*: 164, 180
transcatheter arterial chemoembolization, *V1*: 270, 272
pancreatic cancer, *V1*: 591, 593, 598–602
multiple, *V1*: 593, 600
Gastrinoma triangle, islet cell tumor imaging, *V1*: 598
Gastrin secretion, stomach carcinoids, *V1*: 759
Gastritis, *V1*: 761–764
atrophic, *V1*: 761, 763
Gastroduodenal pseudoaneurysm, *V2*: 1200–1201, 1205–1206
Gastroenteritis, eosinophilic gastroenteritis, small intestine, *V1*: 809
Gastroesophageal reflux disease (GERD), imaging studies, *V1*: 729–730, 732
Gastrointestinal juvenile polyposis, colonic hamartomas, *V1*: 832
Gastrointestinal stromal tumors (GISTs):
colorectal metastases, *V1*: 860, 866
imaging studies, *V1*: 743, 748, 752–758
high-grade GIST, *V1*: 748, 756
intermediate-to high-grade, *V1*: 748, 757
leiomyomas, *V1*: 726–728
liver metastases, sarcomas, *V1*: 147–150
low grade, *V1*: 748, 757–758
small intestine, *V1*: 777, 779, 783–785
Gastrointestinal tract. *See also* Stomach; specific segments, e.g., Esophagus
fetal assessment, *V2*: 1614–1615
MR imaging, *V1*: 725
pediatric imaging, *V2*: 1650
in pregnancy, maternal imaging, *V2*: 1564–1565
Gastrojejunostomy, *V1*: 761, 766
Gastroschisis, fetal assessment, *V2*: 1617
Gaucher disease, spleen imaging and, *V1*: 683
Genetic disease:
breast cancer, *V2*: 1722–1723
hemochromatosis:
liver imaging, *V1*: 354, 362, 365–368
pancreas, *V1*: 546, 548–549
liver, *V1*: 315–318
α1-antitrypsin deficiency, *V1*: 315, 317
Wilson disease, *V1*: 315–318
pancreas:
cystic fibrosis, *V1*: 544–548
primary hemochromatosis, *V1*: 546, 548–549
von Hippel-Lindau syndrome, *V1*: 549–550
Genitalia. *See also* Gonadal differentiation anomalies; Vagina; specific male and female organs, e.g., Penis
ambiguous, *V2*: 1415–1416
Germ cell tumors:
benign ovarian neoplasms, *V2*: 1520–1521, 1526–1529
malignant ovarian neoplasms, *V2*: 1533–1534, 1540–1544
testes lesions, *V2*: 1390–1396
Gestational trophoblastic disease, *V2*: 1628–1629
postpartum uterus, *V2*: 1578–1580
theca-lutein cysts, *V2*: 1504
Ghosting artifacts, breast MRI, *V2*: 1695

Giant cell tumor:
abdominal wall metastases, *V2*: 1274, 1289, 1290
bile duct, *V1*: 511, 514
Giant lymph node hyperplasia, retroperitoneal benign lymphadenopathy, *V2*: 1249–1250
Giardia lamblia, infectious enteritis, differential diagnosis, *V1*: 810, 813–814
Gleason score, prostate cancer, *V2*: 1368
Glomerular disease, *V2*: 1117–1120
renal vein thrombosis, *V2*: 1137, 1144
Glomerular filtration rate (GFR), nephrogenic systemic fibrosis, *V2*: 1781
Glucagonoma, MR imaging, *V1*: 601, 604
Glucocerebroside accumulation, Gaucher disease, *V1*: 683
Gluten-sensitive enteropathy (GSE), small intestine, *V1*: 799, 807–809
Goiter, fetal assessment, *V2*: 1598
Gonadal differentiation anomalies, vagina, *V2*: 1415
Gonadal dysgenesis:
gonadal differentiation anomalies, *V2*: 1415
ovarian anomalies, *V2*: 1503
uterine anomalies, *V2*: 1441–1442
Gonadoblastoma, ovarian anomalies, *V2*: 1503
Gossypiboma, intraperitoneal, *V2*: 945–947
Gradient echo sequences:
abdinomal-pelvic imaging, advantages, *V1*: 2–3
adrenal glands, *V2*: 963–968
aortic dissection, *V2*: 1201, 1208–1212
chest imaging, *V2*: 1654
fat-suppressed gradient echo sequences, *V1*: 4
kidneys:
iron deposition, *V2*: 1121, 1125–1127
renal collecting system dilation, *V2*: 1164, 1172
liver imaging:
contrast agents, *V1*: 51–58
fat/iron deposition, *V1*: 371, 376
fatty liver, *V1*: 371, 373, 377–387
metastases detection and characterization, *V1*: 128, 137–143
portal venous thrombosis, *V1*: 391, 393–400
magnetization-prepared rapid-acquisition gradient echo sequences, *V1*: 5–6
out-of-phase gradient echo sequences, *V1*: 4–5
pancreatic cancer:
adenocarcinoma, staging, *V1*: 575, 577–587
gastrinomas, *V1*: 591, 598–602
pediatric pateients, *V2*: 1637
renal artery disease, *V2*: 1136, 1139–1140
serial MRI examination, *V1*: 24–28
spoiled gradient echo sequences, *V1*: 3–4
T1-weighted magnetic resonance cholangiopancreatography, *V1*: 460
vessel imaging, *V2*: 1195–1200
Gradient system, breast MRI, *V2*: 1693
Graft failure:
aortic graft, postoperative evaluation, *V2*: 1207, 1214, 1216, 1224–1227
hepatic transplantation, *V1*: 287, 292
liver abnormalities, *V1*: 299, 303–306
Graft-*versus*-host disease, small intestine, *V1*: 816–817, 828–829
Gram-negative bacterial, prostate infection, *V2*: 1373–1374
Granulocytic sarcoma:
bladder, *V2*: 1316, 1321
kidney, *V2*: 1109, 1111
Granulomatous disease:
bladder, *V2*: 1326
breast abscess, *V2*: 1712
Granulosa cell tumors, malignant ovarian neoplasms, *V2*: 1540, 1542, 1545–1547
Gynecological malignancies:
bladder metastases, *V2*: 1320–1324
peritoneal metastases, *V2*: 923–924, 932

Half-Fourier acquisition single shot turbo spin-echo (HASTE) sequence:
abdominal pelvic imaging, *V1*: 7
adrenal gland imaging, *V2*: 963–964, 966
adenomas, *V2*: 971, 982–983
aldosteronomas, *V2*: 977, 986–987
cyst/pseudocyst, *V2*: 980–981, 984, 992–993
hypovascular adrenal metastases, *V2*: 994–995, 998, 1000
myelolipoma, *V2*: 977–980, 988–990
bladder imaging, *V2*: 1298
magnetic resonance cholangiopancreatography, *V1*: 456, 460
pancreatic imaging, *V1*: 536–539
pediatric patients, *V2*: 1644
retroperitoneal imaging, *V2*: 1194
scrotal hernia, *V2*: 1390
stomach, *V1*: 734–736
vessel imaging, *V2*: 1200
Hamartomas:
breast, *V2*: 1709, 1711
colonic polyps, *V1*: 832
gastric polyps, *V1*: 736, 739–741
mesenchymal, *V2*: 1620
small intestine polyps, *V1*: 775, 777–778
spleen, *V1*: 690, 693, 695–697
Head imaging, fetal assessment:
anomalies, *V2*: 1598–1599, 1601–1607
normal development, *V2*: 1583
Helicobacter pylori infection:
gastric ulceration and gastritis, *V1*: 761–764
stomach carcinoids, *V1*: 759
HELLP syndrome. *See* Hemolytic anemia, elevated liver function tests, and low platelets (HELLP) syndrome
Hemangioendothelioma, fetal assessment, *V2*: 1620
Hemangiomas:
adrenal glands, *V2*: 993–994
bladder lesiosn, *V2*: 1304
cavernous, *V2*: 1416, 1420
congenital, fetal assessment, *V2*: 1604, 1607
large intestine, infiltration, Kippel-Trenaunay syndrome, *V1*: 832, 841
liver lesions:
capsule-based, *V1*: 90, 101
central filling, *V1*: 73, 84–85
exophytic, *V1*: 101–103
Gd-EOB-DTPA-enhanced imaging, *V1*: 52, 54
giant hemangioma, *V1*: 88, 97–99
liver lesions, *V1*: 70, 72–73, 81, 83–106
metastases, differential diagnosis, *V1*: 165, 177, 190
multiple, *V1*: 72–73, 83
perilesional enhancement, *V1*: 90, 101
metastases, differential diagnosis, *V1*: 147–150
portal vein compression, *V1*: 88, 100, 391
type 1 enhancement, *V1*: 85, 87
type 2 enhancement:
central nodular lesion, *V1*: 85, 91
medium-sized lesion, *V1*: 85, 89–91
small lesion, *V1*: 85–86
small-sized slow-enhancing, *V1*: 88, 94–95
type 3 enhancement:
medium-sized lesion, *V1*: 88, 92–94
small lesion, *V1*: 85, 88
small-sized slow-enhancing, *V1*: 88, 95–96
pancreatic islet cell tumors, differential diagnosis, *V1*: 593
pelvic, *V2*: 1274, 1291–1292
spleen, *V1*: 687–688, 691–693
Hemangiopericytoma, retroperitoneal imaging, *V2*: 1266, 1273
Hematocele, testes, scrotum and epididymis, *V2*: 1388, 1390
Hematocolpometra:
didelphys uterine anomaly, *V2*: 1441, 1444–1446
vaginal duplication, *V2*: 1412, 1414
Hematogenous metastases:
body wall, *V2*: 1274, 1284–1290
ovarian endodermal sinus tumor, *V2*: 1534, 1542
peritoneum, *V2*: 924
Hematomas:
abdominal wall, *V2*: 1274
duodenal, *V1*: 816, 823
hepatic transplantation, *V1*: 292, 294–295
iliacus muscle, *V2*: 1274, 1279–1280

intramural dissecting, *V2*: 1201, 1204, 1213
liver trauma, *V1*: 438–442
pelvic, *V2*: 936, 944
perirenal, *V2*: 1156, 1158
postmyomectomy, *V2*: 1456, 1465
retroperitoneal, *V2*: 1249, 1251
splenic laceration, *V1*: 715, 716–717
subchorionic, in pregnancy, *V2*: 1559–1560
uterine, in pregnancy, *V2*: 1559–1560
postpartum uterus, *V2*: 1575–1580
Hematometra, vaginal agenesis/partial agenesis, *V2*: 1411–1412
Hemochromatosis:
primary:
liver, *V1*: 354, 362, 365–368
pancreas, *V1*: 546, 548–549
secondary, liver imaging, *V1*: 368–374
Hemodialysis:
acquired cystic disease, *V2*: 1049, 1052, 1061–1062
nephrogenic systemic fibrosis prevention, *V2*: 1783
Hemolytic anemia:
adrenal gland myelolipoma, *V2*: 977, 979–980, 988–990
liver imaging, *V1*: 368, 374–375
Hemolytic anemia, elevated liver function tests, and low platelets (HELLP) syndrome, liver imaging, *V1*: 407, 410–411
Hemorrhage:
acute pancreatitis, *V1*: 632, 639–640
adrenal glands, *V2*: 1019–1020
adenomas, *V2*: 971, 982–983
metastases, *V2*: 994–995, 998, 1000
pseudocysts, *V2*: 984, 991–994
cholecystitis, *V1*: 475–477
fetal assessment:
destructive lesions, *V2*: 1596–1601
intraventricular, *V2*: 1598, 1600–1601
hemangiomas and, *V1*: 88, 101, 103
hepatocellular adenoma, *V1*: 51, 107, 110–114
kidney, *V2*: 1156, 1158
liver metastases, *V1*: 165
ovaries:
clear cell carcinoma malignancies, *V2*: 1533, 1540
endometriosis, *V2*: 1506–1507, 1509–1512
hydrosalpinx, *V2*: 1517
paraovarian cysts, *V2*: 1504, 1508
pelvic inflammatory disease, *V2*: 1514, 1516–1517
sex cord-stromal tumor malignancies, *V2*: 1542, 1545–1547
prostate cancer therapy and, *V2*: 1368, 1370
psoas muscle, *V2*: 1274, 1276–1277
renal cell carcinoma, *V2*: 1088–1094
chronic renal failure, *V2*: 1098–1101
retroperitoneum, imaging techniques, *V2*: 1193–1194
small intestine, *V1*: 816, 819–823
stages, *V1*: 442
uterus, leiomyoma, *V2*: 1456, 1458–1459
Hemorrhagic cystitis, bladder, *V2*: 1326, 1329
Hemorrhagic ovarian cysts, *V2*: 1500, 1503
Hemorrhagic/proteinaceous renal cysts, *V2*: 1037, 1042–1047
angiomyolipomas, *V2*: 1063, 1066
dialysis, *V2*: 1049, 1052, 1062
Hemorrhagic pseudocysts:
chronic pancreatitis, *V1*: 656, 665
spleen, *V1*: 683, 687–690
Hemorrhagic telangiectasia, hepatic arteriovenous fistulas, *V1*: 388–392
Hemorrhoids, rectal varices and, *V1*: 838
Hemosiderin deposition:
bladder, hemorrhagic cysts, *V2*: 1326, 1329
spleen imaging, *V1*: 678–681
Hepatectomy, liver regeneration after, *V1*: 256, 259
Hepatic alveolar echinococcosis (HAE), *V1*: 430, 432–433
Hepatic arterial dominant phase (HADP) imaging, gadolinium-based contrast agent, *V2*: 1774–1777
Hepatic artery(ies):
adrenal gland imaging, capillary phase enhancement, *V2*: 964–968
gadolinium-enhanced SGE images, *V1*: 46, 49
gadolinium-enhanced T1-weighted sequences, *V1*: 10–13
hepatic transplant complications, *V1*: 287, 292
hepatocellular carcinoma, *V1*: 192, 198, 202
imaging protocol for, *V1*: 16–20
Mn-DPDP-enhanced SGE imaging, *V1*: 46, 50
obstruction, *V1*: 405, 407–408
Hepatic cysts:
autosomal dominant polycystic kidney disease, *V1*: 67, 71–72
ciliated foregut cysts, *V1*: 60, 66–70
coexistent metastases, *V1*: 165, 190
hemorrhagic cyst, *V1*: 60, 65
hydatid cyst, echinococcal disease, *V1*: 430–431
multilocular cyst, *V1*: 60, 65–66
solitary (nonparasitic), *V1*: 60–66
unilocular cyst, *V1*: 60–61
Hepatic parenchyma:
chronic liver disease:
autoimmune diseases, *V1*: 303–304, 306–315
autoimmune hepatitis, *V1*: 311–314
primary biliary cirrhosis, *V1*: 314–315
primary sclerosing cholangitis, *V1*: 303–304, 306–311
genetic diseases, *V1*: 315–317
α1-antitrypsin deficiency, *V1*: 315, 317
Wilson disease, *V1*: 315–318
hemangiomas, *V1*: 101, 103–106
nonalcoholic fatty liver disease, *V1*: 317, 319–320
radiation-induced hepatitis, *V1*: 321, 331
viral hepatitis, *V1*: 319, 321–330
diseases:
benign masses, *V1*: 60–121
angiomyolipomas, *V1*: 67, 70, 80–81
autosomal dominant polycystic kidney disease, *V1*: 67, 74–77
biliary cystadenoma/cystadenocarcinoma, *V1*: 67, 77–78
ciliated hepatic foregut cysts, *V1*: 60, 66–70
extramedullary hematopoiesis, *V1*: 67, 79–80
focal nodular hyperplasia, *V1*: 119, 121–136
hemangiomas, *V1*: 70, 72–73, 81–106
hepatocellular adenoma, *V1*: 107, 109–118
infantile hemangioendothelioma, *V1*: 106–109
lipomas, *V1*: 70, 82
peliosis hepatis, *V1*: 114–115, 119–120
solitary (nonparasitic cysts), *V1*: 60–66
malignant masses, *V1*: 121, 128, 137–287 (*See also* Liver, metastases)
ablative therapies, *V1*: 278–287
angiosarcoma, *V1*: 240, 242, 249
epithelioid hemangioendothelioma, *V1*: 251–253
fibrolamellar carcinoma, *V1*: 238–239
hepatoblastoma, *V1*: 251, 253–255
hepatocellular carcinoma, diffuse, *V1*: 212, 227–238
hepatocellular carcinoma, focal, *V1*: 188–189, 192–233
intrahepatic/peripheral bile duct carcinoma (cholangiocarcinoma), *V1*: 238–240, 242, 247–249
liver metastases, *V1*: 121, 128, 137–188
lesional/perilesional enhancement, *V1*: 147–150
MRI detection and characterization, *V1*: 127, 128, 137–143
MRI *vs.* CT, *V1*: 141–144
MRI *vs.* CTAP, *V1*: 143, 145–147
primary site features, *V1*: 161–162, 164–192
T1 *vs.* T2 images, *V1*: 143, 147
vascularity and degree of enhancement, *V1*: 149, 151–164
lymphoma, *V1*: 238, 240–245
malignant mesothelioma, *V1*: 242, 250–251

Hepatic parenchyma: (*Contnued*)
multiple myeloma, *V1*: 238, 245–246
postradiation therapy, *V1*: 257, 262–263
posttreatment lesions, *V1*: 256
resections, *V1*: 256–262
systemic chemotherapy, *V1*: 257, 264–270
transcatheter arterial chemoembolization, *V1*: 268, 270–278
undifferentiated sarcoma, *V1*: 251, 256
hepatic arterial dominant phase imaging, gadolinium-based contrast agent, *V2*: 1775–1777
infectious disease:
amebic (nonpyogenic) abscess, *V1*: 430
echinococcal disease, *V1*: 430–433
fungal infection, *V1*: 433, 436–438
metastases, secondary infection, *V1*: 180, 188, 191–192
mycobacterium avium intracellulare, *V1*: 433–435
mycobacterium tuberculosis, *V1*: 433
pyogenic abscess, *V1*: 418, 422–432
inflammatory disease:
hepatic transplantation complication, *V1*: 299–300
inflammatory myofibroblastic tumor (pseudotumor), *V1*: 415, 418–422
sarcoidosis, *V1*: 414–416
Hepatic transplantation:
bile duct obstruction following, *V1*: 292, 299
donor and recipient assessment, *V1*: 287–292
fibrosis, *V1*: 299, 304
fungal infection, *V1*: 299, 305
graft failure, *V1*: 287, 292
liver abnormalities, *V1*: 299, 303–306
hepatic arterial obstruction, *V1*: 405, 407–408
hepatocellular carcinoma recurrence, *V1*: 299, 302
inflammation following, *V1*: 299–300
lymphoma, *V1*: 238, 241
magnetic resonance cholangiopancreatography, bile duct anastomoses, *V1*: 519–520
MR imaging, *V1*: 287–305
posttransplant lymphoproliferative disorder, *V1*: 299–301
vascular complications, *V1*: 292–298
Hepatic venous system:
gadolinium-enhanced T1-weighted imaging:
early phase, *V1*: 11
interstitial phase, *V1*: 13
hepatic transplantation, *V1*: 292–294
hepatocellular carcinoma, *V1*: 192, 198–202
thrombosis, Budd-Chiari syndrome, *V1*: 398, 401–405
Hepatitis:
acute hepatitis, *V1*: 321–324
acute on chronic, *V1*: 321, 327–329
autoimmune hepatitis, *V1*: 311–314
chronic, *V1*: 321, 330
diffuse hepatocellular carcinoma, differential diagnosis, *V1*: 235
hepatitis B, *V1*: 321, 325
hepatitis C, *V1*: 321, 325–327
nonalcoholic steatohepatitis, *V1*: 319–320
radiation-induced, *V1*: 321, 331
viral hepatitis:
hepatocellular carcinoma, *V1*: 202, 212
imaging studies, *V1*: 319, 321, 330
Hepatoblastoma, *V1*: 251, 253–255
Hepatocellular adenoma (HCA):
adenomatosis, *V1*: 114–118
fatty liver and, *V1*: 380, 383
hepatocyte-specific contrast agents, differential diagnosis, *V2*: 1768, 1770–1771
hypervascular liver metastases, differential diagnosis, *V1*: 177, 180
imaging studies, *V1*: 107, 109–118
liver metastases, differential diagnosis, *V1*: 177, 180
carcinoid tumor, *V1*: 164, 183–185
Hepatocellular carcinoma (HCC):
adrenal metastases, *V1*: 192, 199
biliary cystadenoma/cystadenocarcinoma, differential diagnosis, *V1*: 67, 77–78
body wall metastases, *V2*: 1274, 1284–1285
carcinoid tumor, differential diagnosis, *V1*: 164, 183–185
cholangiocarcinoma, differential diagnosis, *V1*: 239–240, 242, 245–247
cirrhosis, differential diagnosis, *V1*: 333
dysplastic nodules, *V1*: 342, 346–354, 357–358
venous thrombosis formation, *V1*: 333
diffuse infiltrative, *V1*: 212, 227, 234–238
fatty liver and, *V1*: 380
genetics, *V1*: 189
hemochromatosis and, *V1*: 354, 367–368
hepatic transplantation and recurrence of, *V1*: 299, 302
hepatic vein thrombosis, *V1*: 405
hepatocyte-specific contrast agents, imaging studies, *V2*: 1768
hypervascular tumors, *V1*: 198, 202, 218–223
hypovascular tumors, *V1*: 192–194, 198, 215–217
incidence and prevalence, *V1*: 188–189, 192
mixed HCC-cholangiocarcinoma, *V1*: 238–240, 242, 248–249
MRI *vs.* CT imaging, *V1*: 192, 203–205
multifocal tumors, *V1*: 192, 194–198, 203–205
peritoneal metastases, *V1*: 192, 200–201; *V2*: 918, 923–924, 931
pleural metastases, *V1*: 192, 202
radiofrequency ablation, *V1*: 278, 280–286
recurrence, *V1*: 256, 260–261
solitary hypovascular tumor, *V1*: 192–194
transcatheter arterial chemoembolization, *V1*: 270, 274–278
venous thrombosis, *V1*: 202, 212, 224–232, 234–238
cirrhosis differential diagnosis, *V1*: 333
well-differentiated tumors, *V1*: 192, 205–212
Hepatocyte function:
hepatocellular carcinoma, *V1*: 189
MRI contrast agent targeting, *V1*: 50–58
gadolinium-based contrast agents, *V2*: 1777
Hepatocyte-specific gadolinium-based contrast agents, *V2*: 1768, 1770–1772, 1777
Hepatomegaly, Reidel lobe, differential diagnosis, *V1*: 58–60
Hepatosplenic candidiasis:
acute, *V1*: 433, 435–436
subacute, *V1*: 433, 436–437
Hepatosplenic sarcoidosis, imaging studies, *V1*: 414–416
Hepatosplenorenal histoplasmosis, *V1*: 709–711
Herlyn-Werner-Wunderlich syndrome, Gartner duct cyst, *V2*: 1416, 1418–1419
Hermaphroditis, gonadal differentiation anomalies, *V2*: 1415
Hernias, *V2*: 904–909
abdominal wall, *V2*: 904, 908–909, 1274
Bochdalek hernia, *V2*: 904–905
fetal assessment, *V2*: 1604–1605, 1608–1609, 1612
congenital diaphragmatic, *V2*: 1604–1605, 1608–1609
hiatus and internal, *V2*: 904, 906–907
scrotal, *V2*: 1390
small intestine, *V1*: 816, 827
Herpes simplex virus (HSV), esophageal infection, *V1*: 731–734
Heterotopias, congenital:
fetal assessment:
Chiari II malformation, *V2*: 1588–1592
subependymal, *V2*: 1595
stomach, *V1*: 736
Heterozygous thalassemia, liver imaging, *V1*: 370, 374–375
Hiatus hernia, *V2*: 904, 906–907
Hilar lymphadenopathy, *V2*: 1666–1667
Histiocytomas, retroperitoneal neoplasms, *V2*: 1265, 1271
Histoplasmosis, hepatosplenorenal histoplasmosis, *V1*: 709–711
Hodgkin lymphoma:
kidneys, *V2*: 1106–1110
liver metastases, *V1*: 238, 241
retroperitoneal lymphadenopathy, *V2*: 1253–1254
spleen malignancies, *V1*: 693–694, 700

Holoprosencephaly, fetal assessment, *V2*: 1585–1592
Homogeneous high-signal-intensity enhancement, spleen, *V1*: 678–681
Hormone therapy, prostate cancer, *V2*: 1368–1369
Horseshoe kidney, *V2*: 1032, 1034
Human chorionic gonadotropin:
  gestational trophoblastic disease, *V2*: 1578–1580, 1628–1629
  theca-lutein ovarian cysts, *V2*: 1504
Human epidermal growth factor receptor 2 (HER2), invasive ductal carcinoma, *V2*: 1723–1727
Human immunodeficiency virus (HIV):
  colonic lymphoma, *V1*: 860, 867
  lymphoma, liver metastases, *V1*: 238, 245
Human papillomavirus, vaginal malignancies, *V2*: 1416, 1420–1426
Hutch diverticula, bladder, *V2*: 1299
Hydatid cyst:
  breast cysts, *V2*: 1701–1703
  liver imaging, *V1*: 430–431
  paraovarian cysts of Morgagni, *V2*: 1504, 1508
  spleen, *V1*: 683, 687–690
Hydatidiform mole, gestational trophoblastic disease, *V2*: 1628–1629
Hydranencephaly, fetal assessment, *V2*: 1598, 1600
Hydrocele, testes, scrotum and epididymis, *V2*: 1388–1392
Hydrocephalus, fetal assessment, brain neoplasms, *V2*: 1598
Hydronephrosis:
  bladder neurofibromas, *V2*: 1304
  fetal assessment, *V2*: 1613–1614
  in pregnancy, maternal imaging, *V2*: 1564, 1566
Hydrops, mesoblastic nephroma, *V2*: 1620
Hydrosalpinx, *V2*: 1517
Hydroureter, in pregnancy, *V2*: 1564
21-Hydroxylase deficiency, female pseudohermaphroditism, *V2*: 1415–1416
Hypergastrinemia, stomach carcinoids, *V1*: 759
Hyperintense gallstones, T1-weighted imaging, *V1*: 464, 469
Hyperplastic kidney, *V2*: 1032, 1037
Hyperplastic polyps:
  gastric polyps, *V1*: 736, 739–741
  small intestine, *V1*: 775, 777–778
Hypersplenism, littoral cell angioma, *V1*: 688, 694
Hypertrophic bladder, *V2*: 1324–1325
Hypertrophic kidney, *V2*: 1032, 1037
Hypertrophic rugal folds, *V1*: 761, 765
Hypervascular liver metastases, *V1*: 128, 138–139. *See also* specific types of cancer
  chemotherapy-related, *V1*: 257, 264–270
  degree of enhancement and, *V1*: 149, 151–162
  focal nodular hyperplasia/hepatic adenocarcinoma, differential diagnosis, *V1*: 177, 180
  hepatocellular carcinoma, *V1*: 198, 202, 218–223
    small satellite tumors, *V1*: 217–218
  pancreatic adenocarcinoma, differential diagnosis, *V1*: 587–589
  perilesional enhancement, *V1*: 149–150
Hypervascular renal tumors, *V2*: 1084, 1086
Hypoplasia, breast, *V2*: 1700–1701
Hypoplastic kidney, *V2*: 1032, 1036
Hypoplastic uterus, *V2*: 1441
Hypoproteinemia, small intestine, *V1*: 816, 824
Hypospadias, *V2*: 1376
Hypovascular liver metastases:
  chemotherapy-related, *V1*: 257, 264–270
  hepatocellular carcinoma, *V1*: 192–194, 198, 215–217
  imaging studies, *V1*: 149, 152–156, 162
Hypovascular renal tumors, *V2*: 1084, 1087
Hysterectomy:
  adenomyosis, *V2*: 1467
  vaginal malignancy recurrence, *V2*: 1416, 1420–1426
Hysterosalpingography, uterus, congenital anomalies, *V2*: 1440

Idiopathic hemochromatosis:
  hepatocellular carcinoma and, *V1*: 354, 367–368
  liver imaging:
    advanced disease, *V1*: 354, 362, 365–366
    early stage, *V1*: 354, 362, 365
Ileal carcinoid, *V1*: 779, 789
Iliacus muscle:
  hematoma, *V2*: 1274, 1279–1280
  melanoma metastases, *V2*: 1273, 1276
Iliac vessels:
  MR imaging, *V2*: 1198–1200
  stenosis, *V2*: 1204, 1207, 1216–1218
  thrombosis, *V2*: 1204, 1207, 1222–1223
Imperforate anus, reconstruction, *V1*: 827, 834
Incisional hernia, abdominal wall imaging, *V2*: 904, 909
Indiana pouch, bladder reconstruction, *V2*: 1331, 1336
Infantile hemangioendothelioma (IHE), imaging studies, *V1*: 106–109
Infants (under 1.5 years), MR imaging techniques, *V2*: 1645
Infarct, splenic, *V1*: 719–722
Infectious colitis, *V1*: 883–884, 888–892
Infectious disease:
  cholangitis, *V1*: 499, 502–507
    cholangiocarcinoma incidence and, *V1*: 515
  esophagus, *V1*: 731–734
  female urethra, *V2*: 1407–1408
hepatic parenchyma:
  amebic (nonpyogenic) abscess, *V1*: 430
  echinococcal disease, *V1*: 430–433
  fungal infection, *V1*: 433, 436–438
  metastases, secondary infection, *V1*: 180, 188, 191–192
  mycobacterium avium intracellulare, *V1*: 433–435
  mycobacterium tuberculosis, *V1*: 433
  pyogenic abscess, *V1*: 418, 422–432
kidneys:
  abscess, *V2*: 1142, 1144, 1149–1152
  acute pyelonephritis, *V2*: 1142, 1147–1149
  malakoplakia, *V2*: 1153–1154
  pyonephrosis, *V2*: 1155–1156
  renal candidiasis, *V2*: 1155
  xanthogranulomatous pyelonephritis, *V2*: 1151–1152
large intestine:
  abdominoperineal resection, *V1*: 892, 894–895
  abscess formation, *V1*: 874, 876–877, 881–886
  appendiceal abscess, *V1*: 874, 881
  appendicitis, *V1*: 874, 879–881
  colonic fistulae, *V1*: 883, 887–888
  Crohn colitis, *V1*: 869, 872–874
  diverticulitis, *V1*: 869, 874–879
  infectious colitis, *V1*: 883–884, 888–892
  radiation enteritis, *V1*: 888, 892–894
  rectal surgery, *V1*: 892, 894–895
  ulcerative colitis, *V1*: 867–868, 870–871
pancreas, *V1*: 664–667
  pancreatic transplants, *V1*: 671–673
penis and urethra, *V2*: 1380
peritoneum:
  abscess, *V2*: 949, 951, 954–959
  mesenteric panniculitis, *V2*: 946, 950
  pancreatitis, *V2*: 940–942, 946, 949
  peritonitis, *V2*: 949, 951–953
prostate gland, *V2*: 1373–1374
seminal vesicles, *V2*: 1383
small intestine:
  Crohn disease, *V1*: 784–785, 791, 793–805
  drug toxicity, *V1*: 810, 817
  eosinophilic gastroenteritis, *V1*: 809
  fistula, *V1*: 810, 812–813
  gluten-sensitive enteropathy, *V1*: 799, 807–809
  graft-*versus*-host disease, *V1*: 816–817, 828–829
  hernia, *V1*: 816, 827
  hypoproteinemia, *V1*: 816, 824
  infectious enteritis, *V1*: 810, 813–814
  inflammatory bowel disease, *V1*: 782, 784
  intussusception, *V1*: 816, 825–826
  ischemia and hemorrhage, *V1*: 816, 819–823
  pancreatitis, *V1*: 810, 815
  pouchitis, *V1*: 810

Infectious disease: (*Continued*)
radiation enteritis, *V1*: 815–816, 818
scleroderma, *V1*: 809
ulcerative colitis, *V1*: 796, 799, 806
spleen, *V1*: 709–711
stomach, *V1*: 761–764
testes, scrotum and epididymis, *V2*: 1397–1398
tubo-ovarian abscess, *V2*: 1514, 1516–1517
Infectious enteritis, small intestine, *V1*: 810, 813–814
Inferior vena cava, retroperitoneal imaging, *V2*: 1216, 1223, 1229
congenital anomalies, *V2*: 1223, 1229–1230
primary malignant tumors, *V2*: 1237–1241
venous thrombosis, *V2*: 1229–1237
Inflammatory aortitis, *V2*: 1201, 1207
Inflammatory bowel disease (IBD):
gastrointestinal tract imaging, *V1*: 725
pregnancy and, *V1*: 868, 871
primary sclerosing cholangitis, *V1*: 494, 497–502
small intestine, *V1*: 782, 784
Inflammatory breast carcinoma (IBC), *V2*: 1737, 1739
Inflammatory disease:
adrenal glands, *V2*: 1019
bladder, *V2*: 1326–1330
esophagus:
corrosive esophagitis, *V1*: 731
radiation esophagitis, *V1*: 730–731
reflux esophagitis, *V1*: 729–730, 732
female urethra, *V2*: 1407–1408
hepatic parenchyma:
hepatic transplantation complication, *V1*: 299–300
inflammatory myofibroblastic tumor (pseudotumor), *V1*: 415, 418–422
sarcoidosis, *V1*: 414–416
large intestine:
abdominoperineal resection, *V1*: 892, 894–895
abscess formation, *V1*: 874, 876–877, 881–886
appendiceal abscess, *V1*: 874, 881
appendicitis, *V1*: 874, 879–881
colonic fistulae, *V1*: 883, 887–888
Crohn colitis, *V1*: 869, 872–874
diverticulitis, *V1*: 869, 874–879
infectious colitis, *V1*: 883–884, 888–892
radiation enteritis, *V1*: 888, 892–894
rectal surgery, *V1*: 892, 894–895
ulcerative colitis, *V1*: 867–868, 870–871
pancreas, *V1*: 625
miscellaneous conditions and infections, *V1*: 664–667
pancreatic transplants, *V1*: 671–673
pancreatitis, *V1*: 625
acute, *V1*: 625, 628, 636–647
autoimmune pancreatitis, *V1*: 656, 664, 666
chemtherapy-induced, *V1*: 664–667
chronic, *V1*: 640, 648–665
hemorrhagic, *V1*: 632, 640–641
mild, *V1*: 625, 632–635
pseudocyst, *V1*: 632, 642–647
pelvic inflammatory disease, tubo-ovarian abscess, *V2*: 1514, 1516–1517
penis and urethra, *V2*: 1380–1381
peritoneum:
abscess, *V2*: 949, 951, 954–959
mesenteric panniculitis, *V2*: 946, 950
pancreatitis, *V2*: 940–942, 946, 949
peritonitis, *V2*: 949, 951–953
primary sclerosing cholangitis, *V1*: 494, 497–502
prostate gland, *V2*: 1373–1374
small intestine:
Crohn disease, *V1*: 784–785, 791, 793–805
drug toxicity, *V1*: 810, 817
eosinophilic gastroenteritis, *V1*: 809
fistula, *V1*: 810–813, 812–813
gluten-sensitive enteropathy, *V1*: 799, 807–809
graft-*versus*-host disease, *V1*: 816–817, 828–829
hernia, *V1*: 816, 827
hypoproteinemia, *V1*: 816, 824
infectious enteritis, *V1*: 810, 813–814
inflammatory bowel disease, *V1*: 782, 784
intussusception, *V1*: 816, 825–826
ischemia and hemorrhage, *V1*: 816, 819–823
pancreatitis, *V1*: 810, 815
pouchitis, *V1*: 810
radiation enteritis, *V1*: 815–816, 818
scleroderma, *V1*: 809
ulcerative colitis, *V1*: 796, 799, 806
stomach, *V1*: 761–764
Inflammatory myofibroblastic tumor:
bladder lesions, *V2*: 1304
hepatic inflammatory disease, *V1*: 415, 418–422
Inflammatory polyps, small intestine, *V1*: 775, 777–778
Infrarenal aorta, thrombotic occlusion, *V2*: 1204, 1207, 1219–1221
Inguinal hernia:
abdominal wall imaging, *V2*: 904, 908
small intestine, *V1*: 816, 827
Initial qualitative enhancement, breast cancer imaging, *V2*: 1723
Insulinomas, pancreatic imaging, *V1*: 601, 603–606
Internal hernia, *V2*: 904, 906–907
International Organization for the Study of Inflammatory Bowel Disease (IOIBD), MRI criteria, *V1*: 796, 803
Interstitial phase imaging:
adrenal pheochromocytomas, *V2*: 1006–1111
gadolinium-based contrast agents, *V2*: 1776–1777
hypervascular liver metastases, *V1*: 149, 157–162
kidneys:
candidiasis infection, *V2*: 1155
medullary sponge kidney, *V2*: 1049, 1060
transitional cell carcinoma, *V2*: 1159–1165
xanthogranulomatous pyelonephritis, *V2*: 1152
renal artery disease, *V2*: 1137
Intraabdominal abscess:
imaging studies, *V1*: 874, 884
peritoneal inflammation, *V2*: 949, 951, 954–959
Intracellular agents, gadolinium-based, *V2*: 1768–1774
Intracranial neoplasms, fetal assessment, *V2*: 1598
Intraductal papillary mucinous neoplasms (IPMN), *V1*: 614
main duct type, *V1*: 614–617
serous cystadenoma, differential diagnosis, *V1*: 612
side-branch type, *V1*: 615, 618–621
Intraductal papilloma, breast imaging, *V2*: 1707–1709, 1738
Intraluminal contrast agent:
peritoneal abscess imaging, *V2*: 951, 954–959
rectal imaging, *V1*: 827, 831
intramural dissecting hematoma, *V2*: 1201, 1204, 1213
Intrapericardial neoplasms, fetal assessment, *V2*: 1612
Intraperitoneal varices, cirrhosis, *V1*: 348, 351, 359
Intrathoracic imaging techniques, *V2*: 1653–1654
Intrauterine contraceptive devices:
pelvic inflammatory disease, *V2*: 1514, 1516–1517
uterine imaging, *V2*: 1433
Intrauterine growth retardation, twin pregnancies, *V2*: 1623
Intravenous urography (IVU), magnetic resonance urography *vs.*,*V2*: 1188
Intussusception:
colonic duplication, *V1*: 827, 832
colonic lipoma, *V1*: 832, 840
large intestine lipomas, *V1*: 832, 839–841
small intestine:
inflammatory/infectious disease, *V1*: 816, 825–826
polyps, *V1*: 775, 777–778
Invasive ductal carcinoma (IDC):
breast implants, *V2*: 1754–1756
classification and staging, *V2*: 1723–1731
neoadjuvant chemotherapy, *V2*: 1749, 1753
postoperative MRI, *V2*: 1744, 1746–1749
Invasive lobular carcinoma (ILC), classification and staging, *V2*: 1727, 1731–1733

Inversion pulse:
fat-suppressed echo-train spin-echo sequences, *V1*: 9–10
magnetization-prepared rapid-acquisition gradient echo sequences, *V1*: 5–6
vessel imaging, *V2*: 1200
Inverted teardrop sign, breast implant rupture, *V2*: 1759
Iodine-based contrast agents, *V2*: 1767
Iron-based contrast agents, *V2*: 1777–1779
large intestine imaging, *V1*: 896–897
Iron-containing structures, out-of-phase (opposed-phase) spoiled gradient echo sequence detection, *V1*: 4–5
Iron deposition:
liver:
cirrhosis, *V1*: 370
coexisting fat and, *V1*: 371, 376
genetic idiopathic hemochromatosis, *V1*: 354, 362, 365–368
secondary hemochromatosis:
hemolytic anemia, *V1*: 368, 370, 374–375
transfusional iron overload, *V1*: 368–373
pancreas, primary hemochromatosis, *V1*: 546, 548–549
renal parenchyma, *V2*: 1121, 1125–1127
spleen imaging, *V1*: 678–681
Iron oxides. *See* Superparamagnetic iron oxide particles (SPIO); Ultrasmall paramagnetic iron oxide particles
Ischemia:
cerebral, fetal assessment, *V2*: 1596–1601
hepatic arterial obstruction, *V1*: 405, 407–408
small intestine, *V1*: 816, 819–823
Ischemic nephropathy, *V2*: 1129, 1131, 1134, 1139
Islet cell tumors:
accessory spleen, differential diagnosis, *V1*: 681–685
pancreatic, *V1*: 590–598
ACTHoma, *V1*: 601, 605
duct obstruction, *V1*: 592
gastrinomas, *V1*: 591, 598–600
glucagonoma, *V1*: 601, 604
insulinomas, *V1*: 601, 603
liver metastases, *V1*: 591, 593–596
somatostatinoma, *V1*: 601, 604–605
thrombus, *V1*: 591, 593, 597
undifferentiated, *V1*: 601
VIPomas, *V1*: 601, 606
pancreatic adenocarcinoma, differential diagnosis, *V1*: 587–589
Isovascular liver metastases:
hepatocellular carcinoma, *V1*: 198, 215–217
imaging studies, *V1*: 149, 151
Ivemark syndrome (asplenia), MR imaging, *V1*: 681, 685

Jejeunal atresia, fetal assessment, *V2*: 1615
Joubert syndrome, fetal assessment, *V2*: 1593–1597
Juvenile hypertrophy, breast, *V2*: 1700–1701
Juvenile polyposis syndrome, colonic adenomatous polyps, *V1*: 832
Juxtarenal process, *V2*: 1172–1173

Kaposi sarcoma, *V1*: 748, 756
Karyotype analysis, gonadal differentiation anomalies, *V2*: 1415
Kasabach-Merritt sequence, fetal assessment, *V2*: 1620
Kawasaki disease, retroperitoneal benign lymphadenopathy, *V2*: 1249–1250
Kidneys. *See also* Renal parenchyma
benign masses:
adenomas, *V2*: 1068
cysts, *V2*: 1035, 1037–1064
acquired dialysis-related cystic disease, *V2*: 1049, 1052, 1061–1062
angiomyolipoma, *V2*: 1063–1068
autosomal dominant polycystic kidney disease, *V2*: 1044, 1047, 1052–1056
autosomal recessive polycystic kidney disease, *V2*: 1047, 1056–1058
calcified cysts, *V2*: 1042, 1048
complex cysts, *V2*: 1037, 1040–1041
fetal assessment, *V2*: 1614–1616
hemhorragic/proteinaceous cysts, *V2*: 1037, 1042–1047
medullary cystic disease, *V2*: 1049, 1059–1060
medullary sponge kidney, *V2*: 1049, 1060
multicystic dysplastic kidney, *V2*: 1047–1049, 1058
multilocular cystic nephroma, *V2*: 1060, 1063–1064
perinephric pseudocysts (parapelvic cysts), *V2*: 1042, 1044, 1050
septated cysts, *V2*: 1042, 1047
simple renal cysts, *V2*: 1035, 1037
thickened wall and infiltration, *V2*: 1043, 1049
tuberous sclerosis, *V2*: 1066, 1069–1071
von Hippel-Lindau disease, *V2*: 1066, 1068, 1072
myelofibrosis, extramedullary hematopoiesis, *V2*: 1068, 1073
oncocytomas, *V2*: 1068, 1072
pattern recognition, *V2*: 1037
collecting system, filling defects, *V2*: 1159, 1166–1169
congenital anomalies, *V2*: 1031–1036
seminal vesicles and, *V2*: 1382, 1384
end-stage kidney disease, *V2*: 1138, 1146–1147
fetal assessment:
anomalies, *V2*: 1612–1613
normal development, *V2*: 1584–1585
hemorrhage, *V2*: 1156–1158
infectious disease:
abscess, *V2*: 1142, 1144, 1149–1152
acute pyelonephritis, *V2*: 1142, 1147–1149
malakoplakia, *V2*: 1153–1154
pyonephrosis, *V2*: 1155–1156
renal candidiasis, *V2*: 1155
xanthogranulomatous pyelonephritis, *V2*: 1152
malignant masses:
carcinoid tumor, *V2*: 1109, 1111
granulocytic sarcoma, *V2*: 1109, 1111
lymphoma, *V2*: 1103, 1106–1110
renal cell carcinoma, *V2*: 1073–1098
chronic renal failure, *V2*: 1098–1101
MR imaging, *V2*: 1098, 1102
radiofrequency ablation, *V2*: 1088–1089, 1095–1096
recurrence, *V2*: 1089, 1096–1097
staging, *V2*: 1073–1095
small cell carcinoma, *V2*: 1110, 1113
Wilms tumor (nephroblastoma), *V2*: 1102–1106
metastases to, *V2*: 1112, 1114–1115, 1159
MR imaging technique, *V2*: 1025–1031
normal anatomy, *V2*: 1025–1030
pediatric imaging, *V2*: 1650
renal collecting system dilation, *V2*: 1164, 1169–1172
renal function, *V2*: 1173, 1175–1177
transplants, *V1*: 671–673, 1173, 1177–1188
trauma, *V2*: 1172–1174
perinephric pseudocysts, *V2*: 1042
Kippel-Trenaunay syndrome, hemangiomatous infiltration, *V1*: 841
Klatskin tumors:
bile duct imaging, *V1*: 515–518, 522–526
biliary stent and, *V1*: 526–527
Klebsiella spp., prostate infection, *V2*: 1373–1374
Krukenberg tumor, ovarian metastases, *V2*: 1547, 1550

LAO projection data, magnetic resonance angiography, *V2*: 1684
Laparoscopic imaging, ovaries, MRI *vs.*, *V2*: 1506–1507
Large intestine. *See also* Colon cancer
benign masses:
hemangiomatous infiltration, Kippel-Trenaunay syndrome, *V1*: 841
lipomas, *V1*: 832, 839
mesenchymal neoplasms (miscellaneous), *V1*: 832, 841
mucocele, *V1*: 832, 838, 841–842
polyps/polyposis syndromes, *V1*: 829, 832, 835–838
varices, *V1*: 838

Large intestine (*Continued*)
congenital anomalies:
anorectal anomalies, *V1*: 827, 833
duplication, *V1*: 827, 832
malrotation, *V1*: 827
inflammatory and infectious disease:
abdominoperineal resection, *V1*: 892, 894–895
abscess formation, *V1*: 874, 876–877, 881–886
appendiceal abscess, *V1*: 874, 881
appendicitis, *V1*: 874, 879–881
colonic fistulae, *V1*: 883, 887–888
Crohn colitis, *V1*: 869, 872–874
diverticulitis, *V1*: 869, 874–879
infectious colitis, *V1*: 883–884, 888–892
radiation enteritis, *V1*: 888, 892–894
rectal surgery, *V1*: 892, 894–895
ulcerative colitis, *V1*: 867–868, 870–871
malignant masses (*See also* Rectal cancer; specific cancers, e.g. Colon cancer)
adenocarcinoma, *V1*: 843–865
TNM staging, *V1*: 843
metastases to, *V1*: 867, 869
gastrointestinal stromal tumors, *V1*: 860, 866
MR imaging techniques, *V1*: 824, 827
intraluminal contrast agents, *V1*: 892, 895–897
normal anatomy, *V1*: 823–824, 827, 830–831
Late hepatic arterial phase (LHAP), gadolinium-based contrast agent, *V2*: 1774–1777
Leiomyomas:
bladder, *V2*: 1300, 1302–1303
broad ligament, *V2*: 1449, 1453–1454
esophageal imaging, *V1*: 726–728
female urethra, *V2*: 1403
ovaries:
benign neoplasms, *V2*: 1525–1526
malignant transformation, *V2*: 1545, 1548
small intestine, *V1*: 775, 780
stomach, *V1*: 736
uterine, *V2*: 1449, 1451–1469
adenomyosis, differential diagnosis, *V2*: 1467, 1469
classification, *V2*: 1451
endometrial carcinoma, *V2*: 1468, 1470, 1473
hemorrhagic degeneration, *V2*: 1456, 1458–1459
intramural, *V2*: 1449, 1451
malignancy, *V2*: 1456, 1465–1466
MR imaging appearance, *V2*: 1452–1469
in pregnancy, maternal imaging, *V2*: 1564, 1567–1570
submucosal, *V2*: 1451–1452, 1454, 1456–1469
vaginal, *V2*: 1416, 1423
Leiomyosarcoma:
inferior vena cava, *V2*: 1237–1241
peritoneal metastases, *V2*: 918, 923–924, 930–931
retroperitoneal neoplasms, *V2*: 1265–1270
uterine, *V2*: 1456, 1465–1466
Lesser sac, intraperitoneal fluid, malignant disease, *V2*: 936, 941
Leukemia, bone metastases, *V2*: 1274, 1288–1290
Linear gadolinium-based contrast agents, *V2*: 1768–1774
Linguine sign, breast implant rupture, *V2*: 1759
Linitus plastica gastric carcinoma, *V1*: 738, 741, 750–751
Lipoleiomyoma, uterus, *V2*: 1456, 1464
Lipomas:
body wall masses, *V2*: 1274, 1283
breast cancer, *V2*: 1739–1740
cecal, *V1*: 832, 839
colonic, *V1*: 832, 840
fatty liver differential diagnosis, *V1*: 383
fetal assessment:
brain, *V2*: 1598–1599
ventriculomegaly, *V2*: 1588–1592
liver lesions, *V1*: 70, 82
pancreatic, *V1*: 551–556
peritoneal, *V2*: 910
small intestine, *V1*: 775
stomach, *V1*: 736, 738, 741
testicular, *V2*: 1386, 1388, 1390
Lipomatosis:
mesenteric, *V2*: 910
pelvic, bladder involvement, *V2*: 1326, 1329–1330
Liposarcoma, retroperitoneal, *V2*: 1265–1266, 1271
Lissencephaly, fetal assessment, *V2*: 1595–1596
Littoral cell angioma (LCA), spleen, *V1*: 688, 694
Liver. *See also* Hepatic cysts; Hepatic parenchyma; Hepatocellular carcinoma (HCC)
abscess:
amebic (nonpyogenic), *V1*: 430
infectious cholangitis, *V1*: 502, 506–507
metastases, secondary infection, *V1*: 180, 188, 191–192
pyogenic, *V1*: 418, 422–432
arteriovenous fistulas, *V1*: 388–392
biliary tree air, *V1*: 411, 413
cirrhosis, *V1*: 321, 331–362
iron overload, *V1*: 370
congestive heart failure, *V1*: 408, 411–413
contrast agents, *V1*: 50–58
diaphragmatic insertion imaging, *V1*: 58, 60
diffuse hyperperfusion abnormality, *V1*: 389–391, 411, 414–415
fat and iron deposition, *V1*: 371, 376
fatty liver, *V1*: 371, 373, 377–387
fetal assessment, *V2*: 1604, 1612
fibrosis, renal cysts, *V2*: 1614–1616
neoplasms, *V2*: 1620
focal hyperperfusion abnormality, *V1*: 414–417
gas bubbles, ablative therapies, *V1*: 286–287
genetic disease, *V1*: 315–318
α1-antitrypsin deficiency, *V1*: 315, 317
Wilson disease, *V1*: 315–318
hepatic arterial obstruction, *V1*: 405, 407–409
hepatic venous thrombosis:
hepatic vein thrombosis, *V1*: 405
hepatocellular carcinoma, *V1*: 202, 224–232
iron overload:
cirrhosis, *V1*: 370
genetic idiopathic hemochromatosis, *V1*: 354, 362, 365–368
secondary hemochromatosis:
hemolytic anemia, *V1*: 368, 370, 374–375
transfusional iron overload, *V1*: 368–373
laceration, hepatic transplantation complication, *V1*: 292, 296
lateral segment elongation imaging, *V1*: 58, 60
lesions:
pattern recognition, *V1*: 51
posttreatment, *V1*: 256
metastases to (*See also* Liver metastases under specific cancers)
ablative therapies, *V1*: 278–287
adrenal cortical carcinoma, *V2*: 998, 1006
adrenal gland neuroblastoma, *V2*: 1013–1017
angiosarcoma, *V1*: 240, 242, 249
avascular, *V1*: 149, 152
benign lesions, differential diagnosis, *V1*: 165, 177, 190
bile duct carcinoma (cholangiocarcinoma), *V1*: 238–240, 242, 247–249
biliary hamartoma, differential diagnosis, *V1*: 67, 73–77
capsule-based metastases, *V1*: 165, 189
hepatocellular carcinoma, *V1*: 202, 224, 232–233
chemotherapy-related, *V1*: 257, 264–270
coexistent cysts, *V1*: 165, 190
colon adenocarcinoma, *V1*: 843, 845, 858, 860
cryotherapy, *V1*: 278, 286–287
epithelioid hemangioendothelioma, *V1*: 251–253
in fatty liver, *V1*: 128, 140–142
fatty liver, imaging interference, *V1*: 371, 377–379
fibrolamellar carcinoma, *V1*: 238–239

focal nodular hyperplasia/hepatocellular adenoma, differential diagnosis, *V1*: 177, 180
hemangiomas, *V1*: 90, 101
hepatoblastoma, *V1*: 251, 253–255
hepatocellular carcinoma, *V1*: 188–189, 192–233
differential diagnosis, *V1*: 235
hypervascular metastases, *V1*: 128, 138–139
hypovascular cystic metastases, *V1*: 149, 152–153
insulinoma, *V1*: 601
islet cell tumors, *V1*: 594–597, 601, 604–606
lymphoma, *V1*: 238, 240–245
malignant mesothelioma, *V1*: 242, 250–251
melanoma, in fatty liver, *V1*: 128, 142
MR imaging techniques, *V1*: 121, 128, 137–147
computed tomography arterial portography *vs.*, *V1*: 143, 145–147
computed tomography *vs.*, *V1*: 141–144
coronal images, *V1*: 128, 143
detection and characterization, *V1*: 128, 137–143
lesional/perilesional enhancement, *V1*: 147–150
vascularity and degree of enhancement, *V1*: 149, 151–162
mucinous cystadenoma/cystadenocarcinoma, *V1*: 614–616
multiple myeloma, *V1*: 238, 245–246
pancreatic adenocarcinoma, *V1*: 552, 580, 584–587
pancreatic gastrinomas, *V1*: 591, 598–602
pancreatic islet cell tumors, *V1*: 591, 593–596
perfusional defect imaging, *V1*: 143, 147, 398–400
postradiation therapy, *V1*: 257, 262–264
posttreatment, *V1*: 256
pyogenic abscess, differential diagnosis, *V1*: 418, 430
rectal carcinoid tumors, *V1*: 867–868
resection, *V1*: 256–262
secondary infection, *V1*: 180, 188, 191–192
small intestine carcinoids, *V1*: 779, 790–791
transcatheter arterial chemoembolization, *V1*: 268, 270–278
undifferentiated sarcoma, *V1*: 251, 256
MR imaging:
basic technique, *V1*: 46–50
gadolinium-based contrast agents, *V2*: 1768, 1770–1772
gadolinium-enhanced T1-weighted images, hepatic arterial dominant (capillary) phase, *V1*: 10–13
protocol for, *V1*: 16–20
whole body imaging, *V1*: 36, 39
mucopolysaccharidoses, *V1*: 384, 387–388
normal anatomy, *V1*: 45–46
variations, *V1*: 58–60
pediatric imaging, *V2*: 1649
porta hepatis lymphadenopathy, *V1*: 352, 354, 362–364
portal venous air, *V1*: 411, 413
portal venous obstruction/thrombosis, *V1*: 388, 391, 393–400
hepatocellular carcinoma, *V1*: 202, 224–232
postradiation therapy, *V1*: 257, 262–264
preeclampsia and eclampsia, *V1*: 407, 410–411
resection, *V1*: 256–262
systemic chemotherapy, *V1*: 257, 264–270
transcatheter arterial chemoembolization, *V1*: 268, 270–278
transplantation, MR imaging, *V1*: 287–305
trauma, *V1*: 438–442
hepatic cysts, *V1*: 60, 65–66
Liver adenomatosis, *V1*: 114–118
Lobar/semilobar holoprosencephaly, fetal assessment, *V2*: 1589–1592
Lobular carcinoma in situ (LCIS), benign breast lesions, *V2*: 1719, 1721–1722
Lobular intraepithelial neoplasia (LIN), fibroadenomas, *V2*: 1702–1706
Lower esophageal sphincter (LES), achalasia, *V1*: 729–730
Lung cancer:
liver metastases, *V1*: 151, 161
squamous cell lung cancer, *V1*: 162, 175–176
MR imaging techniques, *V2*: 1654–1661
pancreatic metastases, *V1*: 619, 625, 629–630
pulmonary nodules, *V2*: 1654, 1657, 1662–1665
small intestine metastases, *V1*: 782, 792
splenic metastases, *V1*: 701, 703–706
stomach metastases, *V1*: 760
Lung imaging, fetal assessment, normal development, *V2*: 1583
Lymphadenopathy:
adrenal glands, retroperitoneal, *V2*: 1017, 1019
colon cancer, *V1*: 858, 860
lymphoma, *V1*: 860, 867
endometrial carcinoma, *V2*: 1474–1481
hilar and mediastinal, *V2*: 1666–1667
MRI signal intensity and, *V1*: 1–2
pancreatic adenocarcinoma, *V1*: 552, 577–578, 580, 584
peritoneal metastases, *V2*: 924–925, 934–935
porta hepatis lymphadenopathy, *V1*: 352, 354, 359, 362–364
retroperitoneum:
benign masses, *V2*: 1247–1250
Hodgkin lymphoma, *V2*: 1253–1254
malignant metastatic, *V2*: 1258–1263
spleen, lymphoma metastases, *V1*: 694, 699–703
Lymphangiomas:
fetal assessment, *V2*: 1598, 1603
pelvic, *V2*: 1274, 1291–1292
spleen, *V1*: 693
Lymphatic dissemination:
ovarian malignancies:
epithelial tumors, *V2*: 1532–1533
metastases to, *V2*: 1547, 1549–1550
peritoneal metastases, *V2*: 924–925, 934–935
carcinoid tumors, *V2*: 936–938
pseudomyxoma peritonei, *V2*: 936–938
testicular cancer, *V2*: 1391–1396
Lymph nodes:
adrenal gland neuroblastoma, *V2*: 1013–1017
bladder cancer, transitional cell carcinoma, *V2*: 1307–1316
breast, *V2*: 1712–1714
cervical cancer metastases, *V2*: 1486–1488
colon cancer imaging, *V1*: 843, 848
endometrial carcinoma, *V2*: 1474–1481
magnetic resonance lymphography, *V1*: 896–897
ovarian malignancies, epithelial tumors, *V2*: 1532–1533
pancreatic adenocarcinoma involvement, *V1*: 575, 578, 580, 584
prostate cancer metastases, *V2*: 1368–1373
psoas muscle tumors, *V2*: 1271, 1273–1274
retroperitoneal necrotic malignant, *V2*: 1258, 1262–1263
Lymphocele:
inferior vena cava thrombus, *V2*: 1237
renal transplants, *V2*: 1178, 1182, 1185
Lymphoma. *See also* Hodgkin lymphoma; Non-Hodgkin lymphoma
adrenal glands, *V2*: 1017, 1019
bile duct/ampulla metastases, *V1*: 520
bladder, *V2*: 1316, 1321
body wall, *V2*: 1274, 1284–1290
breast cancer, *V2*: 1741–1743
colorectal malignancies, *V1*: 860, 867
kidneys, *V2*: 1103, 1106–1110
liver metastases, *V1*: 238, 240–245
angiotropic intravascular, *V1*: 238, 242
Burkitt lymphoma, *V1*: 238, 243–244
HIV patient, *V1*: 238, 245
post-hepatic transplantation, *V1*: 238, 241
primary hepatic, *V1*: 238, 244
ovarian, *V2*: 1545, 1548–1549
renal pelvis and ureter, *V2*: 1159

Lymphoma (*Continued*)
retroperitoneal malignant masses, *V2*: 1253–1257
small intestine, *V1*: 779, 786–791
spleen malignancies, *V1*: 693–694, 699–703
direct tumor invasion, *V1*: 704–705
testicular, *V2*: 1395–1396
vaginal, *V2*: 1421, 1424

Macrocystic serous cystadenoma, MR imaging, *V1*: 607, 611–612
Macrocytic gadolinium-based contrast agents, *V2*: 1768–1774
Magnetic field strength:
breast MRI imaging, *V2*: 1692–1693
pediatric MRI, *V2*: 1644
Magnetic resonance angiography (MRA):
aortic imaging:
abdominal aortic aneurysm, *V2*: 1201–1207
aortic dissection, *V2*: 1201, 1208–1212
chest imaging, *V2*: 1654
hepatic transplantation protocol, *V1*: 287–289, 292
hepatocyte-specific contrast agents, *V2*: 1768
inferior vena cava, *V2*: 1223, 1228–1230
malignancies *vs.* thrombus, differential diagnosis, *V2*: 1240–1241
thrombus, *V2*: 1232–1237
insulinomas, *V1*: 601
kidney imaging, *V2*: 1029
transplants, *V2*: 1177–1184
liver, arteriovenous fistulas, *V1*: 388–392
pancreatic imaging, *V1*: 540
pancreatic transplants, *V1*: 671–673
pulmonary emboli, *V2*: 1673, 1675–1677
pulmonary vascular abnormalities, *V2*: 1673, 1678–1684
renal artery disease, *V2*: 1129, 1131–1133
retroperitoneal imaging, *V2*: 1194
vessels, *V2*: 1194–1200
small intestine, ischemia and hemorrhage, *V1*: 816, 819–823
thoracic, *V2*: 1673, 1679–1684
Magnetic resonance cholangiography, echo-train spin-echo sequences, *V1*: 7
Magnetic resonance cholangiopancreatography (MRCP). *See also* Secretin-enhanced MRCP
3T MR imaging, 8-channel torso coil, *V1*: 35–37
bile duct:
benign disease:
AIDS-related cholangiopathy, *V1*: 505
ampullary adenoma, *V1*: 511, 516
ampullary fibrosis, *V1*: 489, 495–496
ampullary stenosis, *V1*: 489
Caroli disease, *V1*: 505, 511–513
cholecdocholithiasis, *V1*: 488–492
choledochal cyst, *V1*: 505, 508–510
choledochocele, *V1*: 505, 511
cysts, *V1*: 505
infectious cholangitis, *V1*: 499, 502–507
mass lesions, *V1*: 511, 514–520
papillary adenoma, *V1*: 511, 515
papillary dysfunction, *V1*: 489, 493, 497
postsurgical complications, *V1*: 511, 514–515, 517–520
primary sclerosing cholangitis, *V1*: 494, 497–502
sclerosing cholangitis, *V1*: 493–494
imaging studies, *V1*: 483–488
pitfalls, *V1*: 489, 493–494
malignant disease:
carcinoma, intrahepatic/peripheral metastases, *V1*: 238–240, 242, 247–249
cholangiocarcinoma, *V1*: 515–518, 521–526
metastases to, *V1*: 530
periampullary/ampullary carcinoma, *V1*: 518, 520, 527–530
pitfalls of, *V1*: 489, 493–494
biliary anastomoses, *V1*: 464, 466–467
cholecystitis:
acute cholecystitis, *V1*: 468–475
chemoembolization-induced, *V1*: 468, 476
acute on chronic cholecystitis, *V1*: 468, 475
chronic, *V1*: 475, 477–478
hemorrhagic, *V1*: 475–477
xanthogranulomatous, *V1*: 477
gadolinium-based contrast agent, *V2*: 1771–1772
gallstone disease, *V1*: 464–465, 467–469
hepatic transplantation protocol, *V1*: 287–289
intestinal choledochocele, *V1*: 775–776
intraductal papillary mucinous neoplasms, *V1*: 615–621
intraductal papillary mucinous tumor, serous cystadenoma, differential diagnosis, *V1*: 612
MR imaging *vs.*, *V1*: 455
pancreatic imaging, *V1*: 536, 540
acute pancreatitis, *V1*: 625, 632
cystic fibrosis, *V1*: 546
pancreas divisum, *V1*: 541–542
trauma assessment, *V1*: 665, 668–671
in pregnancy, maternal imaging, *V2*: 1564
small intestine, adenocarcinoma, *V1*: 777
T2-weighted sequences, *V1*: 456–461
Magnetic resonance colonography, *V1*: 827
colon cancer polyps, *V1*: 848, 851–852
Magnetic resonance ductography, intraductal papilloma, differential diagnosis, *V2*: 1707–1709
Magnetic resonance imaging (MRI):
emerging developments in, *V1*: 25
liver imaging techniques, *V1*: 46–50
Magnetic resonance lymphography:
imaging contrast agents, *V1*: 896–897
retroperitoneum, malignant metastatic lymphadenopathy, *V2*: 1258–1263
Magnetic resonance spectroscopy:
male pelvis, *V2*: 1343–1344
prostate cancer, adenocarcinoma, *V2*: 1352, 1356–1373
Magnetic resonance urography:
echo-train spin-echo sequences, *V1*: 7
kidney imaging techniques, *V2*: 1184, 1188
perinephric pseudocyst, *V2*: 1042, 1044, 1050
transplants, *V2*: 1177–1184
in pregnancy, maternal imaging, *V2*: 1564, 1566
renal collecting system dilation, *V2*: 1164, 1170
Magnetic susceptibility artifact, breast MRI, *V2*: 1695
Magnetization-prepared rapid-acquisition gradient echo (MP-RAGE) sequences:
abdominal-pelvic imaging, *V1*: 5–6
pediatric patients, *V2*: 1637–1639, 1641–1644
Malakoplakia, *V2*: 1153–1154
Male pseudohermaphroditism, Wilms tumor and, *V2*: 1103–1106
Malignant mixed mesodermal/müllerian tumor:
bladder, *V2*: 1316
uterine sarcoma, *V2*: 1475, 1479–1481
Malrotation:
kidneys, *V2*: 1031
small intestine, *V1*: 770–771
Mammography:
ductal carcinoma in situ, benign lesions, *V2*: 1719–1721
MRI guidance and intervention, *V2*: 1760–1762
Manganese-based (Mn-DPDP (mangofodipir))-enhanced SGE imaging:
biliary tree, normal anatomy, *V1*: 460–461
contrast agenta, *V2*: 1778–1779
liver images, *V1*: 50
hepatocyte targeting, *V1*: 50–58
portal arteriorvenous system, *V1*: 46, 50
T1-weighted magnetic resonance cholangiopancreatography, *V1*: 460–461
Mass enhancement, breast cancer imaging, *V2*: 1723
Mastectomy:
postoperative MRI, *V2*: 1744–1749
prostheses, fat necrosis, *V2*: 1750–1752
Mastitis, inflammatory breast carcinoma, differential diagnosis, *V2*: 1739
Maternal imaging. *See also* pregnancy-related imaging under specific cancers and diseases
amniotic fluid assessment, *V2*: 1622–1623

anticardiolipin antibodies, fetal stroke, *V2*: 1598–1599
metastases in pregnancy, *V2*: 1561–1575
multiple gestation, *V2*: 1623–1624
placental imaging, *V2*: 1623, 1625–1627
postpartum uterus, *V2*: 1575–1580
pregnancy complications, *V2*: 1561–1575
Maximum-intensity projection (MIP):
aortic imaging, *V2*: 1200–1227
aortic dissection, *V2*: 1201, 1208–1212
breast MRI, *V2*: 1693–1694
ductal carcinoma in situ, *V2*: 1721
fibroadenomas, *V2*: 1703, 1706
chest imaging, *V2*: 1654
kidneys, renal artery disease, *V2*: 1129, 1131–1133
magnetic resonance cholangiopancreatography, *V1*: 456, 458–460
thoracic aorta, *V2*: 1679–1684
vessel imaging, *V2*: 1198–1200
inferior vena cava malignancies, *V2*: 1240–1241
Mayer-Rokitansky-Küster-Hauser syndrome:
uterine agenesis/hypoplasia, *V2*: 1441–1443
vaginal agenesis/partial agenesis, *V2*: 1411–1413
Mayo End-Stage Liver Disease (MELD) scale:
autoimmune hepatitis, *V1*: 314
primary sclerosing cholangitis, *V1*: 304, 311
Meckel diverticulum, *V1*: 770, 774
Meckel-Gruber syndrome:
encephalocele, fetal assessment, *V2*: 1595, 1597
renal cysts, fetal assessment, *V2*: 1614–1616
Meconium:
MR imaging, *V2*: 1583–1585
pseudocysts, *V2*: 1617
Mediastinal ascites, *V2*: 936, 942
Mediastinal lymphadenopathy, *V2*: 1666–1667
Medistinal neoplasms, fetal assessment, *V2*: 1612
Medium-vessel disease, renal artery, *V2*: 1136, 1138
Medulla, adrenal. *See* Adrenal glands, medullary masses
Medullary carcinoma, breast cancer, *V2*: 1732–1733
Medullary cystic disease, *V2*: 1049, 1059–1060
Medullary sponge kidney (MSK), *V2*: 1049, 1060
Megacystis-microcolon hyperperistalsis syndrome, fetal assessment, *V2*: 1613–1614
Meigs syndrome, benign ovarian neoplasms, *V2*: 1525–1526, 1529–1531
Melanoma:
anorectal, *V1*: 867, 869
breast metastases, *V2*: 1743–1744
iliacus muscle metastases, *V2*: 1273, 1276
metastases:
to bile duct/ampulla, *V1*: 520
to gallbladder, *V1*: 483, 487
to liver, *V1*: 164, 181–182
to pancreas, *V1*: 625, 628
ovarian metastases, *V2*: 1547, 1549–1550
splenic metastases, *V1*: 701, 703–706
stomach metastases, *V1*: 760
vulvovaginal malignancies, *V2*: 1421, 1424
Membranous nephropathy, glomerular disease, *V2*: 1117–1118
Menstruation, uterine changes, *V2*: 1437–1439
Merkel cell cancer, pancreatic metastases, *V1*: 625, 631
Mesenchymal hamartoma, fetal assessment, *V2*: 1620
Mesenchymal tumors, breast cancer, *V2*: 1739–1740
Mesenteric adenopathy, peritoneal metastases, *V2*: 924–925, 934–935
Mesenteric cysts, *V2*: 907, 910
Mesenteric lipodystrophy, *V2*: 946, 950
Mesenteric lipomatosis, *V2*: 910
Mesenteritis, *V2*: 946, 950
Mesoblastic nephroma, fetal assessment, *V2*: 1620
Mesorectum imaging, colon cancer, *V1*: 848
Mesothelioma, malignant:
liver metastases, *V1*: 242, 250–251
peritoneal diffusion, *V2*: 912, 915–917
Metabolic acidosis, nephrogenic systemic fibrosis and, *V2*: 1782–1783
Metallic artifacts:
bile duct MRCP, *V1*: 489, 493–494, 505
biliary papillomatosis, *V1*: 514–515
single-shot echo-train spin-echo sequences, *V1*: 7–8
Metastatic immature teratoma, peritoneal metastases, *V2*: 918, 923–924, 927
Methemoglobin:
bladder, hemorrhagic cysts, *V2*: 1326, 1329
renal cysts, hemhorragic/proteinaceous cysts, *V2*: 1037, 1046
Microcystic serous cystadenoma, *V1*: 606–607, 609–611
Microvarices, peritoneal, *V2*: 945–946, 948–949
Middle interhemispheric holoprosencephaly (MIH), fetal assessment, ventriculomegaly, *V2*: 1590–1592
Mid-hepatic arterial phase (MHAP) imaging, gadolinium-based contrast agent, *V2*: 1774–1777
Misregistration artifacts, breast MRI, *V2*: 1695
Monodermal teratoma, benign ovarian neoplasm, *V2*: 1521
Mosaic enhancement, liver imaging, congestive heart failure, *V1*: 407, 411–413
Motion-related artifacts:
1.5T *vs.* 3T imaging, *V1*: 35
adnexal imaging, *V2*: 1499–1500
breast MRI, *V2*: 1694–1695
chest imaging, *V2*: 1654
pleural disease, *V2*: 1666, 1671–1672
pregnancy-related MRI, *V2*: 1561
Motion-resistant imaging:
abdominal region, *V1*: 20–24
3T strategy, *V1*: 23–24
pediatric patients, *V2*: 1639, 1641, 1647–1648
Mucinous carcinoma, breast cancer, *V2*: 1732, 1734
Mucinous cystadenoma/cystadenocarcinoma, *V1*: 612–616
mucocele, large intestine, *V1*: 838, 841–842
ovaries:
benign neoplasms, *V2*: 1518–1520, 1521–1522
malignant neoplasms, *V2*: 1533, 1536–1537
Mucin-producing tumors, liver metastases, *V1*: 165, 185–186
Mucocele, appendix, *V1*: 832, 838, 841–842
Mucopolysaccharidoses, liver imaging, *V1*: 384, 387–388
Mucosa-associated lymphoid tissue (MALT), small intestine, *V1*: 779, 786–791
Müllerian duct:
adenocarcinoma, *V2*: 1488, 1491
cancer, ovarian metastases, *V2*: 1547, 1549
congenital anomalies, *V2*: 1439–1448
malignant mixed mesodermal/müllerian duct tumor, bladder, *V2*: 1316
ovarian anomalies, *V2*: 1503
prostate cysts, *V2*: 1344, 1348–1349
vaginal agenesis/partial agenesis, *V2*: 1410–1413
Multicystic dysplastic kidney, *V2*: 1047–1049, 1058
fetal assessment, *V2*: 1614–1616
MultiHance contrast agent (Gd-BOPTA):
classification, *V2*: 1768, 1771–1772
hepatocyt phase, *V2*: 1777
liver imaging, *V1*: 51–58
adenomatosis, *V1*: 114, 118
focal nodular hyperplasia, *V1*: 55–56, 121, 136
metastases characterization, *V1*: 128, 136
T1-weighted magnetic resonance cholangiopancreatography, *V1*: 460
Multilocular cystic nephroma, *V2*: 1060, 1063–1064
Multiplanar reformatting (MPR), renal artery disease, *V2*: 1131

Multiple endocrine neoplasia (MEN) type 1, stomach carcinoids, *V1*: 759
Multiple endocrine neoplasia (MEN) type IIA or IIB, pheochromocytoma, *V2*: 1005
Multiple gestation, MR imaging techniques, *V2*: 1623–1624
Multiple imaging variables, magnetic resonance imaging, *V1*: 13–14
Multiple myeloma:
  liver metastases, *V1*: 238, 245–246
  metastases, gadolinium-based contrast agent imaging, *V2*: 1771–1772
Mumps orchitia, *V2*: 1397–1398
Mural thrombus, abdominal aortic aneurysm, *V2*: 1200–1201, 1205
Mycobacterial infection, liver imaging, *V1*: 433–435
Mycobacterium avium intracellulare (MAI):
  hepatic involvement, *V1*: 433–435
  infectious colitis, *V1*: 884, 888, 891–892
  infectious enteritis, *V1*: 810, 813–814
  retroperitoneal benign lymphadenopathy, *V2*: 1247–1250
Myelofibrosis, kidney, extramedullary hematopoiesis, *V2*: 1068, 1073
Myelolipoma, adrenal glands, *V2*: 977–980, 988–990
Myelomeningocele, fetal assessment, Chiari II malformation, *V2*: 1586–1592
Myofibroblastic tumor, inflammatory:
  bladder lesions, *V2*: 1304
  hepatic inflammatory disease, *V1*: 415, 418–422
Myoglobinuria, renal tubular blockage, *V2*: 1120, 1124
Myometrial hematoma, postpartum uterus, *V2*: 1575–1580
Myometrial metastases, endometrial carcinoma, *V2*: 1470

Nabothian cysts, *V2*: 1467–1468, 1471
Nasopharynx. *See also* Cleft palate
  fetal assessment:
    anomalies, *V2*: 1598–1607
    normal development, *V2*: 1583
Neck imaging, fetal assessment:
  anomalies, *V2*: 1598–1599, 1601–1607
  normal development, *V2*: 1583
Necrosis:
  fetal assessment, destructive lesions, *V2*: 1598–1601
  ovarian fibroma, *V2*: 1526, 1530
Necrotizing granulomatous pancreatitis, inflammation or infection, *V1*: 665–666
Negative oral contrast agents, large intestine imaging, *V1*: 896–897
Neisseria gonorrhoeae:
  Bartholin glands cysts, *V2*: 1416–1418
  tubo-ovarian abscess, *V2*: 1514, 1516–1517
Neoadjuvant chemotherapy (NCT), breast cancer, posttreatment MRI, *V2*: 1744–1753
Neonatal ascites, *V2*: 936, 942
Nephrectomy:
  pancreatic imaging, *V1*: 540–541
  segmental, *V2*: 1142, 1146
Nephroblastoma (Wilms tumor), *V2*: 1102–1106
Nephrogenic systemic fibrosis (NSF):
  circulating fibrocyte hypothesis, *V2*: 1783
  contrast agents, *V2*: 1767
  contrast-induced nephropathy risk *vs.*, *V2*: 1784–1786
  definition, *V2*: 1780
  diagnosis, *V2*: 1783
  epidemiology, *V2*: 1780–1781
  gadolinium-based contrast agent toxicity, *V2*: 1780–1786
    cofactors, *V2*: 1782–1783
    pharmacokinetics, *V2*: 1781–1782
  pathophysiology and risk factors, *V2*: 1781
  pediatric imaging, contrast agents, *V2*: 1647
  pulmonary emboli imaging, *V2*: 1673, 1675–1677
  renal function, *V2*: 1781
  risk minimization guidelines, *V2*: 1783–1784
  treatment and prognosis, *V2*: 1783
  vessel imaging, *V2*: 1195–1200
Nephroma, mesoblastic, fetal assessment, *V2*: 1620
Nephropathy:
  ischemic, *V2*: 1129, 1131, 1134
  reflux nephropathy, *V2*: 1126, 1128, 1130
  Wilms tumor and, *V2*: 1103–1106
Nephrophthisis, *V2*: 1049, 1059–1060
Nephroscleroses, renal artery disease, *V2*: 1137
Nephrotic syndrome, *V2*: 1117, 1120
Neural tube defects, fetal imaging, *V2*: 1585–1592
Neurenteric cysts, fetal assessment, *V2*: 1612
Neurilemmoma, retroperitoneum, *V2*: 1240, 1245–1247
Neuroblastoma:
  adrenal glands, *V2*: 1006, 1012–1017
  fetal assessment, *V2*: 1618, 1620
  retroperitoneum, *V2*: 1266, 1273
Neuroendocrine carcinoma:
  pancreatic cancer, *V1*: 593
  stomach, *V1*: 759
Neurofibromas:
  bladder, *V2*: 1304
  retroperitoneum, plexiform, *V2*: 1240, 1245–1247
  small intestine, *V1*: 775, 779
Neurofibromatosis type 1:
  bladder lesions, *V2*: 1304–1305
  small intestine neurofibromas, *V1*: 775, 779
Neurogenic tumors:
  bladder, *V2*: 1304–1305
  small intestine neurofibromas, *V1*: 775, 779
  stomach, *V1*: 736, 738
Neurovascular bundles, prostate cancer invasion, *V2*: 1368–1373
Neutropenic colitis, *V1*: 884, 890
Nonalcoholic fatty liver disease (NAFLD), imaging studies, *V1*: 317, 319–320
Nonalcoholic steatohepatitis (NASH), *V1*: 319–320
Noncooperative patients, imaging protocols in, *V1*: 25–28
Nonepithelial tumors, bladder cancer, *V2*: 1316
Non-Hodgkin lymphoma:
  adrenal glands, *V2*: 1017, 1019
  colon, *V1*: 860, 867
  kidneys, *V2*: 1103, 1106–1110
  liver metastases, *V1*: 238, 240–245
  pancreas, *V1*: 619, 624–625
  peritoneal metastases, *V2*: 925
  retroperitoneal malignant masses, *V2*: 1253–1257
  small intestine, *V1*: 779, 786–791
  spleen, *V1*: 693–694, 699–703
  stomach, *V1*: 756, 758
Noninvoluting congenital hemangioma, fetal assessment, *V2*: 1604, 1607
Nonmass enhancement, breast cancer imaging, *V2*: 1723
Nonseminomatous tumors, testes, *V2*: 1390–1396
Non-slice selective inversion pulse, magnetization-prepared rapid-acquisition gradient echo sequences, *V1*: 5–6
Noose sign, breast implant rupture, *V2*: 1759
"Nutcracker syndrome," inferior vena cava thrombus, *V2*: 1232–1237

Obesity:
  nonalcoholic fatty liver disease, *V1*: 317, 319–320
  polycystic ovarian syndrome, *V2*: 1507, 1509, 1514
Oligohydramnios:
  encephalocele, fetal assessment, *V2*: 1595, 1597
  kidney anomalies, *V2*: 1612–1613
  twin-twin transfusion syndrome, *V2*: 1623–1624
Omental hypertrophy, cirrhosis, *V1*: 348, 351, 360
  intraperitoneal varices, *V2*: 923–924, 934
Omental metastases, peritoneal, interperitoneal seeding, *V2*: 923–924, 934–935
Omental varices, cirrhosis, *V1*: 348, 351, 359
Omphalocele, fetal assessment, *V2*: 1617
Oncocytomas, renal, *V2*: 1068, 1072
1.5T imaging:
  3T imaging *vs.*, *V1*: 31–36
    gastrointestinal tract, *V1*: 725
  adrenal glands, *V2*: 963–968

breast MRI, *V2*: 1694–1695
lung cancer, pulmonary nodules, *V2*: 1654, 1662
male pelvis, *V2*: 1343–1344
pediatric patients, *V2*: 1637, 1644
receiver coil, *V2*: 1644–1645
renal cell carcinoma, stage 4, 1082, 1084–1085
vaginal carcinoma, *V2*: 1416, 1422
Oral contraceptives:
abdominal fibromatosis, *V2*: 1570
primary ovarian carcinoma protection, *V2*: 1527
uterine changes, *V2*: 1439
Oral contrast agents:
large intestine imaging, *V1*: 892, 895–897
MR imaging strategies, *V1*: 20
pregnancy-related MRI, *V2*: 1561
retroperitoneum imaging, *V2*: 1194
Organs of Zuckerkandl:
benign neoplasms, *V2*: 1247
pheochromocytoma, *V2*: 1005–1111
Oriental cholangitis, MR imaging, *V1*: 502, 507
Oropharynx. *See also* Cleft palate
fetal assessment:
anomalies, *V2*: 1598–1607
normal development, *V2*: 1583
Out-of-phase (opposed-phase) spoiled gradient echo sequences:
adrenal glands, *V2*: 963–968
adenomas, *V2*: 971–985
metastases, *V2*: 998–1002
basic principles, *V1*: 4–5
kidneys, angiomyolipomas, *V2*: 1063–1068
pediatric patients, *V2*: 1645–1646
Ovarian arteries, uterine artery embolization, *V2*: 1456, 1464
Ovarian cancer:
carcinosarcoma, *V2*: 1545, 1548
clear cell carcinoma, *V2*: 1533, 1538–1540
colon metastases, *V1*: 867, 869
epithelial origin, *V2*: 1531–1533
primary peritoneal carcinoma, differential diagnosis, *V2*: 912, 917
gallbladder metastases, *V1*: 483, 487
germ cell origin, *V2*: 1533–1534, 1540–1544
imaging studies, *V2*: 1518
kidney metastases, *V2*: 1112, 1114
liver metastases, *V1*: 151, 158–160, 162, 164, 183–185, 187–188
lymphoma, *V2*: 1545, 1548–1549
mucinous tumors, *V2*: 1533, 1536–1538
peritoneal metastases, intraperitoneal seeding, *V2*: 918–924
in pregnancy, maternal imaging, *V2*: 1569, 1571
primary ovarian carcinoma, *V2*: 1526–1527, 1531
serous tumors, *V2*: 1533–1536
sex cord-stromal origin, *V2*: 1540, 1542, 1545–1547
small intestine metastases, *V1*: 779, 782, 792
uterine leiomyoma, differential diagnosis, *V2*: 1451
Ovarian hyperstimulation syndrome, theca-lutein ovarian cysts, *V2*: 1504, 1507–1508
Ovarian torsion:
paraovarian cysts, *V2*: 1504, 1508
in pregnancy, maternal imaging, *V2*: 1569, 1572
Ovarian vein thrombosis, postpartum uterus, *V2*: 1578–1580
Ovaries. *See also* Adnexa
benign neoplasms, *V2*: 1518–1531
epithelial origin, *V2*: 1518–1523
germ cell origin, *V2*: 1520–1521, 1526–1529
sex cord-stromal origin, *V2*: 1525–1526, 1530–1531
congenital anomalies, *V2*: 1503
cysts, *V2*: 1500, 1502–1503
dermoid cyst, *V2*: 1520–1521, 1526–1529
functional cysts, *V2*: 1500, 1502, 1504–1506
paraovarian/peritoneal cysts, *V2*: 1504, 1508
in pregnancy, differential diagnosis, *V2*: 1567, 1569–1570
theca-lutein cysts, *V2*: 1504, 1507–1508
ectopic pregnancy, *V2*: 1517
endometriosis, *V2*: 1504–1513
hydrosalpinx, *V2*: 1517
metastases to, *V2*: 1546–1547, 1549–1550
endometrial carcinoma, *V2*: 1474, 1476
normal anatomy, *V2*: 1500–1501
ovarian torsion, *V2*: 1509–1510, 1514–1516
pelvic inflammatory disease/tubo-ovarian abscess, *V2*: 1514, 1516–1517
pelvic varices, *V2*: 1517–1518
polycystic ovaries, *V2*: 1507, 1509, 1514
transposed ovary, *V2*: 1500–1502
Overlap syndrome, autoimmune liver disease, *V1*: 313–315
Ovotestes, MRI detection, *V2*: 1503

Paget disease:
of breast, *V2*: 1737–1738
vulvar carcinomas, *V2*: 1421
Palate imaging, fetal assessment, normal development, *V2*: 1583
Pancoast tumor, MR imaging, *V2*: 1654, 1660–1661
Pancreas:
3T MR imaging, *V1*: 35–37
cystic neoplasms, *V1*: 606–625 (*See also* Pancreatic cancer)
ductal dilatation:
chronic pancreatitis, *V1*: 648–652
trauma, *V1*: 665, 668–671
ductal stenosis, traumatic, *V1*: 665, 668–671
genetic disease:
cystic fibrosis, *V1*: 544–548
primary hemochromatosis, *V1*: 546, 548–549
von Hippel-Lindau syndrome, *V1*: 549–550
inflammatory disease, *V1*: 625
miscellaneous conditions and infections, *V1*: 664–667
pancreatitis, *V1*: 625
acute, *V1*: 625, 628, 636–647
autoimmune pancreatitis, *V1*: 656, 664, 666
chemtherapy-induced, *V1*: 664–667
chronic, *V1*: 640, 648–665
hemorrhagic, *V1*: 632, 639–641
mild, *V1*: 625, 632–635
pseudocyst, *V1*: 632, 642–647
metastases to, *V1*: 619, 625–631 (*See also* specific cancers, e.g., Breast cancer)
MR imaging, *V1*: 536–541
mucinous cystadenocarcinoma, liver metastases, *V1*: 165, 185–186
neoplasms (*See also* Pancreatic cancer)
benign solid, lipoma, *V1*: 551–556
focal lesions, pattern recognition, *V1*: 551
malignant solid, *V1*: 552–608
normal anatomy, *V1*: 535–536
pediatric imaging, *V2*: 1649–1650
transplants, *V1*: 671–673
trauma, *V1*: 665, 668–671
Pancreas divisum, MR imaging, *V1*: 541–542
Pancreatic anlage, congenital anomalies, *V1*: 542, 545
Pancreatic cancer:
acinar cell carcinoma, *V1*: 589
ACTHoma, *V1*: 601, 605
adenocarcinoma, *V1*: 552–553, 556–570, 556–589
diffuse, *V1*: 552, 576, 588
staging, *V1*: 575, 577–587
in tail, *V1*: 552, 574–575
vessel involvement, *V1*: 575, 577–578
adrenal gland metastases, *V2*: 998–1002
carcinoid tumors, *V1*: 602, 607–608
chemotherapy and radiation therapy and, *V1*: 589–590
chemotherapy/radiation-treated ductal adenocarcinoma, *V1*: 589–590
chronic pancreatitis, differential diagnosis, *V1*: 648, 656
cystic neoplasms:
cystic fibrosis, *V1*: 546
intraductal papillary mucinous neoplasms, *V1*: 614
main duct type, *V1*: 614–617
side-branch type, *V1*: 615, 618–621
lymphoma, *V1*: 619, 624–625
metastases, *V1*: 619, 625–632
mucinous cystadenoma/cystadenocarcinoma, *V1*: 612–616

Pancreatic cancer: (*Continued*)
pancreatic adenocarcinoma and, *V1*: 564
serous cystadenocarcinoma, *V1*: 612
serous cystadenoma, *V1*: 606–607, 609–612
solid/papillary epithelial neoplasm (papillary cystic neoplasm), *V1*: 619, 622–623
developmental anomalies, *V1*: 541–546
annular pancreas, *V1*: 541–544
pancreas divisum, *V1*: 541–542
pancreatic anlage, congenital absence, *V1*: 542, 545
short pancreas, polysplenia syndrome, *V1*: 544, 546
uneven fatty infiltration, *V1*: 542, 545
ductal adenocarcinoma, liver metastases, *V1*: 162
gastrinomas, *V1*: 591, 598–602
glucagonoma, *V1*: 601, 604
insulinomas, *V1*: 601, 603–604
iron-based contrast agents, differential diagnosis, *V2*: 1778–1779
islet cell tumors, *V1*: 590–598
pancreatic, *V1*: 590–598
gastrinomas, *V1*: 591, 598
undifferentiated, *V1*: 601
pancreatic adenocarcinoma, differential diagnosis, *V1*: 587–589
undifferentiated, *V1*: 590, 597–601
lymphoma, *V1*: 619, 624–625
peritoneal metastases, *V2*: 918, 923–924, 928
schwannoma, *V1*: 594–597, 601
somatostatinoma, *V1*: 601, 604–605
undifferentiated carcinoma, *V1*: 589
VIPoma, *V1*: 601, 606
Pancreatitis, *V1*: 625–667
acute, *V1*: 625, 628, 636–647
autoimmune pancreatitis, *V1*: 656, 664, 666
chemtherapy-induced, *V1*: 666–667
chronic, *V1*: 640, 648–665
pancreatic adenocarcinoma:
differential diagnosis, *V1*: 575
risk for, *V1*: 552, 562–564
focal pancreatitis, *V1*: 649, 652, 665
hemorrhagic, *V1*: 632, 639–641
mild, *V1*: 625, 632–635
necrotizing granulomatous, *V1*: 665–666
pancreas divisum and risk of, *V1*: 541
peritoneal inflammation, *V2*: 940–942, 946, 949
pseudocyst, *V1*: 632, 642–647
small intestine effects, *V1*: 810, 815
Papillary adenoma, bile duct, *V1*: 511, 515
Papillary carcinoma, breast cancer, *V2*: 1733, 1737
Papillary cystic neoplasm, pancreas, *V1*: 619, 622–623
Papillary dysfunction, bile duct, MRCP imaging, *V1*: 489, 493, 497
Papillary epithelial neoplasm, pancreas, *V1*: 619, 622–623
"Papillary lesions," intraductal papilloma, differential diagnosis, *V2*: 1707–1709
Papillary serous carcinoma:
fallopian tube metastases, *V2*: 1551–1552
uterus, *V2*: 1474, 1477
Papilloma:
bladder lesions, *V2*: 1300–1301
intraductal, *V2*: 1707–1709
Papillomatosis, intraductal papilloma, differential diagnosis, *V2*: 1707–1709
Papilomatosis, multiple, diagnostic imaging, *V2*: 1709–1711
Paraesophageal hiatal hernias, *V2*: 904, 906–907
Paraesophageal varices, cirrhosis, *V1*: 351, 361
Parallel-line sign, breast implant rupture, *V2*: 1759
Parallel MR imaging:
evolution of, *V1*: 25, 29–31
non-fat-suppressed *vs*. fat-suppressed images, *V1*: 35–37
pulmonary emboli, *V2*: 1673, 1675–1677
Paramagnetic contrast agents, liver imaging, *V1*: 50–51
Parametrium:
cervical cancer metastases, *V2*: 1486–1487
normal anatomy, *V2*: 1437
papillary serous carcinoma, *V2*: 1474, 1477
Paramtrium, normal anatomy, *V2*: 1437
Paraovarian cysts, *V2*: 1504, 1508
Parapelvic cysts, *V2*: 1042, 1044, 1050
Paraumbilical hernia, abdominal wall imaging, *V2*: 904, 909
Paraumbilical varices, cirrhosis, *V1*: 348, 351, 361
Parenchymal hemorrhage, fetal assessment, *V2*: 1598–1601
Paroxysmal nocturnal hemoglobinuria, iron deposition, renal parenchyma, *V2*: 1121, 1127
Patient preparation and positioning:
breast MRI, *V2*: 1694
MRI guidance and breast intervention, *V2*: 1760–1762
Pediatric patients:
cirrhosis in, *V1*: 317–318
MR imaging techniques, *V2*: 1637–1644
1.5T and 3.0T sequences, *V2*: 1639, 1644
adnexa, *V2*: 1650
adrenal glands, *V2*: 1650
bladder, *V2*: 1650
data acquisition parameters, *V2*: 1644–1645
echo-train spin-echo sqeuence, *V2*: 1644
female urethra/vagina, *V2*: 1650
follow-up procedures, *V2*: 1647–1649
gadolinium-based contrast agents, *V2*: 1647
gallbladder/biliary system, *V2*: 1649
gastrointestinal tract, *V2*: 1650
infants (under 1.5 years), *V2*: 1645
kidneys, *V2*: 1650
liver, *V2*: 1649
magnetic field strength, *V2*: 1644
magnetization-preparied rapid-acquisition gradient-echo sequences, *V2*: 1639, 1644
male pelvis, *V2*: 1650
older children (6–18 years), *V2*: 1645–1646
pancreas, *V2*: 1649–1650
receiver coil, *V2*: 1644–1645
retroperitoneum, *V2*: 1650
sedation technique, *V2*: 1646–1647
single-shot echo-train spin-echo sequence, *V2*: 1644
small children (1–6 years), *V2*: 1641, 1645
spin-echo sequences, *V2*: 1637
spleen, *V2*: 1650
T1-weighted sequences, *V2*: 1637, 1639–1644
T2-weighted sequences, *V2*: 1644
three-dimensional gradient-echo sequences, *V2*: 1639
two-dimensional spoiled gradient echo sequences, *V2*: 1639
uterus and cervix, *V2*: 1650
Peliosis hepatis, *V1*: 114–115, 119–120
Pelvic congestion syndrome, *V2*: 1517–1518
Pelvic floor relaxation, female urethra, *V2*: 1408–1410
Pelvic inflammatory disease (PID), ovarian abscess, *V2*: 1514, 1516–1517
Pelvic kidney, *V2*: 1031–1035
Pelvimetry, MR imaging techniques, *V2*: 1629
Pelvis:
abscesses, *V1*: 874, 884–886
peritoneal inflammation, *V2*: 951, 957–958
Burkitt lymphoma, retroperitoneal malignant masses, *V2*: 1253, 1257
cervical cancer invasion of, *V2*: 1486–1488
Ewing sarcoma pelvic metastases, *V2*: 1274, 1288
extrarenal, *V2*: 1164, 1170
female pelvis (*See* Vagina; specific organs, e.g., Uterus)
bowel peristalsis artifacts, *V2*: 1499
in pregnancy, maternal imaging, *V2*: 1570, 1574
uterine peristalsis, *V2*: 1437–1439
varices, *V2*: 1517–1518
fetal assessment:
anomalies, *V2*: 1612–1617
cysts, *V2*: 1617, 1619
normal development, *V2*: 1583–1585
lipomatosis, bladder involvement, *V2*: 1326, 1329–1330

male pelvis (*See also* specific organs, e.g., Prostate)
MR imaging technique, *V2*: 1343–1344
pediatric imaging, *V2*: 1650
postprostatectomy, *V2*: 1349, 1354
metastases, bladder involvement, *V2*: 1320–1322
protocol for, *V1*: 16–19, 21
whole body imaging, *V1*: 36, 40
Penis:
benign masses, prostheses, *V2*: 1376–1377
congenital anomalies, *V2*: 1376
diffuse disease, *V2*: 1377–1380
infectious disease, *V2*: 1380
inflammatory disease, *V2*: 1380–1381
metastases to, *V2*: 1376–1380
normal anatomy, *V2*: 1375–1376
primary tumors, *V2*: 1377–1380
trauma, *V2*: 1382
Percentage mural enhancement (MRP), Crohn disease imaging criteria, *V1*: 796, 803
Percutaneous gastrostomy tube, *V1*: 761, 766
Perfusional defect imaging, liver metastases, *V1*: 143, 147, 398–400
Periampullary carcinoma, bile duct imaging, *V1*: 518, 520, 527–530
Perianal fistula, *V1*: 883, 887–888
Perilesional enhancement:
liver imaging:
hemangiomas, *V1*: 90, 101
metastases, differential diagnoses, *V1*: 147–150
pancreatic adenocarcinoma, *V1*: 580, 587
uterine leiomyomas, *V2*: 1452–1469
Perinephric pseudocysts, *V2*: 1042, 1044, 1050
Perinephric stranding, renal abscess, *V2*: 1144, 1149–1152
Perineum, carcinomas, *V2*: 1421
Perioarterial lymphoid sheath (PALS), splenic anatomy, *V1*: 678
Periportal halo sign, primary biliary cirrhosis, *V1*: 314–315
Perisplenic varices, splenomegaly and, *V1*: 706–709
Peristalsis. *See* Bowel peristalsis; Uterine peristalsis
Peristomal hernia, abdominal wall imaging, *V2*: 904, 909
Peritoneum. *See also* Retroperitoneum
benign masses:
cysts, *V2*: 907, 910
desmoid tumor (aggressive fibromatosis), *V2*: 912–914
endometriosis, *V2*: 911
lipomas and mesenteric lipomatosis, *V2*: 910
cholangiocarcinoma metastases, *V1*: 520, 526
cirrhosis and enhancement of, *V1*: 348, 351, 360
colon cancer metastases, *V1*: 843, 847–848, 854–858, 860
congenital anomalies, *V2*: 904–907
foreign bodies, *V2*: 945–947
hepatocellular carcinoma metaseses, *V1*: 192, 200–201
hernias, *V2*: 904–909
abdominal wall, *V2*: 904, 908–909
Bochdalek hernia, *V2*: 904–905
hiatus and internal, *V2*: 904, 906–907
inflammatory disease:
abscess, *V2*: 949, 951, 954–959
mesenteric panniculitis, *V2*: 946, 950
pancreatitis, *V2*: 940–942, 946, 949
peritonitis, *V2*: 949, 951–953
intraperitoneal fluid:
ascites, *V2*: 936, 940–942
bile, *V2*: 942
biloma, *V2*: 942, 944–945
blood, *V2*: 936, 943–944
lesser sac involvement, *V2*: 936, 941
postsurgical, *V2*: 936, 940
urine, *V2*: 942
malignant masses:
diffuse malignant mesothelioma, *V2*: 912, 915–917
primary peritoneal carcinoma, *V2*: 912, 917
metastases to, *V2*: 912, 914, 918–936 (*See also* specific cancers)
carcinoid tumors, *V2*: 936, 939–940
contiguous spread, *V2*: 912
hematogenous spread, *V2*: 924
intraperitoneal seeding, *V2*: 914, 918–935
lymphatic dissemination, *V2*: 924–925, 934–935
ovarian cancer, *V2*: 1504–1505, 1533, 1535–1536
ovarian endodermal sinus tumor, *V2*: 1542
pseudomyxoma peritonei, *V2*: 936–938
MR imaging technique, *V2*: 902–903
normal anatomy, *V2*: 901–902
normal variants, *V2*: 904
ovarian cysts, *V2*: 1504, 1508
pancreatic adenocarcinoma metastases, *V1*: 575, 581–583
vascular disease, *V2*: 945–946, 948–949
Peritonitis, *V2*: 949, 951–953
Persistent fetal kidney lobulation, *V2*: 1031
Peutz-Jagers syndrome, colonic adenomatous polyps, *V1*: 832
Peyronie disease, *V2*: 1380–1381
Phase-cancellation artifact, out-of-phase (opposed-phase) spoiled gradient echo sequences, *V1*: 4–5
Phased-array multicoil imaging:
3T MR imaging, 4-channel *vs.* 8-channel, *V1*: 33–34
adnexa, *V2*: 1499
bladder, *V2*: 1298–1299
colon cancer, *V1*: 848
lung cancer, pulmonary nodules, *V2*: 1654, 1657, 1662–1665
male pelvis, *V2*: 1343–1344
pancreatic adenocarcinoma, *V1*: 559
pediatric patients, *V2*: 1644–1645
in pregnancy, *V2*: 1561
retroperitoneal neoplasms, *V2*: 1266
spoiled gradient echo sequences, *V1*: 3
uterus, *V2*: 1433
vessel imaging, *V2*: 1195, 1198–1200
Pheochromocytoma:
adrenal medullary masses, *V2*: 998, 1005–1111
bladder, *V2*: 1303
Phyllodes tumor, *V2*: 1706–1707
Picture archival computing system, vessel imaging, *V2*: 1200
Pince-nez sign, breast implant rupture, *V2*: 1759
Placenta, MR imaging techniques, *V2*: 1623, 1625–1627
Placenta accreta, MR imaging techniques, *V2*: 1623, 1625–1627
Placenta previa, MR imaging techniques, *V2*: 1623, 1625–1627
Pleural disease:
chest imaging, *V2*: 1666, 1671–1672
metastases, *V2*: 1673–1674
Pleural metastases, hepatocellular carcinoma, *V1*: 192, 202
Polycystic ovarian syndrome (PCOS), *V2*: 1507, 1509, 1514
Polygyria, fetal assessment, Chiari II malformation, *V2*: 1588–1592
Polyhydramnios:
encephalocele, fetal assessment, *V2*: 1595, 1597
fetal assessment:
brain neoplasms, *V2*: 1598
epignathi, *V2*: 1599
mesoblastic nephroma, *V2*: 1620
twin-twin transfusion syndrome, *V2*: 1623–1624
Polyorchia, *V2*: 1386
Polyposis coli, *V1*: 829, 832, 838
Polyposis syndromes:
gastric polyps, *V1*: 736, 739–741
large intestine, *V1*: 829, 832, 835–836
small intestinal polyps, *V1*: 775, 777–778
Polyps:
colonic, *V1*: 829, 832, 835–838
endometrial, *V2*: 1448–1450
gallbladder, *V1*: 480, 482–483
gastric, *V1*: 736, 739–741
small intestine, *V1*: 775, 777–778
Polysplenia syndrome:
MR imaging, *V1*: 681, 683, 686
short pancreas, *V1*: 544, 546
Polythelia, breast imaging, *V2*: 1700–1701
Porcelain gallbladder, *V1*: 477, 480
Porta hepatis lymphadenopathy:
hepatitis C and, *V1*: 327, 330
imaging studies, *V1*: 352, 354, 359, 362–365

Portal hypertension:
cirrhosis, *V1*: 348, 351, 359–362
esophageal varices, *V1*: 727, 729
gastric varices, *V1*: 738, 742
omental metastases, differential diagnosis, *V2*: 923–924
pediatric patients, imaging protocols, *V2*: 1637, 1642
rectal varices, *V1*: 838
splenomegaly, *V1*: 706–709
Portal venous system:
biliary tree, air in, *V1*: 411, 413–414
cirrhosis:
cavernous transformation, *V1*: 348, 351, 359
portal hypertension, *V1*: 348, 351, 359–362
gadolinium-enhanced T1-weighted images, *V1*: 11
hemangioma compression, *V1*: 88, 100
hepatic arterial dominant phase imaging, gadolinium-based contrast agent, *V2*: 1776–1777
hepatic transplantation complications, *V1*: 292–294
hepatocellular carcinoma, *V1*: 192, 194–198
MR imaging techniques, *V1*: 46–47, 50
porta hepatis lymphadenopathy, *V1*: 352, 354, 359
thrombosis, *V1*: 388, 391, 393–400
hepatocellular carcinoma, *V1*: 202, 212, 224–232, 234–238
infectious cholangitis, *V1*: 502, 506–507
pancreatic adenocarcinoma, *V1*: 566
Positive intraluminal contrast agents, large intestine imaging, *V1*: 895
Posterior fossa anomalies, fetal assessment, *V2*: 1591, 1593–1597
Posttransplant lymphoproliferative disorder (PTLD):
hepatic transplantation, *V1*: 299–301
renal transplants, *V2*: 1177, 1182, 1184–1185
Pouchitis, *V1*: 810
Pouch of Douglas abscess, *V1*: 874, 882–883
Preeclampsia, liver imaging, *V1*: 407, 410–411
Pregnancy. *See also* Fetal assessment; Gestational trophoblastic disease; Maternal imaging
amniotic fluid assessment, *V2*: 1622–1623
appendicitis diagnostic imaging, *V1*: 874, 880–881, *V2*: 1561–1564
cervical carcinoma in, *V2*: 1482–1483
cervical incompetence, *V2*: 1629–1631
cesarean scar pregnancy, *V2*: 1577–1580
Crohn disease in, *V1*: 796, 802
ectopic pregnancy, *V2*: 1517
endometrioma during, *V2*: 1504, 1513
fetal weight and amniotic fluid, *V2*: 1622–1623
inflammatory bowel disease and, *V1*: 868, 871
intussusception, *V1*: 816, 826
MRI safety in, *V2*: 1559–1561
multiple gestation, *V2*: 1623–1624
ovarian torsion during, *V2*: 1509–1510, 1514–1516
ovarian venous compression and thrombosis, *V2*: 1232, 1237
pelvimetry, *V2*: 1629
placental imaging, *V2*: 1623, 1625–1627
septate uterus, *V2*: 1441, 1447
subchorionic hematoma in, *V2*: 1559–1560
uterine hematoma in, *V2*: 1559–1560
Primary aldosteronism, aldosterone-secreting adrenal adenomas, *V2*: 977, 986–987
Primary biliary cirrhosis (PBC), *V1*: 314–315
Primary hemochromatosis:
liver, *V1*: 354, 362, 365–368
pancreas, *V1*: 546, 548–549
Primary peritoneal carcinoma (PPC), *V2*: 912, 917
Primary sclerosing cholangitis (PSC):
imaging studies, *V1*: 303–304, 306–311
MRCP imaging, *V1*: 494, 497–502
Primovist (Gd-EOB-DTPA) contrast agent, *V2*: 1768
liver imaging, *V1*: 51–58
focal nodular hyperplasia, *V1*: 121, 135
metastases characterization, *V1*: 128, 135
Proctitis:
infectious colitis, *V1*: 888
radiation-induced, *V1*: 888, 893–894
ProHance gadolinium-based contrast agent, classification, *V2*: 1768
Prominent columns of Bertin, kidney anomalies, *V2*: 1031
Prostate cancer:
adenocarcinoma, *V2*: 1352, 1356–1373
anaplastic state, *V2*: 1358, 1366
recurrence, *V2*: 1352, 1354
stage 2, *V2*: 1352, 1356–1357
American Joint Committee staging, *V2*: 1358, 1368
American Urological Committee staging, *V2*: 1368
benign prostatic hyperplasia and, *V2*: 1349–1352
bladder metastases, *V2*: 1320–1323
capsular extension, *V2*: 1352, 1358, 1359–1363, 1367–1373
prostatectomy, *V2*: 1368–1373
radiation therapy, *V2*: 1368–1373
rhabdomyosarcoma, *V2*: 1352, 1355
sarcoma, *V2*: 1352, 1356
squamous cell carcinoma, *V2*: 1352, 1355
Prostatectomy:
bladder changes, *V2*: 1331, 1335
prostate cancer treatment, *V2*: 1368–1373
prostate scarring, *V2*: 1352–1354
Prostate gland:
benign lesions, *V2*: 1349–1354
congenital anomalies, *V2*: 1344, 1347–1349
inflammatory and infectious disease, *V2*: 1373–1374
metastases to, *V2*: 1368–1373
MR imaging techniques, *V2*: 1343–1344
normal anatomy, *V2*: 1344–1346
trauma, *V2*: 1374–1375
Prostatis, chronic, *V2*: 1373
Prostheses:
breast, fat necrosis, *V2*: 1750–1752
breast implants, *V2*: 1754–1759
categories, *V2*: 1754–1755
failure, *V2*: 1687–1689, 1755–1757
fat necrosis, *V2*: 1746, 1749–1752
imaging techniques, *V2*: 1757–1759
postoperative MRI, *V2*: 1744–1749
penile, *V2*: 1376–1377
testicular, *V2*: 1386
Protein synthesis, liver metastases, *V1*: 165, 186
Proteus spp., prostate infection, *V2*: 1373–1374
Proton NMR spectroscopy, breast imaging, *V2*: 1696
fibroadenolipoma, *V2*: 1709, 1711
Proximal descending colon, adenocarcinoma, *V1*: 843, 845
Prune belly syndrome:
bladder anomalies, *V2*: 1299
fetal assessment, *V2*: 1613–1614
wandering spleen and, *V1*: 681
"Pruning," primary sclerosing cholangitis, MRCP imaging, *V1*: 497–502
Pseudoaneurysms:
aorta, *V2*: 1201–1207
renal artery disease, *V2*: 1133, 1135
Pseudocysts:
adrenal glands, *V2*: 980–981, 984, 991–993
intraperitoneal cocoon, *V2*: 945, 947
pancreatic:
acute on chronic pancreatitis, *V1*: 656, 659–664
acute pancreatitis, *V1*: 625, 628, 637, 642–647
hemorrhagic pancreatitis, *V1*: 656, 665
trauma, *V1*: 665, 668–671
perinephric (parapelvic), *V2*: 1042, 1044, 1050
peritoneal, *V2*: 910
ovarian cysts, *V2*: 1504, 1508
peritonitis, *V2*: 949, 951–953
spleen, *V1*: 683, 687–690
Pseudohermaphrodites, *V2*: 1415–1416
Pseudomembranous colitis, *V1*: 883–884, 889
Pseudomonas spp., prostate infection, *V2*: 1373–1374
Pseudomyxoma peritonei:
mucocele, large intestine, *V1*: 838, 841–842
peritoneal metastases, *V2*: 936–938
"Pseudopolyps," ulcerative colitis, *V1*: 867

Pseudotumor:
hepatic inflammatory disease, *V1*: 415, 418–422
retroperitoneal inflammatory, *V2*: 1247
testes, scrotum and epididymis, *V2*: 1388, 1390
Psoas muscle:
abscess, *V2*: 1273–1274, 1276–1279
MR imaging, *V2*: 1271, 1273–1280
neurogenic tumor, *V2*: 1271, 1273
Pulmonary emboli, magnetic resonance angiography, *V2*: 1673, 1675–1677
Pulmonary hyperplasia, fetal assessment, *V2*: 1605
Pulmonary infiltrates, *V2*: 1666, 1668–1671
Pulmonary nodules, MR imaging, *V2*: 1654, 1657, 1662–1665
"Pure gonadal dysgenesis," *V2*: 1415
Pyelonephritis:
acute, *V2*: 1142, 1147–1149
renal transplants, *V2*: 1177, 1179–1180
chronic, *V2*: 1126, 1128, 1130
in pregnancy, maternal imaging, *V2*: 1564, 1566
xanthogranulomatous, *V2*: 1152
Pyeloureteral anastomosis, renal transplants, *V2*: 1184
Pyogenic abscesses, hepatic, *V1*: 418, 422–432
Pyonephrosis, *V2*: 1155–1156
Pyosalpinx. *See* Tubo-ovarian abscess (TOA)

Radial scarring, breast lesions, *V2*: 1714–1715, 1717
Radiation therapy:
bladder changes, *V2*: 1331, 1337
breast cancer, post-therapy imaging, *V2*: 1744, 1747
breast carcinoma from, *V2*: 1743
cervical cancer metastases:
bladder fistulae, *V2*: 1486, 1489
recurrence and posttreatment change, *V2*: 1493–1495
Crohn disease, *V1*: 791
esophagitis, *V1*: 730–731
gastric ulceration and gastritis, *V1*: 761, 763
hepatitis, *V1*: 321, 331
large intestine:
enteritis, *V1*: 888, 892
proctitis, *V1*: 888, 893–894
liver metastases following, *V1*: 257, 262–264
pancreatic cancer and, *V1*: 589–590
peritoneal metastases, differential diagnosis, *V2*: 923–924
prostate cancer, *V2*: 1368–1373
rectosigmoid colon adenocarcinoma, *V1*: 852, 858, 861–865
small intestine, metastases *vs.*, *V1*: 815–816, 818
vaginal effects, *V2*: 1421, 1428
Radiofrequency ablation:
hepatocellular carcinoma, *V1*: 278, 280–286
liver metastases, *V1*: 278–280
renal cell carcinoma, *V2*: 1088–1089, 1095–1096
Radiofrequency power deposition, 3T MR imaging, *V1*: 31
Radiological Diagnostic Oncology Group (RDOG), ovarian cancer, epithelial tumors, *V2*: 1533
Rapid acquisition with relaxation enhancement (RARE) sequences, *V1*: 6
magnetic resonance cholangiopancreatography, *V1*: 456, 460
Rapidly involuting congenital hemangioma (RICH), fetal assessment, *V2*: 1604, 1607
Real-time ("on-the-fly") bolus-tracking method, liver imaging protocol, *V1*: 20
Receiver coil, pediatric MRI, *V2*: 1644–1645
Recipient assessment, hepatic transplantation protocol, *V1*: 287, 291–292
Reconstructive surgery:
bladder, *V2*: 1331, 1335–1336
imperforate anus, *V1*: 827, 834
Rectal cancer:
adenocarcinoma, *V1*: 843, 848–850, 852, 855–857
bone metastases, *V1*: 858, 861–863
bone metastases and sacral invasion, *V1*: 852, 861–863
endorectal coil imaging, *V1*: 850, 857
recurrent, *V1*: 850, 857–866
bladder metastases from, *V2*: 1320, 1323–1324
carcinoid tumors, *V1*: 867–868
MR imaging techniques, *V1*: 843, 848, 850, 852–865
penis and urethra metastases, *V2*: 1376–1377
vaginal metastases, *V2*: 1426–1427
Rectoceles, female urethra, *V2*: 1408–1410
Rectosigmoid colon:
adenocarcinoma, *V1*: 843, 848
fibrosis and, *V1*: 852, 861–863
recurrence rates, *V1*: 850, 857–860
bladder metastases from, *V2*: 1320, 1323–1324
lymphoma, *V1*: 860, 867
Rectourethral fistulas, *V2*: 1408
Rectovaginal fistula, *V2*: 1421, 1426, 1429–1430
Rectum:
anorectal anomalies, *V1*: 827, 831, 833–834
cloacal repair, *V1*: 827, 833
metastases to:
cervical cancer, *V2*: 1492–1495
gastrointestinal stromal tumors, *V1*: 860, 866
vaginal carcinoma, *V2*: 1416, 1423
MR imaging techniques, *V1*: 824, 827
normal anatomy, *V1*: 824, 827, 831
perforation and abscess, *V1*: 874, 886
postsurgical infection, *V1*: 892, 894–895
varices, *V1*: 838
Recurrent malignant disease imaging, echo-train spin-echo sequences, *V1*: 6–7
Recurrent pyogenic cholangitis, MR imaging, *V1*: 502, 507
Redundant sequences, MR imaging strategies and, *V1*: 16–24
Reflux nephropathy, *V2*: 1126, 1128, 1130
Regenerative nodules (RNs), cirrhosis, *V1*: 333–334, 339–345
iron-containing, *V1*: 334, 340, 344–346
Reidel lobe, MR imaging, *V1*: 58–60
Relaxation times, 3T MR imaging, *V1*: 32–36
Reliability issues, parallel MR imaging, *V1*: 29, 31
Remote table motion, MR imaging strategies, *V1*: 20
Renal adenomas, *V2*: 1068
Renal agenesis, fetal assessment, *V2*: 1613
Renal arterial disease, *V2*: 1128–1129, 1131–1133
abdominal aortic aneurysm, *V2*: 1201–1207
renal transplants, *V2*: 1177, 1182–1183
Renal blood flow evaluation, *V2*: 1173
Renal calculi, *V2*: 1159, 1166–1167
Renal cell carcinoma (RCC):
adrenal gland metastases, *V2*: 998–1002
autosomal dominant polycystic kidney disease and, *V2*: 1098, 1101
bilateral cancer, *V2*: 1088, 1093
chronic renal failure, *V2*: 1098–1101
cystic changes with, *V2*: 1088, 1090–1092
cystic disease, differential diagnosis, *V2*: 1052, 1061–1062
granulocytic sarcoma (chloroma), differential diagnosis, *V2*: 1109, 1111
hemorrhage, *V2*: 1088–1094
chronic renal failure, *V2*: 1098–1101
hypervascular tumors, *V2*: 1084, 1086
imaging protocol for, *V1*: 16, 19–20
infiltrative, *V2*: 1088, 1095
metastases, pancreas, *V1*: 619, 625
MR imaging, *V2*: 1098, 1102
radiofrequency ablation, *V2*: 1088–1089, 1095–1096
recurrence, *V2*: 1089, 1096–1097
renal cysts, differential diagnosis, *V2*: 1053, 1098
renal transplants, *V2*: 1177, 1181, 1184
staging, *V2*: 1073–1095
stage 1, *V2*: 1073–1077
stage 2, *V2*: 1076, 1078, 1087–1089
stage 3a, *V2*: 1076–1077, 1079–1081
stage 3b, *V2*: 1077, 1081
stage 3c, *V2*: 1082–1083
stage 4, *V2*: 1082, 1084–1085
subtraction image, *V2*: 1037, 1040
von Hippel-Lindau syndrome, *V1*: 549–550

Renal collecting system:
dilation, *V2*: 1164, 1169–1172
filling defects, *V2*: 1159, 1166–1169
Renal cortical infarcts, *V2*: 1137, 1143–1144
Renal ectopia. *See* Ectopic kidney
Renal filling defects, *V2*: 1159, 1166–1169
Renal function:
imaging studies, *V2*: 1173–1177
nephrogenic systemic fibrosis, *V2*: 1781
renal parenchymal disease, *V2*: 1112, 1116–1117
Renal parenchyma:
acute obstruction, paroxysmal changes, *V2*: 1121, 1127–1130
arterial disease, *V2*: 1127, 1129, 1131–1143
diffuse disease, *V2*: 1112–1124
acute tubular necrosis, *V2*: 1120, 1122
glomerular disease, *V2*: 1117–1120
renal function decline, *V2*: 1112, 1116–1117
tubular blockage, *V2*: 1120, 1123–1124
tubulointerstitial disease, *V2*: 1120–1121
iron deposition, *V2*: 1121, 1124–1127
lesions, pattern recognition, *V2*: 1031, 1037
obstruction, *V2*: 1121, 1125–1126, 1128–1129, 1170–1172
reflux nephropathy and chronic pyelonephritis, *V2*: 1126, 1128, 1130
renal arterial disease, *V2*: 1128–1129, 1131–1144
renal scarring, *V2*: 1128, 1138, 1145–1146
renal vein aneurysm, *V2*: 1138
renal vein thrombosis, *V2*: 1137, 1144
Renal pelvis and ureter:
calyceal diverticulum, *V2*: 1164, 1172
collecting system dilatation, *V2*: 1164, 1169–1172
filling defects, *V2*: 1159, 1166–1169
lymphoma, *V2*: 1159
metastases to, *V2*: 1159
squamous cell carcinoma, *V2*: 1159, 1165
urothelial carcinoma, *V2*: 1155, 1159–1165
Renal vein:
congenital anomalies, *V2*: 1223, 1228–1230
thrombosis, *V2*: 1137–1138, 1144
inferior vena cava thrombus and, *V2*: 1232–1237
nephrotic syndrome, *V2*: 1117, 1120
Rendu-Osler-Weber syndrome, hepatic arteriovenous fistulas, *V1*: 388–392
Repetition time (TR):
3T MR imaging, *V1*: 32–36
small intestine imaging, *V1*: 767–770
Resovist, iron-based contrast agent, *V2*: 1778–1779
Respiration artifacts:
abdominal-pelvic MRI, fast scanning and avoidance of, *V1*: 1–2
magnetic resonance cholangiopancreatography, *V1*: 460
Reticuloendothelial system (RES):
iron-based contrast agents, *V2*: 1777–1779
MRI contrast agent targeting, *V1*: 50–58
spleen imaging, *V1*: 678–681
Retractile mesenteritis, *V2*: 946, 950
Retroperitoneum:
benign masses:
extramedullary hematopoiesis, *V2*: 1249, 1251
fibrosis, *V2*: 1240, 1242–1244
lymphadenopathy, *V2*: 1247–1250
adrenal glands, *V2*: 1017, 1019
retroperitoneal neoplasms, *V2*: 1240, 1245–1247
bladder cancer metastases, transitional cell carcinoma, *V2*: 1308–1316
body wall:
benign neoplasms, *V2*: 1274, 1281–1283
hernias, hematoms, and other lesions, *V2*: 1274, 1290–1293
malignant neoplasms, *V2*: 1274, 1284–1290
malignant masses:
carcinoma, *V2*: 1265–1266
embryonal rhabdomyosarcoma, *V2*: 1265, 1271–1272
hemangiopericytoma, *V2*: 1265, 1271, 1273
leiomyosarcomas, *V2*: 1265–1270
liposarcoma, *V2*: 1265, 1271
lymphadenopathy, *V2*: 1258–1263
adrenal glands, *V2*: 1017, 1019
lymphoma, *V2*: 1253–1257
retroperitoneal fibrosis, *V2*: 1249, 1252–1253
testicular cancer, *V2*: 1258, 1263–1265
MR imaging technique, *V2*: 1193–1194
normal anatomy, *V2*: 1193
pediatric imaging, *V2*: 1650
psoas muscle, *V2*: 1271, 1273–1280
vessel imaging:
aorta, *V2*: 1200–1227
aortic aneurysm, *V2*: 1200–1207
aortic dissection, *V2*: 1201, 1208–1212
aortoiliac atherosclerotic disease/thrombosis, *V2*: 1204, 1207, 1214–1223
penetrating ulcers/intramural dissecting hematoma, *V2*: 1201, 1204, 1213
postoperative graft evaluation, *V2*: 1207, 1214, 1216, 1224–1227
inferior vena cava, *V2*: 1216, 1223, 1229
congenital anomalies, *V2*: 1223, 1229–1230
primary malignant tumors, *V2*: 1237–1241
venous thrombosis, *V2*: 1229–1237
magnetic resonance angiography, *V2*: 1194–1200
Rhabdomyosarcoma:
bladder cancer, *V2*: 1316
embryonal, retroperitoneal imaging, *V2*: 1266, 1272
prostate cancer, *V2*: 1352, 1355
vulvar malignancies, *V2*: 1421, 1423
Rhomboencephalosynapsis, fetal assessment, *V2*: 1593–1597
Ring enhancement imaging:
colon adenocarcinoma, *V1*: 843, 845
colon melanoma, *V1*: 867, 869
hepatosplenic candidiasis, *V1*: 433, 436
liver metastases:
breast cancer, *V1*: 162, 171
gastrinomas, *V1*: 164, 180
hepatocellular carcinoma, *V1*: 202, 232–233
lesional/perilesional enhancement, *V1*: 147–150
ovaries, endometriomas, *V2*: 1506, 1509–1512
pancreas:
insulinomas, *V1*: 601, 603
metastases to, *V1*: 625, 630–631
pancreatic islet cell tumors, *V1*: 593
Robson's renal cell carcinoma classification, *V2*: 1073–1095
Rokitansky-Aschoff sinuses:
gallbladder adenomyomatosis, *V1*: 480, 484
xanthogranulomatous cholecystitis, *V1*: 477

Sacral invasion, rectal adenocarcinoma, *V1*: 852, 861–863
Saddlebag urethral diverticulum, *V2*: 1405, 1407
Safety issues:
3T MR imaging, *V1*: 33
gadolinium-based contrast agents, *V2*: 1779–1786
MRI in pregnancy, *V2*: 1559–1561
whole body MR imaging, *V1*: 41–42
Sagittal-plane imaging:
bladder:
fistulas, *V2*: 1331–1335
metastatic neoplasms, *V2*: 1320–1324
breast MRI, *V2*: 1693–1694
female urethra, malignant masses, *V2*: 1403–1404
renal cell carcinoma:
stage 3a, *V2*: 1076–1077, 1079–1081
stage 4, *V2*: 1082, 1084–1085
vaginal metastases, *V2*: 1421–1426
"Sandwich sign," lymphatic dissemination, peritoneal metastases, *V2*: 925, 935
Santorini ducts, pancreas divisum, *V1*: 541–542

Sarcoidosis:
liver imaging, *V1*: 414–416
retroperitoneal benign lymphadenopathy, *V2*: 1249–1250
spleen, *V1*: 711–713
Sarcoma:
body wall, *V2*: 1274, 1284–1290
granulocytic, kidney, *V2*: 1109, 1111
liver metastases, undifferentiated, *V1*: 251, 256
perirectal metaseses, *V2*: 1274, 1287
peritoneal metastases, *V2*: 918, 923–924, 929–930
prostate cancer, *V2*: 1352, 1356
retroperitoneal, *V2*: 1265–1271
uterine, *V2*: 1475, 1479–1481
undifferentiated, *V2*: 1488–1491
Sarcomatoid carcinoma, bladder, *V2*: 1316
Saturation pulse, fat-suppressed echo-train spin-echo sequences, *V1*: 9–10
Scan time reduction, gradient echo sequences, *V1*: 2–3
Schistosoma baematobium, bladder calculi, *V2*: 1305
Schizencephaly, fetal assessment, *V2*: 1595–1596
Schwannoma:
adrenal glands, *V2*: 1006
gastric, *V1*: 740
pancreatic cancer, *V1*: 594–597, 601
Scleroderma:
reflux esophagitis, *V1*: 730
small intestine, *V1*: 809–810
Sclerosing adenosis, breast changes, *V2*: 1712, 1714, 1716
Sclerosing cholangitis. *See also* Primary sclerosing cholangitis (PSC)
MRCP imaging, *V1*: 493–494
Sclerosing hemangiomas, spleen, *V1*: 688, 693
Sclerosing mesenteritis, *V2*: 946, 950
Sclerosing stromal tumor, ovaries, *V2*: 1525–1526
Scrotum:
benign masses, *V2*: 1388–1392
congenital anomalies, *V2*: 1386
hernia, *V2*: 1390
MR imaging, *V2*: 1385
normal anatomy, *V2*: 1383–1384
Secondary infection, liver metastases, *V1*: 180, 188, 191–192
Secretin-enhanced magnetic resonance cholangiopancreatography (MRCP), chronic pancreatitis imaging, *V1*: 648–649, 652, 655
Sedated patients:
MRI imaging in, *V1*: 25–27
pediatric patients:
age categories, *V2*: 1645
T1-weighted imaging, *V2*: 1637, 1639–1644
technique, *V2*: 1646–1647
Semilobar holoprosoencephaly, fetal assessment, *V2*: 1589–1592
Seminal vesicles:
benign masses, *V2*: 1382
congenital anomalities, *V2*: 1382, 1384
hypoplasia, *V2*: 1344, 1348–1349
malignant masses, *V2*: 1382, 1384–1385
normal anatomy, *V2*: 1382–1384
prostate cancer metastases, *V2*: 1344, 1349, 1363–1365, m1384–1385
hemorrhage, *V2*: 1368, 1370–1372
Seminomas, testes lesions, *V2*: 1390–1396
Sensitivity encoding (SENSE):
parallel MR imaging, *V1*: 25, 29
small intestine imaging, *V1*: 767–770
Septated renal cysts, *V2*: 1042, 1047
Septated vagina, *V2*: 1412, 1414–1415
uterus didelphys, *V2*: 1441, 1444–1446
Septate uterus, *V2*: 1441, 1444, 1447–1449
Septo-optic dysplasia, fetal assessment, *V2*: 1594, 1596
Sequence technology, whole body imaging, *V1*: 40–42
Serial MRI examination, *V1*: 24–25
adrenal glands, *V2*: 964–968
Serosal metastases:
intraperitoneal seeding, *V2*: 923–924
small bowel obstruction, *V1*: 779, 782, 792
Serous cystadenocarcinoma, *V1*: 612
ovarian:
malignant tumors, *V2*: 1533–1535
metastases, *V2*: 1504–1505, 1533, 1535–1536
Serous cystadenoma:
benign ovarian neoplasms, *V2*: 1518–1523
MR imaging, *V1*: 606–607, 609–612
Serpiginous (arciform) enhancement, spleen, *V1*: 678–681
Serratia spp., prostate infection, *V2*: 1373–1374
Sertoli-Leydig cell tumors, malignant ovarian neoplasms, *V2*: 1540, 1542, 1545–1547
Serum creatinine levels, renal function and, *V2*: 1112, 1116–1117
Sex cord-stromal tumors:
benign ovarian neoplasms, *V2*: 1525–1526
malignant ovarian neoplasms, *V2*: 1540, 1542, 1545–1547
Sexual differentiaton disorders:
testicular feminization, *V2*: 1415, 1448
uterine anomalies, *V2*: 1448
Short-tau inversion recovery (STIR):
breast, silicone implants, *V2*: 1757–1759
breast imaging, *V2*: 1694–1695
cysts, *V2*: 1701–1703
cavernous hemangioma, *V2*: 1416, 1420
fat-suppressed echo-train spin-echo sequences, *V1*: 7–10
hepatic cysts, *V1*: 60, 63
liver imaging:
hemangiomas, *V1*: 88, 97–99
hepatic cysts, *V1*: 60, 63
mycobacterium avium intracellulare, *V1*: 433–435
pancreatic adenocarcinoma imaging, *V1*: 573
retroperitoneal lymphoma, *V2*: 1253–1257
spleen, *V1*: 678–681
Sickle cell disease:
hepatic iron overload, *V1*: 368, 370, 374–375
iron deposition, renal parenchyma, *V2*: 1121, 1124–1126
spleen imaging, *V1*: 683, 687
Siderosis, transfusional, liver imaging, *V1*: 368–373
Sigmoid colon:
adenocarcinoma, *V1*: 843, 846–848, 852
lipoma, *V1*: 832
Signal intensity index:
adrenal gland imaging:
adenomas, drop in, *V2*: 971, 974, 982–984
hemangiomas, *V2*: 993–994
metastases, *V2*: 994–1002
pheochromocytoma, *V2*: 1005–1111
breast MRI interpretation guidelines, *V2*: 1696–1700
vessel imaging, *V1*: 14
Signal-to-noise ratio (SNR):
3T imaging, uterus and cervix, *V2*: 1434
3T MR imaging *vs.* 1.5T, *V1*: 31–36
breast MRI, *V2*: 1692–1693
coil systems, *V2*: 1693
liver imaging techniques, *V1*: 46–50
male pelvis imaging, *V2*: 1343–1344
pancreatic imaging, *V1*: 536
parallel MR imaging, *V1*: 29
pediatric patient imaging:
receiver coil, *V2*: 1644–1645
spin-echo sequence, *V2*: 1637
prostate cancer, adenocarcinoma, *V2*: 1352, 1356–1373
Signal-void air, large intestinal abscess imaging, *V1*: 881–886
Silicone breast implants, *V2*: 1754–1759
rupture, *V2*: 1687–1689, 1755–1757
Simultaneous acquisition of spatial harmonics (SMASH), parallel MR imaging, *V1*: 25, 29–31
Single-shot echo-train spin-echo (SS-ETSE) sequences:
abdominal-pelvic imaging, *V1*: 6–8
abdominal wall hernia, *V2*: 904, 908–909
bile duct abnormalities, MRCP imaging, *V1*: 489, 493, 497
colon cancer, *V1*: 843–865
esophagus, *V1*: 726, 728
female urethra, pelvic floor relaxation, *V2*: 1408–1410
fetal assessment, *V2*: 1561
amniotic band syndrome, *V2*: 1621
cleft palate, *V2*: 1603–1607
normal development, *V2*: 1583
gastrointestinal tract, *V1*: 725
gluten-sensitive enteropathy, *V1*: 799, 807–809
hypertrophic rugal folds, *V1*: 761, 765
kidney imaging, *V2*: 1025–1031
filling defects, *V2*: 1159, 1166–1169
multicystic dysplastic kidney, *V2*: 1049, 1058
pyonephrosis, *V2*: 1155–1156

Single-shot echo-train spin-echo (SS-ETSE) sequences: (*Continued*)
large intestine:
abscesses, *V1*: 883–886
diverticulitis, *V1*: 869, 878–879
mucocele, *V1*: 838, 841–842
techniques, *V1*: 824
liver imaging, *V1*: 46–48
echinococcal disease, *V1*: 431–433
hepatic cysts, solitary cysts, *V1*: 60–64
Reidel lobe, differential diagnosis, *V1*: 58–60
unilocular cysts, *V1*: 60–63
magnetic resonance cholangiopancreatography, *V1*: 456–461
noncooperative patients, *V1*: 25
non-fat-suppressed *vs.* fat-suppressed images, *V1*: 35–37
pancreatic imaging, *V1*: 536–539
acute pancreatitis, *V1*: 625, 628, 635–647
pediatric patients, *V2*: 1644
infants, *V2*: 1645
older children, *V2*: 1645–1646
peritoneal metastases, intraperitoneal seeding, *V2*: 918–924
pleural disease imaging, *V2*: 1666, 1671–1672
in pregnancy, maternal imaging:
bowel obstruction, *V2*: 1564
conjoined twins, *V2*: 1623–1624
renal calculi, *V2*: 1159, 1166–1169
retroperitoneum:
lymphoma, *V2*: 1253–1257
primary neoplasms, *V2*: 1271
serial MRI examination, *V1*: 24–28
small intestine:
intussusception, *V1*: 816, 825–826
ischemia and hemorrhage, *V1*: 816, 819–823
small intestine imaging, *V1*: 767–770
adenocarcinoma, *V1*: 777, 781–782
choledochocele, *V1*: 775–776
Crohn disease, *V1*: 785, 791, 793–805
intestinal atresia and stenosis, *V1*: 770, 774
stomach, *V1*: 734–736
duodenal diverticulum, *V1*: 770, 772–774
postoperative evaluation, *V1*: 761, 766
uterine-cervical MRI, *V2*: 1434
Sjögren syndrome, autoimmune pancreatitis, *V1*: 664
Skene glands, urethrovaginal fistulas, *V2*: 1408
"Skip lesions," Crohn disease, *V1*: 785, 791, 797–799
Slice-selective inversion pulse, magnetization-prepared rapid-acquisition gradient echo sequences, *V1*: 5–6
Sliding hernia, *V2*: 904, 906–907
Slow enhancement techniques, liver hemangiomas, *V1*: 88, 90, 95–96
Small bowel. *See* Small intestine
Small cell carcinoma:
kidney, *V2*: 1109, 1111–1113
liver metastases, undifferentiated tumors, *V1*: 164, 177–179
Small intestine:
benign lesions:
leiomyomas, *V1*: 775, 780
lipomas, *V1*: 775
neurofibromas, *V1*: 775, 779
polyps, *V1*: 775, 777–778
varices, *V1*: 775, 781
congenital lesions, *V1*: 770–776
atresia and stenosis, *V1*: 770, 774
choledochocele, *V1*: 775–776
duodenal diverticulum, *V1*: 770, 772–774
Meckel diverticulum, *V1*: 770, 774
rotational abnormalities, *V1*: 770–771
fetal assessment, *V2*: 1615
inflammatory, infectious, and diffuse disease:
Crohn disease, *V1*: 784–785, 791, 793–805
drug toxicity, *V1*: 810, 817
eosinophilic gastroenteritis, *V1*: 809
fistula, *V1*: 810–813, 812–813
gluten-sensitive enteropathy, *V1*: 799, 807–809
graft-*versus*-host disease, *V1*: 816–817, 828–829
hernia, *V1*: 816, 827
hypoproteinemia, *V1*: 816, 824
infectious enteritis, *V1*: 810, 813–814
inflammatory bowel disease, *V1*: 782, 784
intussusception, *V1*: 816, 825–826
ischemia and hemorrhage, *V1*: 816, 819–823
pancreatitis, *V1*: 810, 815
pouchitis, *V1*: 810
radiation enteritis, *V1*: 815–816, 818
scleroderma, *V1*: 809–810
ulcerative colitis, *V1*: 796, 799, 806
leiomyosarcoma, hypervascular liver metastases, *V1*: 161, 163
malignant masses:
adenocarcinomas, *V1*: 777, 781–782
carcinoid tumors, *V1*: 779, 790–791
gastrointestinal stromal tumor, *V1*: 777, 779, 783–785
lymphoma, *V1*: 779, 786–791
metastases to, *V1*: 779, 782, 791–793
MR imaging, *V1*: 767–770
follow-through and enteroclysis, *V1*: 767–770
oral contrast agents, *V1*: 20
normal anatomy, *V1*: 765, 767
polyps, *V1*: 775, 777–778
Small-vessel disease, renal artery, *V2*: 1136–1141
renal transplants, *V2*: 1182, 1184
Solid epithelial neoplasm, pancreas, *V1*: 619, 622–623
Somatostatinoma, MR imaging, *V1*: 601, 604–605
Specific absorption rate (SAR):
echo-train spin-echo sequences, *V1*: 7
MRI in pregnancy, *V2*: 1559–1561
single-shot echo-train spin-echo sequences, *V1*: 36
Spectral (fat)-selective adiabatic inversion pulses (SPAIR), T2-weighted imaging, *V1*: 9–10
Spermatocele, testes, scrotum and epididymis, *V2*: 1388, 1390
Sphincter of Oddi:
abnormalities, MRCP imaging, *V1*: 489, 493, 497
pancreatic anatomy, *V1*: 536
Spigelian hernia, abdominal wall imaging, *V2*: 904, 909
Spin-echo sequence, pediatric patients, *V2*: 1637
Spiral computed tomography (CT):
liver imaging:
hemangiomas, *V1*: 88, 101–102
metastases imaging:
coexistent cysts, *V1*: 190
MR imaging *vs.*, *V1*: 128, 142–147
pancreas, pancreatic adenocarcinoma, *V1*: 552–553, 558–559, 564–565
peritoneal metastases, intraperitoneal seeding, *V2*: 918
renal filling defects, *V2*: 1159, 1166–1169
Spleen:
accessory and wandering spleens, *V1*: 681–685
asplenia, *V1*: 681, 685
benign mass lesions:
cysts, *V1*: 683, 687–690
hamartomas, *V1*: 690, 693, 695–697
hemangiomas, *V1*: 687–688, 691–693
littoral cell angioma, *V1*: 688, 694
lymphangiomas, *V1*: 693
pattern recognition, *V1*: 688
Gamna-Gandy bodies, *V1*: 711, 714
Gaucher disease, *V1*: 683
genetic hemochromatosis and, *V1*: 354
infarcts, *V1*: 719–722, *V2*: 1121
infectious disease, *V1*: 709–711
malignant masses:
lymphoma/hematologic malignancies, *V1*: 693–694, 698–703
metastases to, *V1*: 701, 703–706
angiosarcoma, *V1*: 704, 706
direct tumor invasion, *V1*: 704–705
metastases to:
colonic lymphoma, *V1*: 860, 867
glucagonoma/somatostatinoma, *V1*: 601, 604–605
imaging studies, *V1*: 701, 703–706
islet cell tumors, *V1*: 601, 604–606
MR imaging technique, *V1*: 678–681
normal anatomy, *V1*: 677–678
pediatric imaging, *V2*: 1650
polysplenia, *V1*: 681, 683, 686
portal and splenic thrombosis, *V1*: 388, 391, 394–395
sarcoidosis, *V1*: 711–713
sickle disease, *V1*: 683, 687

splenomegaly and vascular pathologies, *V1*: 706–709
subscapular fluid collection, *V1*: 715, 717
trauma, *V1*: 715–716
Splenic artery aneurysm, splenomegaly and, *V1*: 706–709
Splenic vein:
pancreatic anatomy, *V1*: 535
spleen, normal anatomy, *V1*: 677–678
thrombosis:
esophageal varices, *V1*: 727, 729
gastric varices, *V1*: 738, 742
pancreatic adenocarcinoma, *V1*: 575, 579
splenomegaly and, *V1*: 706–709
Splenic vein-only hepatic arterial phase (SVHADP), gadolinium-based contrast agent, *V2*: 1774–1777
Splenomegaly:
chronic lymphocytic leukemia (CLL), *V1*: 700
lymphoma metastases, *V1*: 694, 699–703
pathology, *V1*: 706–709
Splenorenal shunt, splenomegaly, *V1*: 706–709
Splenosis, *V1*: 715, 717–719
Splenules, MR imaging, *V1*: 681, 684–685
iron-based contrast agents, differential diagnosis, *V2*: 1778–1779
Spoiled gradient echo (SGE) sequences:
abdominal-pelvic imaging, *V1*: 3–4
adnexa, *V2*: 1499–1500
adrenal glands, *V2*: 963–968
appendicitis diagnostic imaging, *V1*: 874, 879–881
bladder, transitional cell carcinoma, *V2*: 1308–1316
chronic pancreatitis imaging, *V1*: 656–665
esophageal imaging, esophageal varices, *V1*: 727, 729
esophagus, malignant masses, *V1*: 729–731
gadolinium-enhanced T1-weighted images, hepatic arterial dominant (capillary) phase, *V1*: 11–13
image parameters, *V1*: 3
large intestine:
abscesses, *V1*: 881–886
colonic adenomatous polyps, *V1*: 832, 835–838
diverticulitis, *V1*: 869, 874–879
infectious colitis, *V1*: 888
liver imaging techniques, *V1*: 46–50
autoimmune hepatitis, *V1*: 312–314
colon cancer metastases, *V1*: 149, 154–155
computed tomography *vs.*, *V1*: 128, 141–144
contrast agents, *V1*: 52–58
diaphragmatic insertion, *V1*: 58, 60
focal nodular hyperplasia, *V1*: 121, 123–125, 127–128
hepatic cysts, solitary cysts, *V1*: 60–64
hepatocellular carcinoma, *V1*: 192–198, 213–217
hypervascular metastases, *V1*: 149, 157–158
hypovascular metastases, *V1*: 149, 153
metastases characterization, *V1*: 128, 137–143
Reidel lobe, differential diagnosis, *V1*: 58–60
squamous cell carcinoma metastases, *V1*: 162, 165–171
unilocular cysts, *V1*: 60–66
viral hepatitis, *V1*: 321–322
male pelvis, *V2*: 1343–1344
noncooperative patients, *V1*: 25
out-of-phase (opposed-phase) spoiled gradient echo sequences, *V1*: 4–5
pancreatic imaging, *V1*: 536–541
pancreatic adenocarcinoma, *V1*: 552, 554–556, 572, 574–575
psoas muscle metastases, *V2*: 1273, 1275
rectal adenocarcinoma, *V1*: 848–850
renal cell carcinoma, *V2*: 1073–1095
retroperitoneum, *V2*: 1193–1194
fibrosis, benign *vs.* malignant, *V2*: 1240, 1242–1244
malignant metastatic lymphadenopathy, *V2*: 1258–1263
small intestine, *V1*: 767–770
gastrointestinal stromal tumor, *V1*: 779, 783–785
metastases to, *V1*: 782, 791–792
polyps, *V1*: 775, 777–778
varices, *V1*: 775, 781
spleen, *V1*: 678–681
hamartomas, *V1*: 693, 695–697
lymphoma metastases, *V1*: 694, 699–703
splenic metastases, *V1*: 701, 703–706
stomach, gastric adenocarcinoma, *V1*: 743
three-dimensional imaging quality improvements, *V1*: 16
TR/TE/flip angle variations, *V1*: 23–24
vessel imaging:
aorta, *V2*: 1200–1227
abdominal aortic aneurysm, *V2*: 1201–1207
aortic dissection, *V2*: 1201, 1208–1212
aortoiliac atherosclerotic disease/thrombosis, *V2*: 1204, 1207, 1214–1223
inferior vena cava, *V2*: 1216, 1223, 1229
inferior vena cava thrombus, *V2*: 1229–1237
"Spoke wheel" pattern, renal oncocytomas, *V2*: 1068, 1072
Squamous cell carcinoma:
anal canal, *V1*: 860, 866
bladder cancer, *V2*: 1316–1318
esophagus, *V1*: 729–731
lung cancer, liver metastases, *V1*: 162, 175–176
prostate cancer, *V2*: 1352, 1355
renal pelvis and ureter, *V2*: 1159, 1165
vaginal malignancies, *V2*: 1416, 1420–1426
vulva, *V2*: 1421, 1427
"Stained glass" lesions, mucinous cystadenocarcinoma, ovarian malignancy, *V2*: 1533, 1536–1537
Steatosis. *See* Fatty liver
Stenosis:
ampullary (bile duct), *V1*: 489
gadolinium-based contrast agent, *V2*: 1771–1773
aqueductal, fetal assessment, *V2*: 1585–1592
bronchial, fetal assessment, *V2*: 1611–1612
cervical, endometriosis and, *V2*: 1506, 1510
iliac arteries, *V2*: 1204, 1207, 1216–1218
intestinal, *V1*: 770, 774
pancreatic duct, *V1*: 665, 668–671
renal artery disease, *V2*: 1131–1132
renal transplants, *V2*: 1178, 1183–1184
Stomach:
benign masses:
bezoar, *V1*: 738, 742
gastric polyps, *V1*: 736, 739–740
leiomyomas, *V1*: 736
neurogenic tumors and lipomas, *V1*: 736, 738, 740–742
varices, *V1*: 738, 742
congenital lesions, *V1*: 736
diverticula, *V1*: 736–738
gastric duplication cysts, *V1*: 736
heterotopias, *V1*: 736
fetal assessment, *V2*: 1615
infectious disease, *V1*: 761–764
inflammatory disease, *V1*: 761–764
malignant masses:
adenocarcinoma, *V1*: 738, 741, 743–751
Peutz-Jeghers syndrome, *V1*: 832
carcinoids, *V1*: 756, 759
carcinomas, *V1*: 741
gastrointestional stromal tumor, *V1*: 743, 748, 752–758
Kaposi sarcoma, *V1*: 748, 756
lymphoma, *V1*: 756, 758
TNM staging, *V1*: 742
metastases to, *V1*: 741, 759–760
MR imaging technique, *V1*: 734–736
normal anatomy, *V1*: 734–735
postoperative conditions, *V1*: 761, 766
Streak gonads:
ovarian anomalies, *V2*: 1503
vaginal anomalies, *V2*: 1415
Streptococcal infection, pyogenic hepatic abscess, *V1*: 418, 427
Stricture:
biliary tree, *V1*: 292, 299
female urethra, *V2*: 1407

Strongoloides stercoralis, infectious enteritis, differential diagnosis, *V1*: 810, 813–814
Struma ovarii, benign ovarian neoplasms, *V2*: 1521, 1528–1529
Subcapsular line sign, breast implant imaging, *V2*: 1759
Subchorionic hematoma, in pregnancy, *V2*: 1559–1560
Subependymal heterotopia, fetal assessment, *V2*: 1595
Subglandular breast implants, *V2*: 1754–1759
Submucosal hemorrhage, small intestine, *V1*: 816, 822–823
Submucosal imaging, ulcerative colitis, *V1*: 867–868, 870
Submucosal leiomyomas, uterine, *V2*: 1449, 1451–1469
Submuscular breast implants, *V2*: 1754–1759
Subscapular fluid collections, splenic trauma, *V1*: 715–717
Subtraction imaging, renal cysts, *V2*: 1037, 1040
Superior mesenteric artery:
  aortic dissection into, *V2*: 1201, 1212
  chronic pancreatitis imaging, *V1*: 648–665
  pancreatic adenocarcinoma involvement, *V1*: 575, 577–578
  vascular graft, branch vessel, *V2*: 1214, 1216, 1227
Superior mesenteric vein, thrombosis, small intestine ischemia and hemorrhage, *V1*: 816, 822
Supernumerary scrotal testes, *V2*: 1386
Superparamagnetic iron oxide particles (SPIO):
  characteristics, *V2*: 1777–1779
  liver imaging, reticuloendothelial system targeting, *V1*: 50, 54–58
  prostate cancer metastases, *V2*: 1368–1373
  spleen imaging, *V1*: 678–681
    accessory/wandering spleens, *V1*: 681–685
    lymphoma metastases, *V1*: 700
    splenic metastases, *V1*: 701, 703–706
Surface coils:
  bladder imaging, *V2*: 1298–1299
  colon cancer imaging, *V1*: 848
  whole body imaging, *V1*: 40–42
Surgical sponge retention, intraperitoneal, *V2*: 945–947
Susceptibility artifact, 3T MR imaging, *V1*: 31–32

T1-relaxivity agents, vessel imaging, *V2*: 1197–1200
T1-weighted imaging:
  abdominal-pelvic disease, *V1*: 2–6
    fat-suppressed gradient echo sequences, *V1*: 4
    gradient echo sequences, *V1*: 3–4
    magnetization -prepared rapid-acquisition gradient echo sequences, *V1*: 5–6
    out-of-phase gradient echo sqeuences, *V1*: 4–5
adnexa, *V2*: 1499–1500
adrenal glands:
  adrenal cortical carcinoma, *V2*: 998, 1002–1006
  metastases, *V2*: 994–1002
  myelolipoma, *V2*: 979–980, 988–990
  neuroblastoma, *V2*: 1013–1017
  pheochromocytoma, *V2*: 1005–1111
  techniques, *V2*: 963–968
aortic dissection, *V2*: 1201, 1208–1212
aortic grafts, *V2*: 1214, 1216, 1224–1227
bile duct:
  ampullary fibrosis, *V1*: 489, 495–496
  cholangiocarcinoma, *V1*: 517–518, 521–526
  infectious cholangitis, *V1*: 502–507
  primary sclerosing cholangitis, *V1*: 499–502
bile duct and parenchymal lesions, *V1*: 460–461
bladder, *V2*: 1298
  congenital anomalies, *V2*: 1299–1301
  hemorrhagic cystitis, *V2*: 1326, 1329
  leiomyomas, *V2*: 1300, 1302–1303
  metastatic neoplasms, *V2*: 1320–1324
  neurofibromas, *V2*: 1304–1305
  squamous cell carcinoma, *V2*: 1317–1319
  transitional cell carcinoma, *V2*: 1307–1316
breast:
  cysts, *V2*: 1701–1703
  fat necrosis, *V2*: 1749
breast cancer:
  invasive ductal carcinoma, *V2*: 1723–1727
  melanoma metastases, *V2*: 1743–1744
cervix, *V2*: 1434
colon cancer:
  melanoma, *V1*: 867, 869
  rectosigmoid carcinoma, *V1*: 850, 857–860
disease conspicuity and, *V1*: 1–2
esophagus, *V1*: 726, 728
  leiomyomas, *V1*: 726–728
female urethra:
  diverticulum, *V2*: 1405–1407
  malignant masses, *V2*: 1403–1404
  normal anatomy, *V2*: 1401–1403
fetal assessment:
  abdomen and pelvis, *V2*: 1583–1585
  brain imaging, *V2*: 1578–1583
  congenital hemangiomas, *V2*: 1604, 1607
  destructive lesions, *V2*: 1598–1601
  head and neck, *V2*: 1583
gadolinium-enhanced images, *V1*: 10–13
  hepatic arterial dominant (capillary) phase, *V1*: 10–13
  hepatic venous (interstitial) phase, *V1*: 11
  portal venous/early hepatic venous phase, *V1*: 11
gallbladder, *V1*: 460, 463
  acute cholecystitis, *V1*: 469–475
  carcinoma, *V1*: 481, 485–486
  gallstone disease, *V1*: 464–465, 467–469
  hemorrhagic cholecystitis, *V1*: 475–477
  polyps, *V1*: 480, 482–483
iron-based contrast agents, *V2*: 1777–1779
kidneys:
  acquired cystic disease, hemodialysis-induced, *V2*: 1052, 1061–1062
  angiomyolipomas, *V2*: 1063–1068
  cysts with thickened walls, *V2*: 1042, 1049
  hemorrhagic/proteinaceous cysts, *V2*: 1037, 1042–1044, 1046
  lymphocele, *V2*: 1182
  perinephric pseudocyst, *V2*: 1042, 1044, 1050
  renal function assessment, *V2*: 1112, 1116–1117
  small-cell carcinoma, *V2*: 1112–1113
  techniques, *V2*: 1025–1031
  trauma, *V2*: 1172–1174
  Wilms tumor, *V2*: 1103–1106
large intestine:
  colonic fistulae, *V1*: 883, 887–888
  intraluminal contrast agents, *V1*: 892, 895–897
  lipomas, *V1*: 832, 839–840
  mucocele, *V1*: 838, 841–842
liver, *V1*: 46–50
  ablative therapies, *V1*: 278–287
  angiosarcoma, *V1*: 242, 249
  bile duct carcinoma, intrahepatic/peripheral metastases, *V1*: 239–240, 242, 247–249
  Budd-Chiari syndrome, hepatic venous thrombosis, *V1*: 398, 401–405
  carcinoid tumor metastases, *V1*: 164, 183–185
  chemotherapy-related metaseases, *V1*: 257, 264–270
  cirrhosis, *V1*: 333–362
    dysplastic nodules, *V1*: 340, 342, 346–354
    regenerative nodules, *V1*: 333–334, 339–345
  contrast agents, *V1*: 51–58
  echinococcal disease, *V1*: 431–433
  fatty liver, *V1*: 371, 373, 377–387
  fibrolamellar carcinoma, *V1*: 238–239
  focal nodular hyperplasia, *V1*: 121
    hepatocellular adenoma, differential diagnosis, *V1*: 177, 180
  fungal infection, *V1*: 437–438
  hemangiomas, *V1*: 73, 81, 83, 85, 87
    chronic liver disease, *V1*: 103–105
    hepatocellular carcinoma, differential diagnosis, *V1*: 106
  hepatic abscess, pyogenic, *V1*: 418, 422–432

hepatic cysts:
foregut hepatic cysts, *V1*: 60, 66–70
solitary (nonparasitic), *V1*: 60–66
hepatic transplantation, *V1*: 292, 299
hepatocellular adenoma, *V1*: 107, 109–113
hepatocellular carcinoma, *V1*: 192, 198, 202–214
diffuse infiltrative, *V1*: 212, 227, 234–238
hypervascular metastases, *V1*: 151–162
inflammatory myofibroblastic tumor, *V1*: 418–422
lesional/perilesional enhancement, *V1*: 147–150
lymphomas, *V1*: 238, 240–245
melanoma metastases, *V1*: 164, 181–182
mesothelioma, malignant, *V1*: 242, 250–251
metastases detection and characterization, *V1*: 128, 137–143
mucin-producing tumors, *V1*: 165, 185–186
multiple myeloma, *V1*: 238, 245–246
pancreatic ductal adenocarcinoma metastases, *V1*: 162
porta hepatis lymphadenopathy, *V1*: 352, 354, 359, 362–365
portal venous air, *V1*: 411, 413
postradiation metastases, *V1*: 257, 262–264
primary biliary cirrhosis, *V1*: 314–315
primary sclerosing cholangitis, *V1*: 304, 306–311
radiation-induced hepatitis, *V1*: 321, 331
resection, metastases following, *V1*: 256–262
squamous cell carcinoma metastases, *V1*: 162, 165–171
T2 images *vs.*, *V1*: 143–147
techniques, *V1*: 46–50
transcatheter arterial embolization, *V1*: 268, 270–278
transfusional iron overload, *V1*: 368–373
trauma, *V1*: 442
undifferentiated sarcoma, *V1*: 251, 256
magnetic resonance cholangiopancreatography, *V1*: 460–461
ovaries:
benign neoplasms:
epithelial origin, *V2*: 1518–1523
germ cell tumors, *V2*: 1520–1521, 1526–1529
sex cord-stromal tumors, *V2*: 1525–1526, 1529–1531
cysts, functional cysts, *V2*: 1500, 1504–1506
endometriomas, *V2*: 1506
functional cysts, *V2*: 1504–1506
hydrosalpinx, *V2*: 1517
lymphoma, *V2*: 1545, 1548–1549
metastases to, *V2*: 1547, 1549–1550
ovarian torsion, *V2*: 1510, 1514–1516
pelvic inflammatory disease, *V2*: 1514, 1516–1517
polycystic ovarian syndrome, *V2*: 1507, 1509, 1514
pancreas, *V1*: 536–541
acute pancreatitis, *V1*: 628, 636–647
annular pancreas, *V1*: 542–544
autoimmune pancreatitis, *V1*: 664, 666
chronic pancreatitis, *V1*: 648–665
cystic fibrosis, *V1*: 545–548
gastrinomas, *V1*: 591, 598–602
insulinomas, *V1*: 601, 603
islet-cell tumors, *V1*: 590–598
metastases to, *V1*: 619, 625–631
mucinous cystadenoma/cystadenocarcinoma, *V1*: 612–616
pancreatic adenocarcinoma, *V1*: 552, 554–558, 562–564, 570, 572, 574–575, 577–587
liver metastases, *V1*: 580, 584–587
lymph node metastases, *V1*: 580, 584
primary hemochromatosis, *V1*: 546, 548–549
serous cystadenoma, *V1*: 607, 611–612
pediatric patients, *V2*: 1637, 1639–1646
pelvic varices, *V2*: 1517–1518
penis and urethra:
inflammatory disease, *V2*: 1380–1381
metastases, *V2*: 1376–1377
normal anatomy, *V2*: 1375–1376
primary tumors, *V2*: 1377–1380
peritoneum:
ascites, *V2*: 936, 940–942
intraperitoneal blood, *V2*: 936, 943–944
in pregnancy, *V2*: 1561
cervical fibroids, *V2*: 1569, 1573
fetal weight and amniotic fluid, *V2*: 1622–1623
postpartum uterus, *V2*: 1575–1580
prostate cancer, *V2*: 1352, 1356–1373
adenocarcinoma, *V2*: 1352, 1356–1373
prostate gland:
benign prostatic hyperplasia, *V2*: 1349–1354
inflammation and infection, *V2*: 1373–1374
normal anatomy, *V2*: 1344–1346
trauma, *V2*: 1374–1375
rectum, *V1*: 827, 831
renal cell carcinoma, *V2*: 1084, 1086
retroperitoneum:
benign lymphadenopathy, *V2*: 1247–1250
primary neoplasms, *V2*: 1265–1271
seminal vesicles:
cysts, *V2*: 1382, 1384
diffuse disease, *V2*: 1382–1383, 1385
normal anatomy, *V2*: 1382–1834
small intestine, *V1*: 767–770
carcinoids, *V1*: 779, 790–791
spleen, *V1*: 678–681
cysts, *V1*: 683, 687–690
hamartomas, *V1*: 690, 693, 695–697
hemangiomas, *V1*: 687–688, 691–693
littoral cell angioma, *V1*: 688, 694
lymphomas, *V1*: 693–694, 699–703
stomach, *V1*: 734
carcinoids, *V1*: 759
gastric adenocarcinoma, *V1*: 738
T3-weighted imaging *vs.*, *V1*: 32–36
testes, scrotum and epididymis, *V2*: 1385
benign neoplasms, *V2*: 1386, 1388–1390
cryptorchidism, *V2*: 1386–1388
infectious disease, *V2*: 1397–1398
malignant tumors, *V2*: 1392–1396
testicular prostheses, *V2*: 1386
trauma, *V2*: 1397
uterus, *V2*: 1434
endometrial carcinoma, *V2*: 1471–1481
endometrial hyperplasia/polyps, *V2*: 1449–1450
leiomyomas, *V2*: 1452–1469
uterine corpus, *V2*: 1434–1436
vagina, *V2*: 1409–1410
Bartholin glands cysts, *V2*: 1416–1418
Gartner duct cyst, *V2*: 1416, 1418–1419
radiation effects, *V2*: 1421, 1428
vaginal malignancies, *V2*: 1420–1426
vessel imaging, *V2*: 1194–1200
inferior vena cava malignancies, *V2*: 1237–1241
T2-weighted imaging:
3T MR imaging, *V1*: 33–36
abdominal-pelvic disease, *V1*: 6–10
adnexa, *V2*: 1499–1500
adrenal glands, *V2*: 964–968
adrenal cortical carcinoma, *V2*: 998, 1002–1006
metastases, *V2*: 994–1002
myelolipoma, *V2*: 979–980, 988–990
neuroblastoma, *V2*: 1013–1017
pheochromocytoma, *V2*: 1005–1111
ambiguous genitalia, *V2*: 1415–1416
aortic grafts, *V2*: 1214, 1216, 1224–1227
bile duct:
ampullary fibrosis, *V1*: 489, 495–496
cholangiocarcinoma, *V1*: 517–518, 521–526
infectious cholangitis, *V1*: 502–507
bile ducts, primary sclerosing cholangitis, *V1*: 499–502
biliary system, gadolinium-based contrast agents, *V2*: 1771
bladder, *V2*: 1298
congenital anomalies, *V2*: 1299–1301
cystitis, *V2*: 1326–1328
hemorrhagic cystitis, *V2*: 1326, 1329
hypertrophic bladder, *V2*: 1324–1325
leiomyomas, *V2*: 1300, 1302–1303
metastatic neoplasms, *V2*: 1320–1324
neurofibromas, *V2*: 1304–1305
transitional cell carcinoma, *V2*: 1307–1316

T2-weighted imaging: (*Continued*)
breast:
cysts, *V2*: 1701–1703
fibroadenomas, *V2*: 1703–1706
phyllodes tumor, *V2*: 1706–1707
protocol, *V2*: 1694–1695
silicone implants, *V2*: 1688–1689, 1757–1759
breast cancer:
invasive ductal carcinoma, *V2*: 1723–1727
melanoma metastases, *V2*: 1743–1744
cervical cancer, *V2*: 1483–1488
cervix, *V2*: 1434
chest, *V2*: 1653–1654
pleural disease, *V2*: 1666, 1671–1672
colon cancer, *V1*: 843–865
disease conspicuity and, *V1*: 1–2
echo-train spin-echo sequences, *V1*: 6–7
esophagus, *V1*: 726, 728
leiomyomas, *V1*: 726–728
fat-suppressed echo-train spin-echo sequences, *V1*: 7–10
female urethra:
diverticulum, *V2*: 1405–1407
malignant masses, *V2*: 1403–1404
normal anatomy, *V2*: 1401–1403
pelvic floor relaxation, *V2*: 1408–1410
fetal assessment:
abdomen and pelvis, *V2*: 1583–1585
central nervous system, *V2*: 1578–1583
congenital hemangiomas, *V2*: 1604, 1607
destructive lesions, *V2*: 1598–1601
head and neck, *V2*: 1583
kidney anomalies, *V2*: 1613
renal cysts, *V2*: 1614–1616
gallbladder:
acute cholecystitis, *V1*: 472–475
carcinoma, *V1*: 481, 485–486
gallstone disease, *V1*: 464–465, 467–469
hemorrhagic cholecystitis, *V1*: 475–477
normal gallbladder, *V1*: 460, 462
polyps, *V1*: 480, 482–483
iron-based contrast agents, *V2*: 1777–1779
kidneys:
adenoma, *V2*: 1068
granulocytic sarcoma (chloroma), *V2*: 1109, 1111
hemorrhagic/proteinaceous cysts, *V2*: 1037, 1042–1044, 1046
iron deposition, *V2*: 1121, 1125–1127
lymphocele, *V2*: 1182
lymphoma, *V2*: 1106–1110
multilocular cystic nephroma, *V2*: 1060, 1063–1064
perinephric pseudocyst, *V2*: 1042, 1044, 1050
simple cysts, *V2*: 1037–1039
techniques, *V2*: 1025–1031
Wilms tumor, *V2*: 1103–1106
large intestine:
colonic fistulae, *V1*: 883, 887–888
intraluminal contrast agents, *V1*: 892, 895–897
mucocele, *V1*: 838, 841–842
rectosigmoid carcinoma, *V1*: 850, 857–860
techniques, *V1*: 824
liver, *V1*: 46–50
ablative therapies, *V1*: 278–287
adenocarcinoma, undifferentiated tumors, *V1*: 162, 164, 177–179
angiosarcoma, *V1*: 242, 249
autoimmune hepatitis, *V1*: 312–314
bile duct carcinoma, intrahepatic/peripheral metastases, *V1*: 239–240, 242, 247–249
Budd-Chiari syndrome, hepatic venous thrombosis, *V1*: 398, 401–405
carcinoid tumor metastases, *V1*: 164, 183–185
chemotherapy-related metaseases, *V1*: 257, 264–270
cirrhosis, *V1*: 333–362
dysplastic nodules, *V1*: 340, 342, 346–354
regenerative nodules, *V1*: 333–334, 339–345
iron-containing, *V1*: 334, 340, 344–346
computed tomography *vs.*, *V1*: 128, 141–144
echinococcal disease, *V1*: 431–433
fat/iron deposition, *V1*: 371, 376
fatty liver, *V1*: 379–387
fibrolamellar carcinoma, *V1*: 238–239
focal nodular hyperplasia, *V1*: 121–126
hepatocellular adenoma, differential diagnosis, *V1*: 177, 180
fungal infection, *V1*: 437–438
hemangiomas, *V1*: 73, 81, 83, 85–86, 89–91
central nodular lesion, *V1*: 85, 91
chronic liver disease, *V1*: 103–105
hepatocellular carcinoma, differential diagnosis, *V1*: 106
hypervascular metastases, differential diagnosis, *V1*: 90, 101–103
medium-sized lesion, *V1*: 85, 89–91
small lesion, *V1*: 85–86
small-sized slow-enhancing, *V1*: 88, 94–95
hepatic abscess, pyogenic, *V1*: 418, 422–432
hepatic arterial obstruction, *V1*: 407
hepatic cysts:
foregut hepatic cysts, *V1*: 60, 66–70
solitary (nonparasitic), *V1*: 60–66
hepatic transplantation, *V1*: 292, 299
hepatocellular adenoma, *V1*: 107, 109–113
hepatocellular carcinoma, *V1*: 192, 198, 202–214
diffuse infiltrative, *V1*: 212, 227, 234–238
hypervascular metastases, *V1*: 151–162
inflammatory myofibroblastic tumor, *V1*: 418–422
lobe abnormalities, *V1*: 58–60
lymphomas, *V1*: 238, 240–245
melanoma metastases, *V1*: 164, 181–182
mesothelioma, malignant, *V1*: 242, 250–251
metastases detection and characterization, *V1*: 128, 137–143
T1 images *vs.*, *V1*: 147–150
multiple myeloma, *V1*: 238, 245–246
mycobacterium avium intracellulare, *V1*: 433–435
pancreatic ductal adenocarcinoma metastases, *V1*: 162
porta hepatis lymphadenopathy, *V1*: 352, 354, 359, 362–365
portal venous air, *V1*: 411, 413
portal venous thrombosis, *V1*: 391, 393–400
postradiation metastases, *V1*: 257, 262–264
preeclampsia and eclampsia, *V1*: 407, 410–411
primary biliary cirrhosis, *V1*: 314–315
primary sclerosing cholangitis, *V1*: 304, 306–311
radiation-induced hepatitis, *V1*: 321, 331
Reidel lobe, differential diagnosis, *V1*: 58–60
secondary infection, metastases, *V1*: 188, 191–192
transcatheter arterial embolization, *V1*: 268, 270–278
transfusional iron overload, *V1*: 368–373
trauma, *V1*: 442
viral hepatitis, *V1*: 321–330
magnetic resonance cholangiopancreatography, *V1*: 456–461
ovaries:
benign neoplasms:
epithelial origin, *V2*: 1518–1523
germ cell tumors, *V2*: 1520–1521, 1526–1529
sex cord-stromal tumors, *V2*: 1525–1526, 1529–1531
cysts, functional cysts, *V2*: 1500, 1504–1506
endometriomas, *V2*: 1506, 1509–1512
functional cysts, *V2*: 1504–1506
hydrosalpinx, *V2*: 1517
lymphoma, *V2*: 1545, 1548–1549
normal anatomy, *V2*: 1500–1501
ovarian torsion, *V2*: 1510, 1514–1516
pelvic inflammatory disease, *V2*: 1514, 1516–1517
polycystic ovarian syndrome, *V2*: 1507, 1509, 1514
pancreas:
acute pancreatitis, *V1*: 628, 636–647
autoimmune pancreatitis, *V1*: 664, 666
chronic pancreatitis, *V1*: 649, 665
gastrinomas, *V1*: 591, 593, 598–602

insulinomas, *V1*: 601, 603
islet-cell tumors, *V1*: 591–598
metastases to, *V1*: 619, 625–631
mucinous cystadenoma/cystadenocarcinoma, *V1*: 612–616
pancreatic adenocarcinoma, *V1*: 552–557
lymph node metastases, *V1*: 580, 584
primary hemochromatosis, *V1*: 546, 548–549
serous cystadenoma, *V1*: 606–607, 609–612
pediatric patients, *V2*: 1644
pelvic varices, *V2*: 1517–1518
penis and urethra:
inflammatory disease, *V2*: 1380–1381
metastases, *V2*: 1376–1377
normal anatomy, *V2*: 1375–1376
primary tumors, *V2*: 1377–1380
prostheses, *V2*: 1376–1377
peritoneum:
ascites, *V2*: 936, 940–942
intraperitoneal blood, *V2*: 936, 943–944
in pregnancy, *V2*: 1561
abdominal fibromatosis, *V2*: 1570
cervical fibroids, *V2*: 1569, 1573
fetal weight and amniotic fluid, *V2*: 1622–1623
postpartum uterus, *V2*: 1575–1580
prostate cancer, *V2*: 1352, 1356–1373
adenocarcinoma, *V2*: 1352, 1356–1373
prostate gland:
inflammation and infection, *V2*: 1373–1374
normal anatomy, *V2*: 1344–1346
trauma, *V2*: 1374–1375
psoas muscle, *V2*: 1271, 1273–1280
rectum, techniques, *V1*: 827, 831
renal cell carcinoma, *V2*: 1084, 1086
recurrence, *V2*: 1089, 1096–1097
retroperitoneum:
fibrosis, benign *vs.* malignant, *V2*: 1240, 1242–1244, 1249, 1252–1253
malignant metastatic lymphadenopathy, *V2*: 1258–1263
neurofibromas, *V2*: 1240, 1245–1247
primary neoplasms, *V2*: 1266–1271
seminal vesicles:
cysts, *V2*: 1382, 1384
diffuse disease, *V2*: 1382–1383, 1385
normal anatomy, *V2*: 1382–1834
single-shot echo-train spin-echo sequences, *V1*: 7–8
small intestine:
carcinoids, *V1*: 779, 790–791
Crohn disease, *V1*: 785, 791, 793–805
spleen, *V1*: 678–681
accessory/wandering spleens, *V1*: 681–685
cysts, *V1*: 683, 687–690
hamartomas, *V1*: 690, 693, 695–697
hemangiomas, *V1*: 687–688, 691–693
littoral cell angioma, *V1*: 688, 694
lymphangiomas, *V1*: 693
lymphomas, *V1*: 693–694, 699–703
stomach, *V1*: 734–736
carcinoids, *V1*: 759
gastric adenocarcinoma, *V1*: 738, 741, 743
gastrointestinal stromal tumors, *V1*: 743, 748, 752–758
testes, scrotum and epididymis, *V2*: 1385
benign neoplasms, *V2*: 1386, 1388, 1390
cryptorchidism, *V2*: 1386–1388
infectious disease, *V2*: 1397–1398
malignant tumors, *V2*: 1392–1396
testicular prostheses, *V2*: 1386
trauma, *V2*: 1397
uterus, *V2*: 1434
adenomyosis, *V2*: 1466–1470
endometrial carcinoma, *V2*: 1471–1481
endometrial hyperplasia/polyps, *V2*: 1448–1450
leiomyomas, *V2*: 1452–1469
menstrual changes, *V2*: 1437–1439
vagina:
agenesis/partial agenesis, *V2*: 1411–1412
Bartholin glands cysts, *V2*: 1416–1418
duplication anomalies, *V2*: 1412, 1414–1415
Gartner duct cyst, *V2*: 1416, 1418–1419
normal anatomy, *V2*: 1409–1410
radiation effects, *V2*: 1421, 1428
vaginal malignancies, *V2*: 1420–1426
vessel imaging, *V2*: 1194–1200
inferior vena cava malignancies, *V2*: 1237–1241
Takayasu arteritis, ischemic nephropathy, *V2*: 1136, 1139
Talipes equinovarus, fetal assessment, *V2*: 1622
Tamoxifen:
endometrial carcinoma, ovarian metastases, *V2*: 1474, 1476
uterine changes, *V2*: 1439–1440
Technetium (^{99m}Tc-pertechnetate) scintigraphy, Meckel divedrticulum, *V1*: 770, 774
Teratomas:
fetal assessment:
fetal mouth, *V2*: 1598, 1604
intracranial, *V2*: 1598–1599, 1602
sacrococcygeal teratoma, *V2*: 1617–1620
ovarian malignancies, *V2*: 1534, 1540, 1543–1544
Terminal duct-lobular units (TDLUs):
breast cancer, risk and prevalence, *V2*: 1723
breast cysts, *V2*: 1700–1703
fibroadenomas, *V2*: 1702–1706
fibrocystic breast changes, *V2*: 1712, 1714–1716
normal breast, *V2*: 1688
Testes:
benign masses:
cystic lesions, *V2*: 1386, 1389
neoplasms, *V2*: 1386, 1388, 1390
testicular prostheses, *V2*: 1386
congenital anomalies, *V2*: 1386
cryptorchidism, *V2*: 1386–1388
infectious disease, *V2*: 1397–1398
malignant masses, *V2*: 1390–1396
MR imaging, *V2*: 1385
normal anatomy, *V2*: 1383–1384
torsion, *V2*: 1396–1397
trauma, *V2*: 1397
Testicular cancer, retroperitoneal imaging, *V2*: 1258, 1263–1265
Testicular feminization, *V2*: 1415
uterine anomalies, *V2*: 1448
Thalassemia:
adrenal gland myelolipoma, *V2*: 977, 979–980, 988–990
hepatic iron overload, *V1*: 368, 370, 374–375
α-Thalassemia, liver imaging, *V1*: 370, 375
Theca-lutein ovarian cysts, *V2*: 1504, 1507–1508
Thecomas, benign ovarian neoplasms, *V2*: 1525–1526, 1531
Thin-collimation source images, magnetic resonance cholangiopancreatography, *V1*: 456, 460
Thorax:
fetal assessment:
anomalies, *V2*: 1604, 1612
normal development, *V2*: 1583
magnetic resonance angiography, *V2*: 1673, 1679–1684
Three-dimensional gradient echo sequences (3D-GE):
adnexa, *V2*: 1499–1500
adrenal glands, *V2*: 963–968
bladder, *V2*: 1298
transitional cell carcinoma, *V2*: 1307–1316
breast imaging, *V2*: 1694–1695
capillary phase imaging, *V1*: 2
chest imaging, *V2*: 1653–1654
hilar and mediastinal lymphadenopathy, *V2*: 1666–1667
pulmonary emboli, *V2*: 1673, 1675–1677
pulmonary infiltrates, *V2*: 1666, 1668–1671
colon cancer, *V1*: 843–865
peritoneal metastases, *V1*: 848, 854–857
dynamic contrast-enhanced imaging, *V1*: 3
esophageal imaging, *V1*: 726, 728
esophagus, malignant masses, *V1*: 729–731
fat-suppressed gradient echo sequences, *V1*: 4

Three-dimensional gradient echo sequences (3D-GE): (*Continued*)
gadolinium-enhanced T1-weighted images, hepatic arterial dominant (capillary) phase, *V1*: 11–13
gastrointestinal tract imaging, *V1*: 725
kidneys:
complex cysts, *V2*: 1037, 1040
fibromuscular dysplasia, *V2*: 1133, 1136–1137
horseshoe kidney, *V2*: 1032, 1034
renal blood flow evaluation, *V2*: 1173
renal filling defects, *V2*: 1159, 1166–1169
techniques, *V2*: 1025–1031
large intestine:
abscesses, *V1*: 881–886
colonic adenomatous polyps, *V1*: 832, 835–838
infectious colitis, *V1*: 888
techniques, *V1*: 824
ulcerative colitis, *V1*: 867–868, 870–871
liver imaging techniques, *V1*: 46–50
lung cancer, pulmonary nodules, *V2*: 1654, 1657, 1662–1665
male pelvis, *V2*: 1343–1344
pancreatic imaging, *V1*: 536–541
pancreatic adenocarcinoma, *V1*: 559, 564–566
pediatric patients, *V2*: 1637
older children, *V2*: 1645–1646
quality improvements, *V1*: 16
rectal adenocarcinoma, *V1*: 848–850
rectal carcinoid tumor, *V1*: 867–868
renal artery disease, *V2*: 1129, 1131–1133
renal cell carcinoma, stage 4, *V2*: 1082, 1084–1085
retroperitoneum, *V2*: 1193–1194
fibrosis, benign *vs.* malignant, *V2*: 1240, 1242–1244
malignant metastatic lymphadenopathy, *V2*: 1258–1263
small intestine, *V1*: 767–770
adenocarcinoma, *V1*: 777, 781–782
gastrointestinal stromal tumor, *V1*: 779, 783–785
infectious enteritis, *V1*: 810, 813–814
metastases to, *V1*: 782, 791–792
pancreatitis, *V1*: 810, 815
polyps, *V1*: 775, 777–778
radiation enteritis, *V1*: 816, 818
varices, *V1*: 775, 781
spleen, *V1*: 678–681
spoiled gradient echo (SGE) sequences, abdominal-pelvic imaging, *V1*: 3–4
stomach, *V1*: 734
gastric adenocarcinoma, *V1*: 743
vessel imaging, *V2*: 1195–1200
aorta, *V2*: 1200–1227
abdominal aortic aneurysm, *V2*: 1201–1207
aortic dissection, *V2*: 1201, 1208–1212
aortic graft evaluation, *V2*: 1214, 1216, 1224–1227
aortoiliac atherosclerotic disease/thrombosis, *V2*: 1204, 1207, 1214–1223
inferior vena cava, *V2*: 1216, 1223, 1229
thrombus, *V2*: 1229–1237
whole body imaging, *V1*: 40–42
Three-dimensional spin echo sequences, *V1*: 7
magnetic resonance cholangiopancreatography, *V1*: 456–461
single-shot echo-train spin-echo sequences, *V1*: 7–8
3.0T imaging:
adnexa, *V2*: 1500
adrenal glands, *V2*: 964–968
aorta, *V2*: 1200–1227
comparisons to 1.5T, *V1*: 31–36
female urethra, normal anatomy, *V2*: 1402–1403
gastrointestinal tract, *V1*: 725
kidney, renal cell carcinoma, stage 4, *V2*: 1082, 1084–1085
kidneys, *V2*: 1029–1031
liver imaging, hemangiomas, *V1*: 81, 83, 85, 88, 92–94, 96–97
lung cancer, pulmonary nodules, *V2*: 1654, 1662
male pelvis, *V2*: 1343–1344
pediatric patients, *V2*: 1637–1644
adnexa, *V2*: 1650
adrenal glands, *V2*: 1650
bladder, *V2*: 1650
data acquisition parameters, *V2*: 1644–1645
female urethra/vagina, *V2*: 1650
follow-up procedures, *V2*: 1647–1649
gadolinium-based contrast agents, *V2*: 1647
gallbladder/biliary system, *V2*: 1649
gastrointestinal tract, *V2*: 1650
imaging protocol, *V2*: 1637, 1644
infants (under 1.5 years), *V2*: 1645
kidneys, *V2*: 1650
liver, *V2*: 1649
magnetic field strength, *V2*: 1644
male pelvis, *V2*: 1650
older children (6–18 years), *V2*: 1645–1646
pancreas, *V2*: 1649–1650
receiver coil, *V2*: 1644–1645
retroperitoneum, *V2*: 1650
sedation technique, *V2*: 1646–1647
small children (1–6 years), *V2*: 1641, 1645
prostate cancer, adenocarcinoma, *V2*: 1352, 1356–1373
uterus and cervix, *V2*: 1434
vagina, vaginal carcinoma, *V2*: 1416, 1422
Thrombotic microangiopathy, renal artery disease, *V2*: 1133, 1137, 1141
Time-intensity curves, breast imaging, *V2*: 1691
Time-of-flight techniques, vessel imaging, *V2*: 1194–1200
TNM staging:
breast cancer, *V2*: 1723–1725
colon cancer, *V1*: 843
female urethral carcinoma, *V2*: 1403
gastric adenocarcinoma, *V1*: 738, 741–742
prostate cancer, *V2*: 1368
renal cell carcinoma (RCC), *V2*: 1073
testicular cancer, *V2*: 1392–1396
transitional cell carcinoma, bladder cancer, *V2*: 1307–1316
vaginal malignancies, *V2*: 1416, 1421
vulvar carcinomas, *V2*: 1421, 1427
Torsion, testicular, *V2*: 1396–1397
Toxicity studies, gadolinium-based contrast agents, *V2*: 1779–1786
Toxic megacolon:
Crohn colitis, *V1*: 869, 872–874
ulcerative colitis and, *V1*: 867–868, 870–781
Trachelectomy, cervical cancer, *V2*: 1493–1495
Transcatheter arterial chemoembolization, liver metastases, *V1*: 268, 270–278
Transfusional iron overload, liver imaging, *V1*: 368–373
Transfusional siderosis, liver imaging, *V1*: 368–373
Transhepatic signal intensity differences (THID), *V1*: 414–415
Transient hepatic arterial defects, *V1*: 414–415
Transitional cell carcinoma (TCC):
bladder:
advanced disease, *V2*: 1308, 1313–1314
diverticulum anomalies and, *V2*: 1300
invasive, *V2*: 1307–1308, 1312
recurrence, *V2*: 1308, 1316
superficial invasion, *V2*: 1307–1312
urothelial neoplasms, *V2*: 1306–1316
pancreatic metastases, *V1*: 619, 625, 627
renal pelvis and ureter, *V2*: 1155, 1159–1165
Transplant procedures:
hepatic transplantation:
bile duct obstruction following, *V1*: 292, 299
donor and recipient assessment, *V1*: 287–292
fibrosis, *V1*: 299, 304
fungal infection, *V1*: 299, 305
graft failure, *V1*: 287, 292
liver abnormalities, *V1*: 299, 303–306
hepatic arterial obstruction, *V1*: 405, 407–408
hepatocellular carcinoma recurrence, *V1*: 299, 302

inflammation following, *V1*: 299–300
lymphoma, *V1*: 238, 241
magnetic resonance cholangiopancreatography, bile duct anastomoses, *V1*: 519–520
MR imaging, *V1*: 287–305
posttransplant lymphoproliferative disorder, *V1*: 299–301
vascular complications, *V1*: 292–298
pancreatic transplants, *V1*: 671–673
renal transplants, *V1*: 671–673, *V2*: 1173, 1177–1188
Transposed ovaries, *V2*: 1500–1502
Transurethral resection of prostate (TURP):
bladder changes, *V2*: 1331, 1335
prostate defects, *V2*: 1352–1354
Transvaginal ultrasound:
pelvic inflammatory disease, *V2*: 1514, 1516–1517
uterus, congenital anomalies, *V2*: 1440
Transverse colon, adenocarcinoma, *V1*: 843, 845
Transverse echo train-STIR imaging, liver, hepatic cysts, *V1*: 60, 63
Transverse mesocolon, pancreatic adenocarcinoma involvement, *V1*: 575, 580
Trauma:
female urethra, *V2*: 1407
fetal assessment, destructive lesions, *V2*: 1596–1601
kidney, *V2*: 1172–1174
liver, *V1*: 438–442
pancreas, *V1*: 665, 668–671
penis and urethra, *V2*: 1382
prostate gland, *V2*: 1374–1375
renal artery injury, *V2*: 1133, 1136
spleen, *V1*: 715–719
testes, scrotum and epididymis, *V2*: 1397
True-FISP. *See* Two-dimensional steady-state precession-balanced echo MRI
Trypsin, pancreatitis and, *V1*: 625
Tuberculosis:
adrenal glands, *V2*: 1019
genitourinary, bladder involvement, *V2*: 1326
mycobacterium tuberculosis, hepatic involvement, *V1*: 433
renal abscess, *V2*: 1144
Tuberculous peritonitis, *V2*: 949, 951
Tuberous sclerosis:
fetal assessment, *V2*: 1595
renal cysts, *V2*: 1066, 1069–1071
Tubo-ovarian abscess (TOA), *V2*: 1514, 1516–1517
Tubular blockage, kdineys, *V2*: 1120, 1123–1124
Tubular carcinoma, breast cancer, *V2*: 1733–1736
Tubular ectasia:
medullary sponge kidney, *V2*: 1049, 1060
testes, scrotum and epididymis, cystic lesions, *V2*: 1386, 1389
Tubulointerstitial kidney disease, *V2*: 1120–1121
Tunnel cluster, endometrial hyperplasia/polyps, *V2*: 1448–1450
Turbo fast low-angle shot (TurboFLASH), abdominal-pelvic imaging, *V1*: 5
Turbo spin-echo sequences, *V1*: 6
magnetic resonance cholangiopancreatography, *V1*: 460
Turner syndrome:
gonadal dysgenesis, *V2*: 1415
uterine hypoplasia, *V2*: 1441–1442
Twin-twin transfusion syndrome, *V2*: 1623–1624
Two-dimensional spin echo sequences, *V1*: 7
breast imaging, *V2*: 1694–1695
magnetic resonance cholangiopancreatography, *V1*: 456–461
pediatric patients, *V2*: 1637
Two-dimensional spoiled gradient echo sequences:
capillary phase imaging, *V1*: 2
kidneys, techniques, *V2*: 1025–1031
magnetization-prepared rapid-acquisition gradient echo sequences, *V1*: 5–6
male pelvis, *V2*: 1343–1344
pancreatic imaging, *V1*: 536–541
spoiled gradient echo (SGE) sequences, abdominal-pelvic imaging, *V1*: 3
vessel imaging, *V2*: 1195–1200
Two-dimensional steady-state precession-balanced echo (True-FISP) MRI:
esophagus, *V1*: 726
esophageal varices, *V1*: 727, 729
fetal assessment, central nervous system, *V2*: 1578–1583
gastrointestinal tract imaging, *V1*: 725
glomerular disease, *V2*: 1117–1120
large intestine, techniques, *V1*: 824
nephrotic syndrome, *V2*: 1117–1120
pulmonary emboli, *V2*: 1673, 1675–1677
small intestinal varices, *V1*: 775, 781
uterus and cervix, *V2*: 1434
vessel imaging, *V2*: 1195–1200
Typhlitis, *V1*: 884, 890

Ulcerated gastric adenocarcinoma, *V1*: 738
Ulcerative colitis:
Crohn disease, *V1*: 785, 867–868, 870–871
differential diagnosis, *V1*: 785, 869, 872–874
large intestine, *V1*: 867–868, 870–871
primary sclerosing cholangitis, *V1*: 494, 497–502
small intestine, *V1*: 797, 806
Ulcers:
aortic, penetrating, *V2*: 1201, 1204, 1213
gastric, *V1*: 761–764
Ultrasmall paramagnetic iron oxide particles:
characteristics, *V2*: 1777–1779
endometrial carcinoma, *V2*: 1474–1481
liver imaging, reticuloendothelial system targeting, *V1*: 50, 54–58
Umbilical vein, cirrhosis and varices in, *V1*: 348, 351, 361
Undifferentiated sarcoma of the liver (USL), *V1*: 251, 256
Undifferentiated uterine carcinoma, *V2*: 1488–1491
Unicornuate uterus, *V2*: 1441, 1444
Uniform low signal intensity enhancement, spleen, *V1*: 678–681
Urachal carcinoma, *V2*: 1316, 1320
Urachal cyst, *V2*: 1300–1301
Uremic medullary cystic disease complex, *V2*: 1049, 1059–1060
Ureter anastomosis, renal transplantation, *V2*: 1182
Ureteric calculi, *V2*: 1159, 1168–1169
Ureterocele:
female urethra, *V2*: 1403
renal duplication, *V2*: 1613
Ureteropelvic junction, fetal assessment, hydronephrosis, *V2*: 1613–1614
Urethra:
female:
caruncles, *V2*: 1407
congenital anomalies, *V2*: 1402
diverticulum, *V2*: 1405–1407
duplication anomaly, *V2*: 1403
leiomyoma, *V2*: 1403
malignant masses, *V2*: 1403–1404
metastases to, *V2*: 1405
MR imaging, *V2*: 1401–1402
normal anatomy, *V2*: 1401–1403
pediatric imaging, *V2*: 1650
pelvic floor relaxation, *V2*: 1408–1410
trauma and strictures, *V2*: 1407
urethritis and fistulae, *V2*: 1407–1408
fetal assessment, hydronephrosis, *V2*: 1613–1614
male:
congenital anomalies, *V2*: 1376
diffuse disease, *V2*: 1377–1380
infectious disease, *V2*: 1380
inflammatory disease, *V2*: 1380–1381
male, normal anatomy, *V2*: 1375–1376
membranous rupture, *V2*: 1373–1374
metastases, *V2*: 1376–1377
primary tumors, *V2*: 1377–1380
trauma, *V2*: 1374–1375, 1382
Urethral carcinoma, female urethra, *V2*: 1403–1404
Urethritis, female urethra, *V2*: 1407–1408
Urethrography, femal urethral diverticulum, *V2*: 1405
Urethrovaginal fistulas, *V2*: 1408
Urinary incontinence, periurethral collagen injection, *V2*: 1408–1409
Urine, intraperitoneal, *V2*: 942
Urinoma, renal transplants, *V2*: 1182, 1184

Urothelial neoplasm:
bladder cancer:
carcinosarcoma, *V2*: 1316
squamous cell carcinoma, *V2*: 1316–1318
transitional cell carcinoma, *V2*: 1306–1316
renal pelvis and ureter carcinoma, *V2*: 1155, 1159–1165
Urthroscopy, femal urethral diverticulum, *V2*: 1405
Usual ductal hyperplasia, benign breast lesions, *V2*: 1715
Uterine artery embolization (UAE):
adenomyosis, *V2*: 1467, 1470
leiomyomas, *V2*: 1451, 1456, 1459–1463
Uterine peristalsis, menstrual cycle and, *V2*: 1437–1439
Uterus:
benign disease:
adenomyosis, *V2*: 1456, 1466–1470
endometrial hyperplasia/polyps, *V2*: 1448–1450
fibroids, *V2*: 1456, 1462–1463
leiomyomas, *V2*: 1449, 1451–1469
lipoleiomyoma, *V2*: 1456, 1464
congenital anomalies:
arcuate uterus, *V2*: 1441, 1444, 1448
bicornuate uterus, *V2*: 1441, 1444, 1446
didelphys uterus, *V2*: 1441, 1444–1446
diethylstilbesterol exposure, *V2*: 1448
Müllerian duct anomalies, *V2*: 1439–1448
segmental agenesis/hypoplasia, *V2*: 1441
septate uterus, *V2*: 1441, 1444, 1447–1449
sexual differentiation disorders, *V2*: 1448
unicornuate uterus, *V2*: 1441, 1444
contractions, *V2*: 1437–1439
dehiscence, postpartum uterus, *V2*: 1577
duplication anomalies, vaginal duplication and, *V2*: 1412, 1414–1415
hematoma, in pregnancy, *V2*: 1559–1560
malignant disease:
adenocarcinoma, undifferentiated carcinoma/sarcoma, *V2*: 1488–1491
endometrial carcinoma, *V2*: 1468, 1470–1481
sarcoma, *V2*: 1475, 1479–1481
menstrual changes, *V2*: 1437–1439
metastases to, *V2*: 1482
leiomyosarcoma, *V2*: 1456, 1465–1466
MR imaging techniques, *V2*: 1433–1434
normal anatomy, uterine corpus, *V2*: 1434–1436
pediatric imaging, *V2*: 1650
in pregnancy, maternal imaging:
leiomyomas, *V2*: 1564, 1567–1570
placental imaging, *V2*: 1623, 1625–1627
postpartum uterus, *V2*: 1575–1580
subserosal leiomyoma, *V2*: 1567, 1570
tamoxifen-induced changes, *V2*: 1439–1440
Utricular cysts, prostate, *V2*: 1344, 1347

Vagina:
agenesis/partial agenesis, *V2*: 1410–1413
ambiguous genitalia, *V2*: 1415–1416
benign masses, *V2*: 1416–1420
Bartholin glands cyst, *V2*: 1416–1418
cavernous hemangioma, *V2*: 1416, 1420
Gartner duct cysts, *V2*: 1416, 1418–1419
cervical cancer metastases, *V2*: 1486–1487
congenital anomalies and variants, *V2*: 1410
duplication/partial duplication, *V2*: 1412, 1414–1415
fistulas, *V2*: 1421, 1426, 1429–1430
gonadal differentiation abnormalities, *V2*: 1415
malignant masses, *V2*: 1416, 1420–1426
staging, *V2*: 1421
metastases to, *V2*: 1420, 1424–1426
cervical cancer, *V2*: 1405
urethral adenocarcinoma, *V2*: 1403–1404
vulvar/perineal carcinomas, *V2*: 1421, 1426–1428
MR imaging techniques, *V2*: 1409–1410
normal anatomy, *V2*: 1401–1403, 1408–1411
pediatric imaging, *V2*: 1650
radiation changes, *V2*: 1421, 1428
Vaginoplasty, vaginal agenesis/partial agenesis, *V2*: 1411
Vanillylmandelic acid (VMA), pheochromocytoma, *V2*: 1005
Varicella virus, splenomegaly and, *V1*: 709–711
Varices:
cirrhosis:
esohpageal, *V1*: 351, 361
fibrosis and, *V1*: 351, 362
gastric, *V1*: 348, 351, 359
subcutaneous, *V2*: 1274, 1290–1291
pelvic, *V2*: 1517–1518
periduodenal/duodenal, *V1*: 775, 781
peritoneal, *V2*: 945–946, 948–949
rectal, *V1*: 838
small intestine, *V1*: 775, 781
splenomegaly and, *V1*: 706–709
Varicocele, testes, scrotum and epididymis, *V2*: 1388–1390, 1392
Vascular disease:
abdominal wall imaging, *V2*: 1274
magnetic resonance angiography, *V2*: 1673, 1679–1684
penis and urethra, *V2*: 1380–1381
peritoneal, *V2*: 945–946, 948–949
renal artery disease, *V2*: 1133–1144
Vascular endothelial growth factor (VEGF), hepatocellular carcinoma, *V1*: 202
Vascular graft, branch vessel, *V2*: 1214, 1216, 1227
Vasculitis, renal artery disease, *V2*: 1136–1137
Vas deferens:
congenital anomalies, *V2*: 1386
cysts, *V2*: 1344, 1347–1349
Vasovist contrast agent, *V2*: 1772, 1774
Venous embolotherapy, pelvic varices, *V2*: 1518
Venous thrombosis:
hepatic venous thrombosis, *V1*: 398, 401–405
hepatocellular carcinoma, *V1*: 202, 212, 224–232, 234–238
inferior vena cava, *V2*: 1229–1237
tumor *vs.* blood thrombus, *V2*: 1229–1237, 1240–1241
nephrotic syndrome, *V2*: 1117, 1120
pancreatic transplants, *V1*: 671–673
portal venous system, obstruction/thrombosis, *V1*: 388, 391, 393–400
renal vein, *V2*: 1137, 1144
splenic vein, pancreatic adenocarcinoma, *V1*: 575, 579
splenomegaly and, *V1*: 706–709
superior mesenteric vein, small intestine ischemia and hemorrhage, *V1*: 816, 822
Ventriculomegaly, fetal imaging, *V2*: 1585–1592
Vermian hypoplasia, fetal assessment, posterior fossa anomalies, *V2*: 1591, 1593–1597
Vesicocervical fistulas, bladder involvement, *V2*: 1331–1335
Vessel imaging:
retroperitoneum:
aorta, *V2*: 1200–1227
aortic aneurysm, *V2*: 1200–1207
aortic dissection, *V2*: 1201, 1208–1212
aortoiliac atherosclerotic disease/thrombosis, *V2*: 1204, 1207, 1214–1223
penetrating ulcers/intramural dissecting hematoma, *V2*: 1201, 1204, 1213
postoperative graft evaluation, *V2*: 1207, 1214, 1216, 1224–1227
inferior vena cava, *V2*: 1216, 1223, 1229
congenital anomalies, *V2*: 1223, 1229–1230
primary malignant tumors, *V2*: 1237–1241
venous thrombosis, *V2*: 1229–1237
magnetic resonance angiography, *V2*: 1194–1200
signal intensity, *V1*: 14

Villous adenoma, large intestine, *V1*: 829, 832, 835–836
VIPoma, MR imaging, *V1*: 601, 606
Viral hepatitis:
  hepatocellular carcinoma, *V1*: 202, 212
  imaging studies, *V1*: 319, 321–330
Von Hippel-Lindau syndrome:
  pancreas, *V1*: 549–550
  renal cysts, *V2*: 1066, 1068, 1072
Von Meyenburg complexes, biliary hamartoma, *V1*: 67, 73–77
Von Recklinghausen disease:
  bladder lesions, *V2*: 1304–1305
  small intestine neurofibromas, *V1*: 775, 779
Vulva:
  carcinomas, *V2*: 1421, 1427–1428
  perivulvar cavernous hemangioma, *V2*: 1416, 1420
  squamous cell carcinoma, *V2*: 1421, 1427

WAGR syndrome, Wilms tumor and, *V2*: 1103–1106
Walker-Warburg syndrome, encephalocele, fetal assessment, *V2*: 1595, 1597
Wandering spleen, MR imaging, *V1*: 681–685
Water excitation T1-weighted magnetization-prepared gradient-echo imaging (WE-MPRAGE), pediatric patients, *V2*: 1645–1650
Weigert-Meyer rule, renal duplication, *V2*: 1613
Whipple procedure, pancreatic adenocarcinoma, *V1*: 588
Whole body imaging:
  3T MR imaging, safety issues, *V1*: 33
  pediatric patients, *V2*: 1637–1650
  performance improvements in, *V1*: 36, 38–42
  protocol for, *V1*: 20, 23
Wilms tumor, *V2*: 1102–1106
Wilson disease, imaging studies, *V1*: 315–318
Wirsung ducts, pancreas divisum, *V1*: 541–542
Wraparound artifacts, breast MRI, *V2*: 1695
Xanthogranulomatous cholecystitis, magnetic resonance cholangiopancreatography, *V1*: 477
Xanthogranulomatous pyelonephritis, *V2*: 1152
X-linked recessive disorder:
  fetal assessment, corpus callosum agenesis, *V2*: 1588–1592
  testicular feminization, *V2*: 1415

Yersinia enterocolitica infection, enteritis, *V1*: 810, 813–814
Yolk sac tumor, peritoneal metastases, *V2*: 918, 923–924, 927

Zellballen masses, pheochromocytoma, adrenal medullary masses, *V2*: 998, 1005–1111
Zollinger-Ellison syndrome:
  hypertrophic rugal folds, *V1*: 761, 765
  pancreatic cancer, *V1*: 591, 598–602
  stomach carcinoids, *V1*: 759

ABDOMINAL-PELVIC MRI

Volume 2

ABDOMINAL-PELVIC MRI

Third Edition

Volume 2

Richard C. Semelka, M.D.
Director, Magnetic Resonance Services
Professor, Vice Chairman of Clinical Research and
Vice Chairman of Quality and Safety
Department of Radiology
University of North Carolina at Chapel Hill

WILEY-BLACKWELL
A JOHN WILEY & SONS, INC., PUBLICATION

Copyright 2010 by John Wiley & Sons, Inc. All rights reserved

Wiley-Blackwell is an imprint of John Wiley & Sons, formed by the merger of Wiley's global Scientific, Technical, and Medical business with Blackwell Publishing.

Published by John Wiley & Sons, Inc., Hoboken, New Jersey
Published simultaneously in Canada

No part of this publication may be reproduced, stored in a retrieval system, or transmitted in any form or by any means, electronic, mechanical, photocopying, recording, scanning, or otherwise, except as permitted under Section 107 or 108 of the 1976 United States Copyright Act, without either the prior written permission of the Publisher, or authorization through payment of the appropriate per-copy fee to the Copyright Clearance Center, Inc., 222 Rosewood Drive, Danvers, MA 01923, (978) 750-8400, fax (978) 750-4470, or on the web at www.copyright.com. Requests to the Publisher for permission should be addressed to the Permissions Department, John Wiley & Sons, Inc., 111 River Street, Hoboken, NJ 07030, (201) 748-6011, fax (201) 748-6008, or online at http://www.wiley.com/go/permission.

Limit of Liability/Disclaimer of Warranty: While the publisher and author have used their best efforts in preparing this book, they make no representations or warranties with respect to the accuracy or completeness of the contents of this book and specifically disclaim any implied warranties of merchantability or fitness for a particular purpose. No warranty may be created or extended by sales representatives or written sales materials. The advice and strategies contained herein may not be suitable for your situation. You should consult with a professional where appropriate. Neither the publisher nor author shall be liable for any loss of profit or any other commercial damages, including but not limited to special, incidental, consequential, or other damages.

For general information on our other products and services or for technical support, please contact our Customer Care Department within the United States at (800) 762-2974, outside the United States at (317) 572-3993 or fax (317) 572-4002.

Wiley also publishes its books in a variety of electronic formats. Some content that appears in print may not be available in electronic formats. For more information about Wiley products, visit our web site at www.wiley.com.

ISBN 978-0-470-48775-4

Library of Congress Cataloging-in-Publication Data is available

Printed in the United States of America

10 9 8 7 6 5 4 3 2 1

This book is dedicated to all the patients whose images we have used to illustrate MR findings. I hope that the MR studies offered positive impact on their lives. Furthermore, I hope that many, many more patients worldwide will benefit from the knowledge conferred to their physicians by the information contained herein.

—Richard Semelka

Christ seated, disputing with the doctors. Etching, 1654. Rembrandt. This etching describes evolution in human thought. New individuals challenge prevailing wisdom, and the end result is the improvement of the human condition.

Christ driving the money-changers from the temple. Etching, 1635. Rembrandt. This etching describes the necessity of being ever vigilant against the excesses of greed. We must constantly challenge ourselves and others that this is not a prime motivation for conduct.

CONTENTS

Volume 1

Preface xi
Contributors xiii

1. DIAGNOSTIC APPROACH TO PROTOCOLING AND INTERPRETING MR STUDIES OF THE ABDOMEN AND PELVIS 1
Puneet Sharma, Diego R. Martin, Brian M. Dale, Busakorn Vachiranubhap, and Richard C. Semelka

2. LIVER 45
Larissa Braga, Diane Armao, Mohamed El Azzazi, and Richard C. Semelka

3. GALLBLADDER AND BILIARY SYSTEM 455
Ersan Altun, Till Bader, Jorge Elias, Jr., Faiq Shaikh, and Richard C. Semelka

4. PANCREAS 535
Ersan Altun, Jorge Elias, Jr., Diane Armao, Busakorn Vachiranubhap, and Richard C. Semelka

5. SPLEEN 677
Ersan Altun, Jorge Elias, Jr., Young Hoon Kim, and Richard C. Semelka

6. GASTROINTESTINAL TRACT 725
Diego R. Martin, Ersan Altun, Jorge Elias, Jr., Mohamed Elazzazi, Miguel Ramalho, Chang-Hee Lee, and Richard C. Semelka

Index I-1

Volume 2

Preface xi
Contributors xiii

7. PERITONEAL CAVITY 901
Ersan Altun, N. Cem Balci, Jorge Elias, Jr., Young Mi Ku, and Richard C. Semelka

8. ADRENAL GLANDS 963
Ersan Altun, Nikolaos L. Kelekis, Jorge Elias, Jr., Penampai Tannaphai, Waqas Qureshi, and Richard C. Semelka

9. KIDNEYS 1025
Larissa Braga, Ersan Altun, Jorge Elias, Jr., Diego R. Martin, Sang Soo Shin, and Richard C. Semelka

10. RETROPERITONEUM AND BODY WALL 1193
Diego R. Martin, Ersan Altun, Jorge Elias, Jr., Young Mi Ku, and Richard C. Semelka

11. BLADDER 1297
Ersan Altun, Corinne Deurdulian, Jorge Elias, Jr., Penampai Tannaphai, and Richard C. Semelka

12. MALE PELVIS 1343
Ersan Altun, Tara Noone, Jorge Elias, Jr., Milena Spirovski, Rahel A. Kubik, Young Mi Ku, and Richard C. Semelka

13. FEMALE URETHRA AND VAGINA 1401
Lara B. Eisenberg, Jorge Elias, Jr., Waqas Qureshi, Young Mi Ku, and Richard C. Semelka

14. UTERUS AND CERVIX 1433
Michèle A. Brown, Sameer A. Patel, Caroline Reinhold, Waqas Qureshi, and Richard C. Semelka

15. ADNEXA 1499
Michèle A. Brown, Mihaela I. Pop, Susan M. Ascher, Mohamed Elazzazi, and Richard C. Semelka

16. PREGNANCY AND FETUS 1559
Lorene Romine, Reena Chopra, Katarina Koprivsek, Waqas Qureshi, Richard C. Semelka, and Michèle A. Brown

17. PEDIATRICS 1637
Waqas Qureshi, Naciye Turan, Thuy Vu, Mohamed Elazzazi, Carlos Gonzalez, Rafael de Campos, and Richard C. Semelka

18. CHEST 1653
Ersan Altun, Jorge Elias, Jr., Katherine R. Birchard, Busakorn Vachiranubhap, Vasco Heredia, and Richard C. Semelka

19. BREAST 1687
Dragana Djilas-Ivanović, Helmuth Schultze-Haack, Dag Pavic, and Richard C. Semelka

20. CONTRAST AGENTS 1767
Ersan Altun, Diego R. Martin, and Richard C. Semelka

Index I-1

PREFACE

Much change has occurred in imaging since the writing of the previous edition of this work. The entity of nephrogenic systemic fibrosis (NSF) has been identified and its association with gadolinium-based contrast agents (GBCAs), especially the linear nonionic agents, has been recognized. Further recognition by the main-stream radiological community of the detrimental nature of excessive medical radiation, that may result in malignancy, and contrast-induced-nephropathy related to the use of iodine-based contrast agents (IBCAs) have simultaneously occurred. These lapses in attention on the subject of safety by the radiology community serve to remind ourselves of our duty to patients of Primum Non Nocere, emphasizing the age-old wisdom of "everything in moderation" and the importance of being ever vigilant when it comes to patient welfare. Positive steps have been taken by individual radiologists and radiological societies and equipment manufacturers to lessen the potential harmful effects of what we have previously assumed to be innocuous imaging studies. Almost all centers have adopted a restrictive GBCA policy that has largely vanquished NSF, and will progressively make the elimination of this condition complete. Policies and programs related to medical radiation, currently foremost amongst them being the Image Gently campaign, a program designed to minimize the amount of radiation sustained by pediatric patients in imaging studies, and operated as a joint venture between many of the large radiology societies, have been developed and instituted.

At the same time, positive advances in MRI have occurred. These include the more widespread adoption and development of 3 T MRI to study diseases of the chest, abdomen and pelvis. 3T possesses higher signal-to-noise, greater image quality especially with 3D-gradient echo imaging, greater sensitivity to GBCA enhancement, and thinner section acquisition. This has allowed further expansion of MRI into more applications in torso imaging.

In recognition of these changes in the imaging terrain, this current edition addresses many of these above mentioned issues and advances. A new chapter on Contrast Agents is included to address the use of MR contrast agents, but also describes GBCA and IBCA issues and safe practice. New chapters on Fetus and Pediatric imaging draw attention to the capacity of MRI to accurately investigate young subjects, to ameliorate the problems with excess medical radiation in this group, who are the most sensitive to radiation damage. Breast imaging has also come of age and is included as a new chapter in this work. Additionally, many of the new images throughout the book are 3T images, emphasizing the high image quality provided at ultrahigh field strength, and illustrating its growing importance.

Despite all these changes, the principles of this book remain unchanged. The emphasis remains on short duration imaging studies that combine comprehensive information and consistent image quality. The major step to widespread implementation of MRI in replacement of other modalities, remains reproducibility and generalizability of information acquired. MRI has to replicate CT images and studies need to be generated with comparable and not excessively longer duration, and image quality must be reliable and consistent, but with the addition of greater and more comprehensive information, and greater safety. Although we touch on new applications in Chapter 1, such as diffusion-weighted imaging and MR elastography, at present I do not consider their roles established in main-stream MRI practice, paying attention to the above mentioned principles, and I recommend that at present their use be restricted to research centers. This text again emphasizes multiple examples of disease processes both rare and common, so that the reader has guidance on the appearances of virtually all diseases processes in the abdomen, pelvis, chest and breast, to compare their own cases against. With all the advances in MRI, and perhaps despite the advances in CT, coupled with the recognition of the hazards intrinsic to CT, especially CT performed with multiple passes of the torso, this work aims to show that much of imaging of these areas can be performed with MRI, by virtue of the depth and breadth of disease processes that can be evaluated well. In many organ systems, as this book reveals, MRI performs extremely well at diagnosing most disease entities, and outperforms CT in many areas, notably the liver. MRI may be the best tool to evaluate cancers in most of the organs described in this text, and much of

the inflammatory diseases. CT remains dominant for major trauma, diffuse lung parenchymal diseases, and renal stone diseases. What remains exciting is that despite the comprehensiveness of this work, it is not the omega work of MRI. We anticipate further exciting advances that may further alter imaging management, perhaps especially, making inroads into more indications in trauma. Those developments may need to wait for the future next edition. With further exciting advances we have to remain vigilant on the subject of safety, MRI is not an innocuous tool, and as we move to even higher field strengths, safety must be cautiously assessed.

RICHARD SEMELKA, M.D.

CONTRIBUTORS

ERSAN ALTUN, M.D., Department of Radiology, University of North Carolina, Chapel Hill, Chapel Hill, North Carolina

DIANE ARMAO, M.D., Department of Radiology, University of North Carolina, Chapel Hill, Chapel Hill, North Carolina

SUSAN M. ASCHER, M.D., Department of Radiology, Georgetown University, Washington, DC

TILL BADER, M.D., Associate Professor of Radiology, Medical University of Vienna, Austria

N. CEM BALCI, M.D., Department of Radiology, St. Louis University, St. Louis, Missouri

KATHERINE R. BIRCHARD, M.D., Department of Radiology, University of North Carolina, Chapel Hill, North Carolina

LARISSA BRAGA, M.D. Ph.D, M.P.H., Department of Radiology, University of Nebraska Medical Center, Omaha, Nebraska

MICHÈLE A. BROWN, M.D., Associate Professor of Radiology, University of California, San Diego, California

REENA CHOPRA, M.D., Clinical Fellow, Department of Radiology, University of California, San Diego, California

BRIAN M. DALE, Ph.D., Siemens Medical Solutions, Inc., Morrisville, North Carolina

RAFAEL DE CAMPOS, M.D., Clinical Research Scholar, MR Section, Department of Radiology, University of North Carolina, Chapel Hill, North Carolina

CORINNE DEURDULIAN, M.D., Imaging Department, VA Medical Center, Salisbury, North Carolina

DRAGANA DJILAS-IVANOVIĆ, M.D., Ph.D., Associate Professor of Radiology, University of Novi Sad, Oncology Institute of Vojvodina, Sremska Kamenica, Serbia

LARA B. EISENBERG, M.D., Chairman of Radiology, Suburban Hospital, Bethesda, Maryland

MOHAMED ELAZZAZI, M.D., Ph.D., Clinical Research Scholar, MR Section, Department of Radiology, University of North Carolina, Chapel Hill, North Carolina; Professor of Radiology, Al-Azhar University, Cairo, Egypt

JORGE ELIAS, JR., M.D., Ph.D., Professor of Radiology, Faculty of Medicine of Ribeirao Preto, University of Sao Paulo, Brazil

CARLOS GONZALEZ, M.D., Clinical Research Scholar, MR Section, Department of Radiology, University of North Carolina, Chapel Hill, North Carolina

VASCO HEREDIA, M.D., Clinical Research Scholar, MR Section, Department of Radiology, University of North Carolina, Chapel Hill, Chapel Hill, North Carolina

NIKOLAOS L. KELEKIS, M.D., Associate Professor of Radiology, National and Kapodistrian University of Athens, General University Hospital "ATTIKON," Athens, Greece

YOUNG HOON KIM, M.D., Clinical Research Scholar, MR Section, Department of Radiology, University of North Carolina, Chapel Hill, North Carolina; Seoul National University College of Medicine and Seoul National University Bundang Hospital, Seongnam-si, Gyeonggi-do, Korea

KATARINA KOPRIVSEK, M.D., Ph.D., Associate Professor of Radiology, University of Novi Sad, Diagnostic Imaging Center, Oncology Institute of Vojvodina, Sremska Kamenica, Serbia

YOUNG MI KU, M.D., Clinical Research Scholar, MR Section, Department of Radiology, University of North Carolina, Chapel Hill, North Carolina; Assistant Professor, Department of Radiology, Uijongbu St. Mary's Hospital, Catholic University of Korea, Uijongu, Korea

RAHEL A. KUBIK, M.D., M.P.H., Department of Medical Services, Cantonal Hospital, Baden, Switzerland

CHANG-HEE LEE, M.D., Ph.D., Clinical Research Scholar, MR Section, Department of Radiology, University of North Carolina, Chapel Hill, North Carolina; Associate

Professor, Department of Radiology, Korea University Guro Hospital, Korea University College of Medicine, Seoul, Korea

DIEGO R. MARTIN, M.D., Professor and Director of MR, Department of Radiology, Emory University, Atlanta, Georgia

TARA NOONE, M.D., President, SEA Imaging, LLC, Mt. Pleasant, South Carolina; Clinical Associate Professor, Medical University of South Carolina, Charleston, South Carolina

SAMEER A. PATEL, M.D., Clinical Fellow, Department of Radiology, University of California, San Diego, California

DAG PAVIC, M.D., Assistant Professor of Radiology, University of North Carolina, Chapel Hill, North Carolina

MIHAELA I. POP, M.D., Clinical Fellow, Department of Radiology, University of California, San Diego, California

WAQAS QURESHI, M.D., Clinical Research Scholar, MR Section, Department of Radiology, University of North Carolina, Chapel Hill, North Carolina

MIGUEL RAMALHO, M.D., Clinical Research Scholar, MR Section, Department of Radiology, University of North Carolina, Chapel Hill, North Carolina

CAROLINE REINHOLD M.D., M.Sc., Professor of Radiology, Gynecology, and Internal Medicine; Director, MR Imaging, McGill University Health Center, Montréal, Québec, Canada

LORENE ROMINE, M.D., Assistant Professor of Radiology, University of California, San Diego, California

HELMUTH SCHULTZE-HAACK, Siemens Medical Solutions USA, Inc., Santa Ana, California

RICHARD C. SEMELKA, M.D., Professor of Radiology, University of North Carolina, Chapel Hill, North Carolina

FAIQ SHAIKH, M.D., Clinical Research Scholar, MR Section, Department of Radiology, University of North Carolina, Chapel Hill, North Carolina

PUNEET SHARMA, Ph.D., Clinical MR Physicist, Department of Radiology, Emory Healthcare, Inc., Atlanta, Georgia

SANG SOO SHIN, M.D., Clinical Research Scholar, MR Section, Department of Radiology, University of North Carolina, Chapel Hill, North Carolina; Assistant Professor, Department of Radiology, Chonnam National University Medical School, Gwanju, Korea

MILENA SPIROVSKI, M.D., Diagnostic Imaging Center, Oncology Institute of Vojvodina, Sremska Kamenica, Serbia

PENAMPAI TANNAPHAI, M.D., Clinical Research Scholar, MR Section, Department of Radiology, University of North Carolina, Chapel Hill, North Carolina

NACIYE TURAN, M.D., Resident, Department of Radiology, University of North Carolina, Chapel Hill, North Carolina

BUSAKORN VACHIRANUBHAP, M.D., Clinical Research Scholar, MR Section, Department of Radiology, University of North Carolina, Chapel Hill, North Carolina

THUY VU, M.D., Resident, Department of Radiology, University of North Carolina, Chapel Hill, Chapel Hill, North Carolina

CHAPTER 7

PERITONEAL CAVITY

ERSAN ALTUN, N. CEM BALCI, JORGE ELIAS, JR., YOUNG MI KU, AND RICHARD C. SEMELKA

NORMAL ANATOMY

The peritoneum is the most extensive and complexly arranged of the serous membranes in the human body. Like the serous membranes that line the pericardial and pleural cavities, the peritoneal cavity is lined by a specialized epithelium termed mesothelium.

The peritoneum can be analogized to an empty yet intricately folded sac. The parietal peritoneum lines the abdominal wall, whereas a continuation of the parietal peritoneum is reflected over viscera as the visceral peritoneum. The free surface of the peritoneum is lined by a smooth layer of mesothelium, moistened by a thin film of serous fluid. In the normal state, viscera are able to glide freely against the wall of the abdominal cavity or upon each other without impediment. Loss of this specialized mesothelial surface may lead to the adherence of underlying tissues. In certain conditions, transformation of mesothelial cells into fibroblasts and proliferation of submesothelial connective tissue can lead to macroscopic adhesions between peritoneal surfaces, disrupting intestinal motility or causing complete obstruction [1].

Some abdominal viscera are completely covered by peritoneum and are suspended from the posterior abdominal wall by a thin sheet of peritoneum-covered connective tissue that contains a network of blood vessels. These folds of peritoneum are termed mesenteries. Peritoneal ligaments are serous membranes, often serving as neurovascular pedicles, extending between two structures. The apronlike greater omentum extends from the greater curvature of the stomach to lie draped over the coils of the small intestine and is reflected back onto the transverse colon. It forms a protective covering over the abdominal contents. The omentum may limit peritoneal infections because it tends to adhere to areas of infection. In a patient with perforation of the appendix, the omentum may wall off the infection to form an abscess, preventing generalized peritonitis. The lesser omentum or gastrohepatic ligament joins the lesser curvature of the stomach to the liver. Its medial free edge is termed the hepatoduodenal ligament, which encloses the portal vein, hepatic artery, and common bile duct. The transverse mesocolon is a broad fold of peritoneum connecting the transverse colon to the posterior abdominal wall. Its layers pass from the pancreas to the transverse colon.

Abdominal-Pelvic MRI, Third Edition, edited by Richard C. Semelka. Copyright © 2010 John Wiley & Sons, Inc.

Because the parietal and visceral layers of the peritoneum are always in sliding contact, the peritoneal "cavity" is, in fact, best viewed as a potential space. The peritoneal cavity is divided into two regions, a main region, termed the greater sac, and a diverticulum, or lesser sac, behind the stomach and the lesser omentum. The opening of the diverticulum, the epiploic foramen, provides communication between the greater and lesser sacs.

The peritoneum has the capacity to exude cells and fluid in response to injury or infection. Certain potential peritoneal spaces or recesses, normally in communication with each other, may be walled off by adhesions and create sites of abnormal fluid collections. With this concept in mind, the greater sac is further divided by the transverse mesocolon into an upper part, the supramesocolic space, and a lower part, the inframesocolic space. The supramesocolic space is subdivided into right and left peritoneal spaces. The right peritoneal space includes the right perihepatic space and the lesser sac, demarcated anteriorly by the lesser omentum. These spaces communicate via the epiploic foramen, which is bounded by the hepatoduodenal ligament of the lesser omentum. The lesser sac is a potential space that distends in the presence of certain disease processes, especially pancreatitis. The right perihepatic space consists of a subphrenic space and a subhepatic space and is partially divided by the right coronary ligament. The posterior aspect of the right subhepatic space encloses a recess between the liver and kidney called the hepatorenal fossa (Morison pouch). This space commonly accumulates fluid in the setting of diseases affecting the gallbladder, the second portion of the duodenum, the liver, or the ascending colon. Malignant disease has a tendency to affect the lesser sac in addition to the greater sac. Benign disease, except for pancreatitis, primarily affects the greater sac [2, 3].

The left peritoneal space can be divided into anterior and posterior perihepatic spaces and anterior and posterior subphrenic spaces. The perihepatic spaces tend to be involved with diseases affecting the left lobe of the liver and stomach, whereas the anterior subphrenic space may also be affected by disease involving the splenic flexure. The posterior subphrenic space is most commonly involved in disease of the spleen.

The inframesocolic compartment of the peritoneal cavity is divided into a small right space and a larger infracolic space. The right side is limited inferiorly by the junction of the distal small bowel mesentery with the cecum, whereas the left infracolic space drains into the pelvis.

The paracolic gutters are located lateral to the peritoneal attachment of the ascending and descending colon. The right paracolic gutter is continuous with the right perihepatic space. On the left side, however, the phrenicocolic ligament forms a partial barrier between the paracolic gutter and the left subphrenic space. The pelvis is the most dependent portion of the peritoneal cavity in both the erect and recumbent positions. Therefore, both benign and malignant fluid preferentially pool in this location [4, 5]. The pelvic cavity consists of the lateral paravesical spaces and the midline rectovaginal space (pouch of Douglas or cul-de-sac) in women and the rectovesical space in men.

The peritoneal reflections are conduits for intraperitoneal fluid, which flows along the path of least resistance. Specifically, flow along the right paracolic gutter and into the pelvis is relatively unimpeded. Greater resistance to flow occurs along the left paracolic gutter, and flow across midline is impeded by the falciform ligament [6].

MRI TECHNIQUE

Techniques that minimize motion and maximize spatial and contrast resolution are well suited for imaging peritoneal disease. The multiplanar capabilities of MRI are also useful. Our standard MRI protocol includes breath-hold T1-weighted SGE and 3D-GE, T2-weighted single-shot echo-train spin-echo, and immediate and delayed postgadolinium SGE or 3D-GE techniques. Precontrast T1-weighted SGE and T2-weighted single-shot echo-train spin-echo sequences are acquired with and without fat suppression. Pre- or postgadolinium T1-weighted 3D-GE sequences are acquired with fat suppression. While immediate postgadolinium T1-weighted SGE sequences are acquired without fat suppression, delayed postgadolinium T1-weighted SGE sequences are acquired with fat suppression. The essential sequence to evaluate peritoneal disease is 2- to 5-min gadolinium-enhanced T1-weighted fat-suppressed SGE or 3D-GE (fig. 7.1).

For fibrotic processes, the T1-weighted non-fat-suppressed SGE technique maximizes contrast resolution between high-signal intraperitoneal fat and low-signal diseased tissue, whereas for inflammatory and neoplastic conditions the gadolinium-enhanced T1-weighted fat-suppressed SGE or 3D-GE techniques are the most sensitive imaging sequence for disease detection. Peritoneal diseases are best studied during the interstitial phase (2–5 min after injection), when leaky capillaries allow contrast to pool in the interstitium. This time course allows for dynamic scanning of a target organ (e.g., the liver) during the capillary phase and a survey of the peritoneum during the interstitial phase. This is particularly advantageous in conditions that simultaneously affect the solid viscera and the peritoneum, such as ovarian, colorectal, pancreatic, and gastric carcinoma.

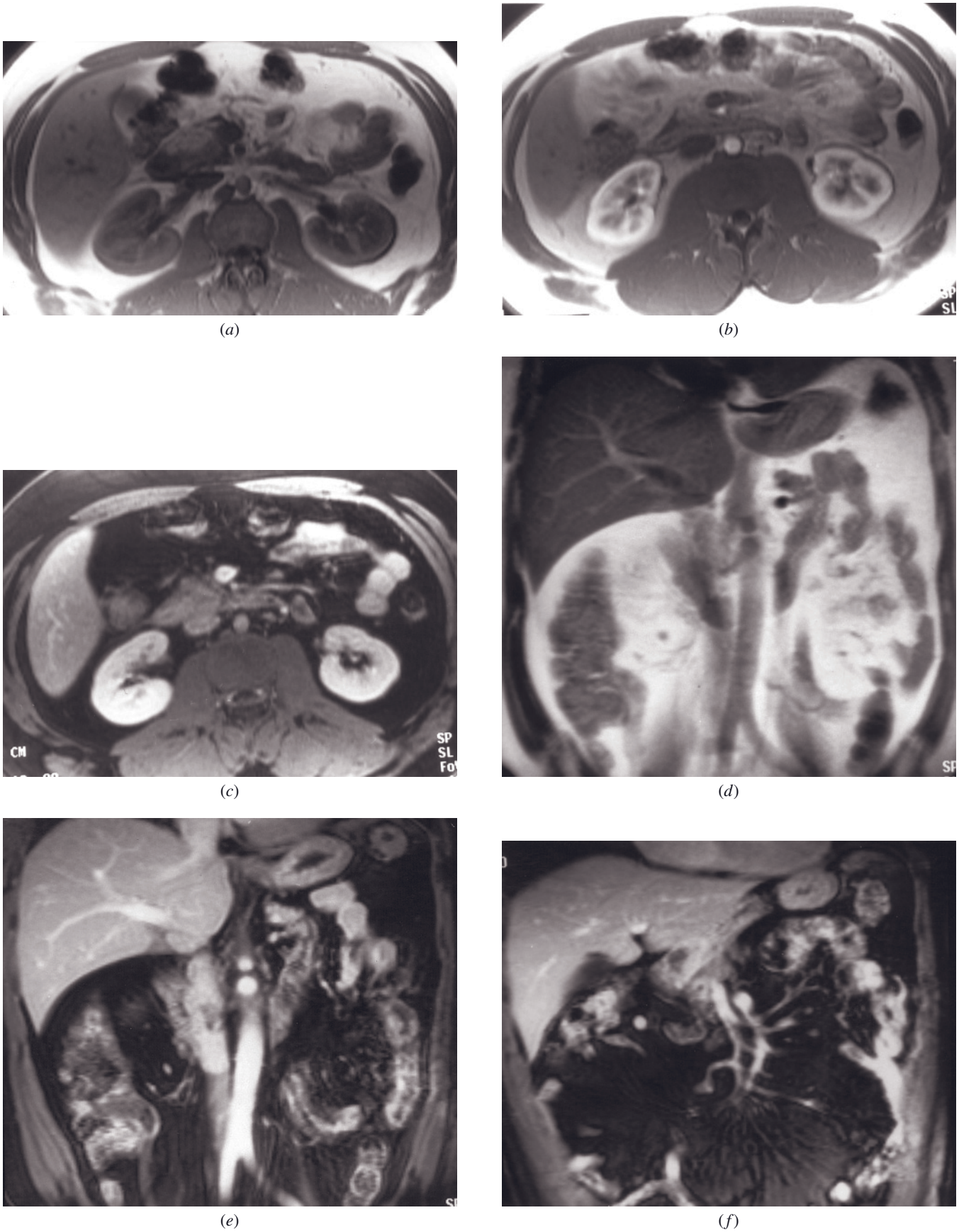

FIG. 7.1 Normal peritoneum. Transverse SGE (*a*) and immediate (*b*) and 90-s postgadolinium fat-suppressed SGE (*c*) images. The normal peritoneum is faintly appreciable with current MRI techniques. The abdominal fat is uniform and provides good contrast with abdominal organs, with a combination of nonsuppressed (*a*, *b*) and fat-suppressed (*c*) sequences. Coronal T2-weighted SS-ETSE (*d*) and coronal interstitial-phase gadolinium-enhanced fat-suppressed SGE (*e*, *f*) images in a second patient. Note that bowel, vessels, and the mesentery are well demarcated.

NORMAL VARIANTS AND CONGENITAL DISEASE

Congenital variations of the peritoneal reflections are rare. They usually are related to malrotation of the bowel or situs anomalies during gestation [7]. Lymphangiomas of the omentum and mesentery are true cysts lined by endothelium. Cystic lymphangioma represents the single most frequent tumor of the omentum in children [8]. Possible pathogenic mechanisms for these lesions include developmental disturbance with abnormality in the lymphatic system or drainage obstruction with secondary expansion of the lymphatic channels. They usually are multiloculated cysts containing serous or chylous fluid, but may be complicated by hemorrhage. The imaging characteristics reflect the cyst contents in that lymphangiomas with high protein content are high in signal intensity on T1-weighted images [9].

HERNIAS

Bochdalek Hernia

Posterolateral defect of the diaphragm is a common congenital diaphragm abnormality. Defective formation and/or fusion of the pleuroperitoneal membrane results in herniation of abdominal contents into the thoracic cavity. This defect, usually unilateral and on the left side, consists of a large opening (referred to as the foramen of Bochdalek) in the posterior aspect of the diaphragm [10]. The discontinuity of the diaphragm may be shown by MRI in multiple planes (fig. 7.2).

Hiatus Hernia and Internal Hernia

Partial congenital herniation of the stomach through an enlarged esophageal hiatus is rare. Most hiatal hernias are acquired lesions occurring during adult life. Esophageal hernias are divided into two types: sliding (axial) and paraesophageal. Paraesophageal hiatal hernias are characterized by herniation of all or part of the stomach into the thorax immediately adjacent and to the left of an undisplaced gastroesophageal junction. In contrast, sliding hiatal hernias are characterized by displacement of the upper stomach and gastroesophageal junction upward into the thorax. Sliding hernias result from weakened or torn phrenoesophageal membranes, resulting in a gastroesophageal junction that is above the esophageal hiatus of the diaphragm (fig. 7.3).

Internal hernia is defined as the herniation of a viscus, usually the small intestine, through a normal or abnormal aperture within the peritoneal cavity (fig. 7.3). The incidence of internal hernia is less than 1%; however, it can cause small bowel obstructions and, if left untreated, has high mortality [10]. Internal hernias can be acquired secondary to surgeries, trauma, or postinflammatory changes. They can also be congenital, including normal patients with normal apertures and patients with abnormal apertures resulting from anomalies of internal rotation and peritoneal attachment. These hernias can be classified according to location: paraduodenal, pericecal, foramen of Winslow, transmesenteric or transmesocolic, intersigmoid, retroanastomatic. MR imaging features of internal hernias include trapping, crowding, and encapsulation of distended bowel loops in a hernia sac located in an abnormal location, segmental small bowel obstruction extending into proximal segments, twisting and engorgement of mesenteric vessels, mesenteric stranding, and increased enhancement in the walls of trapped segments.

Abdominal Wall Hernias

MR images acquired as breath-hold or single-shot techniques identify abdominal wall hernias. This may be helpful in obese patients where physical exam is hampered. Single-shot echo-train spin echo is particularly effective at demonstrating hernias and, in addition, experiences negligible magnetic susceptibility artifact, which improves visualization of bowel wall in the setting of dilated air-filled loops of bowel.

- ***Inguinal hernia:*** Inguinal hernias result from a persistent processus vaginalis, which is that portion of the abdominal peritoneum that enters the deep, or internal, inguinal ring. At birth, the patent processus vaginalis communicates with the peritoneal cavity; it normally closes during infancy. If, however, the processus remains patent, abdominal viscera may protrude into it, forming an inguinal hernia [11] (fig. 7.4).
- ***Spigelian hernia:*** This is a rare hernia of the anterior abdominal wall caused by a defect in the aponeurosis between the transversus abdominis and the rectus abdominis muscle. The peritoneal sac herniates through the rent in the aponeurosis and dissects laterally (fig. 7.5).
- ***Paraumbilical hernia and incisional hernia:*** Paraumbilical hernia arises near the umbilicus and protrudes through the linea alba (fig. 7.6). Although they may be congenital, paraumbilical hernias are more common in obese and multiparous women; diastasis of the recti abdomini is the common underlying factor [11]. Incisional hernia is seen in the abdominal wall after surgeries. Mostly intestinal segments protrude through weakened abdominal wall via a defect. Peristomal hernia is also characterized by herniation of intestinal segments through the abdominal wall defect created for colostomy (fig. 7.6).

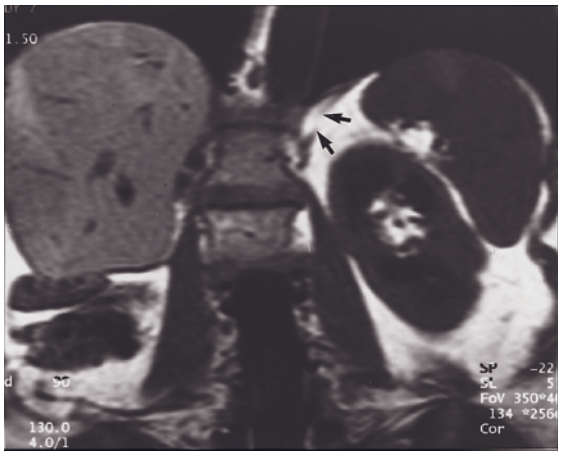

(*a*)

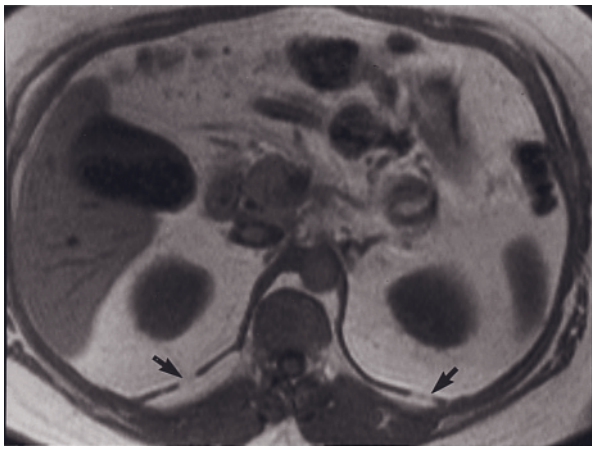

(*b*)

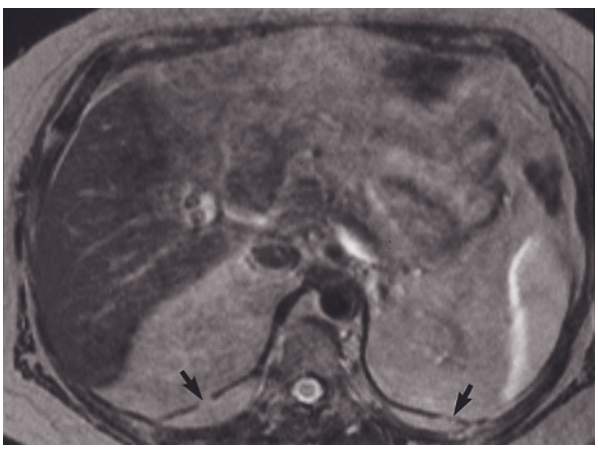

(*c*)

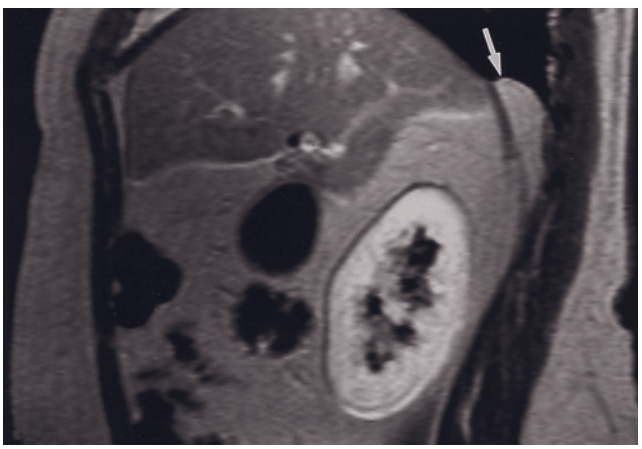

(*d*)

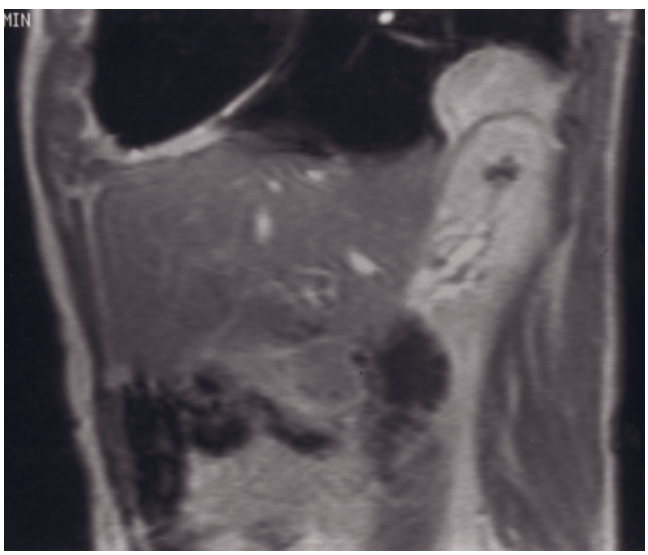

(*e*)

FIG. 7.2 Bochdalek hernia. Coronal breath-hold T1-weighted SGE image (*a*) shows the discontinuity of the posterior diaphragm (arrows). The rent in the diaphragm allows fat and/or viscera to migrate superiorly into the chest. SGE (*b*),T2-weighted spin-echo (*c*), and sagittal 90-s postgadolinium SGE (*d*) images demonstrate rents in the diaphragm bilaterally (arrows, *b*, *c*) and herniation of fat into the pleural space (arrow, *d*). Sagittal-plane gadolinium-enhanced T1-weighted SGE (*e*) image in a third patient shows the herniation of kidney and fat into the thorax.

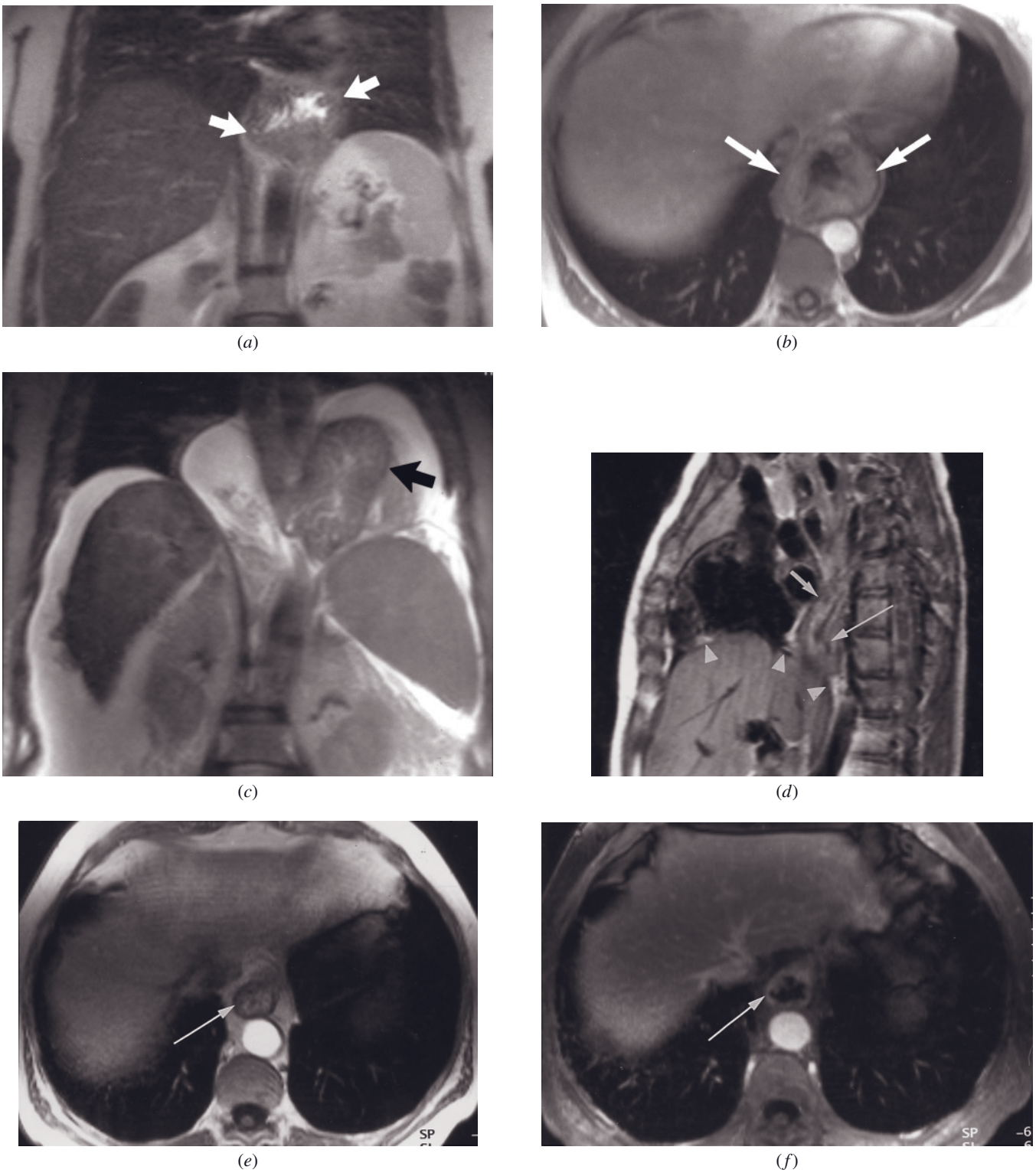

FIG. 7.3 Hiatus hernia and internal hernia. Coronal T2-weighted single-shot echo-train spin-echo (*a*) and transverse immediate postgadolinium SGE (*b*) images. The coronal T2-weighted image demonstrates extension of the stomach (arrows, *a*) above the diaphragm. On the transverse postgadolinium image, the extent of gastric wall enhancement of the herniated part of the stomach (arrows, *b*) is comparable to the remainder of the stomach. Coronal T2-weighted (*c*) image in a second patient. There is a moderately large hiatus hernia (arrow, *c*) in a patient with cirrhosis. Note that stomach, omentum, and ascites protrude through the hernia. Sagittal T1-weighted SGE image (*d*) in a third patient with a history of heartburn. The gastroesophageal junction (long arrow, *d*) is above the diaphragm (arrowheads, *d*), which is diagnostic of a hiatal hernia. Thickening of the esophageal wall (short arrow, *d*) is consistent with reflux esophagitis. Immediate postgadolinium SGE (*e*) and 90-s postgadolinium SGE (*f*) imaging in a fourth patient demonstrate stomach in the lower mediastinum (arrows, *e*, *f*). Gastric rugae are well shown on the gadolinium-enhanced fat-suppressed image (*f*). T2-weighted SSETSE image (*g*) in a fifth patient shows a large hiatal hernia with surrounding herniated fat.

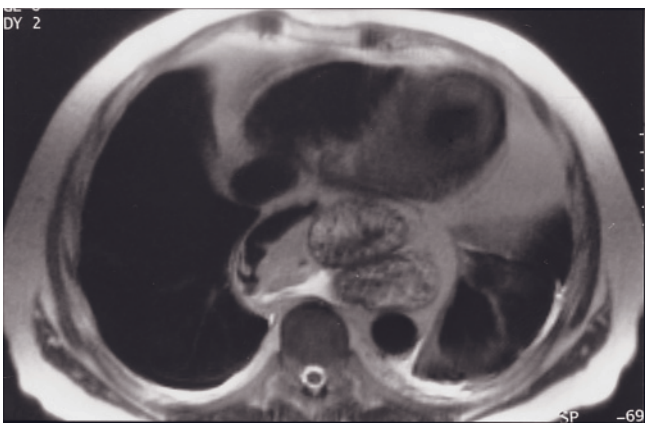

(*g*)

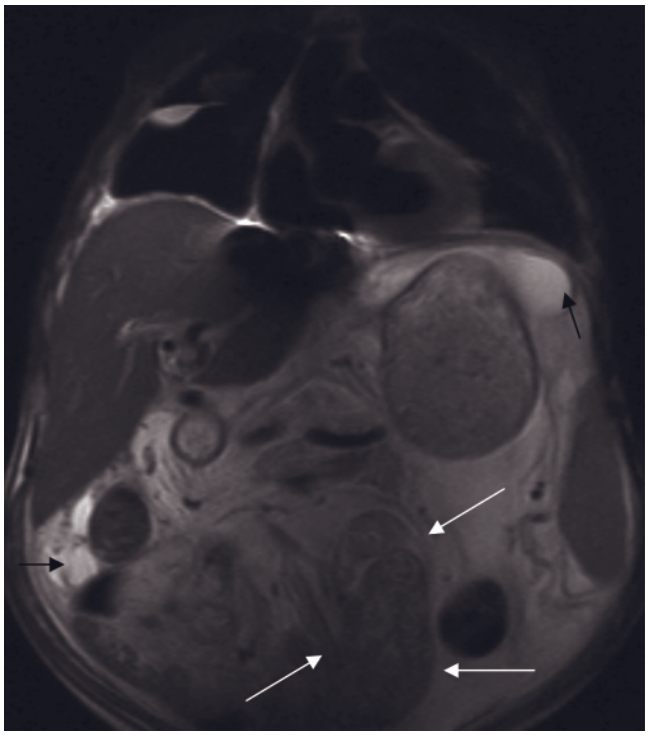

(*h*)

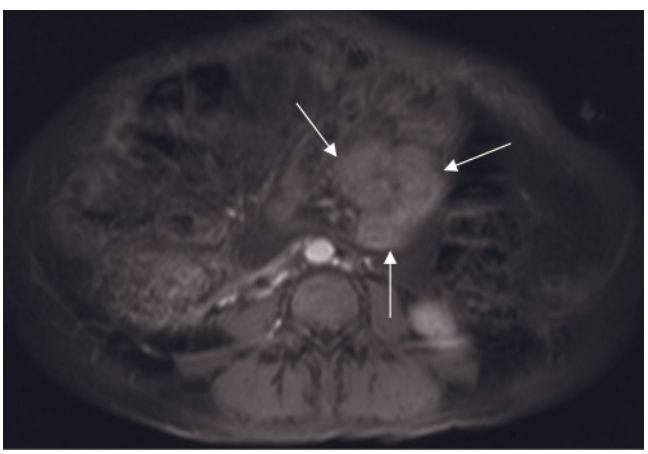

(*i*)

FIG. 7.3 (*Continued*) Coronal T2-weighted single-shot echo-train spin-echo (*h*) and T1-weighted fat-suppressed interstitial-phase postgadolinium 3D-GE (*i*) images in a post-liver transplant patient demonstrate an internal hernia sac (white arrows) in which small intestinal segments are trapped. The stomach is dilated and there is free fluid (black arrows) in the abdomen. Note that right-sided pleural effusion extending into the minor fissure is present as well.

MASS LESIONS

Benign Masses

Cysts

Mesenteric cysts most commonly occur in the small bowel mesentery. Their etiology is not well understood. Although most mesenteric cysts are incidental findings, they can be symptomatic. They may produce chronic or acute pain if complicated by rupture, hemorrhage, torsion, or bowel obstruction. The cysts tend to be singular and thin walled and may contain septae. Different types of mesenteric cysts may be lined by a diversity of cell types including endothelium, mesothelium, and fallopian tube-like epithelium. Their fluid contents may be serous, resembling plasma, or chylous, displaying a white, milky consistency. In complicated cases, blood and/or other proteinaceous fluid predominates [12, 13]. The MRI appearance reflects the cyst contents. Simple cysts will be round, well marginated, low in signal intensity on T1-weighted images, and high in signal intensity on T2-weighted images (fig. 7.7). Cysts complicated by protein or hemorrhage will have higher signal intensity on T1-weighted images and/or heterogeneous signal intensity on T2-weighted images. After contrast administration, the cyst wall and septae, if present, will enhance (see fig. 7.7).

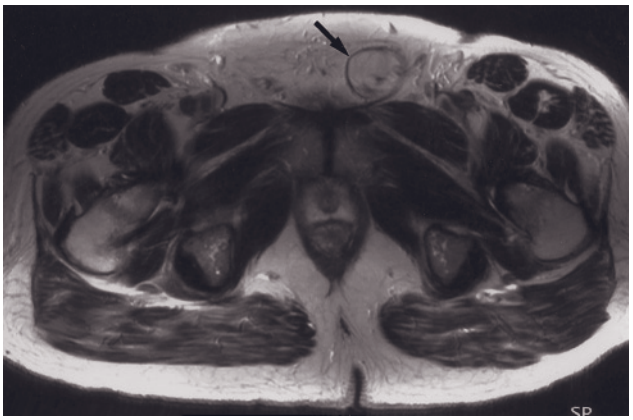

(*a*)

(*b*)

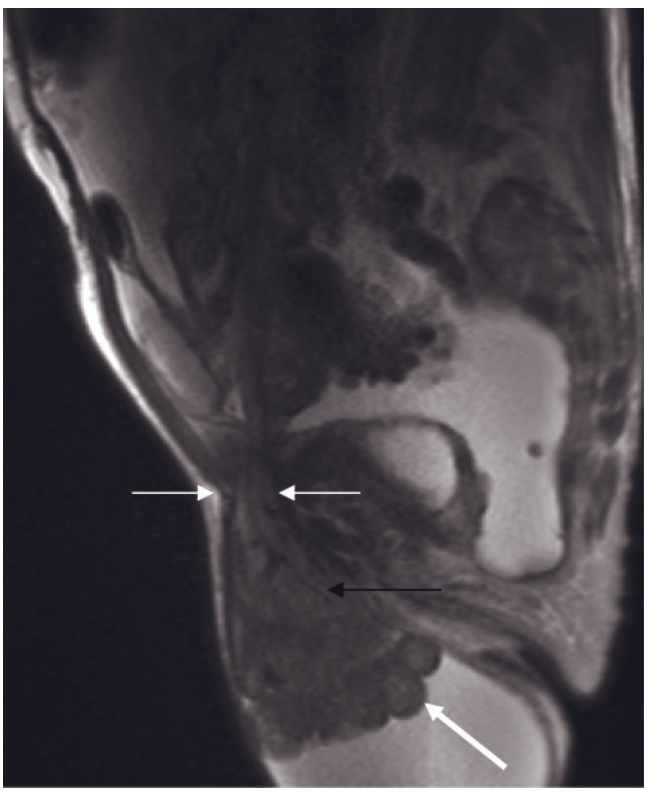

(*c*)

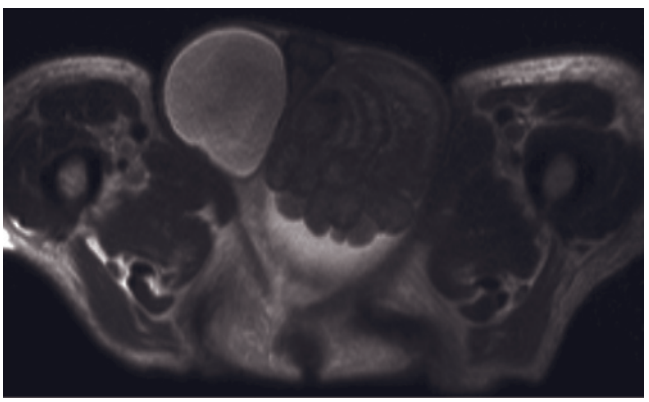

(*d*)

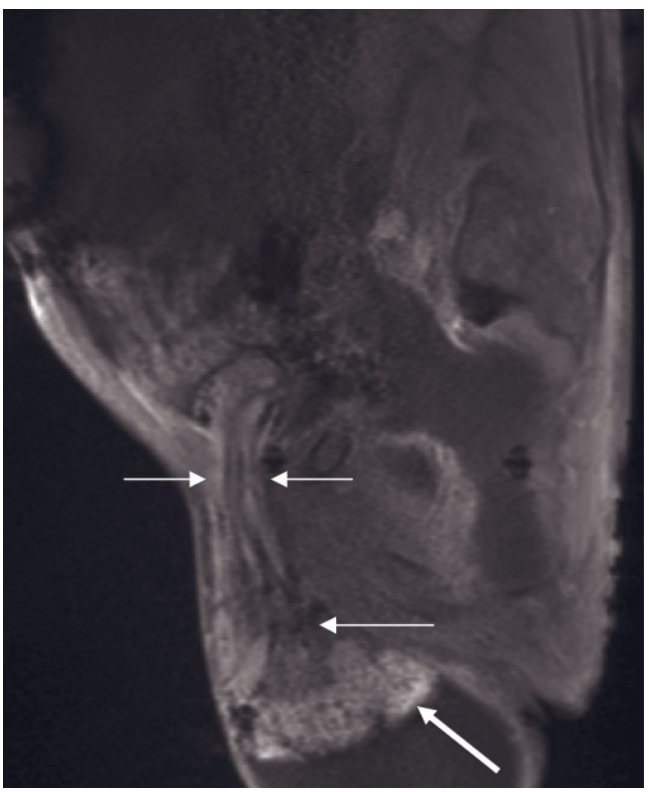

(*e*)

FIG. 7.4 Inguinal hernia. Transverse 512-resolution T2-weighted echo-train spin-echo (*a*) and interstitial-phase gadolinium enhanced fat-suppressed SGE (*b*) images in a patient with inguinal hernia. Expansion of the left inguinal canal (arrow, *a*) is well shown on the T2-weighted image (*a*), which contains high-signal-intensity tissue with an appearance identical to that of surrounding fat. Fat within the expanded inguinal canal diminishes in signal intensity on the fat-suppressed image, and enhancing testicular vessels are well seen (arrows, *b*). Sagittal T2-weighted single-shot echo-train spin-echo (*c*), axial T2-weighted single-shot echo-train spin-echo (*d*), and sagittal T1-weighted postgadolinium interstitial-phase SGE (*e*) images in another patient demonstrate herniation of mesentery (black arrow, *c*) and intestinal segments (white thick arrows, *c*, *e*) through expanded inguinal canal (white thin arrows, *c*, *e*). Free fluid is also detected in the abdominal cavity and scrotum.

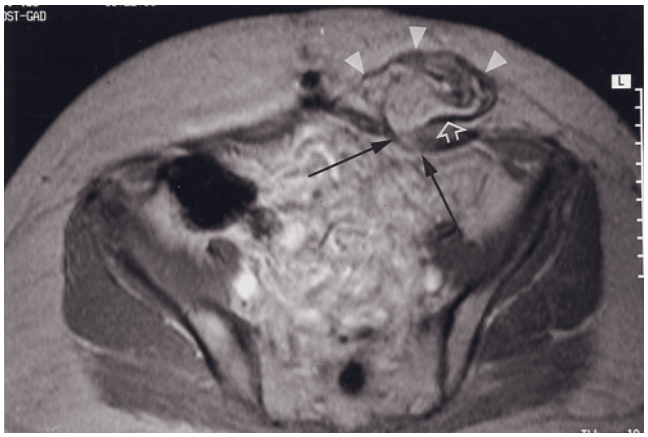

(*a*)

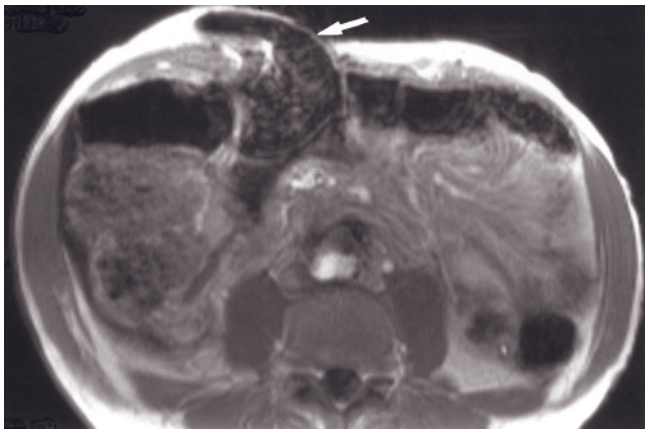

(*b*)

Fig. 7.5 Spigelian hernia. Gadolinium-enhanced T1-weighted SGE image (*a*) in a patient with spigelian hernia. A bowel-containing hernia sac (arrowheads, *a*) protrudes through a defect in the aponeurosis between the transversus and rectus muscles (solid arrows, *a*).The lateral margin of the hernia sac is the intact external oblique muscle and fascia (open arrow, *a*). Transverse immediate postgadolinium T1-weighted SGE image (*b*) in a second patient. A spigelian hernia with protrusion of bowel contents (arrow, *b*) is noted in the right anterior abdomen.

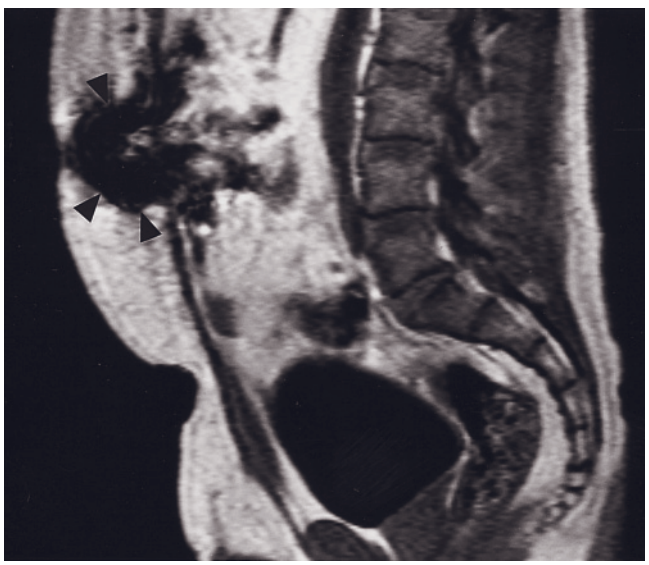

(*a*)

(*b*)

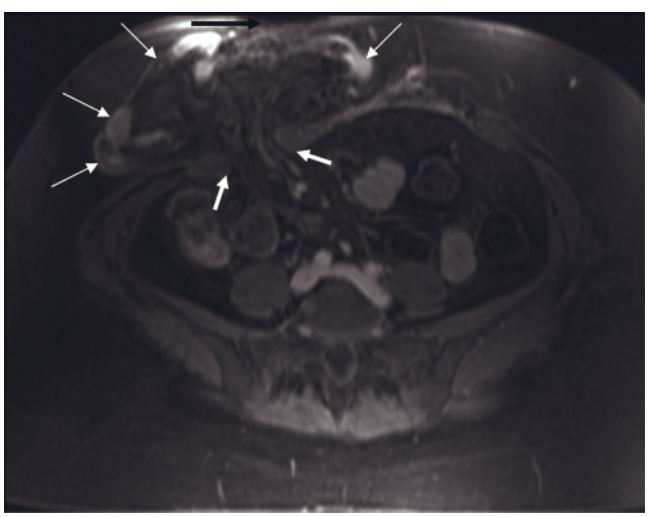

(*c*)

Fig. 7.6 Paraumbilical and incisional hernia. Sagittal T1-weighted SGE image (*a*) shows signal-void air-containing bowel (arrowheads) in the subcutaneous tissues in a patient with a paraumbilical hernia. Coronal T2-weighted single-shot echo-train spin-echo (*b*) and T1-weighted fat-suppressed interstitial-phase postgadolinium 3D-GE (*c*) images in another patient show the herniation of mesentery and intestinal segments (white thin arrows) through the abdominal wall defect (white thick arrows) created for colostomy (black arrow).

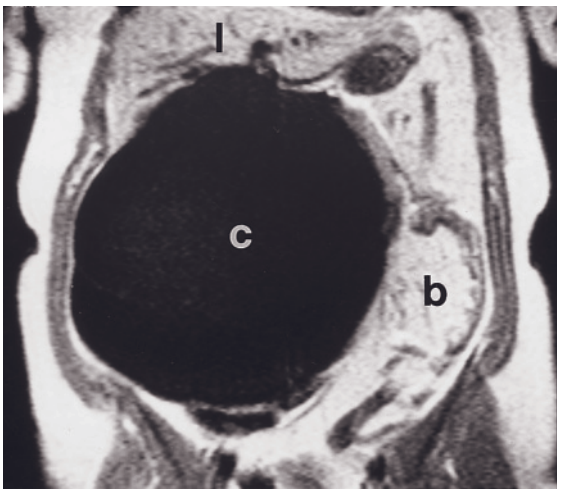

(*a*)

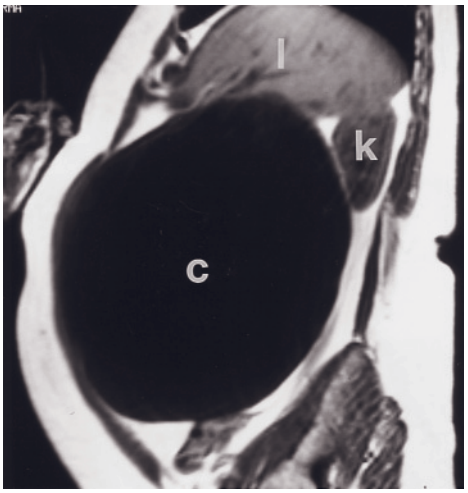

(*b*)

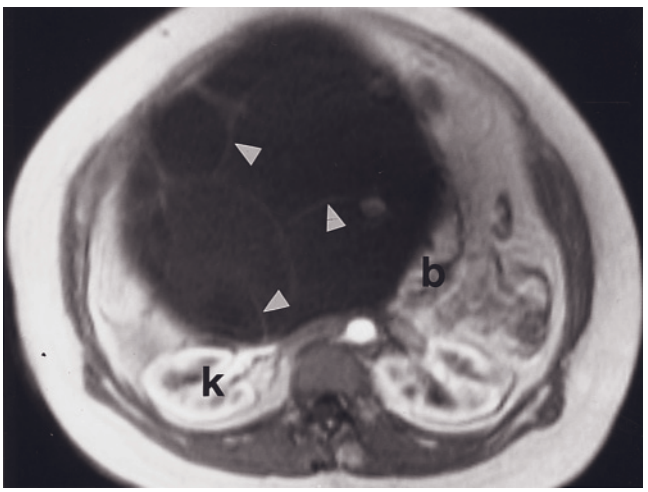

(*c*)

FIG. 7.7 Mesenteric cyst. Coronal T1-weighted magnetization-prepared single-shot gradient echo (*a*), sagittal T1-weighted SGE (*b*), and immediate postgadolinium SGE (*c*) images. A large septated cystic mass (c, *a*, *b*) arising from the small bowel mesentery causes mass effect on the adjacent bowel (b, *a*, *c*), left kidney (k, *b*, *c*), and liver (l, *a*, *b*). Cysts that are low in signal intensity on T1-weighted images (*a*, *b*) and high in signal intensity on T2-weighted images (not shown) are consistent with serous fluid. Immediately after intravenous gadolinium administration (capillary phase), the septae traversing the cyst enhance (arrowheads, *c*). These imaging characteristics are consistent with an uncomplicated mesenteric cyst.

Pseudocysts in the peritoneal cavity lack an epithelial or mesothelial lining. As localized collections of fluid, peritoneal pseudocysts may occur secondary to inflammatory processes such as perforated ulcerative colitis or appendicitis. Pseudocysts may be a rare complication of ventriculo-peritoneal shunt or indwelling peritoneal catheters [14]. In uncomplicated cases, they are low in signal intensity on T1-weighted images and very high in signal intensity on T2-weighted images. Contrast-enhanced T1-weighted images surpass CT imaging and ultrasound by showing that the lesions are encapsulated and contain complex fluid and septations, and by defining the relationship of the pseudocyst to other organs and tissues by direct multiplanar imaging [15]. These findings are more apparent on gadolinium-enhanced fat-suppressed images.

Lipomas and Mesenteric Lipomatosis

Lipomas are benign tumors that rarely involve the peritoneal cavity. Their imaging features parallel those of lipomas elsewhere in the body and are comparable to those of surrounding fat. These lesions are high in signal intensity on non-fat-suppressed T1-weighted images. Because fat signal varies considerably on T2-weighted images depending on the sequence employed, comparison of the signal intensity of the lesion should be made to that of adjacent fat. T1-weighted fat-suppressed SGE images will show loss of the tumor's signal intensity in comparison to non-fat-suppressed images, thereby definitively characterizing their fatty nature. On occasion, excessive proliferation of benign fat may occur within the mesentery, producing a mass effect on adjacent structures simulating malignancy. This benign process may be idiopathic or associated with corticosteroid therapy, Cushing syndrome, or obesity [16, 17].

Cross-sectional imaging is helpful in identifying diffuse or focal prominence of mesenteric fat and excluding the presence of nonfatty soft tissue masses. The signal characteristics of this entity mimic those of benign lipomas [16].

Endometriosis

Endometriosis is defined as the presence of endometrial glands or stroma in abnormal locations outside of the uterus. The three imaging hallmarks of endometriosis are pelvic peritoneal endometrial implants, ovarian endometriomas (endometriotic cysts), and adhesions. The most common peritoneal sites of involvement are, in decreasing order of frequency, the ovaries, uterine ligaments, cul-de-sac, and pelvic peritoneum reflected over the uterus, fallopian tubes, rectosigmoid region, and bladder. Rare extraperitoneal sites include the lungs and the central nervous system [18]. The pathogenesis of endometriosis remains controversial. It likely is related to induction and/or transplantation of endometrial cells into the abdominal cavity [19]. Endometriomas have variable signal intensity but are commonly high in signal intensity on T1-weighted images and heterogeneously high in signal intensity on T2-weighted images [20]. Protein and blood breakdown products tend to demonstrate a gradation of signal intensity on T2-weighted images, which has been termed shading [20]. Noncontrast T1-weighted fat-suppressed imaging is the most sensitive MRI technique for identifying endometriomas (fig. 7.8) [21]. Unfortunately, detecting small peritoneal endometriosis implants remains problematic [22], although contrast-enhanced fat-suppressed imaging has met with mixed results.

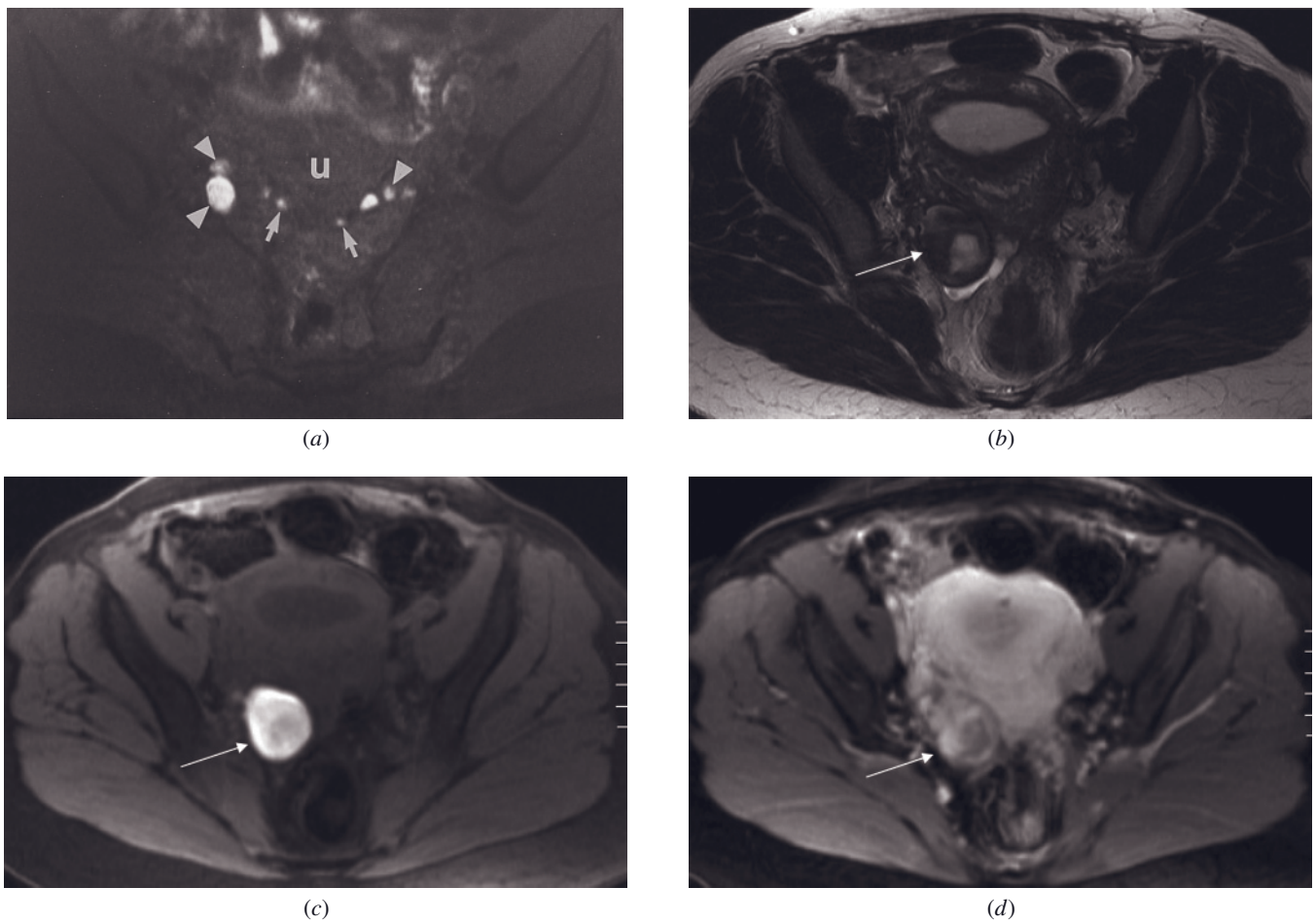

FIG. 7.8 Endometriosis. T1-weighted fat-suppressed spin-echo image demonstrates high-signal-intensity foci of ovarian endometriomas (arrowheads) and smaller endometriosis implants adherent to the uterine serosa (arrows).T1-weighted fat-suppressed spin-echo or SGE or 3D-GE technique is the most sensitive and specific sequence for detecting the blood product-laden deposits of endometriosis. u, Uterus. (Reprinted with permission from Ascher SM, Agrawal R, Bis KG, Brown E et al. Endometriosis: appearance and detection with conventional, fat-suppressed, and contrast-enhanced fat-suppressed spin-echo techniques. *J Magn Reson Imaging* 5: 251–257, 1995.) T2-weighted high-resolution fast spin-echo (*b*), T1-weighted fat-suppressed SGE (*c*), and T1-weighted fat-suppressed interstitial-phase postgadolinium 3D-GE (*d*) images in another patient show a complex structure (arrows) composed of solid-cystic components and subacute stage blood products. The lesion does not demonstrate any enhancement and is located superior to the uterus and adjacent to the right adnexa. The diagnosis is consistent with endometrioma. There are also high-signal-intensity endometrial glands located in the myometrium, suggesting the presence of adenomyosis. Note free fluid located in the endometrial cavity and pelvis.

Desmoid Tumor (Aggressive Fibromatosis)

Desmoid tumor is a rare gastrointestinal mesenchymal tumor whose biological behavior lies in the interface between exuberant fibroproliferations and low-grade fibrosarcoma. Diffuse mesenteric fibromatosis may arise in the postsurgical abdomen or spontaneously [23]. Desmoid tumors are locally invasive lesions that lack the ability to metastasize but tend to recur after incomplete surgical excision [24]. Intra-abdominal desmoids tumors occur in the mesentery or the pelvic wall. These tumors may occur sporadically or in association with Gardner syndrome or familial adenomatous polyposis [25]. Grossly, desmoid tumors vary in size, from 1 to 15 cm in greater diameter. In general, they are unicentric, infiltrative lesions with poorly defined borders (fig. 7.9). Discrete, well-circumscribed tumors also occur (fig. 7.9). Longstanding tumors are low in signal intensity on T1- and T2-weighted images and enhance only minimally after intravenous gadolinium chelate (see fig. 7.9). In the acute phase, tumors may have regions of high signal intensity on T2-weighted images that also show heterogeneous increased enhancement (see fig. 7.9).

Malignant Masses

Diffuse Malignant Mesothelioma

The term mesothelioma is generally used for a malignant tumor derived from mesothelial cells that line serous membranes (e.g., peritoneum, pleura).

Diffuse malignant mesothelioma of the peritoneum is much less common than its counterpart involving the pleura. Heavy exposure to asbestos is an important risk factor. Diffuse malignant peritoneal mesotheliomas have also been described as a late complication of abdominal pelvic therapeutic radiation and after protracted recurrent peritonitis [26]. In the beginning stages of disease, nodules or plaques of tumor may stud the peritoneal surfaces. In time, these lesions become confluent, encasing viscera and mesenteries in a thick mat of tumor. As peritoneal malignant mesothelioma spreads along serosal surfaces, it may invade underlying tissue, especially the wall of the intestine, and adjacent organs such as the liver (fig. 7.10). Peritoneal mesothelioma may be accompanied by intraperitoneal adhesions with dense fibrosis and shortening of the mesentery. Such a desmoplastic response within the mesentery is signified by rigid encasement of vessels and adjacent bowel, creating a stellate appearance on imaging [27–29]. The MR appearance of mesothelioma shows areas of solid tissue with cystic foci within as well as diffuse thickening of the peritoneum alone. Low-grade mesotheliomas will show relatively well-defined margins (fig. 7.10). High-grade mesotheliomas show a more ill-defined infiltrative growth pattern (fig. 7.10). A distinctive feature of mesotheliomas may be the cystic foci interspaced through solid tumor, which may be unusual in many other forms of peritoneal disease (with the exception of ovarian cancer). Although coexistent pleural diseases may be present to aid in the correct diagnosis, we have generally observed peritoneal disease without pleural disease.

Primary Peritoneal Carcinoma

Primary peritoneal carcinoma (PPC) is a rare tumor histologically identical to epithelial ovarian carcinoma (EOC); it is differentiated from EOC based on the extent of gross ovarian involvement and microscopic invasion of the cortex [30]. PPC is a tumor that is often widely distributed over the peritoneal surfaces and is histopathologically indistinguishable from ovarian papillary serous carcinoma. However, in PPC, the ovaries may no longer be present (e.g., after ovariectomy), may appear normal, or may show only minimal surface involvement by tumor. One study evaluated the CT and MR imaging findings of PPC at initial presentation and recurrent disease [30]. The results showed that the most frequent findings were ascites, peritoneal thickening and enhancement, focal or diffuse peritoneal nodules, and bulky mass lesions [30]. Moreover, recurrent disease demonstrated similar findings compared to initial presentation. Nevertheless, these imaging features are nonspecific, and similar appearances are observed for metastatic peritoneal carcinomatosis, peritoneal tuberculosis, lymphomatosis, and malignant mesothelioma [30] (fig. 7.11).

Metastases

Metastatic tumors that involve the peritoneum most commonly arise from the female genital tract, particularly the ovary, followed by colon, stomach, and pancreas [31, 32]. The gross appearance of metastases ranges from single, well-defined nodules to diffuse peritoneal thickening. Peritoneal metastases occasionally appear as large cystic masses with multiple septations and layering of low-signal proteinaceous material in a multitier fashion along the septations. This may be a distinctive appearance for cystic metastasis. Septations are best seen on T2-weighted single-shot echo-train spin-echo images.

Dissemination occurs by several routes: contiguous spread, intraperitoneal seeding, hematogenous spread, and lymphatic dissemination [5, 33].

Contiguous Spread. Primary tumors that are highly invasive may involve adjacent viscera by contiguous extension [31, 34, 35]. This process of direct extension is facilitated by the ligaments that interconnect the various organs (see Chapter 6, *Gastrointestinal Tract,* figs. 6.107–6.119).

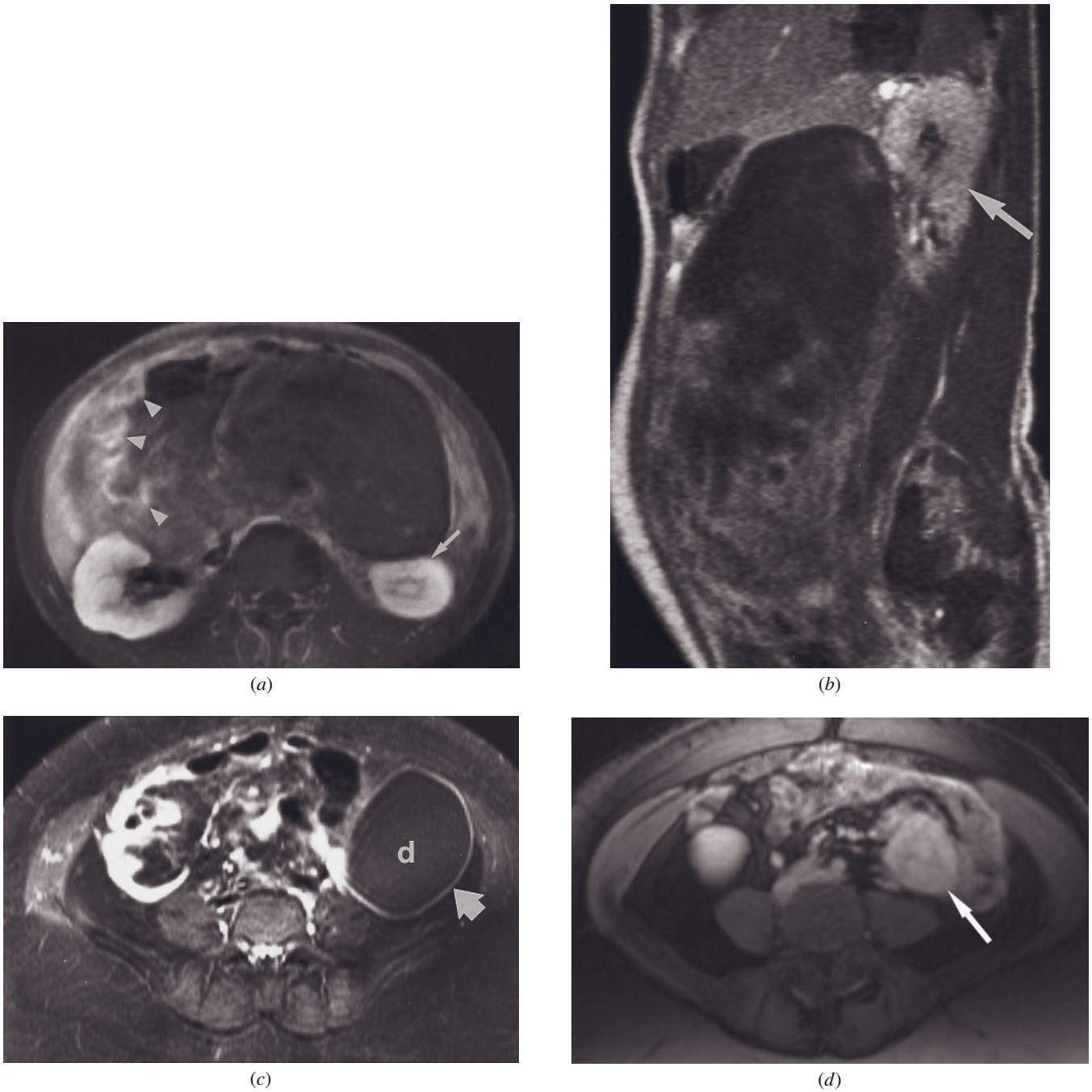

FIG. 7.9 Desmoid tumor. Transverse 90-s second postgadolinium T1-weighted fat-suppressed spin-echo (*a*) and sagittal 10-min postgadolinium SGE (*b*) images in a woman with Gardner syndrome and intra-abdominal desmoid tumor. The right aspect of the mass enhances (arrowheads, *a*) more than the left aspect. The greater enhancement on the right reflects active disease. This large desmoid produces a mass effect on the kidneys (arrows, *a*, *b*). Imaging in the sagittal plane helps define the craniocaudal extent of the tumor. Transverse gadolinium-enhanced T1-weighted fat-suppressed spin-echo image (*c*) in a second woman with Gardner syndrome and intra-abdominal desmoid tumor. The desmoid tumor (d, *c*) exhibits minimal enhancement, confirming its fibrous nature. Thin mural enhancement is apparent (arrow, *c*). On the basis of this image alone, the tumor could be mistaken for a cyst. T2-weighted images distinguish the two: a desmoid tumor remains low in signal intensity, whereas a cyst is high signal intensity. Transverse interstitial-phase postgadolinium T1-weighted fat-suppressed SGE image (*d*) in a third patient with intra-abdominal desmoid tumor demonstrates a moderately enhancing mass (arrow, *d*). Coronal T1-weighted SGE (*e*), axial T1-weighted

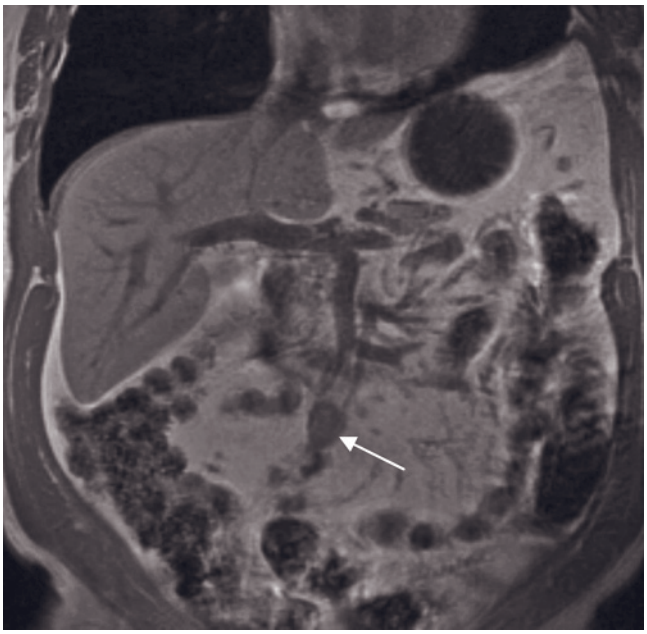

(*e*)

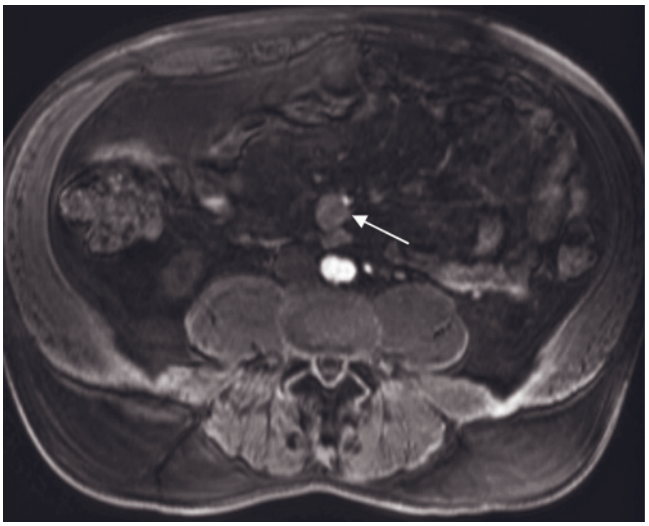

(*f*)

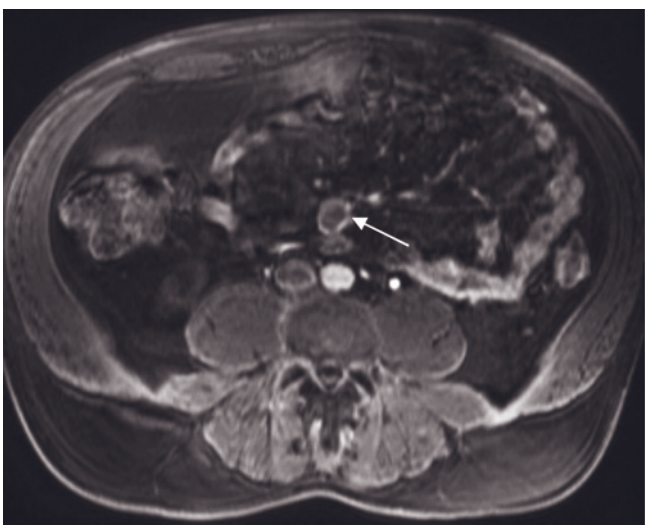

(*g*)

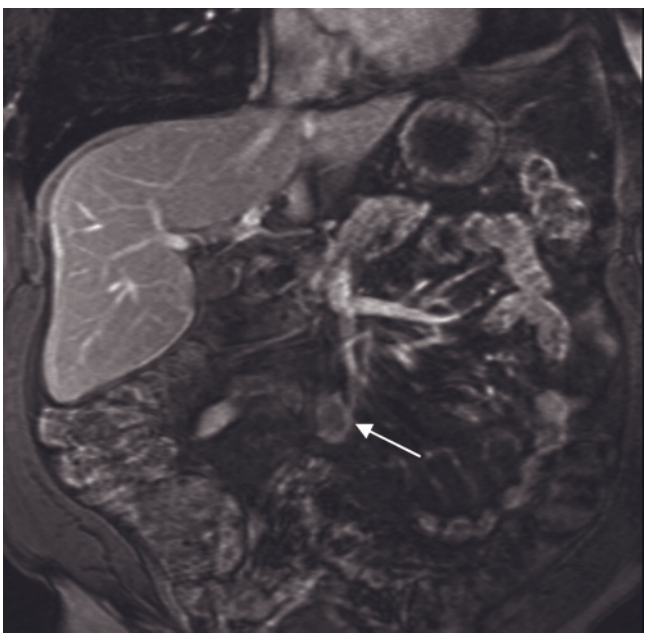

(*h*)

FIG. 7.9 (*Continued*) fat-suppressed 3D-GE (*f*), axial T1-weighted fat-suppressed immediate postgadolinium 3D-GE (*g*), and coronal T1-weighted fat-suppressed interstitial-phase postgadolinium 3D-GE (*h*) images in another patient demonstrate a small desmoid tumor (arrow) located in the mesentery. The tumor shows minimal but predominantly peripheral enhancement.

Intraperitoneal Seeding. Seeding of body cavities and surfaces may occur whenever a malignant tumor invades a natural cavity and gains entrance into an "open field." The peritoneal cavity is most frequently involved in this pathway of spread [36].

Peritoneal metastasis may appear as platelike, small nodular, or large nodular disease, or advanced disease as a combination of these patterns. MR is particularly well suited and superior to CT at showing platelike disease because tumor enhances moderately intensely and is well shown on gadolinium-enhanced T1-weighted fat-suppressed images. The small nodular pattern may be more difficult to see on MRI than on CT, because of the lack of oral contrast on MRI compared to CT, and

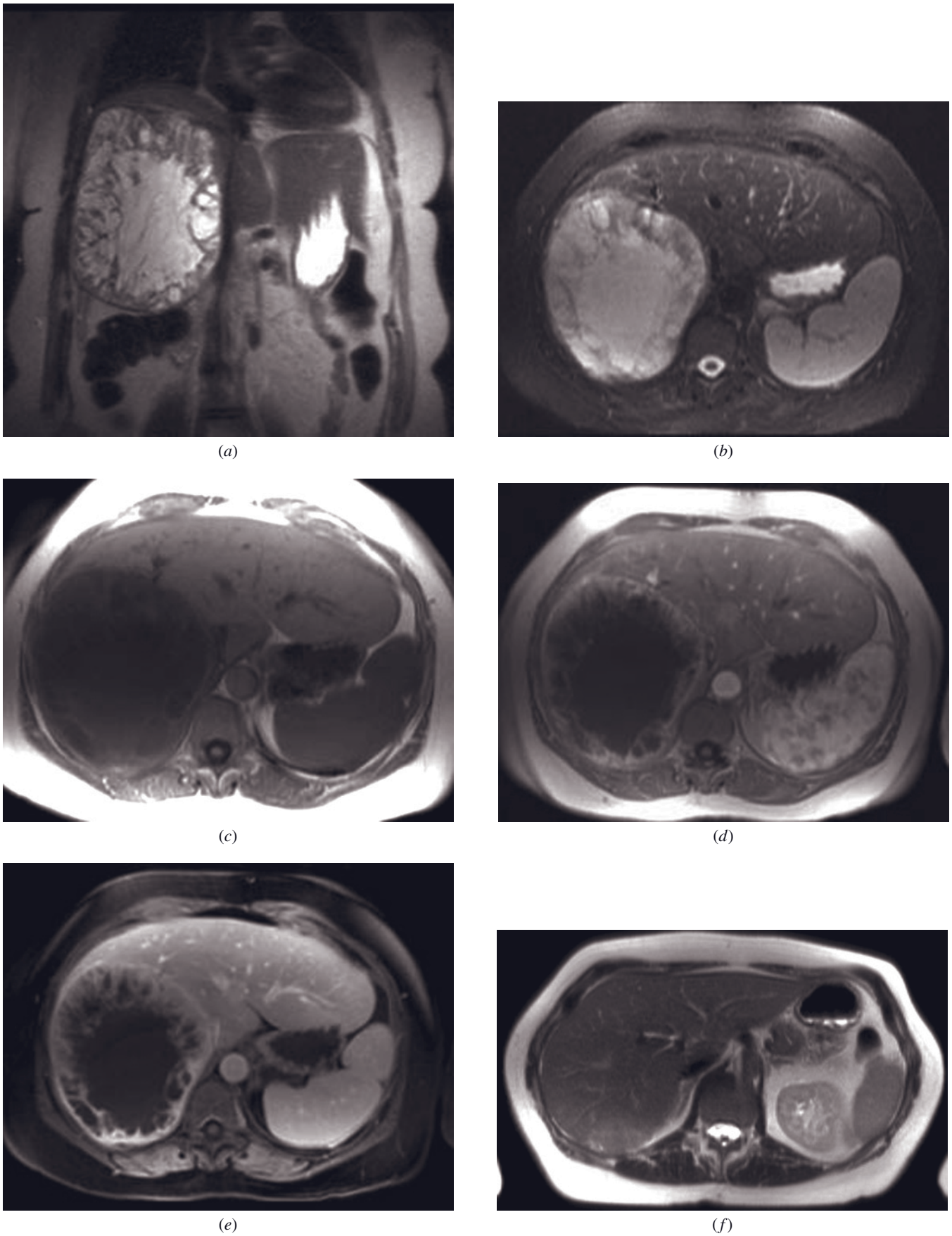

FIG. 7.10 Malignant mesothelioma of the peritoneum. Coronal T2-weighted SS-ETSE (*a*), transverse T2-weighted fat-suppressed SS-ETSE (*b*), transverse precontrast T1-weighted SGE (*c*), and immediate (*d*) and 90-s (*e*) gadolinium-enhanced T1-weighted fat-suppressed SGE images demonstrate a heterogeneous mass that arises from the peritoneal layer along the liver capsule and has well-defined margins and septations. Lack of central enhancement of the lesion is appreciated. These imaging features are consistent with a low-grade malignant mesothelioma. The location along the liver capsule simulates the appearance of a hepatic-origin lesion. T2-weighted SS-ETSE (*f*), immediate postgadolinium T1-weighted SGE (*g*), and T1-weighted interstitial-phase

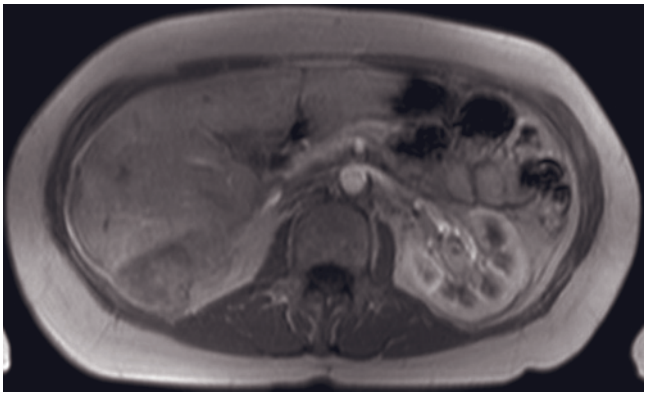

(*g*)

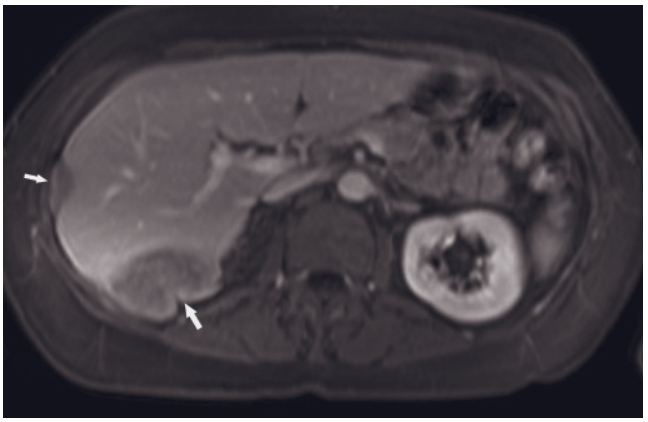

(*h*)

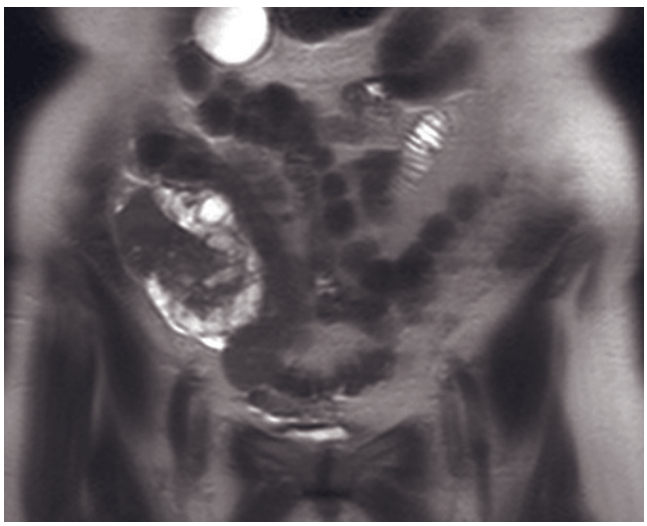

(*i*)

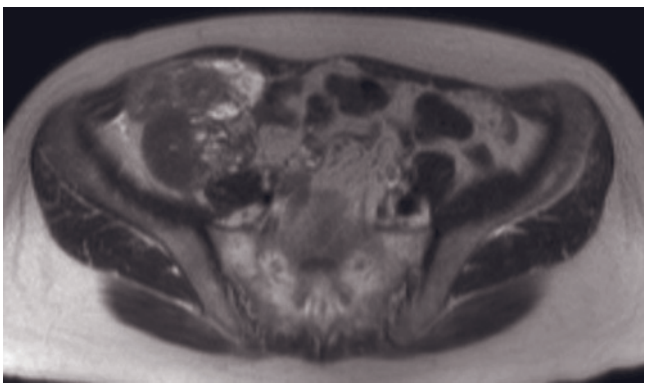

(*j*)

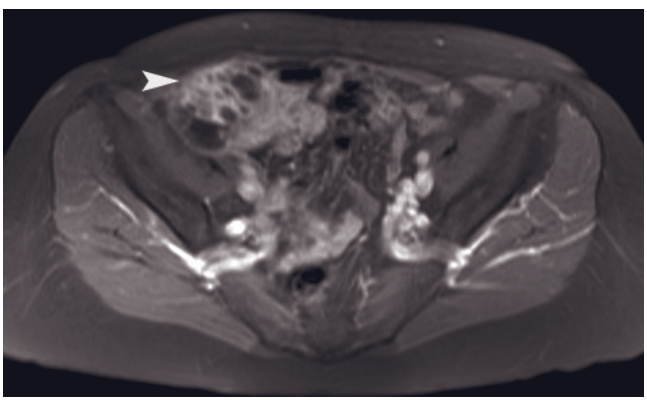

(*k*)

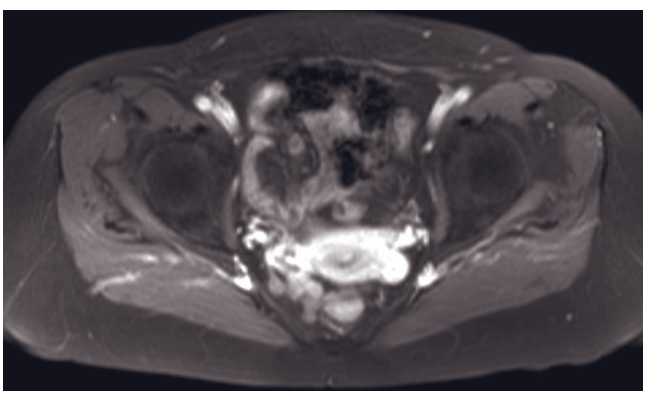

(*l*)

FIG. 7.10 (*Continued*) fat-suppressed SGE (*h*) images of the abdomen and coronal T2-weighted SS-ETSE (*i*), transverse T2-weighted SS-ETSE (*j*), and T1-weighted postgadolinium fat-suppressed SGE (*k*, *l*) images of the pelvis in a patient with diffuse malignant mesothelioma demonstrate extensive peritoneal involvement. Note also the presence of liver metastases (arrows, *h*). A complex cystic mass is appreciated in the pelvis (arrowhead, *k*). These imaging features are consistent with high-grade primary

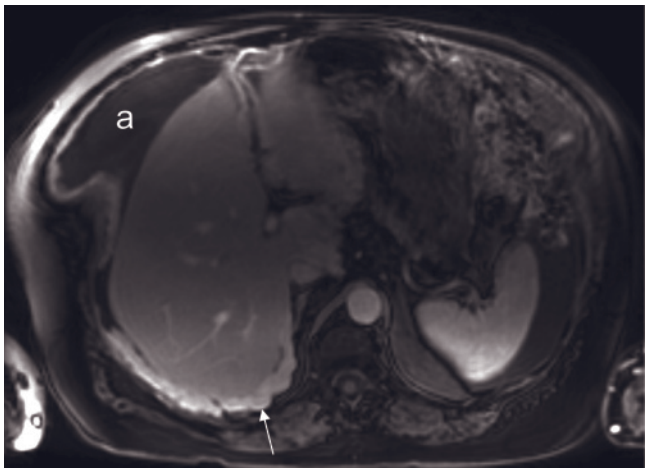

(*m*)

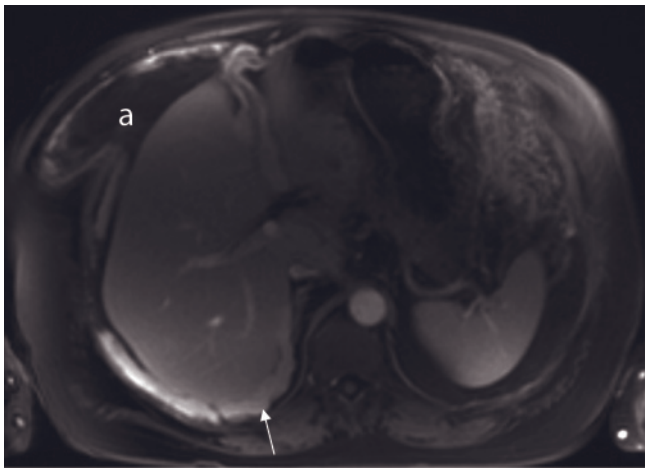

(*n*)

FIG. 7.10 (*Continued*) peritoneal mesothelioma. T1-weighted fat-saturated interstitial-phase postgadolinium 3D-GE (*m*) and T1-weighted interstitial-phase postgadolinium water-excitation magnetization-prepared rapid gradient-echo (*n*) images at 3.0 T show prominent peritoneal thickening (arrows) and intense peritoneal enhancement (arrows) and ascites (a) in another patient. The findings are consistent with diffuse malignant peritoneal mesothelioma.

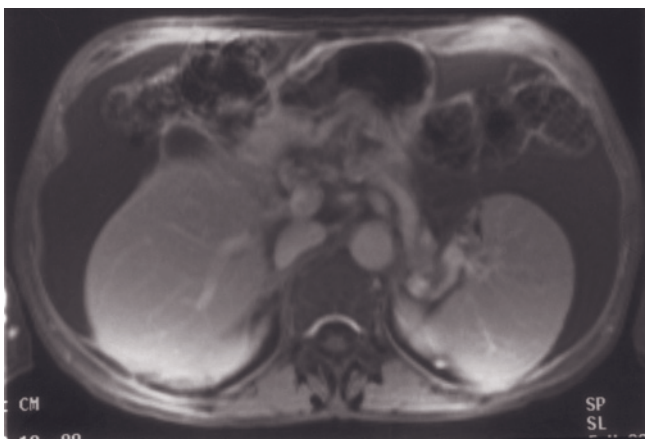

(*a*)

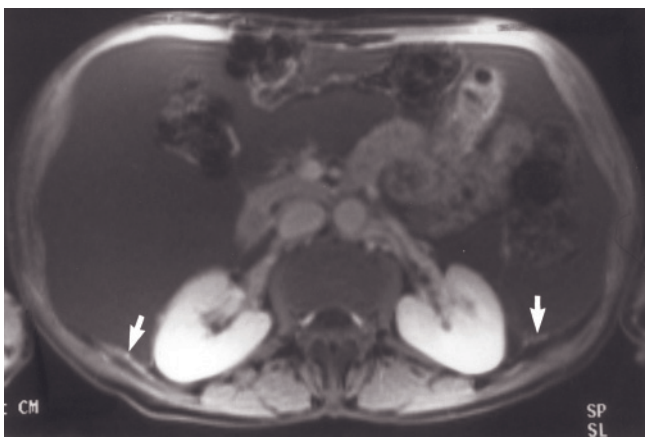

(*b*)

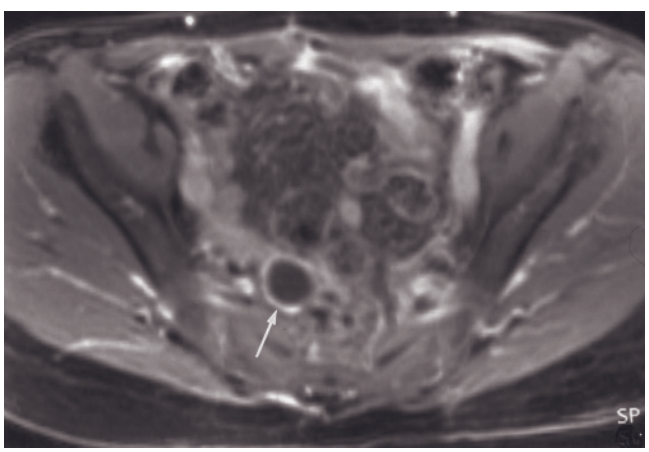

(*c*)

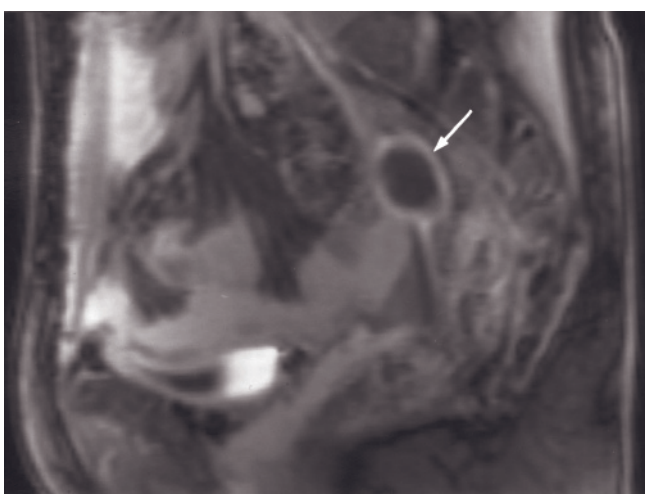

(*d*)

FIG. 7.11 Primary peritoneal papillary carcinoma of the peritoneum. Transverse 90-s gadolinium-enhanced fat-suppressed SGE (*a*) of the abdomen and 5- to 6-min transverse (*b*, *c*) and sagittal (*d*) gadolinium-enhanced fat-suppressed SGE images of the pelvis. Thin-volume diffuse peritoneal thickening with layering in the paracolic gutters (arrows, *b*) is noted in the abdomen. In the pelvis, a 2-cm cystic structure (arrow, *c*) is noted in the right pelvis. The sagittal projection confirms that the lesion is a cystic implant (arrow, *d*) by its oval configuration in both planes, unlike bowel, which would appear tubular in one of the projections.

the large nodular pattern is comparably shown on MRI and CT. Figure 7.12 demonstrates examples of the patterns of peritoneal metastases. The enhancement of peritoneal disease on MR is superior to that on CT, allowing for better detection, especially of thin-volume tumor [37, 38]. The most commonly affected areas are the rectovesical/rectovaginal fossa, sigmoid mesocolon, right paracolic gutter, and the small bowel mesentery near the ileocecal valve [5, 37]. Peritoneal seeding is particularly characteristic of ovarian carcinoma, when peritoneal surfaces become coated with a heavy glaze of tumor. Other malignancies that commonly spread in this manner include colon, stomach, and pancreatic carcinoma. Gadolinium-enhanced T1-weighted fat-suppressed imaging is essential for demonstrating intraperitoneal seeding. Both patterns of peritoneal involvement, whether focal metastatic nodules or confluent thickening of peritoneal surfaces, stand out as high signal against the low signal intensity of the suppressed intraperitoneal fat (figs. 7.13–7.26) [31, 38].

Breathing-independent T2-weighted single-shot echo-train spin-echo imaging is a useful complementary sequence to gadolinium-enhanced T1-weighted fat-suppressed sequence for detecting peritoneal metastases (figs. 7.21 and 7.22). In a large series, gadolinium-enhanced T1-weighted fat-suppressed SGE was shown to be superior to spiral CT for the detection of peritoneal disease [39], confirming findings in earlier studies [38, 40]. Orally and/or rectally administered contrast may improve delineation of bowel [41, 42], with water or enteric CT contrast having been used successfully. Intraluminal air should not be used at 1.5 T, because

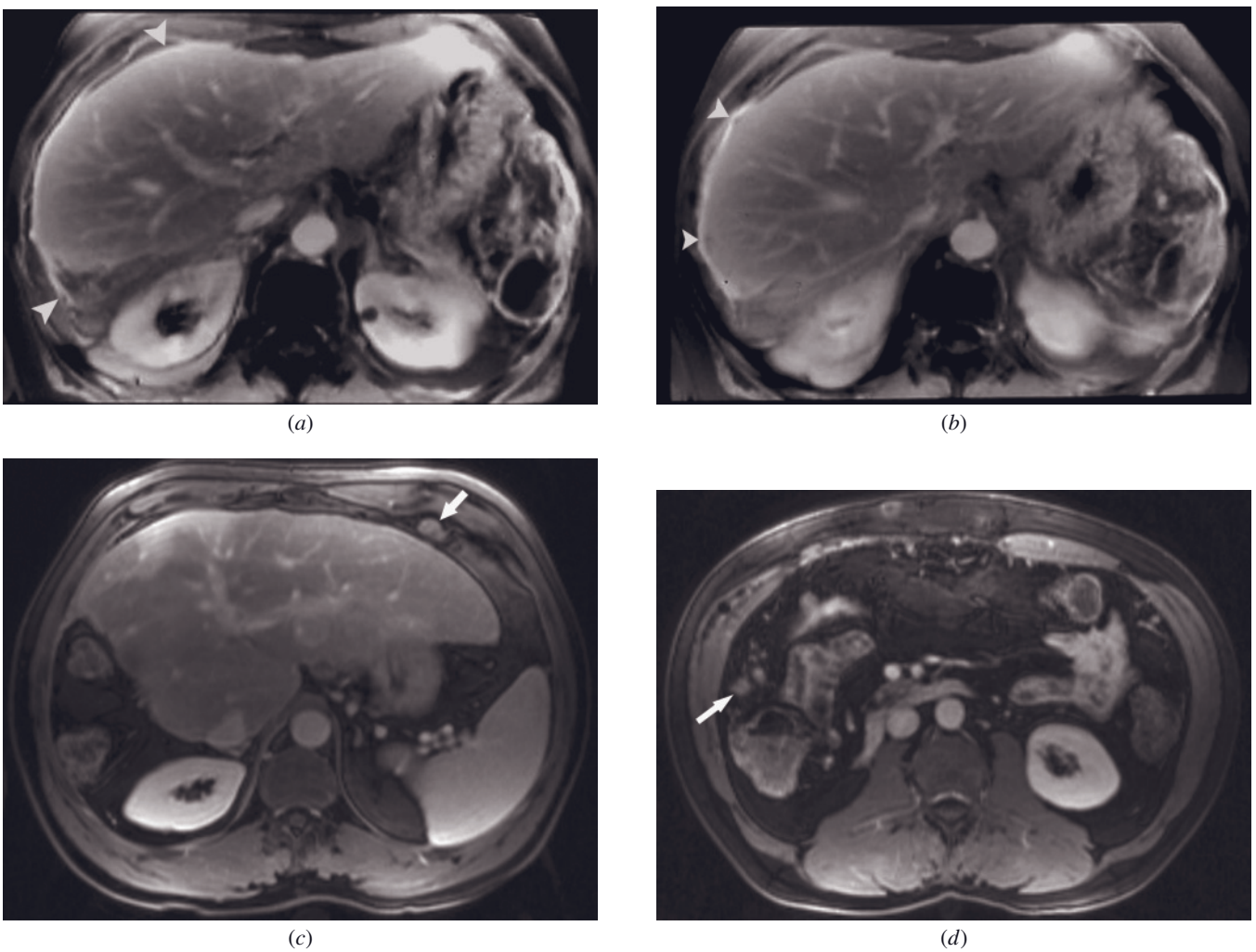

FIG. 7.12 Peritoneal seeding: thin platelike, small nodular, large nodular patterns and advanced disease. Fat-suppressed T1-weighted postgadolinium SGE images (*a*, *b*) in a patient with ovarian cancer demonstrate platelike peritoneal metastasis (arrowheads, *a*, *b*). Fat-suppressed T1-weighted postgadolinium SGE images (*c*, *d*, *e*) in a second patient with ovarian cancer demonstrates small nodular pattern of peritoneal seeding (arrows, *c*, *d*, *e*). T2-weighted fat-suppressed SS-ETSE (*f*), T1-weighted

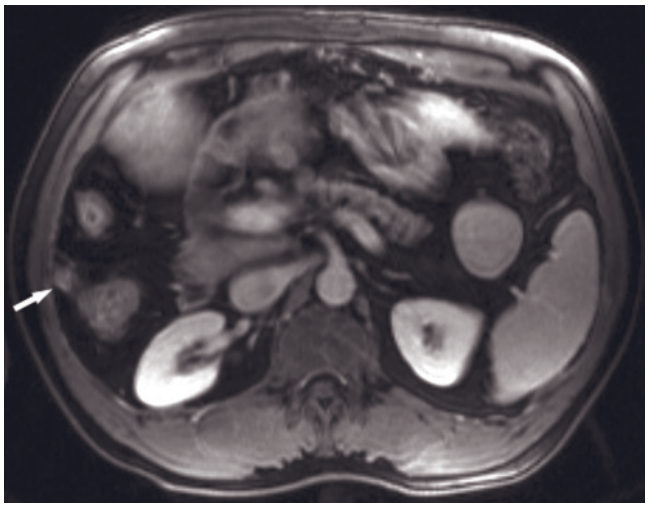

(*e*)

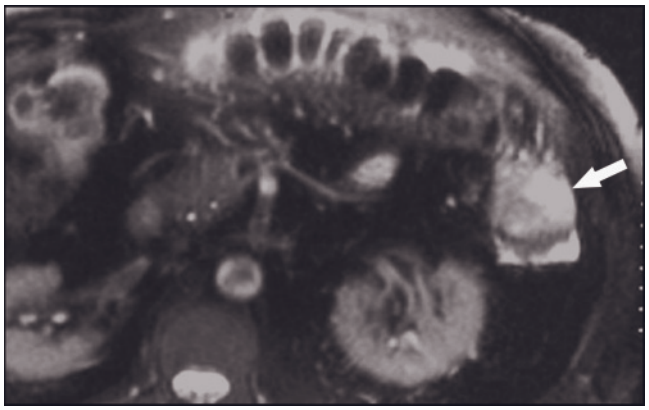

(*f*)

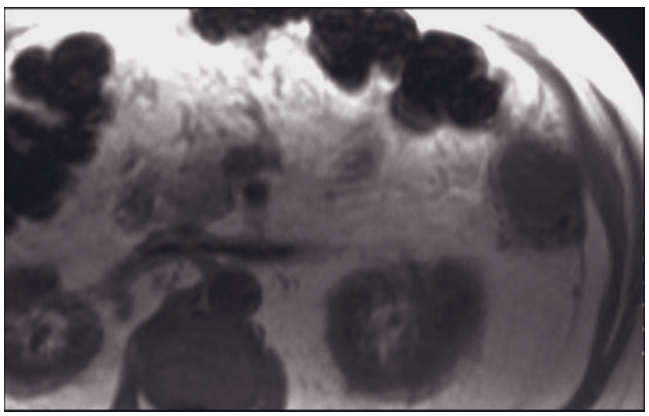

(*g*)

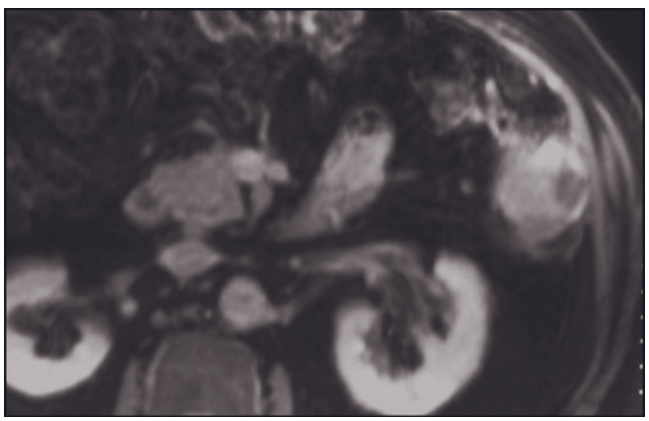

(*h*)

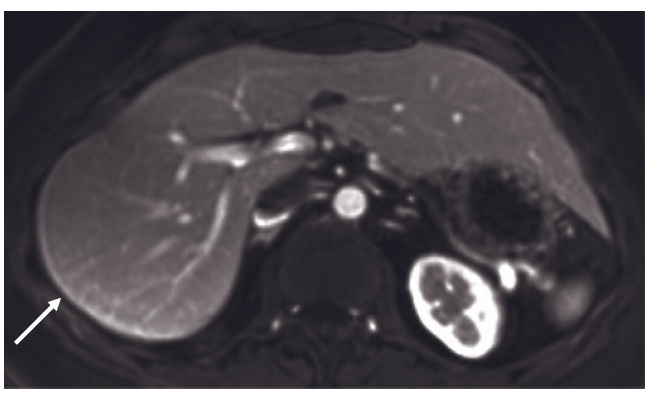

(*i*)

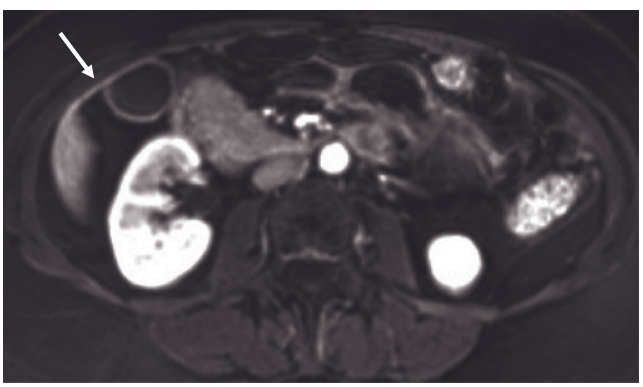

(*j*)

FIG. 7.12 (*Continued*) SGE (*g*), and fat-suppressed T1-weighted postgadolinium SGE (*h*) images in a third patient with ovarian cancer demonstrate large nodules consistent with peritoneal seeding (arrow, *f*). T1-weighted fat-suppressed interstitial phase postgadolinium axial (*i*, *j*, *k*) and sagittal (*l*) 3D-GE images at 3.0 T demonstrate thin platelike (white arrows) and small nodular (black arrow) peritoneal metastases in another patient. T2-weighted single-shot echo-train spin-echo (*m*) and T1-weighted fat-suppressed

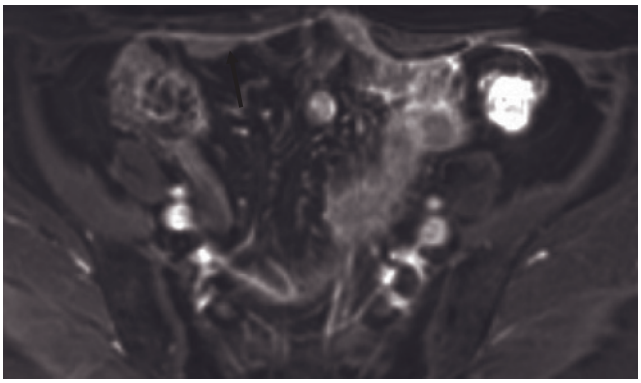

(*k*)

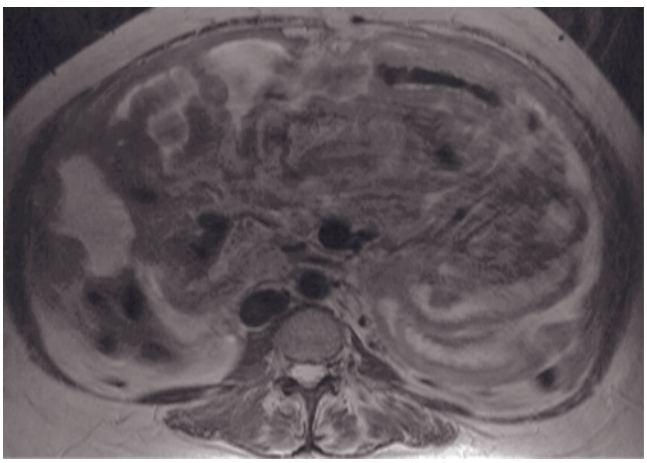

(*m*)

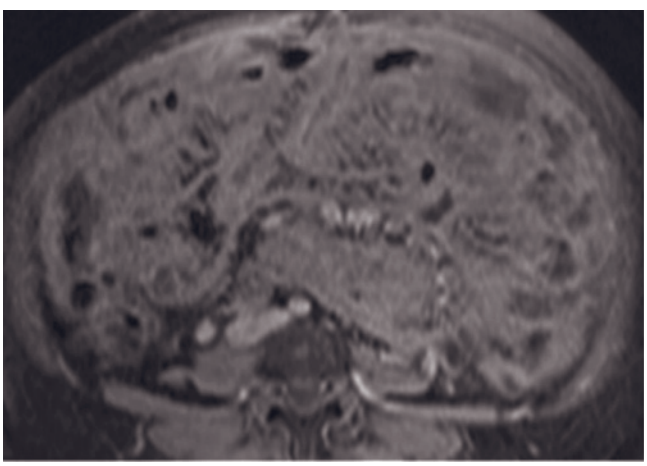

(*n*)

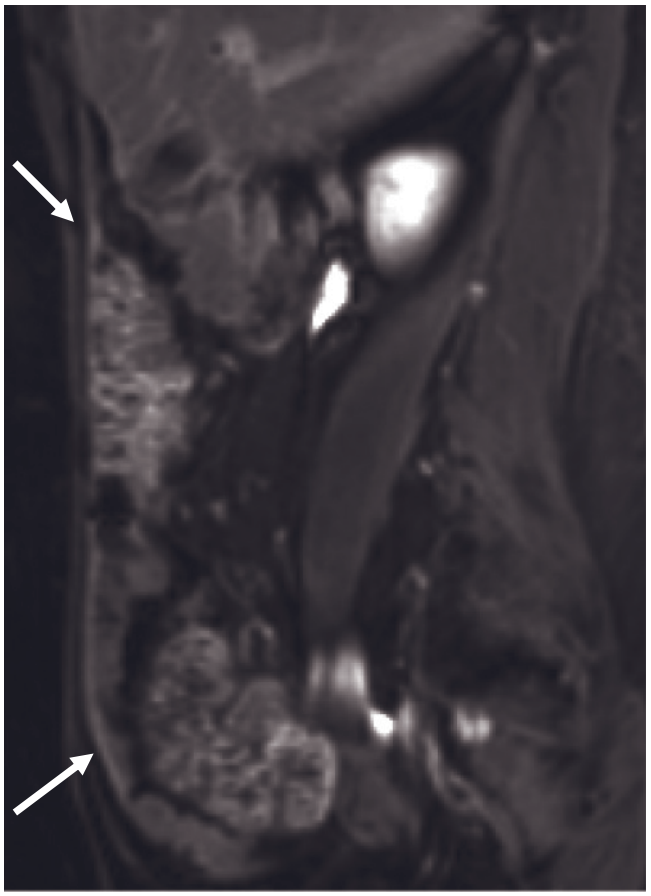

(*l*)

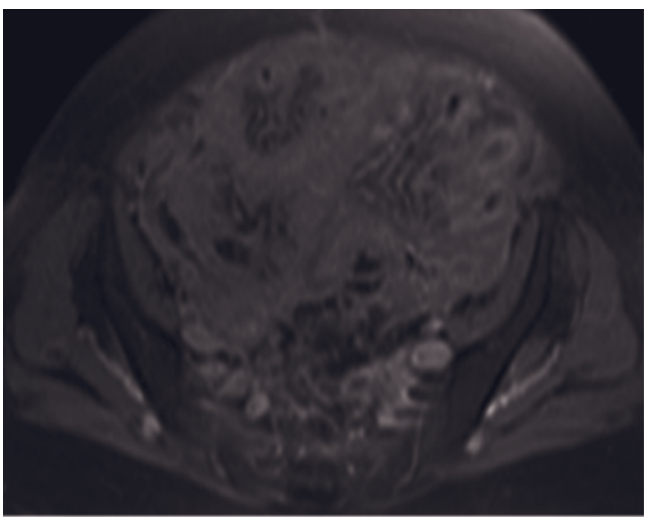

(*o*)

FIG. 7.12 (*Continued*) interstitial-phase postgadolinium 3D-GE (*n*, *o*) images in another patient show advanced peritoneal metastases that are characterized by prominent thickening and intense enhancement of peritoneal surfaces along the abdominal wall and intestines, and mesentery.

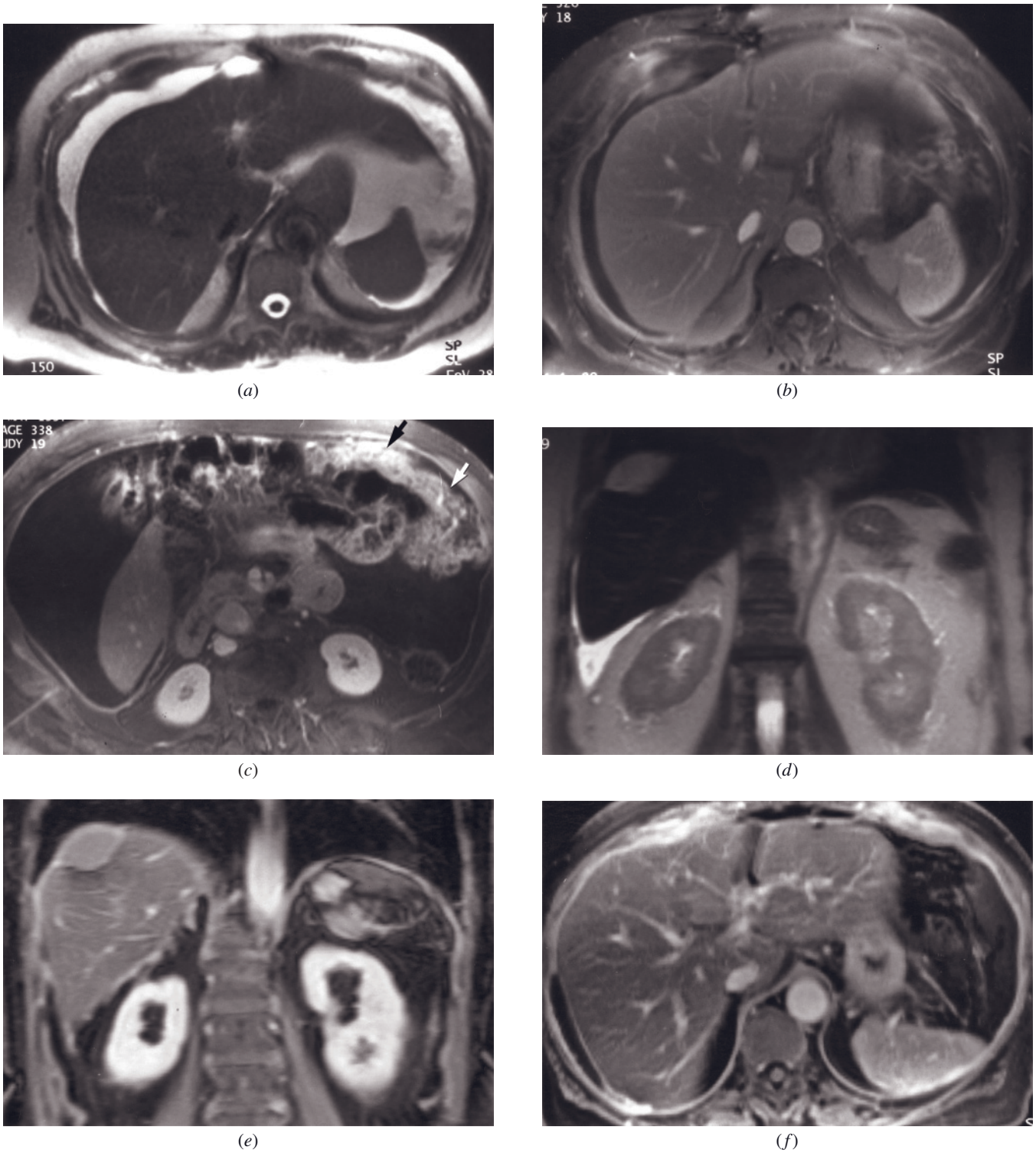

FIG. 7.13 Peritoneal metastases from ovarian cancer. T2-weighted SS-ETSE (*a*) and interstitial-phase gadolinium-enhanced fat-suppressed SGE (*b*, *c*) images in a patient with a history of ovarian cancer. There is a large volume of ascites associated with diffuse thickening and enhancement of peritoneal surfaces on interstitial-phase gadolinium-enhanced images. Omental metastases (arrows, *c*) are also appreciated. Coronal T2-weighted SS-ETSE (*d*), coronal (*e*), and transverse (*f*) interstitial-phase gadolinium-enhanced fat-suppressed SGE images in a second patient. Diffuse and irregular thickening and enhancement of the peritoneum is observed throughout the abdomen. There is nodular thickening and enhancement of the liver capsule and the diaphragm. The coronal projection facilitates detection of diaphragm-based metastases. A large subcapsular metastasis is present in the dome of the liver.

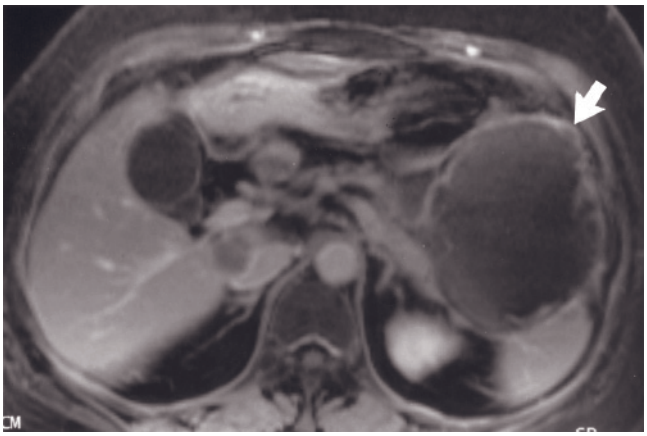

(*a*)

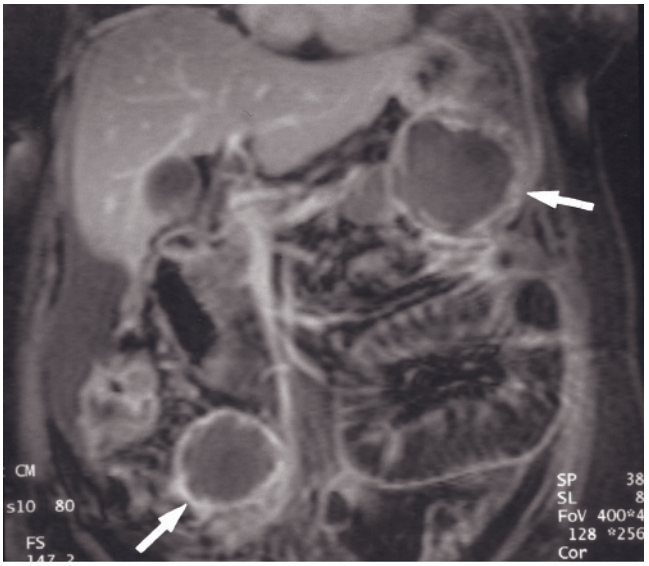

(*b*)

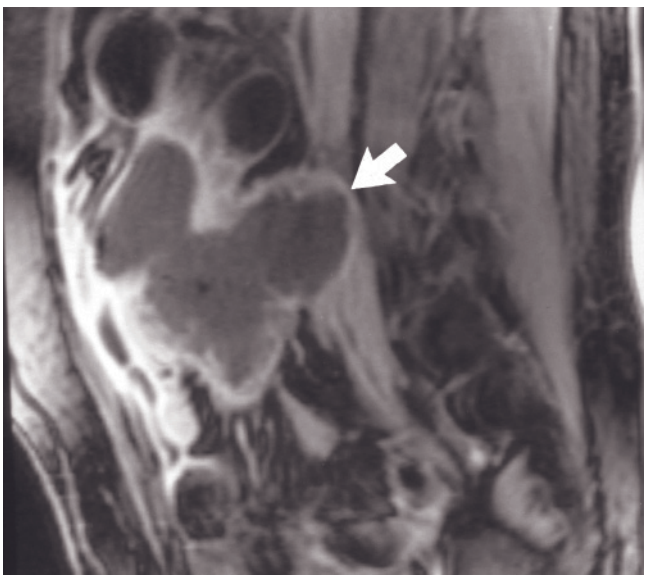

(*c*)

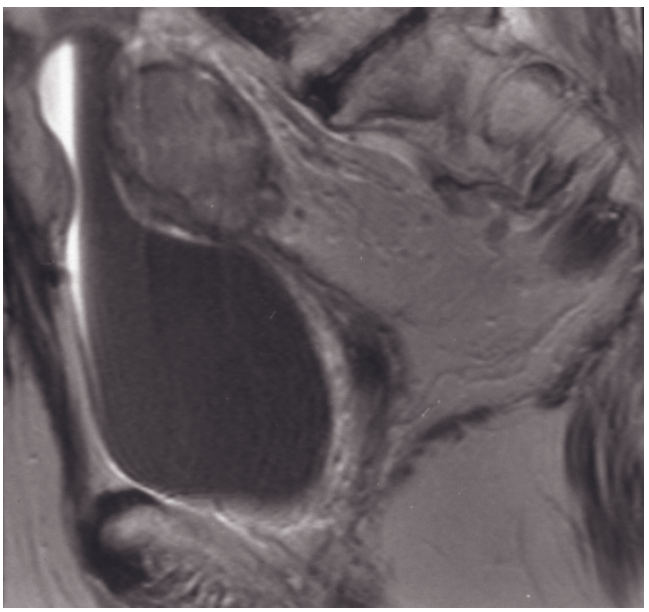

(*d*)

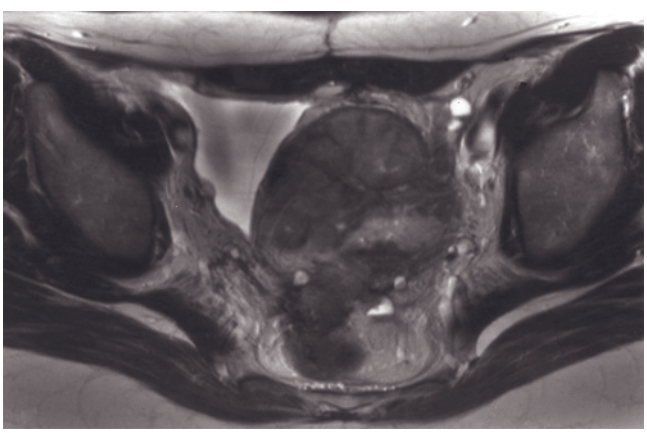

(*e*)

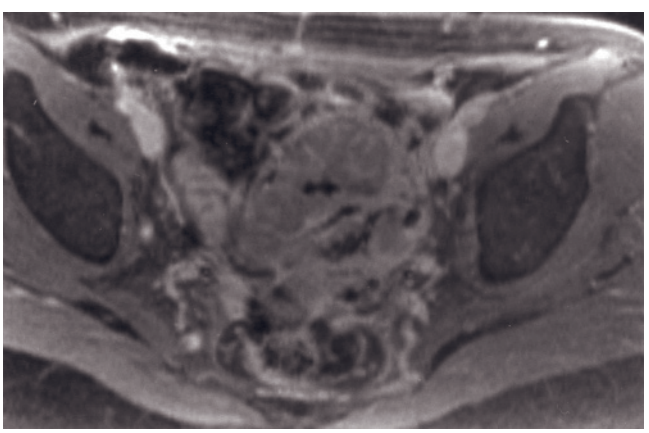

(*f*)

FIG. 7.14 Peritoneal metastases from ovarian cancer. Transverse (*a*), coronal (*b*), and sagittal (*c*) interstitial-phase gadolinium-enhanced fat-suppressed SGE images. There is diffuse enhancement of the peritoneal and serosal surfaces, with multiple peritoneal and serosal-based cystic masses (arrows, *a–c*) throughout the abdomen consistent with metastases. Sagittal (*d*) and transverse (*e*) T2-weighted echo-train spin-echo and interstitial-phase gadolinium-enhanced fat-suppressed SGE (*f*) images in a second patient with ovarian cancer demonstrate the presence of a large metastatic heterogeneous mass in the pelvis that compresses the bladder.

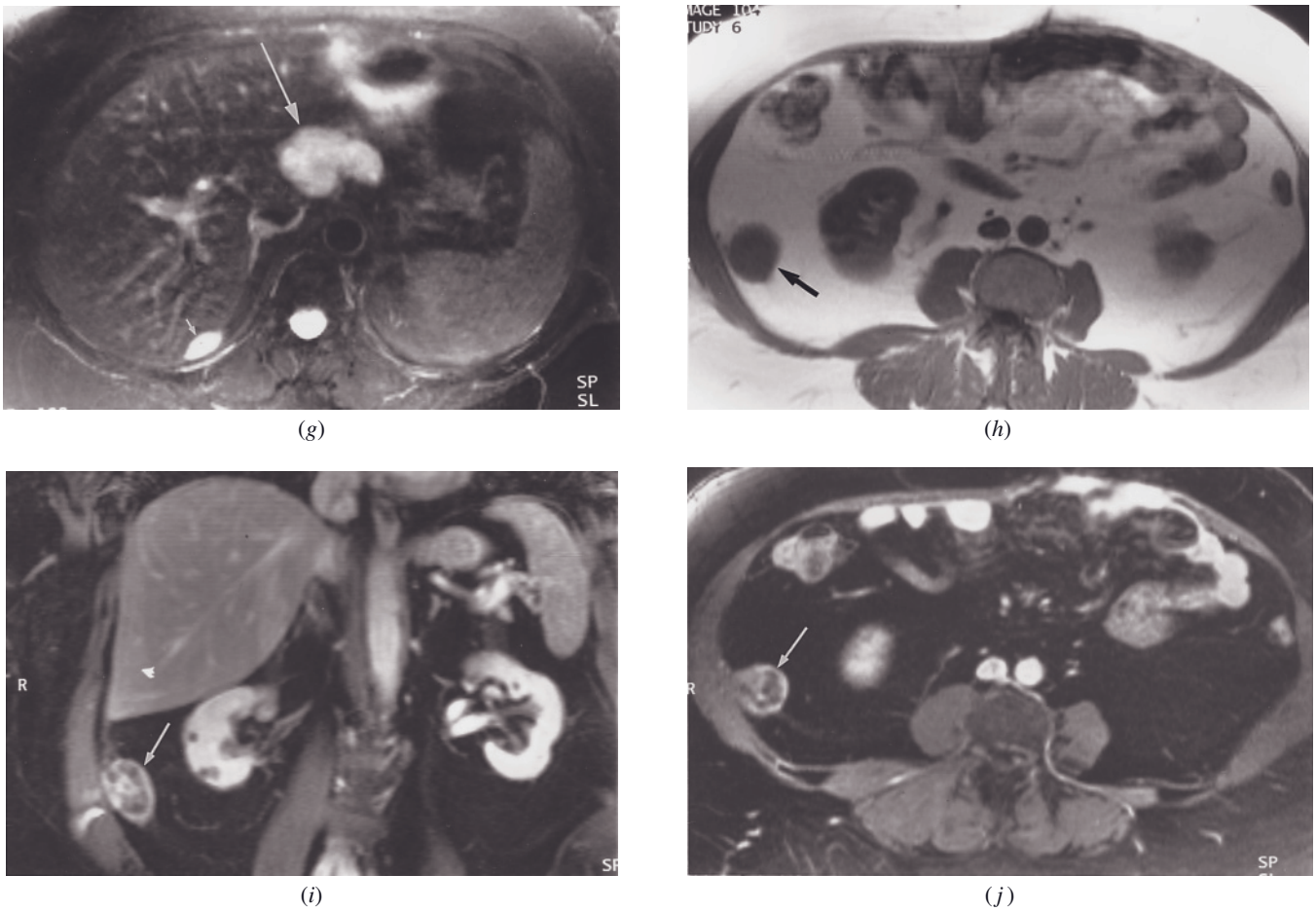

FIG. 7.14 (*Continued*) T2-weighted fat-suppressed echo-train spin-echo (*g*) and SGE (*h*) images of the liver and interstitial-phase gadolinium-enhanced fat-suppressed SGE image in coronal (*i*) and transverse (*j*) planes of the midabdomen. A lobulated 4-cm peritoneal implant along the gastrohepatic ligament is moderately high in signal intensity (arrow, *g*) and contrasts well with moderately low-signal-intensity liver. A subcapsular liver metastasis is also present (small arrow, *g*) that demonstrates a characteristic biconvex lens shape indicating its subcapsular location. Noncontrast SGE image shows a 2-cm low-signal-intensity peritoneal metastasis (arrow, *h*) that contrasts well with high-signal-intensity fat. Gadolinium-enhanced fat-suppressed SGE images demonstrate heterogeneous speckled enhancement of the mass (arrows, *i*, *j*).

of susceptibility effects that may obscure both normal and diseased tissue on gradient-echo sequences. Peritoneal metastases along the liver capsule are also well shown on T2-weighted fat-suppressed echo-train spin-echo images because both the fat and liver are relatively low in signal intensity, rendering moderately high-signal-intensity peritoneal metastases conspicuous. Because breathing artifact is less problematic in the pelvis, peritoneal metastases also may be well shown with T2-weighted echo-train spin-echo imaging. The sagittal plane is particularly effective at showing implants along the bladder surface (fig. 7.25).

Peritoneum- and serosa-based metastases must be distinguished from radiation changes, particularly in patients with gynecological malignancies. Multifocal lesions of peritoneal metastases, regardless of the primary tumor of origin, appear as moderately enhancing masses with slight internal heterogeneity. They lack the round, oval, or tubular contours of bowel and the uniform enhancement of bowel wall, with the associated lack of enhancement of the internal dot or stripe of bowel lumen.

Omental metastases frequently coexist in patients with peritoneal metastases. Four imaging patterns of omental involvement have been described: rounded, cakelike, ill-defined, and stellate [28, 43]. Regardless of contour, these masses enhance after intravenous gadolinium administration (fig. 7.26). Distinction from hypertrophied omentum due to varices in the setting of cirrhosis and portal hypertension can be made by the observation of irregular-enhancing soft tissue on gadolinium-enhanced fat-suppressed SGE images in the

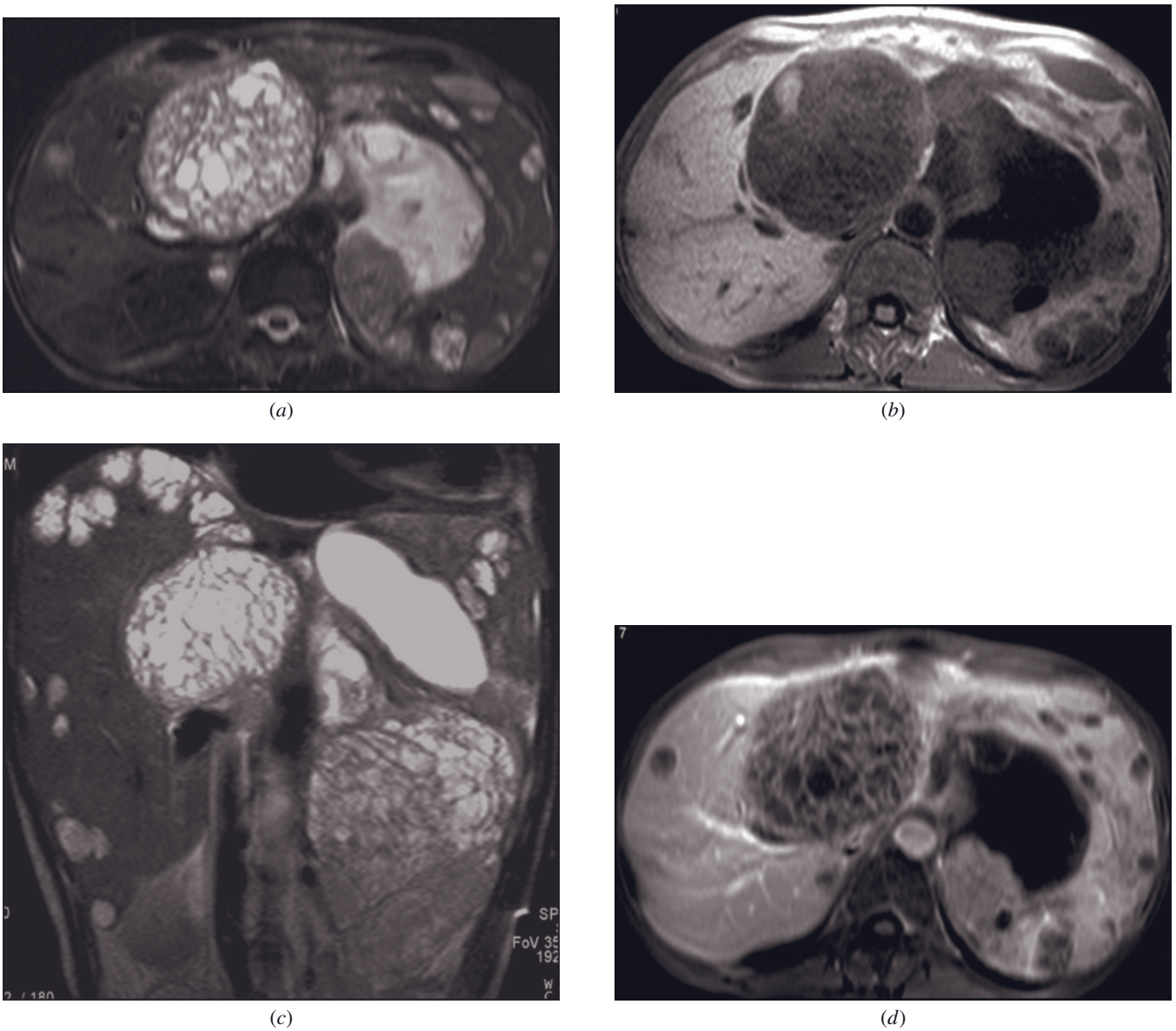

FIG. 7.15 Peritoneal metastases from ovarian cancer. Transverse T2-weighted SS-ETSE (*a*), transverse T1-weighted SGE (*b*), coronal T2-weighted SS-ETSE (*c*), and delayed postgadolinium T1-weighted fat-suppressed SGE (*d*) images in a patient with ovarian cancer demonstrate multiple liver and peritoneal metastases. The largest masses exhibit multiple thin septations that are well shown on single-shot T2-weighted images and reveal enhancement after gadolinium.

setting of tumor and presence of curvilinear-enhancing vessels in omental hypertrophy. The concomitant use of fat suppression emphasizes the presence of ill-defined soft tissue in tumor, and the lack of soft tissue in varices, because the bulky omentum is predominantly fatty in the latter condition and becomes very low in signal on fat-suppressed images, except for the thin curvilinear vessels (fig. 7.27).

Hematogenous Spread. Many malignancies including breast and lung carcinoma and melanoma may metastasize hematogenously to invade structures within the peritoneal cavity. Tumor emboli traverse the mesenteric arteries to the antimesenteric border of the bowel. Hematogenous metastases to bowel are manifest as intramural nodules (see Chapter 6, *Gastrointestinal Tract*, fig. 6.59) [32]. These lesions appear as small enhancing nodules on gadolinium-enhanced T1-weighted fat-suppressed SGE or 3D-GE.

Lymphatic Dissemination. Although permeation of the lymphatic system is the most common route for

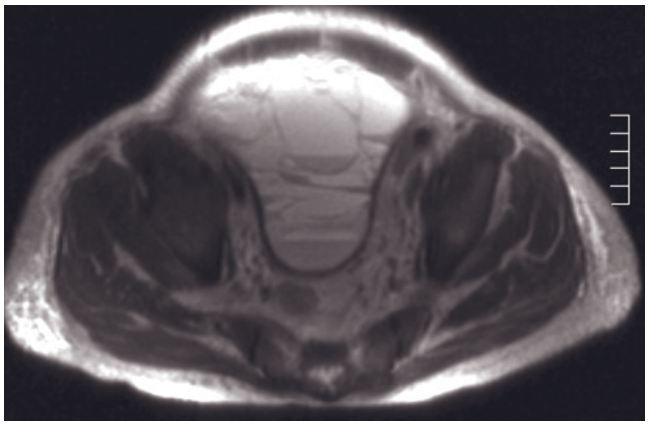

(*a*)

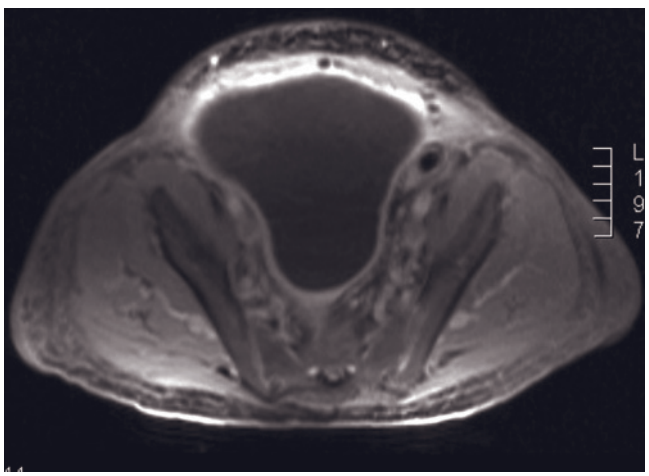

(*c*)

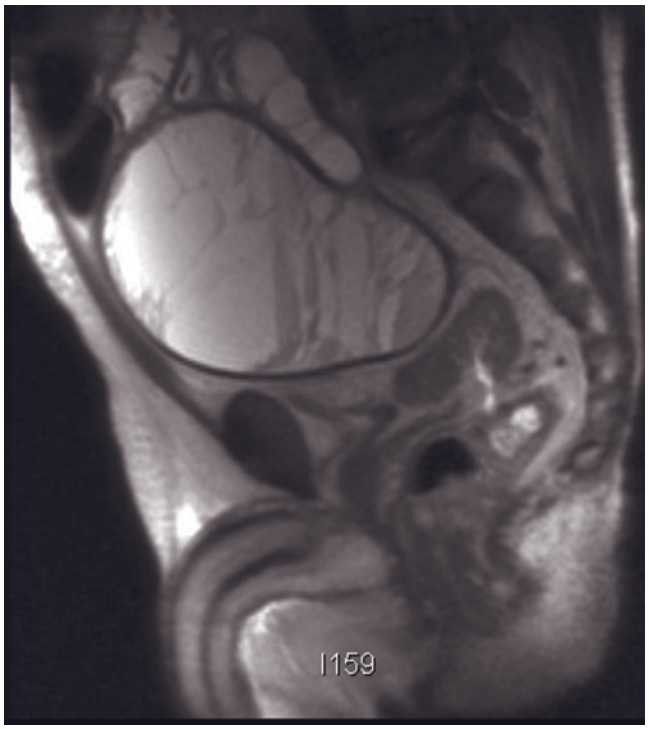

(*b*)

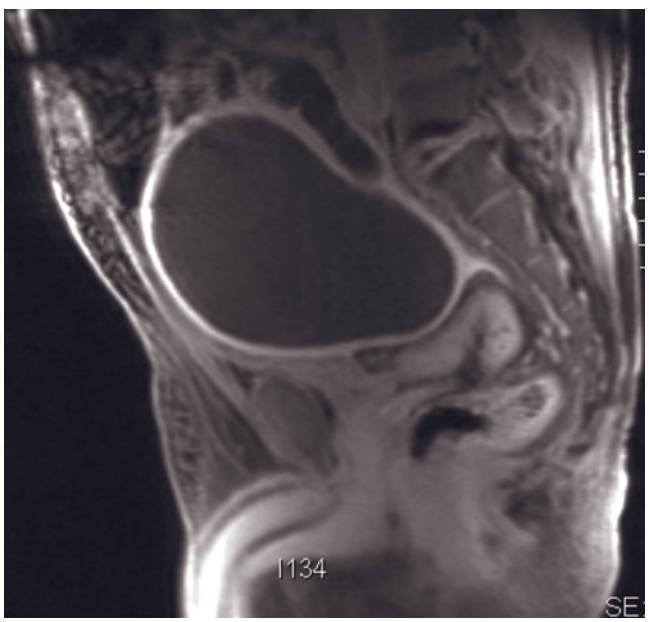

(*d*)

FIG. 7.16 Peritoneal metastases from cholangiocarcinoma. Transverse (*a*) and sagittal (*b*) T2-weighted SS-ETSE and transverse (*c*) and sagittal (*d*) postgadolinium T1-weighted fat-suppressed SGE images in a patient with cholangiocarcinoma demonstrate an intraperitoneal cystic mass with septations. Septations and layering low-intensity material are well shown on T2-weighted images (*a*, *b*) but not well seen on T1-weighted images (*c*, *d*).

initial dissemination of carcinomas, sarcomas may also spread via this route. The presence of mesenteric disease is more typical of non-Hodgkin lymphoma than other malignancies. The morphologic features of involved lymph nodes are variable. Pathologic lymph nodes may form large confluent masses that encircle the splanchnic vessels, the "sandwich sign." Alternatively, a profusion of small, normal-sized, 1-cm lymph nodes may predominate [44–46]. Whereas the former pattern suggests the diagnosis of lymphoma, the latter is nonspecific. MRI has an advantage over other cross-sectional modalities in that the signal intensity of the mesenteric lymph nodes on T2-weighted images and the degree of contrast enhancement reflect their biological activity: tissue that is low in signal intensity on T2-weighted images with minimal contrast enhancement may suggest fibrosis

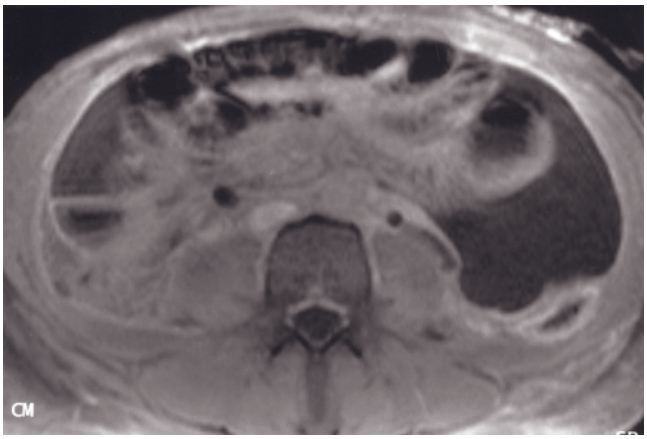

(*a*)

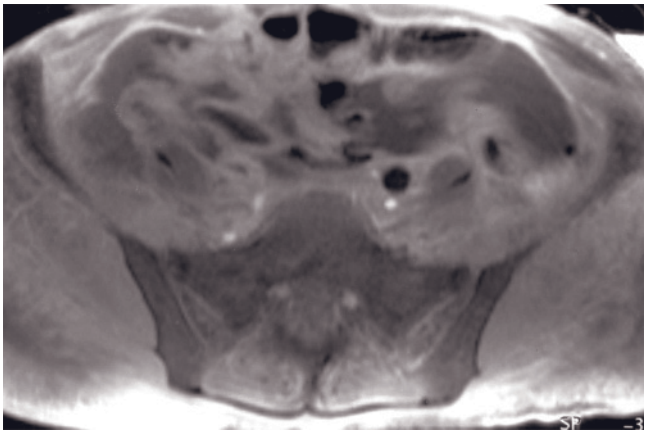

(*b*)

FIG. 7.17 Peritoneal metastases from appendiceal carcinoma. Transverse 90-s postgadolinium fat-suppressed SGE (*a*, *b*) images in a patient with appendiceal carcinoma. A large volume of ascites is present within the abdomen and pelvis. Extensive serosal and peritoneal enhancement is noted, associated with thickening of small bowel loops.

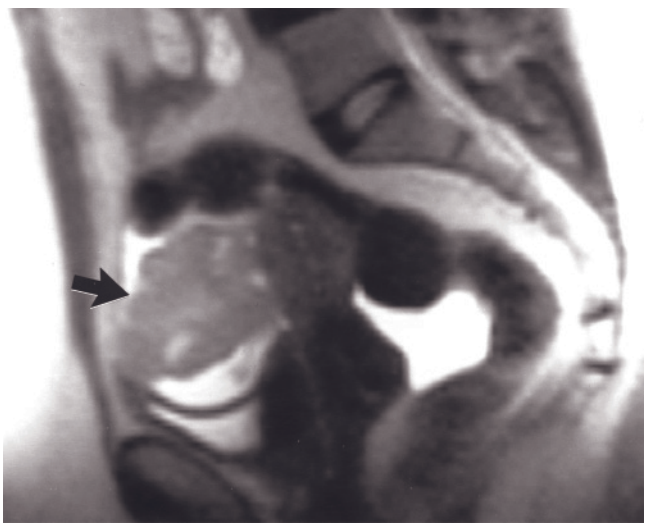

(*a*)

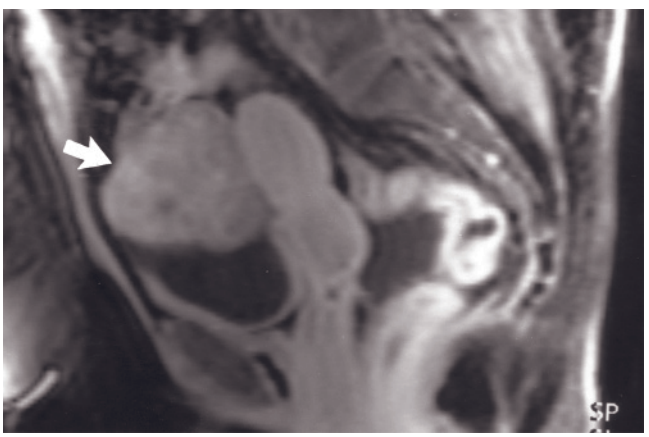

(*b*)

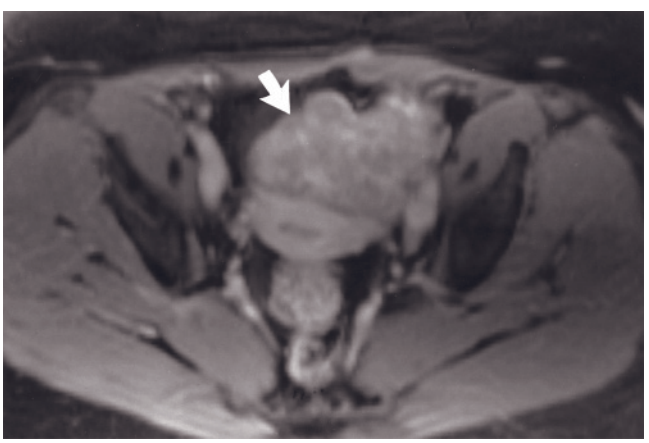

(*c*)

FIG. 7.18 Peritoneal metastases from colon cancer. Sagittal T2-weighted SS-ETSE (*a*) and sagittal (*b*) and transverse (*c*) interstitial-phase gadolinium-enhanced fat-suppressed SGE images in a patient with colon cancer. There is a large heterogeneous metastasis (arrows, *a*–*c*) in the pelvis, anterior to the uterus and superior to the bladder, surrounded by fluid.

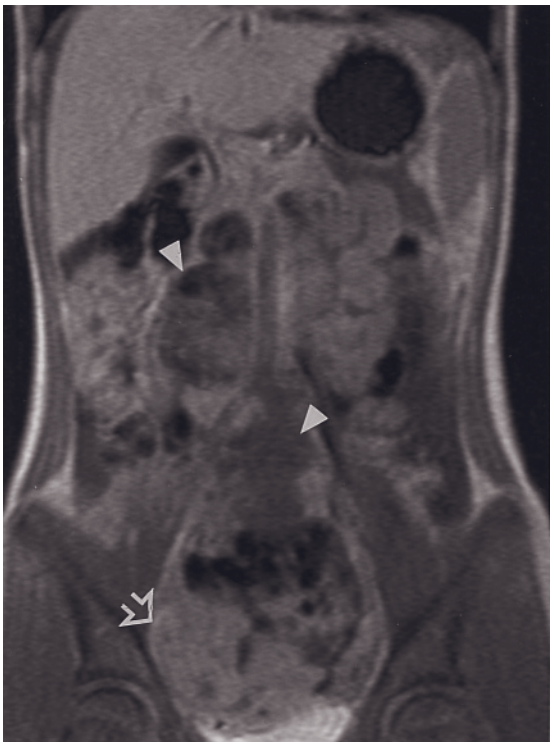

(*a*)

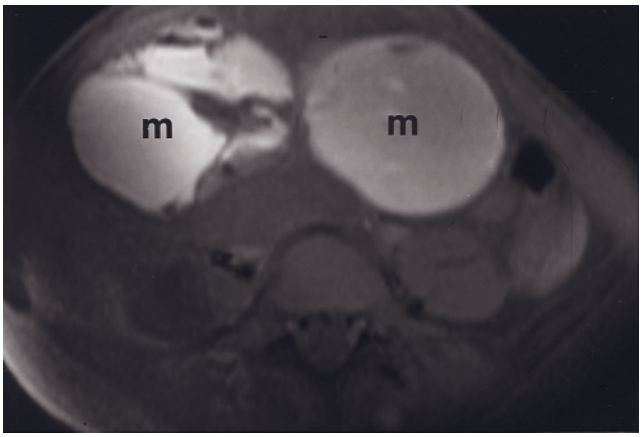

(*b*)

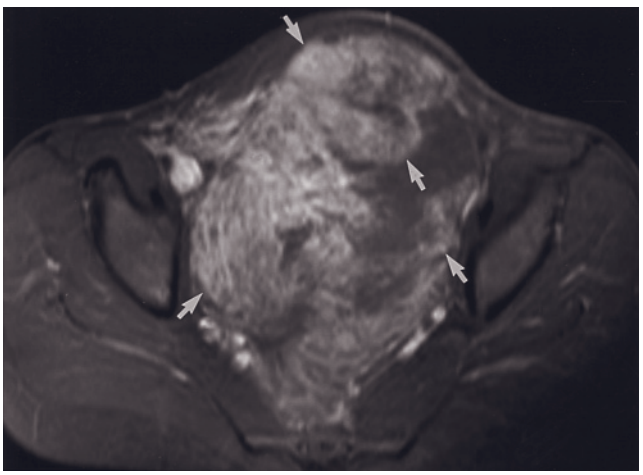

(*c*)

FIG. 7.19 Metastatic immature teratoma. Coronal T1-weighted magnetization-prepared gradient echo (*a*), transverse T1-weighted fat-suppressed spin-echo (*b*), and transverse gadolinium-enhanced T1-weighted fat-suppressed SGE (*c*) images in a patient with metastatic immature teratoma. The primary tumor (open arrow, *a*) originates in the ovary and has spread to the peritoneal cavity (arrowheads, *a*). The unenhanced fat-suppressed image highlights the nonlipomatous metastases (m, *b*). After gadolinium administration, extensive metastases along peritoneal and serosal surfaces are appreciated (arrows, *c*).

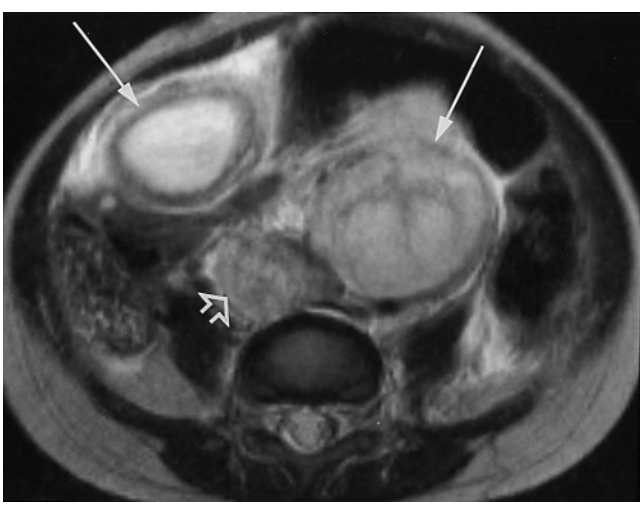

FIG. 7.20 Metastatic yolk sac tumor. Transverse 512-resolution T2-weighted echo-train spin-echo image in a patient with metastatic yolk sac tumor. Ovarian yolk sac tumors spread to the peritoneum (solid arrows), omentum, and retroperitoneal lymph nodes (open arrow).

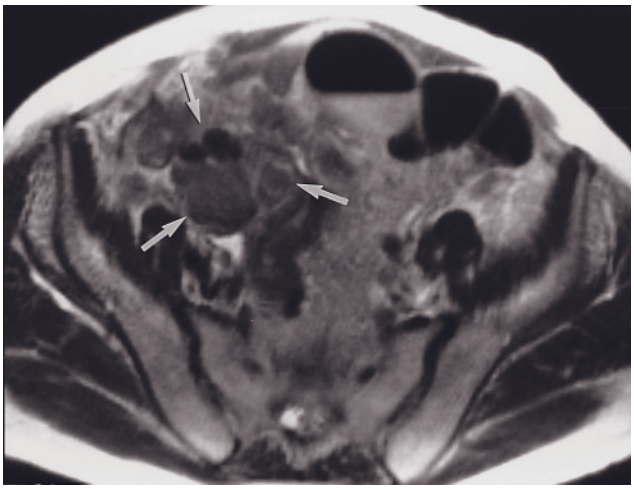

(*a*)

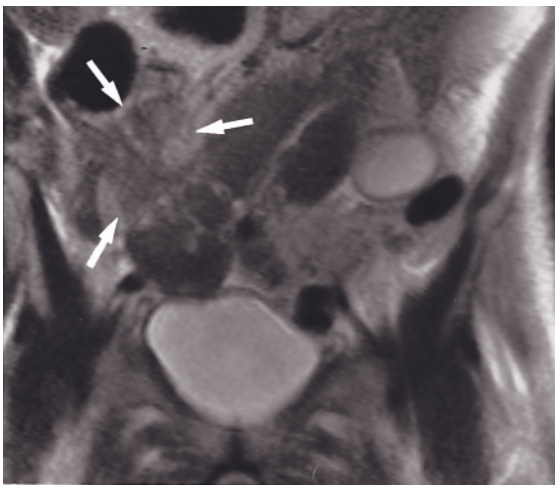

(*b*)

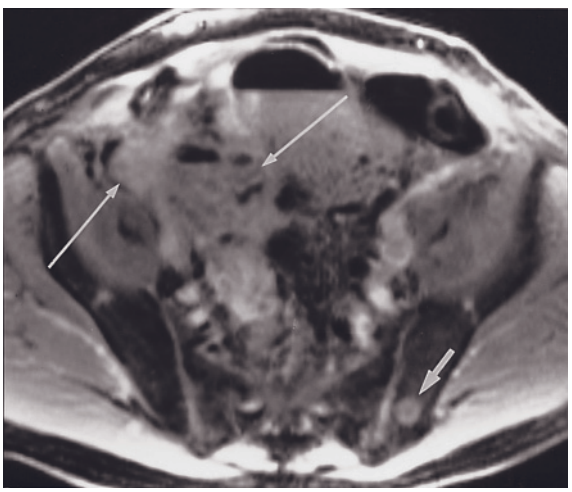

(*c*)

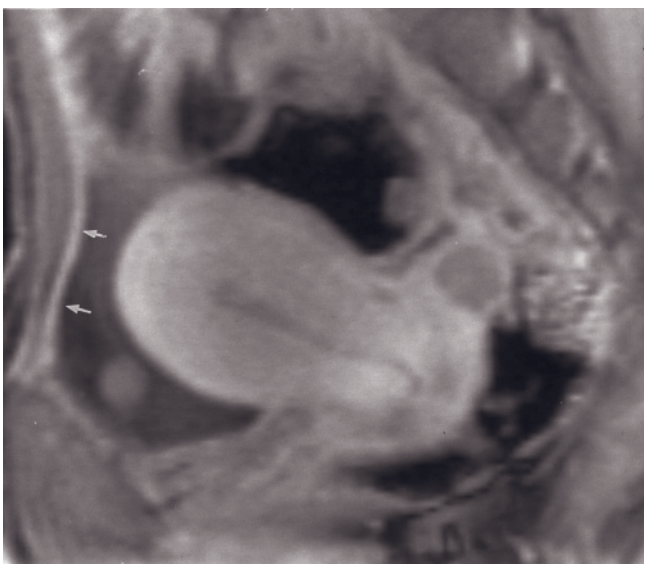

(*d*)

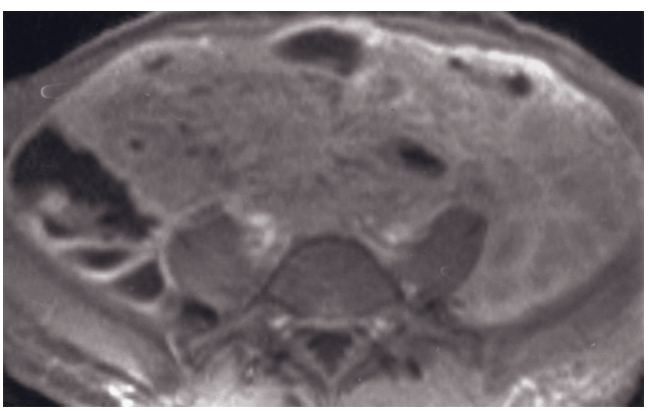

(*e*)

FIG. 7.21 Metastatic pancreatic cancer. Transverse (*a*) and coronal (*b*) T2-weighted single-shot echo-train spin-echo and interstitial-phase gadolinium-enhanced T1-weighted fat-suppressed SGE (*c*) images in a patient with metastatic pancreatic adenocarcinoma. The T2-weighted images show a mass in the right lower quadrant (arrows, *a*, *b*). After intravenous contrast, the serosal and peritoneal metastases enhance (long arrows, *c*). Incidental note is made of an enhancing bone metastasis in the left ilium (short arrow, *c*). Sagittal (*d*) and transverse (*e*) interstitial-phase gadolinium-enhanced fat-suppressed SGE images in a second patient with neuroendocrine pancreatic tumor. There are multiple peritoneum-based metastases throughout the pelvis. Diffuse peritoneal and serosal enhancement is present throughout the peritoneal cavity, consistent with large-volume peritoneal metastases. Virtually no uninvolved intraperitoneal or mesenteric fat is present, as the entire contents of the peritoneal cavity at this level enhance substantially. The sagittal projection is effective at showing metastases along the lower anterior peritoneum (arrows, *d*).

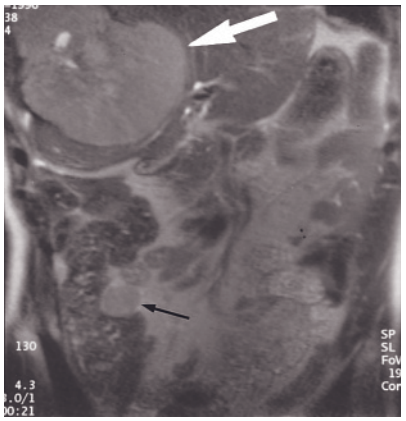

(*a*)

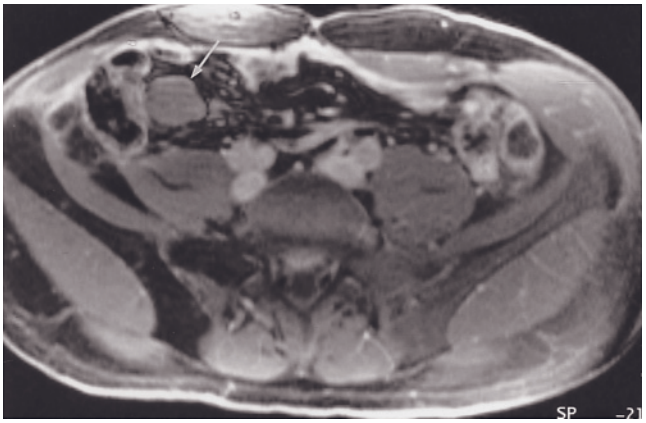

(*b*)

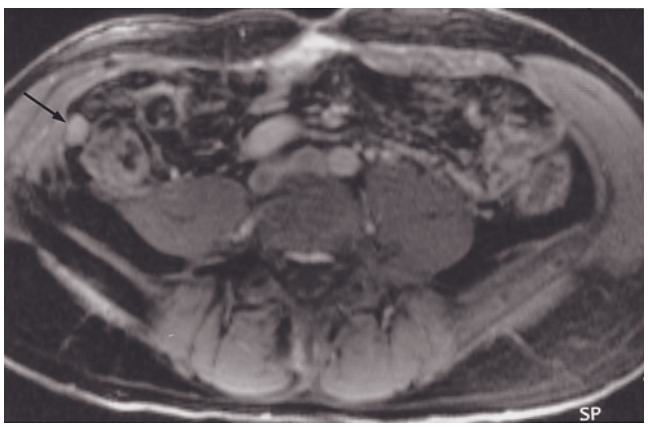

(*c*)

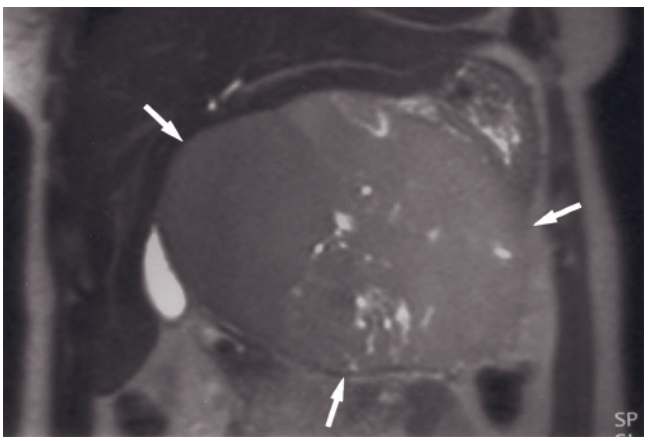

(*d*)

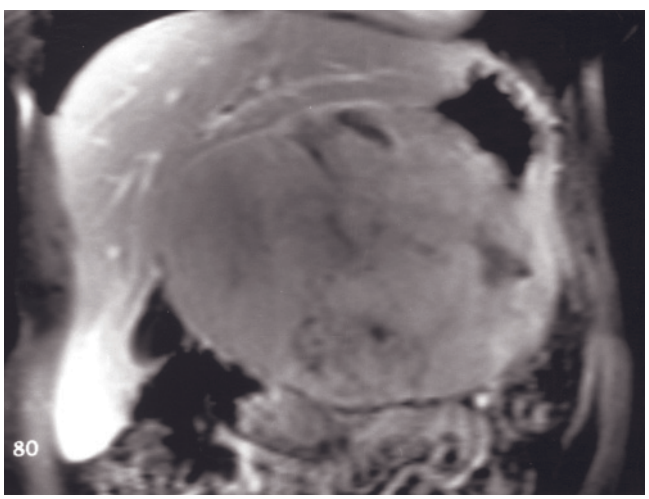

(*e*)

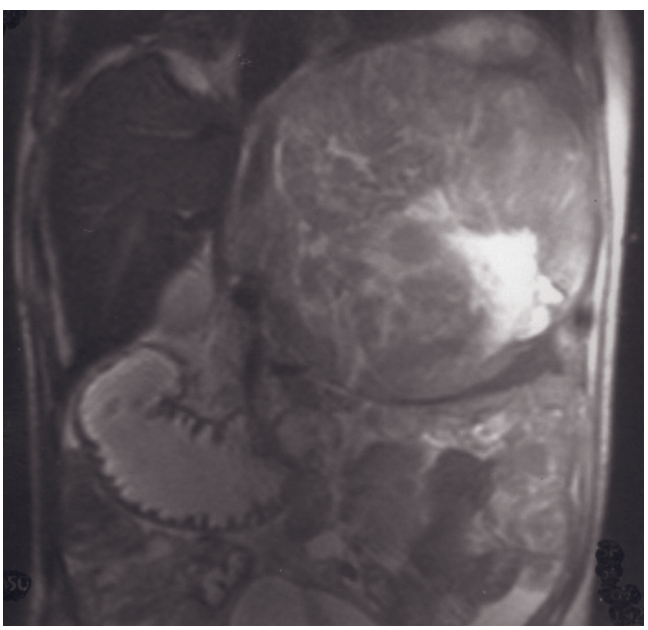

(*f*)

FIG. 7.22 Peritoneal metastases from sarcomas. Coronal SS-ETSE (*a*) and interstitial-phase gadolinium-enhanced T1-weighted fat-suppressed SGE (*b*, *c*) images in a patient with synovial sarcoma. The coronal T2-weighted image demonstrates a large subcapsular liver metastasis (large arrow, *a*) and a 2-cm peritoneal metastasis (small arrow, *a*) medial to the ascending colon. The gadolinium-enhanced fat-suppressed image demonstrates moderate uniform enhancement of this metastatic deposit (arrow, *b*). On a higher tomographic section through the pelvis, a 6-mm moderately enhancing metastatic deposit is well shown (arrow, *c*). Coronal T2-weighted SS-ETSE (*d*) and coronal interstitial-phase gadolinium-enhanced fat-suppressed SGE (*e*) images in a second patient, who has dermatofibrosarcoma. There is a very large, centrally located abdominal soft tissue mass (arrows, *d*) that displaces the liver superiorly and the stomach superiorly and laterally. This mass is mildly hyperintense with small high-signal foci on T2-weighted image (*d*) and has heterogeneous enhancement on the postgadolinium image (*e*). Coronal T2-weighted SS-ETSE (*f*) and

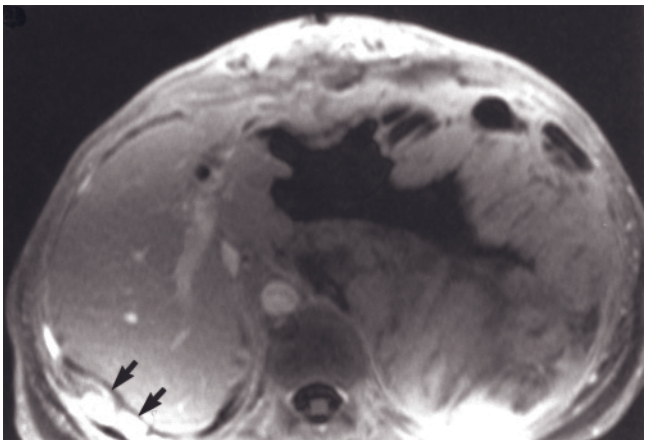

(*g*)

FIG. 7.22 (*Continued*) gadolinium-enhanced magnetization-prepared gradient-echo (*g*) images in a third patient, who has metastatic osteosarcoma. There is a large heterogeneous mass in the left upper quadrant, which has central necrosis. Multiple peritoneal metastases are also present (arrows, *g*).

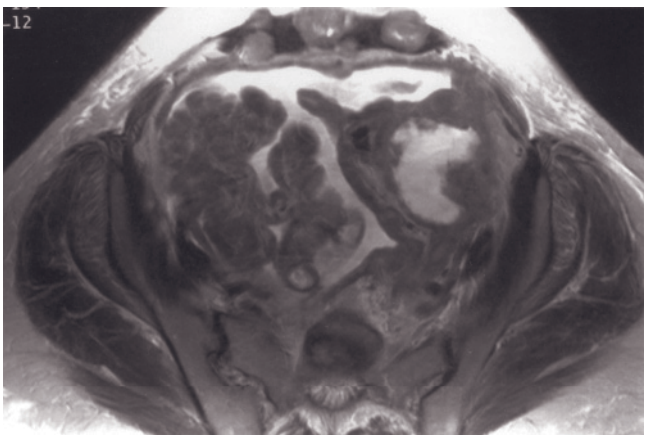

(*a*)

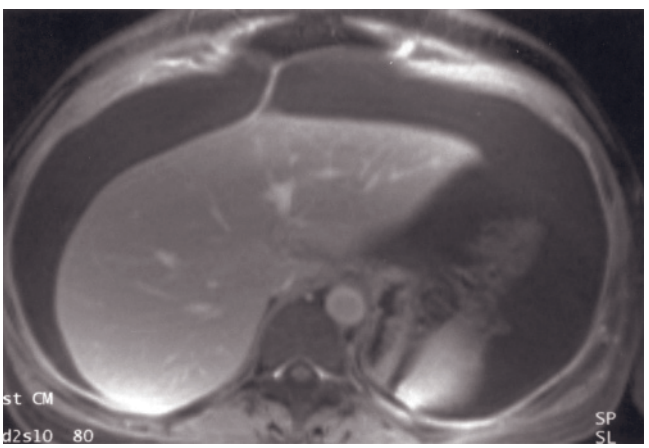

(*b*)

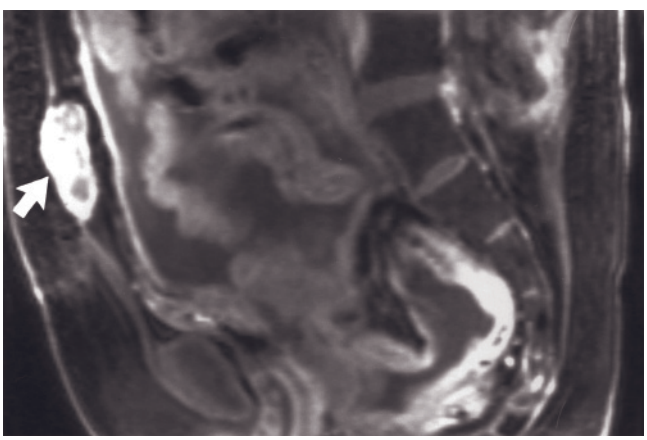

(*c*)

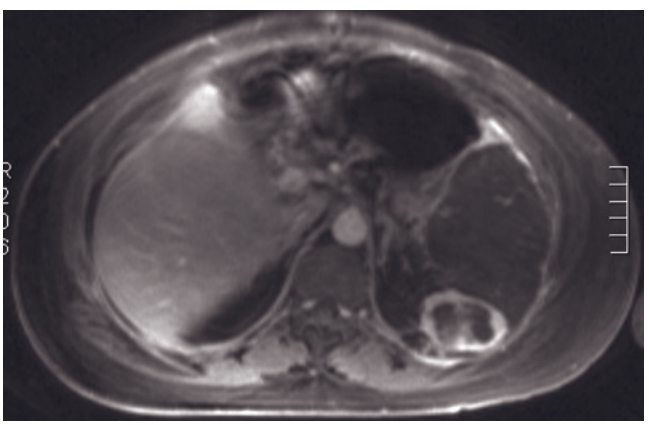

(*d*)

FIG. 7.23 Extensive peritoneal disease in patients with leiomyosarcoma. Transverse T2-weighted ETSE (*a*) and transverse (*b*) and sagittal (*c*) interstitial-phase gadolinium-enhanced fat-suppressed SGE images. A large volume of ascites is present. There is thickening and enhancement of the peritoneal surfaces consistent with metastatic disease. Multiple metastatic deposits are present within the anterior abdominal wall (arrow, *c*). Interstitial-phase gadolinium-enhanced fat-suppressed T1-weighted SGE images (*d*, *e*) in a patient with leiomyosarcoma demonstrate diffuse peritoneal and serosal enhancement throughout the peritoneal cavity

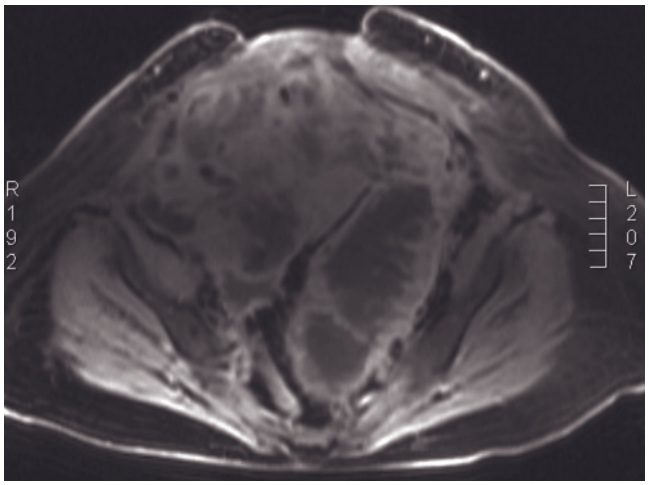

(*e*)

FIG. 7.23 (*Continued*) consistent with large-volume peritoneal metastases. Virtually no uninvolved intraperitoneal or mesenteric fat is present, as the entire contents of the peritoneal cavity at this level enhance substantially.

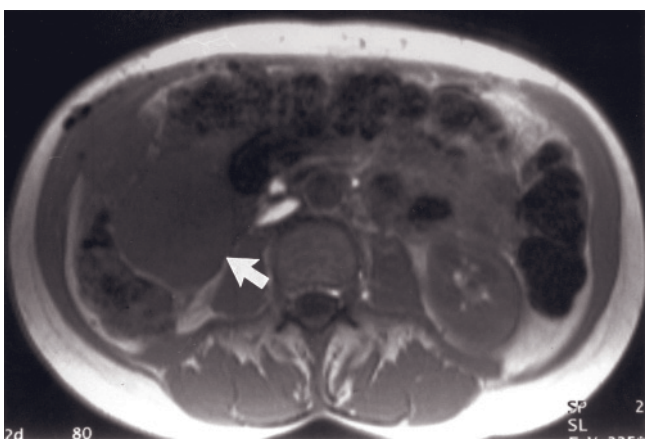

(*a*)

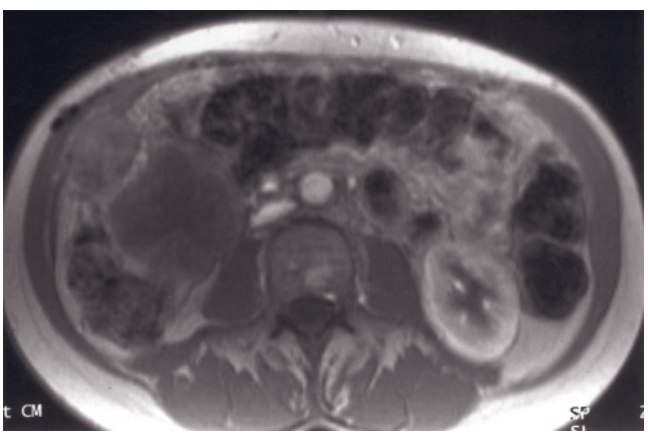

(*b*)

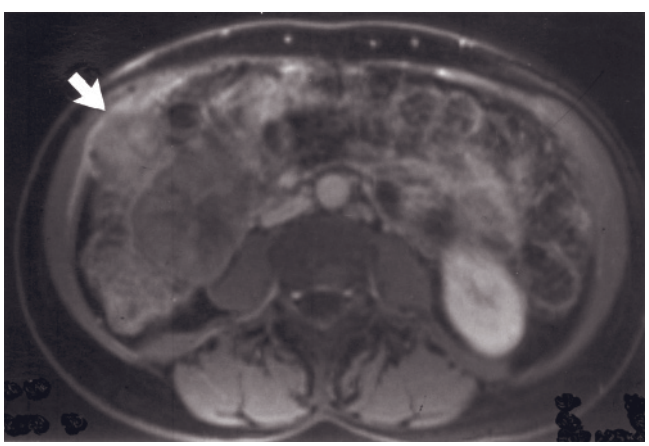

(*c*)

FIG. 7.24 Peritoneal metastatic masses from hepatocellular carcinoma. SGE (*a*), immediate postgadolinium SGE (*b*), and interstitial-phase gadolinium-enhanced fat-suppressed SGE (*c*) images in a patient with hepatocellular carcinoma. There are two large metastases in the right abdomen. The larger mass is applied to the medial aspect of the right colon (arrow, *a*), and the other abuts and extends into the abdominal wall (arrow, *c*). These lesions show mild and heterogeneous enhancement after gadolinium administration.

(*a*)

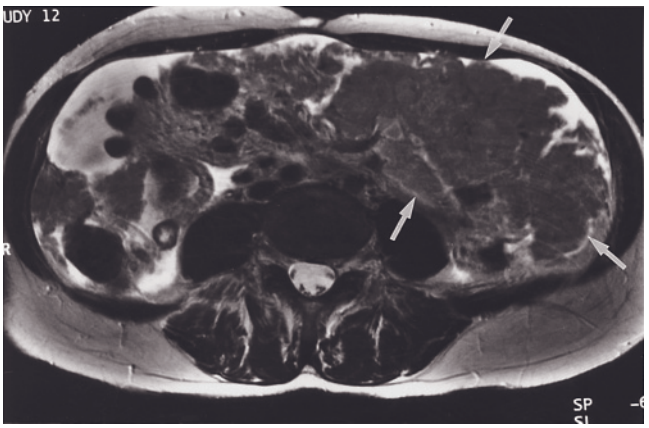

(*b*)

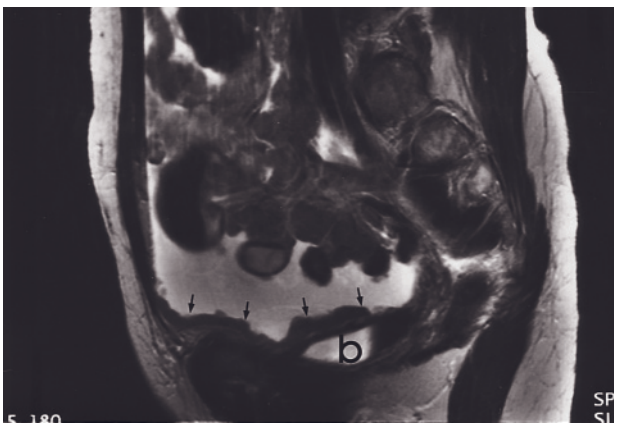

(*c*)

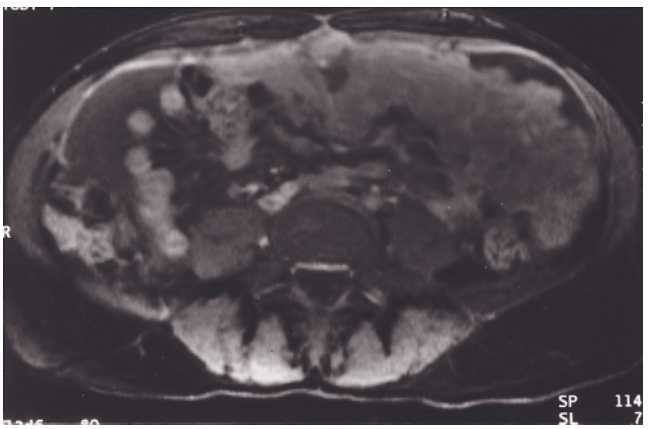

(*d*)

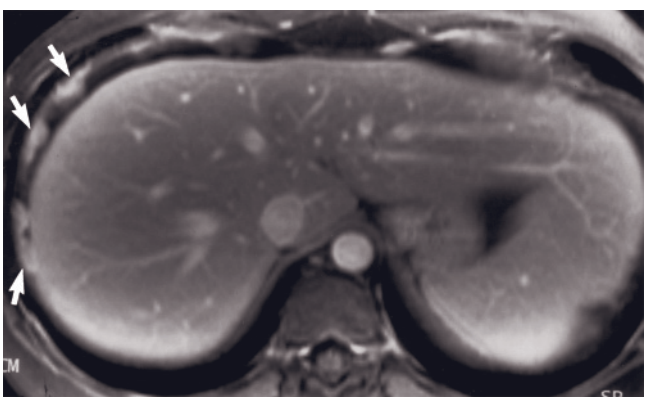

(*e*)

FIG. 7.25 Peritoneal metastases from non-ovary gynecological malignancies. Coronal T2-weighted SS-ETSE (*a*), transverse (*b*) and sagittal (*c*) 512-resolution T2-weighted echo-train spin-echo, and interstitial-phase gadolinium-enhanced SGE (*d*) images in a patient with fallopian tube carcinoma. Extensive peritoneum-based metastases are present that appear intermediate in signal intensity on T2-weighted images (*a–c*). The coronal image demonstrates an irregular layer of metastatic deposit measuring up to 2 cm in thickness along the diaphragmatic surface and the liver capsule (small arrows, *a*). Bulky peritoneal metastases are present in the left lower abdomen (large arrow, *a*) and in the pelvis. The transverse high-resolution T2-weighted image demonstrates extensive bulky peritoneal metastases (arrows, *b*). Peritoneal seeding along the peritoneal reflection over the bladder (b, *c*) is well shown on the sagittal plane image (small arrows, *c*). Heterogeneous and moderate enhancement of the metastases is shown on the gadolinium-enhanced fat-suppressed SGE image obtained at the midabdomen level (*d*). Interstitial-phase gadolinium-enhanced fat-suppressed SGE image (*e*) in a second patient who has endometrial stromal sarcoma demonstrates extensive peritoneal involvement including multiple peritoneal nodules (arrows, *e*).

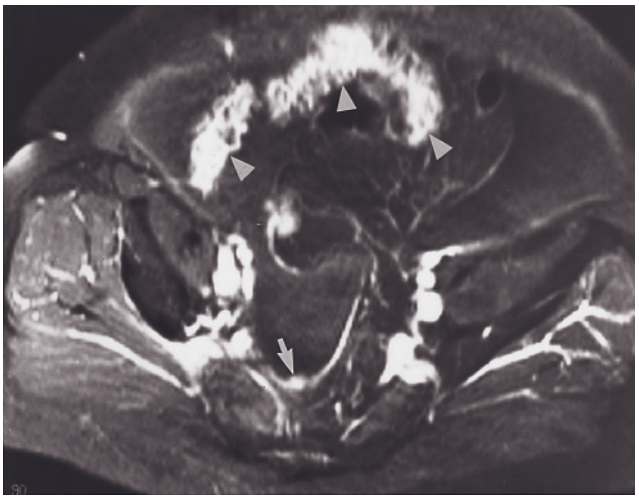

(*a*)

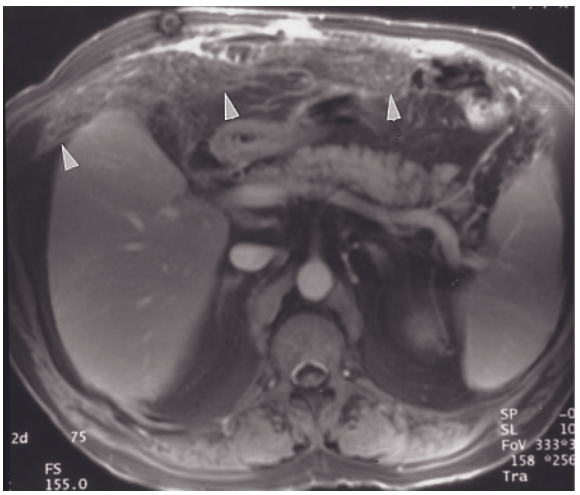

(*b*)

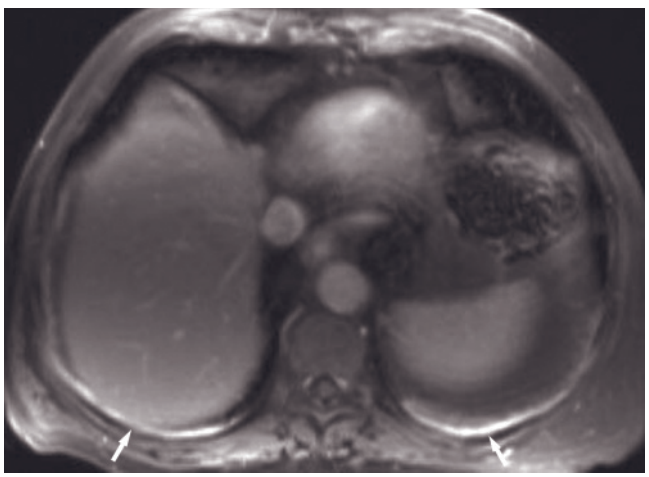

(*c*)

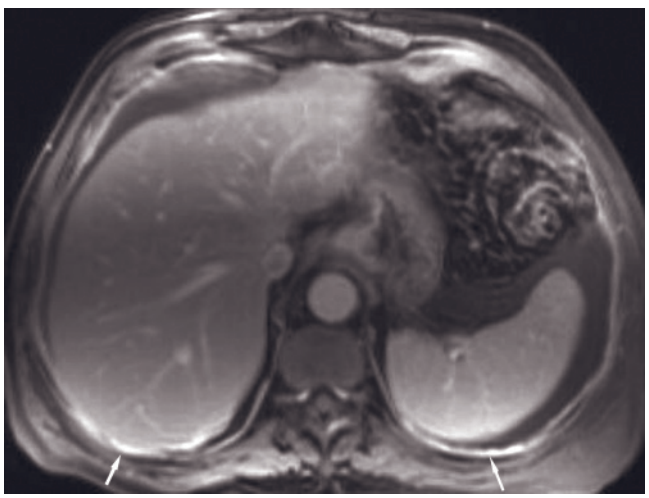

(*d*)

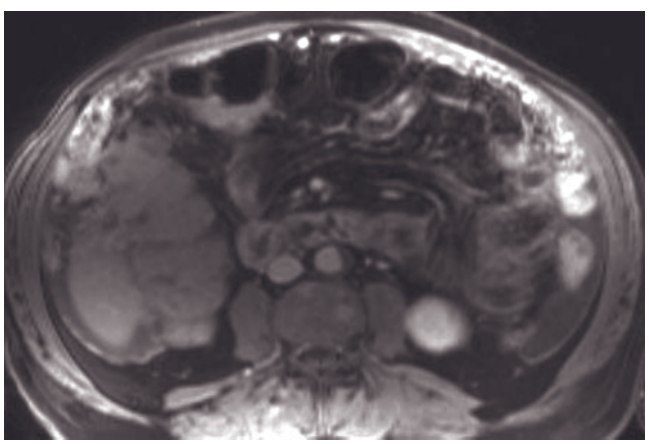

(*e*)

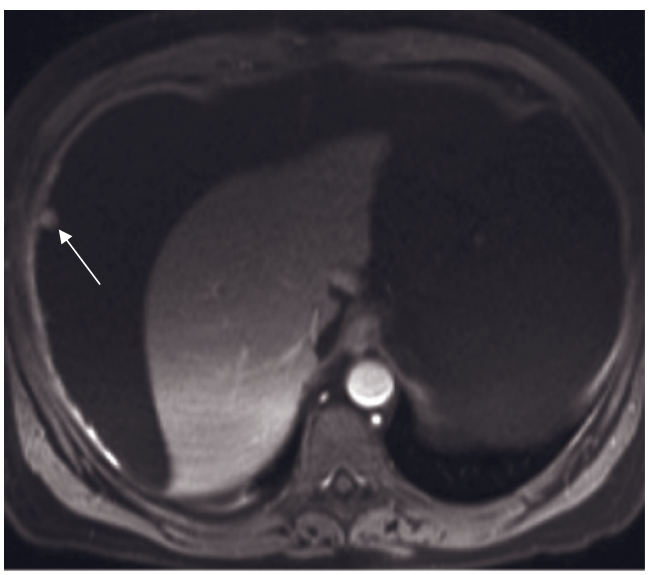

(*f*)

FIG. 7.26 Omental metastases. Transverse gadolinium-enhanced T1-weighted fat-suppressed spin-echo images in a patient with metastatic ovarian carcinoma (*a*) and metastatic leiomyosarcoma (*b*). The enhancing "omental cake" (arrowheads, *a*, *b*) is characteristic of metastatic ovarian carcinoma, but also may be seen with other malignant diseases. Enhancing peritoneal tumor deposits (arrow, *a*) are rendered very conspicuous with suppression of background fat. MRI is superior to CT imaging in detecting small peritoneum-based disease. Interstitial-phase gadolinium-enhanced fat-suppressed T1-weighted SGE images (*c*–*e*) in a third patient with adenocarcinoma demonstrate similar findings. The peritoneum is thickened and enhances intensely (arrows, *c*, *d*). T1-weighted fat-suppressed interstitial-phase postgadolinium 3D-GE images (*f*–*i*) in another patient show multiple omental metastases (white arrows), and thin platelike and small nodular peritoneal metastases (black arrow, *g*).

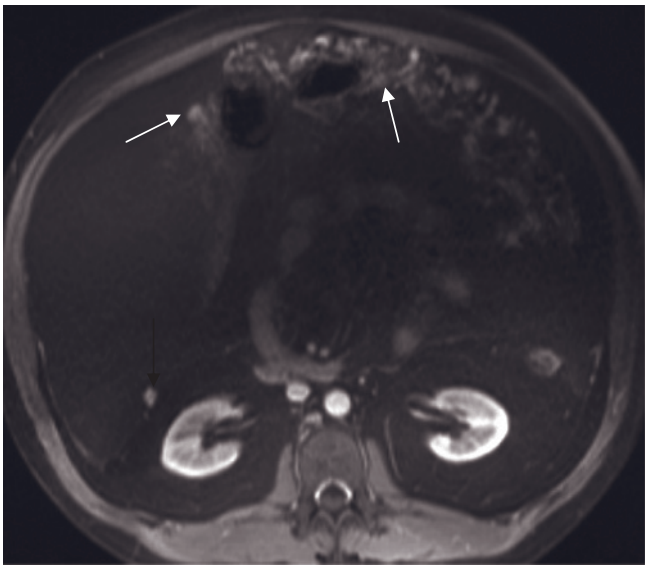

(*g*)

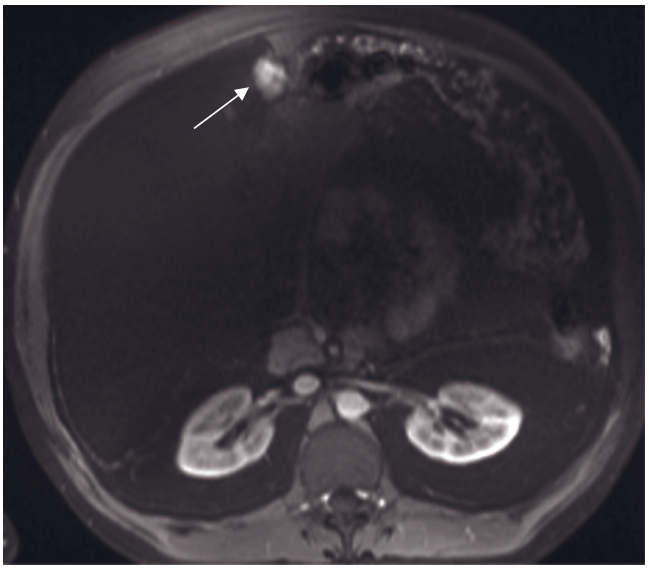

(*h*)

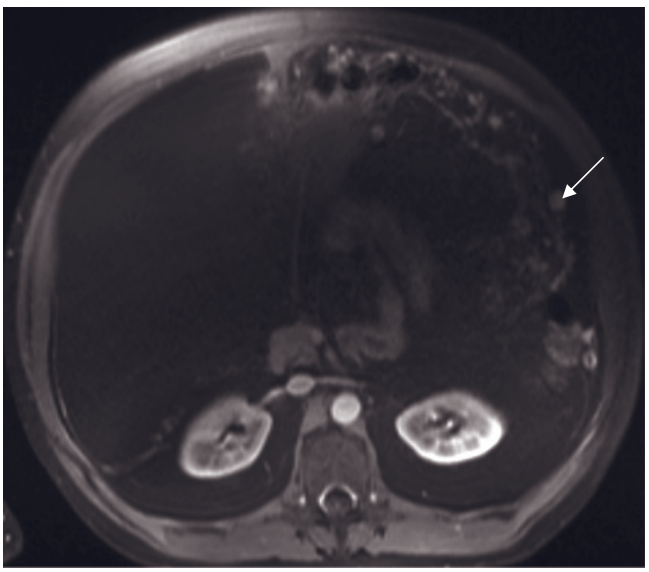

(*i*)

FIG. 7.26 (*Continued*)

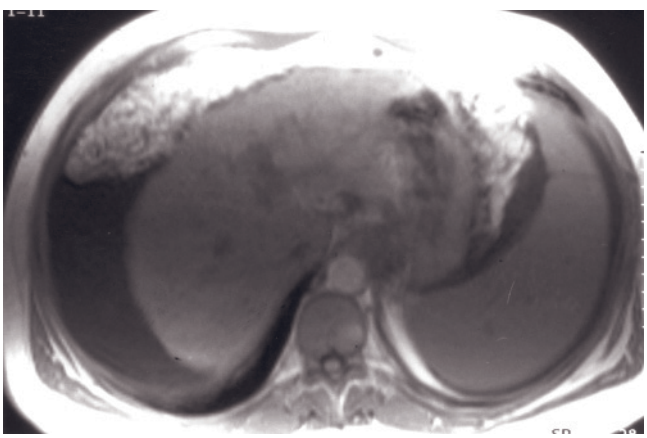

(*a*)

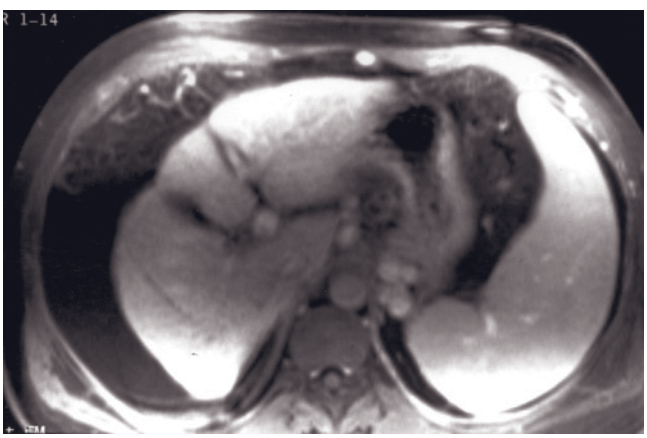

(*b*)

FIG. 7.27 Omental hypertrophy due to varices in the setting of cirrhosis. SGE (*a*) and 90-s postgadolinium fat-suppressed SGE (*b*) images in a patient with cirrhosis. The omentum is enlarged on the basis of hypertrophy in the setting of portal hypertension. This is shown on postgadolinium fat-suppressed images by demonstration of suppression of the omentum and enhancement of thin curvilinear vessels. Note also that the liver is cirrhotic and other features of portal hypertension such as splenomegaly and ascites are present.

rather than recurrent or persistent tumor. Evaluation of degree of contrast enhancement is aided by using T1-weighted fat-suppressed techniques. Various MRI techniques are effective at demonstrating mesenteric lymph nodes. The most consistent demonstration of lymph nodes is with 2- to 5-min gadolinium-enhanced T1-weighted fat-suppressed gradient-echo images. Precontrast T1-weighted fat-suppressed images show most clearly the distinction between mesenteric lymph nodes, which appear intermediate signal intensity, and pancreas, which appears high signal intensity (fig. 7.28). Imaging in multiple planes including sagittal and/or coronal helps distinguish rounded lymph nodes from tubular bowel loops (see fig. 7.28).

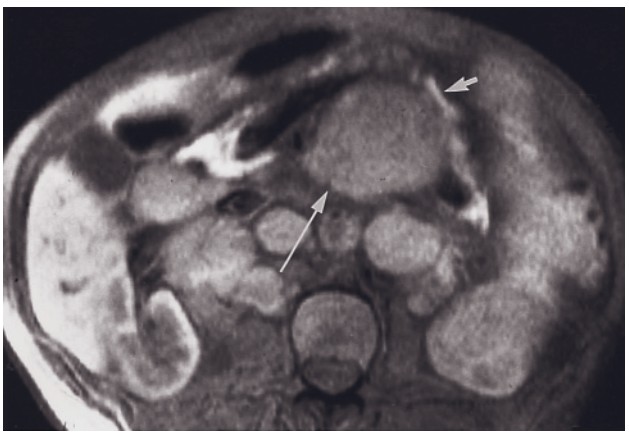

(*a*)

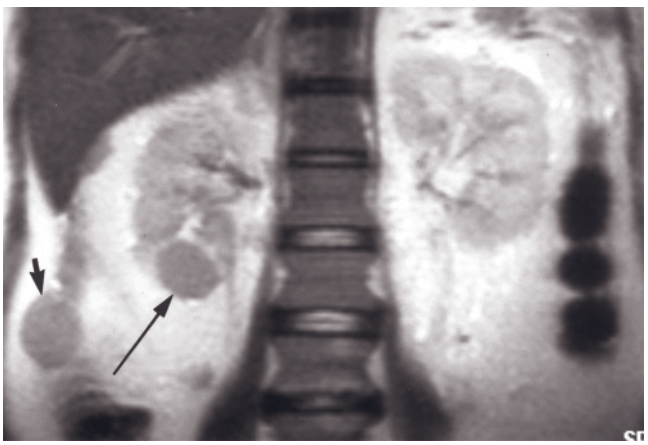

(*b*)

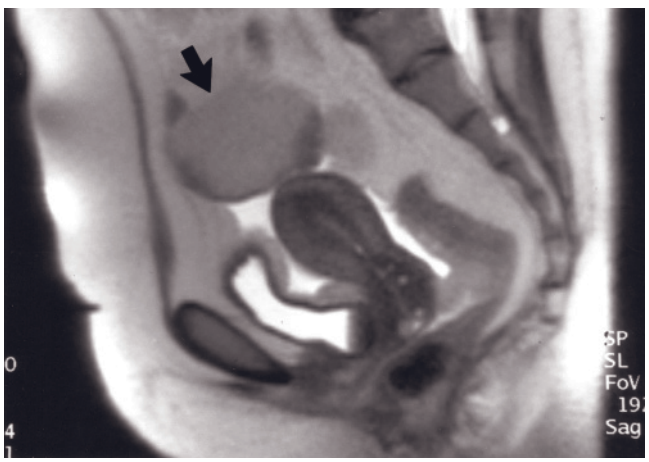

(*c*)

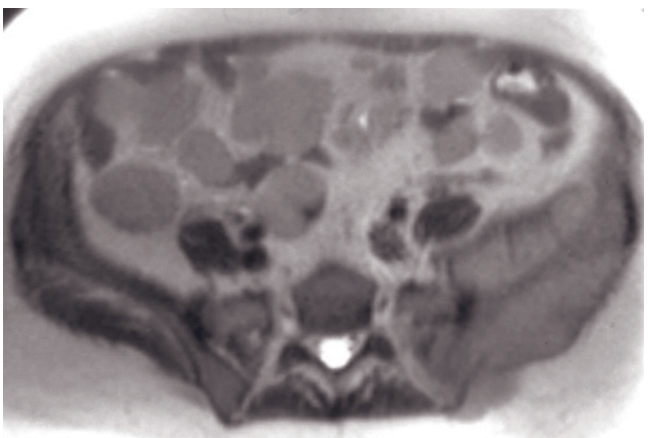

(*d*)

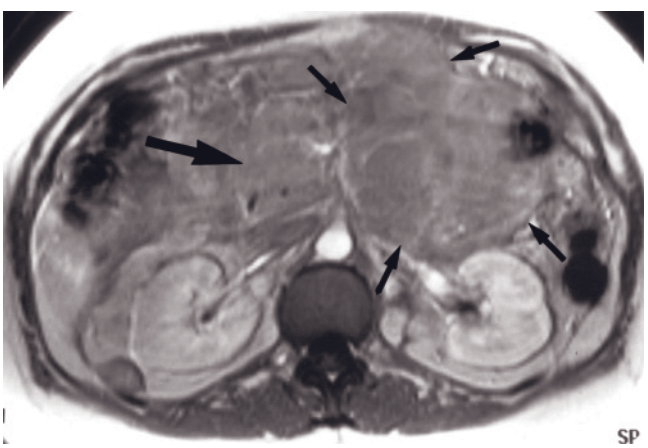

(*e*)

FIG. 7.28 Mesenteric adenopathy. T1-weighted fat-suppressed spin-echo image (*a*) demonstrates an intermediate-signal-intensity lymph node (long arrow, *a*) that is clearly distinguished from high-signal-intensity pancreas (short arrow, *a*). Coronal (*b*), sagittal (*c*), and transverse (*d*) T2-weighted SS-ETSE and transverse 1-min postgadolinium T1-weighted SGE (*e*) images in a patient with Burkitt lymphoma demonstrate multiple masses throughout the peritoneal cavity. The largest mass within the mesentery shows heterogeneous enhancement and lies anterior to the aorta and both kidneys (small arrows, *e*) and invades the anterior abdominal wall. Involvement of the head of the pancreas is also present (large arrow, *e*). Multiple additional mesenteric masses measuring up to 3.0 cm in size are also seen. Note the presence of a retroperitoneal mass (long arrow, *b*) that lies posterior to the right kidney and an abdominal wall mass (short arrow, *b*) in close proximity. The sagittal plane image demonstrates a pelvic mass (arrow, *c*) superior to the uterus.

Pseudomyxoma peritonei

Pseudomyxoma peritonei is a distinctive form of metastatic disease in which the peritoneal cavity becomes distended with tenacious, viscous mucinous material. The primary tumor is usually a malignant neoplasm of the appendix, ovary, or pancreas [47]. The appendix is the primary site of origin of pseudomyxoma in the vast majority of cases [48]. The gelatinous deposits coat the peritoneal surfaces and characteristically indent and scallop the liver margin (fig. 7.29) [49, 50]. The enhancement of even a thick volume of disease may be difficult to appreciate on CT compared to MRI (see fig. 7.29). Septae are also common [31].

Carcinoid Tumors

Intestinal carcinoid tumor may involve the mesentery and produce a characteristic appearance [51]. The release of 5-hydroxytryptophan and serotonin secreted by tumor cells incites a desmoplastic reaction. The result is an irregular, indurated soft tissue mass in the root of the mesentery with associated radiating soft tissue strands [52, 53]. Calcification may be present in up to 70% of tumors [54]. Non-fat-suppressed T1-weighted images are effective at showing these tumors. The tumors appear as low-signal-intensity masses against the high-signal-intensity mesenteric fat (fig. 7.30). T2-weighted single-shot echo-train spin-echo sequences also demonstrate low-signal-intensity tissue in a background of high-signal-intensity fat (see fig. 7.30). Fat-suppressed noncontrast T1-weighted images reduce the contrast between the fibrotic tumor and fat. The desmoplastic nature of this tumor results in minimal enhancement with gadolinium (see fig. 7.30).

INTRAPERITONEAL FLUID

Ascites

Ascites is defined as the collection of excess fluid in the peritoneal cavity. Ascites results from overproduction, impaired resorption, or leakage of fluid. It is a common manifestation of many diseases: cirrhosis, pancreatitis, obstruction (venous or lymphatic), inflammation, low-albumin states, malignancy, and trauma. The signal intensity of the fluid, a function of its protein content, coupled with its distribution, can suggest the underlying etiology. Simple transudates are low in signal intensity on T1-weighted sequences and very high in signal intensity on T2-weighted images (fig. 7.31), whereas exudates, blood, and enteric contents will have higher signal intensity on T1-weighted images and more variable signal intensity on T2-weighted images [2, 55–57] (figs. 7.32 and 7.33). Benign processes favor the greater sac, whereas malignant fluid tends to involve the greater and lesser sacs proportionally [2, 3] (fig. 7.34), although exceptions are common. In simple ascites, small and large bowel tend to float to the anterior abdomen in a central location (fig. 7.35). Malignant or inflammatory ascites tends to tether the bowel in different locations depending on the distribution of the disease process. Breathing-independent T2-weighted imaging is effective in evaluating the distribution and presence of ascites in uncooperative patients and young children (fig. 7.36). Multiplanar imaging facilitates the evaluation of ascites distribution within various abdominal compartments (fig. 7.37). Artifactual heterogeneity of signal in ascites is not uncommon, presumably reflecting dephrasing of signal from breathing-related motion.

Intraperitoneal Blood

Intraperitoneal blood most frequently occurs in the setting of trauma. MRI can readily distinguish blood from ascites. The age of hemorrhage can be determined because of the distinctive signal intensity features of hemoglobin as it undergoes progressive degradation. Balci et al. [58] described the MR features of acute intra-abdominal hemorrhage. Acute blood (<48 h), in the form of deoxyhemoglobin, is low in signal intensity on both T1- and T2-weighted images (fig. 7.38). From 48 h to 7 days methemoglobin may be observed that is high signal on T1- and low or high signal on T2-weighted images. The very low signal of deoxyhemoglobin and intracellular methemoglobin on T2-weighted images is very distinctive, and observation of very low-signal substance in the peritoneal cavity should raise the clinical concern of acute and early subacute hemorrhage, respectively. The near signal void of these blood products can be distinguished from the signal void of air on T2-weighted images, either because of different signal on T1-weighted images or because blood tends to be observed in a dependent location, whereas air is observed in a nondependent location. Late subacute hemorrhage, in the form of extracellular methemoglobin, is high in signal intensity on T1- and T2-weighted images (fig. 7.39). Fat suppression accentuates the conspicuity of this finding. Hematomas also may demonstrate heterogeneity related to hemoglobin breakdown products admixed with blood. Not infrequently, a high-signal-intensity rim surrounding a low signal-intensity center is seen with subacute hematomas (fig. 7.40). A structure with a high-signal rim on noncontrast T1-weighted images is characteristic of subacute hematoma. This distinctive imaging feature represents extracellular methemoglobin encircling the retracting clot [59]. As hematomas age, a low-signal-intensity rim develops around the hematoma on both T1- and T2-weighted sequences. This rim corresponds to hemosiderin and/or fibrosis.

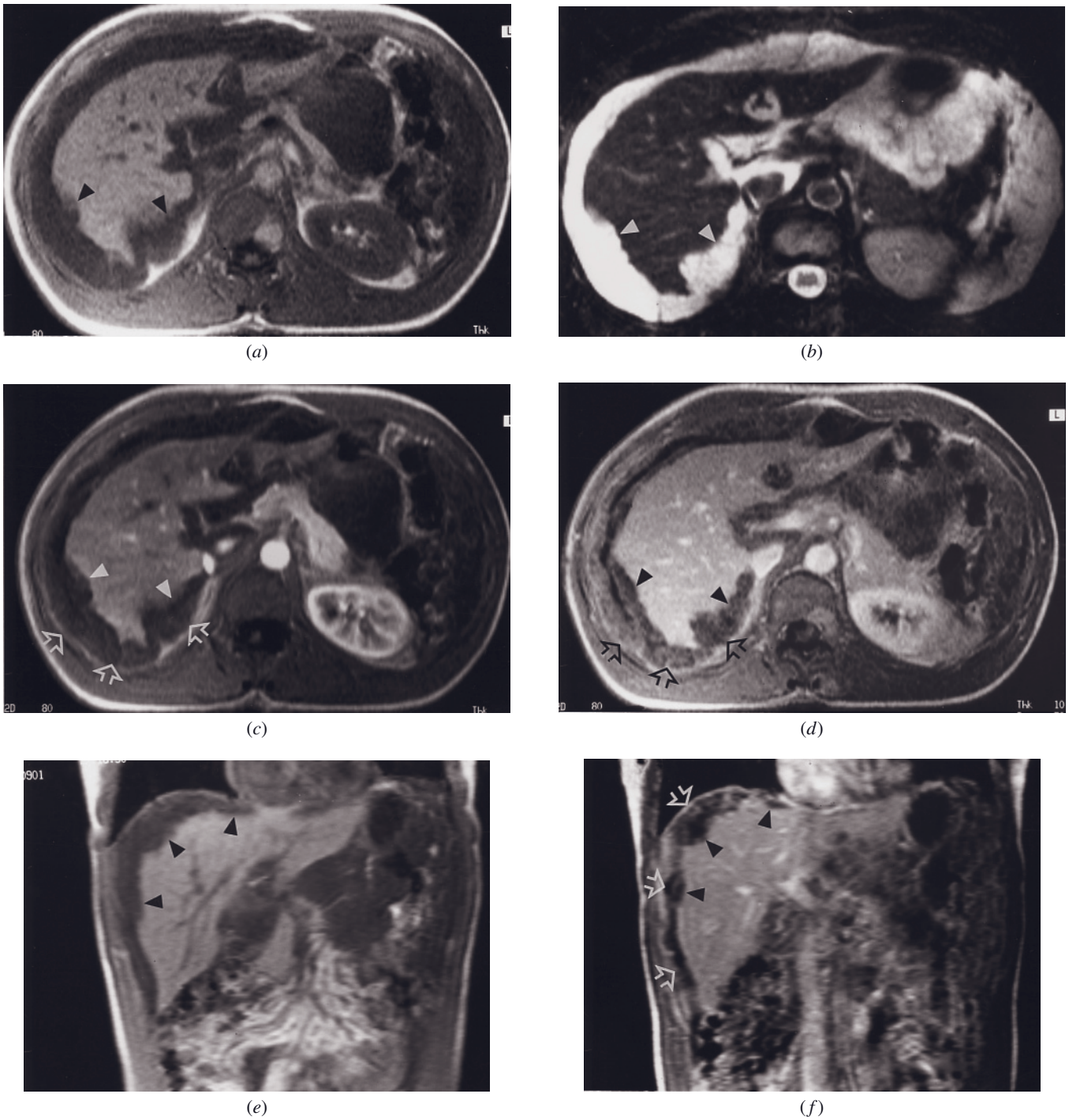

FIG. 7.29 Pseudomyxoma peritonei. SGE (*a*), T2-weighted fat-suppressed echo-train spin-echo (*b*), immediate (*c*) and interstitial-phase (*d*) postgadolinium SGE, and coronal precontrast SGE (*e*) and 5-min postgadolinium SGE (*f*) images in a patient with pseudomyxoma peritonei secondary to rupture of an appendiceal mucinous cystadenocarcinoma. On precontrast T1-weighted SGE (*a*) and T2-weighted fat-suppressed echo-train spin-echo (*b*) images, the gelatinous material surrounding the liver has regions in which the signal intensity resembles that of simple ascites. However, the characteristic scalloping of the liver margin (arrowheads, *a–f*) coupled with the enhancement of the material (open arrows, *c*, *d*, *f*) filling the abdomen establishes the correct diagnosis. Free fluid within the abdomen does not enhance. Coronal images (*e*, *f*) provide a global view of the disease extent and demonstrate subdiaphragmatic disease well. Coronal (*g*) and transverse (*h*) interstitial-phase gadolinium-enhanced fat-suppressed SGE images in

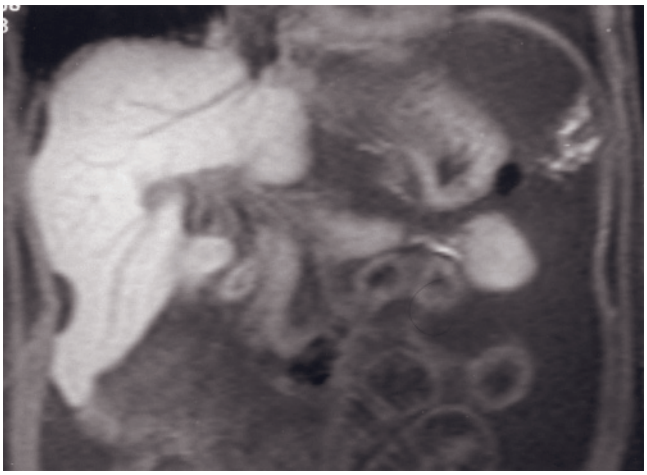

(*g*)

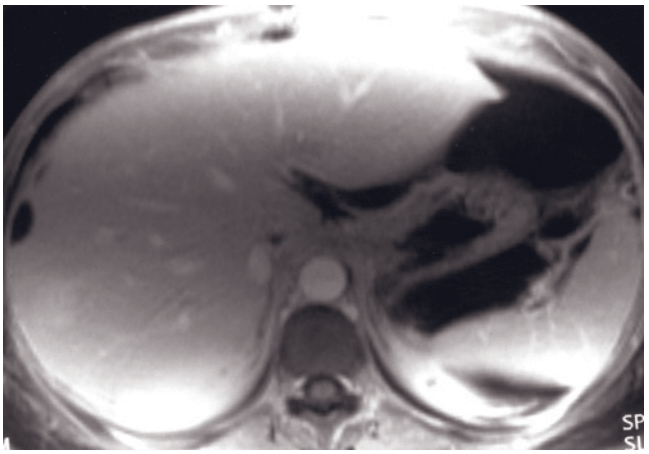

(*h*)

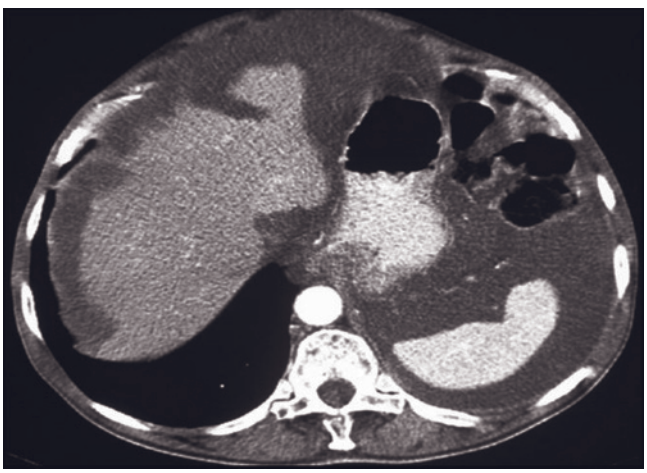

(*i*)

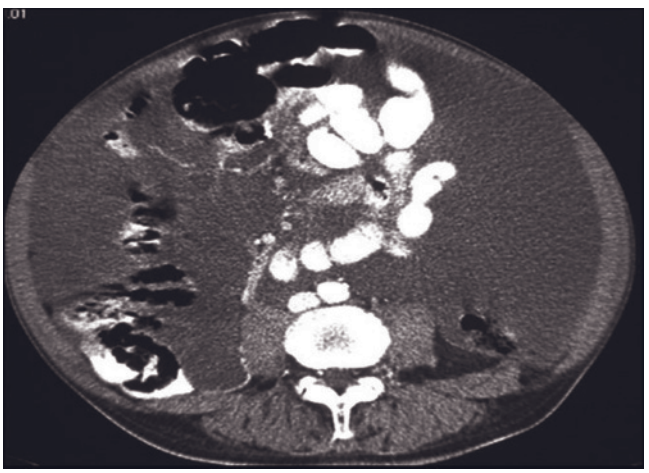

(*j*)

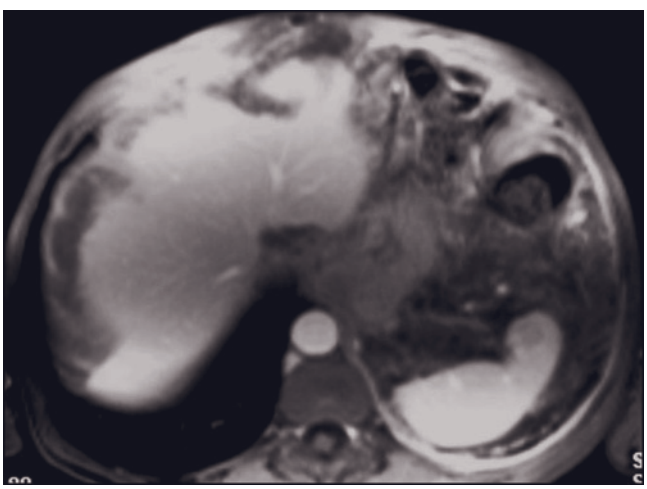

(*k*)

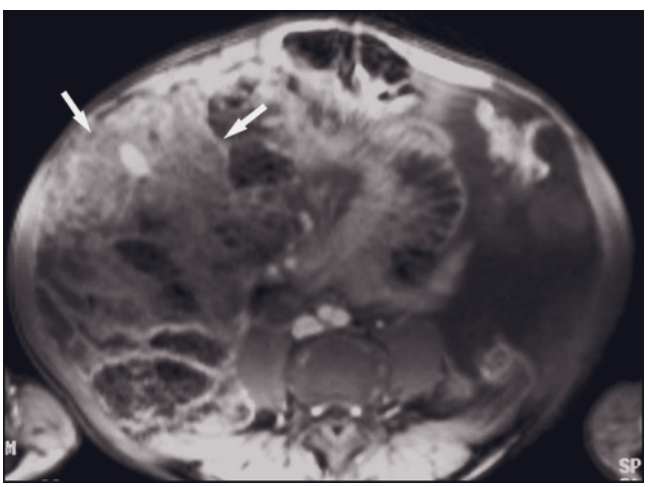

(*l*)

FIG. 7.29 (*Continued*) a second patient, who also has appendiceal mucinous cystadenocarcinoma. A large volume of ascites with extensive peritoneal enhancement is observed, associated with scalloping of the liver surface, features that are characteristic of pseudomyxoma peritonei. Postcontrast CT (*i*, *j*) and gadolinium-enhanced fat-suppressed T1-weighted SGE (*k*, *l*) images in a patient with ovarian cancer. MR images demonstrate thick, extensive peritoneal metastases (*k*, *l*), which encase the ascending colon (arrows, *l*). CT images suggest that there is only thin-volume peritoneal involvement (*i*, *j*).

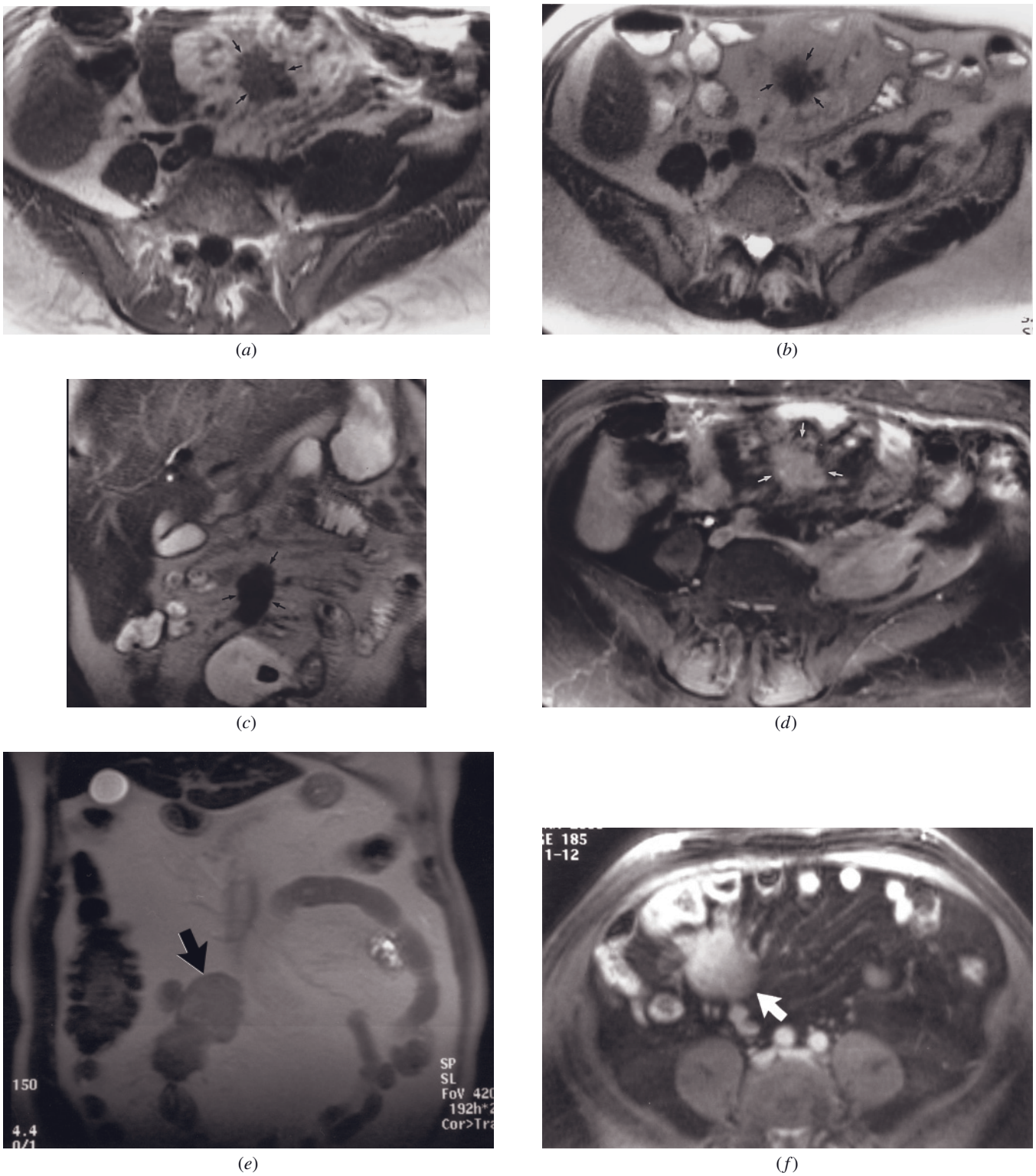

FIG. 7.30 Metastases of carcinoid tumor. SGE (*a*), T2-weighted SS-ETSE (*b*), coronal T2-weighted SS-ETSE (*c*), and 90-s post-gadolinium fat-suppressed SGE (*d*) images in a patient with a carcinoid tumor of the small bowel. Breath-hold T1-weighted SGE images are well suited for imaging the low-signal-intensity metastasis in the root of the small bowel mesentery (arrows, *a*); the radiating strands are highlighted by the surrounding high signal intensity of the intra-abdominal fat. The desmoplastic nature of these tumors is emphasized by low signal intensity on T2-weighted images (arrows, *b*, *c*) and only modest enhancement after intravenous contrast (arrows, *d*). Coronal T2-weighted SS-ETSE (*e*) and interstitial-phase gadolinium-enhanced fat-suppressed SGE (*f*) images in a second patient with mesenteric metastasis from carcinoid tumor demonstrate a spiculated mass (arrows, *e*, *f*) with thin radiating linear strands that extend into the mesentery, which are caused by a desmoplastic fibrous reaction in the surrounding

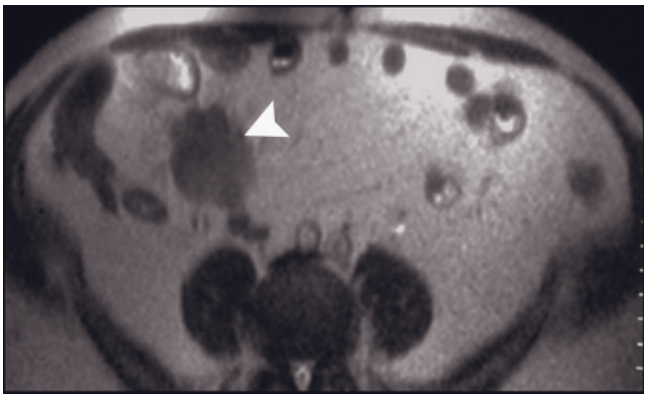

(*g*)

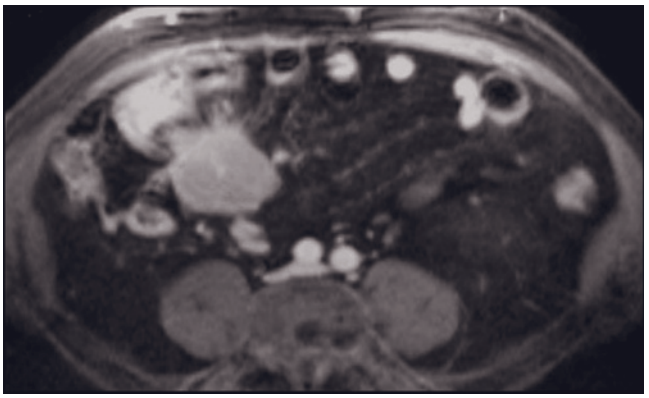

(*h*)

FIG. 7.30 (*Continued*) tissue. T2-weighted SS-ETSE (*g*) and interstitial-phase gadolinium-enhanced fat-suppressed T1-weighted SGE (*h*) images in a third patient with a carcinoid tumor of the ileum demonstrate similar findings (arrowhead, *g*).

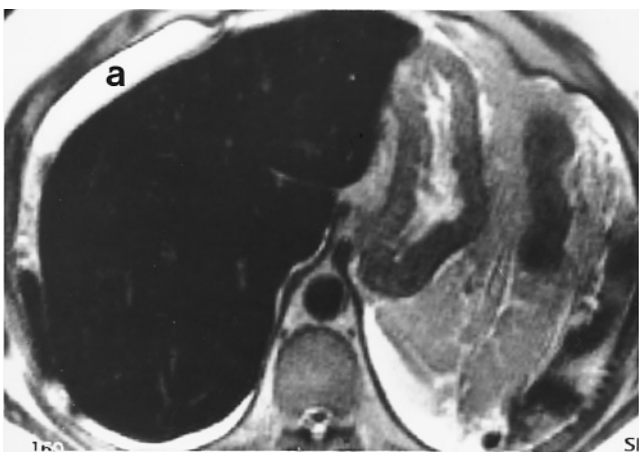

FIG. 7.31 Ascites. T2-weighted SS-ETSE image in a patient with simple transudative ascites. High-signal-intensity ascites (a) surrounds the abdominal viscera. The liver is low in signal intensity secondary to iron overload from multiple transfusions.

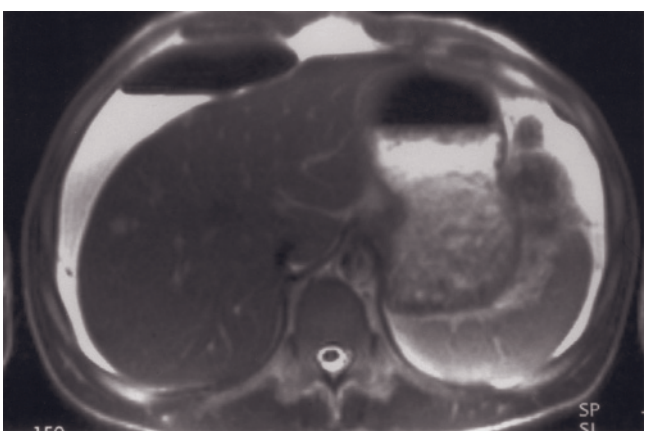

(*a*)

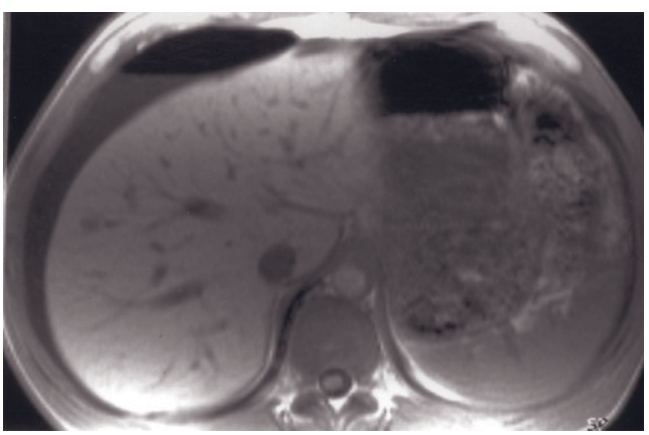

(*b*)

FIG. 7.32 Postsurgical intraperitoneal air and fluid. Transverse T2-weighted SS-ETSE (*a*) and SGE (*b*) images in a patient with a recent history of surgery demonstrate the presence of pneumoperitoneum and ascites. Note that air is invariably located along the most elevated surface in structures.

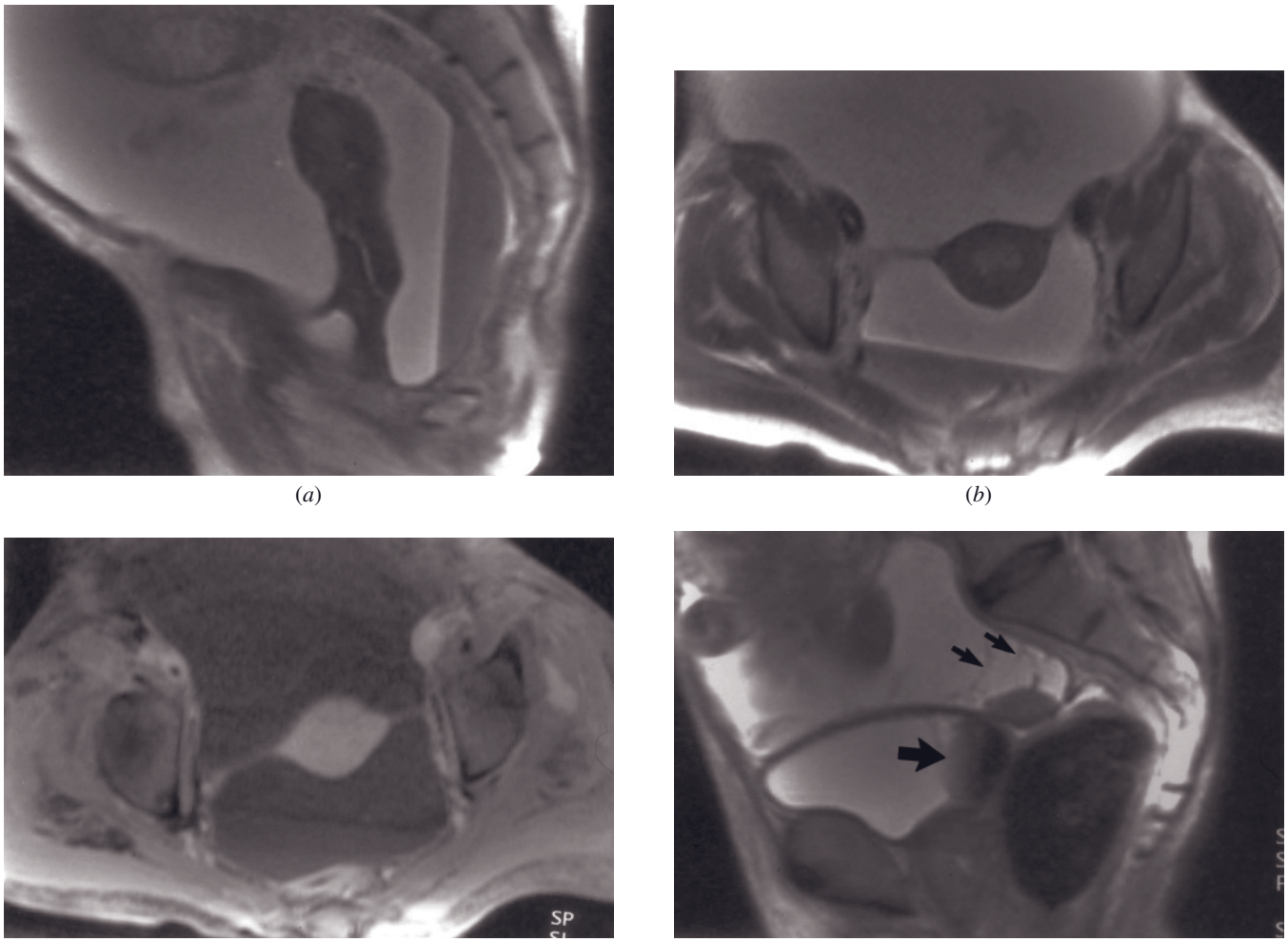

FIG. 7.33 High-protein-content ascites, adhesions. Sagittal (*a*) and transverse (*b*) T2-weighted SS-ETSE and transverse interstitial-phase gadolinium-enhanced fat-suppressed SGE (*c*) images. A large volume of ascites is seen within the pelvis. In the posterior cul-de-sac, a fluid-fluid level is seen on the T2-weighted image with the dependent fluid layer being low in signal, which is consistent with high protein content. Sagittal T2-weighted SS-ETSE image (*d*) in a second patient demonstrates a large volume of ascites in the pelvis with multiple thin septations (small arrows, *d*) and a focal collection of proteinaceous material in the vesicorectal space. Low signal in the dependent portion of the bladder (large arrow, *d*) represents gadolinium.

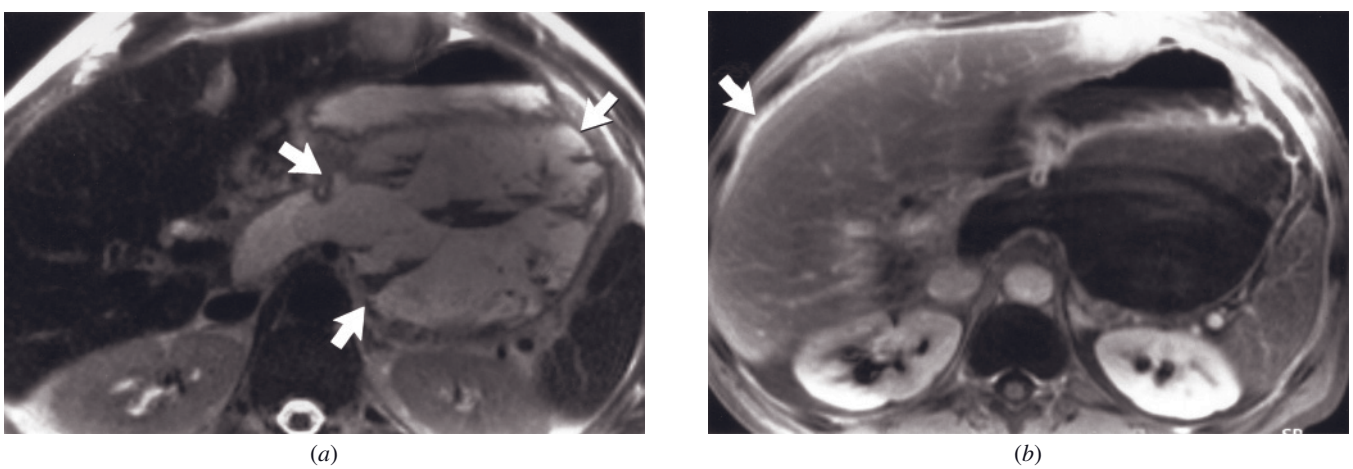

FIG. 7.34 Lesser sac involvement in malignant disease. T2-weighted SS-ETSE (*a*) and 90-s postgadolinium fat-suppressed SGE (*b*) images. There is a dominant fluid collection in the lesser sac (arrows, *a*), which contains multiple septations and multiple fluid-fluid levels from proteinaceous debris as shown on the T2-weighted image (*a*). The gadolinium-enhanced fat-suppressed image (*b*), obtained at the same anatomic level, shows the lesser sac collection but not the internal septations. A thin layer of enhancing peritoneal disease (arrow, *b*) is appreciated on the gadolinium-enhanced fat-suppressed image that is not apparent on the T2-weighted image.

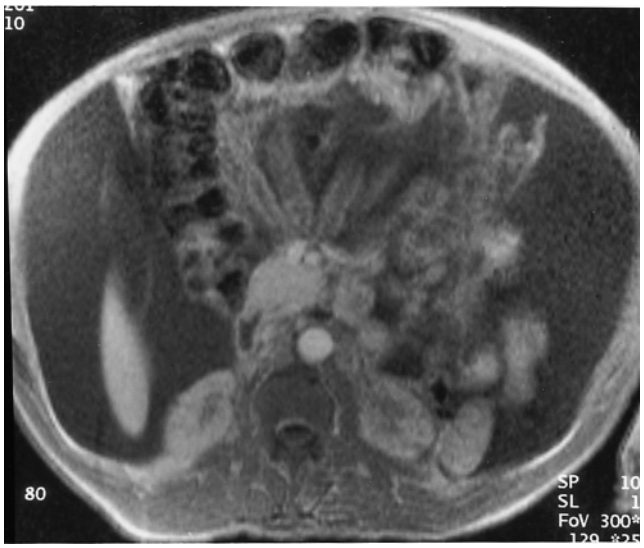

FIG. 7.35 Benign ascites. SGE image demonstrates that small and large bowel have floated anteriorly in a central location. This confirms that ascites is simple, because no tethering of bowel from malignant or inflammatory adhesions has occurred.

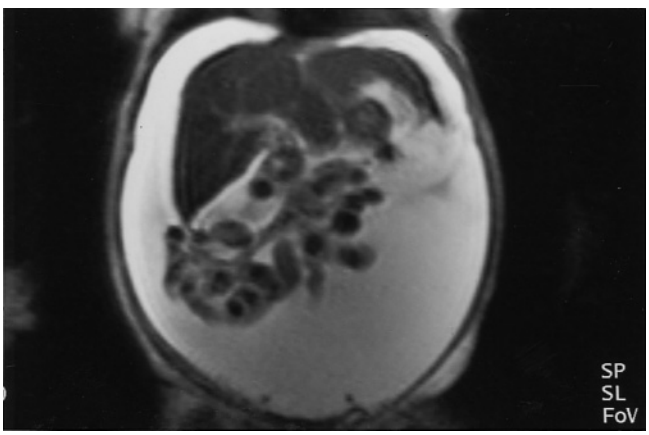

FIG. 7.36 Ascites in a neonate. Coronal SS-ETSE image clearly shows the liver and centrally lying bowel. The central position of the bowel reflects the simple nature of the ascites.

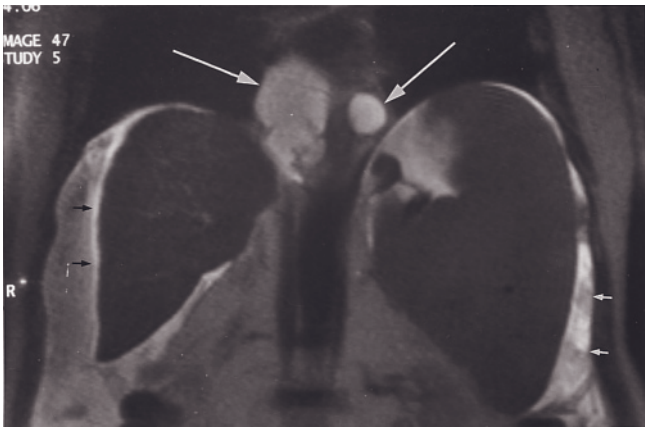

(*a*)

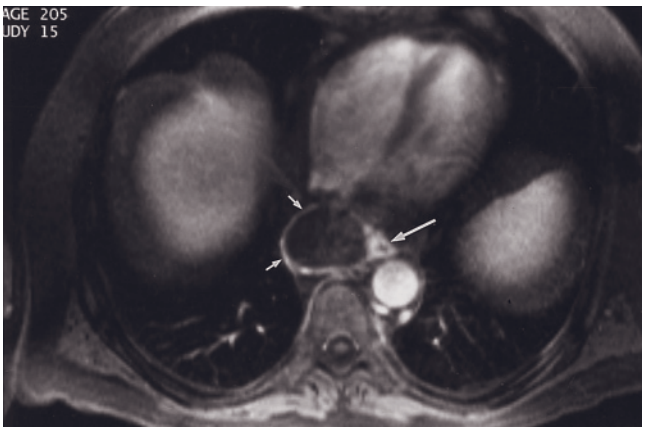

(*b*)

FIG. 7.37 Mediastinal extension of ascites. Coronal SSETSE (*a*) and transverse 45-s postgadolinium fat-suppressed SGE (*b*) images. On the coronal image, ascites is noted along the surfaces of the liver and enlarged spleen (small arrows, *a*) and mediastinal extension of the fluid is apparent (long arrows, *a*). On the gadolinium-enhanced transverse image, the encapsulated collection of ascites in the posterior mediastinum is shown (small arrows, *b*) and close approximation to the esophagus (long arrow, *b*) is apparent.

Intraperitoneal Bile

Free intraperitoneal bile is usually the result of surgery [60]. When present in small amounts, it is clinically occult. However, in the setting of duct injury, bile leakage may result in a biloma or bile peritonitis [60] (fig. 7.41). Free bile preferentially collects in the right upper quadrant, where it incites an inflammatory reaction. A biloma results if the bile is walled off by a pseudocapsule and adhesions. The signal intensity of a biloma is variable and mimics that of the gallbladder. Bilomas may be low, intermediate, or high in signal intensity on T1-weighted images. They are high in signal intensity on T2-weighted images. Enhancement of peritoneum on gadolinium-enhanced T1-weighted images reflects the inflammation associated with bile leak (fig. 7.42).

Intraperitoneal Urine

Bladder rupture leads to extravasation of urine. The location of the free urine is a function of whether the dome or the bladder base is injured. If the base is compromised, urine collects extraperitoneally, whereas injury to the dome results in intraperitoneal urine, also known as urine ascites. On unenhanced images, the signal intensity of urine ascites is nonspecific. Contrast administration establishes the diagnosis as high-signal-intensity gadolinium chelate in urine leaks into the peritoneal cavity.

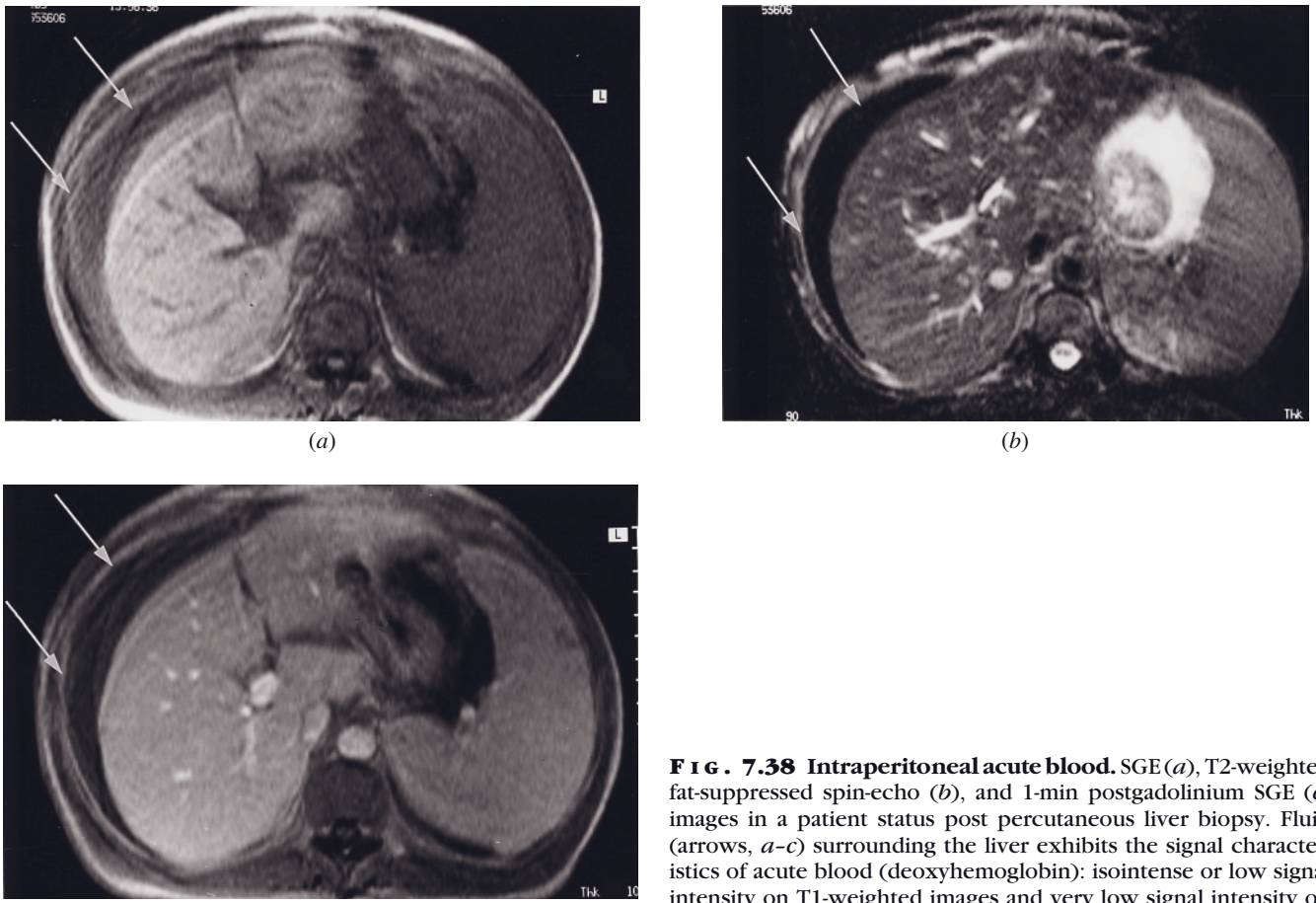

FIG. 7.38 Intraperitoneal acute blood. SGE (*a*), T2-weighted fat-suppressed spin-echo (*b*), and 1-min postgadolinium SGE (*c*) images in a patient status post percutaneous liver biopsy. Fluid (arrows, *a–c*) surrounding the liver exhibits the signal characteristics of acute blood (deoxyhemoglobin): isointense or low signal intensity on T1-weighted images and very low signal intensity on T2-weighted images.

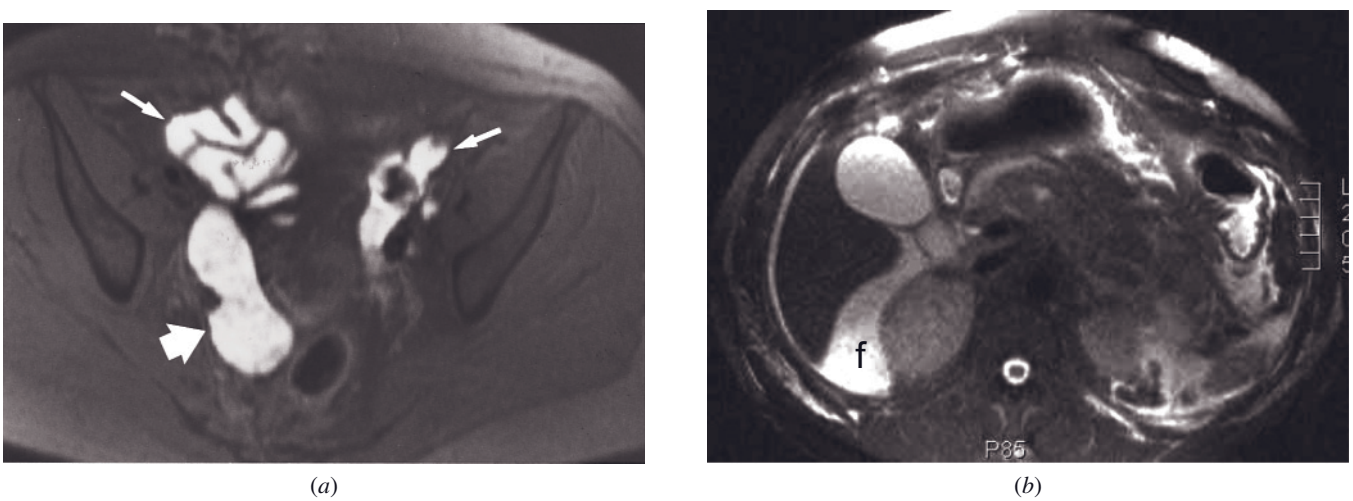

FIG. 7.39 Intraperitoneal blood. T1-weighted fat-suppressed spin-echo image (*a*) in a woman 1 week after hysterectomy. There is a high-signal-intensity collection in the right pelvis, consistent with acute blood (large arrow). T1-weighted fat suppression is particularly sensitive for the detection of blood, but extracellular methemoglobin must be distinguished from the high-signal-intensity proteinaceous intraluminal bowel contents (small arrows). T2-weighted short tau inversion recovery (*b*), T1-weighted fat-suppressed SGE (*c*), and T1-weighted interstitial-phase postgadolinium magnetization-prepared rapid gradient-echo (*d*) images demonstrate acute hemorrhagic pancreatitis in another patient. There is free fluid (f) in the abdominal cavity demonstrating high

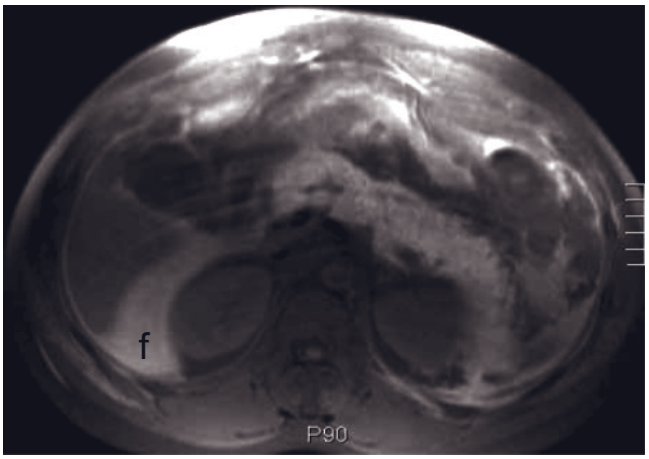

(*c*)

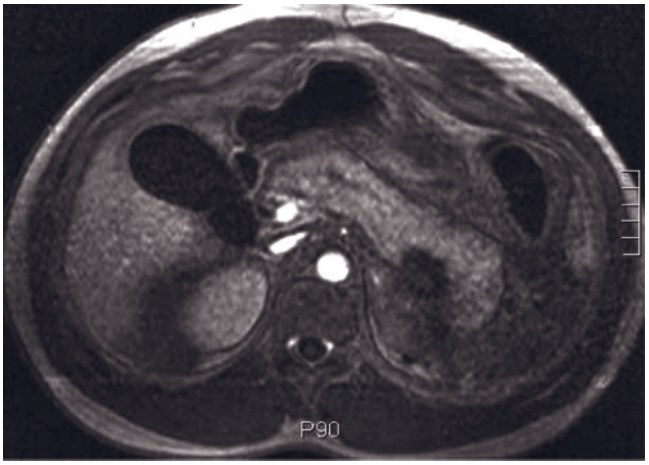

(*d*)

FIG. 7.39 (*Continued*) signal both on T2-weighted (*b*) and fat-suppressed T1-weighted image (*c*), which is consistent with bloody ascites. The enlarged pancreas shows low signal on T2-weighted image (*b*) and high signal on T1-weighted image (*c*), which is consistent with hemorrhagic pancreatitis. The enhancement pattern is also relatively homogeneous on postgadolinium image (*d*).

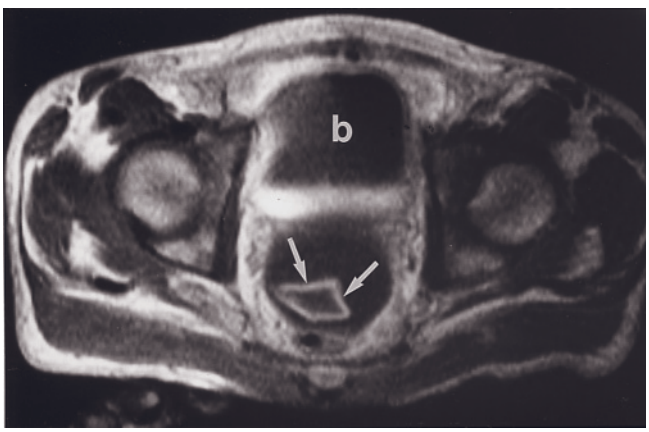

(*a*)

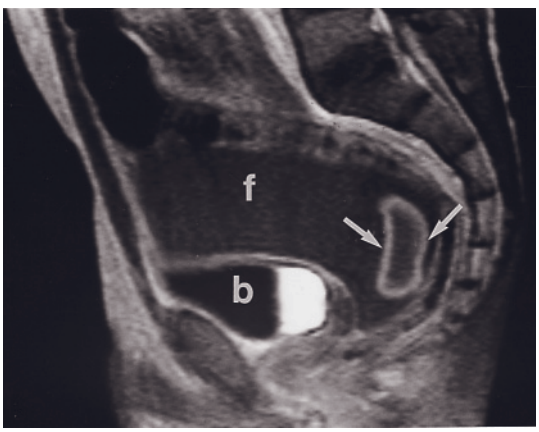

(*b*)

FIG. 7.40 Pelvic hematoma. Transverse (*a*) and sagittal (*b*) interstitial-phase gadolinium-enhanced T1-weighted SGE images in a patient after splenic injury. Subacute hematomas usually have a low-signal-intensity core with a high-signal-intensity surrounding rim (arrows, *a*, *b*) on T1-weighted images. These imaging characteristics reflect the retracting clot surrounded by extracellular methemoglobin. b, Bladder; f, free pelvic fluid.

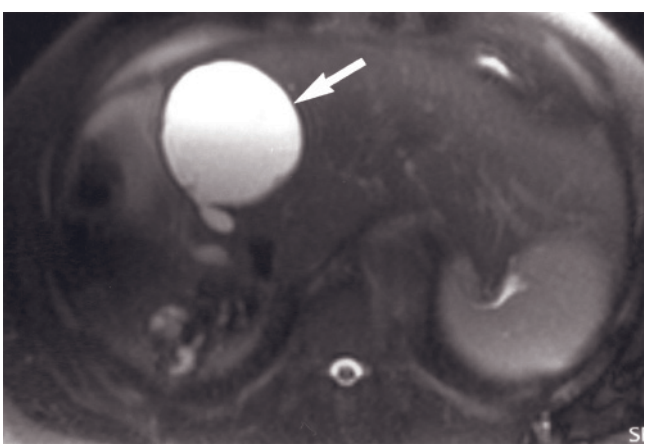

(*a*)

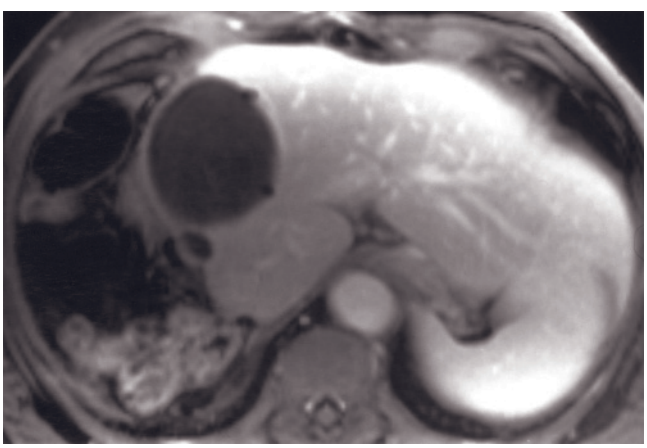

(*b*)

FIG. 7.41 Biloma. T2-weighted fat-suppressed SS-ETSE (*a*) and 90-s postgadolinium fat-suppressed SGE (*b*) images in a patient after right hepatectomy demonstrate a cystic mass along the resected surface of the left lobe (arrow, *a*), consistent with biloma.

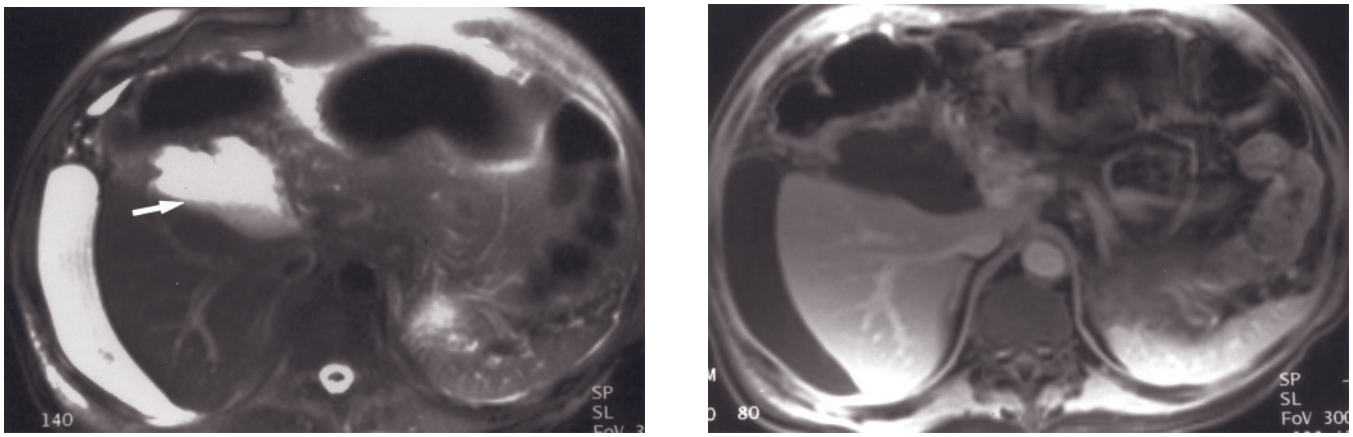

(*a*) (*b*)

FIG. 7.42 Infected biloma. T2-weighted fat-suppressed SS-ETSE (*a*) and 90-s postgadolinium fat-suppressed SGE (*b*) images. There is a fluid collection in the region of the gallbladder fossa that appears somewhat loculated and complex, as evidenced by a fluid-debris level (arrow, *a*) on the T2-weighted image. Note that debris has an irregular linear interface with fluid, unlike high-protein-content ascites, which has a sharp linear fluid-fluid level. A moderate amount of perihepatic ascites is also present, associated with increased peritoneal enhancement. The patient had a recent history of cholecystectomy, and these findings are consistent with infected biloma with peritonitis.

INTRAPERITONEAL FOREIGN BODIES

Retained Surgical Sponge (Gossypiboma)

Gossypiboma is a term used to describe a mass in the body that contains retained surgical sponges and reactive tissue. The term derives from the Latin *gossipium* and the Kiswahili *boma,* which mean "cotton" and a "place of concealment," respectively. A review of 61 retained foreign bodies in 54 patients over 16 years revealed that 69% of the retained substances were surgical sponges [61]. The sponges are inert in human tissue and do not undergo decomposition. There are two types of foreign body reaction at histopathology: an exudative reaction leading to abscess formation or fluid collection and an aseptic fibrinous reaction resulting in adhesion, encapsulation, and eventual formation of granulomas of various sizes. Owing to frequently nonspecific and variable imaging appearances, accurate diagnosis of a gossypiboma may be difficult [61]. The CT findings of gossypiboma include characteristically wavy, striped, and/or spotted appearances, a well-defined round mass with a thick wall, internal heterogeneous densities, and an eccentric high patch. CT imaging is superior to MRI in detecting retained surgical sponge because sponge manufacturers impregnate sponges with material that appears high density on CT and therefore is readily detectable. At present, manufacturers have not included material that is high signal on MRI, and the low signal of these entities is very difficult to appreciate on MRI (fig. 7.43).

Intraperitoneal Catheter

Intraperitoneal catheters are well shown on CT images because of their radiopaque structure. On MRI, catheters are generally signal void. Determination of location of catheters is therefore better performed with CT. Injection of gadolinium into the catheter improves the visibility of catheters and related complications on MR images [62].

Cocoon

A localized collection of inflammatory debris may develop around tubes or catheters (e.g., CSF-peritoneal shunt or indwelling peritoneal catheters) within the peritoneal cavity, with development of a pseudocapsule. This entity is termed a cocoon (fig. 7.44).

VASCULAR DISEASE

In general, abnormalities in the splanchnic circulation are well shown on postgadolinium fat-suppressed SGE images (fig. 7.45). Microvarices within the peritoneal lining and omental hypertrophy are commonly observed in patients with cirrhosis and portal venous hypertension. Microvarices of the peritoneum can be difficult to distinguish from either inflammatory or neoplastic peritoneal disease. Distinctive features of microvarices on gadolinium-enhanced T1-weighted fat-suppressed SGE include the observation of curvilinear, small tubular structures and extension of some of these curvilinear structures into retroperitoneal fat (fig. 7.46). In contrast

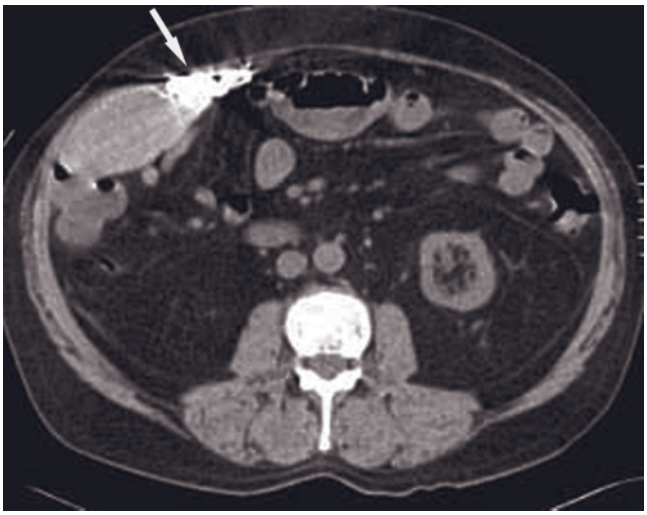

(*a*)

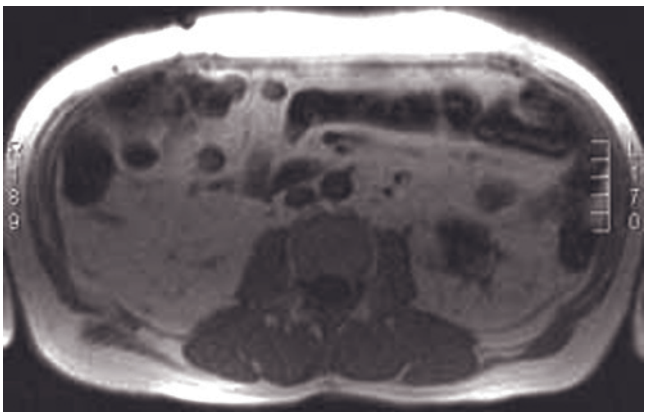

(*b*)

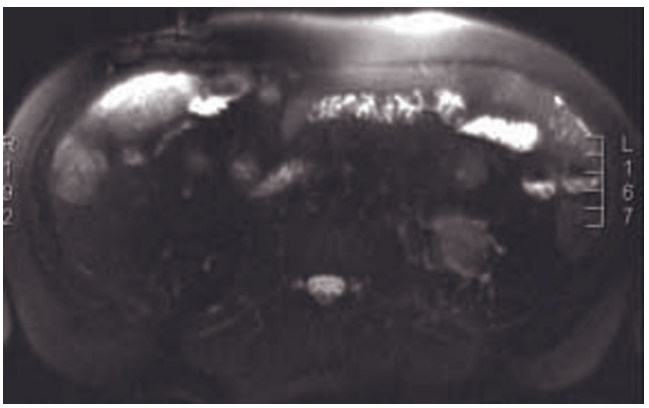

(*c*)

FIG. 7.43 Intraperitoneal retained surgical sponge. Precontrast CT image (*a*) in a patient with intra-abdominal surgical sponge demonstrates intra-abdominal calcified focus (arrow, *a*) that is very difficult to appreciate on T1-weighted SGE (*b*) and T2-weighted fat-suppressed SS-ETSE (*c*) images.

to microvarices, neither distinct curvilinear tubular structures nor their extension into retroperitoneal fat is visualized in inflammatory or malignant peritoneal disease.

INFLAMMATION

Mesenteric Panniculitis (Isolated Lipodystrophy of the Mesentery, Retractile Mesenteritis, Sclerosing Mesenteritis)

Mesenteric panniculitis is a rare disorder characterized grossly by a diffuse, localized, or multinodular fibrofatty thickening of the mesentery of the small and/or large bowel. The disorder is notable for a spectrum of pathologic changes within the mesentery including inflammatory infiltrates, fat necrosis, and fibrosis [63–65]. Although the etiology of mesenteric panniculitis is unclear, infection, trauma, ischemia, autoimmune disorders, and a history of previous abdominal surgery have been suggested as causative factors [64, 66, 67]. The diagnosis of mesenteric panniculitis is supported by the absence of pancreatitis, the most common cause of intra-abdominal fat necrosis, and inflammatory bowel disease. The changes in the mesentery may be focal or diffuse. When diffuse, the mesenteric fat is traversed by low-signal-intensity strands on T1-weighted images [67] (fig. 7.47). In the focal form, heterogeneous nodular masses of fat necrosis are noted. These lesions exhibit varying amounts of fat, fluid, calcification, and soft tissue [67, 68]. A variety of malignant, inflammatory, or infectious etiologies may result in inflammation of the mesentery, which may produce an imaging appearance indistinguishable from that of mesenteric panniculitis. The differential diagnosis includes lymphoma, desmoid tumor, carcinomatosis, and carcinoid tumor [66].

Pancreatitis

Acute pancreatitis is defined as an acute inflammatory condition of the pancreas, which typically presents with

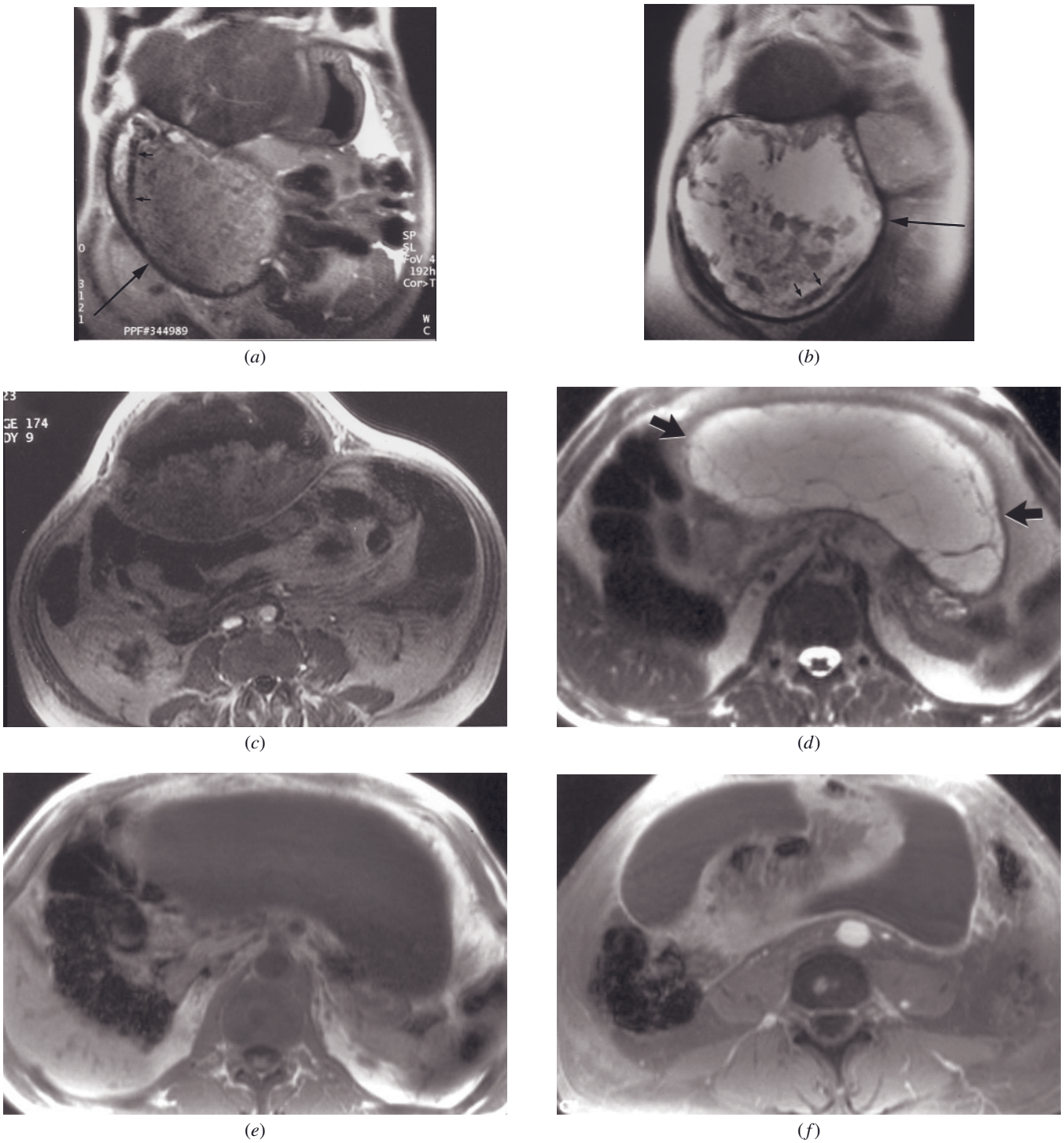

(*a*) (*b*) (*c*) (*d*) (*e*) (*f*)

FIG. 7.44 Pseudocyst surrounding peritoneal catheter (cocoon). Coronal T2-weighted SS-ETSE image from adjacent planes (*a*, *b*; *b* is more anterior) and 90-s postgadolinium SGE (*c*) image. A 14-cm encapsulated debris-containing pseudocyst is present in the midabdomen, immediately beneath the liver. A low-signal-intensity pseudocapsule surrounds the lesion (long arrows, *a*, *b*).The peritoneal catheter is identified within the cocoon (small arrows, *a*, *b*). A substantial volume of particulate debris is present (*a–c*), which is shown to layer on the transverse gadolinium-enhanced SGE image (*c*). Outside CT imaging study had been interpreted as demonstrating a hepatocellular carcinoma (HCC). T2-weighted SS-ESTSE (*d*), SGE (*e*), and 90-s postgadolinium fat-suppressed SGE (*f*) images in a second patient with a peritoneal dialysis catheter demonstrate a large, multiseptated encapsulated fluid collection (arrows, *d*). This fluid collection has an enhancing rim on postgadolinium images (*f*) and extends from the level of the pancreas inferiorly into the upper pelvis.

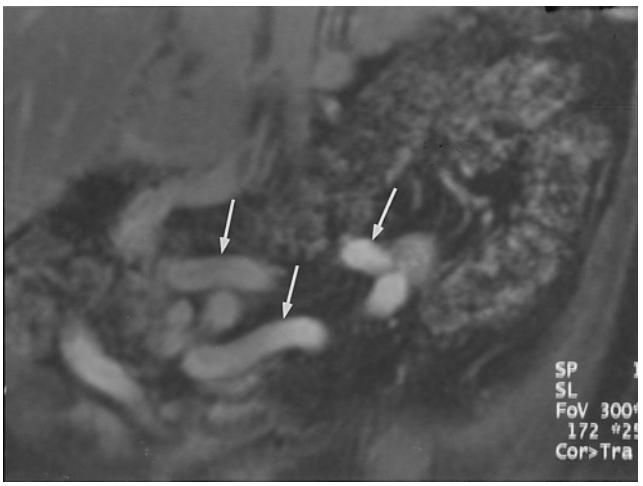

FIG. 7.45 Enlarged collateral of the superior mesenteric vein. Coronal 90-s postgadolinium fat-suppressed SGE image demonstrates an enlarged tortuous collateral vessel of the superior mesenteric vein (arrows).

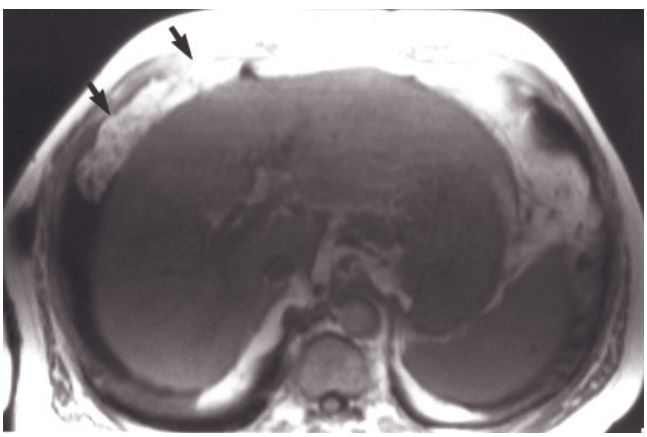

(*a*)

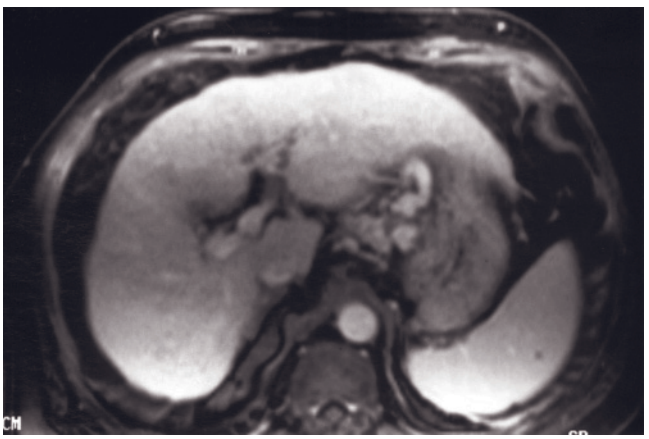

(*b*)

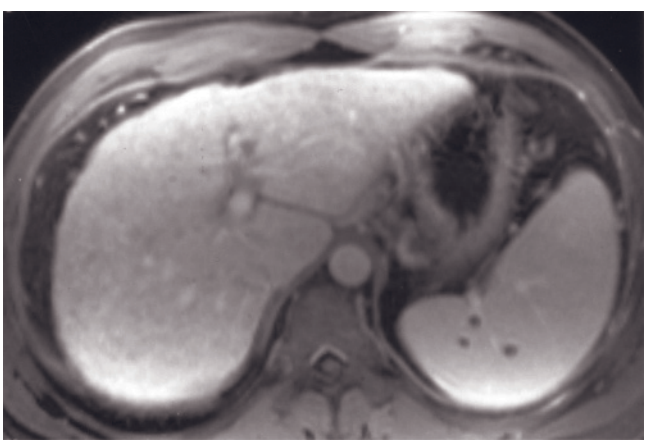

(*c*)

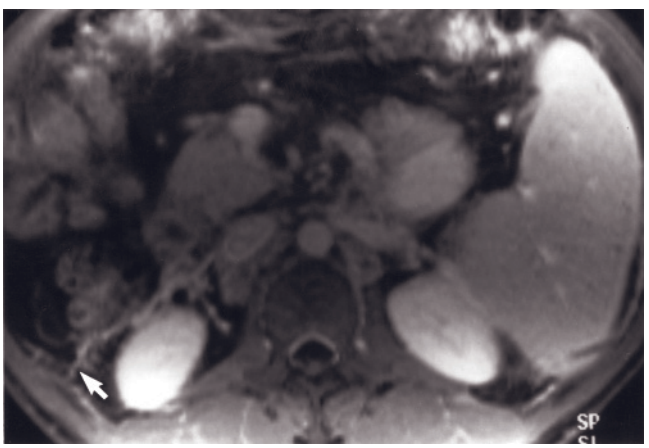

(*d*)

FIG. 7.46 Omental hypertrophy and peritoneal varices. SGE (*a*) and interstitial-phase gadolinium-enhanced fat-suppressed SGE (*b*) images in a cirrhotic patient demonstrate marked hypertrophy of the omentum. On the SGE image, the hypertrophied omentum is high signal (arrows, *a*). On the gadolinium-enhanced fat-suppressed image (*b*), small tubular structures consistent with microvarices are identified. Interstitial-phase gadolinium-enhanced fat-suppressed SGE (*c*) image in a second patient shows features similar to those described above. Fatty tissue anterior and along the lateral liver capsule represents hypertrophied omentum containing vessels. The liver is cirrhotic, and the spleen is enlarged and contains multiple Gamna–Gandy bodies. Interstitial-phase gadolinium-enhanced fat-suppressed SGE (*d*, *e*) images in a third cirrhotic patient demonstrate the presence of peritoneal varices

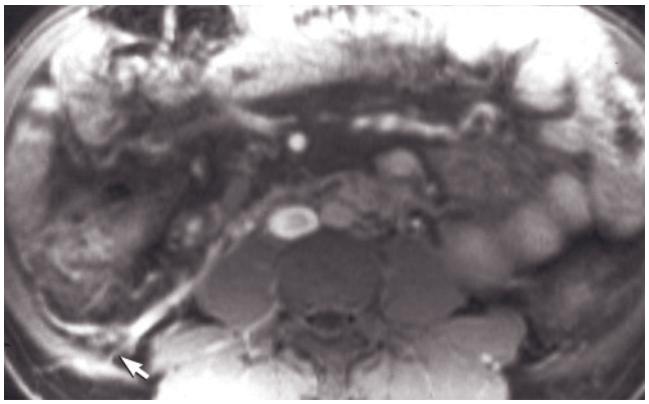

(*e*)

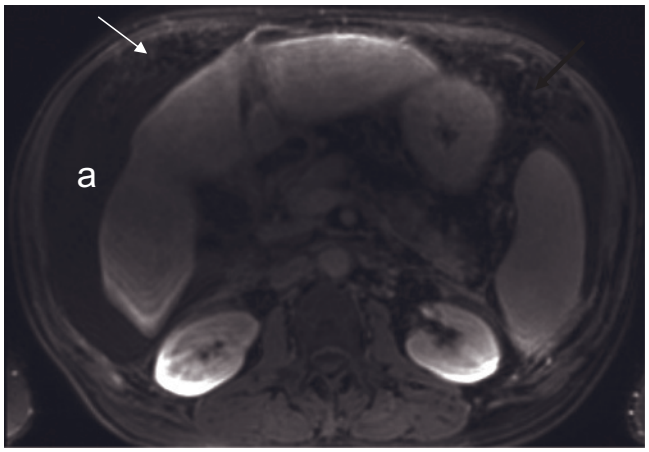

(*f*)

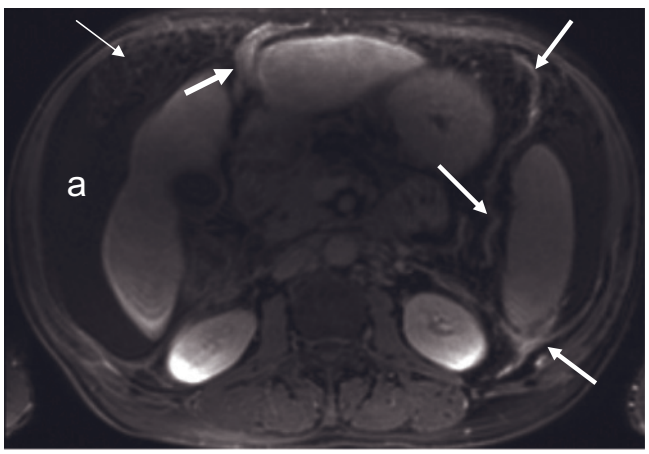

(*g*)

Fig. 7.46 (*Continued*) that appear as enhancing peritoneum in the pericolic gutters, simulating peritoneal metastases. Note that occasional vessels perforate the peritoneum and extend into the retroperitoneum (arrows, *d*, *e*), establishing the diagnosis of microvarices. T1-weighted fat-suppressed interstitial-phase postgadolinium 3D-GE images (*f*, *g*) at 3.0 T in another patient with cirrhosis demonstrate omental hypertrophy (white thin arrows), mesenteric-omental-peritoneal varices (black arrows), patent paraumbilical vein (white thick arrow), and ascites (a).

abdominal pain and is associated with elevated levels of pancreatic enzymes (especially lipase and amylase) in blood and urine.

Patients with pancreatitis usually present with extrapancreatic fluid collections, preferentially in the lesser sac [2]. The enzyme-laden fluid also may dissect into the abdominal cavity and retroperitoneum. Not infrequently, fluid tracks along tissue planes to localize subcapsularly in the liver and/or spleen. Precontrast T1-weighted fat-suppressed SGE or 3D-GE imaging is particularly effective at demonstrating the presence of blood in hemorrhagic pancreatitic ascites (fig. 7.39). The peritoneum typically enhances on gadolinium-enhanced T1-weighted fat-suppressed images because of the caustic nature of the activated pancreatic enzyme-containing fluid.

Peritonitis

Peritonitis may be caused by a variety of infectious or noninfectious causes, many of which are related to bowel perforation. Trauma, complications of surgery, inflammatory bowel disease, and peritoneal dialysis are common underlying causes. Peritonitis appears as diffuse increased enhancement of the peritoneum and mesentery and is most clearly defined on interstitial-phase gadolinium-enhanced fat-suppressed SGE or 3D-GE images (figs. 7.48, 7.49, and 7.50).

Pseudocysts may develop in the setting of peritonitis as walled-off collections of fluid. In uncomplicated cases, they are low in signal intensity on T1-weighted images and very high in signal intensity on T2-weighted images. Complex fluid is characterized by increased signal on T1-weighted images, decreased or heterogeneous signal on T2-weighted images, or a combination of both. Gadolinium-enhanced T1-weighted images reveal increased enhancement and occasionally increased thickness of the inflamed peritoneum, which is more conspicuous in combination with fat suppression.

Abscess

Intra-abdominal abscesses are most often the sequelae of gastrointestinal or biliary surgery, diverticulitis, and

(*a*)

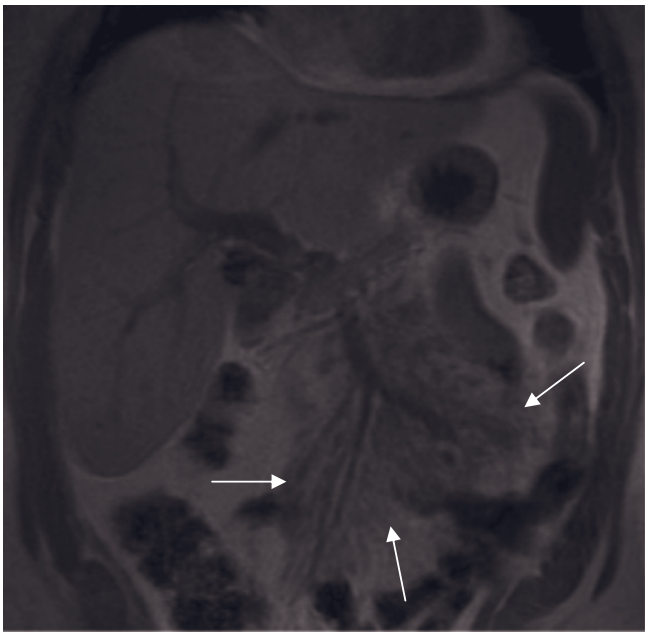

(*b*)

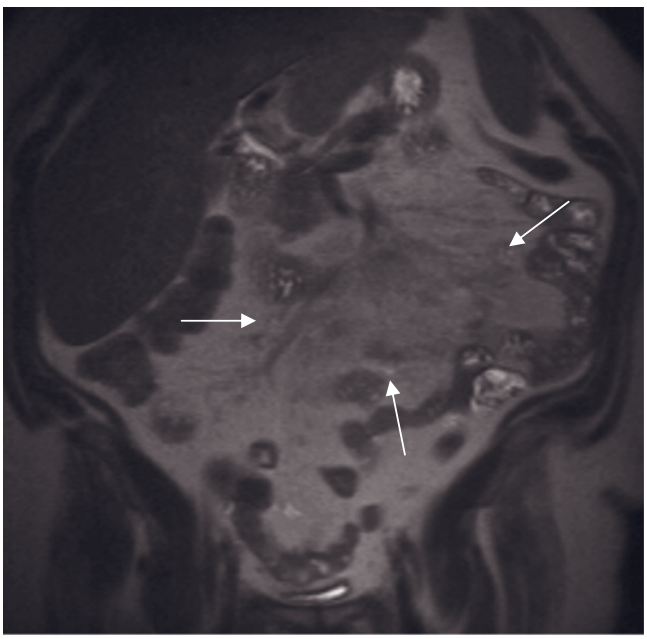

(*c*)

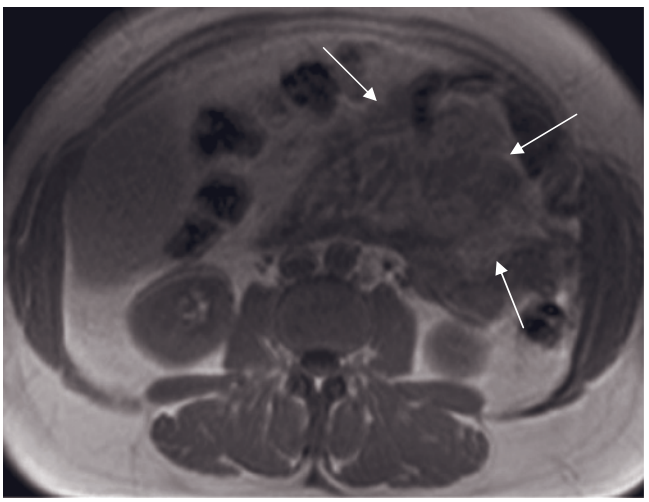

(*d*)

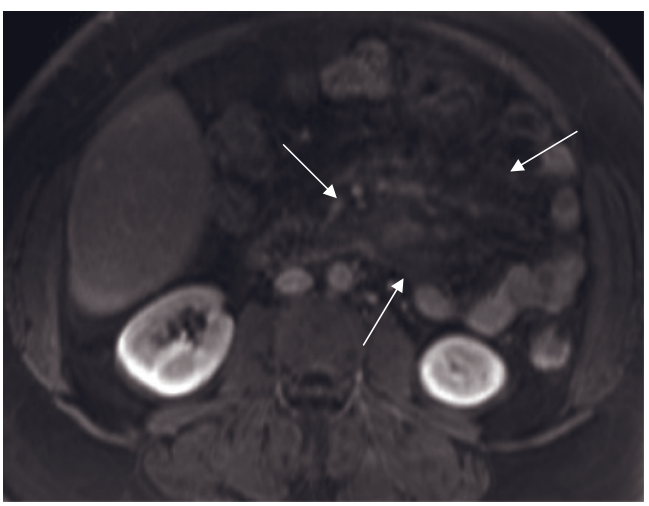

(*e*)

FIG. 7.47 Mesenteric lipodystrophy. T1-weighted SGE image (*a*) demonstrates low-signal-intensity stranding in the fat of the mesentery (long arrows, *a*) consistent with mesenteric lipodystrophy. A small ventral hernia is also present (arrow, *a*). Coronal T1-weighted SGE (*b*) and T2-weighted single-shot echo-train spin-echo (*c*), axial T1-weighted SGE (*d*), and axial T1-weighted fat-suppressed interstitial-phase postgadolinium 3D-GE (*e*) images at 3.0 T in another patient show mesenteric panniculitis (arrows, *b–e*). There is stranding (arrows, *b–e*) along the mesentery that demonstrates low signal intensity both on T1-weighted SGE images and T2-weighted images and mild to moderate enhancement on postgadolinium image.

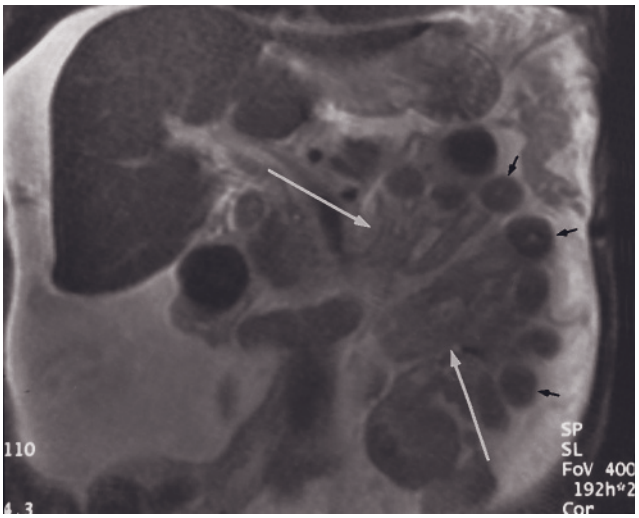

(*a*)

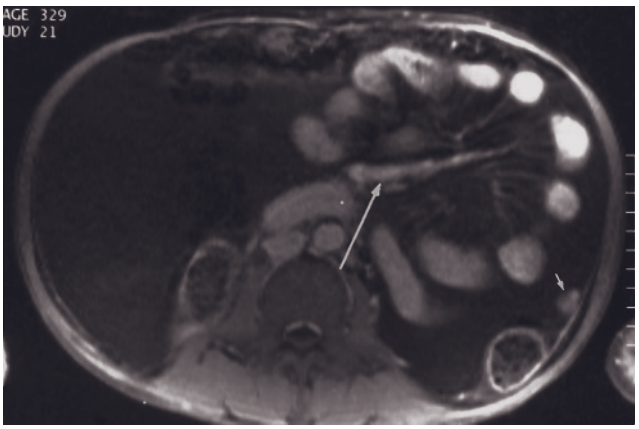

(*b*)

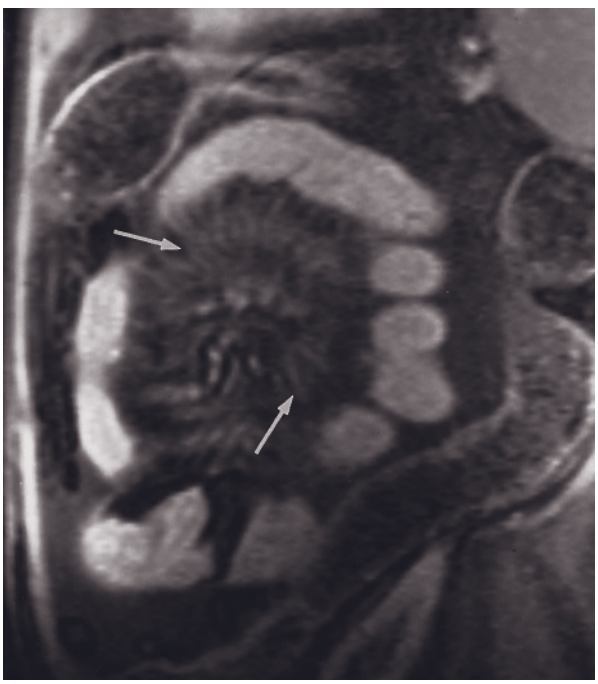

(*c*)

FIG. 7.48 Tuberculous peritonitis. Coronal T2-weighted SSETSE (*a*), transverse (*b*), and sagittal (*c*) interstitial-phase gadolinium-enhanced fat-suppressed T1-weighted SGE images in a second patient, who has tuberculous peritonitis. A large volume of ascites is present. Multiple loops of thickened small bowel are appreciated (short arrows, *a*). The mesentery is infiltrated and intermediate in signal intensity (long arrows, *a*) on the T2-weighted image (*a*). The mesenteric vessels are closely bundled (long arrow, *b*), reflecting adherence of the vessels to each other secondary to the inflammatory process. Terminal branches of the mesenteric vessels (arrows, *c*) fan out to the thickened loops of small bowel, creating a spokewheel type pattern on the sagittal image. Increased enhancement and mild increased thickness of the peritoneum with peritoneum-based nodules (small arrow, *b*) are also appreciated. The appearance is that of retractile mesenteritis, which can be caused by a number of etiologies including tuberculosis.

Crohn disease [69]. In the appropriate clinical setting, a focal fluid collection that demonstrates rim enhancement on gadolinium-enhanced images suggests the correct diagnosis. The addition of fat suppression and image acquisition at 2–5 min after injection (interstitial phase) can highlight the enhancement of the abscess wall and surrounding tissues (figs. 7.51, 7.52, and 7.53). Layering of lower-signal-intensity debris in the dependent portion of the cystic lesion on T2-weighted images is a common finding in abscesses, reflecting the layering of high protein content dependently in abscesses (fig. 7.54). This is a very specific finding for abscess. When air is identified within a fluid collection, active infection and/or fistula to the bowel (fig. 7.55) is present. The combination of breathing-independent T2-weighted echo-train spin-echo, gadolinium-enhanced capillary-phase T1-weighted gradient-echo, interstitial-phase fat-suppressed gradient-echo, and multiplanar imaging renders MRI a very accurate technique for detecting intraperitoneal abscesses. MRI may be the technique of choice in patients who have dense intraluminal barium contrast, renal failure, or allergy to iodine. Noone et al. [70] reported an accuracy of 96% in detecting intraperitoneal abscesses by MR. Multiplanar imaging is also effective at showing the oval-shaped abscess collections, to distinguish them from tubular shaped bowel

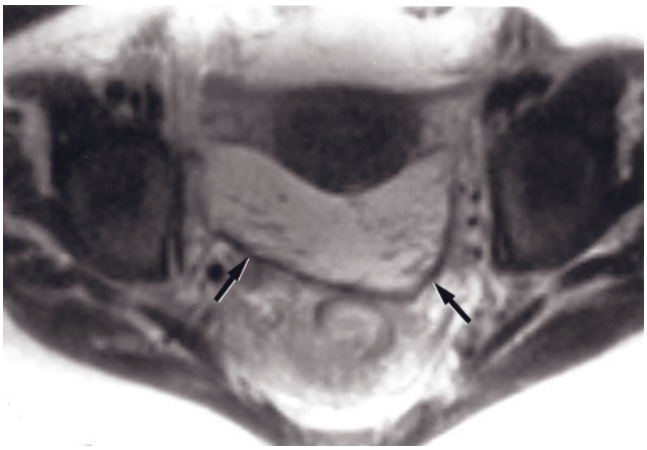

(*a*)

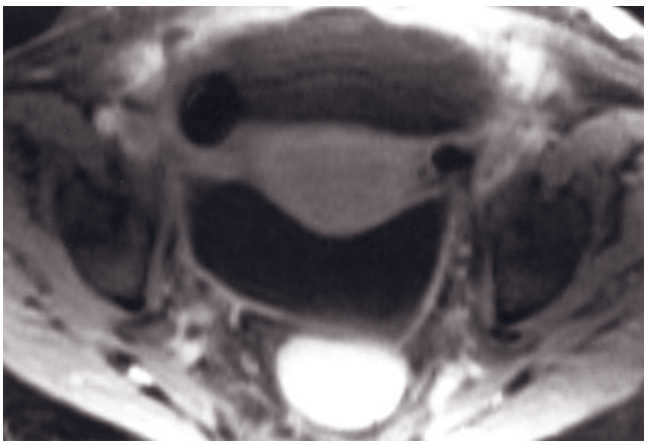

(*b*)

(*c*)

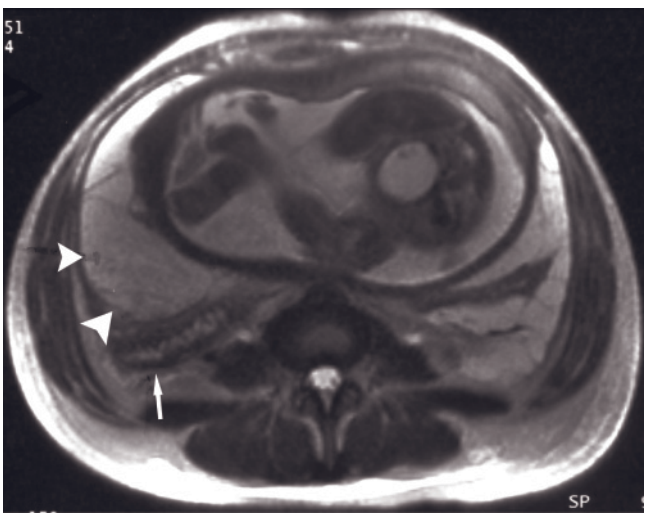

(*d*)

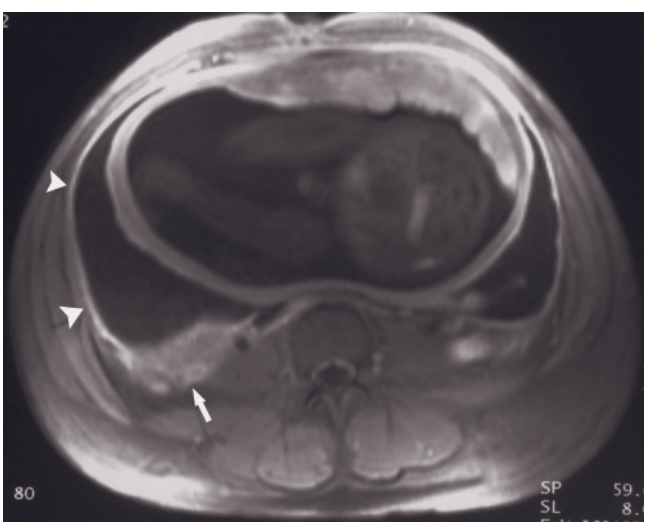

(*e*)

FIG. 7.49 Peritonitis. Transverse T2-weighted SS-ETSE (*a*) and transverse (*b*) and sagittal (*c*) interstitial-phase gadolinium-enhanced SGE images. There is a large volume of ascites seen throughout the abdomen. The ascites in the pelvis appears complex, containing septations (arrows, *a*), best shown on the single-shot T2-weighted sequence (*a*) and increased peritoneal enhancement, shown on the gadolinium-enhanced fat-suppressed images (*b*, *c*), consistent with peritonitis. Continuity of the large volume of ascites extends through a low ventral hernia (arrow, *c*) into the anterior upper thigh. Transverse T2-weighted SS-ETSE (*d*) and gadolinium-enhanced fat-suppressed T1-weighted SGE (*e*) images of a pregnant patient with peritonitis secondary to Crohn disease. Inflammatory debris in the peritoneal cavity is best visualized on T2-weighted SS-ETSE image (arrowheads, *d*); increased peritoneal enhancement is demonstrated on gadolinium-enhanced fat-suppressed SGE images (arrowheads, *e*). Thickened bowel wall is also appreciated (arrows, *d*, *e*). T2-weighted single-shot

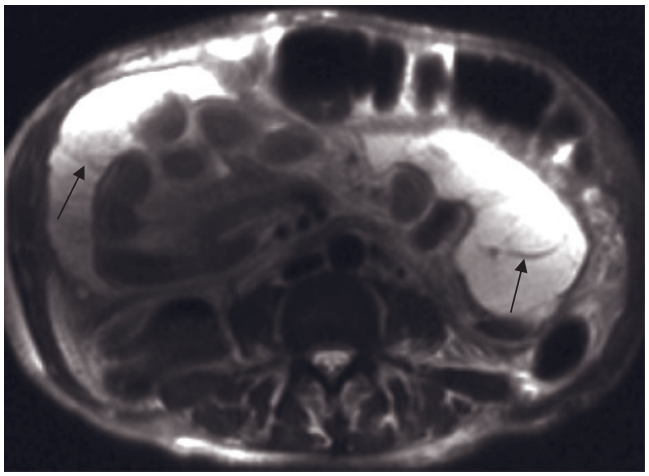

(*f*)

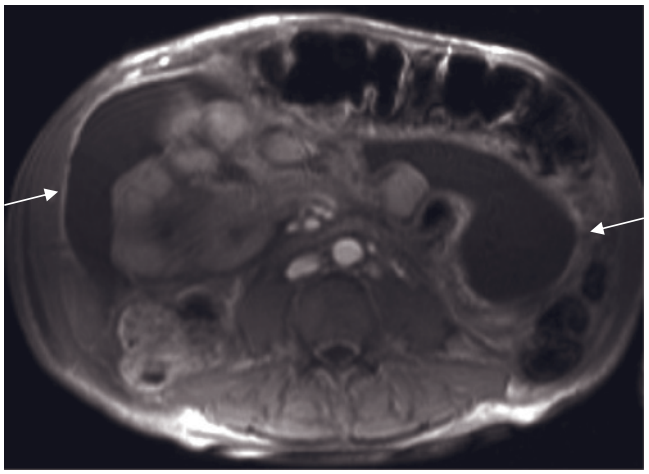

(*g*)

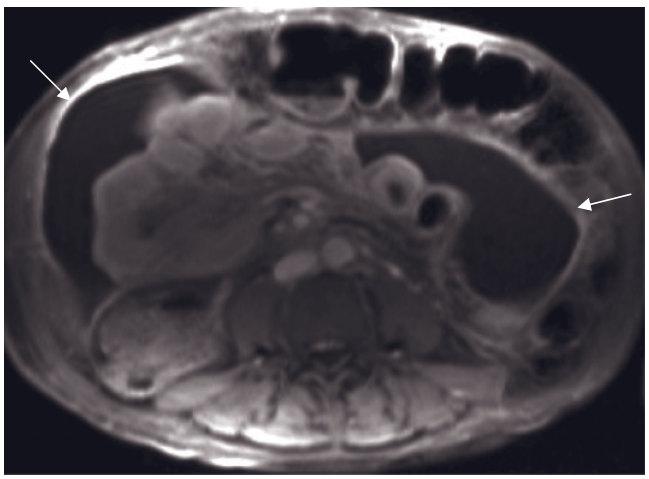

(*h*)

FIG. 7.49 (*Continued*) echo-train spin-echo (*f*), T1-weighted fat-suppressed interstitial-phase postgadolinium SGE (*g*, *h*) images in another patient with peritonitis demonstrate ascites containing septations (black arrows, *f*) and diffuse peritoneal thickening and intense enhancement (white arrows, *g*, *h*).

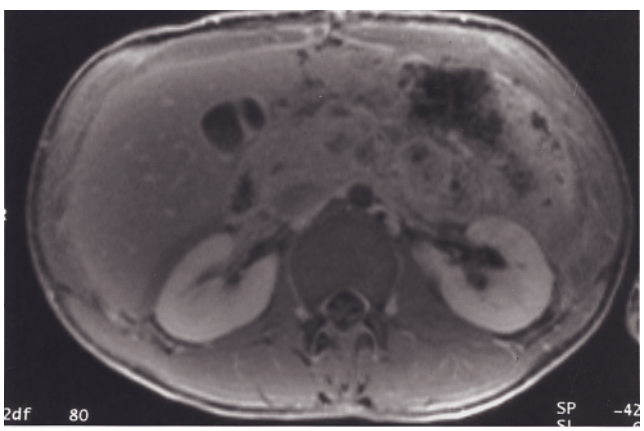

(*a*)

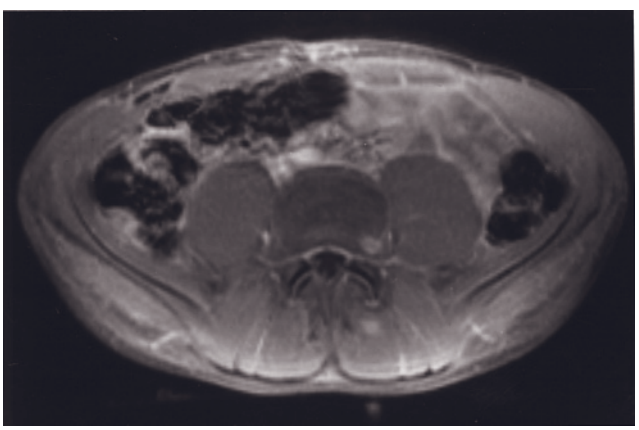

(*b*)

FIG. 7.50 Chemical peritonitis. Interstitial-phase gadolinium-enhanced SGE images from the midabdomen (*a*) and pelvis (*b*) in a patient with chemical peritonitis secondary to intraperitoneal administration of chemotherapeutic agents. Diffuse increased enhancement is present of peritoneal, mesenteric, and serosal surfaces, which has resulted in adherence of bowel loops to each other and linear enhancing strands in the mesentery. Bowel loops and mesenteric planes are ill-defined because of the generalized inflammatory process.

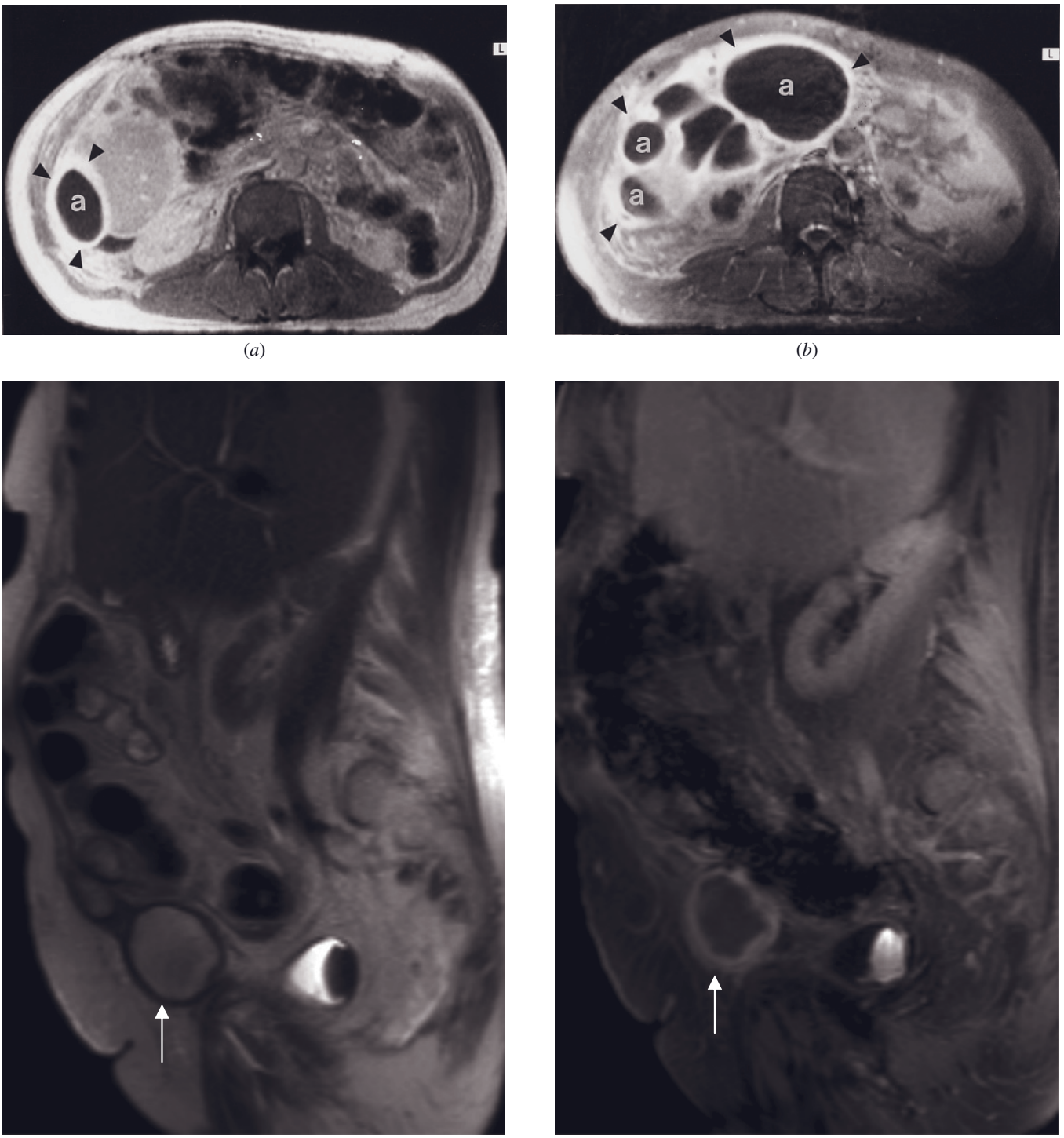

(*a*) (*b*) (*c*) (*d*)

FIG. 7.51 Intra-abdominal abscess. Interstitial-phase gadolinium-enhanced T1-weighted SGE (*a*) and interstitial-phase gadolinium-enhanced T1-weighted fat-suppressed spin-echo (*b*) images in a patient with clinical suspicion of an abscess. Multiple loculated abscess collections are present along the liver capsule and in the right midabdomen (*a*, *b*).The thick enhancing rims (arrowheads, *a*, *b*) are characteristic of the reactive inflammatory capsules associated with abscesses. Sagittal T2-weighted single-shot echo-train spin-echo (*c*) and sagittal T1-weighted fat-suppressed interstitial-phase postgadolinium 3D-GE (*d*) images show an intra-abdominal abscess (arrows) in a post-liver transplantation patient. The abscess has a low-signal-intensity peripheral rim and relatively homogenous high-signal-intensity internal content on T2-weighted image (*c*), and it shows intense peripheral enhancement on the postgadolinium image (*d*). T2-weighted single-shot echo-train spin-echo (*e*) and T1-weighted fat-suppressed interstitial phase

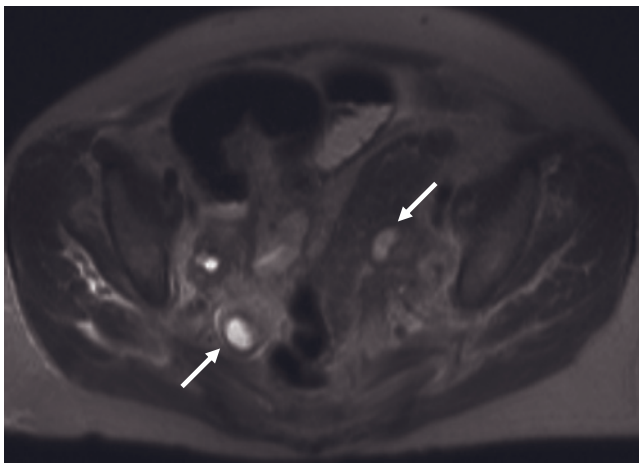

(*e*)

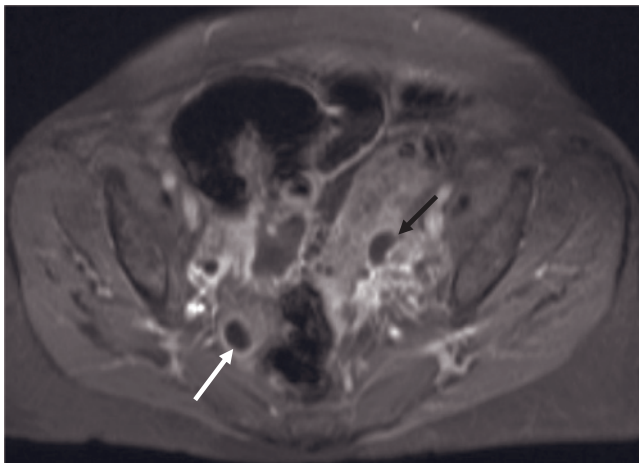

(*f*)

FIG. 7.51 (*Continued*) postgadolinium 3D-GE (*f*) images demonstrate two small abscesses in a patient with diverticulitis. The abscesses are adjacent to the sigmoid colon. They show high signal intensity on T2-weighted image (*e*) and peripheral enhancement on postgadolinium image (*f*).

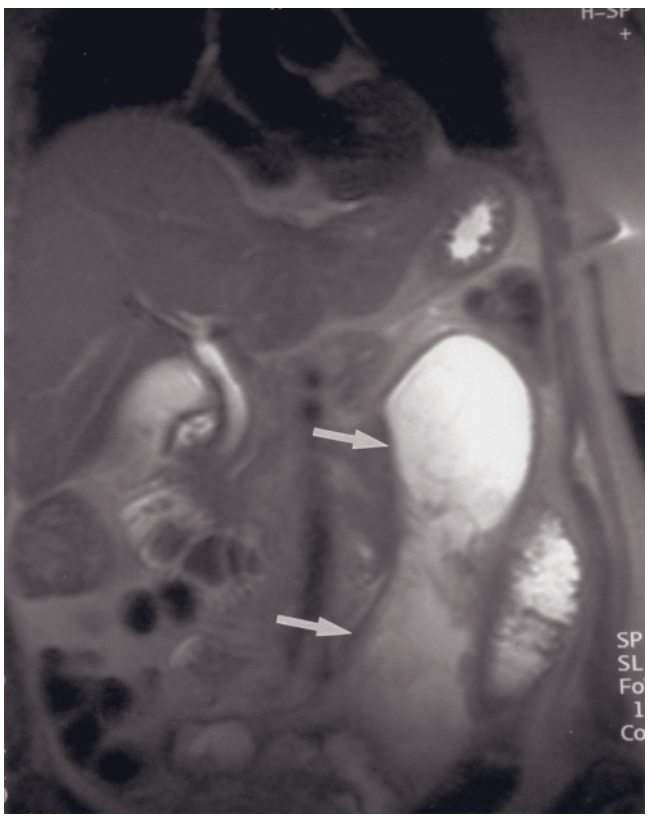

(*a*)

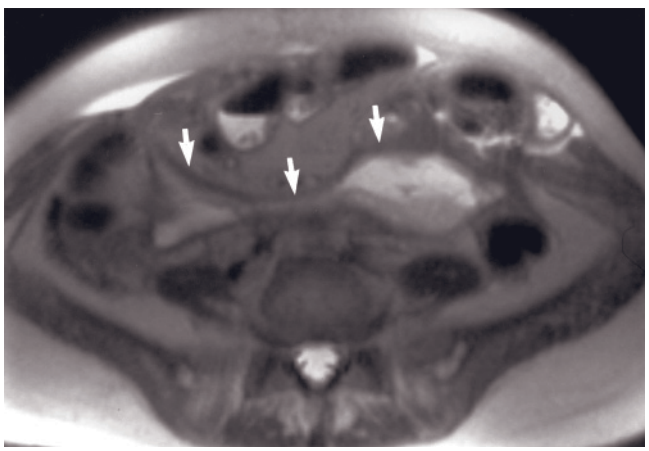

(*b*)

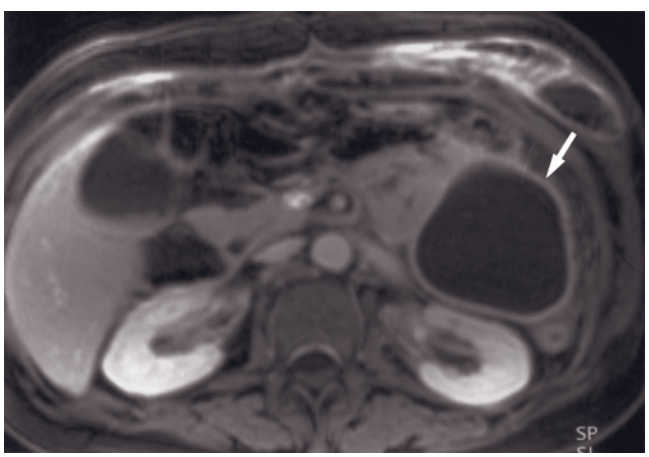

(*c*)

FIG. 7.52 Abdominal abscess. Coronal (*a*) and transverse (*b*) T2-weighted SS-ETSE and transverse interstitial-phase gadolinium-enhanced fat-suppressed SGE (*c*, *d*) images. Within the left hemiabdomen, there is an extremely large fluid collection (arrows, *a*)

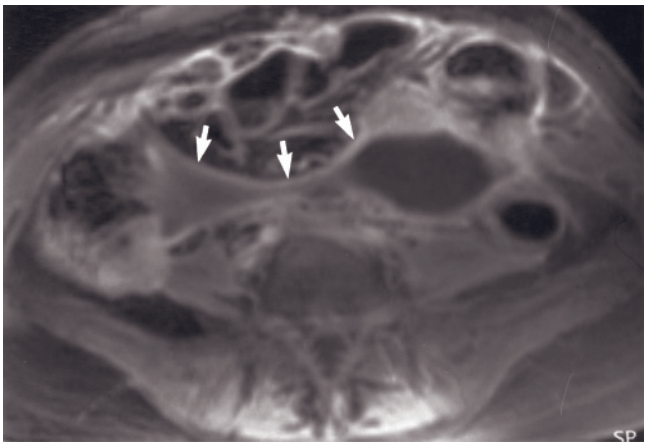

(*d*)

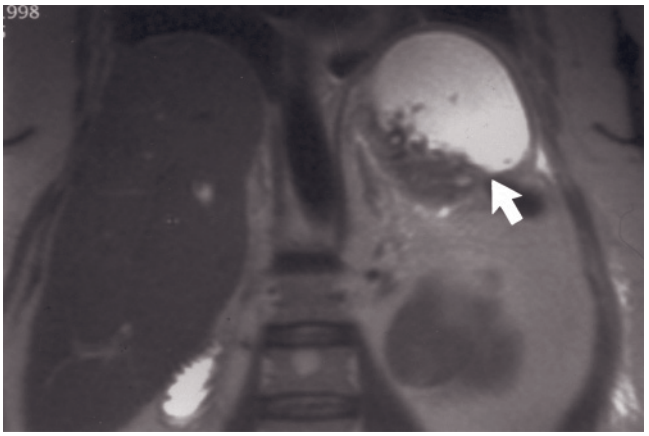

(*e*)

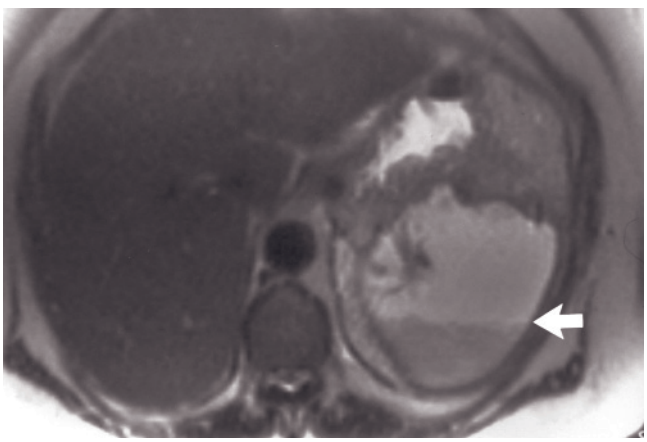

(*f*)

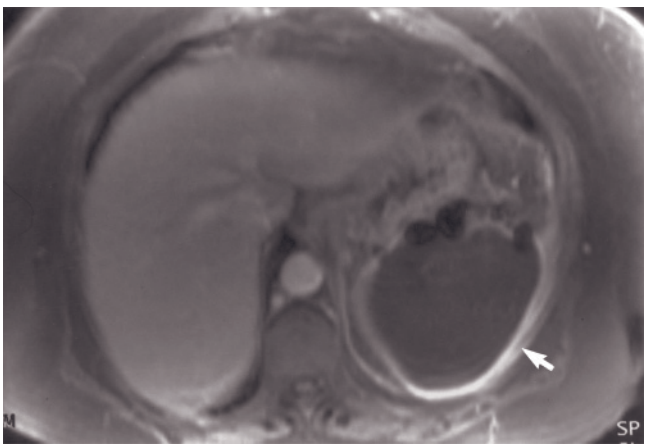

(*g*)

FIG. 7.52 (*Continued*) extending from the lesser sac inferiorly into the pelvis along the left anterior pararenal space. Within the pelvis, it crosses the midline through a narrow track to communicate with another collection located in the right lower quadrant (arrows, *b*). All these fluid collections possess thick enhancing walls (arrows, *c*, *d*) and have layering debris on T2-weighted images (*a*, *b*), consistent with abscesses. Coronal (*e*) and transverse (*f*) T2-weighted SS-ETSE and gadolinium-enhanced fat-suppressed SGE (*g*) images in a second patient, who has an abscess postsplenectomy, demonstrate a large complex fluid collection adjacent to the tail of the pancreas. There is low-signal debris layering in the dependent portion of the fluid collection on the T2-weighted images (arrows, *e*, *f*) and prominent rim enhancement on the gadolinium-enhanced fat-suppressed image (arrow, *g*).

(*a*)

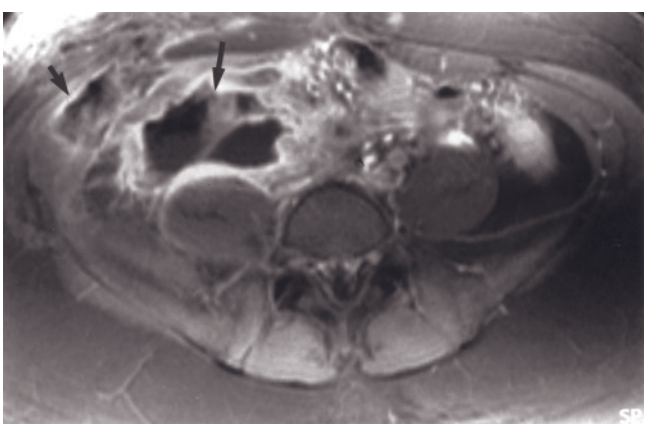

(*b*)

FIG. 7.53 Appendiceal abscess. Sagittal (*a*) and transverse (*b*) interstitial-phase gadolinium-enhanced fat-suppressed SGE images in a patient who underwent appendectomy. A large multilocular fluid-containing abscess (arrows, *b*) is seen in the right lower quadrant of the abdomen associated with substantial enhancement of the surrounding tissues.

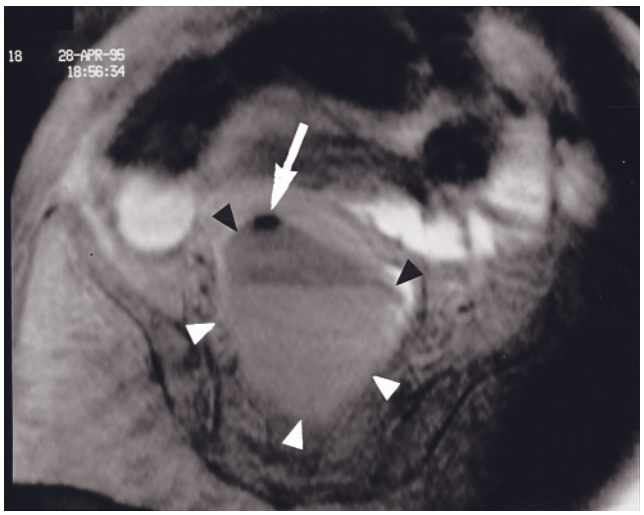

(*a*)

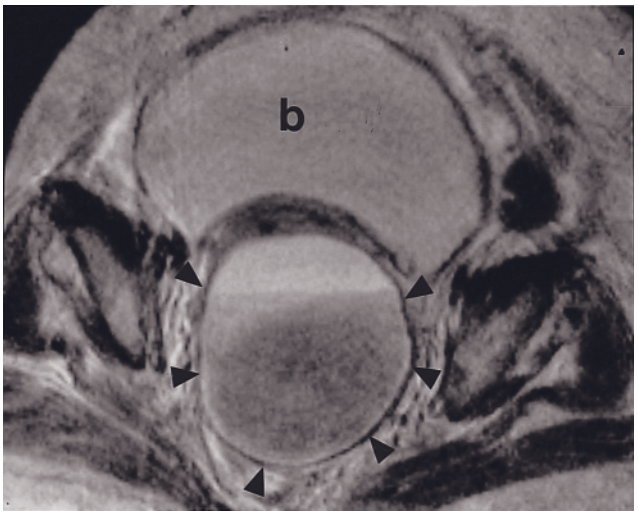

(*b*)

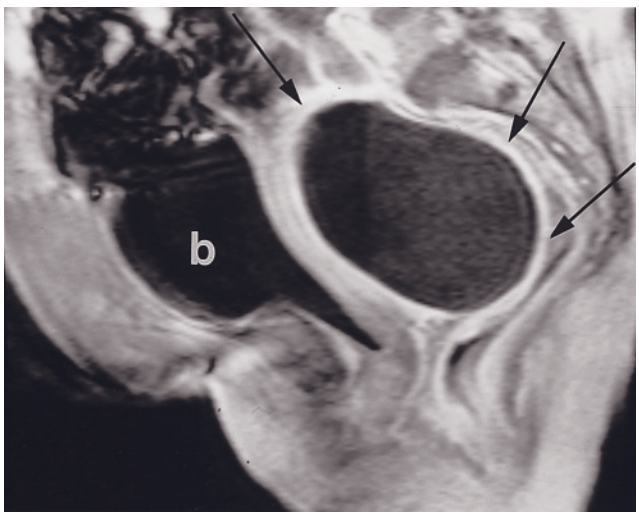

(*c*)

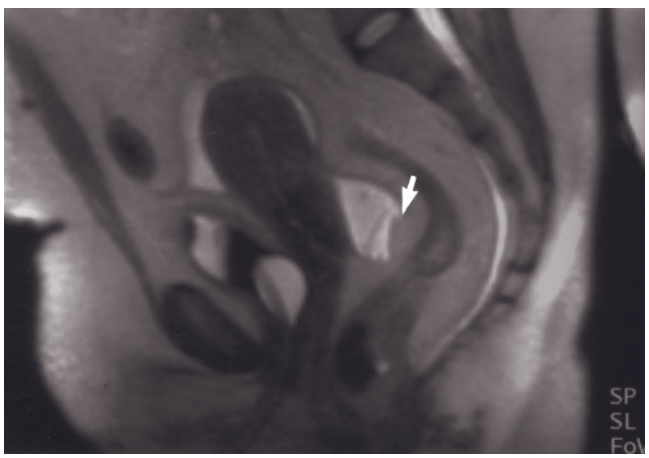

(*d*)

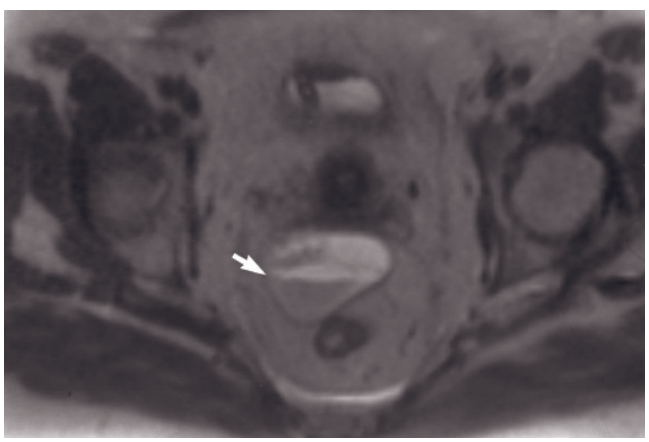

(*e*)

FIG. 7.54 Pelvic abscess. T1-weighted fat-suppressed spin-echo (*a*), T2-weighted fat-suppressed spin-echo (*b*), and sagittal gadolinium-enhanced T1-weighted fat-suppressed SGE (*c*) images in a patient with fever and an elevated white blood cell count. A complex fluid collection (arrowheads, *a*, *b*) is demonstrated in the pelvis. The variable signal intensity on the T1-weighted images reflects its protein content (*a*, *c*). On the T2-weighted image (*b*), low-signal-intensity debris layers in the dependent portion of the abscess. A focus of signal-void air is present (arrow, *a*), which is not uncommonly observed in abscesses. After contrast administration, the wall of the abscess enhances substantially (arrows, *c*). (bladder = b, *b*, *c*). Sagittal (*d*) and transverse (*e*) T2-weighted SS-ETSE images in a second patient show a fluid collection in the cul-de-sac that exhibits layering of low-signal material on T2-weighted images (arrows, *d*, *e*), consistent with abscess. A lesser volume of nonloculated fluid is also observed around the uterus.

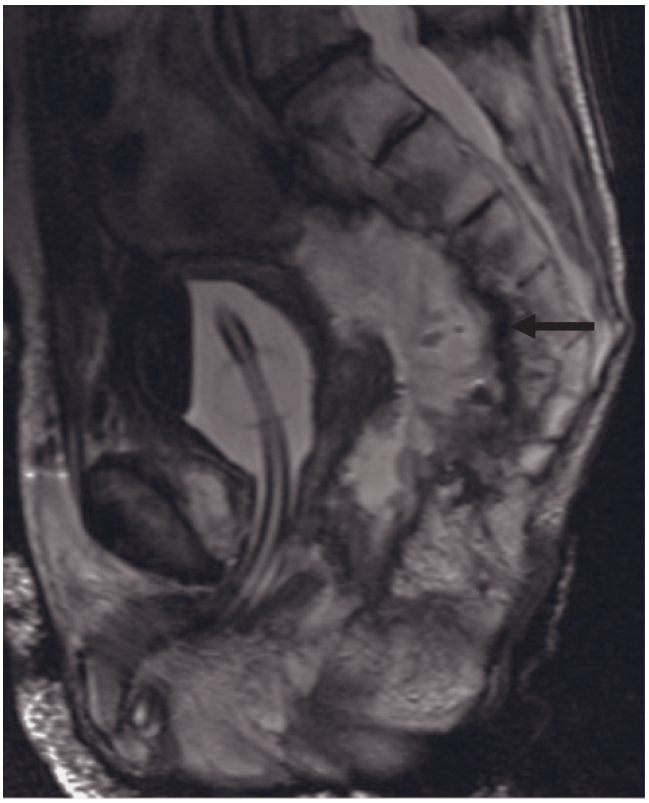

(*f*)

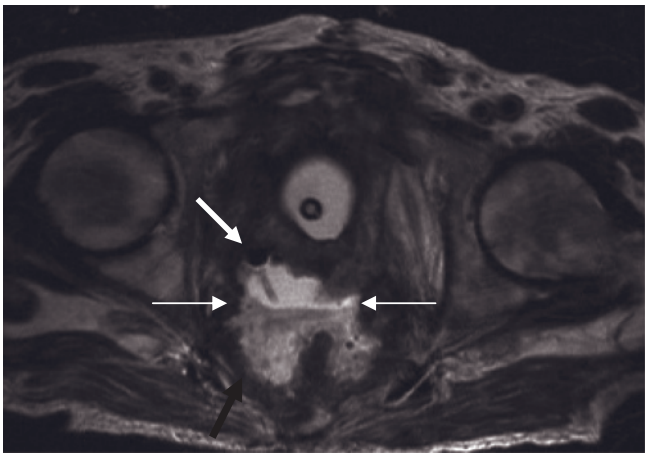

(*g*)

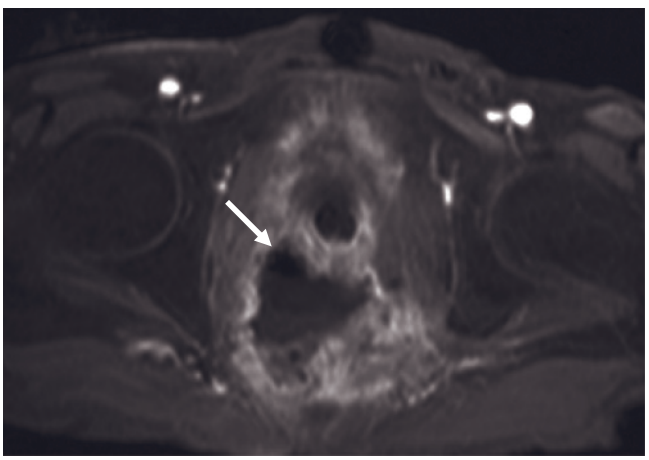

(*i*)

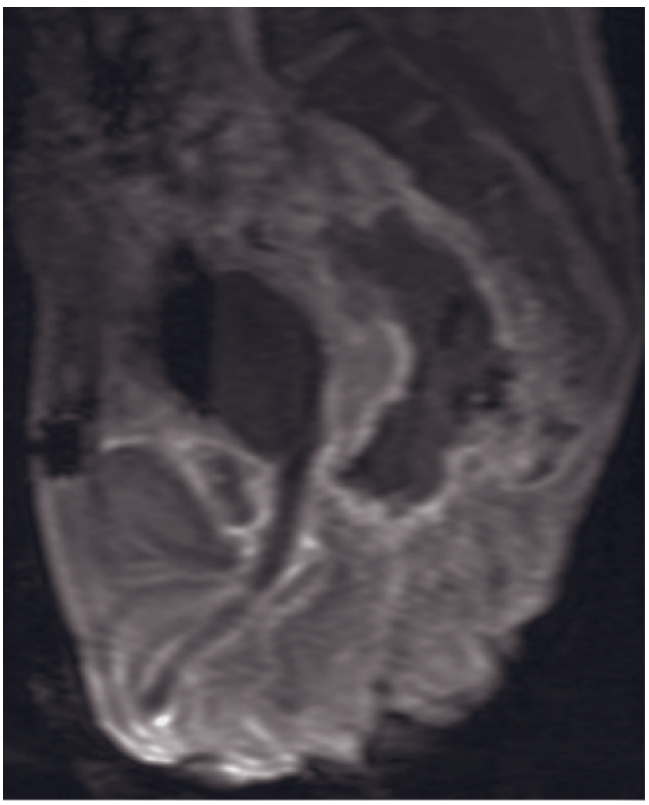

(*h*)

FIG. 7.54 (*Continued*) Sagittal and axial T2-weighted high-resolution fast spin-echo (*f*, *g*), sagittal and axial T1-weighted interstitial-phase fat-suppressed 3D-GE (*h*, *i*) images show a pelvic abscess located posterior to the bladder and anterior to the sacrum in another patient who underwent abdominopelvic resection for rectal cancer. The abscess has a thick and irregular wall (black arrows, *f*, *g*), fluid-fluid level (white thin arrows, *g*), and free air (white thick arrows, *g*, *i*). The thick wall and adjacent soft tissue demonstrates intense enhancement on postgadolinium images. The thick wall may be a sign of residual tumor as well. Adjacent soft tissue inflammation may be a sign of inflammation secondary to the operation, fibrosis secondary to radiation therapy or residual tumoral tissue. Note that bone marrow in the sacrum shows fatty infiltration secondary to radiation therapy. There are also a Foley catheter and air in the bladder.

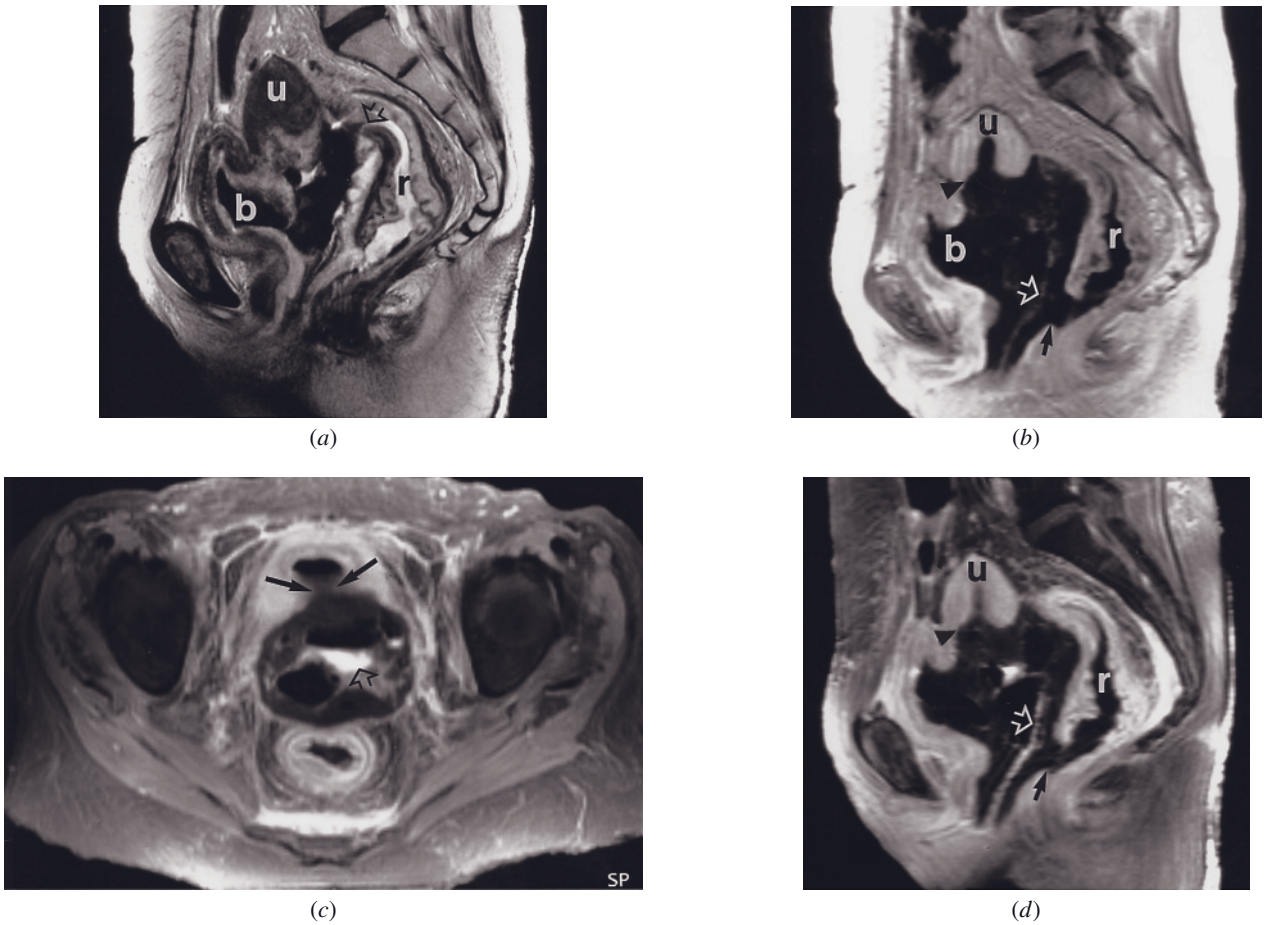

FIG. 7.55 Pelvic abscess and fistulas. Sagittal T2-weighted echo-train spin-echo (*a*), sagittal gadolinium-enhanced T1-weighted SGE (*b*) and axial (*c*) and sagittal (*d*) gadolinium-enhanced T1-weighted fat-suppressed spin-echo images in a patient with cervical cancer who had undergone high-dose radiation therapy. Tumor necrosis, fistula, and abscess formation are not uncommon complications of radiation therapy. A large pelvic cavity is present with communication between bladder, uterus, and rectum, which is clearly defined on the sagittal plane images (*a*, *b*, *d*). The rectal wall is substantially thickened, and submucosal edema is well shown as high signal intensity on the T2-weighted image (*a*). The signal-void regions in the abscess cavity represent air associated with the superior and low inferior rectal fistulas (open arrow, *a* and solid arrow, *d*, respectively) and superimposed infection. There is wide communication of the abscess cavity with the bladder. After intravenous gadolinium administration, high-signal-intensity contrast (open arrow, *c*) exits the bladder through the large fistula (black arrows, *c*) and pools in the abscess. Portions of the uterine corpus and cervix have undergone necrosis; the uterine fundus remains. The posterior wall of the cervix and vagina (open arrow, *b*, *d*) is best shown on the sagittal gadolinium-enhanced T1-weighted fat-suppressed spin-echo image. r, Rectum; u, uterine fundus; b, bladder.

[71]. The sagittal plane is essential in evaluating the pelvis for abscesses, as the relationship to pelvic organs is optimal and layering of low-signal material on T2-weighted images is clearly observed in this projection.

CONCLUSIONS

MRI has become increasingly effective in evaluating diseases involving the peritoneum. This reflects MRI's multiplanar capabilities, robust scanning techniques, and sensitivity to intravenous contrast enhancement. The implementation of gadolinium-enhanced fat-suppressed SGE and 3D-GE sequences and breathing-independent T2-weighted sequences has substantially improved the diagnostic usefulness of MRI. Currently, MRI is useful for evaluating and characterizing diaphragmatic hernias, cysts, pseudocysts, endometriosis, peritoneal carcinomatosis, and intra-abdominal fluid collections.

REFERENCES

1. Williams PL, Bannister LH, Berry MM et al. *Gray's Anatomy*. 38th ed. New York: Churchill Livingstone; 1995, p. 1734–1746.
2. Cohen JM, Weinreb JC, Maravilla KR. Fluid collections in the intraperitoneal and extraperitoneal spaces: comparison of MR and CT. *Radiology* 155(3): 705–708, 1985.

3. Gore RM, Callen PW, Filly RA. Lesser sac fluid in predicting the etiology of ascites: CT findings. *AJR Am J Roentgenol* 139(1): 71–74, 1982.
4. Meyers MA. The spread and localization of acute intraperitoneal effusions. *Radiology* 95(3): 547–554, 1970.
5. Meyers MA. Distribution of intra-abdominal malignant seeding: dependency on dynamics of flow of ascitic fluid. *Am J Roentgenol Radium Ther Nucl Med* 119(1): 198–206, 1973.
6. Meyers MA. *Dynamic Radiology of the Abdomen: Normal and Pathologic Anatomy.* 2nd ed. New York: Springer-Verlag, 1982.
7. Ruess L, Frazier AA, Sivit CJ. CT of the mesentery, omentum, and peritoneum in children. *Radiographics* 15(1): 89–104, 1995.
8. Gonzalez-Crussi F, Sotelo-Avila C, deMello DE. Primary peritoneal, omental, and mesenteric tumors in childhood. *Semin Diagn Pathol* 3(2): 122–137, 1986.
9. Stoupis C, Ros PR, Williams JL. Hemorrhagic lymphangioma mimicking hemoperitoneum: MR imaging diagnosis. *J Magn Reson Imaging* 3(3): 541–542, 1993.
10. Lee GH, Cohen AJ. CT imaging of abdominal hernias. *AJR Am J Roentgenol* 161(6): 1209–1213, 1993.
11. Berger PE. Hernias of the abdominal wall and peritoneal cavity. In: Franken EA, Jr, Smith WL, editors. *Gastrointestinal Imaging in Pediatrics.* Philadelphia: Harper & Row; 1982, p. 446–456.
12. Vanek VW, Phillips AK. Retroperitoneal, mesenteric, and omental cysts. *Arch Surg* 119(7): 838–842, 1984.
13. Haney PJ, Whitley NO. CT of benign cystic abdominal masses in children. *AJR Am J Roentgenol* 142(6): 1279–1281, 1984.
14. Besson R, Hladky JP, Dhellemmes P et al. Peritoneal pseudocyst—ventriculo-peritoneal shunt complications. *Eur J Pediatr Surg* 5(4): 195–197, 1995.
15. Kurachi H, Murakami T, Nakamura H et al. Imaging of peritoneal pseudocysts: value of MR imaging compared with sonography and CT. *AJR Am J Roentgenol* 161(3): 589–591, 1993.
16. Lewis VL, Shaffer HA, Jr., Williamson BR. Pseudotumoral lipomatosis of the abdomen. *J Comput Assist Tomogr* 6(1): 79–82, 1982.
17. Siskind BN, Weiner FR, Frank M et al. Steroid-induced mesenteric lipomatosis. *Comput Radiol* 8(3): 175–177, 1984.
18. Gougoutas CA, Siegelman ES, Hunt J et al. Pelvic endometriosis: various manifestations and MR imaging findings. *AJR Am J Roentgenol* 175(2): 353–358, 2000.
19. Olive DL, Schwartz LB. Endometriosis. *N Engl J Med* 328(24): 1759–1769, 1993.
20. Arrive L, Hricak H, Martin MC. Pelvic endometriosis: MR imaging. *Radiology* 171(3): 687–692, 1989.
21. Sugimura K, Okizuka H, Imaoka I et al. Pelvic endometriosis: detection and diagnosis with chemical shift MR imaging. *Radiology* 188(2): 435–438, 1993.
22. Ascher SM, Agrawal R, Bis KG et al. Endometriosis: appearance and detection with conventional and contrast-enhanced fat-suppressed spin-echo techniques. *J Magn Reson Imaging* 5(3): 251–257, 1995.
23. Reitamo JJ, Hayry P, Nykyri E et al. The desmoid tumor. I. Incidence, sex-, age- and anatomical distribution in the Finnish population. *Am J Clin Pathol* 77(6): 665–673, 1982.
24. Hayry P, Reitamo JJ, Totterman S et al. The desmoid tumor. II. Analysis of factors possibly contributing to the etiology and growth behavior. *Am J Clin Pathol* 77(6): 674–680, 1982.
25. Smith AJ, Lewis JJ, Merchant NB et al. Surgical management of intra-abdominal desmoid tumours. *Br J Surg* 87(5): 608–613, 2000.
26. Daya D, McCaughey WT. Pathology of the peritoneum: a review of selected topics. *Semin Diagn Pathol* 8(4): 277–289, 1991.
27. Smith TR. Malignant peritoneal mesothelioma: marked variability of CT findings. *Abdom Imaging* 19(1): 27–29, 1994.
28. Whitley NO, Bohlman ME, Baker LP. CT patterns of mesenteric disease. *J Comput Assist Tomogr* 6(3): 490–496, 1982.
29. Whitley NO, Brenner DE, Antman KH et al. CT of peritoneal mesothelioma: analysis of eight cases. *AJR Am J Roentgenol* 138(3): 531–535, 1982.
30. Voultsinos V, Semelka RC, Elias J, Jr. et al. Primary peritoneal carcinoma: computed tomography and magnetic resonance findings. *J Comput Assist Tomogr* 32(4): 541–547, 2008.
31. Hamrick-Turner JE, Chiechi MV, Abbitt PL et al. Neoplastic and inflammatory processes of the peritoneum, omentum, and mesentery: diagnosis with CT. *Radiographics* 12(6): 1051–1068, 1992.
32. Meyers MA, McSweeney J. Secondary neoplasms of the bowel. *Radiology* 105(1): 1–11, 1972.
33. Daniel O. The differential diagnosis of malignant disease of the peritoneum. *Br J Surg* 39(154): 147–156, 1951.
34. Meyers MA, Oliphant M, Berne AS et al. The peritoneal ligaments and mesenteries: pathways of intraabdominal spread of disease. *Radiology* 163(3): 593–604, 1987.
35. Oliphant M, Berne AS. Computed tomography of the subperitoneal space: demonstration of direct spread of intraabdominal disease. *J Comput Assist Tomogr* 6(6): 1127–1137, 1982.
36. Cotran RS, Kumar V, Robbins SL. *Pathologic Basis of Disease.* 5th ed. Philadelphia: W.B. Saunders; 1994, p.250.
37. Semelka RC, Lawrence PH, Shoenut JP et al. Primary ovarian cancer: prospective comparison of contrast-enhanced CT and pre-and postcontrast, fat-suppressed MR imaging, with histologic correlation. *J Magn Reson Imaging* 3(1): 99–106, 1993.
38. Low RN, Semelka RC, Worawattanakul S et al. Extrahepatic abdominal imaging in patients with malignancy: comparison of MR imaging and helical CT in 164 patients. *J Magn Reson Imaging* 12(2): 269–277, 2000.
39. Low RN, Semelka RC, Worawattanakul S et al. Extrahepatic abdominal imaging in patients with malignancy: comparison of MR imaging and helical CT, with subsequent surgical correlation. *Radiology* 210(3): 625–632, 1999.
40. Low RN, Carter WD, Saleh F et al. Ovarian cancer: comparison of findings with perfluorocarbon-enhanced MR imaging, In-111-CYT-103 immunoscintigraphy, and CT. *Radiology* 195(2): 391–400, 1995.
41. Chou CK, Liu GC, Chen LT et al. MRI manifestations of peritoneal carcinomatosis. *Gastrointest Radiol* 17(4): 336–338, 1992.
42. Chou CK, Liu GC, Su JH et al. MRI demonstration of peritoneal implants. *Abdom Imaging* 19(2): 95–101, 1994.
43. Novetsky GJ, Berlin L, Epstein AJ et al. Case report. Pseudomyxoma peritonei. *J Comput Assist Tomogr* 6(2): 398–399, 1982.
44. Levitt RG, Sagel SS, Stanley RJ. Detection of neoplastic involvement of the mesentery and omentum by computed tomography. *AJR Am J Roentgenol* 131(5): 835–838, 1978.
45. Mueller PR, Ferrucci JT, Jr., Harbin WP et al. Appearance of lymphomatous involvement of the mesentery by ultrasonography and body computed tomography: the "sandwich sign". *Radiology* 134(2): 467–473, 1980.
46. Picus D, Glazer HS, Levitt RG et al. Computed tomography of abdominal carcinoid tumors. *AJR Am J Roentgenol* 143(3): 581–584, 1984.
47. Rosai J. In: *Ackerman's Surgical Pathology.* 8th ed. St. Louis, MO: Mosby; 1996, p. 2149.
48. Young RH, Gilks CB, Scully RE. Mucinous tumors of the appendix associated with mucinous tumors of the ovary and pseudomyxoma peritonei. A clinicopathological analysis of 22 cases supporting an origin in the appendix. *Am J Surg Pathol* 15(5): 415–429, 1991.
49. Dachman AH, Lichtenstein JE, Friedman AC. Mucocele of the appendix and pseudomyxoma peritonei. *AJR Am J Roentgenol* 144(5): 923–929, 1985.
50. Goffinet DR, Castellino RA, Kim H et al. Staging laparotomies in unselected previously untreated patients with non-Hodgkin's lymphomas. *Cancer* 32(3): 672–681, 1973.

51. Buetow PC, Buck JL, Carr NJ et al. From the archives of the AFIP. Colorectal adenocarcinoma: radiologic-pathologic correlation. *Radiographics* 15(1): 127–146; quiz 148–129, 1995.
52. Cockey BM, Fishman EK, Jones B et al. Computed tomography of abdominal carcinoid tumor. *J Comput Assist Tomogr* 9(1): 38–42, 1985.
53. Terrier F, Revel D, Pajannen H et al. MR imaging of body fluid collections. *J Comput Assist Tomogr* 10(6): 953–962, 1986.
54. Pelage JP, Soyer P, Boudiaf M et al. Carcinoid tumors of the abdomen: CT features. *Abdom Imaging* 24(3): 240–245, 1999.
55. Wall SD, Hricak H, Bailey GD et al. MR imaging of pathologic abdominal fluid collections. *J Comput Assist Tomogr* 10(5): 746–750, 1986.
56. Dooms GC, Fisher MR, Hricak H et al. MR imaging of intramuscular hemorrhage. *J Comput Assist Tomogr* 9(5): 908–913, 1985.
57. Unger EC, Glazer HS, Lee JK et al. MRI of extracranial hematomas: preliminary observations. *AJR Am J Roentgenol* 146(2): 403–407, 1986.
58. Balci NC, Semelka RC, Noone TC et al. Acute and subacute liver-related hemorrhage: MRI findings. *Magn Reson Imaging* 17(2): 207–211, 1999.
59. Hahn PF, Saini S, Stark DD et al. Intraabdominal hematoma: the concentric-ring sign in MR imaging. *AJR Am J Roentgenol* 148(1): 115–119, 1987.
60. Zeman RK, Burrell MI. Hepatobiliary trauma. In: Zeman RK, Burrell MI, editors. *Gallbladder and Bile Duct Imaging: A Clinical Radiologic Approach*. New York: Churchill Livingstone; 1987, p. 677–704.
61. Wan YL, Ko SF, Ng KK et al. Role of CT-guided core needle biopsy in the diagnosis of a gossypiboma: case report. *Abdom Imaging* 29(6): 713–715, 2004.
62. Prokesch RW, Schima W, Schober E et al. Complications of continuous ambulatory peritoneal dialysis: findings on MR peritoneography. *AJR Am J Roentgenol* 174(4): 987–991, 2000.
63. Ogden WW 2nd, Bradburn DM, Rives JD. Mesenteric panniculitis: review of 27 cases. *Ann Surg* 161: 864–875, 1965.
64. Kronthal AJ, Kang YS, Fishman EK et al. MR imaging in sclerosing mesenteritis. *AJR Am J Roentgenol* 156(3): 517–519, 1991.
65. Patel N, Saleeb SF, Teplick SK. General case of the day. Mesenteric panniculitis with extensive inflammatory involvement of the peritoneum and intraperitoneal structures. *Radiographics* 19(4): 1083–1085, 1999.
66. Sabate JM, Torrubia S, Maideu J et al. Sclerosing mesenteritis: imaging findings in 17 patients. *AJR Am J Roentgenol* 172(3): 625–629, 1999.
67. Katz ME, Heiken JP, Glazer HS et al. Intraabdominal panniculitis: clinical, radiographic, and CT features. *AJR Am J Roentgenol* 145(2): 293–296, 1985.
68. Haynes JW, Brewer WH, Walsh JW. Focal fat necrosis presenting as a palpable abdominal mass: CT evaluation. *J Comput Assist Tomogr* 9(3): 568–569, 1985.
69. Wang SM, Wilson SE. Subphrenic abscess. The new epidemiology. *Arch Surg* 112(8): 934–936, 1977.
70. Noone TC, Semelka RC, Worawattanakul S et al. Intraperitoneal abscesses: diagnostic accuracy of and appearances at MR imaging. *Radiology* 208(2): 525–528, 1998.
71. Semelka RC, John G, Kelekis NL et al. Bowel-related abscesses: MR demonstration preliminary results. *Magn Reson Imaging* 16(8): 855–861, 1998.

CHAPTER

8

ADRENAL GLANDS

ERSAN ALTUN, NIKOLAOS L. KELEKIS, JORGE ELIAS, JR., PENAMPAI TANNAPHAI, WAQAS QURESHI, AND RICHARD C. SEMELKA

NORMAL ANATOMY

The adrenal glands are paired organs that lie in the retroperitoneum superomedial to the kidneys. The right adrenal gland is located medial to the right lobe of the liver, lateral to the right crus of the diaphragm, and posterior to the inferior vena cava (IVC). The left adrenal gland is situated posterior to the splenic vein and medial to the left crus of the diaphragm. The adrenal glands are a composite of two endocrine organs, cortex and medulla, the former steroid producing and the latter catecholamine producing.

MRI TECHNIQUE

Techniques that have been employed to examine the adrenal glands include T2-weighted non-fat-suppressed and fat-suppressed single-shot echo-train spin-echo, T1-weighted in-phase and out-of-phase SGE or 3D-GE, T1-weighted fat-suppressed SGE or 3D-GE, and serial gadolinium-enhanced SGE or 3D-GE T1-weighted fat-suppressed sequences [1–26]. The intention of most of these techniques has been to distinguish benign from malignant disease. The approach that appears most reliable is the combined use of in-phase and out-of-phase gradient-echo techniques [9–20, 22, 23, 26]. Benign adenomas have been shown to lose signal intensity on out-of-phase images because of the presence of intracytoplasmic lipid [9–20, 22, 23, 26]. Metastatic lesions do not contain intracytoplasmic lipid, and therefore do not lose signal intensity on out-of-phase images [9–20, 22, 23, 26]. It is important to use an out-of-phase technique without concomitant use of frequency-selective fat suppression because fat suppression will cause minimization of signal dropout [27]. The best approach is to use SGE or 3D-GE [8] technique for both in-phase and out-of-phase imaging. The only variation between sequences should be the echo time (TE), with a TE of 4.2–4.5 ms for in-phase imaging and a TE of 2.2–2.7 ms for out-of-phase imaging at 1.5 T. On the newest MR systems, double-echo (in-phase and out-of-phase) sequences are available that thereby allow accurate comparison between in-phase and out-of-phase images because images are accurate at the same time at the identical level. Use of a longer TE (e.g., 6–7 ms) for

Abdominal-Pelvic MRI, Third Edition, edited by Richard C. Semelka. Copyright © 2010 John Wiley & Sons, Inc.

out-of-phase imaging is less ideal because it introduces T2* signal loss. Current software on modern MR systems results in homogeneous fat suppression consistently surrounding the adrenal glands on T1-weighted images, rendering excellent detail of subtle adrenal gland morphology, especially at 3.0T, which benefits from the ability to acquire even thinner sections of adequate image quality (2mm) [28]; 3.0T imaging facilitates improved spatial resolution for imaging the adrenal glands. This permits better definition of small mass lesions. On the other hand, at the present time, drop in signal is less visually apparent at 3.0T compared to 1.5T on out-of-phase images, which makes the visual recognition of low-lipid-content adenomas more challenging at 3.0T [28]. Different T1 contrast resolution of 3.0T MR imaging and the inability to use exact in-phase/out-of-phase TE times at 3.0T impair the ability to detect fat content in the lesions at 3.0T in a consistent fashion, particularly in small lesions. For this reason, it may be prudent to employ a breath-hold modified Dixon method at 3.0T, in addition to in- and out-of-phase images, as a more quantified fat content measurement can be made with this sequence. Overlap, however, exists between benign and malignant masses with combined in-phase and out-of-phase techniques [11–15, 17–20]. This is because not all benign adrenal adenomas contain intracytoplasmic lipid [15–20] and benign masses of other etiologies (e.g., granulomatous disease) do not contain lipid. There are also rare instances of malignant masses, namely adrenal cortical carcinomas and renal cell cancer metastases, which may contain intracytoplasmic lipid and show drop in signal intensity on out-of-phase images [29–33]. The normal adrenal cortex contains abundant lipid, which is not, however, demonstrated on in-phase and out-of-phase MR imaging [25].

Serial postgadolinium gradient-echo imaging may provide supplemental information to distinguish benign from malignant adrenal masses [6, 7]. Metastases tend to enhance more heterogeneously and retain gadolinium contrast for a more prolonged period than benign adenomas. Chung et al. [34] have reported on the appearance of benign and malignant adrenal masses on images acquired in the capillary phase of enhancement. They observed that 70% of benign adenomas exhibited a relatively intense homogeneous capillary blush, whereas none of the malignant tumors did so. Overlap exists, however, in the enhancement features of metastases and adenomas [11, 18, 34]. Adenomas and metastases may both enhance heterogeneously on immediate postgadolinium images [34], and desmoplastic metastases enhance minimally [8]. The intensity of enhancement of normal adrenal tissue and adrenal adenomas may vary [8, 18, 35]. In fact, the normal adrenals and adrenal adenomas exhibit a capillary phase blush. Optimal timing to observe this blush is in the hepatic arterial dominant phase of liver enhancement, with contrast in portal veins and not yet in hepatic veins [36]. The capillary phase appears to last slightly shorter for the adrenals than for the pancreas, which may simply reflect a smaller capillary bed.

Regarding T2-weighted imaging, high-resolution MR sequences may demonstrate corticomedullary differentiation in the normal gland, which is not present on T1-weighted sequences [25]. Metastases frequently possess a longer T2 and are brighter on T2-weighted images than adenomas. Substantial overlap exists between benign and malignant masses with this technique [4, 5, 11]. Signal intensity on T2-weighted images depends on the fluid content, predominantly in the interstitial space, of the mass. Desmoplastic neoplasms have low fluid content and therefore low signal intensity, whereas some benign lesions have high fluid content and are high in signal intensity [11]. Visual perception of signal intensity on T2-weighted images is also problematic. Most adrenal masses appear at least moderately high in signal intensity on fat-suppressed T2-weighted images because the rendering of fat low signal intensity results in rescaling of the signal intensities of abdominal organs. For similar reasons of signal intensity scaling, most adrenal masses appear moderately low in signal intensity on T2-weighted echo-train spin-echo sequences because of the high signal intensity of background fat.

Because no single technique is more than 90% accurate, a useful approach is to combine in-phase and out-of-phase images with other techniques to increase the confidence of lesion characterization. The combination with capillary-phase gadolinium-enhanced imaging may provide the most consistent results for distinguishing adenoma from metastases [34].

The demonstration of normal adrenal glands and small adrenal masses is well performed with T1-weighted fat-suppressed imaging (fig. 8.1) [8, 12]. The demonstration of renal corticomedullary difference on either noncontrast T1-weighted fat-suppressed images or immediate postgadolinium GE images is helpful in distinguishing adrenal from renal tumors [13, 31]. The multiplanar imaging capability of MRI is also useful for assessing large tumors in the region of the upper pole of the kidney to determine intra- or extrarenal origin by imaging in the coronal or sagittal plane [31, 37]. Sagittal-plane imaging is preferred to coronal-plane imaging [31]. The use of thin-section 3D-GE in one plane of acquisition permits reconstruction of data in other planes to define the location of lesions. The relationship between mass, kidney, and liver or spleen is shown in profile in the sagittal plane (fig. 8.2) and en face in the coronal plane. Origin of tumor is better evaluated when the orientation between these structures is viewed in profile, because partial volume effects may be observed

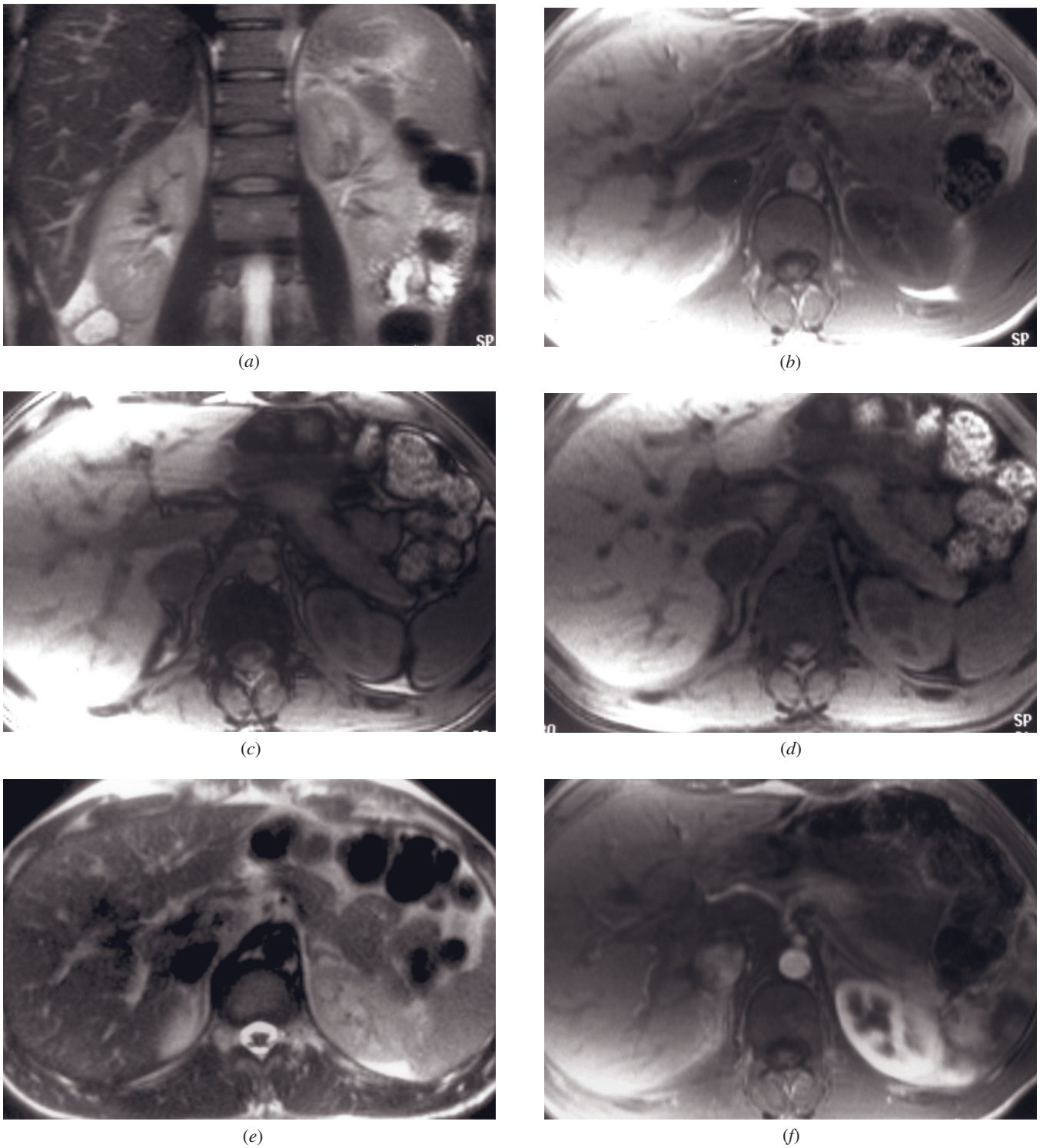

(*a*) (*b*) (*c*) (*d*) (*e*) (*f*)

FIG. 8.1 Normal adrenals. Coronal T2-weighted HASTE (*a*),T1-weighted GE (*b*), T1-weighted fat-suppressed GE (*c*), T1-weighted out-of-phase GE (*d*), HASTE (*e*), immediate postgadolinium T1 GE (*f*), and 90-s postgadolinium T1 fat-suppressed GE (*g*) images.

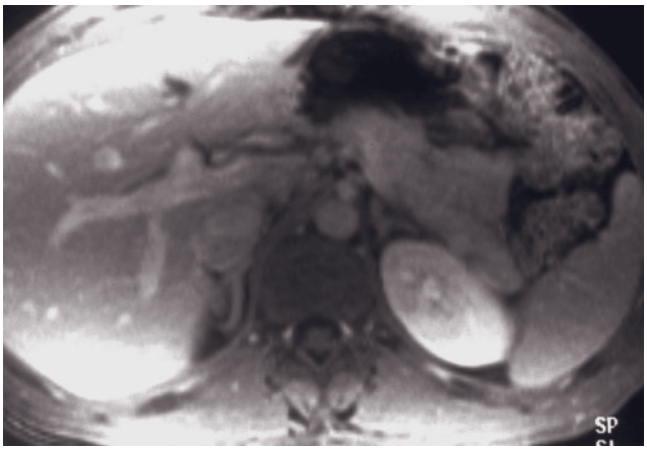

(*g*)

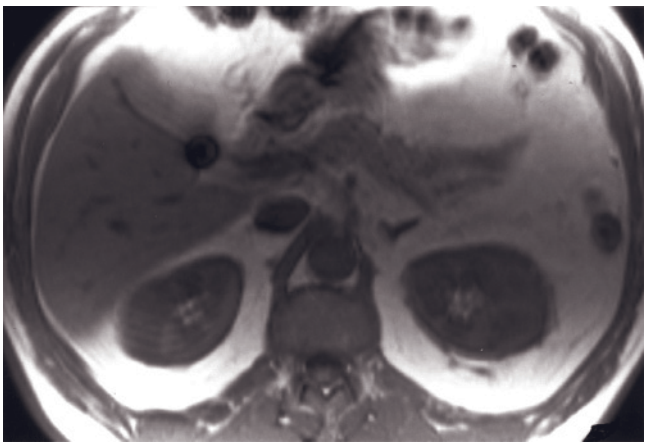

(*h*)

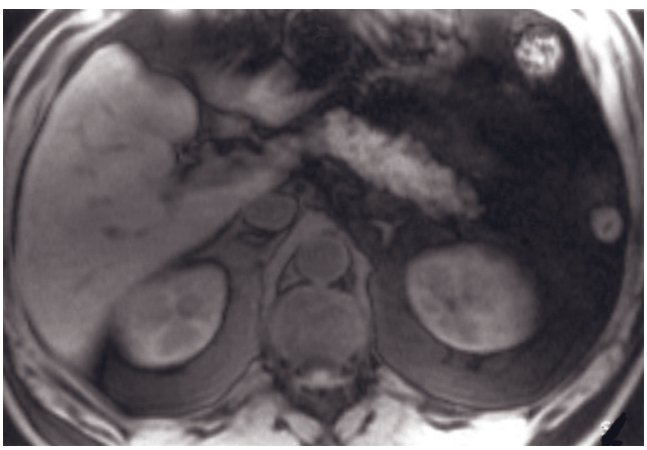

(*i*)

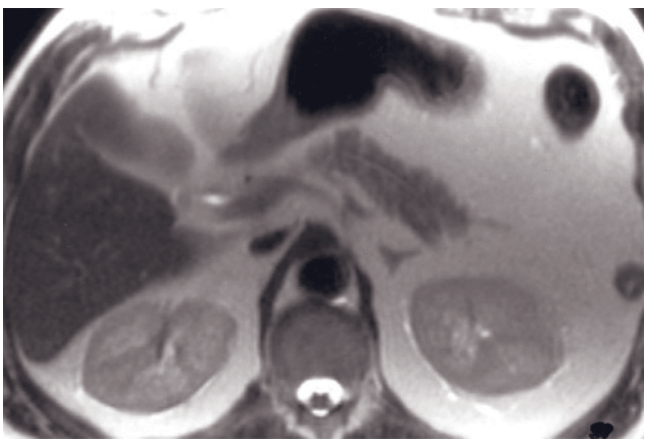

(*j*)

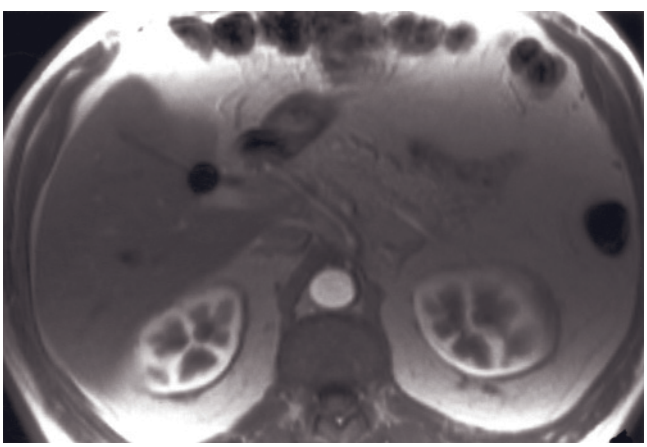

(*k*)

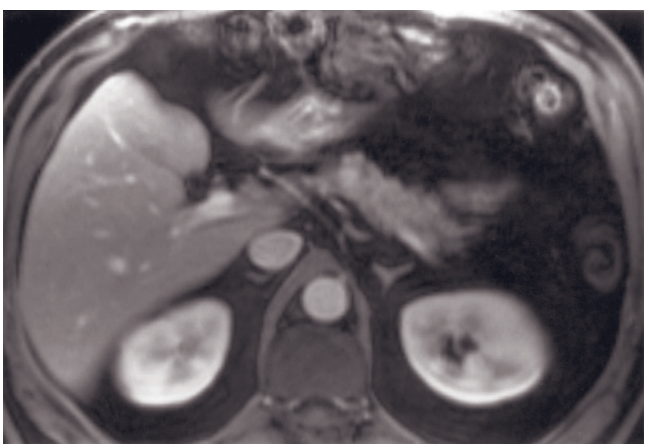

(*l*)

FIG. 8.1 (*Continued*) T1-weighted GE (*h*),T1-weighted fat-suppressed GE (*i*), HASTE (*j*), immediate postgadolinium T1 GE (*k*), and 90-s postgadolinium T1 fat-suppressed GE (*l*) images. Relative to normal liver, normal adrenal glands are typically mildly hypointense on T1 in-phase images (*b*, *h*), are isointense with a signal-void rim on T1 out-of-phase images (*c*), are well defined and isointense on T1-weighted fat-suppressed images (*d*, *i*), are isointense on T2 images (*a*, *e*, *j*), enhance homogeneously on immediate postgadolinium images (*f*, *k*), and fade to isointensity with liver on delayed images (*g*, *l*). T1-weighted SGE (*m*), T1-weighted

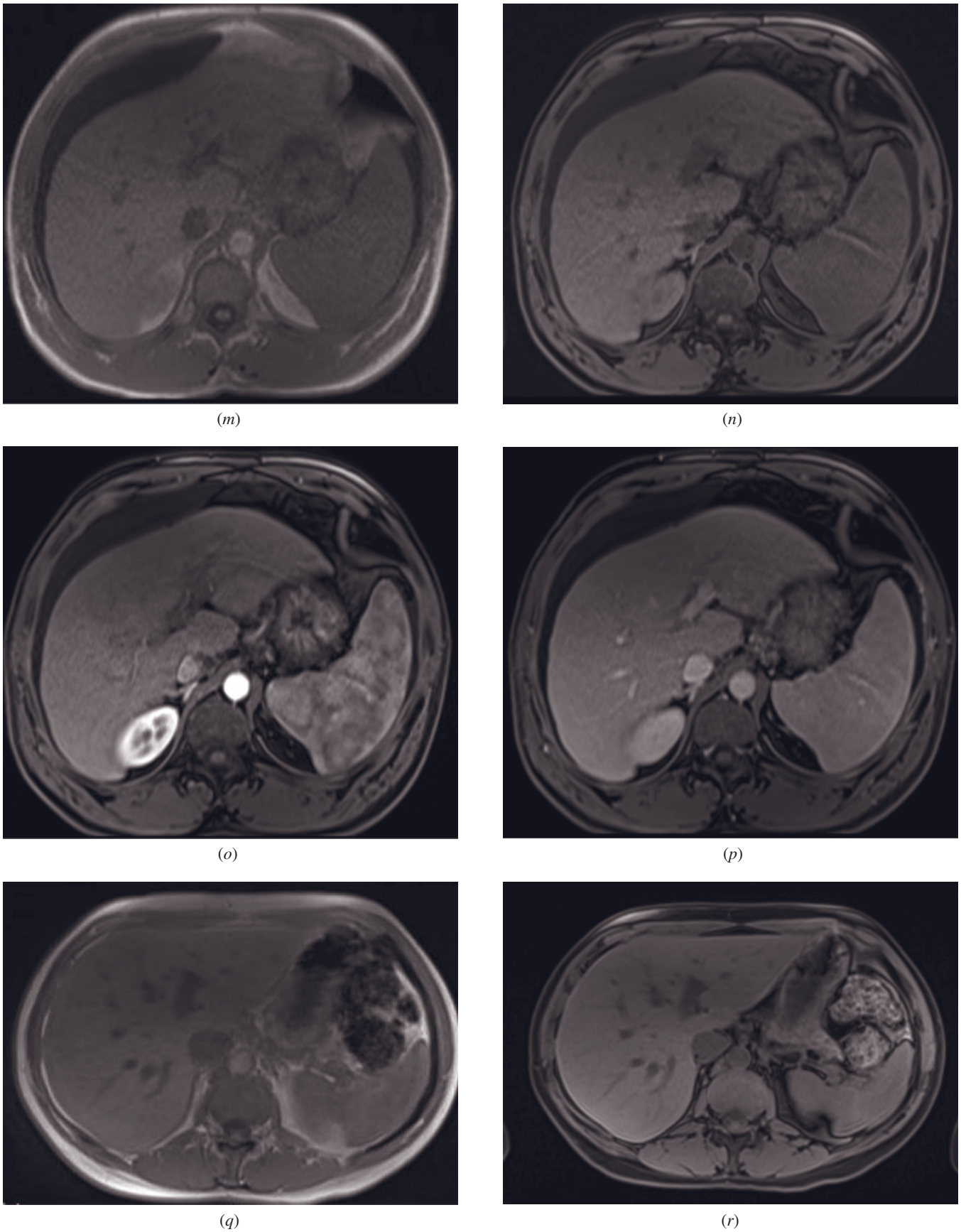

FIG. 8.1 (*Continued*) fat-suppressed 3D-GE (*n*), T1-weighted postgadolinium hepatic arterial dominant-phase (*o*), and interstitial-phase (*p*) fat-suppressed 3D-GE images demonstrate the normal right adrenal gland in another patient. Note the capillary blush in the right adrenal gland. T1-weighted SGE (*q*), T1-weighted fat-suppressed 3D-GE (*r*), T1-weighted postgadolinium hepatic arterial

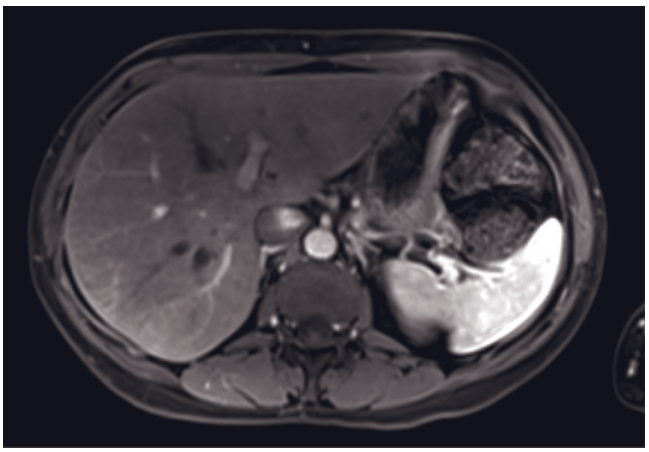

(*s*)

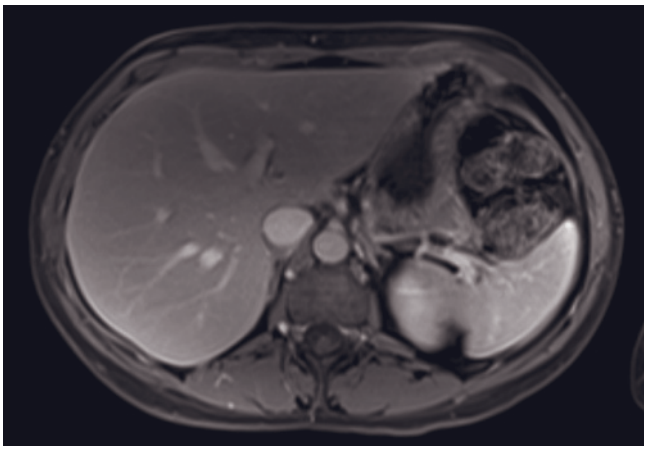

(*t*)

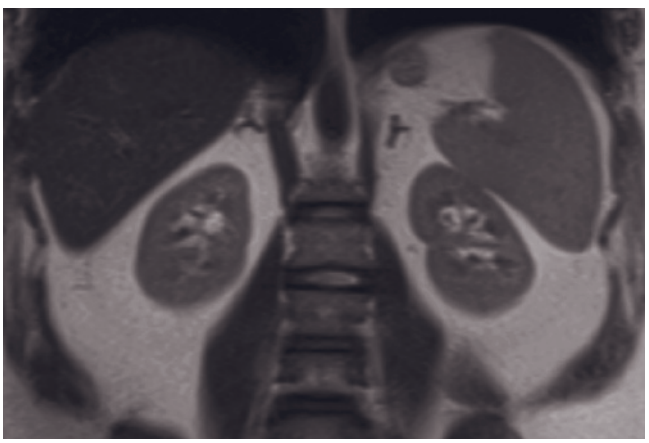

(*u*)

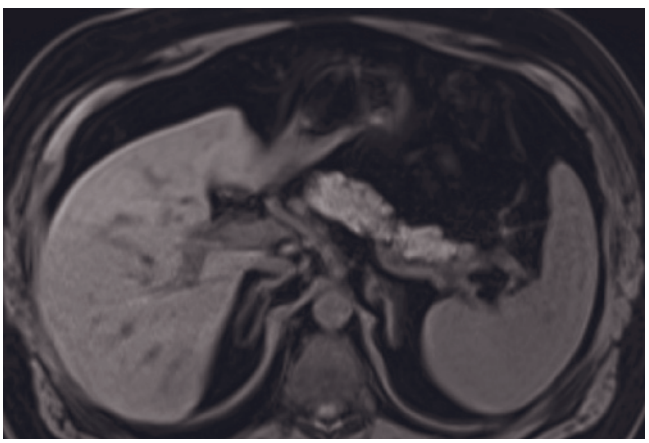

(*v*)

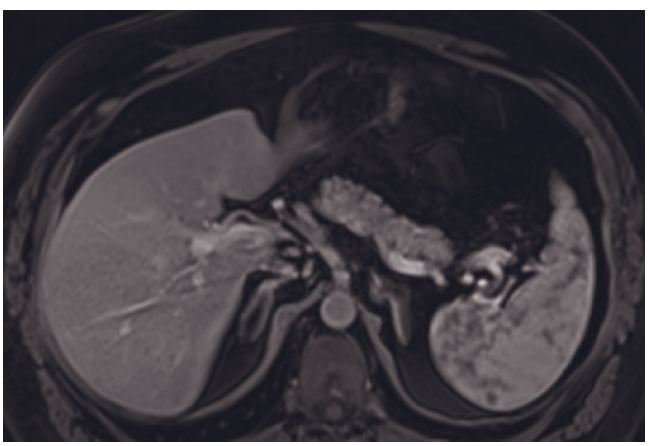

(*w*)

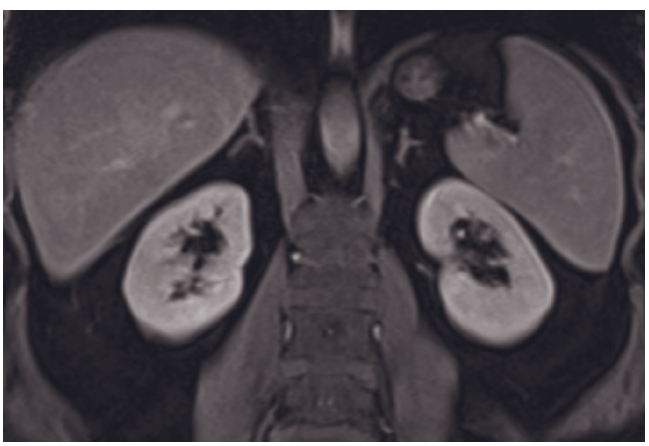

(*x*)

FIG. 8.1 (*Continued*) dominant-phase (*s*), and interstitial-phase (*t*) fat-suppressed 3D-GE images at 3.0 T demonstrate bilateral normal adrenal glands in another patient. Note the capillary blush in adrenals. This capillary blush appears to have a shorter duration than observed in pancreas. Coronal T2-weighted single-shot echo-train spin-echo (*u*), transverse T1-weighted fat-suppressed 3D-GE (*v*), transverse T1-weighted postgadolinium early hepatic venous phase fat-suppressed 3D-GE (*w*), and coronal T1-weighted interstitial phase fat-suppressed 3D-GE (*x*) images demonstrate bilateral normal adrenal glands in another patient. Coronal acquisitions are helpful for the evaluation of adrenal glands.

when the organ margins are viewed en face [31]. T2-weighted images provide information on fluid content of adrenal lesions, and are essential in examining for pheochromocytomas, as their fluid content is consistently higher than that of other adrenal masses.

MASS LESIONS

Diseases of the adrenal glands may affect the cortex or medulla. Diseases of the adrenal cortex can be divided essentially into three categories: 1) disorders associated with hyperfunction and steroid excess, 2) disorders that reduce the output of adrenal steroid, and 3) lesions that have no functional effect. Hyperfunctioning diseases may result from adrenal hyperplasia as well as from benign or malignant tumors. Many mass lesions possess a distinctive MR imaging appearance, which can be described by evaluating the combination of T1, T2, and early and late postgadolinium images (Table 8.1).

FIG. 8.2 Adrenal mass. Adrenal mass is shown in the sagittal plane. Sagittal-plane GE image demonstrates an adrenal adenoma (arrow) that is clearly separated from kidney and spleen (s).

Cortical Lesions

Benign

Hyperplasia. The majority (70%) of patients with Cushing syndrome have adrenal cortical hyperplasia secondary to an ACTH-producing pituitary microadenoma (Cushing disease). Adrenal hyperplasia is also identified in the context of systematic illness, acromegaly, hyperthyroidism, hypertension, diabetes, depression, and malignant disease. Hyperplasia of the adrenal cortex results secondarily to overstimulation of the cortex by ACTH. Primary hyperplasia is relatively uncommon.

Adrenal hyperplasia usually results in bilateral adrenal enlargement, diffuse or nodular, with maintenance of adreniform shape (fig. 8.3). Unilateral adrenal enlargement may, however, also occur [38]. The adrenal glands may also appear normal in size [12]. Hyperplastic glands usually contain microscopic nodules, but macroscopic nodules (12 cm) may be observed [12]. In primary pigmented nodular adrenal dysplasia, multiple tiny (2–5 mm) nodules may be seen bilaterally, with no overall glandular enlargement and normal intervening adrenal tissue. In ACTH-independent macronodular adrenal hyperplasia, both glands may be grossly enlarged and contain larger nodules [39]. Hyperplastic adrenal glands have signal intensity appearances similar to those of normal adrenals on all MR imaging sequences [12].

Adenomas. Adenomas are usually small neoplasms, less than 5 cm, characteristically solitary and well-encapsulated. Adrenal adenomas are the most common adrenal masses and can be divided into two

Table 8.1 Pattern Recognition: Adrenal Lesions

	T1 In-Phase	T1 Out-of-Phase	T2	Early Gd	Late Gd	Other Features
Adenoma	↓–↑	↓–↓↓	∅–↑	Homogeneous intense	Fade	80% drop in signal on out-of-phase; 70% have a homogeneous intense capillary blush;
Metastases	↓–↑	∅	∅–↑	Heterogeneous, variable	Heterogeneous, variable	Heterogeneity increases with increase in lesion size.
Pheochromocytoma	↓–∅	∅	↑–↑↑	Variable, usually minimal	Variable	Heterogeneous and hyperintense on T2-WI; Minimal enhancement with gadolinium
Adrenal Cortical Carcinoma	↓–↑	↓ (portions)	↑	↑ Heterogeneous	Fade	Hemorrhagic and necrotic areas; portions of the tumor may drop on out-of-phase images
Lymphoma	∅	∅	∅	Minimal	Minimal	Mild heterogeneity on all sequences.

↓↓, Moderately to markedly decreased; ↓, mildly decreased; ∅, isointense; ↑, mildly increased; ↑↑, moderately to mildly increased.

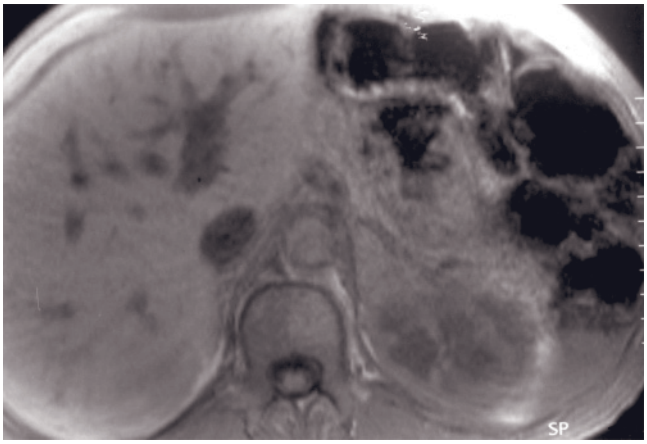

(*a*)

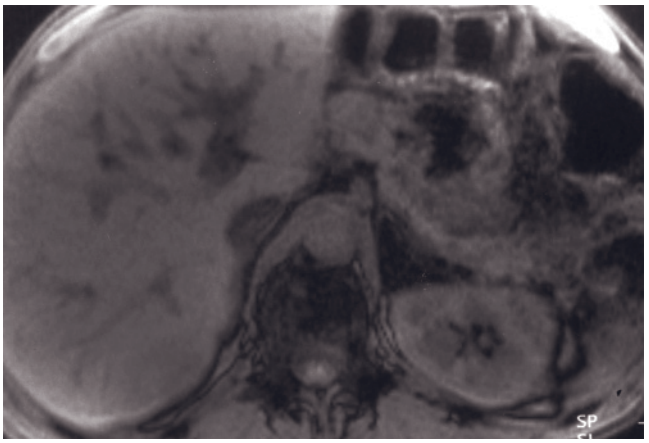

(*b*)

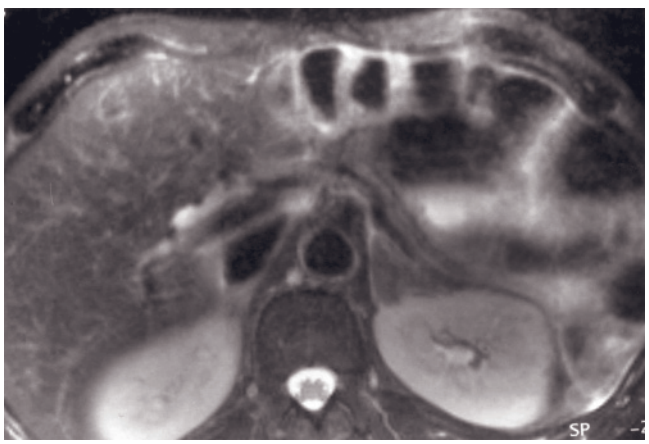

(*c*)

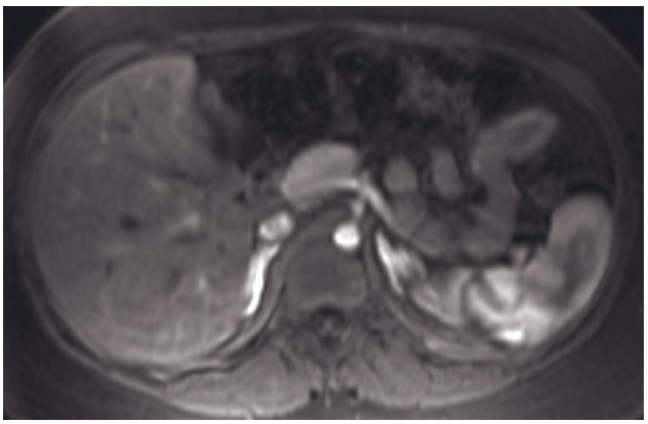

(*d*)

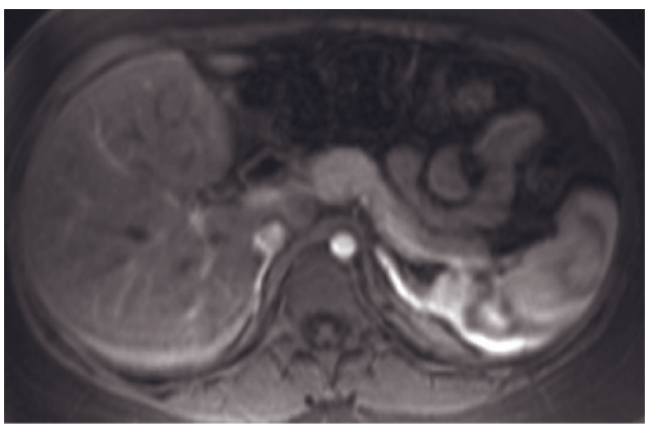

(*e*)

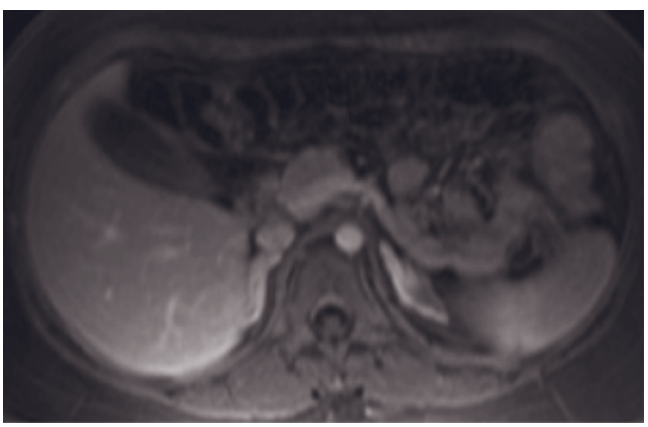

(*f*)

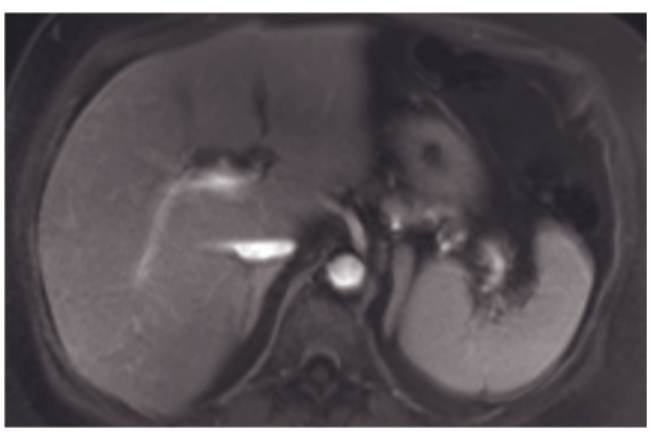

(*g*)

FIG. 8.3 Adrenal hyperplasia. T1-weighted GE (*a*), T1-weighted out-of-phase GE (*b*), and T2-weighted fat suppressed HASTE (*c*) images. The left adrenal is diffusely enlarged, and the adrenaliform shape is maintained. It is isointense to the liver on T1 (*a*), drops significantly in signal intensity on out-of-phase (*b*), and is slightly hypointense on T2 fat-suppressed (*c*) image. The presence of water and fat in the same voxel results in the findings on out-of-phase images. T1-weighted postgadolinium hepatic arterial dominant-phase (*d*, *e*) and interstitial-phase (*f*) fat-suppressed 3D-GE images demonstrate congenital adrenal hyperplasia in another patient. Bilateral adrenal glands are diffusely enlarged, maintaining their adrenaliform shape, and show diffusely intense enhancement. T1-weighted postgadolinium interstitial-phase water-excitation magnetization-prepared gradient-echo image (*g*) at 3.0 T demonstrates diffusely enlarged bilateral adrenal glands that maintain their adrenaliform shapes in another patient with congenital adrenal hyperplasia.

categories: nonhyperfunctioning and hyperfunctioning. Nonhyperfunctioning adenomas are more frequent than hyperfunctioning adenomas. Many adrenal adenomas are found incidentally at autopsy, in 2–8% of autopsy cases, or discovered by imaging studies performed for other reasons. Increased incidence has been reported in patients who are elderly, obese, or hypertensive or have primary malignancies of bladder, kidney, and endometrium. They may rarely be combined with myelolipomas [39, 40]. Hyperfunctioning adenomas are usually larger than 2 cm in diameter and are commonly cortisol secreting. The majority of adenomas are homogeneously iso- or hypointense in comparison to the normal adrenal gland on T2-weighted images (fig. 8.4), whereas adrenal metastases tend to be hyperintense [1–5]. Contrast enhancement on immediate postgadolinium images is variable and ranges from minimal (figs. 8.4–8.6) to moderately intense (figs. 8.7–8.12) [8, 11, 18]. Uniform enhancement of the entire lesion on immediate postgadolinium capillary-phase images is common for adenomas, reported in one series in 70% of cases [34], and rare for other entities. On serial postgadolinium images, rapid washout of contrast may be a feature more typical of benign than malignant masses (fig. 8.7) [6, 7]; however, variation exists (figs. 8.10, 8.11) [11, 18]. These lesions enhance homogeneously and have regular margins on T1-weighted gadolinium-enhanced fat-suppressed images [8]. Small linear or rounded foci of low or high signal intensity may be present on various MR sequences representing small areas of cystic change, hemorrhage, or variations of vascularity (fig. 8.13). These characteristics are also present in adrenal-cortical carcinoma; however, in malignant tumors larger heterogeneous regions are generally observed [41]. Adenomas commonly possess a thin rim of enhancement, best appreciated on interstitial-phase gadolinium-enhanced images [42]. However, a thin rim of adrenal tissue may also be appreciated with small metastases, simulating this appearance.

The most accurate method for demonstrating that a mass is an adenoma is to show loss of signal intensity on out-of-phase images (figs. 8.4–8.9, 8.12, and 8.14) [9–20, 22, 23, 26]. Loss of signal intensity should parallel loss of signal in marrow of the adjacent vertebral body. Caution should be exercised in using liver as the comparative organ to determine signal intensity loss because the liver may also contain fat [17, 27]. The use of spleen may be problematic also, because the spleen may contain iron, and T2* effect will influence signal intensity changes, particularly if a longer echo time (e.g., 6–7 ms) is used for out-of-phase imaging. Renal cortex is less affected by fat or iron deposition and may be a more accurate tissue to use as a visual comparison for signal intensity loss. An echo time-adjusted signal intensity drop greater than 20% is diagnostic for adenomas (fig. 8.14), whereas a 10–20% signal intensity drop is suggestive of adenomas (fig. 8.15), but follow-up may be needed. In a recent study, different methods to differentiate between adrenal adenomas and metastases on chemical-shift MR imaging were evaluated. The signal intensity (SI) index, calculated as [(SI on in-phase imaging − SI on out-of-phase imaging)/(SI on in-phase imaging)] × 100, was shown to be the most accurate method, compared with adrenal-to-spleen ratio, adrenal-to-muscle ratio, and adrenal-to-liver ratio, yielding an accuracy of 100% with appropriate cutoff value (>16.5%) selection [26]. Heterogeneous drop in signal intensity on out-of-phase images is not infrequent (fig. 8.16), and caution should be exercised not to interpret this sign as evidence of malignancy, as most of these tumors were benign adenomas in a recent study [24]. Drop in signal intensity may also be rarely encountered in other benign lesions such as myelolipomas [43].

Benign lesions that do not contain intracytoplasmic lipid may also retain signal on out-of-phase images (fig. 8.17) [11, 20]. If histologic fat content is minimal, negligible signal loss may be observed on out-of-phase images, which has been reported in one series, where this was found in two of seven resected adenomas [20]. T1-weighted fat-suppressed imaging technique has also been useful to differentiate adenomas from malignant masses [44].

MR imaging may well serve as a problem-solving modality in cases of indeterminate adrenal masses discovered on CT. In a recent study, 8 (62%) of 13 adrenal adenomas with density greater than 10 HU on unenhanced CT were definitively characterized with chemical-shift MRI [45]. In another study using a threshold of 20% signal intensity decrease, the overall sensitivity of chemical-shift MR imaging for hyperattenuating (>10 HU) adenoma was 67%. The sensitivity for adenoma was 89% for masses with attenuation of 10–30 HU and 75% for adenomas with attenuation of 20–30 HU, whereas specificity of MRI for the diagnosis of adenoma was 100% [22].

Large adenomas may undergo degenerative changes and contain foci of hemorrhage that appear as punctate high-signal-intensity foci on T1-weighted and/or T2-weighted images (see fig. 8.13) [41].

Functioning adenomas with excess cortisol secretion are responsible for approximately 20% of Cushing syndrome cases. Most of these adenomas measure larger than 2 cm and are well shown on CT and MR images [46]. Hyperfunctioning and nonhyperfunctioning adenomas are presently not distinguishable on MR images because they have similar morphologic and signal intensity features, including the tendency of both to lose signal intensity on out-of-phase images, because they both often contain intracytoplasmic lipid [20]. Functioning adenomas may contain negligible fat

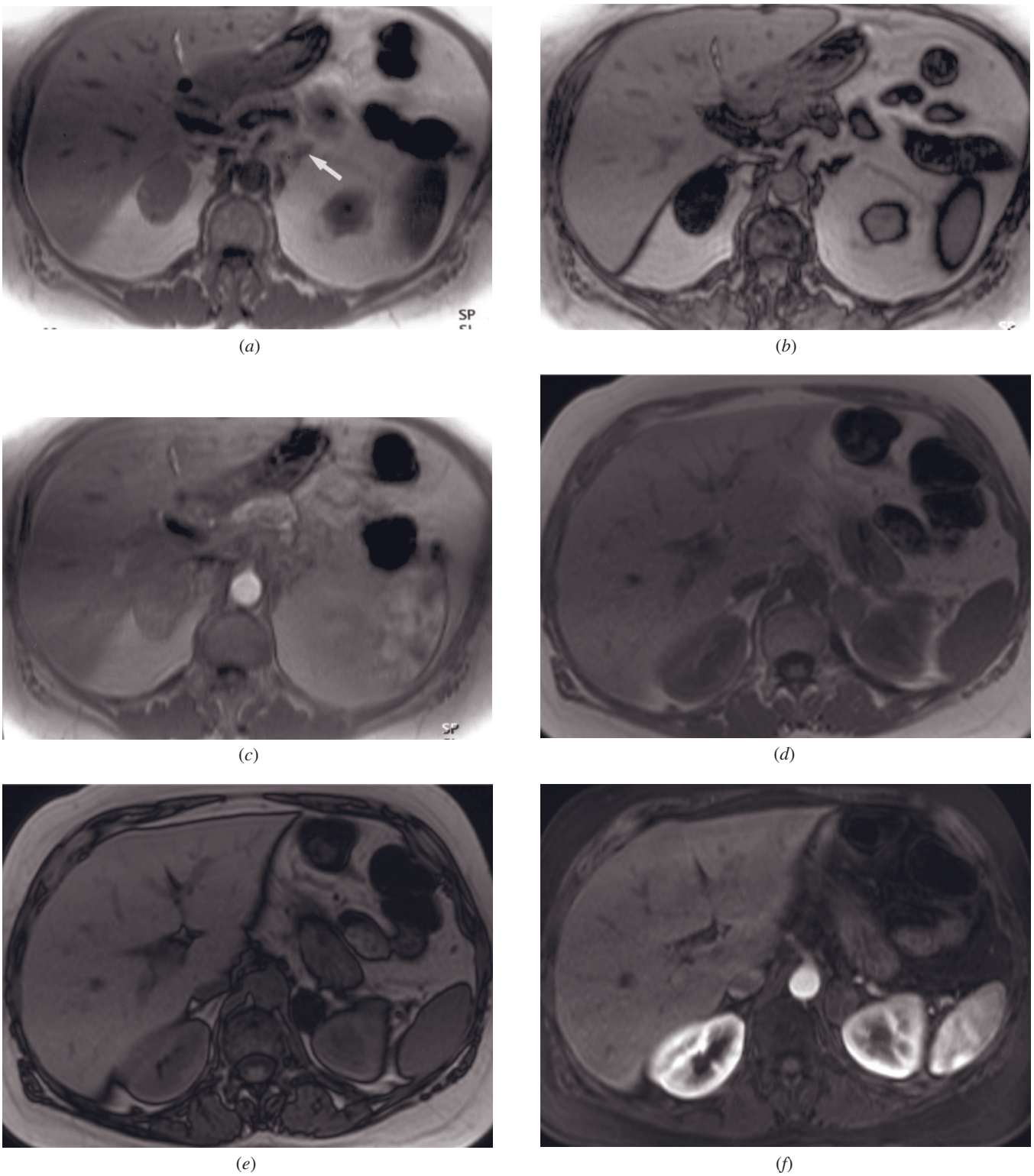

FIG. 8.4 Adrenal adenoma—mild capillary blush. T1-weighted GE (*a*), T1-weighted out-of-phase GE (*b*), and immediate postgadolinium GE (*c*) images. Right adrenal adenoma demonstrates signal drop on out-of-phase image and mild capillary blush on immediate postgadolinium image. Note normal left adrenal (arrow, *a*). T1-weighted in-phase (*d*) and out-of-phase (*e*) SGE, T1-weighted postgadolinium arterial phase (*f*) and hepatic venous phase (*g*) fat-suppressed 3D-GE images at 3.0 T demonstrate left adrenal adenoma in another patient. The adenoma shows signal drop on out-of-phase image (*e*) compared to in-phase image (*d*). Mild capillary blush is detected on the arterial phase image (*f*). **Right adrenal adenoma 1.5 T vs. 3.0 T.** T1-weighted in-phase (*h*)

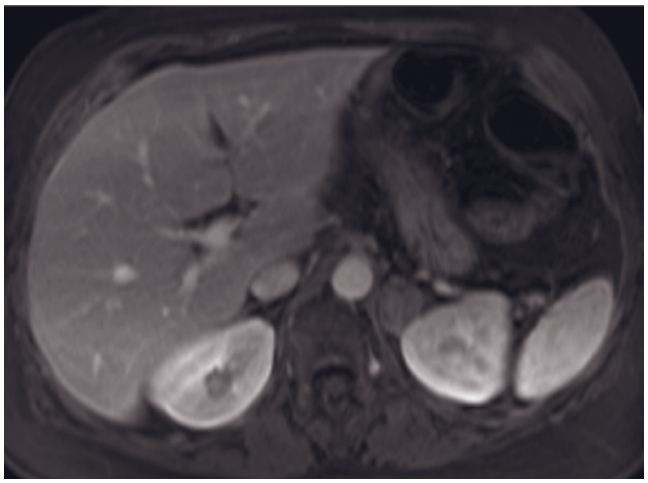

(*g*)

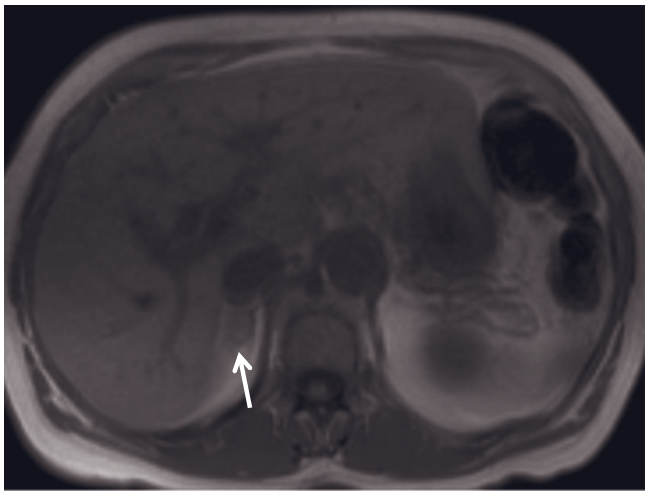

(*h*)

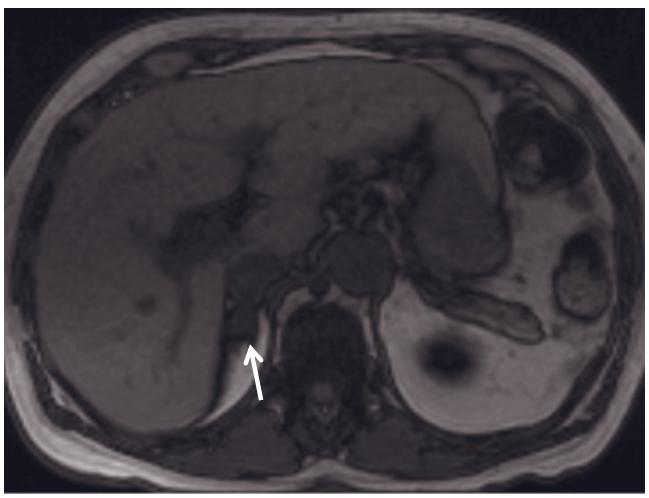

(*i*)

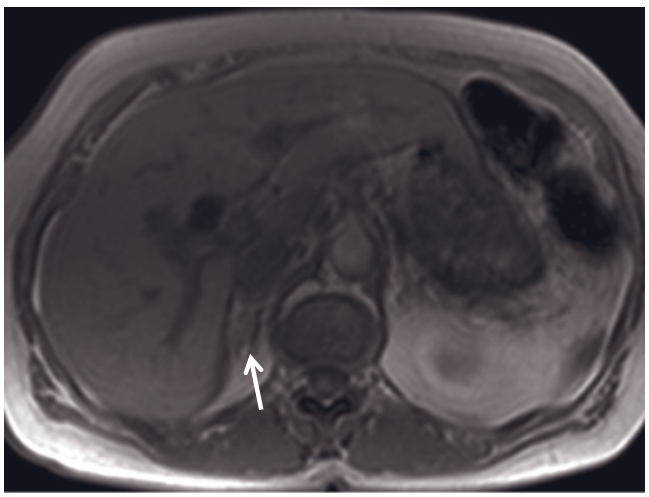

(*j*)

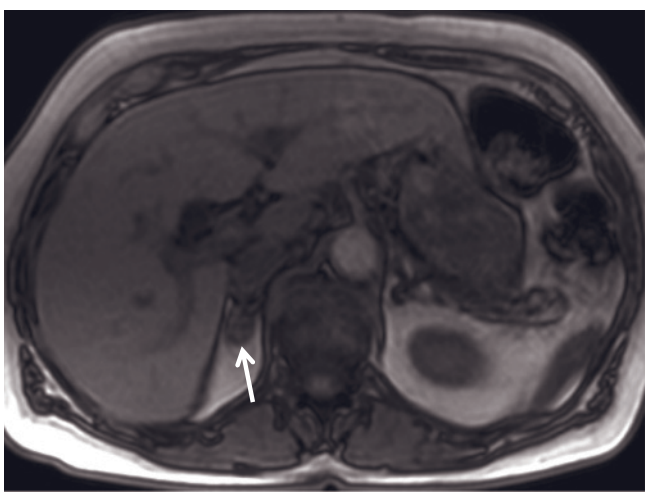

(*k*)

FIG. 8.4 (*Continued*) and out-of-phase (*i*) SGE images at 1.5 T and T1-weighted in-phase (*j*) and out-of-phase (*k*) SGE images at 3.0 T demonstrate right adrenal adenoma in the same patient. The adenoma shows signal drop out-of-phase image (*i*) compared to in-phase image (*h*) at 1.5 T. However, the signal drop on out-of-phase image (*k*) compared to in-phase image (*j*) is less than that at 1.5 T. The different T1 contrast resolution of 3.0 T MR imaging and the inability to use exact in-phase/out-of-phase TE times at 3.0 T impair the ability to detect fat content in the lesions at 3.0 T in a consistent fashion. This is particularly true for small lesions.

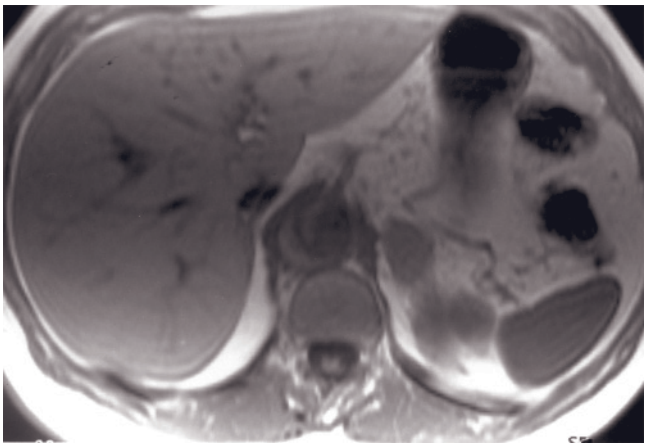

(*a*)

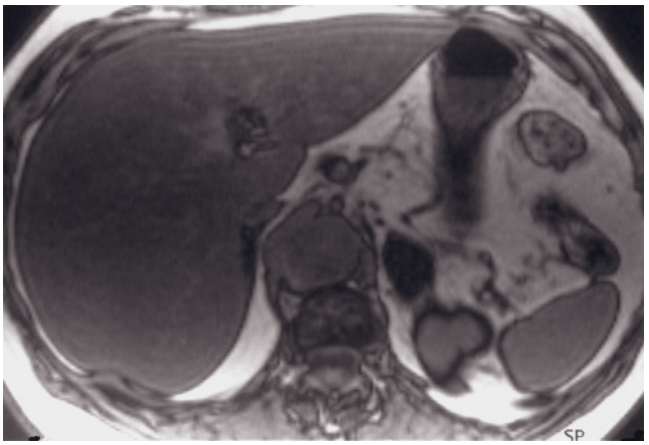

(*b*)

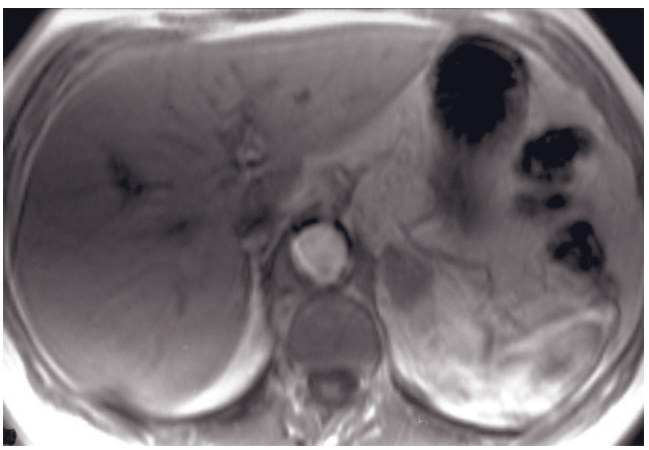

(*c*)

FIG. 8.5 Adrenal adenoma—signal drop and no capillary blush. T1-weighted GE (*a*), T1-weighted out-of-phase GE (*b*), and immediate post gadolinium GE (*c*) images. Left adrenal adenoma demonstrates signal drop on the out-of-phase image (*b*).There is no substantial capillary blush on the immediate postgadolinium image (*c*).

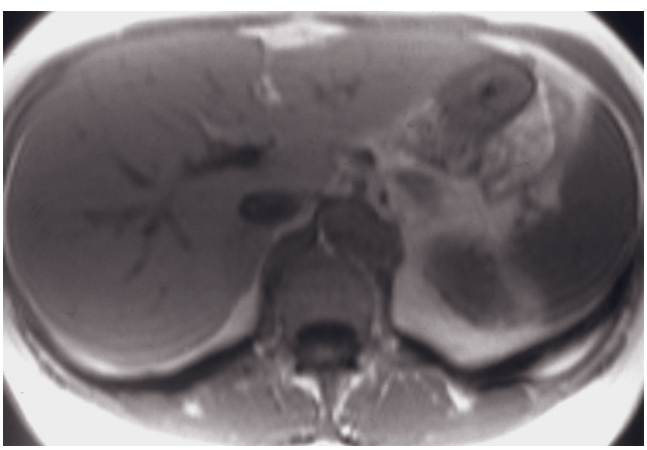

(*a*)

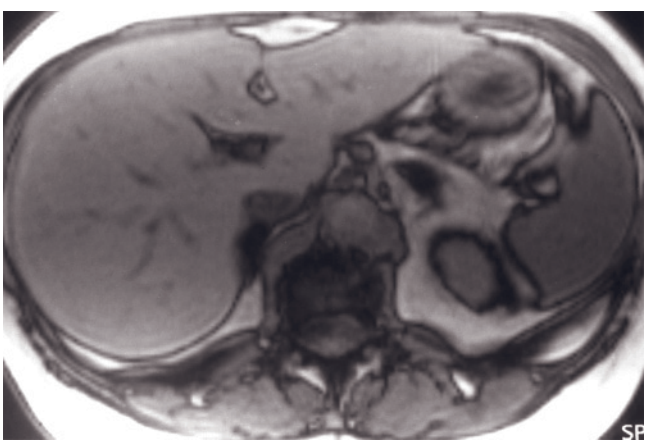

(*b*)

FIG. 8.6 Bilateral adrenal adenomas. T1-weighted GE (*a*), T1-weighted out-of-phase GE (*b*), immediate postgadolinium GE (*c*), and 90-s postgadolinium fat suppressed GE (*d*) images in a patient with bilateral adrenal adenomas. Note that in this patient

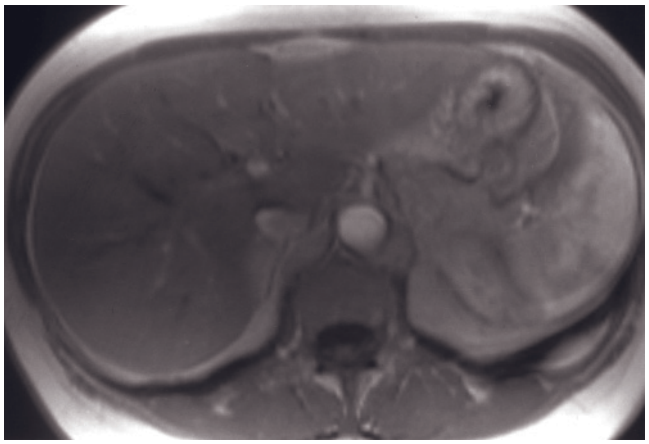

(*c*)

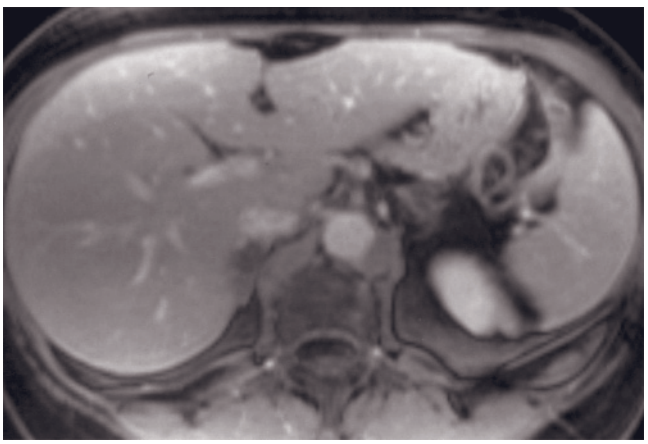

(*d*)

FIG. 8.6 (*Continued*) both adrenals show signal intensity drop on out-of-phase images, but there is no substantial capillary blush after gadolinium administration (*c*). Late enhancement is mildly heterogeneous (*d*).

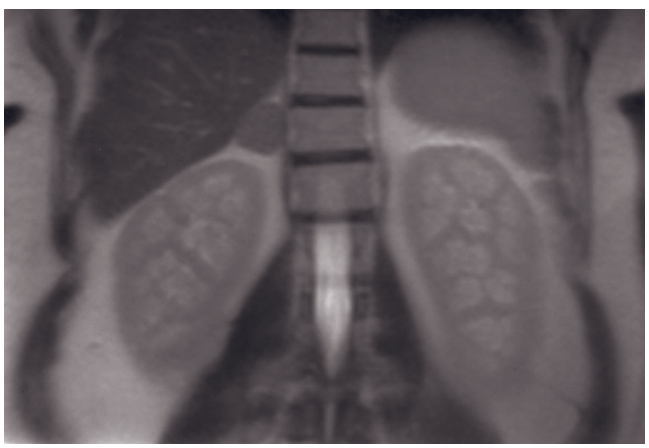

(*a*)

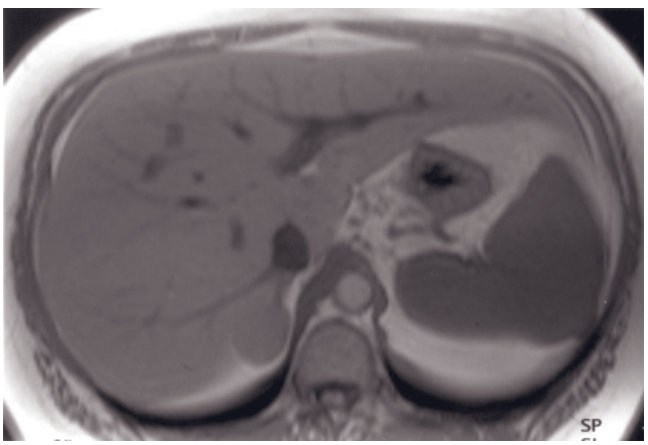

(*b*)

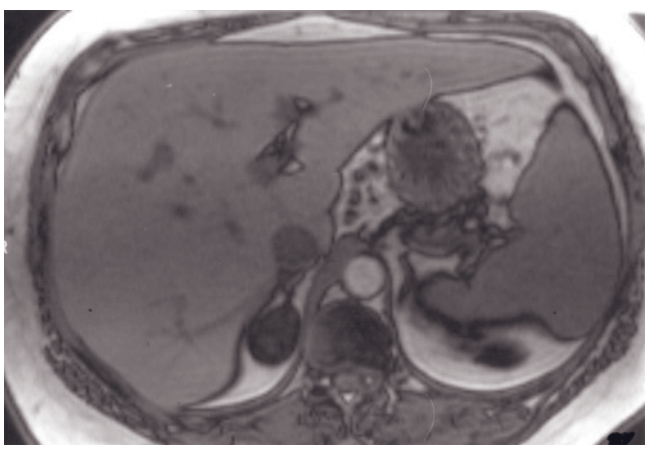

(*c*)

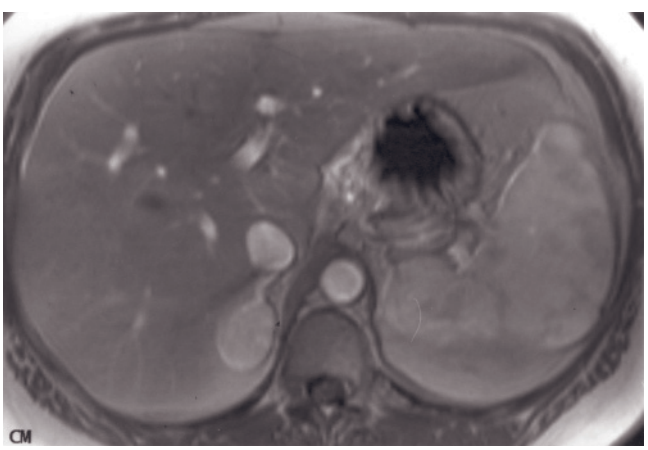

(*d*)

FIG. 8.7 Adrenal adenoma. Coronal T1-weighted GE (*a*), T1-weighted GE (*b*), T1-weighted out-of-phase GE (*c*), immediate postgadolinium GE (*d*), and 90-s postgadolinium fat-suppressed GE (*e*) images. A 3 × 2-cm right adrenal mass shows signal intensity drop on the out-of-phase image (*c*) compared to the in-phase image (*b*). The extent of signal intensity drop is consistent with substantial intracytoplasmic lipid. Immediately after contrast the adenoma demonstrates an early and homogeneous capillary blush (*d*), which washes out on delayed image (*e*).

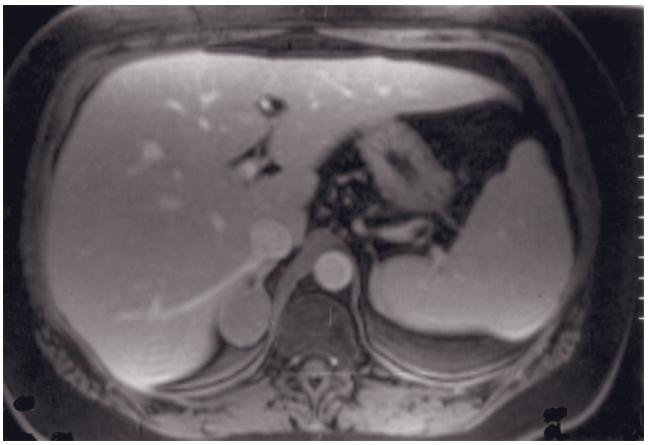

FIG. 8.7 (*Continued*) (*e*)

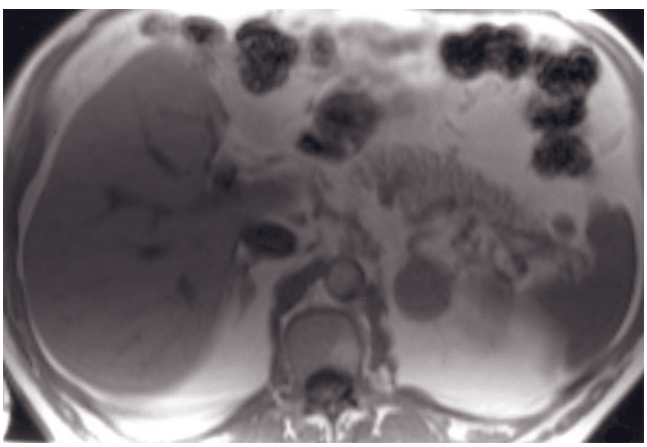

(*a*)

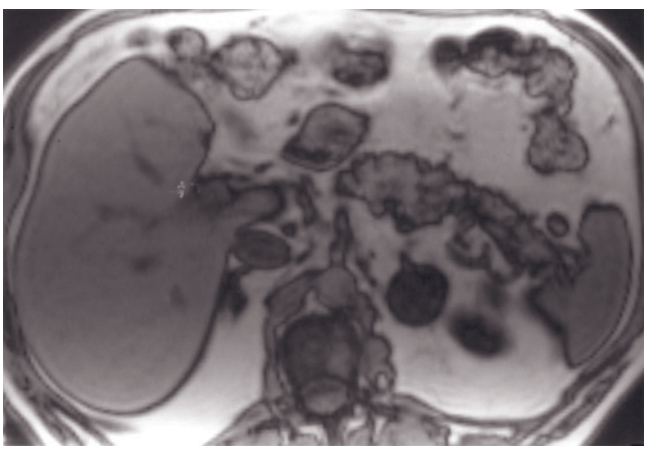

(*b*)

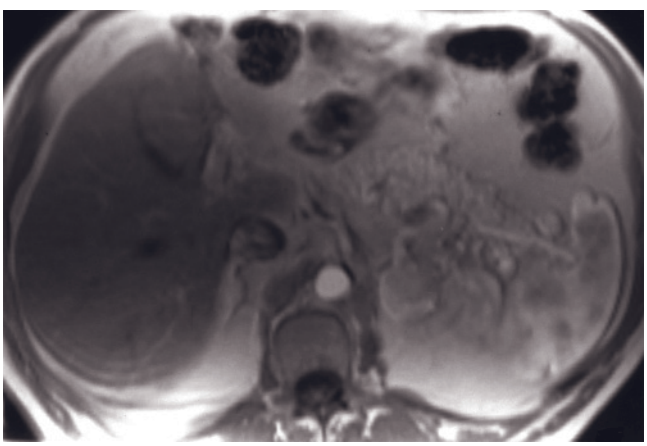

(*c*)

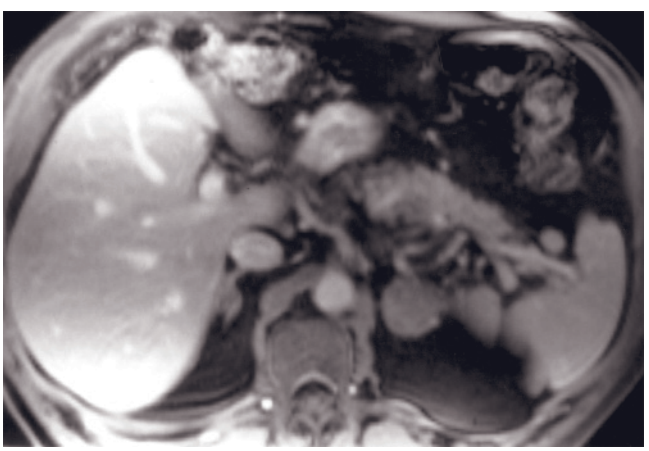

(*d*)

FIG. 8.8 Bilateral adrenal adenoma. T1-weighted GE (*a*),T1-weighted out-of-phase GE (*b*), immediate postgadolinium GE (*c*), and 90-s postgadolinium fat-suppressed GE (*d*) images. Bilateral adrenal adenomas, larger on the left side. Both lesions have signal intensity drop on the out-of-phase image (*b*). There is an intense capillary blush on immediate postgadolinium image (*c*) and a rapid washout on delayed image (*d*).

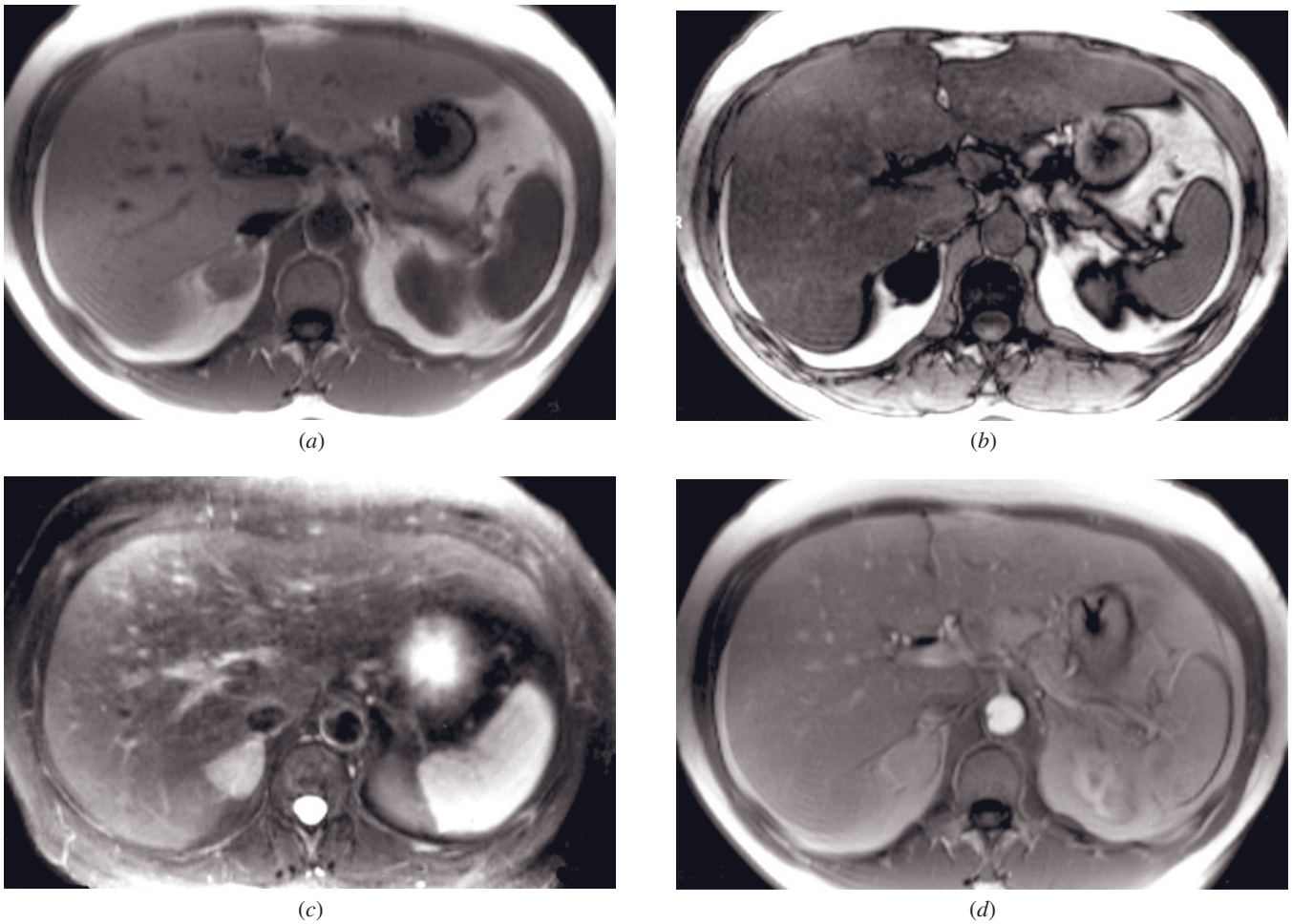

FIG. 8.9 Adrenal adenoma. T1-weighted GE (*a*), T1-weighted out-of-phase GE (*b*), T2-weighted HASTE (*c*), and 45-s postgadolinium GE (*d*) images. Right adrenal adenoma has substantial signal drop from the in-phase (*a*) to the out-of-phase (*b*) image and moderately high signal intensity on fat-suppressed T2 image (*c*). Note intense homogeneous capillary blush after gadolinium administration (*d*).

and therefore not lose signal on out-of-phase images (fig. 8.18).

Aldosterone-secreting adrenal adenomas are rare tumors responsible for 75% of cases of primary aldosteronism (Conn syndrome), with adrenal hyperplasia accounting for 25% [47]. The clinical presentation includes systemic hypertension with hypokalemia, decreased plasma renin activity, and increased plasma aldosterone. These tumors are typically small, measuring less than 3 cm in diameter, and the left adrenal is involved slightly more often than the right. MRI performs well in detecting these tumors [48].

The distinction between adenoma and hyperplasia is important because patients with adenomas will respond to surgical management, whereas patients with hyperplasia are best treated medically [49].

Findings on tomographic images may result in diagnostic errors in patients who have a unilateral adenoma but in whom both adrenals have a nodular appearance. Doppman et al. [50] reported on 24 patients with primary aldosteronism in whom CT images suggested the presence of hyperplasia in six patients, but who had a unilateral aldosteronoma at surgery. T1-weighted fat-suppressed images show clear delineation of the adrenal glands and permit detection of small masses (fig. 8.19) [12]. Aldosteronomas contain intracytoplasmic lipid, likely as a similar percentage as other adenomas (80%), and may therefore lose signal intensity on out-of-phase images (see fig. 8.19) [20].

Other Benign Tumors

Myelolipoma. Myelolipomas are rare benign tumors composed of mature adult adipose tissue and hematopoietic cells [51]. Although usually sporadic, they have been reported in association with thalassemia or chronic hemolytic anemias, suggesting a possible role

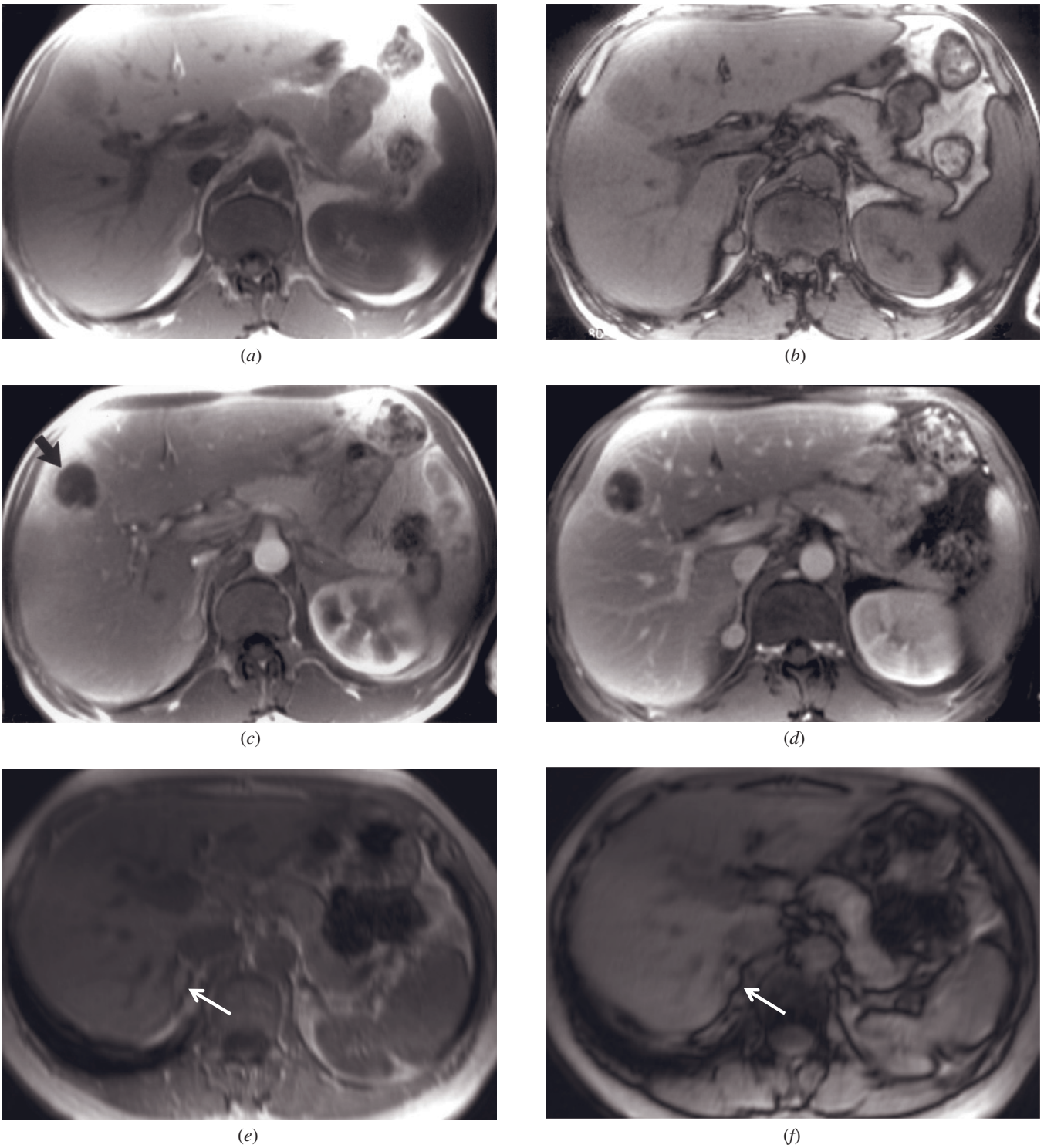

FIG. 8.10 Adrenal adenoma—no signal loss and capillary blush. T1-weighted GE (*a*), T1-weighted out-of-phase GE (*b*), immediate postgadolinium GE (*c*), and 90-s postgadolinium fat-suppressed GE (*d*) images in a patient with a nonfunctioning adenoma. The adrenal adenoma is slightly hypointense to the liver on T1 (*a*) and has no signal drop on the out-of-phase image (*b*). After gadolinium administration, there is a capillary blush of the adrenal adenoma (*c*) and minimal washout of contrast material on the late image (*d*). A 3.5-cm abscess with a thin capsule is present in the liver (arrow, *c*). Note the intense perilesional enhancement on the immediate postgadolinium image. **Adrenal adenoma—no signal loss/Dixon method/capillary blush.** T1-weighted in-phase (*e*), out-of-phase (*f*), water-only (*g*), and fat-only (*h*) images of Dixon technique and T1-weighted postgadolinium

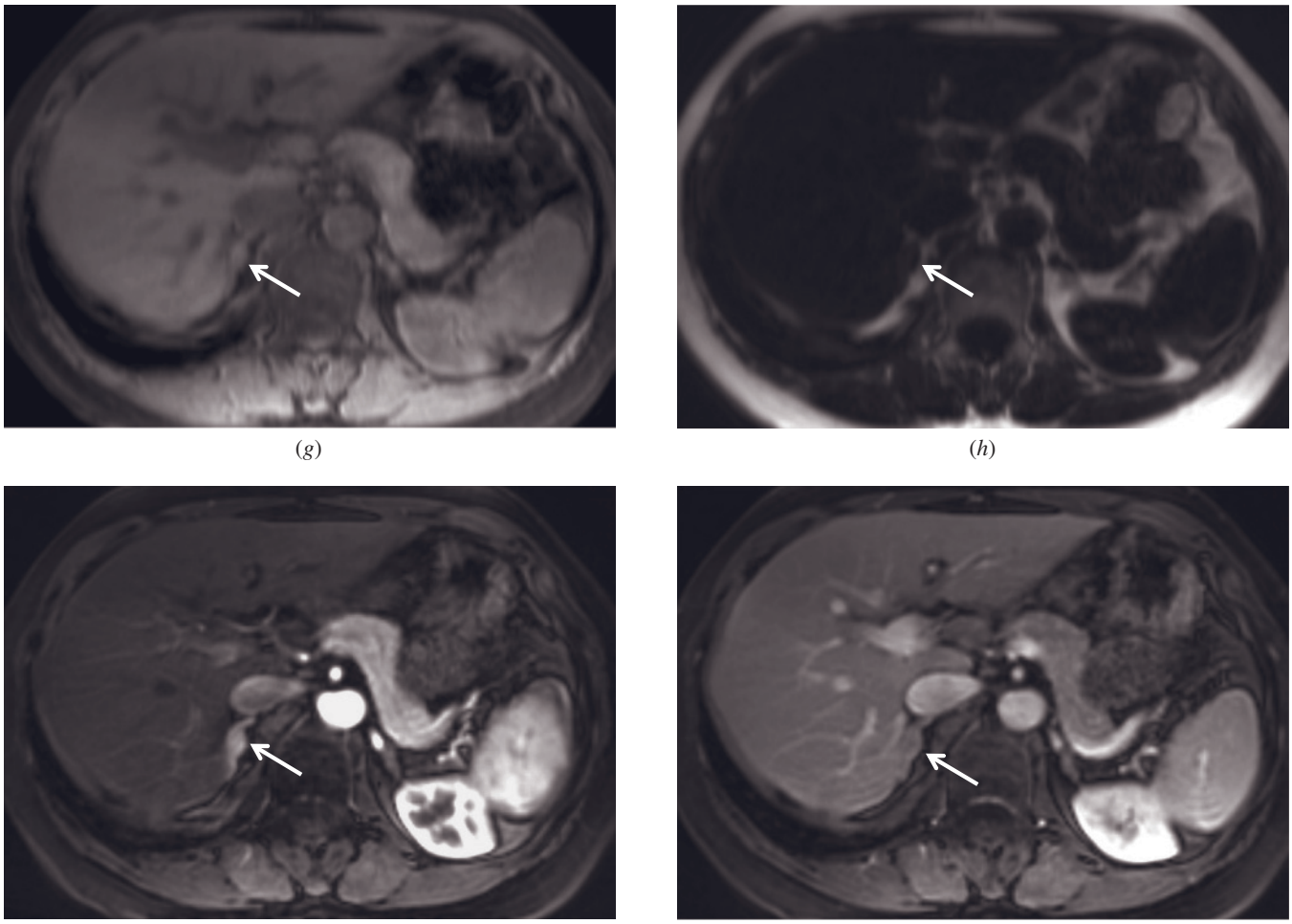

FIG. 8.10 (*Continued*) hepatic arterial phase (*i*) and hepatic venous phase (*j*) fat-suppressed 3D-GE images at 3.0 T demonstrate a small right adrenal adenoma (arrows, *e* and *j*) in another patient. Although no signal drop is detected in the adenoma on out-of-phase image (*f*) compared to in-phase image (*e*), mild increased signal (arrow, *h*) is detected in the adenoma on fat-only image (*h*), suggesting the presence of minimal fat. The adenoma shows capillary blush on the hepatic arterial dominant phase (*i*) and washout on the interstitial phase (*j*).

of increased erythropoietin levels in the pathogenesis of these tumors through stimulation of metaplasia of embryonic stem cells to myeloid tissue [43]. On MR imaging, tumors may demonstrate macroscopic fatty elements, hemorrhagic components, and variable signal intensity on T2-weighted sequences, ranging from hypointensity to moderate hyperintensity [52–54]. They are usually small and unilateral and typically have a high fat content that gives them a pathognomonic appearance on MR images [38, 51, 55–60]. The amount of fat in these lesions may vary. On the basis of T1-weighted images alone, the distinction from a hemorrhagic cyst may be difficult. The diagnosis is virtually certain if the signal of the tumor is hyperintense on T1-weighted images and decreases on fat-suppressed images (fig. 8.20) [12, 38, 60]. Because myelolipomas may be almost entirely fat containing, these tumors may not lose signal intensity on out-of-phase images. Signal loss with the out-of-phase technique occurs when fat and water are of similar proportions in the same voxel. Myelolipomas may exhibit a black ring phase-cancellation artifact if the tumor borders on a water-based organ, but most often the tumor is surrounded by fat and therefore does not exhibit a black ring phase-cancellation artifact. The distinction from adenoma is based on fat content. Adenomas generally do not contain sufficient fat to result in visually apparent signal loss on fat-suppressed images, with rare exceptions [33]. Myelolipomas generally contain such a preponderance of adipose tissue that signal loss does not occur on out-of-phase images, but signal loss is comparable to fat on fat-suppressed images. Coexistence of macroscopic fatty elements with areas of

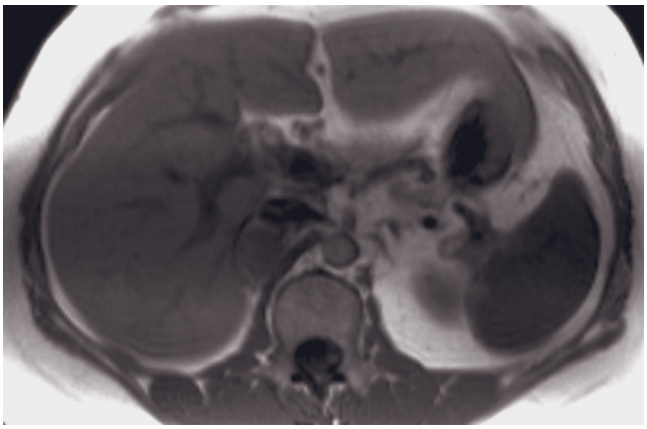

(*a*)

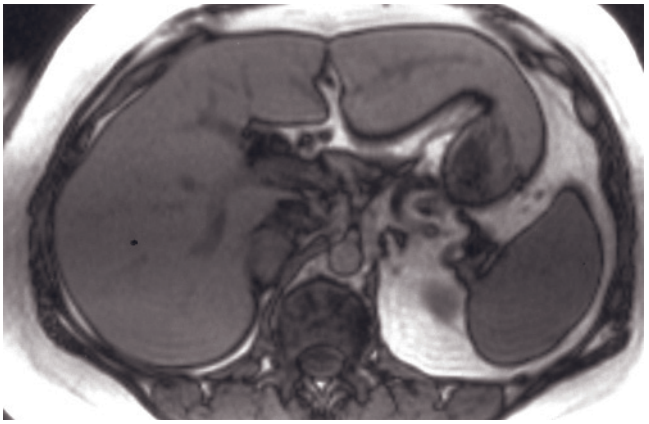

(*b*)

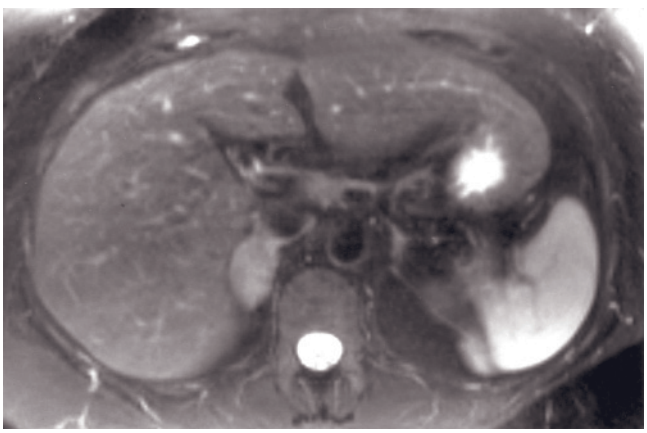

(*c*)

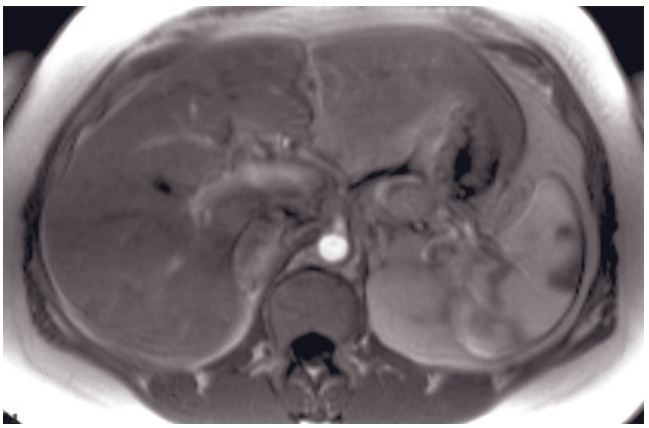

(*d*)

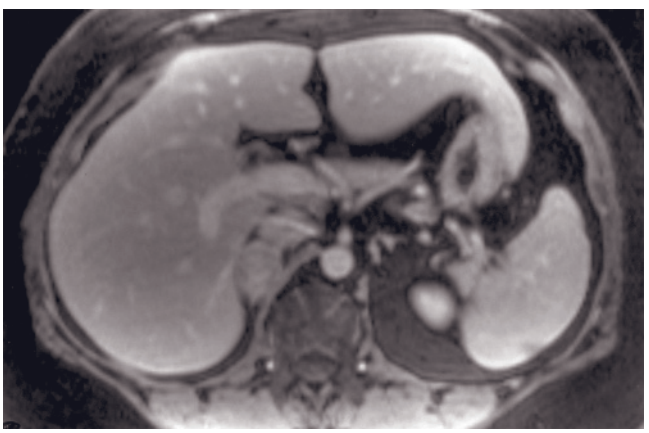

(*e*)

FIG. 8.11 Adrenal adenoma. T1-weighted GE (*a*), T1-weighted out-of-phase GE (*b*), T2-weighted fat-suppressed HASTE (*c*),immediate postgadolinium GE (*d*), and 90-s postgadolinium fat-suppressed GE (*e*) images. A right adrenal adenoma is isointense to the liver on T1 (*a*) and does not drop in signal intensity on out-of-phase image (*b*). The mass is slightly hyperintense on the T2 image, enhances heterogeneously on the immediate postgadolinium image (*d*), and becomes more homogeneous on the late image (*e*).

microscopic lipid, demonstrated by drop in signal intensity on opposed-phase images, has been reported [52], and they may also rarely exhibit signal intensity drop on out-of-phase images (fig. 8.21) with no macroscopic fat component, thus mimicking the appearance of adenomas [43]. Occasionally, myelolipomas may be large [43], and in these cases direct sagittal or coronal imaging may be helpful to demonstrate the extrarenal origin of these tumors [59]. In the presence of hemorrhagic content, they may rarely demonstrate very high signal intensity on T2-weighted images, mimicking the appearance of pheochromocytomas (see fig. 8.21) [43].

Adrenal Cyst and Pseudocyst. Adrenal cysts are an uncommon, heterogeneous group of lesions, with most cases reported as an incidental finding. They have

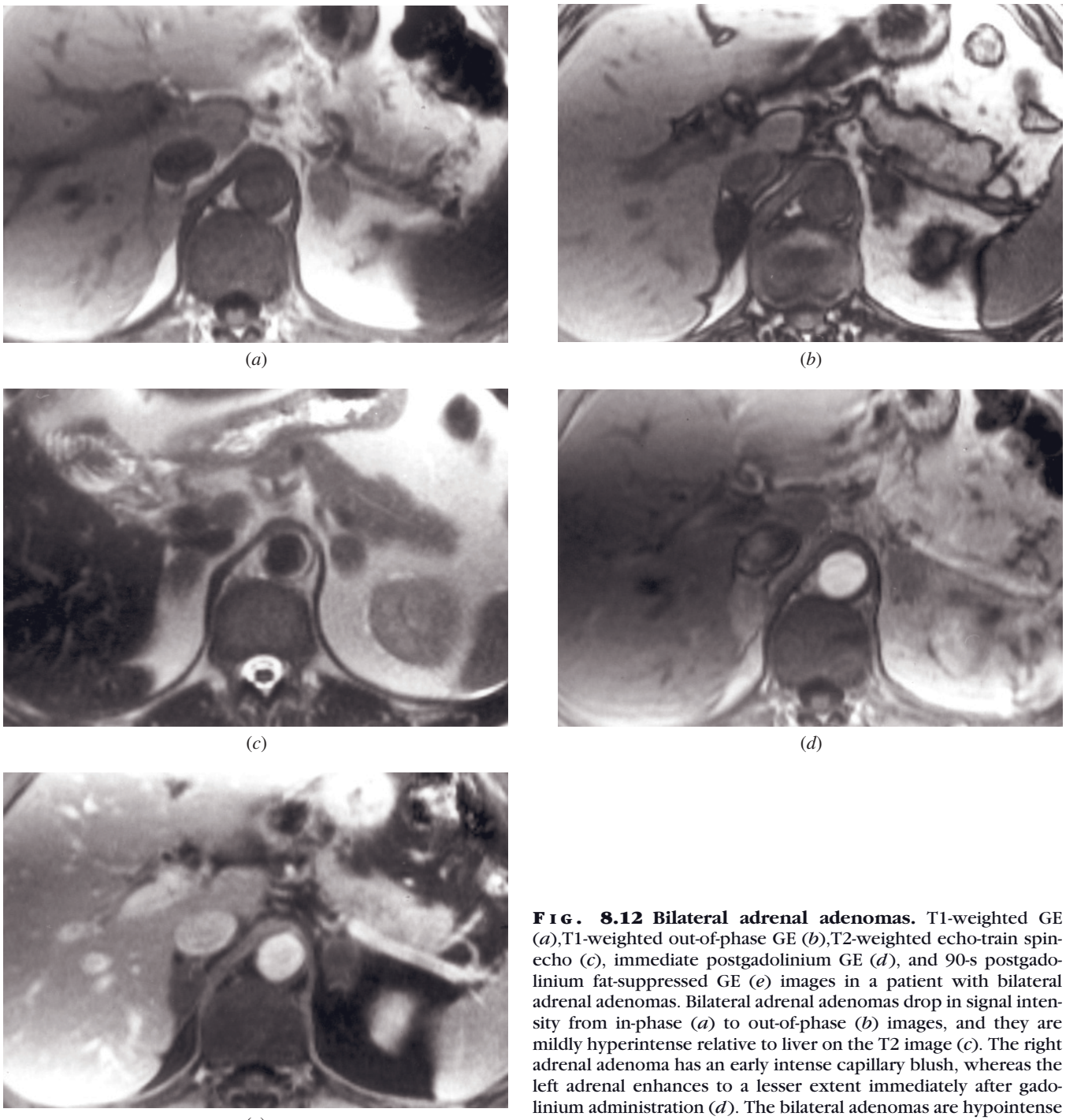

FIG. 8.12 Bilateral adrenal adenomas. T1-weighted GE (*a*),T1-weighted out-of-phase GE (*b*),T2-weighted echo-train spin-echo (*c*), immediate postgadolinium GE (*d*), and 90-s postgadolinium fat-suppressed GE (*e*) images in a patient with bilateral adrenal adenomas. Bilateral adrenal adenomas drop in signal intensity from in-phase (*a*) to out-of-phase (*b*) images, and they are mildly hyperintense relative to liver on the T2 image (*c*). The right adrenal adenoma has an early intense capillary blush, whereas the left adrenal enhances to a lesser extent immediately after gadolinium administration (*d*). The bilateral adenomas are hypointense on the late fat-suppressed image (*e*).

traditionally been divided into four categories: endothelial, hemorrhagic (pseudocyst), epithelial, and parasitic. Endothelial cysts and hemorrhagic pseudocysts are the most common types. Hemorrhagic pseudocysts are usually unilocular cystic masses encased in a fibrous capsule and containing amorphous abnormal material, blood, and fibrin. Microscopic examination reveals numerous irregular, thin-walled vascular channels. In contrast, endothelial cysts are usually multilocular and filled with clear, milky fluid. Histologic examination shows a thin fibrous wall lined by a continuous layer of endothelial cells.

The majority of adrenal cysts and pseudocysts are low in signal intensity on T1-weighted images and high

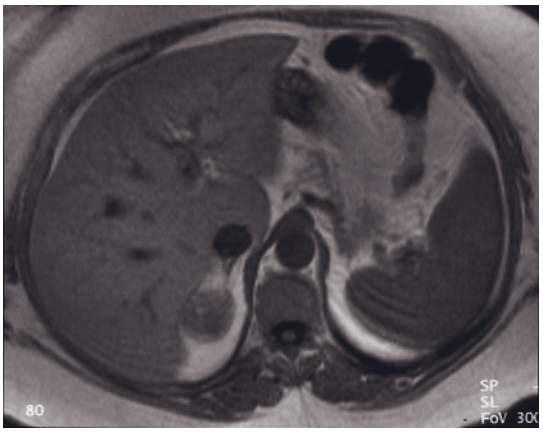

(*a*)

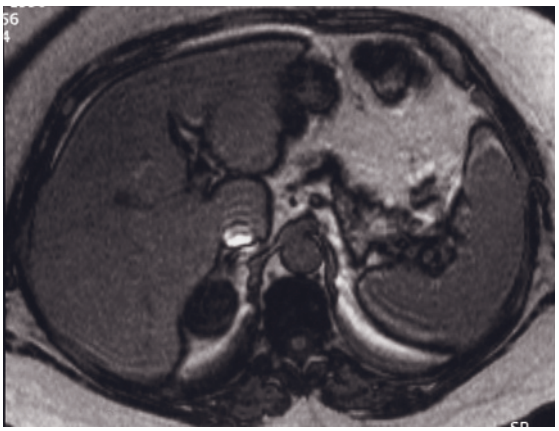

(*b*)

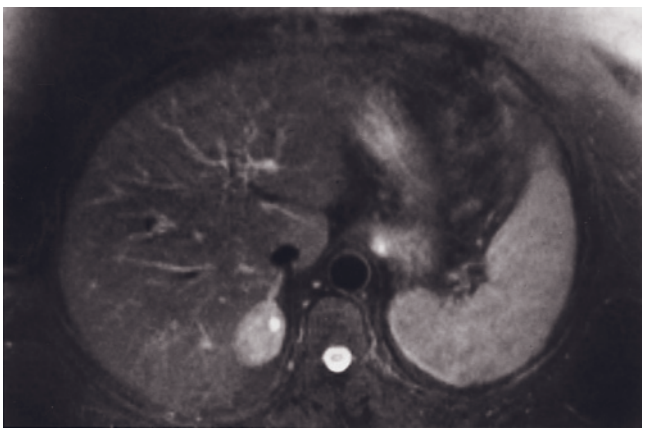

(*c*)

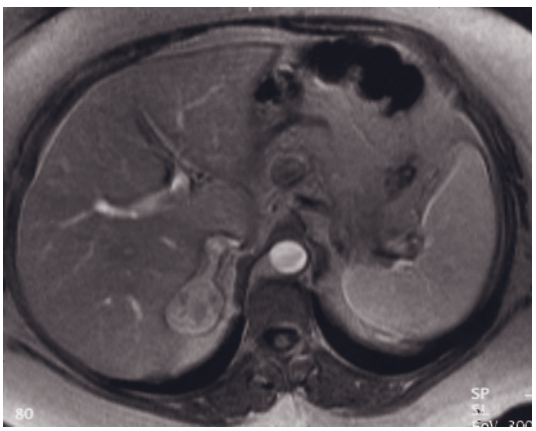

(*d*)

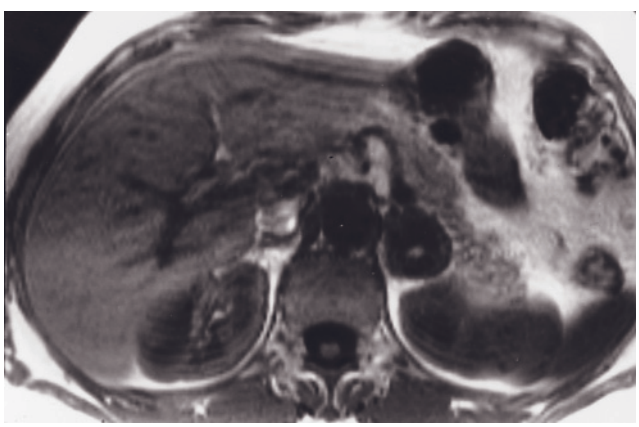

(*e*)

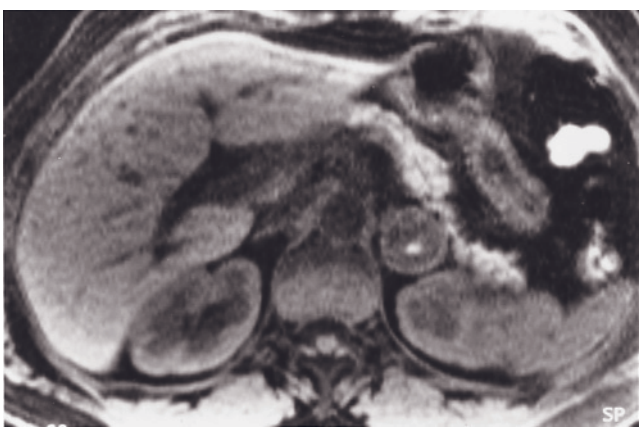

(*f*)

FIG. 8.13 Adrenal adenoma with signal intensity drop and minor hemorrhage. T1-weighted GE (*a*), T1-weighted out-of- phase GE (*b*), T2-weighted fat-suppressed spin-echo (*c*), and immediate postgadolinium GE (*d*) images. Substantial signal intensity drop is present on the right adrenal adenoma comparing in-phase (*a*) to out-of-phase (*b*) GE images. Small high-signal-intensity foci are present on T1 (*a*)- and T2 (*c*)-weighted images, which is consistent with hemorrhage. The adenoma enhances intensely on the immediate postgadolinium GE image (*d*) and contains foci of diminished enhancement that correspond to punctate regions of hemorrhage. T1-weighted GE (*e*), T1-weighted fat-suppressed GE (*f*), T2-weighted fat-suppressed HASTE (*g*), immediate postgadolinium GE (*h*), and 2-min postgadolinium fat-suppressed GE (*i*) images in a second patient. A 3-cm left adrenal adenoma is present that contains foci of high signal intensity on the T1-weighted image (*e*), which do not suppress with fat suppression (*f*). The mass

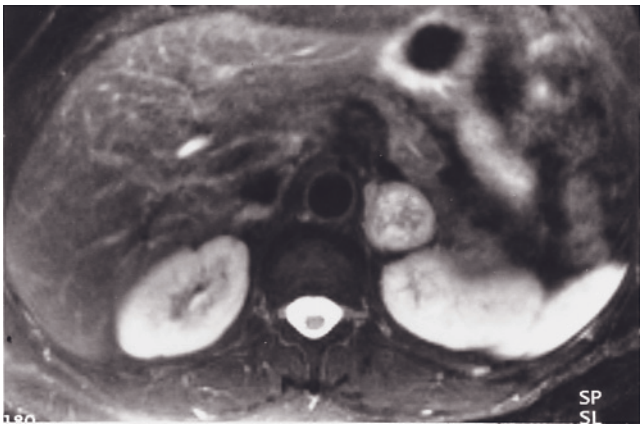

(*g*)

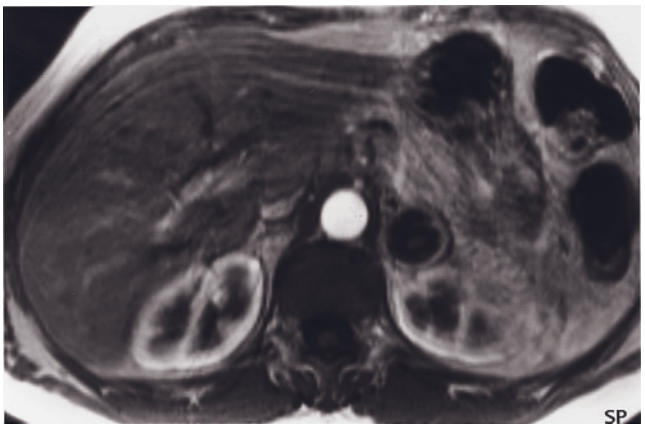

(*h*)

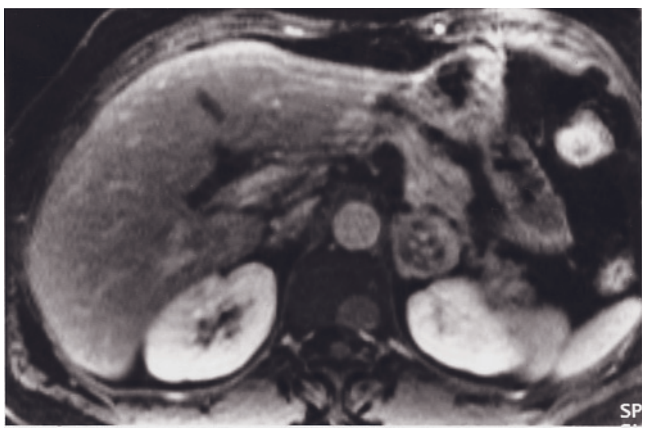

(*i*)

FIG. 8.13 (*Continued*) is heterogeneous on the T2-weighted image (*g*) and contains multiple high-signal-intensity foci. A prominent rim of enhancement is present on the immediate postgadolinium image with minimal internal enhancement (*h*). On the interstitial-phase gadolinium-enhanced fat-suppressed image (*i*), central punctate high-signal intensity foci are apparent.

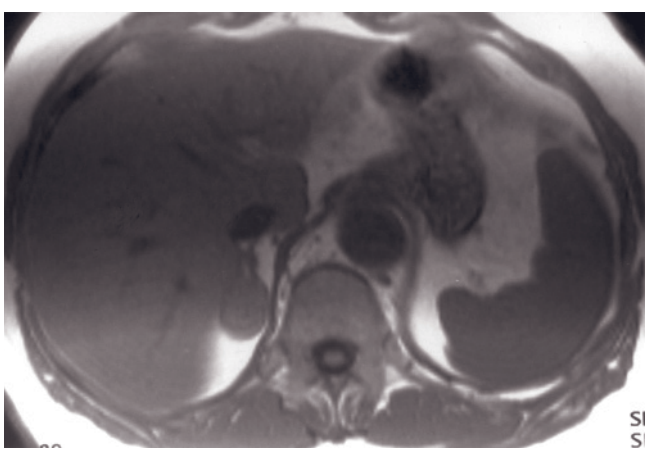

(*a*)

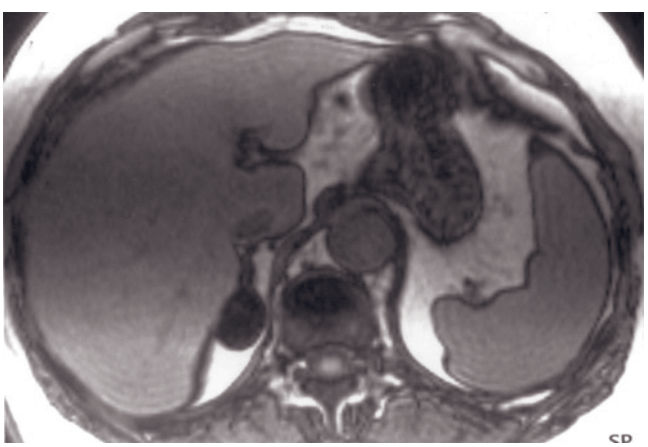

(*b*)

FIG. 8.14 Adrenal adenoma with signal drop on out-of-phase image. T1-weighted GE (*a*) and T1-weighted out-of-phase GE (*b*) images. Substantial signal intensity drop is present on the right adrenal adenoma comparing in-phase (*a*) to out-of-phase (*b*) GE images, consistent with high lipid content.

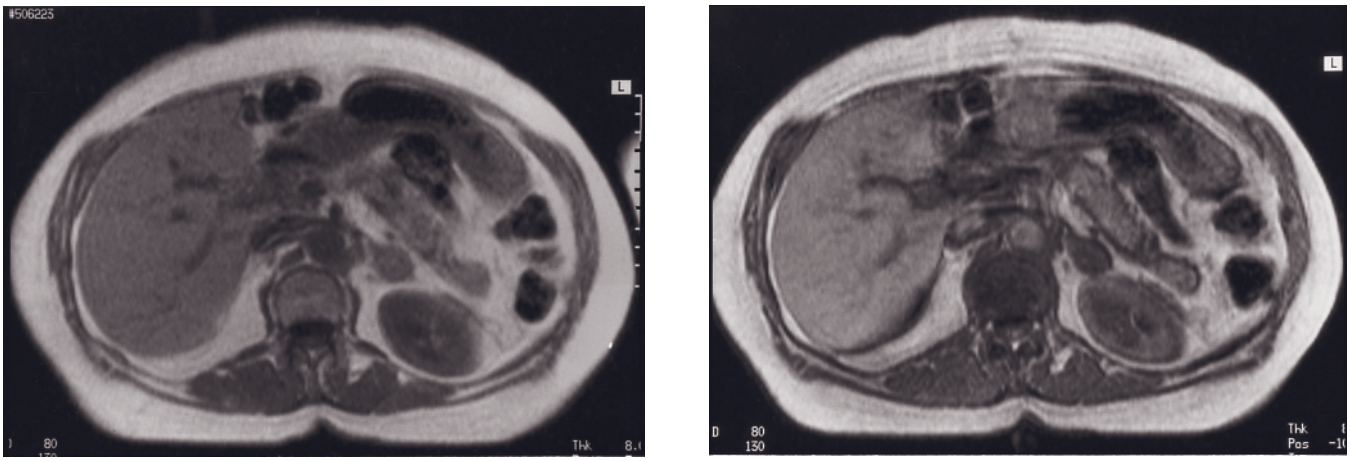

(*a*) (*b*)

FIG. 8.15 Adrenal adenoma—mild signal drop. T1-weighted GE (*a*) and T1-weighted out-of-phase GE (*b*) images. Mild signal intensity loss (approximately 15%) is noted from in-phase (*a*) to out-of-phase (*b*) images, which is in the low range for signal intensity drop to diagnose an adrenal mass as an adenoma. The extent of signal intensity drop is consistent with minimal intracytoplasmic lipid.

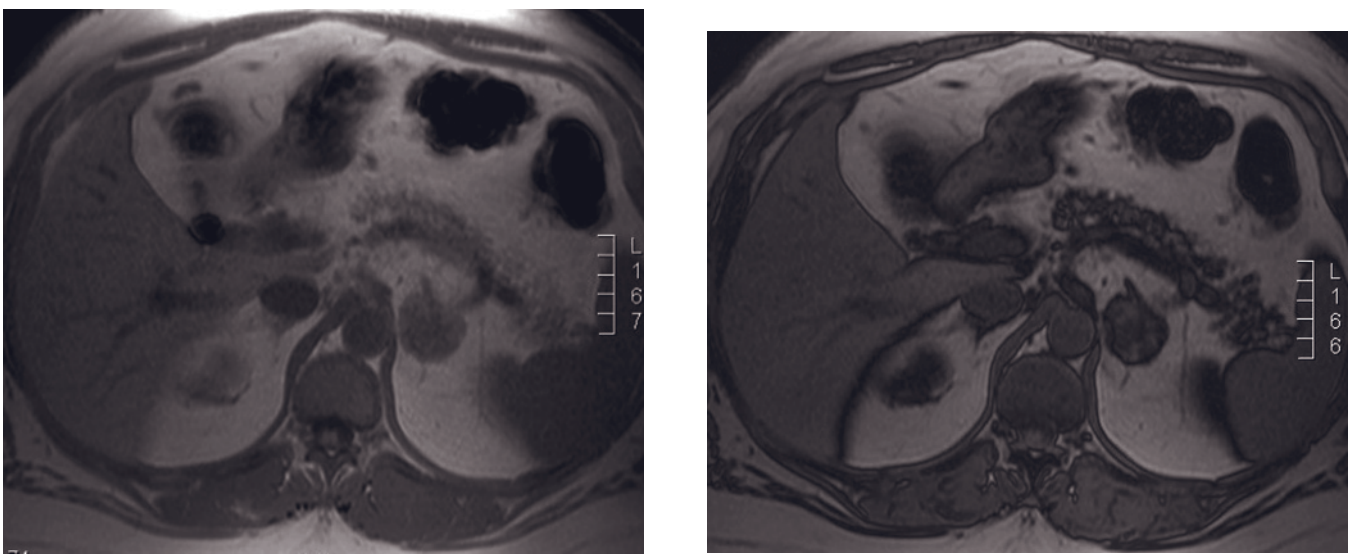

(*a*) (*b*)

FIG. 8.16 Adrenal adenoma—heterogeneous signal intensity and signal drop. T1-weighted GE (*a*) and T1-weighted out-of-phase GE (*b*) images. A left adrenal adenoma with heterogeneous signal intensity is noted on in-phase (*a*) image, with heterogeneous signal drop on out-of-phase (*b*) image. Heterogeneity should not be necessarily interpreted as a sign of malignancy.

in signal intensity on T2-weighted images [12]. Adrenal cysts are sharply marginated and signal void on gadolinium-enhanced MR images. Because most pseudocysts result from adrenal hemorrhage, variable signal intensity on T1- and T2-weighted images may be observed (fig. 8.22) [61]. Pseudocysts that contain a substantial concentration of extracellular methemoglobin from subacute hemorrhage may remain slightly hyperintense on gadolinium-enhanced images. Imaging early and late after gadolinium is useful to ensure that lesions do not enhance over time and therefore are cysts [11]. Hypovascular neoplasms may be nearly signal void on early postcontrast images but enhance on later postgadolinium images. Pseudocysts may be large in size, and sagittal-plane imaging may be useful to demonstrate the location of the mass. Marked hyperintensity

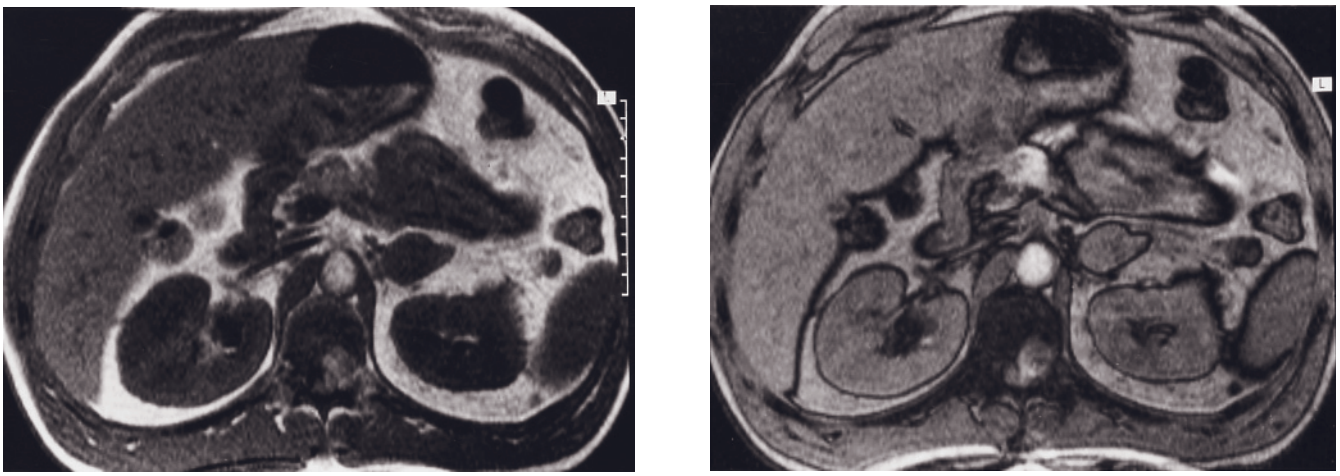

(*a*) (*b*)

FIG. 8.17 Adrenal adenoma—no signal drop. T1-weighted GE (*a*) and T1-weighted out-of-phase GE (*b*) images. No signal intensity drop is noted from in-phase (*a*) to out-of-phase (*b*) images. The lack of signal intensity drop reflects no appreciable intracytoplasmic lipid.

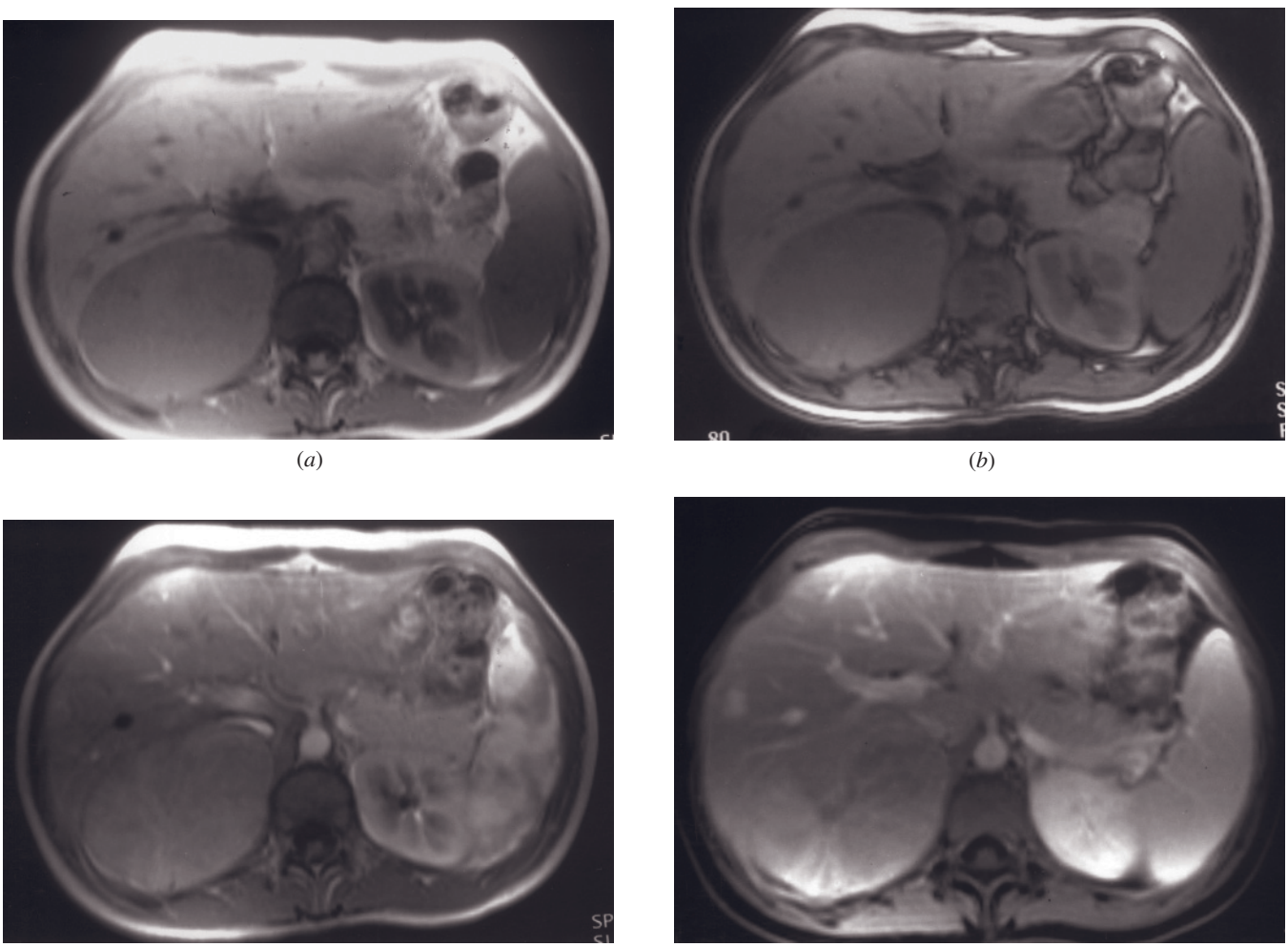

(*a*) (*b*)

(*c*) (*d*)

FIG. 8.18 Large adrenal adenoma. T1-weighted GE (*a*), T1-weighted out-of-phase GE (*b*), immediate postgadolinium GE (*c*), and 90-s postgadolinium fat suppressed GE (*d*) images. A right adrenal mass appears hypointense to the liver on T1 GE image (*a*) and does not drop signal on T1 out-of-phase image (*b*). There is a heterogeneous capillary blush after contrast administration (*c*), which diminishes moderately and remains slightly hypointense on late images (*d*).

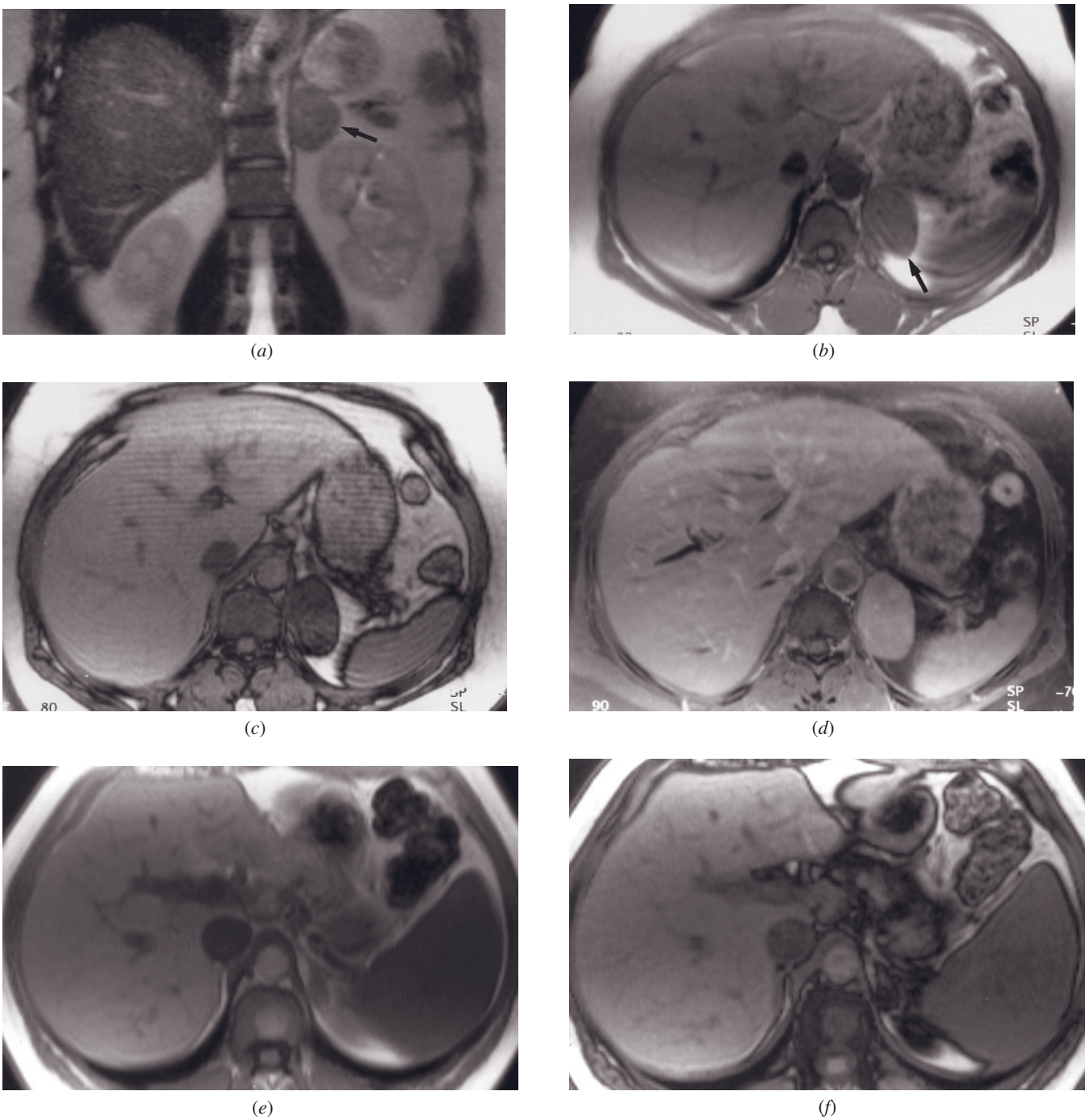

FIG. 8.19 Aldosteronoma. Coronal T2-weighted HASTE (*a*), T1-weighted GE (*b*), T1-weighted out-of-phase GE (*c*), and 90-s postgadolinium fat-suppressed GE (*d*) images. A 3.5-cm left adrenal aldosteronoma is present (arrows, *a*, *b*). The mass is moderately low in signal intensity on the T2-weighted image (*a*). The mass drops in signal from in-phase (*b*) to out-of-phase (*c*) images, reflecting the presence of intracytoplasmic lipid. On the postgadolinium image (*d*) the mass enhances in a relatively homogeneous fashion. T1-weighted GE (*e*), T1-weighted out-of-phase GE (*f*), immediate postgadolinium T1-weighted GE (*g*), and 90-s postgadolinium fat-suppressed GE (*h*) images in a second patient with a small left adrenal aldosteronoma showing the same characteristics as described above.

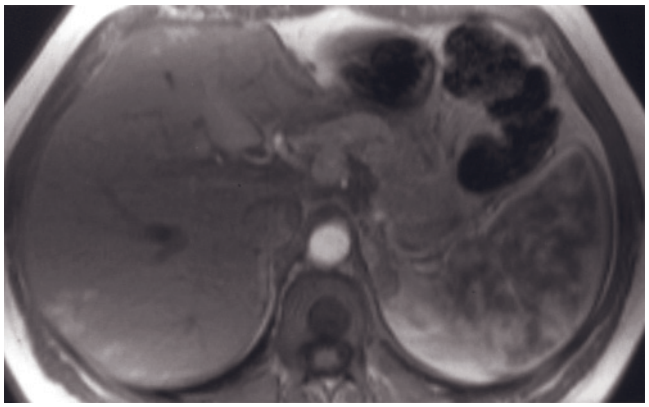

(*g*)

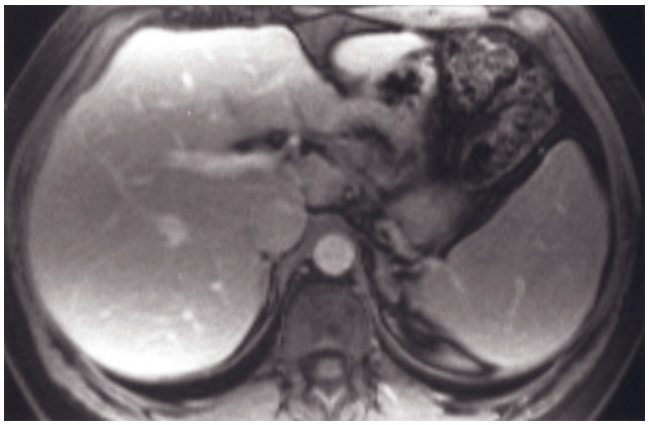

(*h*)

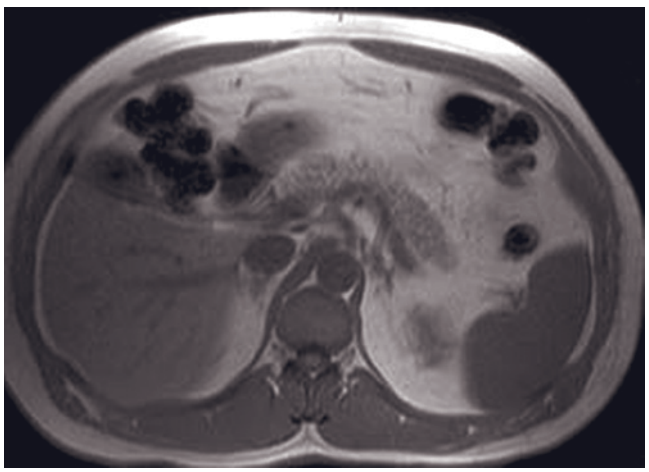

(*i*)

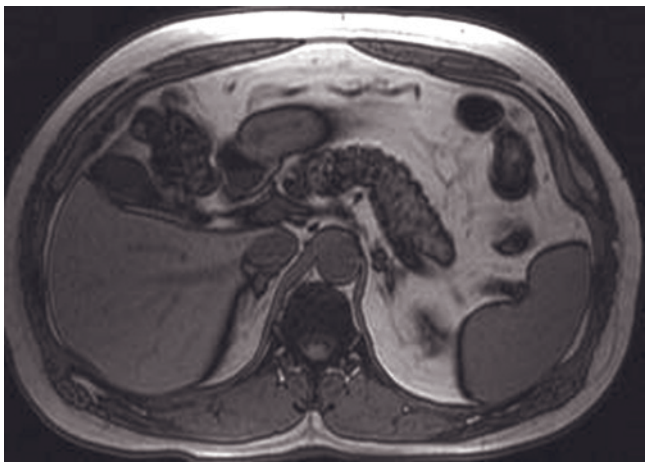

(*j*)

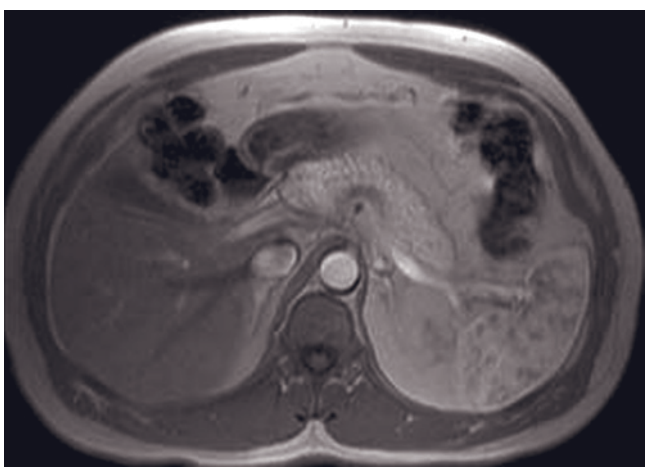

(*k*)

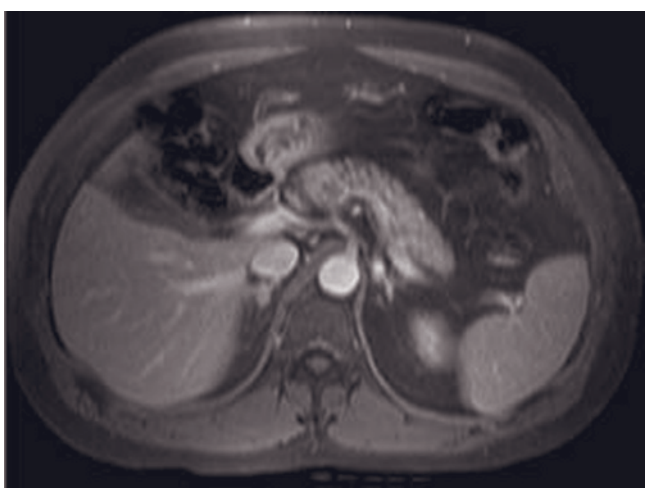

(*l*)

FIG. 8.19 (*Continued*) T1-weighted GE (*i*),T1-weighted out-of-phase GE (*j*), immediate postgadolinium T1-weighted GE (*k*), and 90-s postgadolinium fat-suppressed GE (*l*) images in a third patient with a small adrenal aldosteronoma at the body of the right adrenal demonstrate subtle central drop in signal intensity on out-of-phase GE image, intense homogeneous blush on immediate postgadolinium image, and persistence of enhancement on interstitial-phase gadolinium-enhanced image. These cases illustrate that aldosteronomas have imaging findings similar to those of other benign adrenal adenomas.

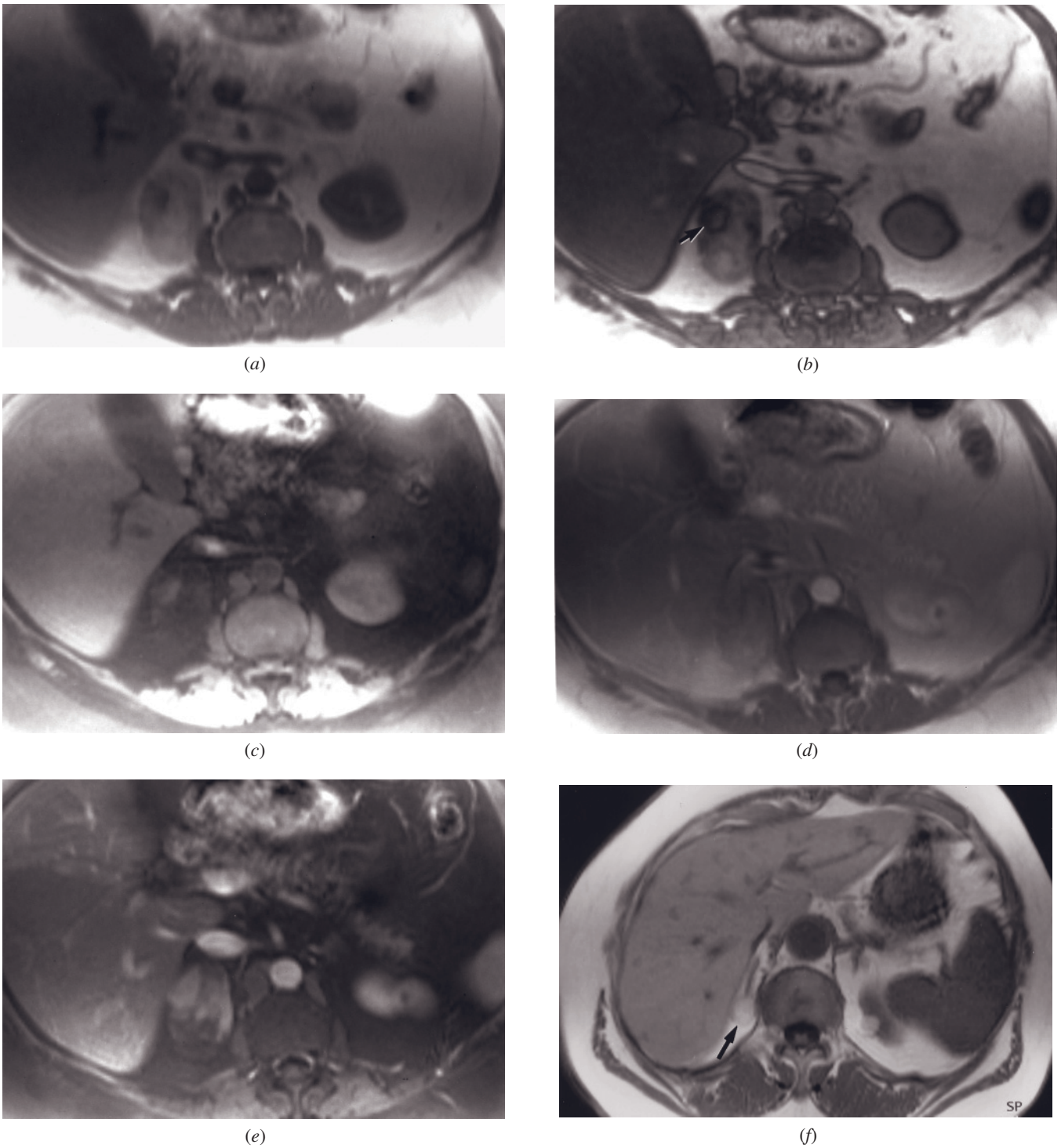

FIG. 8.20 Adrenal myelolipoma. T1-weighted GE (*a*), T1-weighted out-of-phase (*b*), T1-weighted fat-suppressed GE (*c*), immediate postgadolinium GE (*d*), and 90-s postgadolinium GE (*e*) images. The right adrenal myelolipoma is hyperintense on the in-phase (*a*) image and drops in signal on the out-of-phase image (*b*), except for an eccentric focal area that does not drop in signal and possesses a phase-cancellation artifact (arrow, *b*). Myelolipomas may contain focal accumulation of hematopoietic cells within mature adipose tissue, which this focal region represents. The mass is hypointense on T1 fat-suppressed image (*c*), with no suppression of the same focal region. Negligible enhancement on immediate (*d*) and late (*e*) images is appreciated. The predominantly fatty portion of the tumor is low signal on the fat-suppressed image. T1-weighted GE (*f*), T1-weighted out-of-phase GE (*g*), and 90-s postgadolinium fat-suppressed GE (*h*) images in a second patient. A 1.8-cm myelolipoma (arrow, *f*) of the right adrenal is present. The tumor is high in signal intensity on the in-phase GE image because it is composed almost entirely of fat. No drop in

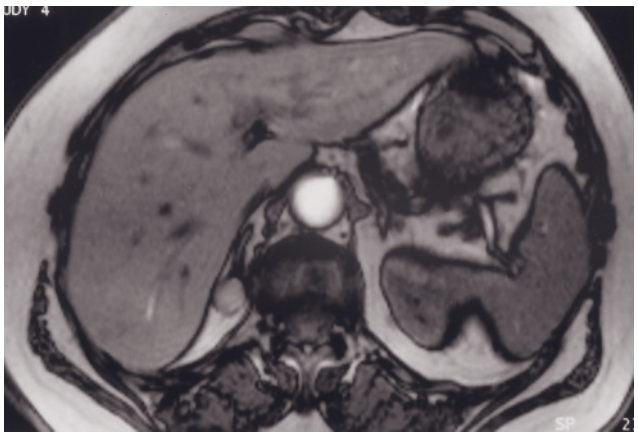

(*g*)

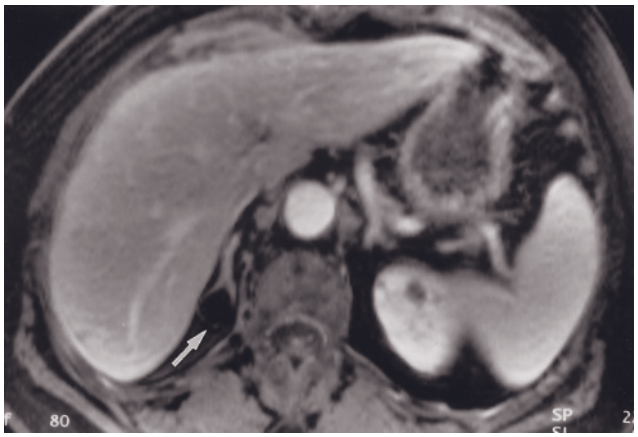

(*h*)

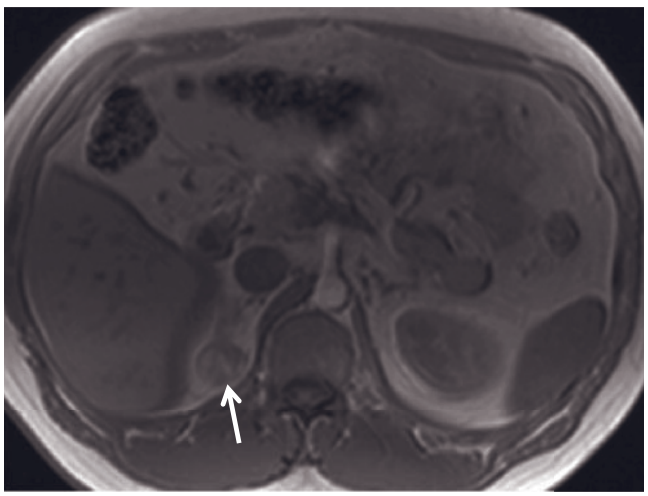

(*i*)

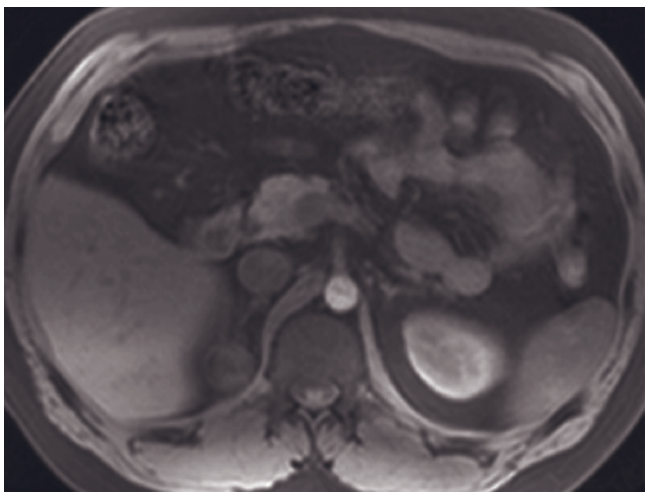

(*j*)

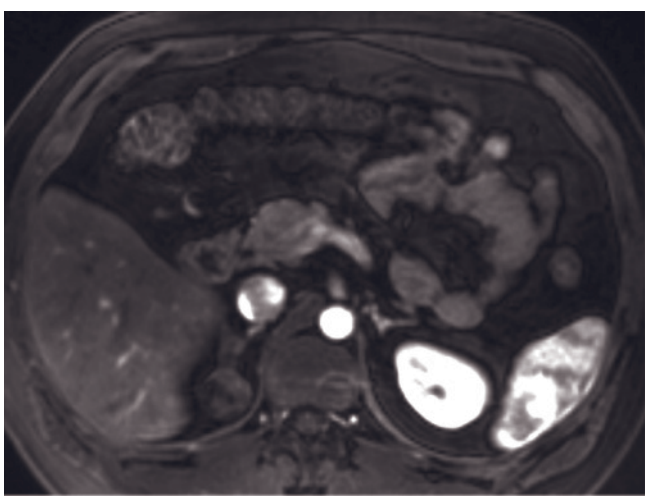

(*k*)

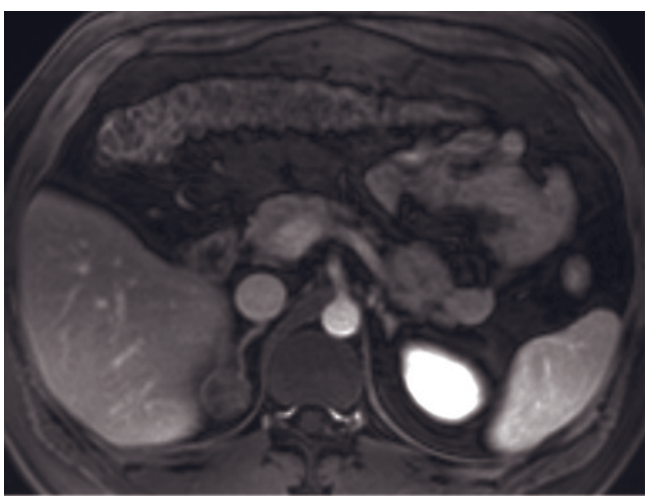

(*l*)

FIG. 8.20 (*Continued*) signal is present on the out-of-phase image (*g*), reflecting the near complete absence of water protons in the mass. On the fat-suppressed image, the mass is near signal void (arrow, *h*), confirming that it is essentially all fatty in composition. T1-weighted SGE (*i*), T1-weighted fat-suppressed SGE (*j*), T1-weighted postgadolinium hepatic arterial dominant phase (*k*) and hepatic venous phase (*l*) images at 3.0 T demonstrate myelolipoma of the right adrenal gland in another patient. High-signal-intensity component of the lesion seen on T1-weighted image (*i*) shows low signal on fat-suppressed images (*j*–*l*). These findings are consistent with the diagnosis of myelolipoma.

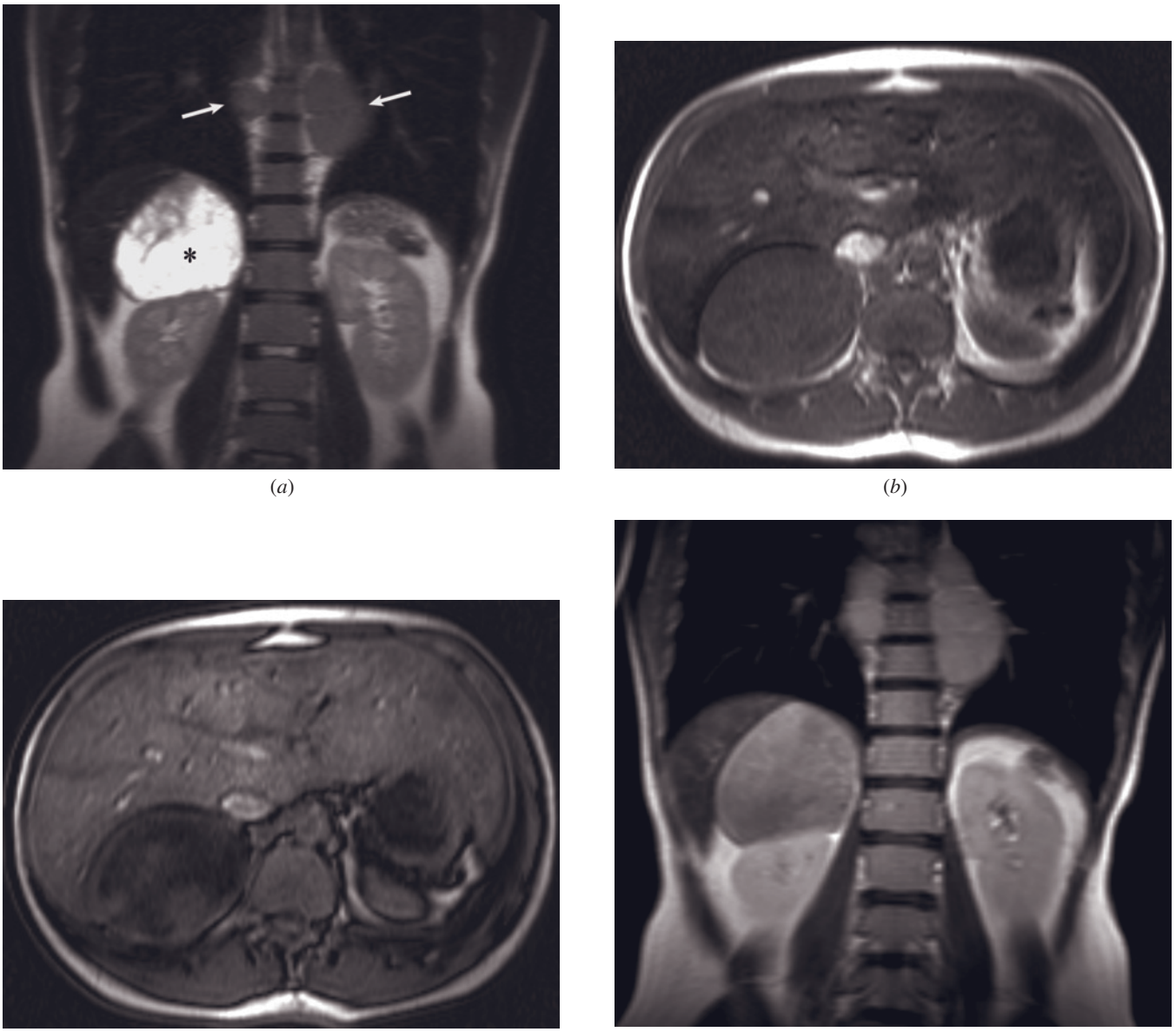

FIG. 8.21 Atypical giant adrenal myelolipoma in a patient with thalassemia. Coronal T2-weighted HASTE (*a*), axial T1-weighted GE (*b*), out-of-phase GE (*c*), and gadolinium enhanced coronal T1-weighted TSE (*d*) images. A large oval-shaped right adrenal mass with well-defined borders demonstrates markedly high and heterogeneous signal intensity (asterisk) on the coronal T2-weighted HASTE (*a*) image, surrounded by a thin low-signal-intensity capsule. Bilateral paraspinal masses of extramedullary hematopoiesis (arrows) are shown as well-defined masses with homogeneous intermediate signal intensity. The liver demonstrates very low signal intensity because of iron deposition. The tumor is heterogeneous on the in-phase GE image (*b*), with foci of mildly increased signal intensity, and demonstrates intense drop in signal intensity on the out-of-phase GE image (*c*) due to microscopic fat content. On the gadolinium-enhanced image (*d*), heterogeneous, mainly peripheral enhancement is noted. This case demonstrates that myelolipomas may mimic imaging findings of other tumors on individual sequences with no macroscopic fat content, and a combined approach is needed to establish diagnosis. (Reprinted with permission from Kelekis NL, Alexopoulou E, Brountzos EN, Ladis V, Boussiotou A, Kelekis DA. Giant adrenal myelolipoma with minimal fat content in a patient with homozygous beta-thalassemia: appearance on MRI. *J Magn Reson Imaging* 18: 608–611, 2003.)

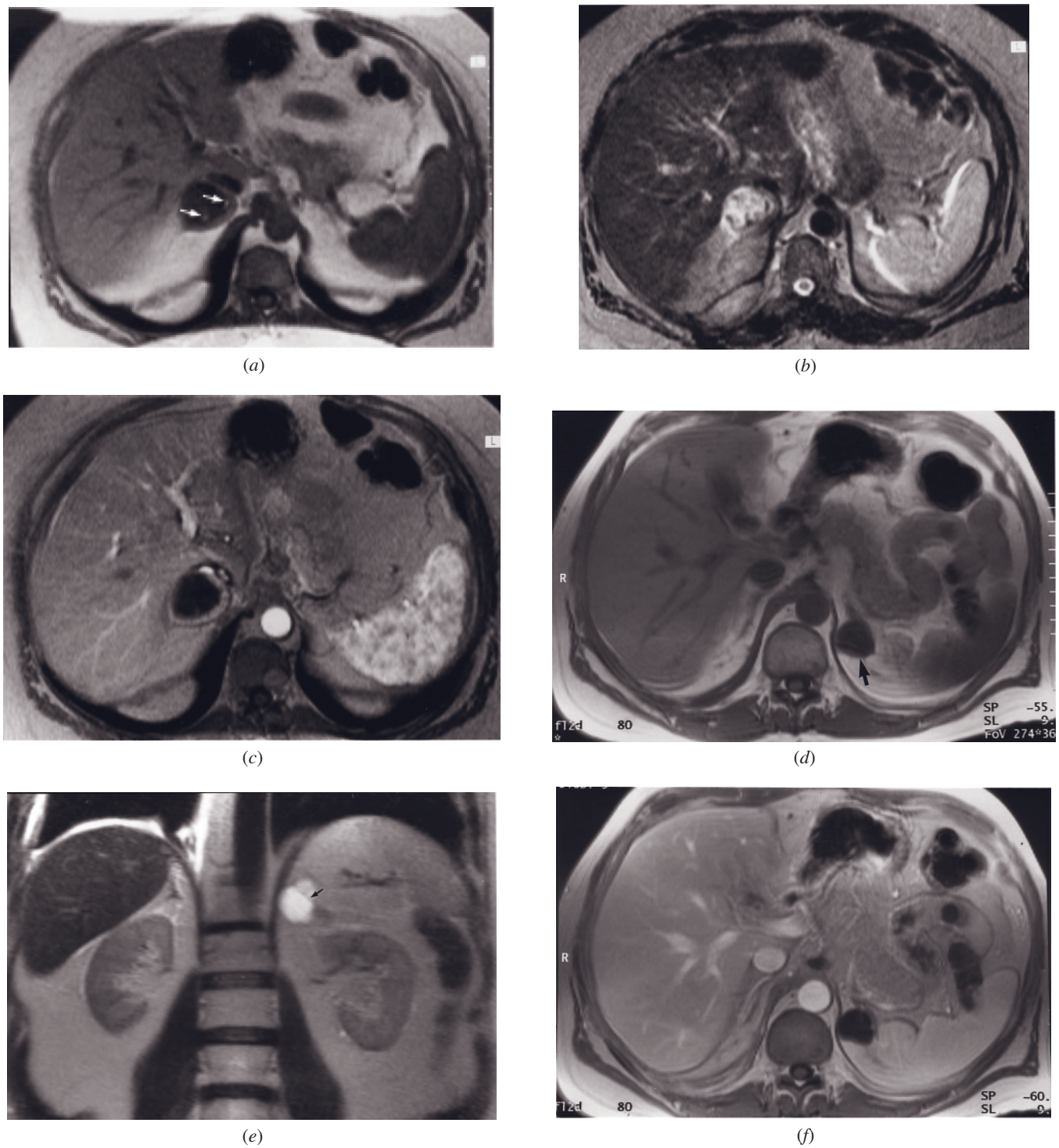

FIG. 8.22 Cyst/pseudocyst. T1-weighted GE (*a*), T2-weighted spin-echo (T2-SE) (*b*), and immediate postgadolinium GE (*c*) images. Small high-signal-intensity foci are noted on the T1 image (arrows, *a*) within the low-signal-intensity pseudocyst, a finding consistent with hemorrhage. The mass is heterogeneous and high in signal intensity on the T2-weighted image (*b*). The heterogeneity reflects the presence of blood products. The lesion is signal void on early (*c*) and late (not shown) postgadolinium images, which are diagnostic features for a cyst. T1-weighted GE (*d*), coronal T2-weighted HASTE (*e*), 45-s postgadolinium GE (*f*), and 90-s postgadolinium fat-suppressed GE (*g*) images in a second patient. An adrenal pseudocyst is identified arising from the left adrenal (arrow, *d*). The pseudocyst is low in signal intensity on the T1-weighted image (*d*) and high in signal intensity on the T2-weighted image (*e*) and does not enhance on early (*f*) or late (*g*) postgadolinium images. Thin septations are present in the pseudocyst

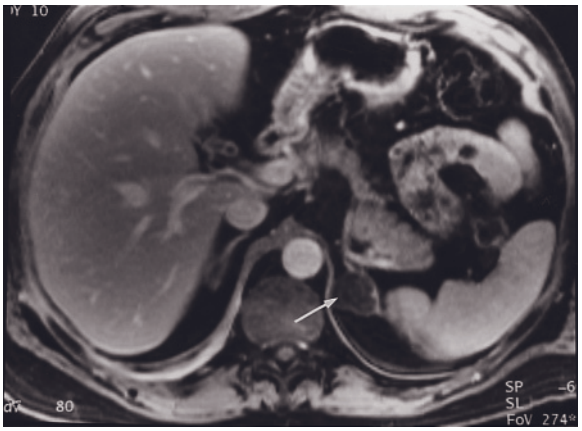

(*g*)

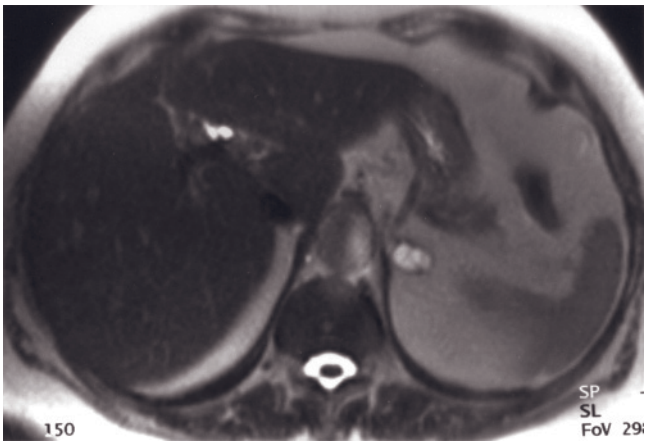

(*h*)

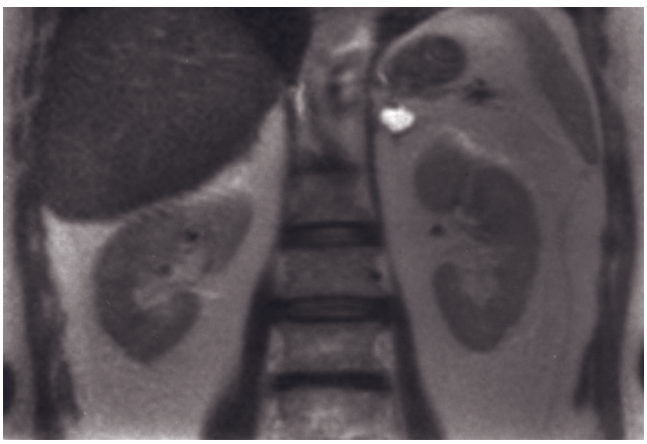

(*i*)

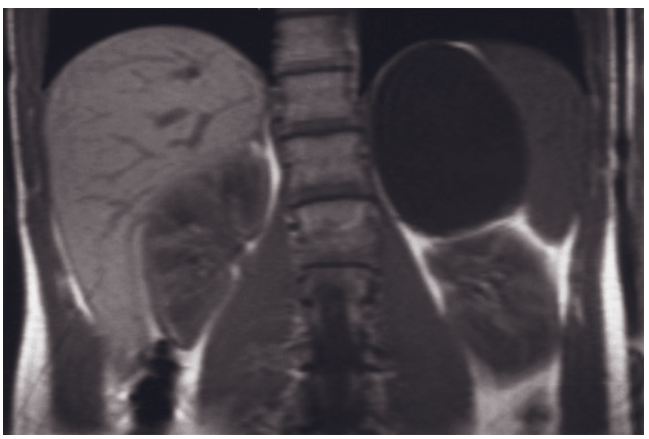

(*j*)

(*k*)

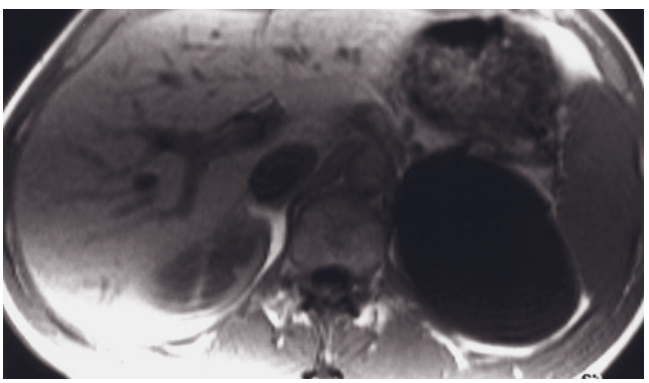

(*l*)

FIG. 8.22 (*Continued*) (arrow, *e*), which are well shown on the breathing-independent T2-weighted image (*d*) and show faint enhancement on the interstitial-phase gadolinium-enhanced fat-suppressed image (arrow, *g*). T2-weighted HASTE (*h*) and coronal T2-weighted HASTE (*i*) images in a third patient. A pseudocyst in the left adrenal appears on the T2 images (*h*, *i*) with hypointense septations. Coronal T1-weighted GE (*j*), coronal T2-weighted HASTE (*k*), T1-weighted GE (*l*), T1-weighted out-of-phase GE (*m*), T2-weighted HASTE (*n*), immediate postgadolinium GE (*o*), 90-s postgadolinium fat-suppressed GE (*p*), and sagittal postgadolinium GE (*q*) images in a fourth patient. A large left adrenal cyst displaces the kidney inferiorly and the spleen anterior and laterally (*j*, *k*, *q*).

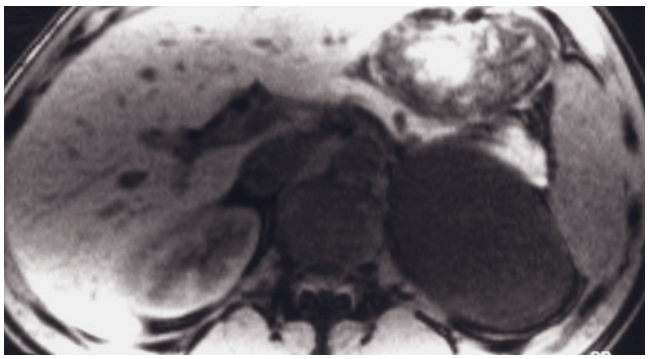

(*m*)

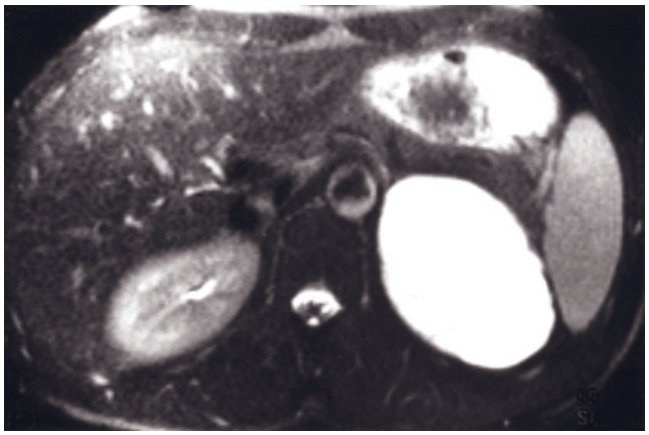

(*n*)

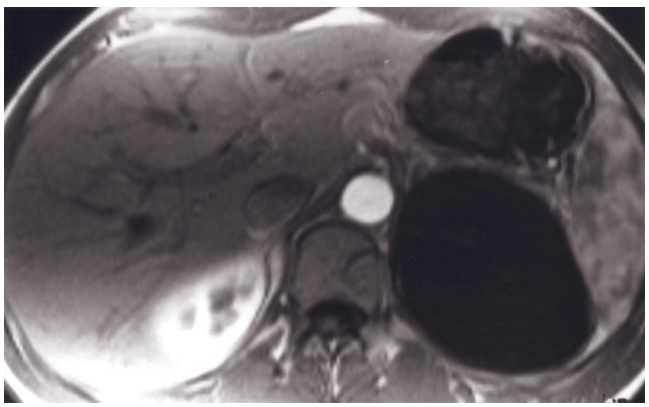

(*o*)

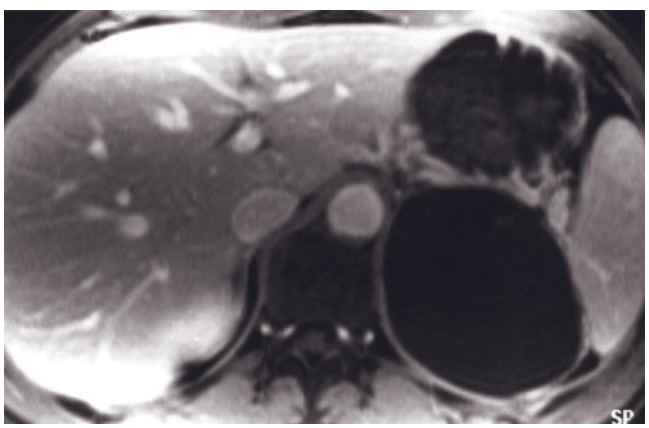

(*p*)

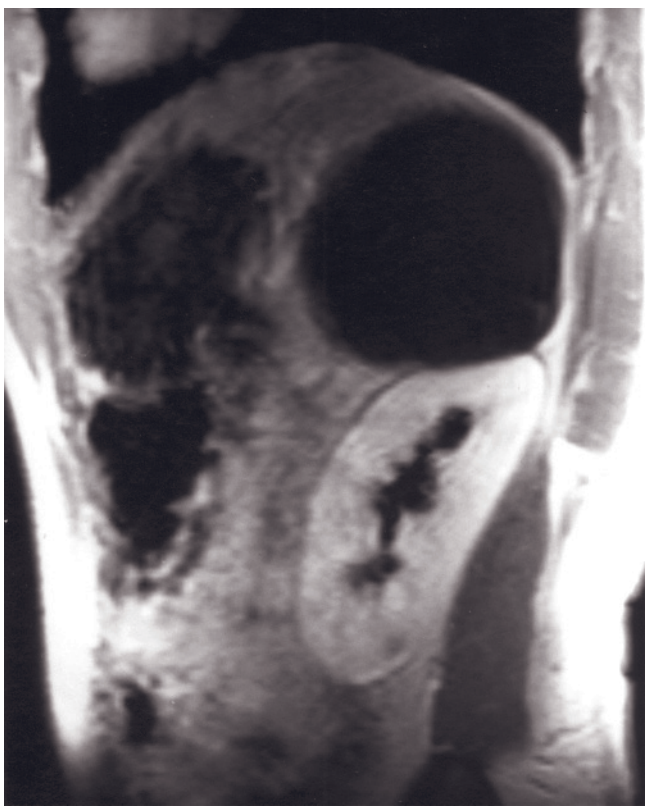

(*q*)

FIG. 8.22 (*Continued*)

on T2-weighted images with hypointense capsule has been reported in patients with adrenal hemorrhage 3–4 wk after liver transplantation [62].

Hemangioma. Adrenal hemangioma is an uncommon, benign vascular tumor composed of mesenchymal cells. The lesions tend to be large (>10 cm) and undergo central necrosis and hemorrhage, which may result in high-signal-intensity foci on T1-weighted images [63, 64]. Peripheral nodules are characteristic of these masses [63], although atypical forms with thin rim enhancement and absence of centripetal enhancement have been reported [64]. Tumors are high in signal intensity centrally on T1- and T2-weighted images

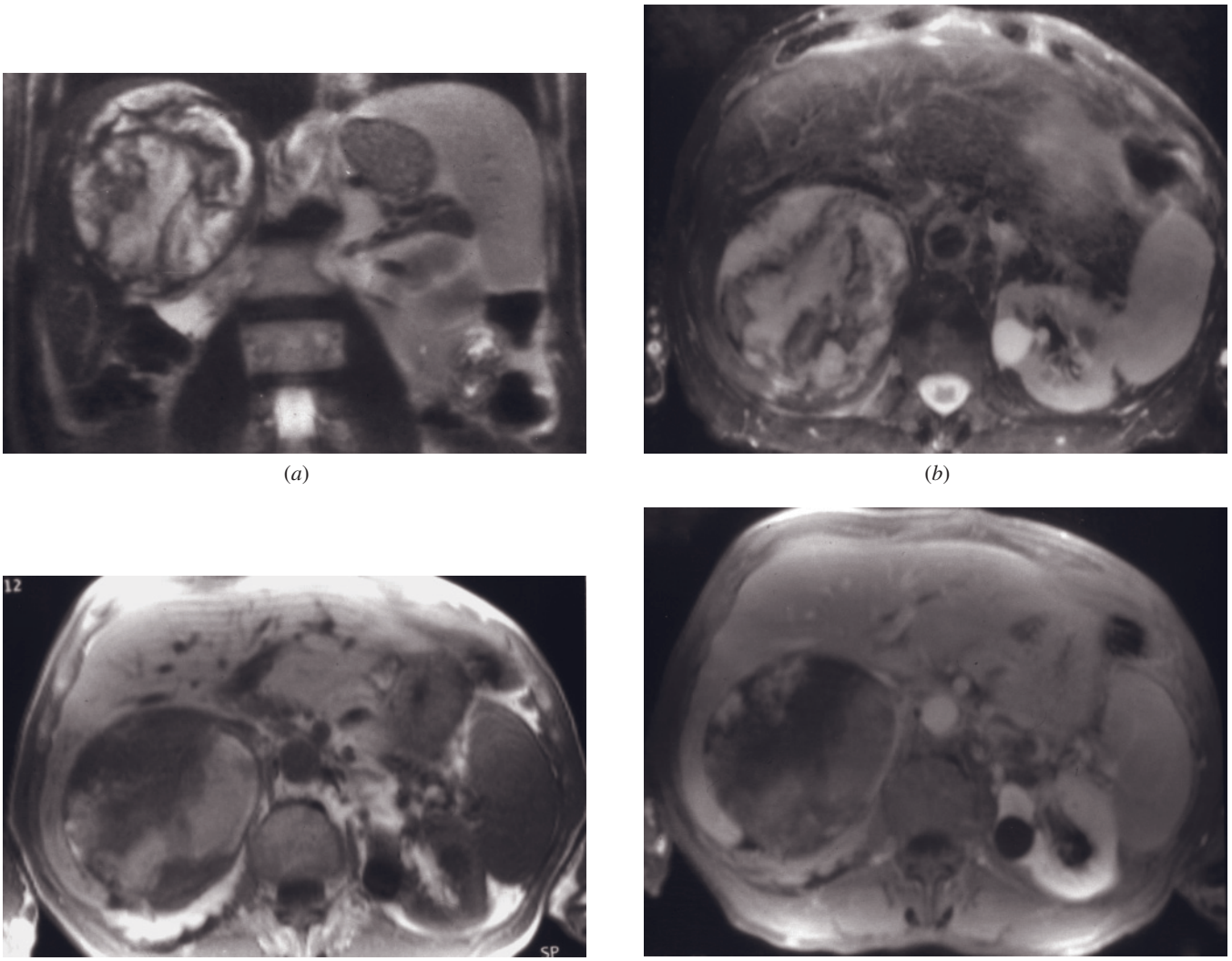

FIG. 8.23 Adrenal hemangioma. Coronal single-shot echo-train spin-echo (*a*), T2-weighted fat-suppressed echo-train spin-echo (*b*), T1-weighted GE (*c*), and 2-min gadolinium-enhanced fat-suppressed GE (*d*) images. A 10-cm mass is present arising from the right adrenal that is mixed signal on T2 (*a*, *b*)- and T1 (*c*)-weighted images, consistent with hemorrhage. Small peripheral nodules of enhancing stroma are appreciated on the postcontrast images (arrow, *d*). Adrenal hemangiomas have a great propensity to undergo hemorrhage and appear as a large hemorrhagic mass.

because of necrosis and hemorrhage [63]. The peripheral nodules enhance intensely with gadolinium, and the centripetal enhancement, which is characteristic of hepatic hemangiomas, is less frequently observed in adrenal hemangiomas because of the substantial central necrosis (fig. 8.23) [53]. These tumors may resemble adrenal cortical carcinomas because of the central necrosis and hemorrhage [31].

Malignant

Metastases. Metastases are the most frequent malignant lesions that involve the adrenal glands. The most common primary tumors originate from lung, breast, gastrointestinal tract, kidney, skin (melanoma), and thyroid gland [65].

Metastatic deposits vary in size from microscopic involvement to large tumor masses. Metastases are most frequently bilateral, but they may be unilateral. On T2-weighted images, metastases have been described as having moderately high signal intensity [1–5] (fig. 8.24). High signal intensity on T2-weighted image should not be relied on. Many metastases, particularly those possessing significant desmoplasia, may be low signal intensity (fig. 8.25) [4, 5], whereas a number of benign lesions may be high signal [37]. Comparison of the signal intensity of the adrenal mass to either the primary

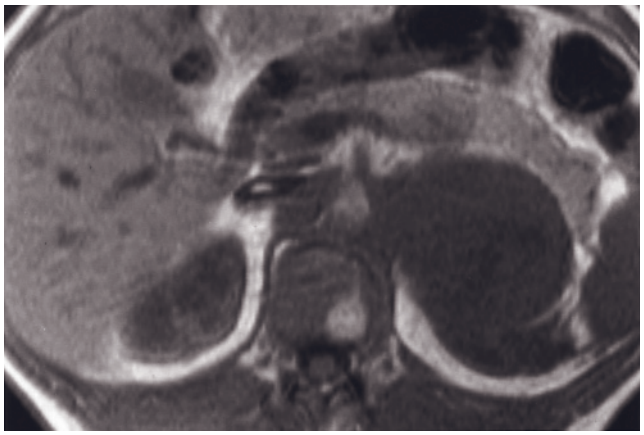

(*a*)

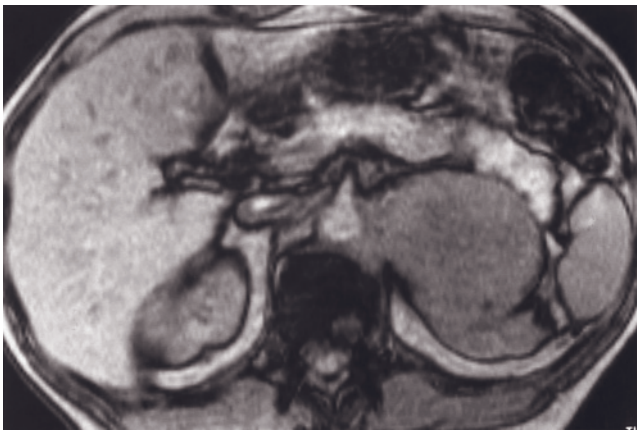

(*b*)

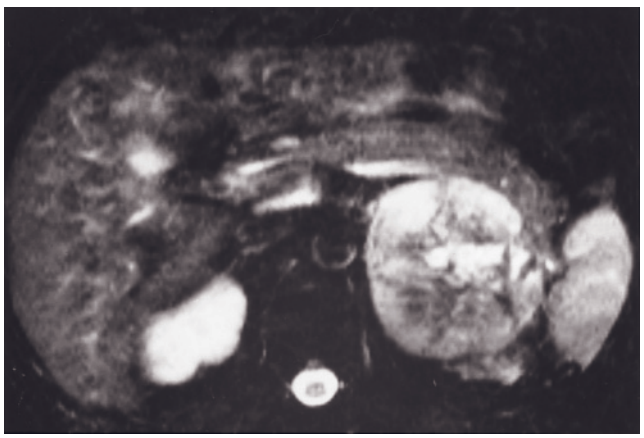

(*c*)

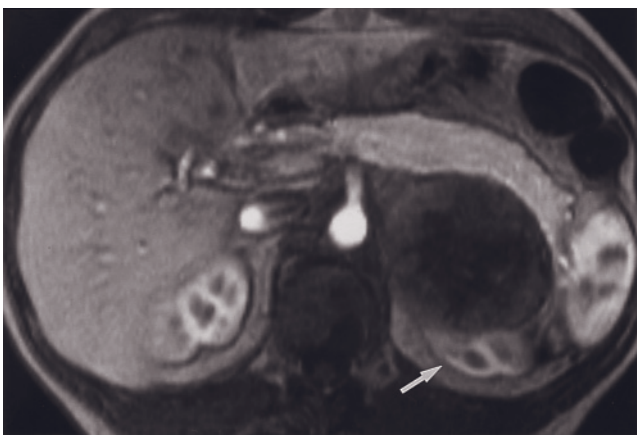

(*d*)

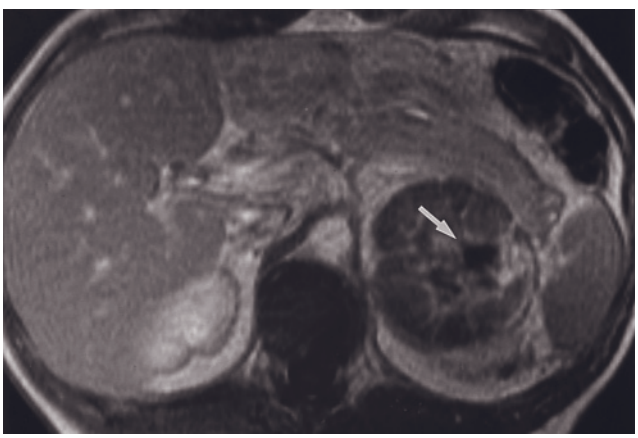

(*e*)

FIG. 8.24 Large left adrenal metastases. T1-weighted GE (*a*), T1-weighted out-of-phase GE (*b*), T2-weighted fat-suppressed spin-echo (*c*), immediate postgadolinium (*d*), and 3-min postgadolinium GE (*e*) images. A large 8-cm left adrenal metastasis is identified that retains signal intensity from in-phase (*a*) to out-of-phase (*b*) images. The mass is heterogeneous and moderately high in signal intensity on T2-weighted images, with a central high-signal-intensity region (*c*). On immediate postgadolinium image (*d*), the mass enhances minimally. On more delayed images, a central low-signal-intensity signal-void region compatible with necrosis is identified (arrow, *e*) that corresponds to the region of high signal intensity on T2-weighted images. The central necrosis and heterogeneity demonstrated on T2-weighted and postgadolinium images further confirm the findings of a malignant mass on out-of-phase images. Distinction between adrenal metastasis and left kidney is best defined on the immediate postgadolinium GE image by the demonstration of corticomedullary differentiation of the kidney (arrow, *d*).

tumor or other metastatic deposits may be helpful in determining whether the lesion is a metastasis, because foci of tumor located in different sites frequently possess similar signal intensity [3]. Metastases frequently have irregular margins and enhance in a heterogeneous fashion, features that are well shown on gadolinium-enhanced T1-weighted fat-suppressed images [8]. Mild, heterogeneous enhancement on early postgadolinium images is commonly observed, with either progressive enhancement or minimal heterogeneous washout on more delayed interstitial-phase images. This pattern is distinct from that manifested by adenomas, which often exhibit a capillary blush. Direct extension of primary tumors may occasionally be seen. This is most

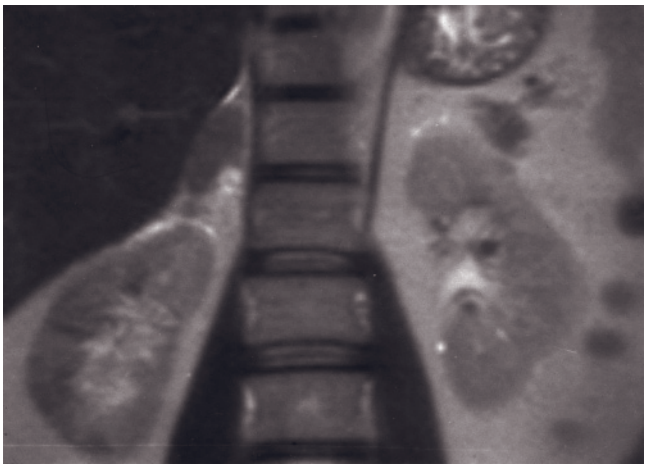

(*a*)

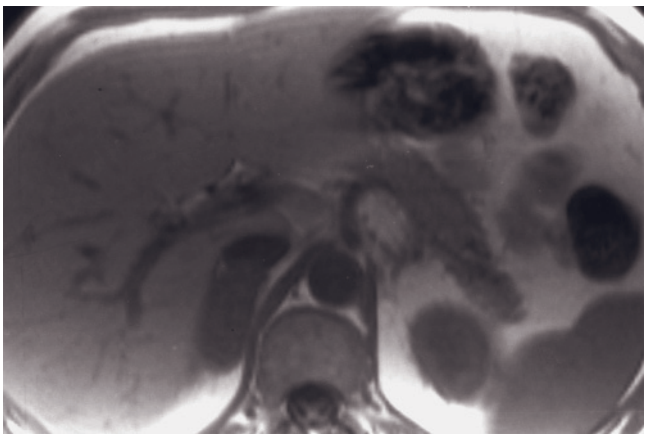

(*b*)

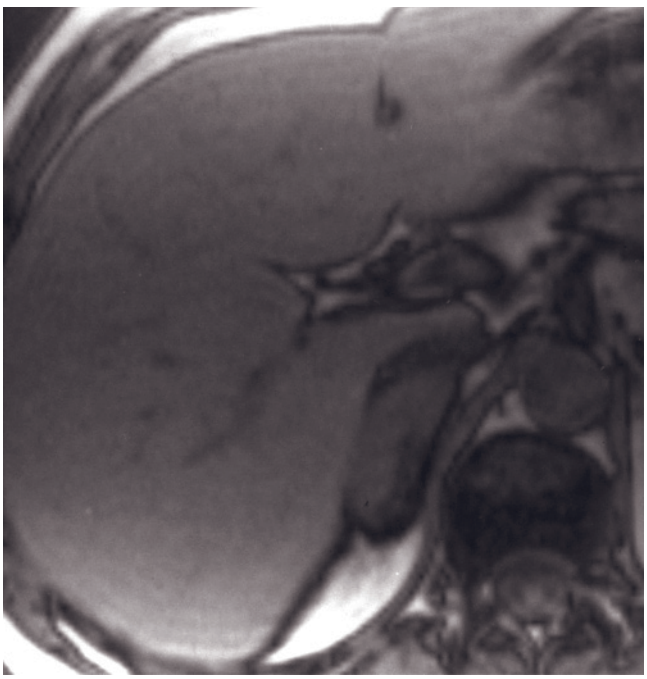

(*c*)

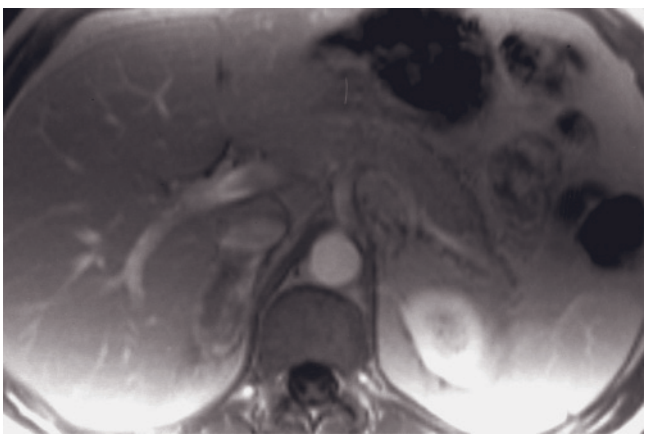

(*d*)

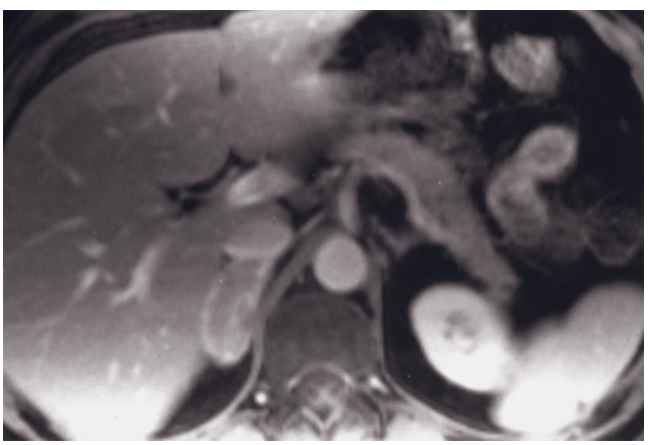

(*e*)

FIG. 8.25 Adrenal metastasis. Coronal T2-weighted echo-train spin-echo (*a*), T1-weighted GE (*b*), T1-weighted out-of-phase GE (*c*), immediate postgadolinium GE (*d*), and 90-s postgadolinium fat-suppressed GE (*e*) images in a patient with primary non-small cell lung cancer. A 5.4 × 2.3-cm oval right adrenal metastasis is slightly hypointense to the liver on T1 (*b*), with the majority of the tumor showing no drop in signal except for a small region of drop of signal on out-of-phase (*c*) images in the posteromedial aspect of the tumor. After contrast administration, there is peripheral, irregular enhancement of the lesion (*d*, *e*). T2-weighted

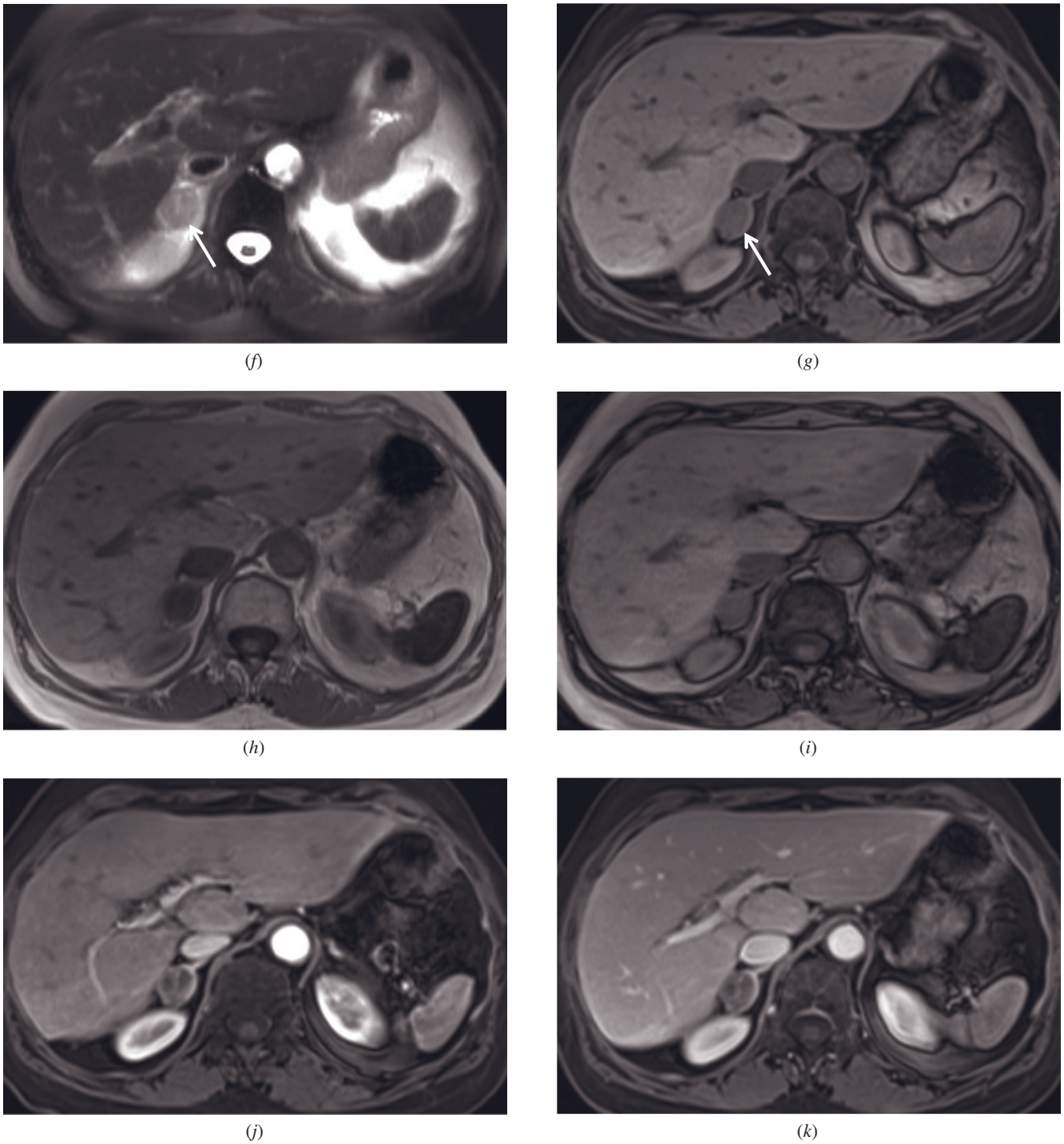

FIG. 8.25 (*Continued*) fat-suppressed single-shot echo-train spin-echo (*f*), T1-weighted fat-suppressed 3D-GE (*g*), T1-weighted in-phase (*h*) and out-of-phase (*i*) 3D-GE, and T1-weighted postgadolinium hepatic arterial dominant phase (*j*) and hepatic venous phase (*k*) fat-suppressed 3D-GE images demonstrate a right adrenal gland metastasis (arrows, *f*, *g*) in another patient. The lesion shows high signal on T2-weighted image (*f*) and low signal on T1-weighted images (*g*, *h*). The lesion does not show any signal drop on out-of-phase image (*i*) compared to in-phase image (*h*). Heterogeneous enhancement is detected in the lesion on postgadolinium images (*j*, *k*).

frequently observed in pancreatic or renal cancer. The adrenal tumor may also invade adjacent structures or organs. Coexistent metastases in other organs are commonly present (fig. 8.26). Necrosis and hemorrhage are not uncommon in large metastatic deposits. Hemorrhage is also a feature more typical of malignant than benign masses and is better shown on MR than CT images (fig. 8.27).

The most reliable MRI feature to suggest that an adrenal mass may represent a metastasis is the demonstration that the lesion does not lose signal on out-of-phase images (fig. 8.28) [9, 10, 20, 22, 23, 26]. This approach is most reliable in the investigation of patients with a known primary malignancy.

Because the accuracy of out-of-phase gradient-echo images in characterizing adrenal masses as benign or malignant is approximately 80%, additional information provided by T2-weighted images and postgadolinium images is useful (figs. 8.26, 8.28, 8.29). CT-guided biopsies are at present not obviated in all cases by MRI examination. To obviate CT-guided biopsy, accuracy of MRI must approach 95% [66]. In a recent large series (229 adrenal masses with histopathology confirmation in 204 patients), the sensitivity of MRI for the differentiation of benign and malignant adrenal masses was 89%, the specificity 99%, and the accuracy 93.9% [67]. Furthermore, not all indeterminate adrenal masses need to be biopsied. In patients with no known primary malignancy, it is acceptable management to serially examine adrenal masses to assess change in size. Reassessment at 3 to 6 months and 1 year is performed at many centers (fig. 8.29) [66, 68, 69]. It may be sufficient to acquire only in-phase and out-of-phase gradient-echo images on follow-up examination to reduce cost.

Adrenal Cortical Carcinoma. Adrenal cortical carcinoma is a very uncommon, aggressive tumor. Tumors may contain intracytoplasmic lipid or fatty regions. The tumor is more common in women, and the age at presentation ranges from 20 to 70 years, although tumor occurrence in patients 20–40 years of age is relatively common [31, 35]. Approximately 50% of the tumors are hyperfunctioning, and hypercortisolism and virilization are common presentations. In contrast to adrenal adenomas, adrenal cortical carcinomas are characteristically large encapsulated tumors, weighing over 100 g and sometimes reaching 1000 g or more before discovery. Areas of necrosis and hemorrhage are frequent [70, 71].

Metastases are frequently found at presentation, with regional and para-aortic lymph nodes, lungs, and liver (fig. 8.30) representing common sites. Tumor thrombus into the IVC is not uncommon at presentation (fig. 8.30). Tumors are frequently necrotic (figs. 8.30–8.32) and hemorrhagic.

In one series, MR images demonstrated central necrosis and hemorrhage in seven of eight adrenal cortical carcinomas [31]. These tumors appear heterogeneous and hyperintense on T1- and T2-weighted images, reflecting central necrosis and hemorrhage. Necrosis is well shown on gadolinium-enhanced images as signal-void regions, and hemorrhage is well shown on precontrast T1-weighted conventional or fat-suppressed images as high-signal-intensity regions (fig. 8.31). Peripheral mural-based nodules may also be observed in these tumors (fig. 8.32) [31]. Although the appearance of a large mass with central hemorrhage and necrosis is characteristic for adrenal cortical carcinoma, a similar appearance may be observed in other tumors including adrenal hemangioma [63] and neuroblastoma [72].

Smaller tumors also tend to have greater enhancement of the tumor periphery than of the center, possibly reflecting their propensity to undergo central necrosis (fig. 8.33) [31]. Fat-suppressed images help delineate large tumors from adjacent pancreas and kidney. Sagittal-plane images are also useful to demonstrate that tumors do not originate from the kidney (fig. 8.31). On T2-weighted images, tumors have a high signal intensity, which partly reflects the frequent occurrence of central necrosis [3, 31, 73]. Because these tumors are functional, they may contain regions of intracytoplasmic lipid that result in irregular foci of signal intensity loss on out-of-phase images (fig. 8.34) [31–33]. The lack of uniform loss of signal intensity helps to distinguish these tumors from adenomas. After resection, local recurrence may occur and tumors demonstrate similar imaging findings (fig. 8.35).

Medullary Masses

The adrenal medulla is composed of neuroendocrine cells derived from the neural crest. As such, it is part of the widely dispersed system of histologically and embryologically similar cells termed the paraganglion system. The most significant disorders arising in the adrenal medulla are neoplasms derived from cell types indigenous to the paraganglion system. These tumors include pheochromocytoma, neuroblastoma, ganglioneuroma, and schwannoma.

Pheochromocytoma

Pheochromocytoma can be defined as a paraganglioma of the adrenal medulla and is a catecholamine-producing tumor. On microscopic examination, a characteristic pattern shows tumor cells arranged in well-defined nests ("Zellballen") surrounded by fibrovascular stroma. There is no morphologic marker of malignancy for this tumor other than the presence of metastases. Pheochromocytomas arise from the adrenal medulla in 90% of cases. The remaining 10% occur in paraganglia

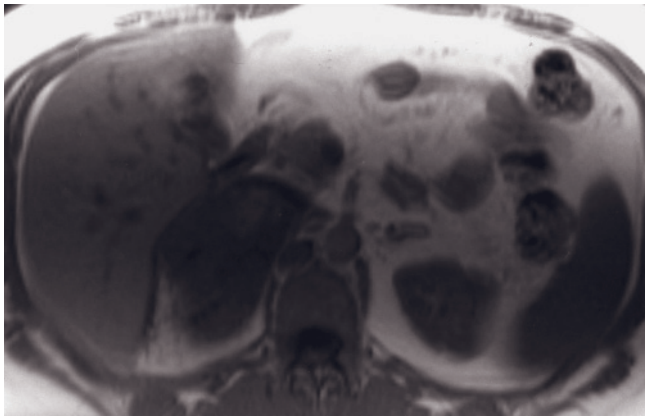

(*a*)

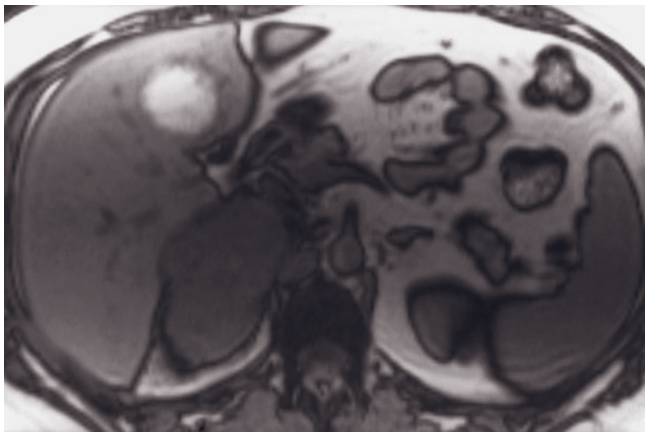

(*b*)

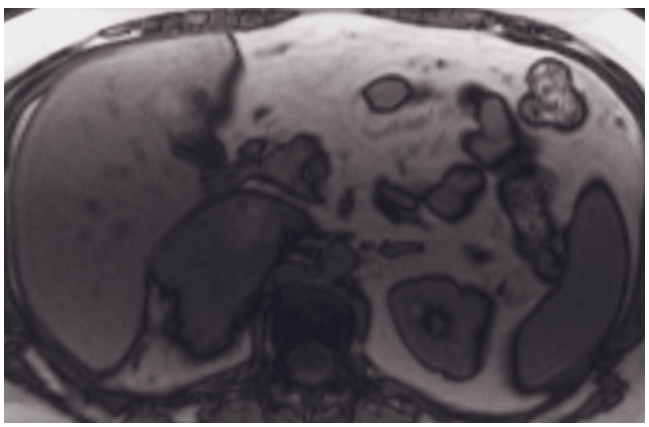

(*c*)

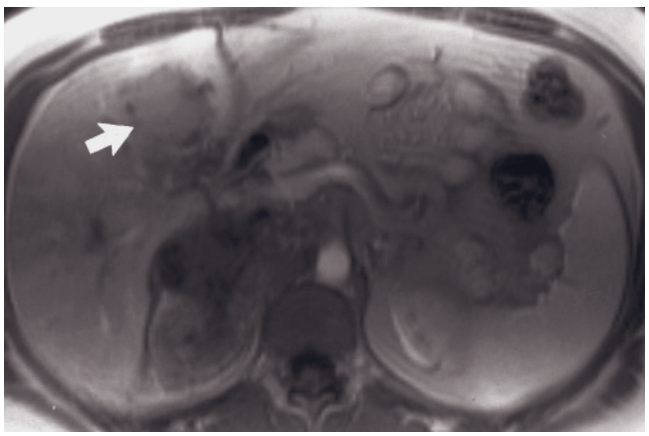

(*d*)

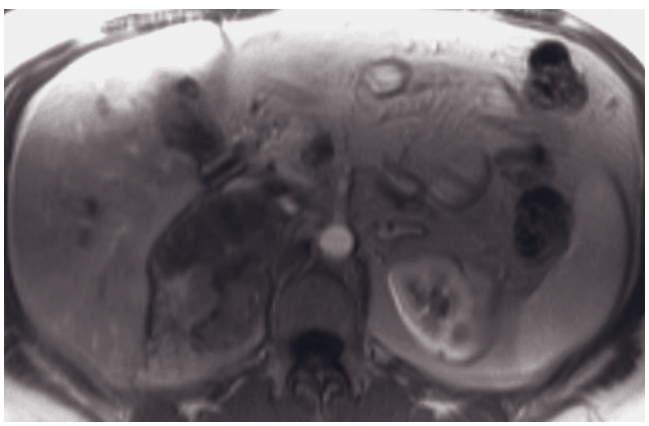

(*e*)

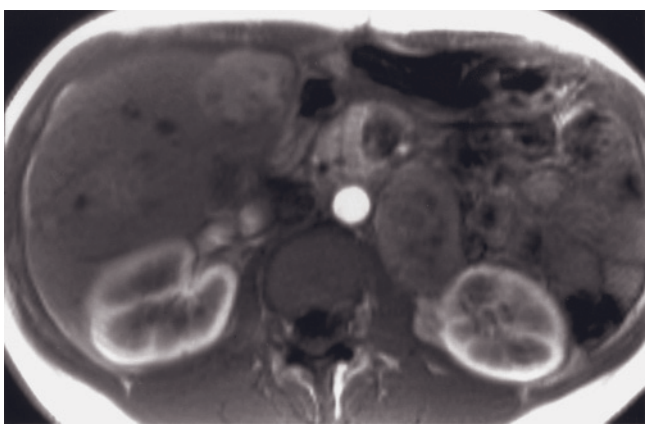

(*f*)

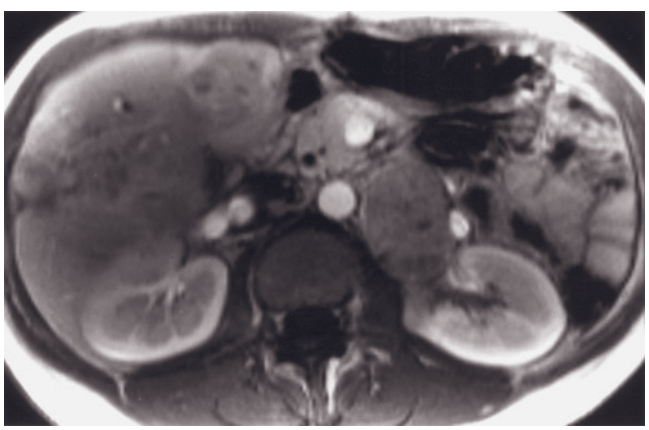

(*g*)

FIG. 8.26 Adrenal metastasis from endometrial cancer. T1-weighted GE (*a*),T1-weighted out-of-phase (*b*, *c*), and immediate postgadolinium GE (*d*, *e*) images. A right adrenal metastasis is invading the upper pole of the right kidney. The tumor is heterogeneous and predominantly hypointense on T1 (*a*), with no signal drop on out-of-phase (*b*, *c*) images. It demonstrates a diminished and heterogeneous enhancement on immediate postgadolinium images (*d*, *e*). Also note hepatic metastasis with irregular margins (arrow, *d*).

Immediate (*f*) and 45-s (*g*) postgadolinium GE images in a second patient. There is a 5-cm metastasis in the left adrenal with irregular patchy enhancement on immediate postgadolinium image (*f*) that persists on the later image (*g*). Liver metastases are also appreciated in this patient with pancreatic gastrinoma.

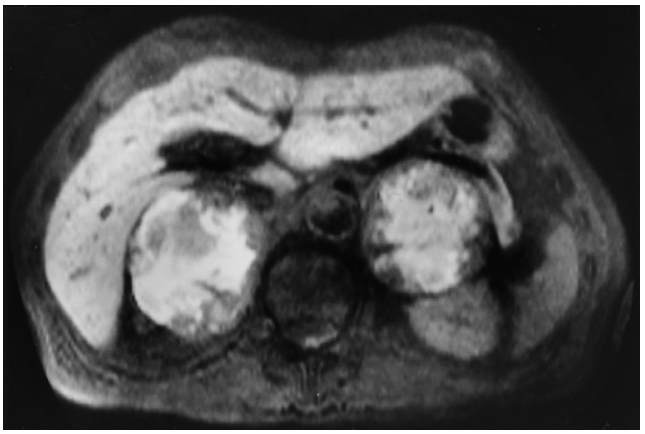

FIG. 8.27 Hemorrhagic adrenal metastases. T1-weighted fat-suppressed spin-echo image demonstrates high-signal-intensity subacute hemorrhage in bilateral adrenal metastases. Metastasis may undergo hemorrhage, simulating primary adrenal cortical carcinoma.

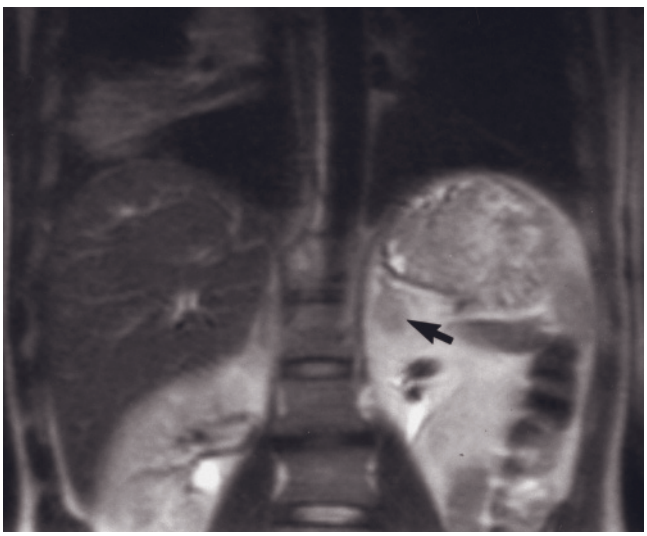

(*a*)

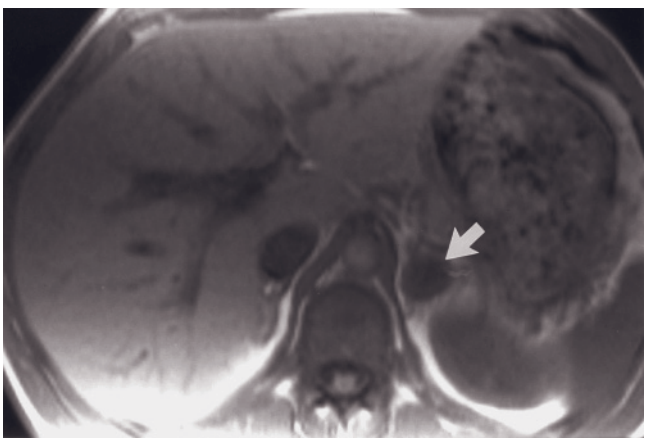

(*b*)

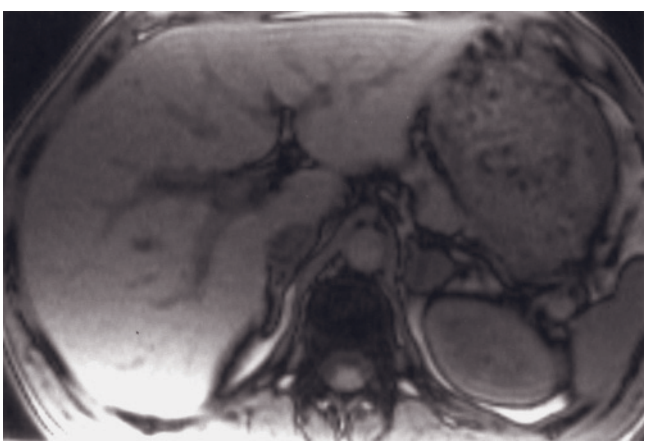

(*c*)

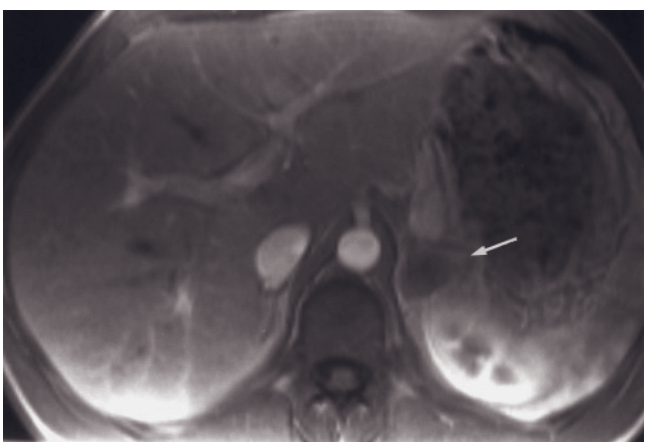

(*d*)

FIG. 8.28 Small left hypovascular adrenal metastasis. Coronal T2-weighted HASTE (*a*), T1-weighted GE (*b*), T1-weighted out-of-phase GE (*c*), and immediate postgadolinium GE (*d*) images. A 1.5-cm metastasis is heterogeneous and moderately high in signal intensity on the T2-weighted image (arrow, *a*).The tumor is hypointense on T1 (arrow, *b*) and does not show signal drop on the out-of-phase image (*c*). On immediate postgadolinium image, the tumor demonstrates negligible enhancement with a thin rim (arrow, *d*).

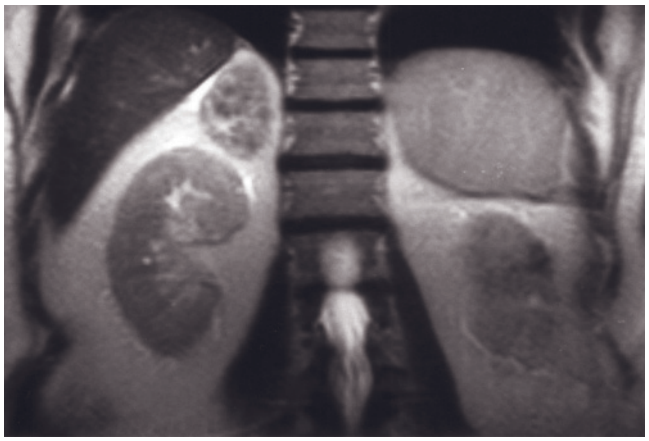

(*a*)

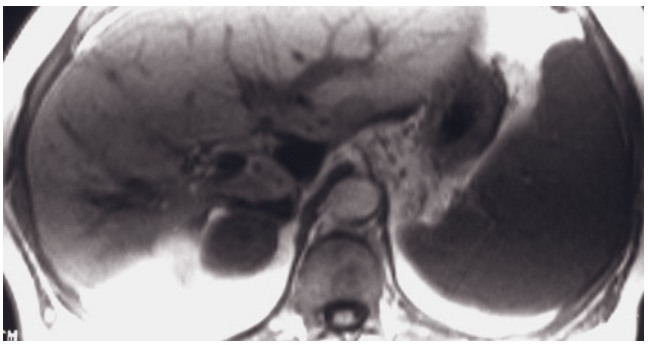

(*b*)

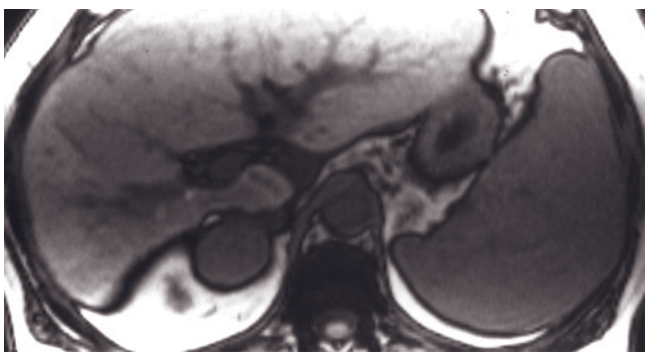

(*c*)

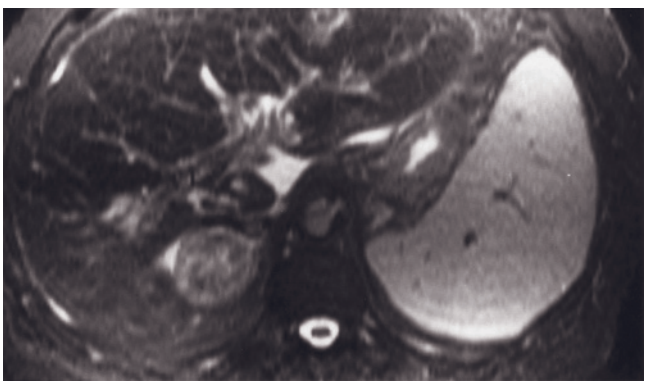

(*d*)

(*e*)

(*f*)

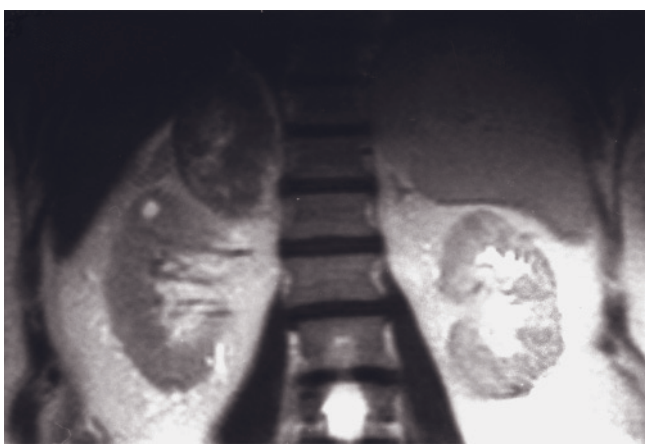

(*g*)

FIG. 8.29 Adrenal metastasis with interval growth. Coronal T2-weighted echo-train spin-echo (*a*), T1-weighted GE (*b*), T1-weighted out-of-phase GE (*c*), T2-weighted echo-train spin-echo (*d*), immediate postgadolinium GE (*e*), and 90-s post-gadolinium fat-suppressed GE (*f*) images. Coronal T2-weighted

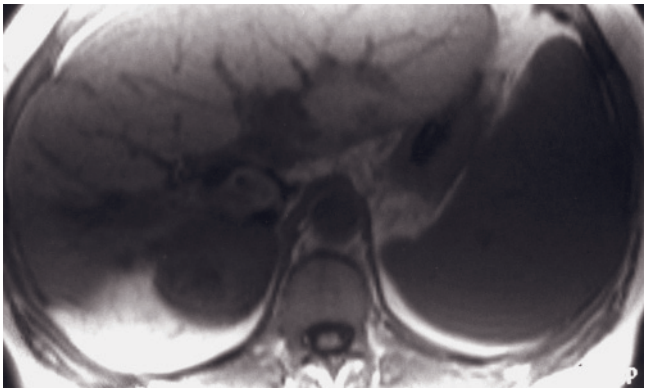

(*h*)

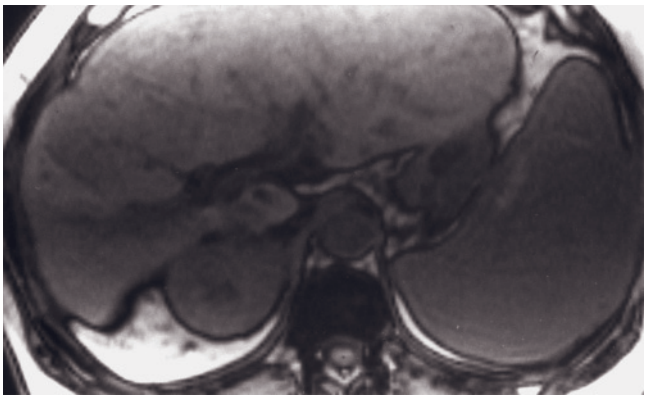

(*i*)

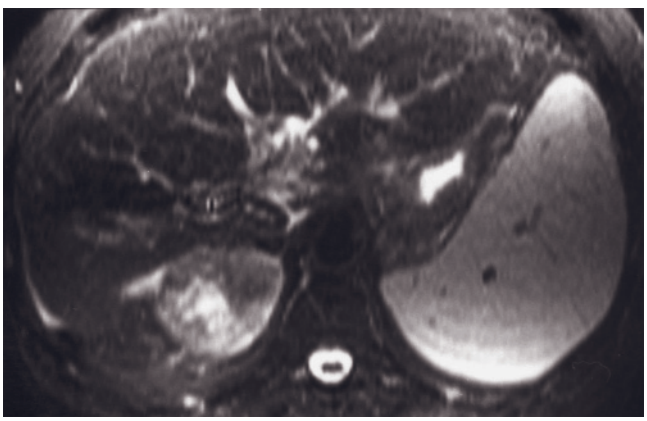

(*j*)

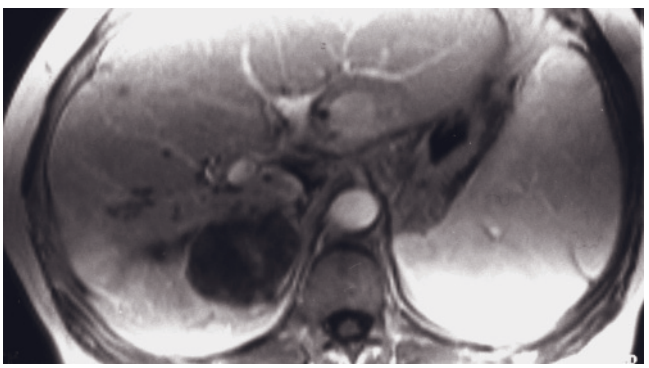

(*k*)

FIG. 8.29 (*Continued*) echo-train spin-echo (*g*), T1-weighted GE (*h*), T1-weighted out-of-phase GE (*i*), T2-STIR (*j*), and immediate postgadolinium GE (*k*) images in the same patient 3 months later. On the T2-weighted image, the adrenal lesion appears heterogeneously hypointense with hyperintense foci (*a, d, g, j*). Interval growth has occurred after a 3-month interval (*g–k*).

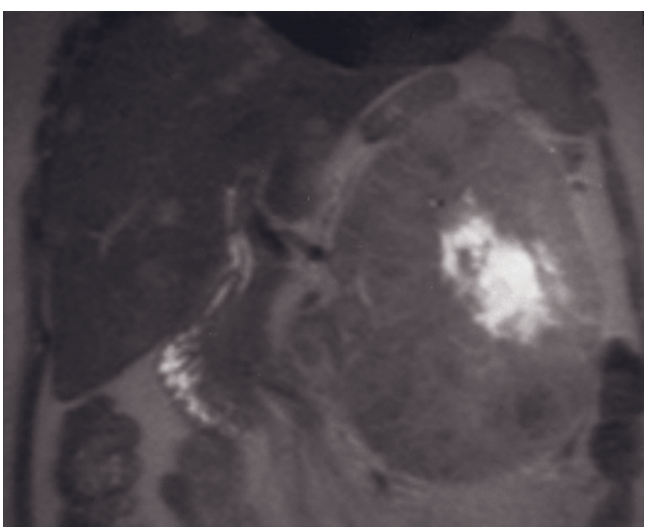

(*a*)

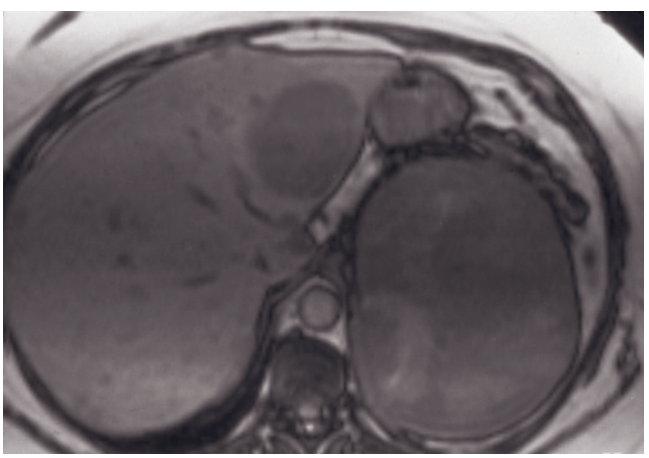

(*b*)

FIG. 8.30 Adrenal cortical carcinoma. Coronal T2-weighted echo-train spin-echo (*a*), T1-weighted out-of-phase GE (*b*), immediate postgadolinium GE (*c*), and 90-s postgadolinium fat-suppressed GE (*d*, *e*) images. The large left adrenal cortical carcinoma is heterogeneous on T2 (*a*). After contrast administration, irregular ring enhancement with a prominent nodular morphology is

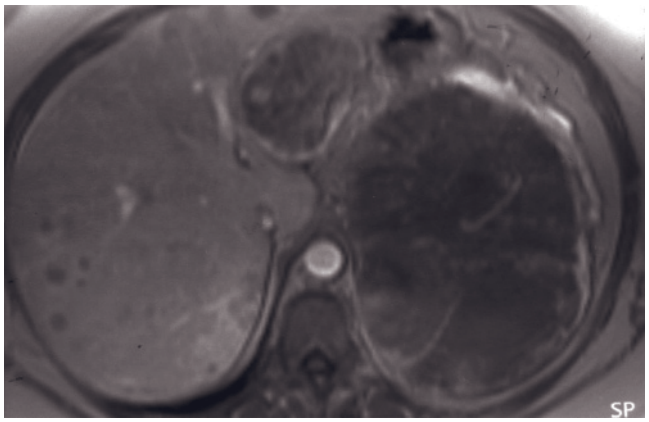

(*c*)

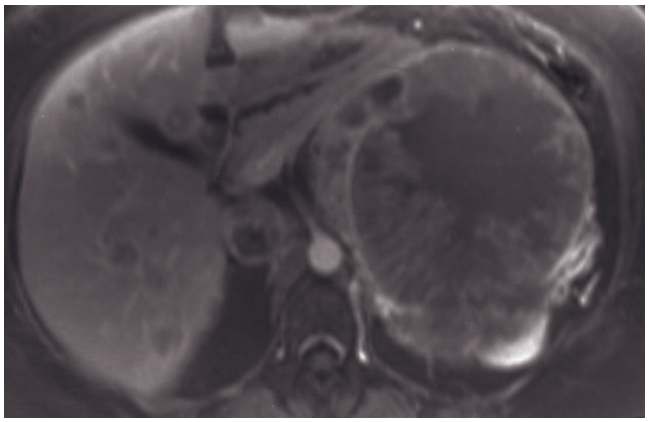

(*d*)

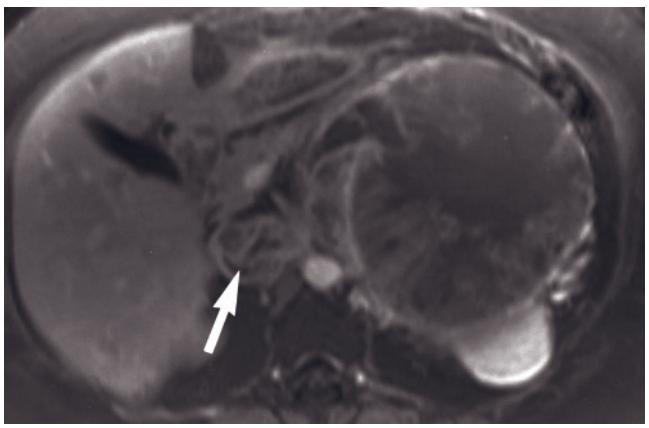

(*e*)

FIG. 8.30 (*Continued*) appreciated, which persists on late images (*c–e*). The central area shows no enhancement, consistent with necrosis. Multiple liver metastases are present. Tumor thrombus in the portal vein is well shown as enhancing thrombus on the gadolinium-enhanced fat-suppressed GE image (arrow, *e*).

(*a*)

(*b*)

FIG. 8.31 Adrenal cortical carcinoma. Sagittal T1-weighted GE (*a*) and 90-s postgadolinium GE (*b*) images in a 25-year-old woman. A 7-cm mass is identified in the right upper abdomen that indents the liver and displaces the right kidney inferiorly. The relationship of the mass to the kidney and liver is clearly defined in profile in the sagittal projection, and the mass is shown to be separate from these organs. High signal intensity is present on precontrast images, a finding consistent with central hemorrhage. The mass enhances heterogeneously after contrast administration and contains signal-void regions of necrosis (arrows, *b*). (Reproduced with permission from Schlund JF, Kenney PJ, Brown ED, Ascher SM, Brown JJ, Semelka RC: Adrenocortical carcinoma: MR imaging appearance with current technique. *J Magn Reson Imaging* 5: 171–174, 1995.)

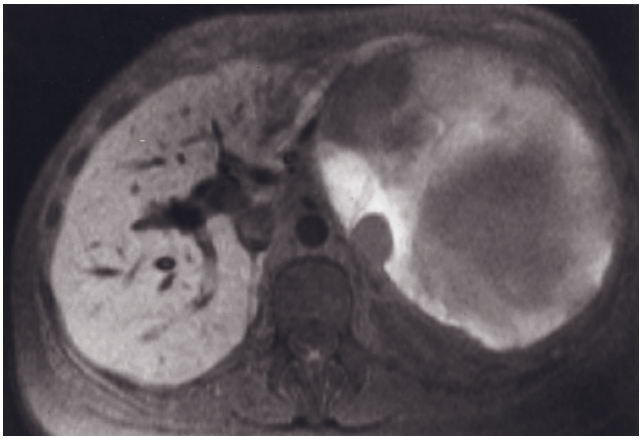

(*a*)

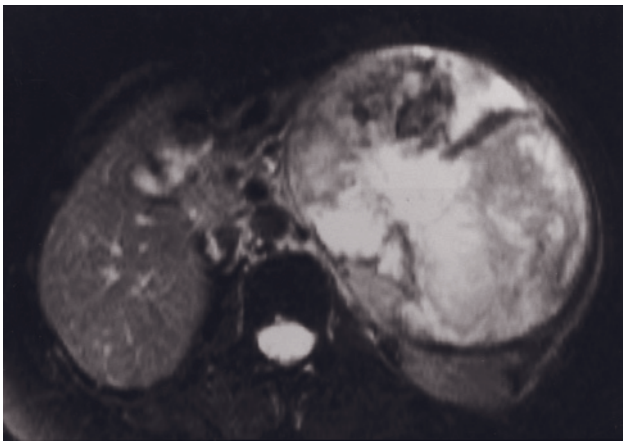

(*b*)

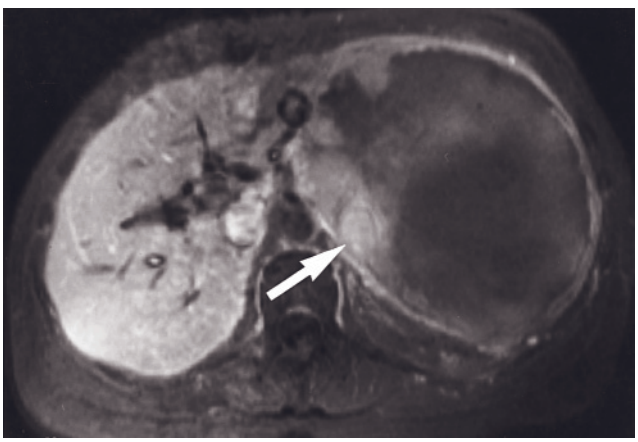

(*c*)

FIG. 8.32 Adrenal cortical carcinoma. T1-weighted fat-suppressed spin-echo (*a*), T2-weighted fat-suppressed spin-echo (*b*), and gadolinium-enhanced fat-suppressed spin-echo (*c*) images in a 41-year-old woman. On the precontrast T1-weighted image, central high signal intensity is present in the tumor, which is consistent with blood (*a*). On the T2-weighted image, the tumor is heterogeneous and high in signal intensity because of the presence of central necrosis and blood products of varying age (*b*). Peripheral nodules enhance after contrast administration (arrow, *c*), and the central portion of the tumor remains largely signal void. (Reproduced with permission from Schlund JF, Kenney PJ, Brown ED, Ascher SM, Brown JJ, Semelka RC. Adrenocortical carcinoma: MR imaging appearance with current technique. *J Magn Reson Imaging* 5: 171–174, 1995.)

FIG. 8.33 Small adrenal cortical carcinoma. Immediate postgadolinium GE image demonstrates a 2.5-cm right adrenal cortical carcinoma (arrow). Note that the tumor has an enhancing rim and is hypovascular centrally. (Reproduced with permission from Semelka RC, Shoenut JP: The adrenal glands. In Semelka RC, Shoenut JP (eds.). *MRI of the Abdomen with CT Correlation.* New York: Raven Press, p. 77–90, 1993.)

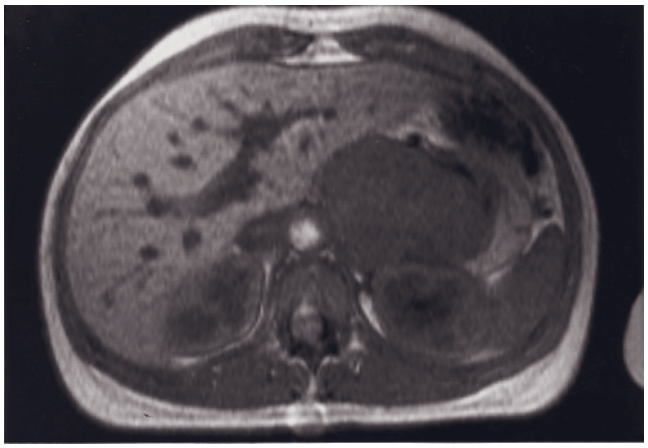

(*a*)

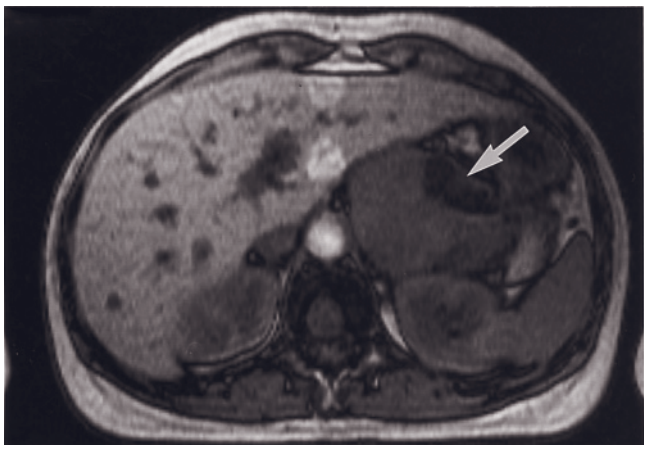

(*b*)

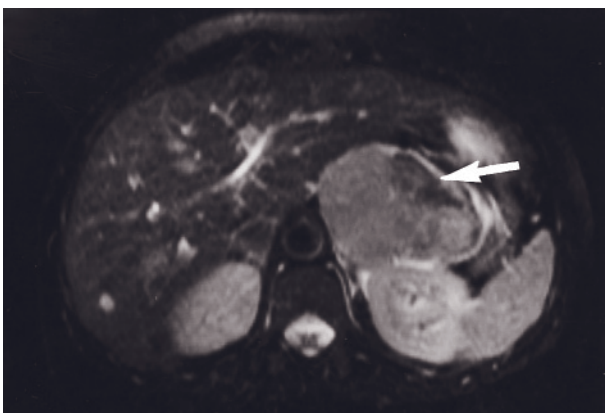

(*c*)

FIG. 8.34 Adrenal cortical carcinoma. T1-weighted GE (*a*), T1-weighted out-of-phase GE (*b*), and T2-weighted fat-suppressed spin-echo (*c*) images in a 37-year-old woman. On the out-of-phase image, a moderate-sized region of the tumor loses signal (arrow, *b*) compared to the in-phase image, a finding consistent with fatty tissue. On the fat-suppressed T2-weighted image (*c*), the tumor is hyperintense and contains a region of low signal (arrow, *c*) representing fat and corresponding to the region of signal drop on the out-of-phase image (*b*). (Reproduced with permission from Schlund JF, Kenney PJ, Brown ED, Ascher SM, Brown JJ, Semelka RC. Adrenocortical carcinoma: MR imaging appearance with current technique. *J Magn Reson Imaging* 5: 171–174, 1995.)

along the course of the sympathetic chain, most frequently in a paraortic or paracaval location including the organs of Zuckerkandl (located at the aortic bifurcation). Mediastinal and bladder wall tumors account for 2% of pheochromocytomas. Most of the tumors are unilateral and frequently greater than 3 cm in diameter at presentation [74]. Pheochromocytomas are bilateral in 10% of cases and malignant in about 10% of cases, with metastatic spread occurring most commonly to lymph nodes, bone, and liver. Extra-adrenal origin tumors are malignant in a greater percentage of cases (40%). Patients present with sustained or paroxysmal hypertension, and the great majority of symptomatic patients have elevated levels of urinary catecholamines and their metabolites, principally vanillylmandelic acid (VMA), and metanephron. Patients with multiple endocrine neoplasia (MEN) type IIA or IIB, neurofibromatosis, von Hippel-Lindau disease, and multiple cutaneous neuromas have increased incidence of pheochromocytomas. Seventy-five percent of patients with MEN II have bilateral tumors, which are rarely extra-adrenal [75, 76]. Cystic pheochromocytomas occur, and distinction from cysts may be difficult [77].

Pheochromocytomas characteristically are hypointense on T1-weighted images and hyperintense on T2-weighted images (fig. 8.36) [1] because of their high interstitial fluid space that in part may reflect necrotic, hemorrhagic, or cystic regions (fig. 8.37) that are observed on gross or microscopic pathologic analysis. Although pheochromocytomas may appear very bright (e.g., "light bulbs") on T2-weighted images, the majority are heterogeneous and moderately high signal, and in rare instances they may have moderate signal intensity [12]. A confounding variable is the signal intensity of background fat, which depends on the type of sequence employed. On echo-train spin-echo images, masses tend to appear lower in signal intensity, whereas on fat-suppressed images masses appear higher in signal intensity. This reflects a signal intensity rescaling effect, reflecting the signal intensity of the background fat; when fat is dark the adrenal mass signal intensity is rescaled and appears brighter. MRI may be the technique of choice to examine for pheochromocytomas because these lesions are most often relatively high in signal intensity on T2-weighted images independent

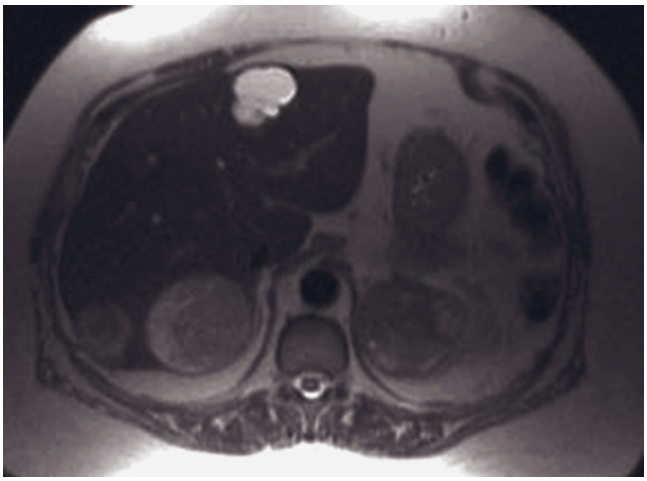

(*a*)

(*b*)

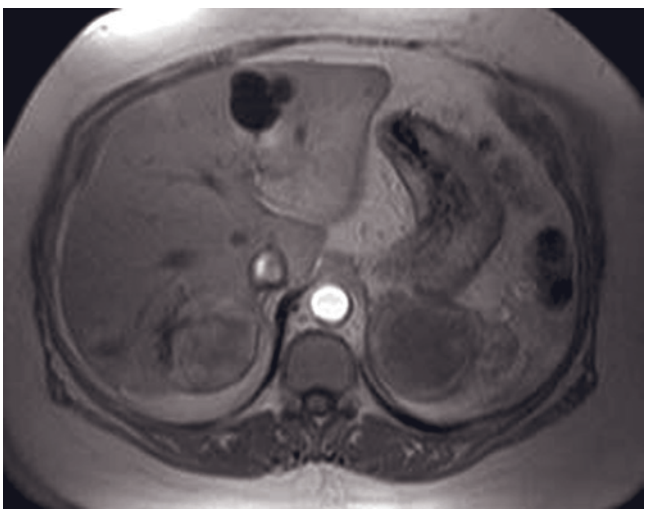

(*c*)

FIG. 8.35 Recurrent adrenal cortical carcinoma with liver metastases. Axial T2-weighted HASTE (*a*), T1-weighted out-of-phase GE (*b*), and immediate postgadolinium GE (*c*) images in a patient with recurrent adrenal cortical carcinoma and liver metastases. A heterogeneous mass on the left is noted on the T2-weighted HASTE image (*a*), with peripheral areas of moderately high signal intensity as well as two liver metastases with similar imaging findings in the upper posterior segment of the right liver lobe. The recurrent mass and liver metastases demonstrate heterogeneous signal intensity on precontrast T1-weighted image (*b*) and intense heterogeneous, mainly peripheral contrast enhancement on the postcontrast GE image (*c*).

of tumor size and location [12, 78]. Therefore, small extra-adrenal lesions are conspicuous on T2-weighted images and are usually distinguishable from other structures such as lymph nodes and bowel, which are lower in signal intensity. Cystic pheochromocytomas are as high in signal intensity as cerebrospinal fluid (CSF) on T2-weighted images [79]. Pheochromocytomas usually enhance minimally on immediate postgadolinium images and demonstrate progressive enhancement on later interstitial-phase images (fig. 8.36), although relatively intense early enhancement may be observed. If early intense enhancement occurs, it reflects the capillary-rich framework within the tumor, which may also contribute to the high signal intensity on T2-weighted images (fig. 8.38). In general, pheochromocytomas do not lose signal intensity on out-of-phase images. Similar imaging findings may be observed in extra-adrenal pheochromocytomas (fig. 8.39).

Neuroblastoma, Ganglioglioma, Ganglioneuroblastoma, and Schwannoma

This group of neoplasms is distinguished by a broad range in differentiation from primitive neuroblastoma at one end of the spectrum to well-differentiated, mature ganglioneuroma at the opposite end. Tumors with intermediary cytological maturation are termed ganglioneuroblastomas.

Neuroblastoma is one of the most common solid tumors of children younger than 5 years of age [80]. Tumors originate from neural crest cells. Neuroblastomas most commonly arise from the adrenal medulla or cells in adjacent retroperitoneal tissue (figs. 8.40 and 8.41). In older patients, extra-adrenal sites increase in frequency [81, 82]. As neuroblastomas occur most commonly in infants, extra-adrenal presentation, although less common than adrenal location, is still relatively frequently observed in these patients (fig. 8.42).

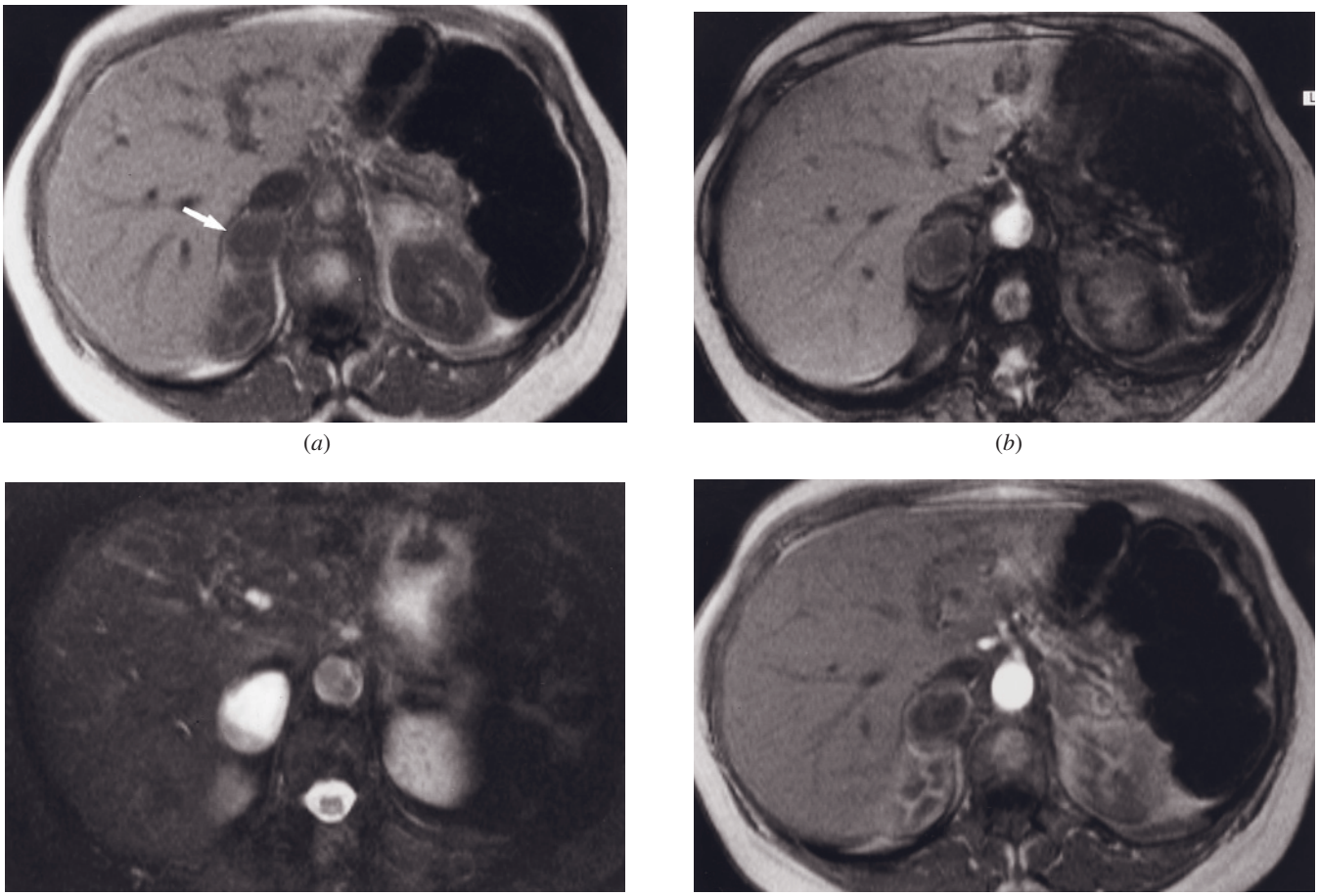

(*a*) (*b*)

(*c*) (*d*)

FIG. 8.36 Pheochromocytoma. T1-weighted GE (*a*), T1-weighted out-of-phase GE (*b*), T2-weighted fat-suppressed spin-echo (*c*), immediate postgadolinium GE (*d*), and 2-min postgadolinium GE (*not shown*) images. A 2.5-cm pheochromocytoma arises from the right adrenal gland (arrow, *a*), which has a moderate-signal-intensity peripheral rim with a low-signal-intensity center on in-phase (*a*) and out-of-phase (*b*) GE images. No appreciable drop of signal intensity is present on the out-of-phase image. On the T2-weighted image, the mass is extremely high in signal intensity, with the peripheral rim appearing slightly low in signal intensity (*c*). On the immediate postgadolinium image, the tumor rim enhances intensely, with minimal central enhancement (*d*). On the more delayed image, the tumor diffusely enhances in a heterogeneous fashion (*not shown*).

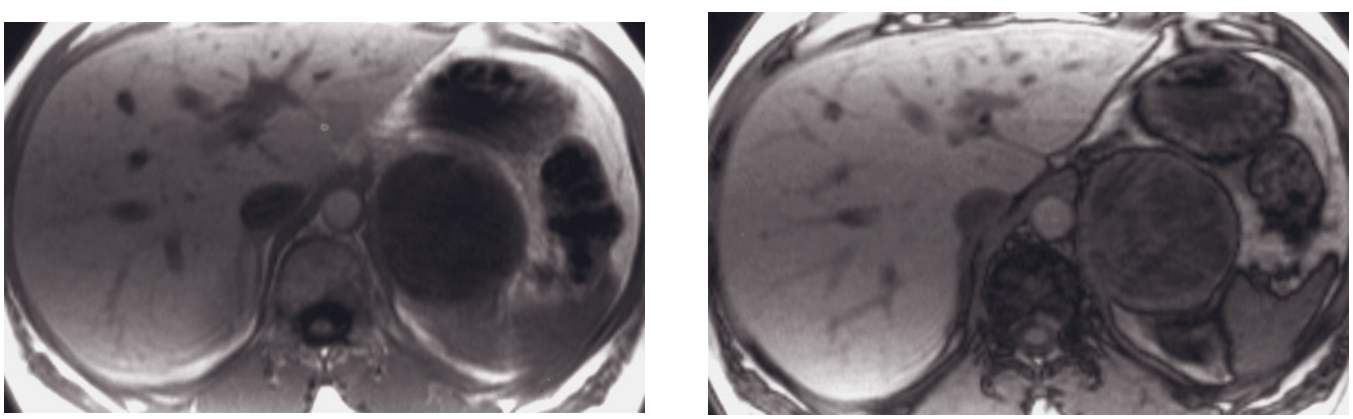

(*a*) (*b*)

FIG. 8.37 Large pheochromocytoma. T1-weighted GE (*a*), T1-weighted out-of-phase GE (*b*), T2-weighted echo-train spin-echo (*c*), immediate postgadolinium GE (*d*), and 90-s postgadolinium fat-suppressed GE (*e*) images. A 6-cm pheochromocytoma is present

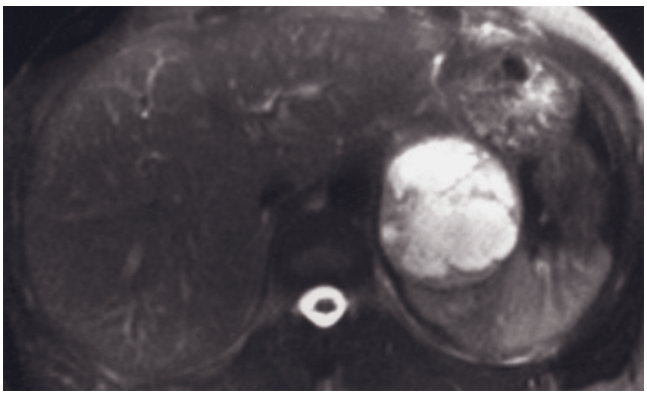

(*c*)

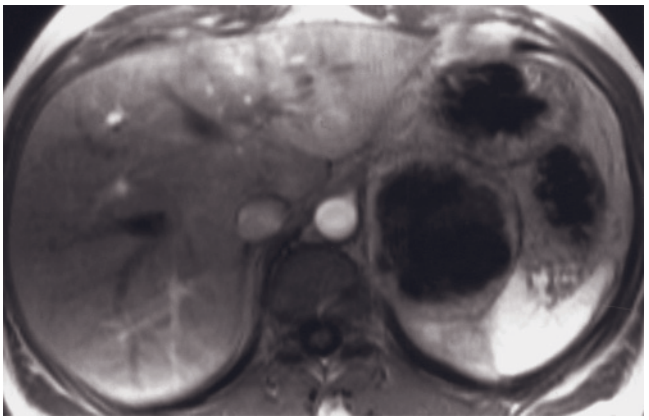

(*d*)

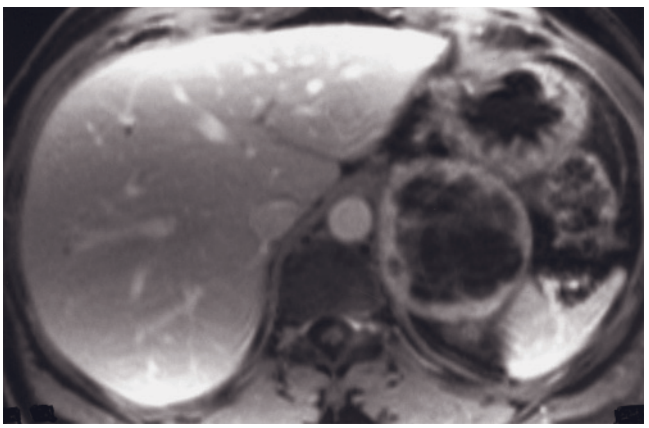

(*e*)

FIG. 8.37 (*Continued*) in the left adrenal, which is hypointense on GE (*a*) and does not drop in signal on the out-of-phase (*b*) image. The tumor is heterogeneous and high in signal intensity on T2 (*c*), and after contrast administration there is an irregular ringlike enhancement (*d*) that persists on late image (*e*).

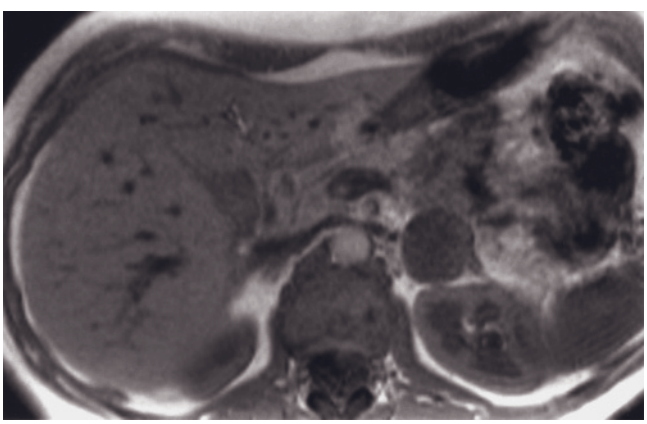

(*a*)

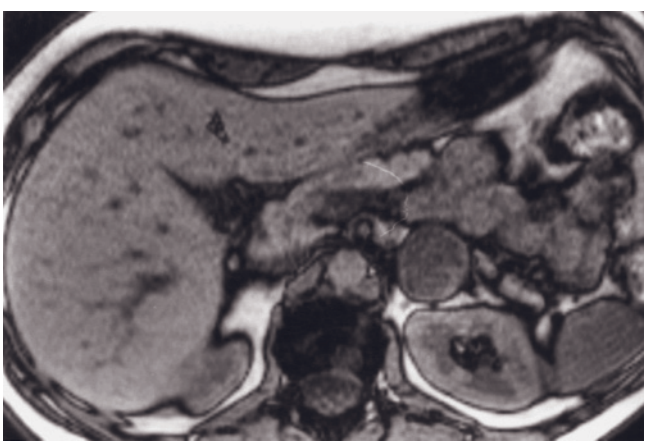

(*b*)

FIG. 8.38 Pheochromocytoma. T1-weighted GE (*a*), T1-weighted out-of-phase GE (*b*), coronal T2-weighted echo-train spin-echo (*c*), T2-weighted echo-train spin-echo (*d*), immediate postgadolinium GE (*e*), and 90-s postgadolinium fat-suppressed GE (*f*) images. A pheochromocytoma is present in the left adrenal, which is mildly low signal intensity on T1 (*a*) and does not drop in signal on the out-of-phase image (*b*). It appears high signal intensity on T2 (*c*, *d*), and after gadolinium administration there is

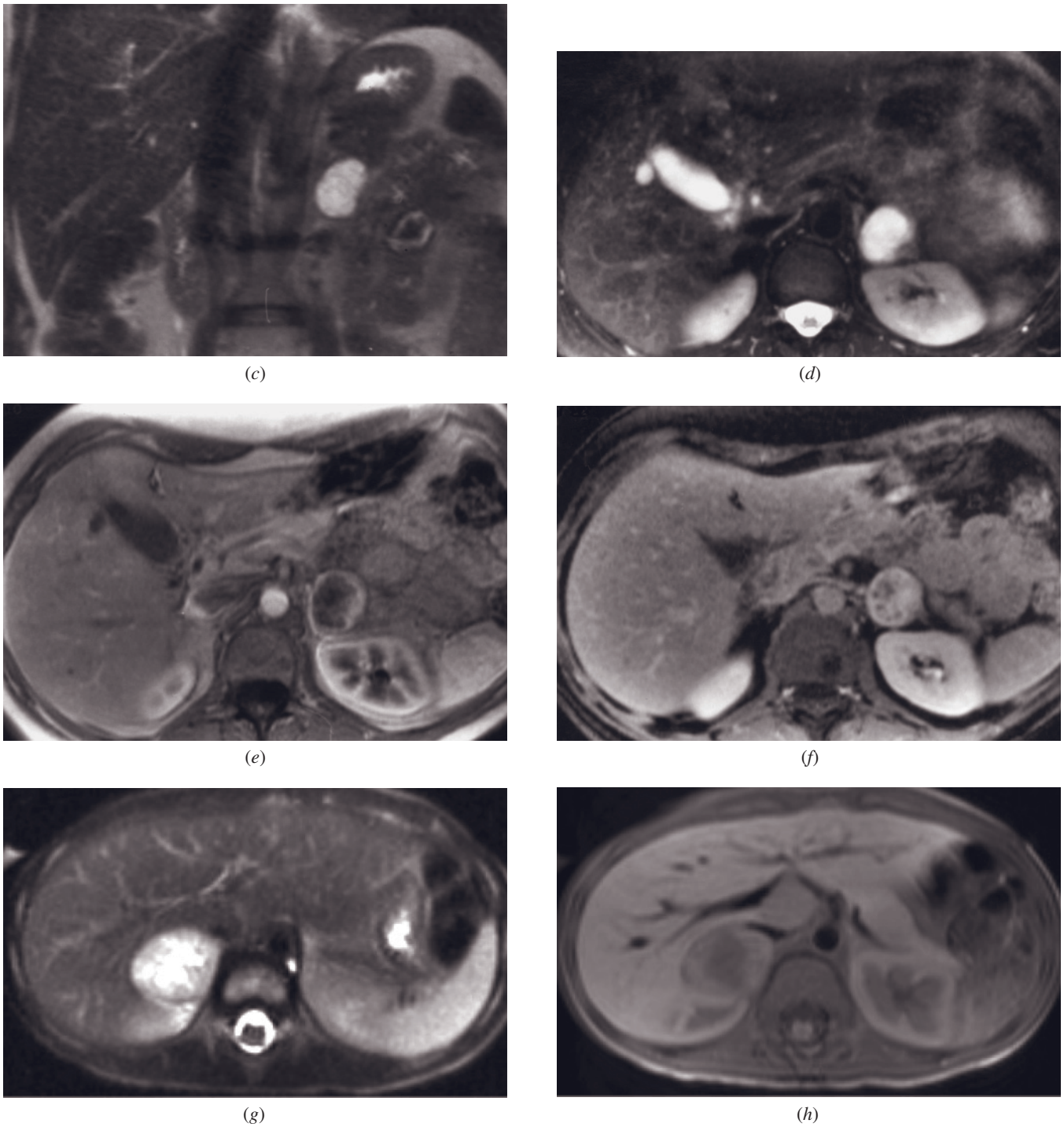

FIG. 8.38 (*Continued*) irregular ringlike enhancement (*e*) with progressive and heterogeneous enhancement on the late image (*f*). Delayed, there is progressive enhancement of gadolinium in the vascular space of the tumor. **Bilateral pheochromocytomas.** T2-weighted fat-suppressed single-shot echo-train spin-echo (*g*, *k*), T1-weighted SGE (*h*, *l*), T1-weighted postgadolinium

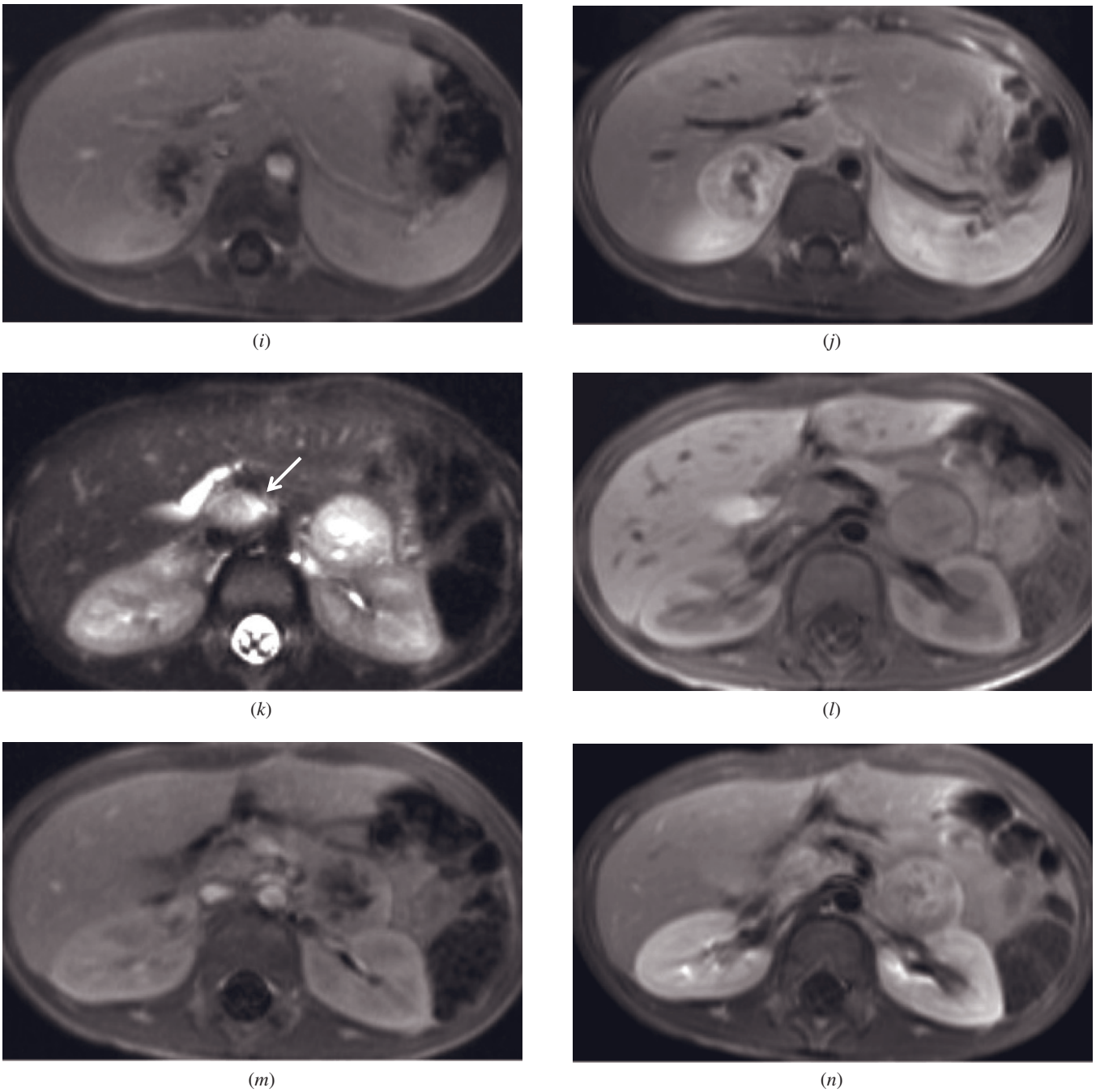

FIG. 8.38 (*Continued*) SGE (*i*, *m*), and T1-weighted postgadolinium fat-suppressed interstitial-phase SGE (*j*, *n*) images demonstrate bilateral pheochromocytomas in another patient. The lesions show high signal on T2-weighted images (*g*, *k*) and progressive heterogeneous enhancement on postgadolinium images (*i*, *j*, *m*, *n*). Central necrosis is present in the lesions. Note that an extra-adrenal pheochromocytoma (arrow, *k*) is also present.

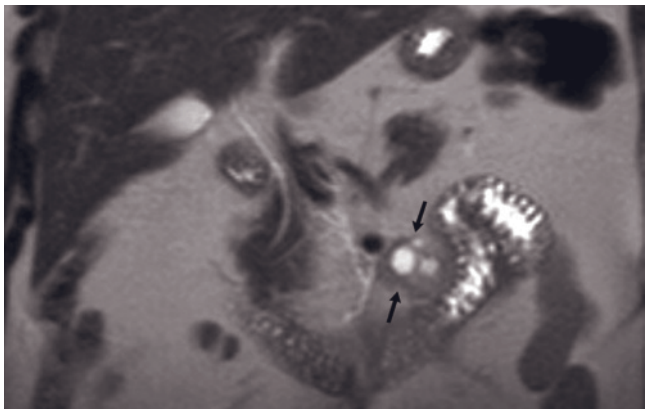

(*a*)

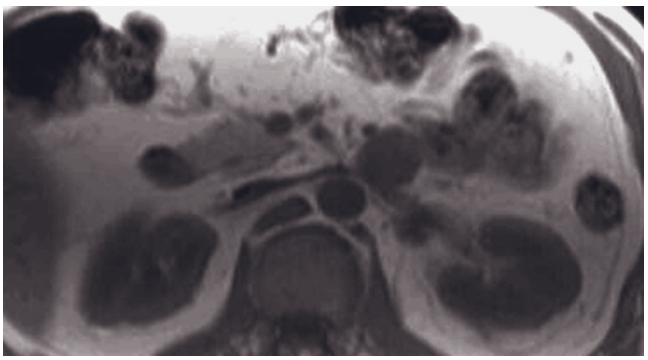

(*b*)

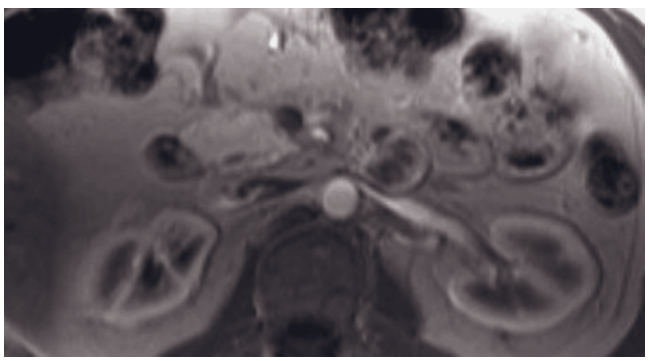

(*c*)

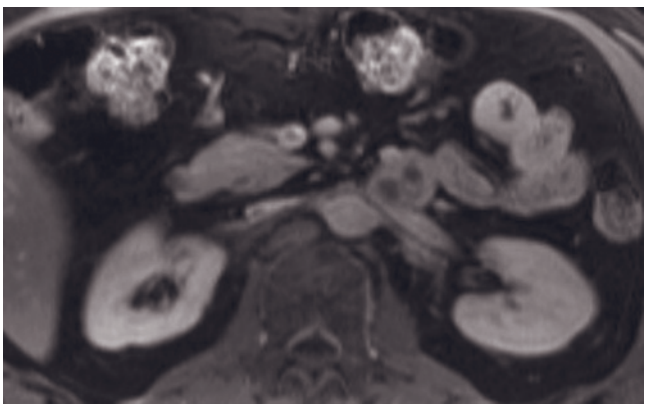

(*d*)

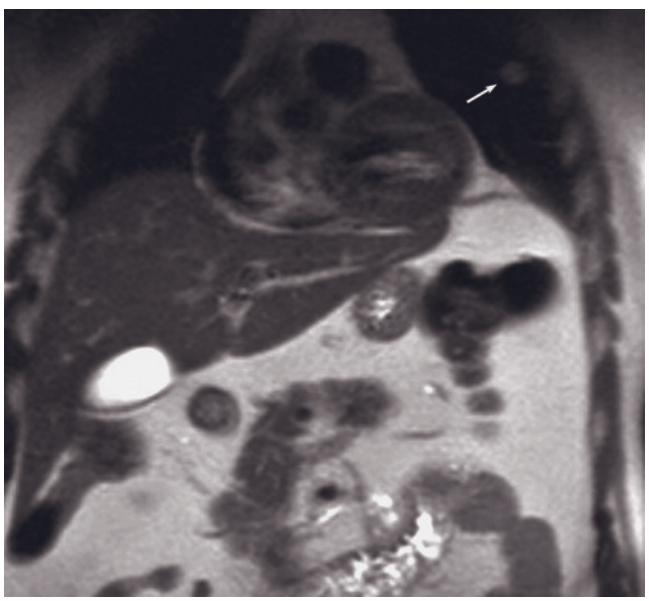

(*e*)

FIG. 8.39 Extra-adrenal cystic malignant pheochromocytoma. Coronal T2-weighted HASTE image (*a*), axial T1-weighted GE image (*b*), immediate postgadolinium GE image (*c*), interstitial-phase fat-suppressed postgadolinium GE image (*d*), and coronal T2-weighted HASTE image (*e*). An extra-adrenal mass (arrows, *a*) is shown between the SMA and 4th portion of the duodenum with well-defined borders and two cystic areas with very high signal intensity on the HASTE images (*a*, *e*).The mass is low signal intensity on the T1-weighted GE image (*b*) and demonstrates intense heterogeneous enhancement on the immediate post-gadolinium image (*c*), which persists on the interstitial-phase fat-suppressed postgadolinium GE image (*d*). A nodular lung metastatic nodule is appreciated on the coronal T2-weighted HASTE image (arrow, *e*).

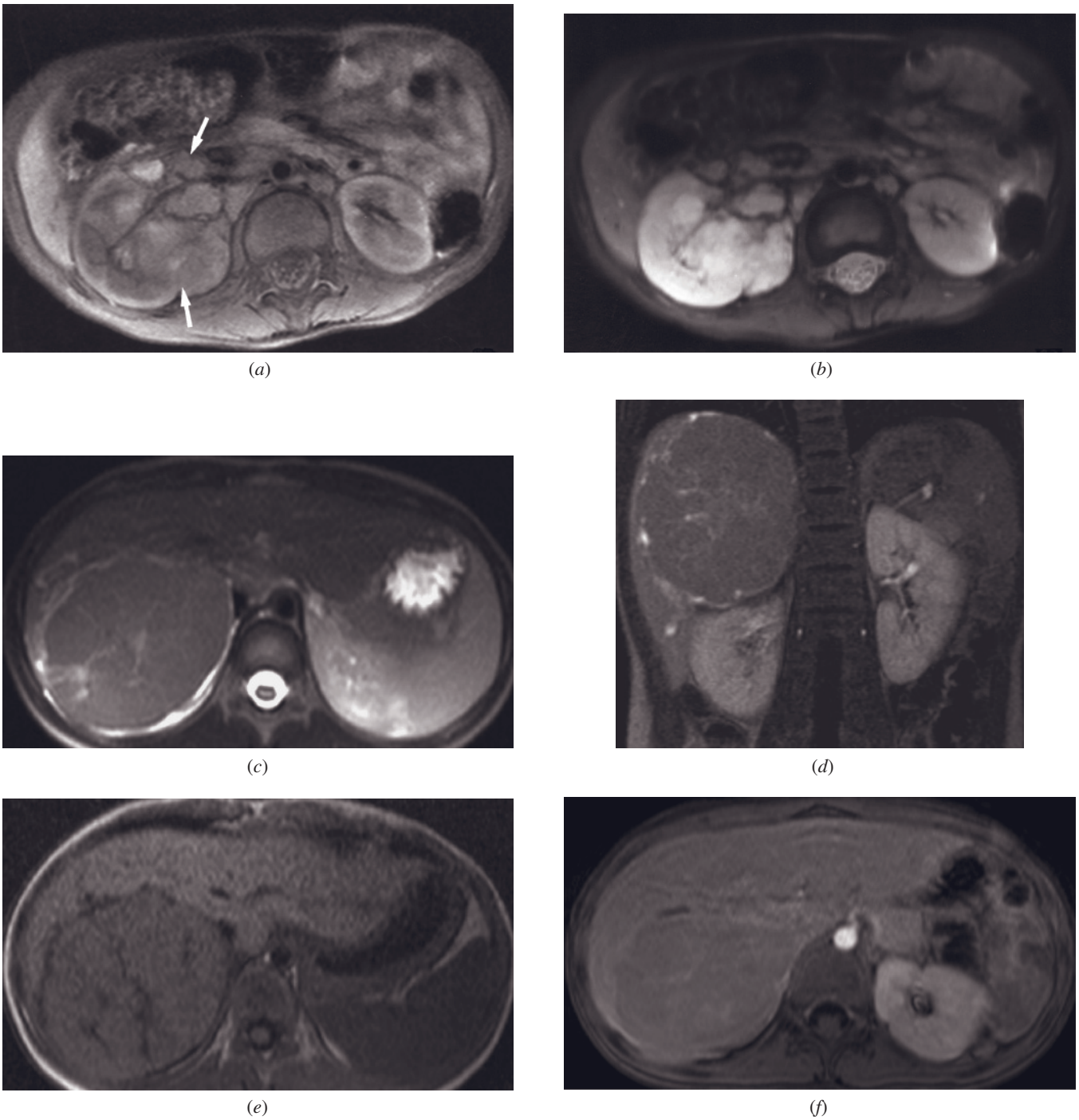

FIG. 8.40 Neuroblastoma. T1-weighted GE (*a*) and T2-weighted fat-suppressed echo-train spin-echo (*b*) images. A right adrenal neuroblastoma is present that invades the right kidney (arrows, *a*). Transverse (*c*) and coronal (*d*) T2-weighted single-shot echo-train spin-echo, transverse T1-weighted magnetization-prepared rapid gradient-echo (*e*), and transverse T1-weighted interstitial-phase SGE (*f*) images demonstrate a neuroblastoma arising from the right adrenal gland. The tumor shows intermediate signal on T2-weighted images (*c*, *d*) and low signal on T1-weighted image (*e*) and enhances intensely on postgadolinium image (*f*).

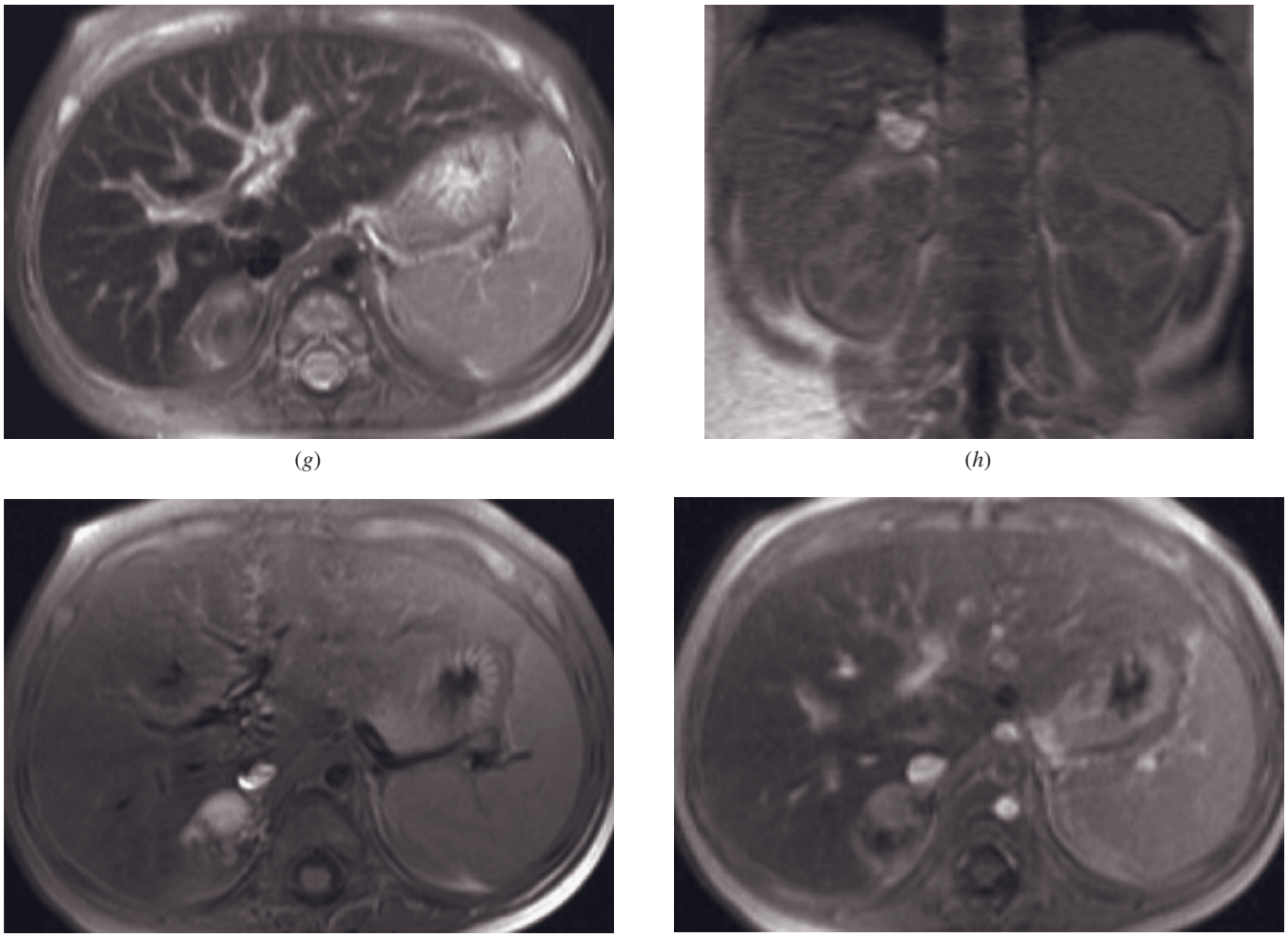

FIG. 8.40 (*Continued*) The tumor abuts on the right kidney. Transverse T2-weighted single-shot echo-train spin-echo (*g*), coronal (*h*) and transverse (*i*) T1-weighted spin-echo, and transverse postgadolinium interstitial-phase spin-echo (*j*) images demonstrate right adrenal neuroblastoma. The lesion contains hemorrhage, which shows high signal on T1-weighted images (*h*, *i*). The lesion shows enhancement on postgadolinium image (*j*).

The most common sites of metastatic disease include the skeletal system, liver (fig. 8.43), and lymph nodes. Tumors are generally high in signal intensity on T2-weighted images and enhance with gadolinium. Extension into the neural canal is a feature of these tumors. Encasement of the aorta and IVC is a common feature of advanced disease (fig. 8.44). MRI is particularly effective at evaluating both the primary tumor and metastases in these patients, who are predominantly pediatric, because of high intrinsic soft tissue contrast resolution, which is beneficial in patients with minimal body fat. Direct multiplanar imaging renders MRI superior to CT imaging for the demonstration of extension into the neural canal, invasion of adjacent organs such as liver [80], and location relative to the diaphragm (fig. 8.42). T2-weighted fat-suppressed spin-echo and pre- and post-contrast T1-weighted fat-suppressed spin-echo images in transverse and sagittal planes demonstrate these tumors well (fig. 8.44). Fat-suppressed spin-echo imaging is generally recommended rather than fat-suppressed gradient-echo techniques because patients are often too young to cooperate with breath holding, and spin-echo imaging has a higher signal-to-noise ratio, which improves image quality in small patients. Neuroblastoma may have an appearance on MRI indistinguishable from adrenal cortical carcinoma in adult patients, with one reported case [32] appearing as a large tumor with central necrosis and hemorrhage and tumor thrombus in the IVC (fig. 8.41).

Unlike neuroblastomas, ganglioneuromas typically occur in older patients [83]. Although all tumors may encase vessels [80], ganglioneuroblastoma and ganglioneuroma tend to be smaller and have better-defined margins (fig. 8.45). On MR images, tumors are intermediate in signal intensity on T1-weighted images and

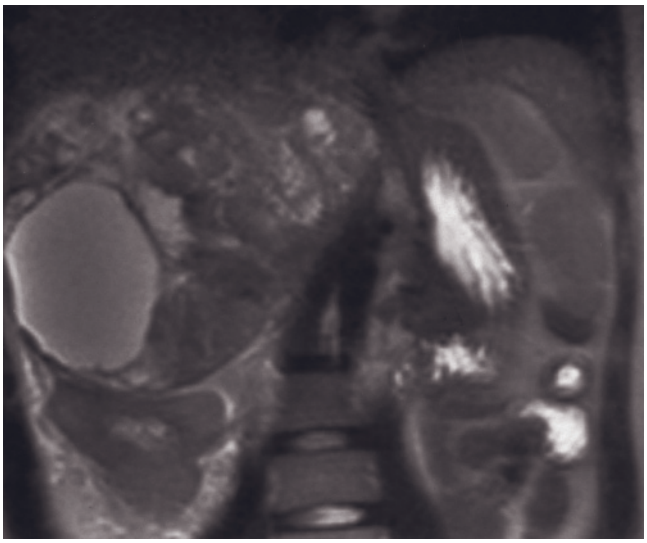

(*a*)

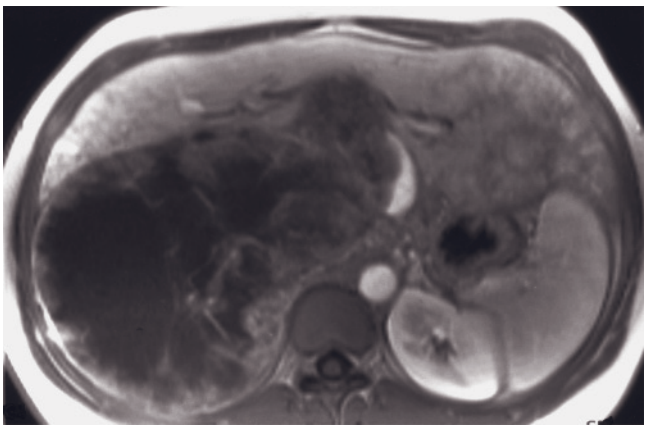

(*b*)

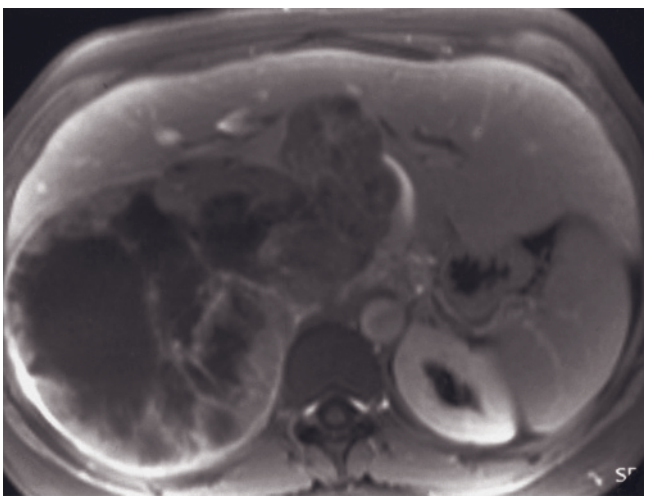

(*c*)

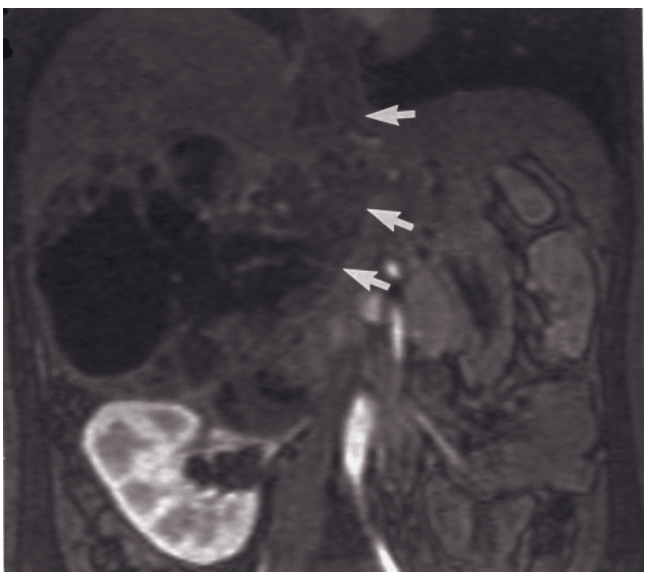

(*d*)

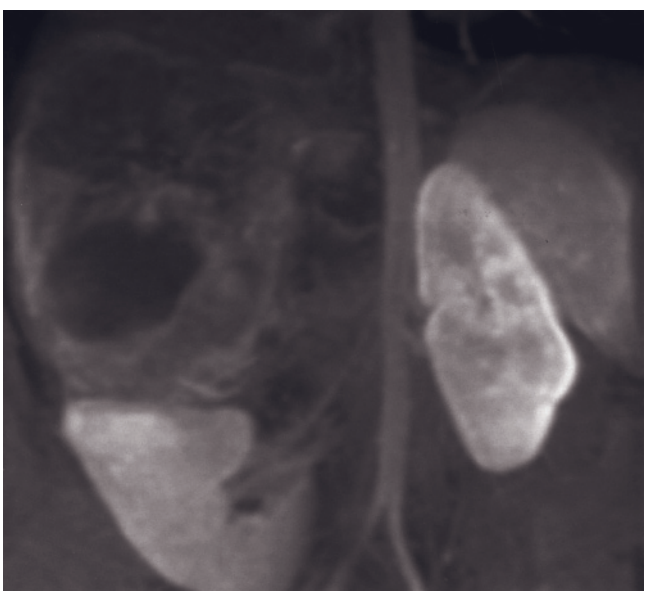

(*e*)

FIG. 8.41 Neuroblastoma. Coronal T2-weighted echo-train spin-echo (*a*), immediate postgadolinium GE (*b*), 90-s postgadolinium fat-suppressed GE (*c*), MRA source-coronal postcontrast fat-suppressed GE (*d*), and MIP reconstruction-3D steady-state free process postgadolinium (*e*) images. A large neuroblastoma arising from the right adrenal is present that displaces the right kidney inferiorly and compresses the liver anteriorly. The mass is heterogeneous with hyperintense areas on T2 (*a*). After gadolinium administration, there is irregular peripheral and internal septa enhancement with central nonenhancing regions that correspond to necrotic areas (*b*, *c*). Hemorrhage, necrosis, and cystic areas may increase as the tumor increases in size. MRA images demonstrates tumor thrombus in the IVC extending to the right atrium (arrows, *d*).

(*a*)

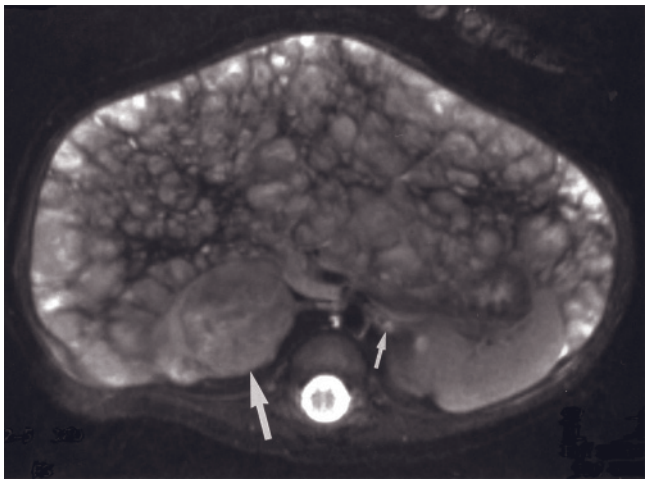

(*b*)

FIG. 8.42 Hepatic metastases from neuroblastoma. T1-weighted fat-suppressed spin-echo (*a*) and T2-weighted fat-suppressed echo-train spin-echo (*b*) images. The liver is massively enlarged, compressing the pancreas (arrows, *a*). Multiple liver metastases are present, which appear minimally hypointense on T1 and markedly hyperintense on T2. The primary tumor in the right adrenal (large arrow, *b*) and contralateral involvement of the left adrenal (small arrow, *b*) have similar signal intensity. Neuroblastoma has a tendency to local infiltration, lymph node metastases, and hematogenous spread to liver, lungs, and bones.

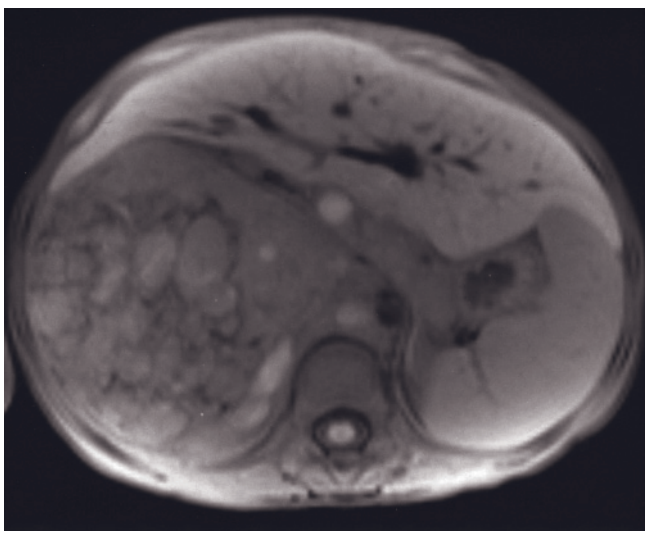

(*a*)

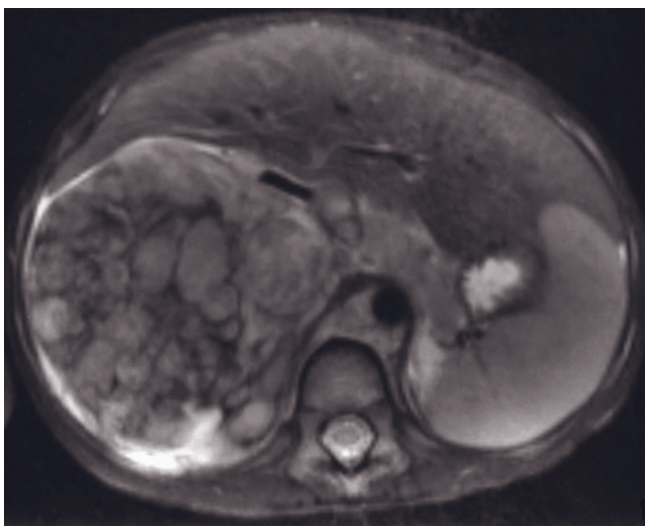

(*b*)

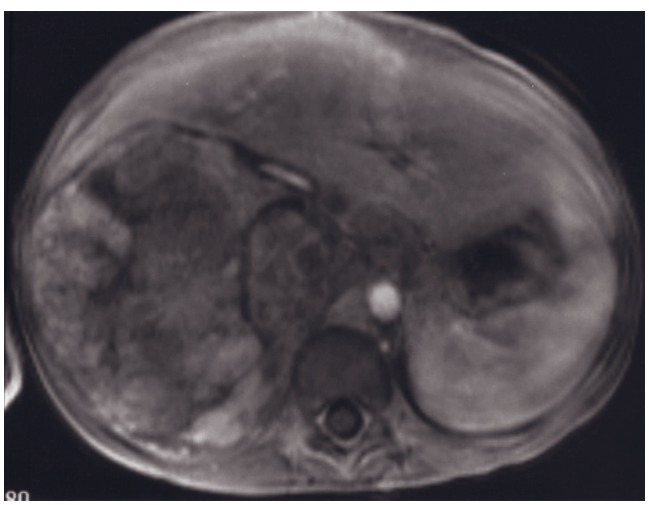

(*c*)

FIG. 8.43 Large neuroblastoma. T1-weighted GE (*a*), T2-weighted echo-train spin-echo (*b*), immediate postgadolinium GE (*c*), coronal T2-weighted echo-train spin-echo (*d*), sagittal 10-min

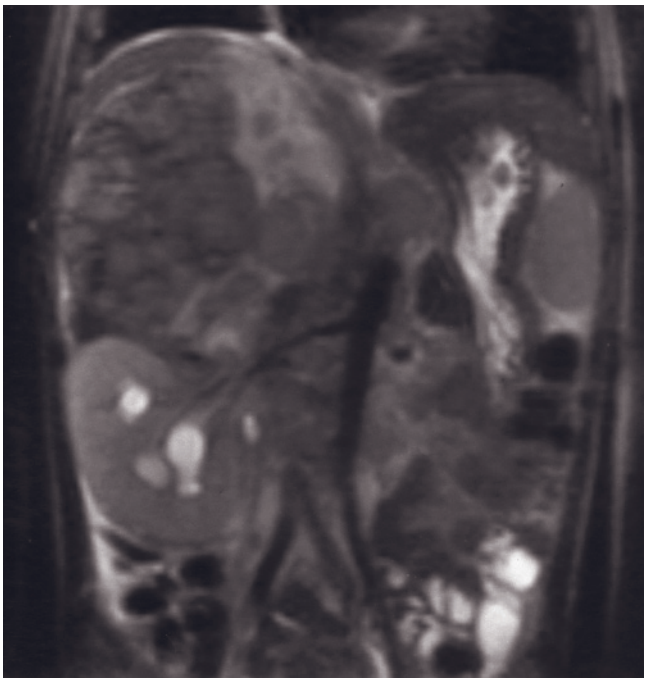

(*d*)

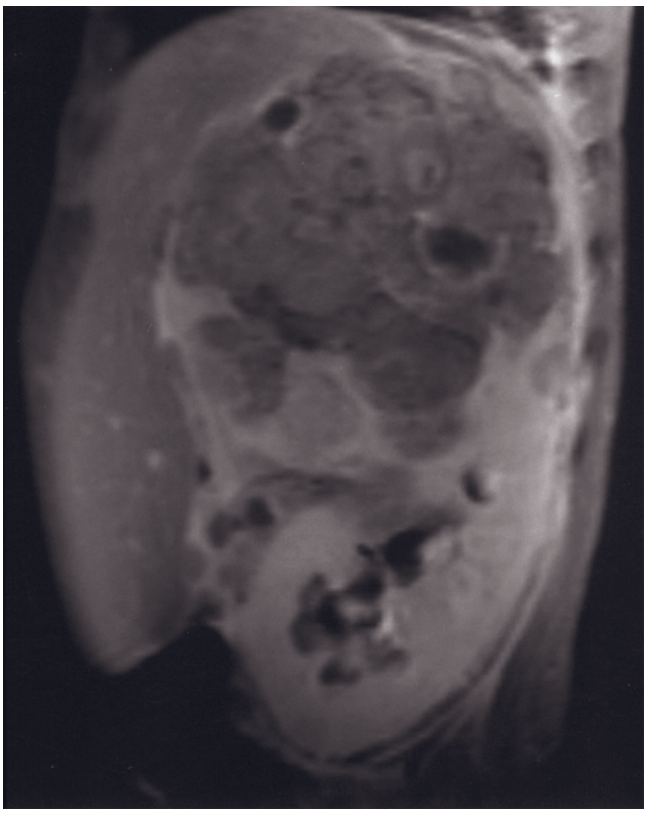

(*e*)

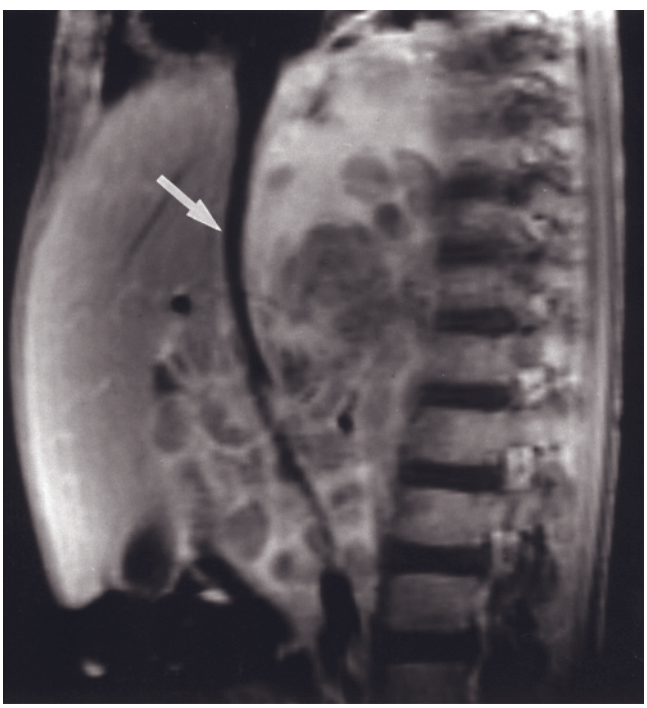

(*f*)

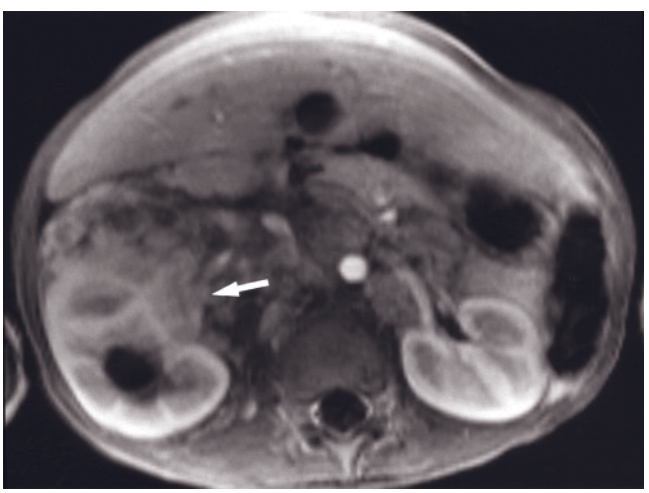

(*g*)

FIG. 8.43 (*Continued*) postgadolinium GE at the level of the left kidney (*e*) and at the level of the IVC (*f*), and immediate postgadolinium GE at the level of the renal hilum (*g*). Neuroblastoma arising from the right adrenal displaces the right kidney inferiorly (*d*, *e*) and surrounds the IVC (arrow, *f*) and right renal hilum (arrow, *g*).The tumor has a multinodular appearance with heterogeneous signal intensity on both T1 (*a*)- and T2 (*b*)-weighted images and peripheral and irregular enhancement on postgadolinium images (*c*, *e*, *f*, *g*).

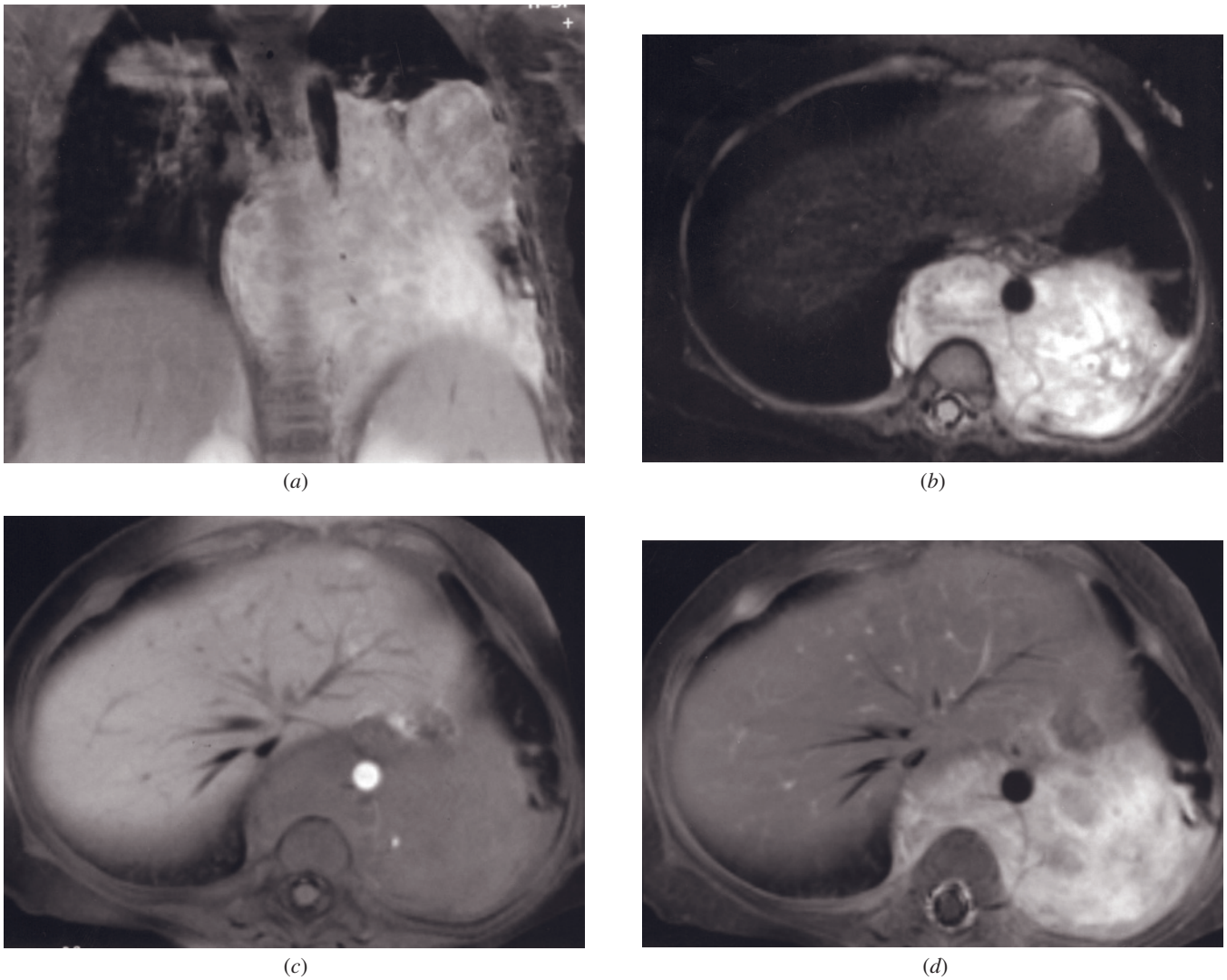

FIG. 8.44 Thoracic neuroblastoma. Coronal T2-weighted echo-train spin-echo of the chest (*a*), T2-weighted fat-suppressed echo-train spin-echo (*b*), T1-weighted GE (*c*), and 90-s fat-suppressed gadolinium-enhanced spin-echo (*d*) images. A large heterogeneously hyperintense mass arises from the left side hemithorax (*a*) and extends into the retrocrural space encasing the descending aorta (*b–d*). After contrast administration, the mass shows diffuse, mildly heterogeneous enhancement on interstitial-phase images (*d*). The posterior mediastinum is the second most common location of neuroblastoma, after adrenal glands.

slightly heterogeneous and high in signal intensity on T2-weighted images [38]. Enhancement with gadolinium is slightly heterogeneous and moderately intense. Adrenal schwannomas (fig. 8.45) can also be seen very rarely.

Lymphoma

Lymphoma occasionally involves the adrenal glands secondarily in patients with disseminated malignant lymphoma. Periadrenal lymphoma has been also reported to mimic an adrenal cortical tumor [84]. The involvement can be uni- or bilateral. Non-Hodgkin lymphoma is the most frequent cell type [85, 86]. Retroperitoneal lymphadenopathy is frequently an associated finding [86]. Signal intensity is intermediate on T1-weighted images and usually intermediate to minimally hyperintense on T2-weighted images. Gadolinium enhancement is variable but is usually minimal on immediate postcontrast images, with increasing enhancement on delayed images (fig. 8.46), which is an enhancement pattern typically observed for lymphoma. Generally, lymphoma enhances throughout its stroma, which reflects the relatively rare occurrence of hemorrhage or necrosis even in large tumors. As with other tumors, if necrosis is present, high signal intensity is observed in this region on T2-weighted images [87], associated with lack of enhancement on postgadolinium images.

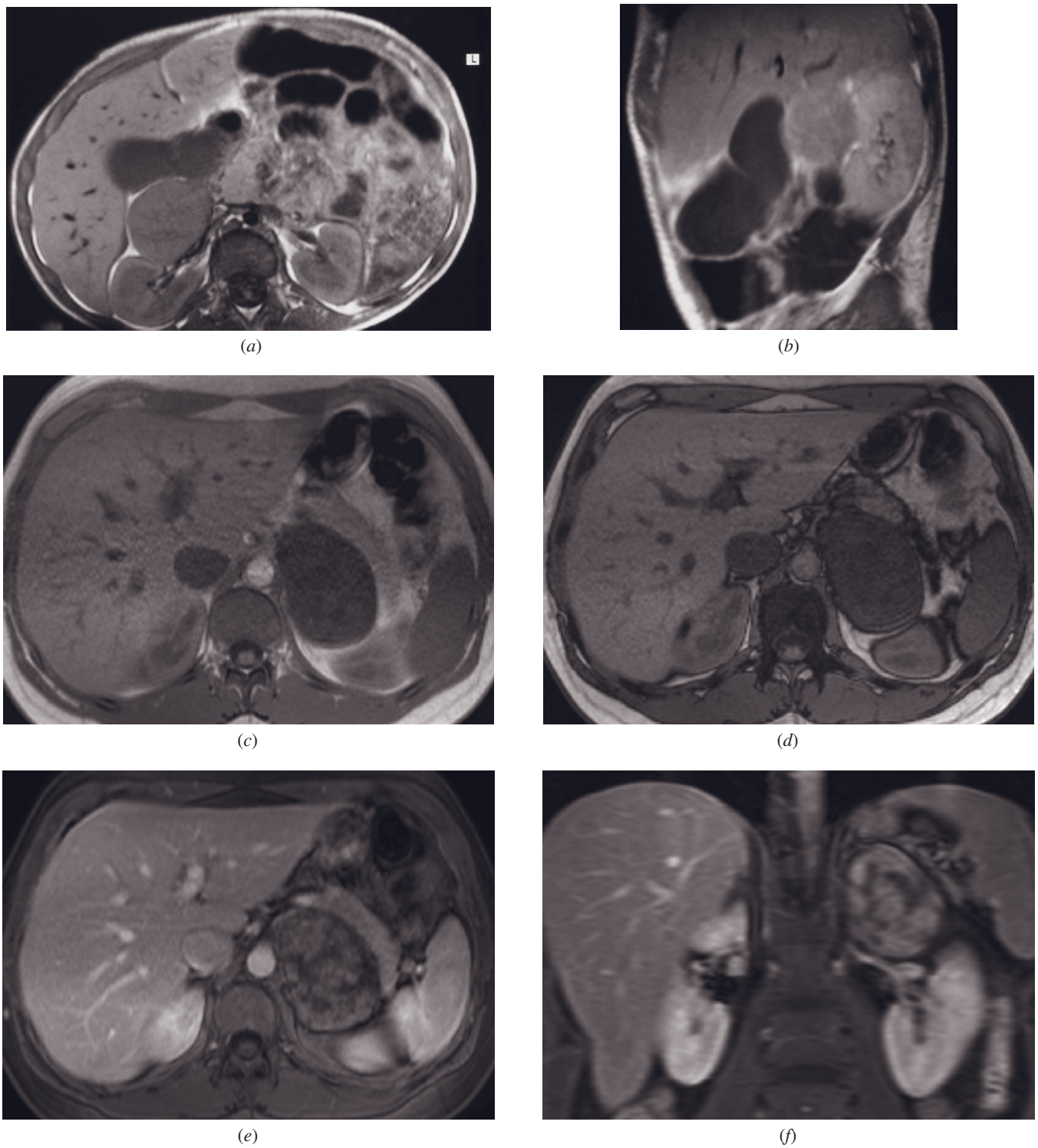

FIG. 8.45 Ganglioneuroblastoma. T1-weighted SE (*a*) and sagittal T1-weighted gadolinium-enhanced SE (*b*) images. A well-defined 3-cm extrarenal mass is identified arising anterior to the upper pole of the right kidney. On the sagittal image, the mass is shown to abut the liver and kidney, with no evidence of invasion. **Schwannoma.** T1-weighted in-phase (*c*) and out-of-phase (*d*) SGE and transverse and coronal T1-weighted postgadolinium interstitial-phase SGE (*e*, *f*) images demonstrate a large heterogeneous mass that does not show signal drop on out-of-phase image and shows heterogeneous enhancement on postgadolinium images. The left adrenal gland is not detected. The diagnosis was schwannoma histopathologically.

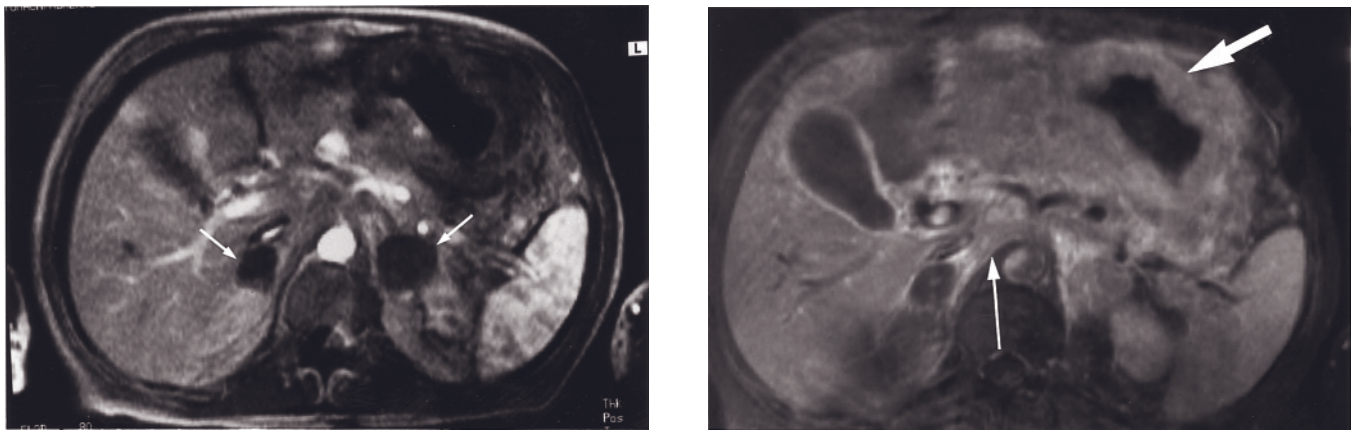

(*a*) (*b*)

FIG. 8.46 Adrenal lymphoma. Immediate postgadolinium GE (*a*) and 4-min fat-suppressed gadolinium-enhanced spin-echo (*b*) images. Minimal enhancement is present of bilateral lymphomatous involvement of the adrenals on the immediate postgadolinium images (arrows, *a*). On the more delayed interstitial-phase images, mild diffuse heterogeneous enhancement is apparent (*b*). On the basis of the immediate postgadolinium images alone, the adrenal masses could be confused with cysts because of the hypovascularity of the tumors. Diffuse gastric wall involvement (large arrow, *b*) and retroperitoneal adenopathy (thin arrow, *b*) are noted.

MISCELLANEOUS

Inflammatory Disease

The adrenal glands may be involved in granulomatous disease, most commonly due to tuberculosis, followed by histoplasmosis and blastomycosis [88–91]. Diffuse enlargement of both adrenal glands is the most common appearance. In rare instances, massive enlargement may be seen. Slight heterogeneity of signal intensity is generally observed on T1- and T2-weighted images [91]. Minimal heterogeneous enhancement on early postgadolinium images, which progresses over time, is also common (fig. 8.47). Signal intensity does not drop on out-of-phase images.

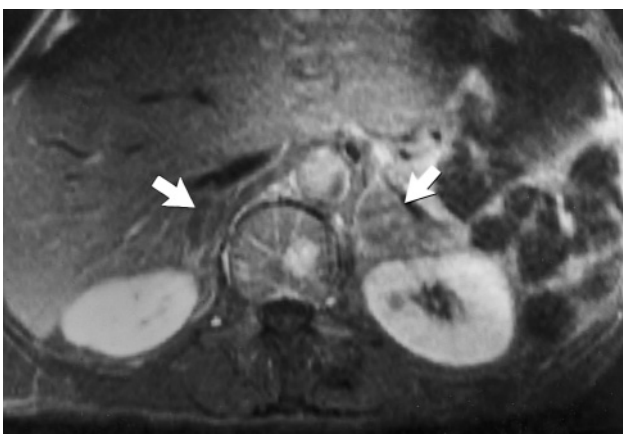

FIG. 8.47 Tuberculosis involvement of the adrenals. Gadolinium-enhanced T1-weighted fat-suppressed spin-echo image demonstrates bilateral adrenal enlargement with heterogeneous mild enhancement (arrows). (Reproduced with permission from Semelka RC, Shoenut JP. The adrenal glands. In Semelka RC, Shoenut JP (eds.). *MRI of the Abdomen with CT Correlation*. New York: Raven Press, p. 77–90, 1993.)

Adrenal Hemorrhage

Adrenal hemorrhage occurs secondary to bleeding diathesis, severe stress, blood loss with resultant hypotension (surgery, childbirth, or sepsis), or trauma [75, 92]. In the setting of primary antiphospholipid syndrome, adrenal infarction may occur with or without MR-detectable hemorrhage, and hemorrhage may extend into the perirenal space [93–95]. Acute awareness of adrenal hemorrhage on tomographic images is important in that clinical findings may be nonspecific and fatal acute adrenal insufficiency may result [96]. MRI is very sensitive for the detection of adrenal hemorrhage and is superior to CT imaging. Subacute hemorrhage is high in signal intensity on T1-weighted images [93, 97–99], and the high signal intensity is more conspicuous on fat-suppressed T1-weighted images (figs. 8.48 and 8.49). Decrease in lesion size over time helps to confirm that the adrenal enlargement is due to hemorrhage (fig. 8.48). In patients after liver transplantation, adrenal hemorrhage may occur and may present as an adrenal mass, which on MRI 3–4 weeks after transplantation is markedly hyperintense on T2-weighted images and demonstrates a hypointense capsule [62].

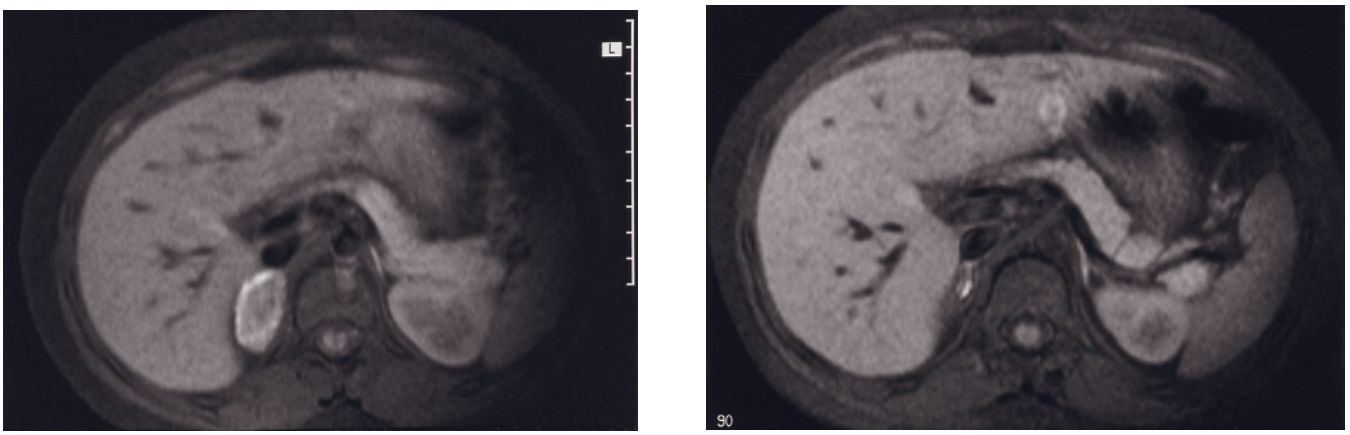

(*a*) (*b*)

FIG. 8.48 Adrenal hemorrhage. T1-weighted fat-suppressed spin-echo image (*a*) and T1-weighted fat-suppressed spin-echo image obtained 7 weeks later (*b*). The T1-weighted fat-suppressed image acquired 1 week after abdominal trauma (*a*) demonstrates a right adrenal mass with a hyperintense peripheral rim. This appearance is classic for a subacute hematoma. Seven weeks later, the mass has diminished in size and remains high in signal intensity because of persistence of extracellular methemoglobin (*b*).

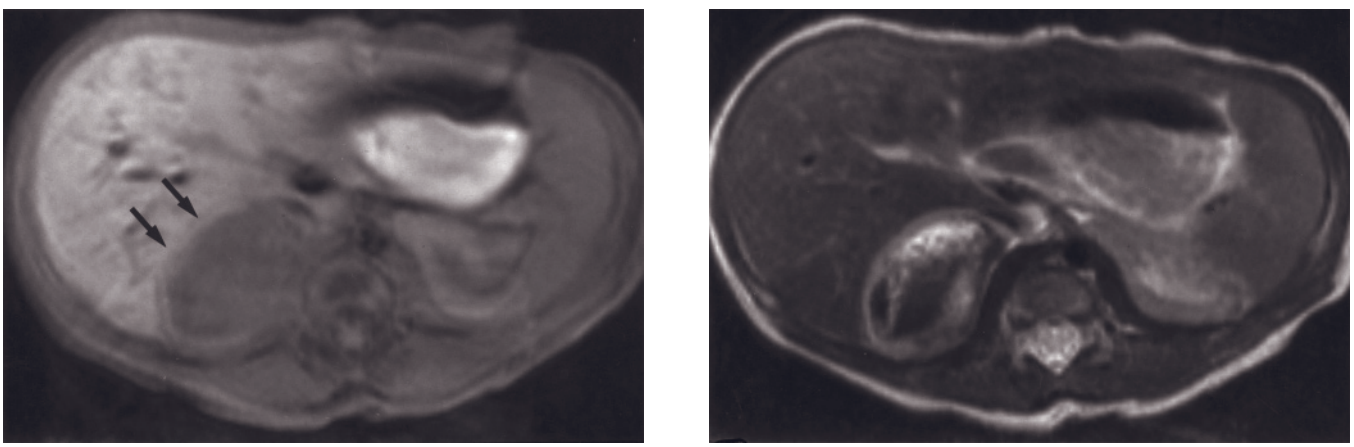

(*a*) (*b*)

FIG. 8.49 Adrenal hemorrhage. T1-weighted fat suppressed GE (*a*) and T2-weighted echo-train spin-echo(*b*) images in a 4-day-old patient. Mass arising from right adrenal is hypointense with a thin hyperintense rim on T1 (*a*) and heterogeneous on T2 (*b*) with hyper- and hypointense areas representing products of hemorrhage. The peripheral high-signal rim on noncontrast T1-weighted fat-suppressed image (arrows, *a*) represents extracellular methemoglobin and is virtually pathognomonic for a subacute hematoma.

Addison Disease

Addison disease results from adrenal insufficiency. The tomographic appearance of the adrenal glands may assist in the diagnosis of the underlying cause [89, 96, 99–101]. Autoimmune disease or pituitary insufficiency is suggested by the presence of atrophic glands [80, 81]. Adrenal hemorrhage may be readily diagnosed by the demonstration of high-signal-intensity substance on T1-weighted images in bilaterally enlarged glands [97–99]. Enlarged glands without hemorrhage suggest granulomatous disease [89]. Metastases may uncommonly result in adrenal insufficiency, and the adrenal glands are massive in this setting.

FUTURE DIRECTIONS

State-of-the-art scanners with phased-array coils permit acquisition of higher-spatial-resolution MR images. MRI of the adrenals may further evolve with the use of parallel imaging techniques, yielding improvement in both spatial and temporal resolution [102].

REFERENCES

1. Reinig JW, Doppman JL, Dwyer AJ et al. Adrenal masses differentiated by MR. *Radiology* 158(1): 81–84, 1986.
2. Reinig JW, Doppman JL, Dwyer AJ et al. MRI of indeterminate adrenal masses. *AJR Am J Roentgenol* 147(3): 493–496, 1986.
3. Chang A, Glazer HS, Lee JK et al. Adrenal gland: MR imaging. *Radiology* 163(1): 123–128, 1987.
4. Baker ME, Blinder R, Spritzer C et al. MR evaluation of adrenal masses at 1.5 T. *AJR Am J Roentgenol* 153(2): 307–312, 1989.
5. Kier R, McCarthy S. MR characterization of adrenal masses: field strength and pulse sequence considerations. *Radiology* 171(3): 671–674, 1989.
6. Krestin GP, Steinbrich W, Friedmann G. Adrenal masses: evaluation with fast gradient-echo MR imaging and Gd-DTPA-enhanced dynamic studies. *Radiology* 171(3): 675–680, 1989.
7. Krestin GP, Freidmann G, Fishbach R et al. Evaluation of adrenal masses in oncologic patients: dynamic contrast-enhanced MR vs. CT. *J Comput Assist Tomogr* 15(1): 104–110, 1991.
8. Semelka RC, Shoenut JP, Lawrence PH et al. Evaluation of adrenal masses with gadolinium enhancement and fat-suppressed MR imaging. *J Magn Reson Imaging* 3(2): 337–343, 1993.
9. Mitchell DG, Crovello M, Matteucci T et al. Benign adrenocortical masses: diagnosis with chemical shift MR imaging. *Radiology* 185(2): 345–351, 1992.
10. Tsushima Y, Ishizaka H, Matsumoto M. Adrenal masses: differentiation with chemical shift, fast low-angle shot MR imaging. *Radiology* 186(3): 705–709, 1993.
11. Reinig JW, Stutley JE, Leonhardt CM et al. Differentiation of adrenal masses with MR imaging: comparison of techniques. *Radiology* 192(1): 41–46, 1994.
12. Lee MJ, Mayo-Smith WW, Hahn PF et al. State-of-the-art MR imaging of the adrenal gland. *Radiographics* 14(5): 1015–1029; discussion 1029–1032, 1994.
13. Bilbey JH, McLoughlin RF, Kurkjian PS et al. MR imaging of adrenal masses: value of chemical-shift imaging for distinguishing adenomas from other tumors. *AJR Am J Roentgenol* 164(3): 637–642, 1995.
14. Korobkin M, Dunnick NR. Characterization of adrenal masses. *AJR Am J Roentgenol* 164(3): 643–644, 1995.
15. Outwater EK, Siegelman ES, Huang AB et al. Adrenal masses: correlation between CT attenuation value and chemical shift ratio at MR imaging with in-phase and opposed-phase sequences. *Radiology* 200(3): 749–752, 1996.
16. Mayo-Smith WW, Lee MJ, McNicholas MM et al. Characterization of adrenal masses (<5 cm) by use of chemical shift MR imaging: observer performance versus quantitative measures. *AJR Am J Roentgenol* 165(1): 91–95, 1995.
17. Outwater EK, Siegelman ES, Radecki PD et al. Distinction between benign and malignant adrenal masses: value of T1-weighted chemical-shift MR imaging. *AJR Am J Roentgenol* 165(3): 579–583, 1995.
18. Korobkin M, Lombardi TJ, Aisen AM et al. Characterization of adrenal masses with chemical shift and gadolinium-enhanced MR imaging. *Radiology* 197(2): 411–418, 1995.
19. McNicholas MM, Lee MJ, Mayo-Smith WW et al. An imaging algorithm for the differential diagnosis of adrenal adenomas and metastases. *AJR Am J Roentgenol* 165(6): 1453–1459, 1995.
20. Korobkin M, Giordano TJ, Brodeur FJ et al. Adrenal adenomas: relationship between histologic lipid and CT and MR findings. *Radiology* 200(3): 743–747, 1996.
21. Schwartz LH, Panicek DM, Koutcher JA et al. Echoplanar MR imaging for characterization of adrenal masses in patients with malignant neoplasms: preliminary evaluation of calculated T2 relaxation values. *AJR Am J Roentgenol* 164(4): 911–915, 1995.
22. Haider MA, Ghai S, Jhaveri K et al. Chemical shift MR imaging of hyperattenuating (>10 HU) adrenal masses: does it still have a role? *Radiology* 231(3): 711–716, 2004.
23. Namimoto T, Yamashita Y, Mitsuzaki K et al. Adrenal masses: quantification of fat content with double-echo chemical shift in-phase and opposed-phase FLASH MR images for differentiation of adrenal adenomas. *Radiology* 218(3): 642–646, 2001.
24. Gabriel H, Pizzitola V, McComb EN et al. Adrenal lesions with heterogeneous suppression on chemical shift imaging: clinical implications. *J Magn Reson Imaging* 19(3): 308–316, 2004.
25. Mitchell DG, Nascimento AB, Alam F et al. Normal adrenal gland: in vivo observations, and high-resolution in vitro chemical shift MR imaging—histologic correlation. *Acad Radiol* 9(4): 430–436, 2002.
26. Fujiyoshi F, Nakajo M, Fukukura Y et al. Characterization of adrenal tumors by chemical shift fast low-angle shot MR imaging: comparison of four methods of quantitative evaluation. *AJR Am J Roentgenol* 180(6): 1649–1657, 2003.
27. Outwater EK, Mitchell DG. Differentiation of adrenal masses with chemical shift MR imaging. *Radiology* 193(3): 877–878, 1994.
28. Merkle EM, Schindera ST. MR imaging of the adrenal glands: 1.5 T versus 3 T. *Magn Reson Imaging Clin N Am* 15(3): 365–372, vii, 2007.
29. Yamada T, Saito H, Moriya T et al. Adrenal carcinoma with a signal loss on chemical shift magnetic resonance imaging. *J Comput Assist Tomogr* 27(4): 606–608, 2003.
30. Shinozaki K, Yoshimitsu K, Honda H et al. Metastatic adrenal tumor from clear-cell renal cell carcinoma: a pitfall of chemical shift MR imaging. *Abdom Imaging* 26(4): 439–442, 2001.
31. Schlund JF, Kenney PJ, Brown ED et al. Adrenocortical carcinoma: MR imaging appearance with current techniques. *J Magn Reson Imaging* 5(2): 171–174, 1995.
32. Ferrozzi F, Bova D. CT and MR demonstration of fat within an adrenal cortical carcinoma. *Abdom Imaging* 20(3): 272–274, 1995.
33. Sato N, Watanabe Y, Saga T et al. Adrenocortical adenoma containing a fat component: CT and MR image evaluation. *Abdom Imaging* 20(5): 489–490, 1995.
34. Chung JJ, Semelka RC, Martin DR. Adrenal adenomas: characteristic postgadolinium capillary blush on dynamic MR imaging. *J Magn Reson Imaging* 13(2): 242–248, 2001.
35. Small WC, Bernardino ME. Gd-DTPA adrenal gland enhancement at 1.5 T. *Magn Reson Imaging* 9(3): 309–312, 1991.
36. Goncalves Neto JA, Altun E, Vaidean G et al. Early contrast enhancement of the liver: exact description of subphases using MRI. *Magn Reson Imaging* 2009.
37. Falke TH, te Strake L, Shaff MI et al. MR imaging of the adrenals: correlation with computed tomography. *J Comput Assist Tomogr* 10(2): 242–253, 1986.
38. McLoughlin RF, Bilbey JH. Tumors of the adrenal gland: findings on CT and MR imaging. *AJR Am J Roentgenol* 163(6): 1413–1418, 1994.
39. Rockall AG, Babar SA, Sohaib SA et al. CT and MR imaging of the adrenal glands in ACTH-independent Cushing syndrome. *Radiographics* 24(2): 435–452, 2004.
40. Matsuda T, Abe H, Takase M et al. Case of combined adrenal cortical adenoma and myelolipoma. *Pathol Int* 54(9): 725–729, 2004.
41. Newhouse JH, Heffess CS, Wagner BJ et al. Large degenerated adrenal adenomas: radiologic-pathologic correlation. *Radiology* 210(2): 385–391, 1999.
42. Ichikawa T, Ohtomo K, Uchiyama G et al. Adrenal adenomas: characteristic hyperintense rim sign on fat-saturated spin-echo MR images. *Radiology* 193(1): 247–250, 1994.

43. Kelekis NL, Alexopoulou E, Brountzos EN et al. Giant adrenal myelolipoma with minimal fat content in a patient with homozygous beta-thalassemia: appearance on MRI. *J Magn Reson Imaging* 18(5): 608–611, 2003.
44. Sohaib SA, Peppercorn PD, Allan C et al. Primary hyperaldosteronism (Conn syndrome): MR imaging findings. *Radiology* 214(2): 527–531, 2000.
45. Israel GM, Korobkin M, Wang C et al. Comparison of unenhanced CT and chemical shift MRI in evaluating lipid-rich adrenal adenomas. *AJR Am J Roentgenol* 183(1): 215–219, 2004.
46. Dunnick NR, Doppman JL, Gill JR Jr. et al. Localization of functional adrenal tumors by computed tomography and venous sampling. *Radiology* 142(2): 429–433, 1982.
47. Ikeda DM, Francis IR, Glazer GM et al. The detection of adrenal tumors and hyperplasia in patients with primary aldosteronism: comparison of scintigraphy, CT, and MR imaging. *AJR Am J Roentgenol* 153(2): 301–306, 1989.
48. Lingam RK, Sohaib SA, Rockall AG et al. Diagnostic performance of CT versus MR in detecting aldosterone-producing adenoma in primary hyperaldosteronism (Conn's syndrome). *Eur Radiol* 14(10): 1787–1792, 2004.
49. Grant CS, Carpenter P, van Heerden JA et al. Primary aldosteronism. Clinical management. *Arch Surg* 119(5): 585–590, 1984.
50. Doppman JL, Gill JR Jr., Miller DL et al. Distinction between hyperaldosteronism due to bilateral hyperplasia and unilateral aldosteronoma: reliability of CT. *Radiology* 184(3): 677–682, 1992.
51. Dieckmann KP, Hamm B, Pickartz H et al. Adrenal myelolipoma: clinical, radiologic, and histologic features. *Urology* 29(1): 1–8, 1987.
52. Rao P, Kenney PJ, Wagner BJ et al. Imaging and pathologic features of myelolipoma. *Radiographics* 17(6): 1373–1385, 1997.
53. Otal P, Escourrou G, Mazerolles C et al. Imaging features of uncommon adrenal masses with histopathologic correlation. *Radiographics* 19(3): 569–581, 1999.
54. Krebs TL, Wagner BJ. MR imaging of the adrenal gland: radiologic-pathologic correlation. *Radiographics* 18(6): 1425–1440, 1998.
55. Palmer WE, Gerard-McFarland EL, Chew FS. Adrenal myelolipoma. *AJR Am J Roentgenol* 156(4): 724, 1991.
56. Musante F, Derchi LE, Bazzocchi M et al. MR imaging of adrenal myelolipomas. *J Comput Assist Tomogr* 15(1): 111–114, 1991.
57. Liessi G, Cesari S, Dell'Antoni C et al. US, CT, MR and percutaneous biopsy of adrenal myelolipomas. *Eur Radiol* (5): 152–155, 1995.
58. Mitchell DG, Outwater EK, Matteucci T et al. Adrenal gland enhancement at MR imaging with Mn-DPDP. *Radiology* 194(3): 783–787, 1995.
59. Casey LR, Cohen AJ, Wile AG et al. Giant adrenal myelolipomas: CT and MRI findings. *Abdom Imaging* 19(2): 165–167, 1994.
60. Cyran KM, Kenney PJ, Memel DS et al. Adrenal myelolipoma. *AJR Am J Roentgenol* 166(2): 395–400, 1996.
61. Aisen AM, Ohl DA, Chenevert TL et al. MR of an adrenal pseudocyst. *Magn Reson Imaging* 10(6): 997–1000, 1992.
62. Prokesch RW, Schima W, Berlakovich G et al. Adrenal hemorrhage after orthotopic liver transplantation: MR appearance. *Eur Radiol* 11(12): 2484–2487, 2001.
63. Hamrick-Turner JE, Cranston PE, Shipkey FH. Cavernous hemangioma of the adrenal gland: MR findings. *Magn Reson Imaging* 12(8): 1263–1267, 1994.
64. Yamada T, Ishibashi T, Saito H et al. Two cases of adrenal hemangioma: CT and MRI findings with pathological correlations. *Radiat Med* 20(1): 51–56, 2002.
65. DeAtkine AB, Dunnick NR. The adrenal glands. *Semin Oncol* 18(2): 131–139, 1991.
66. Silverman SG, Mueller PR, Pinkney LP et al. Predictive value of image-guided adrenal biopsy: analysis of results of 101 biopsies. *Radiology* 187(3): 715–718, 1993.
67. Honigschnabl S, Gallo S, Niederle B et al. How accurate is MR imaging in characterisation of adrenal masses: update of a long-term study. *Eur J Radiol* 41(2): 113–122, 2002.
68. Belldegrun A, Hussain S, Seltzer SE et al. Incidentally discovered mass of the adrenal gland. *Surg Gynecol Obstet* 163(3): 203–208, 1986.
69. Mitnick JS, Bosniak MA, Megibow AJ et al. Non-functioning adrenal adenomas discovered incidentally on computed tomography. *Radiology* 148(2): 495–499, 1983.
70. Rosai J. Chapter 16. Adrenal gland and other paraganglia. In: Rosai J, editor. *Rosai and Ackerman's Surgical Pathology.* 9th ed. Edinburgh: Mosby; 1996. p. 1119–1126.
71. Weissleder R, Wang YM, Papisov M et al. Polymeric contrast agents for MR imaging of adrenal glands. *J Magn Reson Imaging* 3(1): 93–97, 1993.
72. Custodio CM, Semelka RC, Balci NC et al. Adrenal neuroblastoma in an adult with tumor thrombus in the inferior vena cava. *J Magn Reson Imaging* 9(4): 621–623, 1999.
73. Smith SM, Patel SK, Turner DA et al. Magnetic resonance imaging of adrenal cortical carcinoma. *Urol Radiol* 11(1): 1–6, 1989.
74. Tisnado J, Amendola MA, Konerding KF et al. Computed tomography versus angiography in the localization of pheochromocytoma. *J Comput Assist Tomogr* 4(6): 853–859, 1980.
75. Thomas JL, Bernardino ME. Pheochromocytoma in multiple endocrine adenomatosis. Efficacy of computer tomography. *JAMA* 245(14): 1467–1469, 1981.
76. Nguyen L, Niccoli-Sire P, Caron P et al. Pheochromocytoma in multiple endocrine neoplasia type 2: a prospective study. *Eur J Endocrinol* 144(1): 37–44, 2001.
77. Bush WH, Elder JS, Crane RE et al. Cystic pheochromocytoma. *Urology* 25(3): 332–334, 1985.
78. Crecelius SA, Bellah R. Pheochromocytoma of the bladder in an adolescent: sonographic and MR imaging findings. *AJR Am J Roentgenol* 165(1): 101–103, 1995.
79. Belden CJ, Powers C, Ros PR. MR demonstration of a cystic pheochromocytoma. *J Magn Reson Imaging* 5(6): 778–780, 1995.
80. Westra SJ, Zaninovic AC, Hall TR et al. Imaging of the adrenal gland in children. *Radiographics* 14(6): 1323–1340, 1994.
81. Feinstein RS, Gatewood OM, Fishman EK et al. Computed tomography of adult neuroblastoma. *J Comput Assist Tomogr* 8(4): 720–726, 1984.
82. Tateishi U, Hasegawa T, Makimoto A et al. Adult neuroblastoma: radiologic and clinicopathologic features. *J Comput Assist Tomogr* 27(3): 321–326, 2003.
83. Rha SE, Byun JY, Jung SE et al. Neurogenic tumors in the abdomen: tumor types and imaging characteristics. *Radiographics* 23(1): 29–43, 2003.
84. Carnat T, Mai KT, Burns BF. Peri-adrenal malignant lymphoma masquerading as adrenal cortical neoplasm. *Pathology* 36(3): 278–279, 2004.
85. Paling MR, Williamson BR. Adrenal involvement in non-Hodgkin lymphoma. *AJR Am J Roentgenol* 141(2): 303–305, 1983.
86. Glazer HS, Lee JK, Balfe DM et al. Non-Hodgkin lymphoma: computed tomographic demonstration of unusual extranodal involvement. *Radiology* 149(1): 211–217, 1983.
87. Lee FT, Jr., Thornbury JR, Grist TM et al. MR imaging of adrenal lymphoma. *Abdom Imaging* 18(1): 95–96, 1993.
88. Hauser H, Gurret JP. Miliary tuberculosis associated with adrenal enlargement: CT appearance. *J Comput Assist Tomogr* 10(2): 254–256, 1986.
89. Sawczuk IS, Reitelman C, Libby C et al. CT findings in Addison's disease caused by tuberculosis. *Urol Radiol* 8(1): 44–45, 1986.

90. Wilson DA, Muchmore HG, Tisdal RG et al. Histoplasmosis of the adrenal glands studied by CT. *Radiology* 150(3): 779–783, 1984.
91. Kumar N, Singh S, Govil S. Adrenal histoplasmosis: clinical presentation and imaging features in nine cases. *Abdom Imaging* 28(5): 703–708, 2003.
92. Xarli VP, Steele AA, Davis PJ et al. Adrenal hemorrhage in the adult. *Medicine (Baltimore)* 57(3): 211–221, 1978.
93. Provenzale JM, Ortel TL, Nelson RC. Adrenal hemorrhage in patients with primary antiphospholipid syndrome: imaging findings. *AJR Am J Roentgenol* 165(2): 361–364, 1995.
94. Riddell AM, Khalili K. Sequential adrenal infarction without MRI-detectable hemorrhage in primary antiphospholipid-antibody syndrome. *AJR Am J Roentgenol* 183(1): 220–222, 2004.
95. Berneis K, Buitrago-Tellez C, Muller B et al. Antiphospholipid syndrome and endocrine damage: why bilateral adrenal thrombosis? *Eur J Haematol* 71(4): 299–302, 2003.
96. Wolverson MK, Kannegiesser H. CT of bilateral adrenal hemorrhage with acute adrenal insufficiency in the adult. *AJR Am J Roentgenol* 142(2): 311–314, 1984.
97. Koch KJ, Cory DA. Simultaneous renal vein thrombosis and bilateral adrenal hemorrhage: MR demonstration. *J Comput Assist Tomogr* 10(4): 681–683, 1986.
98. Brill PW, Jagannath A, Winchester P et al. Adrenal hemorrhage and renal vein thrombosis in the newborn: MR imaging. *Radiology* 170(1 Pt 1): 95–98, 1989.
99. Wilms G, Tits J, Vanstraelen D et al. Addison's disease due to bilateral post-traumatic adrenal hemorrhage: CT and MR findings. *Eur Radiol* 1: 172–174, 1991.
100. Doppman JL, Gill JR Jr., Nienhuis AW et al. CT findings in Addison's disease. *J Comput Assist Tomogr* 6(4): 757–761, 1982.
101. McMurry JF Jr., Long D, McClure R et al. Addison's disease with adrenal enlargement on computed tomographic scanning. Report on two cases of tuberculosis and review of the literature. *Am J Med* 77(2): 365–368, 1984.
102. Boll DT, Hillenbrand CM, Lewin JS et al. Assessment of parallel acquisition techniques in adrenal magnetic resonance imaging: does increased temporal resolution significantly improve visualization of adrenal lesions? *Acad Radiol* 11(7): 809–816, 2004.

CHAPTER 9

KIDNEYS

LARISSA BRAGA, ERSAN ALTUN, JORGE ELIAS, JR., DIEGO R. MARTIN, SANG SOO SHIN, AND RICHARD C. SEMELKA

NORMAL ANATOMY

The kidneys are paired organs that lie in the retroperitoneum. They are situated within the perirenal space, which contains abundant fat. Kidney and adipose tissue together are enclosed within renal fascia that is called the Gerota fascia posteriorly and the Zuckerlandl fascia anteriorly. The kidney is surrounded by a fibroelastic capsule, usually not visible on tomographic images. The renal capsule is connected to the perirenal fascia through fibrous trabeculae that traverse perirenal fat. At the lateral renal borders, the anterior and posterior fascial layers fuse to form the lateroconal fascia. Superiorly the fascia fuse, whereas inferiorly they are open, forming a potential communication with the anterior and posterior pararenal spaces. Anterior pararenal space is located between anterior perirenal fascia and posterior parietal peritoneum, while posterior pararenal space is located between posterior pararenal fascia and transversalis fascia.

The medial surface of the kidney shows the hilum containing vessels, nerves, and the renal pelvis of the ureter. The hilum leads into a larger space, or renal sinus, containing the calyces, vessels, and fat. The renal parenchyma contains an external cortex and internal medulla. The cortex contains glomeruli and convoluted tubules. The medulla contains convoluted tubules and is seen as conical structures or pyramids.

The cortex arches over the bases of the pyramids and extends between them toward the renal sinus as the renal column of Bertin. The apices of the renal pyramids converge to the renal sinus, where they project into calyces as papillae.

MRI TECHNIQUE

The basic MRI examination of the kidneys involves non-fat-suppressed and fat-suppressed single-shot echo-train spin-echo T2-weighted sequences with pre- and postgadolinium T1-weighted 2D-SGE or 3D-GRE images acquired as non-fat-suppressed and fat-suppressed sequences. The first set of postgadolinium images should be acquired as an immediate postgadolinium hepatic arterial phase or capillary-phase SGE or 3D-GRE sequence. A diagnostically useful protocol is as follows:

Abdominal-Pelvic MRI, Third Edition, edited by Richard C. Semelka. Copyright © 2010 John Wiley & Sons, Inc.

1) coronal T2-weighted single-shot echo-train spin-echo; 2) transverse non-fat-suppressed and fat-suppressed T2-weighted single-shot echo-train spin-echo; 3) transverse precontrast T1-weighted breath-hold in-phase and out-of-phase SGE; 4) transverse precontrast breath-hold T1-weighted fat-suppressed SGE or 3D-GRE; 5) transverse dynamic capillary-phase gadolinium-enhanced T1-weighted SGE or 3D-GRE; and 6) transverse, coronal, and sagittal gadolinium-enhanced interstitial-phase T1-weighted fat-suppressed SGE or 3D-GRE techniques (fig. 9.1) [1].

Pre- and postcontrast image acquisition in the sagittal or coronal plane frequently is helpful to 1) evaluate the superior and inferior borders of renal lesions; 2) characterize lesions as cystic or solid; or 3) demonstrate renal/perirenal location and extension. The advantage

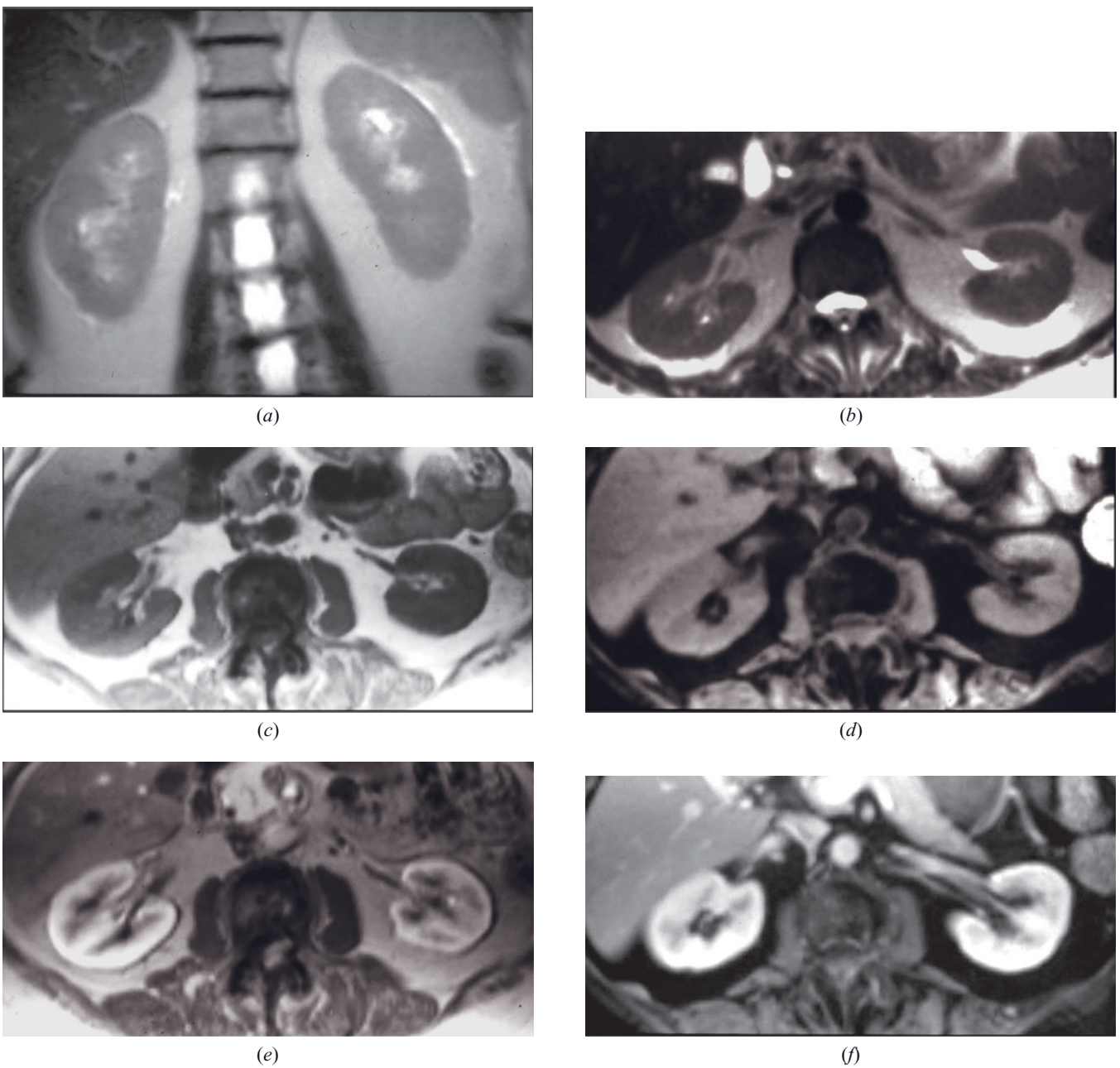

FIG. 9.1 Normal kidneys. Coronal (*a*) and transverse (*b*) T2-weighted SS-ETSE, T1-weighted gradient-echo (*c*), T1-weighted fat-suppressed gradient-echo (*d*), immediate postgadolinium gradient-echo (*e*), and axial (*f*) and sagittal (*g*) interstitial-phase fat-suppressed postgadolinium T1-weighted gradient-echo images. Corticomedullary differentiation is best seen on pregadolinium

(*g*)

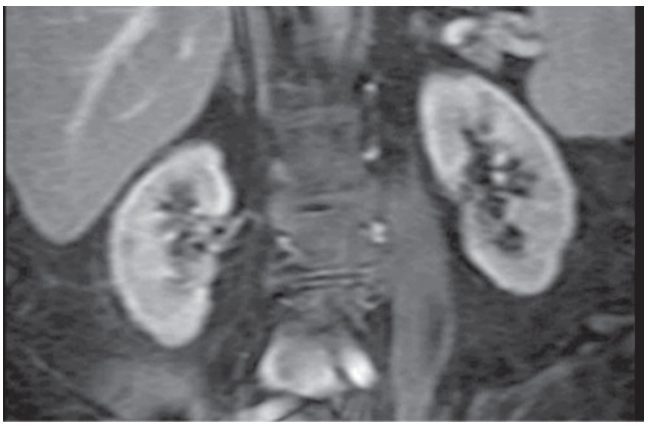

(*h*)

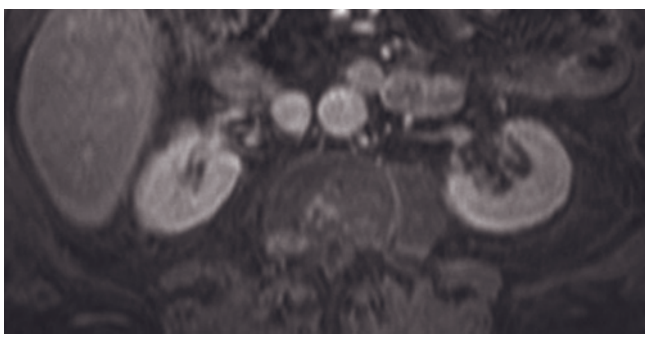

(*i*)

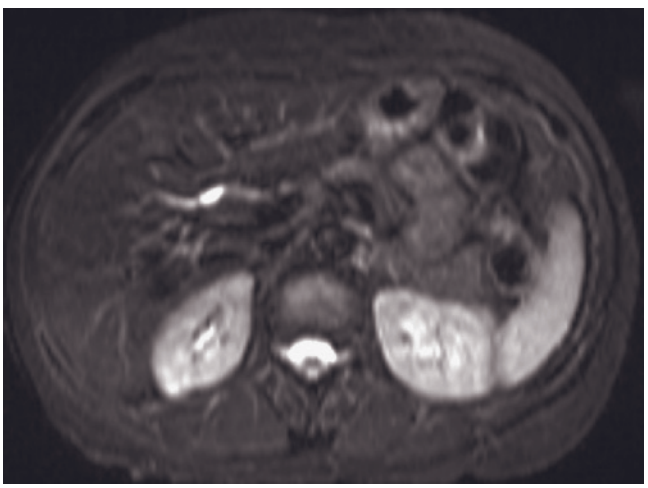

(*j*)

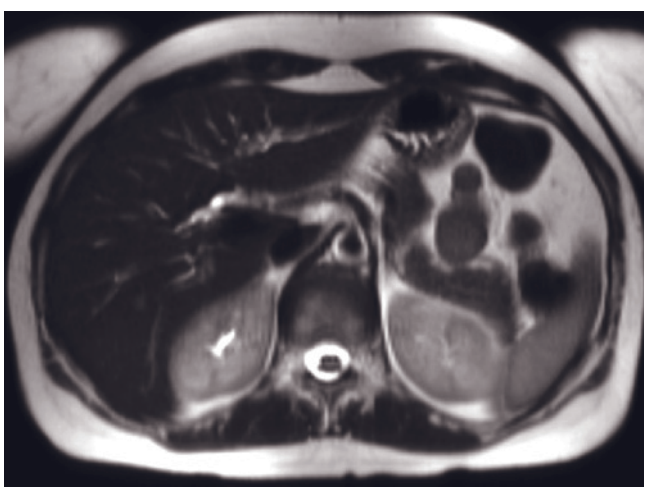

(*k*)

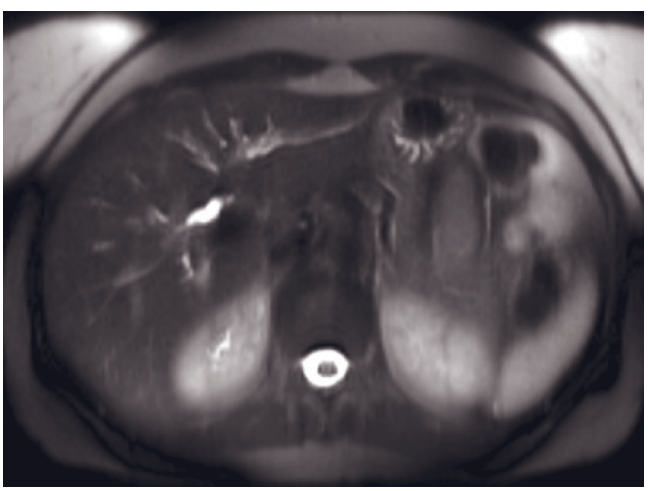

(*l*)

FIG. 9.1 (*Continued*) fat-suppressed T1-weighted images (*d*) and immediate postgadolinium images (*e*). The sagittal plane is effective at showing small lesions in the polar regions of the kidneys. Coronal (*h*) and transverse (*i*) interstitial-phase 3D gradient-echo images in a second patient. 3D gradient echo allows multiplanar reconstruction and is particularly well suited for display of vascular structures, because of the thin slice thickness. T2-weighted short tau inversion recovery (*j*), T2-weighted non-fat-suppressed (*k*) and fat-suppressed (*l*) single-shot echo-train spin-echo, T1-weighted spoiled gradient-echo (SGE) in-phase (*m*) and

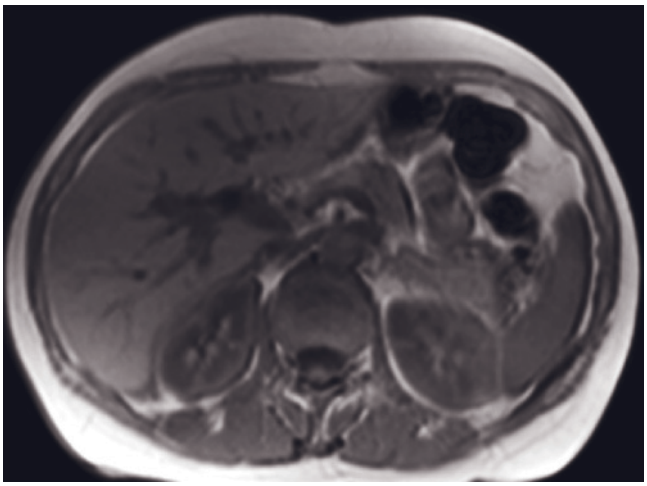

(*m*)

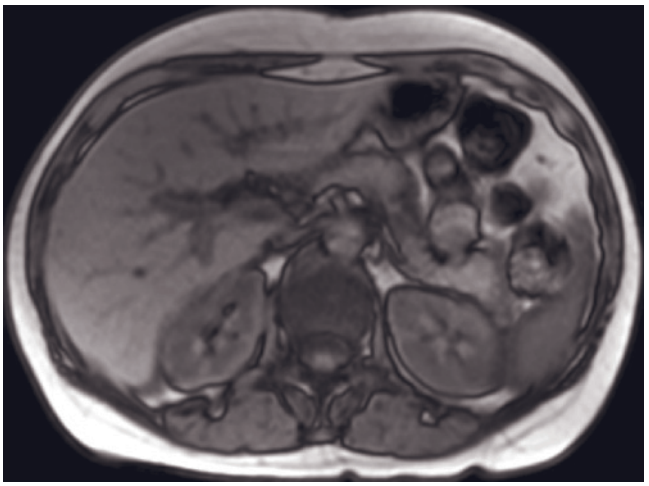

(*n*)

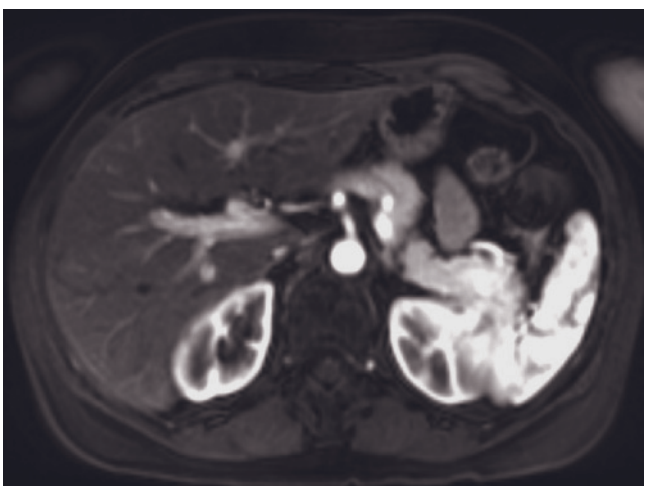

(*o*)

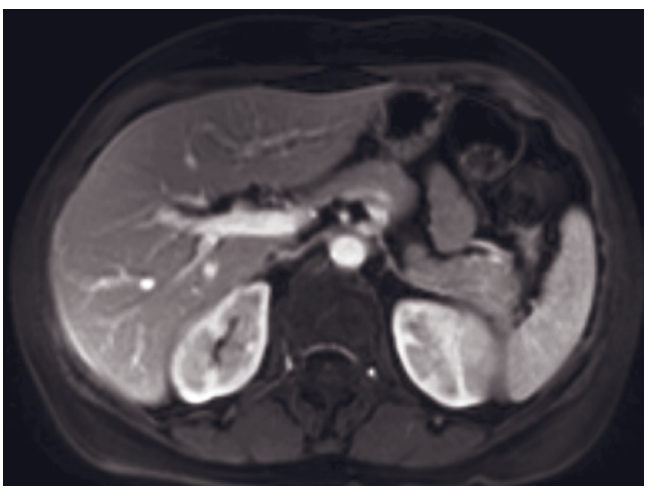

(*p*)

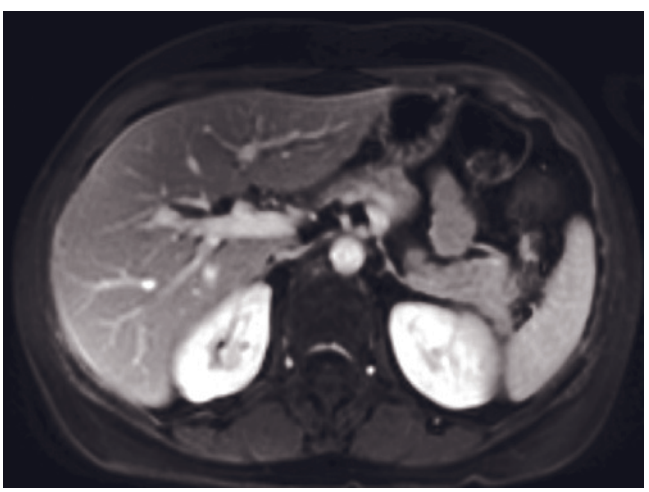

(*q*)

FIG. 9.1 (*Continued*) out-of-phase (*n*), and T1-weighted postgadolinium hepatic arterial dominant-phase (*o*), hepatic venous-phase (*p*), and interstitial-phase (*q*) fat-suppressed 3D-GE images at 3.0 T demonstrate the kidneys in another normal patient with high image quality. The image quality of postgadolinium 3D-GE images is particularly very good. However, the corticomedullary signal difference is not as strong at 3.0 T compared to that at 1.5 T, because of lower contrast resolution of SGE sequences at 3.0 T.

of using a 3D-GRE technique is that it permits acquisition of data in one plane (e.g., coronal or axial) and reconstruction in other planes. 3D-GRE sequences should be preferred in state-of-art MR systems.

MR angiography (MRA) has achieved diagnostically sufficient image quality to reproducibly demonstrate main renal arterial disease (fig. 9.2) [2, 3]. 3D-GRE images may also serve as an MRA sequence, although for detailed vascular studies a dedicated MRA technique (thin-section 3D-GE MRA sequence) may be necessary. Reproducible demonstration of intraparenchymal small vessel disease has not yet been realized.

The echo-train spin-echo (ETSE) technique may be tailored to generate an MR urogram effect, which in early reports has been shown to be effective at elucidating causes of a dilated renal collecting system [4]. Temporal changes in signal intensity of renal cortex and medulla following contrast injection provide information on renal function [5–7]. The ability to generate diverse imaging information on tissue morphology, renal vessels, collecting system, and function renders MRI a comprehensive diagnostic modality for investigating renal disease [8]. Images acquired at 10–15 min after gadolinium may be obtained by using 3D-GRE to create a contrast-enhanced urographic picture.

Gadolinium chelates are freely filtered by renal glomeruli and undergo excretion by renal tubules with no tubular reabsorption or excretion [9]. Because of this elimination pathway, gadolinium chelates are ideal for studying morphology and function of the kidneys. Gadolinium possesses the additional property of changing signal intensity based on concentration. When dilute, gadolinium shortens T1 relaxation and renders urine high in signal intensity. When concentrated, gadolinium induces magnetic susceptibility and signal intensity loss, causing urine to be low in signal intensity [5–7]. The concentrating ability of the kidneys can be evaluated by gadolinium-enhanced MRI, a property that cannot be assessed by dynamic iodine enhanced CT imaging.

3.0 T MR systems have improved the ability of MR imaging by increasing signal-to-noise ratio. Higher signal-to-noise ratio can be translated into higher spatial

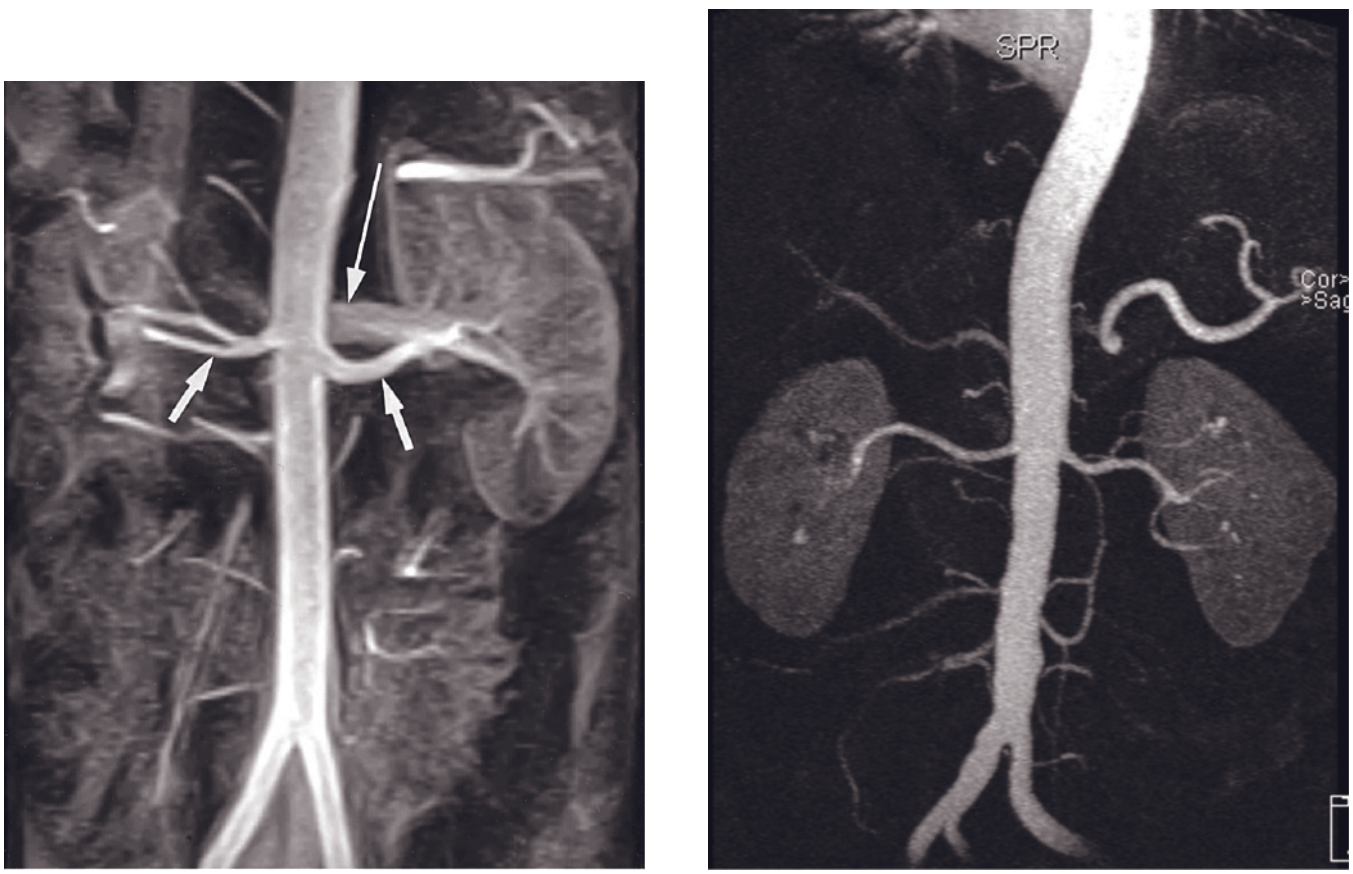

(*a*) (*b*)

FIG. 9.2 MRA of normal kidneys. Coronal MIP of bolus gadolinium-enhanced 3D gradient-echo image (*a*) demonstrates normal renal arteries in sharp detail (arrows). The left renal vein is also opacified (long arrow, *a*). Coronal 3D MIP reconstruction of gadolinium-enhanced source images (*b*) in a second patient demonstrates normal renal arteries with intrarenal branches visualized.

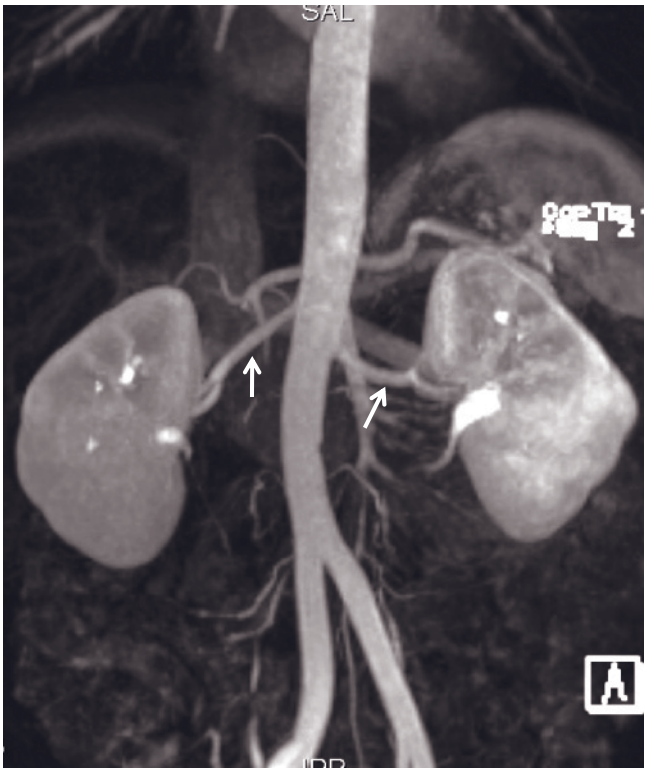

(*c*)

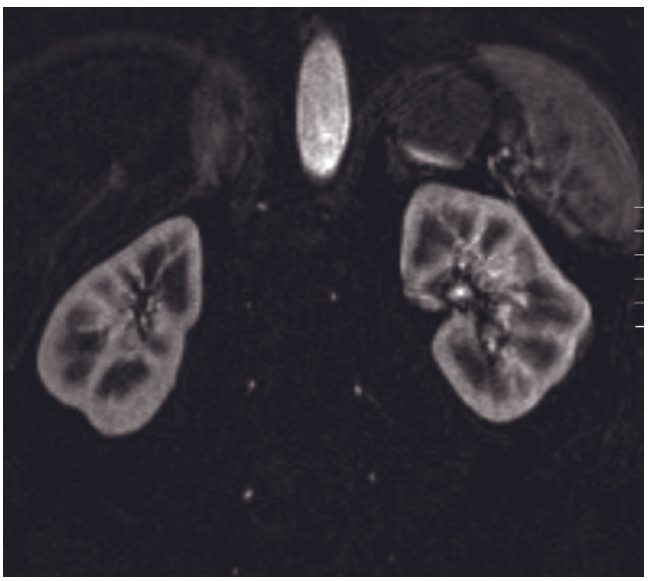

(*d*)

(*e*)

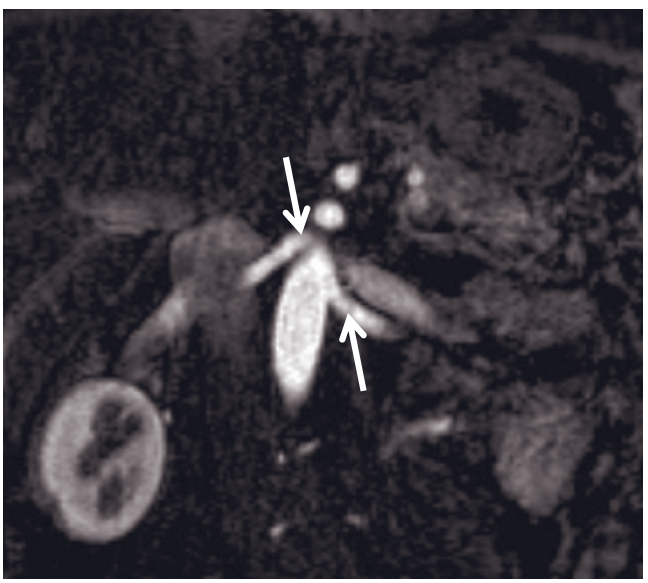

(*f*)

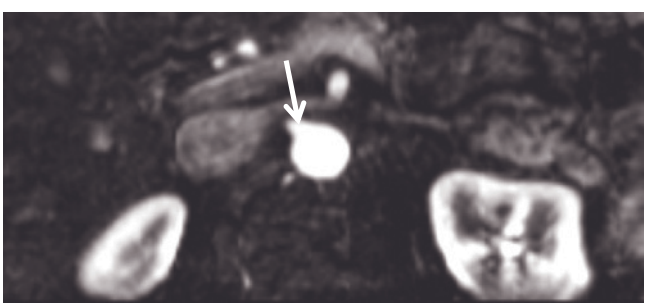

(*g*)

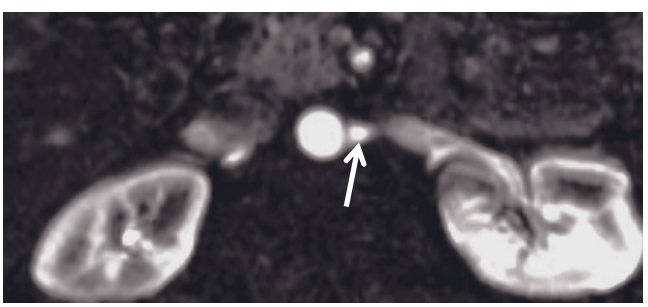

(*h*)

FIG. 9.2 (*Continued*) Coronal 3D reconstructed MIP image of postgadolinium 3D-GE MRA image (*c*), coronal thin-section 3D-GE MRA source images (*d–f*), and transverse thin-section reformatted 3D-GE MRA images (*g*, *h*) at 3.0 T demonstrate bilateral normal renal arteries (arrows, *c*, *e*) and their ostia (arrows, *f–h*) in another patient.

and temporal resolution. Higher spatial and temporal resolution allows acquiring thinner and higher matrix images faster. These advantages may facilitate the detection of small focal lesions or subtle diffuse processes on MRI and MRA images.

NORMAL VARIANTS AND CONGENITAL ANOMALIES

Initially in utero, the kidneys are located in the pelvis, but through growth of the caudal region of the embryo they "ascend" to the abdomen. About 10% of the population is born with potentially significant malformations of the urinary tract [10]. The organogenesis of the kidney is complex, and a diverse array of anomalies affects the urinary tract. The majority relate to abnormalities of renal position (fig. 9.3), form, mass, and number.

Prominent columns of Bertin are frequently observed in kidneys, and it may be difficult to distinguish these from renal masses on other imaging modalities. Columns will follow the signal intensity of renal cortex on all pre- and postgadolinium images. An important observation is that on immediate postgadolinium images the column enhances to the same extent as renal cortex and follows a smooth, continuous contour with cortex. On more delayed images, the enhancement of the column remains isointense with cortex (fig. 9.4).

Persistent fetal lobulation is another common normal variant. Coronal images demonstrate the undulating contour of the kidney. Immediate postgadolinium images show uniform cortical thickness, which excludes the presence of a mass (fig. 9.5).

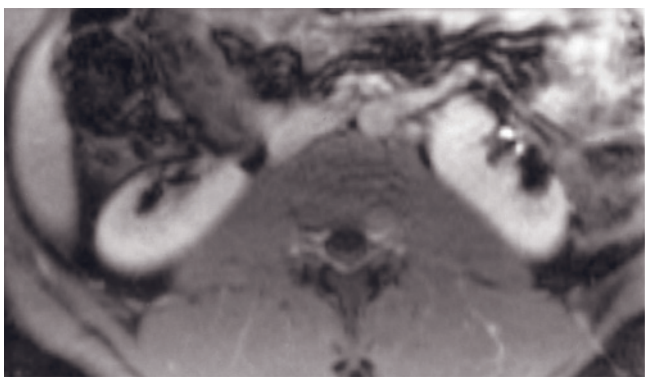

FIG. 9.3 Malrotation. T1-weighted fat-suppressed postgadolinium SGE image. The most common form of malrotation is anterior orientation of the pelvis.

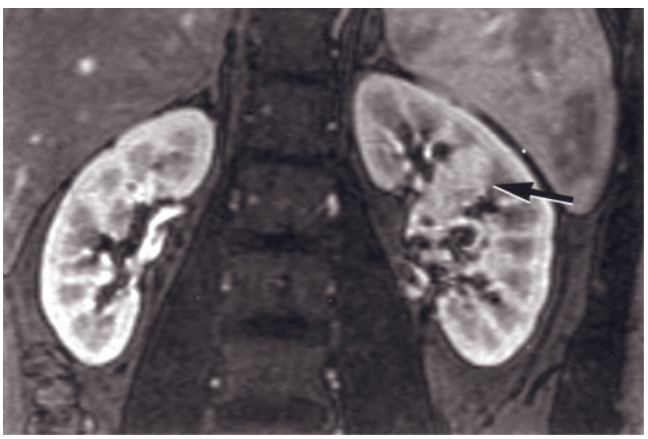

FIG. 9.4 Prominent column of Bertin. Coronal T1-weighted gradient-echo postgadolinium image. Bertin column (arrow) follows a continuous contour and remains isointense with the renal cortex.

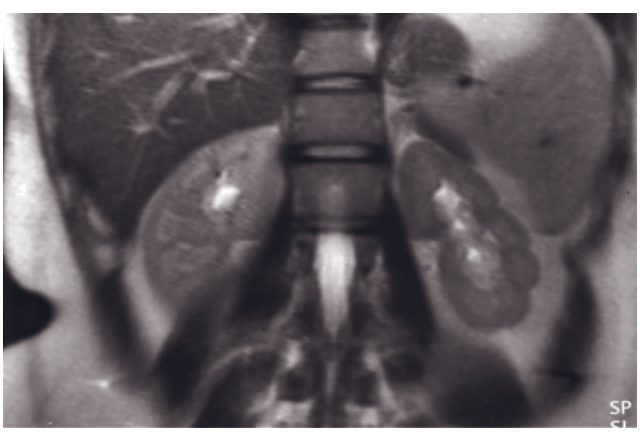

(*a*)

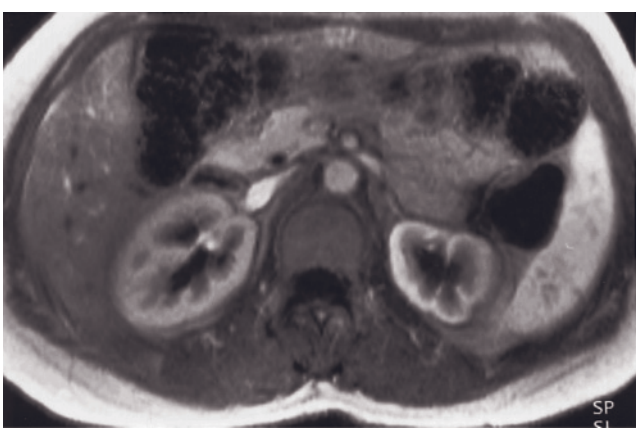

(*b*)

FIG. 9.5 Fetal lobulation. Coronal T2-weighted SS-ETSE (*a*) and transverse T1-weighed immediate postgadolinium SGE (*b*) images. Coronal SS-ETSE image (*a*) demonstrates an undulating contour of the entire left kidney. The immediate postgadolinium SGE image (*b*) shows uniform cortical thickness, excluding the presence of a mass.

Ectopic kidney refers to the malposition of one or both kidneys. Pelvic kidney accounts for most cases of ectopic kidney. In this case the kidneys are often malformed (fig. 9.6). The presence of intense uptake of gadolinium chelates by renal cortex and identification of renal corticomedullary organization allows confident diagnosis of this entity.

Horseshoe kidney occurs in about 1 in every 600 persons and is the most common form of renal fusion. It is defined as the midline fusion of two distinct renal masses, each with its own ureter and pelvis. This entity is demonstrated on tomographic images by the fusion of the lower poles of both kidneys across the midline, immediately anterior to vertebral bodies (fig. 9.7).

Crossed fused ectopia is an uncommon entity. In crossed ectopia, the ectopic kidney is situated opposite the side of insertion of its ureter in the trigone. Fusion with the other kidney is present in 90% of cases. Crossed fused ectopy can be diagnosed on MR images by the identification of corticomedullary organization in the mass. Direct coronal imaging is helpful in demonstrating the fused renal moieties (fig. 9.8). Extrarenal anomalies (genital, skeletal, and anorectal) occur in up to 25% of patients [11]. Pelvic fused kidneys is another uncommon entity (fig. 9.8). Each kidney generally has its own collecting system.

Duplication of the collecting system is a relatively common anomaly, which may sometimes be difficult to detect on transverse tomographic images (fig. 9.9).

Hypoplastic kidney. Renal hypoplasia is defined as failure of the kidney to develop to a normal size. The hypoplastic kidney is a congenitally small (<50% of normal) but otherwise normally developed kidney. The small size of the kidney is usually a manifestation of a marked reduction in the number of renal lobes. The normal adult kidney has a minimum of 10 lobes, each composed of a medullary pyramid surrounded by a cap of cortex. Hypoplastic kidney possesses only one to five lobes. Hypoplastic kidneys have an intact collecting system and normal cortical enhancement. The renal artery, however, is diminutive, suggesting that in utero vascular compromise may be the underlying cause. Renal injury sustained in childhood such as surgery, radiation, or reflux may result in a small, smooth kidney similar in appearance to a true hypoplastic kidney (fig. 9.10).

Hyperplastic (hypertrophic) kidney. Renal hyperplasia that results in renal enlargement occurs in the setting of longstanding compromise or absence of the contralateral kidney. Hyperplasia is most pronounced if the original stimulus for renal enlargement occurs in childhood. Generalized, globular renal enlargement with increased thickness of renal cortex is observed particularly on immediate postgadolinium gradient echo images (fig. 9.11).

DISEASE OF THE RENAL PARENCHYMA

Mass Lesions

A number of renal masses have distinctive MR imaging appearance that can be described on T2-weighted, T1-weighted, and early and late postgadolinium images (Table 9.1).

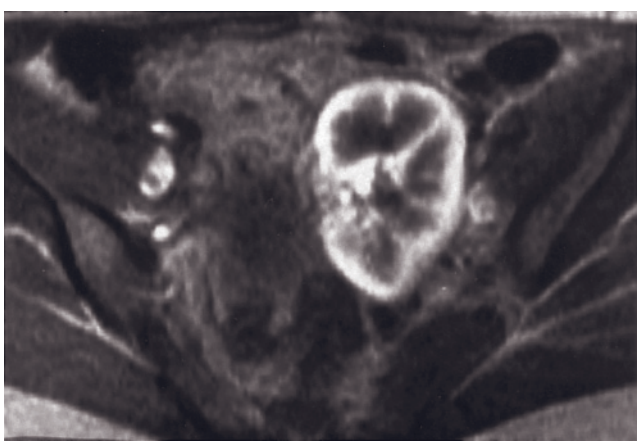

(*a*)

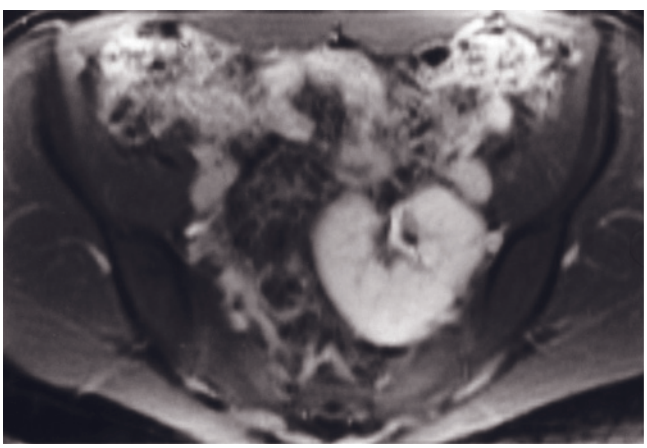

(*b*)

FIG. 9.6 Pelvic kidney. T1-weighted immediate postgadolinium SGE image (*a*). The presence of corticomedullary differentiation identifies the pelvic mass as a kidney. Transverse (*b*) and sagittal (*c*) T1-weighted gadolinium-enhanced fat-suppressed

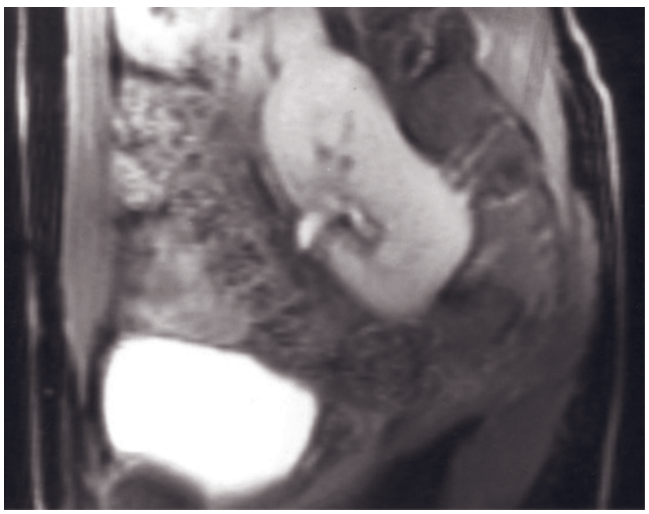

(*c*)

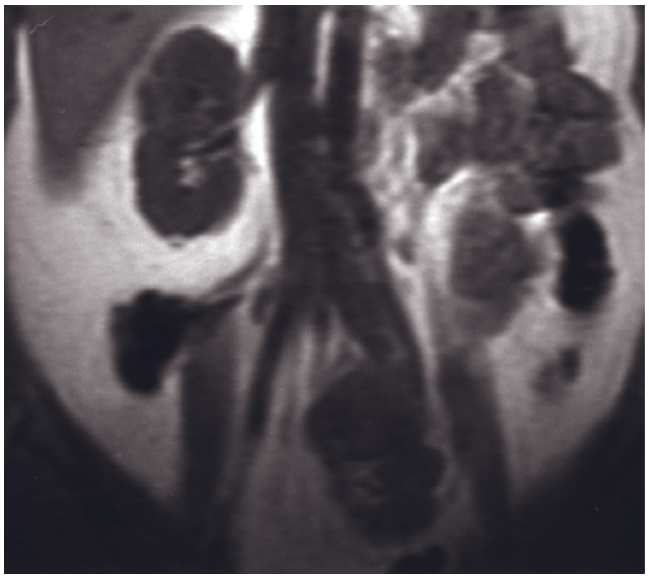

(*d*)

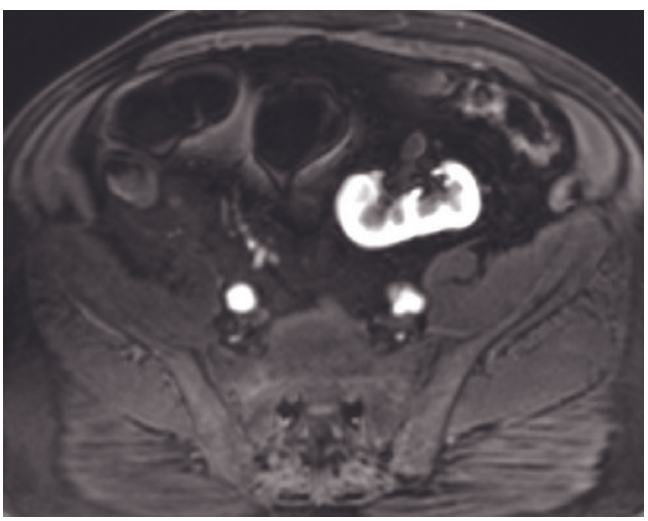

(*e*)

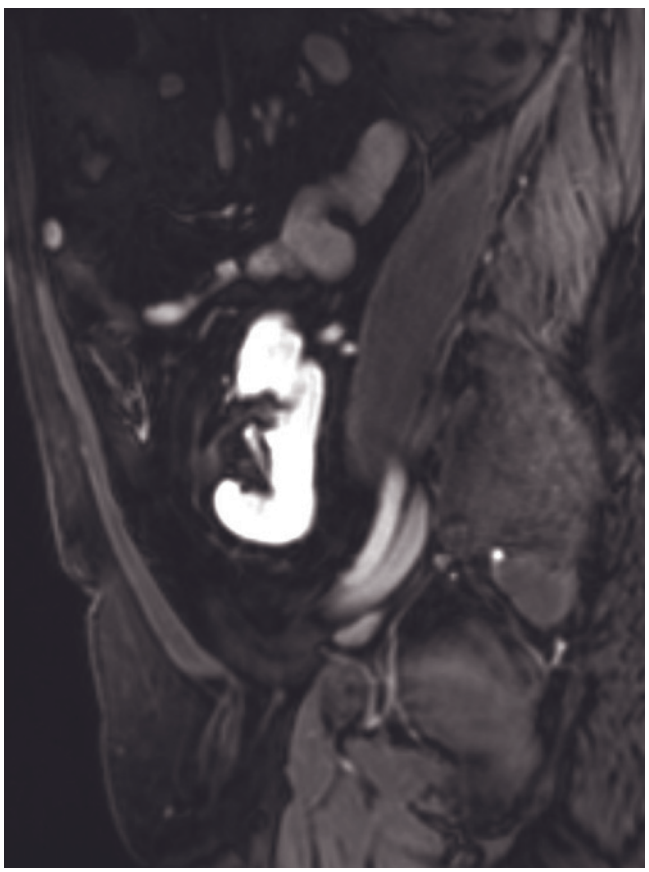

(*f*)

FIG. 9.6 (*Continued*) SGE images in a second patient and coronal T2-weighted SS-ETSE image (*d*) in a third patient demonstrate other examples of a pelvic kidney. Transverse (*e*) and sagittal (*f*) T1-weighted postgadolinium arterial phase 3D-GE images demonstrate the ectopic pelvic kidney in another patient.

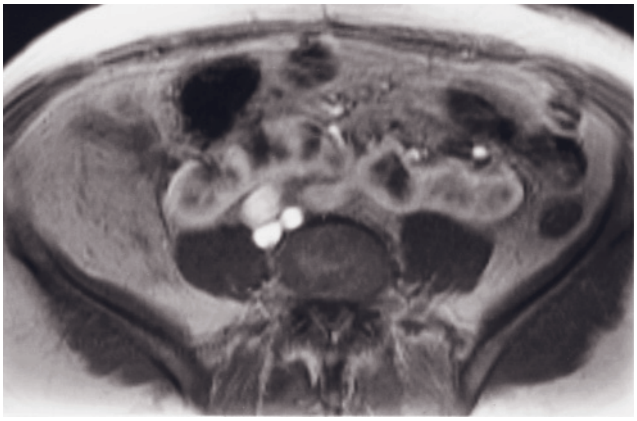

(*a*)

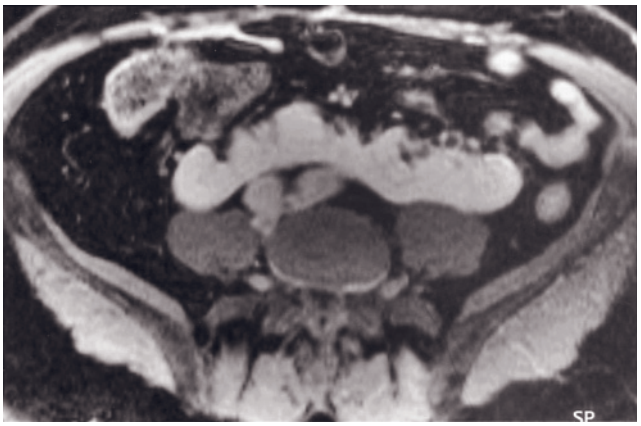

(*b*)

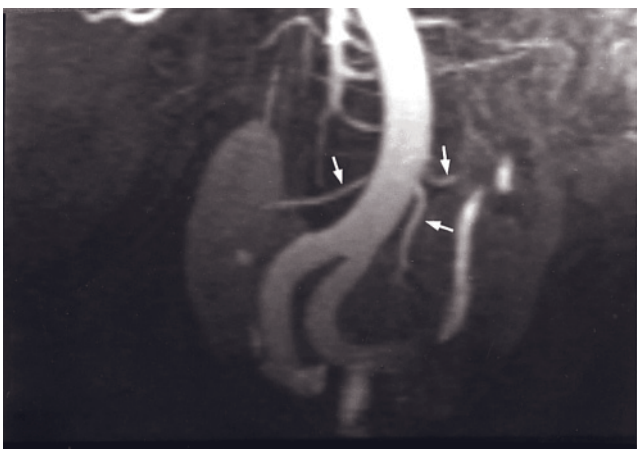

(*c*)

FIG. 9.7 Horseshoe kidney. T1-weighted immediate (*a*) and 90-s fat-suppressed (*b*) postgadolinium SGE and coronal 3D FISP gadolinium-enhanced (*c*) images. The presence of corticomedullary differentiation in the immediate postcontrast image (*a*) demonstrates that the retroperitoneal mass is a horseshoe kidney and that the isthmus contains functional renal parenchyma. Uniform enhancement of the renal parenchyma is present on later images (*b*). Coronal gadolinium-enhanced 3D FISP demonstrates the horseshoe shape of this anomaly, and the renal arteries are well displayed (arrows, *c*).

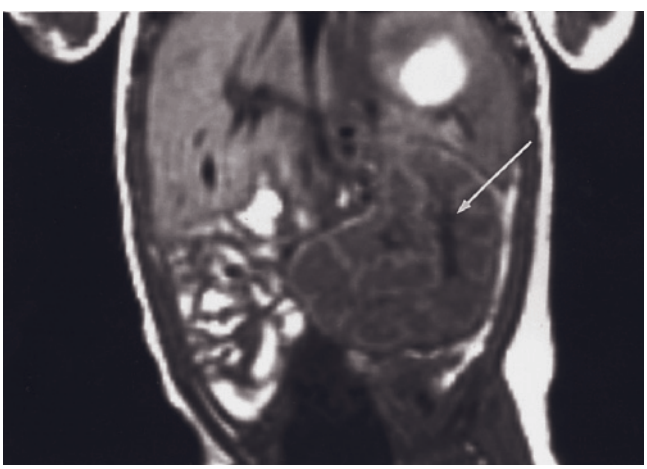

(*a*)

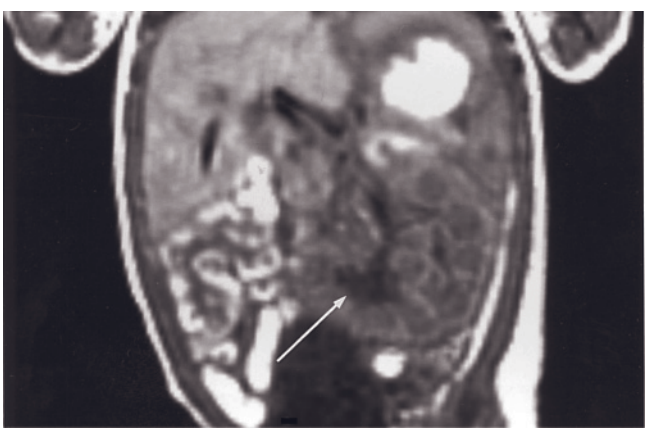

(*b*)

FIG. 9.8 Crossed fused ectopy. Coronal T1-weighted precontrast SE images (*a*, *b*) demonstrate fusion of a small inferomedial kidney to the normal-sized and -positioned left kidney. Clear depiction is rendered by the definition of corticomedullary differentiation. The collecting system of the normally positioned left kidney is normal in size (arrow, *a*), whereas the crossed fused right kidney has a mildly dilated collecting system (arrow, *b*). **Pelvic fused kidneys.** Transverse T2-weighted single-shot echo-train

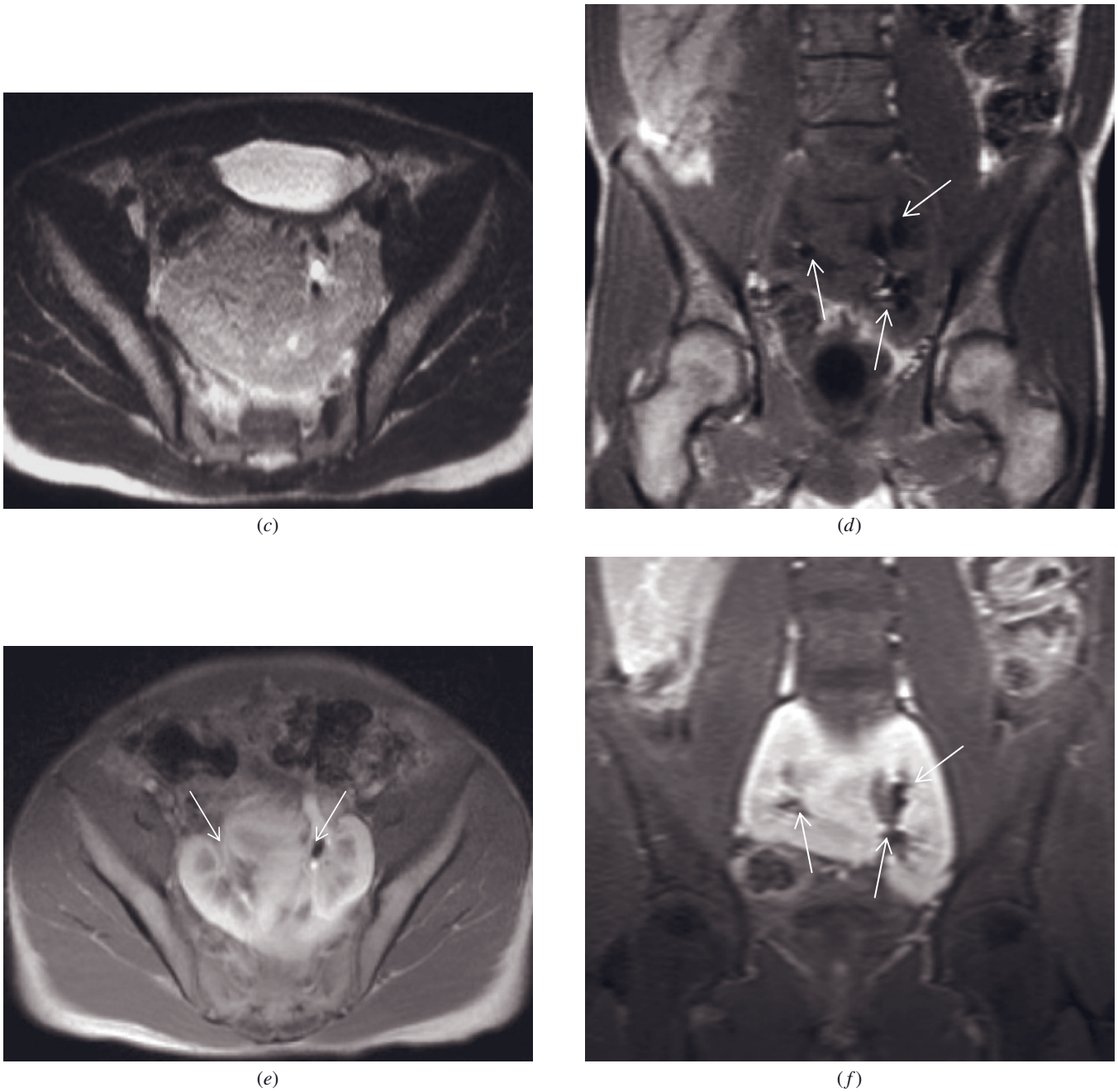

FIG. 9.8 (*Continued*) spin-echo (*c*), coronal T1-weighted SGE (*d*), transverse T1-weighted postgadolinium venous-phase SGE (*e*), and coronal T1-weighted interstitial-phase 3D-GE (*f*) images demonstrate fused pelvic kidneys in another patient. Each kidney has its collecting system (arrows, *d–f*).

Benign Masses

Cysts. Benign cystic diseases of the kidney are a heterogeneous group comprising both hereditary and acquired disorders. These lesions are an important clinical entity [12] for reasons that include:

1. They are common and sometimes present diagnostic challenges for clinicians, radiologists, and pathologists.
2. Forms such as adult polycystic disease are important causes of renal failure.
3. Cysts can occasionally be confused with malignant tumors.

SIMPLE CYSTS. Simple renal cysts are the most common renal lesion in the adult. Number and size of cysts tend to increase with age [13]. Simple cysts occur as single, sometimes multiple, fluid-filled, oval-shaped

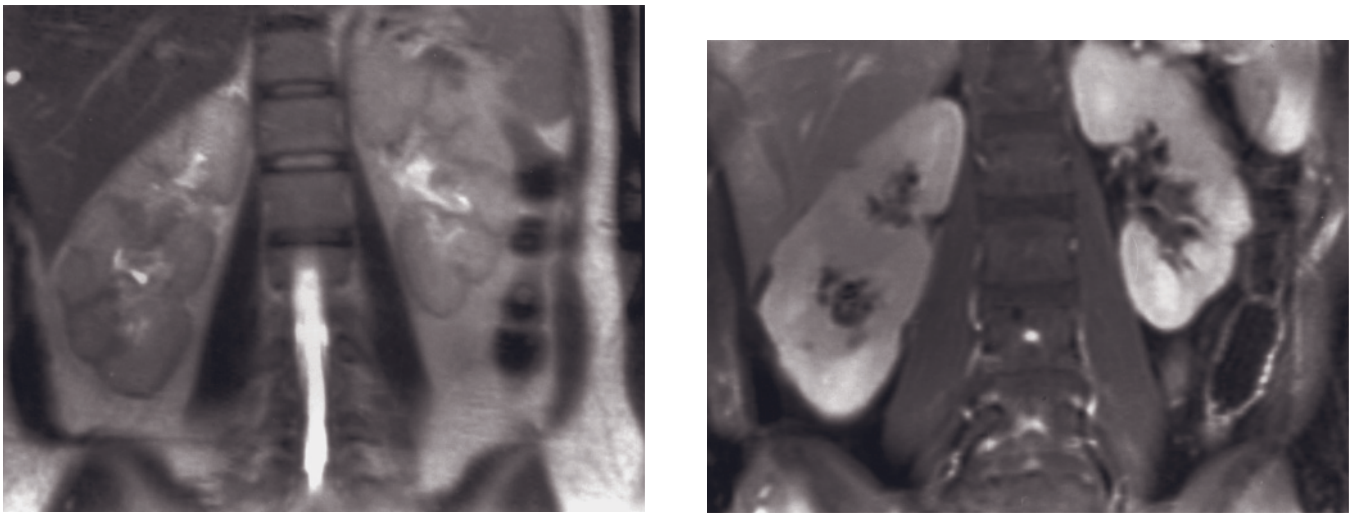

(*a*) (*b*)

FIG. 9.9 Duplex collecting system. Coronal T2-weighted SS-ETSE (*a*) and T1-weighted fat-suppressed postgadolinium SGE (*b*) images demonstrate a duplicated collecting system in the right kidney. Note the thick column of Bertin separating the two pelves.

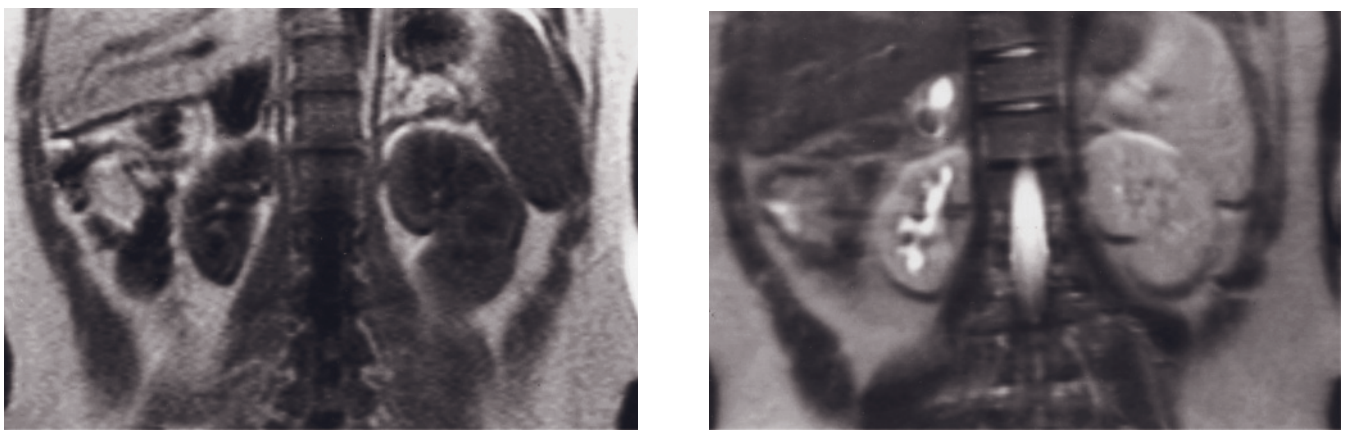

(*a*) (*b*)

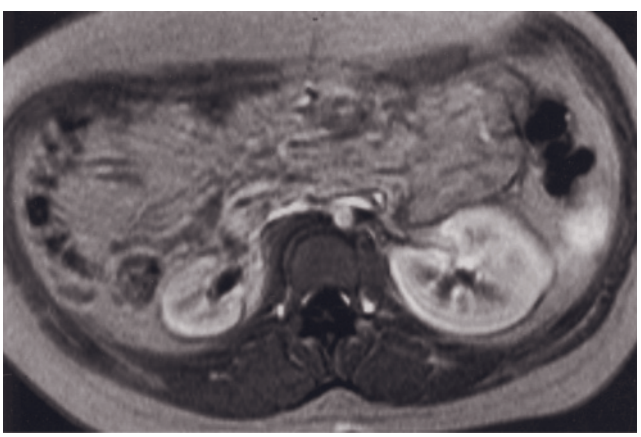

(*c*)

FIG. 9.10 Hypoplastic kidney. Coronal T1-weighted precontrast SGE (*a*), coronal T2-weighted SS-ETSE (*b*), and immediate postgadolinium SGE (*c*) images. Small kidney secondary to ureter reimplantation in infancy. The right kidney is small and smooth in contour and has uniform cortical thickness (*a–c*). Corticomedullary differentiation is preserved on precontrast T1-weighted images. Mild caliectasis with dilatation of the intrarenal collecting system is demonstrated on the T2-weighted image (*b*), reflecting the underlying disease of the collecting system. On the immediate postgadolinium image (*c*), the renal cortex is thin but uniform in thickness, and enhancement is symmetric with the normal left kidney.

structures in the cortex [14]. Cysts are considered simple when they contain clear to amber-colored serous fluid, similar in composition to urine. By MRI, simple cysts are high signal intensity on T2-weighted images and signal void on T1-weighted images and do not enhance after contrast. Cysts are sharply demarcated from adjacent renal parenchyma and have a very thin definable wall when they extend beyond the renal cortex (fig. 9.12) [1, 15]. Simple cysts may be observed as nearly signal-void lesions on postgadolinium images even when they measure 3 to 4 mm in diameter. Sagittal or coronal images permit direct visualization of the superior and inferior margins of cysts.

COMPLEX CYSTS. Cysts are considered complex when they contain hemorrhage, proteinaceous material, septations, calcifications, or thickened wall. Region of interest measurements on pre- and postgadolinium T1-weighted images are useful to ensure lack of contrast enhancement in cysts that are high in signal intensity on pre- and postcontrast images [16]. One approach that can be employed to determine whether stromal enhancement is present in a complex renal lesion is to use subtraction imaging, in which postgadolinium images are subtracted from the same slice position precontrast images (fig. 9.13). This may be best performed with 3D gradient echo imaging, as section thickness is thinner and 3D data sets register more accurately.

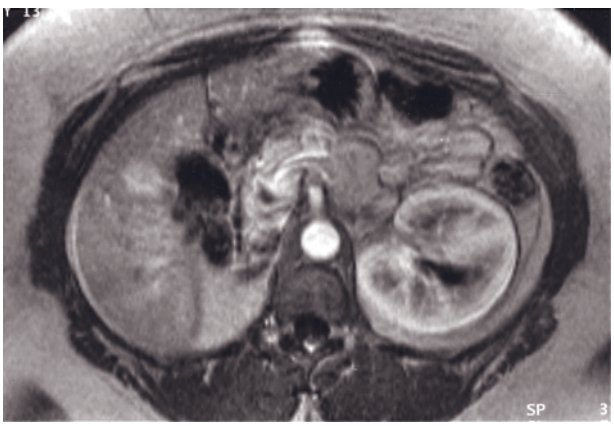

FIG. 9.11 Renal hypertrophy. T1-weighted immediate postgadolinium SGE image demonstrates generalized enlargement of the left kidney with uniform thickness of renal cortex. This adult patient had undergone a right nephrectomy.

A series [17] compared the MR imaging appearance of complex cysts and cystic renal neoplasms. In that series, the combination of mural irregularity and intense mural enhancement in renal cystic lesions was a strong predictor of malignancy (P = 0.0002). In comparison, benign cysts that exhibited a thickened enhancing wall showed more uniform mural thickening. Rarely, benign cysts may contain nodules, which render them suspicious for renal cancer (fig. 9.14).

MR imaging is superior to CT to detect septa in cystic lesions, to delineate the number, thickness, and contour of septa, and to characterize lesions based on the pattern and degree of enhancement. Additional features observed only on MRI may alter the Bosniak classification, which was originally based on CT images, and this may influence the management of some cystic lesions [18].

HEMORRHAGIC/PROTEINACEOUS CYSTS. Hemorrhagic/proteinaceous cysts are commonly encountered on MR examinations. Many of these cysts are not identified as hemorrhagic/proteinaceous on CT examinations, which reflects the higher sensitivity of MRI for the detection of blood and protein. The majority of hemorrhagic cysts are high in signal intensity on T2-weighted and

Table 9.1 Pattern Recognition of Common Renal Lesions on T1, T2, and Early and Late Postgadolinium Images

Lesion	T1	T2	Early	Late	Other
Simple cyst	↓↓	↑↑	○	○	No definable wall
Complex cyst	↓–↑	↓–↑	○	○	Mural enhancement may be present
Angiomyolipoma	↑	∅	○–↑	○–↑	On out-of-phase T1-weighted images, AML shows a black ring phase cancellation artifact; lesions diminish in signal on T1-weighted fat-suppressed images.
Renal cell	↓–↑	∅–↑	↑	↓	The majority are hypervascular. The majority washout on delayed images relative to renal parenchyma.
Lymphoma	∅–↑	∅–↑	Minimal	Minimal	Lymphoma rarely has central necrosis. Most often, the tumor has a large extrarenal retroperitoneal component.

↓↓ moderately to greatly decreased signal intensity
↓ mildly decreased signal intensity
∅ isointense
↑ mildly increased
↑↑ greatly increased
○ absent

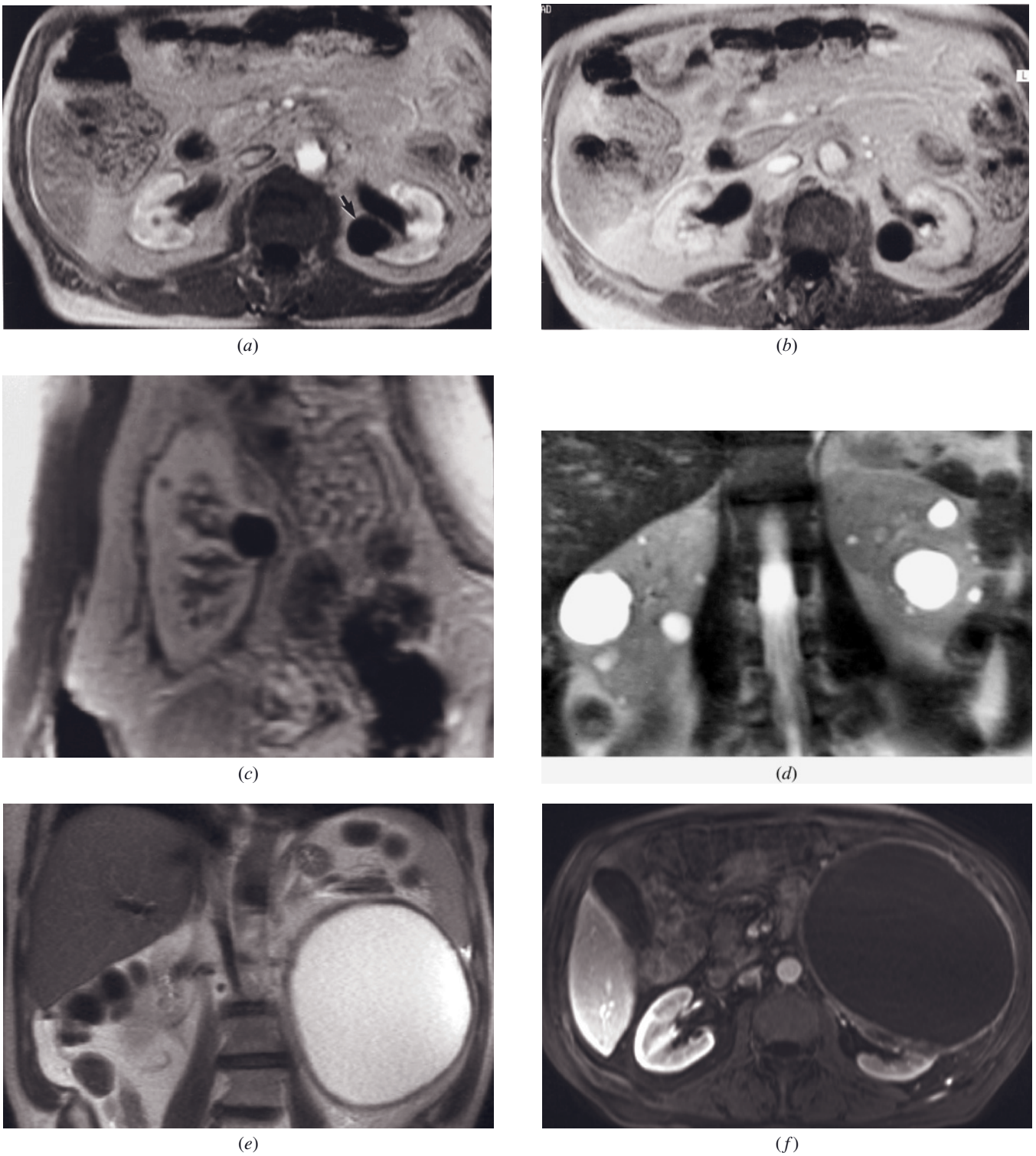

FIG. 9.12 Renal cyst. T1-weighted immediate (*a*) and 5-min (*b*) postgadolinium SGE images. A cyst is present, arising from the posterior aspect of the left kidney. The cyst is sharply marginated and signal void and has no definable wall on the immediate postgadolinium image (arrow, *a*). No change in the appearance of the cyst occurs on the delayed postcontrast image (*b*). Sagittal 5-min postgadolinium SGE image (*c*) of the left kidney in a second patient demonstrates a sharp superior and inferior margin of the renal cyst, confirming that it is a simple cyst. Sagittal T2-weighted SS-ETSE (*d*) image in a third patient shows multiple bilateral simple renal cysts. Coronal T2-weighted single-shot echo-train spin-echo (*e*) and transverse T1-weighted fat-suppressed hepatic arterial dominant (*f*) and interstitial phase (*g*) 3D-GE images demonstrate a large simple cyst with homogeneous internal structure

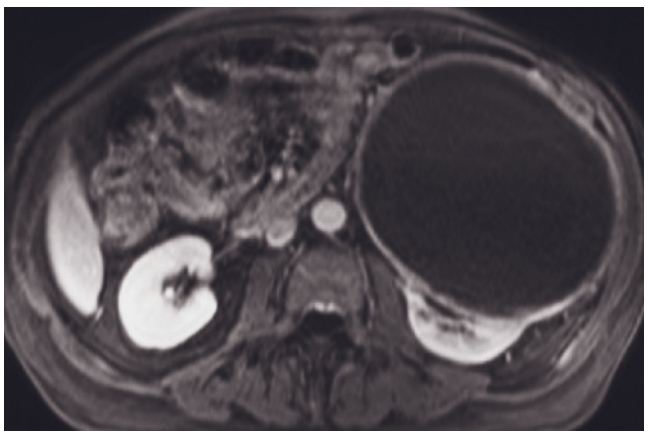

(*g*)

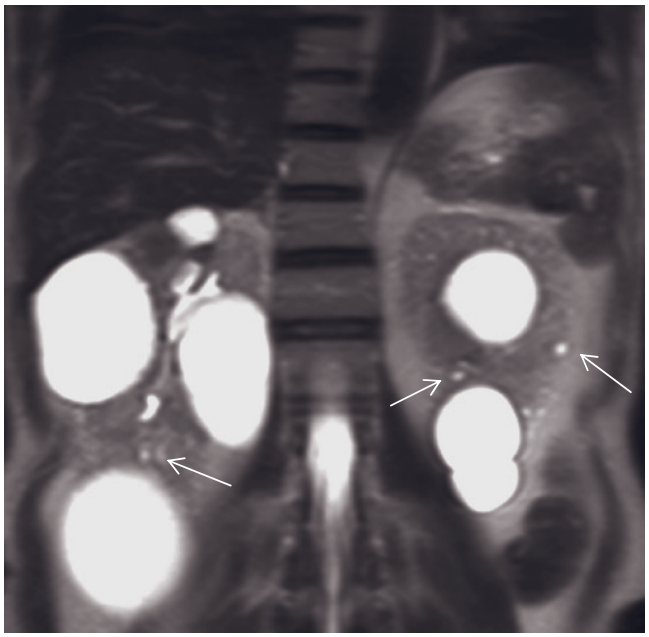

(*h*)

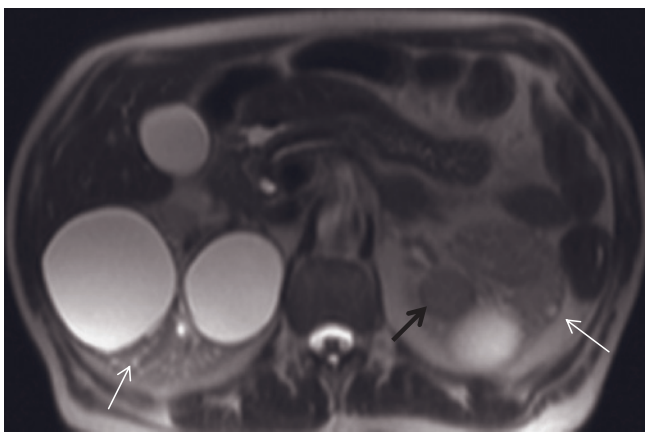

(*i*)

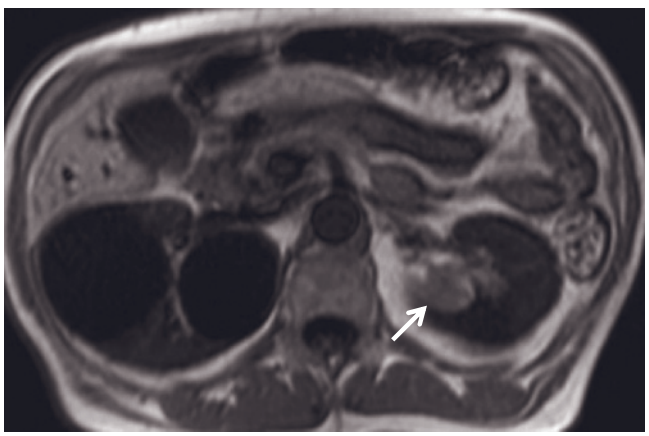

(*j*)

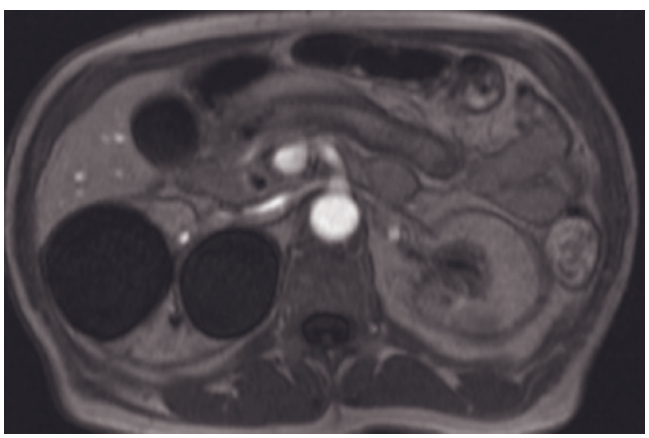

(*k*)

FIG. 9.12 (*Continued*) and relatively thin wall in another patient. The posterior part of the kidney is compressed because of the large size of the simple cyst. Coronal (*h*) and transverse (*i*) T2-weighted single-shot echo-train spin-echo, T1-weighted magnetization-prepared rapid gradient-echo (MPRAGE) (*j*), and T1-weighted postgadolinium interstitial-phase MPRAGE (*k*) images demonstrate multiple cysts in another patient developing secondary to lithium toxicity. Although the presence of small millimetric cysts (arrows, *h*, *i*) is a typical feature of lithium toxicity, large cysts may also be seen, as in this patient. These simple cysts, which are located in both kidneys, have homogeneous internal structure and thin walls and show no enhancement. Note that there is a acute-subacute stage hemorrhagic cyst (black arrows, *i*, *j*), which has low signal on T2-weighted image (*i*) and heterogeneous signal on T1-weighted image (*j*).

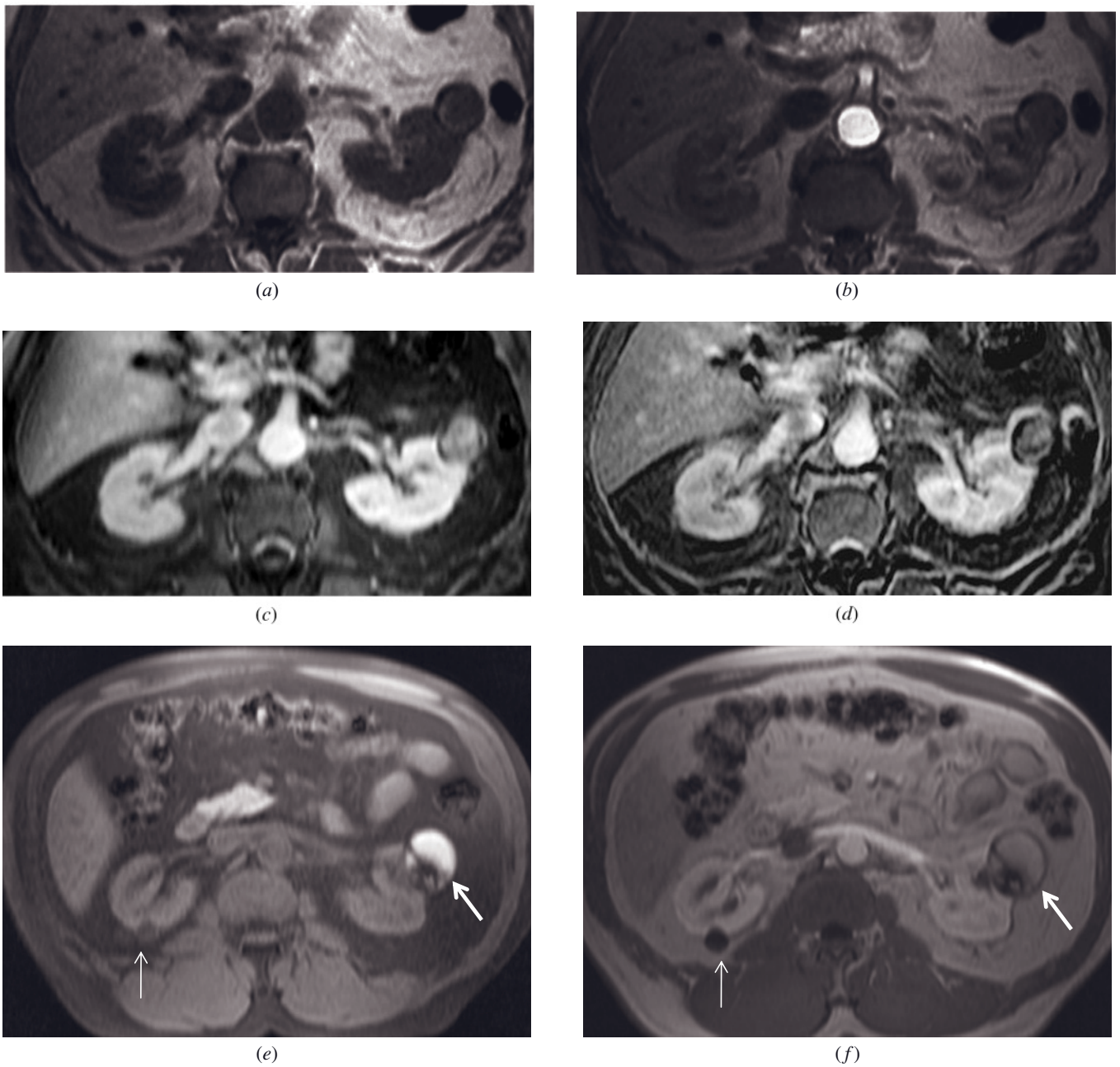

FIG. 9.13 Kidney cancer, subtraction image. SGE (*a*), 1-min postgadolinium SGE (*b*), and 1.5-min postgadolinium fat-suppressed SGE (*c*) images and subtraction image of precontrast from postcontrast image (*d*). The kidney lesion is heterogeneous and slightly high signal on precontrast images, with a heterogeneous postcontrast appearance that is suggestive but not definitive for cancer. The subtraction image clearly reveals that stromal enhancement of the lesion is present, consistent with cancer. **Complex cyst, subtraction image.** Transverse T1-weighted SGE image (*e*), transverse T1-weighted postgadolinium true late hepatic arterial-phase SGE image (*f*), and coronal T1-weighted postgadolinium fat-suppressed interstitial-phase 3D-GE image (*g*) and its corresponding subtraction image (*h*) demonstrate a complex cyst (thick arrows, *e–h*) of the left kidney in another patient. The complex cyst shows heterogeneous high signal on T1-weighted images, suggesting the presence of subacute blood products or proteinaceous material. The complex cyst is septated (*e*, *f*), has a thin wall (*e*, *f*), and contains solid components that show hypointense signal suggesting the presence of chronic hemorrhage or calcification (*e*, *f*). Subtraction image does not show any stromal enhancement in the complex cyst. Note that there is a small simple cyst (thin arrows, *e*, *f*) in the right kidney.

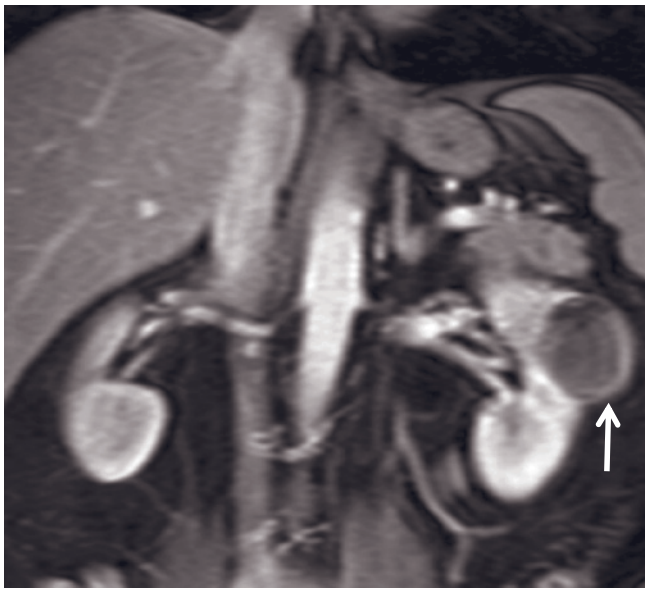

(*g*)

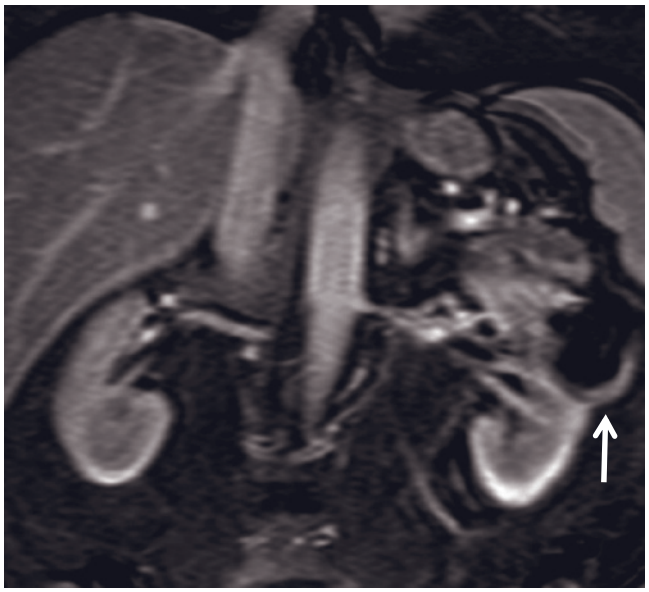

(*h*)

FIG. 9.13 (*Continued*)

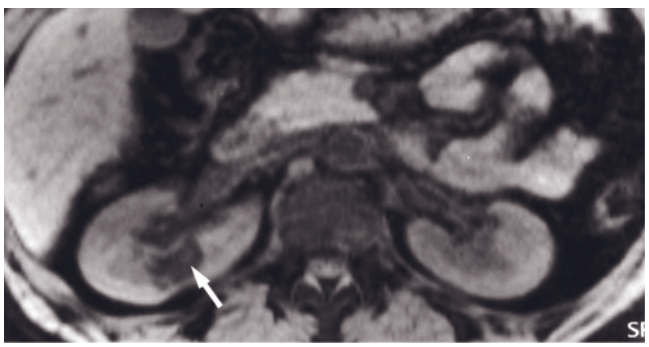

(*a*)

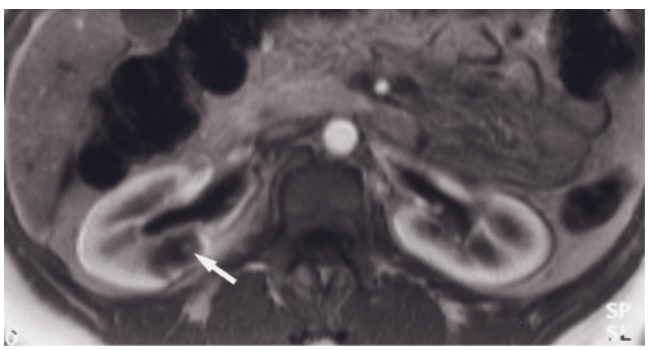

(*b*)

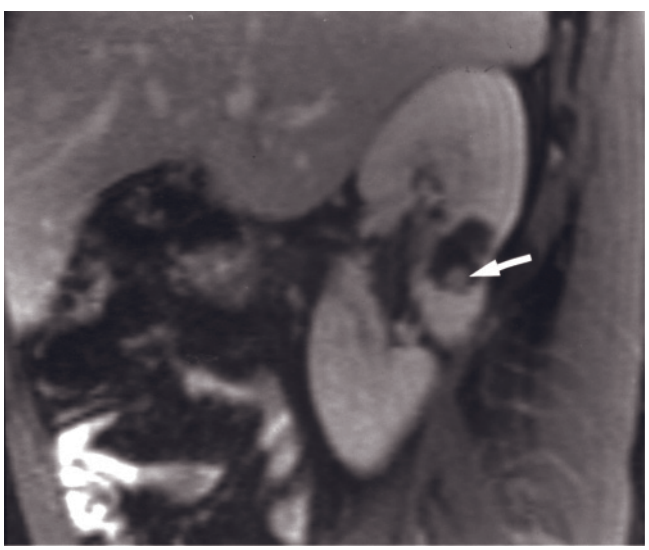

(*c*)

FIG. 9.14 Benign cyst with nodule. Transverse T1-weighted precontrast (*a*) and immediate postgadolinium (*b*) SGE images and sagittal 2-min fat-suppressed postgadolinium SGE image (*c*). In the posterior aspect of the right kidney, there is a small nodule (arrow, *a*) within a cyst that enhances moderately after contrast (arrows, *b*, *c*). At histopathology, the nodule was benign.

T1-weighted images because imaging studies are often acquired in the subacute phase of hemorrhage, which lasts from 1 to 4 weeks after bleeding (fig. 9.15). The observation that most hemorrhagic cysts are high signal intensity on T2- weighted and T1-weighted images reflects the long time period in which blood is present as extracellular methemoglobin. Hemorrhagic cysts may be readily diagnosed as benign if they are homogeneously high in signal intensity on both T2-weighted and T1-weighted images or if they show a fluid-fluid level and have a smooth, thin wall (fig. 9.16). Many cysts that are high in signal intensity on precontrast T1-weighted images are rendered low in signal intensity after gadolinium administration because of rescaling of abdominal tissue signal intensities with the presence of gadolinium (fig. 9.17). Occasionally, organizing hemorrhage contains fibrous strands that make distinction from solid neoplasm difficult.

Acute or early subacute hemorrhage that contains intracellular deoxyhemoglobin or intracellular methemoglobin may pose a diagnostic problem. On T2-weighted images, these cysts may be low in signal intensity and have an appearance resembling solid neoplasm (fig. 9.18). Proteinaceous cysts have a similar appearance. The majority of cysts that are high signal on T1-weighted and low signal on T2-weighted are likely proteinaceous. This can be readily observed because proteinaceous cysts will remain low signal on T2-weighted images for prolonged periods of observation, whereas acute hemorrhagic cysts should eventually appear high signal on T2-weighted images, reflecting conversion of blood breakdown products to extracellular methemoglobin. Because of the occasional occurrence of relatively acute blood or protein in cysts, caution must be exercised in using T2-weighted information to determine whether lesions are cystic or solid. In cysts containing acute hemorrhage, the demonstration of lack of lesion enhancement, and sharp margination with no internal change, on serial postgadolinium images acquired up to 5 min after contrast injection are important imaging findings to show that they are cysts (see fig. 9.18). Clinical history and follow-up MRI at 3 to 6 months also may be required.

SEPTATED CYSTS. Septations in cysts may occur as a result of various events, including fibrin strands after hemorrhage or inflammation, or close juxtaposition of two or more cysts. Demonstration that septations are uniform and thin (≤2 mm), and without enhancing nodular components helps to ascertain that septated cysts are not malignant (fig. 9.19).

CALCIFIED CYSTS. Calcium is generally signal void on MR images. Although calcium is difficult to appreciate on MR images, the lack of signal allows clear visualization of surrounding tissue and internal morphology [15]. Therefore, the presence of tumor tissue is readily determined. An advantage of MRI over CT imaging and ultrasound in the evaluation of calcified cysts is that calcium does not interfere with the evaluation of adjacent soft tissue. MRI is therefore indicated for the evaluation of calcified cysts (fig. 9.20).

CYSTS WITH THICKENED WALLS. Some cysts possess thickened walls that by MR imaging are usually regular in thickness and contour but rarely may be irregular. Cyst contents are occasionally moderate to high in signal intensity on T1-weighted images because of the presence of protein or subacute blood (fig. 9.20). The thickened cyst wall may enhance moderately with gadolinium (fig. 9.21). Histopathologic examination of this category of complex cysts shows prominent reactive macrophage infiltration of either the cyst wall or adjacent renal parenchyma [17]. These cysts occasionally have a prominent perinephric component of inflammatory tissue, greater than that typically seen for cystic renal cancers. However, it may not be possible to distinguish these cysts from cystic renal cancers. Surgery, therefore, cannot be avoided for some of these lesions. If surgery is not performed, close imaging follow-up is recommended.

PERINEPHRIC PSEUDOCYSTS (PARAPELVIC CYSTS). Perinephric pseudocysts are formed from extravasations of urine into perinephric fat in the region of the renal sinus. These lesions may result from blunt trauma to the kidney or surgical procedures in which the renal pelvis or calyces are damaged or the renal capsule is torn, but often the underlying cause is unknown and they are observed as incidental findings observed more commonly in elderly patients. Some degree of accompanying urinary obstruction is not uncommon, and occasionally these cysts may present with urinary obstruction [19]. Perinephric pseudocyst may be solitary or, more commonly, multiple and bilateral. On imaging examinations, they appear as cystic lesions most commonly located in the renal sinus. On MRI, they show high signal intensity on T2-weighted images, low signal intensity on T1-weighted images, and lack of enhancement on postcontrast images. At times these lesions may be difficult to distinguish from a dilated renal collecting system. Images acquired 10–20 min after gadolinium demonstrate that cystic structures in the area of the renal sinus represent perinephric pseudocysts and not dilated collecting system (fig. 9.22). Gadolinium is sufficiently dilute on late postcontrast images to render urine high in signal intensity, which allows differentiation between high signal intensity dilute gadolinium-containing urine in the collecting system and low-signal intensity fluid in perinephric pseudocyst. A MR urogram may also

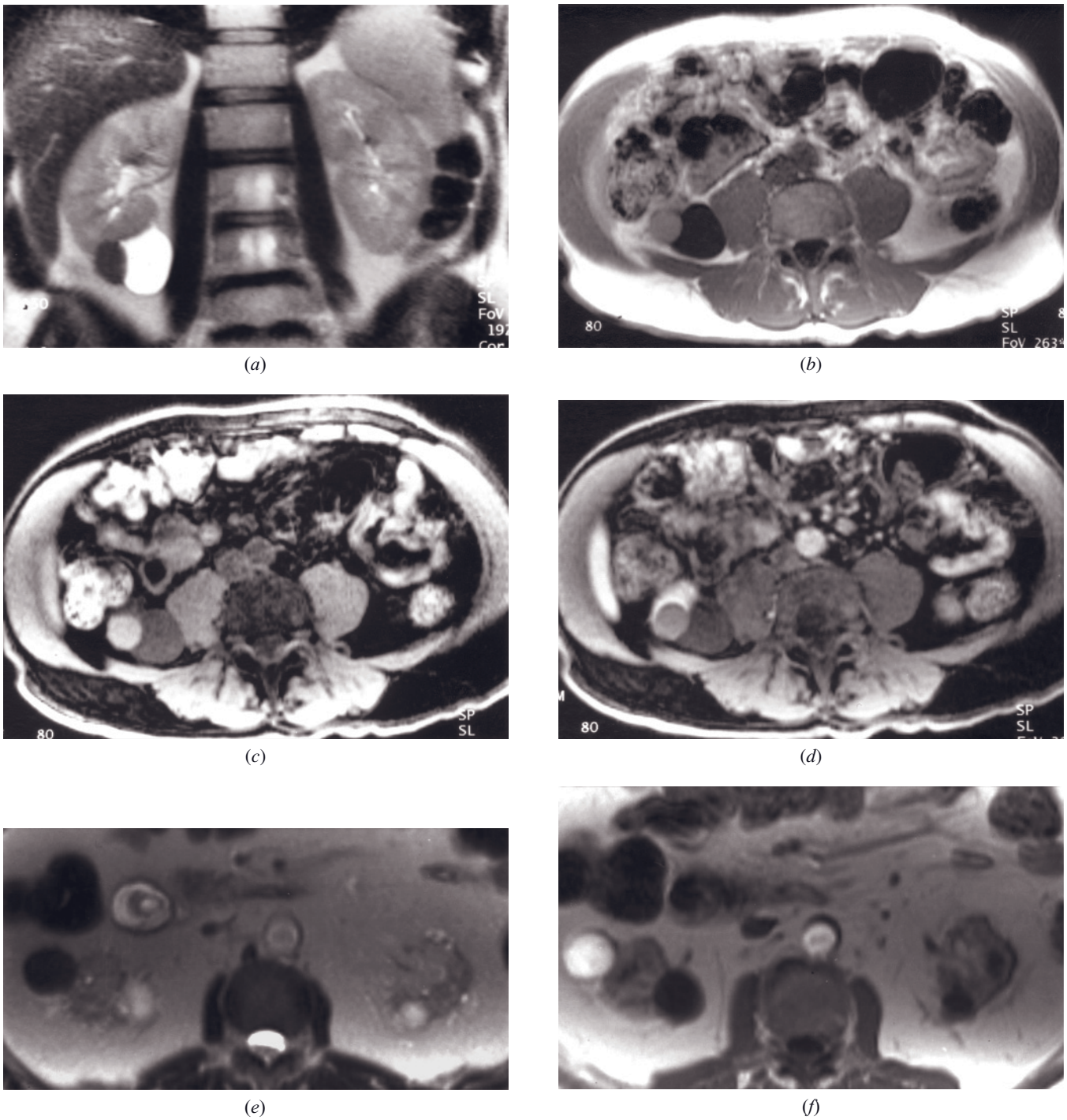

FIG. 9.15 Simple and hemorrhagic cysts. Coronal T2-weighted SS-ETSE (*a*), transverse T1-weighted precontrast (*b*), precontrast fat-suppressed (*c*), and 90-s fat-suppressed postgadolinium (*d*) SGE images. Exophytic simple and hemorrhagic renal cysts are side by side, arising from the lower pole of the right kidney. The hemorrhagic cyst shows low signal intensity on T2-weighted image (*a*) and high signal intensity on T1-weighted precontrast images (*b*, *c*), signal behavior opposite to that of the simple cyst. T2-weighted SS-ETSE (*e*) and immediate postgadolinium SGE (*f*) images in a second patient show bilateral simple renal cysts and, at the same tomographic level arising from the lateral aspect of the right kidney, another cyst with low signal intensity on T2 (*e*)- and increased signal on T1 (*f*)-weighted images, consistent with increased protein content or hemorrhage.

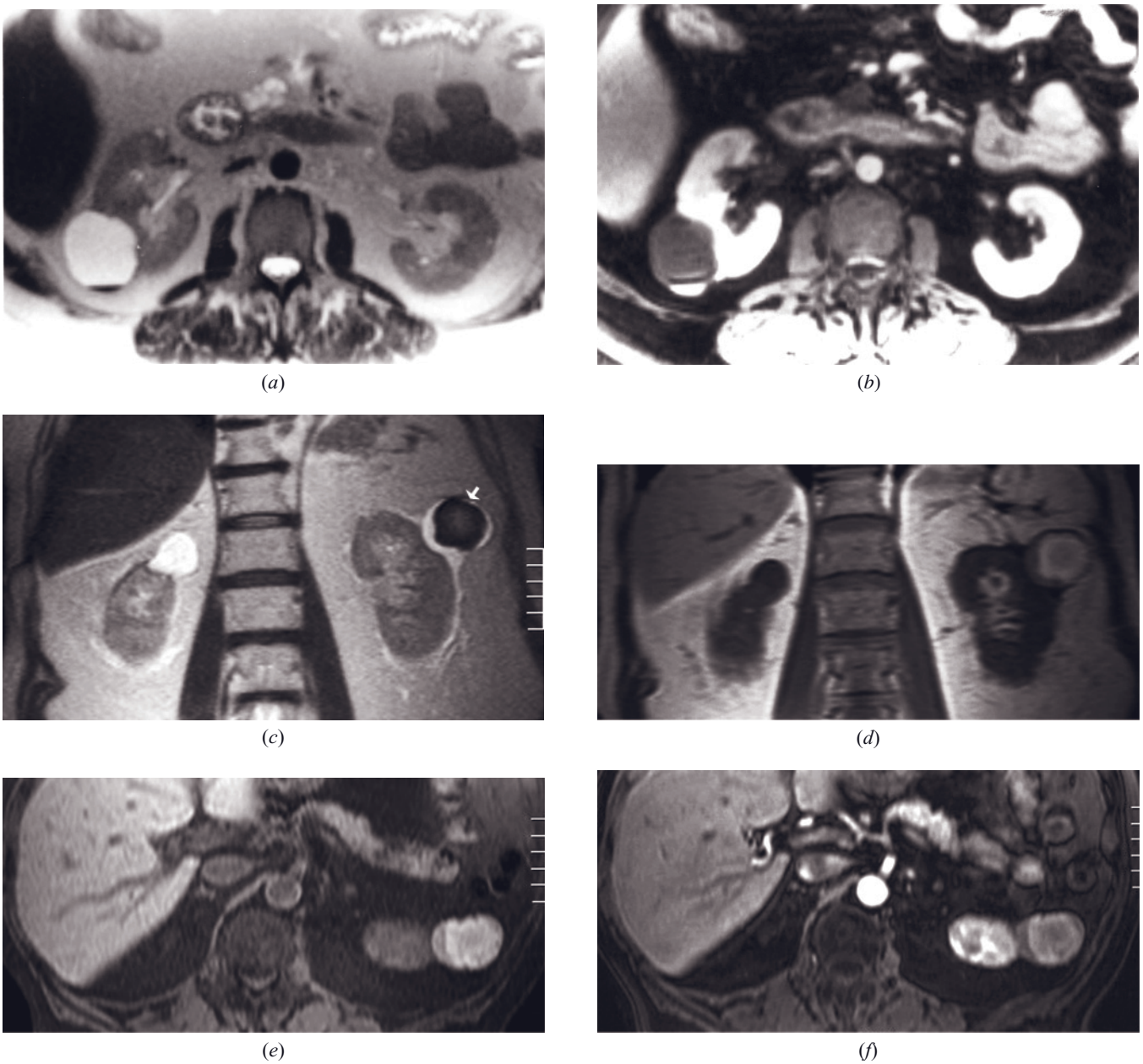

FIG. 9.16 Hemorrhagic cyst. T2-weighted SS-ETSE (*a*) and T1-weighted fat-suppressed postgadolinium SGE (*b*) images. A cyst in the right kidney demonstrates layering material that is low signal on T2 (*a*)- and high signal on T1 (*b*)-weighted images, consistent with hemorrhage. Coronal T2-weighted SS-ETSE (*c*) and T1-weighted gradient-echo (*d*) and transverse T1-weighted fat-suppressed 3D gradient-echo (*e*) and immediate postgadolinium T1-weighted fat-suppressed 3D gradient-echo (*f*) images in a second patient with bilateral renal cyst. The cyst in the left kidney exhibits low signal on T2-weighted (*c*) and high signal on T1-weighted (*d*, *e*) images and shows lack of enhancement on early-phase images (*f*), consistent with acute hemorrhage. In contrast, the cyst in the right kidney shows high signal intensity on T2-weighted images (*d*) and lack of postcontrast enhancement (not shown) consistent with a simple cyst.

demonstrate that these oval-shaped cystic lesions do not communicate with the renal collecting system.

Autosomal Dominant Polycystic Kidney Disease. Autosomal dominant polycystic kidney disease (ADPKD) is characterized by the development of variably sized renal cysts in both kidneys, which progress over time. The disease usually becomes manifest in adult patients, which explains the alternate designation of adult-onset polycystic kidney disease. Patients usually present late in the course of the condition with abdominal masses, hypertension, or after

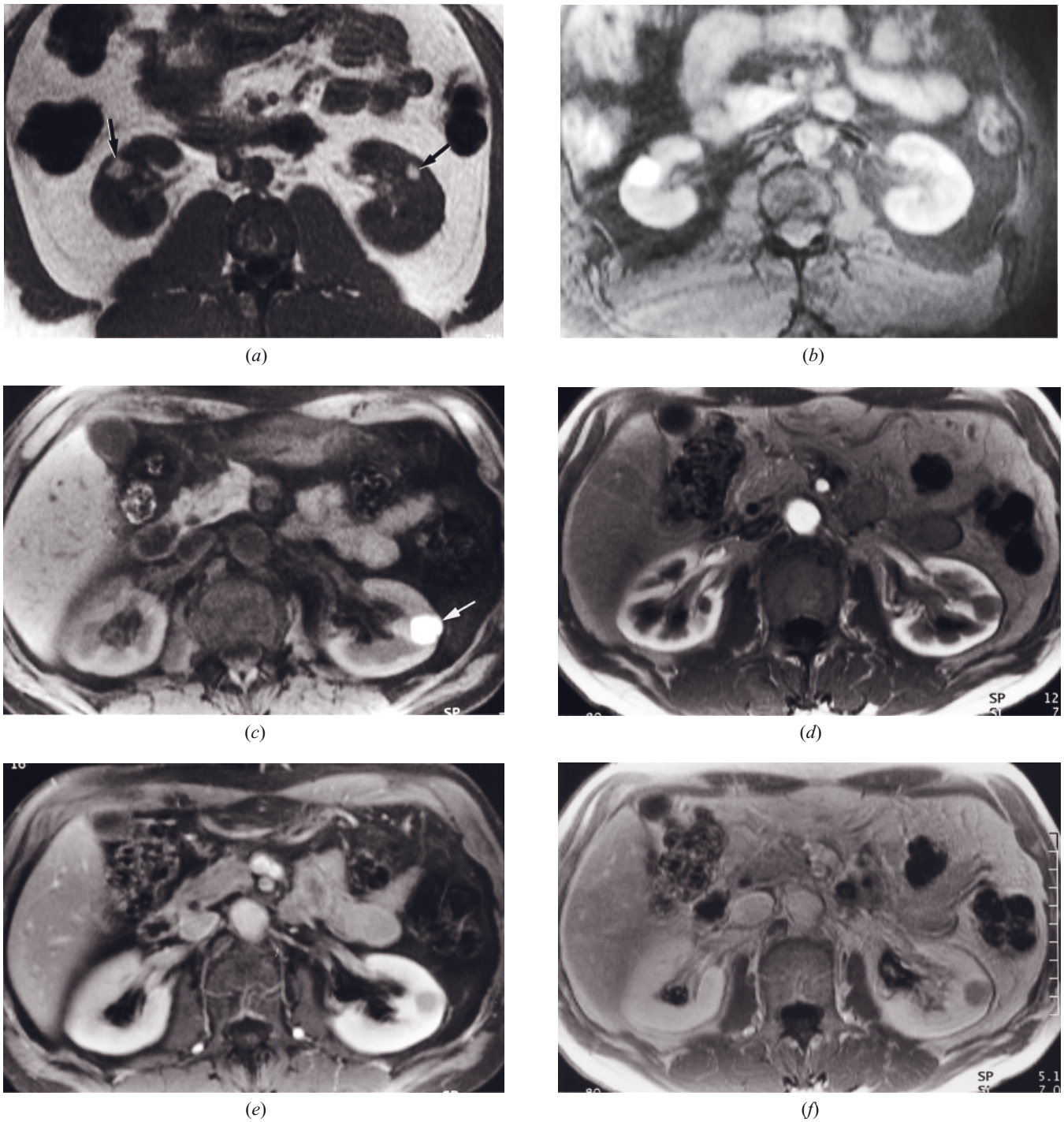

FIG. 9.17 Hemorrhagic renal cysts. T1-weighted precontrast (*a*) and precontrast fat-suppressed (*b*) SGE images. Bilateral renal cysts are apparent on the T1-weighted image (*a*), which are high in signal intensity (arrows, *a*), a finding consistent with subacute blood or fat. T1-weighted image with fat suppression (*b*) demonstrates that these lesions remain high in signal intensity and therefore are not fat containing. Fat suppression accentuates the high signal intensity of these cysts. T1-weighted precontrast fat-suppressed (*c*) and immediate (*d*), 90-s fat-suppressed (*e*), and 5-min (*f*) postgadolinium SGE images in a second patient. A well-defined, uniformly high signal intensity hemorrhagic cyst is present in the left kidney on the fat-suppressed image (arrow, *c*). The cyst does not change in size or shape and does not demonstrate internal enhancement on serial postgadolinium images. Because of the intrinsic high signal intensity of the hemorrhage, the cyst is low in signal but not signal void on the postcontrast images.

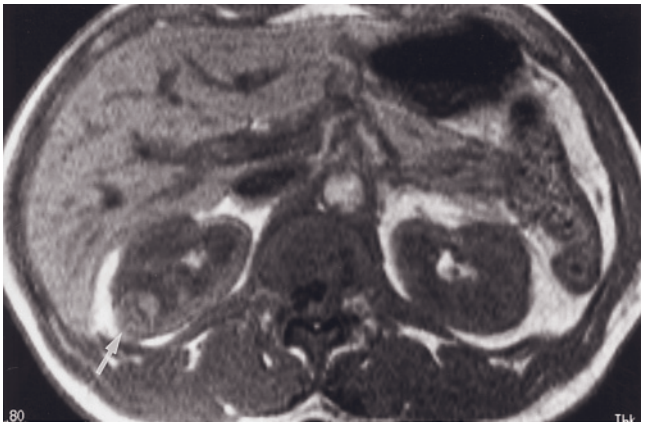

(*a*)

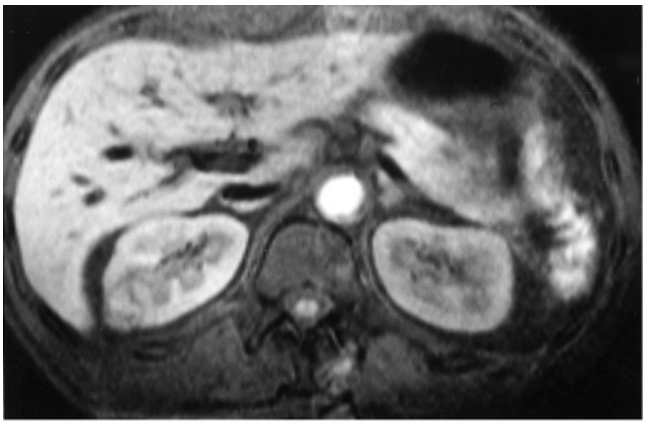

(*b*)

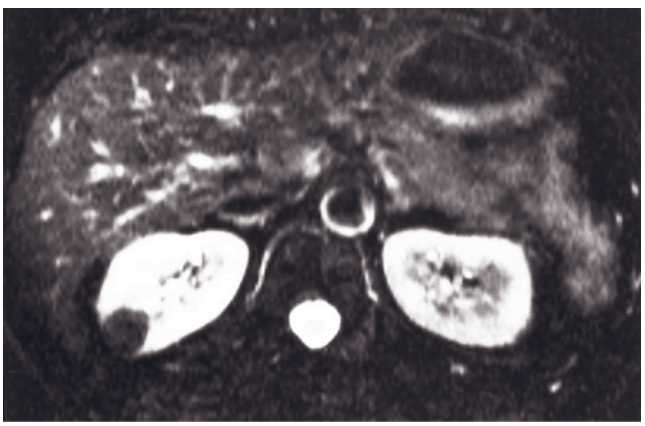

(*c*)

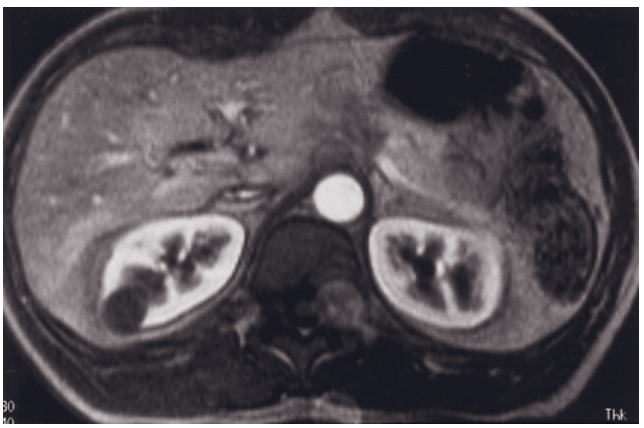

(*d*)

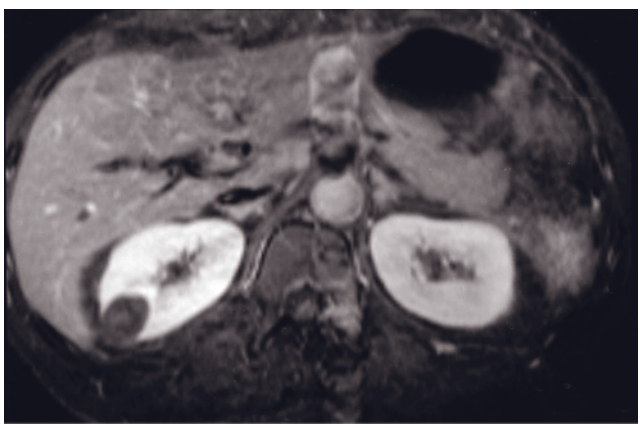

(*e*)

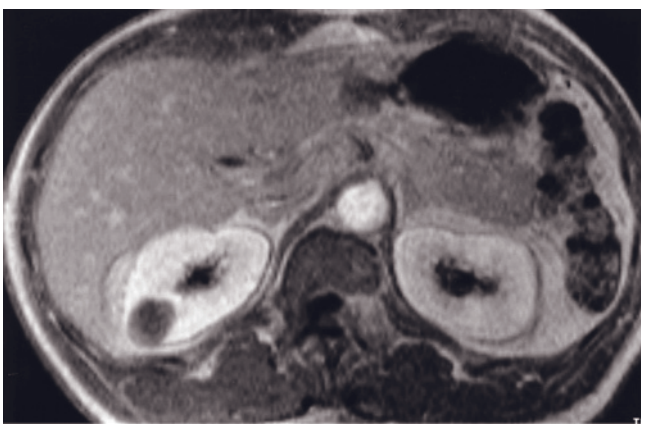

(*f*)

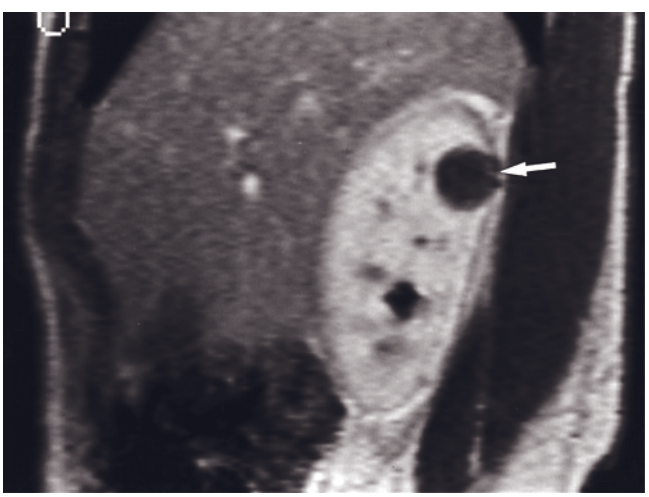

(*g*)

FIG. 9.18 Hemorrhagic cyst containing relatively acute blood (intracellular methemoglobin). T1-weighted precontrast SGE (*a*), T1-weighted precontrast fat-suppressed SE (*b*), T2-weighted fat-suppressed SE (*c*), T1-weighted immediate postgadolinium SGE (*d*), T1-weighted fat-suppressed gadolinium-enhanced SE (*e*), and transverse 8-min (*f*) and sagittal 8.5-min (*g*) postgadolinium SGE images. A lesion is present in the right kidney (arrow, *a*), which is mixed high signal intensity on T1-weighted precontrast images (*a*, *b*), low in signal intensity on T2-weighted image (*c*), and low in signal intensity on early (*d*) and delayed (*e–g*) images. The low signal intensity on the T2-weighted image (*c*) may mimic a solid lesion. Although the lesion is low in signal intensity and not signal void on postcontrast images, it is sharply marginated, has no definable wall or nodularity, and does not change in size and shape between early (*d*) and late (*e–g*) postcontrast images. The postcontrast sagittal plane image demonstrates that the superior and inferior margins of the cyst (arrow, *g*) are sharply defined.

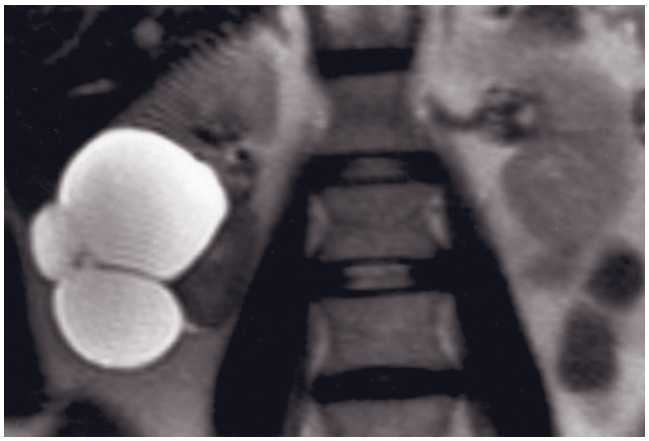

(*a*)

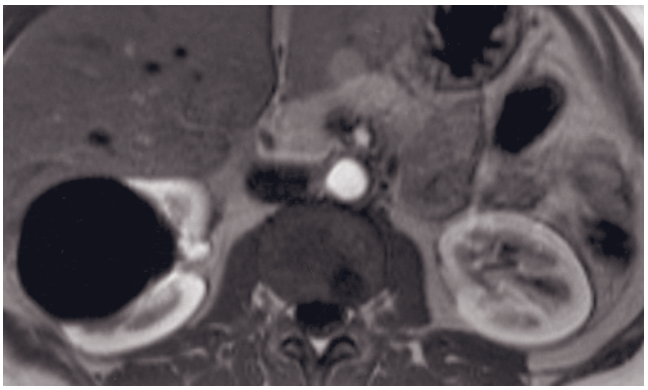

(*b*)

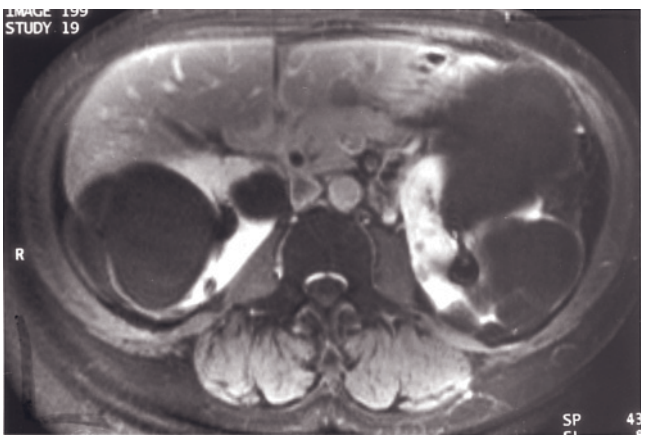

(*c*)

FIG. 9.19 Septated renal cysts. Coronal T2-weighted SS-ETSE (*a*) and transverse T1-weighted immediate (*b*) and 90-s fat-suppressed (*c*) postgadolinium SGE images. Multiple closely grouped cysts are present in both kidneys, which create an appearance of multicystic masses (*a*). Renal parenchyma enhances normally (*b*), and the cysts do not change in size and shape on serial postgadolinium images (*b*, *c*), with no internal enhancement demonstrated.

trauma. Renal failure is a late event. The disease is almost always bilateral, although unilateral disease has been described. Cysts are frequently present in other organs including liver, spleen, and pancreas. Patients are at risk of subarachnoid hemorrhage from ruptured berry aneurysms in the circle of Willis [20].

The typical MR appearance of ADPKD is that of bilaterally enlarged kidneys with multiple renal cysts of varying sizes involving all portions of the renal parenchyma, distorting the normal renal shape and architecture. Early in the course of the disease, the cysts are small (fig. 9.23). Over time, kidneys enlarge massively. Cysts characteristically have varying signal intensities due to the presence of blood products of differing ages (fig. 9.24). Renal cell cancer may be associated with ADPKD, and it presents as a mass that enhances in a heterogeneous fashion. The liver is the organ in which extrarenal cysts are most commonly observed. Liver cysts range in number from solitary to numerous. Even with extensive liver involvement, cysts tend not to distort the hepatic architecture and usually are <2 cm in diameter [21, 22]. On occasion, liver cysts may be large and/or extensive throughout the liver (see Chapter 2, *Liver*).

Autosomal Recessive Polycystic Kidney Disease. Autosomal recessive polycystic kidney disease (ARPKD) is a heritable but phenotypically heterogeneous disorder characterized by nonobstructive renal collecting duct ectasia, hepatic biliary duct ectasia and malformation, and fibrosis of kidneys and liver. Liver pathology is referred to as congenital hepatic fibrosis and is always present in ARPKD [19].

Kidneys are usually bilaterally enlarged, with varying numbers of usually <1-cm cysts scattered through both kidneys. Patients often expire in infancy because of the effects of renal failure. In patients with less severe renal disease, progressive liver disease tends to result in patient death at less than 10 years of age. On MR images, multiple parenchymal cysts <1 cm in diameter are apparent on postgadolinium images (fig. 9.25).

Multicystic Dysplastic Kidney. Multicystic dysplastic kidney results from a congenital failure of fusion

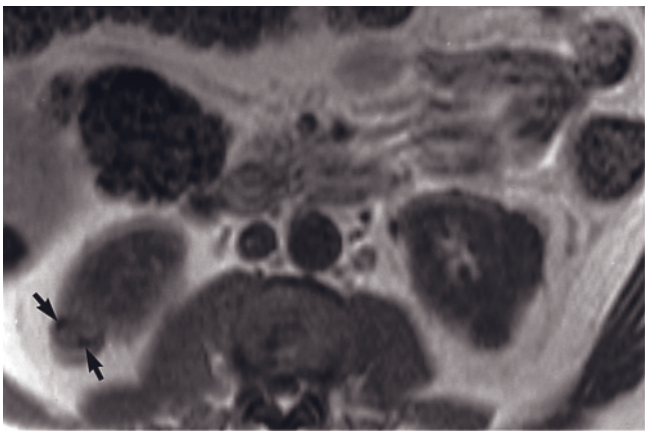

(*a*)

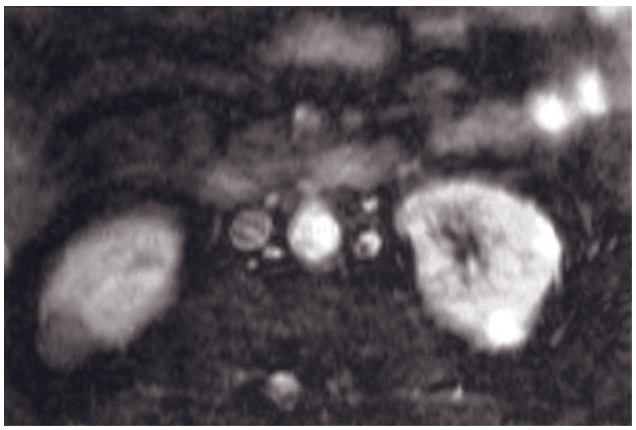

(*b*)

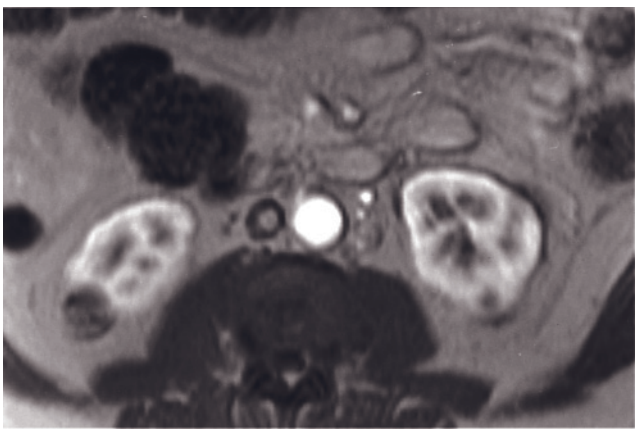

(*c*)

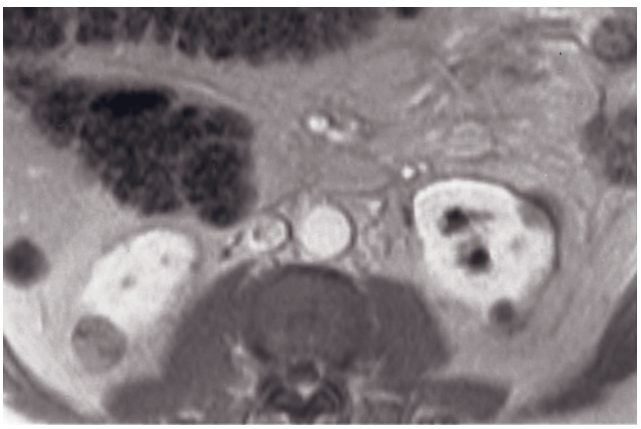

(*d*)

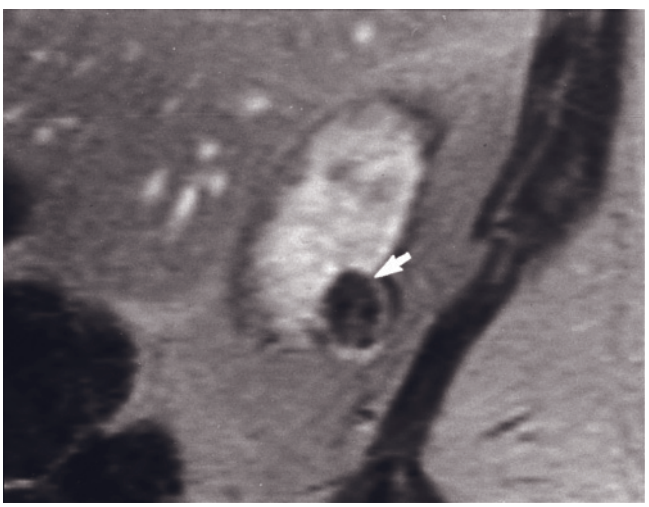

(*e*)

FIG. 9.20 Cyst complicated by the presence of calcification, blood, and thickened wall. Transverse T1-weighted precontrast SGE (*a*), T2-weighted fat-suppressed SE (*b*), and T1-weighted immediate (*c*) and transverse 8-min (*d*) and sagittal 8.5-min (*e*) postgadolinium SGE images. A lesion arises from the posterior aspect of the right kidney, which is mixed in signal intensity and contains signal-void calcifications (arrows, *a*) on the precontrast image. The lesion is mildly low in signal intensity on the T2-weighted image (*b*), which mimics the appearance of a solid tumor. The complicated cyst remains moderate in signal intensity on postcontrast images, but it is sharply defined from adjacent cortex and does not change in size or shape between early (*c*) and late (*d*, *e*) postcontrast images. The superior margin of the cyst is well-defined on the sagittal image (arrow, *e*).

of the metanephrosis and ureteric bud resulting in a nonfunctional cystic renal mass. The ureter is typically atretic. Multicystic dysplastic kidney typically is large in infancy and, if left untreated, atrophies with time. The cyst wall often calcifies during the atrophic process. Multicystic dysplastic kidney may be diagnosed in childhood as a large multicystic mass that lacks organization of a collecting system and shows no evidence of normal renal parenchyma (fig. 9.26). Lesions also may be diagnosed in utero with breathing-independent T2-weighted

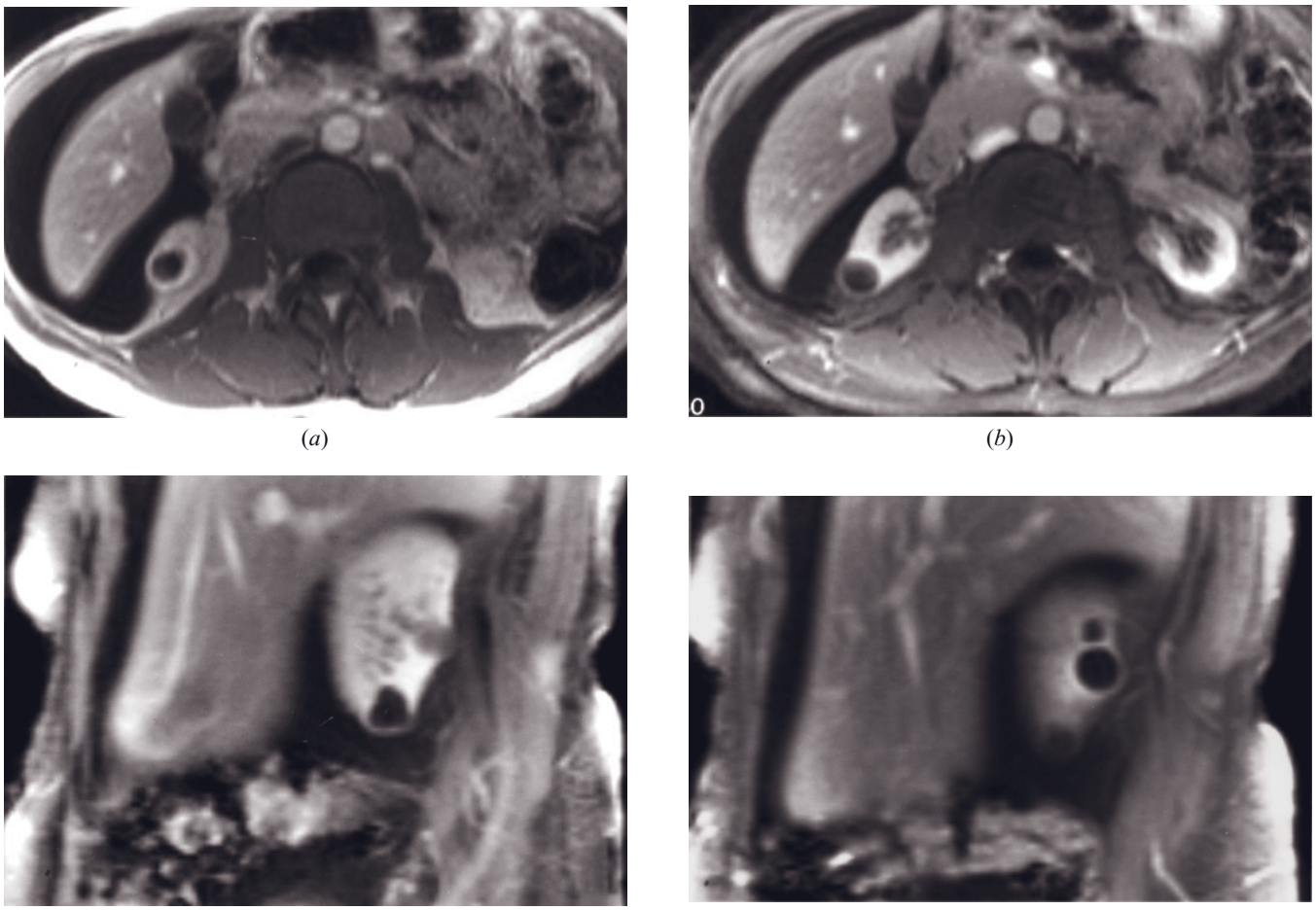

FIG. 9.21 Cyst with thickened wall and reactive cellular infiltrate. Transverse T1-weighed 45-s (*a*) and 90-s fat-suppressed (*b*) postgadolinium SGE images and sagittal T1-weighted 3- to 4-min interstitial-phase (*c*, *d*) postgadolinium SGE images. Note three cysts in the right kidney with thick enhancing walls that show no mural irregularity.

SS-ETSE images (fig. 9.27). Occasionally, a large multicystic dysplastic kidney may be observed in adolescent or adult patients.

Medullary Cystic Disease (Nephronophthisis—Uremic Medullary Cystic Disease Complex). Patients with medullary cystic disease typically present in adolescence with salt-wasting nephropathy and renal failure. On imaging studies, the renal medulla is extensively replaced by 1- to 2-cm cysts (fig. 9.28) [23]. As renal failure progresses, smooth cortical atrophy develops.

Medullary Sponge Kidney. Medullary sponge kidney (MSK) is characterized by multiple cystic dilatations of the papillary collecting ducts. The disease is usually bilateral but may be unilateral or segmental. Patients present with calculi, obstruction, infection, or hematuria. Calculi are frequently present in the cystic cavities.

Tubular ectasia is considered a precursor of MSK. On intravenous urography, tubular ectasia appears as contrast-filled tubular structures that radiate from the calyx into the papilla. A similar appearance may be appreciated on interstitial-phase gadolinium-enhanced MR images, with prominent radiating, enhancing tubular structures demonstrated in the renal papillae (fig. 9.29).

Acquired Cystic Disease of Dialysis. Approximately 50% of patients on long-term hemodialysis develop multiple renal cysts [24–26]. The etiology is uncertain but may relate to ischemia or fibrosis. Kidneys are usually atrophic at the time of development of cystic disease. Cysts tend to be predominantly superficial in location in the renal cortex and tend not to expand the kidney substantially in size, in contrast to ADPKD, in

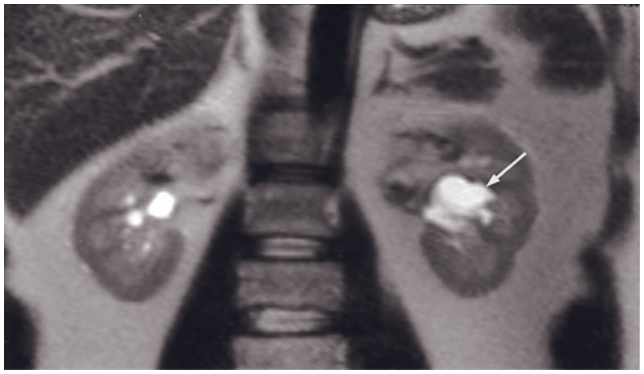

(*a*)

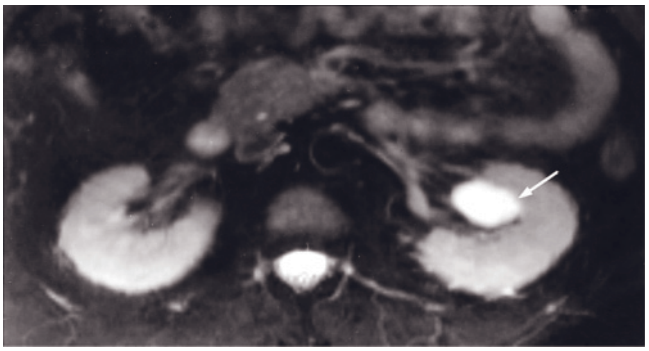

(*b*)

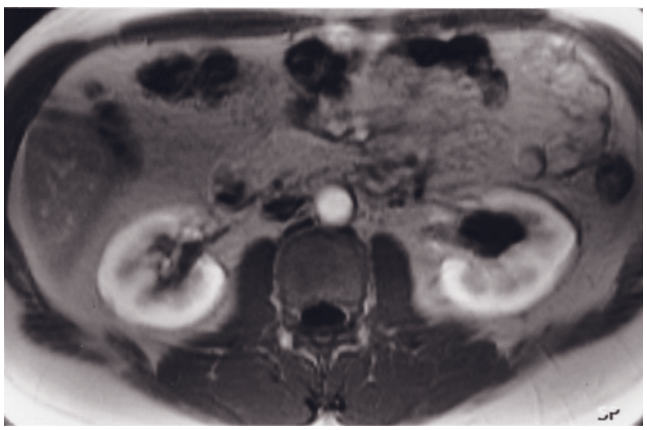

(*c*)

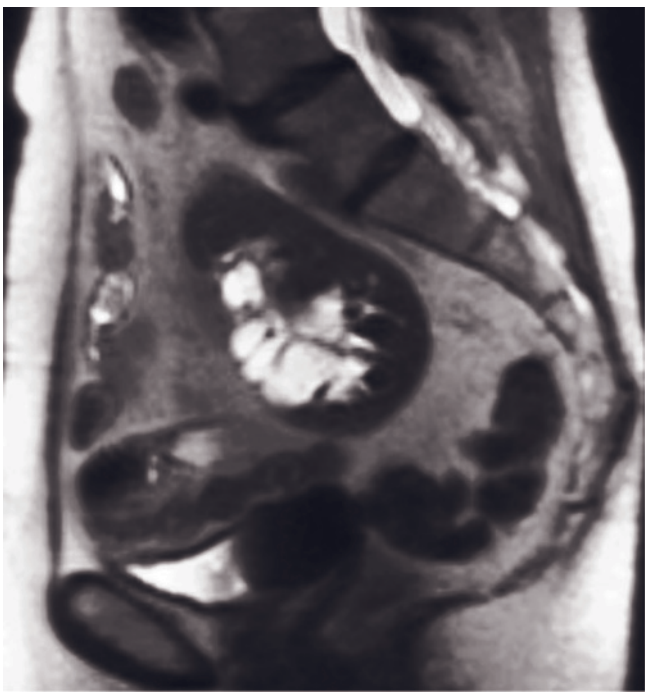

(*d*)

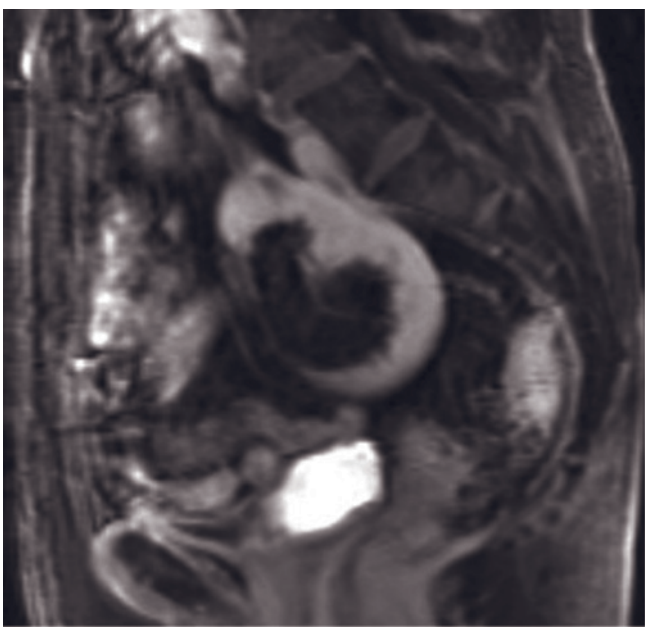

(*e*)

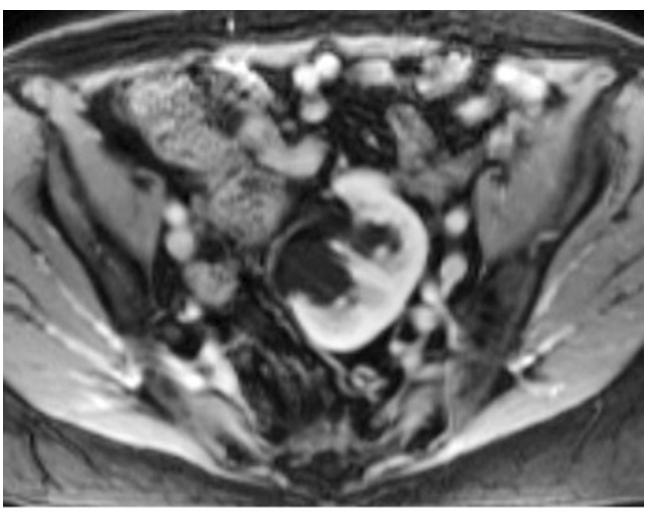

(*f*)

FIG. 9.22 Parapelvic cyst. T2-weighted coronal SS-ETSE (*a*), transverse fat-suppressed SE (*b*), and transverse T1-weighted immediate postgadolinium SGE (*c*) images. An oval-shaped, well-defined parapelvic cyst is present in the left renal sinus, which is separate from the collecting system (arrows, *a*, *b*). The parapelvic cyst is high in signal intensity on T2-weighted images (*a*, *b*) and signal void on the postgadolinium image (*c*). Sagittal SS-ETSE (*d*) and sagittal and transverse 90-s (*e*) and 120-s (*f*) postgadolinium fat-suppressed SGE images in a second patient with a pelvic kidney. Multiple parapelvic cysts are well shown as a grapelike cluster of cysts in the renal pelvis.

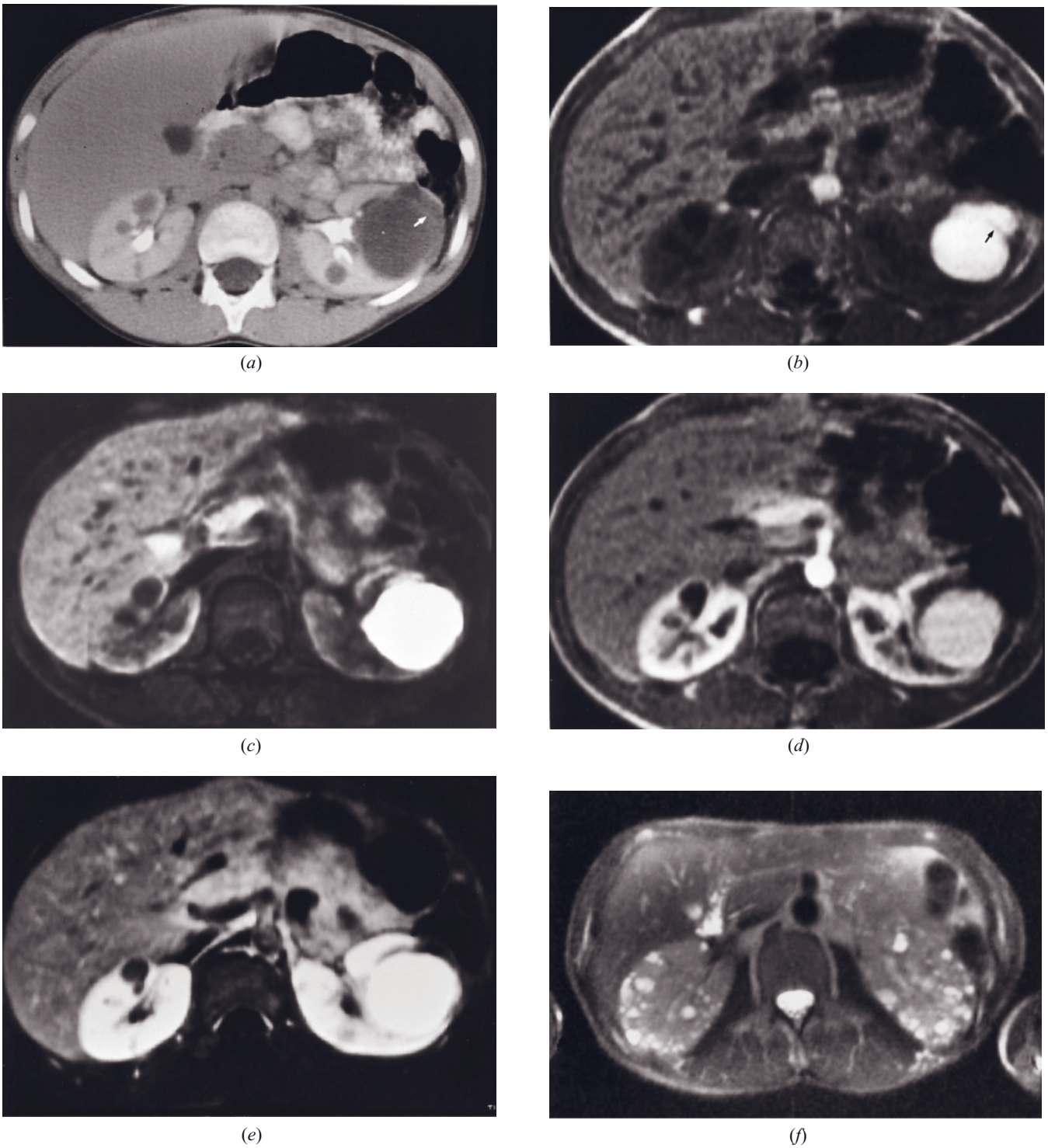

FIG. 9.23 Autosomal dominant polycystic kidney disease in the early stage of development. Contrast-enhanced CT (*a*) and T1-weighted precontrast (*b*), precontrast fat-suppressed (*c*), and immediate (*d*) and late fat-suppressed (*e*) postgadolinium SE images. Multiple small bilateral renal cysts and a large left renal cyst are present. The majority of cysts are <1 cm in diameter, and the renal parenchyma is of normal thickness and not substantially distorted. These findings are consistent with early changes of autosomal dominant polycystic kidney disease. A large left renal cyst contains an internal septation on the CT image (arrow, *a*). Precontrast image (*b*) shows that the cyst is high in signal intensity and contains a low-signal-intensity reticular strand (arrow).This cyst does not suppress with fat suppression (*c*) and does not enhance with gadolinium (*d*), which is consistent with subacute blood in a hemorrhagic cyst. A signal-void rim is appreciated on the postcontrast T1-fat suppressed image (*e*), which probably represents hemosiderin deposition. Transverse T2-weighted fat-suppressed SS-ETSE (*f*) and coronal T1-weighed 90-s postgadolinium SGE (*g*) images in a second patient demonstrate multiple <2-cm cysts scattered throughout the renal parenchyma consistent with early-stage autosomal dominant polycystic kidney disease. Note that kidneys are not substantially enlarged at this point. Coronal T2-weighted

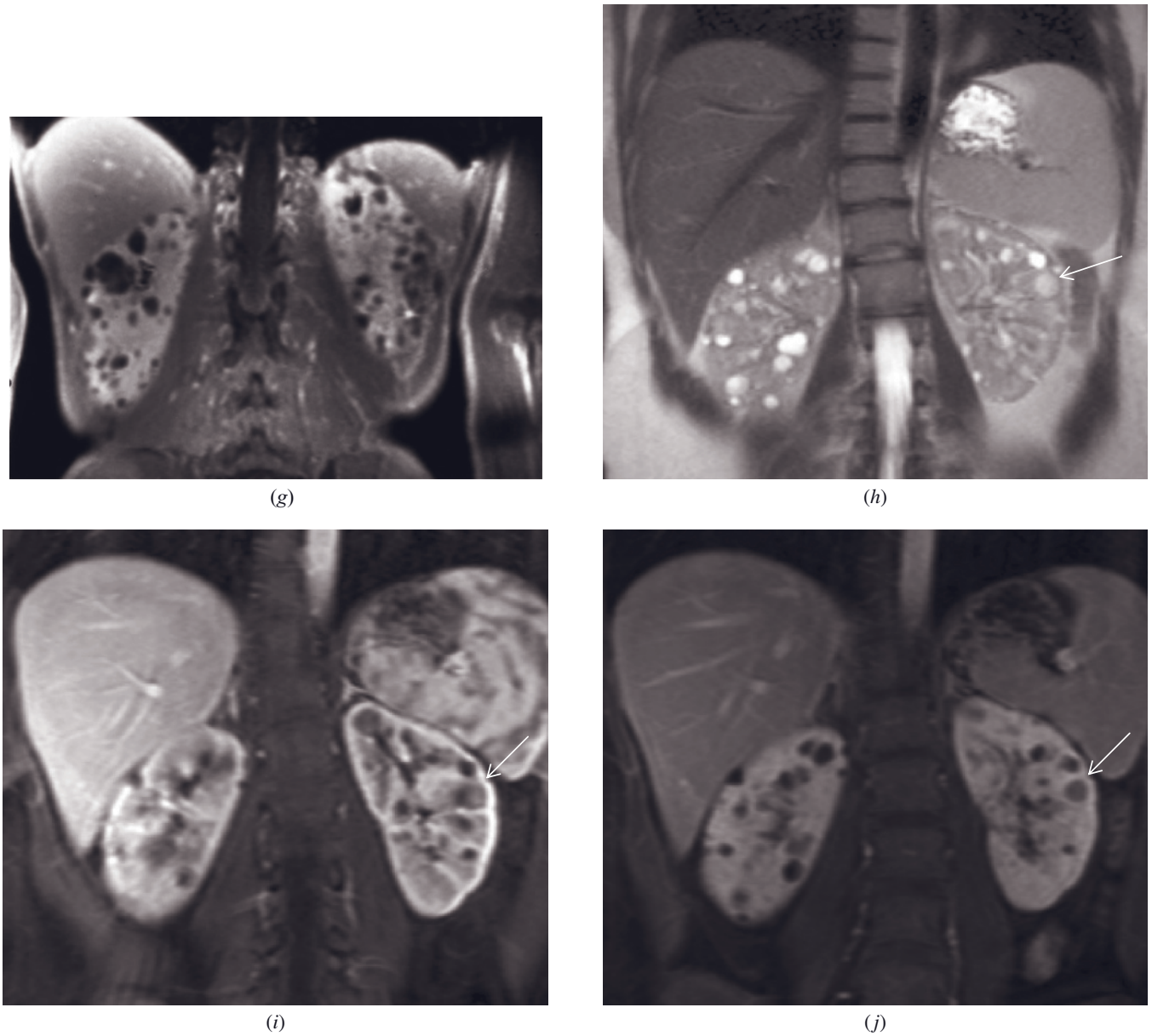

FIG. 9.23 (*Continued*) single-shot echo-train spin-echo (*h*) and coronal T1-weighted postgadolinium hepatic venous-phase (*i*) and interstitial-phase (*j*) fat-suppressed 3D-GE images demonstrate autosomal dominant polycystic kidney disease in the early stage of development in another patient. Multiple cysts that have various signal intensities on T2- and T1-weighted images are detected in both kidneys. Various signal intensities of the cysts reflect various stages of blood products developing secondary to hemorrhage or proteinaceous material. One of these cysts with intermediate signal on both T2-weighted and T1-weighted images is shown with an arrow (*h–j*).

which cysts are scattered throughout the parenchyma and renal size is usually massive. Cysts generally are smaller in size than in ADPKD, measuring <2 cm in diameter. Uncommonly, cysts may also be >2 cm and/or scattered throughout renal parenchyma. Hemorrhage is frequently present in renal cysts in patients with chronic renal failure.

On MR images, multiple small cysts are present in both kidneys, mainly in a superficial renal cortical location (figs. 9.30 and 9.31). Cysts are frequently high in signal intensity on precontrast T1-weighted images because of the presence of subacute blood (fig. 9.32).

MRI is well suited for detection of renal cancer and discrimination between nonenhancing cysts and enhancing cancers. Cysts demonstrate no evidence of enhancement and do not change in morphology on serial postcontrast images, whereas cancers and renal parenchyma will demonstrate evidence of enhancement.

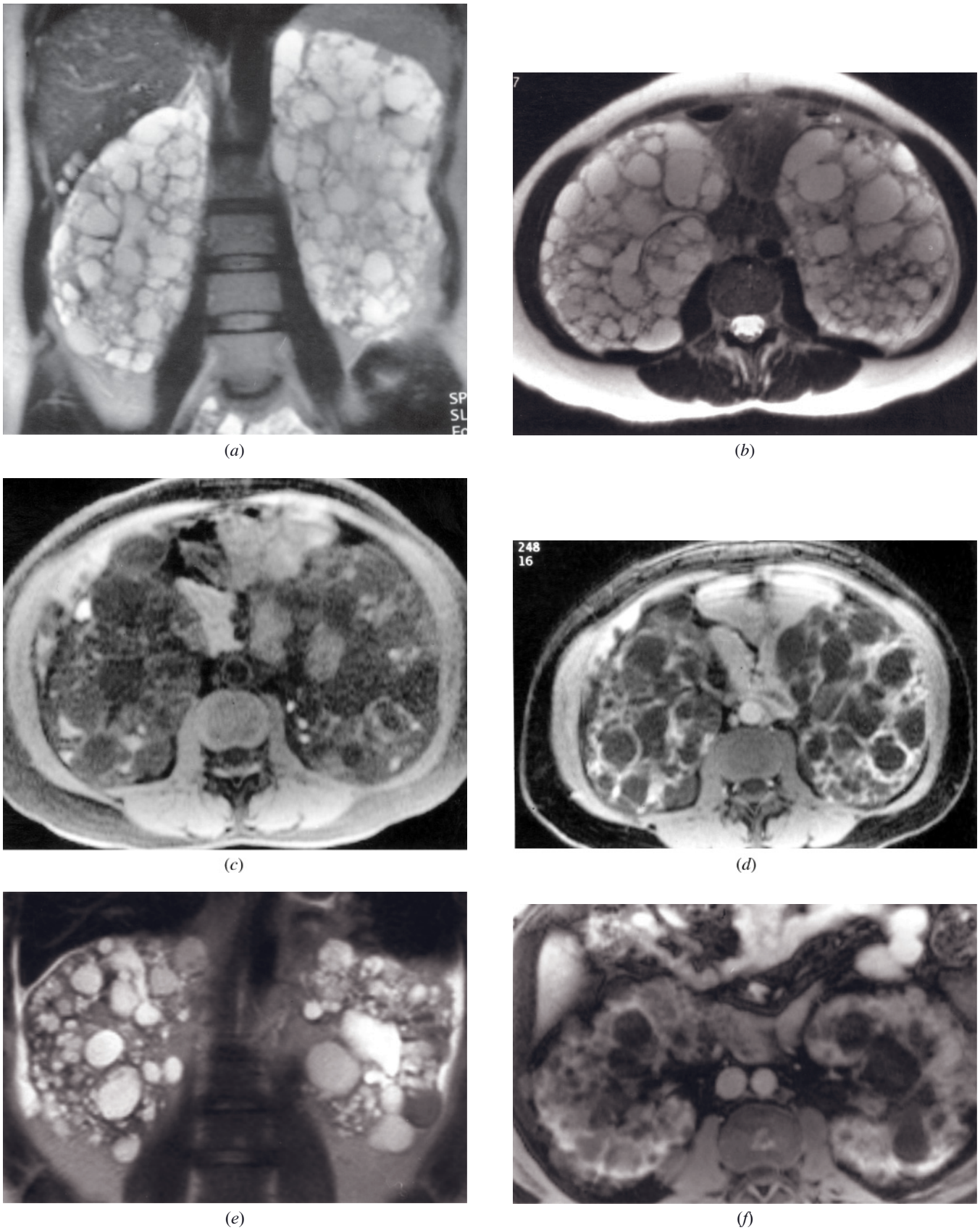

FIG. 9.24 Autosomal dominant polycystic kidney disease. Coronal (*a*) and transverse (*b*) T2-weighed SS-ETSE and transverse T1-weighted precontrast (*c*) and late fat-suppressed postgadolinium (*d*) SGE images. The kidneys are greatly enlarged, with numerous cysts. The majority of the cysts demonstrate high signal intensity on T2- and low signal intensity on T1-weighted images consistent with simple cysts, but a sizable fraction have varying signal consistent with blood products of differing age. Postgadolinium image (*d*) demonstrates no dominant enhancing areas worrisome for neoplasm. Coronal T2-weighted SS-ETSE (*e*) and transverse T1-weighted fat-suppressed postgadolinium SGE (*f*) images in a second patient show the same findings described above. Evaluation for neoplasm in cystic kidneys such as these is difficult because of the varying signal of cysts. Transverse

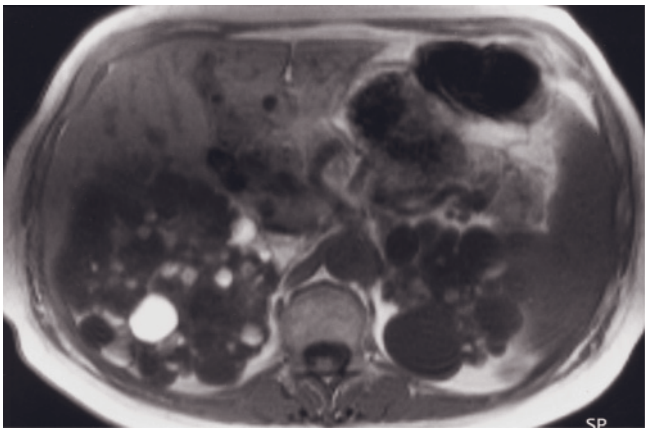

(*g*)

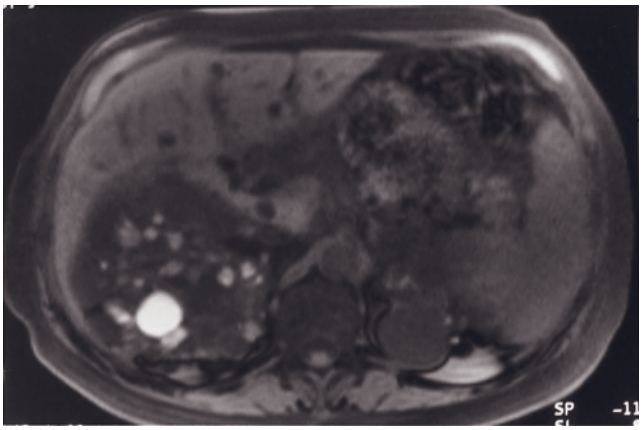

(*h*)

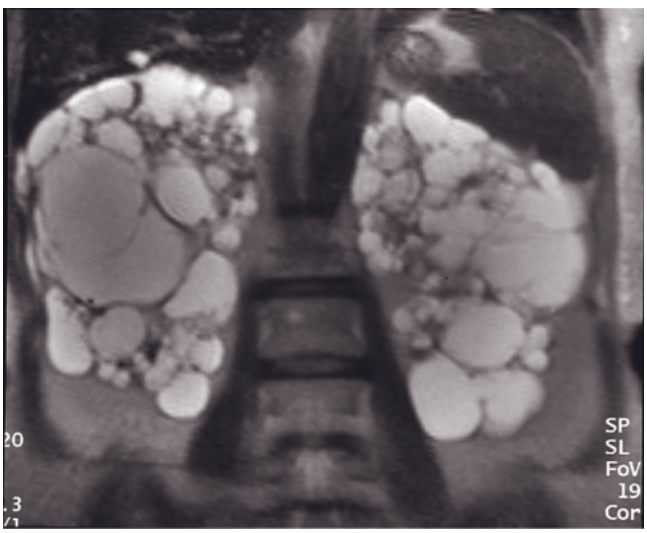

(*i*)

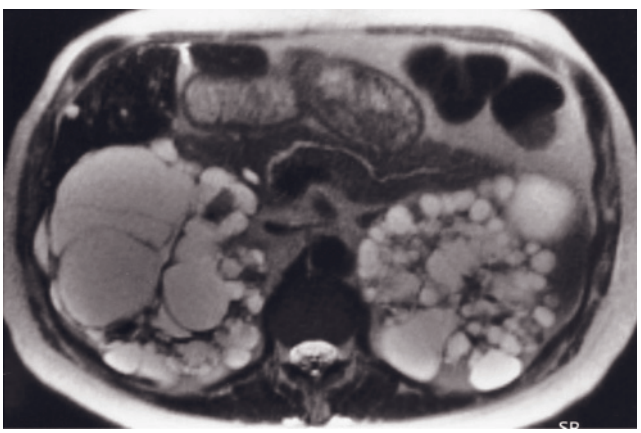

(*j*)

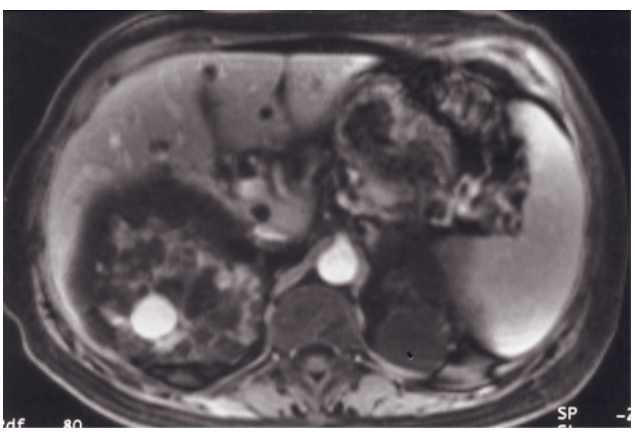

(*k*)

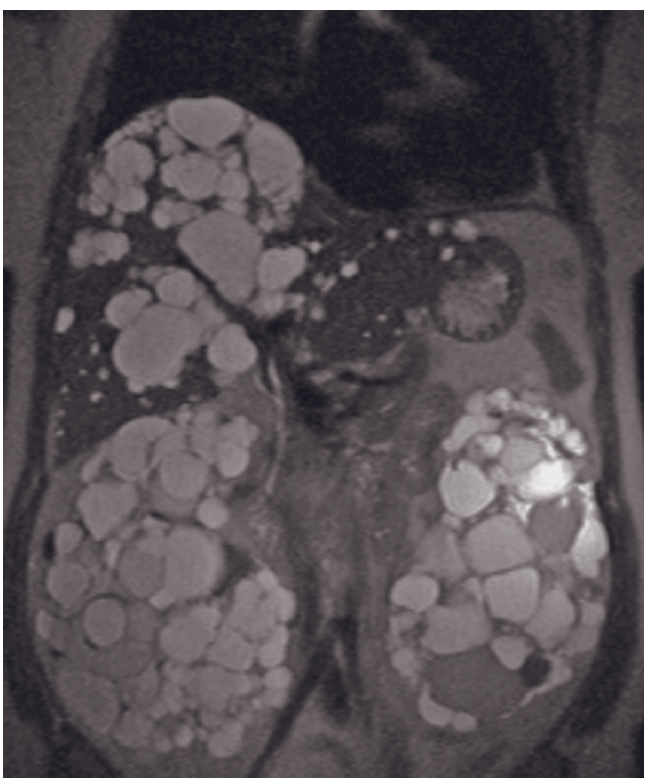

(*l*)

Fig. 9.24 (*Continued*) T1-weighted precontrast (*g*) and precontrast fat-suppressed (*h*) SGE images, coronal (*i*) and transverse (*j*) T2-weighted SS-ETSE images, and T1-weighted 90-s fat-suppressed postgadolinium SGE image (*k*) in a third patient. The kidneys are massively enlarged and contain multiple cysts of varying sizes scattered throughout the renal parenchyma, distorting renal architecture. Several cysts are high in signal intensity on precontrast T1-weighted image (*g*), and the high signal intensity is accentuated on the fat-suppressed image (*h*). The hemorrhagic cysts vary in signal intensity on T2-weighted images (*i*, *j*), consistent with blood products of varying age. Minimal enhancing parenchyma is apparent on late-phase image (*k*). Coronal T2-weighted

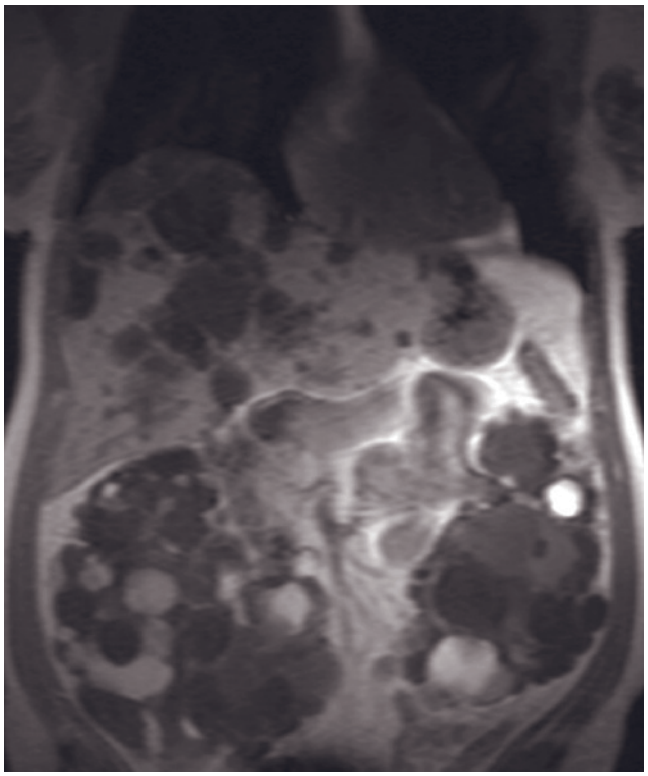

(*m*)

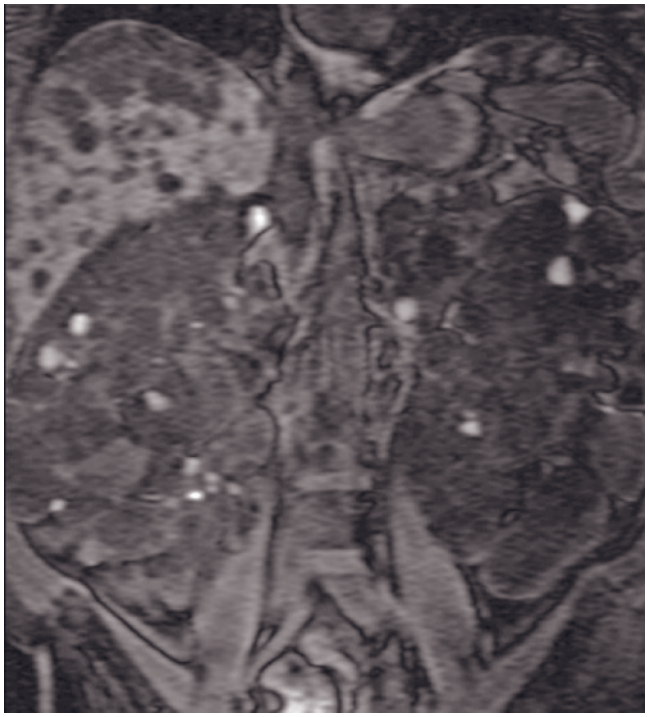

(*n*)

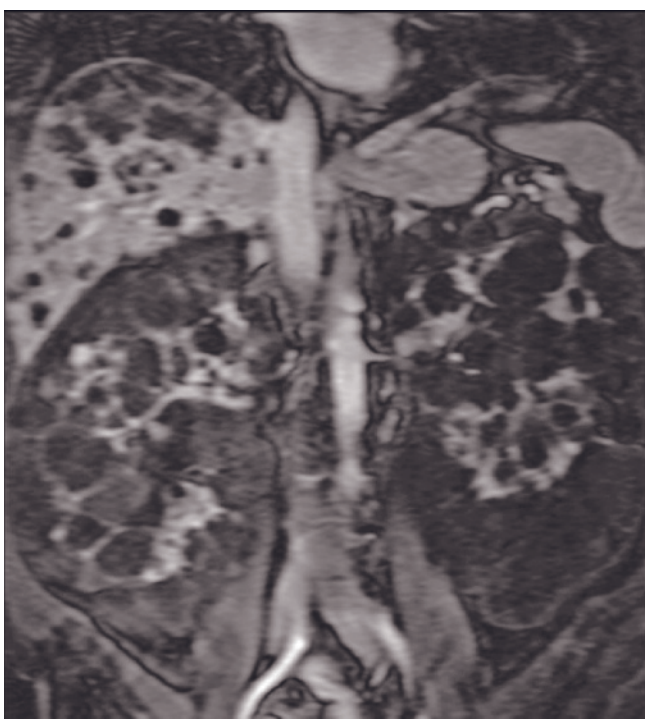

(*o*)

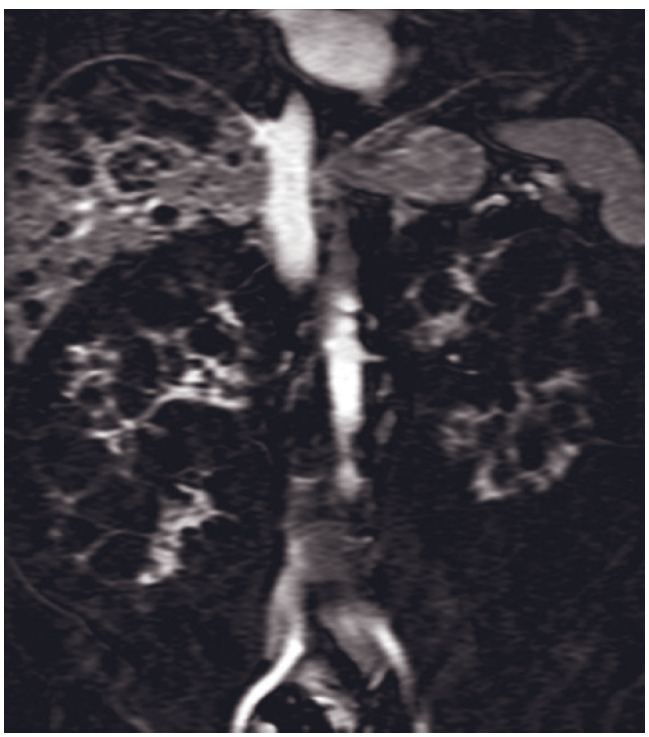

(*p*)

Fig. 9.24 (*Continued*) single-shot echo-train spin-echo image (*l*), coronal T1-weighted SGE image (*m*), coronal T1-weighted fat-suppressed 3D-GE image (*n*), and coronal T1-weighted postgadolinium fat-suppressed venous-phase 3D-GE image (*o*) and its corresponding subtraction image (*p*) demonstrate autosomal dominant polycystic kidney disease in another patient. The kidneys are enlarged, and most of the renal parenchyma is replaced with multiple cysts bilaterally. Note that there are many cysts in the liver as a component of the disease. The cysts show various signal intensities on T2-weighted (*l*) and T1-weighted (*m*) images, suggesting the presence of blood products at various stages, or proteinaceous material. High signal intensity of cysts may impair the detection of renal cell cancers on postgadolinium T1-weighted images; therefore, subtraction images (*p*), which are acquired by the subtraction of precontrast T1-weighted images (*n*) from postgadolinium images (*o*), are particularly helpful for the detection of renal cell cancers. However, the acquisition planes and slice locations should be exactly the same in order to get reliable results. Subtraction image (*p*) shows the enhancement of remaining renal parenchyma but no enhancement of any focal solid mass. T2-weighted short

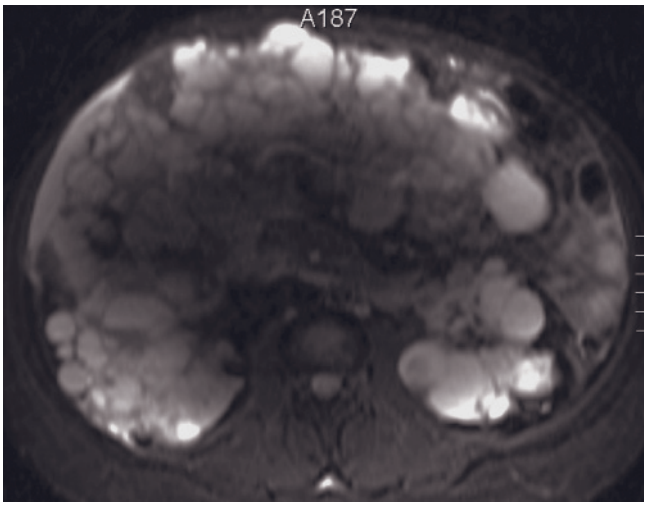

(*q*)

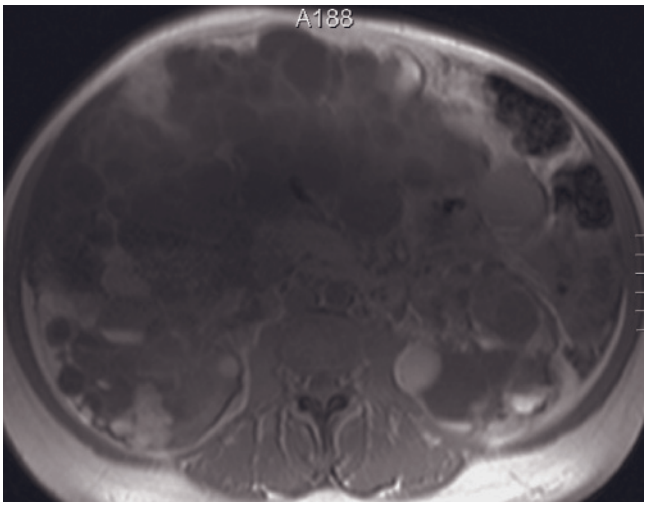

(*r*)

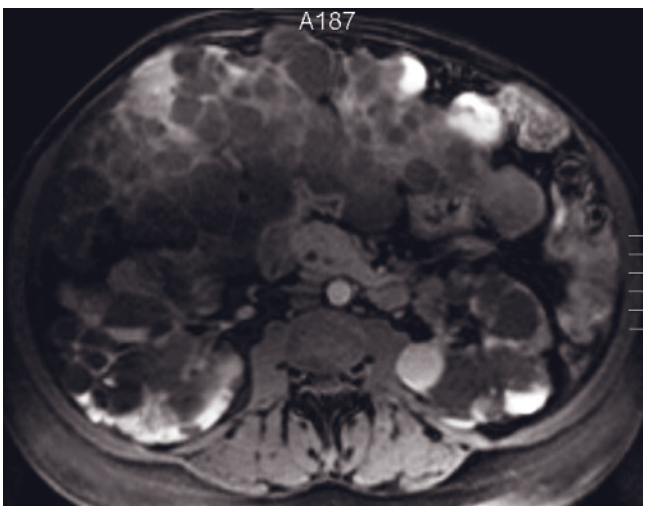

(*s*)

FIG. 9.24 (*Continued*) tau inversion recovery (STIR) (*q*), T1-weighted SGE (*r*), and T1-weighted postgadolinium interstitial-phase fat-suppressed 3D-GE (*s*) images at 3.0 T demonstrate multiple cysts replacing the liver and bilateral renal parenchymas in another patient with autosomal dominant polycystic kidney disease. The cysts show various signal intensities on T2-weighted (*q*) and T1-weighted (*r*) images, suggesting the presence of blood products at various stages, or proteinaceous material. No focal solid mass enhancement is detected on postgadolinium image (*s*). Note that there is a signal loss at the center of STIR and SGE images due to standing wave artifact, which is particularly seen at 3.0 T.

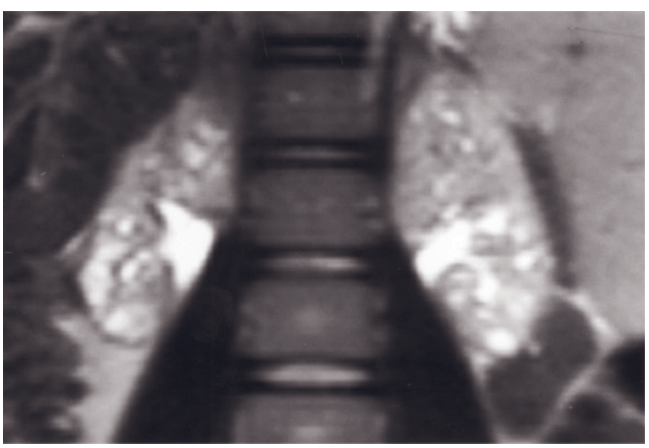

(*a*)

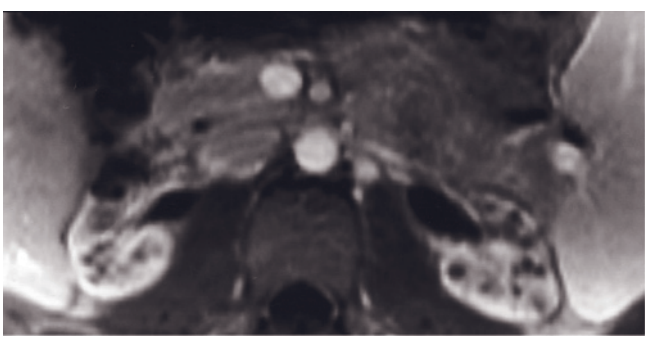

(*b*)

FIG. 9.25 Autosomal recessive polycystic kidney disease. Coronal T2-weighted SS-ETSE (*a*) and transverse T1-weighted immediate (*b*) and 90-s fat-suppressed (*c*) postgadolinium SGE images in a patient with autosomal recessive polycystic kidney disease.

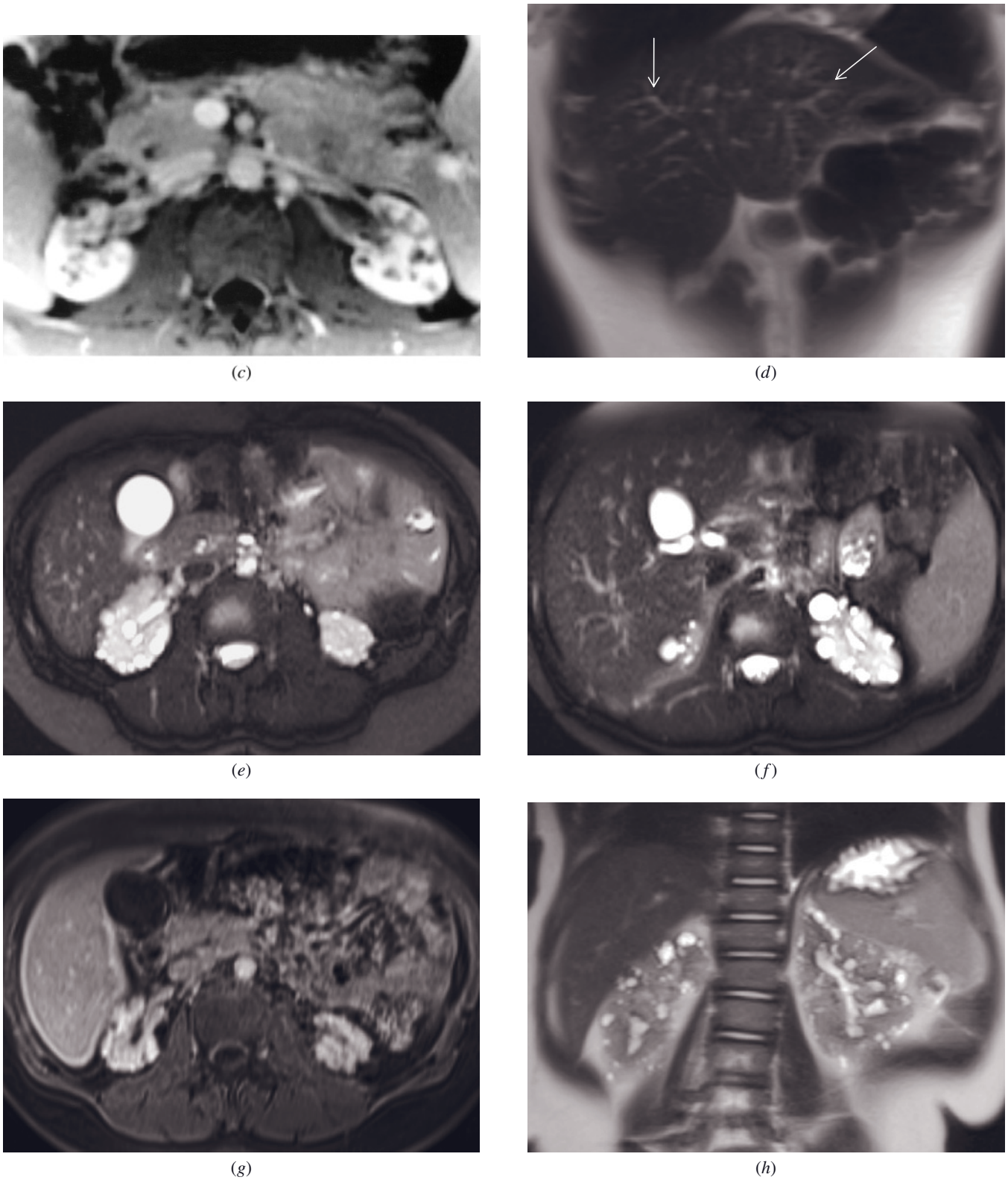

FIG. 9.25 (*Continued*) The kidneys are small, with multiple tiny cysts scattered throughout the renal parenchyma. Coronal T2-weighted single-shot echo-train spin-echo (*d*), transverse T2-weighted fat-suppressed single-shot echo-train spin-echo (*e*, *f*), and T1-weighted postgadolinium interstitial-phase fat-suppressed 3D-GE (*g*) images demonstrate autosomal recessive polycystic kidney disease in another patient. The kidneys are atrophic and have undulated contours. There are multiple small-sized cysts in both kidneys, and bilateral collecting systems are mildly dilated. All cysts show homogeneous internal structure with high signal intensity. Note that the bile ducts are mildly dilated in the liver as well. Coronal T2-weighted single-shot echo-train spin-echo (*h*) and transverse

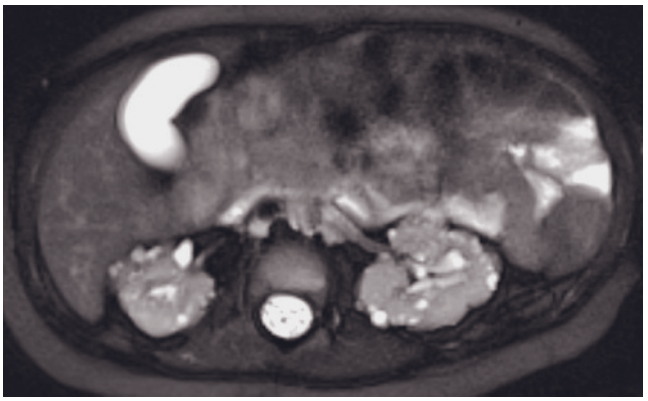

(*i*)

FIG. 9.25 (*Continued*) T2-weighted fat-suppressed single-shot echo-train spin-echo (*i*) images demonstrate autosomal recessive polycystic kidney disease in another patient. Many small cysts that show homogeneous internal structure with high signal intensity are detected in both kidneys. Bilateral collecting systems are mildly dilated, and the kidneys are atrophic.

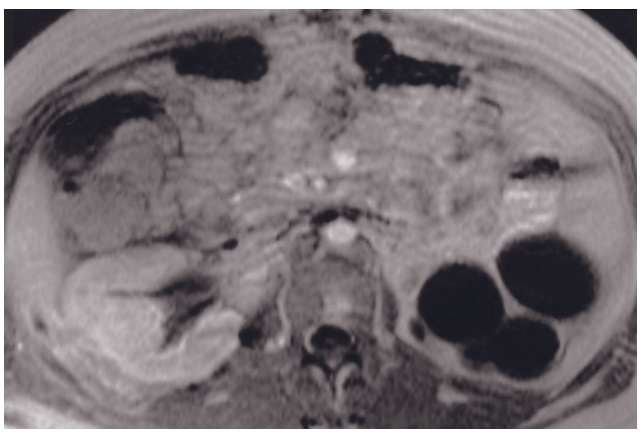

(*a*)

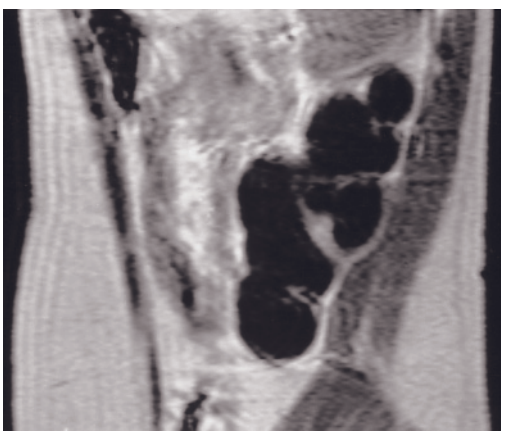

(*b*)

FIG. 9.26 Multicystic dysplastic kidney. Transverse 2-min (*a*) and sagittal 2.5-min (*b*) T1-weighted postgadolinium SGE images. A multicystic dysplastic kidney is present in the left renal fossa that has a cluster of grapes appearance with no evidence of organization into a renal collecting system and no renal parenchyma evident.

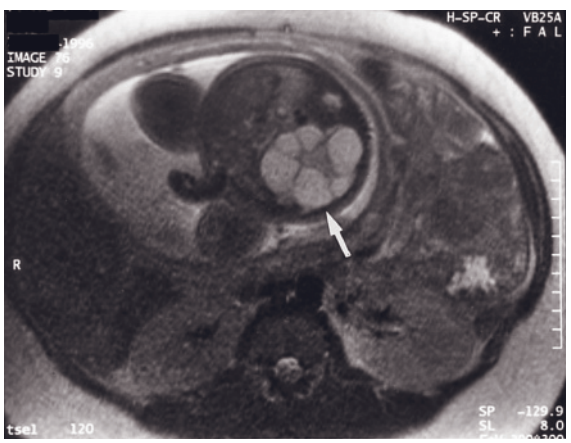

(*a*)

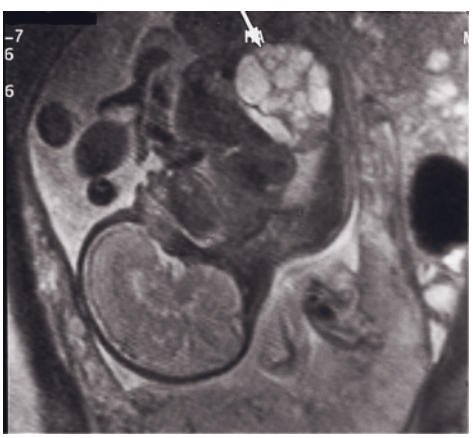

(*b*)

FIG. 9.27 Multicystic dysplastic kidney in fetus. Transverse (*a*) and sagittal (*b*) T2-weighted SS-ETSE images of a fetus demonstrate a multicystic mass in the left renal fossa (arrows, *a*, *b*) with no evidence of organization into a renal collecting system.

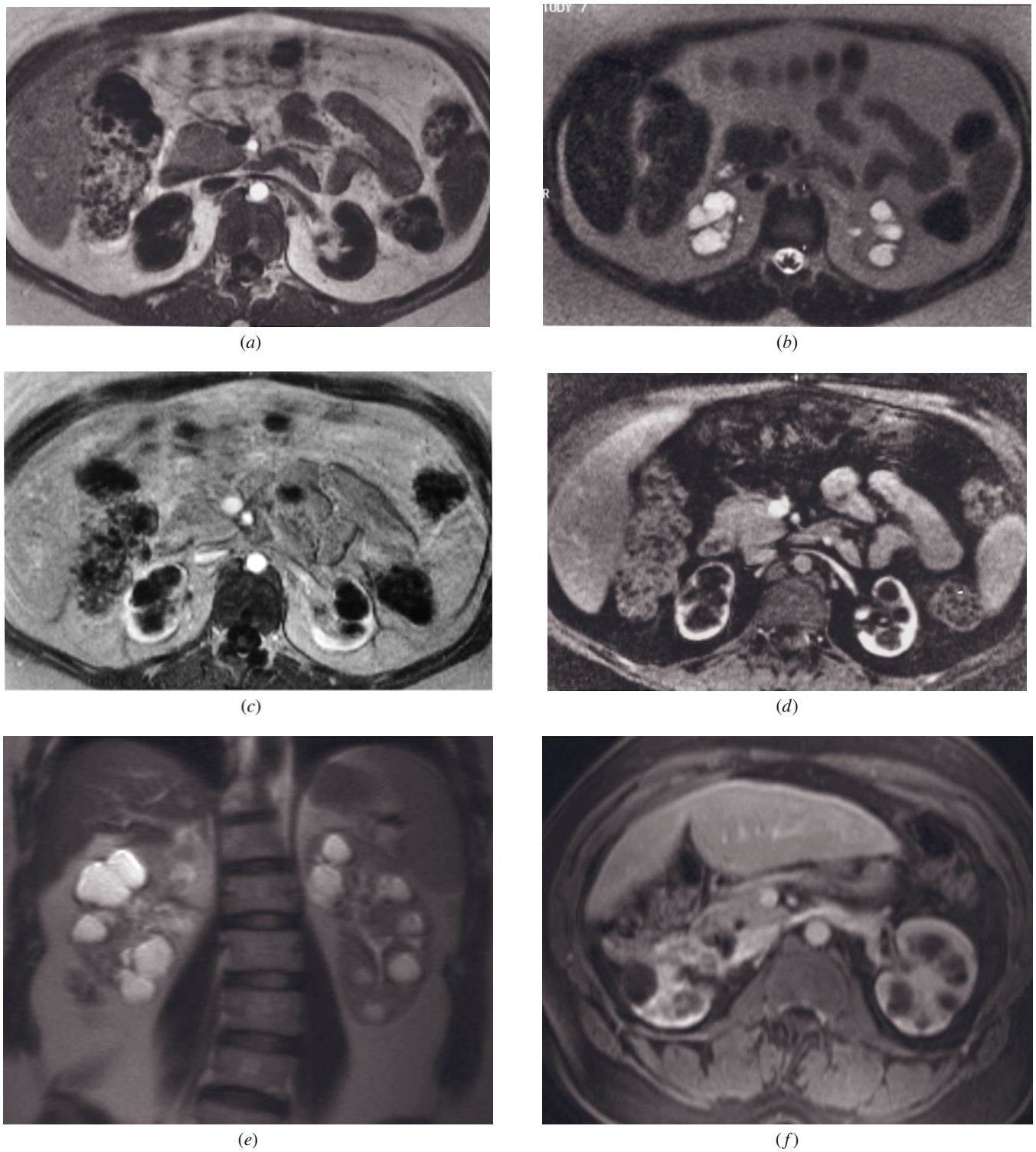

FIG. 9.28 Medullary cystic disease. T1-weighted precontrast SGE (*a*), T2-weighted SS-ETSE (*b*), and T1-weighted immediate (*c*) and 90-s fat-suppressed (*d*) postgadolinium SGE images. Multiple cysts measuring <2 cm in diameter occupy the majority of the renal medulla. These simulate the appearance of corticomedullary differentiation on precontrast images (*a*) in this patient with chronic renal failure. The cysts are homogeneously high in signal intensity on the T2-weighted image (*b*). After gadolinium administration cysts in the renal medulla do not enhance and appear nearly signal void (*c*, *d*). Coronal T2-weighted single-shot echo-train spin-echo (*e*) and transverse T1-weighted postgadolinium interstitial-phase 3D-GE (*f*) images demonstrate medullary cystic disease in another patient. Multiple cysts mainly located in the medulla of both kidneys are detected. These cysts show homogeneous internal structure and high signal on T2-weighted image (*e*) and no enhancement on T1-weighted postgadolinium image (*f*).

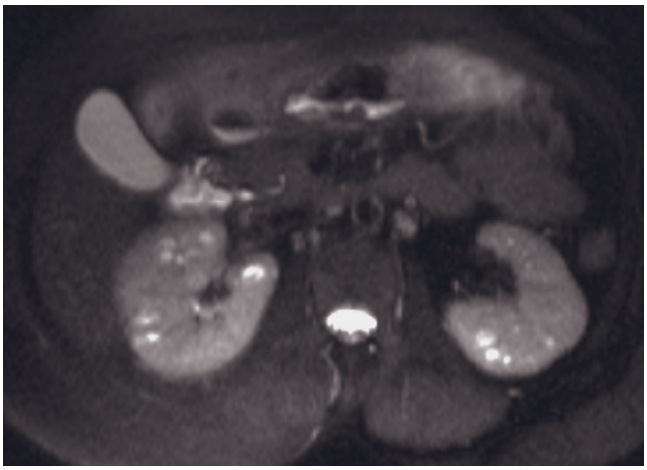

(*g*)

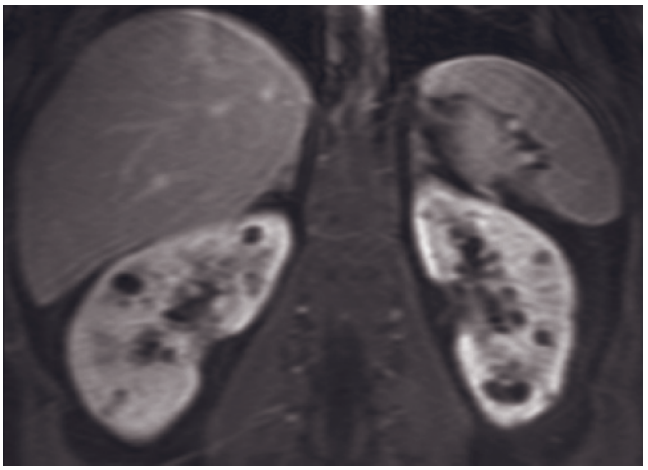

(*h*)

FIG. 9.28 (*Continued*) Transverse T2-weighted fat-suppressed single-shot echo-train spin-echo (*g*) and transverse T1-weighted postgadolinium interstitial-phase fat-suppressed 3D-GE (*h*) images demonstrate multiple medullary cysts in another patient with medullary cystic disease.

(*a*)

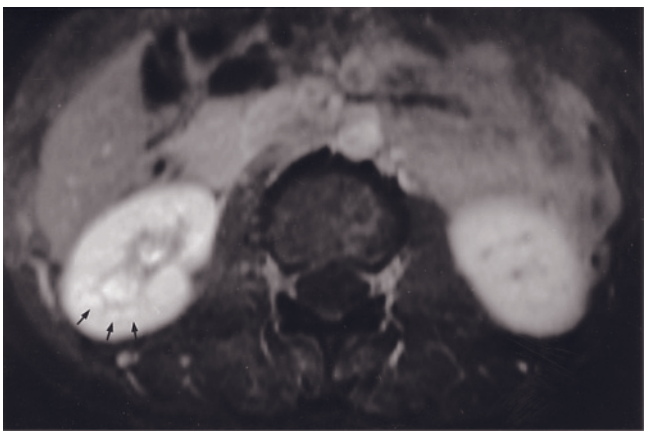

(*b*)

FIG. 9.29 Medullary sponge kidney. Five-minute intravenous urogram (*a*) and T1-weighted 90-s fat-suppressed gadolinium-enhanced SE (*b*) images. Tubular ectasia is apparent on the intravenous urogram (arrows, *a*), and prominent papillary enhancement is present on 90-s gadolinium-enhanced image (arrows, *b*).

Multilocular Cystic Nephroma (Cystic Nephroma). Multilocular cystic nephroma is an uncommon benign lesion, which is usually unilateral, solitary, and sharply demarcated from surrounding uninvolved renal tissue. Cystic nephromas are composed of multiple noncommunicating cysts separated by a fibrous stroma. This lesion has been described as occurring most frequently in boys aged 2 months to 4 years as well as adults, predominantly women, aged 40 years and older [27]. In one MR study [28], adult-type multilocular cystic nephromas were observed in men and women in their 20s and 30s in an approximately equivalent sex distribution. The diagnosis of multilocular cystic nephroma on MR images requires the demonstration of a multicystic renal mass that bulges into the renal pelvis and has thick (2–4 mm), relatively uniform, fibrous septations (fig. 9.33) [28, 29]. Septations are well defined and relatively low in signal intensity on T2-weighted images and enhance on postgadolinium images [28]. Usually cysts are low in signal intensity on T1-weighted images, but not uncommonly they are high in signal intensity, presumably reflecting the presence of proteinaceous material or blood (fig. 9.34) [28, 29]. Transverse images should be supplemented with sagittal or coronal images to demonstrate the indentation into renal pelvis.

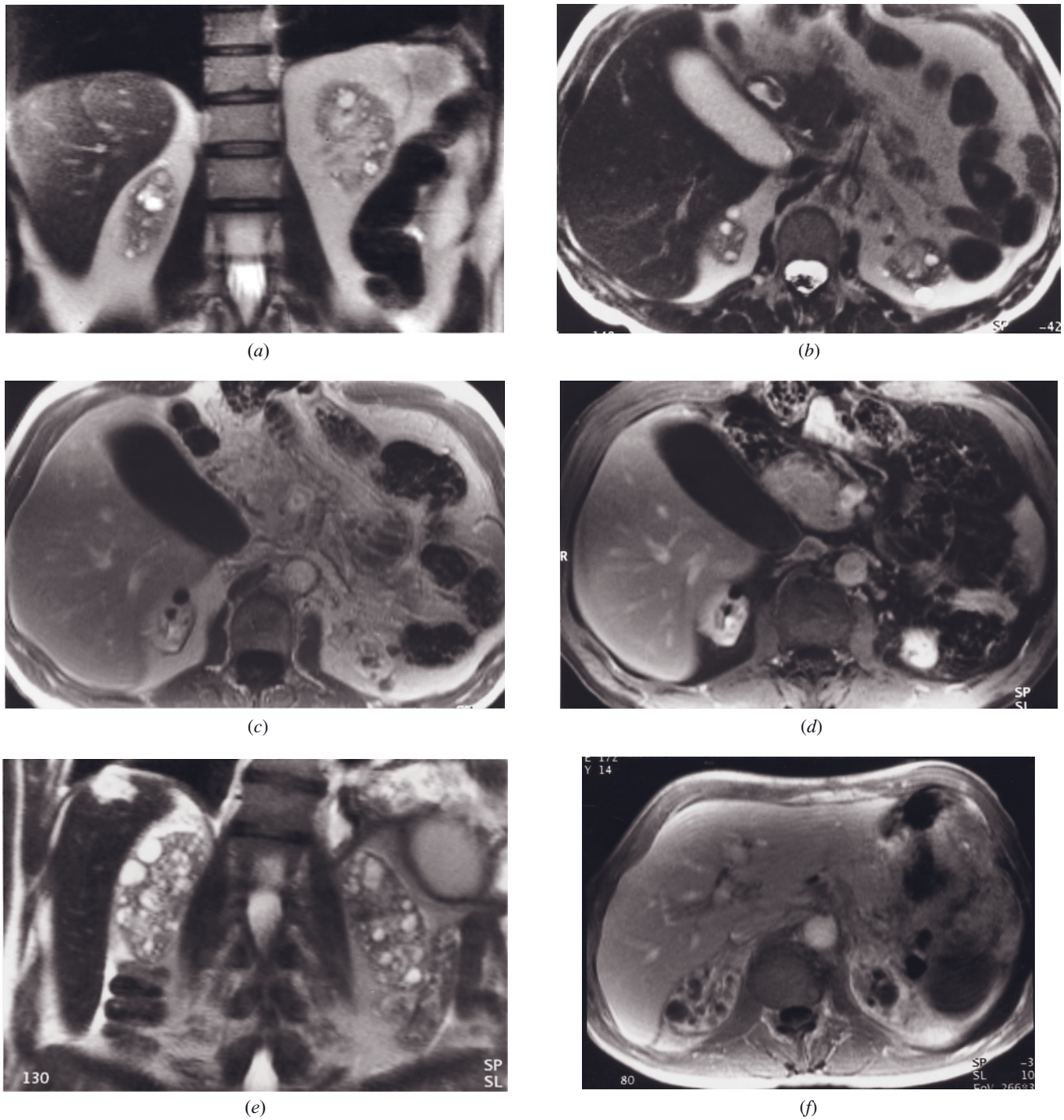

FIG. 9.30 Acquired cystic disease of dialysis. Coronal (*a*) and transverse (*b*) T2-weighted SS-ETSE and transverse T1-weighted immediate (*c*) and 90-s fat-suppressed (*d*) postgadolinium SGE images. Multiple cysts <2 cm in diameter are present in both kidneys, located predominantly in a superficial cortical location. The capillary phase of enhancement (*c*) demonstrates minimal parenchymal enhancement and no corticomedullary differentiation. On the gadolinium-enhanced T1-weighted fat-suppressed spin-echo image (*c*), multiple renal cysts are well shown in a background of moderately enhanced atrophic parenchymal tissue. Coronal T2-weighted SSETSE (*e*) and transverse T1-weighted 90-s fat-suppressed postgadolinium SGE (*f*) images in a second patient on chronic hemodialysis with Alport syndrome. Multiple small cysts are scattered throughout the kidneys.

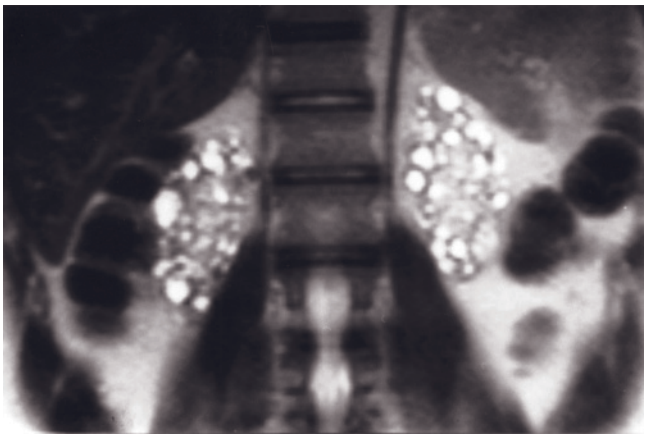

(*a*)

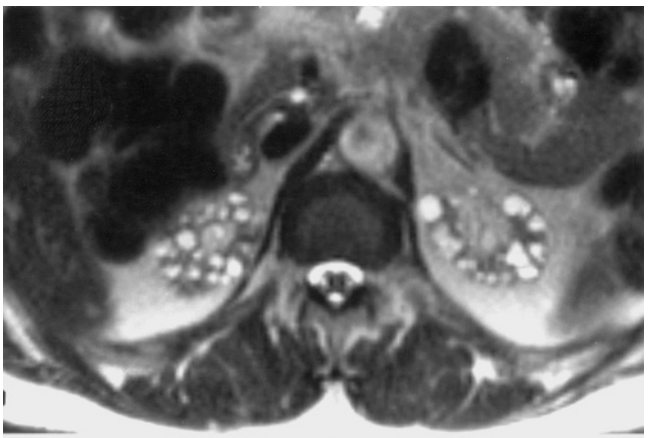

(*b*)

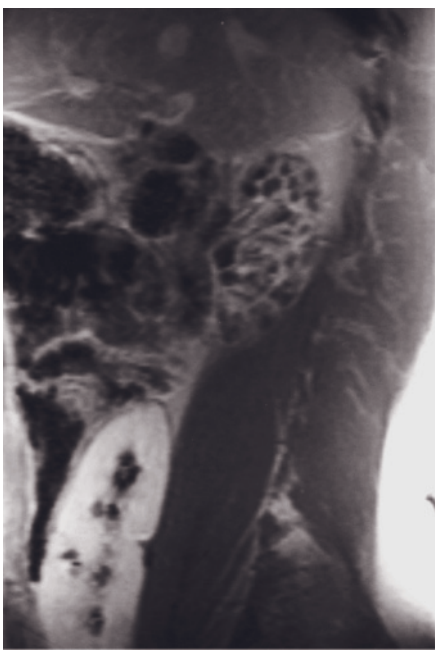

(*c*)

FIG. 9.31 Acquired cystic disease of dialysis. Coronal (*a*) and transverse (*b*) T2-weighted SS-ETSE and sagittal T1-weighted late-phase fat-suppressed postgadolinium SGE (*c*) images. Extensive multiple bilateral renal cysts with high signal on T2-weighted images (*a*, *b*) and low signal on T1-weighted postgadolinium images (*c*) are present in atrophic native kidneys. Note also transplanted kidney in the right pelvis (*c*).

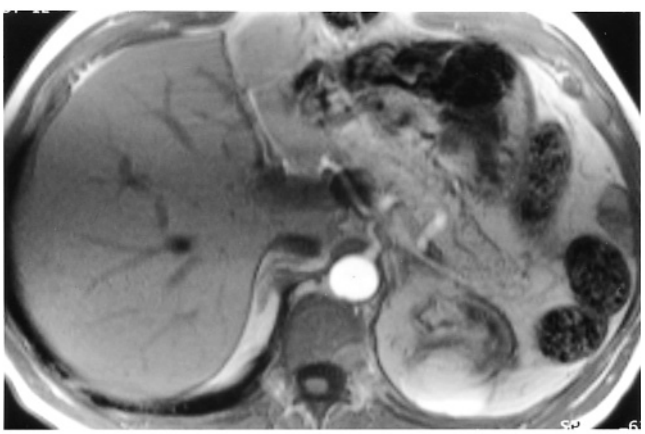

(*a*)

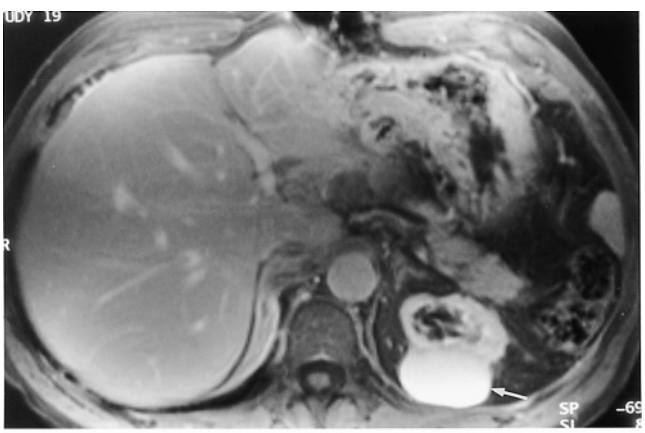

(*b*)

FIG. 9.32 Hemorrhagic large renal cyst in cystic disease of dialysis. T1-weighted immediate (*a*) and 90-s fat-suppressed (*b*) SGE images demonstrate a superficial 4-cm cyst arising from the posterior left renal cortex that is homogeneously high signal intensity on T1-weighted images (arrow, *b*), compatible with hemorrhagic cyst.

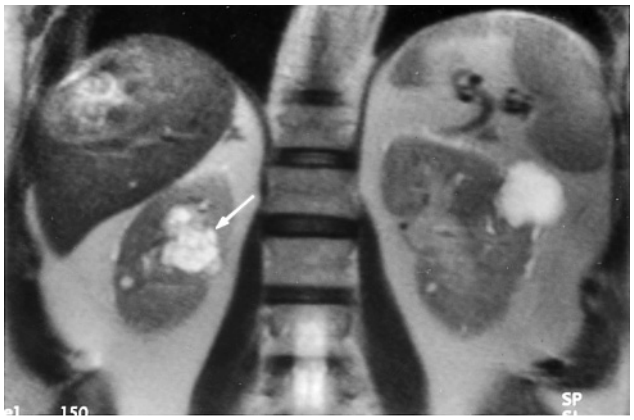

(*a*)

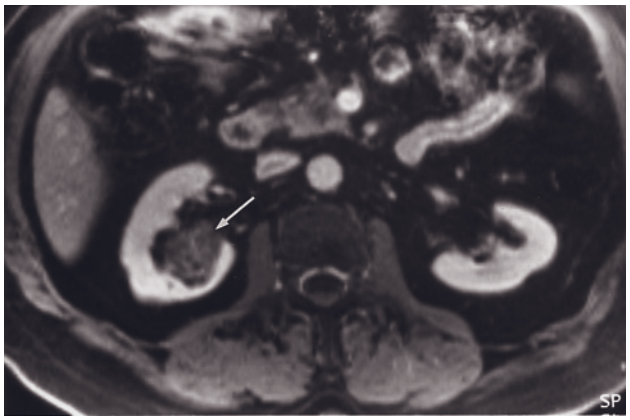

(*b*)

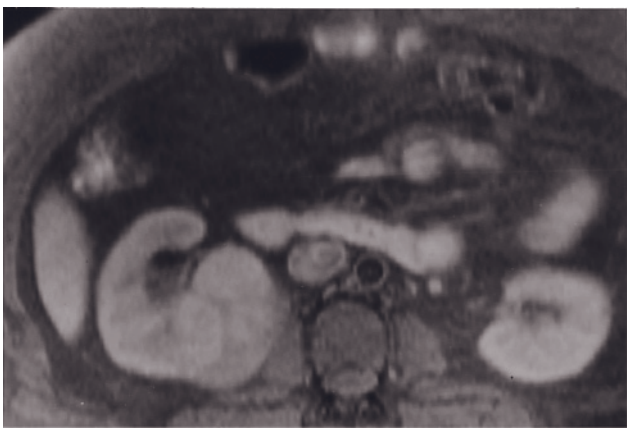

(*c*)

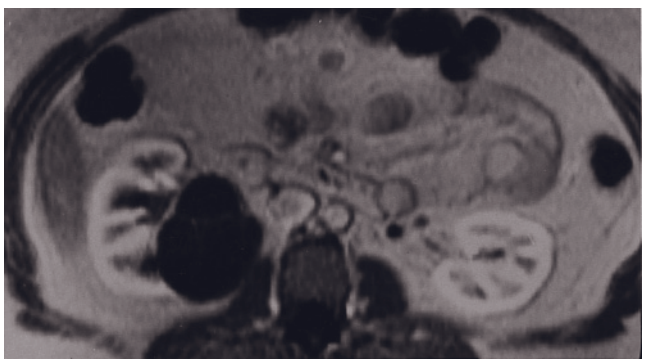

(*d*)

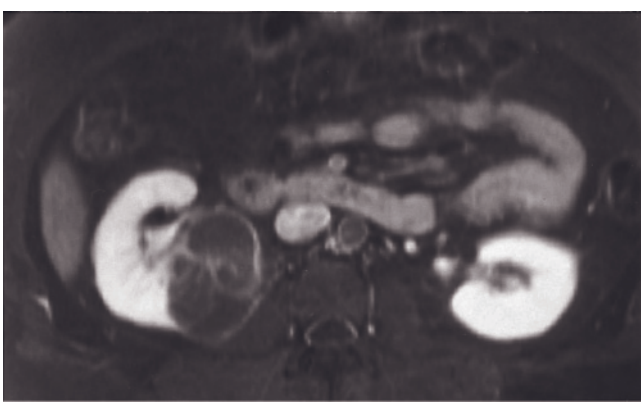

(*e*)

FIG. 9.33 Multilocular cystic nephroma. Coronal T2-weighted SS-ETSE (*a*) and transverse T1-weighted 90-s fat-suppressed gadolinium-enhanced SGE (*b*) images. A well-defined cystic mass arises from the posterior aspect of the right kidney. Internal septations are present, which are low in signal intensity on the T2-weighted image (arrow, *a*) and enhance on the post-contrast T1-weighted image (arrow, *b*).The lesion is noted to bulge into the renal pelvis. These imaging features are typical for multilocular cystic nephroma. This location is also common, arising in the posterior cortex of the kidney at the midrenal level. T1-weighted precontrast fat-suppressed SE (*c*), T1-weighted immediate postgadolinium SGE (*d*), and T1-weighted fat-suppressed gadolinium-enhanced SE (*e*) images in a second patient with multilocular cystic nephroma demonstrate a similar-appearing cystic mass that bulges into the renal pelvis and contains enhancing internal septations. Note that the cyst contents are intermediate in signal intensity on the precontrast T1-weighted image (*c*).

Angiomyolipoma. Angiomyolipomas are benign tumors composed of variable amounts of three elements: 1) thick-walled blood vessels, 2) smooth muscle, and 3) mature fat. The fat component is usually substantial, permitting characterization on CT images and on combined T1-weighted regular (in phase) and fat-suppressed images or combined T1-weighted in-phase and out-of-phase SGE images [30]. Although benign, these tumors may increase in size over time, with larger tumors having greater propensity to bleed [31–33]. Angiomyolipomas have a greater tendency to increase in size when they are multiple than when they are solitary [31–33]. Lesions may be detected and characterized, even when they are <1 cm in diameter, because of the high signal intensity of fat on T1-weighted images that attenuates on fat-suppressed images (fig. 9.35).

FIG. 9.34 Multilocular cystic nephroma. T1-weighted precontrast fat-suppressed SE image demonstrates a multilocular cystic nephroma in the lower pole of the left kidney. Many of the cysts are high in signal intensity, compatible with either subacute blood or protein. Cysts are not uncommonly high in signal intensity on T1-weighted images in multilocular cystic nephroma.

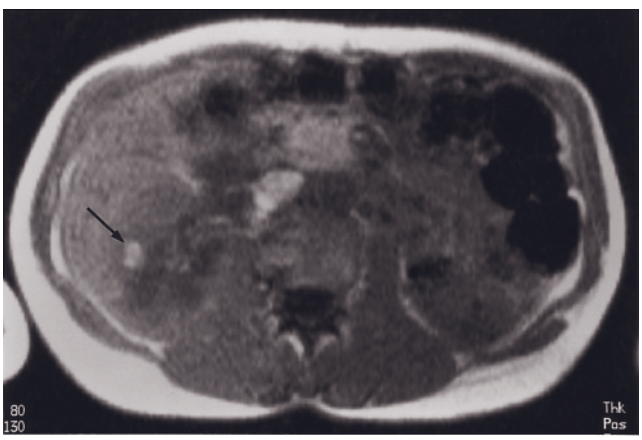

(*a*)

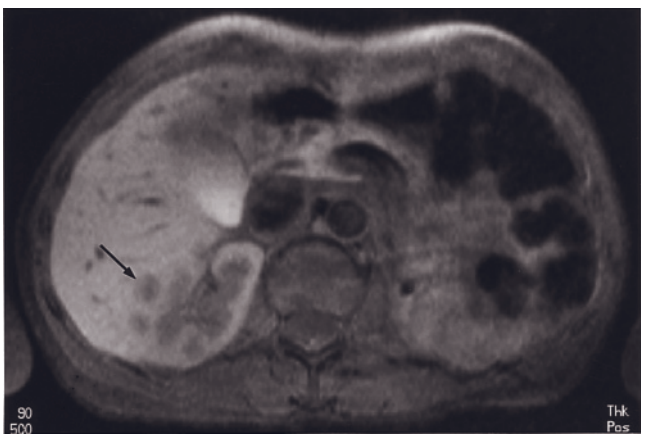

(*b*)

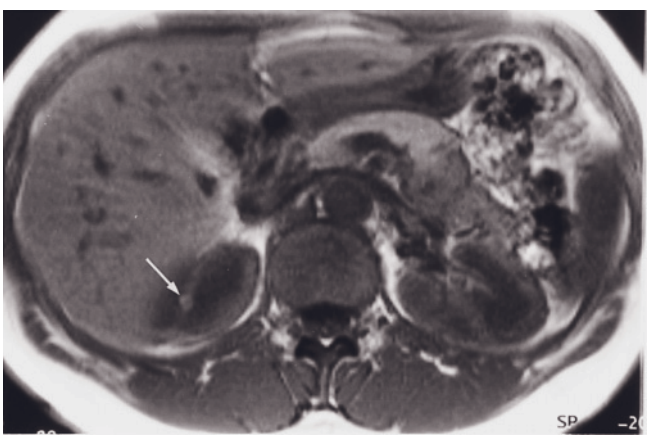

(*c*)

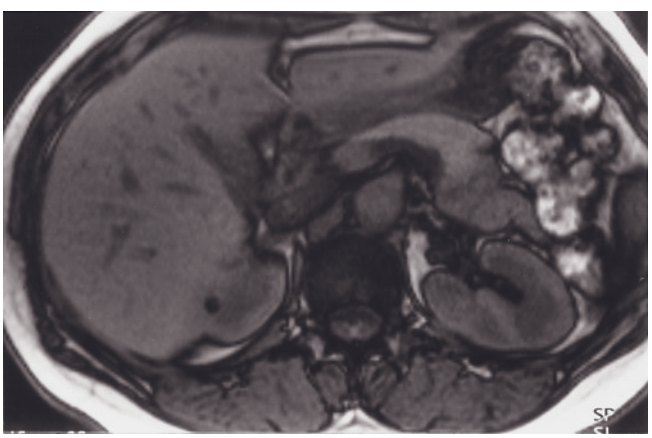

(*d*)

FIG. 9.35 Small angiomyolipoma. T1-weighted precontrast SGE (*a*) and precontrast fat-suppressed SE (*b*) images. A small high-signal-intensity lesion arises from the upper pole of the right kidney on the SGE image (arrow, *a*). Fat suppression decreases the signal intensity of this lesion (arrow, *b*), confirming that it represents an angiomyolipoma. T1-weighted precontrast in-phase (*c*) and out-of-phase (*d*) SGE and 90-s fat-suppressed gadolinium-enhanced SGE (*e*) images in a second patient demonstrate a high-signal-intensity tumor on the in-phase image (arrow, *c*) that becomes signal void on the out-of-phase image (*d*) because of phase-cancellation artifact. The lesion is very low in signal on the postgadolinium fat-suppressed image (*e*). T1-weighted precontrast

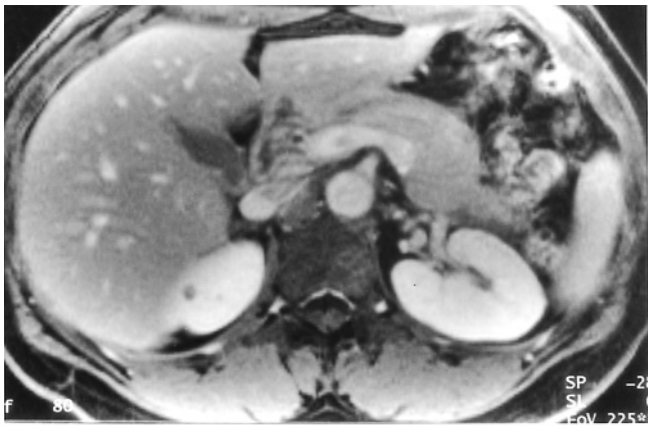

(*e*)

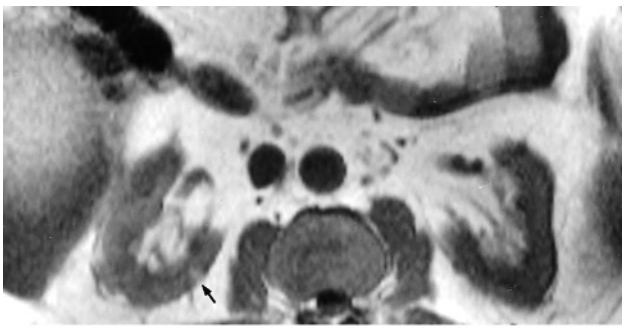

(*f*)

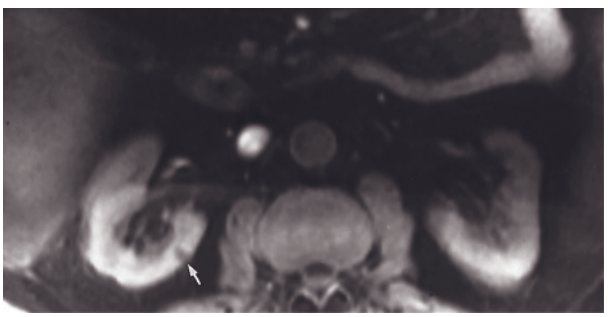

(*g*)

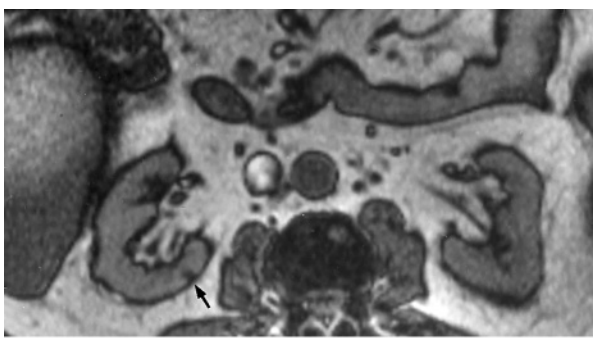

(*h*)

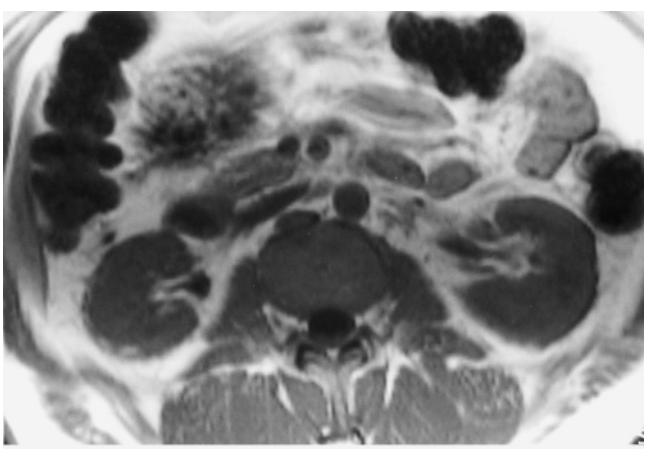

(*i*)

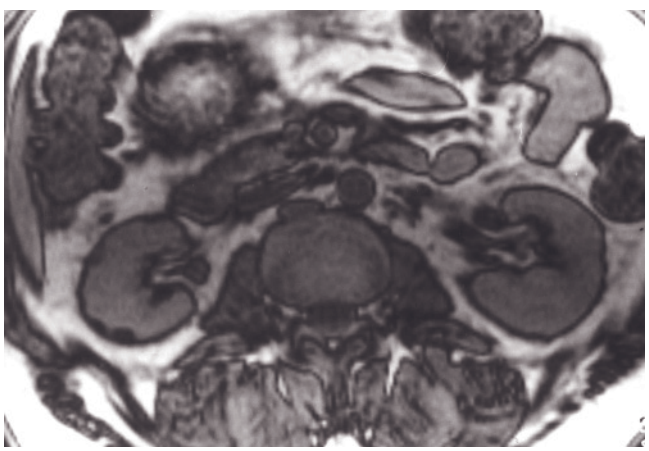

(*j*)

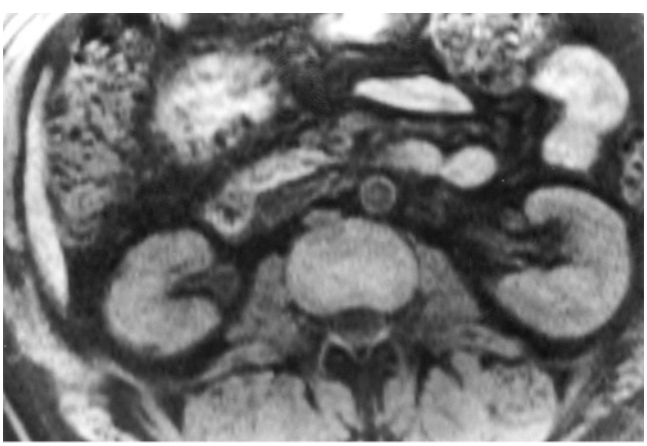

(*k*)

FIG. 9.35 (*Continued*) in-phase (*f*), precontrast fat-suppressed (*g*), and out-of-phase (*h*) SGE images in a third patient. A 6-mm angiomyolipoma is present in the right kidney that is high in signal intensity on the in-phase image (arrow, *f*), suppresses to low signal intensity on the fat-suppressed image (arrow, *g*), and is signal void on the out-of-phase image (arrow, *h*). T1-weighted precontrast in-phase (*i*), out-of-phase (*j*), and fat-suppressed (*k*) SGE images in a fourth patient demonstrate tiny lesions that arise in a subcapsular location in the mid-right kidney. These lesions are high signal on T1, signal void on out-of-phase (phase cancellation), and low signal on fat-suppressed (fat suppression effect) images.

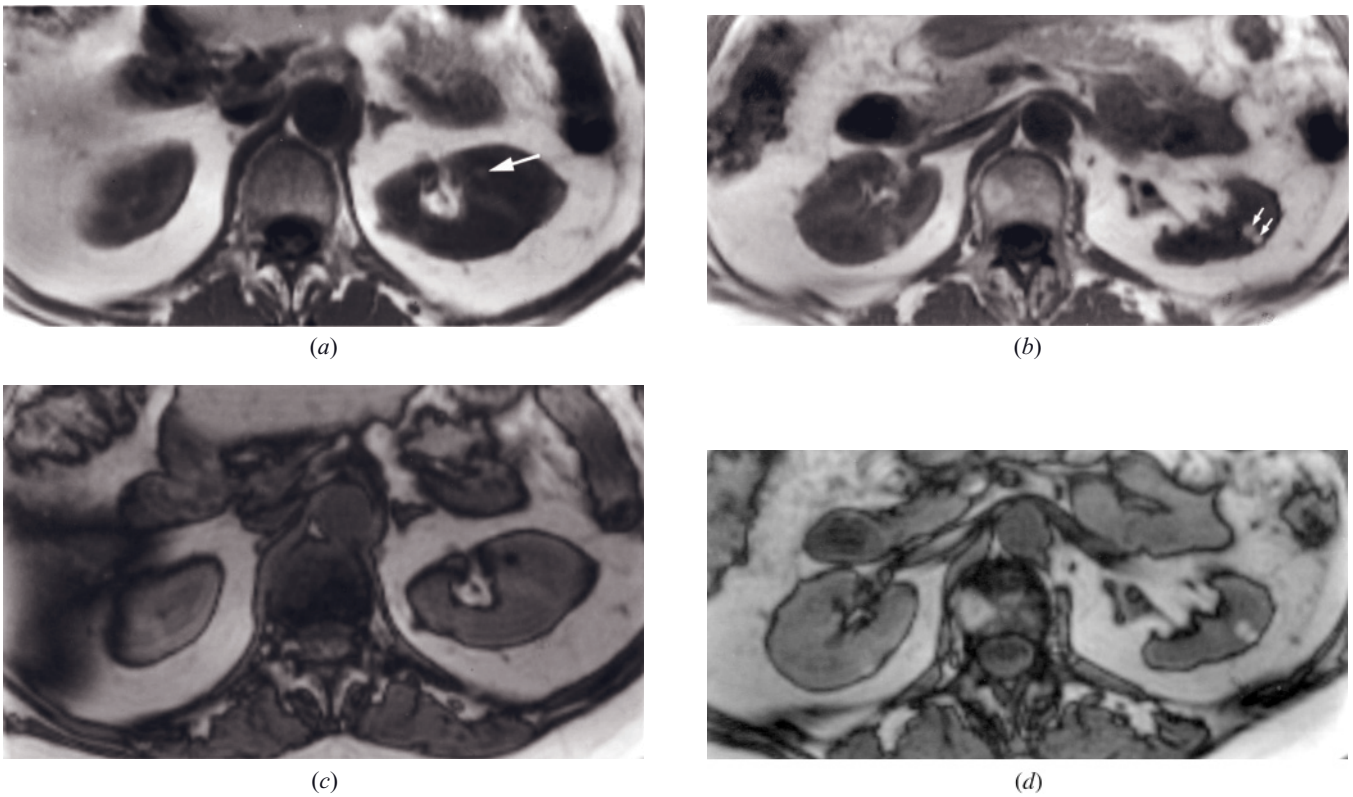

FIG. 9.36 Angiomyolipoma and hemorrhagic cyst. T1-weighted precontrast in-phase (*a*, *b*) and out-of-phase (*c*, *d*) SGE images. The angiomyolipoma (arrow, *a*) is high signal on in-phase and signal void on out-of-phase (*c*) images. The hemorrhagic cysts (arrows, *b*) are high signal on in-phase (*b*) and out-of-phase (*d*) images.

Out-of-phase images are a useful addition to an imaging protocol performed to characterize renal masses as angiomyolipomas (figs. 9.36 and 9.37). A fat-water signal-void phase-cancellation occurs at the boundary between the angiomyolipoma and the adjacent renal parenchyma [34]. When angiomyolipomas are very small (<1 cm) the phase cancellation may occupy the entire lesion and render it signal void (fig. 9.37) [34]. In a small number of cases, when muscle or vascular components predominate, distinction from renal cell cancer may be difficult. When the diagnosis, based on imaging findings, is certain and tumors are <4 cm in size and asymptomatic, imaging follow-up is adequate management [32, 35]. Case reports have described renal cell cancers that contain a small volume of fat [36]. Uniform distribution of a high concentration of fat in renal cell cancer has not been described, unlike angiomyolipoma, in which fat content is usually relatively uniform and prominent. A heterogeneous-appearing mass with foci of fat should be considered an indeterminant lesion.

Tuberous Sclerosis (Bourneville Disease). Tuberous sclerosis is a neurocutaneous syndrome, part of the general category of phacomatoses with autosomal dominant inheritance, although approximately 50% arise from spontaneous mutation. This disorder is characterized by mental retardation, epilepsy, and cutaneous lesions [37].

Patients with tuberous sclerosis have an increased incidence of renal cysts and angiomyolipomas. Cystic disease varies considerably in extent and is usually multiple and bilateral [37–39]. Renal architecture is not uncommonly distorted. Cystic disease may be so extensive that the kidney disease may resemble ADPKD (fig. 9.38). The incidence of angiomyolipomas is 70–95% (fig. 9.38) [37, 40]. Angiomyolipomas in patients with tuberous sclerosis have a tendency to increase in size over time and to be at increased risk of hemorrhage [31, 37, 40]. It is uncertain whether there is an increased incidence of renal cell carcinoma [40]. Angiomyolipomas may also be noted in liver in up to 13% of patients in the setting of tuberous sclerosis [41].

von Hippel–Lindau Disease. von Hippel–Lindau disease is a neurocutaneous syndrome, part of the general category of phacomatoses with autosomal dominant inheritance. Patients with von Hippel–Lindau disease have an increased incidence of renal cysts,

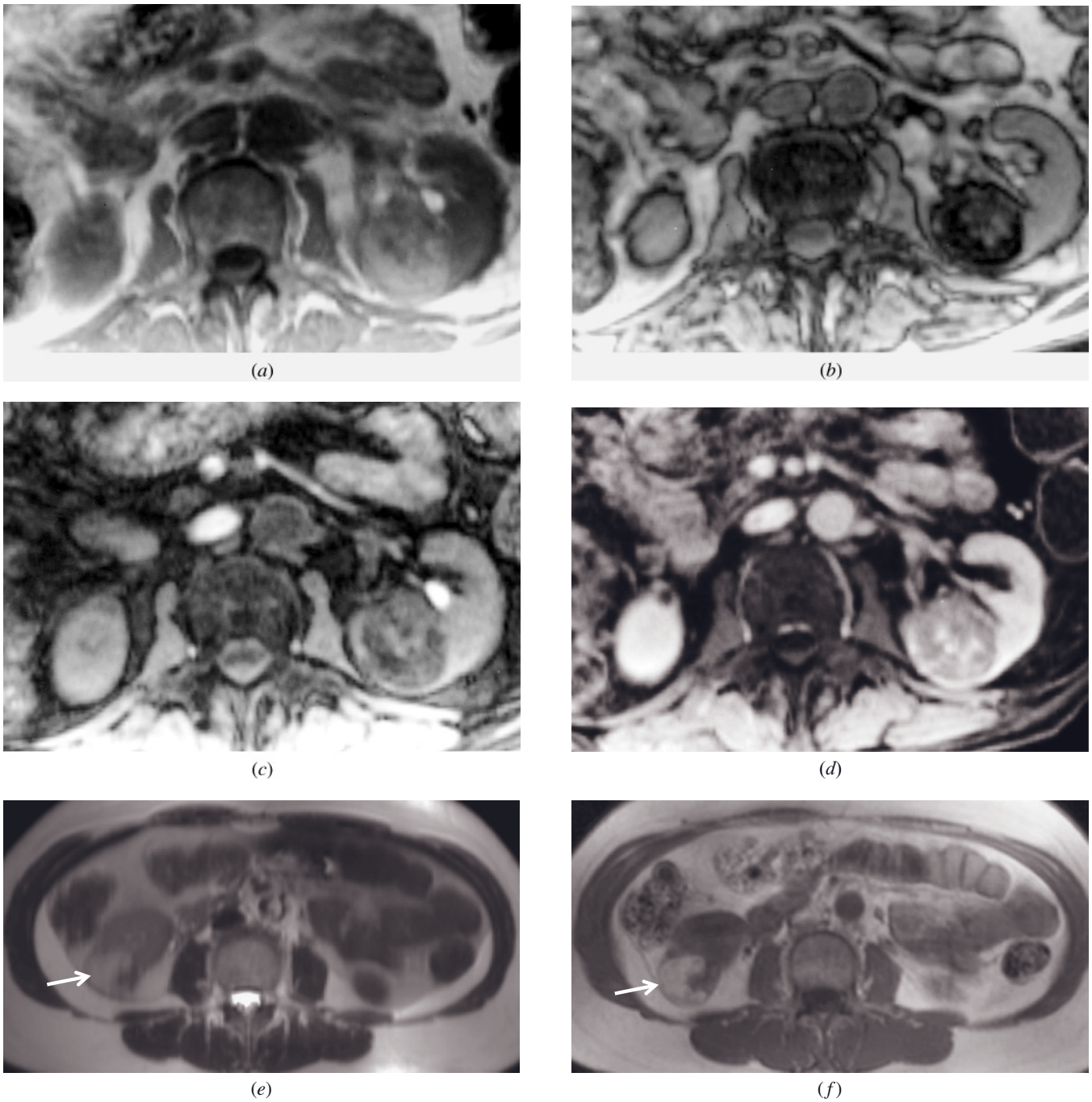

FIG. 9.37 Renal angiomyolipoma. T1-weighted in-phase (*a*) and out-of-phase (*b*) SGE and T1-weighted precontrast (*c*) and postcontrast (*d*) fat-suppressed SGE images. A 4-cm lesion with predominantly high signal on T1-weighted images (*a*) is present in the left kidney, which demonstrates regions of phase cancellation on out-of-phase image (*b*) and decreased signal on precontrast fat-suppressed image (*c*) diagnostic for fat within the lesion that represents an angiomyolipoma. Transverse T2-weighted single-shot echo-train spin-echo (*e*), T1-weighted in-phase (*f*) and out-of-phase (*g*) SGE, and T1-weighted postgadolinium interstitial-phase fat-suppressed 3D-GE (*h*) images at 3.0 T demonstrate an angiomyolipoma (arrows, *e–h*) in another patient. Because the major component of the angiomyolipoma is pure fat, this pure fatty component, which shows high signal intensity on both T2-weighted image and T1-weighted in-phase and out-of-phase images, demonstrates low signal on postgadolinium 3D-GE image because of fat suppression. However, the remaining portion of the angiomyolipoma also shows signal drop on out-of-phase image compared to in-phase image because of its partial fat content. Note that the lesion also shows enhancement due to its vascular and myomatous components.

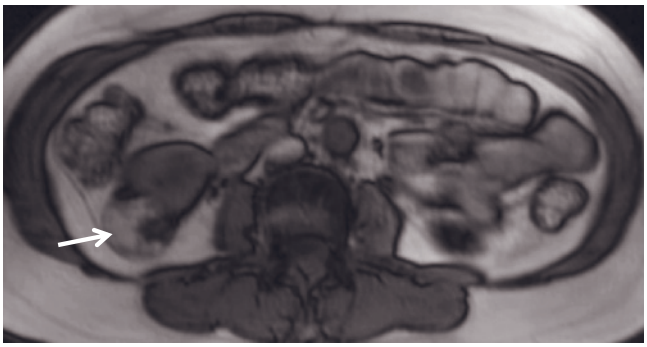

(*g*)

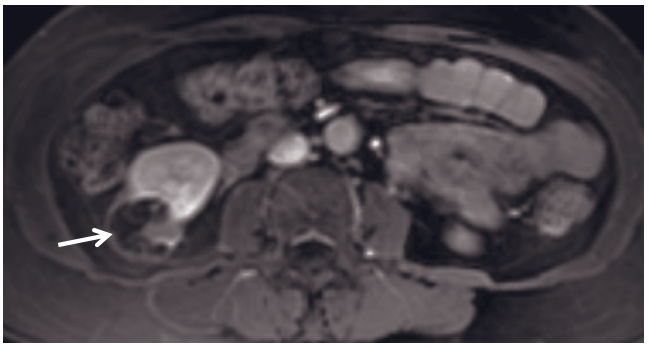

(*h*)

FIG. 9.37 (*Continued*)

adenomas, and carcinoma [42, 43]. Renal cell carcinomas tend to be multicentric and bilateral. On imaging, they present as a solid hypovascular mass or as a complex cystic lesion with thickened septa and mural nodules [43]. T1-weighted fat-suppressed imaging with gadolinium enhancement is the most sensitive technique for detecting and characterizing multiple tumors, many of which are 1 cm in diameter (fig. 9.39) [42, 43].

Adenoma. Renal adenomas are benign tumors of renal cell origin and typically are small solid neoplasms [44]. Renal adenomas are not rare tumors. The relationship of adenomas to renal cell carcinomas is uncertain [33]. They are small cortex-based tumors that are regularly marginated and have generally nonaggressive features. Adenomas cannot be distinguished from papillary renal cell cancers on imaging studies [45, 46]. Depending on the clinical picture, patients with small solid tumors may benefit from serial reassessment to detect tumor growth. An important aspect of their noninvasive diagnosis is that they do not change in size over a >2-year period. Tumor growth raises the concern of malignancy [29, 35, 36, 38, 40, 42, 44]. It may be reasonable to follow a mass at 3 months, 6 months, 1 year, and yearly thereafter. Particularly in elderly patients, close observation likely results in the least patient morbidity [47, 48]. On MR images, adenomas are typically small (<4 cm), round masses that are slightly hyperintense on T2-weighted images and slightly hypointense on T1-weighted images, and enhance in a diffuse intense fashion on capillary-phase images [21]. The relative commonness of renal adenomas suggests that a "watch and wait" approach to small renal tumors in individuals who are not considered good surgical candidates is a prudent course of action.

Oncocytomas are benign epithelial tumors that are generally solid and well encapsulated. A central stellate fibrous scar is often present [49]. Their incidence has been reported as representing 2–15% of primary renal neoplasia [50, 51]. MRI reveals spherical masses that are relatively homogeneous with substantial central enhancement on capillary-phase images (fig. 9.40) [50]. The characteristic early enhancement pattern is described as "spoke wheel" [21] but may not be commonly observed. In comparison, renal cancers tend to exhibit greater peripheral enhancement. Neither pattern of enhancement nor presence of central scar may be specific enough to permit distinction from renal cell carcinoma [46, 52].

Myelofibrosis with Extramedullary Hematopoiesis. Myelofibrosis is a disorder classified as a chronic myeloproliferative disease, characterized by proliferation of bone marrow connective tissue and development of extramedullary hematopoiesis (EMH) [53].

EMH is defined as the formation and development of blood cells within an ectopic site outside the bone marrow. EMH is not always associated with myelofibrosis, and either of these processes may occur in the absence of a hematologic disorder. The liver and spleen are affected most commonly, resulting in hepatosplenomegaly [54]. Reports of renal involvement are rare in the literature (fig. 9.41) [53].

The disease runs a chronic course and typically presents with symptoms related to anemia and splenomegaly that may be observed years before the diagnosis. When EMH involves the kidneys it may lead to renal failure due to either ureteral obstruction or extensive parenchymal involvement [53]. The recognition of EMH as the cause of renal failure is important in these circumstances, as this entity may respond to radiotherapy [55].

In general, the differential diagnosis of a mass encasing the renal pelvis includes transitional cell carcinoma, lymphoma, lipomatosis, and renal cell carcinoma [55]. In the proper clinical setting, renal EMH

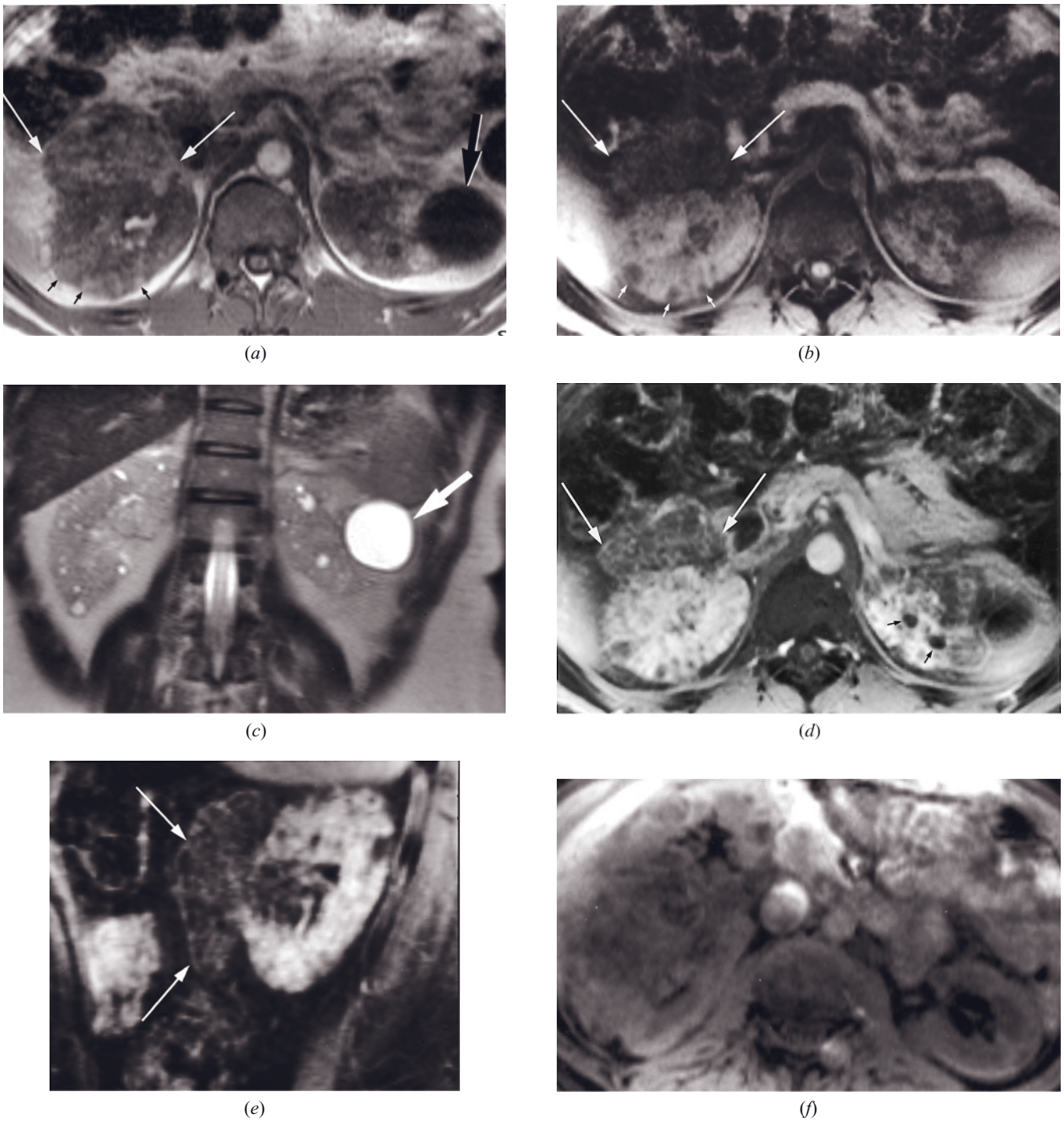

FIG. 9.38 Tuberous sclerosis. Transverse T1-weighted precontrast (*a*) and precontrast fat suppressed (*b*) SGE, coronal T2-weighted SS-ETSE (*c*), and transverse (*d*) and sagittal (*e*) T1-weighted 90-s fat-suppressed SGE images. Numerous angiomyolipomas of various sizes are present throughout both kidneys (small arrows, *a*), including a large exophytic angiomyolipoma with multiple high-signal-intensity punctuate foci of fat (long arrows, *a*). Multiple cysts are also present (large black arrow, *a*). On the precontrast fat-suppressed image, the numerous small angiomyolipomas (small arrows, *b*) and the large angiomyolipoma (long arrows, *b*) decrease in signal intensity. The numerous angiomyolipomas and cysts (arrow) are high in signal intensity on the T2-weighted image (*c*). After gadolinium administration the kidneys are shown to be extensively replaced by angiomyolipomas and cysts (small arrows, *d*). The large exophytic angiomyolipoma (long arrows, *d*, *e*) is well shown on transverse (*d*) and sagittal (*e*) postgadolinium fat-suppressed SGE images. T1-weighted precontrast in-phase (*f*) and out-of-phase (*g*) SGE images in a second patient demonstrate a large heterogeneous mass within the right kidney and multiple small lesions in the left kidney. Note the dramatic phase-cancellation artifact on the out-of-phase sequence in both kidneys, confirming the presence of fat in numerous angiomyolipomas scattered

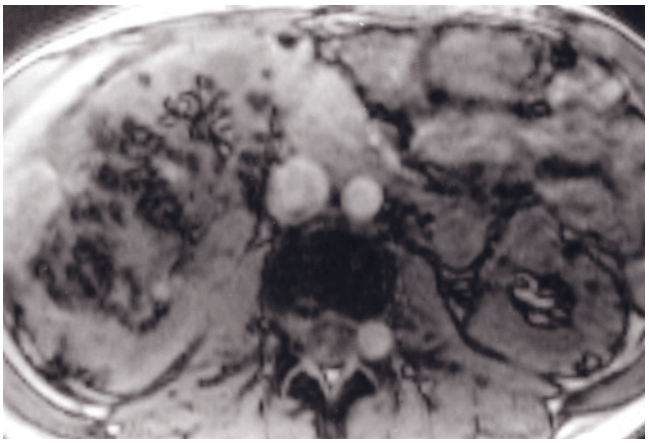

(*g*)

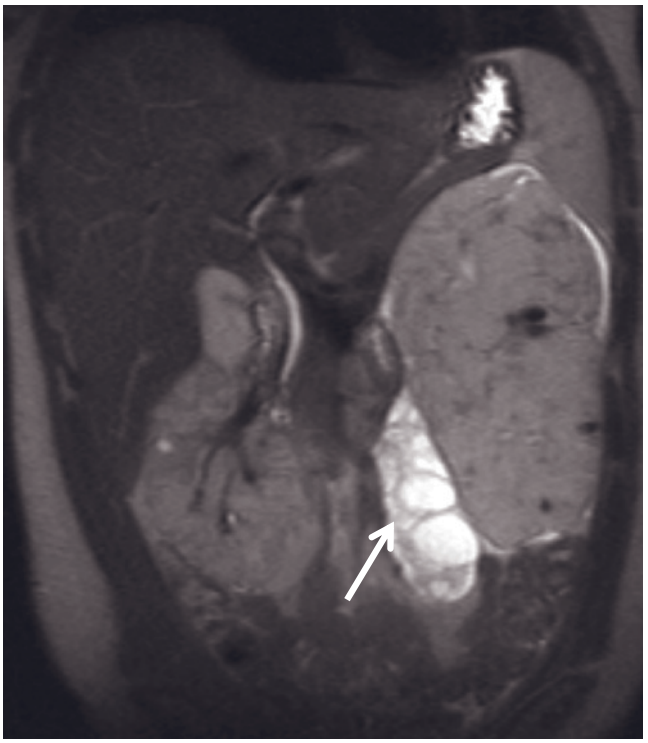

(*h*)

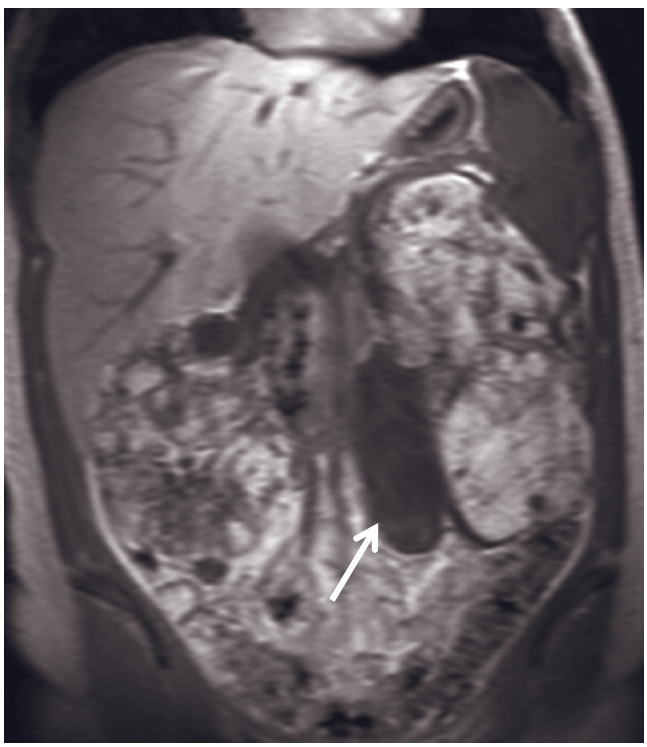

(*i*)

(*j*)

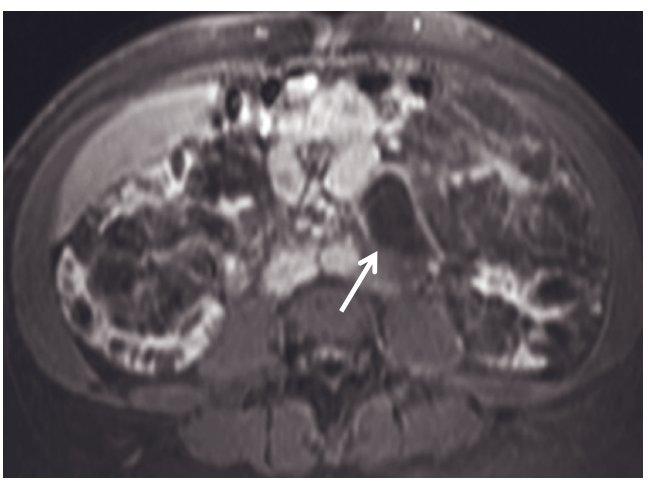

(*k*)

FIG. 9.38 (*Continued*) throughout the kidneys. Coronal T2-weighted single-shot echo-train spin echo (*h*), coronal T1-weighted SGE (*i*), transverse T1-weighted postgadolinium arterial-phase SGE (*j*), and T1-weighted postgadolinium interstitial-phase 3D-GE (*k*) images demonstrate multiple angiomyolipomas in another patient with tuberous sclerosis. The kidneys are enlarged, and normal renal parenchyma are mainly replaced with multiple angiomyolipomas bilaterally. Angiomyolipomas show high signal on T2-weighted (*h*) and non-fat-suppressed T1-weighted (*i*, *j*) images but low signal on fat-suppressed postgadolinium image (*k*) because of fat-suppression. Note that angiomyolipomas are large-sized, show exophytic growth, and occupy most of the abdominal cavity. There is also a multiloculated cystic lesion (arrows, *h*–*k*) medially

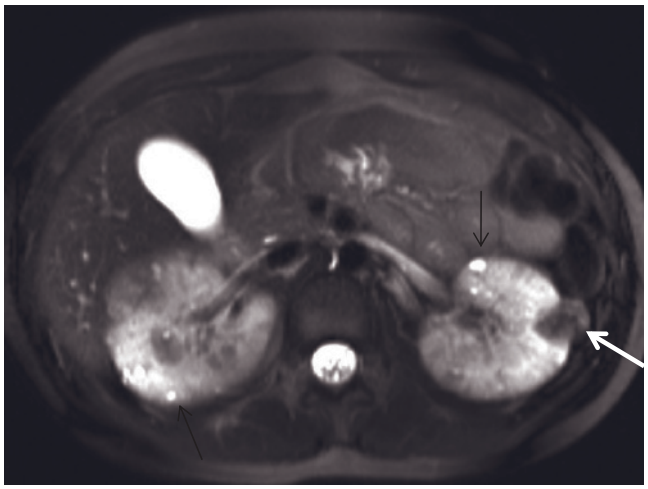

(*l*)

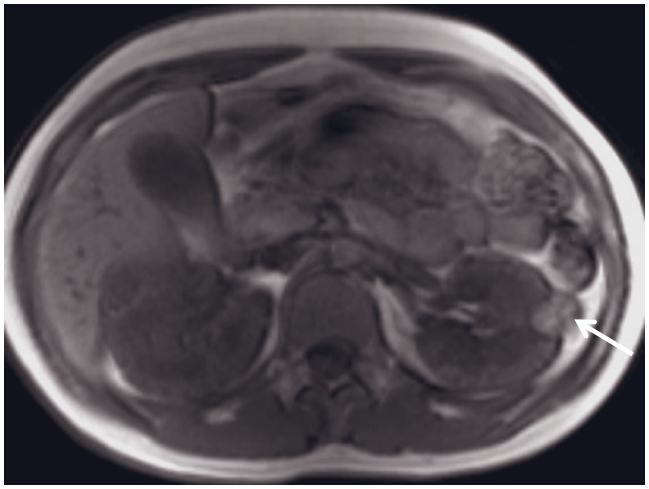

(*m*)

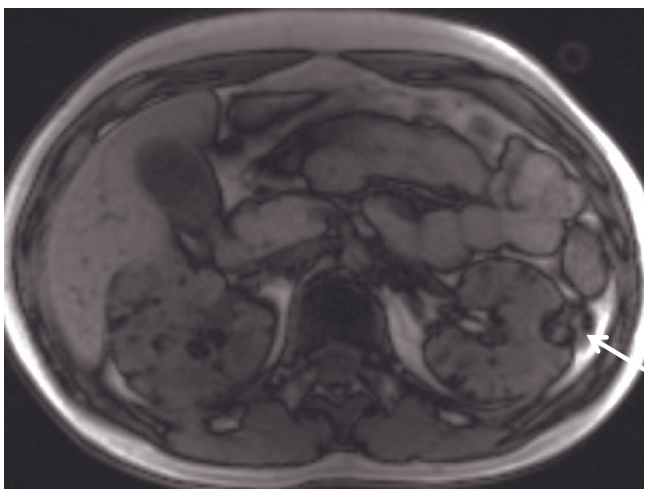

(*n*)

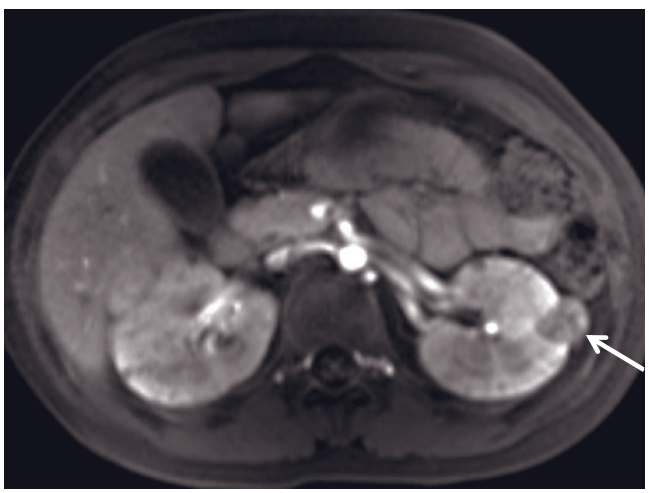

(*o*)

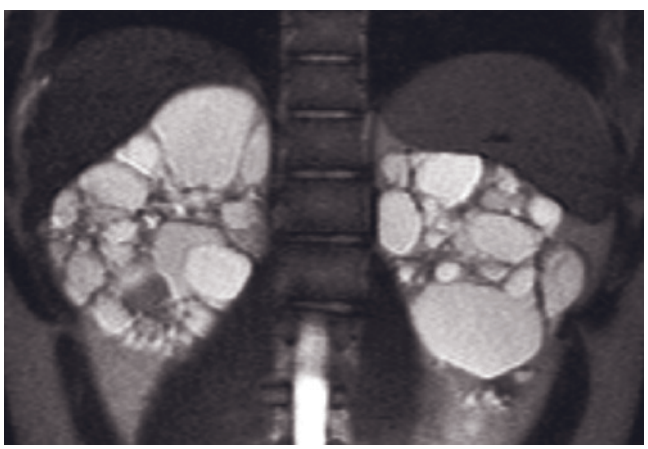

(*p*)

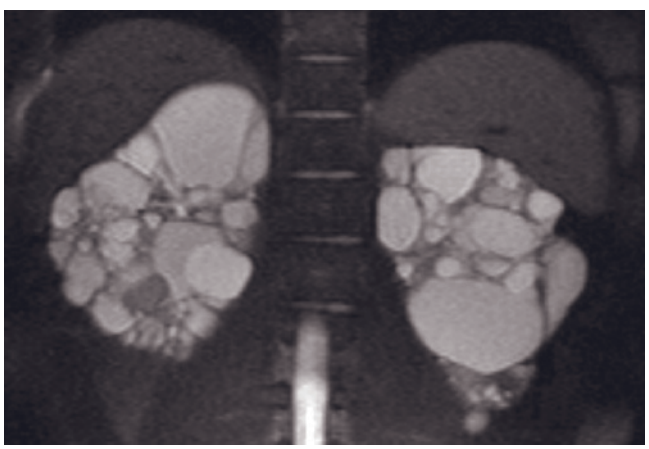

(*q*)

FIG. 9.38 (*Continued*) adjacent to the left kidney and the aorta. T2-weighted fat-suppressed single-shot echo-train spin-echo (*l*), T1-weighted in-phase (*m*) and out-of-phase (*n*) magnetization-prepared rapid gradient-echo, and T1-weighted postgadolinium interstitial-phase water excitation magnetization-prepared rapid gradient-echo (*o*) images at 3.0 T demonstrate multiple angiomyolipomas in another patient with tuberous sclerosis. Angiomyolipomas show signal drop on out-of-phase image (*n*) because of their fat content. The biggest angiomyolipoma (arrows, *l*–*o*) shows signal drop and phase-cancellation artifact on out-of-phase image (*n*). Note that there are small cysts (black arrows) showing high signal intensity on T2-weighted image (*l*) as well. Coronal non-fat-suppressed (*p*) and fat-suppressed (*q*) single-shot echo-train spin-echo images demonstrate multiple cysts in another patient with tuberous sclerosis. Most of the normal renal parenchyma are replaced with multiple cysts bilaterally. The cysts show various signal intensities that reflect the presence of blood products at various ages or proteinaceous material. Multiple renal cysts may be another form of presentation of tuberous sclerosis and may mimic autosomal dominant polycystic kidney disease.

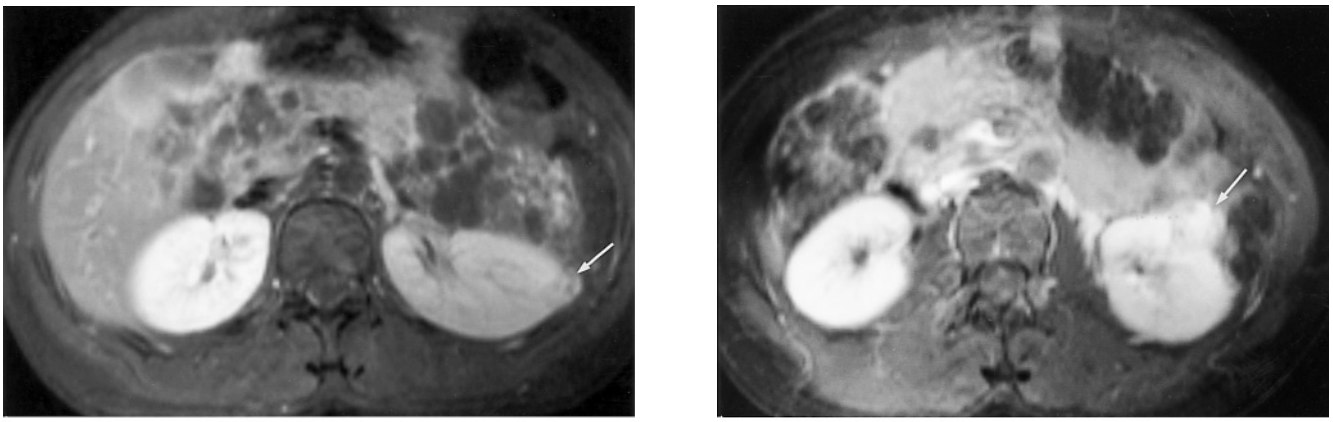

(*a*) (*b*)

FIG. 9.39 von Hippel–Lindau disease. T1-weighted fat suppressed gadolinium-enhanced SE images (*a*, *b*). Two small renal cancers are present in the middle (arrow, *a*) and lower (arrow, *b*) pole of the left kidney. Multiple pancreatic cysts are also appreciated (*a*).

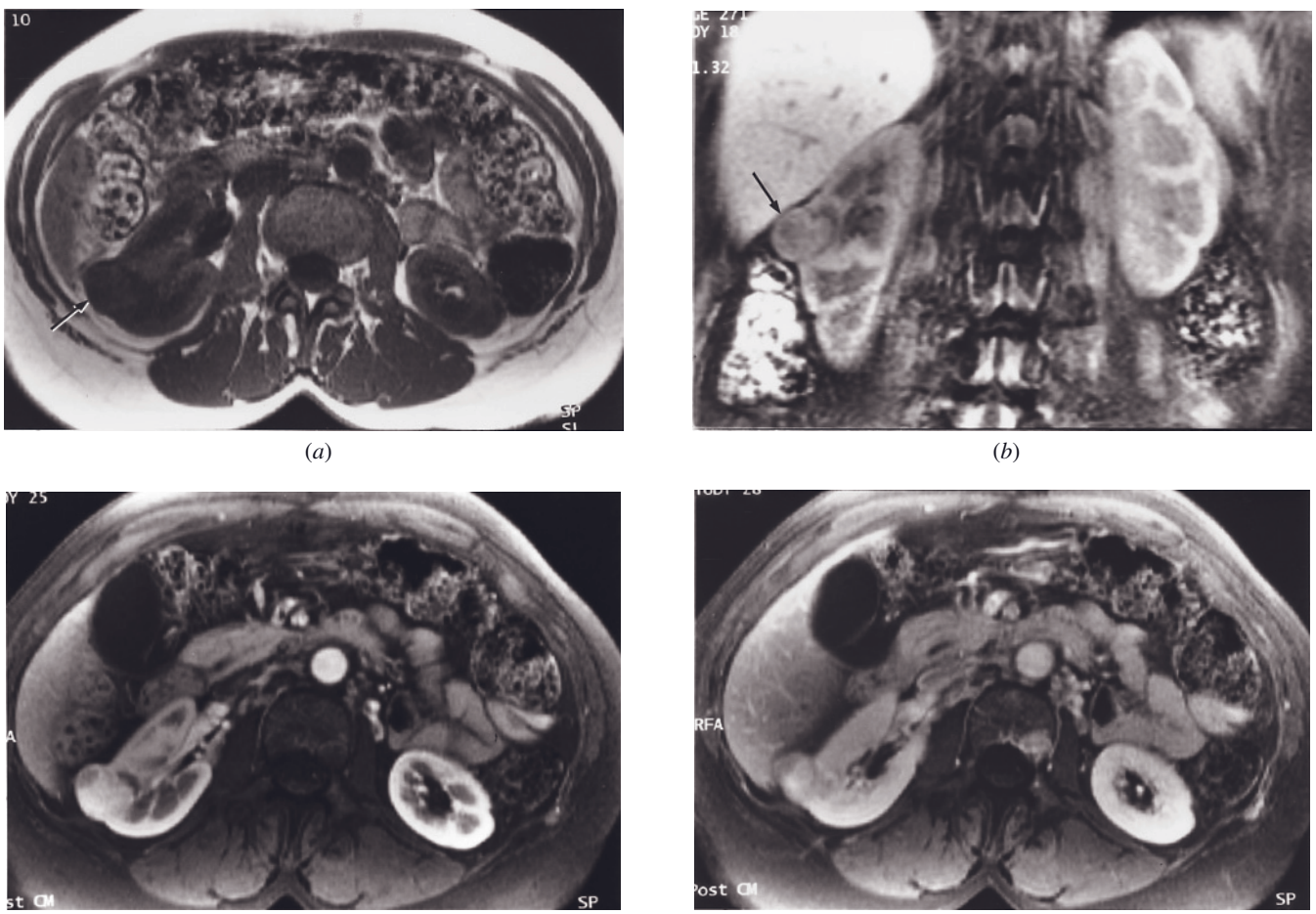

(*a*) (*b*)

(*c*) (*d*)

FIG. 9.40 Renal oncocytoma. Transverse T1-weighted precontrast SGE (*a*), coronal T1-weighted precontrast fat-suppressed SGE (*b*), and T1-weighted immediate (*c*) and 90-s fat suppressed (*d*) gadolinium-enhanced SGE images. A well-defined 2-cm mass is present in the right kidney (arrows, *a*, *b*). The majority of the tumor enhances in a moderately intense fashion on the immediate postgadolinium image (*c*) and shows mild peripheral washout by 90 s (*d*). The appearance is indistinguishable from that of a small renal cancer.

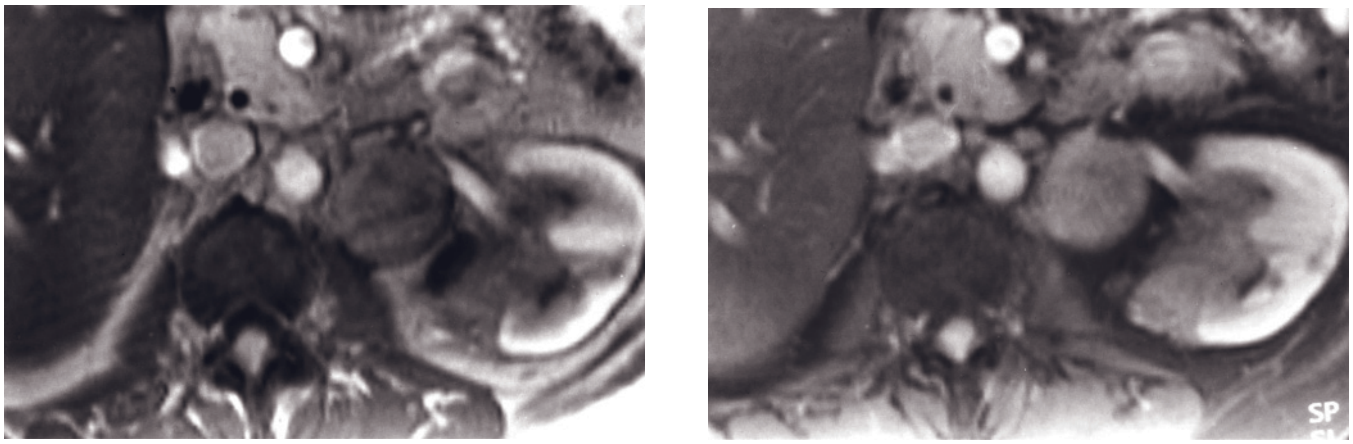

(*a*) (*b*)

FIG. 9.41 Extramedullary hematopoiesis. T1-weighted immediate (*a*) and 90-s fat-suppressed (*b*) postgadolinium SGE images in a patient with myelofibrosis. The left kidney demonstrates an infiltrating soft tissue mass involving the hilum and extending into the renal parenchyma. A large rounded focus of this process is also observed in the left para-aortic region.

should be considered in the differential diagnosis. On MR images, EMH tends to show mild and relatively homogeneous early and late gadolinium enhancement (fig. 9.41).

Malignant Masses

Renal Cell Carcinoma. More than 28,000 new cases of renal neoplasm were diagnosed in 1997, and 11,300 deaths occurred in the United States. Renal cell carcinoma (RCC) is the predominant histology (80–85%) [56]. The peak age of incidence is 50–60 years of age, with a male-to-female ratio of 2 to 1 [57]. Tumors are usually solitary. In approximately 5% of patients, tumors are multiple. Patients commonly present late in the course of the disease when tumors are large and in an advanced stage because of the lack of symptoms with small tumors. RCC is associated with a myriad of presenting features including paraneoplastic phenomena.

Staging of RCC can be performed by either Robson's or TNM classification (Table 9.2) [58]. Robson's classification is frequently used and is described in this text (see below). Both MRI and current-generation CT scanners are able to detect RCC that measure 1 cm in diameter. In a study [59] comparing dynamic contrast-enhanced CT imaging and MRI, these techniques detected 88.5% (54/61) and 95% (58/61), respectively, of renal tumors presented in 53 patients. CT imaging and MRI correctly staged 77.4% (24/31) and 93.5% (29/31) of renal cancers that were resected.

Although conventional MRI sequences may be useful in evaluating large renal tumors to assess the presence of tumor thrombus or extension of tumor to adjacent organs [60], consistent demonstration of small tumors, distinction between cysts and tumors, and reliable evaluation of tumor thrombus and metastases requires the use of intravenous gadolinium. MRI using gadolinium-enhanced breath-hold fat-suppressed 3D-GRE or fat-suppressed and/or non-fat-suppressed SGE sequences is superior to CT imaging in differentiating cysts from solid tumors because of the higher sensitivity of MRI for gadolinium than CT imaging for iodine contrast [1, 15, 59].

Table 9.2 Renal-Cell Cancer Staging Systems

Robson Stage	Description	TNM Stage
I	Tumor contained within renal capsule	
	Small tumor (<2.5 cm)	T1
	Large tumor (>2.5 cm)	T2
II	Tumor spread to perinephric fat	T3a
III-A	Venous tumor thrombus	
	Renal vein tumor thrombus only	T3b
	Infradiaphragmatic caval thrombus	T3c
	Supradiaphragmatic caval thrombus	T4b
III-B	Regional lymph node metastasis	N1–N3
III-C	Venous tumor thrombus and regional lymph node metastasis	
IV-A	Direct invasion of adjacent organs outside Gerota's fascia	T4a
IV-B	Distant metastasis	M1a–M1d, N4

Robson's staging classifications for renal cell carcinoma are described below.

Stage 1 renal carcinomas are confined within the renal capsule (figs. 9.42 and 9.43).

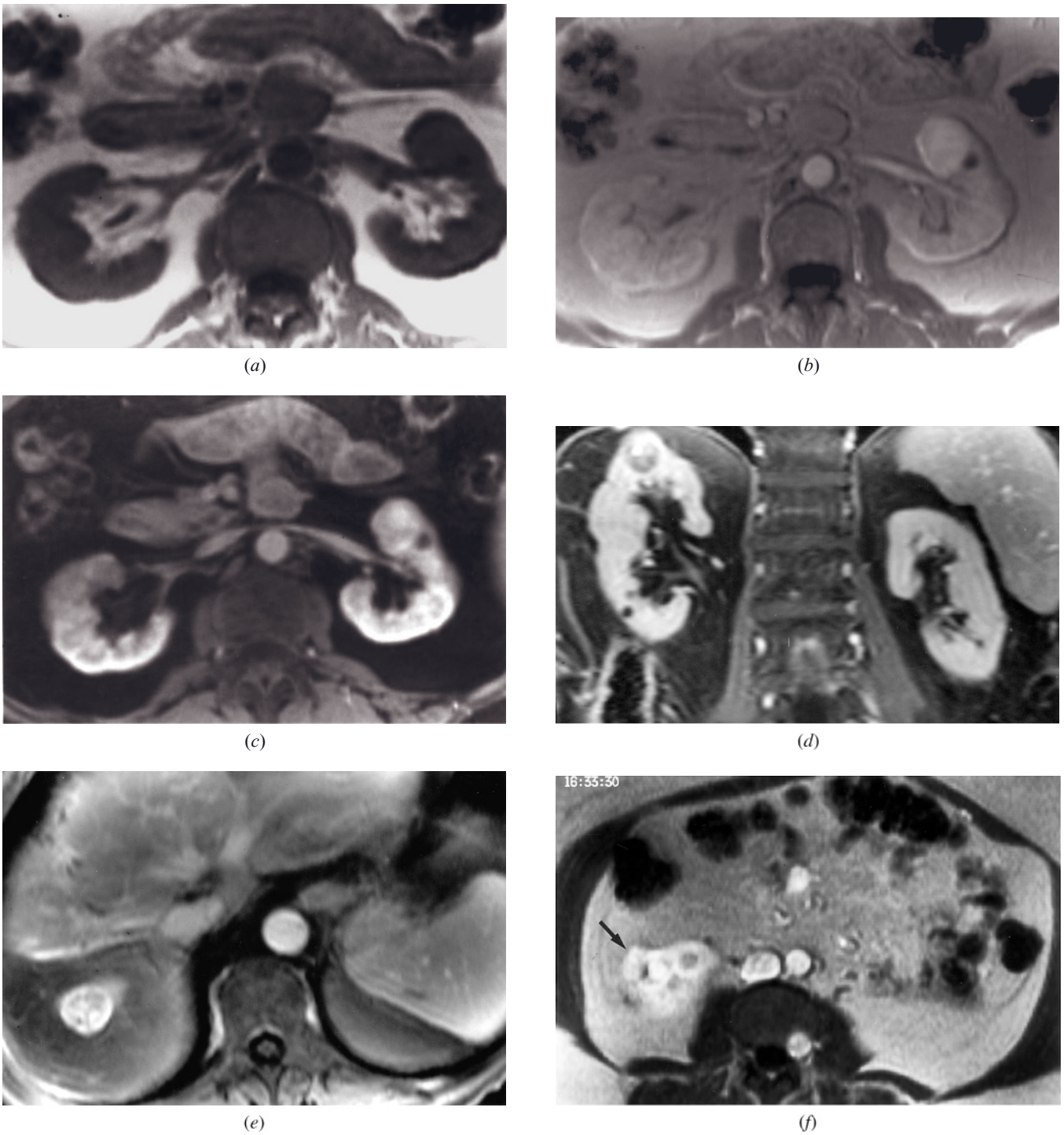

FIG. 9.42 Renal cell cancer—Stage 1. T1-weighted precontrast (*a*) and 45-s (*b*) and 90-s fat-suppressed (*c*) gadolinium-enhanced SGE images. There is a lesion in the anterior aspect of the midpole of the left kidney that is heterogeneous in signal intensity on precontrast image (*a*) and enhances markedly after gadolinium administration, consistent with a renal cell carcinoma. Adjacent to this lesion, a tiny simple cyst is noted. Coronal (*d*) and transverse (*e*) T1-weighted 2- to 3-min fat-suppressed postgadolinium SGE images in a second patient. A 2-cm renal cell cancer arises from the upper pole of the right kidney that exhibits heterogeneous enhancement on interstitial-phase images. T1-weighted transverse immediate (*f*) and sagittal 7-min (*g*) postgadolinium SGE images in a third patient. A small renal cancer arises from the lower pole of the right kidney. The tumor demonstrates intense enhancement immediately after contrast (arrow, *f*) and diminished enhancement on the delayed postcontrast image (arrow, *g*).

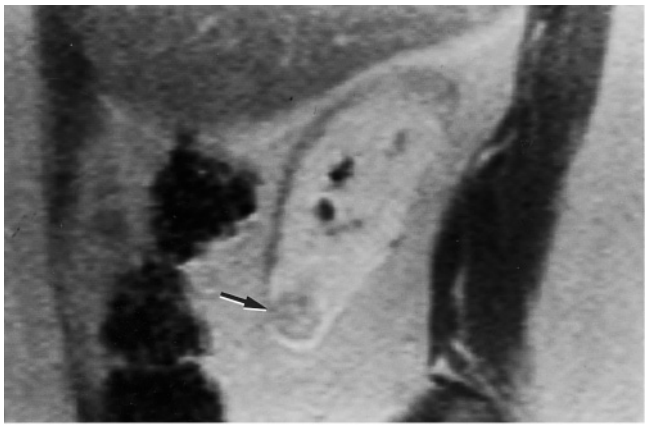

(*g*)

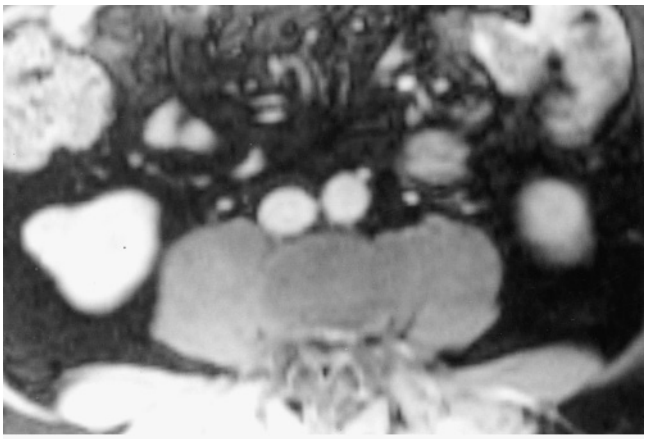

(*h*)

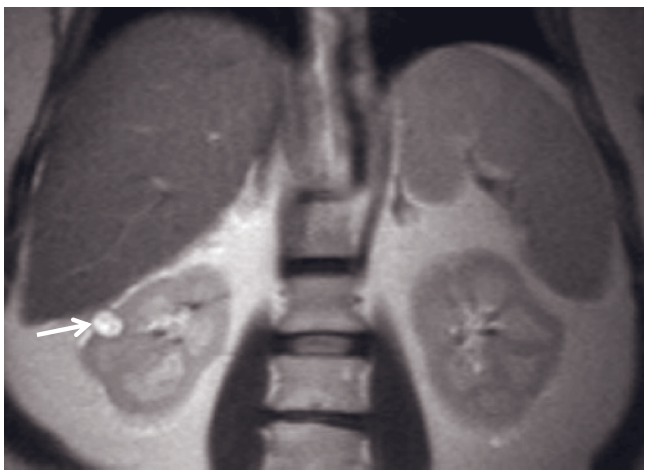

(*i*)

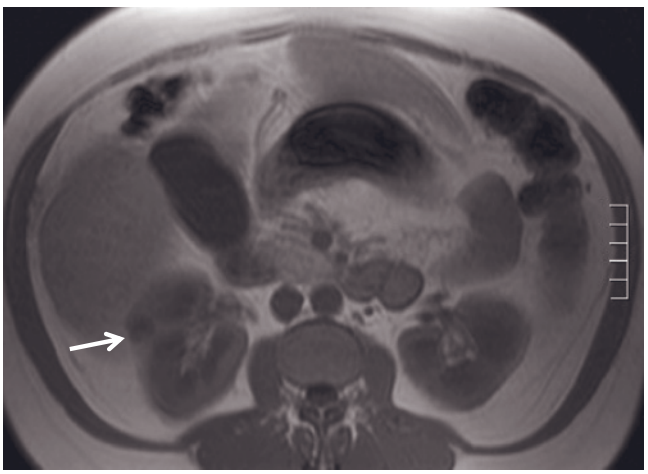

(*j*)

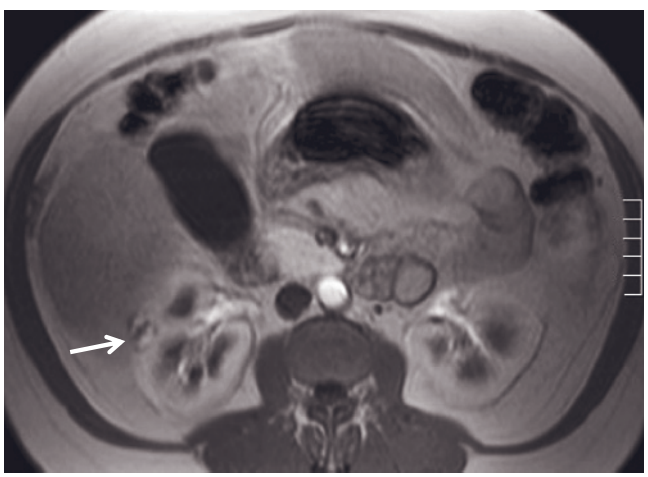

(*k*)

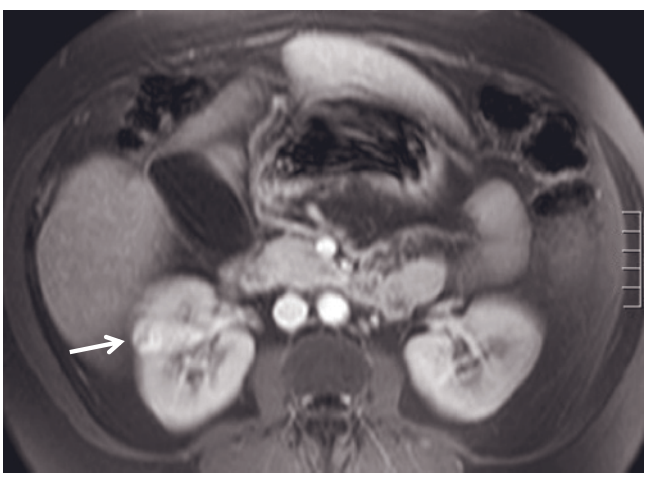

(*l*)

Fig. 9.42 (*Continued*) T1-weighted 90-s fat suppressed postgadolinium SGE image (*h*) in a fourth patient. There is a small lesion in the upper pole of the right kidney that shows intense enhancement after administration of gadolinium. Coronal T2-weighted single-shot echo-train spin-echo (*i*), transverse T1-weighted SGE (*j*), transverse T1-weighted postgadolinium hepatic arterial dominant-phase SGE (*k*), and transverse T1-weighted postgadolinium interstitial-phase fat-suppressed 3D-GE (*l*) images demonstrate a small renal cell cancer of the right kidney in another patient. The tumor shows heterogeneous high signal on T2-weighted (*i*) and low signal on T1-weighted (*j*) images. The tumor, which has a hypervascular nature, enhances intensely and progressively on postgadolinium images (*k*, *l*). Transverse T1-weighted SGE (*m*), transverse T1-weighted fat-suppressed hepatic

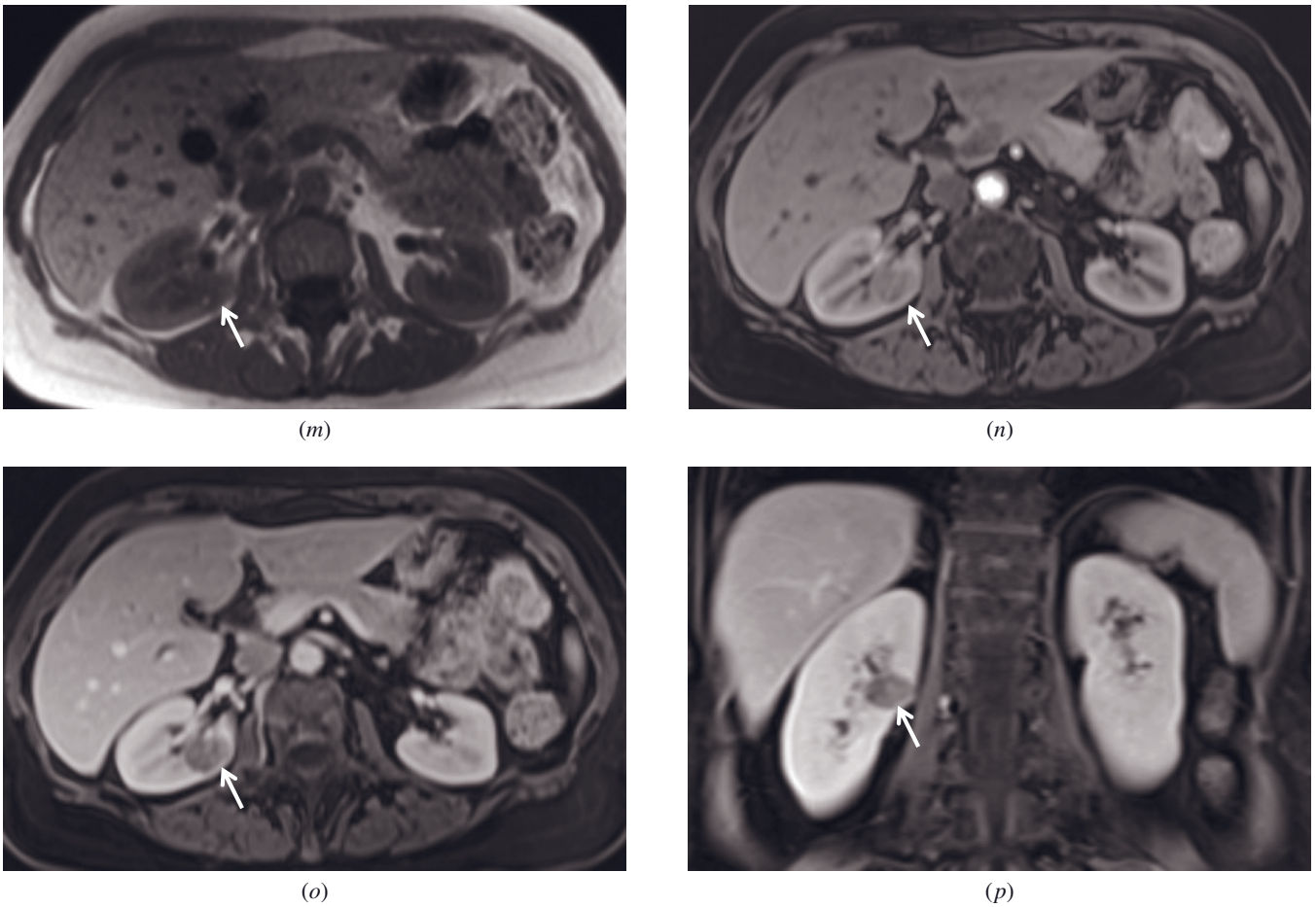

FIG. 9.42 (*Continued*) arterial dominant (*n*) and hepatic venous phase (*o*) fat-suppressed 3D-GE, and coronal T1-weighted fat-suppressed interstitial-phase 3D-GE (*p*) images demonstrate renal cell cancer in the right kidney in another patient. The tumor has a hypovascular nature and shows mild progressive enhancement on postgadolinium images (*n–p*).

Stage 2 carcinomas extend beyond the renal capsule but are confined by perirenal fascia (figs. 9.44 and 9.45). Carcinomas that are completely intraparenchymal are Stage 1 carcinoma. On the basis of imaging features, distinction between Stage 1 and Stage 2 carcinomas cannot be reliably made for tumors that extend beyond the cortical margins. Large exophytic tumors may be Stage 1, and tumors with a small extrarenal component may be Stage 2. Surgical management is identical for disease Stages 1 and 2, so differentiation by imaging is not essential. Renal cell carcinomas Stages 1 and 2 are associated with a high survival rate because the tumor is amenable to complete resection.

Stage 3a renal carcinoma is defined by tumor extension into the renal vein. Tumor thrombus frequently extends into the inferior vena cava (IVC) and grows superiorly with the direction of blood flow toward and, in advanced cases, into the right atrium. Symptoms directly attributable to tumor thrombus are rare, even in the presence of total IVC occlusion, because venous collateralization occurs through the azygos and lumbar systems. Hence, the presence of IVC thrombus is often detected incidentally by radiologic imaging (fig. 9.46) [61].

MRI is superior to CT imaging in determining the presence and superior extent of thrombus and also in determining whether thrombus is composed of blood or tumor. However, in detecting the presence of thrombus, both imaging methods are essentially equivalent. In one series of 431 patients, the sensitivity of MR imaging (90%; 388/431) for detecting IVC thrombus was greater than that of either CT (79%; 340/431) or conventional sonography (68%; 293/431) [61].

Direct coronal- or sagittal-plane images are important for the demonstration of the superior extent of thrombus. This information is useful in that it assists in surgical planning for thrombus extraction. Thrombus extension above the hepatic veins requires a thoracoab-

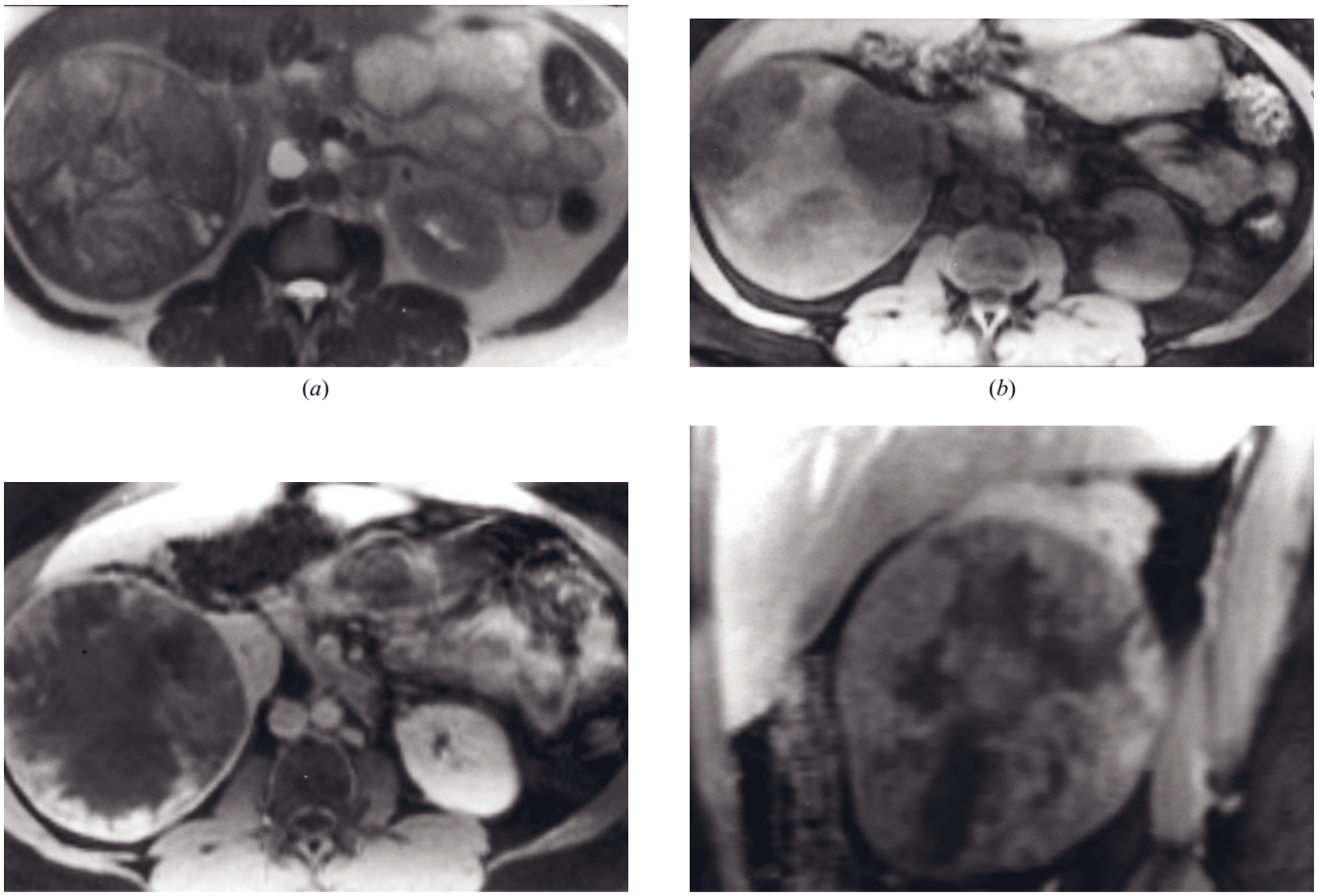

(*a*) (*b*) (*c*) (*d*)

FIG. 9.43 Large renal cell cancer—Stage 1. Transverse T2-weighted SS-ETSE (*a*), T1-weighted precontrast fat-suppressed SE (*b*), and 2- to 3-min fat-suppressed postgadolinium transverse (*c*) and sagittal (*d*) SGE images. A large, well-encapsulated mass is seen involving the mid to lower pole of the right kidney with marked heterogeneity in signal on T2- and T1-weighted images and on postgadolinium images. Despite the relatively large tumor size, this represented a Stage 1 renal cancer. Small areas of central low signal on postgadolinium images represent foci of necrosis.

dominal approach rather than an abdominal approach, whereas the latter approach is used if thrombus extends below the hepatic veins.

Gadolinium administration is generally useful for the evaluation of thrombus composition because tumor thrombus virtually always enhances with gadolinium. Although differentiation of tumor thrombus from bland thrombus may not change surgical treatment, it is an important distinction because the neovascular bed of the tumor thrombus may adhere to the venous wall, whereas a simple tumor clot will not [61], and patient prognosis and likelihood of lung metastases are affected. In comparison, in one CT imaging series, tumor thrombus was correctly detected in 95% (18/19) of patients, but only 16% (3/19) of these thrombi demonstrated appreciable enhancement [62]. A gradient-echo technique that refocuses the signal of flowing blood (e.g., gradient-recalled acquisition in steady state or true-FISP) has been proposed as another method for evaluating tumor thrombus [63]. On these images, tumor thrombus is intermediate in signal intensity (i.e., soft tissue signal intensity) whereas blood thrombus is low in signal intensity because of the presence of blood breakdown products. Because contrast enhancement should be routinely employed in evaluating kidneys and flow-sensitive gradient-echo is rapid to perform, it may be reasonable to use both methods to evaluate thrombus to increase confidence of characterization.

Stage 3b renal carcinoma is defined by the presence of malignant nodes. MRI is occasionally able to detect necrosis in lymph nodes, which appears as irregular low-signal-intensity centers that may not be apparent on CT images (fig. 9.47). In the presence of a necrotic primary tumor, necrosis of lymph nodes may be specific for nodal involvement. The presence of enlarged lymph nodes does not necessarily indicate

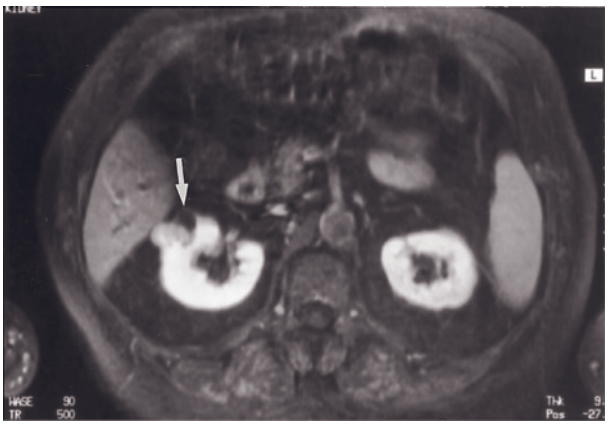

(a)

(*b*)

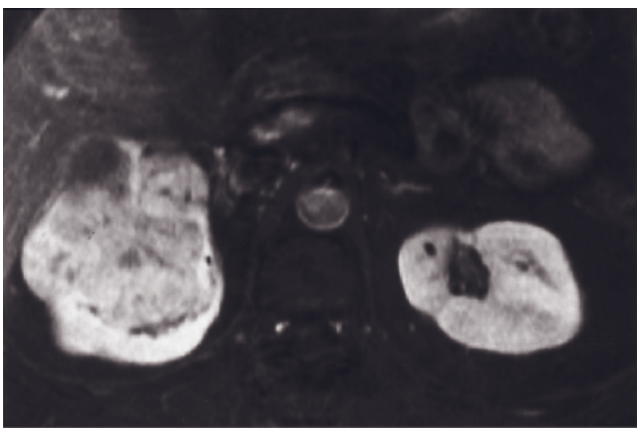

(*c*)

FIG. 9.44 Renal cell cancer—Stage 2. T1-weighted late-phase fat-suppressed gadolinium-enhanced SE images in 3 patients (*a–c*). Stage 2 cancer can vary in size from small (*a*) to large (*c*). Tumors are heterogeneous and lower in signal intensity than adjacent cortex on interstitial-phase images. Larger cancers have a propensity to undergo regions of necrosis that appear nearly signal void on postcontrast images (*c*). A simple renal cyst (arrow, *a*) adjacent to the renal cancer is present in the first of these patients.

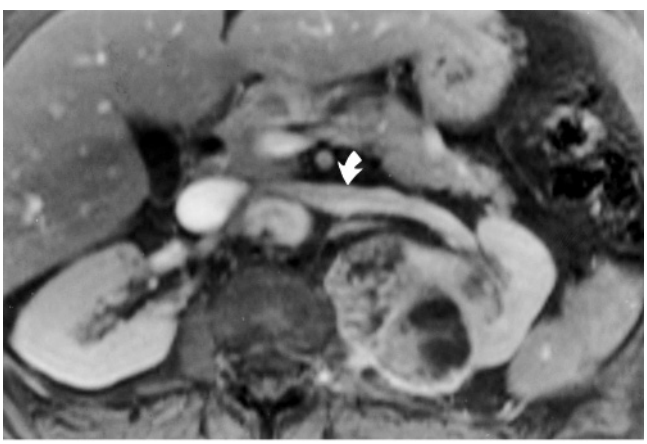

(*a*)

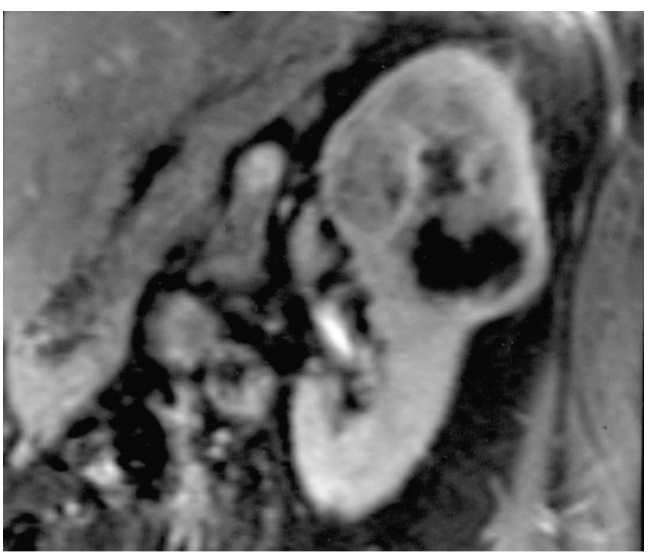

(*b*)

FIG. 9.45 Renal cell cancer—Stage 2. Transverse (*a*) and sagittal (*b*) T1-weighted 2- to 3-min fat-suppressed postgadolinium SGE images. A large renal cancer arises from the upper pole of the left kidney. This mass demonstrates marked heterogeneity of signal on the postgadolinium images, with central areas of necrosis. The renal vein is clearly shown as free of thrombus on the gadolinium-enhanced fat-suppressed image (arrow, *a*). There is no evidence of perinephric fat infiltration.

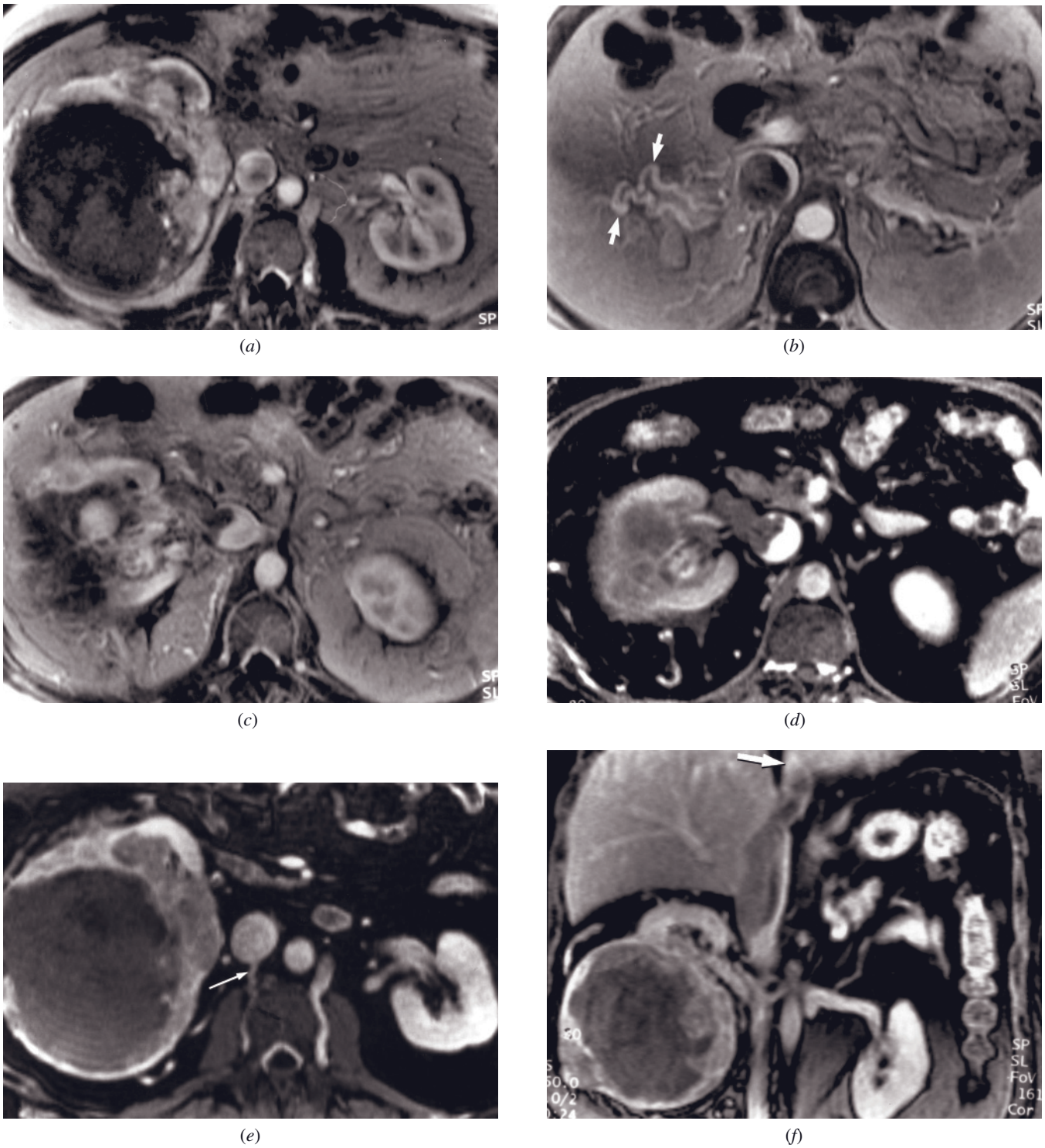

FIG. 9.46 Renal cell cancer—Stage 3a. T1-weighted immediate (*a*) and 45-s (*b*, *c*) and transverse (*d*, *e*), coronal (*f*, *g*), and sagittal (*h*) fat-suppressed gadolinium-enhanced SGE images. A heterogeneous enhancing large renal cancer is present, which originates from the lower two-thirds of the right kidney. An enhancing tumor thrombus is seen within the right renal vein that extends into the inferior vena cava. Direct coronal (*f*, *g*) and sagittal (*h*) images permit evaluation of the superior extent of thrombus (arrow, *f*). Extensive vascular parasitization is appreciated (arrows, *b*) around the tumor. Dilated collateral lumbar veins are identified, one of which communicates with the IVC (arrow, *e*) at the level of the lower aspect of the thrombus. T1-weighted fat-suppressed

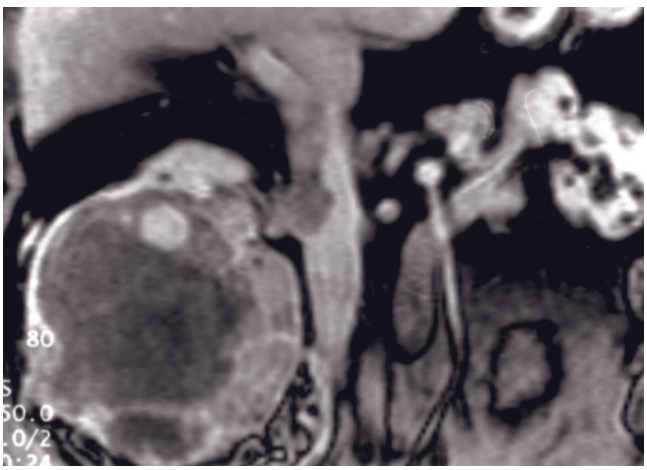

(*g*)

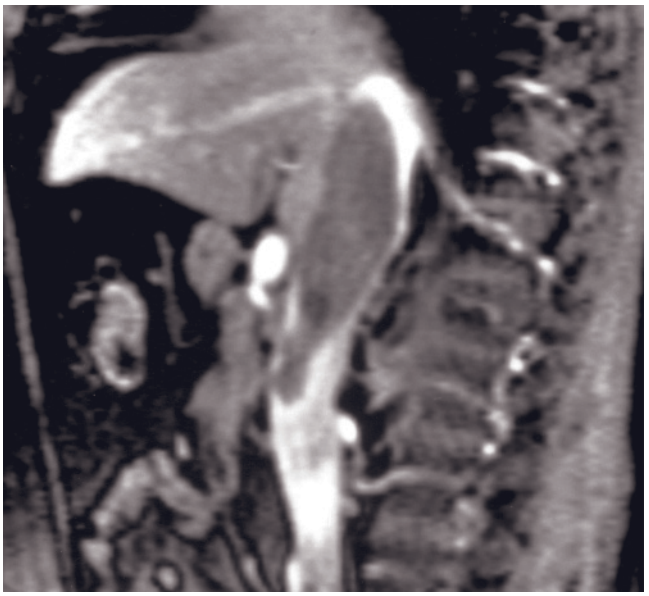

(*h*)

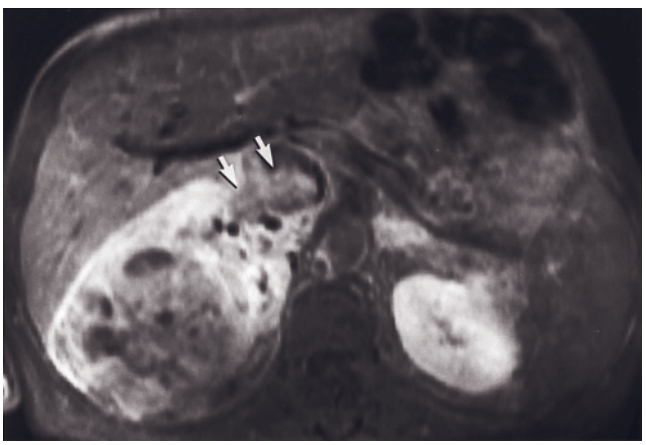

(*i*)

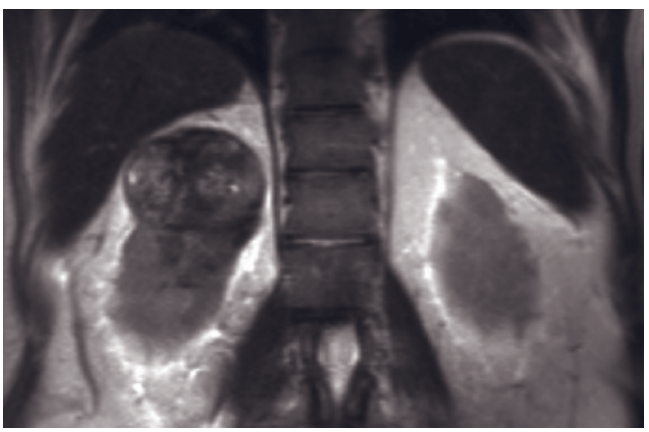

(*j*)

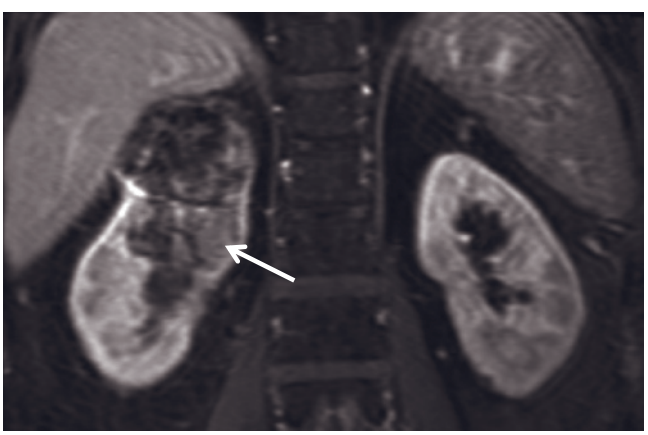

(*k*)

FIG. 9.46 (*Continued*) gadolinium-enhanced SGE image (*i*) in a second patient. Enhancing tumor thrombus can be appreciated extending along the right renal vein into the IVC (arrows, *i*). Enhancement of tumor thrombus is well shown on fat-suppressed postgadolinium images acquired in the interstitial phase. Coronal T2-weighted single-shot echo-train spin-echo (*j*), coronal and transverse postgadolinium interstitial-phase fat-suppressed 3D-GE (*k*, *l*), and transverse postgadolinium hepatic venous-phase fat-suppressed 3D-GE (*m*) images at 3.0 T demonstrate renal cancer in the upper pole of the right kidney in another patient. The tumor shows heterogeneous signal on T2-weighted image (*j*) and heterogeneous enhancement on postgadolinium images (*k*, *l*).

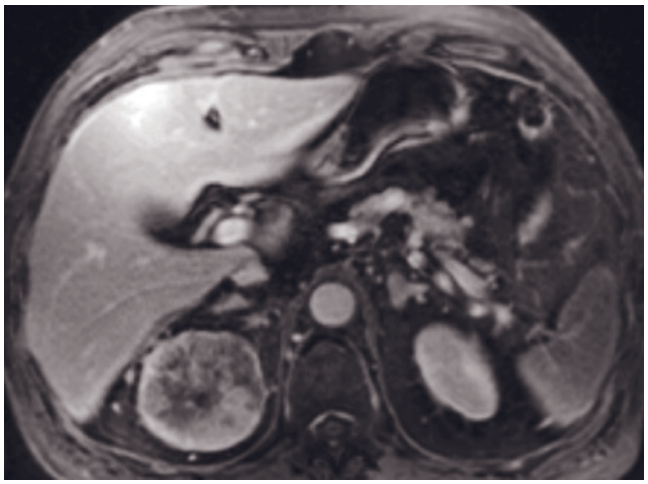

(*l*)

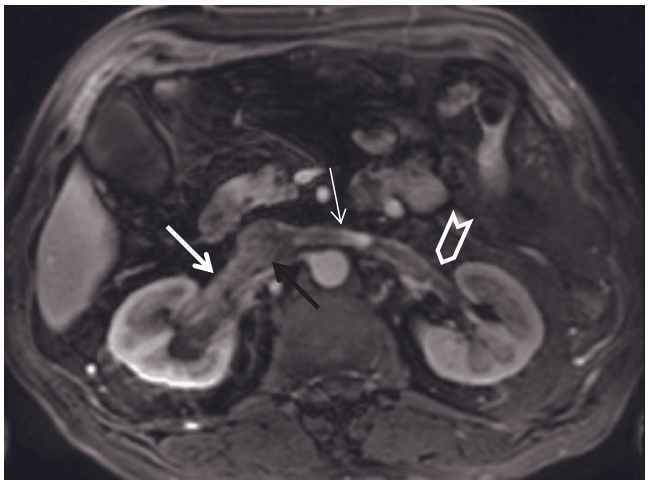

(*m*)

FIG. 9.46 (*Continued*) The tumor invades the renal parenchyma and upper collecting system (white arrow, *k*), and extends into the right renal vein (white thick arrow, *m*) and inferior vena cava (black arrow, *m*). The tumor thrombus in the right renal vein (white thick arrow, *m*) and inferior vena cava (black arrow, *m*) shows enhancement. Additionally, tumor thrombus (white thin arrow, *m*) and bland thrombus (open arrow, *m*) exist in the left renal vein.

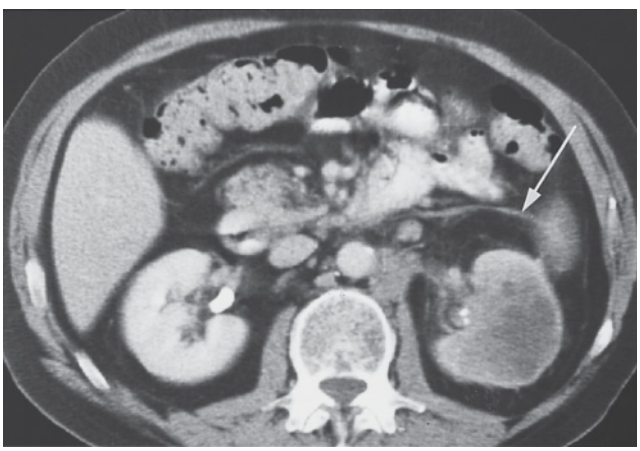

(*a*)

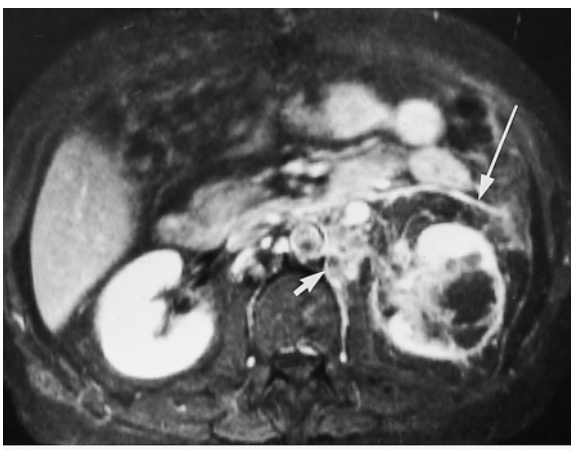

(*b*)

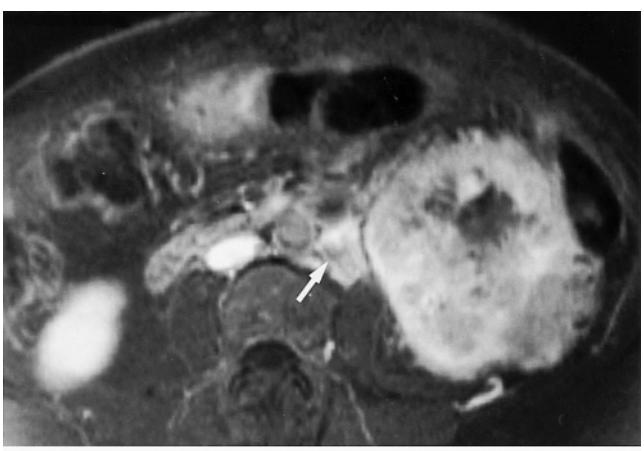

(*c*)

FIG. 9.47 Renal cell cancer—Stage 3b. Contrast-enhanced CT (*a*) and T1-weighted interstitial-phase fat-suppressed gadolinium-enhanced SE (*b*) images. A necrotic 6-cm tumor is present in the left kidney. Enlarged para-aortic nodes are identified on the CT scan. On the postcontrast T1-weighted fat-suppressed image, the nodes enhance in a heterogeneous fashion with central low signal intensity (short arrow, *b*), with an appearance similar to that of the primary tumor. Note the thickening of Gerota fascia (long arrows, *a*, *b*) shown on the CT and MR images. T1-weighted fat-suppressed gadolinium-enhanced image (*c*) of a Stage 3b cancer in a second patient demonstrates a heterogeneous necrotic primary renal cancer of the left kidney with central necrosis and para-aorta lymph nodes with a similar heterogeneous appearance (arrow).

Stage 3b or 3c disease because adenopathy also may be benign. Studer et al. [64] reported that 58% (94/163) of patients with RCC had enlarged hyperplastic lymph nodes.

Stage 3c is tumor extension into the renal vein and nodal involvement (fig. 9.48).

Stage 4 disease is extension to local (4a) or distant (4b) sites. Even when renal cancers are large and have a long interface with adjacent organs (e.g., liver), direct tumor invasion is relatively uncommon (fig. 9.49). Direct multiplanar imaging facilitates recognition of smooth interfaces, implying no invasion, and irregularly marginated interfaces, consistent with invasion. The sagittal plane is particularly effective at evaluating the interface with the liver. Renal cancer metastasizes to lung, adrenal glands, mediastinum, axial skeleton, and liver (fig. 9.50). The lung is the most common site of metastases. Lung metastases measuring 3 mm in diameter are detected on CT images. Reliable detection of metastases measuring 4 mm in diameter may be made with gadolinium-enhanced 3D-GRE at 1.5 T, and 3-mm-sized metastases can be detected at 3.0 T with the same technique. Advantages of this sequence include minimal phase-encoding artifact posterior to the heart, good opacification of pulmonary vessels, and consistent image quality [65], (see Chapter 18, *Chest*).

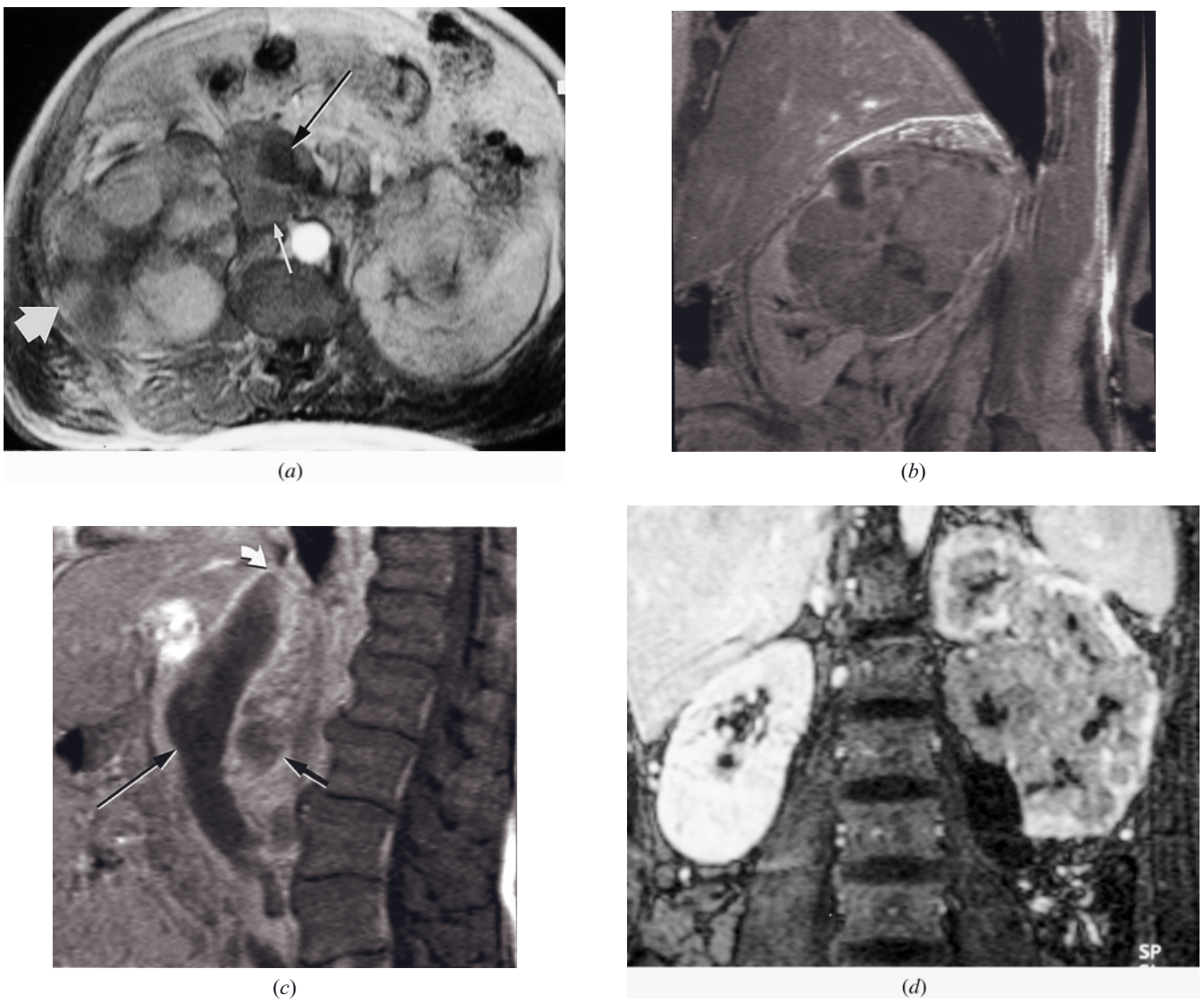

FIG. 9.48 Renal cell cancer—Stage 3c. Transverse 45-s (*a*) and sagittal 90-s (*b*, *c*) T1-weighted postgadolinium SGE images. A 7-cm heterogeneously enhancing renal cancer is present in the right kidney (arrow, *a*). Thrombus is present in the IVC (long arrow, *a*, *c*). Retrocaval (short arrows, *a*, *c*) and paracaval nodes are identified. The thrombus (long arrow, *c*) is noted to terminate approximately 1 cm below the level of the diaphragm on the sagittal projection (curved arrow, *c*). Coronal source image for an MRA (*d*) and transverse (*e*) and sagittal (*f*) 2- to 3-min T1-weighted fat-suppressed postgadolinium SGE and coronal 3D MIP

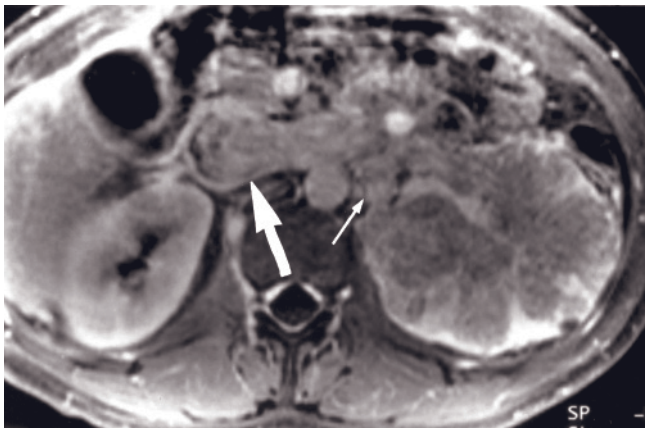

(*e*)

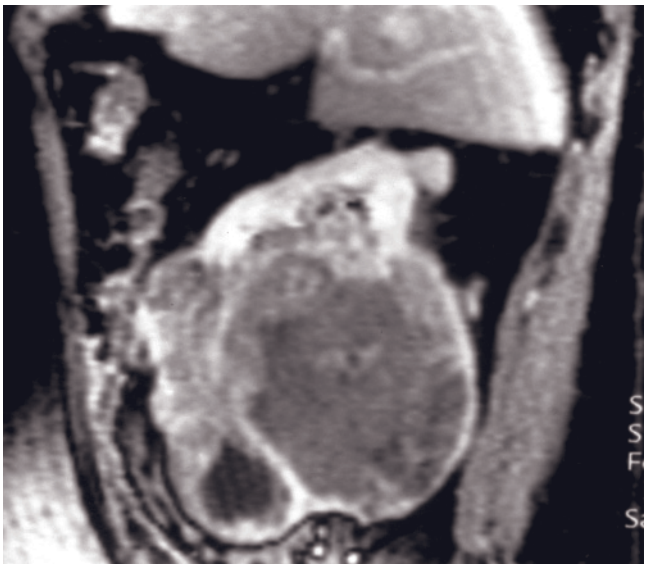

(*f*)

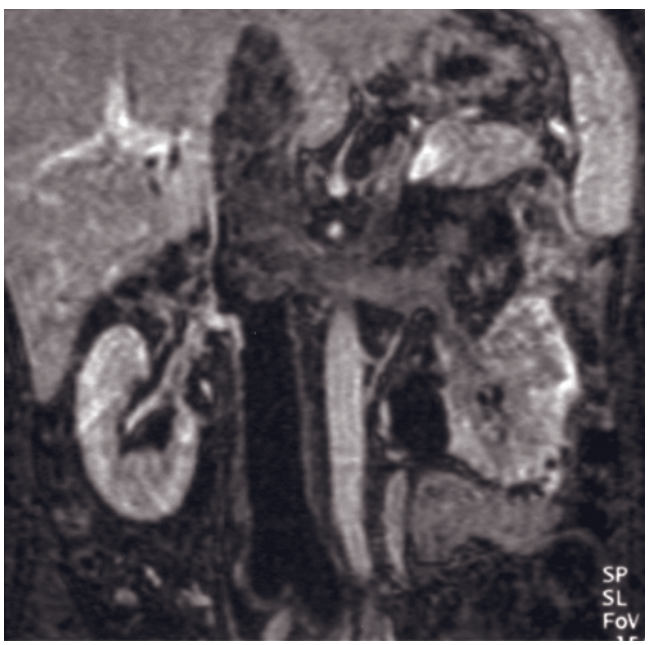

(*g*)

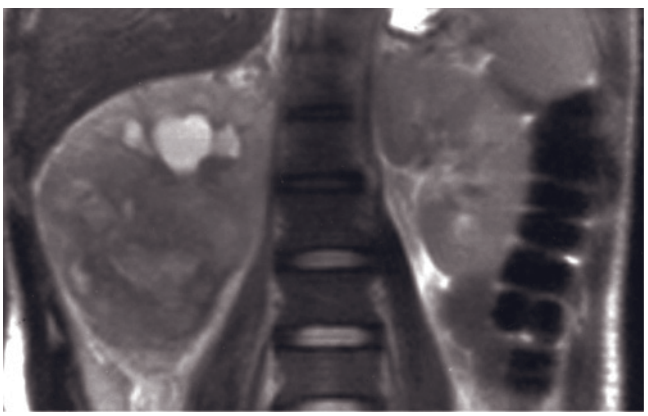

(*h*)

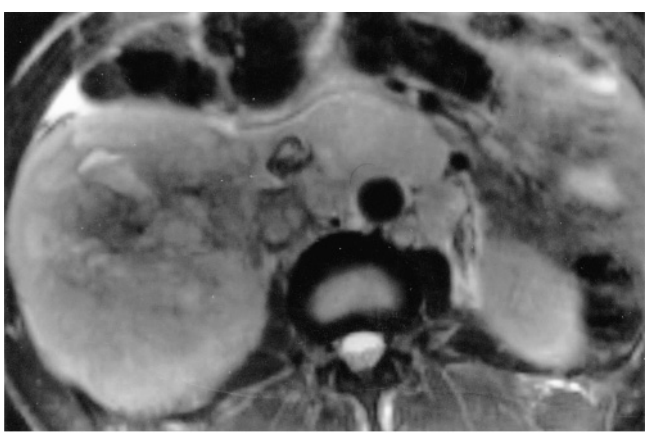

(*i*)

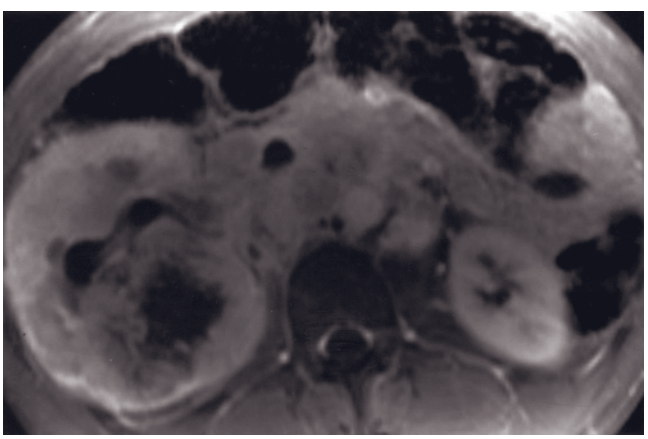

(*j*)

Fig. 9.48 (*Continued*) reconstructed MRA (*g*) images in a second patient. A large heterogeneous infiltrative mass is seen involving the lower two-thirds of the left kidney, which invades the left renal vein and extends into the IVC (large arrow, *e*). Regional lymph node metastases are present (small arrow, *e*). Coronal (*h*) and transverse (*i*) T2-weighted SS-ETSE and 90-s fat-suppressed postgadolinium (*j*) SGE images in a third patient show a large heterogeneous mass in the right kidney associated with IVC thrombosis and extensive enlarged retroperitoneal lymph nodes.

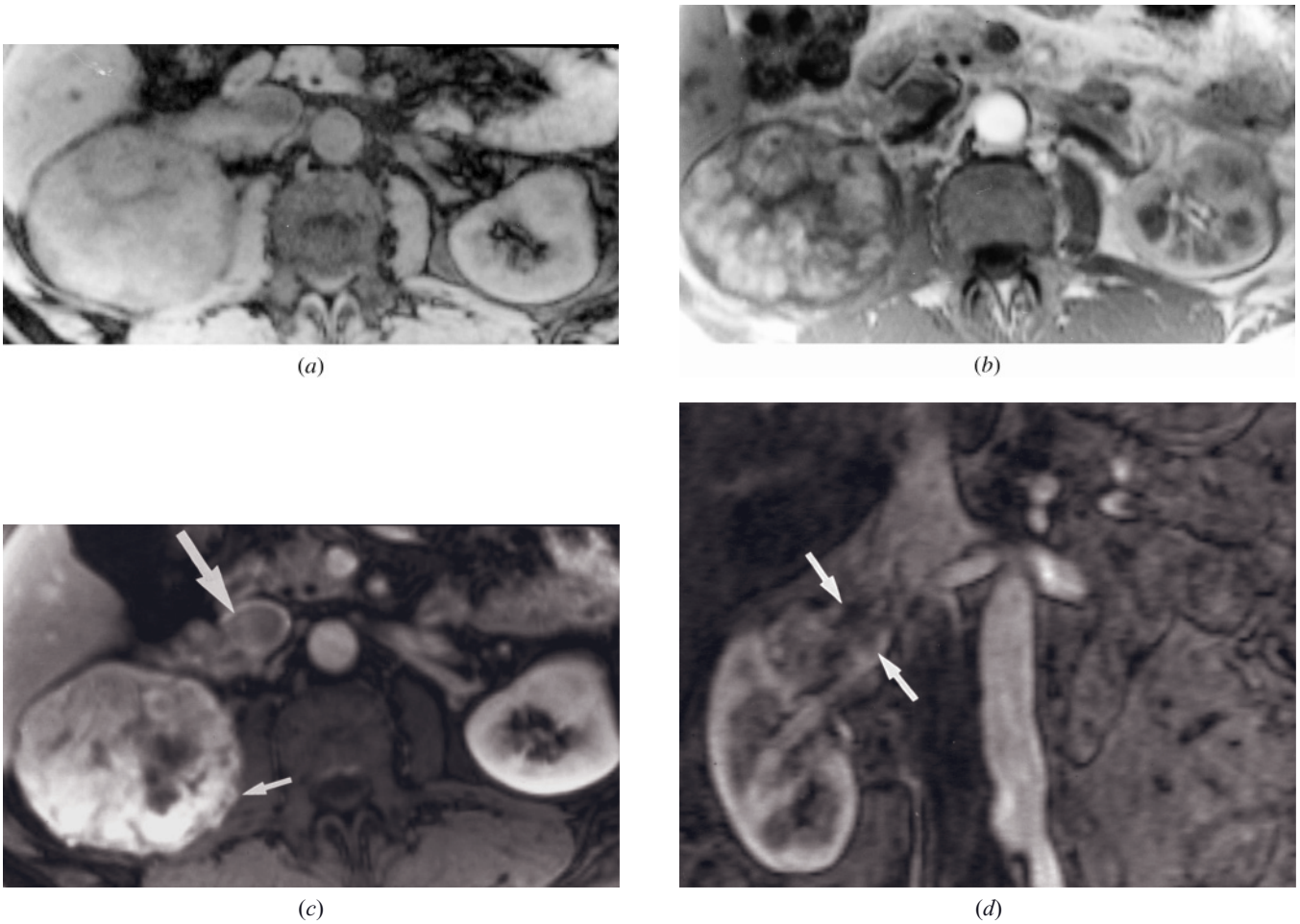

FIG. 9.49 Renal cell cancer—Stage 4a. T1-weighted precontrast fat-suppressed (*a*) and immediate (*b*) and 2-min fat-suppressed (*c*) postgadolinium SGE images and coronal source image for an MRA (*d*). A large cancer arising from the right kidney is present that shows intense heterogeneous enhancement on immediate postgadolinium images (*b*), foci of central necrosis (*c*), tumor thrombus (long arrow, *c*; arrows, *d*), and invasion of the right psoas muscle (short arrow, *c*).

The typical appearance of RCC is an irregular mass with ill-defined margins. Tumors are generally slightly hyperintense on T2-weighted images and slightly hypointense on T1-weighted images relative to renal cortex [60]. The minimal signal difference from renal cortex renders tumors poorly visualized on noncontrast images. RCC are frequently hypervascular and demonstrate intense enhancement on immediate postcontrast images, usually in a heterogeneous fashion with more intense peripheral enhancement. The heterogeneous pattern of enhancement may be due to the presence of central necrosis, which is commonly demonstrated in large, >5-cm, hypervascular tumors. Hypervascular tumors tend to washout of contrast on interstitial-phase images, whereas renal cortex remains high in signal intensity because of retention of contrast in renal tubules (fig. 9.51) [1, 15, 59, 60, 66]. Homogeneous enhancement does occur and is typical of small, low-grade cancers [59]. Homogeneously enhancing small tumors may be difficult to distinguish from renal cortex on immediate post gadolinium images. As a result, it is important that a renal MRI protocol includes not only immediate postgadolinium capillary-phase images but also more delayed interstitial-phase images (fig. 9.51).

Approximately 20% of renal carcinomas may be hypovascular. This MRI finding may be related to a subset of RCC termed papillary renal cell cancer (approximately 15% of all cases). These tumors tend to be large, solid, well-demarcated lesions that are slow growing and show hypovascularity or avascularity on angiography [67]. Hypovascular renal cancers enhance minimally on capillary-phase images and remain low in signal intensity relative to cortex on interstitial-phase images. These tumors may be sharply marginated and may resemble cysts on contrast-enhanced CT images. Diagnosis of a hypovascular renal cancer requires

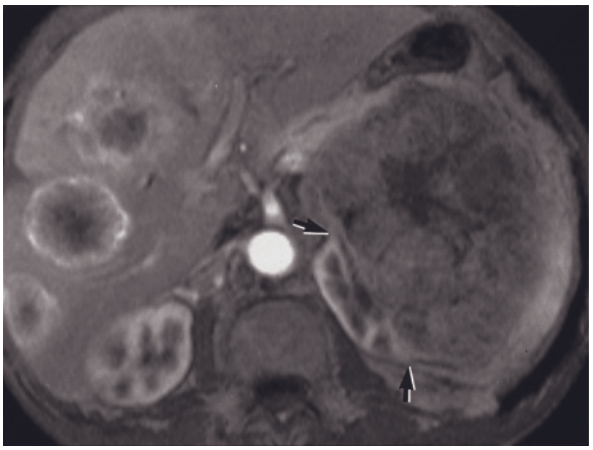

(*a*)

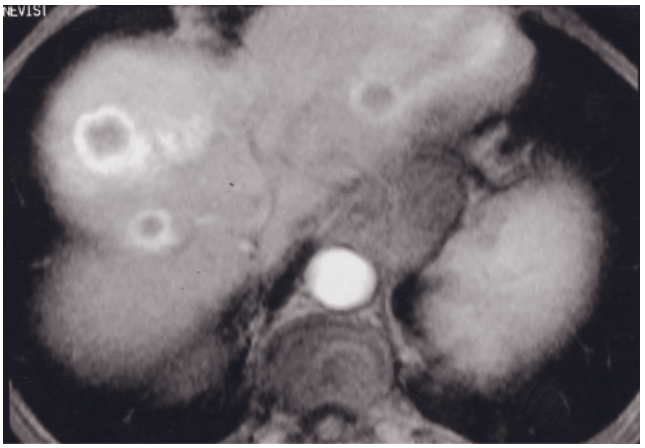

(*b*)

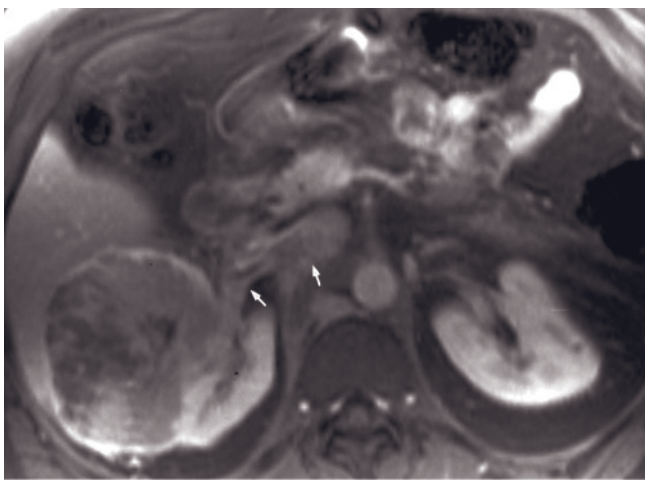

(*c*)

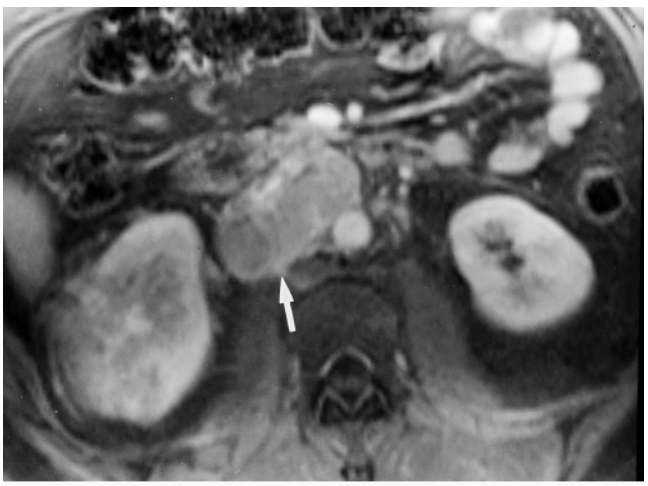

(*d*)

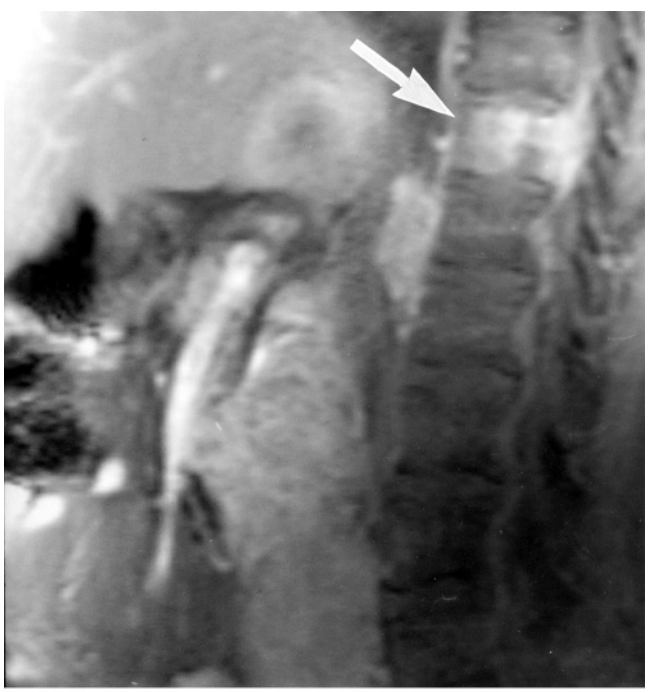

(*e*)

FIG. 9.50 Renal cell cancer—Stage 4b. T1-weighted immediate postgadolinium SGE images (*a*, *b*) demonstrate a 12-cm renal cancer arising from the left kidney (arrows, *a*). Multiple hypervascular ring-enhancing liver metastases are noted. Renal cancer metastases to the liver are frequently hypervascular. Transverse (*c*, *d*) and sagittal (*e*) 2- to 3-min T1-weighted fat-suppressed postgadolinium SGE images in a second patient. There is a large heterogeneous mass in the lateral aspect of the right kidney that invades the renal vein and extends into the IVC (arrows, *c*). Extensive retroperitoneal adenopathy is also present (arrow, *d*). Abnormal increased enhancement of the T11 vertebral body is present (arrow, *e*), consistent with metastatic foci. Gadolinium-enhanced fat-suppressed images are effective at demonstrating bone metastasis, revealing them as high-signal focal masses in a dark background of suppressed fatty marrow.

(*a*)

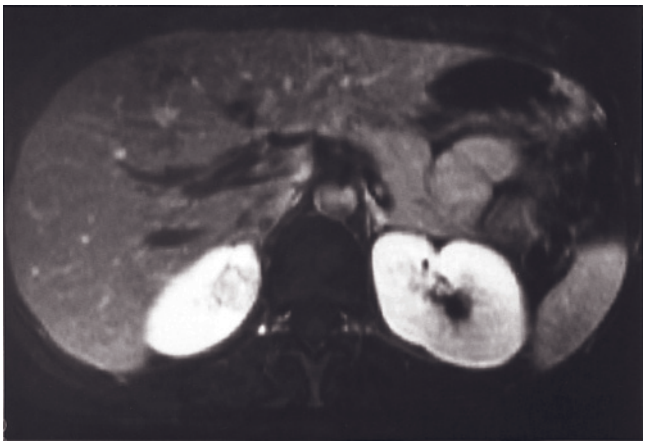

(*b*)

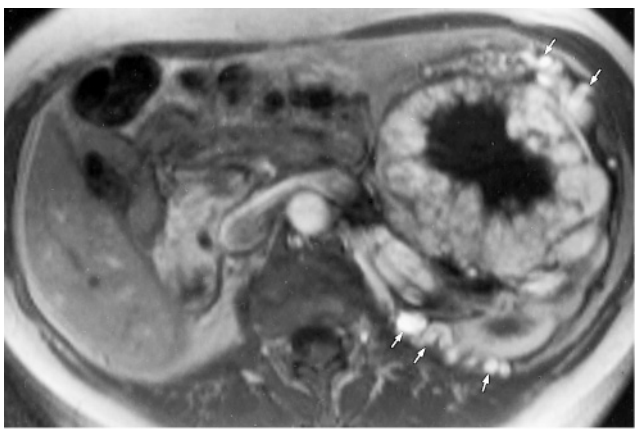

(*c*)

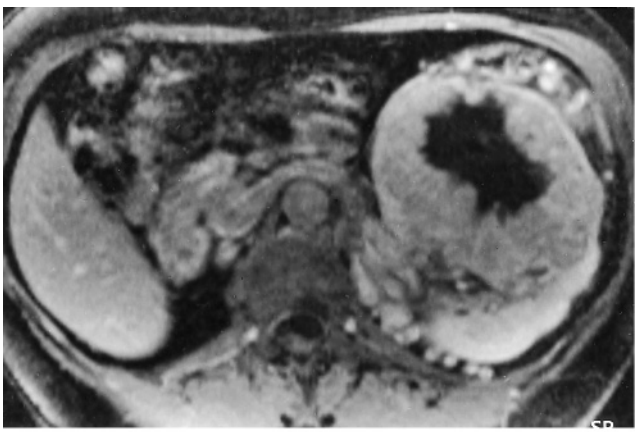

(*d*)

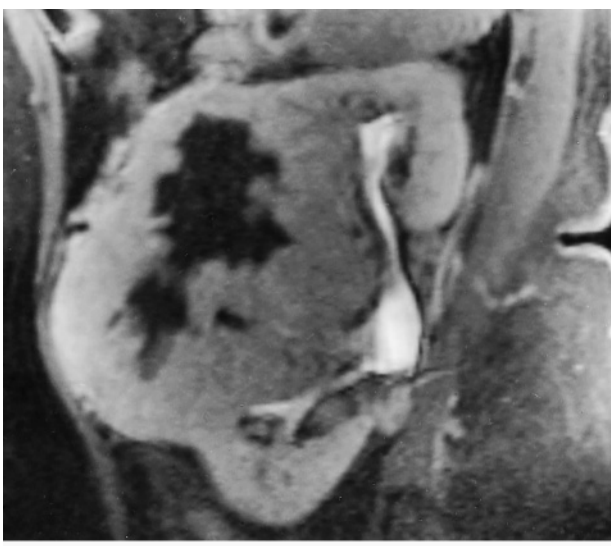

(*e*)

FIG. 9.51 Hypervascular renal cell cancer. T1-weighted immediate postgadolinium SGE (*a*) and T1-weighted fat-suppressed gadolinium-enhanced SE (*b*) images demonstrate a small, uniform-enhancing Stage 1 renal cell cancer. A 2-cm renal cancer arises from the upper pole of the right kidney. The cancer enhances in a uniform intense fashion (arrow, *a*) on the immediate postgadolinium image, comparable in signal intensity to renal cortex. On the later interstitial-phase image (*b*), the tumor is heterogeneous and lower in signal intensity than cortex. Transverse T1-weighted immediate (*c*) and 90-s fat suppressed (*d*) and sagittal 5-min postgadolinium (*e*) SGE images in a second patient demonstrate a 7-cm hypervascular renal cell cancer arising from the left kidney. On the immediate postgadolinium image (*c*), viable tumor enhances intensely, with lack of enhancement of the central portion of the tumor. Intense enhancement of multiple enlarged feeding vessels is present (arrows, *c*). On the 90-s postgadolinium image (*d*), the tumor has diminished in signal lower than renal cortex. The sagittal image (*e*) displays the location of the tumor in the midportion of the kidney.

identification of small, short curvilinear enhanced structures that are present on postgadolinium images but not apparent on precontrast images. Interstitial-phase images acquired with fat suppression are the most reliable at demonstrating these enhancing structures (fig. 9.52). One study [68] reported that negligible enhancement of a renal lesion, particularly a small lesion (<1 cm), after administration of gadolinium may not exclude malignancy in occasional small (<1 cm) hemorrhagic tumors. Subtraction imaging of postgadolinium from

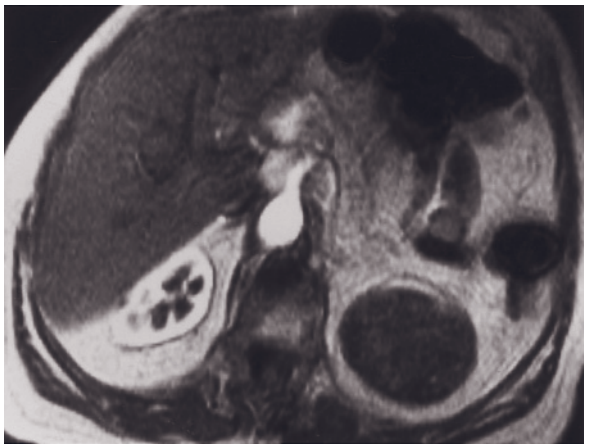

(*a*)

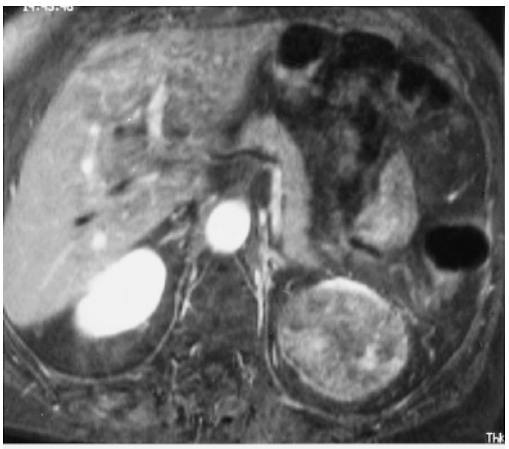

(*b*)

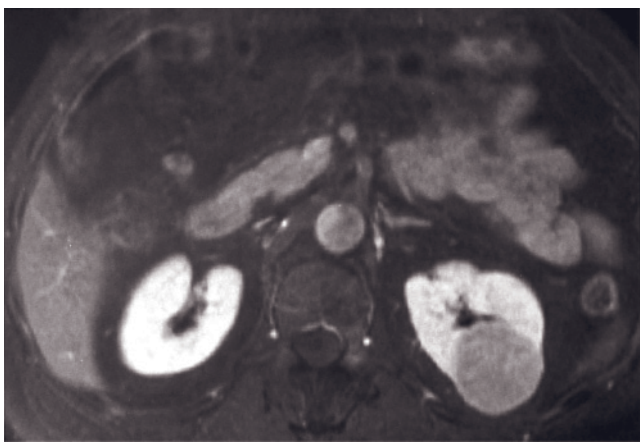

(*c*)

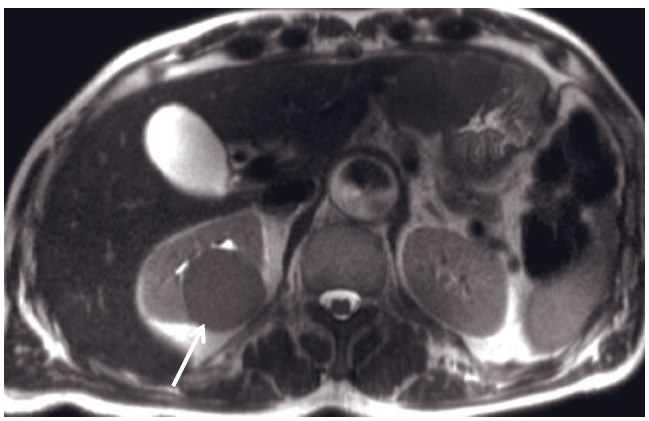

(*d*)

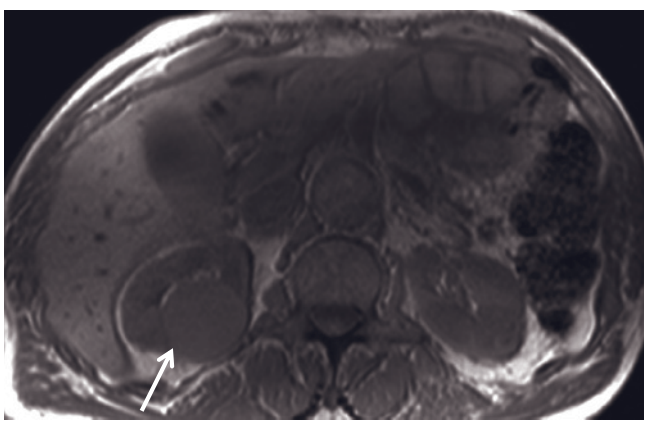

(*e*)

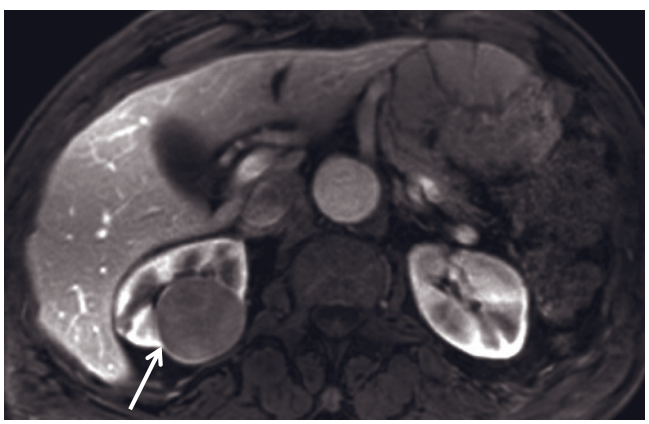

(*f*)

FIG. 9.52 Hypovascular Stage 2 renal cell cancer. T1-weighted immediate postgadolinium SGE (*a*) and T1-weighted late-phase fat-suppressed gadolinium-enhanced SE (*b*) images. The tumor shows diminished enhancement immediately after contrast (*a*).The interstitial-phase fat-suppressed image demonstrates small irregular enhancing structures within the mass (*b*), which distinguishes this lesion from a complicated cyst. T1-weighted interstitial-phase fat-suppressed gadolinium-enhanced SE image (*c*) in a second patient shows small irregular enhancing structures in a hypovascular renal cancer arising from the left kidney. The great majority of hypovascular renal cell cancers are of papillary subtype. Transverse T2-weighted single-shot echo-train spin-echo (*d*), transverse T1-weighted SGE (*e*), transverse T1-weighted postgadolinium hepatic venous-phase fat-suppressed 3D-GE (*f*), and coronal T1-weighted postgadolinium interstitial-phase fat-suppressed 3D-GE (*g*) images at 3.0 T demonstrate a hypovascular renal cell cancer (arrows, *d*–*g*) in the right kidney in another patient. The tumor shows a hypointense signal on both T2-weighted (*d*) and

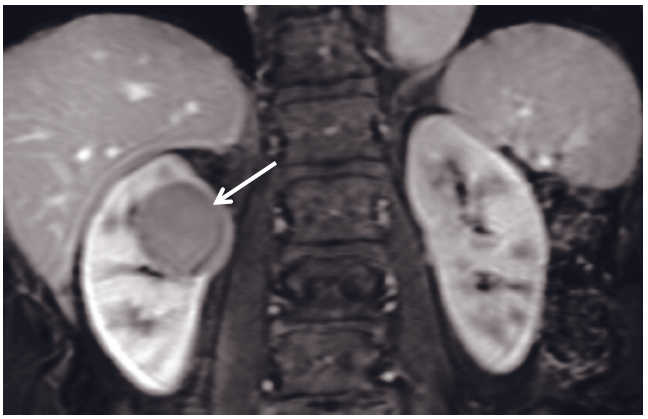

(*g*)

FIG. 9.52 (*Continued*) T1-weighted (*e*) images. The tumor shows mild progressive enhancement (*f*, *g*) reflecting its hypovascular nature. Note that the aorta is dilated.

pregadolinium 3D-GRE imaging may help in this distinction (see fig. 9.13). Careful attention should be paid to the heterogeneity of signal intensity of these lesions on all MR sequences, as this may be an indicator of their solid composition.

Hemorrhage occurs occasionally in tumors in patients with normal renal function. Tumors in patients with chronic renal failure, in contrast, are hemorrhagic relatively commonly (see below). Hemorrhage appears high in signal intensity on noncontrast T1-weighted images (fig. 9.53).

Tumor size is not a reliable criterion for diagnosing renal cancer or for distinguishing cancer from adenoma [46–48, 69–72]. RCC occasionally shows no change in size for intervals of greater than 1 year [47, 72]. Any solid renal tumor that is nonfatty should be considered a possible RCC and should, at minimum, be followed by serial imaging.

In rare instances, RCC is visualized on MRI as largely or completely cystic (fig. 9.54). This radiologic appearance may be best correlated histopathologically with a distinct subtype of RCC termed multilocular cystic renal cell carcinoma. This rare form of RCC has a characteristic gross appearance. In contrast to many RCCs that are primarily solid masses with focal cystic degeneration, multilocular cystic RCC is predominantly cystic with only a modicum of a solid component. Cyst walls are oftentimes densely fibrotic with focal calcifications. Microscopically, tumor cells generally show low-grade cytologic features. Multilocular cystic RCC appears to be an extremely low-grade form of RCC that, if treated early, may be curable [73]. This RCC may have a septated cystic appearance resembling multilocular cystic nephroma on MRI. Septations tend to be thicker and more irregular than those observed in multilocular cystic nephroma, and hemorrhage is common (fig. 9.55).

Cystic changes are relatively common in renal cancer (fig. 9.56). Rarely, lesions may appear virtually identical to a cyst, with a thin layer of tumor cells within the wall. We have observed a propensity for cystic tumors in the setting of multifocal or bilateral renal cancers (fig. 9.57).

Other features that may be observed with renal cancer include substantial hemorrhage in the perinephric space secondary to the extensive vascularity, friable vessels, and the large size that these tumors can attain (fig. 9.58). Although renal cancers usually grow as focal cortex-based neoplasms, poorly differentiated tumors may demonstrate extensive, ill-defined renal parenchymal infiltration resembling transitional cell cancer, lymphoma, or metastases from poorly differentiated tumors (fig. 9.59).

Recent studies have reported that occasionally some clear cell carcinomas and, less commonly, granular cell carcinomas may show a relative focal or diffuse loss of signal intensity on opposed-phase MR images [74, 75]. These lesions have microscopic fat that is not detected on CT or on conventional T1-weighted images. One series [74] demonstrated that mean out-of-phase to in-phase signal intensity ratio of clear cell carcinomas was significantly different from that of other renal cancers ($P < 0.0002$). This study demonstrated that clear cell carcinoma, when compared with other renal cancers, may show a relative focal or diffuse loss of signal intensity. In renal masses, this signal intensity loss, consistent with lipid, does not necessarily indicate angiomyolipoma. It should be noted that fat content in these reported cancers was minimal and/or focal, which contrasts with the majority of angiomyolipomas, in which the fat content is substantial and diffuse. The differential diagnosis is angiomyolipoma with minimal fat content [75].

Radio Frequency Ablation. In patients who are not considered surgical candidates for resection of renal cancer, radiofrequency ablation (RFA) has been employed as a means of tumor eradication. Hemorrhagic

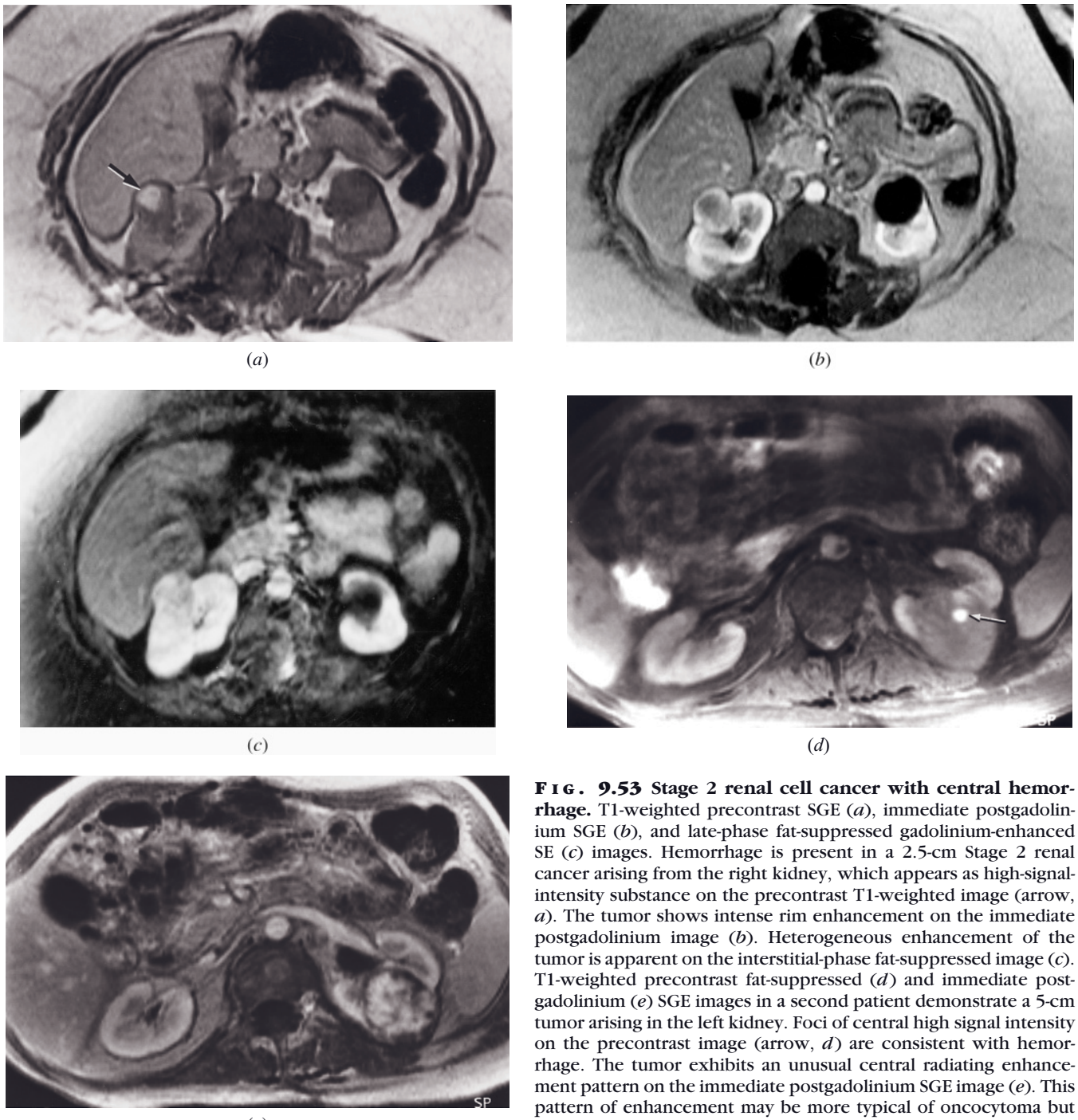

FIG. 9.53 Stage 2 renal cell cancer with central hemorrhage. T1-weighted precontrast SGE (*a*), immediate postgadolinium SGE (*b*), and late-phase fat-suppressed gadolinium-enhanced SE (*c*) images. Hemorrhage is present in a 2.5-cm Stage 2 renal cancer arising from the right kidney, which appears as high-signal-intensity substance on the precontrast T1-weighted image (arrow, *a*). The tumor shows intense rim enhancement on the immediate postgadolinium image (*b*). Heterogeneous enhancement of the tumor is apparent on the interstitial-phase fat-suppressed image (*c*). T1-weighted precontrast fat-suppressed (*d*) and immediate postgadolinium (*e*) SGE images in a second patient demonstrate a 5-cm tumor arising in the left kidney. Foci of central high signal intensity on the precontrast image (arrow, *d*) are consistent with hemorrhage. The tumor exhibits an unusual central radiating enhancement pattern on the immediate postgadolinium SGE image (*e*). This pattern of enhancement may be more typical of oncocytoma but was present in this renal cell cancer.

changes are appreciated after the procedure (fig. 9.60). Persistent or redevelopment of enhancing stroma is consistent with residual or recurrent cancer.

Recurrent Renal Cancer. Renal cancer recurrence occurs most commonly in the resection bed of the resected cancer. Distinction from resection bed fibrosis is usually feasible, as fibrosis tends to appear as linear, small-volume tissue that exhibits low T2-weighted signal and minimal contrast enhancement, whereas tumor recurrence appears more nodular or masslike with relatively high T2-weighted signal and substantial irregular contrast enhancement. Involvement of adjacent organs by the recurrent tumor may be shown. Recurrence may also be manifest as tumor involvement of distant sites (fig. 9.61).

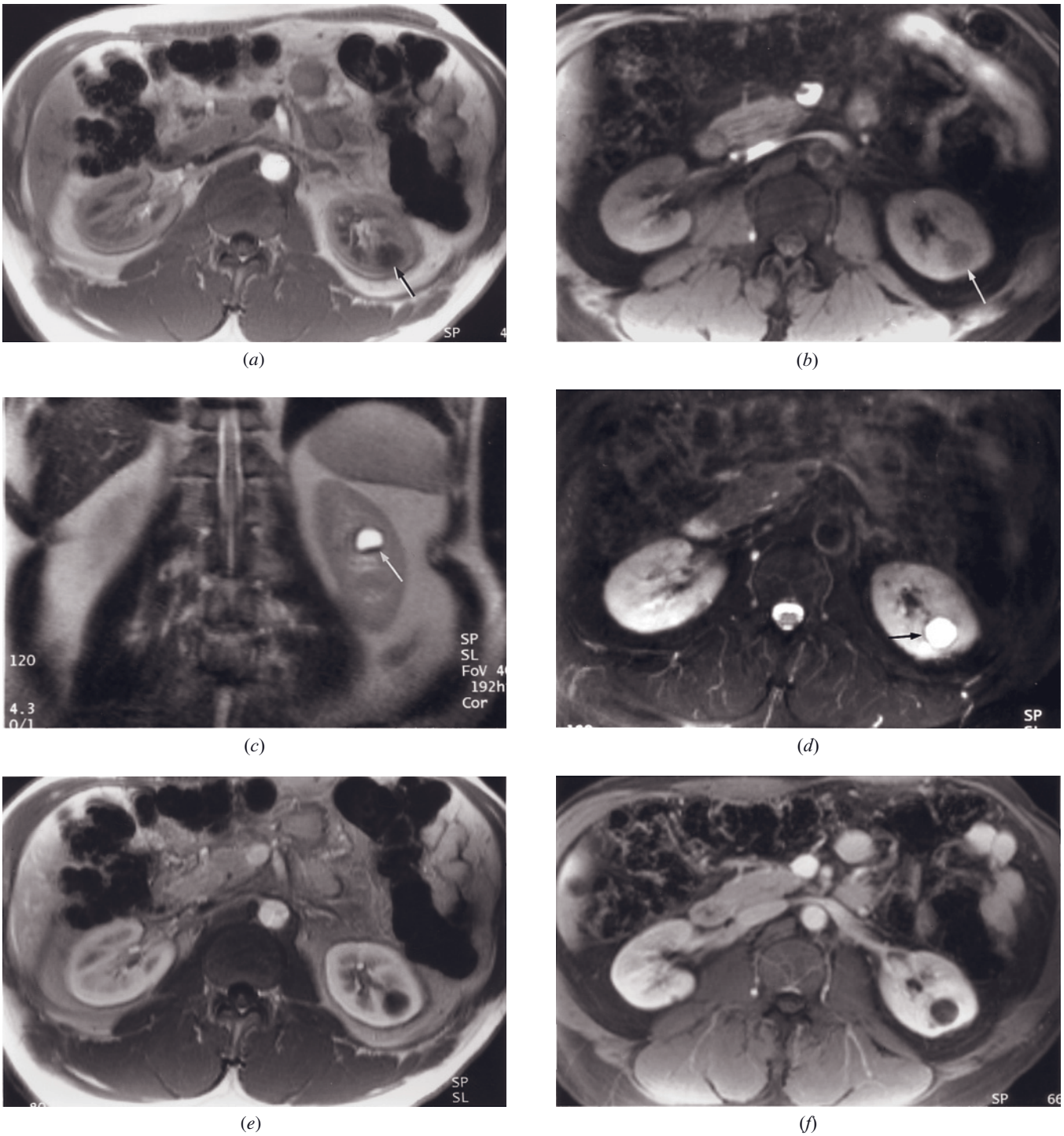

FIG. 9.54 Purely cystic renal cell cancer. T1-weighed precontrast (*a*) and precontrast fat-suppressed (*b*) SGE images, coronal T2-weighed SS-ETSE (*c*) and transverse T2-weighted ETSE (*d*), and T1-weighted immediate (*e*) and interstitial-phase fat-suppressed (*f*) gadolinium-enhanced SGE images. A well-defined cystic lesion with mural calcification was demonstrated on CT images (not shown).The lesion is well circumscribed and low in signal intensity on T1-weighted images (arrows, *a*, *b*) and high in signal intensity on T2-weighted images (*c*, *d*) and does not enhance after gadolinium administration (*e*, *f*). A low-signal-intensity mural rim on the T2-weighted images (arrows, *c*, *d*) corresponds to calcification as shown on the CT image. At surgery, the lesion was considered to represent a cyst, but at histologic examination a thin sheet of tumor cells was present in part of the cyst wall. Coronal T2-weighted

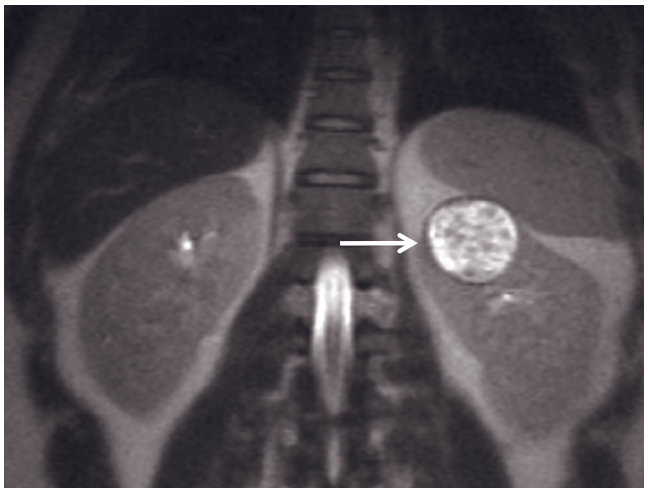

(*g*)

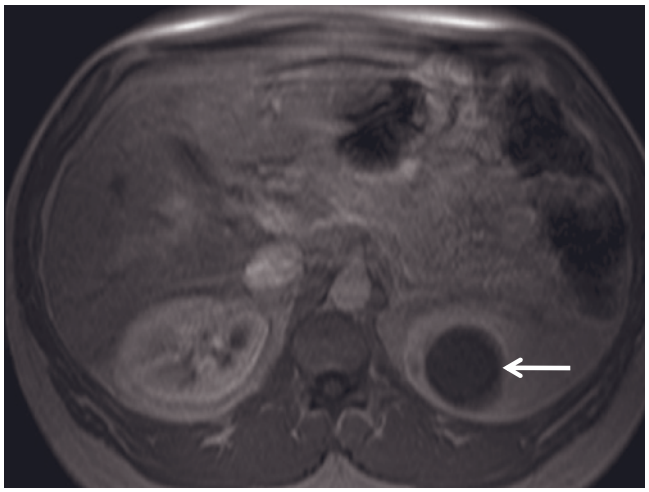

(*h*)

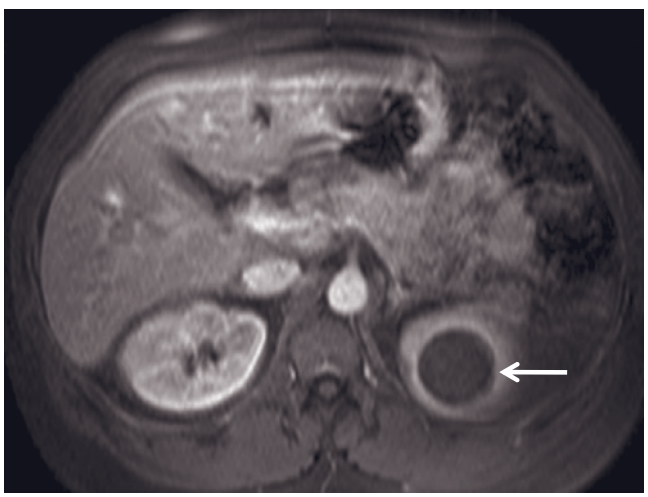

(*i*)

FIG. 9.54 (*Continued*) single-shot echo-train spin-echo (*g*), T1-weighted postgadolinium hepatic arterial dominant SGE (*h*), and fat-suppressed hepatic venous phase 3D-GE (*i*) images demonstrate a cystic renal cell cancer (arrows, *g–i*) in the left kidney in another patient. The cystic tumor shows heterogeneous signal on T2-weighted image (*g*) due to its complex multiloculated structure. The tumor has a thin wall that shows moderate enhancement on postgadolinium images (*h*, *i*). No stromal enhancement is detected on postgadolinium images (*h*, *i*).

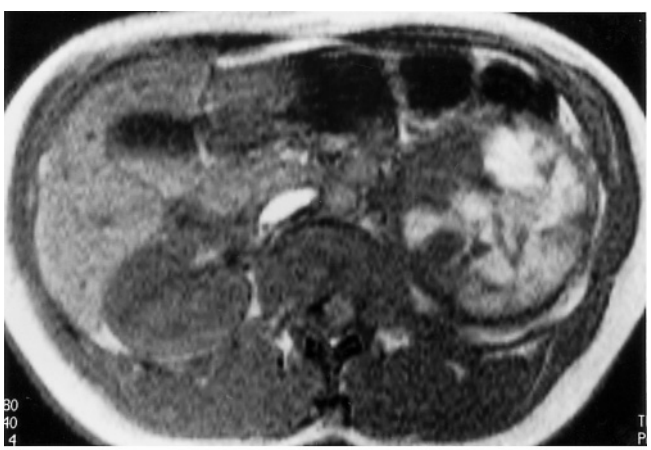

(*a*)

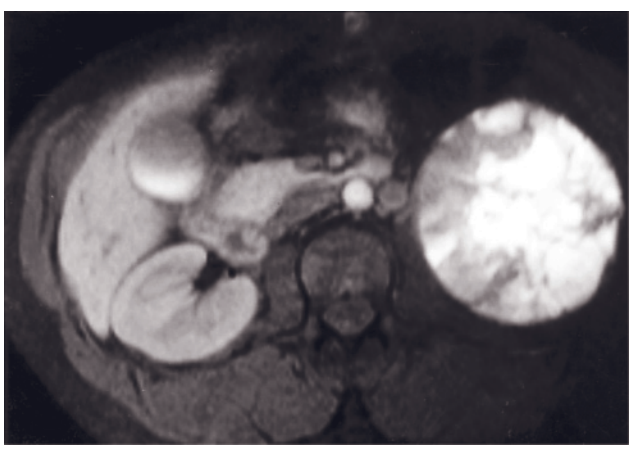

(*b*)

FIG. 9.55 Multicystic hemorrhagic renal cell cancer. T1-weighted precontrast SGE (*a*), precontrast fat-suppressed SE (*b*), and T2-weighted fat-suppressed SE (*c*) images. T1- and T2-weighted images demonstrate an 8-cm tumor arising from the left kidney that contains regions of mixed low and high signal intensity compatible with blood products of varying ages. Small nodular masses of intermediate signal intensity are consistent with solid tumor.

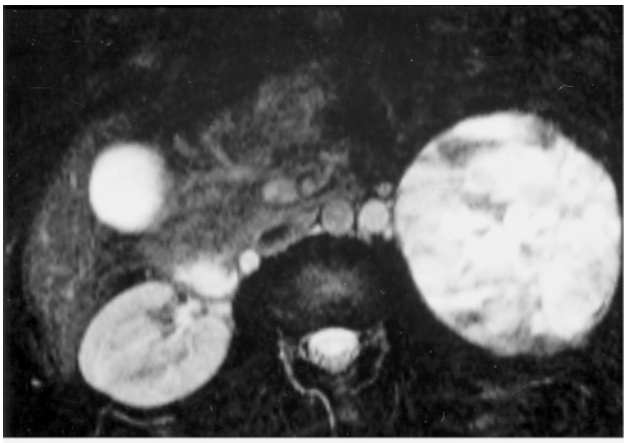

(*c*)

FIG. 9.55 (*Continued*)

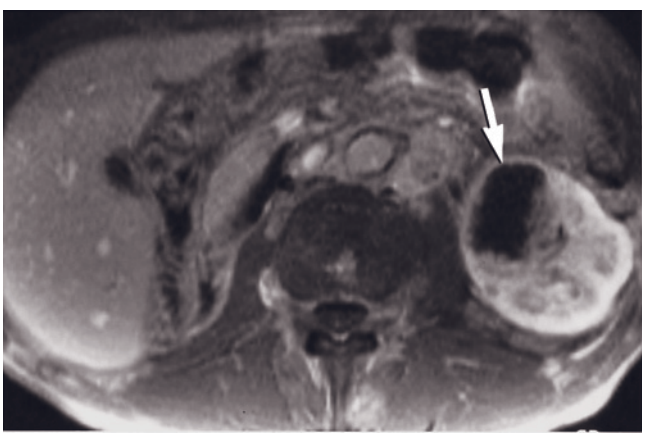

(*a*)

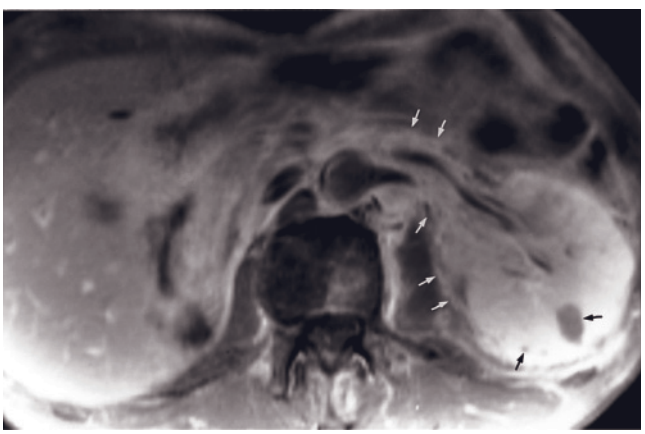

(*b*)

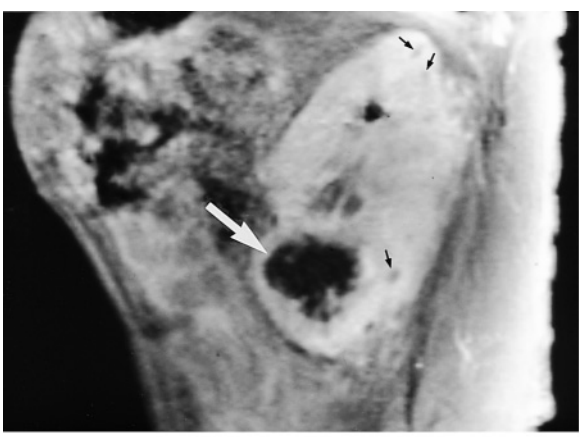

(*c*)

FIG. 9.56 Multifocal renal cell cancer with cystic tumor and sheetlike tumor infiltration. T1-weighted immediate (*a*), transverse interstitial-phase fat-suppressed (*b*), and sagittal interstitial-phase (*c*) postgadolinium SGE images in a patient with prior right nephrectomy for renal cancer. A predominantly cystic renal cancer is present in the lower pole of the left kidney (large arrows, *a*, *c*). Extensive tumor infiltration in a sheetlike pattern is identified along the renal capsule and into the renal hilum (small white arrows, *b*). Numerous small cysts are also present (small black arrows, *b*, *c*), which are seeded with tumor.

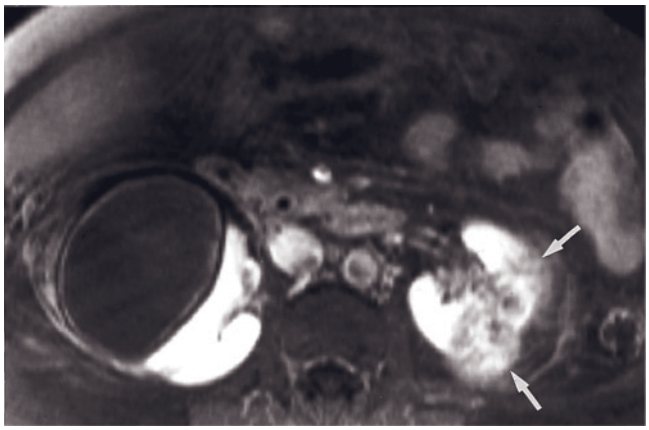

(*a*)

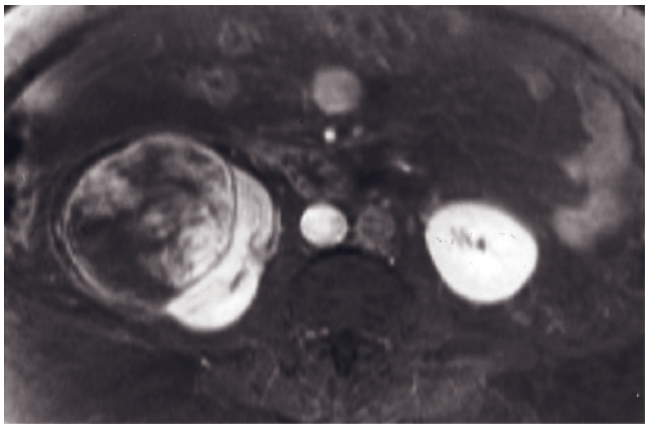

(*b*)

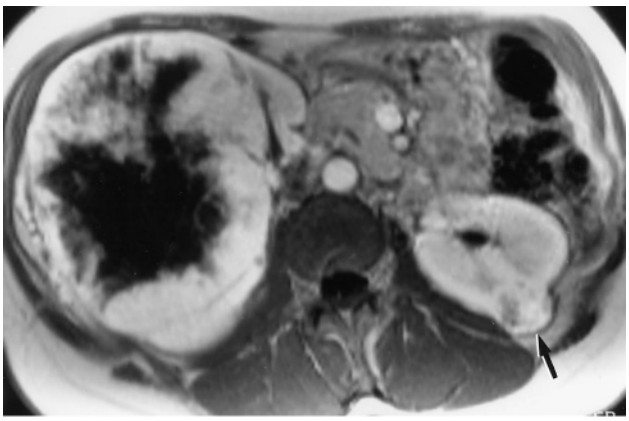

(*c*)

FIG. 9.57 Bilateral renal cell cancer. T1-weighted interstitial-phase fat-suppressed gadolinium-enhanced SE images from midrenal (*a*) and lower renal (*b*) levels. A large cystic/solid renal cancer arises from the right kidney. Two smaller renal cancers (arrows, *a*) are identified at the level of the renal hilum in the left kidney. T1-weighted immediate postgadolinium SGE image (*c*) in a second patient demonstrates bilateral hypervascular renal cell cancers. The large right renal cancer demonstrates a necrotic center, whereas the 2-cm left renal cancer (arrow, *c*) demonstrates intense heterogeneous enhancement.

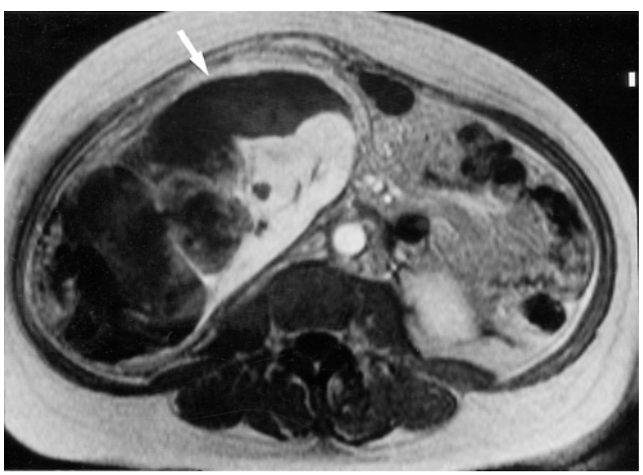

(*a*)

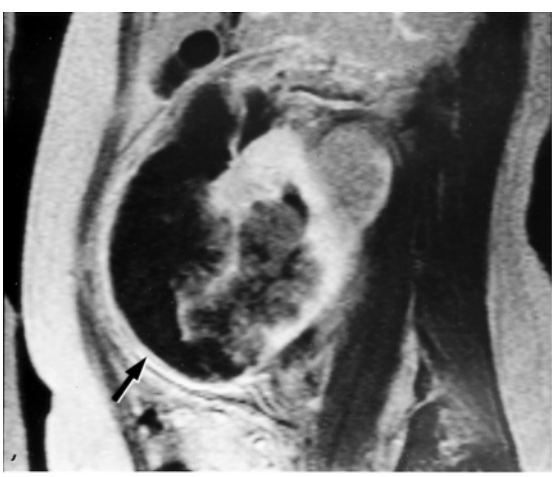

(*b*)

FIG. 9.58 Renal cell cancer with perirenal hemorrhage. T1-weighted transverse 90-s (*a*) and sagittal 120-s (*b*) postgadolinium SGE images. An 8-cm irregular cystic/solid renal cancer arises from the lower two-thirds of the right kidney. A large perirenal collection of blood surrounds the kidney (arrows, *a*, *b*). The blood appears low in signal intensity on postcontrast images

(*c*)

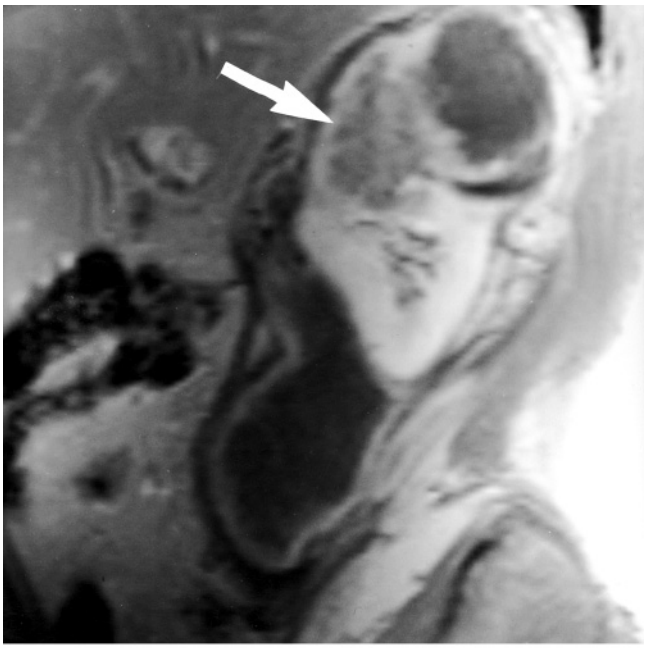

(*d*)

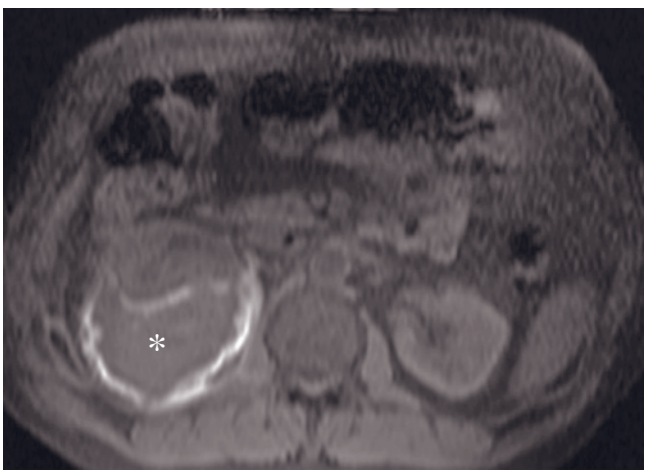

(*e*)

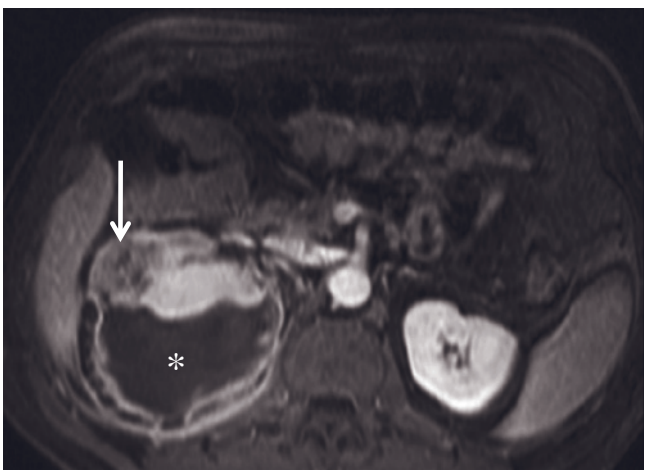

(*f*)

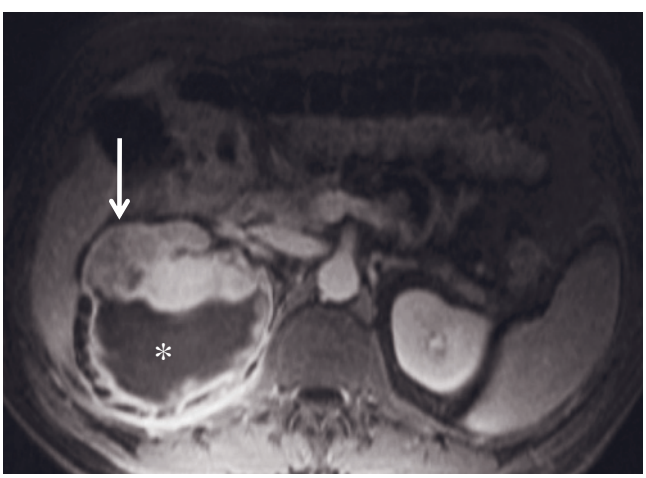

(*g*)

FIG. 9.58 (*Continued*) because of rescaling of abdominal tissue signal intensities. T1-weighted precontrast fat-suppressed SGE (*c*) and sagittal 3-min T1-weighted fat-suppressed postgadolinium SGE (*d*) images in a second patient. A large mass arises in the upper pole of the right kidney. The tumor is heterogeneous on the 3-min postgadolinium image (arrow, *d*). The tumor has resulted in a large perinephric hematoma that has extended inferiorly in the pararenal space (arrow, *c*). The peripheral rim of high signal on the noncontrast T1-weighted image is diagnostic for hemorrhage. Transverse T1-weighted fat-suppressed 3D-GE (*e*) and transverse hepatic venous-phase (*f*) and interstitial- phase (*g*) fat-suppressed 3D-GE images demonstrate renal cancer with subcapsular and perirenal hemorrhage in the right kidney in another patient. The tumor (arrows, *f*, *g*) shows heterogeneous progressive enhancement on postgadolinium images (*f*, *g*). A subcapsular hematoma (*, *e*–*g*) with perirenal extension is detected. The peripheral high signal intensity of the hematoma reflects its subacute nature.

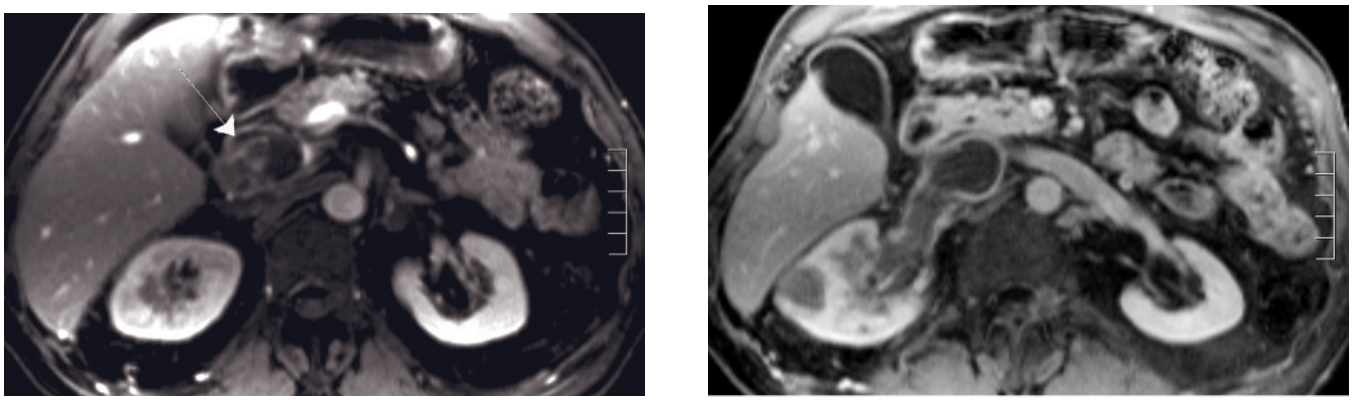

(*a*) (*b*)

FIG. 9.59 Infiltrative renal cell cancer. Gadolinium-enhanced 3D gradient-echo images (*a*, *b*) reveal ill-defined heterogeneous tissue infiltrating the renal medulla, with expansion of the renal vein with heterogeneous and mildly enhancing tissue (arrow, *b*). Infiltrative involvement is an unusual appearance for renal cancer and is consistent with poorly differentiated histology.

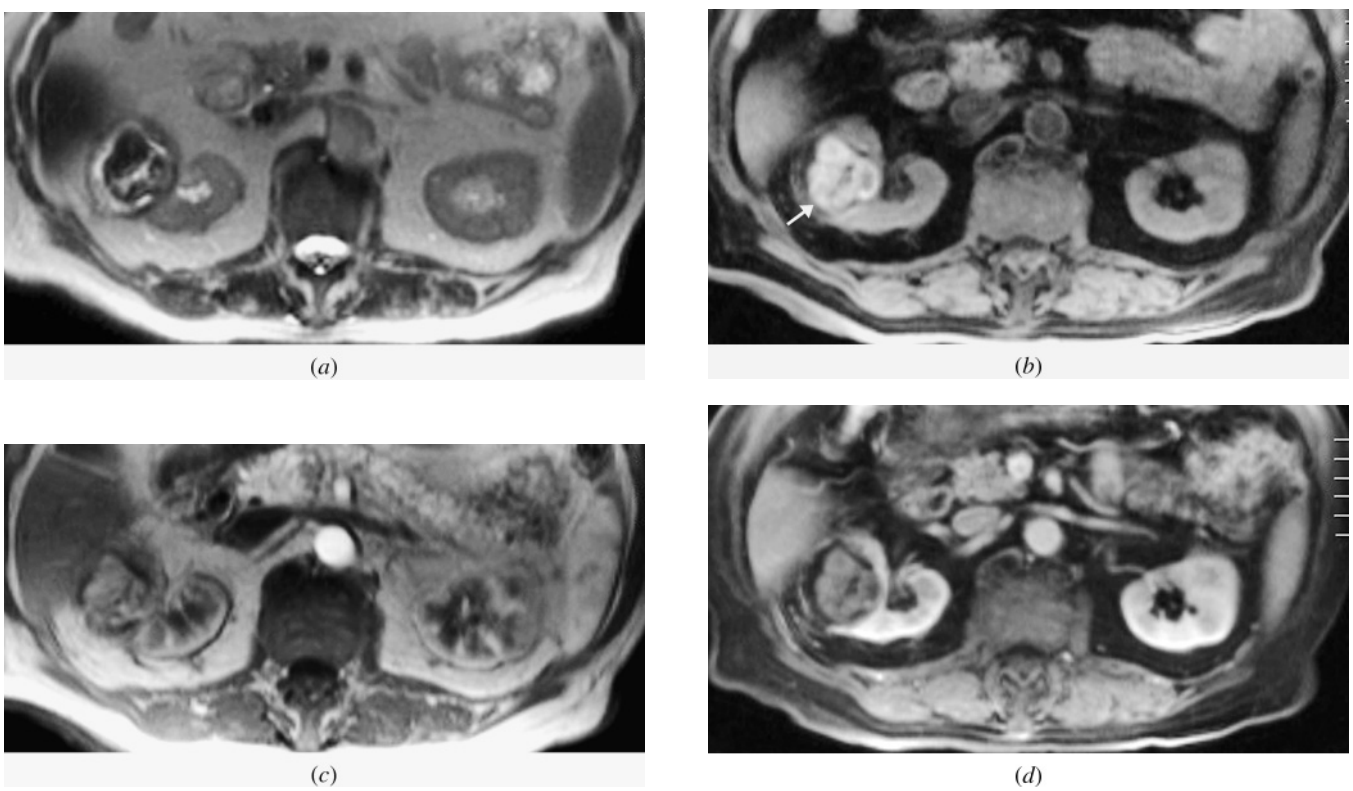

(*a*) (*b*) (*c*) (*d*)

FIG. 9.60 Renal mass after RF ablation. T2-weighted SS-ETSE (*a*), T1-weighted fat-suppressed gradient-echo (*b*), and immediate (*c*) and 90-s (*d*) postgadolinium T1-weighted gradient- echo images. An ablated area is seen in the midaspect of the right kidney, which appears as a region with central decreased signal and peripheral high signal intensity on the T2-weighted image (*a*) and central increased signal intensity and peripheral low signal intensity on the T1-weighted image (arrow, *b*) and shows a lack of enhancement on postgadolinium images (*c* and *d*), consistent with acute hemorrhage after successful RF ablation. Coronal

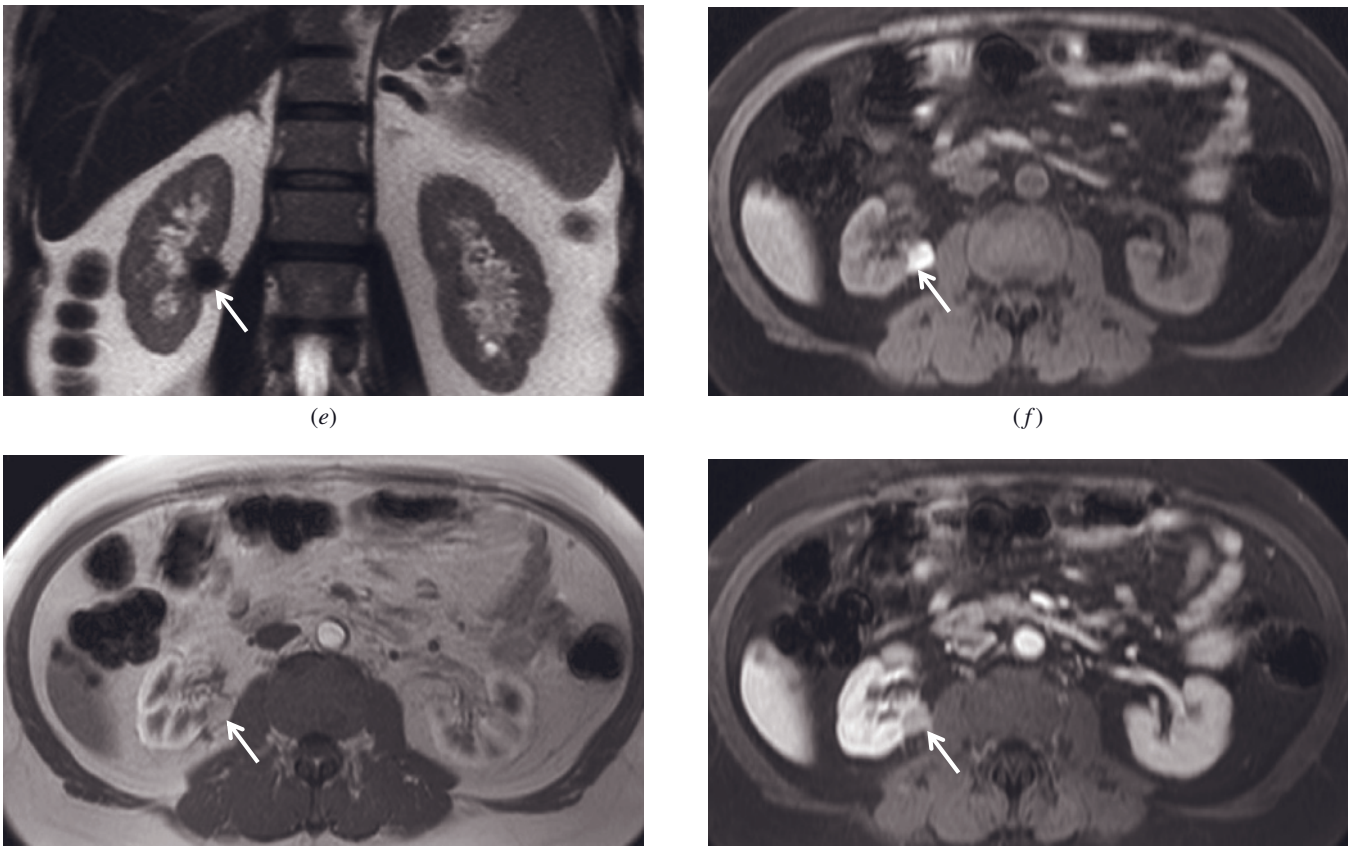

(*e*) (*f*)

(*g*) (*h*)

FIG. 9.60 (*Continued*) T2-weighted single-shot echo-train spin-echo (*e*), transverse T1-weighted fat-suppressed 3D-GE (*f*), transverse T1-weighted postgadolinium hepatic arterial dominant-phase SGE (*g*), and T1-weighted transverse fat-suppressed postgadolinium interstitial-phase 3D-GE (*h*) images demonstrate RF-ablated renal cell cancer (arrows, *e*–*h*) in the right kidney in another patient. RF-ablated lesion shows markedly low signal on T2-weighted image (*e*) and markedly high signal on precontrast T1-weighted image (*f*), which are consistent with blood products secondary to the ablation process. No residual or recurrent tumor enhancement is detected on postgadolinium images (*g*, *h*).

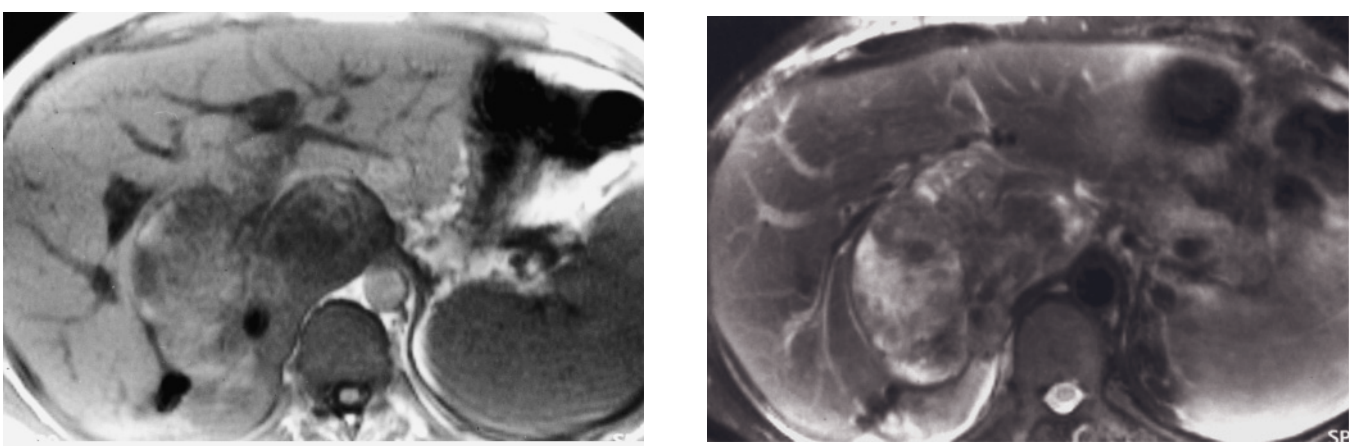

(*a*) (*b*)

FIG. 9.61 Recurrent renal cell cancer. T1-weighted precontrast SGE (*a*), T2-weighted fat-suppressed SGE (*b*), and T1-weighted immediate (*c*) and 2-min fat-suppressed (*d*) postgadolinium SGE images. There is a large heterogeneous mass in the right nephrectomy space consistent with tumor recurrence. The large tumor mass compresses the right lobe of the liver and portal vein with

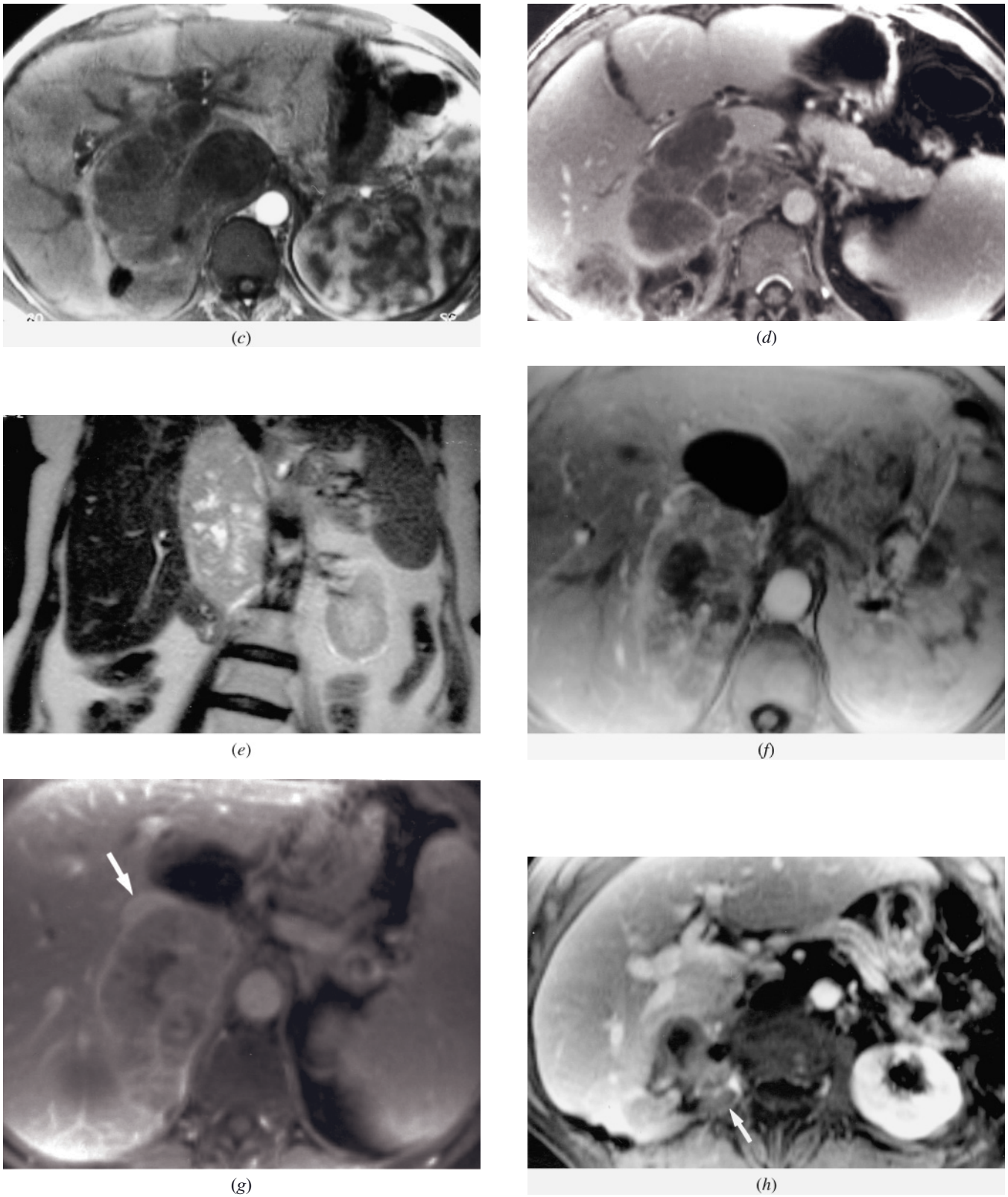

FIG. 9.61 (*Continued*) invasion of the IVC. Coronal T2-weighted SS-ETSE (*e*) and transverse T1-weighted immediate (*f*) and 2-min fat-suppressed (*g*) postgadolinium SGE images in a second patient. There is a large mass in the right upper quadrant that compresses the IVC anteriorly (arrow, *g*). This mass is heterogeneously increased signal on T2-weighted sequences and demonstrates mild heterogeneous enhancement after gadolinium administration. T1-weighted late-phase fat-suppressed postgadolinium SGE (*h*) image in a third patient. An irregular heterogeneous mass is evident in the superior aspect of the right renal fossa. This lesion invades the right psoas muscle (arrow, *h*) and the right hepatic lobe. The tumor also abuts the posterior branch of the right portal vein and the main portal vein.

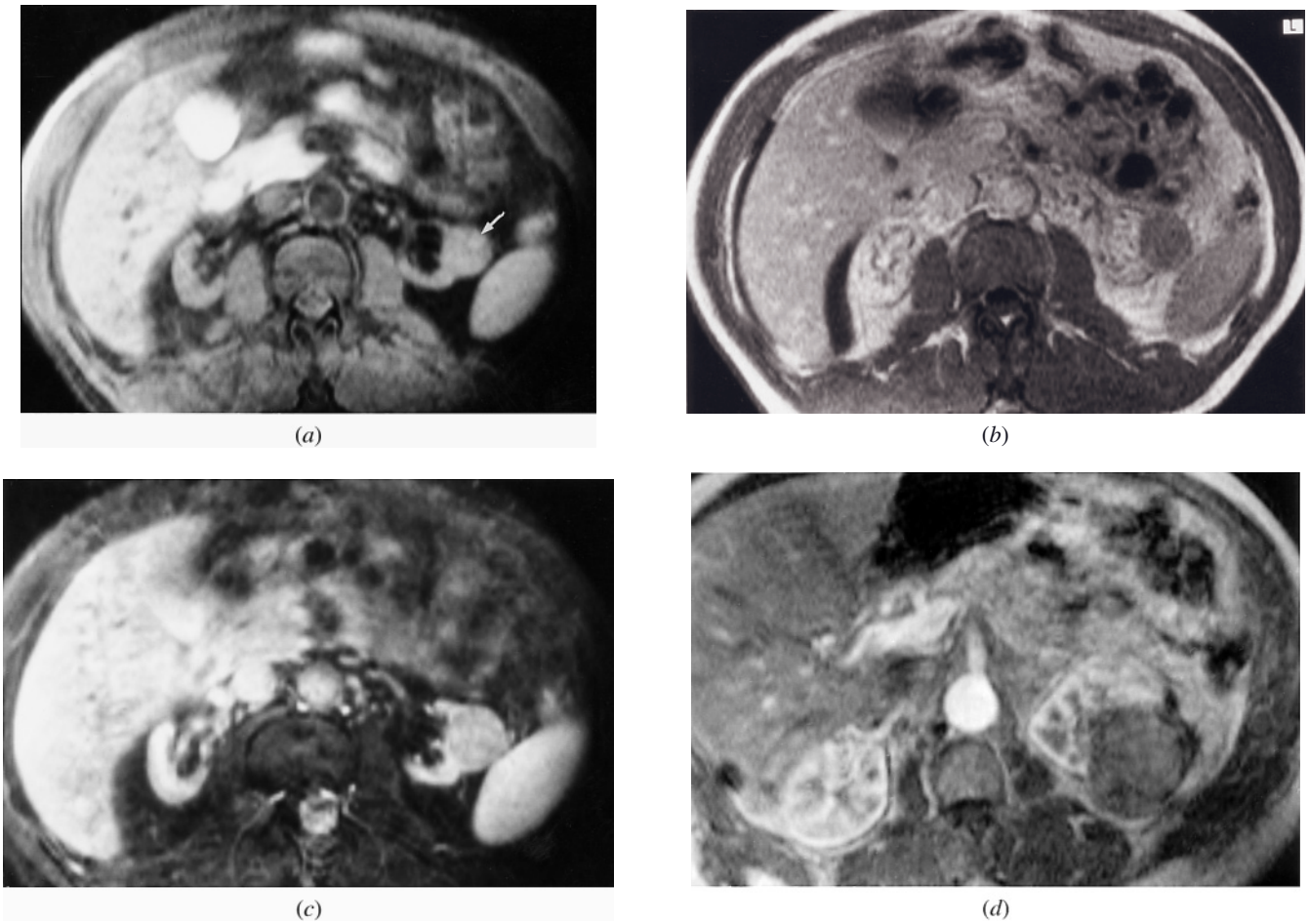

FIG. 9.62 Hypovascular renal cell cancer in chronic renal failure. T1-weighted fat-suppressed SE (*a*), 90-s postgadolinium SGE (*b*), and interstitial-phase gadolinium-enhanced T1-weighted fat-suppressed spin-echo (*c*) images. The kidneys are chronically failed and appear atrophic with no corticomedullary differentiation on the precontrast image. A 2.5-cm renal cancer arises from the lateral aspect of the left kidney and contains a punctate high-signal-intensity focus on the noncontrast T1-weighted image consistent with hemorrhage (arrow, *a*).The tumor enhances minimally on the 90-s postgadolinium SGE image (*b*). Small irregular enhancing structures are apparent on the gadolinium-enhanced T1-weighted fat-suppressed image (*c*), which represent enhancing stroma in a hypovascular renal cancer. T1-weighted immediate postgadolinium SGE image (*d*) in a second patient in chronic renal failure with a hypovascular 5.5-cm renal cancer in the left kidney.

Renal Cancer in Chronic Renal Failure. Patients with chronic renal failure have a substantial risk of developing RCC, which has a reported incidence of approximately 7% [26]. Tumors in patients with chronic renal failure are much more commonly hypovascular than tumors in patients with normal renal function. The frequent occurrence of hypovascular cancers and the suboptimal enhancement of renal parenchyma in patients with chronic renal failure on iodine contrast-enhanced CT images render chronic renal failure patients difficult to evaluate with CT. In comparison, MRI is able to demonstrate diminished heterogeneous enhancement of tumors and moderate enhancement of background renal parenchyma, thereby improving detection of cancer in this patient group (fig. 9.62). Cancers in patients with diminished renal function have a great propensity to undergo hemorrhage (fig. 9.63) [76], which may be so extensive that the cancer can resemble a hemorrhagic cyst (fig. 9.64). Therefore, caution must be exercised in describing heterogeneous hemorrhagic renal lesions as cysts in patients with chronic renal failure. Renal cancer also may arise in patients with other underlying renal diseases such as polycystic kidney disease (fig. 9.65).

Renal Cancer—Role of MRI. MRI is slightly superior to dynamic contrast-enhanced CT imaging for the detection, characterization, and staging of renal cancer [1, 15, 59]. There is, however, little difference between dual-phase spiral or multidetector CT imaging and MRI in the routine investigation of renal masses. There are definite indications for the use of MRI, which include

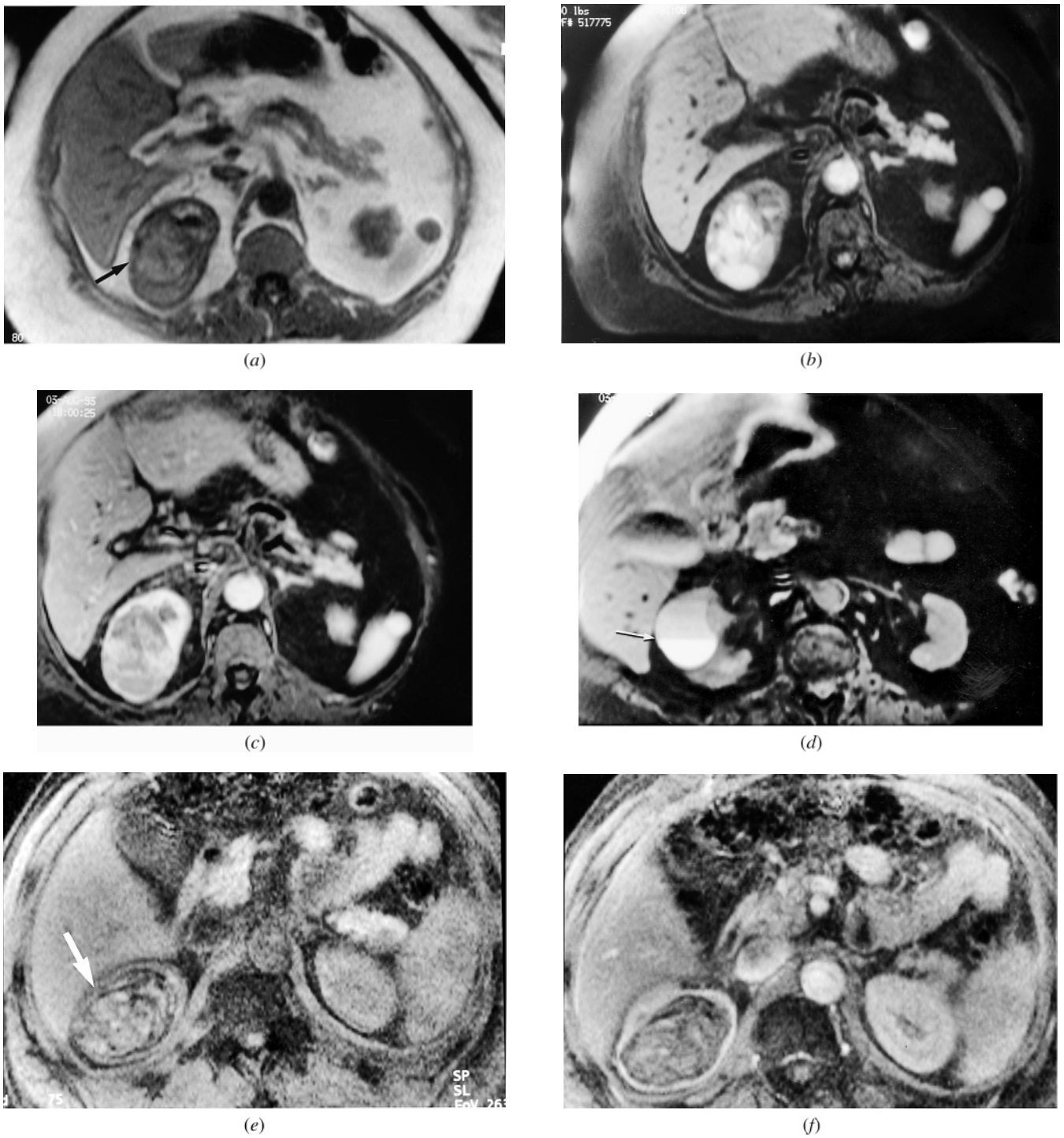

FIG. 9.63 Hemorrhagic renal cancer in chronic renal failure. T1-weighted precontrast SGE (*a*), precontrast fat-suppressed SE (*b*), and interstitial-phase fat-suppressed gadolinium-enhanced SE (*c*) images. A 5-cm renal cancer is present in the right kidney (arrow, *a*) that is heterogeneously high in signal intensity on precontrast T1-weighted images (*a*, *b*), consistent with hemorrhage, and shows heterogeneous high-signal-intensity stroma on the postgadolinium image (*c*). T1-weighted fat-suppressed SE image (*d*) at a level immediately inferior to the renal cancer shows a hemorrhagic renal cyst with a fluid level (arrow, *d*). T1-weighted precontrast fat-suppressed SGE (*e*) and 90-s postgadolinium SGE (*f*) images in a second patient demonstrate a 5-cm tumor that is heterogeneously high in signal intensity on the precontrast fat-suppressed image (arrow, *e*) and is heterogeneously diminished in signal intensity on the postgadolinium image (*f*).

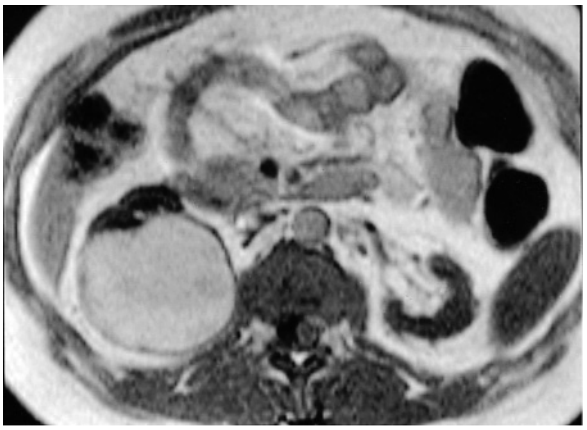

(*a*)

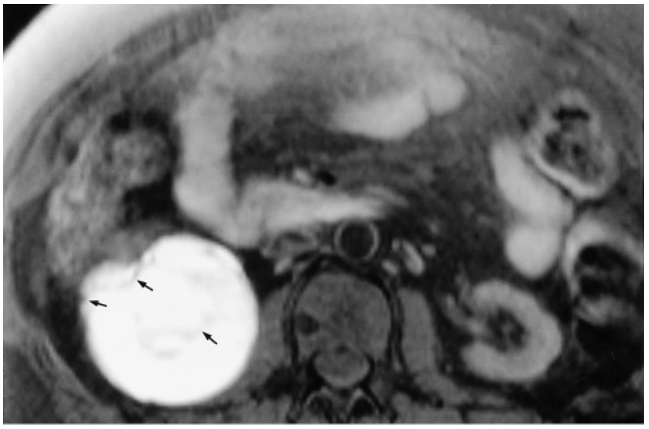

(*b*)

(*c*)

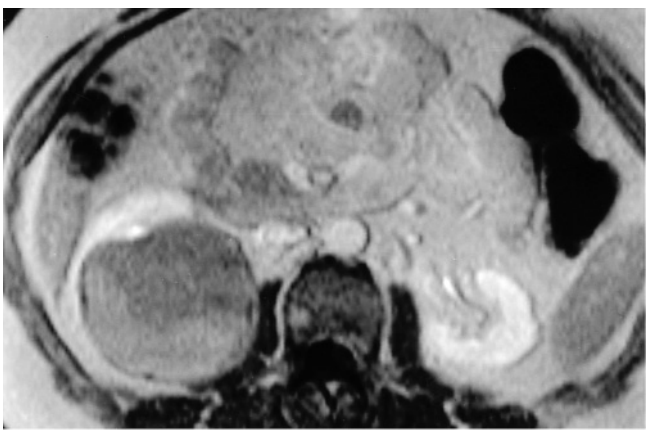

(*d*)

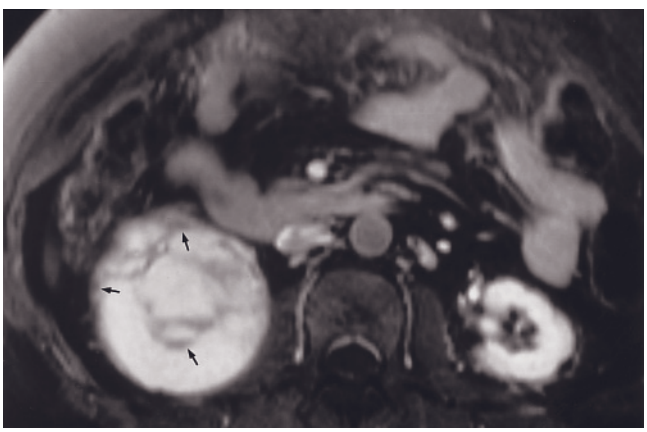

(*e*)

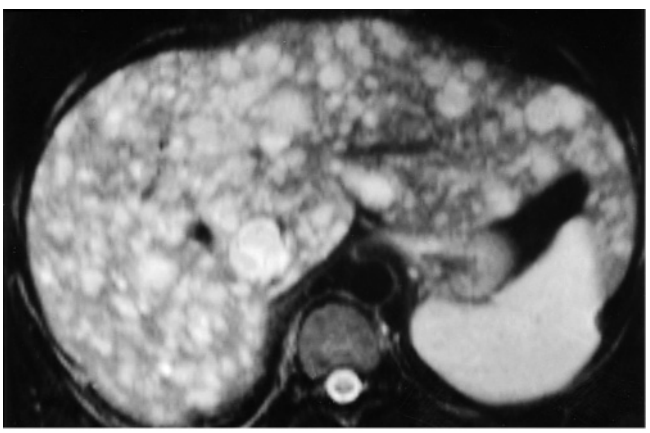

(*f*)

(*g*)

FIG. 9.64 Hemorrhagic cystic renal cell cancer in chronic renal failure. T1-weighted precontrast SGE (*a*), precontrast fat-suppressed SE (*b*), and immediate (*c*), 1-min (*d*), and interstitial-phase fat-suppressed (*e*) gadolinium-enhanced SE images. A largely cystic hemorrhagic renal mass is noted arising from the lower pole of the right kidney. Small murally-based nodular densities and reticular markings are apparent on precontrast and postcontrast images, which are best shown on the fat-suppressed images (arrows, *b*, *e*). Multiple surgical biopsies did not reveal renal cancer. T2-weighted fat-suppressed SE (*f*), T1-weighted immediate (*g*, *h*), and interstitial-phase fat-suppressed (*i*) gadolinium-enhanced SE images obtained 2½ years later. Numerous liver metastases are apparent that are small and high in signal intensity on T2-weighted images (*f*) and enhance in a uniform intense fashion on immediate postgadolinium images (*g*, *h*). An 8-cm hypervascular

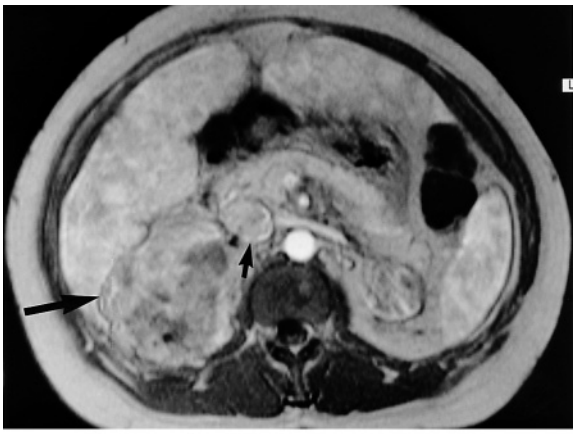

(*h*)

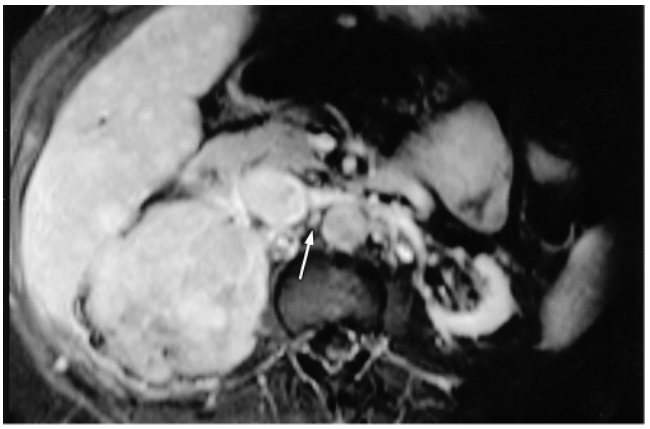

(*i*)

FIG. 9.64 (*Continued*) renal cancer has developed from the cystic cancer (large arrow, *h*), and tumor thrombus expands the IVC (small arrows, *g*, *h*). T1-weighted fat-suppressed gadolinium-enhanced SE image shows the heterogeneous cancer, tumor thrombus, and small lymph nodes (arrow, *i*).

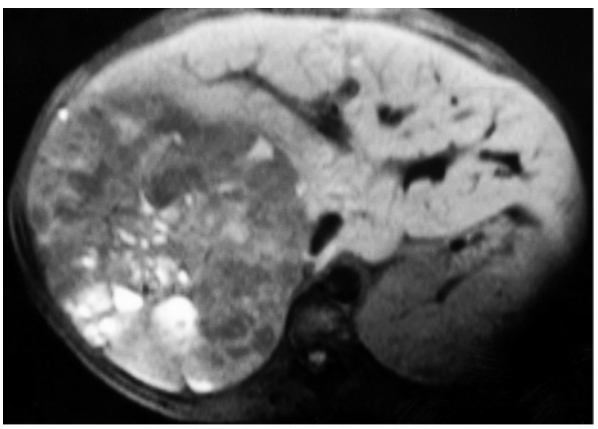

(*a*)

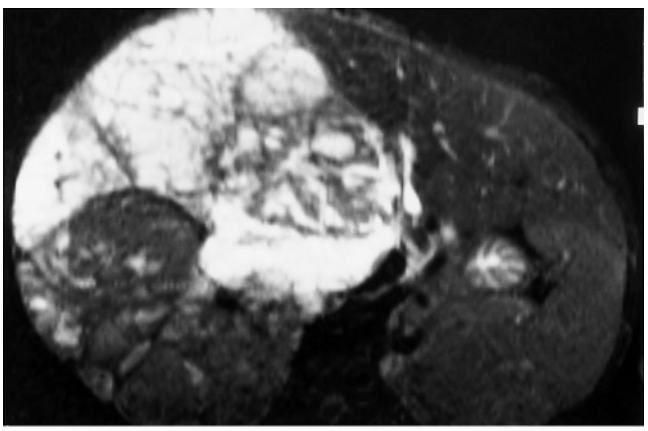

(*b*)

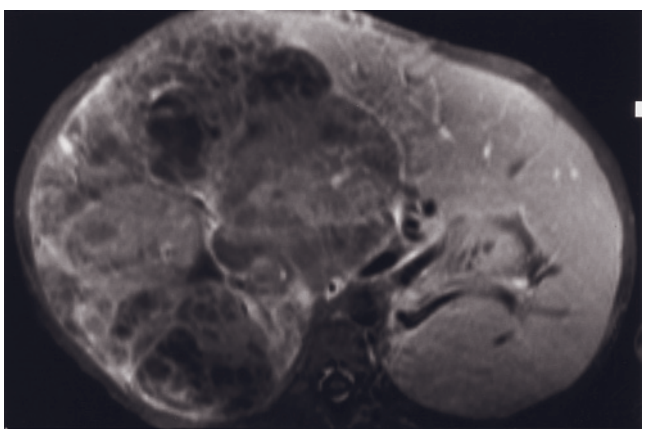

(*c*)

FIG. 9.65 Renal cell cancer in autosomal dominant polycystic kidney disease. T1-weighted precontrast fat-suppressed SE (*a*), T2-weighted fat-suppressed SE (*b*), and T1-weighted transverse fat-suppressed SE (*c*) and sagittal SGE (*d*) interstitial-phase gadolinium-enhanced images. A large multilocular renal mass is present involving the entire right kidney. Cystic spaces vary in signal on T1-weighted (*a*) and T2-weighted (*b*) images, consistent with blood products of differing age. Enhancement of septations

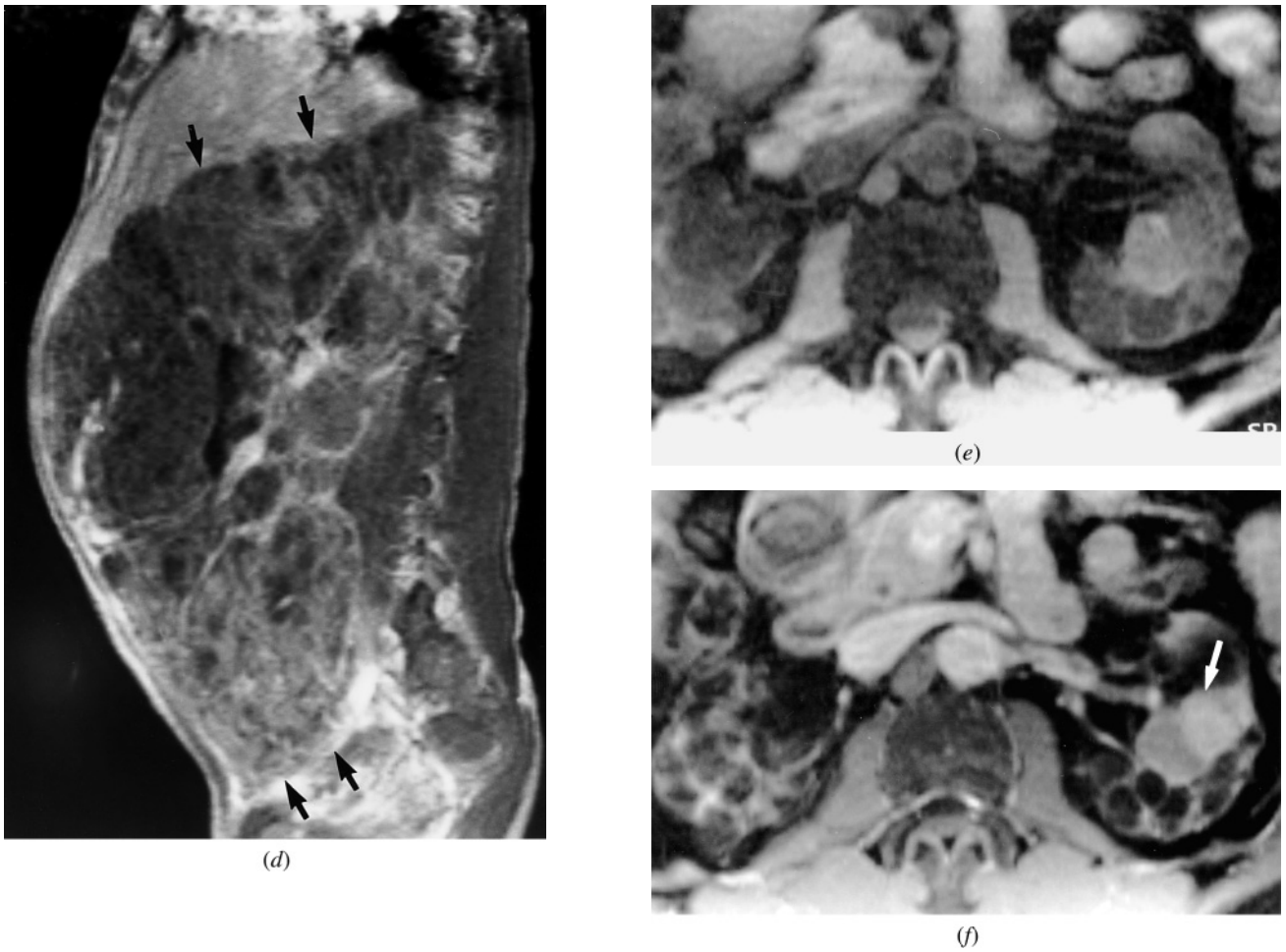

FIG. 9.65 (*Continued*) and more solid tissue is present on postgadolinium images (*c*, *d*). The superior-inferior extent of the massive tumor is shown on the sagittal-plane image (arrows, *d*).Tumor infiltration of the entire kidney was present at histopathology. The left kidney had been removed with the same histologic findings. T1-weighted precontrast (*e*) and 90-s postgadolinium (*f*) fat-suppressed SGE images in a second patient demonstrate a mass in the left kidney. The tumor is not identified on the T1-weighted image and enhances moderately on postgadolinium image (arrow, *f*). This mass represented renal cell cancer. In patients with autosomal dominant polycystic kidney disease it is essential to carefully compare pre- and postgadolinium images to identify areas that show enhancement.

1) allergy to iodine contrast and 2) indeterminate, particularly calcified renal masses. The greater enhancement of renal parenchyma in patients with renal failure and the smaller volume of contrast may be advantageous for the patients with renal failure [77–79]. However, stable gadolinium chelates should be used cautiously in patients with renal failure because of nephrogenic systemic fibrosis considerations (see Chapter 20, *Contrast Agents*). Gadolinium chelates may also be hemodialyzed in patients who already undergo hemodialysis [80]. There may be no indication to perform noncontrast CT imaging alone in the investigation of renal masses. MRI may also be superior for the evaluation of tumor thrombus and liver metastases. Early detection of renal cancer is critical to improving patient survival [69, 81, 82]. Because of the ability of MRI to detect renal tumors <1 cm in diameter, the role of MRI in detecting and characterizing renal masses may become increasingly important in patients with bilateral renal tumors or in patients scheduled for renal-sparing surgery because both CT imaging and ultrasound miss at least 50% of tumors <1 cm [83]. This may have a greater impact in the future, as renal-sparing surgery becomes a more prevalent practice [84, 85].

Wilms Tumor (Nephroblastoma). Wilms tumor is the most common primary renal tumor in childhood. The tumor is diagnosed most frequently in children between the ages of 2 and 5 years. Gross pathologic characteristics of the tumor include a large, homogeneous, well-circumscribed mass that tends to be solitary. Bilaterality or multicentricity occurs in 10% of cases.

Areas of hemorrhage, cyst formation, and necrosis are sometimes encountered. Microscopically, the classic triphasic composition of cell types is usually identified, namely, blastemal ("small, round blue cells"), epithelial, and stromal. Wilms tumors calcify in only 5% of cases, in contrast to neuroblastomas, which calcify in 50% of cases. Unilateral Wilms tumor is associated with a 41% incidence of nephrogenic rests, whereas multifocal Wilms has a 99% incidence of nephrogenic rests [86]. The risk of Wilms tumor is increased in association with at least three recognizable groups of congenital syndromes associated with nephroblastomatosis (the presence of nephrogenic rests). The first group, or WAGR syndrome, is characterized by aniridia, genital anomalies, and mental retardation with a high risk of developing Wilms tumor. The second group has the Denys–Drash syndrome, consisting of gonadal dysgenesis (male pseudohermaphroditism) and nephropathy leading to renal failure. The third group consists of children with Beckwith–Wiedemann syndrome characterized by enlargement of body organs, hemihypertrophy, renal medullary cysts, and abnormal cells in the adrenal cortex. Current staging of Wilms tumors involves a five-stage system in which Stage 1 is a tumor confined to the kidney that has been completely excised; Stage 2 is a tumor that has extended locally beyond the kidney and that has been completely excised; Stage 3 is the presence of residual tumor after surgery that was confined to the abdomen without hematogeneous spread; Stage 4 is hematogeneous metastases; and Stage 5 is bilateral renal involvement [87]. Metastases occur to the lungs, liver, and lymph nodes. Wilms tumor, in rare instances, may be highly cystic. Tumors arise from the kidney with an appearance at times indistinguishable from that of renal cell cancer. Age therefore constitutes a criterion for predicting the diagnosis, because the most common renal malignancy in the pediatric patient is Wilms tumor. A transition occurs in the midteens, after which renal cell cancer is the most common renal tumor. Features suggestive of Wilms tumor are large renal tumors that cross the midline. Central necrosis and tumor thrombus are less common in large Wilms tumors compared to RCC, but this does not provide consistent differentiating information. Wilms tumors commonly contain central hemorrhage.

Wilms tumors are slightly hyperintense on T2-weighted images and slightly hypointense on T1-weighted images. Large cancers are frequently heterogeneous with regions of high signal intensity on T1-weighted images because of the presence of hemorrhage (fig. 9.66). Tumors enhance heterogeneously on postgadolinium images, but tend to be less intensely enhanced and less heterogeneous than renal cell cancer on early postcontrast images. Nephrogenic rests are typically <2 cm and enhance minimally on postgadolinium images (fig. 9.67) [86]. As with renal cancer, tumor thrombus in Wilms tumor is well shown with gadolinium-enhanced MR images and is better defined than on CT images (fig. 9.67) [88].

Lymphoma. Lymphomatous involvement of the kidneys generally occurs in the context of widespread disease. However, isolated focal involvement of the kidney does occur [89–91]. Non-Hodgkin lymphoma

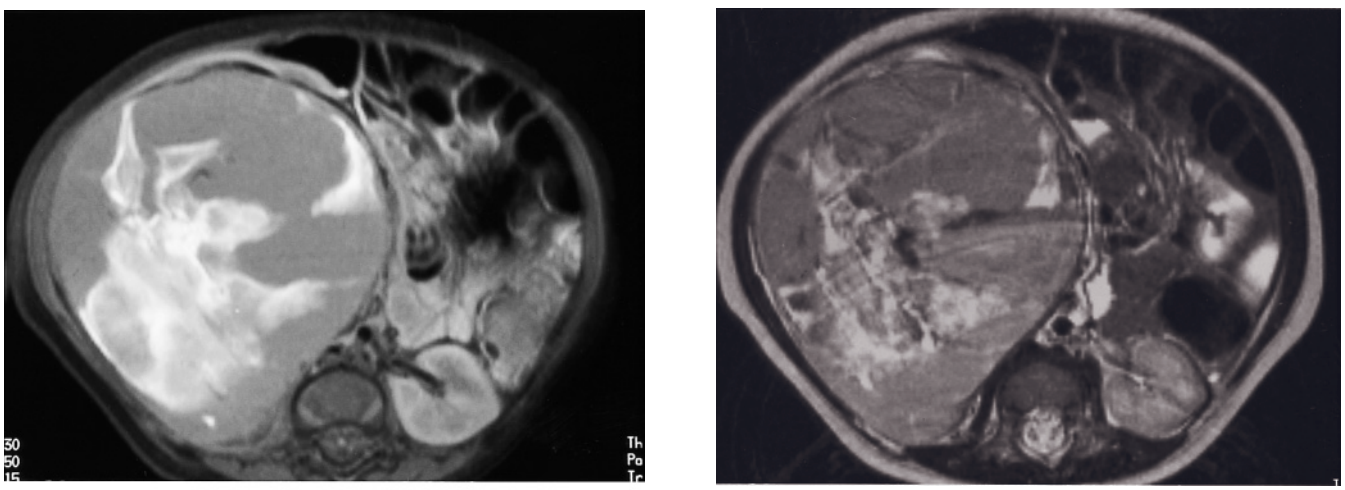

(*a*) (*b*)

FIG. 9.66 Wilms tumor. T1-weighted precontrast fat-suppressed SE (*a*), T2-weighted ETSE (*b*), and T1-weighted interstitial-phase fat-suppressed gadolinium-enhanced SE (*c*) images. A large mass arises from the right kidney and demonstrates central linear

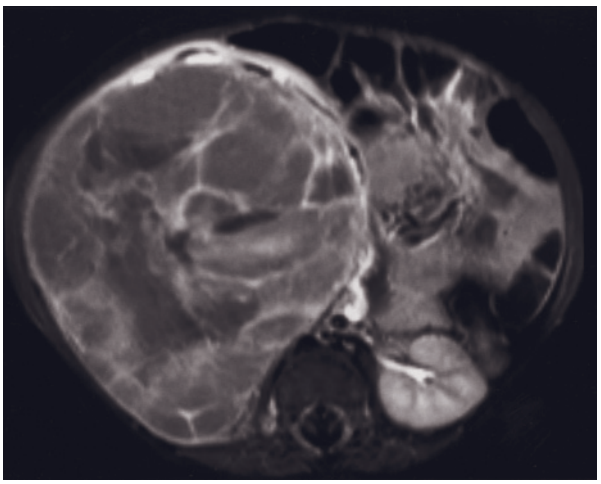

(*c*)

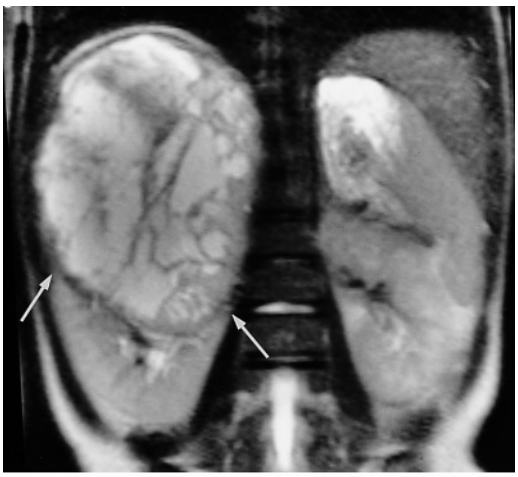

(*d*)

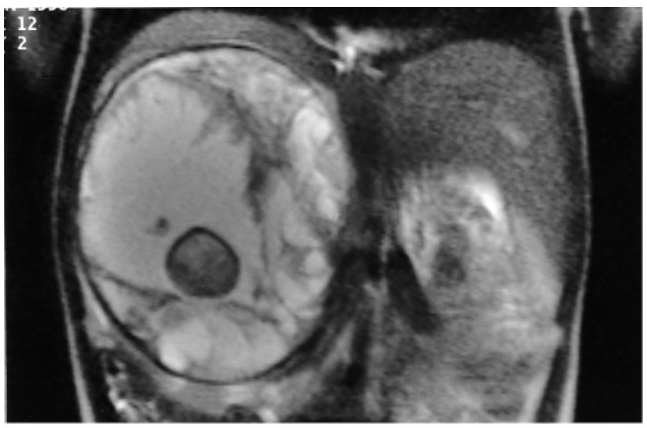

(*e*)

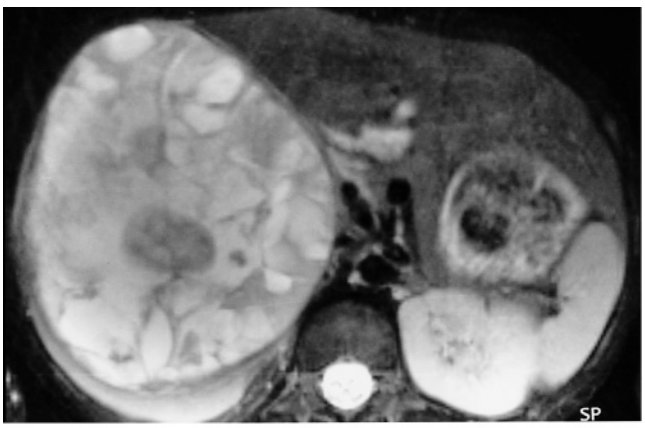

(*f*)

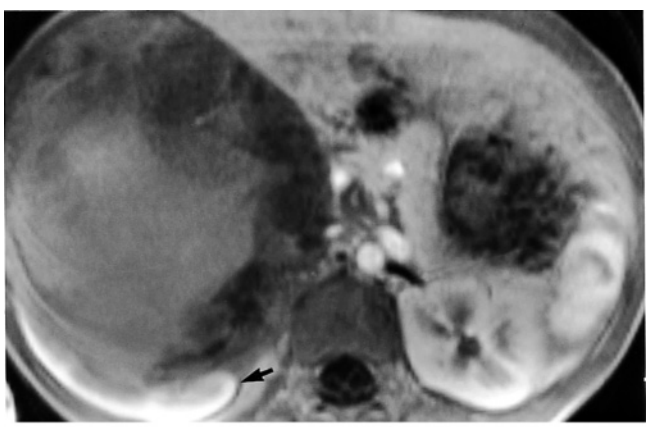

(*g*)

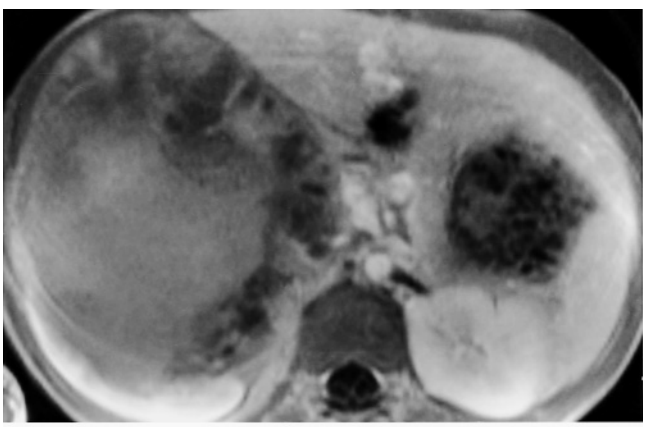

(*h*)

FIG. 9.66 (*Continued*) regions of high signal intensity on T1- and T2-weighted images, consistent with blood. No substantial central necrosis is identified on the postcontrast images despite the large size of the tumor. Coronal T2-weighed SS-ETSE (*d*, *e*), transverse T2-weighted fat-suppressed SE (*f*), and immediate (*g*) and 90-s (*h*) postgadolinium SGE images in a second patient. A large heterogeneous Wilms tumor arises from the upper pole of the right kidney (arrows, *d*). A rim of posterior normal renal cortex is apparent (arrow, *g*).

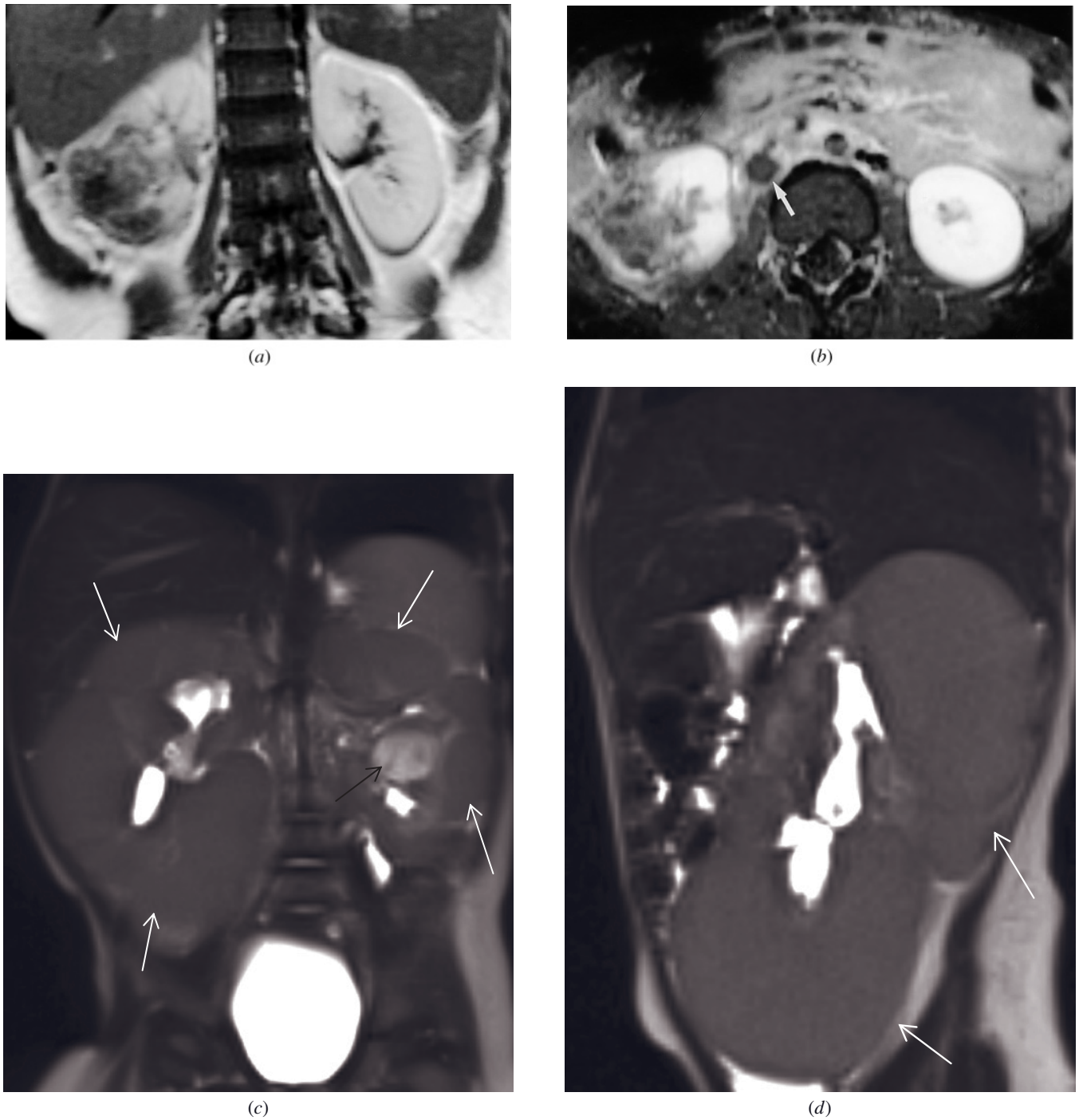

FIG. 9.67 Wilms tumor. Coronal (*a*) and transverse fat-suppressed (*b*) T1-weighted gadolinium-enhanced SE images. A heterogeneously enhancing tumor is present arising from the lower half of the right kidney (*a*, *b*). Thrombus is noted in the IVC (arrow, *b*), which represents blood thrombus at this tomographic section inferior to the renal vein. **Nephroblastomatosis.** Coronal (*c*) and sagittal (*d*) T2-weighted single-shot echo-train spin-echo, coronal T1-weighted magnetization-prepared rapid gradient-echo (MPRAGE) (*e*), transverse T2-weighted single-shot echo-train spin-echo (*f*), and transverse T1-weighted postgadolinium water excitation MPRAGE (*g*) images demonstrate bilateral nephroblastomatosis in another patient. The kidneys are enlarged and have lobulated contours due to the presence of perilobular nephrogenic rests. Nephrogenic rests (arrows, *c*–*g*) show isointense to mildly

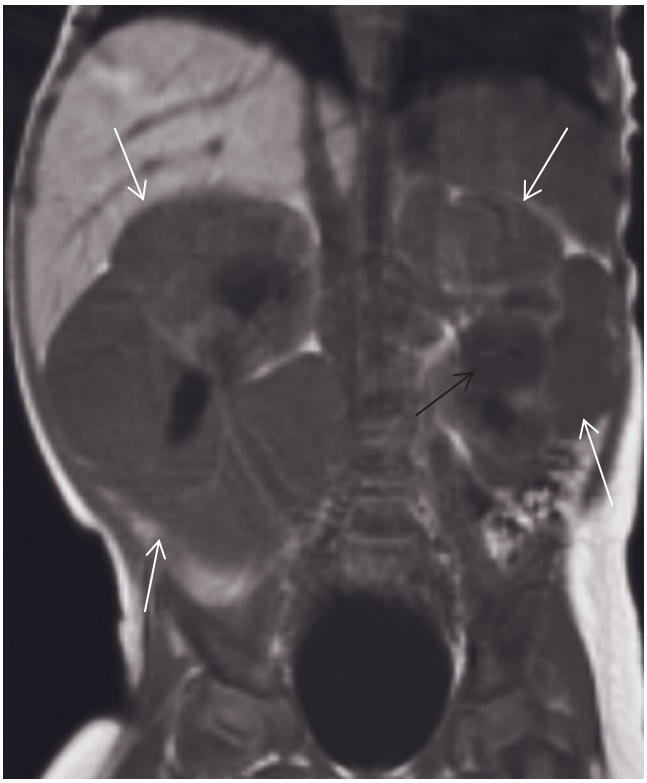

(*e*)

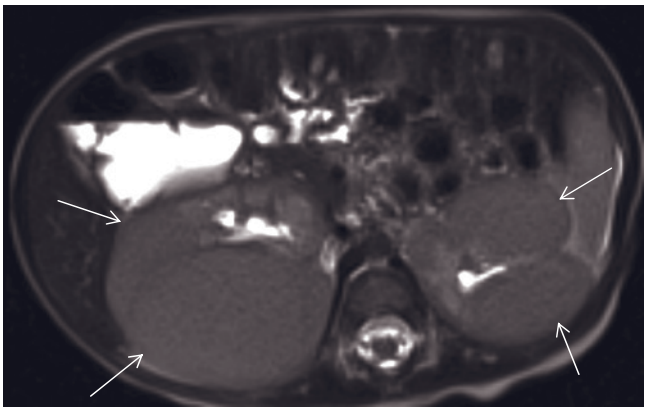

(*f*)

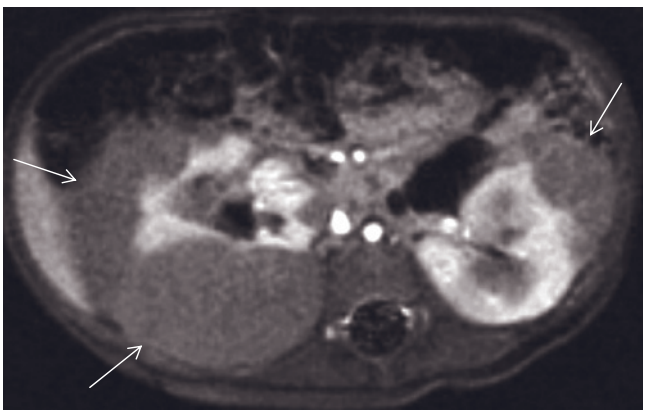

(*g*)

FIG. 9.67 (*Continued*) hypointense signal on T2-weighted (*c*, *d*, *f*) and T1-weighted (*e*) images and lower enhancement compared to normal renal parenchyma on postgadolinium image (*g*). Note that a hyperplastic or neoplastic nodule (black arrows, *c*, *e*) is detected in the left kidney. Bilateral collecting systems are moderately dilated.

more commonly involves the kidneys than Hodgkin lymphoma and is most commonly the B cell type [89]. Three basic patterns of involvement occur: 1) direct invasion from adjacent disease, most commonly large retroperitoneal masses (fig. 9.68), 2) focal masses that may be solitary or multiple (figs. 9.69 and 9.70), and 3) diffuse infiltration (fig. 9.71) [89–91]. Lymphoma commonly extends along the subcapsular surface of the kidney, particularly in the setting of invasion from adjacent disease. Renal parenchyma lacks lymphoid tissue, so primary renal lymphoma usually arises from lymphatic tissue in the renal sinus. Direct invasion of the kidney by a large retroperitoneal nodal mass is the most common form of renal disease and is often observed at initial presentation.

Lymphoma is generally heterogeneous and slightly hypointense to isointense on T2-weighted images and slightly hypointense relative to renal cortex on T1-weighted images. Gadolinium enhancement of most lymphomas is mildly heterogeneous and minimal on early postcontrast images and remains minimal on late postcontrast images [91]. Tumors generally show no appreciable central necrosis, even in the setting of very large tumors.

Lymphoma tends to infiltrate the renal medulla. Retroperitoneal lymphoma that invades the kidney usually extends through the renal sinus into the renal medulla (see fig. 9.68). Diffuse infiltration of the kidney predominantly affects the medulla, with relative sparing of the renal cortex (see fig. 9.71) [88]. Focal masses arise in the renal medulla or cortex (see fig. 9.69). Cortex-based masses tend to enhance more intensely than other forms of renal involvement, which may reflect the greater blood supply of the cortex [91, 92]. As most forms of lymphoma involve the medulla, these tumors can be distinguished from renal carcinoma because renal carcinomas originate in the renal cortex. Other distinguishing features include 1) degree of vascularity (lymphoma shows mild diffuse heterogeneous enhancement, whereas renal cancer shows intense early heterogeneous

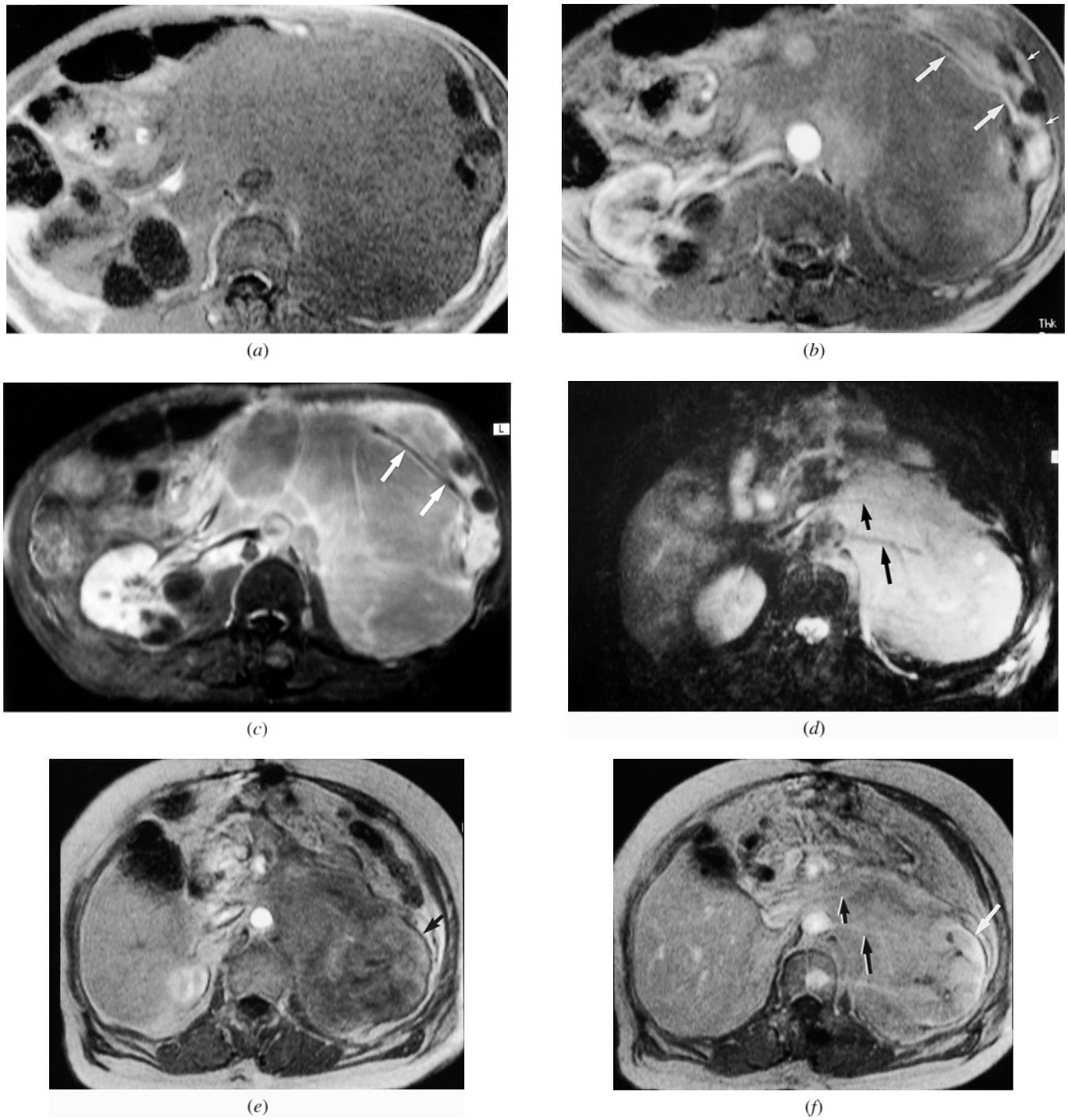

FIG. 9.68 Renal lymphoma, large retroperitoneal mass invading kidney. T1-weighted precontrast SGE (*a*), immediate postgadolinium SGE (*b*), and late-phase fat-suppressed gadolinium-enhanced SE (*c*) images. A large retroperitoneal mass is present that is homogeneous and soft tissue signal intensity on the SGE image (*a*) and enhances minimally on capillary-phase (*b*) and interstitial-phase (*c*) images. On postcontrast, images lymphoma is moderately heterogeneous, with no evidence of necrosis. A thin rim of spared renal cortex is evident (small arrows, *b*), and the kidney is displaced anterolaterally. Tumor invades through the renal pelvis into the renal medulla. The renal artery is patent (arrows, *b*, *c*) but encased by lymphoma. Patency is shown by the presence of high-signal-intensity gadolinium in the artery on the immediate postgadolinium SGE image (*b*) and by flow void on the spin-echo image (*c*). In a second patient, a similar appearance of lymphoma is shown on T2-weighted fat-suppressed SE (*d*), T1-weighted immediate (*e*) and 90-s (*f*) postgadolinium SGE, and late-phase fat-suppressed postgadolinium SE (*g*) images. Lymphoma is mildly hyperintense on the T2-weighted image (*d*) and heterogeneous and mildly enhanced on capillary-phase (*e*) and interstitial-phase (*f*, *g*) gadolinium-enhanced images. The renal artery (arrows, *d*, *f*, *g*) and renal vein (small arrows, *d*, *f*, *g*) are encased by tumor but patent. Patency is demonstrated by the presence of high signal intensity on the SGE image (*f*) and signal void on the SE images (*d*, *g*).

FIG. 9.68 (*Continued*) The involved kidney demonstrates diminished cortical enhancement (arrow, *e*) relative to the normal contralateral right kidney on the capillary-phase image (*e*). Lymphoma has extensively invaded the medulla, but relative sparing of cortex is observed (white arrows, *f*, *g*).

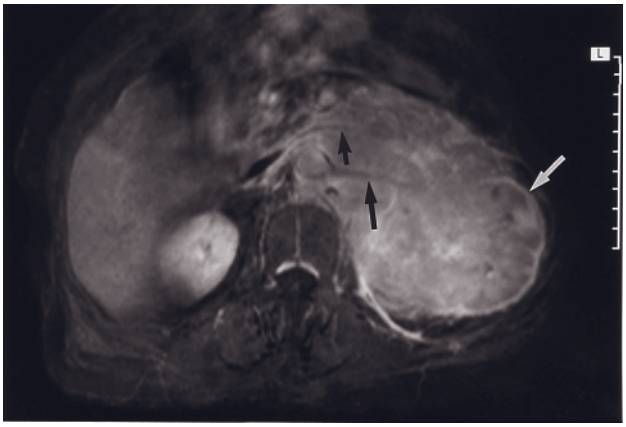

(*g*)

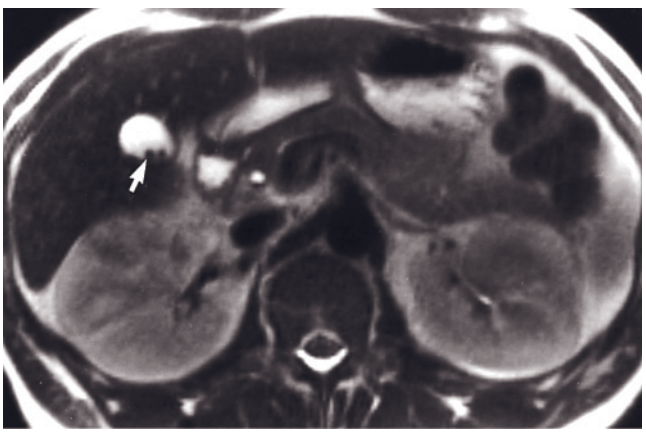

(*a*)

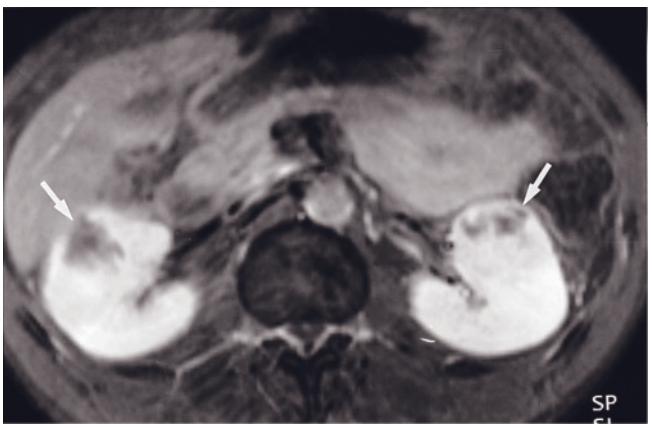

(*b*)

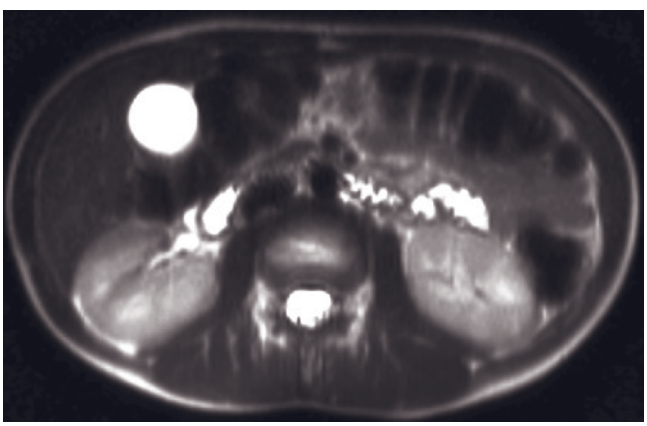

(*c*)

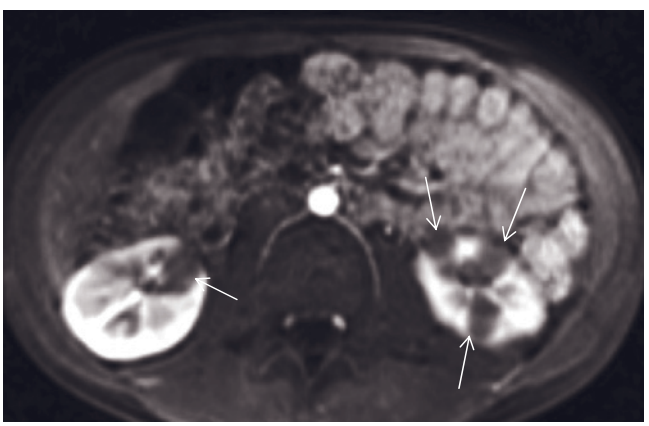

(*d*)

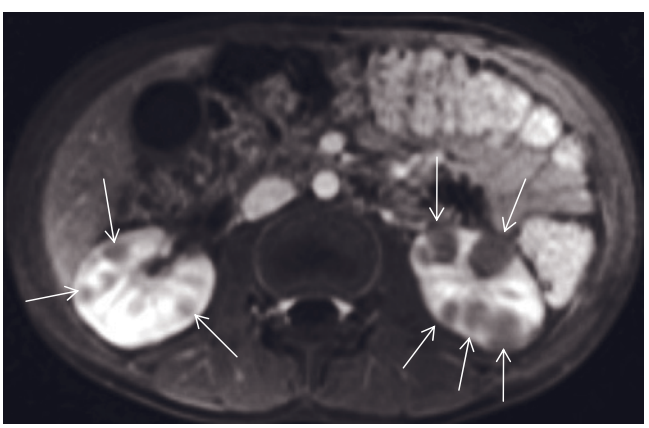

(*e*)

FIG. 9.69 Lymphoma—multifocal renal involvement. T2-weighted breathing-independent SS-ETSE (*a*) and T1-weighted fat-suppressed gadolinium-enhanced SE (*b*) images. Lymphoma masses are mildly hypo- to isointense on T2-weighted images (*a*) and heterogeneous with low-signal-intensity centers (arrows, *b*) on interstitial-phase gadolinium-enhanced images. Incidental note is made of gallstones, which are well shown on the breathing-independent T2-weighted image (arrow, *a*). T2-weighted single-shot echo-train spin-echo (*c*), T1-weighted postgadolinium fat-suppressed hepatic arterial dominant-phase (*d*), and hepatic venous-phase (*e*) 3D-GE images demonstrate multifocal lymphoma (arrows, *d*, *e*) in another patient. The lesions are located in both kidneys and are isointense to the renal cortex on T2-weighted image (*c*). The lesions show less enhancement compared to the normal renal tissue.

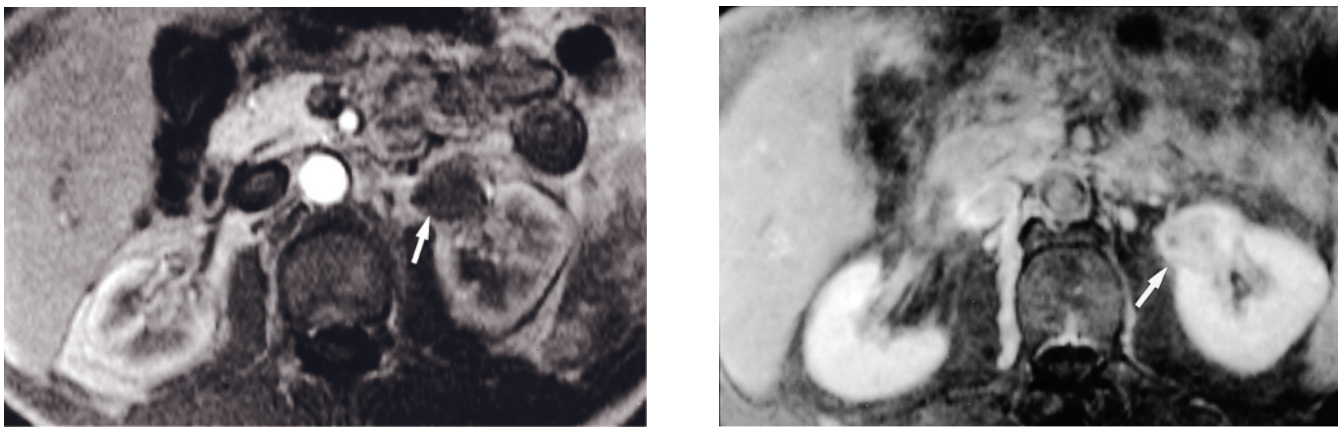

(*a*) (*b*)

FIG. 9.70 Lymphoma, solitary mass. T1-weighted immediate postgadolinium SGE (*a*) and 90-s fat-suppressed gadolinium-enhanced SE (*b*) images. A solitary lymphoma mass is present in the left kidney (arrows, *a*, *b*) that is minimally enhanced on the capillary-phase image (*a*) and heterogeneous and moderately enhanced on the interstitial-phase image (*b*). (Reproduced with permission from Semelka RC, Kelekis NL, Burdeny DA, Mitchell DG, Brown JJ, Siegelman ES: Renal lymphoma: demonstration by MR imaging. *AJR Am J Roentgenol* 166: 823–827, 1996.)

enhancement), 2) presence of necrosis (necrosis is uncommon in lymphoma, even in large masses, whereas central necrosis is very common in large renal carcinomas), 3) presence of tumor thrombus (lymphoma rarely results in tumor thrombus, whereas tumor thrombus is common in large renal carcinomas), 4) location of the center of the tumor (in lymphoma the center is most often outside the contour of the kidney, whereas in renal cancer it is in the renal cortex), 5) presence of renal artery encasement with diminished capillary-phase enhancement of the entire kidney (large retroperitoneal mass and diffusely infiltrative patterns of lymphoma commonly encase the renal artery and result in generalized diminished renal enhancement, which is a rare finding in renal carcinoma) [91], and 6) presence of direct extension and involvement of the psoas muscle (common in lymphoma and rare in renal carcinoma). Solitary focal renal cortical involvement of lymphoma, however, may resemble renal carcinoma. Focal masses usually arise in the setting of recurrent disease, so the history of lymphoma is known, and diagnosis can be established on the basis of clinical history.

Granulocytic Sarcoma (Chloroma). Granulocytic sarcoma or chloroma (from the Greek *chloros*, meaning green) is an uncommon malignant neoplasm that develops in 3–10% of patients with acute myeloblastic leukemia and less commonly in patients with acute lymphocytic leukemia. The incidence of granulocytic sarcomas has increased in recent times because of more prolonged leukemic remission.

Abdominal granulocytic sarcomas show mildly high signal intensity on T2-weighted, moderately low signal intensity on T1-weighted, and minimal enhancement on postgadolinium images. The MR appearance is consistent with hypovascular solid tissue (fig. 9.72).

Renal carcinomas usually have a different appearance in that they are cortex based and generally enhance in an early heterogeneous intense fashion. Hypovascular renal cancers may be difficult to distinguish from granulocytic sarcoma on the basis of imaging appearance, although granulocytic sarcomas usually do not have as regular a spherical shape, fine pattern of small internal vessels, or clear origin from renal cortex as generally observed in hypovascular renal cell cancers. The appearance of granulocytic sarcoma is distinct from renal abscesses and hemorrhage, which are in the differential diagnosis of renal masses in leukemia patients (fig. 9.72) [93].

Carcinoid. A number of very rare primary tumors may occur in the kidney; carcinoid tumor is one such example (fig. 9.72). These malignancies are so rare that at present distinctive MR appearances have not been determined, and their diagnosis is made retrospectively at the time of resection. The fact that these rare tumors do occur should not alter the usual estimation of renal tumors; the great majority of cortex-based tumors are renal cell carcinomas, and cortex-based tumors that are smaller and less aggressive appearing and do not show change in size over a >2-year period are likely renal adenomas.

Small Cell Carcinoma. Small cell carcinoma is a rare primary malignant tumor of the kidney. This tumor occurs most commonly in older females.

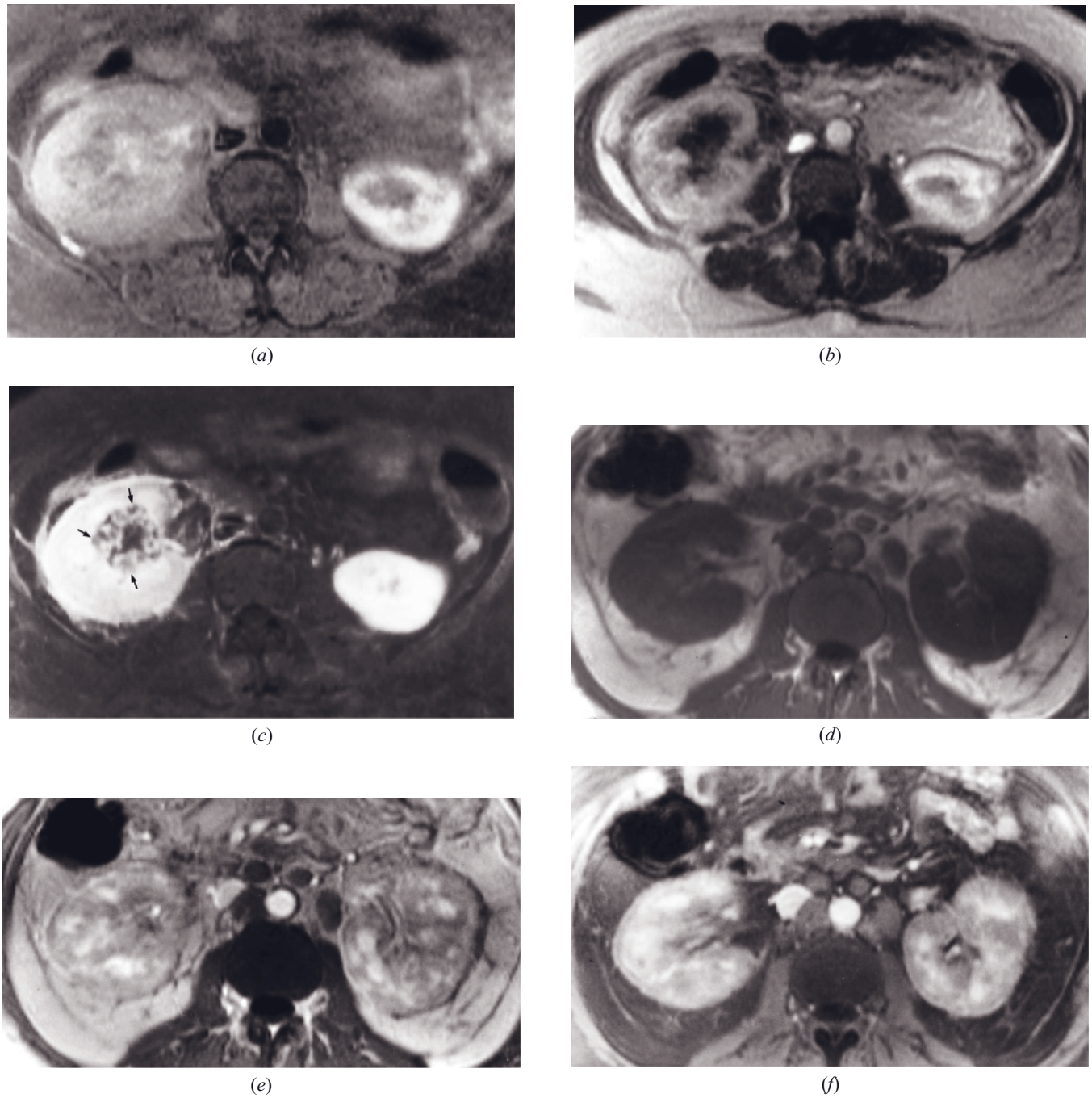

FIG. 9.71 Lymphoma, diffuse infiltration. T1-weighted precontrast fat-suppressed SE (*a*), immediate postgadolinium SGE (*b*), and late-phase fat-suppressed gadolinium-enhanced SE (*c*) images. The right kidney is enlarged in a generalized fashion (*a–c*). CMD is not well shown on the precontrast T1-weighted image (*a*). On the immediate postgadolinium image (*b*), diminished enhancement of the renal cortex is present. However, the cortex has a normal thickness and uniformity. On the later interstitial-phase image, increased enhancement is present in the outer medulla, and multiple low-signal-intensity foci (arrows, *c*) are present in the inner medulla, which likely represent focal aggregates of lymphoma. (Reproduced with permission from Semelka RC, Kelekis NL, Burdeny DA, Mitchell DG, Brown JJ, Siegelman ES: Renal lymphoma: demonstration by MR imaging. *AJR Am J Roentgenol* 166: 823–827, 1996.) T1-weighted precontrast SGE (*d*) and 45-s (*e*) and 90-s fat-suppressed (*f*) postgadolinium SGE images in a second patient. The kidneys show decreased CMD on noncontrast T1-weighted images. There is also decreased, cortical enhancement on the 45-s postcontrast image, with heterogeneous medullary enhancement. The extent of renal enhancement shows negligible changes on the later postcontrast image.

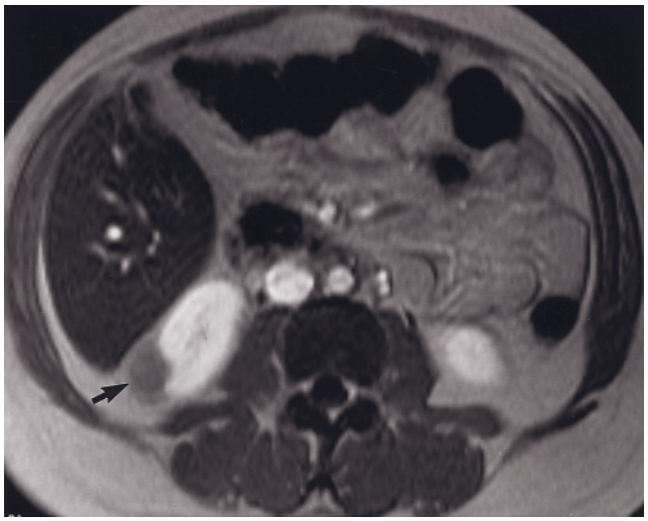

(*a*)

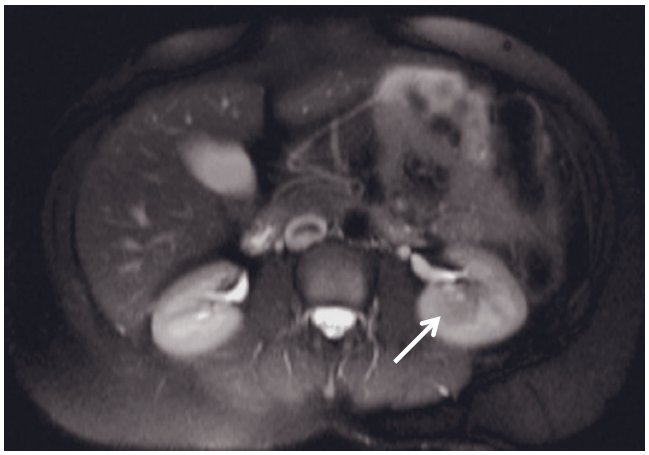

(*b*)

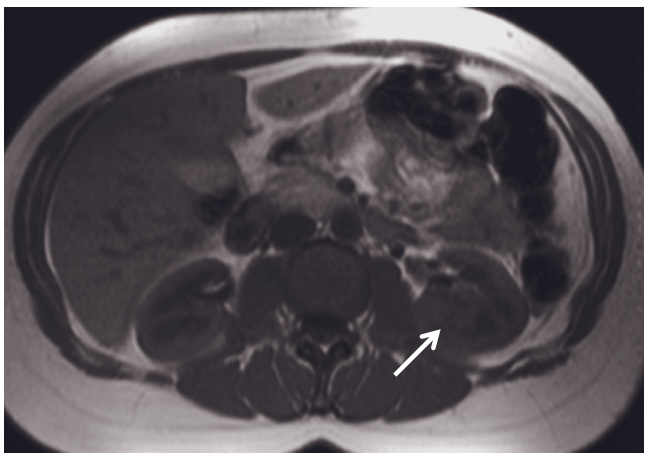

(*c*)

(*d*)

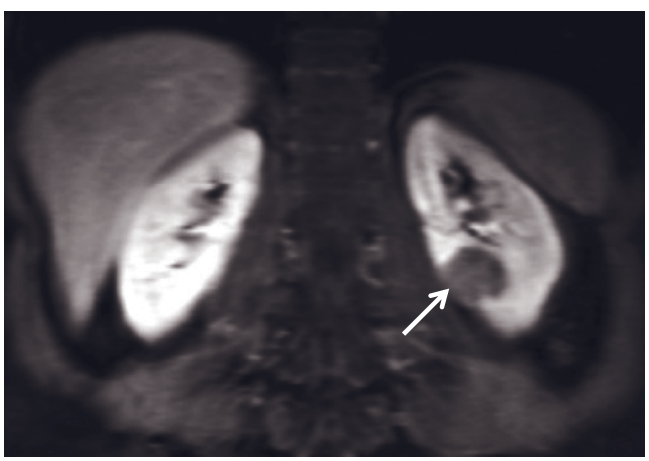

(*e*)

FIG. 9.72 Granulocytic sarcoma. T1-weighted 90-s postgadolinium SGE image (*a*) in a patient with acute myelogenous leukemia. A homogeneous mildly enhanced 2-cm granulocytic sarcoma (arrow, *a*) arises from the upper pole of the right kidney. The liver is low in signal intensity secondary to transfusional hemosiderosis. **Primary renal carcinoid tumor.** Transverse T2-weighted fat-suppressed single-shot echo-train spin-echo (*b*), transverse T1-weighted SGE (*c*), transverse T1-weighted postgadolinium hepatic arterial dominant-phase fat-suppressed 3D-GE (*d*) and coronal T1-weighted postgadolinium interstitial-phase fat-suppressed 3D-GE (*e*) images demonstrate a primary renal carcinoid tumor (arrows, *b*–*e*) in another patient. The tumor shows low signal on T2-weighted image (*b*), isointense signal on T1-weighted image (*c*), and lower but progressive enhancement compared to the normal renal tissue on postgadolinium images (*d*, *e*).

On MR images, the tumor is mildly hyperintense on T2-weighted images and mildly hypointense on T1-weighted images and shows diffuse heterogeneous enhancement on gadolinium-enhanced images [94] (fig. 9.73). Central necrosis is less prominent in small cell carcinomas that are >5 cm in diameter than is typical for renal cell cancer, which may provide a clue to the diagnosis. There may also be a tendency for medullary involvement, with relative sparing of the cortex, that also aids in the distinction from renal cell cancer.

Metastases. Metastases to the kidney are a late manifestation of advanced disease. The most common primary tumors to metastasize to the kidneys are lung (19.8–23.3% of cases), breast (12.3% of cases), and gastric carcinomas, as reported in large autopsy series, but metastases may occur in the setting of many malignant diseases (fig. 9.74) [95]. Metastases usually appear as multiple bilateral renal masses, but solitary masses may occur (fig. 9.75). Metastases from poorly differentiated adenocarcinomas may diffusely infiltrate the kidneys with an appearance similar to that of lymphoma (fig. 9.76).

Diffuse Renal Parenchymal Disease

Diffuse renal parenchymal diseases are common medical conditions. A variety of disease processes may result in parenchymal disease, and they may be classified into the following broad categories: glomerular disease; acute and chronic tubulointerstitial disease; diabetic nephropathy and nephrosclerosis and other forms of microvascular disease; ischemic nephropathy caused by disease of the main renal arteries; obstructive nephropathy; and infectious renal disease [96].

MRI has played a limited role in the evaluation of diffuse renal parenchymal disease. The intrinsic high soft tissue contrast resolution of breath-hold gradient-echo and fat-suppressed images and the clear definition of the renal cortex on immediate postgadolinium gradient-echo images do provide useful information for the evaluation of morphologic changes associated with these entities. The renal cortex is most distinctly shown on immediate postgadolinium gradient-echo images, and alterations of thickness, regularity, and temporal enhancement of the cortex provide information that correlates with underlying pathophysiology [96]. One study [96] described MRI findings for diffuse parenchymal diseases of 121 patients with renal disease. The presence of corticomedullary differentiation (CMD) demonstrated a strong inverse relationship with serum creatinine (sCr) ($r = -0.568$, $P < 0.001$). The mean cortex thicknesses for normal kidney and kidneys with glomerular disease were 8.4 and 7.8 mm, respectively, which were significantly thicker ($P < 0.01$) than renal cortex in patients with microvascular disease (5.2 mm), tubulointerstitial disease secondary to antineoplastic chemotherapy (5.6 mm), ischemic nephropathy (5.5 mm), and obstructive nephropathy (4.3 mm). Irregularity of the renal cortex was common in microvascular disease (60.9%), infectious renal disease (62.5%), obstructive nephropathy (55.6%), and nonchemotherapy tubulointerstitial disease (53.8%) compared with chemotherapy-induced tubulointerstitial disease (5.9%), glomerular disease (3.8%), and normal kidneys (0%). Diffuse high signal intensity of the entire medulla on delayed post-contrast images was observed in 20.7% of patients with diffuse renal disease and in none of the patients with normal kidneys. Combining this information with other imaging findings, such as dilation of the renal collecting system in obstructive nephropathy or atherosclerotic disease of the aorta in ischemic nephropathy and microvascular disease, allows prediction of the probable underlying type of diffuse renal parenchymal disease. Dynamic changes of temporal enhancement of the cortex and medulla in normal kidneys, obstructive nephropathy, and post-extracorporeal shock wave lithotripsy for renal calculus disease have been described [5, 21, 77]. Temporal changes in other causes of diffuse renal parenchymal disease remain to be established.

Currently, because of concerns about nephrogenic systemic fibrosis, stable gadolinium chelates should be used cautiously in patients with diminished renal function (see Chapter 20, *Contrast Agents*).

Diminished Renal Function

Loss of CMD on T1-weighted images in patients with elevated sCr has been described [97]. This is a nonspecific finding observed in virtually all renal diseases that result in diminished renal function. Demonstration of CMD is best made on precontrast T1-weighted fat-suppressed images. Fat-suppressed gradient-echo imaging may be superior to fat-suppressed spin-echo imaging because breath-holding results in greater image sharpness. In one study [97] that described the relationship of CMD to the level of sCr with precontrast T1-weighted fat-suppressed spin-echo and immediate postgadolinium SGE imaging, all patients with sCr ≥ 3.0 mg/dl showed loss of CMD on precontrast images (fig. 9.77). In patients with sCr of 1.5–2.9 mg/dl, the loss of CMD occurred in approximately half of the patients. The loss of CMD on immediate postgadolinium SGE images was not observed until sCr exceeded 8.5 mg/dl. Changes in fluid content between cortex and medulla likely account for the changes on precontrast images. This reflects some combination of increased fluid in the cortex and decreased fluid in the medulla. CMD on immediate postgadolinium images reflects autoregulatory blood flow distribution in the kidney that may be lost in advanced renal disease. This may reflect irreversible renal parenchymal damage.

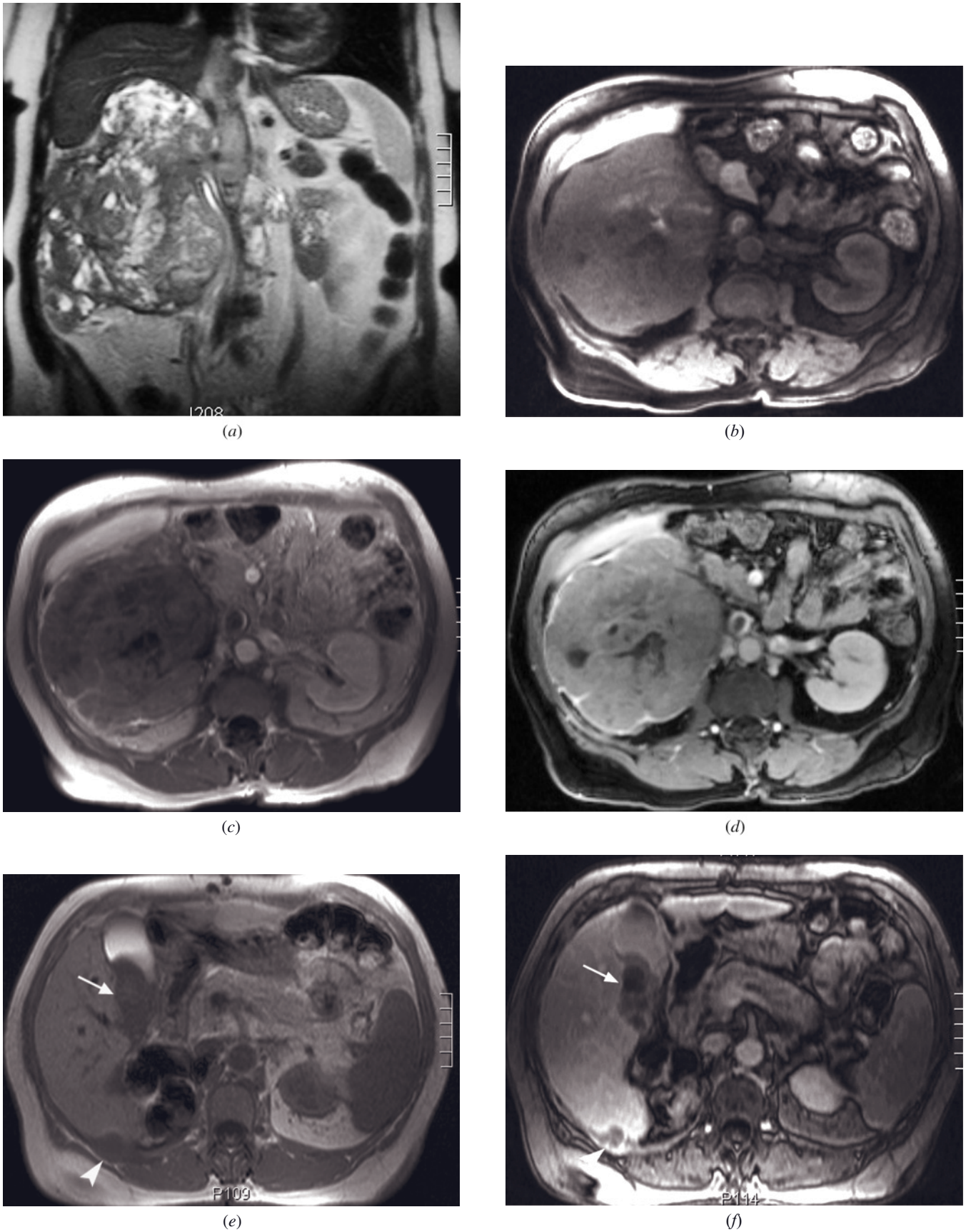

FIG. 9.73 Primary small cell carcinoma of kidney and local recurrence. Coronal T2-weighted SS-ETSE (*a*), T1-weighted fat-suppressed gradient-echo (*b*), immediate postgadolinium T1-weighted gradient-echo (*c*), and interstitial-phase postgadolinium fat-suppressed gradient-echo (*d*) images. There is a large mass arising from the right kidney that demonstrates heterogeneous high signal intensity on T2-weighted image (*a*), low signal intensity on T1-weighted image (*b*), and mild heterogeneous enhancement on early (*c*)- and late (*d*)-phase images. At the periphery of the mass, there is a thin rim of enhancing cortex. T1-weighted gradient echo (*e*) and interstitial-phase postgadolinium fat-suppressed 3D gradient-echo (*f*) images of the same patient 4 months after right nephrectomy demonstrate soft tissue implants near the medial margin of the liver (arrows, *e*, *f*), consistent with local recurrence. There is an additional focus of tumor that tracks along the liver capsule (arrowheads, *e*, *f*).

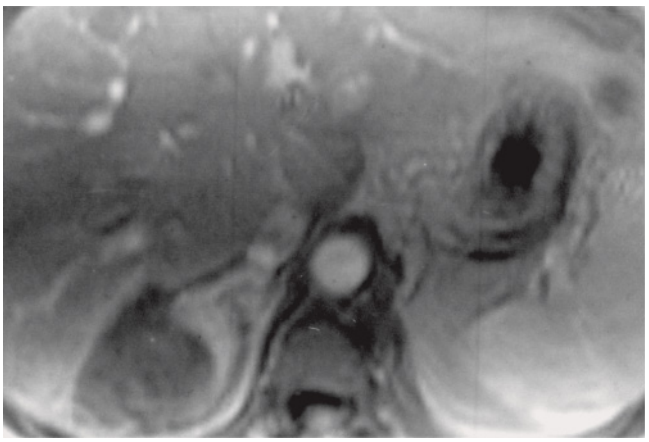

(*a*)

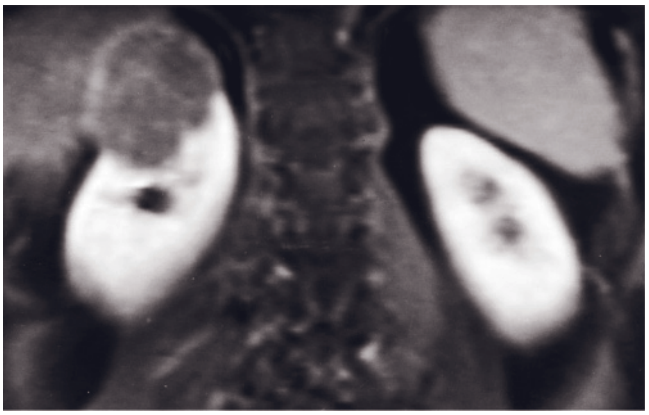

(*b*)

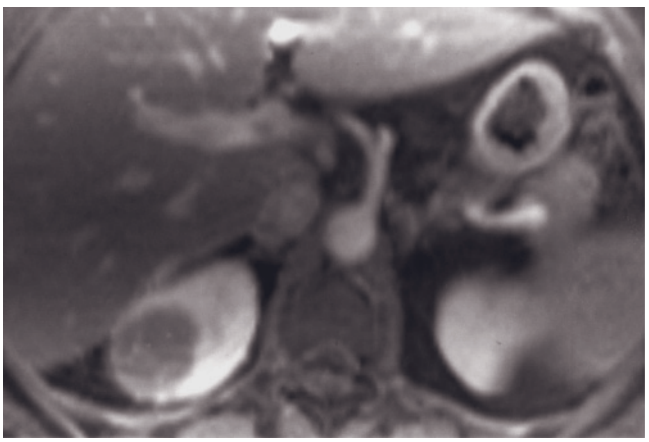

(*c*)

FIG. 9.74 Renal metastases from ovarian cancer. T1-weighted 45-s postgadolinium SGE (*a*) and coronal (*b*) and transverse (*c*) 2- to 3-min fat-suppressed postgadolinium SGE images. A tumor is present in the upper pole of the right kidney that demonstrates mild and heterogeneous enhancement.

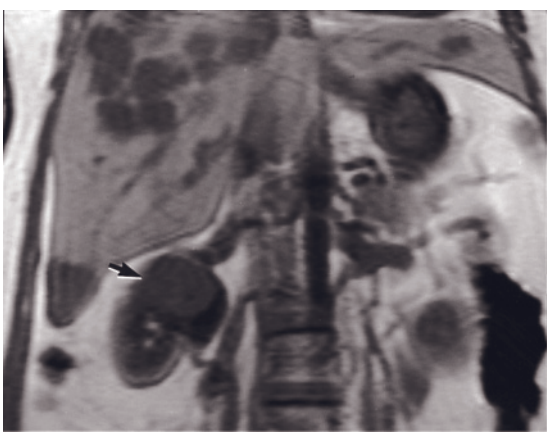

(*a*)

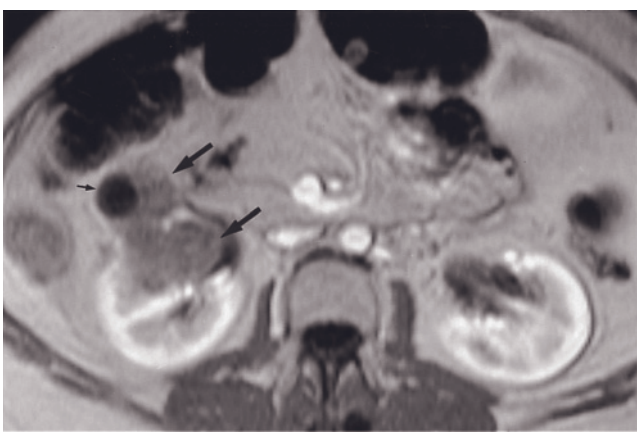

(*b*)

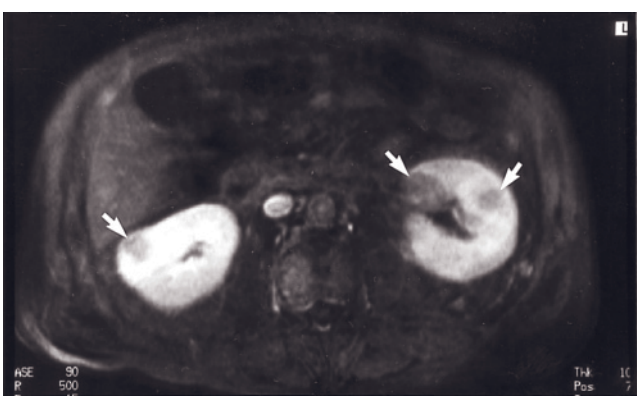

(*c*)

FIG. 9.75 Renal metastases. Coronal T1-weighted precontrast SGE (*a*) and transverse immediate postgadolinium SGE (*b*) images. On the precontrast image (*a*), a homogeneous intermediate-signal-intensity mass is noted in the right kidney (arrow, *a*). In addition, multiple leiomyosarcoma liver metastases are present. On the immediate postcontrast image, the renal metastasis is noted to involve cortex and medulla (arrows, *b*) and extends into the perirenal space. The mass contains a small cystic component (small arrow, *b*). T1-weighted fat-suppressed gadolinium-enhanced image (*c*) in a second patient, who has renal metastases from lung cancer, demonstrates multiple low-signal-intensity metastatic lesions in both kidneys (arrows, *c*). Transverse and coronal

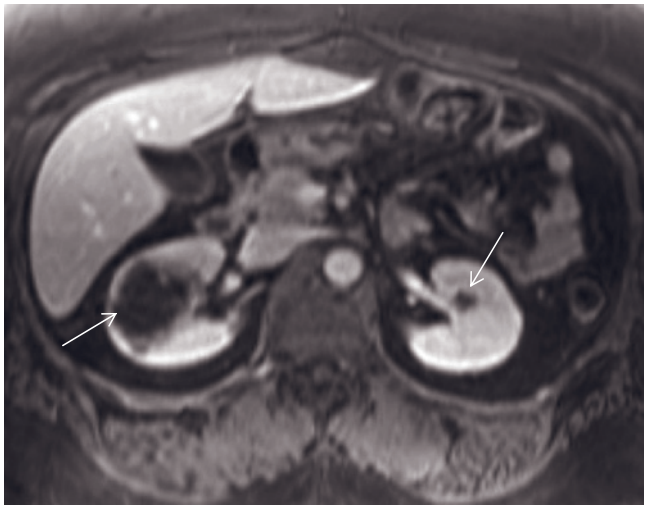

(*d*)

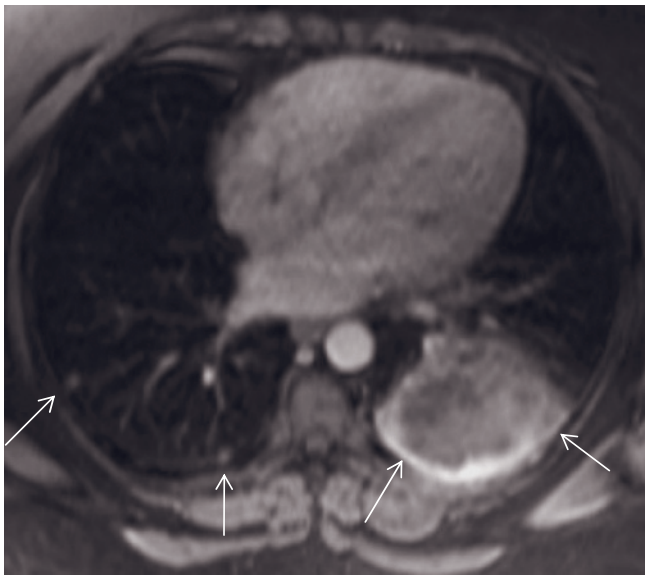

(*e*)

FIG. 9.75 (*Continued*) T1-weighted postgadolinium interstitial-phase fat-suppressed 3D-GE images (*d*, *e*) demonstrate kidney and lung metastases from choriocarcinoma in another patient. Kidney metastases (arrows, *d*) are detected in both kidneys as hypointense irregular masses. Small lung metastases (arrows, *e*) are detected in the right lung. A pleura-based large lung metastasis (arrows, *e*) is detected in left lung.

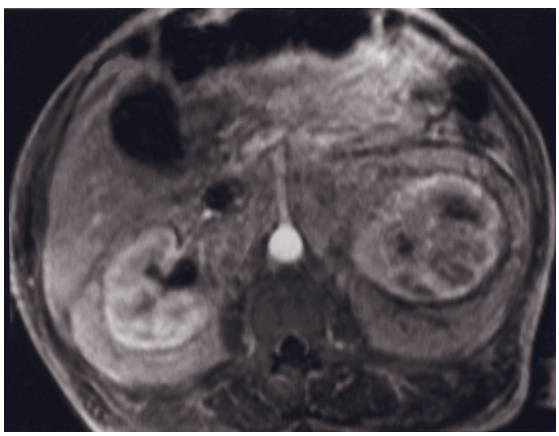

(*a*)

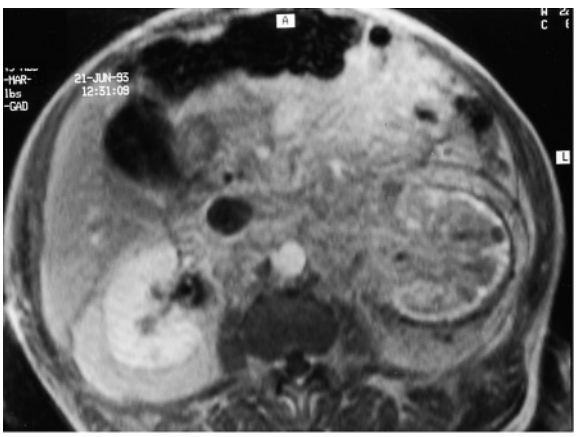

(*b*)

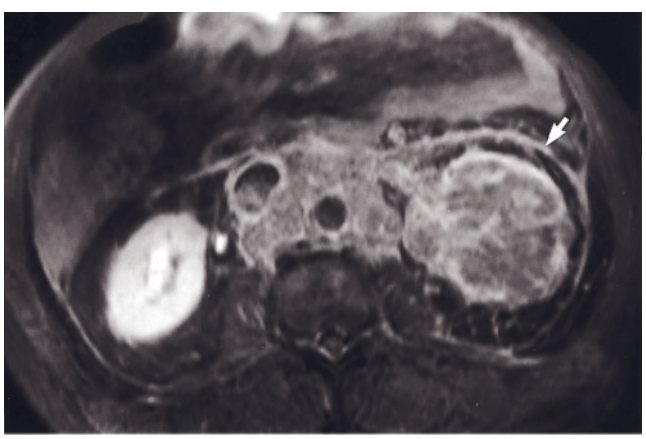

(*c*)

FIG. 9.76 Renal metastases, undifferentiated adenocarcinoma. T1-weighted immediate (*a*) and 90-s (*b*) postgadolinium SGE and interstitial-phase fat-suppressed gadolinium-enhanced SE (*c*) images. Massive retroperitoneal adenopathy with extension through the renal hilum and invasion of the renal medulla is present (*a–c*). Extensive infiltration of the medulla with relative sparing of the cortex is well shown on interstitial-phase images (*b*, *c*). This appearance of renal involvement resembles lymphoma. Thickening of Gerota fascia (arrow, *c*) and retroperitoneal adenopathy are best shown on the gadolinium-enhanced fat-suppressed image, reflecting good conspicuity of enhanced malignant tissue in a background of suppressed fat.

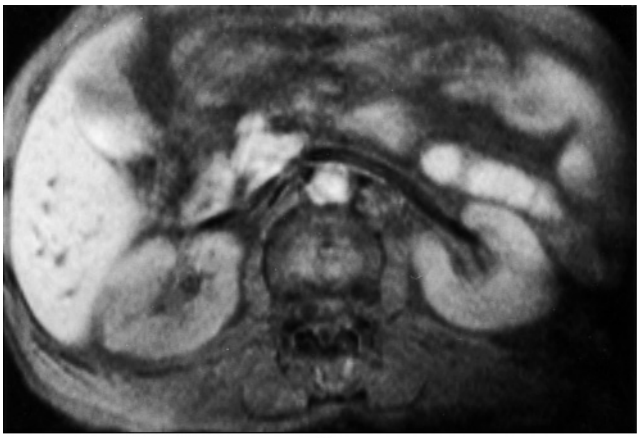

(*a*)

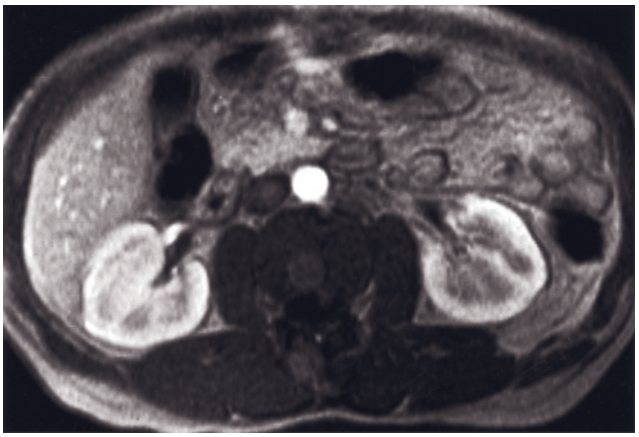

(*b*)

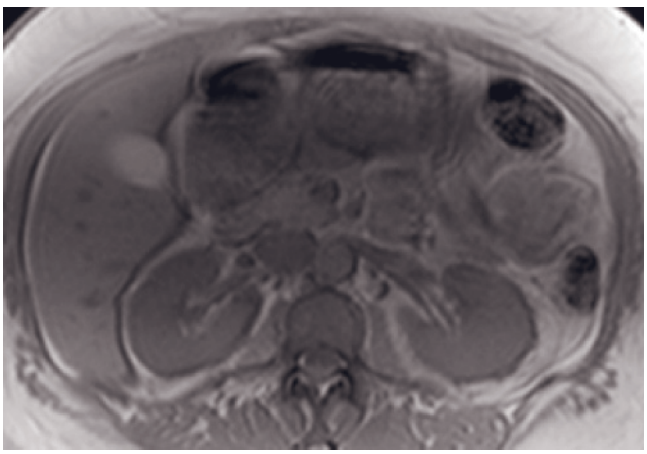

(*c*)

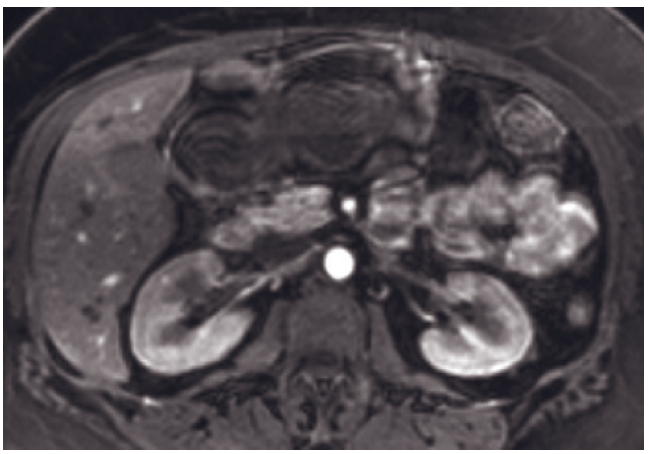

(*d*)

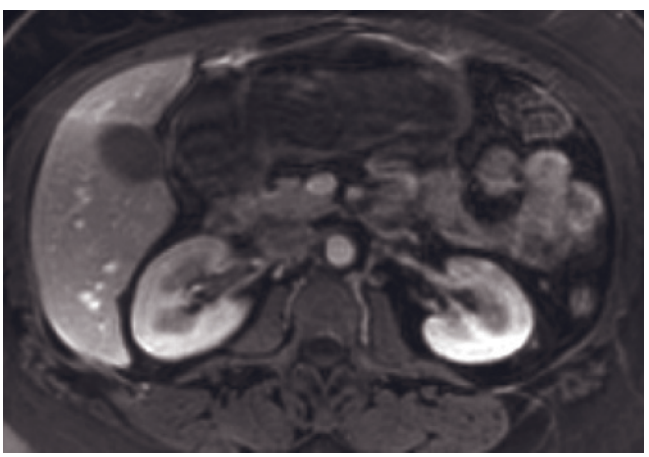

(*e*)

FIG. 9.77 Elevated serum creatinine (3 mg/dl) with loss of CMD. T1-weighted precontrast fat-suppressed SE (*a*) and immediate postgadolinium SGE (*b*) images. Loss of corticomedullary differentiation (CMD) on the precontrast image (*a*) is noted, with preservation of CMD on the immediate postgadolinium SGE (*b*) image. Loss of CMD on precontrast T1-weighted images is a nonspecific finding of diminished renal function. T2-weighted fat-suppressed single-shot echo-train spin-echo (*c*), T1-weighted SGE (*d*), and T1-weighted postgadolinium fat-suppressed hepatic arterial dominant-phase (*d*) and hepatic venous-phase (*e*) 3D-GE images at 3.0 T demonstrate the loss of corticomedullary differentiation in another patient with elevated creatinine level. Corticomedullary signal difference is lost on precontrast T1-weighted image (*c*) and reflects diminished renal function. However, corticomedullary enhancement difference is preserved as seen on postgadolinium images (*d*, *e*). **Advanced renal failure**

(*f*)

FIG. 9.77 (*Continued*) **and elevated serum creatinine (>8.5 mg/dl).** Coronal postgadolinium 3D MIP 3D-GE MRA image (*f*) demonstrates normal renal arteries (arrows) and the absence of enhancement of both kidneys due to advanced renal failure in another patient.

Not all patients with elevated sCr show loss of CMD. Loss of CMD on precontrast images presumably develops over some period of time. Patients with acute renal failure who are imaged within 1 week of onset may show preservation of CMD [96]. A study [98] that evaluated the appearance of CMD in patients with acute renal failure (defined as onset within 2 weeks of the MRI exam) showed that 21 patients with acute renal failure had preservation of CMD on noncontrast T1-weighted images. The conclusion of this study is that caution should be exercised in interpreting renal function based on CMD in patients with acute renal failure, as CMD may be preserved in the setting of severely compromised kidneys. Unlike the situation with chronic renal failure, where the presence of CMD correlates with renal function, this correlation does not exist in the first 2 weeks after the onset of acute renal failure.

Glomerular Disease

The clinical manifestations of glomerular disease are varied and range from asymptomatic urinary abnormalities to acute nephritis, nephrotic syndrome, and chronic renal failure. In patients with nephrotic syndrome, the majority have membranous nephropathy, and MRI findings are generally minimal (fig. 9.78) [96]. Diffuse increased enhancement resulting in high signal intensity of the medulla may be observed on delayed postgadolinium images. In chronic disease, cortical thinning is smooth and regular in contour and medullary atrophy may be substantial (fig. 9.79). Nephrotic syndrome may also be associated with renal vein thrombosis. Renal vein thrombus may be well shown with a number of MRI techniques [59, 63, 96, 99]. Gradient-echo images acquired 45–120 s after gadolinium serve as an effective technique for demonstrating renal vein thrombus (fig. 9.80). True-FISP is an effective noncontrast technique

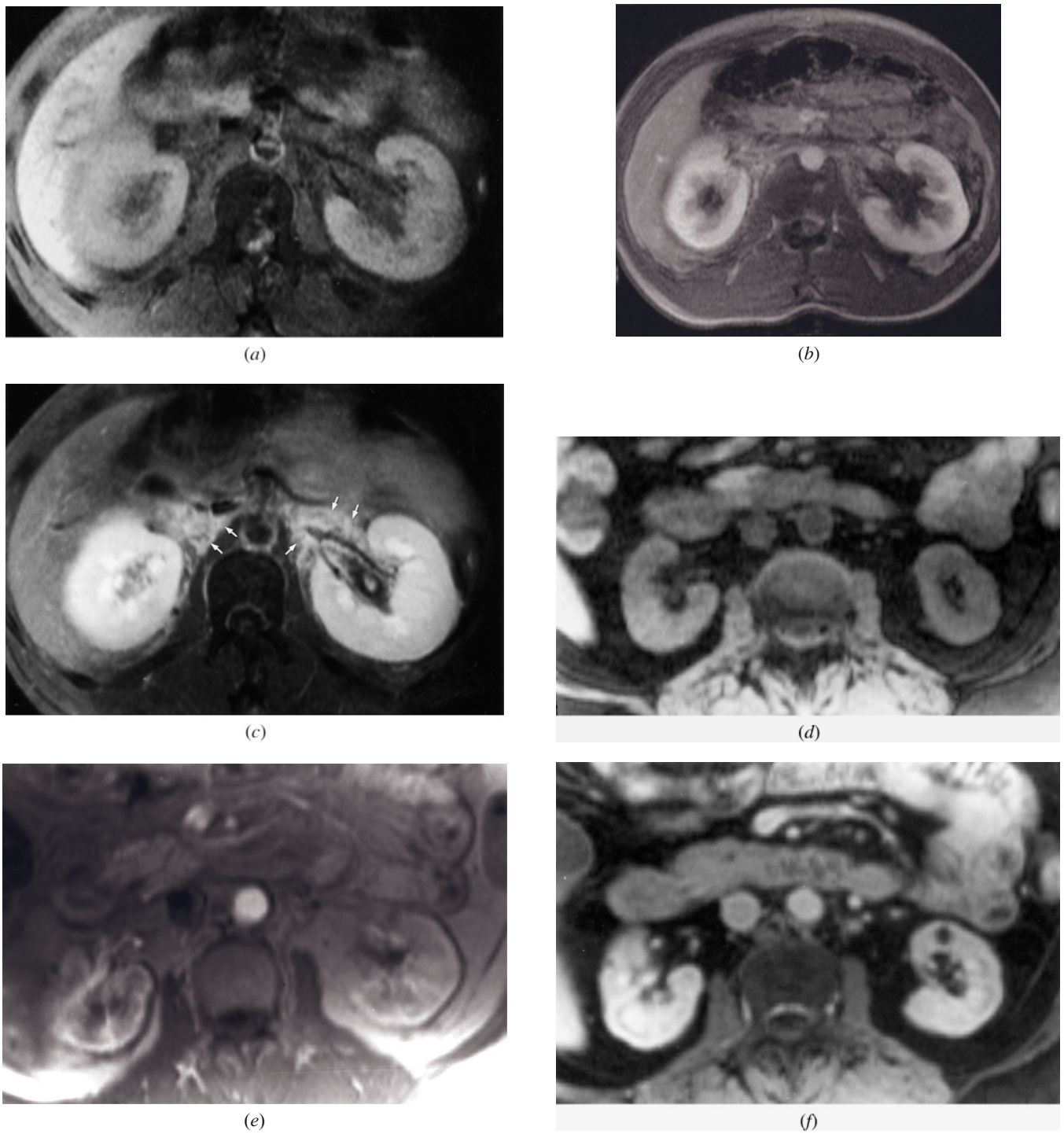

FIG. 9.78 Recent-onset membranous nephropathy. T1-weighted precontrast fat-suppressed SE (*a*) and immediate (*b*) and late-phase fat-suppressed (*c*) gadolinium-enhanced SE images. CMD is diminished on the precontrast image (*a*). Renal cortex is uniform and of normal thickness on the immediate postgadolinium image (*b*). Diffuse increased enhancement of the medulla is noted on the interstitial-phase image (*c*). Enhancing platelike retroperitoneal tissue is present that extends into the left renal hilum (arrows, *c*).This represents acute benign retroperitoneal fibrosis. T1-weighted precontrast fat-suppressed (*d*) and immediate (*e*) and 90-s fat-suppressed (*f*) postgadolinium SGE images in a second patient with chronic renal failure. Decreased CMD is present on the precontrast fat-suppressed image (*d*), and increased medullary enhancement is appreciated on the interstitial-phase image (*f*). Note also a small simple cyst in the left kidney.

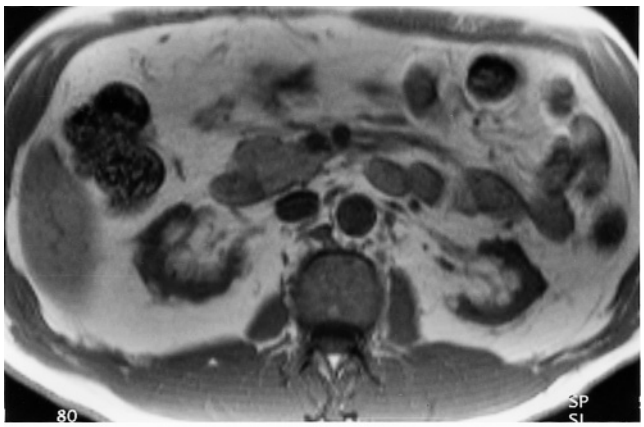

(*a*)

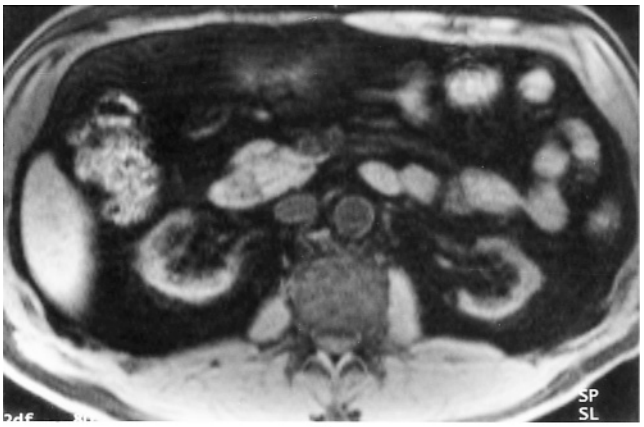

(*b*)

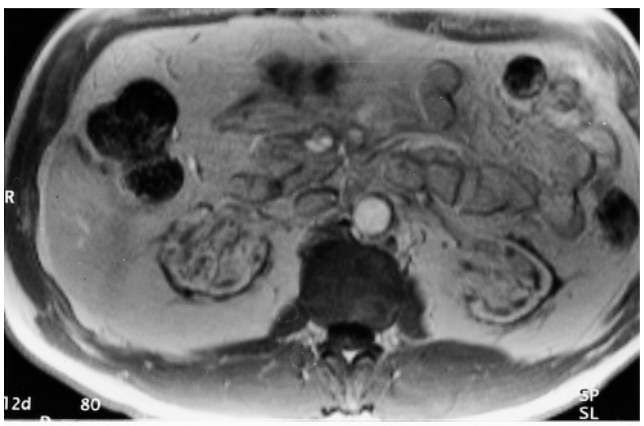

(*c*)

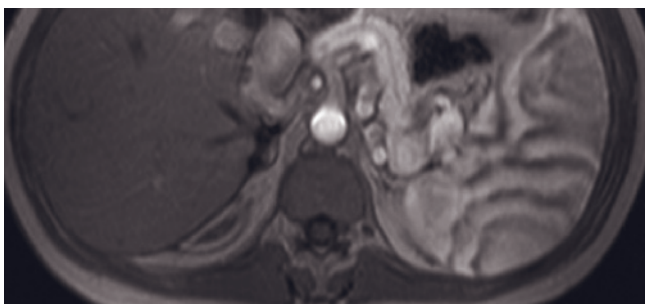

(*d*)

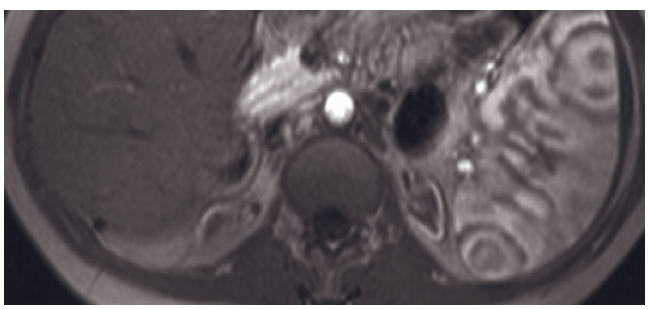

(*e*)

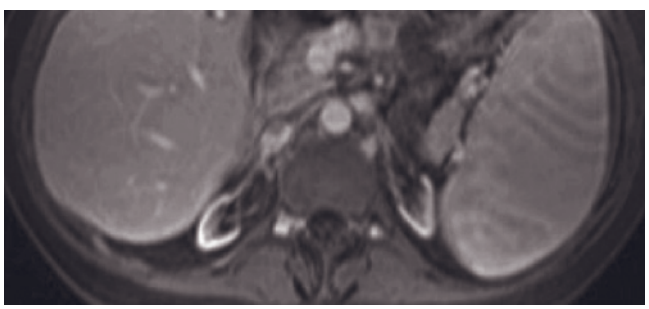

(*f*)

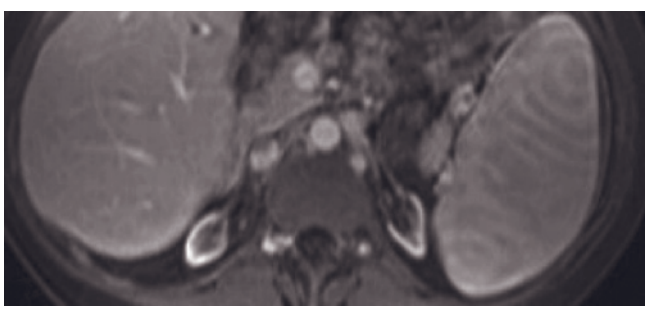

(*g*)

FIG. 9.79 Chronic membranous glomerulonephritis. T1-weighted precontrast (*a*), precontrast fat-suppressed (*b*), and immediate postgadolinium (*c*) SGE images. No CMD is appreciated on precontrast images (*a*, *b*). The immediate postgadolinium image (*c*) demonstrates uniform cortical thinning and disproportionate atrophy of the renal medulla. Fat in the renal sinus has increased in volume to supplant the atrophic medulla. **Chronic renal failure secondary to glomerular disease.** T1-weighted postgadolinium hepatic arterial dominant phase SGE (*d*, *e*) and T1-weighted postgadolinium hepatic venous-phase fat-suppressed 3D-GE (*f*, *g*) images demonstrate bilateral atrophic kidneys developing secondary to glomerular disease in another patient.

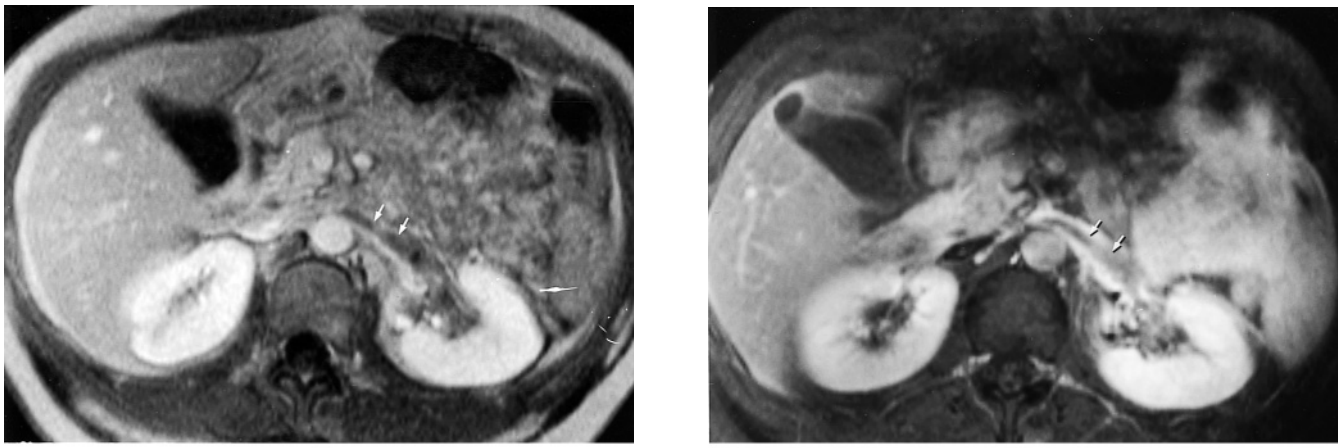

(*a*) (*b*)

FIG. 9.80 Renal vein thrombosis with nephrotic syndrome. T1-weighted 90-s gadolinium-enhanced SGE (*a*) and late-phase fat-suppressed gadolinium-enhanced SE (*b*) images. Low-signal bland thrombus is identified in the left renal vein (arrows, *a*, *b*). Flow in the vein surrounding the thrombus is identified as high signal intensity on these images. Greater conspicuity of gadolinium in the patent periphery of the vein is apparent on the fat-suppressed image because of suppression of the competing signal intensity of fat (*b*).

to show high signal in patent vessels. Detection of thrombus is important because it is treatable with thrombolytic agents and successful treatment may result in improvement of the condition.

Tubulointerstitial Disease

A variety of underlying etiologies may result in tubulointerstitial disease, of which drug-related causes are among the most common. Tubulointerstitial disease secondary to analgesic drug overuse results in irregular cortical thinning (fig. 9.81) [96]. The irregularity presumably reflects the intermittent nature of the insult because drug intake is sporadic. Tubulointerstitial disease from antineoplastic chemotherapy results in more uniform cortical thinning (fig. 9.82) [96]. This presumably reflects the fact that the cortical insult is more constant because of the regular rate of chemotherapy drug administration.

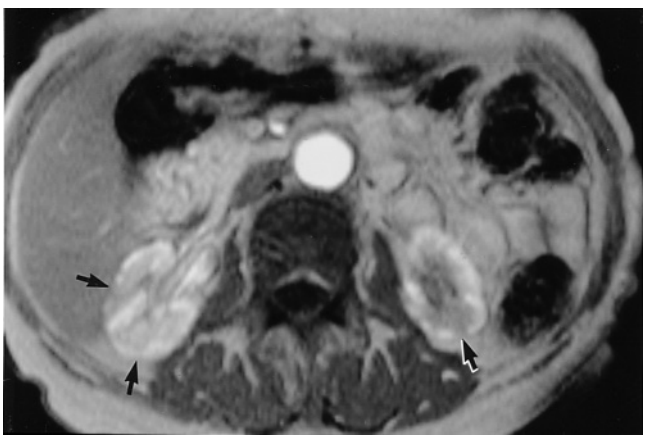

FIG. 9.81 Tubulointerstitial disease secondary to analgesic abuse. T1-weighted immediate postgadolinium SGE image demonstrates irregular cortical thinning ranging in thickness from 1 to 4 mm. Regions of extreme cortical thinning are apparent (arrows) (Reproduced with permission from Kettritz U, Semelka RC, Brown ED, Sharp TJ, Lawing WL, Colindres RE: MR findings in diffuse renal parenchymal disease. *J Magn Reson Imaging* 6: 136–144, 1996.)

Acute Tubular Necrosis

Acute tubular necrosis results from metabolic or toxic etiologies in the majority of cases. Within 1 week of onset of this condition CMD may be preserved despite substantial elevation of sCr (fig. 9.83). This likely reflects the fact that the loss of CMD may take more than 1 week to develop.

Tubular Blockage

A number of etiologic agents may result in tubular blockage. Renal failure may result from blockage of a substantial portion of the renal tubules by various substances. The classic example of diffuse tubular blockage is by Bence Jones proteinuria in multiple myeloma (fig. 9.84).

Another example of renal tubular injury is with high levels of urinary pigments (myoglobinuria), especially in the setting of renal hypoperfusion and ischemia [100]. Many disorders in which myoglobinuria develops result from severe and excessive stress or overuse of striated muscles (fig. 9.84) [101].

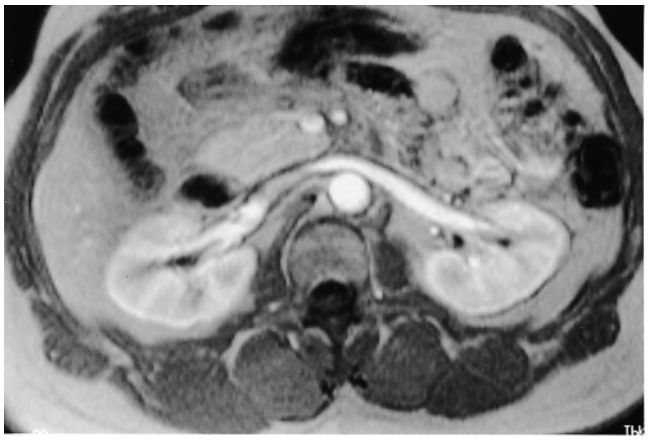

(*a*)

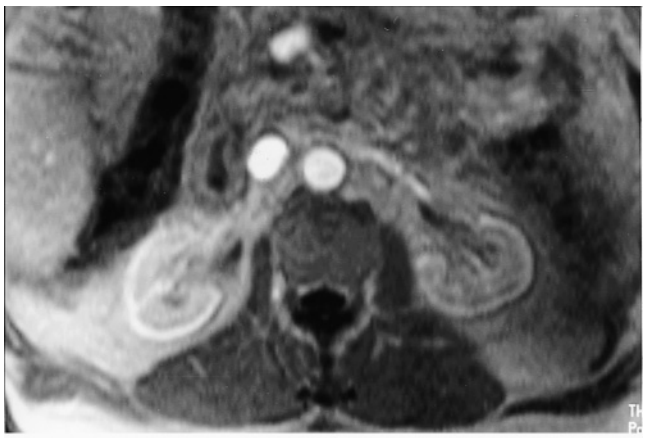

(*b*)

(*c*)

FIG. 9.82 Tubulointerstitial disease secondary to chemotherapy. T1-weighted immediate postgadolinium images in 3 patients (*a–c*) who have a remote history of antineoplastic chemotherapy. Regular cortical thinning is present in all patients. Note the low signal intensity of the liver in the third patient (*c*) due to transfusional siderosis.

Other Parenchymal Diseases

Iron Deposition

Iron deposition occurs in the renal cortex in the setting of intravascular hemolysis with hemoglobin accumulation in renal glomeruli. Sickle cell disease is the most common entity to result in this condition [102, 103]. The usual appearance is low signal intensity of the renal cortex due to the T2*-shortening effects of iron. This is best appreciated on gradient-echo or T2-weighted images (fig. 9.85). On immediate postgadolinium gradient-echo images, the T1-shortening effects of gadolinium usually exceed the T2-shortening effects of the iron in the renal cortex, resulting in high-signal-intensity enhanced renal cortex. On interstitial-phase images, passage of contrast into the tubules and enhancement of the medulla results in signal reversal, with the cortex becoming lower in signal intensity than the medulla (fig. 9.86). Less commonly, dilute-concentration iron in the glomeruli may result in a high-signal-intensity renal cortex on precontrast T1-weighted images. The spleen in sickle cell disease is also affected with iron deposition, and splenic infarcts are observed.

Paroxysmal nocturnal hemoglobinuria results in iron deposition in the renal cortex. Demonstration that the renal cortex becomes higher in signal on a short TE out-of-phase sequence, compared to the longer TE in-phase sequence, confirms the presence of iron in the renal cortex by demonstrating this magnetic susceptibility property (fig. 9.87). Iron deposition in the liver and spleen is variable and related to blood transfusions or portal hypertension [104].

Parenchymal Changes from Obstruction

Acute and chronic obstructions are well shown on MR images. In acute obstruction, kidney size is enlarged and contrast persists in the renal parenchyma for a prolonged period of time, resulting in a prolonged nephrogram phase. The concentration of gadolinium in the collecting system is usually dilute, resulting in high signal (fig. 9.88). This is caused by the combination of the excretion of dilute urine, which occurs in the setting of acute severe obstruction, and the dilutional effect of gadolinium within a large volume of urine in a dilated collecting system. Corticomedullary differentiation is

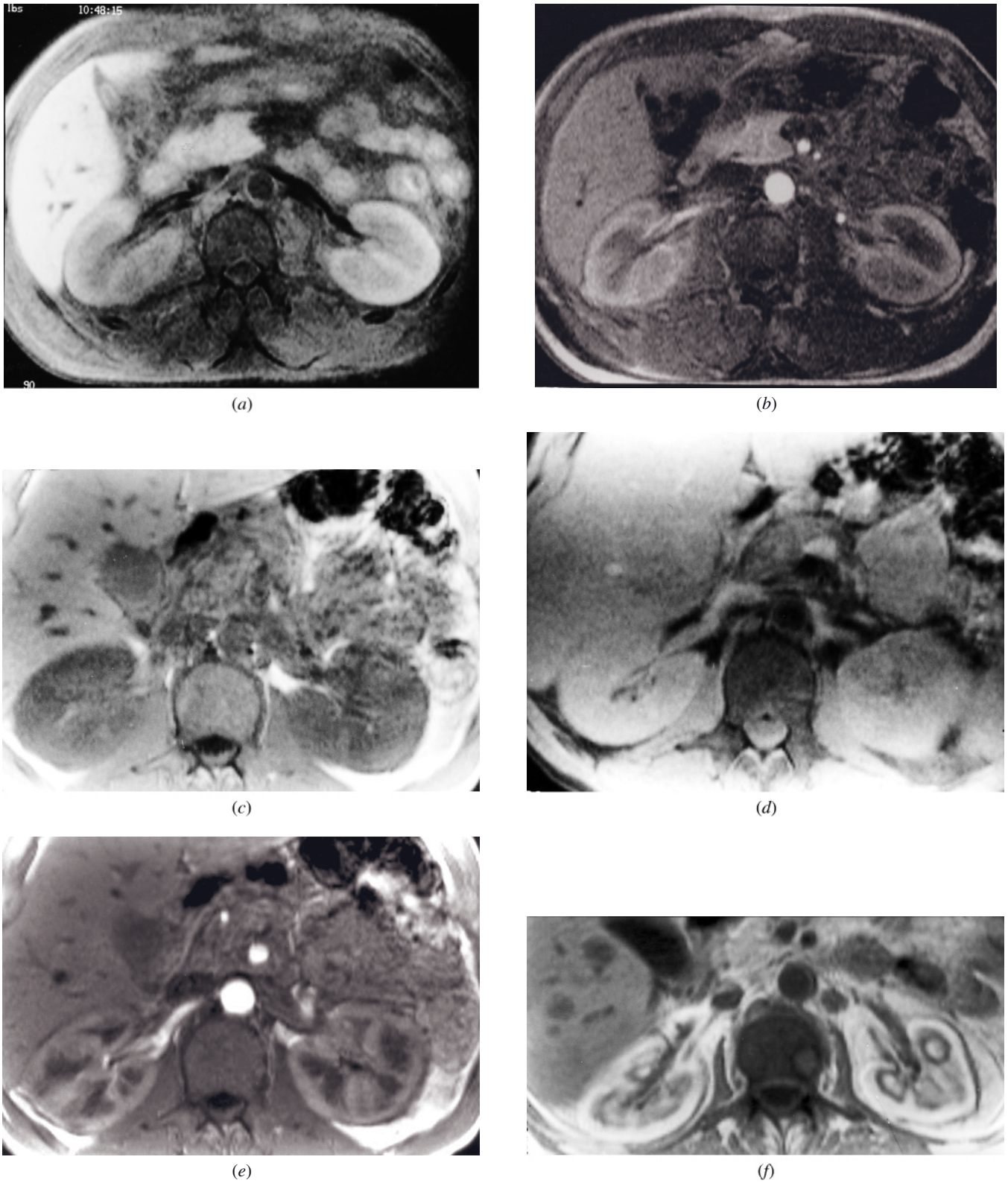

FIG. 9.83 Acute tubular necrosis. T1-weighted precontrast fat-suppressed SE (*a*) and immediate postgadolinium SGE (*b*) images. CMD is demonstrated on both precontrast (*a*) and immediate postcontrast (*b*) images in a patient with acute tubular necrosis and serum creatinine of 6.3 mg/dl. Acute tubular necrosis developed within 1 week before MRI examination, and the acute nature of the injury presumably accounts for the presence of CMD on the precontrast image. T1-weighted precontrast (*c*), precontrast fat-suppressed (*d*), and immediate postgadolinium (*e*) SGE images in a second patient, with acute tubular necrosis of 1-week duration, demonstrate globular-shaped kidneys with decreased CMD on precontrast images (*c*, *d*). T1-weighted precontrast SGE image (*f*) in a third patient shows high signal intensity in the medulla of kidneys on noncontrast T1-weighted images, suggesting infiltration with blood or protein.

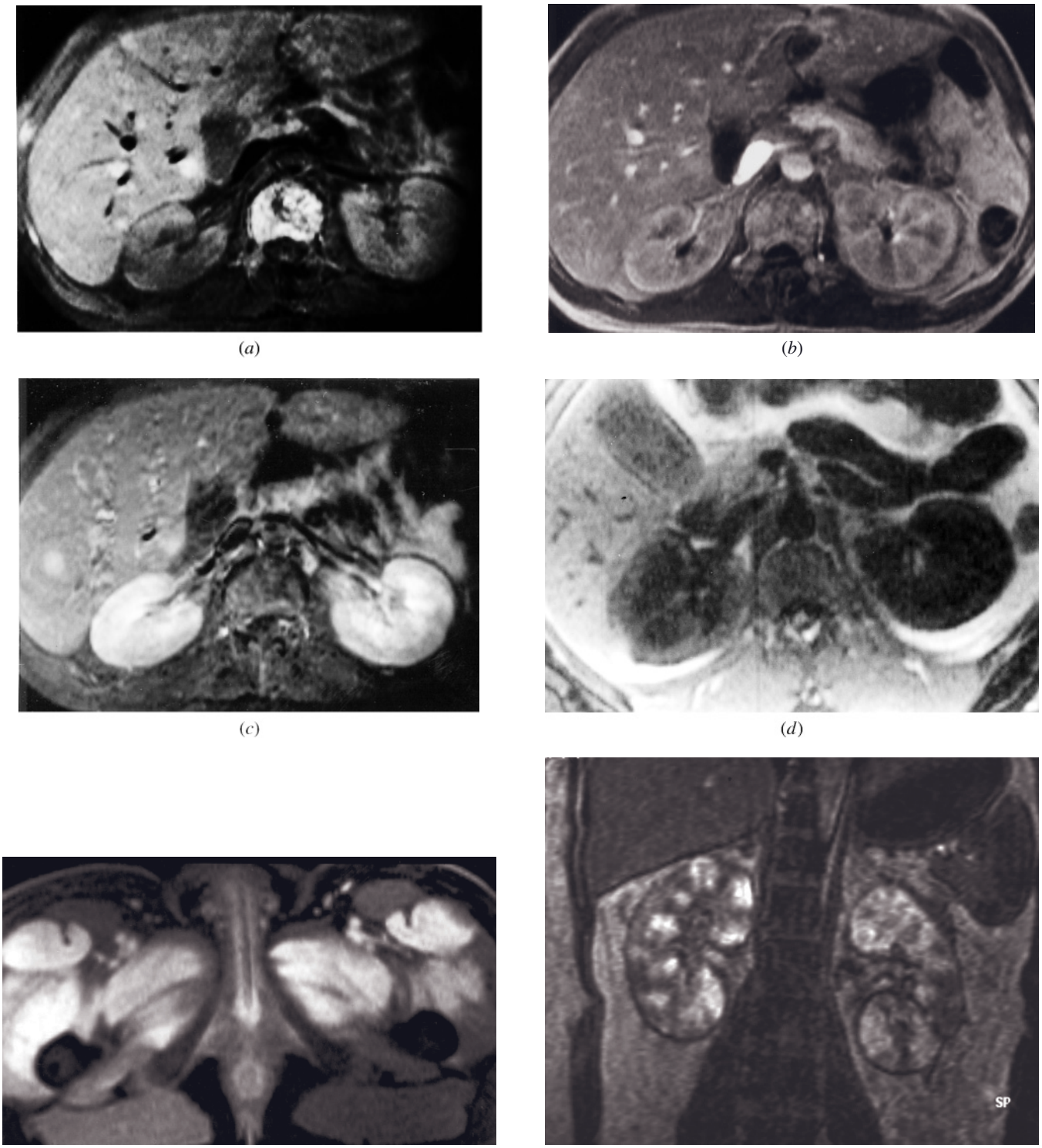

FIG. 9.84 Tubular blockage secondary to Bence Jones proteinuria. T1-weighted precontrast fat-suppressed SE (*a*), immediate postgadolinium SGE (*b*), and late-phase fat-suppressed gadolinium-enhanced SE (*c*) images. This patient with multiple myeloma has high-signal-intensity lesions in the bone marrow and liver and absent CMD on precontrast images (*a*). On immediate postgadolinium image (*b*), CMD is present, but cortical enhancement is not intense. On interstitial-phase image (*c*), diffuse high signal intensity is present in the renal medulla, suggesting the presence of tubular leakage of gadolinium. **Tubular blockage secondary to rhabdomyolysis.** T1-weighted precontrast (*d*) and precontrast fat-suppressed (*e*) SGE images. The kidneys are enlarged, with diminished CMD on the precontrast image. Extensive high signal is present in the muscles of the upper thighs (*e*), which on the noncontrast image reflects diffuse hemorrhagic changes. Coronal T1-weighted gradient-echo (*f*) and T1-weighted fat-suppressed

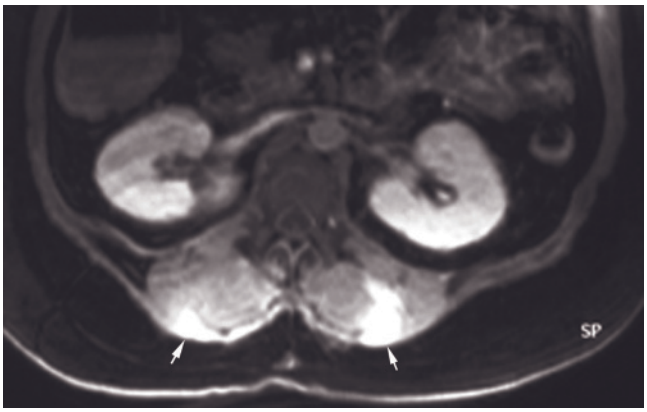

(*g*)

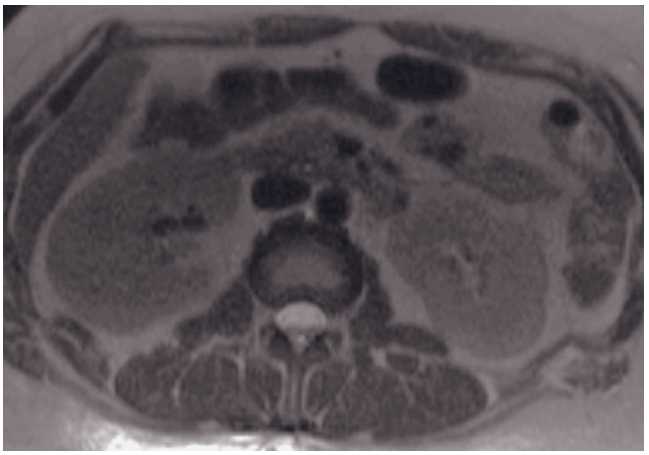

(*h*)

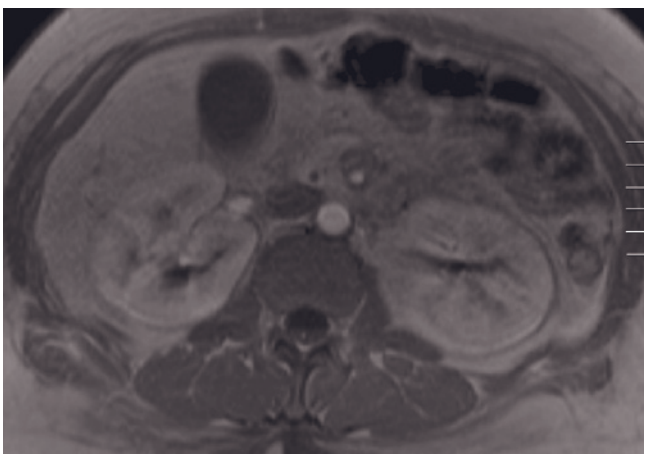

(*i*)

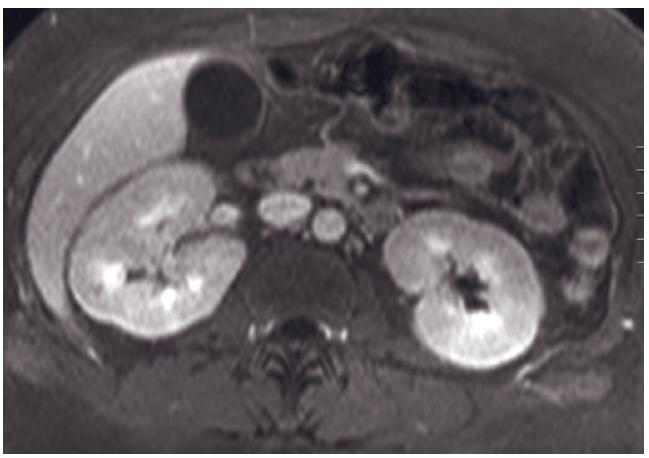

(*j*)

FIG. 9.84 (*Continued*) 90-s postgadolinium (*g*) images in a second patient with a history of rhabdomyolysis. The kidneys are enlarged and exhibit heterogeneous high signal intensity on pregadolinium T1-weighted images more evident in the medullary portion, which is secondary to protein accumulation. Note the abnormal enhancement seen in the paraspinal muscles in the lumbar region (arrows, *g*). **Tubular blockage.** T2-weighted single-shot echo-train spin-echo (*h*), T1-weighted postgadolinium hepatic arterial dominant-phase SGE (*i*), and T1-weighted postgadolinium interstitial-phase fat-suppressed 3D-GE (*j*) images demonstrate tubular blockage in another patient. The kidneys are globular in shape. Corticomedullary enhancement difference is seen on the hepatic arterial dominant-phase image (*i*). On interstitial-phase image (*j*), focal high signal intensity is present in the renal medulla, suggesting the presence of tubular leakage of gadolinium.

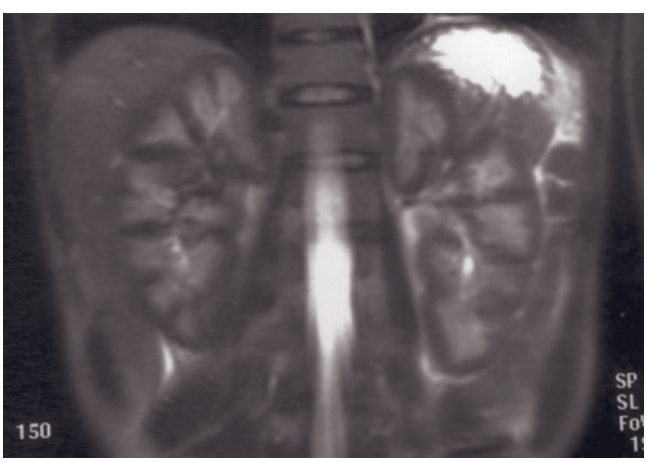

(*a*)

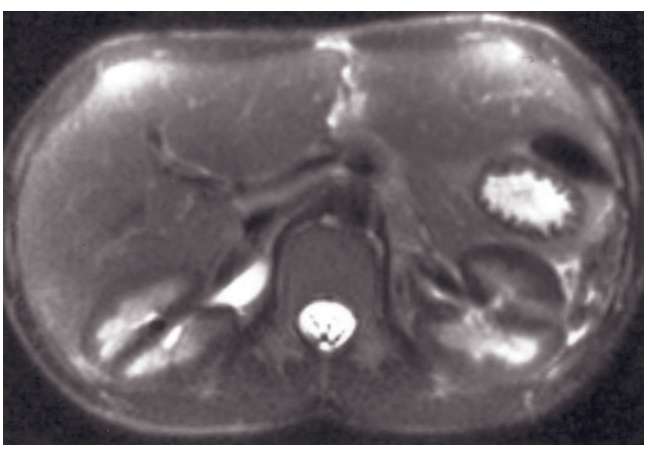

(*b*)

FIG. 9.85 Sickle cell disease. Coronal (*a*) and transverse (*b*) T2-weighted SS-ETSE and T1-weighted precontrast (*c*) and 90-s

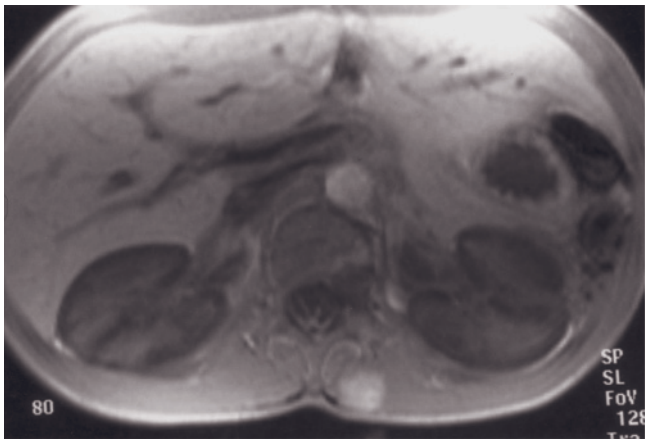

(*c*)

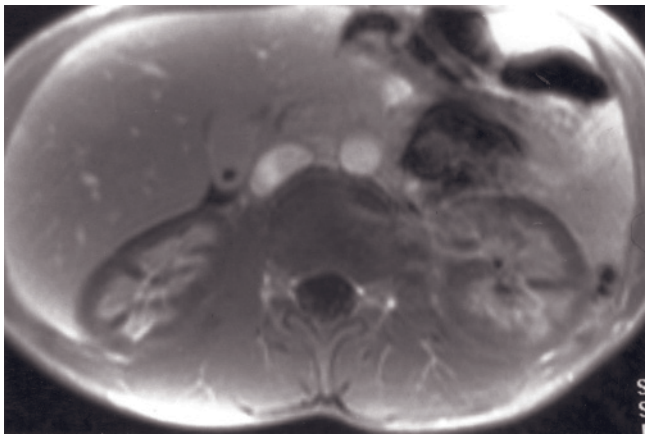

(*d*)

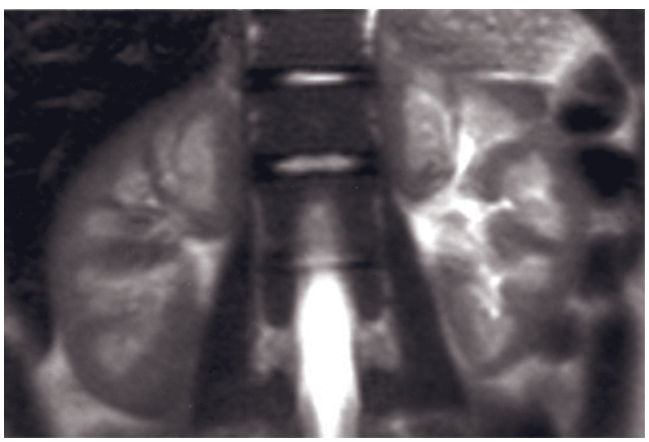

(*e*)

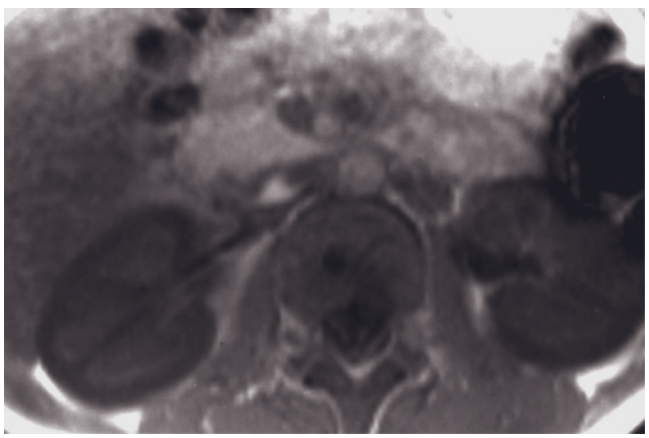

(*f*)

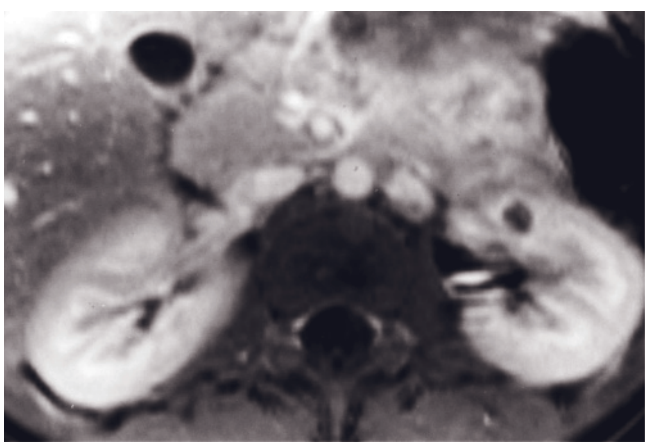

(*g*)

FIG. 9.85 (*Continued*) fat-suppressed postgadolinium (*d*) SGE images. The kidneys are globular shaped, and the renal cortices are low signal on T2- and T1-weighted images, consistent with iron deposition. Coronal T2-weighted SS-ETSE (*e*) and transverse T1-weighted precontrast (*f*) and 90-s fat-suppressed postgadolinium (*g*) SGE images in a second patient reveal similar findings.

diminished on immediate postgadolinium images [5]. In chronic obstruction, the kidney, which is initially enlarged, over time gradually decreases in size and develops diminished renal perfusion (fig. 9.89) [5]. Renal cortical thinning occurs and, in pure renal obstruction, is usually uniform. Irregular cortical thinning, however, is not unusual. The regularity of cortical thinning presumably reflects the tissue pressure experienced in different portions of the kidney. Uniform cortical thinning may reflect a relatively uniform increased pressure throughout the kidney. Irregular thinning may be related to variations in calyceal dilatation and pressure. The presence of associated reflux in some conditions also contributes to irregular cortical

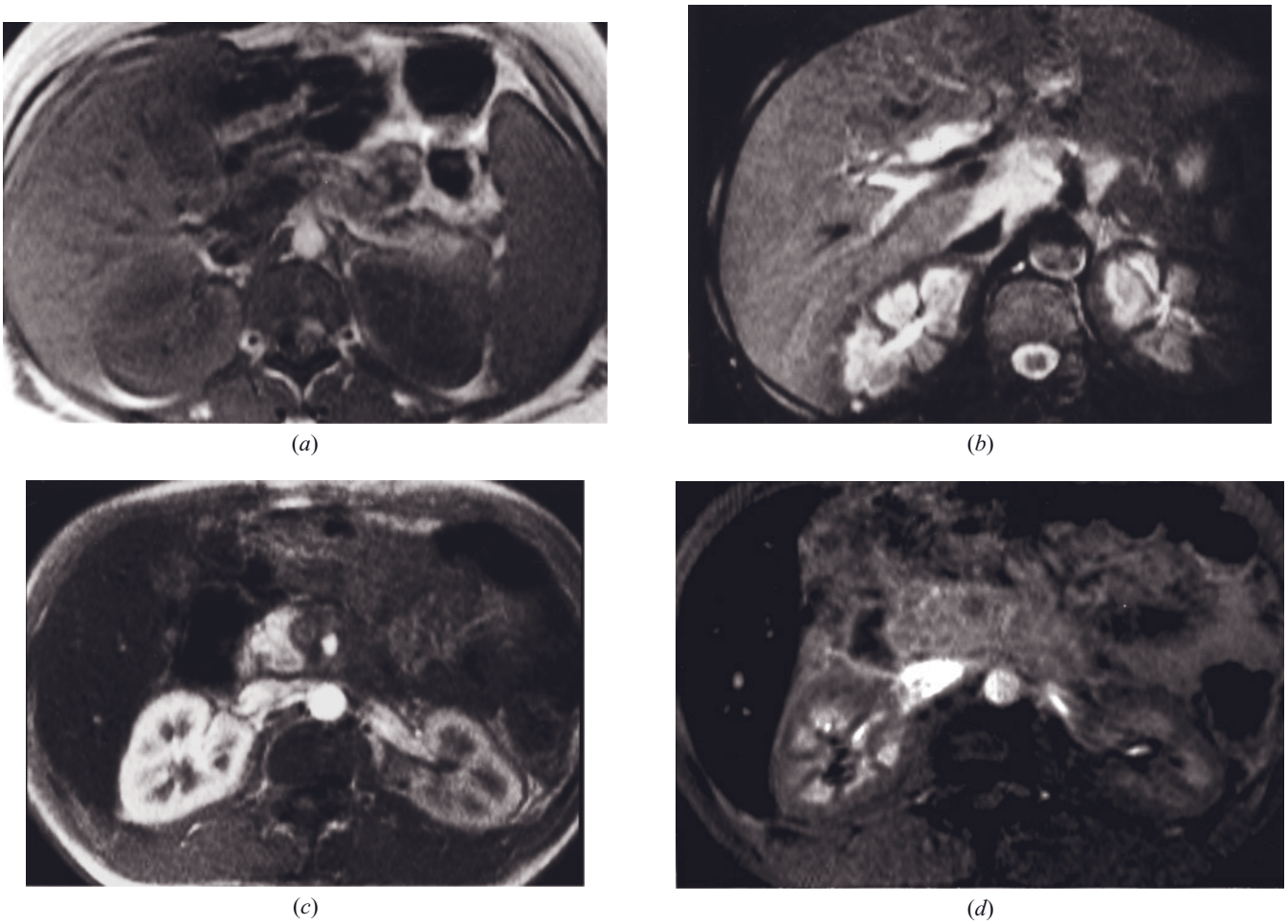

FIG. 9.86 Sickle cell disease. T1-weighted precontrast SGE (*a*) image demonstrates preservation of CMD in a patient with sickle cell disease because of the presence of dilute iron in the renal cortex that results in a T1-shortening paramagnetic effect. T2-weighted fat-suppressed SE image (*b*) in a second patient demonstrates low signal intensity of renal cortex secondary to accumulation of free hemoglobin. High-signal-intensity celiac and porta hepatic nodes are also present. T1-weighted immediate (*c*) and 2-min (*d*) postgadolinium SGE images in a third patient. On the immediate postgadolinium image (*c*), the renal cortex is high in signal intensity, which reflects that the T1-shortening effect of gadolinium exceeds the T2-shortening effects of iron. At 2 min after injection (*d*), the T2 shortening effect of iron in the cortex exceeds the T1 shortening effect of gadolinium, causing diminished signal intensity of the cortex. The relative washout of gadolinium from the cortex coupled with the transit of gadolinium into the medulla results in this signal reversal of cortex and medulla. Signal intensity changes in renal parenchyma on postgadolinium images in patients with sickle cell disease reflect the changing balance of T2-shortening effects of iron and T1-shortening effects of gadolinium.

thinning (fig. 9.90). The collecting system generally remains dilated when the kidney atrophies, which permits distinction from chronic ischemia, in which the collecting system is not dilated.

Reflux Nephropathy and Chronic Pyelonephritis

Reflux nephropathy represents renal parenchymal changes secondary to urine reflux into the renal collecting system. Changes of reflux nephropathy are more common in the upper or lower pole regions of the kidneys because of the presence of compound papillae or fused tips of the medullary pyramids. Owing to the fusion of multiple papillae, the papillary tip is flattened or concave. Normally, large terminal collecting ducts open into the calyces in the area of the papillary tip. In compound papillae, collecting duct orifices are wide, gaping, and permanently opened, and are unable to be compressed in the presence of vesicoureteral reflux. This situation can lead to backflow of urine via the gaping collecting duct openings into the renal tubular system. In simple (unfused) papillae, collecting ducts open in slitlike fashion onto sharply convex papillary tips. This condition favors closure of the ducts when pelvic pressure rises—a protective measure that prevents intrarenal reflux.

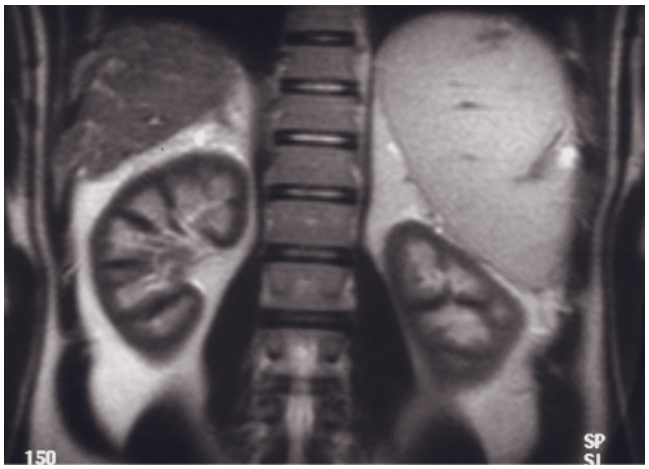

(*a*)

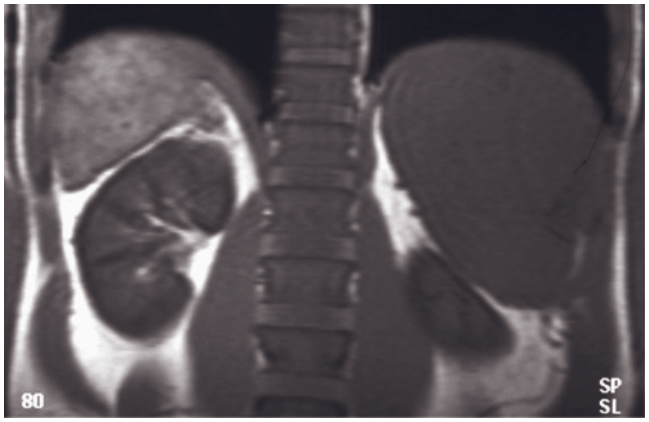

(*b*)

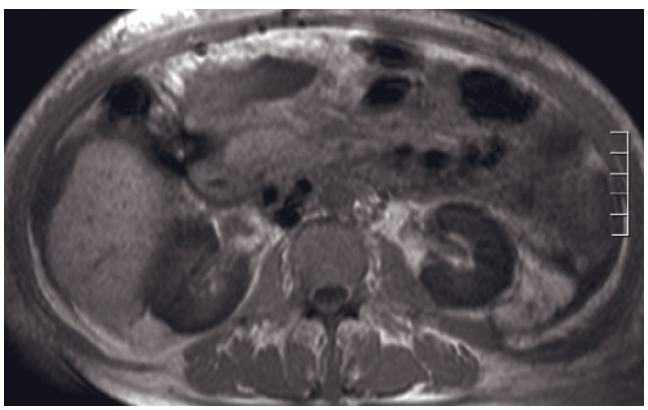

(*c*)

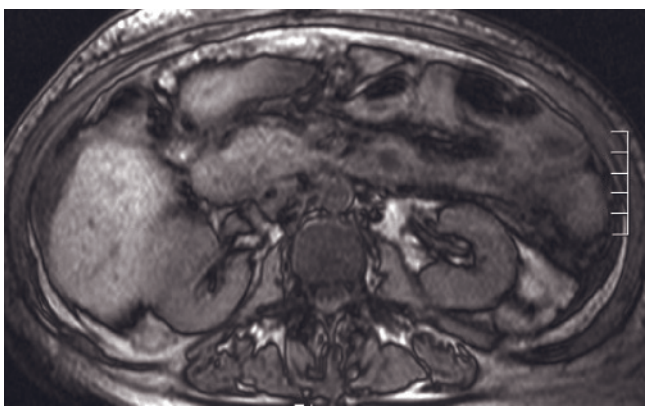

(*d*)

(*e*)

FIG. 9.87 Paroxysmal nocturnal hemoglobinuria. Coronal T2-weighted SS-ETSE (*a*) and T1-weighted gradient-echo (*b*) images in a patient with paroxysmal nocturnal hemoglobinuria. Renal cortices are low in signal intensity on both T1- and T2-weighted images because of iron deposition. This appearance is caused by the T2*-shortening effects of iron. T1-weighted in-phase (*c*) and out-of-phase (*d*) SGE and coronal T2-weighted single-shot echo-train spin-echo (*e*) images demonstrate the deposition of iron in the renal cortex in another patient with paroxysmal nocturnal hemoglobinuria. Bilateral renal cortices show decreased signal on T1-weighted in-phase image (*c*) and relatively high signal on out-of-phase image (*d*) compared to in-phase image. Note that bilateral renal cortices show decreased signal on T2-weighted image (*c*). These findings are consistent with iron deposition in the renal cortices.

Renal scarring is a frequent sequela of reflux nephropathy and occurs superficial to dilated calyces (fig. 9.91). The renal cortex is thin and usually very irregular [96]. The hallmark of chronic pyelonephritis is a coarse, discrete corticomedullary scar overlying a dilated, blunted, or deformed calyx. Most scars are in the upper and lower poles, consistent with the presence of compound papillae and resulting reflux at these sites [105].

Renal Arterial Disease

Disease of the renal arterial system may be thrombotic/arterial wall or embolic in nature. Thrombosis/arterial

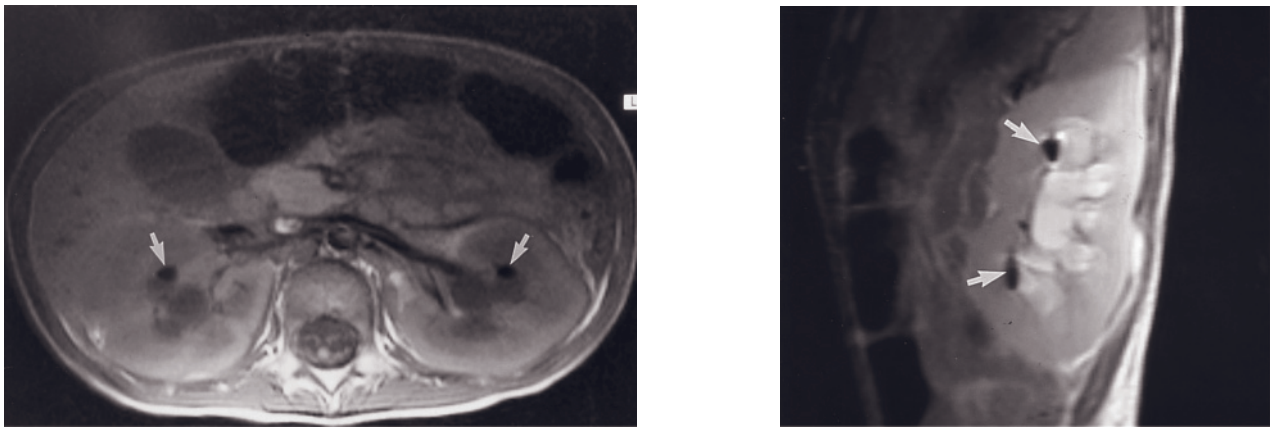

(*a*) (*b*)

FIG. 9.88 Acute obstruction. Transverse T1-weighted precontrast SE (*a*) and sagittal T1-weighted gadolinium-enhanced SE (*b*) images. The kidneys are enlarged in a globular fashion. Corticomedullary differentiation is preserved, reflecting the acuteness of the obstruction (*a*). Gadolinium excreted into the collecting system is dilute and high in signal intensity (*b*). Signal-void foci located in the nondependent portions of the renal collecting system demonstrate blooming artifact (arrows, *a*, *b*) that represents air introduced by Foley catheterization.

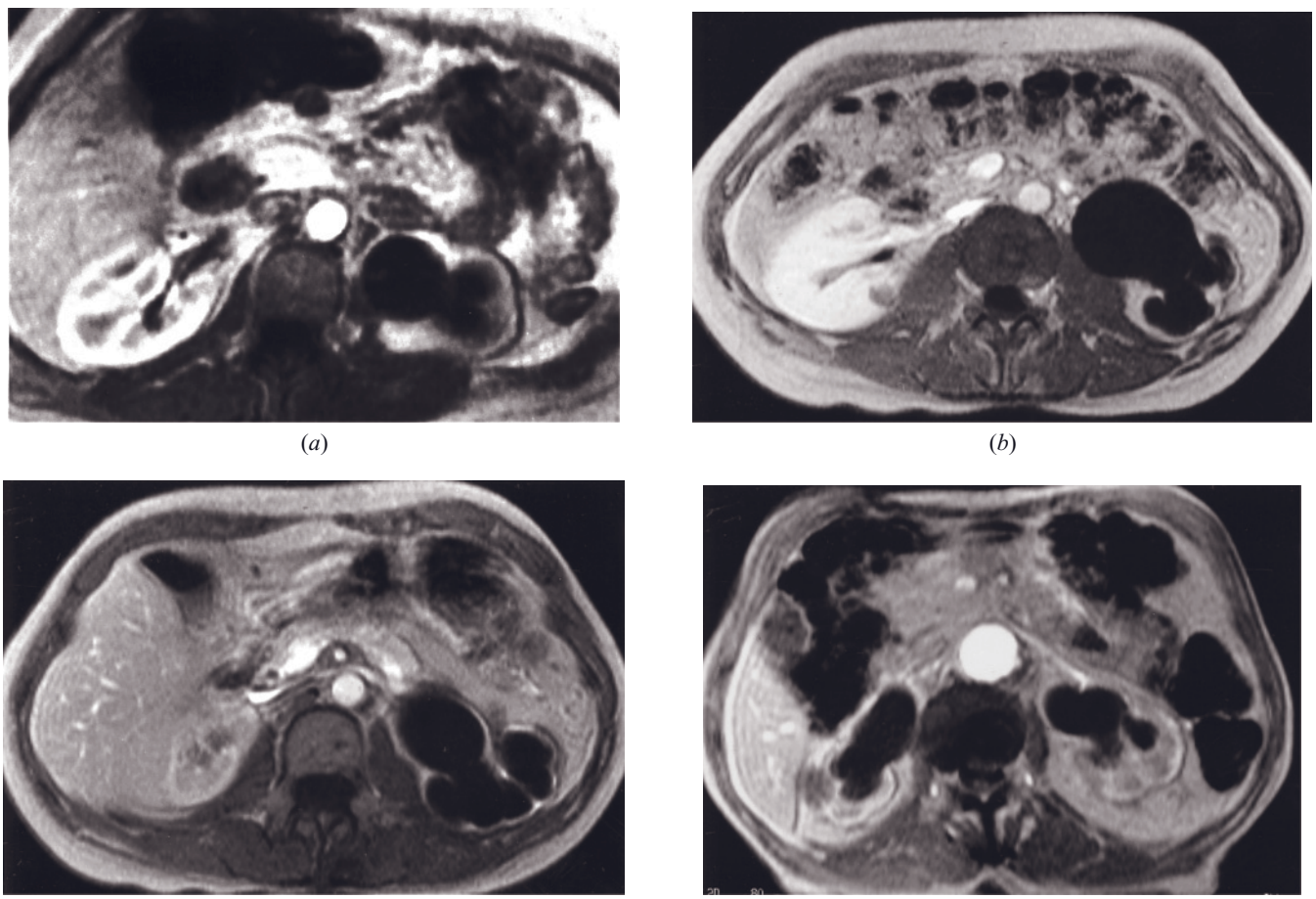

(*a*) (*b*)

(*c*) (*d*)

FIG. 9.89 Chronic renal obstruction. T1-weighted immediate postgadolinium SGE images in 5 patients with chronic renal obstruction (*a–e*). In all cases of unilateral obstruction (*a–c*), the degree of cortical enhancement is less than that of the contralateral normal kidney. Substantial pelvicalyceal dilatation is present in all cases. Corticomedullary differentiation is diminished, and the cortex

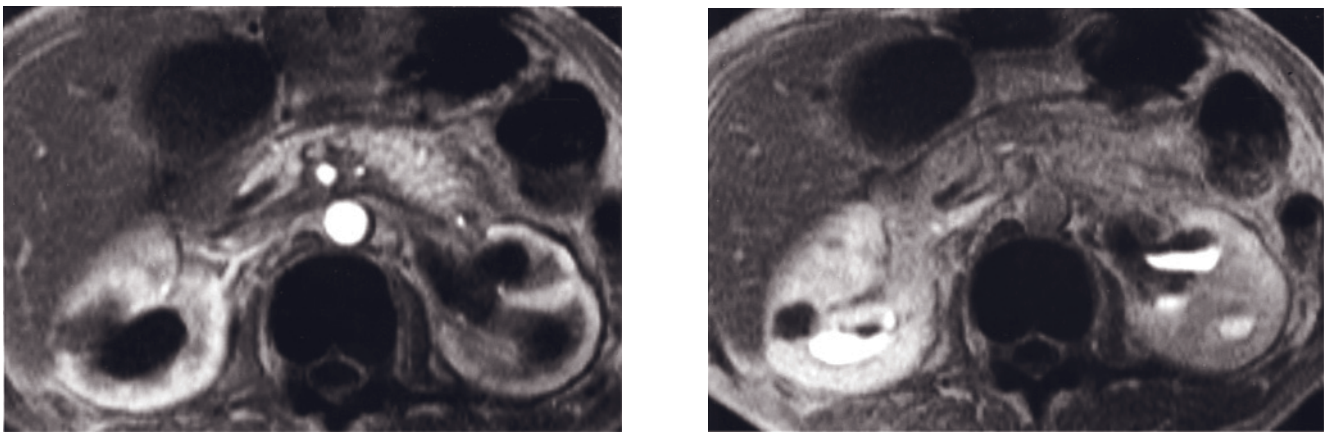

(*e*) (*f*)

FIG. 9.89 (*Continued*) is thinned and relatively smooth. These factors reflect the duration and severity of obstruction. Excreted urine is dilute in the setting of chronic obstruction because kidneys lose concentrating ability. Excretion of dilute gadolinium is shown on a 4-min postgadolinium SGE image (*f*) obtained in the patient illustrated in *e*.

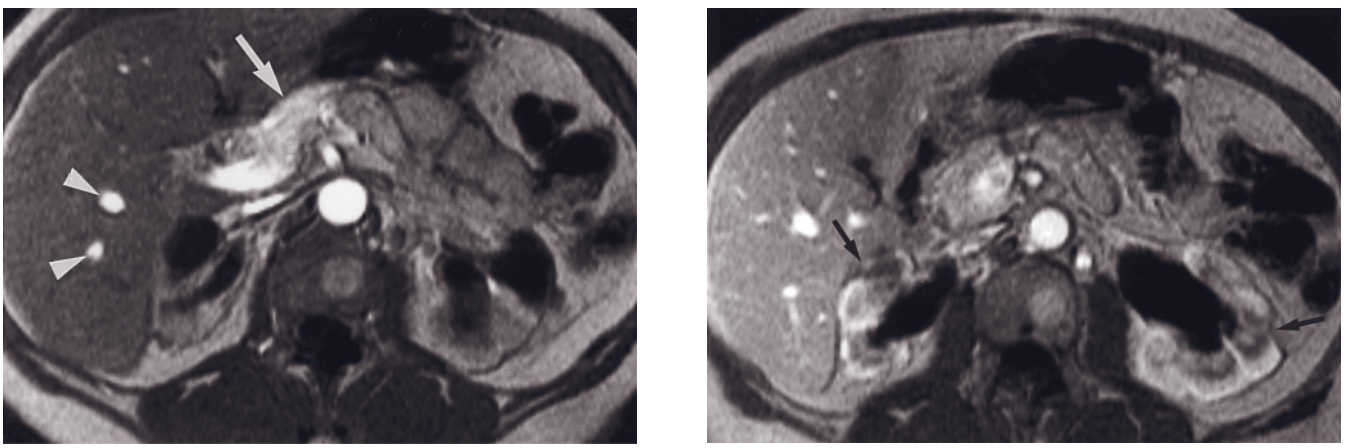

(*a*) (*b*)

FIG. 9.90 Complicated chronic renal obstruction. T1-weighted immediate (*a*) and 45-s (*b*) postgadolinium SGE images. Dilatation of both renal collecting systems has resulted from multiple urological procedures, including creation of an ileal conduit for obstruction of the distal ureters. Minimal cortical enhancement is shown on the immediate postgadolinium image (*a*). Image acquisition has been timed in the capillary phase of enhancement, as evidenced by high signal intensity of the body of the pancreas (arrow, *a*) and contrast in portal veins (arrowheads, *a*). Cortical enhancement has developed in a delayed fashion and is apparent at 45 s. The combination of obstruction associated with reflux has resulted in variation in calyceal dilatation and tissue pressure experienced by the different regions of the kidneys. The result is severe irregularity of the renal cortex (arrows, *b*). (Reproduced with permission from Kettritz U, Semelka RC, Brown ED, Sharp TJ, Lawing WL, Colindres RE: MR findings in diffuse renal parenchymal disease. *J Magn Reson Imaging* 1: 136–144, 1996.)

wall disease may be further subdivided into large-vessel, medium-vessel, and small-vessel disease.

Ischemic nephropathy results from atherosclerotic disease of the main renal artery. Concomitant changes of atherosclerotic disease of the abdominal aorta are virtually always present. MR studies can be tailored to demonstrate both the anatomic change of renal artery disease and the functional consequences of renal artery perfusion and contrast excretion. Anatomic changes of renal artery disease are shown on MR angiographic sequences. The most reproducible technique for demonstrating changes of main artery disease is gadolinium-enhanced 3D gradient-echo MRA [2, 3]. It is critical that, in addition to the 3D reconstructed images, the source images be examined to determine normal arteries (fig. 9.92), the number of arteries, and the presence of stenosis (fig. 9.93). Reconstruction of images in both the coronal and transverse planes is useful. Our practice is to perform maximum intensity projection (MIP) reconstruction in the coronal phase and multiplanar

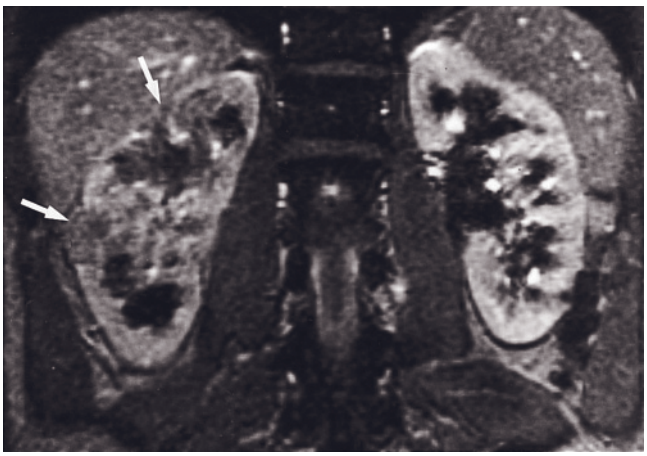

(*a*)

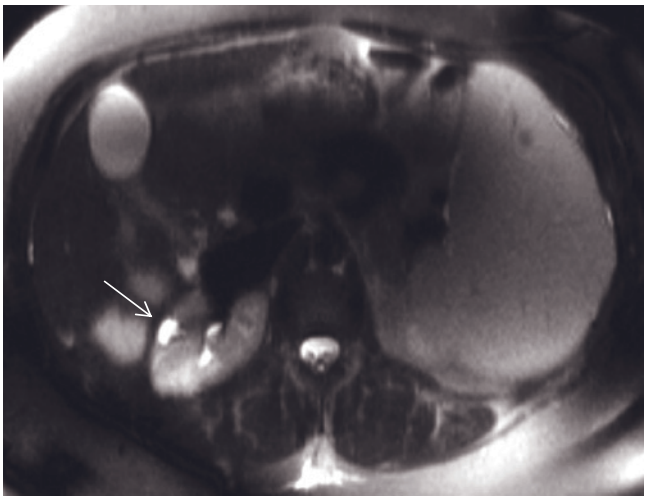

(*b*)

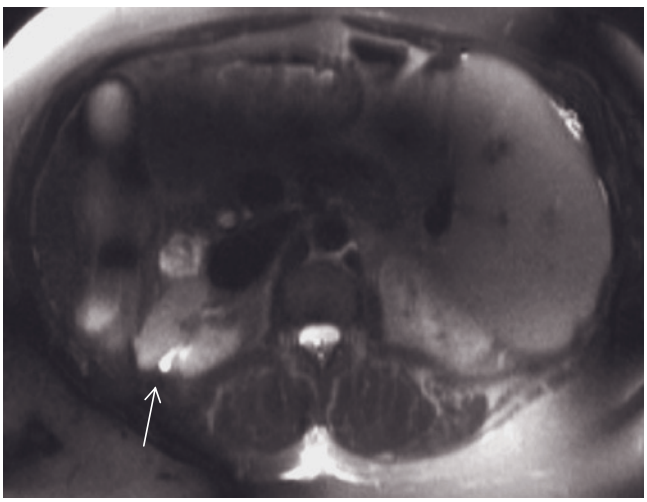

(*c*)

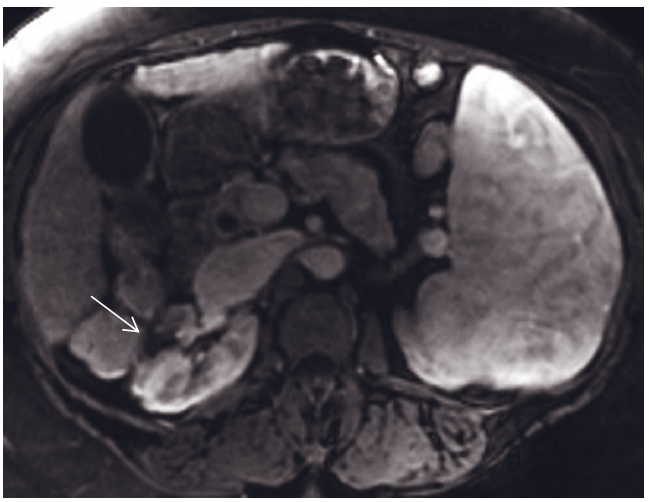

(*d*)

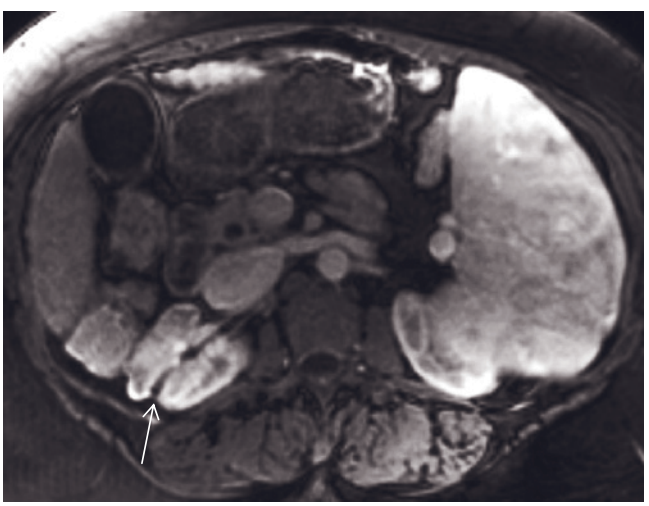

(*e*)

FIG. 9.91 Reflux nephropathy. Coronal 2.5-min postgadolinium gradient-echo image (*a*). Reflux nephropathy of the right kidney is shown by irregular thinning of the renal cortex overlying renal calyces. Damage in this patient is most severe in the upper and midrenal regions (arrows, *a*). T2-weighted fat-suppressed single-shot echo-train spin-echo (*b*, *c*) and T1-weighted postgadolinium hepatic arterial dominant-phase fat-suppressed 3D-GE (*d*, *e*) images demonstrate changes in the renal parenchyma and calyces developing secondary to reflux nephropathy in the right kidney in another patient. The calyces (arrows, *b*–*e*) are dilated, and adjacent renal cortices show scarring and contour irregularities (arrows, *b*–*e*) due to reflux nephropathy.

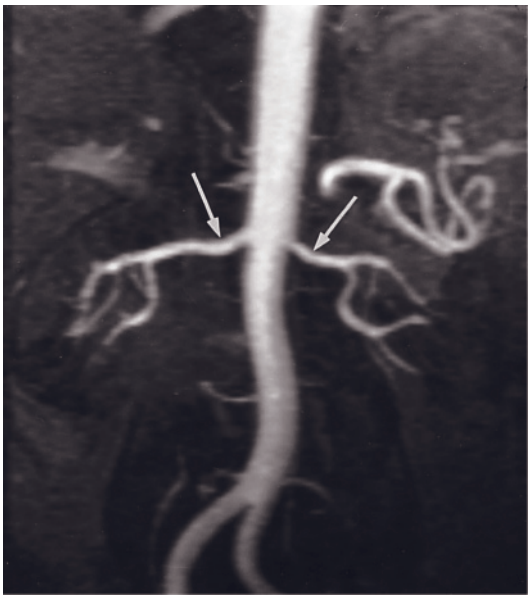

(*a*)

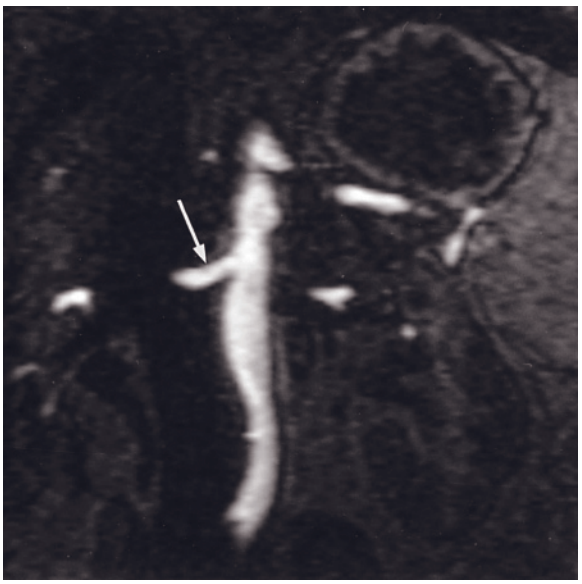

(*b*)

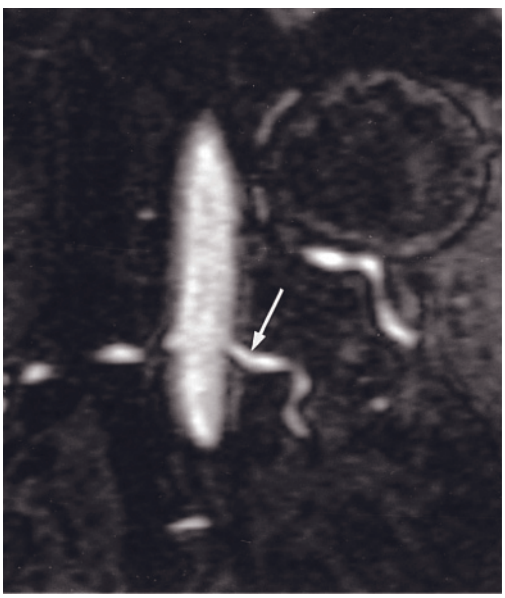

(*c*)

FIG. 9.92 MR angiogram with coronal 3D GE. Coronal MIP reconstructed image (*a*) and individual 2-mm-thin 3D gradient-echo source images of right (*b*) and left (*c*) renal artery origin. The MIP reconstructed image displays a normal aorta and renal arteries (arrows, *a*). Areas of stenosis, however, can be masked in reconstructed images. The individual source images of the right (arrow, *b*) and left (arrow, *c*) renal artery are normal.

reformatting (MPR) in the transverse plane. One study [106] described gadolinium-enhanced MR angiography as an accurate method for the diagnosis of renal artery stenosis, with sensitivities and specificities ranging from 97% to 98% and 90% to 100%, respectively. Sensitivity and specificity were calculated for detection of only grade 2 stenosis and for detection of stenotic or occlusive disease (e.g., stenosis >50%, including occlusions). Another study [107] assessed the ability of dynamic gadolinium administration to demonstrate renal artery stenosis and renal stent patency, using conventional angiography as the gold standard. Severity of renal artery stenosis was classified correctly with an accuracy of 98%, yielding 98% specificity and 100% sensitivity. The renal stents were visualized with 100% accurate patency documentation. The renal arteries are more clearly demonstrated if fat suppression is added to the MRA sequence to remove the competing high signal intensity of fat and render small enhanced vessels more conspicuous. Imaging with 3D sequence acquisition achieves section thickness of 1–2 mm, which markedly improves detection of stenosis.

Kidneys with chronic ischemic nephropathy typically are small and smooth and show minimal early

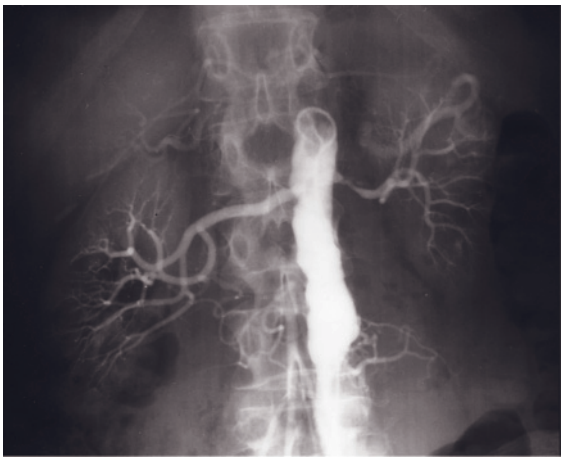

(*a*)

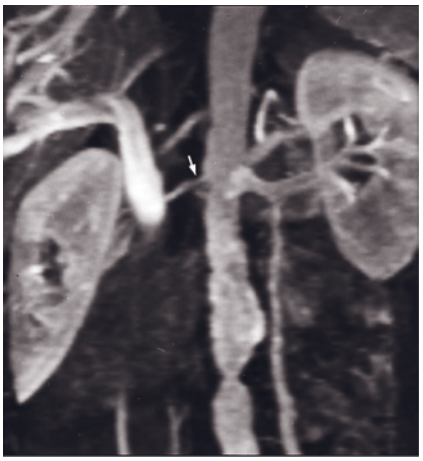

(*b*)

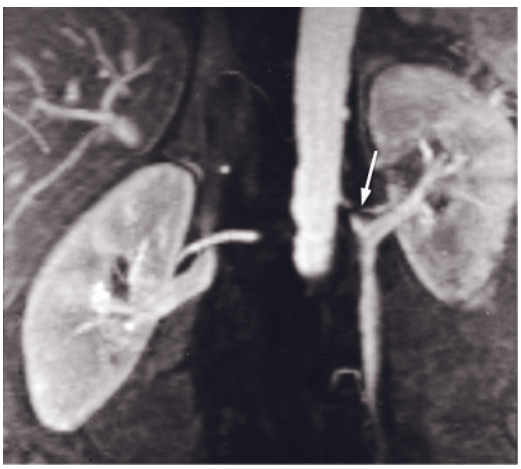

(*c*)

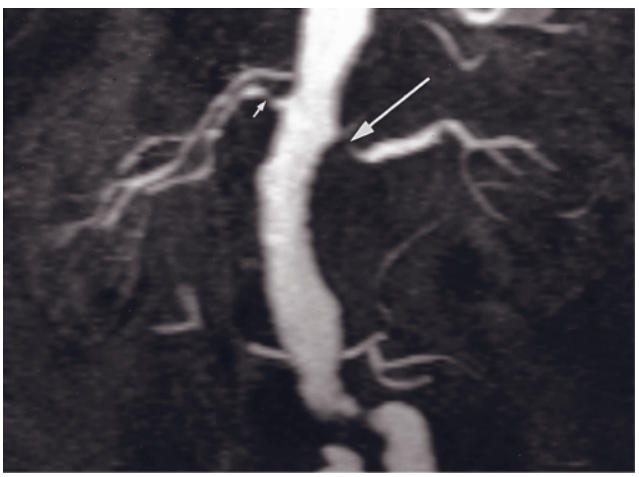

(*d*)

(*e*)

FIG. 9.93 Renal artery stenosis. Angiogram (*a*) and tailored 3D MIP projections, using an interactively selected volume of interest of a gadolinium-enhanced 3D FISP sequence (*b*, *c*). Mild stenosis of the right and severe stenosis of the left renal artery are shown on the angiogram. MIP tailored for the right renal artery demonstrates minimal stenosis (arrow, *b*). MIP tailored for the left renal artery demonstrates severe stenosis (arrow, *c*). Coronal 3D MIP gadolinium-enhanced 3D gradient echo (*d*) in a second patient demonstrates 2 right renal arteries with moderate stenosis of the lower artery (short arrow, *d*) and moderately severe stenosis of a solitary left renal artery (long arrow, *d*). Breath-hold gadolinium-enhanced MR angiography is efficient at depicting the main as well as accessory renal arteries, which is important for preoperative planning (e.g., surgical repair of atherosclerotic aneurysms of the abdominal aorta). MIP reconstructed MRA projection (*e*) and coronal 3D thin-section source (*f*) images.

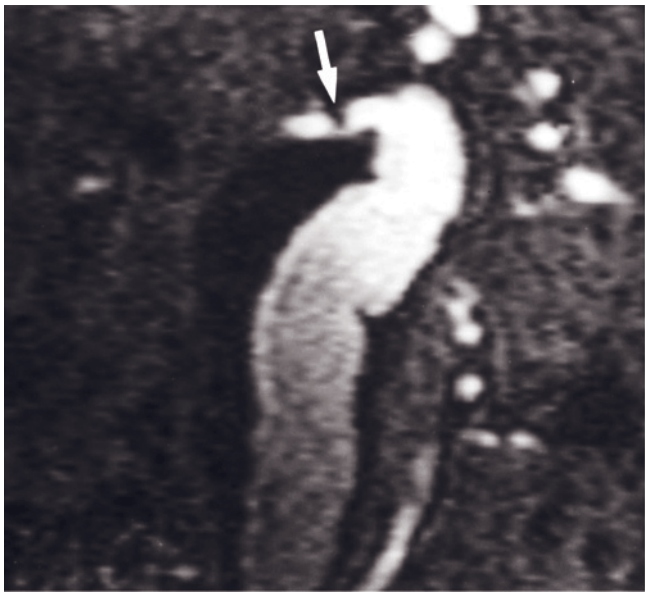

(*f*)

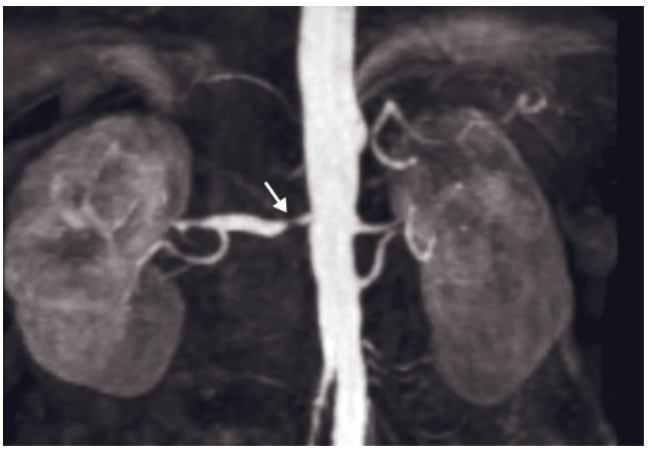

(*g*)

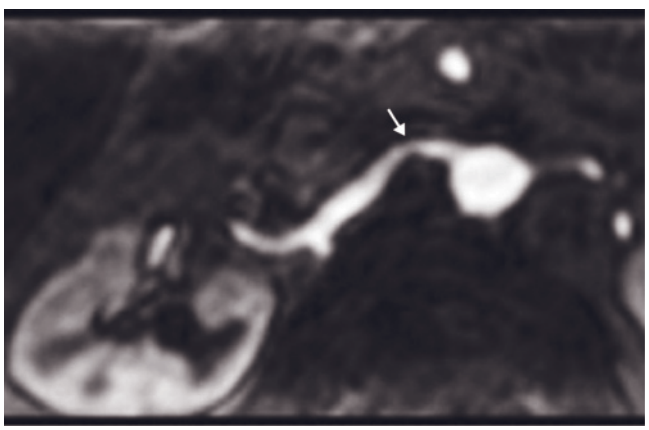

(*h*)

FIG. 9.93 (*Continued*) On the MIP reconstructed image, a short segment of right renal artery is not visualized. On the basis of this image, it is not clear whether this represents stenosis or occlusion. The source image demonstrates that there is a short segment of high-grade stenosis (arrow, *f*). Coronal 3D MIP reconstruction of gadolinium-enhanced source image (*g*) and transverse 3D GE thin-section source image (*h*) in a third patient show mild stenosis at the right renal artery origin (arrows, *g*, *h*).

enhancement on immediate postgadolinium images with delayed development and persistence of CMD (fig. 9.94) [96, 107]. The renal cortex is uniformly thin and frequently smooth, which reflects the global and chronic nature of the ischemic injury (fig. 9.95).

Aortic dissection also may result in changes of diminished renal arterial blood flow to the kidney fed by the false lumen [108]. This may occur either by occlusion/thrombosis of the renal artery by the intimal flap or false channel or by decreased arterial flow through the renal artery fed by the false lumen. Capillary-phase gadolinium-enhanced imaging is effective at demonstrating differences in enhancement between the kidneys, where one is fed by the true lumen and the other (usually the left) is fed by the false lumen (fig. 9.96) [109].

Renal artery pseudoaneurysms are not rare. They may undergo rupture or may come to clinical attention because of pressure effects on other structures. MRA is an effective technique to evaluate size, location, and appearance of pseudoaneurysm (fig. 9.97).

Renal artery injury sustained by trauma or surgery may result in changes of ischemic nephropathy (fig. 9.98). This may result in an acute or chronic ischemic process depending on the time of occurrence. The degree of renal artery compromise affects the extent of renal parenchymal changes. Associated perirenal hemorrhage is usually present.

Fibromuscular dysplasia is a disease that affects the main renal arteries. The disease is characterized by fibrous or fibromuscular thickening affecting any layer of the blood vessel wall. Stenosis of fibromuscular dysplasia often can be differentiated from atherosclerotic stenosis based on the segmental nature of the former, with alternating portions of luminal expansions and narrowings (fig. 9.99). Gadolinium-enhanced 3D MRA may be the most accurate MRI method for demonstrating

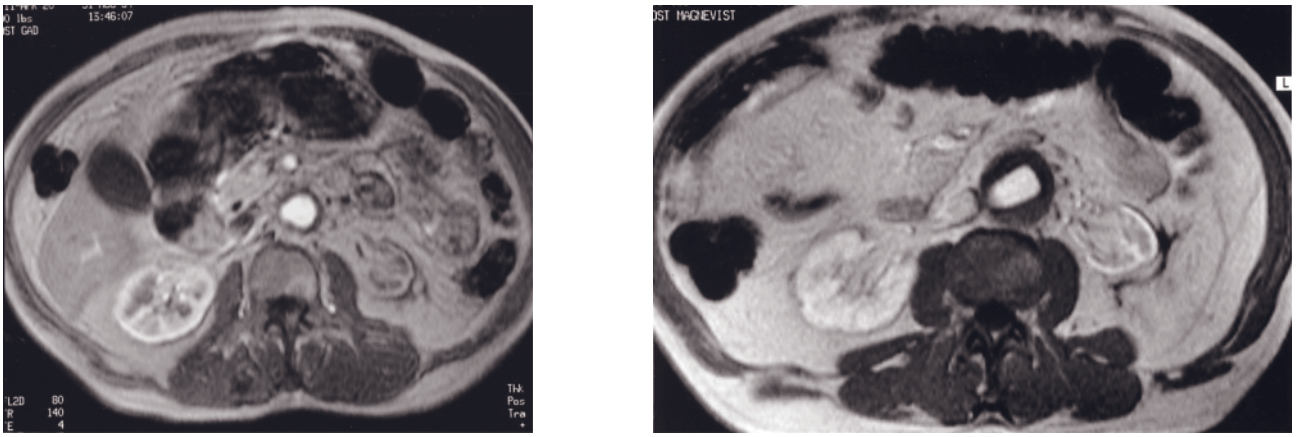

(*a*) (*b*)

FIG. 9.94 Ischemic nephropathy. T1-weighted immediate (*a*) and 2-min (*b*) postgadolinium SGE images in 2 patients. In these patients atherosclerotic disease of the aorta is present, and the involved left kidney is small and smooth and has uniform cortical thinning. The diseased kidney enhances in a diminished fashion compared to the normal right kidney on immediate postgadolinium image (*a*). Corticomedullary differentiation develops later and persists in a more prolonged fashion on late-phase image (*b*).The renal collecting systems are normal in caliber, which is an important observation to exclude obstructive nephropathy.

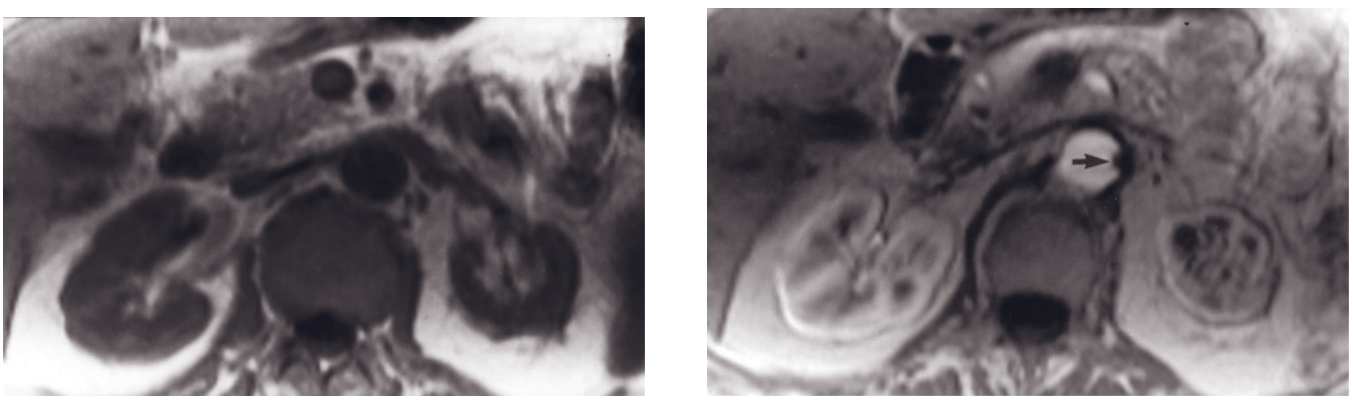

(*a*) (*b*)

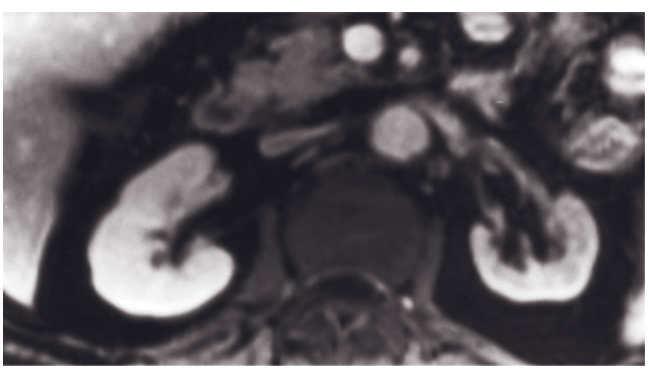

(*c*)

FIG. 9.95 Ischemic nephropathy. T1-weighted precontrast (*a*) and immediate (*b*) and 90-s fat-suppressed (*c*) postgadolinium SGE images. The left kidney is uniformly small, with uniform thinning of the renal cortex observed on postcontrast images (*b*, *c*). Cortical enhancement of the ischemic kidney is diminished on the immediate postgadolinium image (*b*) but shows prolonged and increasing intensity at 90 s (*c*), when corticomedullary differentiation in the contralateral kidney has faded. Note a small, low-signal focus along the left aspect of the aortic wall, which represents atheromatosis plaque at the origin of the left renal artery (arrow, *b*).

(*a*)

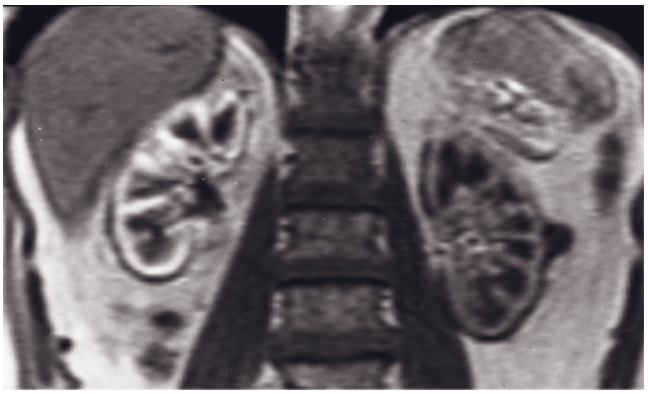

(*b*)

FIG. 9.96 Aortic dissection with differential renal perfusion. Coronal MIP reconstructed projection of coronal immediate postgadolinium 2D SGE image (*a*) and coronal 2D immediate postgadolinium source SGE image (*b*). Aortic dissection (small arrows, *a*) is shown on the MIP reconstructed gadolinium-enhanced SGE image (*a*). On an individual coronal source SGE image (*b*), lesser enhancement of the left renal cortex is present, reflecting diminished perfusion of the kidney due to its blood supply arising from the false lumen, which has slower flow.

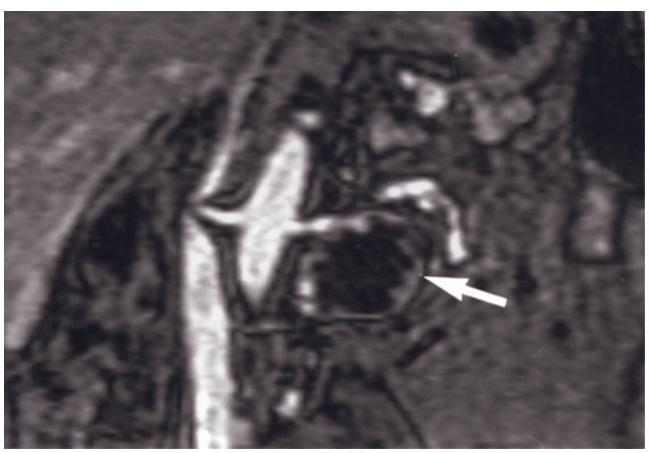

(*a*)

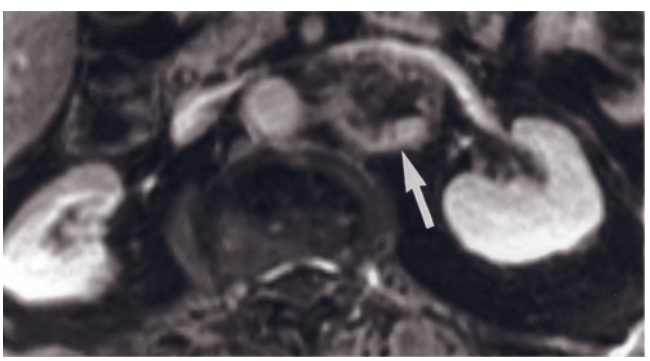

(*b*)

FIG. 9.97 Thrombosed left renal artery pseudoaneurysm. Coronal 3D source (*a*) and transverse 3-min fat-suppressed gadolinium-enhanced SGE (*b*) images. A pseudoaneurysm is identified projecting posteroinferiorly from the left renal artery (arrows, *a*, *b*).The pseudoaneurysm does not fill with contrast on early or late postcontrast images, consistent with thrombosis.

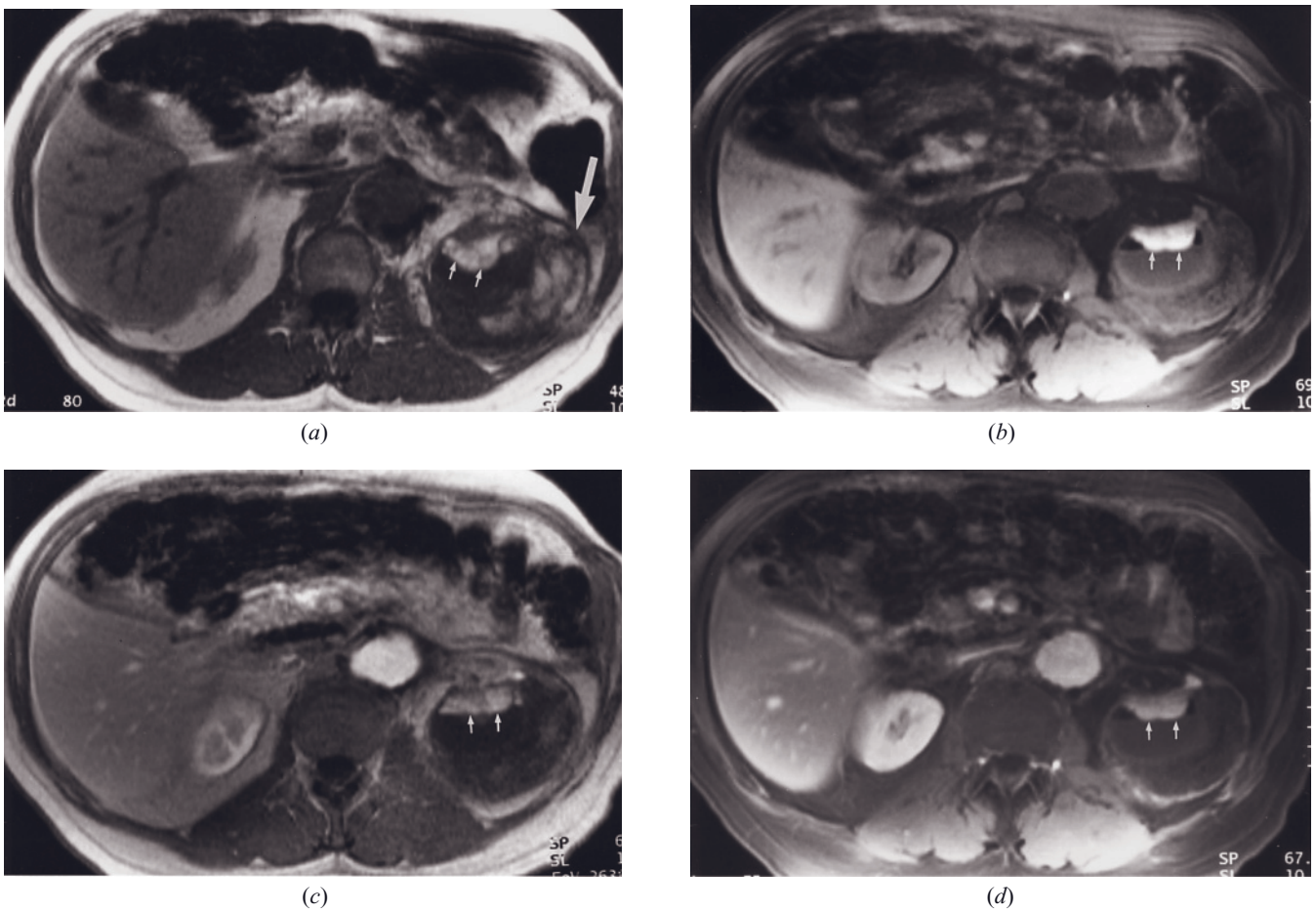

FIG. 9.98 Renal artery injury secondary to abdominal aortic aneurysm surgical repair. T1-weighted precontrast (*a*), precontrast fat-suppressed (*b*), and immediate (*c*) and 90-s fat-suppressed (*d*) postgadolinium SGE images. Abdominal aortic surgery was performed 1 year earlier, in which the left renal artery was injured. The left kidney is atrophic and high in signal intensity on T1-weighted images (small arrows, *a*, *b*), reflecting intraparenchymal hemorrhage. Associated subcapsular fluid collection and high-signal-intensity perirenal fluid (large arrow, *a*) are present. The kidney remains unchanged in signal intensity on postcontrast images (small arrows, *c*, *d*).

this entity. Controlled comparisons with conventional angiography, however, are lacking. Care should be exercised not to misinterpret stepladder image reconstruction artifact for fibromuscular dysplasia. At the present time, MRA may not be a consistent enough technique to demonstrate subtle changes of fibromuscular dysplasia to supplant angiographic approaches.

Medium-vessel disease is often observed in combination with large- or small-vessel disease. Atherosclerotic disease, for example, results in disease of all three types of vessels (fig. 9.100). Various immunologic vasculitides such as Takayasu arteritis, Wegener granulomatosis, or polyarteritis nodosa involve medium and small vessels (fig. 9.101).

Small- vessel disease is a very common cause of renal vascular disease. Nephroscleroses caused by hypertension and/or diabetic angiopathy are the most frequently observed disease entities, but a variety of vasculitides also results in this pattern of renal vascular disease. Antiphospholipase deficiency has more currently received recognition as a cause of severe small-vessel disease. Changes of small-vessel disease are best shown on immediate postgadolinium gradient-echo images as irregular areas of focal cortical thinning or focal perfusion defects [96]. As diabetes and hypertension tend to be chronic and progressive in nature, cortical irregularity is due to irreversible scarring. On serial postgadolinium MR images, areas of cortical thinning appear as fixed irregularities that are unchanged from capillary-phase to interstitial-phase images (fig. 9.102). Vasculitis may be secondary to a number of etiologies, the most common of which are drug effects or collagen vascular diseases. Onset of vascular changes is typically more acute than with diabetes or hypertension. Early in the course of vasculitis, MR images may demonstrate multiple transient perfusional defects that are observed

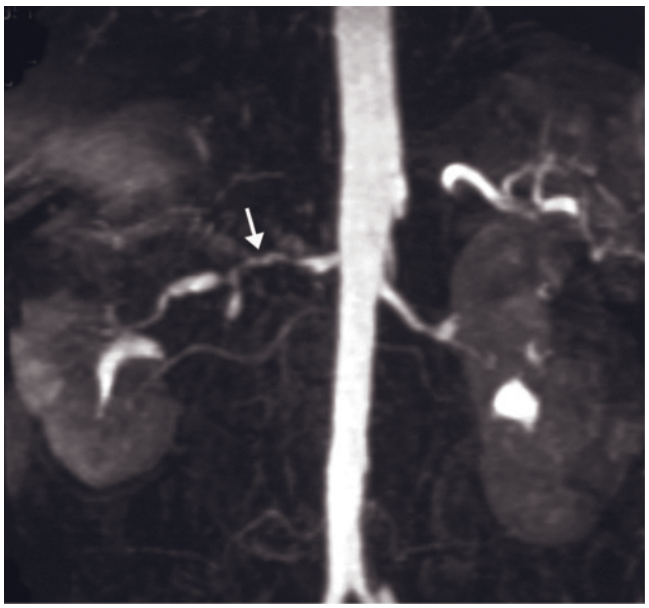

(*a*)

(*b*)

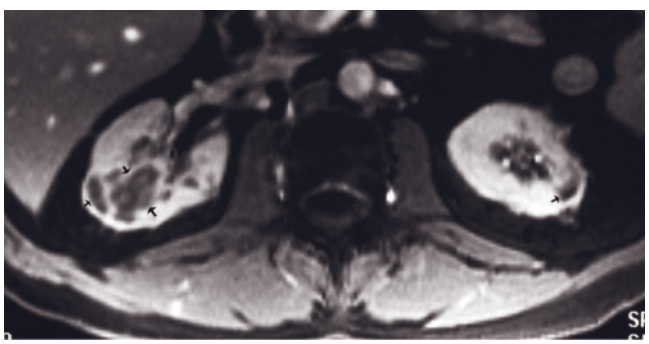

(*c*)

FIG. 9.99 Fibromuscular dysplasia with bilateral renal infarcts. Coronal MIP reconstructed image (*a*), thin-section 3D gradient-echo source image of right renal artery origin (*b*), and 90-s postgadolinium fat-suppressed T1-weighted gradient-echo image (*c*) in a patient with a history of fibromuscular dysplasia. The renal arteries demonstrate irregularities, with a beaded appearance and multiple areas of stricturing, particularly on the right side (arrow, *a*). Bilateral wedge-shaped areas of decreased enhancement are seen on the late-phase images, consistent with infarcts (arrows, *c*) (Courtesy of Günther Schneider, M.D., Ph.D., Department of Radiology, University Hospital of Saarland, Hamburg, Germany).

on immediate postgadolinium gradient-echo images and that resolve on more delayed images (fig. 9.103), which reflect ischemic changes. Acute cortical necrosis may result from rapid-onset diffuse small-vessel disease (fig. 9.104).

Aortic atheroemboli are the most frequent cause of renal emboli [11]. The next most common cause of renal emboli is embolism of cardiac mural thrombi in patients with atrial arrhythmias or prior myocardial infarction. Embolic disease affects the kidneys with some frequency because the kidneys receive approximately 20% of the cardiac output. Renal infarction from embolic events tends to occur between calyces and demonstrates well-defined wedge-shaped defects in the renal outline. A thin enhancing peripheral rim is present because of enhancement of small vessels in the renal capsule (fig. 9.105) [108].

Renal Vein Thrombosis

Renal vein thrombosis may occur as bland or tumor thrombus (see Renal Carcinoma section). Bland thrombus may occur as an acute or chronic process. Acute renal vein thrombosis may be observed in the setting of various hypercoagulable states. In the acute setting, the kidney enlarges because of tissue swelling secondary to the obstruction of egress of blood flow. A progressive and persistent nephrogram is also observed (fig. 9.106). In the setting of chronic thrombosis, the kidney is often normal in size. Association with membranous glomerulonepritis (see Glomerular Disease section) may be observed.

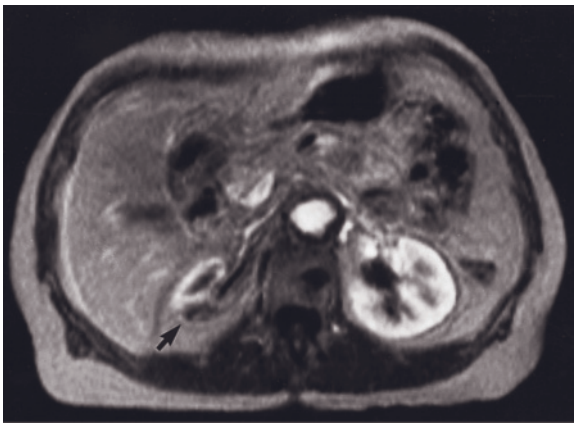

(*a*)

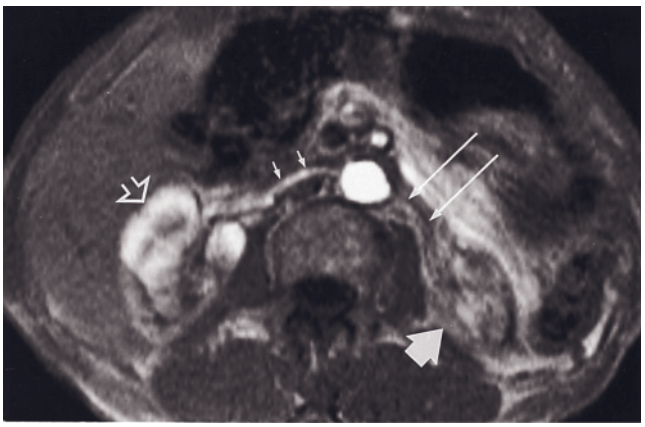

(*b*)

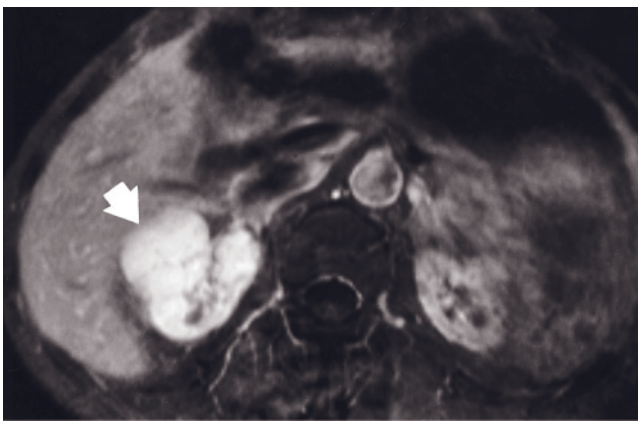

(*c*)

FIG. 9.100 Mixed large-, medium-, and small-vessel disease. T1-weighted immediate postgadolinium SGE image (*a*) demonstrates unilateral renovascular disease The right kidney is noted to be globally small in size with a thin renal cortex. Cortical thinning is greater in the posterior aspect of the kidney (arrow, *a*), associated with greater decrease in enhancement. T1-weighted immediate (*b*) and late-phase fat-suppressed (*c*) gadolinium-enhanced SE images in a second patient demonstrate bilateral renovascular disease. Global severe diminished enhancement of the left kidney and asymmetric renovascular disease of the right kidney are apparent. The posterior portion of the right kidney has severe disease as shown by severe cortical thinning and diminished enhancement (*b*). The main right renal artery is normal in caliber for most of its length (small arrows, *b*), consistent with predominantly medium- and small-vessel disease. The main left renal artery is small in caliber (long arrows, *b*) and, combined with global diminished enhancement of the left kidney (large arrow, *b*), reflects the severity of the main renal artery disease. Hypertrophy of the anterior cortex of the right kidney has developed (open arrow, *b*) in compensation for the renovascular disease of the posterior aspect of the kidney. Uniform cortical thickness with presence of corticomedullary differentiation of the anterior portion of the right kidney on the immediate postgadolinium image shows that the enlargement is due to hypertrophy and not tumor. Later interstitial-phase gadolinium-enhanced T1-weighted fat-suppressed image (*c*) in this patient demonstrates relatively uniform enhancement of this region of renal hypertrophy (large arrow), which mimics the appearance of a tumor. Atherosclerotic disease of the aorta is apparent in both patients.

Renal Vein Aneurysm

Renal vein aneurysm is a rare entity. This entity is well shown with gadolinium enhanced 3D-GRE or MRA techniques in which the patent portion of the aneurysm enhances in the same temporal fashion as the renal vein.

Renal Scarring

Renal scarring results from irreversible damage to renal parenchyma with regional loss of cortex. Scarring arises from a great variety of renal insults, which include vascular and collecting system disease. Scarring defects are well shown on postgadolinium images, with immediate postgadolinium gradient-echo images clearly defining the extent of cortical loss (figs. 9.107 and 9.108).

End-Stage Kidney

End-stage kidney appears as an atrophic diminutive kidney reflecting severe hypovascularity secondary to the loss of renal arterial supply. A variety of diffuse renal

(*a*)

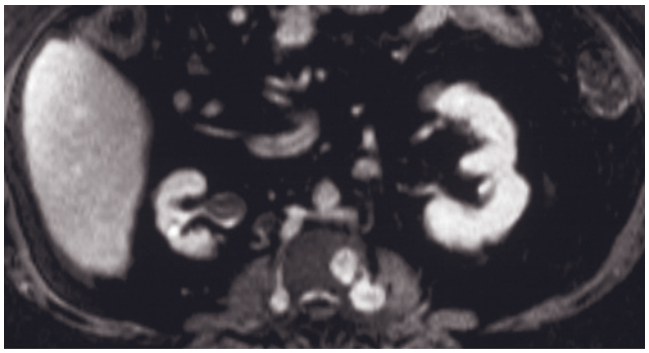

(*b*)

FIG. 9.101 Ischemic nephropathy secondary to Takayasu arteritis. Coronal MIP reconstructed image (*a*) and interstitial-phase postgadolinium T1-weighted fat-suppressed image (*b*) in a patient with Takayasu arteritis. The right kidney is decreased in size and shows irregular contour. The right renal artery is significantly reduced in caliber (arrow, *a*).

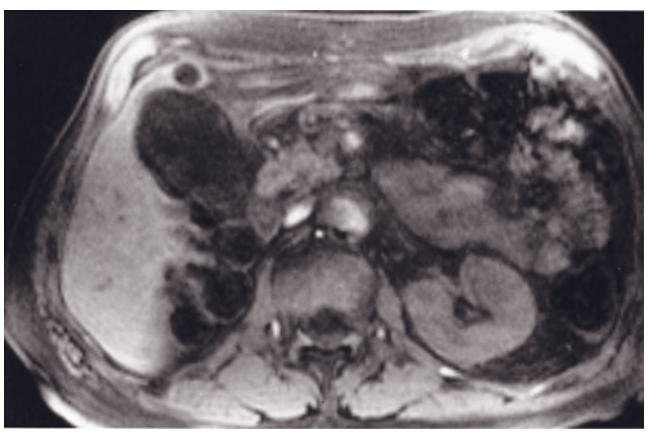

(*a*)

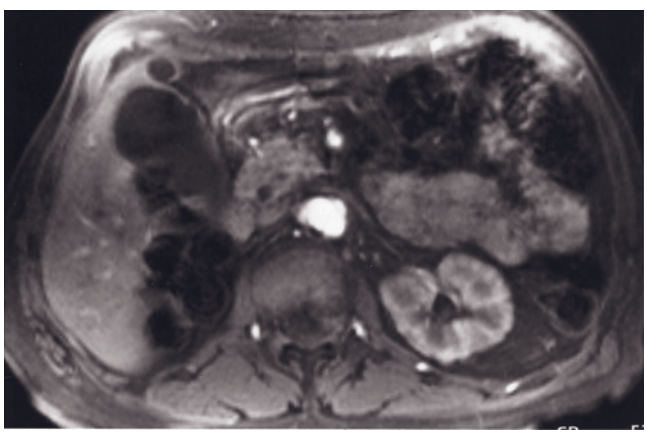

(*b*)

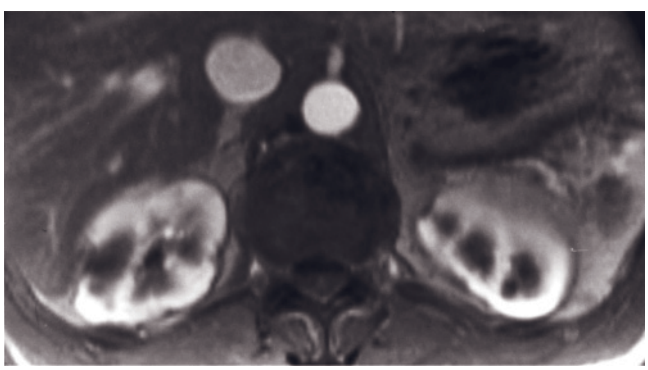

(*c*)

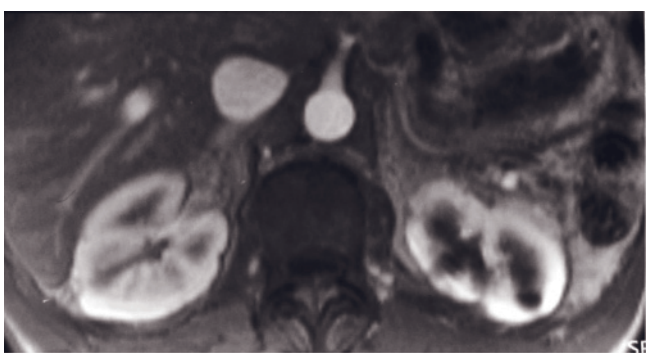

(*d*)

FIG. 9.102 Small-vessel disease. T1-weighted precontrast (*a*) and immediate postgadolinium (*b*) fat-suppressed SGE images. Loss of corticomedullary differentiation in the left kidney is apparent on the precontrast image (*a*), consistent with diminished renal function. On the immediate postgadolinium image (*b*), multiple small cortical defects due to small-vessel disease are present. T1-weighted immediate postgadolinium SGE images (*c*, *d*) in a second patient demonstrate bilateral small, irregular renal cortical defects.

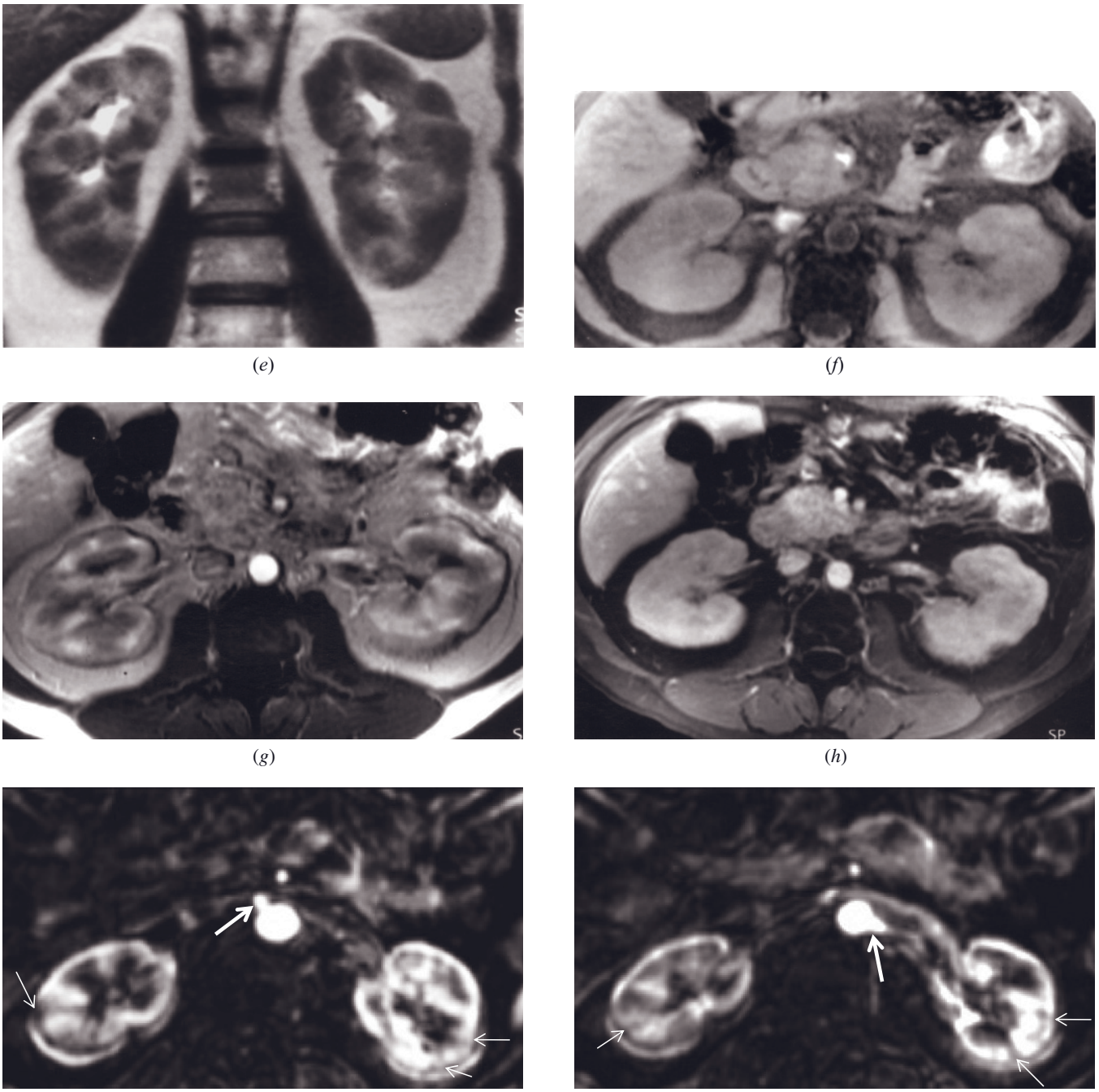

FIG. 9.102 (*Continued*) These changes represent small-vessel disease in this diabetic patient. Coronal T2-weighted SS-ETSE (*e*), T1-weighted precontrast fat-suppressed (*f*), and immediate (*g*) and 90-s fat-suppressed (*h*) postgadolinium SGE images in a third patient with small-vessel disease. This patient is in renal failure, as evidenced by loss of corticomedullary differentiation on precontrast images. Focal patchy areas of diminished enhancement are appreciated on immediate postgadolinium image (*g*), many of which show enhancement by 90 s (*h*). This pattern of enhancement reflects ischemic changes. Transverse reformatted thin-section 3D-GE MRA images (*i*, *j*), coronal 3D MIP 3D-GE MRA image (*k*) and coronal T1-weighted postgadolinium interstitial-phase fat-suppressed 3D-GE image at 3.0 T (*l*) demonstrate small-vessel disease in another patient. Bilateral renal cortices show lesser enhancement than normal, and there are multiple small cortical defects (thin arrows, *i*–*k*) in bilateral renal cortices. Note that the ostia of bilateral renal arteries (thick arrows, *i*, *j*) are normal. Small cortical defects are not seen on the interstitial-phase image (*l*).

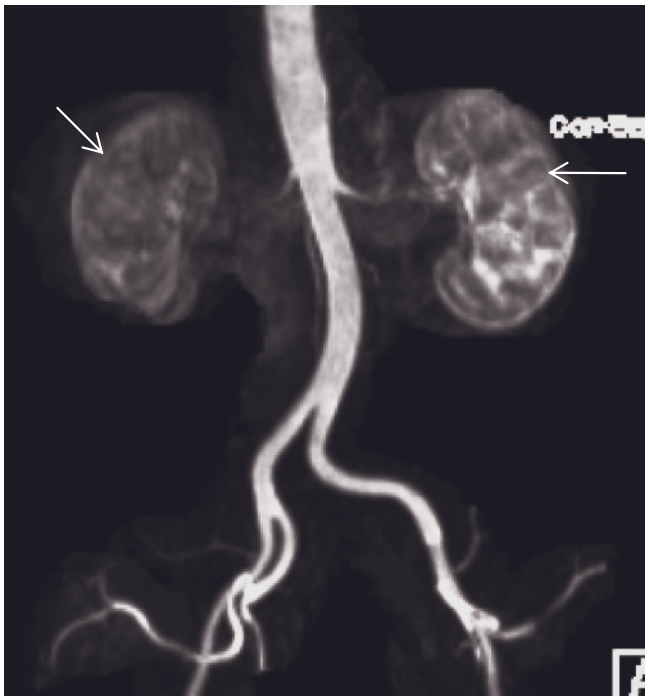

(*k*)

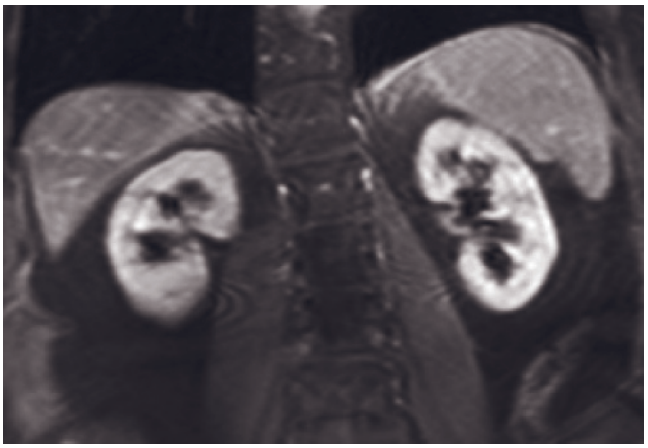

(*l*)

FIG. 9.102 (*Continued*)

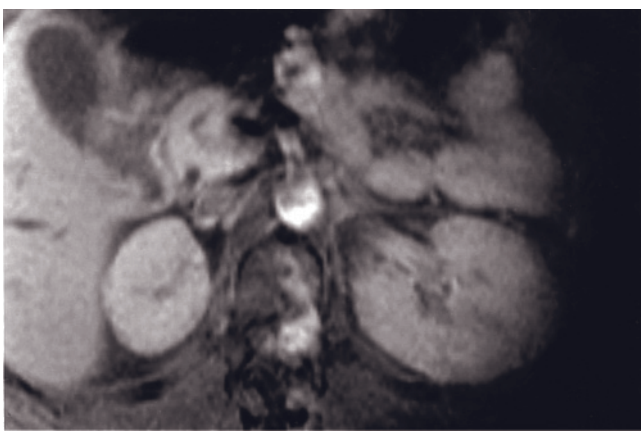

(*a*)

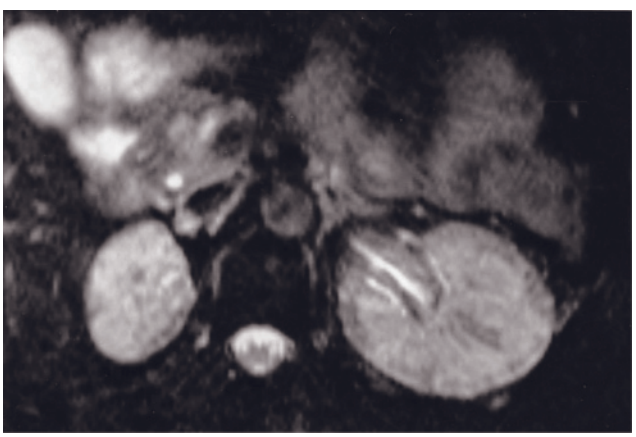

(*b*)

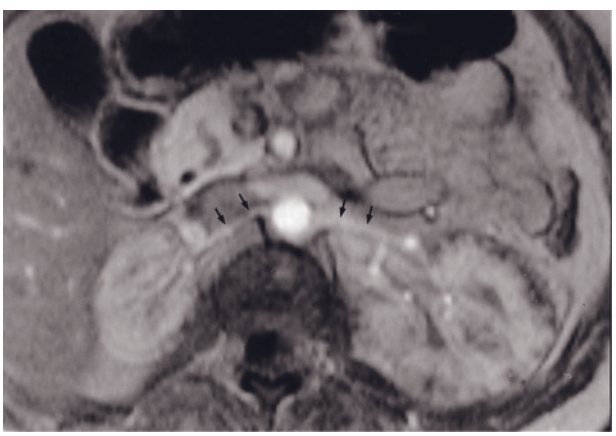

(*c*)

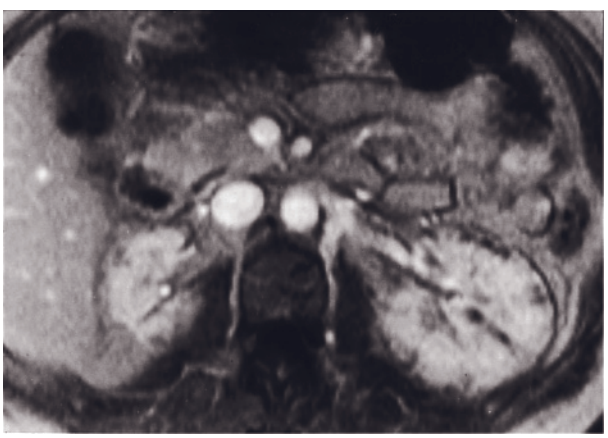

(*d*)

FIG. 9.103 Small-vessel disease due to thrombotic microangiopathy. T1-weighted precontrast fat-suppressed SE (*a*), T2-weighted fat-suppressed SE (*b*), and immediate (*c*) and 90-s (*d*) postgadolinium SGE images. No corticomedullary differentiation is apparent on the precontrast image (*a*). On the T2-weighted image (*b*), numerous 5-mm cortical defects are present. Multiple cortical defects are clearly shown on the immediate postgadolinium image (*c*). In addition, the main renal arteries are noted to be normal (arrows, *c*). On the more delayed image (*d*), some defects have resolved. However, many defects persist, consistent with necrosis. Histology revealed thrombotic microangiopathy with acute tubular necrosis and cortical necrosis.

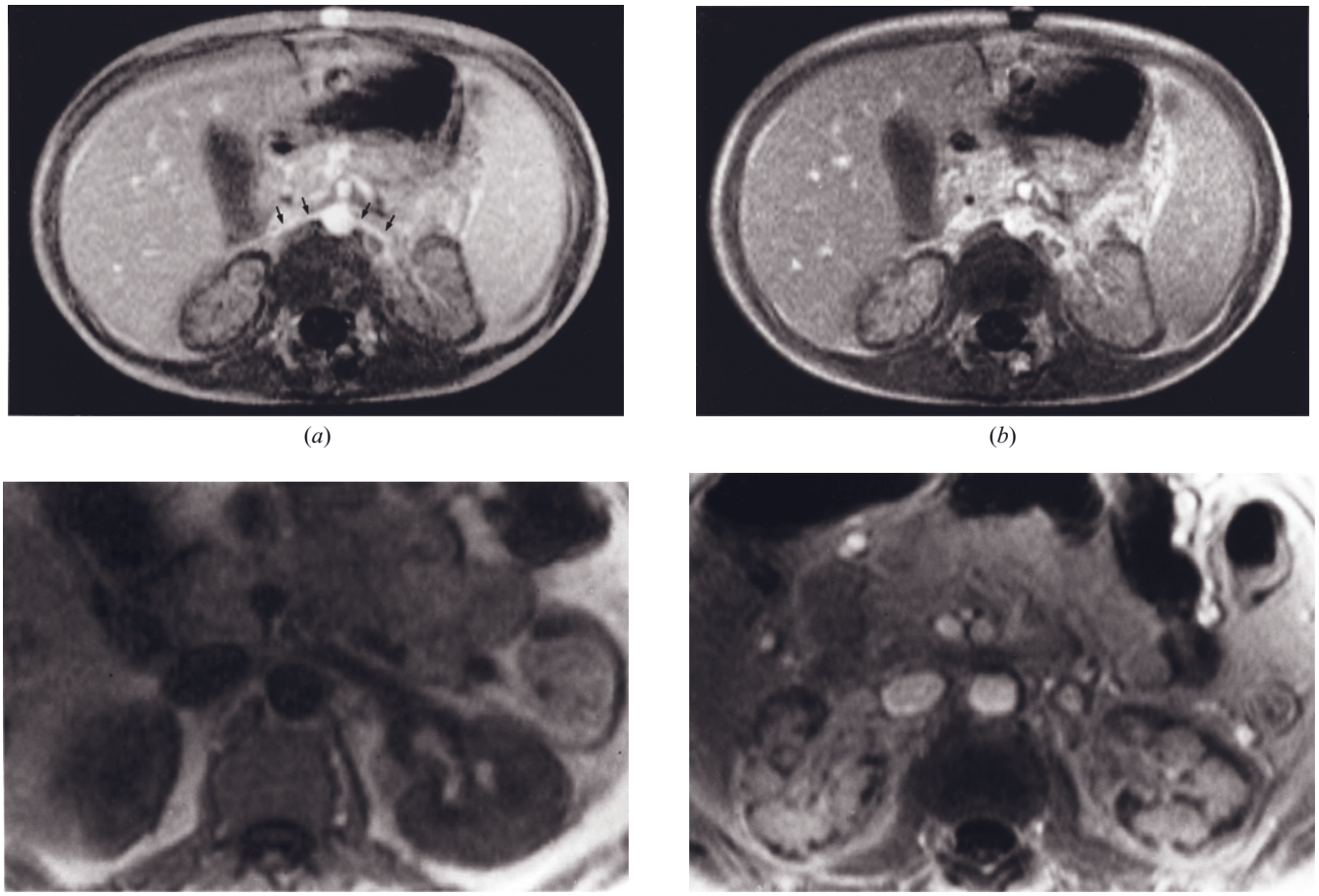

FIG. 9.104 Acute cortical necrosis secondary to small-vessel disease from mixed connective tissue disease. T1-weighted immediate (*a*) and 45-s (*b*) postgadolinium SGE images demonstrate low-signal-intensity renal cortex due to lack of contrast enhancement. This appearance reflects acute cortical necrosis. Normal-appearing main renal arteries are present (arrows, *a*). (Reproduced with permission from Kettritz U, Semelka RC, Brown ED, Sharp TJ, Lawing WL, Colindres RE: MR findings in diffuse renal parenchymal disease. *J Magn Reson Imaging* 1: 136–144, 1996.) T1-weighted precontrast (*c*) and immediate postgadolinium (*d*) SGE images in a second patient with acute cortical necrosis. Extensive irregular linear regions that exhibit lack of enhancement are appreciated on the postcontrast image (*d*).

parenchymal diseases will result in end-stage kidneys, with hypertensive nephropathy the most common cause. Kidneys may be markedly atrophied on MR images and demonstrate the enhancement pattern of scar tissue and negligible capillary-phase enhancement with progressive and minimal enhancement on later postcontrast images (fig. 9.109).

INFECTION

Acute Infection

Acute pyelonephritis is defined as acute suppurative inflammation of the kidney caused by bacterial infection and usually results in enlargement of the infected kidney [109]. The infection is most commonly caused by gram-negative bacilli as an ascending infection from the lower urinary tract. Perinephric fluid may be observed, which is best shown on postgadolinium images (fig. 9.110). Proteinaceous material in the renal tubules may occasionally be visualized as high-signal-intensity substance in the renal medulla on noncontrast T1-weighted fat-suppressed images (see fig. 9.110). MR findings of acute pyelonephritis include a striated nephrogram that radiates from the renal medulla to the cortex, globular renal enlargement, and perinephric fluid (fig. 9.111).

Abscess

Renal abscess usually occurs as a complication of an ascending urinary tract infection, but hematogenous

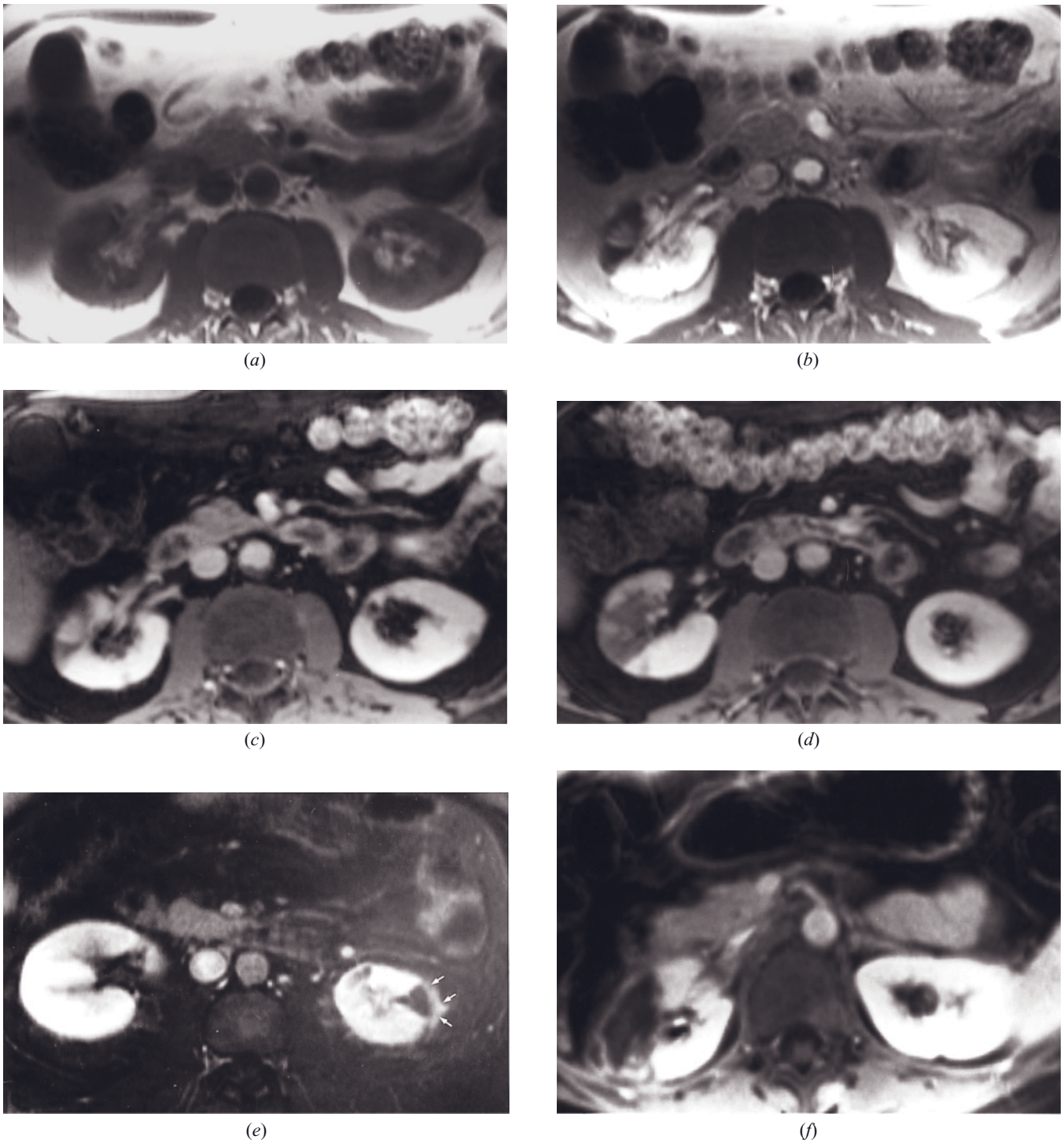

FIG. 9.105 Renal cortical infarcts. T1-weighted precontrast SGE (*a*) and 45-s (*b*) and 90-s fat-suppressed (*c*, *d*) postgadolinium SGE images. There are multiple peripheral wedge-shaped areas of decreased enhancement within the kidneys. A focus of central enhancement is noted within a wedge-shaped defect (*b*, *c*) in the right kidney. The wedge-shaped defects are consistent with areas of infarct, with central sparing in one of the infarcts. T1-weighted interstitial-phase fat-suppressed gadolinium-enhanced SE image (*e*) in a second patient demonstrates a nearly signal-void wedge-shaped defect in the inferior pole of the left kidney. Linear enhancement peripheral to the wedge-shaped defect (arrows, *e*) is due to enhancement of capsule-based vessels. This is a classic feature of renal emboli. (Reproduced with permission from Semelka RC, Shoenut JP, Greenberg HM. The kidney. In: Semelka RC, Shoenut JP (eds.), *MRI of the Abdomen with CT Correlation*. New York: Raven Press, 1993. p. 91–118.) T1-weighted 90-s fat-suppressed postgadolinium T1-weighted SE image (*f*) in a third patient. There is a wedge-shaped defect in the midaspect of the right kidney consistent with a renal infarction. Note thin capsular enhancement along the outer margin of the defect.

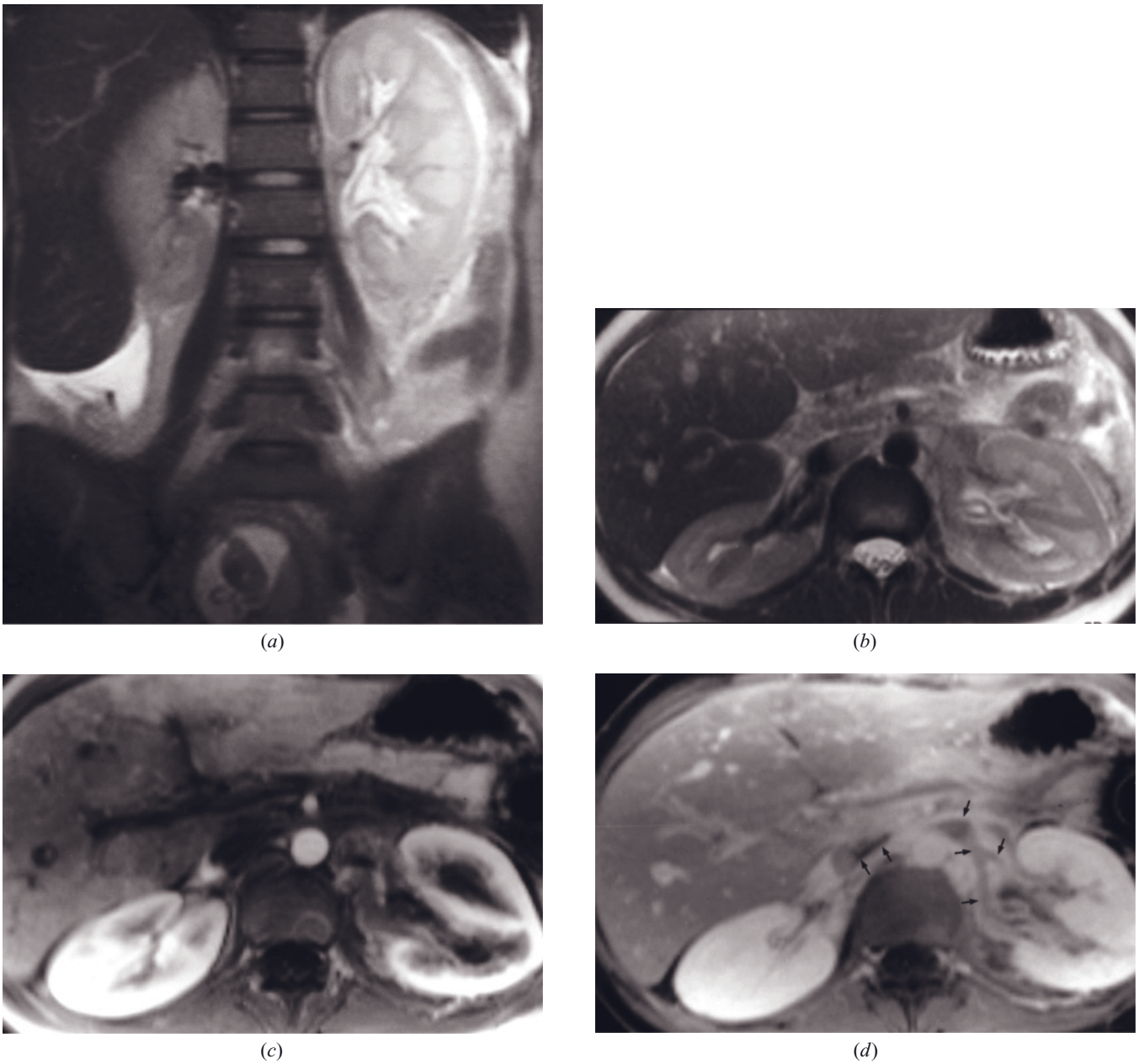

FIG. 9.106 Acute renal vein thrombosis. Coronal (*a*) and transverse (*b*) T2-weighted SS-ETSE and transverse T1-weighted immediate (*c*) and 90-s fat-suppressed (*d*) postgadolinium SGE images. This pregnant patient presented with severe left flank pain. The left kidney is enlarged, and fluid surrounds the collecting system, consistent with edema. Intraluminal clot is appreciated within the left renal vein extending into the IVC (arrows, *d*).

infections also occur [110]. Hematogenous infection may be seen in tuberculosis secondary to disseminated infection, or in the setting of intravenous drug use. On MR images, renal abscesses appear as irregular mass lesions with a signal-void center (figs. 9.112 and 9.113) [111]. Perinephric stranding is frequently prominent [111]. Perinephric linear densities are more prominent in renal abscesses than in necrotic renal cancers because these reflect inflammatory tissue. It may not, however, always be possible to distinguish abscesses from cancer based on imaging findings, and follow-up studies may be needed to ensure resolution after treatment [112]. Patients with multifocal or diffuse renal abscesses frequently have elevated serum creatinine. Ultrasound and noncontrast CT imaging perform poorly at detecting renal abscesses; therefore, MRI may be preferred [111]. However, stable gadolinium chelates should be used with caution because of nephrogenic systemic

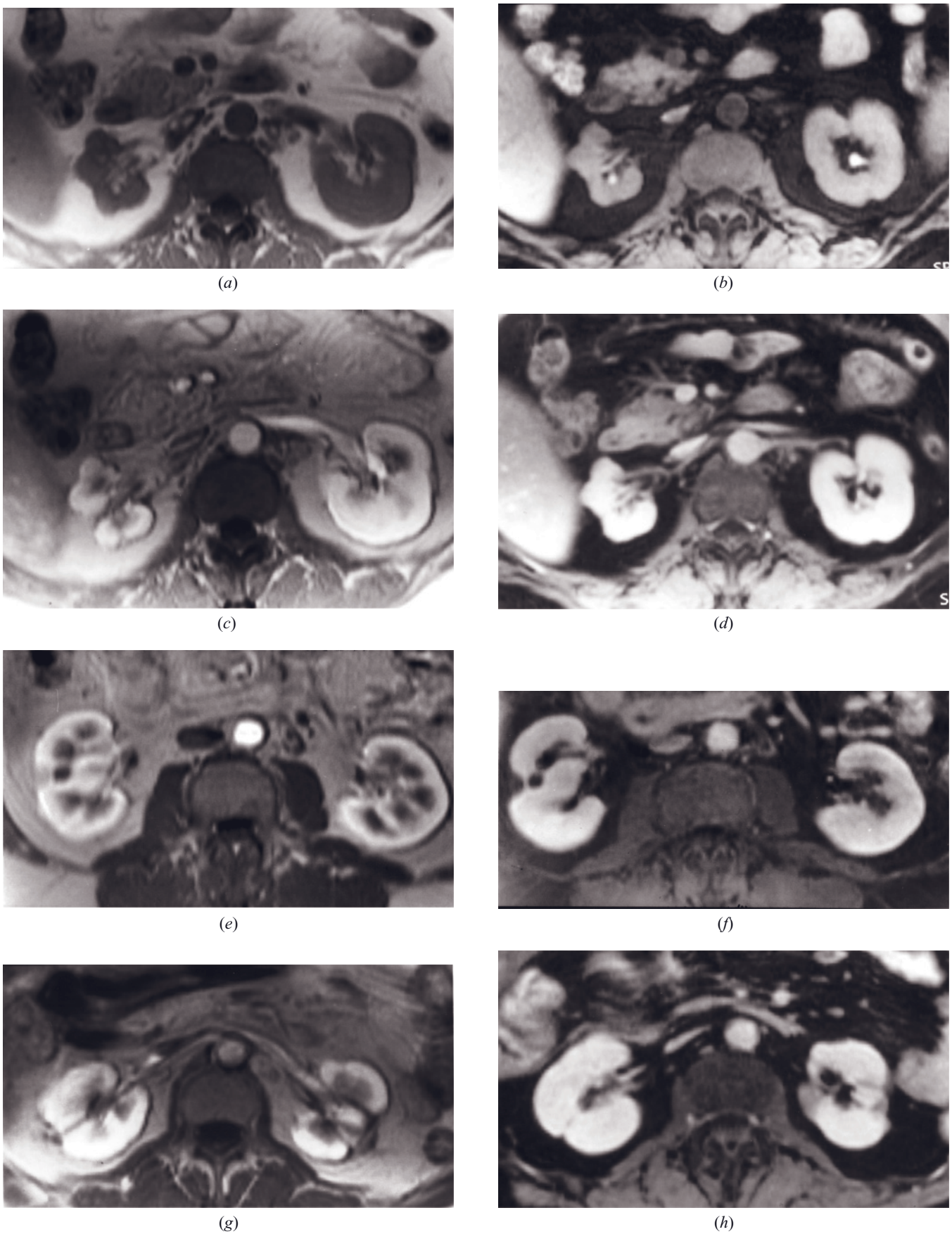

FIG. 9.107 Renal scarring. T1-weighted precontrast (*a*), precontrast fat-suppressed (*b*), and immediate (*c*) and 90-s fat suppressed (*d*) postgadolinium SGE images. The right kidney is small and irregular in contour, consistent with chronic vascular injury, and the left kidney demonstrates compensatory hypertrophy. T1-weighted immediate (*e*) and 90-s fat-suppressed (*f*) postgadolinium SGE images in a second patient demonstrate a cortical defect in the right kidney consistent with a scar. A cyst is noted deep to the infarct. T1-weighted immediate (*g*) and 90-s fat suppressed (*h*) postgadolinium SGE images in a third patient reveal bilateral renal cortical scars more extensive in the left kidney.

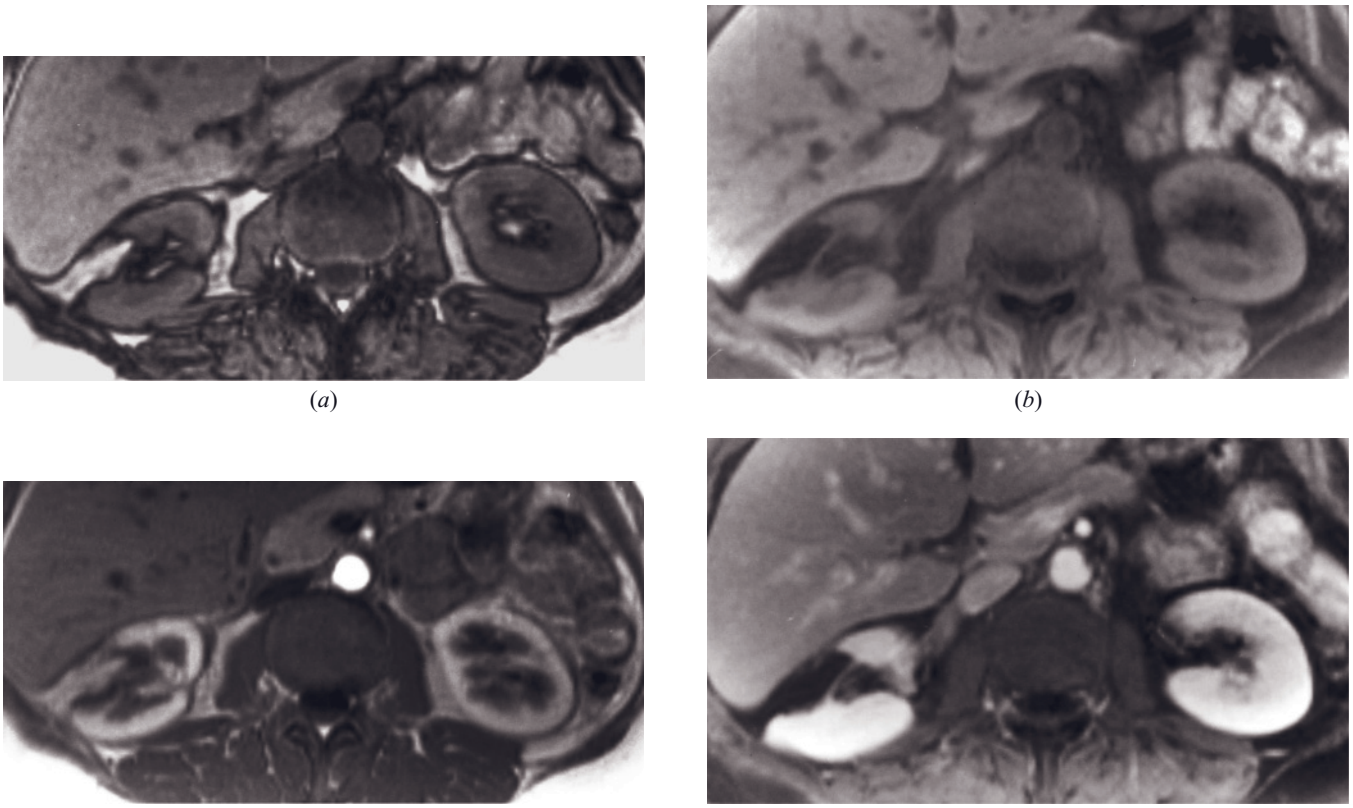

(*a*) (*b*)

(*c*) (*d*)

FIG. 9.108 Segmental nephrectomy. T1-weighted out-of-phase (*a*), fat-suppressed (*b*), and immediate (*c*) and 90-s fat-suppressed (*d*) postgadolinium SGE images. There is a surgical defect in the midpole of the right kidney that has been filled by perirenal fat.

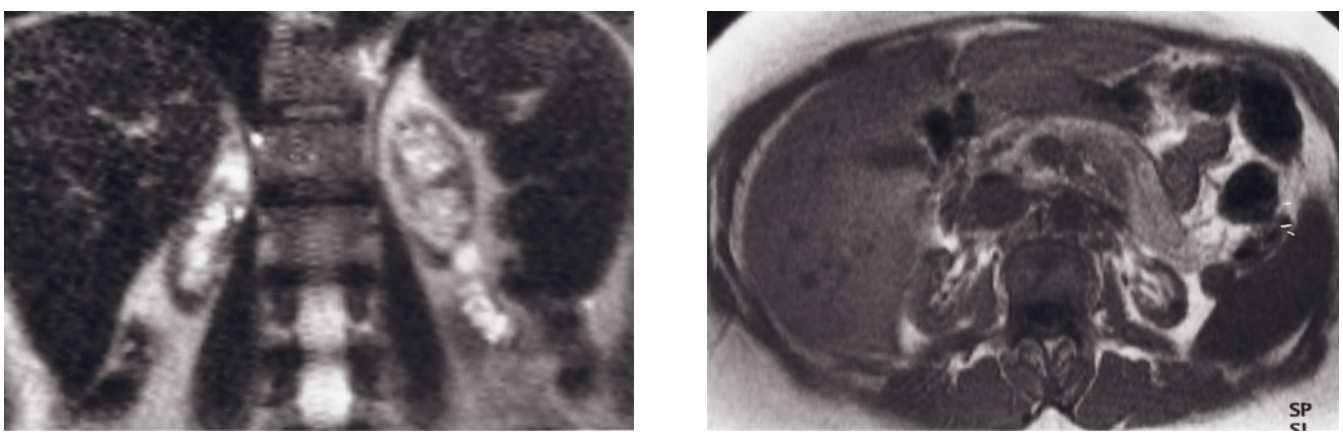

(*a*) (*b*)

FIG. 9.109 End-stage kidneys secondary to sustained hypertension. Coronal T2-weighted SS-ETSE (*a*), transverse T1-weighted precontrast (*b*), and immediate (*c*) and 2-min fat-suppressed (*d*) postgadolinium SGE images. Bilateral diminutive atrophic

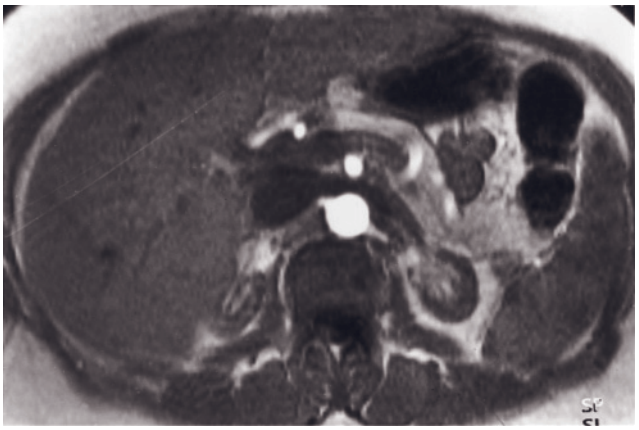

(*c*)

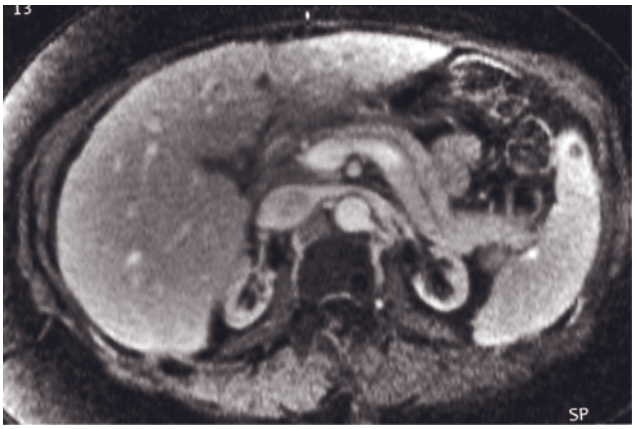

(*d*)

FIG. 9.109 (*Continued*) kidneys are apparent on precontrast images (*a*, *b*). Negligible enhancement is appreciated on the immediate postgadolinium image (*c*). On more delayed image (*d*), renal parenchymal enhancement has increased. This enhancement pattern is observed in fibrotic tissue.

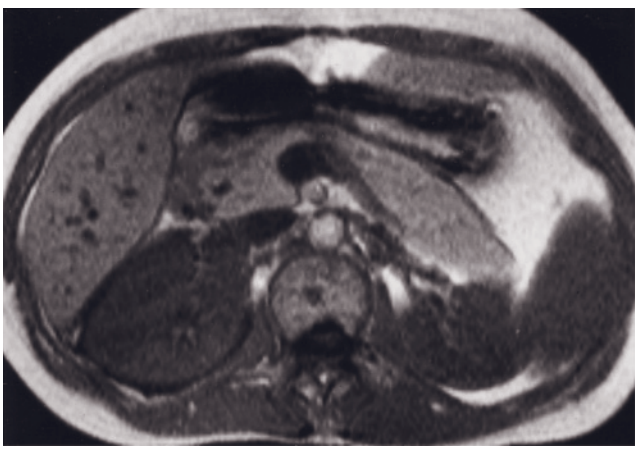

(*a*)

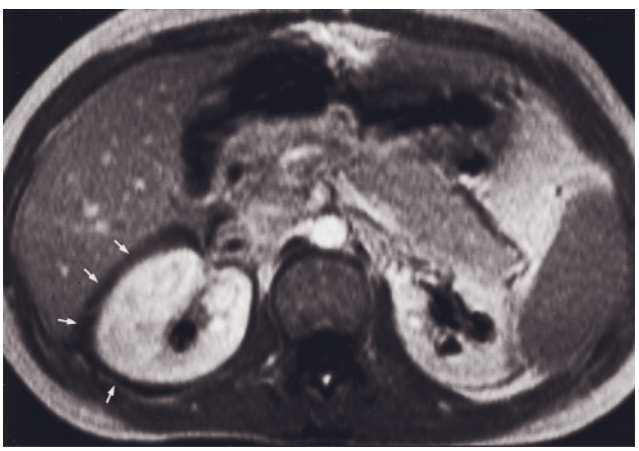

(*b*)

(*c*)

FIG. 9.110 Acute pyelonephritis. T1-weighted precontrast (*a*) and 2-min postgadolinium (*b*) SGE images. The right kidney is swollen, and perinephric fluid (arrows, *b*) is present. No focal parenchymal abnormalities are identified. T1-weighted precontrast fat-suppressed SE image (*c*) in a second patient demonstrates striated, cone-shaped regions of high signal intensity in the medulla of the left kidney, consistent with proteinaceous material in acute pyelonephritis. Hydronephrosis of the right kidney is identified.

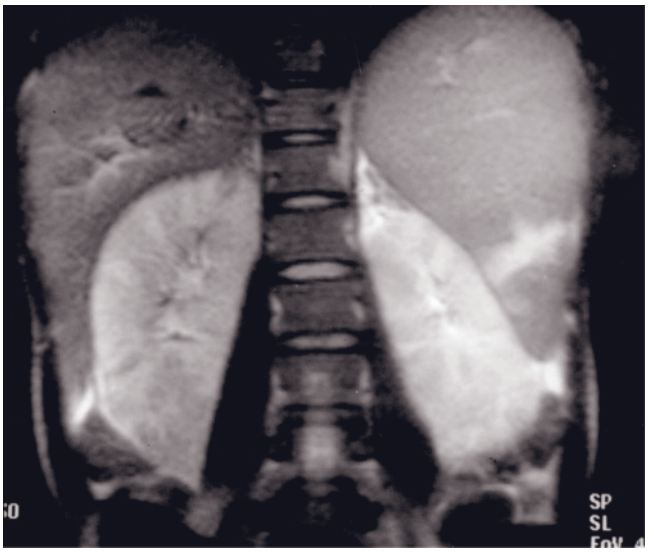

(*a*)

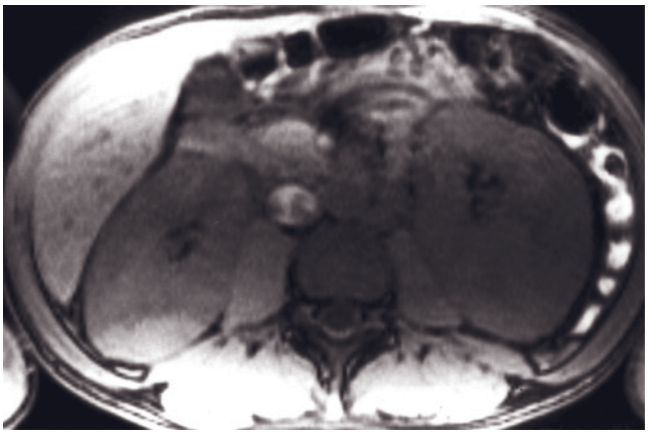

(*b*)

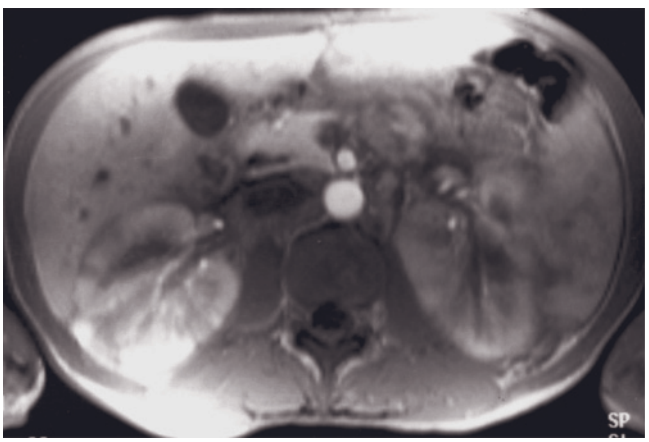

(*c*)

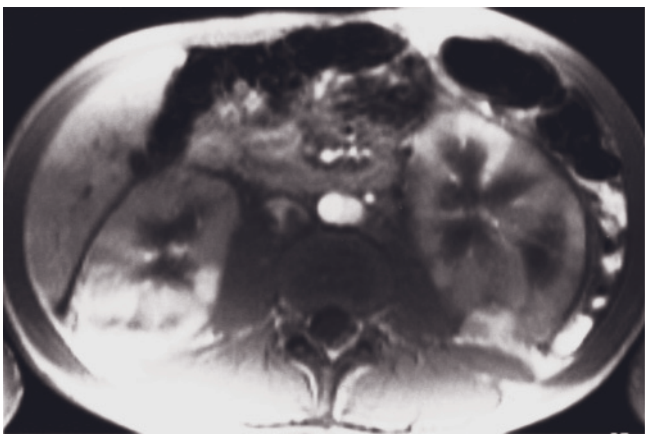

(*d*)

(*e*)

FIG. 9.111 Severe acute bilateral pyelonephritis. Coronal T2-weighted SS-ETSE (*a*) and transverse T1-weighted precontrast (*b*) and immediate postgadolinium (*c*, *d*) SGE images. The kidneys are enlarged and demonstrate heterogeneous signal intensity on T2- and T1-weighted images and heterogeneous enhancement after administration of gadolinium. Note that the heterogeneous enhancement has a striated nephrogram appearance, which is a feature that may be observed in acute pyelonephritis. Coronal T1-weighted SGE and T2-weighted single-shot echo-train spin-echo images (*e*, *f*) demonstrate enlarged right kidney, free fluid adjacent to the inferior pole (arrows, *e*, *f*), and stranding in the adjacent fat tissue (arrows, *e*, *f*) in another pregnant patient with acute pyelonephritis. Based on precontrast images, acute pyelonephritis can be diagnosed in pregnant patients, and gadolinium chelates should not be used in pregnant patients if their use is not deemed essential.

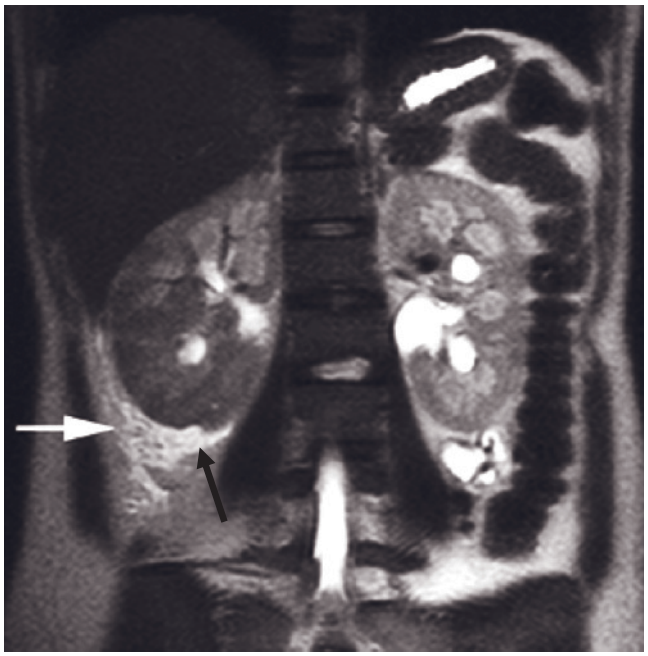

(*f*)

FIG. 9.111 (*Continued*)

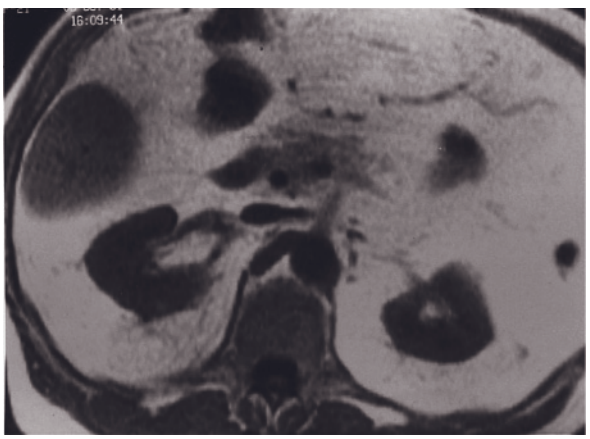

(*a*)

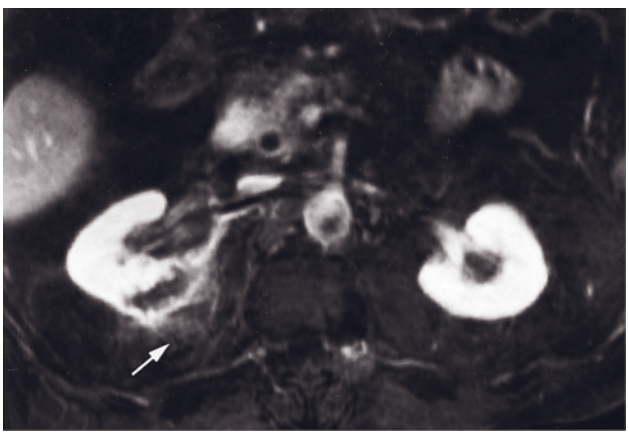

(*b*)

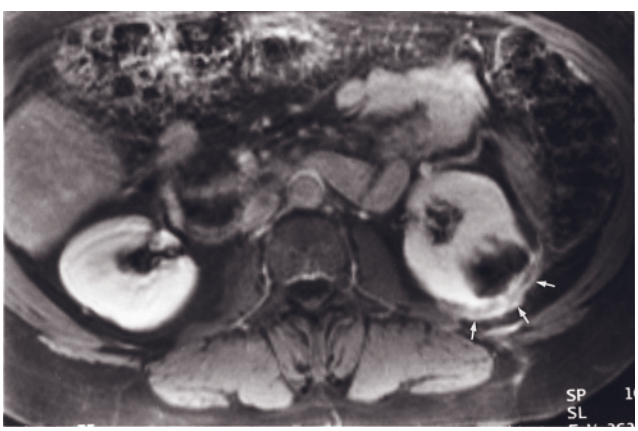

(*c*)

FIG. 9.112 Solitary renal abscess. T1-weighted precontrast SGE (*a*) and late-phase fat-suppressed gadolinium-enhanced SE (*b*) images in a patient with a solitary abscess in the posterior aspect of the right kidney. Perirenal stranding is noted on the precontrast image, but the abscess is not well seen. On the gadolinium-enhanced fat-suppressed image, a signal-void intraparenchymal renal abscess is noted. The inner aspect of the abscess wall is irregular. Prominent perirenal stranding (arrow, *b*) is an important imaging feature of renal abscess. T1-weighted 3-min fat-suppressed postgadolinium SGE image (*c*) in a second patient, who is diabetic. A left renal abscess is present that appears as a low-signal-intensity cystic lesion with an irregular wall. Prominent thickening and increased enhancement of adjacent fascia (small arrows, *c*) are

(*d*)

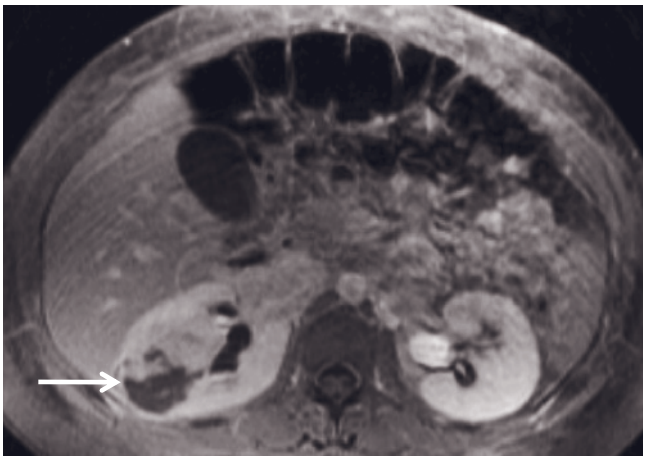

(*e*)

(*f*)

FIG. 9.112 (*Continued*) present. Coronal T2-weighted single-shot echo-train spin-echo (*d*) and transverse (*e*) and sagittal (*f*) T1-weighted interstitial-phase postgadolinium images demonstrate a solitary abscess cavity (arrow, *e*, *f*) in the right kidney in another patient with normal pregnancy. The right kidney is enlarged. Coronal T2-weighted image shows the fetal structures very well (*d*).

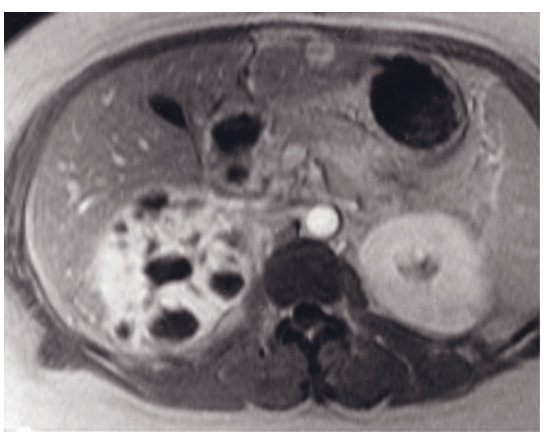

(*a*)

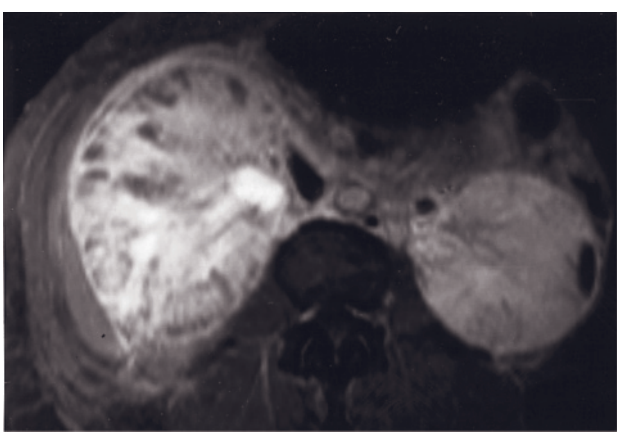

(*b*)

FIG. 9.113 Multiple renal abscesses. T1-weighted 90-s postgadolinium SGE image (*a*) demonstrates multiple signal-void abscesses in the right kidney. T1-weighted fat-suppressed gadolinium-enhanced SE images (*b*, *c*) in a second patient with HIV infection and elevated serum creatinine. Bilateral renal abscesses with substantial renal enlargement are noted on T1-weighted image (*b*). Ultrasound and noncontrast CT imaging demonstrated renal enlargement with no definition of abscesses. A repeat MRI study

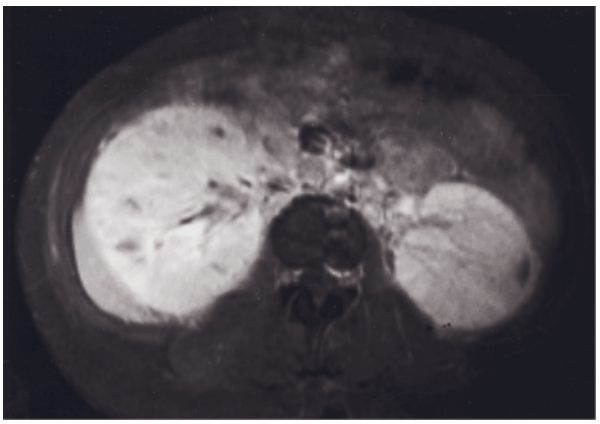

(*c*)

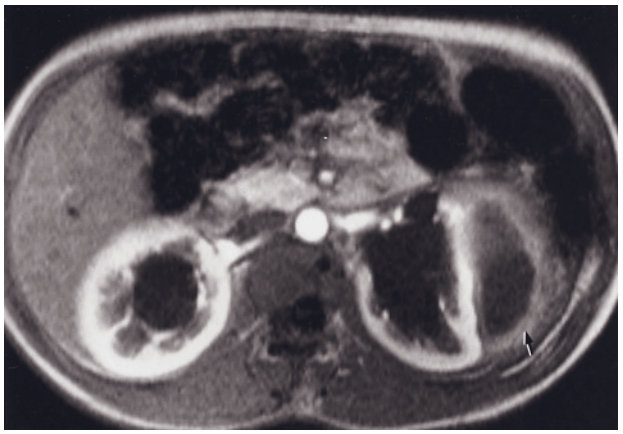

(*d*)

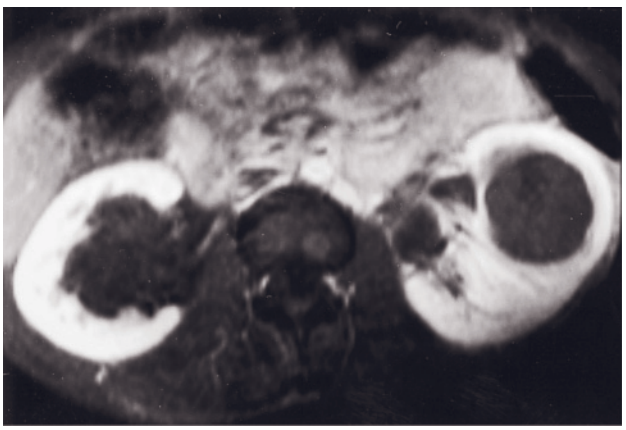

(*e*)

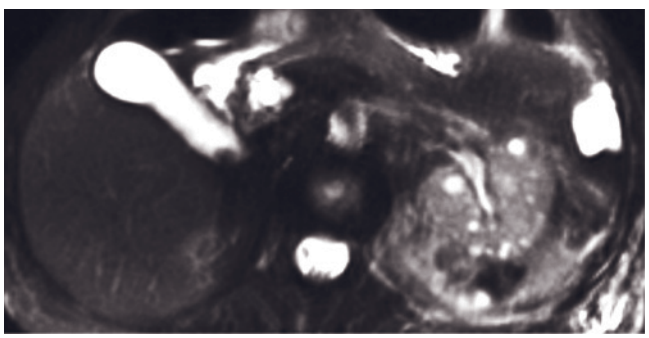

(*f*)

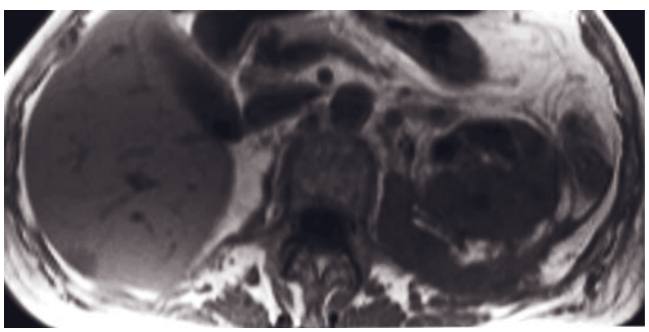

(*g*)

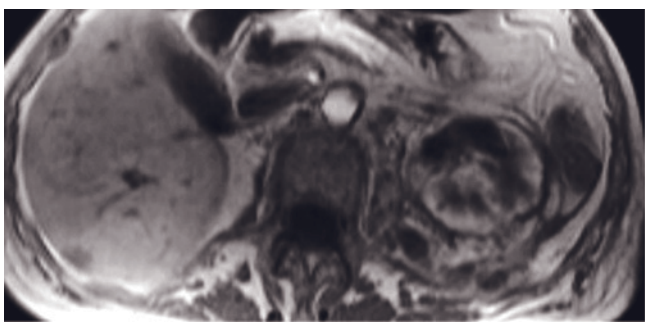

(*h*)

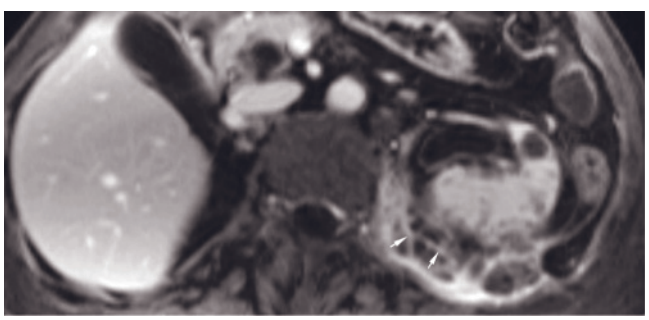

(*i*)

FIG. 9.113 (*Continued*) was performed after a 15-day course of antibiotics (*c*) and showed regression of renal size with decrease in size and number of abscesses. T1-weighted immediate postgadolinium SGE (*d*) and late-phase fat-suppressed postgadolinium SE (*e*) images in a third patient demonstrate a renal abscess with a prominent extrarenal component (arrow, *d*). Multiple parapelvic cysts are present in both kidneys. T2-weighted SS-ETSE (*f*), T1-weighted gradient-echo (*g*), and immediate (*h*) and 90-s (*i*) postgadolinium T1-weighted fat-suppressed gradient-echo images in a fourth patient. There is a complex collection situated posteromedial to the left kidney that demonstrates high signal intensity on T2-weighted images (*f*), low signal intensity on T1-weighted images (*g*), and heterogeneous moderate enhancement on early (*h*) and late-phase (*i*) images. Multiple septations within the collection are best seen on late-phase images (arrows, *i*). Note that multiple small abscesses are appreciated within the kidney.

fibrosis considerations in this group of patients if their administration is necessary (see Chapter 20, *Contrast Agents*).

Xanthogranulomatous Pyelonephritis

Xanthogranulomatous pyelonephritis (XGPN) is an unusual form of chronic pyelonephritis that represents the inflammatory sequela of recurrent suppurative renal infections that develops in the setting of chronic urinary obstruction. The disorder is characterized pathologically by collections of foamy macrophages, "xanthoma cells," acute and chronic inflammatory cells, and multinucleated giant cells. Sixty percent of cases are associated with *Proteus* infection, which usually involves the kidney globally, although focal XGPN has been described [113].

On MR images, the kidney usually is enlarged. After gadolinium administration, minimal enhancement is present on capillary-phase images with progressively intense enhancement on interstitial-phase images (fig. 9.114). This enhancement pattern reflects poor renal perfusion (minimal early enhancement) with substantial capillary leakage due to inflammatory change (increased delayed enhancement). Perinephric inflammatory changes are prominent, with extension to the psoas muscle commonly present. The renal collecting system almost invariably is dilated, and signal-void calculi may be identified. No evidence of gadolinium excretion in the collecting system is appreciated.

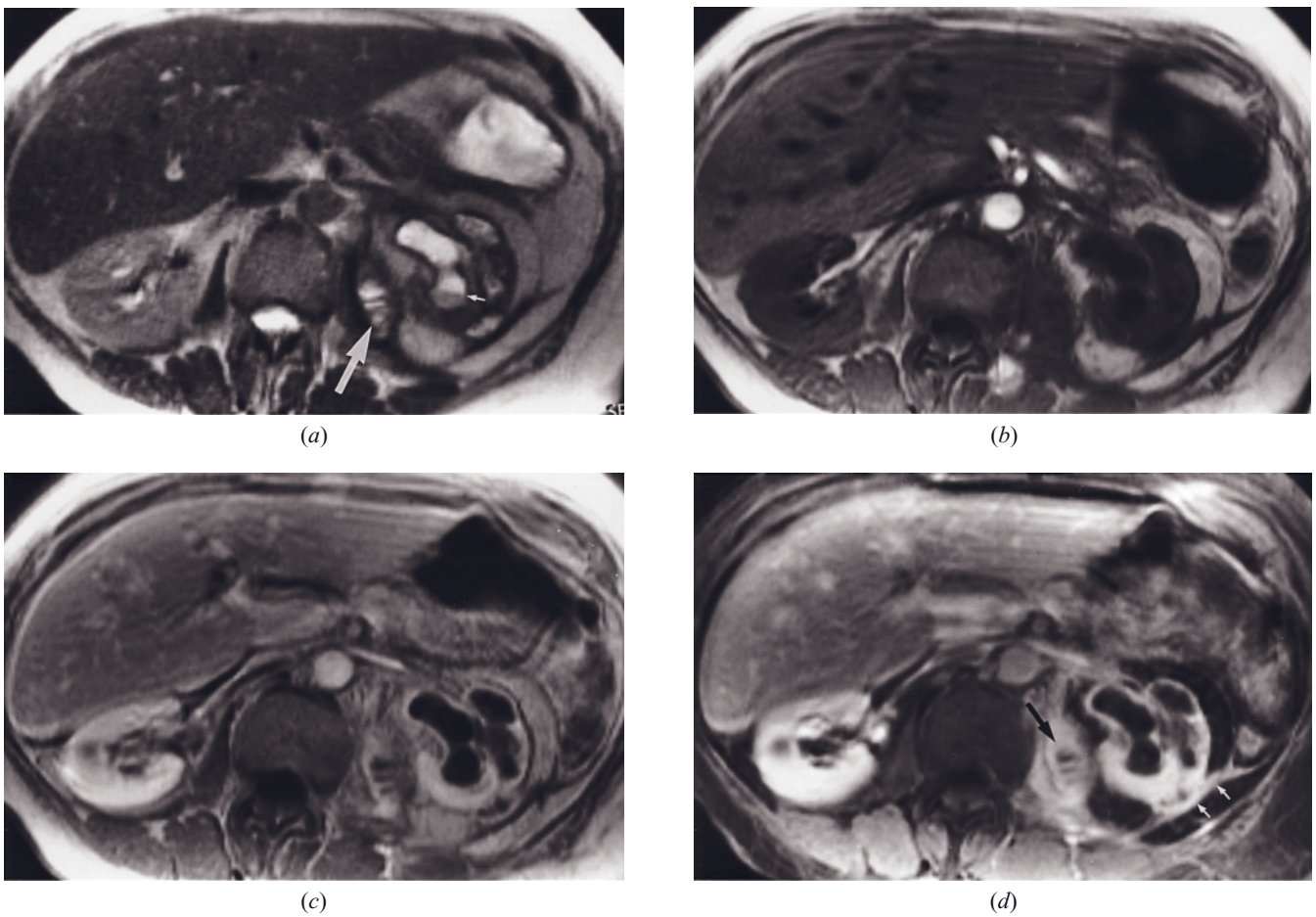

FIG. 9.114 Xanthogranulomatous pyelonephritis. T2-weighted SS-ETSE (*a*) and T1-weighted precontrast (*b*) and 90-s (*c*) and 4-min fat-suppressed (*d*) postgadolinium SGE images. The left renal collecting system is noted to be dilated (*a–d*). A large extrarenal component of the infection is noted in the psoas muscle (arrows, *a*, *d*). Layering of low-signal-intensity material (small arrow, *a*) is noted in calyces on the T2-weighted image. No excretion of gadolinium by the involved kidney is apparent on the 4-min postgadolinium image. Inflammatory changes in Gerota fascia and lateral conal fascia (small arrows, *d*) and psoas abscess are most clearly defined on the gadolinium-enhanced fat-suppressed image. Dilatation of the collecting system, lack of contrast excretion, and prominent extrarenal inflammatory changes are features observed in xanthogranulomatous pyelonephritis.

Malakoplakia

Malakoplakia (*malakos* = soft and *plakos* = plaques) is a rare chronic granulomatous inflammatory process often affecting immunocompromised hosts. The disease is most frequently observed in the urinary tract of middle-aged woman as a complication of recurrent urinary tract infections (coliforms, 90%; *Escherichia coli*, 75%) [114].

The lower urinary tract is more commonly affected, with renal parenchymal involvement being unusual (16% of cases) [114]. The typical mucosal lesion of malakoplakia is a yellow-brown soft plaque with central umbilication. Parenchymal lesions are characterized by nodules of variable size that may be discrete, coalesce to become diffuse, or undergo suppuration with abscess formation. Renal parenchymal malakoplakia can be multifocal or unifocal. In multifocal malakoplakia, the kidneys are enlarged with solid multifocal infiltration, and in unifocal disease a nonspecific mass is present [115]. The clinical presentation and radiologic appearance are often suggestive of a neoplasm. The diagnosis is established on the basis of histopathology. The characteristic histologic feature of the lesion is the presence of Michaelis–Gutmann bodies [116].

Multifocal malakoplakia appears as multiple ill-defined nodules of lower signal intensity on T2- and T1-weighted images, which show minimal enhancement on early and late postgadolinium gradient-echo images, with intervening linear stroma. The kidneys are mildly enlarged (fig. 9.115) [117]. There is currently insufficient experience with MRI to determine the specificity of these findings.

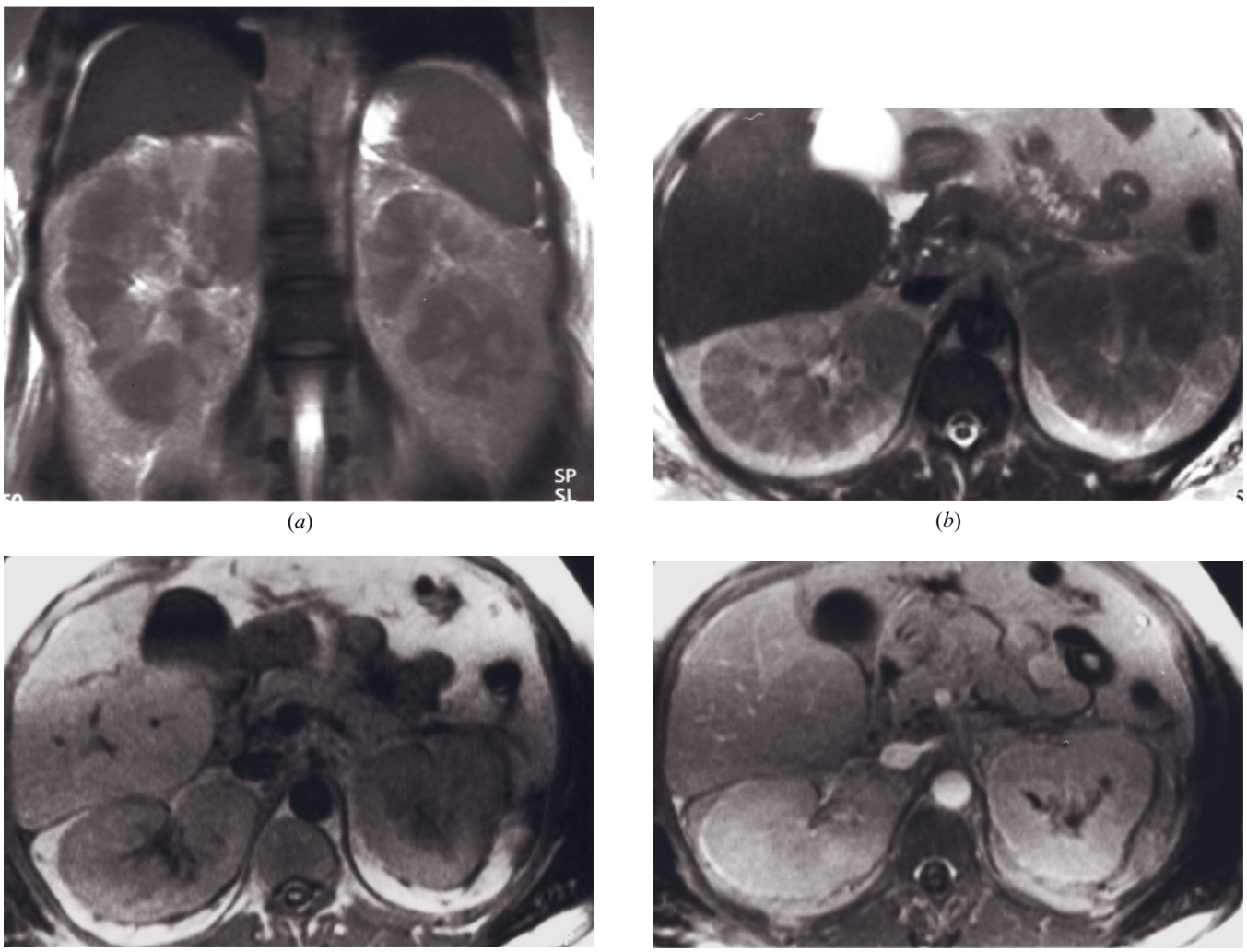

(*a*) (*b*) (*c*) (*d*)

Fig. 9.115 Malakoplakia. Coronal (*a*) and transverse (*b*) T2-weighted SS-ETSE and transverse T1-weighted precontrast (*c*) and 1-min postgadolinium (*d*) SGE images. The kidneys are enlarged, with an extensive multinodular appearance. High-signal septations are appreciated on the T2-weighted sequences (*a*, *b*), which enhance after gadolinium administration (*d*). T2-weighted

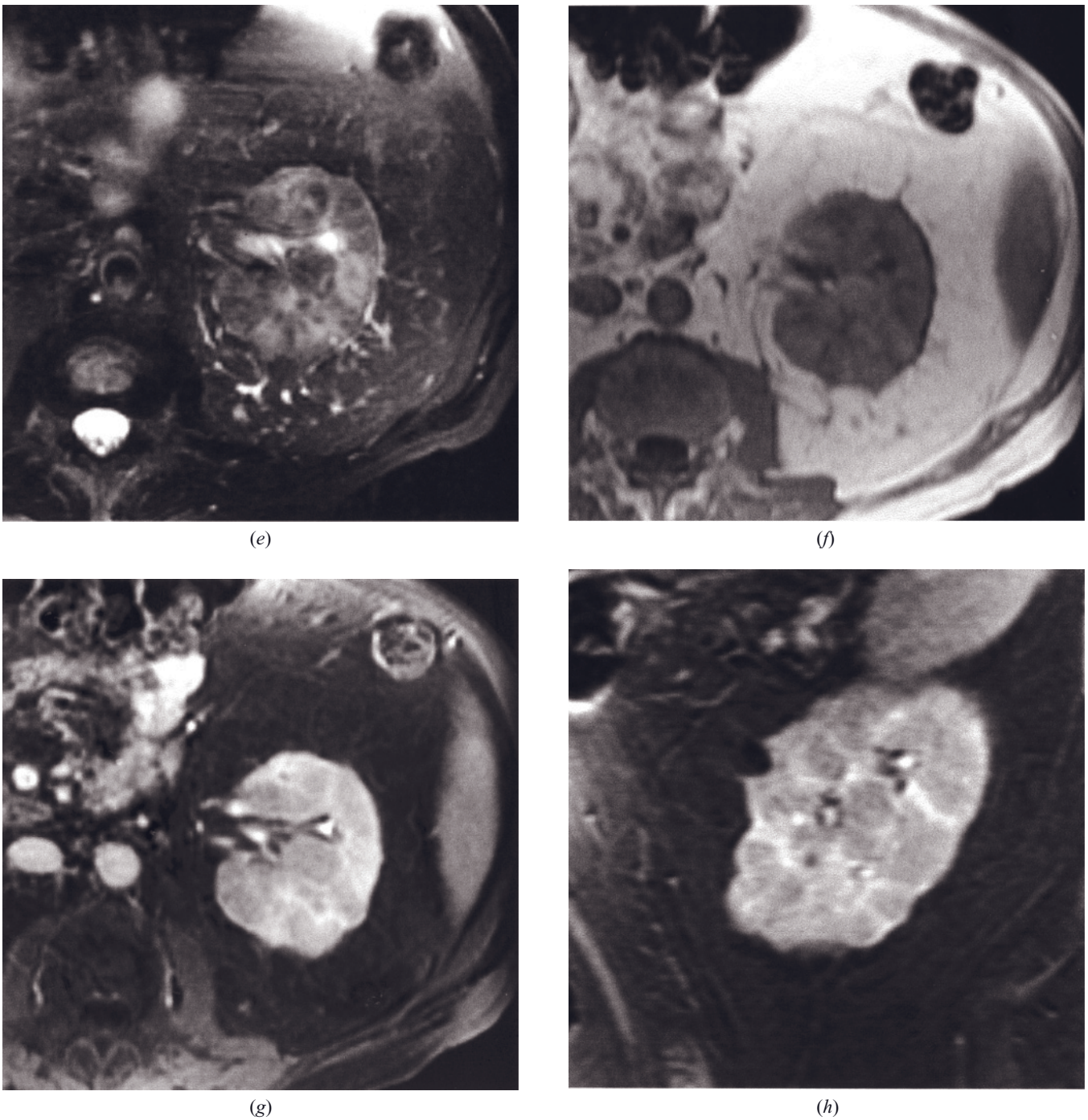

FIG. 9.115 (*Continued*) fat-suppressed ETSE (*e*), T1-weighted precontrast SGE (*f*), and transverse (*g*) and sagittal (*h*) T1-weighted postgadolinium fat-suppressed SGE images in a second patient. This patient, who had undergone liver transplantation, has a similar appearance of extensive multinodular infiltrate in the kidneys with intervening linear stroma that is high signal on T2 (*e*) and enhances after contrast administration (*g*, *h*). (Courtesy of Eric Outwater, M.D., University of Arizona.)

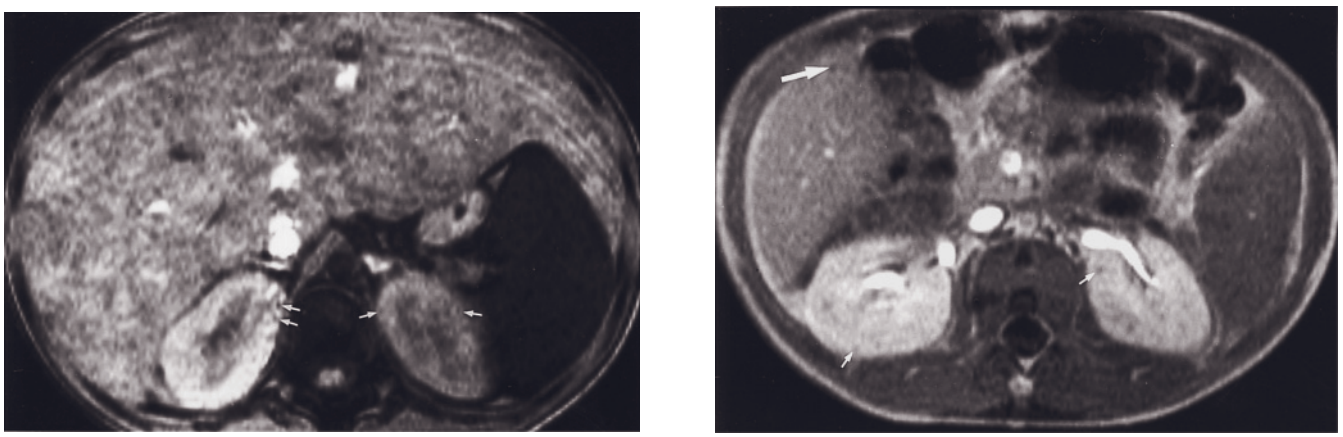

(*a*) (*b*)

FIG. 9.116 Renal candidiasis. T1-weighted immediate (*a*) and 90-s (*b*) postgadolinium SGE images in 2 patients with renal candidiasis. Multiple low-signal-intensity lesions, <5 mm in size, are present in the kidneys of both patients (small arrows, *a*, *b*). Extensive hepatic involvement is apparent in the first patient (*a*), whereas fewer liver lesions are apparent in the second patient (arrow, *b*).

Candidiasis

Renal candidiasis occurs in the context of hepatosplenic candidiasis. These lesions are typically small (5 mm) and well defined. Lesions are best shown on gadolinium-enhanced T1-weighted interstitial-phase fat-suppressed images (fig. 9.116) [118].

Fungus balls also may develop in the collecting system. Diabetes predisposes to this condition.

Pyonephrosis

Pyonephrosis is a complication of acute pyelonephritis and occurs in the setting of total or almost complete urinary tract obstruction, when the suppurative exudate is unable to drain, thus filling the renal pelvis and calyces. MRI features consistent with pyonephrosis include debris layering in the obstructed renal pelvis, most clearly defined on T2-weighted SS-ETSE as dependently layering low-signal-intensity fluid, and moderately intense enhancement of the wall of the renal pelvis on gadolinium-enhanced images (fig. 9.117).

HEMORRHAGE

Renal/perirenal hemorrhage occurs in the context of bleeding disorders, trauma, and neoplasms. Large perinephric hematomas may occur in patients who have undergone renal lithotripsy or renal biopsy. MRI is more sensitive than CT imaging to ascertain the presence of hemorrhage in fluid collections. Parenchymal or subcapsular hemorrhage appears as high- or mixed high-signal-intensity fluid on both T2- and T1-weighted images (fig. 9.118). Perirenal hemorrhage frequently has an unusual multilayered appearance, reflecting the extravasation of blood along the fibrous trabeculae that traverse perirenal fat.

DISEASE OF THE RENAL COLLECTING SYSTEM: RENAL PELVIS AND URETER

Mass Lesions

Primary Tumors

Primary neoplasms of the ureter or renal pelvis are uncommon and collectively are only one-tenth as common as primary neoplasm of the bladder.

Urothelial Carcinoma (Transitional Cell Carcinoma). The majority of primary tumors of the urothelium are malignant. Urothelial cancer, formerly termed transitional cell carcinoma (TCC), is the most common malignancy of the urothelium, accounting for more than 90% of tumors. Squamous cell cancer accounts for 8% and adenocarcinoma for less than 1%. TCC represents 8% of all renal tumors, rarely occurring in patients younger than 30 years of age [119]. TCC of the upper tract is epidemiologically similar to that of the bladder. Males are more commonly affected, in a 3-to-1 ratio with females. Risk factors include analgesics,

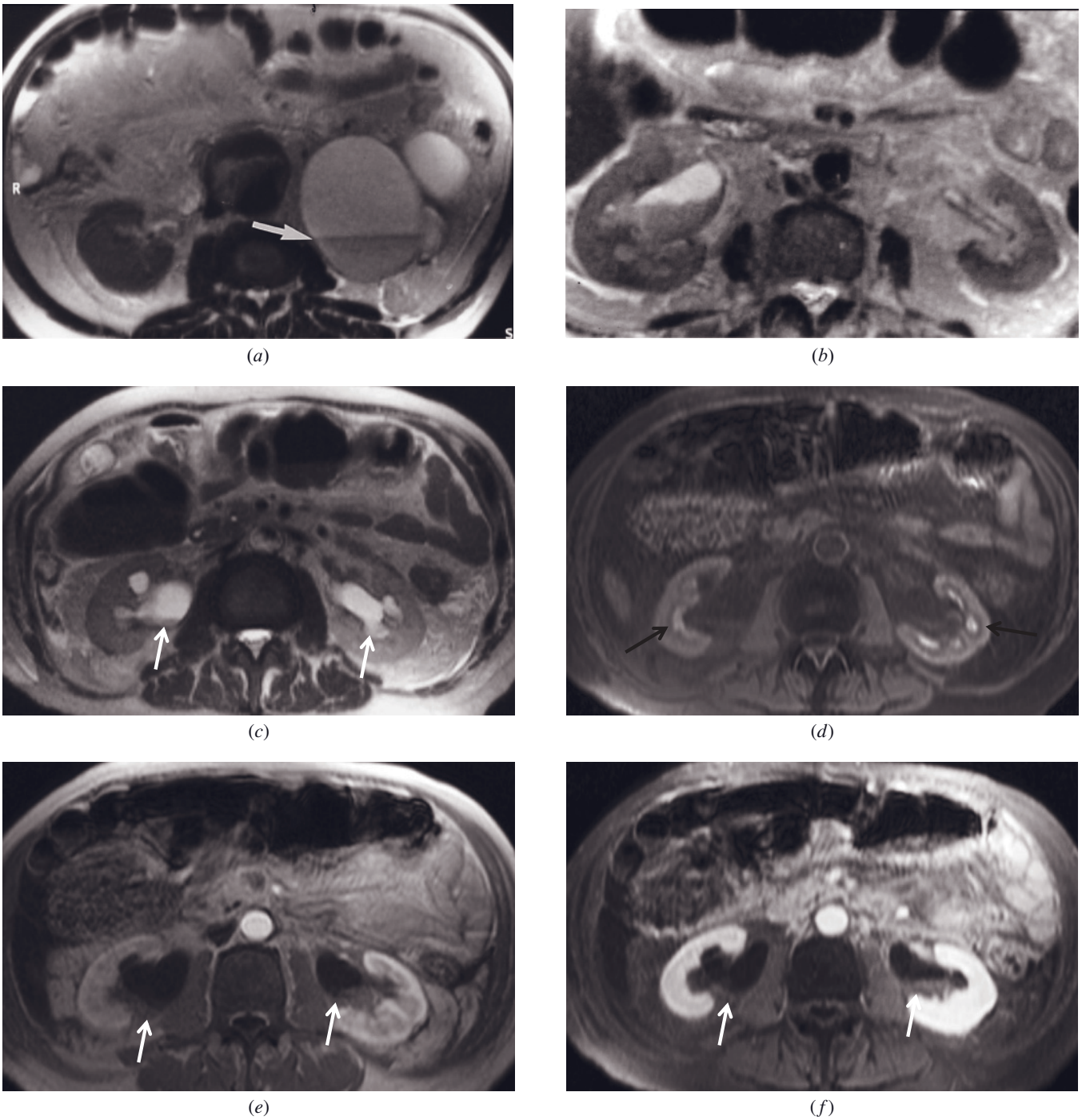

FIG. 9.117 Pyonephrosis. T2-weighted SS-ETSE (*a*) image demonstrates severe dilatation of the collecting system of the left kidney. Layering of low-signal-intensity debris (arrow, *a*) in the dependent portion of the renal pelvis is a common appearance in infection. T2-weighted SS-ETSE (*b*) image in a second patient. There is hydronephrosis of the right kidney with layering of low-signal material consistent with infection within the dilated collecting system. Note also perinephric fluid stranding. T2-weighted single-shot echo-train spin-echo (*c*), T1-weighted fat-suppressed SGE (*d*), T1-weighted postgadolinium arterial-phase SGE (*e*), and T1-weighted postgadolinium fat-suppressed interstitial-phase 3D-GE (*f*) images demonstrate dilated collecting system and pyonephrosis in another patient. Bilateral collecting systems are dilated because of distal obstruction, and low-signal-intensity debris (white arrows, *c–f*) is detected in the dependent portions of bilateral collecting systems, suggesting the presence of pyonephrosis. High-signal-intensity proteinaceous material (black arrows, *d*) due to obstructive renal parenchymal disease is detected in bilateral medullas. Note that the right kidney shows lesser enhancement compared to the left kidney on the arterial-phase image, reflecting the effect of obstructive renal parenchymal disease.

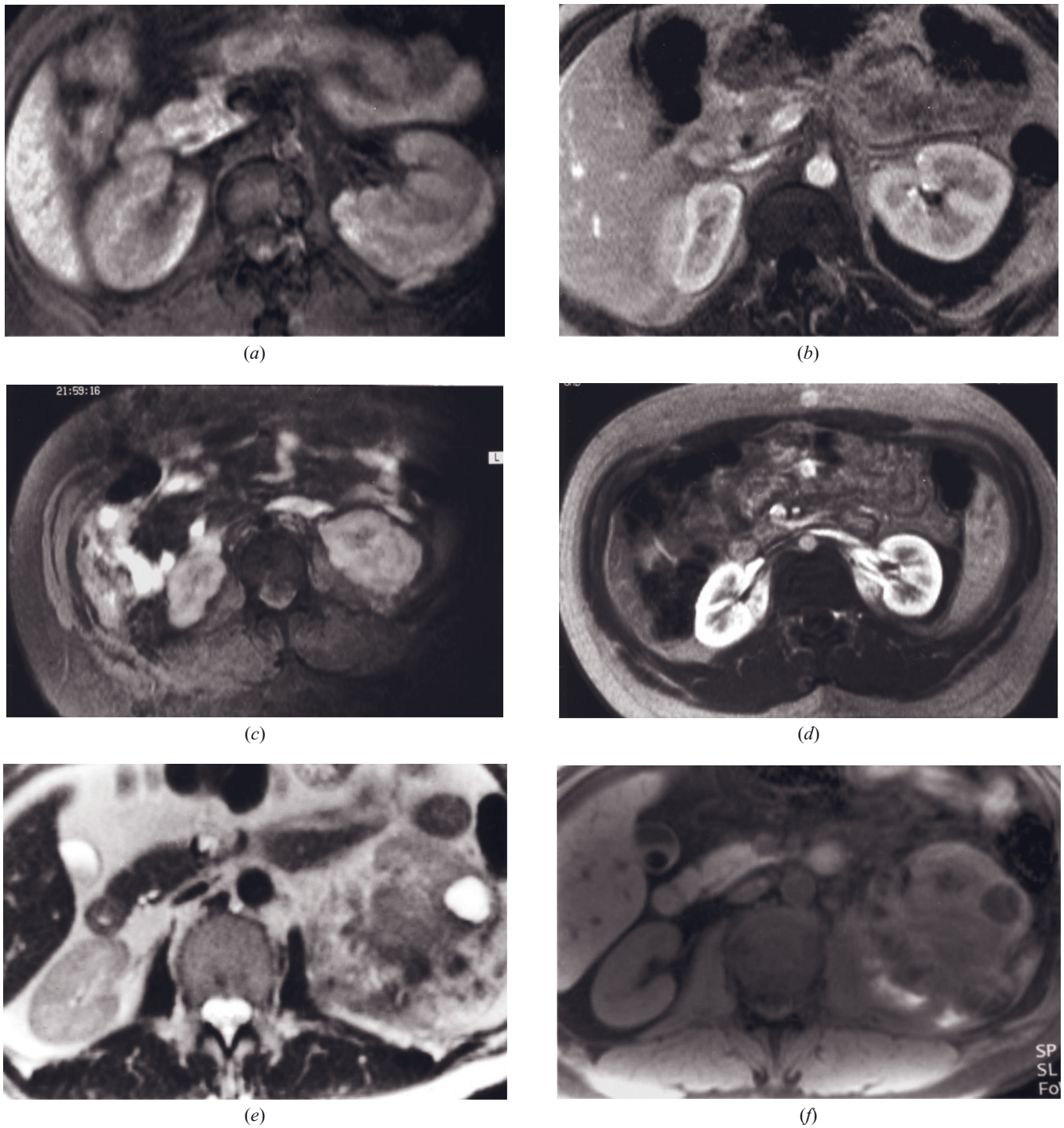

FIG. 9.118 Perirenal hematoma after biopsy. T1-weighted precontrast fat-suppressed SE (*a*) and immediate postgadolinium SGE (*b*) images in 1 patient and the same sequences (*c*, *d*), respectively, in a second patient. On the precontrast images (*a*, *c*) high-signal-intensity fluid is present in the perirenal space of the left kidney, consistent with subacute blood. On the immediate post-gadolinium images (*b*, *d*), the fluid appears low in signal intensity because of rescaling of the tissue signal intensities after gadolinium administration. T2-weighted SS-ETSE (*e*) T1-weighted precontrast (*f*), and postgadolinium (*g*) fat-suppressed SGE images in a third patient. There is heterogeneous-signal-intensity fluid in the left perinephric space on T2 (*e*)- and T1 (*f*)-weighted images, displacing the kidney anterior and laterally, consistent with a perirenal hematoma, after renal biopsy. Note also a thick-walled cyst within

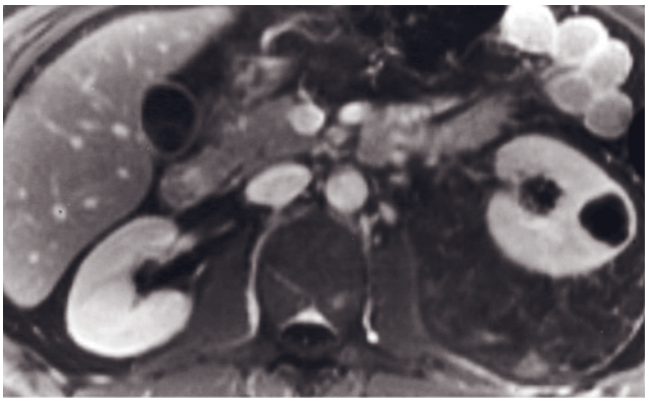

(*g*)

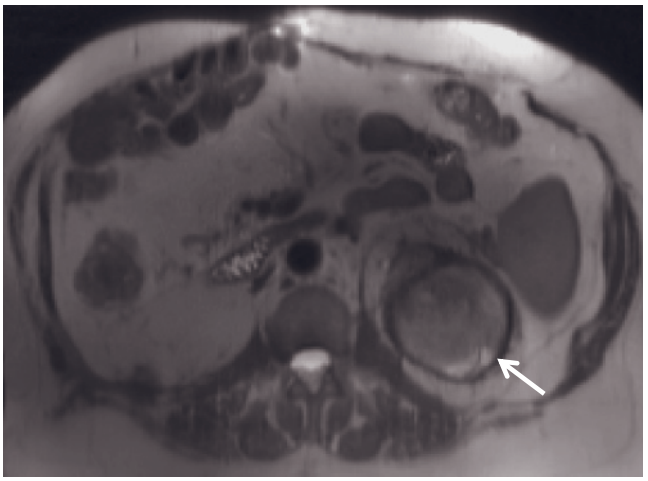

(*h*)

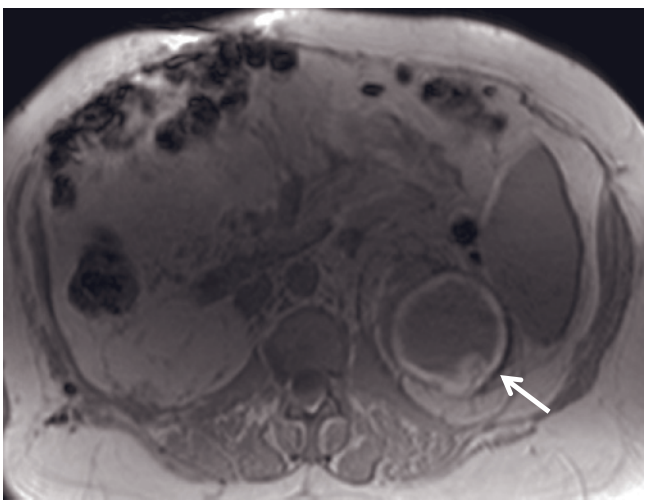

(*i*)

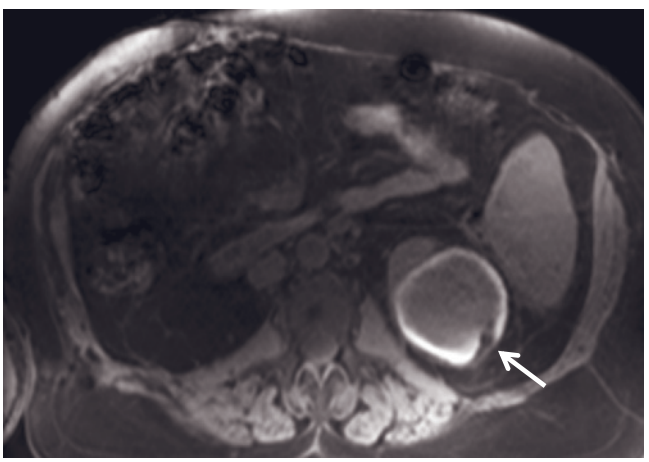

(*j*)

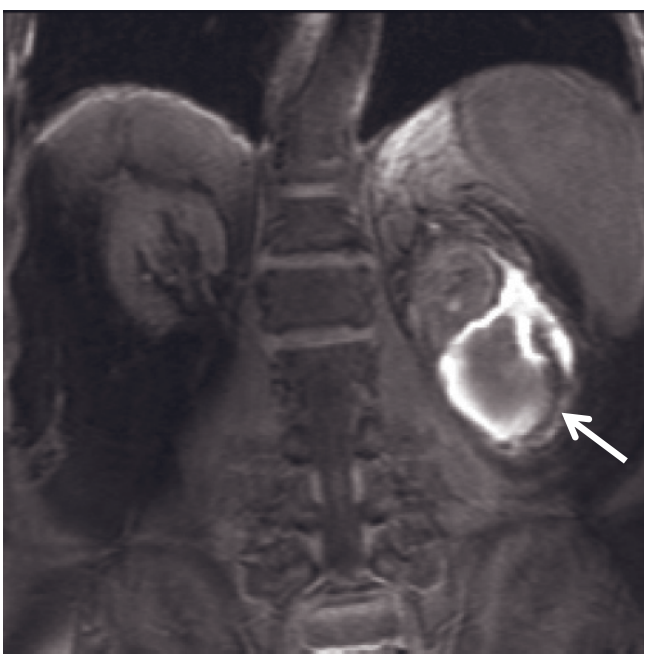

(*k*)

FIG. 9.118 (*Continued*) the left kidney, which is of uniform thickness but has prominent mural enhancement (*g*). **Perirenal hematoma.** Transverse T2-weighted single-shot echo-train spin-echo (*h*), transverse T1-weighted SGE (*i*), and transverse (*j*) and coronal (*k*) T1-weighted fat-suppressed 3D-GE images at 3.0T demonstrate perirenal subacute hematoma in another patient. Low-signal-intensity peripheral rim on T2-weighted image (*h*) and high-signal-intensity peripheral rim on T1-weighted images (*i–k*) reflect the subacute nature of the blood products.

tobacco, caffeine, chronic infection, and urolithiasis. Staging of transitional-cell cancer is as follows: Stage 1, limited to urothelial mucosa and lamina propria; Stage 2, invasion of, but not beyond, pelvic/ureteral muscularis; Stage 3, invasion beyond muscularis into adventitial fat or renal parenchyma; and Stage 4, distant metastasis.

Tumors usually appear as eccentric filling defects in the renal pelvis (fig. 9.119). On occasion, they may cause concentric wall thickening [119, 120]. Tumors usually spread superficially (fig. 9.120), but in rare instances may appear as large focal masses. TCC has a propensity to invade renal parenchyma, but invasion may be difficult to detect. Invasion of or along the IVC may occur and is well depicted on MR images (fig. 9.121) [120, 121]. Although these tumors are hypovascular, they may be moderately high in signal intensity on gadolinium-enhanced interstitial-phase T1-weighted fat-suppressed images, presumably because of diminished clearance of contrast from the interstitial space [120]. Tumors tend to invade locally, with spread to adjacent lymph nodes. There is a great propensity for the tumor to be multifocal; 30–50% of cases are multifocal, and 15–25% are bilateral. The role of MR urography is not established at present. Liver metastases from TCC tend to be hypovascular (fig. 9.122). In rare instances, TCC may have poorly differentiated histology and act as a locally aggressive malignancy (fig. 9.123).

Squamous Cell Carcinoma. A predisposing cause for squamous cell malignancy is usually present. Calculi are present in 50–60% of cases, and chronic infection, leukoplakia, and chronic drug overuse (e.g., phenacetin) are also associated with this malignancy [119]. Squamous cell carcinoma cannot be distinguished from transitional cell cancer on the basis of imaging findings (fig. 9.124). Early tumors tend to spread superficially. As tumors enlarge, they may develop irregular margins, which is somewhat uncommon for transitional cell carcinoma [119].

Secondary Tumors

Lymphoma. Lymphoma is the most common secondary tumor to invade the urothelium. Direct coronal imaging with MRI allows visualization of the extent of disease [96].

Metastases from Other Primary Tumors. Metastases to the ureter are rare. Breast, gastrointestinal tract, prostate, cervix, and kidney cancers are the malignancies that most frequently metastasize to the ureters [119]. Small enhancing nodules of tumor may be appreciated on gadolinium-enhanced fat-suppressed images.

Filling Defects in the Collecting System

Calculi are the most common filling defects in the renal collecting system. Calcium oxalate stones are the most common form of renal calculi in North America, accounting for approximately 65% of cases (fig. 9.125) [122]. Regardless of calcium composition, renal calculi are signal void on MR images (fig. 9.126). To maximize conspicuity of signal-void calculi, they are best displayed on sequences in which urine is high in signal intensity. T2-weighted single-shot echo-train spin-echo (SS-ETSE) sequences generate MR urographic images that can be reconstructed to resemble conventional intravenous urography [4, 123]. MR urography may be effective at demonstrating ureteric calculi because of the high contrast between high-signal-intensity urine in dilated ureter and obstructing low-signal-intensity calculus (fig. 9.127). Because T2-weighted SS-ETSE images have less than 1-s temporal resolution, MRI may be a very time-efficient and cost-effective method of evaluating obstructing calculi. After gadolinium administration, detection of calculi is feasible when gadolinium is sufficiently dilute to render urine high in signal intensity. This is best accomplished by ensuring that the patient is well hydrated and by delay of image acquisition 10–30 min after injection [5]. Signal-void calculi may be detected as small as 1–2 mm in diameter in a background of high-signal-intensity urine. Thin-section 3D-GRE imaging acquired in the coronal plane may be MIP reconstructed to result in MR excretory urographic images. Obstruction by calculi causes alteration in renal parenchymal enhancement and in the transit of contrast material within the kidney, which is well shown on MR images (see Renal Function section below). Because renal calculi are radiopaque in the great majority of cases on noncontrast spiral CT, and are therefore well shown, even when minute and nonobstructing; CT is the procedure of choice for evaluating renal calculi.

Other filling defects such as blood clots or fungus balls are also demonstrable as low-signal-intensity mass lesions in high-signal-intensity urine on T2-weighted sequences and as nonenhancing mass lesions situated in the high-signal-intensity contrast-filled collecting system on delayed postgadolinium gradient-echo images. Foci of air in the collecting system may be distinguished from solid lesions by the presence of susceptibility artifact surrounding the defect and by the observation that air foci locate in nondependent positions and solid lesions tend to layer in dependent positions (fig. 9.128).

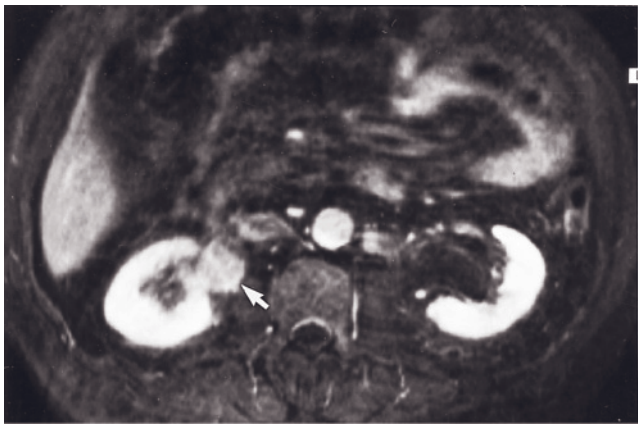

(*a*)

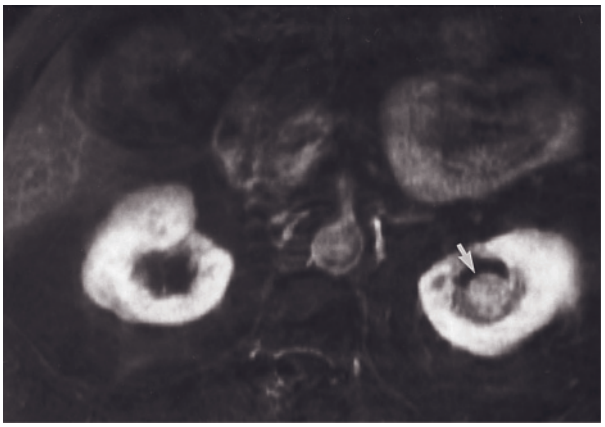

(*b*)

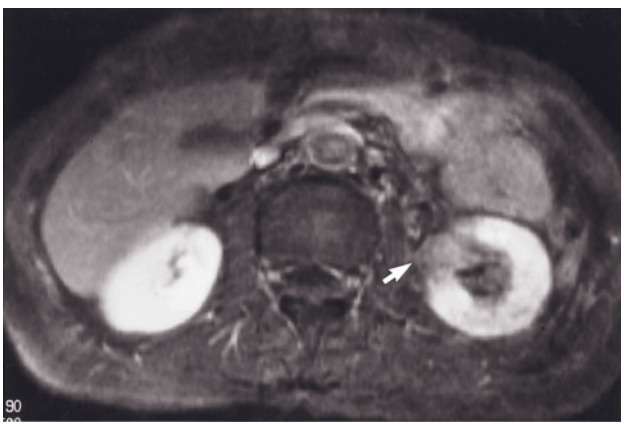

(*c*)

(*d*)

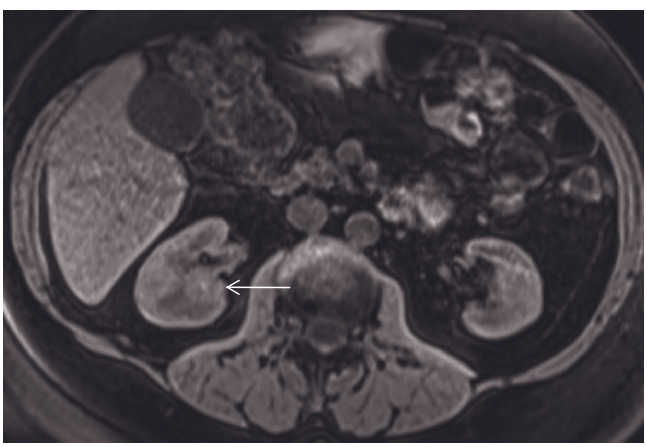

(*e*)

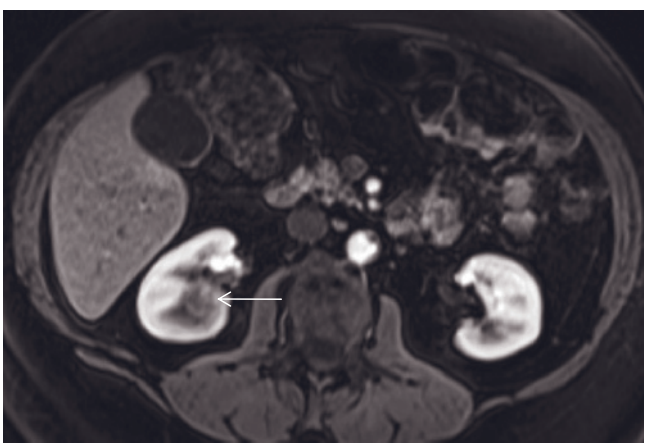

(*f*)

FIG. 9.119 Transitional-cell carcinoma—Stage 2, focal mass type. T1-weighted fat-suppressed gadolinium-enhanced SE images (*a–c*) in 3 patients with transitional cell cancer. Tumors are focal rounded masses (arrows, *a–c*) that show heterogeneous mottled enhancement less than neighboring renal cortex. Note that masses have well-defined margins that correspond to lack of infiltration into surrounding fat. Coronal T2-weighted single-shot echo-train spin-echo (*d*), transverse T1-weighted fat-suppressed 3D-GE (*e*), transverse T1-weighted postgadolinium hepatic arterial dominant-phase (*f*), and coronal T1-weighted postgadolinium interstitial-phase fat-suppressed 3D-GE (*g*) images demonstrate transitional cell carcinoma (arrows, *d–g*) in the right kidney in another patient. The tumor is located in the middle and lower collecting systems and has regular rounded contours. The tumor, which shows progressive enhancement on postgadolinium images, does not show renal parenchymal invasion. Note that the right adrenal gland is enlarged (*g*). Coronal T2-weighted single-shot echo-train spin-echo (*h*), coronal T1-weighted SGE (*i*), and transverse

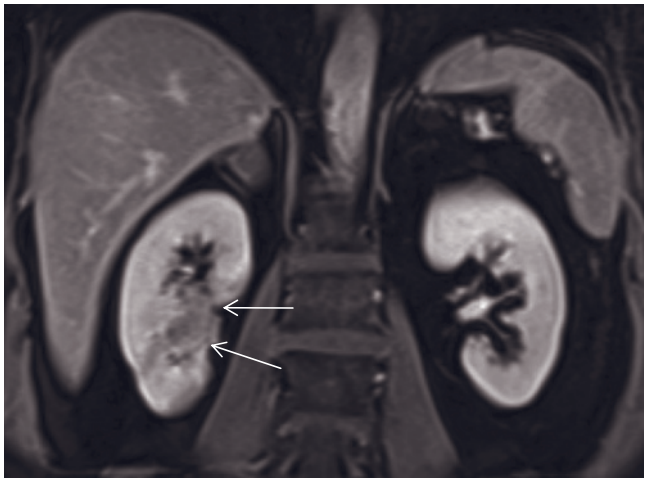

(*g*)

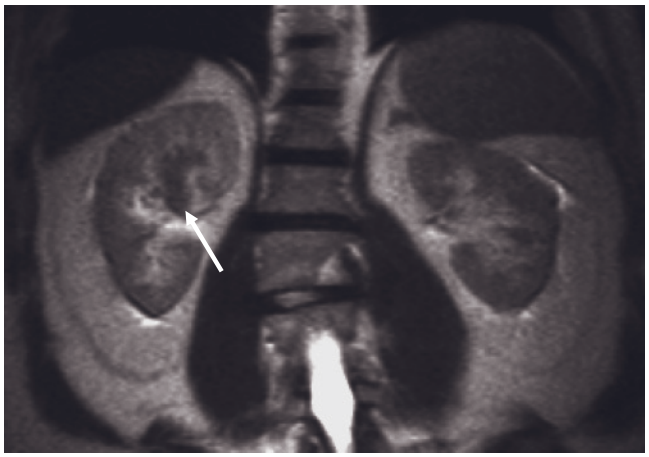

(*h*)

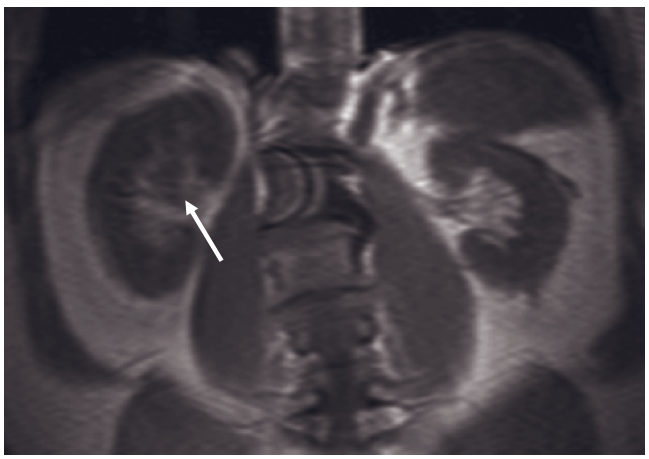

(*i*)

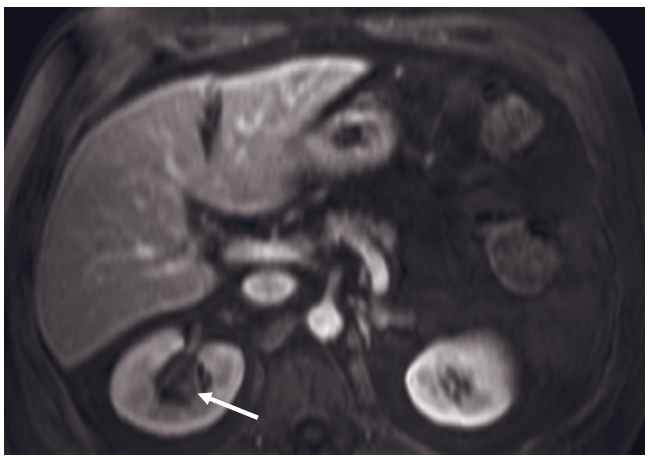

(*j*)

FIG. 9.119 (*Continued*) T1-weighted postgadolinium hepatic venous-phase fat-suppressed 3D-GE (*j*) images demonstrate transitional cell carcinoma (arrows, *h–j*) in the right kidney in another patient. The tumor is located in the upper collecting system and shows low signal on both T2-weighted (*h*) and T1-weighted (*i*) precontrast images. The tumor shows mild enhancement on postgadolinium image (*j*). The tumor does not invade the renal parenchyma.

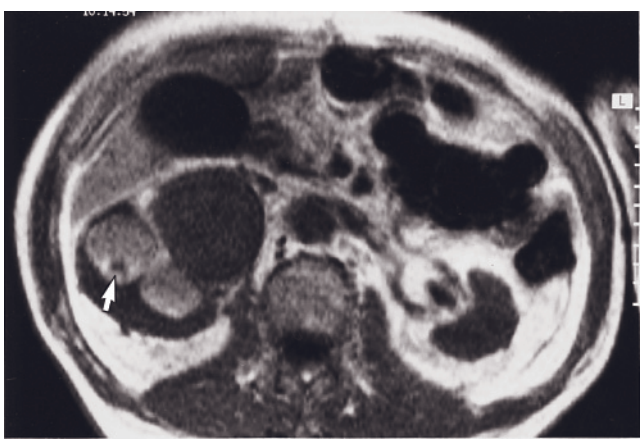

(*a*)

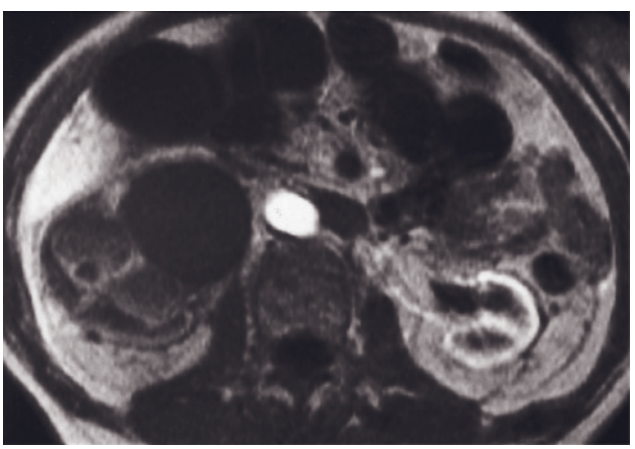

(*b*)

FIG. 9.120 Transitional-cell carcinoma—Stage 3, superficially spreading pattern. T1-weighted precontrast SGE (*a*), immediate postgadolinium SGE (*b*), and late-phase fat-suppressed postgadolinium SE (*c*) images. Severe dilatation of the right renal collecting system is present (*a–c*). Blood is identified as high-signal-intensity substance in dilated calyces on the precontrast image (*a*), and a small low-signal-intensity blood clot is also apparent (arrow). The renal pelvis is filled with a large signal-void blood clot. Diminished cortical enhancement is present on the immediate postgadolinium image (*b*). Thickening of the proximal aspect of

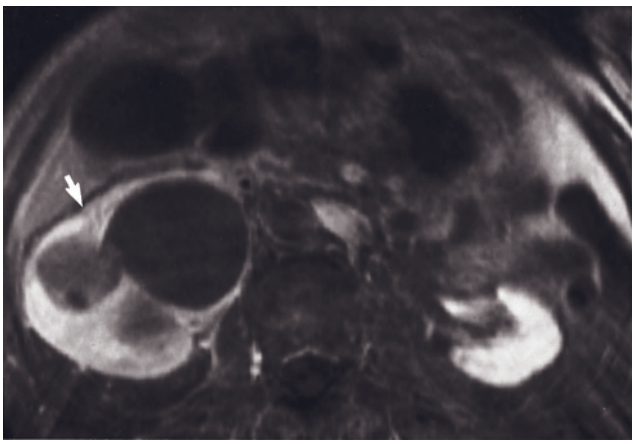

(*c*)

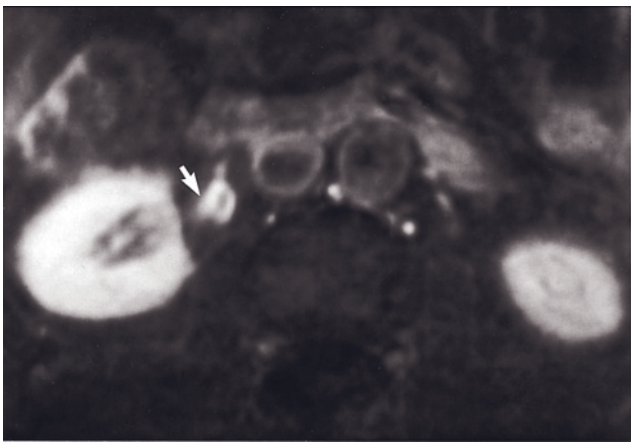

(*d*)

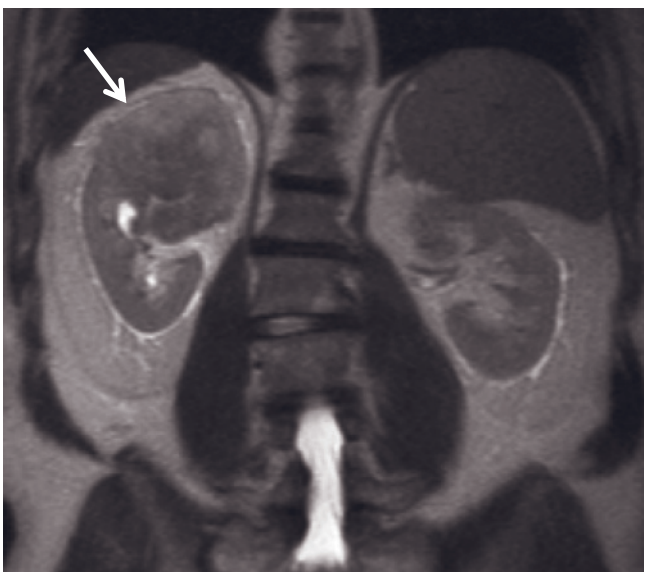

(*e*)

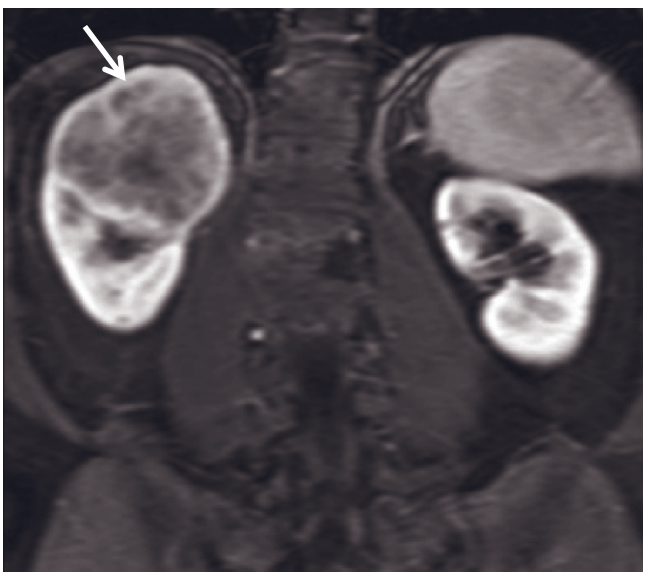

(*f*)

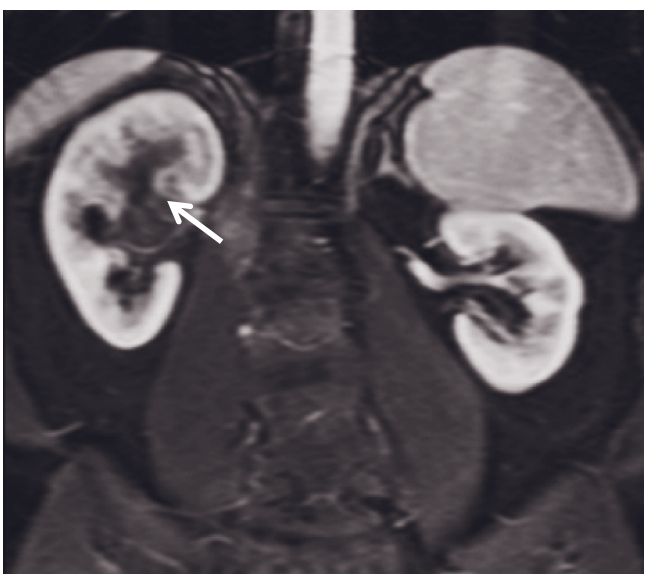

(*g*)

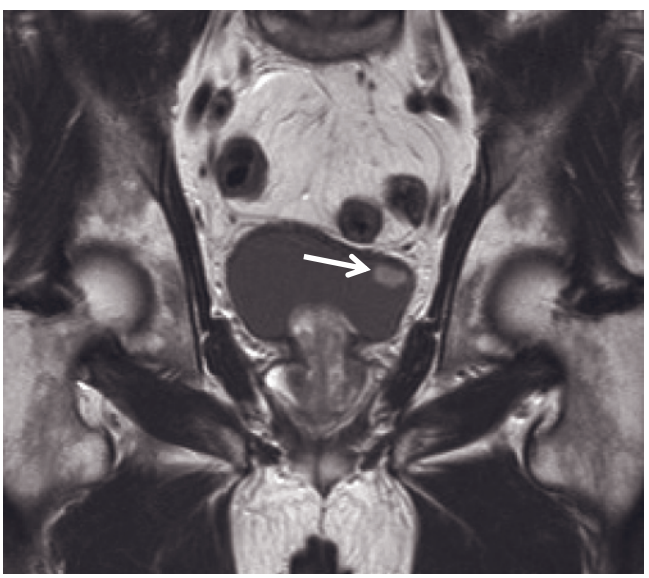

(*h*)

FIG. 9.120 (*Continued*) the renal pelvis urothelium is noted, with invasion of the renal cortex (arrow), which is best appreciated on the gadolinium-enhanced fat-suppressed image (*c*). Gadolinium-enhanced T1-weighted fat-suppressed spin-echo image (*d*) in a second patient shows increased thickness and intense enhancement of the proximal ureter. Ill-defined external margin of the tumor (arrow, *d*) on the lateral aspect of the ureter wall is consistent with tumor extension into the periureteral fat. Coronal T2-weighted single-shot echo-train spin-echo (*e*), coronal T1-weighted postgadolinium hepatic venous-phase fat-suppressed 3D-GE (*f*, *g*), and coronal T2-weighted true-FISP image (*h*) demonstrate multifocal transitional-cell carcinoma in another patient. A large transitional-cell carcinoma (arrows, *e*–*g*) invading the renal parenchyma and showing heterogeneous enhancement is detected in the right kidney. A small focus of transitional-cell carcinoma (arrow, *h*) extending into the lumen is also detected in the superior wall of the bladder.

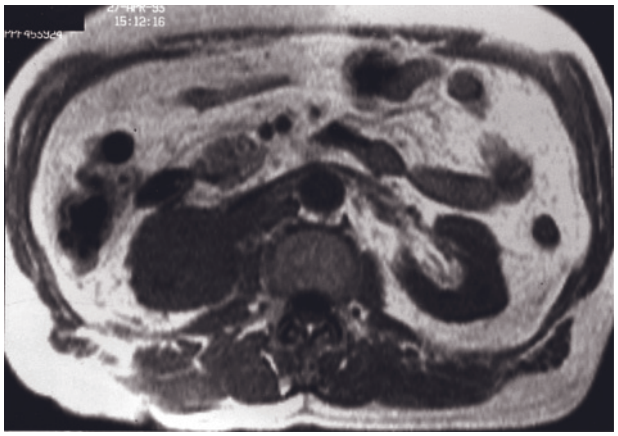

(*a*)

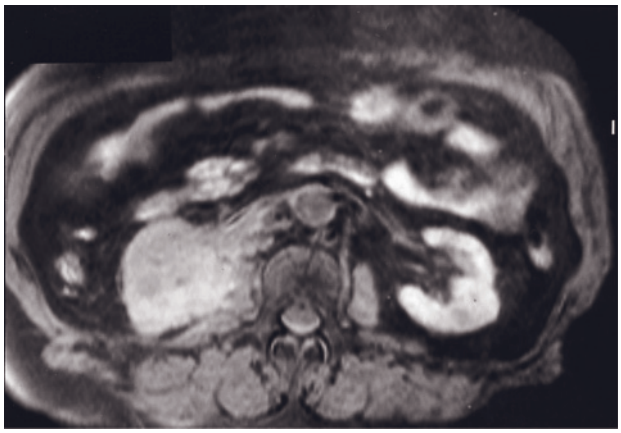

(*b*)

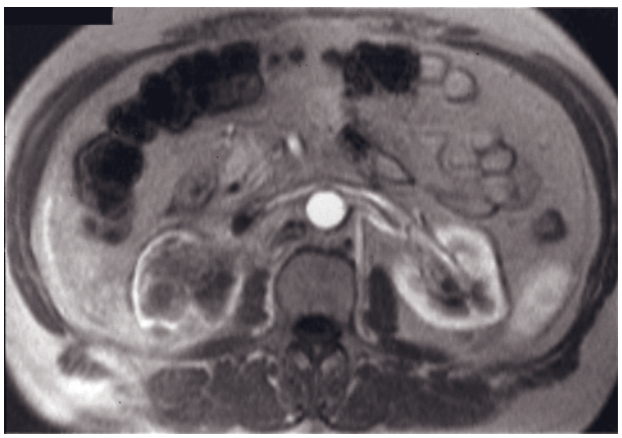

(*c*)

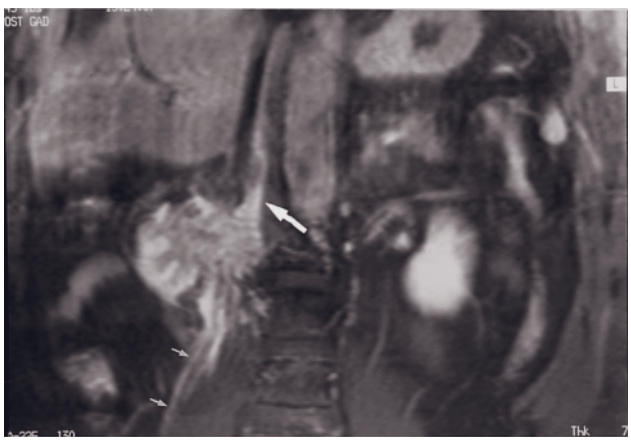

(*d*)

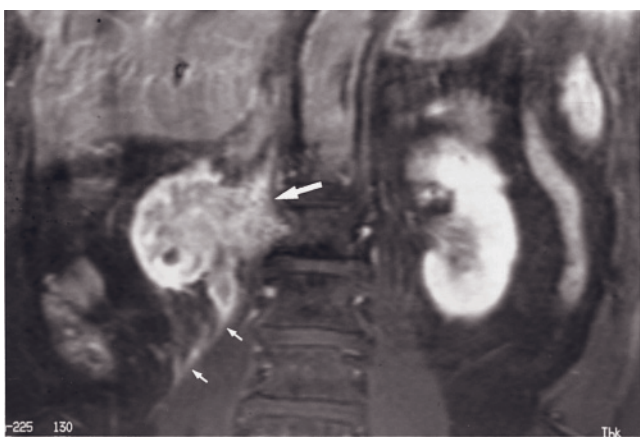

(*e*)

FIG. 9.121 Transitional-cell carcinoma—Stage 4. T1-weighted precontrast SGE (*a*), precontrast fat-suppressed SE (*b*), immediate postgadolinium SGE (*c*), and coronal gadolinium-enhanced T1-weighted fat-suppressed SE images from posterior (*d*) and anterior (*e*) locations. Low-signal-intensity tumor is seen involving kidney and extending posterior to the IVC on the precontrast images (*a*, *b*). On the immediate postgadolinium image (*c*), the tumor is noted to involve predominantly the medulla, with relative sparing of the renal cortex. The extent of tumor is best displayed on the coronal images, in which tumor is shown to extend along the psoas muscle and ureter inferiorly (small arrows, *d*, *e*) and along the vertebral bodies and IVC superiorly (arrows, *d*, *e*).

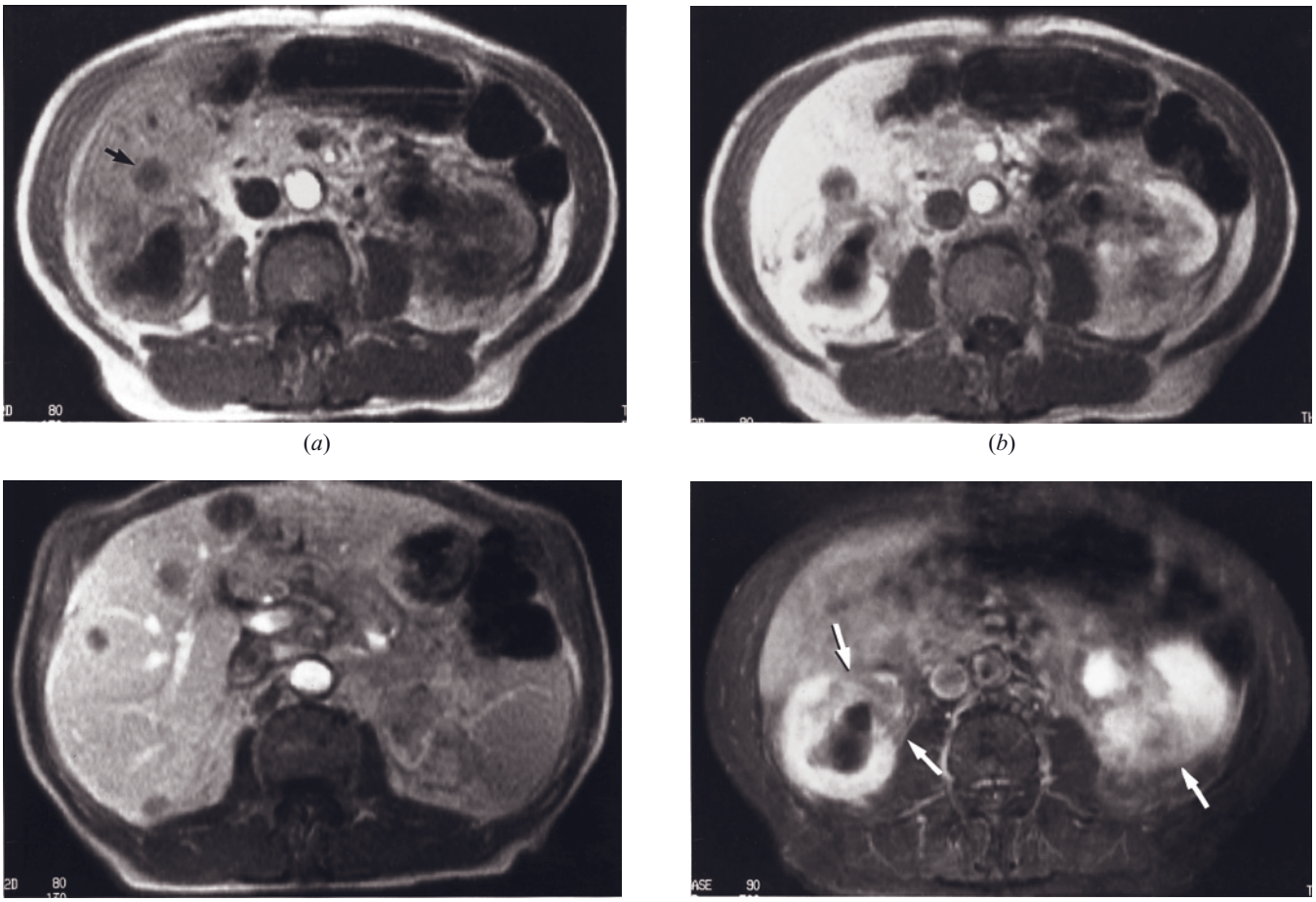

FIG. 9.122 Transitional-cell carcinoma—Stage 4. T1-weighted precontrast SGE (*a*), immediate (*b*) and 90-s (*c*) gadolinium-enhanced SGE, and late-phase fat-suppressed postgadolinium SE (*d*) images. Bilateral infiltrative tumors are present arising from the collection system of both kidneys (*a*, *b*, *d*). The transitional-cell tumors are low in signal intensity on precontrast T1-weighted images (*a*), enhance minimally on immediate postgadolinium images (*b*), and show heterogeneous enhancement less than renal parenchyma on later images (arrows, *d*). Liver metastases are also present (*c*). Liver metastases from transitional cell cancer are generally hypovascular and are low in signal intensity on precontrast T1-weighted images (arrow, *a*), show faint rim enhancement on immediate postgadolinium images (*b*), and often remain well defined and hypointense on later postcontrast images (*c*). Liver metastases frequently are poorly seen on T2-weighted images (not shown) because of their hypovascularity.

Dilation of the Collecting System

Dilation of the renal collecting system may arise as a normal variant (fig. 9.129), a congenital anomaly, an obstruction, reflux related, or after obstruction. MR urography adequately reveals the severity and the level of obstruction of the collecting system (fig. 9.130). The combination of MR urography, tissue imaging sequences to evaluate renal cortex, and dynamic serial postcontrast imaging to assess renal function provides comprehensive information on the morphologic and functional status of kidneys with dilated collecting systems (fig. 9.131). As with intravenous urography and CT imaging, gadolinium-enhanced gradient-echo images can demonstrate delayed excretion of contrast (fig. 9.132).

Calyceal Diverticulum

Calyceal diverticula may be shown on MR images with a combination of MR urography and delayed gadolinium-enhanced images. The MR urogram demonstrates the fluid-filled structure, but the communication with the collecting system is confirmed by demonstration of high-signal-intensity fluid in the diverticulum on delayed images due to the presence of dilute gadolinium (fig. 9.133). Calyceal diverticula frequently contain calculi,

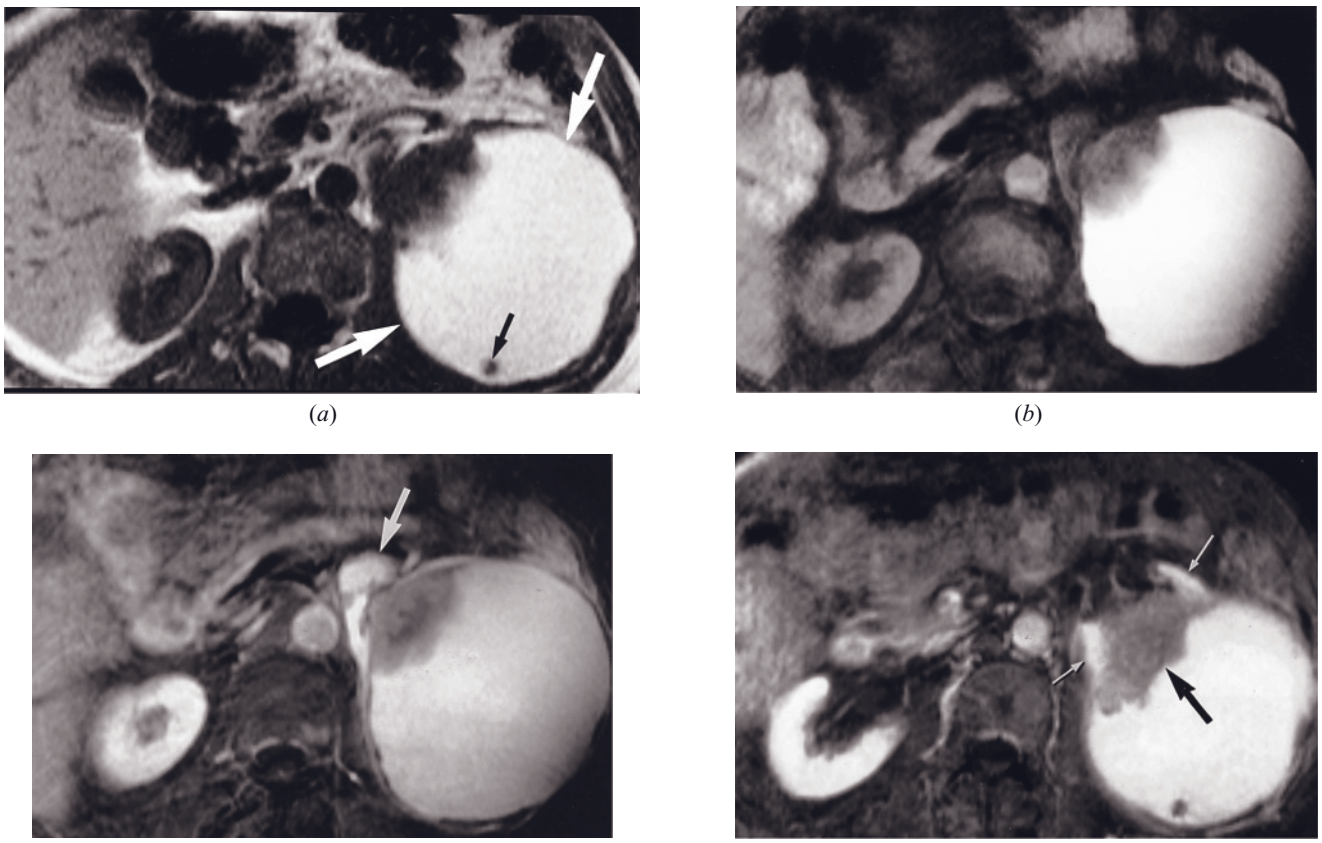

FIG. 9.123 Transitional cell carcinoma, poorly differentiated. T1-weighted precontrast SGE (*a*), precontrast fat-suppressed SE (*b*), and late-phase fat-suppressed gadolinium-enhanced SE (*c*, *d*) images. An irregular tumor arises from the midportion of the kidney and is associated with a large hemorrhagic fluid collection (large arrows, *a*). A small tumor nodule is present in the cystic hemorrhagic component (small arrow, *a*). On the gadolinium-enhanced image, renal parenchyma is well-defined as uniformly enhancing tissue (arrow, *c*).The tumor mass extends from the renal pelvis through the renal parenchyma into the cystic space. Anterior and posterior cortices (small arrows, *d*) are splayed by the irregular tumor mass (black arrow, *d*).

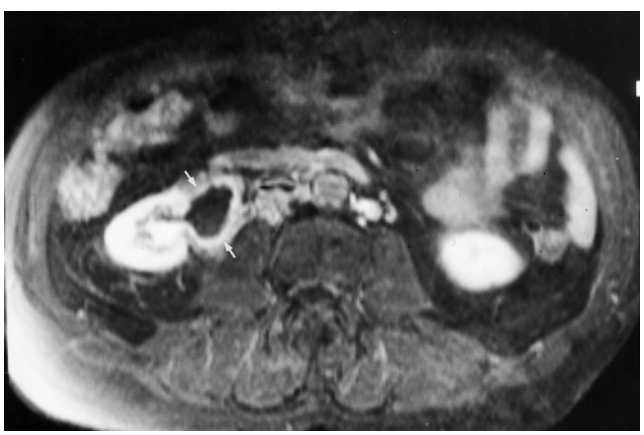

FIG. 9.124 Squamous cell carcinoma. T1-weighted fat-suppressed gadolinium-enhanced SE image demonstrates dilatation of the right renal pelvis with irregularly thickened and intensely enhancing urothelium, which represents squamous cell carcinoma (arrows). Surrounding peripelvic fat contains ill-defined enhancing tissue consistent with tumor extension.

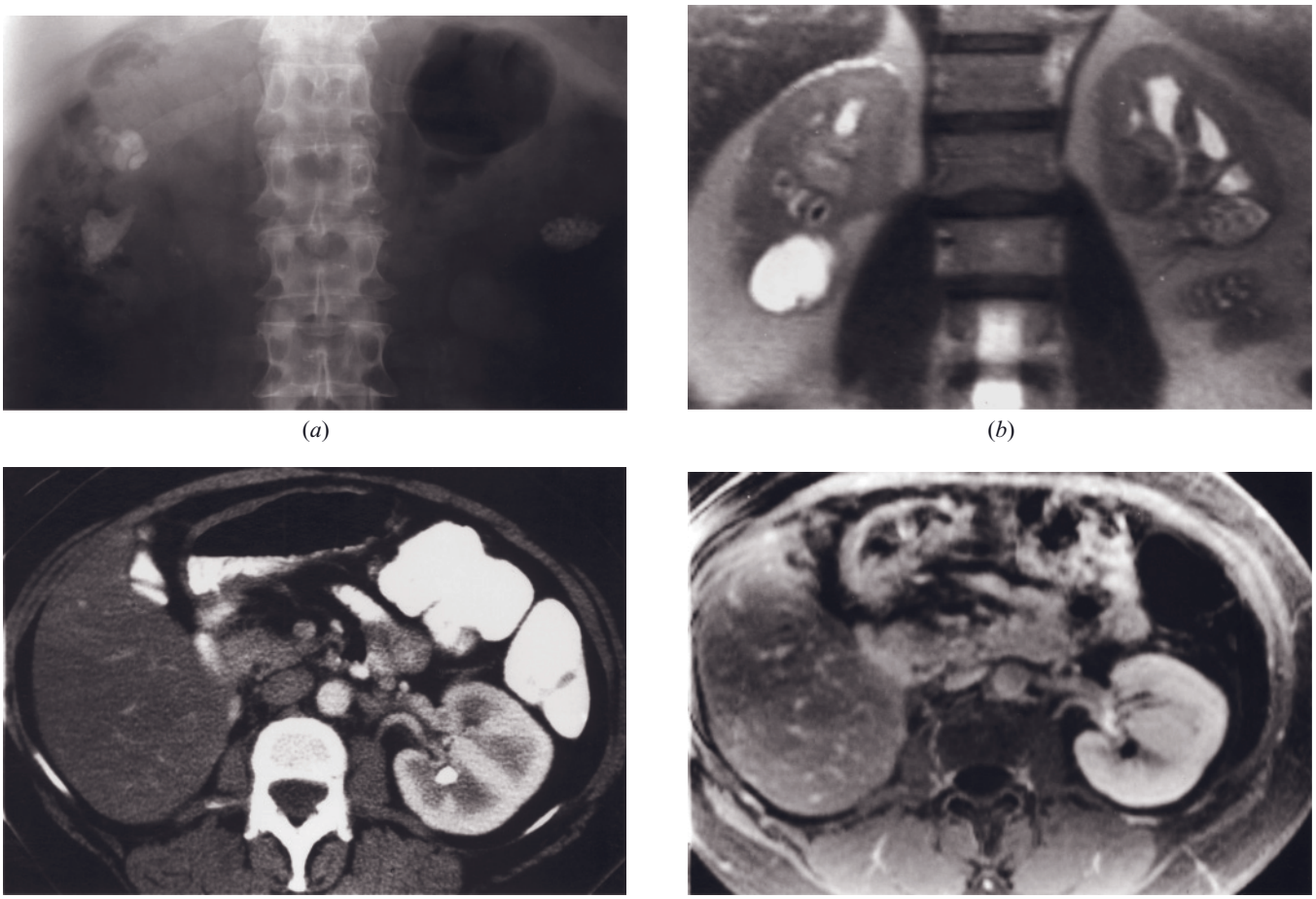

(*a*) (*b*)

(*c*) (*d*)

FIG. 9.125 Renal calculi. Abdominal radiographic (*a*) and coronal T2-weighted SS-ETSE (*b*) images. Radiopaque renal calculi seen on the abdominal radiographic image appears as signal-void defects in high-signal fluid-filled renal collecting systems on the T2-weighted sequence. Contrast enhanced CT (*c*) and T1-weighted 90-s fat-suppressed postgadolinium (*d*) images in a second patient. The radiopaque calculus is clearly shown on CT (*c*) and is apparent as a signal-void focus on the MR image (*d*). The calculus is difficult to appreciate on the MR image.

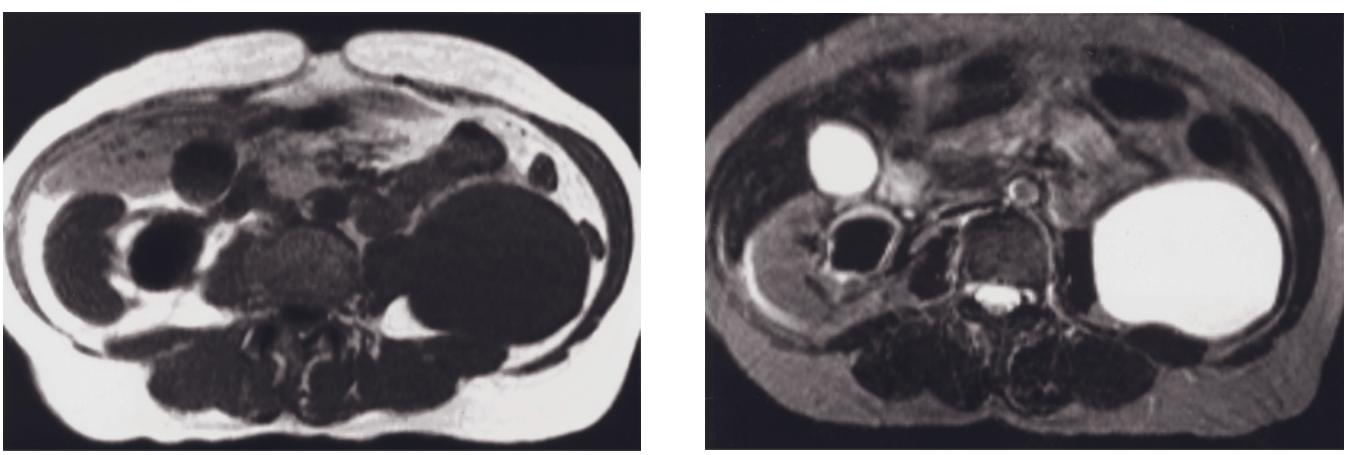

(*a*) (*b*)

FIG. 9.126 Renal calculi. T1-weighted precontrast SGE (*a*), T2-weighted SE (*b*), and T1-weighted 10-min fat-suppressed postgadolinium SE (*c*) images. The renal calculus in the right renal pelvis is signal void on all sequences (*a–c*). Conspicuity of the calculus

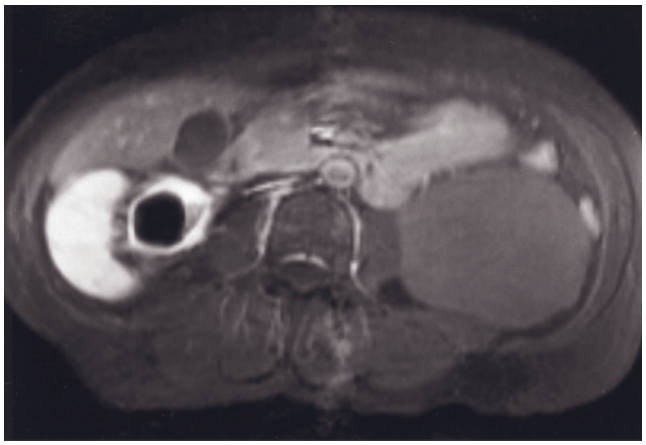

(*c*)

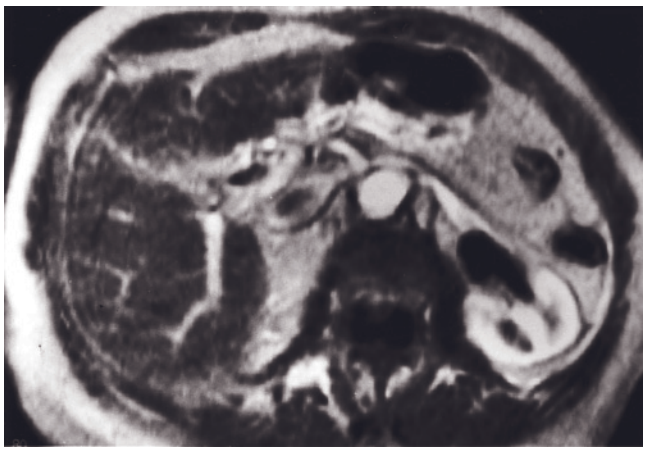

(*d*)

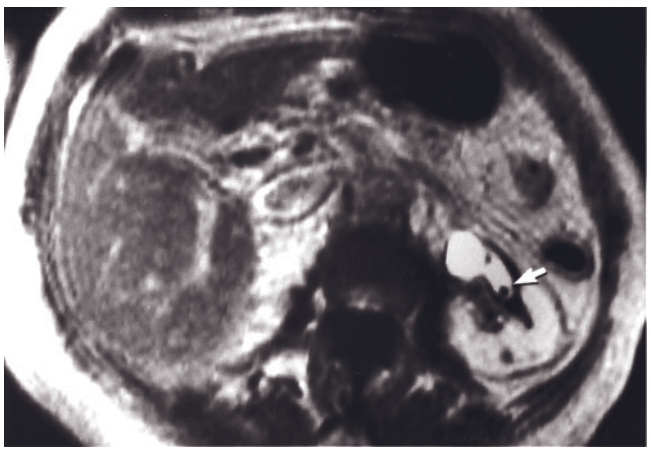

(*e*)

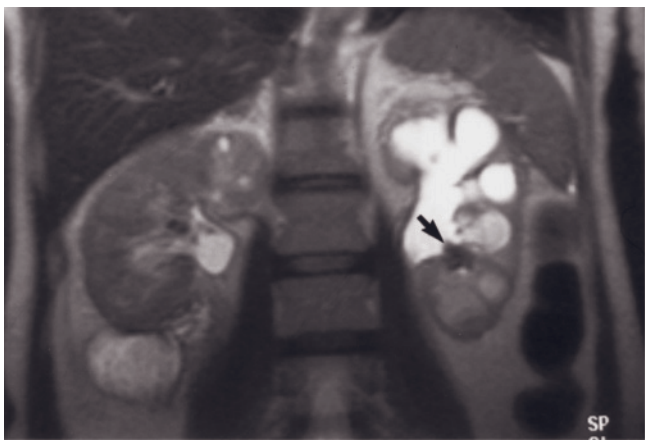

(*f*)

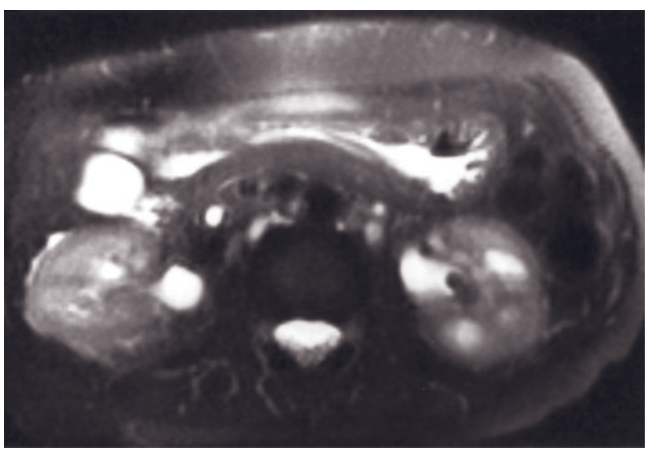

(*g*)

FIG. 9.126 (*Continued*) is greatest on the T2-weighted image and the dilute gadolinium (high signal intensity)-enhanced image. Urine is high in signal intensity on these sequences and contrasts well with the signal-void calculus. T1-weighted immediate (*d*) and 10-min (*e*) postgadolinium images in a second patient demonstrate a small signal-void calculus, which is not apparent in gadolinium-free signal-void urine (*d*) but is well shown on late postgadolinium image (arrow, *e*) because of the high signal intensity of dilute gadolinium-containing urine. Coronal (*f*) and transverse fat-suppressed (*g*) T2-weighted SS-ETSE images in a third patient. A signal-void calculus (arrow, *f*) is present in the lower pole infundibulum of the left kidney. Hydronephrosis is also present.

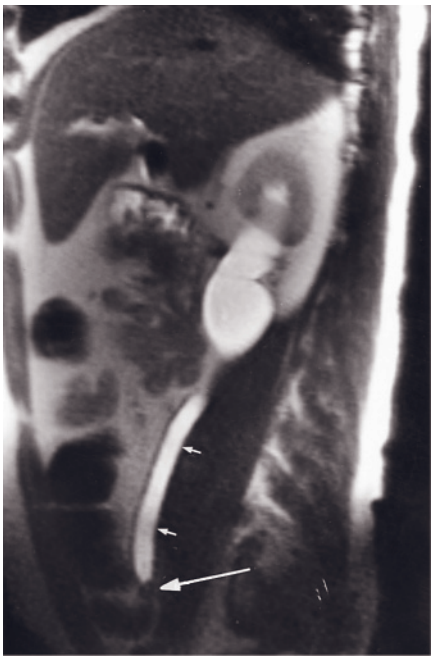

(*a*)

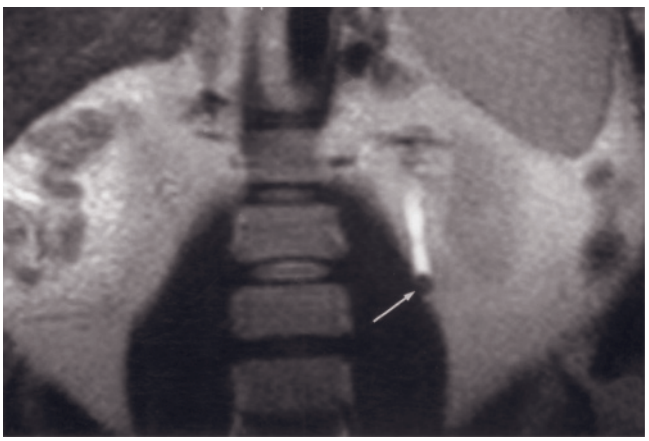

(*b*)

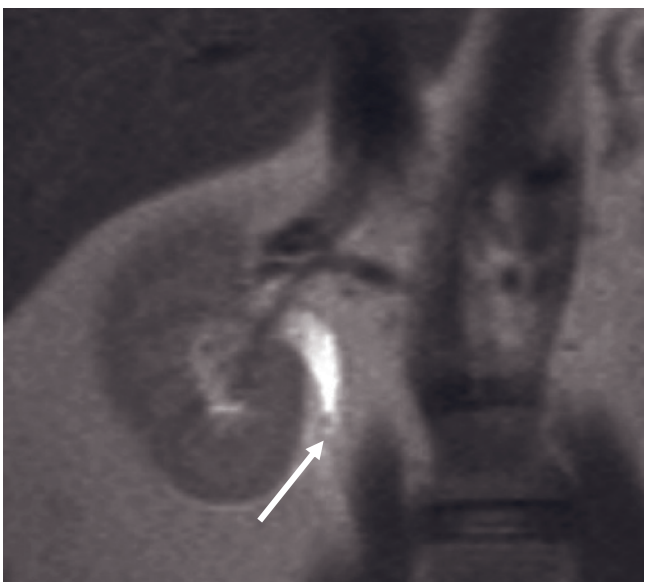

(*c*)

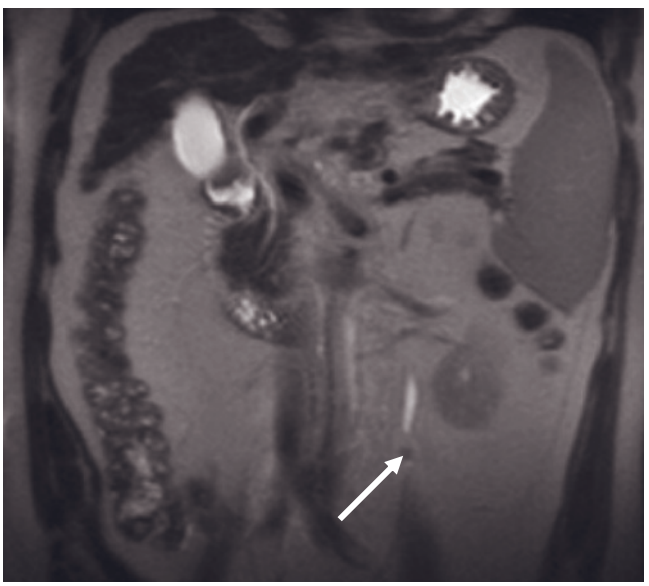

(*d*)

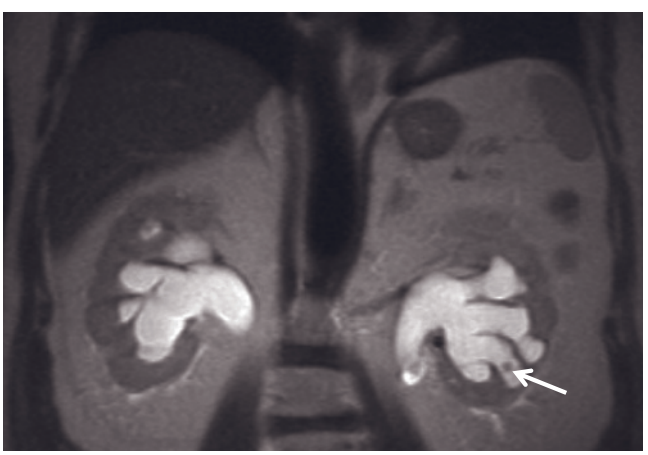

(*e*)

FIG. 9.127 Ureteric calculi. Sagittal T2-weighted SS-ETSE image (*a*).The proximal two-thirds of the ureter are dilated and urine filled, resulting in high signal intensity on the SS-ETSE image (small arrows, *a*). A low-signal-intensity calculus is demonstrated obstructing the ureter (long arrow, *a*), which forms a convex meniscus sign within the urine-filled ureter. Coronal T2-weighted SS-ETSE image (*b*) in a second patient demonstrates mild to moderate left-sided hydronephrosis with an obstructing stone (arrow, *b*) in the proximal left ureter. Coronal T2-weighted single-shot echo-train spin-echo images (*c*, *d*) demonstrate small ureteric calculi (arrows, *c*, *d*) and dilated ureters in another patient. Coronal (*e*) and transverse (*f*) T2-weighted single-shot echo-train spin-echo images demonstrate bilateral hydronephrosis (*e*, *f*), ureteric calculi (arrows, *f*), and a small left kidney stone (arrow, *e*) in another patient. Note that the ureters are dilated.

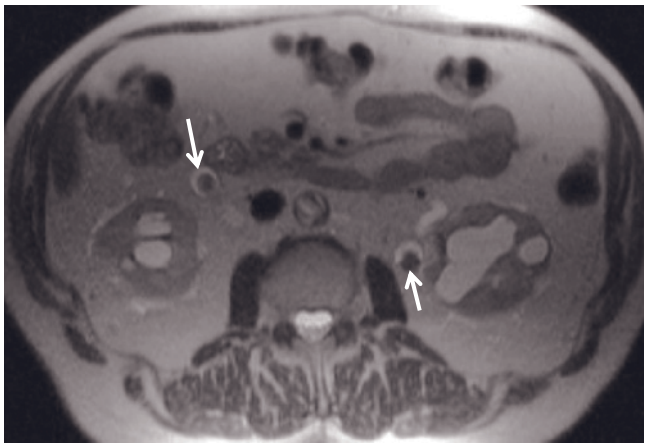

(*f*)

FIG. 9.127 (*Continued*)

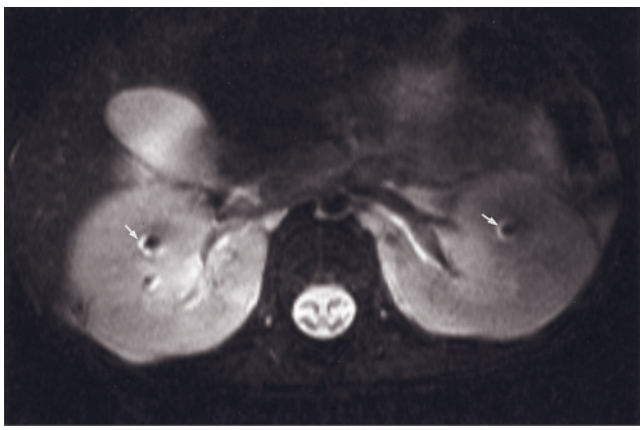

(*a*)

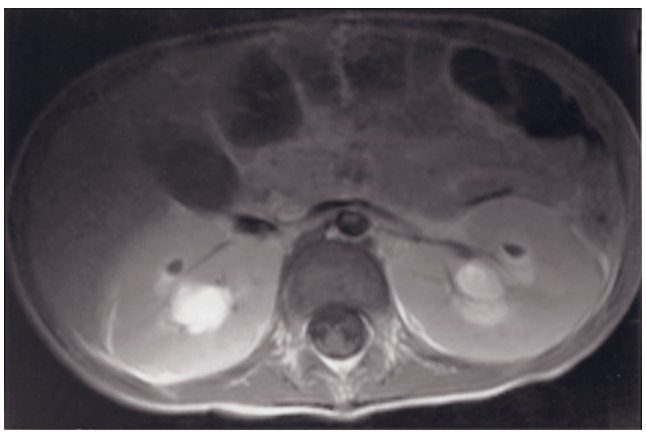

(*b*)

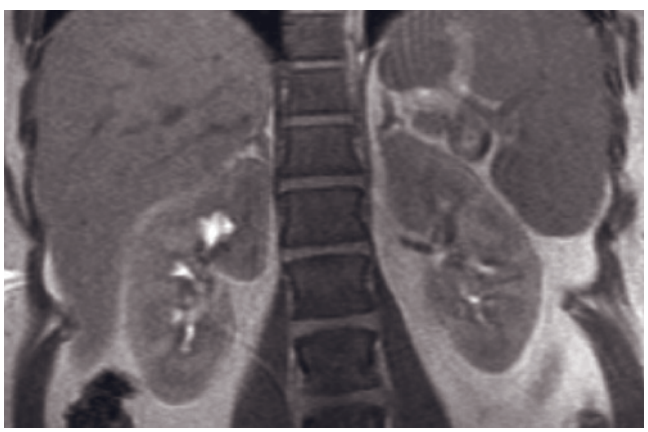

(*c*)

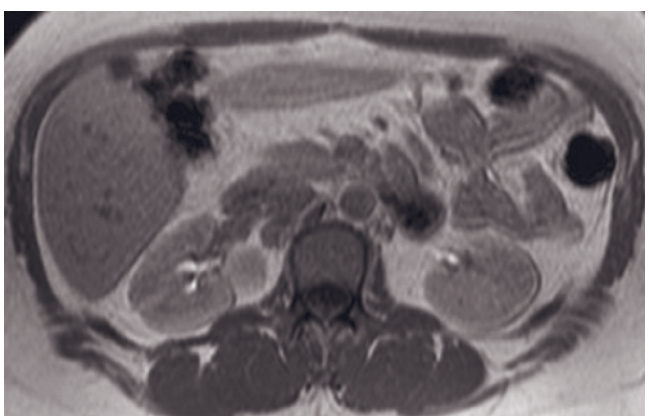

(*d*)

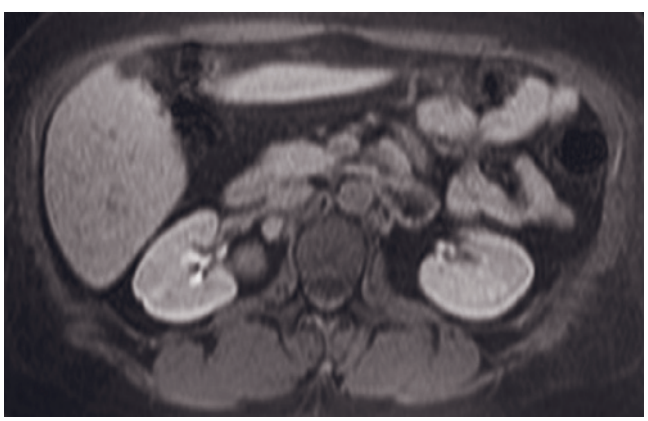

(*e*)

FIG. 9.128 Air in the collecting system. T2-weighted fat-suppressed SE (*a*) and T1-weighted gadolinium-enhanced SE (*b*) images. Multiple foci are present in the nondependent portions of the renal collecting system, demonstrating signal void on both T2-weighted (*a*) and gadolinium-enhanced T1-weighted (*b*) images. These foci possess bright external rings on the T2-weighted images from air-fluid magnetic susceptibility artifact (arrows, *a*). **Blood in the collecting system.** Coronal T1-weighted SGE (*c*) and transverse non-fat-suppressed (*d*) and fat-suppressed (*e*) 3D-GE images demonstrate that bilateral collecting systems are filled with high-signal-intensity material consistent with the presence of subacute blood.

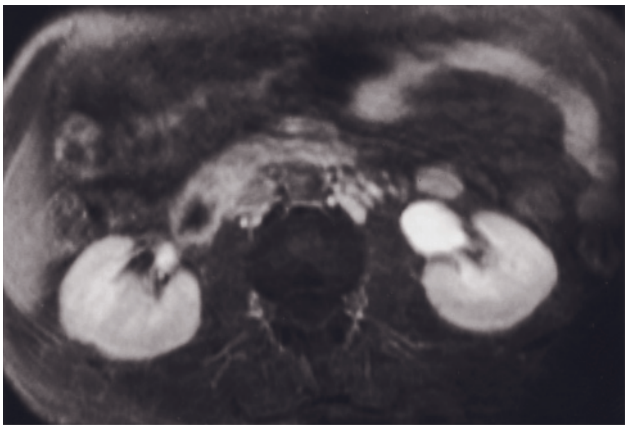

(*a*)

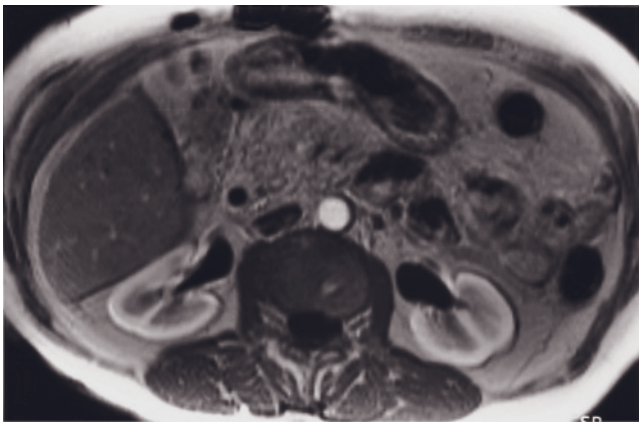

(*b*)

FIG. 9.129 Extrarenal pelvis. T1-weighted fat-suppressed gadolinium-enhanced SE image (*a*). Dilute, high-signal-intensity gadolinium is present in a prominent extrarenal pelvis of the left kidney. The calyces are normal and small in size, reflecting the absence of obstruction. This establishes the diagnosis of extrarenal pelvis. T1-weighted immediate postgadolinium SGE image (*b*) in a second patient demonstrates bilateral extrarenal pelvis. Calyces are normal in size, and cortical enhancement is symmetric and normal.

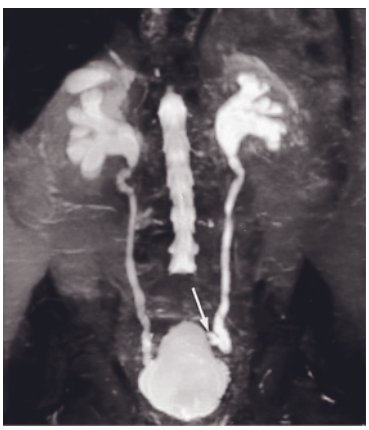

(*a*)

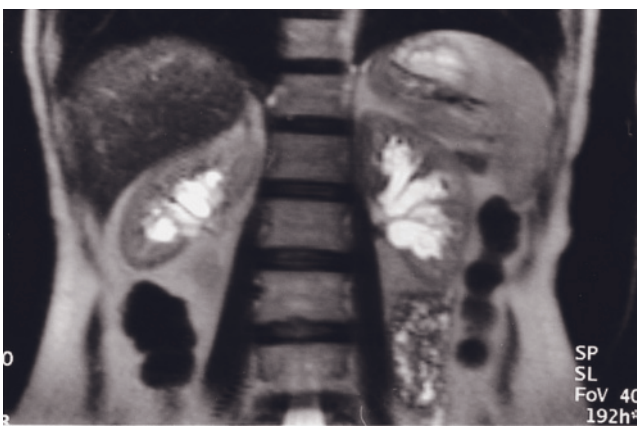

(*b*)

FIG. 9.130 MR urogram. Coronal MIP reconstructed MR urogram from 20 multisession coronal ETSE sections (*a*) demonstrates bilateral severe dilatation of the renal collecting systems secondary to bladder outlet obstruction from prostate cancer. Superior deviation of the left ureter (arrow, *a*) results from superior extension of cancer. Coronal T2-weighted SS-ETSE image (*b*) in a second patient demonstrates moderate calicectasis bilaterally from chronic ureteropelvic junction obstruction.

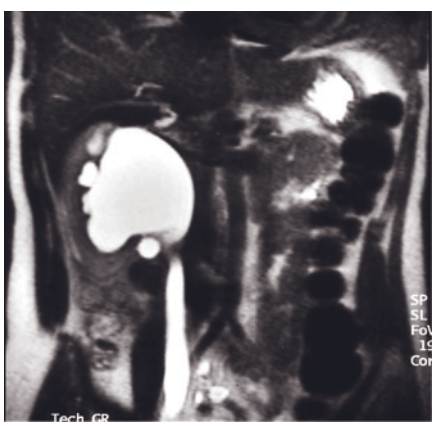

(*a*)

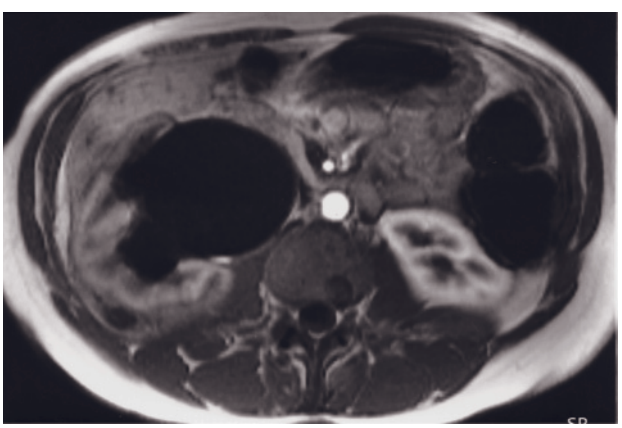

(*b*)

FIG. 9.131 Comprehensive evaluation of renal obstruction. Coronal T2-weighted SS-ETSE (*a*) and transverse immediate (*b*) and coronal 3-min fat-suppressed (*c*) postgadolinium SGE images in a patient with distal ureteral obstruction secondary to

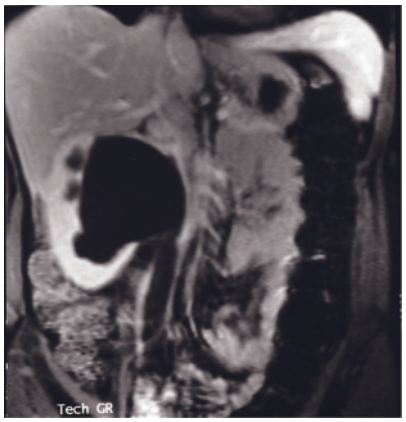

(*c*)

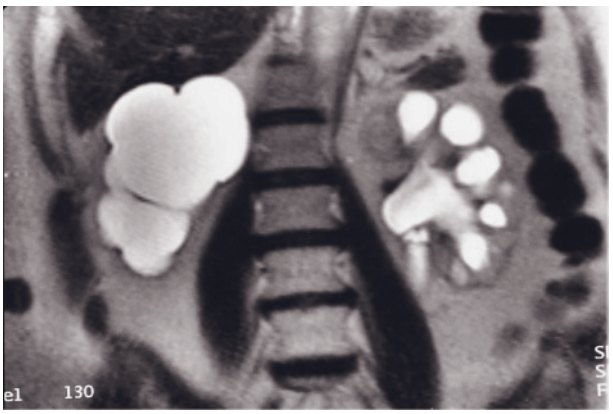

(*d*)

(*e*)

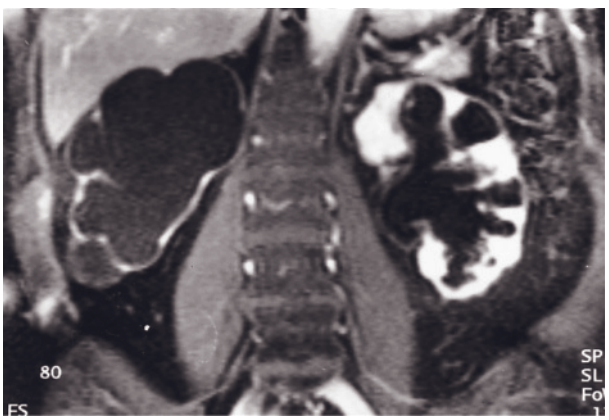

(*f*)

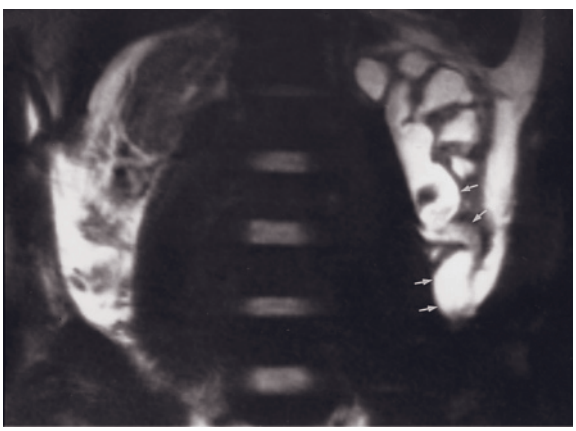

(*g*)

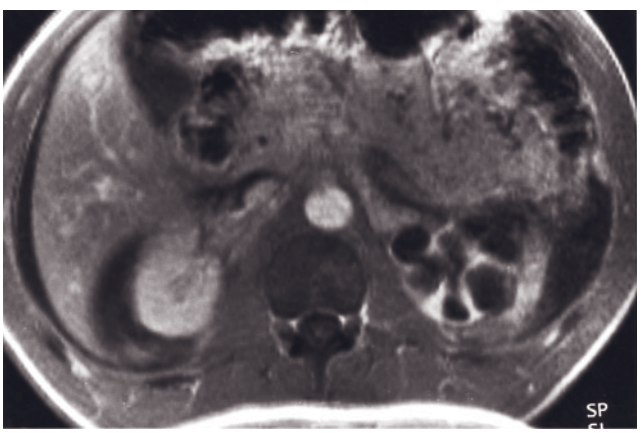

(*h*)

FIG. 9.131 (*Continued*) gynecological malignancy. The coronal T2-weighted image (*a*) demonstrates the severe dilatation of the renal collecting system and ureter. The early-phase image (*b*) demonstrates diminished cortical enhancement of the obstructed right kidney compared to the left. The thickness of the renal cortex is well preserved. The late-phase image (*c*) demonstrates signal-void urine in the ureter and renal pelvis and enhanced renal cortex. Coronal T2-weighted SS-ETSE (*d*, *e*) and coronal 2-min fat-suppressed postgadolinium SGE (*f*) images in a second patient with bilateral distal ureteral obstruction. Massive hydronephrosis is present in the right renal collecting system, and severe dilatation is present in the left (*d*, *e*). After gadolinium administration (*f*), essentially no renal parenchyma is identified in the right kidney, whereas moderately severe thinning is present in the left kidney. Coronal T2-weighted SS-ETSE (*g*) and transverse T1-weighted 90-s fat-suppressed postgadolinium SGE (*h*) images in a third patient with longstanding ureterovesical obstruction secondary to childhood ureteric reimplantation. T2-weighted image (*g*) shows severe hydronephrosis and tortuosity of the ureter (small arrows, *g*) of the left kidney. The transverse gadolinium-enhanced image (*h*) demonstrates extreme thinning of the renal parenchyma in the left kidney, which is effectively nonfunctioning. A normal-appearing right kidney is seen. Intraperitoneal high signal intensity on the T2-weighted image and low signal intensity on the T1-weighted postgadolinium image represent ascites.

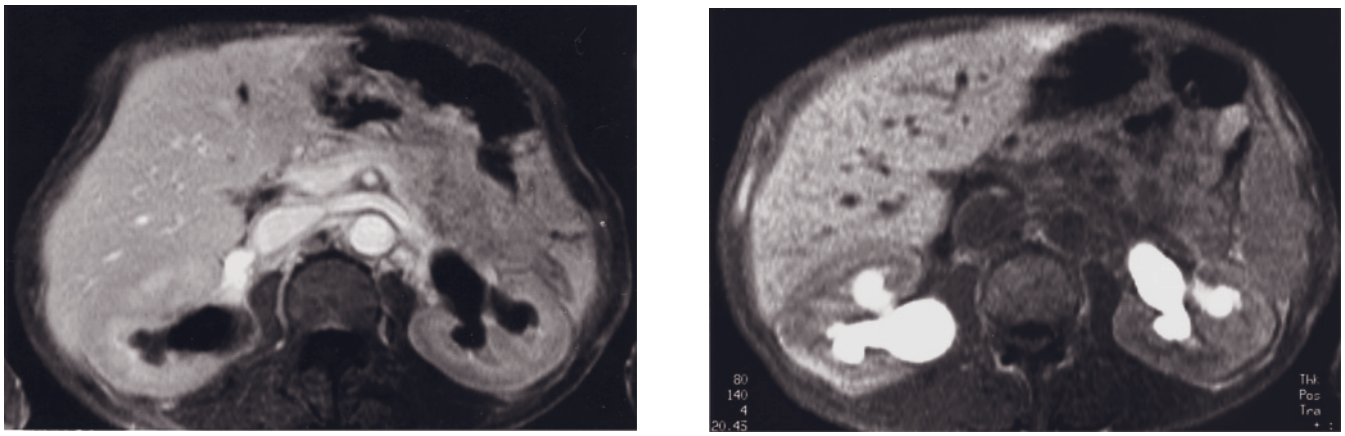

(*a*) (*b*)

FIG. 9.132 Delayed excretion in high-grade obstruction. T1-weighted 2-min postgadolinium fat-suppressed SGE image (*a*) demonstrates severe dilatation of the renal collecting system secondary to bladder cancer. SGE image (*b*) obtained 24 h later demonstrates delayed excretion of gadolinium.

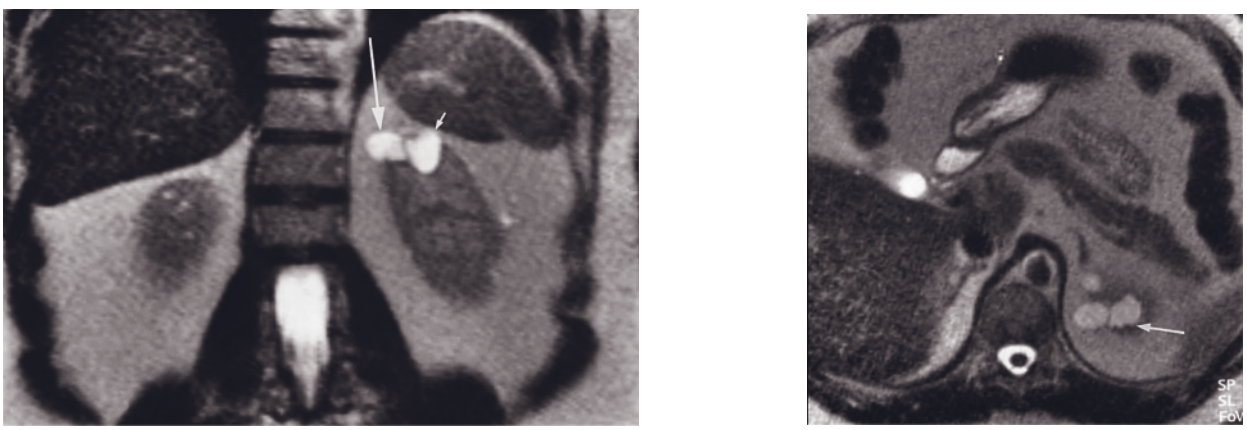

(*a*) (*b*)

FIG. 9.133 Calyceal diverticulum. Coronal (*a*) and transverse (*b*) T2-weighted SS-ETSE images. The coronal image demonstrates a calyceal diverticulum (small arrow, *a*) adjacent to a renal cyst (long arrow, *a*). The calyceal diverticulum extends to the surface of the kidney and contains low-signal-intensity milk of calcium, which is commonly observed in these lesions. Minute low-signal-intensity calculi are apparent in the dependent portion of the diverticulum (arrow) on the transverse image (*b*). Atrophy of the overlying renal cortex is apparent.

which may be well shown with sequences that result in high-signal-intensity urine. Diverticula may uncommonly extend to the cortical surface.

JUXTARENAL PROCESSES

Tumor, hemorrhage, abscesses, and urine leaks all may occur in a juxtarenal location. Urine extravasation most commonly occurs either as a result of trauma or secondary to calyceal rupture due to elevated intracollecting system pressure. Although acute obstruction on the basis of renal calculi is the most common cause of calyceal rupture, this also may be seen in other causes of obstruction (fig. 9.134).

TRAUMA

Renal trauma is a common occurrence in abdominal injury. Tomographic imaging is the most accurate method for assessing the severity of injury, which is generally classified as mild (contusion), moderate (laceration into the collection system), or severe (disruption of renal pedicle or complete crush). Precontrast T1-weighted images, especially fat-suppressed images, are

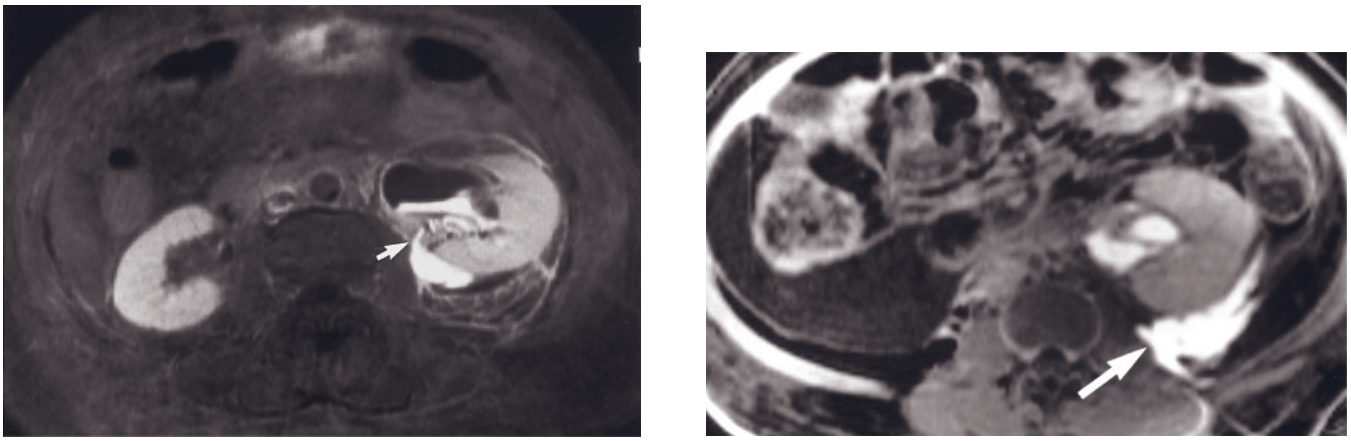

(*a*) (*b*)

FIG. 9.134 Pyelosinus rupture. T1-weighted late-phase fat suppressed gadolinium-enhanced SE image (*a*) demonstrates leakage of dilute, high-signal-intensity gadolinium (arrow) from a dilated, obstructed left renal collecting system. T1-weighted 3-min fat-suppressed postgadolinium SGE image (*b*) in a second patient with a history of trauma. High-signal fluid extravasates into the perinephric space (arrow, *b*) at the same time as high-signal fluid appears in the collecting system.

sensitive to the presence of blood. Dynamic gadolinium-enhanced images demonstrate patent renal vessels as high in signal intensity and are useful for assessing their integrity. Degree of renal injury is well shown on postgadolinium images by the demonstration of lacerations, hemorrhage, or areas of diminished enhancement. Early perinephric leak of contrast material is consistent with vascular injury, whereas >2-min postcontrast leak is indicative of collecting system injury (fig. 9.135) [123].

RENAL FUNCTION

Gadolinium-enhanced dynamic serial imaging of the kidneys demonstrates distinct phases of contrast enhancement based on the location of the bulk of the contrast agent. The phases of enhancement can be separated into 1) capillary, 2) early tubular, 3) ductal, and 4) excretory [5]. Evaluation of the concentrating ability of the kidneys may be made by the observation of signal intensity changes in renal tissue based on the presence of gadolinium of varying concentrations (fig. 9.136). When dilute gadolinium renders tissues high in signal intensity, and when concentrated gadolinium renders tissues signal void. The assessment of these phases of enhancement has been shown to distinguish normal kidneys and those with dilated nonobstructed collecting systems from acute and chronic obstruction. Patients must be mildly dehydrated to provide the physiologic condition for renal concentration. This can be achieved by a 5-h fast. Dilated, nonobstructed kidneys have a temporal pattern of signal intensity changes similar to that of normal kidneys because renal transit is not abnormal (fig. 9.137). Acutely obstructed kidneys are enlarged and have increased renal transit time. This corresponds to an appearance of a prolonged increasing-signal-intensity nephrogram and delayed appearance of contrast in the renal ducts and collecting system (fig. 9.138). Chronic obstruction has diminished cortical enhancement and increased transit time (fig. 9.139).

Functional changes of cortical and medullary enhancement also may be observed in the context of renal ischemia [124].

The renal blood flow (RBF) evaluation can be obtained by using a technique based on intravenous administration of gadolinium chelate and evaluation of first-pass gadolinium chelate perfusion by using a highly accelerated 3D gradient-echo technique on the kidney in freely breathing subjects [125]. This recently described [125] perfusion MR imaging technique helps to evaluate flow rate at the level of the microvasculature within the renal tissue parenchyma, acquiring this data from both kidneys simultaneously. Although this technique allows quantitative assessment of the perfusion to each kidney in terms of blood volume per unit of time per unit of renal volume, its clinical applications remains to be determined.

RENAL TRANSPLANTS

In the United States, 11,000 renal transplants are performed annually [126]. MRI has been used to evaluate potential donors, potential recipients, and recipients after transplantation.

In the evaluation of donors, pretransplantation assessment of the renal vascular anatomy of the potential

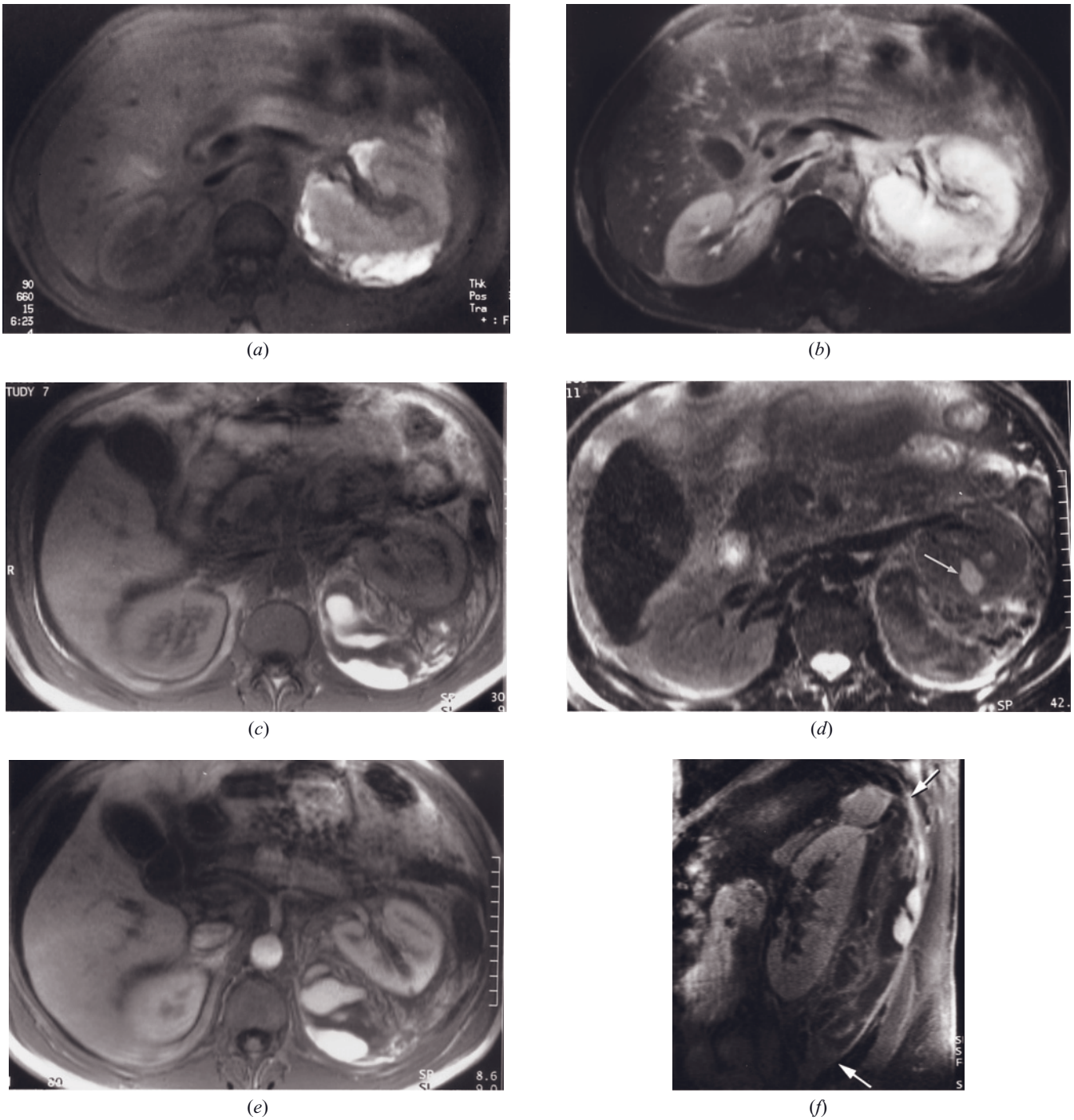

FIG. 9.135 Renal trauma. T1-weighted precontrast (*a*) and 90-s gadolinium-enhanced (*b*) fat-suppressed SE images. High-signal-intensity perirenal hematoma is present surrounding an enlarged left kidney on the precontrast image. The interstitial-phase gadolinium-enhanced image demonstrates greater enhancement of the left kidney, compared to the normal right kidney. This excludes renal artery compromise but implies increased intrarenal tissue pressure, capillary leakage, and/or renal vein compromise. T1-weighted precontrast SGE (*c*), T2-weighted SS-ETSE (*d*), T1-weighted immediate postgadolinium SGE (*e*), and sagittal 90-s fat-suppressed postgadolinium SGE (*f*) images in a second patient who sustained abdominal trauma. High-signal-intensity hemorrhage is noted in the perirenal and posterior pararenal space in the left kidney with a multilayered appearance (*c*). Mixed high signal intensity is apparent on the T2-weighted image (*d*), which is consistent with blood products of varying age. In addition, a tubular-shaped focus of high signal intensity is present, a finding consistent with an intraparenchymal laceration (arrow, *d*). The kidney enhances normally immediately after contrast administration, excluding a major renal arterial injury. The sagittal image (*f*) demonstrates the full renal length and the volume of posterior pararenal blood (arrows).

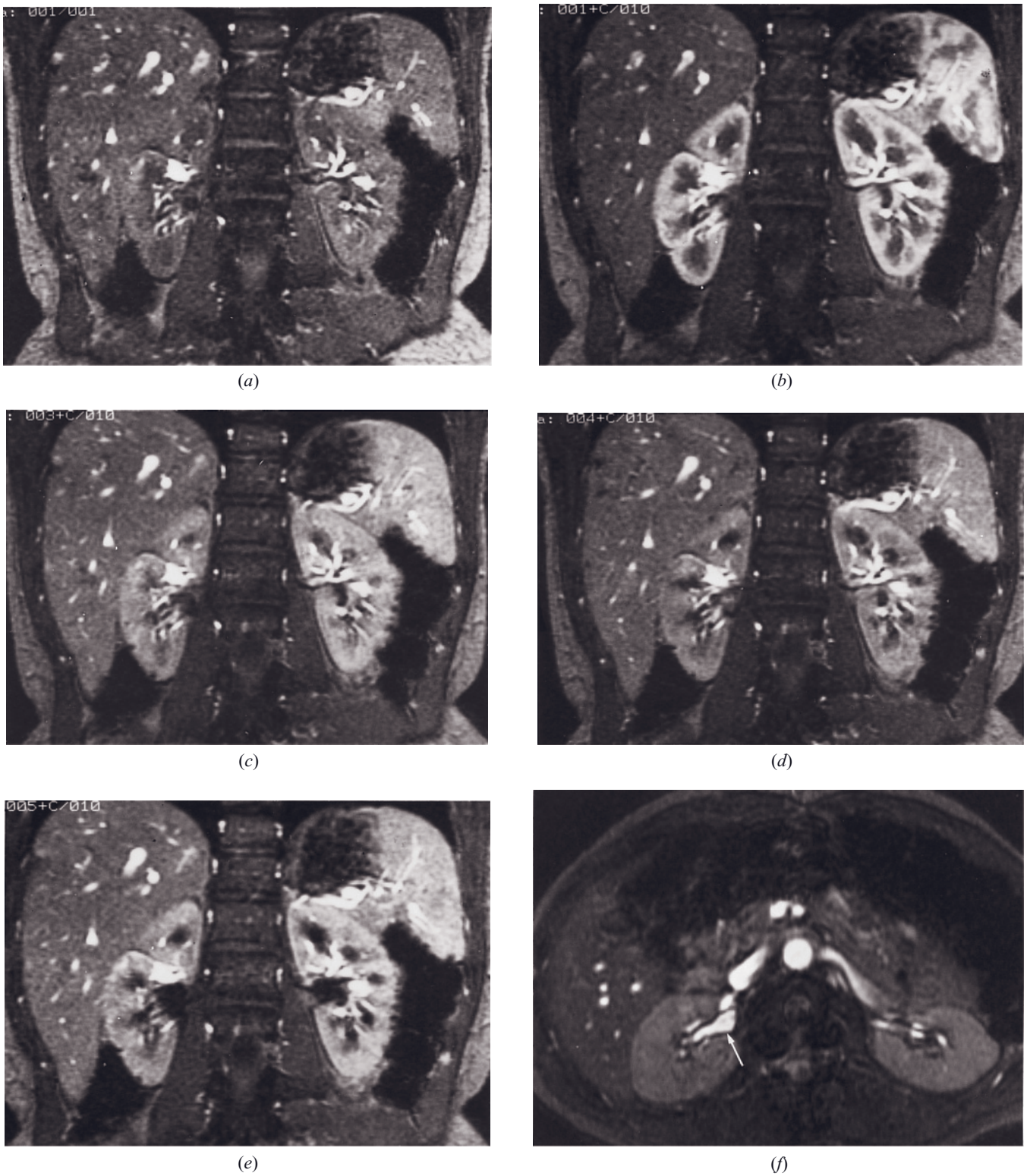

FIG. 9.136 Normal renal function. Precontrast image (*a*). Minimal corticomedullary differentiation is present. Cortical enhancement (capillary)-phase image (*b*). Cortex signal intensity is increased by 17%. Corticomedullary differentiation is distinct because of differential blood flow and increased delivery of gadolinium to the renal cortex. Early tubular-phase image (*c*). Signal intensity of medulla is transiently increased, whereas there is little change in cortical signal intensity. Ductal-phase image (*d*). Signal intensity of medulla is decreased (6% from vascular phase) because of the concentration of gadolinium in distal convoluted tubules and collecting ducts. There is minimal decrease in cortical signal intensity (2%). Decreased signal intensity is apparent in the inner medulla and therefore mainly represents concentrated gadolinium in collecting ducts. Excretory-phase image (*e*). Urine containing concentrated gadolinium appears in renal collecting systems as signal-void fluid. Excretory-phase image (*f*) obtained 15 min after injection. No corticomedullary differentiation is present. Urine contains dilute (high signal intensity) gadolinium (arrow, *f*) because of rapid clearance of gadolinium from the body. (Reprinted with permission from Semelka RC, Hricak H, Tomei E, Floth A, Stoller M: Obstructive nephropathy: evaluation with dynamic Gd-DTPA enhanced MR imaging. *Radiology* 175: 797–803, 1990.)

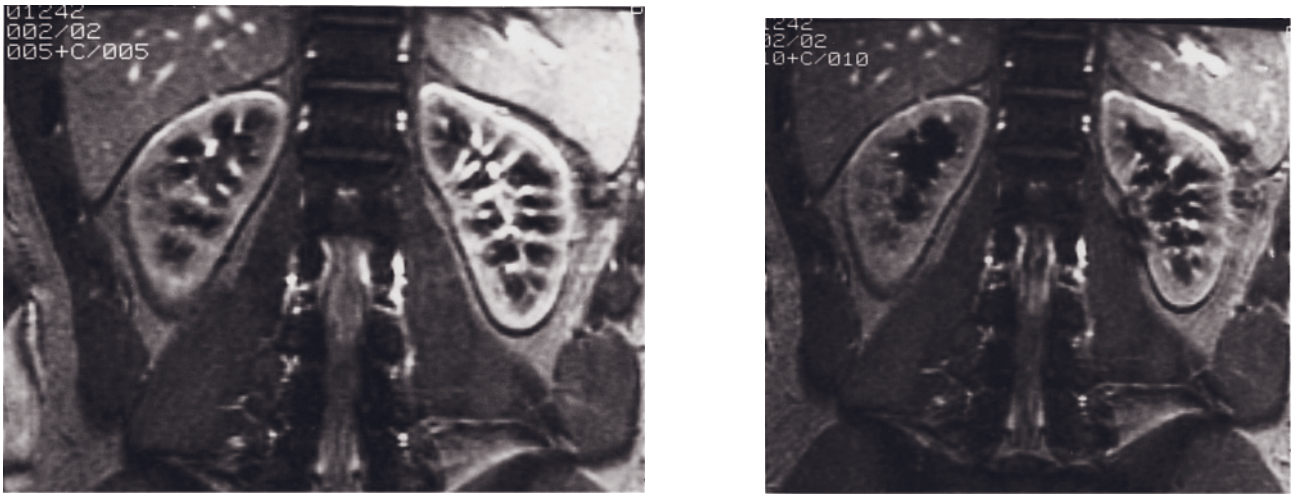

(*a*) (*b*)

FIG. 9.137 Dilated nonobstructed kidney. Gradient-echo images of subject with a dilated nonobstructed right kidney. Ductal-phase image (*a*). Low signal intensity of the medulla appears simultaneously in the dilated nonobstructed right kidney and in the normal left kidney. In the excretory-phase image (*b*), excretion of concentrated urine is bilaterally symmetric. Susceptibility-induced image distortion of the renal collecting systems is due to the high concentration of gadolinium. (Reprinted with permission from Semelka RC, Hricak H, Tomei E, Floth A, Stoller M: Obstructive nephropathy: evaluation with dynamic Gd-DTPA enhanced MR imaging. *Radiology* 175: 797–803, 1990.)

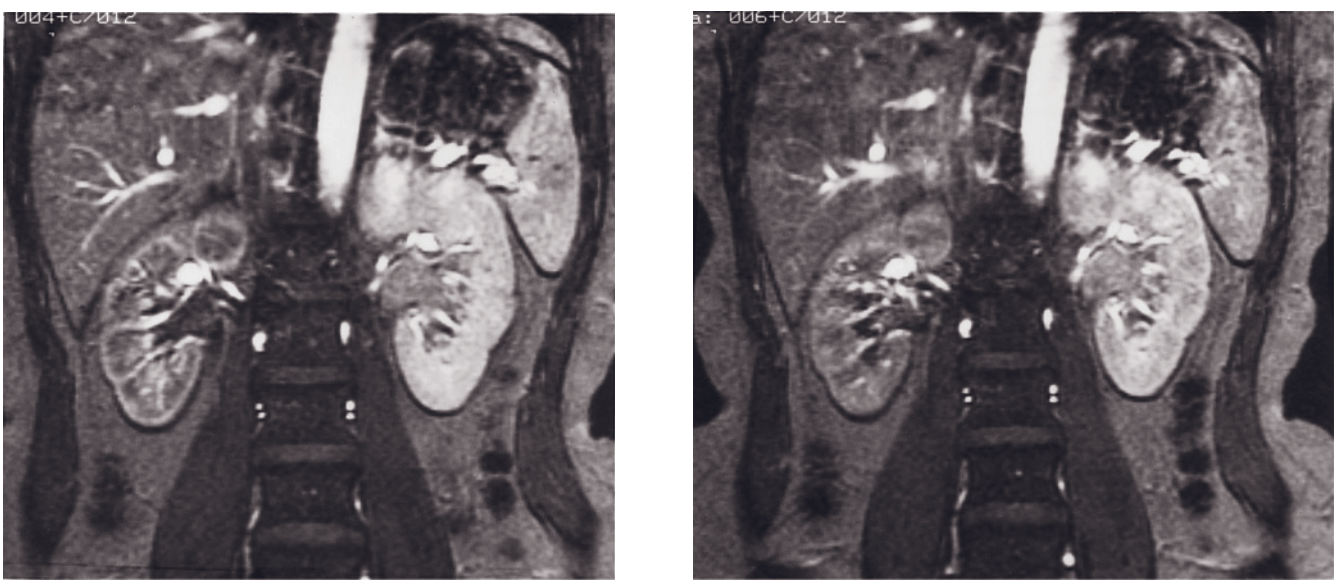

(*a*) (*b*)

FIG. 9.138 Acute obstruction. Gradient-echo images of subject with an acutely obstructed left kidney and a normal right kidney. Cortical enhancement (capillary)-phase image (*a*). The acutely obstructed left kidney is larger and swollen compared with the right kidney. Obstruction to venous drainage results in an abnormal pattern of contrast enhancement of the obstructed kidney. The parenchymal signal intensity is greater, and corticomedullary differentiation is diminished. Ductal-phase image (*b*). Tubular concentration is apparent in the normal right kidney but not on the obstructed left kidney. Cortical enhancement is persistent on the obstructed side, analogous to the persistent nephrogram on intravenous urogram (IVU) examination. Excretory-phase

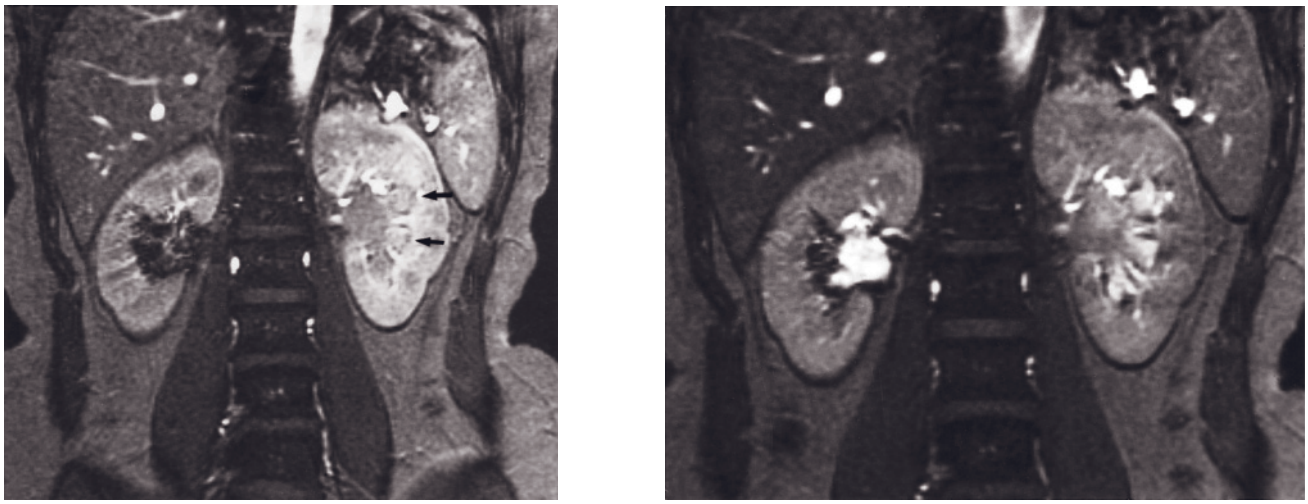

(*c*) (*d*)

FIG. 9.138 (*Continued*) image (*c*). The delayed image obtained at 3.5 min shows dilute (high signal intensity) urine in dilated calyces (arrows, *c*) of the left kidney. Concentrated (low signal intensity) urine is excreted from the right kidney. Excretory-phase image (*d*) obtained 15 min after injection. Dilute urine is excreted by the normal right kidney. Further excretion into the dilated left renal collecting system can be appreciated. (Reprinted with permission from Semelka RC, Hricak H, Tomei E, Floth A, Stoller M: Obstructive nephropathy: evaluation with dynamic Gd-DTPA enhanced MR imaging. *Radiology* 175: 797–803, 1990.)

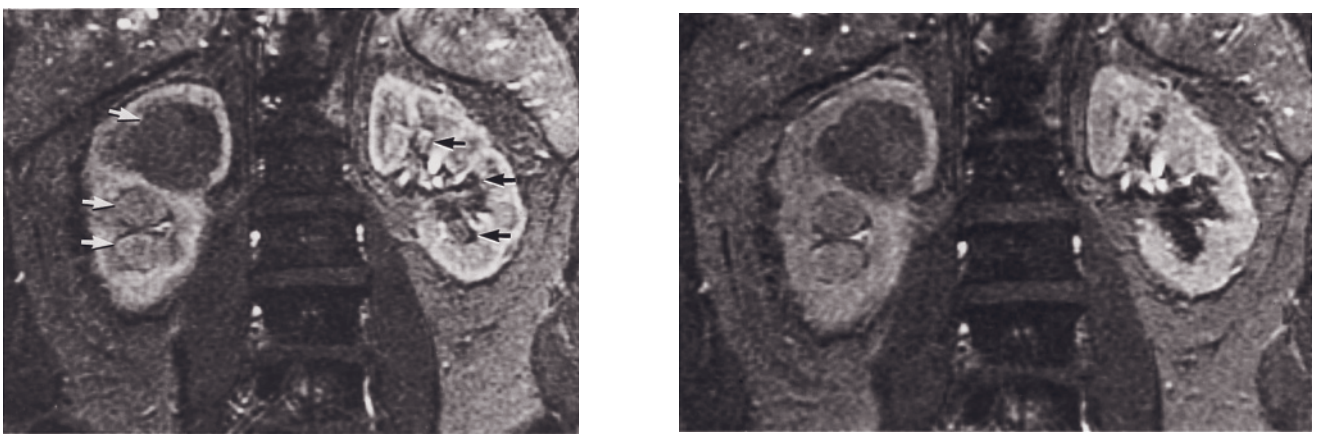

(*a*) (*b*)

FIG. 9.139 Chronic obstruction. Gradient-echo images of a subject with a chronically obstructed right kidney and a dilated nonobstructed left kidney. Cortical enhancement (capillary)-phase image (*a*). Normal cortical enhancement is appreciated in the left kidney, which demonstrates corticomedullary distinction. Cortical enhancement is lower in the chronically obstructed right kidney, with no definition of CMD. Low-signal-intensity gadolinium-free urine is present in both collecting systems (arrows, *a*). On the excretory-phase image (*b*), concentrated urine is excreted by the dilated nonobstructed left kidney. There is no apparent excretion by the chronically obstructed right kidney, no development of corticomedullary differentiation, and no significant changes in parenchymal signal intensity from the cortical enhancement phase. (Reprinted with permission from Semelka RC, Hricak H, Tomei E, Floth A, Stoller M: Obstructive nephropathy: evaluation with dynamic Gd-DTPA enhanced MR imaging. *Radiology* 175: 797–803, 1990.)

renal donor is ancillary information. The incidence of variant arterial anatomy of the kidney is 40%, including early renal artery division or branches, multiple renal arteries (aberrant and accessory renal arteries), and multiple renal veins [126]. Angiography has been the primary modality for the evaluation of renal vascular anatomy. However, in recent articles, excellent sensitivity and accuracy in the depiction of accessory renal arteries has been demonstrated by gadolinium-enhanced 3D MRA [127, 128]. One study [127] showed that combined gadolinium-enhanced 3D MRA, MR urography, and MR nephrography can accurately depict the arterial supply,

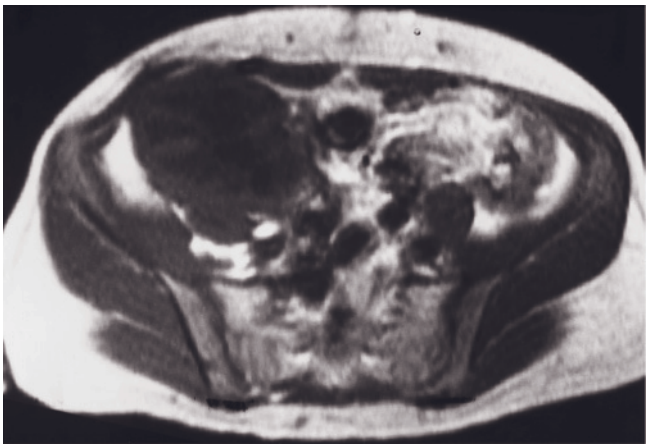

(*a*)

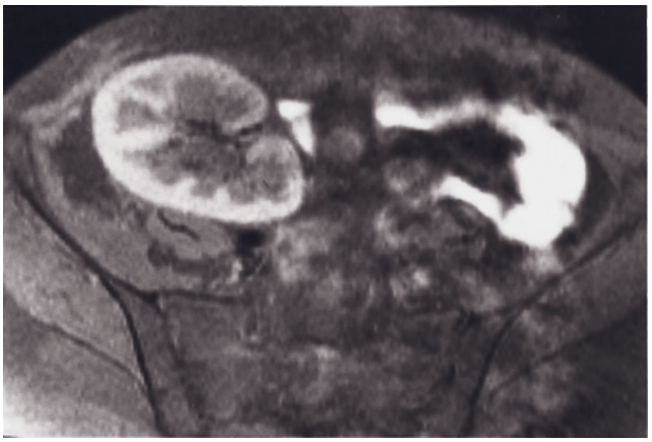

(*b*)

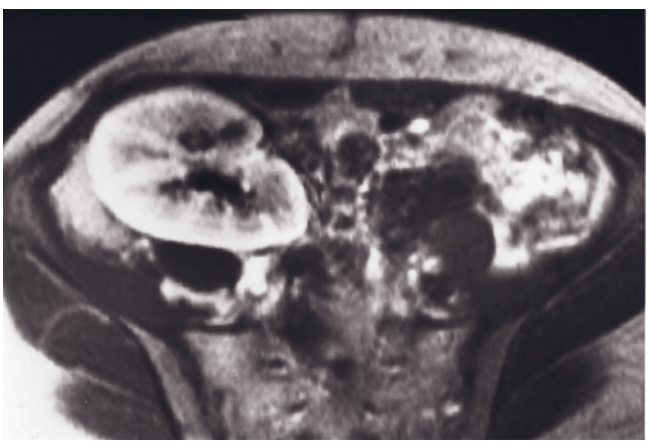

(*c*)

FIG. 9.140 Normal transplant kidney. T1-weighted precontrast SGE (*a*), T1-weighted precontrast fat-suppressed SE (*b*), and T1-weighted immediate postgadolinium SGE (*c*) images of a functioning renal transplant. Normal corticomedullary differentiation is apparent on the precontrast SGE image (*a*) and is clearly defined on the precontrast fat-suppressed SE image (*b*). Corticomedullary differentiation on the immediate postgadolinium image (*c*) is consistent with a normal pattern of renal blood flow. (Reprinted with permission from Semelka RC, Shoenut JP, Greenberg HM: The kidney. In: Semelka RC, Shoenut JP (eds.), *MRI of the Abdomen with CT Correlation*. New York: Raven Press, 1993, p. 91–118.)

collecting system, and renal parenchyma of the donor kidney. In our experience however, depiction of small anomalous renal arteries, particularly when they arise in unusual locations (e.g., distal abdominal aorta, common iliac artery), may elude detection with current MRA technique and yet be clearly defined on angiography. On the newest MR systems, the spatial resolution of MRA sequence with the use of dedicated multireceiver coils may be sufficient to consistently demonstrate the great majority of small anomalous renal arteries.

In the evaluation of potential recipients, MRI may be used to evaluate the native kidneys for disease processes (e.g., development of renal cancer) and the appearance of the common iliac arteries for mural disease or luminal narrowing, particularly if there is a history of prior transplants that have failed.

In the evaluation of recipients after transplantation, normal functioning transplants have good corticomedullary differentiation (CMD) on precontrast T1-weighted fat-suppressed images and immediate postcontrast gradient-echo images (figs. 9.140 and 9.141).

Some immediate postoperative complications may be associated with surgical difficulties; these include renal artery thrombosis or stenosis, renal vein thrombosis, urinary leak, or lymphocele. Others complications include rejection, cyclosporine toxicity, acute tubular necrosis, infection (figs. 9.142 and 9.143), and transplantation-related malignancies such as posttransplantation lymphoproliferative disorder (PTLD) and lymphoma [126, 129–131]. Renal cancer may also arise in the transplant kidney (fig. 9.144).

Regarding immediate complications, allograft renal artery stenosis occurs in 2–10% of cases and may occur as early as 2 days or as late as several years [126]. Gadolinium-enhanced 3D MRA is an accurate reproducible technique for evaluating renal artery complications [2, 3, 126, 128]. Normal transplant arteries and veins are clearly identified (fig. 9.145). Stenosis or thrombosis of artery or vein is similarly demonstrated in a reproducible fashion with this technique (fig. 9.146).

In renal transplant patients, lymphoceles are defined histopathologically as collections of lymphatic fluid (i.e., nonsanguineous or purulent) in the perinephric space

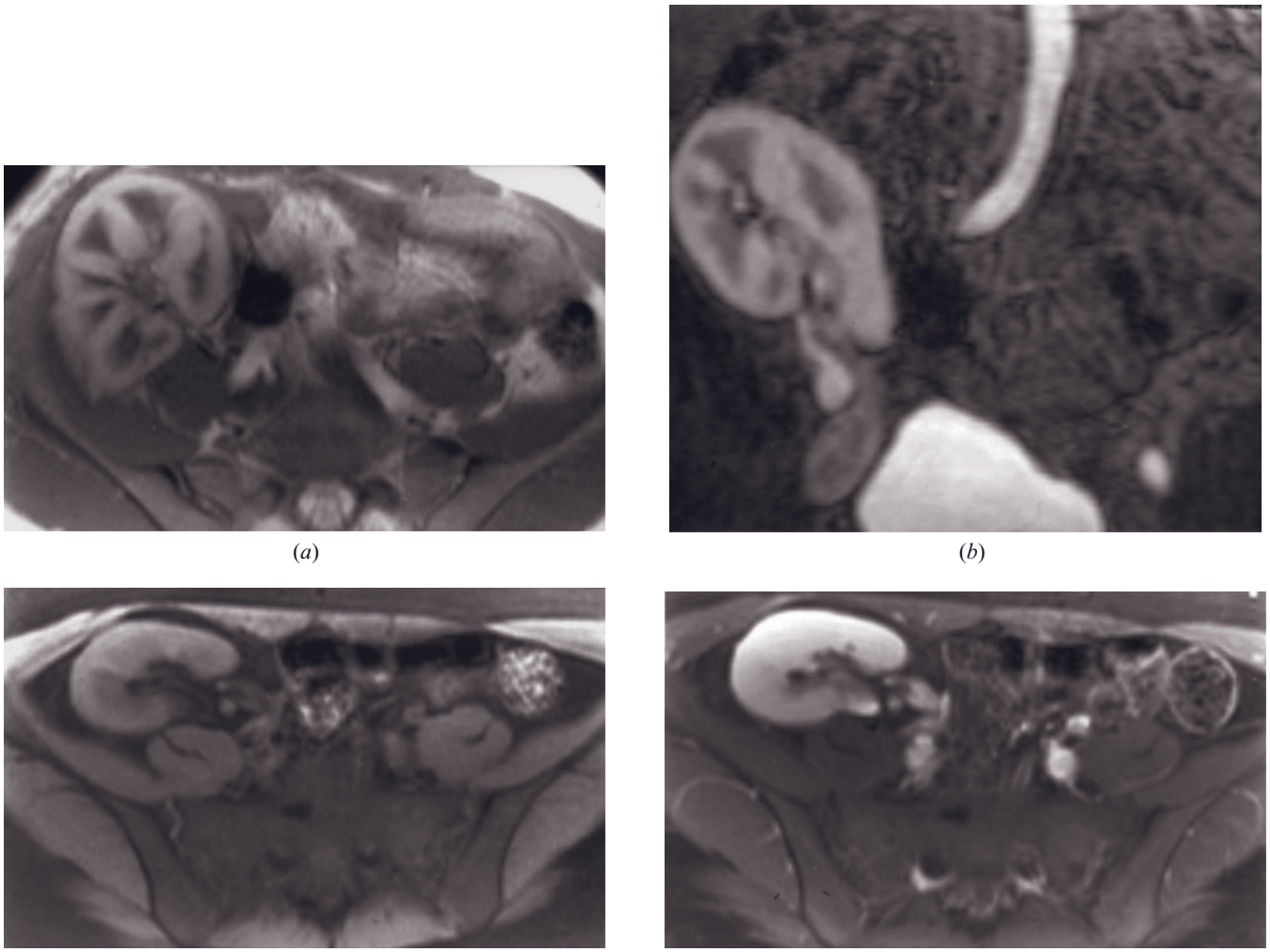

(*a*) (*b*)

(*c*) (*d*)

FIG. 9.141 Normal transplant kidney. Transverse T1-weighted immediate postgadolinium SGE (*a*) and coronal 3D MRA source (*b*) images. The kidney transplant in the right lower quadrant demonstrates normal capillary-phase enhancement. No complications were identified. T1-weighted precontrast (*c*) and 90-s postgadolinium (*d*) fat-suppressed SGE images in a second patient. Corticomedullary differentiation is maintained on the noncontrast image. No complications are evident.

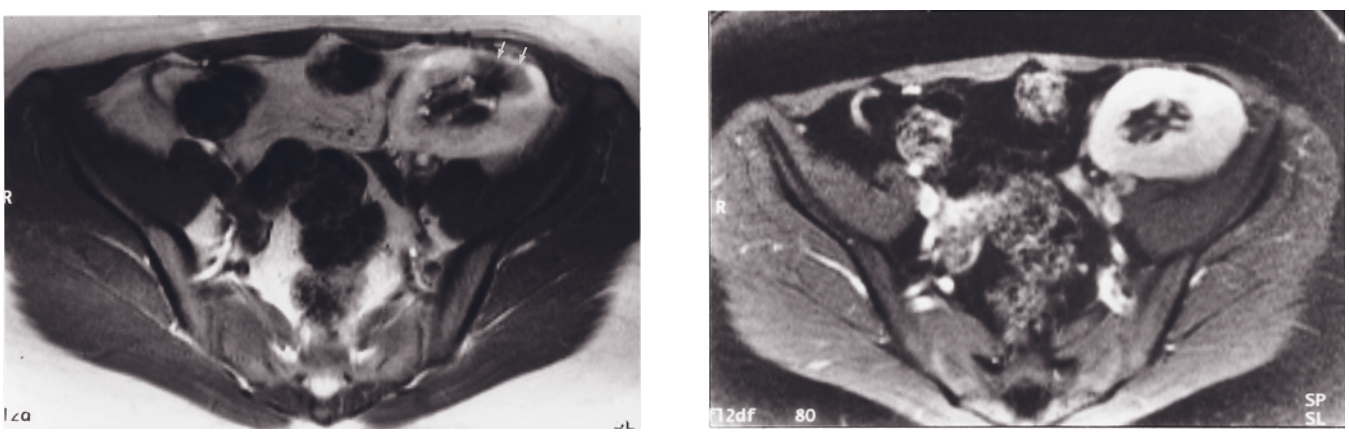

(*a*) (*b*)

FIG. 9.142 Acute focal pyelonephritis in a renal transplant. T1-weighted immediate (*a*) and 90-s fat-suppressed (*b*) postgadolinium SGE images demonstrate a focal region anteriorly in the transplant kidney that shows a striated nephrogram appearance on the capillary-phase image (arrows, *a*) that resolves on the interstitial-phase image (*b*).This appearance is consistent with acute focal pyelonephritis without abscess formation.

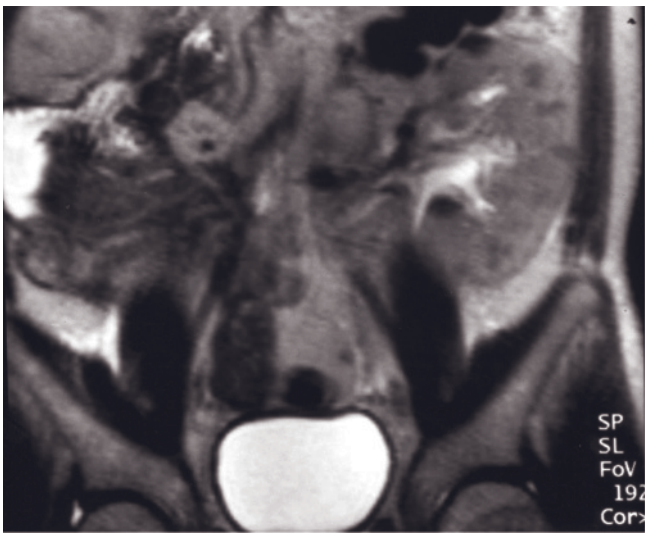

(*a*)

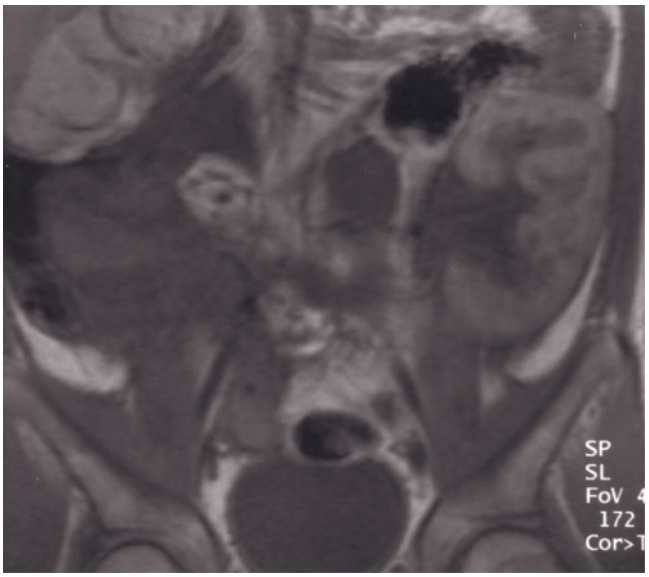

(*b*)

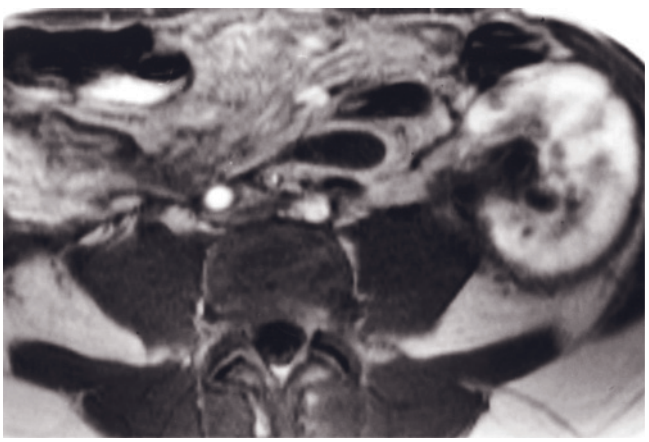

(*c*)

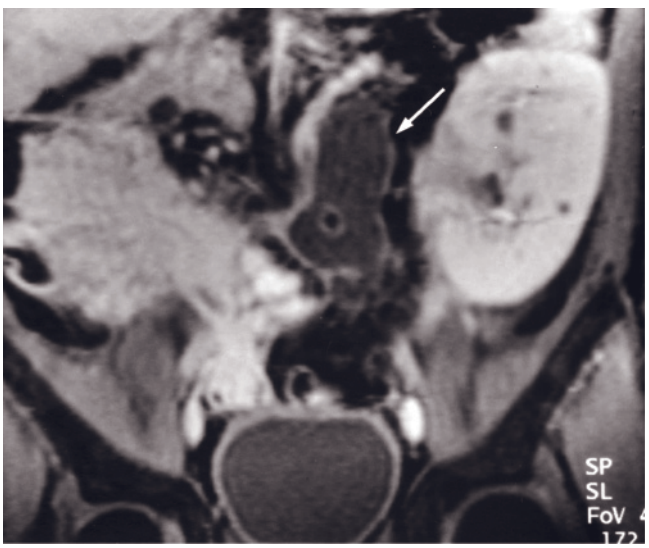

(*d*)

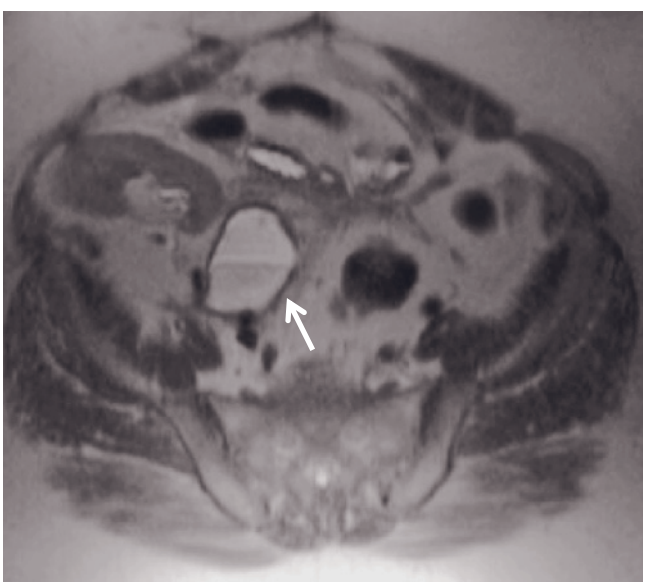

(*e*)

FIG. 9.143 Renal transplant with abscesses. Coronal T2-weighted SS-ETSE (*a*) and T1-weighted precontrast SGE (*b*) images and transverse 90-s postgadolinium SGE (*c*) and coronal T1-weighted 90-s fat-suppressed postgadolinium SGE (*d*) images. There are multiple low-signal-intensity lesions present in the renal transplant. These demonstrate decreased T2-weighted signal and lack of enhancement after contrast. These represent small abscesses, based on their appearance combined with clinical history. There is also a 3-cm well-circumscribed fluid collection present in the central midabdomen, which represents a loculated focal fluid collection or seroma (arrow, *d*). Transverse T2-weighted single-shot echo-train spin-echo (*e*), T1-weighted postgadolinium

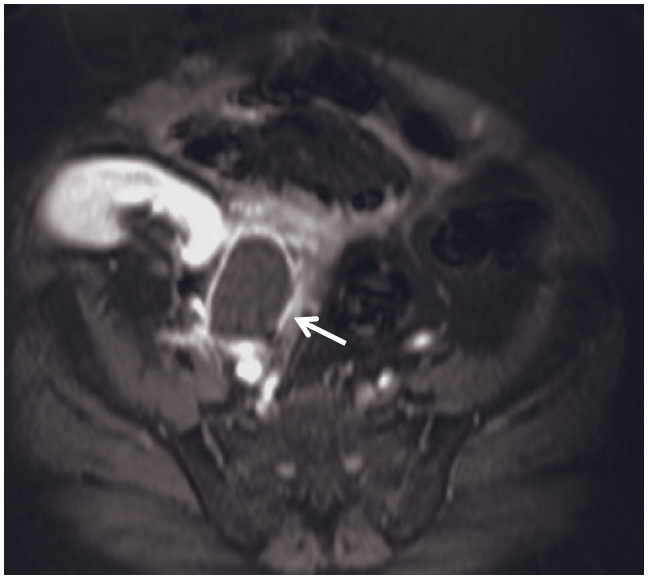

(*f*)

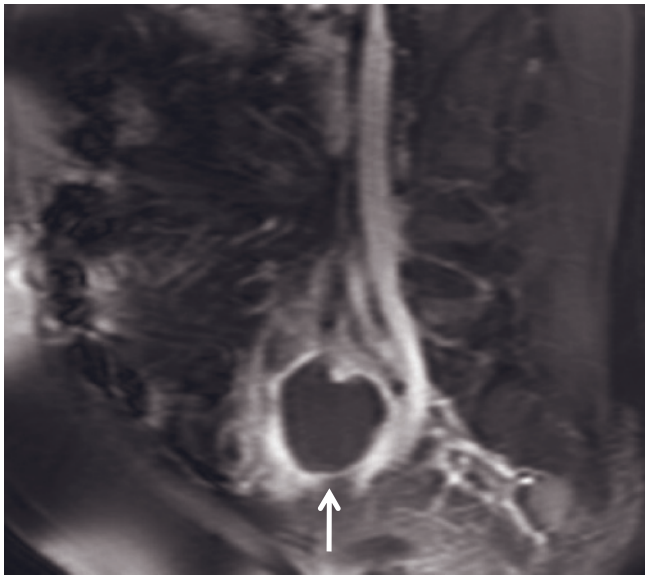

(*g*)

Fig. 9.143 (*Continued*) fat-suppressed interstitial-phase transverse SGE (*f*), and sagittal 3D-GE (*g*) images demonstrate an abscess (arrows, *e–g*) in another patient with renal transplant. A fluid-fluid layer is detected in the abscess cavity. The wall of abscess and adjacent inflammatory tissue shows intense enhancement.

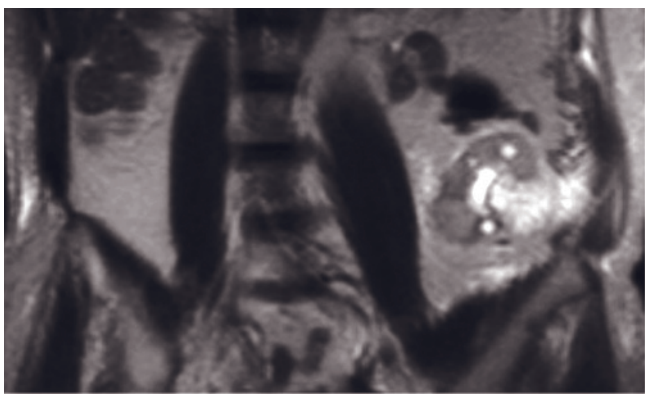

(*a*)

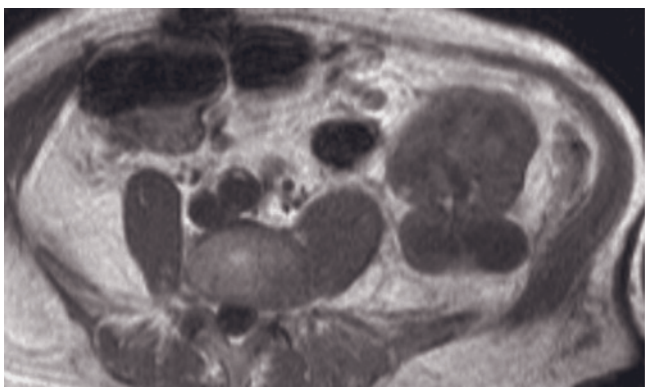

(*b*)

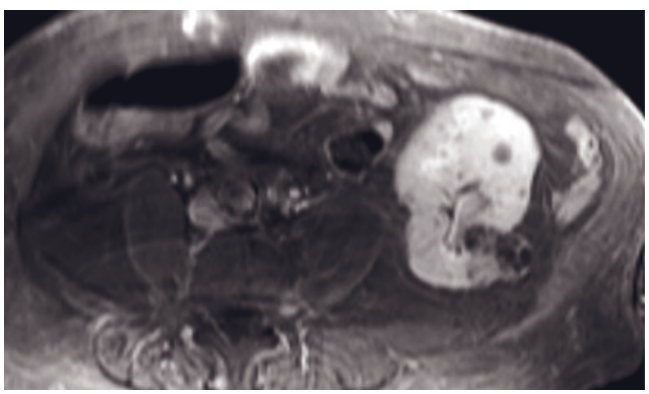

(*c*)

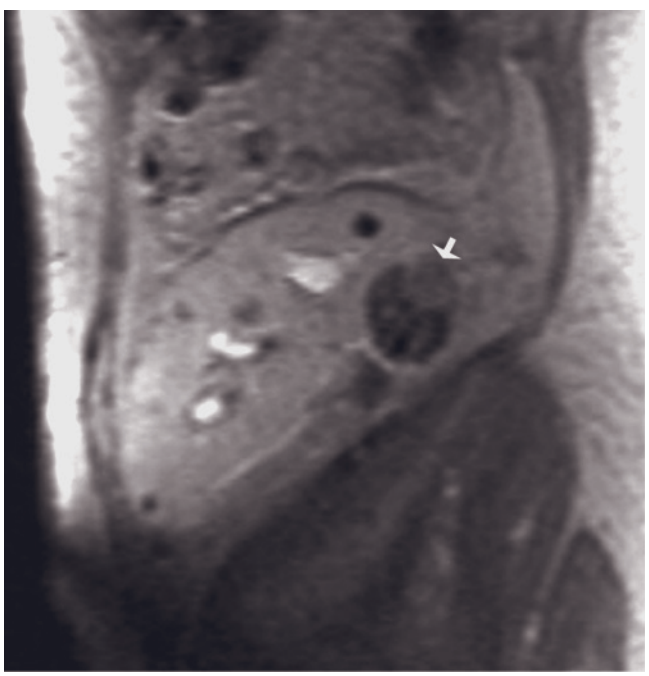

(*d*)

Fig. 9.144 RCC in transplanted kidney. Coronal T2-weighted SS-ETSE (*a*), T1-weighted gradient-echo (*b*), and transverse 90-s fat-suppressed (*c*) and sagittal 90-s (*d*) postgadolinium gradient-echo images. A complex mass is appreciated in the posterior aspect of the transplanted kidney, which appears high signal intensity on the T2-weighted image (*a*) and low signal intensity on the T1-weighted image (*b*) and has mild heterogeneous enhancement on the late-phase image (*c*). There is a small nodule within the mass that shows greater enhancement on the late-phase image, which is best seen on the sagittal plane (arrow, *d*). Multiple additional subcentimeter lesions are identified in the transplanted kidney, likely representing cysts, some of which are complex (*c*, *d*).

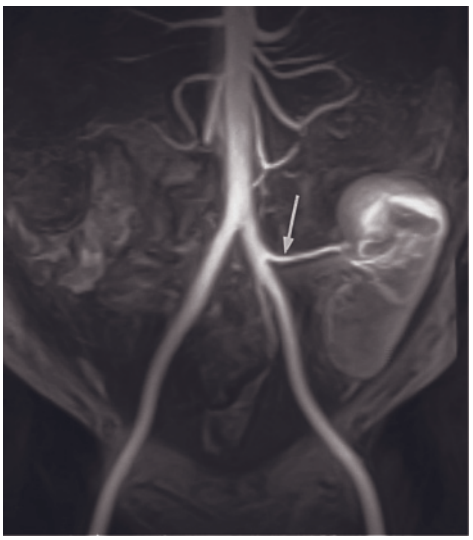

(*a*)

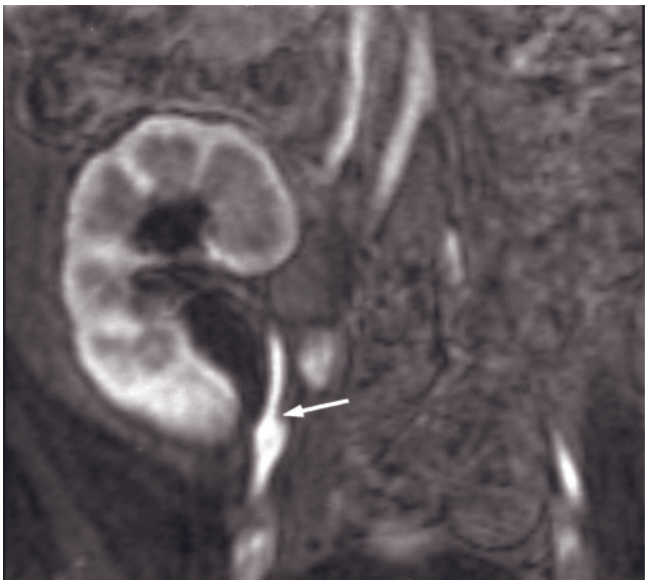

(*b*)

(*c*)

FIG. 9.145 Normal renal artery of a renal transplant. Coronal 3D source image (*a*). The artery is patent, and its anastomosis with the left common iliac artery is well visualized on the source image (arrow, *a*). Coronal 3D source image (*b*) and MIP reconstruction (*c*) image in a second patient demonstrate a normal-caliber renal artery (arrow, *b*). It is important to examine source images in addition to the reconstructed images.

(fig. 9.147). The fluid is derived from the renal lymph vessels, which are not reanastomosed with recipient lymphatics. Clinical differential diagnosis includes urine leak, hematoma, and, rarely, PTLD [132]. Lymphocele after transplant is the most common source of peritransplant fluid collection and occurs up to 18% of cases. Lymphoceles may either occur in the first month because of surgery or later on as a sign of rejection [126]. Lymphocele is high signal on T2-weighted images and low signal on T1-weighted images. Urinoma is formed because of leakage of urine from pyeloureteral anastomosis causing a cystlike fluid-filled structure, and it is more likely to occur in the first 5 weeks after transplantation [126]. There are in general two surgical techniques used for ureter anastomosis in renal transplantation: either implantation of the donor ureter into the recipient

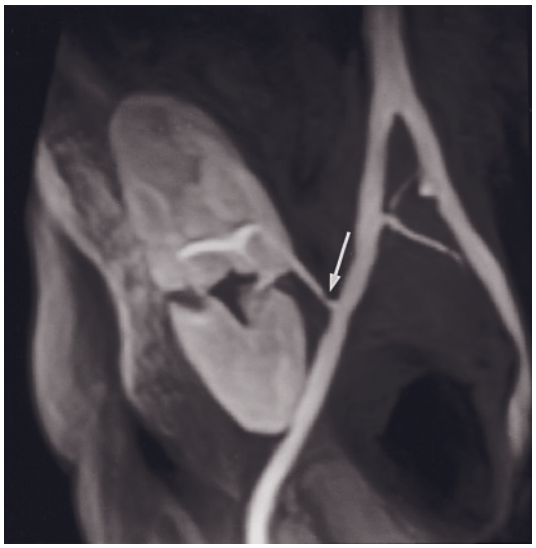

(*a*)

(*b*)

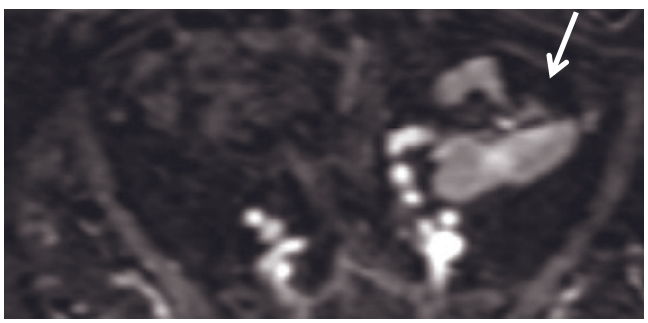

(*c*)

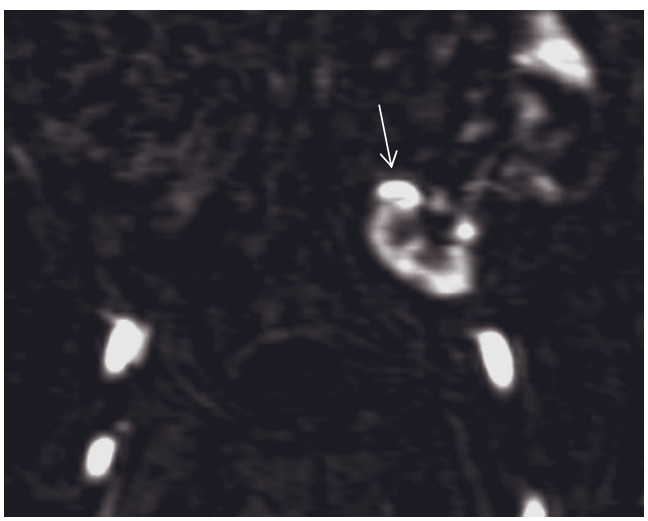

(*d*)

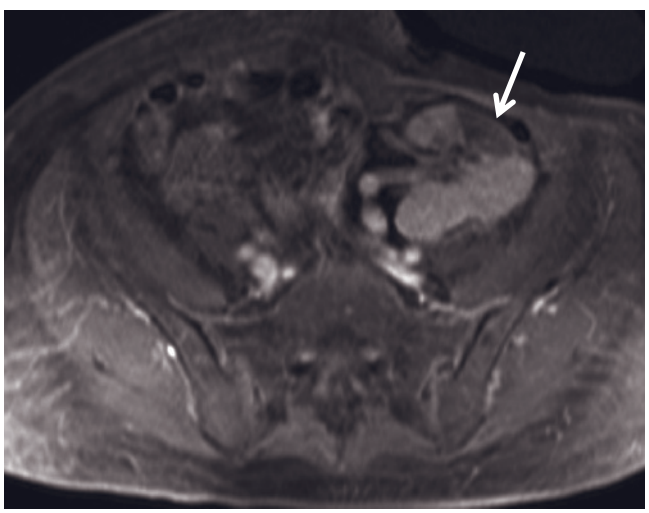

(*e*)

Fig. 9.146 Renal artery stenosis in a transplant kidney. Coronal MRA MIP reconstruction (*a*) demonstrates stenosis of the renal artery (arrow) approximately 2 cm distal to the anastomosis with the internal iliac artery. (Courtesy of Susan M. Ascher, M.D., Department of Radiology, Georgetown University Medical Center.) **Accessory renal artery thrombosis associated with an infarct in the transplanted kidney.** Coronal 3D MIP 3D-GE MRA (*b*), transverse (*c*) and coronal (*d*) thin-section 3D-GE MRA, and transverse T1-weighted postgadolinium interstitial phase fat-suppressed 3D-GE (*e*) images demonstrate a renal infarct (thick arrows, *c*, *e*) due to the thrombosis of an accessory renal artery. The accessory renal artery is not seen because of the thrombosis. The main renal artery (thin arrows, *b*, *d*) is seen on MRA images (*b*–*d*). **Small-vessel disease of the renal transplant.** Coronal

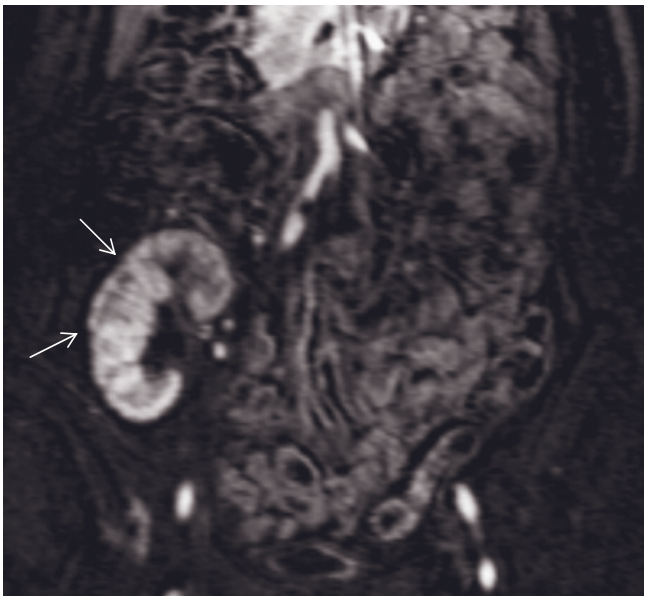

(*f*)

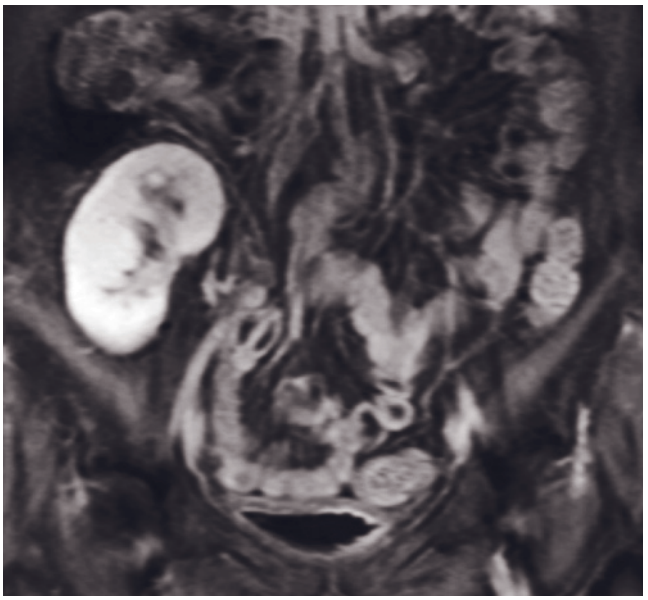

(*g*)

FIG. 9.146 (*Continued*) thin section 3D-GE MRA (*f*) and coronal T1-weighted postgadolinium interstitial-phase fat-suppressed 3D-GE (*g*) images demonstrate small-vessel disease of the renal transplant. Multiple small cortical enhancement defects (arrows) that are consistent with small-vessel disease are seen on MRA image (*f*). These cortical enhancement defects are not seen on the interstitial-phase image (*g*).

bladder or anastomosis of the donor pelvis to the recipient ureter (pyeloureteral anastomosis). Urine leaks are more common in the latter procedure. The incidence of this complication varies from 3% to 10% [133]. The signal characteristic of the urinoma is nonspecific and is high signal intensity on T2-weighted images and low signal intensity on T1-weighted images. Seroma has signal intensity findings similar to lymphocele or urinoma.

Regarding rejection, loss of renal CMD on T1-weighted images is an observation found in renal allografts undergoing rejection (fig. 9.148) [134–136]. In a study comparing the accuracy of MRI, quantitative scintigraphy, and sonography for the detection of renal transplant rejection, the sensitivities for these modalities was 97%, 80%, and 70%, respectively [135]. Loss of CMD, however, is nonspecific and observed also in cyclosporine toxicity and other infiltrative or diffuse renal parenchymal diseases [96, 137]. Chronic rejection results in loss of CMD on T1-weighted fat-suppressed images (fig. 9.149). The degree of loss of CMD on dynamic contrast-enhanced gradient-echo images may correlate with the severity of rejection. Longstanding severe rejection may result in morphologic alterations of the kidney (fig. 9.150).

Malignancies may develop in transplanted kidneys. PTLD often manifests as a mass, predominantly in a hilar location. On MRI, this lesion shows low signal intensity on both T2- and T1-weighted images and mild enhancement after contrast administration [130]. PTLD may arise as early as 6 months after transplantation. Although rare, RCC may also arise in transplanted kidney (see fig. 9.144). Unlike PTLD, renal cancers usually arise late after transplantation. RCC more commonly arises in native failed kidneys.

MR UROGRAPHY

MR urography (MRU) has been performed as a complementary tool to evaluate for urinary tract abnormalities [138–141]. This technique may be performed as a heavily T2-weighted data acquisition or a late (10–15 min) postgadolinium T1-weighted 3D-GRE technique. Techniques employing heavily T2-weighted pulse sequences result in solid organs and moving fluids having a low signal intensity, whereas stationary fluids including bile, urine, cerebrospinal fluid, and bowel fluid have a high signal intensity. In selected cases, postprocessing is performed with a maximum-intensity projection (MIP) that permits three-dimensional rotation, producing views of suspected areas of disease without superimposition of structures. This approach shows the morphologic appearance of the collecting system but does not provide information on renal function.

(*a*)

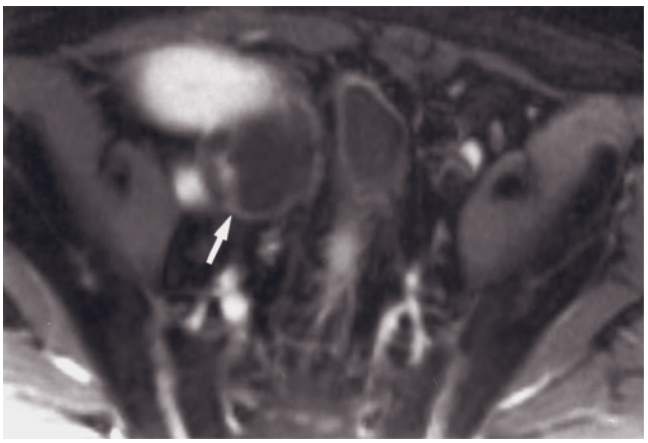

(*b*)

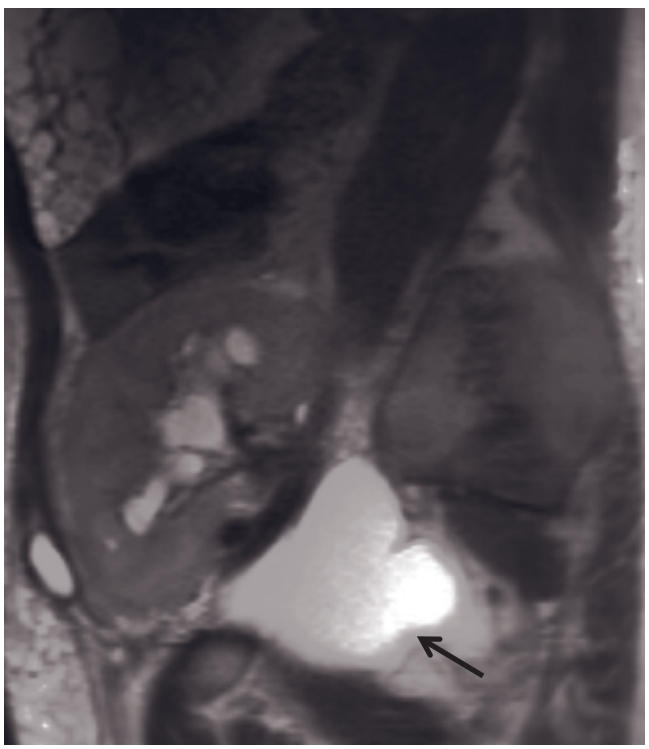

(*c*)

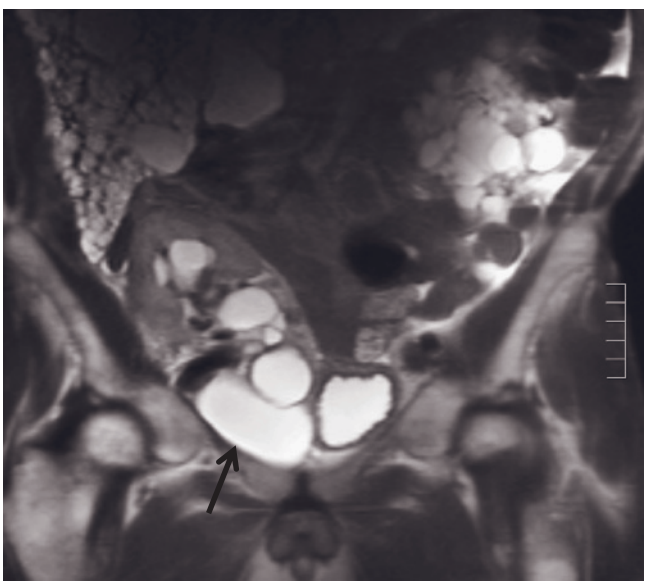

(*d*)

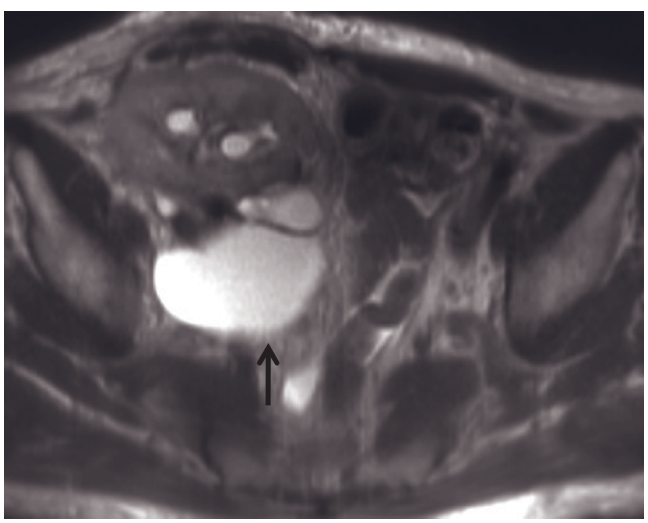

(*e*)

Fig. 9.147 Lymphocele. Transverse T1-weighted 90-s fat-suppressed postgadolinium SGE images (*a*, *b*).There is a right lower quadrant kidney transplant, and projecting inferiorly from the renal hilum there is a well-delineated collection with a thin enhancing capsule (arrow, *b*) that represents a lymphocele. Sagittal (*c*), coronal (*d*) and transverse (*e*) single-shot echo-train spin-echo images demonstrate a lymphocele (arrows, *c–e*) adjacent to the renal transplant with a moderately dilated collecting system in another patient.

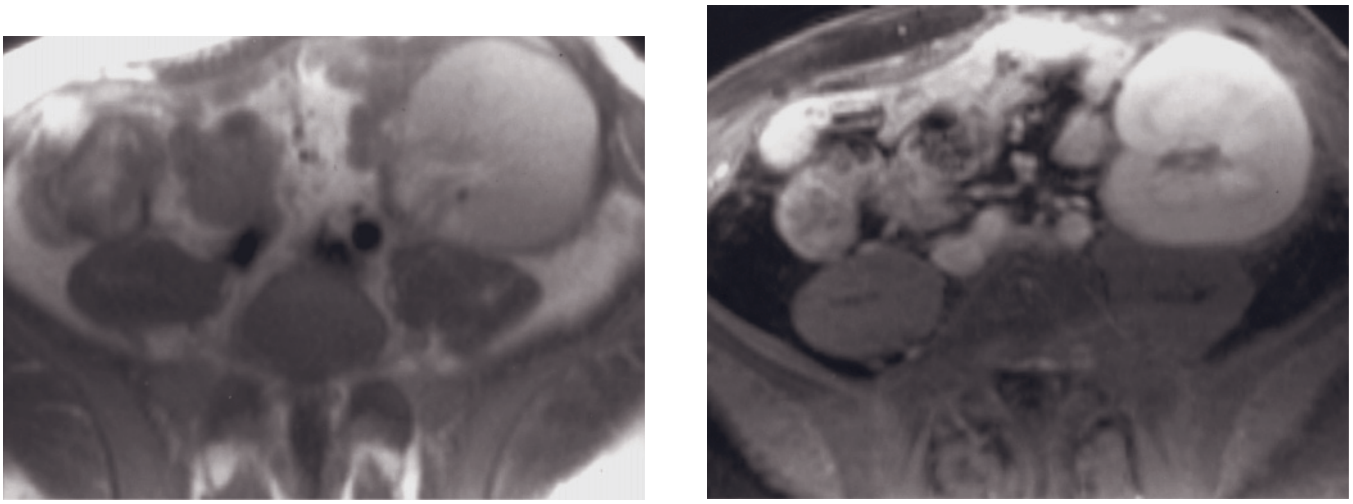

(*a*) (*b*)

FIG. 9.148 Transplanted kidney with rejection. T1-weighted precontrast (*a*) and 90-s fat-suppressed gadolinium-enhanced (*b*) SGE images. The renal transplant in the left pelvic fossa demonstrates decreased corticomedullary differentiation on the precontrast image (*a*) and appears globular or swollen. These findings are consistent with chronic rejection.

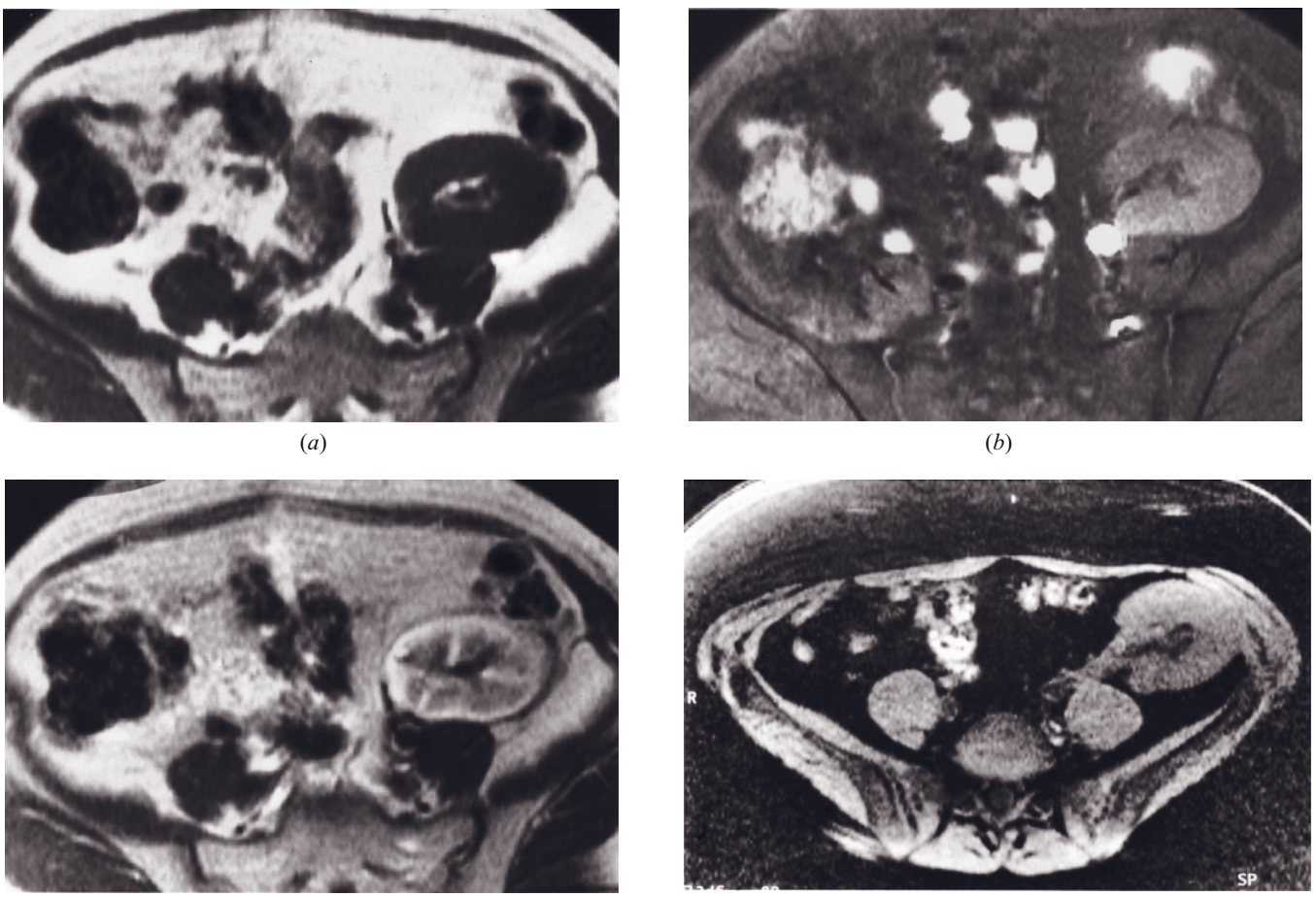

(*a*) (*b*)

(*c*) (*d*)

FIG. 9.149 Chronic rejection of renal transplant. T1-weighted precontrast SGE (*a*), precontrast fat-suppressed SE (*b*), and immediate postgadolinium SGE (*c*) images in a renal transplant undergoing chronic rejection. Loss of corticomedullary differentiation is apparent on precontrast images (*a*, *b*). The presence of corticomedullary differentiation on the capillary-phase image (*c*) shows persistence of a normal pattern of renal blood flow, which is consistent with preservation of some renal function. T1-weighted precontrast fat-suppressed (*d*) and immediate postgadolinium (*e*) SGE images in a second patient with chronic rejection. Loss of

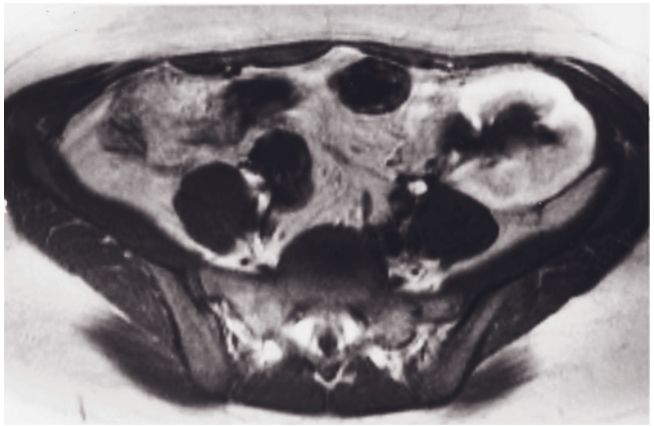

(*e*)

FIG. 9.149 (*Continued*) visualization of the corticomedullary junction is apparent on the precontrast fat-suppressed image (*d*). Corticomedullary differentiation is shown on the immediate post-gadolinium image (*e*), which is consistent with preservation of some renal function.

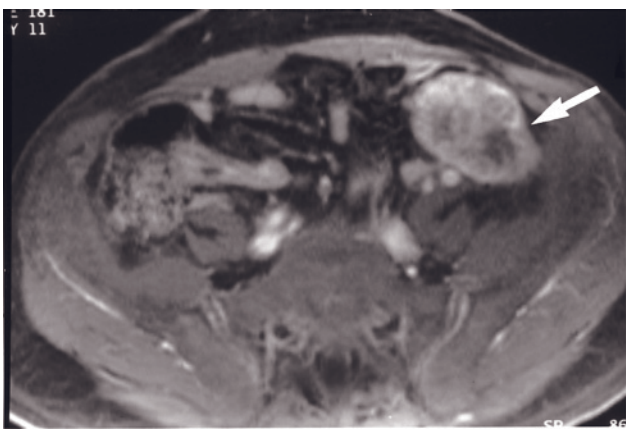

(*a*)

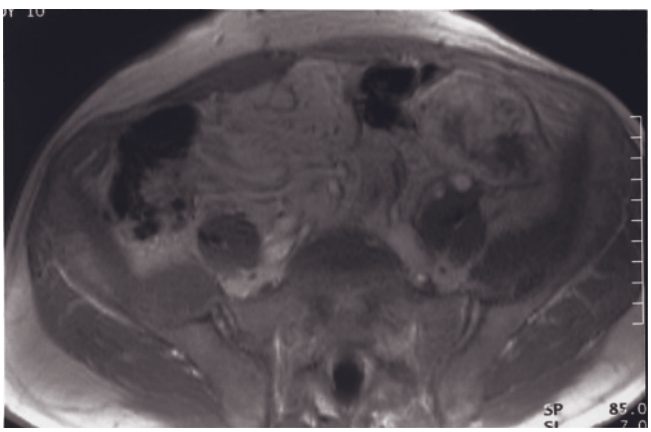

(*b*)

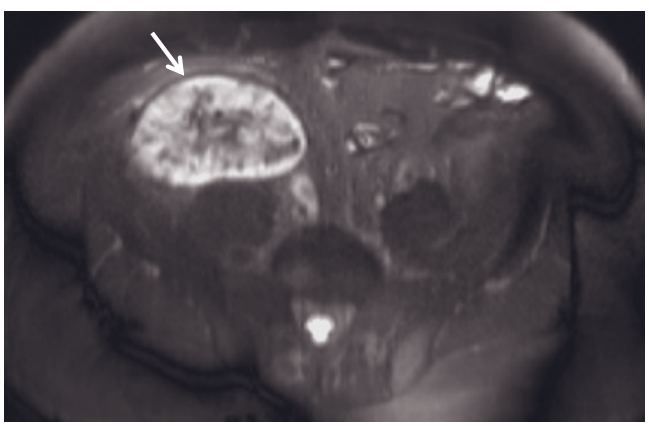

(*c*)

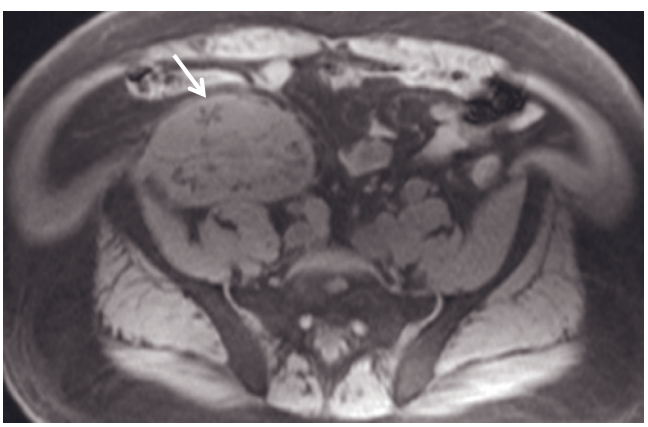

(*d*)

FIG. 9.150 Severe chronic rejection. T1-weighted 45-s fat suppressed (*a*) and 90-s (*b*) postgadolinium images. The transplanted kidney has an irregular contour (arrow, *a*). Irregularly margined central areas of diminished enhancement are present on 45- and 90-s images. By 90 s, enhancement of renal medulla should equilibrate with the cortex; therefore, this central diminished enhancement does not reflect normal medulla. T2-weighted fat-suppressed single-shot echo-train spin-echo (*c*), T1-weighted fat-suppressed 3D-GE (*d*), and T1-weighted postgadolinium venous (*e*)- and interstitial (*f*)-phase fat-suppressed 3D-GE images at 3.0 T

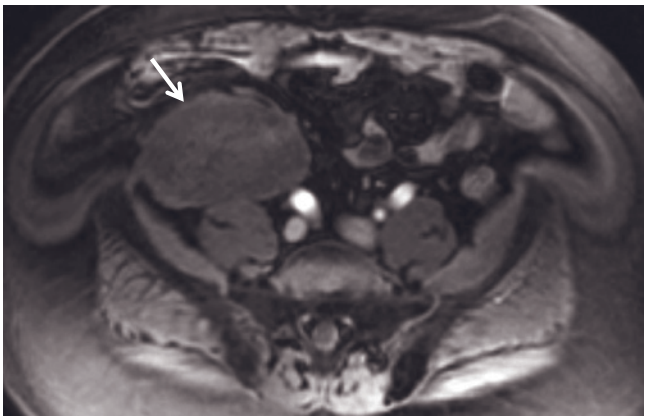

(*e*)

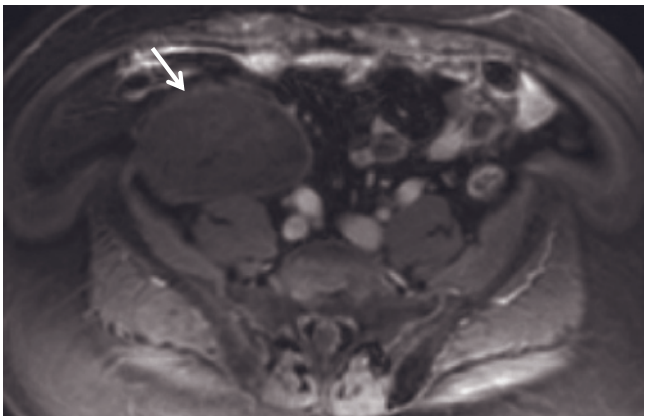

(*f*)

FIG. 9.150 (*Continued*) demonstrate a renal transplant with severe chronic rejection (arrows, *c–f*). Chronically rejected kidney has heterogeneously high signal on T2-weighted image (*c*), and normal renal architecture is lost (*c–f*). No enhancement is seen on postgadolinium images (*e*, *f*).

One study [142] reported that the accuracy of MRU is excellent in the detection of ureterohydronephrosis and superior to conventional intravenous urography (IVU) in cases of renal failure. MRU was equivalent to IVU for the diagnosis of ureterohydronephosis in patients with normal renal function with an accuracy of 100%. No difference was observed in the extent of dilatation as shown as IVU and MRU.

MRU has proven to be efficient in detecting the level of obstruction and permitting an analysis of the type of obstruction. The main disadvantage is the inability of the technique to demonstrate calculi in a consistent fashion, especially small, nonobstructing calculi.

MRU performed as late gadolinium-enhanced 3D-GRE also shows high-signal gadolinium in the collecting system. Advantages of this technique are that there are lesser problems with adjacent competing high-signal fluid (as observed on T2-weighted images) and it provides information on renal function. Additionally, this technique provides information of the integrity of the collecting system (e.g., pyelosinus rupture, ureteral injury) that is not shown on the heavily T2-weighted techniques. Diuretic-induced postgadolinium MR urographic imaging can be performed with the administration of intravenous furosemide. Diuretic-induced MR urographic imaging allows earlier and improved visualization of gadolinium-filled renal collecting system. More consistent demonstration of the majority, or entirety, of the ureters can be achieved with the administration of diuretic. Caution should, however, be exercised when patients have an elevated estimated glomerular filtration rate (eGFR), as the potential nephrotoxic effects of diuretics may result in acute renal failure, thereby creating an environment favorable to the development of nephrogenic systemic fibrosis [143].

FUTURE DIRECTIONS

Anatomic display of kidneys is accurate with current imaging techniques and phased-array multicoil imaging. Although gadolinium-enhanced 3D MRA is the most reproducible technique, advances in noncontrast MRA continue to develop [144–147]. It remains to be determined whether noncontrast MRA may be sufficiently accurate to assess renal transplant donors. Renal function and the functional and morphologic disturbance caused by various renal diseases are currently under investigation [148–154]. Fast imaging techniques such as turboFLASH and echoplanar imaging [136, 151, 155], new contrast agents [147, 156], or a combination of both [150, 151] are being employed to examine renal function. Flow quantification may provide useful information on renal perfusion [152, 153]. Pharmacological stresses also may develop into a clinical routine for evaluating renal vascular disease [154].

REFERENCES

1. Semelka RC, Shoenut JP, Kroeker MA et al. Renal lesions: controlled comparison between CT and 1.5-T MR imaging with nonenhanced and gadolinium-enhanced fat-suppressed spin-echo and breath-hold FLASH techniques. *Radiology* 182(2): 425–430, 1992.
2. Prince MR, Narasimham DL, Stanley JC et al. Breath-hold gadolinium-enhanced MR angiography of the abdominal aorta and its major branches. *Radiology* 197(3): 785–792, 1995.
3. Snidow JJ, Johnson MS, Harris VJ et al. Three-dimensional gadolinium-enhanced MR angiography for aortoiliac inflow assessment plus renal artery screening in a single breath hold. *Radiology* 198(3): 725–732, 1996.
4. Rothpearl A, Frager D, Subramanian A et al. MR urography: technique and application. *Radiology* 194(1): 125–130, 1995.

5. Semelka RC, Hricak H, Tomei E et al. Obstructive nephropathy: evaluation with dynamic Gd-DTPA-enhanced MR imaging. *Radiology* 175(3): 797–803, 1990.
6. Choyke PL, Frank JA, Girton ME et al. Dynamic Gd-DTPA-enhanced MR imaging of the kidney: experimental results. *Radiology* 170(3 Pt 1): 713–720, 1989.
7. Kikinis R, von Schulthess GK, Jager P et al. Normal and hydronephrotic kidney: evaluation of renal function with contrast-enhanced MR imaging. *Radiology* 165(3): 837–842, 1987.
8. Ros PR, Gauger J, Stoupis C et al. Diagnosis of renal artery stenosis: feasibility of combining MR angiography, MR renography, and gadopentetate-based measurements of glomerular filtration rate. *AJR Am J Roentgenol* 165(6): 1447–1451, 1995.
9. Barnhart JL, Kuhnert N, Bakan DA et al. Biodistribution of $GdCl_3$ and Gd-DTPA and their influence on proton magnetic relaxation in rat tissues. *Magn Reson Imaging* 5(3): 221–231, 1987.
10. Jennete JC, Olson JL, Schwartz MM et al. *Hepinstall's Pathology of the Kidney*. 5th ed. Philadelphia: Lippincott-Raven, 1998, p. 1149.
11. Bostwick DG, Eble JN. *Urologic Surgical Pathology*. 1st ed. London: Mosby, 1997, p.14.
12. Cotran R, V. K, Robbins S. *Pathologic Basis of Disease*. 5th ed. Philadelphia: Saunders, 1994.
13. Nascimento AB, Mitchell DG, Zhang XM et al. Rapid MR imaging detection of renal cysts: age-based standards. *Radiology* 221(3): 628–632, 2001.
14. Dalton D, Neiman H, Grayhack JT. The natural history of simple renal cysts: a preliminary study. *J Urol* 135(5): 905–908, 1986.
15. Semelka RC, Hricak H, Stevens SK et al. Combined gadolinium-enhanced and fat-saturation MR imaging of renal masses. *Radiology* 178(3): 803–809, 1991.
16. Ho VB, Allen SF, Hood MN et al. Renal masses: quantitative assessment of enhancement with dynamic MR imaging. *Radiology* 224(3): 695–700, 2002.
17. Balci NC, Semelka RC, Patt RH et al. Complex renal cysts: findings on MR imaging. *AJR Am J Roentgenol* 172(6): 1495–1500, 1999.
18. Israel GM, Hindman N, Bosniak MA. Evaluation of cystic renal masses: comparison of CT and MR imaging by using the Bosniak classification system. *Radiology* 231(2): 365–371, 2004.
19. Jennete JC, Olson JL, Schwartz MM et al. *Hepinstall's Pathology of the Kidney*. 5th ed. Philadelphia: Lippincott-Raven, 1998, p. 1196.
20. Gabow PA. Autosomal dominant polycystic kidney disease. *N Engl J Med* 329(5): 332–342, 1993.
21. Huch Boni RA, Debatin JF, Krestin GP. Contrast-enhanced MR imaging of the kidneys and adrenal glands. *Magn Reson Imaging Clin N Am* 4(1): 101–131, 1996.
22. Mosetti MA, Leonardou P, Motohara T et al. Autosomal dominant polycystic kidney disease: MR imaging evaluation using current techniques. *J Magn Reson Imaging* 18(2): 210–215, 2003.
23. Wise SW, Hartman DS, Hardesty LA et al. Renal medullary cystic disease: assessment by MRI. *Abdom Imaging* 23(6): 649–651, 1998.
24. Cho C, Friedland GW, Swenson RS. Acquired renal cystic disease and renal neoplasms in hemodialysis patients. *Urol Radiol* 6(3-4): 153–157, 1984.
25. Ishikawa I. Uremic acquired cystic disease of kidney. *Urology* 26(2): 101–108, 1985.
26. Levine E, Grantham JJ, Slusher SL et al. CT of acquired cystic kidney disease and renal tumors in long-term dialysis patients. *AJR Am J Roentgenol* 142(1): 125–131, 1984.
27. Agrons GA, Wagner BJ, Davidson AJ et al. Multilocular cystic renal tumor in children: radiologic-pathologic correlation. *Radiographics* 15(3): 653–669, 1995.
28. Kettritz U, Semelka RC, Siegelman ES et al. Multilocular cystic nephroma: MR imaging appearance with current techniques, including gadolinium enhancement. *J Magn Reson Imaging* 6(1): 145–148, 1996.
29. Dikengil A, Benson M, Sanders L et al. MRI of multilocular cystic nephroma. *Urol Radiol* 10(2): 95–99, 1988.
30. Israel GM, Hindman N, Hecht E et al. The use of opposed-phase chemical shift MRI in the diagnosis of renal angiomyolipomas. *AJR Am J Roentgenol* 184(6): 1868–1872, 2005.
31. Lemaitre L, Robert Y, Dubrulle F et al. Renal angiomyolipoma: growth followed up with CT and/or US. *Radiology* 197(3): 598–602, 1995.
32. Steiner MS, Goldman SM, Fishman EK et al. The natural history of renal angiomyolipoma. *J Urol* 150(6): 1782–1786, 1993.
33. Wills JS. Management of small renal neoplasms and angiomyolipoma: a growing problem. *Radiology* 197(3): 583–586, 1995.
34. Burdeny DA, Semelka RC, Kelekis NL et al. Small (<1.5 cm) angiomyolipomas of the kidney: characterization by the combined use of in-phase and fat-attenuated MR techniques. *Magn Reson Imaging* 15(2): 141–145, 1997.
35. Oesterling JE, Fishman EK, Goldman SM et al. The management of renal angiomyolipoma. *J Urol* 135(6): 1121–1124, 1986.
36. Strotzer M, Lehner KB, Becker K. Detection of fat in a renal cell carcinoma mimicking angiomyolipoma. *Radiology* 188(2): 427–428, 1993.
37. van Baal JG, Smits NJ, Keeman JN et al. The evolution of renal angiomyolipomas in patients with tuberous sclerosis. *J Urol* 152(1): 35–38, 1994.
38. Mitnick JS, Bosniak MA, Hilton S et al. Cystic renal disease in tuberous sclerosis. *Radiology* 147(1): 85–87, 1983.
39. Casper KA, Donnelly LF, Chen B et al. Tuberous sclerosis complex: renal imaging findings. *Radiology* 225(2): 451–456, 2002.
40. Reichard EA, Roubidoux MA, Dunnick NR. Renal neoplasms in patients with renal cystic diseases. *Abdom Imaging* 23(3): 237–248, 1998.
41. Fricke BL, Donnelly LF, Casper KA et al. Frequency and imaging appearance of hepatic angiomyolipomas in pediatric and adult patients with tuberous sclerosis. *AJR Am J Roentgenol* 182(4): 1027–1030, 2004.
42. Choyke PL, Glenn GM, Walther MM et al. von Hippel-Lindau disease: genetic, clinical, and imaging features. *Radiology* 194(3): 629–642, 1995.
43. Taouli B, Ghouadni M, Correas JM et al. Spectrum of abdominal imaging findings in von Hippel-Lindau disease. *AJR Am J Roentgenol* 181(4): 1049–1054, 2003.
44. Quinn MJ, Hartman DS, Friedman AC et al. Renal oncocytoma: new observations. *Radiology* 153(1): 49–53, 1984.
45. Press GA, McClennan BL, Melson GL et al. Papillary renal cell carcinoma: CT and sonographic evaluation. *AJR Am J Roentgenol* 143(5): 1005–1009, 1984.
46. Davidson AJ, Hayes WS, Hartman DS et al. Renal oncocytoma and carcinoma: failure of differentiation with CT. *Radiology* 186(3): 693–696, 1993.
47. Bosniak MA, Birnbaum BA, Krinsky GA et al. Small renal parenchymal neoplasms: further observations on growth. *Radiology* 197(3): 589–597, 1995.
48. Bosniak MA, Rofsky NM. Problems in the detection and characterization of small renal masses. *Radiology* 198(3): 638–641, 1996.
49. Jennete JC, Olson JL, Schwartz MM et al. In: *Hepinstall's Pathology of the Kidney*. Philadelphia: Lippincott-Raven, 1998. p. 1548.
50. Newhouse JH, Wagner BJ. Renal oncocytomas. *Abdom Imaging* 23(3): 249–255, 1998.

51. Dechet CB, Bostwick DG, Blute ML et al. Renal oncocytoma: multifocality, bilateralism, metachronous tumor development and coexistent renal cell carcinoma. *J Urol* 162(1): 40–42, 1999.
52. Ball DS, Friedman AC, Hartman DS et al. Scar sign of renal oncocytoma: magnetic resonance imaging appearance and lack of specificity. *Urol Radiol* 8(1): 46–48, 1986.
53. Schnuelle P, Waldherr R, Lehmann KJ et al. Idiopathic myelofibrosis with extramedullary hematopoiesis in the kidneys. *Clin Nephrol* 52(4): 256–262, 1999.
54. Tefferi A. Myelofibrosis with myeloid metaplasia. *N Engl J Med* 342(17): 1255–1265, 2000.
55. Gryspeerdt S, Oyen R, Van Hoe L et al. Extramedullary hematopoiesis encasing the pelvicalyceal system: CT findings. *Ann Hematol* 71(1): 53–56, 1995.
56. Marshall FF, Stewart AK, Menck HR. The National Cancer Data Base: report on kidney cancers. The American College of Surgeons Commission on Cancer and the American Cancer Society. *Cancer* 80(11): 2167–2174, 1997.
57. Boring CC, Squires TS, Tong T. Cancer statistics, 1991. *CA Cancer J Clin* 41(1): 19–36, 1991.
58. Ergen FB, Hussain HK, Caoili EM et al. MRI for preoperative staging of renal cell carcinoma using the 1997 TNM classification: comparison with surgical and pathologic staging. *AJR Am J Roentgenol* 182(1): 217–225, 2004.
59. Semelka RC, Shoenut JP, Magro CM et al. Renal cancer staging: comparison of contrast-enhanced CT and gadolinium-enhanced fat-suppressed spin-echo and gradient-echo MR imaging. *J Magn Reson Imaging* 3(4): 597–602, 1993.
60. Hricak H, Thoeni RF, Carroll PR et al. Detection and staging of renal neoplasms: a reassessment of MR imaging. *Radiology* 166(3): 643–649, 1988.
61. Oto A, Herts BR, Remer EM et al. Inferior vena cava tumor thrombus in renal cell carcinoma: staging by MR imaging and impact on surgical treatment. *AJR Am J Roentgenol* 171(6): 1619–1624, 1998.
62. Zeman RK, Cronan JJ, Rosenfield AT et al. Renal cell carcinoma: dynamic thin-section CT assessment of vascular invasion and tumor vascularity. *Radiology* 167(2): 393–396, 1988.
63. Roubidoux MA, Dunnick NR, Sostman HD et al. Renal carcinoma: detection of venous extension with gradient-echo MR imaging. *Radiology* 182(1): 269–272, 1992.
64. Studer UE, Scherz S, Scheidegger J et al. Enlargement of regional lymph nodes in renal cell carcinoma is often not due to metastases. *J Urol* 144(2 Pt 1): 243–245, 1990.
65. Bader TR, Semelka RC, Pedro MS et al. Magnetic resonance imaging of pulmonary parenchymal disease using a modified breath-hold 3D gradient-echo technique: initial observations. *J Magn Reson Imaging* 15(1): 31–38, 2002.
66. Rominger MB, Kenney PJ, Morgan DE et al. Gadolinium-enhanced MR imaging of renal masses. *Radiographics* 12(6): 1097–1116; discussion 1117–1098, 1992.
67. Bard RH, Lord B, Fromowitz F. Papillary adenocarcinoma of kidney. II. Radiographic and biologic characteristics. *Urology* 19(1): 16–20, 1982.
68. Tello R, Davison BD, O'Malley M et al. MR imaging of renal masses interpreted on CT to be suspicious. *AJR Am J Roentgenol* 174(4): 1017–1022, 2000.
69. Bosniak MA. The small (less than or equal to 3.0 cm) renal parenchymal tumor: detection, diagnosis, and controversies. *Radiology* 179(2): 307–317, 1991.
70. Birnbaum BA, Bosniak MA, Megibow AJ et al. Observations on the growth of renal neoplasms. *Radiology* 176(3): 695–701, 1990.
71. Levine E, Huntrakoon M, Wetzel LH. Small renal neoplasms: clinical, pathologic, and imaging features. *AJR Am J Roentgenol* 153(1): 69–73, 1989.
72. Curry NS. Small renal masses (lesions smaller than 3 cm): imaging evaluation and management. *AJR Am J Roentgenol* 164(2): 355–362, 1995.
73. Murad T, Komaiko W, Oyasu R et al. Multilocular cystic renal cell carcinoma. *Am J Clin Pathol* 95(5): 633–637, 1991.
74. Outwater EK, Bhatia M, Siegelman ES et al. Lipid in renal clear cell carcinoma: detection on opposed-phase gradient-echo MR images. *Radiology* 205(1): 103–107, 1997.
75. Yoshimitsu K, Honda H, Kuroiwa T et al. Fat detection in granular-cell renal cell carcinoma using chemical-shift gradient-echo MR imaging: another renal tumor that contains fat. *Abdom Imaging* 25(1): 100–102, 2000.
76. John G, Semelka RC, Burdeny DA et al. Renal cell cancer: incidence of hemorrhage on MR images in patients with chronic renal insufficiency. *J Magn Reson Imaging* 7(1): 157–160, 1997.
77. Terens WL, Gluck R, Golimbu M et al. Use of gadolinium-DTPA-enhanced MRI to characterize renal mass in patient with renal insufficiency. *Urology* 40(2): 152–154, 1992.
78. Rofsky NM, Weinreb JC, Bosniak MA et al. Renal lesion characterization with gadolinium-enhanced MR imaging: efficacy and safety in patients with renal insufficiency. *Radiology* 180(1): 85–89, 1991.
79. Haustein J, Niendorf HP, Krestin G et al. Renal tolerance of gadolinium-DTPA/dimeglumine in patients with chronic renal failure. *Invest Radiol* 27(2): 153–156, 1992.
80. Choyke PL, Girton ME, Vaughan EM et al. Clearance of gadolinium chelates by hemodialysis: an in vitro study. *J Magn Reson Imaging* 5(4): 470–472, 1995.
81. Thompson IM, Peek M. Improvement in survival of patients with renal cell carcinoma—the role of the serendipitously detected tumor. *J Urol* 140(3): 487–490, 1988.
82. Smith SJ, Bosniak MA, Megibow AJ et al. Renal cell carcinoma: earlier discovery and increased detection. *Radiology* 170(3 Pt 1): 699–703, 1989.
83. Jamis-Dow CA, Choyke PL, Jennings SB et al. Small (<3-cm) renal masses: detection with CT versus US and pathologic correlation. *Radiology* 198(3): 785–788, 1996.
84. Butler BP, Novick AC, Miller DP et al. Management of small unilateral renal cell carcinomas: radical versus nephron-sparing surgery. *Urology* 45(1): 34–40; discussion 40–31, 1995.
85. Provet J, Tessler A, Brown J et al. Partial nephrectomy for renal cell carcinoma: indications, results and implications. *J Urol* 145(3): 472–476, 1991.
86. Gylys-Morin V, Hoffer FA, Kozakewich H et al. Wilms tumor and nephroblastomatosis: imaging characteristics at gadolinium-enhanced MR imaging. *Radiology* 188(2): 517–521, 1993.
87. Cohen MD. Staging of Wilms' tumour. *Clin Radiol* 47(2): 77–81, 1993.
88. Weese DL, Applebaum H, Taber P. Mapping intravascular extension of Wilms' tumor with magnetic resonance imaging. *J Pediatr Surg* 26(1): 64–67, 1991.
89. Richards MA, Mootoosamy I, Reznek RH et al. Renal involvement in patients with non-Hodgkin's lymphoma: clinical and pathological features in 23 cases. *Hematol Oncol* 8(2): 105–110, 1990.
90. Heiken JP, Gold RP, Schnur MJ et al. Computed tomography of renal lymphoma with ultrasound correlation. *J Comput Assist Tomogr* 7(2): 245–250, 1983.
91. Semelka RC, Kelekis NL, Burdeny DA et al. Renal lymphoma: demonstration by MR imaging. *AJR Am J Roentgenol* 166(4): 823–827, 1996.
92. Hauser M, Krestin GP, Hagspiel KD. Bilateral solid multifocal intrarenal and perirenal lesions: differentiation with ultrasonography, computed tomography and magnetic resonance imaging. *Clin Radiol* 50(5): 288–294, 1995.
93. Marcos HB, Semelka RC, Woosley JT. Abdominal granulocytic sarcomas: demonstration by MRI. *Magn Reson Imaging* 15(7): 873–876, 1997.

94. Karadeniz-Bilgili MY, Semelka RC, Hyslop WB et al. MRI findings of primary small-cell carcinoma of kidney. *Magn Reson Imaging* 23(3): 515–517, 2005.
95. Bailey JE, Roubidoux MA, Dunnick NR. Secondary renal neoplasms. *Abdom Imaging* 23(3): 266–274, 1998.
96. Kettritz U, Semelka RC, Brown ED et al. MR findings in diffuse renal parenchymal disease. *J Magn Reson Imaging* 6(1): 136–144, 1996.
97. Semelka RC, Corrigan K, Ascher SM et al. Renal corticomedullary differentiation: observation in patients with differing serum creatinine levels. *Radiology* 190(1): 149–152, 1994.
98. Chung JJ, Semelka RC, Martin DR. Acute renal failure: common occurrence of preservation of corticomedullary differentiation on MR images. *Magn Reson Imaging* 19(6): 789–793, 2001.
99. Tempany CM, Morton RA, Marshall FF. MRI of the renal veins: assessment of nonneoplastic venous thrombosis. *J Comput Assist Tomogr* 16(6): 929–934, 1992.
100. Wyngaarden JB, Smith LH, Bennett JC. *Cecil—Textbook of Medicine* (19th ed.) Philadelphia: WB Saunders, 1992, p. 2263.
101. Engel AG, Franzini C. *Myology*. 2nd ed. New York: McGraw-Hill, 1994, p. 1691.
102. Lande IM, Glazer GM, Sarnaik S et al. Sickle-cell nephropathy: MR imaging. *Radiology* 158(2): 379–383, 1986.
103. Siegelman ES, Outwater E, Hanau CA et al. Abdominal iron distribution in sickle cell disease: MR findings in transfusion and nontransfusion dependent patients. *J Comput Assist Tomogr* 18(1): 63–67, 1994.
104. Roubidoux MA. MR of the kidneys, liver, and spleen in paroxysmal nocturnal hemoglobinuria. *Abdom Imaging* 19(2): 168–173, 1994.
105. Cotran R, Kumar V, Robbins S. *Pathologic Basis of Disease*. 5th ed. Philadelphia: Saunders, 1994, p. 1056.
106. Bakker J, Beek FJ, Beutler JJ et al. Renal artery stenosis and accessory renal arteries: accuracy of detection and visualization with gadolinium-enhanced breath-hold MR angiography. *Radiology* 207(2): 497–504, 1998.
107. Tello R, Thomson KR, Witte D et al. Standard dose Gd-DTPA dynamic MR of renal arteries. *J Magn Reson Imaging* 8(2): 421–426, 1998.
108. Saunders HS, Dyer RB, Shifrin RY et al. The CT nephrogram: implications for evaluation of urinary tract disease. *Radiographics* 15(5): 1069–1085; discussion 1086–1068, 1995.
109. Goldman SM, Fishman EK. Upper urinary tract infection: the current role of CT, ultrasound, and MRI. *Semin Ultrasound CT MR* 12(4): 335–360, 1991.
110. Fowler JE, Jr., Perkins T. Presentation, diagnosis and treatment of renal abscesses: 1972–1988. *J Urol* 151(4): 847–851, 1994.
111. Brown ED, Brown JJ, Kettritz U et al. Renal abscesses: appearance on gadolinium-enhanced magnetic resonance images. *Abdom Imaging* 21(2): 172–176, 1996.
112. Bova JG, Potter JL, Arevalos E et al. Renal and perirenal infection: the role of computerized tomography. *J Urol* 133(3): 375–378, 1985.
113. Mulopulos GP, Patel SK, Pessis D. MR imaging of xanthogranulomatous pyelonephritis. *J Comput Assist Tomogr* 10(1): 154–156, 1986.
114. Ling BN, Delaney VB, Campbell WG, Jr. Acute renal failure due to bilateral renal parenchymal malakoplakia. *Am J Kidney Dis* 13(5): 430–433, 1989.
115. Pamilo M, Kulatunga A, Martikainen J. Renal parenchymal malakoplakia. A report of two cases. The radiological and ultrasound images. *Br J Radiol* 57(680): 751–755, 1984.
116. Esparza AR, McKay DB, Cronan JJ et al. Renal parenchymal malakoplakia. Histologic spectrum and its relationship to megalocytic interstitial nephritis and xanthogranulomatous pyelonephritis. *Am J Surg Pathol* 13(3): 225–236, 1989.
117. Zimina OG, Rezun S, Armao D et al. Renal malacoplakia: demonstration by MR imaging. *Magn Reson Imaging* 20(8): 611–614, 2002.
118. Semelka RC, Shoenut JP, Greenberg HM et al. Detection of acute and treated lesions of hepatosplenic candidiasis: comparison of dynamic contrast-enhanced CT and MR imaging. *J Magn Reson Imaging* 2(3): 341–345, 1992.
119. Winalski CS, Lipman JC, Tumeh SS. Ureteral neoplasms. *Radiographics* 10(2): 271–283, 1990.
120. Weeks SM, Brown ED, Brown JJ et al. Transitional cell carcinoma of the upper urinary tract: staging by MRI. *Abdom Imaging* 20(4): 365–367, 1995.
121. Leo ME, Petrou SP, Barrett DM. Transitional cell carcinoma of the kidney with vena caval involvement: report of 3 cases and a review of the literature. *J Urol* 148(2 Pt 1): 398–400, 1992.
122. Coe FL, Parks JH, Asplin JR. The pathogenesis and treatment of kidney stones. *N Engl J Med* 327(16): 1141–1152, 1992.
123. Marcos HB, Noone TC, Semelka RC. MRI evaluation of acute renal trauma. *J Magn Reson Imaging* 8(4): 989–990, 1998.
124. Laissy JP, Faraggi M, Lebtahi R et al. Functional evaluation of normal and ischemic kidney by means of gadolinium-DOTA enhanced TurboFLASH MR imaging: a preliminary comparison with 99Tc-MAG3 dynamic scintigraphy. *Magn Reson Imaging* 12(3): 413–419, 1994.
125. Martin DR, Sharma P, Salman K et al. Individual kidney blood flow measured with contrast-enhanced first-pass perfusion MR imaging. *Radiology* 246(1): 241–248, 2008.
126. Neimatallah MA, Dong Q, Schoenberg SO et al. Magnetic resonance imaging in renal transplantation. *J Magn Reson Imaging* 10(3): 357–368, 1999.
127. Low RN, Martinez AG, Steinberg SM et al. Potential renal transplant donors: evaluation with gadolinium-enhanced MR angiography and MR urography. *Radiology* 207(1): 165–172, 1998.
128. Hohenwalter MD, Skowlund CJ, Erickson SJ et al. Renal transplant evaluation with MR angiography and MR imaging. *Radiographics* 21(6): 1505–1517, 2001.
129. Kalb B, Martin DR, Salman K et al. Kidney transplantation: structural and functional evaluation using MR nephro-urography. *J Magn Reson Imaging* 28(4): 805–822, 2008.
130. Ali MG, Coakley FV, Hricak H et al. Complex posttransplantation abnormalities of renal allografts: evaluation with MR imaging. *Radiology* 211(1): 95–100, 1999.
131. Kew CE, 2nd, Lopez-Ben R, Smith JK et al. Postransplant lymphoproliferative disorder localized near the allograft in renal transplantation. *Transplantation* 69(5): 809–814, 2000.
132. Jennete JC, Olson JL, Schwartz MM et al. *Hepinstall's Pathology of the Kidney*. 5th ed. Philadelphia: Lippincott-Raven, 1998, p. 1497.
133. Jennete JC, Olson JL, Schwartz MM et al. *Hepinstall's Pathology of the Kidney*. 5th ed. Philadelphia: Lippincott-Raven, 1998, p. 1412.
134. McCreath GT, McMillan N, Patterson J et al. Magnetic resonance imaging of renal transplants: initial experience. *Br J Radiol* 61(722): 113–117, 1988.
135. Hricak H, Terrier F, Marotti M et al. Posttransplant renal rejection: comparison of quantitative scintigraphy, US, and MR imaging. *Radiology* 162(3): 685–688, 1987.
136. Hanna S, Helenon O, Legendre C et al. MR imaging of renal transplant rejection. *Acta Radiol* 32(1): 42–46, 1991.
137. Liou JT, Lee JK, Heiken JP et al. Renal transplants: can acute rejection and acute tubular necrosis be differentiated with MR imaging? *Radiology* 179(1): 61–65, 1991.
138. Kalb B, Votaw JR, Salman K et al. Magnetic resonance nephrourography: current and developing techniques. *Radiol Clin North Am* 46(1): 11–24, v, 2008.

139. Blandino A, Gaeta M, Minutoli F et al. MR urography of the ureter. *AJR Am J Roentgenol* 179(5): 1307–1314, 2002.
140. Rohrschneider WK, Haufe S, Wiesel M et al. Functional and morphologic evaluation of congenital urinary tract dilatation by using combined static-dynamic MR urography: findings in kidneys with a single collecting system. *Radiology* 224(3): 683–694, 2002.
141. Riccabona M, Ruppert-Kohlmayr A, Ring E et al. Potential impact of pediatric MR urography on the imaging algorithm in patients with a functional single kidney. *AJR Am J Roentgenol* 183(3): 795–800, 2004.
142. Roy C, Saussine C, Guth S et al. MR urography in the evaluation of urinary tract obstruction. *Abdom Imaging* 23(1): 27–34, 1998.
143. Ergen FB, Hussain HK, Carlos RC et al. 3D excretory MR urography: improved image quality with intravenous saline and diuretic administration. *J Magn Reson Imaging* 25(4): 783–789, 2007.
144. Edelman RR, Siewert B, Adamis M et al. Signal targeting with alternating radiofrequency (STAR) sequences: application to MR angiography. *Magn Reson Med* 31(2): 233–238, 1994.
145. Li D, Haacke EM, Mugler JP, 3rd et al. Three-dimensional time-of-flight MR angiography using selective inversion recovery RAGE with fat saturation and ECG-triggering: application to renal arteries. *Magn Reson Med* 31(4): 414–422, 1994.
146. Yucel EK, Kaufman JA, Prince M et al. Time of flight renal MR angiography: utility in patients with renal insufficiency. *Magn Reson Imaging* 11(7): 925–930, 1993.
147. Kelekis NL, Semelka RC, Worawattanakul S et al. Magnetic resonance imaging of the abdominal aorta and iliac vessels using combined 3-D gadolinium-enhanced MRA and gadolinium-enhanced fat-suppressed spoiled gradient echo sequences. *Magn Reson Imaging* 17(5): 641–651, 1999.
148. Kim SH, Byun HS, Park JH et al. Renal parenchymal abnormalities associated with renal vein thrombosis: correlation between MR imaging and pathologic findings in rabbits. *AJR Am J Roentgenol* 162(6): 1361–1365, 1994.
149. Vexler VS, Berthezene Y, Clement O et al. Detection of zonal renal ischemia with contrast-enhanced MR imaging with a macromolecular blood pool contrast agent. *J Magn Reson Imaging* 2(3): 311–319, 1992.
150. Trillaud H, Grenier N, Degreze P et al. First-pass evaluation of renal perfusion with TurboFLASH MR imaging and superparamagnetic iron oxide particles. *J Magn Reson Imaging* 3(1): 83–91, 1993.
151. Wolf RL, King BF, Torres VE et al. Measurement of normal renal artery blood flow: cine phase-contrast MR imaging vs clearance of *p*-aminohippurate. *AJR Am J Roentgenol* 161(5): 995–1002, 1993.
152. Wolf GL, Hoop B, Cannillo JA et al. Measurement of renal transit of gadopentetate dimeglumine with echo-planar MR imaging. *J Magn Reson Imaging* 4(3): 365–372, 1994.
153. Debatin JF, Ting RH, Wegmuller H et al. Renal artery blood flow: quantitation with phase-contrast MR imaging with and without breath holding. *Radiology* 190(2): 371–378, 1994.
154. Trillaud H, Roques F, Degreze P et al. Gd-DOTA tubular transit asymmetry induced by angiotensin-converting enzyme inhibitor in experimental renovascular hypertension. *J Magn Reson Imaging* 6(1): 149–155, 1996.
155. Muller MF, Prasad PV, Bimmler D et al. Functional imaging of the kidney by means of measurement of the apparent diffusion coefficient. *Radiology* 193(3): 711–715, 1994.
156. Weishaupt D, Ruhm SG, Binkert CA et al. Equilibrium-phase MR angiography of the aortoiliac and renal arteries using a blood pool contrast agent. *AJR Am J Roentgenol* 175(1): 189–195, 2000.

CHAPTER 10

RETROPERITONEUM AND BODY WALL

DIEGO R. MARTIN, ERSAN ALTUN, JORGE ELIAS, JR., YOUNG MI KU, AND RICHARD C. SEMELKA

NORMAL ANATOMY

The retroperitoneum is limited anteriorly by the parietal peritoneum and posteriorly by the transversalis fascia, extending from the level of the diaphragm to the level of the pelvic inlet. It is divided into the perirenal, anterior pararenal, and posterior pararenal spaces. Additional potential dissection planes exist between the retroperitoneal spaces: the retromesenteric plane, formed by retromesenteric fusion planes anteriorly and the anterior perirenal (Gerota) fascia posteriorly, and the retrorenal plane, formed by retromesenteric fusion planes and the posterior renal (Zuckerkandl) fascia. These potential spaces may form the pathway by which rapidly accumulating fluid collections in the retroperitoneal space may extend to the pelvis [1].

The kidneys, adrenals, and pancreas are retroperitoneal structures and are discussed separately in individual chapters.

Other structures contained within the retroperitoneum include lymph nodes and lymphatic vessels, fat, and nerves. Major vessels include the aorta and inferior vena cava, and major skeletal muscles include the psoas. Neoplastic, infectious, inflammatory, idiopathic, and hemorrhagic processes can arise from, or involve, these particular retroperitoneal structures and are discussed in this chapter.

MRI TECHNIQUE

The retroperitoneum can be reliably assessed by MRI. An imaging protocol should be designed to 1) maximize the signal intensity differences between suspected pathology and background tissues, 2) directly image the full extent of disease processes, and 3) define their boundaries with adjacent organs. The combination of breath-hold and breathing-independent sequences acquired in at least two different planes can achieve these goals without substantially prolonging the examination time. In the investigation of abnormal retroperitoneal tissue, the imaging protocol should include precontrast in-phase and out-of-phase spoiled gradient-echo (SGE), fat-suppressed SGE or 3D-GE, fat-suppressed and non-fat-suppressed T2-weighted, and postgadolinium fat-suppressed SGE or 3D-GE images.

Abdominal-Pelvic MRI, Third Edition, edited by Richard C. Semelka. Copyright © 2010 John Wiley & Sons, Inc.

In the investigation of retroperitoneal hemorrhage, precontrast fat-suppressed SGE or 3D-GE images should be obtained because this technique has the greatest sensitivity for subacute hemorrhage. Postcontrast fat-suppressed SGE or 3D-GE images, using intravenously administered gadolinium chelate, are important for delineation and characterization of retroperitoneal lymph nodes, other masses, inflammation or infection, and fibrosis [2]. Vascular structures are also well defined on postcontrast fat-suppressed SGE or 3D-GE images. Image acquisition in two orthogonal planes permits direct evaluation of the extent of retroperitoneal disease.

Oral contrast also may be used in selected cases to provide better delineation of bowel and to facilitate distinction of bowel from retroperitoneal tissue. Orally administered water provides adequate bowel opacification as a positive contrast medium for short-duration T2-weighted, echo-train spin-echo [e.g., half-Fourier single-shot turbo spin-echo (HASTE)] sequences and as a negative contrast medium for breath-hold T1-weighted (e.g., SGE and 3D-GE) sequences. The selection of sequences may vary according to the clinical history, the other organs that are examined, and the capabilities of the equipment.

MR angiographic techniques, particularly breath-hold three-dimensional (3D) gradient-echo MR angiography (MRA) sequences, play an important role in imaging the aorta and its branches. The combined use of 3D gradient-echo MRA and tissue-imaging sequences provides information on vessel lumen, vessel wall, and surrounding organs.

RETROPERITONEAL VESSELS

MR Angiography (MRA)

The aorta and its branches are well evaluated by MRA using currently available techniques. Generally, techniques can be classified as black blood (flowing blood appears as signal void) or bright blood (flowing blood appears as high signal intensity). Conventional T1- and T2-weighted spin-echo images will generally display the aortic lumen as a signal-void area (dark-blood technique) because the excited blood leaves the slice in the time interval between excitation pulse and echo sampling. Despite the use of presaturation pulses and a long echo time, slow blood flow, as can be seen during diastole in the infrarenal aorta, may appear bright on T1-weighted spin-echo images, which has the potential of appearing similar to thrombus. Cardiac gating can be used to reduce pulsatile motion artifacts and can reduce diastolic slow flow effects by acquiring SE images from inferior to superior, thus obtaining infrarenal aorta images during systole.

Bright-blood techniques include sequences that refocus blood signal intensity with gradient pulses or gadolinium-enhanced gradient-echo sequences. Sequences that refocus blood signal include cine gradient-echo, time-of-flight MR angiography, and phase-contrast MR angiography. Time-of-flight MRA techniques [3–9] rely on the inflow of unsaturated spins into the examined slice (2D) or volume (3D). Although these techniques have been used for head and neck applications, they do not achieve reproducible image quality in the abdomen because of respiratory and peristaltic motion and because of the large volume of examined tissues and vessels. As the majority of these techniques are non-breath hold, they have limited reproducibility in patients who are uncooperative, a circumstance that may be observed in patients with substantial disease. Furthermore, slow or turbulent flow in aortic aneurysms and poststenotic turbulent flow (e.g., in aortic occlusive disease or renal artery stenoses) cause dephasing that leads to signal loss and impaired vessel visualization [6, 9–11]. Phase-contrast techniques may be used when flow velocity and direction information is required (fig. 10.1). They require cardiac triggering and can be rela-

FIG. 10.1 Phase map of the normal aorta. The abdominal aorta (encircled) appears high in signal intensity on this phase map in the systolic phase of antegrade blood flow. A blood velocity tracing obtained throughout the cardiac cycle is superimposed on the phase image, demonstrating the normal velocity profile of blood in the abdominal aorta. (Reproduced with permission from Semelka RC, Shoenut JP, Kroeker MA: The retroperitoneum and the abdominal wall. In: Semelka RC, Shoenut JP (eds.), *MRI of the Abdomen with CT Correlation.* New York: Raven Press, p. 13–41, 1993.)

tively long acquisition sequences, predominantly used for assessment of critical aortic stenosis or for assessment of cardiac valvular disease.

The disadvantages of the time-of-flight techniques include signal loss in low-flow and turbulent-flow states and saturation of in-plane flow. To overcome these disadvantages, gadolinium enhancement has been employed in conjunction with 2D or 3D fast gradient-echo acquisitions, yielding good, reproducible results [10–16]. The 3D gadolinium-enhanced gradient-echo MRA technique does not rely on time-of-flight effects but rather on the T1 shortening provided by gadolinium [17]. Advantages compared with 2D techniques include a high signal-to-noise ratio permitting nearly isotropic resolution (typically 2-mm effective slice thickness), acquisition of the central phase-encoding steps at the same time point for all the slices, and avoidance of slice misregistration [11]. Recent advances in MRI, including the use of phased-array coils that increase the signal-to-noise ratio and faster-rising gradient times, have led to the implementation of fast 3D gradient-echo acquisitions in a breath hold [17, 18]. Typically, 0.1 mmol/kg body weight of gadolinium [high-dose gadolinium injections including 0.2 mmol/kg or higher doses should be avoided because of nephrogenic systemic fibrosis (NSF) considerations, and high T1-relaxivity agents should be preferred particularly for MRA applications] is administered into an arm vein with a dual-chamber power injector at a rate of 2–3 cc/s, followed by 15 cc of saline to clear lines and veins. A tight bolus technique is useful when examining renal arteries because the venous return from the kidneys is rapid and overlap from renal veins is more difficult to control with infusion techniques. A slower infusion technique may be used when smaller and/or distal vessels are imaged, as in combined examinations of aortoiliac and lower extremity vessels.

Timing of the injection depends on the vessels studied, the patient's cardiac output, and the total acquisition time of the 3D gradient MRA sequence, with the objective being to maximize intravascular gadolinium concentration during acquisition of the central phase-encoding steps [13, 17]. It is these central encoding steps that are responsible for generating image contrast. To simplify timing, 3D gradient-echo MRA sequences have been designed to reorder phase-encoding steps, obtaining image contrast information at the beginning of the acquisition. Such techniques include helical, helicocentric, or elliptocentric 3D gradient MRA sequences. For aortic imaging, the time interval between initiation of contrast injection and initiation of the imaging sequence can be determined with a timed bolus technique. This is accomplished by placing a sagittal gradient-echo slice centered on the descending thoracic aorta and imaging one image every 2 s as a 2- or 3-cc gadolinium injection is administered. Alternatively, an automated system can be employed such that the control software measures signal intensity arising from within a region of interest, placed within the aortic lumen, and the entire intravenous gadolinium bolus is then administered such that a prescribed 3D gradient MRA acquisition is triggered when the system detects a rise in intraluminal aortic signal intensity.

Automation has progressed further such that a bolus-chase technique, similar in concept to conventional fluoroscopic angiography, is now possible. This is performed by prescribing up to three consecutive fields of view having three separate centering points, which can extend from the aortic arch to the vessels of both lower extremities and feet (fig. 10.2). Each field of view can overlap slightly with the neighboring field by 2 cm, with each field typically measuring between 34 and 40 cm in length. Imaging of the superior field is acquired with initiation determined by a timed-bolus or automated preparation technique. Subsequent middle and lower fields are imaged as previously prescribed, with the table moving the patient to the appropriate new center point automatically. In this way, the bolus of arterial gadolinium contrast can be chased into the lower extremities. Venous filling can then be chased in reverse sequence from the feet to the IVC. Although the time interval between initiation of contrast injection and initiation of imaging of the superior first station can be determined by prior bolus timing or by automated bolus detection, the subsequent imaging at the second and third inferior stations is timed empirically. To include the aorta, bilateral iliac, and bilateral lower extremity vessels, coronal 3D volumes are used. The ankles are elevated to keep the calf arteries within a level horizontal plane. More recent faster image acquisition sequencing, such as true free induction in steady-state precession (e.g., true FISP or FIESTA) sequences, in combination with gadolinium, can be used for obtaining high spatial resolution, high contrast, and high temporal resolution, allowing more eloquent bolus-chase imaging. For example, a single bolus of contrast can now be imaged as the contrast first passes through the respective right heart, pulmonary arteries and veins, left heart, and then into the aorta (fig. 10.3). Generally, as temporal resolution improves, optimal image timing becomes easier, arterial-venous delineation is superior, and the required dose of contrast decreases; 3.0 T MR imaging enables the acquisition of higher-quality images because of its higher spatial and temporal resolution compared to 1.5 T. Previously, an aortic run-off study would require a combination of two or three stations, each treated as an individual exam requiring a total of two or three doses of gadolinium, typically at 0.1 mmol/kg each. Caution should currently be exercised in using high-dose volumes of gadolinium-based contrast agents for MRA studies. Many of the reported cases of NSF have

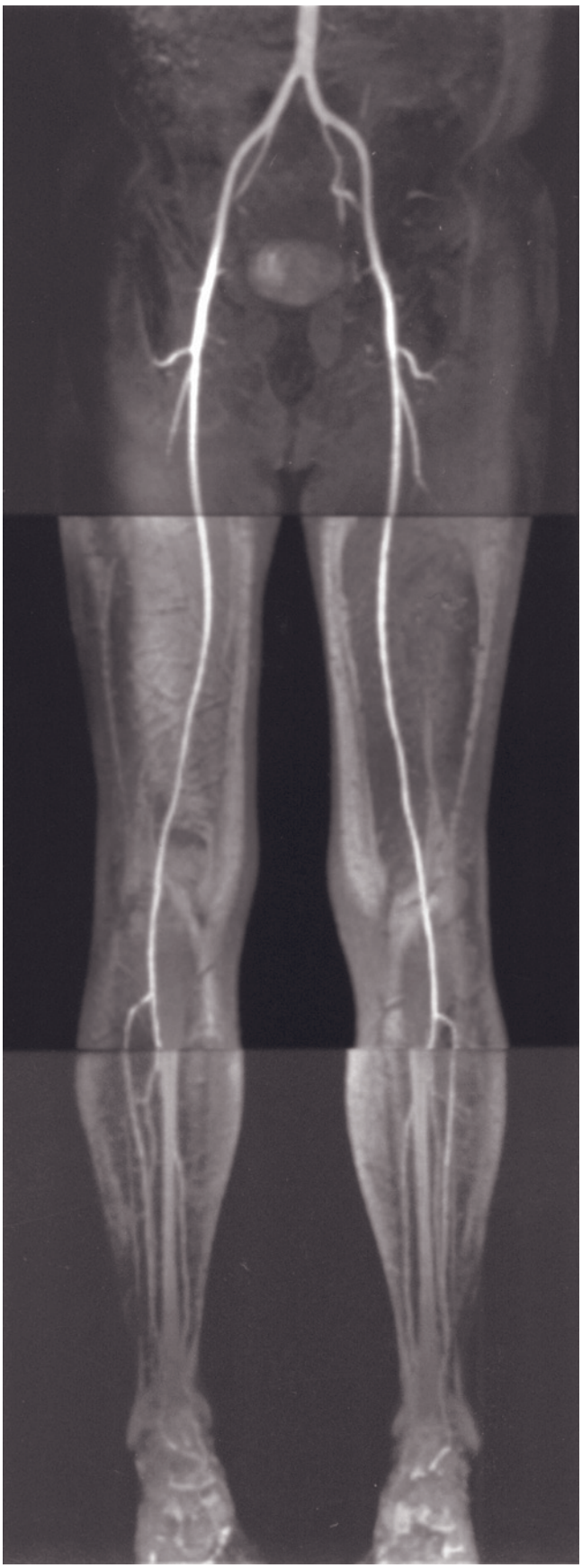

(*a*)

(*b*)

FIG. 10.2 Extended-coverage MR angiography (MRA). Aortic run-off 3-station 3D gradient-echo MRA showing normal (*a* and *b*), abnormal (*c*, right side), and conventional fluoroscopic digital subtraction angiogram (*c*, left side). A normal patient was

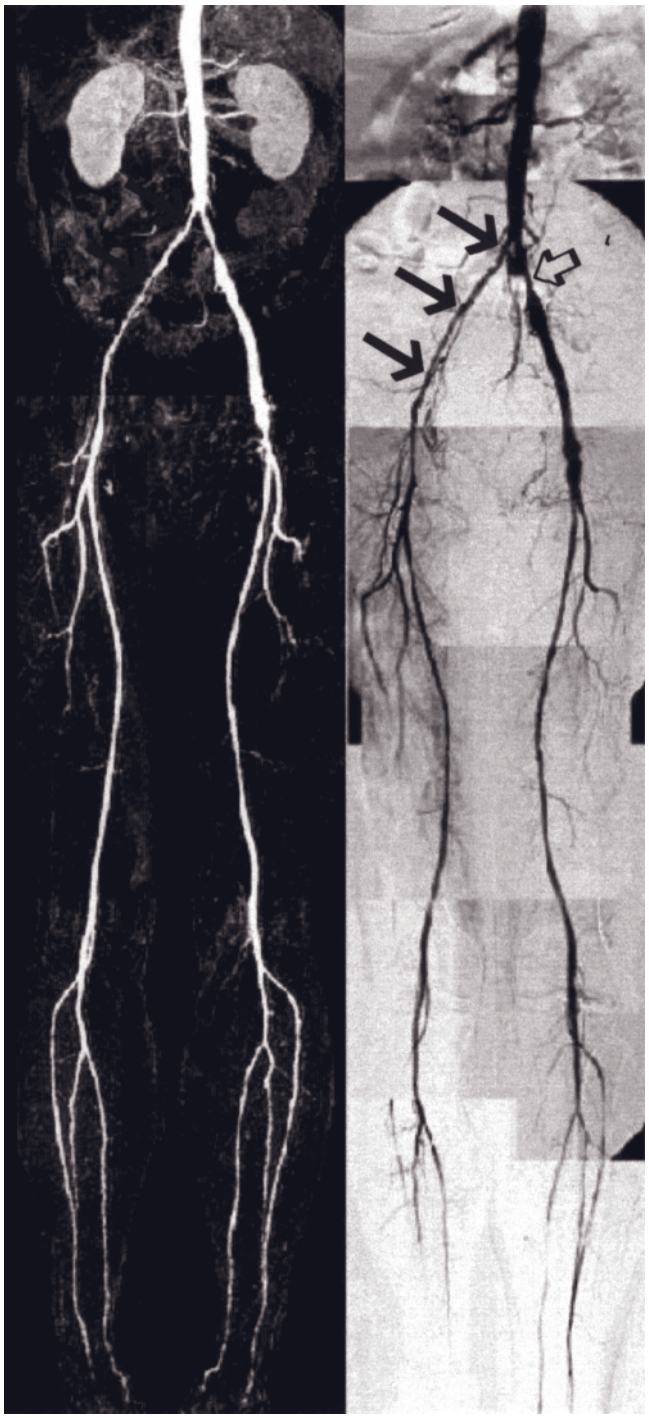

(*c*)

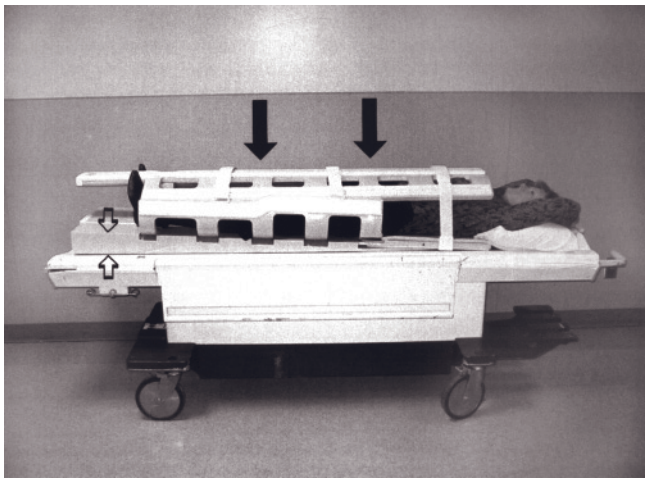

(*d*)

FIG. 10.2 (*Continued*) scanned using a peripheral vascular 3-station phased-array coil (*d*) having 2-cm overlaps between upper and middle (junction at the midsuperficial femoral artery) and again between middle and bifurcation into the peroneal and posterior tibial arteries. The data were processed by maximum intensity projection (MIP) software analysis and are shown with no background subtraction and with soft tissue window and level (*a*) and after background subtraction using a high-contrast window and level (*b*) to eliminate soft tissues. Surgical planning often requires soft tissue visualization for spatial reference (*a*), although vascular detail may be more easily appreciated after removal of the soft tissue (*b*). Image *c* compares an MRA run-off study performed as in *a* and *b*, but with atherosclerotic irregular narrowing demonstrated over a long segment of right common and external iliac artery and a short segment of proximal to mid-left common iliac artery. Nearly identical results are demonstrated on a conventional fluoroscopic angiogram using iodinated contrast agent, performed on the same patient and shown on the right (arrows, right common and external iliac artery; open arrow, proximal left common iliac artery).

been reported after either the cumulative effects of multiple doses of these agents experienced with repeated studies or in the setting of high-dose applications such as MRA [19]. Our current recommendation is to not use more gadolinium-based contrast agent than a single-dose application (i.e., 0.1 mmol/kg). High T1-relaxivity agents [gadobenate dimeglumine (MultiHance), gadoxetic acid (Eovist), gadofosveset trisodium (Vasovist)] may be preferred for MRA applications. High T1-relaxivity agents provide higher signal-to-noise ratio at the standard doses (i.e., 0.1 mmol/kg) of other gadolinium agents with standard T1 relaxivity. They can either be used at standard doses (i.e., 0.1 mmol/kg) to obtain higher image quality or can be used at

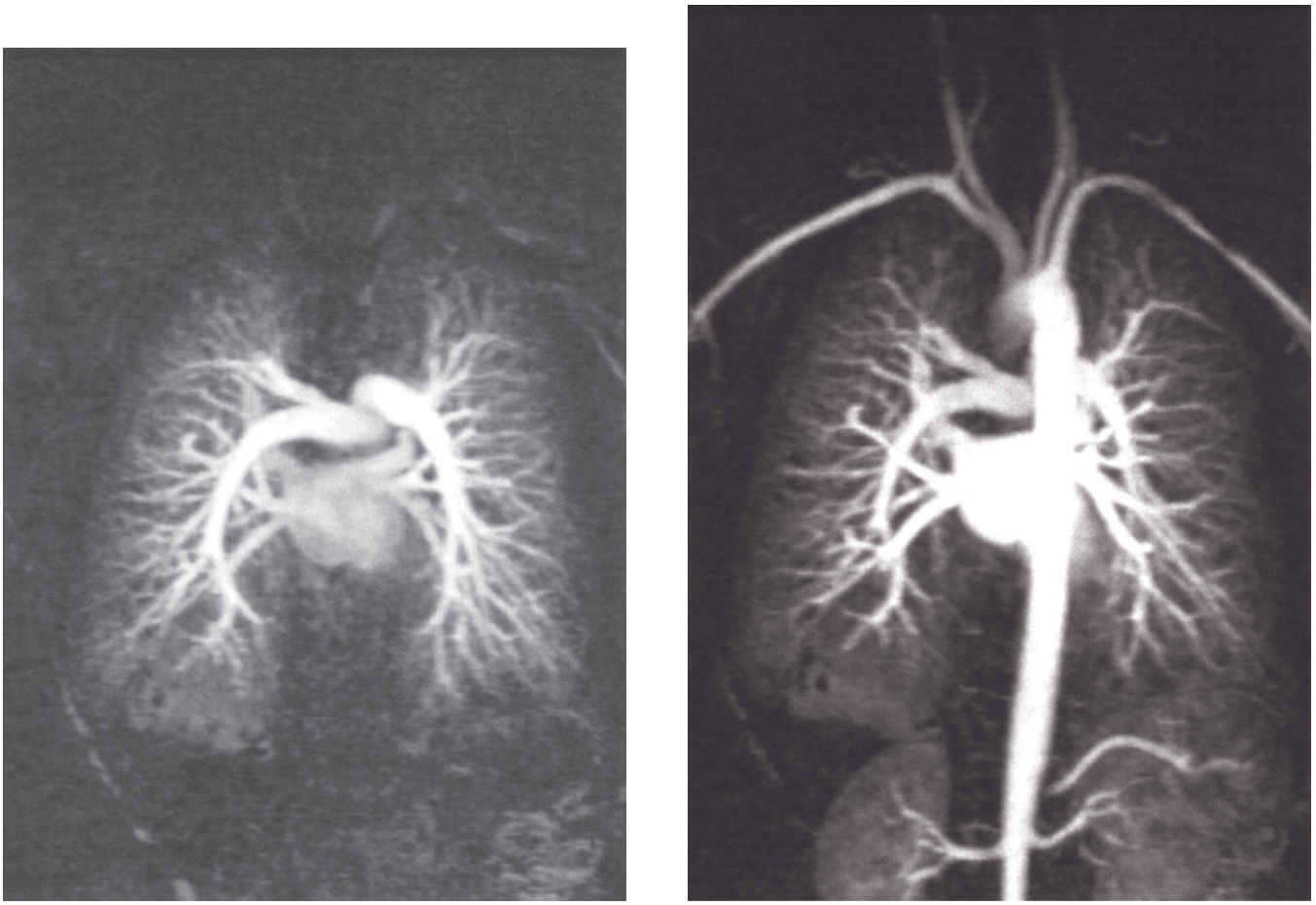

(*a*) (*b*)

FIG. 10.3 Normal pulmonary MRA. Coronal 3D gradient-echo (*a* and *b*) images. The acquisition of image data over a short time period, after rapid injection of a small volume of gadolinium contrast, allows better temporal resolution, obtaining an image with contrast predominantly within the pulmonary arteries and just starting to fill pulmonary veins and left atrium. The image acquired immediately after the pulmonary angiogram (*b*) shows contrast within the pulmonary veins, left atrium, aorta, and major aortic arch vessels and starting to fill the renal arteries.

lower doses (i.e., less than 0.1 mmol/kg) to obtain similar image quality compared to other gadolinium agents with standard T1 relaxivity. Therefore, these agents may be particularly advantageous to minimize the risk of NSF because they can be used at lower doses in patients at risk for NSF. Also, gadofosveset trisodium (Vasovist) is a gadolinium-based contrast agent with higher relaxivity and with prolonged intravascular retention due to being extensively and reversibly bound to human serum albumin, which should be considered for use [20, 21]. More experience with this agent, and more data regarding stability are necessary before we are prepared to state that this agent should be preferred for MRA procedures.

Another development necessary for multiple consecutive field-of-view imaging for aortic run-off exams has been specialized peripheral vascular phased-array coils that can cover from the chest to the feet (see fig. 10.2). Without such coil designs, a solitary phased-array torso coil would require repositioning or, more simply, the built-in body coil could be used. However, signal-to-noise ratio is significantly improved with surface coils.

The data acquired can be postprocessed either by multiplanar reconstructions or by 3D reconstruction using a maximum-intensity projection (MIP) algorithm. The small size of the individual slices permits reconstructions and 3D MIP projections at any level without image degradation. MIP images provide a quick overview and are useful in tracking vessels that have a tortuous course in and out of the section plane. They are also useful for identifying smaller vessels (e.g., accessory renal arteries) (fig. 10.4). The diagnosis, however, is usually based on the individual source sections, and evaluation should not rely solely on the MIP images. The source images are superior to MIP reconstructions

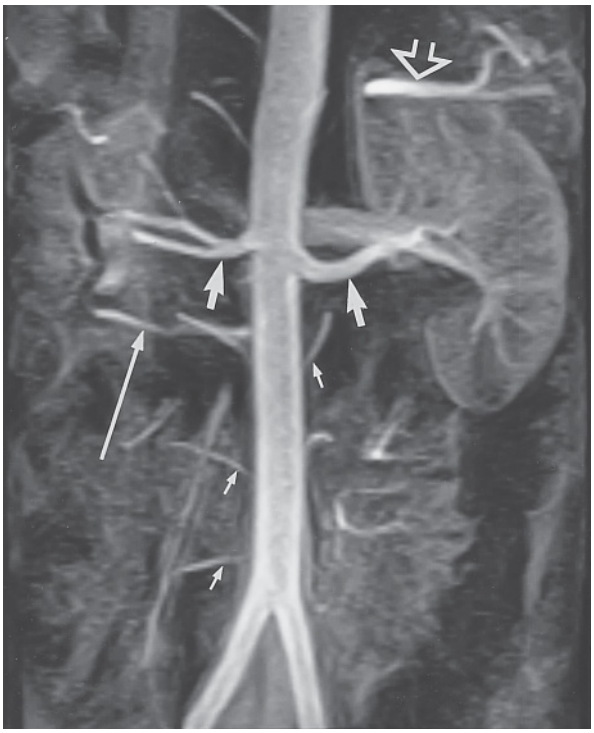

(*a*)

(*b*)

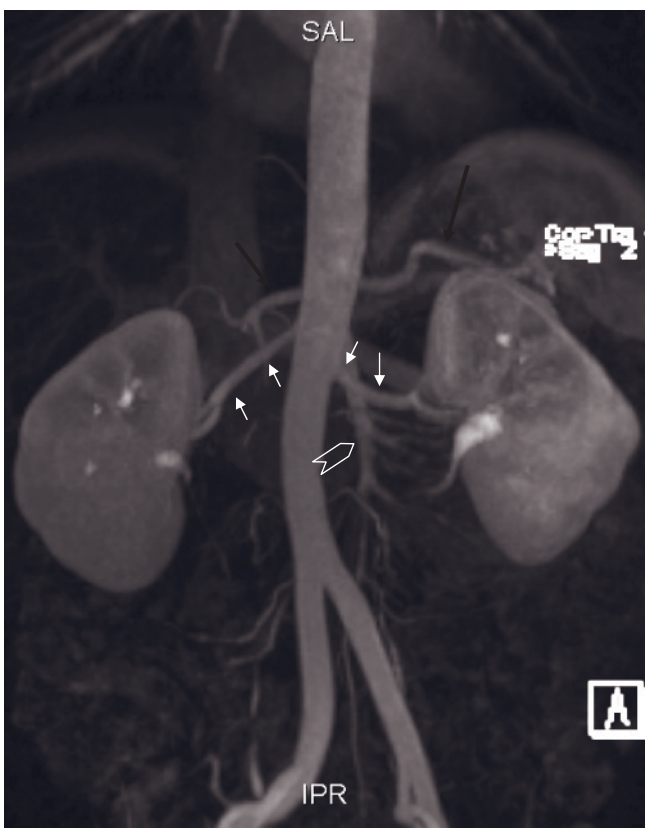

(*c*)

FIG. 10.4 Normal abdominal aorta and iliac vessels. Anteroposterior projection (*a*) from a 3D MIP reconstruction of a set of immediate postgadolinium coronal breath-hold 3D gradient-echo sections with effective slice thickness of 2 mm. The abdominal aorta, left and right renal arteries (arrows, *a*) and a right accessory lower pole renal artery (long arrow, *a*), common iliac arteries, and lumbar arteries (small arrows, *a*) are well visualized, with good lumen enhancement and smooth contours. The celiac axis and superior mesenteric artery are not visualized because they course outside the narrow (4 cm) coronal slab. A segment of the splenic artery is identified reentering the acquired slab in its posterior course toward the hilum of the spleen (open arrow, *a*). Anteroposterior projection (*b*) from a 3D MIP reconstruction of a set of immediate postgadolinium coronal breath-hold 3D gradient-echo sections with effective slice thickness of 2 mm in a second patient. The normal aorta, renal arteries (arrows, *b*), and lumbar arteries (small arrows, *b*) are well demonstrated. 3D MIP reconstruction image (*c*) of a set of immediate postgadolinium coronal breath-hold 3D-GE MRA sections acquired at 3.0 T demonstrates the abdominal aorta, common iliac arteries, bilateral renal arteries (white short arrows, *c*), common hepatic artery (short black arrow, *c*) and its branches, splenic artery (long black arrow, *c*) and superior mesenteric artery (open arrow, *c*) and its branches in another patient with normal MRA findings. 3D MIP reconstruction

(*d*) (*e*)

FIG. 10.4 (*Continued*) image (*d*) of a set of immediate postgadolinium sagittal breath-hold 3D-GE MRA sections and sagittal 3D-GE angiographic source image (*e*) demonstrate common celiac-mesenteric trunk in another patient. Celiac-mesenteric trunk is a rare variant seen in less than 1% of the population. MRA is also effective at demonstrating vascular anatomic variations. Note that pulmonary arterial vasculature is also shown.

in the depiction of vessel wall, presence of mural thrombus, renal artery ostia, and intimal flap in aortic dissections [4]. Of critical importance for viewing and interpretation of large MRA data sets is a picture archival computing system (PACS) that has viewing workstations with software capable of image stacking and scrolling (i.e., rapid paging from one image slice to the next).

A useful adjunct, particularly in uncooperative patients, is a single-shot echo-train spin-echo technique (e.g., HASTE) combined with a set of preparatory inversion pulses (black-blood technique): A non-slice-selective 180° inversion pulse is applied, which is followed by a slice-selective 180° inversion pulse before the start of the echo-train sequence. The first pulse inverts the longitudinal magnetization of the whole body, whereas the second pulse selectively restores the longitudinal magnetization of the examined slice. The time delay of the first inversion pulse is selected so that the central phase-encoding steps are acquired when blood reaches the null point, resulting in no signal from blood [22].

For clinical examinations, it may be of value to obtain a bright-blood and a black-blood technique for studying the aorta [5, 23]. An attractive feature of MRI is its ability to image the aorta along its longitudinal length, which has a particular advantage in studying the length of a disease process such as aneurysm [5, 16, 23].

For the assessment of aortic pathology, early (up to 2 min after injection) postgadolinium images obtained for investigation of diseases of solid abdominal organs provide a fast and reproducible technique incorporated into the routine abdominal MRI protocol [24]. Immediate postgadolinium SGE or 3D-GE images also generate information on capillary blood flow, which may provide important insight into the impact of anatomic vessel abnormalities on organ perfusion [24]. When angiographic sequences are not available, an anteroposterior projection of an MIP reconstruction using immediate postgadolinium coronal 3D-GE sections (3.5 mm) results in angiographic-like images. The acquisition of thinner sections (2 or 3 mm) at 3.0 T also improves the use of 3D-GE soft tissue imaging sequence for the assessment of vessels [24].

Aorta

Aortic Aneurysm

Abdominal aortic aneurysm (AAA) is a common disease entity in North America. The incidence is 21.1 per 100,000, and men are five times more likely than women

to be affected by AAA. The median age at diagnosis is 69 years for men and 78 years for women [25]. Important diagnostic information for patient management includes the diameter of the aneurysm, its longitudinal length, and its relationship to renal, common iliac, and femoral arteries. Spontaneous rupture is a frequent complication of aneurysms 6 cm or more in diameter, but it is relatively uncommon for AAAs smaller than 5 cm [26, 27]. MR images with black-blood and bright-blood techniques are successful at demonstrating aneurysms [5, 16, 23, 28–32]. Gadolinium-enhanced 3D gradient-echo MR angiography (e.g., 3D FISP) demonstrates the full extent of the aneurysm and its relationship to the renal arteries, celiac axis, and superior mesenteric artery (SMA) (fig. 10.5). In patients with atherosclerotic disease, renal artery stenosis may coexist and is well depicted on gadolinium-enhanced 3D FISP images. Stenosis of the SMA also can be assessed reliably, and this is of importance in patients with suprarenal aortic aneurysms because postoperative bowel ischemia may complicate aneurysm repair [32]. Assessment of the aortic wall, mural thrombus, and abdominal viscera is accomplished on postgadolinium SGE or 3D-GE (fig. 10.6) or fat-suppressed SGE or 3D-GE images after the 3D acquisition.

A pseudoaneurysm represents enlargement of the artery resulting from blood accumulating beyond the intimal layer and typically trapped within the serosa or outer layer of the arterial wall. Etiology may be related to ruptured atheroma, dissection, or trauma (fig. 10.7).

Inflammatory aortitis, also termed inflammatory aortic aneurysm, is an uncommon entity in which an inflammatory reaction develops around an aortic aneurysm [33]. Etiologic factors proposed by some investigators include an immune response to ceroid produced in atheromatous plaque [30], whereas other investigators have found evidence of vasculitis involving the aortic wall in patients with inflammatory aortic aneurysms and have postulated that the combination of retroperitoneal fibrosis, vasculitis, and aortic aneurysm may represent a distinct pathological entity [33]. Gadolinium-enhanced fat-suppressed SGE or 3D-GE images demonstrate infiltrative enhancing tissue surrounding an aortic aneurysm (fig. 10.8).

Aortic Dissection

Aortic dissection usually originates in the thoracic aorta. MRI with MRA has been shown to be accurate in the detection of aortic dissection [32, 34, 35]. The noninvasive nature of the technique and the absence of ionizing radiation are important features of MRI. Strengths of MRI include the ability to demonstrate the intimal flap [34] and entry site [11], to examine the whole length of the aorta, and occasionally to demonstrate so-called "aortic cobwebs," which are fibroelastic bands formed during the dissection process that project from the false lumen wall [36]. Detection of these bands facilitates the distinction of the false from the true lumen because they are located in the false lumen. On spin-echo images, flow in the true lumen is usually signal void, whereas flow in the false lumen can be signal void or high in signal intensity depending upon the velocity of blood flow (fig. 10.9). Slow flow in the false lumen of a dissection may be difficult to differentiate from thrombosis on spin-echo images.

The role of conventional spin-echo imaging is limited because gadolinium-enhanced 3D gradient-echo MRA (e.g., 3D FISP) and gadolinium-enhanced fat-suppressed GE (2D or 3D) imaging are all fast, accurate, and reproducible techniques for the demonstration of dissection. Gadolinium-enhanced SGE or 3D-GE and 3D gradient-echo MRA techniques reliably differentiate slow flow, which is high in signal intensity on these images, from thrombus, which is low to intermediate in signal intensity (fig. 10.9). Breath-hold gadolinium-enhanced 3D gradient-echo MRA images provide sharp detail and demonstrate the full extent of dissection, the entry site, the location of the intimal flap, and the relation of the visceral vessels to the true and false lumen (fig. 10.10). The entry site, intimal flap, and origins of the vessels are better shown on the individual sections than on the 3D MIP reconstructions. The acquisition of two data sets provides dynamic flow information, which often demonstrates delayed enhancement of the false lumen, which is apparent in cases with slow flow. Breath-hold immediate postgadolinium SGE or 3D-GE images may also provide this information. Postgadolinium non-fat-suppressed and fat-suppressed SGE or 3D-GE images delineate the intimal flap, demonstrate the origins of the aortic branches, and can assess extension of the dissection into the splanchnic vessels (see fig. 10.11). This extension is evaluated better on transverse- than on sagittal- or coronal-plane images. In rare instances the only finding may be wall thickening with or without high-signal-intensity foci on T1-weighted images [37, 38]. The high-signal-intensity foci on T1-weighted images reflect the presence of intramural hematoma. This pattern may be missed on angiography and has been postulated to represent the early stage of dissection with hemorrhage from the vasa vasorum that leads to aortic wall weakening and subsequent intimal rupture [37, 38]. In one report, the transition from this appearance to classic dissection with intimal flap and blood flow in the false lumen was documented on follow-up studies in two patients [38].

Penetrating Aortic Ulcers and Intramural Dissecting Hematoma

Penetrating aortic ulcers result from ulcerated atherosclerotic plaques that penetrate the internal elastic

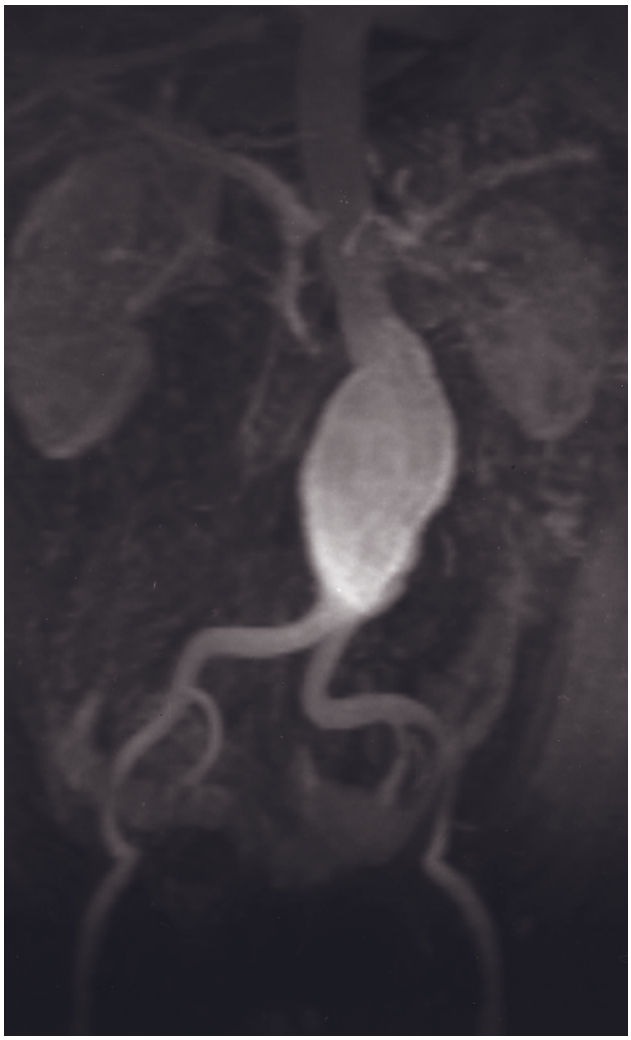

(*a*)

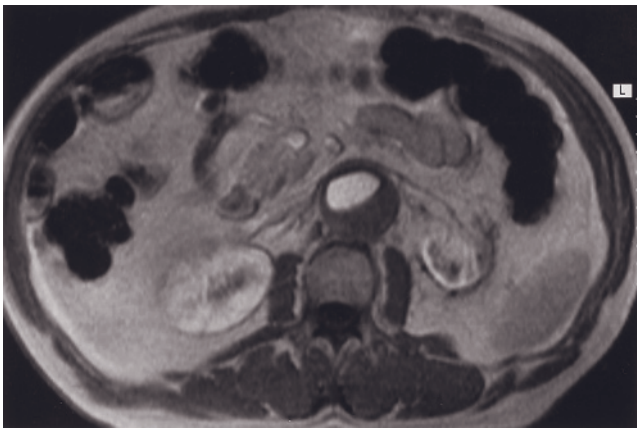

(*b*)

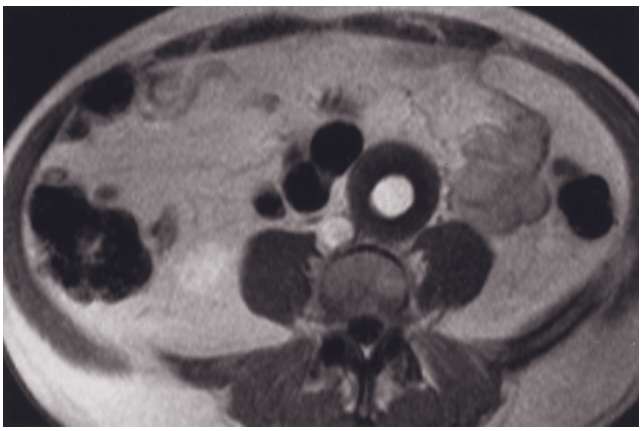

(*c*)

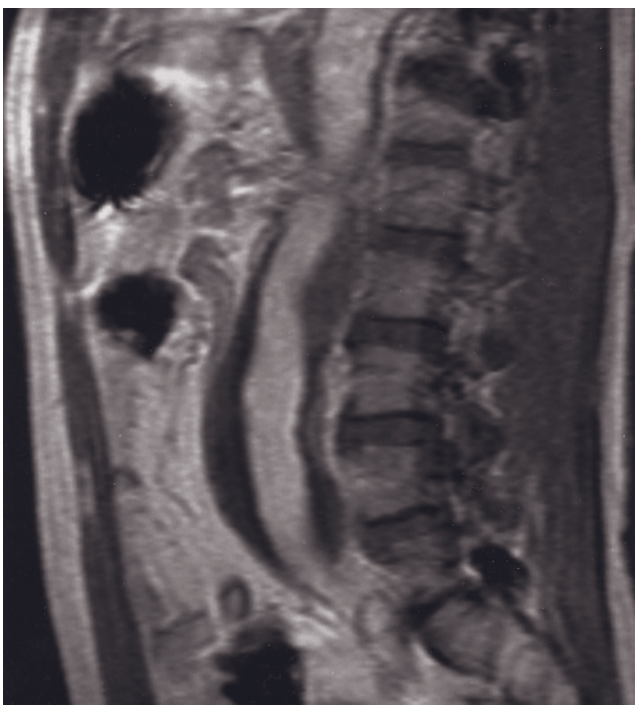

(*d*)

FIG. 10.5 Atherosclerotic aortic aneurysm of the abdominal aorta. Coronal MIP reconstruction (*a*) of a set of gadolinium-enhanced 2-mm thin-section coronal 3D gradient-echo sections in a patient with an infrarenal aortic aneurysm. The MIP images demonstrate a large fusiform infrarenal aortic aneurysm. The aneurysm is shown not to extend into the common iliac arteries. Transverse 45-s postgadolinium SGE (*b*), interstitial-phase gadolinium-enhanced SGE (*c*), and sagittal interstitial-phase SGE (*d*) images in a second patient. An abdominal aortic aneurysm containing high-signal-intensity gadolinium in the lumen and low-signal-intensity wall thrombus is evident on the 45-s postgadolinium SGE image (*b*). The left kidney is small and demonstrates delayed enhancement of a uniform thin cortex, findings consistent with left renal artery stenosis. Note that the signal intensity of the cortex and medulla of the right kidney has equilibrated at this tubular phase of enhancement. Good delineation of the patent lumen and mural thrombus is provided by gadolinium enhancement on early postgadolinium SGE images (*b, c*), whereas imaging in the sagittal plane demonstrates the longitudinal extent of disease. Immediate postgadolinium (*e*) and transverse (*f, g, h*) and

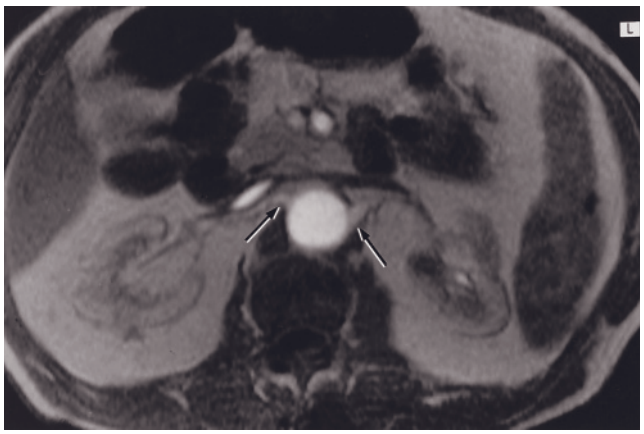

(*e*)

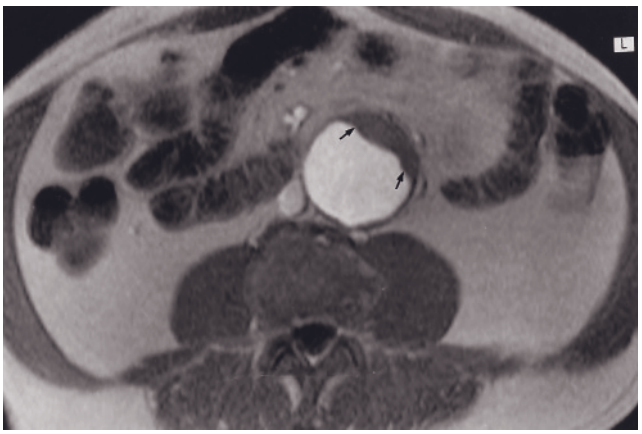

(*f*)

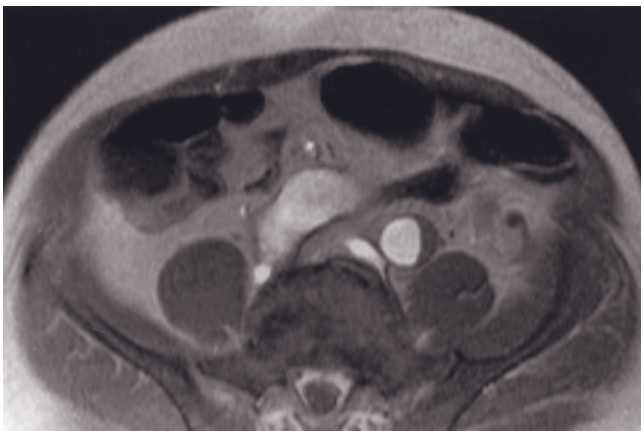

(*g*)

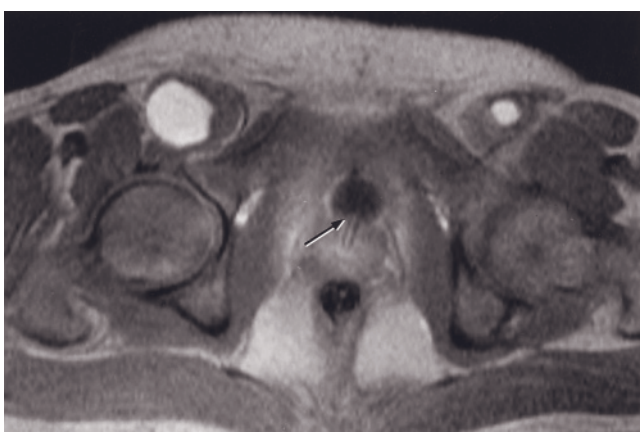

(*h*)

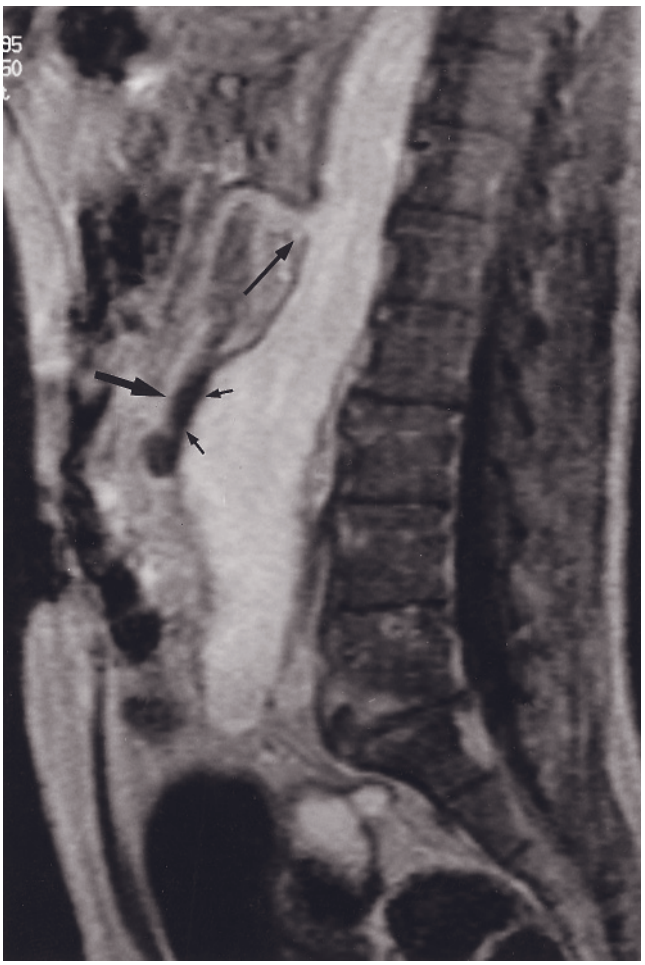

(*i*)

FIG. 10.5 (*Continued*) sagittal (*i*) interstitial-phase gadolinium-enhanced SGE images in a third patient. The abdominal aorta is normal in diameter at the level of the origins (arrows, *e*) of the renal arteries. At lower tomographic levels (*f–h*), enlargement of the aortic lumen with sharp demarcation of the high-signal-intensity patent lumen and low-signal-intensity wall thrombus (small arrows, *f*) is noted. Involvement of the infrarenal aorta (*f*), common iliac arteries (*g*), and common femoral arteries (*h*) is demonstrated. A Foley catheter is also noted in place (arrow, *h*).The sagittal interstitial-phase image provides direct visualization of the site of maximal anteroposterior diameter (arrow, *i*) with depiction of low-signal-intensity thrombus (small arrows, *i*) in the anterior aortic wall. The origin of the superior mesenteric artery (thin arrow, *i*) is also demonstrated. Coronal 2-mm gadolinium-enhanced

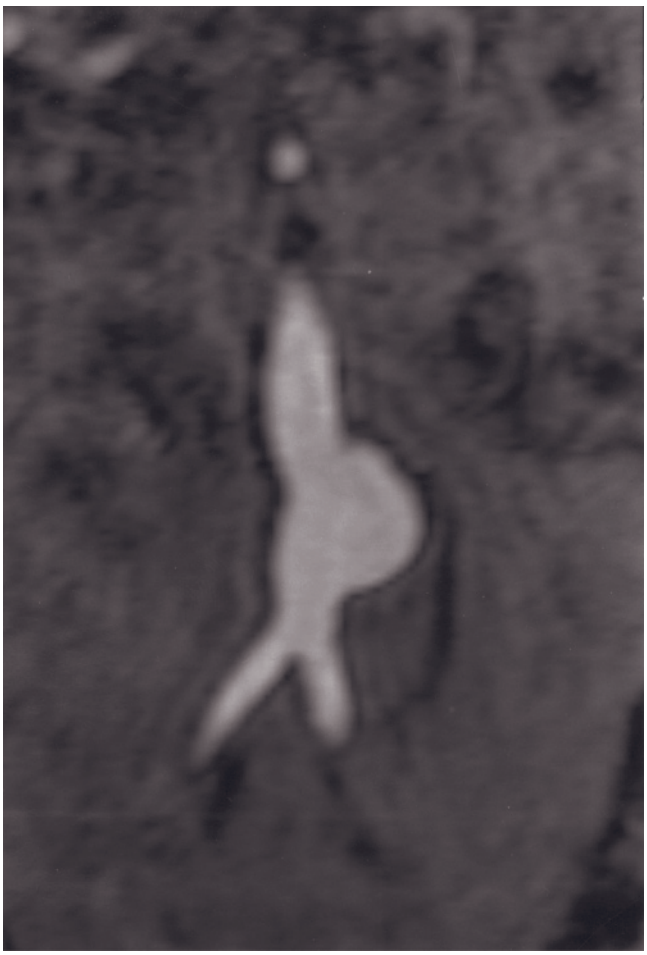

(*j*)

(*k*)

FIG. 10.5 (*Continued*) 3D gradient-echo source image (*j*) and MIP reconstruction of the 2-mm 3D gradient echo sections (*k*) in a fourth patient. The source image (*j*) most clearly defines the vascular abnormalities, whereas the MIP reconstructed image provides the overall topographic display (*k*). In this patient, a saccular infrarenal aortic aneurysm is clearly shown.

lamina and may lead to hematoma formation within the media of the aortic wall, false aneurysm, and finally transmural rupture of the aorta. They are more commonly located in the descending thoracic or upper abdominal aorta (fig. 10.12) [39]. In cases of intramural dissecting hematoma, the intimal flap is not often seen and is irregular and thick. The intramural hematoma rarely fills with contrast and is usually seen to extend both cephalad and caudal to the entry site, which is at the penetrating atherosclerotic ulcer. Extensive atherosclerotic changes are usually present in the aorta [39]. It is important to differentiate this entity from aortic dissection because management may be different. MRI can demonstrate the intramural hematoma, atherosclerotic ulcer, and false aneurysm [39, 40] and is superior to angiography in depicting the extent of intramural thrombus. MRI may be similar or superior to CT imaging in differentiating acute hematoma from atherosclerotic plaque and chronic thrombus [40]. Intramural hematoma is high in signal intensity on both T1- and T2-weighted images and can be differentiated from chronic mural thrombus, which is low in signal intensity [40]. The combination of gadolinium-enhanced 3D gradient-echo MRA images to define the aortic lumen and gadolinium-enhanced fat-suppressed SGE or 3D-GE images to demonstrate the wall thickness in deep aortic ulcers may be the most effective means for evaluating this entity (see fig. 10.12).

Aortoiliac Atherosclerotic Disease—Thrombosis

Gadolinium-enhanced SGE or fat-suppressed SGE and 3D-GE images may demonstrate gross atherosclerotic

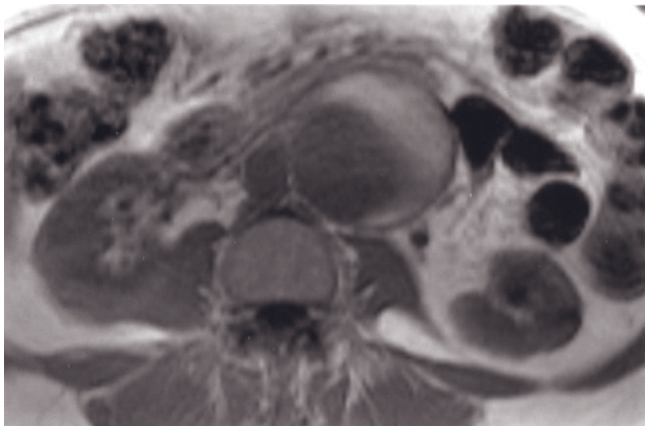

(*a*)

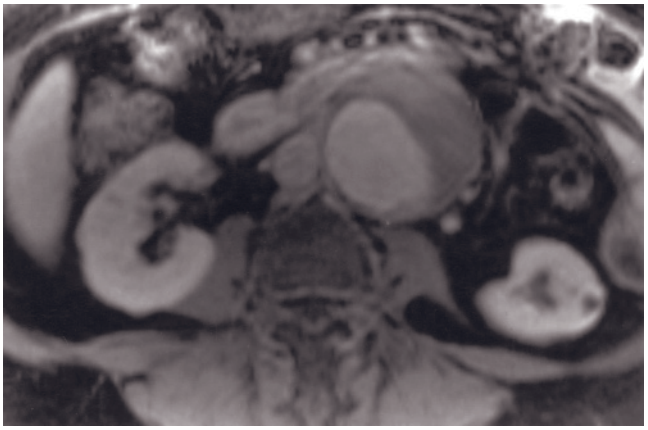

(*b*)

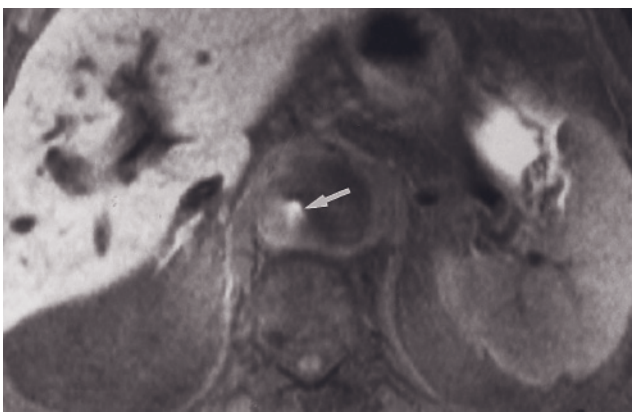

(*c*)

FIG. 10.6 High-signal-intensity mural thrombus. Precontrast SGE (*a*) and gadolinium-enhanced fat-suppressed SGE (*b*) images. An abdominal aortic aneurysm containing high-signal-intensity thrombus (arrow, *a*) is observed on the precontrast SGE image. On the postcontrast image, the lumen is opacified and the thrombus becomes relatively low signal. T1-weighted fat-suppressed spin-echo image (*c*) in a second patient with aortic aneurysm demonstrates an aortic aneurysm with atherosclerotic plaque in its right posterior aortic wall with a high-signal-intensity focus (arrow, *c*) representing clot of more recent origin.

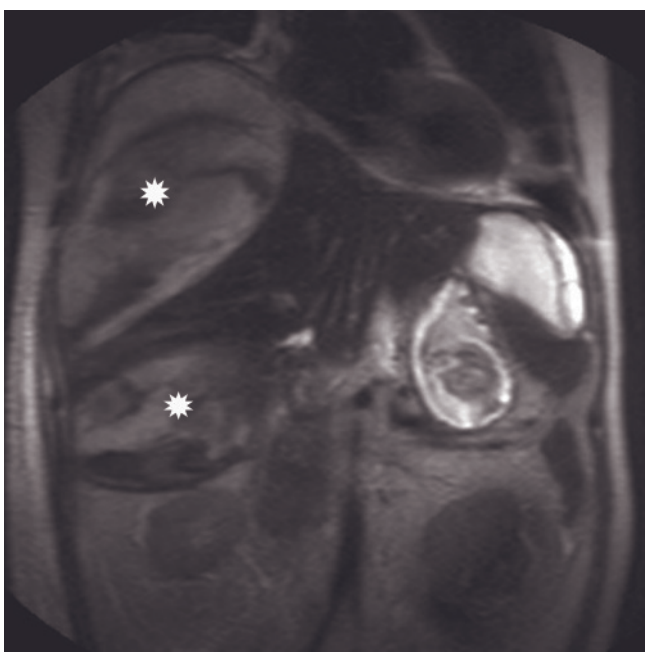

(*a*)

(*b*)

FIG. 10.7 Gastroduodenal pseudoaneurysm. The patient presented with upper quadrant abdominal pain after a partial pancreatectomy and diminished renal function. An MR angiogram was performed and included precontrast imaging that showed a massive subcapsular hemorrhagic collection (stars, *a*) on coronal T2-weighted single-shot echo-train imaging with blood tracking along the porta hepatis. Postgadolinium imaging was obtained by bolus tracking timed imaging to capture the arterial phase (*b*), and subsequent delayed-phase axial 3D GRE imaging was performed to have an overview of the relationship of blood vessels and surrounding soft tissues (*c*). The MRA image (*b*) is displayed as a single selected maximum-intensity projection (MIP) from a series of multiple-projection reconstruction (MPR) images and shows the proper hepatic artery (arrowhead, *b*), the origin of the gastroduodenal artery (large arrow, *b*), and the pseudoaneurysm arising from the gastroduodenal artery (small arrows, *b*). The pseudoaneurysm

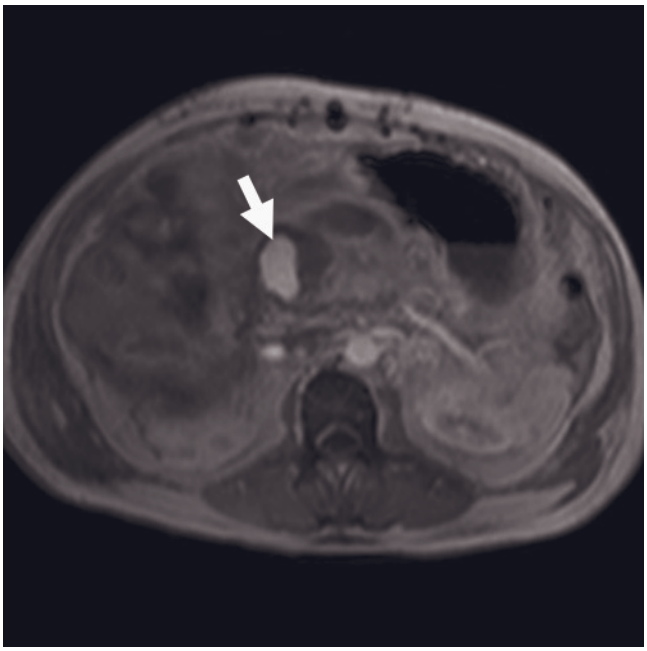

(*c*)

(*d*)

(*e*)

FIG. 10.7 (*Continued*) is also demonstrated on axial 3D GRE imaging (arrow, *c*). After the MRA, the patient had an angiographically directed interventional procedure with successful thrombosis of the pseudoaneurysm by coil placement. With the use of the MRA to assist in catheter guidance, only 10 cc of iodinated contrast was required for the interventional procedure, representing a small fraction of the total dose burden that would have been required without the MRA and minimizing the risk for further acute impairment of renal function. **Renal artery aneurysm.** 3D MIP reconstruction image (*d*) of a set of immediate postgadolinium coronal breath-hold 3D-GE MRA sections and coronal 3D-GE angiographic source image (*e*) at 3.0 T demonstrate a small renal artery aneurysm in another patient.

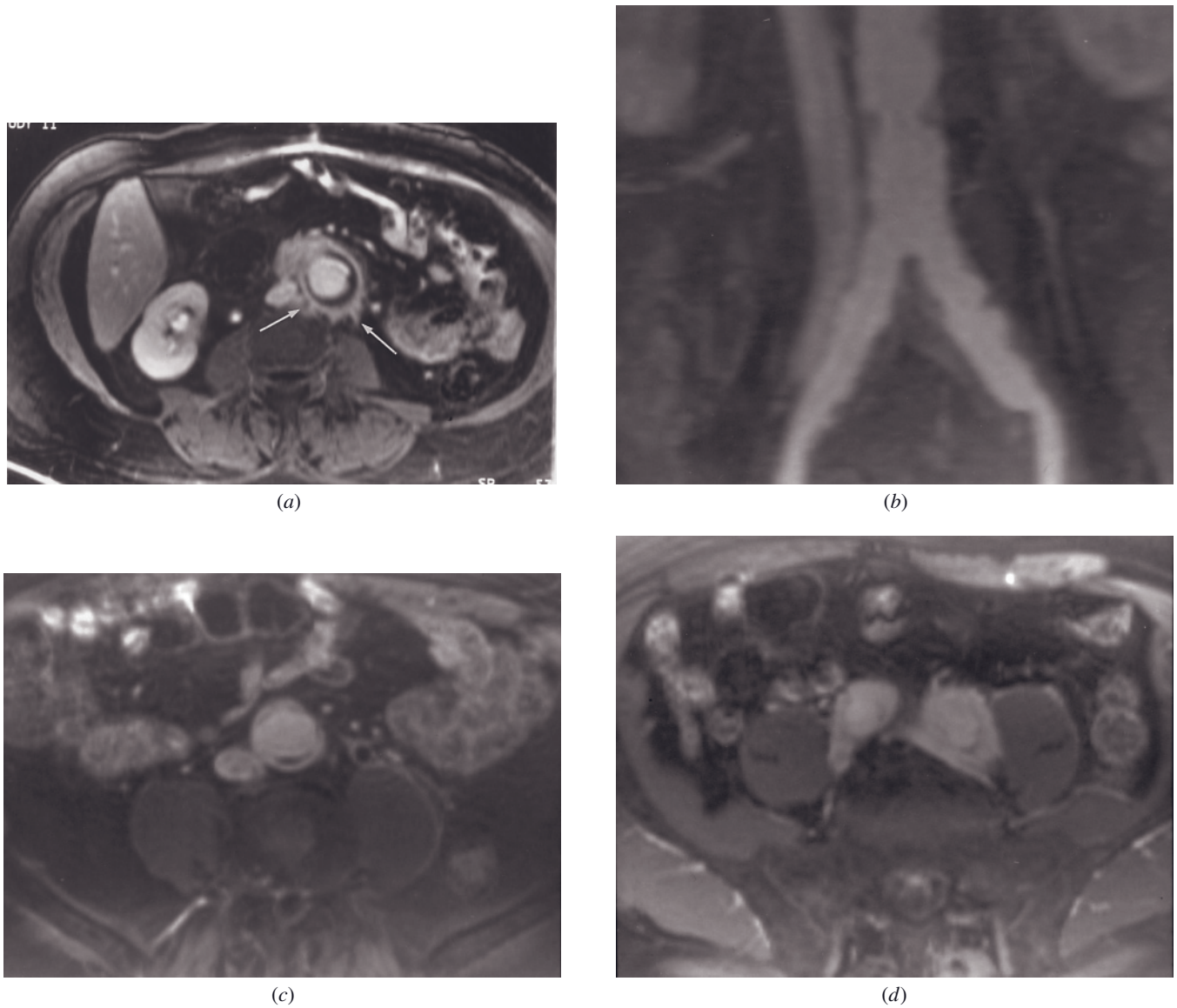

FIG. 10.8 Inflammatory aortitis. Interstitial-phase gadolinium-enhanced fat-suppressed SGE image (*a*). An aortic aneurysm is present with diffusely thickened wall and enhancing ill-defined tissue that projects (arrows) into the retroperitoneal fat surrounding the aneurysm. Enhancement of the lumen and nearly signal-void mural thrombus are also shown. Coronal 3D MIP reconstruction (*b*) and transverse gadolinium-enhanced fat-suppressed SGE (*c*, *d*) images in a second patient demonstrate dilatation of the infrarenal aorta and common iliac arteries. Note the homogeneous enhancing tissue surrounding these vessels, consistent with perianeurysmal inflammation.

changes of the aorta and iliac arteries. Gadolinium-enhanced 3D gradient-echo MRA images can reliably assess atherosclerotic changes and stenoses of the aorta (fig. 10.13) and iliac arteries (figs. 10.14 and 10.15) and are able to demonstrate the lumen of the stenotic segment and the immediate poststenotic area (see fig. 10.14) because they do not suffer from dephasing, reverse flow, or in-plane saturation phenomena compared with time-of-flight techniques.

Occlusion of the abdominal aorta and its branches may occur in advanced thrombotic disease or dissection. Gadolinium-enhanced SGE or 3D-GE images permit clear distinction between high-signal-intensity patent lumen and low-signal-intensity thrombosed lumen (fig. 10.16). Coronal or sagittal images are useful to confirm the level of occlusion (figs. 10.16 and 10.17).

Postoperative Aortic Graft Evaluation

Postoperative complications of abdominal aortic graft surgery include occlusion, hemorrhage with false aneurysm formation, infection, and aortoenteric fistula formation. Complications are well shown on MR images

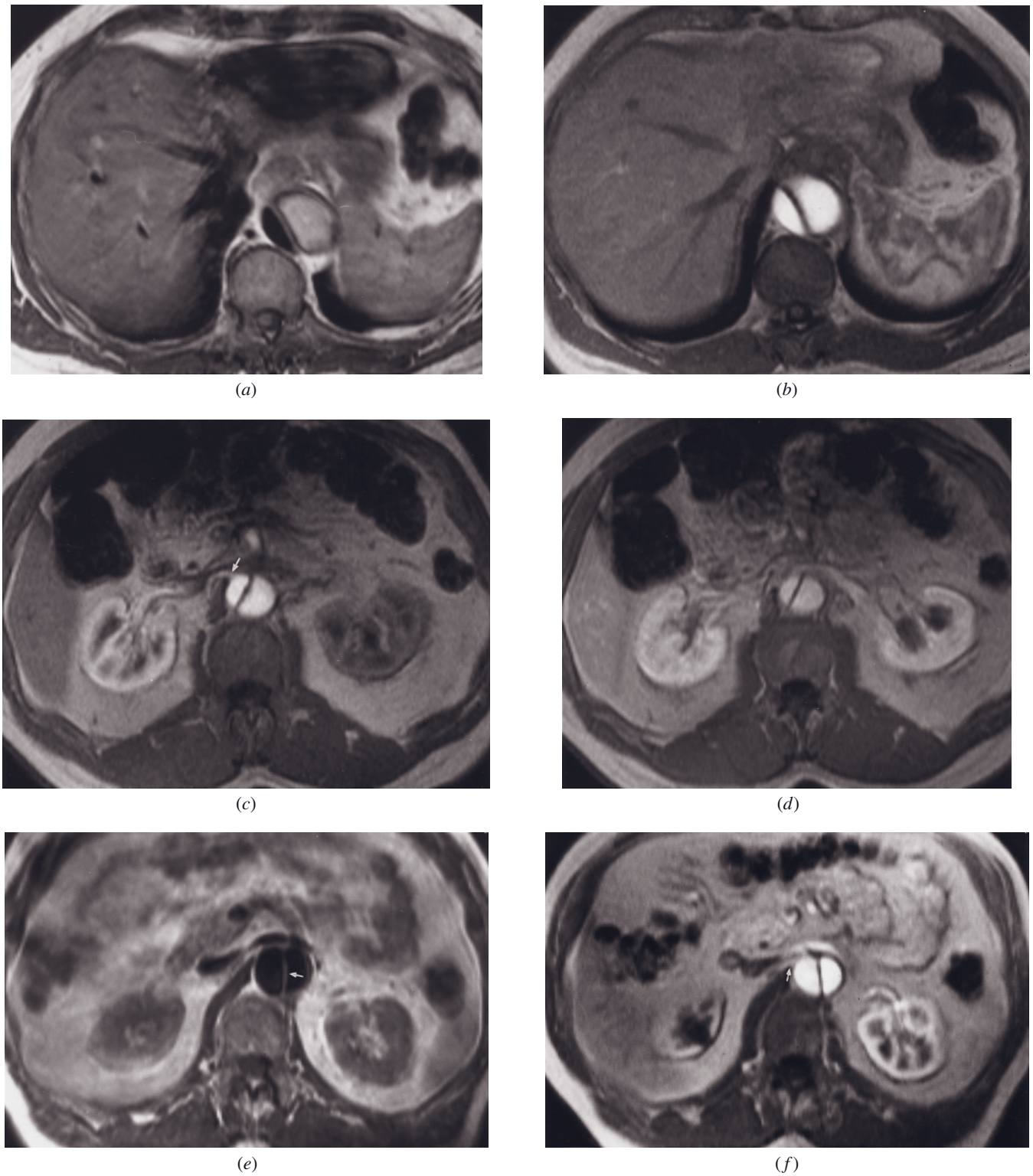

FIG. 10.9 Aortic dissection with perfusion differential between the kidneys. T1-weighted spin-echo (*a*) and immediate (*b, c*) and 90-s (*d*) postgadolinium SGE images. The T1-weighted spin-echo image (*a*) shows enlargement of the abdominal aorta, which contains an intimal flap and has a true and a false lumen. High signal intensity is noted in the false lumen because of slow flow. Note that the true lumen has a biconvex configuration because of the higher blood pressure. The immediate postgadolinium SGE image (*b*) acquired at the same tomographic level shows enhancement of both lumens with sharp demarcation of the intimal flap. The false lumen enhances substantially less than the true lumen on the immediate postgadolinium SGE image (*c*) at a lower tomographic level because of diminished contrast delivery secondary to slow flow in the false lumen. The right renal artery (arrow, *c*) is demonstrated originating from the true lumen. Intense cortical enhancement of the right kidney and minimal cortical enhancement of the left kidney is evident, reflecting the origin of the left renal artery from the false lumen. Note that on the 90-s postgadolinium SGE image (*d*) lumen and kidneys enhance to the same extent. T1-weighted spin-echo (*e*) and immediate postgadolinium SGE (*f*) images in a second patient with aortic dissection. The T1-weighted spin-echo image shows an aortic aneurysm with an intimal flap (arrow, *e*). Both lumens are signal void on this image, reflecting higher blood velocity in the false lumen than observed in the first patient. The right lumen has a biconvex configuration consistent with the true lumen. High flow in both lumens is also reflected as equal enhancement on the immediate postgadolinium SGE image. The origin of the right renal artery (arrow, *f*) from the true lumen is well shown. Immediate postgadolinium SGE images in patients with aortic dissection provide hemodynamic information that is helpful in determining true and false lumens and abdominal organ arterial perfusion.

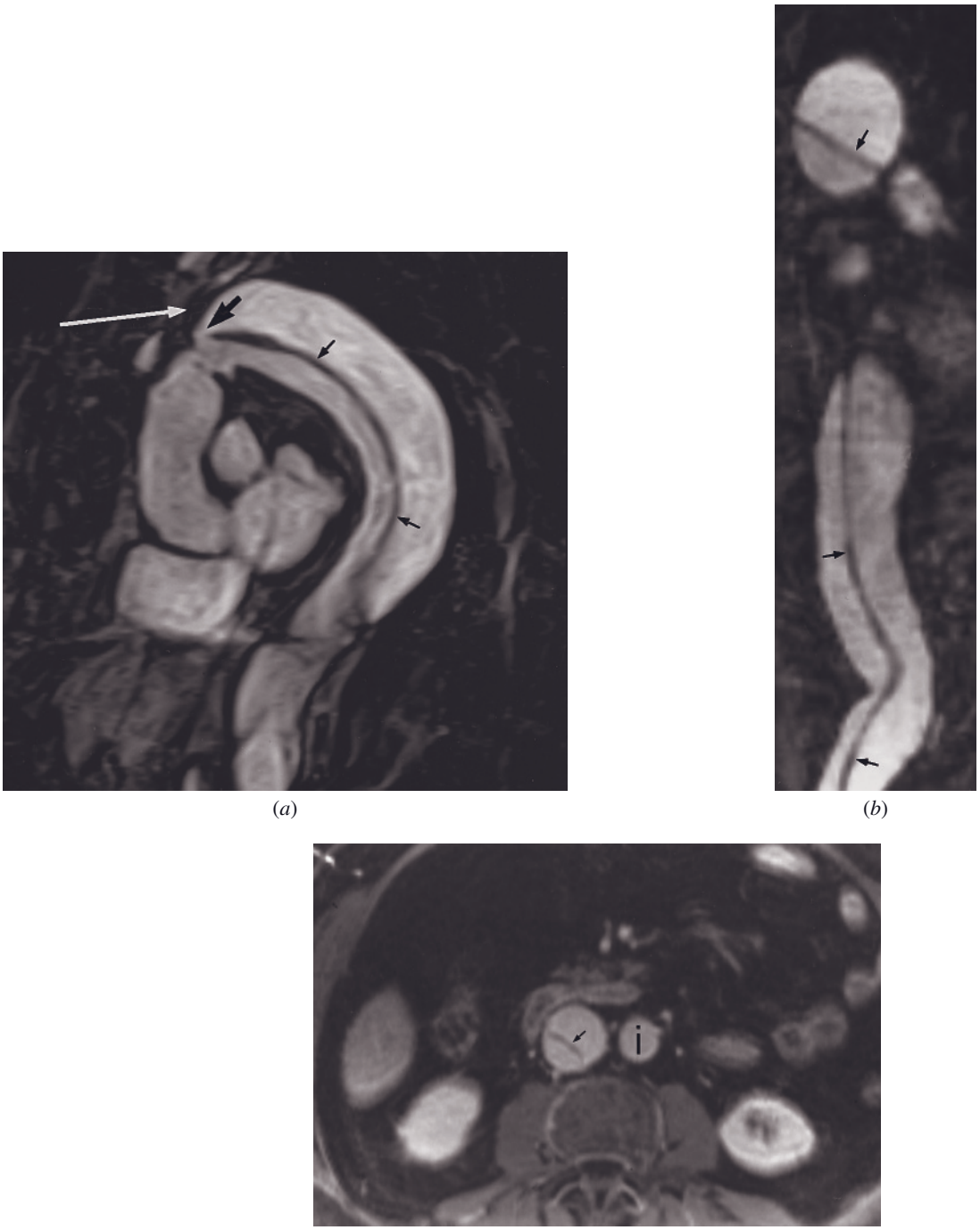

FIG. 10.10 Aortic dissection. Gadolinium-enhanced 2-mm thin-section 3D gradient-echo image (*a*) obtained in an oblique sagittal plane through the center of the lumen of the aortic arch, coronal multiplanar reconstruction (*b*) from the set of gadolinium-enhanced 2-mm thin oblique sagittal 3D gradient-echo sections, and transverse interstitial-phase gadolinium-enhanced fat-suppressed SGE images (*c*) in a patient with type B aortic dissection. The oblique sagittal gadolinium-enhanced 3D gradient-echo image (*a*) demonstrates an aortic dissection originating in the thoracic aorta. The intimal flap (small arrows, *a–c*) is readily demonstrated as a low-signal-intensity curvilinear structure. The entry site (arrow, *a*) is identified immediately distal to the origin of the left subclavian artery (long arrow, *a*). The multiplanar reconstruction (*b*) outlines the course of the dissection and demonstrates the intimal flap (small arrows, *b*) from the thoracic to the abdominal aorta. The intimal flap is well seen on the interstitial-phase gadolinium-enhanced fat-suppressed SGE image (*c*) at the level of the abdominal aorta. Incidental note is made of a left-sided IVC (i, *c*). Coronal 2-mm

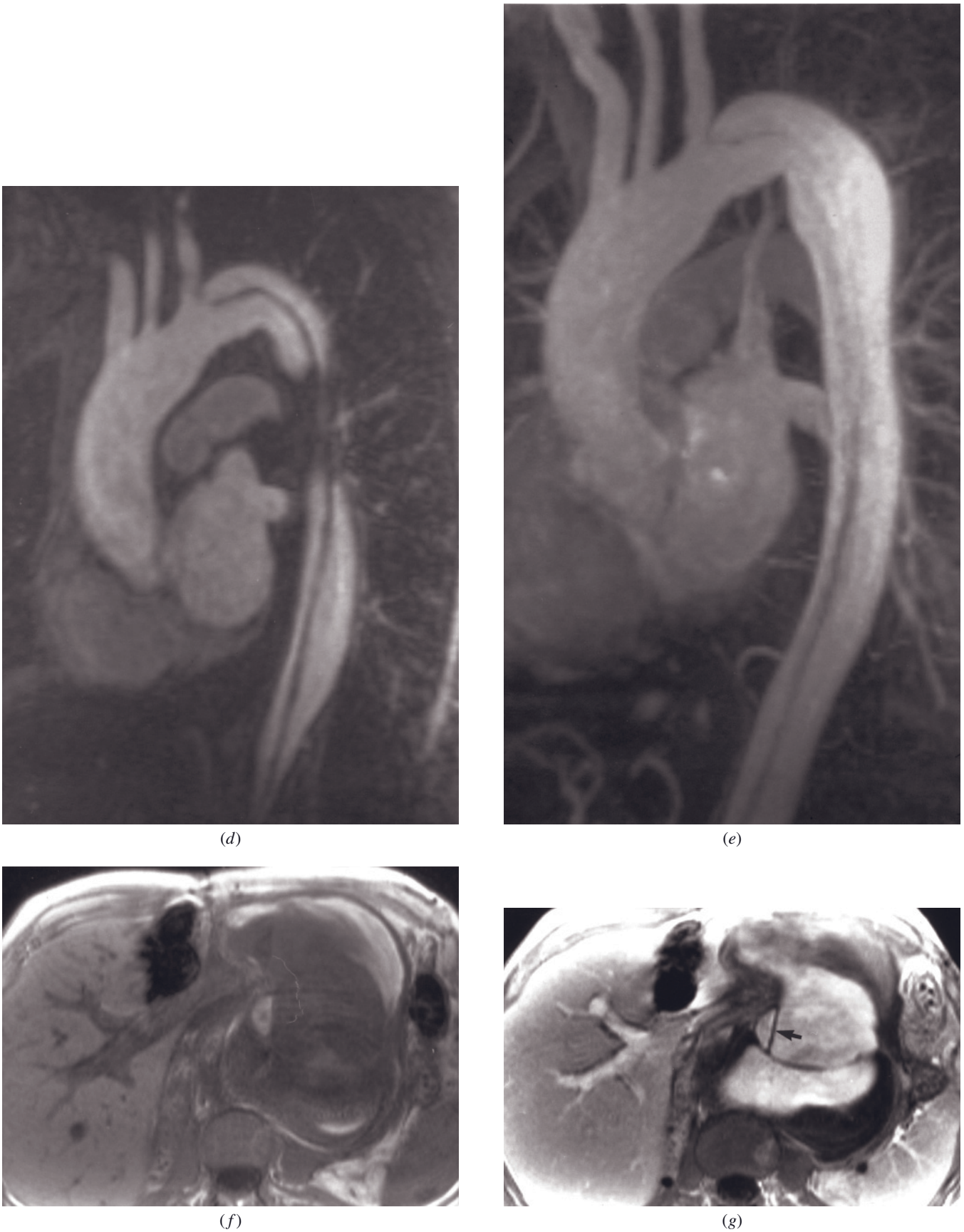

(*d*) (*e*)

(*f*) (*g*)

FIG. 10.10 (*Continued*) gadolinium-enhanced 3D gradient-echo source image (*d*) and 3D MIP reconstruction of the 2-mm 3D gradient-echo sections (*e*) from a second patient show similar features of an aortic dissection. Transverse SGE (*f*) and immediate postgadolinium SGE (*g*) images in a third patient. There is a large complex abdominal aortic saccular aneurysm associated with thrombus and dissection. The intimal flap is clearly shown (arrow, *g*) after contrast administration. 3D MIP reconstruction

(*h*)

(*i*)

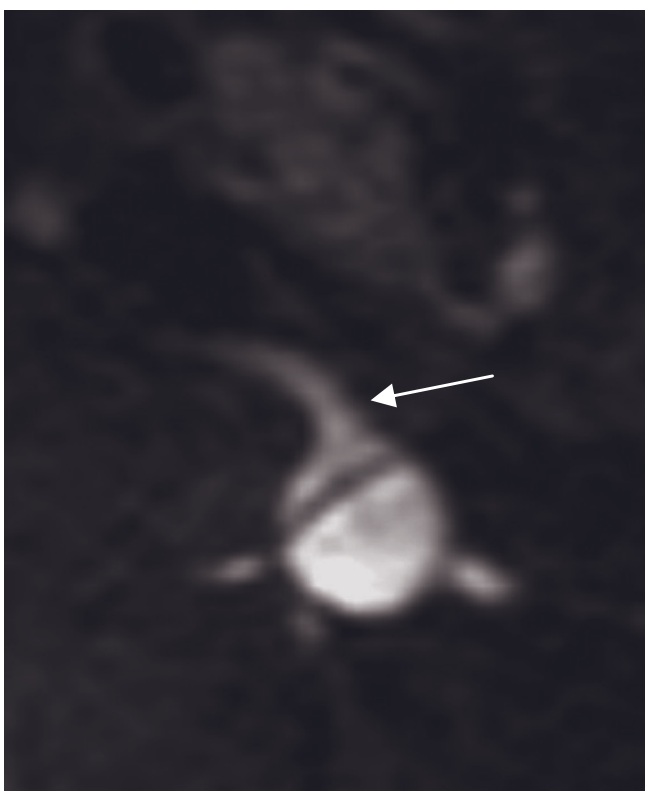

(*j*)

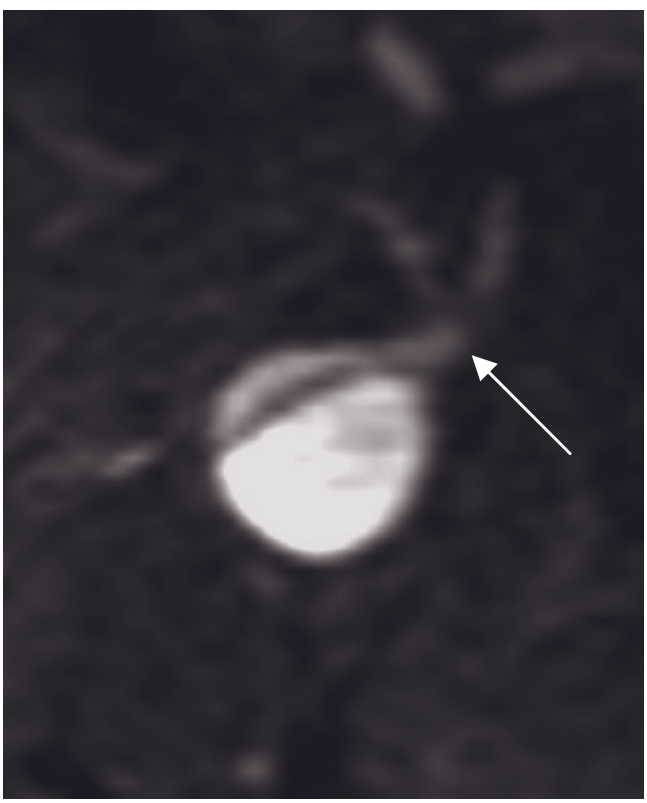

(*k*)

FIG. 10.10 (*Continued*) image (*h*) of a set of immediate postgadolinium sagittal breath-hold 3D-GE MRA sections, sagittal 3D-GE angiographic source image (*i*), and reformatted transverse 3D-GE angiographic images (*j, k*) demonstrate type B aortic dissection in another patient. Intimal dissection flap (black arrows, *h, i*) originates distal to the left subclavian artery. Celiac artery (arrow, *j*) and superior mesenteric artery (arrow, *k*) originate from the small true lumen. Note the bronchial arteries (white arrows, *h*) originating from the descending aorta.

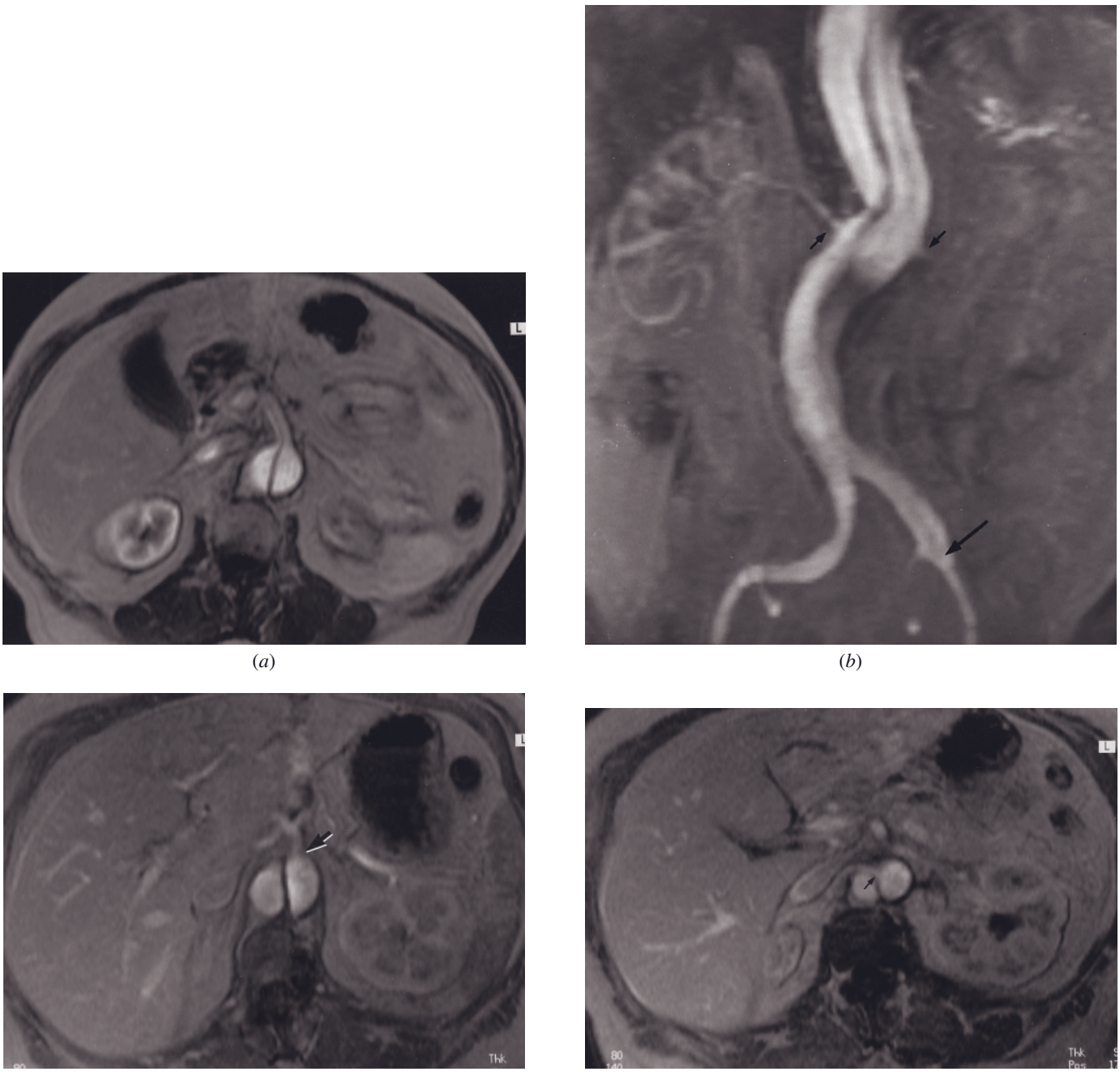

FIG. 10.11 Aortic dissection with extension into the superior mesenteric artery. Immediate postgadolinium SGE image (*a*) and coronal projection (*b*) from 3D MIP reconstruction of a set of coronal immediate postgadolinium SGE images obtained in a follow-up study. The immediate postgadolinium SGE image (*a*) at the level of the origin of the superior mesenteric artery shows high signal intensity, gadolinium-containing true (right) and false (left) lumens, and extension of the intimal flap into the superior mesenteric artery. The coronal projection from the 3D MIP reconstruction shows the abdominal aorta and iliac arteries, with the intimal flap extending into the external iliac artery (arrow, *b*). The ostia of the renal arteries are clearly depicted (small arrows, *b*), whereas the left renal artery and kidney are not visualized because of decreased enhancement from slow blood flow in the false lumen. Immediate postgadolinium SGE images (*c, d*) at two tomographic levels in a second patient. The high-signal-intensity gadolinium-containing aorta is clearly shown on both images. The intimal flap is well shown, as are the origins of the celiac axis (arrow, *c*) and right renal artery (small arrow, *d*) from the true lumen.

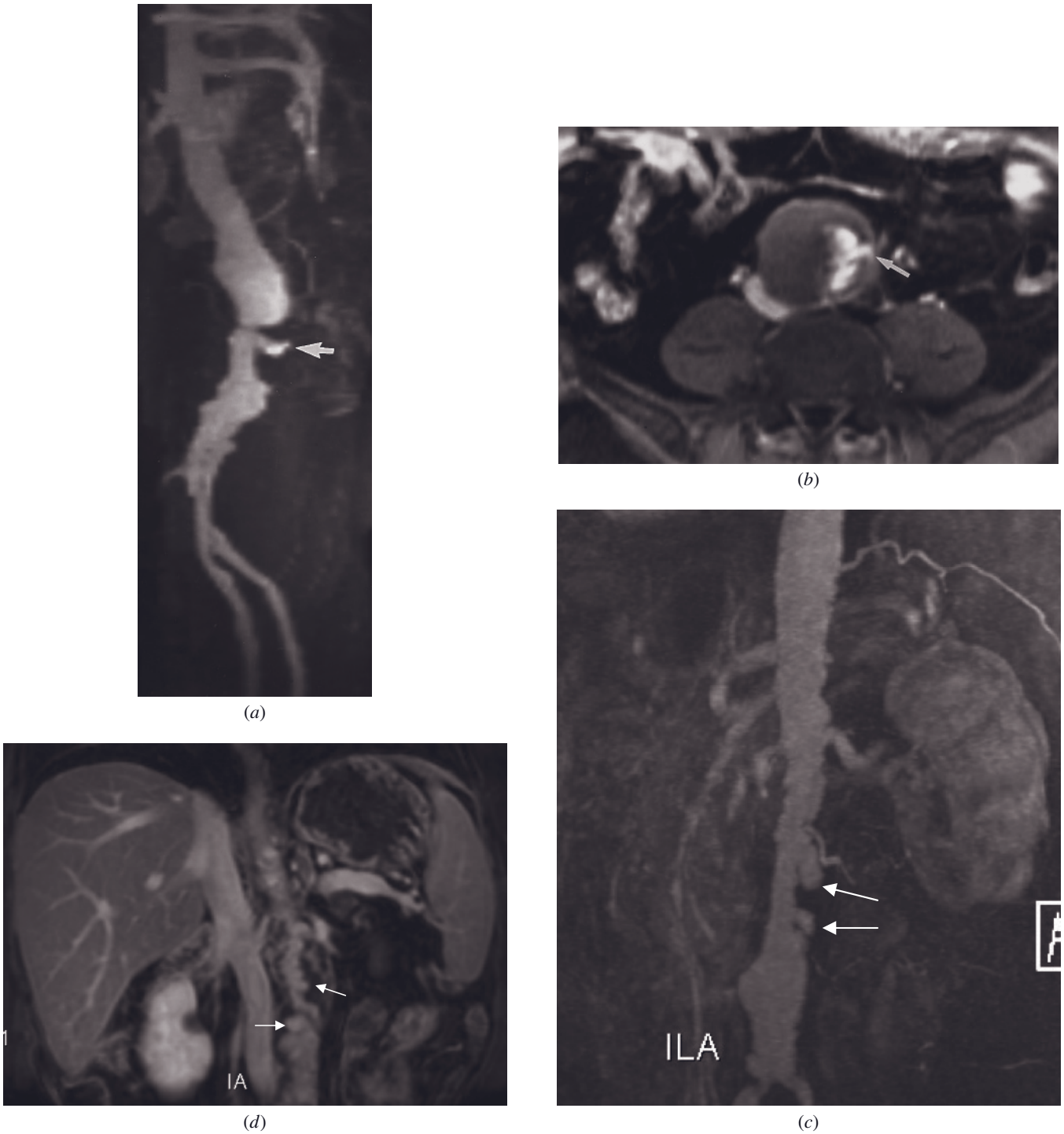

FIG. 10.12 Penetrating aortic ulcer. Lateral MIP projection of a set of gadolinium-enhanced 2-mm coronal 3D gradient-echo sections (*a*) and transverse interstitial-phase gadolinium-enhanced fat-suppressed SGE image (*b*). An atherosclerotic aneurysm of the infrarenal abdominal aorta is present. An ulceration of the atherosclerotic plaque (arrow, *a, b*) is demonstrated on the lateral MIP projection. On the interstitial-phase gadolinium-enhanced fat-suppressed SGE image (*b*), the diameter of the aortic aneurysm and the presence of mural thrombus are well evaluated. The depth of the ulceration in relation to the outer aortic wall is appreciated. Interstitial-phase gadolinium-enhanced fat-suppressed SGE images provide information on the aortic wall and the surrounding tissues that are not available on MR angiographic images. 3D MIP reconstruction image (*c*) of a set of immediate postgadolinium coronal breath-hold 3D-GE MRA sections and T1-weighted postgadolinium fat-suppressed hepatic venous phase 3D-GE image (*d*) at 3.0 T demonstrate atherosclerotic changes in the abdominal aorta in another patient. Penetrating ulcers (arrows, *c, d*) in the abdominal wall are seen on both images. Note that an aortic aneurysm is also present proximal to the bifurcation.

[23, 41]. Although some of these complications can occur acutely in the postoperative period, it is generally agreed that MR imaging should not be performed before 4–6 weeks after surgery to allow endothelial repair and reduction of risk for injury due to surgical clip dislodgement. However, nonferromagnetic MR compatible stents that can be applied endovascularly can be examined earlier. Fluid is frequently present surrounding the graft within 3 months after surgery (fig. 10.18). Fluid surrounding the graft beyond 3 months or an increasing volume of perigraft fluid after 3 months is suggestive of infection on T1- and T2-weighted images [23, 42, 43]. Gadolinium-enhanced fat-suppressed imaging may also be an ideal technique for evaluating inflammatory enhancement in aortic graft infections (fig. 10.19). Gadolinium-enhanced fat-suppressed SGE or 3D-GE images are preferable to gadolinium-enhanced T1-weighted fat-suppressed spin-echo images because patency of the graft lumen can also be assessed reliably with the SGE and 3D-GE sequence. Patent lumen is high in signal intensity, and intraluminal thrombus is low to intermediate in signal intensity. Inflammatory tissue shows substantial enhancement, and fluid collections/abscesses will have low central signal intensity.

Endoluminal placement of aortic grafts is a procedure that is gaining in popularity because of the lower

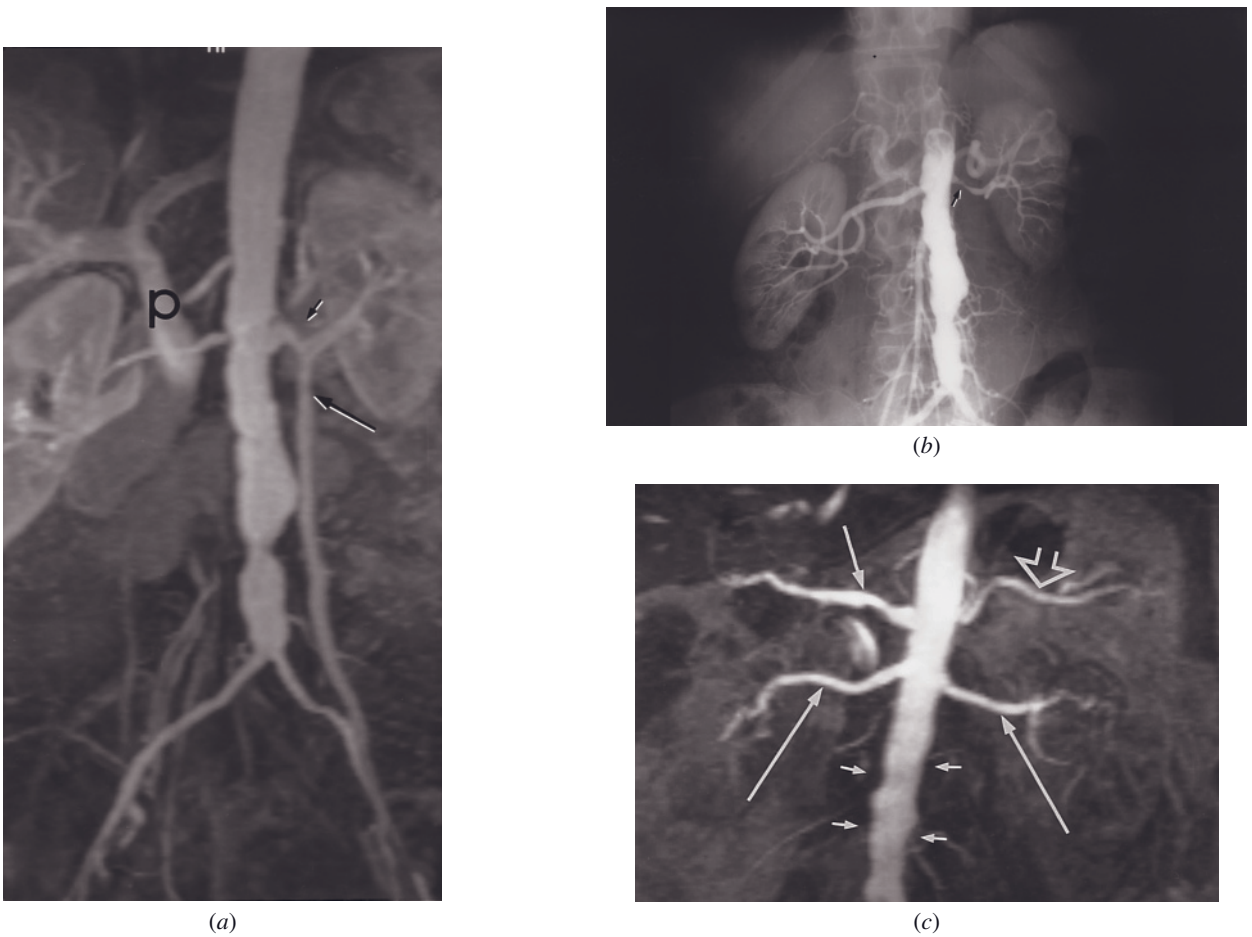

FIG. 10.13 Atherosclerotic disease of the abdominal aorta. Coronal 3D MIP reconstruction of gadolinium-enhanced 2-mm source images (*a*) and anteroposterior conventional arteriography image (*b*). Diffuse atherosclerotic disease of the abdominal aorta with irregularity of the contour and focal stenotic and dilated segments is demonstrated on the 3D MIP image (*a*). Close correlation of the MRI findings with the intra-arterial catheter angiographic image (*b*) is present. The image acquisition timing in this case was slightly delayed, and the 3D gradient-echo images were acquired during the capillary rather than the arterial phase of enhancement, as evidenced by the presence of enhanced portal vein (p, *a*) and right renal vein. Enhancement of the left renal vein partially masks a stenosis (small arrow, *a, b*) of the left renal artery. Targeted 3D MIP reconstructions of the left renal artery revealed this stenosis. Note early retrograde filling of the left ovarian vein (arrow, *a*). Coronal 3D MIP reconstruction of gadolinium-enhanced 2-mm source images (*c*) in a second patient shows irregular contour of the aorta (small arrows, *c*) due to diffuse atherosclerotic changes. Note normal renal arteries (long arrows, *c*) bilaterally. The common hepatic artery (short arrow, *c*) and splenic artery (open arrow, *c*) are also demonstrated. Coronal 3D MIP reconstruction of gadolinium-enhanced 2-mm source images (*d*) in a third patient

(*d*)

(*e*)

(*f*)

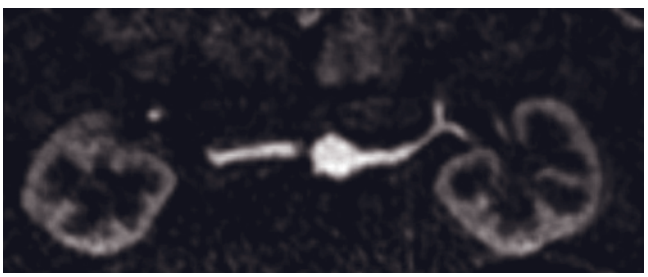

(*g*)

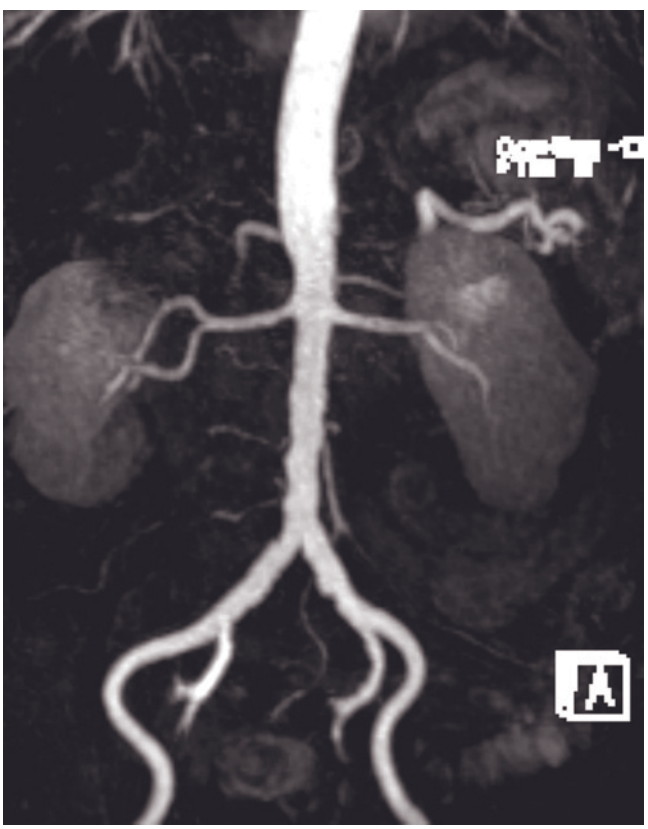

(*h*)

Fig. 10.13 (*Continued*) demonstrates slight irregularity of the abdominal aorta associated with stenoses of the celiac axis and superior mesenteric artery and occlusion of the right common iliac artery (arrow). Coronal 3D-GE immediate postgadolinium breath-hold source MRA images (*e*, *f*), transverse reformated MRA image (*g*) and 3D MIP reconstruction image (*h*) of immediate postgadolinium coronal source images at 3.0 T demonstrate diffuse contour irregularity of the abdominal aortic wall due to atherosclerosis in another patient. Note that the renal arteries are patent.

(*a*)

(*b*)

(*c*)

FIG. 10.14 Stenosis of the left common and external iliac arteries. Coronal (*a*) and right anterior oblique (*b*) 3D MIP reconstructions of gadolinium-enhanced 2-mm source images. High-grade stenoses are demonstrated of the left common iliac (black arrow, *a*) and left external iliac (small black arrow, *a*) arteries. Irregularity of the vessel contour from diffuse atherosclerotic disease and a more prominent eccentric plaque at the right common femoral artery (white arrow, *a*) are also noted. On the oblique image (*b*) vessel lumen distal to the high-grade stenoses and the lumen of the stenotic segment (small arrows) are well visualized, reflecting negligible signal loss from dephasing. This is due to the very short echo time of the sequence combined with the T1 shortening from gadolinium enhancement. The internal iliac arteries are not adequately visualized because of their location outside the obtained 3D slab. Coronal 3D MIP reconstruction of gadolinium-enhanced 2-mm source images (*c*) in a second patient with diabetes mellitus and recent onset of impotence. A high-grade stenosis (arrow, *c*) of the right internal iliac artery is demonstrated 1 cm from its origin. The lumen immediately distal to the stenotic area is well visualized because of minimized dephasing despite turbulent flow. An ulcerated atherosclerotic plaque (small arrow, *c*) in the left common iliac artery is also present. The peripheral segments of the internal iliac arteries are not visualized because of their course outside the acquired 3D slab.

risks associated with this procedure compared with open surgical graft placement. MRI may be used to ensure adequate position of the graft (figs. 10.20 and 10.21) and to examine for complications.

Inferior Vena Cava

As with the aorta, the IVC may be evaluated with bright-blood and black-blood techniques [44, 45]. The IVC may be evaluated for the presence of thrombus, differentiation of blood from tumor thrombus, and in rare instances for the evaluation of primary tumors. In the vast majority of cases, an abdominal protocol employing precontrast SGE and fat-suppressed 3D-GE and postgadolinium SGE and fat-suppressed SGE or 3D-GE images provides sufficient evaluation of the IVC for patient management. At least one sequence should be performed in the sagittal or coronal plane, such as gadolinium-enhanced SGE or, preferably, fat-suppressed SGE or 3D-GE images, because this permits direct visualization of the longitudinal extent of the IVC, which is ideal in examining for the extent of blood or tumor thrombus. Breath-hold

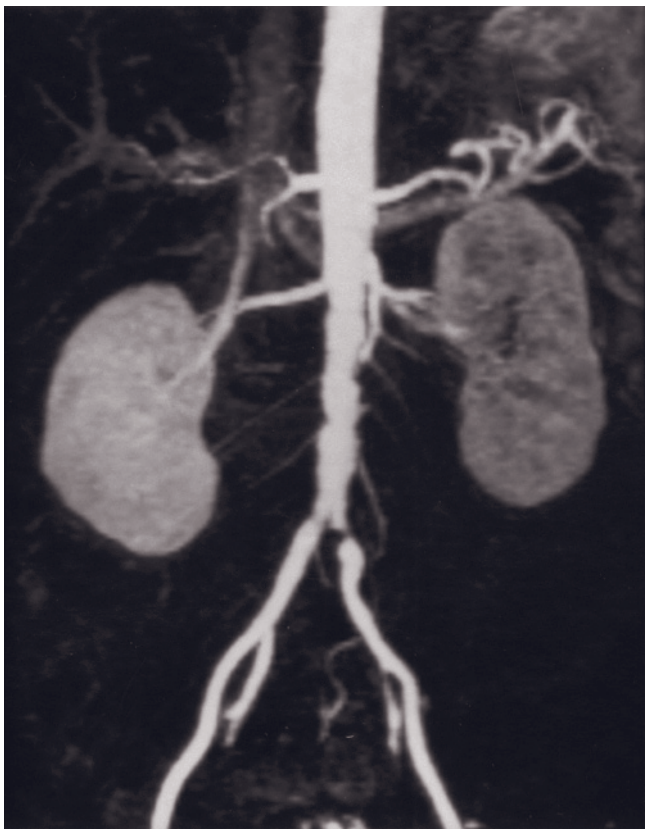

(*a*)

(*b*)

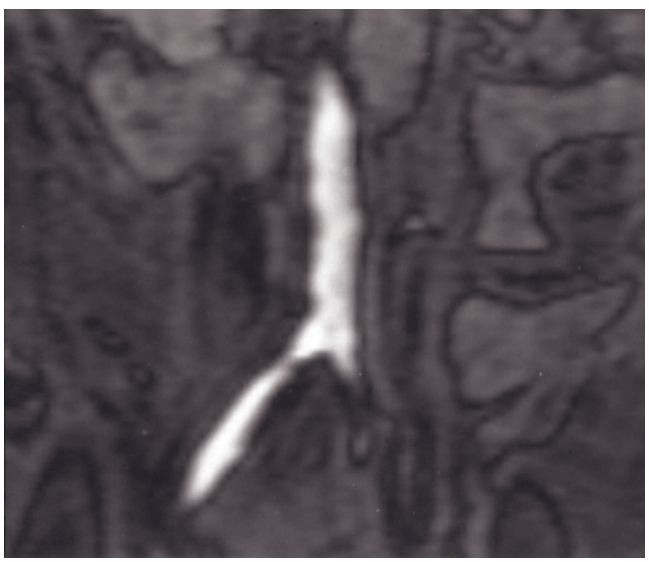

(*c*)

FIG. 10.15 Stenosis of the iliac arteries. Coronal 3D MIP reconstructions of gadolinium-enhanced 2-mm source images from abdominal (*a*) and pelvic (*b*) acquisitions demonstrate stenosis of the left common and left internal left iliac arteries. Note irregularity of the infrarenal abdominal aorta from atherosclerotic disease. Coronal gadolinium-enhanced 2-mm 3D gradient-echo source image (*c*) and 3D MIP reconstruction of the 3D gradient-echo

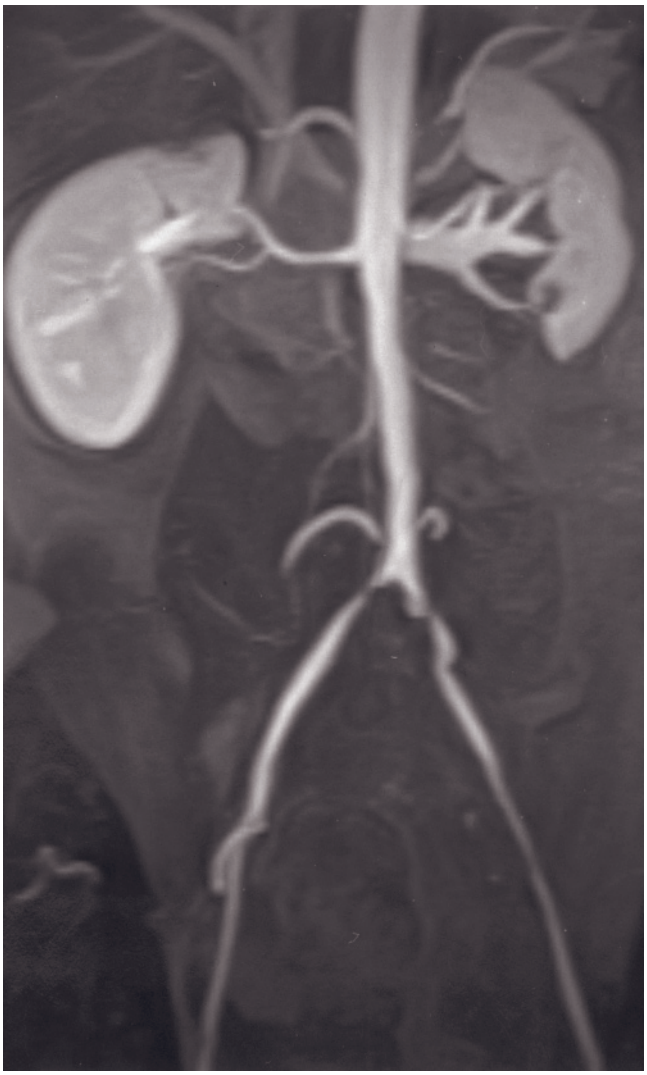

(*d*)

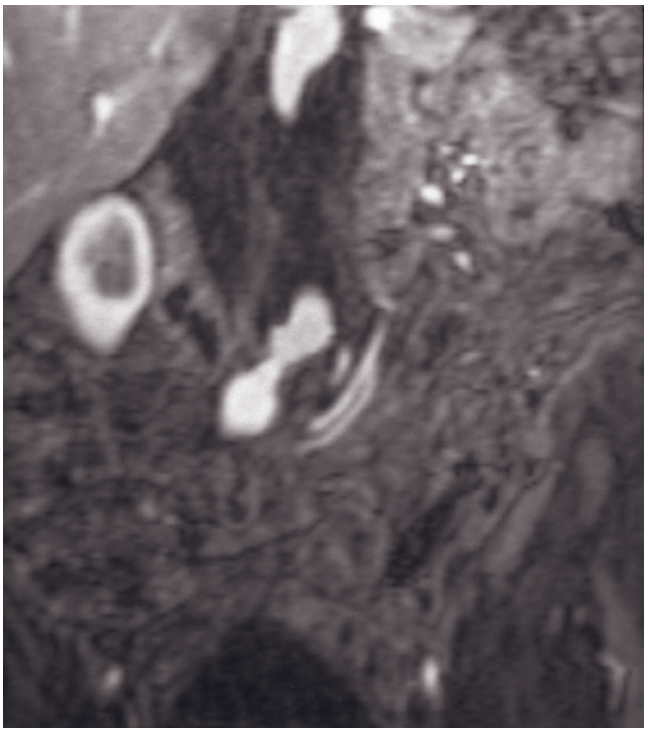

(*e*)

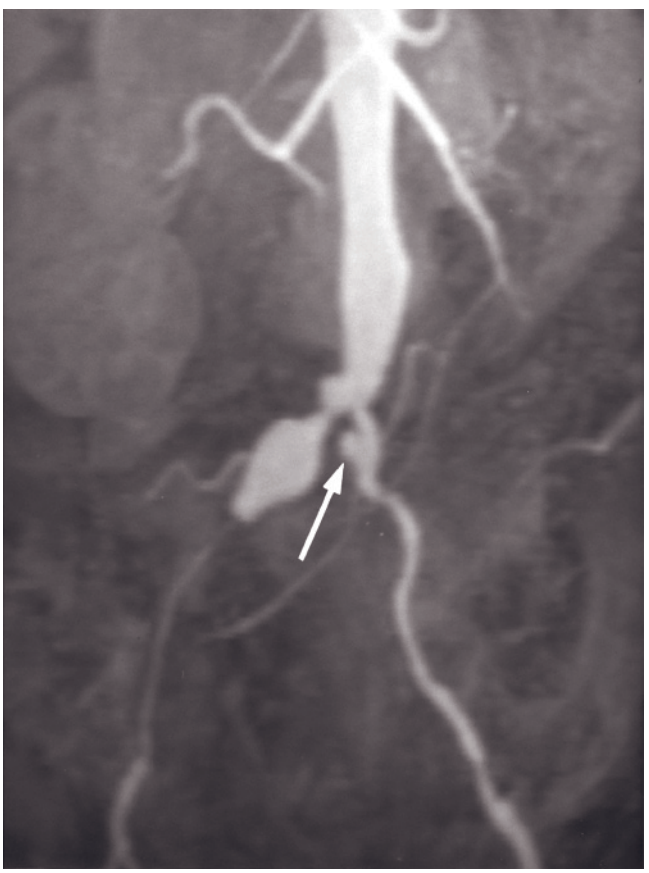

(*f*)

FIG. 10.15 (*Continued*) images (*d*) in a second patient. There are bilateral stenoses of the common iliac arteries, more severe on the left. The source image better defines the severity of stenosis. Coronal gadolinium-enhanced 2-mm 3D gradient-echo source image (*e*) and 3D MIP reconstruction of the 3D gradient-echo images (*f*) in a third patient. Moderate stenosis at the bifurcation of the abdominal aorta is seen associated with severe stenosis at the origin of the right common iliac artery. There is a fusiform expansion of the right common iliac artery just distal to the stenosis, with another segment of severe stenosis more distal. Note also a moderate stenosis of the origin of the left common iliac artery, with a small saccular aneurysm (arrow, *f*). The source image (*e*) identifies the true extent of stenosis.

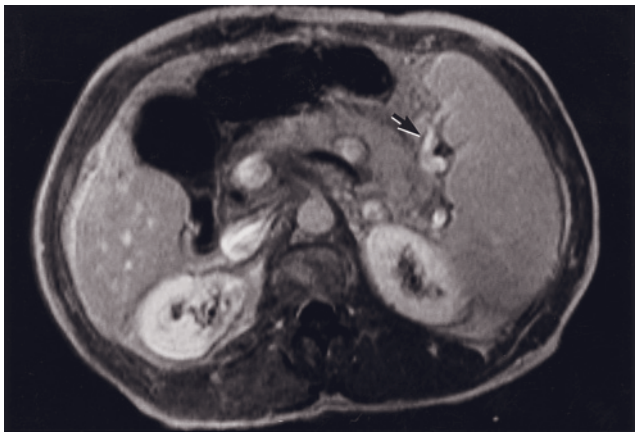

(*a*)

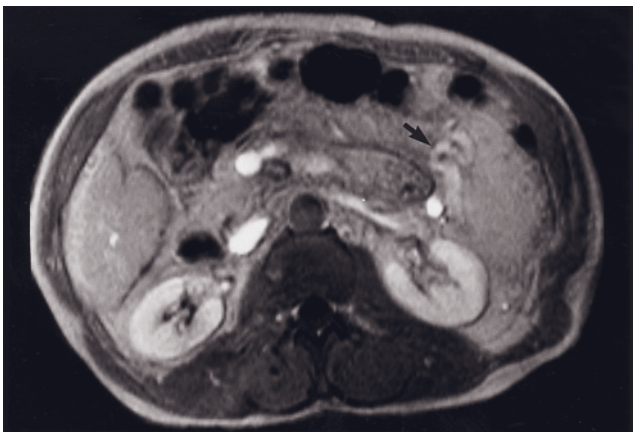

(*b*)

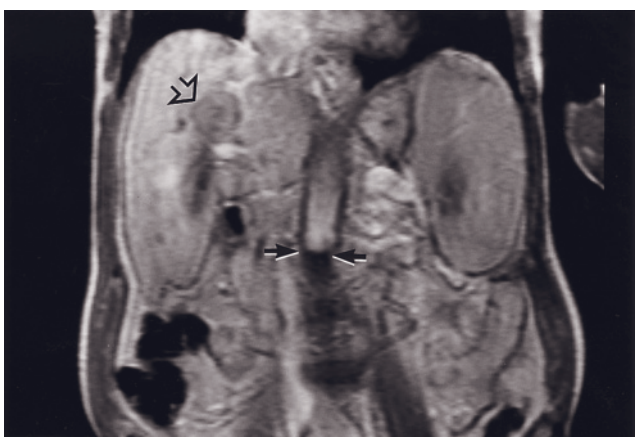

(*c*)

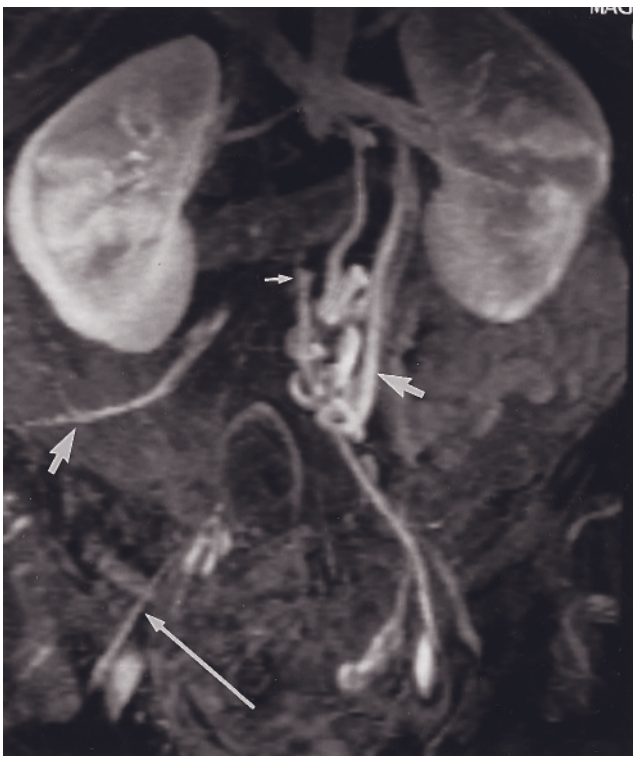

(*d*)

FIG. 10.16 Thrombotic occlusion of the infrarenal aorta. Transverse (*a, b*) and coronal (*c*) interstitial-phase gadolinium-enhanced SGE images. The lumen of the abdominal aorta demonstrates normal enhancement at the level of celiac axis origin (*a*). On the SGE image at a lower tomographic level (*b*), lack of enhancement of the aortic lumen reflects thrombotic occlusion. The abrupt transition (arrows, *c*) of enhancing patent to low-signal-intensity thrombosed lumen is demonstrated on the coronal image. This patient was assessed for multifocal hepatocellular carcinoma, and a tumor nodule (open arrow, *c*) is demonstrated in the right lobe of the liver. Splenomegaly with varices (arrows, *a, b*) is also present in this patient because of portal hypertension secondary to alcoholic cirrhosis. Coronal MIP reconstruction of gadolinium-enhanced 2-mm source images (*d*), coronal interstitial-phase gadolinium-enhanced fat-suppressed SGE image (*e*), and sagittal multiplanar reconstruction of gadolinium-enhanced 2-mm source images (*f*) in a second patient with infrarenal aortic occlusion. Complete occlusion of the infrarenal aorta 1 cm below the level of the renal arteries is demonstrated on the coronal MIP image (*d*). The lumen of the aorta (small arrow, *d*) is reconstituted distally, through numerous retroperitoneal collateral vessels (arrows, *d*). The left common iliac artery is patent, whereas the right common iliac artery is occluded at its origin with reconstitution at the level of the distal external iliac artery (long arrow, *d*). Thrombus

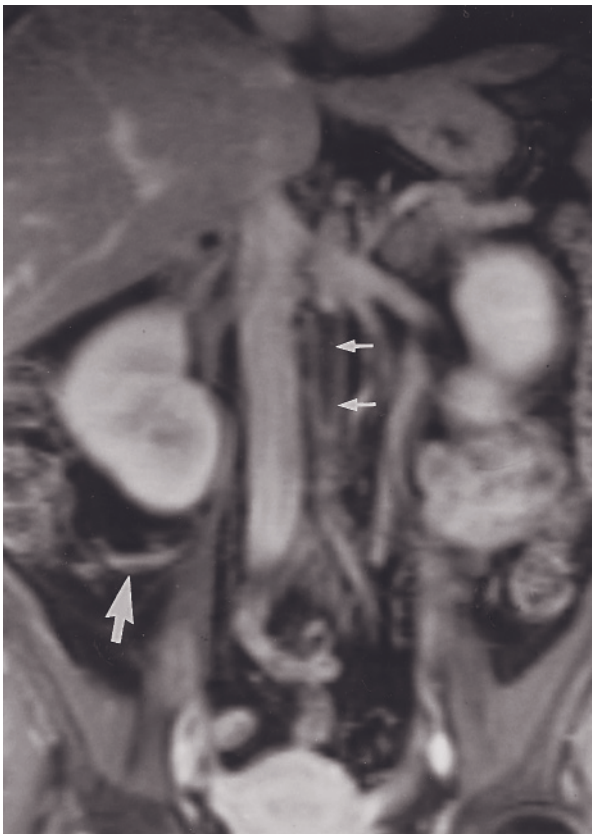

(*e*)

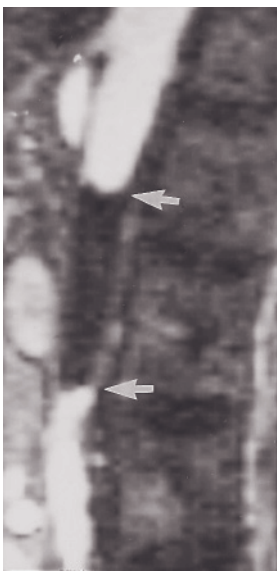

(*f*)

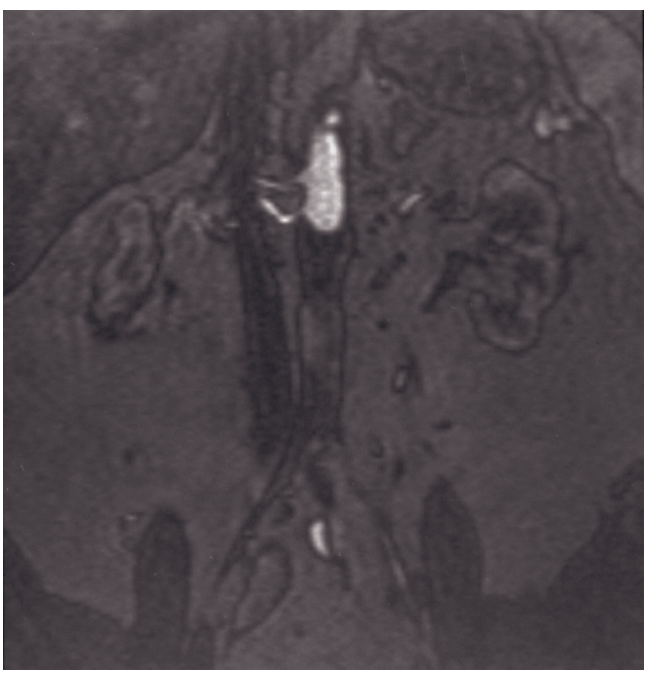

(*g*)

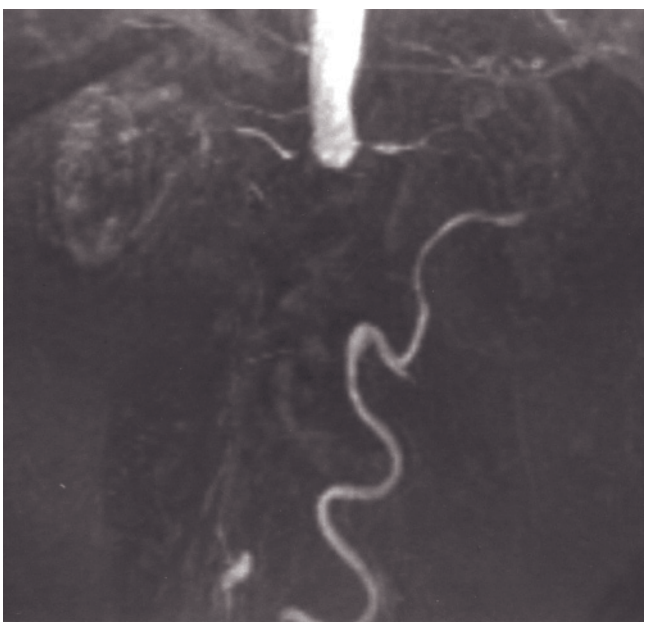

(*h*)

FIG. 10.16 (*Continued*) (small arrows) in the infrarenal aorta and a large retroperitoneal collateral (arrow) are demonstrated on the interstitial-phase gadolinium-enhanced fat-suppressed SGE image (*e*) in a third patient. The sagittal 2-mm thin reconstruction (*f*) through the center of the aortic lumen clearly demonstrates the superior and inferior margins (arrows, *f*) of the near signal-void thrombus against the homogeneous high-signal-intensity gadolinium-enhanced patent lumen. The acquisition of a volume of data with thin sections permits excellent resolution for multiplanar reconstructions. Coronal gadolinium-enhanced 2-mm 3D gradient-echo source image (*g*), 3D MIP reconstruction of the 3D gradient-echo images (*h*), and transverse interstitial-phase

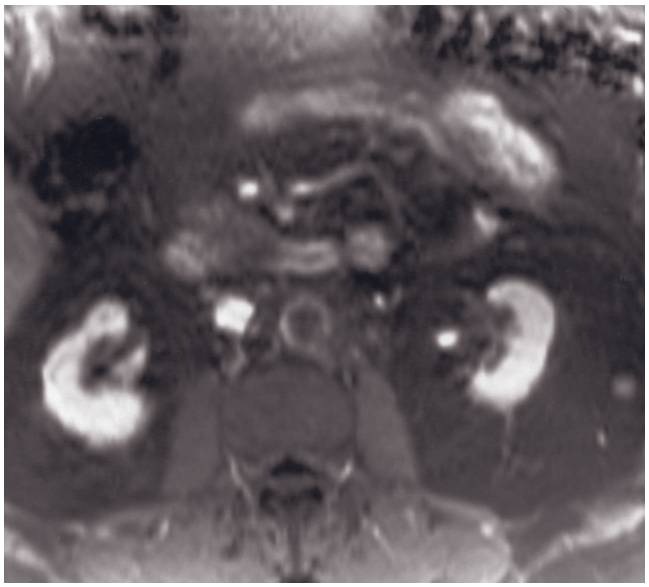

(*i*)

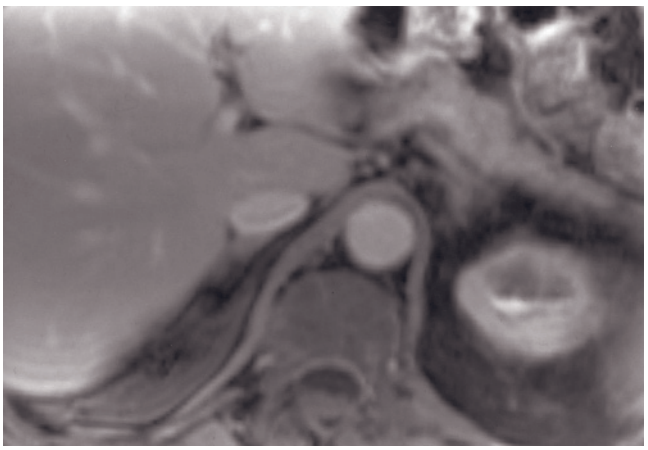

(*j*)

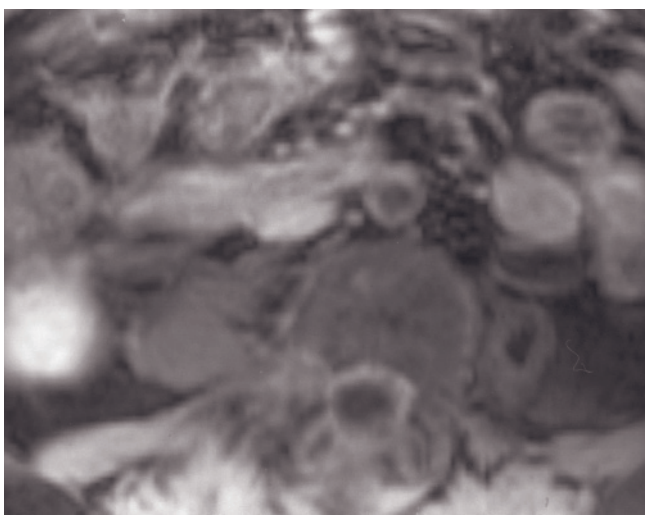

(*k*)

(*l*)

FIG. 10.16 (*Continued*) gadolinium-enhanced fat-suppressed SGE (*i*) images in a fourth patient also demonstrate complete aortic obstruction. Note the lack of enhancement of the distal abdominal aorta (*i*). The MRA images demonstrate that the renal arteries are patent, there are two right renal arteries, and bilateral moderate renal artery stenosis is present. Transverse interstitial-phase gadolinium-enhanced fat-suppressed SGE (*j, k*) and coronal gadolinium-enhanced 2-mm 3D gradient-echo source (*l*) images in a fifth patient. Note the transition of opacified (*j*) to nonopacified (*k*) lumen on transverse images, which is clearly shown in the coronal plane.

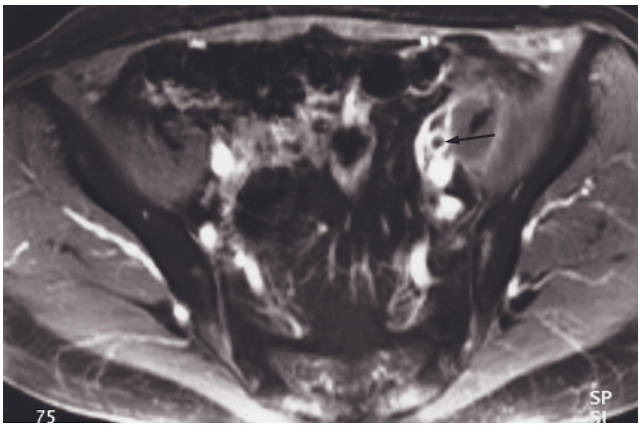

(*a*)

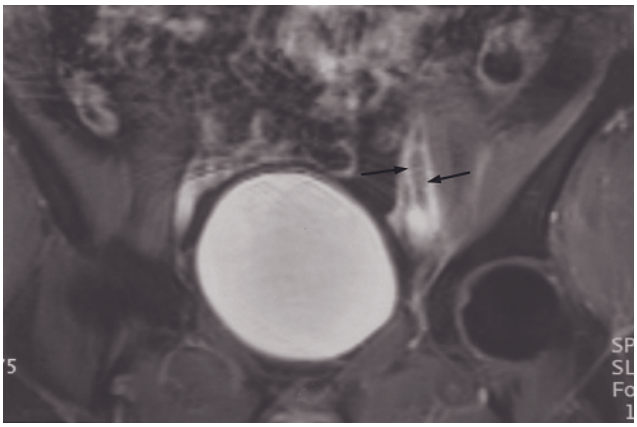

(*b*)

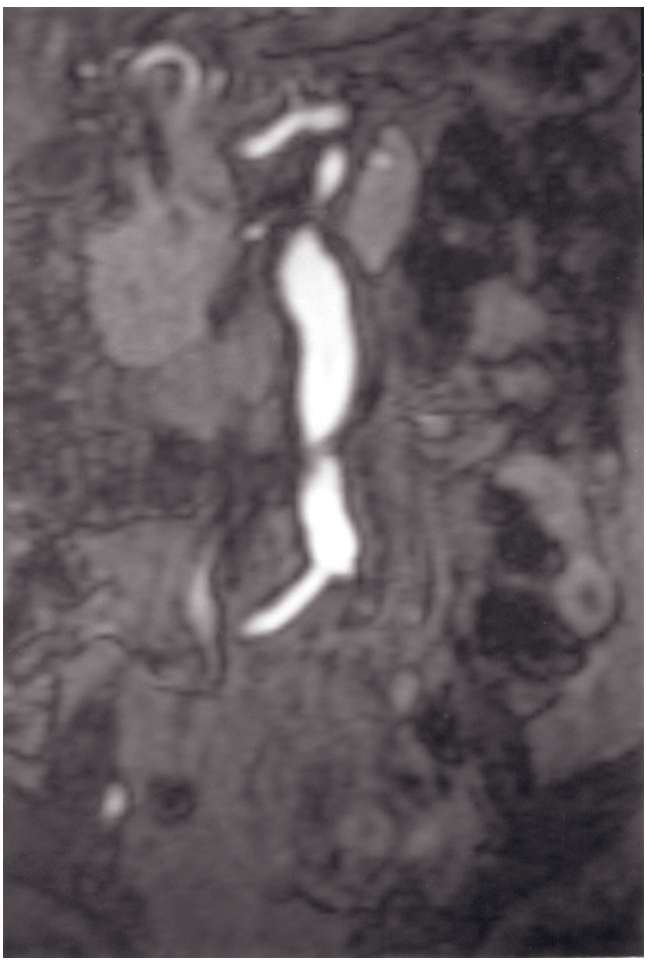

(*c*)

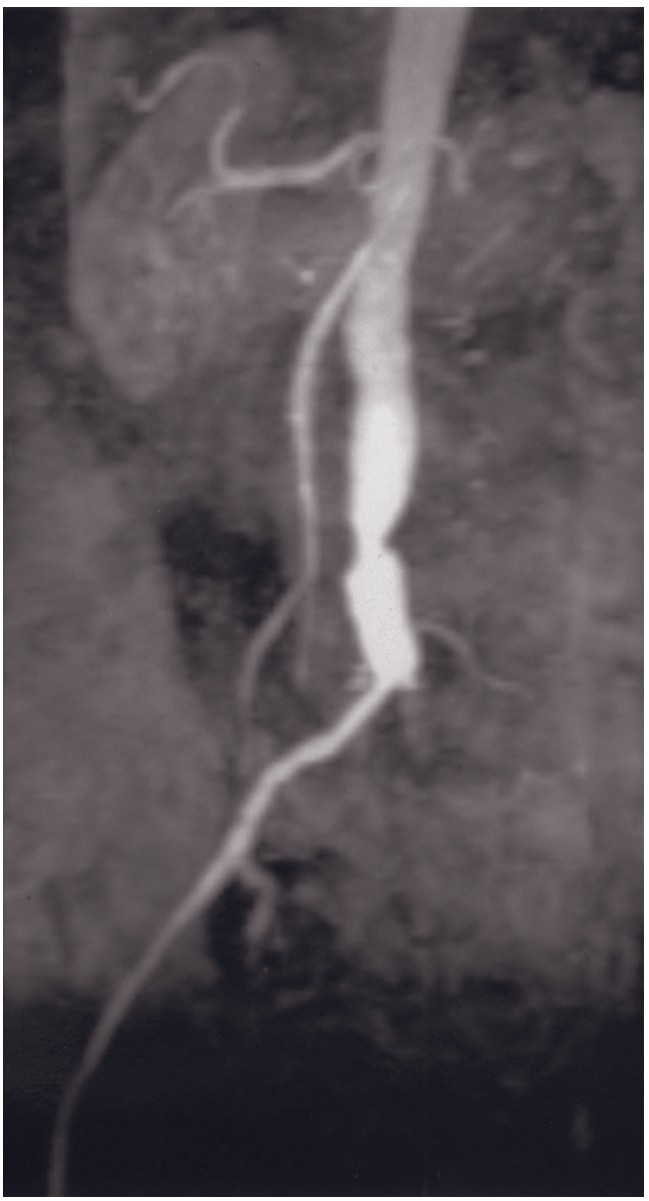

(*d*)

FIG. 10.17 Iliac artery thrombosis. Transverse (*a*) and coronal (*b*) interstitial-phase gadolinium-enhanced fat-suppressed SGE images. The left external iliac artery is identified medial to the psoas muscle on the transverse image (*a*) and contains low-signal-intensity thrombus (arrow, *a*). The presence of intraluminal thrombus (arrows, *b*) is confirmed on the coronal image. Postgadolinium SGE images, acquired within 2 min after gadolinium injection and performed as part of routine abdominal and pelvic MR imaging protocols, provide a reproducible technique for the assessment of the patency of large and medium-sized arteries and veins. Coronal gadolinium-enhanced 2-mm 3D gradient-echo source image (*c*) and 3D MIP reconstruction of the 3D gradient-echo images (*d*) in a second patient demonstrate distal abdominal aortic stenosis and occlusion of the left common iliac artery. Careful attention to the source images (*c*) reveals no contiguous distal opacification of the vessel. Coronal

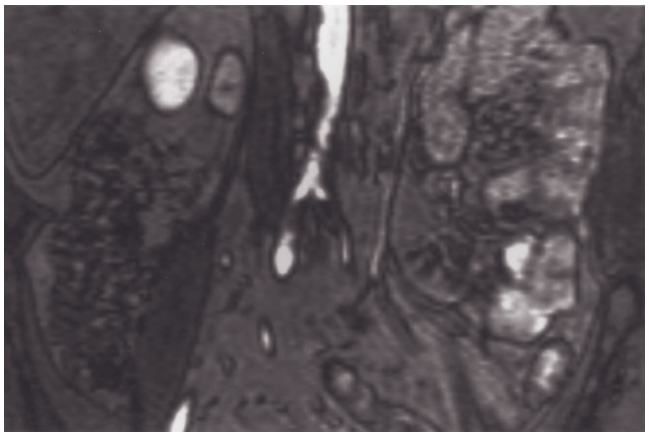

(*e*)

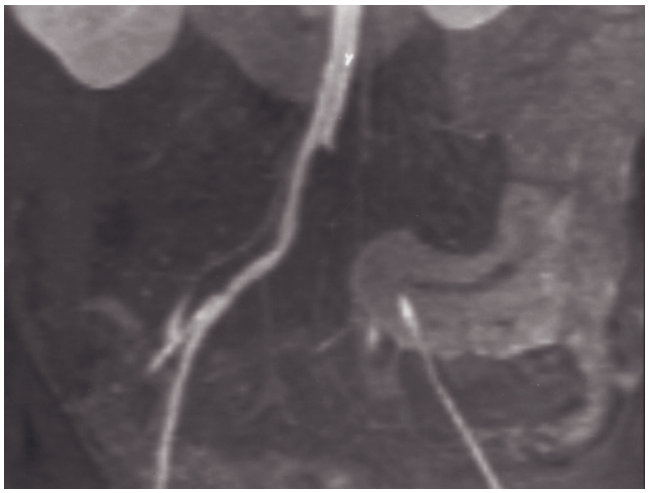

(*f*)

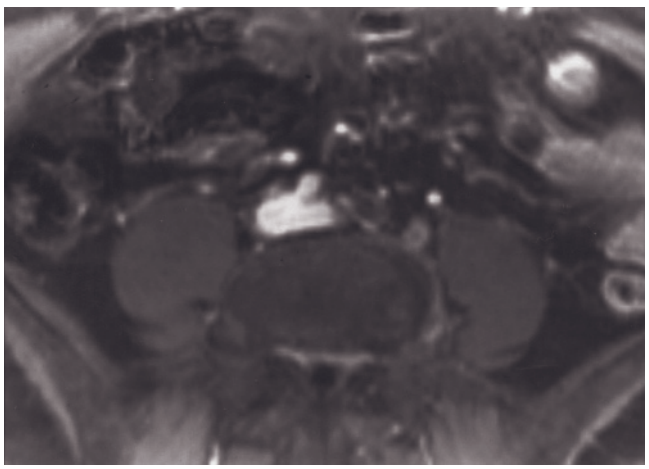

(*g*)

FIG. 10.17 (*Continued*) gadolinium-enhanced 2-mm 3D gradient-echo source image (*e*), 3D MIP reconstruction of the 3D gradient-echo images (*f*), and transverse interstitial-phase gadolinium-enhanced fat-suppressed SGE image (*g*) in a third patient show obstruction of the left common iliac artery.

time-of-flight techniques are less effective at demonstrating slow flow than gadolinium-enhanced SGE and 3D-GE techniques. Gadolinium-enhanced MRA of the IVC is not usually performed because preferential venous enhancement requires suppression of the arterial signal by presaturation pulses, which are not effective at overcoming the extreme T1 shortening caused by gadolinium. Alternatively, when 3D venography-like MRA images are required to answer complicated clinical problems, immediate postgadolinium breath-hold 3D gradient-echo MRA techniques (e.g., breath-hold coronal 3D FISP acquisition) may be performed during the simultaneous injection of gadolinium in peripheral veins of both legs. This technique provides thin (2 mm) slice resolution but is seldom needed in routine clinical practice. There is also the theoretical risk of dislodgement of deep venous thrombi leading to pulmonary emboli, particularly in nonambulatory patients.

Congenital Abnormalities

Congenital abnormalities of the inferior vena cava and related veins are common [44–48]. The most common venous anomalies are those of the left renal vein. Retroaortic left renal vein is the most common (fig. 10.22) [46–48], with other anomalies such as circumaortic left renal vein (fig. 10.23) being less common. A combination of a black-blood technique (e.g., T1-weighted spin-echo or SGE with inferior presaturation pulses) and a bright-blood technique (dynamic gadolinium-enhanced SGE or, preferably, fat-suppressed SGE or 3D-GE imaging) is useful to determine whether rounded or tubular retroperitoneal structures are vascular in nature [49]. Left-sided vena cava (fig. 10.24), duplicated vena cava (fig. 10.25), and IVC interruption with azygous/hemiazygous continuation are not uncommon anomalies that are well shown by MRI. Gadolinium enhancement is useful because in noncontrast images

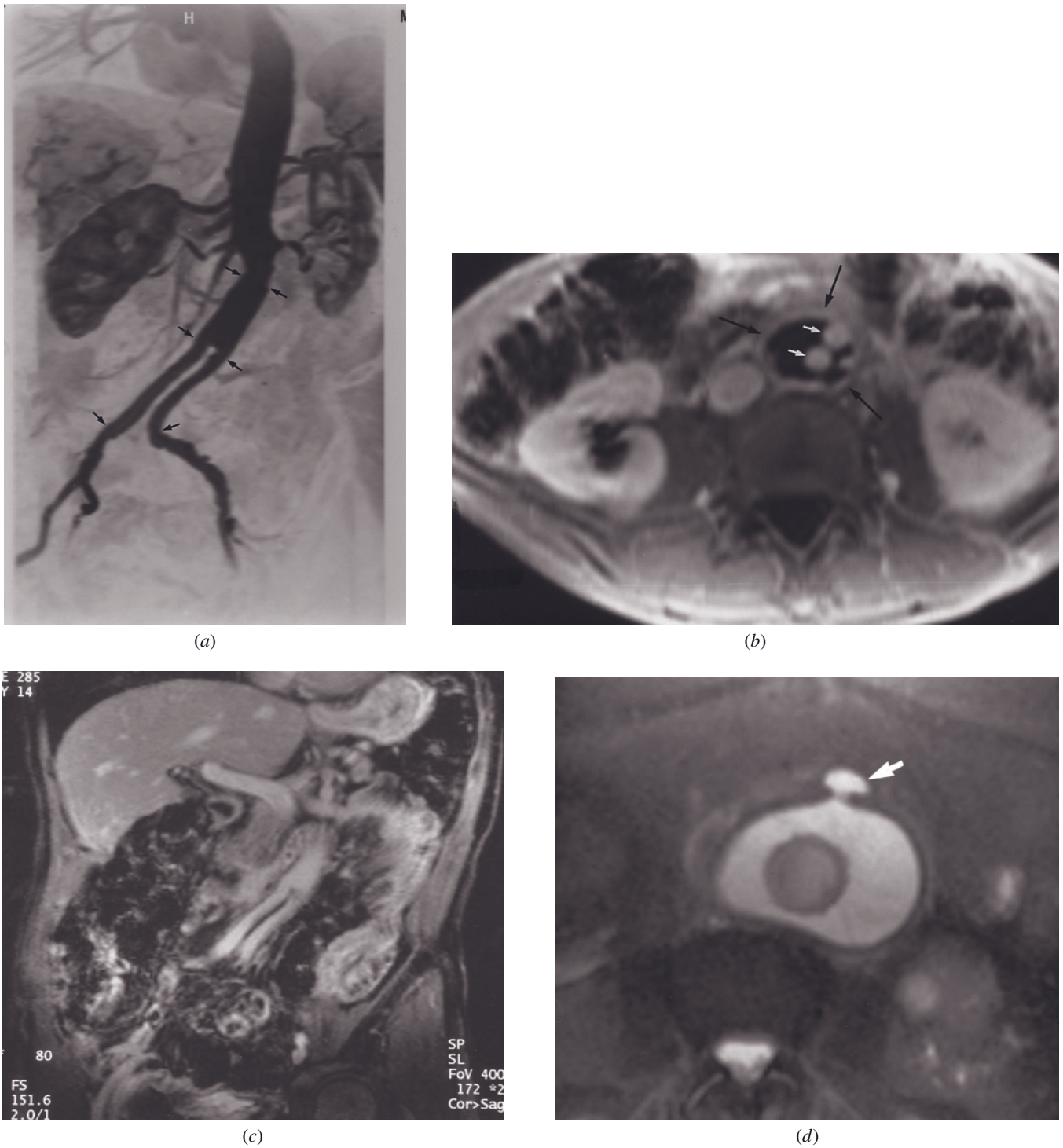

FIG. 10.18 Aortobifemoral graft after surgery. A 3D MIP reconstruction of gadolinium-enhanced 2-mm source images (*a*) and transverse (*b*) and coronal (*c*) interstitial-phase gadolinium-enhanced fat-suppressed SGE images in a patient with Marfan syndrome 1 month after surgery. The MIP image (*a*) demonstrates an abdominal aortic aneurysm with a maximal diameter of 4.5 cm at the level of the upper pole of the left kidney. More distally within the abdominal aorta, an aortoiliac graft is identified (small arrows, *a*). Irregularity of the luminal contour is noted distal to the graft because of atherosclerotic disease. The transverse 1-min postgadolinium fat-suppressed SGE image shows the patent lumens of the limbs of the graft (small arrows, *b*) surrounded by low-signal-intensity postoperative fluid contained within the wall (arrows, *b*) of the native aorta. The patency of the graft is also shown on the coronal interstitial-phase gadolinium-enhanced fat-suppressed SGE image (*c*). T2-weighted fat-suppressed SS-ETSE (*d*),

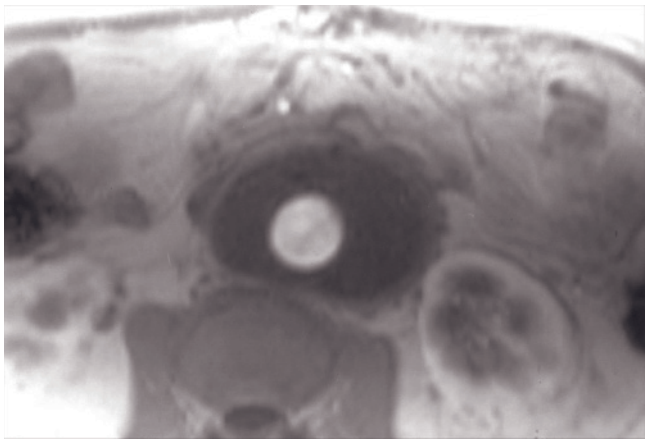

(*e*)

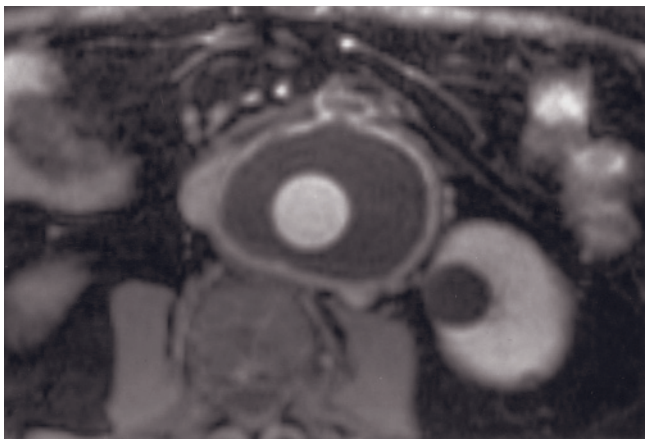

(*f*)

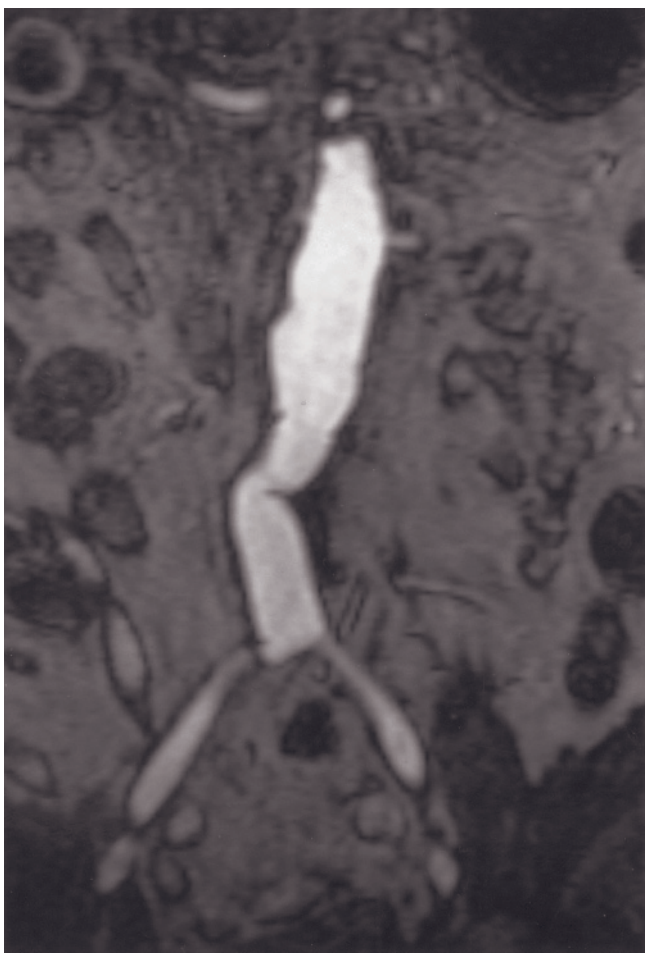

(*g*)

(*h*)

FIG. 10.18 (*Continued*) immediate postgadolinium SGE (*e*), and interstitial-phase gadolinium-enhanced fat-suppressed SGE (*f*) images in a second patient, with recent history of aortobifemoral graft surgery, demonstrate the presence of perigraft fluid. A small pocket of fluid is noted along the incision margin of the aneurysm (arrow, *d*). Coronal immediate postgadolinium 2-mm 3D gradient-echo source image (*g*) and MIP reconstruction of the 2-mm 3D source images (*h*) demonstrate a normal appearance for the vascular graft.

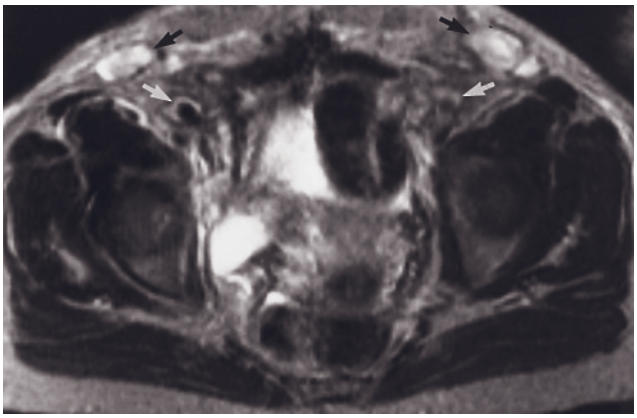

(*a*)

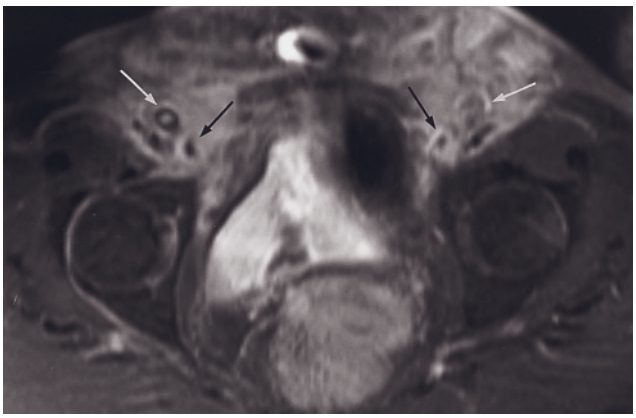

(*b*)

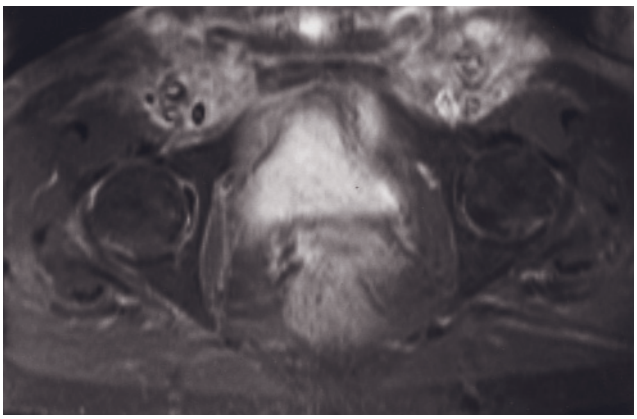

(*c*)

FIG. 10.19 Infected aortobifemoral graft. T2-weighted spin-echo (*a*) and gadolinium-enhanced T1-weighted fat-suppressed spin-echo (*b, c*) images. High-signal-intensity fluid (white arrows, *a*) is demonstrated on the T2-weighted image (*a*) surrounding the wall of the infected graft. The subcutaneous fat in the groins and anterior abdominal wall is heterogeneously high in signal intensity, reflecting the presence of inflammation, and bilateral enlarged inguinal lymph nodes (black arrows, *a*) are noted. Intense enhancement of the surrounding soft tissue and the walls of the grafts (black arrows, *b*) as well as the walls of the common femoral veins (white arrows, *b*) is demonstrated on gadolinium-enhanced T1-weighted fat-suppressed spin-echo images, reflecting severe inflammatory changes.

FIG. 10.20 Endovascular graft. Coronal 3D MIP reconstruction of gadolinium-enhanced 2-mm source images demonstrates an abdominal aortic aneurysm and the presence of a patent endovascular stent graft.

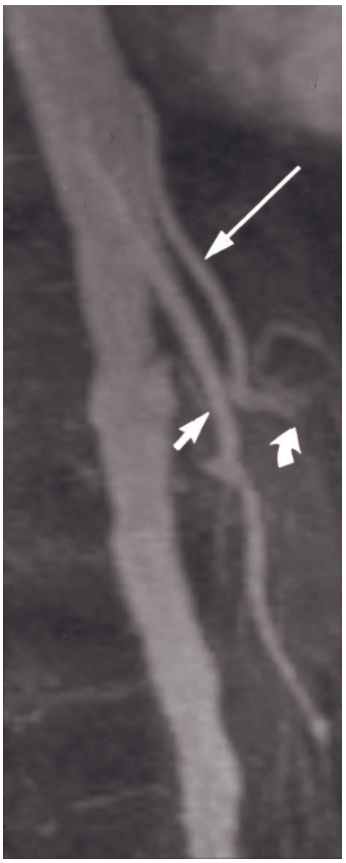

(*a*)

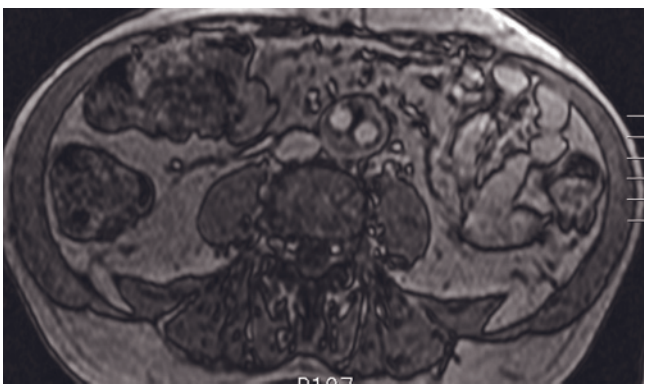

(*b*)

(*c*)

FIG. 10.21 Vascular graft to branch vessel. Sagittal 3D MIP reconstruction of gadolinium-enhanced 2-mm source images in a patient with thoracic aortic grafts, one to the celiac axis (long arrow) and another to the SMA (short arrow). The SMA distal to the graft is patent. The splenic artery distal to the celiac graft is thrombosed (curved arrow, *a*). Transverse T1-weighted out-of-phase 2D-GE image (*b*) and coronal 3D MIP reconstruction MRA image (*c*) demonstrate the presence of endovascular aortic stent-graft extending into the common iliac arteries in another patient with abdominal aortic aneurysm.

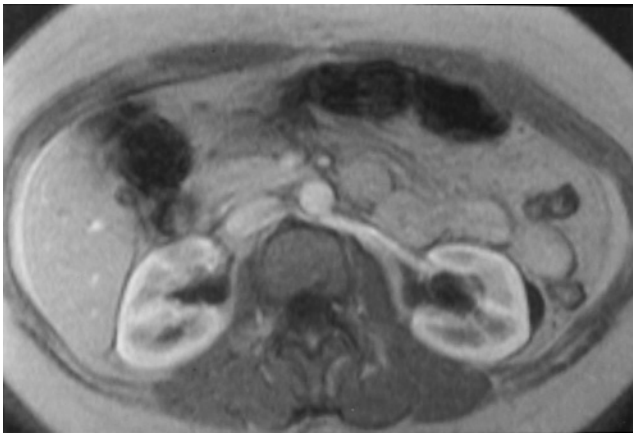

FIG. 10.22 Retroaortic left renal vein. Immediate post-gadolinium SGE image demonstrates a retroaortic left renal vein entering the IVC.

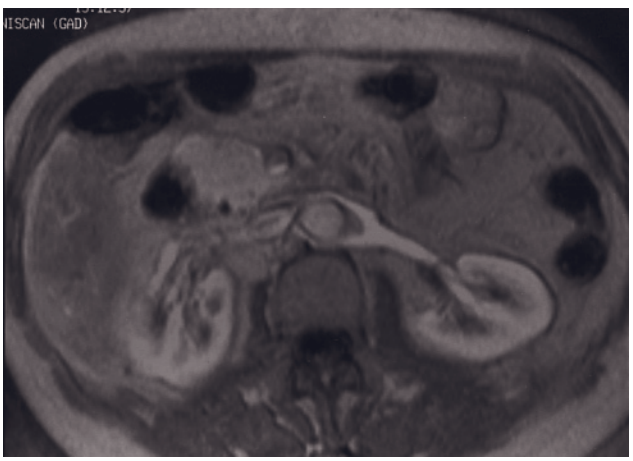

(*a*)

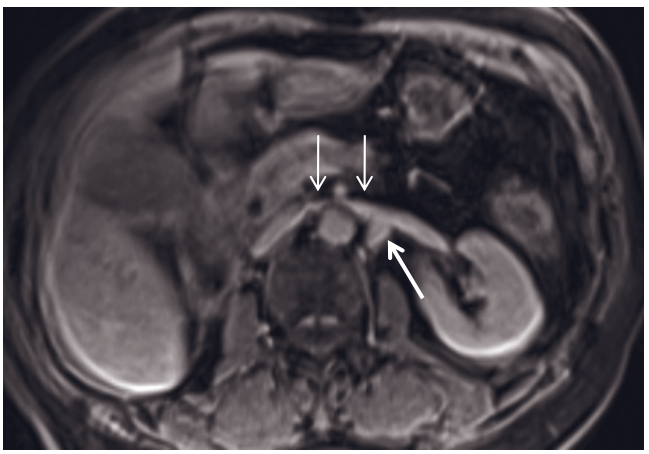

(*b*)

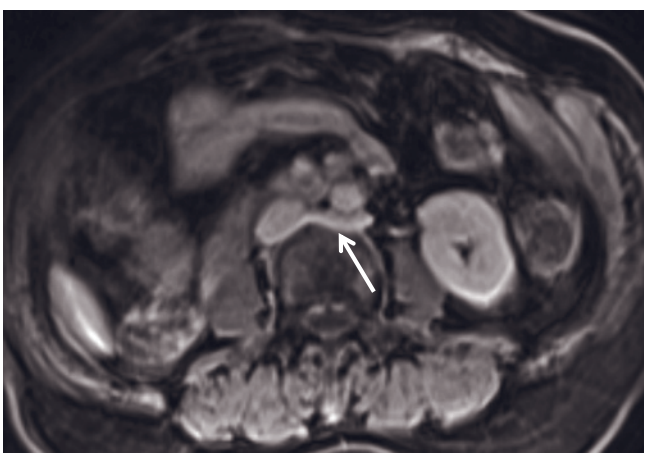

(*c*)

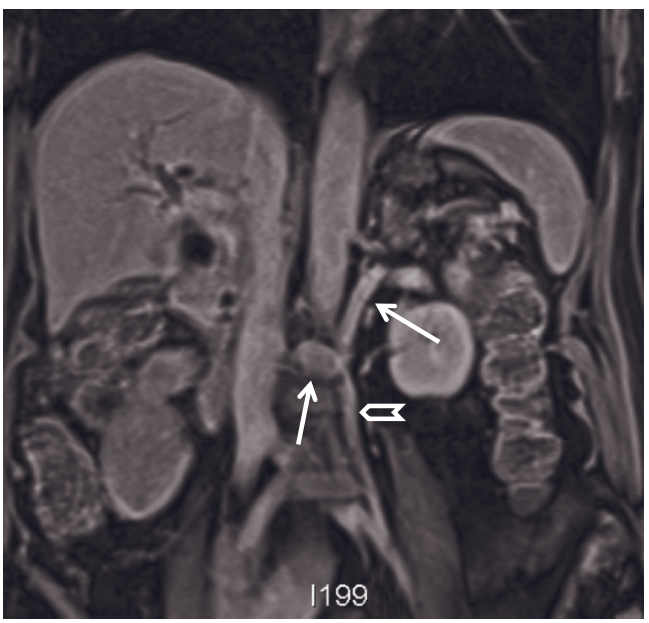

(*d*)

FIG. 10.23 Circumaortic left renal vein. Immediate postgadolinium SGE image clearly defines both limbs of the circumaortic left renal vein with their entry into the IVC (*a*). Transverse (*b*, *c*) and coronal (*d*) T1-weighted postgadolinium interstitial phase fat-suppressed 3D-GE images demonstrate circumferential left renal vein in another patient. The left renal vein bifurcates and its posterior limb (white thick arrows; *b–d*) course inferiorly and turn right to drain into the IVC. The anterior limb (white thin arrows; *b*) directly continues its horizontal course to drain to the IVC. The left gonadal vein (arrowhead; *d*) also drains into the posterior limb of the left renal vein. The limbs of the circumferential left renal vein more commonly drain into the IVC at different levels.

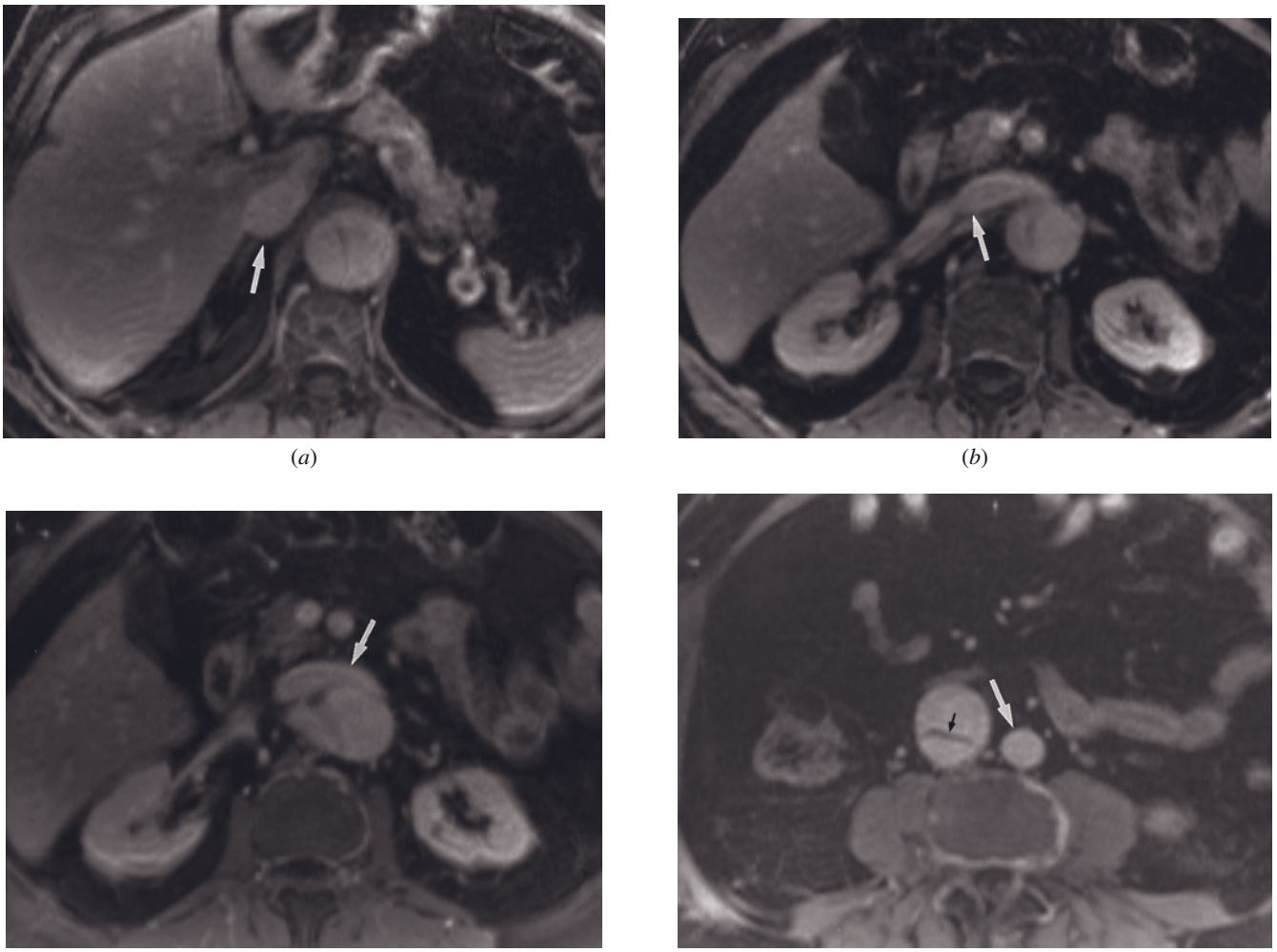

(*a*) (*b*) (*c*) (*d*)

FIG. 10.24 Left-sided IVC. Transverse 90-s postgadolinium fat-suppressed SGE images at different tomographic levels (*a–d*). A right-sided suprarenal IVC is demonstrated on the most cranial image (arrow, *a*). At the level of the renal veins, the IVC (arrow, *b*) crosses over the aorta to the left and the infrarenal IVC (arrow, *c*, *d*) is left-sided (*c*). An aortic dissection is also present with the intimal flap (small arrow, *d*) shown in the contrast-enhanced aortic lumen.

duplicated IVC, thrombophlebitis of the left-sided IVC, and existing retroperitoneal collateral vessels may mimic retroperitoneal lymphadenopathy [50].

Venous Thrombosis

MRI performs well in evaluating IVC thrombosis [51, 52] and distinguishing tumor from blood thrombus. Gadolinium-enhanced SGE or fat-suppressed SGE or 3D-GE images are useful for these determinations. Tumor thrombus enhances, whereas blood (also termed bland) thrombus does not enhance with contrast (figs. 10.26 and 10.27) [53]. Signal intensity measurements of thrombus before and after gadolinium administration may be necessary because blood thrombus, which is subacute or responding to anticoagulant therapy, may be high in signal intensity on precontrast images. Lack of increase in signal intensity on postcontrast images would confirm the blood nature of the thrombus. Flow-sensitive gradient-echo techniques with a lower flip angle (30–45°) may distinguish tumor from blood thrombus. Tumor thrombus is intermediate (soft tissue) in signal intensity on these sequences, whereas blood thrombus is generally very low in signal intensity [54]. Blood thrombus frequently exists at the tail of tumor thrombus (fig. 10.28), and the two components can be distinguished readily on postgadolinium SGE and fat-suppressed SGE or 3D-GE images. Evaluation of the degree of expansion of the IVC is also contributory, as pronounced expansion of the lumen is characteristic of tumor thrombus but atypical of blood thrombus. MRI, because of its higher soft tissue contrast resolution, is superior to CT imaging in determining the presence and extent of tumor thrombus. MRI outperforms CT imaging in detecting the extension of tumor thrombus supradiaphragmatically into the right atrium. This is an important evaluation in the preoperative setting, as supradiaphragmatic thrombus requires

combined thoracoabdominal surgery, whereas tumor thrombus with superior extension that ends below the hepatic veins may require only an abdominal approach.

In cases of chronic venous thrombosis the affected vessel may not be identified if the thrombus is organized and the vein is highly contracted. In these cases careful evaluation may reveal the absence of a vein in its expected location in combination with the presence of collateral vessel networks (fig. 10.29). IVC filters can be recognized by the symmetric arrangement of their

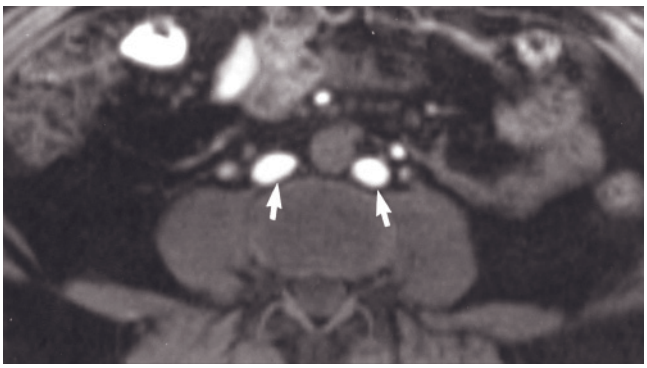

(*a*)

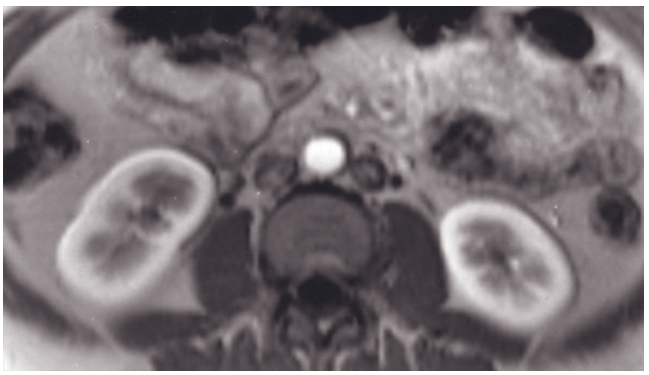

(*b*)

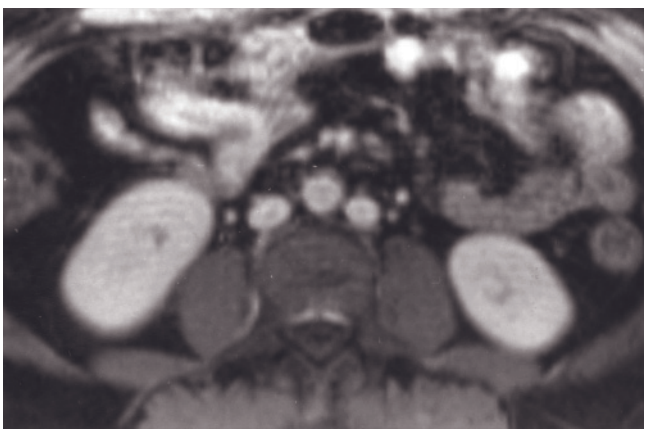

(*c*)

FIG. 10.25 Duplicated IVC. Noncontrast fat-suppressed SGE (*a*), immediate postgadolinium (*b*), and interstitial-phase gadolinium-enhanced SGE (*c*) images in a patient with duplicated IVC. The noncontrast T1-weighted image shows high-signal time-of-flight effects in venous structures on the inferior sections of the data acquisition. The bilateral IVCs (arrows, *a*) are clearly appreciated with the time-of-flight effects. The capillary-phase image (*b*) shows lack of enhancement of the IVCs early after contrast, which then become opacified on the interstitial-phase image (*c*). Combining morphologic and directional flow information on the precontrast images with dynamic temporal flow information on serial postgadolinium SGE images permits evaluation of congenital vascular variations and malformations.

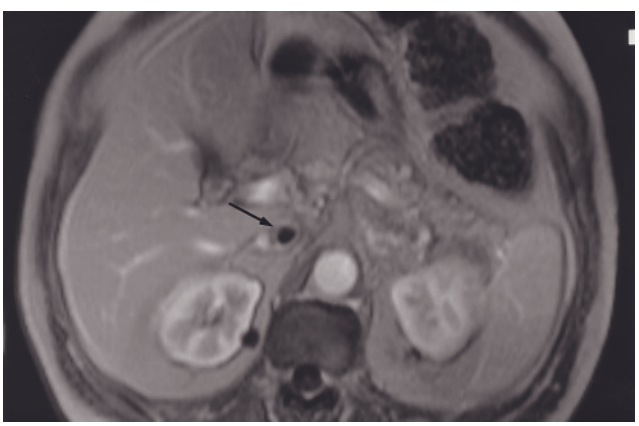

(*a*)

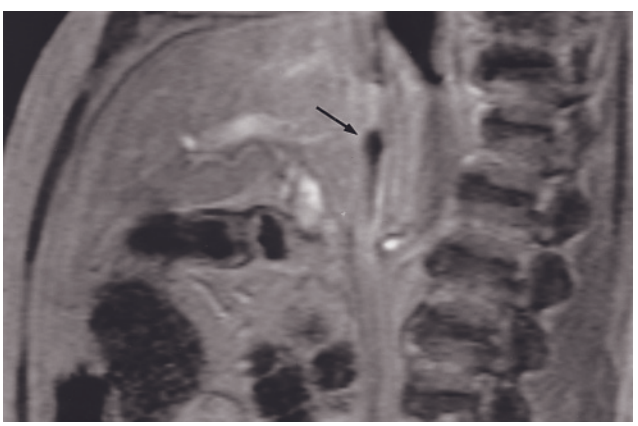

(*b*)

FIG. 10.26 IVC thrombosis. Transverse 45-s (*a*) and sagittal 90-s (*b*) postgadolinium SGE images. Bland thrombus (arrow, *a*, *b*) appears nearly signal void on gadolinium-enhanced SGE images. The 45-s postgadolinium SGE image (*c*) in a second patient demonstrates low- to intermediate-signal-intensity thrombus (arrow, *c*) attached to the posterior wall of the IVC. The combination of intense enhancement of the IVC on gadolinium-enhanced SGE images with multiplanar imaging makes MRI an excellent, minimally invasive modality for the assessment of venous thrombosis. Gadolinium-enhanced interstitial-phase SGE images (*d, e*)

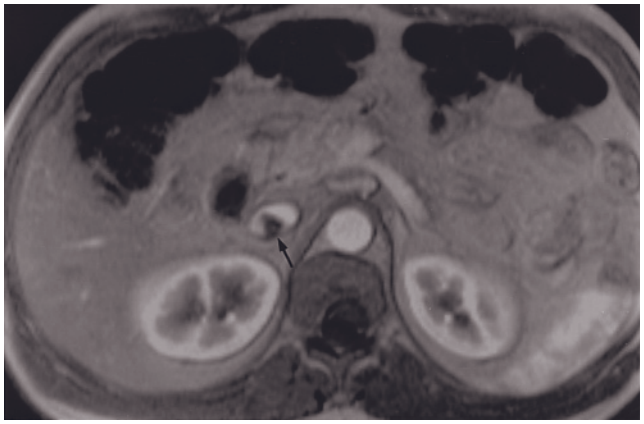

(*c*)

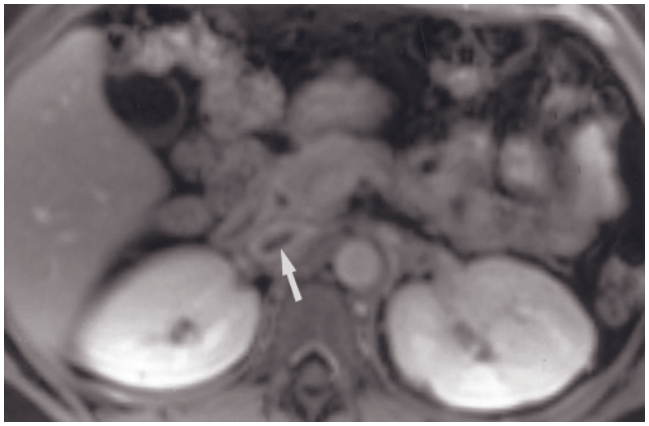

(*d*)

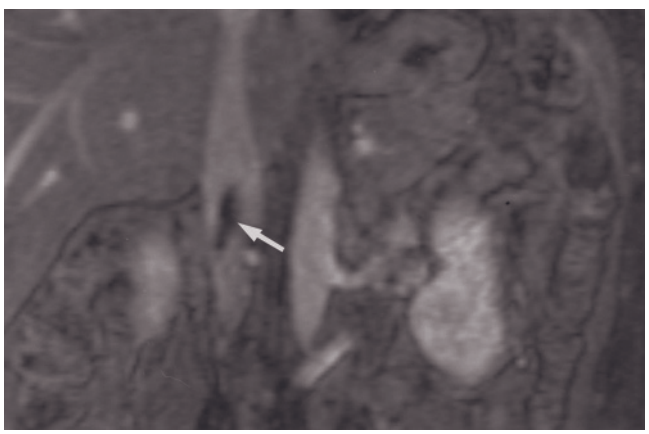

(*e*)

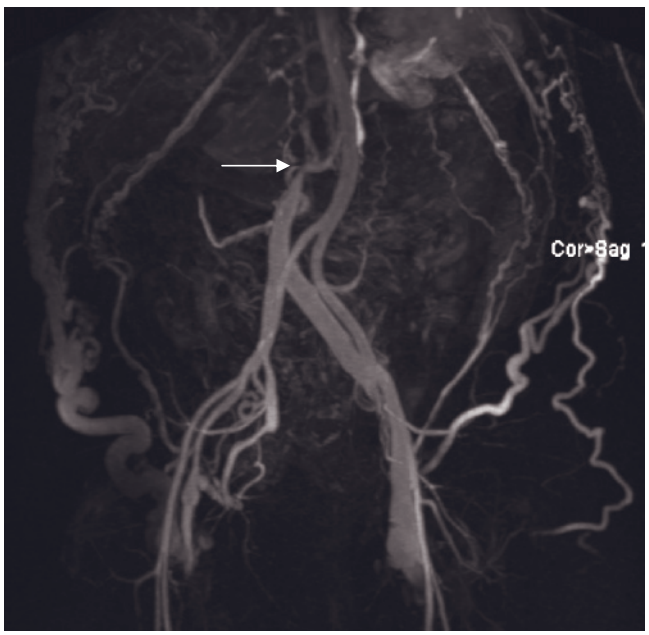

(*f*)

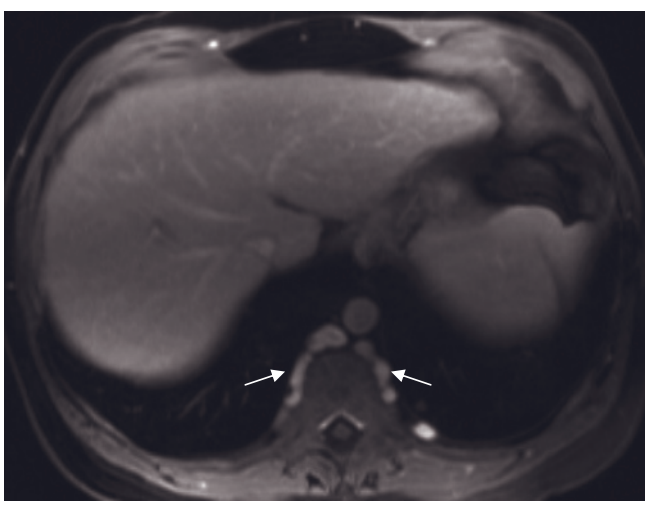

(*g*)

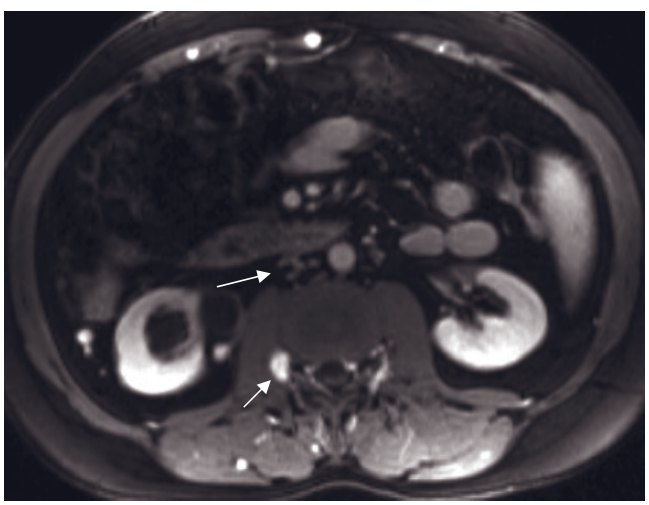

(*h*)

FIG. 10.26 (*Continued*) in a third patient show a nonocclusive low-signal-intensity structure (arrows, *d, e*) within the lumen of the infrahepatic IVC consistent with thrombus. Imaging in two planes is useful to verify patency or thrombosis of vessels. 3D MIP reconstruction image (*f*) of a set of venous-phase postgadolinium coronal breath-hold 3D-GE MRA sections in another patient with chronic IVC thrombosis demonstrate abrupt cutoff (arrow, *f*) of IVC proximal to its bifurcation. The presence of extensive venous collaterals and recanalization in the IVC indicates the chronic nature of IVC thrombosis. T1-weighted postgadolinium fat-suppressed SGE images (*g, h*) demonstrate the absence of intrahepatic IVC (arrow, *h*) in combination with the presence of dilated azygos and hemiazygos veins and venous collaterals (arrows, *g, h*) located in the abdominal wall and paraspinal region in another patient with chronic venous thrombosis.

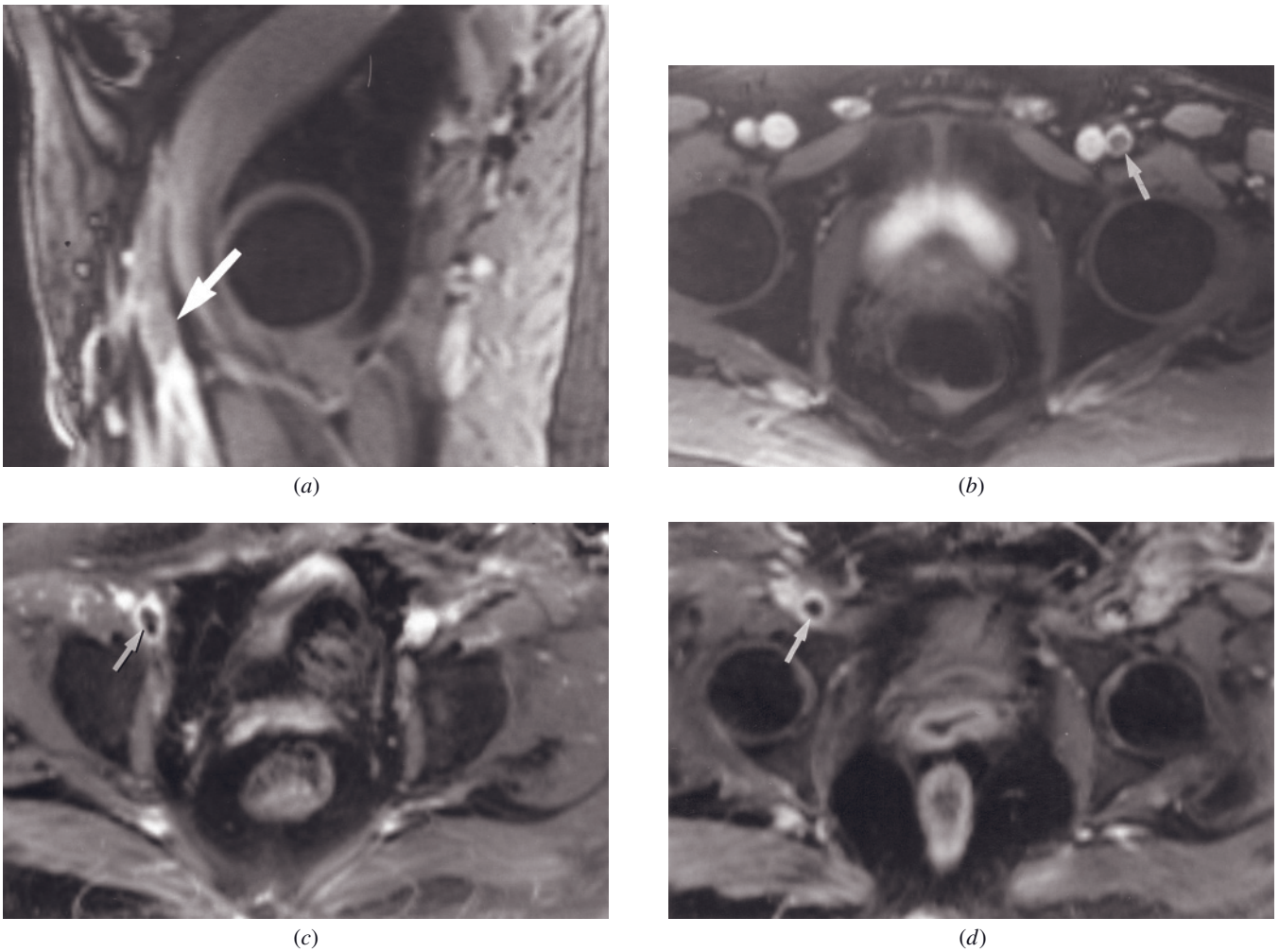

FIG. 10.27 Venous thrombosis. Sagittal (*a*) and transverse (*b*) interstitial-phase gadolinium-enhanced fat-suppressed SGE images demonstrate nonenhancing very low-signal-intensity tissue (arrows, *a*, *b*) within the lumen of the left external iliac vein consistent with venous thrombus. Transverse interstitial-phase gadolinium-enhanced fat-suppressed SGE images (*c, d*) in a second patient show the same finding within the right iliac vein (arrows, *c, d*).

elements and the magnetic susceptibility artifact on SGE or 3D-GE images (fig. 10.30).

In a fashion similar to that of IVC evaluation, MRI is effective at demonstrating renal and gonadal veins as well as retroperitoneal collaterals in cases of venous thrombosis (fig. 10.31) [45]. Compression of the left renal vein between the aorta and superior mesenteric artery may result in the "nutcracker syndrome," and when a pressure gradient is present, it may occasionally lead to development of varicocele, ovarian vein or pelviureteral varices, hematuria, and flank pain [55]. Thrombosed, enlarged retroperitoneal collateral veins may mimic lymphadenopathy on imaging studies [50]. In these cases, careful visual assessment of the course of the structures on transverse images may indicate the vascular nature of the masses [50]. Direct coronal or sagittal imaging is also helpful because these planes demonstrate the tubular shape of these vessels. Gadolinium-enhanced fat-suppressed SGE or 3D-GE images provide a definitive answer because they demonstrate lack of enhancement in thrombosed vessels compared to moderate enhancement of lymph nodes. Gonadal veins may be enlarged in cases of varicoceles in men and varices of the ovarian venous plexus in women (fig. 10.32). Early retrograde filling of a large and/or tortuous gonadal vein may be demonstrated on immediate postgadolinium SGE and 3D-GE images or arterial-phase bolus-enhanced 3D gradient-echo MRA images (see fig. 10.32). Markedly enlarged ovarian veins are commonly encountered during pregnancy because of compression by the pregnant uterus and increased venous flow (fig. 10.33). Thrombosis of the ovarian veins may complicate puerperal infection and is readily detected on gadolinium-enhanced fat-suppressed SGE or 3D-GE images. Congenital abnormalities of lymphatic channels

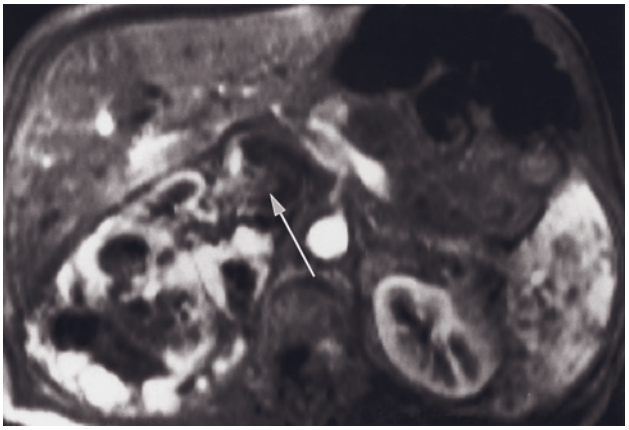

(*a*)

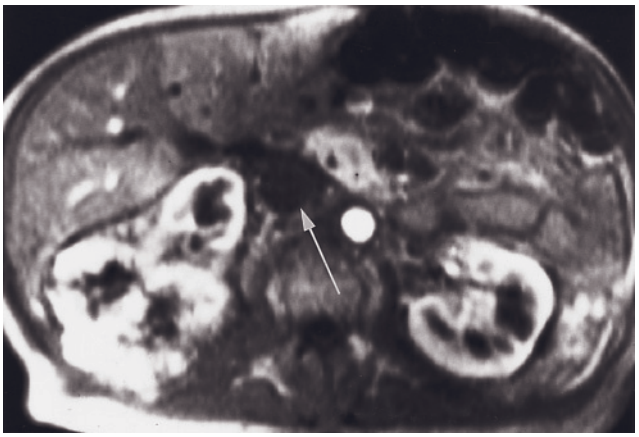

(*b*)

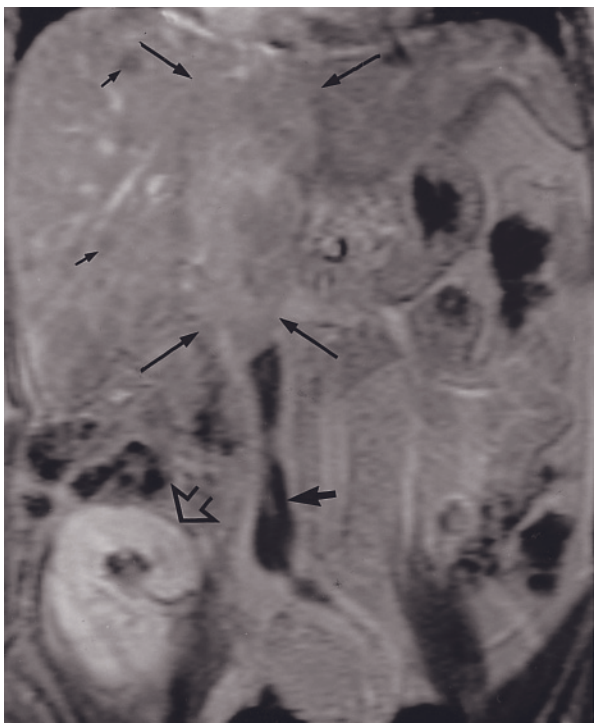

(*c*)

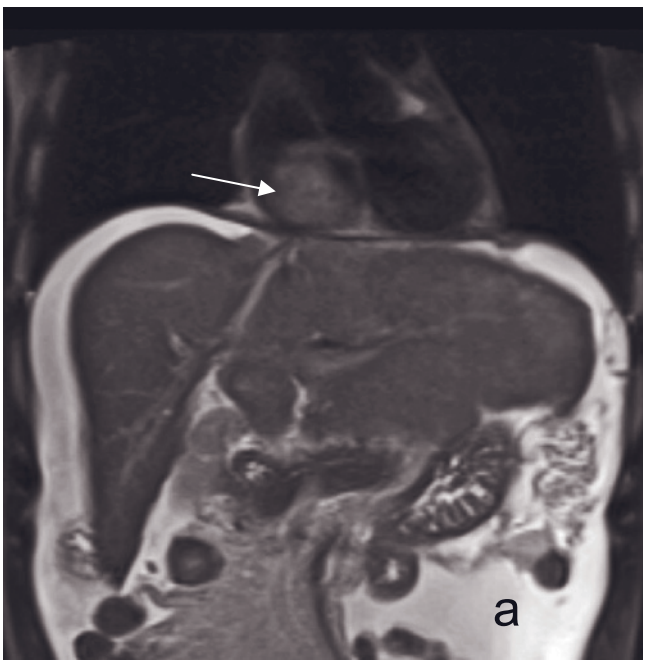

(*d*)

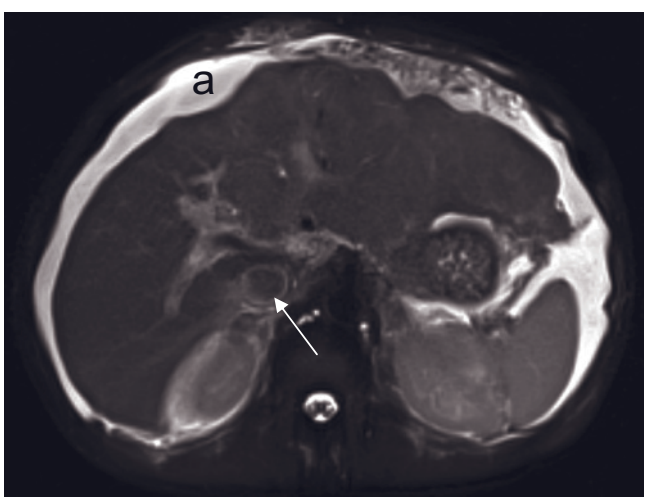

(*e*)

FIG. 10.28 Tumor and blood thrombus. Immediate postgadolinium SGE images (*a, b*). A large hypervascular renal cell carcinoma is present in the right kidney. Extension into the inferior vena cava is depicted on the higher tomographic level image (*a*), with tumor thrombus (long arrow, *a*) demonstrating heterogeneous enhancement. The SGE image at a lower tomographic level demonstrates blood thrombus (long arrow, *b*) to be nearly signal void. MRI using postgadolinium SGE images can reliably differentiate tumor from bland thrombus. Interstitial-phase gadolinium-enhanced SGE image (*c*) in a second patient shows a renal cell carcinoma with enhancing tumor thrombus (long arrows, *c*) and signal-void blood thrombus (arrow, *c*) extending distally to the left common iliac vein. Multiple hepatic metastases (small arrows, *c*) and a renal transplant (open arrow, *c*) are also noted. Coronal T2-weighted single-shot echo-train spin-echo (*d*), transverse T2-weighted fat-suppressed single-shot echo-train spin-echo (*e*),

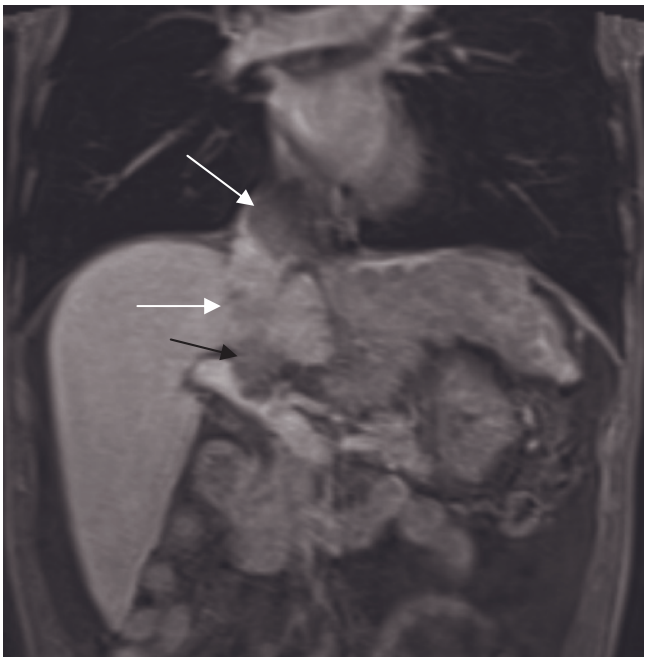

(*f*)

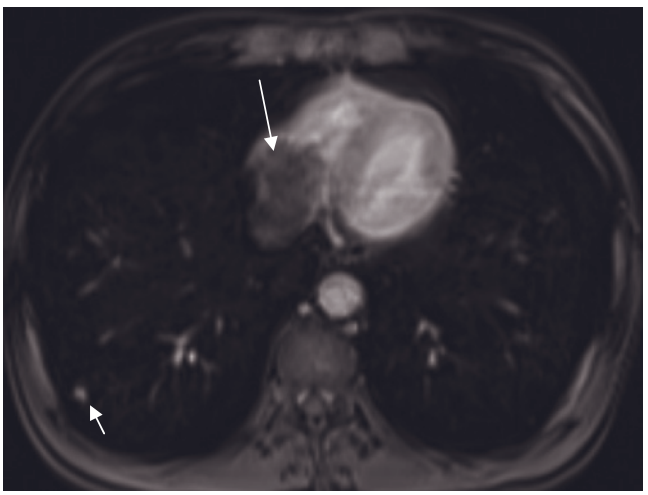

(*g*)

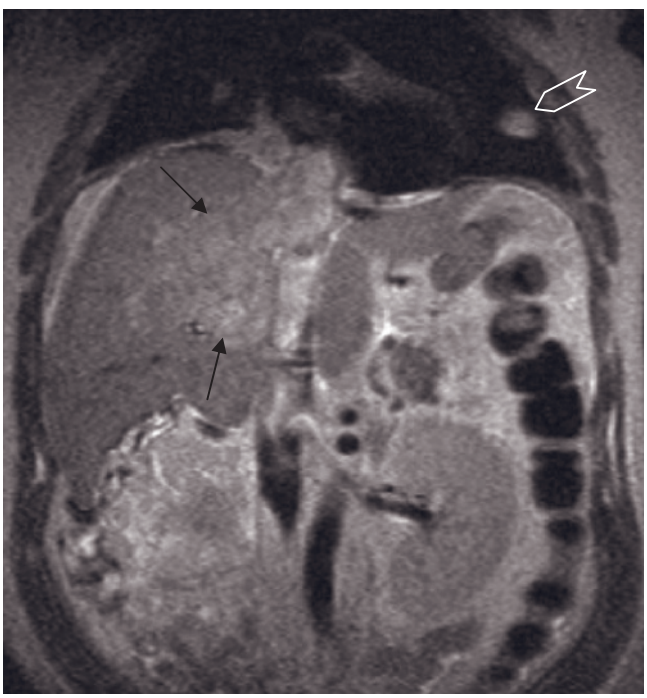

(*h*)

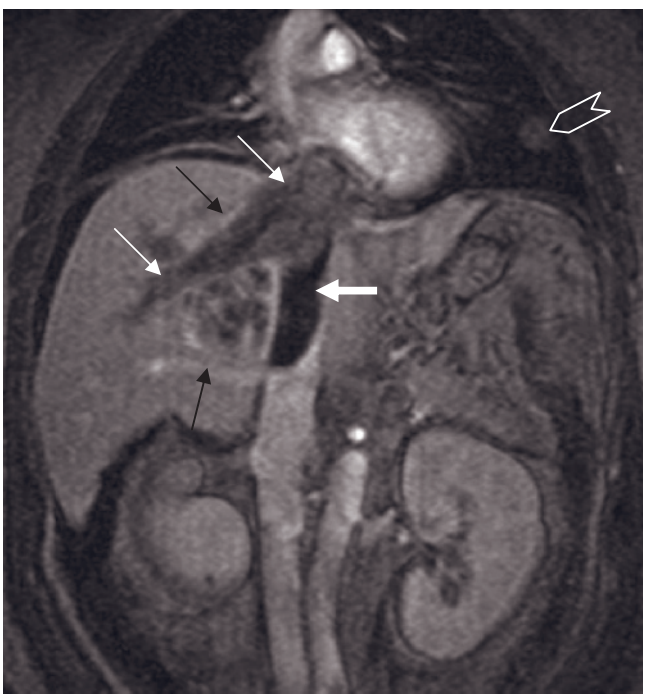

(*i*)

FIG. 10.28 (*Continued*) and coronal (*f*) and transverse (*g*) T1-weighted postgadolinium interstitial-phase fat-suppressed 3D-GE images at 3.0 T demonstrate diffuse hepatocellular carcinoma (HCC) in another patient. Diffuse HCC mainly involves the left lobe of the liver. The left lobe is irregularly enlarged and shows heterogeneous enhancement on postgadolinium image (*f*). The tumor also causes IVC thrombosis extending into right atrium (white long arrows, *d–g*). Thrombus shows enhancement due to its tumoral content. The invasion of portal vein (black arrow, *f*) by the tumor is detected. There is a small metastasis (short arrow, *g*) from HCC in the right lung. Note the presence of ascites (a, *d, e*). Coronal T2-weighted single-shot echo-train spin-echo (*h*) and coronal postgadolinium magnetization-prepared rapid gradient-echo (*i*) images demonstrate diffuse HCC (black arrows, *h, i*) in another patient. Diffuse HCC causes tumor thrombus (white thin arrows, *i*) and bland thrombus (white thick arrow, *i*). The tumor thrombus extends into the right atrium and right hepatic vein and shows enhancement. The bland thrombus does not show any enhancement. Note that there is a lung metastasis (open arrow, *h, i*) from HCC in the left lung. T2-weighted fat-suppressed echo-train

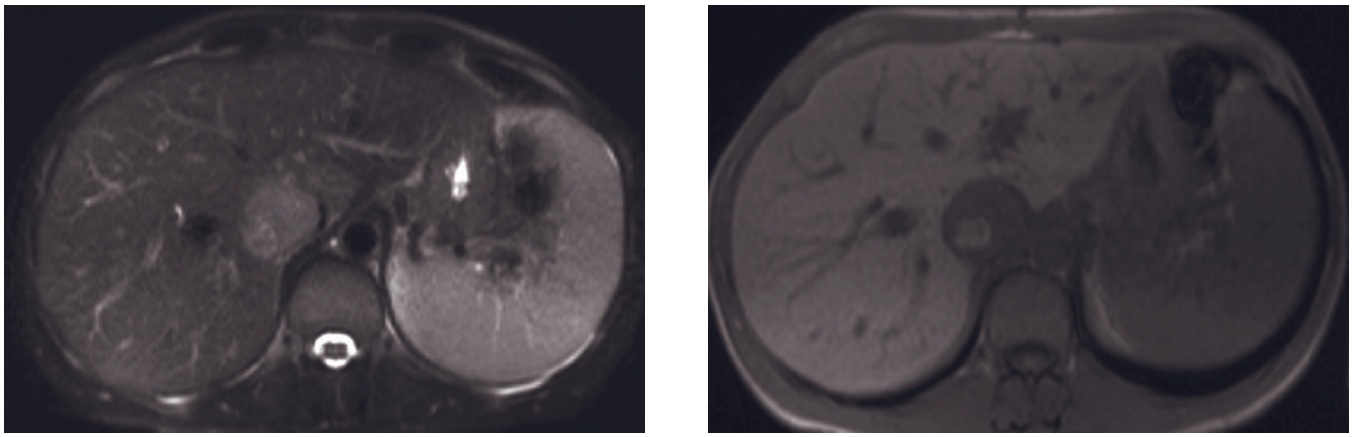

(*j*) (*k*)

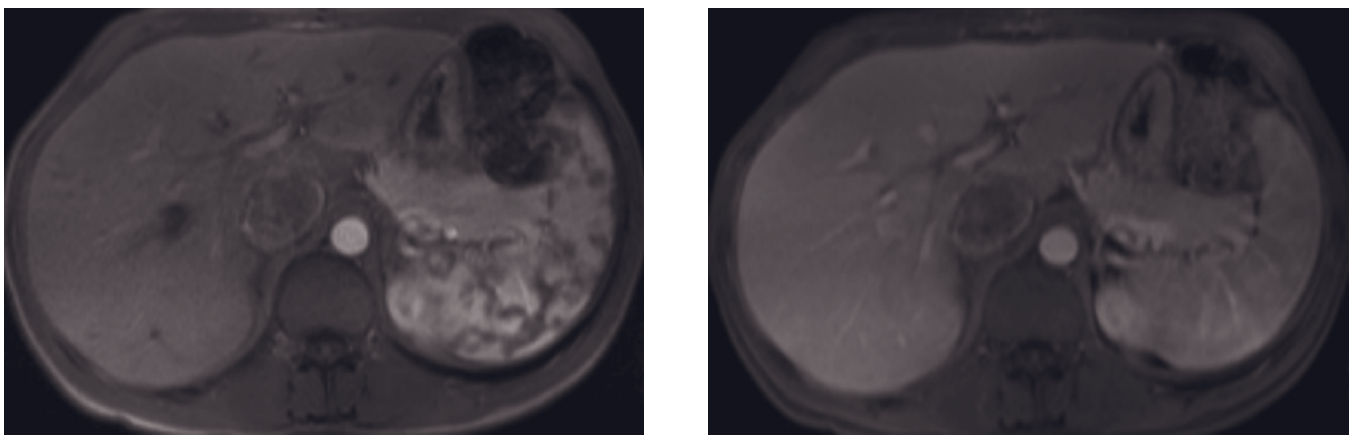

(*l*) (*m*)

FIG. 10.28 (*Continued*) spin-echo (*j*), T1-weighted in-phase SGE (*k*), T1-weighted postgadolinium hepatic arterial dominant-phase SGE (*l*), and T1-weighted postgadolinium hepatic venous-phase fat-suppressed 3D-GE (*m*) images demonstrate the tumor thrombus in the IVC developing secondary to adrenocortical carcinoma in another patient. The thrombus is heterogeneous on precontrast images (*j, k*) and shows heterogeneous enhancement on postgadolinium images (*l, m*).

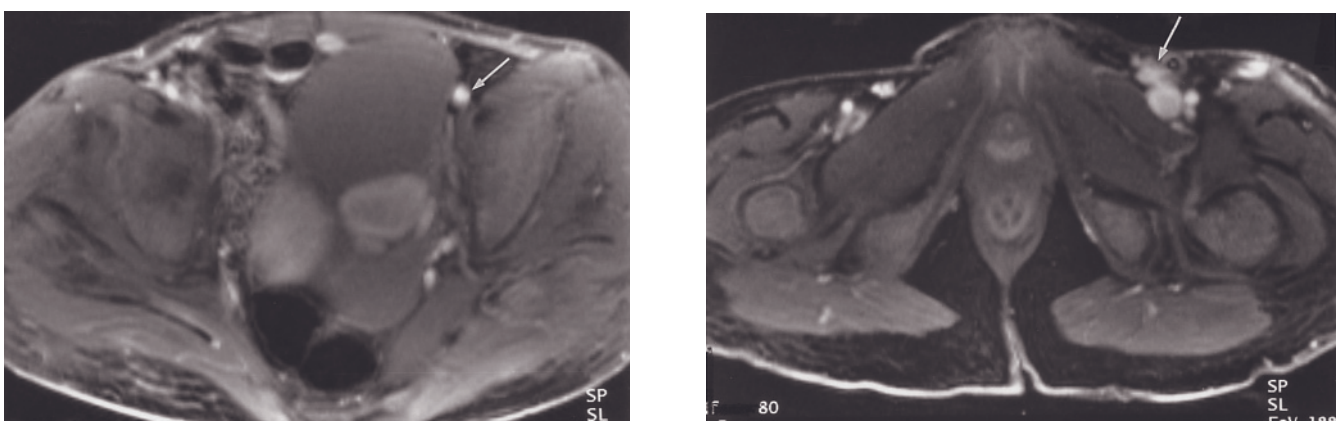

(*a*) (*b*)

FIG. 10.29 Chronic venous thrombosis. Interstitial-phase gadolinium-enhanced fat-suppressed SGE images at superior (*a*) and more inferior (*b*) tomographic levels. At the level of the midpelvis, only the left external iliac artery (arrow, *a*) is identified, whereas the chronically thrombosed left external iliac vein appears as linear nonenhancing tissue immediately posterior to the artery. A collateral enhancing vessel (arrow, *b*) is noted, reconstituting the left common femoral vein at a lower tomographic level (*b*). SGE images obtained from 45 s to 2 min after gadolinium administration provide reproducible uniform intense enhancement of normal veins, rendering this technique sensitive to the presence of thrombus even in medium- and small-diameter vessels. Imaging within 40 s permits evaluation of arteries, often without the presence of contrast in veins.

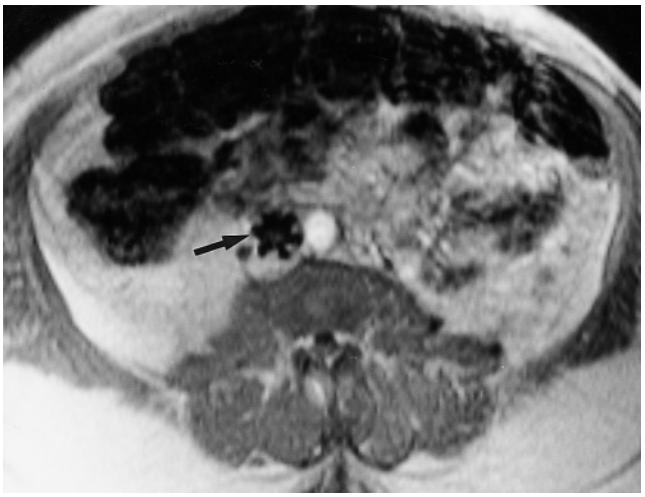

FIG. 10.30 IVC filter. A 45-s postgadolinium SGE image demonstrates a Gianturco IVC filter (arrow) in the inferior vena cava. The filter is readily recognized by the magnetic susceptibility effect and the symmetric configuration of its pedicles.

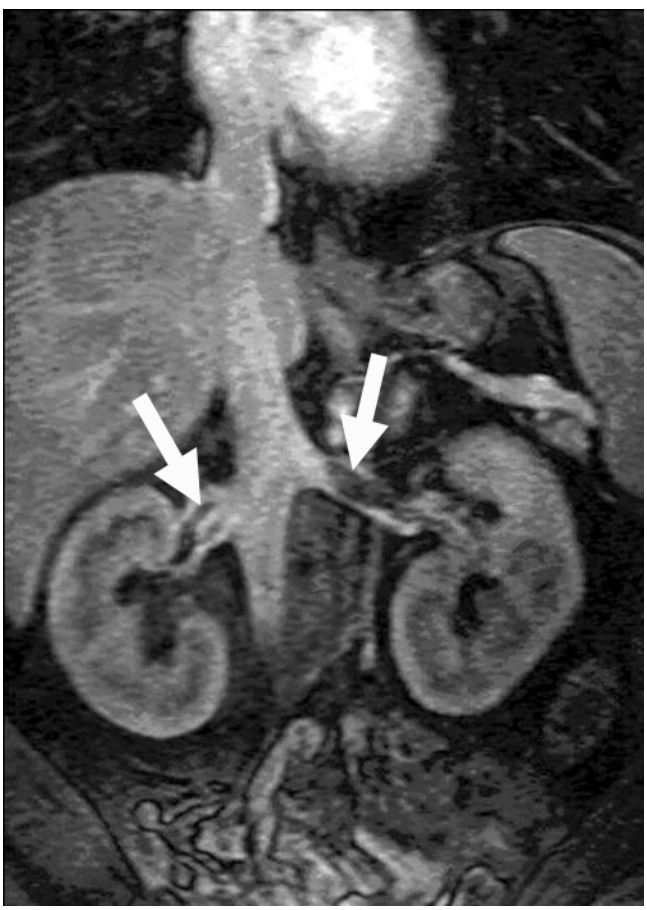

FIG. 10.31 Bilateral renal vein partial thrombosis. Coronal MRA shows filling defects in both renal veins partially occluding the lumen, with contrast seen passing around the defects, in keeping with nonocclusive thrombus.

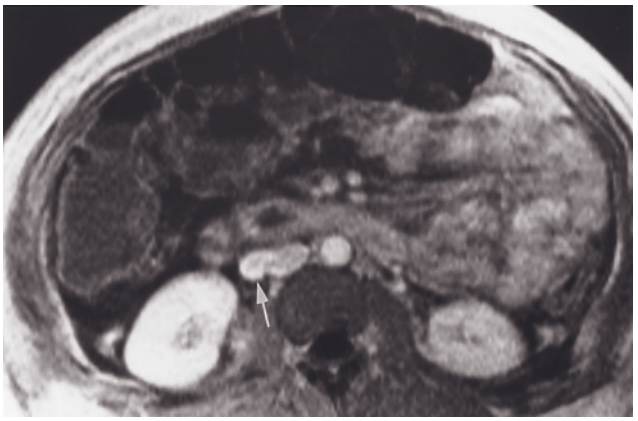

(*a*)

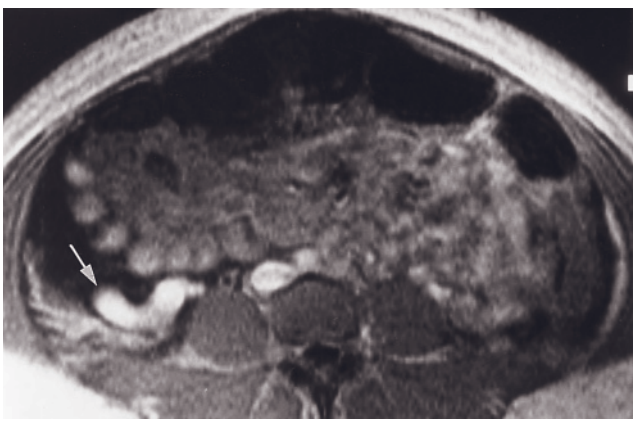

(*b*)

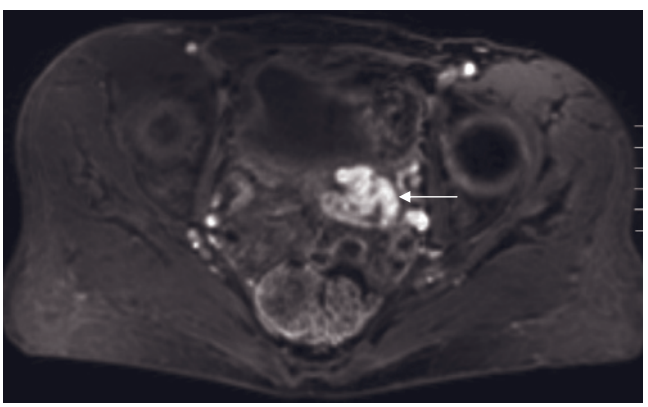

(*c*)

FIG. 10.32 Dilated gonadal vein. Transverse 90-s postgadolinium SGE images at superior (*a*) and more inferior (*b*) tomographic levels. A dilated right gonadal vein is demonstrated at its drainage into the IVC (arrow, *a*). At the lower tomographic level, the enhancing vessel (arrow, *b*) follows a serpiginous course. Low-signal-intensity ascites with centrally displaced bowel loops is also identified. T1-weighted postgadolinium interstitial-phase fat-suppressed 3D-GE image (*c*) at 3.0 T in another patient demonstrates dilated ovarian venous plexus (arrow) in another patient.

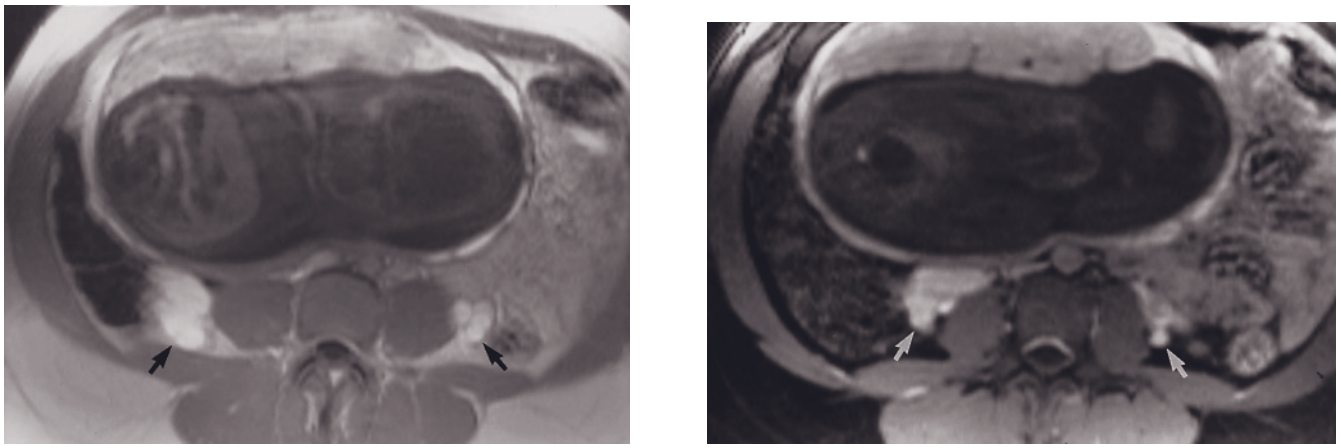

(*a*) (*b*)

FIG. 10.33 Dilated ovarian veins during pregnancy. Interstitial-phase gadolinium-enhanced SGE (*a*) and fat-suppressed SGE (*b*) images in a pregnant woman. The inferior vena cava is compressed by the pregnant uterus, and the ovarian veins (arrows, *a*, *b*) are enlarged, more prominent on the right. The patient was scanned for evaluation of persistent right flank pain, and her pain was attributed to the venous engorgement.

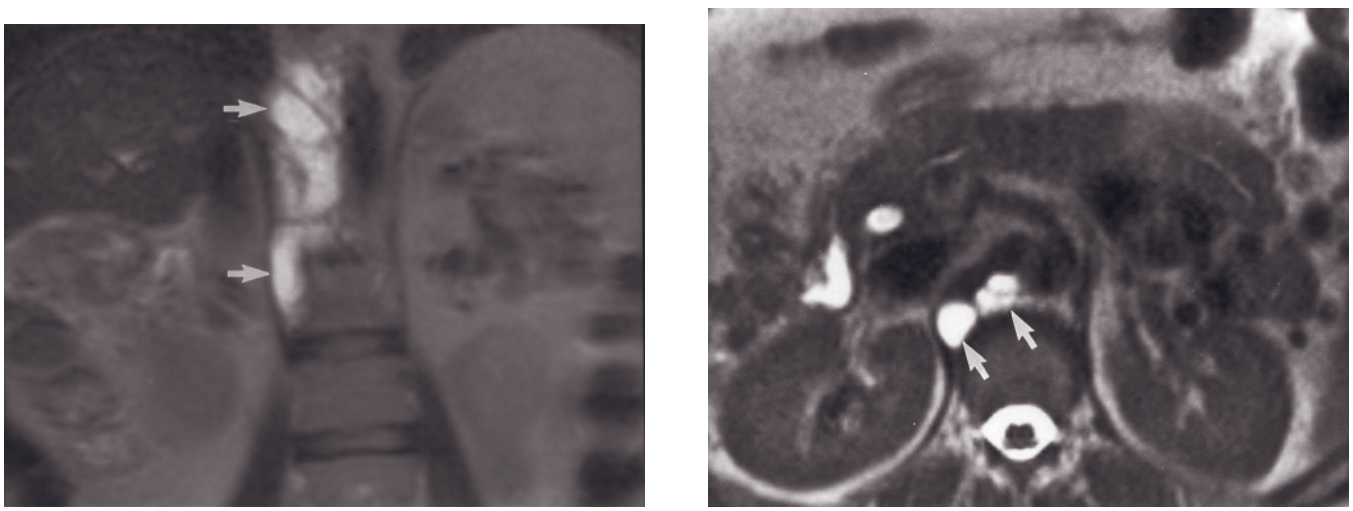

(*a*) (*b*)

FIG. 10.34 Dilated cysterna chyli. Coronal (*a*) and transverse (*b*) SS-ETSE images demonstrate multiple tortuous dilated tubular structures (arrows, *a*, *b*) that do not conform to arteries or veins and are situated in the location of the cysterna chyli.

are relatively rare. Dilatation of the cisterna chyli is one example (fig. 10.34). Lymphangioma and lymphangioma/hemangioma are described below. Postsurgical changes of lymphatic obstruction or lymphoceles are not uncommon complications, which usually do not have long-term morbidity complications.

Primary Malignant Tumors

Primary malignant tumors of the IVC are rare. The most common histologic type is leiomyosarcoma, followed by angiosarcoma [56]. In a review of leiomyosarcomas of the retroperitoneum and IVC, leiomyosarcomas involving the IVC have been classified as Pattern 2 when completely intraluminal and Pattern 3 in cases of combined extraluminal and intraluminal components, which comprise 5% and 33%, respectively, of the total cases [16]. Pattern 1 has no major IVC components and is discussed below in the primary retroperitoneal neoplasm subsection. These tumors are frequently large at presentation (fig. 10.35) but tend to present earlier than their completely extraluminal counterparts, because of symptoms related to obstruction of the IVC. Signal intensity of these tumors is moderately low on T1-weighted images and mixed moderate to high on

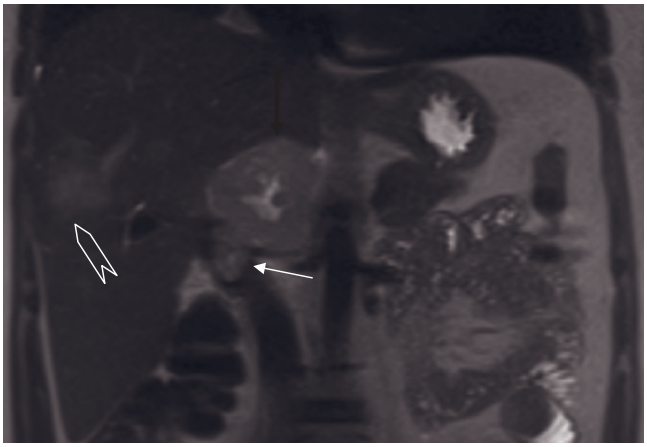

(*a*)

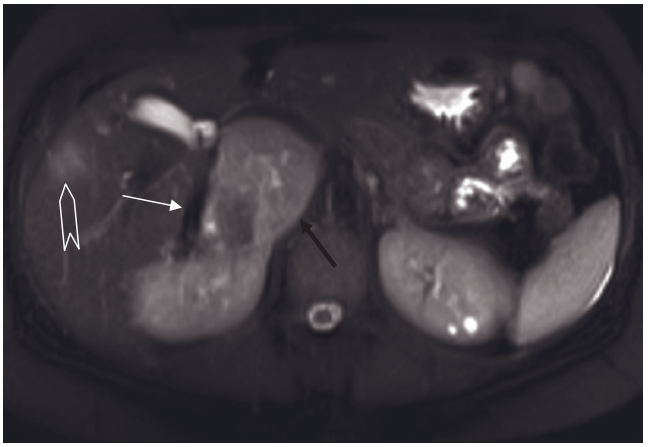

(*b*)

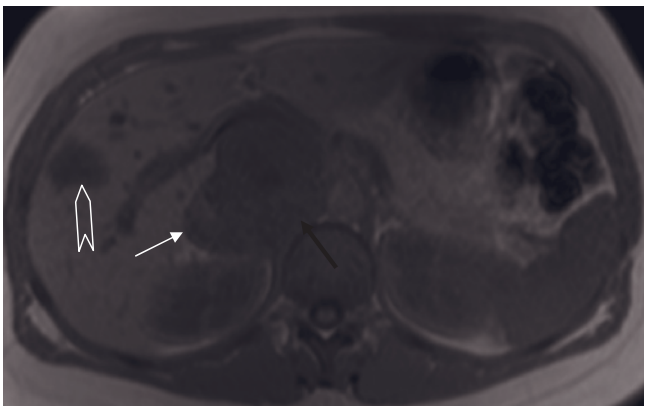

(*c*)

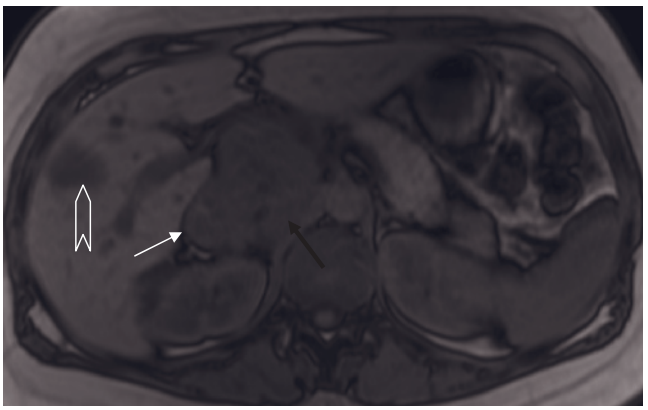

(*d*)

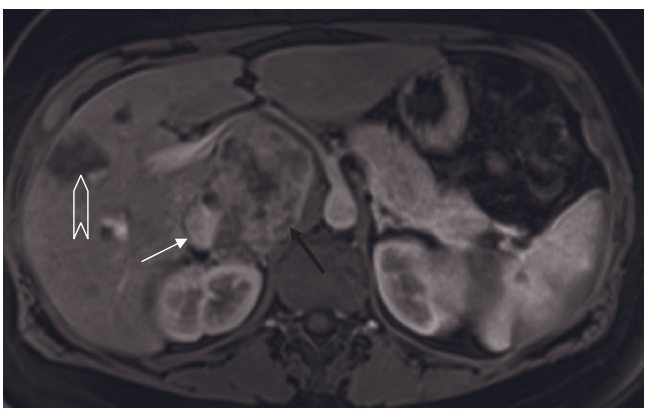

(*e*)

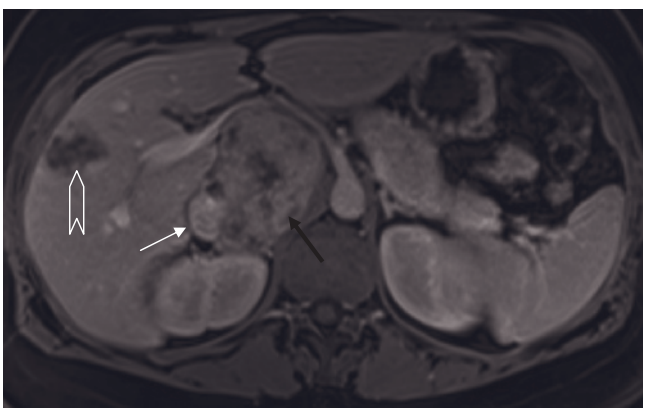

(*f*)

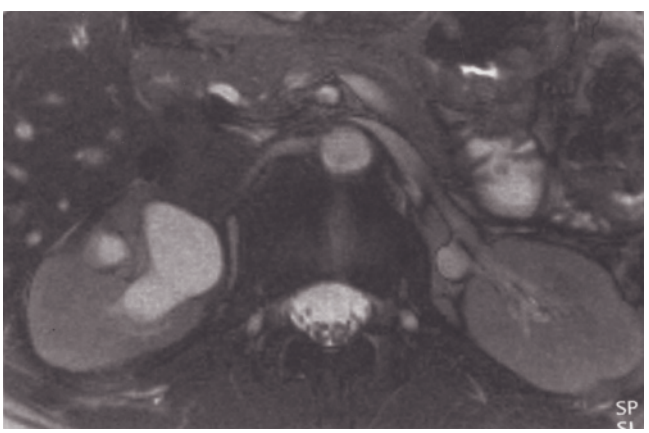

(*g*)

FIG. 10.35 Leiomyosarcoma of the IVC. Coronal (*a*) and transverse (*b*) T2-weighted single-shot echo-train spin-echo, T1-weighted in-phase (*c*) and out-of-phase (*d*) SGE, and T1-weighted postgadolinium hepatic arterial dominant-phase (*e*) and hepatic venous-phase (*f*) fat-suppressed 3D-GE images demonstrate leiomyosarcoma (black arrows, *a–f*) originating from the IVC. The IVC (white arrows, *a–f*) is compressed and displaced laterally. The tumor originates from the medial side of the IVC and extend into the lumen (white arrows, *a*, *c–f*). The tumor displaces the main portal vein anteriorly as well. It has central necrosis seen as high-signal-intensity region on T2-weighted images. The tumor shows high signal on T2-weighted images, low signal on T1-weighted precontrast images, and heterogeneous progressive enhancement on postgadolinium images. Note that there is a liver metastasis (open arrows, *a–f*) enhancing heterogeneously in the liver. T2-weighted fat-suppressed SS-ETSE (*g*), immediate

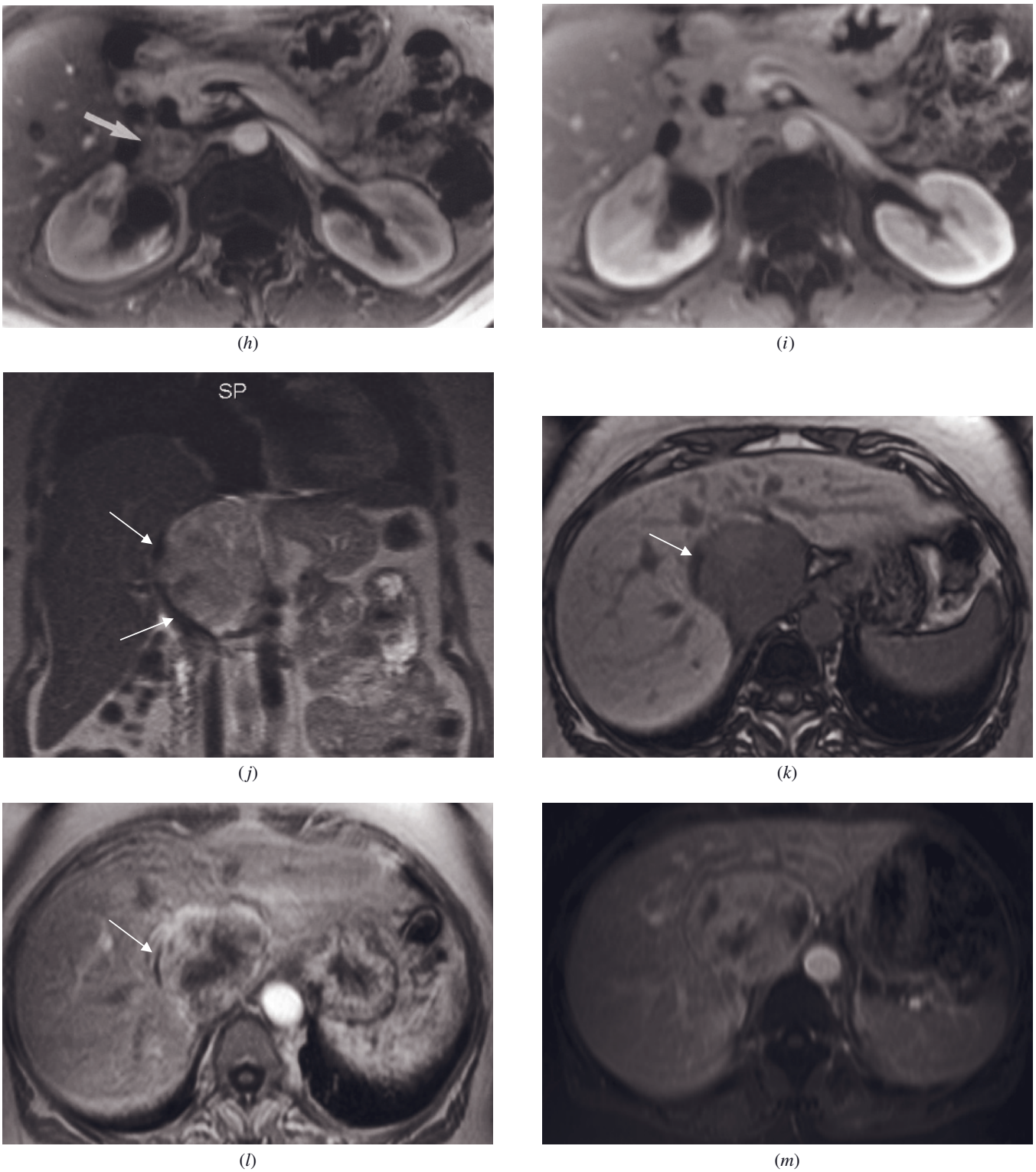

FIG. 10.35 (*Continued*) postgadolinium SGE (*h*), and interstitial-phase gadolinium-enhanced fat-suppressed SGE (*i*) images in a second patient. The IVC is enlarged by the presence of a mass that is hypointense on the T2-weighted image (*g*) and enhances heterogeneously on early (arrow, *h*) and late postgadolinium images. Note also the presence of hydronephrosis of the right kidney, secondary to ureteral involvement by the mass. Coronal T2-weighted single-shot echo-train spin-echo (*j*), T1-weighted out-of-phase (*k*), T1-weighted postgadolinium hepatic arterial dominant-phase SGE (*l*), and T1-weighted postgadolinium hepatic venous-phase fat-suppressed 3D-GE (*m*) images demonstrate leiomyosarcoma originating from IVC in another patient. IVC (arrows, *j–l*) is compressed and displaced laterally by the tumor. The tumor originates from the medial aspect of IVC. The IVC is partly signal void on precontrast images; however, the lateral wall of IVC shows thickening and prominent enhancement on postgadolinium images, suggesting the invasion of the lateral wall (arrow, *l*).

T2-weighted images. Areas of intermixed tumor and blood thrombus may have bright signal intensity on the T1-weighted images, a finding accentuated on fat-suppressed images (fig. 10.36). These tumors, which are usually hypervascular, demonstrate intense heterogeneous enhancement on gadolinium-enhanced images [57]. Bright-blood MRI techniques are useful for demonstrating IVC patency and extent of tumor [57]. Gadolinium-enhanced 3D MRA may demonstrate the extent of tumor well with MIP reconstructions. On occasion, it may be difficult to distinguish neoplasms, with completely intraluminal growth, from tumor thrombus. Expansion of the IVC and enhancement on postgadolinium SGE or 3D-GE images are features favoring neoplasm and tumor thrombus. In rare cases of hypovascular neoplasms (e.g., malignant fibrous histiocytoma), IVC expansion and demonstration of arterial feeders on immediate postgadolinium SGE or 3D-GE images may help to distinguish the neoplasm from blood thrombus (fig. 10.36) [57]. In rare instances, leiomyosarcomas originating in the renal veins may extend intraluminally into the IVC, and they may appear as tumors in the medial portion of the kidney with tumor thrombus in the renal vein and IVC [58].

RETROPERITONEAL MASSES

Benign Masses

Retroperitoneal Fibrosis

Retroperitoneal fibrosis is most frequently an idiopathic disease [2]. Benign retroperitoneal fibrosis also may arise secondary to certain drugs (classically methysergide), inflammatory aortic aneurysm, retroperitoneal hemorrhage, infection, surgery, or radiation therapy [59]. Idiopathic retroperitoneal fibrosis is considered part of a more extensive systemic fibrotic disorder related to mediastinal fibrosis, sclerosing cholangitis, Riedel thyroiditis, orbital and sinus pseudotumors [60, 61], and pulmonary hyalinizing granulomas [62, 63].

The most important differential diagnosis is between idiopathic benign and malignant retroperitoneal fibrosis, particularly as malignant neoplasms may coexist with benign retroperitoneal fibrosis [64]. Retroperitoneal fibrosis most commonly appears as oval-shaped tissue that encases the aorta. The extent of disease may vary from a focal region of fibrosis to dense infiltration of the retroperitoneum encasing the aorta, inferior vena cava (IVC), and ureters. The disease in its acute stage may present as a focal unilateral mass in the region of the common iliac vessels. Over time, fibrosis extends superiorly in the retroperitoneum along the major vessels. In rare instances, thrombosis of the iliac veins [65] and portal vein [66] may be encountered. In the majority of cases the fibrous tissue is located around the abdominal aorta below the level of the renal vessels. A feature distinguishing retroperitoneal fibrosis from retroperitoneal malignant adenopathy and lymphomas is that the fibrous tissue envelopes the aorta, IVC, and ureters but does not displace the aorta substantially anteriorly. Lymph nodes have a rounded, nodular configuration of retroperitoneal masses, whereas retroperitoneal fibrosis has a more platelike, curvilinear morphology.

Early reports suggested that MRI might be able to distinguish benign from malignant retroperitoneal fibrosis [59, 67]. Acute benign retroperitoneal fibrosis may, however, resemble malignant retroperitoneal fibrosis because both may enhance substantially with contrast and may be high in signal intensity on T2-weighted sequences (fig. 10.37) [68–70]. This enhancement pattern is due to the extensive capillary network of acute benign granulation tissue comparable to that in the postoperative spine [71]. Morphologically, acute benign retroperitoneal fibrosis has very infiltrative margins and may be very extensive throughout the retroperitoneum. Over time, the margins of benign retroperitoneal fibrosis become better defined and the tissue becomes more confluent and contracted around the aorta, IVC, and ureters. Eventually, the granulation tissue alters to a more collagenous fibrotic form after approximately 1 year of development. During the course of maturation, signal intensity on T2-weighted images decreases, enhancement on immediate postgadolinium SGE images decreases, and the pattern of enhancement appears as a delayed, progressive increase in signal intensity (fig. 10.38). Granulation tissue on T2-weighted images generally shows decrease in signal intensity after approximately 1 year. Interstitial-phase gadolinium-enhanced fat-suppressed SGE or 3D-GE images may show enhancement of fibrous tissue for approximately 1.5 year from onset. Mature chronic benign retroperitoneal fibrosis is low in signal intensity on T2-weighted images and demonstrates negligible contrast enhancement, facilitating differentiation from malignancy. Imaging findings that may favor benign fibrosis include a well-marginated mass with smooth borders and a decrease in size and/or progressive smoothing of the borders on follow-up examinations.

Benign Retroperitoneal Neoplasms

Benign retroperitoneal tumors are rare [72]. Therefore, any retroperitoneal tumor should initially be considered malignant. Retroperitoneal neurilemmoma may have characteristic high signal intensity on T2-weighted images [73]. Retroperitoneal plexiform neurofibromas are usually bilateral [74], slightly higher in signal intensity than muscles on T1-weighted images, and high in signal intensity on T2-weighted images [75–77] (fig. 10.39).

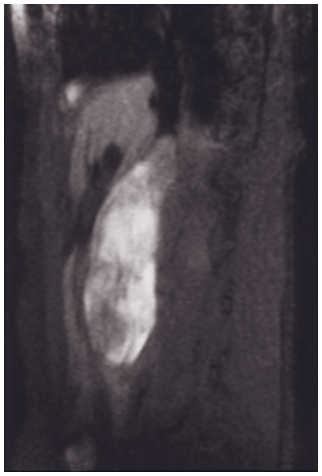

(*a*)

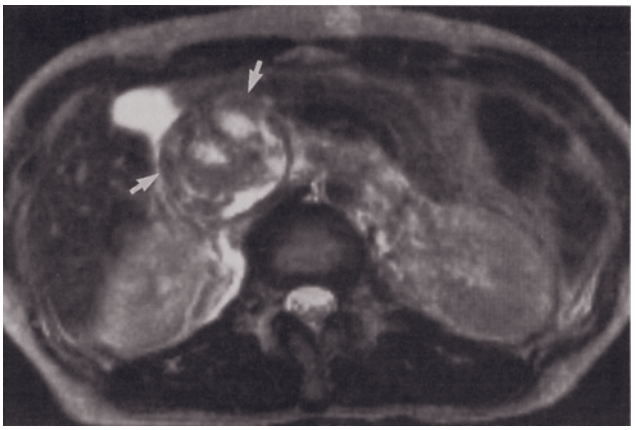

(*b*)

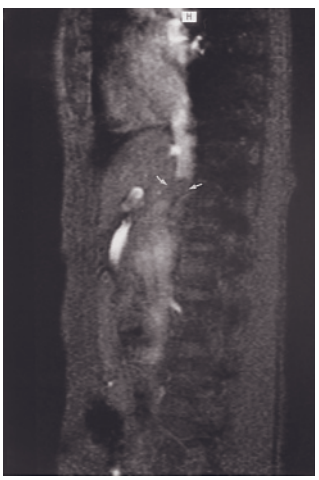

(*c*)

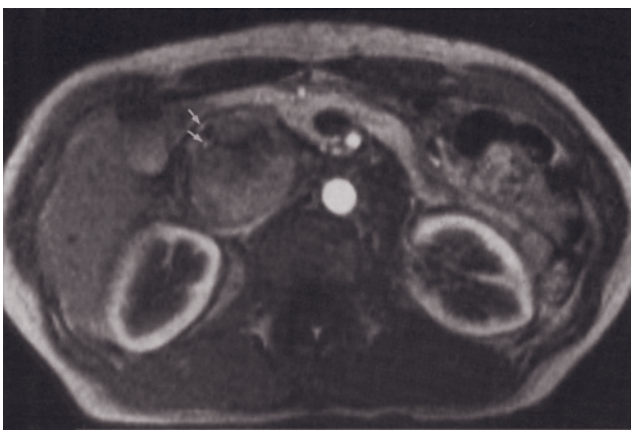

(*d*)

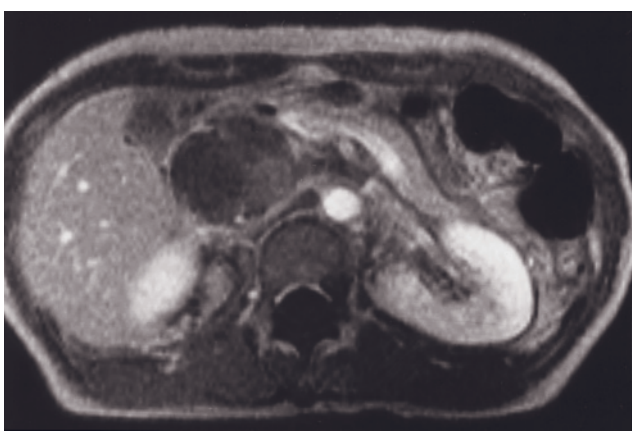

(*e*)

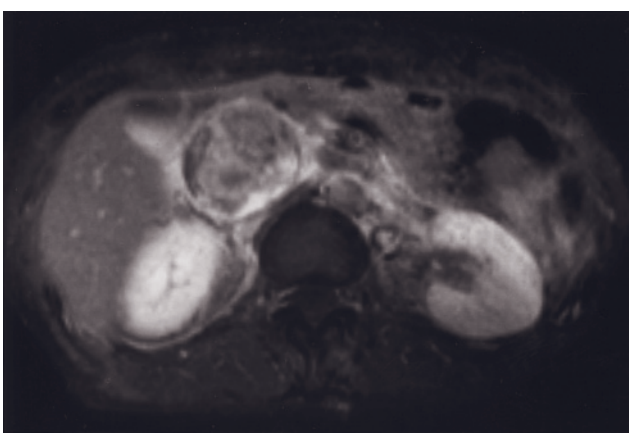

(*f*)

FIG. 10.36 Primary malignant fibrous histiocytoma of the IVC. Sagittal T1-weighted fat-suppressed spin-echo (*a*), T2-weighted spin-echo (*b*), sagittal gradient-refocused (time-of-flight) SGE (*c*), immediate (*d*) and 90-s (*e*) postgadolinium SGE, and transverse gadolinium-enhanced T1-weighted fat-suppressed spin-echo (*f*) images. The tumor (arrows, *b*) is heterogeneous in signal intensity on the T1 (*a*)- and T2 (*b*)-weighted images and contains areas of high signal intensity on the T1-weighted fat-suppressed spin-echo image (*a*), reflecting the presence of subacute methemoglobin in the thrombus. The neoplasm expands the IVC but is contained within the vessel lumen, which is consistent with its primary origin from the vessel wall. The superior extent of the neoplasm (small arrows) is clearly depicted at the level of the intrahepatic IVC, the patent portion of which is high in signal on the flow-sensitive gradient-refocused SGE image (*c*). Feeding arterioles (small arrows) within the tumor are demonstrated as tubular enhancing structures on the immediate postgadolinium SGE image (*d*).The neoplasm enhances minimally in a heterogeneous fashion on the immediate (*d*) and 90-s (*e*) postgadolinium SGE images, reflecting its hypovascular nature. Progressive enhancement is noted on the more delayed T1-weighted fat-suppressed spin-echo image (*f*), which is consistent with delayed enhancement of fibrotic tumor components. The superior extension of tumor thrombus in the IVC is important for surgical planning because the demonstration of supradiaphragmatic extension requires a combined abdominothoracic surgical approach. Sagittal images are superior to transverse sections for demonstrating the craniocaudal extent and defining the superior border of tumor thrombus in the IVC.

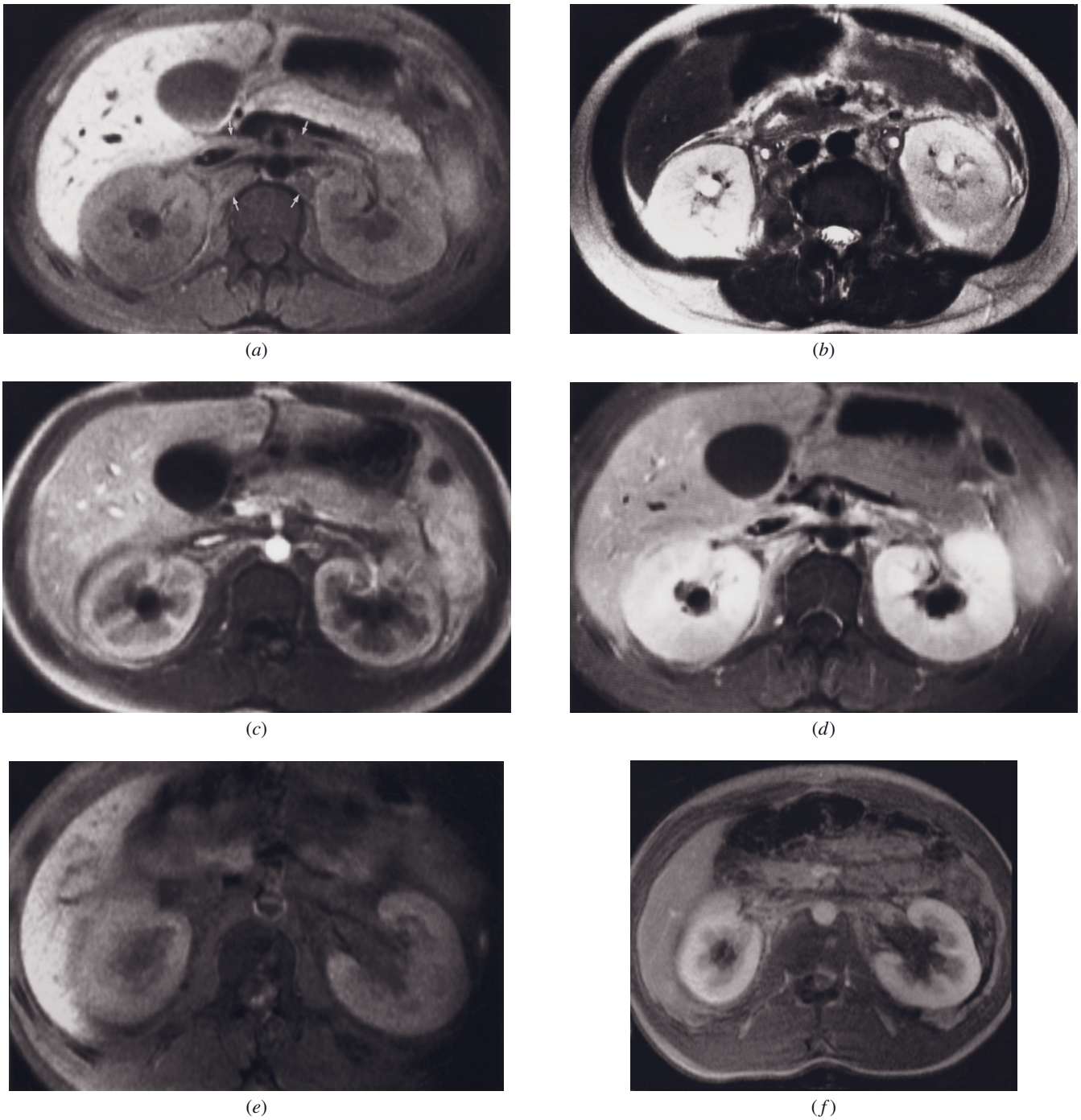

FIG. 10.37 Acute benign retroperitoneal fibrosis. T1-weighted fat-suppressed spin-echo (*a*), T2-weighted spin-echo (T2-SE) (*b*), immediate postgadolinium SGE (*c*), and delayed postgadolinium T1-weighted fat-suppressed spin-echo (*d*) images. The aorta, IVC, renal arteries, and ureters are encased by soft tissue (arrows, *a*), which is low in signal intensity on T1-weighted (*a*) and heterogeneously high in signal intensity on T2-weighted (*b*) images and has ill-defined margins. There is bilateral hydronephrosis and ureteral dilatation (*b*) caused by ureteral obstruction at a lower level. The fibrous tissue demonstrates heterogeneous enhancement on the immediate postgadolinium SGE image (*c*), which progresses on the more delayed T1-weighted fat-suppressed spin-echo image (*d*). Precontrast T1-weighted fat-suppressed spin-echo (*e*), immediate postgadolinium SGE (*f*), and gadolinium-enhanced T1-weighted fat-suppressed spin-echo (*g*) images in a second patient with biopsy-proven membranous glomerulonephritis and benign retroperitoneal fibrosis. Ill-defined extensive infiltrative soft tissue is present in the retroperitoneum. The fibrous tissue is low signal on the precontrast T1-weighted image (*e*), demonstrates moderate heterogeneous enhancement on the immediate postgadolinium image (*f*), and is more conspicuous on the gadolinium-enhanced T1-weighted fat-suppressed spin-echo image (*g*) because of the removal of the competing high signal intensity of the fat and progressive enhancement of the fibrous tissue. Corticomedullary differentiation is absent in both kidneys on the precontrast T1-weighted fat-suppressed spin-echo image (*e*) because of elevated serum creatinine level. Corticomedullary differentiation, however, is present on the immediate postgadolinium SGE image (*f*), reflecting some preservation of renal function. Increased medullary enhancement is shown in both kidneys on

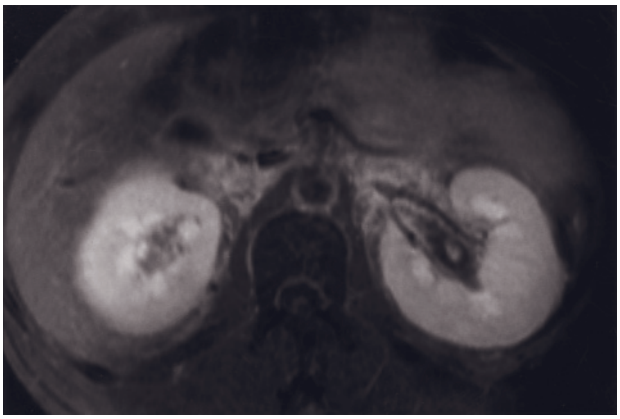

(*g*)

FIG. 10.37 (*Continued*) the gadolinium-enhanced T1-weighted fat-suppressed spin-echo image (*g*), reflecting tubulointerstitial damage.

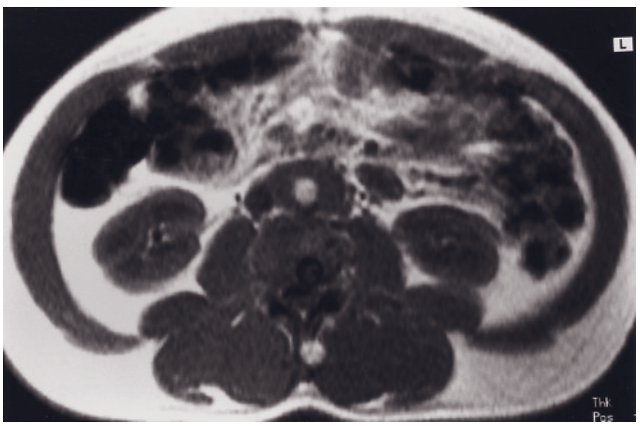

(*a*)

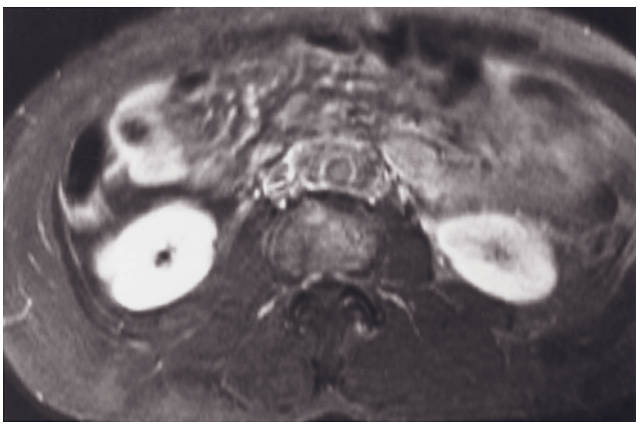

(*b*)

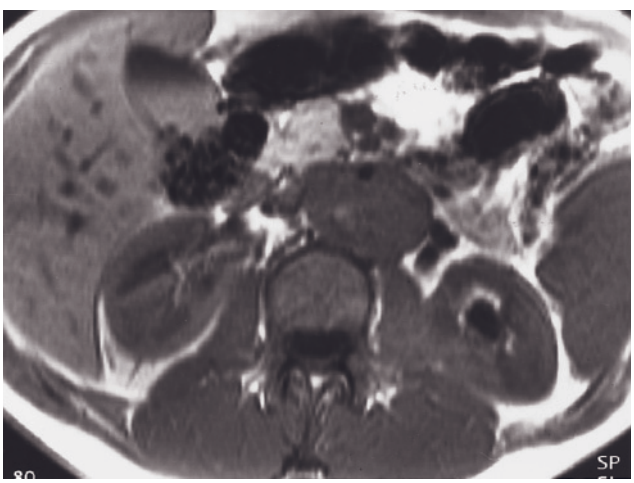

(*c*)

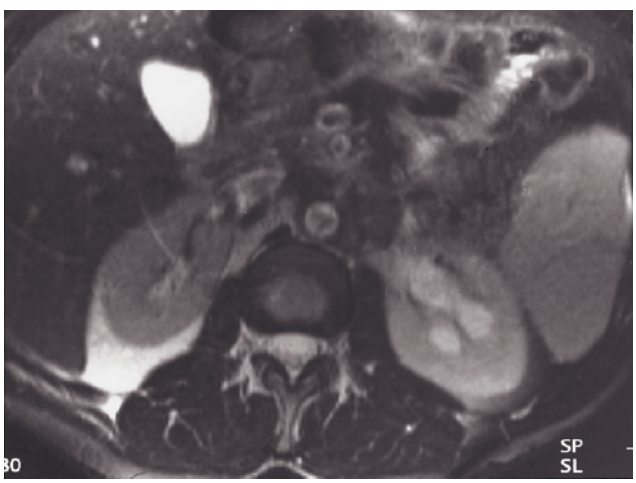

(*d*)

FIG. 10.38 Chronic benign retroperitoneal fibrosis. SGE (*a*) and interstitial-phase gadolinium-enhanced fat-suppressed spin-echo (*b*) images. Low-signal intensity oval-shaped tissue surrounds the aorta. The fibrous tissue has well-defined margins and shows minimal enhancement on the gadolinium-enhanced T1-weighted fat-suppressed spin-echo image (*b*), findings that are typical of mature fibrous tissue. SGE (*c*), T2-weighted echo-train spin-echo (*d*), arterial-phase (*e*) and capillary-phase (*f*) postgadolinium SGE, and 90-s postgadolinium fat-suppressed SGE (*g*) images in a second patient. The fibrotic tissue is oval-shaped with well-defined margins and encases the aorta. Note that, despite its size, the tissue does not substantially displace the aorta anteriorly. The fibrotic tissue is low in signal intensity on the T1-weighted image (*c*) and heterogeneously low with focal areas of high signal intensity on the T2-weighted image (*d*), demonstrates minimal enhancement on the arterial-phase (*e*) and capillary-phase (*f*) postgadolinium SGE images, and enhances moderately on the more delayed fat-suppressed SGE (*g*) image. Delayed enhancement is characteristic

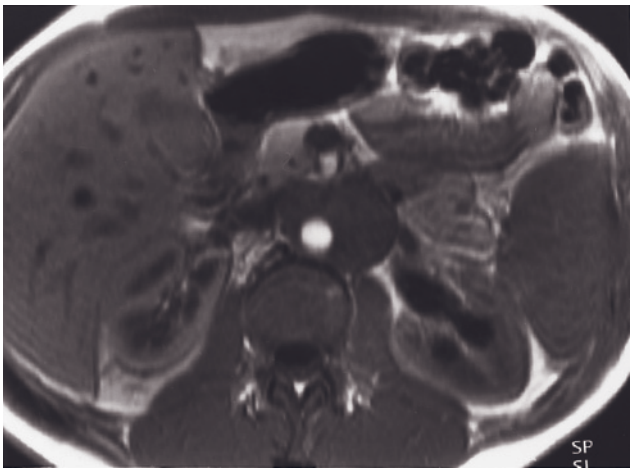

(*e*)

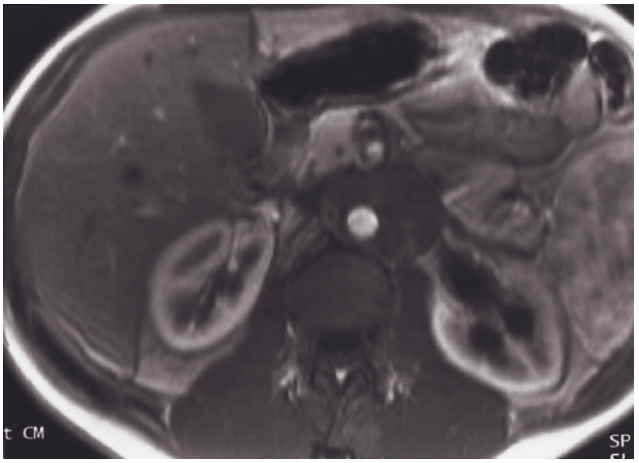

(*f*)

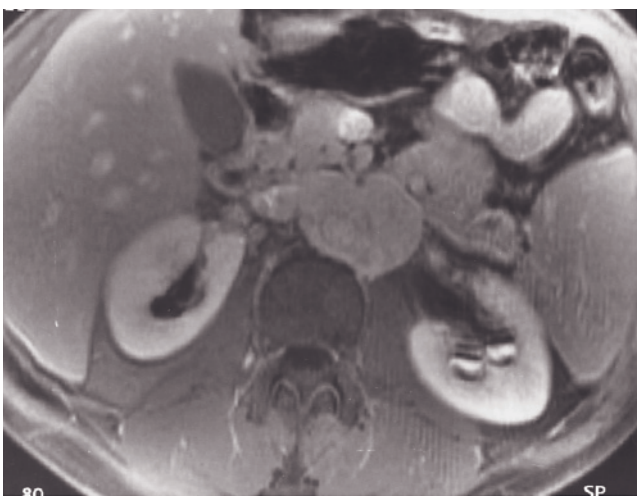

(*g*)

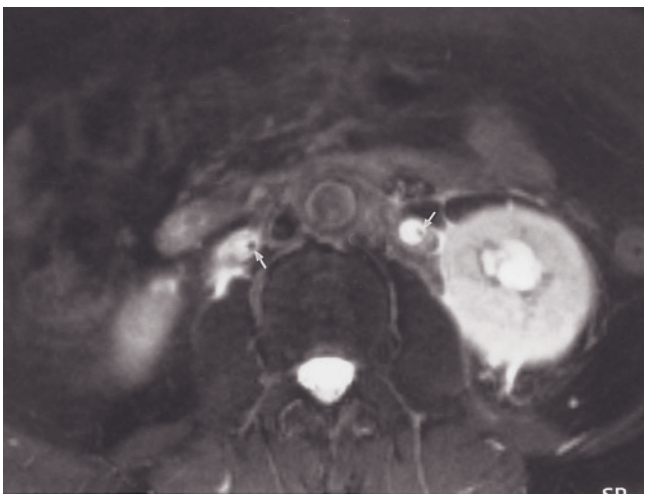

(*h*)

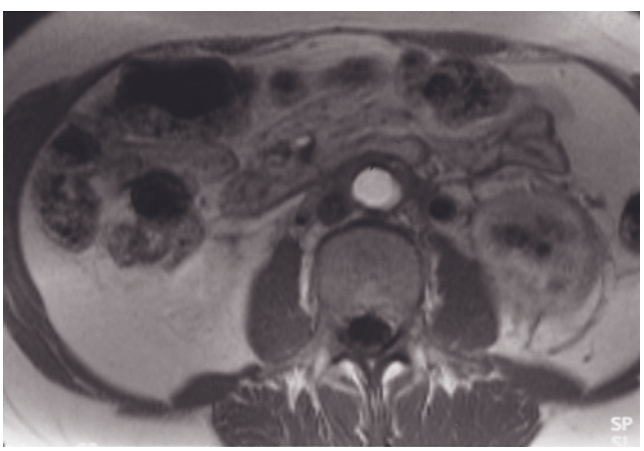

(*i*)

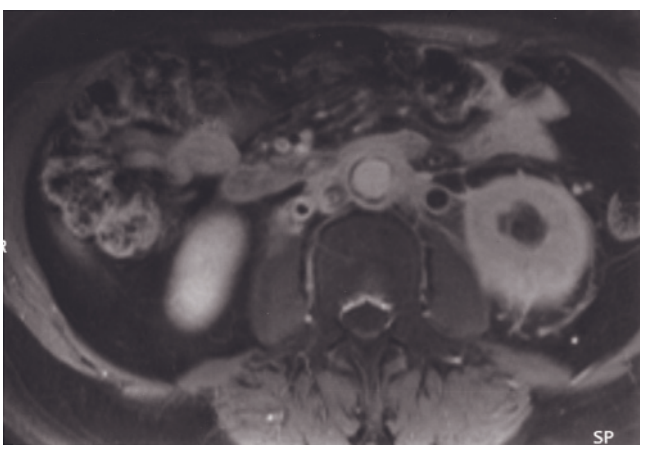

(*j*)

FIG. 10.38 (*Continued*) of relatively mature fibrous tissue. Greater enhancement of the fibrotic tissue in the second patient reflects a more active stage in the transition between acute and chronic fibrosis than in the first patient. The pyelocalyceal system of the left kidney is dilated because of concomitant ureteral obstruction. T2-weighted echo-train spin-echo (*h*), immediate post-gadolinium SGE (*i*), and interstitial-phase gadolinium-enhanced fat-suppressed SGE (*j*) images in a third patient. Again noted is relatively well-marginated oval tissue encasing the aorta, IVC, and both ureters. The fibrous tissue is heterogeneously low in signal intensity on the T2-weighted image (*h*) and demonstrates minimal enhancement on the immediate postgadolinium SGE image (*i*), progressing to moderate enhancement on the interstitial-phase gadolinium-enhanced fat-suppressed SGE image (*j*), indicating mature fibrous tissue. Bilateral ureteral obstruction with hydronephrosis is present and signal-void ureteral stents (arrows) are demonstrated in both ureters on the T2-weighted image (*h*).The majority of the fibrous tissue is located anterior to the aorta and IVC, and these vessels are not displaced substantially anteriorly.

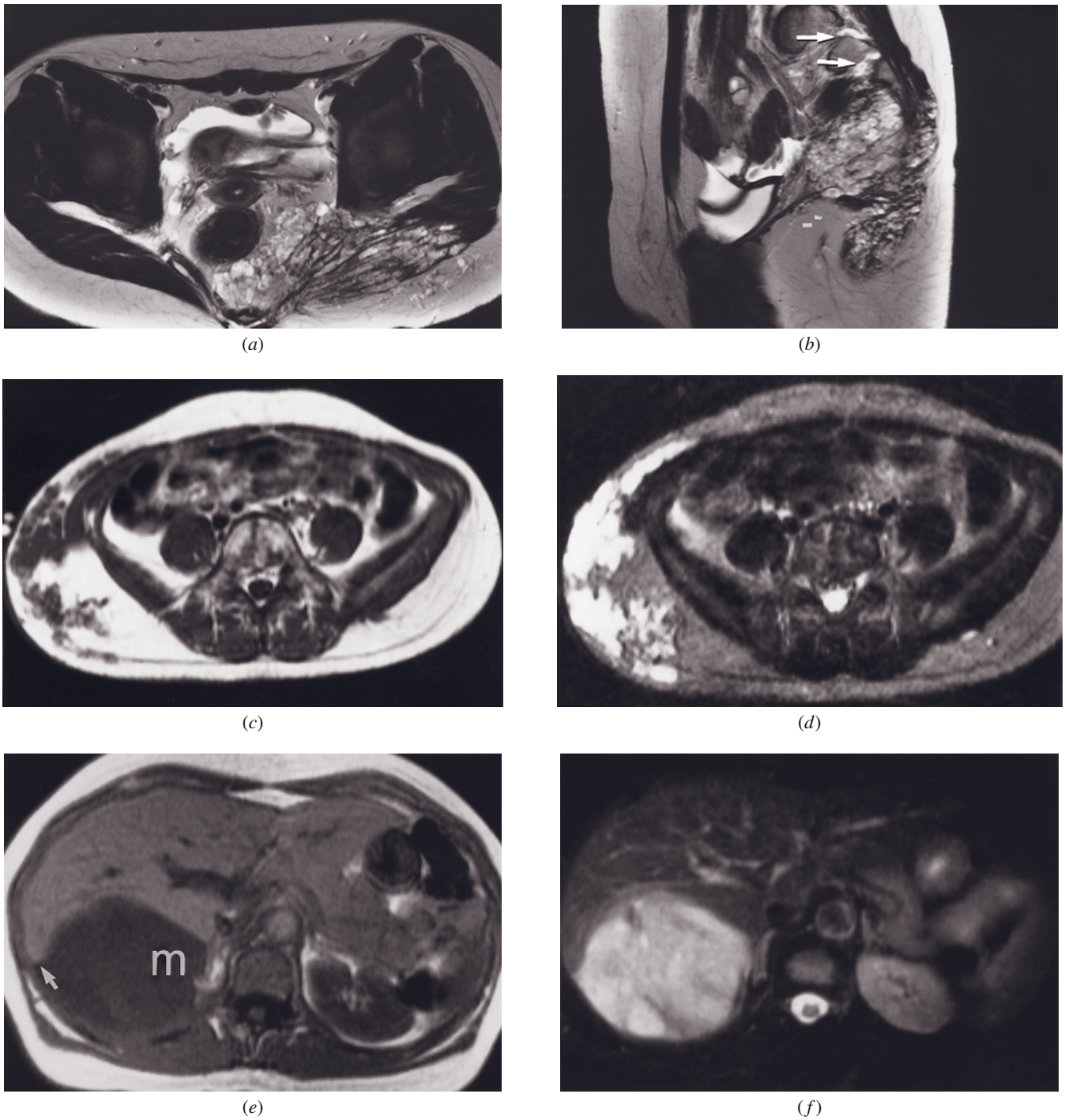

FIG. 10.39 Benign retroperitoneal tumors. Transverse (*a*) and sagittal (*b*) 512-resolution T2-weighted echo-train spin-echo images in a patient with plexiform neurofibroma of the pelvis and neurofibromatosis type 1. The plexiform neurofibroma appears as a large heterogeneous mass that occupies the majority of the left posterior pelvis and infiltrates the left gluteus maximus and pyriformis muscles. Extension into the sacral neural foramina is present (arrows, *b*). T1-weighted spin-echo (*c*) and T2-weighted spin-echo (*d*) images in a second patient demonstrate an extensive plexiform neurofibroma in the right subcutaneous tissues that is low in signal intensity on the T1-weighted image (*c*) and high in signal intensity on the T2-weighted image (*d*). The tumors are high in signal intensity on the T2-weighted images in both patients, which is characteristic for tumors of neural origin. SGE (*e*), T2-weighted fat-suppressed echo-train spin-echo (*f*), and immediate postgadolinium SGE (*g*) images in a patient with inflammatory pseudotumor arising from the renal capsule. A large mass (mass = m, *e*) is noted posterior to the liver. The mass is well-marginated, heterogeneous, and low in signal intensity on the T1-weighted image (*e*) and moderately high in signal on the T2-weighted image (*f*) and demonstrates intense diffuse heterogeneous enhancement on the immediate postgadolinium SGE image. The posterior liver margin at the interface with the mass forms an obtuse angle consistent with an extrahepatic origin of the mass. The right kidney (not shown) was displaced but not invaded by the mass. Inflammatory pseudotumor may have an aggressive appearance that mimics

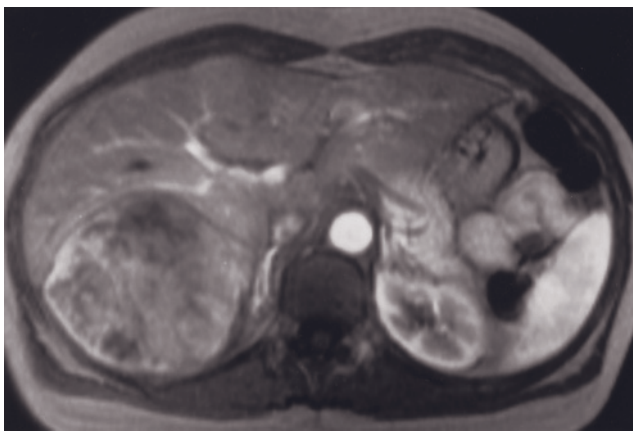

(*g*)

(*h*)

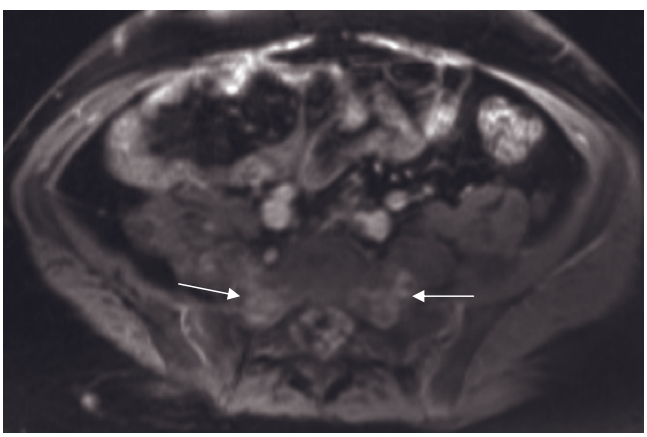

(*i*)

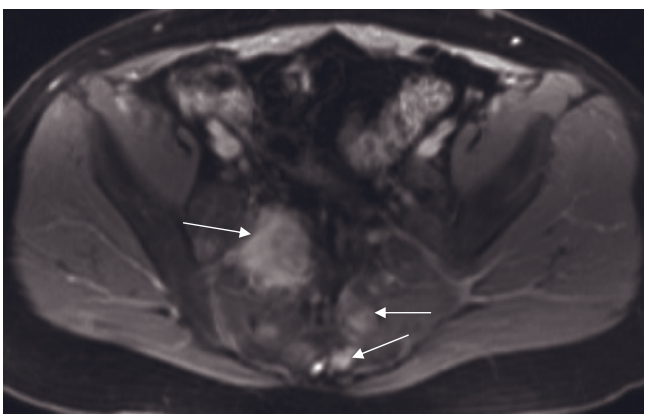

(*j*)

(*k*)

FIG. 10.39 (*Continued*) the appearance of a malignant tumor. Coronal T2-weighted single-shot echo-train spin-echo (*h*) and T1-weighted postgadolinium fat-suppressed interstitial-phase SGE (*i, j*) images demonstrate multiple neurofibromas (arrows, *h–j*) in another patient with neurofibromatosis. Neurofibromas (arrows, *h–j*) demonstrate markedly high signal on T2-weighted image and prominent enhancement on postgadolinium images (*i, j*) Transverse T1-weighted SGE (*k*), sagittal T2-weighted high-resolution fast spin-echo (*l*), transverse T1-weighted postgadolinium hepatic arterial dominant-phase SGE (*m*), and transverse T1-weighted postgadolinium fat-suppressed 3D-GE (*n*) images demonstrate a large pedunculated paraspinal neurogenic tumor extending into the dilated neural foramen (arrows, *k–n*) in another

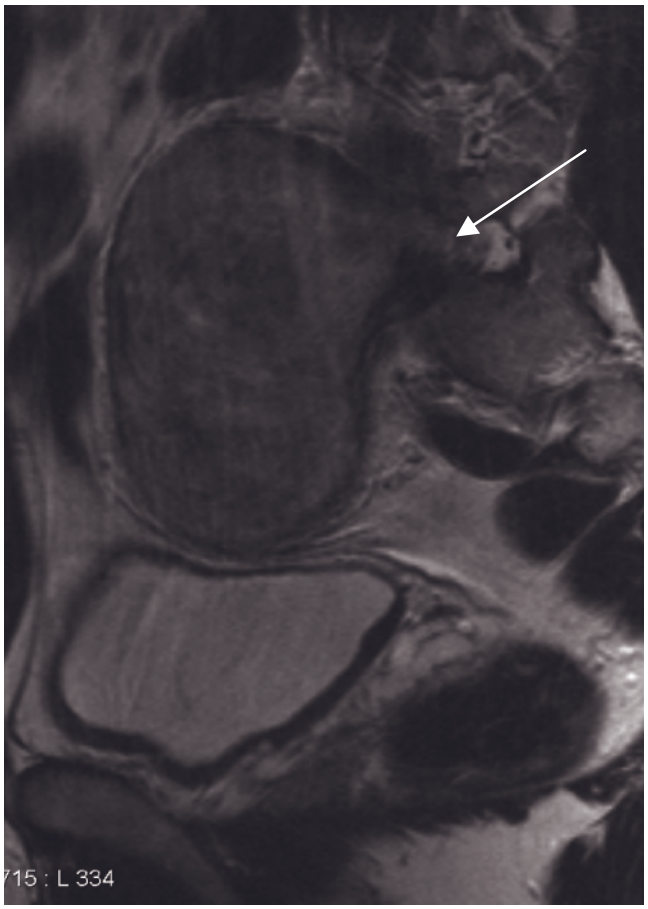

(*l*)

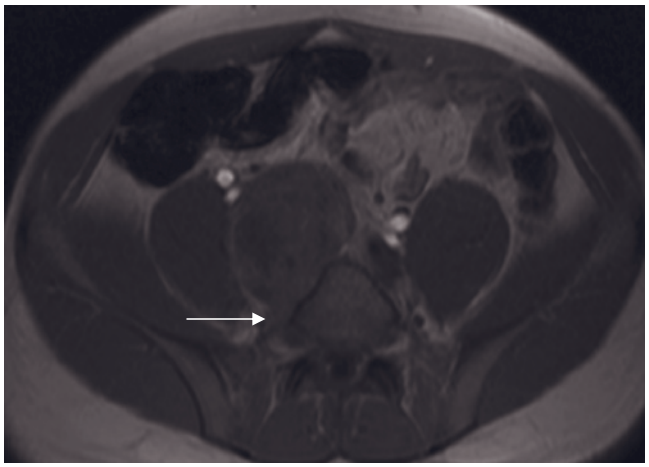

(*m*)

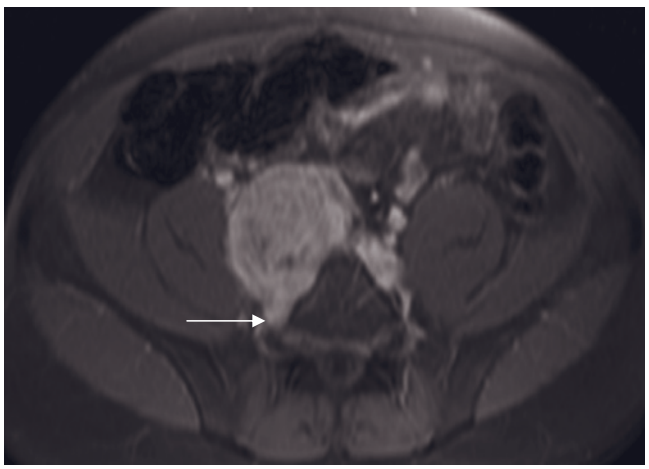

(*n*)

FIG. 10.39 (*Continued*) patient. Right psoas muscle is displaced laterally because of mass effect. The tumor shows heterogeneous mildly high signal on T2-weighted image (*l*) and prominent enhancement on postgadolinium interstitial-phase image (*n*).

Other rare neoplasms include paragangliomas, hemangiomas/lymphangiomas, and lipomas [72]. Paragangliomas of Zuckerkandl's organ may be hormone secreting. Imaging follow-up after surgery is advisable because 30% of these tumors are malignant and show late manifestation of remote disease [78]. Inflammatory pseudotumor is a rare benign mass lesion that is minimally low in signal intensity on T1-weighted images and heterogeneous and moderately high in signal intensity on T2-weighted images and demonstrates moderately intense diffuse heterogeneous enhancement on immediate postgadolinium SGE or 3D-GE images. This appearance may mimic that of malignant tumors.

Benign Lymphadenopathy

Benign lymphadenopathy may occur secondary to inflammatory or infectious disease. Sequences suited for detection of lymph nodes include precontrast T1-weighted SE or SGE, fat-suppressed T2-weighted spin-echo or echo-train spin-echo, and gadolinium-enhanced fat-suppressed SGE techniques (fig. 10.40). In each of these techniques, the signal difference between lymph nodes and background tissue is substantial. The enlarged lymph nodes appear low in signal on precontrast SGE in a background of high-signal fat, and nodes are moderately high in signal on fat-suppressed T2-weighted and gadolinium-enhanced T1-weighted images, set in a background of low-signal suppressed fat. Fat-suppressed T2-weighted images are very sensitive for the detection of lymph nodes and exceed CT imaging, particularly in pediatric patients or patients with minimal retroperitoneal fat (fig. 10.41). *Mycobacterium avium-intracellulare* infection is not uncommon in immunocompromised patients and may exhibit enlarged lymph nodes and evidence of liver involvement (see fig. 10.41). Massive retroperitoneal adenopathy mimicking lymphoma may

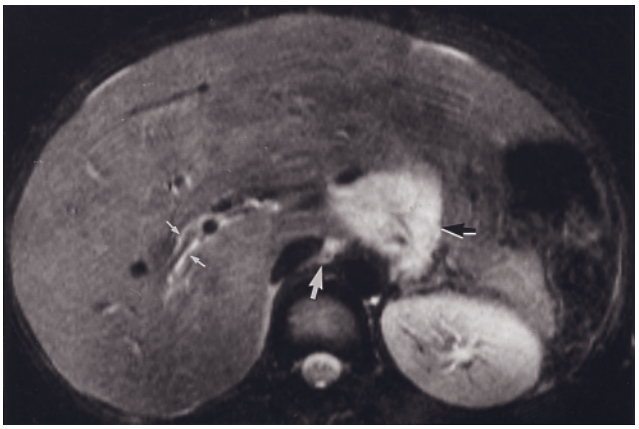

(*a*)

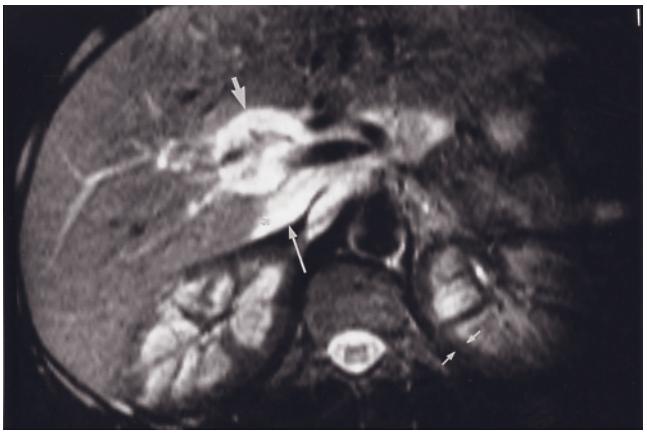

(*b*)

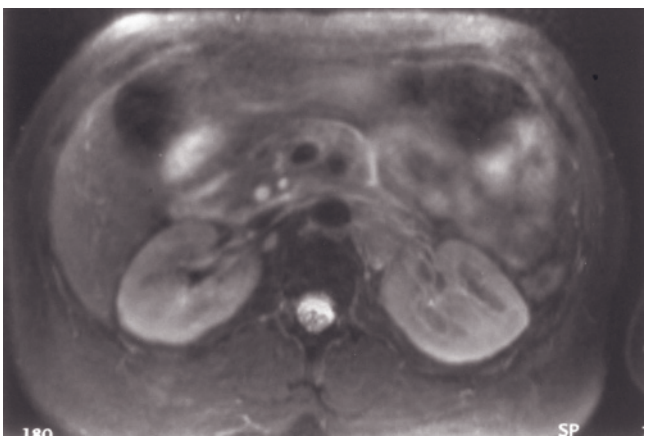

(*c*)

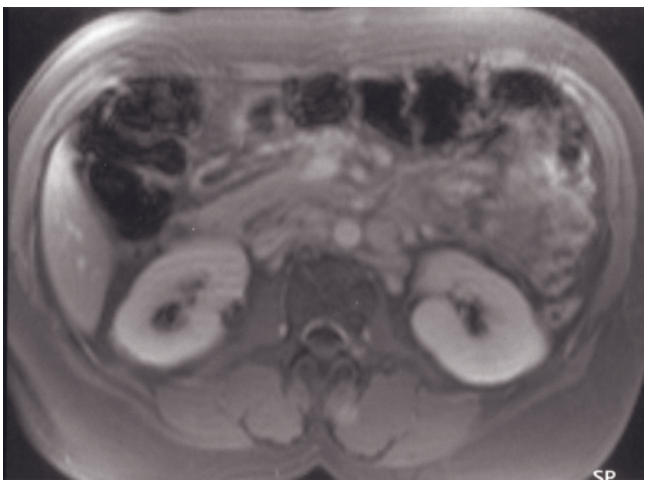

(*d*)

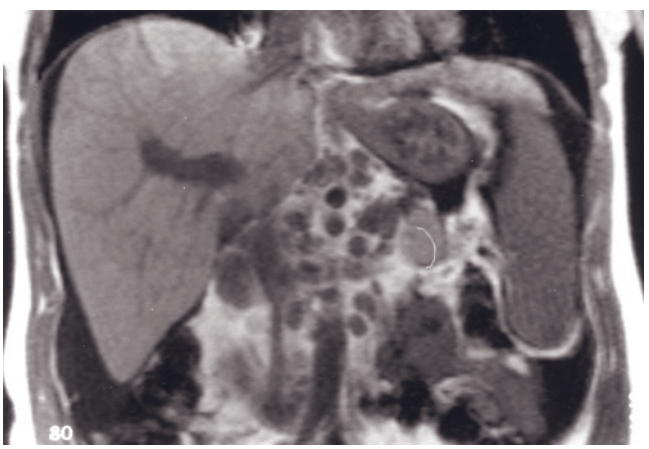

(*e*)

FIG. 10.40 Benign retroperitoneal adenopathy. T2-weighted fat-suppressed spin-echo image (*a*) in a patient with sclerosing cholangitis demonstrates para-aortic (black arrow) and aortocaval (white arrow) lymphadenopathy. Enlarged lymph nodes are readily distinguished in a dark background. Periportal high signal intensity is also noted (small arrows). T2-weighted fat-suppressed image in a second patient (*b*) shows inflammatory portal (arrow) and portocaval (thin arrow) nodes as high-signal-intensity structures. Note also that the cortex of the kidneys (small arrows, *b*) in this patient with sickle cell anemia is low in signal intensity secondary to iron deposition. Transverse T2-weighted fat-suppressed SS-ETSE (*c*) and interstitial-phase gadolinium-enhanced fat-suppressed SGE (*d*) images in a third patient demonstrate extensive retroperitoneal lymphadenopathy. These two sequences allow good distinction between low-signal background tissue and moderate-signal lymph nodes. Coronal SGE (*e*) image in a fourth patient shows multiple enlarged retroperitoneal lymph nodes that are low signal intensity compared to the background fat. The coronal plane is effective at showing rounded retroperitoneal nodes, which are distinguishable from tubule-shaped vessels.

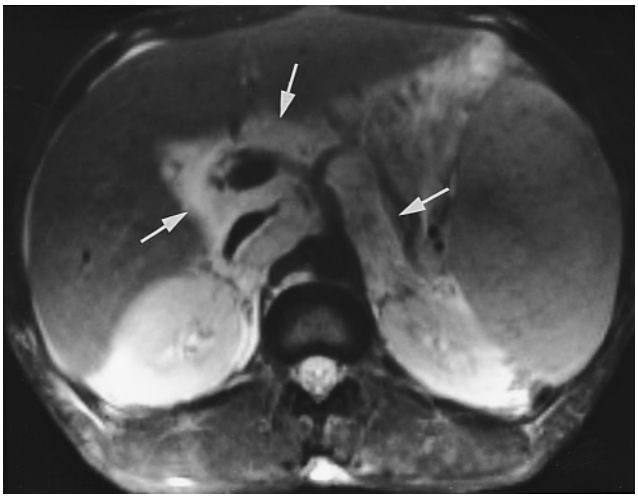

FIG. 10.41 Retroperitoneal lymphadenopathy from *Mycobacterium avium intracellulare* in a 13-year-old female patient. T2-weighted fat-suppressed echo-train spin-echo image shows extensive para-aortic, aortocaval, paracaval, portocaval, and celiac lymphadenopathy (arrows). Retroperitoneal lymph nodes are conspicuous on T2-weighted fat-suppressed images as high-signal-intensity masses, and this permits detection of small lymph nodes, which appear moderate signal in thin or pediatric patients, who have little retroperitoneal fat.

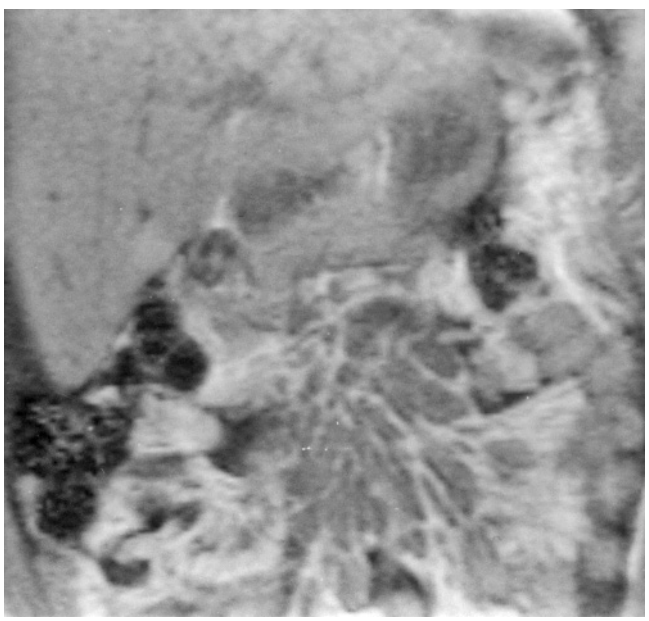

FIG. 10.42 Sarcoidosis. Coronal SGE image demonstrates diffuse mesenteric lymphadenopathy in a patient with sarcoidosis.

be an uncommon manifestation of sarcoidosis (fig. 10.42). Lymph nodes enhance with gadolinium and may have a speckled appearance on T2-weighted images [79, 80]. Substantial benign adenopathy resembling malignant disease may also be found in Castleman disease (fig. 10.43), also known as giant lymph node hyperplasia. The lymph nodes have a heterogeneous appearance on the MR images and may show increased vascularity of the adjacent fat [81]. Retroperitoneal adenopathy is commonly observed in Kawasaki disease, and involved lymph nodes are hemorrhagic, demonstrating characteristic high signal intensity on T1-weighted images (fig. 10.44).

Miscellaneous

Masses of extramedullary hematopoiesis are more commonly found in patients with hereditary hemolytic anemias, particularly thalassemia major, but may be encountered in chronic leukemias, polycythemia vera, and diseases with extensive bone marrow infiltration [82]. Common retroperitoneal locations are the retrocrural and presacral spaces. Occasionally, they have an aggressive appearance and may result in bone destruction [82]. The masses are intermediate in signal intensity on T1-weighted images and intermediate to moderately high in signal intensity on T2-weighted images and enhance moderately after gadolinium administration (fig. 10.45).

Retroperitoneal hematomas may occur in patients with coagulation disorders or hemophilia and after renal biopsy (fig. 10.46).

Malignant Masses

Malignant Retroperitoneal Fibrosis

Malignant retroperitoneal fibrosis is most commonly associated with cervical, bowel, breast, prostate, lung, and kidney cancers [59, 83]. The tumor consists of malignant cell infiltration of the retroperitoneum with associated desmoplastic reaction and encases the aorta, IVC, and ureters. The contour of the mass is not lobular, distinguishing malignant retroperitoneal fibrosis from adenopathy, and may be infiltrative and irregular (fig. 10.47), a finding that favors malignant rather than benign retroperitoneal fibrosis. Ureteral obstruction with bilateral hydronephrosis is common. Malignant retroperitoneal fibrosis is usually moderately high in signal intensity on T2-weighted images, exhibiting moderately intense enhancement with gadolinium [59, 67, 68]. Malignant retroperitoneal fibrosis will usually demonstrate enhancement on immediate postgadolinium images. MRI can distinguish chronic benign from malignant retroperitoneal fibrosis, but distinction from acute benign retroperitoneal fibrosis is not always possible. Findings favoring malignancy include a more irregular contour and increase in size and irregularity on follow-up examinations. Acute benign retroperitoneal fibrosis has a wispier infiltrative pattern compared to malignant disease, which is more solid and irregular. Clinical

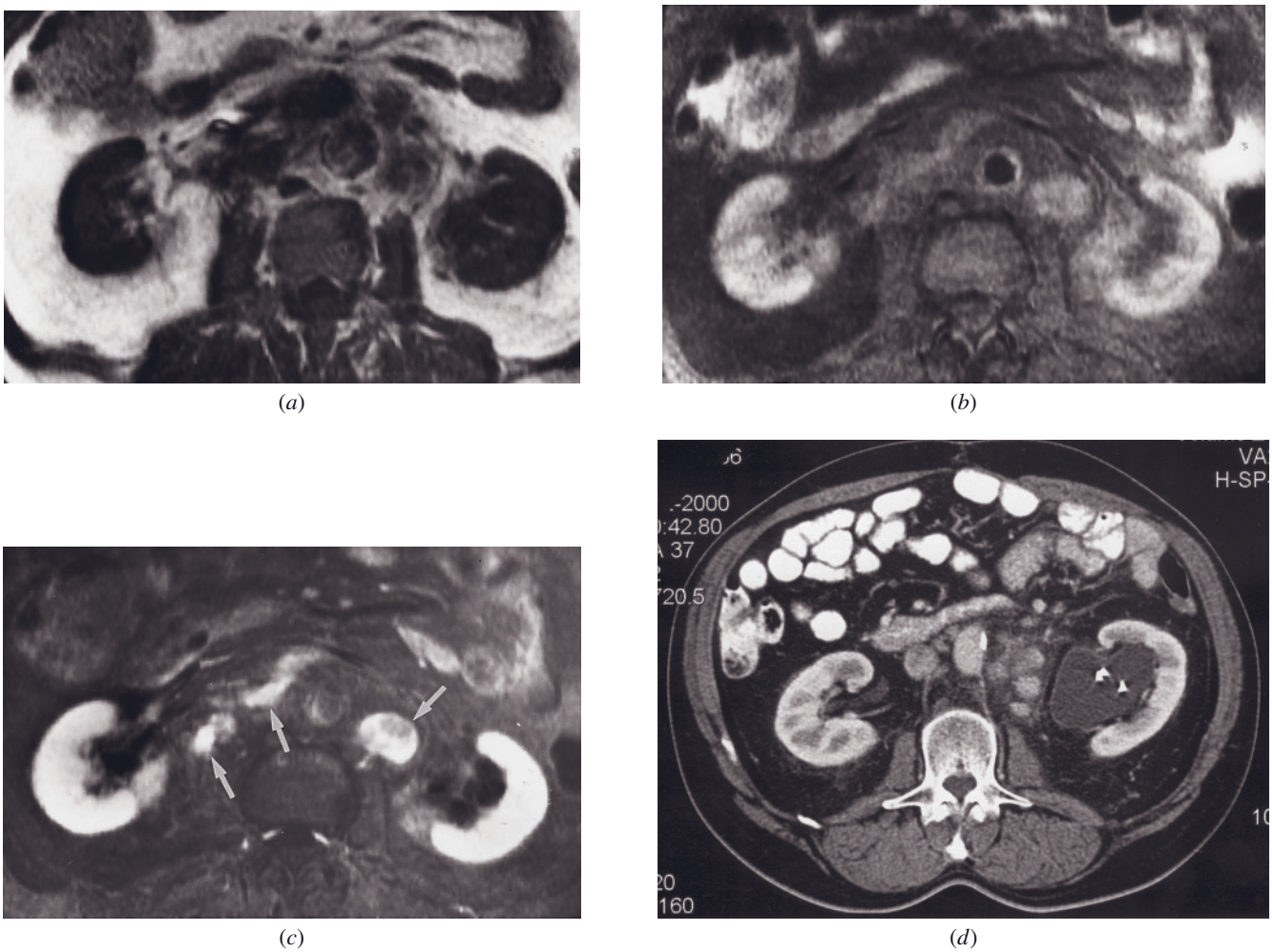

FIG. 10.43 Castleman disease. SGE (*a*), T1-weighted fat-suppressed spin-echo (*b*), and gadolinium-enhanced T1-weighted fat-suppressed spin-echo (*c*) images. Enlarged retroperitoneal lymph nodes are present. The lymph nodes are low in signal intensity on the SGE image (*a*) and intermediate to moderate in signal intensity on the T1-weighted fat-suppressed spin-echo image (*b*), with several of them demonstrating substantial enhancement (arrows, *c*) on the gadolinium-enhanced image (*c*). Ill-defined stranding is also present in the retroperitoneum (*a*). (Reproduced with permission from Semelka RC, Shoenut JP, Kroeker MA: The retroperitoneum and the abdominal wall. In Semelka RC, Shoenut JP (eds.), *MRI of the Abdomen with CT Correlation*. New York: Raven Press, p. 13–41, 1993.) Iodine-contrast enhanced spiral CT image (*d*) in a second patient demonstrates enlarged lymph nodes and ill-defined retroperitoneal tissue. Associated hydronephrosis is present because of entrapment of the ureters by strandy tissue. (Courtesy of Andrea Baur, M.D., Klinikum Grosshadern, University of Munich.)

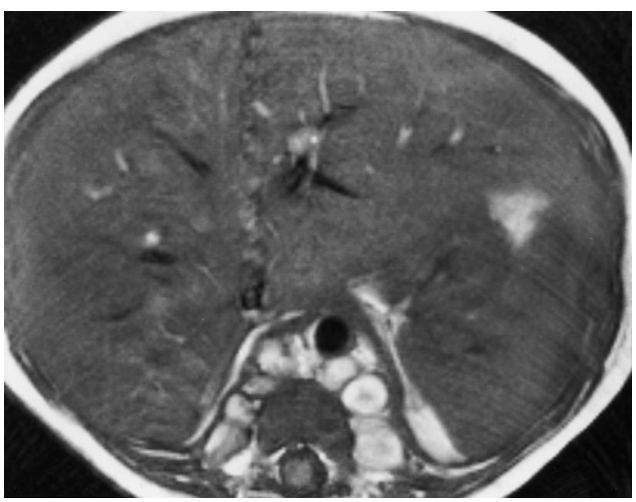

FIG. 10.44 Hemorrhagic lymph nodes in Kawasaki disease. T1-SE image shows multiple retrocrural lymph nodes that are high in signal intensity because of the presence of subacute blood. (Reproduced with permission from Semelka RC, Shoenut JP, Kroeker MA: The retroperitoneum and the abdominal wall. In Semelka RC, Shoenut JP (eds.), *MRI of the Abdomen with CT Correlation.* New York: Raven Press, p. 13–41, 1993.)

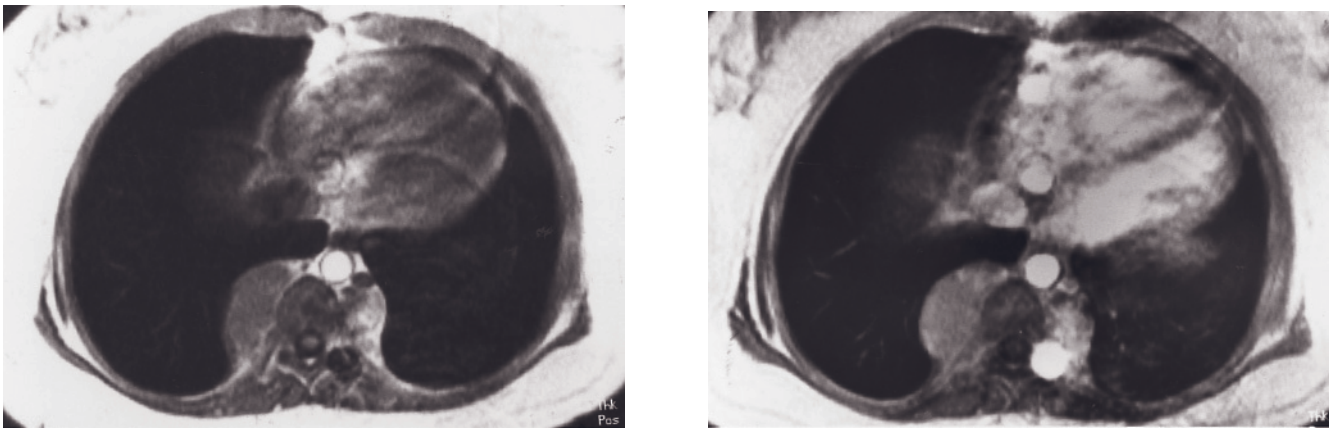

(*a*) (*b*)

FIG. 10.45 Extramedullary hematopoiesis in thalassemia major. SGE (*a*) and immediate postgadolinium SGE (*b*) images. Soft tissue paravertebral masses in the lower thorax and abdomen are demonstrated. The hematopoietic masses are low in signal intensity on the SGE image (*a*) and demonstrate moderate enhancement on the immediate postgadolinium SGE image (*b*). (Reproduced with permission from Semelka RC, Shoenut JP, Kroeker MA: The retroperitoneum and the abdominal wall. In Semelka RC, Shoenut JP (eds.), *MRI of the Abdomen with CT Correlation*. New York: Raven Press, p. 13–41, 1993.)

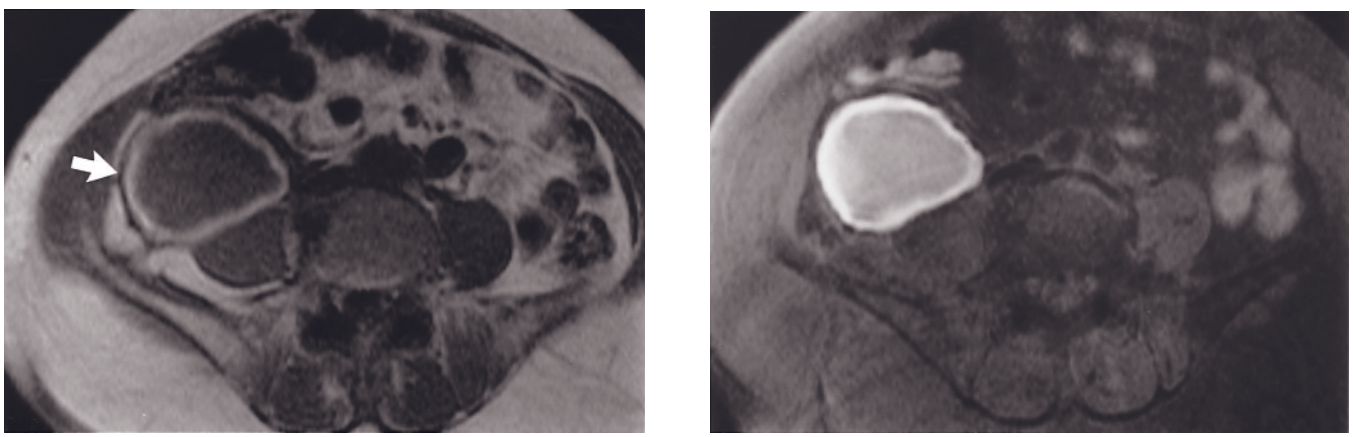

(*a*) (*b*)

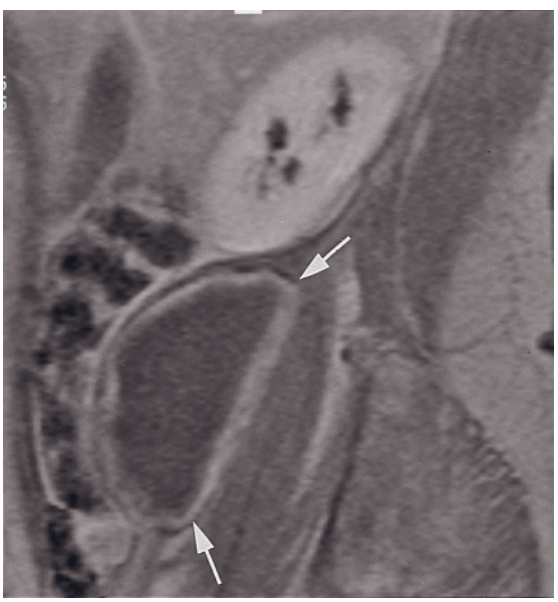

(*c*)

FIG. 10.46 Retroperitoneal hematoma. SGE (*a*), fat-suppressed T1-weighted spin-echo (*b*), and interstitial-phase gadolinium-enhanced SGE (*c*) images. A 7.5-cm well-defined hematoma (arrow, *a*) is noted along the anterior margin of the right psoas muscle. The periphery of the hematoma is hyperintense on the precontrast SGE image (*a*). The hyperintensity is markedly accentuated on the T1-weighted fat-suppressed spin-echo image (*b*), confirming that fat is not the cause of hyperintensity. A thin rim that is low in signal intensity on both T1- and T2-weighted (not shown) images reflects the presence of hemosiderin and suggests chronicity of the hematoma. After gadolinium administration, no enhancing tissue components are identified in the hematoma (arrows, *c*), which excludes tumor as the cause.

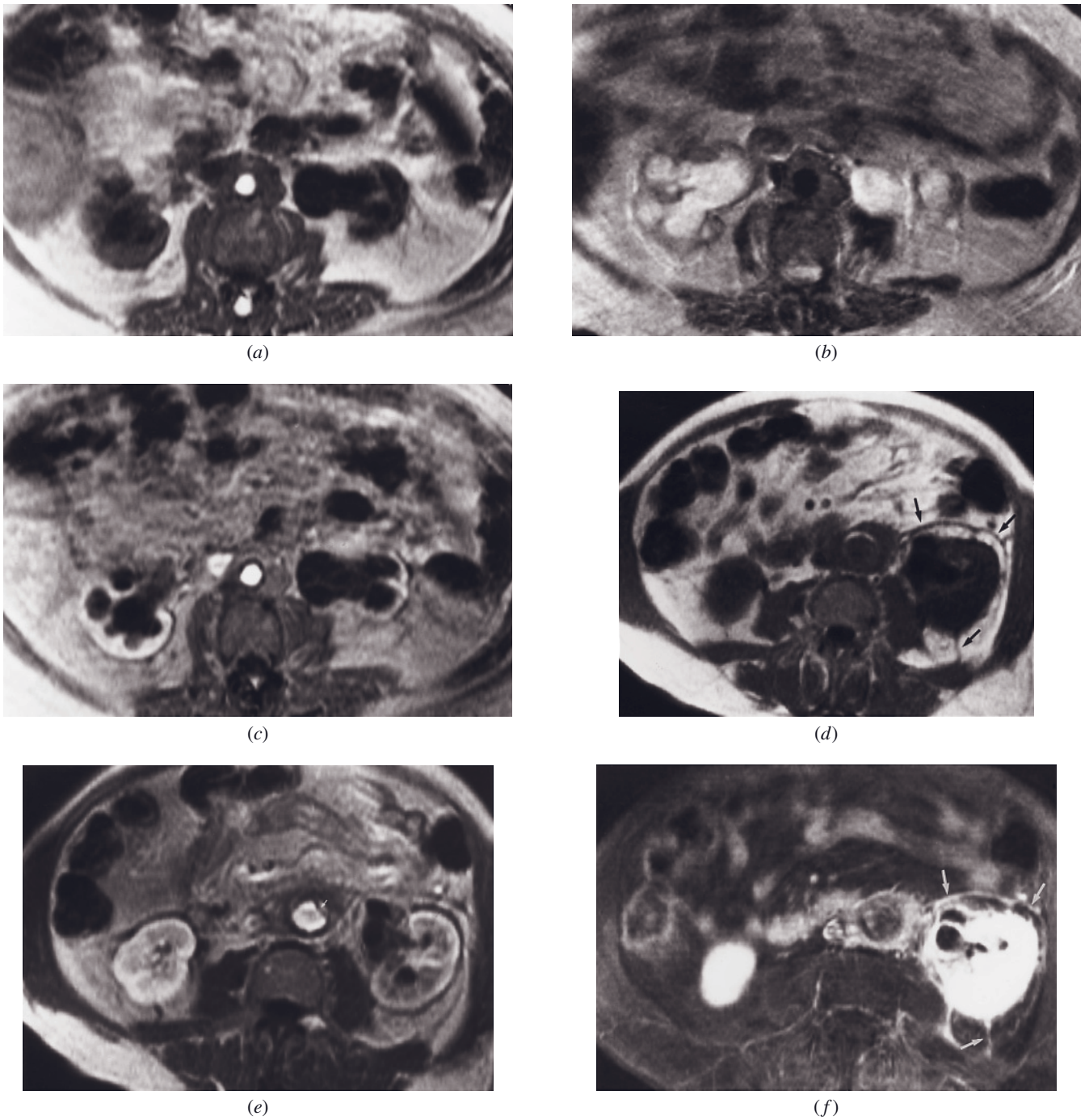

FIG. 10.47 Malignant retroperitoneal fibrosis from cervical cancer. SGE (*a*), T2-weighted echo-train spin-echo (*b*), and immediate postgadolinium SGE (*c*) images. The aorta is encased by abnormal soft tissue, which has slightly ill-defined margins. The soft tissue is low in signal intensity on the SGE image (*a*) and heterogeneous and moderate in signal intensity on the T2-weighted echo-train spin-echo image (*b*) and demonstrates diffuse heterogeneous enhancement after gadolinium administration (*c*). This appearance is compatible with active malignant rather than chronic benign retroperitoneal fibrosis. Note bilateral hydronephrosis resulting from ureteral obstruction at a lower level. SGE (*d*), immediate postgadolinium SGE (*e*), and postgadolinium T1-weighted fat-suppressed spin-echo (*f*) images in a second patient with malignant retroperitoneal fibrosis. An oval-shaped mass encases the aorta. The mass is low in signal intensity on the SGE image (*d*) and demonstrates moderate heterogeneous enhancement on the immediate postgadolinium image (*e*) that progresses on the postgadolinium T1-weighted fat-suppressed spin-echo image (*f*). The mass has aggressive infiltrating margins (arrows, *f*).The left perirenal fascia and perirenal septae are thickened (arrows, *d*) and demonstrate enhancement (arrows) on the gadolinium-enhanced T1-weighted fat-suppressed spin-echo image (*f*). Also noted is a dissection involving the abdominal aorta with good demonstration of the intimal flap (small arrow, *e*). T2-weighted single-shot

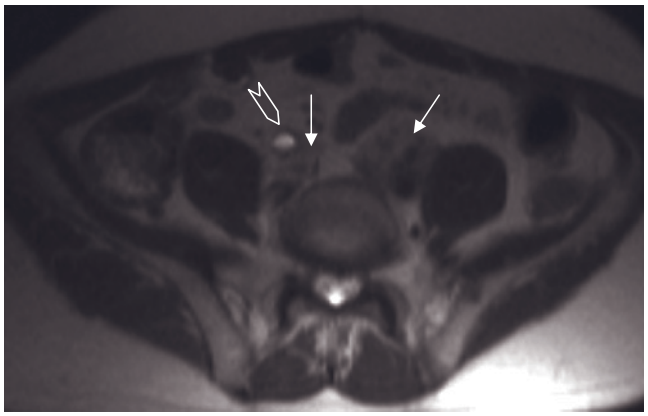

(*g*)

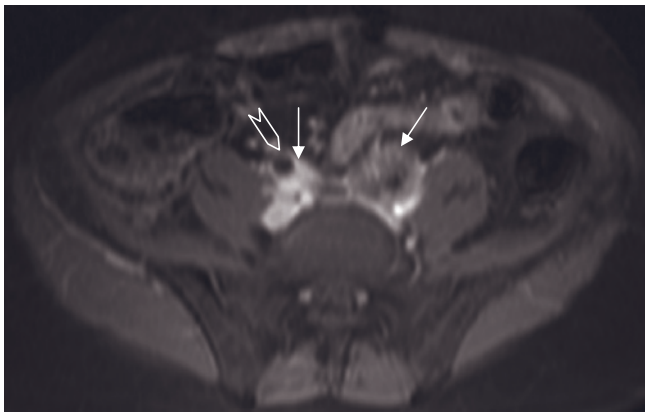

(*h*)

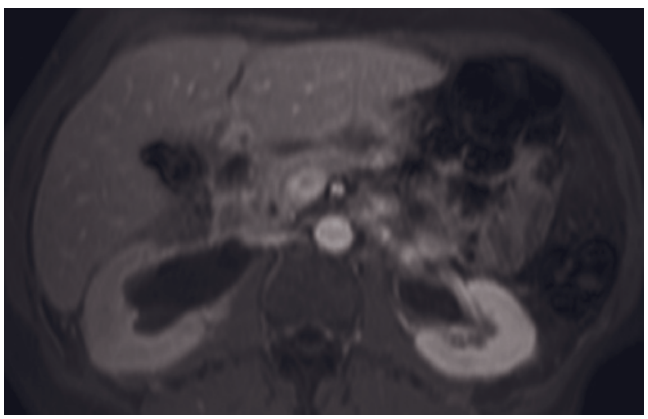

(*i*)

FIG. 10.47 (*Continued*) echo-train spin-echo (*g*) and T1-weighted postgadolinium interstitial-phase fat-suppressed 3D-GE (*h, i*) images show infiltrative retroperitoneal tissue extending from the level of renal hilum to the pelvic inlet in another patient with malignant retroperitoneal fibrosis. The infiltrative tissue (arrows, *g*, *h*) show intermediate signal on T2-weighted image and prominent enhancement on postgadolinium image (*h*). The right ureter (open arrows, *g, h*) is dilated because of fibrosis. Infiltrative malignant tissue is also detected at the level of the kidneys (*i*), and the collecting systems of both kidneys are also dilated because of fibrosis.

history is also helpful, as acute benign retroperitoneal fibrosis is often observed in younger patients (20–40 years) with no pre-existent malignant disease and malignant retroperitoneal fibrosis is more commonly observed in older patients (>40 years). Indeterminate cases that have somewhat well-defined borders, high signal intensity on T2-weighted images, and increased enhancement on immediate postgadolinium SGE or 3D-GE images are findings that should be evaluated with caution. Biopsies from multiple sites should be obtained because benign retroperitoneal fibrosis may coexist with malignant neoplasms that are known to induce malignant retroperitoneal fibrosis [64].

Lymphoma

Lymphoma is the most common retroperitoneal malignancy, and both Hodgkin and non-Hodgkin lymphomas may involve the retroperitoneum [84–88]. Non-Hodgkin lymphoma more commonly involves a variety of nodal groups (in particular, mesenteric nodes are involved in >50% of the cases) and extranodal sites [85]. Intra-abdominal Hodgkin lymphoma tends to be limited to the spleen and retroperitoneum, with spread of disease to contiguous nodes [84].

MRI performs well in the demonstration of enlarged lymph nodes (figs. 10.48–10.50) [88–90] and outperforms CT imaging in evaluation of the upper abdominal para-aortic and porta hepatis regions and in thin patients [88]. Short tau inversion recovery (STIR), T2-weighted fat-suppressed spin-echo, and echo-train spin-echo techniques result in excellent conspicuity of moderately high-signal-intensity nodes in a suppressed background. The fat-suppressed single-shot echo-train spin-echo sequence may be used as an alternative in uncooperative or pediatric patients, and results are generally good with this technique. Persistent tissue after therapy also may be better characterized by MRI as recurrent disease or fibrosis [84, 86, 91]. After approximately 1 year, fibrotic tissue is low in signal intensity on T2-weighted images, unlike recurrent disease, which is high or mixed high in signal intensity on T2-weighted images. Chronic fibrotic tissue will enhance minimally with gadolinium compared with the enhancement of persistent or recurrent disease, which is moderate or marked and often heterogeneous. In rare instances, lymphoma may appear as a large solitary retroperitoneal mass (fig. 10.49) that mimics the appearance of a primary malignant retroperitoneal tumor.

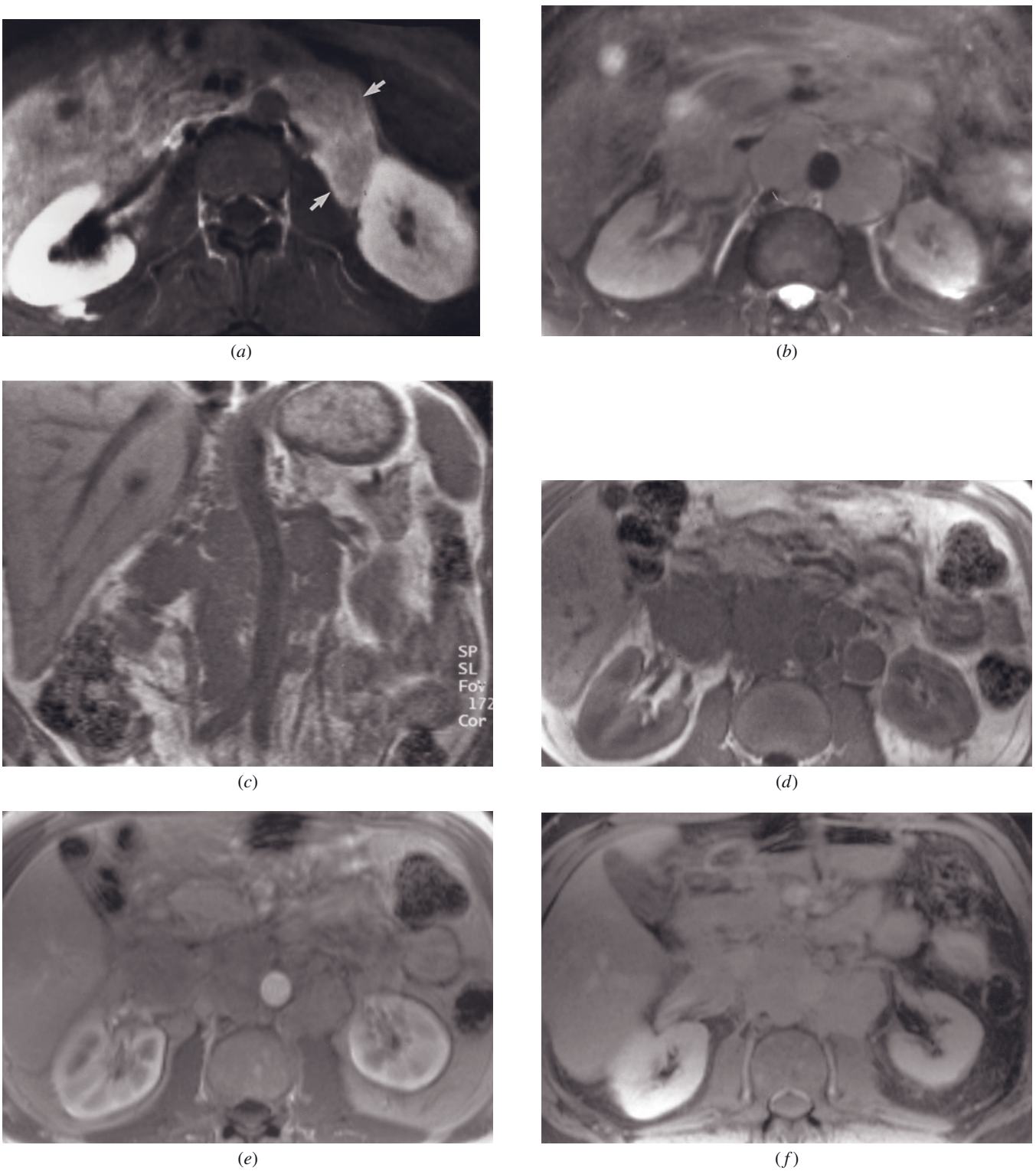

FIG. 10.48 Retroperitoneal lymphadenopathy from Hodgkin lymphoma. Gadolinium-enhanced T1-weighted fat-suppressed spin-echo image (*a*) shows a 4-cm moderately enhancing lymphomatous nodal mass (arrows) in a left periaortic location at the level of the left renal hilum. (Reproduced with permission from Semelka RC, Shoenut JP, Kroeker MA: The retroperitoneum and the abdominal wall. In Semelka RC, Shoenut JP (eds.), *MRI of the Abdomen with CT Correlation*. New York: Raven Press, p. 13–41, 1993.) Transverse fat-suppressed T2-weighted SS-ETSE (*b*), coronal (*c*) and transverse (*d*) SGE, immediate postgadolinium SGE (*e*), and gadolinium-enhanced fat-suppressed SGE (*f*) images in a second patient with Hodgkin lymphoma. Extensive retroperitoneal adenopathy is shown.

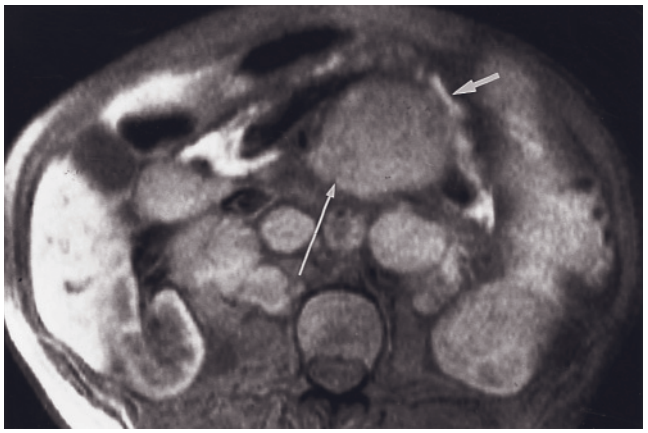

(*a*)

(*b*)

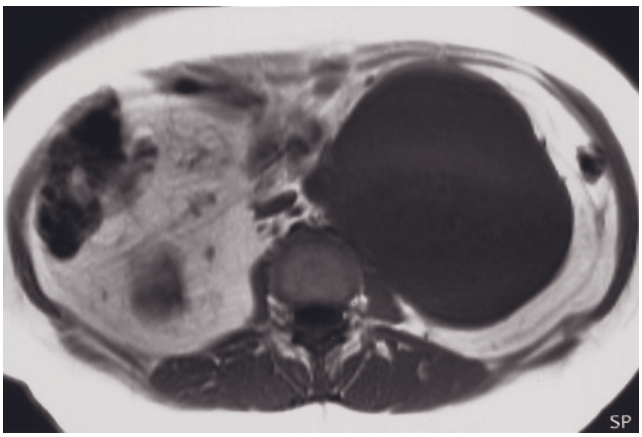

(*c*)

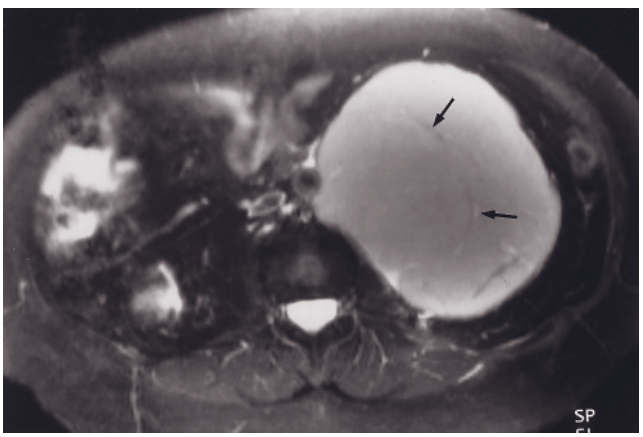

(*d*)

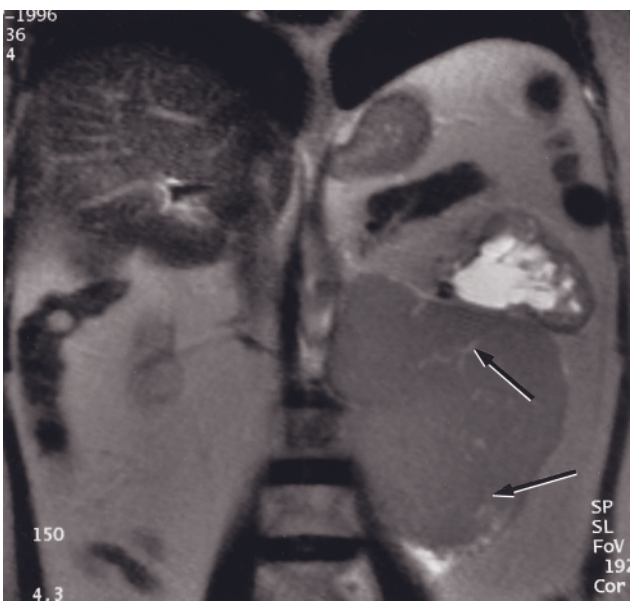

(*e*)

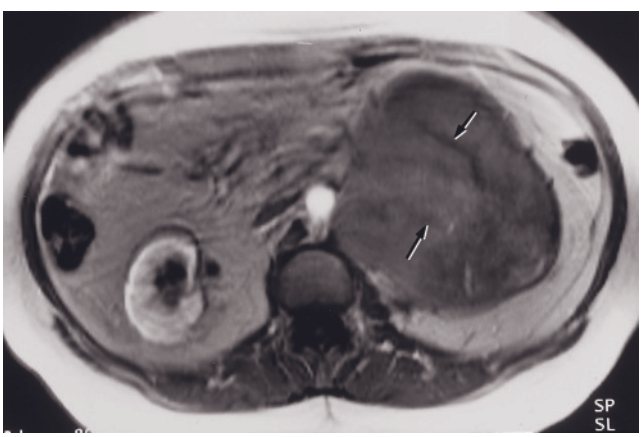

(*f*)

Fig. 10.49 Non-Hodgkin lymphoma. Precontrast (*a*) and gadolinium-enhanced (*b*) T1-weighted fat-suppressed spin-echo images in a patient with retroperitoneal lymphadenopathy from non-Hodgkin lymphoma. Extensive retroperitoneal and mesenteric lymphadenopathy is noted. The precontrast T1-weighted fat-suppressed spin-echo image (*a*) permits distinction of the normal high-signal-intensity pancreas (short white arrow) from the retropancreatic nodal mass (long white arrow) and documents the extrapancreatic location of the mass. The nodal masses show moderate to intense enhancement on the gadolinium-enhanced image (*b*), whereas abnormal enhancement of the spleen (arrow, *b*) reflects lymphomatous infiltration. (Reproduced with permission from Semelka RC, Shoenut JP, Kroeker MA: The retroperitoneum and the abdominal wall. In Semelka RC, Shoenut JP (eds.), *MRI of the Abdomen with CT Correlation*. New York: Raven Press, p. 13–41, 1993.) SGE (*c*), T2-weighted fat-suppressed echo-train spin-echo (*d*), coronal T2-weighted SS-ETSE (*e*), immediate postgadolinium SGE (*f*), and transverse (*g*) and sagittal (*h*) interstitial-phase gadolinium-enhanced fat-suppressed SGE images in a patient with lymphoma presenting as a solitary retroperitoneal mass. A large, well-defined retroperitoneal mass is present. The mass is mildly heterogeneous and low in signal intensity on the T1-weighted image (*c*) and moderately high signal intensity on the T2-weighted image (*d*). Thin septations (arrows, *d, e*) are present in the mass.

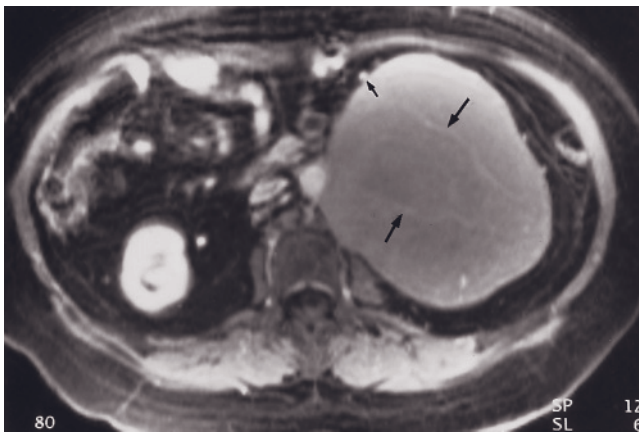

(*g*)

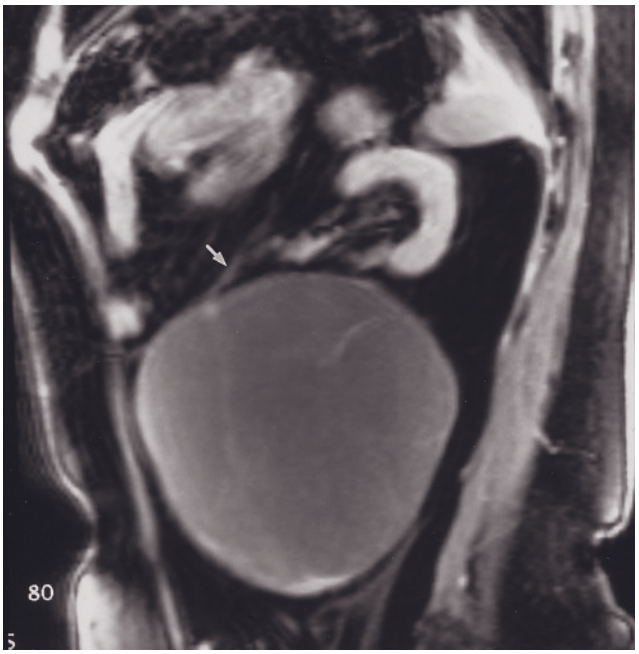

(*h*)

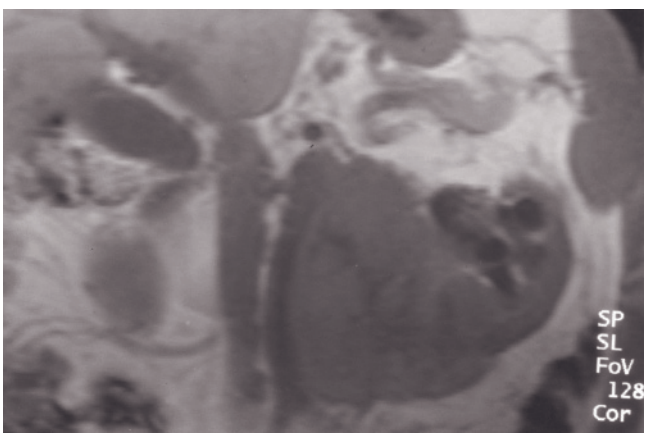

(*i*)

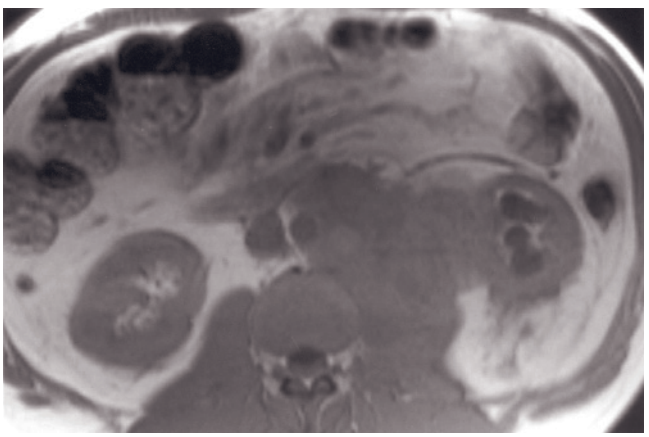

(*j*)

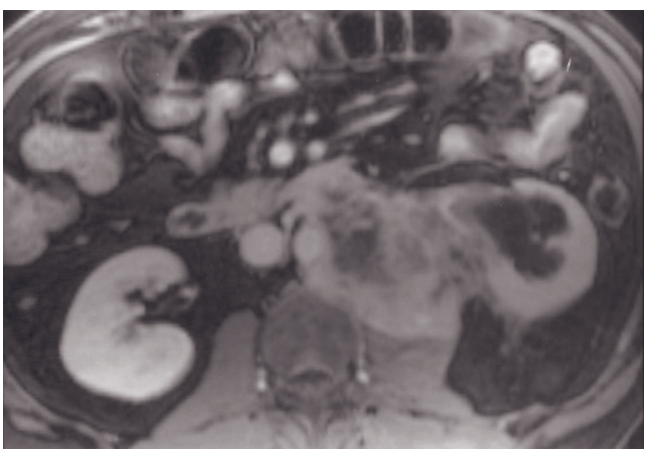

(*k*)

Fig. 10.49 (*Continued*) The coronal T2-weighted SS-ETSE image demonstrates superior displacement and hydronephrosis of the left kidney secondary to ureteral compression caused by the mass. The lymphoma mass demonstrates mild to moderate diffuse heterogeneous enhancement on the immediate postgadolinium SGE image (*f*), which becomes more homogeneous over time on the interstitial-phase fat-suppressed SGE image (*g*). Note that the internal septations (arrows, *f, g*) show minimal enhancement on the immediate postgadolinium SGE image (*f*) and show progressive enhancement on the more delayed fat-suppressed SGE images (*g, h*), consistent with fibrous tissue. The anteriorly displaced ureter is identified at the anterior margin of the mass on the interstitial-phase fat-suppressed SGE image (small arrow, *g*). Note that the sagittal image clearly demonstrates the fat plane between the kidney and the mass and depicts a segment of the anterosuperiorly displaced ureter (small arrow, *h*). A solitary mass lesion with no evidence of other sites of nodal or organ disease is a rare appearance for lymphoma. Coronal (*i*) and transverse (*j*) SGE and 90-s gadolinium-enhanced fat-suppressed SGE (*k*) images. There is a large heterogeneous mass originating in the retroperitoneum on the left that extends from the celiac axis inferiorly to the aortic bifurcation. This mass is isointense on noncontrast T1-weighted images (*i, j*) and enhances heterogeneously (*k*). The mass encases the left renal artery and vein, as well as the ureter, resulting in hydronephrosis. This pattern is the most common form of kidney involvement by lymphoma. The psoas muscle is also compressed. This lesion represented large cell lymphoma at histopathology.

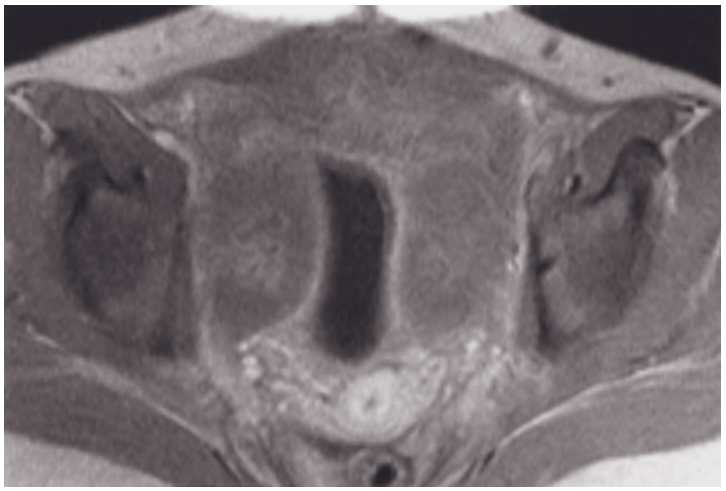

(*a*)

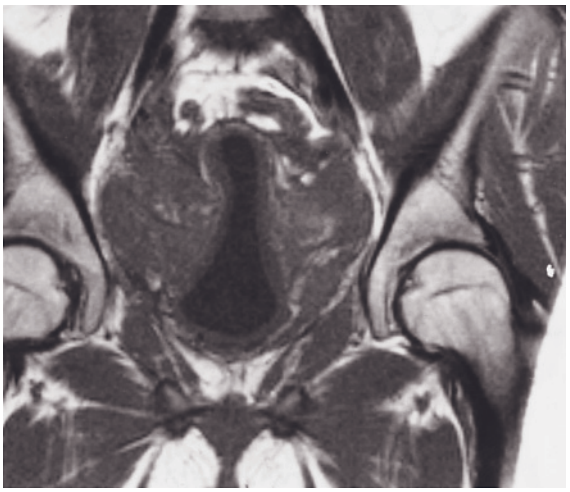

(*b*)

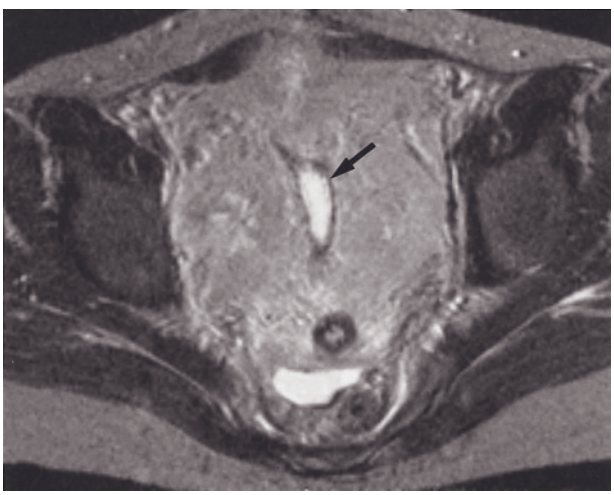

(*c*)

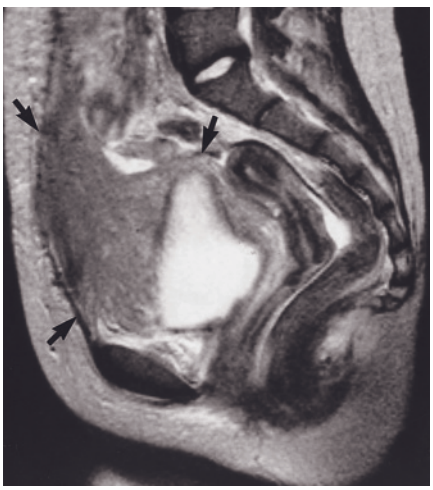

(*d*)

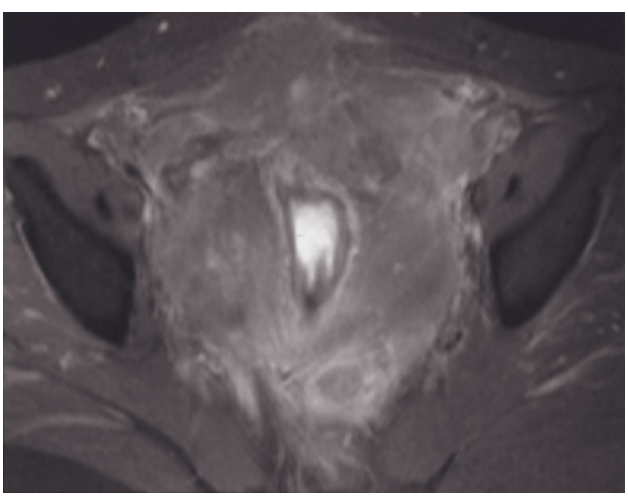

(*e*)

FIG. 10.50 Burkitt lymphoma of the pelvis. SGE (*a*), coronal T1-SE (*b*), T2-SE (*c*), sagittal T2-SE (*d*), and gadolinium-enhanced fat-suppressed T1-weighted spin-echo (*e*) images. Large lymphoma masses are present in the pelvis that cause compression of the urinary bladder (arrow, *c*), which has an hourglass configuration, well shown on the coronal T1-SE image (*b*). The sagittal T2-SE image depicts the large lymphomatous mass (arrows, *d*) that extends along the dome of the bladder into the uterovesicular space. The masses are heterogeneous on both T1- and T2-weighted images and show minimal enhancement after gadolinium administration (*e*).

Malignant Metastatic Lymphadenopathy

Carcinomas associated with retroperitoneal lymphadenopathy include kidney, colon, pancreas, lung, breast, testes, and melanoma [92, 93]. Enlarged lymph nodes are usually moderate in signal intensity on T2-weighted images and higher than adjacent psoas muscle (figs. 10.51 and 10.53). T2-weighted fat-suppressed spin-echo or echo-train spin-echo images are particularly effective at demonstrating nodes in patients who are thin. The addition of fat suppression is important, particularly when echo-train spin-echo sequences are used, because fat is high in signal intensity on these images (fig. 10.52). Adenopathy, whether benign or malignant, will enhance on postgadolinium SGE or 3D-GE images. A feature favoring malignancy is the depiction of necrotic lymph nodes (fig. 10.53) in a patient in whom the primary tumor is also necrotic. The MRI and CT imaging criterion for describing lymph nodes as pathologically enlarged is lymph node minimum transverse diameter greater than 1.5 cm. Unfortunately, sensitivity and specificity of measurements are not high, as benign reactive lymph nodes may exceed 2 cm in diameter in the vicinity of malignant neoplasms and gastrointestinal and pancreatic cancers and cholangiocarcinoma usually involve lymph nodes without causing nodal enlargement. Tissue-specific contrast agents may increase the diagnostic accuracy of MRI in characterizing retroperitoneal lymphadenopathy. MR lymphography using iron oxide particle technique has been shown to distinguish contrast-enhanced, low-signal-intensity benign lymph nodes from nonenhanced, intermediate, heterogeneous-signal-intensity malignant nodes on T2-weighted images in animal models [94]. However, the role of this technique in the evaluation of malignancies has not yet been definitely established.

Testicular Cancer

Testicular cancer may arise in an undescended testis located in the retroperitoneum [95], in the mediastinum or the retroperitoneum without evidence of primary testicular tumor [72], or in the testicles, metastasizing along the lymphatic pathway of testicular arteries and veins into para-aortic and paracaval nodes at the level of the renal hila (fig. 10.54). It is the most common solid cancer in men between the ages of 15 and 34 years, and in 95% of the cases it is of germ cell origin, either seminomatous (40%) or nonseminomatous (embryonal cell tumors, teratocarcinomas, teratomas, choriocarcinomas, and mixed-histology tumors). The remaining 5% are of stromal origin (Sertoli, Leydig, or mesenchymal cell carcinomas). MRI and CT imaging have comparable ability to detect lymphadenopathy associated with testicular cancer [96]. MRI is useful in detecting undescended testes, which may be the site of origin of testicular neoplasms. T2-weighted fat-suppressed images may show the undescended testis as a moderate- to high-signal-intensity structure along the anatomic course of the spermatic vessels. In tumors arising in undescended testes, MRI may perform better than CT imaging in lesion characterization [95].

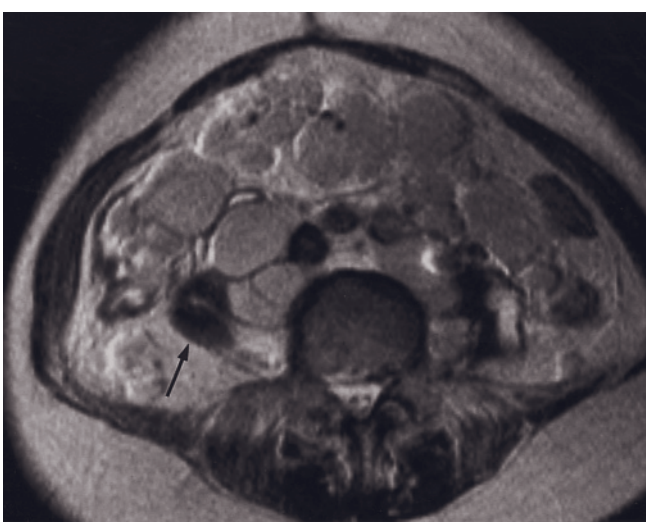

(*a*)

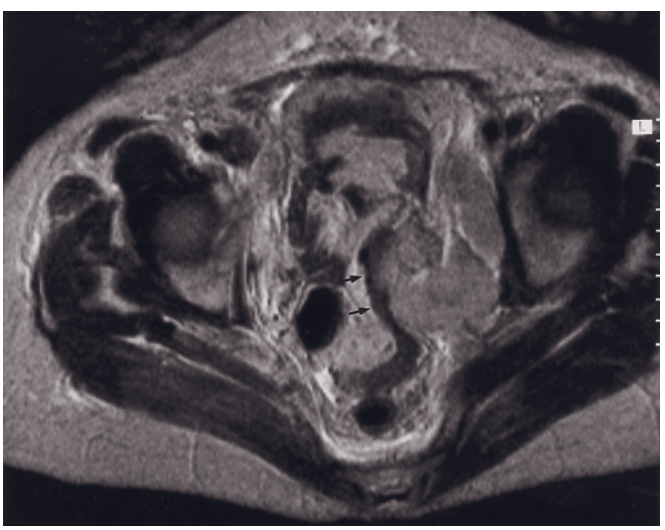

(*b*)

FIG. 10.51 Malignant retroperitoneal adenopathy. T2-weighted spin-echo images from cranial (*a*) and more caudal (*b*) levels. Enlarged retroperitoneal lymph nodes are demonstrated as rounded, well-defined masses of moderate signal intensity on both images. Note lateral displacement of the right psoas muscle (arrow, *a*) by enlarged paracaval lymph nodes and medial displacement of the sigmoid colon (arrows, *b*) by enlarged left obturator lymph nodes. SGE (*c*), T2-weighted fat-suppressed spin-echo (*d*),

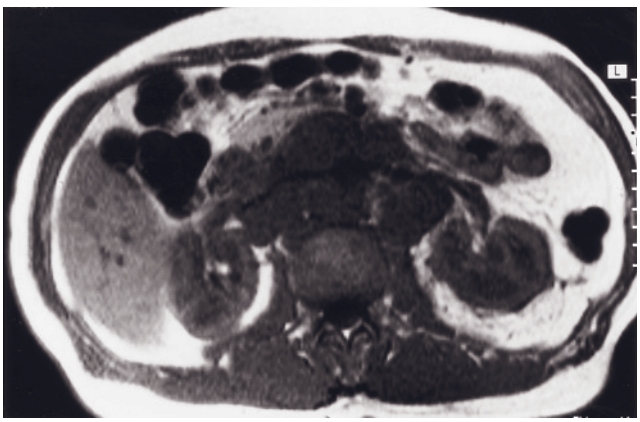

(*c*)

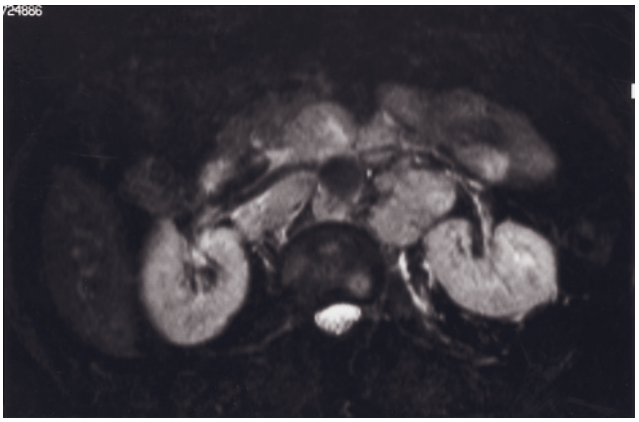

(*d*)

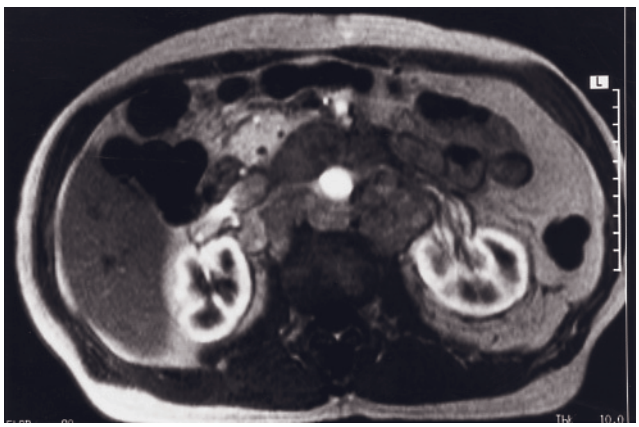

(*e*)

(*f*)

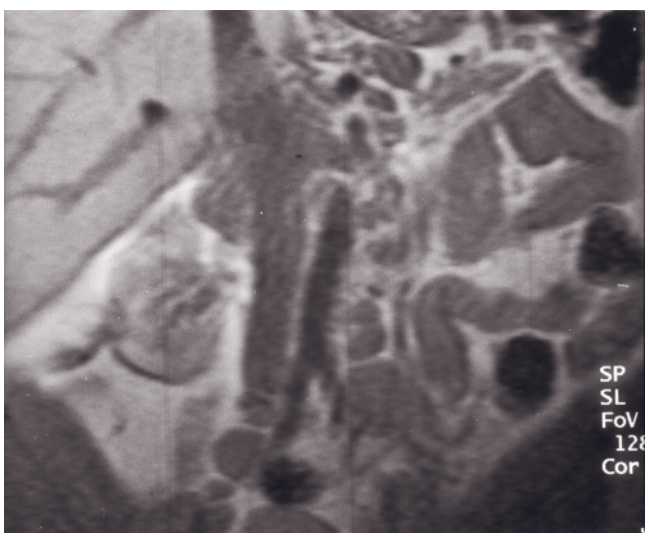

(*g*)

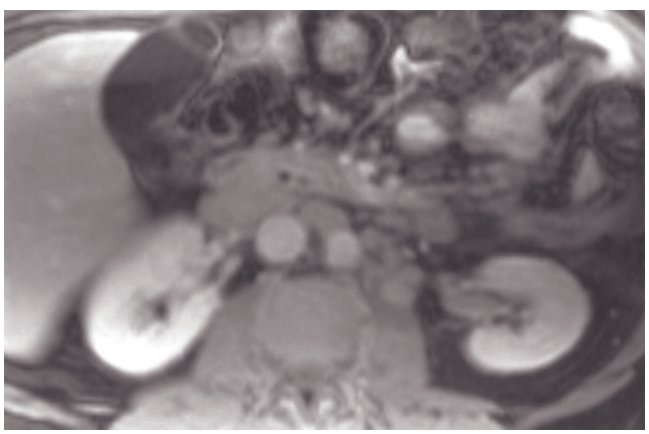

(*h*)

FIG. 10.51 (*Continued*) and immediate (*e*) and 90-s (*f*) postgadolinium SGE images in a second patient who has prostate cancer. Multiple enlarged lymph nodes are present in the retroperitoneum, displacing the aorta and the IVC anteriorly. The lymph nodes are low in signal intensity on the SGE image (*c*) and high in signal intensity on the T2-weighted fat-suppressed spin-echo image (*d*). Fat suppression removes the competing high signal intensity of fat and renders the lymph nodes particularly conspicuous on the T2-weighted image. The lymph nodes enhance minimally on the immediate postgadolinium SGE image (*e*) and show progressive enhancement on the 90-s postgadolinium SGE image (*f*). Coronal SGE (*g*) and interstitial-phase gadolinium-enhanced fat-suppressed SGE (*h*) images in third patient who has chronic lymphocytic leukemia. Diffuse abdominal adenopathy is appreciated in portocaval, periaortic, and iliac chains.

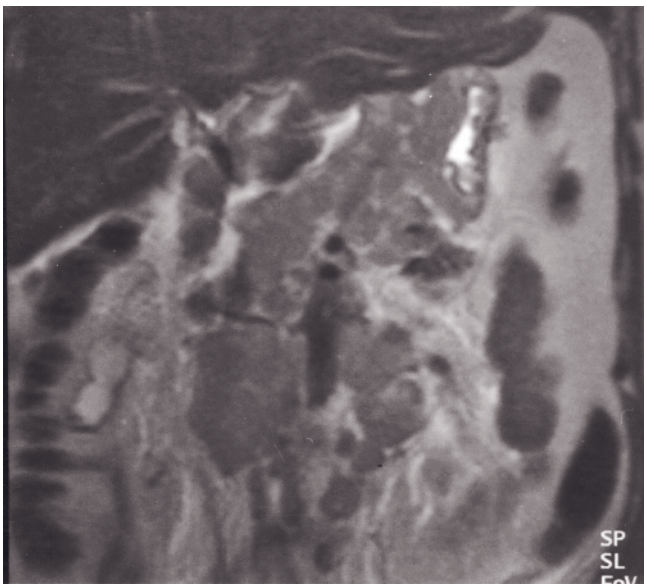

(*a*)

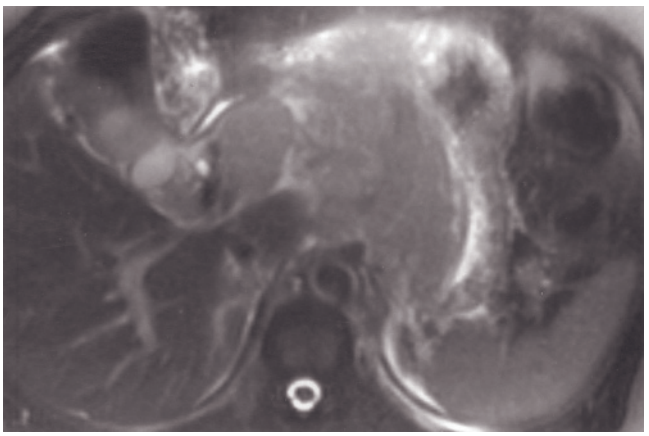

(*b*)

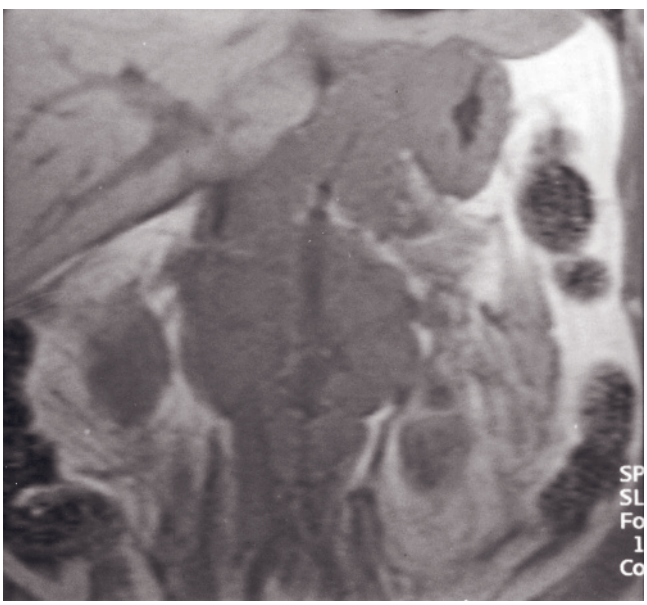

(*c*)

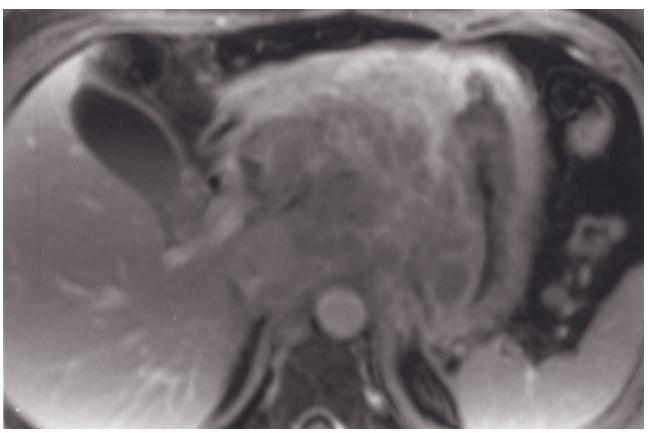

(*d*)

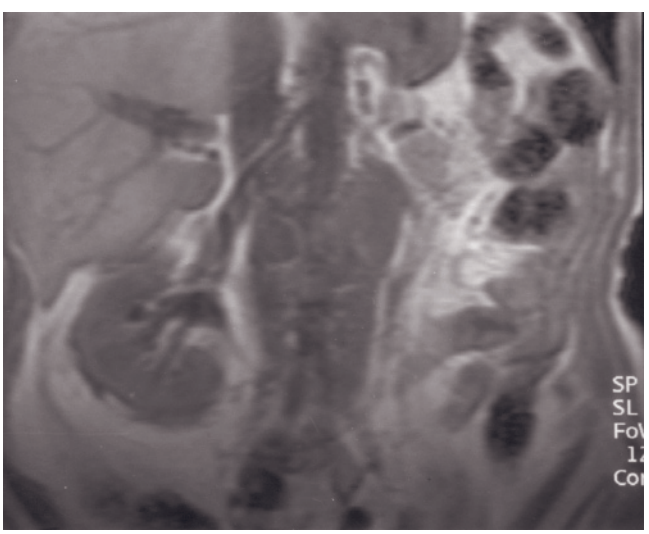

(*e*)

FIG. 10.52 Malignant retroperitoneal lymphadenopathy. Coronal T2-weighted SS-ETSE (*a*), transverse fat-suppressed T2-weighted SS-ETSE (*b*), coronal SGE (*c*), and interstitial-phase gadolinium-enhanced fat-suppressed SGE (*d*) images in a patient with gastric adenocarcinoma. There is a large, mildly heterogeneous lobulated mass involving the lesser curvature and extending into the gastrohepatic ligament (*d*). Extensive retroperitoneal lymph nodes are also appreciated. Coronal SGE (*e*), immediate

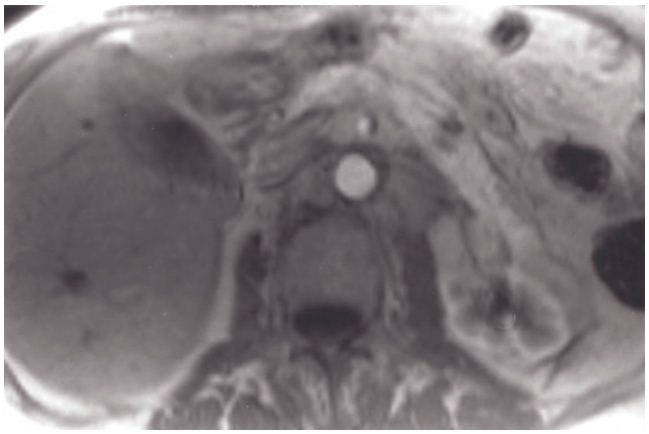

(*f*)

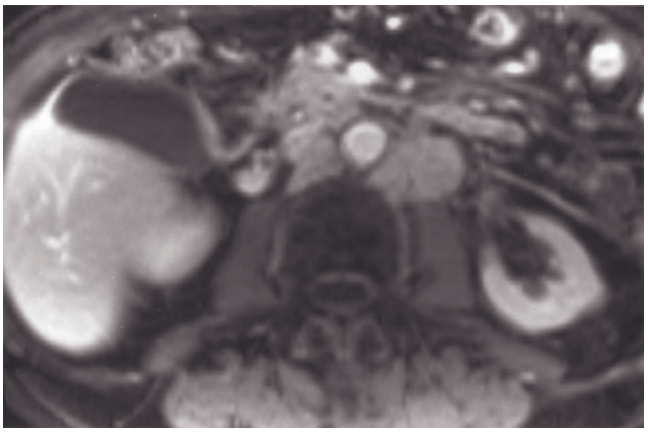

(*g*)

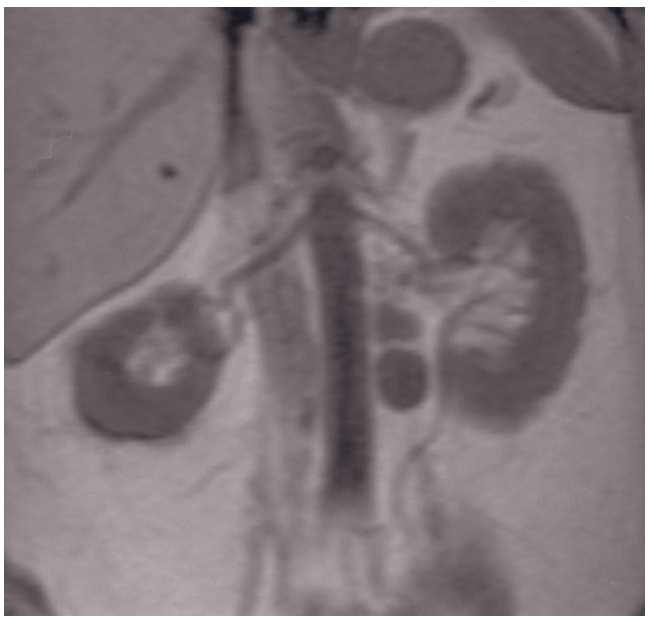

(*h*)

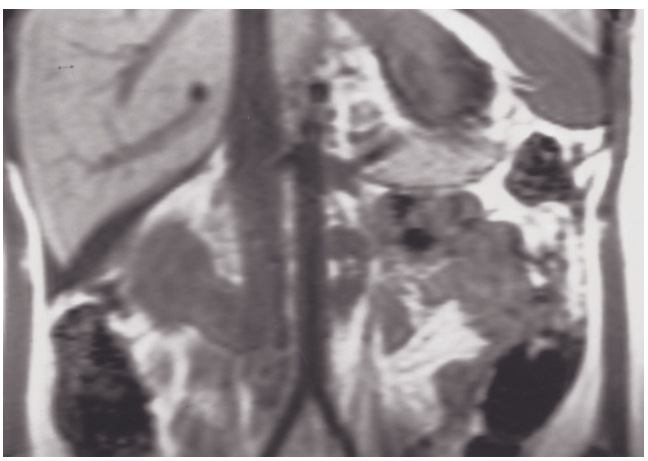

(*i*)

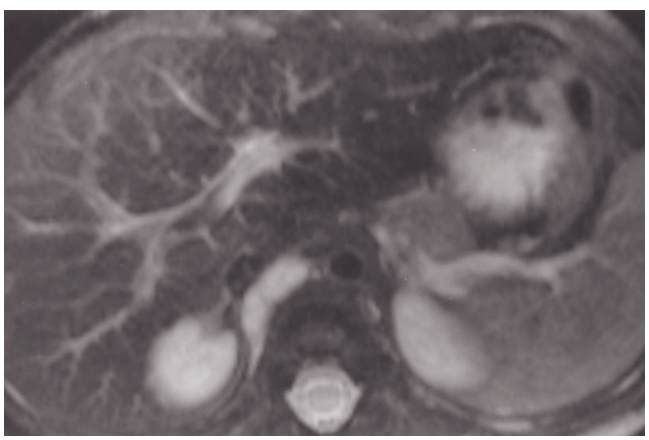

(*j*)

FIG. 10.52 (*Continued*) postgadolinium SGE (*f*), and interstitial-phase gadolinium-enhanced fat-suppressed SGE (*g*) images in a second patient with recurrent colon cancer demonstrate the presence of aortocaval and left para-aortic bulky lymphadenopathy that extend superiorly to the level of the kidneys. Coronal SGE image (*h*) in a third patient, who has carcinoma of the uterus, shows enlarged left para-aortic lymph nodes consistent with metastatic lymphadenopathy. Coronal SGE image (*i*) in a fourth patient, who has endometrial stromal sarcoma, also demonstrates left para-aortic retroperitoneal adenopathy. Transverse T2-weighted fat-suppressed SS-ETSE image (*j*) in a fifth patient with neuroblastoma shows the presence of retrocrural lymph nodes that represent recurrent disease.

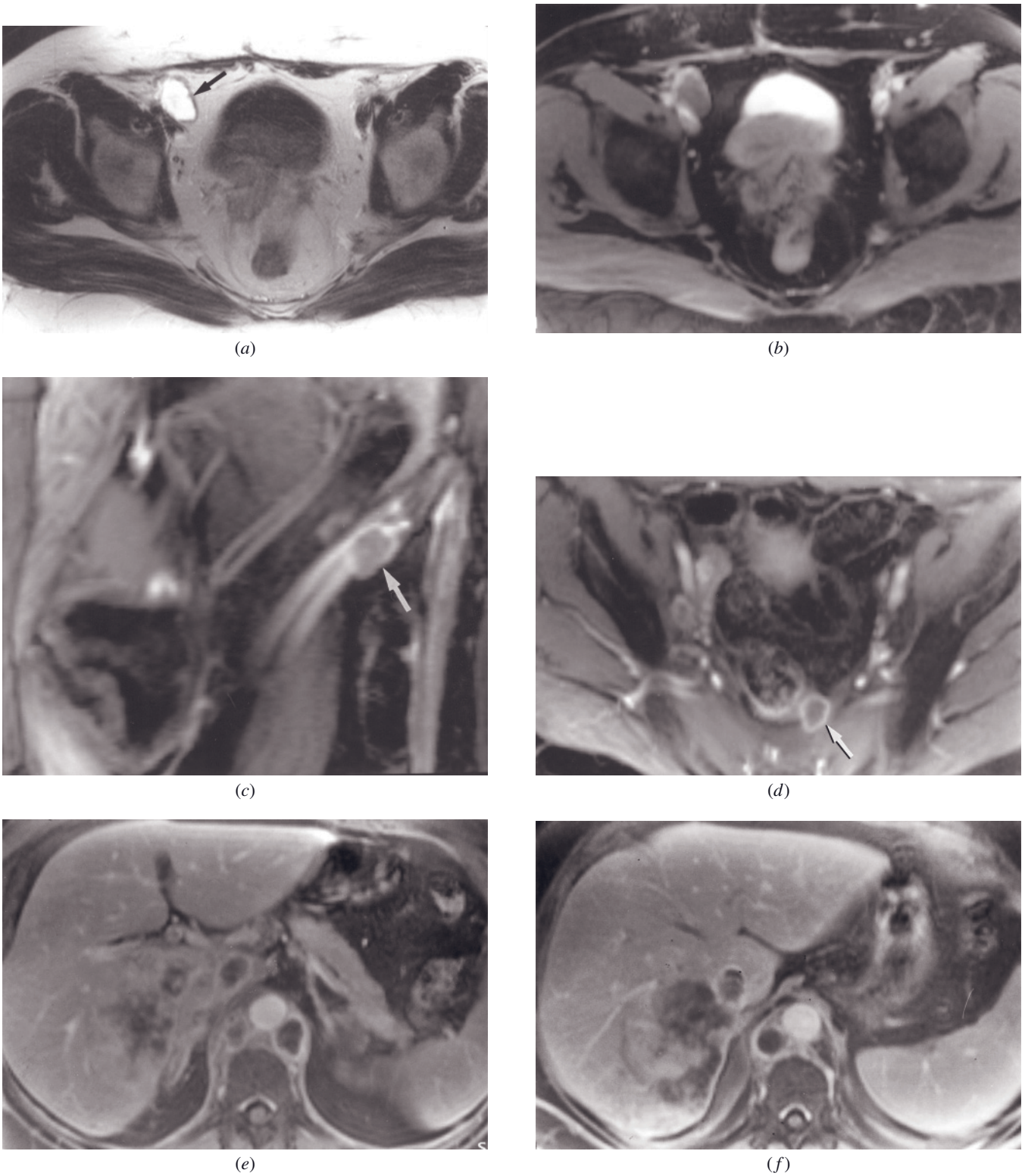

FIG. 10.53 Necrotic malignant lymph nodes. T2-weighted ETSE (*a*) and interstitial-phase gadolinium-enhanced fat-suppressed SGE (*b*) images in a patient with ovarian cancer. There is a large right external iliac lymph node (arrow, *a*) that is high signal on T2 (*a*) and is centrally near signal void with a thin peripheral rim of enhancement on the postgadolinium image (*b*). Sagittal (*c*) and transverse (*d*) interstitial-phase gadolinium-enhanced fat-suppressed SGE images in a second patient, who has cervical cancer, demonstrate a left perirectal lymph node that is low signal and has a thin rim enhancement (arrow, *c, d*). The combination of sagittal- and transverse-plane images permits identification of the rounded configuration of the mass in multiple planes. Interstitial-phase gadolinium-enhanced fat-suppressed SGE images (*e*, *f*) in a third patient, who has unknown primary adenocarcinoma, show multiple necrotic metastatic lymph nodes associated with metastatic liver lesions. Interstitial-phase gadolinium-enhanced

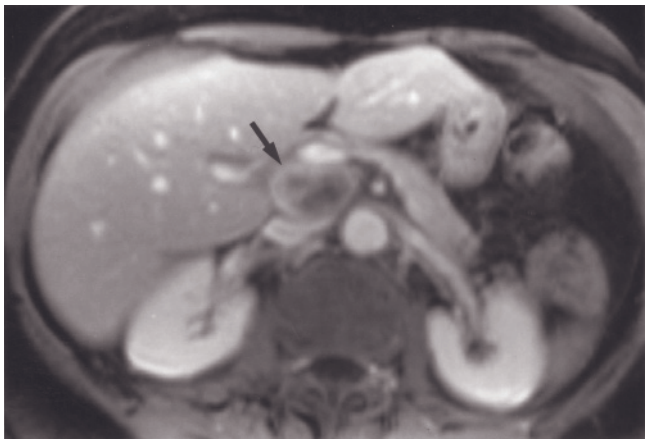

(*g*)

FIG. 10.53 (*Continued*) fat-suppressed SGE image (*g*) in a fourth patient, who has ovarian cancer, demonstrates a necrotic lymph node in the porta hepatis (arrow, *g*).

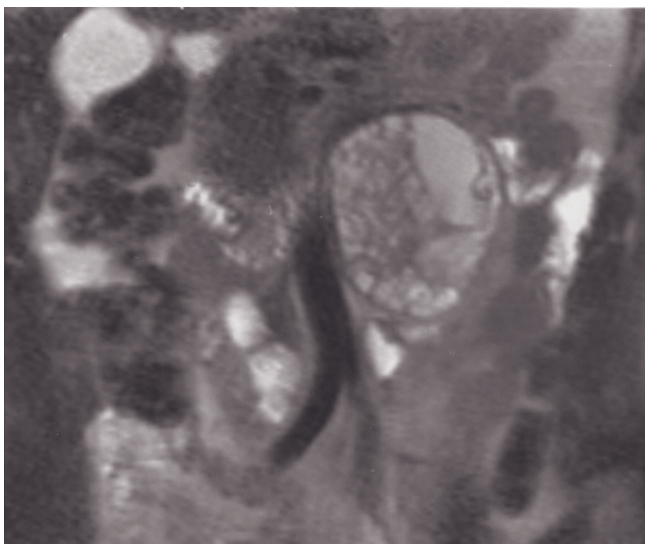

(*a*)

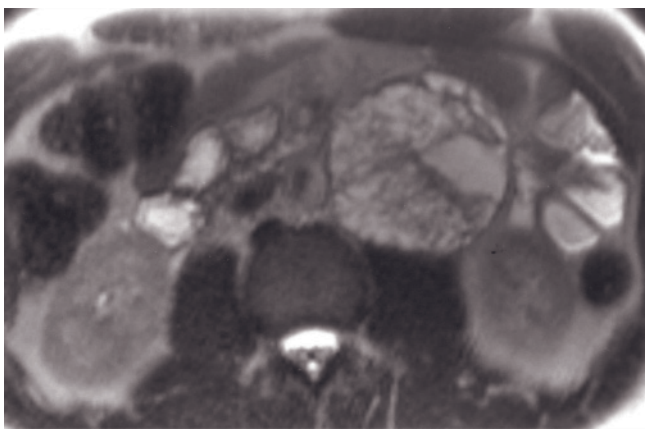

(*b*)

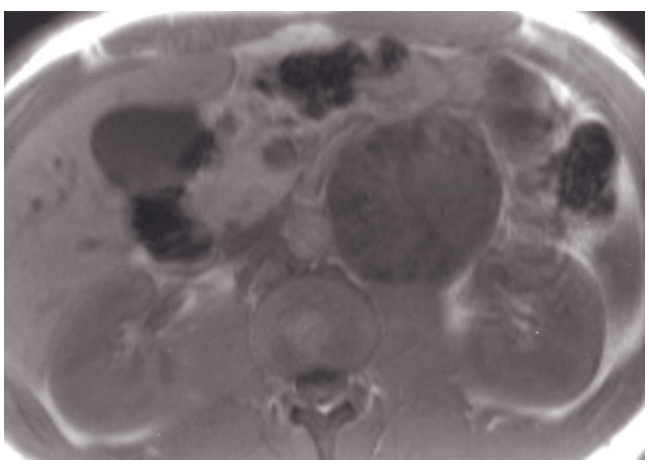

(*c*)

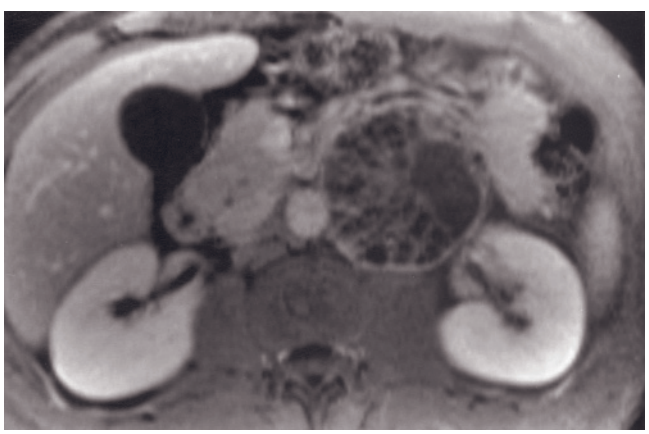

(*d*)

FIG. 10.54 Testicular cancer. Coronal (*a*) and transverse (*b*) T2-weighted SS-ETSE, transverse SGE (*c*), and interstitial-phase gadolinium-enhanced fat-suppressed SGE (*d*) images. There is a large left retroperitoneal mass that demonstrates heterogeneous internal signal on T1- and T2-weighted images and possesses thin septations that enhance after contrast administration. This is consistent with a large nodal mass secondary to nonseminomatous testicular cancer. Coronal T2-weighted SS-ETSE (*e*), transverse

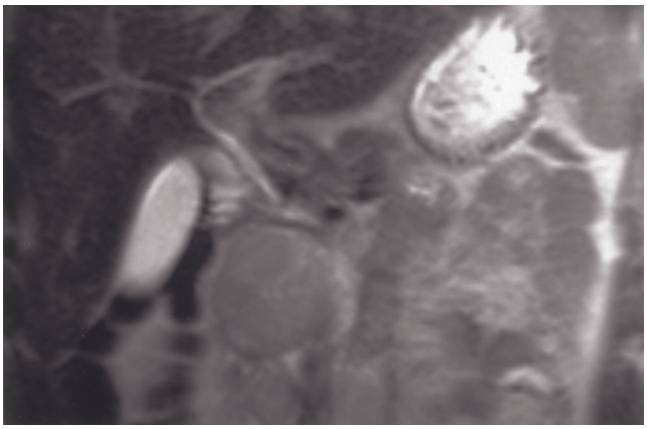

(*e*)

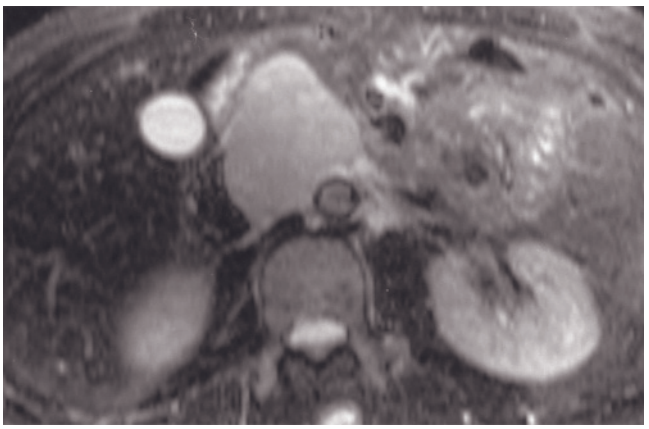

(*f*)

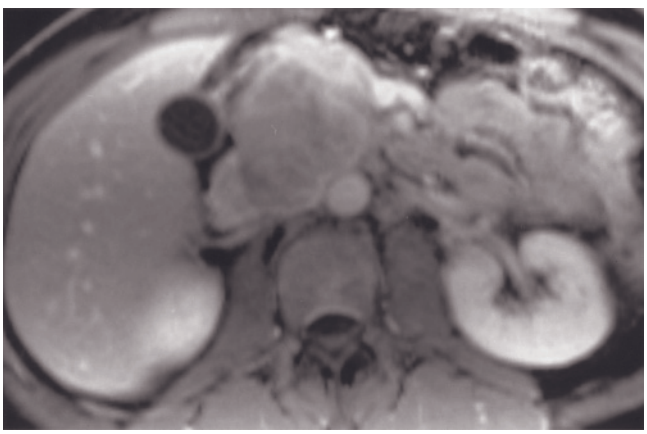

(*g*)

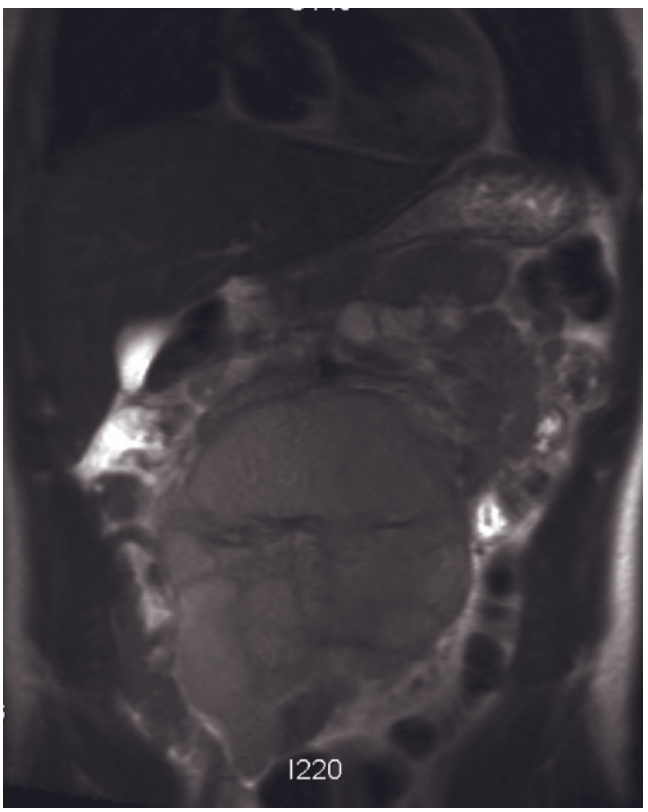

(*h*)

(*i*)

FIG. 10.54 (*Continued*) T2-weighted fat-suppressed SS-ETSE (*f*), and transverse interstitial-phase gadolinium-enhanced SGE (*g*) images in a second patient, who has right testis rhabdomyosarcoma. There is a nodal mass in the aortocaval region that displaces the pancreas anteriorly and the inferior vena cava laterally. Left para-aortic lymph nodes are also identified. Coronal T2-weighted single-shot echo-train spin-echo (*h*), transverse T1-weighted SGE (*i*), and transverse T1-weighted postgadolinium interstitial-phase

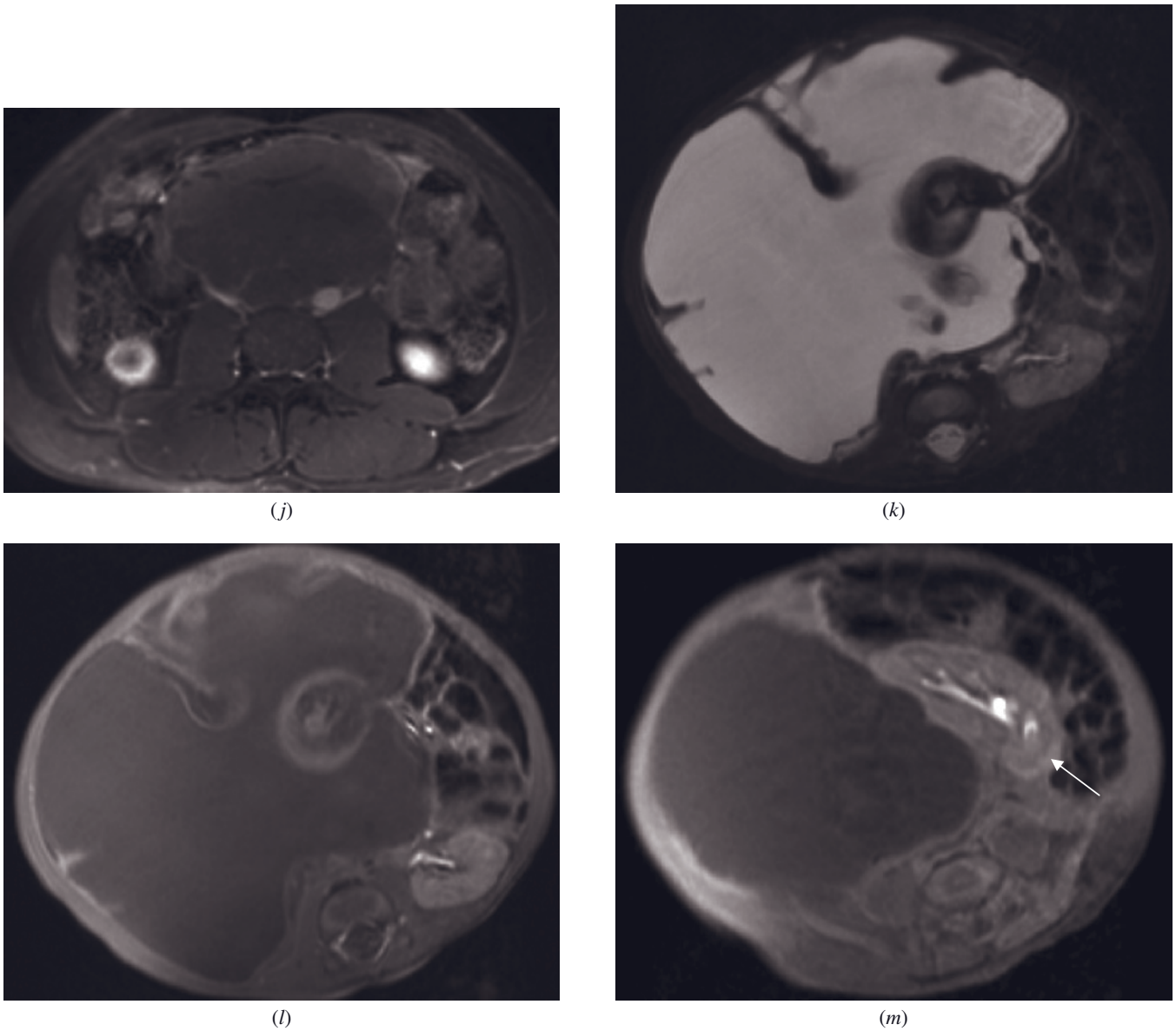

Fig. 10.54 (*Continued*) fat-suppressed 3D-GE (*j*) images at 3.0 T show a large retroperitoneal seminoma in another patient. The tumor shows high signal and fibrous septa on T2-weighted image (*h*) and mild enhancement on postgadolinium image (*j*). The aorta and IVC are compressed and displaced laterally. T2-weighted fat-suppressed single-shot echo-train spin-echo (*k*) and T1-weighted postgadolinium interstitial-phase fat-suppressed SGE (*l, m*) images demonstrate a germ cell tumor in another patient. The patient is an infant. The large tumor occupies most of the abdominal cavity and compresses and displaced the bowel to the left lateral side. The right kidney (arrow, *m*) is displaced by the retroperitoneal mass to the left side. The axis of the right kidney is also deviated. The contrast is present in the collecting systems of both kidneys. The tumor has a complex structure consisting of cystic and solid components.

Primary Retroperitoneal Neoplasms

The majority of primary retroperitoneal tumors (70–90%) are malignant (figs. 10.55–10.59) [97–100]. The most common histologic type is liposarcoma, followed by leiomyosarcoma and malignant fibrous histiocytoma [72, 99–101]. A male predominance exists for liposarcomas and malignant fibrous histiocytomas, whereas leiomyosarcomas are more common in women [72, 101]. The tumors are typically large at presentation (see figs. 10.55 and 10.56), because of their silent clinical course. Presenting symptoms include abdominal mass, pain, weight loss, and nausea and vomiting [101]. In a review of leiomyosarcomas of the retroperitoneum and IVC, leiomyosarcomas with no major vascular involvement have been classified as Pattern 1 and comprise 62% of the total cases [101]. On MR images, tumors are generally mixed low and intermediate in signal intensity on T1-weighted images and mixed medium and high in

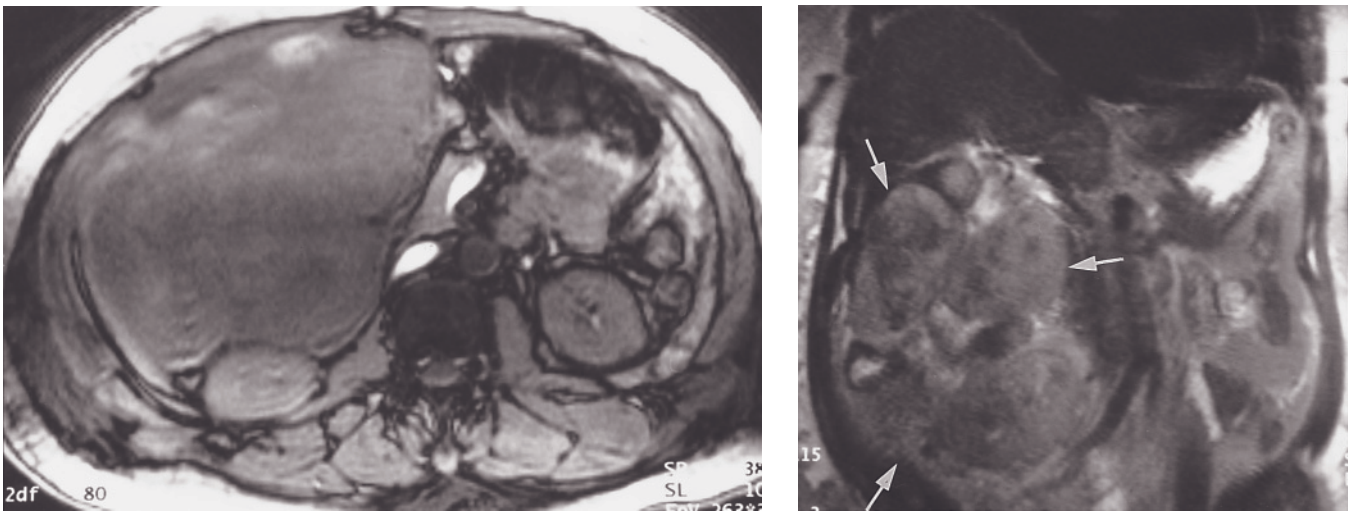

(*a*) (*b*)

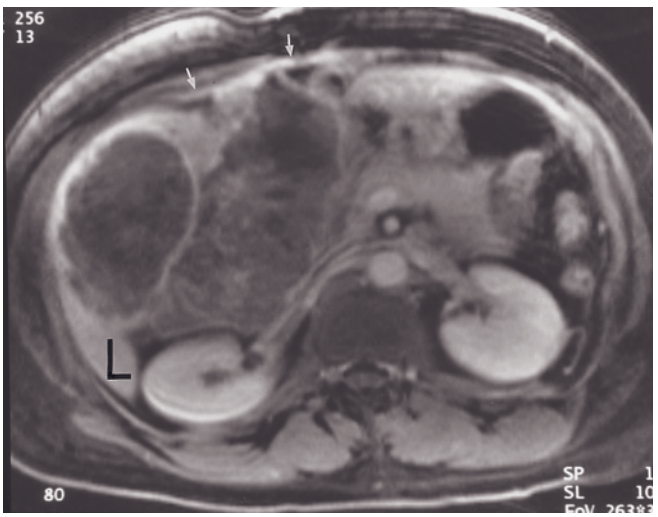

(*c*)

FIG. 10.55 Retroperitoneal carcinoma. Out-of-phase SGE (*a*), coronal T2-weighted SS-ETSE (*b*), and interstitial-phase gadolinium-enhanced fat-suppressed SGE (*c*) images. A large, lobulated, heterogeneous mass is located in the right abdomen. The mass is heterogeneous on both T1 (*a*)- and T2 (arrows, *b*)-weighted images, displacing the aorta and IVC medially and the right kidney posteriorly. Areas of high signal intensity on the T2-weighted image (*b*) represent necrotic areas. The mass demonstrates peripheral and patchy heterogeneous enhancement on the interstitial-phase gadolinium-enhanced fat-suppressed SGE image (*c*). Invasion of the right lobe of the liver (L, *c*) is clearly demonstrated. The mass abuts the anterior abdominal wall, and enhancement of the anterior peritoneum (small arrows, *c*) is evident secondary to a recent laparotomy attempt, which was aborted because of the large size of the mass.

signal intensity on T2-weighted images [100, 101]. Tumors enhance in a heterogeneous fashion, and leiomyosarcomas, in particular, are hypervascular and demonstrate intense enhancement (see fig. 10.56). Areas of necrosis may be present, which is common in leiomyosarcomas [72, 101], and are demonstrated as areas that are low signal intensity on T1-weighted images and high signal intensity on T2-weighted images and lack enhancement on postgadolinium images. Hemorrhage occasionally occurs in the liquefied necrotic areas and appears mixed high signal intensity on T1-weighted images and mixed low and high signal intensity on T2-weighted images, with occasional demonstration of a dependent low-signal layer on T2-weighted images [101]. The various histologic types share common MRI appearances, and differentiation may not be feasible. In rare cases liposarcomas may be sufficiently well differentiated (lipogenic liposarcoma) to contain mature fat, which is high in signal intensity on T1- and T2-weighted echo-train spin-echo images and intermediate in signal intensity on T2-weighted spin-echo images and suppresses on fat-suppressed images (fig. 10.57). In these cases, soft tissue strands are present within the fatty mass, and tumor nodules may enhance after gadolinium administration. These tumors are well assessed by MRI, which provides direct imaging of the craniocaudal and transverse extent of the tumor.

Neuroblastoma (fig. 10.59) and ganglioneuroblastoma are tumors discussed in Chapter 8, *Adrenal Glands*. Extra-adrenal involvement increases with age [102]. MRI with the use of phased-array multicoil, T2-weighted fat-suppressed echo-train spin-echo, and gadolinium-enhanced T1-weighted fat-suppressed images provides excellent morphologic detail and tumor/background

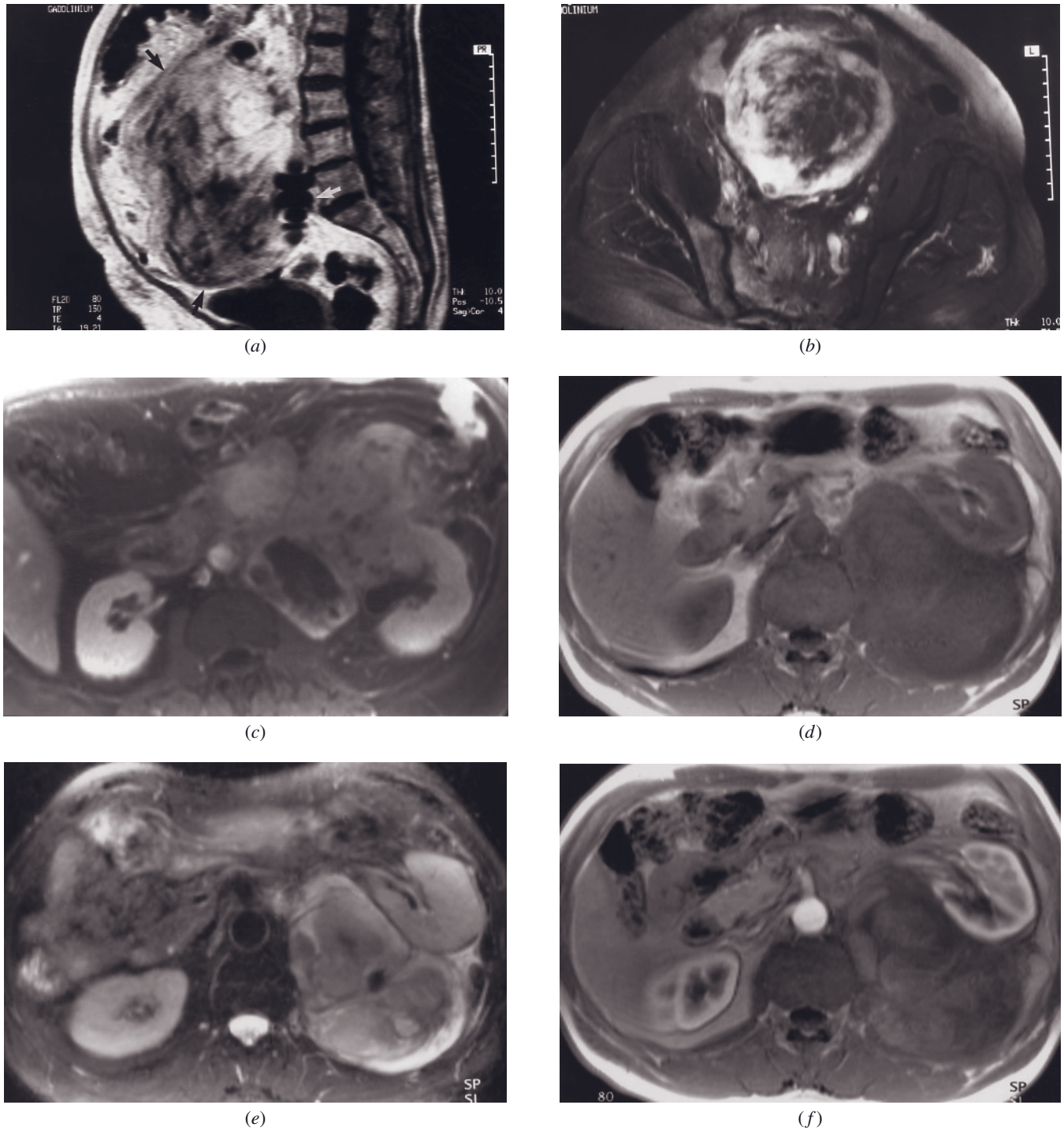

(*a*) (*b*) (*c*) (*d*) (*e*) (*f*)

FIG. 10.56 Retroperitoneal sarcoma. Sagittal T1-SE (*a*) and postgadolinium T1-weighted fat-suppressed spin-echo (*b*) images in a patient with recurrent retroperitoneal leiomyosarcoma. A large, markedly heterogeneous mass (arrows, *a*) arises in the retroperitoneum immediately anterior to the lumbar spine and extends inferiorly to the pelvis. The mass demonstrates intense heterogeneous enhancement on interstitial-phase gadolinium-enhanced images. Magnetic susceptibility artifacts are present, caused by surgical clips (white arrow, *a*). Transverse interstitial-phase gadolinium-enhanced fat-suppressed SGE image (*c*) in a second patient, who has retroperitoneal leiomyosarcoma, demonstrates a large left-sided retroperitoneal mass that is heterogeneous in appearance and invades the lower and medial aspect of the left kidney. SGE (*d*), T2-weighted fat-suppressed echo-train spin-echo (*e*), immediate postgadolinium SGE (*f*), and transverse (*g*) and sagittal (*h*) interstitial-phase gadolinium-enhanced fat-suppressed SGE images in a third patient, who has pleomorphic rhabdomyosarcoma. A large, left-sided retroperitoneal rhabdomyosarcoma mass is present. The mass displaces the left kidney anterolaterally, consistent with the retroperitoneal origin of the mass. The mass is heterogeneous and low in signal intensity on the precontrast SGE image (*d*) and heterogeneous and mixed high signal intensity on the T2-weighted image (*e*). The mass demonstrates moderate and heterogeneous enhancement on the immediate postgadolinium SGE image (*f*)

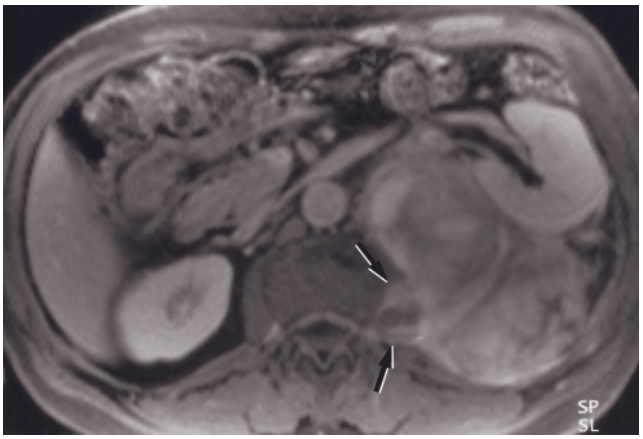

(*g*)

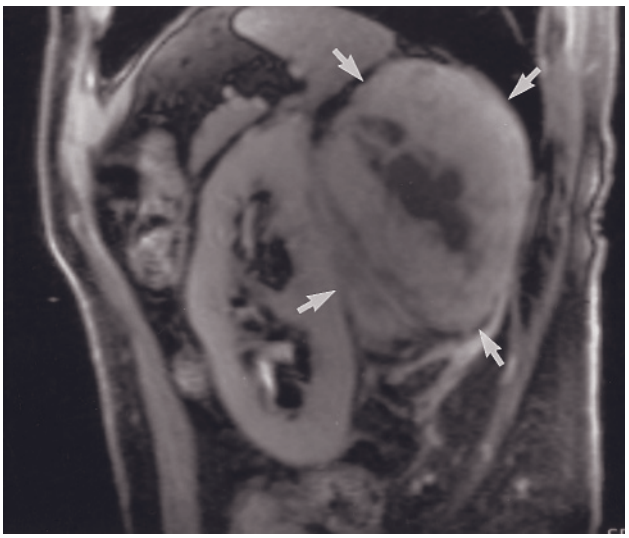

(*h*)

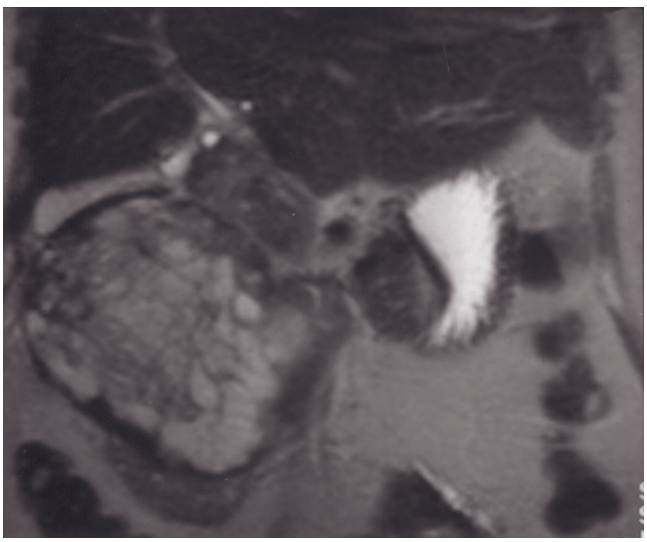

(*i*)

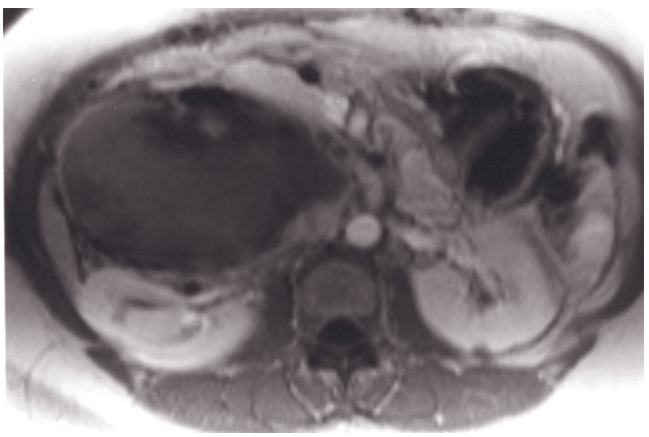

(*j*)

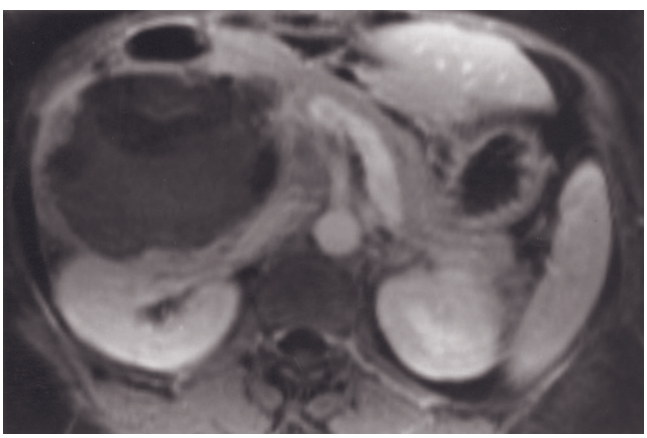

(*k*)

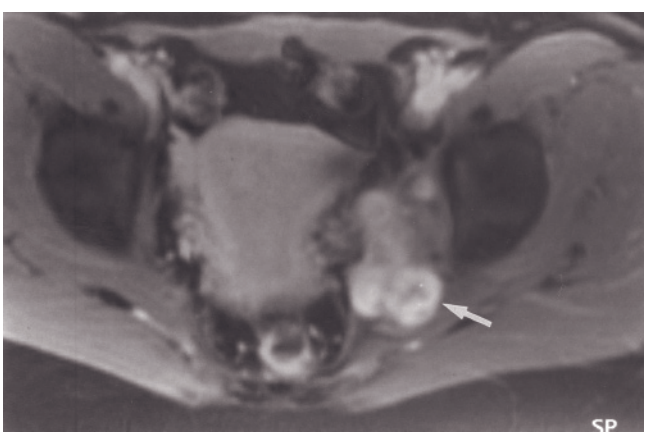

(*l*)

Fig. 10.56 (*Continued*) with progressive enhancement on the interstitial-phase fat-suppressed SGE images (*g*, *h*). Invasion of the left psoas muscle (arrows) is well shown on the interstitial-phase fat-suppressed SGE image (*g*) as an enhancing area with irregular margins within the muscle. The sagittal image demonstrates the longitudinal extent of the mass (arrows, *h*) and anterior displacement of the kidney. Central necrosis is present that appears as a central area of lack of enhancement within the mass. Coronal SS-ETSE (*i*), interstitial-phase postgadolinium SGE (*j*), and interstitial-phase gadolinium-enhanced fat-suppressed SGE (*k*) images in a fourth patient, who has retroperitoneal sarcoma. A large and heterogeneously enhancing tumor with septations and necrosis is seen in the right abdomen, abutting the head of the pancreas, porta hepatis, the right kidney, and the inferior vena cava. Interstitial-phase gadolinium-enhanced fat-suppressed SGE (*l*) image in a fifth patient, who has retroperitoneal sarcoma. A heterogeneous, moderately intense mass (arrow, *l*) is present in the left pelvis. Involvement of the obturator internus and pyriformis muscles

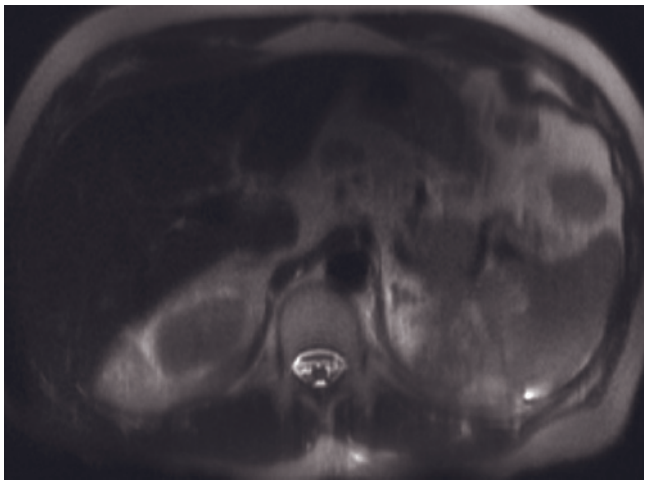

(*m*)

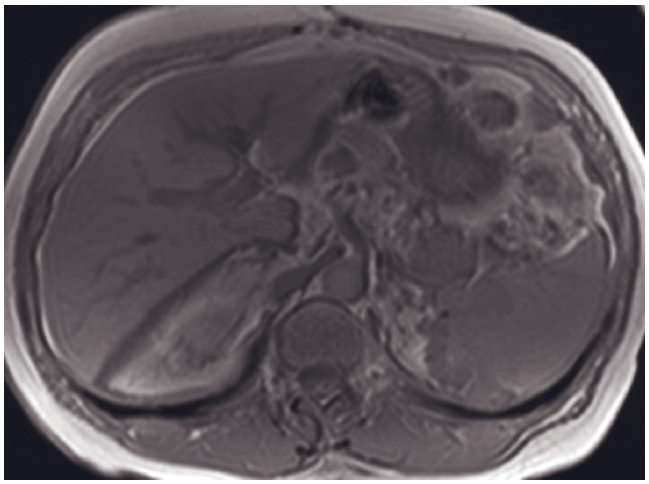

(*n*)

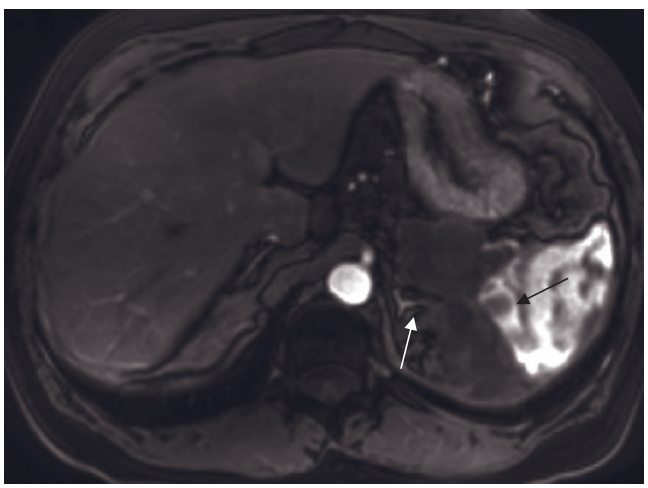

(*o*)

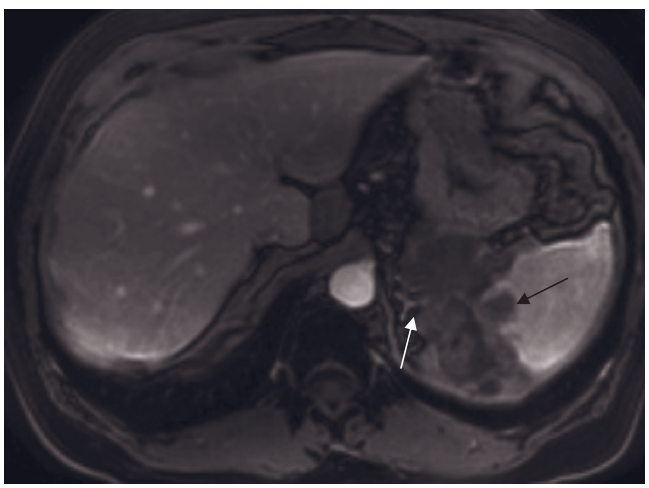

(*p*)

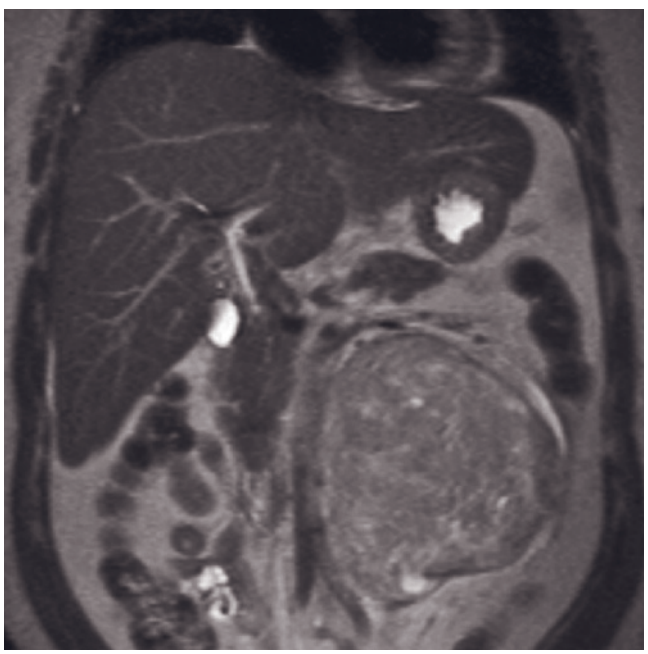

(*q*)

FIG. 10.56 (*Continued*) is apparent. T2-weighted single-shot echo-train spin-echo (*m*), T1-weighted SGE (*n*), T1-weighted postgadolinium hepatic arterial dominant-phase (*o*) and interstitial-phase (*p*) fat-suppressed 3D-GE images at 3.0 T demonstrate retroperitoneal sarcoma in another patient. The tumor invades the spleen (black arrows, *o, p*) and lateral limb of the left adrenal gland (white arrows, *o*, *p*) and shows progressive enhancement on postgadolinium images. Invasion of the diaphragm is most clearly shown of the interstitial phase fat-suppressed images (*p*). Coronal T2-weighted single-shot echo-train spin-echo (*q*), transverse T1-weighted postgadolinium hepatic arterial dominant-phase SGE (*r*), and transverse T1-weighted postgadolinium interstitial-phase fat-suppressed 3D-GE (*s*) images from another patient with a large retroperitoneal sarcoma, which show a high signal on T2-weighted image (*q*) and heterogeneous enhancement on postgadolinium images (*r, s*). The tumor deviates the aorta medially and compresses the left psoas muscle. Transverse T1-weighted

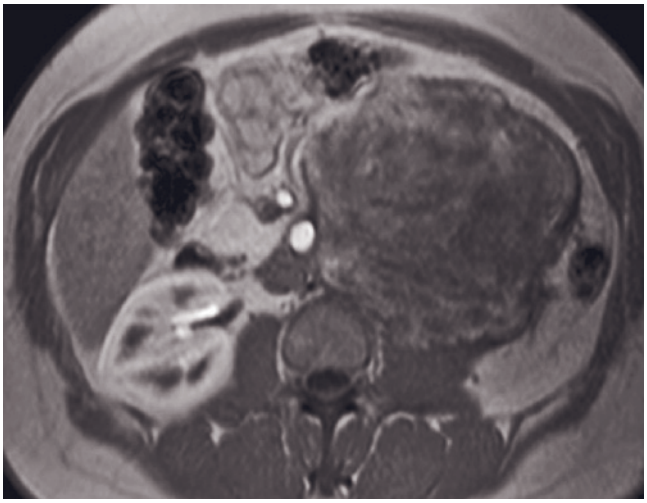

(*r*)

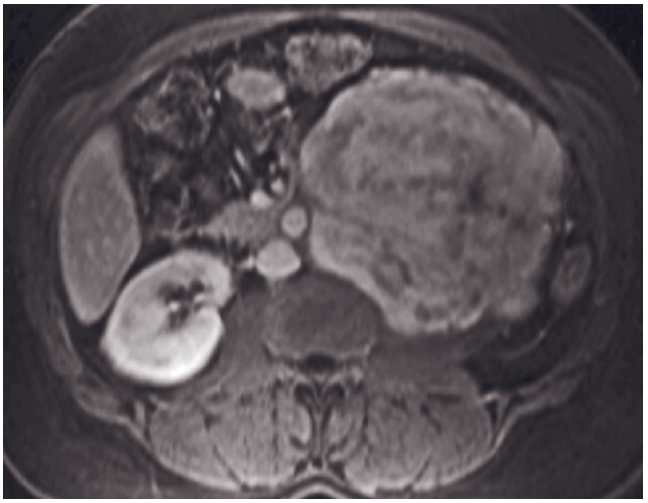

(*s*)

(*t*)

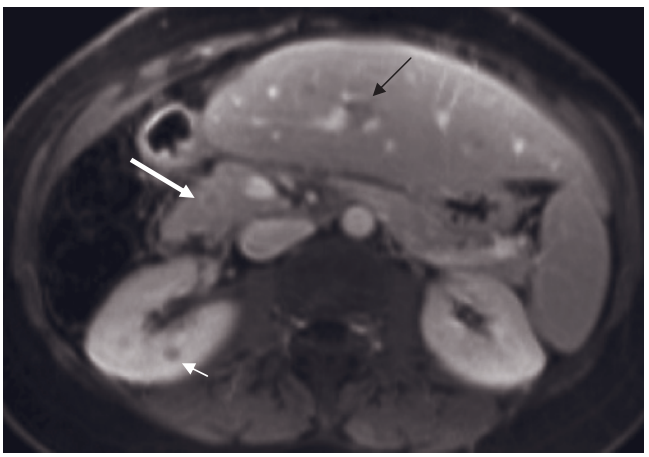

(*u*)

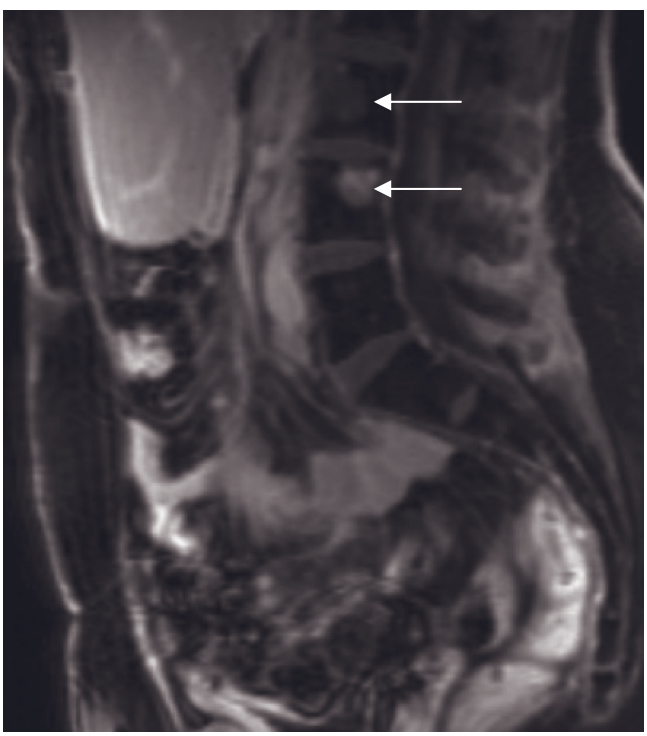

(*v*)

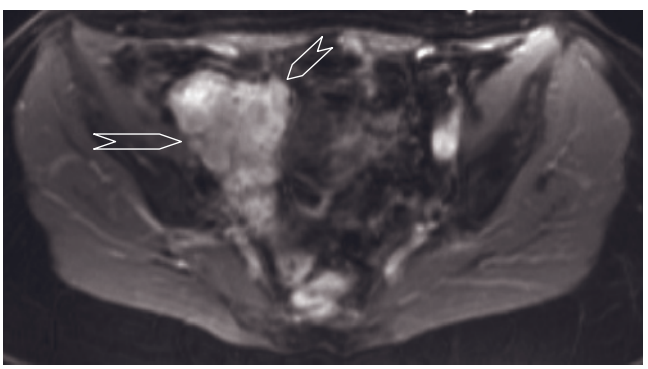

(*w*)

Fig. 10.56 (*Continued*) postgadolinium hepatic arterial dominant-phase SGE (*t*), transverse T1-weighted postgadolinium hepatic venous-phase fat-suppressed SGE (*u*), sagittal T1-weighted postgadolinium interstitial-phase fat-suppressed SGE (*v*), and transverse T1-weighted postgadolinium interstitial-phase fat-suppressed SGE (*w*) images demonstrate a recurrent retroperitoneal sarcoma (open arrows, *w*) in another patient with pancreas (white long thick arrows, *t, u*), liver (black arrows, *t, u*), kidney (white thin short arrow, *u*), and bone (white long thin arrows, *v*) metastases. The liver metastasis that shows intense enhancement on the hepatic arterial dominant phase and washout on the hepatic venous phase is hypervascular. The pancreatic metastasis shows peripheral ring enhancement progressively on postgadolinium images. The kidney metastasis is seen as hypointense focus on the interstitial-phase image. Sagittal plane is helpful for the demonstration of vertebral metastases that demonstrate intense enhancement on the interstitial phase. Note that bone marrow signal is low because of prior blood transfusions.

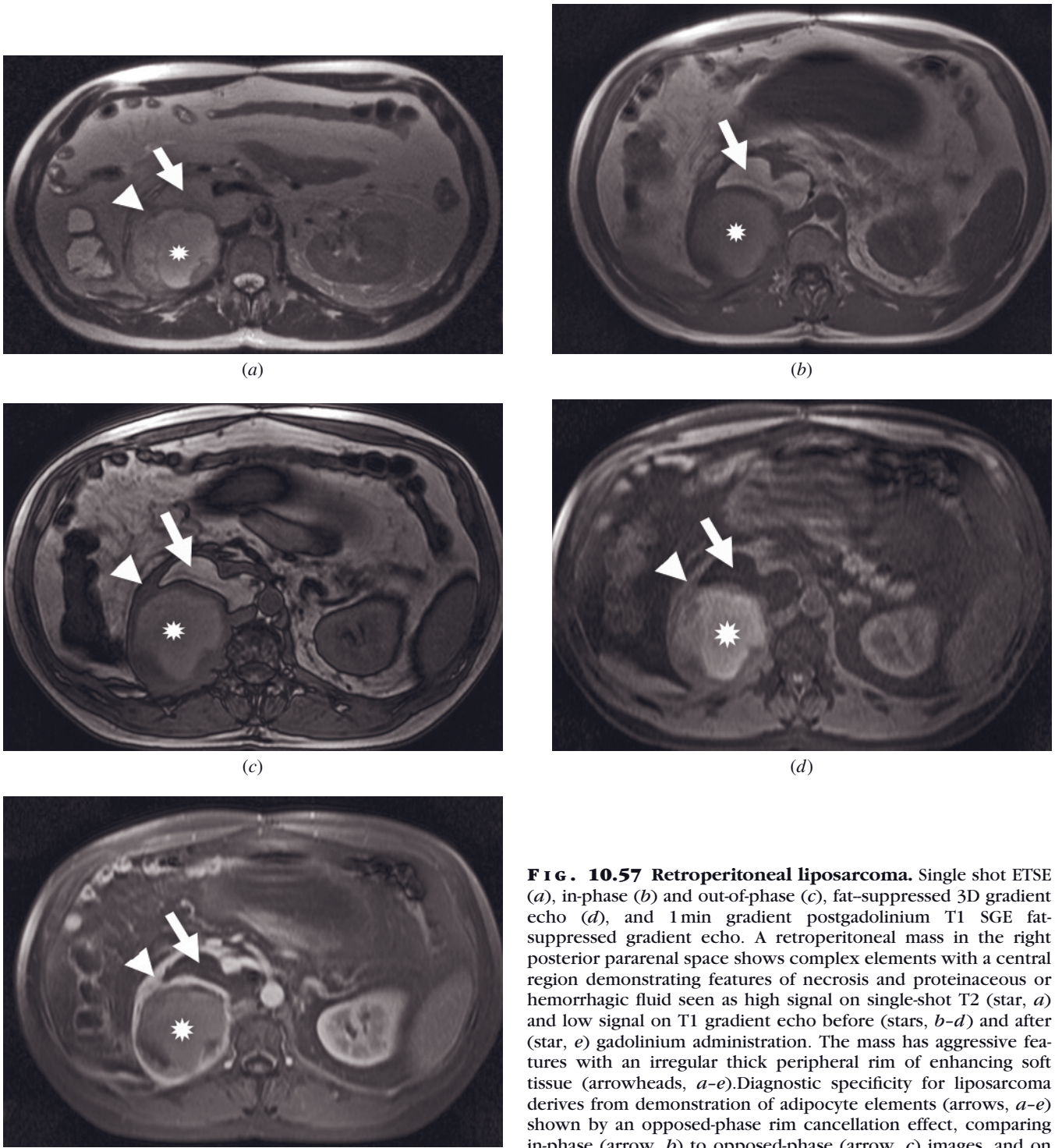

FIG. 10.57 Retroperitoneal liposarcoma. Single shot ETSE (*a*), in-phase (*b*) and out-of-phase (*c*), fat–suppressed 3D gradient echo (*d*), and 1 min gradient postgadolinium T1 SGE fat-suppressed gradient echo. A retroperitoneal mass in the right posterior pararenal space shows complex elements with a central region demonstrating features of necrosis and proteinaceous or hemorrhagic fluid seen as high signal on single-shot T2 (star, *a*) and low signal on T1 gradient echo before (stars, *b–d*) and after (star, *e*) gadolinium administration. The mass has aggressive features with an irregular thick peripheral rim of enhancing soft tissue (arrowheads, *a–e*).Diagnostic specificity for liposarcoma derives from demonstration of adipocyte elements (arrows, *a–e*) shown by an opposed-phase rim cancellation effect, comparing in-phase (arrow, *b*) to opposed-phase (arrow, *c*) images, and on fat-suppressed image that demonstrates drop in signal (arrow, *d*).

contrast. MRI may be superior to CT imaging because CT imaging may not detect small tumor masses or involved lymph nodes in this mainly pediatric population because of small patient size and lack of retroperitoneal fat. The T2-weighted single-shot echo-train spin-echo sequence should be part of the imaging protocol as it is very resistant to motion artifacts from movement or respiration. This is important in pediatric patients, who may move during the acquisition, and in problematic areas such as the subdiaphragmatic paraspinal retroperitoneum. Added advantages of MRI include the lack of ionizing radiation and higher soft tissue

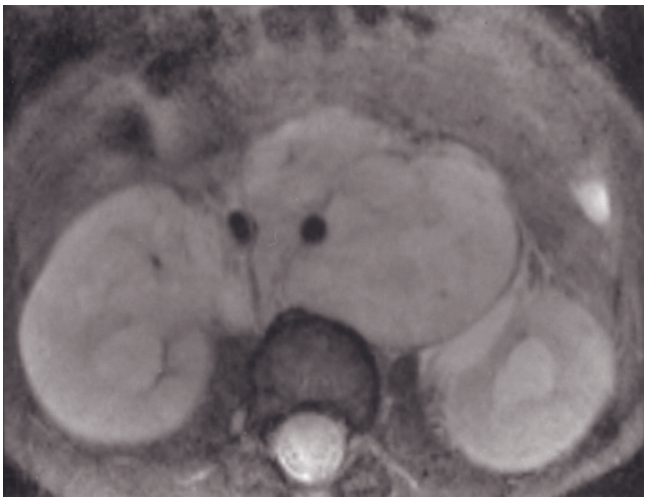

(*a*)

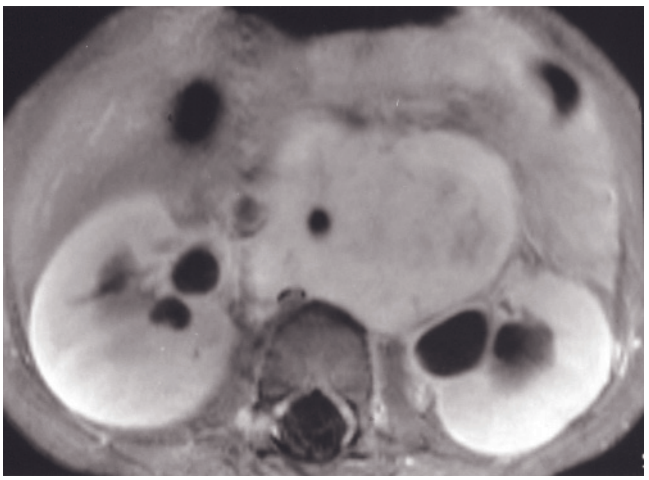

(*b*)

(*c*)

FIG. 10.58 Embryonal rhabdomyosarcoma. T2-weighted ETSE fat-suppressed (*a*) and transverse (*b*) and sagittal (*c*) interstitial-phase gadolinium-enhanced T1-weighted fat-suppressed SE images in a 21-month-old patient with embryonal rhabdomyosarcoma. There is massive enhancing retroperitoneal adenopathy that lifts and encases the aorta, iliac vessels, and IVC. The lymph nodes are moderately hyperintense on T2-weighted images (*a*) and enhance moderately intensely with mild heterogeneity on postgadolinium images (*b, c*).

contrast resolution. Furthermore, MRI is the method of choice for imaging of the spine and delineation of tumor involving neural and perineural structures.

PSOAS MUSCLE

Diseases affecting the psoas muscle more commonly originate from adjacent structures and involve the muscle by direct extension. These include malignant and infectious processes of the spine, kidney, bowel, pancreas, and retroperitoneal lymph nodes [103, 104]. Atrophy of the iliopsoas from neuromuscular disease can occur. Spontaneous hemorrhage may also occur in the iliopsoas muscle and is most frequently observed in patients on anticoagulant therapy or in hemophiliacs. Primary tumors of the muscle are rare, but the psoas can be the site of metastatic deposits.

The psoas muscle is well evaluated by MRI. The normal muscle is low in signal intensity on T2-weighted images. As most disease processes are high in signal intensity on T2-weighted images (fig. 10.60), they are usually clearly shown [103, 104]. Imaging in the coronal or sagittal plane provides direct evaluation of the full

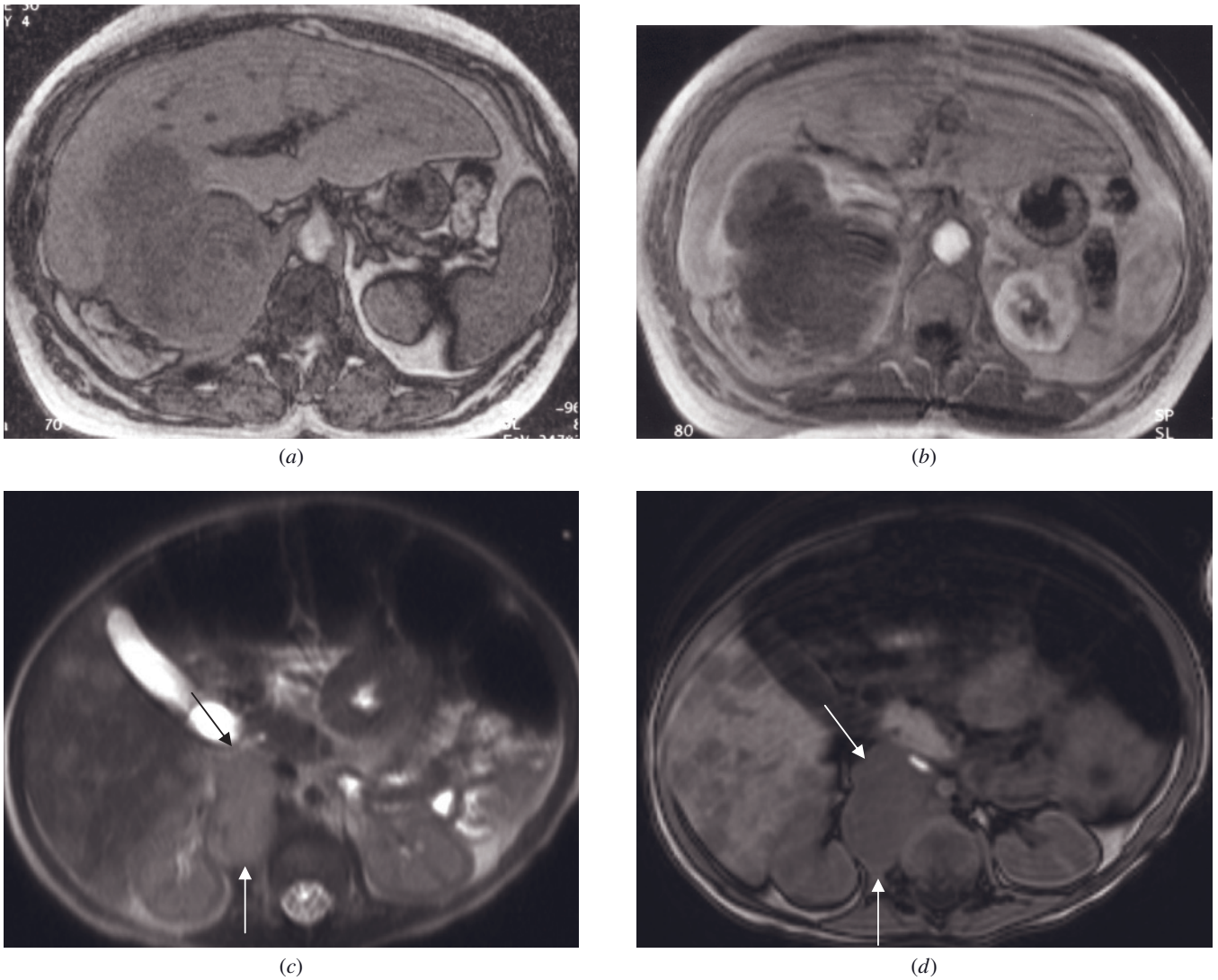

(*a*) (*b*)

(*c*) (*d*)

FIG. 10.59 Hemangiopericytoma. Transverse out-of-phase SGE (*a*) and immediate postgadolinium SGE (*b*) images show a large lobulated necrotic mass in the right abdomen that invades the right kidney and the liver. Histopathologic examination established the diagnosis of hemangiopericytoma. **Neuroblastoma.** T2-weighted single-shot echo-train spin-echo (*c*) and T1-weighted out-of-phase SGE (*d*) images demonstrate a large retroperitoneal mass and multiple liver metastases in an infant patient with neuroblastoma. The mass compresses the pancreatic head and displaces the pancreatic head anteriorly and the IVC anteromedially.

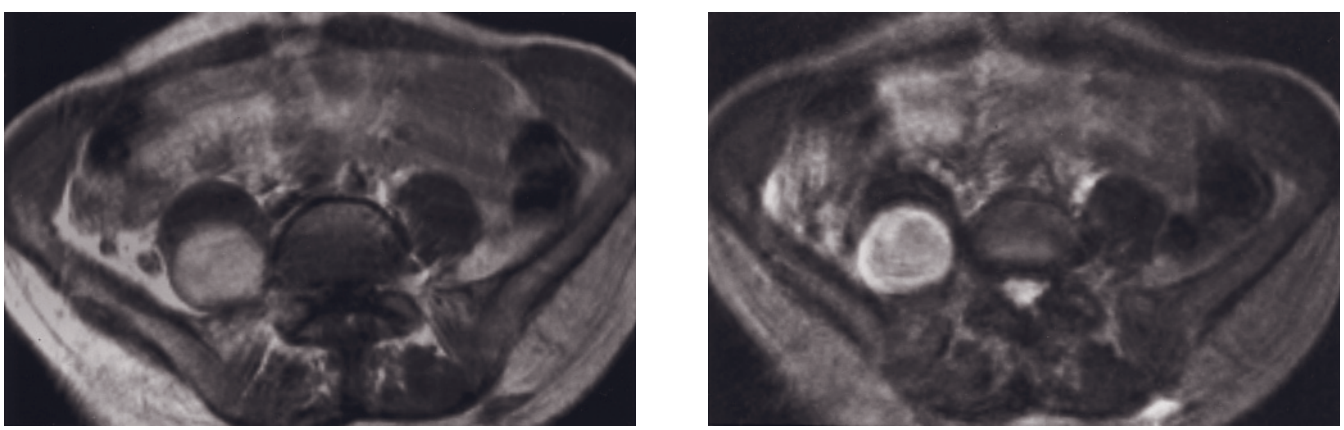

(*a*) (*b*)

FIG. 10.60 Neurogenic psoas tumor. T1-weighted spin-echo (*a*) and T2-weighted spin-echo (*b*) images. A well-defined rounded tumor is noted in the right psoas muscle. The tumor is moderate in signal intensity on the T1-weighted image and high in signal intensity on the T2-weighted image. High signal intensity on T2-weighted images is a common feature of tumors of neural origin.

craniocaudal extent of the muscle. Lymph nodes are well evaluated on precontrast sagittal SGE images in a background of retroperitoneal fat, but they are isointense with psoas muscle. Lymph nodes are readily distinguished from psoas muscle on T2-weighted images because muscle is low in signal intensity compared to the moderate signal intensity of lymph nodes [103, 104]. Metastatic disease to the iliopsoas muscle is moderate to high in signal intensity on T2-weighted images and shows substantial enhancement on gadolinium-enhanced fat-suppressed T1-weighted SGE images (figs. 10.61 and 10.62). Infection is well shown on MR images as high-signal-intensity areas on fat-suppressed T2-weighted images and intense enhancement on gadolinium-enhanced fat-suppressed SGE or 3D-GE images (fig. 10.63). Destruction of adjacent vertebral body is common with associated extension into the disk space. Disk space involvement is more typical of infection than of malignancy. On postgadolinium images, abscesses are shown as expansile lesions with signal-void centers, intense peripheral enhancement, and enhancement of the periabscess tissues (see fig. 10.63).

Hemorrhage is well shown on MR images because of the high signal intensity of subacute blood on T1-weighted images [105–107]. The appearance of a fluid structure that possesses a high-signal peripheral rim in noncontrast T1-weighted fat-suppressed images is virtually pathognomonic for subacute hematoma. The use of fat suppression permits the detection of even small amounts of blood, and imaging in different planes provides direct evaluation of the dimensions and extent of the hematoma (fig. 10.64).

THE BODY WALL

Neoplasms

Benign Tumors

Desmoid tumors and cysts (fig. 10.65) are two common benign body wall tumors [108]. Desmoids may be encountered in the setting of Gardner syndrome and are relatively avascular, locally aggressive masses with a propensity for recurrence, occurring more commonly in middle-aged women [109]. They arise most commonly from the aponeurosis of the rectus abdominis muscle and may on occasion be very large, mimicking intra-abdominal masses [109]. They are readily detected on T1-weighted images as low-signal-intensity masses in a background of high-signal-intensity fat (fig. 10.65). In mature desmoids, areas of abundant fibrosis result in low signal intensity on T2-weighted images [109].

The body wall also may be involved in cases of endometriosis occurring almost exclusively along scars from previous surgery (fig. 10.65). Endometriomas are generally shown better on noncontrast T1-weighted fat-suppressed SGE or 3D-GE images as high-signal-intensity foci. Lipomas are also common lesions, and they can be easily diagnosed with their characteristic MR appearance.

Malignant Tumors

Direct tumor spread, hematogenous metastases (figs. 10.66 and 10.67), sarcomas (figs. 10.68 and 10.69), and lymphomas can involve the body wall. Tumors are medium-signal-intensity masses that are well defined in the background of high-signal-intensity subcutaneous fat on T1-weighted SE or SGE images. On gadolinium-enhanced fat-suppressed T1-weighted images they are moderate to high in signal intensity in a background of low-signal-intensity fat. Imaging in the sagittal plane permits direct visualization of the extent of the tumor and its relationship to the abdominal wall muscles.

Tumors arising in or involving the skeletal structures of the abdomen and pelvis are well-shown on a combination of T1-weighted images, T2-weighted fat-suppressed images, and gadolinium-enhanced fat-suppressed SGE or 3D-GE images (figs. 10.70 and 10.71).

Miscellaneous

Hernias, hematomas, infection, arteriovenous malformations, and varices (fig. 10.72) may involve the abdominal wall. (Hernias are discussed in Chapter 7, *Peritoneal Cavity.*) Malignant or vascular lesions are well shown on SGE and gadolinium-enhanced fat-suppressed SGE images. Vascular structures are shown as low-signal-intensity structures on SGE images and enhance after gadolinium administration. The enhancement is rendered more conspicuous with the addition of fat suppression on postcontrast images. Involvement of the abdominal wall in cases of hemangiomas/lymphangiomas is not infrequent and may be part of a larger mass, usually of congenital origin. MRI demonstrates multiple ovoid and tubular structures infiltrating subcutaneous tissue and abdominal wall muscles (fig. 10.73). The hemangiomatous component is comprised of smaller vascular spaces that may enhance after gadolinium administration, whereas the lymphangiomatous components, which are generally cystic, larger in size, and high in signal intensity on T1-weighted images, demonstrate dependent low-signal-intensity layers on T2-weighted images (fig. 10.73). MRI using multiplanar imaging demonstrates the extent of the abnormality and degree of infiltration of muscles and abdominal structures. Heavily T2-weighted echo-train spin-echo images have been used to image patients with generalized lymphangiomatosis, because the fluid-filled cystic spaces are high in signal intensity on these images. Differentiation from hemangiomatous

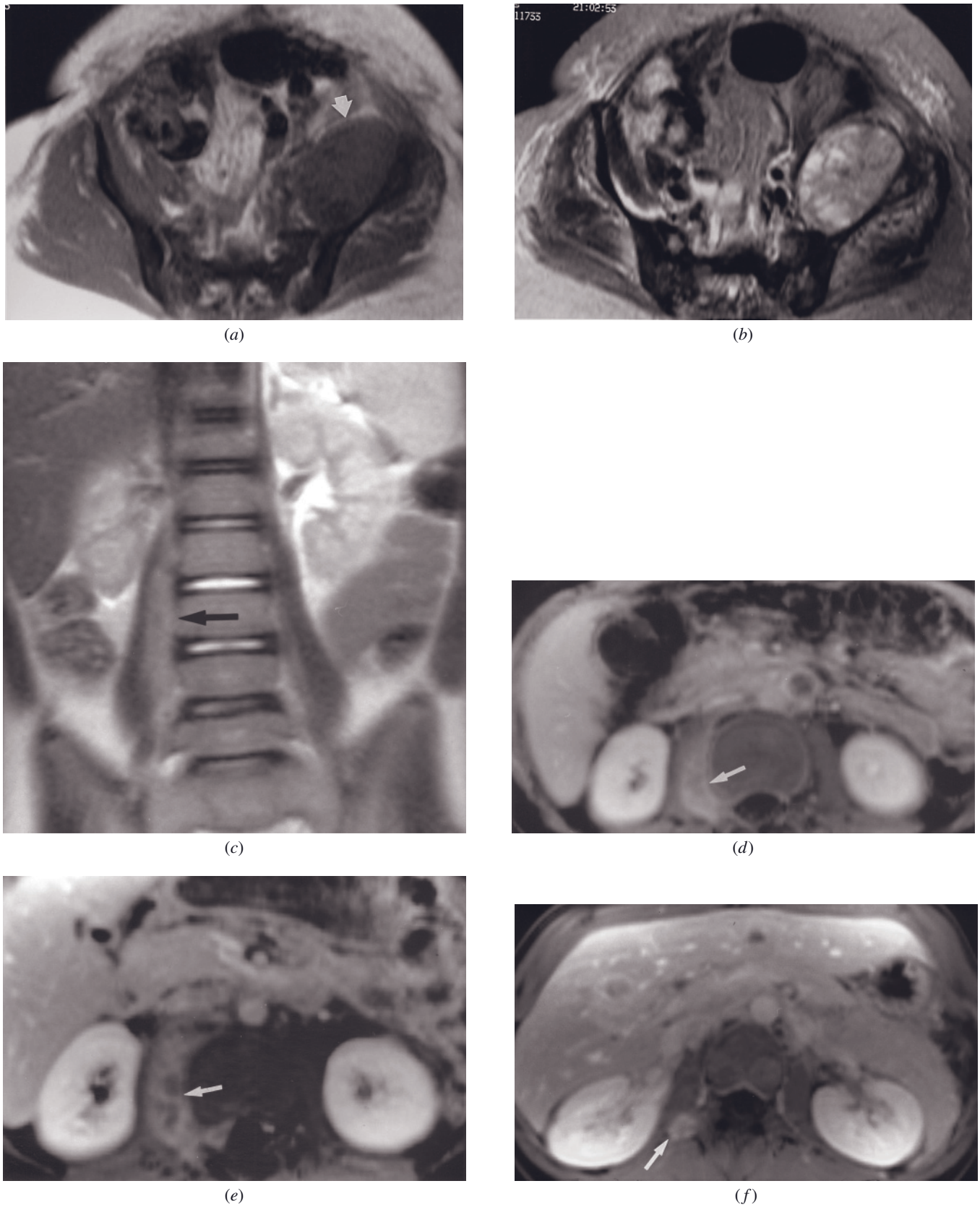

FIG. 10.61 Metastasis. SGE (*a*) and T2-weighted spin-echo (*b*) images. A large heterogeneous mass (arrow, *a*) is present in the left iliopsoas muscle, consistent with metastasis from breast cancer. The metastasis is low in signal intensity on the SGE image (*a*) and high in signal intensity on the T2-weighted spin-echo image (*b*). Coronal T2-weighted SS-ETSE (*c*) and transverse 90-s gadolinium-enhanced fat-suppressed SGE (*d*) images in a second patient, who has a history of neuroblastoma, demonstrate an area within the medial right psoas muscle with high signal on the T2-weighted image (arrow, *c*) and peripheral enhancement after contrast administration (*d*), which represents a metastasis. Transverse 90-s gadolinium-enhanced fat-suppressed SGE images (*e, f*) in 2 additional patients with cancer demonstrate metastatic masses (arrow, *e, f*) involving the right psoas muscle. The greater enhancement of the metastases relative to the psoas muscle increases their conspicuity.

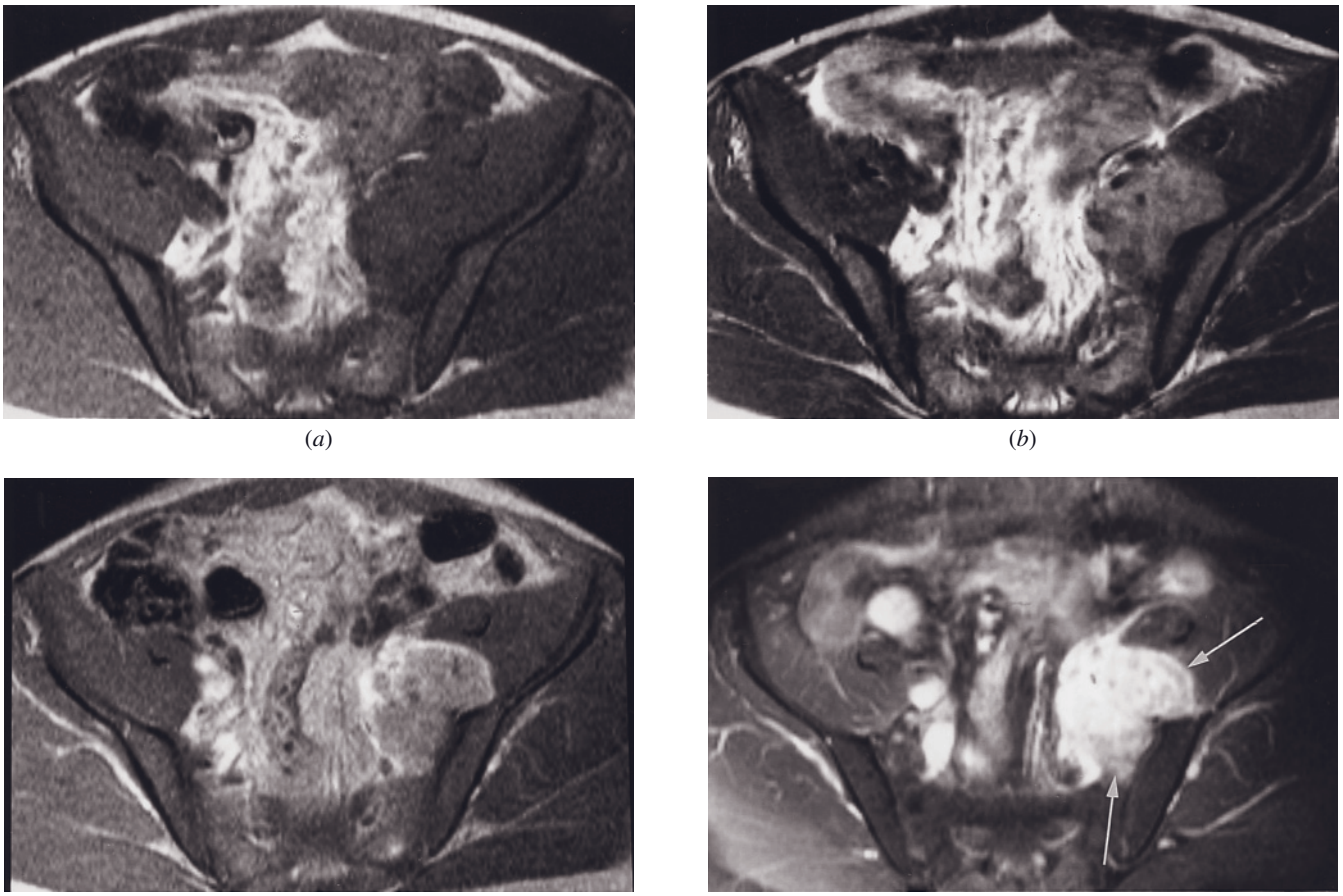

(*a*) (*b*) (*c*) (*d*)

FIG. 10.62 Metastasis to the iliacus muscle from melanoma. SGE (*a*), T2-weighted spin-echo (*b*), 45-s postgadolinium (*c*), and gadolinium-enhanced T1-weighted fat-suppressed spin-echo (*d*) images. A mass is identified in the posterior portion of the left iliacus muscle. The mass is isointense to muscle on the SGE image (*a*) and heterogeneously high in signal intensity on the T2-weighted image (*b*) and enhances in a heterogeneous fashion after gadolinium administration (*c, d*).The degree of enhancement and delineation of its borders are best appreciated on the postgadolinium T1-weighted fat-suppressed spin-echo image (arrows, *d*).

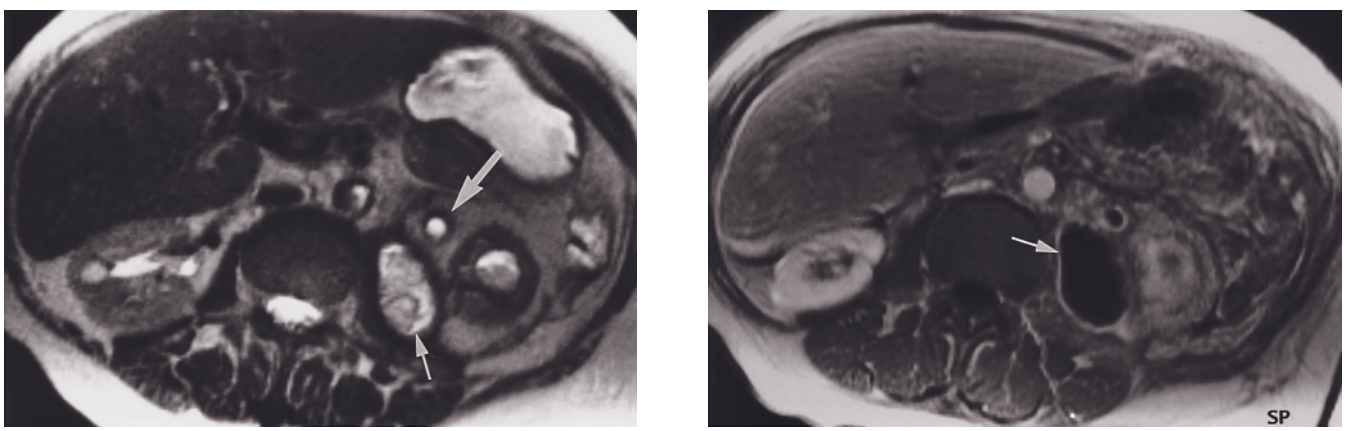

(*a*) (*b*)

FIG. 10.63 Psoas abscess. T2-weighted SS-ETSE (*a*), 45-s postgadolinium SGE (*b*), and transverse (*c*) and coronal (*d*) interstitial-phase gadolinium-enhanced fat-suppressed SGE images. A complex fluid collection is present in an enlarged left psoas muscle. The fluid is heterogeneously high in signal intensity on the T2-weighted image (arrow, *a*) and contains low-signal-intensity necrotic debris. The left ureter (large arrow, *a*) is dilated and has a thick wall. The abscess wall (arrow, *b*) and the ureteral wall demonstrate

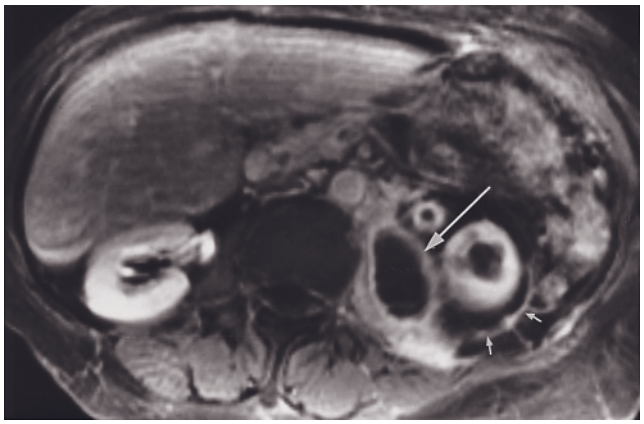

(*c*)

(*d*)

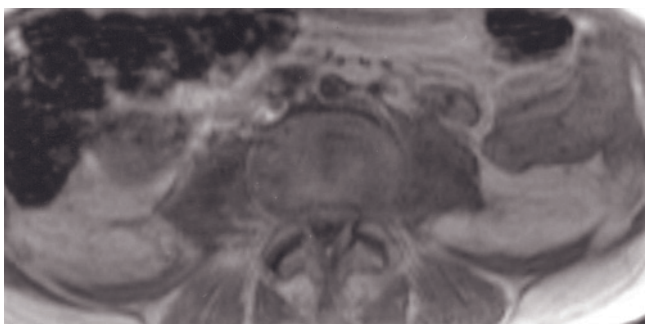

(*e*)

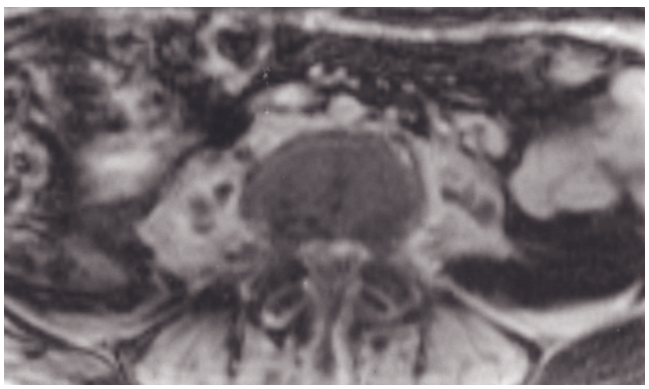

(*f*)

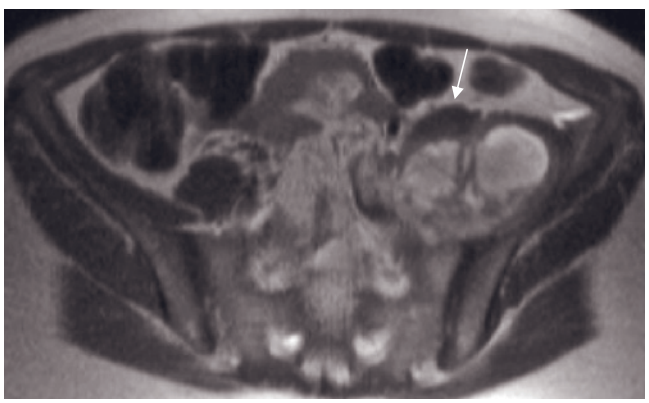

(*g*)

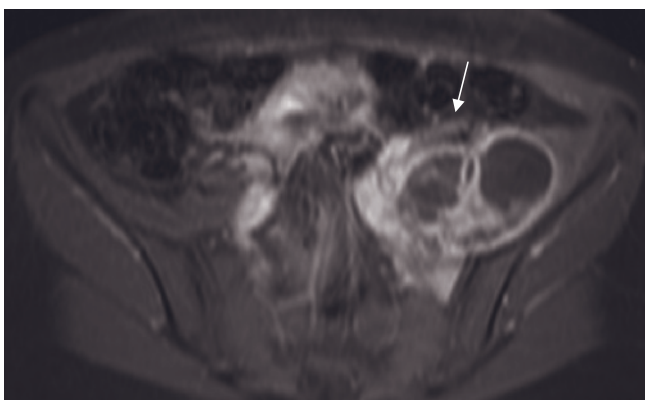

(*h*)

Fig. 10.63 (*Continued*) enhancement on the 45-s postgadolinium SGE image (*b*), which progresses on the interstitial-phase images (*c, d*) to intense enhancement of the abscess-containing psoas muscle (long arrows, *c, d*) and the ureteral wall. Ill-defined borders with linear enhancing strands reflect the extension of the inflammation into the pararenal and perirenal fat. Enhancement of the thickened left perirenal fascia (small arrows, *c*) is also noted. The contents of the abscess are signal void on the postgadolinium images (*b–d*). Imaging in the coronal plane (*d*) provides direct evaluation of the craniocaudal extent of the abscess. The right psoas muscle is uninvolved and remains low in signal intensity on the postgadolinium images. The collecting system of the left kidney is dilated and low in signal intensity on the interstitial-phase gadolinium-enhanced fat-suppressed SGE images (*c, d*) because of absent gadolinium excretion in a kidney with xanthogranulomatous pyelonephritis. SGE (*e*) and interstitial-phase gadolinium-enhanced fat-suppressed SGE (*f*) images in a second patient demonstrate increased enhancement of the psoas muscles bilaterally, which contain fluid collections that have central low-signal areas with peripheral rim enhancement, consistent with abscesses. T2-weighted single-shot echo-train spin-echo (*g*), T1-weighted postgadolinium interstitial-phase fat-suppressed SGE (*h*) images demonstrate left iliopsoas abscess in another patient. Septations are present in the abscess cavity. The uninvolved part of psoas muscle (arrows, *g, h*) is anterior to the abscess cavity. T2-weighted single-shot echo-train spin-echo (*i*) and T1-weighted

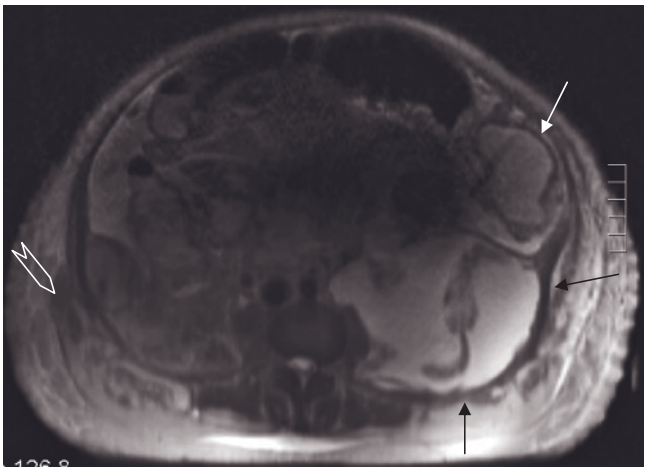

(*i*)

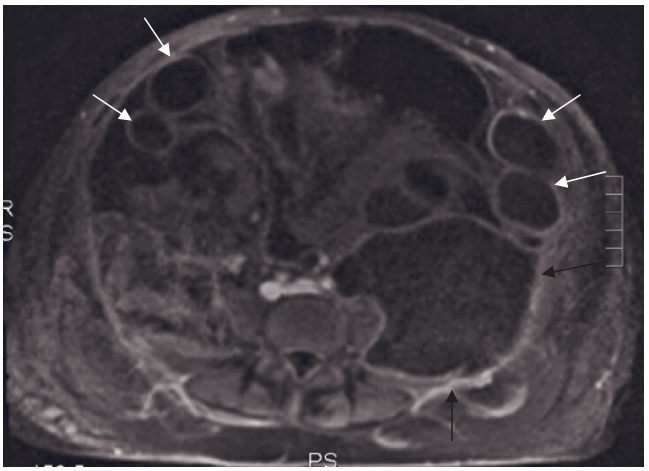

(*j*)

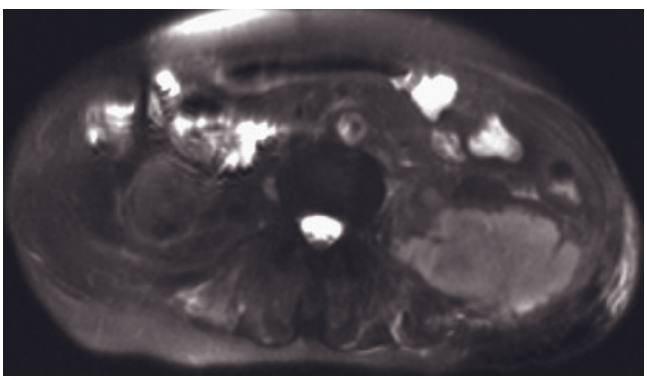

(*k*)

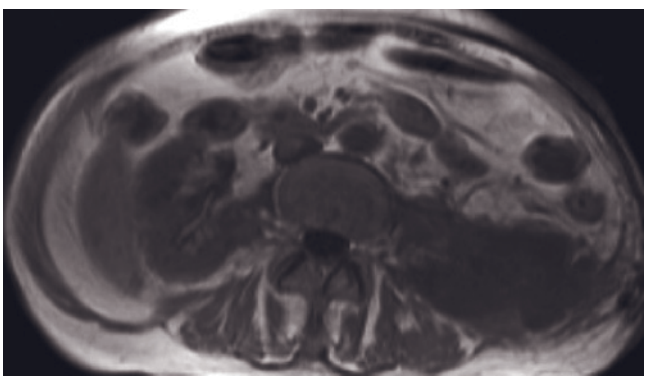

(*l*)

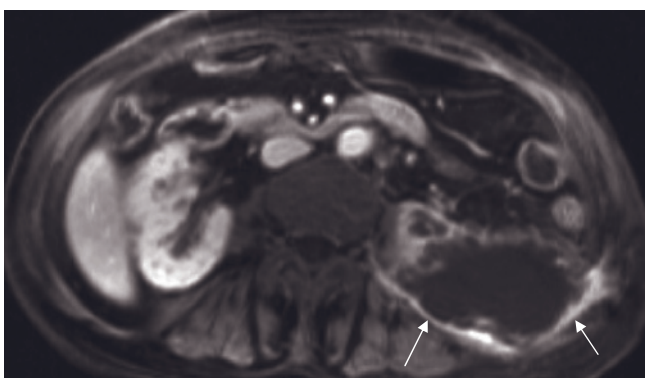

(*m*)

FIG. 10.63 (*Continued*) postgadolinium interstitial-phase magnetization prepared rapid gradient echo (*j*) images at 3.0 T demonstrate multiple retroperitoneal (black arrows, *i, j*), intraperitoneal, and subcutaneous abscess in another noncooperative patient with similar findings. T2-weighted fat-suppressed single-shot echo-train spin-echo (*k*), T1-weighted SGE (*l*), and T1-weighted postgadolinium interstitial- phase fat-suppressed SGE (*m*) images demonstrate left iliopsoas abscess in another patient. Septations are again present in the abscess cavity. The left psoas muscle shows intense inflammatory enhancement on postgadolinium image. The transversalis fascia (arrows, *m*) also shows intense enhancement. Note that there is inflammation in the left subcutaneous region adjacent to the abscess cavity as well.

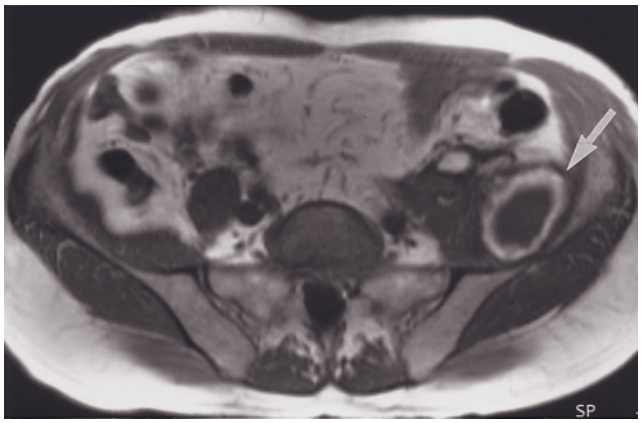

(*a*)

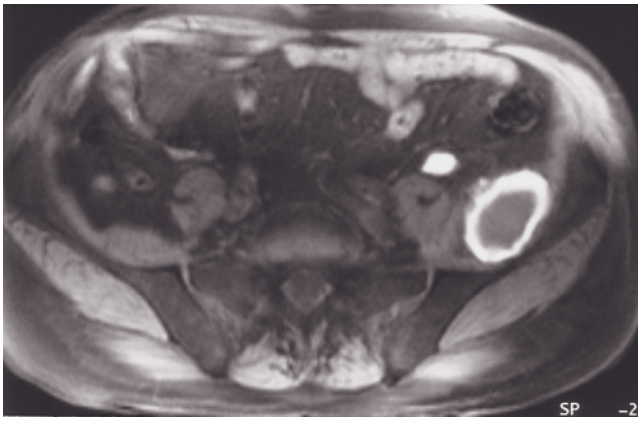

(*b*)

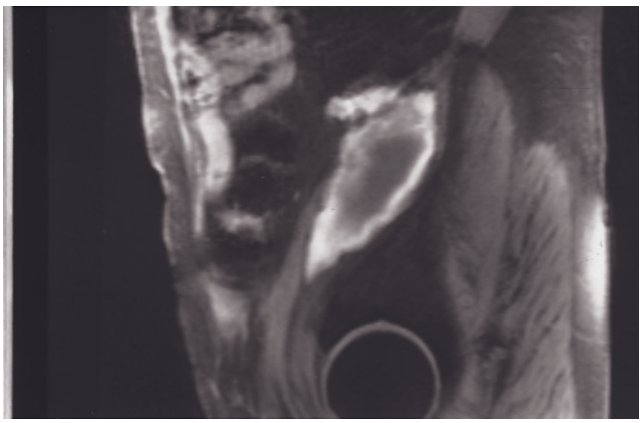

(*c*)

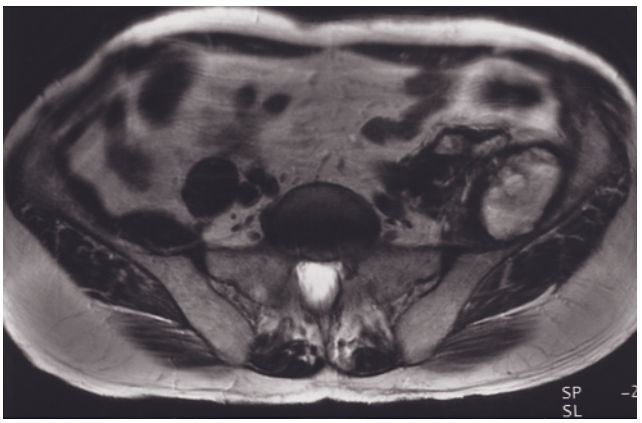

(*d*)

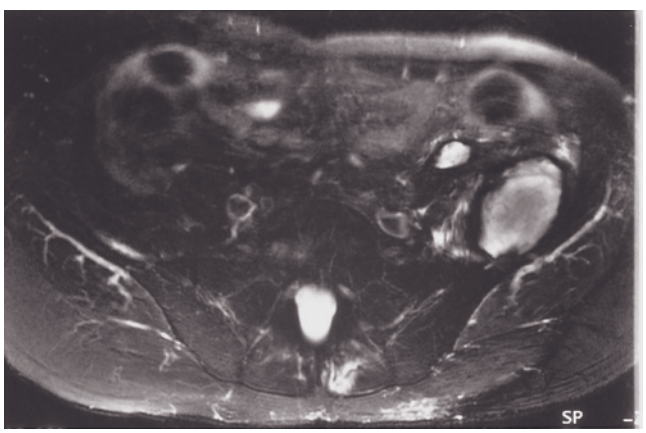

(*e*)

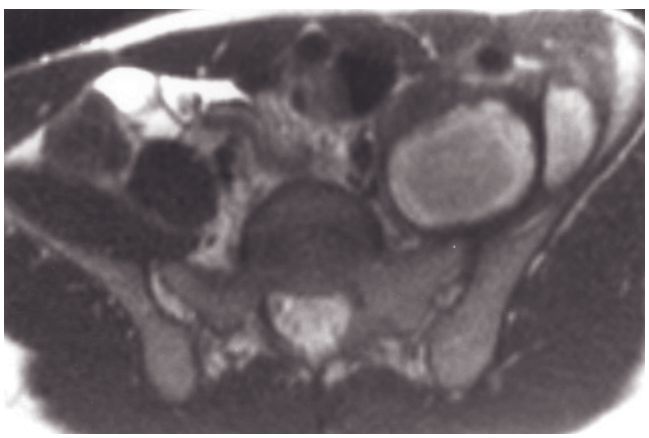

(*f*)

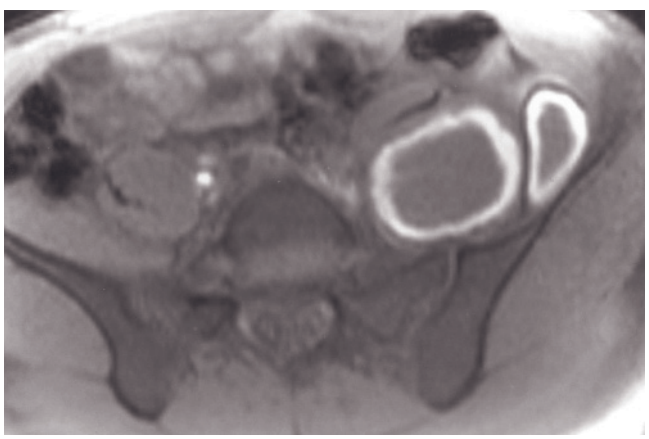

(*g*)

Fig. 10.64 Hematoma in the left iliacus muscle. SGE (*a*), transverse (*b*) and sagittal (*c*) fat-suppressed SGE, T2-weighted echo-train spin-echo (*d*), and T2-weighted fat-suppressed echo-train spin-echo (*e*) images. The left iliacus is enlarged and contains a complex fluid collection that is low in signal intensity centrally with a high-signal-intensity peripheral rim (arrow, *a*) on the T1-weighted images (*a–c*) and heterogeneously high in signal intensity on the T2-weighted images (*d, e*). The hyperintensity of the peripheral rim is accentuated with the use of fat suppression on the T1-weighted images (*b, c*). The sagittal fat-suppressed SGE image (*c*) demonstrates the craniocaudal extent of the hematoma. The mixed signal intensity of the hematoma reflects blood products in different stages of degradation. T2-weighted SS-ETSE (*f*) and transverse (*g*), coronal (*h*), and sagittal (*i*) fat-suppressed SGE images in a second patient demonstrate a similar appearance of hematomas involving the left iliopsoas muscle.

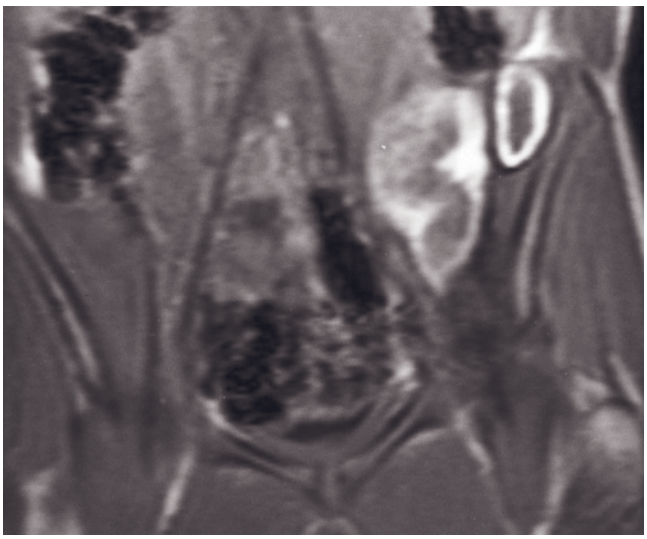

(*h*)

(*i*)

FIG. 10.64 (*Continued*)

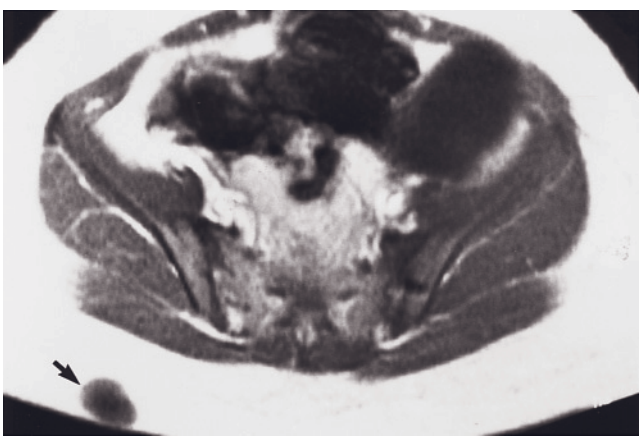

(*a*)

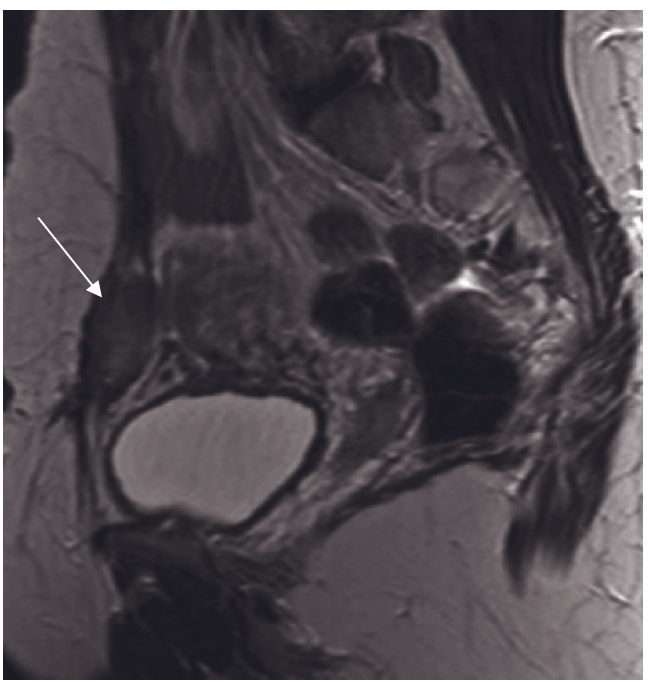

(*b*)

FIG. 10.65 Desmoid. SGE image (*a*) in a patient with Gardner syndrome demonstrates a subcutaneous desmoid (arrow, *a*) in the right gluteal region. Fibrous tumors are low in signal intensity on T1-weighted images and are readily detected against a background of high-signal-intensity fat. Sagittal T2-weighted high-resolution fast spin-echo (*b*), transverse T1-weighted SGE (*c*),

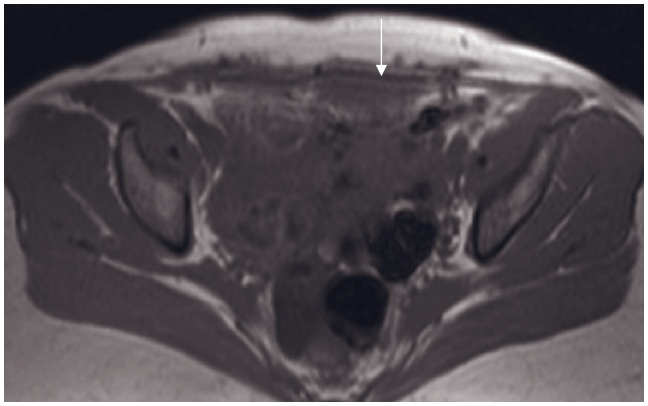

(*c*)

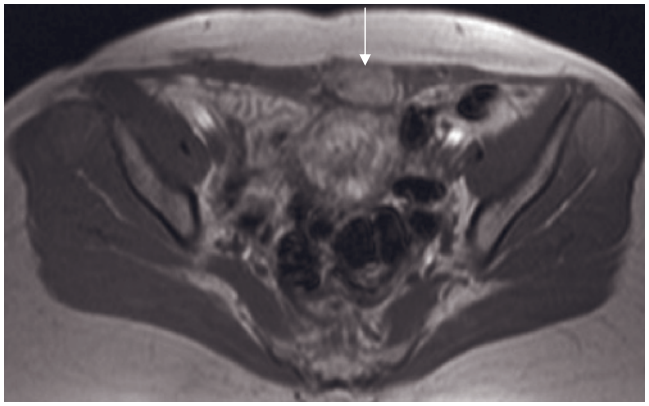

(*d*)

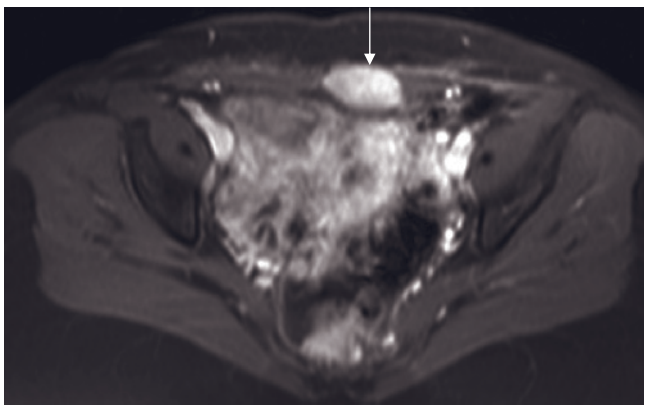

(*e*)

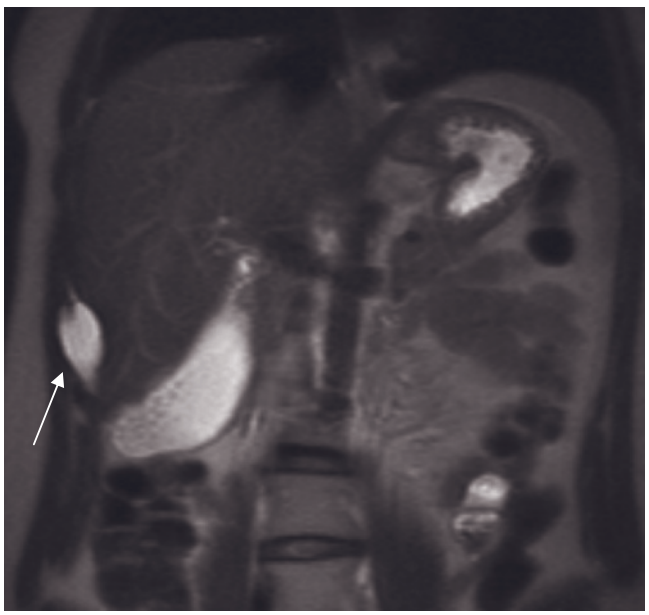

(*f*)

(*g*)

Fig. 10.65 (*Continued*) transverse T1-weighted postgadolinium immediate SGE (*d*), and transverse T1-weighted postgadolinium interstitial-phase fat-suppressed 3D-GE (*e*) images demonstrate a desmoid tumor (arrows, *b–e*) located in the rectus abdominis muscle in another patient. The tumor, which shows low signal on T2-weighted image because of its fibrotic nature, enhances progressively on postgadolinium images. **Cyst.** Coronal T2-weighted single-shot echo-train spin-echo (*f*), coronal T1-weighted SGE (*g*), T1-weighted postgadolinium hepatic arterial

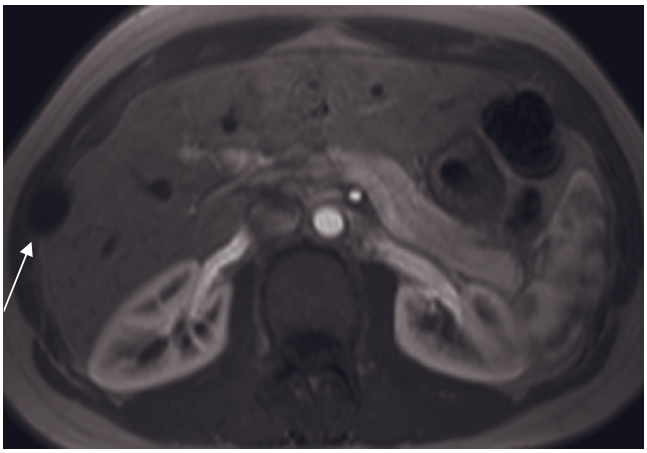

(*h*)

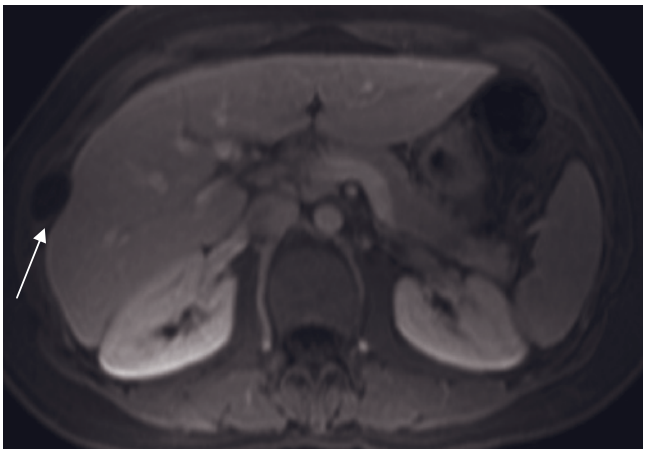

(*i*)

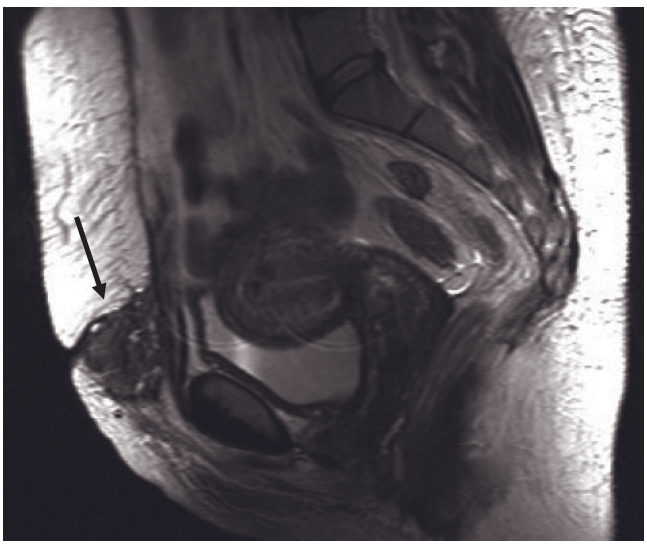

(*j*)

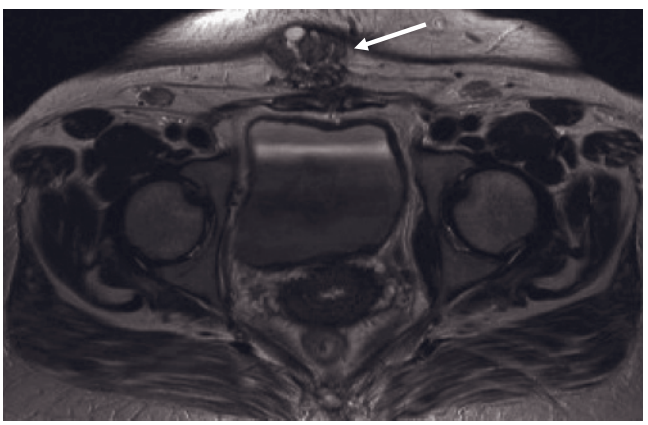

(*k*)

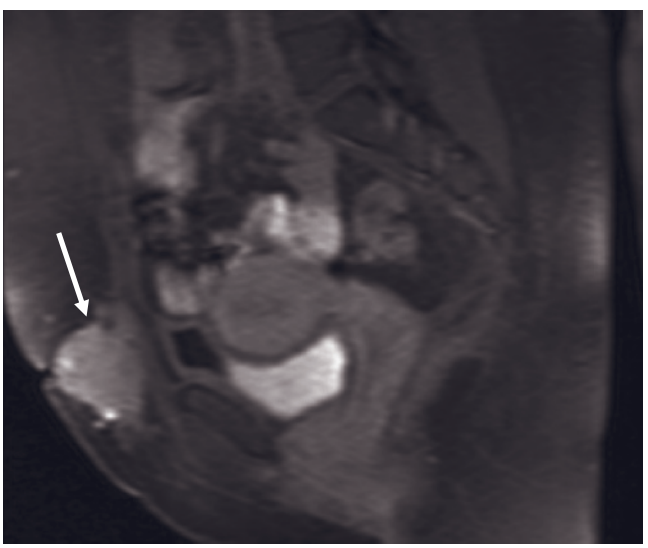

(*l*)

FIG. 10.65 (*Continued*) dominant-phase SGE (*h*), and T1-weighted postgadolinium interstitial-phase fat-suppressed 3D-GE (*i*) images demonstrate an abdominal wall cyst (arrows, *f–i*) in another patient. The structure of the cyst is homogeneous and shows high signal on T2-weighted image and low signal on T1-weighted precontrast image. The cyst does not demonstrate any enhancement on postgadolinium images. Note that the cyst is at different positions on coronal precontrast images because of respiration. **Endometriosis.** Sagittal (*j*) and transverse (*k*) high-resolution fast spin-echo T2-weighted and sagittal (*l*) and

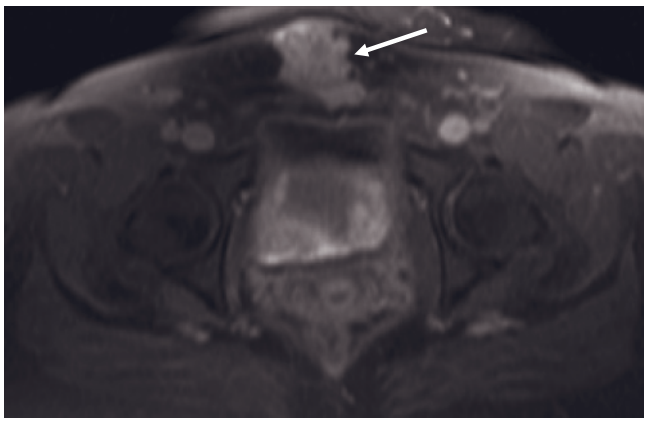

(*m*)

(*n*)

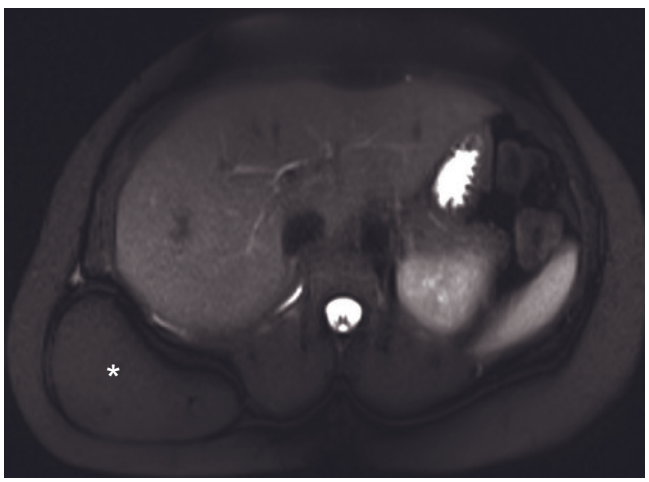

(*o*)

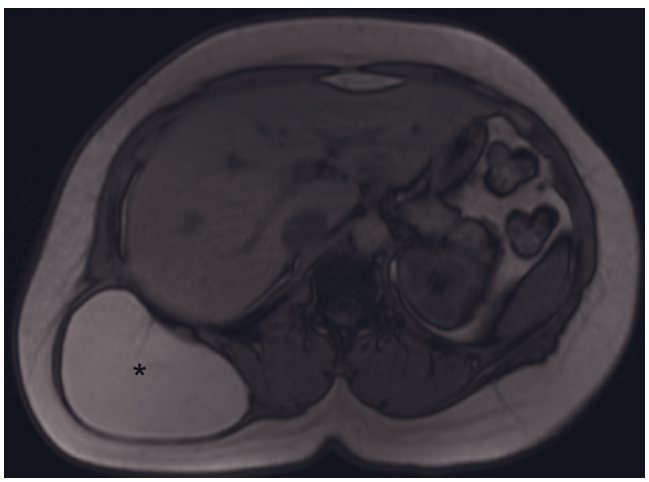

(*p*)

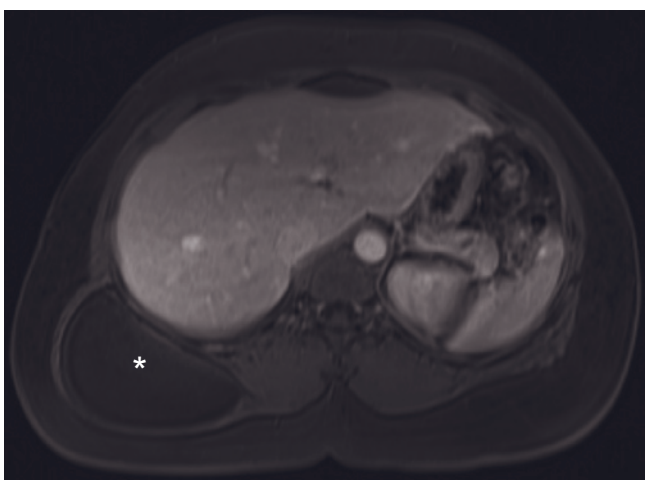

(*q*)

Fig. 10.65 (*Continued*) transverse (*m*) T1-weighted postgadolinium interstitial-phase fat-suppressed 3D-GE images demonstrate endometriosis (arrows, *j–m*) located along the scar in the subcutaneous tissue of anterior abdominal wall in another patient. Endometriosis shows heterogeneously low signal on T2-weighted images and prominent enhancement on postgadolinium images. Note the enlarged uterus and widened junctional zone in the uterus, which are consistent with adenomyosis. **Lipoma.** Coronal T2-weighted single-shot echo-train spin echo (*n*), transverse T2-weighted fat-suppressed single-shot echo-train spin-echo (*o*), T1-weighted out-of-phase SGE (*p*), and T1-weighted postgadolinium fat-suppressed interstitial phase 3D-GE (*q*) images demonstrate a large lipoma (*) in the right posterior body wall. The lipoma shows high signal on T2 (*n*)- and T1 (*p*)-weighted out-of-phase images and low signal on fat-suppressed T2 (*o*) and T1 (*q*)-weighted images. Note that there is phase cancellation artifact around the lipoma on out-of-phase image (*p*). These findings demonstrate the fat content of the lipoma.

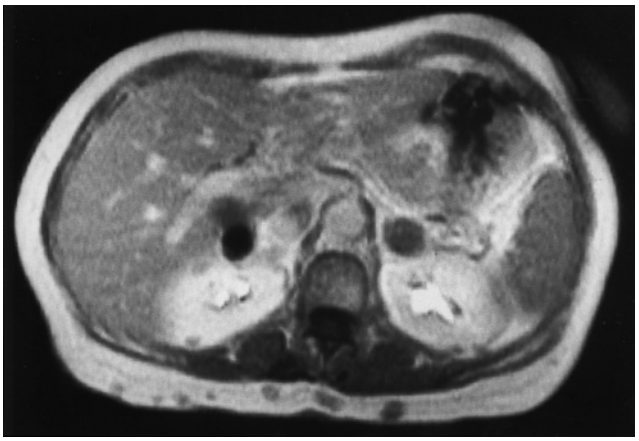

FIG. 10.66 Subcutaneous metastases. Delayed postgadolinium SGE image demonstrates multiple subcutaneous metastases from breast cancer.

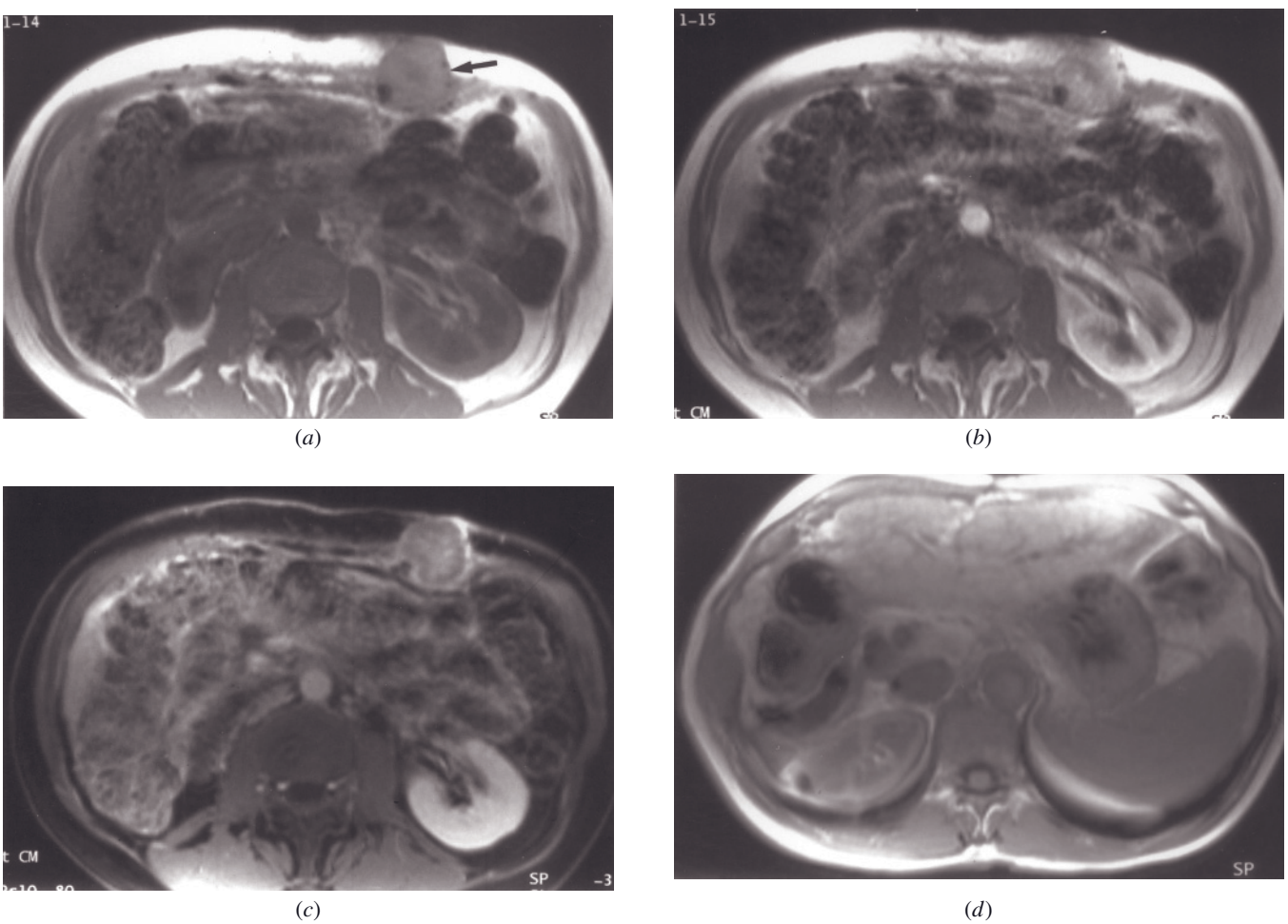

FIG. 10.67 Abdominal wall metastases from hepatocellular carcinoma (HCC). SGE (*a*), immediate postgadolinium SGE (*b*), and 90-s gadolinium-enhanced fat-suppressed SGE (*c*) images. An abdominal wall metastasis is present (arrow, *a*) that is isointense in T1 (*a*) and demonstrates moderate enhancement with mild heterogeneity on immediate postgadolinium image (*b*) and heterogeneous enhancement on delayed fat-suppressed image (*c*). The mass is well shown on sequences that have good contrast between tumor and background tissue, such as SGE and gadolinium-enhanced fat-suppressed SGE. Precontrast SGE (*d*) and interstitial-phase gadolinium-enhanced fat-suppressed SGE (*e*) images in a second patient, with recurrent HCC after right hepatectomy, demonstrate an oval mass within the right upper abdominal wall musculature that shows moderate enhancement (arrow, *e*).

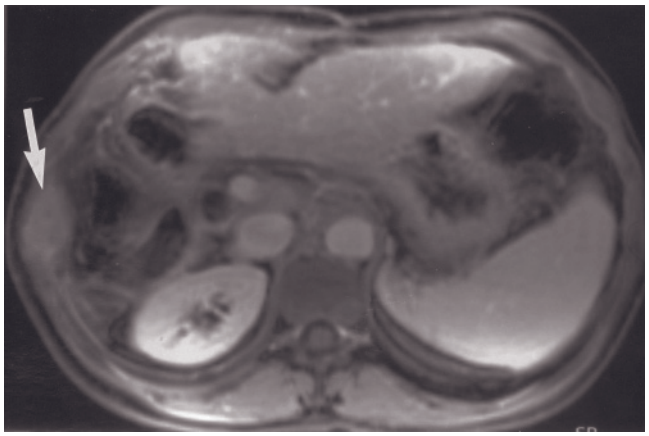

(*e*)

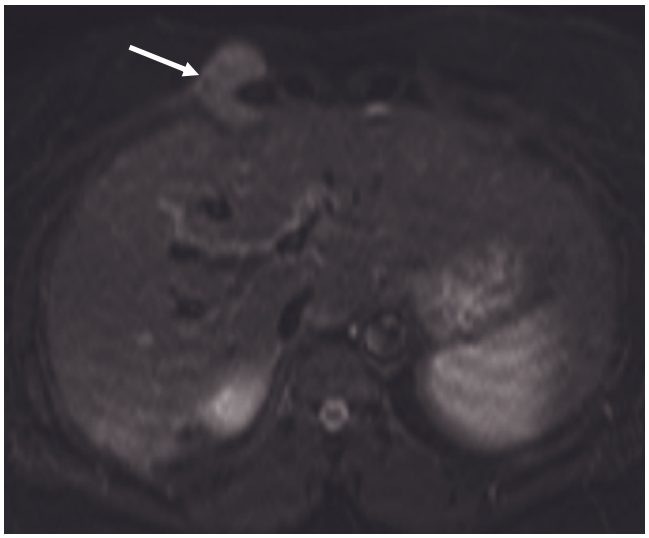

(*f*)

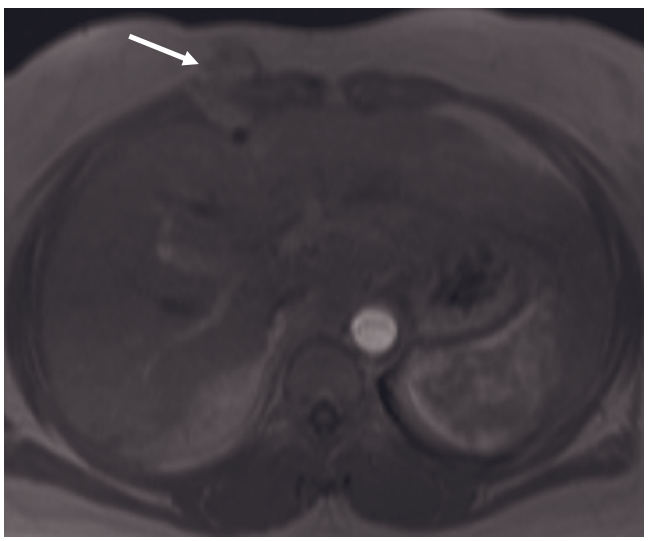

(*g*)

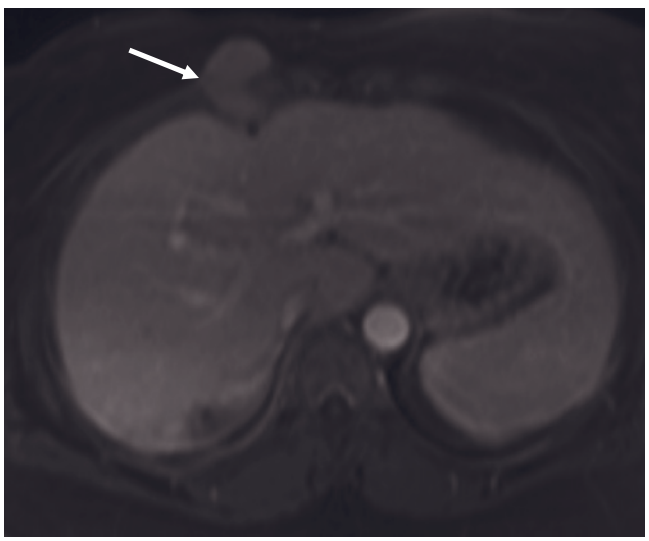

(*h*)

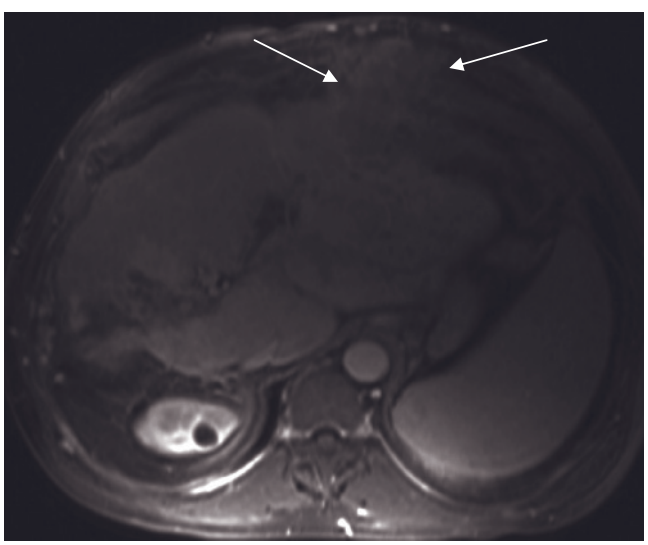

(*i*)

Fig. 10.67 (*Continued*) T2-weighted short tau inversion recovery (*f*), T1-weighted postgadolinium hepatic arterial dominant-phase SGE (*g*), and T1-weighted postgadolinium interstitial phase fat-suppressed 3D-GE (*h*) images demonstrate anterior abdominal wall metastasis (arrows, *f–h*) from HCC due to biopsy tract seeding in another patient. T1-weighted postgadolinium interstitial phase image (*i*) demonstrates the invasion of anterior abdominal wall by a large HCC in another patient.

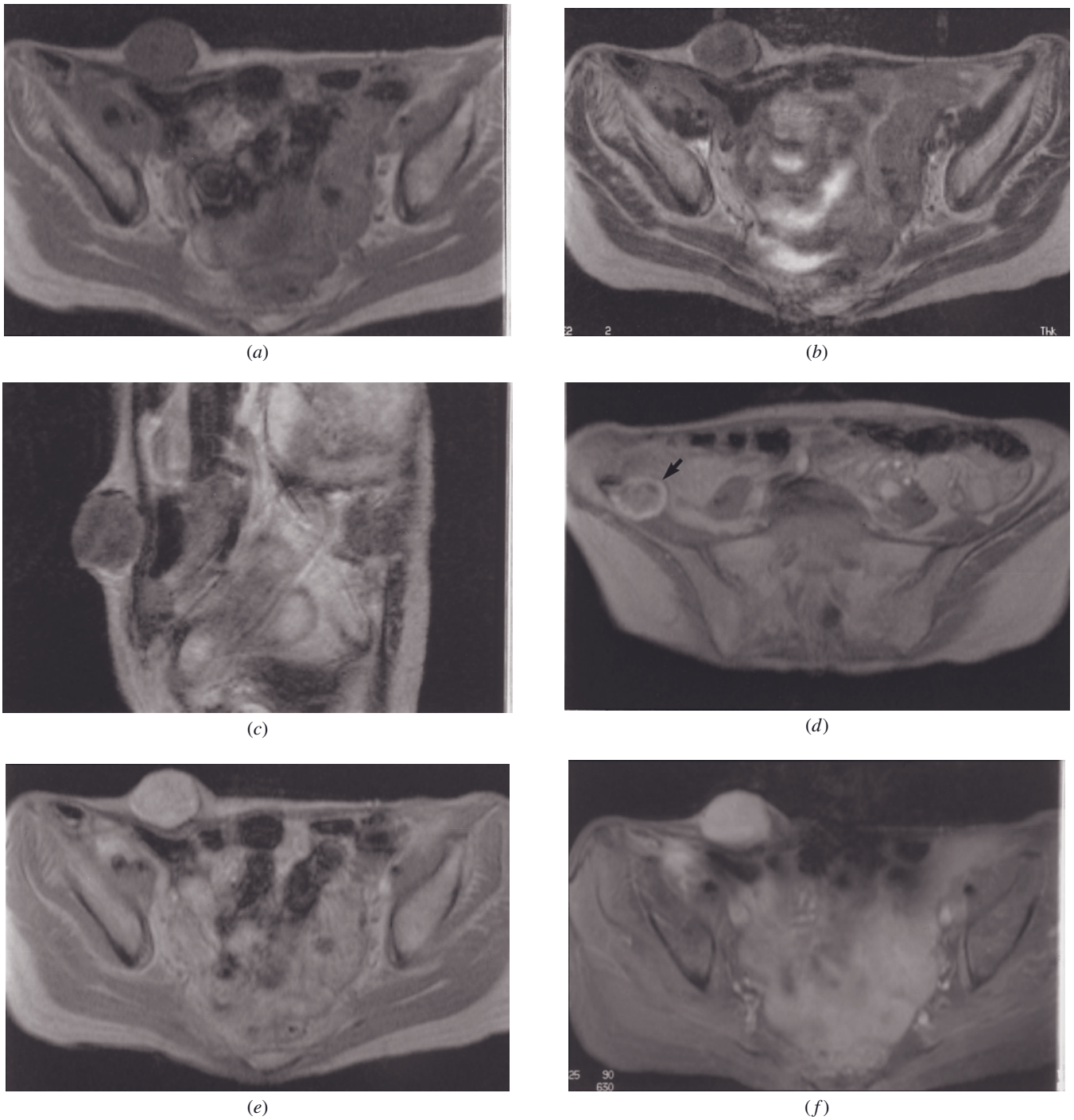

FIG. 10.68 Malignant fibrous histiocytoma of the right anterior abdominal wall. SGE (*a*), transverse (*b*) and sagittal (*c*) T2-weighted echo-train spin-echo, 90-s postgadolinium SGE at superior (*d*) and inferior (*e*) tomographic levels, and gadolinium-enhanced T1-weighted fat-suppressed spin-echo (*f*) images. The tumor is readily identified as a low-signal-intensity well-defined mass against the high-signal-intensity background of subcutaneous fat on the T1-weighted image (*a*) and is heterogeneously low to intermediate in signal intensity on the T2-weighted images (*b, c*).The tumor abuts and displaces the right rectus abdominis muscle, which is well shown on the sagittal T2-weighted image (*c*). The tumor enhances in a mildly heterogeneous fashion on the 45-s postgadolinium SGE image (*e*). A metastatic tumor nodule (arrow, *d*) with predominantly peripheral heterogeneous enhancement is also present at a higher tomographic level (*d*) in the right iliacus muscle. Enhancement of the tumor is more uniform on the more delayed gadolinium-enhanced T1-weighted fat-suppressed spin-echo image (*f*), reflecting delayed enhancement of the fibrotic components of the tumor. The use of fat suppression increases the conspicuity of the abnormally enhancing tumor.

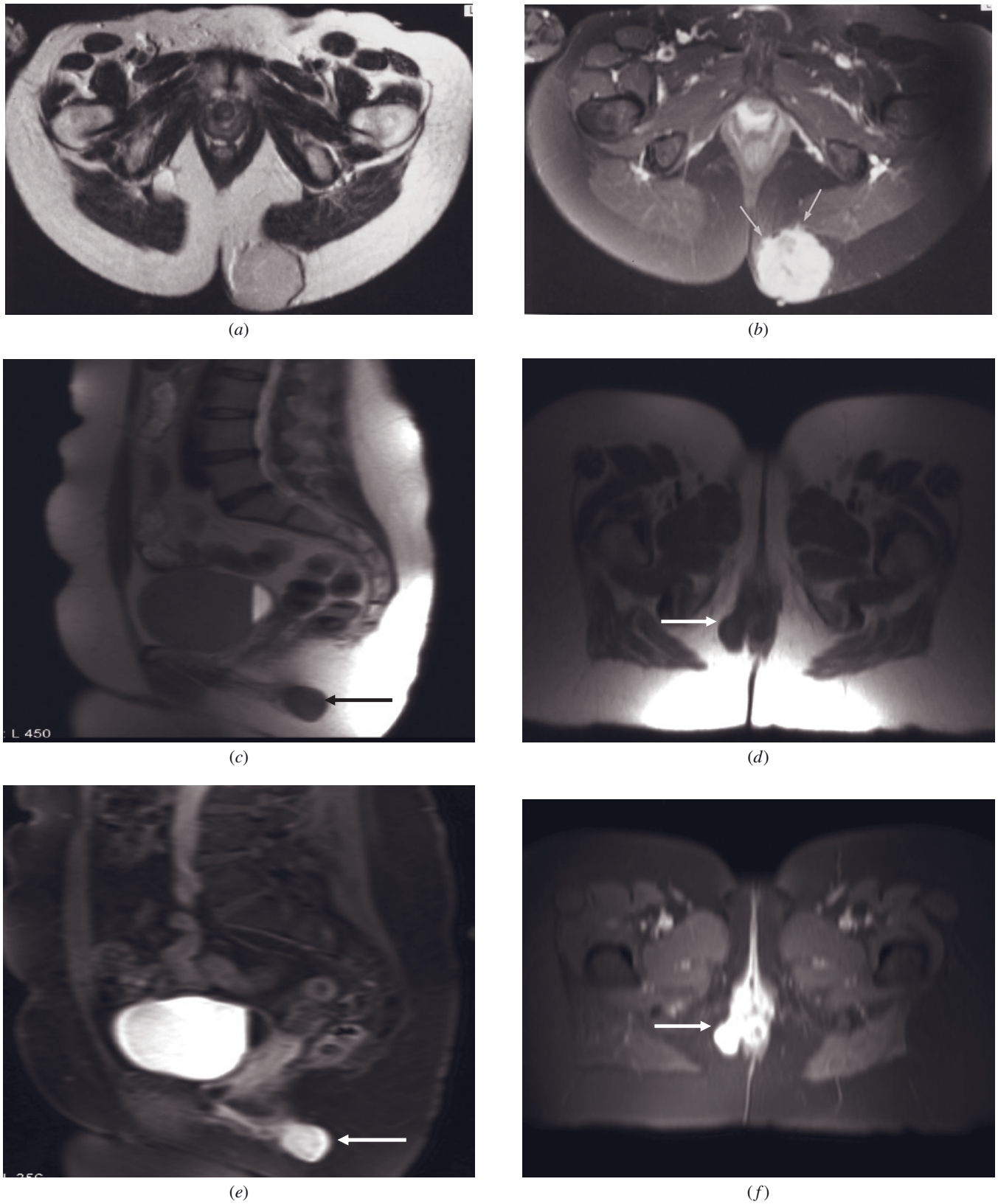

FIG. 10.69 Well-differentiated subcutaneous fibrosarcoma. T2-weighted spin-echo (*a*) and gadolinium-enhanced T1-weighted fat-suppressed spin-echo (*b*) images. The tumor is located in the subcutaneous tissue of the left buttock, is moderate in signal intensity on the T2-weighted image (*a*), and shows intense enhancement on the gadolinium-enhanced T1-weighted fat-suppressed image (*b*). The anterior margin of the mass appears irregular (arrows, *b*) and abuts the gluteus maximus muscle. Note the presence of chemical-shift artifact on the lateral edges of the mass on the T2-weighted image (*a*). **Perirectal sarcoma.** Sagittal (*c*) and transverse (*d*) T2-weighted single-shot echo-train spin-echo and sagittal (*e*) and transverse (*f*) T1-weighted postgadolinium interstitial-phase fat-suppressed 3D-GE images demonstrate a perirectal sarcoma in another patient. The lesion shows intense enhancement on postgadolinium images.

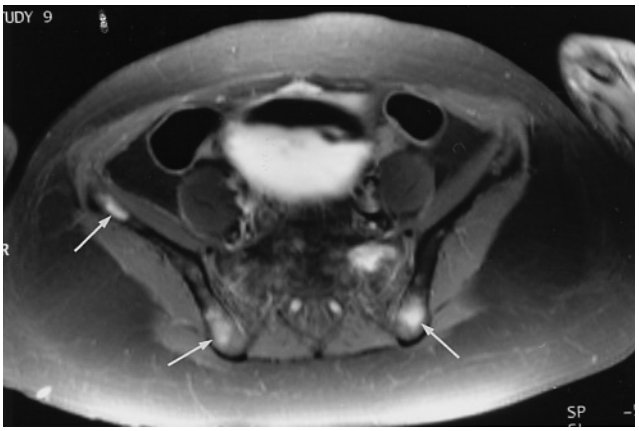

FIG. 10.70 Leukemic bone infiltrates. Gadolinium-enhanced T1-weighted fat-suppressed spin-echo image in a patient with leukemia shows focal enhancing leukemic lesions (arrows) in the bone marrow of the iliac bones bilaterally. Normal fat-containing marrow is low in signal intensity, rendering enhancing tumors conspicuous.

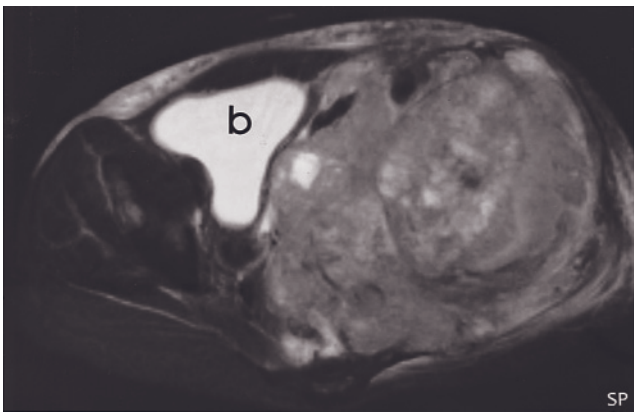

(*a*)

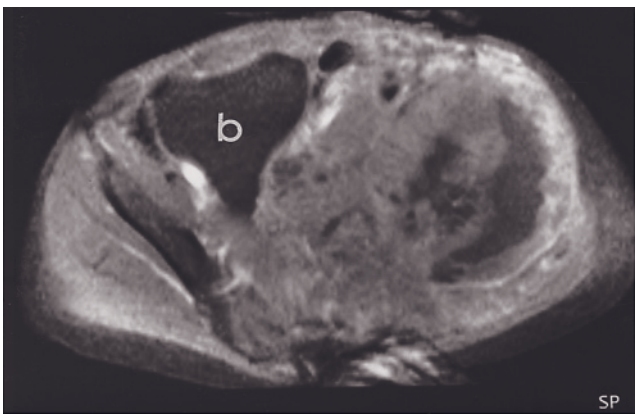

(*b*)

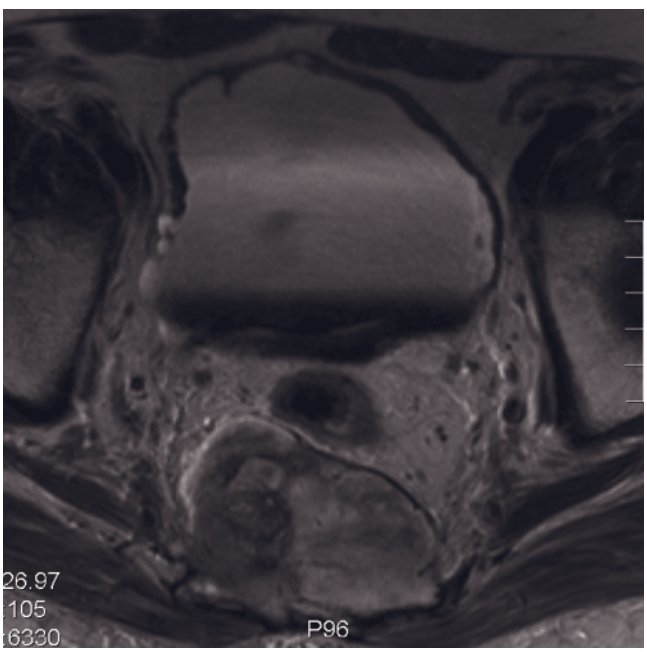

(*c*)

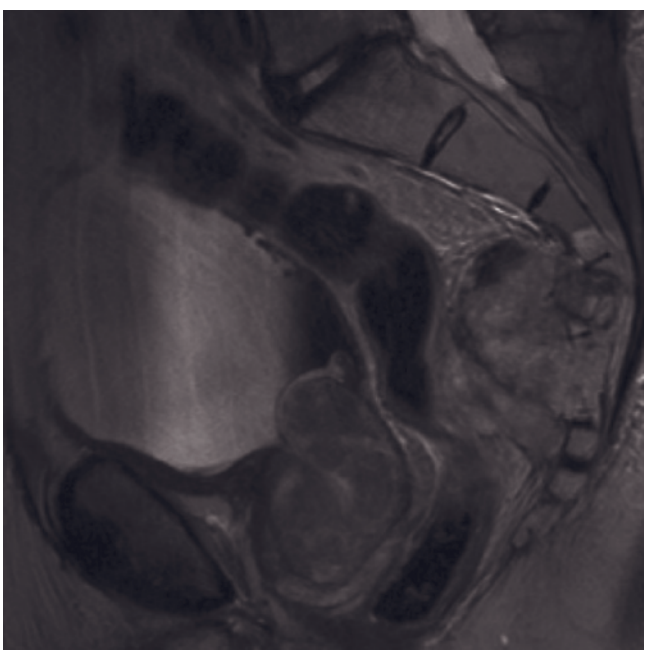

(*d*)

FIG. 10.71 Extensive Ewing sarcoma of the pelvis. T2-weighted fat-suppressed echo-train spin-echo (*a*) and gadolinium-enhanced fat-suppressed SGE (*b*) images. An extensive heterogeneous mass originating from the left iliac bone is demonstrated. The mass invades all the muscles of the left pelvis and displaces the bladder (b, *a, b*) to the right. The tumor is heterogeneous with mixed high-signal-intensity areas on the T2-weighted image (*a*) and demonstrates heterogeneous enhancement after gadolinium administration (*b*). **Chordoma.** Transverse (*c*) and sagittal (*d*) high-resolution fast spin-echo T2-weighted, T1-weighted postgadolinium

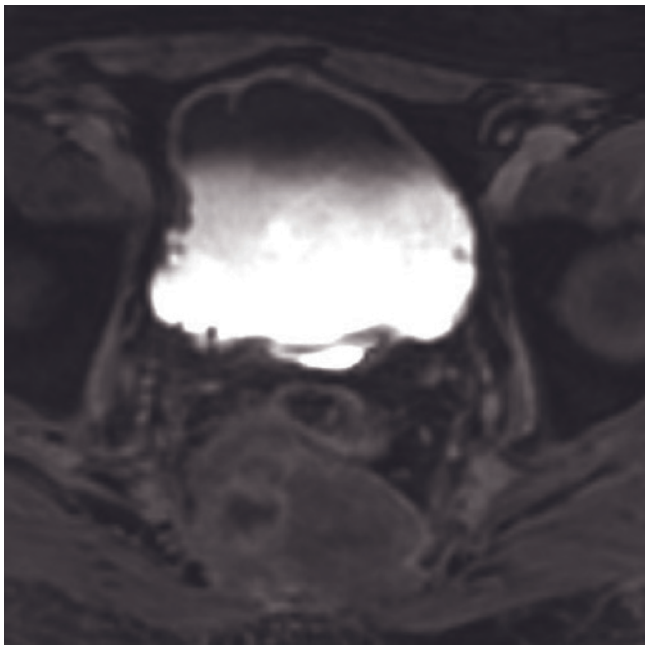

(*e*)

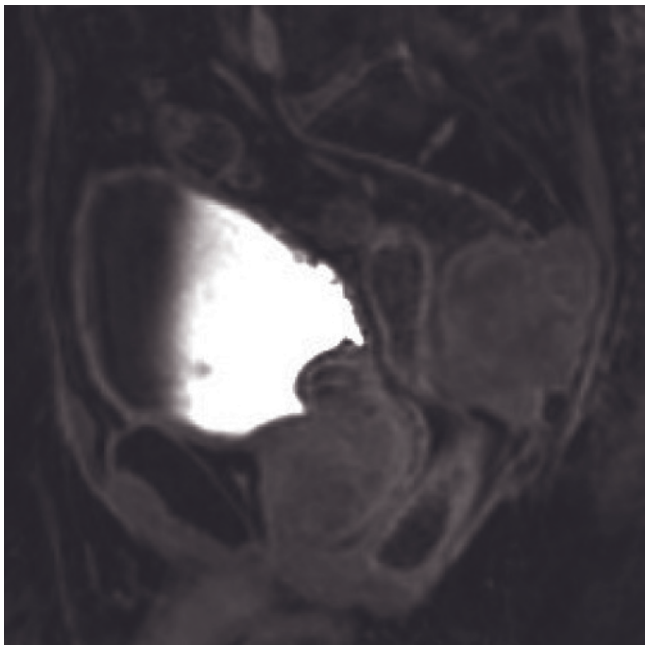

(*f*)

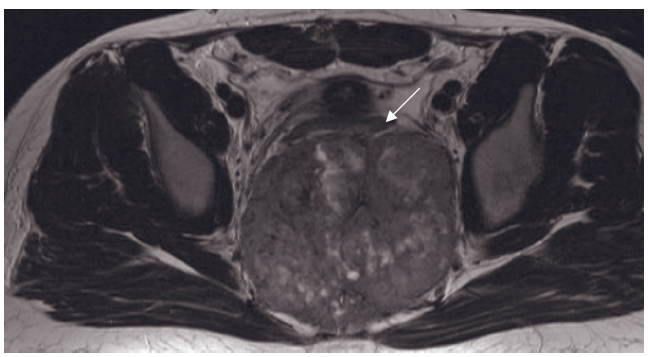

(*g*)

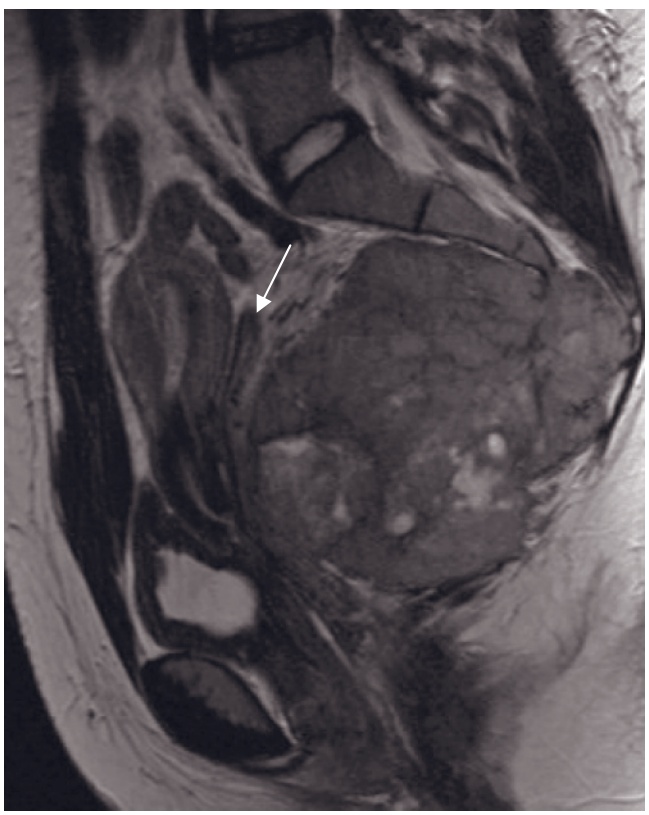

(*h*)

FIG. 10.71 (*Continued*) interstitial-phase fat-suppressed transverse (*e*) and sagittal (*f*) 3D-GE images at 3.0 T demonstrate chordoma originating from sacrum in another patient with enlarged prostate. The chordoma shows heterogeneous high signal on T2-weighted images and moderate heterogeneous enhancement. Chordomas are low-grade malignancies and the most common neoplasms originating from the sacrum. Note that the bladder wall is trabeculated and irregular because of outlet obstruction. **Giant cell tumor.** Transverse (*g*) and sagittal (*h*) high-resolution fast spin-echo T2-weighted and T1-weighted post-gadolinium interstitial-phase fat-suppressed SGE transverse (*i*) and sagittal (*j*) images demonstrate giant cell tumor of sacrum in another patient. The large tumor is very heterogeneous. It shows intermediate signal on T2-weighted images and heterogeneous enhancement on postgadolinium images. There are scattered areas of central necrosis in the tumor. The tumor is located in the rectosacral space and originates from the sacrum and coccyx. The uterus and rectum (arrows, *g, h*) are compressed and displaced anteriorly by the tumor. Although giant cell tumors of the sacrum are benign, they can show malignant transformation. They are the second most common neoplasms originating from the sacrum after chordomas.

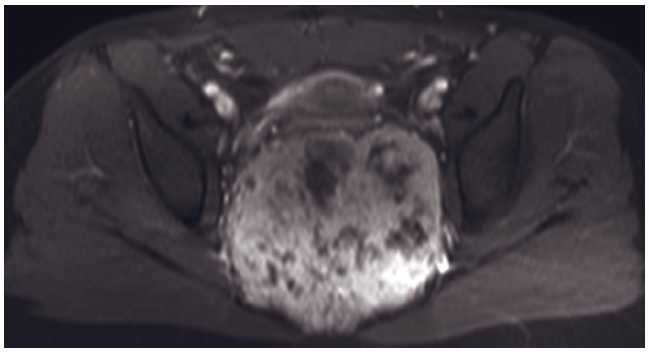

(*i*)

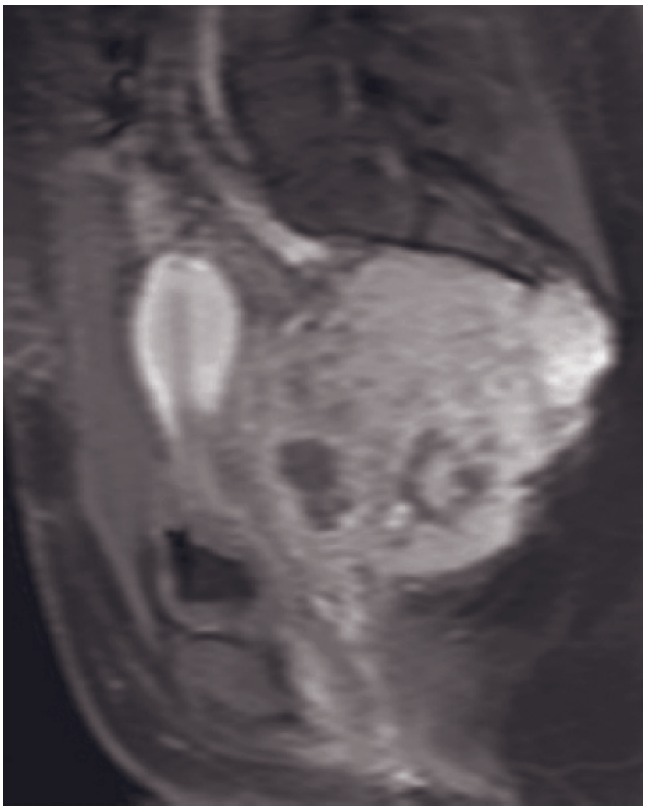

(*j*)

FIG. 10.71 (*Continued*)

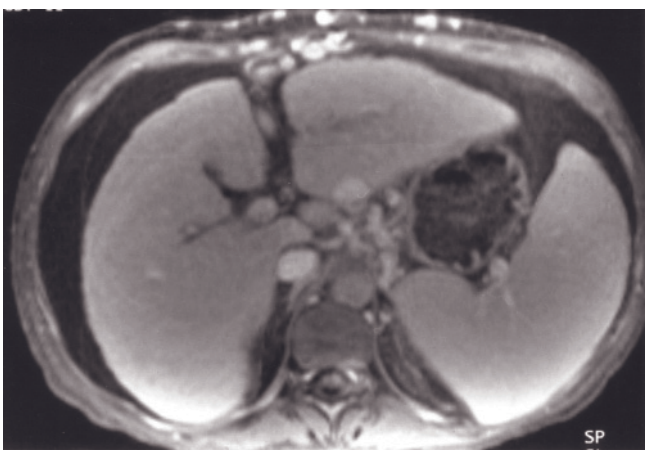

(*a*)

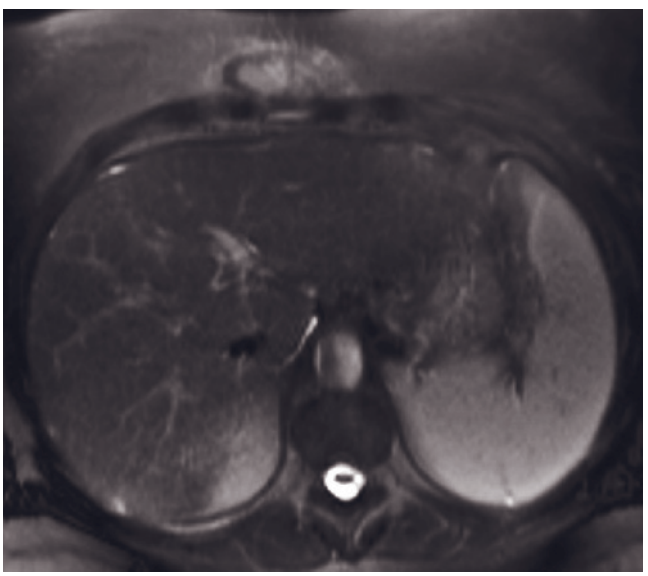

(*b*)

FIG. 10.72 Subcutaneous varices in a patient with cirrhosis. Interstitial-phase gadolinium-enhanced fat-suppressed SGE image (*a*) demonstrates numerous enhancing serpiginous vessels within the anterior abdominal wall, consistent with varices. Multiple varices at the gastroesophageal junction are also present. **Infection.** T2-weighted fat-suppressed single-shot echo-train spin-echo (*b*), T1-weighted fat-suppressed 3D-GE (*c*), T1-weighted postgadolinium hepatic arterial dominant-phase 3D-GE (*d*), and

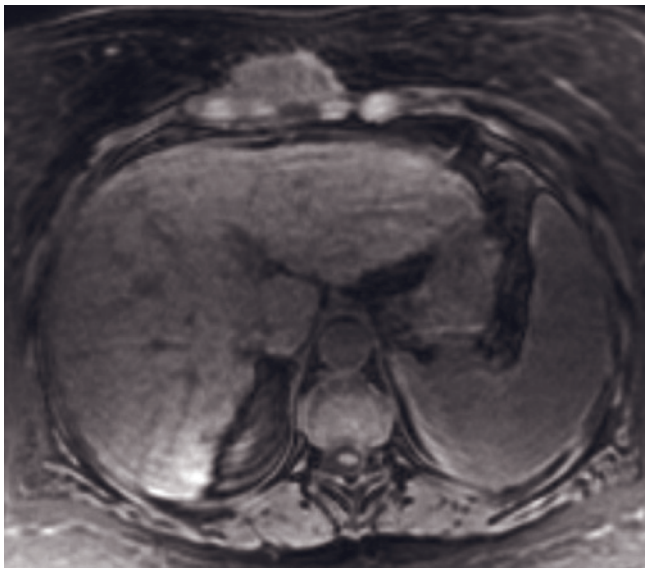

(*c*)

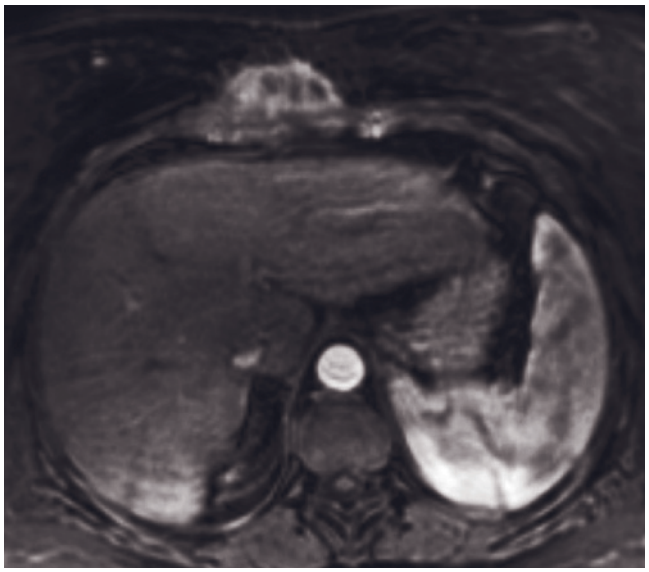

(*d*)

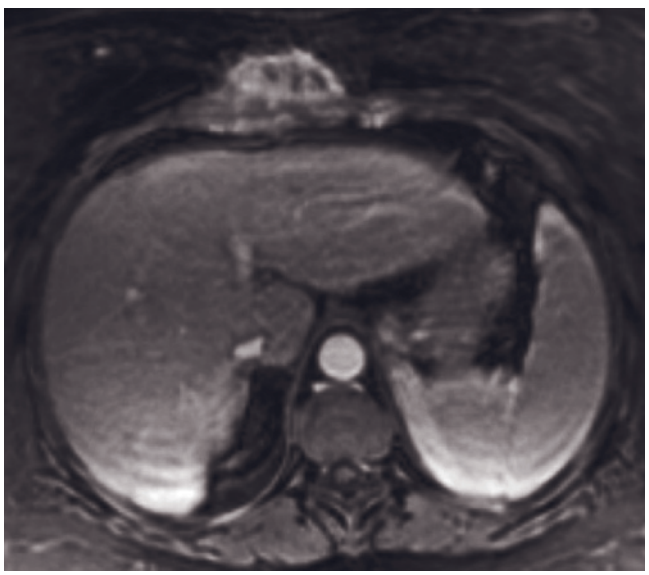

(*e*)

FIG. 10.72 (*Continued*) T1-weighted postgadolinium interstitial-phase fat-suppressed 3D-GE (*e*) images at 3.0 T demonstrate granulomatous infection involving the costochondral junctions and anterior abdominal wall in another patient. The lesion is very irregular and shows marked heterogeneous enhancement. Peripheral spiculations and stranding are present around the lesion. The appearance of the lesion mimics sarcomas.

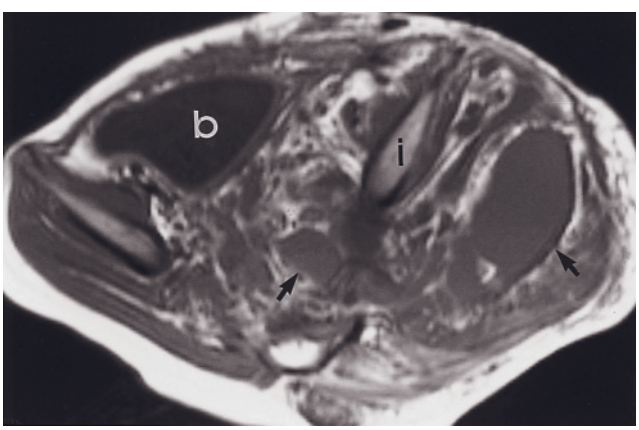

(*a*)

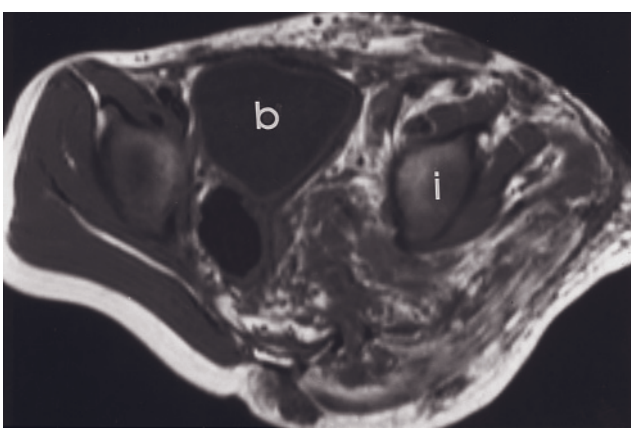

(*b*)

FIG. 10.73 Lymphangioma-hemangioma of the pelvis. Transverse (*a, b*) and coronal (*c, d*) T1-weighted spin-echo and

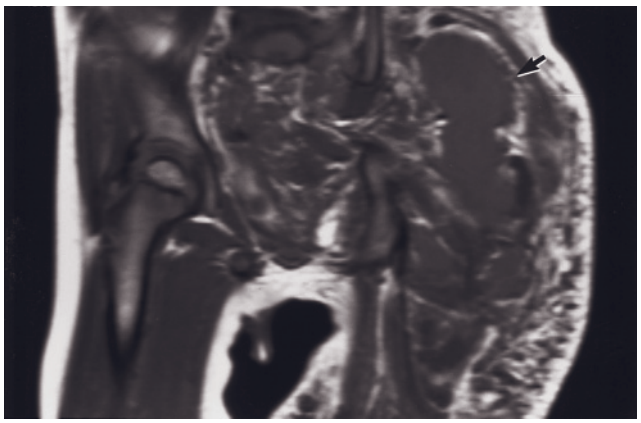

(*c*)

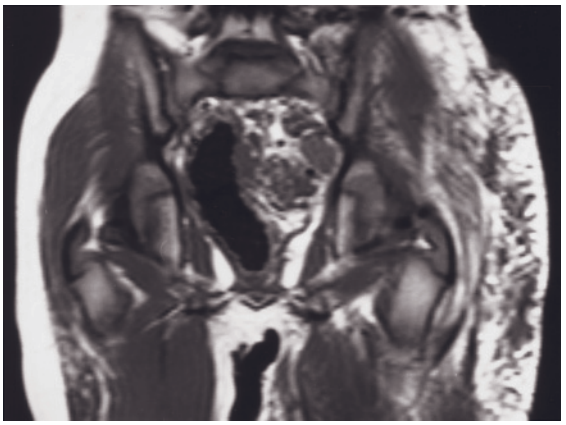

(*d*)

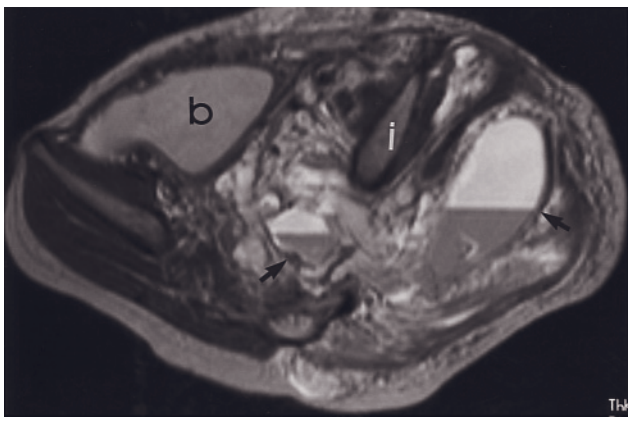

(*e*)

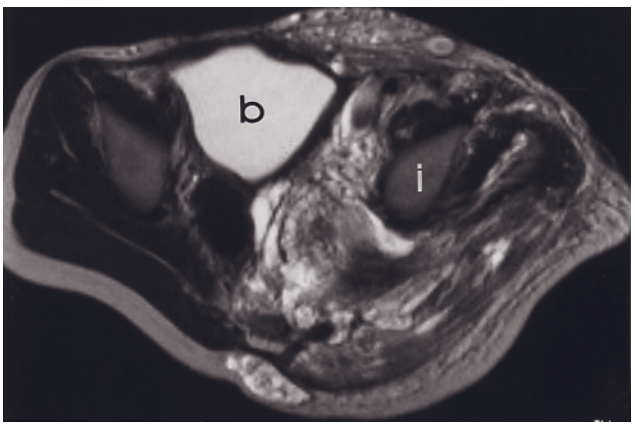

(*f*)

(*g*)

FIG. 10.73 (*Continued*) transverse (*e*, *f*) and sagittal (*g*) T2-weighted spin-echo images. An extensive heterogeneous mass is present in the left and central pelvis. The mass infiltrates the subcutaneous tissue of the entire left hemipelvis, the gluteus maximus, intermedius, and minor muscles and extends into the true pelvis, causing extensive deformity and displacing the bladder (b, *a, b, e–g*) and left iliac bone (i, *a, b, e, f*) anteriorly to the right. The mass consists of numerous tubular and ovoid cystic structures, representing malformed blood and lymph vessels. The cystic spaces are low in signal intensity on the T1-weighted images and high in signal intensity on the T2-weighted images, reflecting their fluid content. Larger fluid-filled cystic spaces (arrows, *a, c, e*) have fluid-fluid levels on the T2-weighted image (*e*) with the dependent lower-signal-intensity level representing fluid of higher protein concentration. The presence of large fluid-filled cystic spaces is characteristic of lymphangiomatous rather than hemangiomatous malformations. The coronal images (*c, d*) demonstrate the extent of the pelvic deformity and extension of the vascular malformation to the muscles and subcutaneous tissues of the left thigh, which are enlarged compared with the contralateral side.

malformations or the hemangiomatous component of mixed malformations may also be possible with this technique because the vascular hemangiomatous spaces will be lower in signal intensity on these images [110]. Cellulitis can be differentiated from abscess on MR images by the demonstration of a signal-void center in an abscess. The extent of inflammatory or infectious disease is well-defined on gadolinium-enhanced fat-suppressed SGE images by the extent and intensity of high-signal enhancing tissue.

CONCLUSION

MRI should be considered as a primary diagnostic technique for assessment of most benign and malignant disease processes affecting the retroperitoneum and body wall. Continued advances in MRA, with improvements in dynamic gadolinium-enhanced gradient-echo and true-FISP sequencing techniques, the routine use of 3.0 T MRI, and improved automated multistation surface phased-array coil and table movement systems, have resulted in an increasing role for MRI in the evaluation of aortoiliac disease.

REFERENCES

1. Molmenti EP, Balfe DM, Kanterman RY et al. Anatomy of the retroperitoneum: observations of the distribution of pathologic fluid collections. *Radiology* 200(1): 95–103, 1996.
2. Kottra JJ, Dunnick NR. Retroperitoneal fibrosis. *Radiol Clin North Am* 34(6): 1259–1275, 1996.
3. Swan JS, Grist TM, Weber DM et al. MR angiography of the pelvis with variable velocity encoding and a phased-array coil. *Radiology* 190(2): 363–369, 1994.
4. Arlart IP, Guhl L, Hausmann R. [The evaluation of 2D- and 3D-"time of flight" magnetic resonance angiography (MRA) in the diagnosis of renal artery stenoses]. *Rofo* 157(1): 59–64, 1992.
5. Sallevelt PE, Barentsz JO, Ruijs SJ et al. Role of MR imaging in the preoperative evaluation of atherosclerotic abdominal aortic aneurysms. *Radiographics* 14(1): 87–98; discussion 99, 1994.
6. Kim D, Edelman RR, Kent KC et al. Abdominal aorta and renal artery stenosis: evaluation with MR angiography. *Radiology* 174(3 Pt 1): 727–731, 1990.
7. Mulligan SA, Doyle M, Matsuda T et al. Aortoiliac disease: two-dimensional inflow MR angiography with lipid suppression. *J Magn Reson Imaging* 3(6): 829–834, 1993.
8. Ecklund K, Hartnell GG, Hughes LA et al. MR angiography as the sole method in evaluating abdominal aortic aneurysms: correlation with conventional techniques and surgery. *Radiology* 192(2): 345–350, 1994.
9. Durham JR, Hackworth CA, Tober JC et al. Magnetic resonance angiography in the preoperative evaluation of abdominal aortic aneurysms. *Am J Surg* 166(2): 173–177; discussion 177–178, 1993.
10. Kaufman JA, Geller SC, Petersen MJ et al. MR imaging (including MR angiography) of abdominal aortic aneurysms: comparison with conventional angiography. *AJR Am J Roentgenol* 163(1): 203–210, 1994.
11. Prince MR, Narasimham DL, Jacoby WT et al. Three-dimensional gadolinium-enhanced MR angiography of the thoracic aorta. *AJR Am J Roentgenol* 166(6): 1387–1397, 1996.
12. Douek PC, Revel D, Chazel S et al. Fast MR angiography of the aortoiliac arteries and arteries of the lower extremity: value of bolus-enhanced, whole-volume subtraction technique. *AJR Am J Roentgenol* 165(2): 431–437, 1995.
13. Prince MR, Yucel EK, Kaufman JA et al. Dynamic gadolinium-enhanced three-dimensional abdominal MR arteriography. *J Magn Reson Imaging* 3(6): 877–881, 1993.
14. Snidow JJ, Aisen AM, Harris VJ et al. Iliac artery MR angiography: comparison of three-dimensional gadolinium-enhanced and two-dimensional time-of-flight techniques. *Radiology* 196(2): 371–378, 1995.
15. Sivananthan UM, Ridgway JP, Bann K et al. Fast magnetic resonance angiography using turbo-FLASH sequences in advanced aortoiliac disease. *Br J Radiol* 66(792): 1103–1110, 1993.
16. Prince MR. Gadolinium-enhanced MR aortography. *Radiology* 191(1): 155–164, 1994.
17. Kelekis NL, Semelka RC, Worawattanakul S et al. Magnetic resonance imaging of the abdominal aorta and iliac vessels using combined 3-D gadolinium-enhanced MRA and gadolinium-enhanced fat-suppressed spoiled gradient echo sequences. *Magn Reson Imaging* 17(5): 641–651, 1999.
18. Leung DA, McKinnon GC, Davis CP et al. Breath-hold, contrast-enhanced, three-dimensional MR angiography. *Radiology* 200(2): 569–571, 1996.
19. Shellock FG, Spinazzi A. MRI safety update 2008: part 1, MRI contrast agents and nephrogenic systemic fibrosis. *AJR Am J Roentgenol* 191(4): 1129–1139, 2008.
20. Meaney JF, Goyen M. Recent advances in contrast-enhanced magnetic resonance angiography. *Eur Radiol* 17 Suppl 2: B2–6, 2007.
21. Fink C, Goyen M, Lotz J. Magnetic resonance angiography with blood-pool contrast agents: future applications. *Eur Radiol* 17 Suppl 2: B38–44, 2007.
22. Sinha S. Improved depiction of vascular lumen. *Proceedings of the ISMRM fourth scientific meeting and exhibition* 2: 1265, 1996.
23. Thurnher S, Cejna M. Imaging of aortic stent-grafts and endoleaks. *Radiol Clin North Am* 40(4): 799–833, 2002.
24. Ramalho M, Altun E, Heredia V et al. Liver MR imaging: 1.5T versus 3T. *Magn Reson Imaging Clin N Am* 15(3): 321–347, vi, 2007.
25. Wolf YG, Bernstein EF. A current perspective on the natural history of abdominal aortic aneurysms. *Cardiovasc Surg* 2(1): 16–22, 1994.
26. Sakalihasan N, Limet R, Defawe OD. Abdominal aortic aneurysm. *Lancet* 365(9470): 1577–1589, 2005.
27. Fisher ER, Stern EJ, Godwin JD 2nd et al. Acute aortic dissection: typical and atypical imaging features. *Radiographics* 14(6): 1263–1271, 1994.
28. Yuan C, Kerwin WS. MRI of atherosclerosis. *J Magn Reson Imaging* 19(6): 710–719, 2004.
29. Grist TM. MRA of the abdominal aorta and lower extremities. *J Magn Reson Imaging* 11(1): 32–43, 2000.
30. Flak B, Li DK, Ho BY et al. Magnetic resonance imaging of aneurysms of the abdominal aorta. *AJR Am J Roentgenol* 144(5): 991–996, 1985.
31. Vosshenrich R, Fischer U. Contrast-enhanced MR angiography of abdominal vessels: is there still a role for angiography? *Eur Radiol* 12(1): 218–230, 2002.
32. LaRoy LL, Cormier PJ, Matalon TA et al. Imaging of abdominal aortic aneurysms. *AJR Am J Roentgenol* 152(4): 785–792, 1989.
33. Lindell OI, Sariola HV, Lehtonen TA. The occurrence of vasculitis in perianeurysmal fibrosis. *J Urol* 138(4): 727–729, 1987.

34. Roberts DA. Magnetic resonance imaging of thoracic aortic aneurysm and dissection. *Semin Roentgenol* 36(4): 295–308, 2001.
35. Geisinger MA, Risius B, O'Donnell JA et al. Thoracic aortic dissections: magnetic resonance imaging. *Radiology* 155(2): 407–412, 1985.
36. Williams DM, Joshi A, Dake MD et al. Aortic cobwebs: an anatomic marker identifying the false lumen in aortic dissection—imaging and pathologic correlation. *Radiology* 190(1): 167–174, 1994.
37. Yamada T, Tada S, Harada J. Aortic dissection without intimal rupture: diagnosis with MR imaging and CT. *Radiology* 168(2): 347–352, 1988.
38. Wolff KA, Herold CJ, Tempany CM et al. Aortic dissection: atypical patterns seen at MR imaging. *Radiology* 181(2): 489–495, 1991.
39. Welch TJ, Stanson AW, Sheedy PF 2nd et al. Radiologic evaluation of penetrating aortic atherosclerotic ulcer. *Radiographics* 10(4): 675–685, 1990.
40. Yucel EK, Steinberg FL, Egglin TK et al. Penetrating aortic ulcers: diagnosis with MR imaging. *Radiology* 177(3): 779–781, 1990.
41. Schwope RB, Alper HJ, Talenfeld AD et al. MR angiography for patient surveillance after endovascular repair of abdominal aortic aneurysms. *AJR Am J Roentgenol* 188(4): W334–340, 2007.
42. Justich E, Amparo EG, Hricak H et al. Infected aortoiliofemoral grafts: magnetic resonance imaging. *Radiology* 154(1): 133–136, 1985.
43. Auffermann W, Olofsson PA, Rabahie GN et al. Incorporation versus infection of retroperitoneal aortic grafts: MR imaging features. *Radiology* 172(2): 359–362, 1989.
44. Hricak H, Amparo E, Fisher MR et al. Abdominal venous system: assessment using MR. *Radiology* 156(2): 415–422, 1985.
45. Colletti PM, Oide CT, Terk MR et al. Magnetic resonance of the inferior vena cava. *Magn Reson Imaging* 10(2): 177–185, 1992.
46. Cory DA, Ellis JH, Bies JR et al. Retroaortic left renal vein demonstrated by nuclear magnetic resonance imaging. *J Comput Assist Tomogr* 8(2): 339–340, 1984.
47. Schultz CL, Morrison S, Bryan PJ. Azygos continuation of the inferior vena cava: demonstration by NMR imaging. *J Comput Assist Tomogr* 8(4): 774–776, 1984.
48. Fisher MR, Hricak H, Higgins CB. Magnetic resonance imaging of developmental venous anomalies. *AJR Am J Roentgenol* 145(4): 705–709, 1985.
49. Semelka RC, Shoenut JP, Kroeker MA. The retroperitoneum and the abdominal wall. In: Semelka RC, Shoenut JP, editors. *MRI of the abdomen with CT correlation.* New York: Raven Press, 1993, p. 13–41.
50. Silverman SG, Hillstrom MM, Doyle CJ et al. Thrombophlebitic retroperitoneal collateral veins mimicking lymphadenopathy: MR and CT appearance. *Abdom Imaging* 20(5): 474–476, 1995.
51. Erdman WA, Weinreb JC, Cohen JM et al. Venous thrombosis: clinical and experimental MR imaging. *Radiology* 161(1): 233–238, 1986.
52. Higgins CB, Goldberg H, Hricak H et al. Nuclear magnetic resonance imaging of vasculature of abdominal viscera: normal and pathologic features. *AJR Am J Roentgenol* 140(6): 1217–1225, 1983.
53. Semelka RC, Shoenut JP, Magro CM et al. Renal cancer staging: comparison of contrast-enhanced CT and gadolinium-enhanced fat-suppressed spin-echo and gradient-echo MR imaging. *J Magn Reson Imaging* 3(4): 597–602, 1993.
54. Roubidoux MA, Dunnick NR, Sostman HD et al. Renal carcinoma: detection of venous extension with gradient-echo MR imaging. *Radiology* 182(1): 269–272, 1992.
55. Wendel RG, Crawford ED, Hehman KN. The "nutcracker" phenomenon: an unusual cause for renal varicosities with hematuria. *J Urol* 123(5): 761–763, 1980.
56. Cyran KM, Kenney PJ. Leiomyosarcoma of abdominal veins: value of MRI with gadolinium DTPA. *Abdom Imaging* 19(4): 335–338, 1994.
57. Kelekis NL, Semelka RC, Hill ML et al. Malignant fibrous histiocytoma of the inferior vena cava: appearances on contrast-enhanced spiral CT and MRI. *Abdom Imaging* 21(5): 461–463, 1996.
58. Lipton M, Sprayregen S, Kutcher R et al. Venous invasion in renal vein leiomyosarcoma: case report and review of the literature. *Abdom Imaging* 20(1): 64–67, 1995.
59. Arrive L, Hricak H, Tavares NJ et al. Malignant versus nonmalignant retroperitoneal fibrosis: differentiation with MR imaging. *Radiology* 172(1): 139–143, 1989.
60. Comings DE, Skubi KB, Van Eyes J et al. Familial multifocal fibrosclerosis. Findings suggesting that retroperitoneal fibrosis, mediastinal fibrosis, sclerosing cholangitis, Riedel's thyroiditis, and pseudotumor of the orbit may be different manifestations of a single disease. *Ann Intern Med* 66(5): 884–892, 1967.
61. Van Hoe L, Oyen R, Gryspeerdt S et al. Case report: pseudotumoral pelvic retroperitoneal fibrosis associated with orbital fibrosis. *Br J Radiol* 68(808): 421–423, 1995.
62. Dent RG, Godden DJ, Stovin PG et al. Pulmonary hyalinising granuloma in association with retroperitoneal fibrosis. *Thorax* 38(12): 955–956, 1983.
63. Young AS, Binkovitz LA, Adler BH et al. Pulmonary hyalinizing granuloma and retroperitoneal fibrosis in an adolescent. *Pediatr Radiol* 37(1): 91–95, 2007.
64. Connolly J, Eisner D, Goldman S et al. Benign retroperitoneal fibrosis and renal cell carcinoma. *J Urol* 149(6): 1535–1537, 1993.
65. Rhee RY, Gloviczki P, Luthra HS et al. Iliocaval complications of retroperitoneal fibrosis. *Am J Surg* 168(2): 179–183, 1994.
66. Gatanaga H, Ohnishi S, Miura H et al. Retroperitoneal fibrosis leading to extrahepatic portal vein obstruction. *Intern Med* 33(6): 346–350, 1994.
67. Hricak H, Higgins CB, Williams RD. Nuclear magnetic resonance imaging in retroperitoneal fibrosis. *AJR Am J Roentgenol* 141(1): 35–38, 1983.
68. Mulligan SA, Holley HC, Koehler RE et al. CT and MR imaging in the evaluation of retroperitoneal fibrosis. *J Comput Assist Tomogr* 13(2): 277–281, 1989.
69. Rubenstein WA, Gray G, Auh YH et al. CT of fibrous tissues and tumors with sonographic correlation. *AJR Am J Roentgenol* 147(5): 1067–1074, 1986.
70. Cullenward MJ, Scanlan KA, Pozniak MA et al. Inflammatory aortic aneurysm (periaortic fibrosis): radiologic imaging. *Radiology* 159(1): 75–82, 1986.
71. Ross JS, Delamarter R, Hueftle MG et al. Gadolinium-DTPA-enhanced MR imaging of the postoperative lumbar spine: time course and mechanism of enhancement. *AJR Am J Roentgenol* 152(4): 825–834, 1989.
72. Lane RH, Stephens DH, Reiman HM. Primary retroperitoneal neoplasms: CT findings in 90 cases with clinical and pathologic correlation. *AJR Am J Roentgenol* 152(1): 83–89, 1989.
73. Kim SH, Choi BI, Han MC et al. Retroperitoneal neurilemoma: CT and MR findings. *AJR Am J Roentgenol* 159(5): 1023–1026, 1992.
74. Bass JC, Korobkin M, Francis IR et al. Retroperitoneal plexiform neurofibromas: CT findings. *AJR Am J Roentgenol* 163(3): 617–620, 1994.
75. Ros PR, Eshaghi N. Plexiform neurofibroma of the pelvis: CT and MRI findings. *Magn Reson Imaging* 9(3): 463–465, 1991.
76. Bequet D, Labauge P, Larroque P et al. [Peripheral neurofibromatosis and involvement of lumbosacral nerves. Value of imaging]. *Rev Neurol (Paris)* 146(12): 757–761, 1990.
77. Burk DL Jr., Brunberg JA, Kanal E et al. Spinal and paraspinal neurofibromatosis: surface coil MR imaging at 1.5 T1. *Radiology* 162(3): 797–801, 1987.

78. Pagliano G, Michel P, la Fay T et al. [Paraganglioma of the organ of Zuckerkandl]. *Chirurgie* 120(3): 128–133, 1994.
79. Kessler A, Mitchell DG, Israel HL et al. Hepatic and splenic sarcoidosis: ultrasound and MR imaging. *Abdom Imaging* 18(2): 159–163, 1993.
80. Warshauer DM, Semelka RC, Ascher SM. Nodular sarcoidosis of the liver and spleen: appearance on MR images. *J Magn Reson Imaging* 4(4): 553–557, 1994.
81. Johnson WK, Ros PR, Powers C et al. Castleman disease mimicking an aggressive retroperitoneal neoplasm. *Abdom Imaging* 19(4): 342–344, 1994.
82. Vlahos L, Trakadas S, Gouliamos A et al. Retrocrural masses of extramedullary hemopoiesis in beta-thalassemia. *Magn Reson Imaging* 11(8): 1227–1229, 1993.
83. Vivas I, Nicolas AI, Velazquez P et al. Retroperitoneal fibrosis: typical and atypical manifestations. *Br J Radiol* 73(866): 214–222, 2000.
84. Gossmann A, Eich HT, Engert A et al. CT and MR imaging in Hodgkin's disease—present and future. *Eur J Haematol Suppl* (66): 83–89, 2005.
85. Neumann CH, Robert NJ, Canellos G et al. Computed tomography of the abdomen and pelvis in non-Hodgkin lymphoma. *J Comput Assist Tomogr* 7(5): 846–850, 1983.
86. Rahmouni A, Tempany C, Jones R et al. Lymphoma: monitoring tumor size and signal intensity with MR imaging. *Radiology* 188(2): 445–451, 1993.
87. Amparo EG, Hoddick WK, Hricak H et al. Comparison of magnetic resonance imaging and ultrasonography in the evaluation of abdominal aortic aneurysms. *Radiology* 154(2): 451–456, 1985.
88. Hanna SL, Fletcher BD, Boulden TF et al. MR imaging of infradiaphragmatic lymphadenopathy in children and adolescents with Hodgkin disease: comparison with lymphography and CT. *J Magn Reson Imaging* 3(3): 461–470, 1993.
89. Lee JK, Heiken JP, Ling D et al. Magnetic resonance imaging of abdominal and pelvic lymphadenopathy. *Radiology* 153(1): 181–188, 1984.
90. Dooms GC, Hricak H, Crooks LE et al. Magnetic resonance imaging of the lymph nodes: comparison with CT. *Radiology* 153(3): 719–728, 1984.
91. Glazer HS, Lee JK, Levitt RG et al. Radiation fibrosis: differentiation from recurrent tumor by MR imaging. *Radiology* 156(3): 721–726, 1985.
92. Hricak H, Demas BE, Williams RD et al. Magnetic resonance imaging in the diagnosis and staging of renal and perirenal neoplasms. *Radiology* 154(3): 709–715, 1985.
93. Fein AB, Lee JK, Balfe DM et al. Diagnosis and staging of renal cell carcinoma: a comparison of MR imaging and CT. *AJR Am J Roentgenol* 148(4): 749–753, 1987.
94. Anzai Y, Blackwell KE, Hirschowitz SL et al. Initial clinical experience with dextran-coated superparamagnetic iron oxide for detection of lymph node metastases in patients with head and neck cancer. *Radiology* 192(3): 709–715, 1994.
95. Williams WM, Kosovsky PA, Rafal RB et al. Retroperitoneal germ cell neoplasm: MR and CT. *Magn Reson Imaging* 10(2): 325–331, 1992.
96. Ellis JH, Bies JR, Kopecky KK et al. Comparison of NMR and CT imaging in the evaluation of metastatic retroperitoneal lymphadenopathy from testicular carcinoma. *J Comput Assist Tomogr* 8(4): 709–719, 1984.
97. Nishino M, Hayakawa K, Minami M et al. Primary retroperitoneal neoplasms: CT and MR imaging findings with anatomic and pathologic diagnostic clues. *Radiographics* 23(1): 45–57, 2003.
98. Elsayes KM, Staveteig PT, Narra VR et al. Retroperitoneal masses: magnetic resonance imaging findings with pathologic correlation. *Curr Probl Diagn Radiol* 36(3): 97–106, 2007.
99. Cohan RH, Baker ME, Cooper C et al. Computed tomography of primary retroperitoneal malignancies. *J Comput Assist Tomogr* 12(5): 804–810, 1988.
100. Bretan PN, Jr., Williams RD, Hricak H. Preoperative assessment of retroperitoneal pathology by magnetic resonance imaging. Primary leiomyosarcoma of inferior vena cava. *Urology* 28(3): 251–255, 1986.
101. Hartman DS, Hayes WS, Choyke PL et al. From the archives of the AFIP. Leiomyosarcoma of the retroperitoneum and inferior vena cava: radiologic-pathologic correlation. *Radiographics* 12(6): 1203–1220, 1992.
102. Feinstein RS, Gatewood OM, Fishman EK et al. Computed tomography of adult neuroblastoma. *J Comput Assist Tomogr* 8(4): 720–726, 1984.
103. Lee JK, Glazer HS. Psoas muscle disorders: MR imaging. *Radiology* 160(3): 683–687, 1986.
104. Weinreb JC, Cohen JM, Maravilla KR. Iliopsoas muscles: MR study of normal anatomy and disease. *Radiology* 156(2): 435–440, 1985.
105. Hahn PF, Saini S, Stark DD et al. Intraabdominal hematoma: the concentric-ring sign in MR imaging. *AJR Am J Roentgenol* 148(1): 115–119, 1987.
106. Rubin JI, Gomori JM, Grossman RI et al. High-field MR imaging of extracranial hematomas. *AJR Am J Roentgenol* 148(4): 813–817, 1987.
107. Unger EC, Glazer HS, Lee JK et al. MRI of extracranial hematomas: preliminary observations. *AJR Am J Roentgenol* 146(2): 403–407, 1986.
108. Brasfield RD, Das Gupta TK. Desmoid tumors of the anterior abdominal wall. *Surgery* 65(2): 241–246, 1969.
109. Ichikawa T, Koyama A, Fujimoto H et al. Abdominal wall desmoid mimicking intra-abdominal mass: MR features. *Magn Reson Imaging* 12(3): 541–544, 1994.
110. Stover B, Laubenberger J, Hennig J et al. Value of RARE-MRI sequences in the diagnosis of lymphangiomatosis in children. *Magn Reson Imaging* 13(3): 481–488, 1995.

CHAPTER 11

BLADDER

ERSAN ALTUN, CORINNE DEURDULIAN, JORGE ELIAS, JR., PENAMPAI TANNAPHAI, AND RICHARD C. SEMELKA

NORMAL ANATOMY

The bladder is located posterior to the symphysis, the retropubic fat pad, and the space of Retzius. It is pyramidal in shape, with its apex pointing anteriorly toward the superior portion of the pubic symphysis. From the apex, the median umbilical fold passes up to the umbilicus. This is a fold of peritoneum raised by the median umbilical ligament, which is the remnant of the urachus. The superior surface of the bladder is covered by peritoneum, which dips down posteriorly to form the anterior wall of the rectovesical (male) or uterovesical (female) pouch. The obturator internus muscles are located laterally, and the levator ani muscles are situated inferiorly [1, 2]. The bladder consists of four layers: an outer adventitial layer of connective tissue, a nonstriated muscle layer (the detrusor muscle, consisting of outer and inner longitudinal fibers, enclosing a middle circular layer), a lamina propria (submucosal connective tissue), and an inner layer of mucosa. The mucosa is rugose in the underdistended state and becomes smoother as filling proceeds, with the exception of the trigone, which is always smooth [3]. When fully distended, the bladder is 2 mm thick. The ureteric orifices are placed at the angles of the trigone and are usually slitlike. The internal urethral orifice is at the apex of the trigone, the lowest part of the bladder.

The bladder receives its principal blood supply from the superior and inferior vesical arteries, which are branches of the internal iliac artery. Branches from the obturator and inferior gluteal arteries, as well as branches of the uterine and vaginal arteries in the female, also supply the bladder. Venous drainage is via an intricate plexus on the inferolateral surface, which eventually drains into the internal iliac veins. Lymphatics from the bladder drain mainly to the internal or common iliac chain [3].

MRI TECHNIQUES

A variety of MRI techniques have been employed to study the bladder. As in other organ systems, it is useful to combine imaging techniques that demonstrate different tissue contrast. In the bladder, it is useful to combine sequences that demonstrate high-signal-intensity urine

Abdominal-Pelvic MRI, Third Edition, edited by Richard C. Semelka. Copyright © 2010 John Wiley & Sons, Inc.

(i.e., T2-weighted imaging and delayed postgadolinium imaging) with techniques that demonstrate low-signal intensity urine (noncontrast T1-weighted imaging with or without fat suppression and immediate postgadolinium dynamic SGE or 3D-GE imaging). Images that show this contrast between urine and bladder wall are important in effectively evaluating abnormalities in the bladder wall and lumen. Techniques that are particularly useful include T2-weighted echo-train spin-echo, pre- and postgadolinium T1-weighted fat-suppressed SGE or 3D-GE, and T1-weighted dynamic immediate postgadolinium SGE or fat-suppressed 3D-GE sequences. T1-weighted images are effective at demonstrating morphology but are not effective as the aforementioned techniques at demonstrating depth of tumor invasion. T1-weighted images performed as breath-hold SGE or 3D-GE sequences have shown good spatial and temporal resolution. Implementation of breath-hold T2-weighted echo-train spin-echo sequences has been effective in examining the pelvis. One version of this, the half-Fourier single-shot turbo spin-echo (HASTE) technique, has the additional advantage of being breathing-independent. The multiplanar imaging capability of MRI permits image acquisition in different planes to minimize partial volume effects when evaluating depth of penetration of bladder cancer [4] (i.e., sagittal imaging for anterior and posterior wall and dome lesions and coronal imaging for lateral wall and dome lesions). If a tumor is not aligned in one of the three standard planes, volume averaging of tumor and bladder wall may occur and lead to potential overstaging [4, 5]. The use of thinner slices or high-resolution imaging may reduce these potential disadvantages.

The critical artifacts in MRI of the bladder include motion, degree of bladder distension, chemical shift, and, occasionally, abnormal mixing of intravenous contrast. Involuntary motion artifacts include motion from respiration, intestinal peristalsis, and bladder motion. Respiratory movements can be reduced by the use of a tight abdominal band; however, a phased-array torso coil can achieve a similar effect. Bowel peristalsis can be minimized with administration of 1 mg of glucagon intramuscularly immediately before the exam. Glucagon should not be given to patients with a history of pheochromocytoma, insulin-dependent diabetes, or insulinoma or prior hypersensitivity reaction [3]. Moderate bladder distention is important. If the bladder is not distended, the detrusor muscle is thickened, mimicking thickening from disease states and making it difficult to recognize small tumors. If the bladder is too distended, the patient becomes uncomfortable, and flat tumors can be missed secondary to overstretching of the muscle layer. It has been suggested that optimal bladder filling is achieved by asking the patient to void 2–3 h before the exam and not again until after the exam or by clamping the Foley catheter for a similar time period [6, 7]. Chemical-shift artifact occurs at the water-fat interface and appears as a dark band along the lateral wall on one side and a bright band along the lateral wall on the opposite side [8]. This appearance can mimic or mask an invasive bladder cancer. To correct for this, chemically selective fat suppression can be performed or the frequency-encoding gradient can be rotated to select the direction that least interferes with examination of bladder wall adjacent to tumor [8, 9]. Intravenously administered contrast can also result in artifacts in the bladder by causing a linear layering effect if settled or an artifact mimicking a tumor mass if mixing heterogeneously (fig. 11.1). The latter is most prominent at the ureteral orifices, which helps establish the artifactual nature of the signal abnormalities. The use of thinner slices or high-resolution imaging may reduce these potential artifacts.

The use of surface coils can significantly improve the image quality of the pelvic structures. Double surface coils have been shown to improve pelvic MR imaging [6, 9, 10]. Even greater image improvements occur with the use of a phased-array multicoil.

Endorectal coils can be used to obtain high-resolution images of the bladder. However, these are usually most useful for imaging of tumors along the posterior wall of the bladder base [6].

NORMAL

On MRI images, the thickness of the normal bladder wall ranges from 2 to 8 mm. The normal wall appears as a low-signal-intensity band on noncontrast T1-weighted images, with urine appearing near signal void. On T2-weighted images, the bladder wall appears as a low-signal-intensity band, which represents the entire muscular layer. More recently, this band has been divided into two bands, of low signal intensity (inner) and intermediate signal intensity (outer), corresponding to the compact inner and looser outer smooth muscle layers [11].

The normal bladder wall does not enhance substantially on images acquired immediately after gadolinium administration, which becomes important in tumor imaging. However, there is delayed enhancement of bladder wall, best seen by combining fat saturation with gadolinium enhancement [3, 12].

NORMAL VARIANTS AND CONGENITAL DISEASE

Congenital anomalies of the urinary bladder include agenesis, hypoplasia, duplication, exstrophy, prune

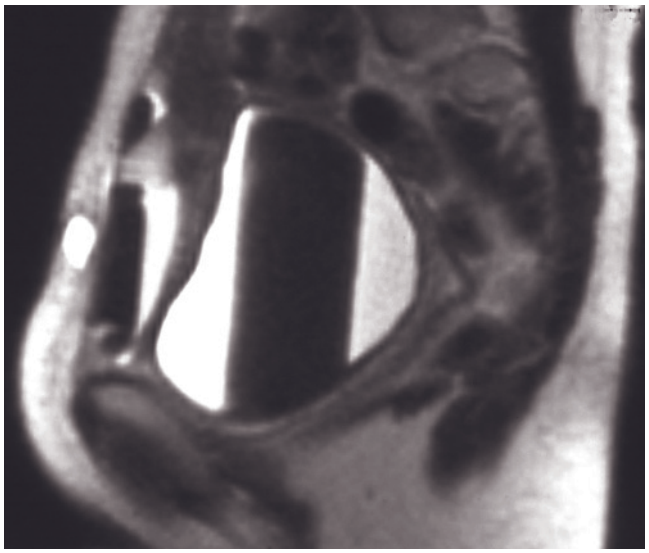

(*a*)

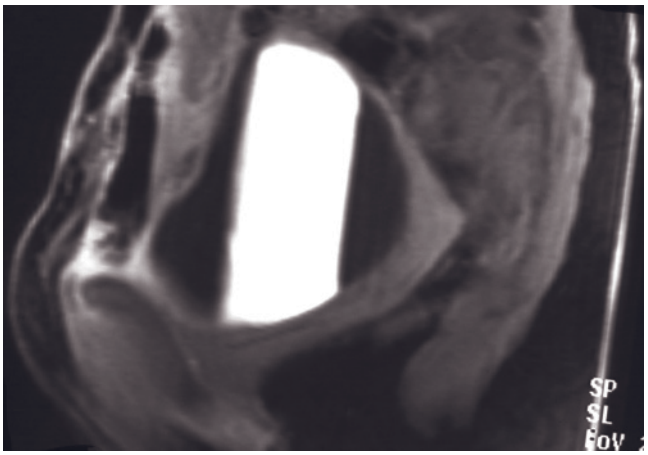

(*b*)

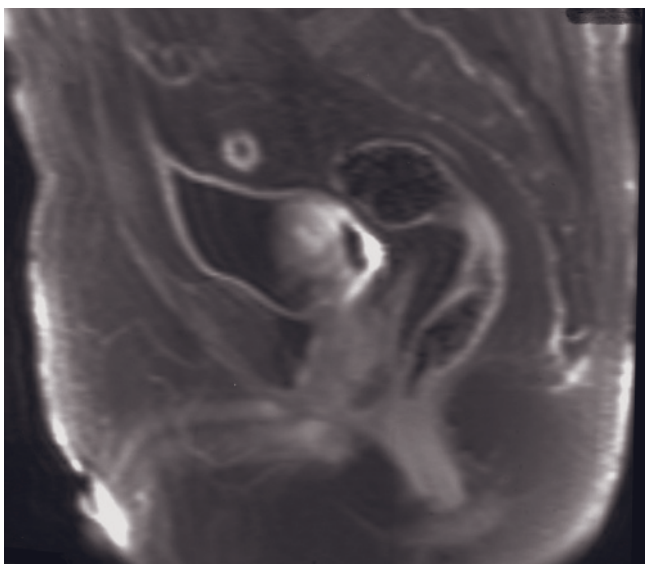

(*c*)

FIG. 11.1 Artifacts in the bladder from intravenous contrast. Sagittal T2-weighted SS-ETSE (*a*) and T1-weighted gadolinium-enhanced fat-suppressed SGE (*b*) images demonstrate discrete layers in the bladder from settling of intravenous contrast. Sagittal T1-weighted gadolinium-enhanced fat-suppressed SGE image (*c*) in a second patient demonstrates a whorl of contrast in the bladder, simulating an enhancing mass.

belly syndrome, diverticula, and patent urachus. Agenesis and hypoplasia are extremely rare. Duplication of the bladder can be demonstrated with MR imaging. The septum dividing the two bladder cavities is low in signal on both T1- and T2-weighted images. The bladder wall of both cavities is of the same thickness and signal intensity. Although bladder exstrophy, the most common congenital bladder lesion, is a clinical diagnosis, MR imaging may contribute important information about the skeletal, muscular, and peritoneal anomalies associated with bladder exstrophy as well as the position of the sex organs [13]. MR is similarly helpful in identifying associated anomalies of prune belly syndrome. In this rare syndrome, the bladder is often enlarged, lacks trabeculation, and may be associated with a patent urachus. The bladder wall is thickened because of replacement of normal smooth muscle with connective tissue [14].

Congenital bladder diverticula are herniations of bladder mucosa through areas of weakness in the detrusor muscle of the bladder. Most are seen in young males, and most occur at the level of the bladder base. When they originate at the ureteral meatus, they are called Hutch diverticula. These may be associated with ureteral obstruction. On MR images, bladder diverticula are seen as outpouchings from the native bladder (fig. 11.2). The wall of the diverticulum is thin and hypointense on T2-weighted images. On T1-weighted images acquired after gadolinium administration, the diverticulum fills with contrast-enhanced urine. Diverticula may

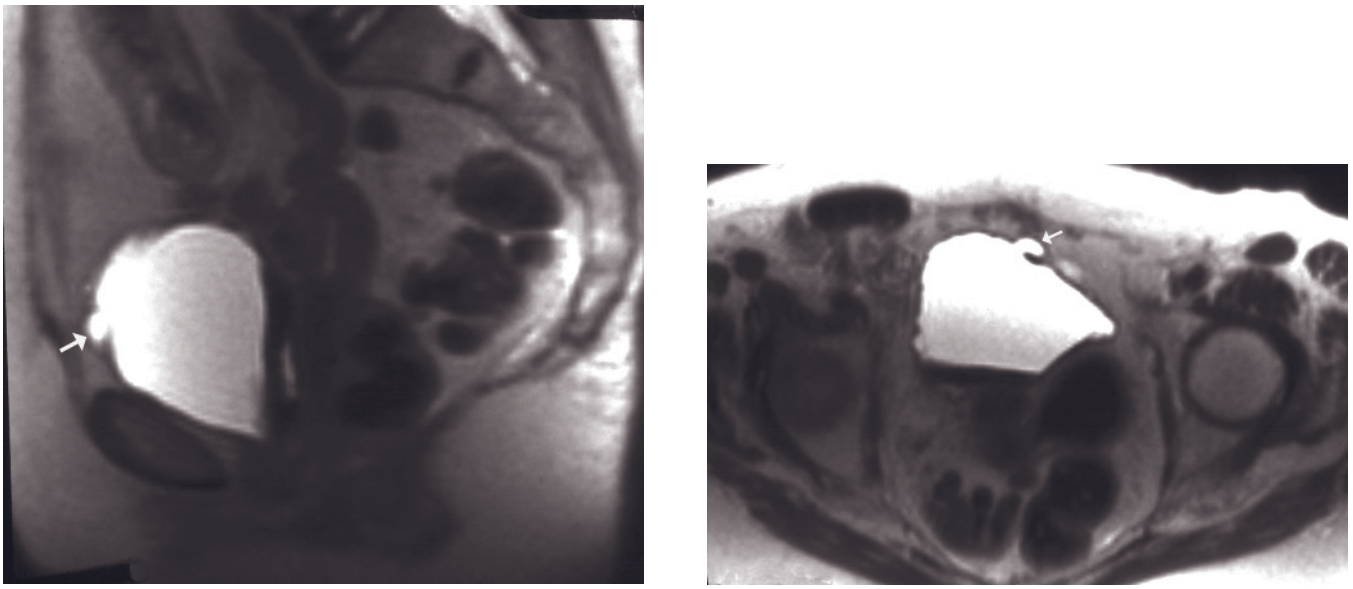

(*a*) (*b*)

FIG. 11.2 Bladder diverticula. Sagittal (*a*) and transverse (*b*) T2-weighted SS-ETSE images demonstrate focal outpouchings of the bladder representing diverticula (arrows, *a*, *b*).

be associated with urinary stasis, leading to chronic infection, inflammation, dysplasia, leukoplakia, and squamous metaplasia. This process may precede the development of a malignant tumor in the diverticulum. Tumors originating within diverticula are rare, occurring in 2–7% of patients with vesical diverticula. The most common cell type is transitional cell carcinoma (78%), followed by squamous cell carcinoma (17%), a combination of transitional and squamous cell types (2%), and adenocarcinoma (2%) [15].

The urachus is a vestigial structure, representing the remnant of the embryonic allantoids and cloaca. In adults, this persists as a midline musculofibrous tube that can extend from the bladder dome to the umbilicus. Incomplete obliteration may persist as a patent urachus or urachal cyst (fig. 11.3), sinus, or diverticulum [14]. A patent urachus may coexist with posterior urethral valves, prune belly syndrome, or ventral abdominal wall defects. Urachal adenocarcinoma is rare and is described later in this chapter.

MASS LESIONS

Benign Masses

Papilloma

Transitional cell papilloma accounts for 2–3% of all primary bladder tumors and is histologically benign but may recur or become malignant. The tumor consists of an axial fibrovascular core, which is covered by well-differentiated urothelial layers [16]. Bladder papillomas are most clearly shown on immediate postgadolinium MR images as small enhancing masses arising from lesser-enhancing wall. Dynamic gadolinium-enhanced MR images (15–45 s) may be most useful to demonstrate the superficial nature of these lesions (fig. 11.4).

Leiomyoma

Leiomyoma is the most common of the rare benign bladder tumors, affecting women 30–55 years of age. The lesion most commonly arises at the trigone but may be found on the lateral and posterior walls. Lesions may be intravesicular (60%), extravesicular (30%), or intramural (10%) (fig. 11.5). Intramural and extravesicular tumors do not cause symptoms, but intravesical lesions may present with hematuria or dysuria. Bladder neck tumors causing bladder outlet obstruction have been reported. The lesion is intermediate in signal intensity on T1-weighted images and well shown against a background of low-signal-intensity urine. On T2-weighted images, leiomyomas may vary from mildly hypointense to moderately hyperintense and are often slightly heterogeneous with variable enhancement [17]. Intramural extent is often well shown. Degenerating leiomyomas can have various appearances, including medium to high signal intensity on T1-weighted images and heterogeneous mixed signal intensity on T2-weighted images. These appearances are thought to be secondary to hemorrhage, calcification, or cystic transformation [18]. Leiomyomas and leiomyosarcomas cannot be

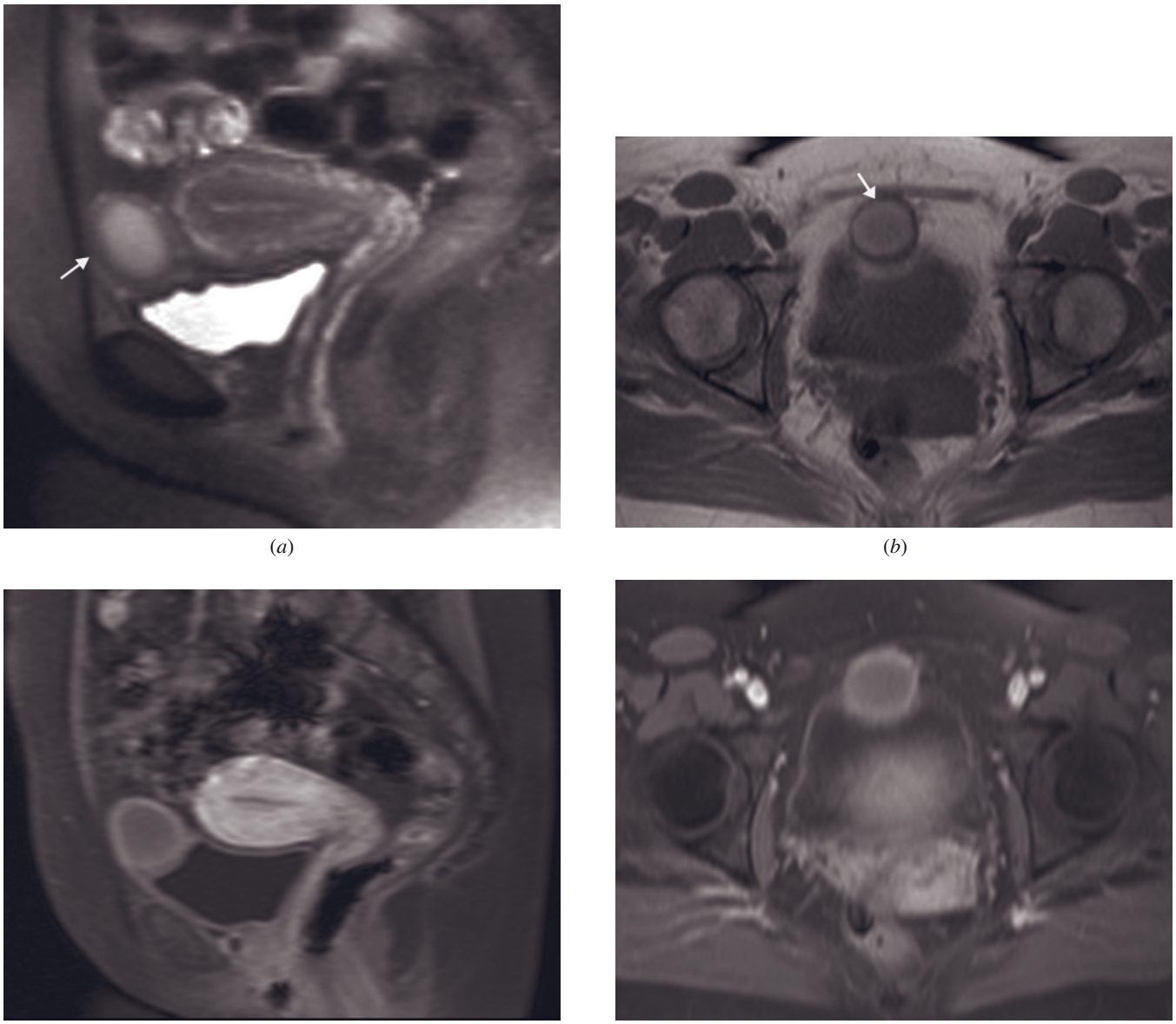

(*a*) (*b*)

(*c*) (*d*)

FIG. 11.3 Urachal cyst. Sagittal T2-weighted fat-suppressed SS-ETSE (*a*), transverse T1-weighted SGE (*b*), and sagittal (*c*) and transverse (*d*) T1-weighted gadolinium-enhanced fat-suppressed SGE images. There is a round lesion anterior and superior to the bladder that shows increased T1 and T2 signal, likely from proteinaceous or mucinous contents (arrow, *a*, *b*). There is no internal enhancement after contrast administration, but the wall enhances similar to the bladder wall (*c*, *d*).

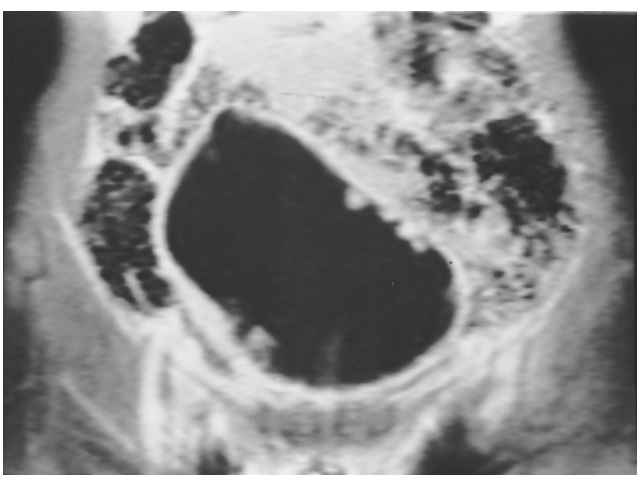

FIG. 11.4 Multiple papillary tumors. Coronal T1-weighted gadolinium-enhanced fat-suppressed spin-echo image. The enhancing papillomas are well shown as enhancing mass lesions in a background of low signal intensity of non-gadolinium-containing urine.

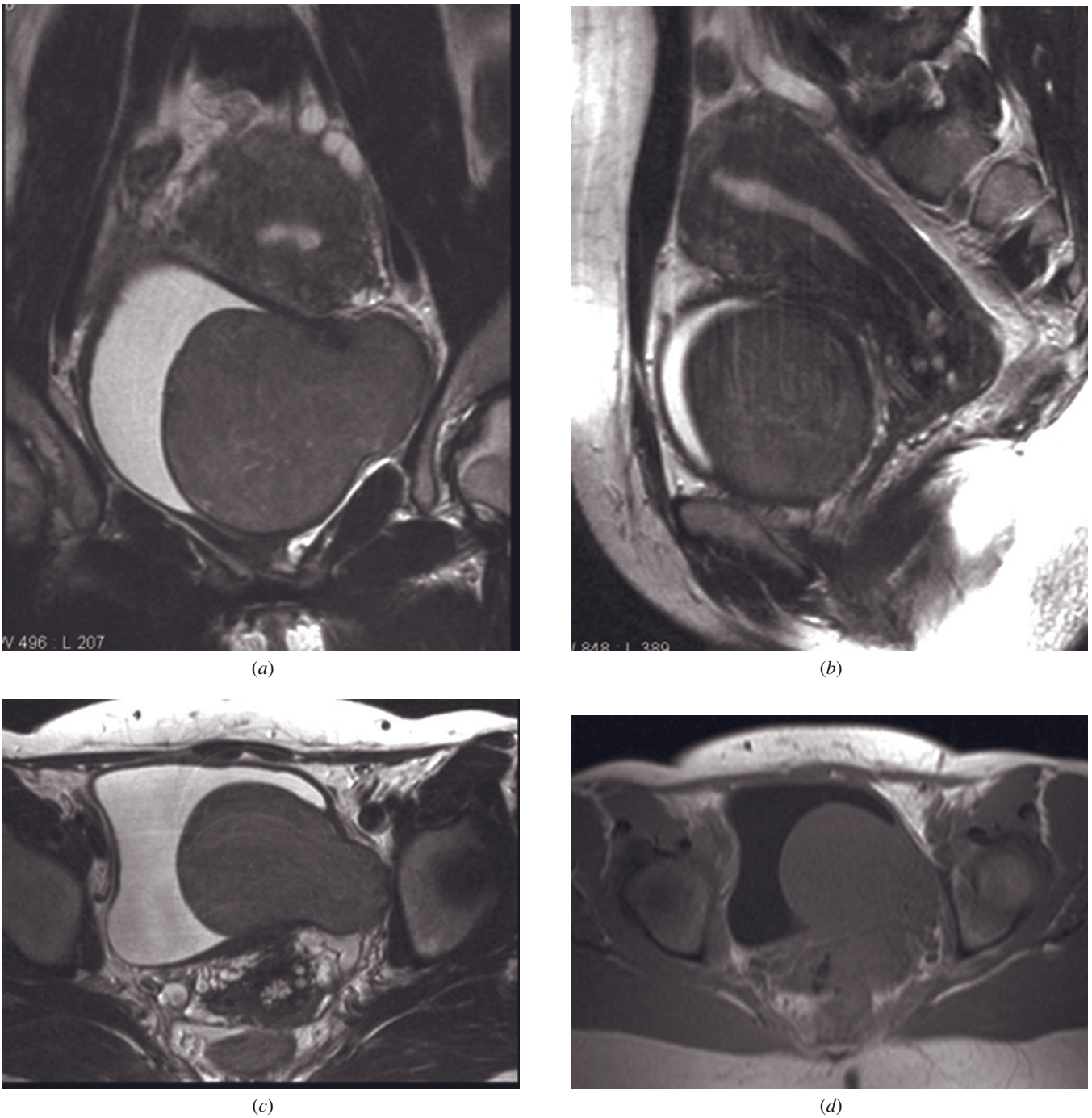

FIG. 11.5 Leiomyoma. Coronal (*a*), sagittal (*b*), and transverse (*c*) 512-resolution T2-weighted ETSE, transverse T1-weighted SGE (*d*), immediate transverse T1-weighted gadolinium-enhanced SGE (*e*), and delayed (2 min) transverse T1-weighted gadolinium-enhanced SGE (*f*) and sagittal (*g*) T1-weighted gadolinium-enhanced fat-suppressed SGE images demonstrate a large mass involving the left lateral wall and trigone of the bladder. The mass is hypointense on T2 (*a–c*)- and T1 (*d*)-weighted images, reflecting low fluid content characteristic for leiomyomas. There is mild heterogeneous enhancement on the immediate gadolinium-enhanced T1-weighted image (*e*), with progressive enhancement on the delayed images (*f*, *g*).

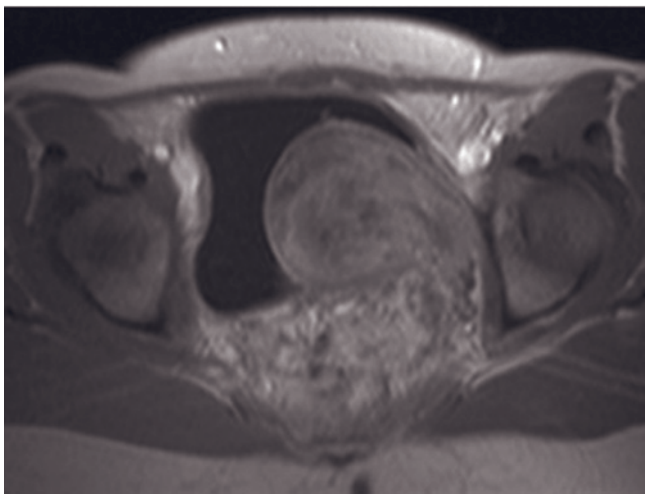

(*e*)

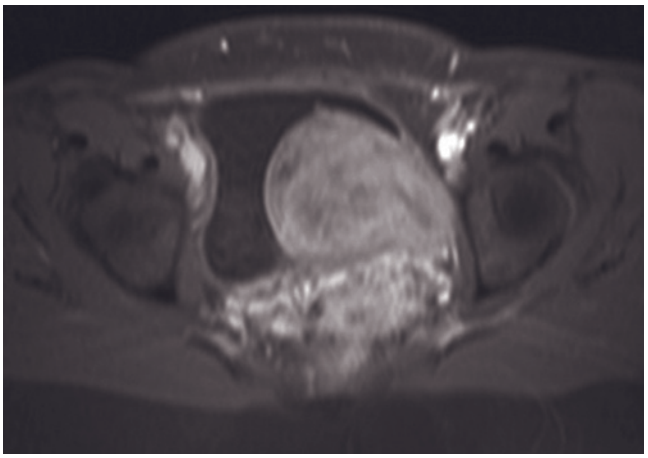

(*f*)

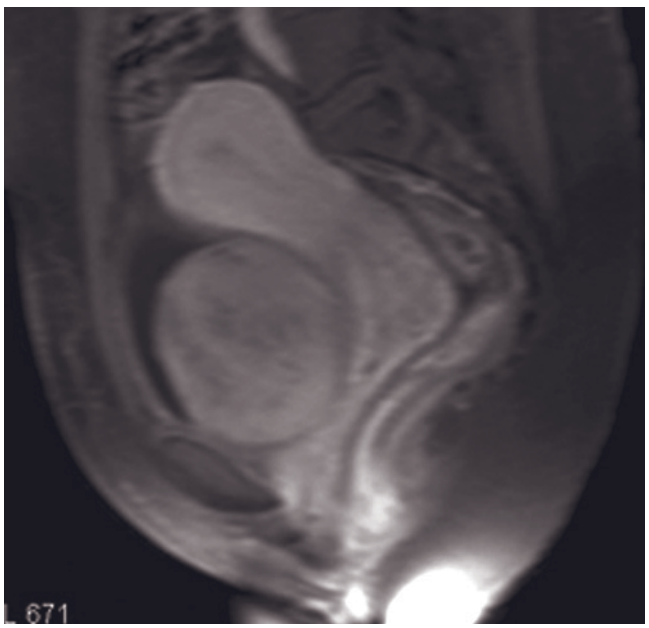

(*g*)

FIG. 11.5 (*Continued*)

consistently distinguished on MR images [3]. However, large size, heterogeneity, and irregular margins are features suggestive of malignancy.

Pheochromocytoma

Pheochromocytomas are catecholamine-producing tumors that arise from chromaffin cells and can occur anywhere along the sympathetic nervous system from the neck to the sacrum. Ten to fifteen percent occur in an extra-adrenal location. One percent are located in the bladder and have a predilection for the trigone, followed by the region near the ureteral orifices. They are found less frequently in the dome and lateral walls of the bladder. Seven percent of bladder pheochromocytomas are malignant [16]. Males and females have an equal incidence, with a mean age of 41 years. About half of the cases present with the clinical triad of hypertension, gross intermittent hematuria, and attacks of sweating, headache, and palpitations induced by micturition [19]. Characteristic MRI features help to distinguish this tumor from other tumors, including carcinoma [19, 20]. Typically, these tumors show markedly increased, homogeneous signal intensity on T2-weighted spin-echo sequences [21–23]. However, signal can be heterogeneously increased on T2-weighted images [24]. T1-weighted images demonstrate hypointense or isointense signal intensity [17, 18]. They enhance intensely after gadolinium administration.

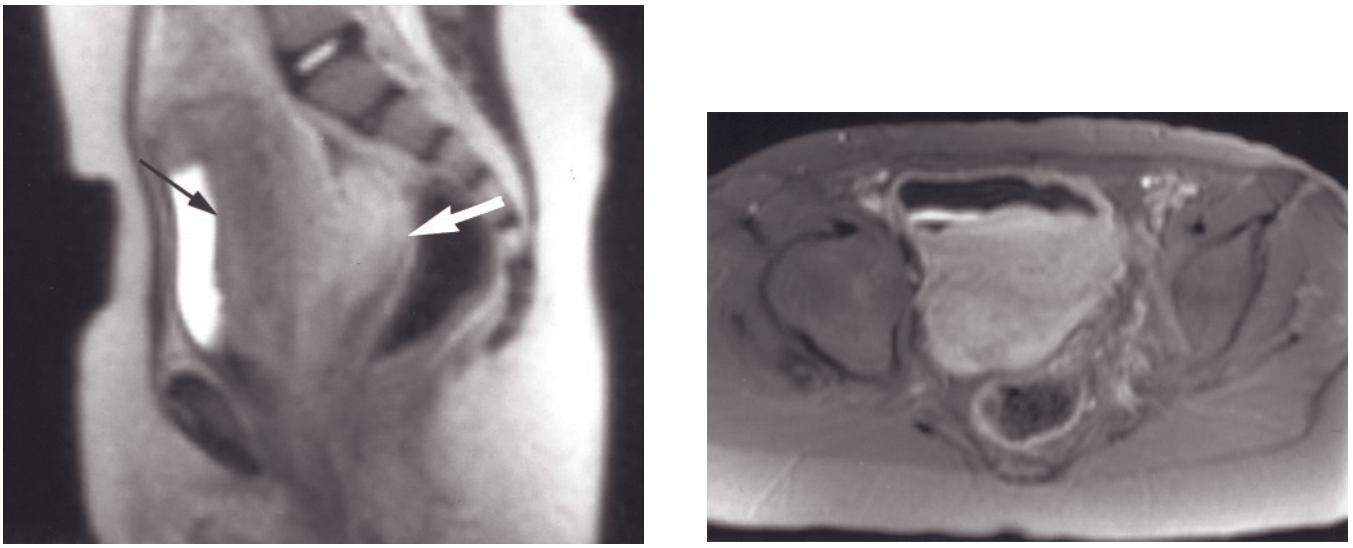

(*a*) (*b*)

FIG. 11.6 Neurofibroma. Sagittal T2-weighted single-shot echo-train spin-echo (*a*) and T1-weighted gadolinium-enhanced fat-suppressed spin-echo (*b*) images in a patient with history of neurofibromatosis. There is a mildly heterogeneous and hypointense mass (black arrow, *a*) on the T2-weighted image that involves the posterior aspect of the bladder wall and uterus (white arrow, *a*) and displaces the rectum posteriorly. After gadolinium administration, there is moderately intense and slightly heterogeneous enhancement of the tumor (*b*). Histopathology demonstrated a plexiform neurofibroma in the bladder wall.

Neurogenic Tumors

Neurofibromatosis, the most common phakomatosis, is characterized by café au lait spots, optic gliomas, Lisch nodules, distinctive bone lesions, and neurofibromas. Genitourinary tract neurofibromas are rare, but most commonly affect the bladder (fig. 11.6). Obstructive hydronephrosis, a common complication, is presumably due to neurofibromas involving the trigone. Pelvic sidewall tumors appear nodular and may extend into the obturator foramina. Neurofibromas demonstrate distinct MRI features that allow better characterization of the extent of the tumor within the bladder, pelvic sidewalls, and surrounding soft tissues than CT imaging. The MRI appearance for type 1 neurofibromatosis (von Recklinghausen disease) is T1-weighted signal intensity slightly greater than that of skeletal muscle and markedly increased signal intensity relative to the surrounding tissues on T2-weighted images. Larger tumors may be inhomogeneous, with markedly increased signal intensity and well-defined central areas of decreased signal intensity on T2-weighted images. Most demonstrate enhancement with gadolinium administration (fig. 11.6) [25]. Malignant degeneration may occur in plexiform neurofibromas but is rare in isolated neurofibromas [17].

Ganglioneuromas have a similar appearance; they are isointense to skeletal muscle on T1-weighted images and hyperintense on T2-weighted images and enhance substantially with gadolinium (fig. 11.7).

Hemangiomas

Hemangioma is a rare mesenchymal benign tumor of the bladder that is more common in children but may occur at any age [17]. The most common presenting symptom is gross, painless hematuria. The tumor has been reported to be low to intermediate signal intensity on T1-weighted images, with a multilocular pattern. The lesion is of very high signal intensity on T2-weighted images [26].

Inflammatory Myofibroblastic Tumor

Inflammatory myofibroblastic tumor (also described as inflammatory pseudosarcoma) is a rare mesenchymal benign bladder lesion of spindle cell origin. It can occur at any age; patients may present with hematuria, urinary frequency, dysuria, or nocturia. Usually these lesions are exophytic and extend into the bladder lumen, but they may be intramural and may extend into the perivesical tissues. This lesion is reported to have low T1 signal intensity, inhomogeneous high T2 signal intensity, and heterogeneous enhancement with areas of necrosis [17].

Calcifications

Bladder calculi may be the result of foreign body nidus, stasis, or migration of upper tract calculi, or they may be idiopathic. Foreign bodies include catheters, nonabsorbable sutures, hair, or bone fragments. Stasis may result from bladder outlet obstruction, diverticula, cys-

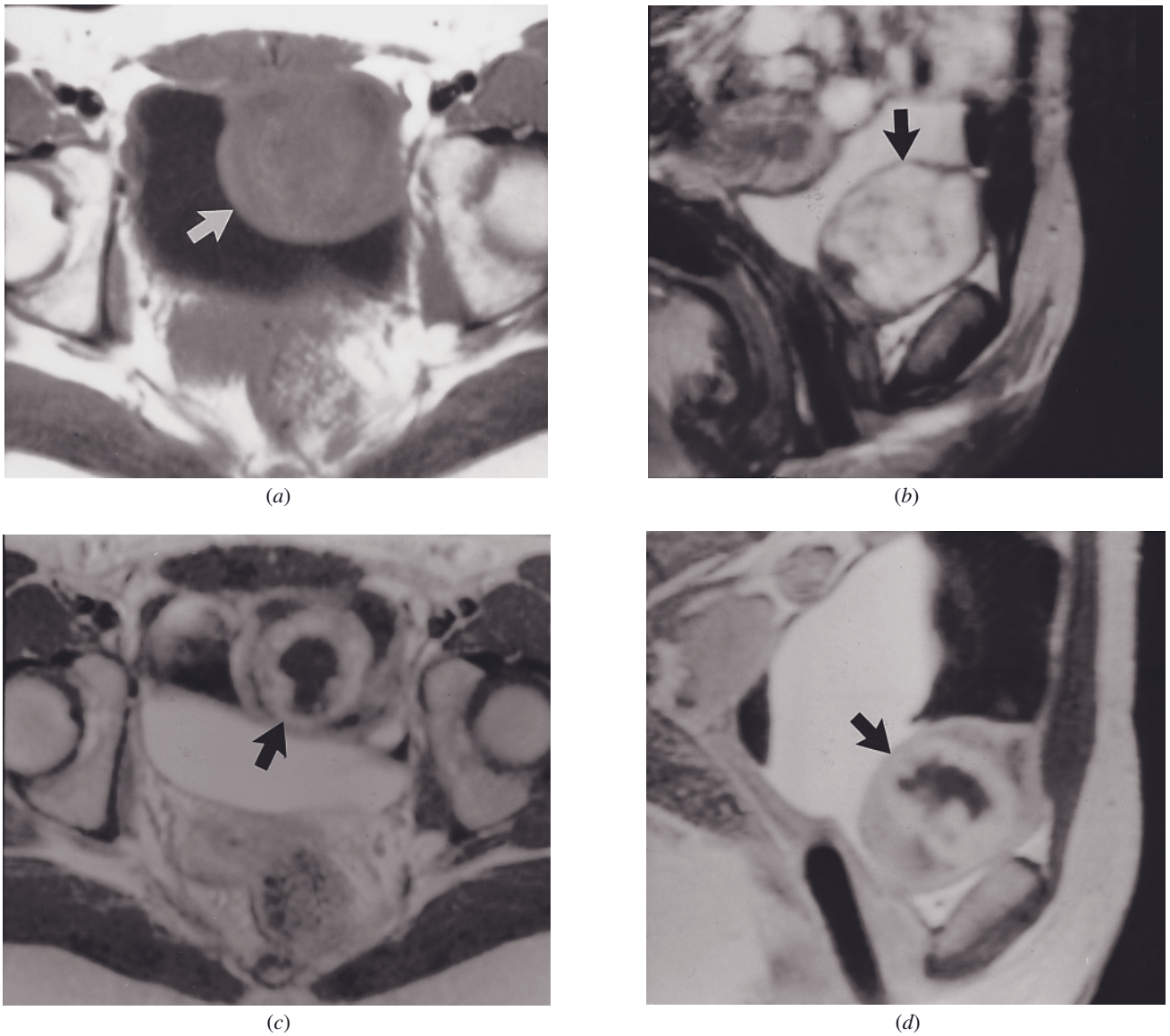

FIG. 11.7 Ganglioneuroma. T1-weighted spin-echo (*a*), sagittal T2-weighted spin-echo (*b*), and transverse (*c*) and sagittal (*d*) gadolinium-enhanced T1-weighted spin-echo images. A 4-cm ganglioneuroma arises from the anteroinferior bladder wall. The tumor is intermediate in signal intensity on the T1-weighted image (arrow, *a*) and moderately hyperintense on the T2-weighted image (arrow, *b*) and shows substantial enhancement on interstitial-phase gadolinium-enhanced images (arrows, *c*, *d*) with central necrosis. (Courtesy of Hedvig Hricak, M.D., Ph.D.).

tocele, or postoperative states. Bladder calculi are well shown on T2-weighted images or late postgadolinium T1-weighted images. These sequences show good contrast between high-signal-intensity urine and signal-void calculi (fig. 11.8) [27].

Bilharziosis is caused by the organism *Schistosoma haematobium* in the majority of cases. Patients present with frequency urgency, dysuria, flank pain, and hematuria. The characteristic calcifications are linear and continuous along the bladder wall. These bladder wall calcifications are signal void on all MRI sequences [28].

Malignant Masses

Bladder cancer is the most common cancer of the urinary tract. It accounts for 4.5% of all new malignant neoplasms and 1.9% of all cancer deaths in the United States [29]. Its incidence appears to be rising, believed to be caused by an increased exposure to multiple environmental carcinogens such as tobacco, artificial sweeteners, coffee, cyclophosphamides, and various aromatic amines. The incidence of bladder cancer increases with age, and it is most commonly seen in

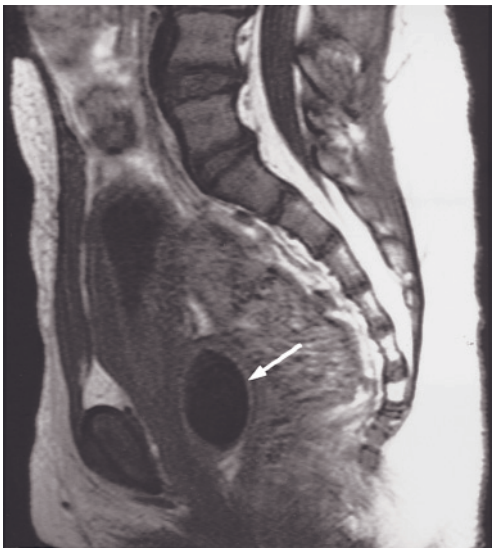

(*a*)

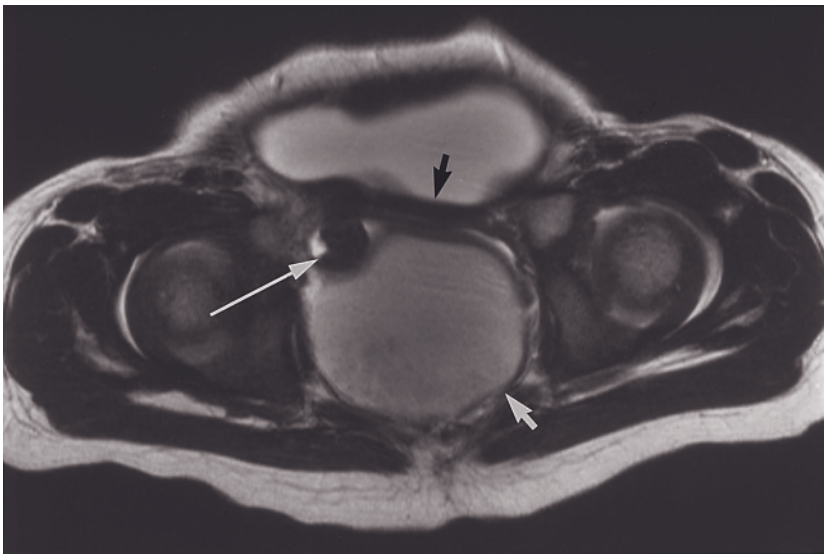

(*b*)

(*c*)

FIG. 11.8 Bladder calculus in a patient with a surgically repaired persistent cloaca. Sagittal T1-weighted spin-echo (*a*), T2-weighted fat-suppressed echo-train spin-echo (*b*), and sagittal 512 resolution T2-weighted echo-train spin-echo (*c*) images. A nearly signal-void oval structure (long white arrows, *a–c*) on the T1- and T2-weighted images represents a calculus in a bladder diverticulum. The bladder wall is thickened (black arrows, *b*, *c*), and the reconstructed rectum is dilated (short white arrow, *b*).

the sixth and seventh decades. However, it is being found in an increasing number of patients less than 30 years old. Bladder cancer is three times more common in men than in women [13]. Classification of bladder tumors is based on three criteria: cell type (urothelial, squamous, or glandular), pattern of growth (papillary, nonpapillary, noninfiltrating, or infiltrating), and grading (degree of cellular differentiation). The nonpapillary urothelial tumors include invasive transitional cell carcinoma, squamous cell carcinoma, adenocarcinoma, and carcinosarcoma.

Primary Urothelial Neoplasm

Transitional Cell Carcinoma. Transitional cell carcinoma is the most common primary bladder malignancy and accounts for 85% of all bladder malignancies. Nonpapillary or sessile urothelial tumors are typically more invasive and of a higher grade than exophytic types. Most patients have a prior history of papillary tumors, which arise from epithelial abnormalities adjacent to papillary neoplasia. Invasive urothelial cancer initially spreads radially through the wall of the bladder and then circumferentially through the muscular layer. It may then invade the perivesical fat and, depending on the location of the neoplasm, may invade the prostate, seminal vesicles, or obturator internus muscles. In women, it rarely invades the uterus or cervix. Invasion of the ureters or urethra is common when the tumor originates near one of these structures [30]. Transitional cell carcinoma most commonly rises from the lateral

wall and can cause hydronephrosis or hydroureter if it extends around the ureteral orifices [31].

Seventy to eighty percent of bladder cancers are diagnosed as early stage, associated with a 5-year survival rate of 81 percent. Patients with invasive tumors are at high risk of disease progression, and, despite definitive therapy, the overall 5-year mortality rate is almost 50% [13]. Selection of appropriate treatment for bladder cancer depends on accurate diagnosis and staging. Superficial neoplasm can be treated with transurethral resection and instillation of chemotherapeutic agents, BCG therapy, or both. Patients with involvement of the superficial muscle layer are candidates for segmental cystectomy. Invasive neoplasms and those with limited perivesical fat involvement require radical cystectomy. Presurgical chemotherapy or palliative radiation therapy is used when extension has occurred outside of the bladder into adjacent pelvic structures [3].

The TNM staging of bladder neoplasms is as follows (fig. 11.9) [32]:

T0	No evidence of primary tumor
Ta	Noninvasive papillary carcinoma
Tis	Carcinoma in situ: "flat tumor"
T1	Tumor invades subepithelial connective tissue
T2a	Tumor invades superficial muscle (inner half)
T2b	Tumor invades deep muscle (outer half)
T3a	Tumor invades perivesical tissue microscopically
T3b	Tumor invades perivesical tissue macroscopically (extravesical mass)
T4a	Tumor invades prostate, uterus, or vagina
T4b	Tumor invades pelvic wall or abdominal wall
N0	No regional lymph node metastases
N1	Metastasis in a single lymph node ≤2 cm in greatest dimension
N2	Metastasis in a single lymph node >2 cm but ≤5 cm in greatest dimension, or multiple lymph nodes
N3	Metastasis in a single lymph node >5 cm in greatest dimension
M0	No distant metastases
M1	Distant metastases

Both T1- and T2-weighted images are useful in staging bladder cancers [6, 28, 33–40]. The mass on T1-weighted images demonstrates intermediate signal intensity similar to that of muscle [31, 41]. The use of T1-weighted sequences is recommended to determine invasion of the perivesical fat and surrounding organs (except the prostate) and involvement of lymph nodes and bone marrow. On T2-weighted images, the mass has similar to slightly higher signal intensity than the bladder wall [31, 41]. T2-weighted images are recommended for assessment of the extent of tumor invasion

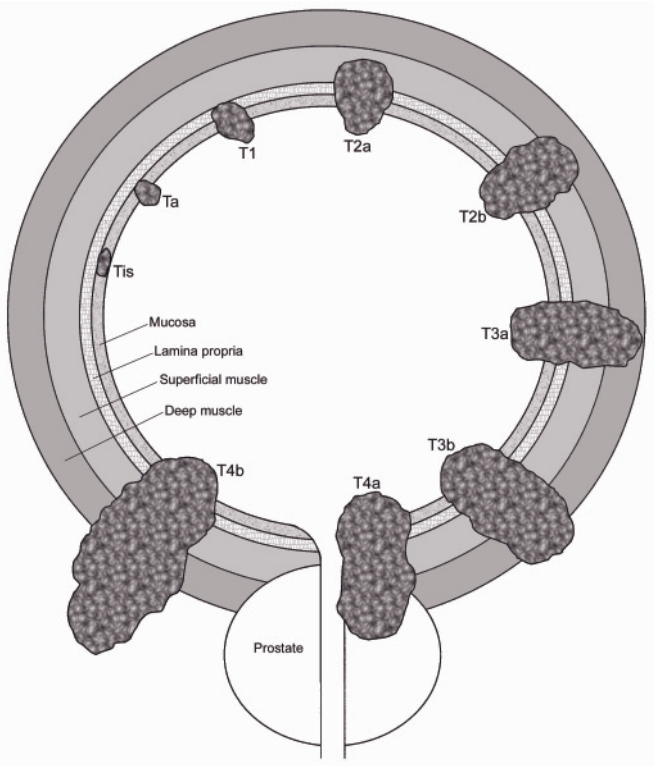

FIG. 11.9 T staging of urothelial carcinoma. (Drawing by Donald Eknoyan, MD.)

into the muscle layer of the bladder wall and prostate [6, 8, 28, 33–36, 42].

The use of intravenous gadolinium contrast agents has improved the imaging of bladder carcinomas. Gadolinium quickly distributes in the extracellular space without passing through intact cell membranes [42] and typically provides substantial enhancement of urinary bladder carcinomas [5, 43–51]. Bladder carcinomas tend to enhance more than the surrounding bladder wall early after injection of contrast because of neovascularity. Tumors are well seen approximately 5–15 s after arterial enhancement [47]. This early phase of enhancement also demonstrates good conspicuity of bladder tumor against gadolinium-free urine in the bladder. Given the tendency of transitional cell carcinoma to be multiple or multifocal, the identification of more than one area of enhancement is important [41]. Fast dynamic MR imaging may also be able to differentiate between tumor and postbiopsy change, because tumor enhances earlier than postbiopsy tissue (6.5 s vs. 13.6 s) [6]. Delayed (>5 min) postcontrast T1-weighted images show high signal intensity of urine, and the intraluminal portion of a bladder tumor is usually well delineated, although small tumors may be obscured. Two- to five-minute postcontrast fat-suppressed SGE or 3D-GE images are the most reliable to show lymph nodes and bone marrow metastases in a consistent fashion.

MRI offers several advantages over CT imaging, including higher contrast resolution and higher sensitivity to contrast agents, which permits better imaging of the bladder dome, trigone, perivesical fat, prostate, and seminal vesicles. Bladder tumors at the base or dome and smaller tumors [41] are better staged with MRI. Overall, accuracy of MRI in the staging of bladder carcinoma has been reported to range from 69% to 89%. Acquisition of MR images in oblique planes to demonstrate the tumor-bladder wall interface in profile has been effective for assessing depth of bladder wall invasion, with overall staging accuracy of 78% for gadolinium-enhanced T1-weighted images and 60% for T2-weighted images. Staging of small tumors, in particular, is improved with the use of immediate postgadolinium imaging [46, 48, 49, 51].

Immediate postgadolinium SGE or 3D-GE images acquired in an oblique projection to demonstrate tumor-bladder wall interface in profile has been an effective approach, especially in the differentiation of superficial tumors and tumors with superficial muscle invasion [5]. The use of thinner slices and high-resolution imaging may also help in the differentiation of superficial tumors and tumors with superficial muscle invasion.

MRI is able to differentiate between superficial (stage T1) (fig. 11.10) and deep (stage T2b) (fig. 11.11) invasion of the muscular layer of the bladder wall with high accuracy [43]. In general, if a clearly defined dark bladder wall is visualized and appears intact on T2-weighted images, the tumor should be classified as stage Tis, T1, or T2a, whereas if the bladder wall is breached, the tumor should be staged as T2b or higher. The higher contrast resolution is most useful in the differentiation between muscular invasion (stage T2b) and invasion into the perivesical fat (stage T3b) [5, 28–32, 34]. For deeply infiltrative tumors (stages T3b, T4a, and T4b), MRI is generally considered the most accurate method of staging (fig. 11.12) [43, 52], with postgadolinium fat-suppressed images most useful. The most common cause of staging error in MRI and CT imaging studies is overstaging, and prior cystoscopic biopsy is likely a common cause of this overstaging [41, 53]. For this reason, it is recommended that MRI studies be performed at least 3 weeks after bladder biopsy.

In the staging of lymph node metastases, MRI and CT imaging appear to be comparable. Accuracy is 83–97% for CT imaging and 73–98% for MRI. At present, distinction between enlarged hyperplastic nodes and malignant nodes cannot be made, which can result in overstaging of tumors (fig. 11.13). Additionally, because the criterion for pathologic enlargement of nodes in the pelvis is greater than 1 cm, small, involved nodes will not be detected. Nodes involved in the spread of bladder cancer include the anterior and lateral paravesical, presacral, hypogastric, obturator, and external iliac nodes, followed by common iliac and para-aortic lymph nodes [7]. Retroperitoneal nodal involvement is not often seen in patients with bladder cancer at the time of initial diagnosis, but if present, the pelvic nodes are also usually involved [38]. After treatment with radiotherapy, relapse in retroperitoneal nodes may be seen without evidence of nodal disease in the pelvis [38]. In treated patients, it is therefore probably prudent to examine the retroperitoneum as well as the pelvis. T1-weighted images are useful for imaging lymph nodes, as their signal intensity is lower than that of the surrounding fatty tissue [6]. Postgadolinium T1-weighted images with fat saturation are particularly useful for the evaluation of adenopathy, as the moderate signal intensity of enhanced nodes is conspicuous in the background of low-signal-intensity fat. Three-dimensional imaging may be helpful in providing information not only about size of nodes but also about their shape [6].

MRI is superior to CT imaging in the diagnosis of bone marrow metastases [54]. T1-weighted images are useful in detection of bone marrow metastases, because lesions will have similar signal characteristics as the primary tumor (typically intermediate intensity) and will be conspicuous against the high signal intensity of fatty marrow [53]. The most accurate technique for the detection of bone marrow metastases is gadolinium-enhanced T1-weighted fat-suppressed imaging. Metastases appear as rounded or geographic regions of enhancement in a background of suppressed background fatty marrow. Unlike noncontrast T1-weighted images that have relatively low specificity, as a number of entities in addition to metastases are low to intermediate in signal, gadolinium-enhanced fat-suppressed images have higher specificity because focal regions of enhancement are quite characteristic for metastases. Sensitivity is also higher for gadolinium-enhanced fat-suppressed images, as areas of enhancement are more conspicuous than areas of low signal.

MRI is useful in the distinction between late fibrosis and recurrence of carcinoma. One year after transurethral resection, after resolution of the acute edema, residual scar can be distinguished from recurrence of tumor with T2-weighted images [5, 6, 39, 40, 42, 44–51]. Fibrosis is low in signal intensity, whereas tumor recurrence is heterogeneous and moderate in signal intensity. Before resolution of the edema, distinction between granulation tissue and recurrence is problematic [6, 46, 48, 49, 51]. Diagnosing tumor recurrence is also aided by the observation that recurrent tumor appears as soft tissue that enhances similarly to the primary tumor (fig. 11.14) [41].

MRI and clinical staging have complementary roles, and staging of urinary bladder tumors is best achieved with the use of both approaches. Because of the limitations in differentiating acute edema from tumor

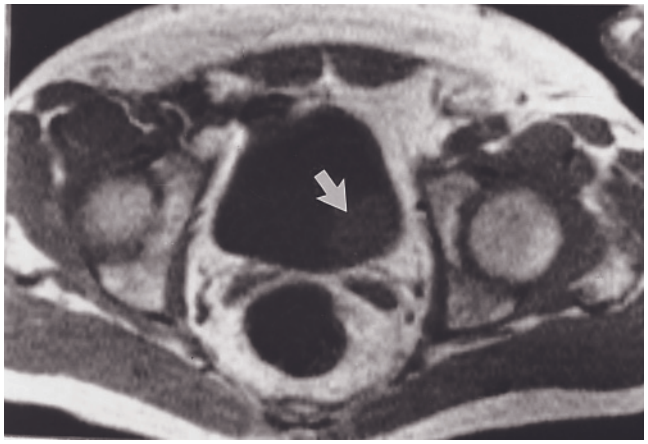

(*a*)

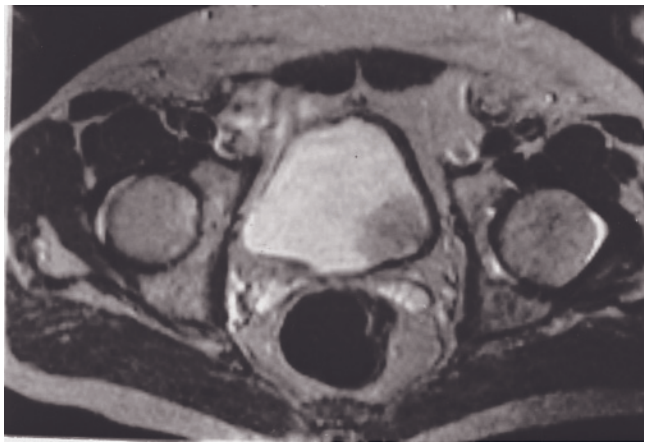

(*b*)

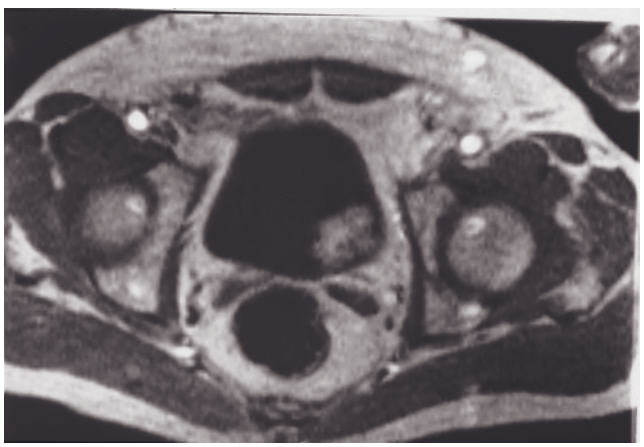

(*c*)

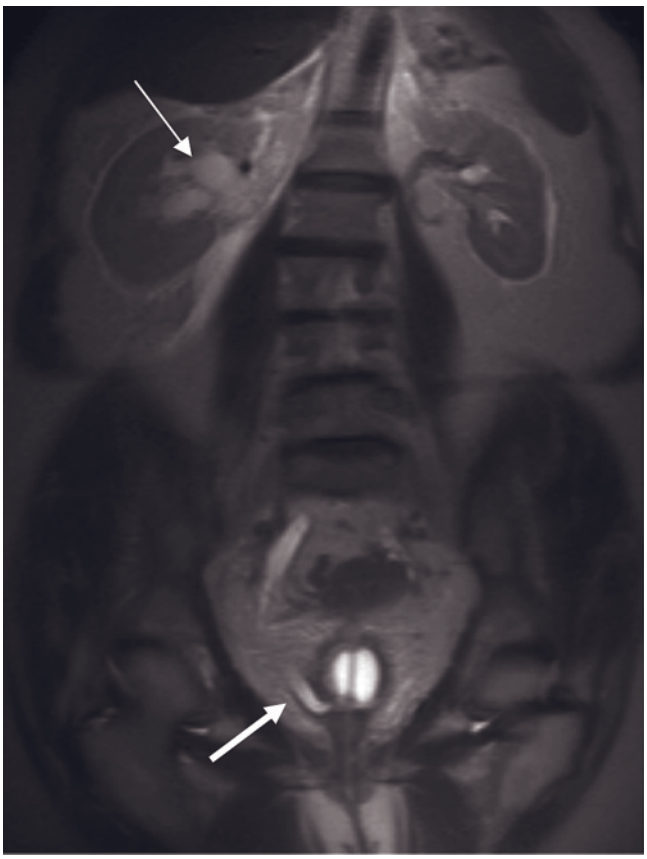

(*d*)

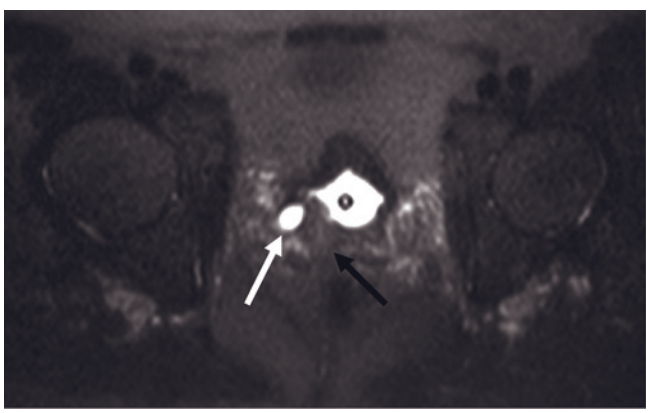

(*e*)

FIG. 11.10 Transitional cell cancer, superficial invasion. T1-weighted SGE (*a*), T2-weighted echo-train spin-echo (*b*), and immediate postgadolinium SGE (*c*) images in a patient with superficial T1 transitional cell bladder cancer. The tumor is intermediate in signal intensity on the T1-weighted image (arrow, *a*) and moderately high in signal intensity on the T2-weighted image (*b*). Moderately intense tumor enhancement is appreciated on the postgadolinium image (*c*), and lack of wall invasion is shown. Intact low-signal-intensity muscular wall deep to the tumor is appreciated on the T2-weighted (*b*) and immediate postgadolinium SGE (*c*) images. Coronal and axial T2-weighted single-shot echo-train spin-echo (*d*, *e*), MR urography (*f*), and transverse 45-s postgadolinium fat-suppressed 3D-GE (*g*) images in another patient with transitional cell cancer. Dilated right ureter (white thick arrows, *d*, *e*) and right hydronephrosis (white thin arrow, *d*) are demonstrated on T2-weighted single-shot echo-train spin-echo images (*d*, *e*). MR urography image (*f*) shows dilated right ureter

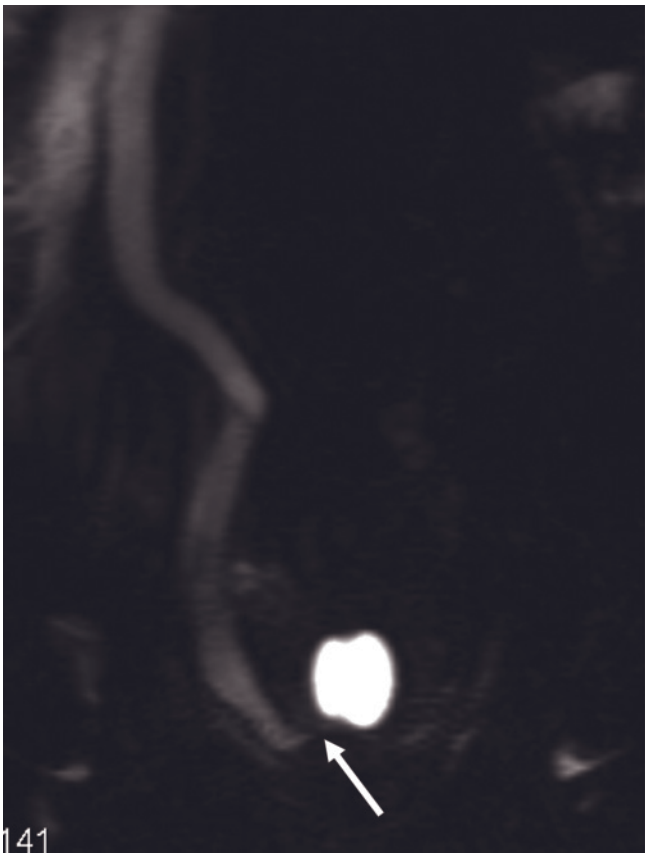

(*f*)

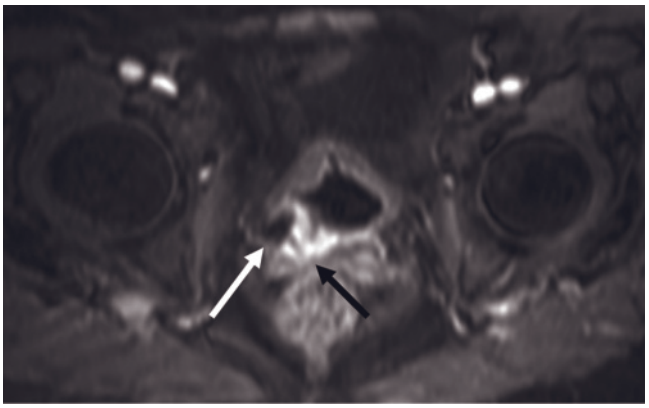

(*g*)

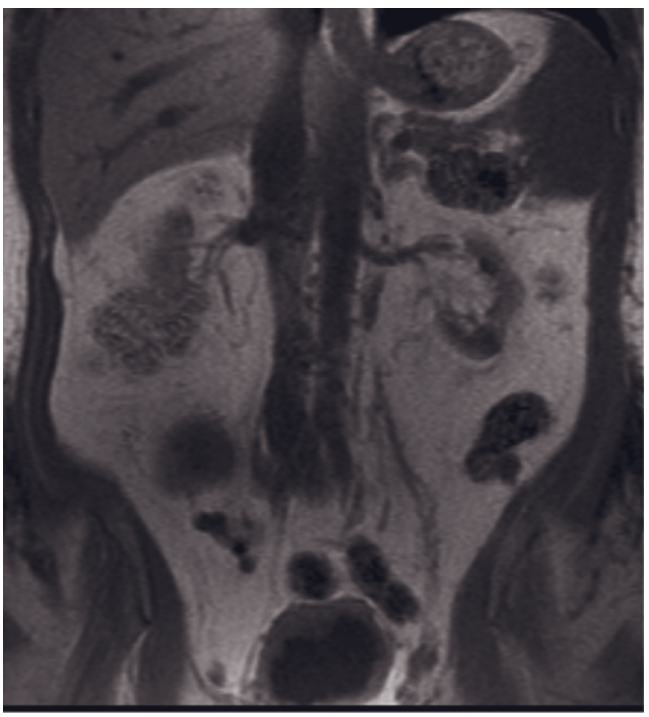

(*h*)

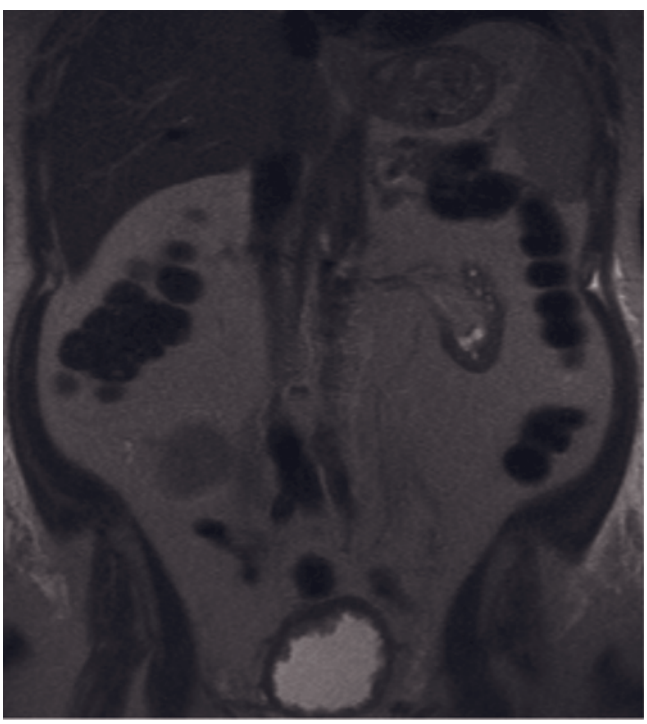

(*i*)

FIG. 11.10 (*Continued*) and its abrupt cutoff at vesicoureteral junction (white thick arrow). A soft tissue mass obstructing the right ureter at vesicoureteral junction is seen as a hyperintense structure (black arrow) compared to the remaining bladder wall on transverse T2-weighted image (*e*). The tumor shows intense enhancement (black arrow) on postgadolinium image (*g*). Enhancement of the tumor does not extend beyond the limits of bladder wall. Intact wall is present deep to the enhancing tumor. Note the Foley catheter in the bladder lumen. Coronal T1-weighted SGE (*h*), T2-weighted single-shot echo-train spin-echo (*i*), and 90-s

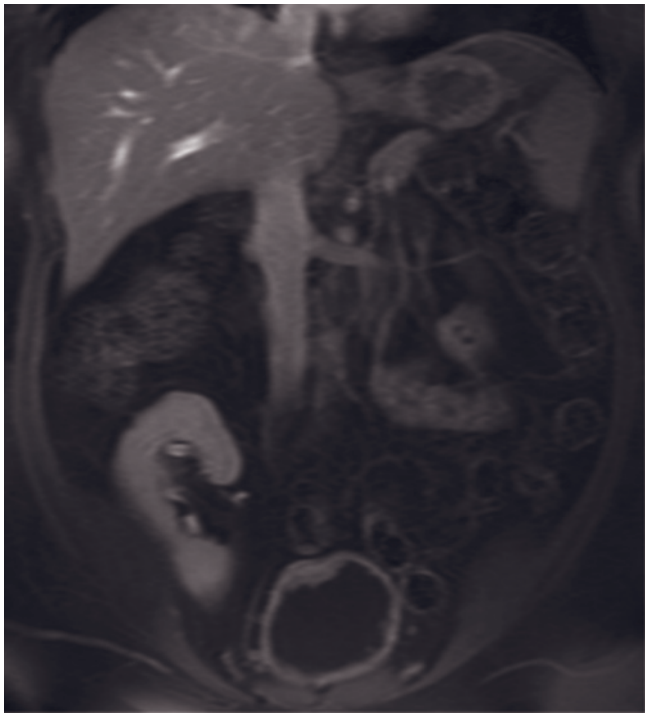

(*j*)

FIG. 11.10 (*Continued*) postgadolinium fat-suppressed 3D-GE (*j*) images demonstrate transitional cell cancer in another patient with atrophic kidneys and renal transplant located in the right lower quadrant. The bladder wall is diffusely thickened, and there are multiple polypoid projections extending into the lumen. The thickened bladder wall and its projections show homogenous enhancement on postgadolinium image (*j*). The tumor does not extend beyond the limits of bladder wall. Intact low-signal-intensity muscular wall deep to the tumor is appreciated on T2-weighted image.

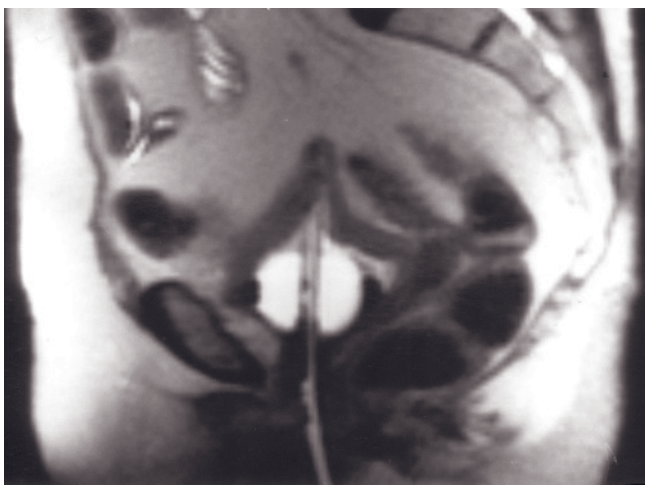

(*a*)

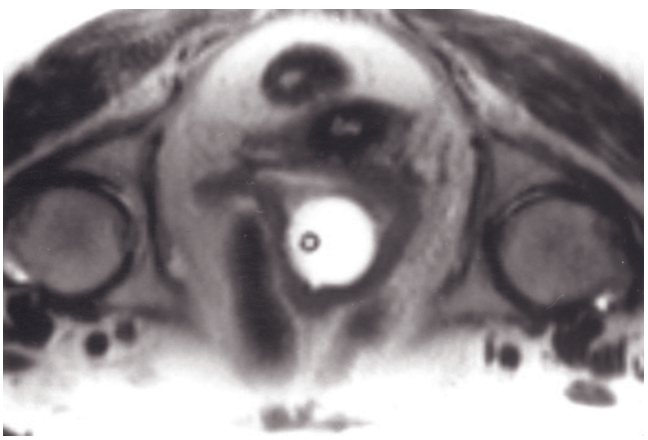

(*b*)

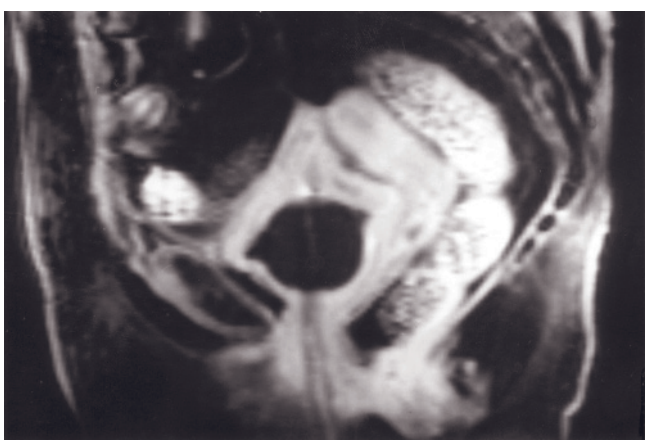

(*c*)

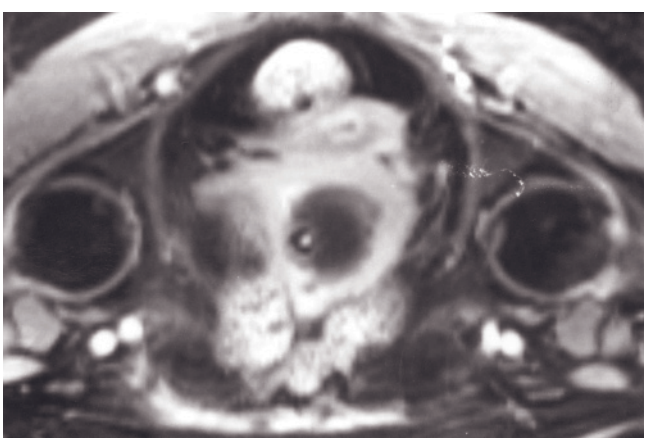

(*d*)

FIG. 11.11 Invasive transitional cell carcinoma. Sagittal (*a*) and transverse (*b*) T2-weighted single-shot echo-train spin-echo and sagittal (*c*) and transverse (*d*) T1-weighted gadolinium-enhanced fat-suppressed SGE images. Markedly diffuse thickening of the bladder wall (*a*, *b*) is present, which represents diffuse tumor involvement. The tumor enhances intensely after gadolinium administration (*c*, *d*). T2-weighted echo-train spin-echo (*e*), T1-weighted gadolinium-enhanced fat-suppressed spin-echo (*f*), and coronal

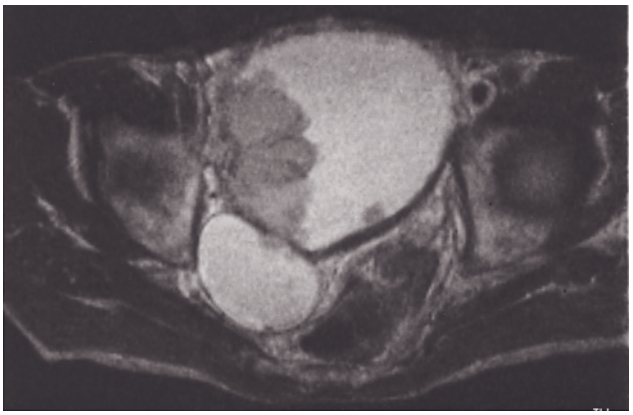

(*e*)

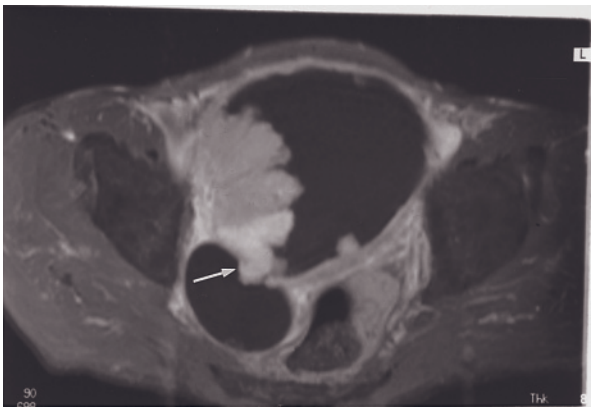

(*f*)

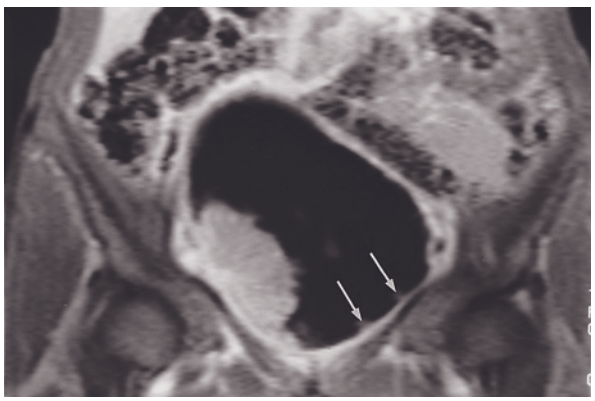

(*g*)

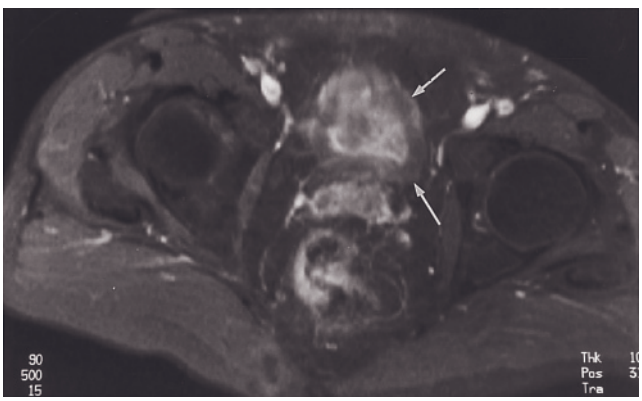

(*h*)

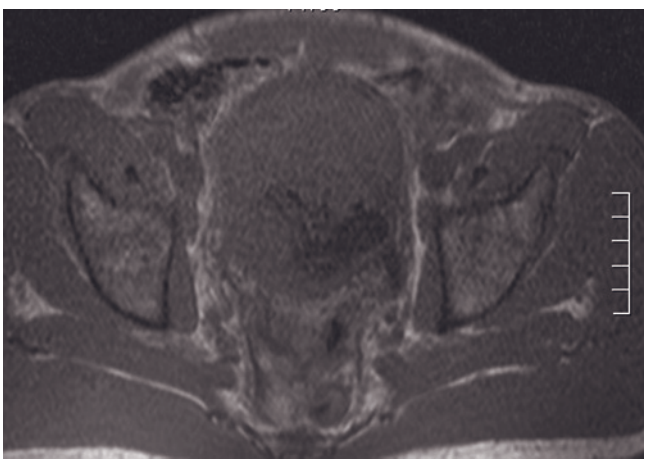

(*i*)

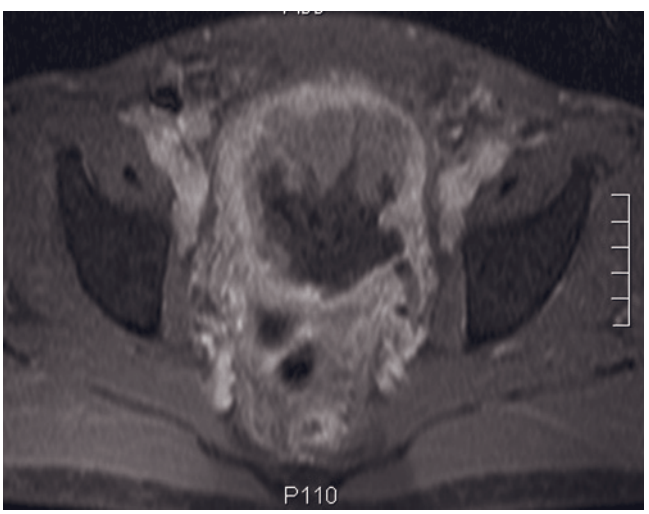

(*j*)

FIG. 11.11 (*Continued*) interstitial-phase gadolinium-enhanced SGE (*g*) images in a second patient. A frondlike stage T3a papillary transitional cell cancer is demonstrated arising from the right lateral wall of the bladder. Note that the lesion extends into a diverticulum (arrow, *f*). On the T2-weighted image, the low-signal-intensity muscular wall is not infiltrated by tumor (*e*). Multiple small papillomas are also identified (arrows, *g*). T1-weighted postgadolinium fat-suppressed image (*h*) in a third patient. There is diffuse, relatively symmetric thickening of the bladder wall from transitional cell cancer with heterogeneous moderate enhancement. T1-weighted SGE (*i*) and T1-weighted gadolinium-enhanced fat-suppressed SGE (*j*) images in a fourth patient demonstrate an irregular enhancing mass arising from the anterior aspect of the bladder with irregular circumferential thickening of the bladder wall.

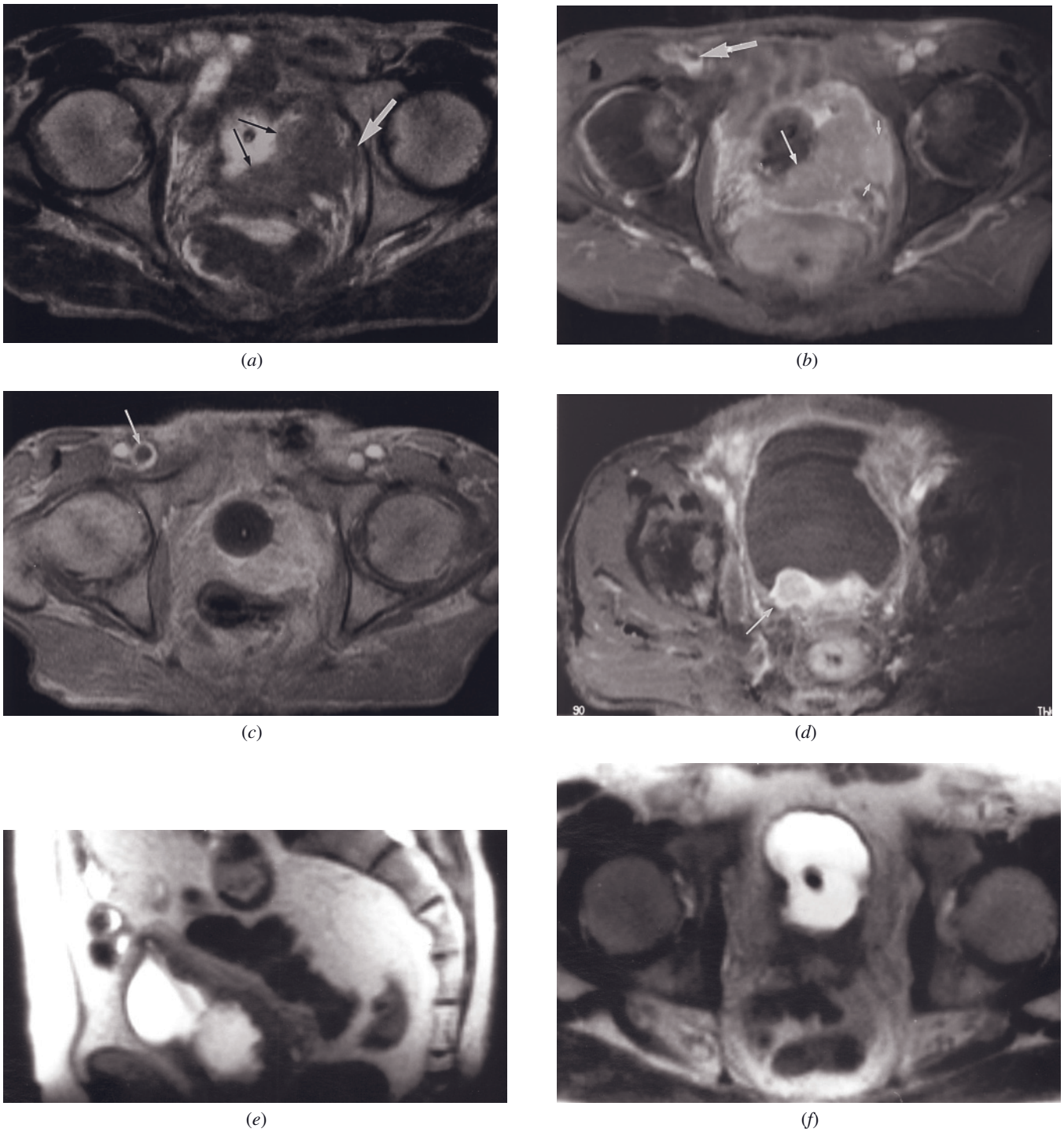

FIG. 11.12 Transitional cell cancer, advanced disease. T2-weighted spin-echo (*a*), T1-weighted gadolinium-enhanced fat-suppressed spin-echo (*b*), and T1-weighted postgadolinium SGE (*c*) images in a patient with T4bN1M0 transitional cell carcinoma. A large cancer arises from the left and posterior aspect of the bladder (black arrows, *a*). Invasion of the obturator internus muscle is shown (large arrow, *a*). The tumor enhances heterogeneously after gadolinium administration (thin white arrow, *b*). Tumor extension into the obturator internus (small arrows, *b*) is relatively high in signal intensity compared to muscle. Thrombus in the right common iliac vein is identified (large arrow, *b* and arrow, *c*). A Foley catheter is present in the bladder (*c*). T1-weighted gadolinium-enhanced fat-suppressed (*d*) image in a second patient with deeply invasive transitional cell cancer. The tumor invades the posterior wall of the bladder. Deep invasion is evidenced by irregular enhancing tissue that extends through the full thickness of the bladder wall (arrow, *d*). Sagittal (*e*) and transverse (*f*) T2-weighted single-shot echo-train spin-echo and sagittal (*g*) and transverse (*h*) T1-weighted gadolinium-enhanced fat-suppressed images in a third patient with high-grade invasive transitional cell carcinoma. The bladder wall is diffusely thickened and irregular (*e*, *f*), with moderately intense enhancement after gadolinium

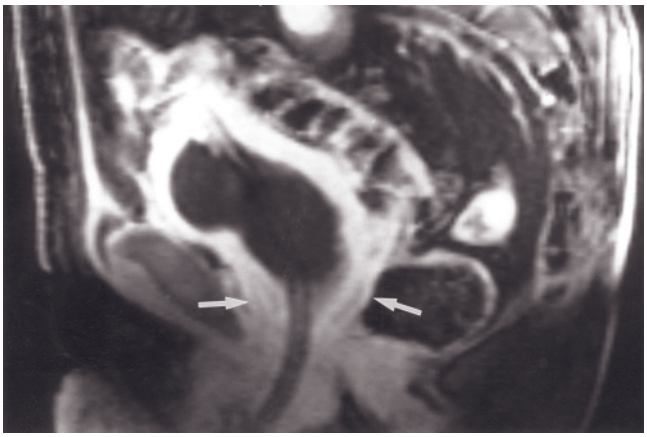

(*g*)

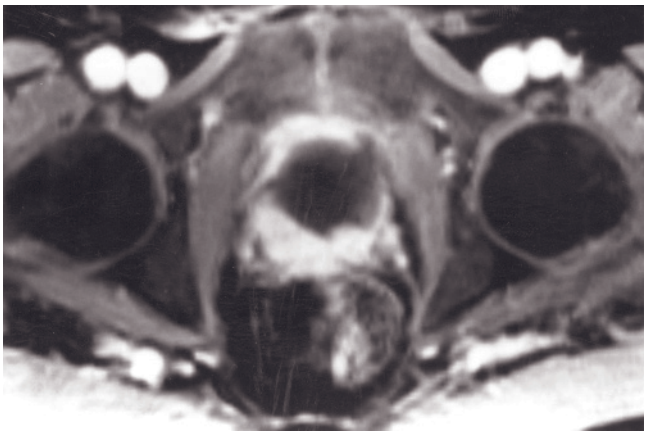

(*h*)

(*i*)

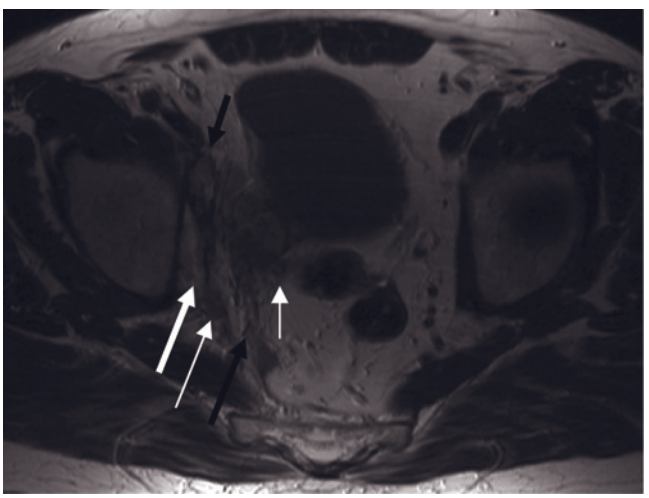

(*j*)

(*k*)

FIG. 11.12 (*Continued*) administration (*g*, *h*). The tumor extends inferiorly and invades the prostate gland (arrows, *g*). Note the Foley catheter in the bladder lumen. Coronal and transverse high-resolution T2-weighted fast spin-echo (*i*, *j*) and transverse 90-s postgadolinium fat-suppressed 3D-GE (*k*) images demonstrate an advanced case of transitional cell cancer in another patient. The bladder is filled with contrast, and therefore it is hypointense on T2-weighted images. A large exophytic aggressive tumor originating from the right posterolateral wall of the bladder invades right perivesical soft tissue, right internal obturator muscle laterally (white long thick arrow, *j*, *k*), right sacrotuberous ligament posterolaterally (white long thin arrow, *j*), and right ischiorectal fascia posteriorly (long black arrow, *j*) and extends to the right external iliac vessels (short black arrow, *i*–*k*) and right psoas muscle anterolaterally (short black arrow, *j*, *k*), rectum posteromedially (white short thin arrow, *j*, *k*), and right piriformis more posteriorly (white short thick arrow, *k*). The tumor invades the bladder wall and enhances intensely.

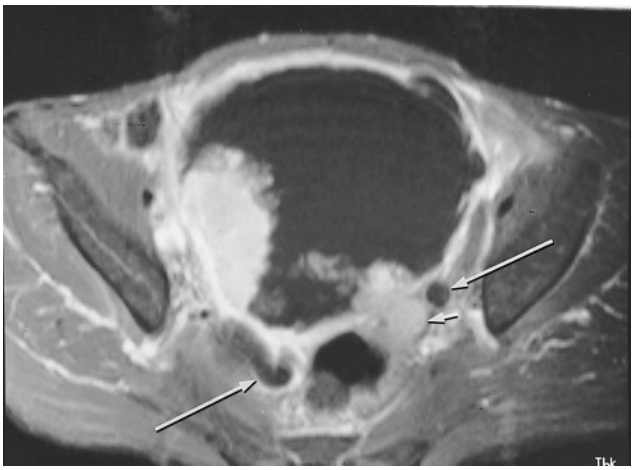

FIG. 11.13 Transitional cell cancer and hyperplasic lymph node. T1-weighted gadolinium-enhanced fat-suppressed spin-echo image. Multiple varying-sized papillary cancers are present with substantial enhancement of the mucosa after gadolinium administration. A 1.2-cm lymph node (small arrow) is shown, which was considered consistent with nodal disease. At histopathology the enlarged nodes were benign and hyperplastic. Note also the dilated ureters (long arrows).

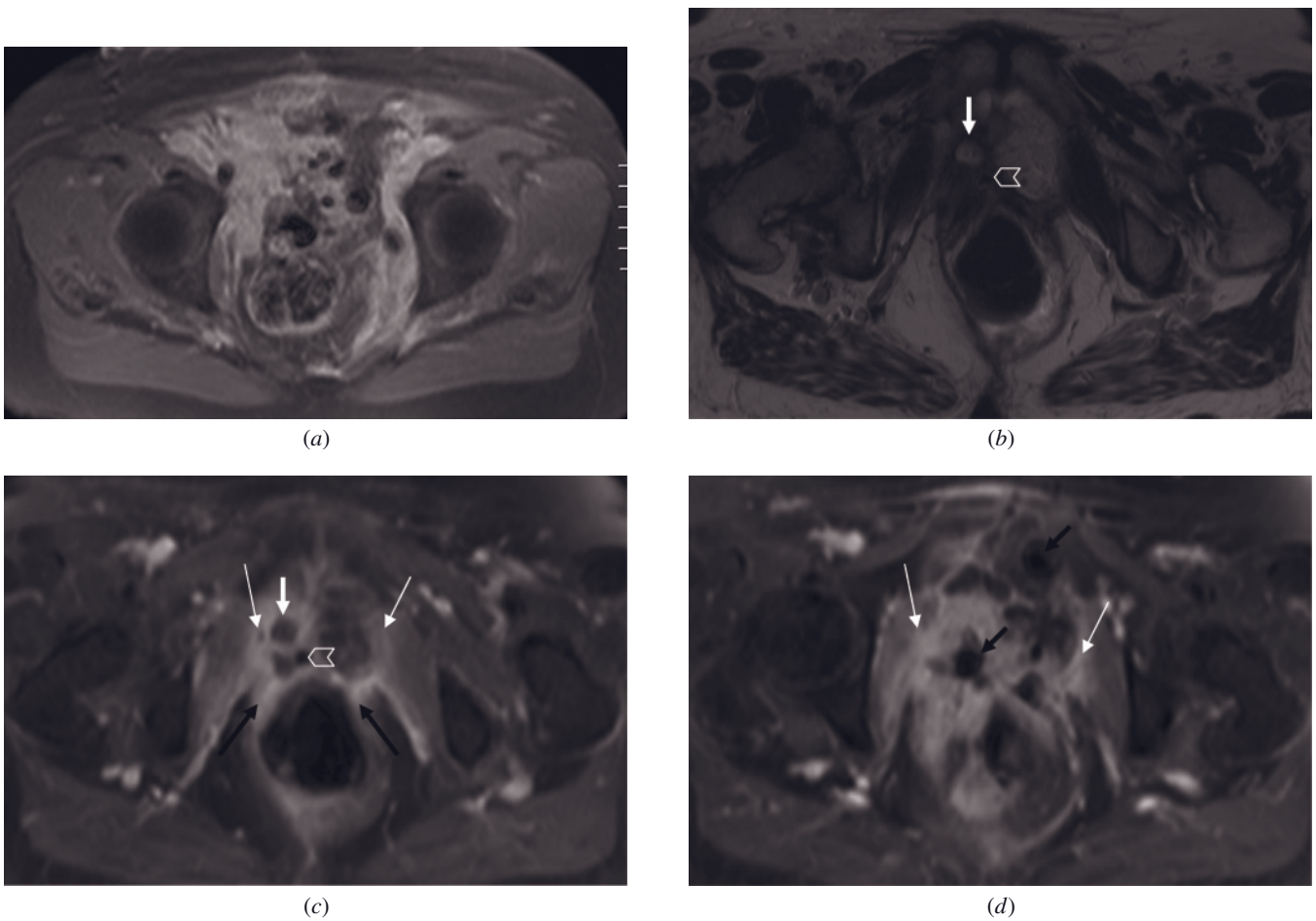

FIG. 11.14 Tumor recurrence. Transverse T1-weighted gadolinium-enhanced fat-suppressed SGE image (*a*) in patient with history of urothelial cancer, status post radical cystoprostatectomy, ileal conduit, and pelvic lymph node dissection 14 months previously. A large volume of soft tissue extends along both pelvic sidewalls and along the regions of prior nodal dissection with substantial contrast enhancement consistent with recurrent disease. T2-weighted high-resolution fast spin-echo (*b*) and T1-weighted 90-s postgadolinium fat-suppressed 3D-GE (*c*, *d*) images in a patient with bladder cancer and tumor recurrence. The recurrent tumor is seen in the perineal region as an irregular soft tissue that enhances intensely on postgadolinium images (*c*, *d*). It invades the vagina, bilateral internal obturator (white long thin arrows, *c*, *d*) and levator ani (black long arrows) muscles (predominantly the right side) and perirectal-perivaginal soft tissue. There are also small fluid collections (white short thick arrows, *b*, *c*) adjacent to the vagina (arrowhead) and postoperative surgical clips creating susceptibility artifacts (black short arrow, *d*) in the perineal region.

tissue, MRI is most helpful if performed before clinical staging [6].

Squamous Cell Carcinoma. Squamous cell carcinoma is the most common form of neoplasia in patients with chronic inflammation of the urinary bladder [13]. It is rare in Western countries but is the most frequent form of bladder neoplasm (55%) in patients with schistosomiasis and is often associated with squamous metaplasia. It is also more common in women. Histologically, these tumors form squamous pearls and are graded based on the varying degrees of cellular differentiation and histologic appearance [16]. Tumors are intermediate in signal intensity on T1-weighted images and enhance with gadolinium (fig. 11.15). Their appearance is usually not distinguishable from that of transitional cell carcinoma. However, metastases of squamous cell carcinoma often occur in the bone, lung, and bowel, rather than the regional lymph nodes [55].

Adenocarcinoma. Adenocarcinoma of the bladder is rare and is the most common tumor to arise at the vesicourachal remnant of the bladder dome (fig. 11.16). The tumor may, however, arise in any location. It is also found in patients with exstrophy of the bladder and cystitis glandularis [55]. Adenocarcinoma most commonly arises secondarily as extension from adjacent organs (see discussion below). As with squamous cell carcinoma, the prognosis is poor.

Carcinosarcoma. Carcinosarcoma, also known as malignant mixed mesodermal/müllerian tumor or sarcomatoid carcinoma, is a highly aggressive neoplasm with malignant epithelial and sarcomatous elements. The epithelial component is most often transitional cell carcinoma. The sarcomatous component is made up of a variable mixture of chondrosarcoma, osteosarcoma, rhabdomyosarcoma, and spindle cells (leiomyosarcoma-like) [56]. Gross hematuria is the most common symptom. Most tumors present as single, large polypoid masses, ranging from 1.5 to 12 cm, usually at the bladder base, followed by the trigone and lateral walls [57]. These tumors are bulky and invariably deeply invade the bladder wall. On MRI, the tumors are isointense on T1-weighted images and heterogeneous on T2-weighted images and show variable enhancement. Prognosis is poor, as local recurrence after radical cystectomy is common [16, 57].

Malignant Nonepithelial Neoplasms

Malignant nonepithelial tumors include leiomyosarcoma, rhabdomyosarcoma, and lymphoma and collectively account for less than 10% of all primary bladder tumors [13]. The bladder and prostate are the most common sites of rhabdomyosarcoma in children. The MRI appearance of rhabdomyosarcoma has been reported as isointense on T1-weighted images and high in signal on T2-weighted images. Intravesical disease is obscured on T2-weighted images because of the similarity in signal intensity between urine and tumor. Gadolinium-enhanced T1-weighted images are helpful in some cases for detecting bladder wall involvement, as with transitional cell and other epithelial tumors. Imaging early after gadolinium administration is important as the increased signal intensity of the urine and layering effect on later postgadolinium images obscure the intravesical component of the tumor [58].

Lymphoma and Chloroma

Bladder involvement is more common in non-Hodgkin lymphoma than in Hodgkin disease. Secondary bladder lymphoma, associated with more generalized disease, is more common than primary bladder lymphoma. Primary bladder lymphoma has a relatively good prognosis, with the tumor remaining localized for a long period of time [59]. Spread may eventually occur to local nodes and then become generalized. In contrast, secondary lymphoma occurs late in patients with disease; involvement of the bladder is usually by direct invasion from adjacent pelvic masses [59]. MRI appearance of bladder lymphoma appears as thickened bladder wall, with intermediate signal intensity on both T1- and T2-weighted images and mild gadolinium enhancement on early and late images. In secondary bladder lymphoma, the tumor is of similar signal intensity to involved regional lymph nodes [59].

Chloroma or granulocytic sarcoma is a rare solid tumor composed of precursors of the granulocytic series of white blood cells. This tumor is seen associated with acute myelogenous or chronic myelogenous leukemia and other myeloproliferative disorders. This tumor rarely seen involves the bladder (fig. 11.17).

Urachal Carcinoma

Neoplastic involvement of the urachal remnant is rare but can extend anywhere along the course of the urachus. Annual incidence of urachal carcinoma is estimated to be 1 in 5 million. The majority occur in men between the ages of 40 and 70 years [60]. At presentation, the tumor is usually advanced, with a resultant poor prognosis. Overall, 5-year survival is about 10% [60]. Approximately 90% of tumors arise from the umbilical segment, and 4% arise from the umbilical end of the urachus [61]. The majority of urachal cancers are adenocarcinomas. Seventy-five percent are mucin producing and thus can be associated with calcifications on CT [60]. Demonstration of a mass in the characteristic midline supravesical location, adjacent to the anterior abdominal wall in the space of Retzius, should suggest the urachal origin of the lesion. On MR images, urachal

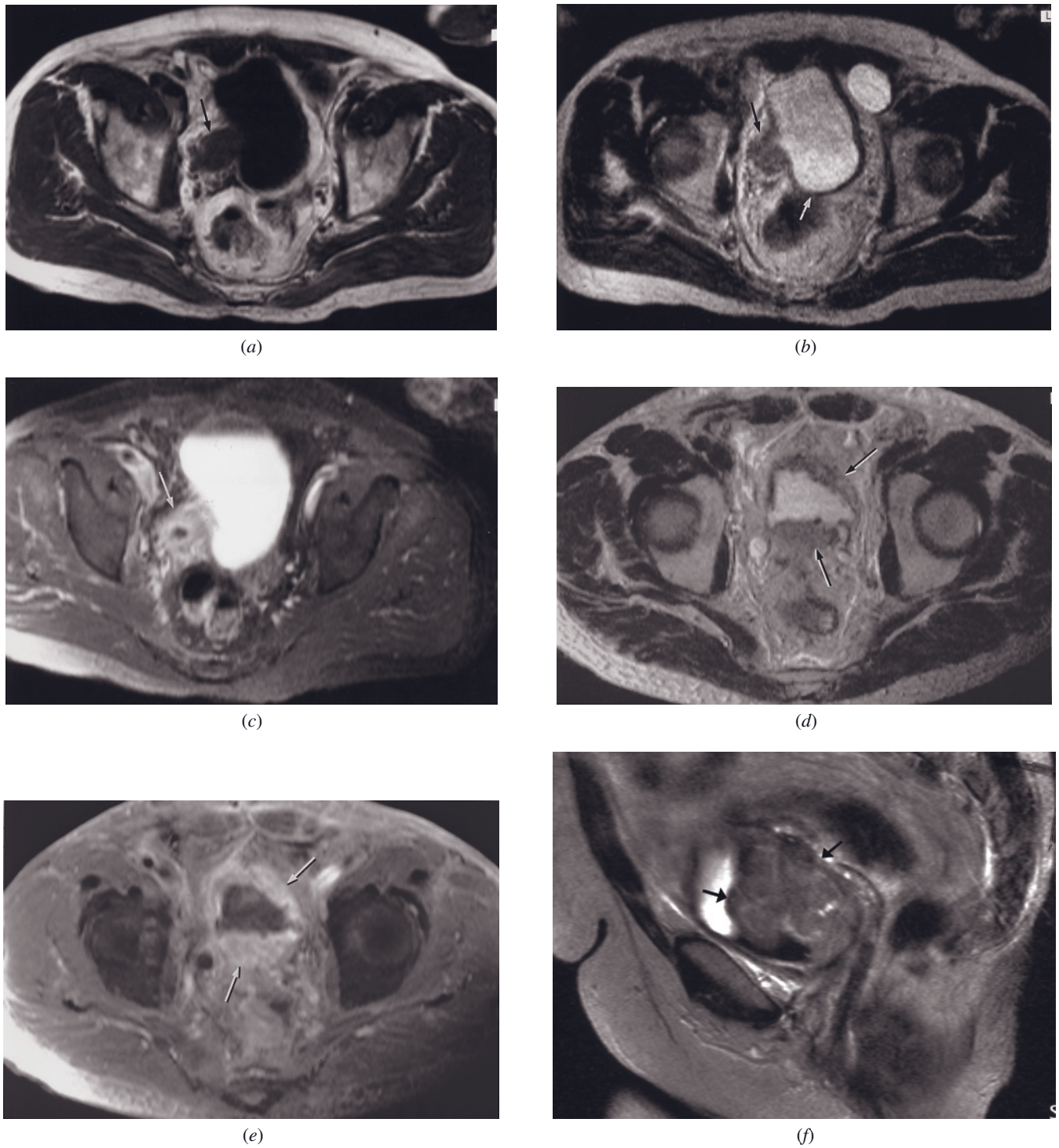

FIG. 11.15 Squamous cell cancer. T1-weighted spin-echo (*a*), T2-weighted spin-echo (*b*), and T1-weighted gadolinium-enhanced fat-suppressed spin-echo (*c*) images. Squamous cell cancer involving the distal right ureter and adjacent bladder wall is shown. The tumor is low to intermediate signal intensity on the T1-weighted image (arrow, *a*) and minimally hyperintense on the T2-weighted image (black arrow, *b*). Note that there is a transition between the involved bladder wall, which is intermediate signal intensity, and the normal wall, which is low signal intensity (white arrow, *b*). After contrast administration the tumor shows moderate, heterogeneous enhancement (arrow, *c*), and the fat planes around the tumor are ill-defined with high-signal-intensity reticular strands, consistent with perivesicular fat infiltration. T2-weighted spin-echo (*d*) and T1-weighted gadolinium-enhanced fat-suppressed spin-echo (*e*) images in a second patient with squamous cell cancer of the bladder. The tumor is irregular in contour and heterogeneously and minimally hyperintense on the T2-weighted spin-echo image (arrows, *d*). After gadolinium administration there is heterogeneous enhancement of the tumor (arrows, *e*). Sagittal (*f*) and transverse (*g*) 512-resolution T2-weighted ETSE and

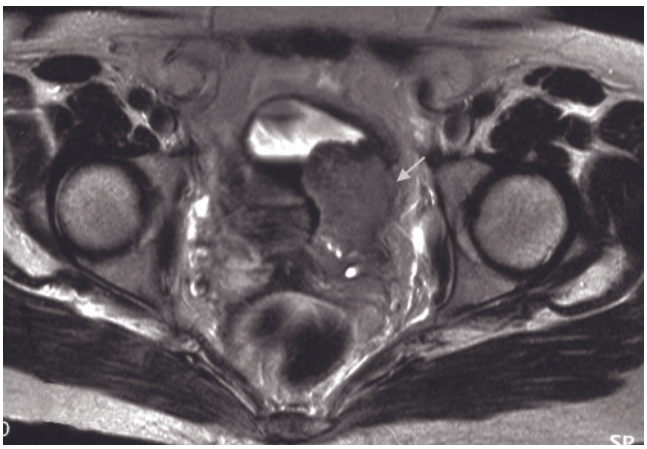

(*g*)

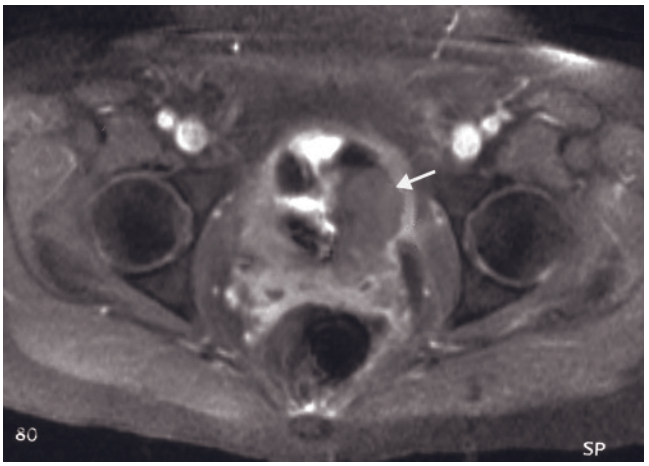

(*h*)

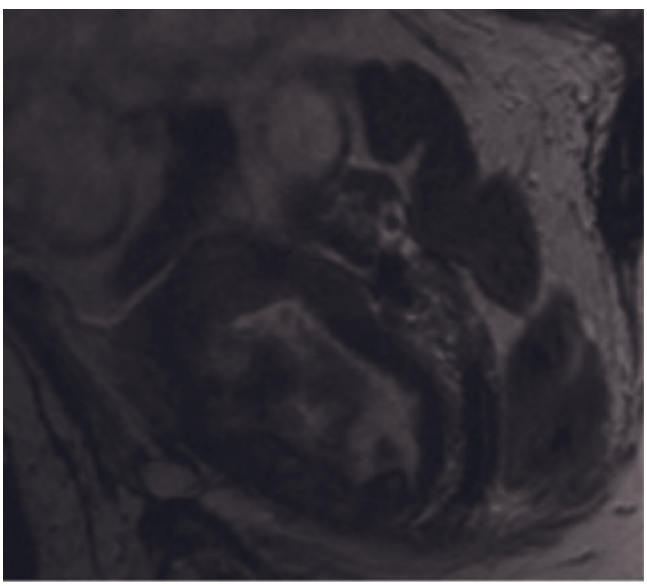

(*i*)

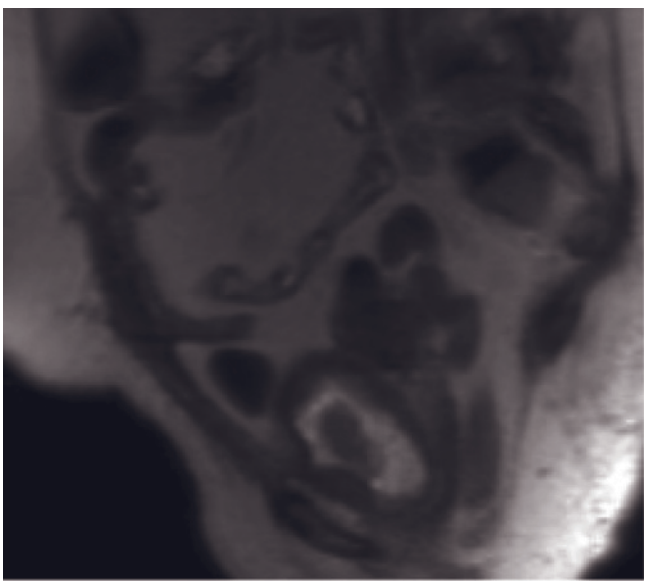

(*j*)

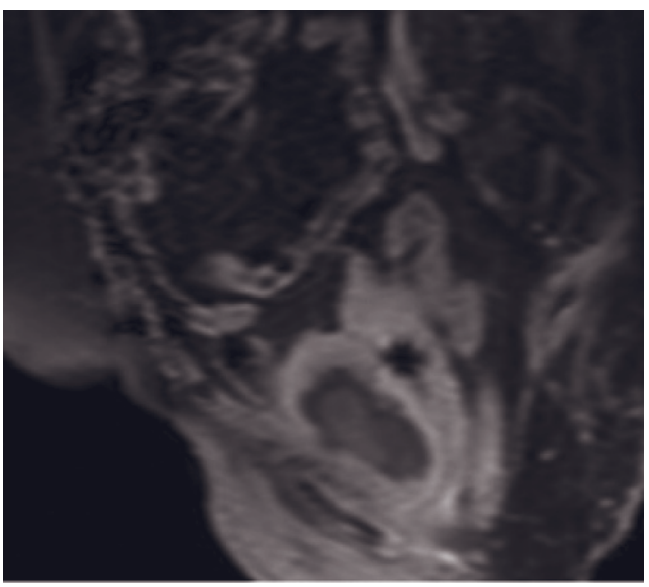

(*k*)

FIG. 11.15 (*Continued*) T1-weighted gadolinium-enhanced fat-suppressed SGE (*h*) images in a third patient demonstrate a mildly enhancing soft-tissue mass that arises from the left posterolateral bladder and extends into the paravesical fat (arrows, *f–h*). Sagittal T2-weighted high-resolution fast spin-echo (*i*), single-shot echo-train spin-echo (*j*), and T1-weighted 90-s postgadolinium fat-suppressed 3D-GE (*k*) images in another patient with squamous cell cancer images show diffuse thickening of the bladder wall. The bladder wall demonstrates irregular thickening and heterogeneous signal on high-resolution T2-weighted image (*i*) but enhances homogenously on postgadolinium image (*k*). In the bladder lumen, there is hematoma showing low signal on T2-weighted images (*j*) and intermediate signal and no enhancement on postgadolinium image (*k*).

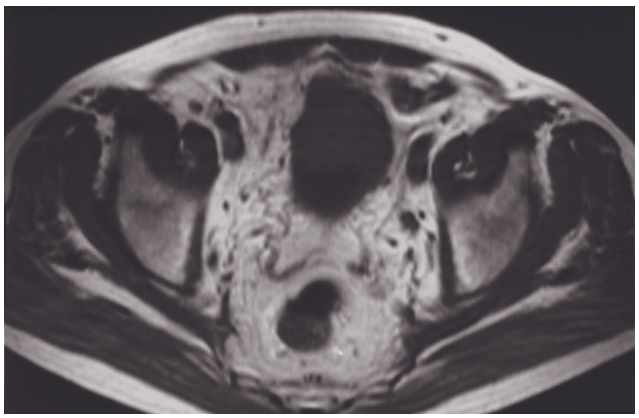

(*a*)

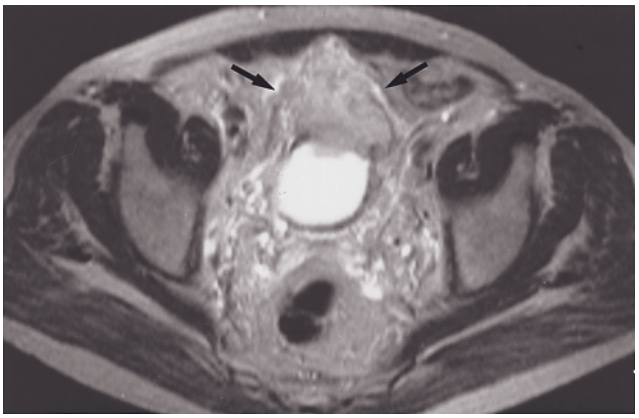

(*b*)

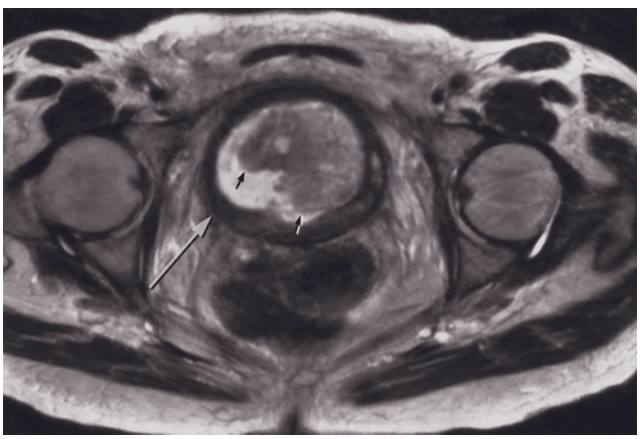

(*c*)

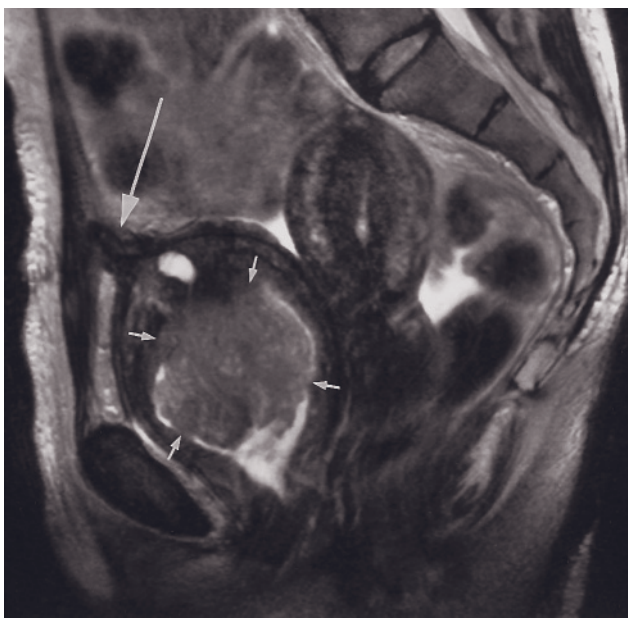

(*d*)

(*e*)

Fig. 11.16 Adenocarcinoma. T1-weighted spin-echo (*a*) and T2-weighted spin-echo (*b*) images in a patient with a patent urachus. There is a tumor arising from the bladder and extending anteriorly along the urachus, which appears low in signal intensity on the T1-weighted image (*a*) and heterogeneous and moderately high in signal intensity on the T2-weighted image (arrows, *b*). T2-weighted echo-train spin-echo (*c*), sagittal T2-weighted echo-train spin-echo (*d*), and sagittal (*e*) and coronal (*f*) T1-weighted gadolinium-enhanced fat-suppressed SGE images in a second patient. A large pedunculated adenocarcinoma (short arrows, *c*–*f*) arises from the dome of the bladder. Diffuse bladder wall thickening is noted (long arrow, *c*). Heterogeneous signal of the bladder wall on the T2-weighted image reflects deep bladder wall invasion. The bladder wall is more homogeneous on the postgadolinium image because it was acquired late after contrast administration. Definition of tumor invasion of the wall is not feasible on these late postcontrast images because of equilibration of contrast between wall and tumor. A urachal remnant is apparent on sagittal plane images (long arrow, *d*, *e*). Sagittal T2-weighted single-shot echo-train spin-echo (*g*) and

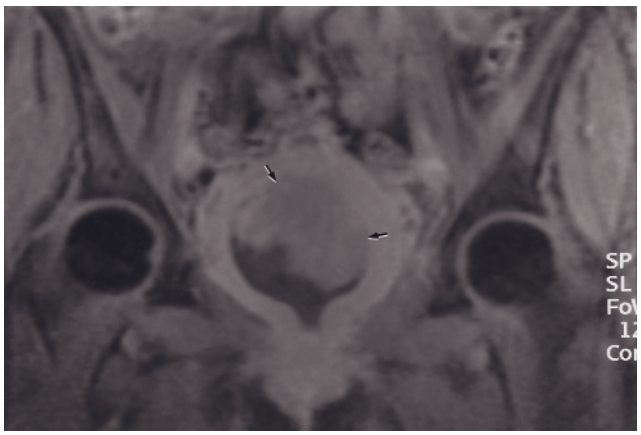

(*f*)

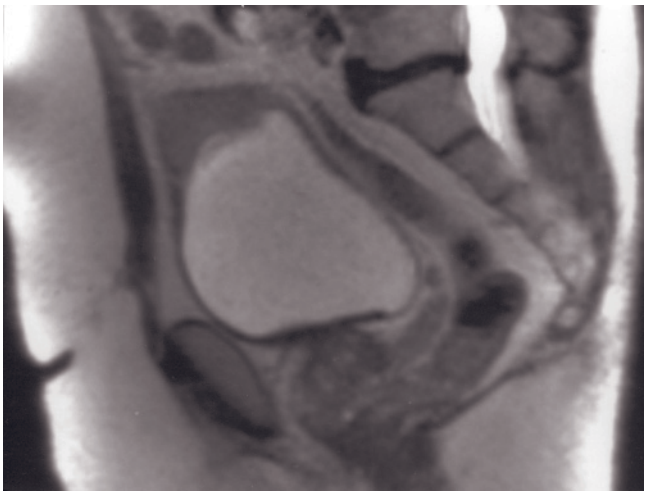

(*g*)

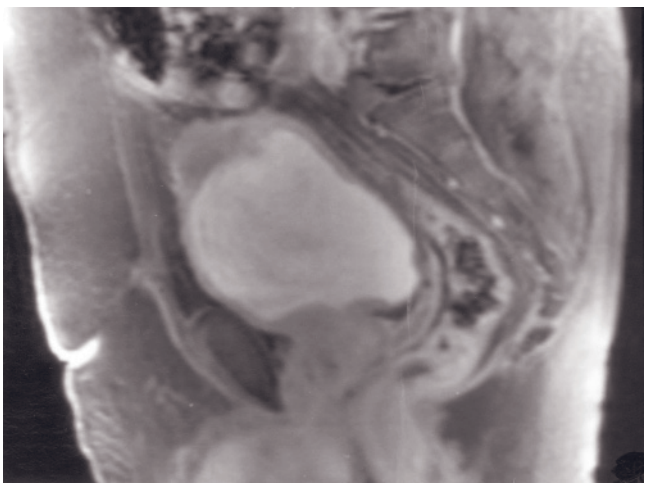

(*h*)

FIG. 11.16 (*Continued*) sagittal T1-weighted postgadolinium fat-suppressed SGE (*h*) images in a third patient with adenocarcinoma. There is an irregular mass lesion arising from the anterosuperior aspect of the bladder wall, which is minimally hyperintense on T2 (*g*) and enhances mildly after gadolinium administration (*h*).

carcinoma appears as low signal on T1-weighted images and heterogeneous high signal on T2-weighted images [61], although signal characteristics vary, possibly secondary to differences in mucin content or presence of necrosis.

Metastatic Neoplasms

Direct invasion of the bladder may occur secondary to prostate (fig. 11.18), rectosigmoid (fig. 11.19*a–e*), and uterine adenocarcinomas, and adenocarcinomas of stomach and breast and malignant melanoma (fig. 11.19*f–h*) may metastasize to the bladder [16]. The most common metastases to the bladder from distant sites are melanoma and gastric carcinoma. However, more commonly, metastases to the bladder arise from direct extension of pelvic neoplasms. The diagnostic accuracy of MRI in the detection of bladder mucosal invasion by pelvic tumors was reported to be 81% in one series [62]. The types of tumors studied in this series were cervical, colon, urethral, vaginal, vulvar, and lymphoid tissue. False-negative findings may arise from microscopic foci of invasion, whereas false-positive findings may stem from muscularis invasion without mucosal invasion. In this series, it was noted that postradiation changes and bullous edema are distinguishable from tumor [62]. Multiplanar imaging with precontrast T1- and T2-weighted images as well as postcontrast T1-weighted images is effective at defining tumor extension to the bladder (figs. 11.18 and 11.19). Sagittal-plane imaging is particularly effective for rectal and gynecologic malignancies, and fat suppression combined with gadolinium enhancement is useful. Cervical carcinoma stage 4a has a particular propensity to invade bladder mucosa. This invasion is well shown with the use of sagittal-plane imaging and gadolinium-enhanced T1-weighted images, which provide accurate diagnosis [63, 64].

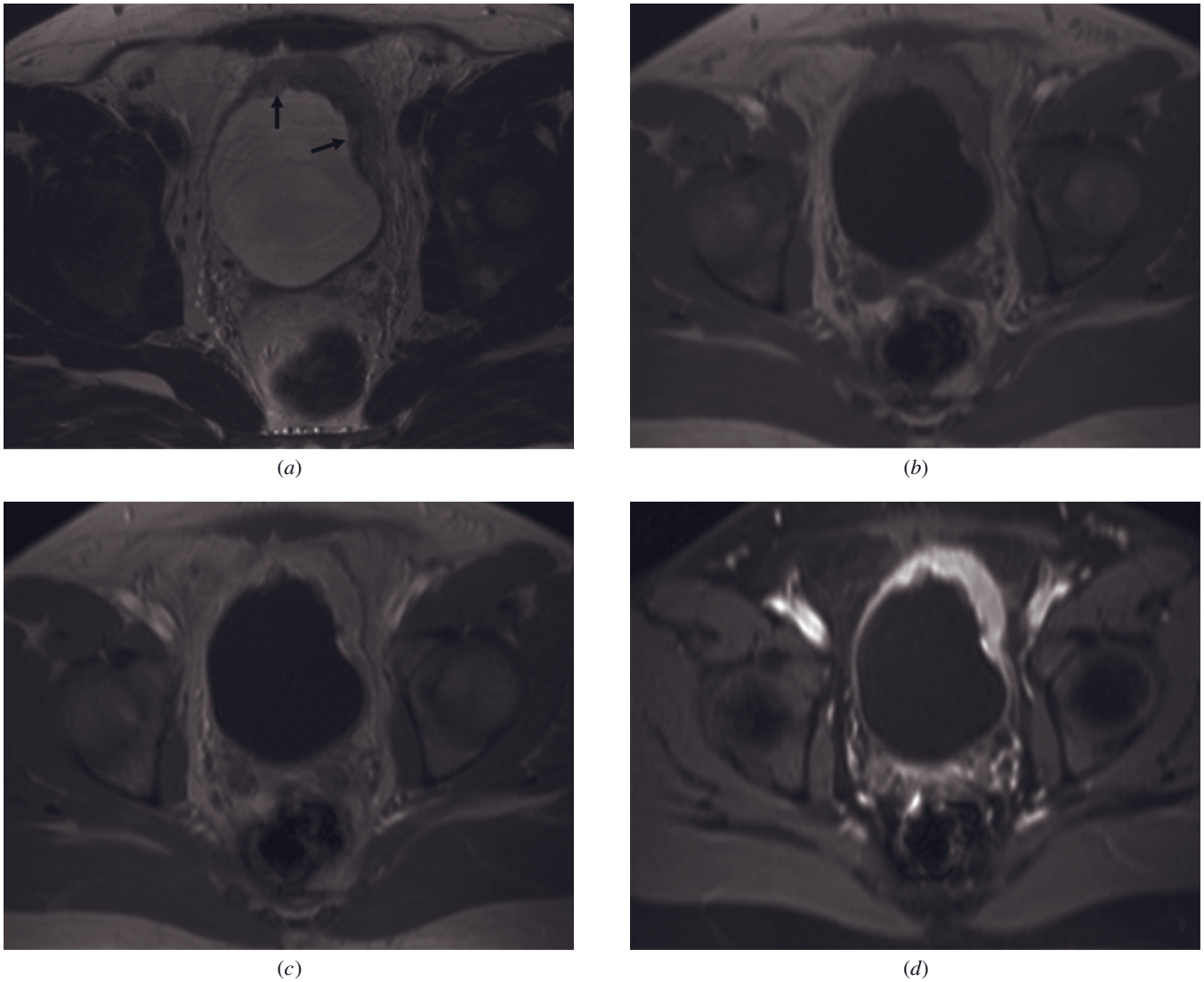

(*a*) (*b*) (*c*) (*d*)

FIG. 11.17 Bladder chloroma. T2-weighted high-resolution fast spin-echo (*a*), T1-weighted SGE (*b*), T1-weighted 45-s postgadolinium SGE (*c*), and T1-weighted 90-s postgadolinium fat-suppressed 3D-GE (*d*) images show bladder wall chloroma in a patient with acute leukemia. An exophytic tumor originates from the anterior and left lateral bladder wall. The tumor also invades the bladder wall (black arrows, *a*), and it is hyperintense compared to the normal bladder wall on T2-weighted image (*a*). The tumor shows prominent enhancement on postgadolinium images (*c*, *d*).

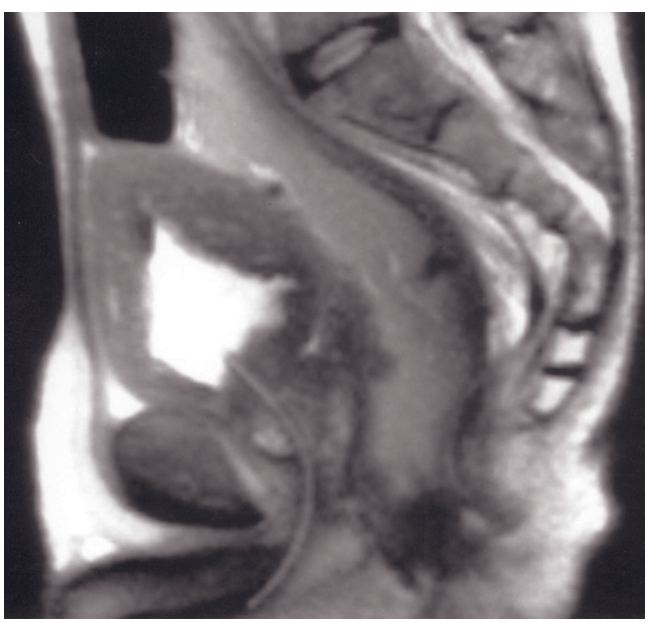

(*a*)

FIG. 11.18 Bladder invasion by malignant disease. Sagittal T2-weighted single-shot echo-train spin-echo (*a*), sagittal

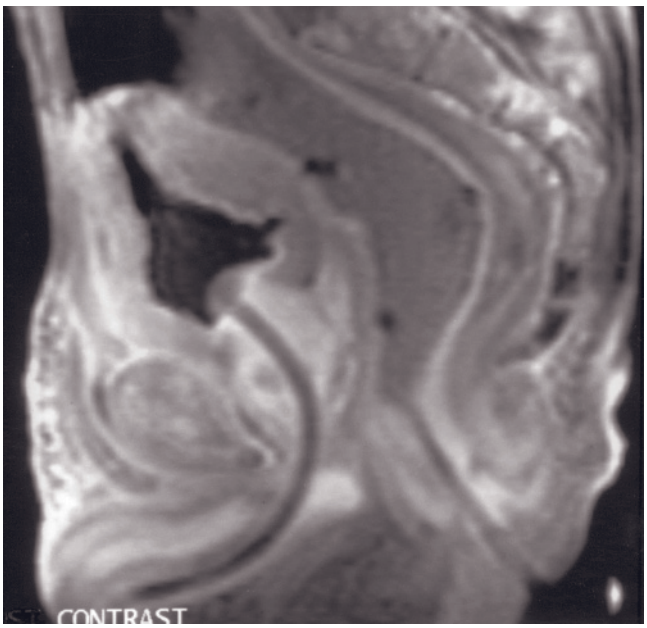

(*b*)

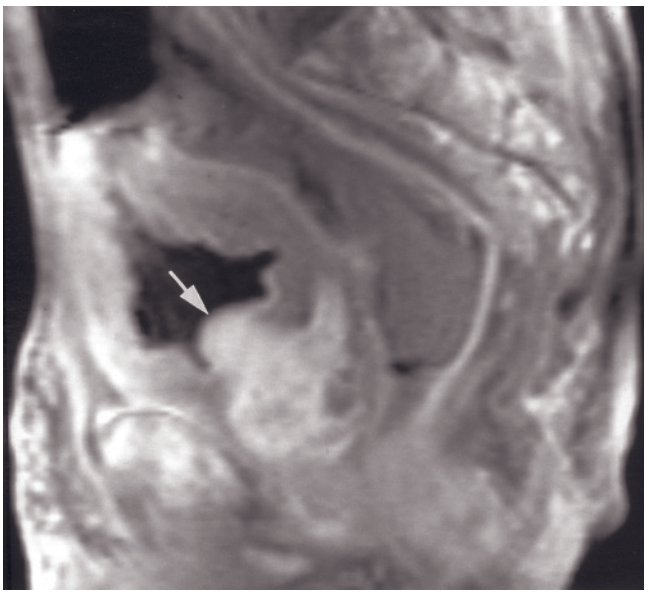

(*c*)

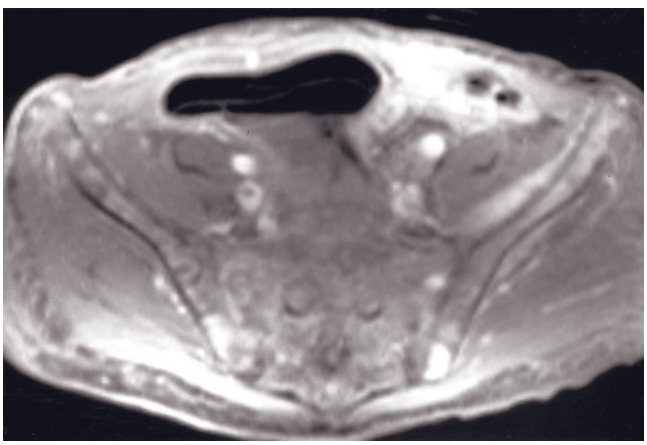

(*d*)

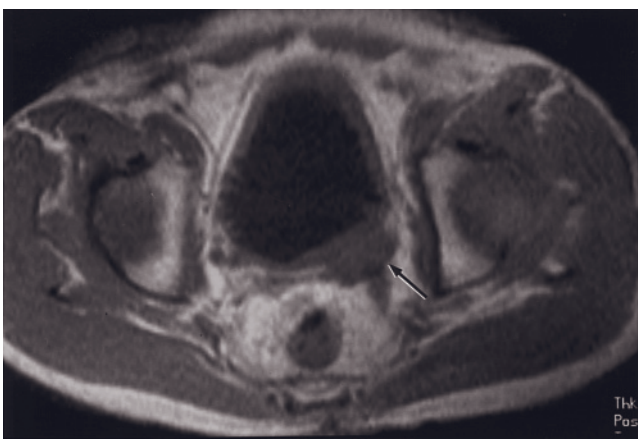

(*e*)

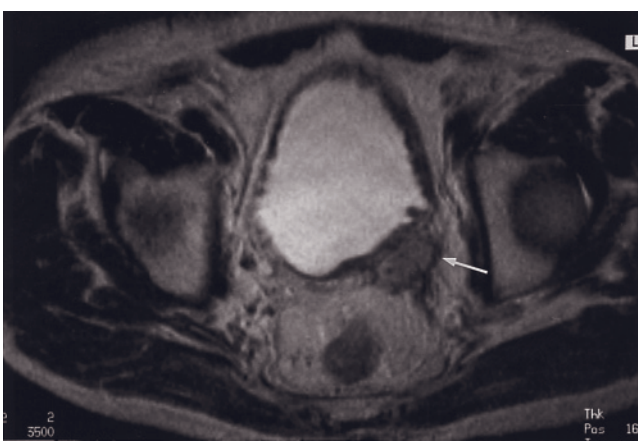

(*f*)

FIG. 11.18 (*Continued*) T1-weighted gadolinium-enhanced SGE (*b*, *c*), and T1-weighted gadolinium-enhanced fat-suppressed SGE (*d*) images in a patient with prostate cancer. The bladder wall is diffusely thickened (*a*, *b*) and shows heterogeneous enhancement of the anterior wall. The prostate gland is irregularly enlarged and enhances heterogeneously after contrast administration (*b*, *c*). A nodule of tumor, extending superiorly from the prostate to the trigone region, enhances substantially (arrow, *c*). Note multiple bone metastases in the iliac wings that appear as high-signal enhancing foci (*d*). T1-weighted SGE (*e*), T2-weighted single-shot echo-train spin-echo (*f*), and T1-weighted postgadolinium SGE (*g*) images in a second patient with recurrent prostate cancer invading the bladder. Tumor is intermediate in signal intensity on T1 (arrow, *e*)- and T2 (arrow, *f*)-weighted images and enhances minimally with gadolinium (arrow, *g*).

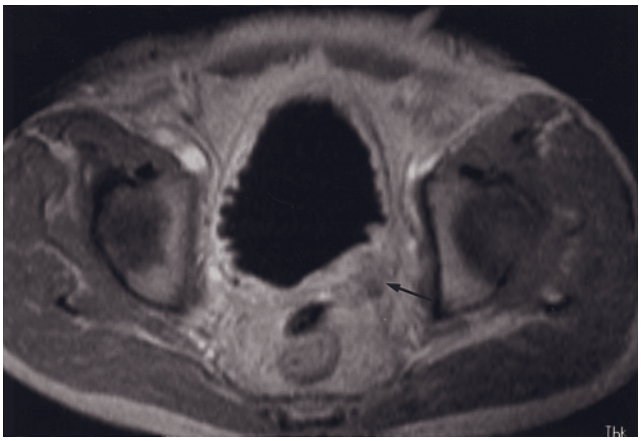

(*g*)

FIG. 11.18 (*Continued*)

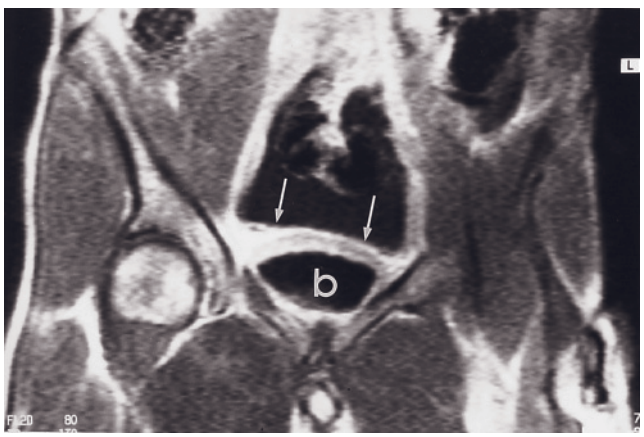

(*a*)

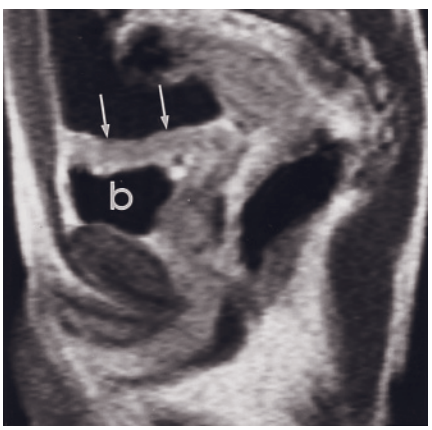

(*b*)

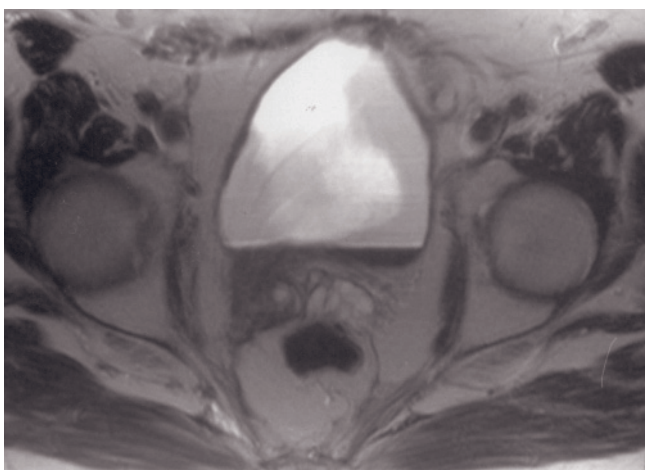

(*c*)

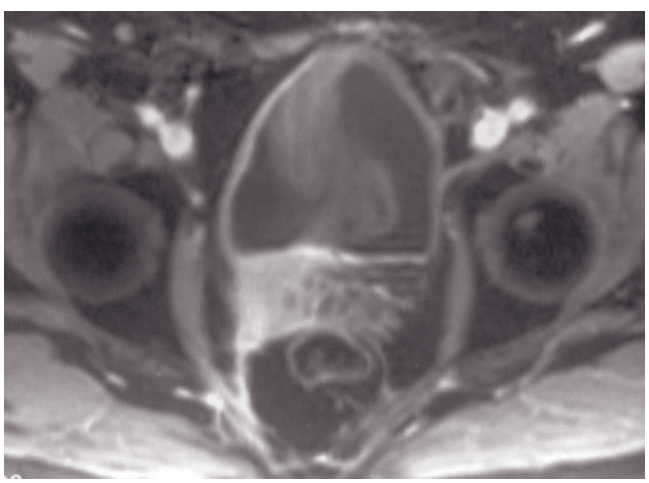

(*d*)

FIG. 11.19 Bladder invasion by malignant disease. Coronal T1-weighted SGE (*a*) and sagittal T1-weighted immediate post-gadolinium SGE (*b*) images in a patient with rectal cancer. Tumor is identified arising from the rectum and extending along the superior bladder (b) wall (arrows, *a*, *b*). T2-weighted single-shot echo-train spin-echo (*c*) and T1-weighted gadolinium-enhanced fat-suppressed SGE (*d*) images in a second patient with recurrent colorectal adenocarcinoma. The right posterior aspect of the bladder wall and the right seminal vesicle are thickened, with loss of the high signal of the seminal vesicle on the T2-weighted image (*c*). Tumor enhances intensely on the postgadolinium image (*d*), clearly defining the extent of the tumor. T1-weighted

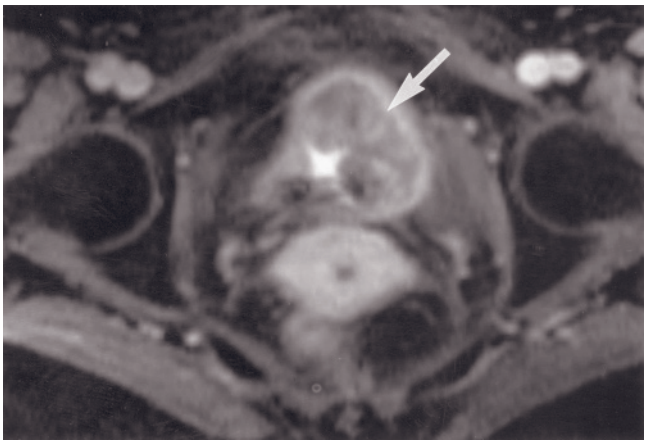

(*e*)

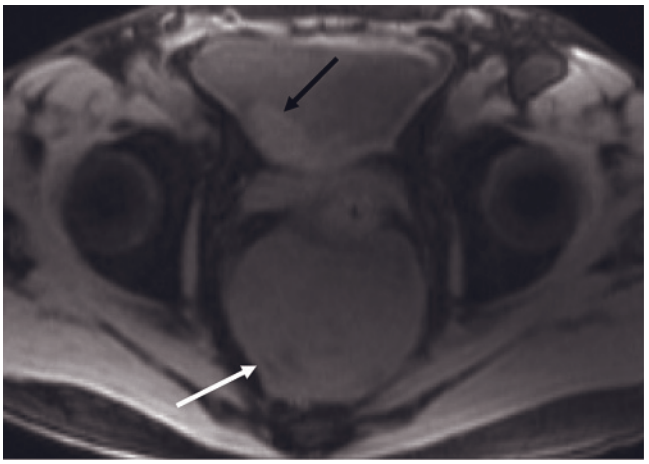

(*f*)

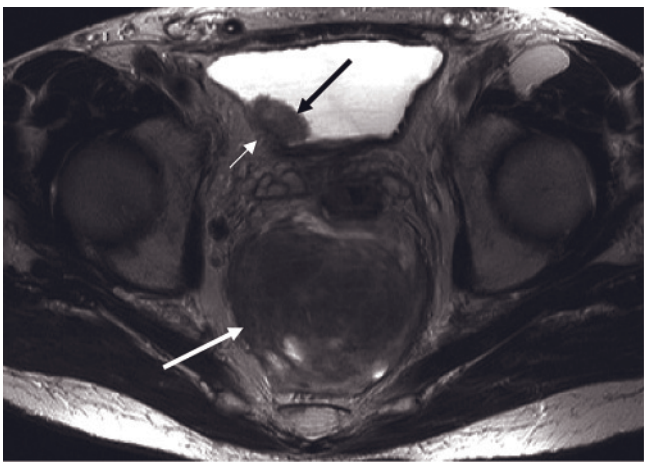

(*g*)

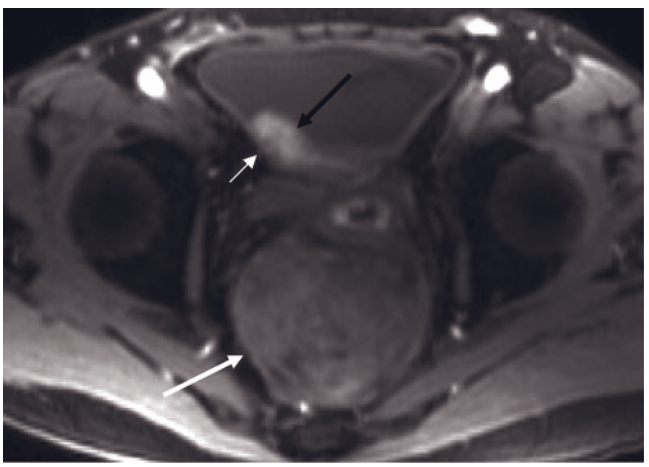

(*h*)

FIG. 11.19 (*Continued*) gadolinium-enhanced fat-suppressed SGE image (*e*) in a third patient with rectal cancer involving the bladder. A large tumor mass is present (arrow, *e*), which fills much of the lumen of the bladder. T1-weighted fat-suppressed SGE (*f*), T2-weighted high resolution fast spin-echo (*g*), and T1-weighted immediate postgadolinium fat-suppressed 3D-GE (*h*) images in a patient with metastatic malignant melanoma. There is a large tumor mass (white long arrows, *f–h*) in the rectosacral space, which shows intermediate to mildly high signal on T1-weighted image (*f*), heterogeneously low signal on T2-weighted image (*g*), and heterogeneous enhancement on postgadolinium image. Additionally, there is another tumoral mass (black arrows, *f–h*) in the bladder lumen that invades the bladder wall (white short arrows, *g*, *h*) as well. This lesion shows signal and enhancement characteristics similar to the large tumoral mass located in the rectosacral space. The intermediate to mildly high signal on T1-weighted image suggests the diagnosis of malignant melanoma.

MISCELLANEOUS

Edema

Edema of the bladder wall as a result of acute bladder disease can be distinguished from bladder wall hypertrophy by its longer T2, which renders it high in signal intensity on T2-weighted images [65].

Hypertrophy

Muscular hypertrophy of the bladder wall results from bladder outlet obstruction. Underlying causes include benign prostatic enlargement (the most common cause in males), prostatic cancer, large pelvic tumors, bladder neck obstruction (functional or anatomic), and hydrocolpos.

Bladder wall hypertrophy appears as an increased thickness of the bladder wall, which is low in signal intensity on T2-weighted images and does not enhance substantially with gadolinium. Signal intensity features are similar to those of normal bladder wall (fig. 11.20). Mucosal edema related to bladder outlet obstruction is usually located around the urethral orifice and is high signal intensity on T2-weighted images.

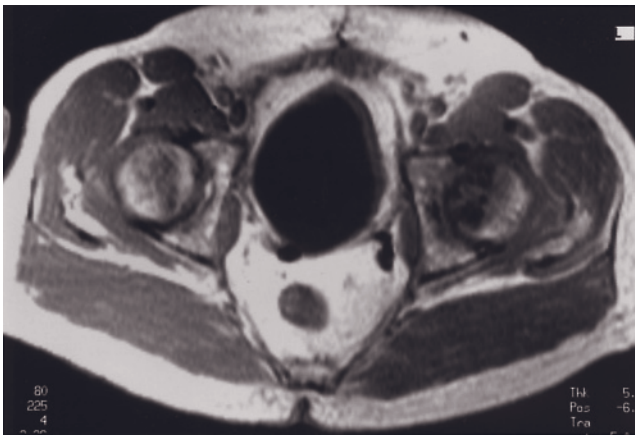

(*a*)

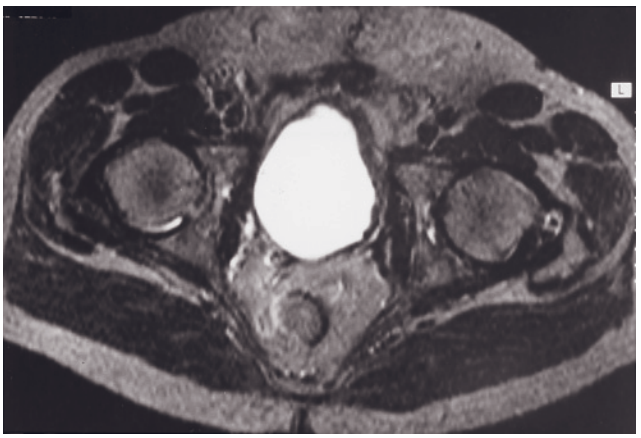

(*b*)

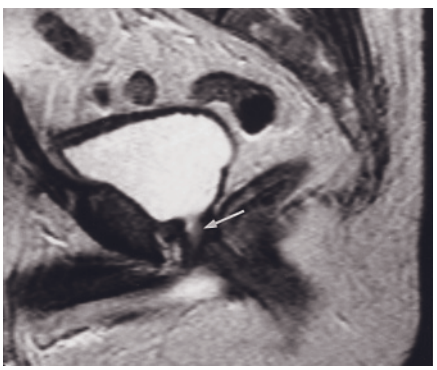

(*c*)

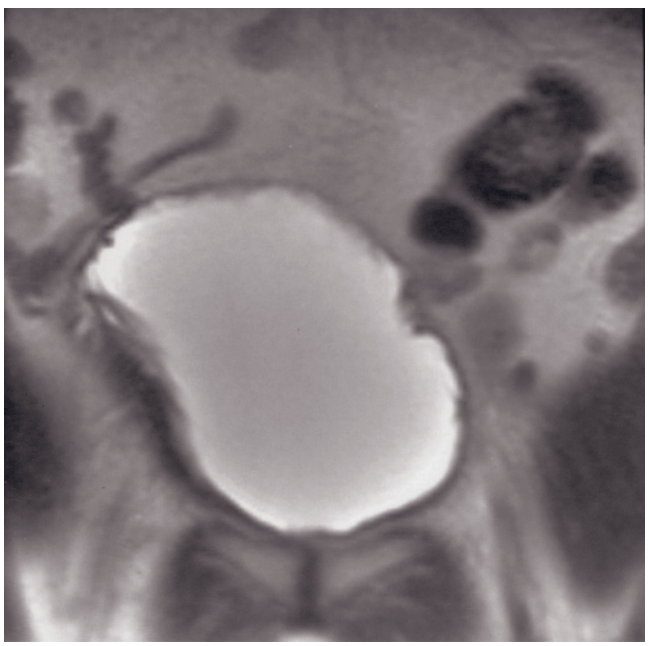

(*d*)

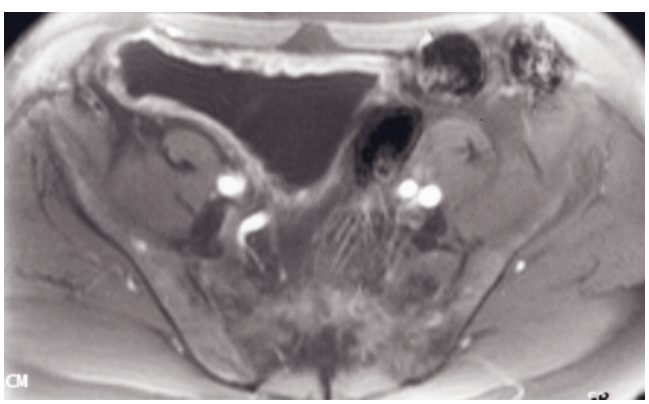

(*e*)

FIG. 11.20 Bladder wall hypertrophy. T1-weighted SGE (*a*) and transverse (*b*) and sagittal (*c*) T2-weighted echo-train spin-echo images in a patient with chronic outlet obstruction from prostate enlargement. The bladder wall is asymmetrically thickened, with low signal intensity on T1- and T2-weighted images. Note the transurethral prostatectomy defect in the bladder base on the sagittal image (arrow, *c*). Coronal T2-weighted single-shot echo-train spin-echo (*d*) and T1-weighted gadolinium-enhanced fat-suppressed SGE (*e*) images in a second patient. The bladder is dilated with a thickened, trabeculated wall secondary to outlet obstruction from prostate enlargement. Note the moderately increased enhancement of the bladder mucosa reflecting inflammatory change (*e*). The prostate was also enlarged (image not shown), demonstrating that outlet obstruction was present.

Cystitis

Inflammation of the bladder wall may be the result of infection, foreign bodies within the bladder, peritonitis, drug toxicity, or other causes. The appearance is a thickened bladder wall that may be focal or diffuse. On T2-weighted images, four layers can be appreciated within the inflamed bladder wall. An innermost low-signal-intensity band and an inner high-signal-intensity band represent the thickened epithelium and lamina propria, respectively. An outer low-signal-intensity band and outermost intermediate-signal-intensity bands represent the inner compact muscle layer and outer loose muscle layer, respectively [11]. Increased enhancement after gadolinium administration is observed. The extent of enhancement reflects the severity of the inflammatory process (fig. 11.21).

Hemorrhagic Cystitis

Hemorrhagic cystitis is a severe form of cystitis characterized by hematuria. It may be secondary to radiation of the pelvis or infectious agents including *Escherichia coli* and viruses.

Hemorrhagic cystitis demonstrates a complex appearance on MR images based on the T1 and T2 characteristics of aging blood products. Active bleeding (oxyhemoglobin) has limited paramagnetic properties and behaves like simple fluid with a long T1 (low signal intensity on T1-weighted images) and a long T2 (high signal intensity on T2-weighted images). Acute blood (intracellular deoxyhemoglobin) has a long T1 (low signal intensity on T1-weighted images) and a short T2 (low signal intensity on T2-weighted images). Intracellular methemoglobin has a short T1 (high signal intensity on T1-weighted images) and a short T2 (low signal intensity on T2-weighted images). Extracellular methemoglobin has a short T1 (high signal intensity on T1-weighted images) and a long T2 (high signal intensity on T2-weighted images), and this appearance is most typical for subacute hemorrhage. Intracellular hemosiderin in an old hematoma has a medium T1 (intermediate signal intensity on T1-weighted images) and a short T2 (low signal intensity on T2-weighted images) [66]. Thus the appearance of hemorrhagic cystitis demonstrates not only a thickened bladder wall but also the complex signal characteristics of hemorrhage (fig. 11.22).

Cystitis Cystica

Cystitis cystica is a cystic lesion that appears in the lamina propria. The lesion may be an incidental finding at biopsy but is more common in the clinical setting of chronic cystitis related to *E. coli* infection. Grossly, the appearance may be that of large cysts, resembling cobblestones (fig. 11.23*a* and *b*) [16].

Cystitis Glandularis

Cystitis glandularis is a premalignant condition associated with chronic or recurrent infections and may be associated with pelvic lipomatosis and development of adenocarcinoma. The glandular structures appear as irregular mucosal lesions that mimic bladder cancer [12].

Granulomatous Disease

In the setting of genitourinary tuberculosis, bladder involvement is common. Patients present with dysuria and frequency. The earliest manifestations are mucosal edema and ulcerations, primarily surrounding the ureteral orifices, which can produce obstruction. Tuberculomas in the bladder wall can be large and simulate mass lesions [67]. Focal granulomatous reactions appear as intravesical lesions with high signal intensity on T2-weighted images [27]. Epithelioid granulomatous lesions, which can occur in patients undergoing immunotherapy for the treatment of malignant bladder lesions, may appear similar to malignant tumors on MRI. Although MRI accurately shows these lesions to be confined to the vesical wall, their presence can lead to false-positive findings [27].

Endometriosis

Urinary tract involvement of endometriosis is rare, with the bladder being the most common site. The endometrial tissue may invade the bladder muscle and may protrude into the bladder lumen [12]. Endometrial masses are typically hyperintense on T1-weighted images and relatively hypointense on T2-weighted images with a gradient. This entity is further described in Chapter 15, *Adnexa*, on the ovary.

Pelvic Lipomatosis

Pelvic lipomatosis predominantly affects black males between the ages of 25 and 55 years. Some patients present with frequency, dysuria, perineal pain, or suprapubic discomfort. Although the process is benign, the effects may be damaging, including renal failure and rectal compression [68].

The diagnosis of pelvic lipomatosis can be supported with the use of MRI. It characteristically appears as an extensive amount of fat, which appears high in signal intensity on T1-weighted images surrounding the bladder (fig. 11.23*c*–*e*) [69].

Fistulas

Pelvic fistulas may result from obstetrical procedures, surgery, trauma, radiation, infection, inflammatory

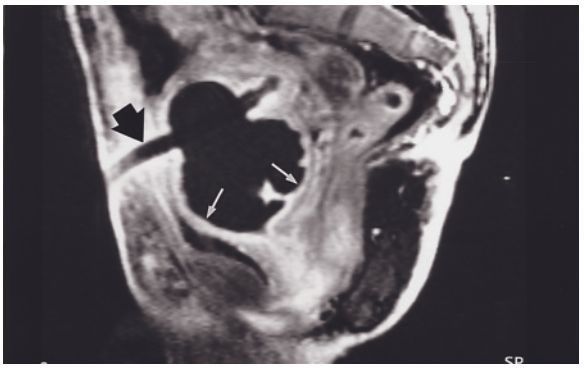

(*a*)

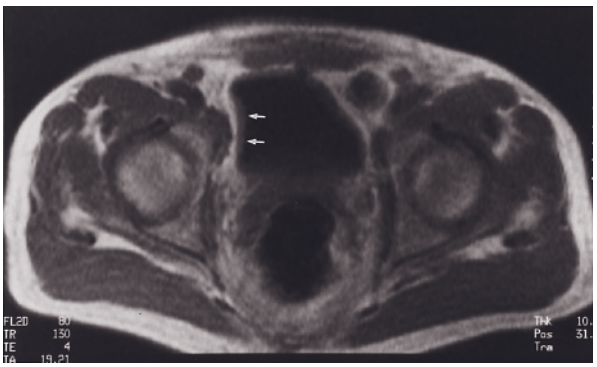

(*b*)

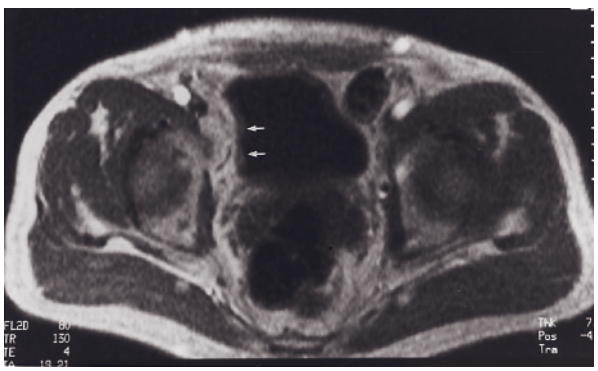

(*c*)

(*d*)

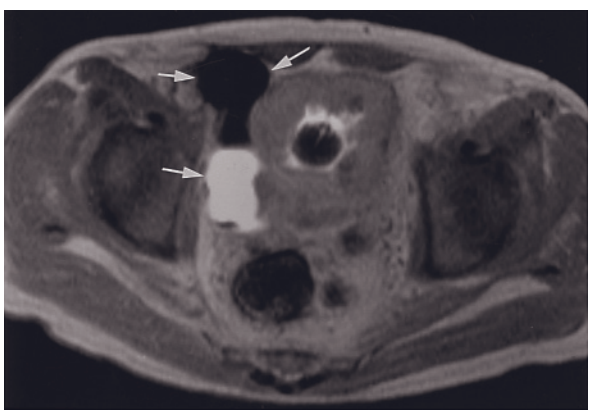

(*e*)

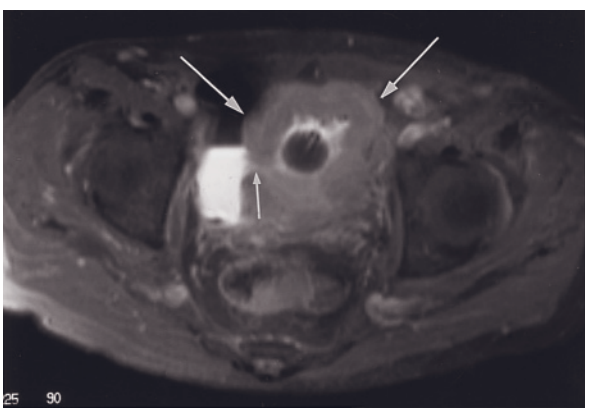

(*f*)

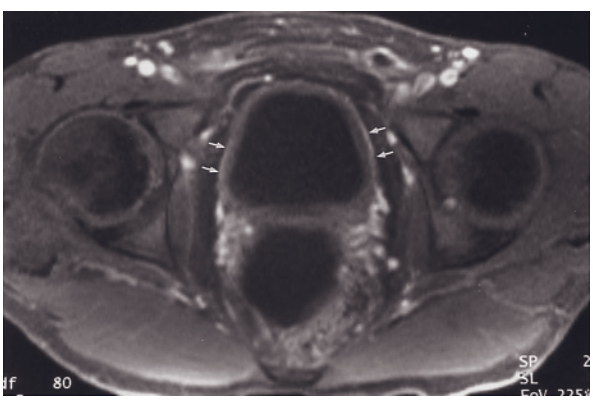

(*g*)

FIG. 11.21 Bladder inflammation. Sagittal T1-weighted immediate postgadolinium SGE image (*a*) in a patient with a suprapubic catheter (black arrow). Substantial enhancement of the bladder wall is demonstrated (small arrows, *a*). T1-weighted SGE (*b*), immediate postgadolinium SGE (*c*), and sagittal 5-min postgadolinium SGE (*d*) images in a second patient with mild inflammatory cystitis. The bladder wall is irregularly thickened (arrows, *b*), with minimal enhancement after contrast administration (arrows, *c*, *d*). Ninety-second postgadolinium SGE (*e*) and T1-weighted postgadolinium fat-suppressed spin-echo (*f*) images in a third patient with inflammation secondary to infection. Diffuse bladder wall thickening is present (arrows, *f*), and a large gadolinium-containing diverticulum (arrows, *e*) is identified arising from the right aspect of the bladder. A small high-signal-intensity tract represents the communication between the bladder and the diverticulum (short arrow, *f*). Ninety-second postgadolinium fat-suppressed SGE image (*g*) in a fourth patient who had undergone intraperitoneal chemotherapy. Increased enhancement of the serosal surface of the bladder (small arrows, *g*) is present, which represents chemical peritonitis. Transverse T2-weighted

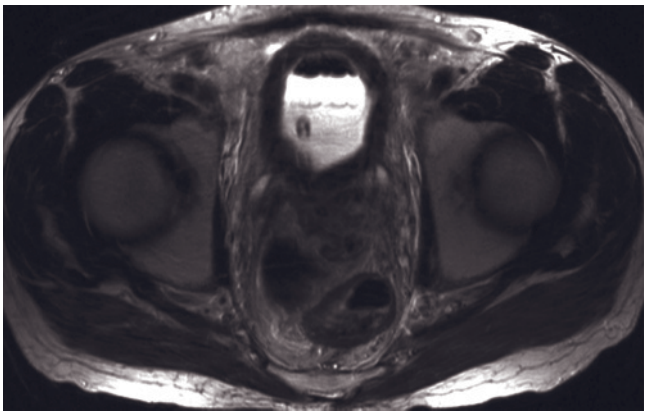

(*h*)

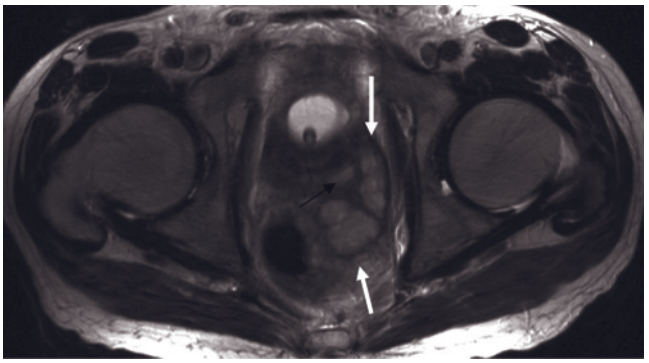

(*i*)

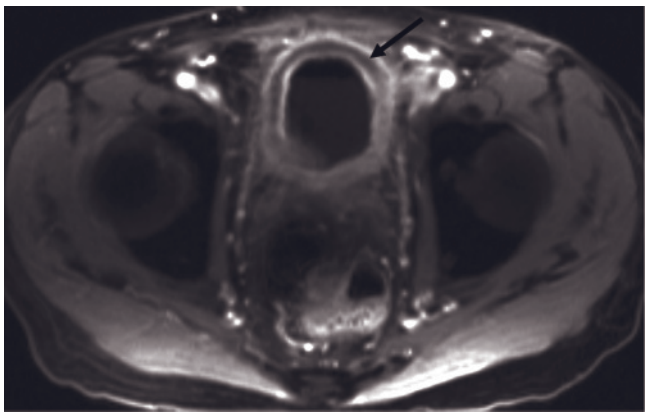

(*j*)

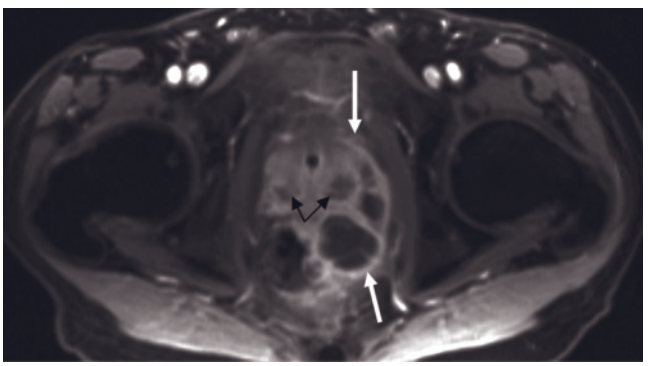

(*k*)

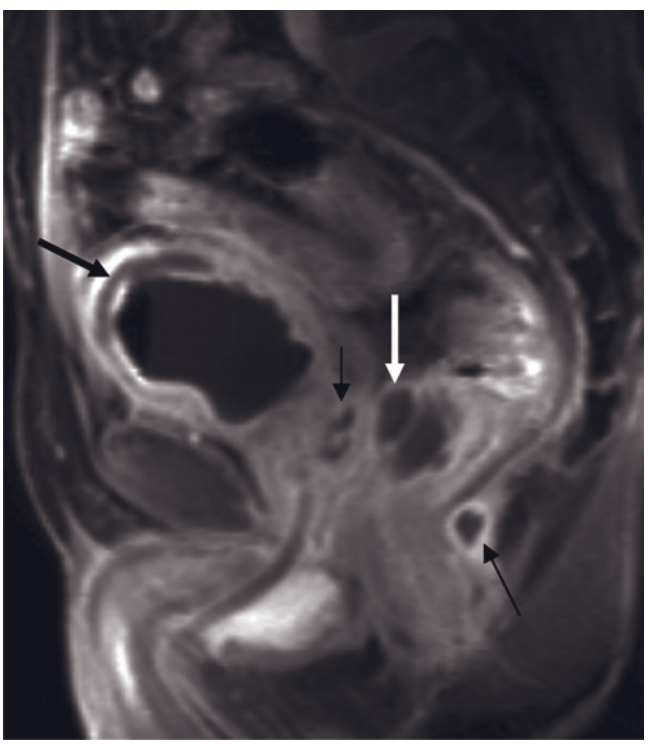

(*l*)

FIG. 11.21 (*Continued*) high-resolution fast spin-echo (*h*, *i*), transverse T1-weighted postgadolinium 45-s fat-suppressed 3D-GE (*j*, *k*), and sagittal T1-weighted postgadolinium 90-s fat-suppressed 3D-GE (*l*) images in another patient with pelvic abscess and inflammation involving the bladder, prostate, and rectum. Pelvic abscess (white thick arrows, *i*, *k*, *l*) is located in the rectovesical pouch, predominantly on the right side. It is located posterior to the bladder wall, posterolateral to the prostate, and anterior to the rectum. The abscess shows high signal on T2-weighted images and prominent peripheral enhancement on postgadolinium images. Additionally, there are two areas of fluid collections in the peripheral zone of the prostate gland (black short thin arrows, *i*, *k*, *l*), one area of fluid collection in the anterior bladder wall (black long thick arrows, *j*, *l*), and one area of fluid collection posterior to the rectum (black long thin arrow, *l*). These areas also show prominent peripheral enhancement on postgadolinium images. The soft tissue adjacent to the abscess, the bladder wall, prostate, and rectal wall also shows prominent enhancement due to inflammation. Note that there is a Foley catheter and free air in the bladder lumen.

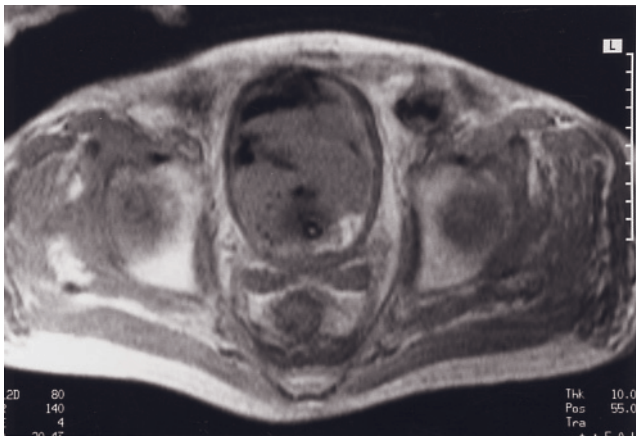

(*a*)

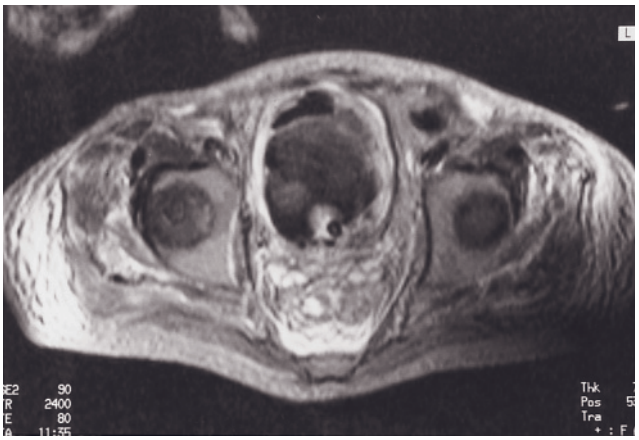

(*b*)

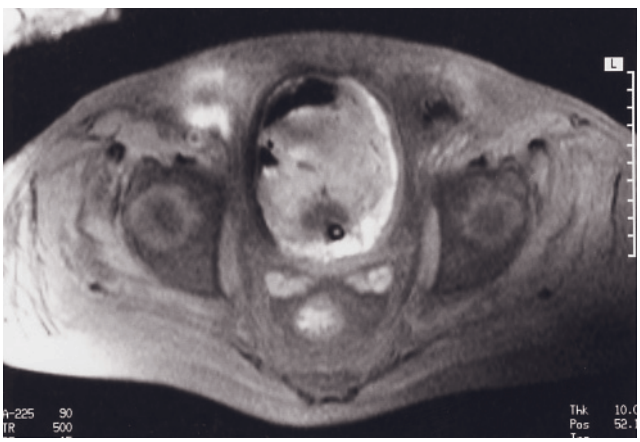

(*c*)

FIG. 11.22 Hemorrhagic cystitis. T1-weighted SGE (*a*), T2-weighted spin-echo (*b*), and T1-weighted fat-suppressed spin-echo (*c*) images in a patient with hemorrhagic cystitis. The bladder wall and intraluminal fluid show varying signal intensities, which represent the different phases of hemoglobin degradation.

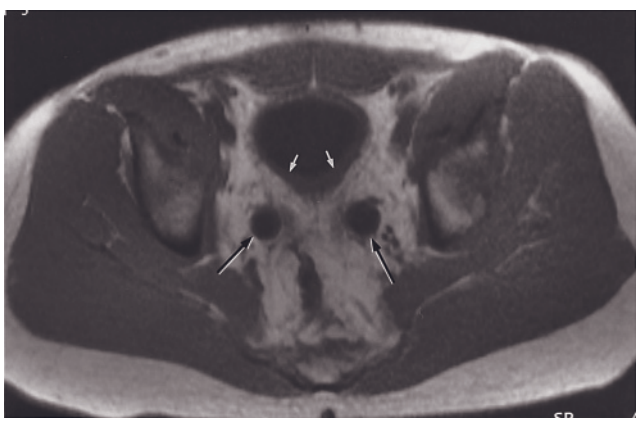

(*a*)

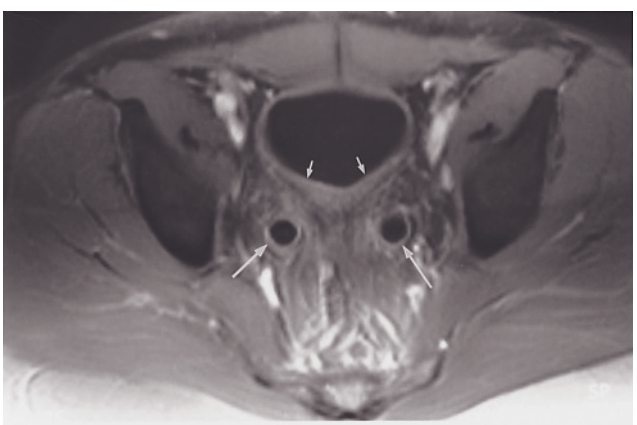

(*b*)

FIG. 11.23 Cystitis cystica and pelvic lipomatosis. T1-weighted SGE (*a*) and 90-s postgadolinium fat-suppressed SGE (*b*) images. Note that the bladder wall is uniformly thickened (short arrows) and the distal ureters are thick walled and substantially dilated (long arrows). Coronal T2-weighted single-shot echo-train spin-echo (*c*), coronal T1-weighted SGE (*d*), and coronal

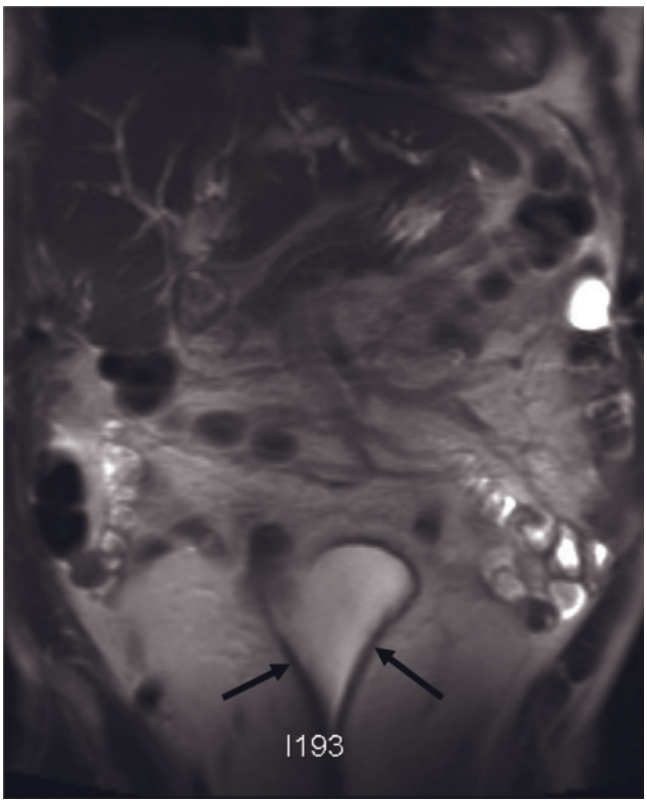

(*c*)

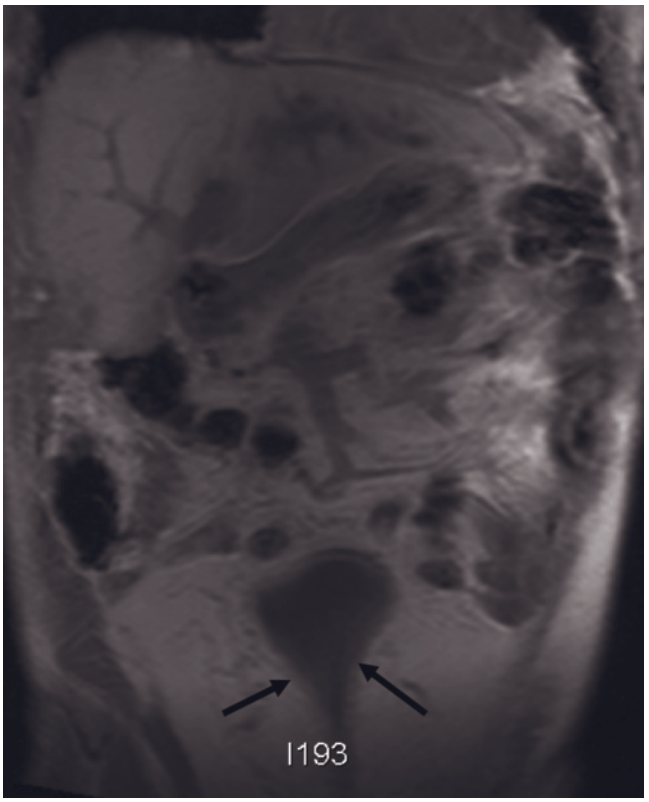

(*d*)

(*e*)

FIG. 11.23 (*Continued*) T2-weighted single-shot echo-train spin-echo (*e*) images at 3.0 T in a patient with pelvic lipomatosis show large amount of fat located in the pelvis compressing the bladder. The bladder is pear-shaped (black arrows, *c*, *d*), and there is right hydronephrosis (*e*) due to obstructive effects of pelvic lipomatosis.

bowel disease, or pelvic malignancies. Typically, patients present with urinary or fecal incontinence, pneumaturia, fecaluria, or vaginal discharge. Patients can be evaluated with cystoscopy, vaginoscopy, colonoscopy, fistulography, gastrointestinal contrast radiographic studies, sonography, scintigraphy, computed tomography, or magnetic resonance.

The sagittal plane is particularly effective at demonstrating vesicocervical fistulas because it displays these fistulas in profile (fig. 11.24). They typically insert low in the bladder, a region less well evaluated on transverse images because of volume averaging of the pelvic floor musculature. Gadolinium-enhanced T1-weighted images best demonstrate bladder fistulas. On early postgadolinium images, the fistula wall has high signal intensity and the tract has low signal intensity. Late postgadolinium images may show high-signal-intensity fluid within the fistula tract [70]. The addition of fat suppression increases the conspicuity of enhancing fistulous tract walls (fig. 11.25).

Postoperative Changes

Widening of the prostatic urethra occurs after all forms of prostatectomies. Immediately after prostatectomy, the prostatic fossa is quite wide, but it rapidly involutes to a more normal configuration over several weeks. However, a residual prostatectomy defect typically is observed for years. The configuration of the widening after cryocaustic prostate surgery is bottle shaped and different from that of transurethral resection (fig. 11.26) [71].

Bladder Reconstruction

A variety of bladder surgical procedures are performed to alter the native bladder (e.g., bladder augmentation) (fig. 11.27) or to create a neobladder (e.g., Indiana pouch) (fig. 11.28). MRI may be used to evaluate the reconstructed bladder and to examine for surgical complications or status of the kidneys.

Radiation Changes

As a sequela of pelvic radiation, bullous edema may arise in the bladder and may persist for months or years. Over time, patients may develop radiation cystitis with fibrosis and a contracted bladder.

Radiation changes in the bladder increase with increasing radiation dose. Radiation-induced disease is common when the dose exceeds 4500 cGy. In one study, the incidence of bladder changes increased from 8% to 51% as the dose surpassed 4500 cGy [72].

In patients with moderate or severe symptoms, radiation changes are detectable on MRI. However, abnormalities on MRI may be present in the absence of symptoms. Postradiation changes of the bladder have MRI appearances that correlate with the severity of histologic features. The mildest form of radiation change results in a high signal intensity of the bladder mucosa with preservation of the bladder wall thickness on T2-weighted images. The high signal intensity typically is seen at the trigone but may spread to involve the entire mucosa and could be the result of mucosal edema. With more severe injury, the wall increases in thickness

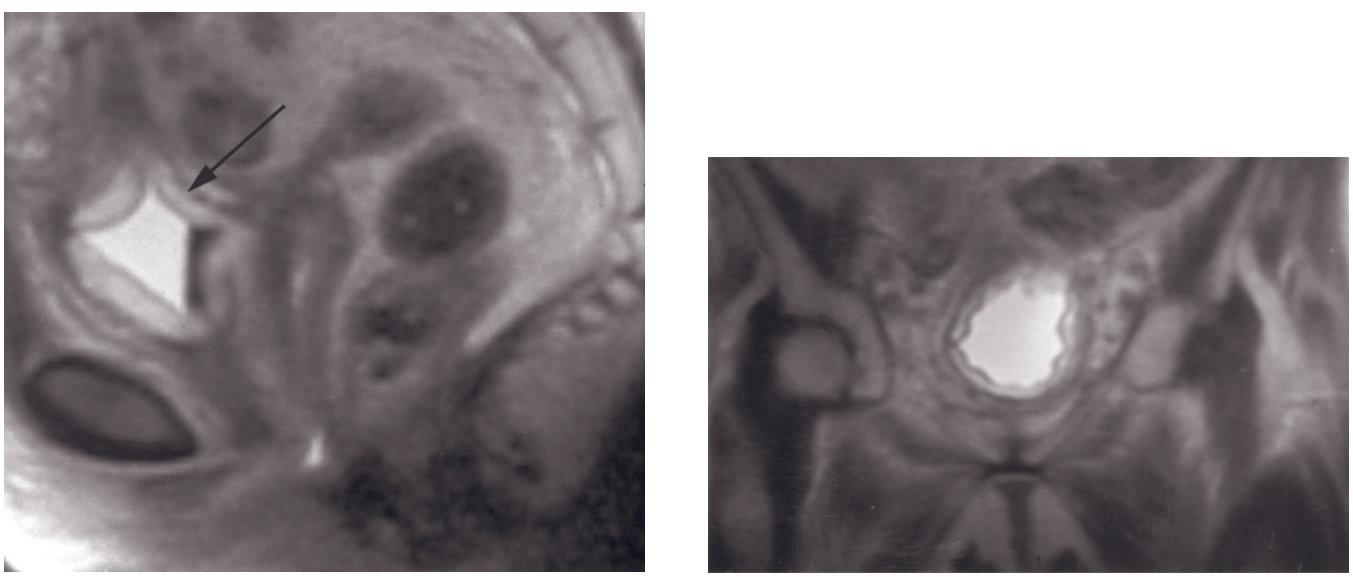

(*a*) (*b*)

FIG. 11.24 Bladder fistula. Sagittal (*a*), coronal (*b*), and transverse (*c*) T2-weighted single-shot echo-train spin-echo and sagittal T1-weighted gadolinium-enhanced fat-suppressed SGE (*d*) images in a patient after radiation therapy for ovarian cancer. The vaginal

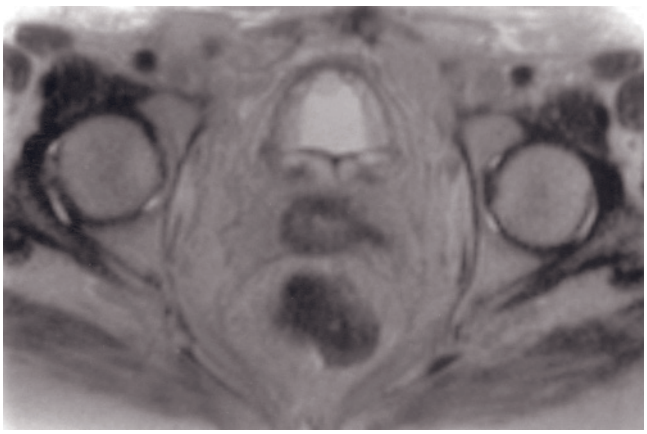

(*c*)

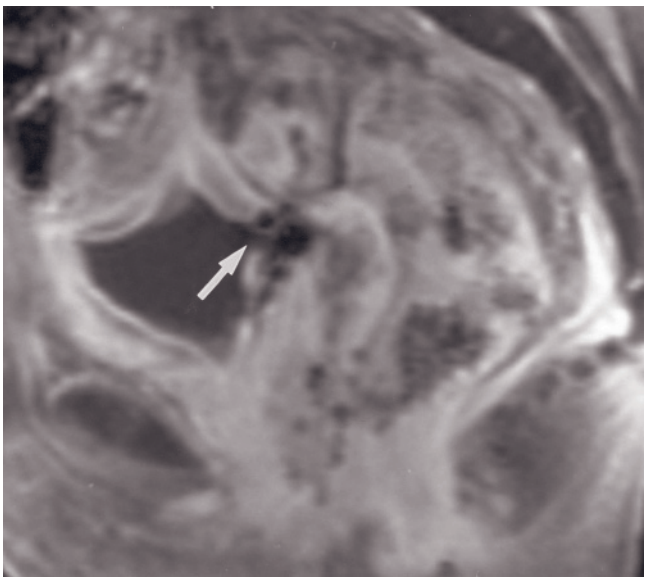

(*d*)

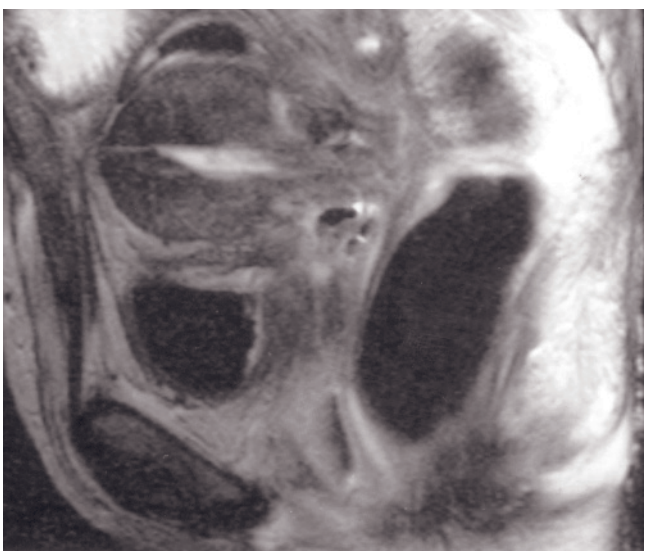

(*e*)

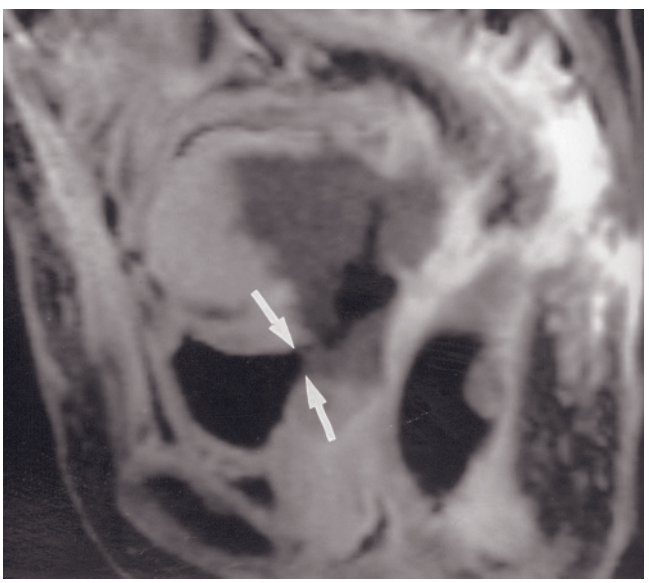

(*f*)

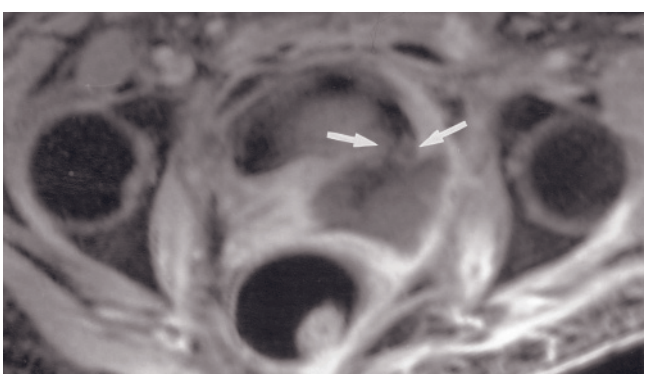

(*g*)

FIG. 11.24 (*Continued*) and bladder walls are thickened, and a fistula between the bladder and vagina (arrow, *d*) is apparent. Sagittal-plane, T1-weighted gadolinium-enhanced fat-suppressed images are particularly effective at demonstrating fistula between female pelvic organs and the bladder. Substantial submucosal edema of the bladder is appreciated as high signal on T2 (arrow, *a*) and lack of enhancement on postgadolinium images (*d*). Sagittal T2-weighted single-shot echo-train spin-echo (*e*) and sagittal (*f*) and transverse (*g*) T1-weighted gadolinium-enhanced fat-suppressed SGE images in a second patient with cervical cancer after radiation therapy. Enlarged tissue in the region of the cervix is heterogeneous on T2- and hypointense on postgadolinium T1-weighted images (*f*, *g*), consistent with cervical necrosis. The necrotic tissue is in continuity with the posterior bladder wall, and a low-signal-intensity fistulous tract is apparent on sagittal and transverse images (arrows, *f*, *g*). Sagittal T2-weighted single-shot

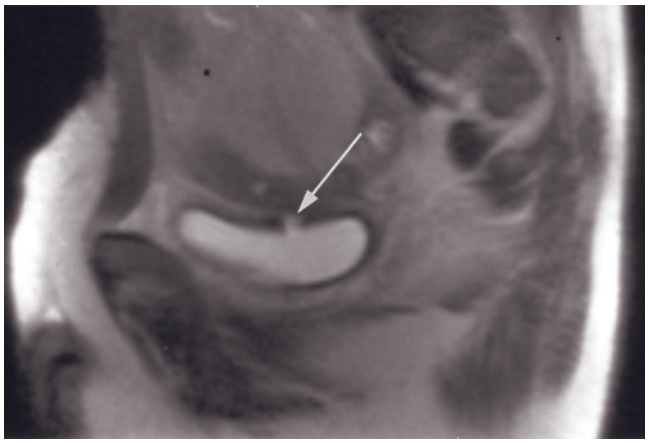

(*h*)

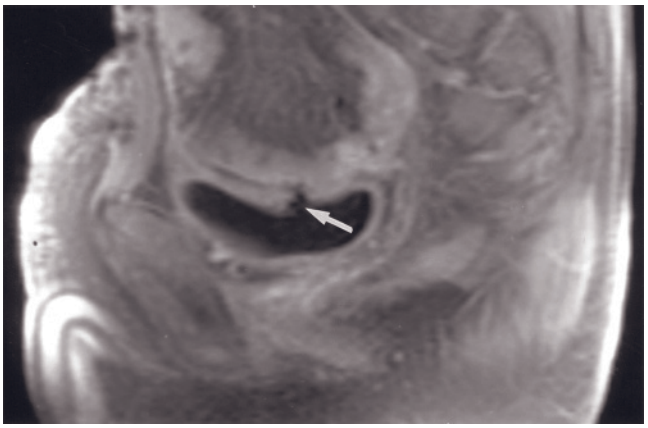

(*i*)

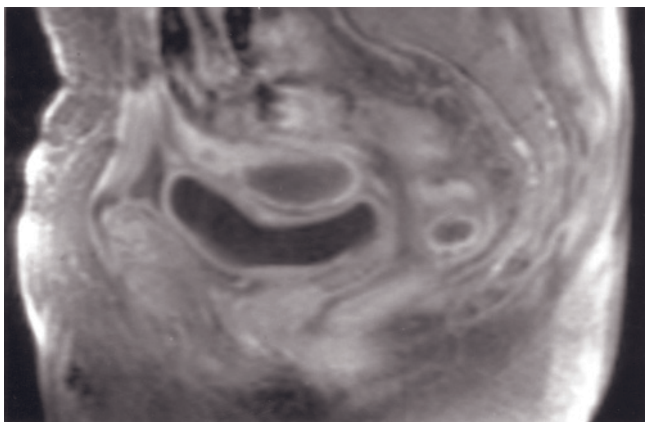

(*j*)

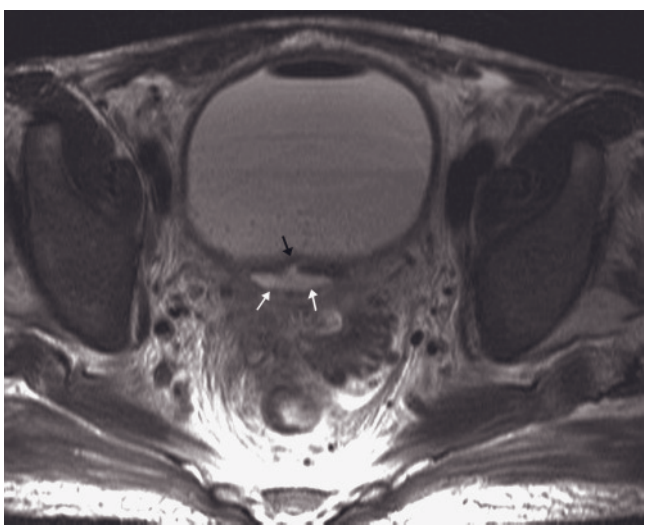

(*l*)

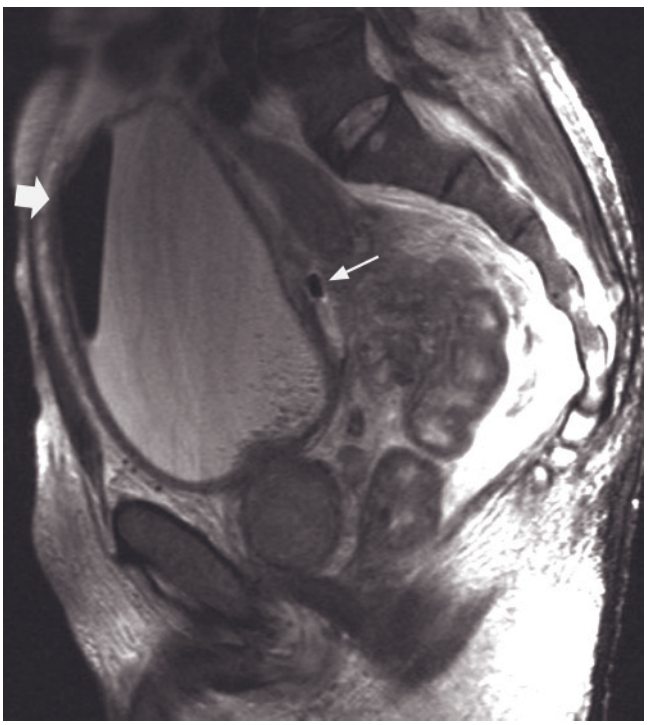

(*k*)

FIG. 11.24 (*Continued*) echo-train spin-echo (*h*) and sagittal T1-weighted gadolinium-enhanced fat-suppressed SGE (*i*, *j*) images in a third patient with colovesical fistula. A fistulous tract is present in the bladder dome (arrows, *h*, *i*). Adjacent sigmoid colon is thickened and demonstrates increased enhancement (*j*). Sagittal (*k*) and transverse (*l*) 512-resolution T2-weighted ETSE images in a fourth patient with diverticulitis. There is a signal-void layer superior to the urine in the bladder, consistent with air (large arrow, *k*). A smaller focus of air is located posterior to the bladder wall (small arrow, *k*). A small fluid collection (white arrows, *l*) posterior to the bladder is shown to connect to the bladder by a thin fistulous track (black arrow, *l*).

(*a*)

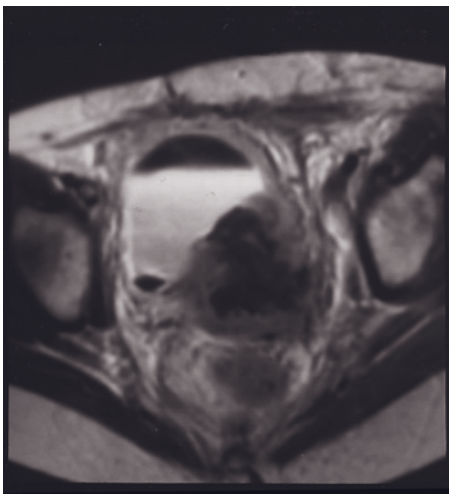

(*b*)

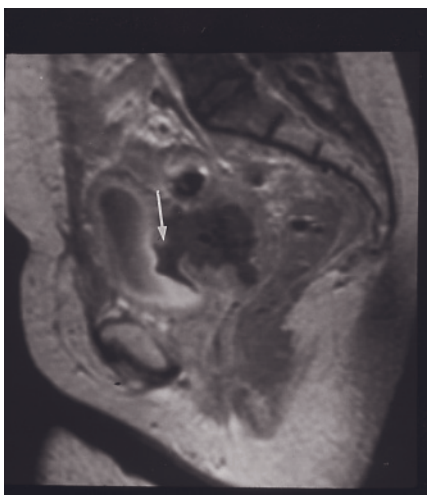

(*c*)

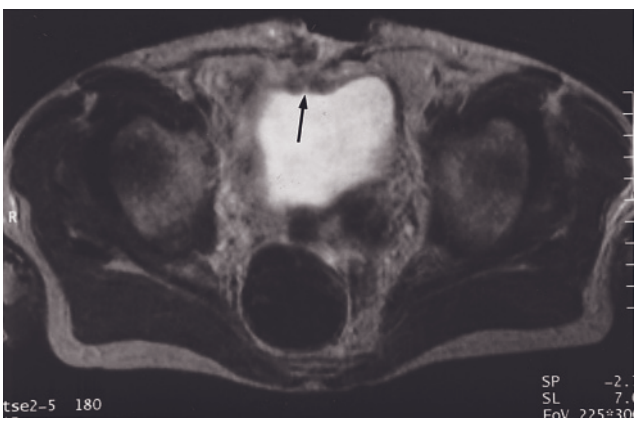

(*d*)

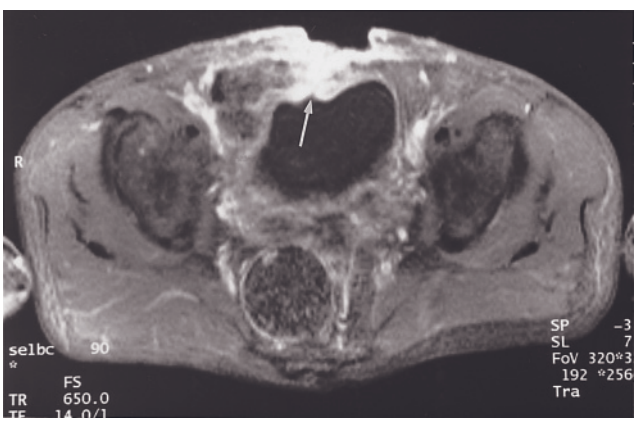

(*e*)

FIG. 11.25 Bladder fistula. T2-weighted spin-echo (*a*) and transverse (*b*) and sagittal (*c*) gadolinium-enhanced T1-weighted spin-echo images. There is a cervicovesical fistula formation after radiation for cervical cancer. The fistula tract is best shown on the sagittal postgadolinium image (arrow, *c*). (Courtesy of Hedvig Hricak, M.D., Ph.D.). T2-weighted echo-train spin-echo (*d*) and T1-weighted gadolinium-enhanced fat-suppressed spin-echo (*e*) images in a second patient with vesicocutaneous fistula. The bladder wall shows focal irregular thickening with an overlying skin defect. A thin fistula tract is apparent and is high in signal intensity on the T2-weighted image (arrow, *d*) and low in signal intensity on the postgadolinium image (arrow, *e*). On the gadolinium-enhanced fat-suppressed image, substantial enhancement of the soft tissues surrounding the fistula and the skin is present, which is consistent with inflammatory changes.

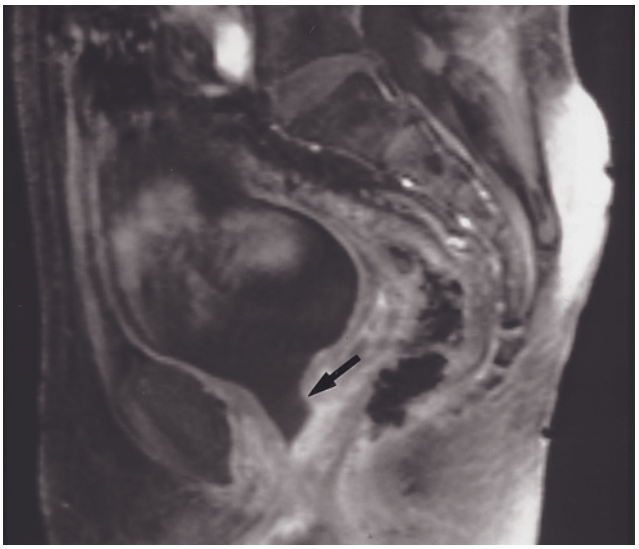

(*a*)

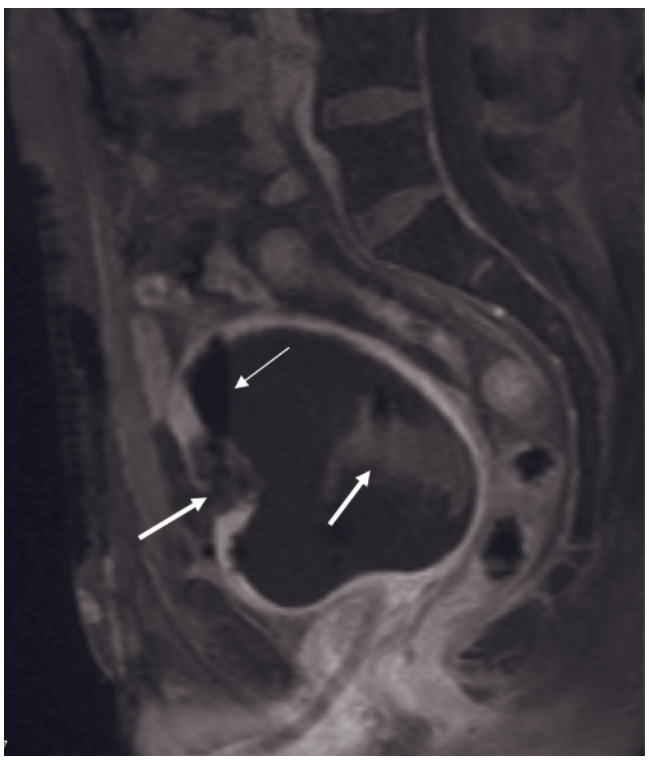

(*b*)

FIG. 11.26 Postoperative changes. Sagittal T1-weighted gadolinium-enhanced fat-suppressed SGE image (*a*) showing the characteristic widening and defect of the prostatic urethra (arrow) following transurethral prostatectomy. T1-weighted 90-s postgadolinium fat-suppressed 3D-GE (*b*) in a patient with a history of bladder rupture demonstrates postoperative changes in the anterior bladder wall secondary to the repair. There is a fibrotic tissue in the operation area demonstrating less enhancement compared to the normal bladder wall. Additionally, free air and hematoma are seen in the bladder lumen. Note the postoperative changes in the anterior abdominal wall.

(*a*)

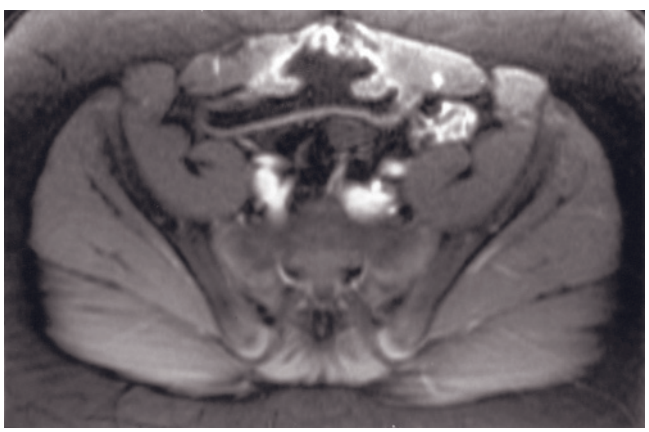

(*b*)

FIG. 11.27 Enterocystoplasty. Sagittal (*a*) and transverse (*b*) T1-weighted gadolinium-enhanced fat-suppressed images in a patient with enterocystoplasty using small bowel for the augmentation procedure for primary bladder exstrophy. The augmented bladder (*a*, *b*) has a large, capacious appearance with mucosal infoldings observed in bowel.

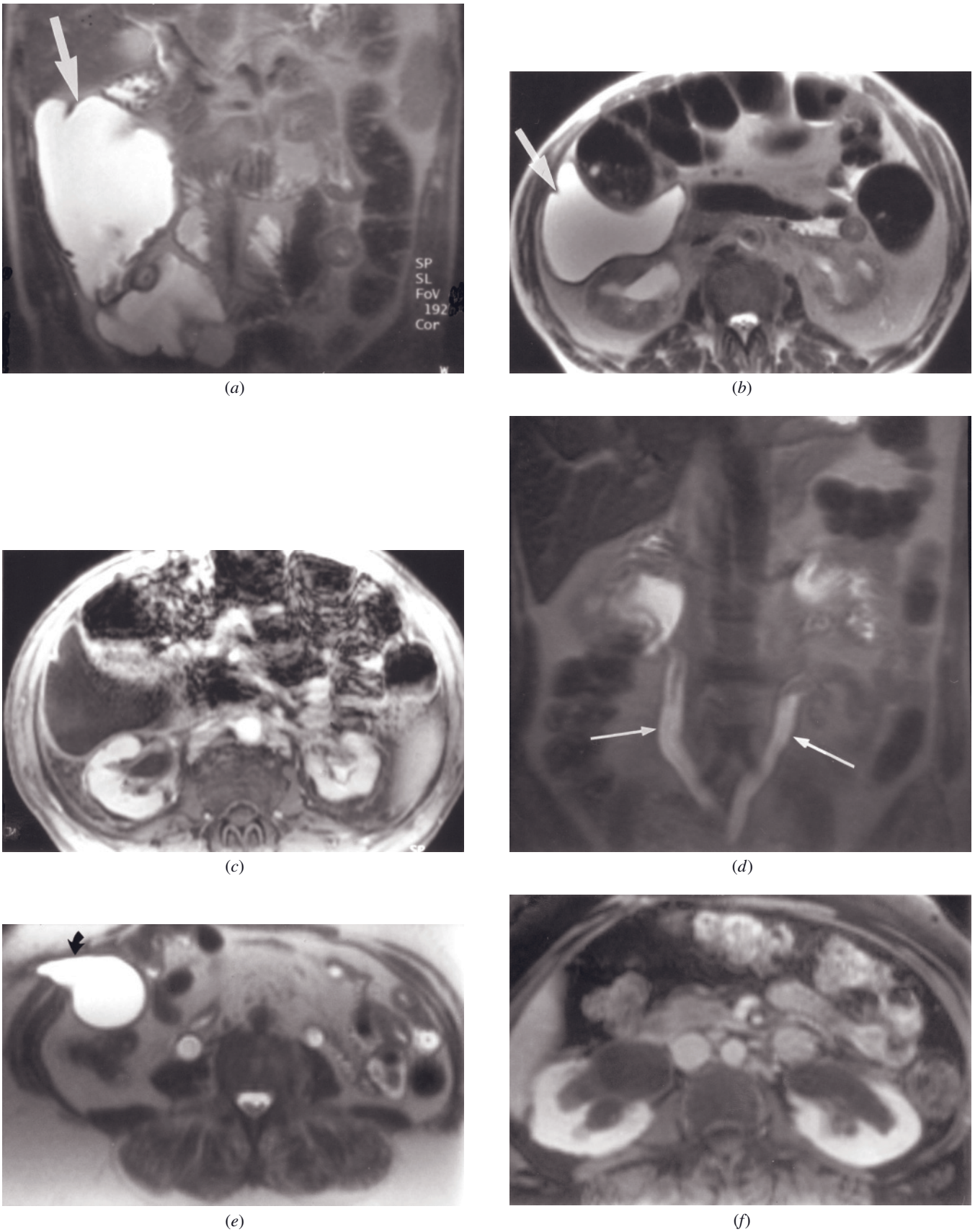

FIG. 11.28 Cystectomy with Indiana pouch. Coronal (*a*) and transverse (*b*) T2-weighted single-shot echo-train spin-echo and T1-weighted gadolinium-enhanced fat-suppressed SGE (*c*) images in a patient with primary transitional cell carcinoma who underwent radical cystectomy with Indiana pouch construction. The Indiana pouch is fluid filled and located in the right anterior peritoneal cavity (arrows, *a*, *b*). Note prominent renal pelvis bilaterally with atrophy of the left kidney (*b*, *c*). Coronal (*d*) and transverse (*e*) T2-weighted single-shot echo-train spin-echo and T1-weighted gadolinium-enhanced fat-suppressed SGE (*f*) images in a second patient with an Indiana pouch. The coronal T2-weighted image provides an MRU appearance of moderately dilated ureters bilaterally (arrows, *d*). The Indiana pouch is observed in the right anterior abdomen (arrow, *e*). Dilated renal collecting systems are present on the gadolinium-enhanced image (*f*). Delayed excretion of gadolinium is evidenced by lack of visualization of gadolinium in the collecting systems by 5 min.

(greater than 5 mm when fully distended), and the signal characteristics are one of two patterns. The wall has either uniformly high signal intensity or low signal intensity in the inner layer with high signal intensity at the periphery. On gadolinium-enhanced studies, the bladder wall shows increased enhancement, sometimes without other morphologic changes on noncontrast images. This enhancement may occur up to 2.5 years after irradiation [73]. With extreme radiation change, formations of fistula or sinus tracts are seen. Other findings of radiation changes are commonly present (fig. 11.29).

CONCLUSION

MRI is an effective technique for evaluating the full range of bladder disease. Staging of transitional cell carcinoma is the most common indication for bladder MRI investigation and is well performed with a combination of breath-hold SGE or fat-suppressed 3D-GE, 512-resolution T2-weighted echo-train spin-echo, and immediate and delayed postgadolinium fat-suppressed SGE or 3D-GE techniques, with image acquisition in multiple planes and the concurrent use of a phased-array multicoil.

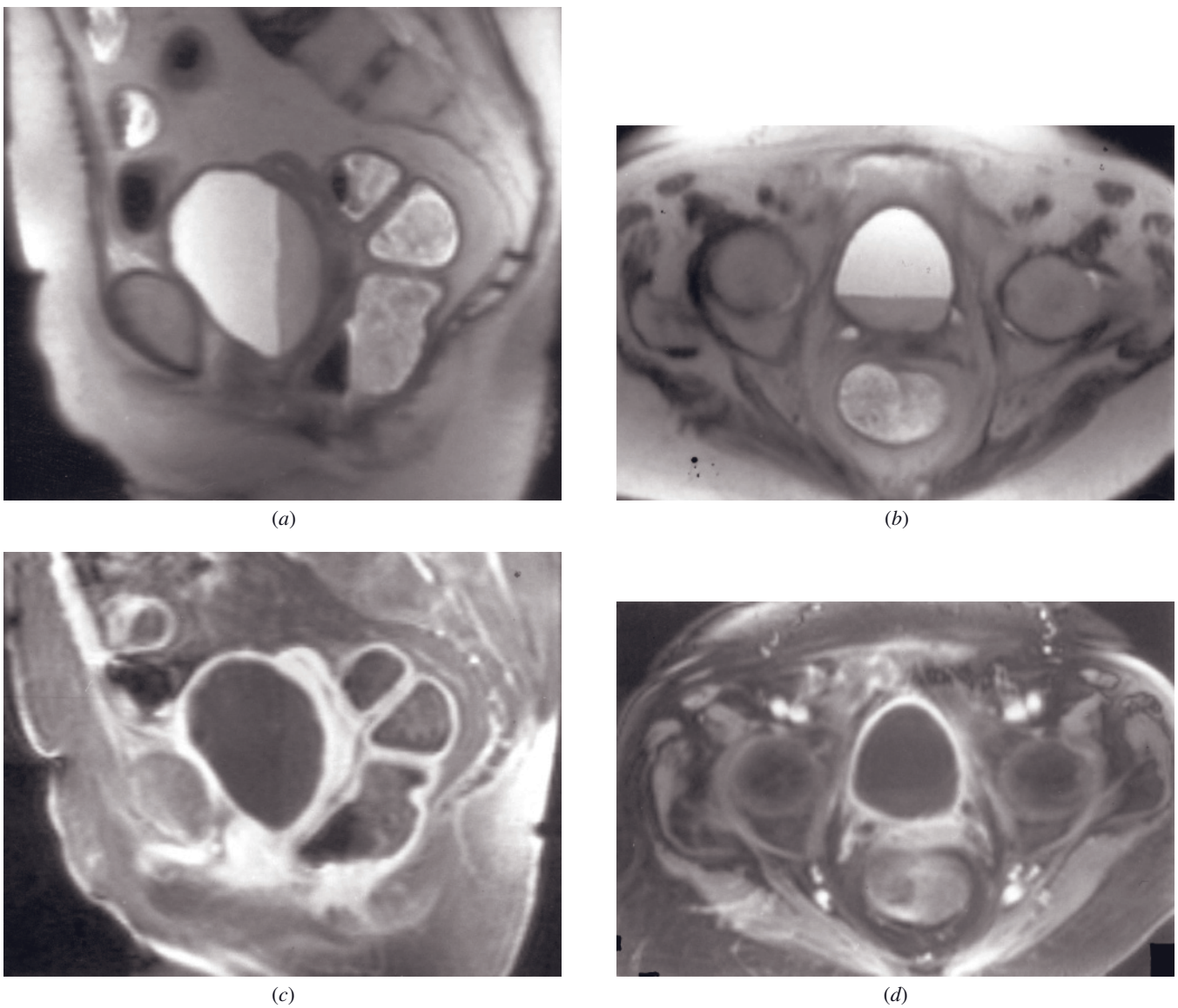

FIG. 11.29 Radiation changes. Sagittal (*a*) and transverse (*b*) T2-weighted single-shot echo-train spin-echo and sagittal (*c*) and transverse (*d*) T1-weighted gadolinium-enhanced fat-suppressed SGE images in a patient with primary cervical cancer who underwent radiation therapy. The bladder wall is diffusely thickened (*a–d*), and it enhances intensely and homogeneously after gadolinium administration (*c*, *d*). Note the dependently layering low-signal material in the bladder on the T2-weighted images, compatible with proteinaceous material and a clinical history of hematuria. Reticular strands in the perivesical fat and colorectal wall also enhance intensely because of inflammatory changes. T1-weighted fat-suppressed SGE (*e*) and T2-weighted fat-suppressed spin-echo (*f*) images

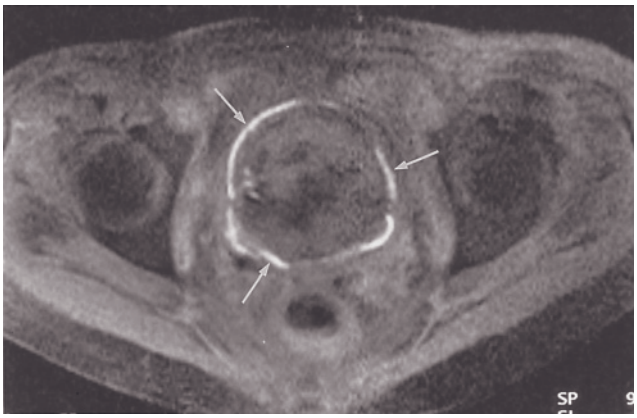

(*e*)

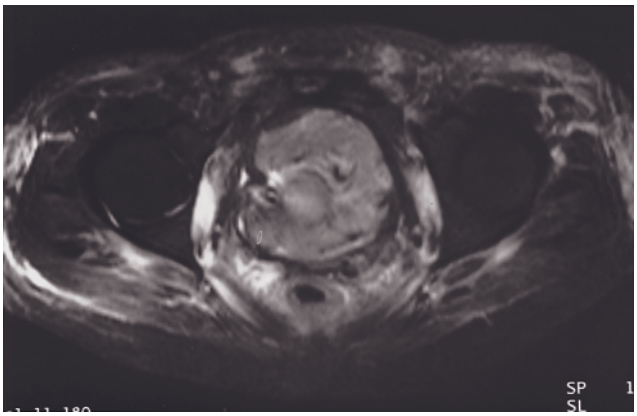

(*f*)

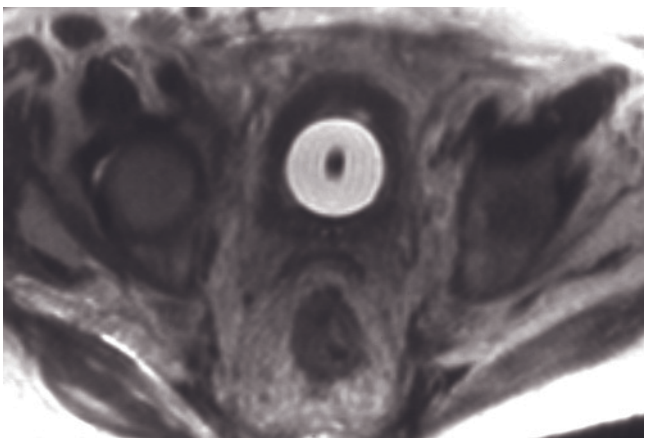

(*g*)

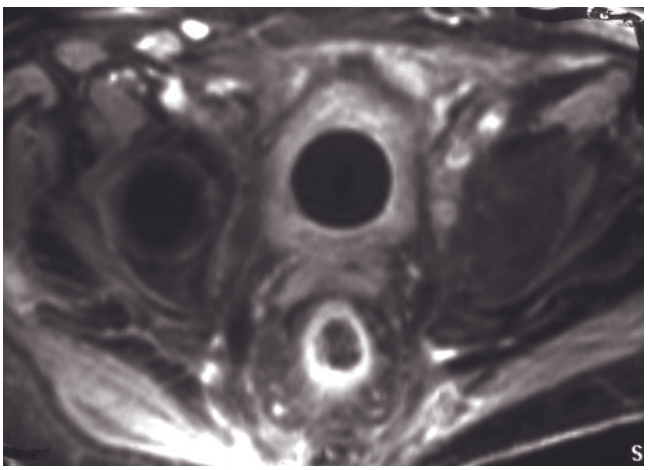

(*h*)

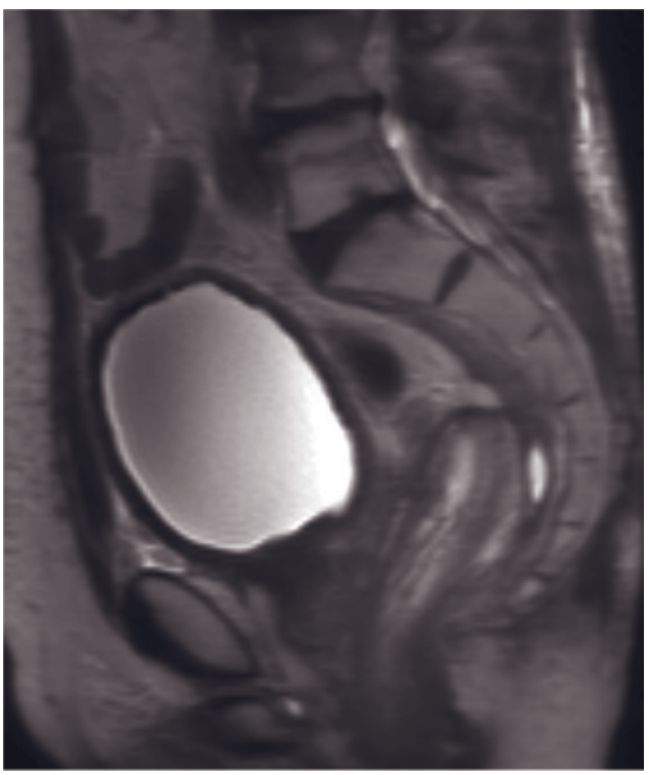

(*i*)

FIG. 11.29 (*Continued*) in a second patient. On the T2-weighted image, there is high signal intensity of the obturator internus muscles and high-signal-intensity strands in the perirectal space, consistent with radiation-induced tissue damage. High signal intensity within the bladder wall on the T1-weighted fat-suppressed SGE (*e*) and low signal intensity on the T2-weighted fat-suppressed spin-echo (*f*) images are consistent with intracellular methemoglobin due to the radiation-induced hemorrhagic cystitis. The fluid in the bladder is predominantly high in signal intensity on T1- and T2-weighted images, which is consistent with extracellular methemoglobin. T2-weighted SS-ETSE (*g*) and T1-weighted gadolinium enhanced fat-suppressed SGE (*h*) images in a third patient demonstrate uniform circumferential bladder wall thickening, a sequela of radiation therapy to the pelvis for endometrial carcinoma. Sagittal T2-weighted fast spin echo (*i*),

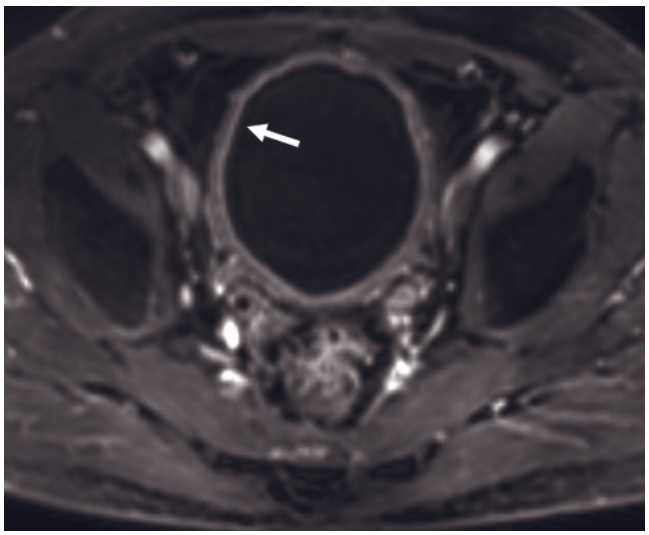

(*j*)

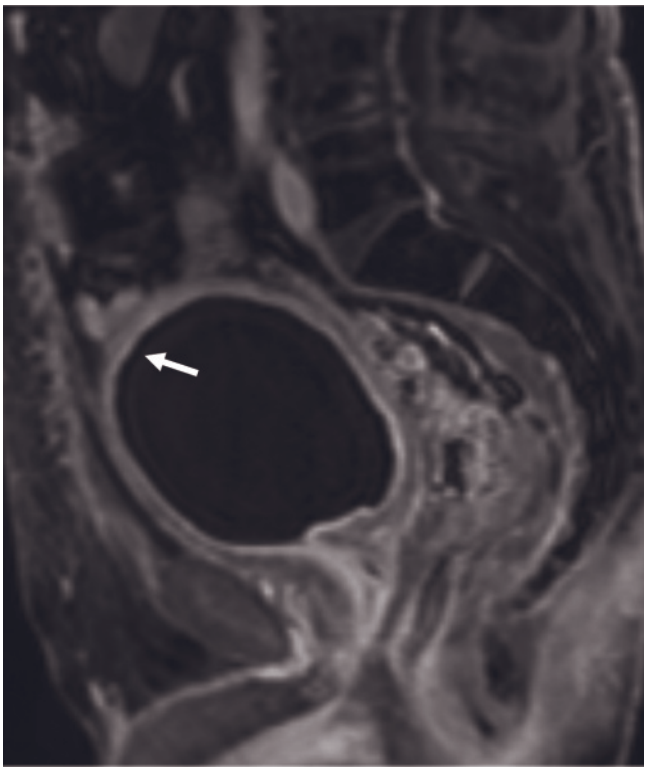

(*k*)

FIG. 11.29 (*Continued*) transverse T1-weighted postgadolinium 45-s fat-suppressed 3D-GE image (*j*), and sagittal T1-weighted postgadolinium 90 s fat-suppressed 3D-GE image (*k*) at 3.0 T demonstrate diffuse thickening and prominent enhancement of the wall, particularly the mucosa (arrow) in a patient who underwent pelvic radiation therapy. The findings are consistent with radiation cystitis.

Use of cine MRI may provide dynamic information regarding pattern of bladder emptying as a function of time [74]. Lymph node-specific contrast agents have been investigated that may permit differentiation of lymph node malignant involvement versus hyperplastic enlargement. Thus the staging of bladder carcinomas may be improved [75].

REFERENCES

1. Banson ML. Normal MR anatomy and techniques for imaging of the male pelvis. *Magn Reson Imaging Clin N Am* 4(3): 481–496, 1996.
2. Fritzsche PJ, Wilbur MJ. The male pelvis. *Semin Ultrasound CT MR* 10(1): 11–28, 1989.
3. Teeger S, Sica GT. MR imaging of bladder diseases. *Magn Reson Imaging Clin N Am* 4(3): 565–581, 1996.
4. Feinstein RS, Gatewood OM, Fishman EK et al. Computed tomography of adult neuroblastoma. *J Comput Assist Tomogr* 8(4): 720–726, 1984.
5. Narumi Y, Kadota T, Inoue E et al. Bladder tumors: staging with gadolinium-enhanced oblique MR imaging. *Radiology* 187(1): 145–150, 1993.
6. Sallevelt PE, Barentsz JO, Ruijs SJ et al. Role of MR imaging in the preoperative evaluation of atherosclerotic abdominal aortic aneurysms. *Radiographics* 14(1): 87–98; discussion 99, 1994.
7. Lawler LP. MR imaging of the bladder. *Radiol Clin North Am* 41(1): 161–177, 2003.
8. Lee JK, Rholl KS. MRI of the bladder and prostate. *AJR Am J Roentgenol* 147(4): 732–736, 1986.
9. Piccoli CW, Rifkin MD. Magnetic resonance imaging of the prostate and bladder. *Top Magn Reson Imaging* 2(3): 51–66, 1990.
10. Lane RH, Stephens DH, Reiman HM. Primary retroperitoneal neoplasms: CT findings in 90 cases with clinical and pathologic correlation. *AJR Am J Roentgenol* 152(1): 83–89, 1989.
11. Narumi Y, Kadota T, Inoue E et al. Bladder wall morphology: in vitro MR imaging—histopathologic correlation. *Radiology* 187(1): 151–155, 1993.
12. Balci NC, Semelka RC, Siegelman ES. Tumors of the bladder and urethra. In: Bragg DG, Rubin P, Hricak H, editors. *Oncologic Imaging*. Philadelphia: WB Saunders, 2002, p. 629–646.
13. Hricak H. The bladder and female urethra. In: Hricak H, Carrington BM, editors. *MRI of the pelvis: A Text Atlas*. London: Martin Dunitz, 1991, p. 417–461.
14. Berrocal T, Lopez-Pereira P, Arjonilla A et al. Anomalies of the distal ureter, bladder, and urethra in children: embryologic, radiologic, and pathologic features. *Radiographics* 22(5): 1139–1164, 2002.
15. Dondalski M, White EM, Ghahremani GG et al. Carcinoma arising in urinary bladder diverticula: imaging findings in six patients. *AJR Am J Roentgenol* 161(4): 817–820, 1993.
16. Hahn PF, Saini S, Stark DD et al. Intraabdominal hematoma: the concentric-ring sign in MR imaging. *AJR Am J Roentgenol* 148(1): 115–119, 1987.

17. Elsayes KM, Staveteig PT, Narra VR et al. Retroperitoneal masses: magnetic resonance imaging findings with pathologic correlation. *Curr Probl Diagn Radiol* 36(3): 97–106, 2007.
18. Maya MM, Slywotzky C. Urinary bladder leiomyoma: magnetic resonance imaging findings. *Urol Radiol* 14(3): 197–199, 1992.
19. Warshawsky R, Bow SN, Waldbaum RS et al. Bladder pheochromocytoma with MR correlation. *J Comput Assist Tomogr* 13(4): 714–716, 1989.
20. Heyman J, Cheung Y, Ghali V et al. Bladder pheochromocytoma: evaluation with magnetic resonance imaging. *J Urol* 141(6): 1424–1426, 1989.
21. Fink C, Goyen M, Lotz J. Magnetic resonance angiography with blood-pool contrast agents: future applications. *Eur Radiol* 17 Suppl 2: B38–B44, 2007.
22. Falke TH, te Strake L, Shaff MI et al. MR imaging of the adrenals: correlation with computed tomography. *J Comput Assist Tomogr* 10(2): 242–253, 1986.
23. Quint LE, Glazer GM, Francis IR et al. Pheochromocytoma and paraganglioma: comparison of MR imaging with CT and I-131 MIBG scintigraphy. *Radiology* 165(1): 89–93, 1987.
24. Hencey JF, Verness M, Norman J. Urinary bladder pheochromocytoma in a patient with familial pheochromocytoma: MR and CT features. *Int Med Image Registry* 1: 123–124, 1995.
25. Shonnard KM, Jelinek JS, Benedikt RA et al. CT and MR of neurofibromatosis of the bladder. *J Comput Assist Tomogr* 16(3): 433–438, 1992.
26. Amano T, Kunimi K, Hisazumi H et al. Magnetic resonance imaging of bladder hemangioma. *Abdom Imaging* 18(1): 97–99, 1993.
27. Arrive L, Hricak H, Tavares NJ et al. Malignant versus nonmalignant retroperitoneal fibrosis: differentiation with MR imaging. *Radiology* 172(1): 139–143, 1989.
28. Schultz CL, Morrison S, Bryan PJ. Azygos continuation of the inferior vena cava: demonstration by NMR imaging. *J Comput Assist Tomogr* 8(4): 774–776, 1984.
29. Rozanski TA, Grossman HB. Recent developments in the pathophysiology of bladder cancer. *AJR Am J Roentgenol* 163(4): 789–792, 1994.
30. Heiken JP, Forman HP, Brown JJ. Neoplasms of the bladder, prostate, and testis. *Radiol Clin North Am* 32(1): 81–98, 1994.
31. Tekes A, Kamel IR, Imam K et al. MR imaging features of transitional cell carcinoma of the urinary bladder. *AJR Am J Roentgenol* 180(3): 771–777, 2003.
32. Sobin LH, Wittekind CH. *TNM Classification of Malignant Tumors.* 5th ed. New York: John Wiley & Sons, Inc., 1997.
33. Fisher MR, Hricak H, Tanagho EA. Urinary bladder MR imaging. Part II. Neoplasm. *Radiology* 157(2): 471–477, 1985.
34. Amendola MA, Glazer GM, Grossman HB et al. Staging of bladder carcinoma: MRI-CT-surgical correlation. *AJR Am J Roentgenol* 146(6): 1179–1183, 1986.
35. Rholl KS, Lee JK, Heiken JP et al. Primary bladder carcinoma: evaluation with MR imaging. *Radiology* 163(1): 117–121, 1987.
36. Buy JN, Moss AA, Guinet C et al. MR staging of bladder carcinoma: correlation with pathologic findings. *Radiology* 169(3): 695–700, 1988.
37. Koelbel G, Schmiedl U, Griebel J et al. MR imaging of urinary bladder neoplasms. *J Comput Assist Tomogr* 12(1): 98–103, 1988.
38. Husband JE, Olliff JF, Williams MP et al. Bladder cancer: staging with CT and MR imaging. *Radiology* 173(2): 435–440, 1989.
39. Cheng D, Tempany CM. MR imaging of the prostate and bladder. *Semin Ultrasound CT MR* 19(1): 67–89, 1998.
40. Mallampati GK, Siegelman ES. MR imaging of the bladder. *Magn Reson Imaging Clin N Am* 12(3): 545–555, vii, 2004.
41. MacVicar AD. Bladder cancer staging. *BJU Int* 86 Suppl 1: 111–122, 2000.
42. Persad R, Kabala J, Gillatt D et al. Magnetic resonance imaging in the staging of bladder cancer. *Br J Urol* 71(5): 566–573, 1993.
43. Tekes A, Kamel I, Imam K et al. Dynamic MRI of bladder cancer: evaluation of staging accuracy. *AJR Am J Roentgenol* 184(1): 121–127, 2005.
44. Ebner F, Kressel HY, Mintz MC et al. Tumor recurrence versus fibrosis in the female pelvis: differentiation with MR imaging at 1.5 T. *Radiology* 166(2): 333–340, 1988.
45. Strich G, Hagan PL, Gerber KH et al. Tissue distribution and magnetic resonance spin lattice relaxation effects of gadolinium-DTPA. *Radiology* 154(3): 723–726, 1985.
46. Tachibana M, Baba S, Deguchi N et al. Efficacy of gadolinium-diethylenetriaminepentaacetic acid-enhanced magnetic resonance imaging for differentiation between superficial and muscle-invasive tumor of the bladder: a comparative study with computerized tomography and transurethral ultrasonography. *J Urol* 145(6): 1169–1173, 1991.
47. Neuerburg JM, Bohndorf K, Sohn M et al. Urinary bladder neoplasms: evaluation with contrast-enhanced MR imaging. *Radiology* 172(3): 739–743, 1989.
48. Neuerburg JM, Bohndorf K, Sohn M et al. Staging of urinary bladder neoplasms with MR imaging: is Gd-DTPA helpful? *J Comput Assist Tomogr* 15(5): 780–786, 1991.
49. Sohn M, Neuerburg J, Teufl F et al. Gadolinium-enhanced magnetic resonance imaging in the staging of urinary bladder neoplasms. *Urol Int* 45(3): 142–147, 1990.
50. Jager GJ, Ruijter ET, van de Kaa CA et al. Dynamic TurboFLASH subtraction technique for contrast-enhanced MR imaging of the prostate: correlation with histopathologic results. *Radiology* 203(3): 645–652, 1997.
51. Sparenberg A, Hamm B, Hammerer P et al. [The diagnosis of bladder carcinomas by NMR tomography: an improvement with Gd-DTPA?] *Rofo* 155(2): 117–122, 1991.
52. Newhouse JH. Clinical use of urinary tract magnetic resonance imaging. *Radiol Clin North Am* 29(3): 455–474, 1991.
53. Kim B, Semelka RC, Ascher SM et al. Bladder tumor staging: comparison of contrast-enhanced CT, T1- and T2-weighted MR imaging, dynamic gadolinium-enhanced imaging, and late gadolinium-enhanced imaging. *Radiology* 193(1): 239–245, 1994.
54. Algra PR, Bloem JL, Tissing H et al. Detection of vertebral metastases: comparison between MR imaging and bone scintigraphy. *Radiographics* 11(2): 219–232, 1991.
55. Tekes A, Kamel IR, Chan TY et al. MR imaging features of non-transitional cell carcinoma of the urinary bladder with pathologic correlation. *AJR Am J Roentgenol* 180(3): 779–784, 2003.
56. Perret L, Chaubert P, Hessler D et al. Primary heterologous carcinosarcoma (metaplastic carcinoma) of the urinary bladder: a clinicopathologic, immunohistochemical, and ultrastructural analysis of eight cases and a review of the literature. *Cancer* 82(8): 1535–1549, 1998.
57. Tekes A, Kamel IR, Szarf G et al. Carcinosarcoma of the urinary bladder: dynamic contrast-enhanced MR imaging with clinical and pathologic correlation. *AJR Am J Roentgenol* 181(1): 139–142, 2003.
58. Hanna SL, Fletcher BD, Boulden TF et al. MR imaging of infradiaphragmatic lymphadenopathy in children and adolescents with Hodgkin disease: comparison with lymphography and CT. *J Magn Reson Imaging* 3(3): 461–470, 1993.
59. Yeoman LJ, Mason MD, Olliff JF. Non-Hodgkin's lymphoma of the bladder—CT and MRI appearances. *Clin Radiol* 44(6): 389–392, 1991.
60. Krysiewicz S. Diagnosis of urachal carcinoma by computed tomography and magnetic resonance imaging. *Clin Imaging* 14(3): 251–254, 1990.
61. Williams WM, Kosovsky PA, Rafal RB et al. Retroperitoneal germ cell neoplasm: MR and CT. *Magn Reson Imaging* 10(2): 325–331, 1992.

62. Popovich MJ, Hricak H, Sugimura K et al. The role of MR imaging in determining surgical eligibility for pelvic exenteration. *AJR Am J Roentgenol* 160(3): 525–531, 1993.
63. Hricak H, Hamm B, Semelka RC et al. Carcinoma of the uterus: use of gadopentetate dimeglumine in MR imaging. *Radiology* 181(1): 95–106, 1991.
64. Janus CL, Mendelson DS, Moore S et al. Staging of cervical carcinoma: accuracy of magnetic resonance imaging and computed tomography. *Clin Imaging* 13(2): 114–116, 1989.
65. Rifkin MD, Piccoli CW. Male pelvis and bladder. In: Stark DD, editor. *Magnetic Resonance Imaging*. Baltimore: Mosby, 1992, p. 2044–2057.
66. Bradley WG Jr. Hemorrhage and brain iron. In: Stark DD, Bradley WG Jr, editors. *Magnetic Resonance Imaging*. Baltimore: Mosby, 1992, p. 721–728.
67. Jung YY, Kim JK, Cho KS. Genitourinary tuberculosis: comprehensive cross-sectional imaging. *AJR Am J Roentgenol* 184(1): 143–150, 2005.
68. Saxton HM. Pelvic lipomatosis. In: Pollack, editor. *Clinical Urography*, 1990.
69. Schnall MD, Connick T, Hayes CE et al. MR imaging of the pelvis with an endorectal-external multicoil array. *J Magn Reson Imaging* 2(2): 229–232, 1992.
70. Kelekis NL, Semelka RC, Molina PL et al. Immediate postgadolinium spoiled gradient-echo MRI for evaluating the abdominal aorta in the setting of abdominal MR examination. *J Magn Reson Imaging* 7(4): 652–656, 1997.
71. Mindell HJ, Quiogue T. postoperative uroradiological appearances. In: Pollack, editor. *Clinical Urography*, 1990.
72. Sugimura K, Carrington BM, Quivey JM et al. Postirradiation changes in the pelvis: assessment with MR imaging. *Radiology* 175(3): 805–813, 1990.
73. Hricak H. Magnetic resonance imaging evaluation of the irradiated female pelvis. *Semin Roentgenol* 29(1): 70–80, 1994.
74. Brasfield RD, Das Gupta TK. Desmoid tumors of the anterior abdominal wall. *Surgery* 65(2): 241–246, 1969.
75. Guimaraes R, Clement O, Bittoun J et al. MR lymphography with superparamagnetic iron nanoparticles in rats: pathologic basis for contrast enhancement. *AJR Am J Roentgenol* 162(1): 201–207, 1994.

CHAPTER 12

MALE PELVIS

ERSAN ALTUN, TARA NOONE, JORGE ELIAS, JR., MILENA SPIROVSKI, RAHEL A. KUBIK, YOUNG MI KU, AND RICHARD C. SEMELKA

MRI TECHNIQUE

MRI is an effective modality for the diagnosis, staging, and posttreatment follow-up of a variety of diseases occurring within the male pelvis. The routine use of a phased-array multicoil results in reproducible high image quality. Several reports have emphasized the value of the high spatial resolution achieved with endorectal coil imaging [1–3]. A combination of endorectal coil and pelvis phased-array coil imaging is an alternative, widely accepted technique. Signal-to-noise ratio is substantially improved at 3.0T compared to 1.5T [4, 5]. Higher signal-to-noise ratio can be translated into higher spatial and/or temporal and/or spectral resolution. Therefore, thinner sections can be acquired faster at 3.0T compared to 1.5T, because of high spatial and temporal resolutions. Isotropic spatial resolution, which may also be achieved at 3.0T, can also be useful for radiation planning treatment strategies. Higher spectral resolution at 3.0T improves the quality of MR spectroscopy and may obviate the need for endorectal coils to achieve adequate signal-to-noise ratio. Because of the higher spectral resolution, metabolites that may be obscured at 1.5T can routinely be detected at 3.0T.

Our standard male pelvis imaging protocol includes 512-resolution transverse, coronal and sagittal T2-weighted echo-train spin-echo, as well as postgadolinium transverse and sagittal fat-suppressed gradient-echo (GE) sequences including three-dimensional (3D) or two-dimensional (2D or SGE) techniques. Supplemental precontrast non-fat-suppressed and fat-suppressed T1-weighted imaging with 3D-GE or SGE sequences through the abdomen and pelvis should be performed to assess for lymphadenopathy, hemorrhage, and fat content of the lesions. Thinner slices are acquired with 3D-GE sequence compared to SGE sequence, and 3D-GE sequences should be preferred at the state-of-the-art MR systems at 1.5T and 3.0T.

Magnetic resonance spectroscopy (MRS) and dynamic gadolinium-enhanced MR imaging of the prostate [6–11] have been reported to increase the sensitivity and specificity in diagnosis and evaluation of prostate cancer. Therefore, it has been reported that either MRS or dynamic gadolinium-enhanced MR imaging or both should be used in conjunction with the standard MR

Abdominal-Pelvic MRI, Third Edition, edited by Richard C. Semelka. Copyright © 2010 John Wiley & Sons, Inc.

protocol [6–8]. However, although these techniques are routinely used at some institutions, there is a need for further research to establish and improve their definitive roles in the diagnosis of prostate cancer.

PROSTATE AND POSTERIOR URETHRA

Normal Anatomy

Approximately 70% of the prostate consists of glandular tissue, and the remaining 30% is composed of nonglandular tissue [6–8]. The prostatic urethra and the anterior fibromuscular band are the elements of nonglandular tissue [6–8]. The prostate is divided anatomically into central, transitional, and peripheral zones. The central zone is situated superiorly within the base of the gland and forms about 25% of the glandular prostate [6–8]. It surrounds the ejaculatory ducts. The transitional zone is located predominantly within the base of the gland and accounts for 5% of the glandular tissue [6–8]. The transitional zone increases in size with patient age. The transitional zone surrounds the prostatic urethra, which is located at the posterior part of the transitional zone superiorly. The periurethral glandular tissue composes less than 1% of the glandular prostate. The peripheral zone comprises 70% of the gland and is most extensive within the prostatic apex, where it forms the majority of the gland, and in the midgland, where it is posterior and posterolateral in location. The peripheral zone surrounds the prostatic urethra inferiorly.

The prostate appears homogeneous and intermediate in signal intensity on T1-weighted images, and zonal anatomy is not demonstrable. The zonal anatomy of the prostate is well demonstrated on T2-weighted images (fig. 12.1). Signal intensity on T2-weighted images is directly related to the proportion of glandular elements and inversely related to the density of stromal or muscular elements. Thus there is increased signal intensity in the peripheral zone, where there is abundant glandular material, and decreased signal intensity in the central zone, where more striated muscle and stroma are present. The signal intensity of the transitional zone, where there is also a large volume of stroma, is similar to that of the central zone. Differentiation between the two cannot be made by imaging appearances but is based primarily on anatomic location.

The anterolateral prostate is cloaked by the anterior fibromuscular band, which is low in signal intensity on both T1- and T2-weighted images (fig. 12.1). It serves as a landmark, dividing the prostate from the tissues of the preprostatic space. The prostatic capsule also is comprised of fibromuscular tissue and is low in signal intensity on T2-weighted images (fig. 12.1). The verumontanum, a central ovoid low-signal-intensity structure, is located in the periurethral region at the midgland level (fig. 12.1). The neurovascular bundles are located posterolaterally at 5 and 7 o'clock within the rectoprostatic angles in the transverse plane (fig. 12.1). MR spectroscopy can show the relative concentrations of metabolic chemical compounds in the prostate tissue. Normal prostate tissue contains high levels of citrate and low levels of choline and creatine (fig. 12.1).

The prostatic and membranous portions of the urethra form the posterior urethra. The distal prostatic urethra is demonstrated as a low-signal-intensity rounded structure within the high-signal-intensity peripheral zone at the apex of the prostate (fig. 12.2). The membranous urethra extends from the prostatic apex to the bulb of the penis. The muscular wall of the membranous urethra forms the external sphincter, and embedded within its adventitia are the paired Cowper glands.

Disease Entities

Congenital Abnormalities

Cysts are the most commonly encountered congenital anomalies of the prostate. Congenital prostatic cysts are generally high in signal intensity on T2-weighted images and of variable signal intensity on T1-weighted images, depending on the presence of infection or hemorrhage. Characterized by location, which may be midline, paramedian, or lateral, they occur between the prostatic urethra or bladder anteriorly and the rectum posteriorly.

Midline cysts include utricular and müllerian duct cysts. Utricular cysts arise from dilatation of the prostatic utricle, originating from the verumontanum. Frequently associated with other genital anomalies, they are usually teardrop-shaped and communicate with the posterior urethra (fig. 12.3) [12, 13].

In contrast, müllerian duct cysts do not communicate with the posterior urethra but are connected to the verumontanum by a stalk. Generally retrovesical in location (fig. 12.4), they are remnants of the müllerian ductal system and rarely are associated with renal agenesis. Patients may present with urinary retention, infection, and stone formation. There are associated increased incidences of both squamous cell and adenocarcinomas [12–14].

Cysts arising from the vas deferens or ejaculatory ducts are paramedian in location. Ejaculatory duct cysts may be either congenital or postinflammatory and generally result from obstruction along the expected course of the ductal system. Cysts of the vas deferens, although extremely rare, most frequently involve the ampulla. When large, either of these paramedian cystic structures may appear identical to utricular or müllerian duct cysts.

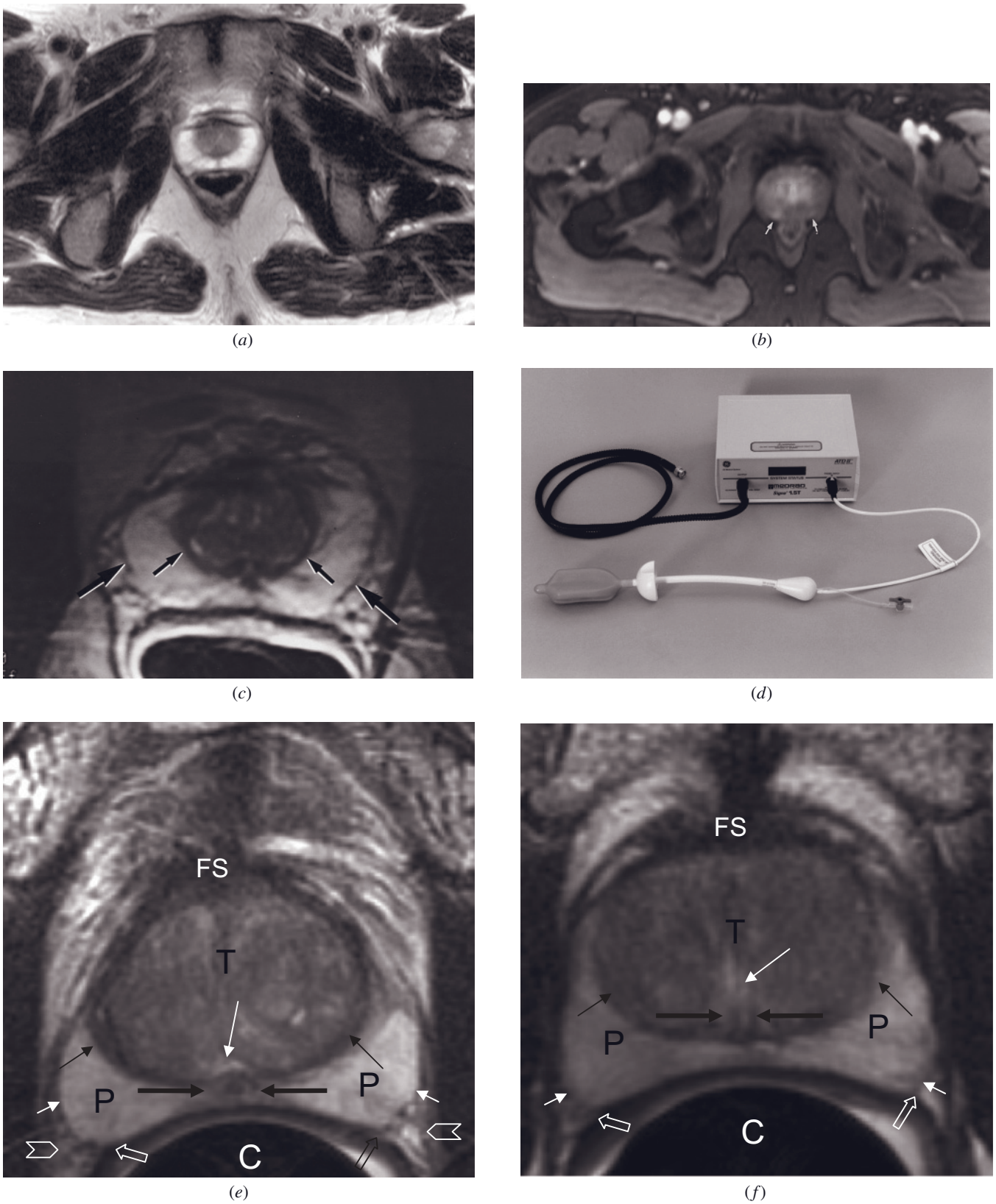

FIG. 12.1 Normal prostate. Transverse T2-weighted echo-train spin-echo (ETSE) image (*a*). The peripheral zone is high in signal intensity on T2-weighted images and surrounds the lower-signal-intensity transitional and central zones. Transverse immediate postgadolinium fat-suppressed T1-weighted gradient-echo (*b*) image in a second patient. Note the vascular enhancement delineating the neurovascular bundles (arrows, *b*) on the postgadolinium image. T2-weighted endorectal coil image (*c*) in a third patient with normal prostate. The zonal anatomy of the prostate is well demonstrated on T2-weighted images. The normal central zone and transitional zones are low in signal intensity (short arrows, *c*), and the normal peripheral zone is high in signal intensity (long arrows, *c*). The endorectal coil (*d*) has a balloon tip, which is inflated when the coil is placed. Normal anatomy of prostate gland is demonstrated on T2-weighted images (*e–b*) acquired with endorectal coil (Courtesy of Fergus V. Coakley, M.D.). P, peripheral zone. T,

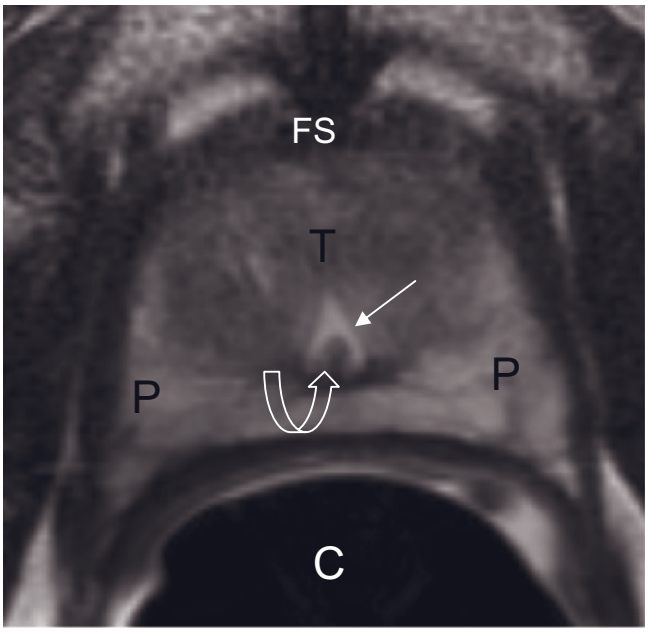

(*g*)

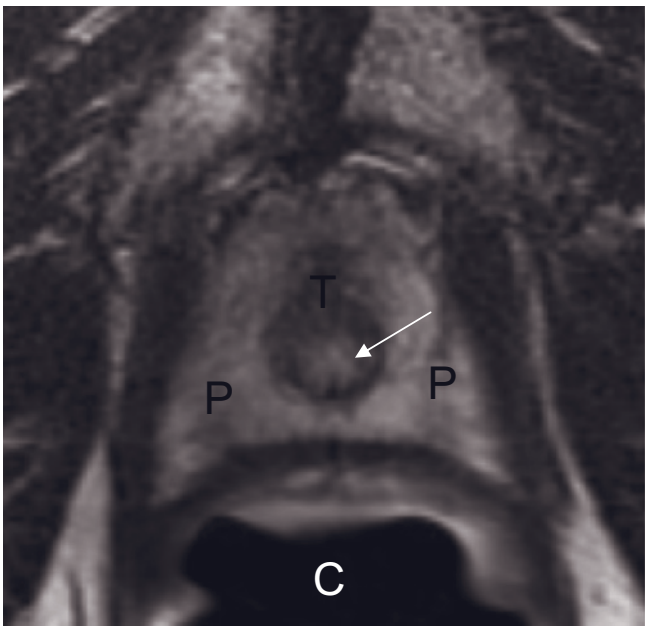

(*h*)

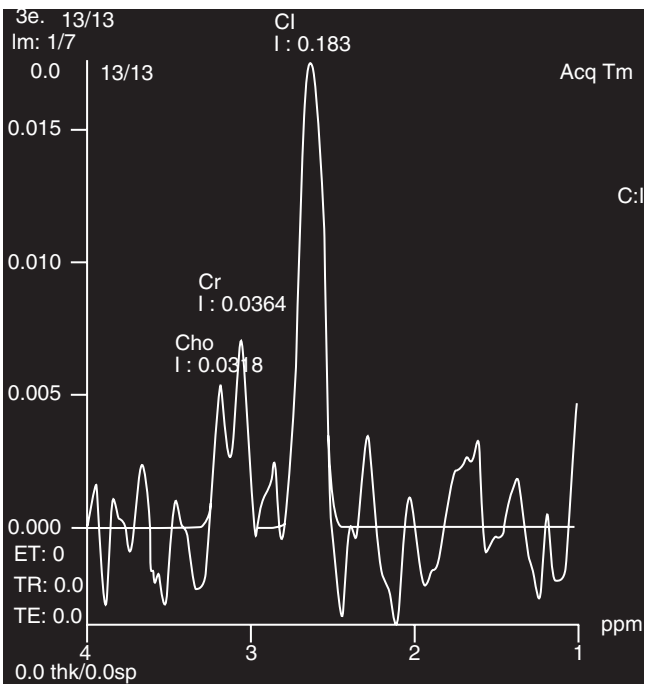

(*i*)

FIG. 12.1 (*Continued*) transitional zone. FS, anterior fibromuscular stroma. White arrows, urethra. Open arrowheads, rectoprostatic angle. Open arrows, neurovascular bundle. Short white arrows, true capsule. Black thin arrows, pseudocapsule. Black thick arrows, ejaculatory ducts. Curved arrow, verumontanum. C, coil in the rectum. MR spectroscopy of the prostate, normal spectrum (*i*). In vivo proton spectroscopy of the prostate determines the levels or concentrations of citrate (Ci), choline (Cho), and creatine (Cr) (*i*). Normal prostate tissue demonstrates high levels of citrate. However, prostate cancer tissue shows high levels of choline and often diminished citrate levels.

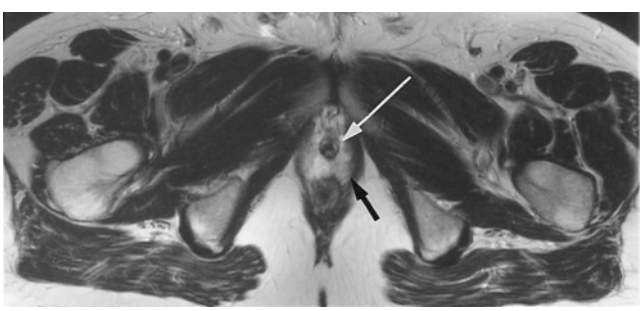

FIG. 12.2 Normal prostate level of apex. Transverse T2-weighted ETSE image. At the level of the prostatic apex, the gland is comprised predominantly of the peripheral zone, which is high in signal intensity on T2-weighted images (black arrow). The muscular wall of the urethra, which is low in signal intensity on T2-weighted images, is clearly depicted (white arrow).

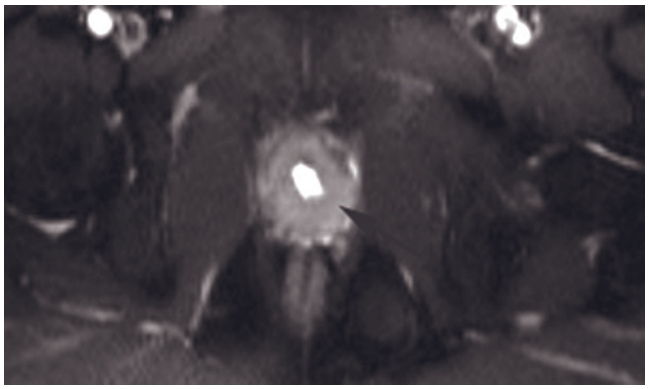

(*a*)

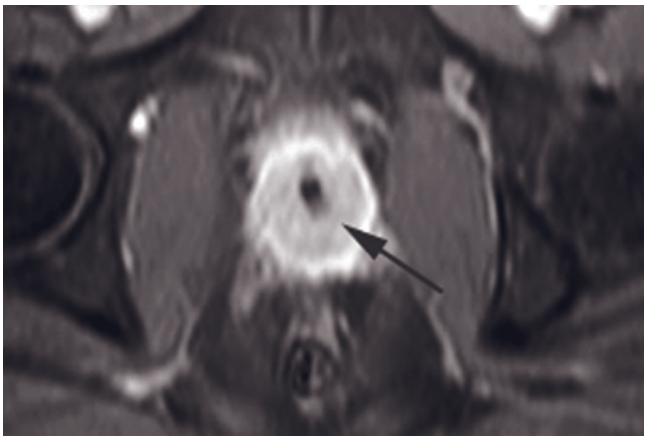

(*b*)

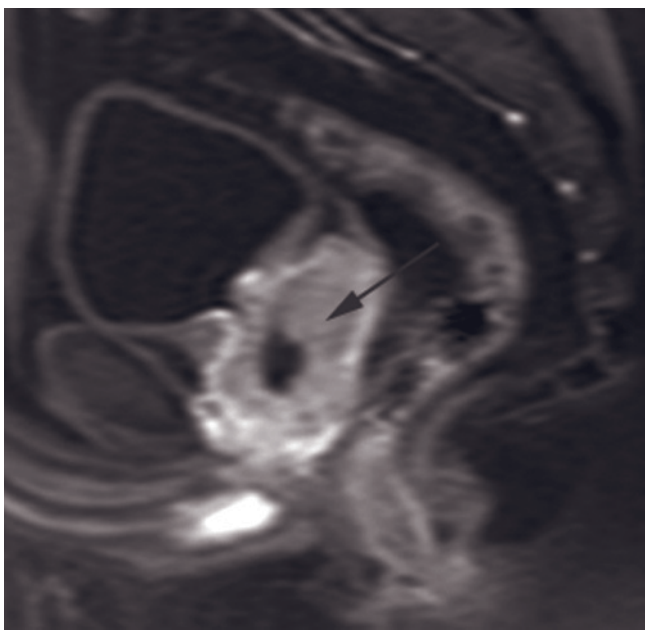

(*c*)

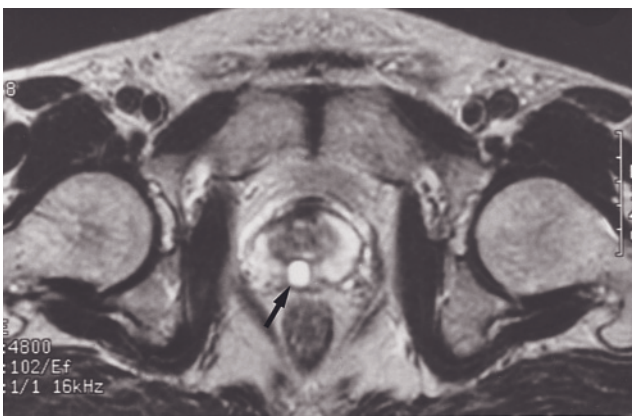

(*d*)

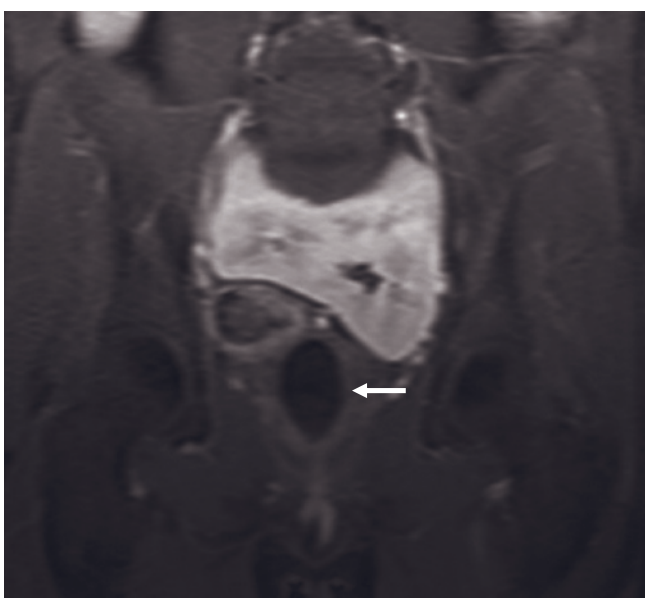

(*e*)

FIG. 12.3 Utricular cysts. Transverse T2-weighted echo-train spin-echo with fat suppression (*a*) and transverse (*b*) and sagittal (*c*) T1-weighted fat-suppressed gradient-echo images. A rounded, central structure, which is high in signal intensity on the T2-weighted images, represents a utricular cyst (arrow, *a*). Note the lack of enhancement in the cyst relative to the surrounding prostatic parenchyma (arrows, *b*, *c*).Transverse T2-weighted spin-echo image (*d*) in a second patient. A utricular cyst located in the region of the verumontanum is high in signal intensity on this T2-weighted image (arrow, *d*). T1-weighted postgadolinium interstitial phase 3D-GE image (*e*) demonstrates the midline cystic structure (arrow) in the prostate that is consistent with utricle cyst in another patient. Note the fused ectopic pelvic kidney located in the pelvis.

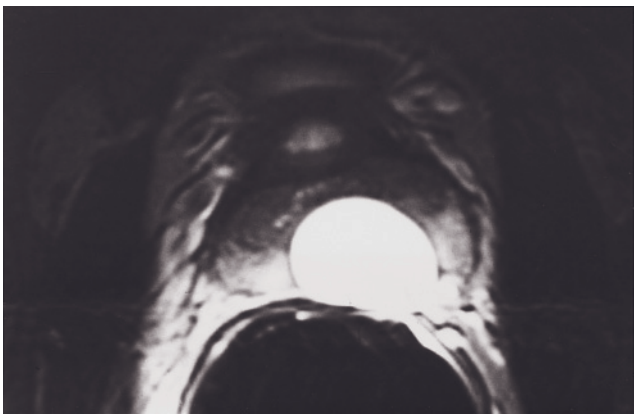

(*a*)

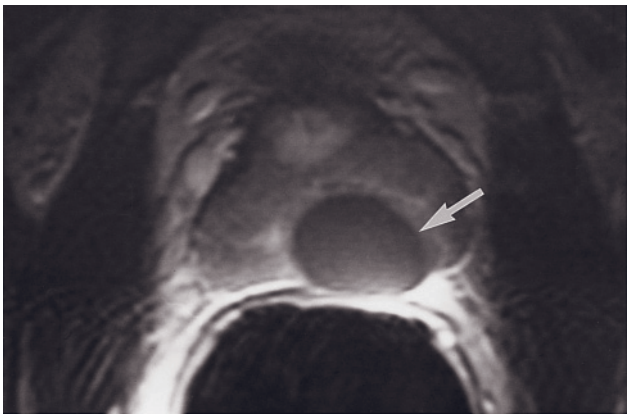

(*b*)

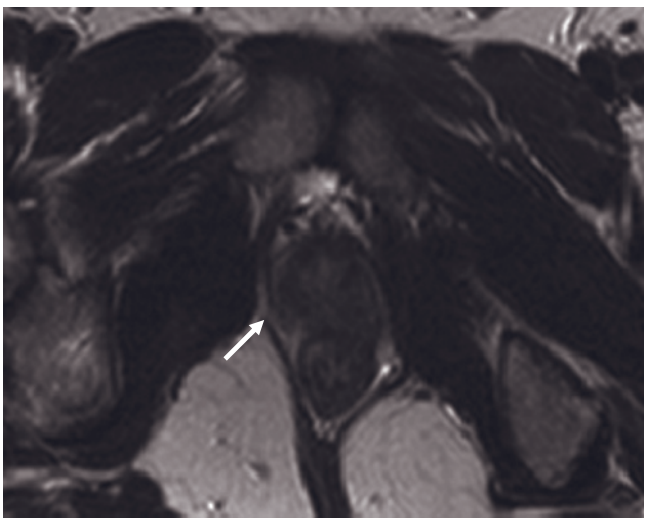

(*c*)

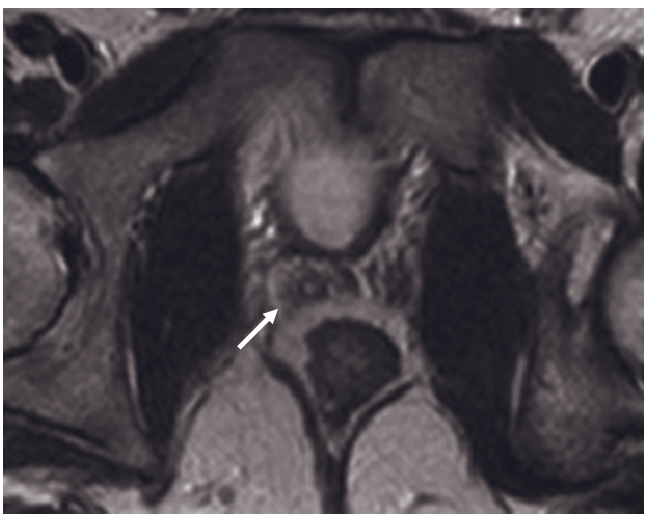

(*d*)

(*e*)

FIG. 12.4 Müllerian cyst. Transverse T2-weighted spin-echo (*a*) and immediate postgadolinium fat-suppressed T1-weighted gradient-echo (*b*) endorectal coil images. A large, ovoid müllerian cyst is seen in the dorsal aspect of the prostate near the midline, which is high in signal intensity on the T2-weighted image (*a*) and intermediate in signal intensity on the postgadolinium image (white arrow, *b*). **Prostate and seminal vesicle hypoplasia.** Transverse (*c*, *d*) and sagittal (*e*) high-resolution T2-weighted fast spin-echo images demonstrate prostate (arrow, *c*, *e*) and seminal vesicle (arrow, *d*, *e*) hypoplasia in another patient. The prostate and seminal vesicles (arrows, *c*–*e*) are hypoplastic in a young patient with no history of ejaculation. The bladder is larger than normal and elongated. Note that there is sacrum hypoplasia and coccyx aplasia as well.

Aspirated cyst fluid contains spermatozoa, permitting differentiation from müllerian duct cysts [12, 13, 15, 16]. Cysts are high in signal intensity on high-resolution T2-weighted images and appear signal void on postgadolinium images. Prostatic agenesis and hypoplasia with or without associated seminal vesicle agenesis or hypoplasia, much rarer anomalies (fig. 12.4), often are associated with other anomalies of the genitourinary tract.

Mass Lesions

Benign Masses. Proliferation of glandular, or, less commonly, interstitial elements of the transitional zone leads to benign prostatic hyperplasia (BPH), a disease entity observed in approximately 50% of the male population older than 45 years of age [17]. When changes are focal, they may result in the formation of nodules or adenomyomata.

Glandular hyperplasia frequently results in enlargement of the central aspect of the prostate. BPH is low in signal intensity on T1-weighted images. On T2-weighted images, BPH may be homogeneous or heterogeneous in appearance, ranging from medium to high in signal intensity [18–20]. Compression of the adjacent peripheral zone results in a low-signal-intensity band referred to as the surgical pseudocapsule [20, 21]. Adenomatous changes may result in focal, nodular enlargement of the gland. Signal characteristics may be variable on T2-weighted images [18, 22]. BPH commonly occurs in conjunction with prostate cancer because both are disease processes that increase in incidence with patient age (fig. 12.5).

Distinction between interstitial hyperplasia and glandular hyperplasia has been described on MR images [19, 23]. Hyperplastic changes that predominantly involve the interstitium result in heterogeneous low signal intensity of the enlarged gland on T2-weighted images [19]. Focal alterations in signal intensity may result from infarction or cystic changes within nodules of glandular BPH [13, 23–25]. Areas of infarction may demonstrate low signal intensity on T2-weighted images [25]. Cystic ectasia, corresponding to dilatation of glandular elements, results in high signal intensity on T2-weighted images (fig. 12.6) [19, 23]. BPH may occasionally infiltrate the peripheral zone, making its distinction from carcinoma problematic [23].

Progressive enlargement of the central portion of the prostate with resultant protrusion into the bladder leads to partial bladder outlet obstruction (fig. 12.7) [19].

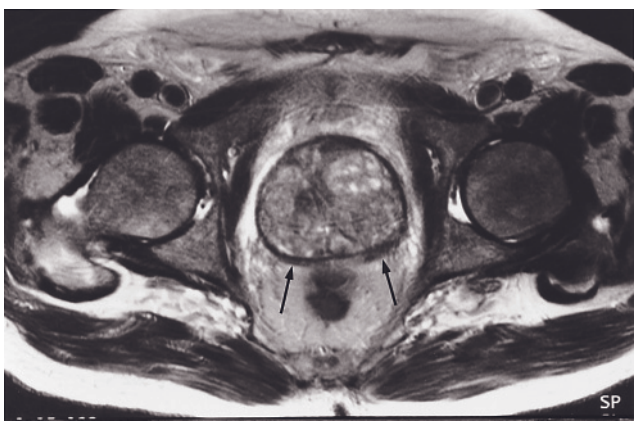

(*a*)

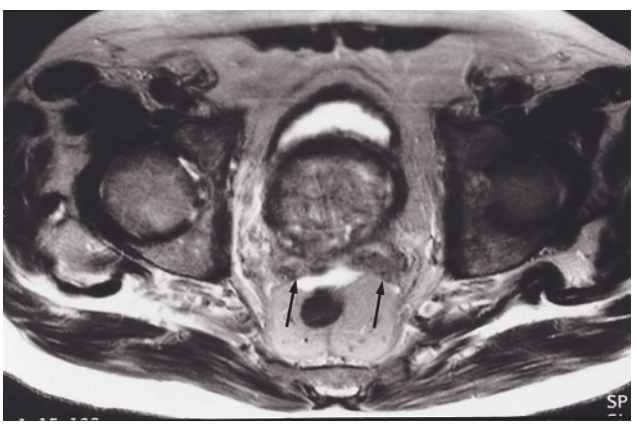

(*b*)

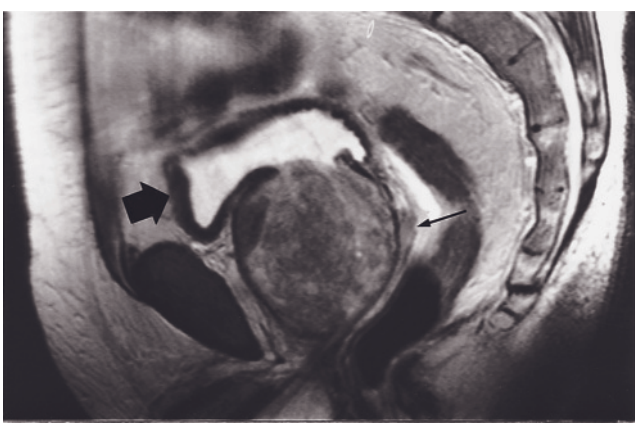

(*c*)

FIG. 12.5 Prostate cancer with seminal vesicle extension in the setting of massive BPH. Transverse (*a*, *b*) and sagittal (*c*) T2-weighted ETSE images. The transitional zone, which is greatly enlarged, is heterogeneous and moderately high in signal intensity. The peripheral zone of the prostate (thin arrows) is thin and diffusely low in signal intensity secondary to tumor involvement (*a*). The seminal vesicles (thin arrows, *b*, *c*) also are low in signal intensity secondary to invasion by tumor (*b*, *c*).The bladder (large arrow, *c*) is elevated by the enlarged prostate and thick walled from resultant outlet obstruction. The prostate is enlarged, with heterogeneous signal intensities scattered throughout the central and peripheral zones of the prostate. The margins of the prostate are intact. Adenocarcinoma was present at histopathology.

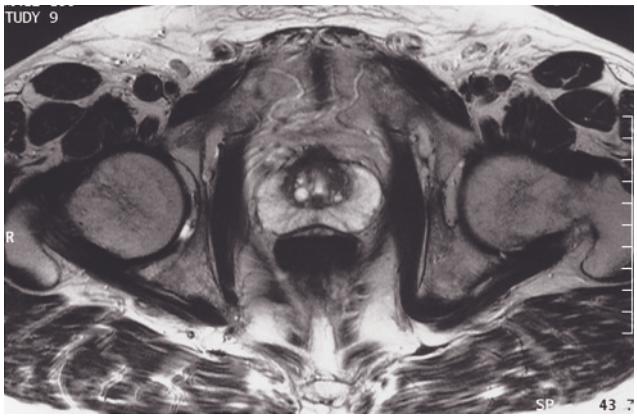

(*a*)

(*b*)

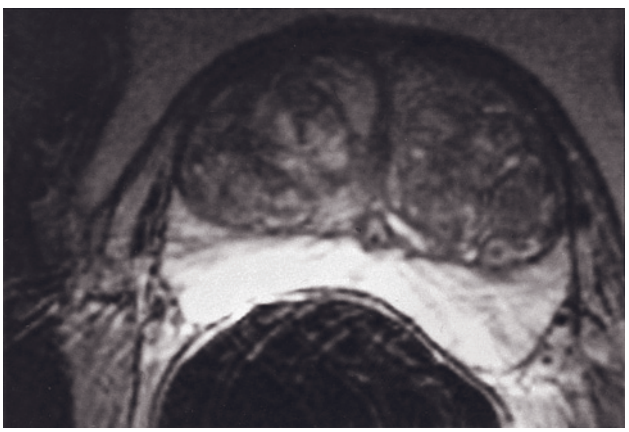

(*c*)

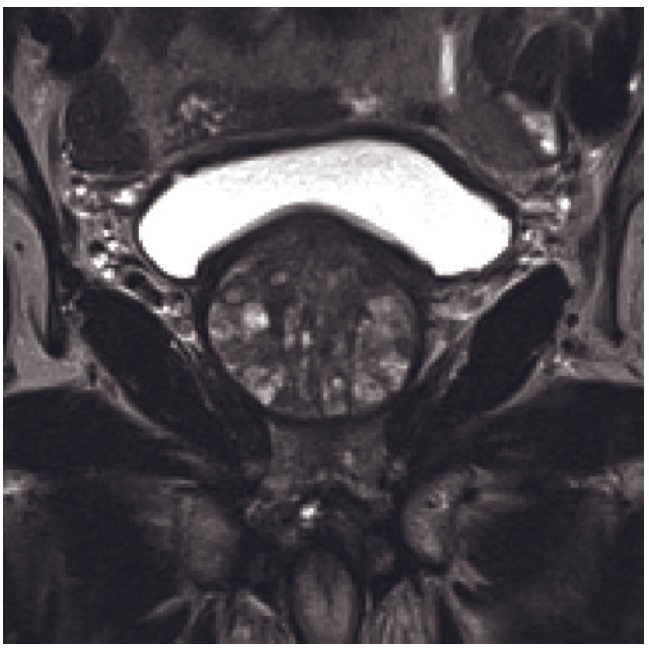

(*d*)

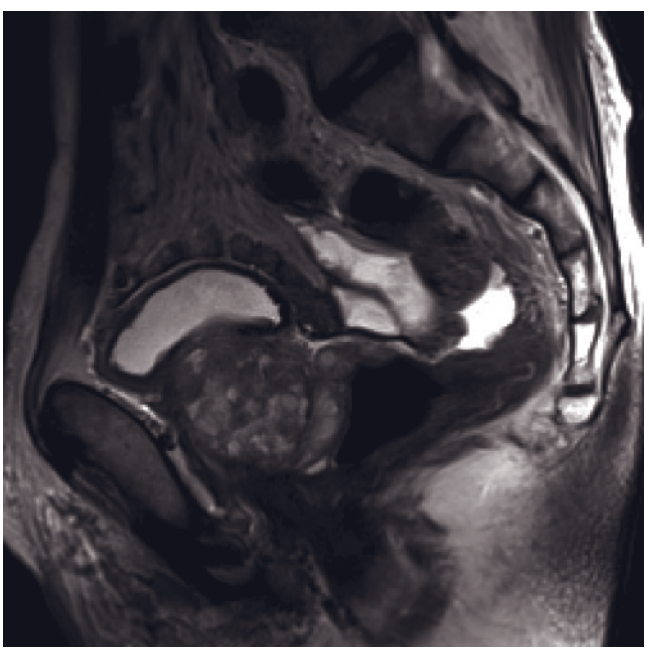

(*e*)

FIG. 12.6 Benign prostatic hyperplasia. Transverse (*a*) and sagittal (*b*) T2-weighted ETSE image. High-signal-intensity foci are present, representing cystic elements of interstitial BPH (long arrow, *b*). Normal signal intensity is seen within the surrounding peripheral zone (short arrows, *b*).Transverse T2-weighted ETSE endorectal coil image (*c*) in a second patient. Diffuse heterogeneous low signal intensity within an enlarged central gland is consistent with the predominantly glandular subtype of BPH. Coronal (*d*) and sagittal (*e*) high-resolution T2-weighted echo-train spin-echo images demonstrate enlarged transitional zone with bladder impression in another patient with benign prostatic hyperplasia. Hyperplasia is a mixed type containing glandular and interstitial elements. The peripheral zone is very thin because of the compression of central gland hyperplasia. Note the trabeculations of thickened bladder wall.

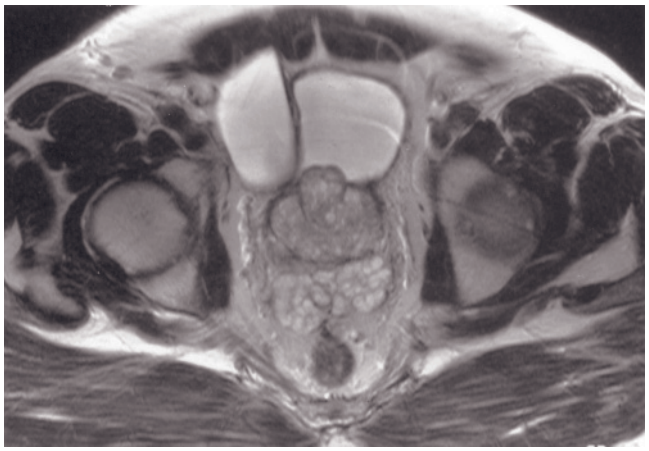

(*a*)

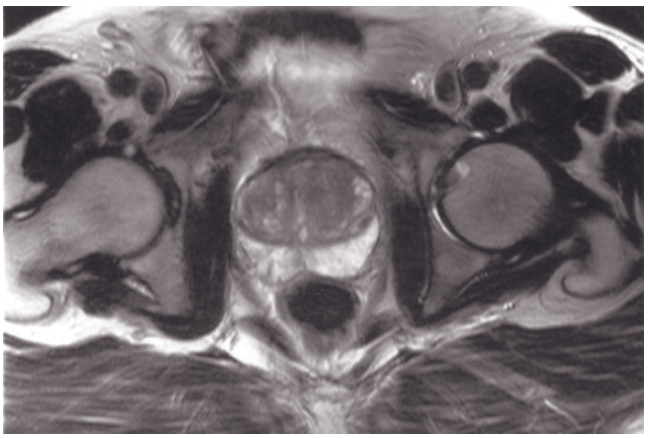

(*b*)

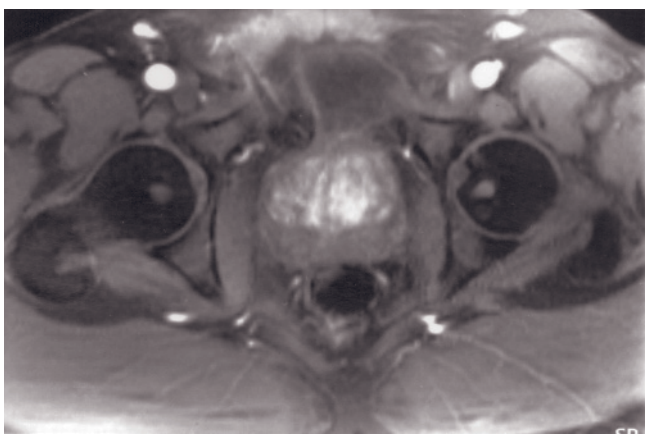

(*c*)

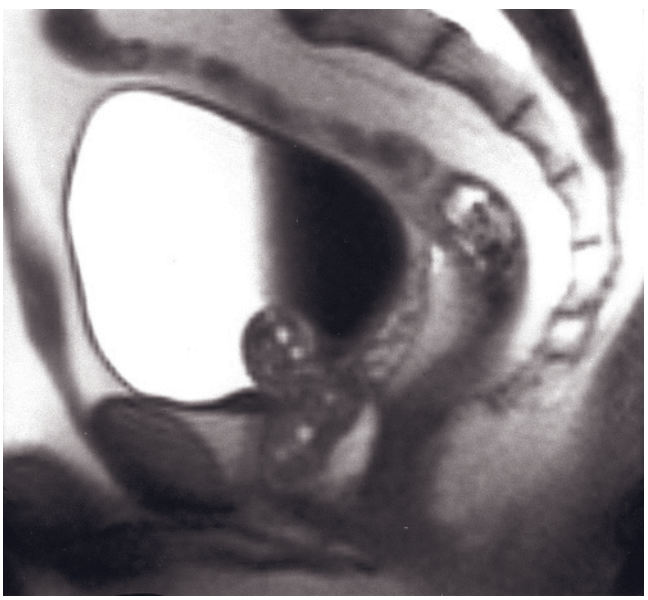

(*d*)

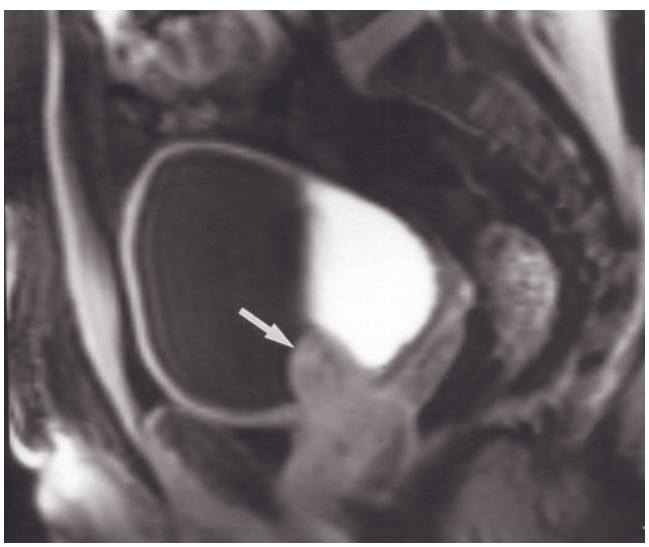

(*e*)

FIG. 12.7 Benign prostatic hyperplasia with bladder impression. Transverse T2-weighted ETSE (*a*, *b*) and T1-weighted gradient-echo postgadolinium fat-suppressed (*c*) images. The prostate is enlarged, asymmetrically nodular, and heterogeneous in appearance, causing bladder impression. Note that the transitional zone is largely low signal, consistent with interstitial hyperplasia. Sagittal SS-ETSE (*d*) and T1-weighted gradient-echo fat-suppressed interstitial-phase (*e*) images in a second patient. A prominent nodule arises from the transitional zone and indents the base of the bladder (arrow, *e*). Note the high-signal foci in the transitional zone, consistent with glandular hyperplasia.

After the surgical removal of periurethral tissue by transurethral, transvesical, or retropubic approaches, the adjacent prostatic urethra dilates to the level of the verumontanum. Residual hyperplastic tissue may be low to medium in signal intensity on T2-weighted images (fig. 12.8) [16]. Radical prostatectomy may result in periurethral scarring, which also is low in signal intensity on T2-weighted images (fig. 12.9). Fibrosis in the bed of the prostate and seminal vesicles after total prostatectomy is low in signal intensity on T2-weighted images and may mimic the appearance of a small, low-signal-intensity prostate and seminal vesicles.

Malignant Masses

RARE TUMORS. Squamous cell cancer, transitional cell cancer, and sarcoma are uncommon malignancies that involve the prostate and account for less than 5% of malignant tumors (fig. 12.10). In the pediatric population, prostate rhabdomyosarcoma is the most common tumor to arise from the bladder region (fig. 12.10) [16].

PROSTATE ADENOCARCINOMA. Approximately 95% of malignant prostate lesions are adenocarcinomas. Prostatic carcinoma is frequently latent. It may occur in as many as 80% of men 80 years of age or older and in as many as 50% of men 50 years of age or older [23]. Its behavior depends on histologic grade/stage and tumor volume [26–28]. Thus tremendous controversy regarding diagnostic and treatment options remains.

Approximately 70% of prostate cancers arise from the peripheral zone, and the remainder arise in the transitional and central zones. Prostate cancers arising from the peripheral zone are more easily detected with MRI compared to the prostate cancers arising from the transitional and central zones. Prostate cancers arising from all zones are generally isointense relative to surrounding tissue on T1-weighted images. The majority of prostate cancers arising from the peripheral zone are hypointense on T2-weighted images (fig. 12.11). In rare instances, tumors may be isointense or hyperintense [29–31]. These tumors frequently contain numerous mucinous elements [31, 32]. When isolated to the transitional or central zone, adenocarcinomas may appear heterogeneous, isointense, or hypointense relative to surrounding tissue [24]. Thus these lesions may be difficult to differentiate from BPH. Prostate cancers can be markedly, moderately, or mildly hypervascular compared to surrounding normal prostate tissue. Markedly hypervascular tumors demonstrate increased enhancement on immediate postgadolinium fat-suppressed gradient-echo images, and they can be easily detected on immediate postgadolinium images, particularly if they are located in the peripheral zone (fig. 12.12). The detection of moderately or mildly hypervascular tumors is more difficult, particularly if they are located in the transitional and central zone in the presence of BPH.

The higher signal-to-noise ratio, higher spatial resolution, and lack of difficulty with localization achievable with endorectal coils have resulted in clinical applicability of spectroscopy for the detection of prostate cancer [33–35]. However, 3.0T MR imaging may obviate the need for the use of endorectal coil in the near future because of its higher signal-to-noise ratio. MRS may be used particularly as a useful adjunct to the standard MR evaluation of prostate cancer. The addition of a spectroscopic sequence to routine MR evaluation of the prostate can provide direct correlation between morphologic and biochemical alterations [34]. This may be either single or multivoxel study. Multivoxel study is more advantageous because it provides metabolic information for a larger area. Studies have revealed increased levels of choline relative to that of citrate in the prostate cancer patient [36–38]. The choline level is elevated owing to a high phospholipid cell membrane turnover in the proliferating malignant tissue. Because the creatine peak is very close to the choline peak in the spectrum, it may not be possible to separate their peaks, and therefore the ratio of choline and creatine to citrate is used in the analysis for practical purposes. Citrate levels are decreased in the presence of prostate cancer because of a conversion from citrate-producing to citrate-oxidating metabolism. However, citrate levels may not be decreased. Therefore, tumor detection is based on the presence of an increased choline citrate level, or, if the choline and creatine peaks are not fully separable, the combined choline and creatine ratio to citrate (figs 12.13, 12.14, and 12.15) [7]. Although these metabolites show variations between the zones of the prostate and in the presence of BPH with increasing age, it has been reported that the use of MRS in combination with MRI increases the sensitivity and specificity of prostate cancer detection in the peripheral and transitional zones in nontreated patients. It may be possible to differentiate between normal tissue, BPH, and carcinoma by identifying the metabolite ratios [35], although there may be overlaps between BPH and carcinoma, particularly in the transitional zone. An increase in overall accuracy and specificity has been reported in the detection of tumor within the postbiopsy prostate [39]. MRS also may prove helpful in the evaluation of recurrent disease, as well as the far lateral peripheral zone and prostatic apex, which are less amenable to traditional biopsy [40–42].

However, the role of MRS has not been well established yet for the detection of prostate cancer or

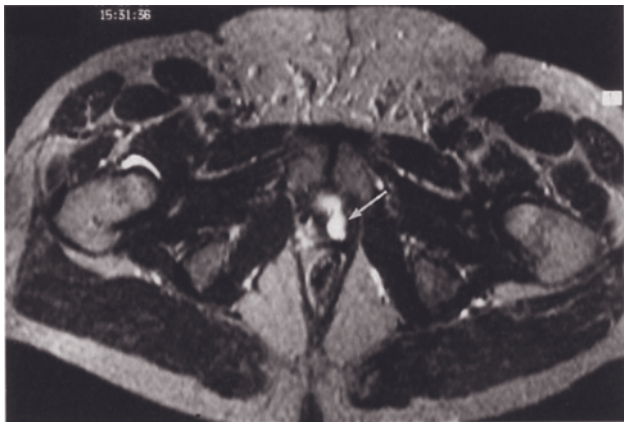

(*a*)

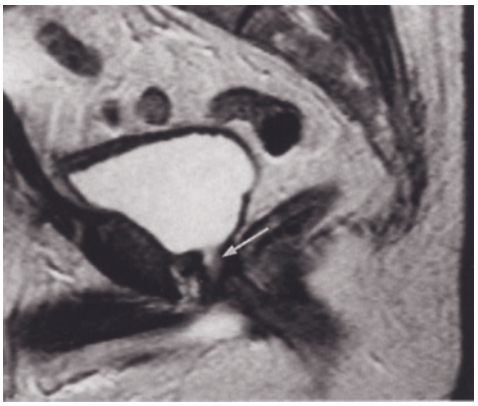

(*b*)

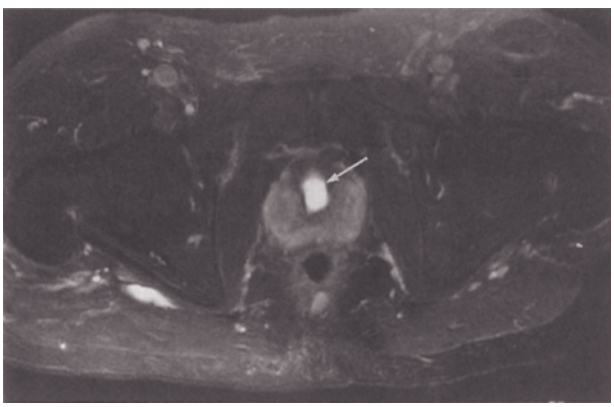

(*c*)

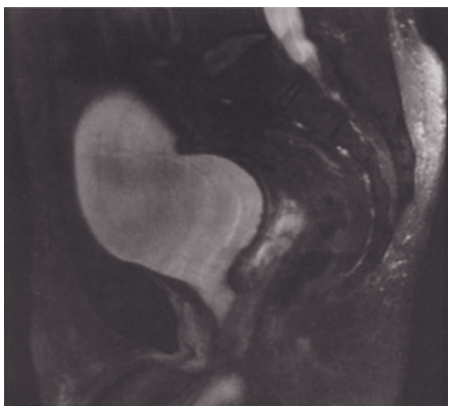

(*d*)

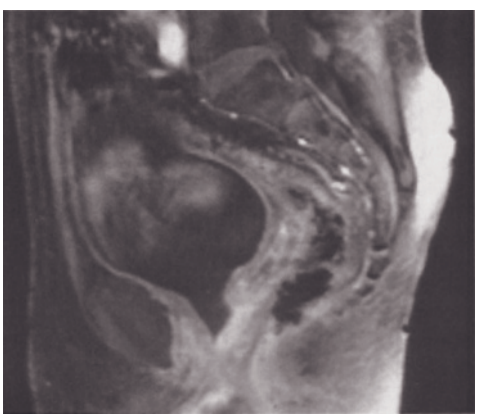

(*e*)

(*f*)

FIG. 12.8 Defect from transurethral resection of the prostate (TURP). Transverse (*a*) and sagittal (*b*) T2-weighted ETSE images. The TURP defect is seen within the base of the prostate. The posterior urethra (arrows, *a*, *b*) is dilated after the surgical removal of periurethral tissue. Transverse T2-weighted fat-suppressed ETSE (*c*), sagittal T2-weighted fat-suppressed ETSE (*d*), and sagittal postgadolinium T1-weighted fat-suppressed gradient-echo (*e*) images in a second patient. Dilatation of the prostatic urethra (arrow, *c*) is observed after TURP. Coronal T2-weighted fat-suppressed endorectal coil image (*f*) of a patient after TURP. Note slight irregularity of the TURP defect in the prostate.

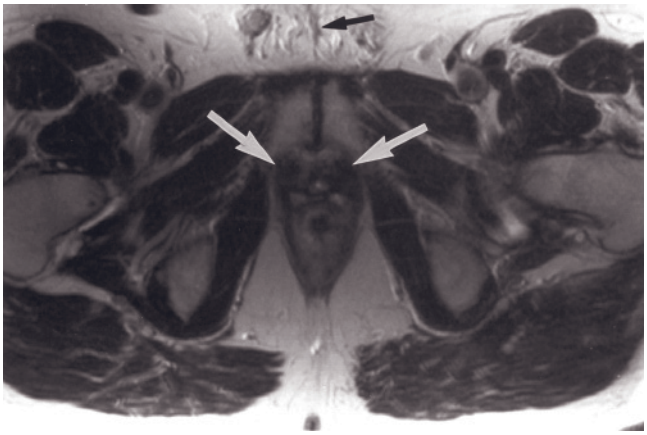

(*a*)

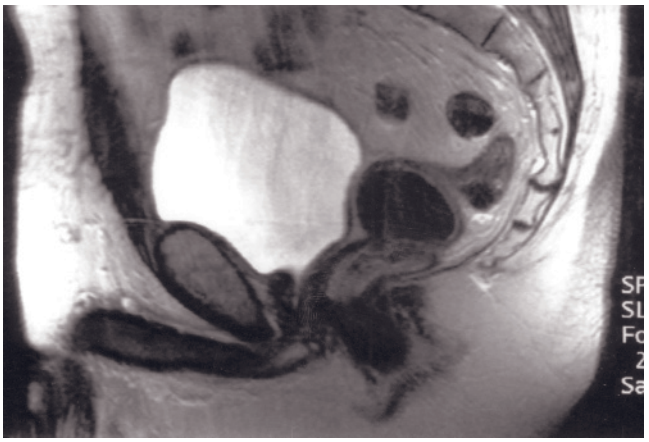

(*b*)

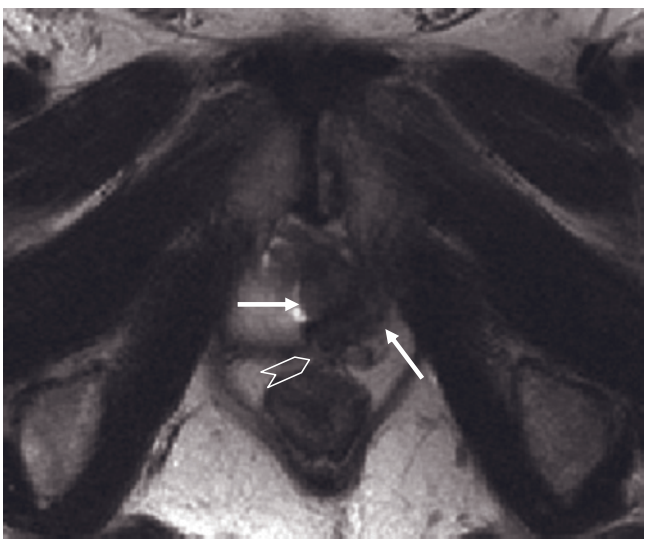

(*c*)

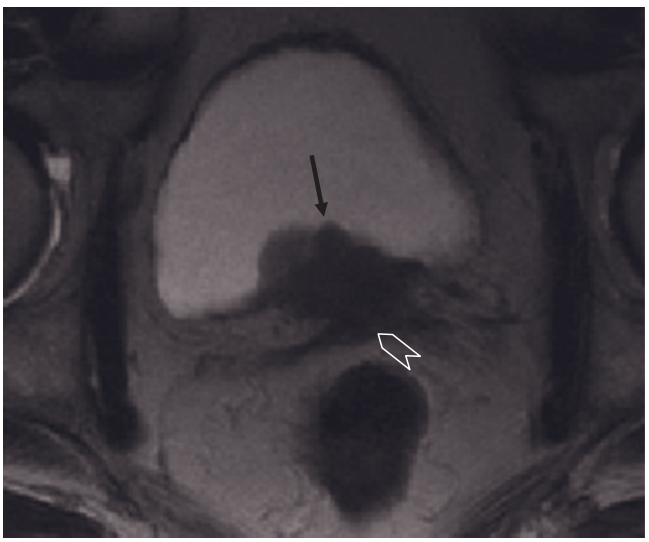

(*d*)

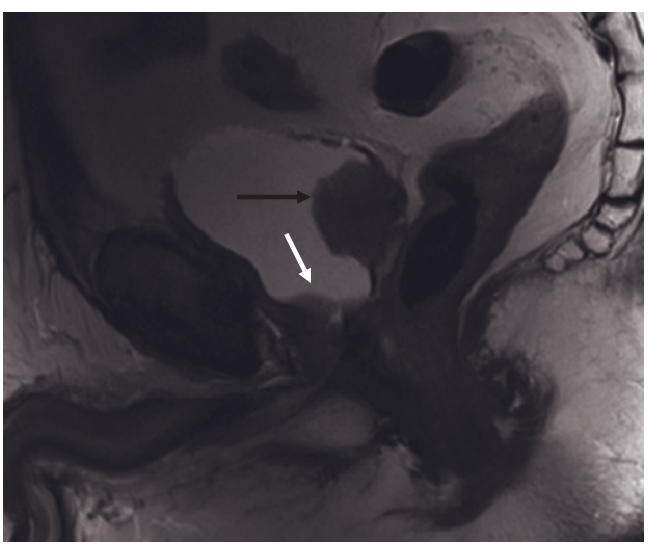

(*e*)

FIG. 12.9 Postprostatectomy pelvis. Transverse (*a*) and sagittal (*b*) T2-weighted ETSE images. Low-signal-intensity tissue surrounds the posterior urethra within the prostatic bed (white arrows, *a*) of this patient after prostatectomy. This appearance results from fibrosis and scarring at the operative site. Note the midline scar in the subcutaneous tissue (black arrow, *a*), which is a constant observation in postprostatectomy patients. **Prostate carcinoma recurrence after radical prostatectomy.** Transverse (*c*, *d*) and sagittal (*e*) high-resolution T2-weighted fast spin-echo images at 3.0T demonstrate hypointense recurrent tumor (white arrows, *c*, *e*) at the level of prostate bed in another patient with radical prostatectomy. There is another tumor infiltrating the posterior bladder wall (black arrow, *d*, *e*). Both tumors invade the perirectal fascia (open arrows, *c*, *d*) and the perirectal fascia is thickened anteriorly because of tumor involvement. Note that there is stranding in the left rectovesical space. Small lymph nodes adjacent to the tumor are also detected.

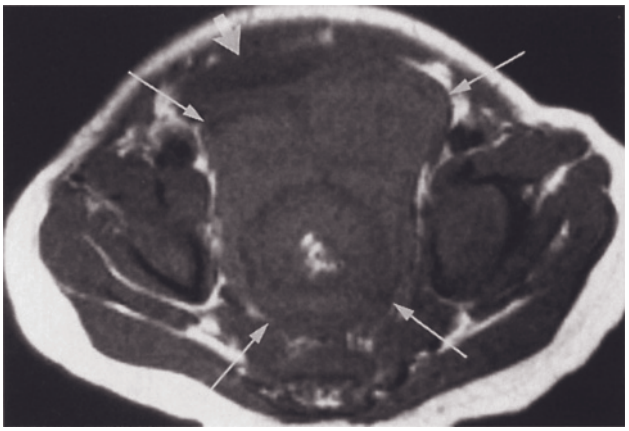

(*a*)

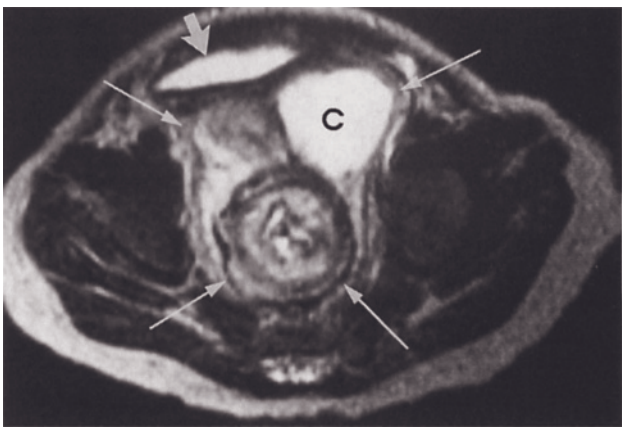

(*b*)

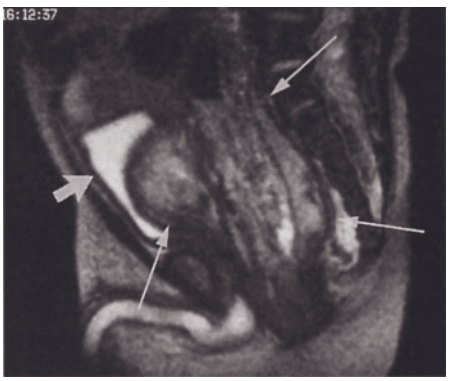

(*c*)

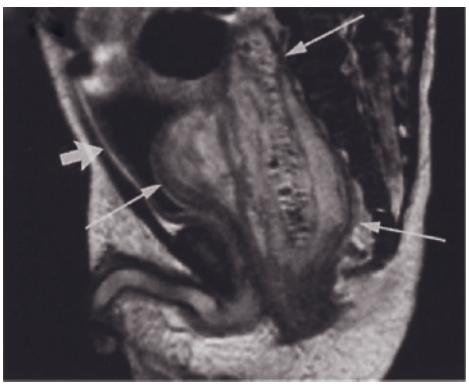

(*d*)

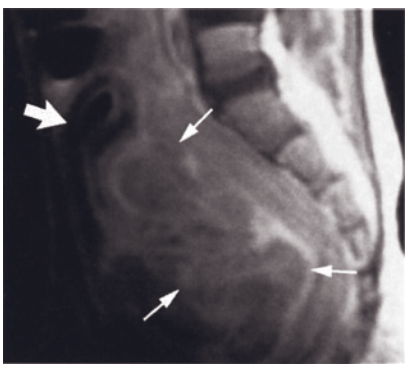

(*e*)

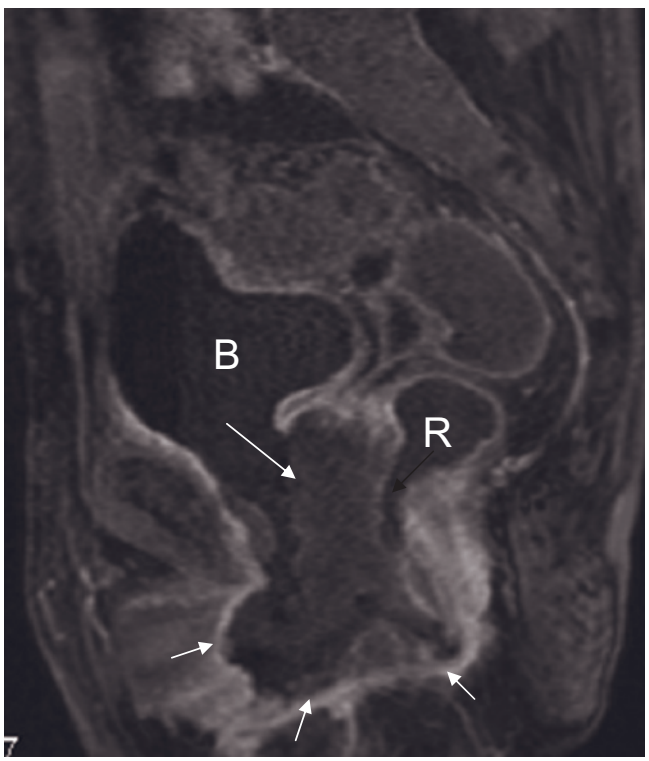

(*f*)

FIG. 12.10 Prostatic rhabdomyosarcoma. Transverse T1-weighted spin-echo (*a*), transverse T2-weighted spin-echo (*b*), sagittal T2-weighted spin-echo (*c*), and sagittal postgadolinium T1-weighted spin-echo (*d*) images. A complex, predominantly solid mass (long arrows, *a–c*) compresses and displaces the bladder anteriorly (arrow, *a–d*). An area of cystic (c, *b*) change within the left aspect of the tumor is shown on the T2-weighted image (*b*). Sagittal immediate postgadolinium T1-weighted gradient-echo image (*e*) in a second patient with prostatic rhabdomyosarcoma. A predominantly solid, complex mass (thin arrows, *e*) impresses upon the bladder posteriorly and displaces it anteriorly. There is bladder wall thickening from outlet obstruction (large arrow, *e*). **Prostate sarcoma.** T1-weighted sagittal (*f*) and

FIG. 12.10 (*Continued*) transverse (*g*) postgadolinium 3D-GE images demonstrate prostate sarcoma in another patient. A large sarcoma originating from the prostate invades the posterior bladder wall (white arrow, *f*) and anterior rectal wall (black arrow, *f*). The tumor also infiltrates the bladder and rectal walls. The tumor invades the inferior, anterior, and left lateral pelvic wall. The left internal obturator muscle (white arrow, *g*) is thickened because of tumor infiltration. Note that the disease also involves the peritoneal surfaces and adjacent bowel loops. Air is present in the bladder. B, bladder. R, rectum.

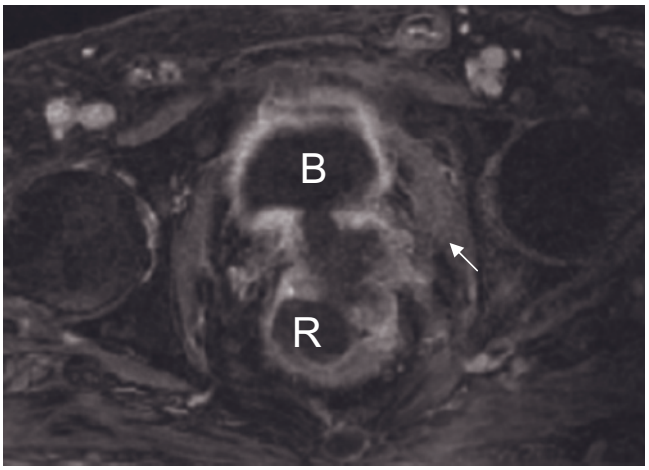

(*g*)

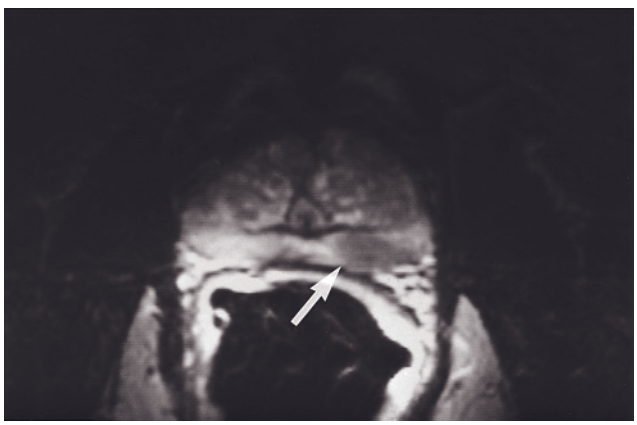

(*a*)

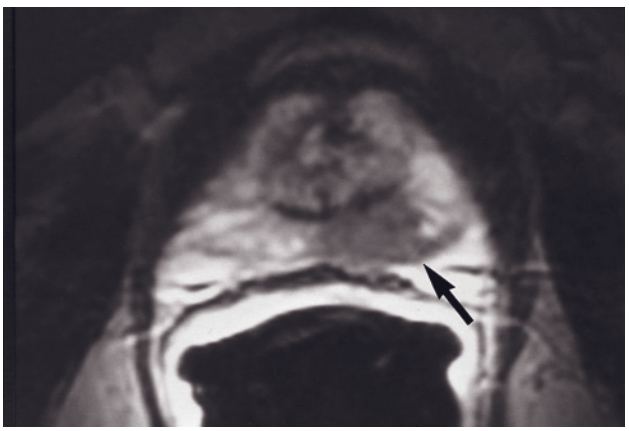

(*b*)

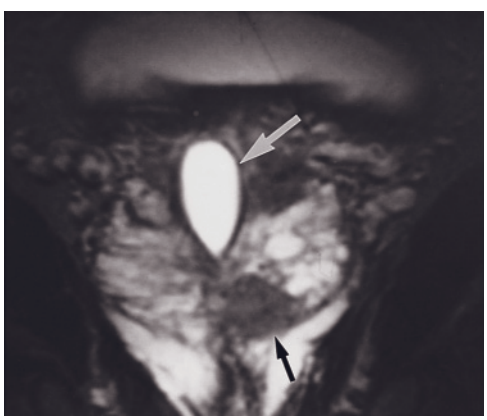

(*c*)

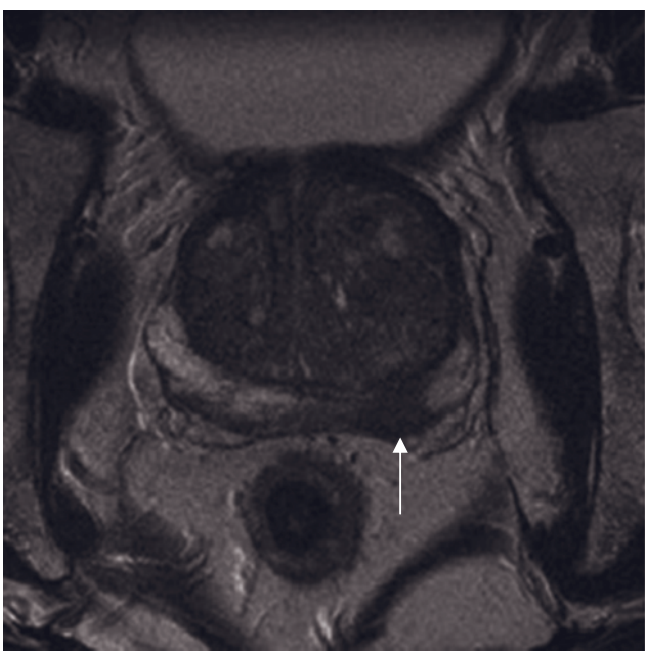

(*d*)

FIG. 12.11 Prostate adenocarcinoma Stage T2. Transverse T2-weighted ETSE endorectal image (*a*). A focus of low signal intensity is seen within the peripheral zone in this patient with Stage T2 adenocarcinoma of the prostate (arrow, *a*). Endorectal transverse T2-weighted ETSE image (*b*) in a second patient with prostate carcinoma. A hypointense tumor is seen within the peripheral zone of the prostate at the level of the apex (arrow, *b*). Endorectal coronal T2-weighted ETSE image (*c*) in a third patient with prostate carcinoma. A low-signal-intensity focus within the apex of the prostate represents primary adenocarcinoma (black arrow, *c*). Note the incidental midline utricular cyst, which is high in signal intensity on the T2-weighted image (white arrow, *c*).

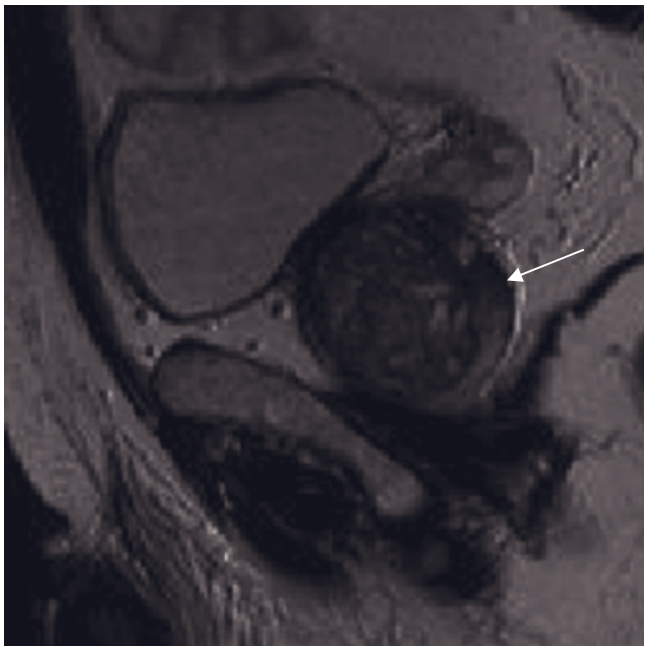

(*e*)

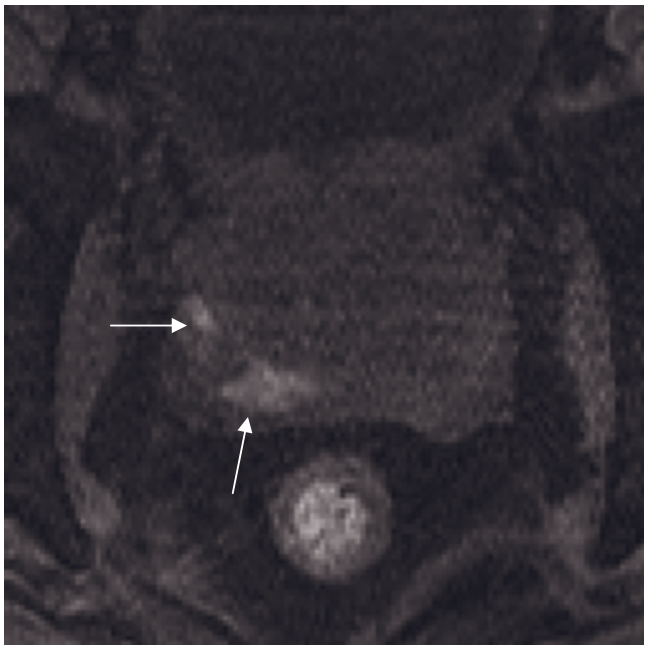

(*f*)

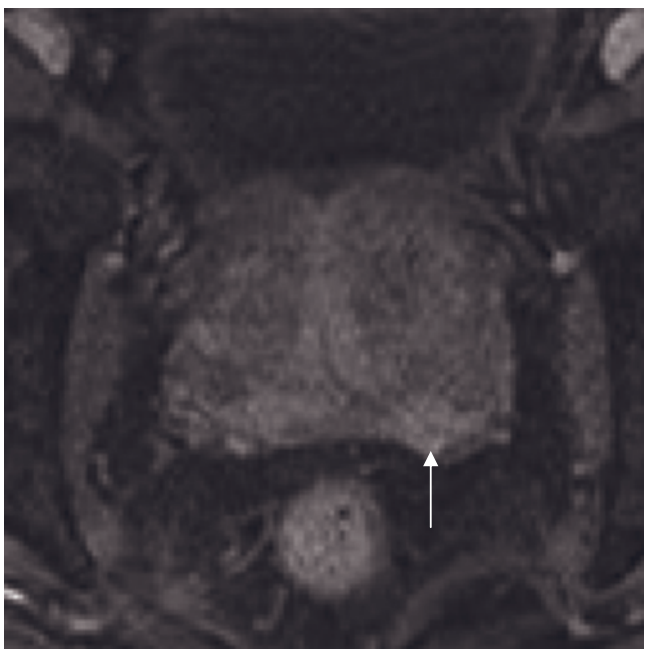

(*g*)

FIG. 12.11 (*Continued*) **Prostate carcinoma, Stage T2.** Transverse (*d*) and sagittal (*e*) high-resolution T2-weighted fast spin-echo images and transverse fat-suppressed T1-weighted 3D-GE (*f*) and transverse postgadolinium fat-suppressed 3D-GE (*g*) images at the level of the midgland of the prostate. A hypointense tumor is seen within the left peripheral zone of the prostate (arrows, *d*, *e*), with moderate enhancement on postcontrast image (arrow, *g*). There is no extracapsular extension. Hyperintense areas on precontrast T1-weighted image in the right peripheral zone are consistent with postbiopsy hemorrhage (arrow, *f*).

recurrence of prostate cancer in patients following biopsy or in patients with chronic prostatitis, prostate atrophy due to hormonal treatment, and fibrosis due to radiation treatment or surgery [6–11]. The changes in the metabolites may mimic prostate cancer in patients with chronic prostatitis and fibrosis of the prostate or prostate bed due to radiation treatment or surgery [6–11]. Additionally, the loss of metabolites in patients with prostate atrophy following hormonal therapy and spectral degradation following biopsy may prevent MRS from reaching a diagnostic conclusion [6–11]. Therefore, MRI findings should be used in combination with MRS in these patients [6–11].

Dynamic gadolinium enhanced MR imaging of the prostate has been reported to be successful in the detection of prostate cancers, although the role of

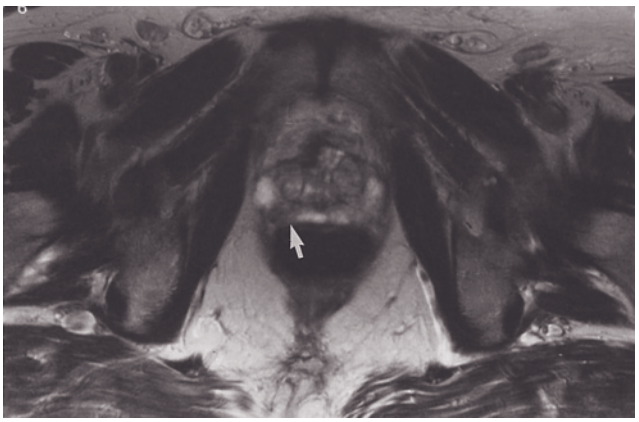

(*a*)

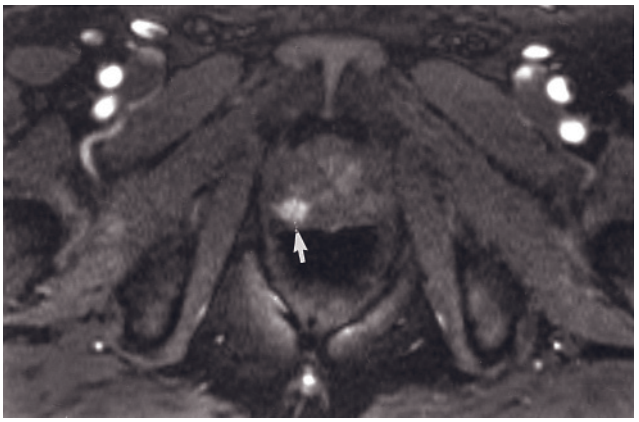

(*b*)

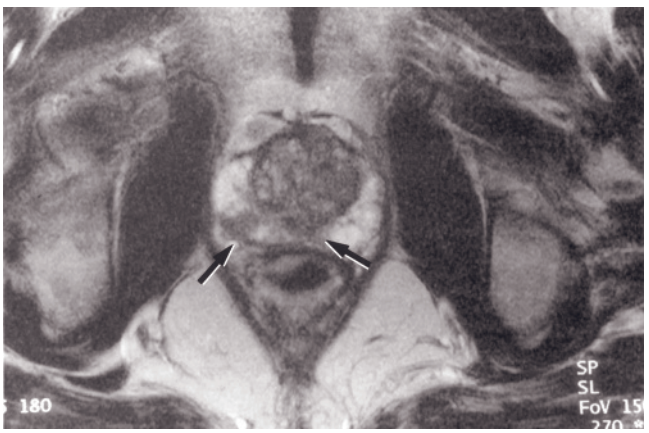

(*c*)

FIG. 12.12 Prostate carcinoma. Transverse T2-weighted ETSE (*a*) and transverse immediate postgadolinium fat-suppressed T1-weighted gradient-echo (*b*) images. High-resolution T2-weighted image (*a*) reveals a well-defined carcinoma within the peripheral zone of the right lobe of the prostate (arrow). Smaller tumor volume is present within the left lobe (*a*). Immediate post-gadolinium image demonstrates enhancement of the tumor focus within the right lobe (arrow, *b*). More ill-defined enhancement is seen within the left lobe (*b*). Transverse T2-weighted ETSE (*c*) images in a second patient. There is a heterogeneous enlargement of the central aspect of the prostate consistent with prostatic hypertrophy. Several foci of low signal are noted at the 6 and 8 o'clock positions (arrows, *c*) within the gland, consistent with prostate cancer.

this technique has not yet been well established [6, 8]. Because of angiogenesis, increased vascular permeability, and greater interstitial space, cancerous tissue shows a hypervascular enhancement pattern that is different from that of normal tissue [6, 8]. This enhancement pattern can be detected with very fast dynamic gradient-echo sequences, and resultant perfusion data can be obtained [6, 8]. These perfusion data can be presented as a time-signal intensity curve (figs 12.13, 12.14, and 12.15). The tumoral tissue shows strong early enhancement (wash-in) and rapid wash-out compared to normal prostate tissue [6, 8]. However, although this enhancement pattern is detected in markedly hypervascular tumors, mildly or moderately hypervascular tumors may not demonstrate this enhancement pattern and this may lead to false negative diagnoses [6, 8]. The enhancement patterns of transitional zone cancers may also not be differentiated from BPH tissue, and this constitutes another disadvantage of the technique [6, 8]. Additionally, there is no consensus on the acquisition protocols and optimal perfusion parameters differentiating cancer from normal tissue [6, 8].

Tumors spread first to penetrate the prostatic capsule (fig. 12.13). After capsular penetration, tumor extends to the neurovascular bundles and seminal vesicles (figs. 12.14 and 12.15). Bladder invasion occurs commonly in advanced-stage prostate cancer and may be extensive (figs. 12.15 and 12.16). The most common sites of metastasis are the bone marrow and lymph nodes. Infiltration of the pelvic lymphatics, particularly the obturator, external, and internal iliac chains, precedes distant metastases to the bones and retroperitoneum. Bone marrow in the iliac bones is frequently marbled in signal intensity on T1- and T2-weighted images, rendering detection of bone metastases at times problematic. On gadolinium-enhanced fat-suppressed images, metastases appear as relatively well-defined focal mass lesions or diffusely enhancing extensive bony infiltration in a low-signal-intensity background of fatty or fibrotic marrow (fig. 12.17). The emergence of managed care and fiscal constraint has led to the search for comprehensive imaging evaluation of the oncology patient with a single modality. In addition to the promise of a combined approach, employing contrasted MRI and

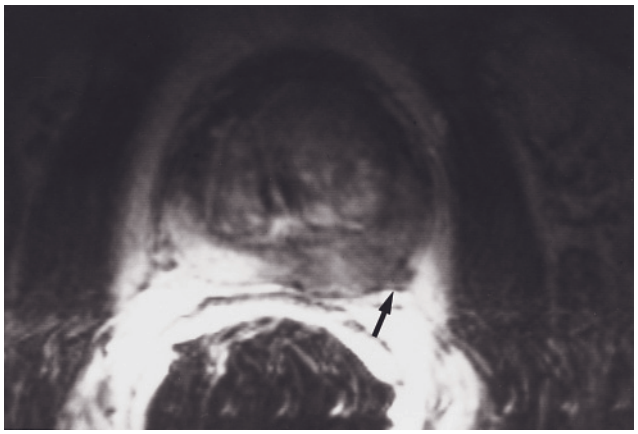

(*a*)

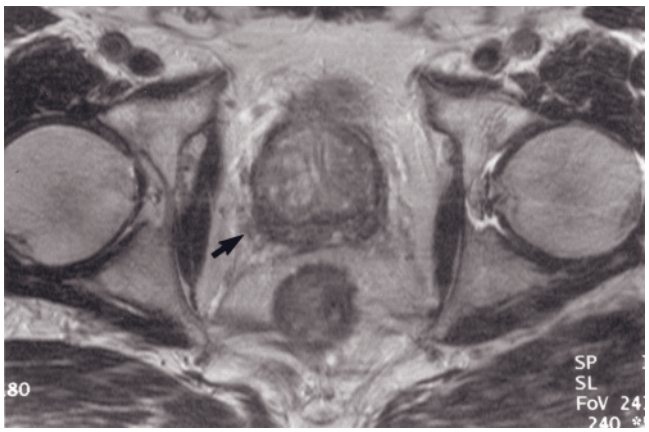

(*b*)

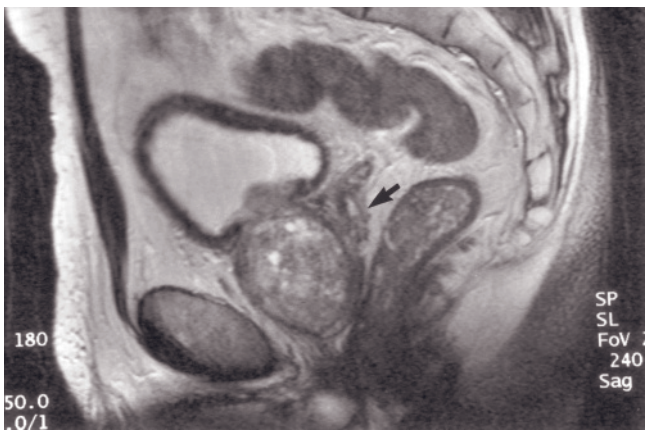

(*c*)

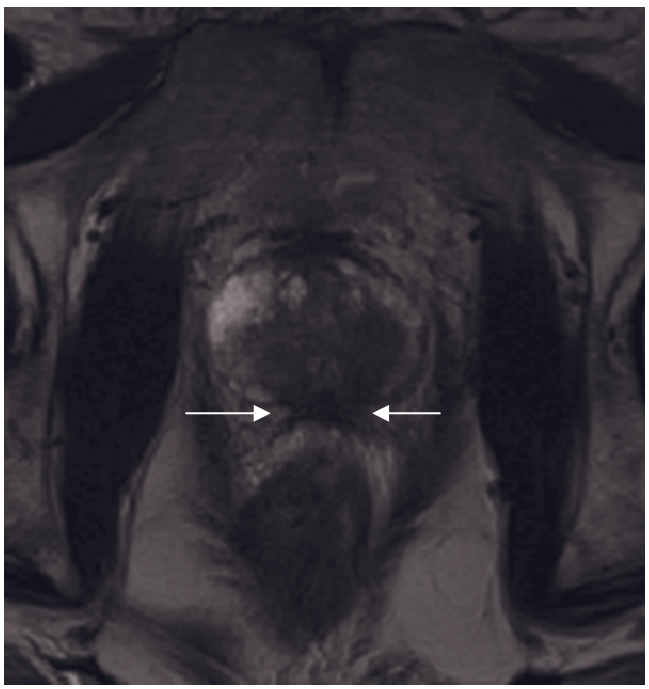

(*d*)

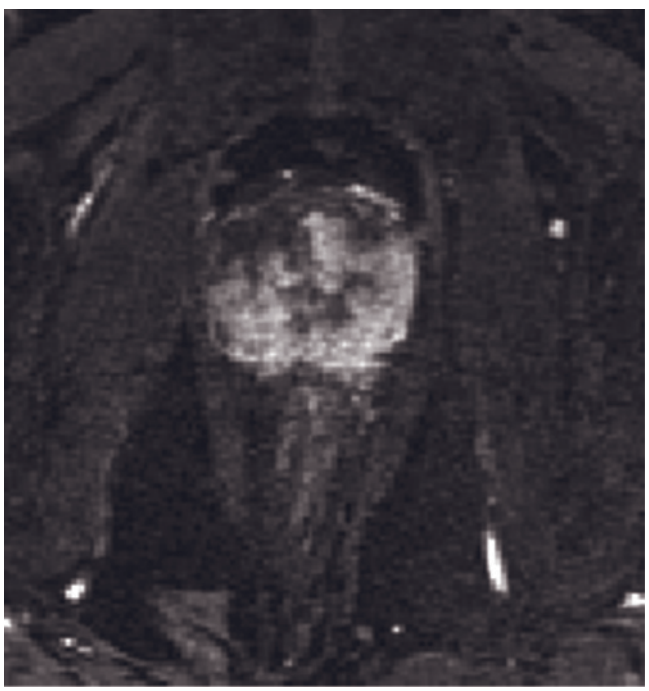

(*e*)

FIG. 12.13 Prostate carcinoma with capsular penetration. T2-weighted ETSE endorectal image (*a*) demonstrates low-signal-intensity tumor within the peripheral zone of the prostate that extends posterolaterally (arrow, *a*), indicating capsular penetration. Transverse (*b*) and sagittal (*c*) T2-weighted ETSE images in a second patient demonstrate diffuse low signal intensity of the peripheral zone, consistent with diffuse carcinoma. Capsular penetration is observed at the 8 o'clock position (arrow, *b*). Seminal vesicle invasion is clearly shown in the sagittal projection (arrow, *c*), with involvement of the bladder base also appreciated. **Prostate carcinoma with extracapsular extension, Stage T3a.** Transverse high-resolution T2-weighted fast spin-echo image (*d*) demonstrates low-signal-intensity tumor within the transitional and peripheral zones of the prostate bilaterally showing extracapsular extension (arrows), invasion of anterior perirectal fascia (arrows), and obliteration of rectoprostatic angles (arrows). The tumor and its extracapsular extension show prominent enhancement on transverse arterial-phase postgadolinium fat-suppressed 3D-GE image (*e*). Time-signal intensity curve of the dynamic 3D-GE

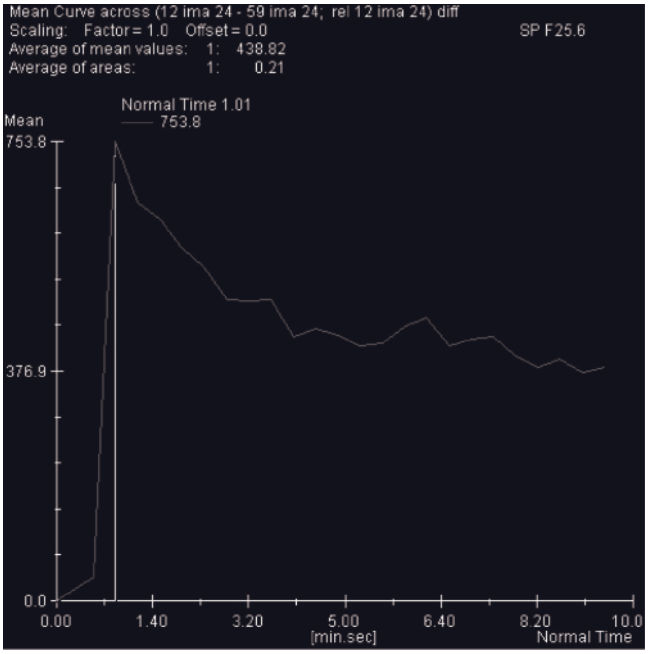

(*f*)

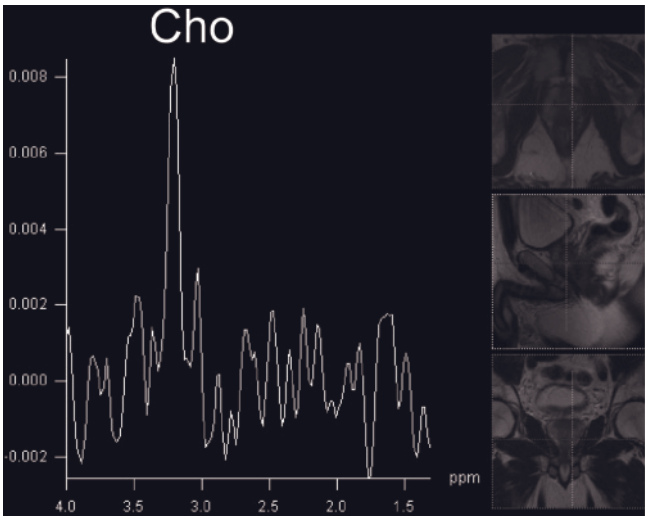

(*g*)

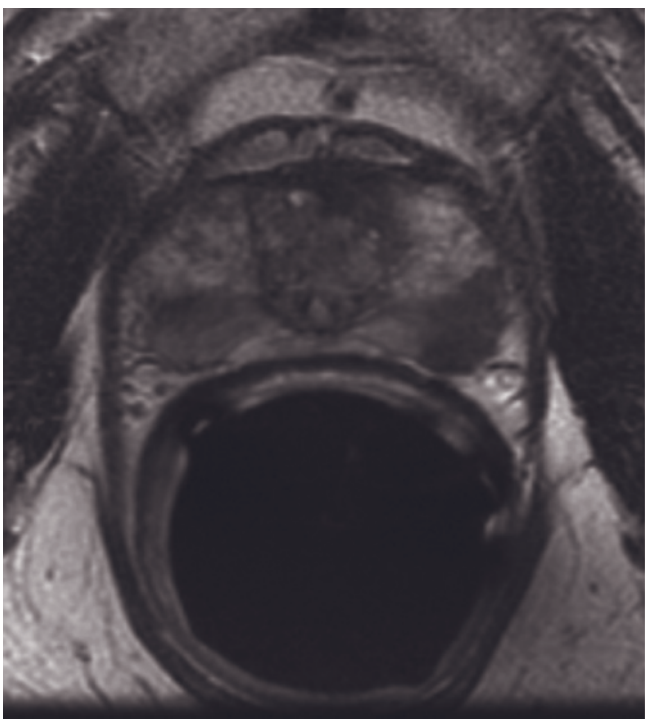

(*h*)

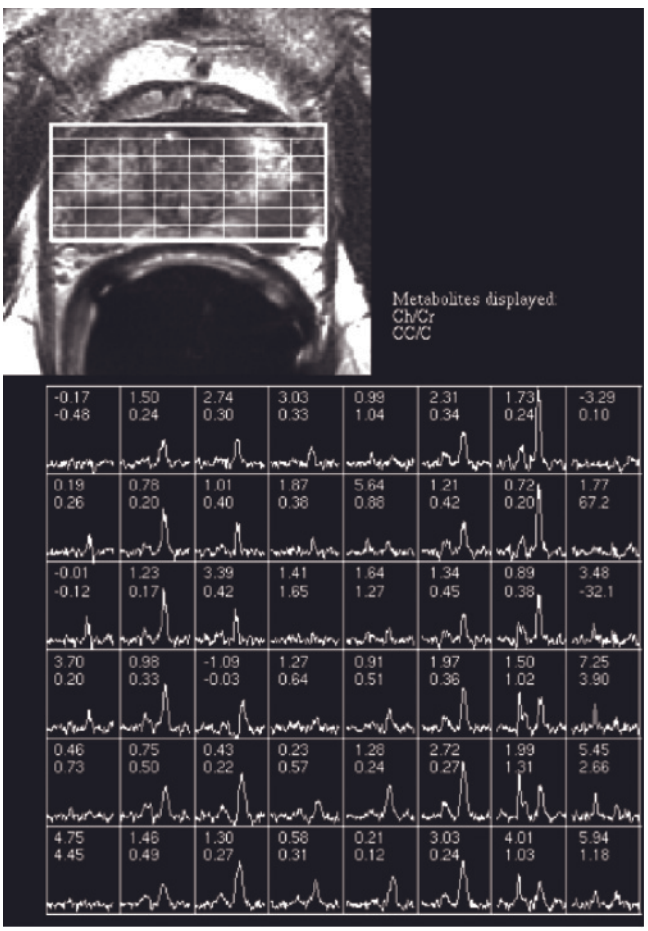

(*i*)

FIG. 12.13 (*Continued*) imaging (*f*) demonstrates fast and strong enhancement (washin) and fast washout of the tumor, suggestive of prostate cancer. Single-voxel MR spectroscopy (*g*) demonstrates the absence of citrate peak and the elevation of choline (Cho) peak, suggestive of prostate cancer. **Prostate carcinoma with extracapsular extension, Stage T3a.** Transverse high resolution T2-weighted fast spin-echo image (*h*) demonstrates low-signal tumor with extracapsular extension located in the left peripheral zone. Multivoxel MR spectroscopy (*i*) demonstrates the characteristic absence of citrate peak and the elevation of choline-creatine peak in the designated voxels (*), suggestive of prostate cancer. (Courtesy of Fergus V. Coakley, M.D.)

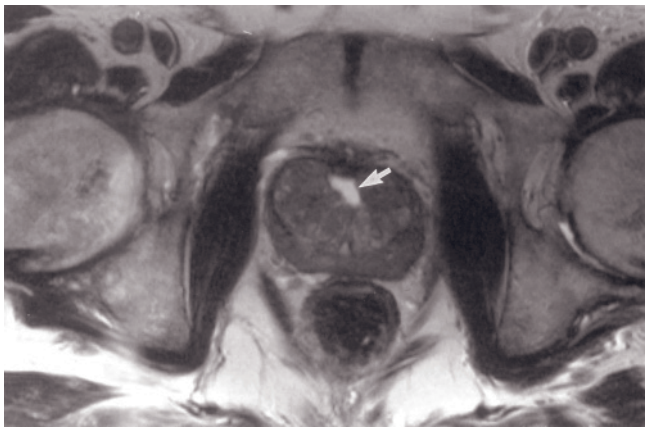

(*a*)

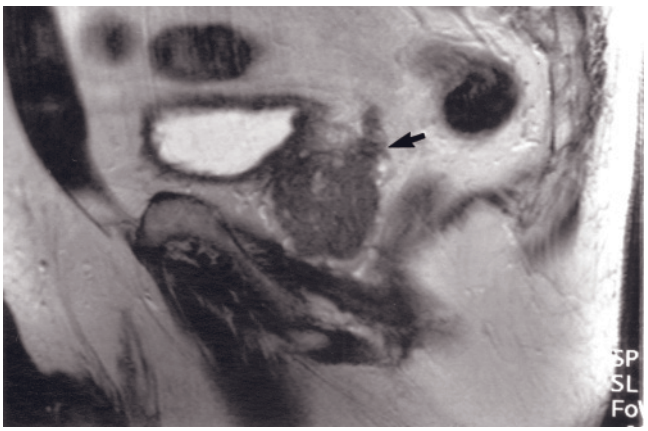

(*b*)

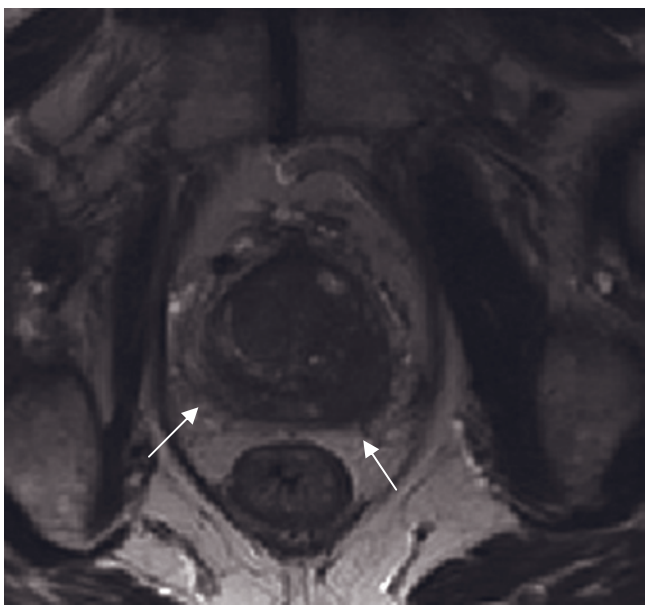

(*c*)

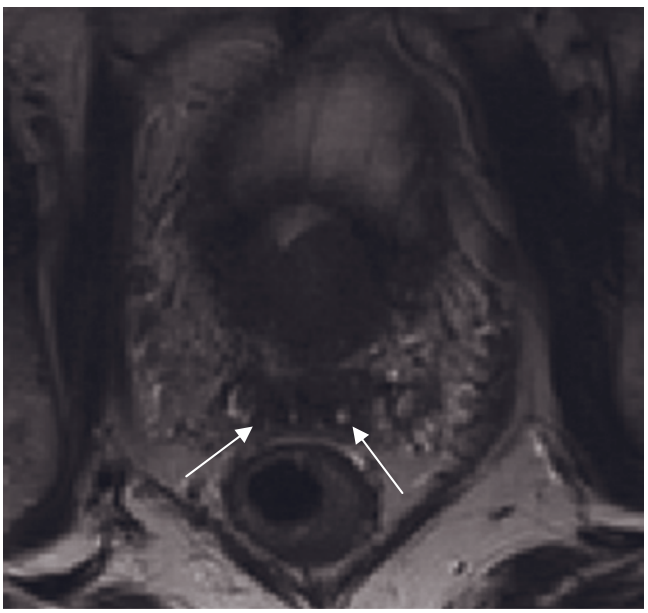

(*d*)

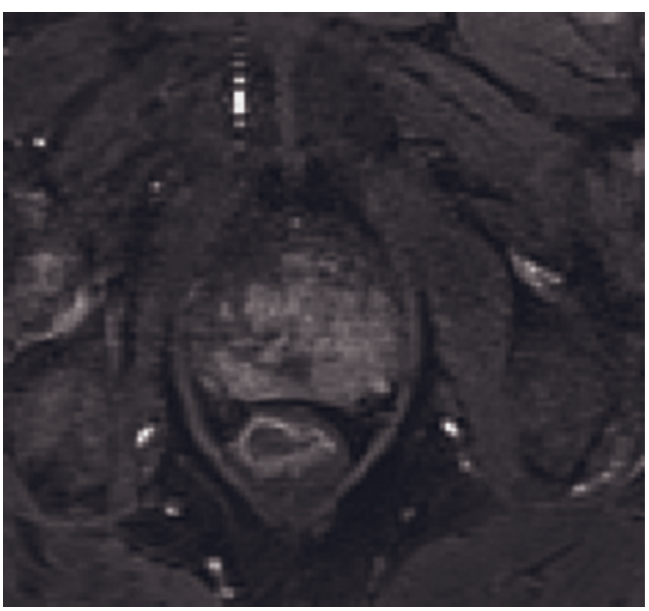

(*e*)

FIG. 12.14 Prostate carcinoma, diffuse involvement. Transverse (*a*) and sagittal (*b*) SS-ETSE images. The prostate is enlarged with a transurethral prostatic resection defect in the superior aspect of the gland (arrow, *a*).The peripheral zone of the prostate is diffusely low signal on T2-weighted images, consistent with diffuse tumor infiltration. This is shown on both transverse and sagittal projection. Note seminal vesicle involvement on the sagittal projection (arrow, *b*). **Prostate carcinoma, diffuse involvement with extracapsular extension and seminal vesicle invasion, Stage T3b.** Transverse high-resolution T2-weighted fast spin-echo images at 3.0 T (*c*, *d*) demonstrate low-signal-intensity tumor within the transitional and peripheral zones of the prostate bilaterally showing extracapsular extension (arrows, *c*) and invasion of seminal vesicles (arrows, *d*). Seminal vesicles are seen as hypointense structures because of the invasion. The tumor shows strong enhancement on transverse fat-suppressed postgadolinium arterial phase 3D-GE image at 3.0 T (*e*). Time-signal intensity curve of the dynamic 3D-GE imaging (*f*)

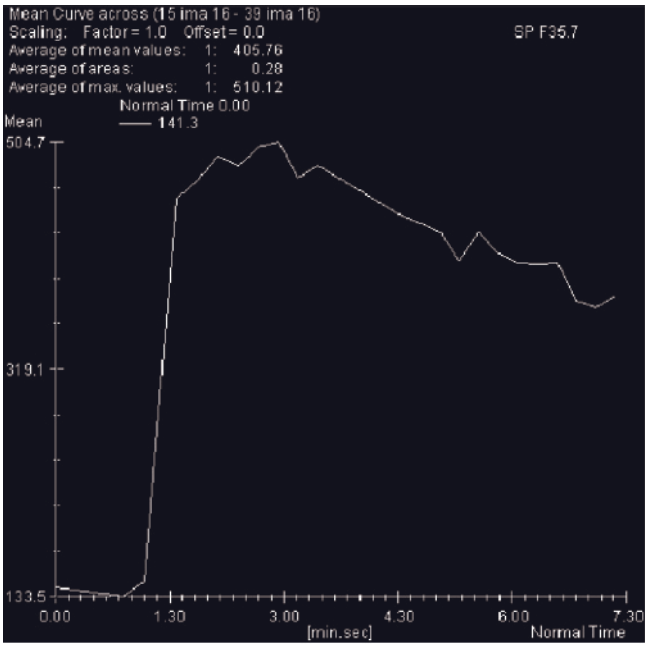

(*f*)

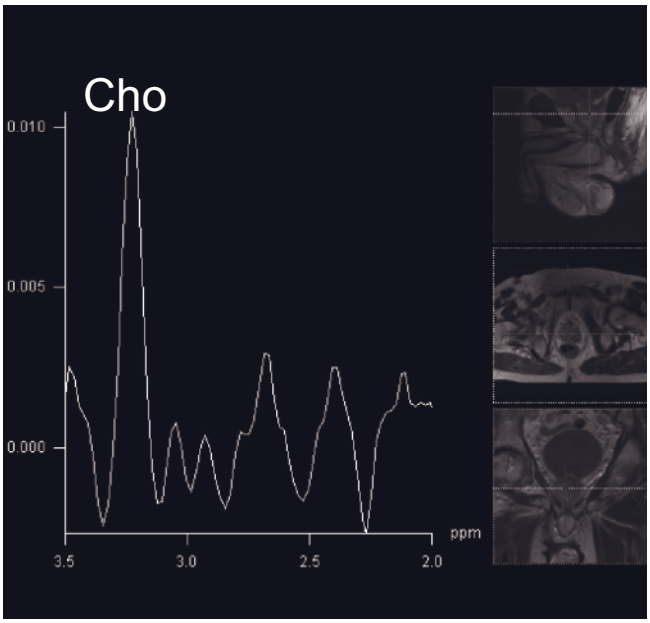

(*g*)

FIG. 12.14 (*Continued*) demonstrates fast and strong enhancement (washin) and fast washout of the tumor, suggestive of prostate cancer. Single-voxel MR spectroscopy (*g*) demonstrates the absence of citrate peak and the elevation of choline (Cho) peak, suggestive of prostate cancer. Note the presence of small periprostatic lymph nodes. (Figures *c–g*, courtesy of Fergus V. Coakley, M.D.)

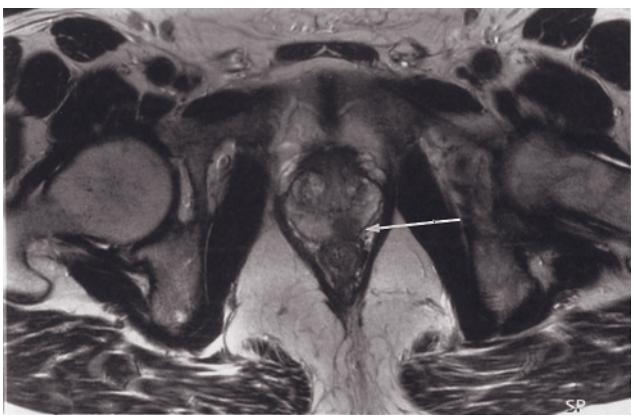

(*a*)

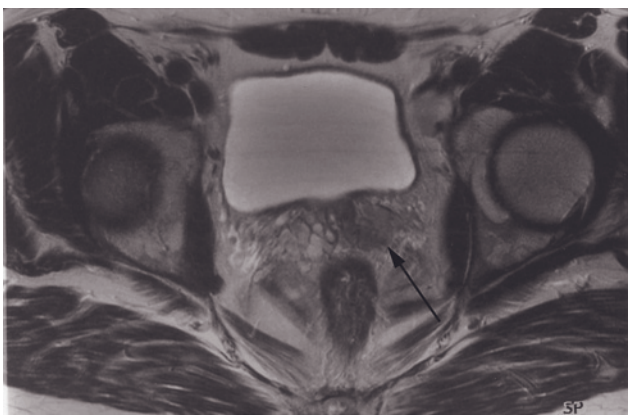

(*b*)

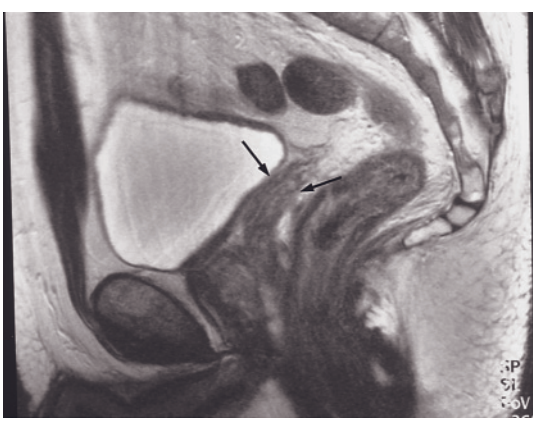

(*c*)

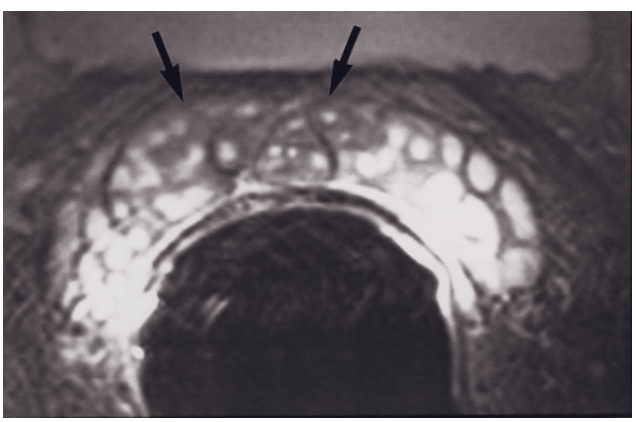

(*d*)

FIG. 12.15 Prostate cancer with seminal vesicle invasion. Transverse (*a*, *b*) and sagittal (*c*) T2-weighted ETSE images. A 1-cm tumor (white arrow) within the left aspect of the prostate at the midgland level is low in signal intensity on the T2-weighted image (*a*). The left seminal vesicle (black arrow, *b*) is diffusely low in signal intensity secondary to diffuse tumor involvement. Note the normal high-signal-intensity cluster of grapes appearance of the right seminal vesicle (*b*). Loss of normal architecture and diffuse low signal intensity of the left seminal vesicle (black arrows) is confirmed on the sagittal image (*c*). Transverse T2-weighted ETSE

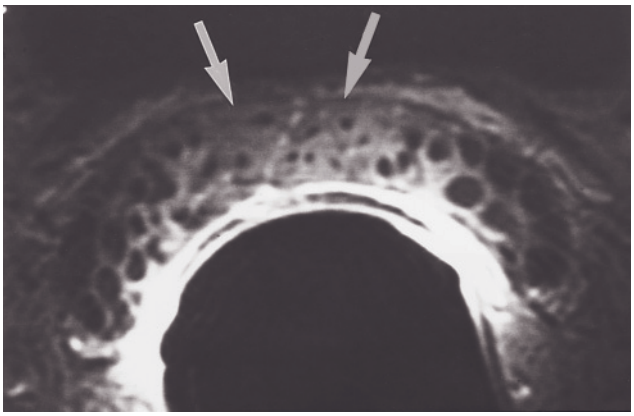

(*e*)

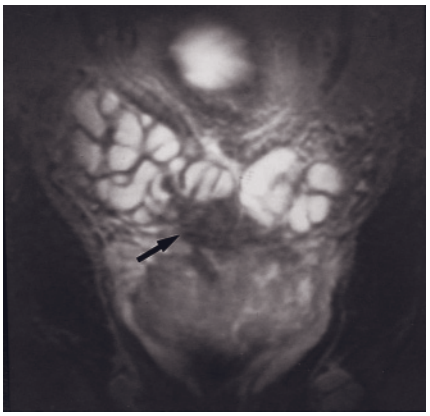

(*f*)

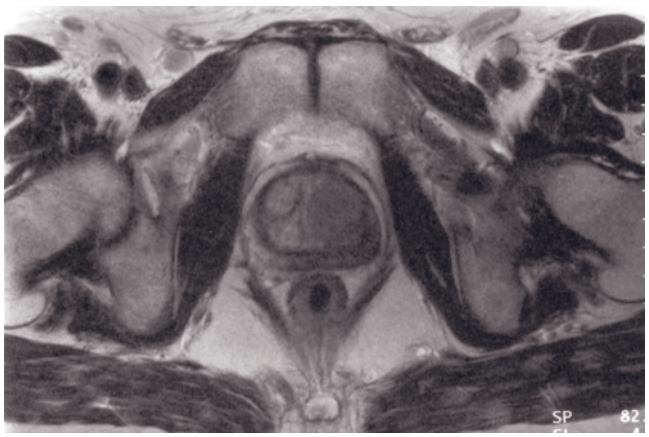

(*g*)

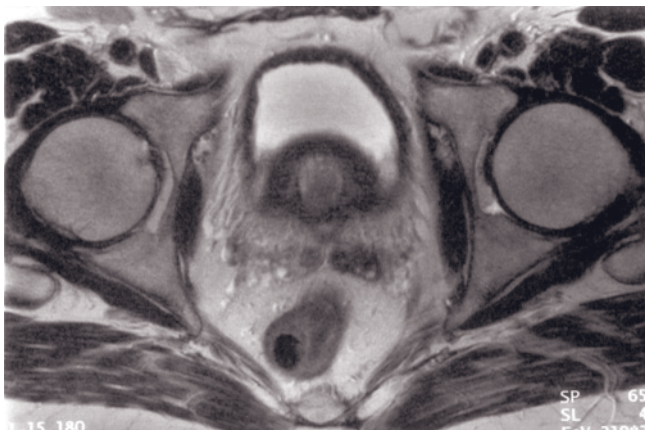

(*h*)

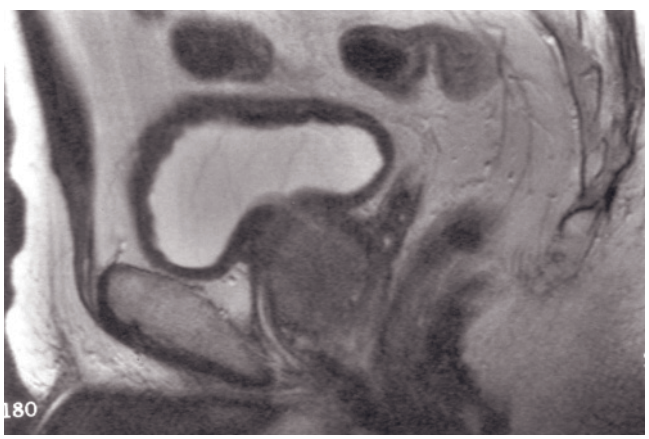

(*i*)

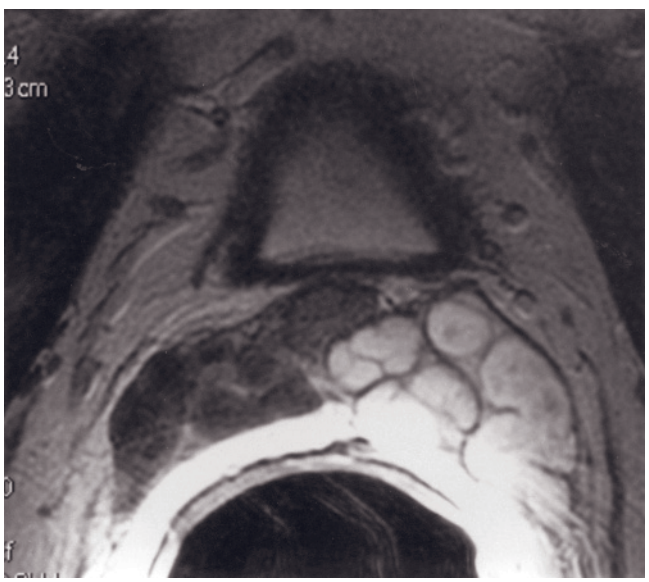

(*j*)

Fig. 12.15 (*Continued*) endorectal coil (*d*) and postgadolinium T1-weighted fat-suppressed T1-weighted gradient-echo endorectal coil (*e*) images in a second patient. There is ill-defined low-signal-intensity tissue (arrows) within the medial aspects of the seminal vesicles on the T2-weighted image (*d*), corresponding to tumor invasion. Loss of the normal architecture of the seminal vesicles medially (arrows) indicates tumor invasion on the postgadolinium T1-weighted image (*e*). Coronal T2-weighted ETSE endorectal coil image (*f*) in a third patient with seminal vesicle invasion. There is low signal intensity within the inferomedial aspects of the seminal vesicles (arrow, *f*) secondary to tumor invasion. Transverse (*g*, *h*) and sagittal (*i*) T2-weighted ETSE images in a fourth patient. There is low-signal-intensity tumor in the peripheral zone of the prostate at the midgland level extending from the 2:30 to 7:00 o'clock positions. Transverse and sagittal projections of the seminal vesicle demonstrate tumor involvement. Endorectal coil T2-weighted echo-train spin-echo image (*j*) in a fifth patient demonstrates involvement of the right seminal vesicle. Endorectal

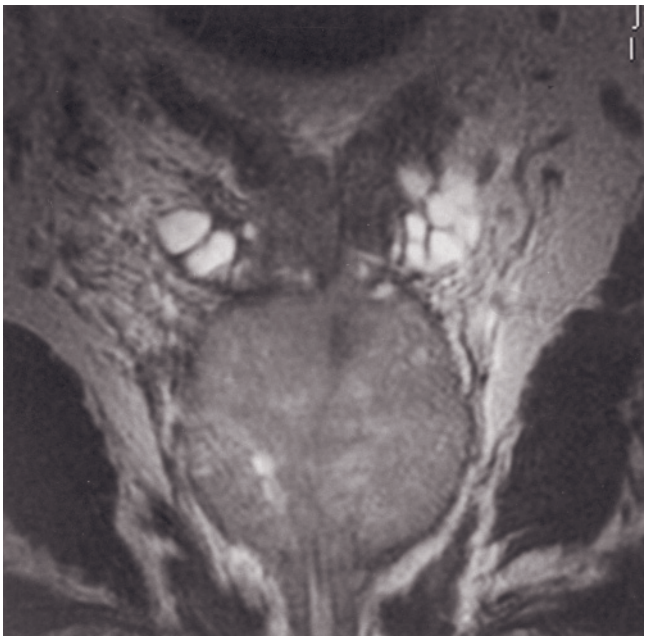

(*k*)

(*l*)

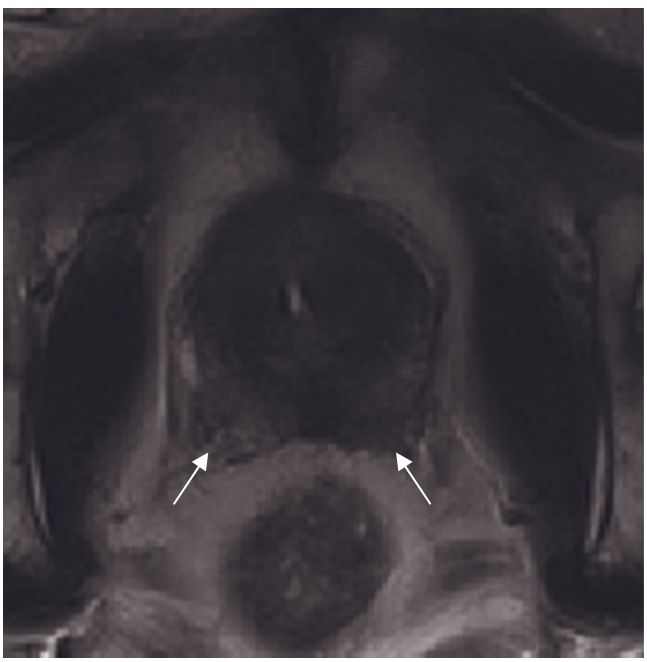

(*m*)

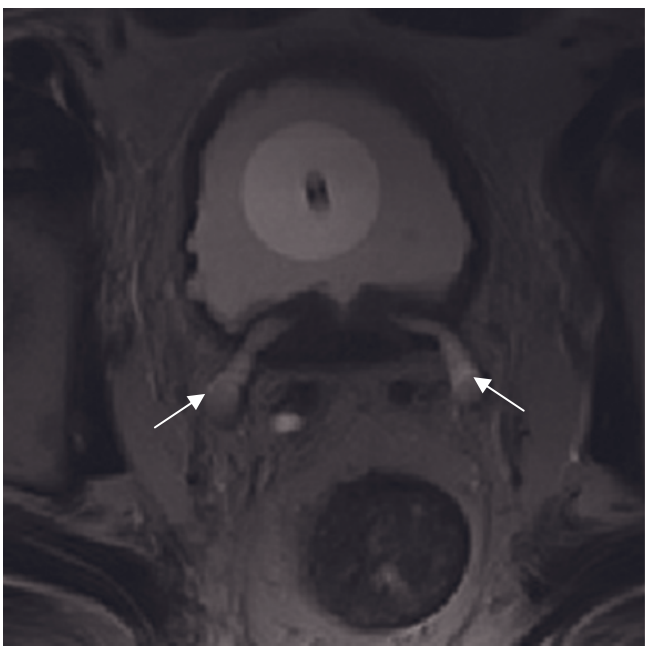

(*n*)

FIG. 12.15 (*Continued*) T2-weighted echo-train spin-echo coronal (*k*) and transverse (*l*) images in a sixth patient demonstrate involvement of the medial portions of bilateral seminal vesicles. Imaging in two planes provides increased observer confidence of diagnosing tumor involvement. **Prostate carcinoma, diffuse involvement with extracapsular extension, seminal vesicle and bladder invasion, Stage T4.** Transverse (*m*, *n*) and sagittal (*o*) high-resolution T2-weighted fast spin-echo images at 3.0T demonstrate diffuse low-signal-intensity tumor involving the peripheral and transitional zones of the prostate. The contour bulging and extracapsular spiculations suggest the extracapsular extension bilaterally and posterolaterally. There is also neurovascular bundle invasion (arrows, *m*, *p*). The tumor invades the bladder wall and trigone and causes obstruction of bilateral ureters (arrows, *n*, *o*). The seminal vesicles (open arrow, *o*) are seen as hypointense structures because of the tumor invasion. The tumor shows

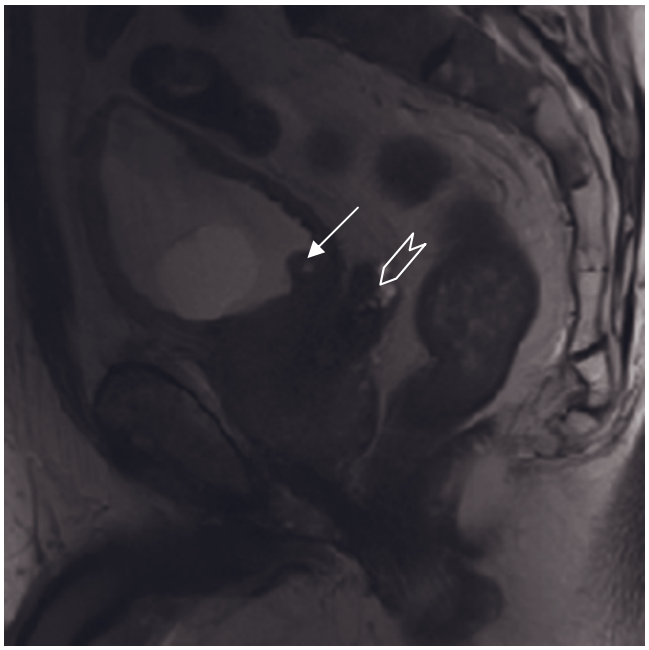

(*o*)

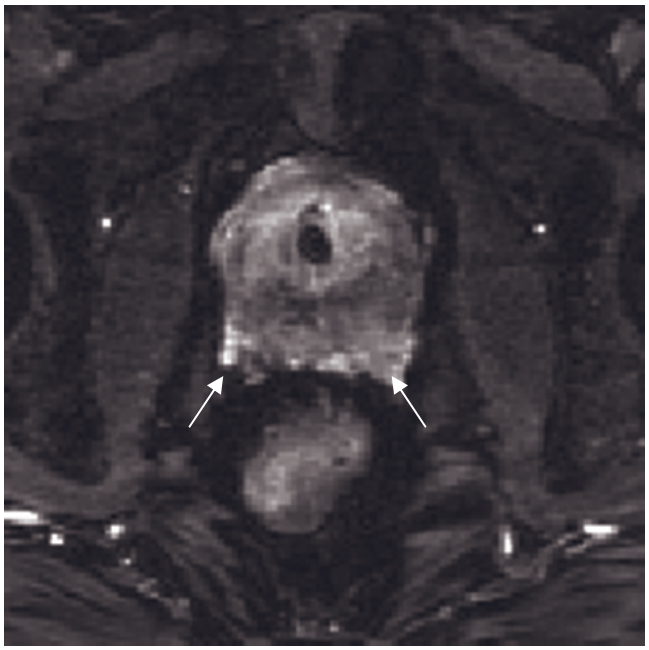

(*p*)

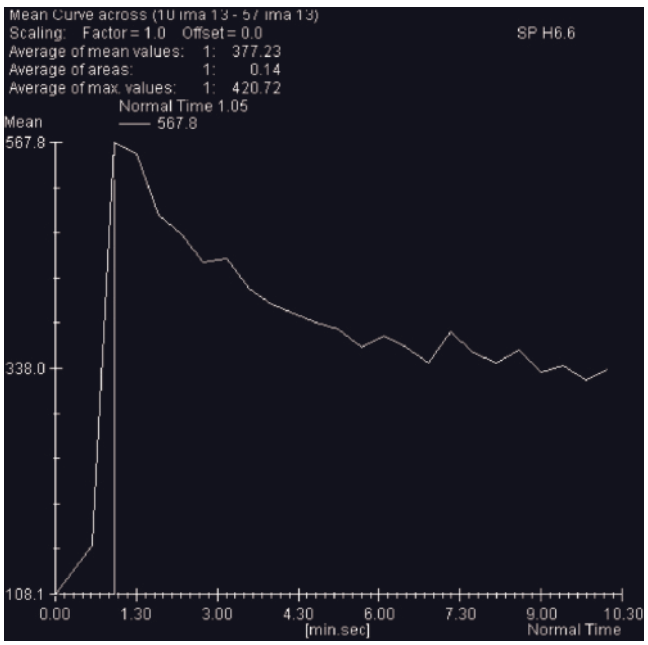

(*q*)

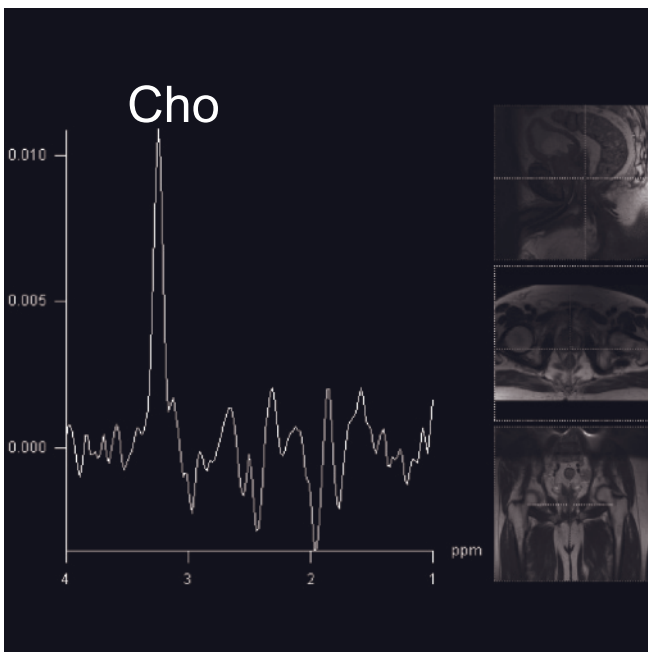

(*r*)

FIG. 12.15 (*Continued*) strong enhancement on transverse fat-suppressed postgadolinium arterial-phase 3D-GE image at 3.0 T (*p*). Time-signal intensity curve of the dynamic 3D-GE imaging (*q*) demonstrates fast and strong enhancement (washin) and fast washout of the tumor, suggestive of prostate cancer. Single-voxel MR spectroscopy (*r*) demonstrates the absence of citrate peak and the elevation of choline (Cho) peak, suggestive of prostate cancer. (Figures *m–r* courtesy of Fergus V. Coakley, M.D.)

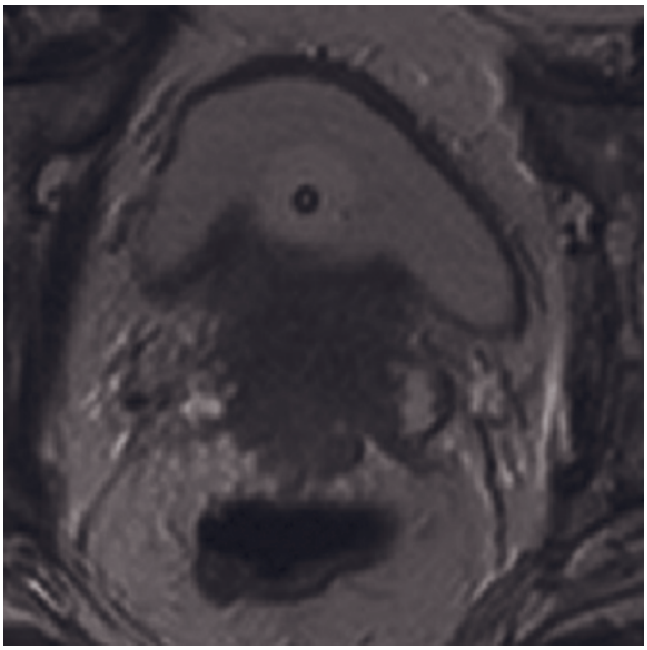

(*s*)

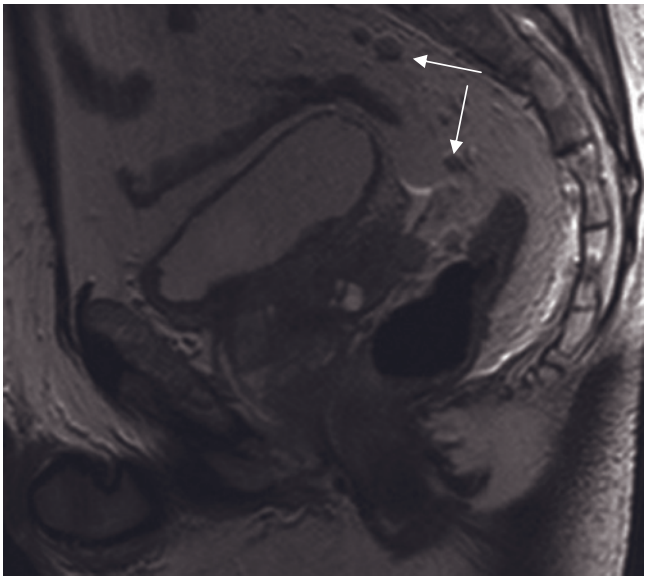

(*t*)

FIG. 12.15 (*Continued*) **Prostate carcinoma, Stage T4.** Transverse (*s*) and sagittal (*t*) high-resolution T2-weighted fast spin-echo images in another patient demonstrate a large prostate carcinoma that invades the seminal vesicles, posterior bladder wall, anterior perirectal fascia, and adjacent fat tissue. Note enlarged presacral lymph nodes as well (arrows, *t*). A Foley catheter is present in the bladder (*s*).

FIG. 12.16 Anaplastic prostate carcinoma. Coronal T2-weighted ETSE endorectal coil image. Lobular low-signal-intensity tissue invading the urinary bladder (arrows) represents invasive prostate carcinoma in this patient with a normal prostate-specific antigen level.

MRS, a survey examination for osseous metastatic disease may be merited for patients at higher risk. These examinations could include a limited number of sequences for the assessment of those anatomic areas most likely to harbor metastases: the spine, pelvis, and femora. The sequence with the greatest consistency in the detection of osseous metastases is T1-weighted, gadolinium-enhanced, fat-suppressed gradient echo. This can be performed in imaging planes complementary to sequences employed in the evaluation of the

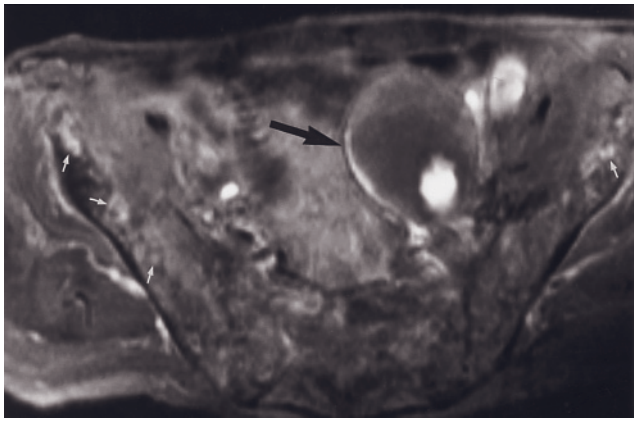

(*a*)

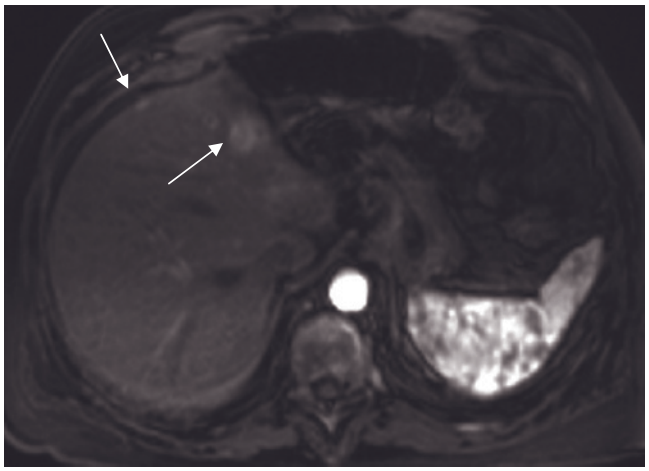

(*b*)

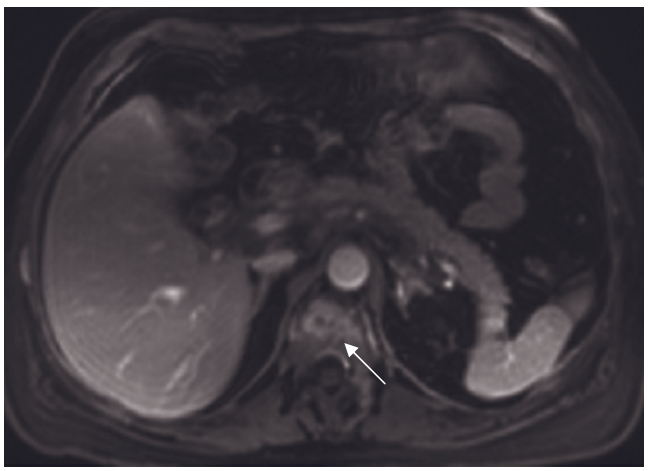

(*c*)

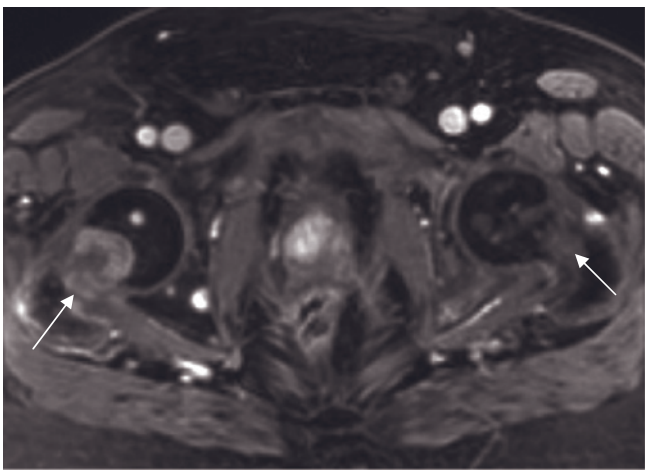

(*d*)

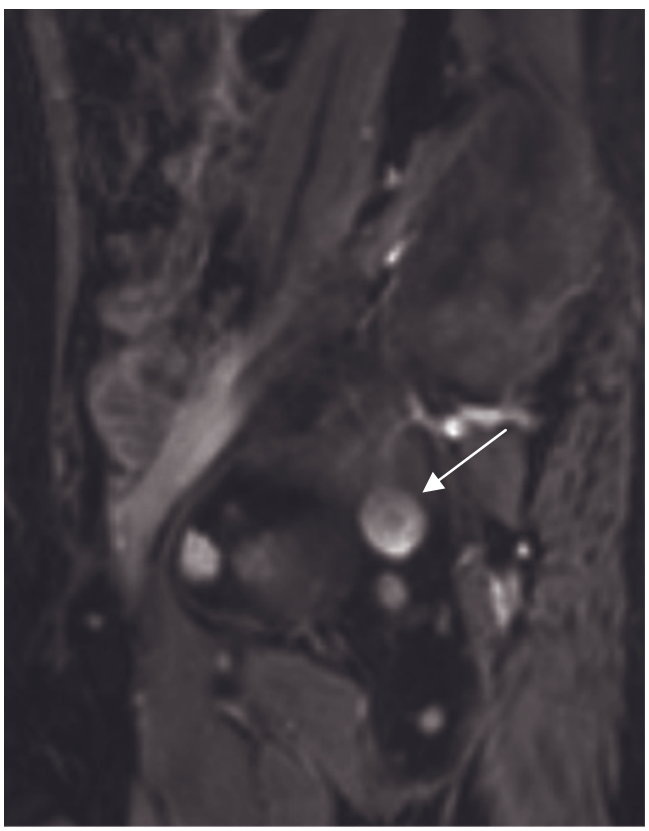

(*e*)

FIG. 12.17 Osseous metastases secondary to prostate carcinoma. Transverse 90-s postgadolinium fat-suppressed T1-weighted gradient-echo image (*a*). Metastatic lesions are focal, well-defined enhancing lesions in a background of low-signal-intensity fatty marrow on gadolinium-enhanced fat-suppressed images. Gadolinium-enhanced fat-suppressed technique enables accurate differentiation of enhancing metastatic foci (white arrows) from the frequently marbled appearance of normal bone marrow in the older patient. High-signal-intensity intraluminal flow surrounded by low-signal-intensity mural thrombus is seen in an incidental left internal iliac artery aneurysm (black arrow). **Prostate cancer metastases.** T1-weighted postgadolinium fat-suppressed hepatic arterial dominant-phase (*b*) and interstitial-phase (*c–e*) images at 3.0T demonstrate liver metastases (arrows, *b*) and bone metastases (arrows, *c–e*), which show prominent enhancement in another patient with prostate cancer.

Table 12.1 American Joint Committee on Cancer Staging of Prostate

Carcinoma
Primary Tumor
T0 No evidence of primary tumor
T1 Clinically inapparent, not visible by imaging
T2 Tumor confined to the prostate (may involve capsule)
T3 Tumor extends beyond capsule (T3a, unilateral or bilateral extracapsular extension/T3b, seminal vesicle invasion)
T4 Invasion of adjacent structures other than seminal vesicles (bladder, rectum, levator m.)
Regional Lymph Nodes
N0 No regional lymph node metastasis
N1 Regional lymph node metastasis
Distant Metastasis
M0 No distant metastasis
M1 Distant metastasis (regional nodes, bone, other sites)

Table 12.2 American Urological Association Staging of Prostate Carcinoma

A	Clinically inapparent
B	Tumor confined to the prostate
C	Tumor extends beyond capsule (may involve seminal vesicles)
D	Metastatic disease to pelvic or distant nodes, bones, soft tissues, or organs

primary tumor to minimize the overall duration of scanning.

Table 12.1 outlines the American Joint Committee on Cancer's TNM staging classification of prostate carcinoma [28]. The American Urological Association staging system, developed by Whitmore and Jewett, assigns alphabetical stages (A through D) to disease extent that correspond roughly to the primary tumor staging (T1 through T4) of the TNM system [43], which is outlined briefly in Table 12.2. Histologic grading may be by degree of anaplasia, DNA ploidy (diploid, tetraploid, or anaploid), or Gleason score, which sums the scores of the two most predominant glandular patterns of the tumor to predict aggressivity.

Currently accepted therapies for Stage T1, T2, and T3 disease include radical prostatectomy and radiation therapy, including both external beam irradiation and radioisotope implants. Radical prostatectomy is generally reserved for patients with either Stage T1 or Stage T2 disease. Stage T4 disease is treated palliatively with either hormonal or radiation therapies. Clinical assessment and treatment decisions are based on imaging stage, pathological grade, and prostate-specific antigen levels, as well as the patient's age and general state of health. Accurate tumor staging is essential for appropriate clinical decision making.

Detection of extracapsular extension precludes radical prostatectomy in the younger patient. A variety of signs have been used to predict extracapsular extension by MRI. These include focal contour abnormalities of the prostatic capsule including angulation and spiculation, obliteration of rectoprostatic angles, tumor volume, apical location, broad margins with the prostate capsule, infiltration of the periprostatic fat with a breech of the capsule, and asymmetry or tumor envelopment of neurovascular bundle [6, 18, 32, 44, 45]. Seminal vesicle invasion is demonstrated by low signal intensity on T2-weighted images, enlarged low-signal-intensity ejaculatory ducts, enlarged low-signal-intensity seminal vesicles, direct tumor invasion, and obliteration of the angle between the prostate and seminal vesicles (fig. 12.15) [6]. Increased staging accuracy can be achieved with the use of T2-weighted endorectal coil MRI and prostate-specific antigen values [46–48].

Identification of invasion of the neurovascular bundles can have important clinical implications because preservation of one or both bundles during radical prostatectomy results in a significantly decreased incidence of postoperative impotence. Identification of direct tumor extension posterolaterally into the neurovascular bundles, decreased signal intensity obliterating the rectoprostatic angle, and focal contour abnormalities within the posterolateral aspect of the gland on transverse T2-weighted images have been shown to be valuable in the prediction of neurovascular invasion [49].

Hormonal (fig. 12.18) and radiation (fig. 12.19) therapies may result in low signal intensity within the prostate. Postbiopsy changes also may mask prostate cancer. High signal intensity in the peripheral zone (fig. 12.20) or seminal vesicles on T1- and T2-weighted images reflects postbiopsy hemorrhage, which can thereby conceal underlying tumor (fig. 12.21). Cryosurgery may result in necrosis and loss of zonal anatomy [44, 50]. Because either recent biopsy or cryosurgery may hinder differentiation from residual carcinoma, MRI should generally be delayed at least 3 weeks after intervention [44].

A variety of tumors may metastasize to the prostate. The appearance of metastases may mimic primary tumors (fig. 12.22). A history of another primary site of malignancy usually is present.

The detection of small malignant lymph nodes with lymphotropic superparamagnetic nanoparticles has been reported. However, the role of this technique has not yet been well established, and there is need for further research.

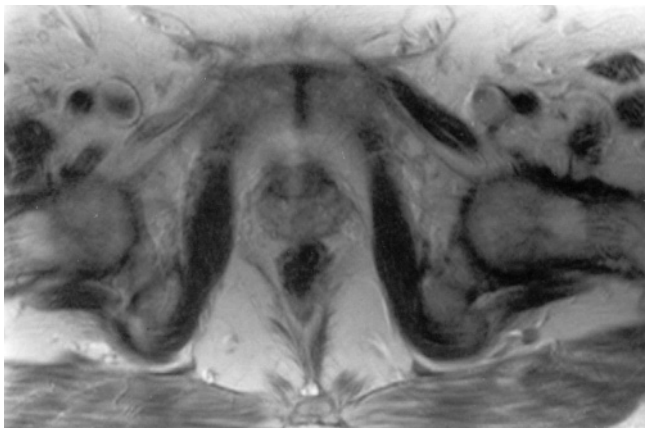

FIG. 12.18 Prostatic cancer after hormone therapy. Transverse ETSE image demonstrates a small, globule-shaped heterogeneously dark prostate. This appearance, which includes decrease in prostate size and signal intensity, is typical for hormone therapy.

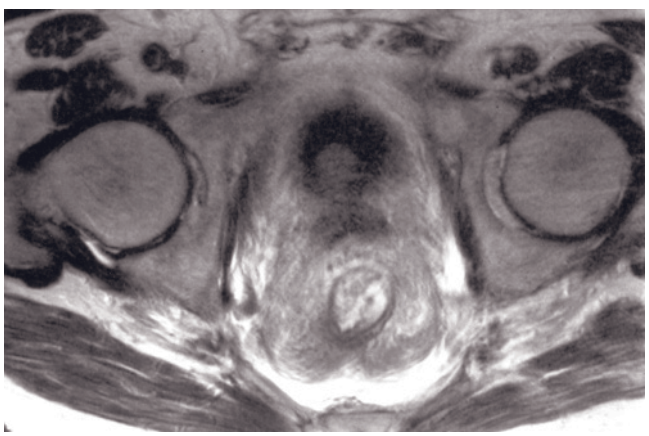

(*a*)

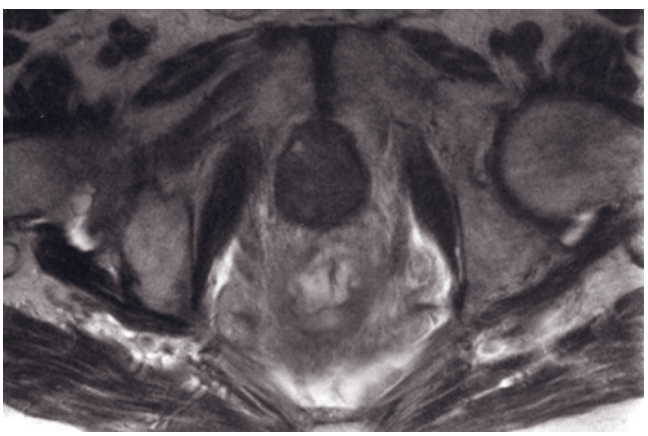

(*b*)

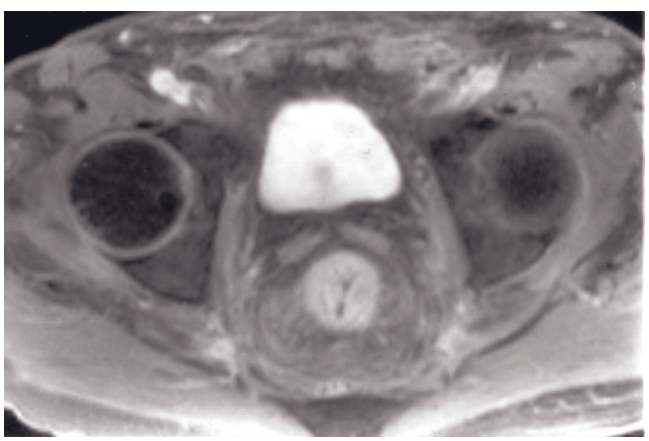

(*c*)

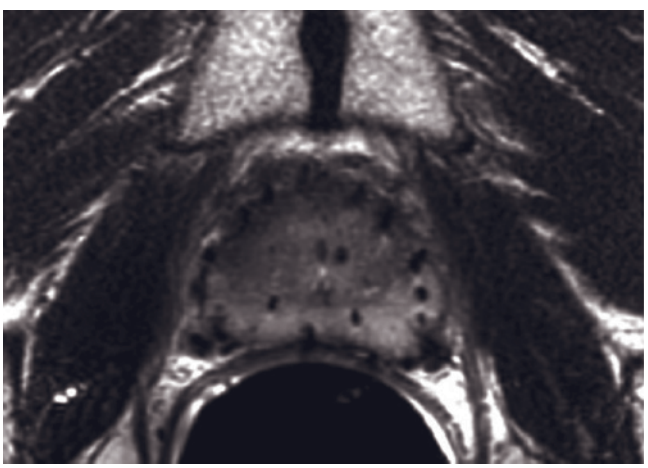

(*d*)

FIG. 12.19 Postradiation changes. Transverse T2-weighted ETSE (*a*, *b*) and 90-s gadolinium-enhanced fat-suppressed T1-weighted gradient-echo (*c*) images. The prostate is enlarged, with diffuse low signal intensity of the entire gland. Radiation changes and hormonal therapy result in diffuse low-signal changes, which makes detection of persistent cancer not feasible. Substantial thickening is noted of the rectal wall (*c*) with extensive perirectal stranding (*a*, *c*) consistent with radiation changes. **Brachytherapy seeds.** T2-weighted high-resolution fast spin-echo image (*d*) demonstrates brachytherapy seeds as low-signal-intensity structures in the prostate gland. (Courtesy of Fergus V. Coakley, M.D.)

(*a*)

(*b*)

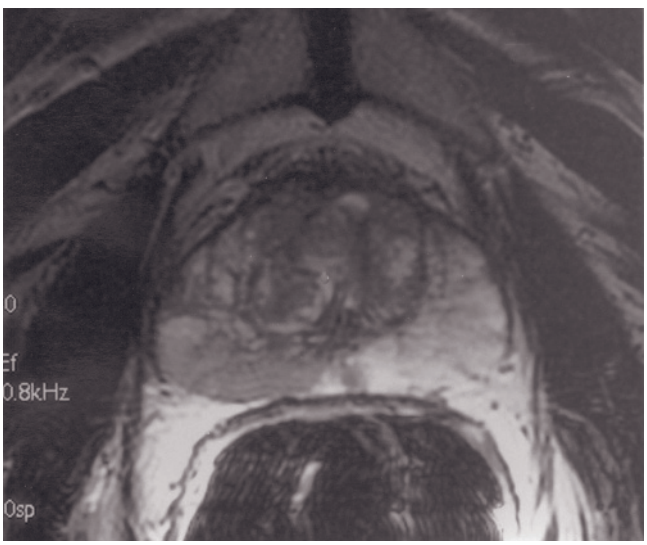

(*c*)

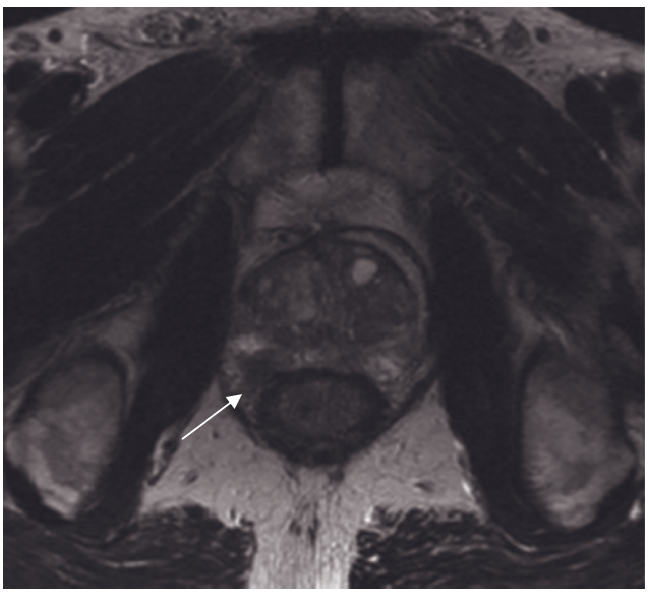

(*d*)

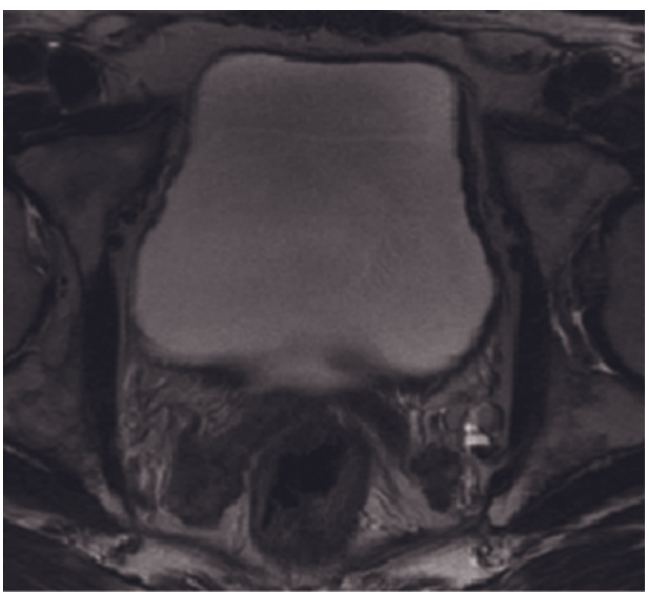

(*e*)

FIG. 12.20 Postbiopsy hemorrhage within the prostate. Transverse fat-suppressed T1-weighted gradient-echo (*a*) image. There are two high-signal-intensity foci in the anterior apex of the gland, consistent with postbiopsy hemorrhage. T1-weighted spin-echo (*b*) and endorectal coil T2-weighted echo-train spin-echo (*c*) images in a second patient demonstrate biopsy changes in the right aspect of the peripheral zone that appear high signal on T1 and low signal on T2. Biopsy changes may simulate or mask prostate cancer on T2-weighted images. Appreciation of high signal on T1-weighted images identifies the presence of hemorrhage. **Postbiopsy hemorrhage within the seminal vesicles.** Transverse high-resolution T2-weighted fast spin-echo (*d*, *e*), transverse T1-weighted fat-suppressed 3D-GE (*f*), and transverse T1-weighted postgadolinium fat-suppressed 3D-GE (*g*) images at 3.0 T demonstrate postbiopsy hemorrhage in another patient with prostate carcinoma with extracapsular extension. A focus of low signal intensity is seen within the peripheral zone of the right lobe of the prostate on T2-weighted image (*d*), and the tumor shows extracapsular extension (arrow, *d*). The seminal vesicles

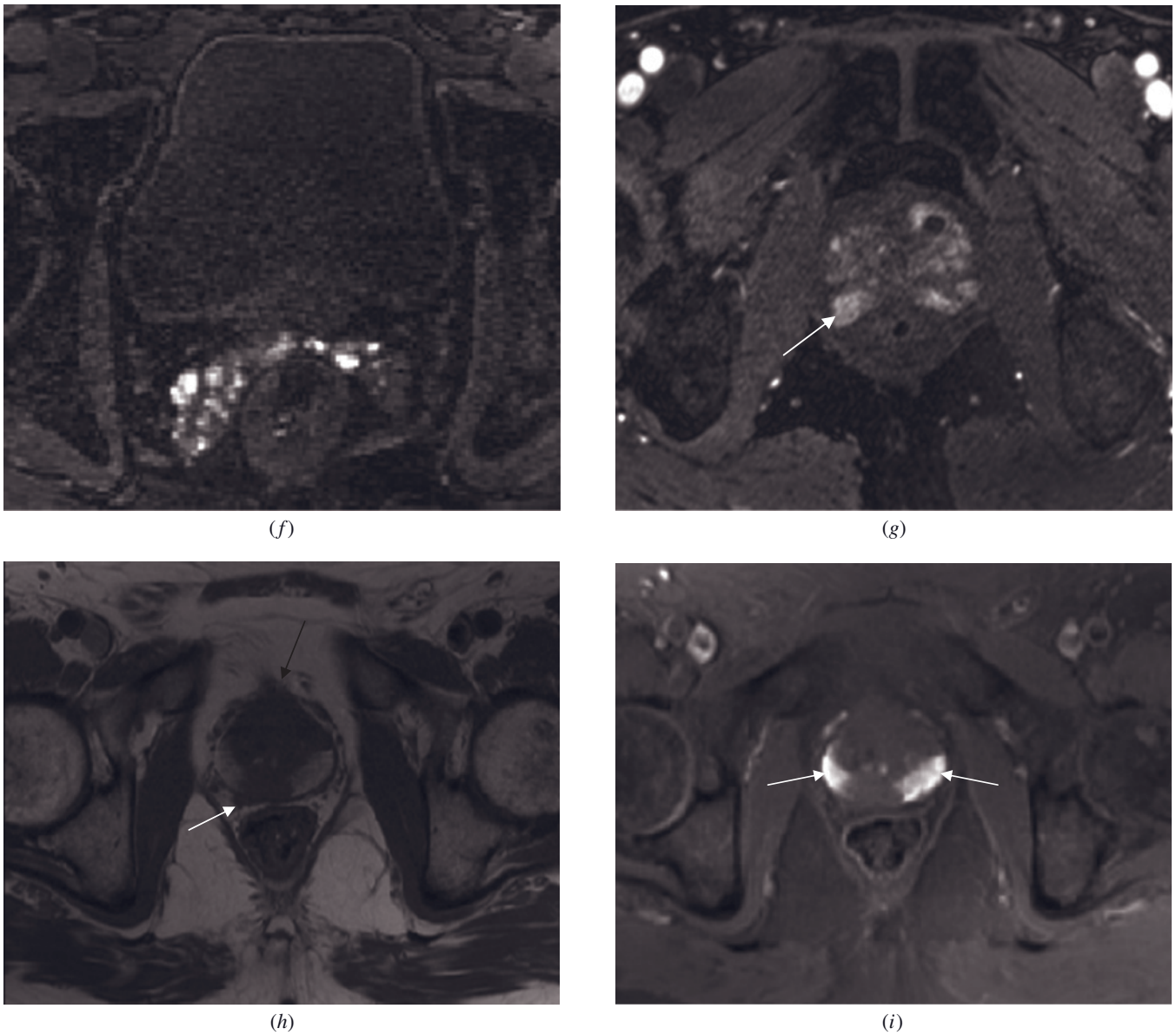

FIG. 12.20 (*Continued*) demonstrate low signal on T2 weighted image (*e*) and high signal on T1-weighted image (*f*) due to blood products secondary to the biopsy procedure. The prostate gland including the tumor (arrow) shows heterogeneous moderate enhancement on postgadolinium image (*g*). **Postbiopsy hemorrhage within the prostate.** Transverse high-resolution T2-weighted fast spin-echo (*h*) and transverse T1-weighted fat-suppressed arterial-phase 3D-GE (*i*) images demonstrate postbiopsy hemorrhage in another patient with prostate carcinoma with extracapsular extension. The tumor, which shows markedly low signal on T2-weighted image, invades the fibromuscular stroma anteriorly (black arrow, *h*) and the capsule posterolaterally on the right side (white arrow, *h*). Areas of markedly increased signal (arrows, *i*) on T1-weighted image demonstrate moderately high signal on T2-weighted image (*h*), and these findings are consistent with blood products secondary to the biopsy procedure.

Diffuse Disease

Prostatic Calcifications. Prostatic calcifications may be either primary or secondary in origin. Primary prostatic calcifications form within the ductal and acinar components of the gland. Acquired calcifications include those arising within the prostatic urethra or secondary to other etiologies, including infection, obstruction, necrosis, and radiation therapy [51].

Calcification appears as a signal-void focus on both T1- and T2-weighted images. Primary prostatic calcifications classically have a curvilinear configuration. Secondary dystrophic calculi are generally larger and more irregular in appearance [16, 21, 51]. Several age-related changes within the prostate are well recognized. The peripheral zone enlarges approximately 67%, and the central gland, which includes both the central

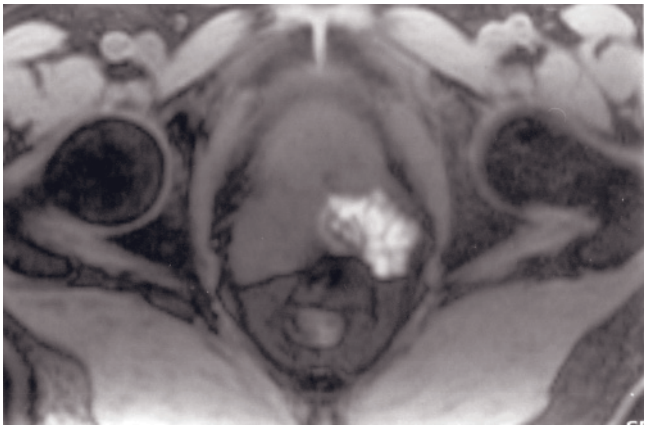

(*a*)

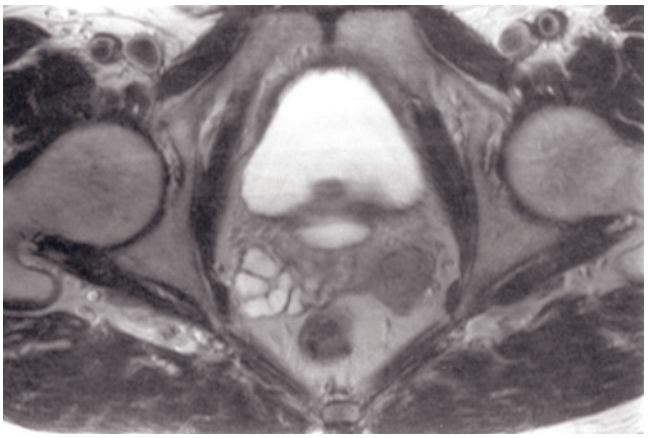

(*b*)

FIG. 12.21 Prostate cancer with hemorrhage in the left seminal vesicle after biopsy. Fat-suppressed T1-weighted gradient-echo (*a*) and T2-weighted ETSE (*b*) images. Diffuse increased signal intensity in the left seminal vesicle on T1-weighted images (*a*) and diffuse low signal on T2-weighted images (*b*) are consistent with hemorrhage related to biopsy changes.

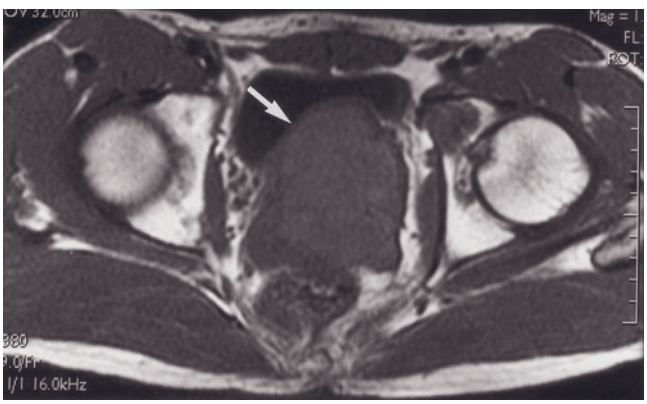

(*a*)

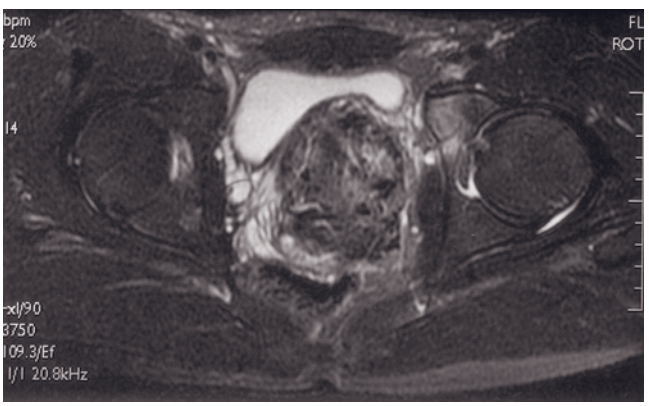

(*b*)

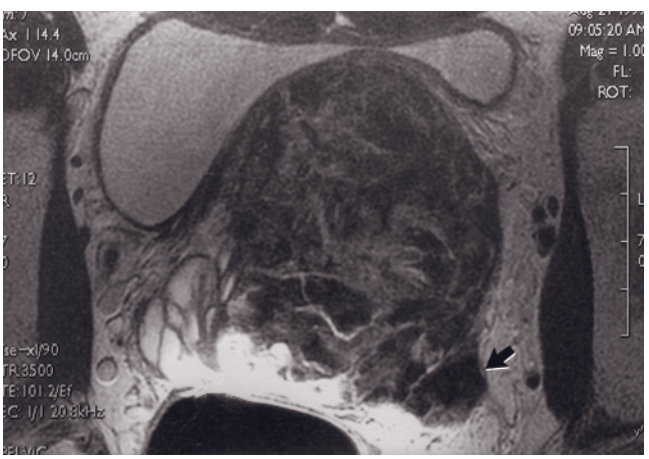

(*c*)

FIG. 12.22 Prostate metastasis. T1-weighted spin-echo (*a*), T2-weighted echo-train spin-echo (*b*), and endorectal coil transverse T2-weighted echo-train spin-echo (*c*) images in a patient with colon cancer. A large metastasis is present in the prostate that is isointense on T1-weighted imaging (arrow, *a*) and heterogeneous and slightly hypointense on T2-weighted imaging (*b*, *c*). The left seminal vesicle is also extensively invaded (arrow, *c*).

and transitional zones, enlarges approximately 175% between the second and eighth decades [52]. Although the zonal anatomy becomes more clearly defined, the periprostatic venous plexus and anterior fibromuscular stroma are less easily distinguished in the older patient [52, 53].

Inflammation and Infection. Inflammatory processes of the prostate may be classified as either bacterial or nonbacterial in origin. Gram-negative organisms are responsible for 90–95% of infectious prostatitis cases. Approximately 80% of these result from infection with *Escherichia coli*, whereas 10–15% are the consequences of *Klebsiella*, *Serratia*, *Proteus*, *Pseudomonas*, and *Enterobacter* infections. The remaining cases result from infection by gram-positive organisms, including Enterococcus, Streptococcus, and Staphylococcus [54].

MRI of acute prostatitis frequently reveals an enlarged gland with abnormal signal intensity within the peripheral zone. Low signal intensity on T1-weighted images and higher signal intensity on T2-weighted images are often observed. Areas of inflammation demonstrate diffusely increased signal intensity after intravenous administration of gadolinium. Infiltration of the adjacent periprostatic fat and involvement of the seminal vesicles are frequent associated findings [16]. Chronic prostatitis results in lesser inflammatory changes. Focal low signal intensity within the peripheral zone may result from chronic granulomatous prostatitis, simulating the MRI appearance of prostate carcinoma (fig. 12.23) [55].

Abscesses can result in ill-defined, focal enlargement of the prostate that is appreciable on T1- and T2-weighted images. Abscesses are often very high in signal intensity on T2-weighted images (fig. 12.24). There are frequently associated inflammatory changes in the periprostatic fat [21]. Enhancement of the abscess wall and inflammatory tissue surrounding a signal-void center is demonstrated on gadolinium-enhanced T1-weighted fat-suppressed images.

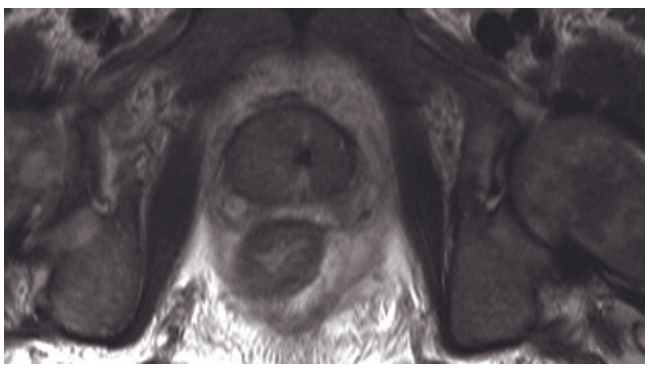

(*a*)

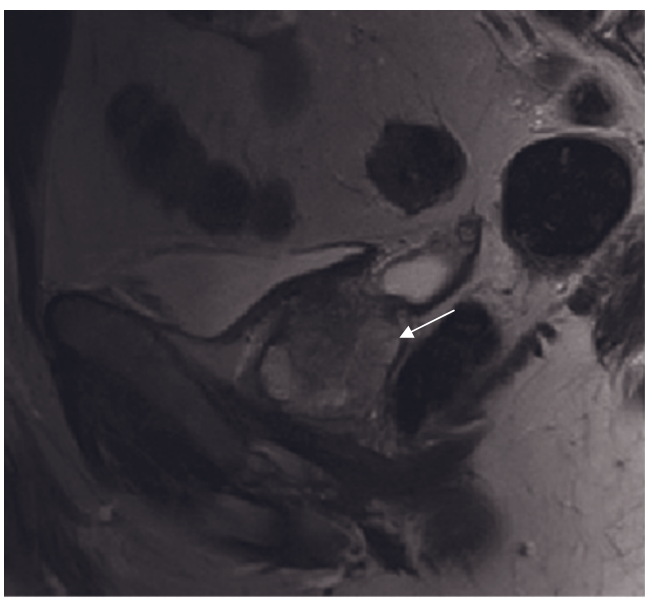

(*c*)

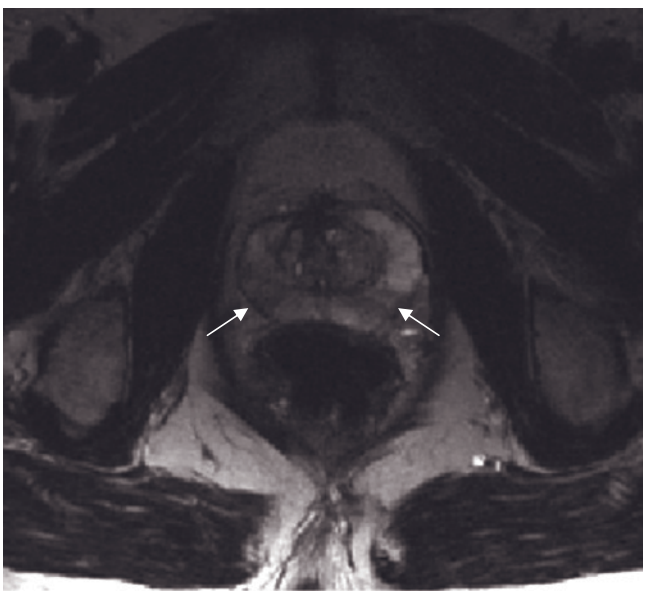

(*b*)

FIG. 12.23 Chronic prostatitis. Transverse T2-weighted ETSE image (*a*) at the midgland level reveals low signal intensity within the peripheral zone of the prostate. This entity may mimic the appearance of carcinoma. Transverse (*b*) and sagittal (*c*) high-resolution T2-weighted fast spin-echo images demonstrate mildly low signal (arrows, *b*, *c*) in the peripheral zone bilaterally, which is consistent with chronic prostatitis. Note that there is a seminal vesicle cyst.

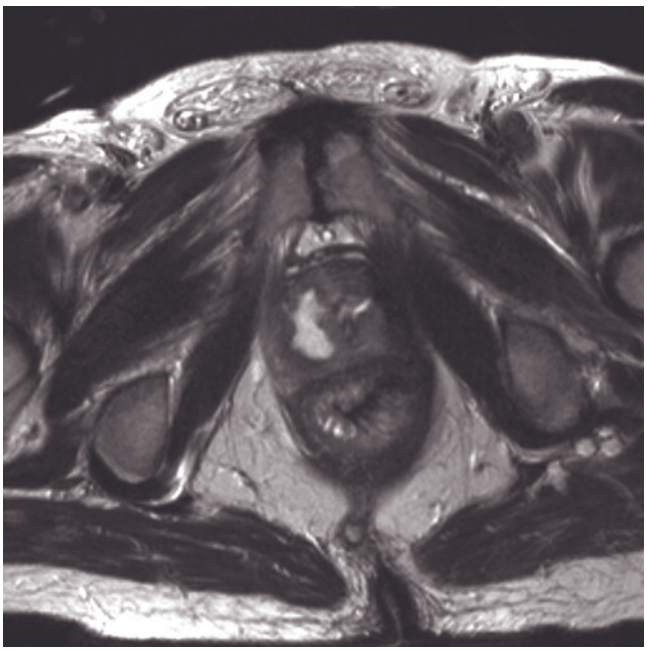

(*a*)

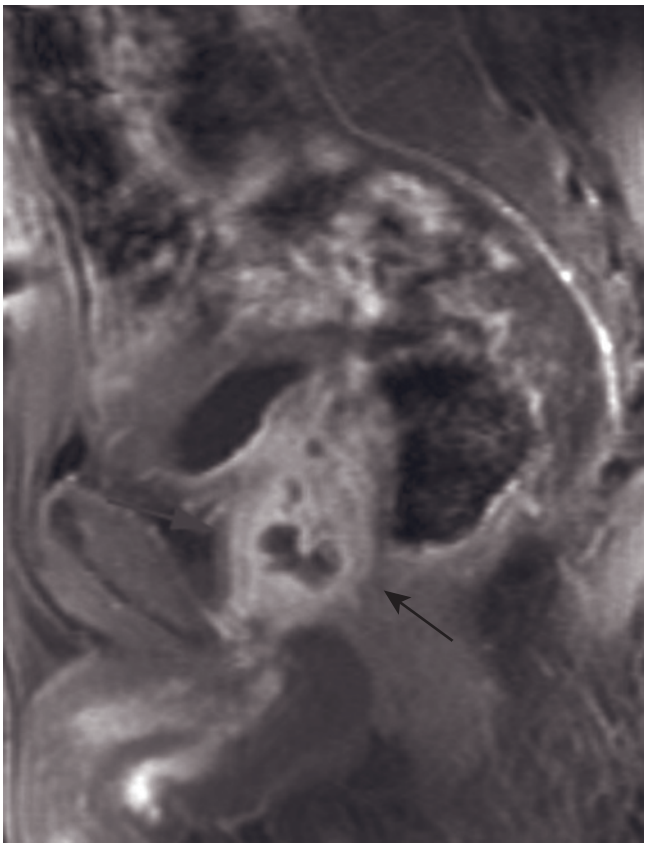

(*b*)

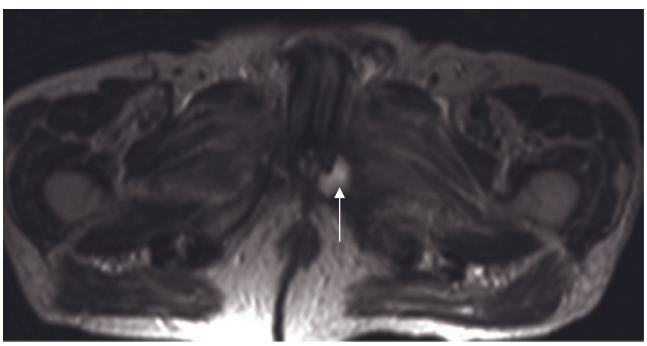

(*c*)

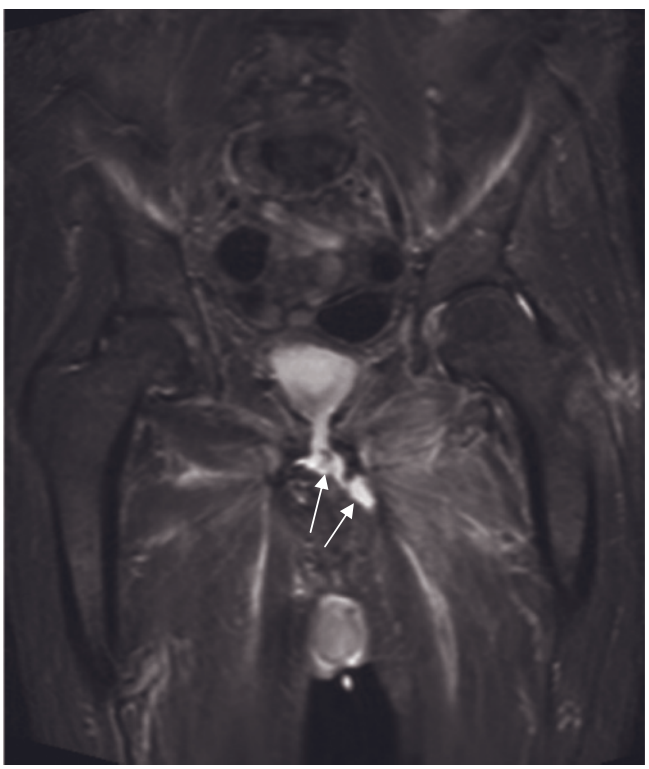

(*d*)

FIG. 12.24 Prostate abscess. Transverse T2-weighted echo-train spin-echo (*a*) and sagittal gadolinium-enhanced, fat-suppressed T1-weighted gradient-echo (*b*) images. The prostate contains multiple, irregular, fluid-filled spaces. There is extensive rim and perilesional enhancement (arrow, *b*). **Rupture of membranous urethra.** Transverse T2-weighted single-shot echo-train spin-echo (*c*) and coronal T1-weighted fat-suppressed postgadolinium interstitial-phase 3D-GE (*d*) images in another patient with traumatic rupture of membranous urethra. A fluid collection (arrow) adjacent to the corpus spongiosum and left corpus cavernosum is detected on T2-weighted image (*c*). Contrast leak and accumulation (arrows) are detected adjacent to the membranous urethra on postgadolinium image (*d*). Adductor muscle on the left thigh also shows high signal on postgadolinium image (*d*) due to trauma.

Trauma

Posterior urethral trauma may occur in association with crush injuries or extensive pelvic fracturing (fig. 12.24). There may be complete disruption of the prostatomembranous urethra, with resultant erectile dysfunction and stricture formation. Demonstration of superior prostatic displacement on imaging studies is useful because it may alter the surgical approach [56].

Disruption of the posterior urethra is identified by urethral discontinuity and a low-signal-intensity band on T2-weighted images. Stricture-associated fibrosis is shown on T1- and T2-weighted images as low-signal-intensity tissue. Sagittal T2-weighted images clearly depict displacement and elevation of the prostatic apex above the pubic symphysis, which may necessitate a suprapubic approach or pubectomy [16, 56, 57].

PENIS AND ANTERIOR URETHRA

Normal Anatomy

The anterior urethra is separated into bulbous and penile portions by the suspensory ligament of the penis. It is surrounded by the corpus spongiosum, which in turn is enveloped by a thin layer of the tunica albuginea. These structures comprise the ventral compartment of the penis. The dorsal compartment contains the paired corpora cavernosa. The two compartments are separated by Buck fascia, which encases both the thin layer of tunica albuginea surrounding the ventral compartment and a thicker layer surrounding the dorsal compartment [57].

The posterior portion of the corpus spongiosum expands to form the bulb of the penis, which is attached to the urogenital diaphragm. Immediately inferior and lateral to the bulb lies the bulbospongiosus muscle. The posterior aspects of the corpora cavernosa form the crura, which are attached to the ischiopubic ramus and are contiguous with the ischiocavernosus muscles inferomedially [58].

MRI studies should be performed with a circular surface coil or a phased-array multicoil to achieve a good signal-to-noise ratio and spatial resolution. On T1-weighted images, both the corpora spongiosa and cavernosa demonstrate homogeneous, medium signal intensity. The corpus spongiosum demonstrates a homogeneous high signal intensity on T2-weighted images, whereas the corpora cavernosa may demonstrate homogeneous or heterogeneous increases in signal intensity, depending on perfusion distribution (fig. 12.25). The bulb of the penis is a useful landmark because of its high signal intensity on T2-weighted images.

The urethra and cavernous arteries are identified as low-signal-intensity tubular structures within the centers of the corpus spongiosum and corpora cavernosa, respectively. The fascial layers demonstrate low signal intensity on both T1- and T2-weighted images. Gadolinium administration results in an increased signal intensity of both the corpus spongiosum and corpora cavernosa, enabling improved differentiation from the surrounding muscle and fascial layers (fig. 12.26). Greater delineation of anterior urethral and penile anatomy is achieved with the application of fat saturation techniques.

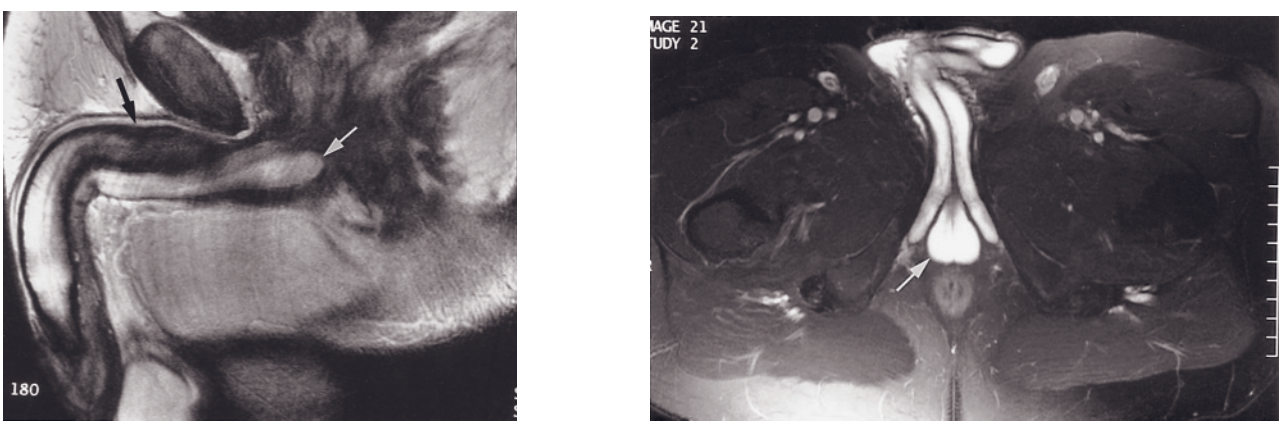

(*a*) (*b*)

FIG. 12.25 Normal penis. Sagittal T2-weighted ETSE image (*a*). The corpus cavernosum is high in signal intensity on the T2-weighted image (black arrow, *a*).The high signal intensity of the bulb of the penis is seen posteriorly (white arrow, *a*). A T2-weighted fat-suppressed ETSE image (*b*) in a second patient. The bulb of the penis is well defined as a high-signal-intensity structure (white arrow, *b*).

FIG. 12.26 Normal progression of enhancement of the penis. Coronal immediate postgadolinium T1-weighted gradient-echo image. Enhancement of the corpus spongiosum (arrow) and corpora cavernosa commences proximally and centrally, as seen on this immediate postgadolinium image. There is subsequent progression of enhancement outward and distally within the erectile bodies.

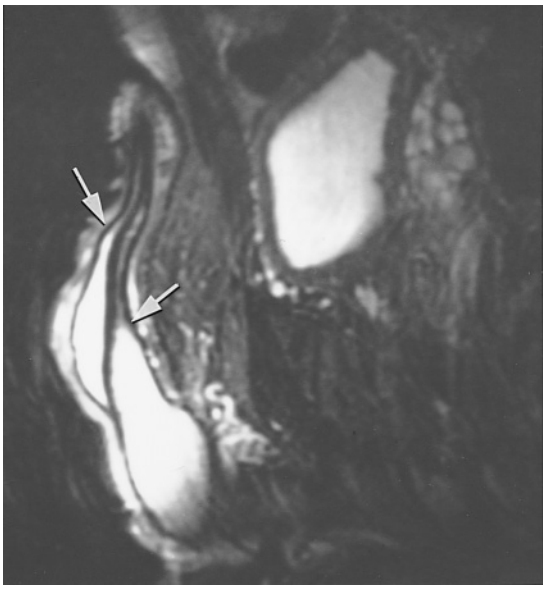

FIG. 12.27 Partial aplasia of the corpora cavernosa and spongiosum. Sagittal T2-weighted ETSE image. The distal aspects of the corpora cavernosa and spongiosa are atrophic and demonstrate a dramatic change in caliber (arrows) in this patient presenting with distal erectile dysfunction. The patient had other concomitant urogenital anomalies.

Disease Entities

Congenital Abnormalities

Epispadias is a rare anomaly characterized by absence of the dorsal covering of the distal urethra and ectopic placement of the proximal urethral aperture, which may be located anywhere along the length of the penis. This entity is almost always associated with bladder exstrophy and accompanying pubic diastasis. MRI reveals separation of the corpora cavernosa and inversion of their normal relationship with the corpus spongiosum at the level of the pubic symphysis. Hence, the urethra assumes a more cephalad position. The detailed anatomic display provided by MRI enables careful surgical planning.

Hypospadias denotes a proximal, ventral location of the meatus. Perineal hypospadias is frequently associated with a ventral fibrous band, resulting in a chordee deformity. There may be foreshortening of the urethra with either epispadias or hypospadias [59].

In rare instances, partial aplasia of the corpora cavernosa may lead to erectile dysfunction. Patients frequently have other associated anomalies within the genitourinary tract. Irregularity of length and caliber are well shown on T2-weighted images (fig. 12.27). Diphallus is another rare anomaly, resulting in partial or complete duplication of the erectile bodies and urethra. Frequently, there is associated shortening of the perineum or asymmetric development of the corpora cavernosa and ischiocavernosus muscles. Again, the detailed anatomic information provided by MRI permits accurate surgical planning. The MRI signal characteristics of the supernumerary corpora are identical to those of normally configured corpora [57, 58].

Mass Lesions

Benign Masses

PENILE PROSTHESES. MRI may be helpful in the postoperative evaluation of penile prostheses. These are identified as tubular structures within the central corpora cavernosa. Solid silicone prostheses appear signal void on all imaging sequences. Inflatable prostheses, however, follow the signal characteristics of the fluid they contain (fig. 12.28). Progressive decreased signal intensity on T2-weighted images within the corpora cavernosa may reflect the development of fibrosis. Other complications detected by MRI include infection and hematoma formation [57, 58].

Malignant Masses

METASTASES. Metastases from a variety of primary tumors may involve the penis. Metastatic penile lesions may result from contiguous spread of prostatic, testicular, urethral, bladder, rectal (fig. 12.29), and osseous neoplasms, as well as from disseminated leukemia and lymphoma [57, 58]. Metastases generally have an appearance similar to primary penile tumors when they occur within the penile shaft (fig. 12.30). Direct invasion of pelvic tumors may occur to the corpora cavernosa and spongiosum, and the site of the primary tumor is usually evident. Metastatic lesions show low or intermediate signal intensity on T1-weighted images, but they may appear hypointense, isointense, or hyperintense relative to the corpus spongiosum on T2-weighted images.

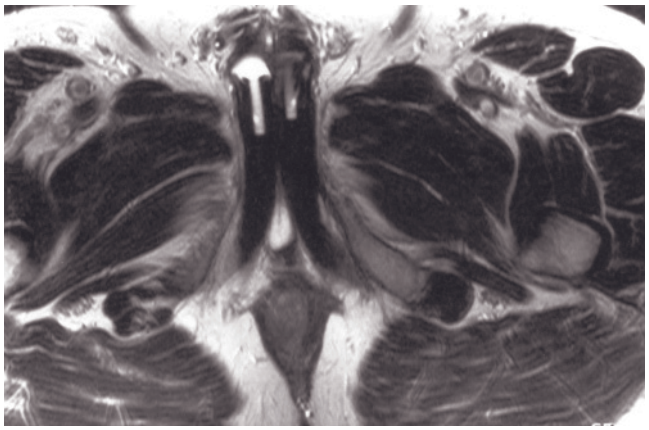

(*a*)

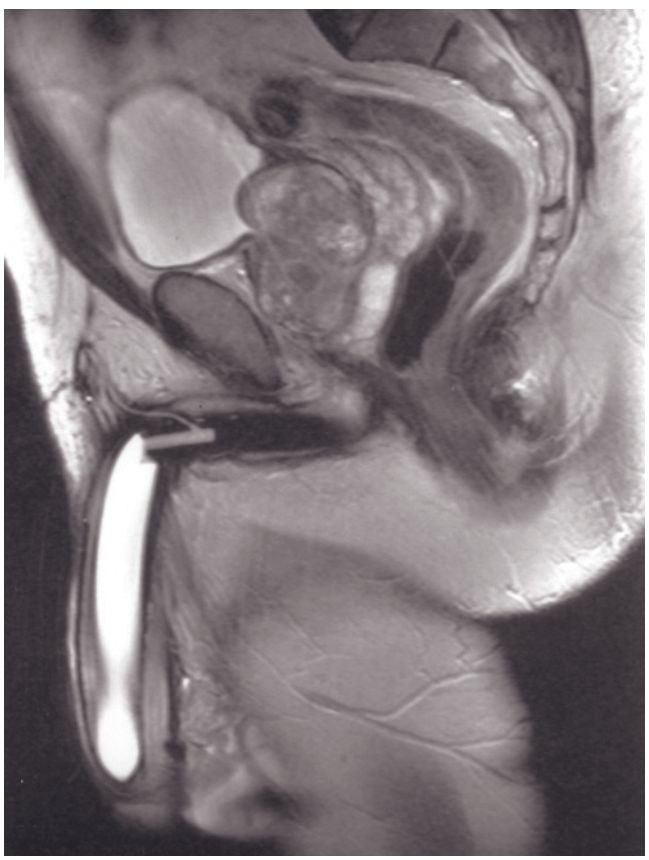

(*b*)

FIG. 12.28 Penile prosthesis. Transverse (*a*) and sagittal (*b*) T2-weighted ETSE images. An inflatable penile prosthesis is present in the corpora cavernosa. On the sagittal image (*b*) the prostate is enlarged and asymmetrically nodular and protrudes into the base of the bladder.

They show homogenous or heterogeneous enhancement depending on the size.

PRIMARY TUMORS. Carcinomas of the urethra and penis are extremely rare, accounting for less than 1% of genitourinary cancers in males. Histologic examination reveals squamous cell carcinoma in more than 95% of cases of penile malignancies. Approximately 78% of urethral carcinomas demonstrate this histology, whereas transitional cell carcinomas constitute approximately 15% of tumors. Adenocarcinomas account for 6% of cases and undifferentiated carcinomas for the remainder [58, 60]. Sarcomas constitute less than 5% of penile malignancies.

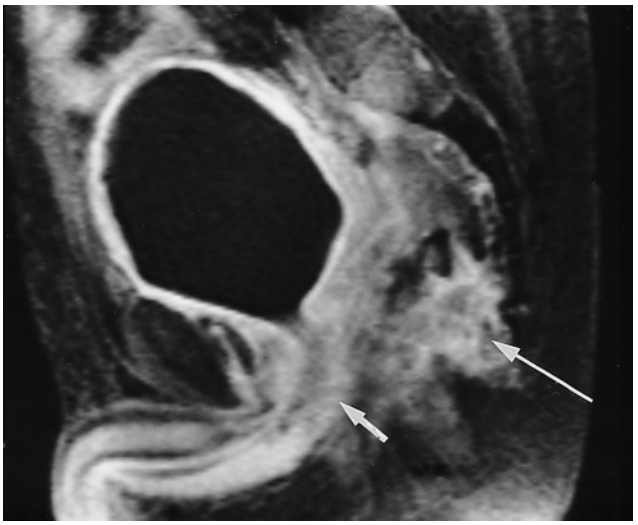

FIG. 12.29 Invasion of prostate and membranous urethra by recurrent rectal carcinoma. Sagittal 90-s postgadolinium fat-suppressed T1-weighted gradient-echo image. Heterogeneously enhancing recurrent rectal carcinoma is seen in the presacral space (long arrow).There is invasion of the prostate and membranous urethra (short arrow). Note the increased enhancement of the bladder wall secondary to radiation changes.

Primary neoplasms of the urethra and penis demonstrate isointense to low signal intensity relative to the surrounding corpus spongiosum on both T1- and T2-weighted images (fig. 12.30). Heterogeneous enhancement is usually seen (fig. 12.30). Regardless of the organ of origin, MRI aids in the delineation of the extent of tumor dissemination, enabling detection of invasion into the corpora cavernosa or tunica albuginea.

Diffuse Disease

MRI may be employed to evaluate normal and abnormal flow phenomena within the corpora spongiosum and cavernosa. Alteration in the normal vascular flow progression, which extends from the central cavernosal arteries outward and distally, may provide evidence for erectile dysfunction. Vascular disorders may result from impairment of the arterial supply, intracorporeal sinusoids, or venous drainage networks [61].

Amyloid may also affect the anterior urethra. Although the majority of cases represent amyloid

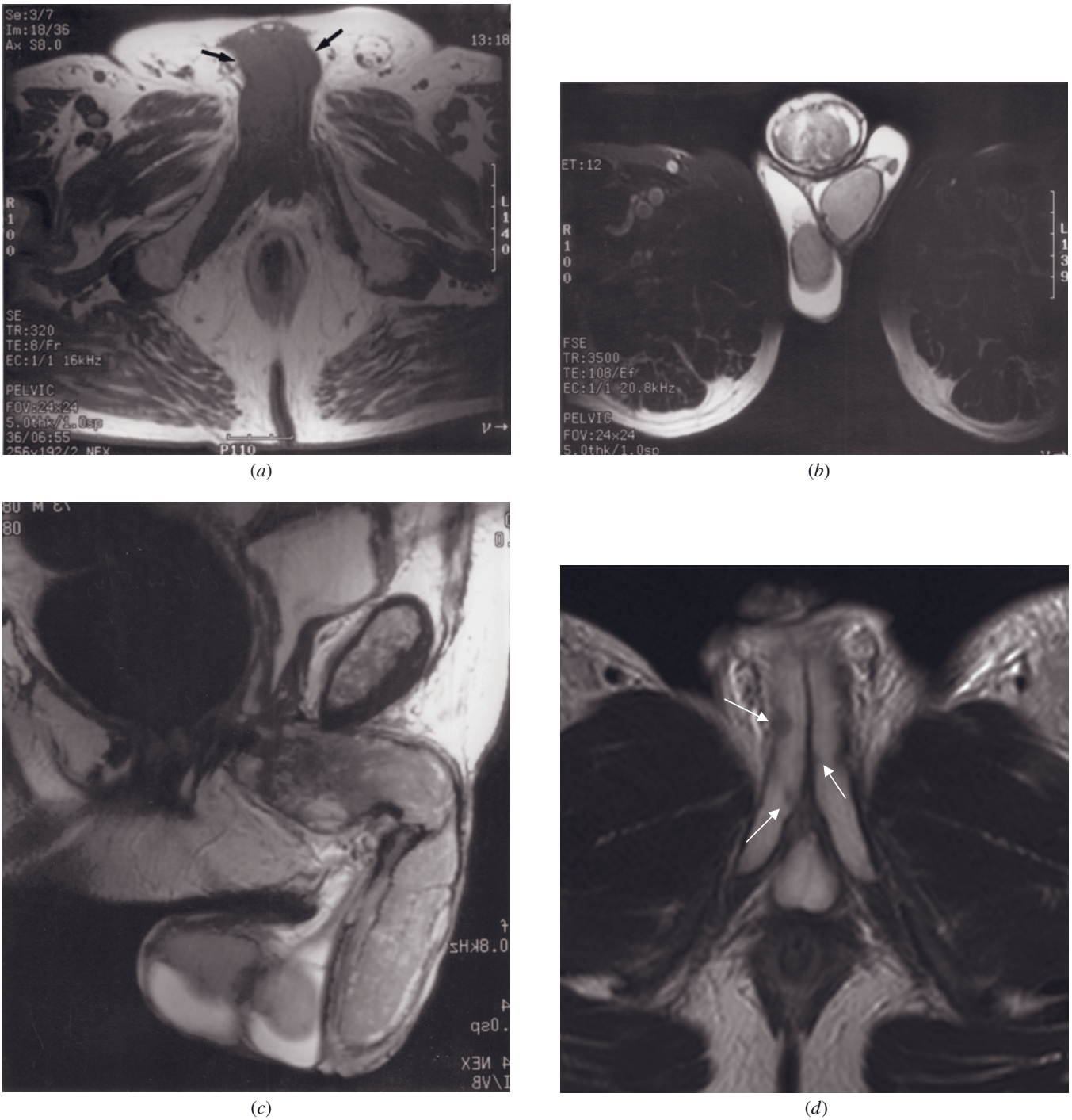

(*a*) (*b*)

(*c*) (*d*)

FIG. 12.30 Penile metastasis. T1-weighted spin-echo (*a*) and transverse (*b*) and sagittal (*c*) surface coil T2-weighted echo-train spin-echo images in a patient with transitional carcinoma of the urinary bladder. Enlargement of the corpora cavernosa (arrows, *a*) with loss of tissue planes by an isointense mass is appreciated on the T1-weighted image. On the T2-weighted images (*b*, *c*), the corpora cavernosa are enlarged and heterogeneous and lack well-defined tissue planes. **Penile metastases.** T2-weighted transverse (*d*) and sagittal (*e*) high-resolution fast spin-echo images demonstrate multiple hypointense metastases (arrows, *d*, *e*) in the corpora

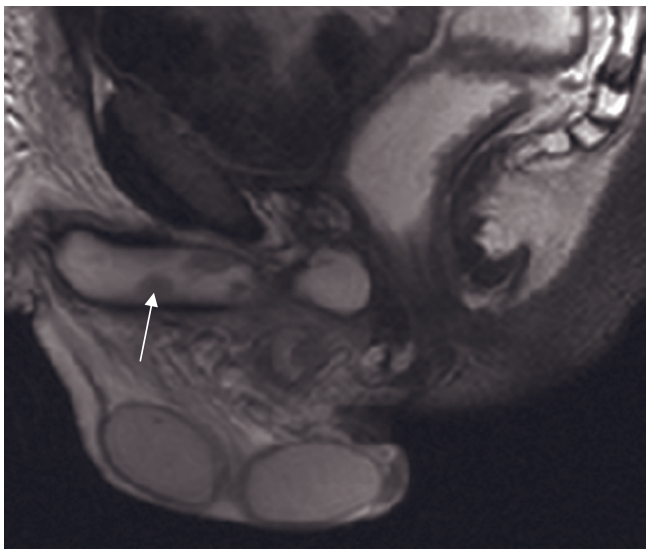

(*e*)

(*f*)

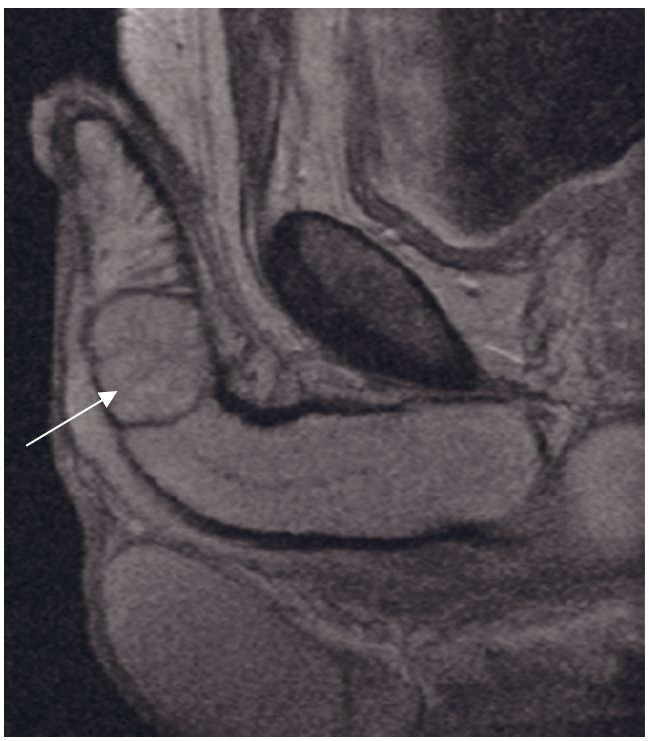

(*g*)

(*h*)

FIG. 12.30 (*Continued*) cavernosa from recurrent urethral planocellular carcinoma in another patient. The patient has a history of previous penectomy for the urethral planocelullar carcinoma. Note the normal testes in the scrotum. **Primary penile cancer.** T2-weighted high-resolution fast spin-echo image (*f*) demonstrates the tumor (arrow) located in the corpus spongiosum. T2-weighted high-resolution fast spin-echo sagittal (*g*) and transverse (*h*) images and sagittal (*i*) and transverse (*j*) fat-suppressed

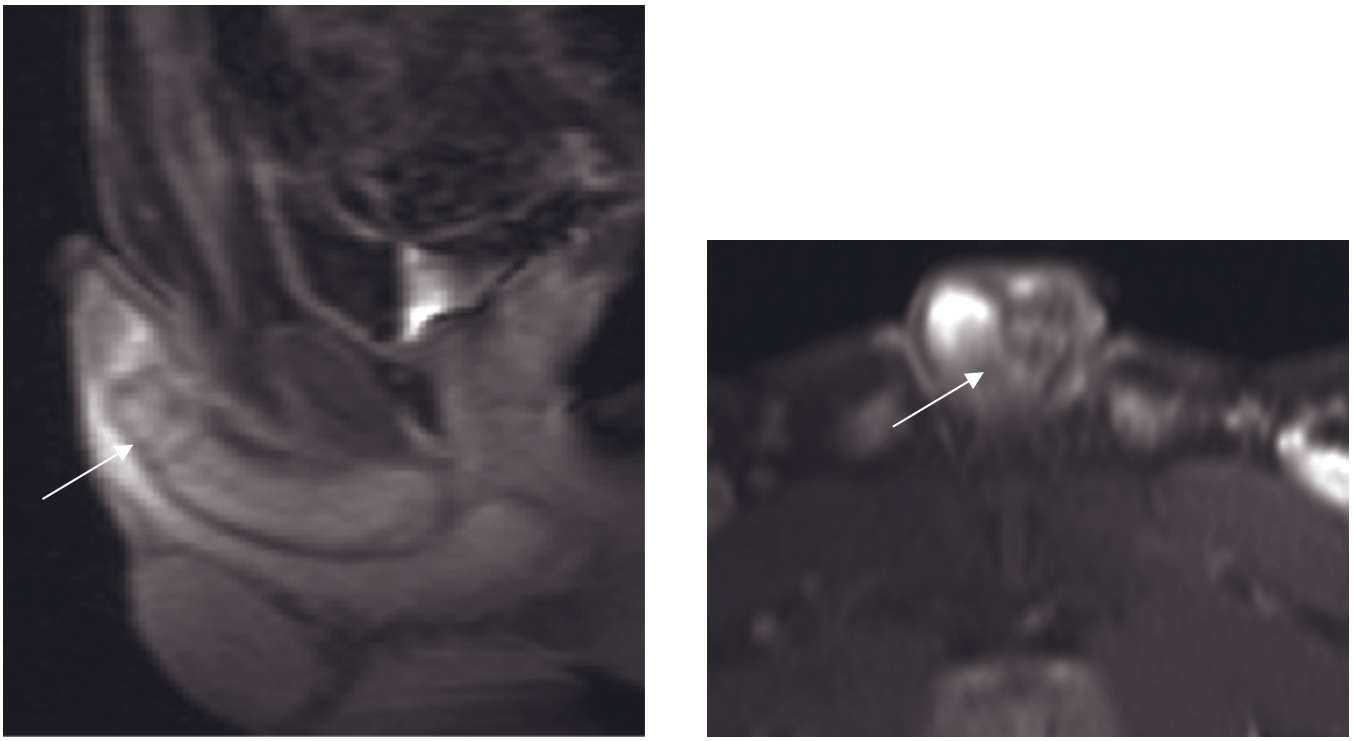

(*i*) (*j*)

FIG. 12.30 (*Continued*) postgadolinium interstitial-phase 3D-GE images demonstrate a leiomyosarcoma (arrows, *g–i*) of the penis in another patient. The tumor invades both corpora cavernosa and corpus spongiosum and shows heterogeneous enhancement on postgadolinium image.

secondary to other disease states, very rarely primary amyloid of the urethra occurs, which is identified by immunohistochemical stains. The disease may result in stricture formation and calcified plaques within the anterior urethra [62]. Focal low signal intensity on T2-weighted images may reflect amyloid deposition.

Inflammation. Peyronie disease (induratio penis plastica) is caused by focal inflammation of the tunica albuginea and corpora cavernosa. Resultant fibrosis and plaque formation lead to painful, deviated erections. Various etiologies including trauma, diabetes, gout, and hormonal dysfunction have been implicated in the development of the disease. It is most commonly observed in patients between the ages of 30 and 60 years, although occasional cases have been reported in men younger than 20 [63, 64].

On T2-weighted images, heterogeneity of the corpora cavernosa may be demonstrated. In addition, low-signal-intensity plaques may be visualized within the corpora cavernosa and tunica albuginea on T1- and T2-weighted images [57, 63]. Plaque detection is improved by the administration of gadolinium, with increased enhancement apparent in areas of active inflammation [63].

In rare instances, fibrosis may affect Buck fascia. This entity may be observed in cases of early Peyronie disease. Alternatively, it may represent extension of fibrosis resulting from other causes including trauma, sustained priapism, and collagen vascular disease (fig. 12.31).

Infection. Urethritis may be secondary to infection with *Neisseria gonococcus*, *Chlamydia trachomatis*, *Condylomata acuminatum*, or *Mycobacterium tuberculosis*. The periurethral glands of Littre may become distended with bacteria and leukocytes. Spread to adjacent periurethral tissues may lead to abscess formation. Aggressive infections also may result in perineal or scrotal sinus formation [65]. MRI may prove helpful in the detection of these associated complications.

Vascular. Thrombosis of the corpus cavernosum has been reported. Partial priapism and/or induration over the corpus cavernosum are the most common presenting findings. The affected corpus cavernosum is distended (fig. 12.31). The signal intensity of the affected segment reflects the age of the thrombus (fig. 12.31). It is usually hyperintense relative to the normal corpus cavernosum on T1-weighted images and hypointense on T2-weighted images [66].

FIG. 12.31 Fibrosis of Buck fascia. Transverse T1-weighted gradient-echo (*a*) and 90-s postgadolinium fat-suppressed gradient-echo (*b*) images. There is increased thickness of the left aspect of Buck fascia (black arrow, *a*). Note the low-signal-intensity linear markings in the adjacent fat (*a*). The thickened fascia enhances diffusely after gadolinium administration (white arrow, *b*). These changes are compatible with early Peyronie disease. **Partial cavernosal thrombosis.** Transverse T1-weighted fat-suppressed SGE (*c*), transverse (*d*) and sagittal (*e*) T2-weighted high-resolution fast spin-echo, and transverse 45-s postgadolinium SGE (*f*) images demonstrate the partial thrombosis of left corpus cavernosum in another patient. The left corpus cavernosum (arrows, *c–f*) is enlarged. The left corpus cavernosum shows isointense to mild hyperintense signal (arrow, *c*) on T1-weighted image (*c*) and low signal (arrow, *d*, *e*) on T2-weighted images (*d*, *e*). These findings are consistent with blood products secondary to the thrombosis. The thrombosis (arrow) does not show any enhancement on postgadolinium image (*f*).

Trauma

Penile trauma usually results from direct, blunt injury. The most common finding is a tear in the tunica albuginea. An adjacent hematoma is frequently visualized. There also may be fracture or avulsion of the corpora cavernosa from their ischial attachments.

MRI demonstrates discontinuity of the normal low-signal-intensity ring of the tunica albuginea on T2-weighted images after a tear. Discontinuity between the corpus cavernosum and ischium also results in focal low signal intensity on T2-weighted images. Signal characteristics of associated hematomas reflect the acuity of the traumatic event [56–58]. MRI has been shown to alter surgical planning in as many as 26% of cases [56].

SEMINAL VESICLES

Normal Anatomy

The seminal vesicles are paired accessory glands located superior to the prostate gland. Each is comprised of a single tube coiled upon itself. It is surrounded by a dense fibromuscular sheet and narrows medially, forming an excretory duct that joins with the vas deferens to form the ejaculatory duct.

Both the width and fluid content of the seminal vesicles increase after puberty, peaking within the fifth and sixth decades. On T1-weighted images, the seminal vesicles demonstrate homogeneous signal intensity similar to that of muscle tissue. On T2-weighted images, the signal intensity varies with the composition of fluid content. In normal men younger than 60 years of age, fluid is abundant and the seminal vesicles appear as high-signal-intensity "cluster of grapes" structures (fig. 12.32). After the administration of intravenous gadolinium, the convoluted walls of the vesicles enhance. The walls can be more clearly defined, with concomitant application of fat saturation techniques. The surrounding walls appear higher in signal intensity than the fluid with these techniques (see fig. 12.32). The high contrast resolution for the appearance of normally uninvolved seminal vesicles is an important feature in the staging of prostate cancer by MRI (fig. 12.33).

Beyond 60 years of age, fluid content decreases and the seminal vesicles may appear progressively lower in signal intensity. In the normal process of aging, low signal intensity is symmetric bilaterally and associated with a decrease in size.

Disease Entities

Congenital Abnormalities

Congenital abnormalities of the seminal vesicles including ectopia, hypoplasia, and agenesis are frequently associated with other anomalies of the genitourinary tract. Detection of congenital seminal vesicle abnormalities therefore warrants evaluation of the remainder of the genitourinary tract. Congenital seminal vesicle cysts are the most commonly encountered abnormalities (fig. 12.33). Approximately 80% of cases are associated with ipsilateral renal dysgenesis and approximately 8% with collecting system duplication. Seminal vesicle cysts are frequently asymptomatic but may become large enough to cause dysuria, perineal pain, increased frequency, or bladder outlet obstruction [67, 68]. Seminal vesicle cysts are easily differentiated from müllerian or utricular cysts on MRI because of their typical lack of connection to the prostate. They are of variable signal intensity on T1-weighted-images and high in signal intensity on T2-weighted images. Variable signal intensity on T1-weighted images reflects the presence of hemorrhage or highly proteinaceous material.

Mass Lesions

Benign Masses. Vesicular tumors are rare, and among benign mass lesions leiomyomas are the most common histologic type. They generally appear well circumscribed and are of intermediate signal intensity on T1-weighted images and high signal intensity on T2-weighted images. In rare cases, lipomas, fibromas, cystadenomas, and angiomas may occur in the seminal vesicles.

Malignant Masses. Most malignant disease of the seminal vesicles results from local extension of prostatic, urinary bladder, or rectal carcinomas. Invasion by prostate carcinoma results in loss of normal architecture and decreased signal intensity on T2-weighted images (see figs. 12.5, 12.14, and 12.15). Primary malignancies are rare and are usually adenocarcinomas. Leiomyosarcomas and fibrosarcomas also have been reported.

Diffuse Disease

Calcifications within the seminal vesicles are most commonly associated with diabetes mellitus. Less often, calcifications may arise secondary to infectious etiologies, which include tuberculosis and schistosomiasis [68]. Calcifications are low in signal intensity on both T1- and T2-weighted images (fig. 12.34). Abnormally low signal intensity on T2-weighted images also may be seen after prostatic biopsy [69]. This finding, if confused with tumor invasion, may prevent radical prostatectomy in eligible patients. Senile amyloidosis of the seminal vesicles is a common finding at autopsy. Appearing as low signal intensity on T2-weighted images, it also can mimic malignancy (fig. 12.34) [32, 70].

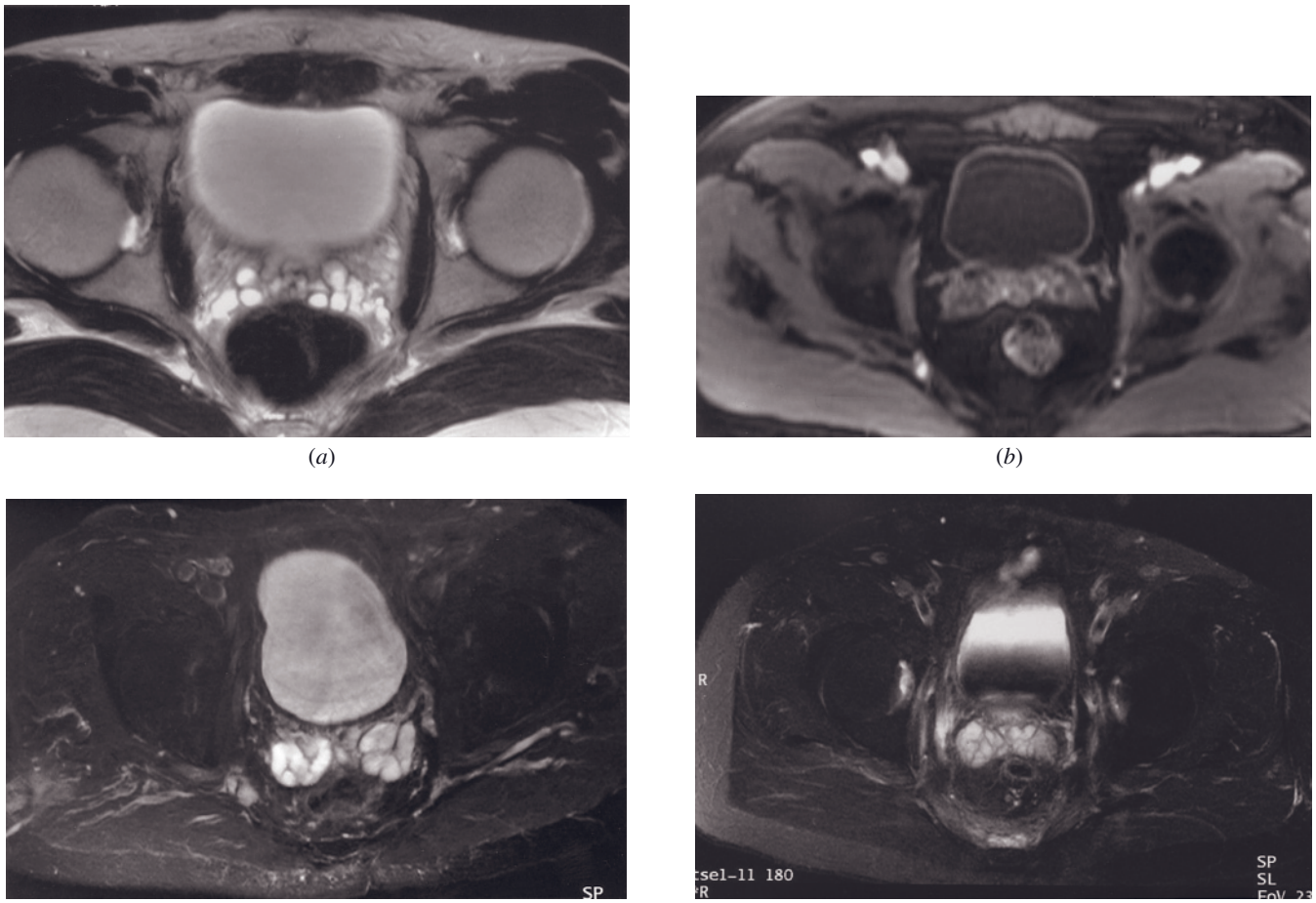

FIG. 12.32 Normal seminal vesicles. Transverse T2-weighted ETSE (*a*) image. High signal intensity is seen within the normal fluid-filled seminal vesicles on the T2-weighted image (*a*). Immediate postgadolinium fat-suppressed T1-weighted gradient-echo image (*b*) in a second patient. Note how fat suppression increases conspicuity of the convoluted walls of the seminal vesicles, which enhance relative to the fluid that they contain (*b*). Transverse T2-weighted fat-suppressed ETSE image (*c*) in a third patient. Normal, fluid-filled seminal vesicles exhibit high signal intensity on T2-weighted images. The low signal intensity of the walls of the tubules gives the glands a cluster of grapes appearance. The external borders are clearly demarcated after the application of fat suppression. Transverse T2-weighted fat-suppressed ETSE image (*d*) in a fourth patient. The seminal vesicles are high in signal intensity on this high-resolution T2-weighted image. Image acquisition after gadolinium administration accounts for the low signal intensity within the dependent portion of the urinary bladder.

Infection. Infection of the seminal vesicles is diagnosed primarily on the basis of clinical presentation. Patients usually have associated prostatitis or epididymitis. Rare, isolated infection of the seminal vesicles classically results in hemospermia. Signal characteristics on MR images therefore reflect the presence or absence of blood products. The acutely inflamed gland also may appear enlarged and of lower signal intensity than the contralateral side. Chronic infection may result in fibrosis with concomitant loss of fluid content and a resultant decrease in signal intensity on T1- and T2-weighted images. Abscess formation may manifest as an ill-defined focus of decreased signal intensity on T1-weighted images.

TESTES, EPIDIDYMIS, AND SCROTUM

Normal Anatomy

The testes lie within the scrotum, a sac comprised of internal cremasteric and external fascial layers, dartos muscle, and skin. They are encased by the tunica albuginea, a fibrous capsule that invaginates into the testis posteriorly to form the mediastinum testis. The processus vaginalis represents an extension of peritoneum, projecting between the tunica albuginea and dartos layers. The posterior testis and mediastinum

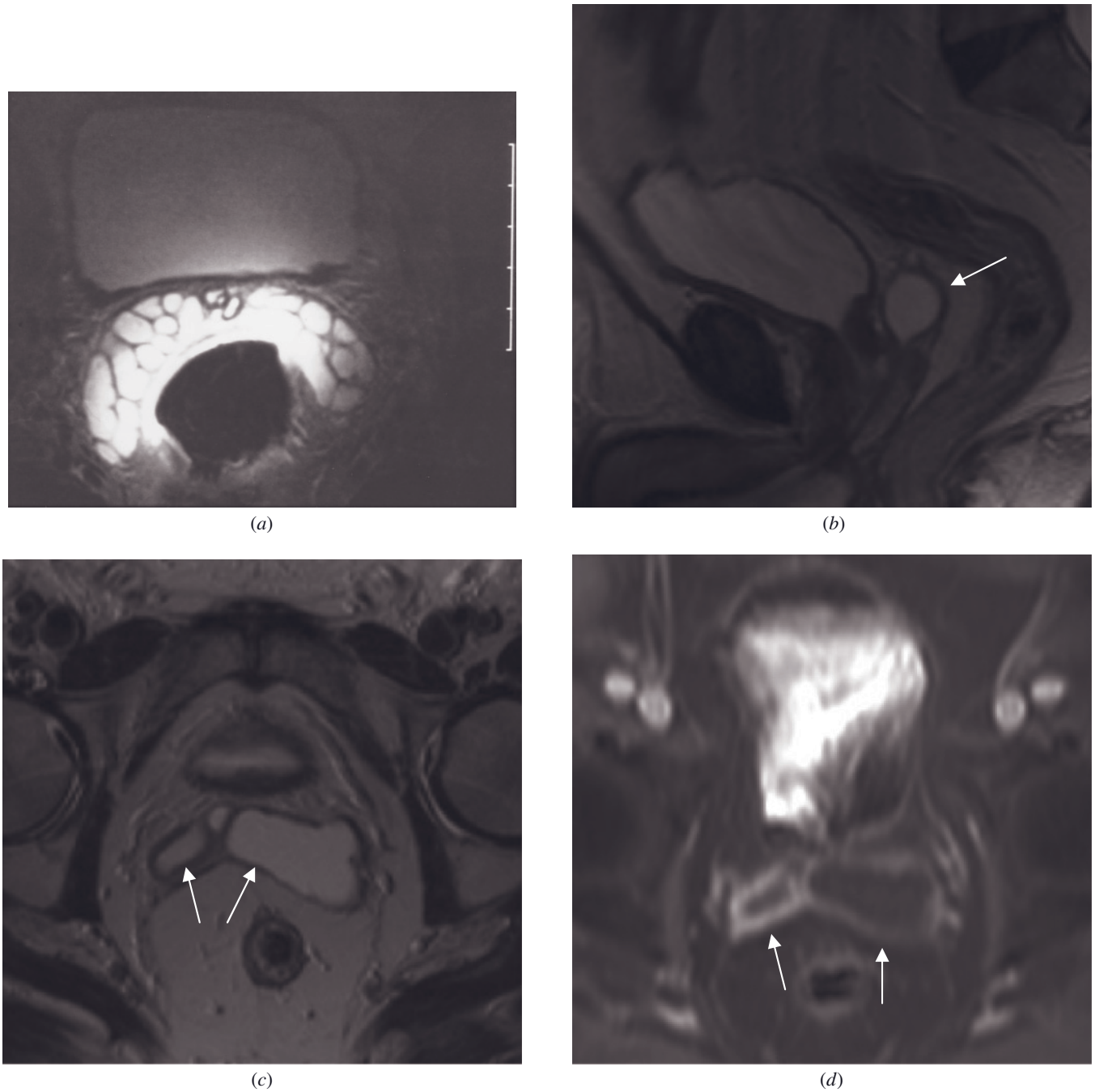

FIG. 12.33 Normal seminal vesicles in the presence of adenocarcinoma of the prostate. Transverse T2-weighted fat-suppressed ETSE endorectal coil image (*a*). Normal, high signal intensity is present within the seminal vesicles in this patient with Stage T2 adenocarcinoma of the prostate. **Seminal vesicle cysts.** Sagittal (*b*) and transverse (*c*) high-resolution T2-weighted images and T1-weighted postgadolinium fat-suppressed 3D-GE image (*d*) demonstrate bilateral seminal vesicle cysts (arrows, *b–d*) in another patient. The cyst walls show enhancement on postgadolinium image (*d*).

testis are not covered by the tunica vaginalis, resulting in the bare area through which vascular structures and tubules pass. Approximately 400–600 seminiferous tubules are coiled within each testis. These converge to form the rete testis and, ultimately, the efferent ductules. The efferent ductules form the epididymal head posterior to the testis. They then unify into a single coiled duct representing the epididymal body. The narrowed tail of the epididymis ultimately leads into the vas deferens.

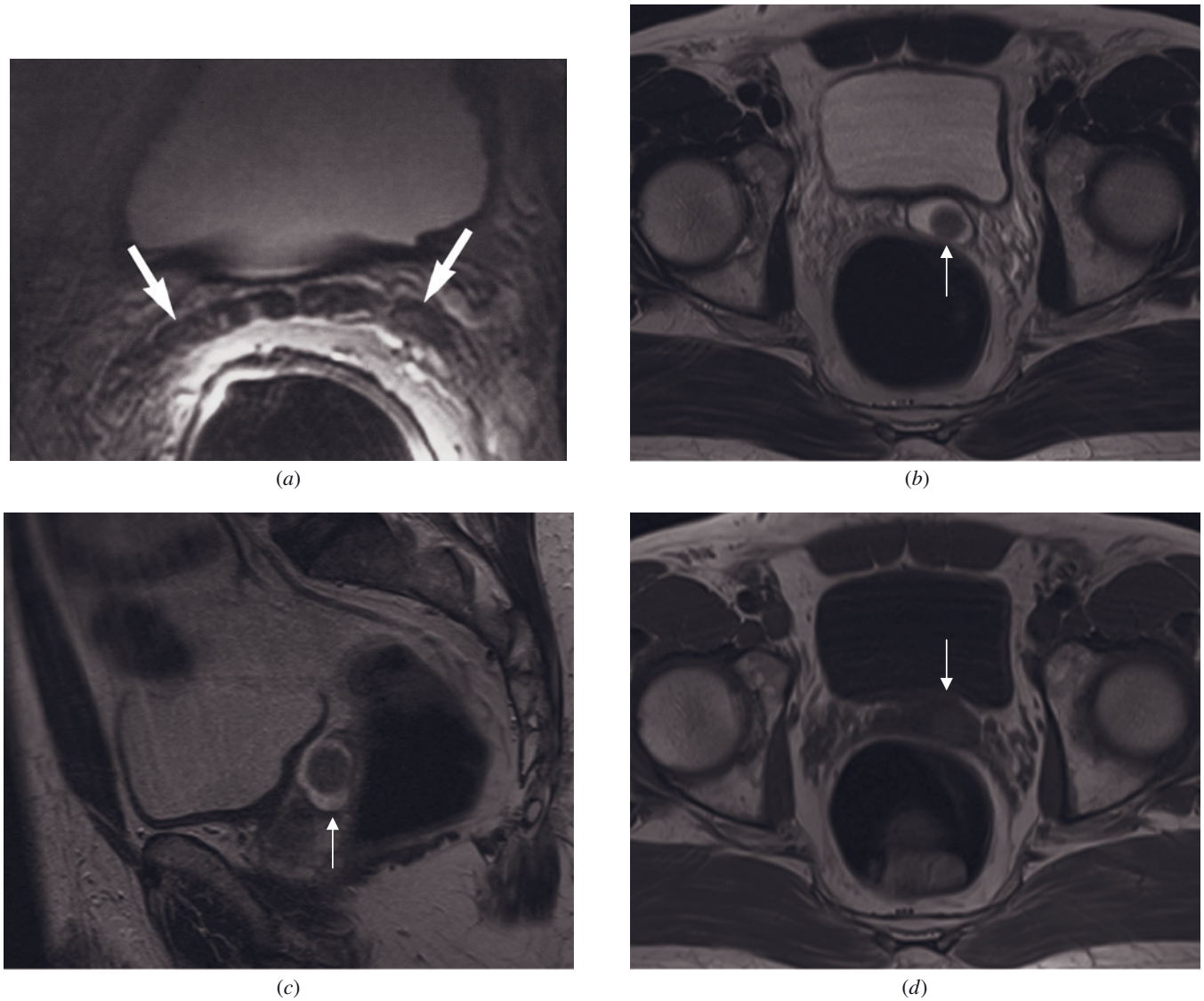

FIG. 12.34 Amyloidosis of the seminal vesicles. Transverse T2-weighted ETSE endorectal coil image (*a*). There is bilateral decreased signal intensity of the seminal vesicles secondary to amyloid deposition (arrows, *a*). **Seminal vesicle cyst and stone.** Transverse (*b*) and sagittal (*c*) high-resolution T2-weighted images and T1-weighted fast spin-echo image (*d*) demonstrate a seminal vesicle cyst (arrows, *b–d*) in another patient. A stone, which shows low signal on T1- and T2-weighted images, is also detected in the cyst.

MRI Technique

MRI studies should be performed with a phased-array surface coil or a circular surface coil overlying the testes, which should be elevated above a folded towel placed between the thighs. The testes are clearly demarcated on both T1- and T2-weighted images by the low signal intensity of the surrounding tunica albuginea. The testes are homogeneous and isointense to muscle on T1-weighted images and higher in signal intensity on T2-weighted images. The mediastinum testis can be identified as a low-signal-intensity band within the posterior testis on T2-weighted images. Low-signal-intensity fibrous projections emanating from the mediastinum testis represent septulae, which divide the testis into lobules. The gubernaculum may be recognized on T2-weighted images as a low-signal-intensity curvilinear rim along the inferoposterior aspect of the testis. The signal intensity of the epididymis is slightly heterogeneous and hypo- to isointense to the testis on T1-weighted images. The epididymis is more clearly differentiated from the testis on T2-weighted images because it is lower in signal intensity than the adjacent testis. Gadolinium administration results in hyperintensity of the epididymis relative to the testis [71].

Disease Entities

Congenital Abnormalities

Congenital abnormalities of the testes include unilateral or bilateral hypoplasia and agenesis, as well as duplication and cryptorchidism. Congenitally duplicated testes may be classified by their location within the scrotum, inguinal canal, or retroperitoneum. Supernumerary scrotal testes are usually associated with duplication of the vas deferens and epididymis. There may be an associated ipsilateral inguinal hernia. Inguinal testes have duplicated draining systems in the majority of cases and also may have associated inguinal hernias. Retroperitoneal testes, frequently occurring near the deep inguinal ring, are always associated with ipsilateral inguinal hernias. They may or may not demonstrate separate draining structures. Polyorchia is associated with an increased incidence of testicular malignancy [72].

Cryptorchidism. MRI may be employed to localize a clinically suspected undescended testis. The testes normally descend into the scrotum during the eighth month of gestation, accounting for the increased incidence of cryptorchidism in premature births. Approximately 80% of undescended testes are located distal to the external inguinal ring [73]. A significant number of cryptorchid testes will descend spontaneously during an infant's first year of life. Fibrosis and impaired spermatogonia have been observed in undescended testes not surgically corrected by 2 years of age. Hence, as a result of subsequent increased incidences of both infertility and carcinoma, it is recommended that orchiopexy be performed between the first and second years of life [74, 75].

Undescended testes demonstrate low signal intensity on T1-weighted images and intermediate to high signal intensity on T2-weighted images. Low signal intensity on T2-weighted images may be observed in more fibrotic or atrophic testes [20, 75]. Identification of the undescended testis may be aided by identifying the mediastinum testis as a low-signal-intensity structure on T2-weighted images and recognizing that undescended testes often have a larger transverse than anteroposterior (AP) diameter (fig. 12.35). In comparison, lymph nodes usually have a larger AP than transverse diameter. The low-signal-intensity remnant of the gubernaculum testis on coronal T2-weighted images also serves as a helpful landmark because the testis frequently lies along its medial border [75].

Mass Lesions

Benign Masses

TESTICULAR PROSTHESES. Testicular prostheses usually contain silicone. The older, fluid-filled silicone prostheses demonstrate low signal intensity on both T1- and T2-weighted images. Newer prostheses are composed of solid elastomers and demonstrate signal characteristics similar to those of native testes: They are of intermediate signal intensity on T1-weighted images and of high signal intensity on T2-weighted images. They are generally recognized by the presence of chemical-shift artifact and the absence of spermatic cord or other scrotal structures [76].

CYSTIC LESIONS. Intratesticular cysts may be solitary or multiple and may occur in up to 10% of the male population. They are characterized by distinct margins and most commonly demonstrate simple fluid signal characteristics [20].

Seminiferous tubular ectasia in the region of the rete testis may produce ovoid lesions in continuity with the edge of the testis. These cystic lesions, which contain spermatozoa, are bilateral in approximately 71% of cases and associated with an ipsilateral spermatocele in approximately 92% of cases. Centered at the mediastinum testis, they are contiguous with the adjacent spermatocele along the bare area of the testis. Seminiferous tubular ectasia is lower in signal intensity than the normal surrounding testis on T1-weighted images and nearly isointense to the surrounding testis on T2-weighted images. It has been postulated that pure intratesticular cysts originate from progressive seminiferous tubular ectasia [77]. Occasionally, cysts also may be localized to the tunica albuginea [71].

Epididymal cysts can occur along the length of the epididymis. They contain simple fluid and are low in signal intensity on T1-weighted images and high in signal intensity on T2-weighted images [20]. Spermatoceles, small cystic structures that occur most commonly in the epididymal head, may be either solitary or multiloculated. They demonstrate variable signal intensity, depending on the presence of spermatozoa, fat, lymphocytes, and cellular debris (fig. 12.36) [20, 78].

BENIGN NEOPLASMS. Only 5% of testicular neoplasms are benign. Of these, 90% are non-germ cell tumors. They may arise from Leydig cells, Sertoli cells, or connective tissue stroma [78].

The most common extratesticular neoplasm is the adenomatoid tumor. It most commonly arises in the epididymis but may be located in the spermatic cord or tunica. Adenomatoid tumor may be round and well defined (fig. 12.37) or, occasionally, plaquelike and less well defined [79, 80]. Lipomas also may arise within the spermatic cord. They demonstrate high signal intensity on T1-weighted images and follow the signal intensity of other adipose tissues on T2-weighted images [81]. As with other fatty lesions, loss of signal intensity on fat-suppressed images is a diagnostic finding.

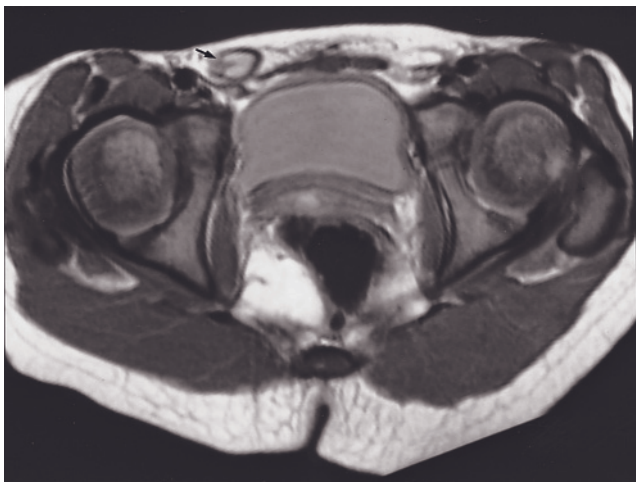

(*a*)

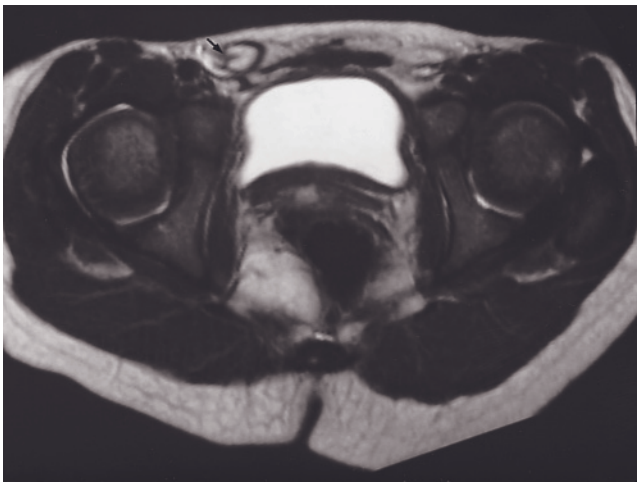

(*b*)

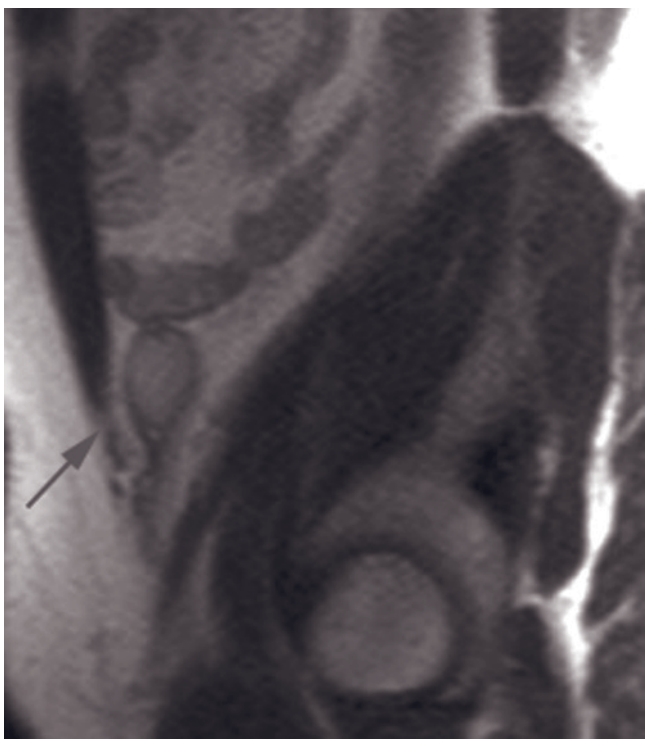

(*c*)

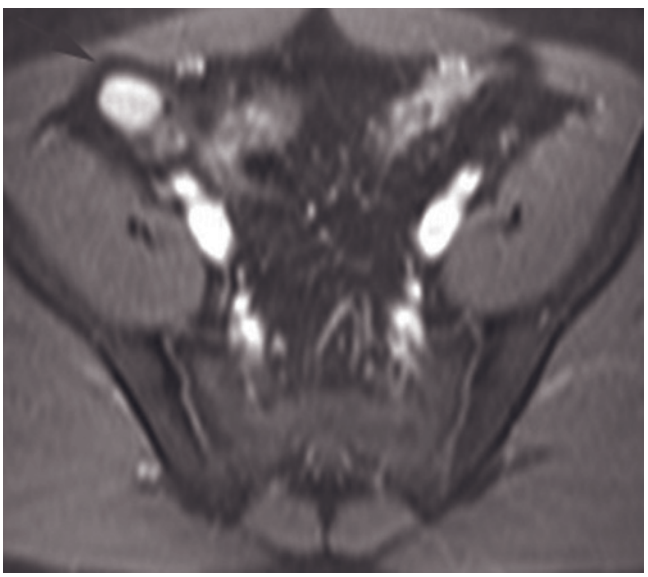

(*d*)

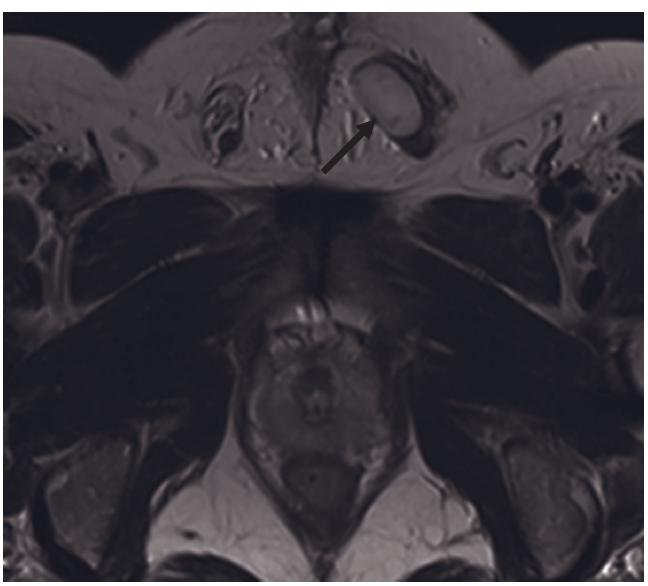

(*e*)

FIG. 12.35 Cryptorchidism. Transverse T1-weighted spin-echo (*a*) and T2-weighted ETSE (*b*) images. The undescended testis within the right inguinal canal is intermediate to high in signal intensity on both T1- and T2-weighted images. The mediastinum testis is shown as a low-signal-intensity transverse band (arrows, *a*, *b*). Sagittal T2-weighted ETSE (*c*) and transverse T1-weighted 3-min postgadolinium fat-suppressed gradient-echo (*d*) images in a second patient. The undescended testis in the right inguinal canal (arrow, *c*) is intermediate to high in signal intensity on the T2-weighted sequence and enhances homogeneously (arrow, *d*) on the postgadolinium T1-weighted images. Note the greater transverse than anteroposterior dimension of the ovoid testis, aiding differentiation from inguinal adenopathy.

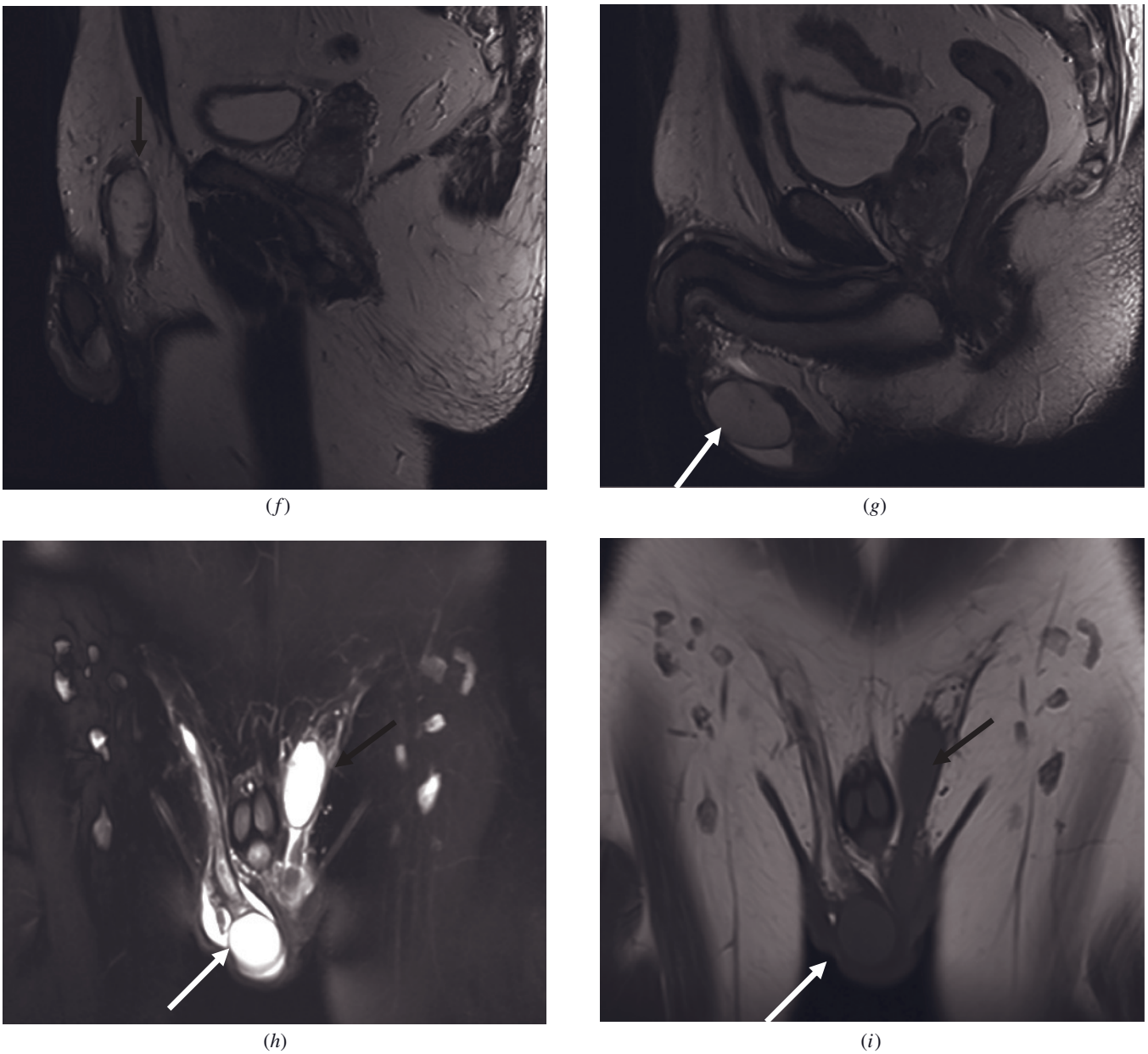

FIG. 12.35 (*Continued*) T2-weighted transverse (*e*) and sagittal (*f*, *g*) high-resolution fast spin-echo, coronal T2-weighted fat-suppressed high-resolution fast spin-echo (*h*), and coronal T1-weighted high-resolution T1-weighted fast spin-echo (*i*) images demonstrate cryptorchidism in another patient. The left testis (black arrows, *e*, *f*, *h*, *i*) is located in the left inguinal canal. The right testis (white arrows, *g*–*i*) is located in the scrotum. Note minimal hydrocele in the right testis and inguinal lymph nodes.

The paratesticular tissues also may harbor benign, fibroproliferative tumors classified as fibrous pseudotumors. They are the second most common extratesticular neoplasm after adenomatoid tumors. They may originate from the tunica albuginea or vaginalis, spermatic cord, or epididymis [82], and their etiology is uncertain [83, 84].

Patients most commonly present with painless masses. Slightly less than half of fibrous pseudotumors are associated with hydroceles or hematoceles [82]. These masses are frequently lobulated, demonstrating frondlike projections, but they also may be characterized by circumferential thickening of the tunica albuginea. They are low in signal intensity on both T1- and T2-weighted images and enhance negligibly with gadolinium [81, 82].

OTHER BENIGN SCROTAL LESIONS. Fluid may accumulate between the parietal and visceral layers of the tunica vaginalis, producing hydroceles, pyoceles, or

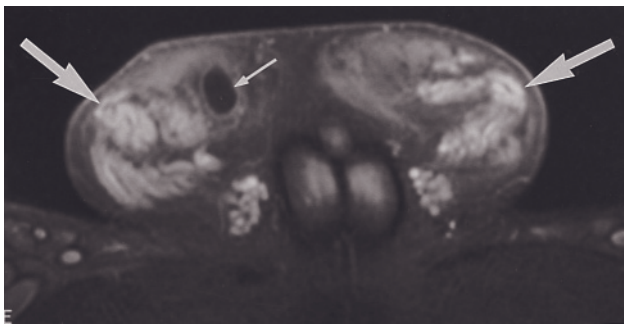

(*a*)

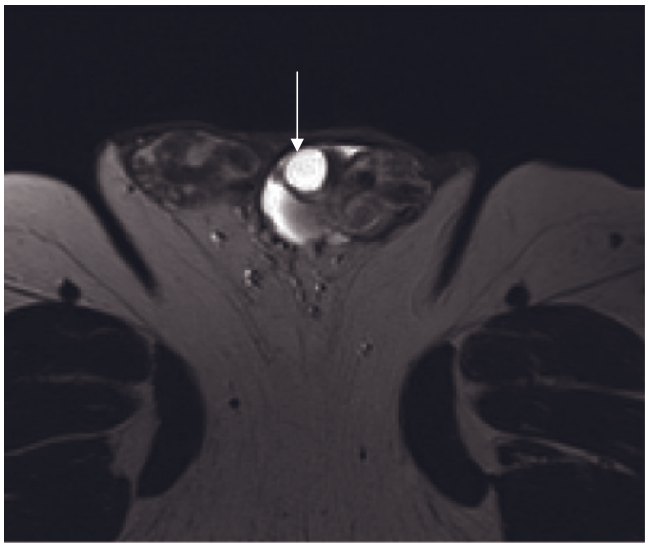

(*b*)

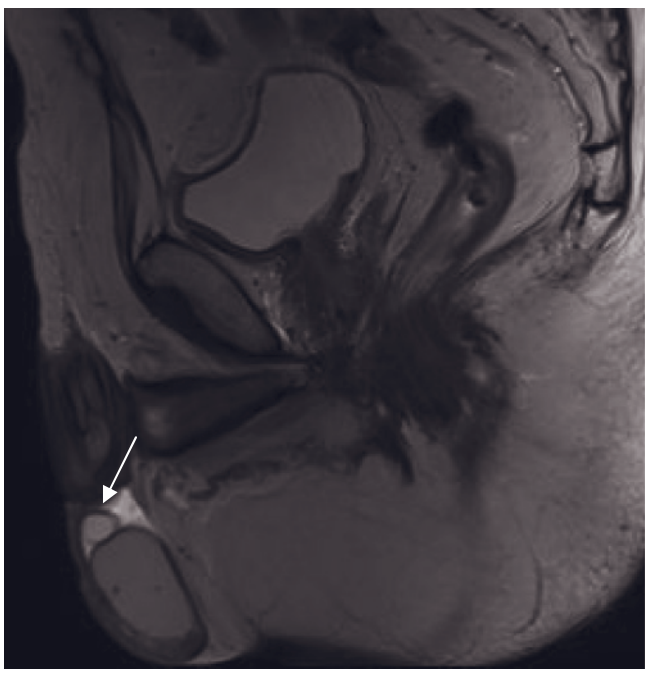

(*c*)

FIG. 12.36 Spermatocele and bilateral varicoceles. Transverse gadolinium-enhanced T1-weighted fat-suppressed spin-echo image (*a*) demonstrates a nonenhancing ovoid structure within the right epididymal head consistent with a spermatocele (small arrow, *a*). There are also bilateral enhancing varicoceles (large arrows). **Epididymal cyst.** Transverse (*b*) and sagittal (*c*) T2-weighted high-resolution fast spin-echo images demonstrate a simple cyst (arrows, *b*, *c*) located in the head of the left epididymis in another patient. The left testis shows its normal high signal intensity on T2-weighted images.

hematoceles. Hydroceles may occur in association with infection, tumor, or trauma. They demonstrate signal characteristics typical of simple fluid and are low in signal intensity on T1-weighted images, high in signal intensity on T2-weighted images, and nearly signal void on postgadolinium images (fig. 12.38). Pyoceles may appear complicated with heterogeneous low signal intensity on T1-weighted images and heterogeneous high signal intensity on T2-weighted images. Hematoceles may exhibit varied signal characteristics, depending on the chronicity of the blood products they contain.

Varicoceles may occur as the result of thrombosis or extrinsic compression of the testicular venous system by organomegaly or retroperitoneal masses. They are more commonly left-sided as a result of testicular vein drainage into the left renal vein, which is lengthier and more prone to compression than the right testicular vein. MRI reveals multiple serpiginous structures in the region of the pampiniform plexus, epididymal head, and spermatic cord. Signal intensity is dependent on flow velocity. Varicoceles often appear intermediate in signal intensity on T1-weighted images and higher in

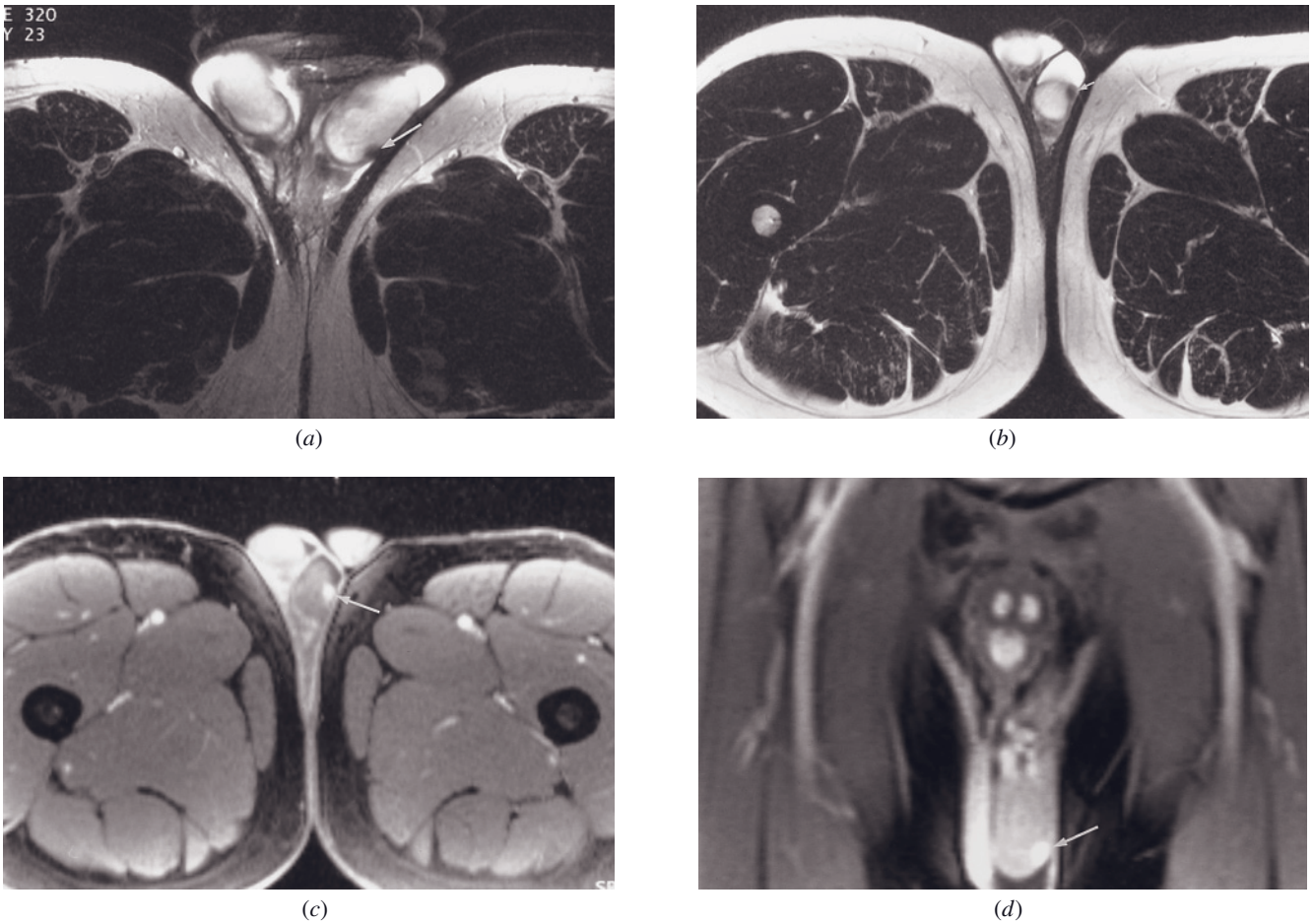

FIG. 12.37 Adenomatoid neoplasm. Transverse phased-array body coil T2-weighted ETSE (*a*), transverse circular surface coil T2-weighted ETSE (*b*), transverse phased-array body coil T1-weighted immediate postgadolinium fat-suppressed gradient-echo (*c*), and coronal phased-array coil T1-weighted immediate postgadolinium fat-suppressed gradient-echo (*d*) images. The tumor is hypointense relative to the normal surrounding testis on T2-weighted imaging (arrows, *a*, *b*). After the administration of gadolinium, there is immediate increased enhancement of the tumor relative to the surrounding testis (arrows, *c*, *d*). Note that the higher signal-to-noise ratio of the circular surface coil permits higher spatial resolution imaging (*b*) compared to the phased-array body coil (*a*). This is useful for imaging superficial structures such as the testicles.

signal intensity on T2-weighted images [20, 78, 81]. On early postgadolinium gradient-echo images, varicoceles are well shown as high-signal-intensity tubular structures (fig. 12.39). Varicoceles often exist with hydroceles (see fig. 12.39).

Scrotal hernias are most frequently diagnosed by clinical inspection. MRI evaluation may prove helpful in equivocal cases, particularly when there is marked associated pain or when physical examination is limited.

The MRI appearance of the hernia may vary with its contents. A complex mass is frequently visualized within an enlarged inguinal canal. Mesenteric fat, loops of bowel, and intraluminal air may be visualized within the scrotal sac. Imaging with a half-Fourier single-shot turbo spin-echo (HASTE) and immediate postgadolinium T1-weighted fat-suppressed gradient-echo (GE) sequence may provide helpful information regarding entrapped bowel viability.

Malignant Masses. Although testicular carcinomas comprise less than 1% of tumors in the male population, a significant number of these occur in males under the age of 40 years and approximately 95% are malignant [85, 86]. Early detection and treatment are crucial, particularly for seminomas, which are chemotherapy- and radiotherapy-sensitive.

Testicular carcinomas may be divided into germ cell and non-germ cell subtypes. Approximately 95% of malignant neoplasms are of germ cell origin [87]. These include seminomas (approximately 40%) and nonseminomatous tumors. Nonseminomatous tumors may be subclassified into embryonal carcinomas (~30%),

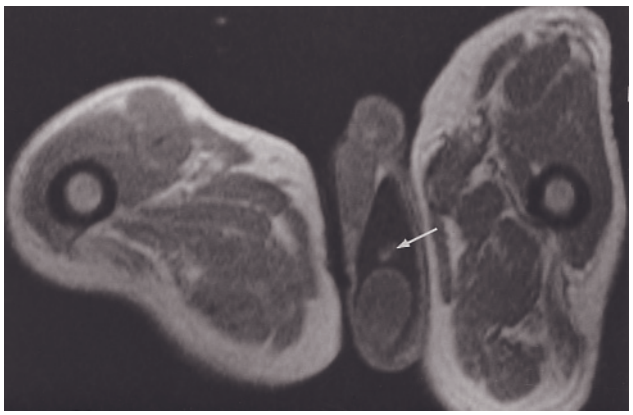

(*a*)

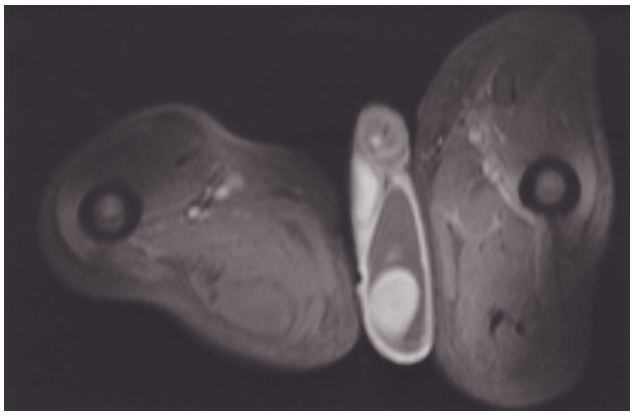

(*b*)

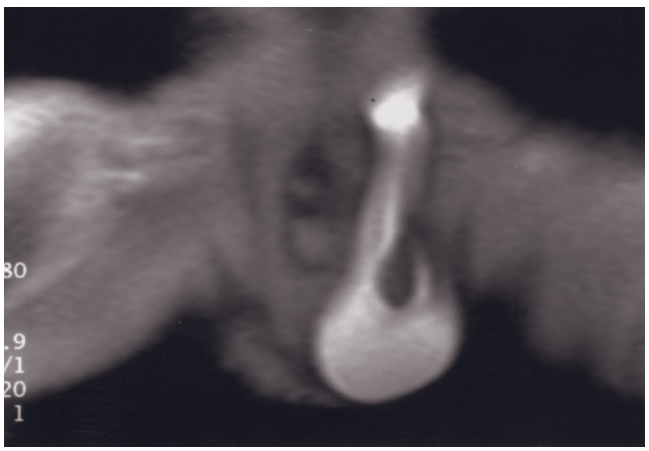

(*c*)

(*d*)

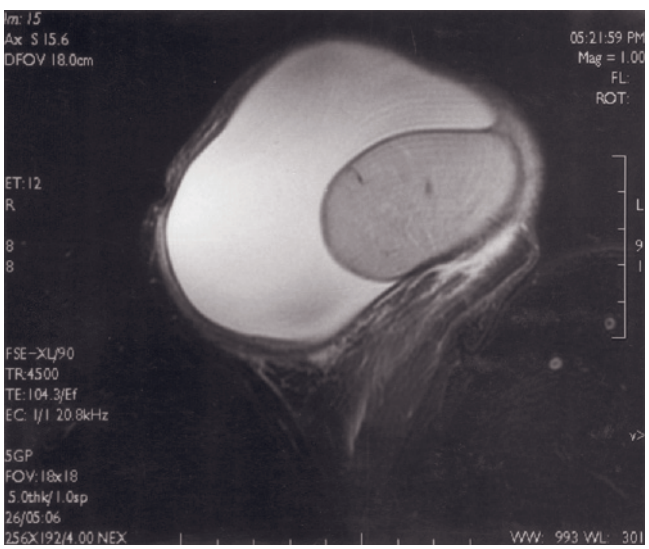

(*e*)

FIG. 12.38 Hydrocele. Transverse T1-weighted gradient echo (*a*) and transverse 1-min postgadolinium T1-weighted fat-suppressed gradient-echo (*b*) images. A left-sided hydrocele is low in signal intensity on the T1-weighted image (*a*). A focus of high signal intensity within the fluid represents the spermatic cord (arrow, *a*). There is uniform enhancement of the testes on the postgadolinium image (*b*). Coronal SS-ETSE (*c*) and gradient-echo fat-suppressed postgadolinium (*d*) images in a second patient, a neonate, demonstrate a large left hydrocele. The testicle is low signal on T2 (*c*) but enhances moderately intensely on the postgadolinium image (*d*). Surface coil T2-weighted echo-train spin-echo image (*e*) in a third patient demonstrates a moderate-sized hydrocele.

teratocarcinomas (~25%), teratoma (10%), and choriocarcinomas (1%). Another 30% of the cases are of mixed histology [87, 88]. The remainder are comprised of Sertoli, Leydig, or mesenchymal cell carcinomas. There may also be involvement by leukemia, lymphoma, or, in rare instances, metastatic disease from lung, melanoma, genitourinary, or gastrointestinal malignancies [78, 88]. Lymphatic drainage of the testes follows the gonadal vessels to the retroperitoneum. In the presence of epididymis or spermatic cord invasion, lymphatic

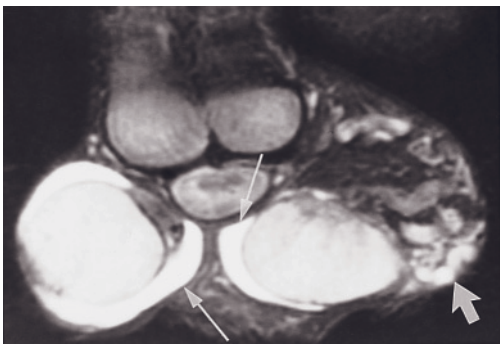

(*a*)

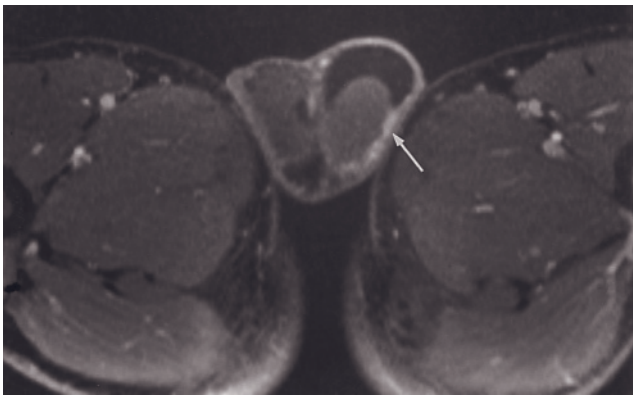

(*b*)

(*c*)

FIG. 12.39 Varicocele with bilateral hydroceles. Coronal T2-weighted ETSE image (*a*) demonstrates high-signal-intensity, serpiginous structures within the left scrotal sac representing a varicocele (thick arrow). There are also bilateral hydroceles (thin arrows, *a*). Transverse 90-s postgadolinium fat-suppressed T1-weighted gradient-echo image (*b*) in a second patient with a varicocele and bilateral hydroceles. High-signal-intensity tubular structures represent a varicocele (arrow, *b*). Coronal 3-min postgadolinium T1-weighted gradient-echo image (*c*) in a third patient with varicocele and bilateral hydroceles with an appearance similar to the prior case.

drainage also extends to the pelvic nodes. Tumors are staged according to TNM criteria as outlined in Table 12.3 [89].

MRI of testicular neoplasms may reveal relative enlargement of the involved testis. Tumors are low in signal intensity on T2-weighted images, and there is degradation of normal testicular morphology. Lack of visualization of the normal septulae has been found to be a sensitive indicator of malignant infiltration [81].

Seminomas are isointense to normal tissue on T1-weighted images and hypointense to normal tissue on T2-weighted images. They most commonly demonstrate homogeneous low signal intensity on T2-weighted images (fig. 12.40) [73, 81]. They may exhibit lobulation or, occasionally, central necrosis [81, 86]. Tumors enhance to a lesser degree than normal testicular tissue. Thus gadolinium administration may increase lesion conspicuity and aid detection of extension into the surrounding tunica albuginea [71, 81].

Nonseminomatous tumors appear more heterogeneous on T2-weighted images and have more ill-defined margins (fig. 12.41). Areas of increased and decreased signal intensity on T1- and T2-weighted images correspond to foci of hemorrhage and necrosis, respectively,

Table 12.3 American Joint Committee on Cancer Staging of Testicular Carcinoma

Carcinoma
Primary Tumor
T0 No evidence of primary tumor
T1 Tumor limited to testis and epididymis, may invade tunica albuginea but not tunica vaginalis
T2 Tumor extends beyond tunica albuginea with involvement of the tunica vaginalis
T3 Tumor invades spermatic cord
T4 Tumor invades scrotum
Lymph Nodes
N0 No lymph node metastasis
N1 Metastasis to a lymph node mass or multiple lymph nodes that are 2 cm or smaller
N2 Metastasis to a lymph node mass or multiple lymph node masses or nodes that are between 2 and 5 cm in size
N3 Metastasis to a lymph node mass larger than 5 cm
Distant Metastases
M0 No distant metastases
M1 Distant metastases (M1a, nonregional nodal or pulmonary metastases/M1b, other distant metastases

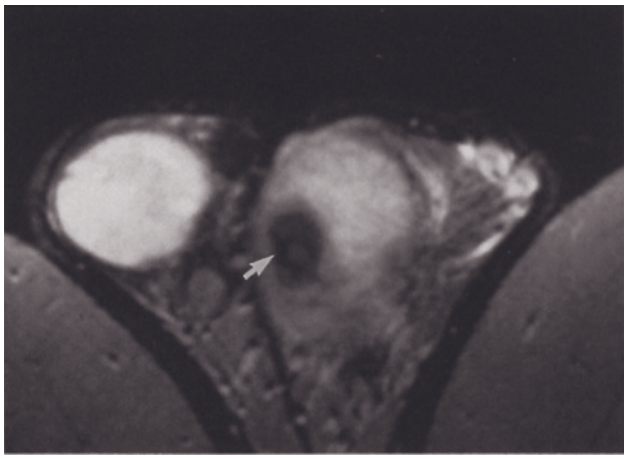

(*a*)

(*b*)

(*c*)

FIG. 12.40 Testicular seminoma. T2-weighted fat-suppressed ETSE image (*a*) using a surface coil demonstrates a well-defined, homogeneously low-signal-intensity 1-cm seminoma (arrow, *a*) arising in the left testicle. (Courtesy of Evan S. Siegelman, M.D., Hospital of the University of Pennsylvania.) Surface coil transverse (*b*) and coronal (*c*) T2-weighted echo-train spin-echo images demonstrate a heterogeneous low-signal-intensity mass that exhibits extensive infiltration of the testicle. Remnants of uninvolved testicle appear high signal.

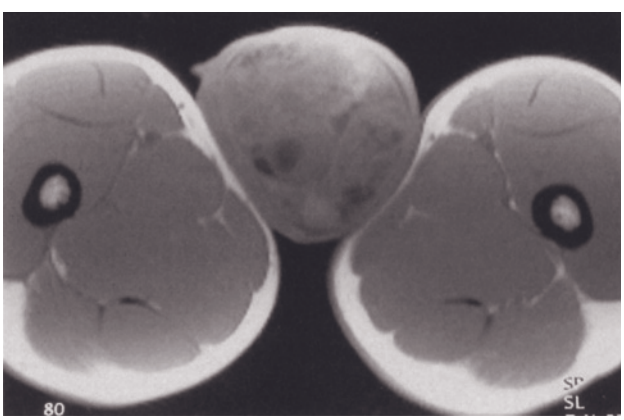

(*a*)

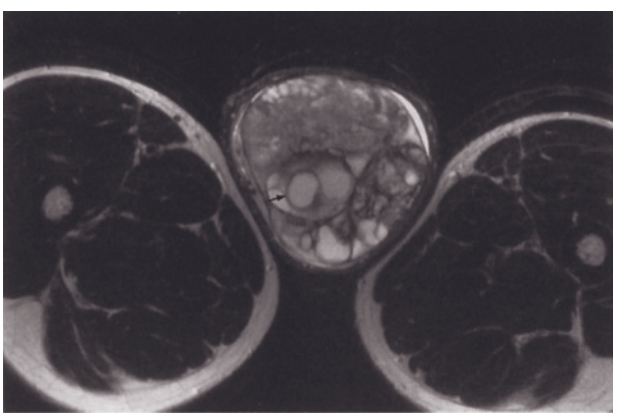

(*b*)

FIG. 12.41 Nonseminomatous testicular neoplasm. T1-weighted gradient-echo (*a*), T2-weighted ETSE (*b*), and 45-s transverse (*c*) and 90-s coronal (*d*) gadolinium-enhanced fat-suppressed T1-weighted gradient-echo images. The left testicle is greatly enlarged, measuring 5 cm in diameter. Tumor replaces the testicle and is mildly heterogeneous on the T1-weighted image (*a*) and considerably heterogeneous on the T2-weighted image (*b*). The tumor contains multiple cystic spaces that are well-defined, high-signal-intensity foci (arrow, *b*) on the T2-weighted image and show lack of enhancement on the postgadolinium images (arrow, *c*).

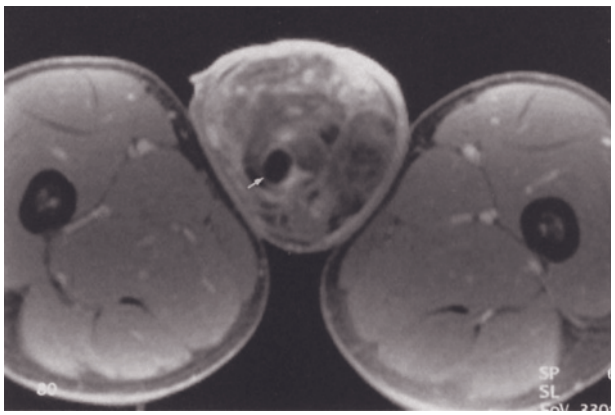

(*c*)

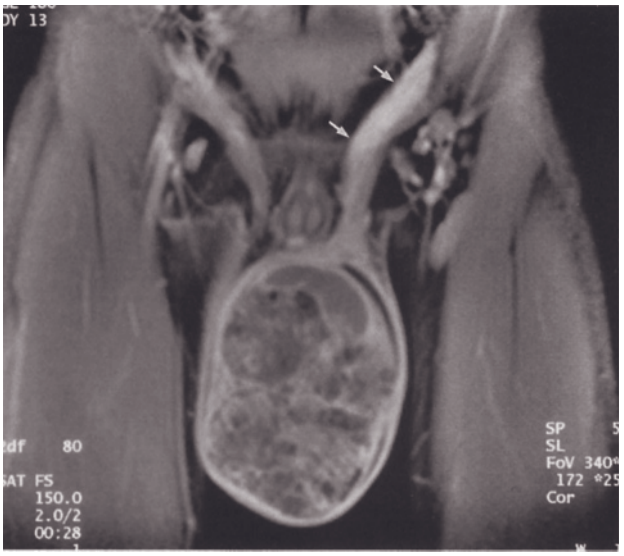

(*d*)

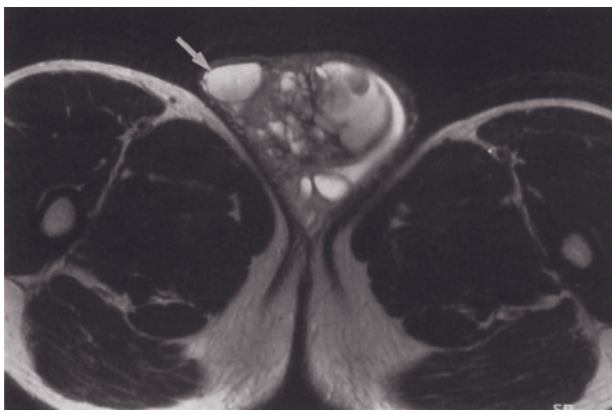

(*e*)

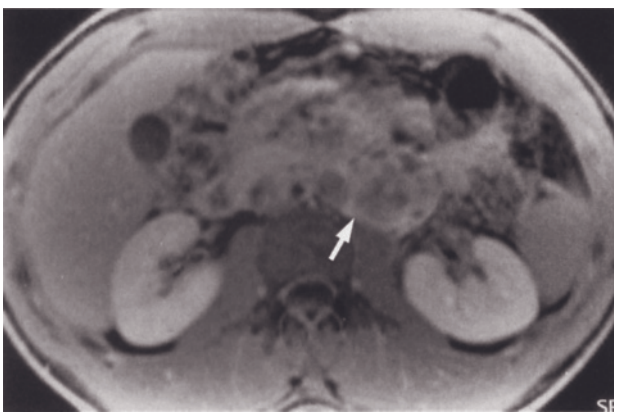

(*f*)

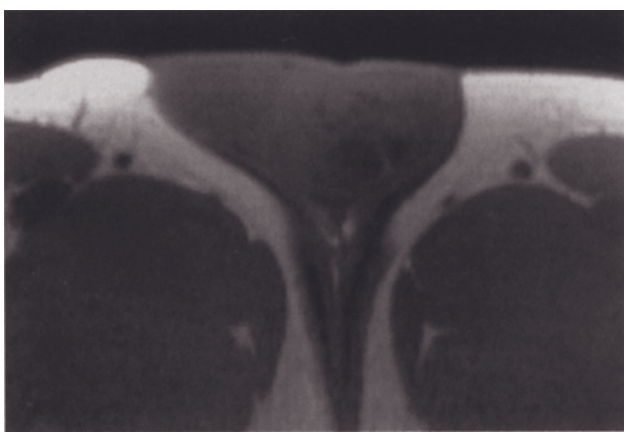

(*g*)

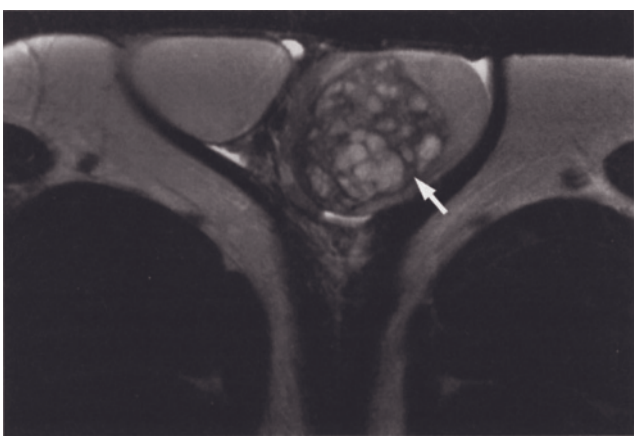

(*h*)

FIG. 12.41 (*Continued*) The coronal image demonstrates the vertical size of the tumor and enlargement of testicular vessels in the left inguinal canal (arrows, *d*). T2-weighted echo-train spin-echo image (*e*) from a more superior tomographic section through the scrotum demonstrates a normal high-signal-intensity right testicle (arrow). On a 3-min postgadolinium fat-suppressed T1-weighted gradient echo image (*f*), a 3-cm left para-aortic lymph node (arrow) is present at the level of the left renal hilum that demonstrates a heterogeneous appearance similar to the primary tumor. T1-weighted gradient-echo (*g*), T2-weighted ETSE (*h*), and coronal interstitial-phase gadolinium-enhanced fat-suppressed T1-weighted gradient-echo (*i*) images in a second patient. A 2.5-cm tumor is present in the left testicle (arrow, *h*).The appearance is similar to the prior case. Note in particular the well-defined high-signal-intensity foci within the mass on the T2-weighted image (*h*). Heterogeneous appearance of the involved left para-aortic lymph

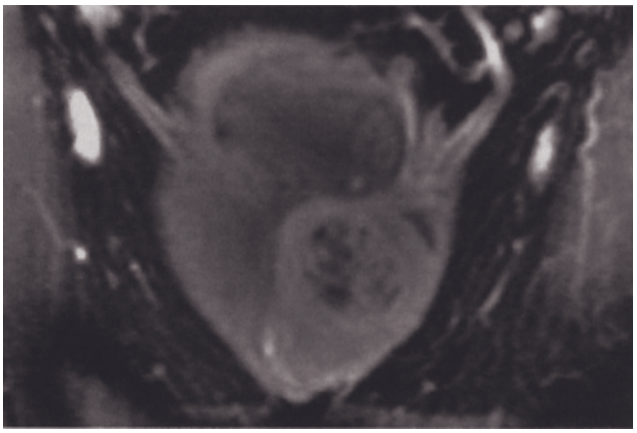

(*i*)

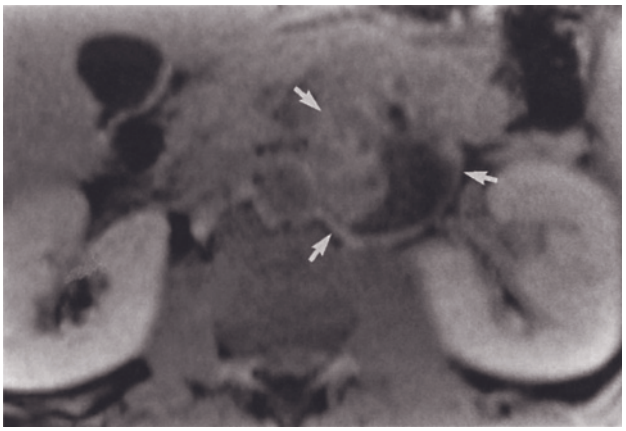

(*j*)

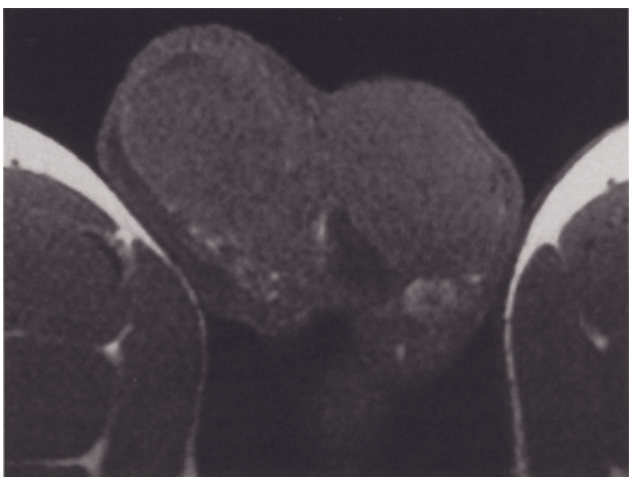

(*k*)

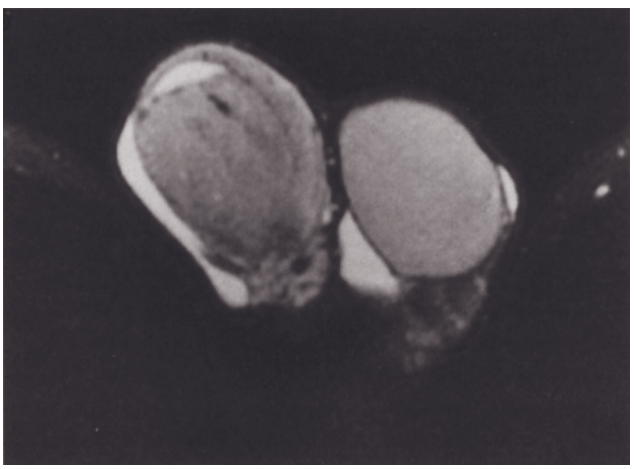

(*l*)

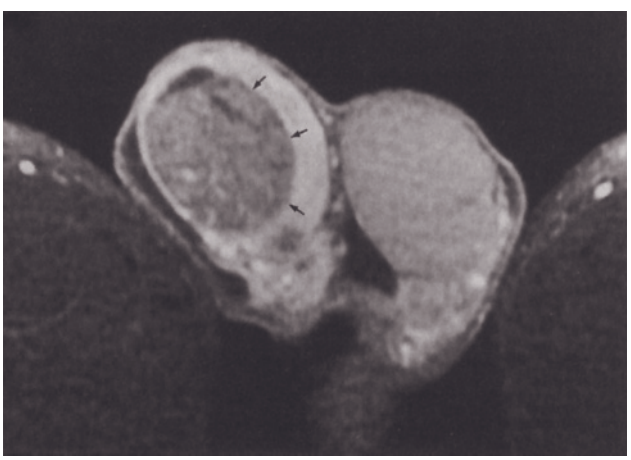

(*m*)

Fig. 12.41 (*Continued*) nodes on the interstitial-phase gadolinium-enhanced fat-suppressed T1-weighted gradient-echo image (arrows, *j*) is also comparable. T1-weighted spin-echo (*k*), T2-weighted ETSE (*l*), and gadolinium-enhanced T1-weighted spin-echo (*m*) images in a third patient. The tumor in this patient is mixed embryonal carcinoma-seminoma. The tumor has a relatively homogeneous and mildly low signal intensity on the T2-weighted image (*l*). Tumor enhancement is slightly heterogeneous on postgadolinium images (*m*) and has a relatively sharp margination (arrows, *m*) from background testicle.

on histologic specimens [73, 86]. These features are most marked within tumors demonstrating mixed histologies [81, 86]. Lymph nodes have a characteristic multicystic appearance.

Lymphomatous infiltration may result in diffuse testicular enlargement, relative hypointensity on T2-weighted images, and involvement of the draining lymphatics. Lymphoma typically has a more homogeneous appearance than other neoplasms (fig. 12.42). Associated adenopathy is similarly homogeneous. This differs from the appearance of nonseminomatous tumors, which have a more multicystic appearance.

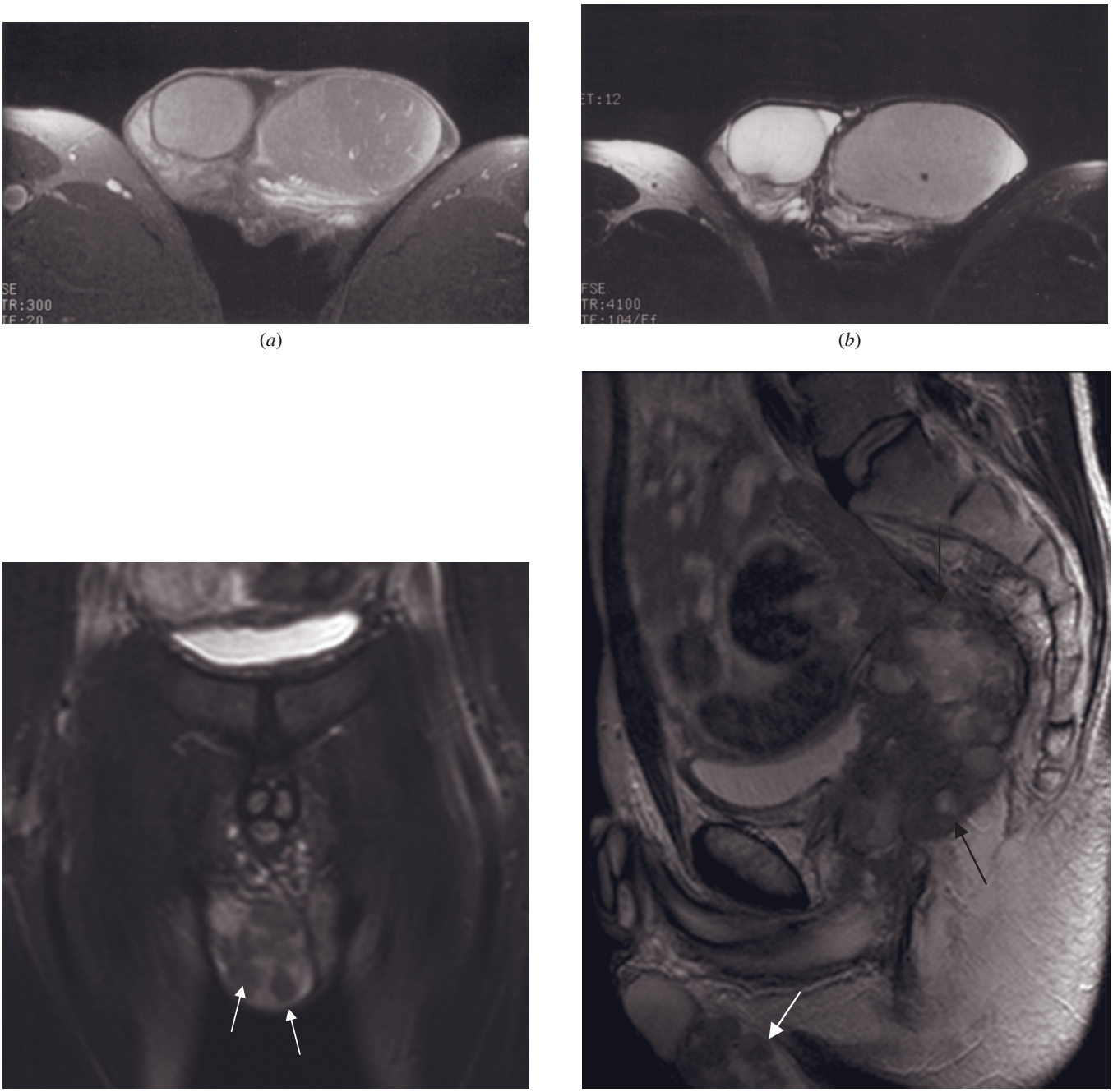

(*a*) (*b*)

(*c*) (*d*)

FIG. 12.42 Testicular lymphoma. T1-weighted SE (*a*) and T2-weighted echo-train spin-echo (*b*) images. The left testicle is enlarged and exhibits diffuse infiltration with homogeneous tumor that is isointense on T1 and mildly hypointense on T2. Lymphoma is typically more homogeneous in appearance than other neoplasms. **Testicular metastases.** Coronal (*c*) and sagittal (*d*) T2-weighted high-resolution fast spin-echo images demonstrate multiple hypointense metastases (white arrows, *c*, *d*) in the right testis in another patient with rectal cancer. The large rectal tumor (black arrows, *d*) invades the posterior bladder wall, seminal vesicles, and prostate.

Metastases are uncommon and usually occur in patients with a known malignancy in an advanced stage. The most common primary tumors are prostate, lung, malignant melanoma, colon (fig. 12.42), and kidney tumors [90].

Testicular Torsion

Acute testicular torsion arises when the bare area is not sufficiently broad to anchor the testis and its supporting structures in place, resulting in a "bell clapper" defor-

mity. It results in irreversible ischemia in fewer than 30% of cases if diagnosis and surgical correction occur within 12 h of the event. The salvage rate decreases rapidly thereafter, with minimal surgical success after 24 hours of ischemia [91]. Ultrasound and nuclear medicine examinations enable timely diagnosis in the acute setting. However, bilateral orchiopexy is still indicated in the subacute period, when findings may be equivocal with either of these modalities. In the setting of subacute torsion, MRI may provide assistance in differentiating this entity from epididymoorchitis.

Common findings on MRI in the subacute setting include an enlarged spermatic cord with diminished flow, diffusely decreased signal intensity of the testis, decreased testicular size, and mild to moderate thickening of the tunica albuginea and epididymis [91]. There also may be increased-signal-intensity foci on T1-weighted images, reflecting hemorrhage, visualization of the pedicular attachment of the testicle in a bell clapper deformity, or an associated hematocele. The identification of a whirling pattern within the spermatic cord and an associated low-signal-intensity knot at the point of maximal torsion on T2-weighted images provides specific evidence for the diagnosis [81, 91]. Initial studies with ^{31}P MR spectroscopy in an animal model have revealed additional promise for the evaluation of testicular torsion in the acute setting [92, 93].

Infection

The vast majority of acute epididymitis cases are isolated, but up to 20% may be associated with orchitis [78]. Therapy is conservative and limited to antibiotics unless there is concomitant infarction from extensive edema or abscess formation necessitating surgery [91]. With the exception of mumps orchitis, isolated acute infection of the testes is rare [54]. When pyogenic abscesses occur, they are frequently accompanied by pyoceles [78, 91]. On MRI, epididymal inflammation is most commonly manifested by generalized enlargement of the organ [71, 81]. The involved epididymis may be hyperintense on T1-weighted images and of variable signal intensity relative to the contralateral side on T2-weighted images [71, 78, 81]. There is heterogeneous enhancement after gadolinium administration [71].

Testicular inflammation also is commonly manifested by generalized enlargement (fig. 12.43) [20, 71, 91]. There is frequently decreased signal intensity of the involved testis on T2-weighted images [71, 78, 81]. The testicular septulae remain well defined but thickened, a finding that is in contrast to the loss of normal architecture frequently observed with invasive neoplastic disease [81]. Intense enhancement of the involved testis is seen after gadolinium administration [71]. Abscesses are accompanied by pyoceles in the majority of patients [91]. Heterogeneous high signal intensity on T2-weighted images is observed both in these extratesticular fluid collections and in the infected fluid intercalating between the testicular septulae (fig. 12.44) [81].

Acute inflammation often results in enlargement and edema of the spermatic cord [71, 91]. However, in contrast to the avascularity of the cord observed in cases of torsion, there is increased vascularity of the cord in the setting of infection. On gadolinium-enhanced images, there is marked enhancement of the inflamed structure and surrounding tissues [71]. These findings serve as helpful differentiating factors in equivocal cases. Identification of the bare area of the testis also virtually excludes the possibility of a bell clapper deformity, and thus of torsion as well [91].

Trauma

MRI may provide information important for clinical management after testicular trauma. Hemorrhage is well demonstrated on T1- and T2-weighted images. Intratesticular hematomas may appear high in signal intensity on T1-weighted images and variable in signal intensity on T2-weighted images [71, 81]. They may also result in alternating bands of increased and decreased signal intensity on T1-weighted images [81]. Blood intersecting between the layers of the tunica vaginalis may result in hematoceles, which also follow the signal intensity of blood products.

Contusion in the absence of focal hemorrhage may also be detected by MRI. There is a resultant decrease in signal intensity of the involved testis on T2-weighted images as well as a relative decrease in gadolinium enhancement [71].

Careful inspection of the tunica albuginea is necessary to evaluate for the possibility of acute testicular rupture. This may be manifested by discontinuity in the normal low signal intensity of the tunica albuginea on T2-weighted images. Detection of testicular rupture often necessitates surgical intervention [81].

CONCLUSIONS

MRI is an effective modality for detecting the full range of disease entities involving the male pelvis because of high intrinsic soft tissue contrast resolution, high spatial resolution, and multiplanar imaging. Although MRI is excellent at evaluating testicular disease, the lower cost and acceptable accuracy of other imaging approaches have relegated MRI primarily to a problem-solving modality. The greatest role for MRI has been in the staging of prostate cancer. The variety of diagnostic options and uncertainty in patient outcome after therapeutic intervention have limited the widespread use of MRI in this setting. Continued refinement of MR

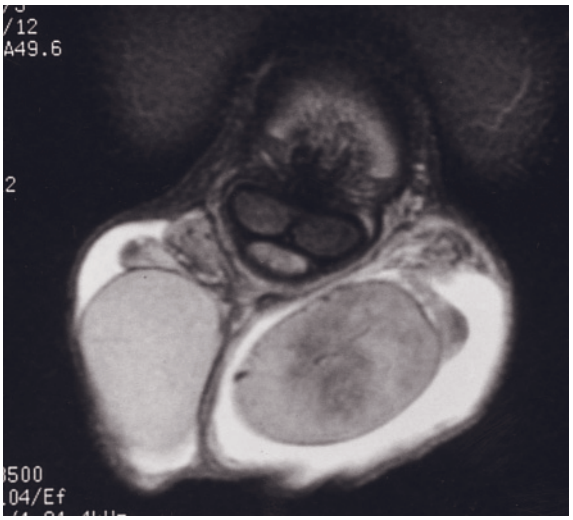

(*a*)

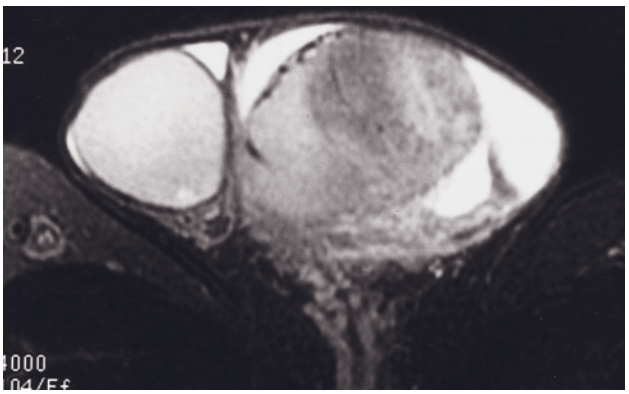

(*b*)

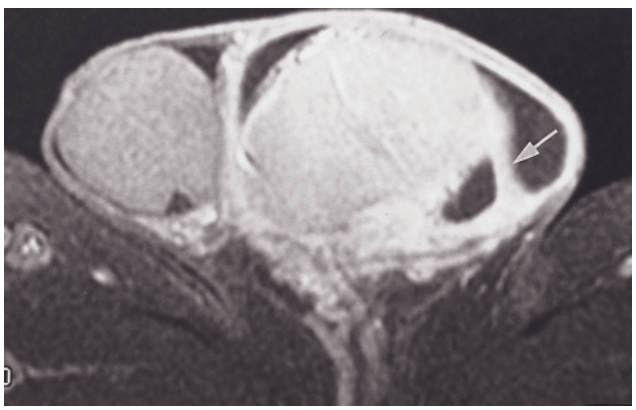

(*c*)

FIG. 12.43 Mumps orchitis. Coronal T2-weighted fat-suppressed echo-train spin-echo (*a*), transverse T2-weighted fat-suppressed ETSE (*b*), and T1-weighted postgadolinium fat-suppressed spin-echo (*c*) images. There is enlargement of the left testis relative to the contralateral side (*b*, *c*).The affected testis is heterogeneous and low in signal intensity on the T2-weighted images (*a*, *b*) and enhances slightly more than the unaffected testis on the postgadolinium image (*c*). Note the enhancing, thickened septations within the scrotal sac (arrow, *c*). There are accompanying hydroceles bilaterally.

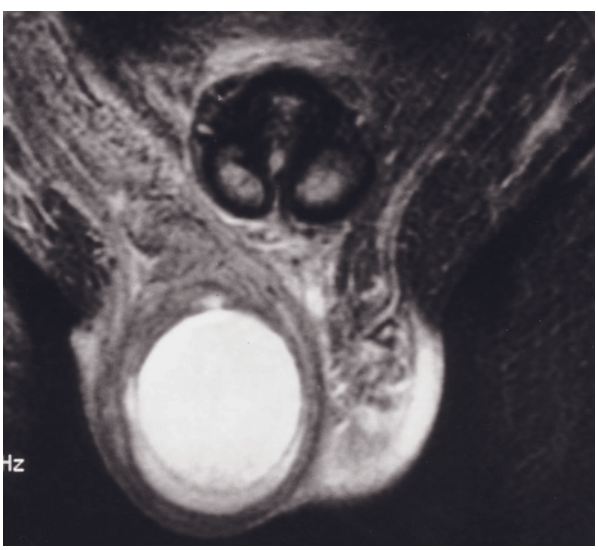

(*a*)

(*b*)

FIG. 12.44 Testicular abscess. Coronal T2-weighted ETSE (*a*) and gadolinium-enhanced T1-weighted spin-echo (*b*) images. A complex fluid collection within the right testis is heterogeneously high in signal intensity on the T2-weighted image (*a*) and heterogeneously low in signal intensity on the postgadolinium T1-weighted image (*b*), which is consistent with an abscess. There is extensive enhancement of the surrounding scrotal tissues secondary to adjacent inflammatory changes (arrow, *b*).

spectroscopy techniques may ultimately permit comprehensive imaging evaluation of the oncology patient.

REFERENCES

1. Mirowitz SA, Heiken JP, Brown JJ. Evaluation of fat saturation technique for T2-weighted endorectal coil MRI of the prostate. *Magn Reson Imaging* 12(5): 743–747, 1994.
2. Nunes LW, Schiebler MS, Rauschning W et al. The normal prostate and periprostatic structures: correlation between MR images made with an endorectal coil and cadaveric microtome sections. *AJR Am J Roentgenol* 164(4): 923–927, 1995.
3. Hricak H, White S, Vigneron D et al. Carcinoma of the prostate gland: MR imaging with pelvic phased-array coils versus integrated endorectal—pelvic phased-array coils. *Radiology* 193(3): 703–709, 1994.
4. Cornfeld D, Weinreb J. MR imaging of the prostate: 1.5T versus 3.0T. *Magn Reson Imaging Clin N Am* 15: 433–448, 2007.
5. Kim CK, Park BK. Update of prostate magnetic resonance imaging at 3T. *J Comput Assist Tomogr* 32(2): 163–172, 2008.
6. Hricak H, Choyke PL, Eberhardt SC et al. Imaging prostate cancer: a multidisciplinary perspective. *Radiology* 243(1): 28–53, 2007.
7. Claus FG, Hricak H, Hattery RR. Pretreatment evaluation of prostate cancer: role of MR imaging and ^{1}H MR spectroscopy. *Radiographics* 24 (Suppl 1): S167–S180, 2004.
8. Choi YJ, Kim JK, Kim N et al. Functional MR imaging of prostate cancer. *Radiographics* 27(1): 63–75; discussion 75–67, 2007.
9. Shukla-Dave A, Hricak H, Eberhardt SC et al. Chronic prostatitis: MR imaging and ^{1}H MR spectroscopic imaging findings—initial observations. *Radiology* 231(3): 717–724, 2004.
10. Pucar D, Shukla-Dave A, Hricak H et al. Prostate cancer: correlation of MR imaging and MR spectroscopy with pathologic findings after radiation therapy—initial experience. *Radiology* 236(2): 545–553, 2005.
11. Mueller-Lisse UG, Vigneron DB, Hricak H et al. Localized prostate cancer: effect of hormone deprivation therapy measured by using combined three-dimensional ^{1}H MR spectroscopy and MR imaging: clinicopathologic case-controlled study. *Radiology* 221(2): 380–390, 2001.
12. McDermott VG, Meakem TJ 3rd, Stolpen AH et al. Prostatic and periprostatic cysts: findings on MR imaging. *AJR Am J Roentgenol* 164(1): 123–127, 1995.
13. Nghiem HT, Kellman GM, Sandberg SA et al. Cystic lesions of the prostate. *Radiographics* 10(4): 635–650, 1990.
14. Thurnher S, Hricak H, Tanagho EA. Mullerian duct cyst: diagnosis with MR imaging. *Radiology* 168(1): 25–28, 1988.
15. Gevenois PA, Van Sinoy ML, Sintzoff SA Jr. et al. Cysts of the prostate and seminal vesicles: MR imaging findings in 11 cases. *AJR Am J Roentgenol* 155(5): 1021–1024, 1990.
16. Hricak H. The prostate gland. In: Hricak H, Carrington B, editors. *MRI of the pelvis*. Norwalk, CT: Appleton & Lange, 1991, p. 249–312.
17. Keetch DW, Andriole GL. Medical therapy for benign prostatic hyperplasia. *AJR Am J Roentgenol* 164(1): 11–15; discussion 16–17, 1995.
18. Kahn T, Burrig K, Schmitz-Drager B et al. Prostatic carcinoma and benign prostatic hyperplasia: MR imaging with histopathologic correlation. *Radiology* 173(3): 847–851, 1989.
19. Schiebler ML, Tomaszewski JE, Bezzi M et al. Prostatic carcinoma and benign prostatic hyperplasia: correlation of high-resolution MR and histopathologic findings. *Radiology* 172(1): 131–137, 1989.
20. Fritzsche PJ, Wilbur MJ. The male pelvis. *Semin Ultrasound CT MR* 10(1): 11–28, 1989.
21. Chang Y, Hricak H. Magnetic resonance imaging of the prostate gland. *Semin Ultrasound CT MR* 9(5): 343–351, 1988.
22. Way WG, Jr. Brown JJ, Lee JK et al. MR imaging of benign prostatic hypertrophy using a Helmholtz-type surface coil. *Magn Reson Imaging* 10(3): 341–349, 1992.
23. Lovett K, Rifkin MD, McCue PA et al. MR imaging characteristics of noncancerous lesions of the prostate. *J Magn Reson Imaging* 2(1): 35–39, 1992.
24. Sommer FG, Nghiem HV, Herfkens R et al. Gadolinium-enhanced MRI of the abnormal prostate. *Magn Reson Imaging* 11(7): 941–948, 1993.
25. Phillips ME, Kressel HY, Spritzer CE et al. Prostatic disorders: MR imaging at 1.5T. *Radiology* 164(2): 386–392, 1987.
26. Hricak H. Imaging prostate carcinoma. *Radiology* 169(2): 569–571, 1988.
27. Hricak H, Thoeni R. Neoplasms of the prostate gland. In: Pollack H, editor. *Clinical Urography*. Philadelphia: WB Saunders, 1990, p. 1382–1383.
28. Prostate. In: Greene FL, Compton CC, Fritz AG et al., editors. *AJCC Cancer Staging Atlas*. ed. New York: Springer, 2006, p. 293–301.
29. Schnall MD, Imai Y, Tomaszewski J et al. Prostate cancer: local staging with endorectal surface coil MR imaging. *Radiology* 178(3): 797–802, 1991.
30. Carter HB, Brem RF, Tempany CM et al. Nonpalpable prostate cancer: detection with MR imaging. *Radiology* 178(2): 523–525, 1991.
31. Outwater E, Schiebler ML, Tomaszewski JE et al. Mucinous carcinomas involving the prostate: atypical findings at MR imaging. *J Magn Reson Imaging* 2(5): 597–600, 1992.
32. Schiebler ML, Schnall MD, Pollack HM et al. Current role of MR imaging in the staging of adenocarcinoma of the prostate. *Radiology* 189(2): 339–352, 1993.
33. Cornel EB, Smits GA, Oosterhof GO et al. Characterization of human prostate cancer, benign prostatic hyperplasia and normal prostate by in vitro ^{1}H and ^{31}P magnetic resonance spectroscopy. *J Urol* 150(6): 2019–2024, 1993.
34. van Dorsten FA, van der Graaf M, Engelbrecht MR et al. Combined quantitative dynamic contrast-enhanced MR imaging and ^{1}H MR spectroscopic imaging of human prostate cancer. *J Magn Reson Imaging* 20(2): 279–287, 2004.
35. Yu KK, Hricak H. Imaging prostate cancer. *Radiol Clin North Am* 38(1): 59–85, viii, 2000.
36. Garcia-Segura JM, Sanchez-Chapado M, Ibarburen C et al. In vivo proton magnetic resonance spectroscopy of diseased prostate: spectroscopic features of malignant versus benign pathology. *Magn Reson Imaging* 17(5): 755–765, 1999.
37. van der Graaf M, van den Boogert HJ, Jager GJ et al. Human prostate: multisection proton MR spectroscopic imaging with a single spin-echo sequence—preliminary experience. *Radiology* 213(3): 919–925, 1999.
38. Heerschap A, Jager GJ, van der Graaf M et al. In vivo proton MR spectroscopy reveals altered metabolite content in malignant prostate tissue. *Anticancer Res* 17(3A): 1455–1460, 1997.
39. Kaji Y, Kurhanewicz J, Hricak H et al. Localizing prostate cancer in the presence of postbiopsy changes on MR images: role of proton MR spectroscopic imaging. *Radiology* 206(3): 785–790, 1998.
40. Bahnson RR. Editorial: improving prostate cancer detection. *J Urol* 164(2): 405, 2000.
41. Parivar F, Hricak H, Shinohara K et al. Detection of locally recurrent prostate cancer after cryosurgery: evaluation by transrectal ultrasound, magnetic resonance imaging, and three-dimensional proton magnetic resonance spectroscopy. *Urology* 48(4): 594–599, 1996.
42. Coakley FV, Teh HS, Qayyum A et al. Endorectal MR imaging and MR spectroscopic imaging for locally recurrent prostate cancer after external beam radiation therapy: preliminary experience. *Radiology* 233(2): 441–448, 2004.

43. Steinfeld AD. Questions regarding the treatment of localized prostate cancer. *Radiology* 184(3): 593–598, 1992.
44. Quinn SF, Franzini DA, Demlow TA, et al. MR imaging of prostate cancer with an endorectal surface coil technique: correlation with whole-mount specimens. *Radiology* 190(2): 323–327, 1994.
45. Harris RD, Schned AR, Heaney JA. Staging of prostate cancer with endorectal MR imaging: lessons from a learning curve. *Radiographics* 15(4): 813–829; discussion 829–832, 1995.
46. Huch Boni RA, Boner JA, Debatin JF et al. Optimization of prostate carcinoma staging: comparison of imaging and clinical methods. *Clin Radiol* 50(9): 593–600, 1995.
47. Huch Boni RA, Boner JA, Lutolf UM et al. Contrast-enhanced endorectal coil MRI in local staging of prostate carcinoma. *J Comput Assist Tomogr* 19(2): 232–237, 1995.
48. Huch Boni RA, Meyenberger C, Pok Lundquist J et al. Value of endorectal coil versus body coil MRI for diagnosis of recurrent pelvic malignancies. *Abdom Imaging* 21(4): 345–352, 1996.
49. Tempany CM, Rahmouni AD, Epstein JI et al. Invasion of the neurovascular bundle by prostate cancer: evaluation with MR imaging. *Radiology* 181(1): 107–112, 1991.
50. Kalbhen CL, Hricak H, Shinohara K et al. Prostate carcinoma: MR imaging findings after cryosurgery. *Radiology* 198(3): 807–811, 1996.
51. McCollum RW, Banner MP. Calculous disease of the urinary tract. In: Pollack H, editor. *Clinical Urography*. 1990, p. 1908–1912.
52. Allen KS, Kressel HY, Arger PH et al. Age-related changes of the prostate: evaluation by MR imaging. *AJR Am J Roentgenol* 152(1): 77–81, 1989.
53. Hricak H, Dooms GC, Jeffrey RB et al. Prostatic carcinoma: staging by clinical assessment, CT, and MR imaging. *Radiology* 162(2): 331–336, 1987.
54. Rifkin M. Inflammation of the lower urinary tract. In: Pollack H, editor. *Clinical Urography*. 1990, p. 940–960.
55. Engelbrecht MR, Huisman HJ, Laheij RJ et al. Discrimination of prostate cancer from normal peripheral zone and central gland tissue by using dynamic contrast-enhanced MR imaging. *Radiology* 229(1): 248–254, 2003.
56. Narumi Y, Hricak H, Armenakas NA et al. MR imaging of traumatic posterior urethral injury. *Radiology* 188(2): 439–443, 1993.
57. Hricak H, Marotti M, Gilbert TJ et al. Normal penile anatomy and abnormal penile conditions: evaluation with MR imaging. *Radiology* 169(3): 683–690, 1988.
58. Hricak H. The penis and male urethra. In: Hricak H, Carrington B, editors. *MRI of the pelvis*. Norwalk, CT: Appleton & Lange, 1991, p. 383–416.
59. Amis ES, Newhouse JH. *Essentials of Uroradiology*. Boston: Little, Brown, & Company, 1991, p. 69.
60. McCollum RW. Ureteral Neoplasms. In: Pollack H, editor. *Clinical Urography*. 1990, p. 1406–1409.
61. Kaneko K, De Mouy EH, Lee BE. Sequential contrast-enhanced MR imaging of the penis. *Radiology* 191(1): 75–77, 1994.
62. Ichioka K, Utsunomiya N, Ueda N et al. Primary localized amyloidosis of urethra: magnetic resonance imaging findings. *Urology* 64(2): 376–378, 2004.
63. Helweg G, Judmaier W, Buchberger W et al. Peyronie's disease: MR findings in 28 patients. *AJR Am J Roentgenol* 158(6): 1261–1264, 1992.
64. Schneider HJ, Rugendorff EW, Rohrborn C. Pathogenesis, diagnosis and therapy of induratio penis plastica (IPP). *Int Urol Nephrol* 17(3): 235–244, 1985.
65. Di Santis D. Ureteral Neoplasms. In: Pollack H, editor. *Clinical Urography*, 1990, p. 925–939.
66. Pretorius ES, Siegelman ES, Ramchandani P et al. MR imaging of the penis. *Radiographics* 21 Spec No: S283–298; discussion S298–289, 2001.
67. King BF, Hattery RR, Lieber MM et al. Congenital cystic disease of the seminal vesicle. *Radiology* 178(1): 207–211, 1991.
68. King BF, Hattery RR, Lieber MM et al. Seminal vesicle imaging. *Radiographics* 9(4): 653–676, 1989.
69. Mirowitz SA. Seminal vesicles: biopsy-related hemorrhage simulating tumor invasion at endorectal MR imaging. *Radiology* 185(2): 373–376, 1992.
70. Furuya S, Masumori N, Furuya R et al. Characterization of localized seminal vesicle amyloidosis causing hemospermia: an analysis using immunohistochemistry and magnetic resonance imaging. *J Urol* 173(4): 1273–1277, 2005.
71. Muller-Leisse C, Bohndorf K, Stargardt A et al. Gadolinium-enhanced T1-weighted versus T2-weighted imaging of scrotal disorders: is there an indication for MR imaging? *J Magn Reson Imaging* 4(3): 389–395, 1994.
72. Hancock RA, Hodgins TE. Polyorchidism. *Urology* 24(4): 303–307, 1984.
73. Johnson JO, Mattrey RF, Phillipson J. Differentiation of seminomatous from nonseminomatous testicular tumors with MR imaging. *AJR Am J Roentgenol* 154(3): 539–543, 1990.
74. Giwercman A, Grindsted J, Hansen B et al. Testicular cancer risk in boys with maldescended testis: a cohort study. *J Urol* 138(5): 1214–1216, 1987.
75. Kier R, McCarthy S, Rosenfield AT et al. Nonpalpable testes in young boys: evaluation with MR imaging. *Radiology* 169(2): 429–433, 1988.
76. Semelka R, Anderson M, Hricak H. Prosthetic testicle: appearance at MR imaging. *Radiology* 173(2): 561–562, 1989.
77. Tartar VM, Trambert MA, Balsara ZN et al. Tubular ectasia of the testicle: sonographic and MR imaging appearance. *AJR Am J Roentgenol* 160(3): 539–542, 1993.
78. Hricak H. The testis. In: Hricak H, Carrington B, editors. *MRI of the pelvis*. Norwalk, CT: Appleton & Lange, 1991, p. 343–382.
79. Faysal MH, Strefling A, Kosek JC. Epididymal neoplasms: a case report and review. *J Urol* 129(4): 843–844, 1983.
80. Pavone-Macaluso M, Smith PH, Bagshaw MA. *Testicular Cancer and Other Tumors of the Genito-Urinary Tract*. New York, NY: Plenum Press, 1985.
81. Cramer BM, Schlegel EA, Thueroff JW. MR imaging in the differential diagnosis of scrotal and testicular disease. *Radiographics* 11(1): 9–21, 1991.
82. Grebenc ML, Gorman JD, Sumida FK. Fibrous pseudotumor of the tunica vaginalis testis: imaging appearance. *Abdom Imaging* 20(4): 379–380, 1995.
83. Sajjad SM, Azizi MR, Llamas L. Fibrous pseudotumor of testicular tunic. *Urology* 19(1): 86–88, 1982.
84. Parveen T, Fleischmann J, Petrelli M. Benign fibrous tumor of the tunica vaginalis testis. Report of a case with light, electron microscopic, and immunocytochemical study, and review of the literature. *Arch Pathol Lab Med* 116(3): 277–280, 1992.
85. Parker SL, Tong T, Bolden S et al. Cancer statistics, 1996. *CA Cancer J Clin* 46(1): 5–27, 1996.
86. Buckley DL, Roberts C, Parker GJ et al. Prostate cancer: evaluation of vascular characteristics with dynamic contrast-enhanced T1-weighted MR imaging—initial experience. *Radiology* 233(3): 709–715, 2004.
87. Richie JP. Detection and treatment of testicular cancer. *CA Cancer J Clin* 43(3): 151–175, 1993.
88. Mostofi FK. Proceedings: Testicular tumors. Epidemiologic, etiologic, and pathologic features. *Cancer* 32(5): 1186–1201, 1973.
89. Testis. In: Greene FL, Compton CC, Fritz AG, et al., editors. *AJCC Cancer Staging Atlas*. New York: Springer, 2006, p. 303–314.
90. Dogra VS, Gottlieb RH, Oka M et al. Sonography of the scrotum. *Radiology* 227(1): 18–36, 2003.
91. Trambert MA, Mattrey RF, Levine D et al. Subacute scrotal pain: evaluation of torsion versus epididymitis with MR imaging. *Radiology* 175(1): 53–56, 1990.
92. Tzika AA, Vigneron DB, Hricak H et al. P-31 MR spectroscopy in assessing testicular torsion: rat model. *Radiology* 172(3): 753–757, 1989.
93. Chew WM, Hricak H. Phosphorus-31 MRS of human testicular function and viability. *Invest Radiol* 24(12): 997–1000, 1989.

CHAPTER 13

FEMALE URETHRA AND VAGINA

LARA B. EISENBERG, JORGE ELIAS, JR., WAQAS QURESHI, YOUNG MI KU, AND RICHARD C. SEMELKA

FEMALE URETHRA

Introduction

Evaluation and diagnosis of pathology involving the female urethra have been challenging and difficult because of the poor specificity of clinical symptoms and the lack of a suitable imaging modality. Because of its multiplanar imaging capability and superior soft tissue contrast, MRI has proven to be the most sensitive modality for the detection and staging of benign and malignant urethral pathology.

Normal Anatomy

The female urethra originates at the trigone of the bladder and terminates anterior to the opening of the vagina. It is a thin-walled muscular channel and measures approximately 4 cm in length. The lower two-thirds of the urethra is lined by stratified squamous epithelium, whereas the proximal one-third, like the urinary bladder, has a transitional cell epithelial lining. The urethra has a three-layered zonal anatomy, which consists of the inner mucosal layer, the highly vascular submucosal layer, and the outer muscular layer. The muscular layer consists of an inner longitudinal smooth muscle layer and an outer striated circular muscle layer. Extensions of the endopelvic fascia, the urethropelvic and pubourethral ligaments, help to stabilize the urethra in addition to contributing to urinary continence. The submucosal and striated muscle fibers of the urethra aid in urinary continence as well. The paraurethral and periurethral submucosal glands are not typically seen [1–3].

MRI Technique

Routine imaging for urethral pathology should include transverse, high-resolution, small-field-of-view T1-weighted images before and after intravenous contrast administration, particularly in cases of suspected tumor. The addition of fat suppression may increase conspicuity of disease. Orthogonal transverse and sagittal high-resolution T2-weighted images are also routinely obtained [1, 4].

Coronal high-resolution T2-weighted images may be helpful in select cases. Endorectal and endovaginal

Abdominal-Pelvic MRI, Third Edition, edited by Richard C. Semelka. Copyright © 2010 John Wiley & Sons, Inc.

coil imaging provides superior anatomic resolution and can help better delineate the zonal anatomy of the urethra as well as define extent of disease processes. However, near-field high signal intensity and the small field of view can limit image quality with these techniques [4–6]. Imaging at 3T can provide superior spatial resolution, but several challenges exist when imaging at 3T, such as RF field inhomogeneity, which can lead to imaging artifacts and local variation in signal intensity.

Normal

On transverse T2- and enhanced T1-weighted images the female urethra demonstrates a "target" appearance,, with a low-signal-intensity outer ring, a high-signal-intensity middle ring, and a low-signal-intensity central dot (fig. 13.1) [1, 4]. The dark outer ring corresponds to both the outer striated and inner longitudinal and circular smooth muscle layers [4, 7–10]. The middle high-signal-intensity ring represents the vascular submucosal layer, whereas the dark central dot represents the mucosal layer. This target appearance is seen more commonly in the middle urethra than in the proximal or distal urethra. The low-signal-intensity outer layer thins toward the distal urethra. Occasionally, a tiny dot of high signal intensity is seen in the center of the urethra on high-resolution T2-weighted images and is thought to be due to urine or mucus in the lumen [10, 11]. With endovaginal coil imaging, the separate muscle layers of the urethra can be discerned [12]. The zonal anatomy of the urethra is not always apparent in post-

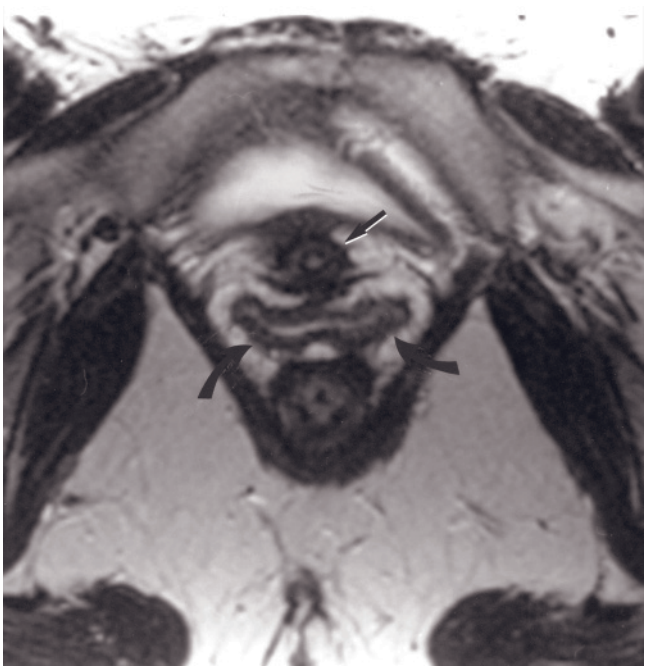

(*a*)

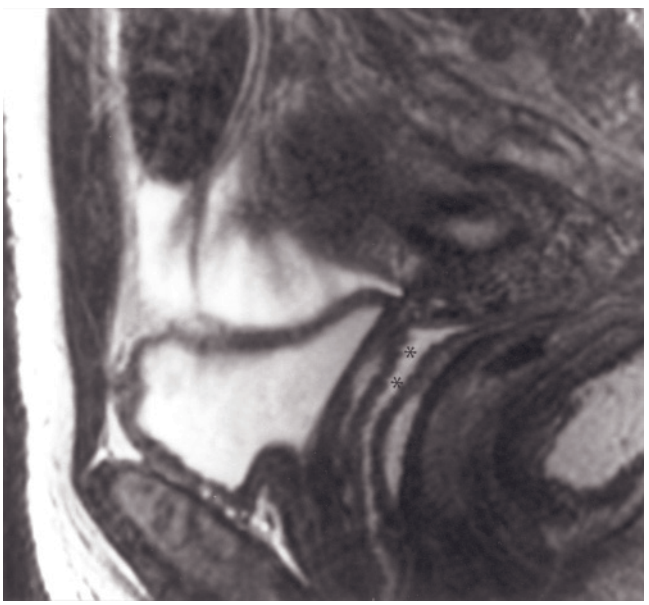

(*b*)

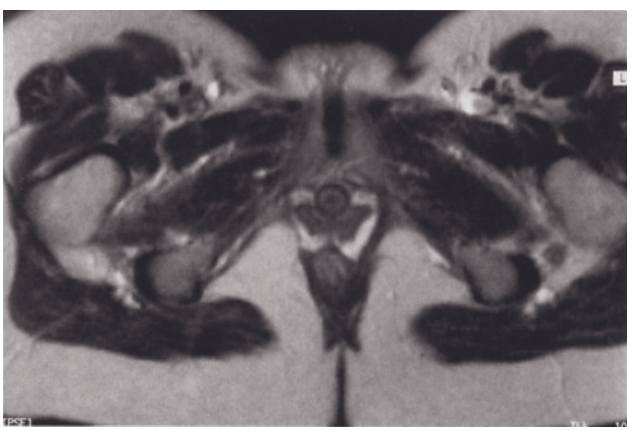

(*c*)

FIG. 13.1 Normal anatomy of the female urethra and vagina. Transverse (*a*) and sagittal (*b*) ETSE images show the normal urethral zonal anatomy (from central to peripheral): high-signal-intensity central spot, low-signal-intensity mucosa, moderately high-signal-intensity submucosa, and low-signal-intensity muscularis (arrow, *a*). The vagina is located posteriorly and reveals (from central to peripheral) high-signal mucosa/secretions, low-signal-intensity muscular wall (curved arrows, *a*), and high-signal-intensity perivaginal venous plexus. The normal rugae of the vaginal wall are well depicted (**, *b*). T2-weighted ETSE image (*c*) in a second patient demonstrates the central low-signal-intensity mucosal layer, higher-signal-intensity surrounding submucosal layer, and low-signal-intensity outer ring representing the muscular layer.

menopausal women, and decreased zonal definition should not be assumed to be abnormal. On enhanced T1-weighted images, the most common pattern seen is marked enhancement in the middle submucosal layer with little to no enhancement of the remaining urethra [1, 10].

Normal Variants and Congenital Disease

Duplication. Urethral duplication is caused by delayed fusion of the urogenital sinus and müllerian ducts. It may occur alone or in concert with bladder duplication or other abnormalities of the genitalia. It is typically discovered in infants, but affected adults may present with a double urinary stream, incontinence, or recurrent urinary infections [13, 14]. The accessory urethra usually drains into the clitoris. Surface coil imaging and postgadolinium T1-weighted fat-suppressed gradient-echo techniques may be useful in the evaluation of suspected urethral duplication.

Ectopic Ureterocele. A cause of urinary incontinence, ectopic ureters can drain into the urethrovaginal septum, into a urethral diverticulum, or into the posterior urethral wall [15–17]. Ectopic ureters are often associated with ureteral duplication.

Table 13.1 TNM Staging for Female Urethral Carcinoma

Primary Tumor	
Tx	Primary tumor cannot be assessed
T0	No evidence of primary tumor
Tis	Carcinoma in situ
T1	Tumor invades subepithelial, connective tissue
T2	Tumor invades periurethral muscle
T3	Tumor invades the bladder neck or anterior vaginal wall
T4	Tumor invades other adjacent organs
Regional Lymph Nodes	
Nx	Regional lymph nodes cannot be assessed
N0	No regional lymph node metastasis
N1	Metastasis in one lymph node is 2 cm or smaller
N2	Metastasis on one node in between 2 and 5 cm in size
N3	Metastasis in one node is larger than 5 cm
Metastases	
Mx	Distant metastases cannot be assessed
M1	No distant metastases
M2	Distant metastases

Mass Lesions

Benign Masses

Urethral Leiomyoma. Urethral leiomyomas are unusual benign tumors that arise from the smooth muscle layer of the urethra [18, 19]. Presenting clinical symptoms of dysuria or a palpable mass may be mistaken for a urethral diverticulum [19, 20]. Like uterine fibroids, these masses may grow during pregnancy. Urethral leiomyomas are usually of low to intermediate signal intensity on T1- and T2-weighted images secondary to their smooth muscle content [4, 21, 22]. Malignant degeneration has not been reported. Symptomatic tumors can often be removed by transurethral resection [18].

Other. Fibrous polyps and hemangiomas are other, less common benign urethral masses.

Malignant Masses

Primary Urethral Carcinomas. Primary urethral carcinoma is an uncommon entity that occurs in middle-aged or older women. Most urethral carcinomas are of squamous cell origin and arise from the distal (anterior) urethra. Transitional cell carcinomas and adenocarcinomas most commonly originate from the proximal (posterior) urethra [23, 24]. Posterior urethral tumors are more often high grade and aggressive. A TNM staging approach is used for urethral carcinomas (Table 13.1). Urethral carcinoma spreads contiguously to adjacent sites and then lymphatically to distant sites. Regional nodal involvement relates to the initial location of the tumor. Anterior urethral lesions usually involve the inguinal nodes, with subsequent spread to pelvic nodal groups. Posterior urethral lesions drain to iliac, obturator, and para-aortic lymph nodes [1, 23, 25]. Patients often present with advanced disease because of nonspecific symptomatology combined with difficulty in detecting lesions clinically. Treatment for advanced lesions includes anterior pelvic exenteration, radiation, or chemotherapy [25, 26]. Lesions that are Stage 2a N0M0 or less may be treated with surgery alone.

The combination of T2- and T1-weighted images before and after contrast administration provides complementary information (figs. 13.2 and 13.3). Tumors are typically of low signal intensity on T1-weighted images and relatively high signal intensity on T2-weighted images. Transverse and sagittal T2-weighted images are useful for depicting tumor invasion of the muscular wall of the bladder, vagina, and pelvic floor. T1-weighted images, on the other hand, demonstrate extension into periurethral fat [8]. MRI has been reported to be 90% accurate in estimating local tumor extension [1]. Although proven to be a sensitive modality for this entity, MRI is limited by difficulty in differentiating tumor from secondary inflammatory change, which can lead to overestimation of disease extent [1, 10].

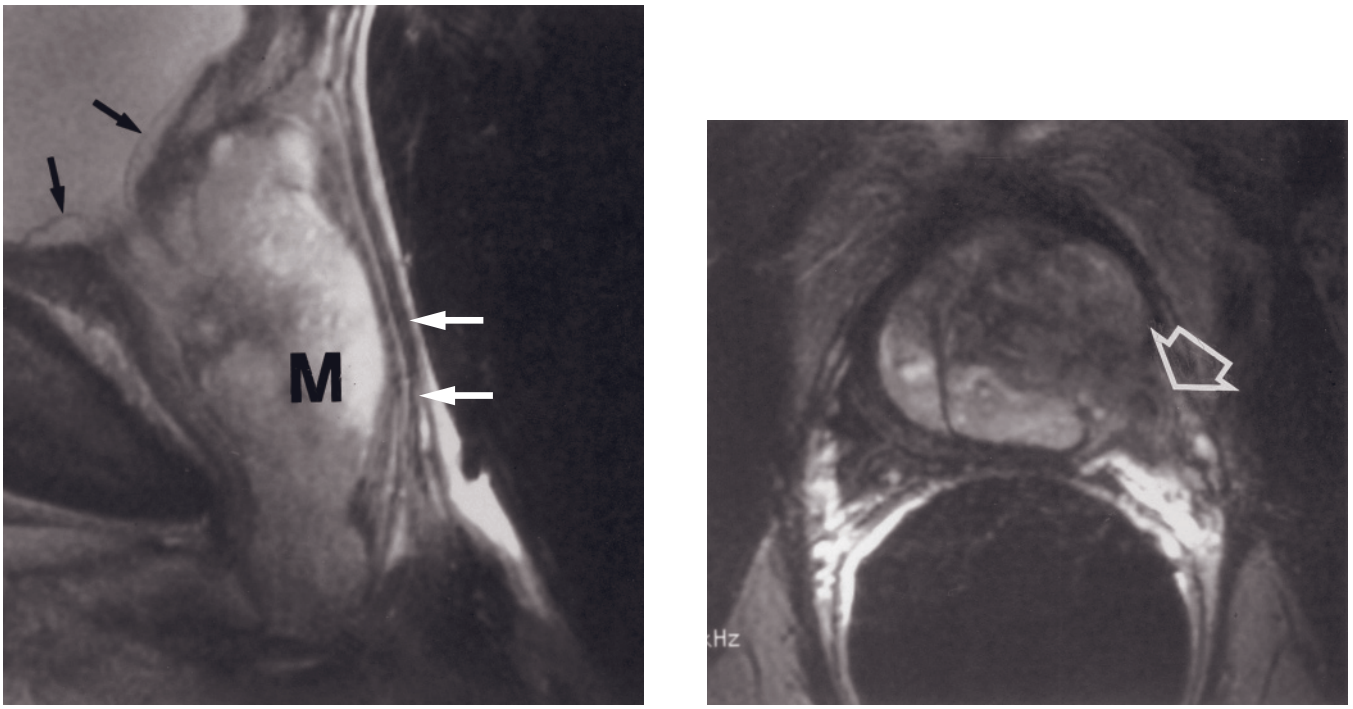

(*a*) (*b*)

FIG. 13.2 Poorly differentiated adenocarcinoma of the urethra with vaginal invasion. Sagittal (*a*) and transverse (*b*) ETSE endorectal coil images in a 50-year-old woman with palpable urethral mass. Sagittal image (*a*) shows a heterogeneous high-signal-intensity mass (M) whose center is in the posterior urethra. The mass extends from the widened bladder neck (arrows, *a*) to the meatus. Normal collapsed high-signal-intensity vaginal mucosa can be seen posterior to the mass. Transverse image (*b*) at the level of the proximal urethra shows a tumor-filled widened bladder neck, as well as thinning and poor definition of the left posterior urethral muscularis and anterior vaginal wall, with gross tumor involvement of the left paravaginal/paraurethral venous plexus (open arrow, *b*) representing contiguous spread of tumor.

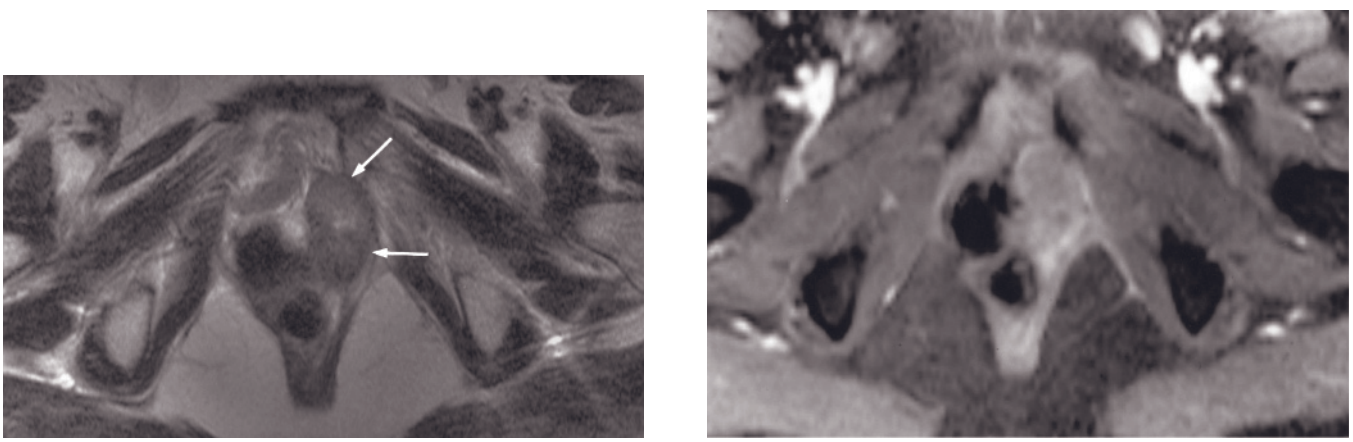

(*a*) (*b*)

FIG. 13.3 Recurrent urethral cancer. Transverse T2-weighted ETSE (*a*) and gadolinium-enhanced fat-suppressed SGE (*b*) images in a patient who underwent anterior pelvic exenteration for urethral cancer show an irregular left-sided mass (arrows, *a*) with heterogeneous enhancement (*b*) consistent with local recurrence.

Secondary Urethral Malignancies. Secondary urethral malignancies include metastases from renal cell carcinoma or melanoma and contiguous spread from carcinomas of the bladder, uterus, cervix, and vagina (fig. 13.4). MRI is useful in demonstrating the extent of involvement in these cases and thereby influencing staging and treatment [27].

Miscellaneous

Urethral Diverticulum

Urethral diverticula are saccular outpouchings from the urethra that are thought to result from recurrent infection and obstruction of the periurethral glands [28–30]. The dilated glands then rupture and drain into the urethral lumen. They are often asymptomatic but can become infected, form stones, or, less often, cause dyspareunia, dribbling, or a palpable mass [31]. Diverticula typically arise from the posterolateral wall in the midportion of the urethra. These lesions often are difficult to diagnose because of nonspecific symptomatology [32]. Traditional evaluation for urethral diverticula has been done with voiding cystourethrography, double-balloon urethrography, and/or urethroscopy. These modalities are not always successful [1, 33]. Ultrasound has been advocated by some as an economical way to evaluate this condition, but ultrasound may not be able to distinguish a diverticulum from a paravaginal cyst, nor can it often localize the ostium of the diverticulum [34, 35].

MRI is an excellent imaging modality for evaluation of symptomatic urethral diverticula. Its accuracy and sensitivity exceed both urethrography and urethroscopy, and MRI has the added advantages of visualizing the surrounding anatomy and being a noninvasive test [35]. MRI findings include an enlarged urethra with a focal area of low signal intensity on T1-weighted images and high signal intensity on T2-weighted images corresponding to the diverticulum. Multiplanar T2-weighted images are useful for the accurate localization of diverticula (figs. 13.5 and 13.6). Gadolinium-enhanced T1-weighted fat-suppressed images have proven useful in demonstrating the cystic nature of diverticula. Contrast-enhanced images may also detect the presence of granulation tissue or carcinoma [35, 36]. Carcinomas arising within diverticula are very rare and are most often adenocarcinomas, reflecting the ductal origin of the diverticula [37]. The ability of MRI to clearly delineate the anatomy of the diverticulum and its relationship to the bladder neck significantly aids in planning the surgical repair of these lesions [30, 33, 35, 37–39].

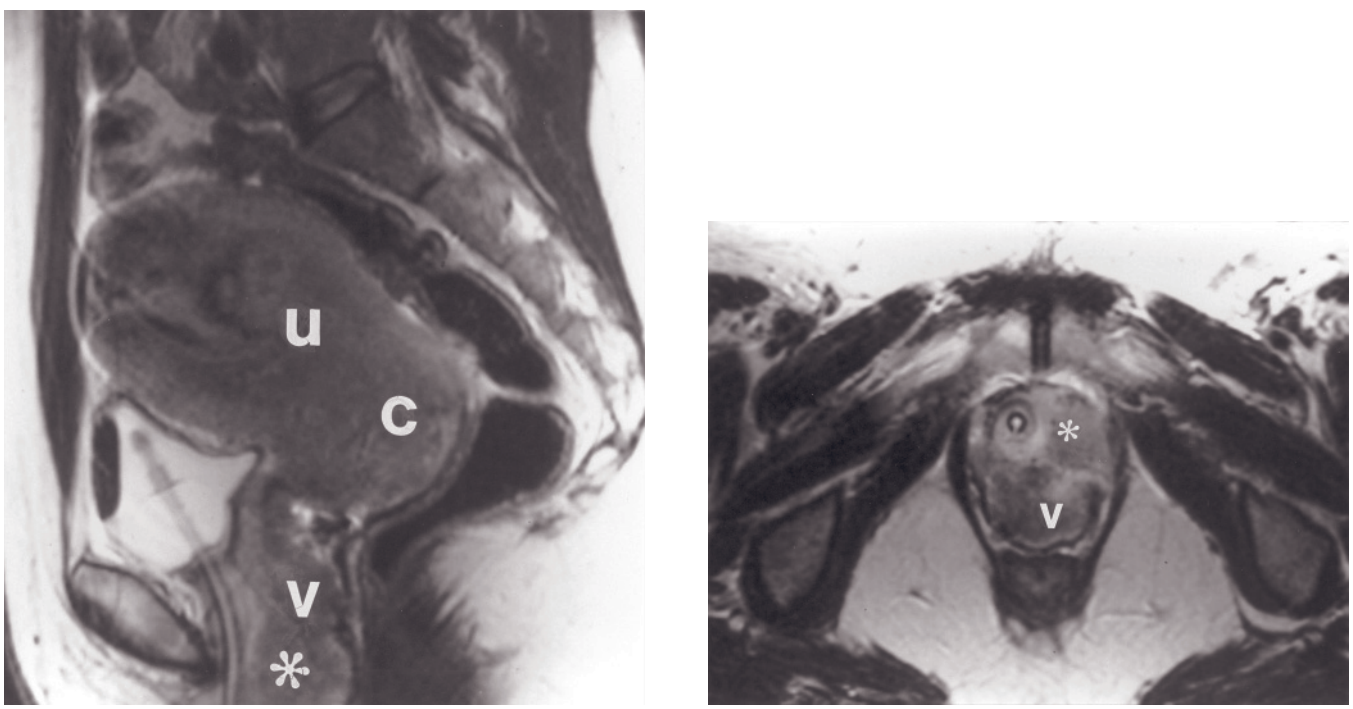

(*a*) (*b*)

FIG. 13.4 Poorly differentiated cervical carcinoma with vaginal and urethral invasion. Sagittal (*a*) and transverse (*b*) ETSE images show an aggressive mass centered within the cervix (c) with proximal extension into the uterus (u) and distal spread inferiorly through the cervix into the anterior vagina (v) and periurethral soft tissues (*). A Foley catheter reveals the urethral lumen.

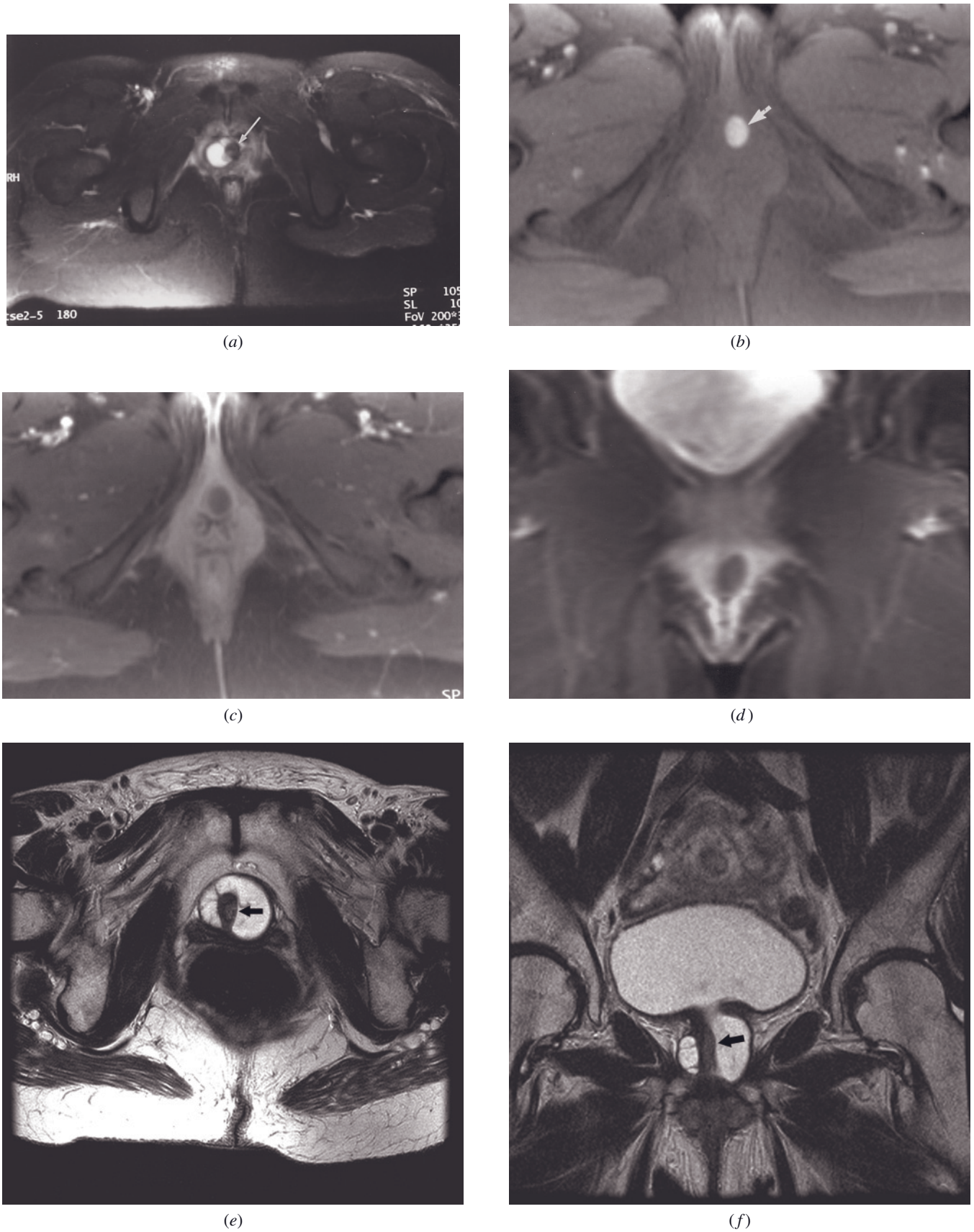

(*a*) (*b*) (*c*) (*d*) (*e*) (*f*)

FIG. 13.5 Urethral diverticulum. Transverse T2-weighted fat-suppressed ETSE image shows the high-signal-intensity diverticulum surrounding the lower-signal-intensity urethra (arrow, *a*), which is displaced laterally. Transverse T1-weighted fat-suppressed SGE (*b*) and transverse (*c*) and coronal (*d*) gadolinium-enhanced fat-suppressed SGE images in a second patient also demonstrate a urethral diverticulum (arrow, *b*), which is high signal on the noncontrast T1-weighted fat-suppressed image, reflecting retained mucous and other proteinaceous material, and low signal on the contrast-enhanced T1-weighted images. Transverse (*e*) and coronal (*f*) ETSE images in a third patient show a septated saddlebag diverticulum that also has a wide-mouthed direct connection to the bladder base. The urethra (arrows, *e*, *f*) is seen surrounded by the diverticulum on both images.

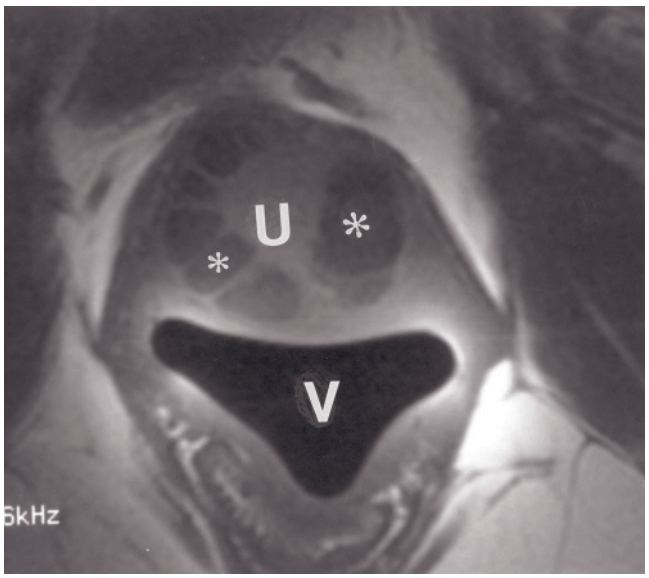

(*a*)

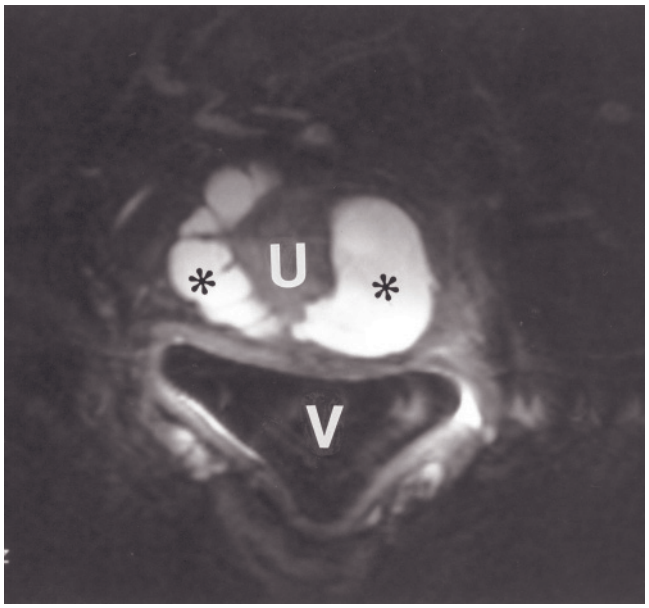

(*b*)

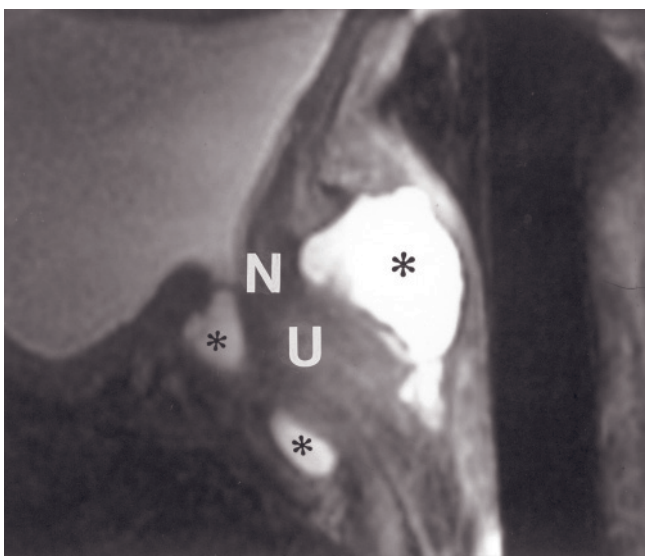

(*c*)

FIG. 13.6 Endovaginal coil demonstration of a saddlebag urethral diverticulum. Transverse T1-weighted (*a*) and transverse (*b*) and sagittal (*c*) T2-weighted ETSE endovaginal coil images show the multiloculated diverticulum (*) that almost entirely surrounds the circumference of the urethra (U). The vaginal coil (V) is positioned posterior to the urethra. Sagittal T2-weighted image (*c*) reveals the superior extent of the diverticulum relative to the bladder neck (N) and also shows the portions of the diverticulum located anterior to the urethra (U).

Caruncle

Urethral caruncles are small, benign, often asymptomatic inflammatory masses that typically occur in older postmenopausal women and arise on or near the external meatus. Occasionally, these lesions can cause pain or hematuria [28]. Histologically, caruncles demonstrate hyperplastic squamous epithelium with underlying submucosal vascularity, fibrosis, and inflammation [40]. This entity has become uncommon with the widespread use of estrogen replacement in the postmenopausal population. MR imaging is useful in localizing the lesion to the urethral meatus and in excluding adenopathy that would suggest a malignant neoplasm [4, 41].

Urethral Trauma and Strictures

MRI is useful in the evaluation of urethral trauma in males by demonstrating in detail the anatomy of the urethral and periurethral tissues. For the same reasons, MR imaging has been useful in preoperative evaluation of posttraumatic and postinfectious strictures in men [42–44]. Urethral trauma and strictures are very rare in women, and the MR appearance has not yet been described [24].

Urethritis and Urethral Fistulas

MRI is useful in evaluation of inflammatory conditions of the urethra and periurethral tissues, often the result

of infection or pelvic irradiation. Urethral inflammation usually manifests as a thickened urethra with intermediate T2 signal intensity and diffuse enhancement. [45].

Urethrovaginal fistulas occur most often as a complication of urethral diverticulectomy or vaginal surgery [46]. Crohn disease and Behçet disease are uncommon causes, whereas traumatic childbirth is a common cause in developing countries [47–49]. Infection of Skene glands can lead to formation of sinus tracts or periurethral abscesses that may be difficult to differentiate from urethral diverticula. Rectourethral fistulas are usually developmental abnormalities and are usually associated with complex anorectal abnormalities [50]. Spinal cord injury patients with decubitus ulcers are at risk for developing urethroperineal fistulas [51]. Infection with gonorrhea or tuberculosis can cause periurethral abscesses that can rupture through the skin and form urethroperineal fistulas as well. Sinus tracts are well seen on transverse and sagittal T2-weighted images, whereas postgadolinium T1-weighted fat-saturated images can demonstrate the enhancing sinus tract walls.

Pelvic Floor Relaxation

Pelvic floor relaxation and pelvic organ prolapse is a very prevalent condition that can be quite debilitating. Prolapsed structures can include the urethra, vagina, rectum, cervix, uterus, bladder, colon, and/or small bowel. Common symptoms include incontinence, difficult defecation, constipation, urinary retention, pain, and pressure. Physical examination is the primary method of diagnosis. Traditionally, fluoroscopic defecography was the mainstay for radiologic imaging of these conditions. MRI has the advantages of being noninvasive, not using ionizing radiation, and being able to best demonstrate the soft tissue structures and associated pathology to best advantage [52–54].

A variety of MR techniques have been used to evaluate the pelvic floor. Commonly, multiplanar single-shot fast spin-echo sequences are performed during rest and straining. Rectal contrast, typically ultrasound gel, is administered before the exam. Some sites have also used vaginal markers, rectal markers, and bladder, urethral, and/or vaginal contrast [55–64].

Urethral hypermobility is depicted at MR imaging by a change in the normal vertical orientation of the urethra to a horizontal orientation during straining [57]. Urethral hypermobility can be treated with surgical urethral suspension, collagen injection, or mechanical sphincters. Periurethral collagen is well shown on T2-weighted images and appears high in signal intensity (fig. 13.7) [65–68]. Complications of mechanical sphincters such as fistula formation, periurethral abscess, and erosion can also be depicted [69]. The sagittal single-shot echo-train spin-echo technique is also valuable for demonstrating enteroceles and cystoceles, which are also associated with pelvic floor relaxation [57, 70, 71].

Cystoceles are caused by defects in the pubocervical fascia. The loss of support allows the bladder to bulge into the anterior vaginal wall and extend inferiorly. Symptoms of pelvic pressure, tissue bulging, and heaviness can be exacerbated by voiding, prolonged standing, and physical exertion. Cystoceles can be repaired surgically, or symptoms can be controlled with a pessary device [59, 72]. Similar symptoms can occur with prolapse of the uterus, vagina, and/or cervix. When severe, these organs can completely prolapse through the introitus.

Rectoceles often occur because of weakness or defects in the puborectalis sling. Many patients are asymptomatic, but difficult defecation is often present, sometimes requiring manual pressure through the vagina to assist with defecation. Bulging of the posterior vaginal wall is seen at physical examination as well as with MR imaging. Rectoceles are usually diagnosed when the rectum bulges more than 2–3 cm anterior of a line drawn through the anterior wall of the anal canal [59, 73, 74] (fig. 13.8). These abnormalities are often repaired surgically. Other abnormalities seen at pelvic floor imaging include enteroceles, hernias, and bulging or defects in the pelvic floor musculature.

Conclusion

MRI is the ideal imaging modality for the evaluation of urethral abnormalities because of its superior contrast resolution, lack of ionizing radiation, multiplanar capability, and nonnephrotoxic contrast material. Most common indications include evaluation of incontinence and pelvic floor relaxation and evaluation for diverticula in patients with recurrent infection. MRI is also excellent for evaluation of the more uncommon conditions of malignancy and congenital abnormalities.

THE VAGINA

High contrast resolution, the ability to achieve both small and large fields of view, and multiplanar capability render MRI superior to CT imaging and ultrasound for evaluation of many benign and malignant conditions of the vagina. In addition, the lack of invasiveness and added extraluminal anatomic detail make MRI preferable to vaginography for the evaluation of congenital anomalies [75].

Normal Anatomy

The vagina is a 7- to 9-cm-long fibromuscular tube lying between the bladder and rectum. The upper one-third is derived from müllerian duct fusion, whereas the lower

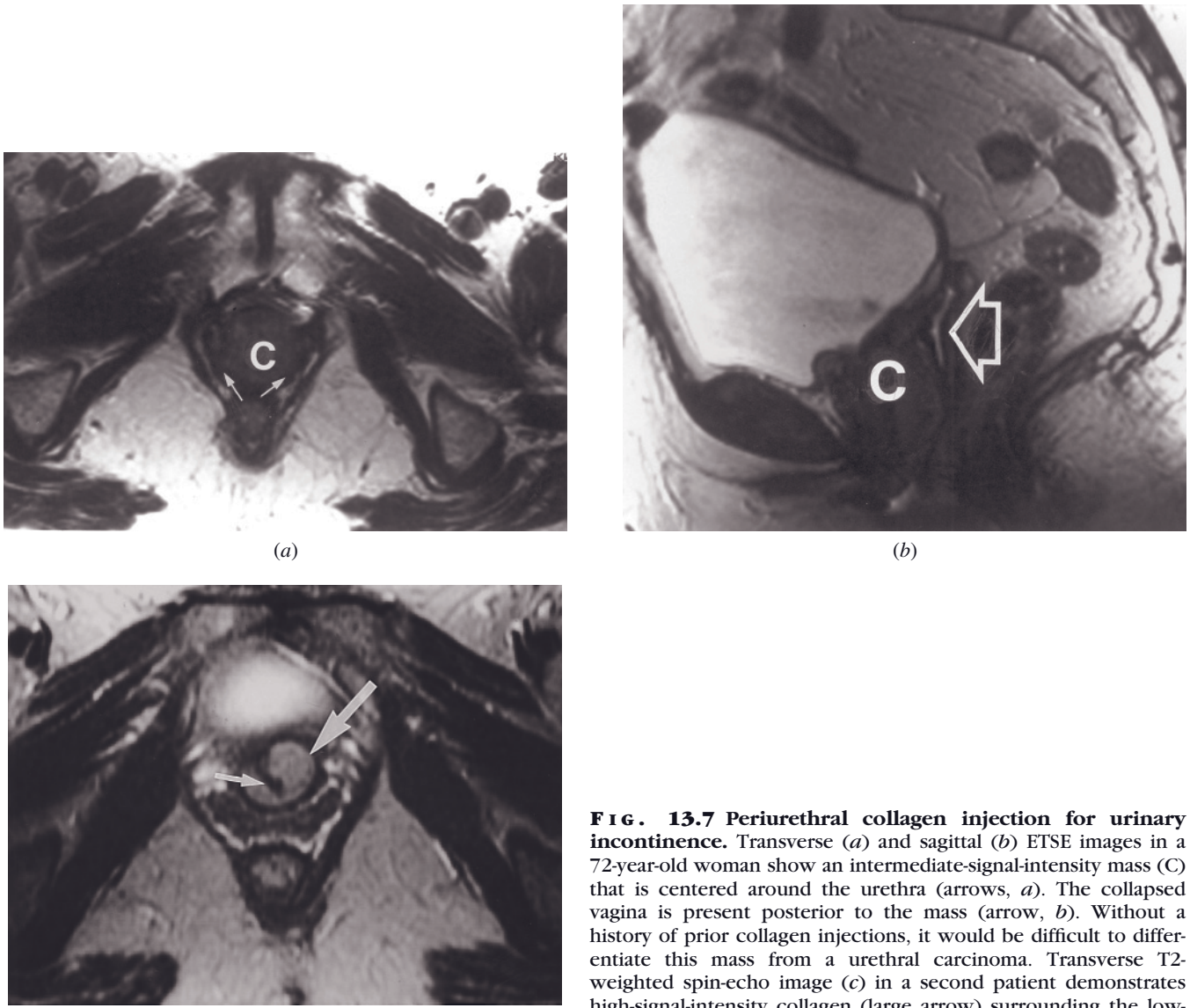

(*a*) (*b*) (*c*)

FIG. 13.7 Periurethral collagen injection for urinary incontinence. Transverse (*a*) and sagittal (*b*) ETSE images in a 72-year-old woman show an intermediate-signal-intensity mass (C) that is centered around the urethra (arrows, *a*). The collapsed vagina is present posterior to the mass (arrow, *b*). Without a history of prior collagen injections, it would be difficult to differentiate this mass from a urethral carcinoma. Transverse T2-weighted spin-echo image (*c*) in a second patient demonstrates high-signal-intensity collagen (large arrow) surrounding the low-signal-intensity urethra (small arrow).

two-thirds originates from the urogenital sinus [76]. The layers of the vagina consist of the inner mucosal layer, the middle submucosal and muscular layer, and an outer adventitial layer that contains the vaginal venous plexus [10, 77]. The anterior, posterior, and lateral fornices of the vagina surround the cervix and are best seen on sagittal and transverse images. For descriptive purposes, it is useful to divide the vagina into thirds. The upper third is considered to be at the level of the lateral fornices, the middle third at the level of the base of the bladder, and the lower third at the level of the urethra.

MRI Technique

As in the evaluation of the pelvis in general, T2-weighted images are critical because they differentiate the layers of the vaginal wall to best advantage. T1-weighted images are complementary, particularly combining fat suppression with gadolinium administration. Fat suppression is required to differentiate fat from proteinaceous or hemorrhagic contents [78] and for detection of peritoneal enhancement or tumor [79]. The transverse plane is ideal for the evaluation of pathology with respect to the vaginal wall, and sagittal plane imaging demonstrates the relationship to the bladder and rectum. Coronal images can demonstrate levator ani muscle involvement. Thin (≤5 mm) sections are preferable. Patients should be asked to remove tampons before imaging to avoid obscuring detail. Routine use of torso or pelvic phased-array coils is ideal to allow acquisition of high-resolution, small field-of-view images [80, 81]. When even smaller field-of-view and higher-resolution

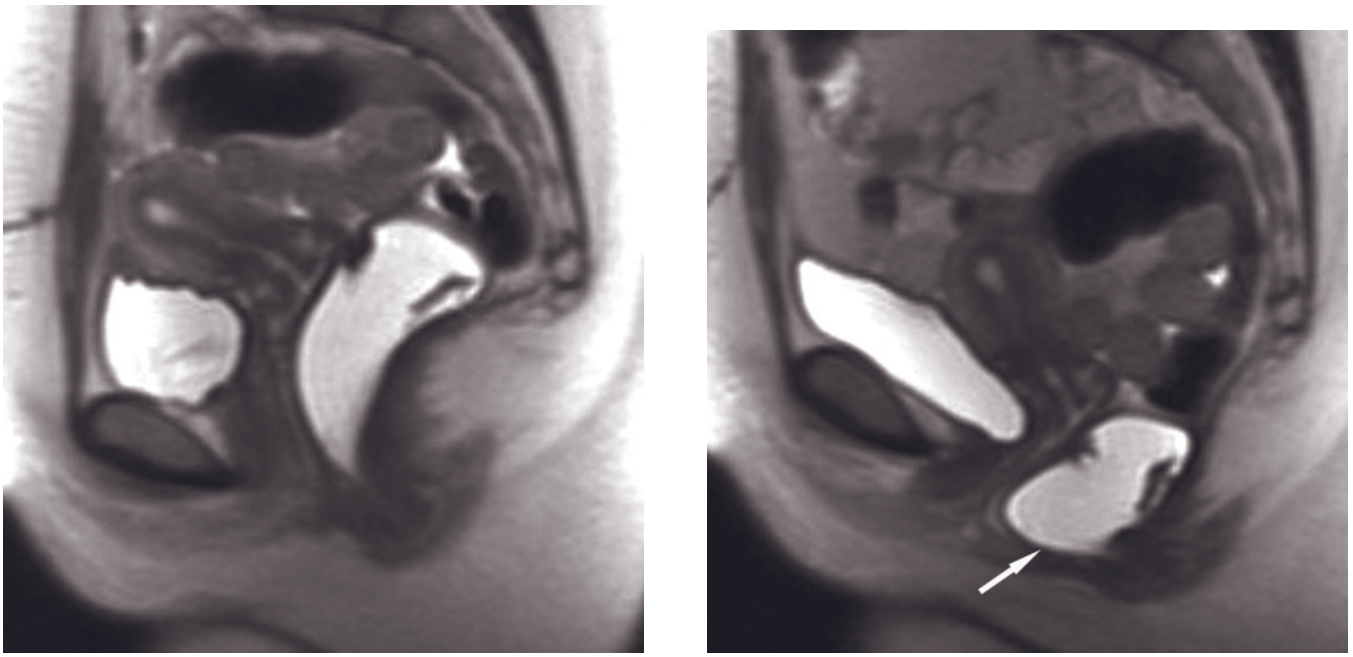

(*a*) (*b*)

FIG. 13.8 Rectocele and urethral hypermobility. Sagittal SSFSE images in a 35-year-old woman were obtained after placement of rectal contrast. During relaxation (*a*), the rectum and urethra are normal in position. During straining (*b*), the urethra assumes a more horizontal orientation consistent with hypermobility. The rectum bulges (arrow, *b*) significantly anterior to the anterior wall of the anal canal, consistent with a rectocele.

images are needed, endovaginal or endorectal coils may be employed [5]. As with 3T imaging of the urethra, improved spatial resolution is possible, but imaging can sometimes be challenging because of artifacts such as from field inhomogeneity.

Normal

The mucosal layer and any intraluminal fluid and mucus appear as a central area of low signal intensity on T1-weighted images and high signal intensity on T2-weighted images (fig. 13.9) [77]. The thickness of the endoluminal mucus has been shown to correlate with estrogen levels and becomes more prominent during the late proliferative and early secretory phases of the menstrual cycle. Pregnant patients often have medium to high signal intensity of the mucus layer, vaginal wall, and surrounding tissues. In contrast, premenarchal females and postmenopausal females have a low-signal-intensity wall and a very thin high-signal-intensity mucus layer. The middle layer of the vagina is low in signal intensity on both T1- and T2-weighted images and consists of the submucosa and muscularis layers. The muscularis consists of inner longitudinal and outer circular smooth muscle layers. The vaginal venous plexus in the adventitial layer is high in signal intensity on T2-weighted images because of slow venous flow. After gadolinium administration, the vaginal wall enhances, and occasionally a low-signal-intensity line is present centrally, which may represent the lumen or inner epithelial layer [10].

Normal Variants and Congenital Disease

Congenital and developmental anomalies of the vagina can be divided into four categories: absence and partial absence, duplication and partial duplication, abnormalities of gonadal differentiation, and ambiguous genitalia. MRI provides a noninvasive method of determining the presence of the uterus, cervix, vagina, gonads, and penile bulb and thus is ideally suited for evaluation of these abnormalities [82–87].

Vaginal Agenesis and Partial Agenesis. Vaginal agenesis and partial agenesis are rare conditions that are classified under the larger category of müllerian duct anomalies. The incidence of all müllerian duct anomalies in women has been reported to be 1–15%. One in 4000–5000 women is estimated to have vaginal agenesis [84, 88]. These patients typically have normal ovaries and external genitalia but can have associated abnormalities of the uterus, cervix, upper urinary tract, and skeleton (fig. 13.10). If no functioning endometrium is present, these patients will often present with primary amenorrhea. If functioning endometrium is present,

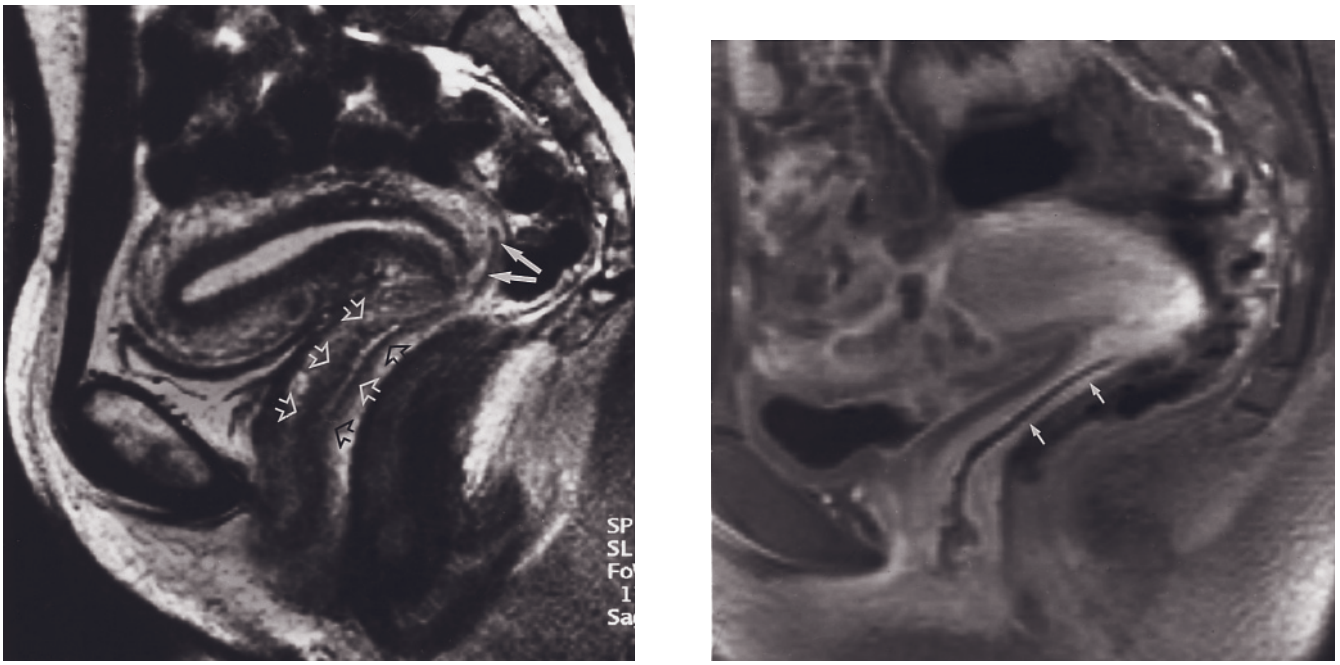

(*a*) (*b*)

FIG. 13.9 Normal vagina. Sagittal T2-weighted echo-train spin-echo (*a*) and immediate postgadolinium fat-suppressed SGE (*b*) images. On the T2-weighted images, the low-signal-intensity muscular wall and the central higher-signal-intensity mucosal layer of the vagina are apparent. The sagittal T2-weighted image (*a*) shows vagina (open arrows) as well as the posterior vaginal fornix (solid arrows). Relationship with uterus and cervix is well seen. On the immediate postgadolinium fat-suppressed image (*b*), intense enhancement of vaginal mucosa (arrows) is present. (Courtesy of Susan M. Asher, M.D., Dept. of Radiology, Georgetown University Medical Center, Washington, DC.)

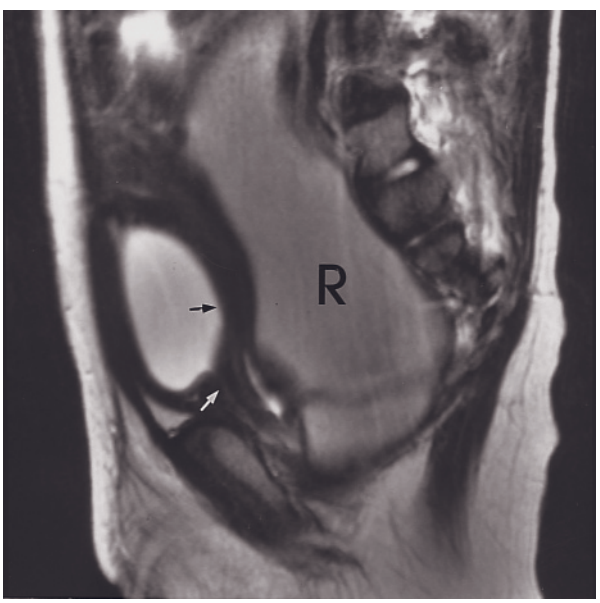

FIG. 13.10 Vaginal agenesis in patient with surgically repaired persistent cloaca. Sagittal SS-ETSE image. No vagina is seen. The urethra (white arrow) is elongated and superiorly positioned. The bladder has a thickened wall (black arrow).The reconstructed rectum (R) is dilated.

however, patients present after menarche with pain and mass effect from hematometra (fig. 13.11).

The surgical management of these patients is determined by the presence of functioning endometrium and a cervix. Complete vaginal agenesis with no functioning endometrium and only a small uterine bulb is treated with vaginoplasty. If the uterine bulb contains functioning endometrium, vaginoplasty along with open surgery to remove the uterine remnant are required to prevent endometriosis. When a uterus with endometrium but no cervix accompanies complete agenesis, hysterectomy and vaginoplasty are required. If patients have a partial vaginal agenesis with a normal uterus and cervix, creation of an external vaginal opening alone is required, and pregnancy is possible [88].

Mayer–Rokitansky–Küster–Hauser syndrome is the name given to the müllerian duct anomaly with vaginal and uterine agenesis, normal tubes and ovaries, and variable urinary tract anomalies (fig. 13.12). This disorder occurs in approximately 1 in 5000 female births, with most patients having a normal karyotype [89]. Uterine and/or vaginal rudiments may be present, and documentation of their presence is also important for planning of the surgical approach [83]. Vaginal agenesis,

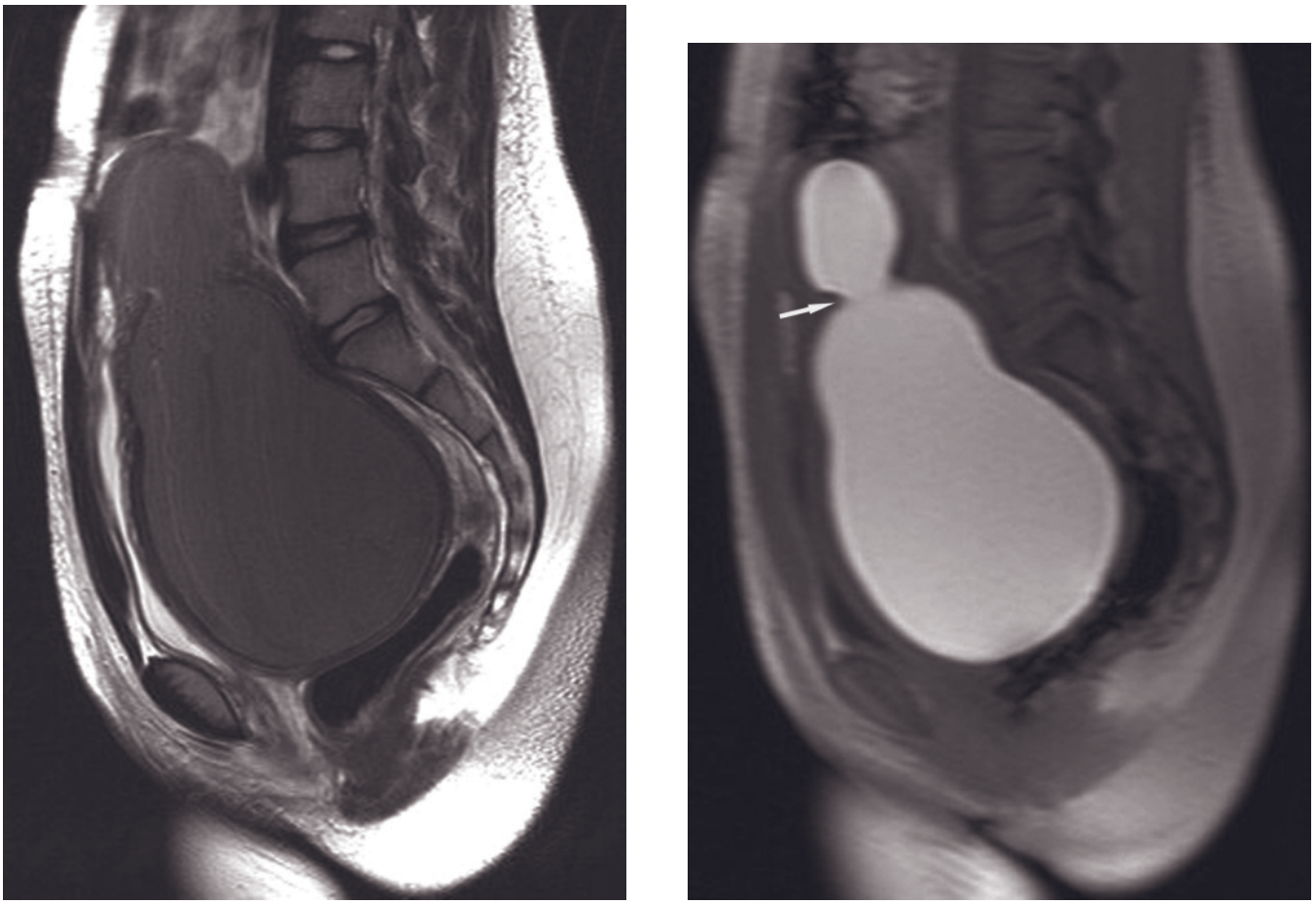

(*a*) (*b*)

FIG. 13.11 Vaginal atresia with hematometra. Sagittal-plane high-resolution 512 matrix T2-weighted echo-train spin-echo (*a*) and T1-weighted 2D-SGE gradient-echo (*b*) images. The upper vagina and uterus are dilated and blood filled. Narrowing of the blood-filled structures is noted at the level of the cervix (arrow, *b*).

partial agenesis, and cloacal abnormalities are best imaged with MRI. Thin-section T2-weighted transverse images accurately demonstrate agenesis, and in cases of partial agenesis combined transverse and sagittal images delineate vaginal length, which is important in surgical planning [83, 86, 90, 91]. MRI also shows the presence or absence of the uterus, cervix, and kidneys. Exquisite sensitivity in evaluating blood makes MRI ideal for identifying functioning endometrium.

Duplication and Partial Duplication. Duplication and partial duplication of the vagina are typically seen in association with the didelphys anomaly of the uterus. This anomaly is well seen on transverse T2-weighted images. Vaginal duplication can result in a longitudinal vaginal septum that can be a cause of dyspareunia [92]. T2-weighted images demonstrate the low-signal-intensity septum contrasted by the high signal intensity of the adjacent vaginal secretions and mucosal layer. Vaginal and uterine duplication can also be complicated by a transverse vaginal septum causing obstruction of the affected hemivagina and its associated uterine cavity [93]. Patients begin menses at a normal age at puberty, because of the presence of the nonobstructed uterine horn, but can present with a palpable mass. Untreated cases can result in the development of endometriosis [92, 94]. This abnormality is also associated with ipsilateral renal agenesis.

A transverse vaginal septum is the result of failure of fusion of the down-growing müllerian duct with the up-growing urogenital sinus. Like patients with imperforate hymen, these patients present at puberty with amenorrhea and cyclical abdominal pain (fig. 13.13). Treatment of transverse vaginal septum includes resection of the septum and vaginal reconstruction. In more severe cases, agenesis of the cervix is also

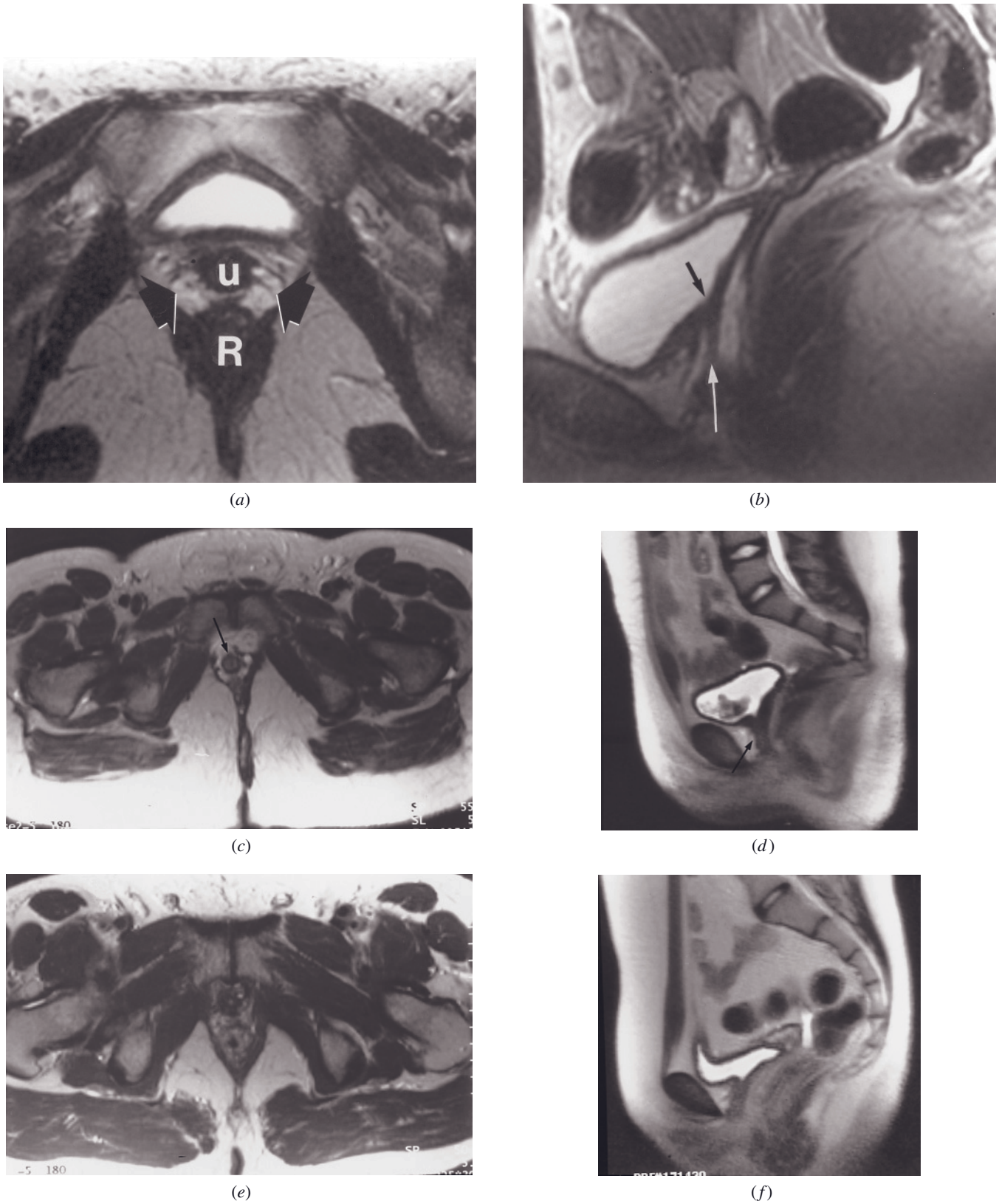

FIG. 13.12 Mayer-Rokitansky-Küster-Hauser syndrome. Transverse (*a*) and sagittal (*b*) T2-weighted ETSE images in a 17-year-old female with primary amenorrhea show a normal urethra (u, *a*), rectum (R, *a*), and vaginal venous plexus (arrows, *a*). No normal vaginal wall is present (compare to fig.13.8). On the sagittal image (*b*) the absence of the uterus, cervix, and vagina is well demonstrated. Transverse (*c*) and sagittal (*d*) SS-ETSE images in a second patient .The vagina and uterus are absent, and the urethra (arrows, *c*, *d*) is more posteriorly positioned than normal. Partial absence of the sacrum with abnormal elevation of the pelvic floor is present. Transverse 512-resolution echo-train spin-echo (*e*) and sagittal SS-ETSE (*f*) images in a third patient demonstrate similar findings of absent vagina and uterus with posterior positioned urethra.

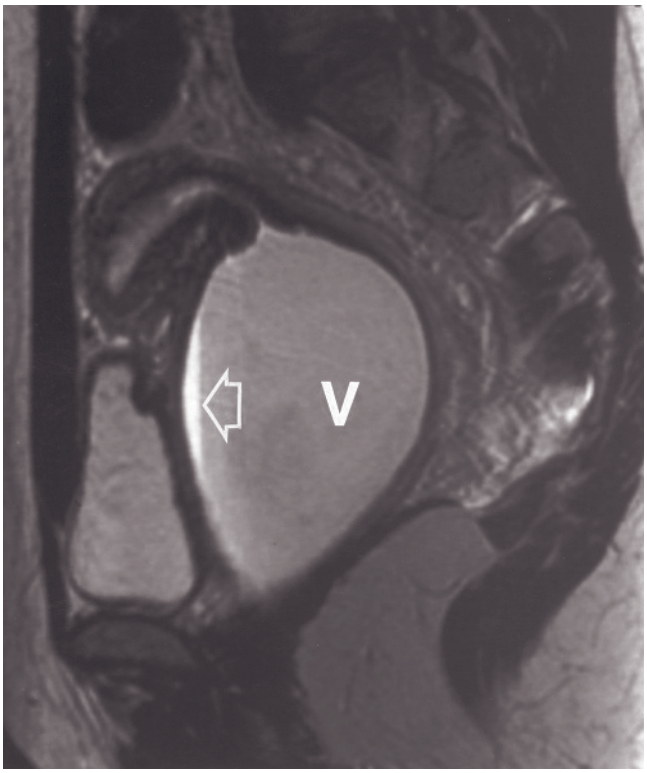

(*a*)

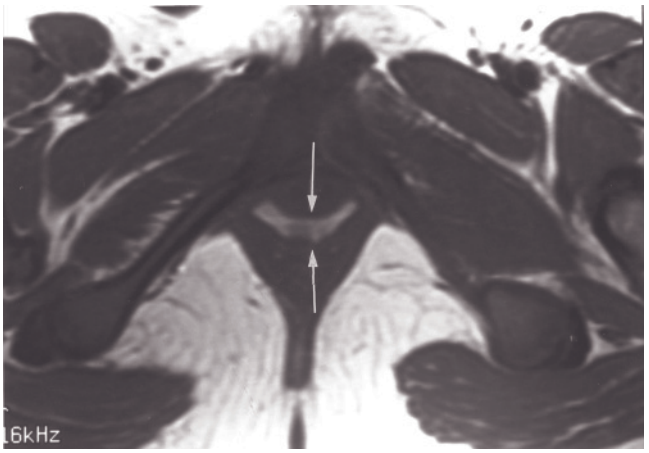

(*b*)

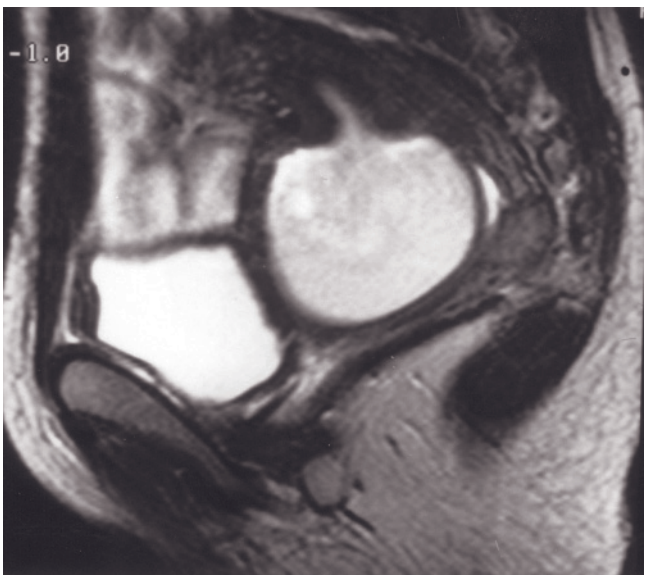

(*c*)

(*d*)

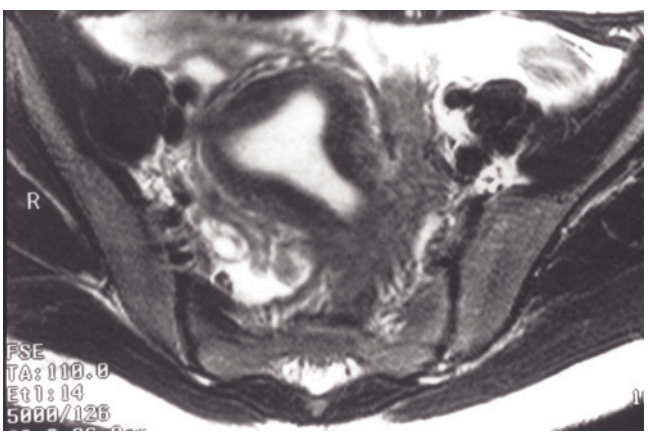

(*e*)

FIG. 13.13 Low transverse vaginal septum and hematocolpos. Sagittal T2-weighted ETSE (*a*) and transverse T1-weighted (*b*) images in a 12-year-old girl with pelvic pain show a distended vaginal canal (V) that is filled with complex fluid with a fluid-fluid level (arrow, *a*). T1-weighted image (*b*) obtained through the lower vagina shows that the distended vaginal canal contains high signal intensity (arrows, *b*) representing the T1-shortening effects of protein and/or methemoglobin within subacute blood. A low transverse septum may have an appearance similar to an imperforate hymen on MR imaging. The treatment of the two conditions, however, is similar. Sagittal (*c*, *d*) and transverse (*e*) T2-weighted ETSE images in a second patient, who has a transverse vaginal septum, demonstrate marked distension of the vagina and uterine cavity consistent with hematocolpometra. (Courtesy of Andrea Oliveira, M.D., Brasilia, Brazil.)

found and hysterectomy with vaginoplasty is required [92, 95, 96].

Abnormalities of Gonadal Differentiation. Abnormalities of gonadal differentiation include true hermaphroditism and gonadal dysgenesis. True hermaphrodites have both ovarian and testicular tissues, which can exist together as an ovotestis or in separate discrete gonads [97, 98]. Although the internal genitalia are variable, most patients have a uterus. Ovotestes and testes are often intra-abdominal or cryptorchid, whereas ovaries are typically intra-abdominal [98]. Most (80%) have XX karyotype, with the remaining 20% evenly divided between XY and mosaic karyotypes [82, 83]. Development of the internal ducts usually corresponds with the gonad on that side. Sex assignment of true hermaphrodites is usually made by the external genitalia, which are variable in appearance. MRI evaluation can be helpful in demonstrating the internal anatomy. Presence of the vagina or prostate is well established with transverse imaging, and sagittal views display the uterus, penile bulb, and prostate well [77, 82, 86, 98]. The gonads in these patients are at increased risk of neoplasms.

The term "pure gonadal dysgenesis" refers to the presence of bilateral streak gonads, which are fibrous in nature and contain no germ cells [98]. The basic underlying defect is typically an abnormal second sex chromosome. The majority of these patients are of the XO phenotype known as Turner syndrome. These patients have infantile external genitalia, a uterus and a vagina, as well as bilateral streak ovaries. They often have other abnormalities such as a webbed neck and short stature. Other karyotypes occur with gonadal dysgenesis, including mixed gonadal dysgenesis in which the patients have a mosaic karyotype (XO/XY, XO/XYY). These patients have one testis and one streak gonad [98]. A 46 XY combination also exists with abnormal testicular development. This entity differs from testicular feminization in that female internal ducts are usually present as well as external female genitalia. The feminization may be incomplete if the testes are able to produce some testosterone or müllerian regression factor [98]. In patients with gonadal dysgenesis, Y chromosome-containing gonads are at increased risk for malignant transformation and should be removed. Although karyotype analysis is the most critical in the evaluation of these patients, MRI can be helpful in demonstrating the degree of differentiation of internal organs as well as identifying streak gonads, seen as low signal intensity on T2-weighted images.

Ambiguous Genitalia. Patients with normal genotype but ambiguous genitalia are classified as pseudohermaphrodites. Male pseudohermaphrodites have testes but possess ambiguous internal and/or external genitalia [98]. The most common etiology is testicular feminization (fig. 13.14), which is an X-linked recessive disorder in which there is an absence of cytoplasmic testosterone receptors. These patients are phenotypically female but have a blind-ended vagina with no uterus or fallopian tubes because the testes make normal müllerian regression factor [97]. T2-weighted MR imaging is helpful in preoperative location of the testes, which are removed because of increased risk of malignancy [98]. Other forms of male pseudohermaphroditism include incomplete testicular feminization with partially masculinized genitalia, inability of tissues to convert testosterone to dihydrotestosterone, congenital errors of testosterone synthesis, and inability of the testes to respond to hypothalamic gonadotropin [82].

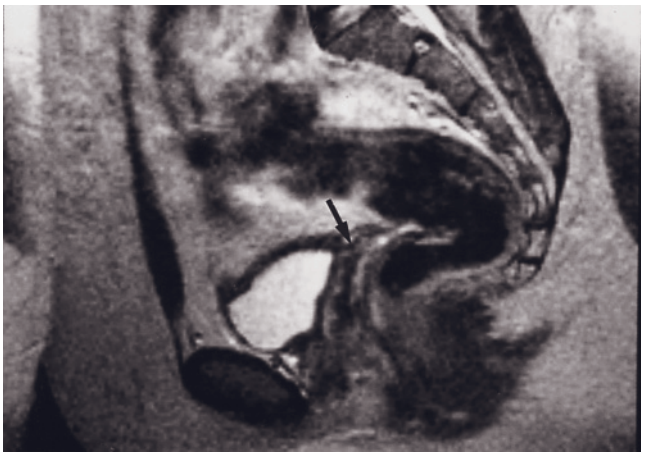

FIG. 13.14 Testicular feminization. Sagittal T2-weighted echo-train spin-echo image. Note absence of the uterus and the blind-ended vagina (arrow).

Female pseudohermaphrodites have normal 46 XX karyotypes and normal ovaries but have virilized external genitalia because of androgen exposure in utero [77, 98]. The most common etiology is 21-hydroxylase deficiency, which is one form of congenital adrenal hyperplasia. This deficiency leads to an excess of androgenic sex steroids, which leads in turn to ambiguous genitalia if exposure occurs before the 12th week of gestation and to clitoromegaly if exposure occurs later. Development of male internal genitalia does not occur because this requires local androgen exposure rather than systemic exposure. Other, rarer causes of female pseudohermaphroditism include androgen-producing ovarian or adrenal tumors or maternal ingestion of androgen-containing drugs during the first trimester. With surgical and/or hormonal treatment, these females can have normal fertility and

near-normal female phenotype. MRI is important in identifying uterus, ovaries, vagina, and penile bulb if it is present.

Mass Lesions

Benign Masses

Bartholin Cyst. Bartholin glands are mucus-secreting glands that open into the posterolateral aspect of the vaginal vestibule. Trauma or chronic inflammation in this region is thought to lead to retention of secretion in these glands and cyst formation. Unless these cysts become infected, they usually do not incite symptoms. *Neisseria gonorrhoeae* is the most common infecting organism. In addition to antibiotic therapy, aspiration, incision and drainage, laser vaporization, and marsupialization can be employed [99, 100]. These cysts are seen on MR images as small fluid-filled structures in the lower third of the vagina. They are high in signal intensity on T2-weighted images and medium to high in signal intensity on T1-weighted images, depending on the protein content of the fluid [75, 101] (fig. 13.15). Rim enhancement after gadolinium administration suggests infection of the cyst.

Gartner Duct Cyst. Gartner duct cysts are formed from mesonephric duct or wolffian duct remnants and represent the most common benign vulvovaginal lesion in children. Usually asymptomatic, these lesions are found incidentally in 1–2% of female pelvic MRI examinations [75]. Occasionally larger lesions are seen and may cause dyspareunia or difficult vaginal delivery. Gartner duct cysts arise from the anterolateral wall of the proximal vagina. These lesions have signal characteristics typical for cysts that are low in signal intensity on T1-weighted images and high in signal intensity on T2-weighted images. These cysts can exhibit high signal intensity on T1-weighted images when the contents are proteinaceous or hemorrhagic (fig. 13.16) [102]. Rim enhancement is not a typical feature. Gartner duct cysts can be associated with genitourinary abnormalities such as Herlyn–Werner–Wunderlich syndrome, where they are associated with ipsilateral renal agenesis [103]. Communication of an ectopic ureter with a Gartner duct cyst has been reported and is a cause of incontinence [104].

Cavernous Hemangioma. Cavernous hemangiomas of the vulva or vagina are most common in infants and tend to stabilize or regress during childhood and adolescence. Symptoms are unusual but can include bleeding, ulceration, or hemorrhage during vaginal delivery [105–107]. STIR and fat-suppressed T2-weighted images demonstrate high signal intensity in the serpiginous vascular lakes that make up the neoplasm (fig. 13.17) [108].

Malignant Masses

Primary Vaginal Malignancies. Relatively rare lesions, vaginal carcinomas account for less than 3% of all gynecological malignancies. Up to 95% of primary vaginal malignancies are of squamous cell histology, and they are usually well-differentiated [109, 110]. This entity affects older patients, with a peak age incidence of 60–70 years. Infection with human papillomavirus has been shown to be a risk factor for these tumors [111]. Patients are often asymptomatic but can present with increased vaginal discharge or spotting. Either TNM or FIGO classification schemes can be used for staging (Table 13.2). These lesions typically arise from the upper posterior vagina and then spread through the wall to invade adjacent pelvic structures. Lesions in the upper third of the vagina spread to the iliac nodes, whereas tumors in the lower two-thirds initially involve the inguinal nodes.

Clear cell adenocarcinomas make up 3% of primary vaginal malignancies and occur in less than 0.14% of women who have suffered in utero diethylstilbestrol (DES) exposure [112–114]. Most of these patients were born between 1951 and 1953. These tumors most often arise from the anterior aspect of the upper third of the vagina (fig. 13.18). There is an 80% 5-year survival rate for women presenting with vaginally confined disease and only 20% 5-year survival for women with locally advanced or metastatic tumors [111].

The contrast resolution of MRI has made it the modality of choice in the evaluation of vaginal tumors. It can be used to assess the extent of disease at initial presentation, and it can be used to detect tumor recurrence [115]. Differentiation of inflammatory changes from primary or metastatic lesions may be problematic, but one group of investigators has shown MRI to be 92% accurate in demonstrating metastatic disease and 82% accurate in depicting recurrence [116]. Vaginal tumors are of intermediate signal intensity on T1-weighted images and may be occult when small. However, these lesions are well seen on T2-weighted images and demonstrate moderately high signal intensity [115, 117]. Vaginal neoplasms show variable enhancement after gadolinium administration (figs. 13.19, 13.20, and 13.21).

Detection of tumor recurrence after hysterectomy may be an important role for MRI. The vaginal cuff can have a very irregular appearance due to postoperative fibrosis and granulation tissue. Tumor is generally irregular in contour and usually high in signal intensity on T2-weighted images, whereas fibrosis and granulation tissue are low in signal intensity on T2-weighted images [116, 118]. Recurrent tumor frequently enhances in a heterogeneous intense fashion on gadolinium-enhanced fat-suppressed images. Inflammatory changes within 9 months to 1 year after radiation therapy result in

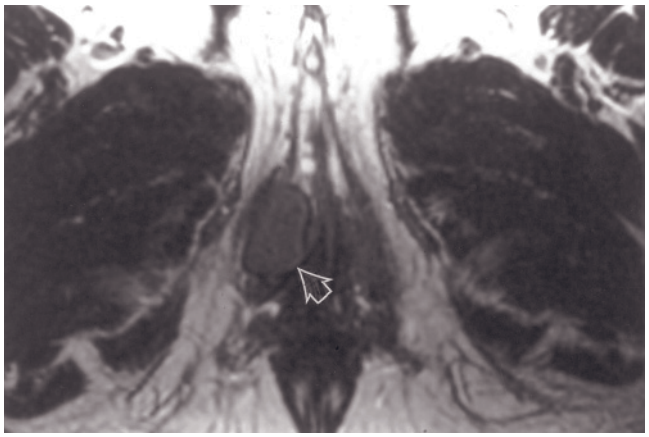

(*a*)

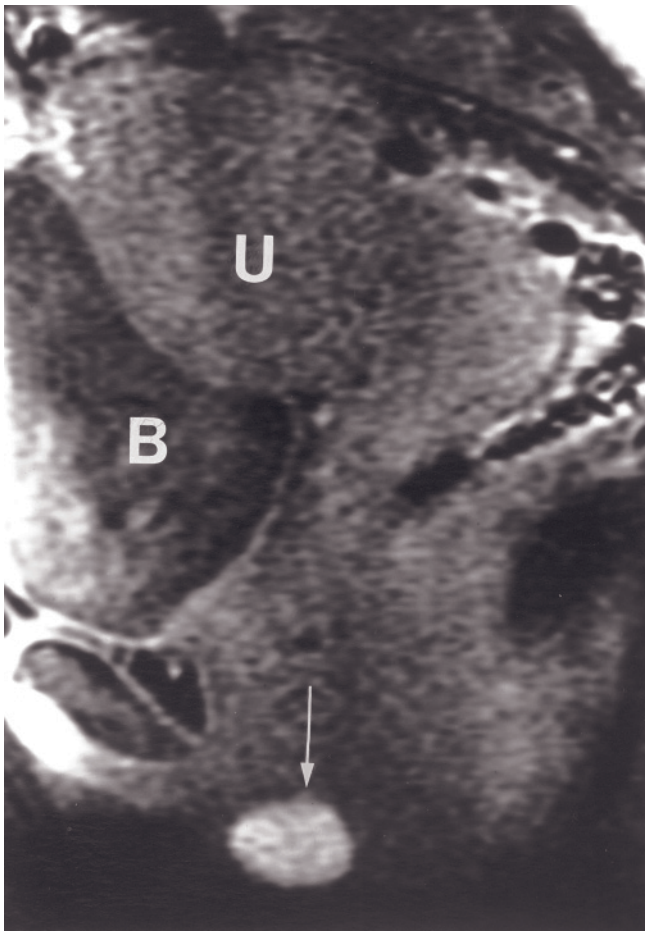

(*b*)

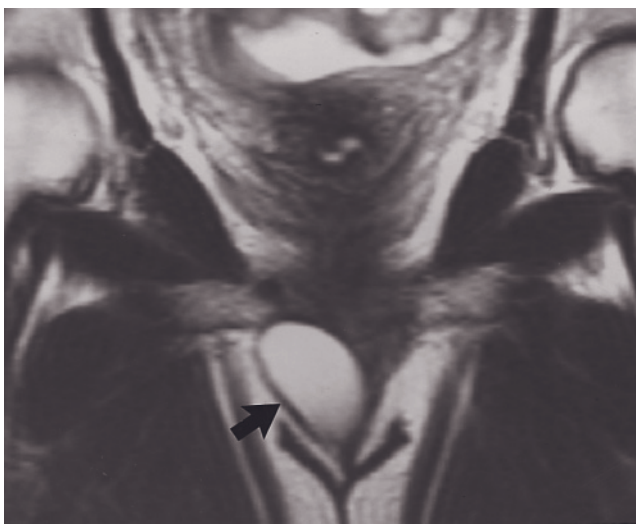

(*c*)

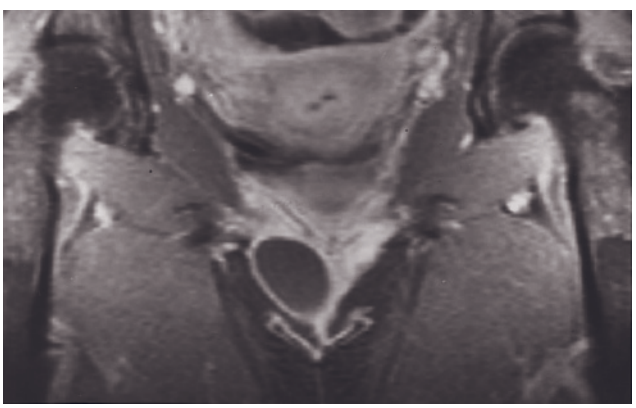

(*d*)

(*e*)

FIG. 13.15 Asymptomatic Bartholin gland cyst. Transverse T2-weighted ETSE (*a*) and sagittal T1-weighted fat-suppressed SGE (*b*) images show a low-signal-intensity mass on the T2-weighted image (arrow, *a*) within the lateral aspect of the distal vagina near the introitus. On the sagittal T1-weighted fat-suppressed image this mass appears high signal intensity because of high protein content (arrow, *b*). B, bladder; U, uterus. Coronal T2-weighted ETSE (*c*) and coronal gadolinium-enhanced fat-suppressed SGE (*d*) images in a second patient. The cyst is high in signal intensity on the T2-weighted image (arrow, *c*) and demonstrates an enhancing cyst wall with low-signal-intensity cyst contents on the postgadolinium image (*d*). Sagittal 512-resolution T2-weighted ETSE (*e*, *f*) images in two other patients show Bartholin duct cysts (arrows, *e*, *f*).

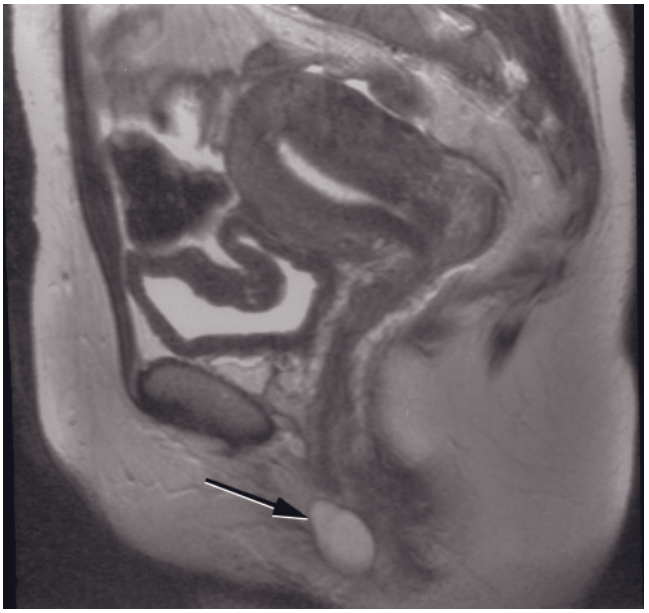

FIG. 13.15 (*Continued*) (*f*)

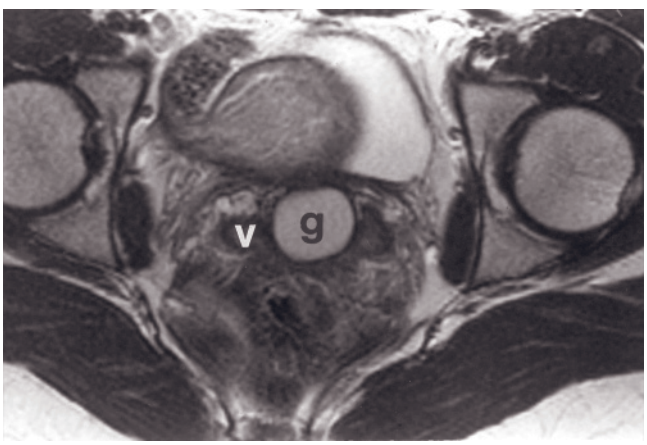

(*a*)

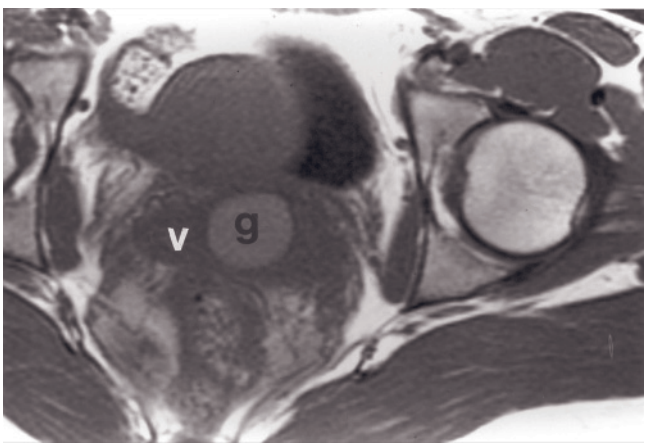

(*b*)

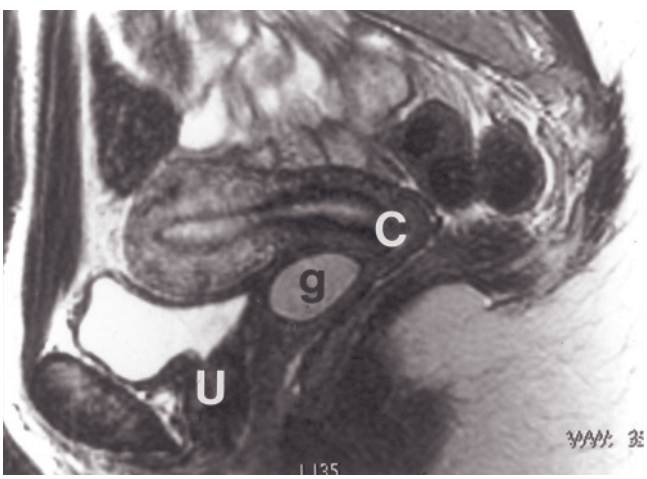

(*c*)

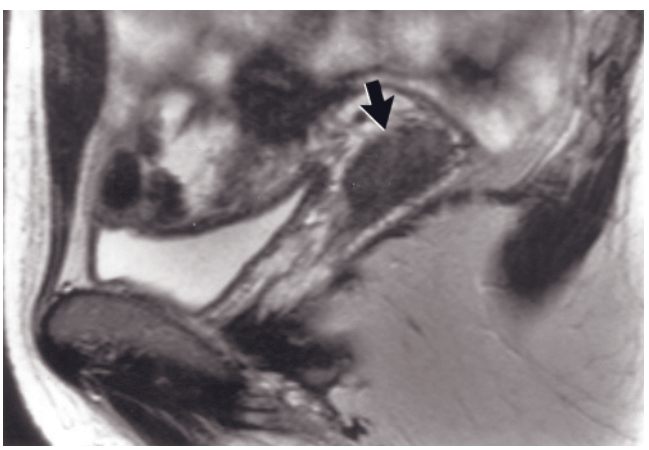

(*d*)

FIG. 13.16 Gartner duct cyst. Transverse T2-weighed ESTE (*a*), transverse T1-weighted ETSE (*b*), and sagittal T2-weighted ETSE (*c*) images in a 22-year-old woman with an asymptomatic palpable paracervical mass. There is a well-circumscribed mass with high-signal intensity on T1- and T2-weighted images (g, *a–c*), centered within the left side of the proximal vagina (v, *a*, *b*). The high signal on T1 reflects intracystic protein. Sagittal T2-weighted image (*c*) reveals that the mass is located above the urethra (U, *c*) and below the cervix (C, *c*) within the proximal vagina. The normal zonal anatomy of the uterus is present. Sagittal (*d*) and

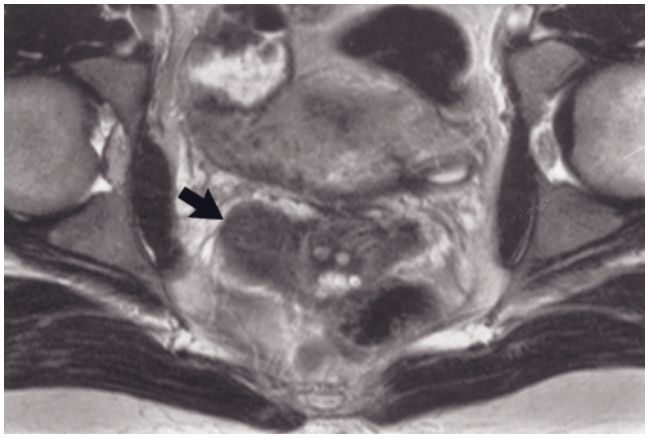

(*e*)

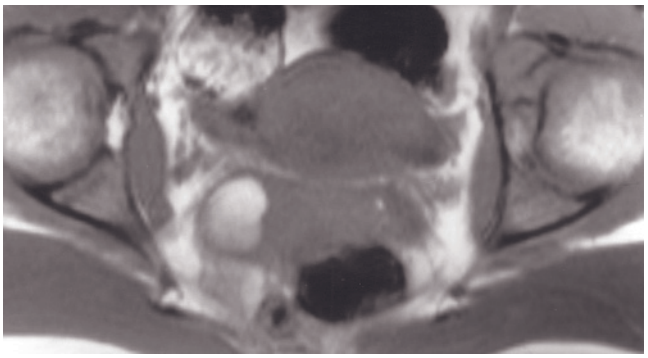

(*f*)

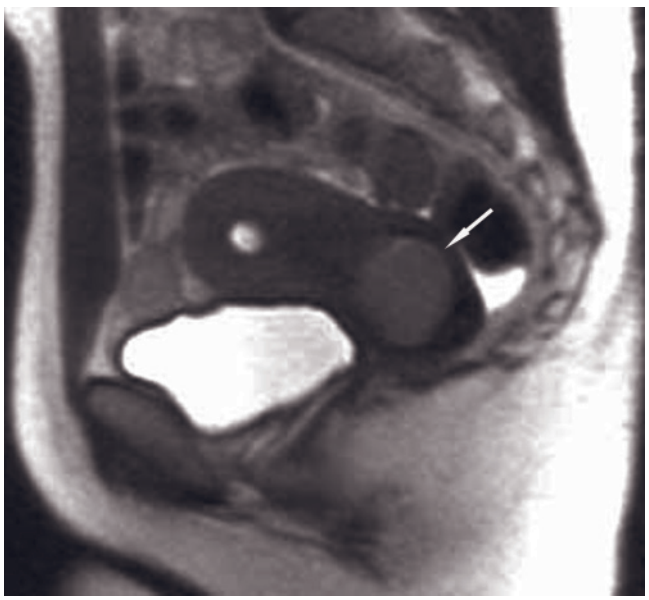

(*g*)

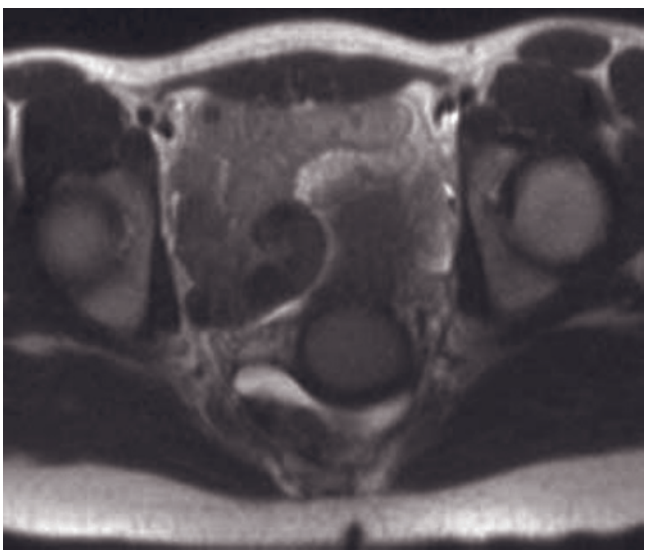

(*h*)

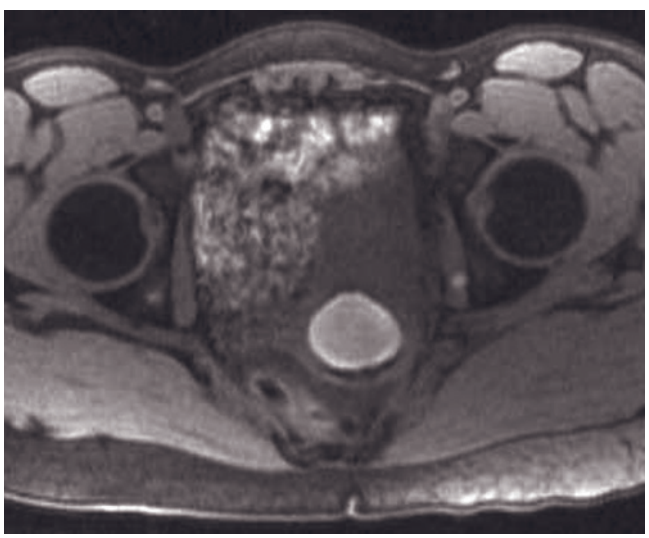

(*i*)

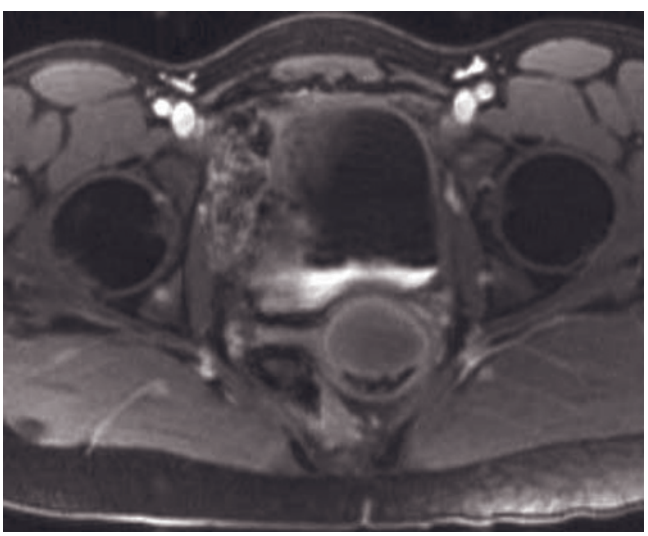

(*j*)

FIG. 13.16 (*Continued*) transverse (*e*) T2-weighted ETSE and transverse SGE (*f*) images in a second patient. There is a round, well-defined lesion in the upper vagina in the right lateral fornix (arrows, *d*, *e*). The cyst is high signal on the T1-weighted image (*f*) and low signal on T2-weighted images (*d*, *e*), consistent with intracystic protein in a Gartner cyst. Sagittal T2-weighted single-shot echo-train (*g*), transverse (*h*), T1-weighted fat-suppressed SGE (*i*), and postgadolinium T1-weighted fat-suppressed SGE (*j*) images in a third patient demonstrate findings similar to the second patient (arrow, *g*).

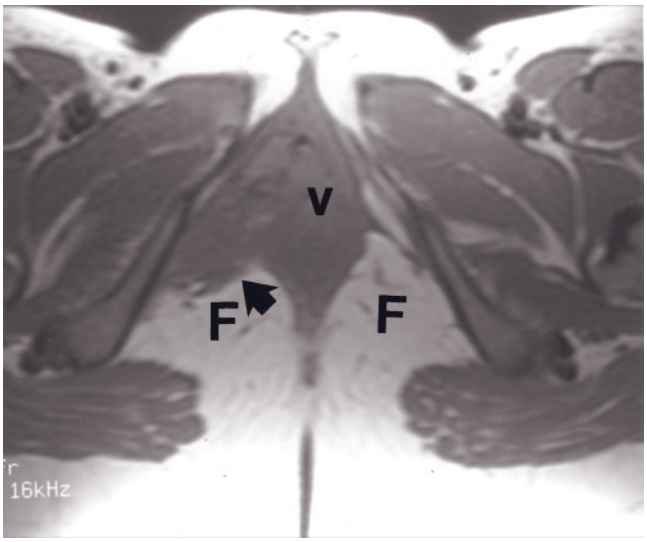

(*a*)

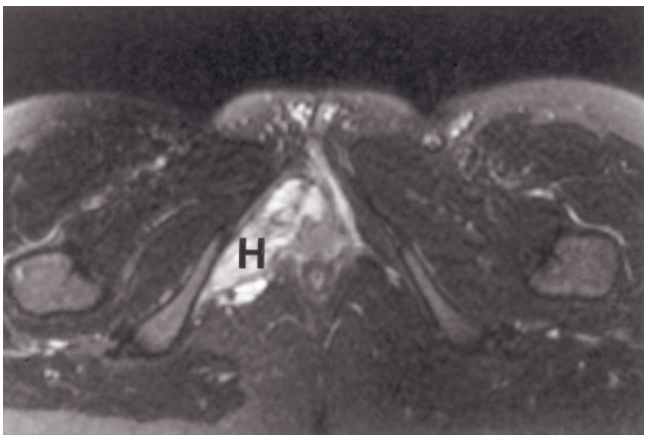

(*b*)

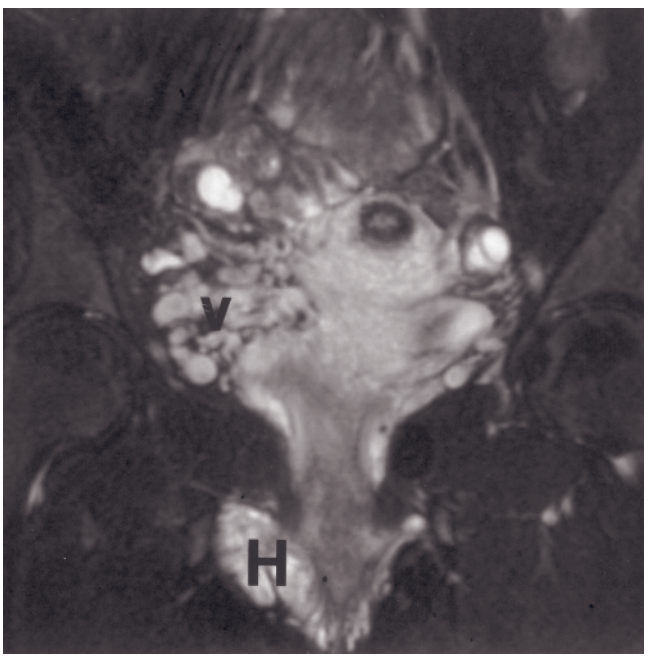

(*c*)

FIG. 13.17 Recurrent perivulvar cavernous hemangioma. Transverse T1-weighted (*a*) and transverse (*b*) and coronal (*c*) T2-weighted ETSE images in a 26-year-old woman who underwent resection of perivulvar hemangioma 12 years before imaging. The T1-weighted image (*a*) at the level of the perineum shows effacement (arrow) of the anterior ischiorectal fat (F) adjacent to the right side of the vagina (v). On T2-weighted images (*b*, *c*), this area is ill-defined and shows high signal intensity (H, *b*) representing the patient's known vascular malformation. Coronal image (*c*) shows the longitudinal extent of the lobular malformation (H). Note the asymmetry of the more central pelvic veins (v, *c*) because of the increased venous outflow of the malformation.

increased signal intensity on T2-weighted images and may mimic tumor recurrence [119]. Close follow-up with MRI may be useful in selected cases.

Other rare primary vaginal malignancies include leiomyosarcomas in adults, endodermal sinus tumors in infants, embryonal rhabdomyosarcoma (sarcoma botryoides) in children (fig. 13.22), melanoma (fig. 13.23), and lymphoma (fig. 13.24) [115, 120–122]. Leiomyosarcoma and endodermal sinus tumors are highly malignant with poor prognosis. Melanoma may be high in signal intensity on T1-weighted images [117]. The high signal intensity within melanin can be either secondary to intratumoral hemorrhage or from the T1-shortening effects of paramagnetic metals such as iron that are associated with melanin [123]. Primary vaginal leiomyomas have as appearance similar to uterine fibroids. Tumors that are not degenerated reveal homogenous low signal intensity on T2-weighted images secondary to the smooth muscle content of the tumor (see fig. 13.21) [22, 124].

Vaginal Metastases. Secondary vaginal malignancies make up 80% of all vaginal tumors [98]. Local spread from cervical and endometrial carcinoma comprise the majority of reported cases (figs. 13.25 and 13.26) [125].

Table 13.2 TNM Staging for Vaginal Carcinoma

Primary Tumor	
Tx	Primary tumor cannot be assessed
T0	No evidence of primary tumor
Tis	Carcinoma in situ
T1	Tumor confined to the vagina
T2	Tumor invades paravaginal tissues but does not extend to the pelvic wall
T3	Tumor extends to the pelvic wall
T4	Tumor invades mucosa of bladder or rectum and/or extends beyond
Regional Lymph Nodes	
Nx	Regional lymph nodes cannot be assessed
N0	No regional lymph node metastasis
Upper two-thirds of vagina	
N1	Regional lymph node metastasis
Lower third of vagina	
N2	Regional lymph node metastasis Bilateral inguinal lymph node metastasis
Metastases	
M1	Distant metastases

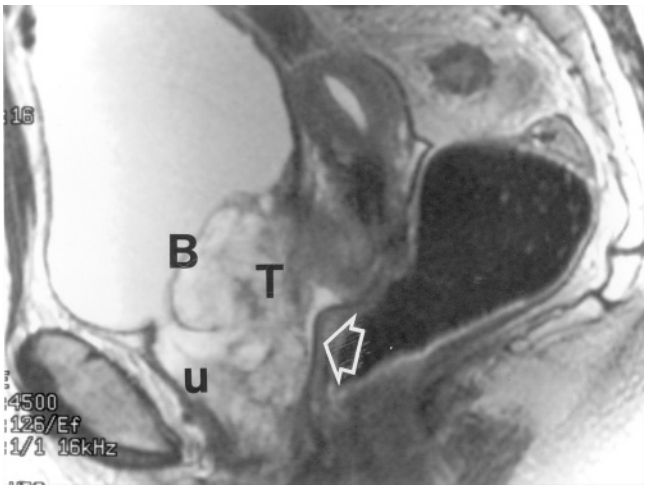

FIG. 13.18 Invasive clear cell adenocarcinoma of the vagina. Sagittal T2-weighted ETSE image in a in a 68-year-old woman unrelated to DES exposure shows a large heterogeneous intermediate- to high-signal-intensity mass (T) in the anterior wall of the proximal vagina with gross invasion of the posterior bladder wall (B) and the posterior urethra (u). The posterior vaginal wall is preserved (open arrow).

Sagittal- and transverse-plane images are useful for the demonstration of tumor extension to the vagina. Both T2-weighted fast spin-echo images and gadolinium-enhanced T1-weighted fat-suppressed images define tumor involvement.

Vulvar and Perineal Carcinomas. Vulvar carcinomas are uncommon lesions that occur in older patients and are typically of squamous cell origin. Most of the patients have vulvar pruritus, although pain, bleeding, and palpable mass are often typical symptoms. A TNM system is used for staging (Table 13.3). Modern treatment includes local resection with inguinal lymphadenectomy. Postoperative adjuvant radiation therapy has replaced pelvic lymphadenectomy [126, 127]. MRI is a sensitive modality for the evaluation of both primary and recurrent vulvar carcinoma (figs. 13.27 and 13.28).

Other more rare malignancies involving the vulva include Bartholin gland carcinoma, Paget disease, melanoma, basal cell carcinoma, rhabdomyosarcoma, and aggressive angiomyxoma [75, 122, 128].

Bartholin gland carcinomas are very rare, with fewer than 50 reported cases in the literature [129]. Most are adenoid cystic carcinomas and grow slowly, with local spread preceding metastatic disease. Treatment includes radical vulvectomy with regional nodal dissection and adjuvant radiation if complete resection is not obtained [130]. At least in part because of the slow rate of growth of this neoplasm, greater than 80% 5-year survival is usually seen.

Miscellaneous

Radiation Change

The appearance of radiation changes of the vagina varies depending on the time interval between therapy and imaging. Acute radiation changes of less than 1 year reflect histologic changes of interstitial edema and capillary leakage. The vaginal wall shows generalized thickening and is high in signal intensity on T2-weighted and gadolinium-enhanced T1-weighted images (fig. 13.29). Chronic changes after more than 1 year result in fibrosis, diminished interstitial fluid, and diminished vascularity. The vaginal wall may become atrophic, has low signal intensity on T2-weighted images, and demonstrates diminished enhancement after gadolinium administration. Necrosis of the vaginal wall with secondary fistula formation can also occur [119, 131, 132].

Fistulas

Fistulas to the vagina occur most commonly in the setting of gynecological malignancy after radiation therapy, hysterectomy, inflammatory bowel disease, or a combination of these. Imaging in the sagittal and

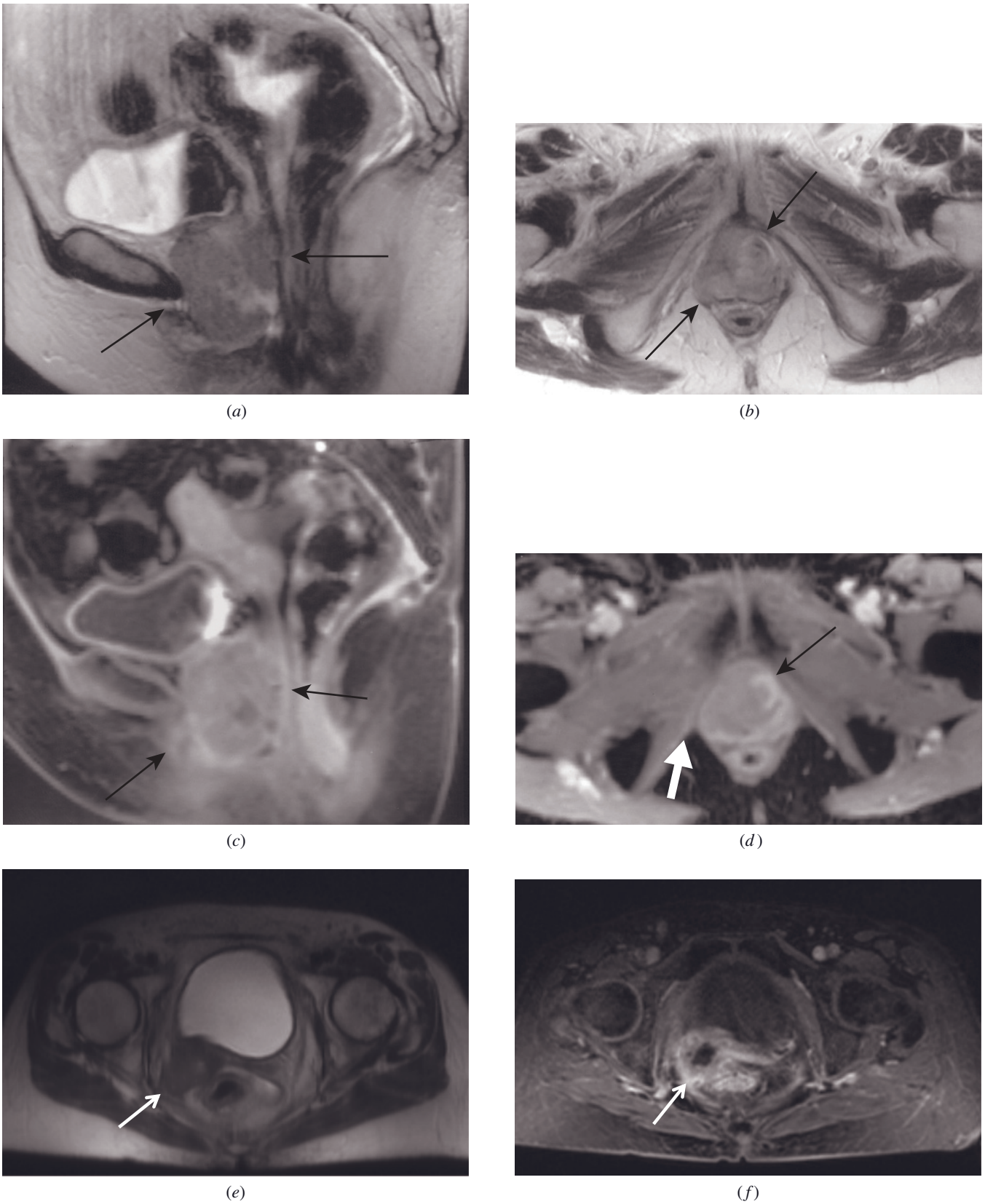

FIG. 13.19 Vaginal carcinoma at 1.5 and 3 T. Sagittal (*a*) and transverse (*b*) T2-weighted ETSE and sagittal (*c*) and transverse (*d*) interstitial-phase gadolinium-enhanced fat-suppressed SGE images at 1.5 T. There is a large, irregular soft tissue mass arising from the vagina and involving the urethra (arrows, *a–d*). The uterus is small and low signal secondary to prior radiation therapy. In a second patient, transverse T2-SE (*e*) and interstitial-phase gadolinium-enhanced fat-suppressed 3D gradient echo (*f*) images at 3 T show an irregular, enhancing, partially necrotic vaginal mass (arrow *e*, *f*).

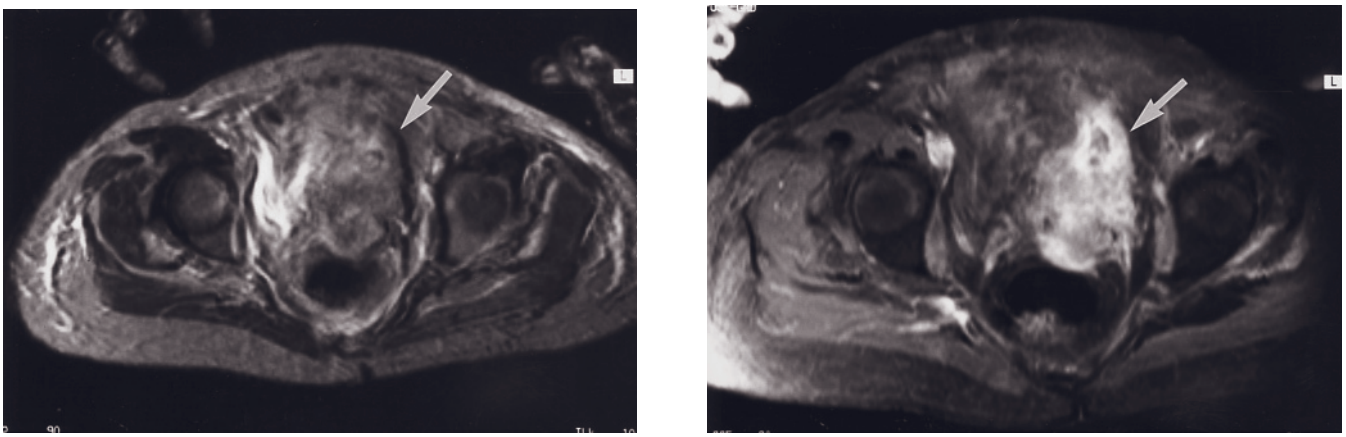

(*a*) (*b*)

FIG. 13.20 Vaginal carcinoma with bladder and rectum invasion. Transverse T2-weighted spin-echo (*a*) and transverse gadolinium-enhanced T1-weighted fat-suppressed spin-echo (*b*) images. A large heterogeneous vaginal cancer is identified on the T2-weighted image (arrow, *a*) arising from the anterior vaginal wall. Postradiation changes in the pelvis are also heterogeneous in signal intensity, and the margins of the tumor are not well-defined. The tumor enhances heterogeneously and intensely after gadolinium administration (arrow, *b*), and invasion of the bladder is clearly shown.

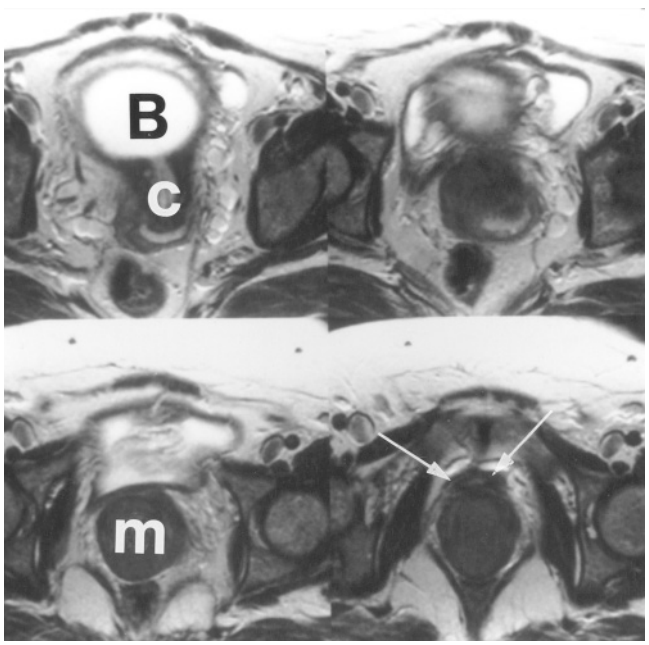

FIG. 13.21 Primary vaginal leiomyoma in a 40-year-old woman. Four consecutive transverse T2-weighted ETSE images show a homogeneous low-signal-intensity mass (m) that is separate from the cervix (c) and urethra (arrows). The low signal intensity on T2 reflects the smooth muscle content of the tumor. B, bladder.

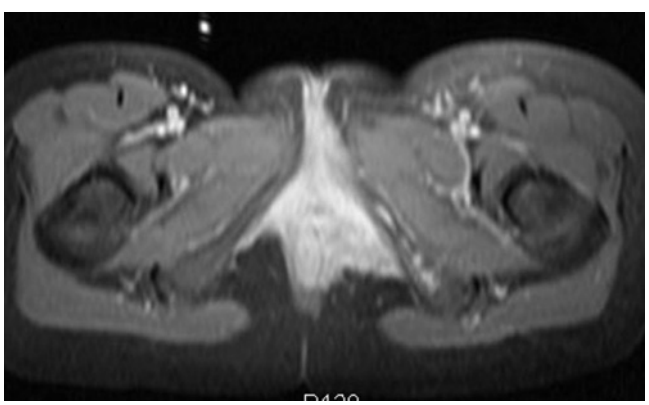

FIG. 13.22 Vaginal rhabdomyosarcoma in a 14-year-old female. Transverse gadolinium-enhanced T1-weighted fat-suppressed spin-echo image demonstrates an irregular enhancing mass extending outside the vagina to involve the vulva and perineal region. Enhancing bony metastasis of the left inferior pubic ramus is also seen.

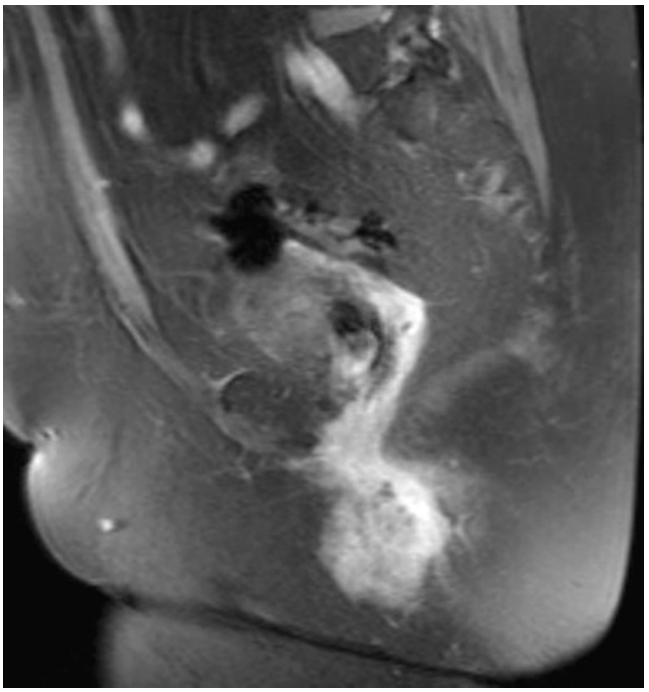

FIG. 13.23 68-year-old female with vaginal melanoma recurrence. Sagittal gadolinium-enhanced T1-weighted fat-suppressed spin-echo image demonstrates an irregular enhancement of the vaginal area extending into the soft tissues anteriorly.

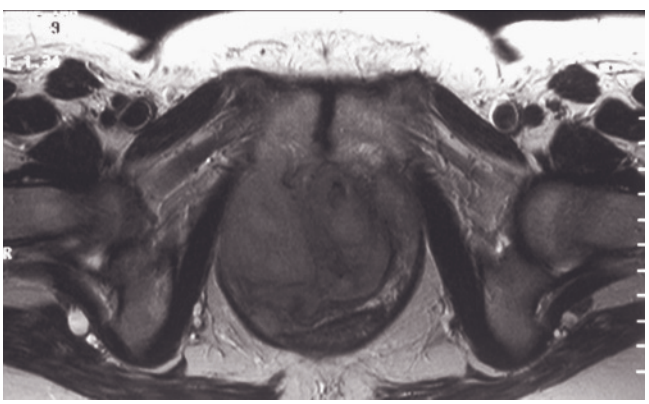

(*a*)

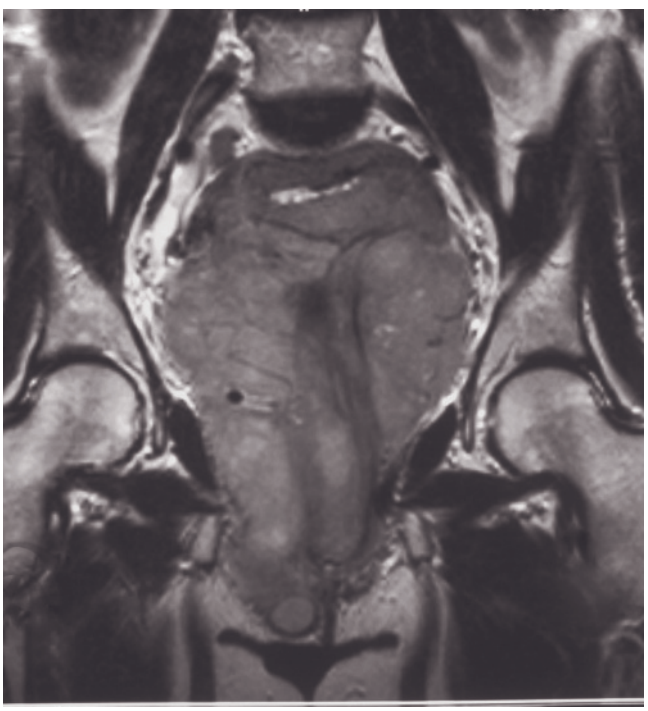

(*b*)

FIG. 13.24 Extensive vaginal lymphoma. Axial (*a*) and coronal (*b*) T2-weighted ETSE images demonstrate a large, lobulated intermediate-signal-intensity mass filling the vaginal canal, displacing the uterus, and extending through the introitus.

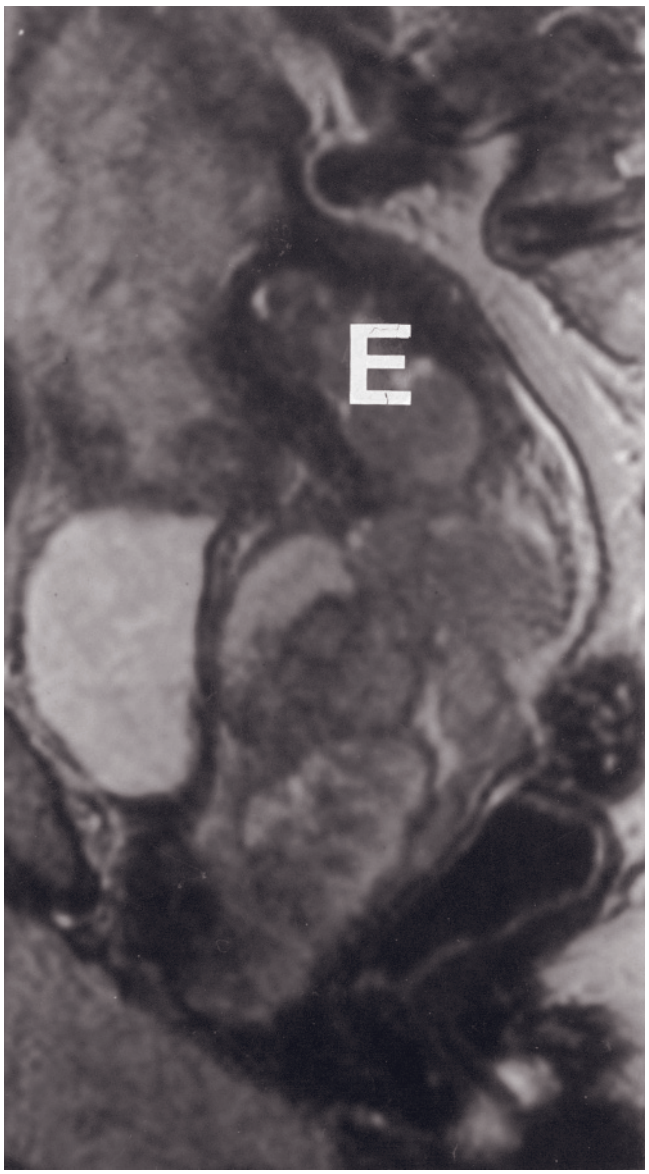

(*a*)

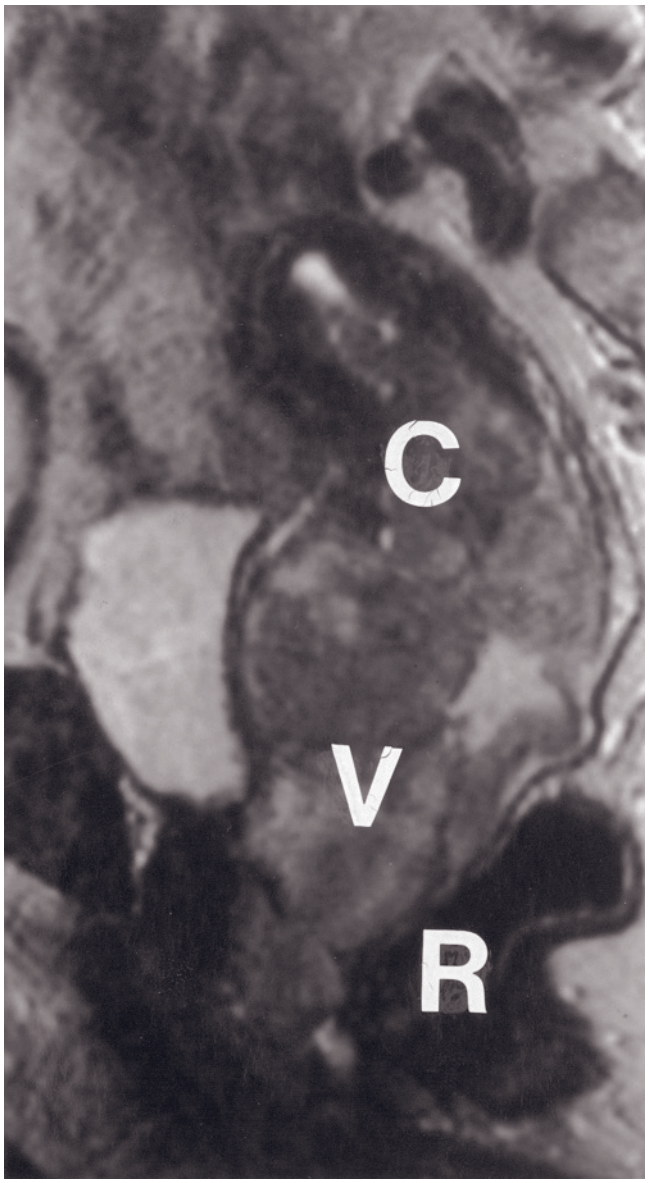

(*b*)

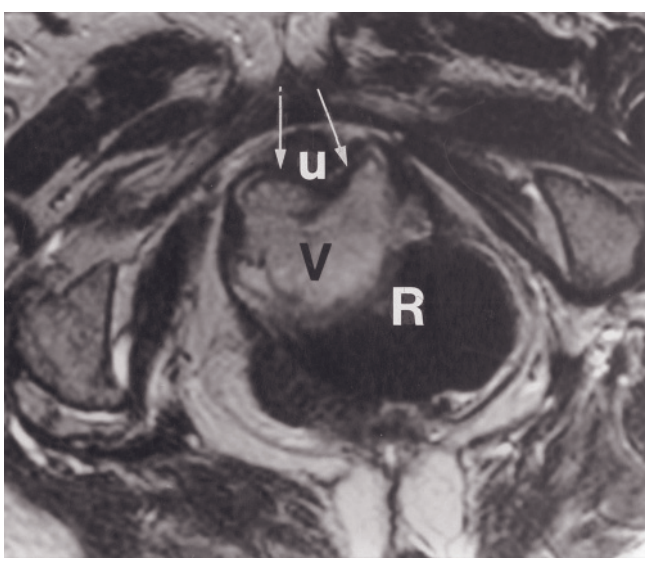

(*c*)

FIG. 13.25 Vaginal invasion. Sagittal (*a*, *b*) and transverse (*c*) T2-weighted ETSE images in a 78-year-old woman who has endometrial carcinoma and presents with an introital mass show distended endometrial (E), cervical (C), rectal (R), and vaginal (V) canals that are filled with solid tumor. Transverse image (*c*) demonstrates that the anterior vaginal wall is intact (white arrows) and the urethra (u) is spared. However, the posterior vaginal wall and rectovaginal septum are indistinct, indicating invasive adenocarcinoma. Transverse T2-weighted spin-echo image (*d*) in

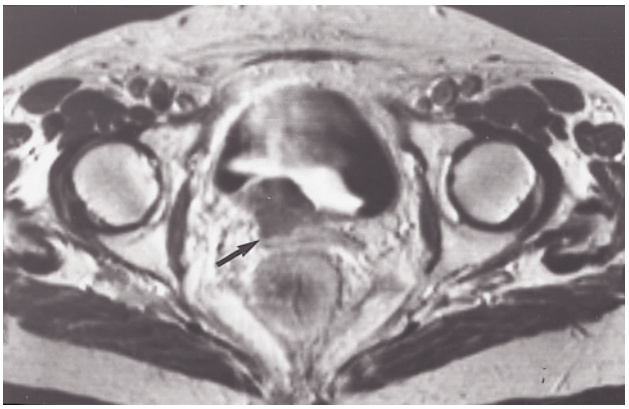

(*d*)

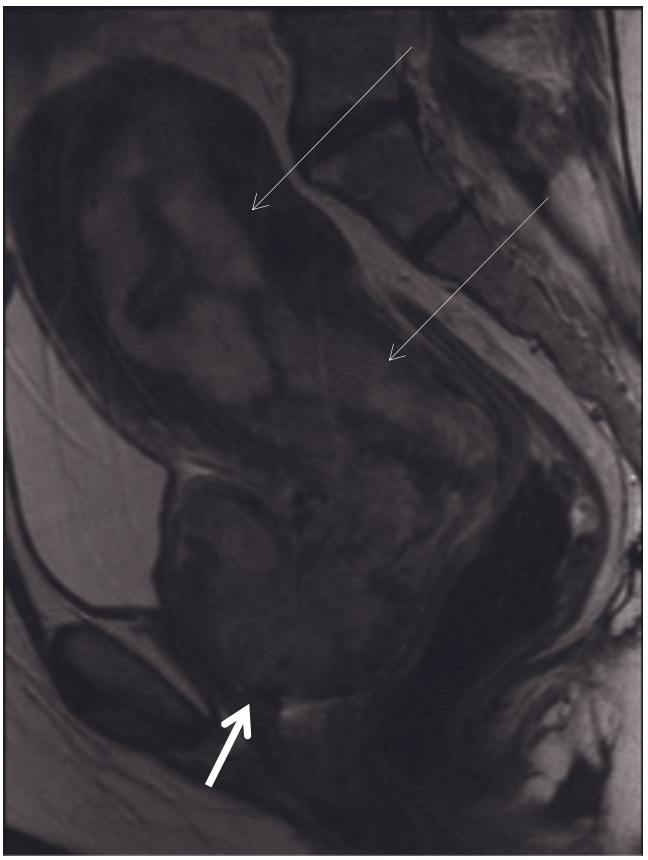

(*e*)

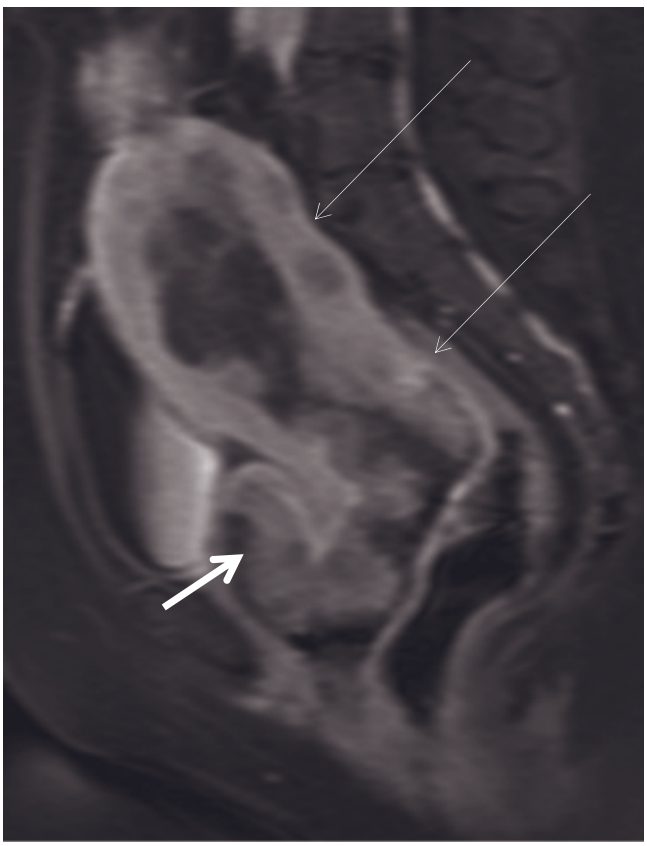

(*f*)

FIG. 13.25 (*Continued*) a second patient, who has bladder cancer. The bladder cancer (arrow, *d*) arises from the posterior wall and invades the anterior wall of the vagina. In a third patient, sagittal T2-weighted ETSE (*e*) and interstitial-phase gadolinium-enhanced fat-suppressed 3D-gradient echo (*f*) images at 3 T show cervical carcinoma with extensive uterine (long arrows, *e*, *f*) and vaginal invasion (short arrow, *e*, *f*).

transverse planes with T2-weighted and postgadolinium T1-weighted images is important to maximize detection (fig. 13.30). The addition of fat suppression to the T1-weighted images increases the conspicuity of the enhancing sinus tract walls. Vaginal fistulas can be diagnosed with vaginography, contrast enema, and retrograde cystography, but MR imaging has the added advantage of being able to evaluate the surrounding soft tissue structures, which can often determine whether the fistula is due to benign or malignant disease [133–135].

Conclusion

MRI is the modality of choice for evaluation of vaginal pathology. The noninvasive nature of the test, the lack of ionizing radiation, and its ability to demonstrate the surrounding soft tissue structures make it superior to vaginography for evaluation of congenital abnormalities. Multiplanar capability, high soft tissue contrast, and nonnephrotoxic contrast media make it the examination of choice for evaluation of benign or malignant masses.

FIG. 13.26 Rectal carcinoma with spread to posterior vaginal fornix. Sagittal immediate postgadolinium fat-suppressed SGE image. A lobulated intermediate-signal-intensity mass (arrow) extends from the lower rectum anteriorly to involve the posterior vaginal fornix (long arrow), which appears expanded.

Table 13.3 TNM Staging for Carcinoma of the Vulva

Primary Tumor	
T1	Tumor 2cm or smaller confined to the vulva
T2	Tumor larger than 2 cm confined to the vulva
T3	Tumor of any size with adjacent spread to the urethra and/or perineum
T4	Tumor of any size infiltrating the bladder mucosa and/or the rectum
Regional Lymph Nodes	
N0	No nodes palpable
N1	Noes palpable in either groin, not enlarged, mobile
N2	Nodes palpable in either one or both groins, enlarged, firm, and mobile
N3	Fixed or ulcerated nodes
Metastases	
M0	No clinical metastases
M1	Palpable deep pelvic lymph nodes
M2	Other distant metastases

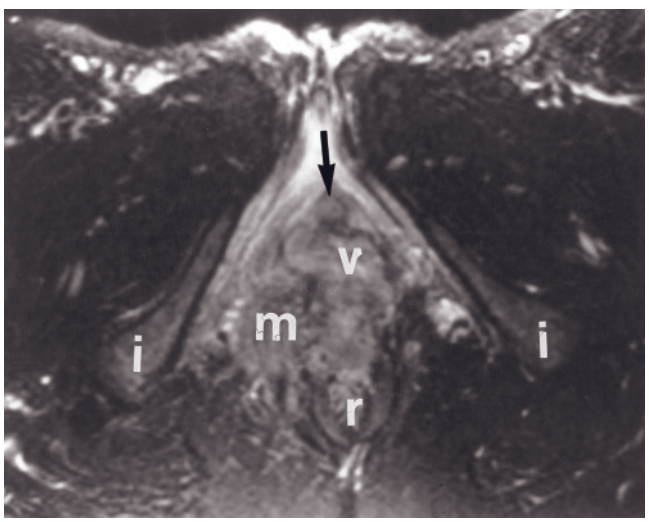

(*a*)

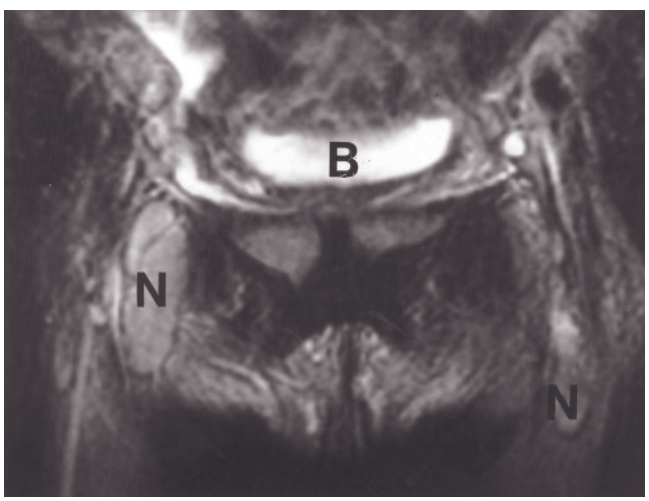

(*b*)

FIG. 13.27 Invasive squamous cell carcinoma of the vulva. Transverse (*a*) and coronal (*b*) T2-weighted fat-suppressed ETSE images in a 37-year-old woman with history of human papillomavirus infection and condylomata accuminata. There is a heterogeneous mass (m, *a*) of intermediate to high signal intensity in the perineum, with obliteration of the expected location of the normal low-signal-intensity anterior rectal wall (r, *a*) and posterior vaginal wall (v, *a*).The distal urethra is not involved (arrow, *a*). Coronal image (*b*) shows bilateral inguinal adenopathy (N). This image alone is not specific for metastatic adenopathy. The presence of central necrosis within lymph nodes on postcontrast MR and CT images is very specific for malignancy in the setting of squamous cell carcinomas of the pelvis. i, Ischial tuberosities; B, bladder.

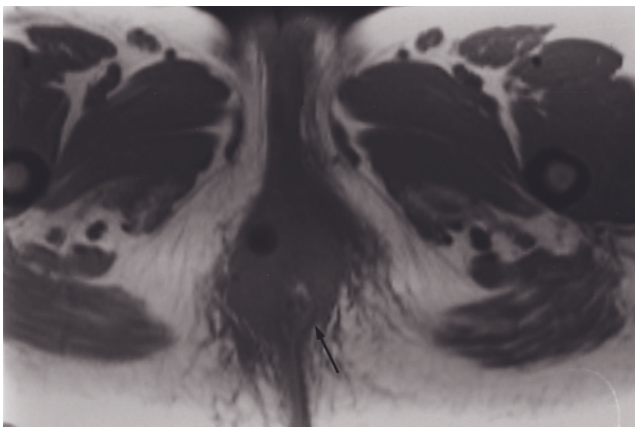

(*a*)

(*b*)

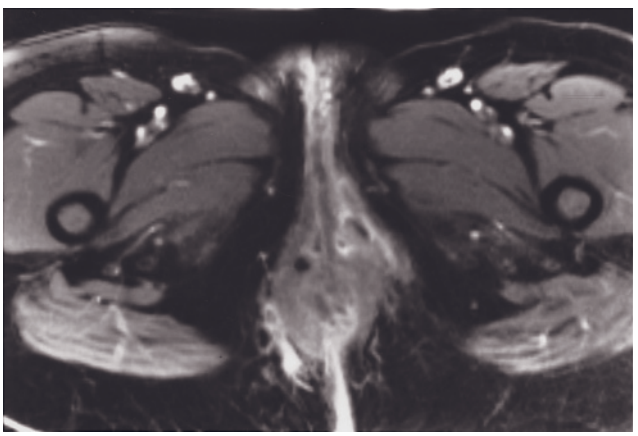

(*c*)

FIG. 13.28 Vulvar carcinoma. Transverse SGE (*a*), 512-resolution T2-weighted echo-train spin-echo (*b*), and 90-s post-gadolinium fat-suppressed SGE (*c*) images. The T1-weighted image (*a*) shows an irregular low-signal-intensity mass arising from the vulva with posterior extension to involve the anus (arrow, *a*). On the T2-weighted image (*b*) the mass is intermediate in signal intensity. In part, this reflects the high signal intensity of fat on echo-train spin-echo sequences. Heterogeneous enhancement of tumor is seen on postgadolinium imaging (*c*).

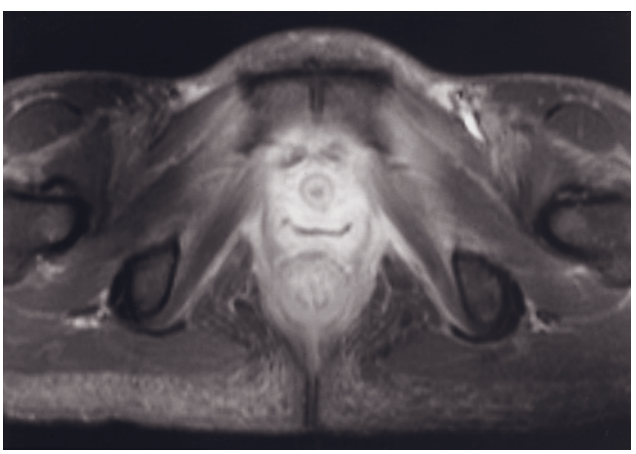

FIG. 13.29 Radiation changes after treatment for vaginal carcinoma. Transverse gadolinium-enhanced T1-weighted fat-suppressed spin-echo image. Enhancing tissue is seen involving the urethra, vagina, and anal canal, giving a "grinning pig" appearance. Diffuse thickening of the vaginal wall is appreciated. Enhancement from acute radiation changes cannot be easily distinguished from tumor, but symmetric changes favor benign disease.

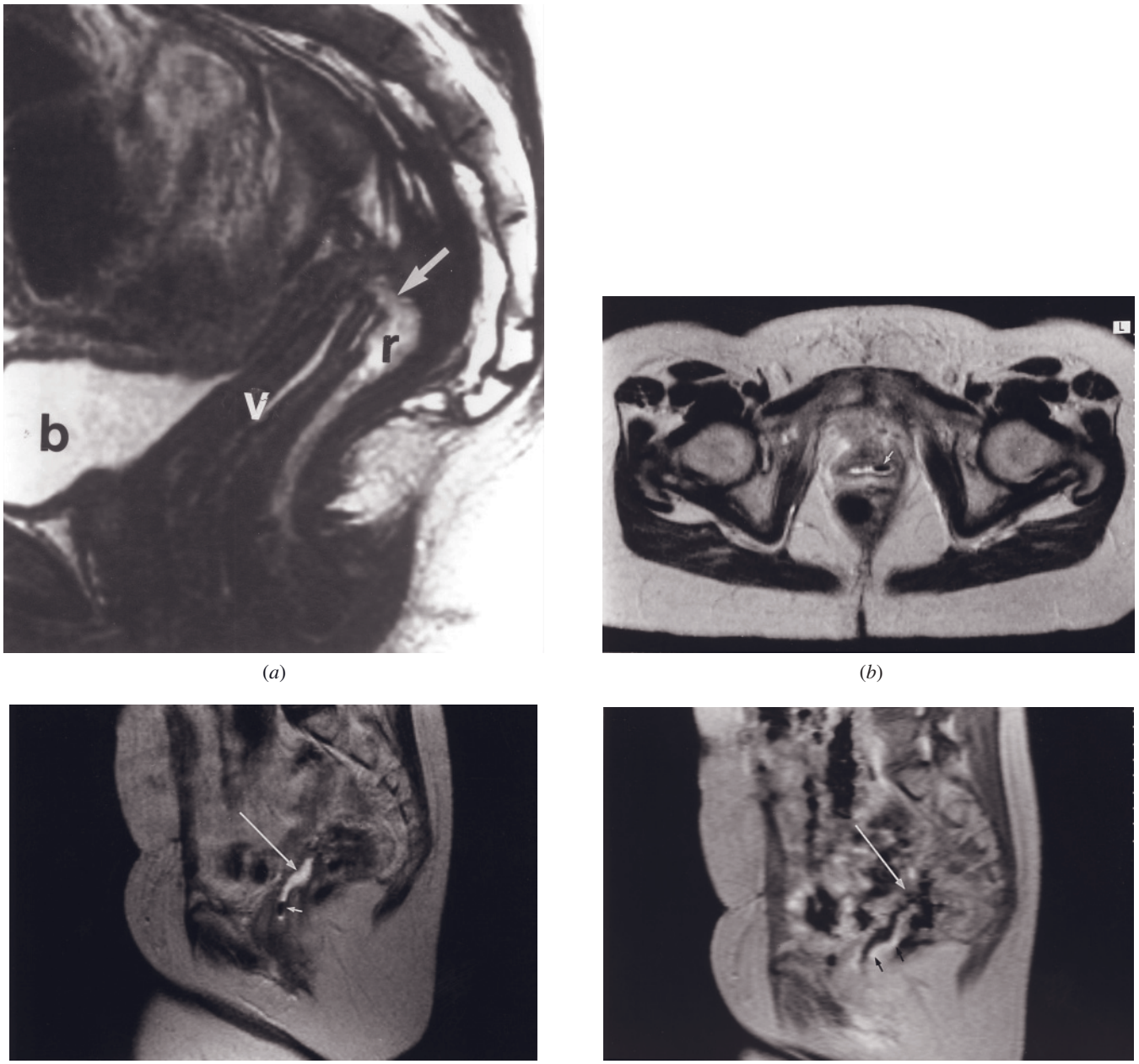

(*a*) (*b*) (*c*) (*d*)

FIG. 13.30 Rectovaginal fistula. Sagittal T2-weighted ETSE image (*a*) in a 36-year-old woman with history of inflammatory bowel disease and prior subtotal colectomy reveals high-signal-intensity content of the fistula (arrow) that is continuous with the remaining rectal segment (r) and the vagina (v). b, Bladder. Transverse 512-resolution T2-weighted echo-train spin-echo (*b*), sagittal 512-resolution T2-weighted echo-train spin-echo (*c*), and sagittal 45-s postgadolinium SGE (*d*) images in a second patient who is status post hysterectomy for cervical cancer. A signal void focus of air is present in the vagina on T2-weighted images (small arrows, *b*, *c*), consistent with a fistulous communication with bowel. The superior aspect of the vagina expands into an abscess cavity (long arrow, *c*), which is well shown on sagittal-plane images. The gadolinium-enhanced image shows increased enhancement and thickness of the vaginal wall, which is consistent with inflammatory changes (short arrow, *d*). A fistulous tract is apparent on this sagittal image (long arrow, *d*) in continuity with adjacent bowel.

REFERENCES

1. Hricak H, Secaf E, Buckley DW et al. Female urethra: MR imaging. *Radiology* 178(2): 527–535, 1991.
2. Moore K. *Clinically Oriented Anatomy.* 2nd ed. Baltimore: Williams and Wilkins, 1985.
3. Countouris N. [The mucosal zones of the female urethra]. *Urologe A* 31(2): 81–84, 1992.
4. Siegelman ES, Banner MP, Ramchandani P et al. Multicoil MR imaging of symptomatic female urethral and periurethral disease. *Radiographics* 17(2): 349–365, 1997.
5. Tan IL, Stoker J, Lameris JS. Magnetic resonance imaging of the female pelvic floor and urethra: body coil versus endovaginal coil. *Magma* 5(1): 59–63, 1997.
6. Nurenberg P, Zimmern PE. Role of MR imaging with transrectal coil in the evaluation of complex urethral abnormalities. *AJR Am J Roentgenol* 169(5): 1335–1338, 1997.
7. Strohbehn K, Quint LE, Prince MR et al. Magnetic resonance imaging anatomy of the female urethra: a direct histologic comparison. *Obstet Gynecol* 88(5): 750–756, 1996.
8. Klutke CG, Siegel CL. Functional female pelvic anatomy. *Urol Clin North Am* 22(3): 487–498, 1995.
9. Sugimura K, Yoshikawa K, Okizuka H et al. [Normal female urethra and paraurethral structure—evaluation with MR imaging]. *Nippon Igaku Hoshasen Gakkai Zasshi* 51(8): 901–905, 1991.
10. Lipson SA, Hricak H. The urinary bladder and female urethra. In: Higgins CB, Hricak H, Helms CA, editors. *Magnetic Resonance Imaging of the Body.* 3rd ed. New York: Lippincott-Raven, 1997, p. 929–956.
11. Tempany CMC. Normal magnetic resonance imaging anatomy. In: Tempany CMC, editor. *MR and Imaging of the Female Pelvis.* Philadelphia: Mosby, 1995. p. 35–54.
12. Preidler KW, Tamussino K, Szolar DM et al. Staging of cervical carcinomas. Comparison of body-coil magnetic resonance imaging and endorectal surface coil magnetic resonance imaging with histopathologic correlation. *Invest Radiol* 31(7): 458–462, 1996.
13. Bellinger MF, Duckett JW. Accessory phallic urethra in the female patient. *J Urol* 127(6): 1159–1164, 1982.
14. Ramon J, Mekras JA, Webster GD. Accessory phallic urethra in adult female. *Urology* 36(3): 280–282, 1990.
15. Nino-Murcia M, Friedland GW, DeVries PA. Congenital anomalies of the papillae, calyces, renal pelvis, ureter, and ureteral orifice. In: Pollack HM, McClennan BL, editors. *Clinical Urography.* 2nd ed. Philadelphia: W. B. Saunders, 2000, p. 764–825.
16. Hochhauser L, Alton DJ. Prolapse of an ectopic ureterocele into both urethra and ipsilateral orthotopic ureter. *Pediatr Radiol* 16(2): 167–168, 1986.
17. Leese T, Osborn DE. Ectopic ureterocele in an adult with prolapse through the urethra. *J Urol* 133(2): 269–270, 1985.
18. Cornella JL, Larson TR, Lee RA et al. Leiomyoma of the female urethra and bladder: report of twenty-three patients and review of the literature. *Am J Obstet Gynecol* 176(6): 1278–1285, 1997.
19. Leidinger RJ, Das S. Leiomyoma of the female urethra. A report of two cases. *J Reprod Med* 40(3): 229–231, 1995.
20. Cheng C, Mac-Moune Lai F, Chan PS. Leiomyoma of the female urethra: a case report and review. *J Urol* 148(5): 1526–1527, 1992.
21. Siegelman SS, Khouri NF, Scott WW Jr. et al. Pulmonary hamartoma: CT findings. *Radiology* 160(2): 313–317, 1986.
22. Siegelman ES, Outwater EK. Tissue characterization in the female pelvis by means of MR imaging. *Radiology* 212(1): 5–18, 1999.
23. Benson RC, Jr., Tunca JC, Buchler DA et al. Primary carcinoma of the female urethra. *Gynecol Oncol* 14(3): 313–318, 1982.
24. Hayes WS. The urethra. In: Davidson AJ, Hartman DS, editors. *Radiology of the Kidney and Urinary Tract.* Philadelphia: W.B. Saunders, 1994, p. 649–667.
25. Narayan P, Konety B. Surgical treatment of female urethral carcinoma. *Urol Clin North Am* 19(2): 373–382, 1992.
26. Gheiler EL, Tefilli MV, Tiguert R et al. Management of primary urethral cancer. *Urology* 52(3): 487–493, 1998.
27. De Paepe ME, Andre R, Mahadevia P. Urethral involvement in female patients with bladder cancer. A study of 22 cystectomy specimens. *Cancer* 65(5): 1237–1241, 1990.
28. Dmochowski RR, Ganabathi K, Zimmern PE et al. Benign female periurethral masses. *J Urol* 152(6 Pt 1): 1943–1951, 1994.
29. Lee RA. Diverticulum of the urethra: clinical presentation, diagnosis, and management. *Clin Obstet Gynecol* 27(2): 490–498, 1984.
30. Khati NJ, Javitt MC, Schwartz AM et al. MR imaging diagnosis of a urethral diverticulum. *Radiographics* 18(2): 517–522, 1998.
31. Di Santis SJ. Inflammatory conditions of the urethra. In: Pollack HM, McClennan BL, editors. *Clinical Urography.* 2nd ed. Philadelphia: W. B. Saunders, 2000, p. 1041–1057.
32. Romanzi LJ, Groutz A, Blaivas JG. Urethral diverticulum in women: diverse presentations resulting in diagnostic delay and mismanagement. *J Urol* 164(2): 428–433, 2000.
33. Neitlich JD, Foster HE Jr., Glickman MG et al. Detection of urethral diverticula in women: comparison of a high resolution fast spin echo technique with double balloon urethrography. *J Urol* 159(2): 408–410, 1998.
34. Keefe B, Warshauer DM, Tucker MS et al. Diverticula of the female urethra: diagnosis by endovaginal and transperineal sonography. *AJR Am J Roentgenol* 156(6): 1195–1197, 1991.
35. Kim B, Hricak H, Tanagho EA. Diagnosis of urethral diverticula in women: value of MR imaging. *AJR Am J Roentgenol* 161(4): 809–815, 1993.
36. Hickey N, Murphy J, Herschorn S. Carcinoma in a urethral diverticulum: magnetic resonance imaging and sonographic appearance. *Urology* 55(4): 588–589, 2000.
37. Thomas RB, Maguire B. Adenocarcinoma in a female urethral diverticulum. *Aust NZ J Surg* 61(11): 869–871, 1991.
38. Blander DS, Broderick GA, Rovner ES. Images in clinical urology. Magnetic resonance imaging of a "saddle bag" urethral diverticulum. *Urology* 53(4): 818–819, 1999.
39. Daneshgari F, Zimmern PE, Jacomides L. Magnetic resonance imaging detection of symptomatic noncommunicating intraurethral wall diverticula in women. *J Urol* 161(4): 1259–1261; discussion 1261–1252, 1999.
40. Marshall FC, Uson AC, Melicow MM. Neoplasma and caruncles of the female urethra. *Surg Gynecol Obstet* 110: 723–733, 1960.
41. Khatib RA, Khalil AM, Tawil AN et al. Non-Hodgkin's lymphoma presenting as a urethral caruncle. *Gynecol Oncol* 50(3): 389–393, 1993.
42. Narumi Y, Hricak H, Armenakas NA et al. MR imaging of traumatic posterior urethral injury. *Radiology* 188(2): 439–443, 1993.
43. Dixon CM, Hricak H, McAninch JW. Magnetic resonance imaging of traumatic posterior urethral defects and pelvic crush injuries. *J Urol* 148(4): 1162–1165, 1992.
44. Maubon AJ, Roux JO, Faix A et al. Penile fracture: MRI demonstration of a urethral tear associated with a rupture of the corpus cavernosum. *Eur Radiol* 8(3): 469–470, 1998.
45. Ryu J, Kim B. MR imaging of the male and female urethra. *Radiographics* 21(5): 1169–1185, 2001.
46. Lee RA, Symmonds RE, Williams TJ. Current status of genitourinary fistula. *Obstet Gynecol* 72(3 Pt 1): 313–319, 1988.
47. Jafri SZH, Roberts JL, Berger BD. Fistulas of the genitourinary tract. In: Pollack HM, McClennan BL, editors. *Clinical Urography.* 2nd ed. Philadelphia: W. B. Saunders, 2000. p. 2992–3012.
48. Gerber GS, Schoenberg HW. Female urinary tract fistulas. *J Urol* 149(2): 229–236, 1993.

49. Waidelich RM, Brunschweiger SM, Schmeller NT. [Urethrovaginal fistula in Behcet disease]. *Urologe A* 33(2): 163–166, 1994.
50. Takamatsu H, Noguchi H, Tahara H et al. Ano-urethral fistula, a special type of anomaly: report of two cases. *Surg Today* 23(12): 1116–1118, 1993.
51. Rousson B, Verzeaux E, Leriche A et al. [Urethroplasty using polyglactin mesh in urethral fistula caused by decubitus ulcer of the perineum in spinal cord injuries. Apropos of 7 cases]. *Ann Chir Plast Esthet* 39(1): 10–14, 1994.
52. Constantinou CE, Hvistendahl G, Ryhammer A et al. Determining the displacement of the pelvic floor and pelvic organs during voluntary contractions using magnetic resonance imaging in younger and older women. *BJU Int* 90(4): 408–414, 2002.
53. deSouza NM, Daniels OJ, Williams AD et al. Female urinary genuine stress incontinence: anatomic considerations at MR imaging of the paravaginal fascia and urethra initial observations. *Radiology* 225(2): 433–439, 2002.
54. Kim JK, Kim YJ, Choo MS et al. The urethra and its supporting structures in women with stress urinary incontinence: MR imaging using an endovaginal coil. *AJR Am J Roentgenol* 180(4): 1037–1044, 2003.
55. Comiter CV, Vasavada SP, Barbaric ZL et al. Grading pelvic prolapse and pelvic floor relaxation using dynamic magnetic resonance imaging. *Urology* 54(3): 454–457, 1999.
56. Mostwin JL, Yang A, Sanders R et al. Radiography, sonography, and magnetic resonance imaging for stress incontinence. Contributions, uses, and limitations. *Urol Clin North Am* 22(3): 539–549, 1995.
57. Pannu HK, Kaufman HS, Cundiff GW et al. Dynamic MR imaging of pelvic organ prolapse: spectrum of abnormalities. *Radiographics* 20(6): 1567–1582, 2000.
58. Yang A, Mostwin JL, Rosenshein NB et al. Pelvic floor descent in women: dynamic evaluation with fast MR imaging and cinematic display. *Radiology* 179(1): 25–33, 1991.
59. Pannu HK. Dynamic MR imaging of female organ prolapse. *Radiol Clin North Am* 41(2): 409–423, 2003.
60. Fielding JR, Versi E, Mulkern RV et al. MR imaging of the female pelvic floor in the supine and upright positions. *J Magn Reson Imaging* 6(6): 961–963, 1996.
61. Kelvin FM, Maglinte DD, Hale DS et al. Female pelvic organ prolapse: a comparison of triphasic dynamic MR imaging and triphasic fluoroscopic cystocolpoproctography. *AJR Am J Roentgenol* 174(1): 81–88, 2000.
62. Huddleston HT, Dunnihoo DR, Huddleston PM 3rd et al. Magnetic resonance imaging of defects in DeLancey's vaginal support levels I, II, and III. *Am J Obstet Gynecol* 172(6): 1778–1782; discussion 1782–1774, 1995.
63. Lienemann A, Anthuber C, Baron A et al. Dynamic MR colpocystorectography assessing pelvic-floor descent. *Eur Radiol* 7(8): 1309–1317, 1997.
64. Healy JC, Halligan S, Reznek RH et al. Magnetic resonance imaging of the pelvic floor in patients with obstructed defaecation. *Br J Surg* 84(11): 1555–1558, 1997.
65. McGuire EJ, English SF. Periurethral collagen injection for male and female sphincteric incontinence: indications, techniques, and result. *World J Urol* 15(5): 306–309, 1997.
66. Maki DD, Banner MP, Ramchandani P et al. Injected periurethral collagen for postprostatectomy urinary incontinence: MR and CT appearance. *Abdom Imaging* 25(6): 658–662, 2000.
67. Carr LK, Herschorn S, Leonhardt C. Magnetic resonance imaging after intraurethral collagen injected for stress urinary incontinence. *J Urol* 155(4): 1253–1255, 1996.
68. Corcos J, Fournier C. Periurethral collagen injection for the treatment of female stress urinary incontinence: 4-year follow-up results. *Urology* 54(5): 815–818, 1999.
69. Martins FE, Boyd SD. Post-operative risk factors associated with artificial urinary sphincter infection-erosion. *Br J Urol* 75(3): 354–358, 1995.
70. Kirschner-Hermanns R, Wein B, Niehaus S et al. The contribution of magnetic resonance imaging of the pelvic floor to the understanding of urinary incontinence. *Br J Urol* 72(5 Pt 2): 715–718, 1993.
71. Fielding JR, Griffiths DJ, Versi E et al. MR imaging of pelvic floor continence mechanisms in the supine and sitting positions. *AJR Am J Roentgenol* 171(6): 1607–1610, 1998.
72. Brubacker LT, Saclarides TJ. *The Female Pelvic Floor: Disorders of Function and Support*. Philadelphia: Davis, 1996.
73. Pannu HK. MRI of pelvic organ prolapse. *Eur Radiol* 14(8): 1456–1464, 2004.
74. Yoshioka K, Matsui Y, Yamada O et al. Physiologic and anatomic assessment of patients with rectocele. *Dis Colon Rectum* 34(8): 704–708, 1991.
75. Siegelman ES, Outwater EK, Banner MP et al. High-resolution MR imaging of the vagina. *Radiographics* 17(5): 1183–1203, 1997.
76. Hopkins KL, Nino-Murcia M, Friedland GW et al. Miscellaneous congenital anomalies of the genitourinary tract. In: Pollack HM, McClennan BL, editors. *Clinical Urography*. 2nd ed. Philadelphia: W. B. Saunders, 2000, p. 892–911.
77. Hricak H, Chang YC, Thurnher S. Vagina: evaluation with MR imaging. Part I. Normal anatomy and congenital anomalies. *Radiology* 169(1): 169–174, 1988.
78. Gougoutas CA, Siegelman ES, Hunt J et al. Pelvic endometriosis: various manifestations and MR imaging findings. *AJR Am J Roentgenol* 175(2): 353–358, 2000.
79. Low RN, Barone RM, Lacey C et al. Peritoneal tumor: MR imaging with dilute oral barium and intravenous gadolinium-containing contrast agents compared with unenhanced MR imaging and CT. *Radiology* 204(2): 513–520, 1997.
80. Outwater EK, Mitchell DG. Magnetic resonance imaging techniques in the pelvis. *Magn Reson Imaging Clin N Am* 2(2): 161–188, 1994.
81. Smith RC. Magnetic resonance imaging of the female pelvis: technical considerations. *Top Magn Reson Imaging* 7(1): 3–25, 1995.
82. Secaf E, Hricak H, Gooding CA et al. Role of MRI in the evaluation of ambiguous genitalia. *Pediatr Radiol* 24(4): 231–235, 1994.
83. Fedele L, Dorta M, Brioschi D et al. Magnetic resonance imaging in Mayer-Rokitansky-Kuster-Hauser syndrome. *Obstet Gynecol* 76(4): 593–596, 1990.
84. Togashi K, Nishimura K, Itoh K et al. Vaginal agenesis: classification by MR imaging. *Radiology* 162(3): 675–677, 1987.
85. Carrington BM, Hricak H, Nuruddin RN et al. Mullerian duct anomalies: MR imaging evaluation. *Radiology* 176(3): 715–720, 1990.
86. Reinhold C, Hricak H, Forstner R et al. Primary amenorrhea: evaluation with MR imaging. *Radiology* 203(2): 383–390, 1997.
87. Fielding JR. MR imaging of Mullerian anomalies: impact on therapy. *AJR Am J Roentgenol* 167(6): 1491–1495, 1996.
88. Capraro VJ, Gallego MB. Vaginal agenesis. *Am J Obstet Gynecol* 124(1): 98–107, 1976.
89. Strubbe EH, Willemsen WN, Lemmens JA et al. Mayer-Rokitansky-Kuster-Hauser syndrome: distinction between two forms based on excretory urographic, sonographic, and laparoscopic findings. *AJR Am J Roentgenol* 160(2): 331–334, 1993.
90. Letterie GS. Combined congenital absence of the vagina and cervix. Diagnosis with magnetic resonance imaging and surgical management. *Gynecol Obstet Invest* 46(1): 65–67, 1998.
91. Lang IM, Babyn P, Oliver GD. MR imaging of paediatric utero-vaginal anomalies. *Pediatr Radiol* 29(3): 163–170, 1999.

92. Rock JA, Azziz R. Genital anomalies in childhood. *Clin Obstet Gynecol* 30(3): 682–696, 1987.
93. Tanaka YO, Kurosaki Y, Kobayashi T et al. Uterus didelphys associated with obstructed hemivagina and ipsilateral renal agenesis: MR findings in seven cases. *Abdom Imaging* 23(4): 437–441, 1998.
94. Lin CC, Chen AC, Chen TY. Double uterus with an obstructed hemivagina and ipsilateral renal agenesis: report of 5 cases and a review of the literature. *J Formos Med Assoc* 90(2): 195–201, 1991.
95. Niver DH, Barrette G, Jewelewicz R. Congenital atresia of the uterine cervix and vagina: three cases. *Fertil Steril* 33(1): 25–29, 1980.
96. Neal MR, Angtuaco TL, Shah HR. Case of the day. 4. Diagnosis: vaginal agenesis. *J Ultrasound Med* 13(4): 333–334, 1994.
97. Saenger P. Abnormal sex differentiation. *J Pediatr* 104(1): 1–17, 1984.
98. Gambino J, Caldwell B, Dietrich R et al. Congenital disorders of sexual differentiation: MR findings. *AJR Am J Roentgenol* 158(2): 363–367, 1992.
99. Cheetham DR. Bartholin's cyst: marsupialization or aspiration? *Am J Obstet Gynecol* 152(5): 569–570, 1985.
100. Andersen PG, Christensen S, Detlefsen GU et al. Treatment of Bartholin's abscess. Marsupialization versus incision, curettage and suture under antibiotic cover. A randomized study with 6 months' follow-up. *Acta Obstet Gynecol Scand* 71(1): 59–62, 1992.
101. Kier R. Nonovarian gynecologic cysts: MR imaging findings. *AJR Am J Roentgenol* 158(6): 1265–1269, 1992.
102. Moulopoulos LA, Varma DG, Charnsangavej C et al. Magnetic resonance imaging and computed tomography appearance of asymptomatic paravaginal cysts. *Clin Imaging* 17(2): 126–132, 1993.
103. Lee MJ, Yoder IC, Papanicolaou N et al. Large Gartner duct cyst associated with a solitary crossed ectopic kidney: imaging features. *J Comput Assist Tomogr* 15(1): 149–151, 1991.
104. Rosenfeld DL, Lis E. Gartner's duct cyst with a single vaginal ectopic ureter and associated renal dysplasia or agenesis. *J Ultrasound Med* 12(12): 775–778, 1993.
105. Haley JC, Mirowski GW, Hood AF. Benign vulvar tumors. *Semin Cutan Med Surg* 17(3): 196–204, 1998.
106. Lazarou G, Goldberg MI. Vulvar arteriovenous hemangioma. A case report. *J Reprod Med* 45(5): 439–441, 2000.
107. O'Neal MF, Amparo EG. MR demonstration of extensive pelvic involvement in vulvar hemangiomas. *J Comput Assist Tomogr* 12(2): 219–221, 1988.
108. Saks AM, Paterson FC, Irvine AT et al. Improved MR venography: use of fast short inversion time inversion-recovery technique in evaluation of venous angiomas. *Radiology* 194(3): 908–911, 1995.
109. Dixit S, Singhal S, Baboo HA. Squamous cell carcinoma of the vagina: a review of 70 cases. *Gynecol Oncol* 48(1): 80–87, 1993.
110. Piura B, Rabinovich A, Cohen Y et al. Primary squamous cell carcinoma of the vagina: report of four cases and review of the literature. *Eur J Gynaecol Oncol* 19(1): 60–63, 1998.
111. Merino MJ. Vaginal cancer: the role of infectious and environmental factors. *Am J Obstet Gynecol* 165(4 Pt 2): 1255–1262, 1991.
112. Herbst AL, Anderson D. Clear cell adenocarcinoma of the vagina and cervix secondary to intrauterine exposure to diethylstilbestrol. *Semin Surg Oncol* 6(6): 343–346, 1990.
113. Herbst AL, Anderson D. Clear cell adenocarcinoma of cervix and vagina and DES-related abnormalities. In: Coppleson M, editor. *Gynecologic Oncology*. New York: Churchill Livingstone, 1992, p. 523–540.
114. Mittendorf R. Teratogen update: carcinogenesis and teratogenesis associated with exposure to diethylstilbestrol (DES) in utero. *Teratology* 51(6): 435–445, 1995.
115. Tsuda K, Murakami T, Kurachi H et al. MR imaging of nonsquamous vaginal tumors. *Eur Radiol* 9(6): 1214–1218, 1999.
116. Chang YC, Hricak H, Thurnher S et al. Vagina: evaluation with MR imaging. Part II. Neoplasms. *Radiology* 169(1): 175–179, 1988.
117. Gilles R, Michel G, Chancelier MD et al. Case report: clear cell adenocarcinoma of the vagina: MR features. *Br J Radiol* 66(782): 168–170, 1993.
118. Brown JJ, Gutierrez ED, Lee JK. MR appearance of the normal and abnormal vagina after hysterectomy. *AJR Am J Roentgenol* 158(1): 95–99, 1992.
119. Blomlie V, Rofstad EK, Tvera K et al. Noncritical soft tissues of the female pelvis: serial MR imaging before, during, and after radiation therapy. *Radiology* 199(2): 461–468, 1996.
120. McNicholas MM, Fennelly JJ, MacErlaine DP. Imaging of primary vaginal lymphoma. *Clin Radiol* 49(2): 130–132, 1994.
121. Moon WK, Kim SH, Han MC. MR findings of malignant melanoma of the vagina. *Clin Radiol* 48(5): 326–328, 1993.
122. Piura B, Rabinovich A, Dgani R. Malignant melanoma of the vulva: report of six cases and review of the literature. *Eur J Gynaecol Oncol* 20(3): 182–186, 1999.
123. Enochs WS, Petherick P, Bogdanova A et al. Paramagnetic metal scavenging by melanin: MR imaging. *Radiology* 204(2): 417–423, 1997.
124. Murase E, Siegelman ES, Outwater EK et al. Uterine leiomyomas: histopathologic features, MR imaging findings, differential diagnosis, and treatment. *Radiographics* 19(5): 1179–1197, 1999.
125. Outwater EK. CT and MRI of neoplasms metastatic to the genital tract. In: Andersen JC, editor. *Gynecologic Imaging*. London: Churchill Livingstone, 1999, p. 519–534.
126. Morgan MA, Mikuta JJ. Surgical management of vulvar cancer. *Semin Surg Oncol* 17(3): 168–172, 1999.
127. Hacker NF. Radical resection of vulvar malignancies: a paradigm shift in surgical approaches. *Curr Opin Obstet Gynecol* 11(1): 61–64, 1999.
128. Outwater EK, Marchetto BE, Wagner BJ et al. Aggressive angiomyxoma: findings on CT and MR imaging. *AJR Am J Roentgenol* 172(2): 435–438, 1999.
129. DePasquale SE, McGuinness TB, Mangan CE et al. Adenoid cystic carcinoma of Bartholin's gland: a review of the literature and report of a patient. *Gynecol Oncol* 61(1): 122–125, 1996.
130. Duun S. Adenoid cystic carcinoma of Bartholin's gland—a review of the literature and report of a patient. *Acta Obstet Gynecol Scand* 74(1): 78–80, 1995.
131. Blomlie V, Rofstad EK, Trope C et al. Critical soft tissues of the female pelvis: serial MR imaging before, during, and after radiation therapy. *Radiology* 203(2): 391–397, 1997.
132. Grigsby PW, Russell A, Bruner D et al. Late injury of cancer therapy on the female reproductive tract. *Int J Radiat Oncol Biol Phys* 31(5): 1281–1299, 1995.
133. Healy JC, Phillips RR, Reznek RH et al. The MR appearance of vaginal fistulas. *AJR Am J Roentgenol* 167(6): 1487–1489, 1996.
134. Outwater E, Schiebler ML. Pelvic fistulas: findings on MR images. *AJR Am J Roentgenol* 160(2): 327–330, 1993.
135. Semelka RC, Hricak H, Kim B et al. Pelvic fistulas: appearances on MR images. *Abdom Imaging* 22(1): 91–95, 1997.

CHAPTER 14

UTERUS AND CERVIX

MICHÈLE A. BROWN, SAMEER A. PATEL, CAROLINE REINHOLD, WAQAS QURESHI, AND RICHARD C. SEMELKA

Magnetic resonance imaging (MRI) provides excellent visualization of the uterus and cervix. MRI has become the imaging modality of choice for the diagnosis of congenital uterine anomalies and benign acquired gynecological disease. MRI has been shown to be effective for preoperative characterization and staging of endometrial and cervical carcinoma. Because MRI does not employ ionizing radiation, it is also well suited for imaging women of reproductive age.

MRI TECHNIQUE

Patients are best imaged with an empty bladder after fasting for at least 4 hours. A distended bladder may produce motion-related artifact in the phase-encoding direction and displace the uterine fundus superiorly, where it is more affected by bowel peristalsis. Also, uterine compression may obscure the normally visible fat plane between the uterus and urinary bladder, an important landmark for evaluation of tumor invasion in gynecologic cancer staging. Antispasmodics such as glucagon (1 mg intramuscularly or intravenously) may be used to decrease motion artifact related to bowel peristalsis. Some centers use intravaginal gel to distend the vaginal fornices [1]. Imaging is performed with the patient supine unless she is in late pregnancy, in which case a decubitus position is preferred to decrease pressure on the inferior vena cava.

Patients with intrauterine contraceptive devices are safely imaged. The device demonstrates a signal void on T1- and T2-weighted sequences and does not cause sufficient signal loss to significantly limit the examination [2]. A phased-array coil should be used. It is helpful to place a saturation band over the fat in the anterior abdominal wall to minimize artifact on non-fat-suppressed sagittal images, and it may be helpful to use an anterioposterior frequency-encoding direction for axial images. Endoluminal coils are not currently commonly used for imaging of the uterus [3]. One study showed that endoluminal coils would add cost without improving overall staging in patients with cervical carcinoma [4]. However, another study showed endovaginal coils to be useful for evaluation of small-volume disease and parametrial extension in patients with cervical cancer [5].

Abdominal-Pelvic MRI, Third Edition, edited by Richard C. Semelka. Copyright © 2010 John Wiley & Sons, Inc.

There are many MR sequence protocol options for imaging the female pelvis. The appropriate choice depends on the specific clinical question as well as the available equipment and expertise. The following general protocol suggestions employ current widely available sequences. First, a large-field-of-view coronal and axial T2-weighted single shot echo train spin-echo image is obtained, such as half-Fourier single-shot turbo spin-echo. Subsequent images are obtained with a small field of view (20–24 cm) to maximize spatial resolution and are angled to the uterus based on the axial single-shot echo-train spin echo because the uterus is frequently oriented toward the left or right [6]. Small-field-of-view images include axial and sagittal T2-weighted echo-train spin echo and axial T1-weighted spoiled gradient echo in and out of phase. Sequence planes are angled to the uterus or cervix to provide true long- and short-axis views of these structures. An oblique section obtained perpendicular to the cervical canal results in a short-axis view and allows accurate assessment of cervical zonal anatomy and facilitates cervical carcinoma staging [7].

The necessary oblique planes can be obtained by first obtaining T2-weighted echo-train spin-echo or T2-/T1-weighted steady state-free precession images axial to the patient. These sequences delineate the endometrial and endocervical canals and are used to prescribe oblique sagittal T2-weighted images oriented parallel to the endometrial or endocervical canal. From the oblique sagittal images, oblique axial T2-weighted and dual-echo T1-weighted images are prescribed in a plane perpendicular to the endometrial or endocervical canal (short-axis view). In some conditions, such as uterine anomalies, oblique coronal T2-weighted images are also obtained (fig. 14.1). Fat saturation is not routinely applied to T2-weighted sequences in the female pelvis; however, fat-suppressed T1-weighted images are helpful in cases of suspected endometriosis to detect small endometrial deposits. A three-dimensional T2-weighted acquisition may be helpful if the necessary plane proves difficult to obtain in cases of suspected uterine anomalies. Cine imaging using ultrafast imaging such as single-shot echo-train spin echo has been shown to depict uterine peristalsis and the development and resolution of sustained uterine contractions [8–10]. This can be accomplished by imaging midsagittal to the uterus every 2–3 seconds for 1–2 minutes for a cine consisting of between 20 and 60 individual images.

For benign disease, exclusive use of breath-hold sequences is usually sufficient and serves to minimize examination time. For evaluation of cancer, longer-duration high-resolution T2-weighted echo-train spin-echo and postgadolinium fat-suppressed T1-weighted images are needed. Sequential postgadolinium breath-hold three-dimensional fast gradient-echo images are used for dynamic imaging.

Imaging at 3T

The movement toward higher-field MR systems requires adaptation of techniques for female pelvis imaging. The essential advantage of high-field MR imaging is an increase in signal-to-noise ratio (SNR), which depends on main magnetic field strength, B_0. There is a potential twofold increase in SNR at 3T compared to 1.5T. Alternatively, similar SNR can be obtained at a faster speed. However, several challenges are encountered when imaging at 3T. Higher-field imaging is associated with increased specific absorption rates (SAR) that require modifications for most breath-hold rapid acquisition sequences. Also, there are increased signal inhomogeneities that arise from the greater shimming challenge for the extrinsic magnetic field as well as intrinsic field distortions due to increased susceptibility effects and chemical-shift effects. Particularly problematic in the female pelvis is signal shading problems magnified by dielectric effects increased at higher field strengths. One tool that helps decrease focal signal loss in the female pelvis is a dielectric pad, or radiofrequency cushion, available from several vendors. The pad is placed between the patient and the surface coil.

Certain sequences require compromises for implementation at 3T, including single-shot T2 and balanced-echo techniques [11, 12]. Other sequences benefit from imaging at higher field strength, such as 3D gradient echo and echo-train spin echo. Standard echo-train spin echo is not limited by SAR effects, because of the relatively long TR and short echo-train lengths, and can more fully take advantage of the increased SNR at 3T. 3D gradient echo may be optimized at 3T by taking advantage of the higher signal to increase the bandwidth, which allows a decrease in the TE and TR. Shorter TE leads to decreased susceptibility effects, and shorter TR allows for reduction in scan time.

Because of the current advantages and disadvantages of 3T imaging, consideration should be made before imaging a particular patient at 3T rather than 1.5T. For instance, at the present time it is recommended that fetal imaging not be performed at 3T because of prominent standing wave effects from amniotic fluid as well as concerns regarding safety [13]. For nonpregnant patients, careful optimization of imaging parameters can lead to high-quality images at 3T with acceptable scan times and SAR [10, 14].

NORMAL ANATOMY

Uterine Corpus

The uterus is divided into three major segments: 1) the fundus. 2) the body or corpus, and 3) the cervix. In women of reproductive age the entire uterus measures

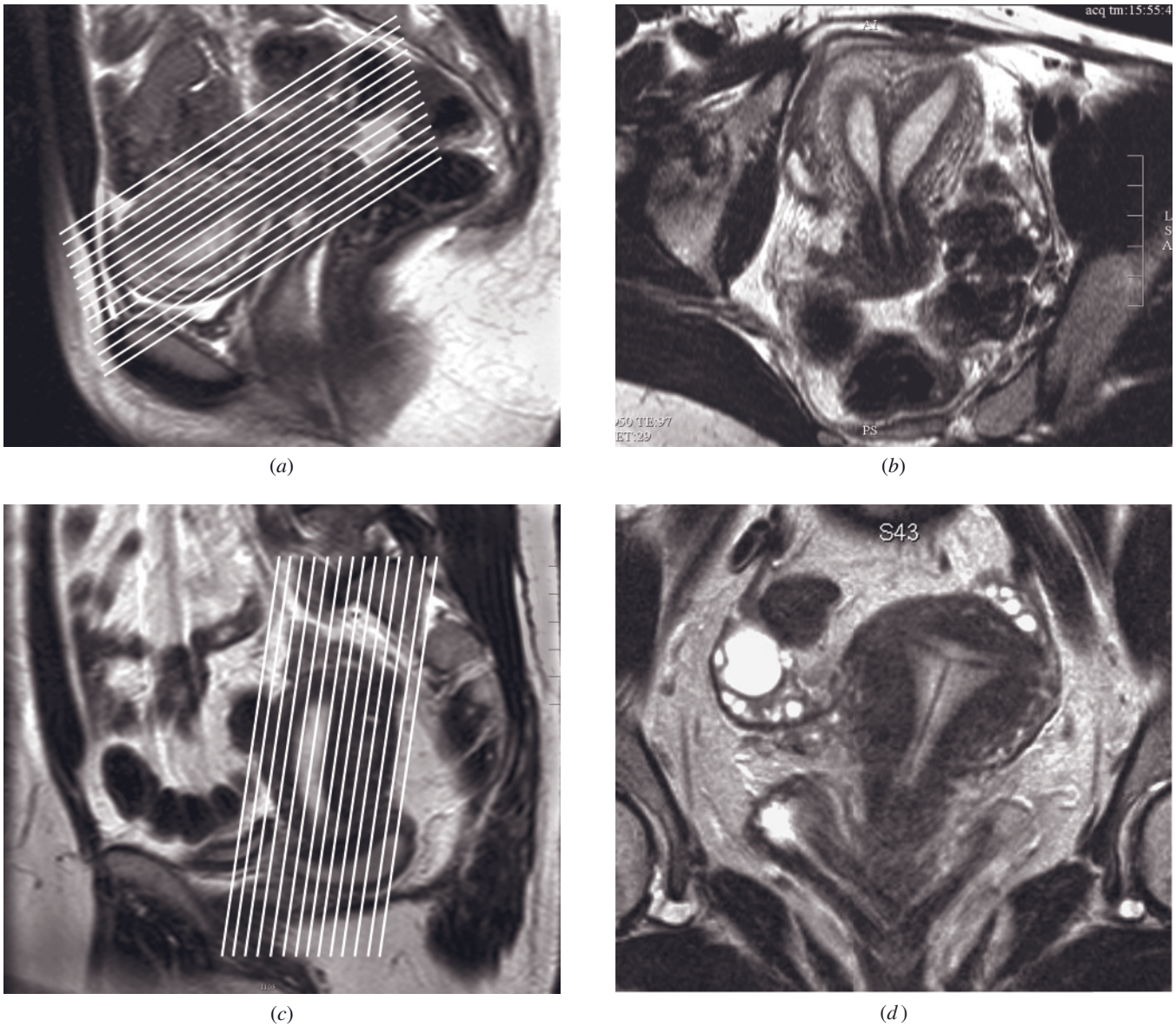

(*a*) (*b*) (*c*) (*d*)

FIG. 14.1 Long-axis view of the uterus in two patients. Sagittal (*a*) and oblique (*b*) T2-weighted ETSE images of a septate uterus. On the sagittal section (*a*), an imaging plane parallel to the endometrium is prescribed. The resultant long-axis view of the uterus (*b*) shows a muscular and fibrous septum with a normal convex fundal contour, which helps differentiate septate from bicornuate uteri. Sagittal (*c*) and oblique (*d*) T2-weighted ETSE images of a normal uterus. A sagittal image (*c*) is used to prescribe an oblique plane parallel to the endometrial canal. The long-axis view of the uterus (*d*) shows a correctly positioned IUD, seen as a hypointense T-shape within the endometrial cavity.

6–9 cm in length with the uterine corpus measuring 4–6 cm; the cervix 2.5–3.2 cm. The uterus measures approximately 4 cm in thickness and 6 cm in its maximal transverse dimension. Histologically, the uterine corpus is divided into three layers: 1) the serosa, which consists of peritoneum; 2) the myometrium, which consists of smooth muscle; and 3) the endometrium.

On T1-weighted images, the entire uterus is of intermediate signal intensity similar to muscle; the zonal anatomy is usually unapparent. On T2-weighted imaging, three distinct zones can be recognized in women of reproductive age: 1) a high-signal-intensity stripe representing the normal endometrium and secretions within the endometrial cavity, 2) the junctional zone, a band of low signal intensity histologically corresponding to the innermost layer of the myometrium, and 3) the outer myometrium of intermediate signal intensity [15–17] (figs. 14.2 and 14.3). The low-signal-intensity junctional zone is seen immediately subjacent to the endometrial stripe and represents the innermost layer of the

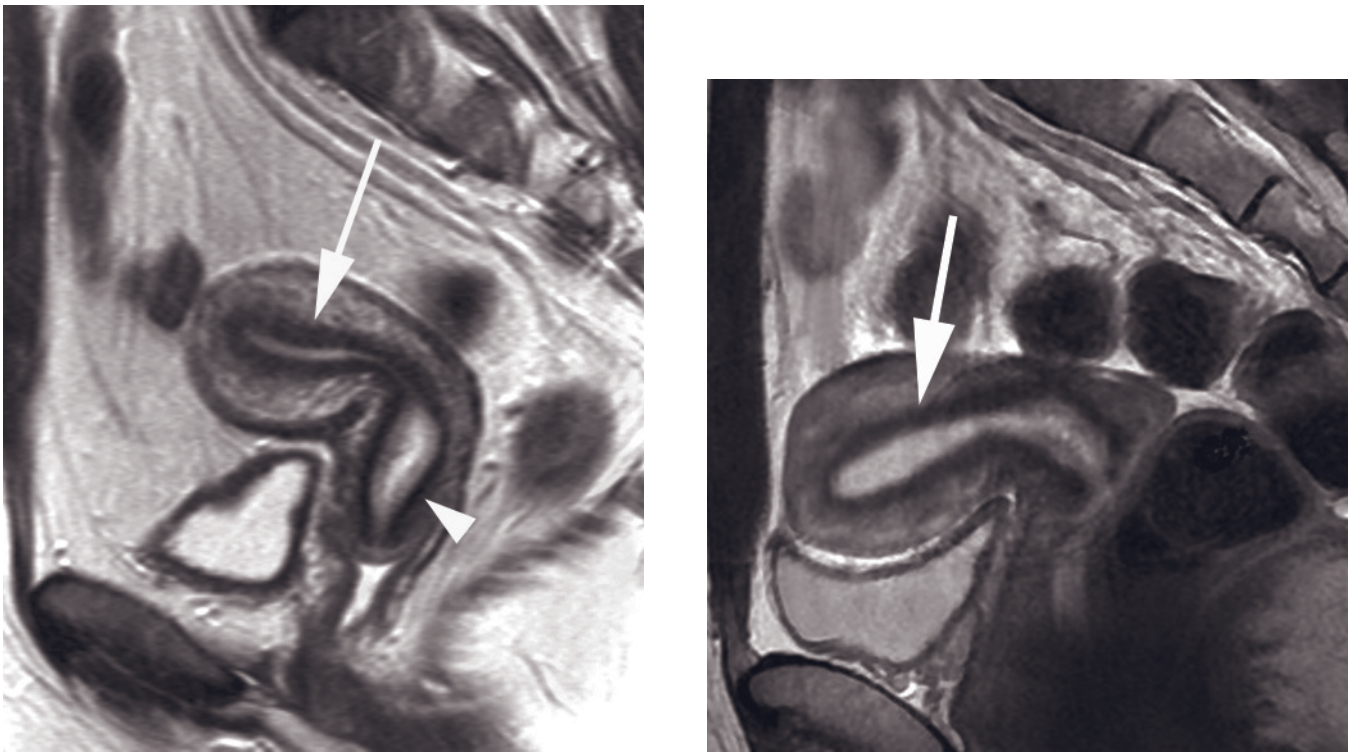

(*a*) (*b*)

FIG. 14.2 Zonal anatomy of the uterine corpus and cervix. (*a*) Sagittal T2-weighted ETSE image of the uterine corpus and cervix. The central hyperintensity in the uterine corpus represents the endometrium. The band of low signal intensity represents the junctional zone (arrow), which appears continuous with the fibrous stroma of the cervix (arrowhead). The outer layer of the myometrium is of intermediate signal intensity. **Zonal anatomy of the uterine corpus and cervix at 3T.** Sagittal T2-weighted ETSE image of the uterine corpus and cervix in a different patient (*b*) shows the myometrial layers including the junctional zone (arrow).

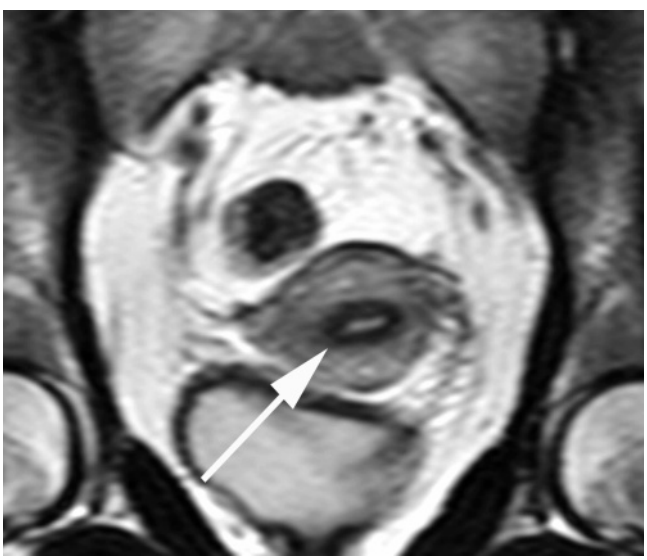

FIG. 14.3 Short-axis view of the uterus. T2-weighted ETSE sequence perpendicular to the endometrial canal shows the uterine zonal anatomy: central hyperintense endometrium, low-signal-intensity junctional zone (arrow) representing the innermost myometrium, and outer intermediate-signal-intensity myometrium.

myometrium. [18, 19]. The junctional zone differs from the outer myometrium structurally and functionally. The histological basis for the low signal intensity of the junction zone is multifactorial. First, the water content of the junctional zone is lower than that of the endometrium and outer myometrium [18]. The compact smooth muscle bundles, as well as the orientation of the fibers within the junctional zone, may also contribute to the low signal on T2-weighted images [19]. There is also a threefold increase in percentage of nuclear area in the junctional zone in comparison with the outer myometrium, reflecting an increase in both size and number of nuclei [20]. Considerable variation in the normal thickness of the junctional zone has been reported, with a mean thickness ranging from 2 to 8 mm [15, 19]. In women taking oral contraceptives, the junctional zone may be indistinct.

Cervix

The cervix is separated from the corpus of the uterus by the internal os, which corresponds to a slight constriction visible externally and by the entrance of

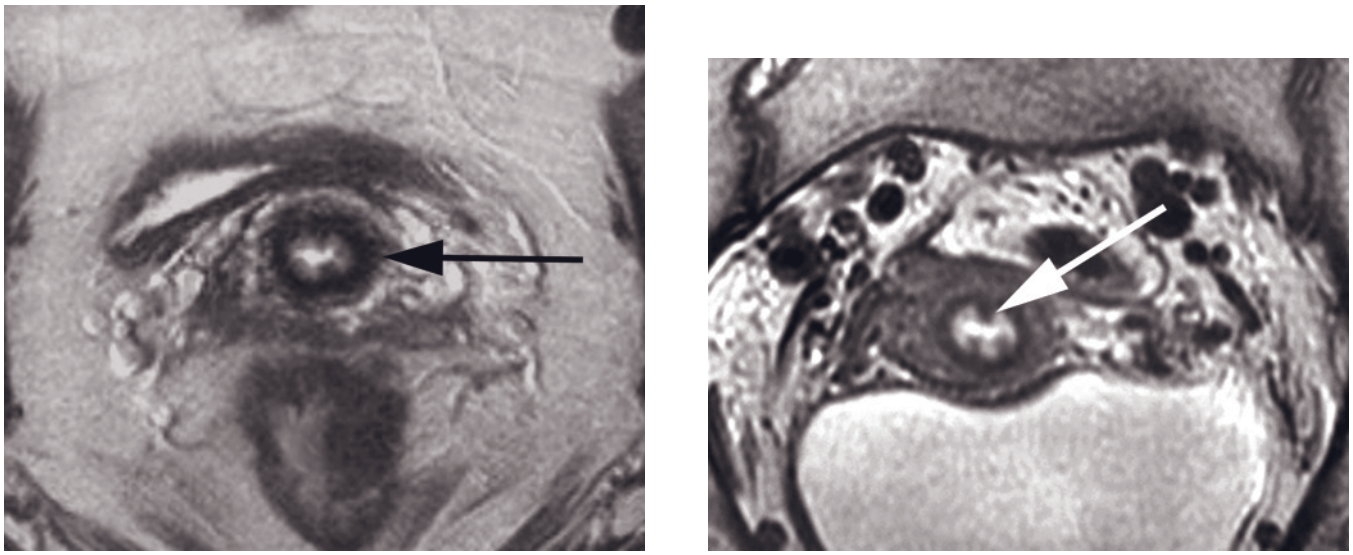

(*a*) (*b*)

FIG. 14.4 Short-axis view of the cervix. (*a*) T2-weighted ETSE image perpendicular to the endocervical canal shows the cervical zonal anatomy: central hyperintense mucus, high signal-intensity mucosa, hypointense fibrous stroma (arrow), and outer intermediate-signal-intensity loose stroma. **Short-axis view of the cervix at 3T.** T2-weighted ETSE image (*b*) perpendicular to the endocervical canal in a different patient shows the cervical zonal anatomy including prominent vertical folds (arrow) due to plicae palmatae.

the uterine vessels. On high-resolution T2-weighted sequences, the cervix demonstrates four distinct zones: 1) central hyperintense mucous within the endocervical canal, 2) high-signal-intensity endocervix composed of columnar epithelium, 3) hypointense fibrous stroma, and 4) outer intermediate-signal-intensity loose stroma (figs. 14.2 and 14.4). The combined thickness of the endocervical canal and mucosa ranges from 2 to 3 mm, and the surrounding hypointense fibrous stroma is of 3- to 8-mm thickness [21]. This layer contains a high concentration of elastic fibrous tissues and appears continuous with the junctional zone. Smooth muscle strands predominate toward the periphery of the cervix in the outer intermediate-signal-intensity layer, which is continuous with the outer myometrium of the uterine corpus. In contrast to the zonal anatomy of the uterus, the MRI appearance of the cervical zonal anatomy does not appear to vary with the hormonal status of women. On T1-weighted precontrast images, the zonal anatomy of the cervix usually is not apparent. After gadolinium administration, the endocervical mucosa enhances rapidly, whereas the stroma shows more gradual enhancement. The fibrous stroma enhances at a slower rate relative to the outer zone of smooth muscle.

Parametrium

The parametrium is located between the layers of the broad ligament adjacent to the lateral margins of the uterine corpus and cervix. It may serve as a pathway for local spread of disease, for example, tumor extension of cervical carcinoma. The parametrium is composed largely of loose connective tissue and contains a high amount of blood and lymphatic vessels. It is therefore usually of intermediate signal intensity on T1-weighted sequences and iso- or hyperintense to fat on T2-weighted sequences. On contrast-enhanced images, intense enhancement of the parametrium is often noted.

Menstrual Changes

Endometrial thickness varies with the menstrual cycle and is thinnest at time of menstruation. The endometrium increases in width rapidly during the proliferative phase and continues to increase more slowly during the secretory phase [22]. The thickness of the endometrial stripe is reported to vary widely from 3 to 6 mm in the follicular phase to 5–13 mm during the secretory phase (fig. 14.5) [16, 23]. The junctional zone has been shown to be the site of uterine contractions, which may be sustained or transient (uterine peristalsis). Sustained contractions typical of pregnancy also occur in non-pregnant women and may mimic fibroids or adenomyosis [8, 9, 24, 25]. They may be differentiated by their tendency to appear or resolve over the course of the examination (fig. 14.6). Uterine peristalsis occurs continuously in women of childbearing age, and the direction of the peristaltic wave depends on the phase of the menstrual cycle. Peristalsis has been demonstrated with MRI using fast T2-weighted imaging as

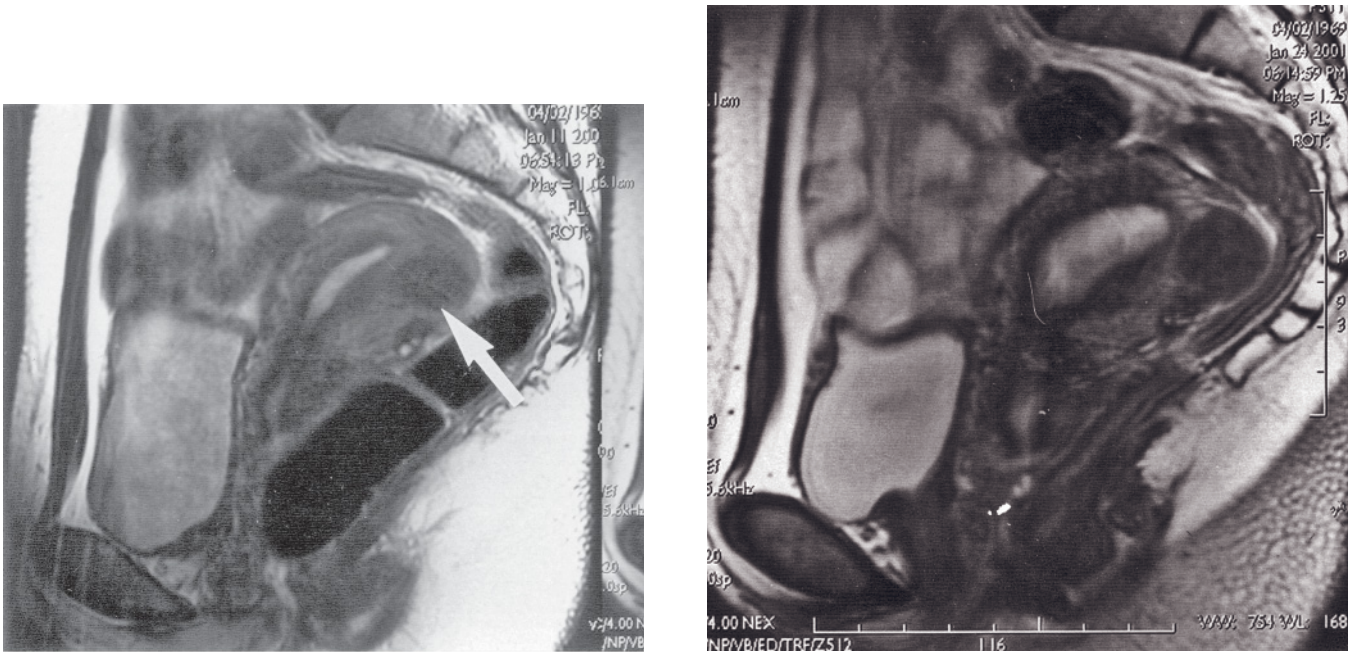

(*a*) (*b*)

FIG. 14.5 Physiological changes during menstrual cycle in a 32-year-old woman. Sagittal T2-weighted ETSE images at different phases of the menstrual cycle. A retroverted uterus with a small hypointense intramural leiomyoma (arrow, *a*) is apparent. During the follicular phase (day 5) (*a*), the hyperintense endometrial stripe is thin. During the secretory phase (day 18) (*b*), the endometrial stripe widens considerably, and the endometrial complex and myometrium show increased signal intensity.

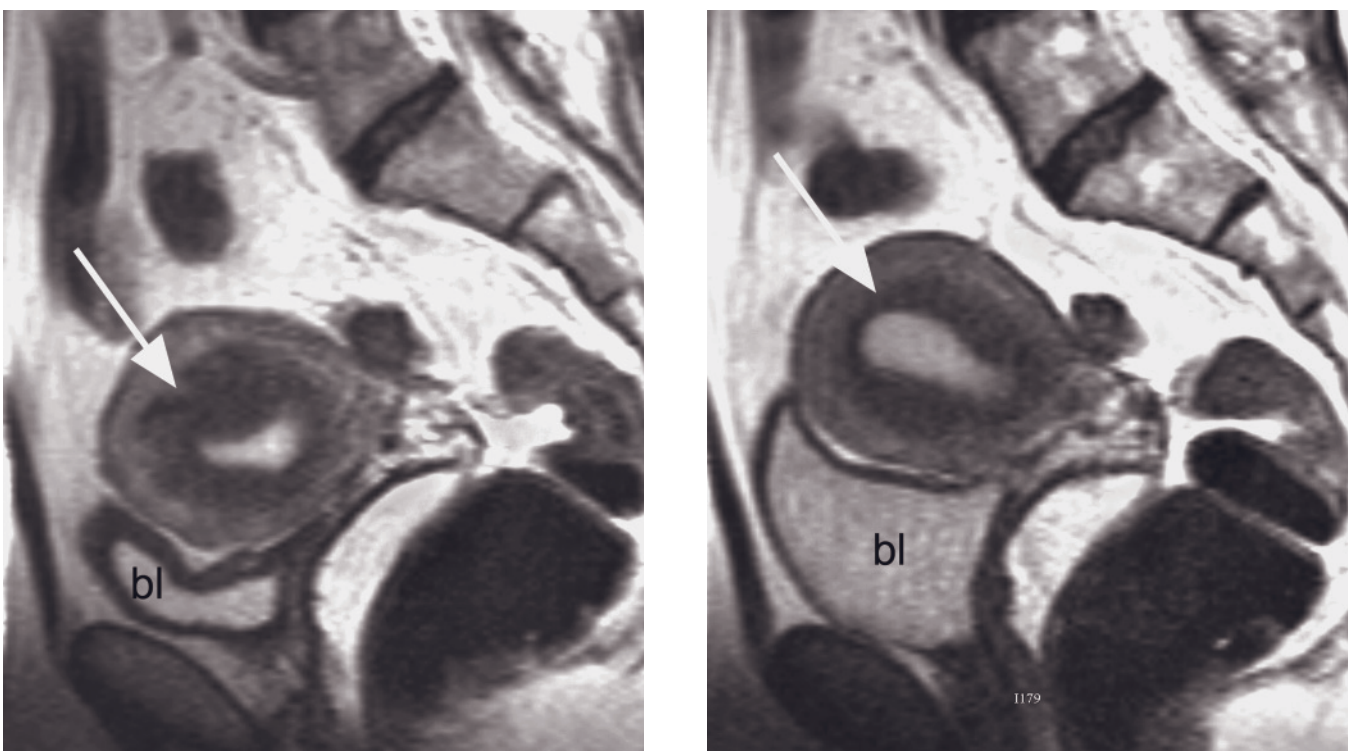

(*a*) (*b*)

FIG. 14.6 Uterine contraction. Sagittal T2-weighted ETSE images separated by 25 min. The early image (*a*) shows a focal thickening of the junctional zone with slight mass effect on endometrial canal (arrow, *a*). After 25 min (*b*), the contraction is no longer seen and the junctional zone appears normal (arrow, *b*). Also note the movement of the uterus with bladder (bl) filling during the time interval.

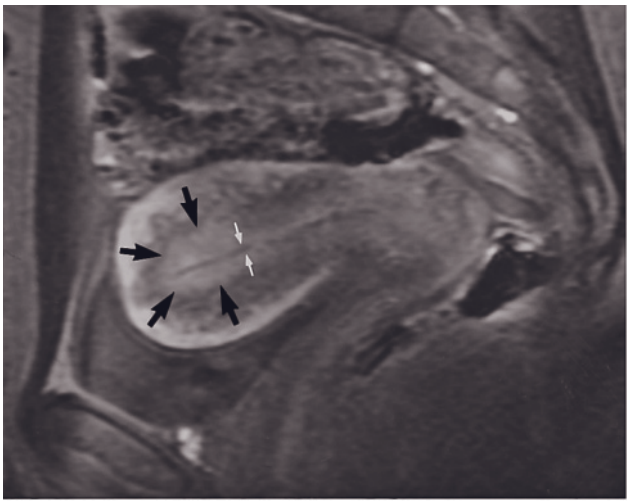

FIG. 14.7 Variable patterns of uterine enhancement. Sagittal T1-weighted gadolinium-enhanced fat-suppressed gradient-echo image. Early enhancement of the inner myometrium may be observed during the menstrual phase. The endometrial stripe is thin and hypointense (small arrows). There is early enhancement of the junctional zone (arrows) relative to the outer myometrium.

transient thickening that moves up or down the junctional zone, depending on menstrual cycle phase [24, 25]. The outer layer of the myometrium is of intermediate signal intensity on T2-weighted images; it increases in signal intensity in the midsecretory phase. During the menstrual cycle, the thickness of the myometrium increases slightly and is greatest during the secretory phase [23].

Uterine enhancement varies with the menstrual cycle. A very thin layer of the innermost myometrium enhances early during the proliferative phase. The entire junctional zone enhances early during menstruation (fig. 14.7) [26]. The outer myometrium enhances slightly later, and the endometrium enhances in a delayed fashion [26, 27]. On delayed gadolinium-enhanced images, the zonal anatomy may be apparent with the same relative signal intensities as on T2-weighted images, although there is less contrast between zones.

In postmenopausal women, the uterus is small with indistinct zonal anatomy. The signal intensity of the myometrium on T2-weighted sequences is decreased, and the junctional zone is not consistently visualized. On T2-weighted sequences, the endometrial stripe can be identified as a thin, hyperintense structure. A maximal endometrial thickness of 3 mm in women not receiving exogenous hormones and a thickness of 4–6 mm in women receiving hormonal replacement therapy has been reported [17].

With prolonged use of oral contraceptives, a decrease in uterine size may be seen, the endometrial thickness averages 2 mm, and no variation with the course of the menstrual cycle is seen. The junctional zone is less prominent, and the signal intensity of the myometrium on T2-weighted imaging is increased compared to women who do not use oral contraceptives [16, 24, 28].

Tamoxifen

Tamoxifen is an orally administered nonsteroidal antiestrogen used as an adjuvant therapy in women with breast carcinoma. In addition to its antiestrogen effects on breast tissue, tamoxifen acts as a weak estrogen agonist on the postmenopausal endometrium of the uterus. A spectrum of endometrial abnormalities has been reported in patients receiving tamoxifen therapy, including proliferative changes, hyperplasia, polyps, and carcinoma [26, 29–31]. Postmenopausal women taking tamoxifen are more likely to develop fibroids or adenomyosis, particularly the cystic variety [27, 32, 33]. Currently, no definitive screening guidelines for monitoring patients on tamoxifen therapy have been established, but a combination of endovaginal ultrasound and endometrial sampling is most frequently used [27]. The role of MRI in evaluating this group of patients is limited. In patients undergoing MR imaging, two different imaging patterns have been described: 1) a T2-weighted homogeneously hyperintense endometrium with a mean thickness of 0.5 mm, contrast material enhancement of the endometrial-myometrial interface, and a signal void within the lumen on gadolinium-enhanced images as well as 2) a T2-weighted heterogeneous, widened endometrium (mean thickness 1.8 cm) with enhancement of the endometrial-myometrial interface and a latticelike enhancement circumscribing well-defined cystic spaces on gadolinium-enhanced images (fig. 14.8).

CONGENITAL UTERINE ANOMALIES

Müllerian Duct Anomalies

The prevalence of congenital müllerian duct anomalies (MDA) among women of reproductive age is approximately 1%. These congenital uterine anomalies result from nondevelopment or nonfusion of the müllerian ducts. Anomalies are divided into classes with similar clinical features, prognoses, and treatment options (fig. 14.9). Failure of the paired müllerian ducts to develop results in various degrees of uterine, cervical, and vaginal agenesis. Didelphys or bicornuate uteri result from absent or incomplete fusion of the uterine horns, respectively. If fusion does occur but is followed by absent or incomplete resorption of the septum between müllerian duct components, a septate uterus will result.

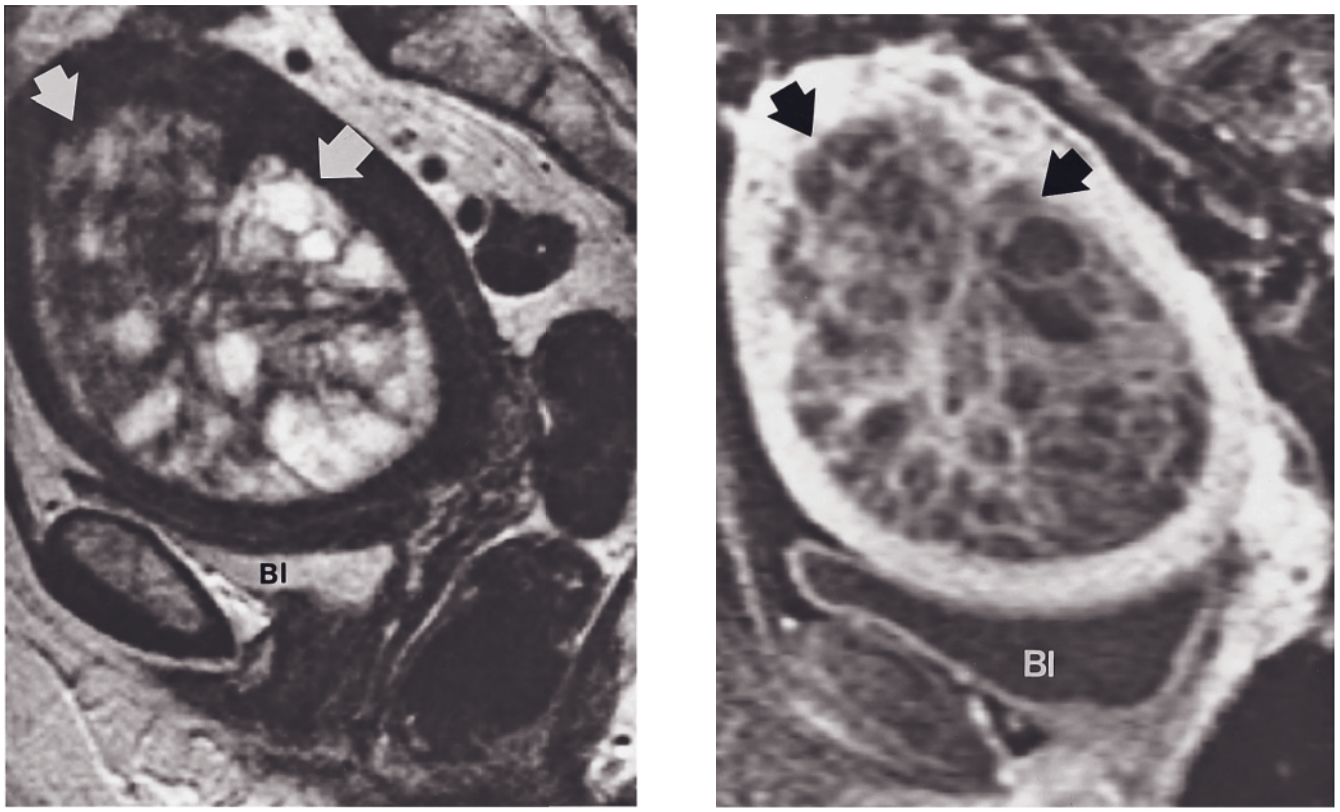

(*a*) (*b*)

FIG. 14.8 Tamoxifen-induced changes. Sagittal T2-weighted ETSE (*a*) and gadolinium-enhanced fat-suppressed gradient-echo (*b*) images. The endometrial complex is markedly enlarged (arrows, *a*, *b*) and shows heterogeneous signal intensity. A latticelike pattern of enhancement is present. A benign polyp was found at histopathology. Bl, bladder.

Because of the proximity of the müllerian and wolffian systems embryologically, MDAs are frequently associated with urinary tract anomalies, particularly renal agenesis or ectopia. Many of these uterine abnormalities are entirely asymptomatic. It is estimated that reproductive difficulties occur in 25% of women with MDAs compared to 10% of all women. MDAs do not cause primary infertility but are associated with recurrent miscarriage, premature labor, dystocia, cervical incompetence, and intrauterine growth retardation.

Role of MRI

Transvaginal ultrasound and hysterosalpingography (HSG) are widely used for imaging diagnosis; however, each has limitations in classifying patients with uterine anomalies. During HSG, only horns that communicate with the main endometrial cavity are opacified, and the external contour of the uterus cannot be evaluated. MRI is currently the imaging modality of choice. In patients undergoing MRI for suspected MDA, an additional sequence oriented coronal to the uterus should be performed to evaluate the fundal contour. Occasionally the anatomy is such that it is difficult to obtain this view, in which case a T2-weighted three-dimensional acquisition may be acquired to be viewed in any plane. If not routinely performed, a large-field-of-view coronal image should be obtained to diagnose renal agenesis or ectopia, unless this was investigated before MRI by US or excretory urography [34, 35]. MR hysterosalpingography is at present still in an experimental state but might become a promising technique as an adjunct to conventional MR pelvic imaging in the future [36].

The treatment options for different uterine anomalies vary considerably, and accurate preoperative diagnosis is essential for appropriate patient management.

Described below is the widely used modified Buttram and Gibbons classification and corresponding MR imaging features [37, 38]. Despite the classification scheme, these anomalies represent a spectrum of disease, and complex anomalies may show characteristics of multiple classes. In the case of a complex anomaly, it is important to describe the individual components rather than placing it into the class it most resembles [38–40].

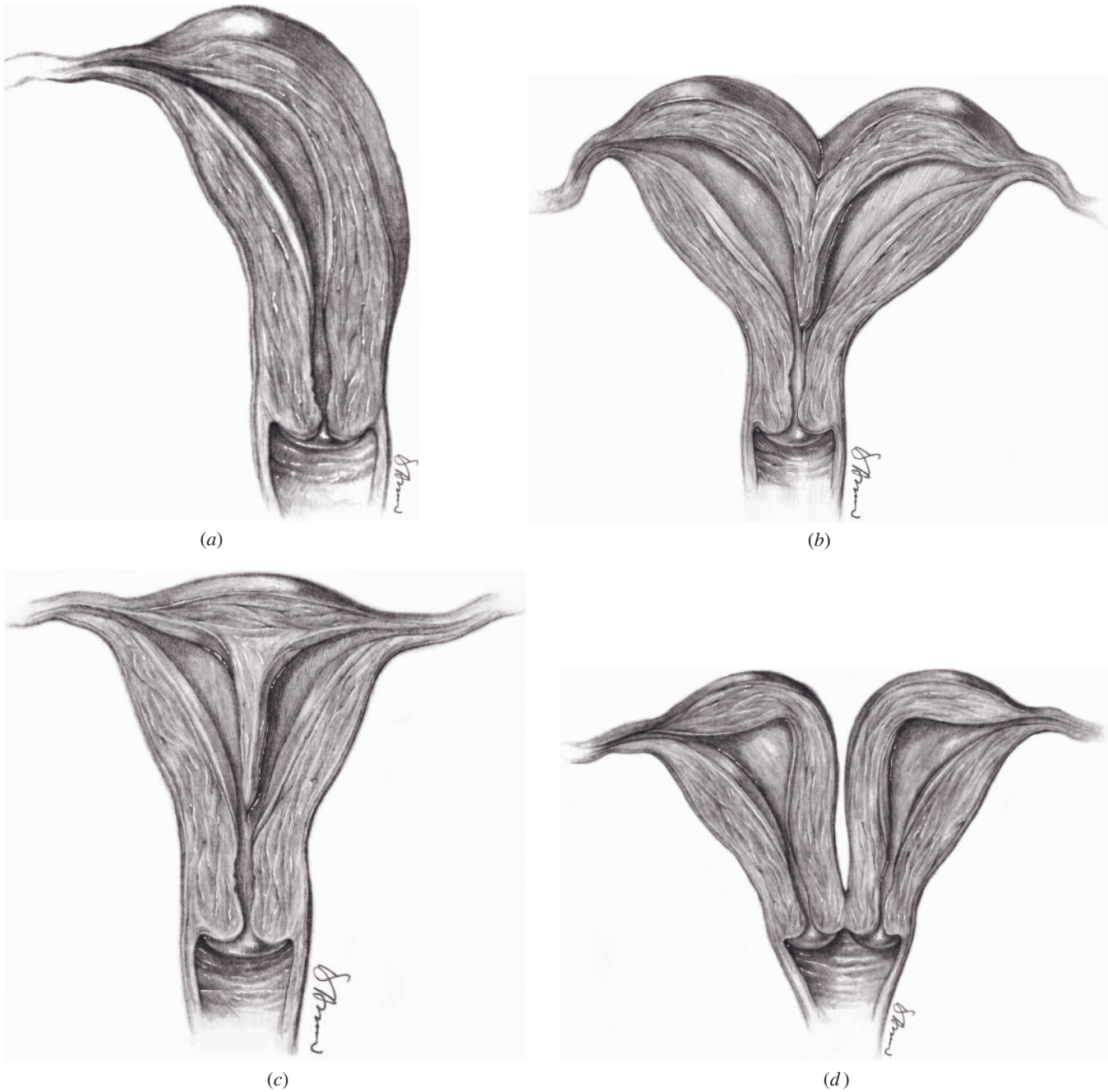

FIG. 14.9 Uterine anomalies. Unicornuate uterus (*a*), bicornuate uterus (*b*), septate uterus (*c*), uterus didelphys (*d*).

MRI Appearance

Class I: Segmental Agenesis or Hypoplasia. These anomalies result from abnormal development of the müllerian ducts. This may occur as part of a congenital syndrome or as a result of chromosomal defects (fig. 14.10). MR imaging reveals an absent or very small uterus, cervix, or vagina depending on the affected segment. Uterovaginal agenesis is typically best seen on sagittal T2-weighted sequences. The most common type of class I MDA is the combined form as seen in patients with Mayer–Rokitansky–Küster–Hauser syndrome. In patients with this syndrome, the presence of vaginal agenesis or hypoplasia with intact ovaries and fallopian tubes is accompanied by variable anomalies of the uterus, urinary tract, and skeletal system. Primary amenorrhea is the leading symptom in these patients (fig. 14.11) [41, 42].

Class II: Unicornuate Uterus. This anomaly is the result of nondevelopment or rudimentary development

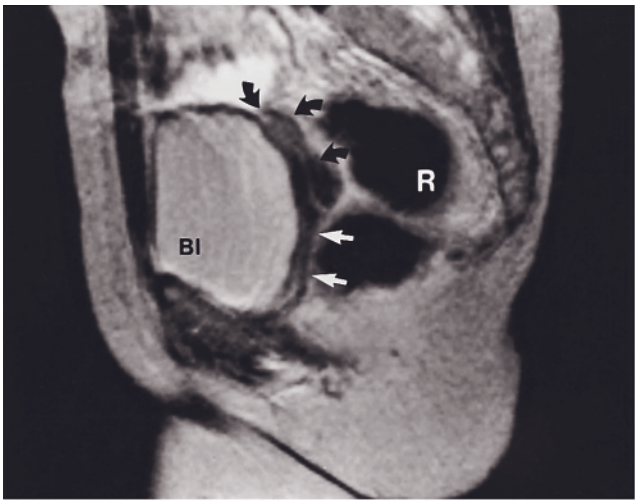

FIG. 14.10 Gonadal dysgenesis. Sagittal T2-weighted spin-echo image in a patient with Turner syndrome. There is uterine hypoplasia (curved arrows) with a uterus-to-cervix ratio of 1:1. Vaginal hypoplasia (arrows) is also noted. Ovaries were not identified. Bl, bladder; R, rectum. (Reprinted with permission from Reinhold C, Hricak H, Forstner R et al.: Primary amenorrhea: evaluation with MR imaging. *Radiology* 203(2): 383–390, 1997.)

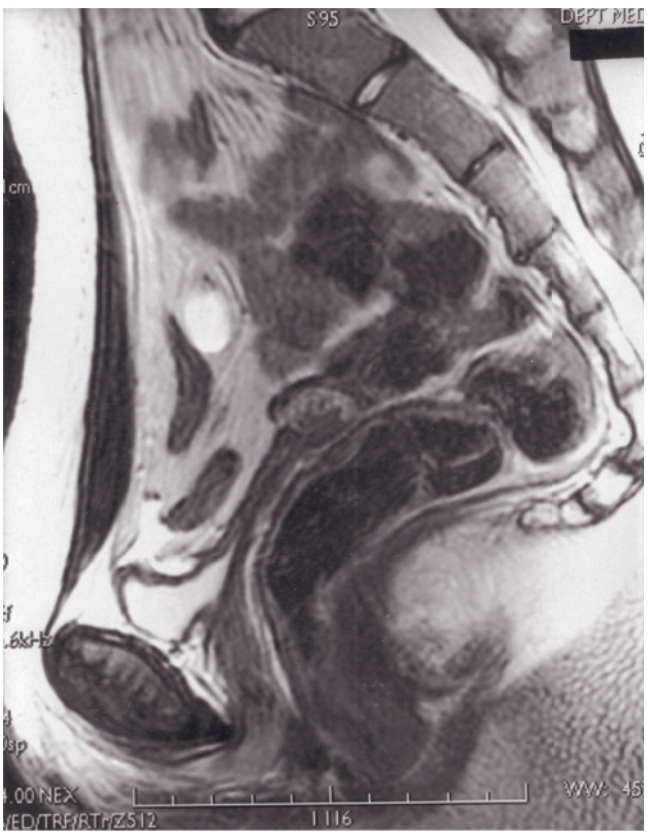

(*a*)

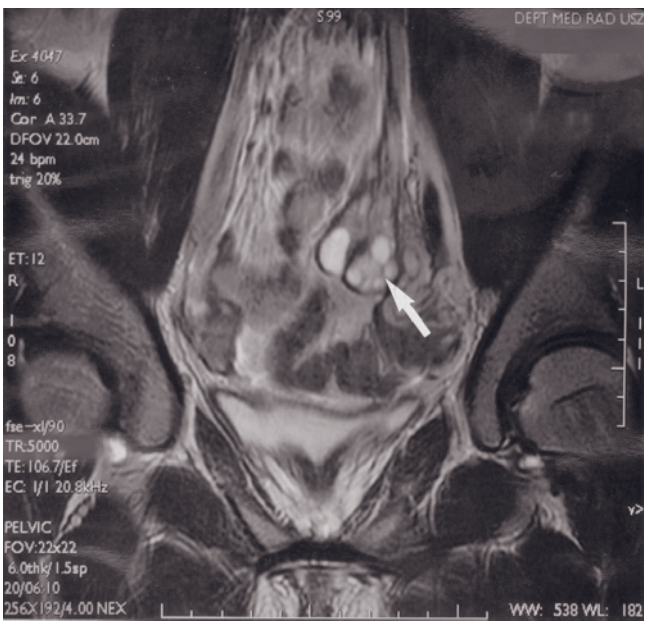

(*b*)

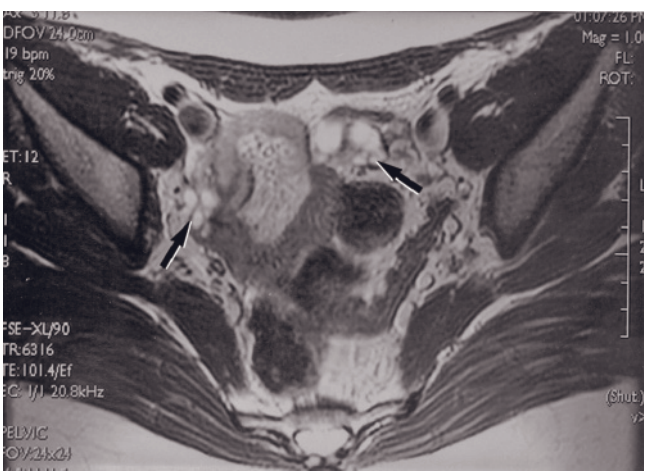

(*c*)

FIG. 14.11 Mayer-Rokitansky-Küster-Hauser (MRKH) syndrome. Sagittal (*a*), coronal (*c*), and axial (*b*, *d*) T2-weighted ETSE images in a 16-year-old patient presenting with primary amenorrhea. There is vaginal and uterine agenesis, with no evidence of these structures on sagittal (*a*) or axial (*c*, *d*) images. Both ovaries (arrows, *b* and *c*) and kidneys (not shown) were present. **Mayer-Rokitansky-Küster-Hauser syndrome at 3T.**

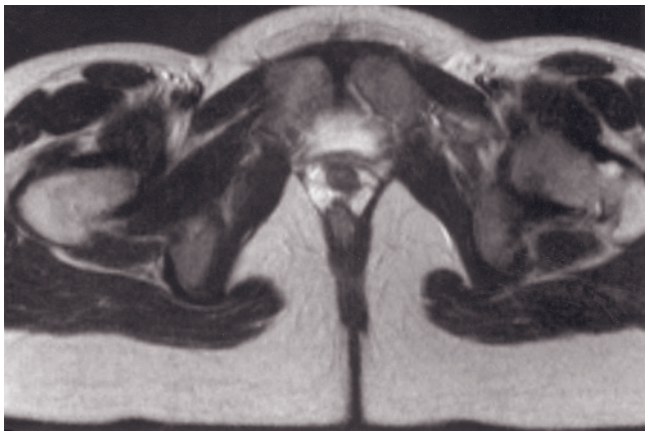

(*d*)

(*f*)

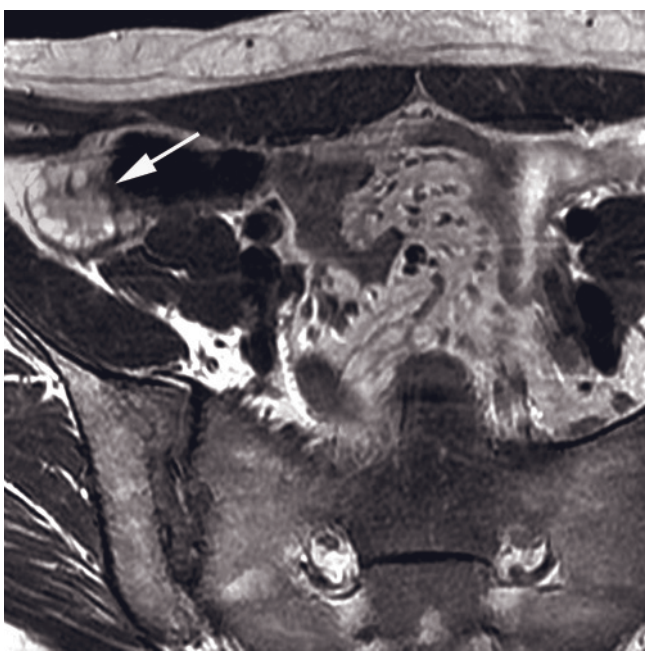

(*h*)

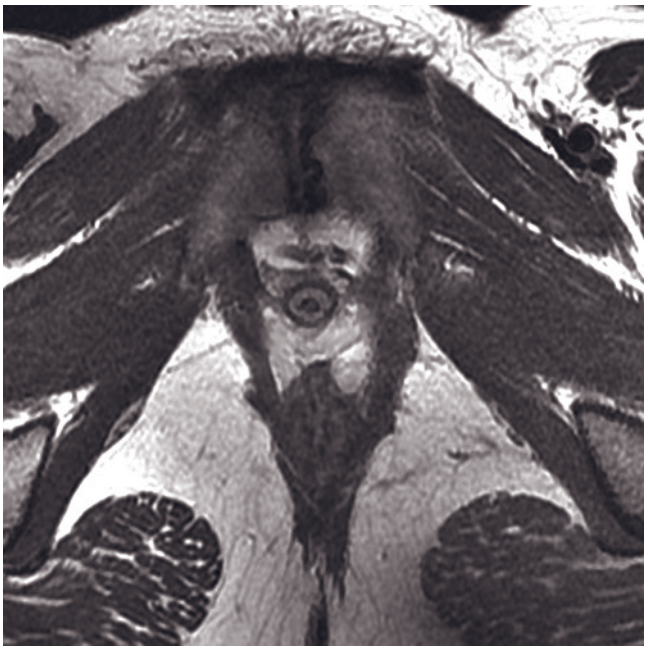

(*e*)

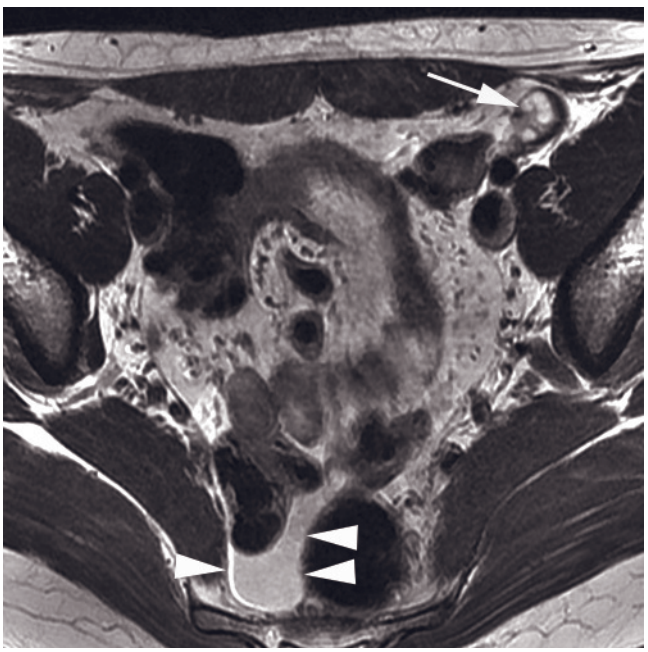

(*g*)

Fig. 14.11 (*Continued*) Transverse T2-weighted ETSE images in a 21-year-old patient show vaginal and uterine agenesis with only fat seen between the urethra and rectum. Both ovaries (arrows, *g*, *h*) are superiorly positioned but otherwise normal; note physiologic fluid in the pelvis (arrowheads, *g*).

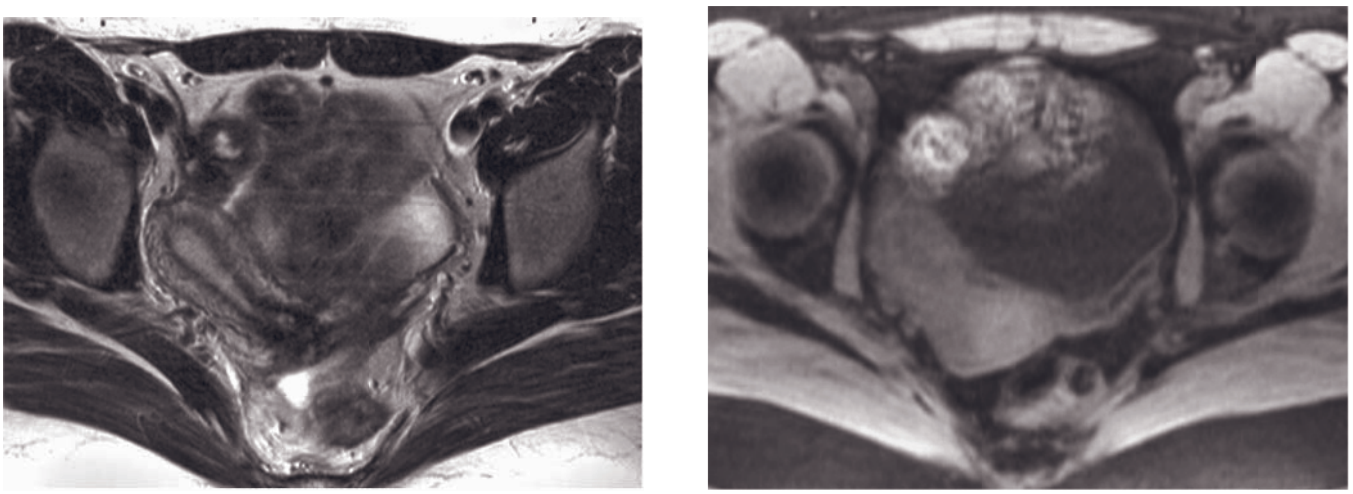

(*a*) (*b*)

FIG. 14.12 Unicornuate uterus. Transverse T2-weighted ETSE (*a*) and fat-suppressed T1-weighted gradient-echo (*b*) images. The uterus is elongated and extends toward the right with normal zonal anatomy. No rudimentary horn was seen.

of one müllerian duct. MR imaging shows an elongated uterus with normal zonal anatomy, but the overall uterine volume is reduced (fig. 14.12). When there is incomplete development of the second müllerian duct, a rudimentary horn is seen that may or may not contain endometrium. If a rudimentary horn contains endometrium, surgical removal is often indicated. T2-weighted short- and long-axis views, as well as parasagittal sections, are used to image the rudimentary horn. The presence or absence of the hyperintense endometrial stripe, as well as its continuity with the main uterine cavity, can be accurately determined with MRI [34, 35, 43]. Of all the MDAs, unicornuate uterus has the highest association with renal anomalies, most commonly agenesis.

Class III: Uterus Didelphys. MR imaging shows two separate uteri and cervices, often widely separated. Although a septate vagina may be seen with any of the MDAs, it is most commonly associated with uterus didelphys (figs. 14.13 and 14.14). When transverse, the septum can obstruct the outflow of blood into the vagina and result in hematocolpometra. In these cases, MRI demonstrates a distended vagina and uterine horn whose contents follow the signal characteristics of blood on T1- and T2-weighted sequences [34, 35].

Class IV: Bicornuate Uterus. MR imaging reveals divergent uterine horns more than 4 cm apart divided by a muscular and fibrous septum. An indentation in the fundus of more than 1 cm in depth suggests bicornuate over septate uterus, and this is best seen on a true coronal image oriented to the uterus (fig. 14.15). The septum of a bicornuate uterus may terminate at the level of the internal os (uterus bicornuate unicollis) or extend down to the external os (uterus bicornuate bicollis). At times it may be difficult to differentiate a double cervix from a cervical septation at MRI. Although a bicornuate uterus infrequently requires surgery, a transabdominal approach is used to fuse the uterine horns in symptomatic patients [34, 35].

Class V: Septate Uterus. Failure of resorption of the final fibrous septum between the two müllerian ducts results in a septate uterus. This is the most common MDA and has a high association with infertility. MR imaging shows a convex or minimally indented (<1 cm) fundus, a fibrous septum, and normal distance between the uterine horns (2–4 cm) [35, 43]. To differentiate from a bicornuate uterus, it is helpful to obtain a true coronal (long axis) image oriented to the uterus (figs. 14.16 and 14.17). Until recently, laparoscopy was the only reliable method of differentiating these entities. Several studies have demonstrated the accuracy of MRI in diagnosing septate and bicornuate uteri [34, 35, 44]. Septate uteri have a convex, flat, or minimally indented fundal contour, whereas bicornuate uteri have a large fundal cleft [34]. Accurate distinction between septate and bicornuate uteri is important for proper patient management. Septate uteri are associated with a higher rate of reproductive failure, with two-thirds of pregnancies terminating in abortion. In contrast to bicornuate uteri, septate uteri are successfully treated with hysteroscopic excision of the septum and do not require abdominal surgery.

Class VI: Arcuate Uterus. Considered a mild septate uterus in the original classification and a normal

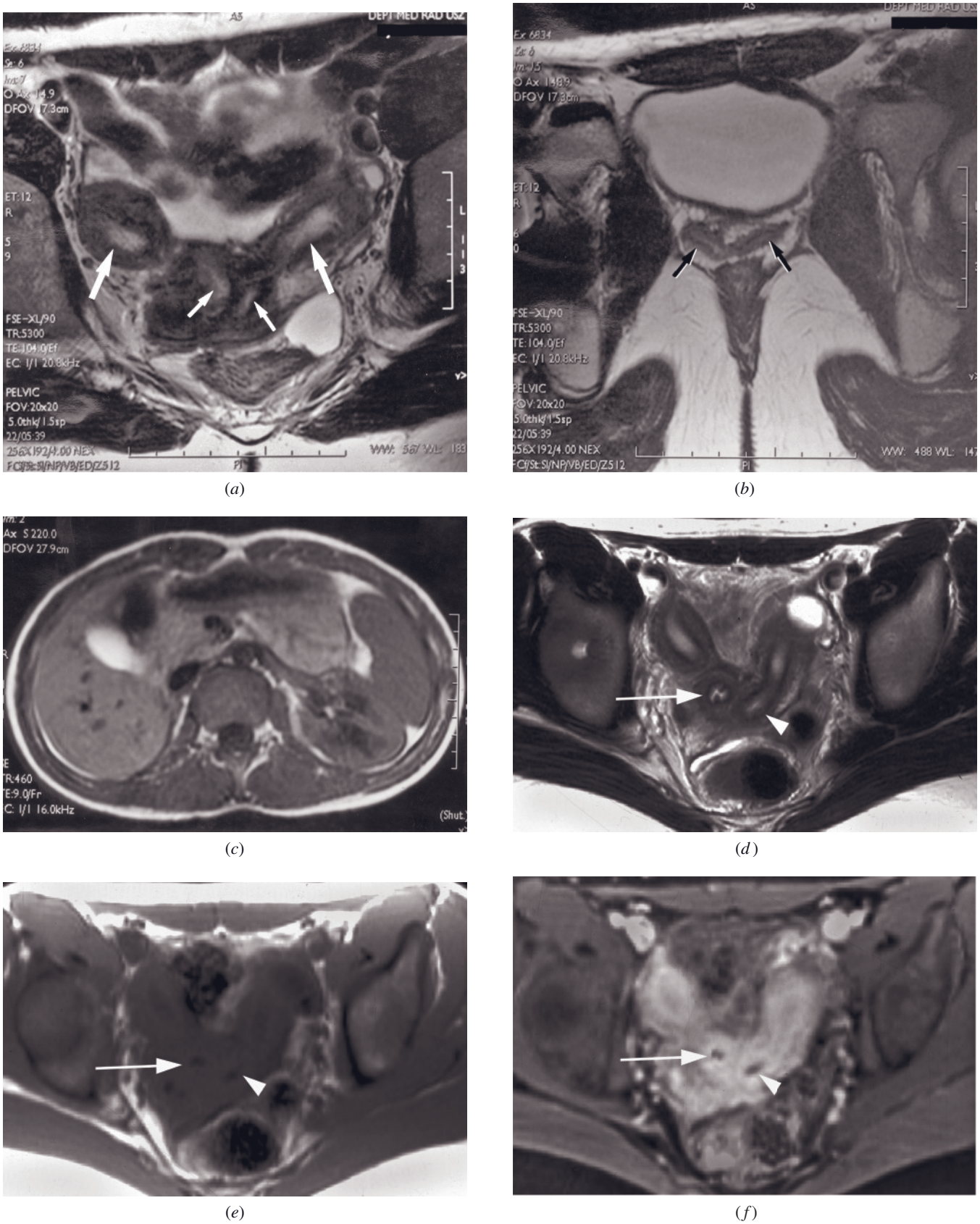

FIG. 14.13 Uterus didelphys in two patients. Transverse T2-weighted ETSE images at the level of the uterine corpus (*a*) and vagina (*b*) and T1-weighted spin-echo image of the upper abdomen (*c*). Complete uterine duplication with two separate, normal sized corpora (arrows, *a*) as well a double cervix can be seen with two hyperintense endocervical canals (small arrows, *a*). Two separate vaginas are present (arrows, *b*), as well as right renal agenesis (*c*). Transverse T2-weighted ETSE (*d*), T1-weighted gradient echo (*e*), and gadolinium-enhanced fat-suppressed T1-weighted gradient-echo (*f*) images in a second patient. A double cervix is present, one seen in short axis (arrow, *d–f*) and one in long axis (arrowhead, *d–f*), and two divergent uteri are present. Normal zonal anatomy and enhancement are seen.

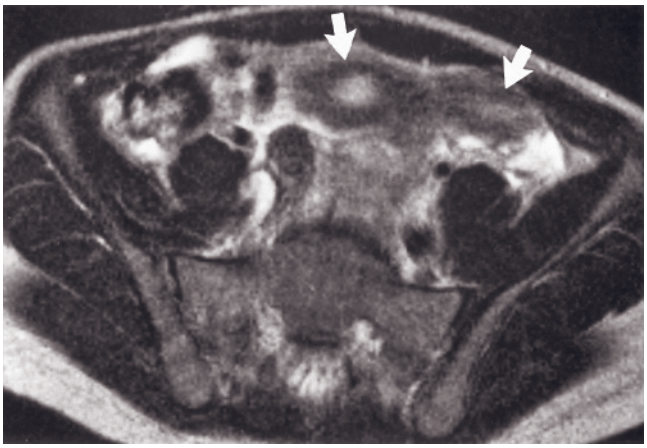

(*a*)

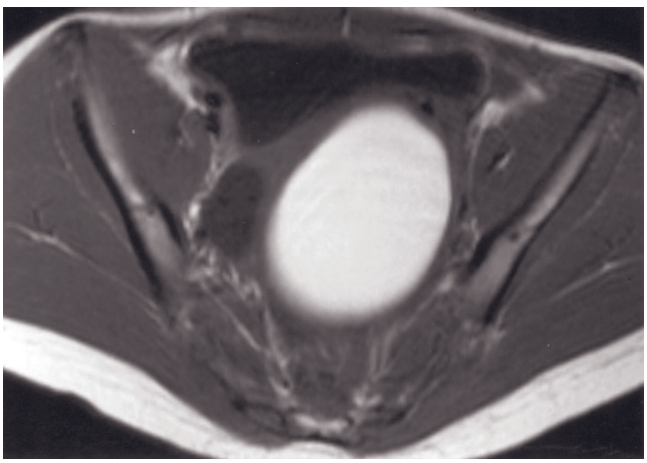

(*b*)

(*c*)

FIG. 14.14 Uterus didelphys with obstructing vaginal septum. Transverse T2-weighted ETSE (*a*),T1-weighted gradient-echo (*b*), and gadolinium-enhanced T1-weighted gradient-echo (*c*) images show two separate uteri (arrows, *a*) with distension of the right endometrial cavity and vagina by hyperintense material, consistent with hematocolpometra. The right kidney is absent (*c*).

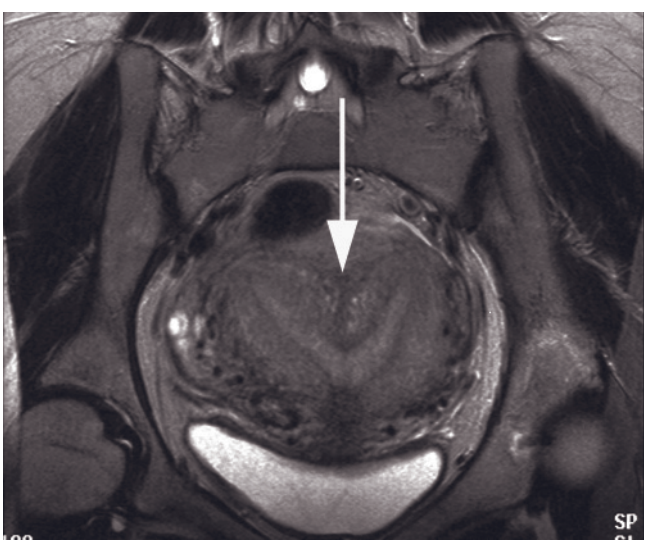

FIG. 14.15 Bicornuate uterus. T2-weighted ETSE long-axis view of the uterus demonstrates widely divergent uterine horns and a concave fundus (arrow).

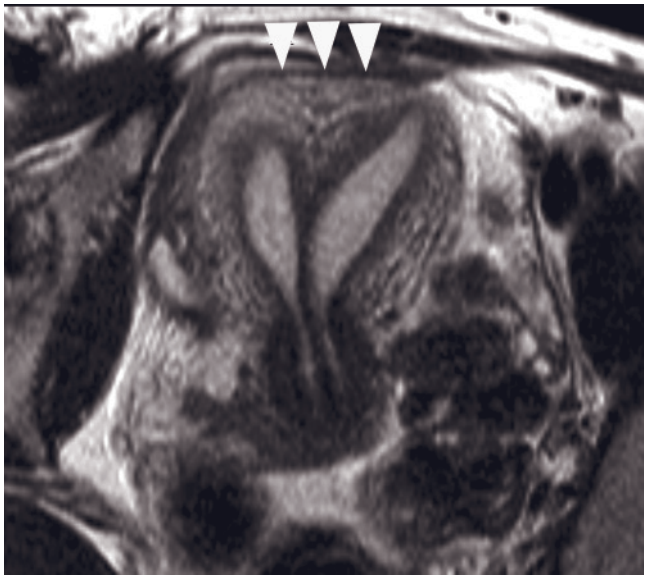

(*a*)

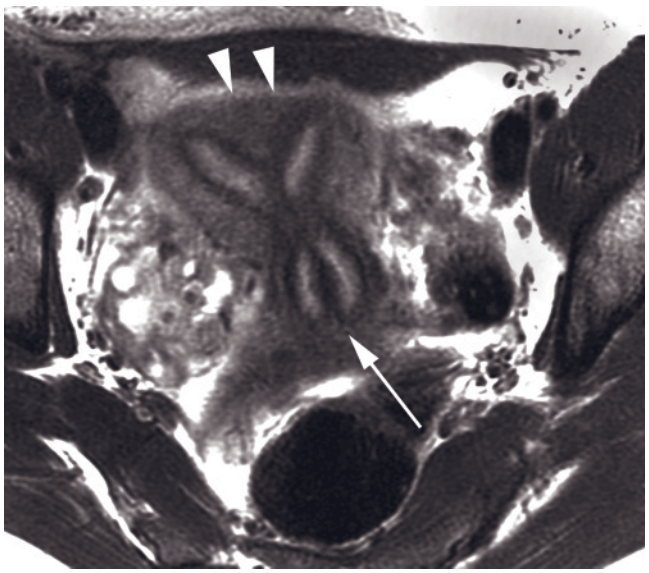

(*b*)

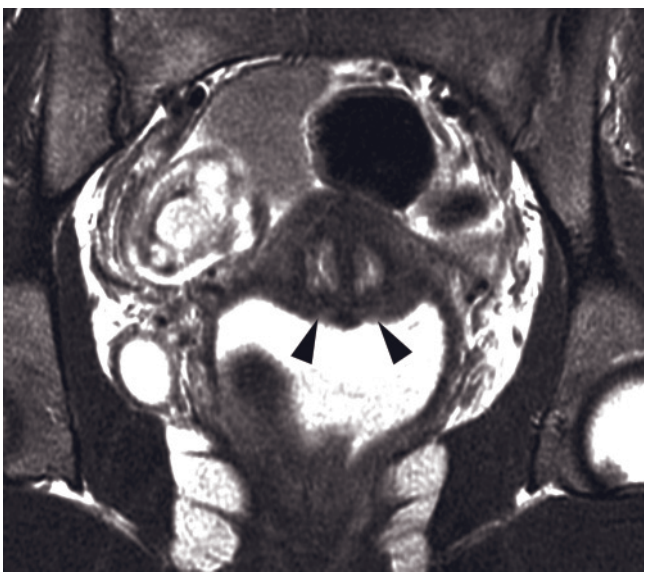

(*c*)

Fig. 14.16 Septate uterus. (*a*) T2-weighted ETSE long-axis view of the uterus demonstrates a hypointense septum extending into the cervix with a convex uterine fundus (arrowheads). (Courtesy of Claude Sirlin, M.D., University of California, San Diego). **Septate uterus with cervical duplication at 3T.** Oblique T2-weighted images in a different patient obtained coronal to the uterine body (*b*) and cervix (*c*) show a septate configuration of the fundus (arrowheads, *b*) and two separate cervices (arrow, *b*). The portio vaginalis of each cervix can be seen protruding into the vagina, distended with gel (arrowheads, *c*). Combined anomalies may not fit into a single class according to common classification schemes; in reporting such cases, all individual components should be described.

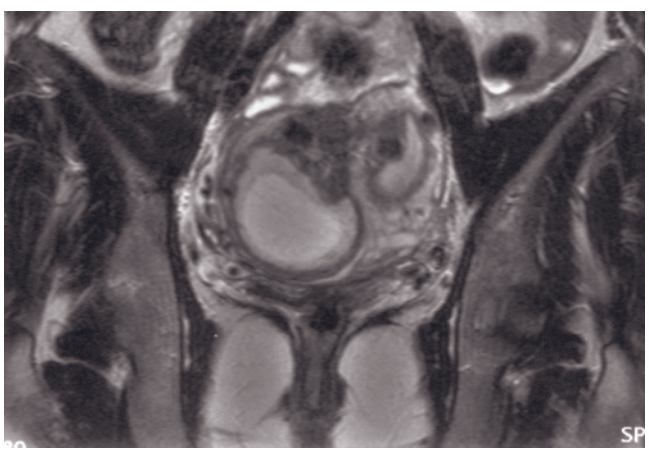

(*a*)

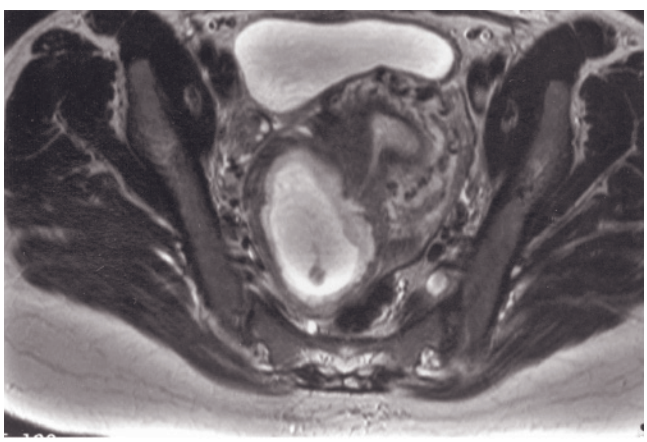

(*b*)

Fig. 14.17 Septate uterus with pregnancy in right horn. Coronal (*a*) and transverse (*b*) ETSE images in a patient with a septate uterus and first-trimester pregnancy. A gestational sac is identified in the right horn of the uterus. Incidental note is made of multiple small leiomyomas in the left horn (*a*).

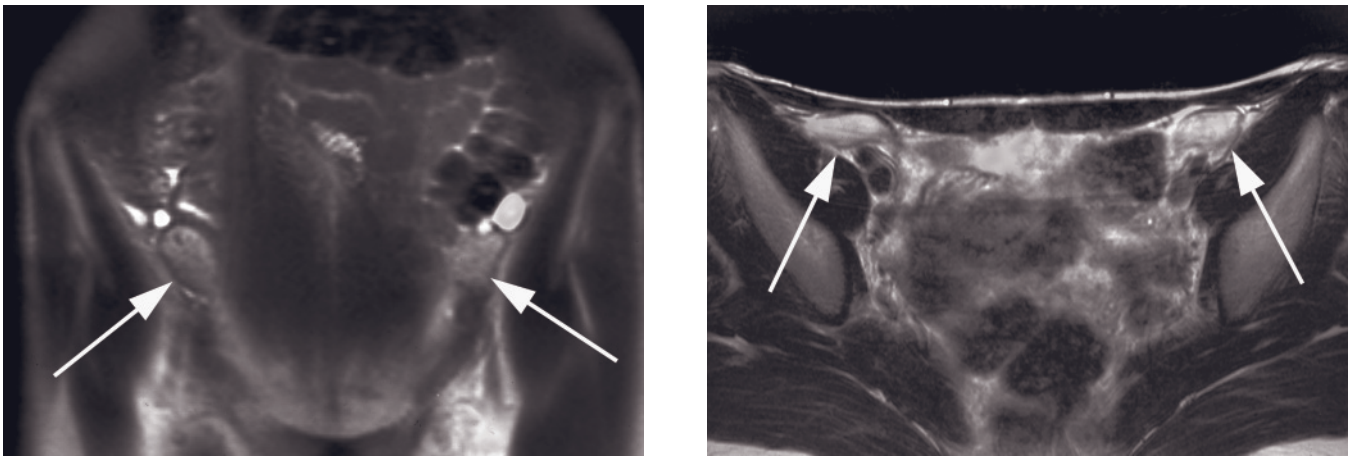

(*a*) (*b*)

FIG. 14.18 Testicular feminization. Coronal T2-weighted SS-ETSE (*a*) and transverse (*b*) T2-weighted ETSE images in a patient with complete androgen insensitivity.The uterus is absent. Bilateral rounded structures (arrows, *a*, *b*) with no follicles are seen at the internal inguinal ring, representing testes.

variant by some, an arcuate uterus has questionable impact on fertility. MR imaging shows a short, broad septum.

Class VII: Diethylstilbesterol Exposure. Diethylstilbesterol (DES), a synthetic estrogen agent, was frequently used until the 1970s in pregnant women with vaginal bleeding in an attempt to prevent miscarriage. This category includes various anomalies associated with DES such as hypoplasia, T-shaped uterus, constrictions, polypoid defects, synechiae, and marginal irregularities. These patients are also at risk for developing clear cell carcinoma of the vagina. On MR imaging, a T-shaped endometrium is best seen on oblique coronal images parallel to the endometrium, and constrictions are seen as focal thickening of the junctional zone. Hypoplasia of the cervix and uterine cavity is seen, whereas the normal zonal uterine anatomy is preserved. No increased incidence of urinary tract anomalies has been reported in patients with DES exposure [45].

Congenital Disorders of Sexual Differentiation

Congenital disorders of sexual differentiation are divided into four categories: male and female pseudohermaphroditism, mixed gonadal dysgenesis, and true hermaphroditism. A multidisciplinary approach is usually required in these patients, including hormonal studies, karyotyping, and anatomic information for accurate diagnosis and treatment. The excellent soft tissue differentiation and multiplanar imaging capability of MRI make it a useful noninvasive tool to determine the presence or absence of a uterus and vagina as well as to preoperatively identify the position of undescended testes (fig. 14.18) [46].

BENIGN DISEASE OF THE UTERINE CORPUS

Endometrial Hyperplasia and Endometrial Polyps

Endometrial hyperplasia is typically seen in postmenopausal women and presents with abnormal bleeding. Premenopausal women with polycystic ovary syndrome or women with estrogen-secreting tumors may also develop endometrial hyperplasia.

Role of MRI

Ultrasound is often used for initial imaging evaluation of the endometrium; however, the diagnosis of malignancy generally requires tissue sampling as the sonographic finding of endometrial thickening is nonspecific. MRI is helpful in patients with indeterminate ultrasound findings and unsuccessful biopsy due to distorted anatomy or cervical stenosis.

MRI Appearance

Endometrial hyperplasia usually appears as diffuse thickening of the endometrial stripe on T2-weighted images (fig. 14.19). The signal intensity of the endometrial stripe is isointense or slightly hypointense to normal endometrium. These imaging characteristics, however, are nonspecific and may also be seen with endometrial carcinoma. Polyps of the endometrium are seen in about 10% of all uteri, typically in postmenopausal

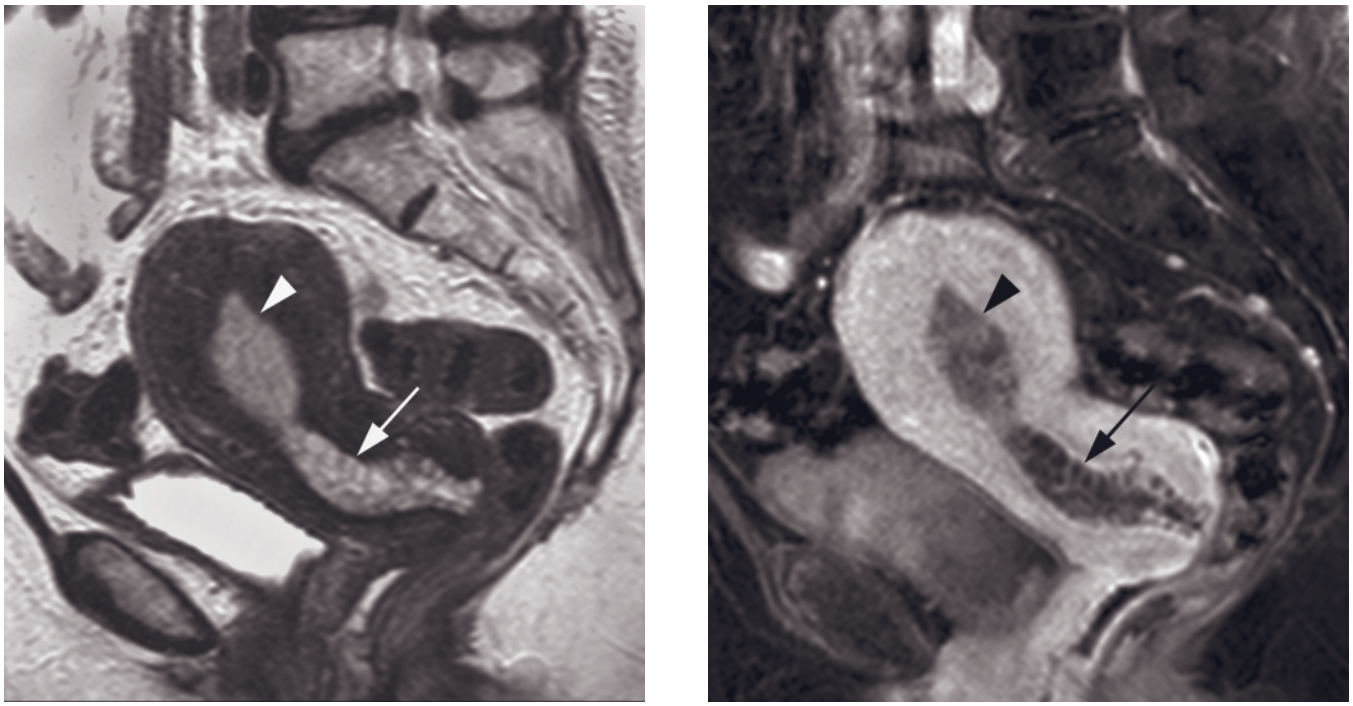

(*a*) (*b*)

FIG. 14.19 Endometrial hyperplasia and tunnel cluster. Sagittal T2-weighted ETSE (*a*) and gadolinium-enhanced fat-suppressed T1-weighted (*b*) images show thickening of the endometrial stripe (arrowhead,*a*,*b*), which enhances less than myometrium on postgadolinium images (*b*).Also note innumerable small cystic lesions lining the endocervical canal (arrow). Examination of the hysterectomy specimen revealed endometrial hyperplasia and tunnel cluster, a benign cervical glandular condition similar to nabothian cysts that may mimic minimum deviation adenocarcinoma (adenoma malignum) on gross and histologic inspection.

patients. In many cases they are asymptomatic, but they may cause irregular or persistent bleeding. Malignant transformation into endometrial cancer is seen in less than 1% of cases [47, 48].

On T2-weighted images, endometrial polyps most frequently present as masses isointense or slightly hypointense relative to normal endometrium. At times, however, they may be entirely isointense and present as diffuse or focal thickening of the endometrial stripe. Large polyps result in distension of the endometrial cavity and often appear heterogeneous. Identification of a vascular stalk or cystic areas favors the diagnosis. On the basis of signal intensity, they can be distinguished from submucosal leiomyomas by means of MRI, the latter typically appearing hypointense on T2-weighted sequences (fig. 14.20) [48]. Polyps show pronounced early enhancement on gadolinium-enhanced T1-weighted sequences. This helps distinguish them from endometrial carcinoma, which typically shows only mild enhancement. However, it is important to realize that although MRI can help to distinguish most polyps from endometrial carcinoma on the basis of morphologic features, accuracy is not sufficient to obviate biopsy, partly because carcinomas and polyps frequently coexist [49].

Leiomyomas

Leiomyomas (synonyms: fibroids, fibroleiomyoma) are benign neoplasm of smooth muscle cell origin and are the most common reproductive tract tumor. Leiomyomas are usually classified according to location: submucosal, intramural, subserosal, or cervical (figs. 14.21–14.24). Uncommonly, a leiomyoma may be situated in the broad ligament (fig. 14.25) or entirely detached from the uterus, parasitizing the blood supply from other vascular beds, usually the omentum [50]. Although leiomyomas are entirely asymptomatic, in most cases presenting as incidental findings, they may be associated with a variety of symptoms, usually abnormal bleeding. Other symptoms include pressure effects, infertility, second-trimester abortions, dystocia, or palpable pelvic-abdominal mass. Torsion, infection, and sarcomatous degeneration are rare complications. Pain is usually the result of acute degeneration, for example, in hemorrhagic infarction of a leiomyoma during pregnancy or torsion of a pedunculated subserosal leiomyoma. Patients may also present with prolapse of a submucosal leiomyoma (fig. 14.26) [48, 51]. For patients with symptomatic leiomyomas, treatment options include medical therapy with gonadotropin-releasing hormone

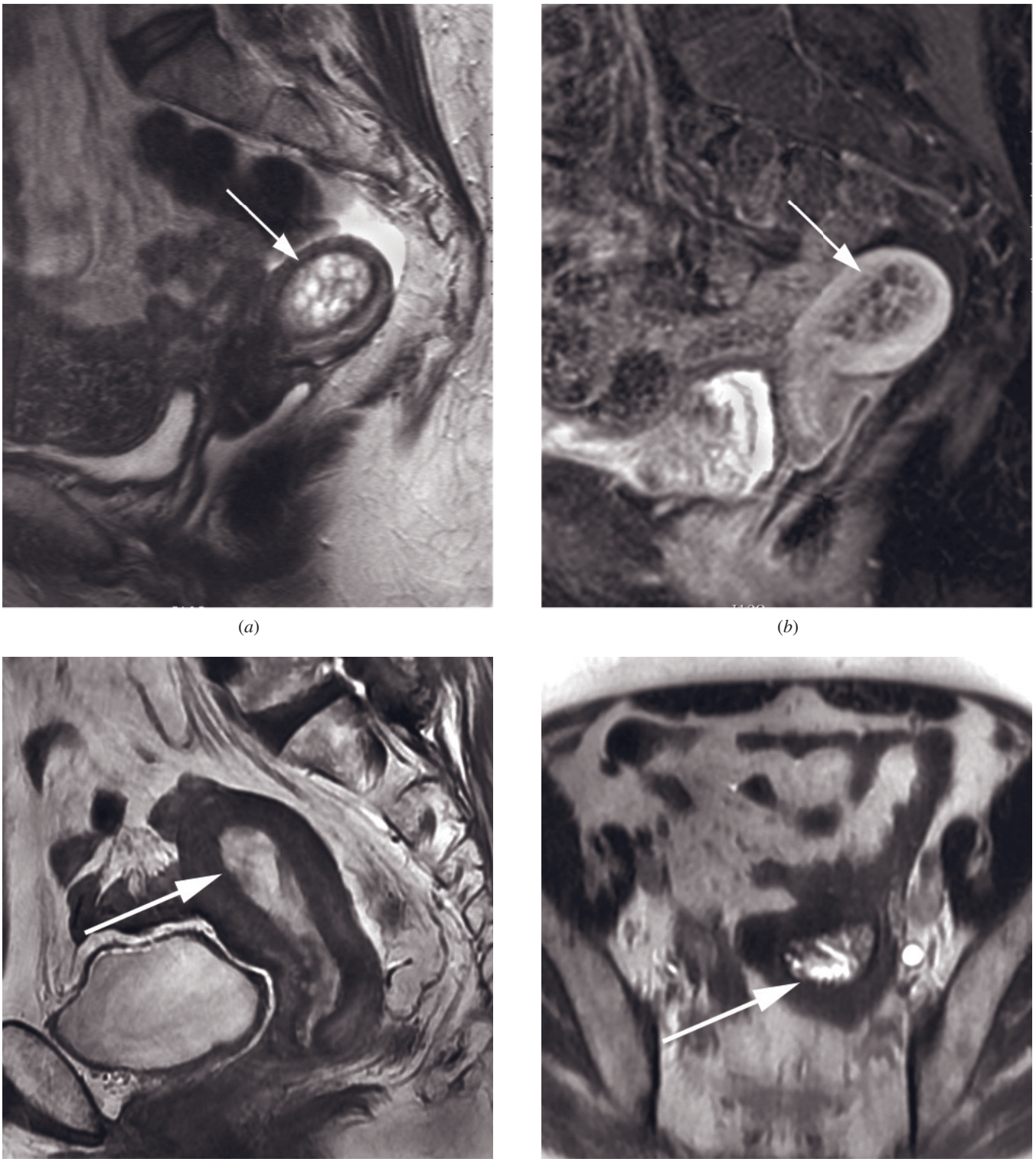

FIG. 14.20 Endometrial polyp. Sagittal T2-weighted ETSE (*a*) and gadolinium-enhanced fat-suppressed T1-weighted gradient-echo (*b*) images show an endometrial mass (arrow, *a*, *b*). On T2-weighted images (*a*), hyperintense cystic spaces are seen within the polyp. On postgadolinium images (*b*), reticular enhancement outlines the cystic foci. **Endometrial polyp at 3T.** Sagittal T2-weighted ETSE (*c*) and axial single-shot ETSE (*d*) images in a different patient show an endometrial mass (arrow, *c*, *d*) with hyperintense cystic spaces seen within the polyp.

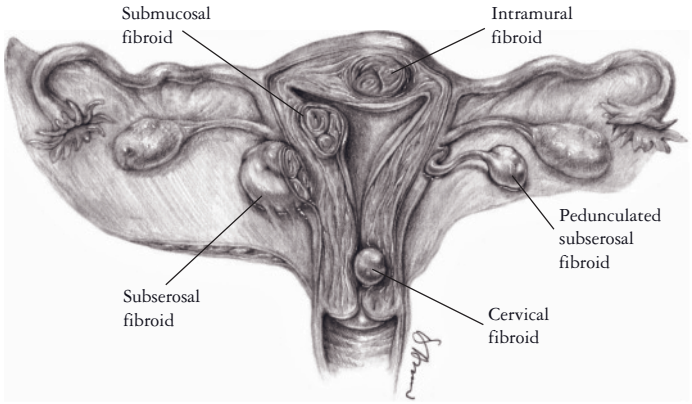

FIG. 14.21 Classification of uterine leiomyomas.

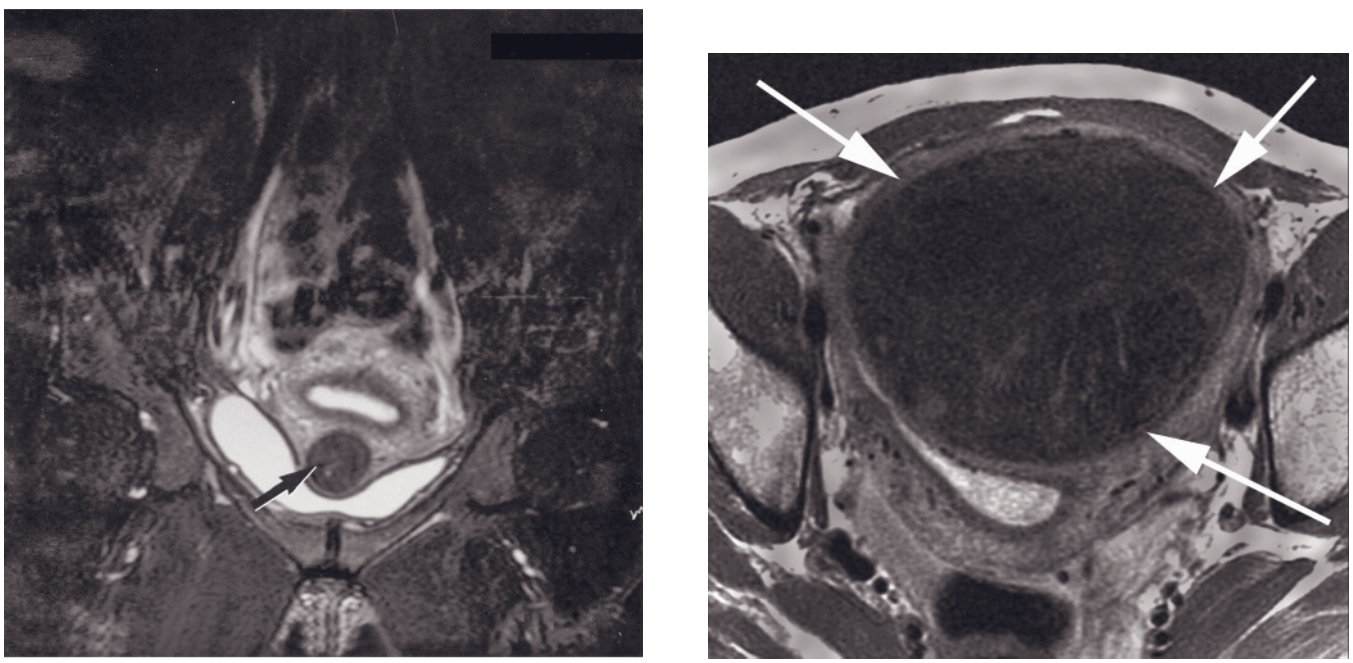

(*a*) (*b*)

FIG. 14.22 Intramural leiomyoma. (*a*) Coronal T2-weighted fat-saturated ETSE image demonstrates a small sharply marginated, hypointense intramural leiomyoma (arrow). **Intramural leiomyoma at 3T.** Coronal T2-weighted fat-saturated ETSE image in a different patient (*b*) demonstrates a larger sharply marginated, hypointense intramural leiomyoma (arrows).

(GnRH) analogs, surgical treatment with hysterectomy or myomectomy, or uterine artery embolization (UAE). As a percutaneous interventional technique, this procedure offers the advantages of avoidance of surgical risks, potential preservation of fertility, and shorter hospitalization [51, 52]. MRI-guided focused ultrasound is another treatment method gaining acceptance [53, 54].

Role of MRI

The role of imaging in evaluating patients with suspected leiomyomas includes lesion detection, characterization, and localization. MRI is used in selected cases as a problem-solving modality, for example, to distinguish between a pedunculated leiomyoma and a solid ovarian mass, to demonstrate the exact size and location of the lesion (i.e., subserosal, intramural, or submucosal origin) before uterine-sparing surgery, to distinguish leiomyomas from adenomyosis, or to visualize the endometrium in a patient with multiple leiomyomas and indeterminate ultrasound. MRI has been shown to be superior to ultrasound for the detection and localization of uterine leiomyomas and to be a useful adjunct for differentiating leiomyomas from other pathological conditions. Accurate preoperative localization of leiomyomas is of great importance in planning myomectomy because submucosal leiomyomas may be resected

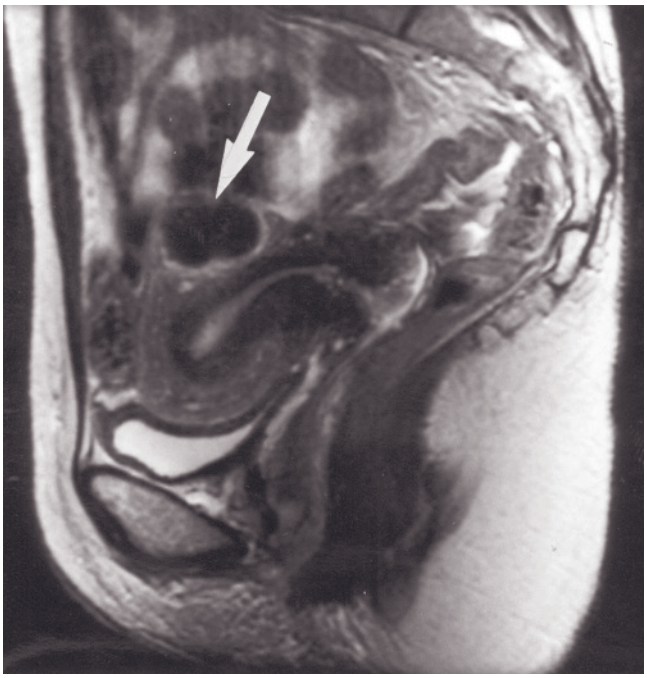

FIG. 14.23 Subserosal leiomyoma. Sagittal T2-weighted ETSE image demonstrates a subserosal sharply marginated, hypointense lesion with a hyperintense rim (arrow).

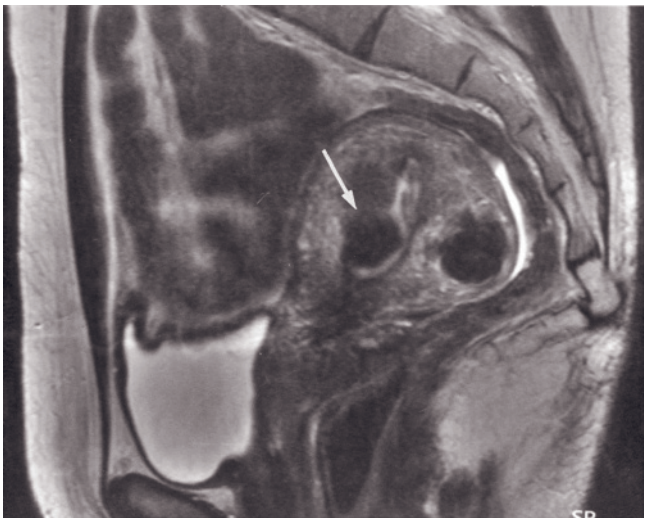

(*a*)

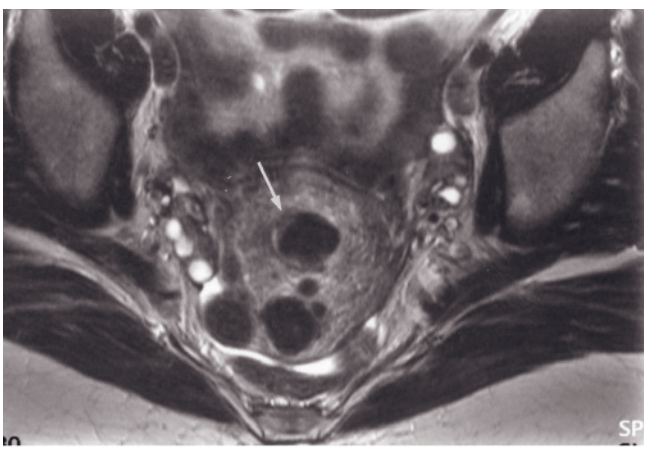

(*b*)

FIG. 14.24 Submucosal leiomyoma. Sagittal (*a*) and transverse (*b*) T2-weighted ETSE images demonstrate multiple welldefined hypointense leiomyomas including a submucosal leiomyoma (arrows, *a*, *b*) that arises in the anterior uterine wall and deviates the endometrial canal.

hysteroscopically, whereas laparoscopic or transabdominal myomectomy is required for intramural or subserosal leiomyomas. It can also demonstrate postprocedural complications such as hematoma, abscess, uterine rupture, and peritoneal inclusion cyst.

MRI has also been used to aid patient selection for uterine artery embolization (UAE) and monitoring the result of embolization by demonstrating the degree of shrinkage and loss of enhancement of the leiomyomas [51, 56–58]. It has been shown that in this subpopulation of patients undergoing uterine arterial embolization, MRI is helpful. MRI characteristics of leiomyomas before embolization can help predict the success of the procedure, and MRI can monitor outcome [51, 56–59]. It has been shown that leiomyomas that do not enhance respond poorly to UAE, presumably because they have already undergone infarction. MRI not only evaluates tissue enhancement characteristics before embolization, but also delineates arterial supply [60, 61]. MRI also enables quantitative monitoring of GnRH analog therapy, documenting the change in size of individual leiomyomas.

MRI Appearance

Leiomyomas of the uterus have a typical appearance on MRI. They are depicted as sharply marginated lesions of low signal intensity not only on T1- but also T2-weighted sequences. Dark signal on T2-weighted images permits differentiation from malignant tumors (figs. 14.21–14.27). The lesions are surrounded by a pseudocapsule of compressed neighboring tissue. A small hyperintense rim due to dilated lymphatic clefts, dilated veins, as well as slight edema surrounding the leiomyoma may be seen on T2-weighted imaging (fig. 14.23). These histologic findings have been shown to correspond to perilesional rim enhancement on contrast-enhanced images. In addition to standard sagittal and axial views, coronal or oblique views may be indicated for accurate localization and for establishing the myometrial origin of a lesion. The presence of a fat plane on T1-weighted sequences may aid in differentiating a pedunculated leiomyoma from a solid adnexal mass. Most leiomyomas enhance similar to the

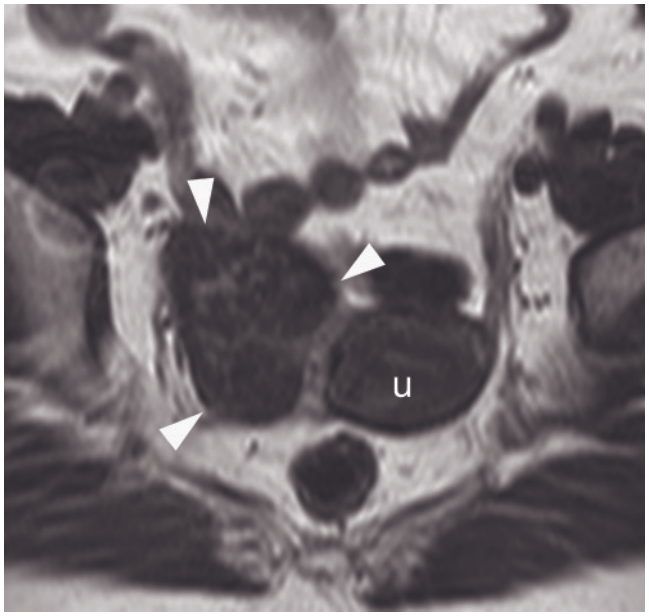

(*a*)

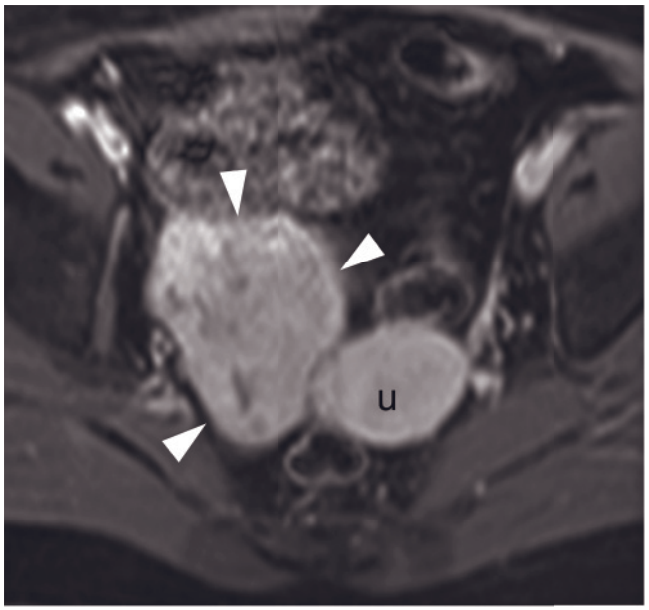

(*b*)

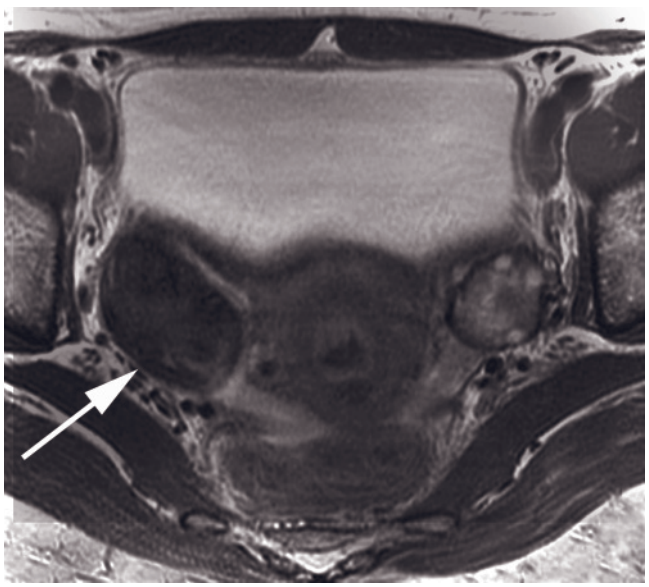

(*c*)

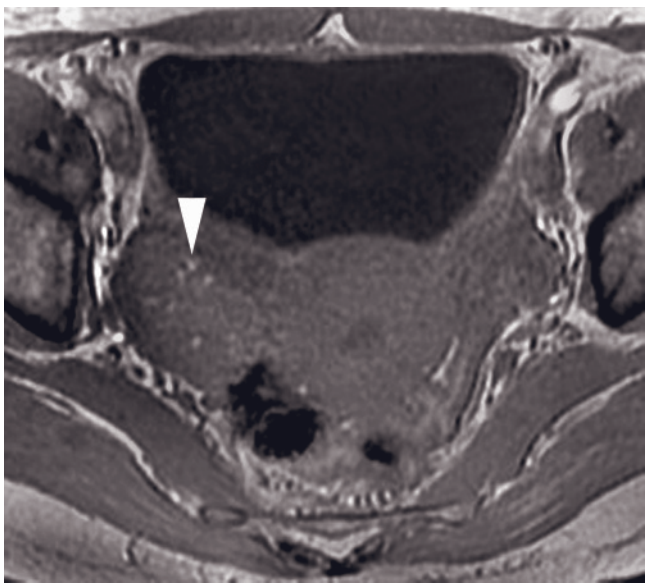

(*d*)

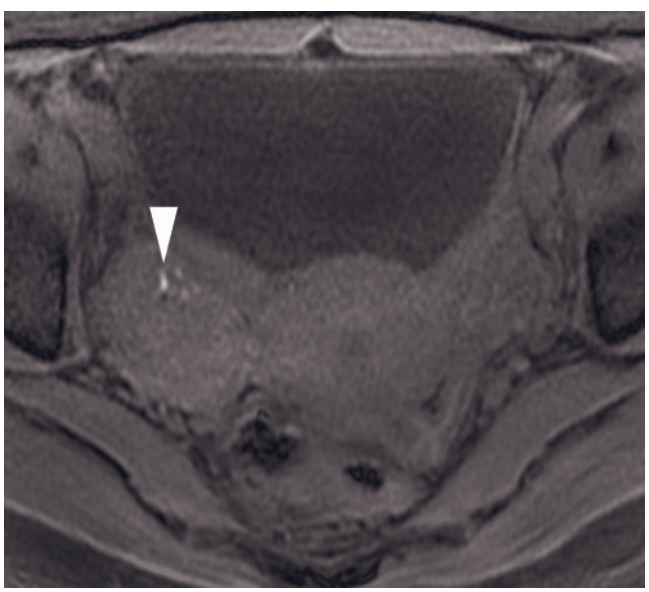

(*e*)

Fig. 14.25 Broad ligament leiomyoma. Transverse T2-weighted ETSE (*a*) and gadolinium-enhanced fat-suppressed T1-weighted gradient-echo (*b*) images show a right adnexal mass (arrowheads, *a*) that is hypointense on T2-weighted images (*a*) and enhances fairly homogeneously on postgadolinium images (*b*). The mass was resected and found to be a leiomyoma within the broad ligament. **Broad ligament adenomyoma.** Transverse T2-weighted ETSE (*c*), T1-weighted gradient-echo without (*d*) and with (*e*) fat suppression, and gadolinium-enhanced fat-suppressed T1-weighted gradient-echo (*f*) images in another patient show a right adnexal mass (arrows, *c*, *f*) that is hypointense on T2-weighted images (*c*) and enhances fairly homogeneously on post-gadolinium images (*d*). Note high-signal-intensity foci (arrowhead, *d*, *e*) on T1-weighted images. The mass was removed and found to be an extrauterine adenomyoma within the broad ligament.

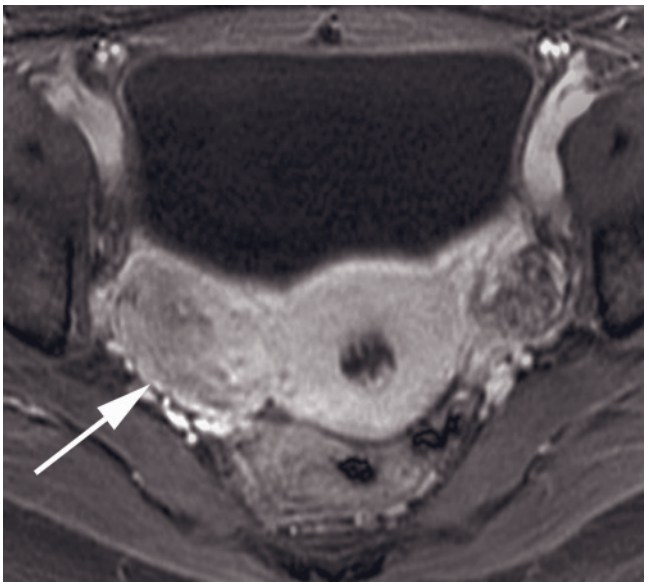

FIG. 14.25 (*Continued*) (*f*)

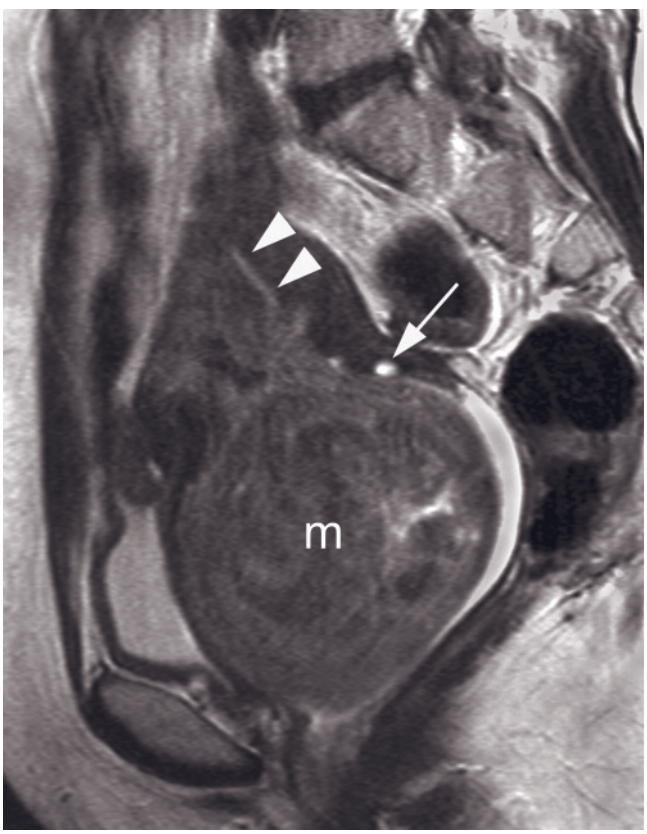

(*a*)

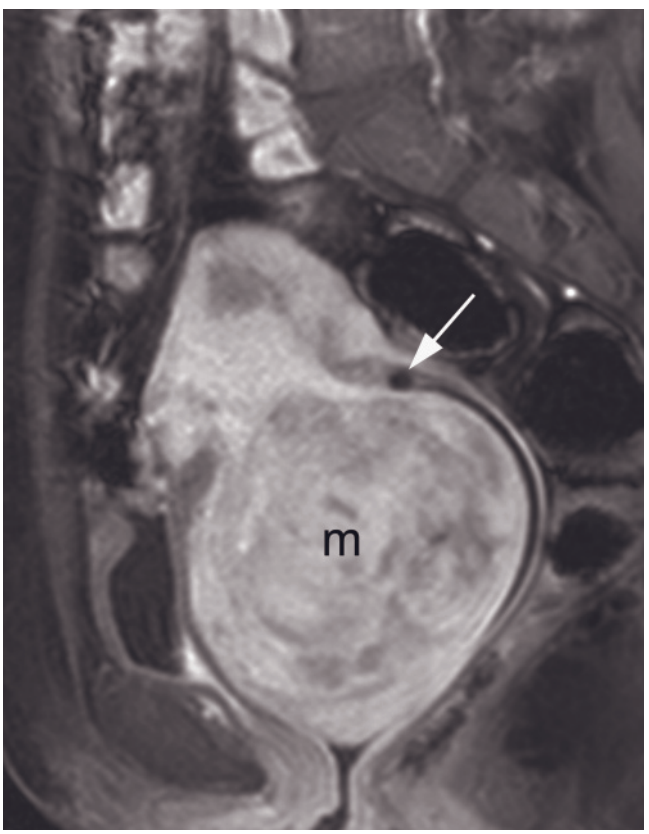

(*b*)

FIG. 14.26 Prolapsed submucosal leiomyoma. Sagittal T2-weighted (*a*) and gadolinium-enhanced fat-suppressed T1-weighted (*b*) images show a large mass (m, *a*, *b*) arising from the uterine wall, anterior to the endometrial stripe (arrowheads, *a*).The mass extends through the cervix into the vagina. At surgery, the cervix was found to be dilated 10 cm to accommodate the leiomyoma. Note the nabothian cyst, which identifies the posterior aspect of the dilated cervix (arrow, *a*, *b*).

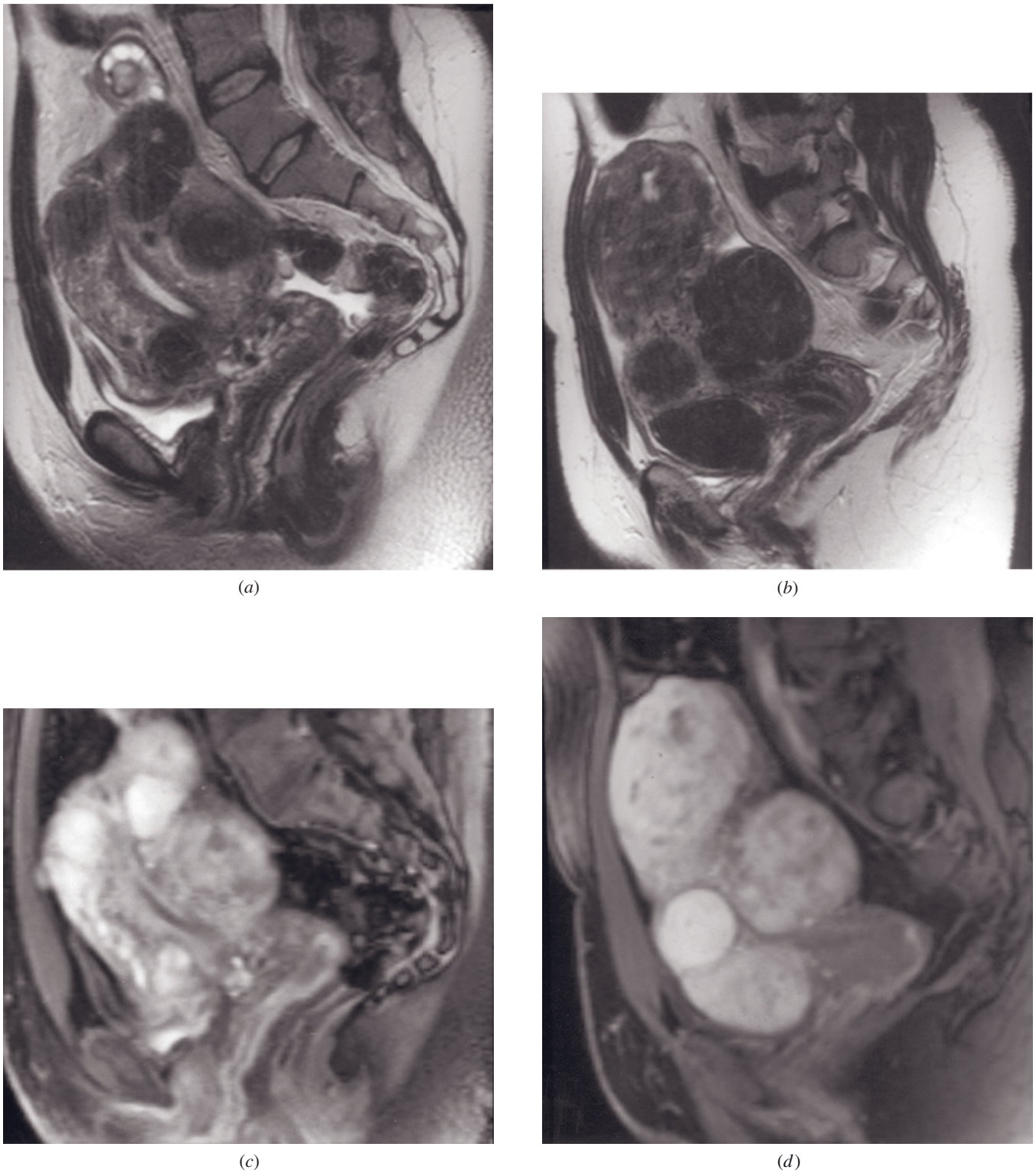

FIG. 14.27 Multiple uterine leiomyomas with gadolinium enhancement. Sagittal T2-weighted ETSE (*a*, *b*) and gadolinium-enhanced fat-suppressed T1-weighted gradient-echo (*c*, *d*) images show multiple well-defined hypointense masses on T2-weighted images that enhance avidly with gadolinium. Enhancement of leiomyomas varies with the cellular components and degree of degeneration.

surrounding myometrium and remain well marginated (figs. 14.26 and 14.27).

Leiomyomas may undergo degenerative changes resulting in various, nonspecific MR appearances, but predominantly presenting with inhomogeneous high signal intensity on T2-weighted sequences and a lack of contrast-enhancement on gadolinium-enhanced T1-weighted sequences (fig. 14.28). In leiomyomas undergoing hemorrhagic or red degeneration, hyperintense areas on T1-weighted images are typically seen, and there is no enhancement (fig. 14.29) [51]. For patients undergoing UAE, MRI aids patient selection and monitors change in size of leiomyomas, which is variable (fig. 14.30). UAE results in hemorrhagic infarction and results in high signal on T1-weighted images and lack of enhancement in successfully treated leiomyomas; evidence of poor enhancement before embolization is a predictor of poor outcome (fig. 14.31). Cellular leiomyomas are a subtype that demonstrates uniform high signal intensity on T2-weighted images because of their unique histologic composition. These leiomyomas typically enhance homogeneously and respond well to embolization. In addition to demonstrating enhancement characteristics, MRI can evaluate arterial supply, which may predict or explain poor outcome of UAE. Leiomyomas may parasitize blood supply from other sources such as ovarian arteries, and response to UAE may be minimal (fig. 14.32).

Secondary calcification occurs in about 4% of leiomyomas [62]. Although the demonstration of these characteristic calcifications is difficult by MRI within the hypointense lesion, this is irrelevant as the correct diagnosis will be made by the characteristic appearance of leiomyomas [48].

Lipoleiomyoma is a rare, specific type of leiomyoma that contains a substantial amount of fat presenting on MRI with signal intensity characteristic of fat on all pulse sequences [62] (fig. 14.33).

MRI can be useful in differentiating leiomyomas from other solid pelvic masses [55]. Establishing the myometrial origin of a mass by demonstrating splaying of the uterine serosa or myometrium usually allows a confident diagnosis of leiomyoma to be made. Signal characteristics will give additional information. If a mass is predominantly of low signal intensity relative to myometrium on T2-weighted images, the diagnosis of leiomyoma is probable. Signal characteristics of leiomyomas may be indistinguishable from those of ovarian fibroma and Brenner tumors of the ovary; however, differentiation is unlikely to be important for clinical management because these tumors are rarely malignant [55].

Submucosal leiomyomas may be differentiated from endometrial pathology such as endometrial polyps, hyperplasia, or endometrial carcinoma by confirmation of their myometrial origin and by their typical low signal intensity on T2-weighted images (fig. 14.24). However, leiomyomas may exhibit variable signal intensities, and overlap in signal characteristics between leiomyomas and endometrial pathologies has been described. In women undergoing myomectomy, the surgical bed may be seen as an area of moderately high signal intensity on both T1- and T2-weighted sequences. These signal characteristics suggest the presence of a subacute hematoma within the myometrium at the myomectomy site (fig. 14.34) [51].

Benign metastasizing leiomyoma is an unusual variant that consists of smooth muscle cell tumors in the lungs, lymph nodes, or abdomen that appear to have originated from a benign uterine leiomyoma usually removed many years earlier [62].

Malignant degeneration occurs in less than 1% of leiomyomas, and leiomyosarcomas also occur de novo. There are no MRI signal characteristics that reliably distinguish leiomyomas from leiomyosarcomas. Malignancy should be considered if a leiomyoma enlarges suddenly after menopause or demonstrates an irregular configuration with indistinct borders; however, the most suggestive finding is evidence of metastatic disease (figs. 14.35 and 14.36).

Adenomyosis

Uterine adenomyosis is a common disease that affects women of reproductive age. Symptoms may be similar to those of leiomyomata and include dysmenorrhea and menorrhagia. Adenomyosis is defined as the presence of aberrant endometrial stroma and glands within the myometrium. The ectopic endometrium consists almost exclusively of the basal layer and is not affected by hormonal stimulation, unlike the ectopic functional endometrium found in endometriosis. Adenomyosis is commonly associated with leiomyomas. Adenomyosis may be microscopic, focal, or diffuse. The term adenomyoma is reserved for the focal, nodular form of adenomyosis [48, 63–66].

Adenomyosis may be entirely asymptomatic or present with symptoms of pelvic pain, hypermenorrhea, and uterine enlargement. Symptoms typically manifest in the fourth to fifth decade, with a higher incidence in multiparous women. These symptoms and signs, however, are nonspecific and can be seen in other common gynecological disorders such as dysfunctional uterine bleeding, leiomyomas, and endometriosis. Physical examination demonstrates an enlarged uterus that is not as firm as a myomatous uterus.

Role of MRI

The findings of adenomyosis on endovaginal ultrasound are subtle, although correct diagnosis is sometimes established when ultrasound is performed meticulously

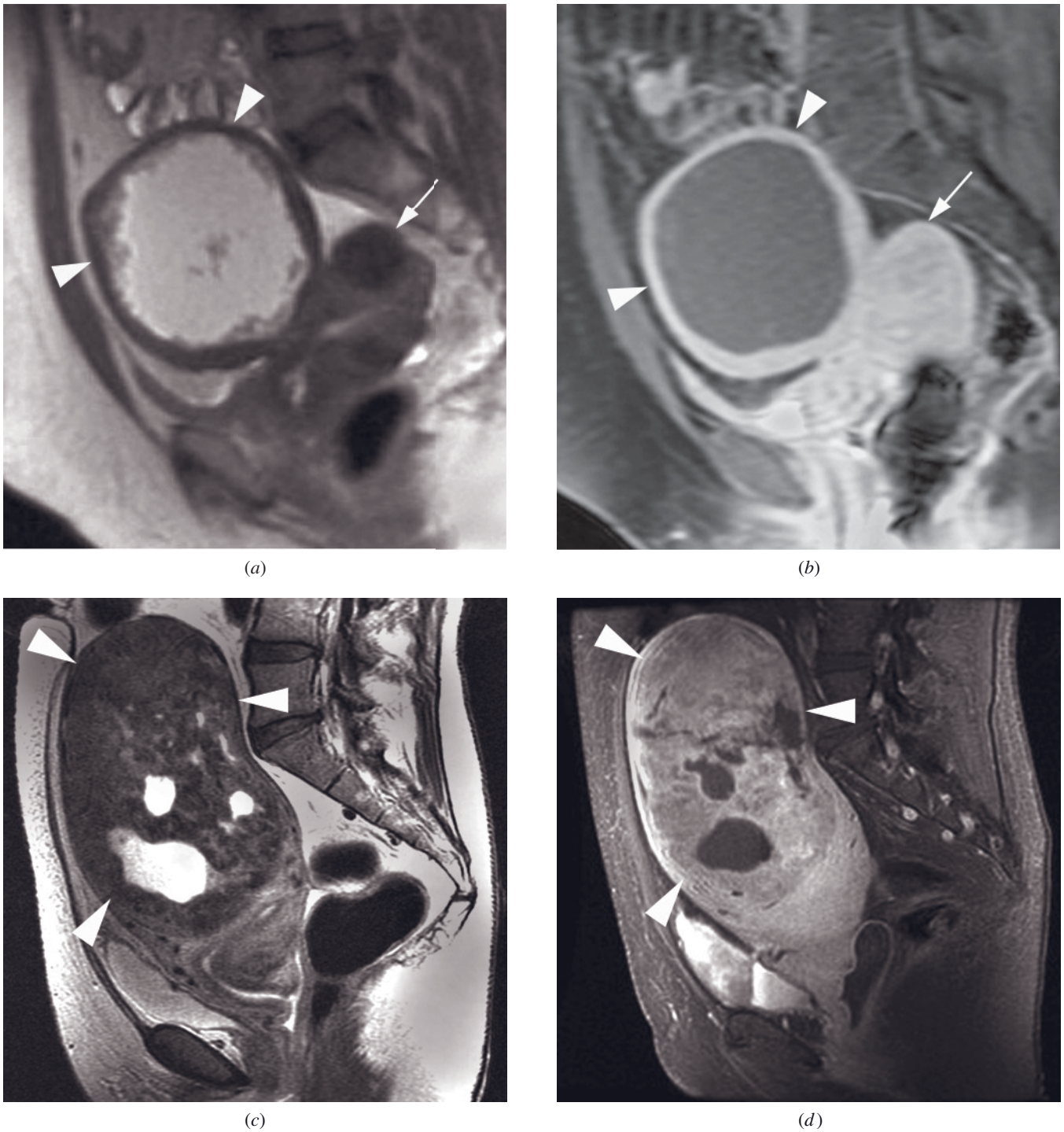

FIG. 14.28 Degenerated uterine leiomyoma. Sagittal T2-weighted ETSE (*a*) and contrast-enhanced T1-weighted fat-suppressed gradient-echo (*b*) images show a large subserosal leiomyoma (arrowheads, *a*, *b*) arising from the anterior uterus that is high signal intensity on T2-weighted images and does not enhance with gadolinium. Note the smaller leiomyoma in the fundus (arrow, *a*, *b*), which shows typical low signal intensity on T2-weighted images and homogeneous enhancement with gadolinium. **Uterine leiomyoma with degeneration at 3T.** Sagittal T2-weighted ETSE (*c*) and contrast-enhanced T1-weighted fat-suppressed gradient-echo (*d*) images in a different patient show a large subserosal leiomyoma (arrowheads, *c*, *d*) arising from the anterior uterus that contains areas of high signal intensity on T2-weighted images that do not enhance with gadolinium.

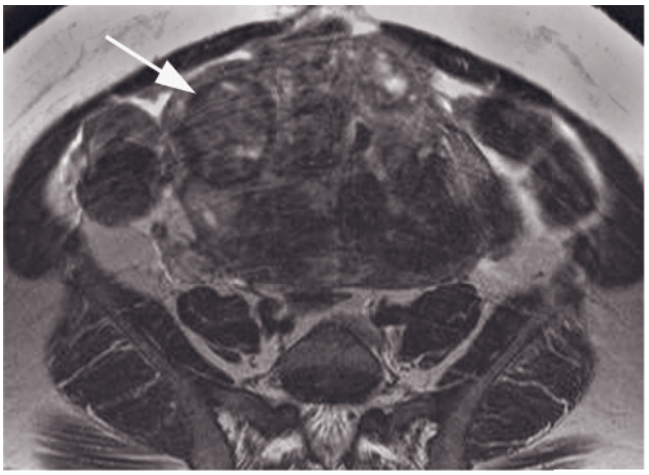

(*a*)

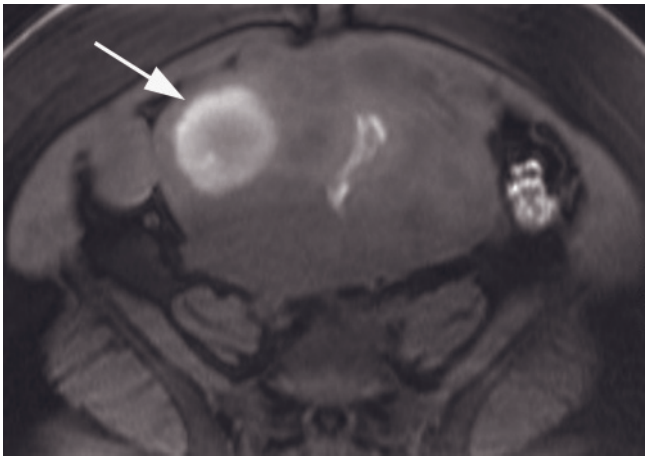

(*b*)

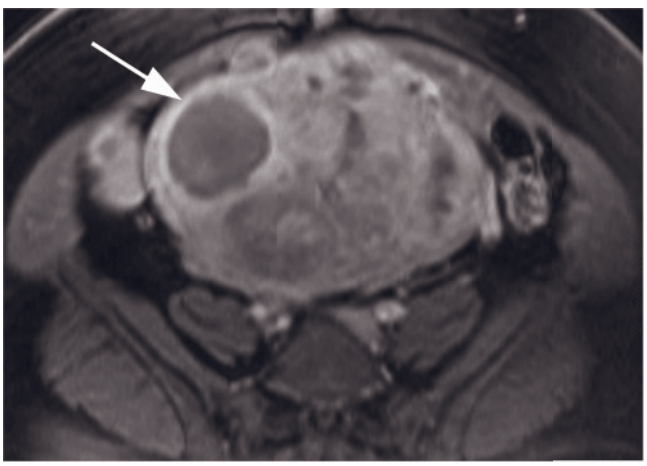

(*c*)

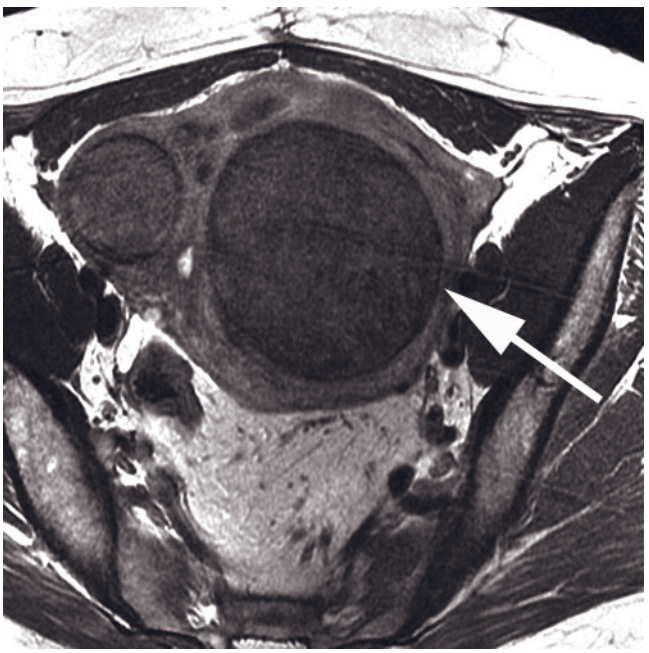

(*d*)

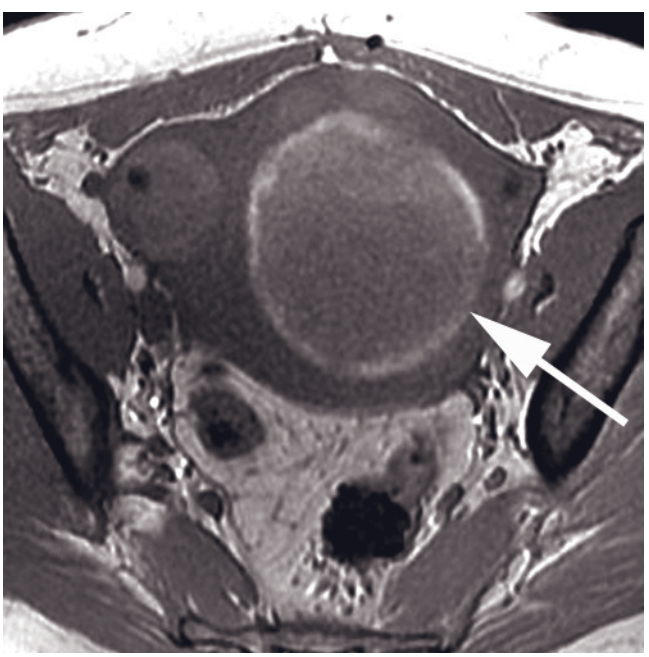

(*e*)

Fig. 14.29 Hemorrhagic degeneration in a leiomyoma. Transverse T2-weighted ETSE (*a*), fat-suppressed T1-weighted gradient-echo (*b*), and gadolinium-enhanced fat-suppressed T1-weighted gradient-echo (*c*) images show multiple uterine fibroids, one of which exhibits hemorrhagic degeneration (arrow, *a–c*) with high signal intensity on T1-weighted images (*b*) and lack of enhancement on postgadolinium images (*c*). **Hemorrhagic degeneration in a leiomyoma at 3T.** Transverse T2-weighted ETSE (*d*), T1-weighted gradient-echo (*e*), and gadolinium-enhanced fat-suppressed T1-weighted gradient-echo (*f*) images in another patient show multiple uterine fibroids, one of which exhibits hemorrhagic degeneration (arrows, *d–f*) with high signal intensity on T1-weighted images (*e*) and lack of enhancement on postgadolinium images (*f*).

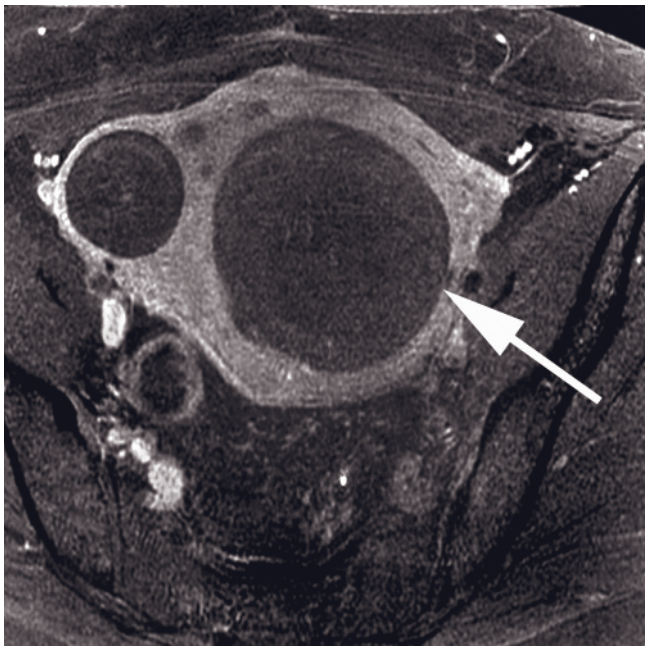

(*f*)

FIG. 14.29 (*Continued*)

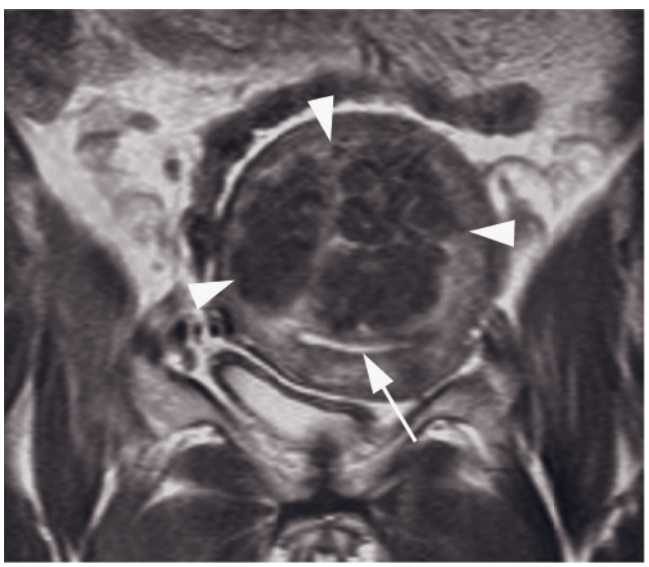

(*a*)

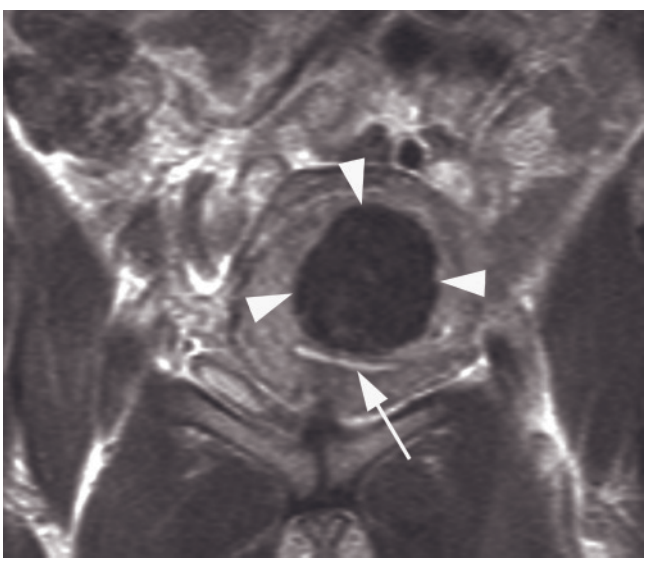

(*b*)

FIG. 14.30 Leiomyomas before and after uterine artery embolization in two patients. Coronal T2-weighted ETSE images before (*a*) and after (*b*) uterine artery embolization (UAE) show a leiomyoma (arrowheads) in the posterior uterus that displaces the endometrial stripe (arrow). The leiomyoma is larger before UAE (*a*) and decreases in size after UAE (*b*). Sagittal T2-weighted

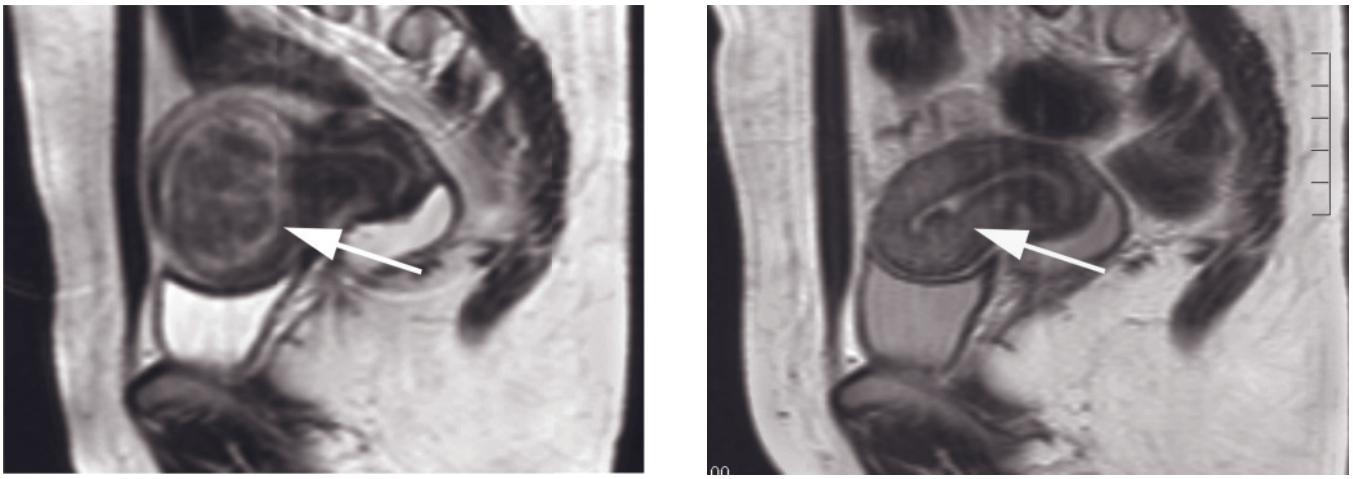

(*c*) (*d*)

FIG. 14.30 (*Continued*) ETSE images before (*c*) and after (*d*) UAE in a second patient show a large leiomyoma before UAE (arrow, *c*) that decreases in size dramatically after UAE (arrow, *d*).

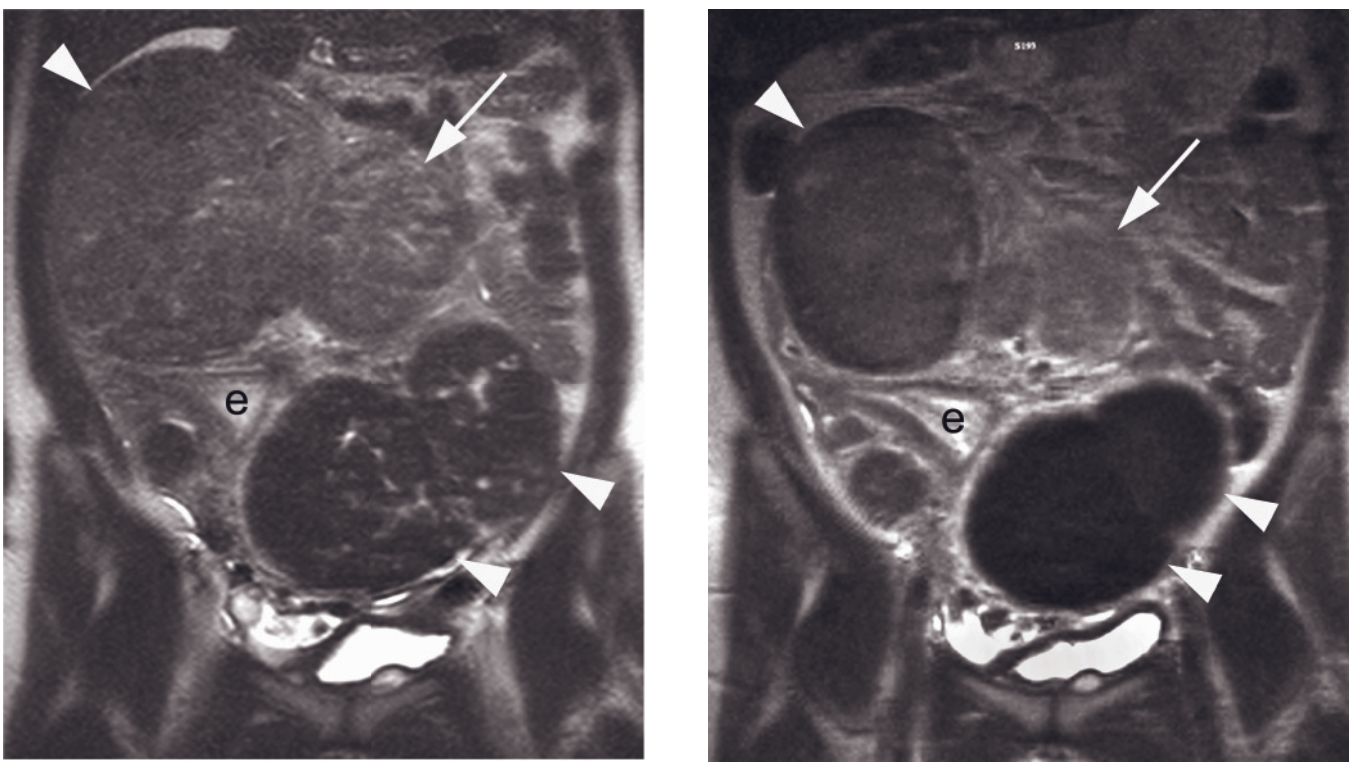

(*a*) (*b*)

FIG. 14.31 Multiple uterine leiomyomas before and after uterine artery embolization. Coronal T2-weighted SS-ETSE (*a*, *b*) and gadolinium-enhanced fat-suppressed T1-weighted gradient echo (*c*, *d*) and sagittal T1-weighted gradient echo (*e*, *f*) images. Images are obtained before (*a*, *c*, *e*) and after (*b*, *d*, *f*) uterine artery embolization (UAE). The large fibroids that show

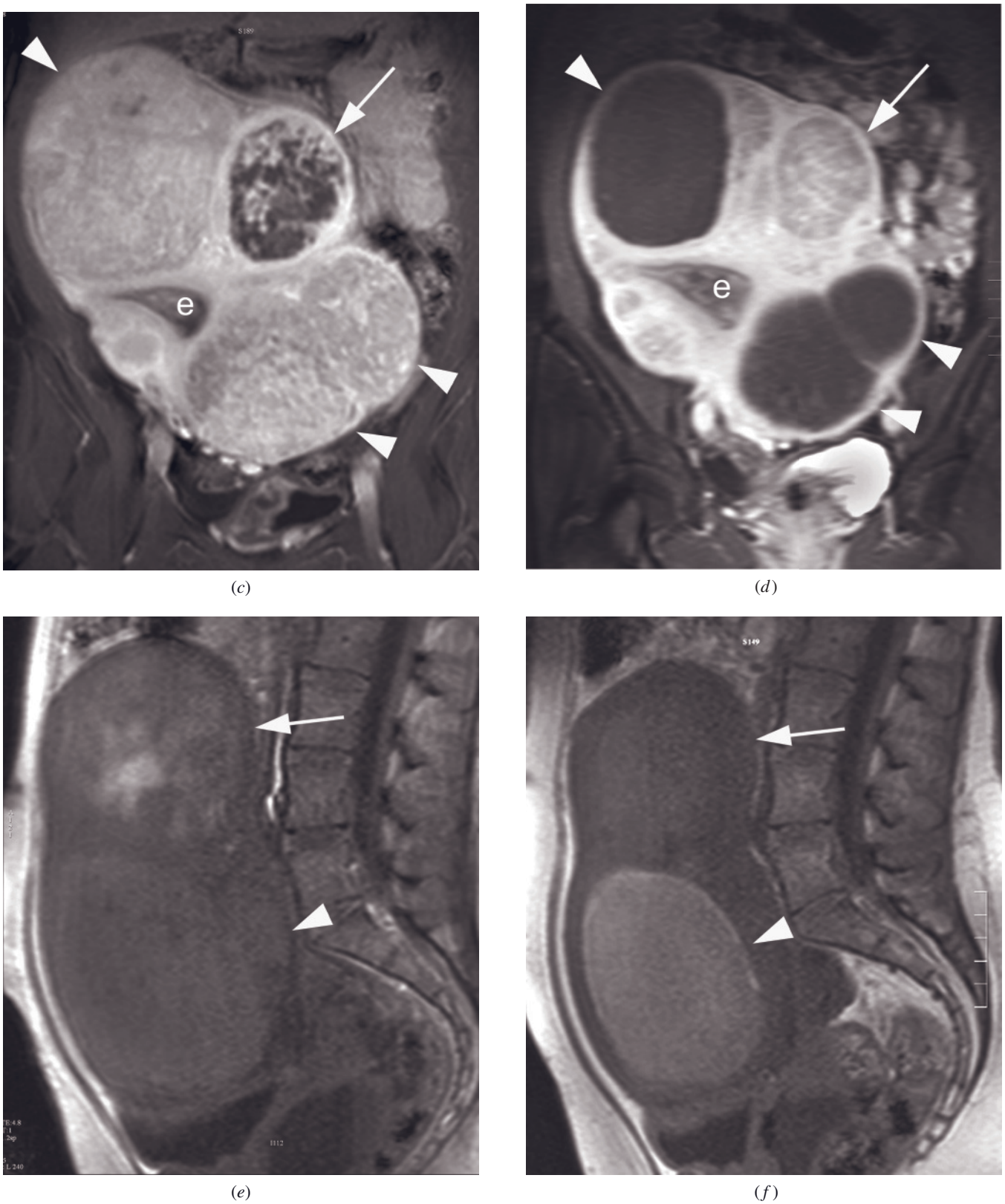

(*c*) (*d*)

(*e*) (*f*)

FIG. 14.31 (*Continued*) typical signal characteristics and diffuse enhancement before UAE (arrowheads, *a*, *c*, *e*) show decreased size and lack of enhancement after UAE (arrows, *b*, *d*, *f*). The fibroid with evidence of degeneration before UAE (arrow, *a*, *c*, *e*) shows enhancement after UAE (arrows *b*, *d*, *f*). e, Endometrium. **Fibroids before embolization at 1.5T and after embolization**

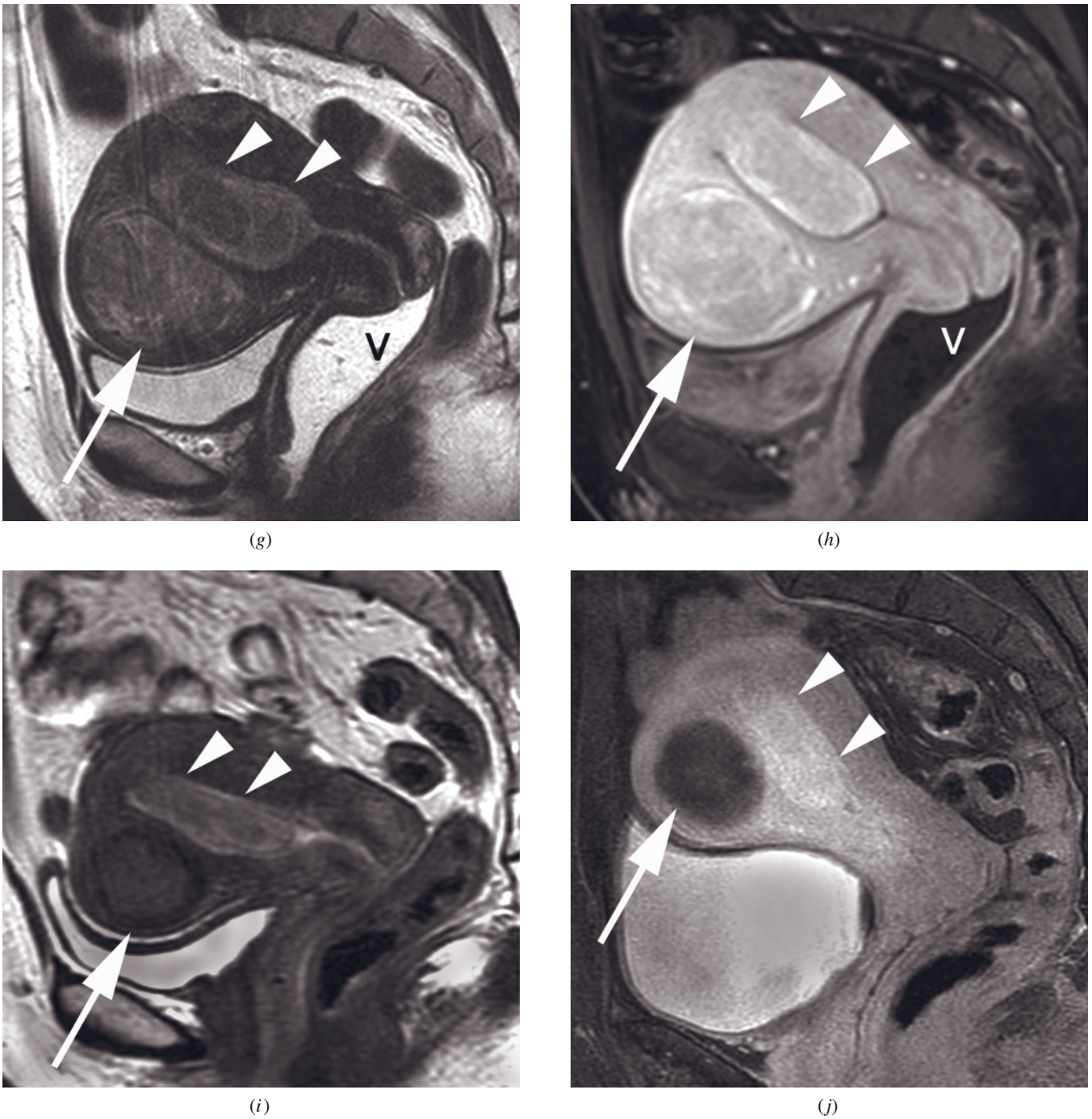

(*g*) (*h*)

(*i*) (*j*)

FIG. 14.31 (*Continued*) **at 3T.** Sagittal T2-weighted ETSE (*g*, *i*) and gadolinium-enhanced fat-suppressed T1-weighted gradient-echo (*h*, *j*) images before (*g*, *h*) and after (*i*, *j*) embolization in a different patient show expected infarction of the intramural fibroid (arrow) and persistent enhancement of the pedunculated submucosal fibroid (arrowheads), which was subsequently resected hysteroscopically. The preembolization images were performed at 1.5 T, using gel to distend the vaginal canal (v, *g*, *h*), whereas the postembolization images were performed without gel at 3 T.

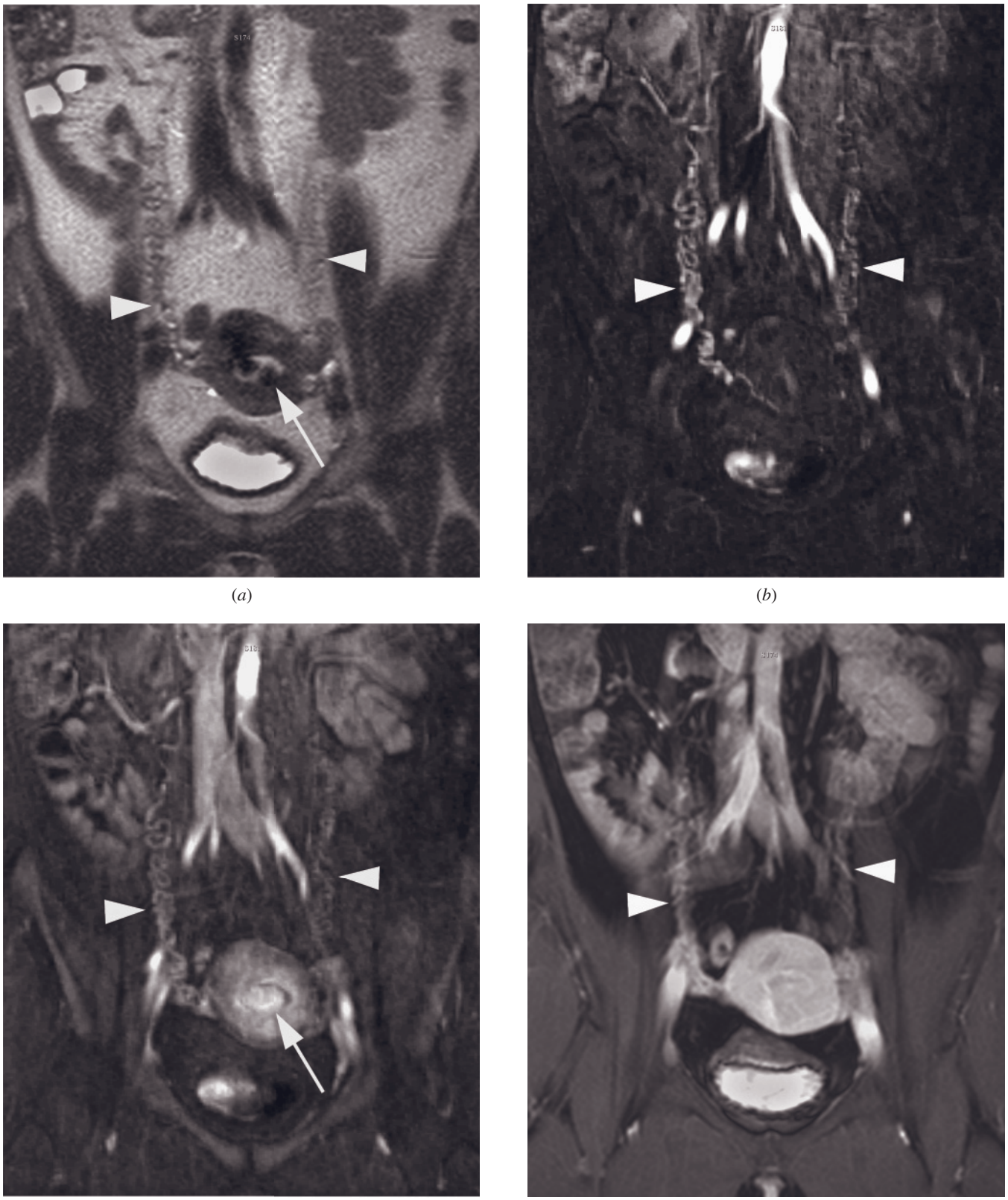

FIG. 14.32 Unsuccessful uterine artery embolization due to recruitment of ovarian arteries. Coronal T2-weighted SSETSE (*a*), dynamic gadolinium-enhanced MRA in early (*a*) and late (*b*) arterial phases, and delayed gadolinium-enhanced fat-suppressed T1-weighted gradient-echo (*d*) images in a patient status post uterine artery embolization without relief of symptoms. Submucosal fibroids are seen that are hyperintense on T2-weighted images (arrow, *a*) and show marked enhancement on late arterial phase images (arrow, *c*). Enlarged ovarian arteries, right larger than left, are seen (arrowheads, *a–d*).

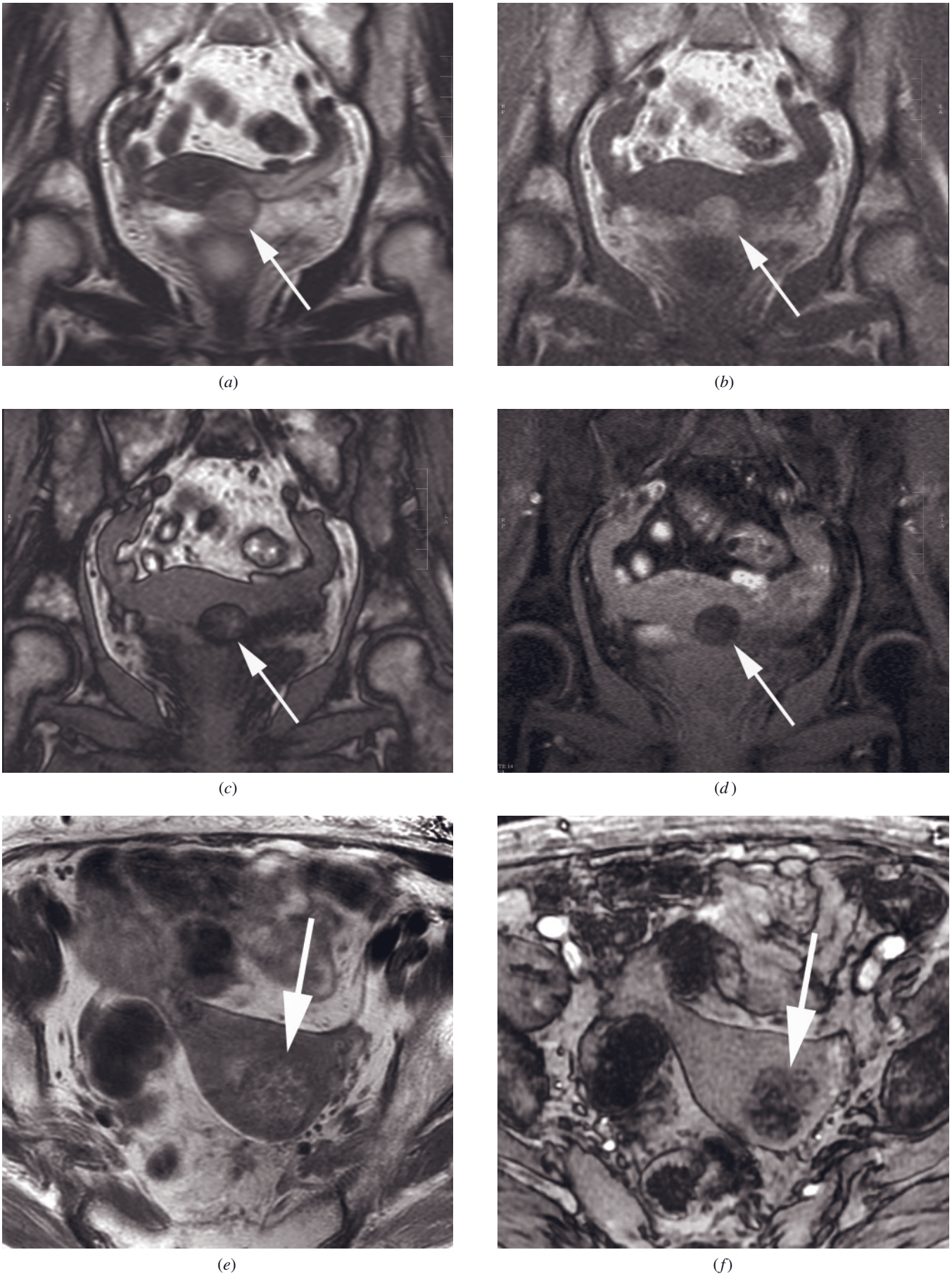

Fig. 14.33 Lipoleiomyoma. Coronal T2-weighted ETSE image (*a*) and T1-weighted gradient-echo images obtained in phase (*b*), out of phase (*c*), and with fat suppression (*d*) show a round mass (arrow) arising from the uterus with signal characteristics that indicate intralesional fat: chemical shift artifact seen on out-of-phase images (*c*) and signal loss throughout the lesion on chemically selective fat-suppression images (*d*). **Lipoleiomyoma at 3T.** Transverse T1-weighted gradient echo obtained in phase (*e*) and out of phase (*f*) in another patient show a round myometrial mass (arrows, *e*, *f*) with chemical-shift artifact seen on out-of-phase images.

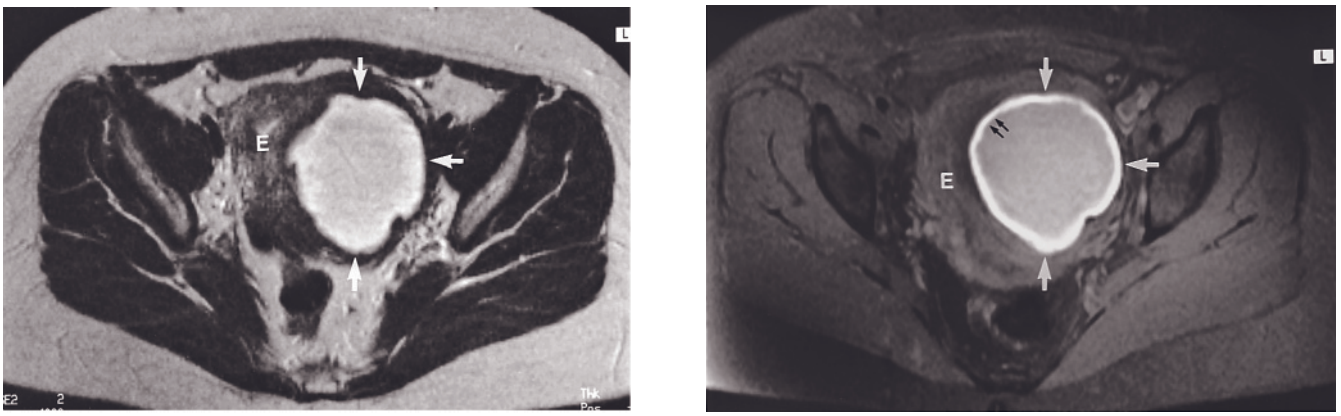

(*a*) (*b*)

FIG. 14.34 Postmyomectomy hematoma. Transverse T2-weighted ETSE (*a*) and fat-suppressed T1-weighted gradient-echo (*b*) images.A well delineated mass of moderately high signal intensity (arrows, *a*, *b*) consistent with a hematoma is present in the surgical bed. Note the peripheral rim of higher signal intensity (small arrows, *b*), which is typical of a subacute hematoma. E, Endometrium.

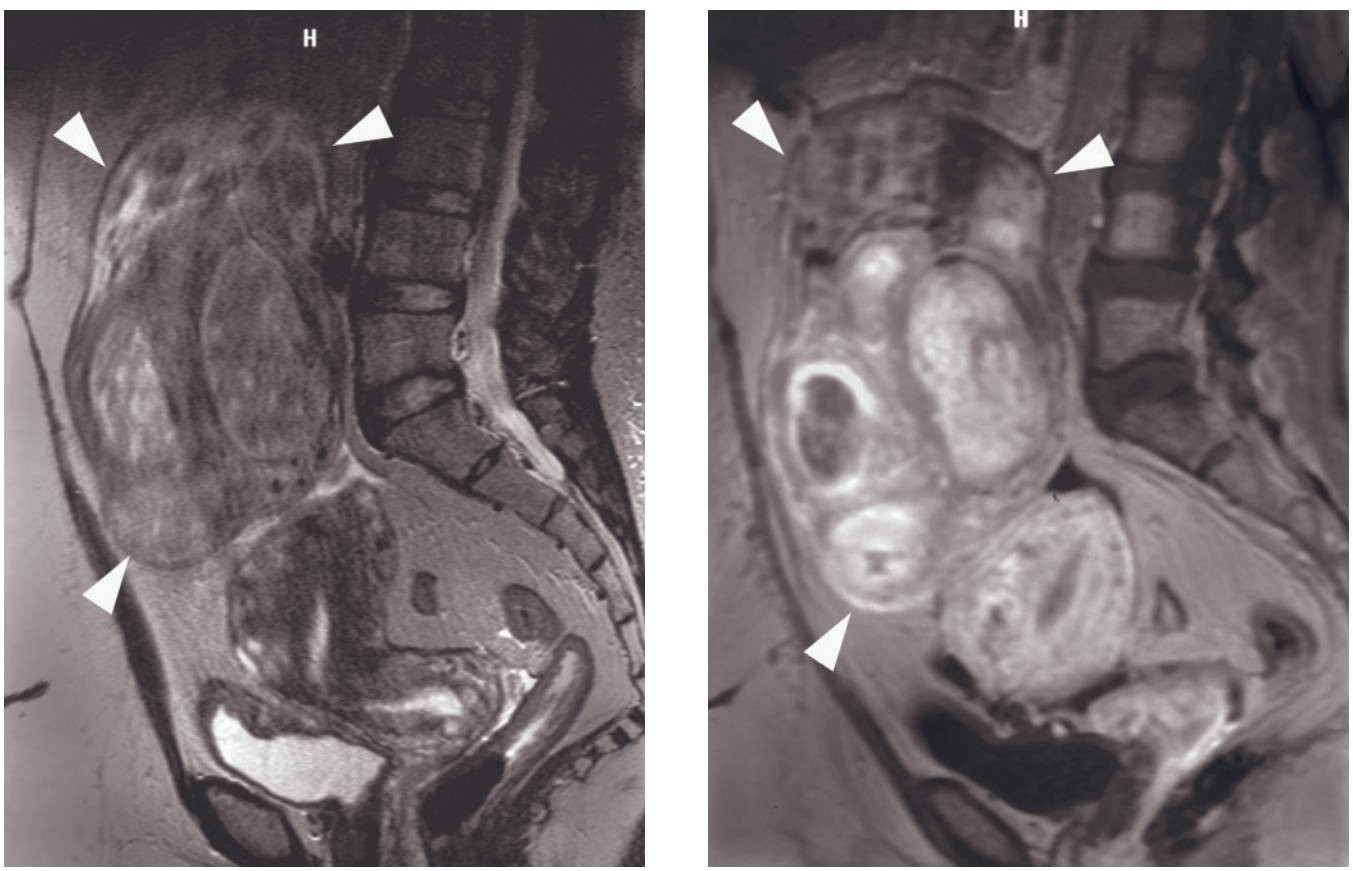

(*a*) (*b*)

FIG. 14.35 Low-grade leiomyosarcoma. Sagittal T2-weighted ETSE (*a*) and gadolinium-enhanced fat-suppressed T1-weighted gradient-echo (*b*) images show a large exophytic subserosal uterine mass (arrowheads) with areas of high signal intensity on T2-weighted images and heterogeneous enhancement that was found to be low-grade leiomyosarcoma.

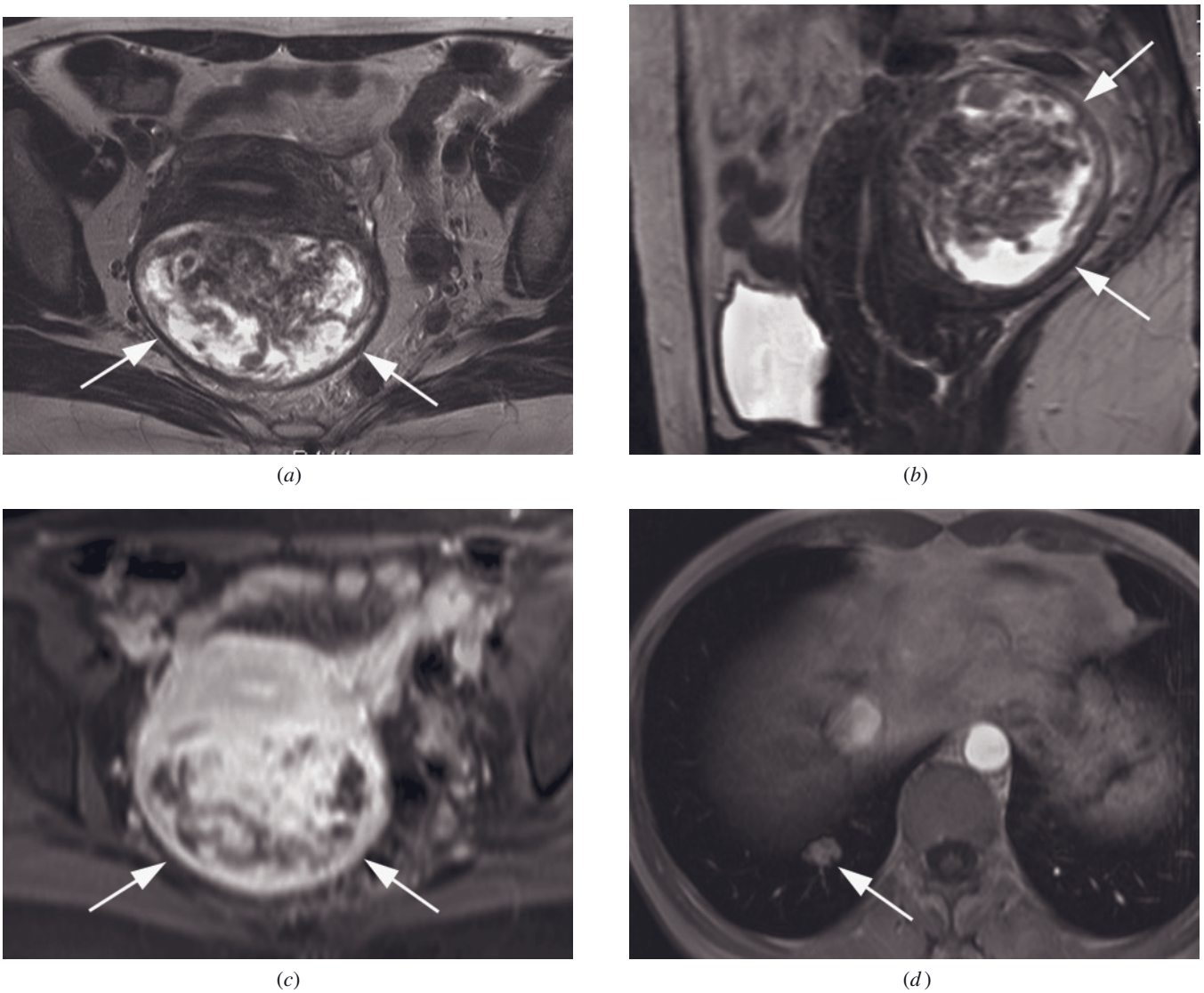

FIG. 14.36 Metastatic leiomyosarcoma. Transverse (*a*) and sagittal (*b*) T2-weighted ETSE, and transverse gadolinium-enhanced fat-suppressed T1-weighted gradient-echo (*c*, *d*) images show a heterogeneous mass (arrow, *a*, *c*) arising from the posterior uterine wall and a right lower lobe lung metastasis (arrow, *d*).

by an experienced operator. The correct diagnosis is important because uterine-conserving therapy is possible with leiomyomas, whereas hysterectomy is considered the definitive treatment for debilitating adenomyosis [58]. MRI is an accurate means of diagnosis, with sensitivity and specificity ranging from 86% to 100% [65, 66]. MRI is especially helpful in patients with adenomyosis and leiomyomas. Ultrasound is difficult in these patients, and detection of associated adenomyosis may change management.

MRI Appearance

On MRI, adenomyosis is diagnosed on T2-weighted sequences. Pathologic thickening of the hypointense junctional zone of 12 mm or more is typical (fig. 14.37). The use of a lower threshold value is problematic because of the wide range of normal and transient causes of thickening such as myometrial contractions and diffuse physiological thickening related to menses. Although published data are limited, some investigators have reported normal junctional zone thickness in excess of 12 mm on days 1 and 2 of the menstrual cycle [66]. For this reason, caution should be used when making the diagnosis of adenomyosis based only on junctional zone thickness. On T2-weighted images, multiple spots of hyperintensity are frequently seen, most likely representing islands of ectopic endometrium, cystically dilated endometrial glands, or hemor-

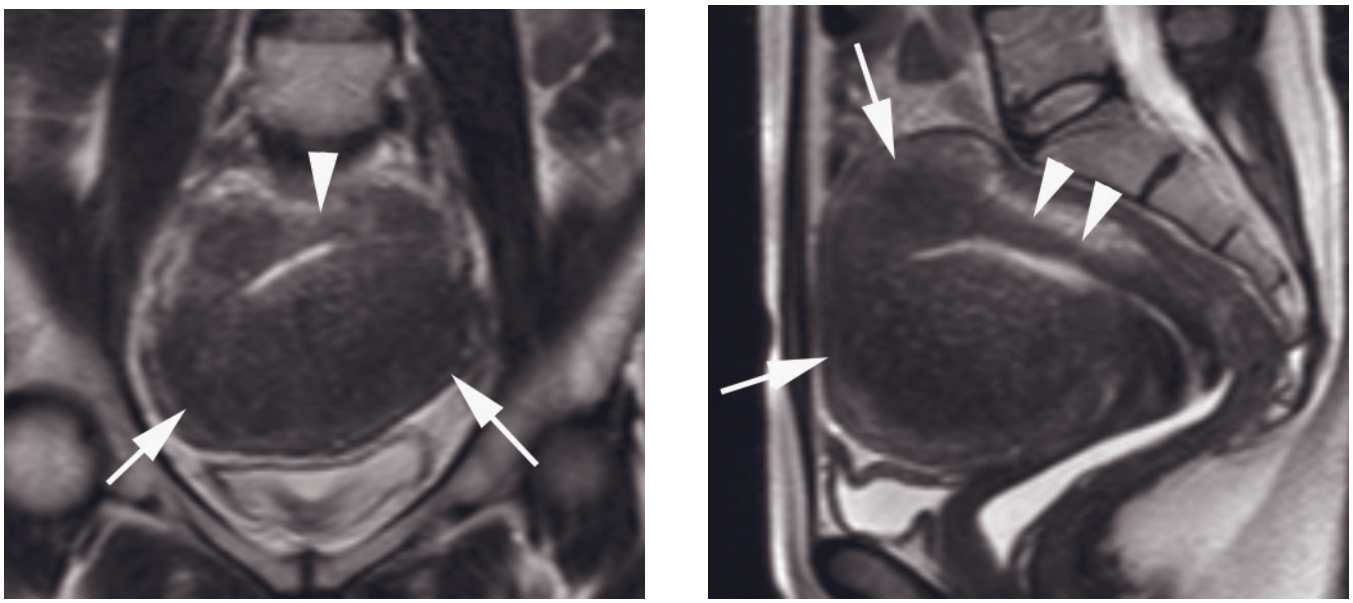

(*a*) (*b*)

FIG. 14.37 Diffuse asymmetric adenomyosis. Coronal (*a*) and sagittal (*b*) T2-weighted ETSE images show a markedly thickened junctional zone with greater involvement of the anterior uterus (arrows) and a small area of sparing in the posterior uterus where the junctional zone is nearly normal (arrowheads). Diffuse adenomyosis frequently has an asymmetric distribution. Note the punctate high signal foci throughout the lesion.

rhagic fluid (fig. 14.38) [66]. Bright foci on T1-weighted images are seen much less frequently and correspond to areas of hemorrhage (fig. 14.39). The exact mechanism of hemorrhage is unclear because adenomyosis involves only the basal, nonfunctional layer of the endometrium. When the degree of hemorrhage is extensive, cystic adenomyosis can result, presenting with well-circumscribed, cystic myometrial lesions with hemorrhage in different stages of organization [66].

The diffuse form of adenomyosis affects the entire uterus (figs. 14.37 and 14.38), which may result in uterine enlargement. The focal form, the so-called adenomyoma, is characterized by a thickening of the junctional zone with an indistinct outer margin (fig. 14.39). Contrast-enhanced sequences may show uniform enhancement similar to many leiomyomas [48, 66]. In some cases, the dilated center of the endometrial glands does not enhance, leading to a speckled appearance (fig. 14.38).

An important differential diagnosis of focal adenomyosis on MRI is leiomyoma. Although MRI is shown to be highly accurate in differentiating adenomyosis from leiomyomas, the imaging characteristics may overlap. Features favoring the diagnosis of adenomyosis include poorly defined borders, elliptical rather than round shape, minimal mass effect on the endometrium, and linear striations radiating out from endometrium into the myometrium [28, 67]. Myometrial contractions may also mimic adenomyosis but typically change during the examination (fig. 14.6).

While hysterectomy is the only well-established definitive treatment for adenomyosis, there are reports of success with endometrial ablation, medical therapy with GnRH analogs, and UAE (fig. 14.40). Reports suggest that patients with adenomyosis experience improvement in symptoms after UAE [59]. However, long-term results are not well established, and there is evidence that symptoms may recur in many patients [63, 67].

BENIGN DISEASE OF THE CERVIX

Nabothian Cysts

Nabothian cysts result from mucous distention of endocervical glands or clefts. They can be the result of an inflammatory process or due to squamous metaplasia. The cysts are common and only rarely present with symptoms, thus usually not requiring treatment. They may, however, reach up to 4 cm in diameter and, when multiple, may result in marked enlargement of the cervix.

On MRI, nabothian cysts are well depicted on T2-weighted sagittal and axial images. Nabothian cysts demonstrate variable signal intensity on T1-weighted images and are hyperintense on T2-weighted images (fig. 14.41). They show no enhancement after contrast administration. Nabothian cysts are differentiated from cervical carcinoma by their well-defined margins and

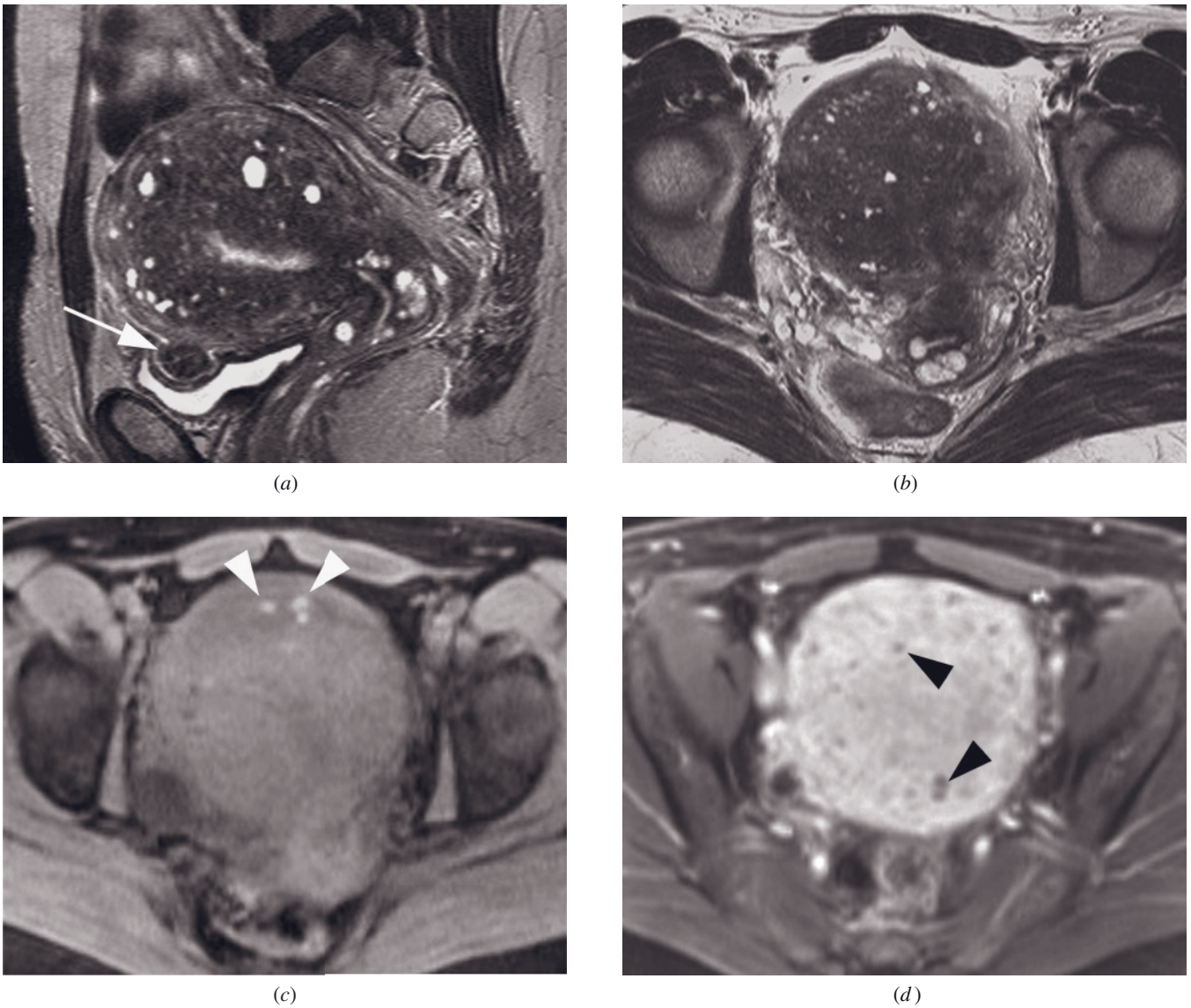

FIG. 14.38 Diffuse adenomyosis: findings on T2- and T1-weighted images. Sagittal (*a*) and transverse (*b*) T2-weighted ETSE, transverse fat-suppressed T1-weighted gradient-echo (*c*), and transverse gadolinium-enhanced fat-suppressed T1-weighted gradient-echo (*d*) images show diffuse thickening of the junctional zone with numerous foci of hyperintense signal on T2-weighted images (*a*, *b*) and several foci of hyperintense signal on T1-weighted images (arrowheads, *c*). Enhancement of adenomyosis is variable; however, nonenhancing foci (arrowheads, *d*) may be seen.Also note the small subserosal leiomyoma (arrow, *a*).

very high signal intensity on T2-weighted images. However, deep nabothian cysts and other benign cervical glandular conditions may have imaging and histologic findings that mimic malignancy. One of these benign conditions called tunnel cluster involves multicystic dilatation of endocervical glands (fig. 14.19) and may on occasion appear similar to adenoma malignum (minimal deviation adenocarcinoma). A solid component within or around multiple cysts should raise suspicion for malignancy. Endocervical polyps are also benign cervical masses, and they are a common cause of abnormal bleeding. MR may show a cystic or solid polypoid mass in the endocervical canal or vagina [68, 69].

MALIGNANT DISEASE OF THE UTERINE CORPUS AND CERVIX

Endometrial Carcinoma

Endometrial carcinoma is the most common malignancy of the female genital tract, primarily occurring in postmenopausal women. Postmenopausal bleeding often

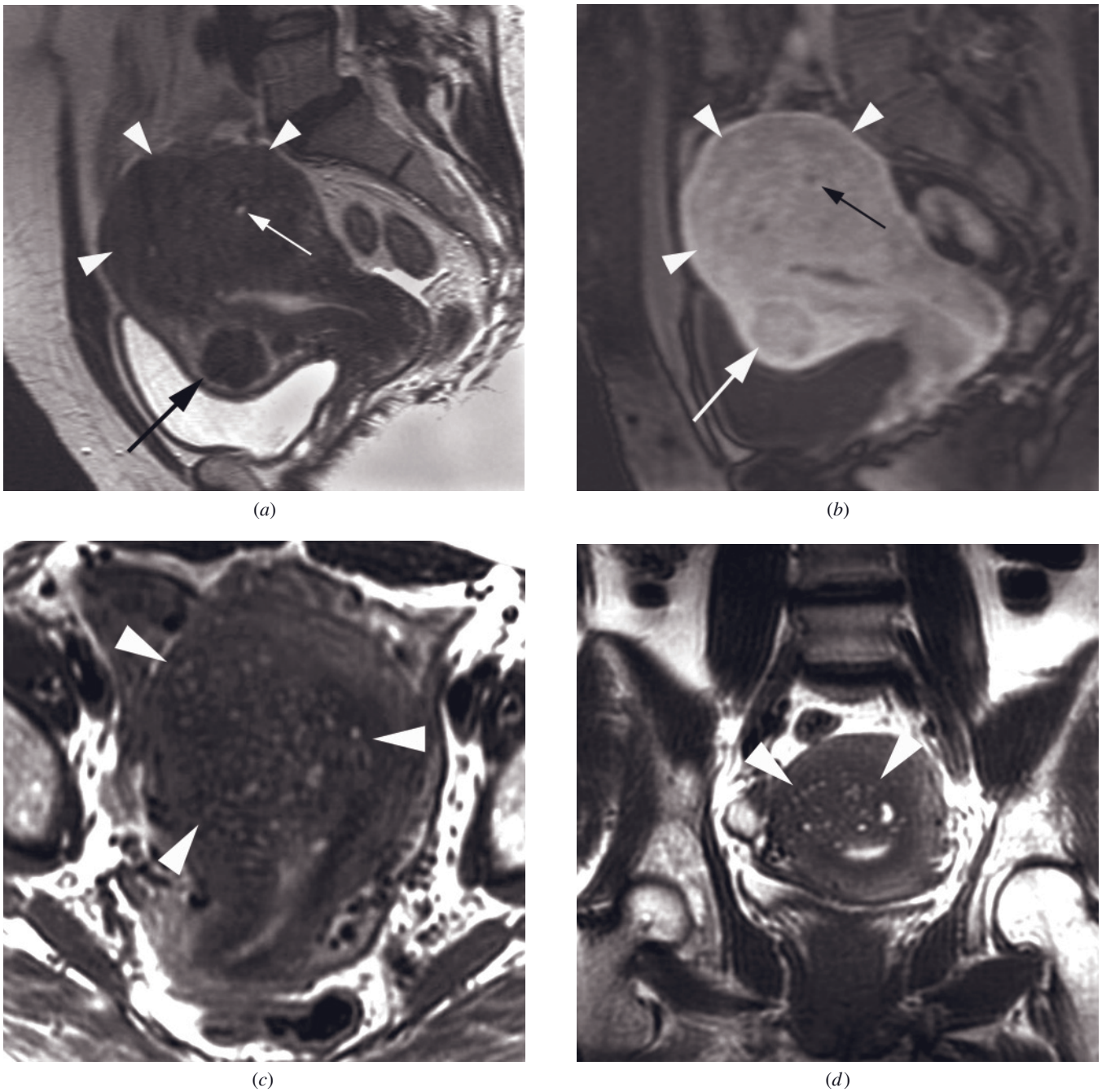

FIG. 14.39 Focal adenomyosis and leiomyoma. Sagittal T2-weighted ETSE (*a*) and fat-suppressed T1-weighted gradient-echo (*b*) images show a hypointense masslike region in the uterine fundus (arrowheads) that is continuous with the junctional zone. The mass contains punctate foci that are hyperintense on T2-weighted images (white arrow,*a*) and hypointense on gadolinium-enhanced images (black arrow, *b*). Also note that the mass effect on the endometrium is minimal given the size of the lesion, even less than that of the smaller leiomyoma (black arrow, *a*; white arrow, *b*). Adenomyomas are generally oblong rather than round and do not have the hyperintense rim on T2-weighted images that is often seen in leiomyomas (black arrow, *a*). **Focal adenomyosis at 3T.** Transverse (*c*) and coronal (*d*) T2-weighted ETSE images in another patient show a hypointense masslike region in the posterior uterine wall (arrowheads) that is continuous with the junctional zone and contains punctate hyperintense foci characteristic of adenomyosis.

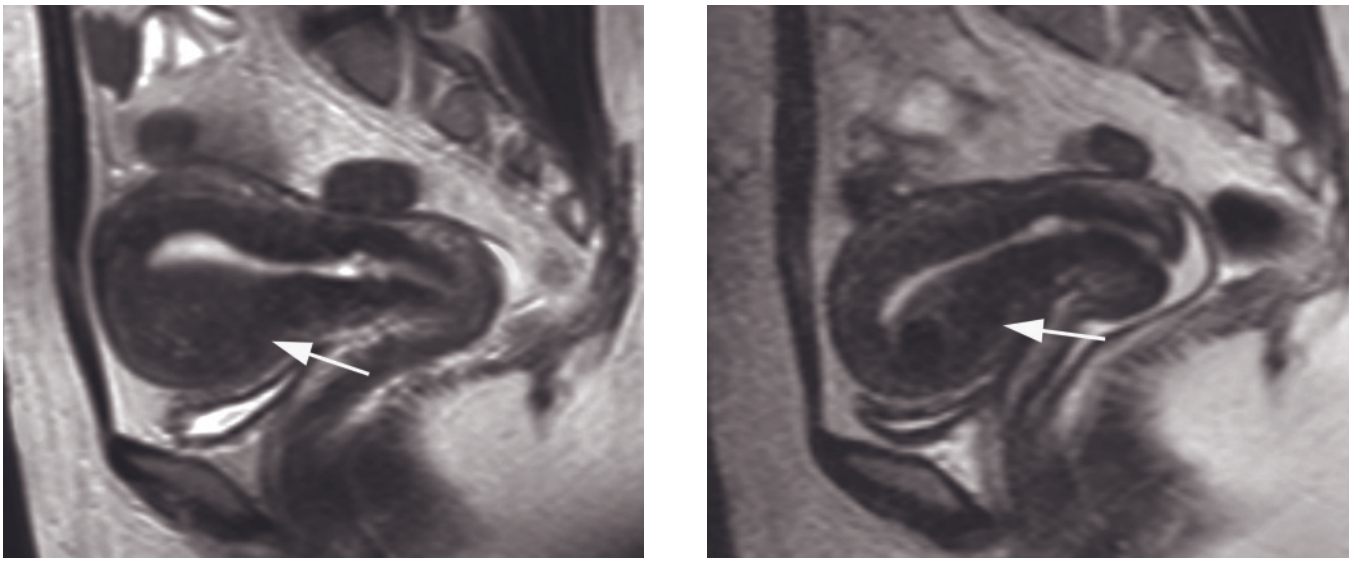

(*a*) (*b*)

FIG. 14.40 Adenomyosis before and after uterine artery embolization. Sagittal T2-weighted ETSE images before (*a*) and 9 months after (*b*) uterine artery embolization (UAE) show an adenomyoma (arrow, *a*) that decreases in size after UAE (arrow, *b*). There are reports of successful treatment of adenomyosis with UAE, although consistent long-term efficacy has not been established. (Courtesy of Claude Sirlin, M.D., University of California, San Diego).

occurs early in the disease. Most patients present with stage I disease, which carries a good prognosis. Adenocarcinomas account for 80–90% of all endometrial carcinomas. The remainder consists of adenosquamous, papillary serous, and clear cell carcinomas. Papillary and clear cell subtypes tend to be more aggressive tumors and carry a worse prognosis; however, imaging cannot predict cell type. The FIGO classification is used for tumor staging (Table 14.1) [70]. In general, endometrial carcinoma invades the myometrium but rarely extends through the serosa into the abdominal cavity. The cervix is involved at time of diagnosis in approximately 10% of cases. Lymphatic and hematogenous spread occurs later in endometrial carcinoma than in cervical carcinoma, and there is a strong correlation between the depth of myometrial invasion and the presence of positive lymph nodes. Superficial myometrial invasion (FIGO stage Ib) is associated with lymph node metastases in 3% of cases, while deep myometrial invasion (FIGO stage Ic) is associated with lymph node metastases in 40% of patients. The extent of myometrial invasion is considered the factor most responsible for the extreme variation in the 5-year survival of patients with stage I disease: from 49–60% in the most invasive cases to 90–100% in cases with little or no myometrial involvement. Histologic grade (1–3) of the tumor is another important prognostic factor. Adenocarcinomas and adenosquamous carcinomas are graded based on histologic differentiation, while clear cell and papillary serous carcinomas, characterized by particularly aggressive behavior, are considered high grade by definition [71]. Prognosis depends on histological grade, extension into the cervical stroma, and depth of myometrial invasion, which independently predicts lymph node involvement, recurrence, and 5-year survival.

Para-aortic lymphadenopathy may occur without involvement of pelvic lymph nodes if the tumor spreads via lymphatics accompanying the ovarian vessels. Hematogenous metastases occur in patients with disseminated disease and most frequently involve the lungs [48, 72]. Peritoneal spread may also occur and is most associated with papillary and clear cell subtypes.

Role of MRI

MRI is the imaging modality of choice for preoperative staging of endometrial carcinoma proven by fractional abrasion. The presence of deep myometrial invasion correlates well with lymph node invasion [73] and is well evaluated with MRI [74]. The likelihood of myometrial invasion increases with histologic tumor grade, which is used to select patients for lymphadenectomy and possible specialist referral. MRI used for preoperative assessment of the myometrium has been shown to improve patient selection for lymphadenectomy for all grades of tumor [75]. In addition, MRI is helpful for patients with an established or suspected diagnosis of endometrial cancer in cases of technically limited ultrasound, difficult biopsy, clinically advanced disease, aggressive histologic subtypes, or adenocarcinoma on cervical biopsy that may be either endometrial or cervi-

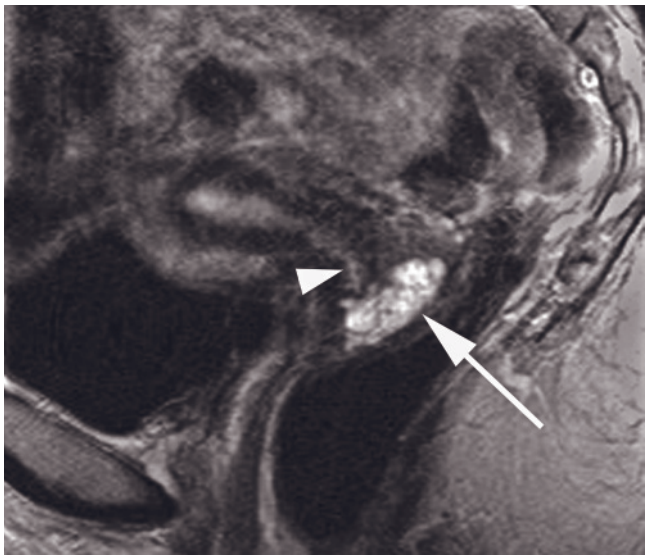

(*a*)

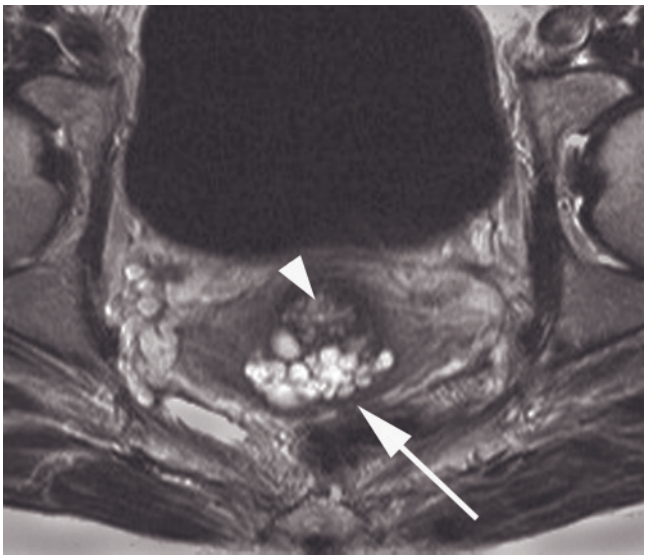

(*b*)

(*c*)

FIG. 14.41 Nabothian cysts in two patients. Sagittal (*a*) and transverse (*b*) T2-weighted ETSE images show hyperintense round lesions consistent with nabothian cysts (arrow, *a*, *b*). In this patient, the cysts are small and clustered posterior to the endocervical canal (arrowhead, *a*, *b*). Sagittal T2-weighted ETSE image in a second patient (*c*) shows several 1-cm well-defined hyperintense nabothian cysts in the cervix (arrows, *c*). The uterus is retroverted.

cal in origin. MRI also detects cervical stromal involvement, which is another important prognostic indicator. For patients with adenocarcinoma diagnosed by cervical biopsy, MRI helps differentiate between tumors of endometrial and cervical origin.

MRI Appearance

T2-weighted sequences depict the uterine zonal anatomy and are used to identify and stage endometrial carcinoma. In addition to standard sagittal and axial imaging planes, short-axis views of the uterine corpus are helpful for assessing myometrial invasion. Signal intensities of small endometrial tumors are similar to that of normal endometrium on T2-weighted sequences, limiting the ability of tumor delineation, while larger tumors result in the widening of the endometrial cavity. A disruption of the junctional zone by the hyperintense tumor is indicative of myometrial invasion. A problem, however, is that the junctional zone is not always visualized in postmenopausal women, making correct imaging interpretation difficult in these cases. Deep myometrial invasion is suggested by the presence of hyperintense tumor in the outer half of the myometrium. Intravenous administration of gadolinium agents is helpful for MR staging

Table 14.1 Revised FIGO Staging of Endometrial Carcinoma with Corresponding MRI Findings

Revised FIGO Staging[1]		
Stage 0		Carcinoma in situ
Stage I		Tumor confined to corpus
	IA	Tumor limited to endometrium
	IB	Invasion <50% of myometrium
	IC	Invasion >50% of myometrium
Stage II		Tumor invades cervix but does not extend beyond uterus
	IIA	Invasion of endocervix
	IIB	Cervical stromal invasion
Stage III		Tumor extends beyond uterus but not outside true pelvis
	IIIA	Invasion of serosa, adnexa, or positive peritoneal cytology
	IIIB	Invasion of vagina
	IIIC	Pelvic and/or para-aortic lymphadenopathy
Stage IV		Tumor extends outside of true pelvis of invades bladder or rectal mucosa
	IVA	Invasion of bladder or rectal mcosa
	IVB	Distant metastases (includes intraabdominal or inguinal lymphadenopathy)
Corresponding MR Findings[2]		
Stage 0		Normal or thickened endometrial stripe
Stage I	IA	Thickened endometrial stripe with diffuse or focal abnormal signal intensity. Endometrial stripe may be normal.
		Intact junctional zone with smooth endometrial-myometrial interface[3]
	IB	Signal intensity of tumor extends into myometrium <50%
		Partial or full-thickness disruption of junctional zone with irregular endometrial-myometrial interface
	IC	Signal intensity of tumor extends into myometrium >50%
		Full-thickness disruption of junctional zone[3]
		Intact stripe of normal outer myometrium
Stage II	IIA	Internal os and endocervical canal are widened
		Low signal intensity of fibrous stroma remains intact
	IIB	Disruption of fibrous stroma
Stage III	IIIA	Disruption of continuity of outer myometrium
		Irregular uterine configuration
	IIIB	Segmental loss of hypointense vaginal wall
	IIIC	Regional lymph nodes >1.0 cm in diameter
Stage IV	IVA	Tumor signal disrupts normal tissue planes with loss of low signal intensity of bladder or rectal wall
	IVB	Tumor masses in distant organs or anatomic sites

[1]All stages are further subdivided into three tumor grades (not shown).
[2]MRI findings seen on T2-weighted or contrast-enhanced T1-weighted images.
[3]For patients with adenomyosis, criteria may not apply.

of endometrial carcinoma, with the cancer demonstrating less pronounced contrast-enhancement compared to the surrounding tissues. Most studies report that contrast-enhanced sequences further improve assessment of myometrial invasion, the differentiation of vital tumor from necrosis or fluid-accumulation, as well as the differentiation of tumor from debris or hematometra [48, 75, 76]. Leiomyomas and adenomyosis may also enhance less than normal myometrium, and correlation should be made between contrast-enhanced T1-weighted images and T2-weighted images. These benign myometrial conditions are pitfalls that lead to less accurate staging both by MR imaging and by pathological assessment [31].

The MR appearance of noninvasive endometrial carcinoma (FIGO stage IA) is nonspecific. The uterus may appear entirely normal, or the endometrial carcinoma may present as a widening of the endometrial stripe in postmenopausal women. In some cases, a heterogeneous mass with areas of high and low signal intensity distending the endometrial cavity may be noted. Since these changes are also seen in endometrial hyperplasia, endometrial polyps, or coagulated blood, MRI has no role as a screening modality and histologic sampling is required to establish the diagnosis. After gadolinium administration, endometrial carcinoma typically enhances to a lesser extent than the adjacent myometrium. In patients with FIGO stage IA disease, the junctional zone will remain intact (fig. 14.42), while in patients with myometrial invasion (stages FIGO Ib and Ic) segmental or complete disruption of the junctional zone by the tumor may be seen on T2-weighted sequences (Table 14.1; figs. 14.43 and 14.44). The accuracy of MRI in differentiating noninvasive from invasive endometrial carcinoma has been reported to range from 69% to 88% [76, 77]. Gadolinium-enhanced images improve accuracy, especially in postmenopausal women, in whom the junctional zone is often indistinct. Stage IA disease may involve the ectopic endometrial glands of adenomyosis without true myometrial invasion (fig. 14.45). Histologically, endometrial carcinoma involving adenomyosis is not considered invasive if endometrial stroma is seen between tumor cells and myometrium [66].

Tumor extension to the cervix indicates at least stage II disease (fig. 14.46). Superficial extension of endometrial carcinoma to the cervical mucosa (FIGO stage IIA) is best seen on sagittal T2-weighted images by direct tumor visualization and widening of the endocervical canal. Invasion of the cervical fibrous stroma (FIGO stage IIB) is diagnosed when hypointense cervical stroma is disrupted by the hyperintense tumor mass. An angled short-axis view of the cervix is helpful to evaluate the fibrous stroma. The ovaries may be involved by contiguous spread or metastases. Secondary

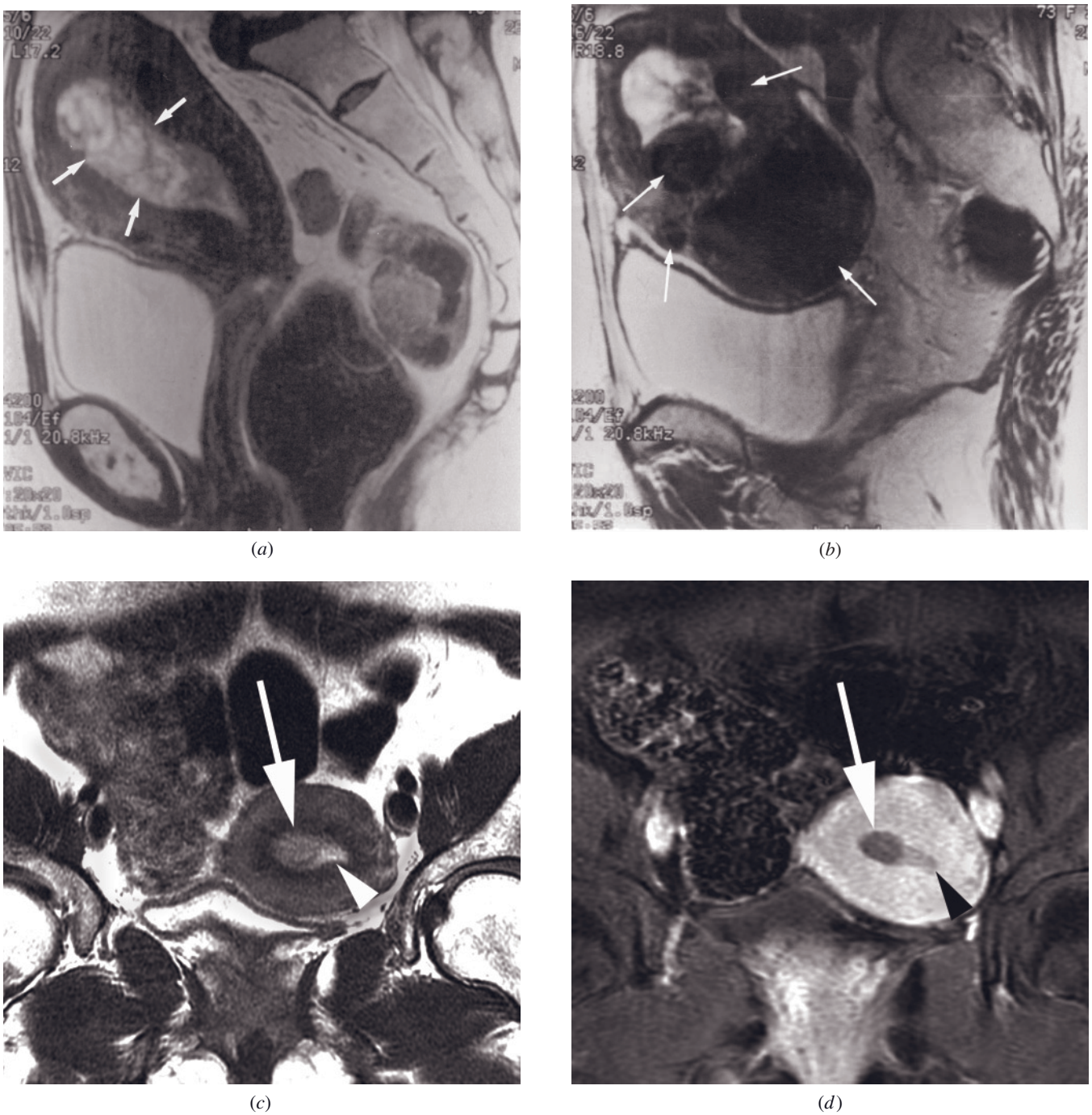

(*a*) (*b*) (*c*) (*d*)

FIG. 14.42 Endometrial carcinoma stage IA, multiple leiomyomas. Sagittal T2-weighted ETSE images (*a*, *b*) in a patient referred to MRI for staging of endometrial carcinoma proven by D&C. Clinically advanced tumor stage was suspected. MRI shows widening of the endometrial cavity due to heterogeneously hyperintense tumor. The junctional zone (arrows,*a*),however,was intact and thus stage IA was diagnosed. The large uterus found at clinical examination and prompting the suspicion of advanced tumor stage could be explained by multiple sharply delineated, hypointense leiomyomas (arrows, *b*.). **Endometrial carcinoma stage IA at 3T.** T2-weighted ETSE (*c*) and gadolinium-enhanced fat-suppressed T1-weighted gradient-echo (*d*) images in an oblique plane axial to the uterine body in a different patient show asymmetric widening of the endometrial cavity on the right that is darker than normal endometrium on T2-weighted images and enhances less than normal endometrium on the delayed postgadolinium images (arrows, *c*, *d*). The junctional zone appears intact. Normal appearance of the adjacent endometrium is also seen (arrowheads, *c*, *d*).

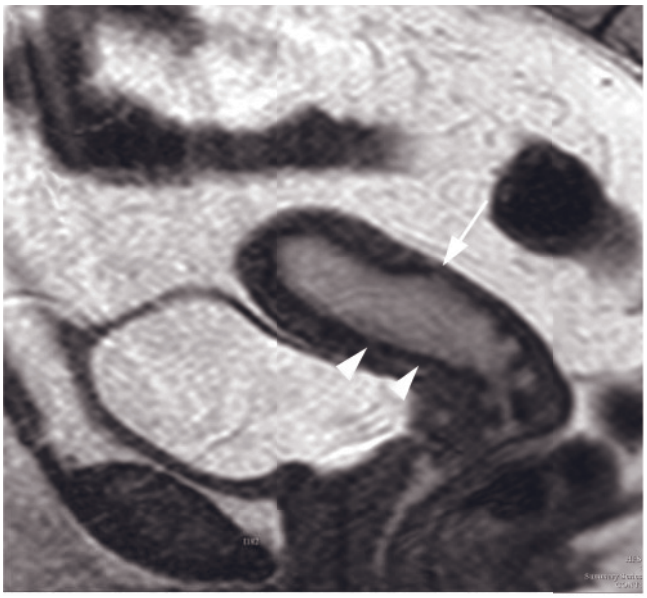

(*a*)

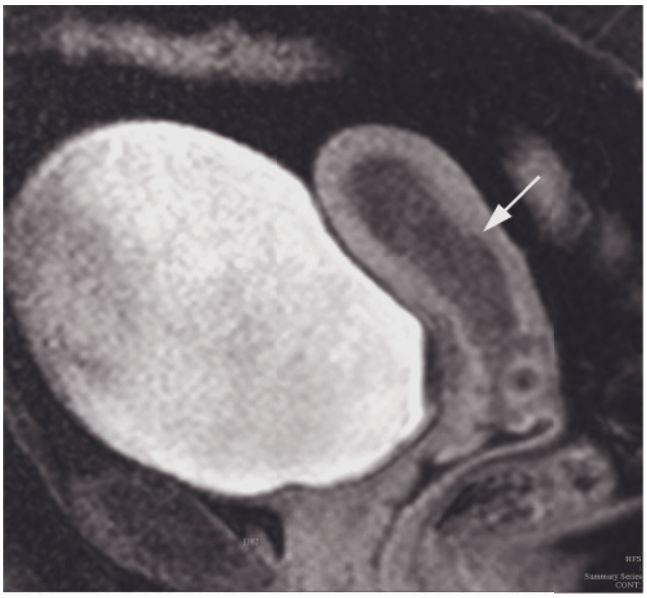

(*b*)

FIG. 14.43 Endometrial carcinoma stage IB. Sagittal T2-weighted ETSE (*a*) and gadolinium-enhanced fat-suppressed T1-weighted gradient-echo (*b*) images show endometrial thickening and focal disruption of the inner myometrium posteriorly (arrow). The junctional zone is intact anteriorly (arrowheads, *a*). Gadolinium-enhanced images are particularly helpful if the junctional zone is indistinct, as it may be in postmenopausal women.

involvement of the ovaries is suggested whenever a mass with indeterminate signal characteristics is noted within the ovary (figs. 14.46 and 14.47). Stage FIGO III and stage FIGO IV are characterized by tumor extension beyond the uterus (figs. 14.46–14.50). Stage IIIA may appear as full-thickness myometrial invasion with uterine contour changes or a suspicious ovarian mass. The ovaries may be involved either by contiguous spread or metastases and should be suspected if any indeterminate lesion is noted within the ovary. Invasion of the vagina indicates stage IIIB disease, and enlarged pelvic or paraaortic lymph nodes suggest stage IIIC disease. Stage IV disease is present if the tumor spreads to the bladder or rectal mucosa, or if there are distant metastases including involvement of abdominal or inguinal lymph nodes. Ascites may also be present in advanced disease.

Lymph nodes are well seen on T1-weighted images because of the good soft tissue contrast between low- to moderate-signal-intensity nodes and the high-signal-intensity surrounding fat. Assessment of metastatic lymphadenopathy in patients with endometrial and cervical carcinoma on MRI is based on the size of lymph nodes; however, size is not specific for metastatic involvement. Nodes with a size exceeding 1.0 cm short-axis diameter are considered pathologic [77]. The administration of lymph node-specific contrast agents (ultrasmall superparamagnetic iron oxide, USPIO) may potentially improve MR accuracy in lymph node staging [78].

FIG. 14.44 Endometrial carcinoma stage IC. Sagittal T2-weighted ETSE image shows endometrial carcinoma, which is isointense relative to endometrium, resulting in asymmetric widening of the endometrial.The junctional zone (arrows) can be delineated anteriorly, and the tumor invades the inner myometrium along the posterior aspect.

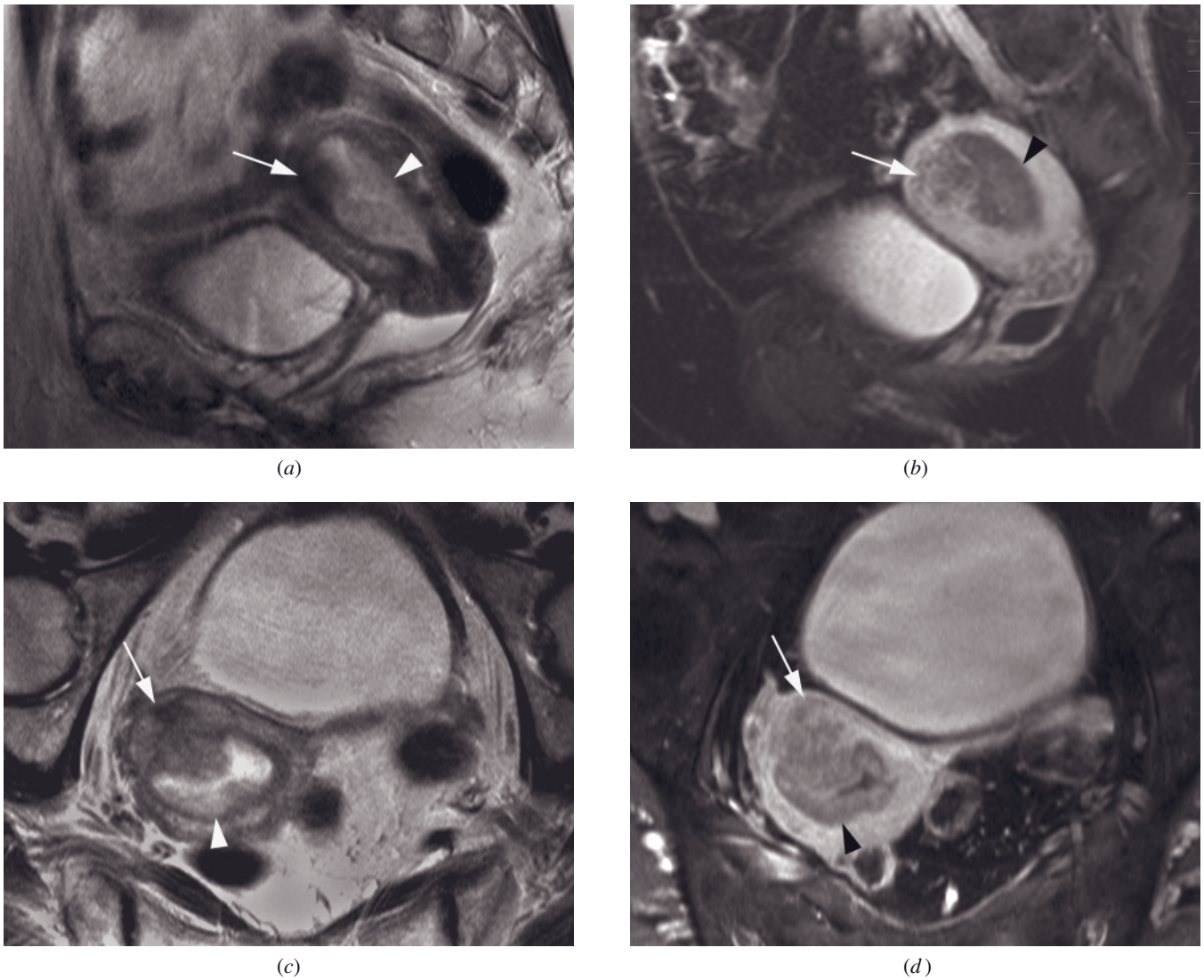

FIG. 14.45 Endometrial carcinoma stage IA with involvement of adenomyosis. Sagittal T2-weighted ETSE (*a*) and gadolinium-enhanced fat-suppressed T1-weighted gradient-echo (*b*) and short-axis uterus view T2-weighted ETSE (*c*) and gadoliniumenhanced fat-suppressed T1-weighted gradient-echo (*c*) images show endometrial carcinoma expanding the endometrial canal (arrowhead). The junctional zone is largely intact; however, a focal masslike region is seen in the anterior fundus (arrow) that is hypointense on T2-weighted images (*a*, *c*) and enhances less than adjacent myometrium on postgadolinium images (*b*, *d*). Pathological evaluation revealed stage IA disease within the endometrial canal and within adenomyosis with no evidence of myometrial invasion.

Uterine Sarcoma

Uterine sarcomas are rare, constituting only 2–3% of all uterine malignancies. They encompass four histologic subtypes: carcinosarcomas, also called malignant mixed müllerian tumors (MMMT), leiomyosarcomas, endometrial stromal sarcomas, and adenosarcomas. MMMT, containing both carcinomatous and sarcomatous features, is the most common subtype and is associated with prior radiation therapy in one-third of cases (figs. 14.51 and 14.52). Leiomyosarcoma, the second most common subtype, was discussed previously and may occur from malignant degeneration of a benign leiomyoma or arise de novo (figs. 14.34 and 14.35). Endometrial stromal sarcoma is the third most common subtype (figs. 14.53 and 14.54).

No specific staging system exists for uterine sarcomas. Uterine sarcomas invade blood vessels, lymphatics, and contiguous pelvic structures once they have extended beyond the uterus. The lung is the most common site of distant metastases. MRI signal characteristics are not reliable in differentiating between the various sarcomas, and it is often difficult to distinguish uterine sarcoma from endometrial adenocarcinoma. MR features that favor sarcoma over endometrial carcinoma include large size, heterogeneous signal with

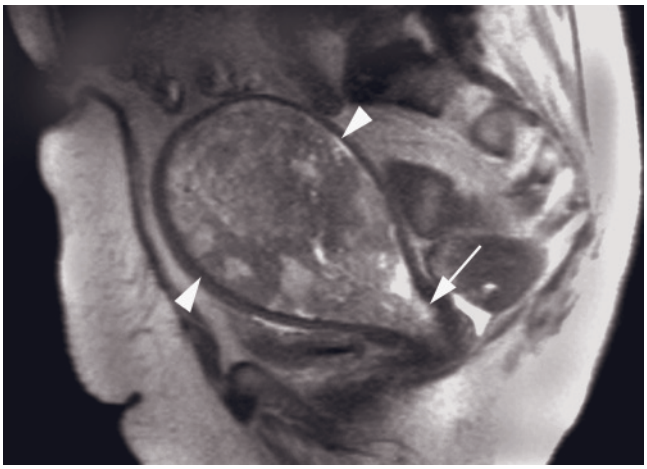

(*a*)

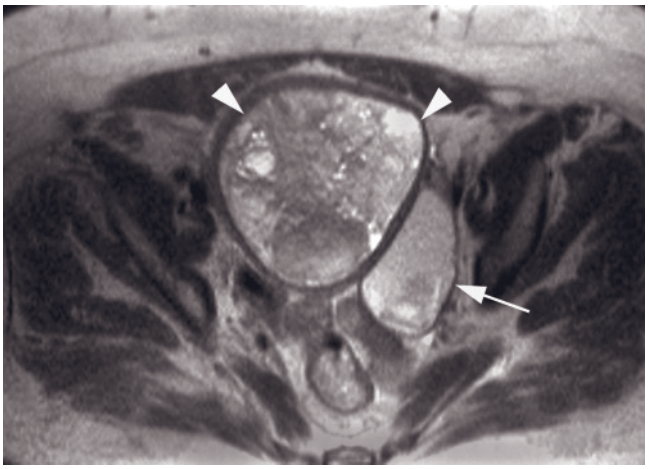

(*b*)

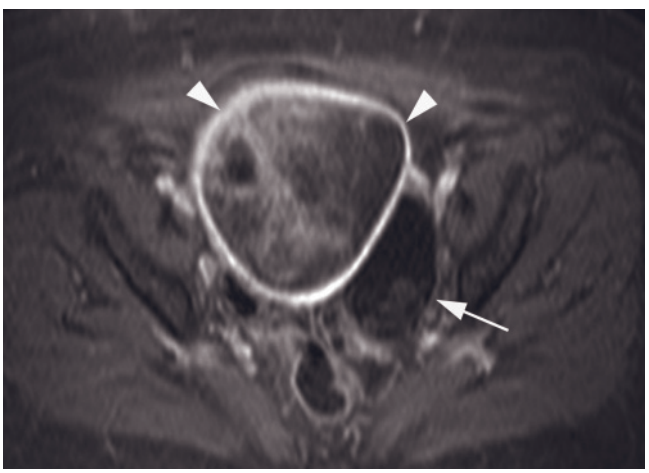

(*c*)

FIG. 14.46 Endometrial carcinoma with ovarian metastasis in a patient taking tamoxifen. Sagittal (*a*) and transverse (*b*) T2-weighted ETSE and transverse gadolinium-enhanced fat-suppressed T1-weighted gradient-echo (*c*) images show a large mass expanding the endometrial canal (arrowheads) and a left ovarian mass (arrow, *b*, *c*). Also note widening of the cervical canal indicating extension of tumor into the cervix (arrow, *a*). Tamoxifen is associated with increased risk of endometrial carcinoma.

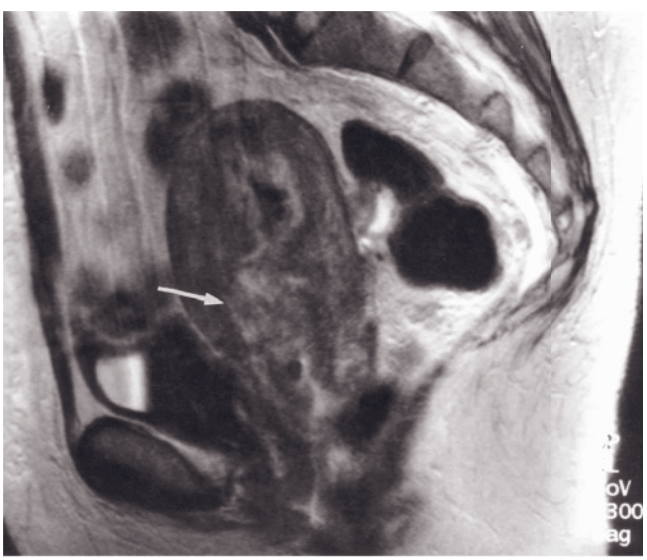

(*a*)

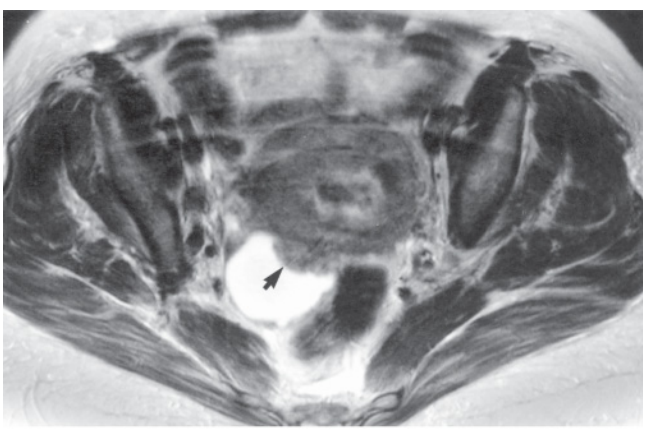

(*b*)

FIG. 14.47 Endometrial carcinoma with right adnexal metastasis. Sagittal (*a*) and transverse (*b*) T2-weighted ETSE and transverse gadolinium-enhanced fat-suppressed T1-weighted gradient-echo (*c*) images. There is a heterogeneous endometrial mass that invades the myometrium (arrow, *a*). A cystic right adnexal mass with an anterior solid nodule (arrows,*b*,*c*) is seen, consistent

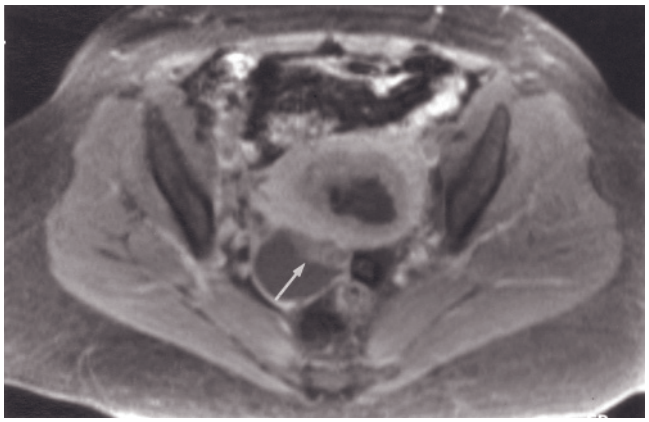

(*c*)

FIG. 14.47 (*Continued*) with metastatic disease. Gadolinium enhancement allows distinction between enhancing endometrial cancer and nonenhnacing fluid in the endometrial canal.

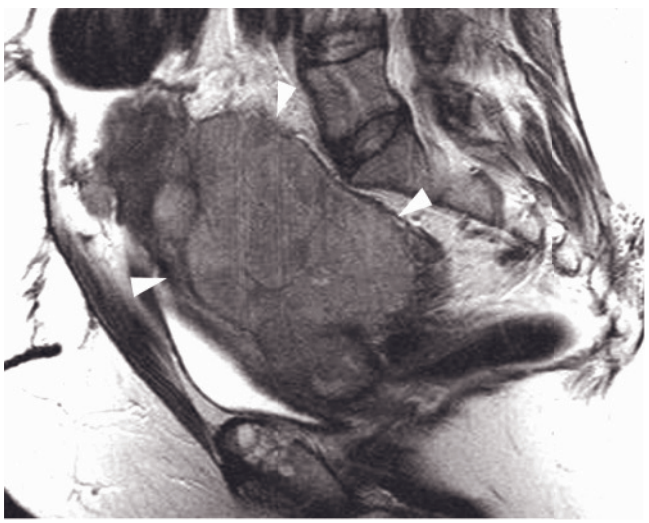

(*a*)

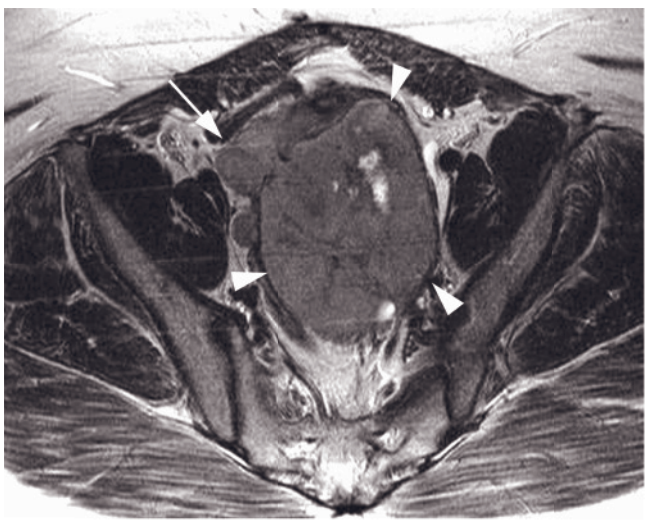

(*b*)

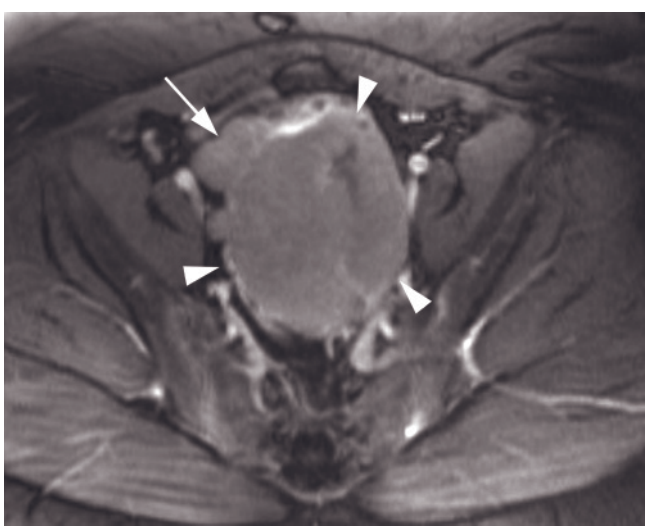

(*c*)

FIG. 14.48 Papillary serous carcinoma with parametrial extension. Sagittal (*a*) and transverse (*b*) T2-weighted ETSE and transverse gadolinium-enhanced fat-suppressed T1-weighted gradient-echo (*c*) images show a large tumor (arrowheads) that replaces the uterus and extends beyond the uterine serosa (arrow, *b*, *c*). Papillary serous and clear cell endometrial carcinomas tend to be more aggressive than adenocarcinoma.

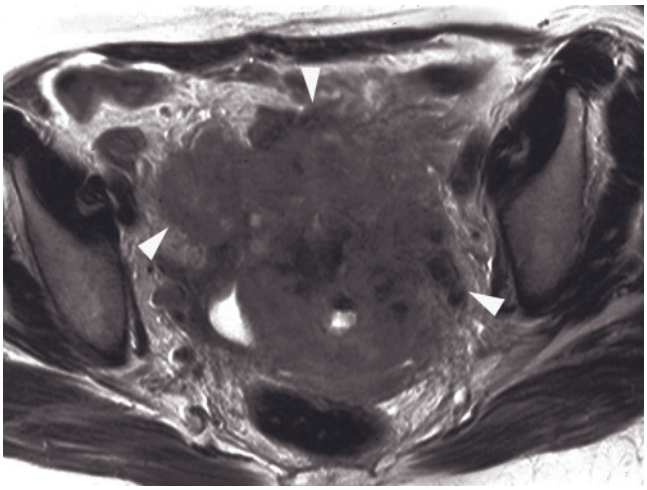

(*a*)

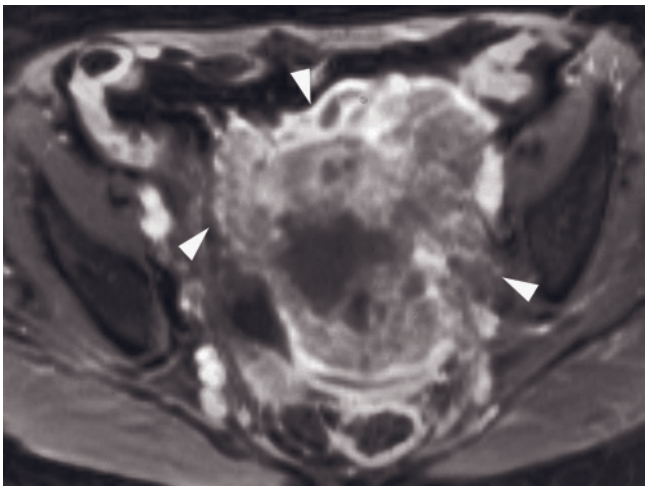

(*b*)

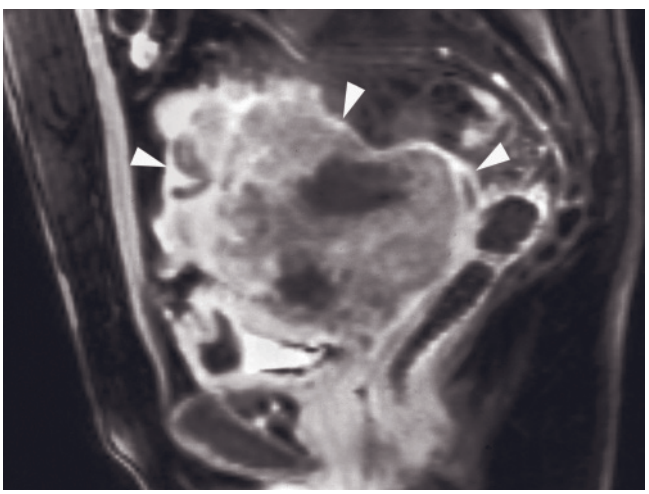

(*c*)

FIG. 14.49 Poorly-differentiated endometrioid adenocarcinoma. Transverse T2-weighted ETSE (*a*) and transverse (*b*) and sagittal (*c*) gadolinium-enhanced fat-suppressed T1-weighted gradient-echo images show a large heterogeneous mass (arrowheads) with extrauterine extension.

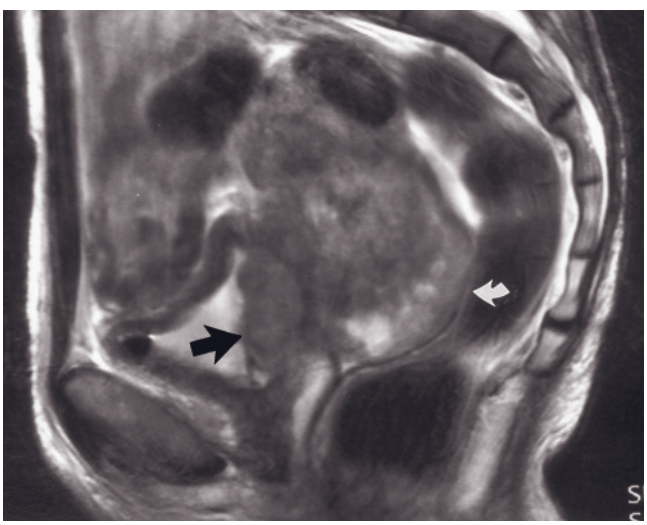

(*a*)

(*b*)

FIG. 14.50 Endometrial carcinoma, extensive disease. Sagittal (*a*, *b*) and transverse (*c*) T2-weighted ETSE and gadolinium-enhanced fat-suppressed SGE (*d*) images show a large necrotic endometrial mass with invasion of the posterior wall of the urinary bladder (arrows, *a*–*c*) as well as extension to the left pelvic sidewall (arrow, *d*). This mass extends to the sigmoid colon and rectum (curved arrow, *a*). Liver metastases (not shown) were also identified.

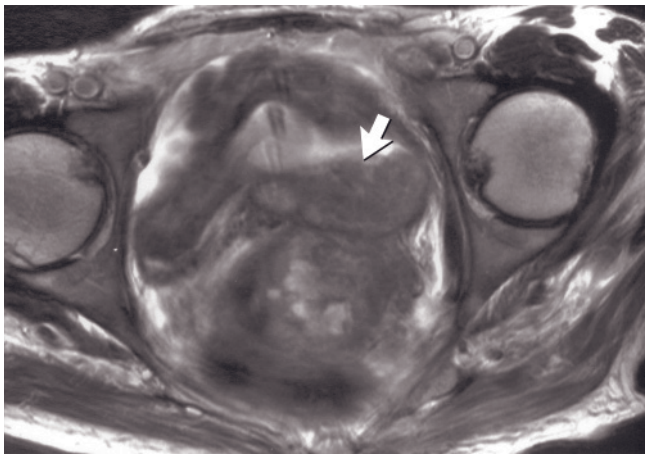

(*c*)

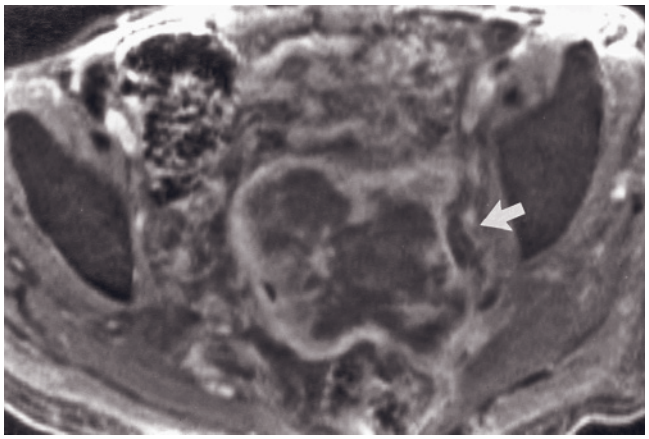

(*d*)

FIG. 14.50 (*Continued*)

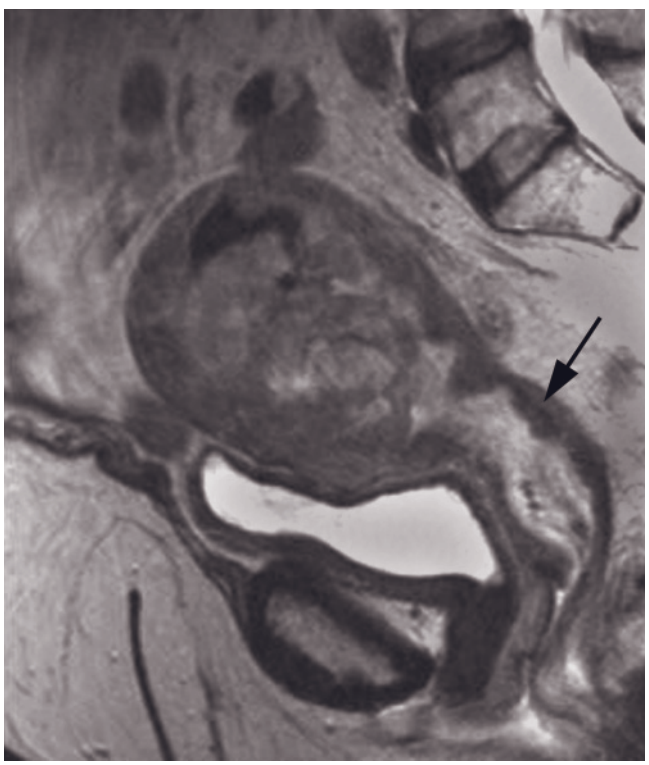

(*a*)

(*b*)

FIG. 14.51 Uterine carcinosarcoma. Sagittal (*a*) and coronal (*b*) T2-weighted ETSE images in a patient with prior pelvic radiation therapy show a large, heterogeneous uterine tumor extending into the cervix (arrow, *a*). There is also evidence of bladder wall invasion (arrow, *b*). **Uterine carcinosarcoma.** Sagittal T2-weighted SS-ETSE (*c*), transverse T2-weighted ETSE (*d*), and

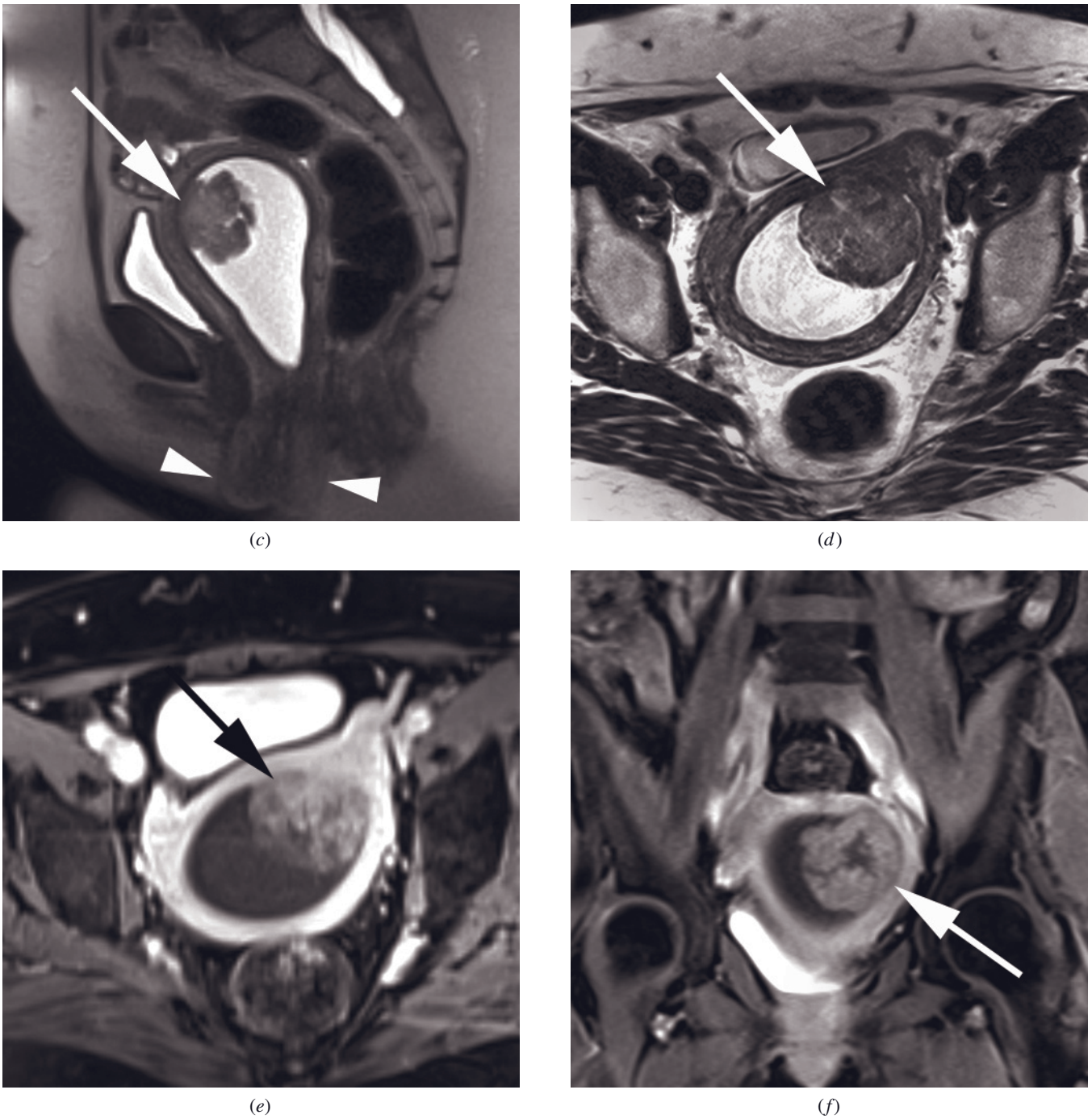

FIG. 14.51 (*Continued*) transverse (*e*) and coronal (*f*) gadolinium-enhanced fat-suppressed T1-weighted gradient-echo images in a different patient show a heterogeneous uterine tumor (arrows, *c–f*) without evidence of deep myometrial invasion. Also note significant uterine prolapse, with the cervix located at the introitus (arrowheads, *c*).

hemorrhage and necrosis, areas of marked delayed enhancement, and invasive or metastatic disease at the time of diagnoses [79]. MR cannot reliably differentiate leiomyosarcomas from benign leiomyomas or those pathologically characterized as smooth muscle tumors of uncertain malignant potential [80]. Features that raise concern are large tumor size in an older patient, rapid growth, and ill-defined margins [81, 82]. Other features of leiomyosarcomas include high signal on T2-weighted images in more than 50% of the tumor, high-signal foci on T1-weighted images, and nonenhanced areas [80].

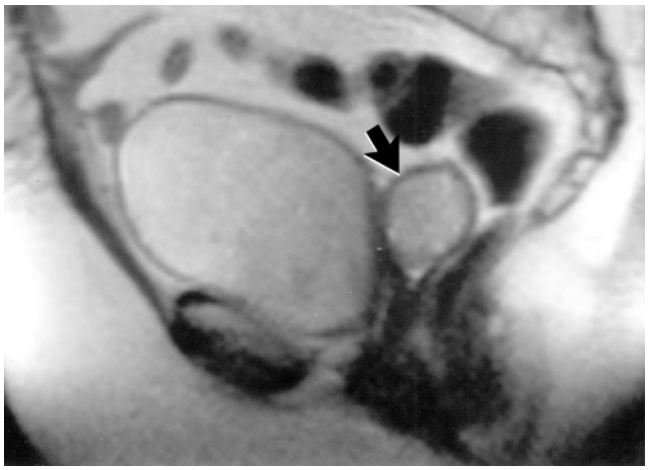

FIG. 14.52 Recurrent uterine carcinosarcoma. Sagittal T2-weighted ETSE image demonstrates a soft tissue mass (arrow) at the superior aspect of the vaginal cuff.

FIG. 14.53 Endometrial sarcoma. Sagittal T2-weighted ETSE image shows a large, heterogeneous uterine mass with indistinct borders.

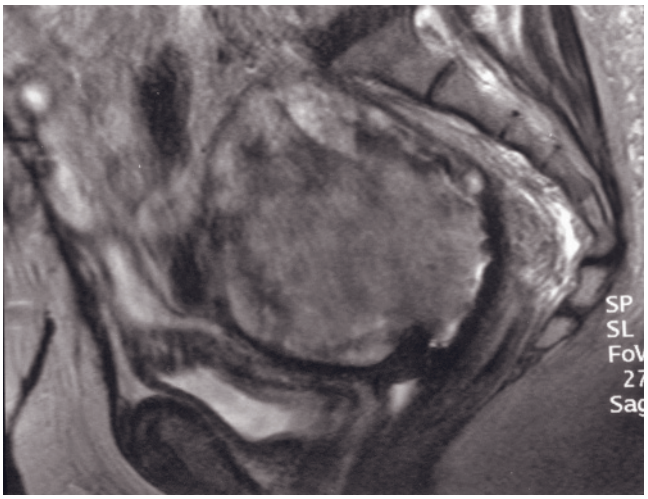

(*a*)

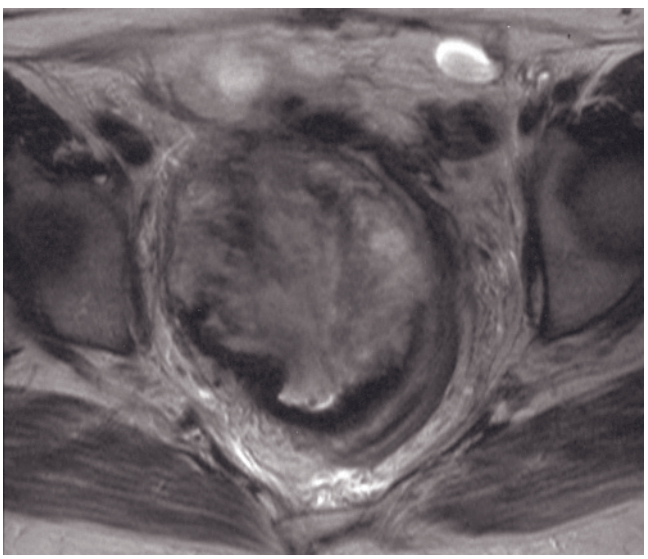

(*b*)

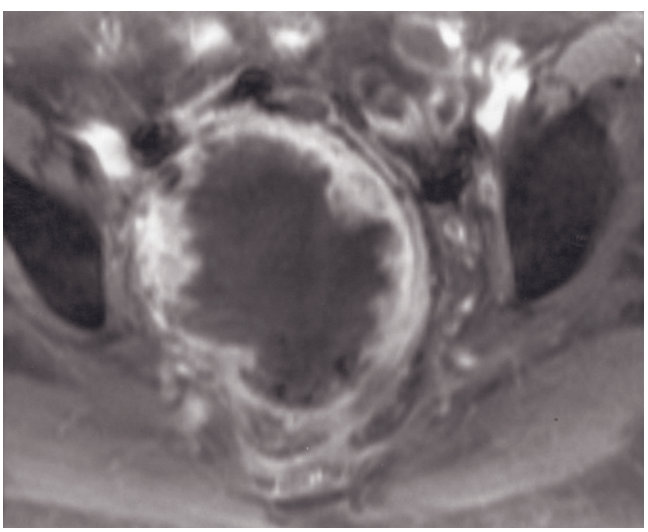

(*c*)

FIG. 14.54 Endometrial sarcoma. Sagittal (*a*) and transverse (*b*) T2-weighted ETSE and gadolinium-enhanced fatsuppressed T1-weighted (*c*) images demonstrate a large, heterogeneous uterine mass with indistinct borders, central necrosis, and peripheral enhancement.

Uterine Metastases

Metastatic disease involving the uterus is uncommon. Involvement of the uterus by nonuterine primary cancer usually occurs by direct extension. Rarely hematogenous or lymphatic spread involves the uterus. The diagnosis of uterine metastasis is considered in patients with known metastatic disease and diffuse uterine enlargement [83].

Cervical Carcinoma

Invasive cervical carcinoma is the third most common malignancy of the female genital tract and is typically seen in younger women. The average age at diagnosis is 45 years. Early cytological detection of cervical intraepithelial neoplasia (CIN), a precursor lesion of cervical carcinoma, with routine cervical Papanicolaou (Pap) smears has led to a significant reduction in mortality. Approximately 80% of new cases occur in developing countries. Vaccines against oncogenic human papillomaviruses may reduce incidence further and could potentially lead to a significant decrease in cervical cancer deaths throughout the world [84]. The Pap smear is most sensitive for squamous cell carcinomas, and where screening programs exist there has been a relative increase in adenocarcinomas, which carry an overall poorer prognosis.

When symptomatic, abnormal bleeding is the most common symptom. Currently approximately 85% of all cervical carcinomas are squamous cell carcinomas. The remaining 15% are adenocarcinomas, adenosquamous carcinomas, undifferentiated carcinomas, and sarcomas. Indicators of a poor prognosis include tumor cell type, young age, advanced stage at presentation, lymphadenopathy, tumor diameter larger than 4 cm, depth of stromal invasion greater than 5 mm, and lymphovascular invasion.

Cervical carcinoma spreads by direct extension and lymphatics. Because of the upward migration of the squamocolumnar junction with age, exophytic growth is typical in younger patients, while endophytic growth is typical in older patients. The external iliac chain is the most common site of lymph node involvement, followed by obturator, common iliac, and internal iliac chains. Para-aortic lymph nodes are involved in approximately 45% of cases with tumor extension to the pelvic sidewall or lower vagina. As tumor extends to the lower vagina, inguinal lymph nodes may become involved. Hematogenous spread is rare and occurs only in the presence of advanced disease. The liver and lung are the most common sites of hematogenous metastases.

Cervical carcinoma is staged clinically according to the FIGO staging system (Table 14.2) [70]. Correct preoperative assessment of tumor stage influences prognosis and choice of treatment. Patients with FIGO stage Ia are usually treated with simple hysterectomy or fertility-preserving surgery such as trachelectomy [85], whereas patients with invasive carcinoma (FIGO stage

Table 14.2 FIGO Staging of Cervical Carcinoma with Corresponding MRI Findings

FIGO Staging[1]		
Stage 0		Carcinoma in situ
Stage I		Tumor confined to cervix (extension to corpus should be disregarded)
	IA	Microinvasion
	IB	Clinically invasive. Invasive component >5 mm in depth and >7 mm in horizontal spread
Stage II		Tumor extends beyond cervix but not to pelvic side wall or lower third of vagina
	IIA	Vaginal invasion (no parametrial invasion)
	IIB	Parametrial invasion
Stage III		Tumor extends to lower third of vagina or pelvic sidewall; ureter obstruction
	IIIA	Invasion of lower third of vagina (no pelvic sidewall extension)
	IIIB	Pelvic sidewall extension or ureteral obstruction
Stage IV		Tumor extends outside true pelvis of invades bladder or rectal mucosa
	IVA	Invasion of bladder or rectal mucosa
	IVB	Distant metastases
Corresponding MRI findings[2]		
Stage 0		No tumor mass present
Stage I	IA	No tumor mass or localized widening of the endocervical canal with a small tumor mass
		Fibrous stroma intact and symmetric
	IB	Partial or complete disruption of low-signal-intensity fibrous stroma
		Rim of intact cervical tissue surrounding tumor
Stage II	IIA	Segmental disruption of hypointense vaginal wall (upper two-thirds)
	IIB	Complete disruption of low signal intensity fibrous stroma with tumor signal extending into parametrium
Stage III	IIIA	Segmental disruption of hypointense vaginal wall (lower third)
	IIIB	Same findings as IIB with tumor signal, most frequently extending to involve obturator internus, piriformis, or levator ani muscles
		Dilated ureter
Stage IV	IVA	Tumor signal disrupts normal tissue planes with loss of low signal intensity of bladder or rectal wall
	IVB	Tumor masses in distant organs or anatomic sites

[1]The presence of metastatic lymph nodes is not included in the FIGO classification.
[2]MRI findings seen on T2-weighted or contrast-enhanced T1-weighted images.

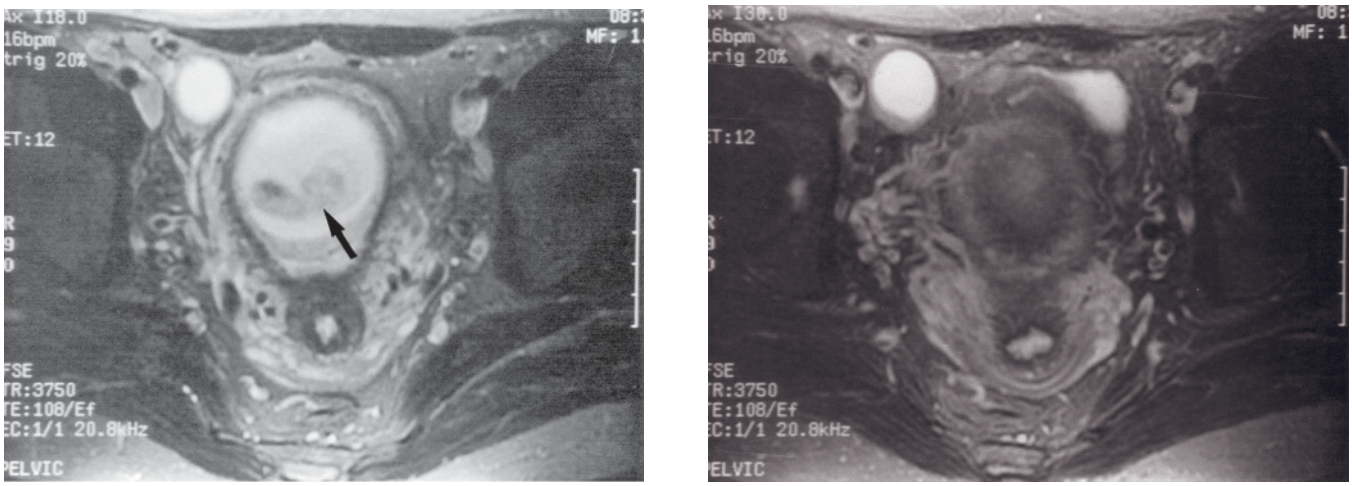

FIG. 14.55 FIGO stage I cervical carcinoma in a pregnant patient at 11 weeks of gestation. Transverse T2-weighted ETSE images (*a*, *b*).Although the cervical carcinoma itself is not clearly visualized, the hypointense cervical stroma is not disrupted and therefore parametrial invasion could be excluded. Trachelectomy was performed, and definitive treatment was delayed until delivery (arrow, *a*: fetus).

Ib) or tumor extending to the upper vagina (FIGO stage IIa) are generally treated with radical hysterectomy and pelvic lymph node dissection. Patients with more advanced disease (stage IIB or beyond) are treated with radiation therapy.

Despite well-known limitations of the FIGO staging system, clinical staging remains the standard that determines treatment in patients with invasive cervical carcinoma [86]. Staging errors of clinical staging ranging from 17% to 32% for stage IB disease and from 39% to 64% for stage II disease have been reported [87]. Furthermore, although the presence of lymphadenopathy, large tumor volume, and tumor extension to the uterine corpus have important prognostic and therapeutic implications, these factors are not evaluated in the FIGO staging system.

Role of MRI

The role of imaging in preoperative assessment of cervical carcinoma has steadily increased. Imaging is not used for detection of carcinoma, but for staging of cytologically proven disease. MRI surpasses CT in the local staging of cervical carcinoma, showing superior accuracy for assessment of depth of stromal and parametrial invasion [88, 89]. A recent cost-effectiveness study demonstrated significant cost savings with MRI compared to traditional evaluation including tests such as cystoscopy, barium enema, and intravenous pyelography [86].

Currently MRI may not be indicated in all patients with cervical carcinoma. Patients with tumors larger than 2 cm in size or with tumors located entirely within the endocervical canal have been shown to benefit most from undergoing MRI evaluation [86]. Furthermore, MRI is particularly useful in patients with biopsy-proved adenocarcinoma or coexistent pelvic masses and in pregnant patients with cervical carcinoma (fig. 14.55).

MRI Appearance

On MRI, the T2-weighted sequence is the most important sequence for the staging of cervical disease, providing optimal contrast between the tumor and the residual cervix. Axial and sagittal sequences are routinely performed. It was shown that additional oblique images, perpendicular to the cervical canal, further improve staging accuracy [7]. The tumor is of high signal intensity compared to the hypointense cervical stroma. Stage FIGO I disease is restricted to the cervix (figs. 14.55–14.57). Stage IA disease may not be visible, while stage IB disease is seen as a high-signal-intensity mass on T2-weighted images surrounded by a preserved hypointense rim of cervical stroma (fig. 14.58).

A tumor is classified as stage IIA when it invades the upper two-thirds of the vagina (figs. 14.59 and 14.60) (see Table 14.2). On MRI, this is best assessed on sagittal T2-weighted images. Disruption of the low-signal-intensity vaginal wall or the presence of a thickened hyperintense vagina indicate tumor invasion. An important criterion for management is the presence or absence of parametrial invasion, which indicates FIGO stage IIb disease. Parametrial extension is diagnosed with MRI when there is complete disruption of the cervical stroma, often associated with irregularity or stranding within the parametrial fat (fig. 14.61). A

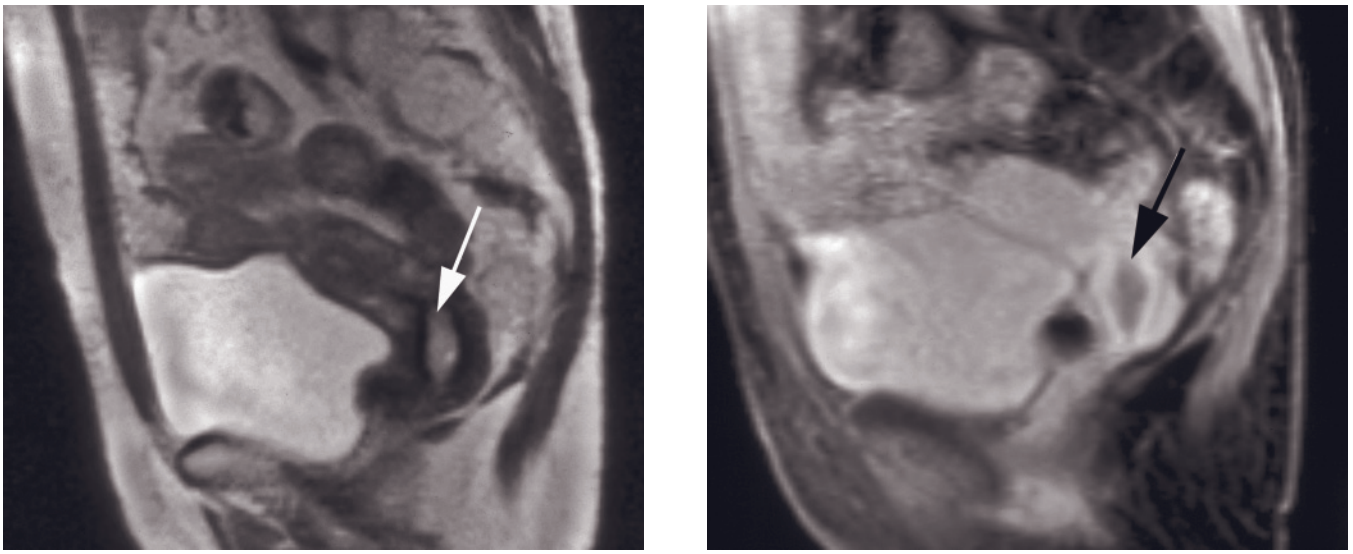

(*a*) (*b*)

FIG. 14.56 Stage I cervical carcinoma. Sagittal T2-weighted ETSE (*a*) and gadolinium-enhanced fat-suppressed T1-weighted gradient-echo (*b*) images show a small endocervical mass (arrow) surrounded by intact fibrous stroma. The tumor is high signal intensity on T2-weighted images (*a*) and enhances less than myometrium on postgadolinium images (*b*).

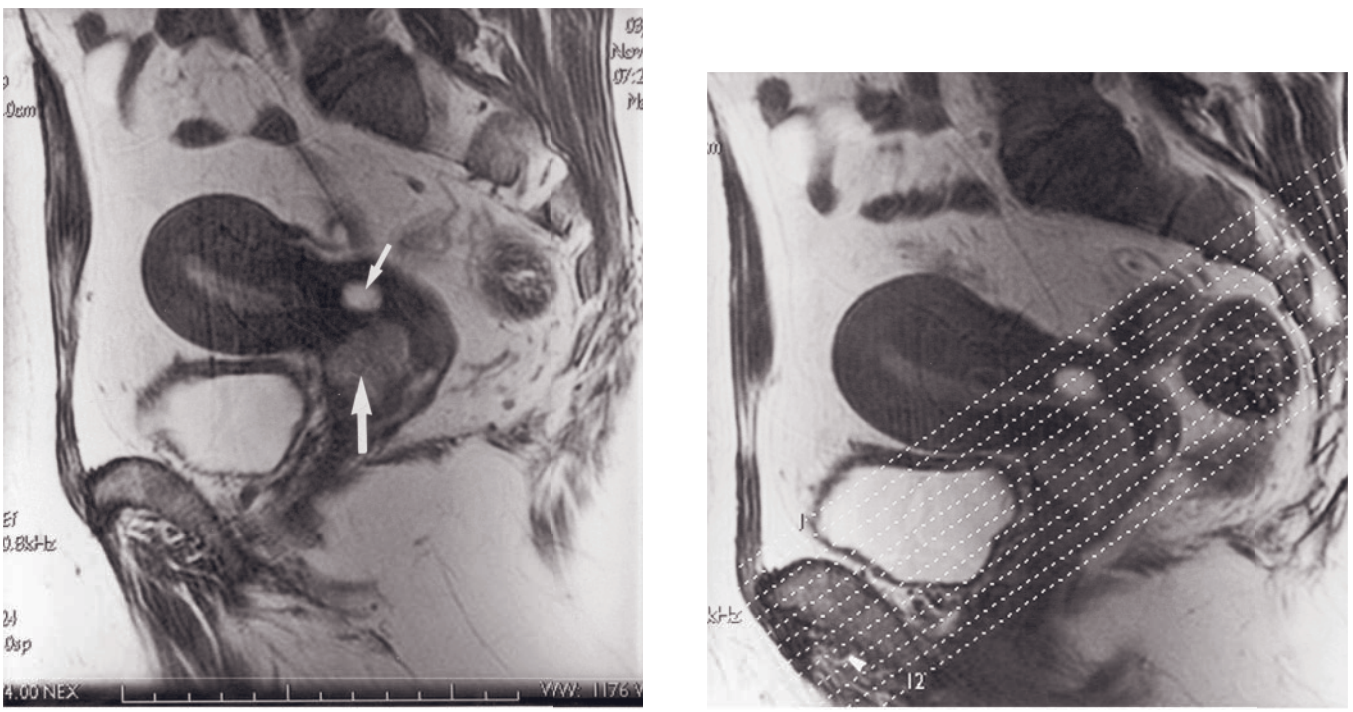

(*a*) (*b*)

FIG. 14.57 Cervical carcinoma stage IB. Sagittal (*a*,*b*) and oblique (*c*) T2-weighted ETSE images. On the sagittal image, oblique imaging plane perpendicular to the cervical canal is prescribed graphically (*b*), resulting in a short-axis view of the cervix (*c*). A tumor (arrow, *a*) of intermediate signal is seen within the cervix. The tumor is entirely surrounded by normal hypointense cervical stroma (arrowheads, *c*), excluding parametrial invasion.A nabothian cyst (small arrow, *a*) is also seen within the cervix.

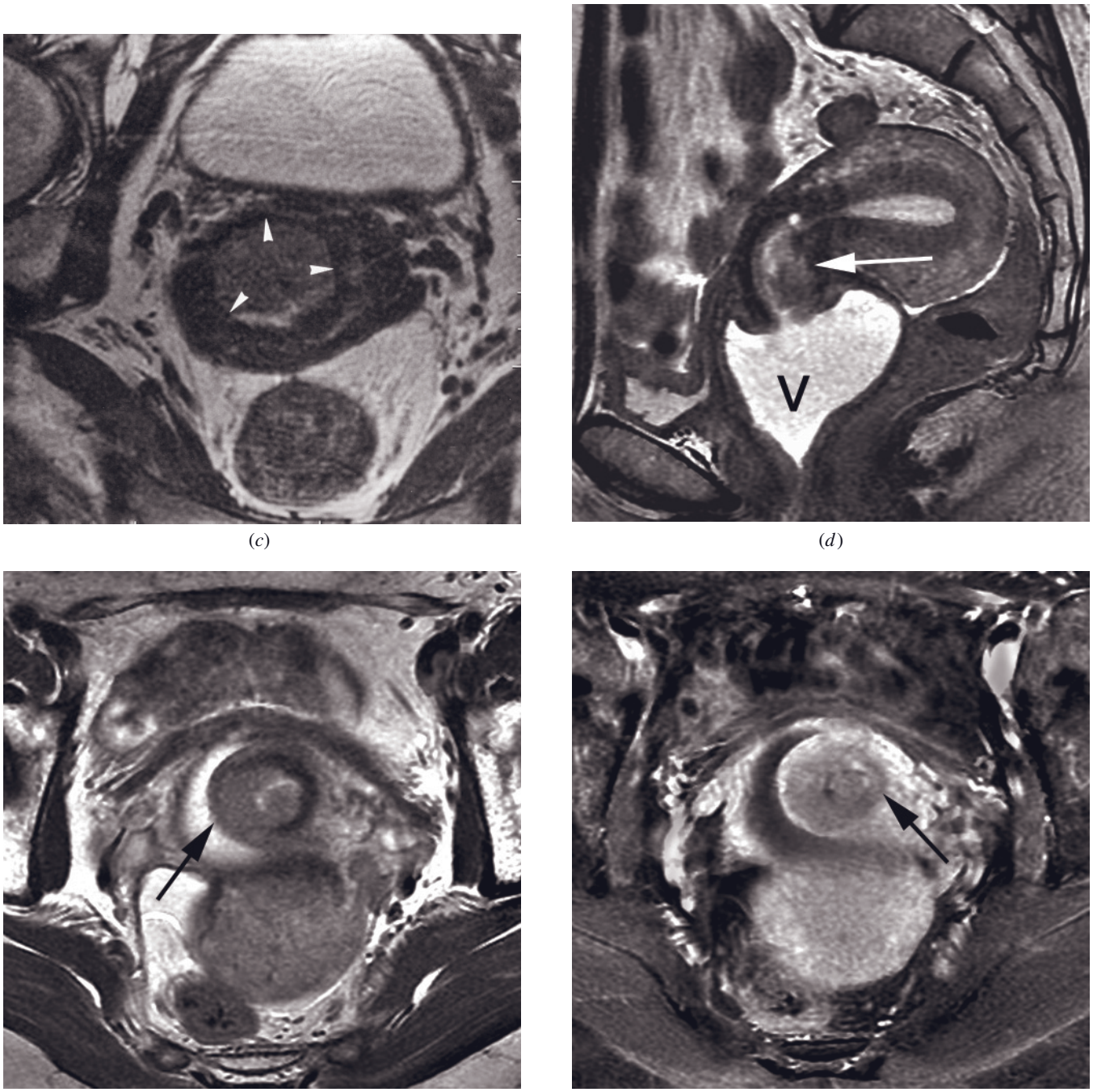

(*c*) (*d*) (*e*) (*f*)

FIG. 14.57 (*Continued*) **Cervical carcinoma stage IB at 3T.** Sagittal (*d*) and oblique axial (*e*) T2-weighted ETSE and oblique axial gadolinium-enhanced fat-suppressed T1-weighted gradient-echo (*f*) images in a different patient. The vaginal canal (v, *d*) is distended with gel. A tumor is seen of intermediate signal on T2-weighted images and hypointense to the surrounding cervical stroma after gadolinium (arrows, *d*, *f*). The tumor is not entirely surrounded by normal hypointense cervical stroma (arrowhead, *e*) but is contained within the cervix. Apparent disruption of the fibrous stromal ring is suggestive but not diagnostic of extracervical invasion, whereas an intact fibrous ring essentially excludes parametrial invasion.

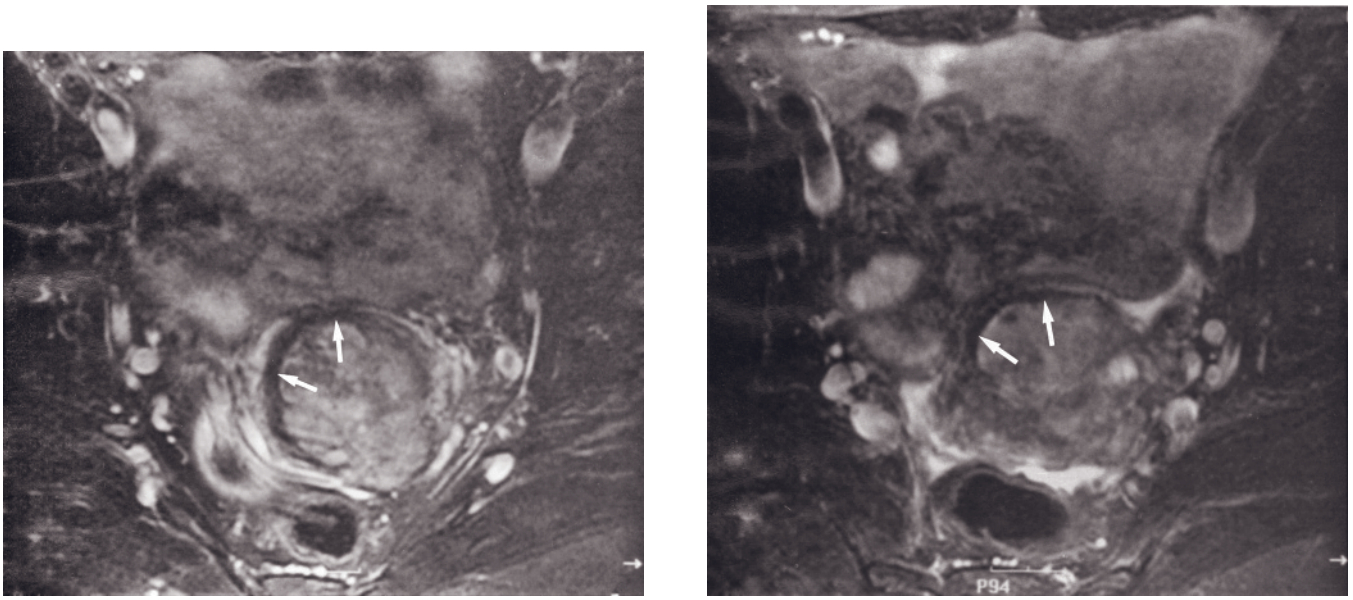

(*a*) (*b*)

FIG. 14.58 Cervical carcinoma stage IIB. Transverse T2-weighted fat-suppressed ETSE images (*a*, *b*) show a large, heterogeneously hyperintense cervical tumor. Normal hypointense cervical stroma is seen anteriorly (arrows, *a*, *b*) but is disrupted posteriorly.The diagnosis of parametrial invasion was histologically confirmed.

FIG. 14.59 Cervical carcinoma with vaginal extension. Sagittal T2-weighted ETSE image shows hyperintense cervical carcinoma (arrow) with extension to the vagina. The tumor results in cervical stenosis with fluid retention within the uterus. Note that the fat planes between the cervix and the urinary bladder and between the cervix and the rectal wall are preserved (arrowheads), excluding bladder or rectal wall infiltration.

completely intact ring of low-signal-intensity cervical stroma is highly accurate in excluding parametrial invasion (fig. 14.58).

In FIGO stage IIIa disease, the tumor mass can be seen extending to the lower third of the vagina. This is best evaluated on sagittal T2-weighted images. Because of the lymphatic drainage of the distal vagina, enlarged inguinal nodes may be seen with distal vaginal invasion (fig. 14.62).

Infiltration of the pelvic wall or obstruction of one or both ureters corresponds to stage IIIb disease. A dilated ureter can be well delineated on the psoas muscle on axial fat-saturated T2-weighted images. Pelvic sidewall invasion is suggested when the normal low signal intensity of the levator ani, pyriformis, or obturator internus muscle is disrupted on T2-weighted images. Invasion of the urinary bladder or rectal wall (stage IVa) is suspected when the normally present fat planes between the organs are obliterated. Furthermore, a hyperintense disruption of the otherwise hypointense urinary bladder or rectal wall might be seen and a nodular wall thickening or intraluminal masses may be present (figs. 14.62 and 14.63) [48].

Lymph node metastases are not part of FIGO staging but do affect prognosis and treatment decisions. As in the case of endometrial carcinoma, accuracy for detecting lymph node metastases based on size is poor. Yang et al. showed that central necrosis of a lymph node is an accurate criterion to diagnose metastasis in a pelvic

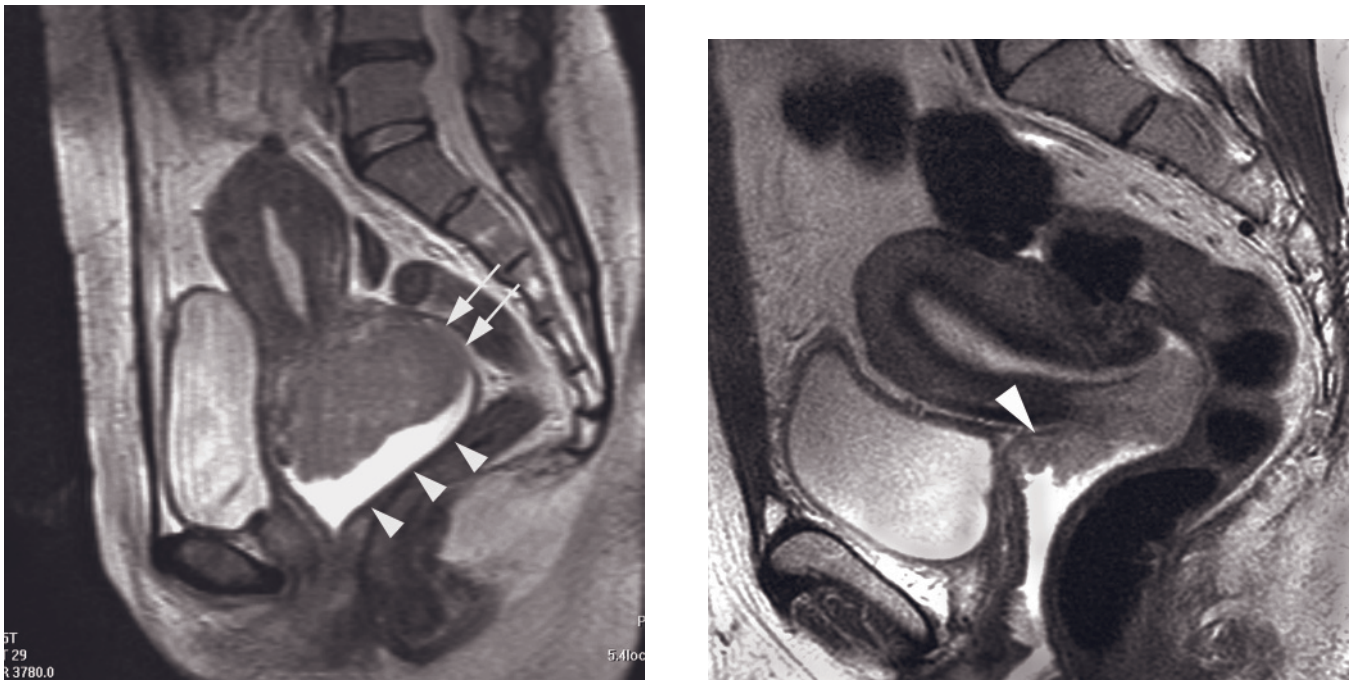

(*a*) (*b*)

FIG. 14.60 Cervical carcinoma with vaginal extension: use of vaginal gel. (*a*) Sagittal T2-weighted ETSE image shows a large cervical carcinoma with exophytic growth pattern in a 44-year-old woman. There is focal disruption of the low-signal vaginal wall in the posterior fornix (arrow). The anterior wall and the remainder of the posterior wall (arrowheads) are well delineated and intact. (Courtesy of Claude Sirlin, M.D., University of California, San Diego). **Cervical carcinoma with vaginal extension at 3T.** Sagittal T2-weighted ETSE image in a 42-year-old woman (*b*) shows a cervical carcinoma with invasion of the anterior vaginal wall.

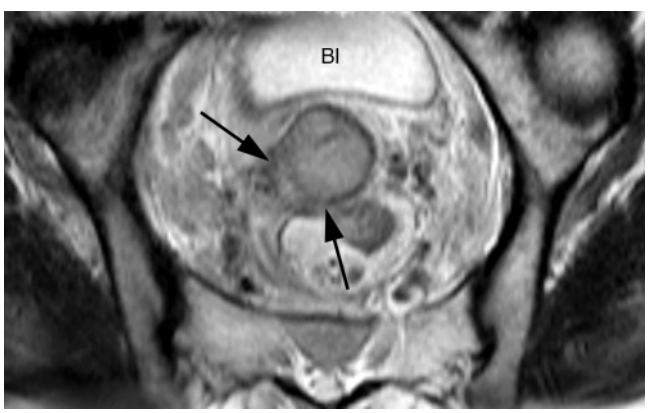

FIG. 14.61 Cervical carcinoma with parametrial invasion. Oblique transverse T2-weighted ETSE image obtained perpendicular to the cervical canal (short-axis view) shows parametrial extension of tumor with disruption of the hypointense ring of fibrous stroma (arrows). The short-axis view of the cervix minimizes partial volume effects and may improve staging accuracy. (Bl = bladder.)

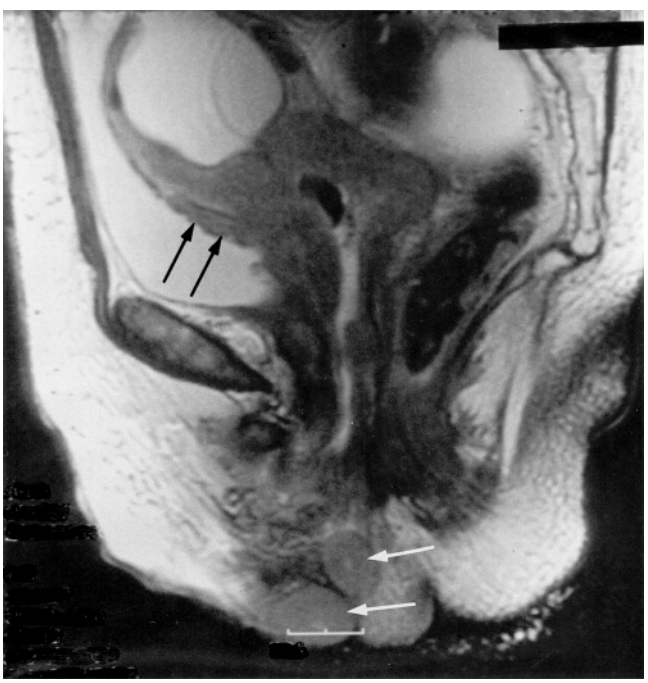

FIG. 14.62 Cervical carcinoma, extensive disease. Sagittal T2-weighted ETSE image shows hyperintense cervical carcinoma with extension to the vagina, labia majora (white arrows), and urinary bladder (black arrows). Fluid in the uterus is caused by cervical obstruction from the tumor.

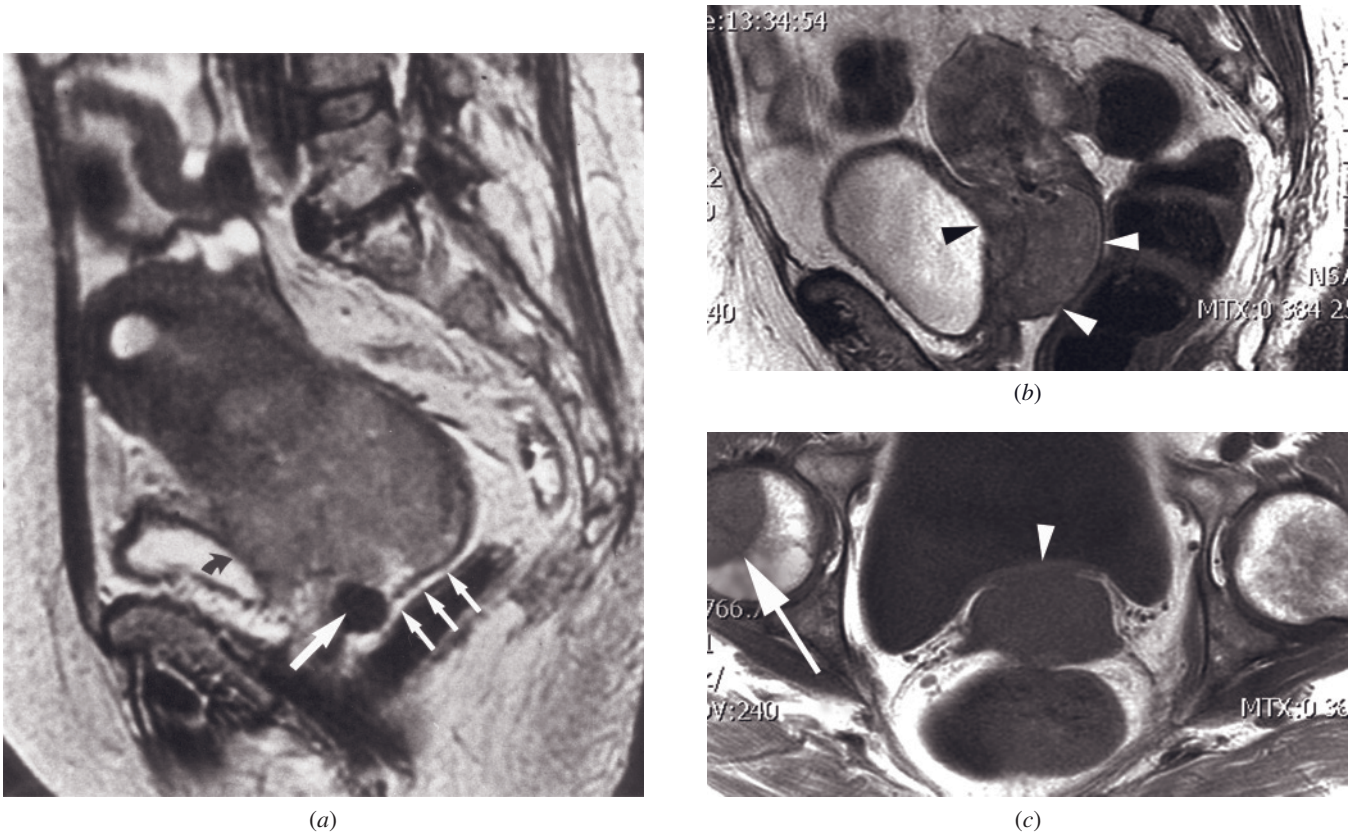

FIG. 14.63 Cervical carcinoma with urinary bladder invasion (FIGO stage IV). (*a*) Sagittal T2-weighted ETSE image shows hyperintense cervical carcinoma with extension to the vagina (large arrow: tampon) and urinary bladder (curved arrow). Note that the fat plane between cervix and rectal wall is well seen (small arrows), excluding rectal invasion. **Stage IV cervical carcinoma at 3T.** Sagittal T2-weighted ETSE (*b*) and transverse T1-weighted gradient-echo (*c*) images show a large cervical mass (white arrowheads, *b*) with abnormal thickening of the bladder wall (black arrowhead, *b*; white arrowhead, *c*). Stage IV disease was diagnosed based on the large femoral metastasis (arrow, *c*).

node [90]. Others have reported that spiculated or lobulated shape is predictive of metastasis [91].

Contrast-enhanced images are also useful in cases of suspected invasion of the bladder or rectum or if the tumor volume is large and necrotic areas or fistulas are suspected, particularly in the postradiation setting (fig. 14.64) [48, 92–94].

Cervical carcinoma may result in cervical outlet obstruction and, when high grade, hematometra or pyometra. On MRI, the uterine cavity is distended by material of variable signal intensity, depending on its composition, for example, retained secretions, blood, or tumor. Other causes of cervical stenosis include congenital, inflammatory, neoplastic, or iatrogenic origins as well as the presence of endometrial carcinoma.

Adenocarcinoma, Undifferentiated Carcinoma, and Sarcoma

Adenocarcinomas, undifferentiated carcinomas, and sarcomas comprise 15% of cervical carcinomas and are associated with a worse prognosis. The relative incidence of adenocarcinoma is increasing because of the success of the screening programs, which are more sensitive for squamous cell carcinoma. Adenocarcinomas may be higher in signal intensity on T2-weighted images with less enhancement on delayed gadolinium-enhanced T1-weighted images; however, the MRI appearance overlaps with that of squamous cell carcinoma. Because up to 30% of cervical adenocarcinomas have endometrioid elements, pathological differentiation from endometrial carcinoma may be difficult [95]. In patients with adenocarcinoma diagnosed by cervical biopsy, MRI may reveal the origin and guide proper management. MR features that favor endometrial origin include endometrial thickening or distension by a mass, invasion of the myometrium directly from endometrium, and the presence of a complex ovarian mass. If myometrial invasion is seen from the region of the cervix only, the origin is likely cervical (fig. 14.65). However, some tumors have an intermediate appearance, and it is not possible to determine tumor origin based on MRI appearance. Adenosquamous carci-

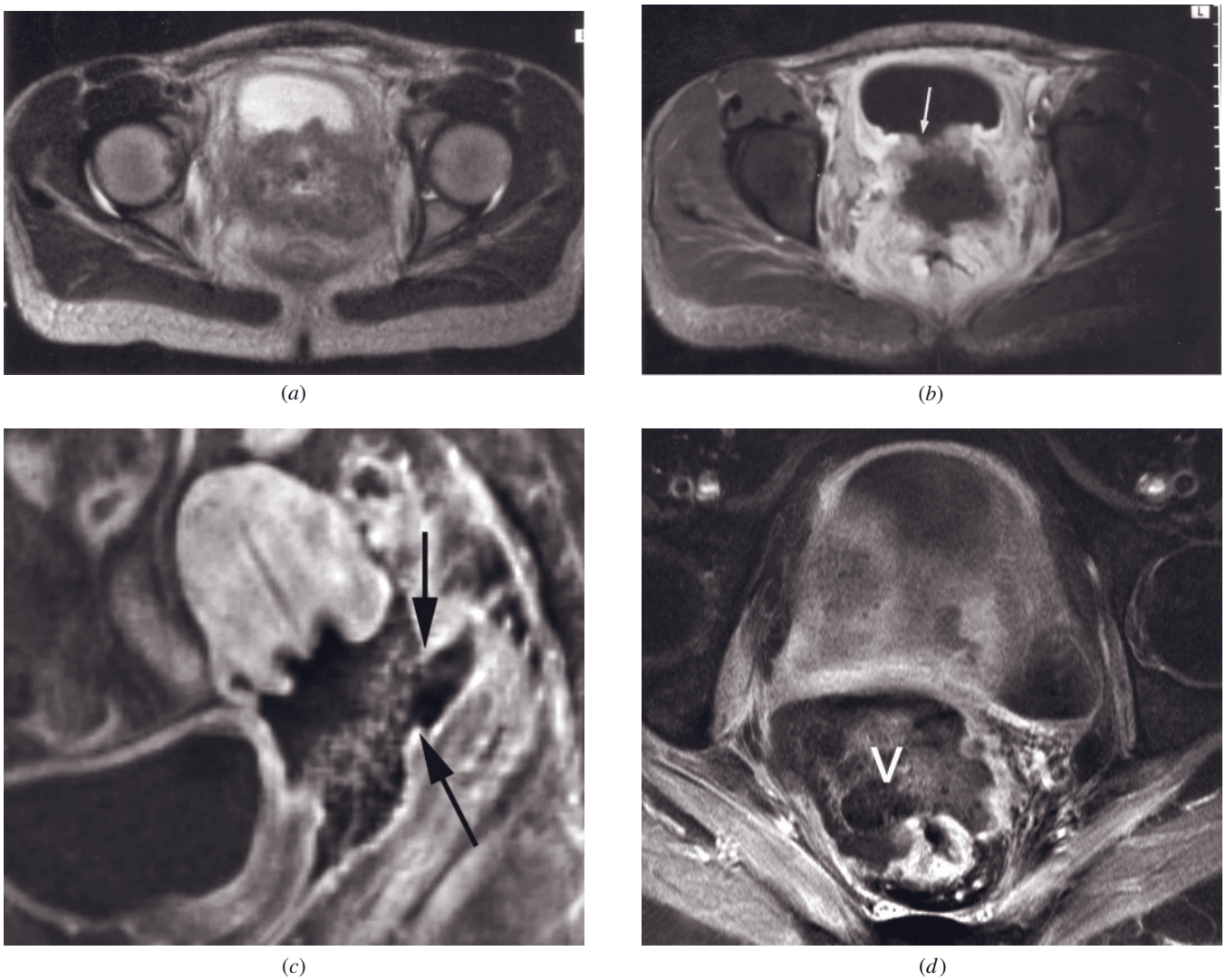

FIG. 14.64 Large cervical cancer after radiation therapy with necrosis and bladder fistula. Transverse T2-weighted ETSE (*a*) and transverse gadolinium-enhanced fat-suppressed gradient-echo (*b*) images. The T2-weighted image (*a*) demonstrates a large mass in the cervix. After gadolinium enhancement (*b*), extensive necrosis secondary to radiation therapy and a fistula to the bladder (arrow, *b*) are seen. Bladder fistulae are usually best shown on postgadolinium images as a low-signal linear structure, reflecting lack of enhancement of the tract, often associated with increased enhancement of the tract wall. **Cervical cancer after radiation therapy with necrosis and rectal fistula.** Sagittal (*c*) and transverse (*d*) gadolinium-enhanced fat-suppressed gradient-echo images in a different patient show extensive necrosis secondary to radiation therapy and a large fistula to the rectum (arrows, *c*) as well as abundant stool in the distended vaginal vault (v, *d*) between the bladder and rectum.

noma has a worse prognosis than either squamous cell carcinoma or adenocarcinoma [96]. Müllerian adenosarcoma is a rare low-grade malignancy that may occur in the endometrium or cervix. Adenosarcoma present as recurrent cervical polyps (fig. 14.65*e*, *f*) [97].

Adenoma Malignum

Adenoma malignum (also called minimal deviation adenocarcinoma) is a rare subtype of mucinous adenocarcinoma, comprising about 3% of cervical adenocarcinomas. There is an association with Peutz–Jeghers syndrome [68]. It carries a poor prognosis and classically presents with the nonspecific symptom of watery discharge. The MRI appearance of adenoma malignum has been described. A multicystic mass extends from the endocervix into the cervical stroma (fig. 14.66). The mass typically has solid enhancing components that help differentiate it from benign nabothian cysts, which may also appear as a multicystic mass (figs. 14.40 and 14.41). It may not be possible to distinguish adenoma malignum from cervical hyperplasia, polyps, or other benign cystic lesions [68, 69, 95].

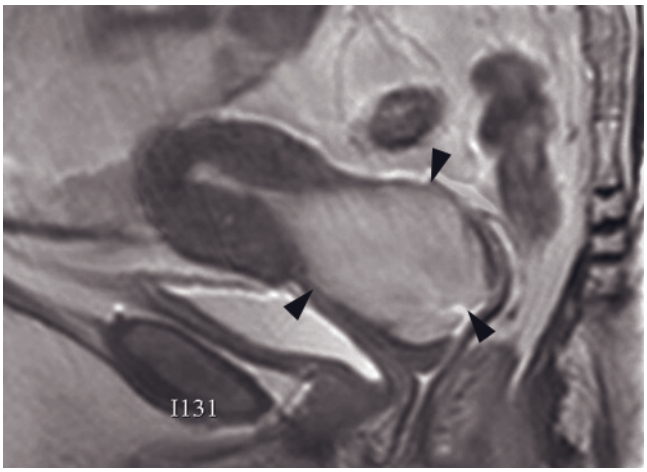

(*a*)

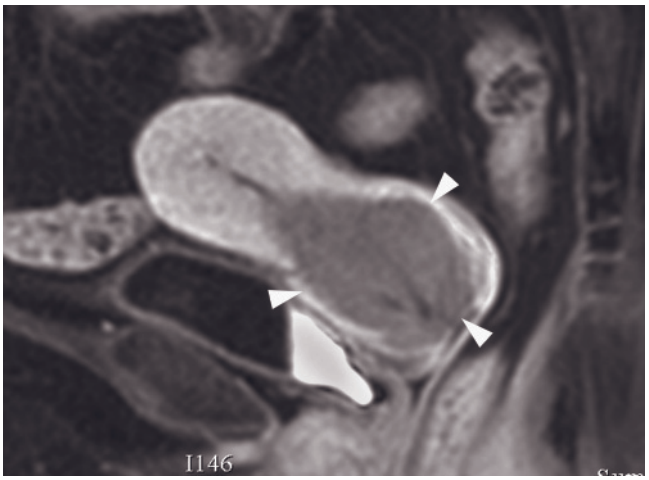

(*b*)

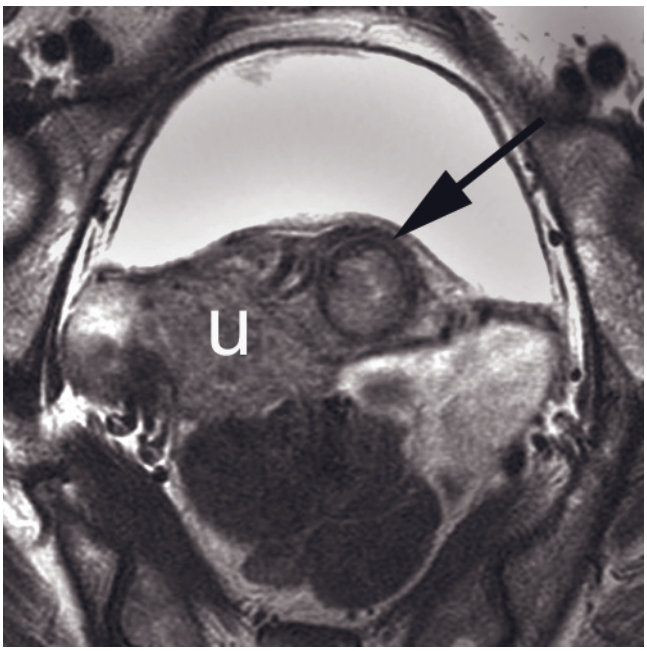

(*c*)

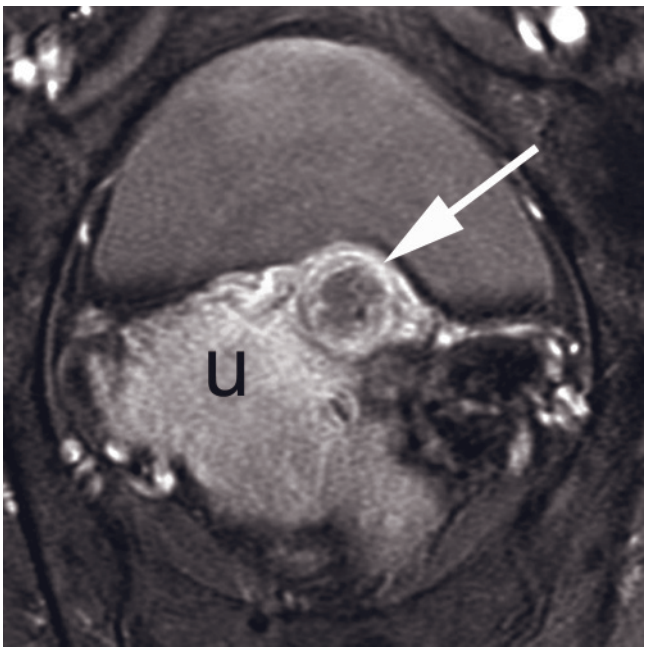

(*d*)

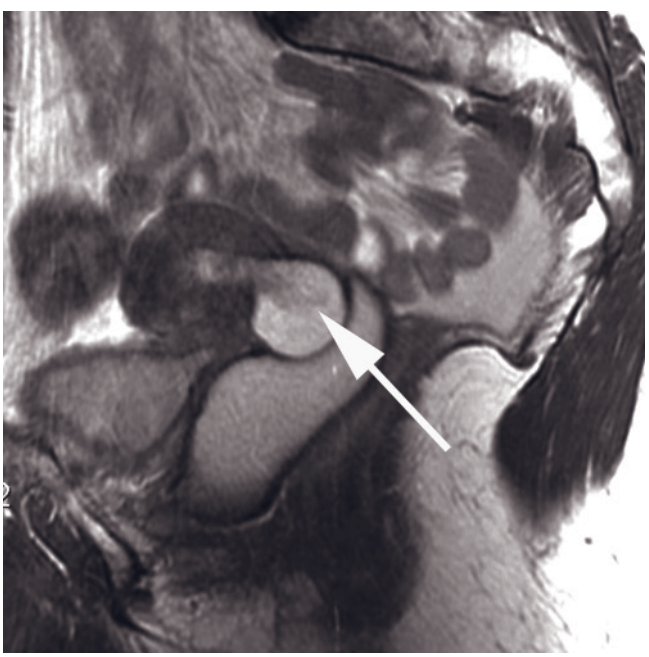

(*e*)

Fig. 14.65 Cervical adenocarcinoma. Sagittal T2-weighted ETSE (*a*) and gadolinium-enhanced fat-suppressed T1-weighted gradient-echo (*b*) images in a 55-year-old woman show a large cervical mass with endophytic growth (arrowheads). MRI is helpful to determine whether biopsy-proven adenocarcinoma is endometrial or cervical in origin. **Cervical adenocarcinoma at 3T.** Oblique axial T2-weighted ETSE (*c*) and gadolinium-enhanced fat-suppressed T1-weighted gradient-echo (*d*) images oriented to the cervix in another patient show a smaller cervical adenocarcinoma (arrows, *c*, *d*) confined to the cervix. A portion of the retroflexed and angulated uterine body is also seen (u, *c*, *d*).

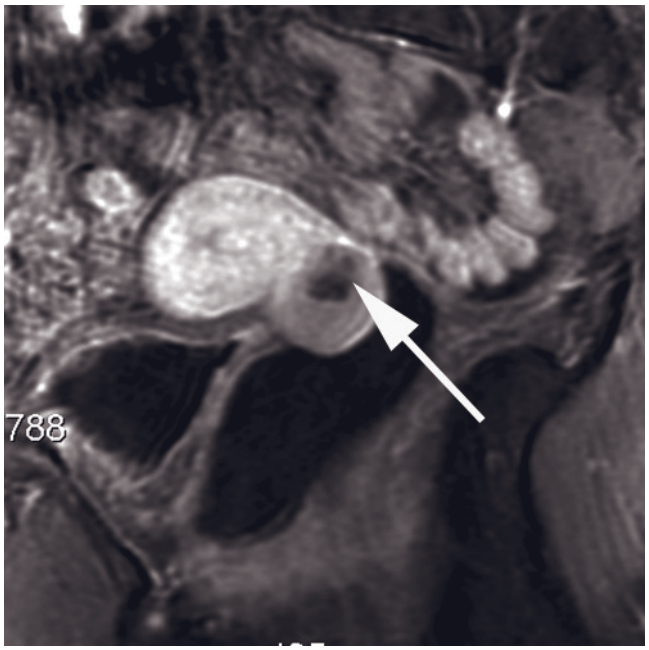

(*f*)

FIG. 14.65 (*Continued*) **Müllerian adenosarcoma at 3T.** Sagittal T2-weighted ETSE (*e*) and gadolinium-enhanced fat-suppressed T1-weighted gradient-echo (*f*) images in a third patient show a polypoid mass (arrows, *e*, *f*) projecting into the cervix, which is distended because of stenosis of the external os. Adenosarcoma is a rare low-grade malignancy that may present as cervical polyps and has a tendency for recurrence.

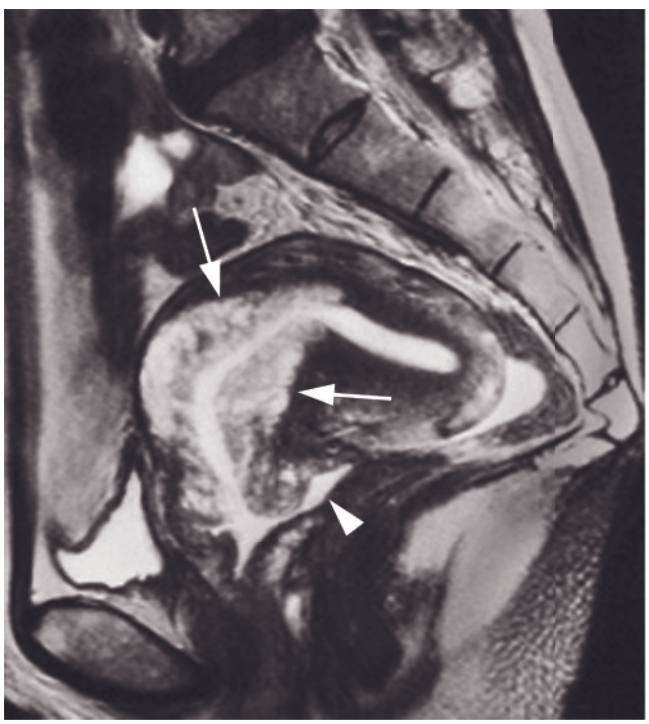

(*a*)

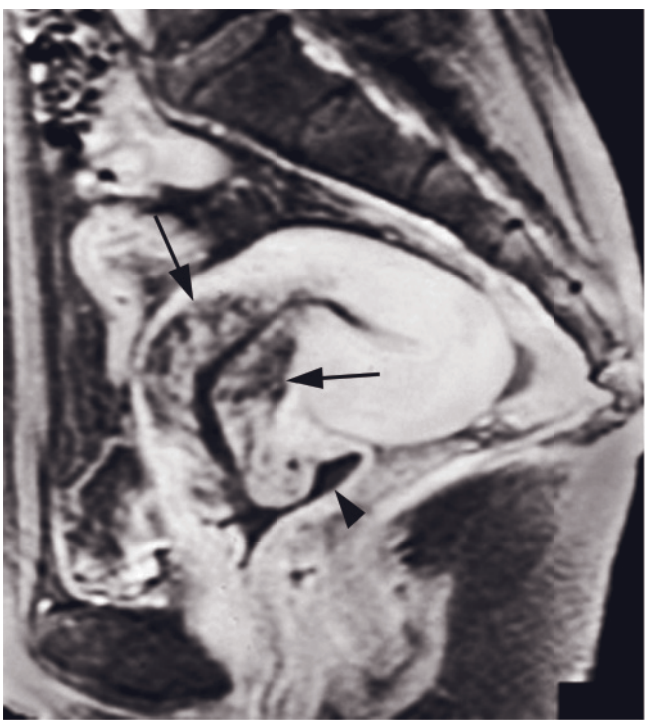

(*b*)

FIG. 14.66 Adenoma malignum. Sagittal T2-weighted ETSE (*a*) and gadolinium-enhanced fat-suppressed T1-weighted gradient-echo (*b*) images in a 47-year-old woman with watery vaginal discharge.A multicystic mass extends from the endocervical glands to the deep cervical stroma (arrows). Note distension of the vaginal fornices with mucin produced by the tumor (arrowhead). (Courtesy of Kaori Togashi, M.D., Ph.D., Department of Nuclear Medicine and Diagnostic Imaging, Graduate School of Medicine, Kyoto University.)

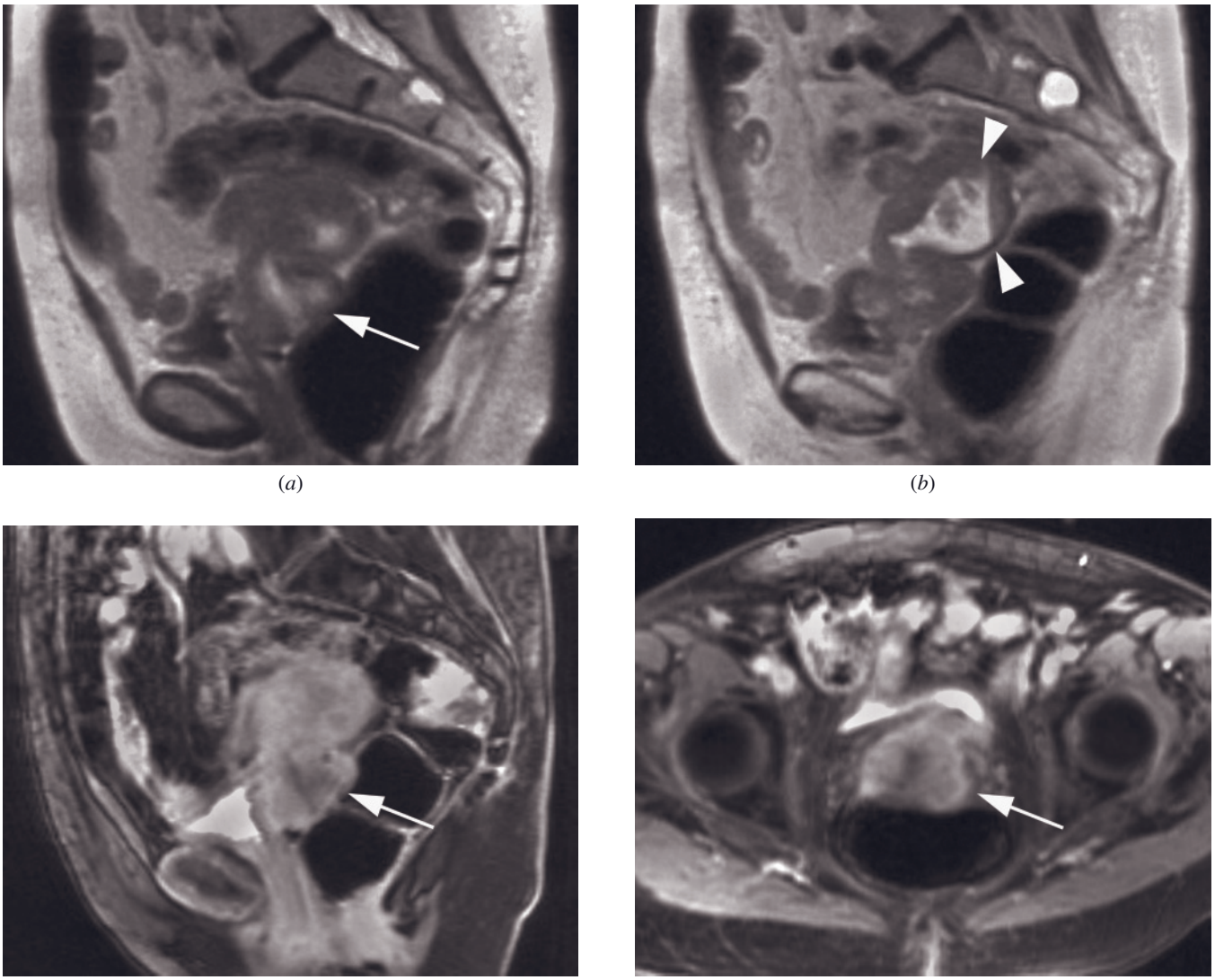

(*a*) (*b*) (*c*) (*d*)

FIG. 14.67 Cervical metastasis. Sagittal T2-weighted ETSE (*a*, *b*) and sagittal (*c*) and transverse (*d*) gadolinium-enhanced fat-suppressed T1-weighted gradient-echo images in a patient with colon cancer show an irregular cervical mass (arrow, *a*, *c*, *d*) causing uterine obstruction with hematometra (arrowheads, *b*).

Cervical Metastases

The cervix and uterine corpus are both uncommon sites of metastatic disease and usually involved by direct extension from bladder or colorectal cancer (fig. 14.67). Rarely, hematogenous or lymphatic spread reaches the cervix.

Recurrent Cervical Carcinoma and Posttreatment Change

After treatment of cervical carcinoma, recurrent disease may occur in multiple locations. Most recurrence occurs within 2 years of treatment, frequently in the pelvis. Less commonly, liver, bone, or peritoneal recurrence is seen. Approximately 30% of women with invasive cervical carcinoma will die as the result of recurrent or persistent disease [98]. Recurrent disease may be detected by surveillance imaging studies or become symptomatic, causing swelling of the lower extremities due to lymphatic obstruction or pain due to nerve compression or ureteral obstruction. MRI and CT are comparable for detection of distant recurrence; however, MRI is superior for detection of local recurrence in the pelvis (figs. 14.68 and 14.69).

Patients who have undergone radiation therapy present a diagnostic challenge. It may be difficult to differentiate between radiation changes and tumor. MRI

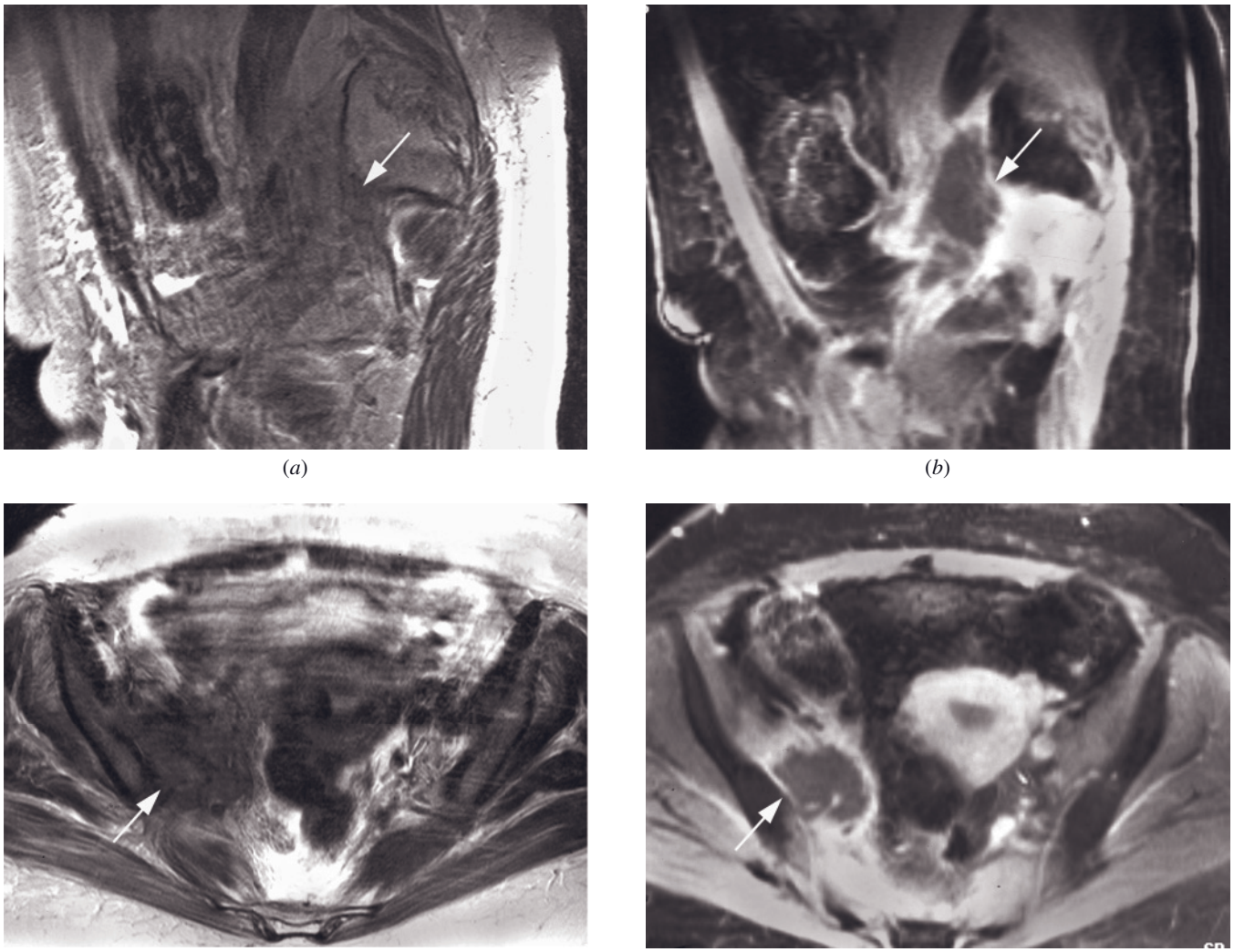

FIG. 14.68 Recurrent cervical carcinoma. Sagittal T2-weighted ETSE (*a*) and gadolinium-enhanced fat-suppressed T1-weighted gradient-echo (*b*) and transverse T2-weighted ETSE (*c*) and gadolinium-enhanced fat-suppressed T1-weighted gradient-echo (*d*) images show a right pelvic sidewall mass that is low signal intensity on T2-weighted images (arrow, *a*, *c*) and enhances on postgadolinium images with central necrosis (arrow, *b*, *d*).

was shown to be of value in this subpopulation of patients and to be superior to CT [99–103]. Irradiation of the uterus in premenopausal patients results in a decrease in the size of the uterus, thinning of the endometrium, decreased signal intensity of the myometrium, and loss of uterine zonal anatomy on T2-weighted sequences. These changes likely reflect a combination of direct radiation effects on the uterus and loss of hormonal stimulation from ovarian function suppression.

Recurrent tumor is hyperintense relative to muscle on T2-weighted imaging, whereas radiation fibrosis remains hypointense when imaged more than 12 months after radiation therapy. During the initial 6–12 months after treatment, areas of radiation fibrosis may demonstrate increased signal intensity on T2-weighted sequences because of associated inflammation, edema, and increased capillary vascularity. Both tumor recurrence and radiation fibrosis demonstrate low signal intensity on T1-weighted sequences; however, the presence of an identifiable mass lesion favors recurrence [101, 102]. Increased enhancement of the cervix after gadolinium is nonspecific and can be observed in recurrent tumor as well as postradiation fibrosis, inflammation, and radiation necrosis [94]; however, early enhancement on dynamic imaging is considered more worrisome for tumor. Gadolinium-enhanced imaging is helpful in demonstrating parametrial and pelvic sidewall recurrence [100].

Radical trachelectomy is a fertility-conserving treatment for early-stage cervical cancer. Usually performed

(*a*)

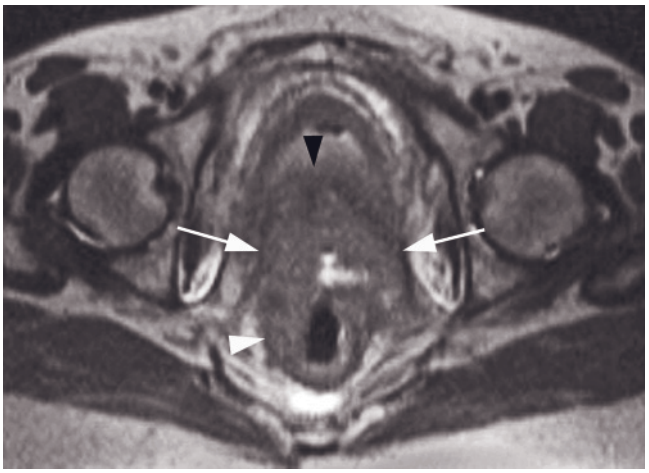

(*b*)

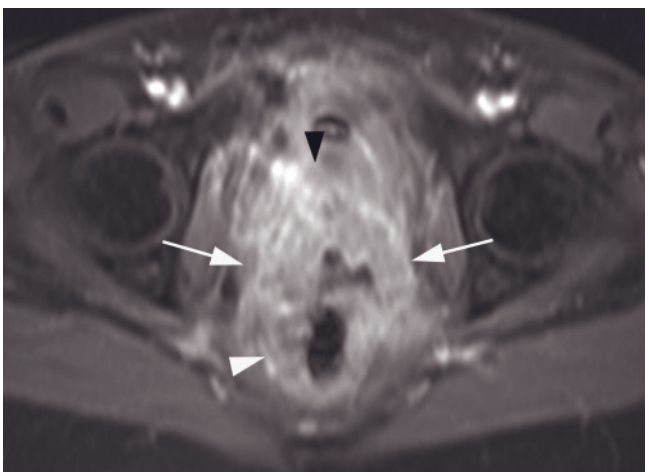

(*c*)

Fig. 14.69 Recurrent cervical carcinoma with invasion of the rectum and bladder. Sagittal (*a*) and transverse (*b*) T2-weighted ETSE and transverse gadolinium-enhanced fat-suppressed T1-weighted gradient-echo (*c*) images show an ill-defined mass involving the vaginal cuff (arrow, *a–c*) with extension to the rectum (white arrowhead, *a–c*) and bladder (black arrowhead, *a–c*).

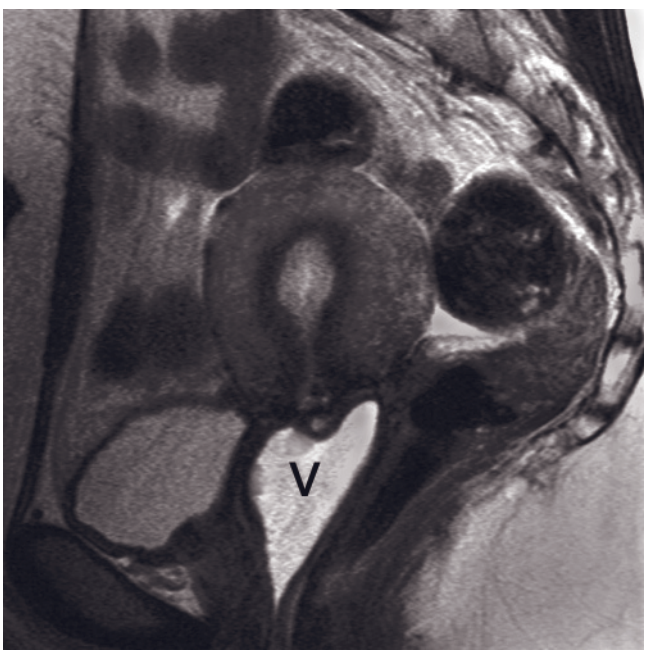

(*a*)

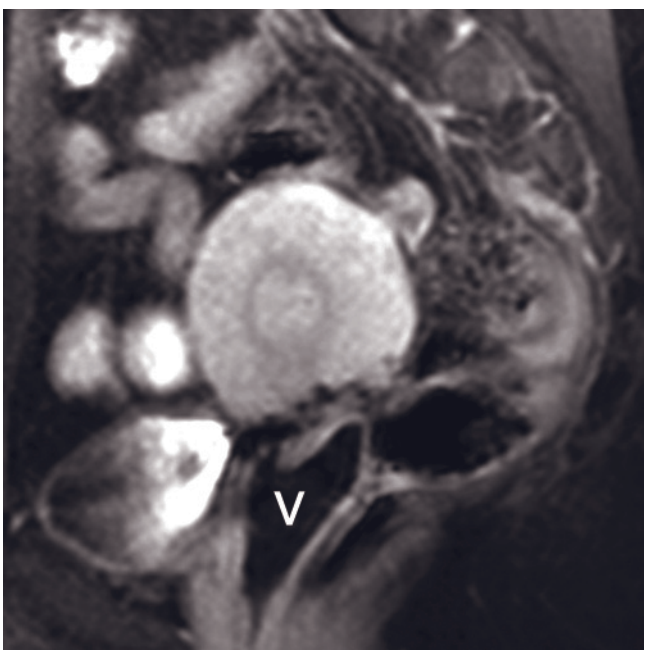

(*b*)

Fig. 14.70 Normal postoperative appearance after trachelectomy. Sagittal T2-weighted ETSE (*a*) and gadolinium-enhanced fat-suppressed T1-weighted gradient-echo (*b*) images show the absence of the cervix after fertility-sparing surgery for cervical carcinoma. The vaginal canal (v) was distended with gel.

transvaginally in association with laparoscopic lymph node resection, the procedure consists of resection of the cervix, formation of an end-to-end anastamosis between the uterine corpus and vagina, and placement of a cerclage suture [103]. The postoperative MR appearance has been described and reflects these anatomical changes [104] (fig. 14.70). In some cases, the appearance may mimic that of prior irradiation, resulting in a very small cervix, although in the case of trachelectomy prominent suture susceptibility artifact may be seen.

CONCLUSION

MRI has an established role in the investigation of the uterus and cervix. Detection and characterization of benign disease, such as leiomyomata and adenomyosis, is routinely performed at many centers. MRI is excellent for staging of malignancy, although the exact clinical role has not been universally established.

REFERENCES

1. Brown MA, Mattrey RF, Stamato S, Sirlin CB. MRI of the female pelvic using vaginal gel. *AJR Am J Roentgenol* 185: 1221–1227, 2005.
2. Pasquale SA, Russer TJ et al. Lack of interaction between magnetic resonance imaging and the copper-T380A IUD. *Contraception* 55: 169–173, 1997.
3. Kubik Huch RA, Hailemariam S et al. CT and MRI of the male genital tract: radiologic-pathologic correlation. *Eur Radiol* 9: 16–28, 1999.
4. Kim MJ, Chung JJ et al. Comparison of the use of the transrectal surface coil and the pelvic phased-array coil in MR imaging for preoperative evaluation of uterine cervical carcinoma. *AJR Am J Roentgenol* 168: 1215–1221, 1997.
5. deSouza NM, Dina R, McIndoe GA, Soutter WP. Cervical cancer: value of an endovaginal coil magnetic resonance imaging technique in detecting small volume disease and assessing parametrial extension. *Gynecol Oncol* 102: 80–85, 2006.
6. Hauth EA, Jaeger HJ, Libera H, Lange S, Forsting M. MR imaging of the uterus and cervix in healthy women: determination of normal values. *Eur Radiol* 17: 734–742, 2006.
7. Shiraiwa M, Joja I et al. Cervical carcinoma: Efficacy of thin-section oblique axial T2-weighted images for evaluating parametrial invasion. *Abdom Imaging* 24: 514–519, 1999.
8. Matsui T, Katayama M et al. Changes in myometrial and junctional zone thickness and signal intensity: demonstration with kinematic T2-weighted MRI. *Radiology* 235: 124–131, 2001.
9. Nakai A, Togashi K et al. Uterine persistalsis shown on cine MRI using ultrafast sequence. *J Magn Reson Imaging* 18: 726–733, 2003.
10. Kataoka M, Kido A et al. MRI of the female pelvis at 3T compared to 1.5T: evaluation on high-resolution T2-weighted and HASTE images. *J Magn Reson Imaging* 25: 527–534, 2007.
11. Martin DR, Friel H, Danrad R, De Becker J, Hussain S. Approach to abdominal imaging at 1.5 Tesla and optimization at 3 Tesla. *Magn Reson Imaging Clin N Am* 13: 241–254, 2005.
12. Hussain SM, van den Bos IC, Oliveto JM, Martin JR. MR imaging of the female pelvis at 3T. *Magn Reson Imaging Clin N Am* 14: 537–544, 2006.
13. Merkle EM, Dale BM. Abdominal MRI at 3.0T: the basics revisited. *AJR Am J Roentgenol* 186: 1524–1532, 2006.
14. Morakkabati-Spitz N, Schild HH, Kuhl CK et al. Female pelvis: MR imaging at 3.0T with sensitivity encoding and flip-angle sweep technique. *Radiology* 241: 538–545, 2006.
15. Lee JK, Gersell DJ et al. The uterus: in vitro MR-anatomic correlation of normal and abnormal specimens. *Radiology* 157: 175–189, 1985.
16. McCarthy S, Tauber C et al. Female pelvic anatomy: MR assessment of variations during the menstrual cycle and with use of oral contraceptives. *Radiology* 160: 119–123, 1986.
17. Hricak H, Alpers C et al. Magnetic resonance imaging of the female pelvis: initial experience. *AJR Am J Roentgenol* 141: 1119–1128, 1983.
18. McCarthy S, Scott G et al. Uterine junctional zone: MR study of water content and relaxation properties. *Radiology* 171: 241–253, 1989.
19. Brown HK, Stoll BS et al. Uterine junctional zone: correlation between histologic findings and MR imaging. *Radiology* 179: 409–413, 1991.
20. Scoutt LM, Flynn SD et al. Junctional zone of the uterus: correlation of MR imaging and histologic examination of hysterectomy specimens. *Radiology* 179: 403–407, 1991.
21. Scoutt LM, McCauley TR et al. Zonal anatomy of the cervix: correlation of MR imaging and histologic examination of hysterectomy specimens. *Radiology* 186: 159–162, 1993.
22. Haynor DR, Mack LA et al. Changing appearance of the normal uterus during the menstrual cycle: MR studies. *Radiology* 161: 459–462, 1986.
23. Janus CL, Bateman B et al. Evaluation of the stimulated menstrual cycle by magnetic resonance imaging. *Fertil Steril* 54: 1017–1020, 1990.
24. Togashi K, Nakai A, Sugimura K. Anatomy and physiology of the female pelvis: MR imaging revisited. *J Magn Reson Imaging* 13: 842–849, 2001.
25. Kataoka M, Togashi K, Kido A et al. Dysmenorrhea: evaluation with cine-mode-display MR imaging—initial experience. *Radiology* 235: 124–131, 2005.
26. Yamashita Y, Harada M et al. Normal uterus and FIGO stage I endometrial carcinoma: dynamic gadolinium-enhanced MR imaging. *Radiology* 186: 495–501, 1993.
27. Chaudhry S, Reinhold C, Guermazi A, Khalili I, Maheshwari S. Benign and malignant diseases of the endometrium. *Top Magn Reson Imaging* 14: 339–57, 2003.
28. Ascher SM, Jha RC, Reinhold C. Benign myometrial conditions: leiomyomas and adenomyosis. *Top Magn Reson Imaging* 14: 281–304, 2000.
29. Fong K, Causer P, Atri M, Lytwyn A, Kung R. Transvaginal US and hysterosonography in postmenopausal women with breast cancer receiving tamoxifen: correlation with hysteroscopy and pathologic study. *Radiographics* 23: 137–50, 2003.
30. De Muylder X, Neven P et al. Endometrial lesions in patients undergoing tamoxifen therapy. *Int J Gynaecol Obstet* 36: 127–130, 1991.
31. Ascher SM, Johnson JC et al. MR imaging appearance of the uterus in postmenopausal women receiving tamoxifen therapy for breast cancer: histopathologic correlation. *Radiology* 200: 105–110, 1996.
32. Ascher SM, Imaoka I, Lage JM. Tamoxifen-induced uterine abnormalities: the role of imaging. *Radiology* 214: 29–38, 2000.
33. McCluggage WG, Desai V, Manek S. Tamoxifen-associated postmenopausal adenomyosis exhibits stromal fibrosis, glandular dilatation and epithelial metaplasias. *Histopathology* 37: 340–346, 2000.
34. Pellerito JS, McCarthy SM et al. Diagnosis of uterine anomalies: relative accuracy of MR imaging, endovaginal sonography, and hysterosalpingography. *Radiology* 183: 795–800, 1992.

35. Carrington BM, Hricak H et al. Mullerian duct anomalies: MR imaging evaluation. *Radiology* 176: 715–720, 1990.
36. Frye RE, Ascher SM et al. MR hysterosalpingography: protocol development and refinement for simulating normal and abnormal fallopian tube patency—feasibility study with a phantom. *Radiology* 214: 107–112, 2000.
37. Troiano RN, McCarthy SM. Mullerian duct anomalies: imaging and clinical issues. *Radiology* 233: 19–34, 2004.
38. The American Fertility Society classifications of adnexal adhesions, distal tubal obstruction, tubal occlusion secondary to tubal ligation, tubal pregnancies, mullerian anomalies and intrauterine adhesions. *Fertil Steril* 49: 944–955, 1988.
39. Pavone ME, King JA, Vlahos N. Septate uterus with cervical duplication and a longitudinal vaginal septum: a mullerian anomaly without a classification. *Fertil Steril* 85: 494.e9–e10, 2006.
40. Oppelt P, Renner SP, Brucker S, Strissel PL, Strick R, Oppelt PG et al. The VCUAM (Vagina Cervix Uterus Adnex-associated Malformation) classification: a new classification for genital malformations. *Fertil Steril* 84: 1493–1497, 2005.
41. Reinhold C, Hricak H et al. Primary amenorrhea: evaluation with MR imaging. *Radiology* 203: 383–390, 1997.
42. Wiesner W, Kubik Huch RA et al. [Mayer-(von)Rokitansky-Kuster syndrome] Original title: Mayer-(von)Rokitansky-Kuster-Syndrom. *Schweiz Rundsch Med Prax* 87: 1257–1259, 1998.
43. Fedele L, Dorta M et al. Magnetic resonance imaging of unicornuate uterus. *Acta Obstet Gynecol Scand* 69: 511–513, 1990.
44. Woodward PJ, Wagner BJ et al. MR imaging in the evaluation of female infertility. *Radiographics* 13: 293–310, 1993.
45. Van Gils AP, Tham RT et al. Abnormalities of the uterus and cervix after diethylstilbestrol exposure: Correlation of findings on MR and hysterosalpingography. *AJR Am J Roentgenol* 153: 1235–1238, 1989.
46. Gambino J, Caldwell B et al. Congenital disorders of sexual differentiation: MR findings. *AJR Am J Roentgenol* 158: 363–367, 1992.
47. Atri M, Nazarnia S et al. Transvaginal US appearance of endometrial abnormalities. *Radiographics* 14: 483–492, 1994.
48. Hamm B, Kubik Huch RA et al. MR imaging and CT of the female pelvis: radiologic-pathologic correlation. *Eur Radiol* 9: 3–15, 1999.
49. Grasel RP, Outwater EK et al. Endometrial polyps: MR imaging features and distinction from endometrial carcinoma. *Radiology* 214: 47–52, 2000.
50. Rader JS, Binette SP et al. Ileal hemorrhage caused by a parasitic uterine leiomyoma. *Obstet Gynecol* 76: 531–534, 1990.
51. Murase E, Siegelman ES et al. Uterine leiomyomas: histopathologic features, MR imaging findings, differential diagnosis, and treatment. *Radiographics* 19: 1179–1197, 1999.
52. Siskin GP, Shlansky-Goldberg RD, Goodwin SC et al. A prospective multicenter comparative study between myomectomy and uterine artery embolization with polyvinyl alcohol microspheres: long-term clinical outcomes in patients with symptomatic uterine fibroids. *J Vasc Interv Radiol* 17: 1287–1295, 2006.
53. Hindley J, Gedroyc WM, Regan L, Stewart E, Tempany C, Hynnen K et al. MRI guidance of focused ultrasound therapy of uterine fibroids: early results. *AJR Am J Roentgenol* 183: 1713–1719, 2004.
54. Stewart EA, Rabinovici J, Tempany CM et al. Clinical outcomes of focused ultrasound surgery for the treatment of uterine fibroids. *Fertil Steril* 85: 22–29, 2006.
55. Weinreb JC, Barkoff ND et al. The value of MR imaging in distinguishing leiomyomas from other solid pelvic masses when sonography is indeterminate. *AJR Am J Roentgenol* 154: 295–299, 1990.
56. Burn PR, McCall JM et al. Uterine fibroleiomyoma: MR imaging appearances before and after embolization of uterine arteries. *Radiology* 214: 729–734, 2000.
57. Jha RC, Ascher SM et al. Symptomatic fibroleiomyomata: MR imaging of the uterus before and after uterine arterial embolization. *Radiology* 217: 228–235, 2000.
58. Pelage JP, Guaou NG, Jha RC, Ascher SM, Spies JB. Uterine fibroid tumors: long-term MR imaging outcome after embolization. *Radiology* 30: 803–809, 2004.
59. Jha RC, Takahama J, Imaoka I, Korangy SJ, Spies JB, Cooper C, Ascher SM. Adenomyosis: MRI of the uterus treated with uterine artery embolization. *AJR Am J Roentgenol* 181: 851–856, 2003.
60. Spielmann AL, Keogh C, Forster BB, Martin ML, Machan LS. Comparison of MRI and sonography in the preliminary evaluation for fibroid embolization. *AJR Am J Roentgenol* 187: 1499–1504, 2006.
61. Kroencke TJ, Scheurig C, Kluner C, Taupitz M, Schnorr J, Hamm B. Uterine fibroids: contrast-enhanced MR angiography to predict ovarian artery supply—initial experience. *Radiology* 241: 181–189, 2006.
62. Ueda H, Togashi K et al. Unusual appearances of uterine leiomyomas: MR imaging findings and their histopathologic backgrounds. *Radiographics* 19: 131–145, 1999.
63. Pelage JP, Jacob D, Fazel A, Namur J, Laurent A, Rymer R, Le Dref O. Midterm results of uterine artery embolization for symptomatic adenomyosis: initial experience. *Radiology* 234: 948–953, 2005.
64. Byun JY, Kim SE et al. Diffuse and focal adenomyosis: MR imaging findings. *Radiographics* 19: 161–170, 1999.
65. Reinhold C, Tafazoli F et al. Uterine adenomyosis: endovaginal US and MR imaging features with histopathologic correlation. *Radiographics* 19: 147–160, 1999.
66. Tamai K, Togashi K, Ito T, Morisawa N, Fujiwara T, Koyama T. MR imaging findings of adenomyosis: correlation with histopathologic features and diagnostic pitfalls. *Radiographics* 25: 21–40, 2005.
67. Kim MD, Kim S, Kim NK et al. Long-term results of uterine artery embolization for symptomatic adenomyosis. *AJR Am J Roentgenol* 188: 176–181, 2007.
68. Okamoto Y, Tanaka YO, Nishida M, Tsunoda H, Yoshikawa H, Itai Y. MR imaging of the uterine cervix: imaging-pathologic correlation. *Radiographics* 23: 425–445, 2003.
69. Okamoto Y, Tanaka YO, Nishida M, Tsunoda H, Yoshikawa H. Pelvic imaging: multicystic uterine cervical lesions. Can magnetic resonance imaging differentiate benignancy from malignancy? *Acta Radiol* 45: 102–108, 2004.
70. American Joint Committee on Cancer. *Cancer Staging Manual* (6th ed.). New York: Springer, pp. 259–270, 2002.
71. Amant F, Moerman P, Neven P, Timmerman D, Van Limbergen E, Vergote I. Endometrial cancer. *Lancet* 366: 491–505, 2005.
72. Piver MS, Lele SB et al. Paraaortic lymph node evaluation in stage I endometrial carcinoma. *Obstet Gynecol* 59: 97–100, 1982.
73. Larson DM, Connor GP, Broste SK, Krawisz BR, Johnson KK. Prognostic significance of gross myometrial invasion with endometrial cancer. *Obstet Gynecol* 88: 394–398, 1996.
74. Kinkel K, Kaji Y, Yu KK et al. Radiologic staging in patients with endometrial cancer: a meta-analysis. *Radiology* 212: 711–718, 1999.
75. Frei KA, Kinkel K et al. Prediction of deep myometrial invasion in patients with endometrial cancer: clinical utility of contrast-enhanced MR imaging—a meta-analysis and Bayesian analysis. *Radiology* 216: 444–449, 2000.
76. Yamashita Y, Mizutani H et al. Assessment of myometrial invasion by endometrial carcinoma: Transvaginal sonography vs contrast-enhanced MR imaging. *AJR Am J Roentgenol* 161: 595–599, 1993.
77. Popovich MJ, Hricak H et al. The role of MR imaging in determining surgical eligibility for pelvic exenteration. *AJR Am J Roentgenol* 160: 525–531, 1993.

78. Harisinghani MG, Saini S et al. MR lymphangiography using ultrasmall superparamagnetic iron oxide in patients with primary abdominal and pelvic malignancies: radiographic-pathologic correlation. *AJR Am J Roentgenol* 172: 1347–1351, 1999.
79. Ohguri T, Aoki T, Watanabe H et al. MRI findings including gadolinium-enhanced dynamic studies of malignant, mixed mesodermal tumors of the uterus: differentiation from endometrial carcinomas. *Eur Radiol* 12: 2737–2742, 2002.
80. Tanaka YO, Nishida M, Tsunoda H, Okamoto Y, Yoshikawa H. Smooth muscle tumors of uncertain malignant potential and leiomyosarcomas of the uterus: MR findings. *J Magn Reson Imaging* 20: 998–1007, 2004.
81. Shapeero LG, Hricak H. Mixed mullerian sarcoma of the uterus: MR imaging findings. *AJR Am J Roentgenol* 153: 317–319, 1989.
82. Rha SE, Byun JY, Jung SE et al. CT and MRI of uterine sarcomas and their mimickers. *AJR Am J Roentgenol* 181: 1369–1374, 2003.
83. Metser U, Haider MA, Khalili K, Boerner S. MR imaging findings and patterns of spread in secondary tumor involvement of the uterine body and cervix. *AJR Am J Roentgenol* 180: 765–769, 2003.
84. Schiller JT, Lowy DR. Prospects for cervical cancer prevention by human papillomavirus vaccination. *Cancer Res* 66: 10229–10232, 2006.
85. Peppercorn PD, Jeyarajah AR et al. Role of MR imaging in the selection of patients with early cervical carcinoma for fertility-preserving surgery: initial experience. *Radiology* 212: 395–399, 1999.
86. Hricak H, Powell CB et al. Invasive cervical carcinoma: role of MR imaging in pretreatment work-up—cost minimization and diagnostic efficacy analysis. *Radiology* 198: 403–409, 1996.
87. Lagasse LD, Creasman WT et al. Results and complications of operative staging in cervical cancer: experience of the Gynecologic Oncology Group. *Gynecol Oncol* 9: 90–98, 1980.
88. Sironi S, De Cobelli F et al. Carcinoma of the cervix: value of plain and gadolinium-enhanced MR imaging in assessing degree of invasiveness. *Radiology* 188: 780–797, 1993.
89. Subak LL, Hricak H et al. Cervical carcinoma: computed tomography and magnetic resonance imaging for preoperative staging. *Obstet Gynecol* 86: 43–50, 1995.
90. Yang WT, Lam WW et al. Comparison of dynamic helical CT and dynamic MR imaging in the evaluation of pelvic lymph nodes in cervical carcinoma. *AJR Am J Roentgenol* 175: 759–766, 2000.
91. Choi HJ, Kim SH, Seo SS et al. MRI for pretreatment lymph node staging in uterine cervical cancer. *AJR Am J Roentgenol* 187: W538–W543, 2006.
92. Hawighorst H, Knapstein PG et al. Cervical carcinoma: comparison of standard and pharmacokinetic MR imaging. *Radiology* 201: 531–539, 1996.
93. Semelka RC, Hricak H et al. Pelvic fistulas: appearances on MR images. *Abdom Imaging* 22: 91–95, 1997.
94. Scheidler J, Heuck AF et al. Parametrial invasion in cervical carcinoma: evaluation of detection at MR imaging with fat suppression. *Radiology* 206: 125–129, 1998.
95. Oguri H, Maeda N, Izumiya C, Kusume T, Yamamoto Y, Fukaya T. MRI of endocervical glandular disorders: three cases of a deep nabothian cyst and three cases of a minimal-deviation adenocarcinoma. *Magn Reson Imaging* 22: 1333–7, 2004.
96. Farley JH, Hickey KW, Carlson JW, Rose GS, Kost ER, Harrison TA. Adenosquamous histology predicts a poor outcome for patients with advanced-stage, but not early-stage, cervical carcinoma. *Cancer* 97: 2196–2202, 2003.
97. Manoharan M, Noor Azma MA, Soosay G, Mould T, Weekes AR. Mullerian adenosarcoma of the uterine cervix: report of three cases and review of the literature. *Gynecol Oncol* 105: 256–260, 2007.
98. Cannistra SA, Niloff JM. Cancer of the uterine cervix. *N Engl J Med* 334: 1030–1038, 1996.
99. Flueckiger F, Ebner F et al. Cervical cancer: serial MR imaging before and after primary radiation therapy—a 2-year follow-up study. *Radiology* 184: 89–93, 1992.
100. Hricak H, Swift PS et al. Irradiation of the cervix uteri: value of unenhanced and contrast-enhanced MR imaging. *Radiology* 189: 381–388, 1993.
101. Weber TM, Sostman HD et al. Cervical carcinoma: determination of recurrent tumor extent versus radiation changes with MR imaging. *Radiology* 194: 135–139, 1995.
102. Yamashita Y, Harada M et al. Dynamic MR imaging of recurrent postoperative cervical cancer. *J Magn Reson Imaging* 6: 167–171, 1996.
103. Hertel H, Kohler C, Grund D et al. German Association of Gynecologic Oncologists (AGO). Radical vaginal trachelectomy (RVT) combined with laparoscopic pelvic lymphadenectomy: prospective multicenter study of 100 patients with early cervical cancer. *Gynecol Oncol* 103: 506–511, 2006.
104. Sahdev A, Jones J, Shepherd JH, Reznek RH. MR imaging appearances of the female pelvis after trachelectomy. *Radiographics* 25: 41–52, 2005.

CHAPTER 15

ADNEXA

MICHÈLE A. BROWN, MIHAELA I. POP, SUSAN M. ASCHER, MOHAMED ELAZZAZI, AND RICHARD C. SEMELKA

MRI plays an increasingly important role in the evaluation of patients with adnexal disease. Accurate tissue characterization often allows definitive diagnosis not possible with other imaging modalities. MRI characteristics help predict the likelihood of malignancy in order to direct proper management and limit surgical intervention for benign disease [1, 2]. In women who are of childbearing age or pregnant, MRI provides detailed evaluation of adnexal disease without ionizing radiation or other harmful effects on the fetus [3]. This chapter describes the MRI appearance of a variety of benign and malignant adnexal diseases.

MRI TECHNIQUE

Bowel peristalsis can cause significant degradation of images in the pelvis. To reduce this artifact, patients should fast for 4–6 hours before scanning, or an antiperistaltic drug such as glucagon may be used. A dose of 1 mg given intramuscularly 15–30 min before the examination is effective. To reduce the presence of flow-related artifacts, saturation pulses can be placed above and below the volume of interest. In addition, having the patient void before imaging improves comfort and decreases motion artifact.

A phased-array coil should be used routinely. Phased-array coils improve signal-to-noise ratio in the center of the body compared to conventional body coils [4–6]. Because of near field sensitivity of the coil, fat beneath the coil is bright in signal intensity and motion-related ghost artifact may be a problem [7]. A variety of techniques have been described to moderate this effect [8, 9]. It is helpful to place a saturation band over the anterior body wall for non-fat-suppressed sagittal images and use an anterioposterior frequency-encoding direction for axial images.

Standard sequences used for the adnexa include transverse T1-weighted spoiled gradient-echo, transverse T1-weighted gradient-echo with fat suppression, transverse echo-train spin-echo, T2-weighted, sagittal or coronal breath-hold or single-shot echo-train spin-echo, and postgadolinium gradient-echo with fat suppression. Sequential fast 3D gradient-echo sequences are used for dynamic postgadolinium imaging.

Abdominal-Pelvic MRI, Third Edition, edited by Richard C. Semelka. Copyright © 2010 John Wiley & Sons, Inc.

Imaging at 3 T

There has been increasing use of 3 T systems to image the female pelvis, including the ovaries [10]. The technical challenges and potential solutions are similar to those encountered when imaging the uterus, as discussed in Chapter 14. Please refer to that discussion for more detail regarding optimization of 3 T imaging techniques for female pelvic imaging.

NORMAL ANATOMY

From the Latin *adnectere* (to bind to), adnexa are accessory or adjoining anatomic parts. In the female pelvis, the adnexa are the appendages of the uterus: the ovaries, the fallopian tubes, and the ligaments that support the uterus.

Ovary

During the first year of life, the ovaries migrate into the true pelvis to lie within the ovarian fossa, a depression within the pelvic sidewall. The ovarian fossa is defined by the external iliac vessels anteriorly and the ureter and internal iliac vessels posteriorly. Although this is the typical location of the ovaries, there is some variability based on multiparity, the size of the bladder and uterus, and prior surgery. The ovaries are held in position by the ovarian suspensory ligament (or infundibulopelvic ligament) superiorly and medially, by the broad ligament (proper ovarian ligament) inferiorly and anteriorly, and by the mesovarium anteriorly. In general, the ovaries are lateral to the uterus and inferior to the fallopian tubes.

The blood supply of the ovaries is derived from the ovarian artery and the ovarian branch of the uterine artery. These anastomose to form an arcade of approximately 10 arterial branches that penetrate the ovary. The ovarian artery and vein pass through the ovarian suspensory ligament. The venous drainage of the ovaries differs slightly between left and right, with the left ovarian vein draining into the left renal vein and the right ovarian vein draining directly into the IVC near the right renal vein. The lymphatic drainage of the ovaries follows the venous drainage into para-aortic nodes.

Ovarian size varies with age; in the neonate, ovaries measure approximately 1.5 × 2.5 × 3 mm [11]. In the premenopausal female, ovarian volume is 5–8 g, with increases during ovulation and pregnancy. A decrease in size begins at age 30, and after menopause ovarian atrophy is more pronounced [12]. The use of hormonal replacement therapy may affect the rate of atrophy.

Histologically, the ovary is divided into medullary (central) and cortical (peripheral) regions. The medulla contains the stromal cells, lymphatics, blood vessels, and nerves. The cortex is composed of follicles differing in their stage of maturation; the number of follicles is greatest at birth and progressively declines, disappearing after menopause [11]. During the reproductive years, one graafian follicle matures each month, releasing an ovum and becoming a corpus luteum. In the absence of pregnancy, the corpus luteum degenerates into a corpus albicans and eventually completely involutes. Oral contraceptives interfere with this process, suppressing graafian follicle maturation and ovum release.

In a study of MRI features of the ovary [13], two patterns of ovarian anatomy were seen with T2-weighted images. The first is a lower-signal-intensity cortex and stroma with higher signal in the medulla; this pattern is more prevalent in premenopausal subjects (fig. 15.1). The second pattern is a more homogeneous low signal of the cortex and medulla. This pattern is more common in postmenopausal women. On T1-weighted images, the ovaries have signal intensity homogeneously isointense to the myometrium. After the administration of gadolinium, ovarian enhancement differs with hormonal status. In premenopausal women, ovarian enhancement tends to be less than the enhancement of the myometrium, while in postmenopausal women enhancement is equivalent [14].

Transposed ovaries have imaging patterns similar to normal ovaries (fig. 15.2).

Functional cysts have very high signal on T2-weighted images and are of low to intermediate signal on T1-weighted images. These include follicular, corpus luteal, and corpus albicans cysts. Cysts are common in ovaries regardless of age and hormonal status. In one series of asymptomatic postmenopausal women, 17% had at least one cyst [15]. Cyst walls are generally of decreased signal intensity on T2-weighted images; wall enhancement after gadolinium is variable (fig. 15.3). Corpus luteal cysts have thick and often irregular walls, which enhance early and intensely after contrast (fig. 15.4) [16]. Corpus luteal cysts may also contain proteinaceous material or blood, altering their T1- and T2-weighted signal characteristics (fig. 15.5).

Fallopian Tubes

The fallopian tubes form from the unfused proximal portions of the müllerian ducts during the third phase of müllerian development [17]. They are encased within the superior portion of the broad ligament and assume a relatively horizontal orientation during the migration of the ovaries. The normal tube is approximately 10 cm in length and has a 1- to 4-mm luminal diameter [18]. Four segments are recognized (medial to lateral): interstitial portion, isthmus, ampulla, and infundibulum or fimbriated end. The wall of the fallopian tube is complex, consisting of longitudinal folds and mucosal rugae

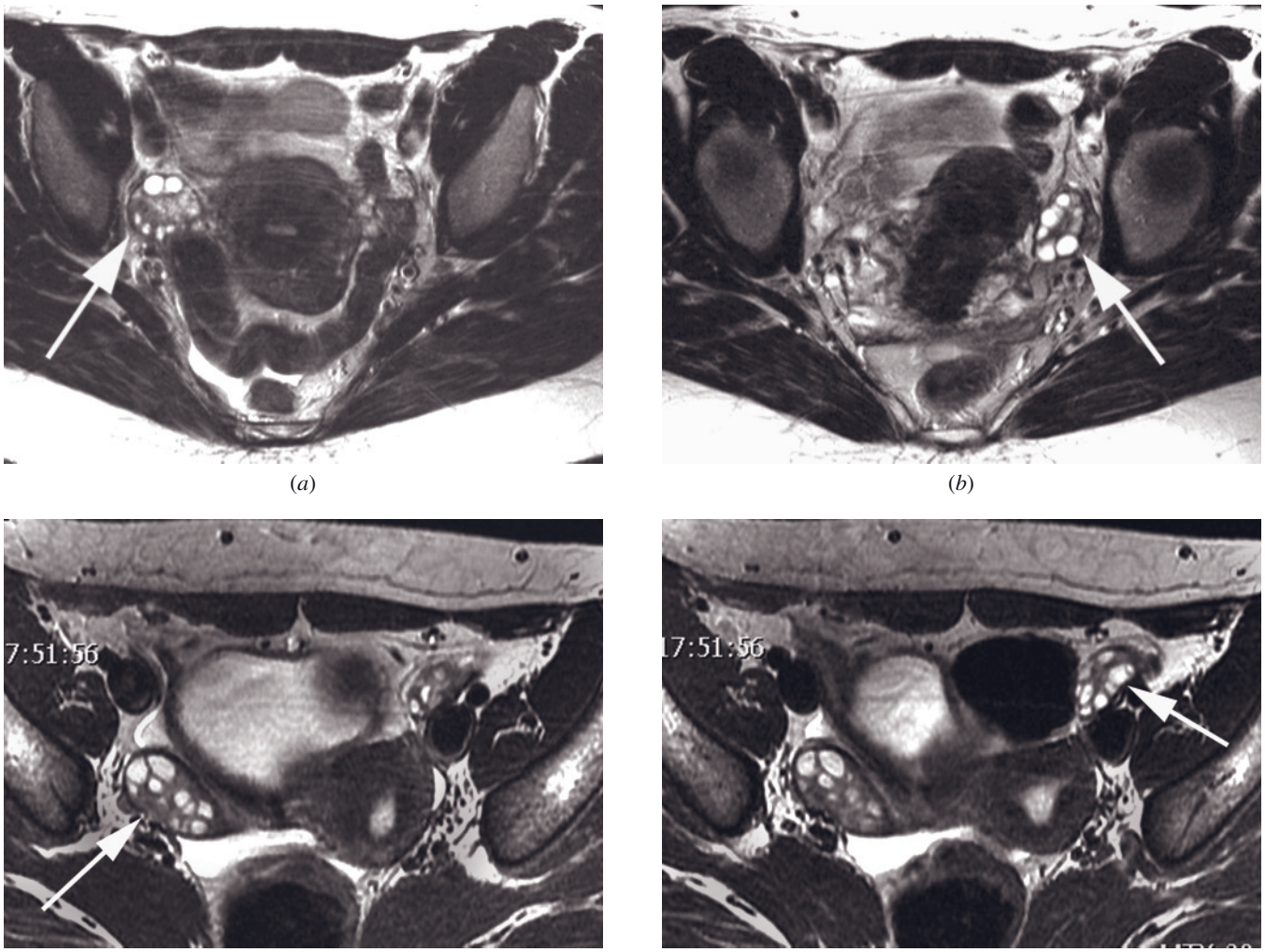

FIG. 15.1 Normal ovaries. Transverse T2-weighted ETSE images demonstrate normal ovaries (arrows, *a*, *b*) with multiple small hyperintense follicles. **Normal ovaries at 3 T.** Transverse T2-weighted ETSE images demonstrate normal ovaries (arrows, *a*, *b*) with multiple small, hyperintense follicles.

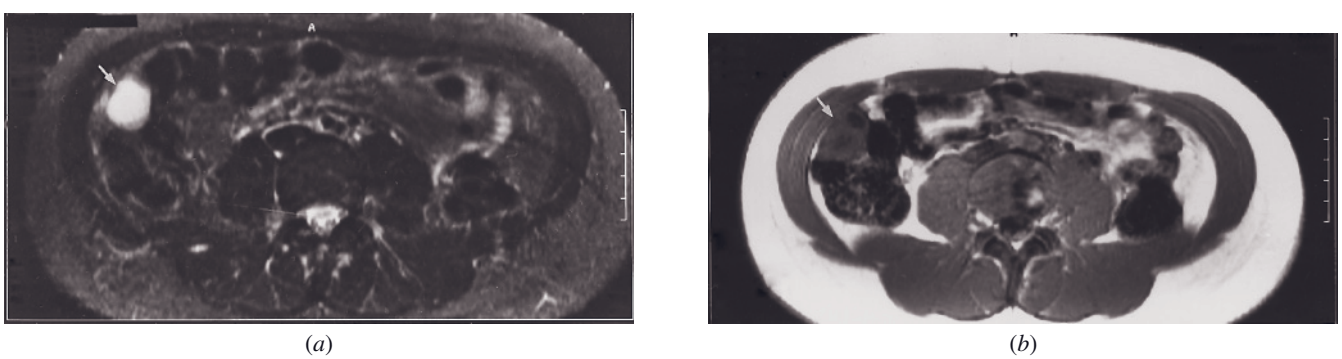

FIG. 15.2 Transposed right ovary. T2-weighted ETSE (*a*) and T1-weighted gradient-echo (*b*) images of a transposed normal right ovary (arrows, *a*, *b*) in a woman with cervical cancer treated with radiation therapy. **Transposed ovaries with**

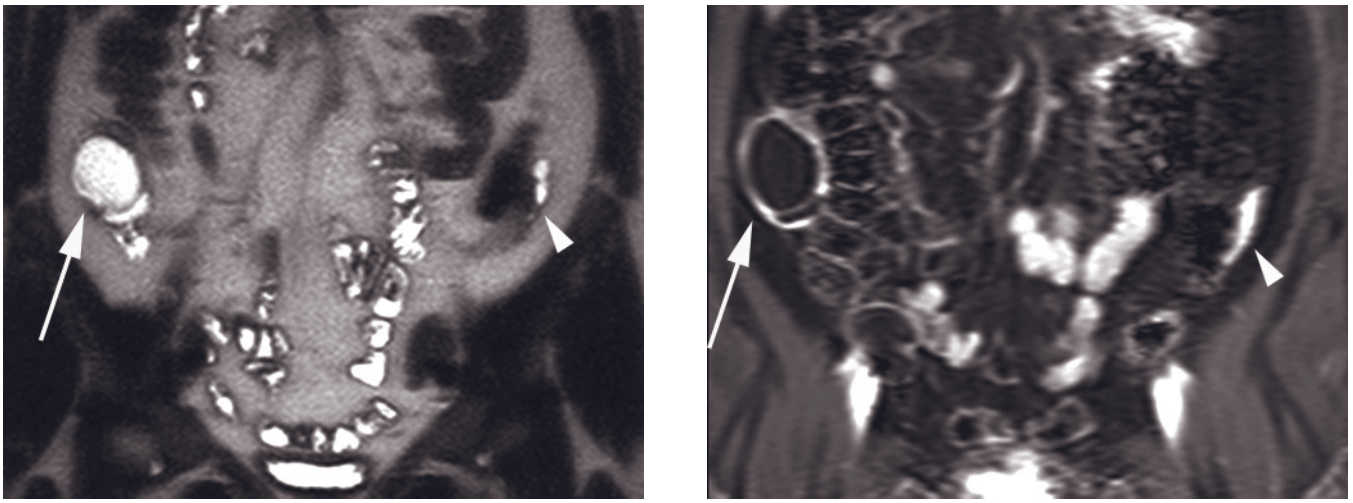

(*c*) (*d*)

FIG. 15.2 (*Continued*) **physiological cyst on the right.** Coronal T2-weighted SS-ETSE (*c*) and gadolinium-enhanced fat-suppressed T1-weighted gradient-echo (*d*) images show transposed ovaries in a different patient with cervical carcinoma. There is a physiological cyst in the right ovary (arrows, *c*, *d*). A portion of the normal left ovary is also seen (arrowheads, *c*, *d*).

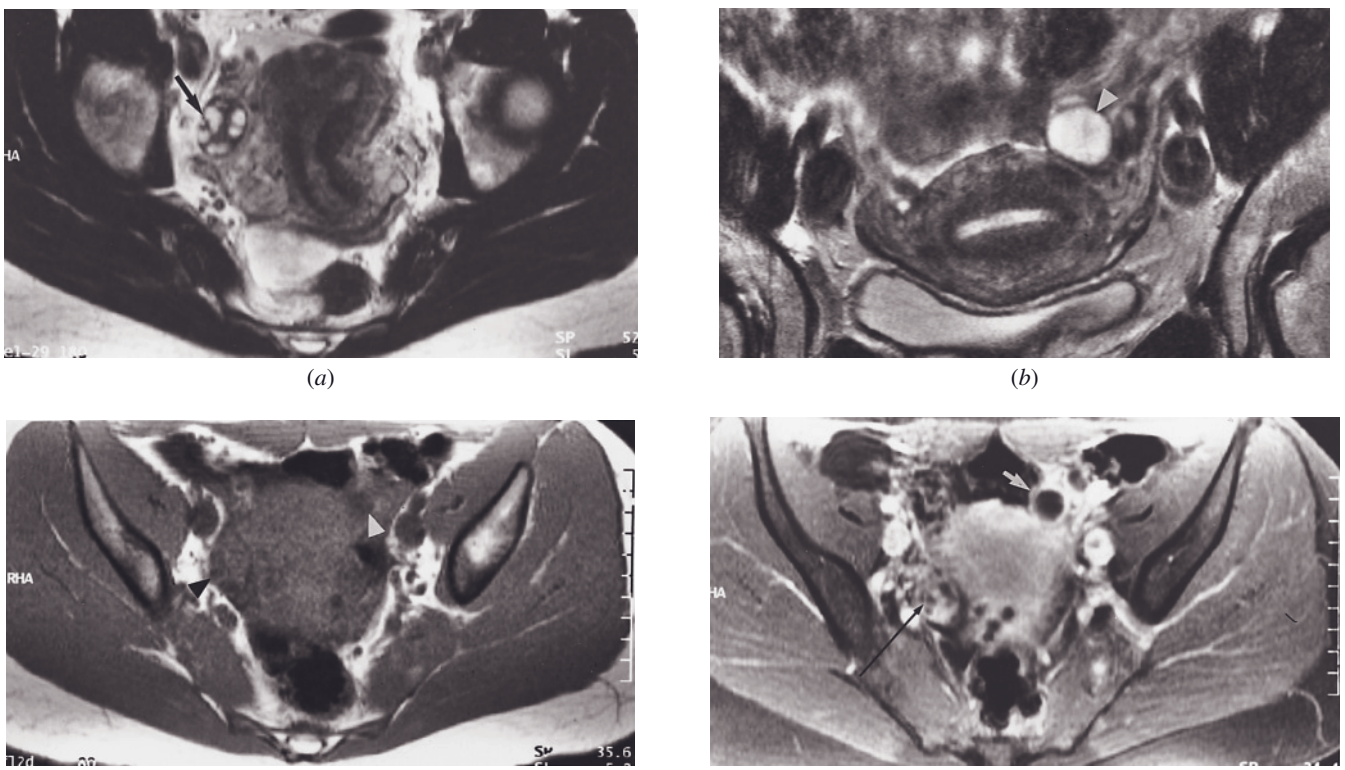

(*a*) (*b*)

(*c*) (*d*)

FIG. 15.3 Normal ovary with a functional cyst. Transverse (*a*) and coronal (*b*) 512-resolution T2-weighted ETSE,T1-weighted gradient-echo (*c*), and transverse gadolinium-enhanced T1-weighted fat-suppressed gradient-echo (*d*) images in a woman with normal ovaries. The high-resolution T2-weighted images (*a*, *b*) show follicles within the right ovary (arrow, *a*) and a cyst within the left ovary (arrowhead, *b*). The cortex containing the follicles is lower in signal intensity than the medulla. On the unenhanced T1-weighted image, the ovarian stroma is isointense to the uterus, with the follicles and functional cyst being lower in signal intensity (arrowheads, *c*). After contrast, the ovarian parenchyma enhances, including the rims of the follicles (long arrow, *d*) and cyst (short arrow, *d*). Simple functional cysts are low to intermediate in signal intensity on T1-weighted images and high in signal intensity on T2-weighted images and have variable thin mural enhancement after contrast administration.

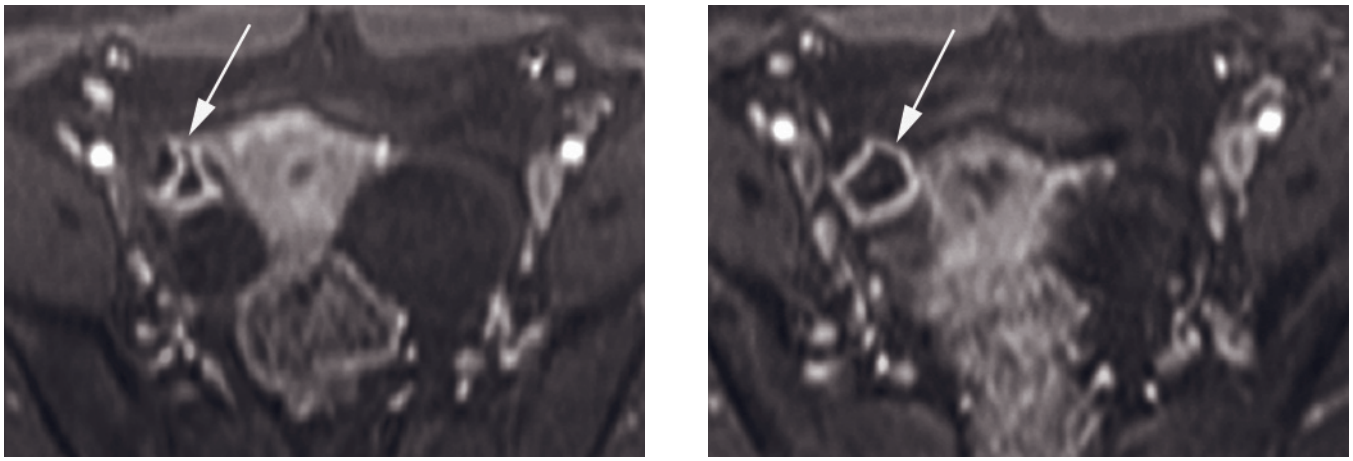

(*a*) (*b*)

FIG. 15.4 Corpus luteal cyst. Transverse gadolinium-enhanced fat-suppressed T1-weighted gradient-echo images obtained in late arterial phase show an intensely enhancing, irregularly shaped cyst (arrow, *a*, *b*). Intense early enhancement and thick, irregular walls are characteristics of corpus luteal cysts on MR images.

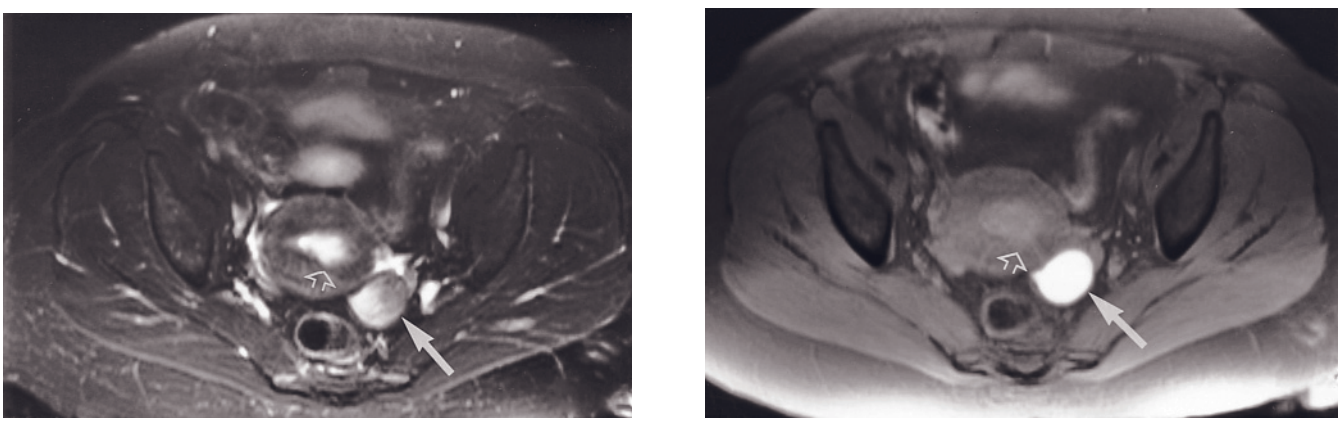

(*a*) (*b*)

FIG. 15.5 Hemorrhagic cyst in a patient with endometrial carcinoma. T2-weighted fat-suppressed ETSE (*a*) and T1-weighted fat-suppressed gradient-echo (*b*) images. Hemorrhagic cysts can mimic endometriomas with high signal intensity on T1-weighted images (arrow, *b*) and heterogeneous high signal intensity on T2-weighted images (arrow, *a*). Note the endometrial thickening due to endometrial carcinoma with focal thinning of the junctional zone (open arrows, *a*, *b*).

whose size and number increase from medial to lateral. The mucosal surface contains ciliated cells that aid in the passage of the ovum to the uterine cavity. The normal fallopian tube is not routinely seen with MR imaging.

CONGENITAL ABNORMALITIES

Congenital abnormalities of the ovaries include complete and mixed gonadal dysgenesis as well as true and pseudohermaphroditism. MRI is very important in demonstrating the internal reproductive organs and can identify the presence of normal ovaries, streak gonads, or ovotestes [19, 20]. Gonadoblastoma, a neoplasm occurring in up to one-third of patients with mixed gonadal dysgenesis, can also be detected [19, 21].

The Buttram classification of müllerian duct defects includes tubal disorders. Class I anomalies include fallopian tube agenesis, which is a bilateral condition [18]. Class II anomalies include unicornuate uterus, which may be associated with one aplastic tube. Diethylstilbestrol-related anomalies may involve shortened, convoluted tubes with withered fimbria, narrow fimbrial openings, and bandlike constrictions in the intramural portion of the tube [22].

BENIGN DISEASE OF THE ADNEXA

Benign adnexal disease consists of neoplastic and nonneoplastic processes. Benign neoplastic disease primarily involves ovarian tumors, as benign fallopian tube tumors are exceedingly rare. Nonneoplastic disease such as infection and endometriosis may affect the fallopian tubes as well as the ovaries. Specific benign masses such as endometriomas and mature cystic teratomas demonstrate specific MRI features that, when present, allow confident diagnosis. MRI may also predict the likelihood of malignancy in an adnexal mass with several MRI criteria that have been described; these are discussed in greater detail in the following section on malignant disease. It is important to appreciate that overlap exists between the MRI appearance of benign and malignant ovarian masses, and proper management of nonspecific masses may include serial imaging and often resection.

Nonneoplastic Disease

Functional Ovarian Cysts

When uncomplicated, functional cysts are not a diagnostic dilemma. However, when complicated by hemorrhage, differentiation from endometriomas and neoplasm may be difficult. Resolution of a cyst on serial imaging easily classifies it as functional. On a single study, certain features aid differentiation. Papillary projections are an important feature of neoplastic cysts (fig. 15.6) not present in functional cysts (fig. 15.7) [23]. Endometriomas generally have profound T1-shortening that causes high signal on T1-weighted images and T2 shortening that causes low signal on T2-weighted images [24]. Low signal on T2-weighted images (shading) is a feature of endometrioma that is reported to be unusual in corpus luteal cysts. In the absence of multiplicity or T2 shading, the distinction is often difficult and follow-up imaging may be helpful.

Theca-Lutein Cysts

Elevated circulating levels of human chorionic gonadotropin (β-hCG), usually seen in women with gestational trophoblastic disease, cause gross enlargement of the ovaries due to the presence of multiple theca-lutein cysts. Of women with gestational trophoblastic disease, up to 46% are found to have theca-lutein cysts [25]. Numerous cysts, often multilocular and measuring up to 4 cm, may be seen. The ovaries are generally between 6 and 12 cm but may enlarge to upwards of 20 cm [25]. While usually asymptomatic, women may present with pain if there is cyst rupture or hemorrhage or if the ovary torses.

On MRI, theca-lutein cysts have a variable appearance with low to high signal on T1- and high signal on T2-weighted sequences [26, 27]. If there is an associated hypervascular endometrial mass, gestational trophoblastic disease is likely (fig. 15.8). Women undergoing ovulation induction for infertility may have a similar ovarian response. Accompanying simple or hemorrhagic ascites may indicate ovarian hyperstimulation syndrome given the appropriate clinical scenario. In these cases, an intrauterine or ectopic gestation may also be evident (fig. 15.9).

Paraovarian and Peritoneal Cysts

Almost any sort of benign or malignant ovarian cyst can arise adjacent to the ovary within the broad ligament or parovarium, and collectively these cysts are termed paraovarian cysts [12]. They may account for 10–20% of adnexal masses, based on surgical reports [28]. A common subset of these cysts is hydatid cysts of Morgagni that arise from müllerian duct remnants. These occur at the fimbriated end of the fallopian tube and are generally asymptomatic. Large cysts may undergo torsion or develop hemorrhage. On MRI, uncomplicated paraovarian cysts have signal characteristics of simple fluid. Multiplicity and bilaterality have been reported. Paraovarian cysts are round or ovoid and may be indistinguishable from ovarian cysts unless a normal ipsilateral ovary is identified separate from the cystic lesion.

Peritoneal inclusion cysts or peritoneal pseudocysts require two conditions for formation: an ipsilateral functioning ovary and adhesions. Most often seen in women with prior abdominopelvic surgery or endometriosis, these are pseudocysts that lack true walls. Because they are fluid collections contained by mesothelium-lined adhesions, they conform to the surrounding structures and are often triangular or irregular in shape, rather than round. This distinguishing feature is well shown by MRI, and in one series MRI was more useful than CT or US in their diagnosis [29]. Inclusion cysts can also mimic other adnexal cysts [30]. If left untreated, they tend to grow because of continued accumulation of fluid (fig. 15.10).

Endometriosis

Endometriosis is a generally benign entity that affects women in their reproductive years. It may be an incidental finding or may present with pain or infertility. Malignant transformation occurs in less than 1% of cases, most commonly to endometrioid carcinoma, clear cell carcinoma, and carcinosarcoma [12, 31]. Enlargement of an endometrioma during pregnancy may be the result of changes in the hormonal milieu and does not necessarily indicate malignant transformation [32]. By strict pathological criteria, ectopic endometrial glands with surrounding endometrial stroma must be found; however, repeated hemorrhage often causes oblitera-

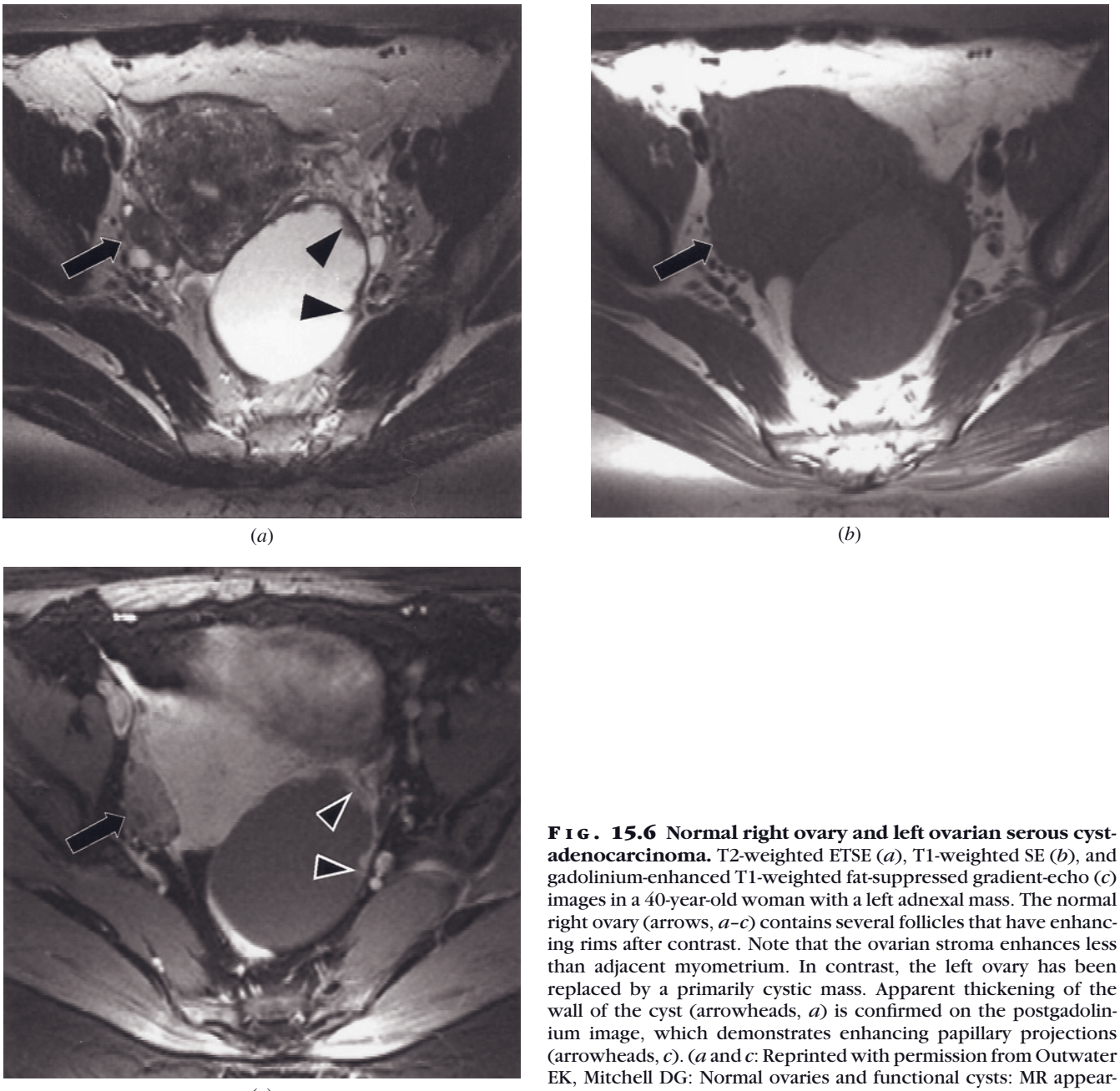

(*a*) (*b*) (*c*)

FIG. 15.6 Normal right ovary and left ovarian serous cystadenocarcinoma. T2-weighted ETSE (*a*), T1-weighted SE (*b*), and gadolinium-enhanced T1-weighted fat-suppressed gradient-echo (*c*) images in a 40-year-old woman with a left adnexal mass. The normal right ovary (arrows, *a–c*) contains several follicles that have enhancing rims after contrast. Note that the ovarian stroma enhances less than adjacent myometrium. In contrast, the left ovary has been replaced by a primarily cystic mass. Apparent thickening of the wall of the cyst (arrowheads, *a*) is confirmed on the postgadolinium image, which demonstrates enhancing papillary projections (arrowheads, *c*). (*a* and *c*: Reprinted with permission from Outwater EK, Mitchell DG: Normal ovaries and functional cysts: MR appearance. *Radiology* 198: 397–402, 1996.)

tion of the endometrial lining [33, 34]. In order of decreasing frequency, the most common sites of involvement are the ovaries, cul-de-sac and posterior uterine wall, uterosacral ligaments, anterior uterine wall, and bladder dome [34–36]. Other potential sites of involvement are the sigmoid colon, fallopian tubes, and distal ureters. Hypothesized etiologies include three major mechanisms: 1) metastatic: reflux of endometrial cells through the fallopian tubes with implantation onto pelvic structures or spread through blood vessels, lymphatics, or surgery; 2) metaplastic: coelomic cells are transformed by repeated exposure to hormonal stimuli; and 3) induction: endometrial substances induce undifferentiated mesenchymal cells [37]. Metastatic deposition is the most accepted theory, specifically retrograde menstruation. Retrograde menstruation has been associated with disordered myometrial contractions that may alter the direction of flow during menses [38].

On MRI, endometriomas are typically thick-walled cysts with extensive surrounding fibrosis and adhesions to adjacent structures. Imaging studies most often detect endometriomas rather than small endometrial implants,

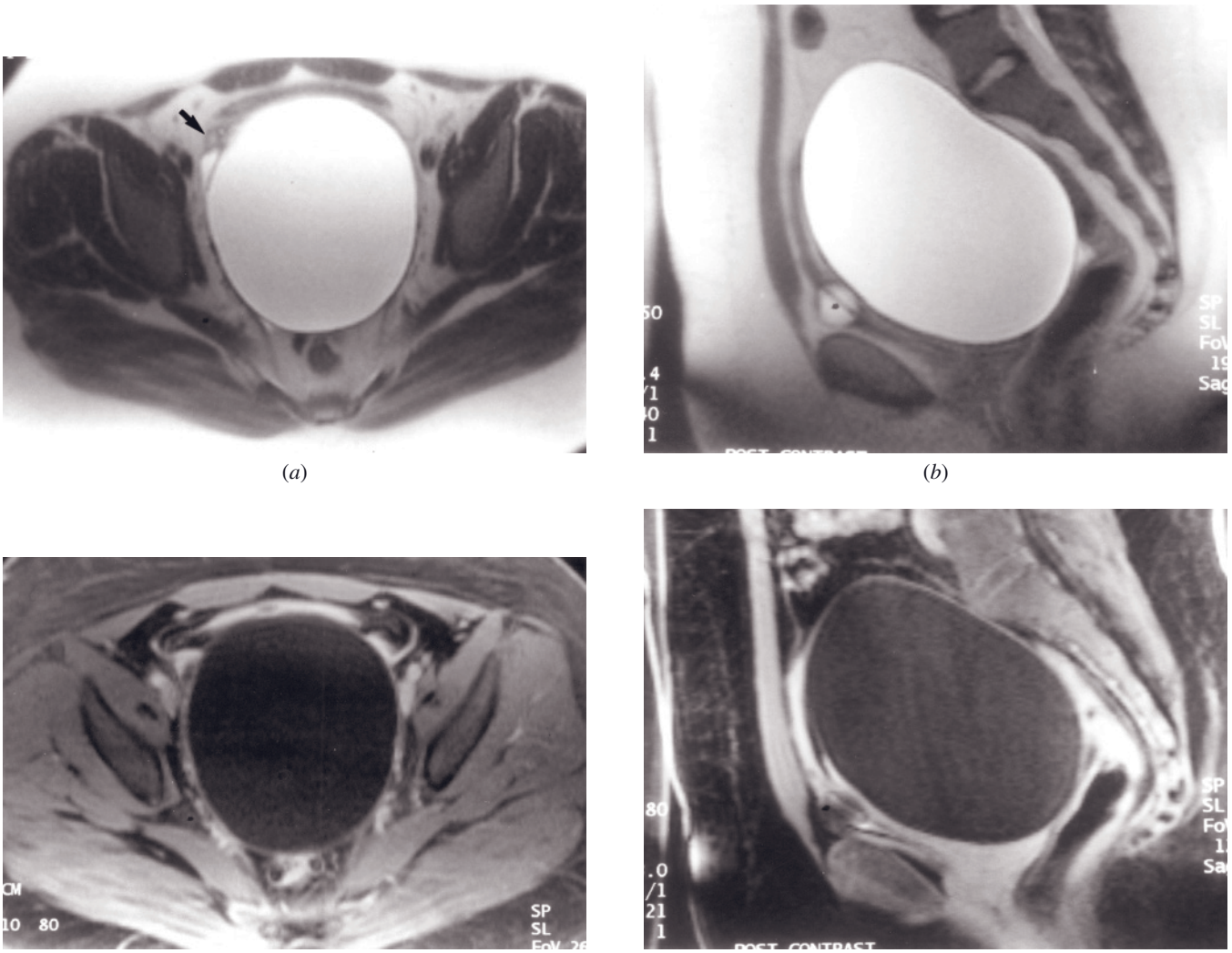

FIG. 15.7 Ovarian cyst. Transverse (*a*) and sagittal (*b*) T2-weighted SS-ETSE and transverse (*c*) and sagittal (*d*) gadolinium-enhanced fat-suppressed images. A large, well-defined cyst with simple fluid content and no mural irregularity is apparent arising from the right ovary (arrow, *a*).

which are often difficult to detect. On T1-weighted images, endometriomas are of high signal intensity. The high signal intensity is more conspicuous with the use of fat suppression; lesions less than 1 cm in size can be detected on fat-suppressed T1-weighted images [39–41]. On T2-weighted images, endometriomas demonstrate low signal intensity (shading), presumably due to repeated bleeding and the accumulation of blood products that shorten T2 (figs. 15.11–15.13). This profound T2 shortening is uncommon in functional or hemorrhagic cysts [16]. When these signal characteristics are used as diagnostic criteria, the sensitivity of MR for detecting endometriomas ranges from 90% to 92%, and the specificity ranges from 91% to 98% [39, 42, 43]. Smooth ringlike mural enhancement is typical of endometriomas, although solid lesions also occur (fig. 15.14). The characteristic ring enhancement may cause confusion with other processes such as tubo-ovarian abscess or hemorrhagic cysts if all sequences are not considered [42, 44, 45].

The diagnosis of endometrial implants is more elusive. High-resolution MR imaging may detect implants as high-signal lesions on T1-weighted sequences, especially with fat suppression [39, 40]. Some implants also exhibit enhancement after gadolinium [42]. High signal on T2-weighted images has also been described, presumably due to actual endometrial glands within the implants [58]. Typically, implants are low-signal-intensity masses on T2-weighted images due to surrounding fibrosis, and foci of hemorrhage may also be

(*a*)

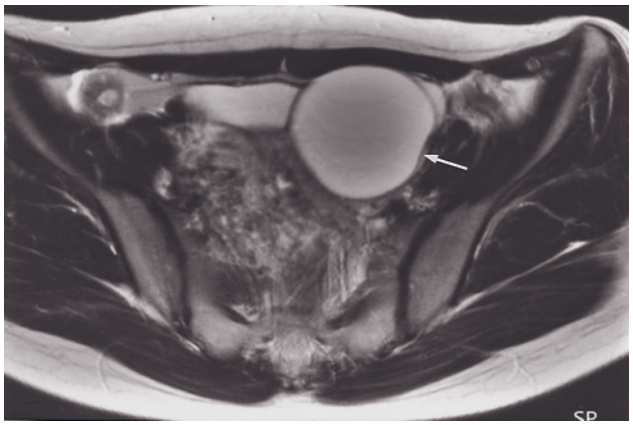

(*b*)

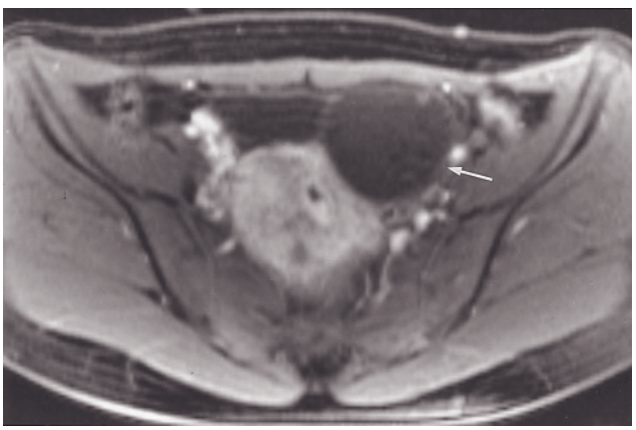

(*c*)

FIG. 15.8 Theca-lutein cysts. Sagittal (*a*) and transverse (*b*) 512-resolution T2-weighted ETSE and gadolinium-enhanced fatsuppressed T1-weighted SGE (*c*) images in a woman with an invasive mole. The combination of an infiltrating endometrial mass and enlarged and cystic ovaries (long arrows, *a–c*) should suggest the diagnosis of gestational trophoblastic disease. Note the high signal of myometrium in the area of marked molar invasion (arrowheads, *a*) versus the area where it is relatively spared (short arrows, *a*). Whereas theca-lutein cysts are present in up to one-third of women with gestational trophoblastic disease, they also occur in other conditions associated with elevated human chorionic gonadotropin (β-hCG) levels.

detected [46]. Laparoscopic or surgical diagnosis, staging, and treatment are still often necessary, as the sensitivity of MR for detecting mild endometriosis has been reported to be 75% [47]. MR imaging may not detect very small superficial lesions seen at laparoscopy; however, MR imaging may surpass laparoscopy at detecting deep pelvic endometriosis, which is more frequently symptomatic [48].

Polycystic Ovaries

Polycystic ovarian syndrome (PCOS) represents a spectrum of disease that may manifest clinically with hirsutism, irregular bleeding, or infertility. Obesity is an associated characteristic but does not define the disease [49]. The most common cause is a hormone imbalance leading to stimulation of the ovaries without maturation of a dominant follicle. As a result, the ovaries are left with numerous follicles of nearly the same size, generally at the periphery of the ovary. When present, ovarian enlargement is due to an increase in the stromal tissues; capsular hypertrophy is also present [12, 50]. On MR images, polycystic ovaries are normal to large in size, with multiple small peripheral follicles of uniform size. A dark capsule and central stroma can be seen on T2-weighted images (fig. 15.15) [51, 52]. Unlike normal ovaries, the small uniform follicles do not become hemorrhagic and are consistently bright on T2-weighted images and dark on T1-weighted images [51]. It should be noted that overlap exists between the MRI appearance of normal and polycystic ovaries, and even classic imaging findings are neither sufficient nor necessary for the diagnosis of PCOS [52]. The significance of polycystic ovaries in asymptomatic women is not currently well understood. PCOS patients are typically treated for a

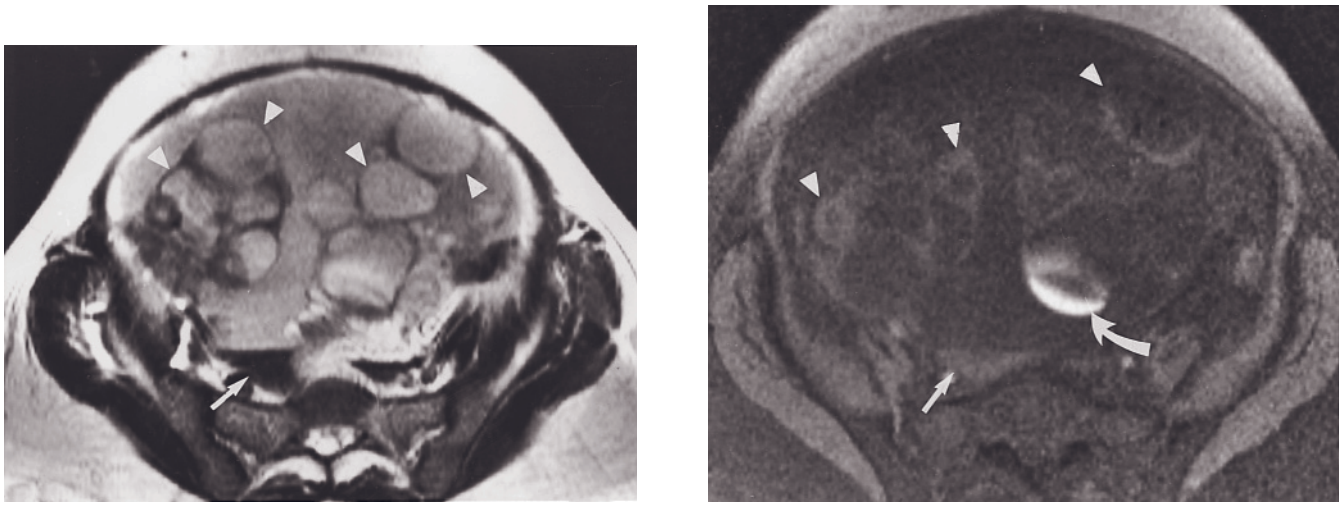

(*a*) (*b*)

FIG. 15.9 Theca-lutein cysts in ovarian hyperstimulation syndrome. Transverse T2-weighted ETSE (*a*) and T1-weighted gradient-echo fat-suppressed gradient echo (*b*) images in a patient on ovulation induction medicine who presented with acute pain and hypotension. Bilateral multilocular ovarian cysts (arrowheads, *a*, *b*) are identified in association with a gravid uterus (not shown) and marked free abdominopelvic fluid. Some of the cysts are complicated by hemorrhage, which is best seen on the fat-suppressed T1-weighted images (curved arrow, *b*). There is also evidence of hemoperitoneum. Note that the dependent fluid is intermediate in signal intensity on the T1-weighted images and is decreased in signal intensity on T2-weighted images, which is consistent with intracellular methemoglobin (arrows, *a*, *b*). The hyperstimulation syndrome is a well-recognized, life-threatening complication of ovulation induction therapy for infertility.

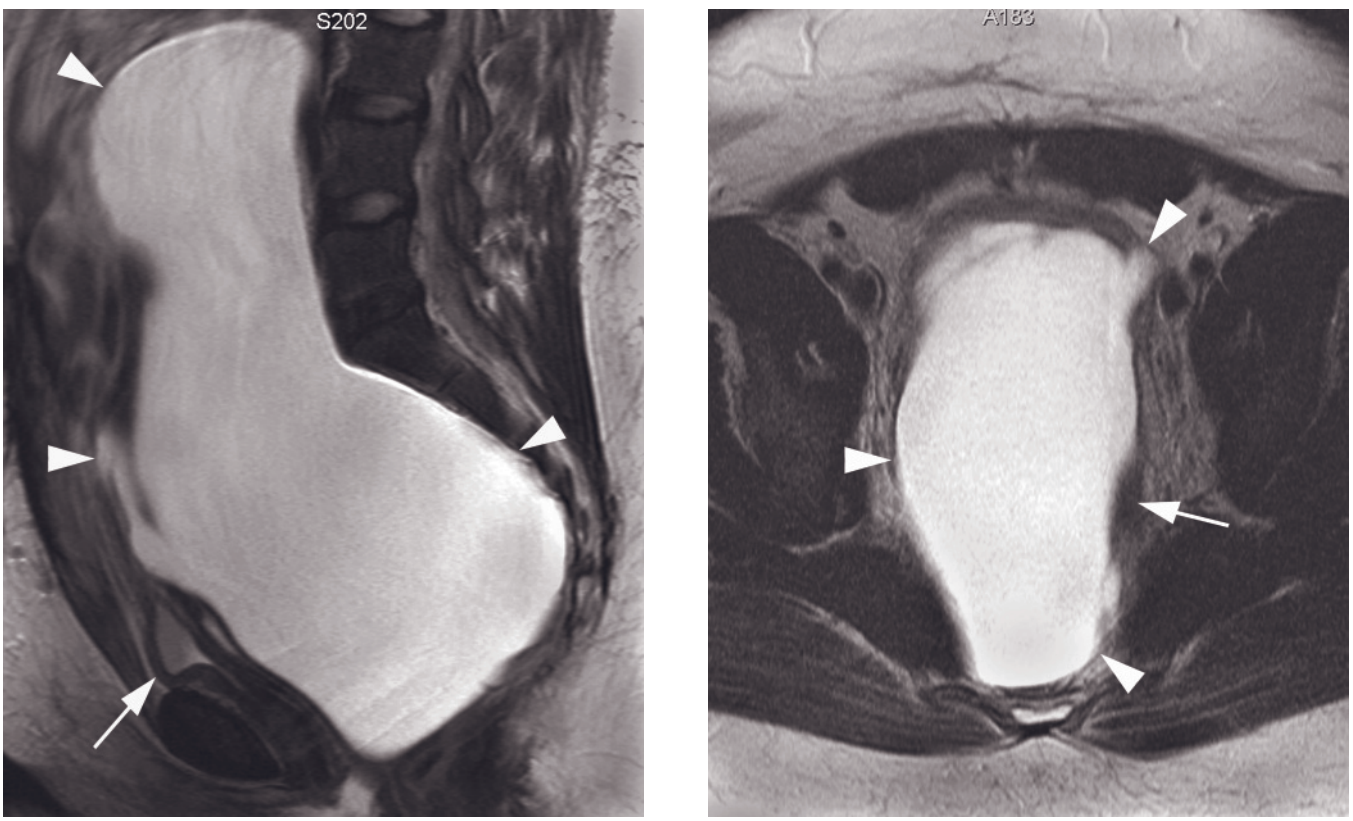

(*a*) (*b*)

FIG. 15.10 Peritoneal inclusion cyst. Sagittal (*a*) and transverse (*b*) T2-weighted ETSE images in a woman with a history of abdominopelvic surgery. A large, irregularly shaped cystic mass (arrowheads, *a*, *b*) displaces the bladder (arrow, *a*) and sigmoid colon (arrow, *b*). The mass was found to be a benign peritoneal cyst.

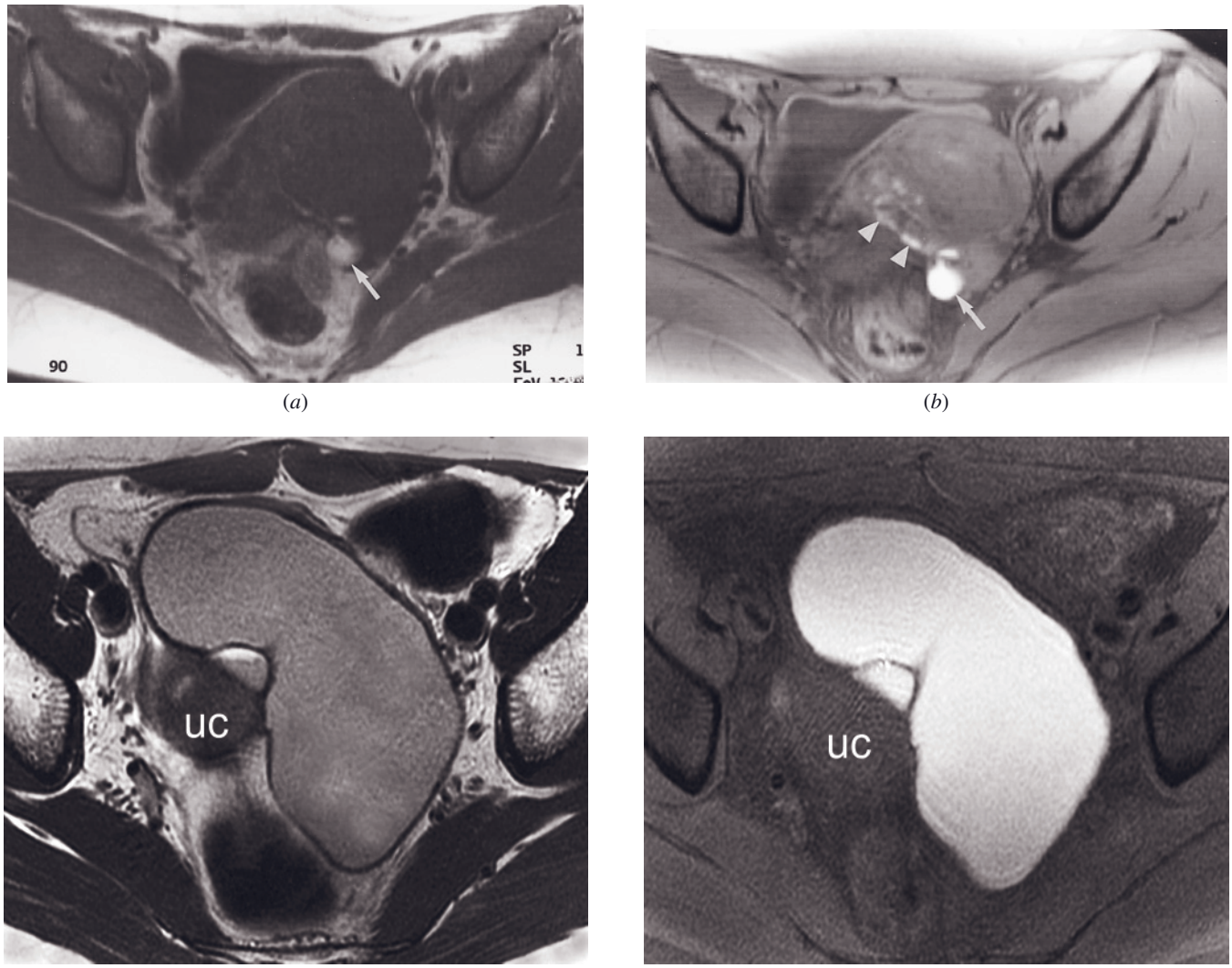

FIG. 15.11 Endometriosis: benefit of fat-suppression. T1-weighted SE (*a*) and T1-weighted fat-suppressed gradient-echo (*b*) images in a patient with bilateral adnexal masses shown on transvaginal ultrasound. There is a high-signal-intensity mass applied to the left ovary on the T1-weighted image (arrow, *a*), which is more conspicuous on the fat-suppressed image (arrow, *b*). Note that the small endometrial implants applied to the uterine serosa are well seen with the fat suppression technique (arrowheads, *b*). **Large endometrioma at 3 T.** Transverse T2-weighted ETSE (*c*) and T1-weighted fat-suppressed T1-weighted gradient-echo (*d*) images in a different patient show a large endometrioma with a single septation adjacent to the uterine cervix (uc). In this case, no additional small implants were seen on fat-suppressed images.

presenting complaint of infertility, menstrual irregularity, or androgen excess; however, there are important long-term health implications, including diabetes and its associated cardiovascular risks. Also, because of the unopposed estrogen seen in anovulation, patients with PCOS are at increased risk for endometrial cancer (fig. 15.16) [49].

Ovarian Torsion

Torsion of the ovary occurs most frequently in prepubertal girls and during pregnancy [53]. The presence of an underlying ovarian mass predisposes the ovary to torsion. While most patients present with acute onset of pelvic pain, some patients present with episodic pain, presumably related to intermittent ovarian torsion. The pathologic and imaging changes reflect the degree of vascular compromise. In the earliest stages, only the venous flow is restricted; this causes enlargement of the ovary from congestion, edema, and interstitial hemorrhage. As arterial flow is restricted, necrosis of the ovary and any associated mass will commence.

Three MRI findings have been described that are together considered diagnostic of acute ovarian torsion: 1) an adnexal protrusion continuous with the uterus or

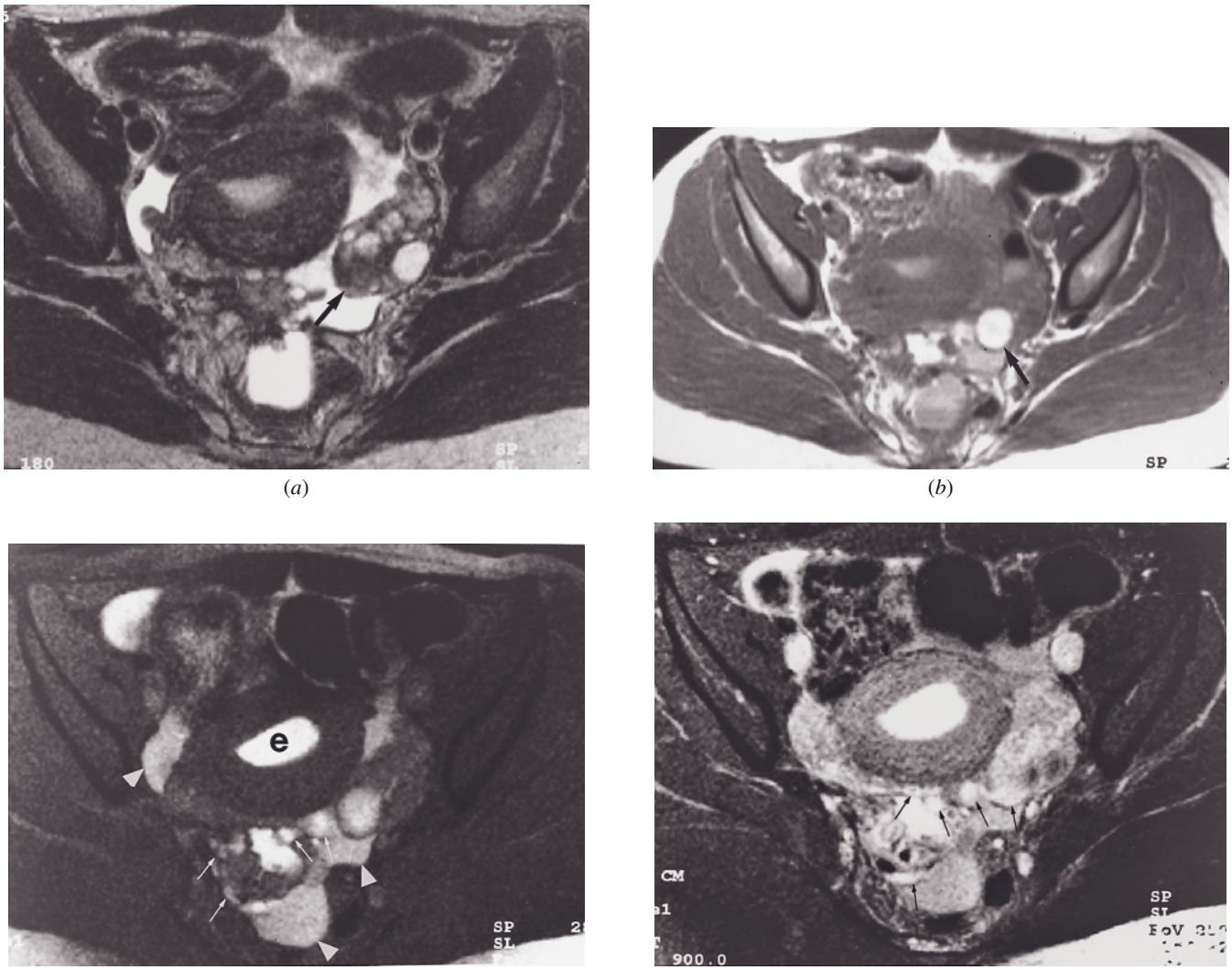

FIG. 15.12 Endometriosis in a patient with cervical stenosis. Transverse T2-weighted ETSE (*a*), T1-weighted SE (*b*), T1-weighted fat-suppressed SE (*c*), and gadolinium-enhanced T1-weighted fat-suppressed SE (*d*) images in an adolescent girl with amenorrhea and pelvic pain. High-signal-intensity endometriomas on the conventional T1-weighted images (arrow, *b*) demonstrate characteristic low signal on the T2-weighted images (arrow, *a*).With the addition of fat suppression, small endometriosis implants that were indistinguishable from pelvic fat on nonsuppressed images become more conspicuous (arrows, *c*). Note that the endometrial canal (e, *c*) and free fluid (arrowheads, *c*) in the pelvis are higher in signal intensity than usual, which is consistent with hematometra and hemoperitoneum, respectively. The endometriomas and endometriosis implants have variable enhancement after contrast administration (arrows, *d*). This patient had cervical atresia and retrograde menses, which presumably account for her endometriosis. Surgery confirmed endometriosis and hemorrhagic free pelvic fluid; the hysterectomy specimen revealed cervical agenesis.

to which engorged blood vessels converge, 2) thick, straight vessels draped around the lesion, and 3) complete absence of enhancement [54]. The first sign, the adnexal protrusion, is felt to represent the pedicle connecting the ovary and/or lesion to the uterus or vascular supply. This torsion knot is generally of low signal intensity on T1- and T2-weighted images (fig. 15.17), but areas of high signal may be seen, reflecting the presence of hemorrhage or congestion [51, 54]. The second sign, draping vessels, are vessels on the surface of the ovary distal to the torsion. The third sign, lack of enhancement, indicates significant arterial compromise; when the torsion involves only the vein or incompletely involves the artery, some enhancement will still be detected. This enhancement may be better seen with the use of MR subtraction imaging [55]. Multiple small peripheral follicles are also seen. Occasionally, a high-signal-intensity rim surrounds the adnexal mass on T1-weighted images. This reflects the presence of hemorrhage within the lesion but is a nonspecific finding

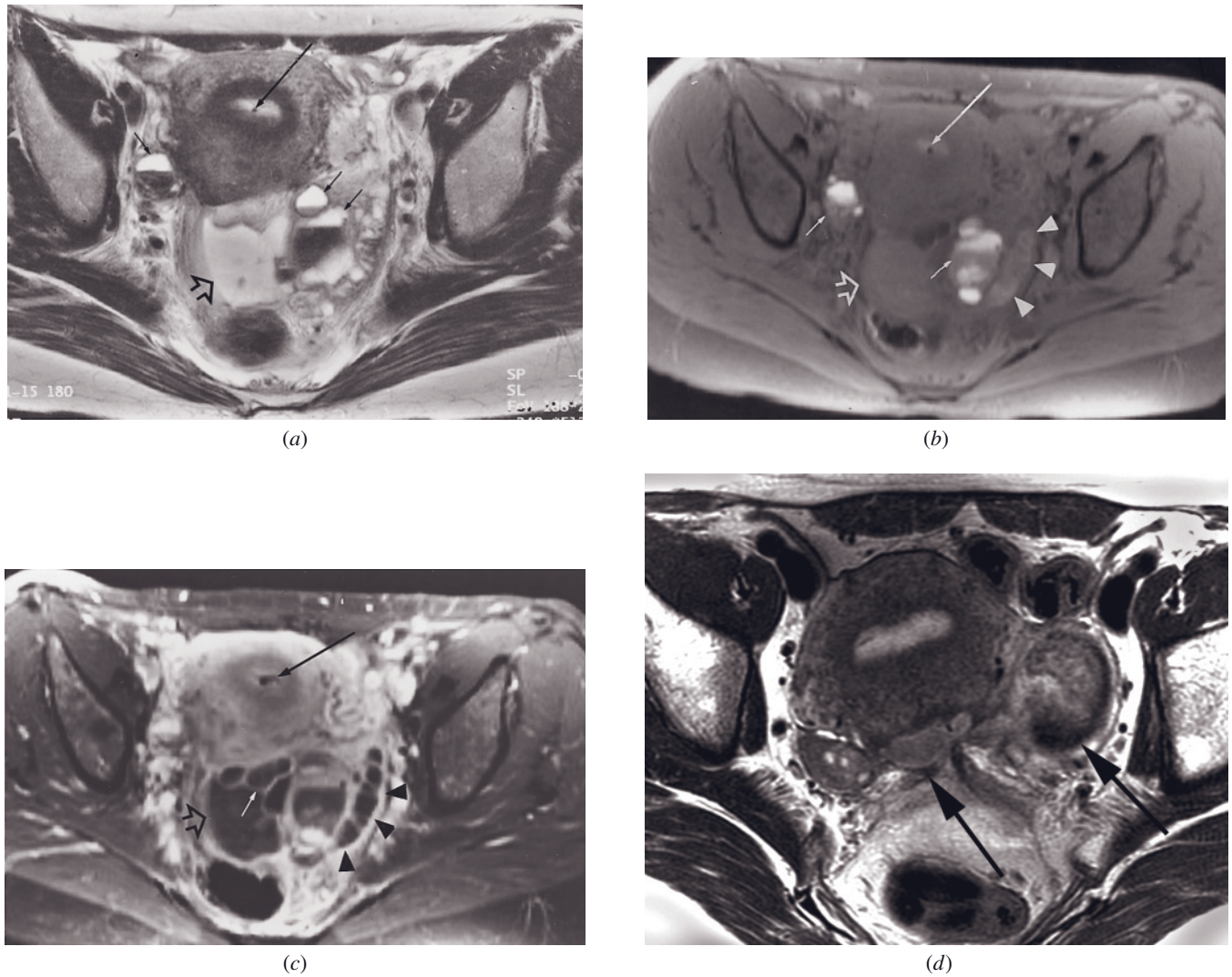

FIG. 15.13 Endometriosis: T2 shortening with fluid-fluid levels. Transverse 512-resolution T2-weighted ETSE (*a*), T1-weighted fat-suppressed SE (*b*), and gadolinium-enhanced T1-weighted fat-suppressed SE (*c*) images in a 42-year-old woman with a 2-month history of pelvic pain, elevated CA-125, and complex adnexal masses on transvaginal sonography. Bilateral adnexal masses have high-signal-intensity components on T1-weighted images, which demonstrate fluid-fluid levels on T2-weighted images consistent with endometriomas (short solid arrows, *a*, *b*). Note the serpentine left hydro/hematosalpinx (arrowheads, *b*, *c*). Posterior to the uterus is a polygonal fluid collection (open arrow, *a–c*). After contrast, the septations of the masses (short solid arrow, *c*) enhance, as do the walls of the dilated left fallopian tube (arrowheads, *c*). The polygonal fluid collection has similar enhancement characteristics. Orthogonal views confirm the findings. Note the IUD within the endometrium (long solid arrows, *a–c*). At laparoscopy, bilateral endometriomas, endometriosis implants, left hydro/hematosalpinx, adhesions, and a peritoneal pseudocyst behind the uterus were found. MRI can add specificity to the finding of an elevated CA-125. **Endometriosis at 3 T.** Transverse T2-weighted ETSE (*d*), T1-weighted gradient-echo (*e*), and T1-weighted fat-suppressed gradient echo (*f*) images in a different patient show pelvic masses (arrows, *d–f*) with low signal on T2-weighted images and high-signal-intensity components on T1-weighted images that suppress with fat saturation. Also note evidence of adhesions, characteristic of severe endometriosis.

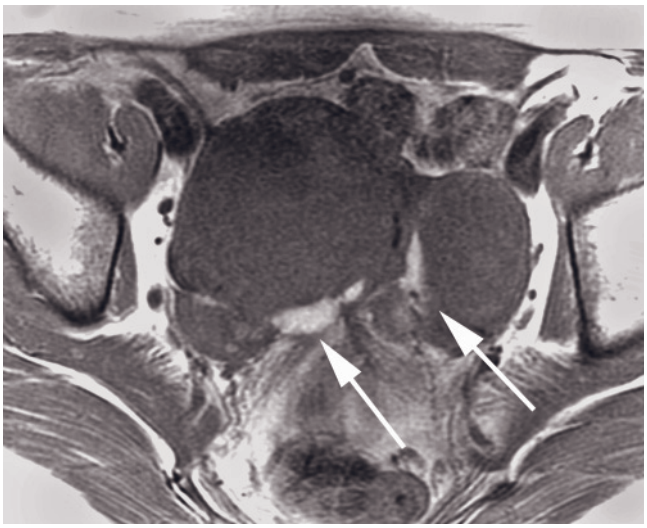

(*e*)

(*f*)

FIG. 15.13 (*Continued*)

(*a*)

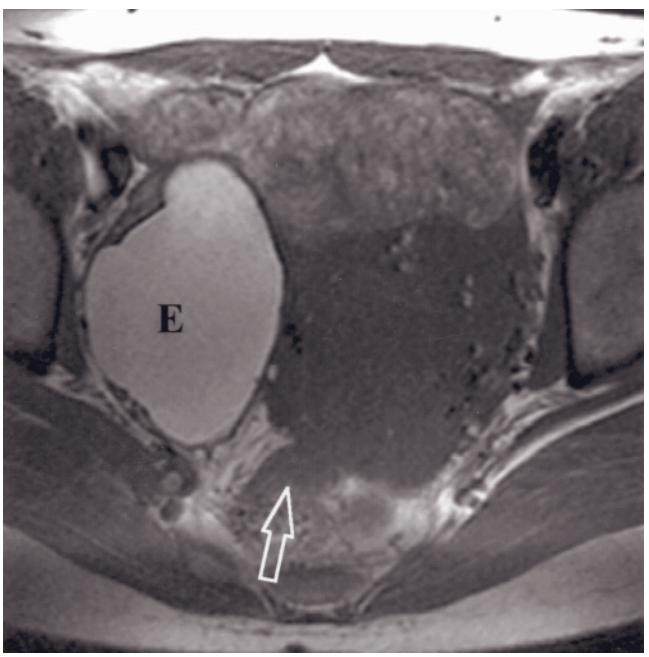

(*b*)

FIG. 15.14 Solid endometrioma. T2-weighted echo-train spin-echo (*a*), T1-weighted spin-echo (*b*), and gadolinium-enhanced T1-weighted fat-suppressed gradient-echo (*c*) images in a patient with right endometrioma and cul-de-sac endometrial implants. The T2-weighted image (*a*) shows the endometrioma (E, *b*) with low signal intensity (arrow, *a*). A fibrotic cul-de-sac solid endometrioma implant (open arrows, *a–c*) infiltrates the perirectal fat (A = adenomyosis, *a*). Gadolinium-enhanced T1-weighted fat-suppressed

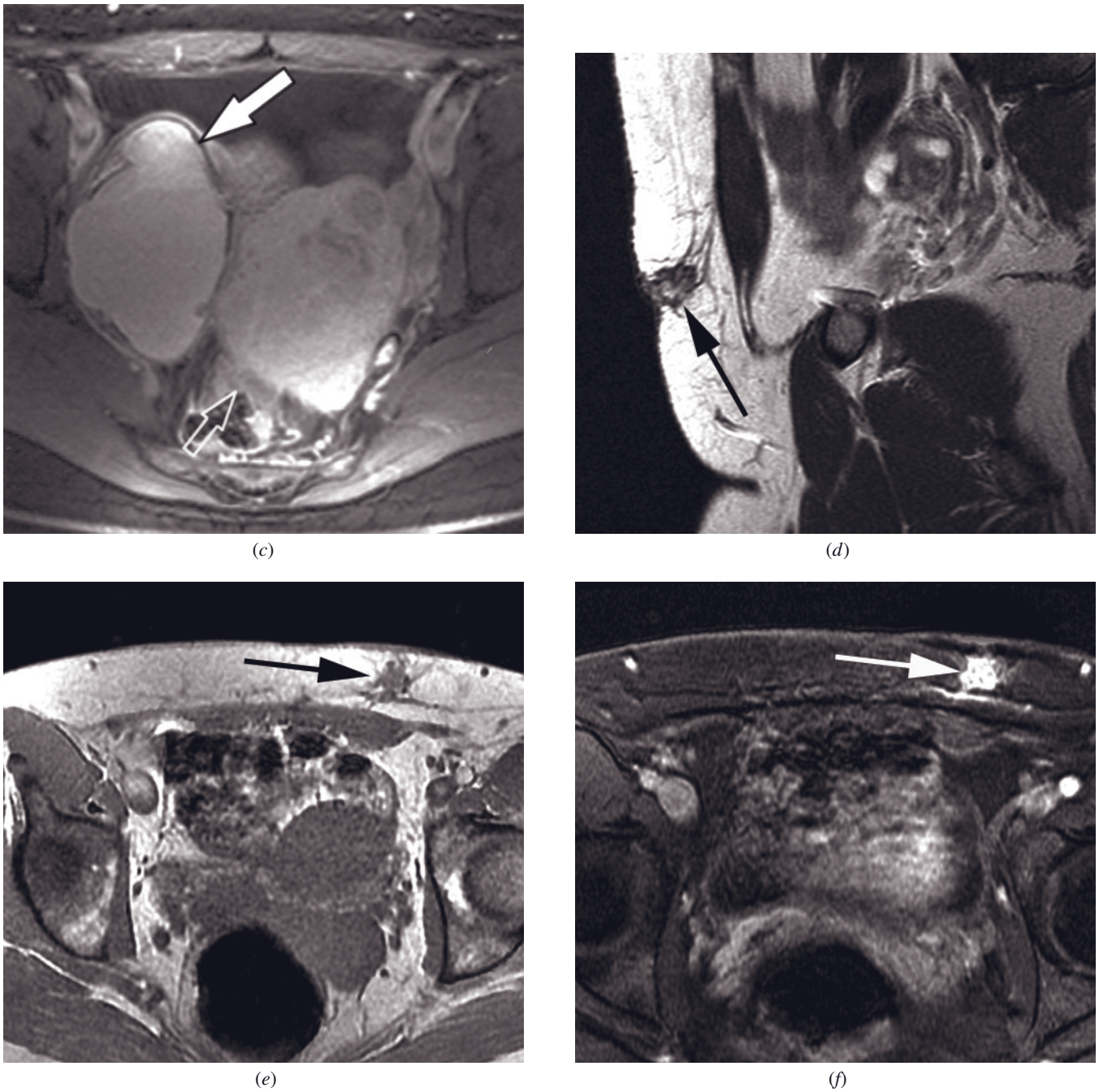

FIG. 15.14 (*Continued*) gradient-echo image (*c*) shows a layered appearance to the endometrioma (arrow, *c*) with a high-signal-intensity superior layer (arrow, *c*), corresponding to the low-signal layer on T2, reflecting paramagnetic effects of blood products. **Abdominal wall endometriosis at 3 T.** Sagittal T2-weighted echo-train spin-echo (*d*), T1-weighted gradient-echo (*e*), and gadolinium-enhanced T1-weighted fat-suppressed gradient-echo (*f*) images in a different patient with prior cesarean section and pain. A small mass is seen at the left aspect of the abdominal scar (arrows, *d–f*) that is low signal on T2-weighted images and enhances with gadolinium. Abdominal wall endometriosis implants may appear solid with marked enhancement.

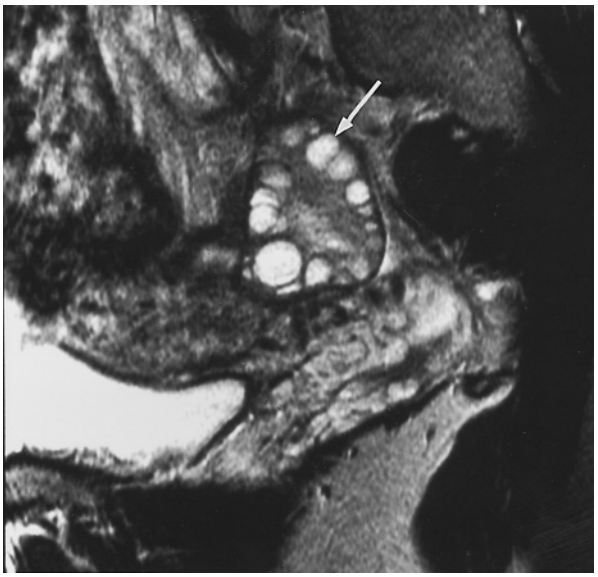

FIG. 15.15 Polycystic ovaries. Sagittal 512-resolution T2-weighted ETSE image demonstrates a mildly enlarged ovary that contains multiple, similar-sized cysts (arrow). Central ovarian tissue is low in signal intensity, reflecting increased medullary cellular stroma.

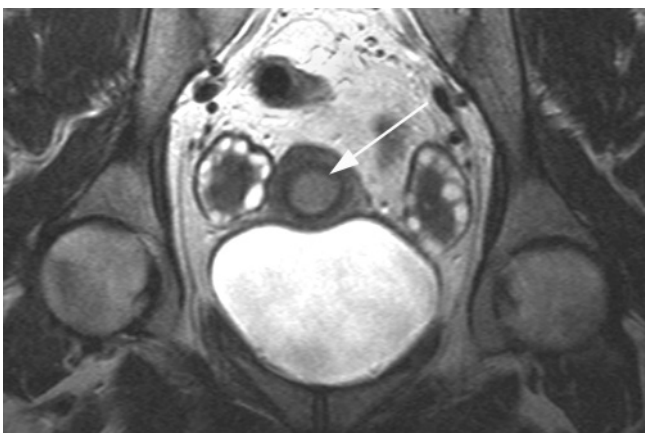

FIG. 15.16 Endometrial carcinoma in a patient with polycystic ovary syndrome. Oblique (short-axis view of the uterus) T2-weighted ETSE image shows low-signal-intensity central ovarian stroma and capsule with numerous small peripheral follicles. The endometrium is thickened (arrow). Biopsy revealed endometrial carcinoma.

seen in any subacute hematoma [56, 57]. Diffusion imaging has also been used with success in the evaluation of ovarian torsion [58].

The MRI findings of massive ovarian edema have also been described. This occurs when there is twisting of the vascular pedicle without hemorrhagic infarction, and there is typically no underlying mass. The most common finding is marked enlargement of the ovary (up to 40 cm) with increased signal intensity on T2-weighted images (fig. 15.18) [59–61].

Pelvic Inflammatory Disease/Tubo-Ovarian Abscess

Pelvic inflammatory disease (PID) is a condition of women of reproductive age and refers to a variety of pelvic infections. The route of spread of the infection is ascending; women who have undergone hysterectomy are not at risk. A variety of microorganisms may be involved, most commonly *Chlamydia trachomatis* and *Neisseria gonorrhoeae*. Other causes include *Bacteroides* species and a variety of other gram-negative and -positive aerobic and anaerobic bacteria, and mixed infections are also common. Women at particularly high risk for PID are those with an intrauterine device (IUD). Actinomycosis is especially common in these women [62]. Women with PID present with fever and abdominal and pelvic pain; cervical motion tenderness and a discharge may be detected during the physical examination. An associated palpable adnexal mass suggests a concurrent tubo-ovarian abscess (TOA) or pyosalpinx. Uncomplicated PID (myometritis, endometritis, and oophoritis) is typically managed conservatively with antibiotics. TOA or pyosalpinx may require percutaneous or surgical drainage for cure. Long-term sequelae of PID include infertility, chronic pelvic pain, and increased risk of ectopic pregnancy.

Most patients with PID/TOA are diagnosed based on clinical picture, physical examination, and ultrasound. In one series of highly selected patients admitted to the hospital for suspicion of PID, MRI proved more accurate in the diagnosis of PID than transvaginal US [63]. MR was also helpful in detecting other causes of symptoms. MRI depicts the extent of inflammation as ill-defined hyperintensity on fat-suppressed T2-weighted images that enhances markedly on postgadolinium fat suppressed T1-weighted images (fig. 15.19) [62]. These areas are also seen as curvilinear and hypointense on routine T1-weighted imaging. TOA has a variable appearance but is usually seen as a round or tubular thick-walled, fluid-filled mass in the adnexal region (fig. 15.20). In one series, the abscesses were most often hypointense on T1-weighted images and hyperintense or heterogeneous on T2-weighted images [64]. Within the innermost portion of the abscess wall, a thin rim was observed that was hyperintense or intermediate signal intensity on T1-weighted images and hypointense on T2-weighted images in almost every case. Dense enhancement was observed after gadolinium administration. This rim corresponds histologically with a layer of granulation tissue, heavily infiltrated by inflammatory cells and containing fresh hemorrhage. The differential diagnosis of TOA includes endometrioma, ovarian neoplasm, infected ovarian cyst, and abscess from another

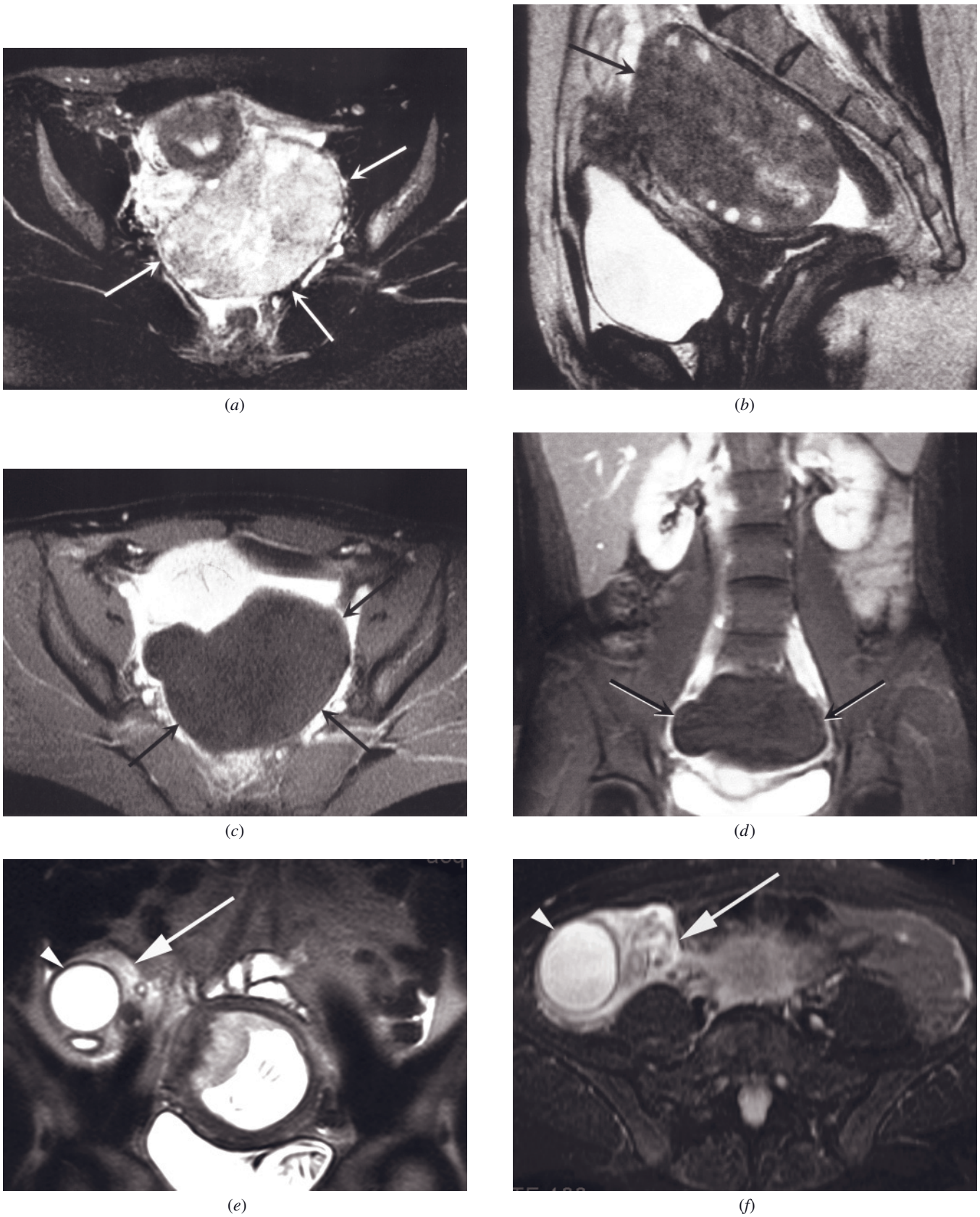

FIG. 15.17 Ovarian torsion. Transverse (*a*) and sagittal (*b*) T2-weighted ETSE and transverse (*c*) and coronal (*d*) gadolinium-enhanced T1-weighted gradient-echo images in a patient with pelvic pain, low-grade fever, and mild leukocytosis. T2-weighted images (*a*, *b*) show a large, solid pelvic mass (arrows, *a*, *b*) posterior to the uterus. Peripheral follicles are noted on the sagittal image (*b*), indicating that the mass is a markedly enlarged ovary. Gadolinium-enhanced T1-weighted images (*c*, *d*) show no enhancement of the pelvic mass (arrows, *c*, *d*) consistent with infarction. Surgery confirmed ovarian torsion with an infarcted ovary. Histopathologic evaluation showed an infarcted ovary with hemorrhagic necrosis. (Courtesy of Russell Low, M.D., Sharp Clinic, San Diego, CA.) **Ovarian torsion in a pregnant patient.** Coronal T2-weighted SS-ETSE (*e*) and transverse T2-weighted SS-ETSE with fat suppression (*f*) in a different patient show a large right ovary with edematous stroma (arrows, *e*, *f*) and prominent cyst (arrowheads, *e*, *f*). Pregnant patients are predisposed to ovarian torsion.

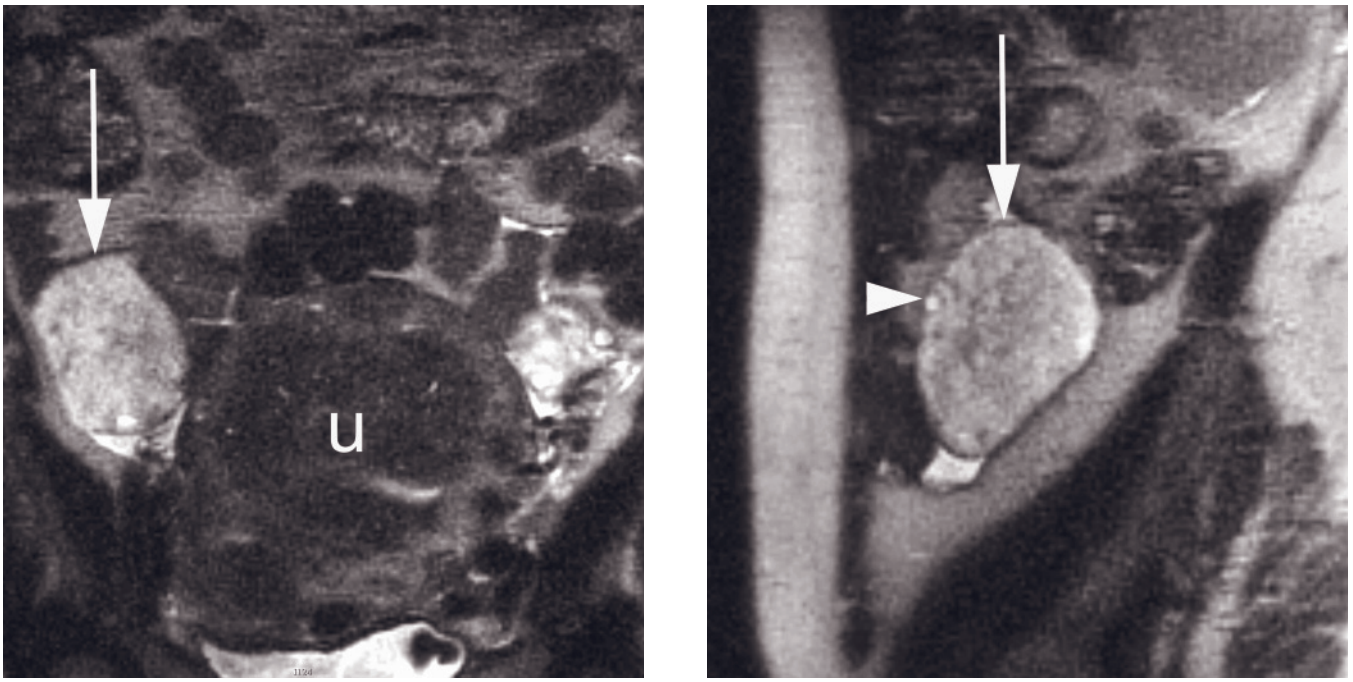

(*a*) (*b*)

FIG. 15.18 Massive ovarian edema. Coronal (*a*) and sagittal (*b*) T2-weighted SS-ETSE images show an enlarged right ovary (arrow, *a*, *b*) with increased stromal signal intensity and few small peripheral follicles (arrowhead, *b*). Note the enlarged uterus (u, *a*) due to adenomyosis and leiomyomata.

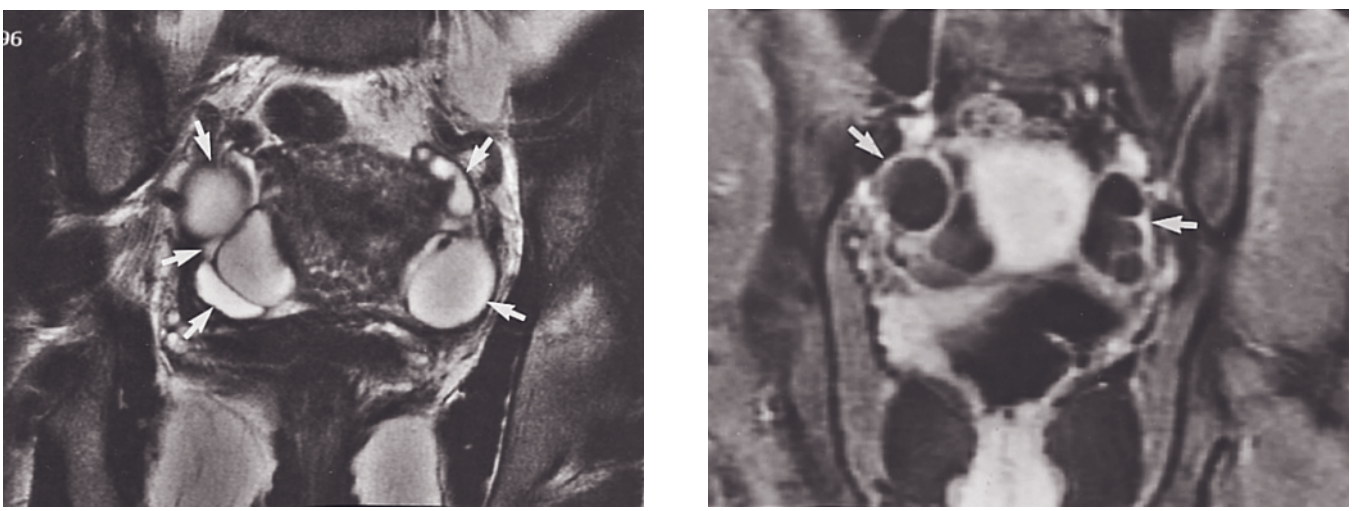

(*a*) (*b*)

FIG. 15.19 Pelvic inflammatory disease. Coronal 512-resolution T2-weighted ETSE (*a*) and gadolinium-enhanced T1-weighted fat-suppressed gradient-echo (*b*) images in a patient with acute pelvic pain and fever. Bilateral complex cystic masses are not ovarian cysts but the inflamed, dilated fallopian tubes folded upon themselves (arrows, *a*), flanking the uterus. After contrast the tube walls enhance and further demonstrate that the masses are not adjacent discrete cysts, but rather continuous structures (arrows, *b*).

source such as Crohn disease, appendicitis, or diverticulitis. Chronic PID/TOA results in similar but less severe changes. Findings of salpingitis include tubal enlargement due to obstruction of the fimbriated end of the tube. On MR images, a serpentine adnexal lesion is seen; the central signal varies with the tube contents. Purulent material is of variable signal intensity on T1- and T2-weighted images but may show a fluid-debris level. After the administration of gadolinium, the tube wall enhances.

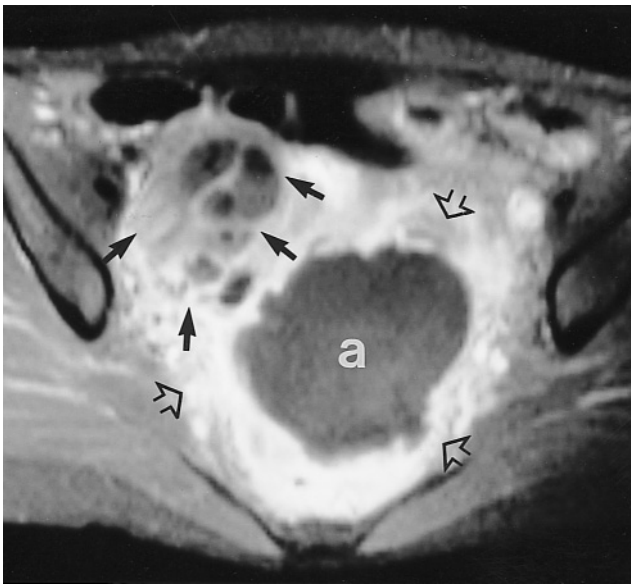

FIG. 15.20 Tubo-ovarian abscess. Transverse gadolinium-enhanced T1-weighted fat-suppressed SE image in a woman with fever and a fluctuant adnexal mass on bimanual exam. A large loculated abscess occupies the posterior pelvis (a). The right ovary is enlarged (solid arrows) and is invested with an abscess ("a"). The well-formed abscess capsule and septations enhance markedly, as does the inflammation in the surrounding fat (open arrows). Associated inflammatory changes are more conspicuous on fat-suppressed images. Tubo-ovarian abscess is a well-recognized complication of PID, and whereas most cases of PID can be managed conservatively, the presence of an abscess usually necessitates surgical intervention.

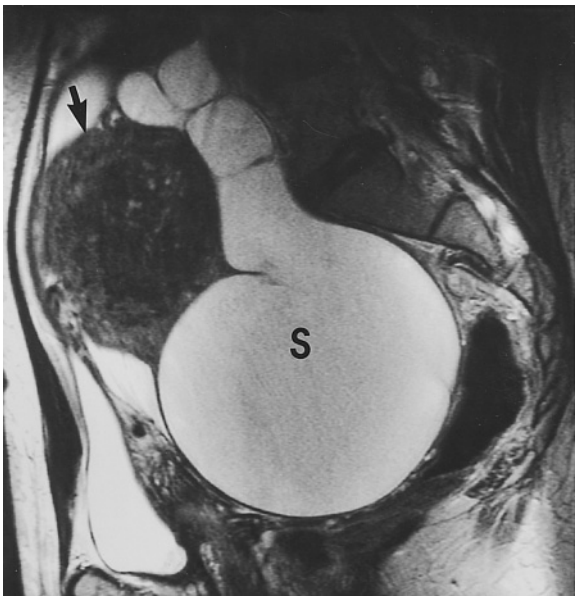

FIG. 15.21 Hydrosalpinx. Sagittal 512-resolution T2-weighted ETSE image demonstrates a large hydrosalpinx (S). Adenomyosis of the uterus (arrow) is also present.

Hydrosalpinx

Occlusion of the fimbriated end of the tube uncomplicated by hemorrhage or infection produces tubal dilation resulting in a hydrosalpinx. If complicated by hemorrhage the term hematosalpinx may be applied; if complicated by infection, the term pyosalpinx is used. The causes of tubal obstruction include PID, endometriosis, adjacent tumors, and adhesions from prior surgery. On MR images, a dilated fallopian tube appears as a tubular fluid-filled structure folded on itself to form an S or C shape (fig. 15.21) [65]. The multiplanar capability of MR is especially useful in proving that a multicystic structure is actually a dilated tube. The signal intensity of the fluid on T1- and T2-weighted images may suggest the cause of the obstruction. Fluid that is of increased signal on T1-weighted images is associated with endometriosis.

Ectopic Pregnancy

The most common sites for extrauterine pregnancy are the fallopian tubes, followed by the ovaries. Because of the increased use of ovulation-stimulating drugs, the incidence of ectopic pregnancy is increasing. Most ectopic pregnancies are confirmed with transvaginal ultrasound, and few reports of the MRI appearance have been published [66–69] A potential advantage of MRI is its ability to precisely localize the implantation site of a cornual or cervical ectopic pregnancy, which is important for proper management. MRI features include fallopian tube hematoma, enhancement of the fallopian tube wall, a gestational sac-like structure, bloody ascites, and a heterogeneous adnexal mass. The hematoma is of intermediate to high signal intensity on T1-weighted images [68], and the ascites is of increased signal intensity on fat-suppressed T1-weighted images. An enhancing treelike region within the heterogeneous mass has been reported to represent villus-containing fibrin strands in the fetoplacental tissue [66].

Pelvic Varices

Pelvic varices and enlarged ovarian veins may be detected as part of an evaluation of pelvic pain or may be noted incidentally [70, 71]. Primary pelvic varices are associated with the pelvic pain syndrome (also called pelvic congestion syndrome), in which patients present with chronic pelvic pain without obvious cause. Pelvic congestion syndrome generally affects multiparous women of reproductive age; patients complain of a deep, dull pelvic ache made worse by activity or actions that increase intra-abdominal pressure [72]. The clinical diagnosis is challenging; patients suspected of having this condition often undergo venography, which is invasive and frequently negative. MR imaging provides a noninvasive venogram, and the addition of routine sequences

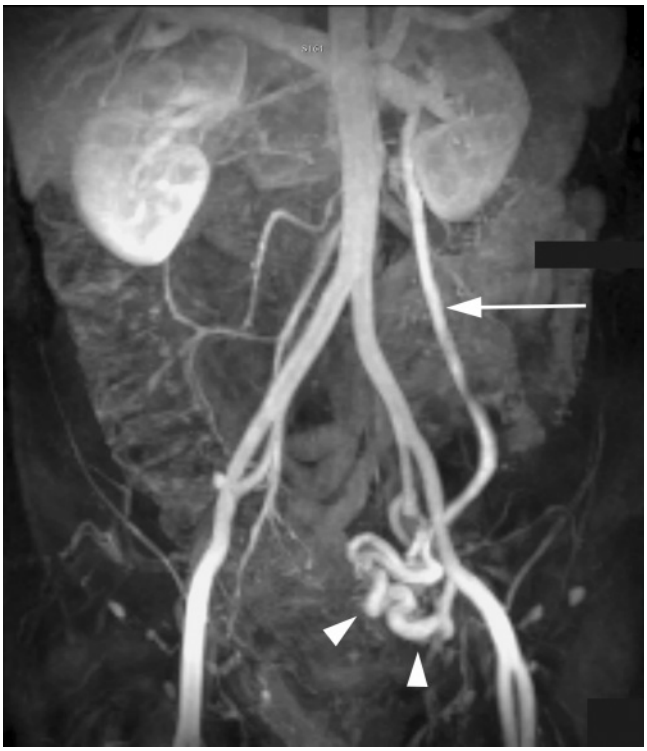

FIG. 15.22 Pelvic varices. Coronal oblique maximum-intensity projection of an MR angiogram approximately 45 s after gadolinium injection in a patient with chronic pelvic pain. There is reflux of contrast down a large left ovarian vein (arrow) with filling of left pelvic varices (arrowheads).

for evaluation of pelvic anatomy permits diagnosis of other possible causes of pain such as adenomyosis. On T1-weighted and T2-weighted images, serpentine parauterine and paraovarian vessels are noted. With dynamic gadolinium-enhanced imaging, reflux can be seen down enlarged gonadal veins on early images, and the pelvic varices enhance intensely (fig. 15.22). In patients with pain due to pelvic varices, venous embolotherapy has been reported to lead to significant improvement in pain [73]. Secondary pelvic varices are not generally associated with pain but do signal a potentially serious underlying abnormality such as inferior vena caval obstruction, portal hypertension, increased pelvic blood flow, or vascular malformations [72].

Benign Ovarian Neoplasms

Benign ovarian neoplasms are classified together with their malignant counterparts according to cell type (Table 15.1).

Table 15.1 Benign and Malignant Primary Ovarian Neoplasms

Epithelial Cell (~70%)	Germ Cell (~20%)	Sex Cord-Stroma (~10%)
Serous tumor	Mature cystic teratoma	Fibroma
Mucinous tumor	Immature teratoma	Granulosa-theca cell tumor
Endometrioid tumor	Dysgerminoma	Sertoli–Leydig tumor
Clear cell tumor	Endodermal sinus tumor	Sclerosing stromal cell tumor
Brenner tumor	Embryonal cell tumor	
Cystadenofibroma	Choriocarcinoma	

Epithelial Origin

Benign epithelial tumors may be serous, mucinous, or transitional cell (Brenner tumors). Endometrioid and clear cell epithelial tumors are usually malignant, although rare benign varieties exist. Most benign epithelial tumors are cystadenomas, usually serous or mucinous. Tumors with fibrous stroma are considered cystadenofibromas or adenofibromas. Serous and mucinous cystadenomas each have characteristic MRI features; however, overlap exists. The distinction is often not possible, which is not important because treatment is the same.

Serous cystadenomas are common and account for approximately 20% of benign ovarian neoplasms [12]. While the malignant variation of this lesion tends to occur in older women, benign cystadenomas develop in women between 20 and 50 years of age. About 20% are bilateral, in contrast to the malignant version, which is more frequently bilateral [74]. The most common presentation is of a thin-walled unilocular cyst, although there may be papillary projections [75]. These projections are very important to recognize because they are the hallmark of epithelial neoplasms and may be a predictor of malignancy [76]. Benign epithelial tumors have fewer and smaller projections than borderline or frankly malignant tumors [23]. When benign, these lesions can be treated by simple resection or unilateral oophorectomy. On MR images, uncomplicated serous cystadenomas have signal intensity similar to water on all sequences, and they appear dark on T1- and bright on T2-weighted sequences (fig. 15.23). If complicated by hemorrhage, the T1 and T2 signal characteristics are altered because of shortening of relaxation times. Unilocular and thin-walled lesions may be mistaken for simple functional cysts, while multilocular lesions may mimic mucinous cystadenomas or, more importantly, malignant tumors (fig. 15.24). Papillary projections may occur in benign epithelial tumors but should raise suspicion of malignancy (fig. 15.25).

Mucinous cystadenomas are also of epithelial origin and account for another 20% of benign ovarian

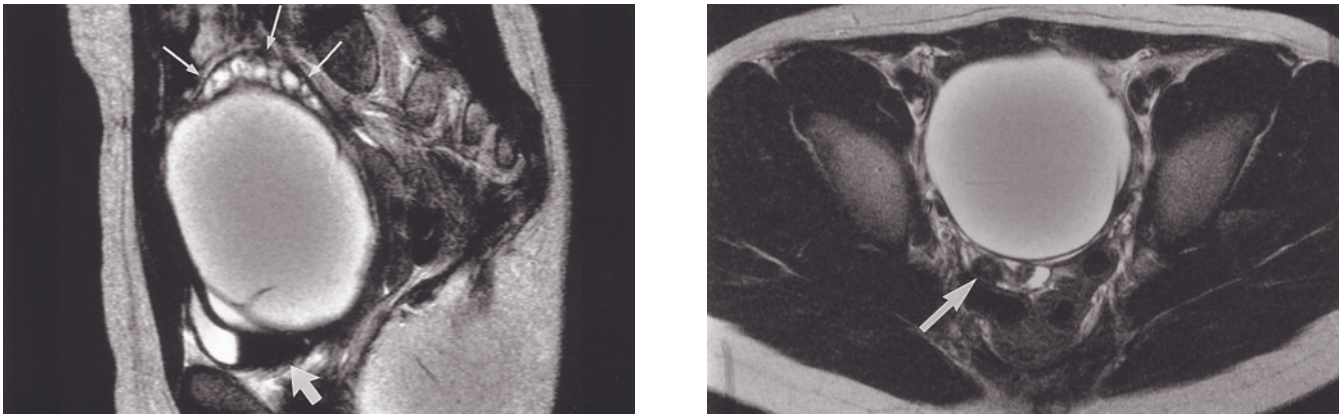

(*a*) (*b*)

FIG. 15.23 Serous cystadenoma. Sagittal (*a*) and transverse (*b*) 512-resolution T2-weighted ETSE images in a 10-year-old girl with precocious puberty. A large septate mass occupies the pelvis. Note the pubertal-sized, follicle-containing ovary draped over the mass (long arrows, *a*). The signal-void area in the dependent portion of bladder reflects the T2* effects of concentrated gadolinium (short arrow, *a*). The ovarian mass displaces the uterine corpus and cervix (arrow, *b*) posteriorly. At surgery, a benign serous cystadenoma was resected.

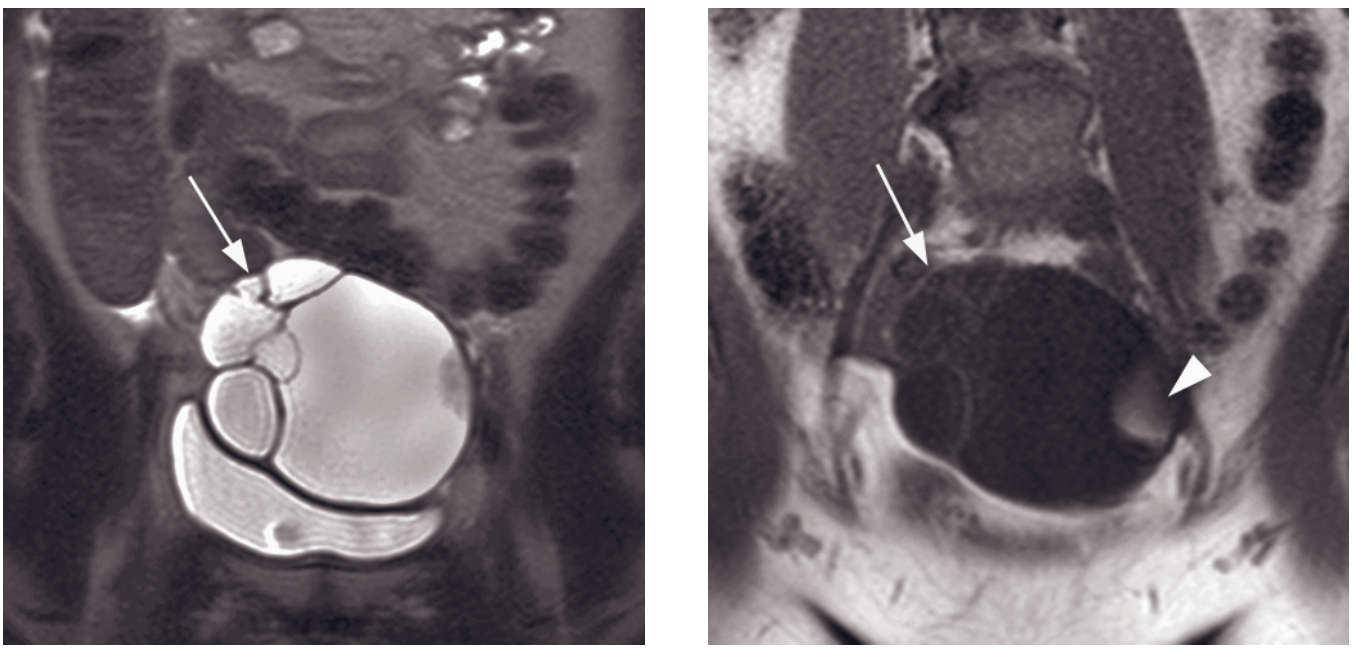

(*a*) (*b*)

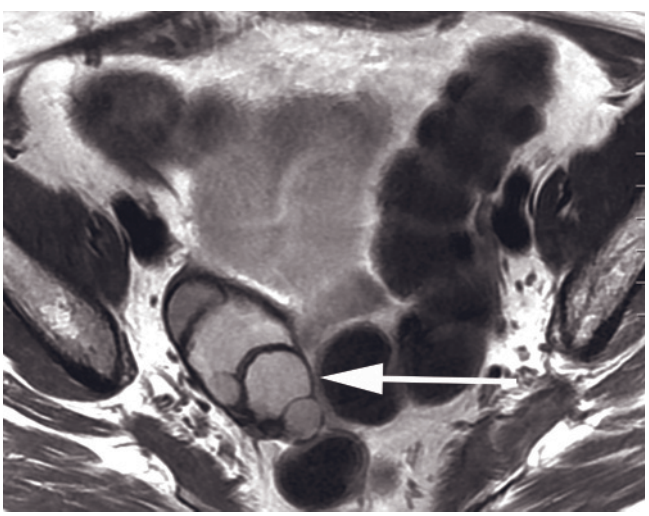

(*c*)

FIG. 15.24 Multilocular serous cystadenoma. Coronal T2-weighed SS-ETSE (*a*) and T1-weighted gradient-echo (*b*) images show a multilocular mass (arrow). A focus of high-signal-intensity material on T1-weighted images (arrowhead, *b*) indicates hemorrhage within a locule. (Courtesy of Claude Sirlin, M.D., Department of Radiology, University of California, San Diego). **Multilocular serous cystadenoma at 3 T.** Transverse T2-weighted ETSE image in a different patient (*c*) show a multiseptate mass in the right adnexa found to be a benign serous cystadenoma on resection.

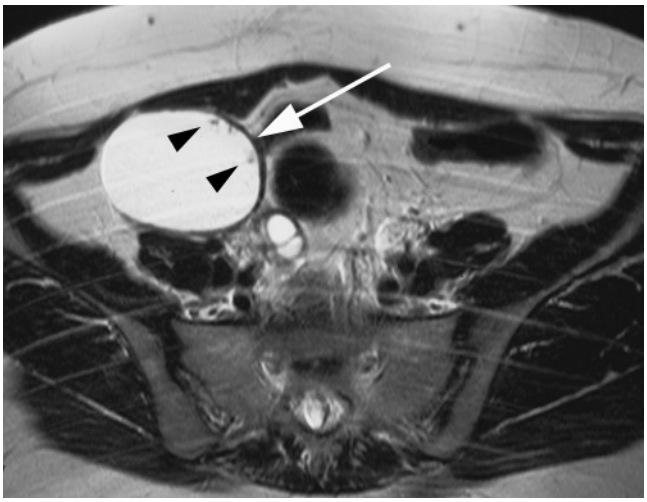

FIG. 15.25 Serous cystadenoma with papillary projections. Transverse T2-weighted ETSE image shows a unilocular right adnexal mass (arrow) with a small number of papillary projects (arrowheads). Benign serous tumors may have papillary projections, but they tend to be fewer and smaller than those typically seen in malignant serous tumors.

neoplasms. They are less frequently bilateral (about 5%) and are more common after age 40 [12]. These lesions tend to be multilocular and lack papillary projections, which may help distinguish them from the serous type. Distinction may not be possible, and it is unlikely to be important because treatment is the same. Mucinous cystadenomas also tend to be larger than serous cystadenomas. On MR images, mucinous cystadenomas classically demonstrate multiple locules with varying signal intensity on T1- and T2-weighted images due to their protein content [76]. Hemorrhage may also be seen in one or more locules, causing further variation in T1 and T2 signal (fig. 15.26) [75]. Mucinous cystadenomas may also be unilocular or have very few septa (fig. 15.27). As in serous cystadenomas, papillary projections are suggestive of malignancy.

Cystadenofibromas are cystic epithelial neoplasms in which fibrous stroma is a major component in addition to epithelial cells. Adenofibromas contain an even more prominent fibrous component. Like other epithelial tumors, cystadenofibromas and adenofibromas may be serous, mucinous, or, less commonly, endometrioid or clear cell. These tumors are usually benign; however, borderline and malignant varieties exist. The MRI appearance has been reported to be variable. They may contain solid components that are very low signal on T2-weighted images, suggesting their fibrous nature [77]. However, cystadenofibromas may also appear nearly entirely cystic on MR images, mimicking cystadenomas (fig. 15.28) [78]. Endometrioid tumors are typically malignant but may occur as benign adenofibromas. There is an association of endometrioid and clear cell tumors with endometriosis, and they may arise from endometriotic cysts (fig. 15.29).

A variety of adenofibroma is the Brenner tumor or transitional cell tumor, which arises from the surface epithelium of the ovary and contain nests of urothelium-like cells [79]. These account for 2–3% of all ovarian neoplasms; the majority of these are benign, with few reports of borderline or malignant counterparts. Benign Brenner tumors have signal characteristics similar to fibromas, with decreased homogeneous signal intensity on T2-weighted images [80]. Larger tumors may show cystic areas [79]. Brenner tumors are associated with other ovarian tumors in approximately 30% of cases, usually in the ipsilateral ovary.

Germ Cell Origin

The only benign tumor of germ cell origin is the mature cystic teratoma or dermoid cyst, which is the most common ovarian neoplasm and accounts for 26–44% [12]. The peak incidence is during the midreproductive years, although they can be detected at any age. Approximately 90% are unilateral, and the mean size is 6 cm. Patients are usually asymptomatic. When present, symptoms are related to mass effect or torsion. Rarely, infection or rupture may occur. Malignant transformation occurs in 1–3% [12], most frequently in postmenopausal women.

Mature cystic teratomas are composed of varying amounts of endodermal, mesodermal, and ectodermal elements. Bone, teeth, hair, cartilage, skin, muscle, fat, bronchus, salivary gland, thyroid, pancreas, neural tissue, and retina have been found within them [12]. They are typically unilocular, although septations may be present. The cysts have an ectodermal lining and contain keratin and sebum, secreted by sebaceous glands. Management consists of conservative surgery with cystectomy, oophorectomy, or salpingo-oophorectomy depending on the size of the tumor and the desire to preserve fertility. Rarely, malignant transformation occurs, usually to squamous cell carcinoma. Other cell types reported include adenocarcinoma, sarcoma, transitional cell carcinoma, and melanoma [12, 81, 82]. The prognosis after malignant transformation is poor; most patients survive less than 1 year [12].

The characteristic MRI feature is fat, which is present in approximately 95% of mature cystic teratomas (figs. 15.30–15.32). Other findings include fluid-fluid levels, layering debris, low-signal-intensity calcification (usually teeth), and Rokitansky nodules (dermoid plugs attached to the cyst wall) [83–86]. The fat within the lesion has signal characteristics of gross fat signal on all sequences. Interfaces between the fat and water and/or soft tissue in the lesion also cause chemical shift artifact, present in about 60% of cases [87]. Standard T1- and T2-weighted

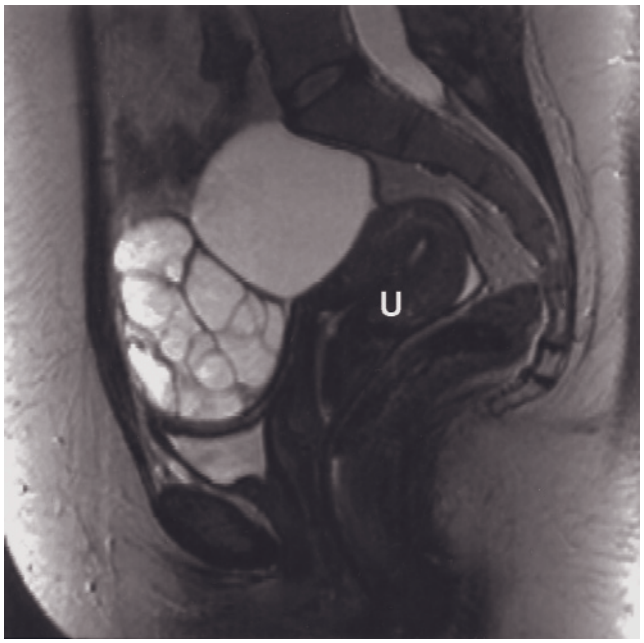

(*a*)

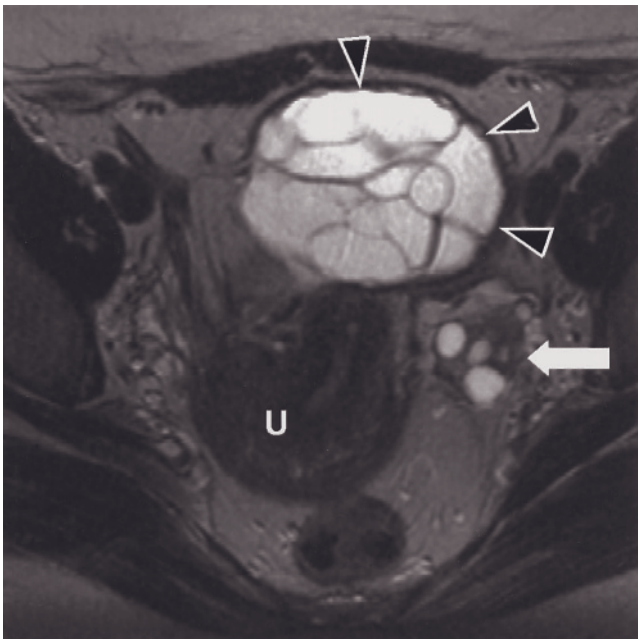

(*b*)

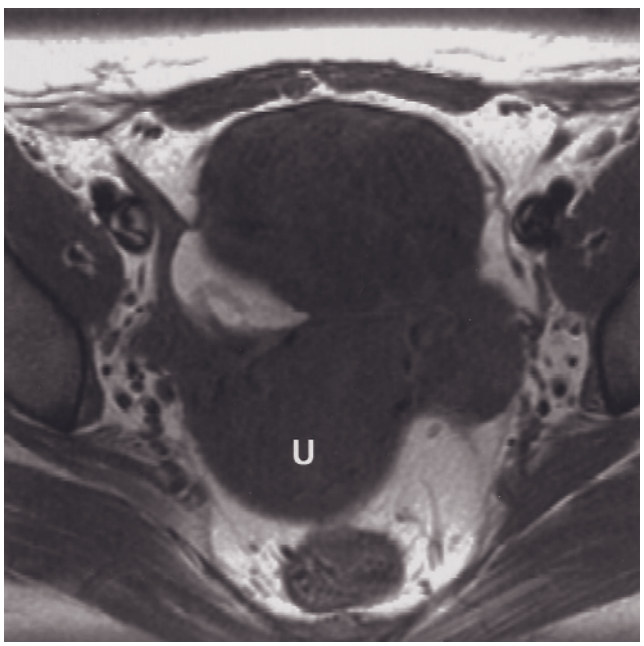

(*c*)

FIG. 15.26 Mucinous cystadenoma. Sagittal (*a*) and transverse (*b*) T2-weighted ETSE and transverse T1-weighted SE (*c*) images. Multiple internal cysts and septations are typical findings in mucinous cystadenoma. The low-signal-intensity fibrotic wall of the mass (arrowheads, *b*) and the adjacent normal left ovary (arrow, *b*) are noted. The sagittal image (*a*) demonstrates displacement of the uterus (u) posteriorly by the mass.

imaging sequences support the diagnosis of a teratoma; however, T1-weighted images obtained out of phase or with chemically selective fat suppression improve diagnostic confidence [87–89]. Accuracies up to 96% have been reported with these techniques [87]. Out-of-phase imaging may have a particular advantage in lesions with only small amounts of fat (fig. 15.33) [90].

Monodermal teratomas are a subset of teratomas that are composed of one tissue type, such as struma ovarii and struma carcinoid. Most reports in the literature describe struma ovarii as complex multilocular masses with solid components [91–94]. The different locules may have variable signal intensity due to the differences in viscosity within the fluid; the signal is often low to intermediate on T1- and very low on T2-weighted images [95]. The solid components demonstrate significant enhancement after gadolinium and correspond to thyroid tissue (fig. 15.34) [95]. Cases have been reported that lack a solid component [96]; however, the same signal pattern within the locules was noted.

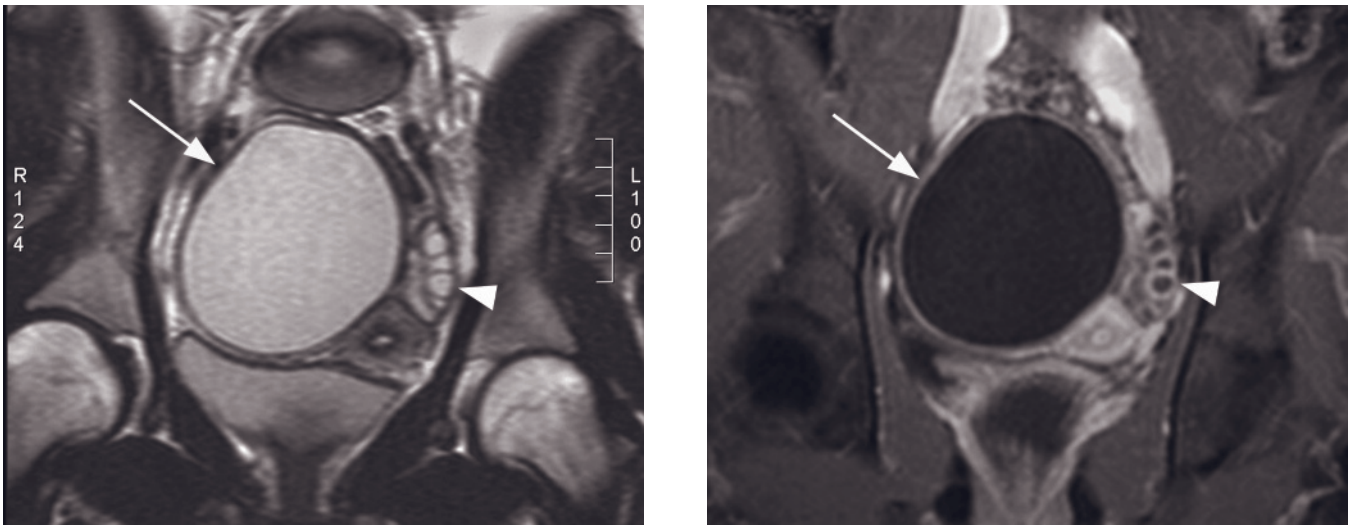

(*a*) (*b*)

FIG. 15.27 Mucinous cystadenoma. Coronal T2-weighted ETSE (*a*) and gadolinium-enhanced fat-suppressed T1-weighted gradient-echo (*b*) images show a unilocular cystic right ovarian mass (arrow) without mural nodularity, adjacent to the normal left ovary containing multiple follicles (arrowhead).

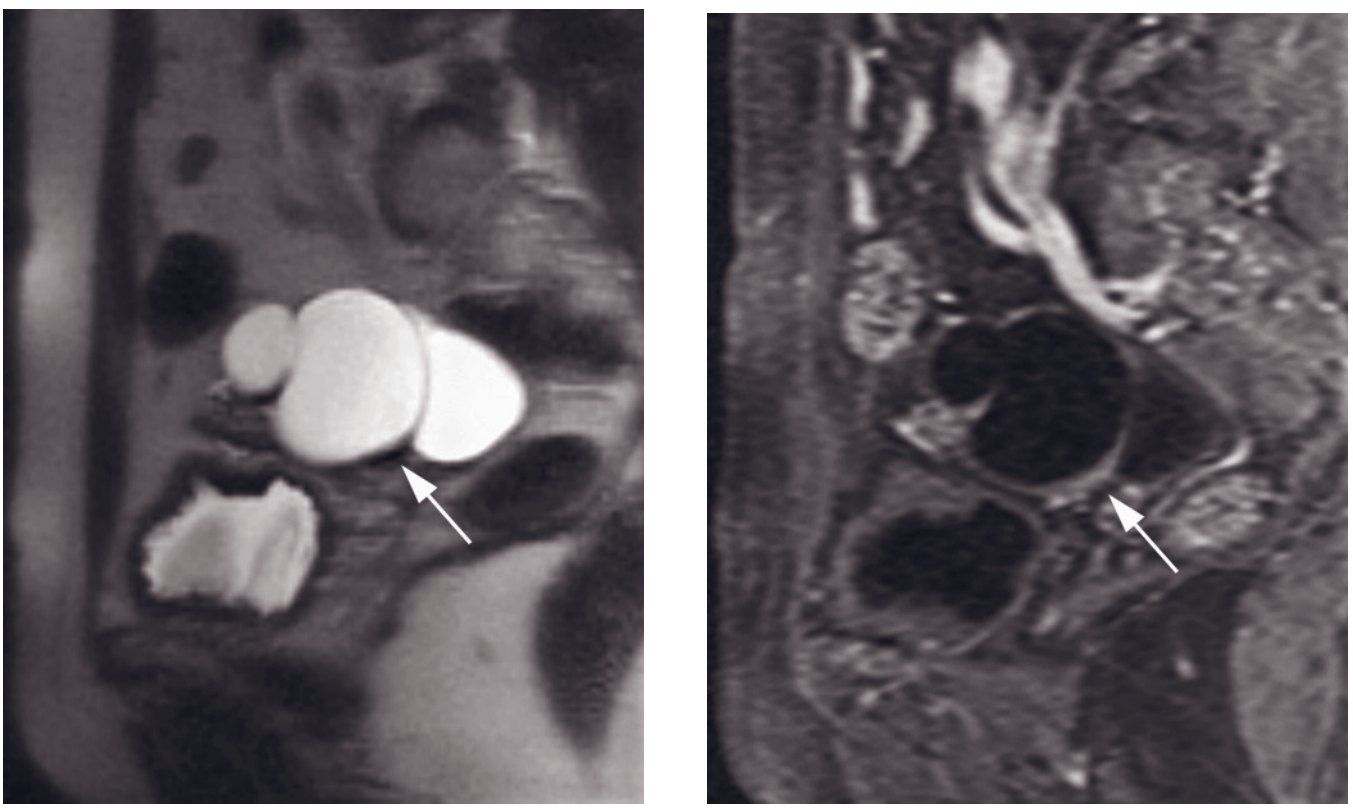

(*a*) (*b*)

FIG. 15.28 Serous cystadenofibroma. Sagittal T2-weighted ETSE (*a*) and gadolinium-enhanced T1-weighted gradient-echo (*b*) images show a septated mass containing simple fluid. The small solid portions are hypointense on T2-weighted images (arrow, *a*), presumably reflect fibrous content, and enhance on postgadolinium images (arrow, *b*).

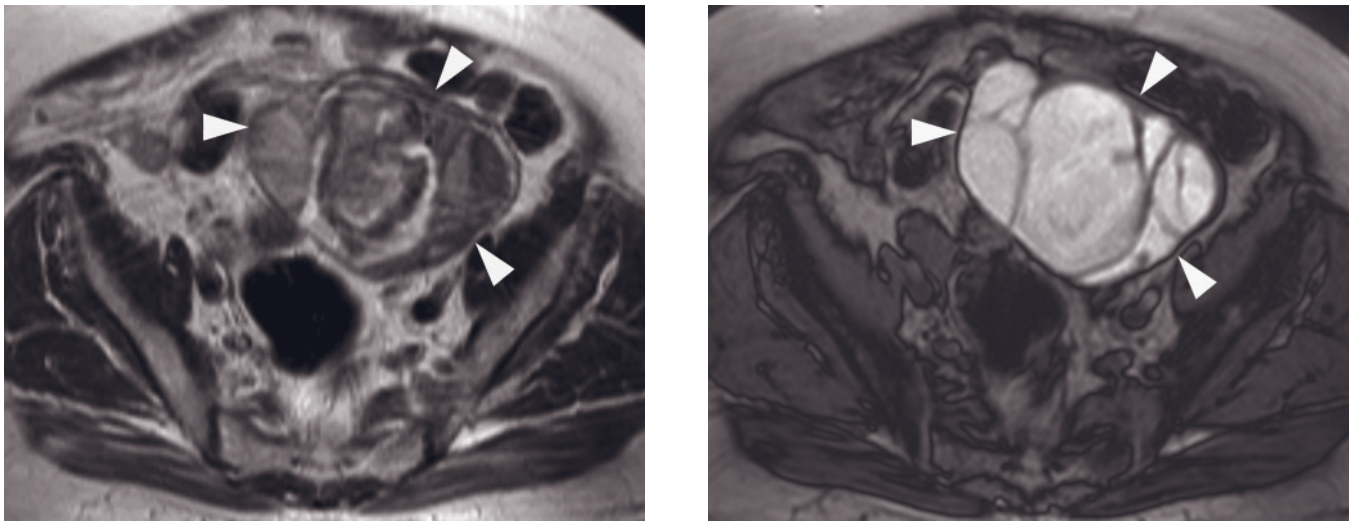

(*a*) (*b*)

FIG. 15.29 Endometrioid adenofibroma arising in an endometriotic cyst. Transverse T2-weighted ETSE (*a*) and out-of-phase T1-weighted gradient-echo (*b*) images show a septated mass (arrowheads, *a*, *b*) with heterogeneous high and low signal intensity on T2-weighted images (*a*) and slightly heterogeneous high signal intensity on T1-weighted images (*b*), consistent with blood products. Pathologic evaluation of the resected mass revealed benign endometrioid adenofibroma in an endometriotic cyst. (Courtesy of Claude Sirlin, M.D., Department of Radiology, University of California, San Diego).

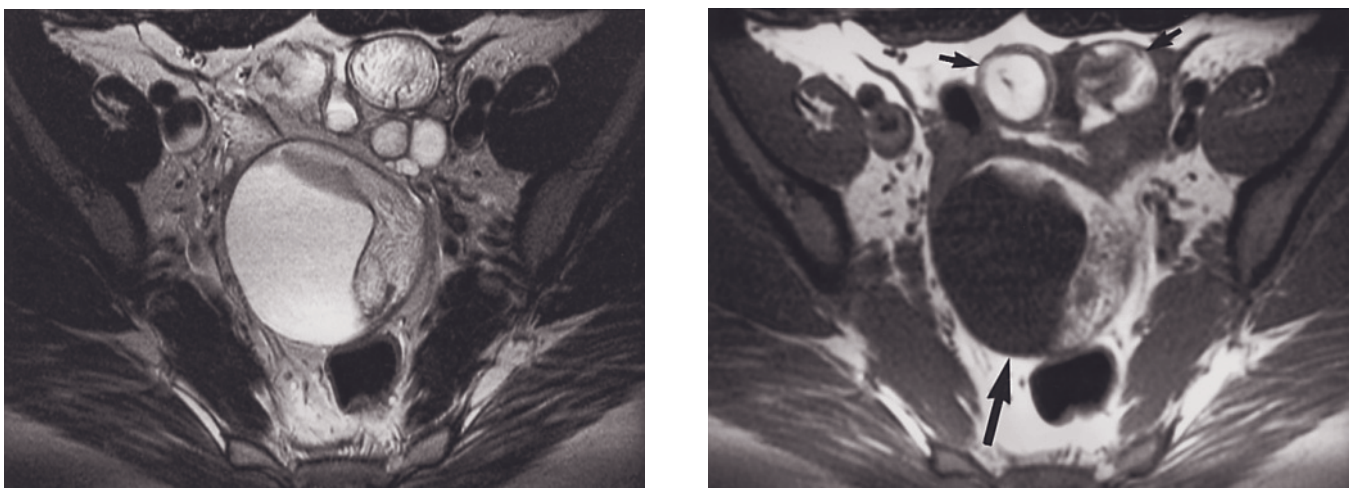

(*a*) (*b*)

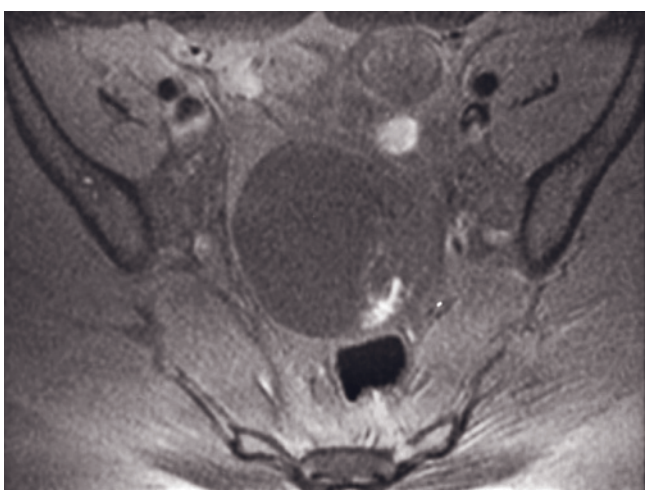

(*c*)

FIG. 15.30 Mature cystic teratoma. Transverse 512-resolution T2-weighted ETSE (*a*), T1-weighted SE (*b*), and T1-weighted fat-suppressed SE (*c*) images in a patient with bilateral dermoids. A large right (large arrow, *b*) and two smaller left (small arrows, *b*) ovarian dermoids are present. The signal intensity is heterogeneous because of the variety of substances within the masses. The fat components suppress on the fat-suppressed image (*c*).

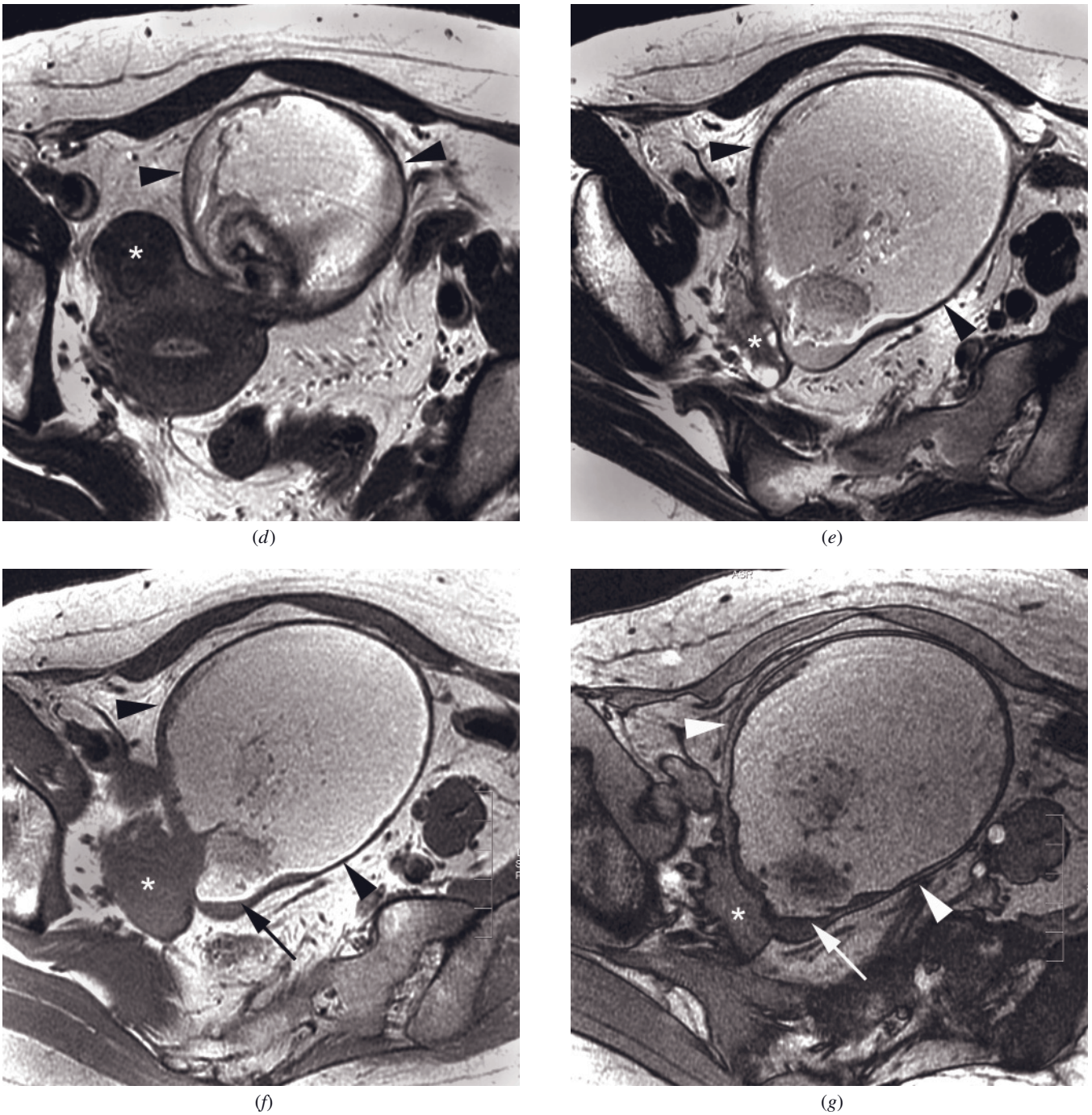

FIG. 15.30 (*Continued*) **Mature cystic teratoma at 3 T.** Transverse T2-weighted ETSE (*d*, *e*) and T1-weighted gradient echo in-phase (*f*) and out-of-phase (*g*) images show a large left ovarian dermoid (arrowheads, *d–g*). The adjacent uterus contains a fibroid (*, *d*), and part of the normal right ovary is seen (*, *e–g*). In- and out-of-phase T1-weighted images, showing artifact within the mass due to chemical shift of the second kind, confirm gross fat, fat-fluid level (arrow, *f*, *g*), and small foci centrally that may represent hair. Also note the prominent spatial misregistration artifact due to chemical shift of the first kind best seen on the T2-weighted images; this artifact is increased at 3 T compared to 1.5 T.

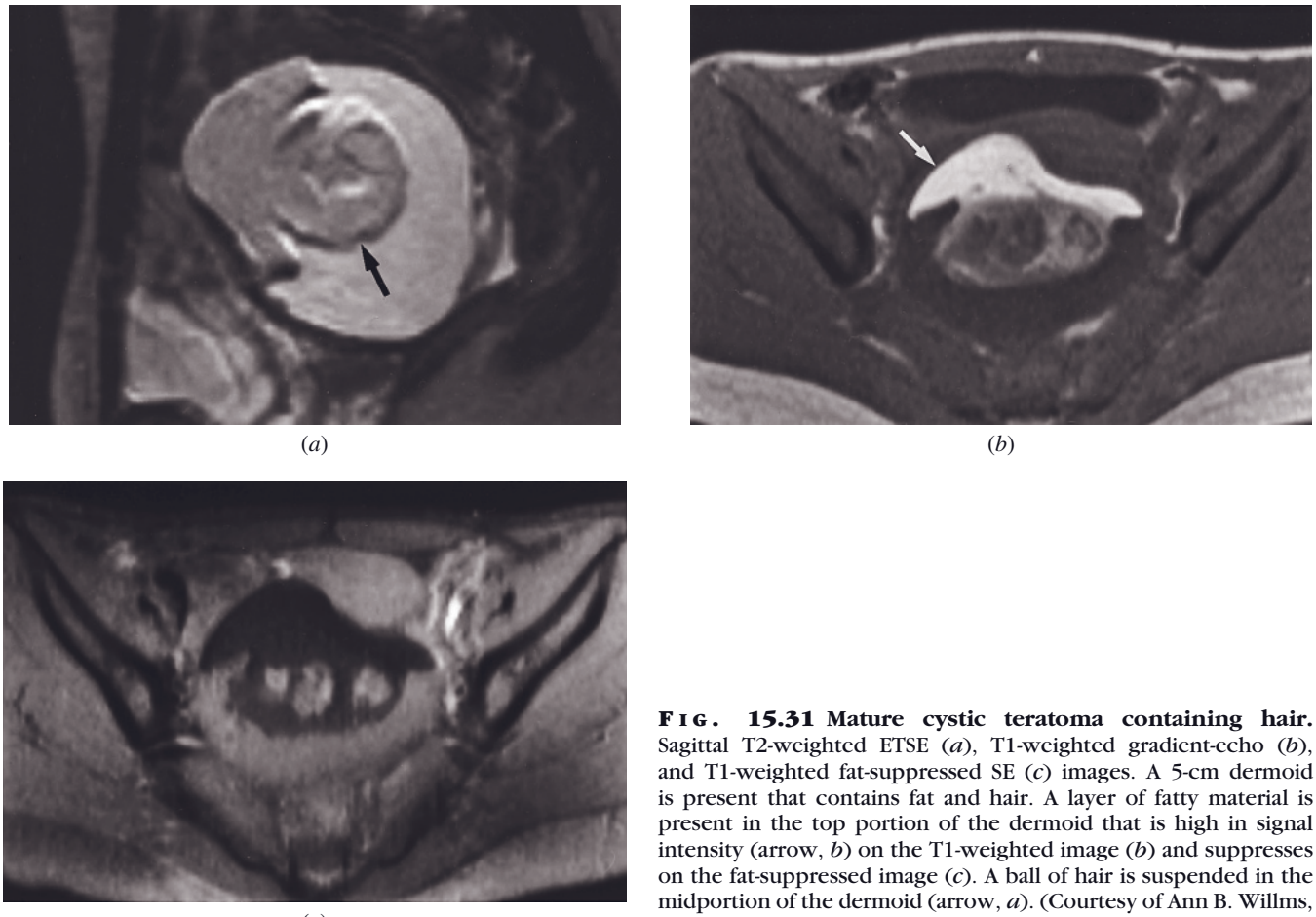

(*a*) (*b*) (*c*)

FIG. 15.31 Mature cystic teratoma containing hair. Sagittal T2-weighted ETSE (*a*), T1-weighted gradient-echo (*b*), and T1-weighted fat-suppressed SE (*c*) images. A 5-cm dermoid is present that contains fat and hair. A layer of fatty material is present in the top portion of the dermoid that is high in signal intensity (arrow, *b*) on the T1-weighted image (*b*) and suppresses on the fat-suppressed image (*c*). A ball of hair is suspended in the midportion of the dermoid (arrow, *a*). (Courtesy of Ann B. Willms, M.D.)

Sex Cord-Stromal Origin

The most common benign solid ovarian tumors arise from the stromal elements of the ovary and are composed of fibrous cells, thecal cells, or a combination of the two. If purely one or the other, they are termed fibromas or thecomas. Because the histologic appearance can overlap, the term fibrothecoma may be more appropriate in many cases. Tumors that contain thecal cells are associated with increased estrogen. Pure thecomas arise most often in menopausal or perimenopausal women; 15% have concomitant endometrial hyperplasia, and 29% have frank endometrial carcinoma [12]. Given the associated endometrial disease, many of these tumors are discovered during evaluation of abnormal bleeding. Other symptoms are nonspecific and include pelvic pain or discomfort. Pure fibromas are diagnosed more frequently in women under 50 and are usually asymptomatic. Rarely, patients can present with ascites. If a right pleural effusion is also present, this is termed Meigs syndrome, which is a rare presentation of fibroma [12]. These tumors are treated by surgical excision.

The MR characteristics of fibromas, thecomas, and fibrothecomas are similar: hypointensity on both T1-and T2-weighted images (figs. 15.35 and 15.36). Because of the similar signal characteristics, these tumors are difficult to distinguish from pedunculated leiomyomata [97]. Exophytic leiomyomas will often exhibit what has been termed the "bridging vascular sign," to describe curvilinear tortuous vascular structures crossing between the uterus and the pelvic mass [98]. Detection of compressed ovarian tissue surrounding an ovarian tumor is also useful. After the administration of gadolinium, these tumors have variable enhancement, with reports of negligible and avid enhancement [77, 99–101]. Atypical high T2 signal due to pronounced microscopic myxomatous change has been reported [102]. One series reported a high association with ascites [103].

A less common benign sex cord-stromal tumor is sclerosing stromal tumor of the ovary [104–108]. These tumors are usually diagnosed in women less than 30 years of age who present with menstrual irregularity, although only a minority are hormonally active.

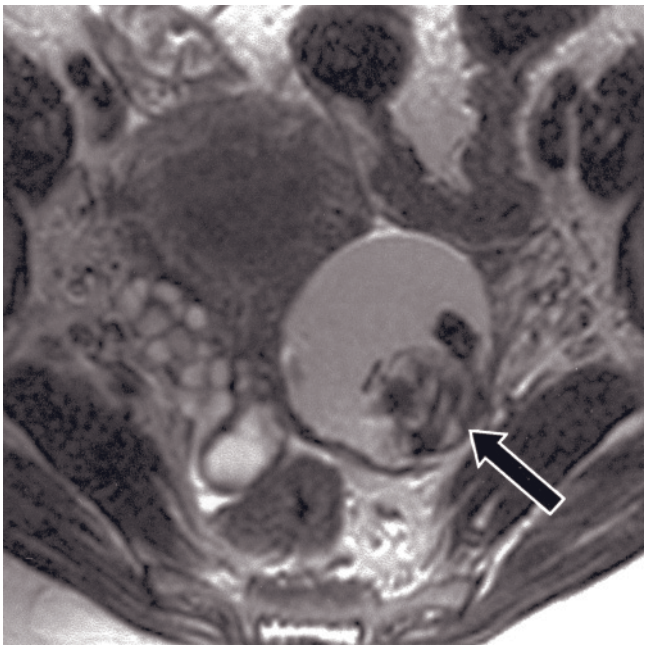

(*a*)

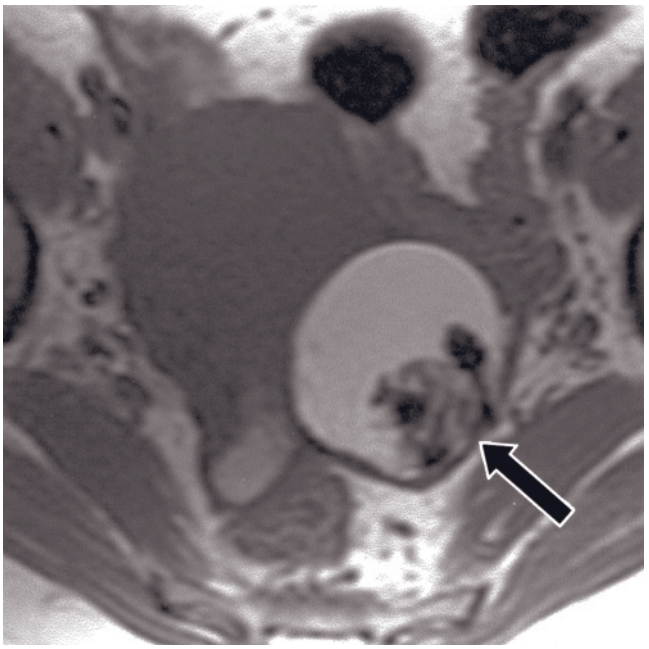

(*b*)

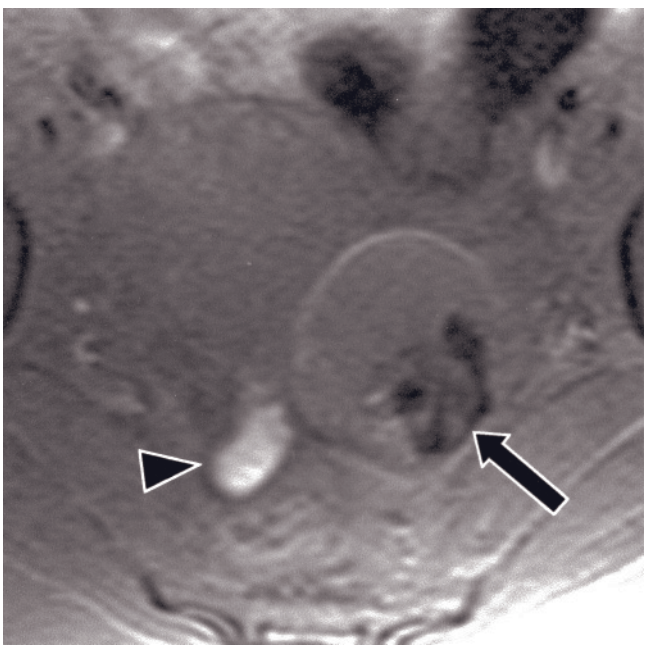

(*c*)

FIG. 15.32 Mature cystic teratoma containing teeth. T2-weighted ETSE (*a*), T1-weighted SE (*b*), and T1-weighted fat-suppressed gradient-echo (*c*) images. T2-weighted image shows a high-signal-intensity mature cystic teratoma (arrow, *a*) in the left ovary. The Rokitansky nodule contains areas that are high signal intensity, representing fat, and signal voids representing teeth. T1-weighted spin-echo image shows the signal voids that represent teeth in the Rokitansky nodule (arrow, *b*). T1-weighted fat-suppressed gradient-echo image (*c*) shows suppression of the substantial fat content both within the cyst and within the Rokitansky nodule itself. The high-signal-intensity hematosalpinx (arrowhead, *c*) does not suppress.

Hormone-producing sclerosing stromal tumors may secrete both estrogenic and androgenic hormones. Resection is curative. An MRI pattern has been described as pseudolobular, reflecting the histopathologic features of the tumor: Low-signal peripheral nodules contrast against high-signal stroma on T2-weighted images [108]. These tumors are highly vascular and are reported to show intense early contrast enhancement that progresses in a centripetal fashion.

MALIGNANT DISEASE OF THE ADNEXA

Primary Ovarian Carcinoma

Ovarian cancer accounts for 4% of all cancers in women and is the number one cause of death from reproductive tract malignancies. Ovarian cancer is primarily a diagnosis of middle-aged and older women, with the inci-

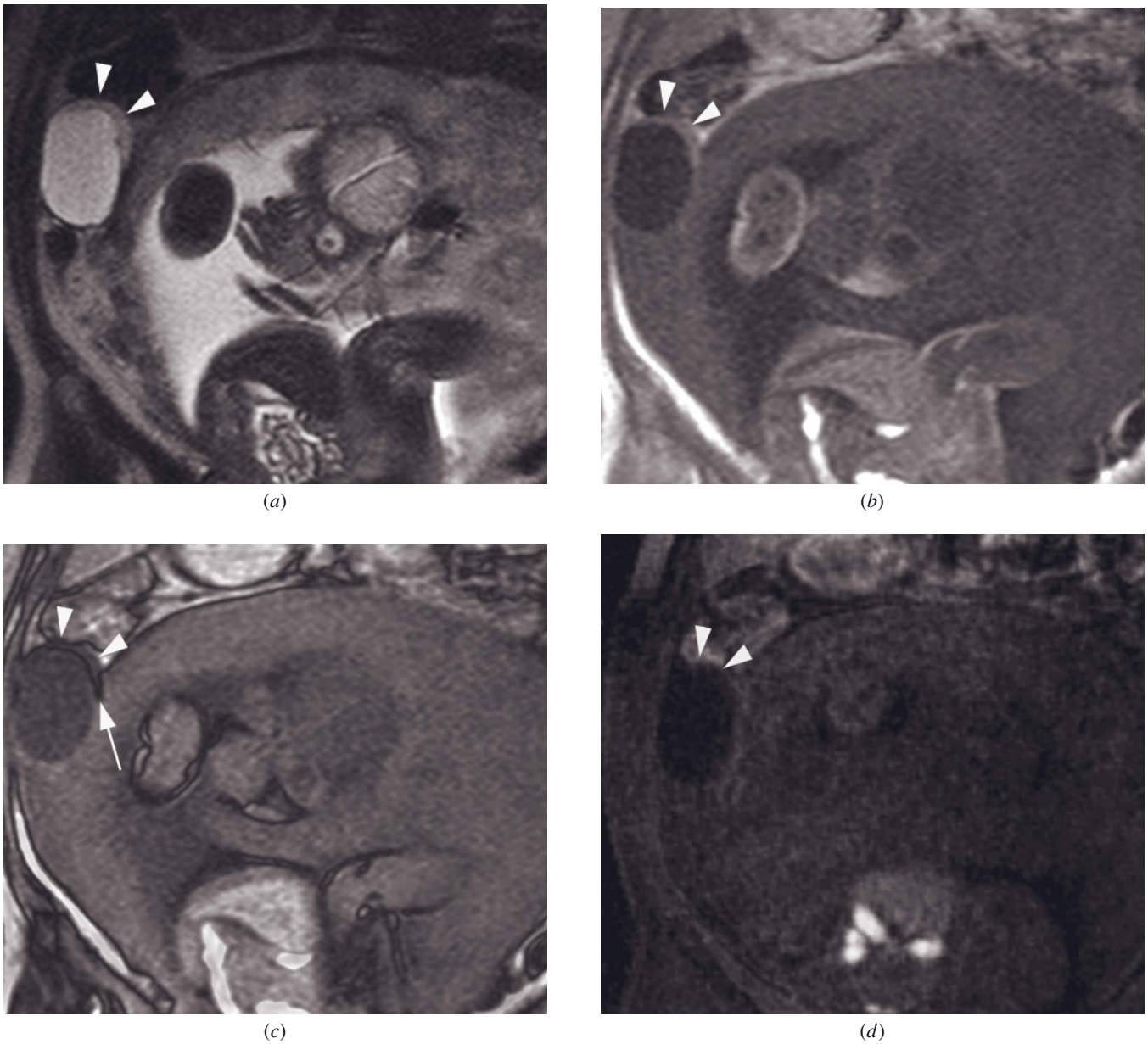

FIG. 15.33 Mature cystic teratoma with a small amount of fat. Coronal T2-weighted SS-ETSE image (*a*), T1-weighted gradient-echo in-phase (*b*) and out-of-phase (*c*) images obtained as a dual echo, and fat-suppressed T1-weighted gradient echo image (*d*) in a pregnant woman with an adnexal mass. A cystic mass is seen in the right adnexa with a small amount of tissue superiorly that does not have signal characteristics of simple fluid (arrowheads). The out-of-phase T1-weighted image reveals signal loss at the interface of the tissue and the fluid within the cyst, indicating that the tissue is fat and the lesion is a benign teratoma. The fat-suppressed T1-weighted image (*d*) may fail to confirm the presence of small amounts of fat because of spatial misregistration and inhomogeneous fat suppression.

dence increasing with age. The median age at diagnosis is 61 years. Risk factors associated with ovarian cancer include early menarche, low parity, older age at first pregnancy, infertility, late menopause, and family history of the disease. Oral contraceptives appear to have a protective effect. There have also been suggestions of environmental risk factors, but none has been conclusively proven responsible [109]. Survival depends on tumor stage at diagnosis. Because most women present with advanced disease, the overall 5-year survival is poor. If women present with localized disease, the 5-year survival is 93%. With disease spread beyond the pelvis, 5-year survival drops to 25% [110]. Screening efforts have not yet been successful.

The main strength of MR in the diagnosis of women with pelvic masses is the ability to accurately determine

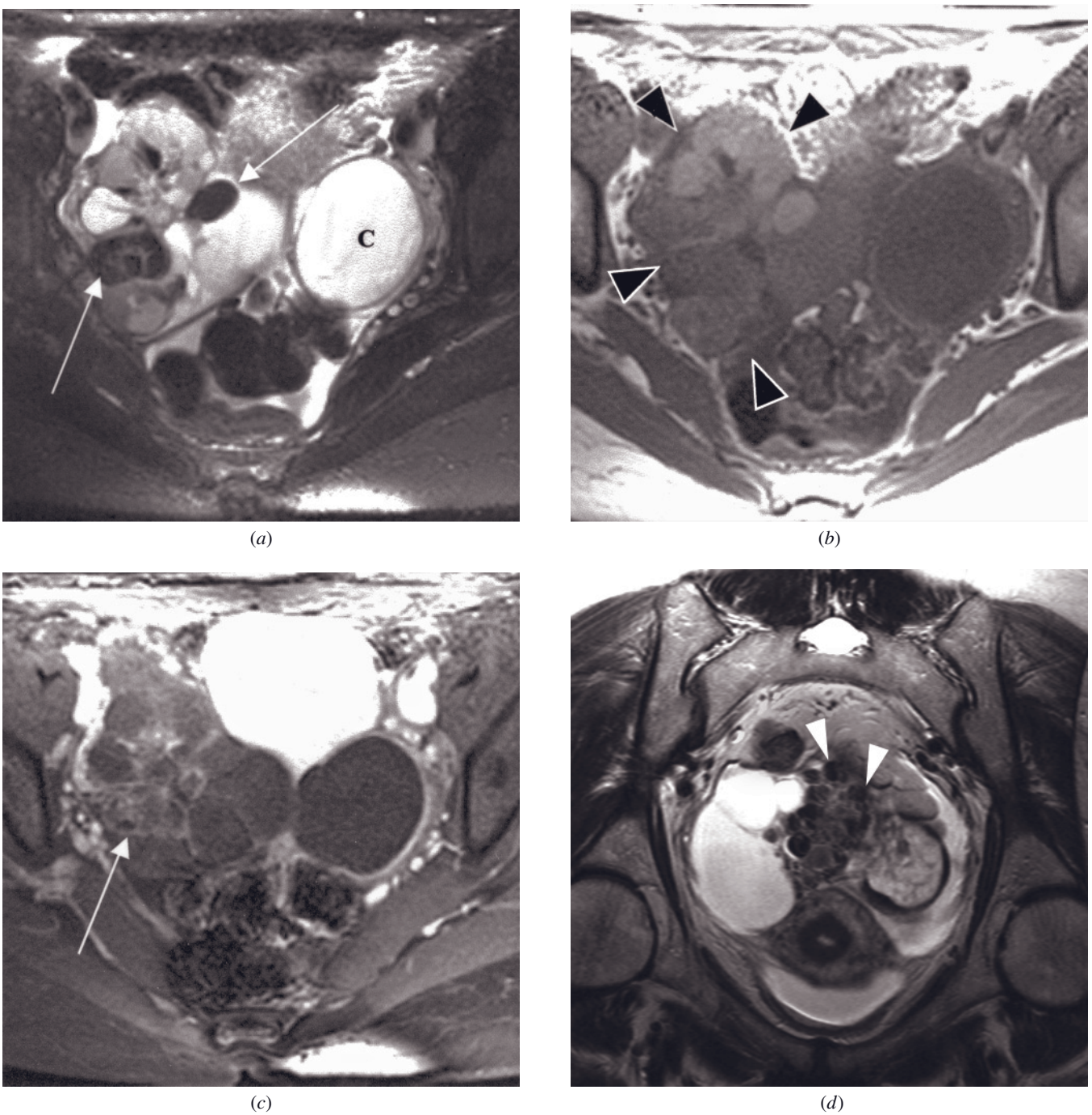

FIG. 15.34 Struma ovarii. T2-weighted ETSE (*a*), T1-weighted SE (*b*), and gadolinium-enhanced T1-weighted fat-suppressed gradient-echo (*c*) images in a patient with struma ovarii. Note the multiloculated mass in the right ovary (arrowheads, *b*), which shows lacelike enhancement on postgadolinium images (arrow, *c*). Some cysts show low signal intensity on T2-weighted images (arrows, *a*). Struma ovarii is a monodermal teratoma that may produce thyroid hormones. (C, ovarian cyst.)

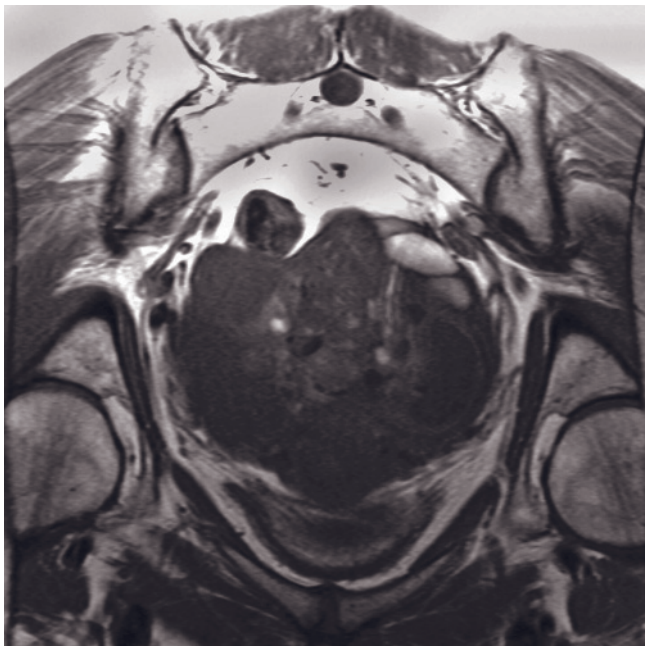

(*e*)

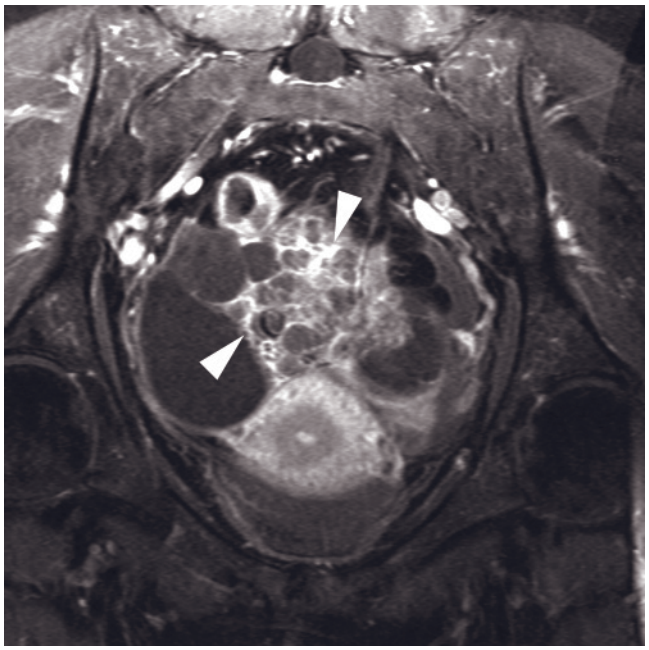

(*f*)

FIG. 15.34 (*Continued*) **Struma ovarii.** Oblique T2-weighted ETSE (*d*), T1-weighted gradient echo (*e*), and gadolinium-enhanced T1-weighted fat-suppressed gradient echo (*f*) images in a different patient with struma ovarii. Note a multiloculated mass with characteristic low-signal-intensity locules on T2-weighted images (arrowheads, *d*) and lacelike enhancement on postgadolinium images (arrowheads, *f*).

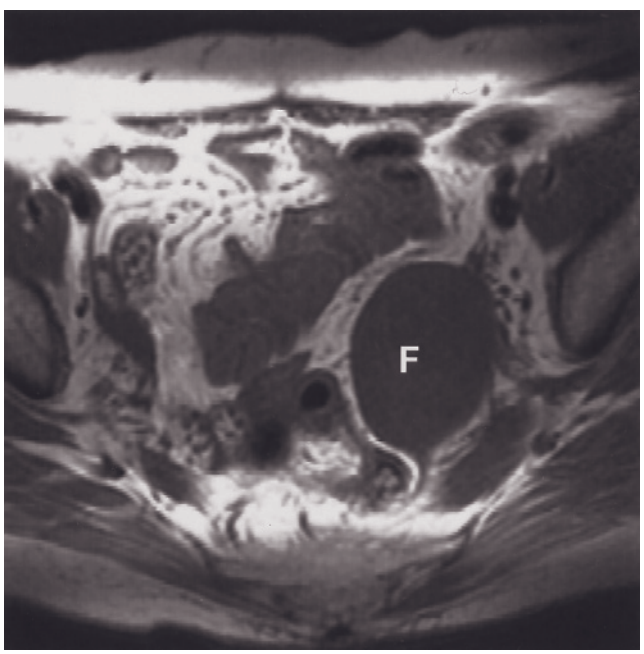

(*a*)

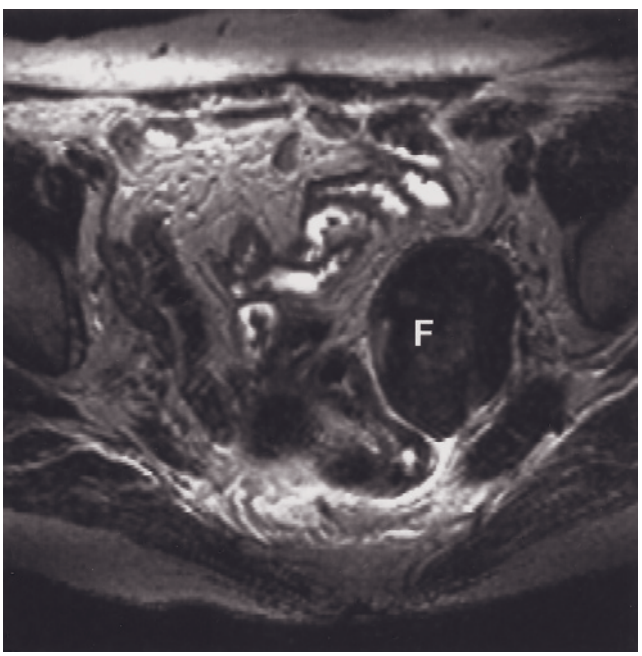

(*b*)

FIG. 15.35 Ovarian fibroma. T1-weighted SE (*a*) and transverse (*b*) and sagittal (*c*) T2-weighted ETSE images show a left ovarian fibroma (F). The tumor is well defined and low in signal intensity on T1-weighted (*a*) and T2-weighted (*b*, *c*) images.

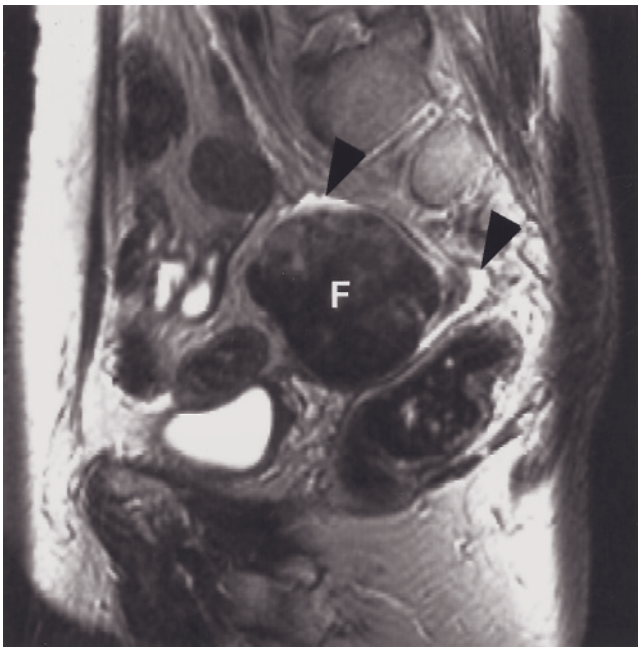

(*c*)

FIG. 15.35 (*Continued*) A small volume of pelvic fluid (arrowheads, *c*) is noted posterior and adjacent to the mass.

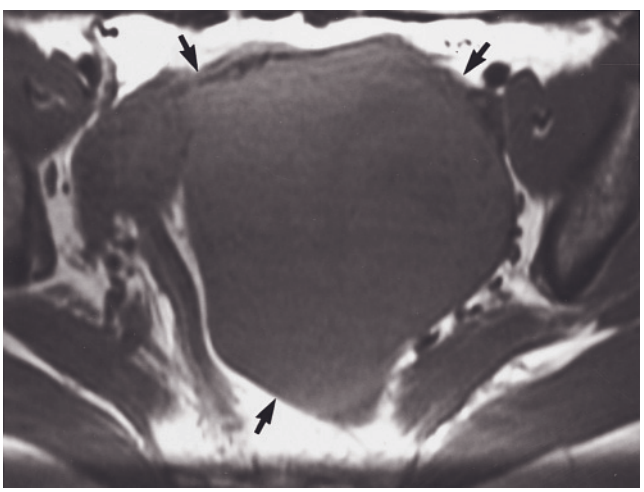

(*a*)

(*b*)

FIG. 15.36 Large ovarian fibroma with necrosis. T1-weighted SE (*a*), sagittal 512-resolution T2-weighted ETSE (*b*), and gadolinium-enhanced T1-weighted SE (*c*) images show an ovarian fibroma. A 12 cm mass is present in the pelvis that is homogeneous in signal intensity on the T1-weighted image (arrows, *a*), heterogeneous on the T2-weighted image (*b*), and enhances in a mild and heterogeneous

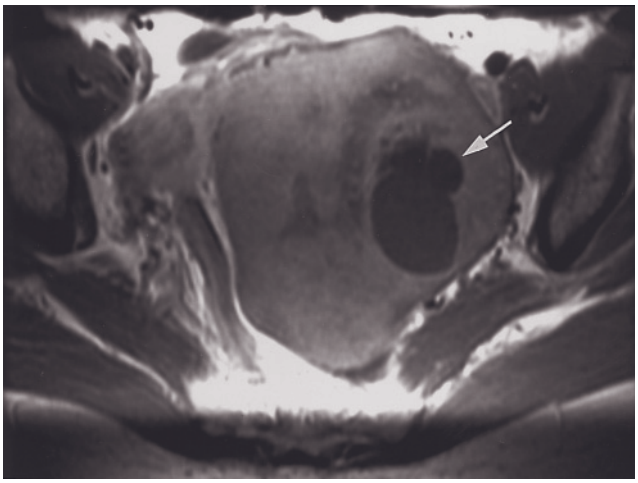

(*c*)

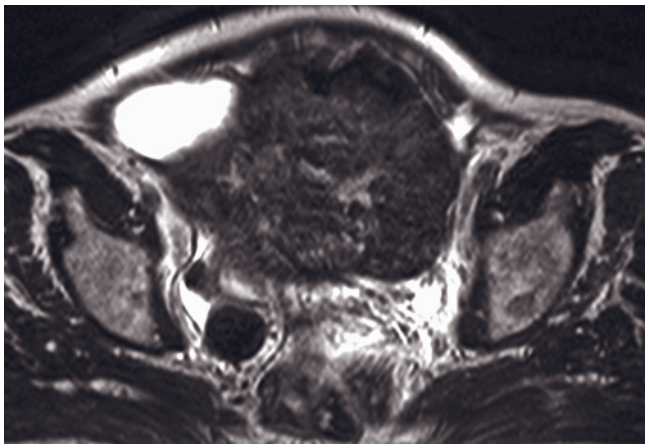

(*d*)

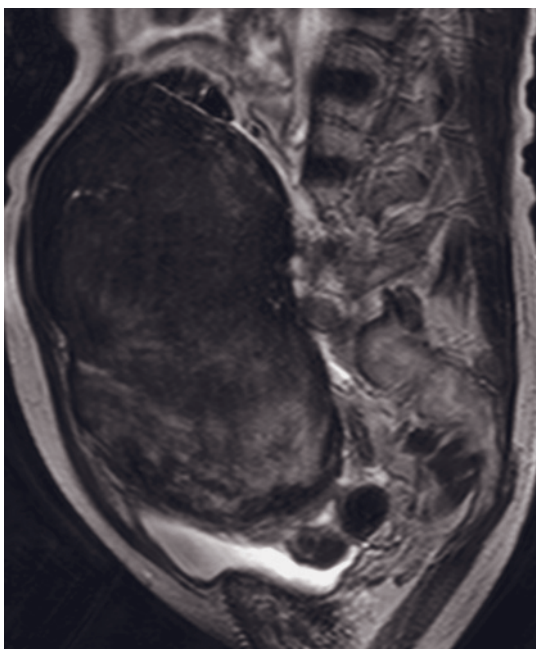

(*e*)

(*f*)

Fig. 15.36 (*Continued*) fashion with cystic areas (arrow, *c*). **Ovarian thecoma.** Transverse (*d*) and sagittal (*e*) T2-weighted ETSE images show a large mass with low signal intensity. Photograph of the resected solid tumor is also shown (*f*).

the origin of a pelvic mass, to determine whether an ovarian mass is likely neoplastic, and to determine whether a neoplastic mass is likely benign or malignant. Studies have reported high accuracy rates for these determinations [42, 87, 111–116]. Several criteria suggestive of malignancy have been described, including large size (>4–6 cm, depending on series), solid and cystic components, papillary projections, and necrosis. [115–117]. Extraovarian findings of malignancy include ascites, peritoneal implants, and lymphadenopathy [113, 115, 116]. Several studies have shown gadolinium to improve accuracy [115, 117, 118]. In addition to characterizing adnexal masses, MRI can also evaluate patients for preoperative chemotherapy and monitor recurrence after treatment.

Epithelial Origin

Ovarian carcinoma derives most often from the epithelium of the ovary. There are four major cell types of ovarian epithelium: serous, mucinous, clear cell, and endometrioid. Tumors arising from these cell types account for 60% of all ovarian neoplasms and 85% of malignant neoplasms [119]. The benign lesions arising from these cell types were discussed above. A second category of tumor includes those that have borderline features (fig. 15.37) or low malignant potential. These tumors have an excellent prognosis despite sharing histologic features of frankly malignant masses; the quality they lack is destructive growth (invasion) [109]. The final category includes tumors that are overtly malignant.

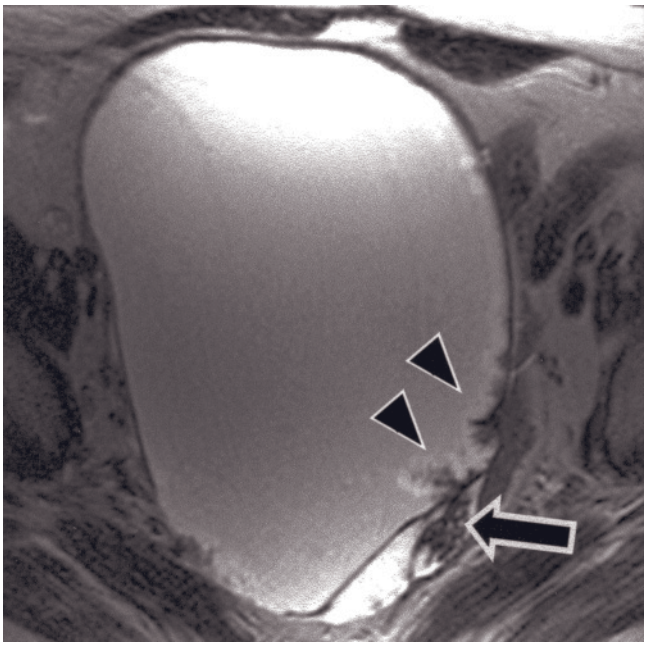

(*a*)

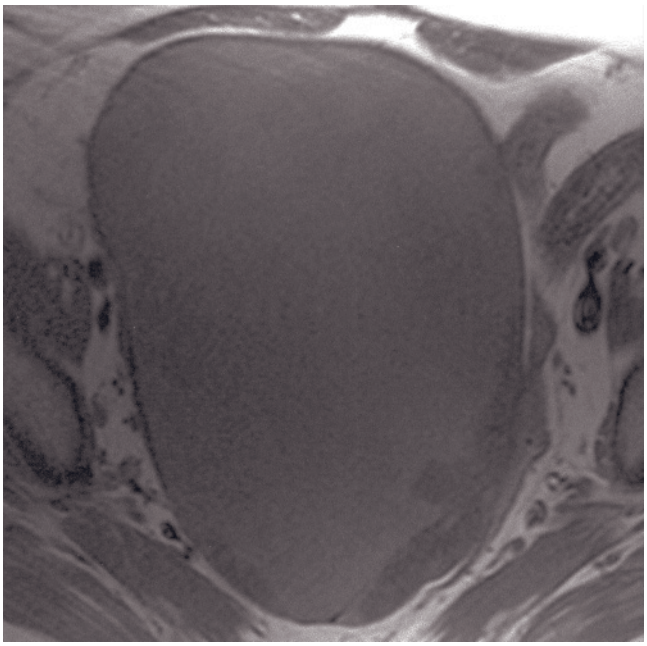

(*b*)

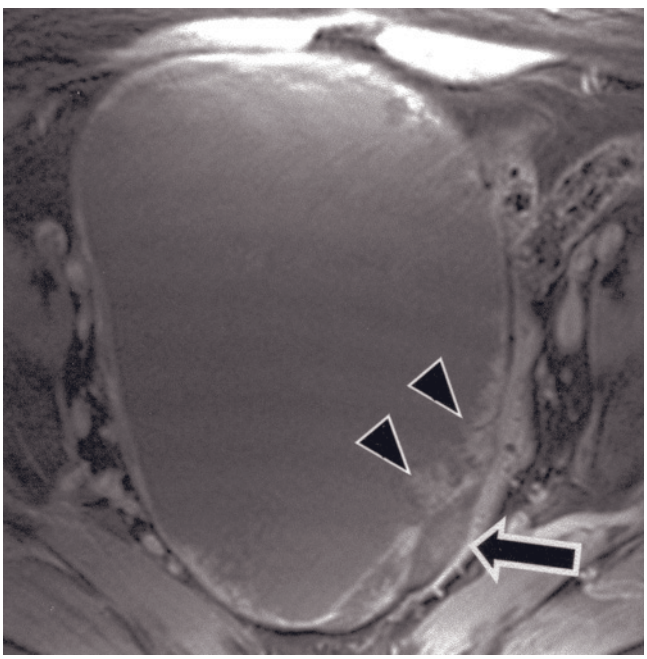

(*c*)

FIG. 15.37 Cystadenofibroma with borderline features. T2-weighted echo-train spin-echo (*a*), T1-weighted spin-echo (*b*), and gadolinium-enhanced T1-weighted fat-suppressed gradient-echo (*c*) images in a patient with cystadenofibroma with borderline features. T2-weighted image (*a*) shows papillary projections (arrowheads, *a*) consisting of low-signal-intensity fibrous core and barely visible edematous stroma. A prominent, very low-signal-intensity fibrous component (arrow, *a*) is seen in the wall. Gadolinium-enhanced T1-weighted fat-suppressed gradient-echo image (*c*) shows enhancement of the papillary projections (arrowheads, *c*) but less enhancement of the fibrous component (arrow, *c*).

Approximately 75–85% of patients with epithelial neoplasms present with peritoneal disease, and even women with apparently localized disease may have metastases detected in peritoneal washings or biopsy of the omentum or diaphragm [109]. Tumor may also spread through lymphatic channels to the para-aortic lymph nodes. Lymphatics also facilitate spread along the broad ligament to pelvic lymph nodes. Most patients present with nonspecific symptoms such as abdominal discomfort, pain, or distension. The latter is attributable to malignant ascites or a large primary mass. Traditionally, complete staging requires surgical removal of the uterus, ovaries, and fallopian tubes, sampling of the para-aortic and retroperitoneal lymph nodes, excision of the omentum, biopsies of the peritoneum and diaphragm, and evaluation of peritoneal washings. Stages are assigned according to the International Federation of Gynecology and Obstetrics (FIGO) schema. Many investigators have attempted to prove the worth of noninvasive methods for staging. A major initiative of

the Radiological Diagnostic Oncology Group (RDOG) is to examine the diagnostic accuracy of Doppler US, CT, and MR in the diagnosis and staging of ovarian cancer. A primary analysis showed no difference for the three modalities [120], while a subsequent study of advanced disease (stages III and IV) showed an advantage of using MRI or CT over US in these patients [121]. Prognosis depends on tumor stage, residual disease after initial surgery, and tumor grade. In up to 80% of cases, the CA-125 level will be elevated at presentation, and the level can be followed to assess for response to treatment. However, a normal value does not exclude the presence of tumor [122]. After surgery and chemotherapy, MRI may be helpful to detect residual disease. In one series of 69 patients, MRI accurately determined the presence of residual or recurrent subclinical disease in 20 of 23 patients [122].

The MR appearance of primary epithelial neoplasms is a variable combination of cystic and solid components. Gadolinium administration is useful for the detection of solid and necrotic components as well as intraperitoneal implants. There is considerable overlap in the appearance of tumors of the various cell types, but some features are more characteristic of a particular cell type.

Serous. Cancers arising from the serous cell type account for approximately one-half of all ovarian malignancies [123, 124]. In 50% of these patients, the disease is bilateral. Serous cancers are predominantly unilocular cysts (figs. 15.38 and 15.39). As the degree of cellular differentiation decreases, the incidence of hemorrhage, solid elements, and necrosis increases. On MRI, papillary projections seen as intermediate-signal-intensity projections within a cystic lesion that enhance with gadolinium indicate tumors of serous origin. They are suggestive of but not specific for malignancy, as they are also seen in some benign serous cystadenomas. Approximately 30% contain psammoma bodies [123], which are not well seen on MRI. Many patients have peritoneal disease at the time of diagnosis (fig. 15.40).

Mucinous. Cancers arising from the mucinous cell type are typically larger and more often unilateral compared to serous tumors. On MR images, these tumors appear multilocular more frequently than serous tumors, with septations of variable thickness that enhance with gadolinium. Mucinous tumors have been called "stained glass" lesions because of the different signal intensities of locules based on variable content. Septae between locules may enhance with gadolinium in benign or malignant lesions; however, areas of hemorrhage, necrosis, and solid elements are more suggestive of malignancy (figs. 15.41–15.43*a–c*). Another potentially helpful feature is the number of locules, which have been reported to be more numerous in borderline mucinous tumors and mucinous cystadenocarcinomas compared to benign mucinous cystadenomas [125].

Endometrioid. Cancers arising from the endometrioid cell type are usually malignant rather than benign. Endometrioid tumors comprise 15% of ovarian cancers and may arise within the ovary or within foci of endometriosis. These tumors are associated with endometrial hyperplasia or frank endometrial carcinoma in up to one-third of cases. Despite this association, they are felt to represent separate tumors and not metastatic disease. They are less commonly bilateral (approximately 25%) than serous or mucinous tumors and are generally composed of a mixture of cystic and solid elements (fig. 15.43*d–f*). Rarely, lesions are purely solid.

Clear Cell. Cancers arising from the clear cell type are less common, comprising 5% of ovarian cancers. Like endometrioid tumors, clear cell tumors are nearly always malignant. Unlike the other cell types, clear cell carcinoma presents more often with local disease, and carries a better overall prognosis. Clear cell cancers are less frequently bilateral (approximately 13%) than other epithelial cancers (figs. 15.44 and 15.45). These are generally unilocular tumors with mural nodules, which may be few in number, and these tumors can mimic serous tumors. Benign and borderline clear cell tumors are rare and nearly always of the adenofibromatous subtype (fig. 15.45*c*, *d*). The presence of proteinaceous material or hemorrhage may alter T1- and T2-weighted imaging characteristics of clear cell carcinomas (fig. 15.46) [126]. In the case of a hemorrhagic mass that is very bright on T1-weighted images, it may be difficult to detect nodule enhancement, and subtraction images may be helpful.

Undifferentiated. A final classification is the undifferentiated epithelial neoplasm. These do not fit into any category based on one of the four cell types of origin. These carry the poorest prognosis, with widespread disease generally present at diagnosis (fig. 15.47).

Germ Cell Origin

Dysgerminomas are the most common malignant germ cell neoplasm in children and young women under 20 years of age. Most patients present with stage I disease, in which case the tumor is bilateral in up to 15% [127]. Conservative surgery with postoperative chemotherapy is a fertility-preserving option that has been reported to be successful. These tumors are generally large, lobulated, and solid.

Endodermal sinus tumors are the second most common malignant germ cell tumor and have a similar age distribution. The MRI appearance has been described

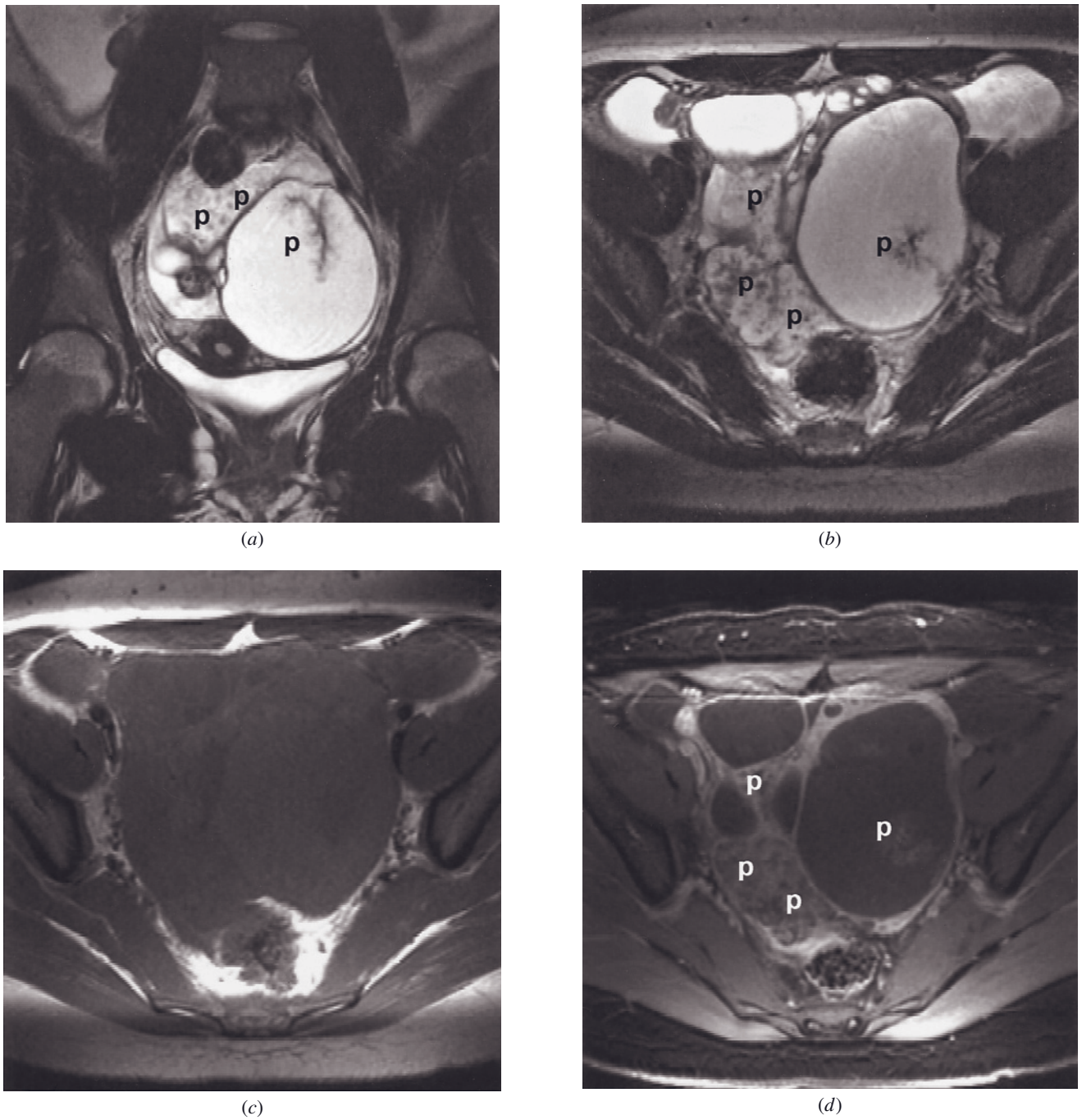

FIG. 15.38 Serous cystadenocarcinoma. Coronal (*a*) and transverse (*b*) T2-weighted ETSE, T1-weighted gradient-echo (*c*), and gadolinium-enhanced fat-suppressed T1-weighted (*d*) SE images in a 19-year-old woman with a low malignant potential serous tumor. Complex bilateral adnexal masses are noted. The T2-weighted images demonstrate papillary projections (p, *a*, *b*) After gadolinium administration, the papillary projections show marked enhancement (p, *d*). Contrast administration helps to differentiate between vascularized solid elements and debris within cystic masses.

as large, solid masses with internal cysts, necrosis, and vascularity; however, imaging features are not specific (figs. 15.48 and 15.49). Rupture and ascites are not uncommon [127]. Elevated serum α-fetoprotein is seen in these patients and is used to monitor treatment outcome. Treatment is surgery and chemotherapy. The prognosis is poor in patients who do not respond to chemotherapy [128–130].

Immature teratomas are rare and comprise about 1% of germ cell tumors. Histologically these tumors are comprised of tissues normally seen in the human embryo. They tend to occur in younger patients and

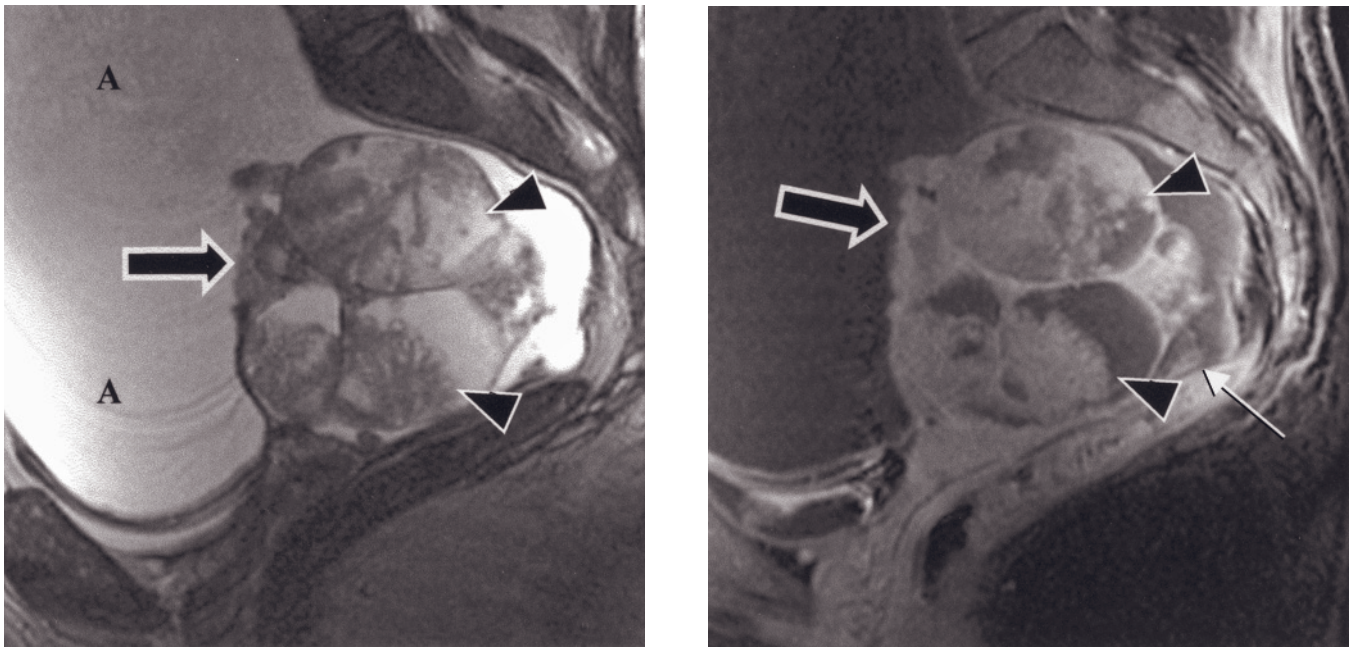

(*a*) (*b*)

FIG. 15.39 Serous cystadenocarcinoma. Sagittal T2-weighted ETSE image (*a*) and sagittal T1-weighted fat-suppressed gradient-echo (*b*) images. T2-weighted image shows a right ovarian mass with irregular solid components (arrow, *a*) and florid intracystic papillary projections (arrowheads, *a*). Ascites (A) is present, with implants in the cul-de-sac. Gadolinium-enhanced T1-weighted fat-suppressed gradient-echo image (*b*) shows enhancement of the papillary projections (arrowheads, *b*) and solid components (arrow, *b*) and implants (thin arrow, *b*).

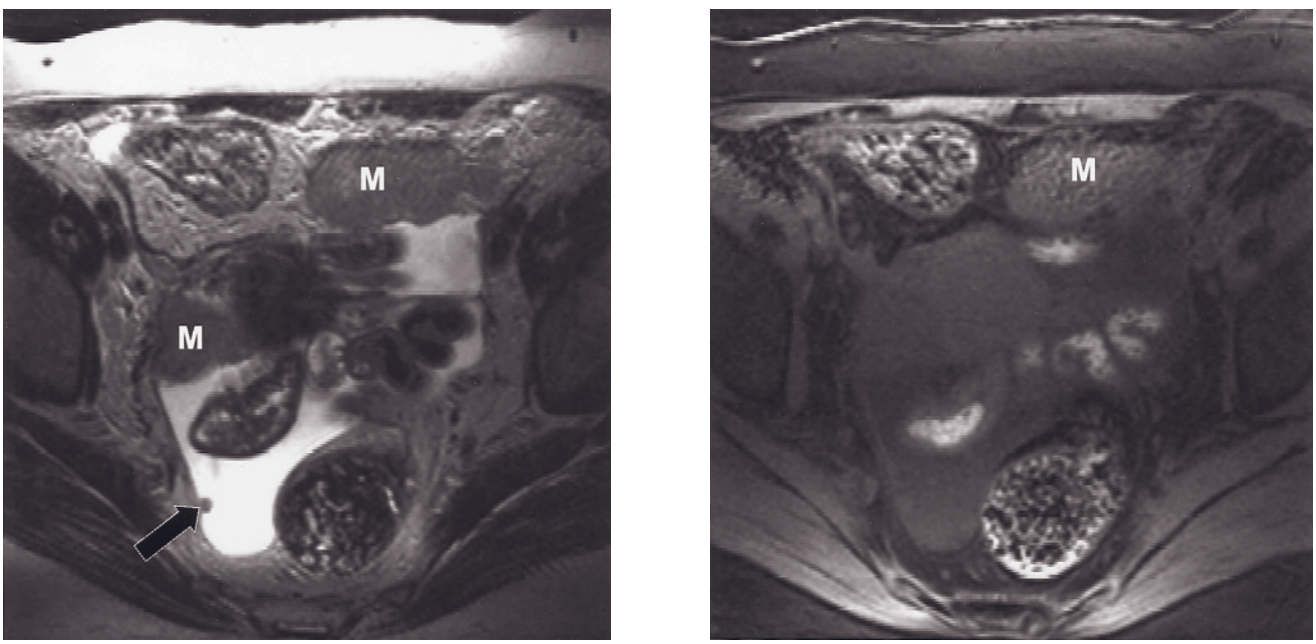

(*a*) (*b*)

FIG. 15.40 Peritoneal metastases. T2-weighted ETSE (*a*), T1-weighted fat-suppressed (*b*), and gadolinium-enhanced T1-weighted fat-suppressed (*c*) SE images in a 69-year-old woman with advanced ovarian carcinoma, stage III. The peritoneum is diffusely thickened and has superimposed nodules. Peritoneal metastases (arrow, *a*) are most conspicuous on T2-weighted images in the setting of ascites and after gadolinium administration on T1-weighted fat-suppressed images (arrows, *c*). Note the larger metastatic masses distributed in the pelvis (M, *a–c*). Contrast-enhanced T1-weighted fat-suppressed technique increases staging accuracy of ovarian carcinomas.

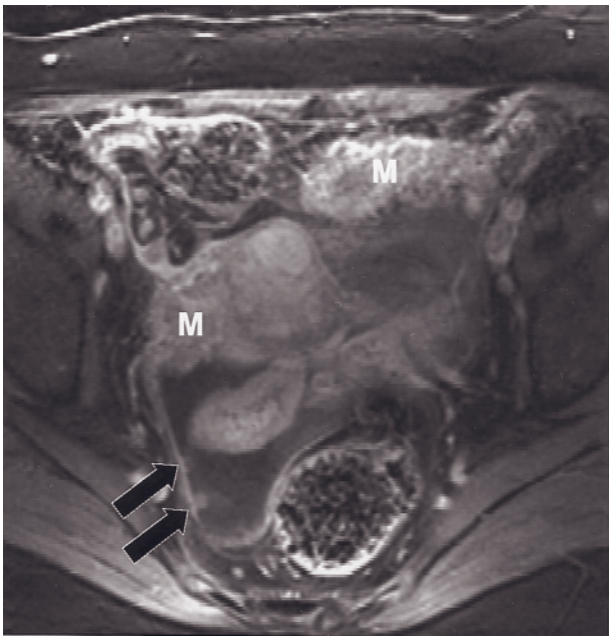

(*c*)

Fig. 15.40 (*Continued*)

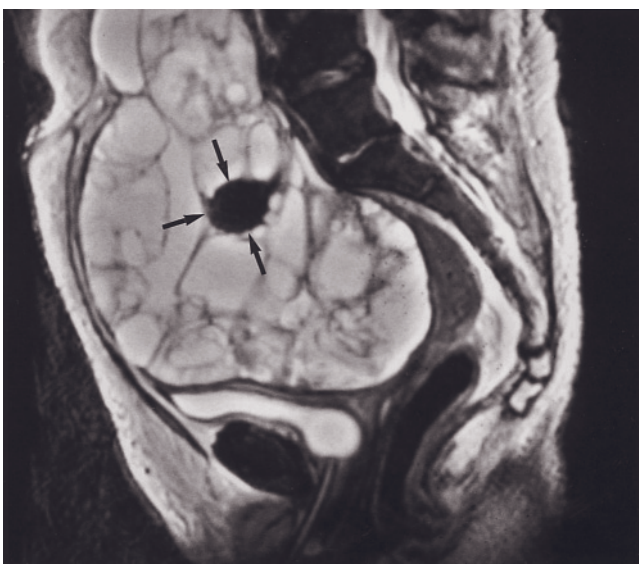

(*a*)

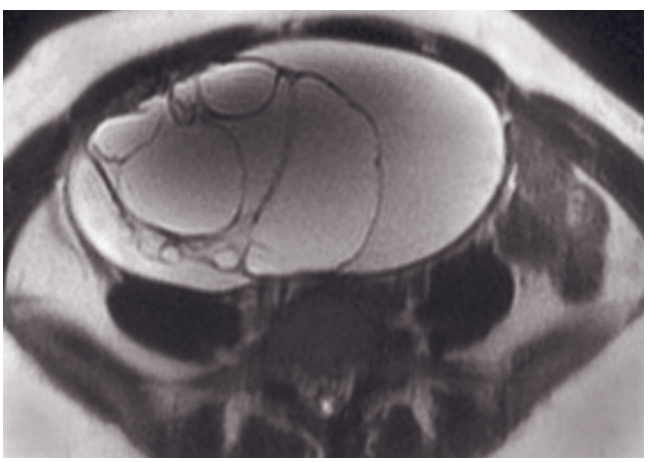

(*b*)

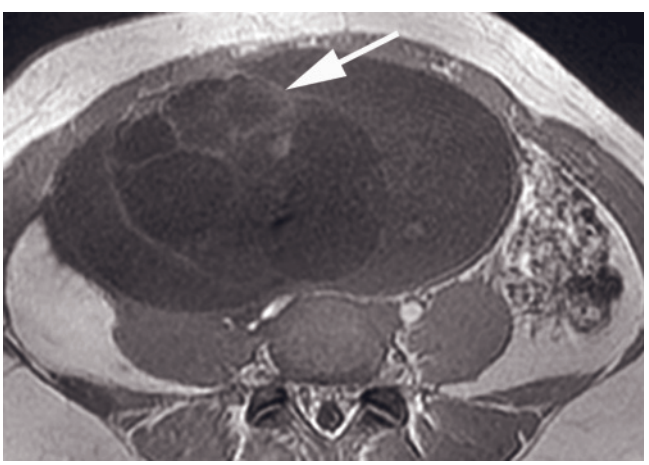

(*c*)

Fig. 15.41 Mucinous cystadenocarcinoma. (*a*) Sagittal T2-weighted ETSE image in a patient with a large multiloculated mucinous cystadenocarcinoma. One of the locules is complicated by hemorrhage; intracellular methemoglobin is low in signal intensity on T2-weighted images (arrows). Hemorrhage into a tumor locule is common with mucinous neoplasms. **Borderline mucinous tumor at 3 T.** Transverse T2-weighted ETSE (*b*) and T1-weighted gradient-echo (*c*) images in a different patient show a large multiloculated mucinous that had borderline features on histological evaluation. Note the differing signal intensity within the locules, best seen on the T1-weighted image (arrow, *c*).

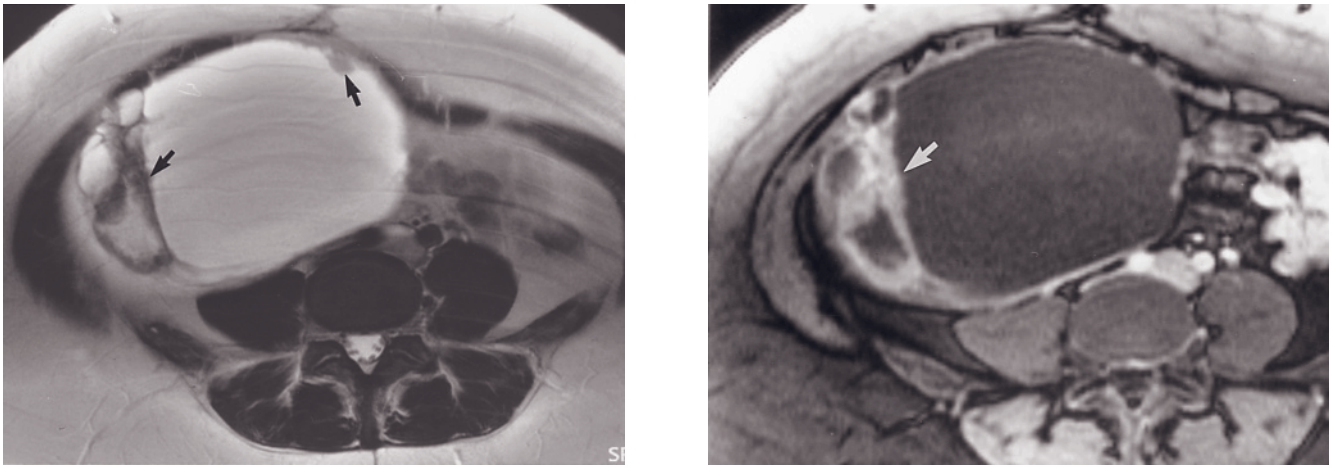

(*a*) (*b*)

Fig. 15.42 Mucinous cystadenocarcinoma. Transverse 512-resolution T2-weighted ETSE (*a*) and gadolinium-enhanced T1-weighted fat-suppressed gradient-echo (*b*) images in a patient with advanced mucinous ovarian cancer. A large cystic mass with septations and nodules (arrows, *a*) is present. After contrast, the enhancing tumor excrescences are well shown (arrow, *b*).

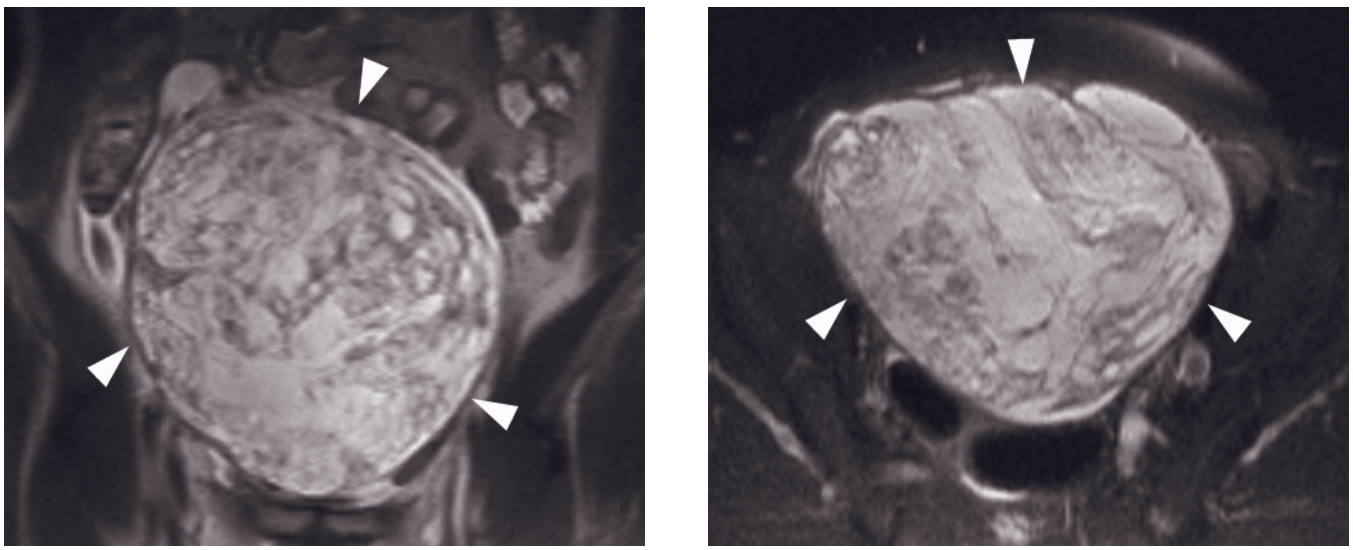

(*a*) (*b*)

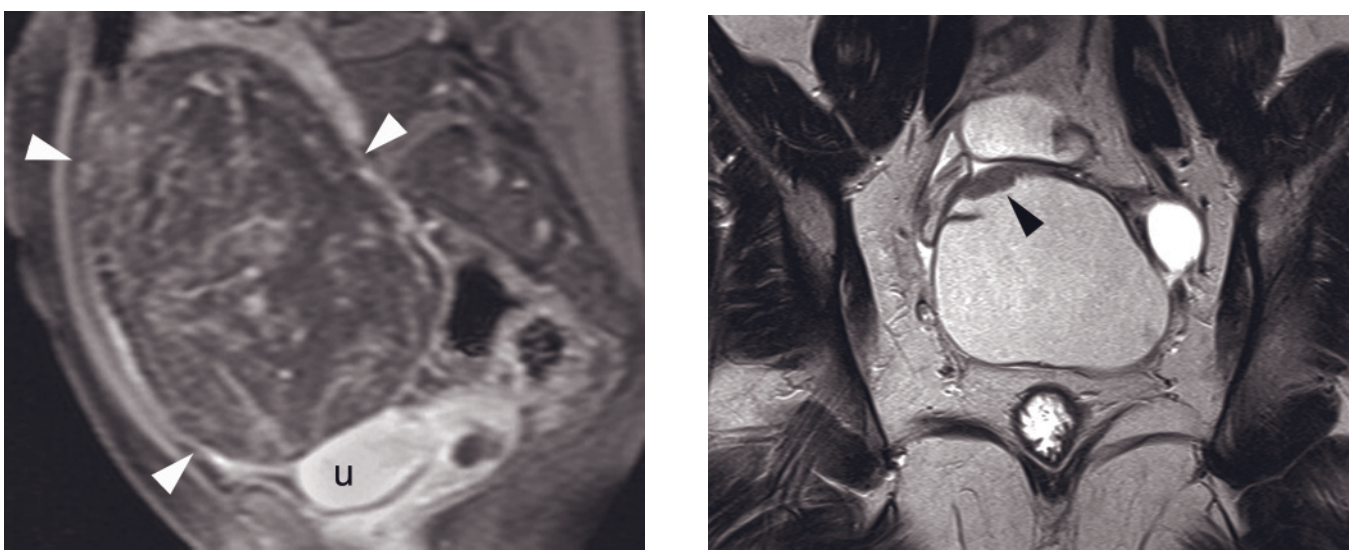

(*c*) (*d*)

Fig. 15.43 Mucinous cystadenocarcinoma. Coronal T2-weighted SS-ETSE (*a*), transverse fat-suppressed T2-weighted ETSE (*b*), and sagittal gadolinium-enhanced fat-suppressed T1-weighted gradient-echo (*c*) images show a large multiseptated mass (arrowheads). The postgadolinium image (*c*) shows enhancement of the septations and mass effect on the uterus (u, *c*).

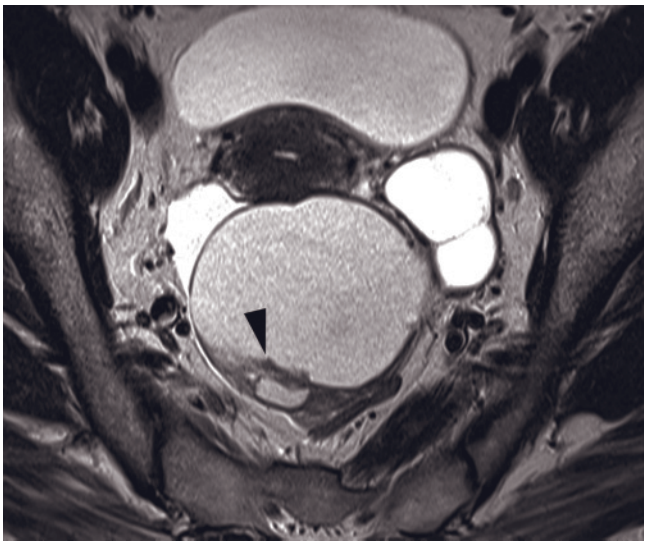

(*e*)

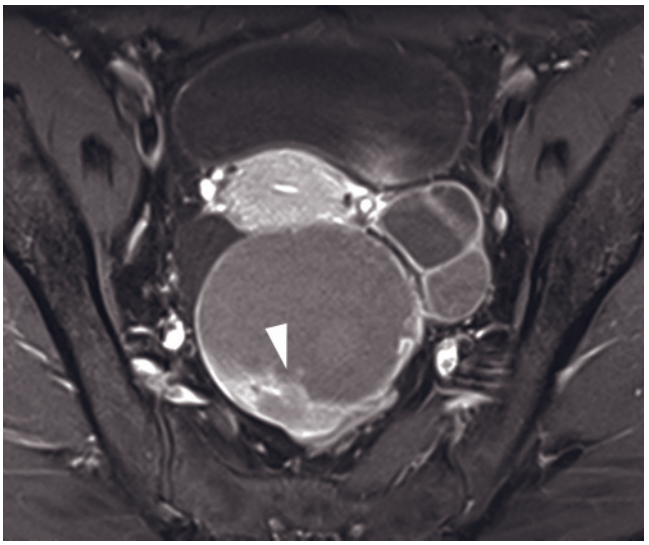

(*f*)

FIG. 15.43 (*Continued*) **Endometrioid adenocarcinoma.** Coronal (*d*) and transverse (*e*) T2-weighted ETSE and transverse gadolinium-enhanced fat-suppressed T1-weighted gradient-echo (*f*) images in a different patient show a left ovarian mass that is predominantly cystic with solid components (arrowheads, *d–f*).

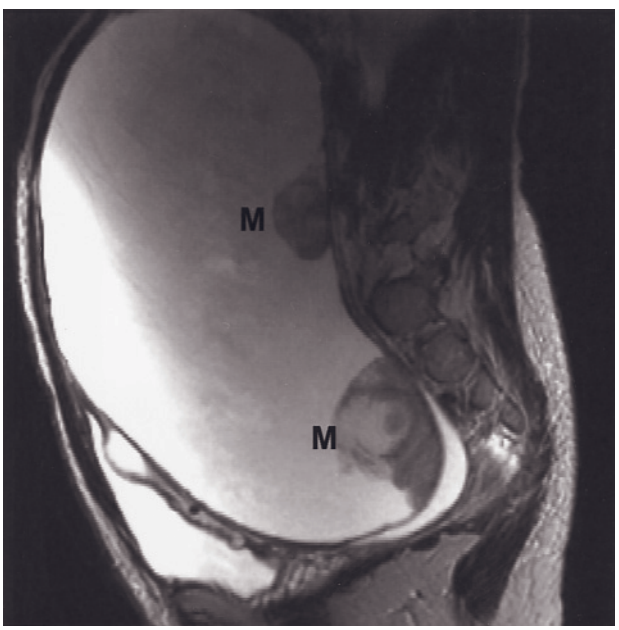

(*a*)

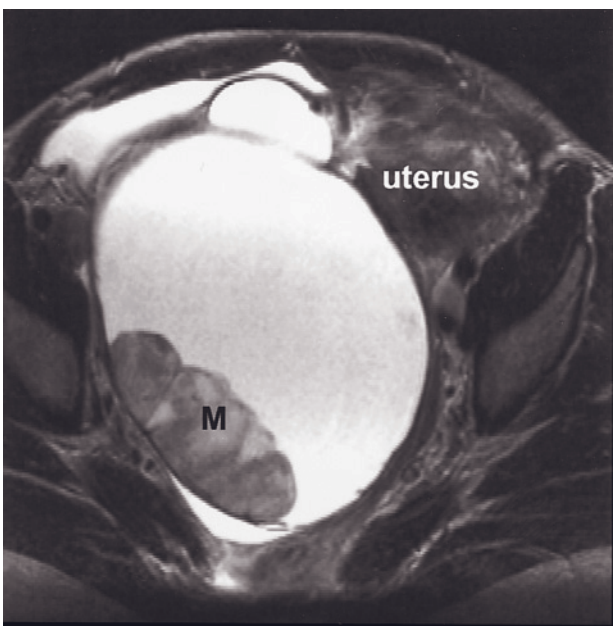

(*b*)

FIG. 15.44 Clear cell carcinoma. Sagittal (*a*) and transverse (*b*) T2-weighted ETSE, T1-weighted SE (*c*), and gadolinium-enhanced T1-weighted fat-suppressed gradient-echo (*d*) images in a 51-year-old woman with an ovarian mass. A large, primarily unilocular cystic lesion with peripheral masses (M, *a–c*) arises from the pelvis. The masses enhance after contrast (M, *d*).This appearance is typical of clear cell carcinoma.

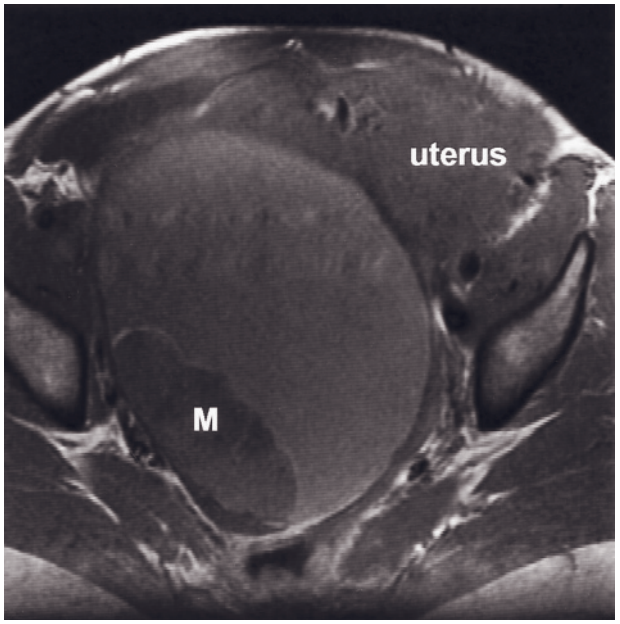

(*c*)

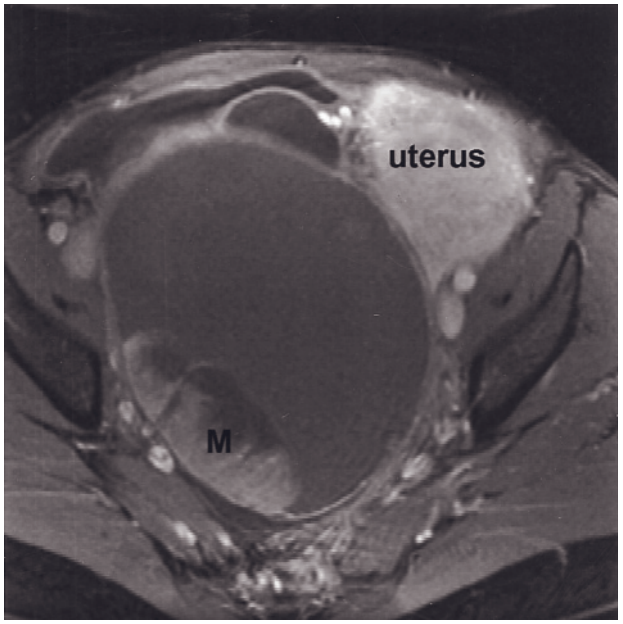

(*d*)

FIG. 15.44 (*Continued*)

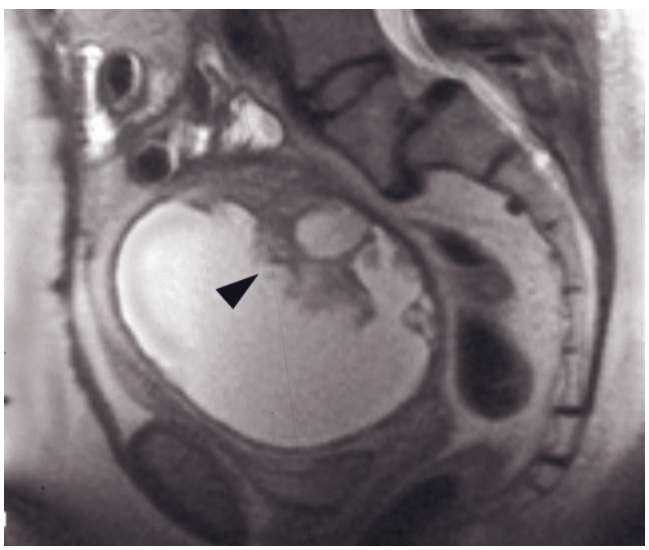

(*a*)

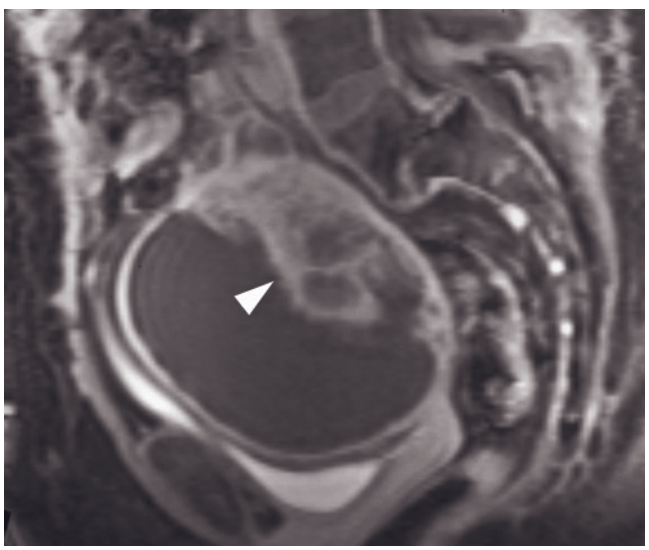

(*b*)

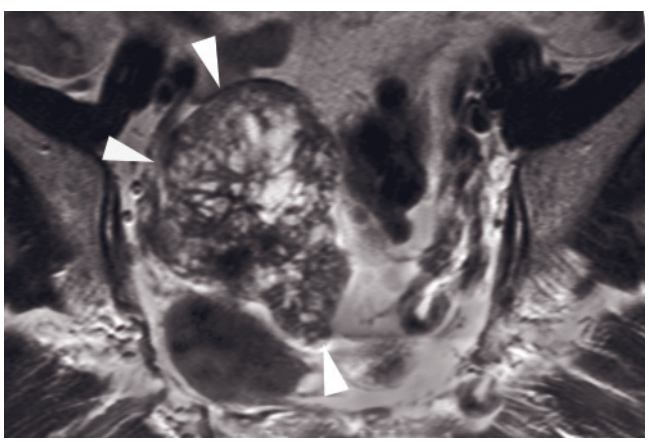

(*c*)

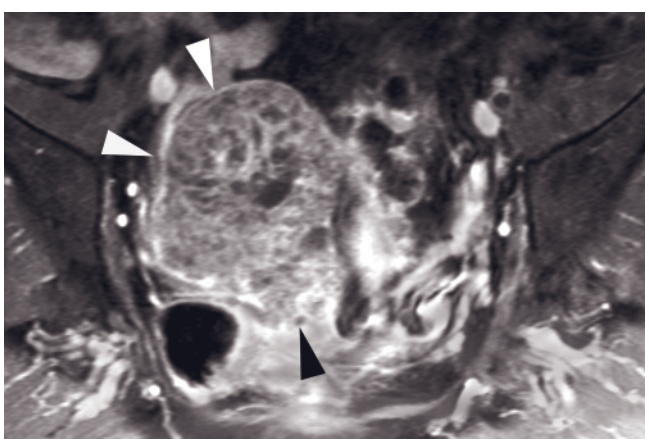

(*d*)

FIG. 15.45 Clear cell carcinoma. Sagittal T2-weighted ETSE (*a*) and gadolinium-enhanced fat-suppressed T1-weighted gradient-echo (*b*) images show a cystic mass with solid enhancing components (arrowheads). **Borderline clear cell adenofibromatous tumor.** Transverse T2-weighted ETSE (*c*) and gadolinium-enhanced fat-suppressed T1-weighted gradient-echo (*d*) images show a complex multicystic mass with solid enhancing components with a spongy appearance.

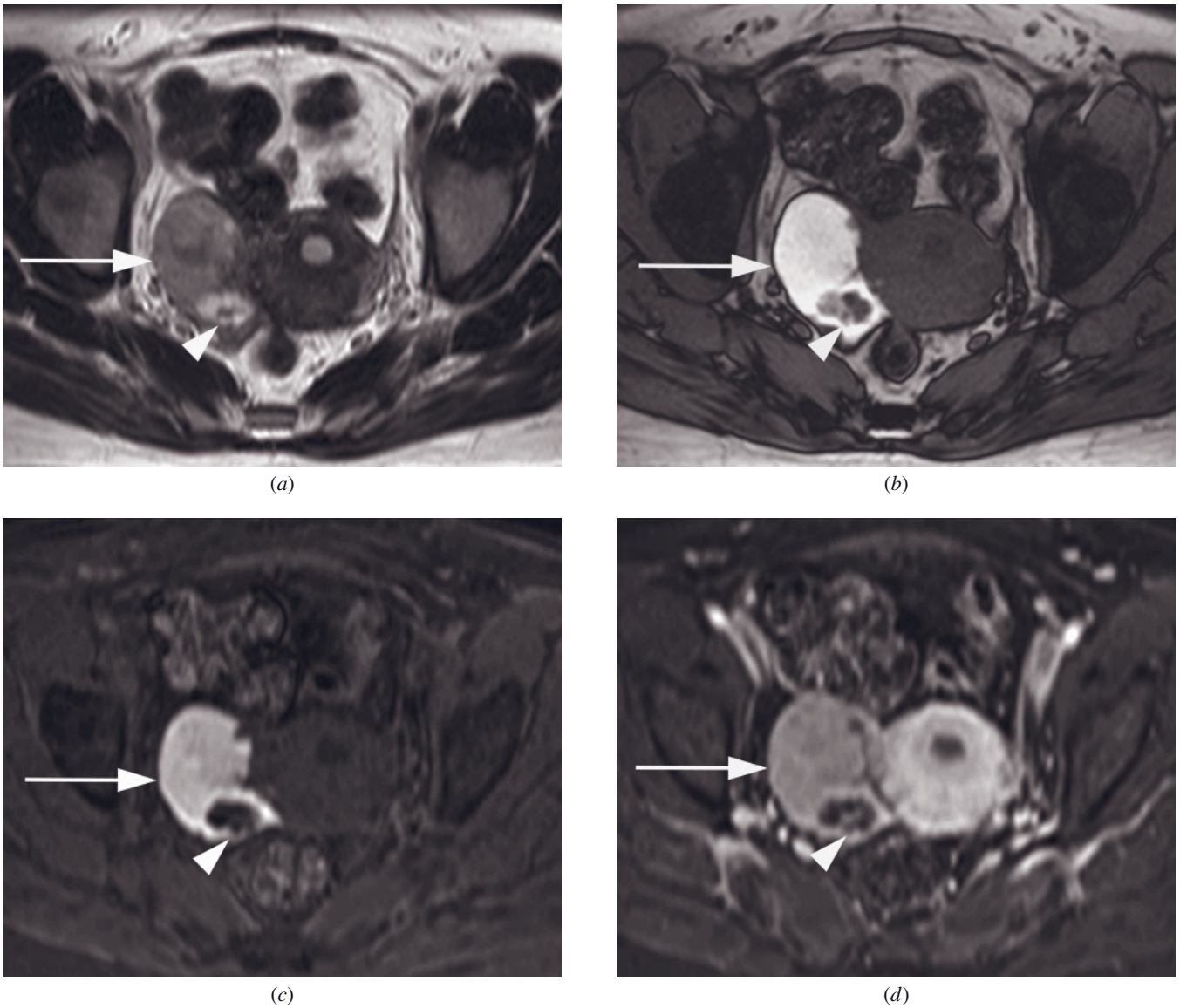

FIG. 15.46 Clear cell carcinoma with hemorrhage. Transverse T2-weighted ETSE (*a*) and out-of-phase (*b*), fat-suppressed (*c*), and gadolinium-enhanced fat-suppressed (*d*) T1-weighted gradient echo images show a right ovarian mass (arrow) with signal intensity consistent with hemorrhage and a small nodular component (arrowhead). A small amount of enhancement is seen, although difficult to appreciate in a background of high-signal-intensity blood products because of dynamic range effects. Pathologic evaluation revealed clear cell carcinoma with no evidence of endometriosis.

are usually large (average 18 cm) and unilateral [12]. Identification of fat within a large, invasive ovarian mass suggests the diagnosis (figs. 15.50 and 15.51). They tend to spread by seeding the peritoneum. The peritoneal implants may show spontaneous maturation into benign tissues, typically glial [127].

Other, rarer malignant germ cell tumors do not have specific imaging characteristics but also tend to present as aggressive ovarian masses in young women. These include mixed malignant germ cell tumor, embryonal cell tumor, and primary ovarian choriocarcinoma.

Sex Cord-Stromal Origin

Masses arising from the specialized gonadal stroma account for 5% of all ovarian neoplasms [127]. These are classified according to differentiation toward ovarian follicles, testicular tubules, Leydig cells, or adrenal cortical cells [127]. Granulosa cell tumors are the most common of this category, followed by fibrothecoma/fibroma (benign tumors), and Sertoli–Leydig cell tumors. Granulosa cell tumors are divided into adult and juvenile types, and both excrete estrogen. This can cause pseudoprecocious puberty in children and uterine

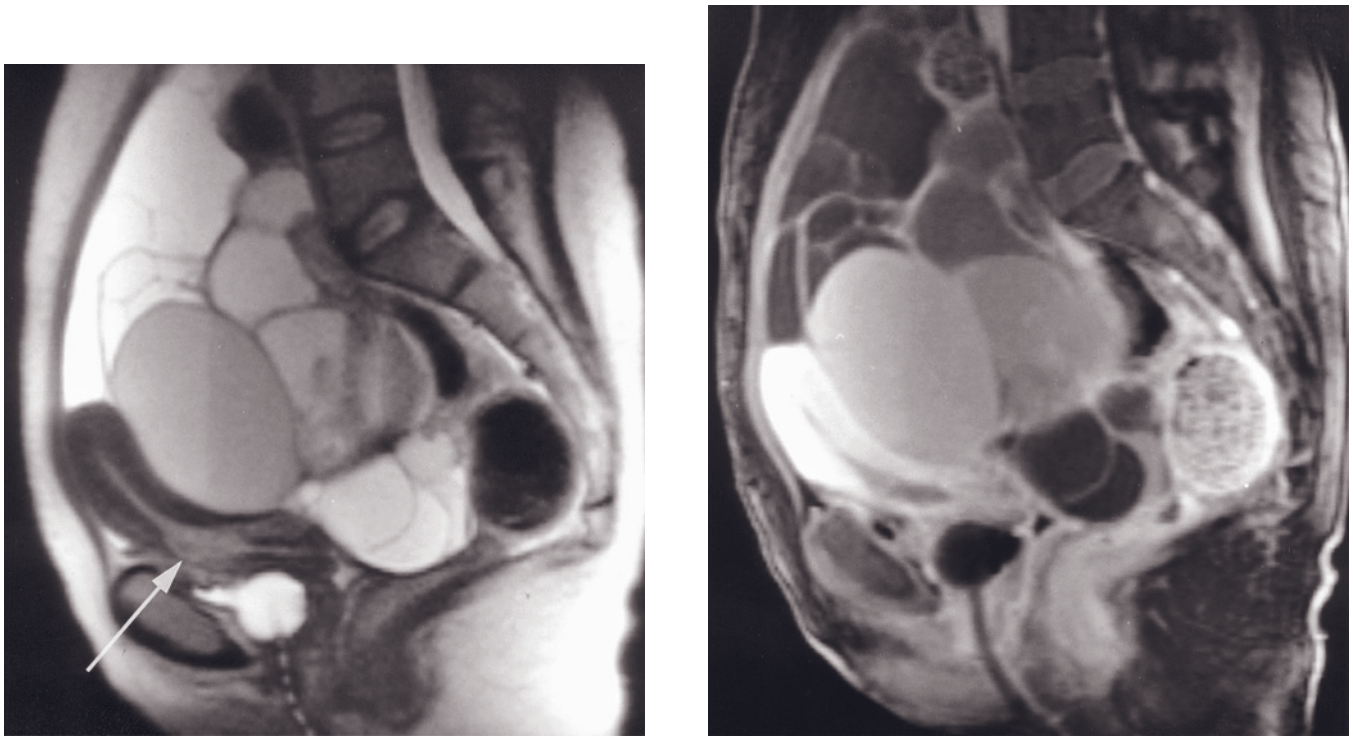

(*a*) (*b*)

FIG. 15.47 Poorly differentiated adenocarcinoma. Sagittal T2-weighted ETSE (*a*) and gadolinium-enhanced T1-weighted fat-suppressed gradient-echo (*b*) images in a patient with poorly-differentiated ovarian adenocarcinoma and endometrial cancer. A large cystic/solid mass is present in the pelvis, representing ovarian carcinoma. A separate high-signal tumor (arrow, *a*) is appreciated in the lower endometrial canal, consistent with endometrial carcinoma.

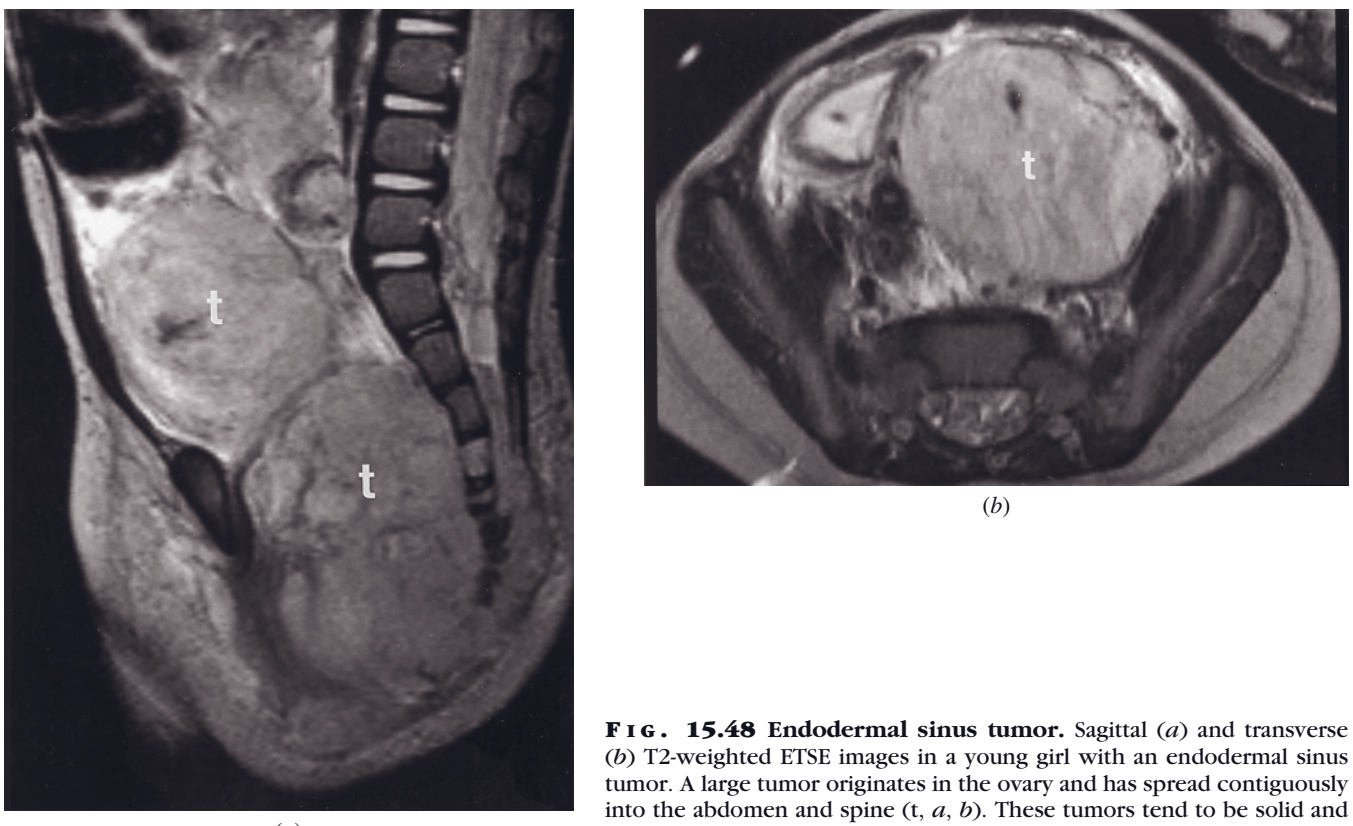

(*a*) (*b*)

FIG. 15.48 Endodermal sinus tumor. Sagittal (*a*) and transverse (*b*) T2-weighted ETSE images in a young girl with an endodermal sinus tumor. A large tumor originates in the ovary and has spread contiguously into the abdomen and spine (t, *a*, *b*). These tumors tend to be solid and are very aggressive, with rapid growth and a poor prognosis.

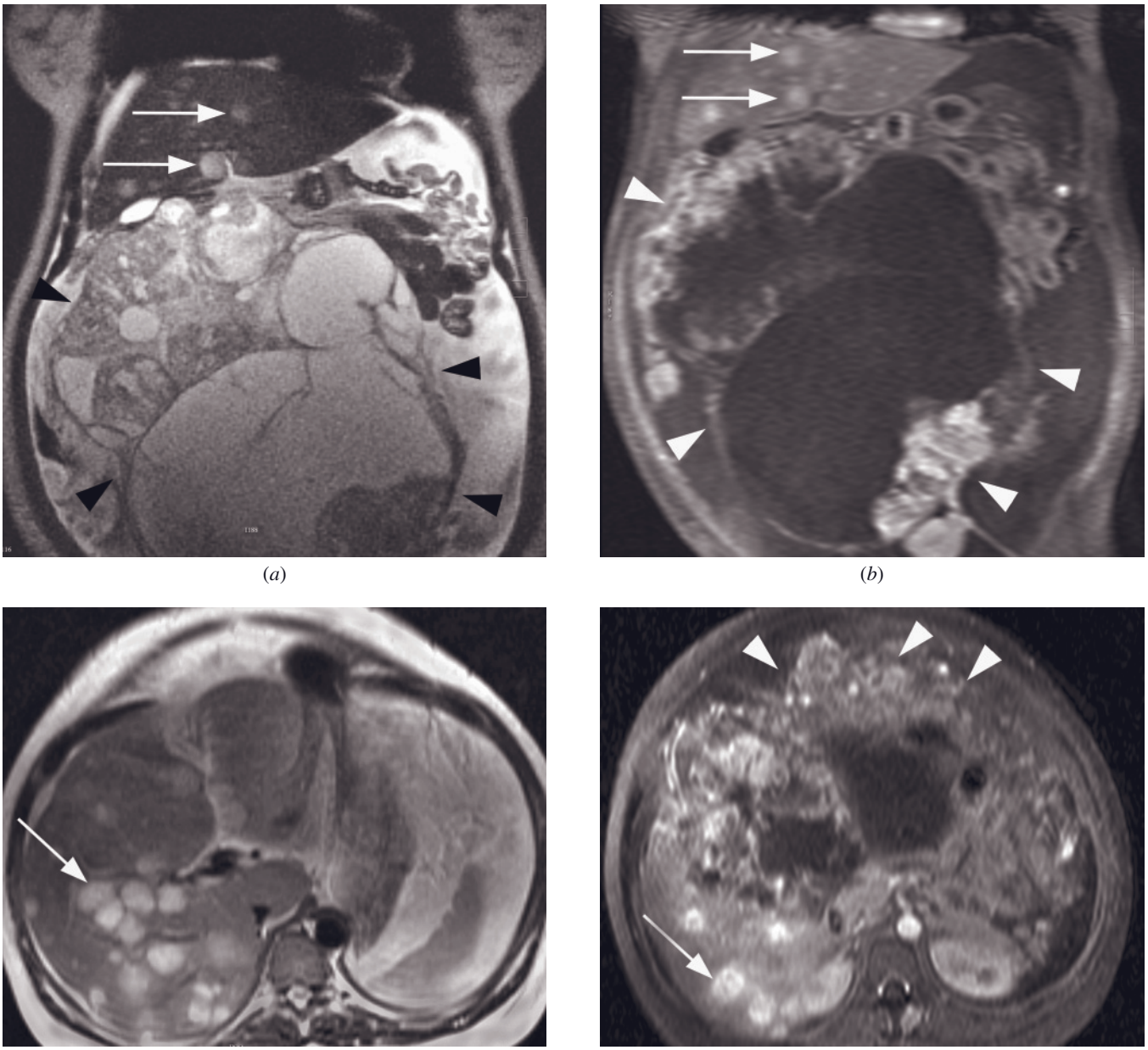

FIG. 15.49 Endodermal sinus tumor with peritoneal and hematogenous metastases. Coronal T2-weighted SS-ETSE (*a*) and gadolinium-enhanced fat-suppressed T1-weighted gradient-echo (*b*) and axial T2-weighted ETSE (*c*) and gadolinium-enhanced fat-suppressed T1-weighted gradient-echo (*d*) images show a large mass (arrowheads, *a*, *b*) with cystic and solid components emanating from the pelvis. Liver metastases (arrows, *a–d*) and ascites are present, with seeding of the omentum (arrowheads, *d*).

bleeding in adults. There is an association with endometrial hyperplasia, polyps, and cancer. A variety of histologic patterns are seen, and the gross appearance is also variable, ranging from predominantly solid to unilocular to multicystic [128]. On MR images, granulosa cell tumors are typically solid, with variable amounts of cystic change and intratumoral hemorrhage (fig. 15.52). These tumors are of intermediate signal intensity on T1-weighted images and heterogeneously high signal intensity on T2-weighted images. After gadolinium, solid areas enhance while areas of cystic change or hemorrhage do not. Local invasion, especially into the sacrum, is well seen with sagittal imaging. Also well demonstrated on sagittal images are the associated uterine changes due to hormone elaboration, which are seen in most patients and include uterine enlargement and thickening of the endometrium (fig. 15.53) [106, 129]. Because of early presentation, surgery is often

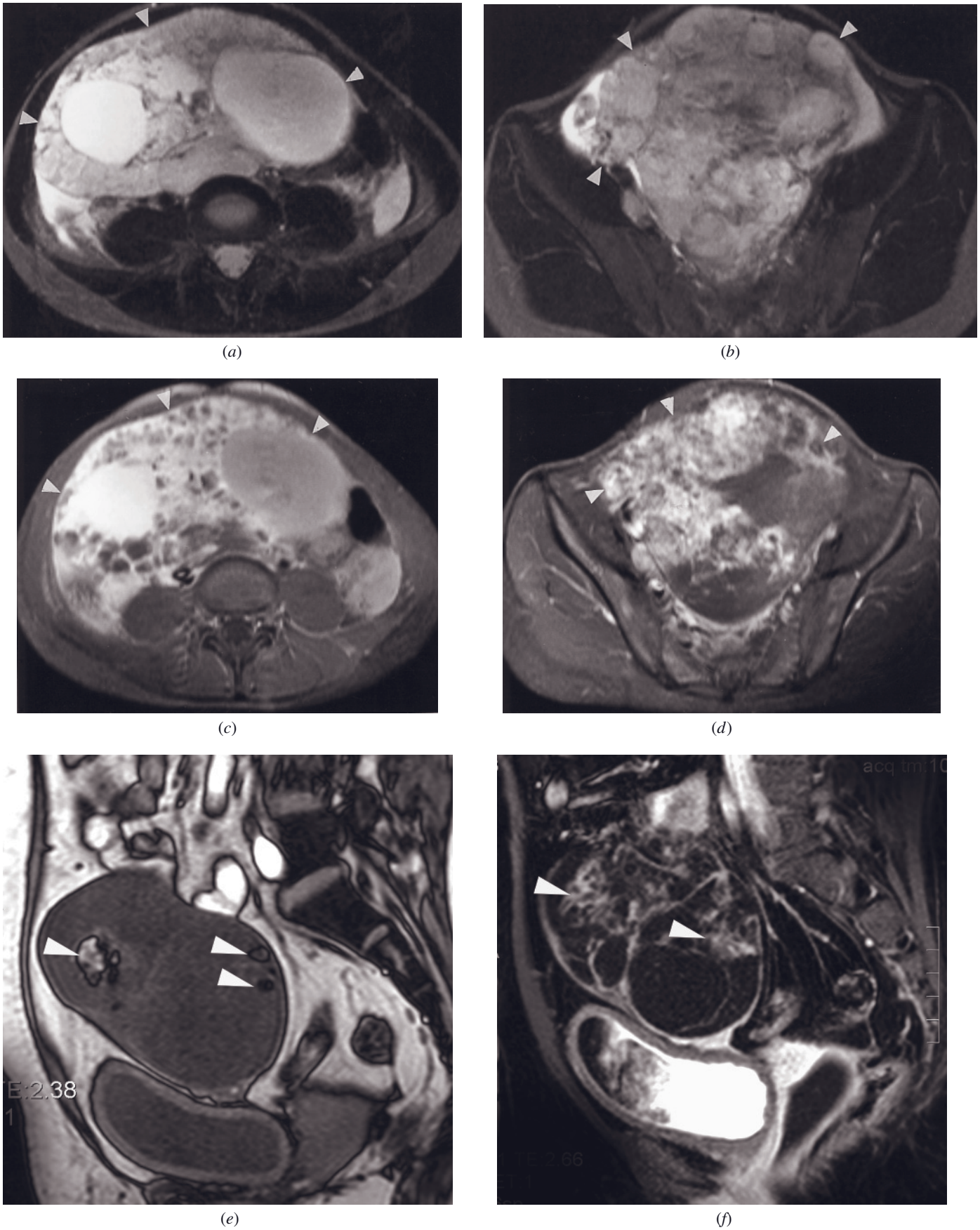

FIG. 15.50 Immature teratoma. Transverse T2-weighted ETSE (*a*, *b*) and contrast-enhanced T1-weighted fat-suppressed gradient-echo (*c*, *d*) images. A complex cystic and solid mass occupies the abdomen and pelvis (arrowheads, *a–d*). Immature teratomas are composed of amorphous embryonic elements, which accounts for their markedly disorganized appearance in contrast to the more regular and recognizable elements associated with mature teratomas. **Immature teratoma.** Sagittal T1-weighted gradient echo out-of-phase (*e*) and gadolinium-enhanced T1-weighted fat-suppressed gradient-echo (*f*) images in a different patient show a complex cystic with small foci of fat (arrowheads, *e*) and extensive internal enhancement (arrowheads, *f*).

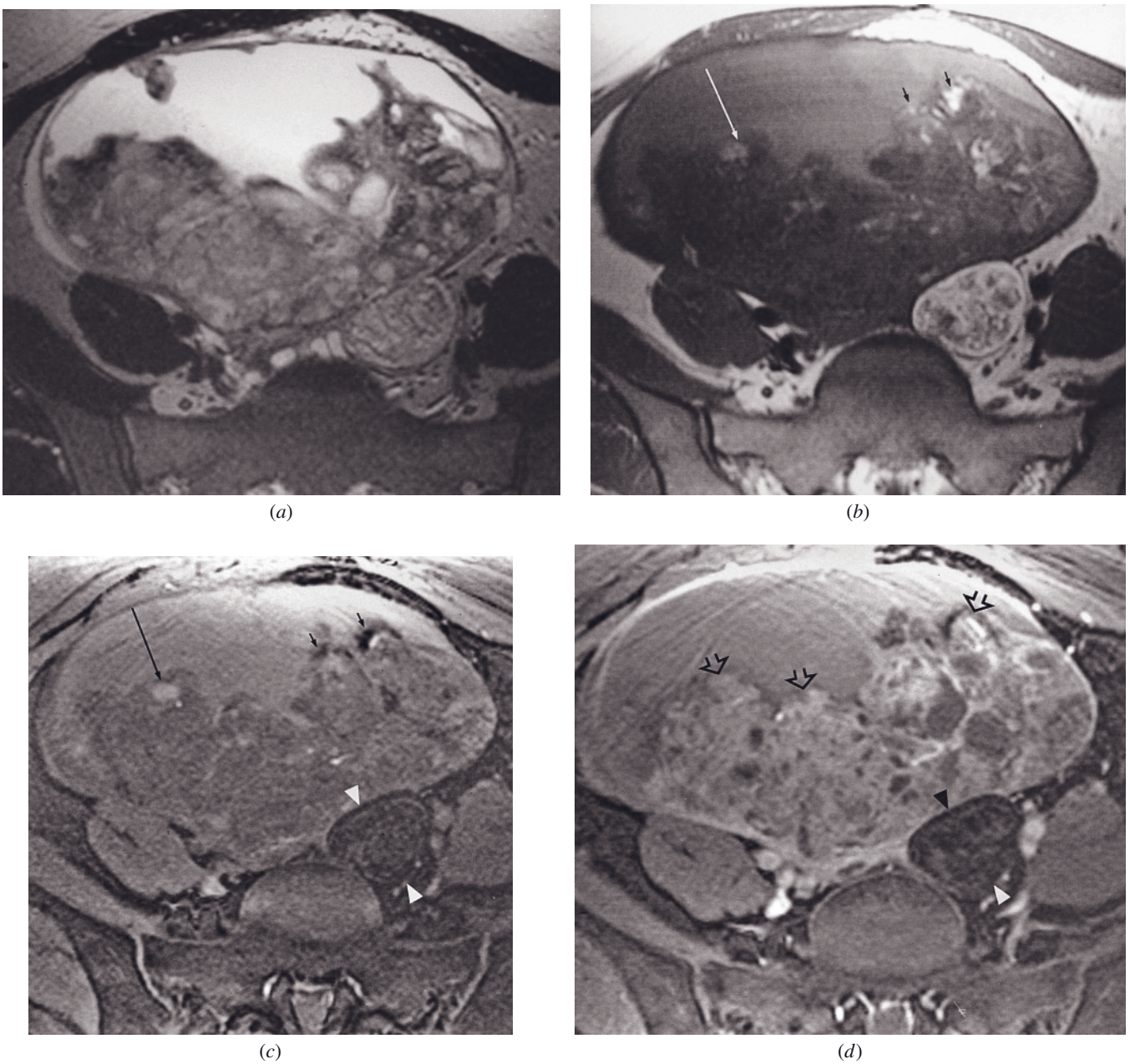

FIG. 15.51 Mature and immature teratomas. T2-weighted ETSE (*a*), T1-weighted SE (*b*), T1-weighted fat-suppressed gradient-echo (*c*), and gadolinium-enhanced T1-weighted fat-suppressed gradient-echo (*d*) images in a patient with complex right adnexal masses. The two masses have variable amounts of fatty elements, which are high in signal intensity on the conventional T1-weighted SE image and suppress on the fat-suppressed images (short arrows, *b*, *c*). Note that some of the high-signal-intensity foci in the larger mass retain their high signal intensity on the fat-suppressed images, which is consistent with coexisting hemorrhage (long arrow, *b*, *c*). The smaller posterior mass shows nearly complete suppression on the fat-suppressed image (arrowheads, *c*). After contrast, there is a profusion of solid tissue enhancing in the larger mass (open arrows, *d*). The smaller mass does not enhance appreciably, which is consistent with a cystic structure (arrowheads, *d*). Extensive solid elements in a fat-containing mass are atypical of a dermoid cyst and should raise the suspicion of an immature teratoma. This was proven at surgery, whereas the posterolateral mass turned out to be a mature teratoma (dermoid cyst). (reprinted with permission from Outwater EK, Dunton CJ: Imaging of the ovary and adnexa: clinical issues and applications of MR imaging. *Radiology* 194: 1–18, 1992.)

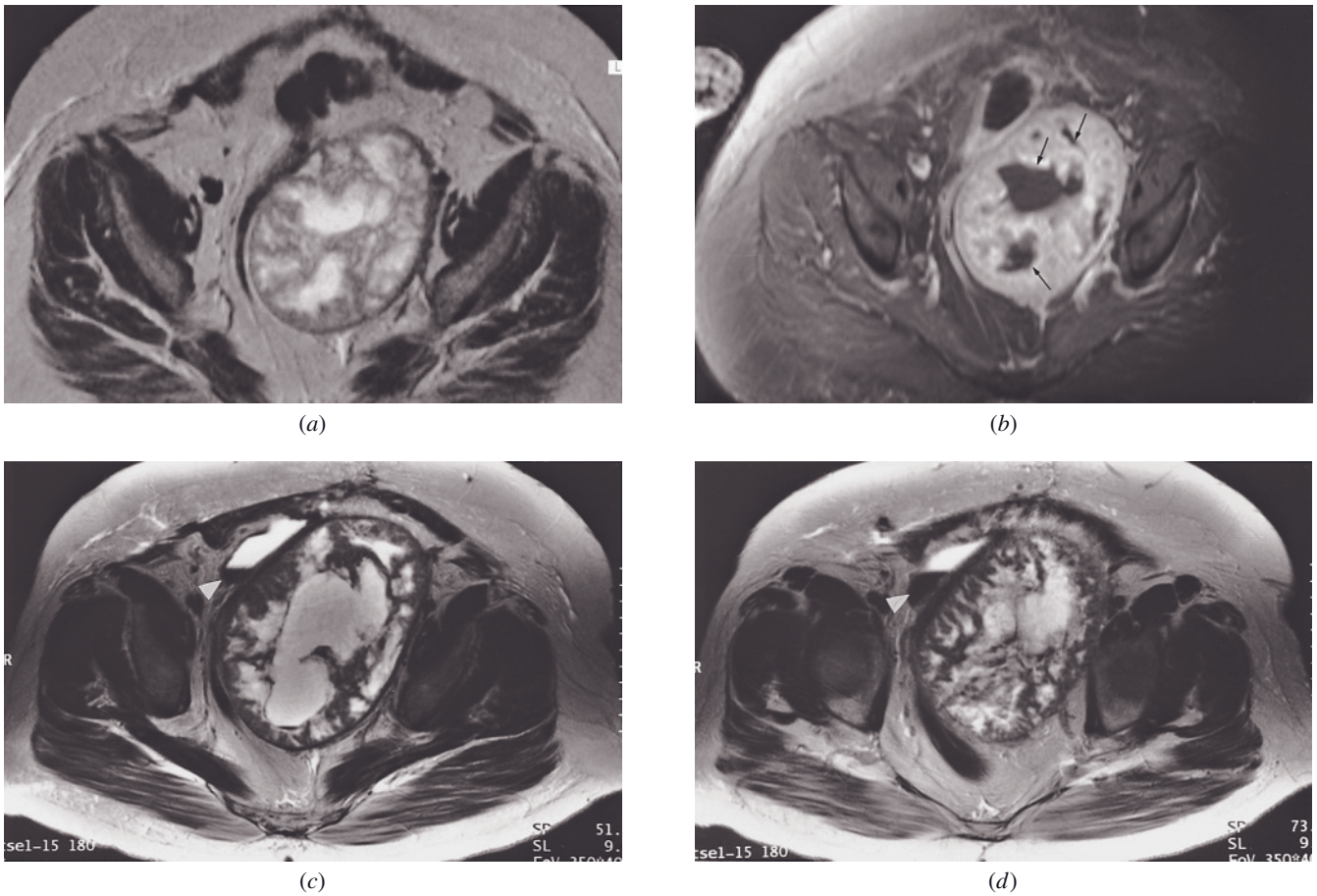

FIG. 15.52 Granulosa cell tumor. Transverse T2-weighted ETSE (*a*) and gadolinium-enhanced T1-weighted fat-suppressed gradient-echo (*b*) images in a woman with a granulosa cell ovarian tumor. The tumor is heterogeneous on the T2-weighted image, and after contrast the solid elements enhance. Necrotic foci interspersed in an otherwise solid mass are a common feature of granulosa-cell tumors (arrows, *b*). Transverse 512-resolution T2-weighted ETSE (*c*, *d*) images 9 months later show interval growth of tumor and increasing necrosis. Note that the bladder is displaced anterolaterally by the mass. Low signal intensity in the dependent portion of the bladder reflects excreted concentrated gadolinium (arrowheads, *c*, *d*).

curative; however, they have been reported to recur (fig. 15.54).

Other Primary Ovarian Tumors

Almost all types of soft tissue tumors, benign and malignant, have been reported to arise within the ovary. These tumors are similar in appearance to their counterparts elsewhere within the body. The most common mesenchymal tumors are those of smooth muscle origin, mostly benign leiomyomas. The MRI appearance of malignant transformation of a benign leiomyoma has been reported [131]. Leiomyosarcomas are rare [12]. Also reported are carcinosarcoma (also called malignant mixed müllerian tumor) (fig. 15.55), lipoleiomyoma, hemangioma, myxoma, fibrosarcoma, rhabdomyosarcoma, schwannoma, osteosarcoma, chondrosarcoma, fibrosarcoma, lymphoma, and endometrial stromal sarcoma [12].

Secondary Ovarian Malignancy

Lymphoma

Although rare cases of primary ovarian lymphoma have been reported, with curative oophorectomy [12], most ovarian involvement with lymphoma is part of disseminated disease (fig. 15.56). The most common forms of lymphoma to involve the ovary are non-Hodgkin in children and younger women and large cell, typically in adults. The diagnosis of lymphoma may be suspected when bilateral masses are seen with homogeneous hypointensity on T1-weighted images and homogeneous slight hyperintensity on T2-weighted images. Contrast enhancement is mild to moderate and best

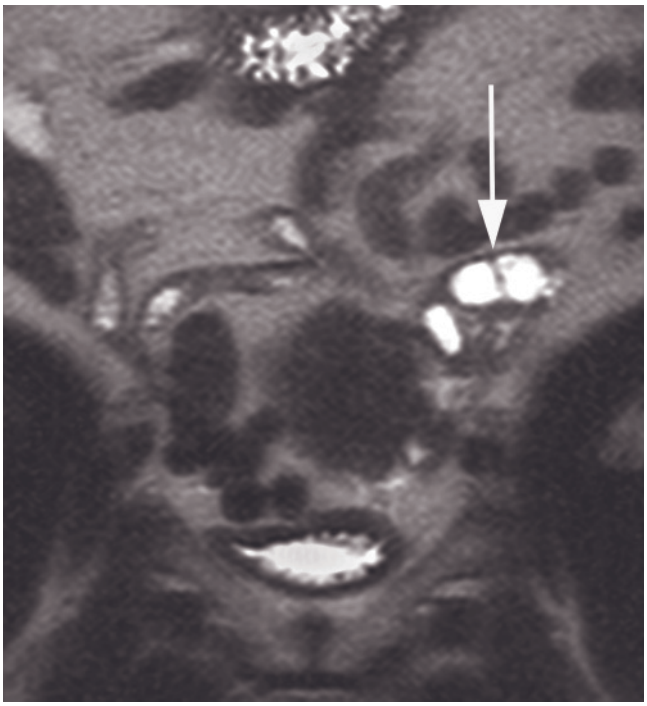

(*a*)

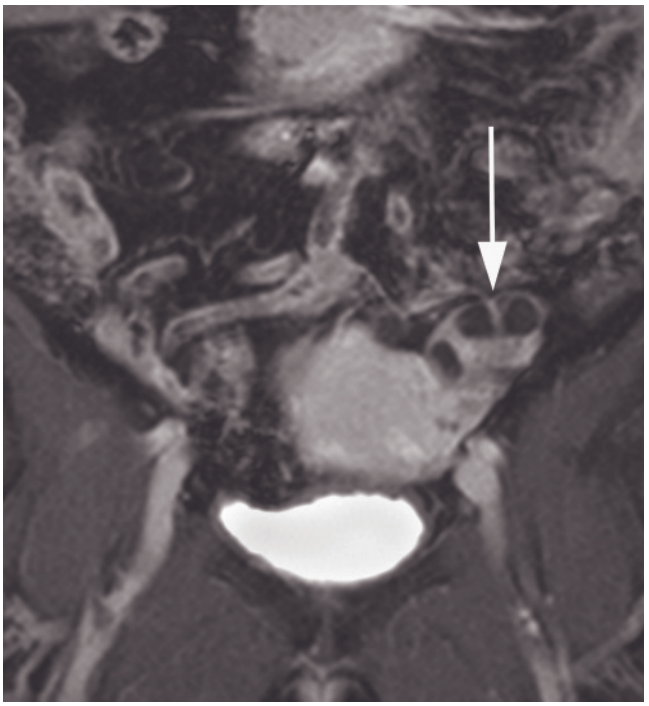

(*b*)

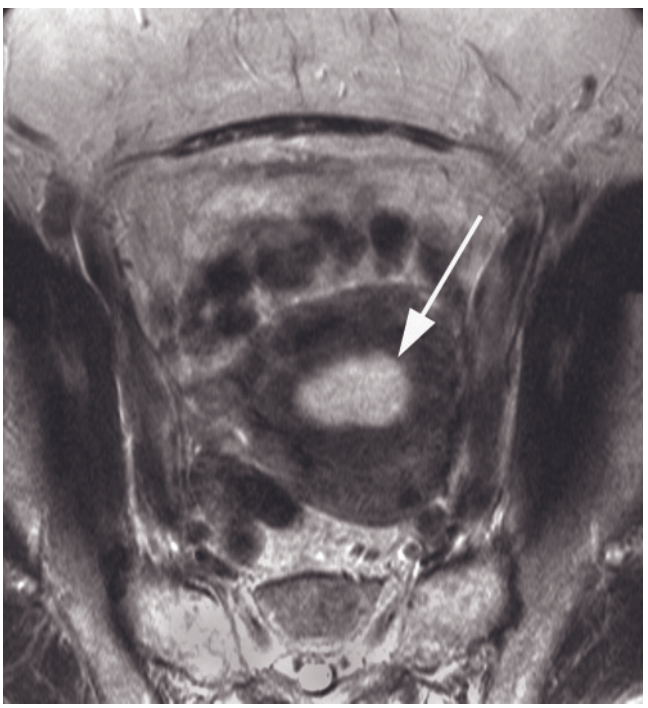

(*c*)

FIG. 15.53 Granulosa cell tumor and endometrial hyperplasia. Coronal T2-weighted SS-ETSE (*a*) and gadolinium-enhanced fat-suppressed T1-weighted gradient-echo (*b*) images and oblique T2-weighted ETSE short-axis view of the uterus (*c*) in a patient with postmenopausal bleeding show a left ovarian mass with solid and cystic components (arrow, *a*, *b*) and a thickened endometrium (arrow, *c*).

seen with fat suppression techniques [132]. Physiologic follicles may be preserved [133].

Metastases

Metastases account for 10% of tumors seen in surgical series; however, few present as a primary ovarian mass [12]. The most common sites of origin are colon, stomach, breast, and hematopoietic tissues [134]. The functioning, highly vascularized ovaries of premenopausal women are more receptive to metastatic deposits than the ovaries of older women. Of patients with the common primary malignancies, those with ovarian

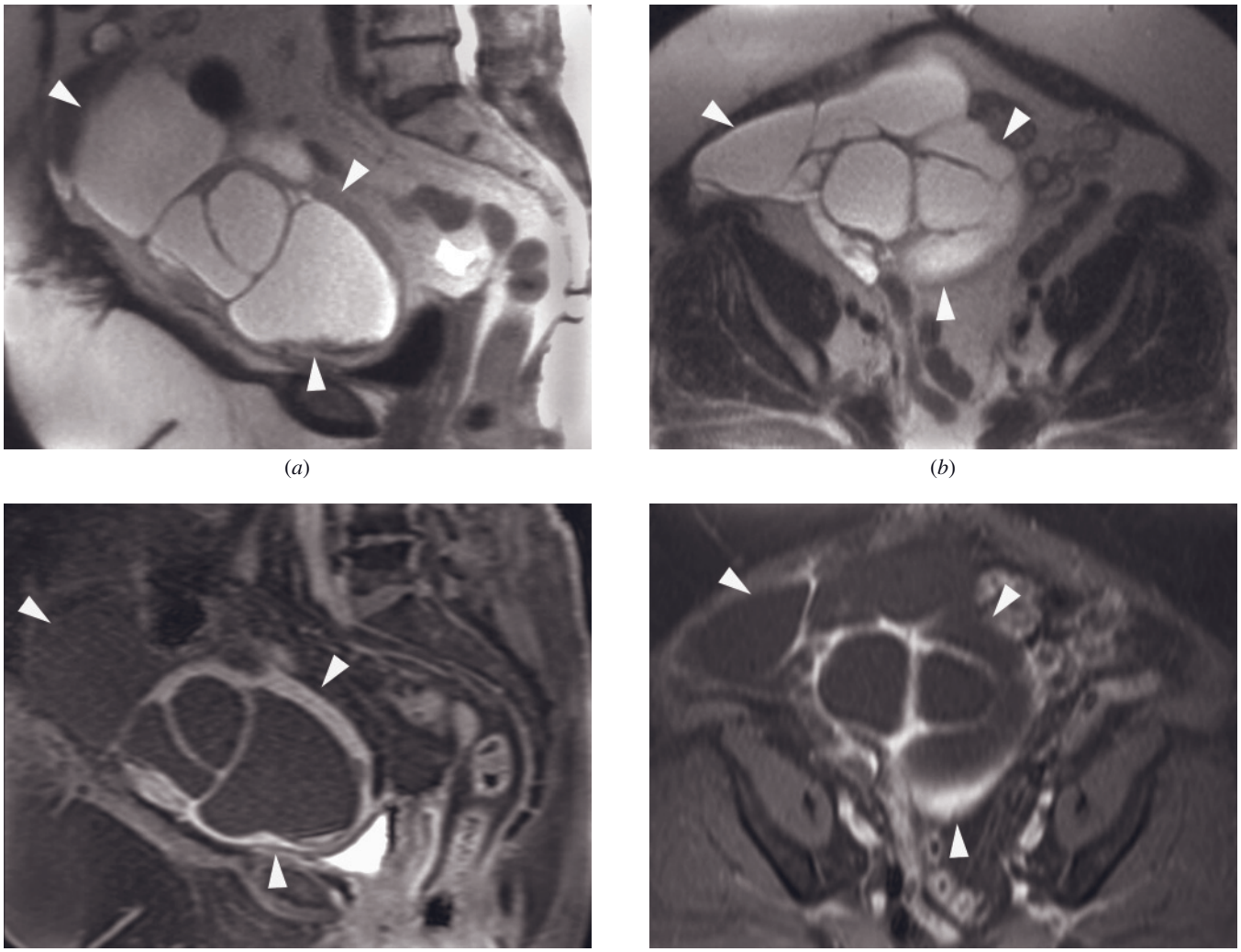

FIG. 15.54 Recurrent granulosa cell tumor. Sagittal (*a*) and transverse (*b*) T2-weighted SS-ETSE and sagittal (*c*) and transverse (*d*) gadolinium-enhanced fat-suppressed T1-weighted gradient-echo images in a patient treated for granulosa cell tumor show a large, multiseptated mass (arrowheads). The septations and solid components enhance on postgadolinium images (*c*, *d*).

involvement are on average significantly younger than women without ovarian involvement [134]. The mode of spread of metastatic disease can be one of several: direct extension from adjacent organs, hematogenous, lymphatic, or serosal implantation of cells shed into the peritoneal cavity. The term Krukenberg tumor specifically refers to tumors in which malignant mucin-filled signet ring cells are found within the abundant and hypercellular ovarian stroma [12]. While this term is classically associated with tumors of gastric origin, tumors arising from the breast, colon, and appendix can also give rise to these histologic features. Tumors from the gallbladder, pancreas, biliary tract, urinary bladder, and cervix are less common sources of this tumor type [134]. Almost all patients die within a year of diagnosis of Krukenberg tumors.

The gross appearance of metastatic disease to the ovaries varies with the primary malignancy and route of spread. The ovary may retain its shape but enlarge, may be replaced by a multicystic mass with solid components, or may exhibit tumor nodules on its surface. Ovaries may also be of normal size but have widespread lymphatic involvement. The MR appearance of metastatic disease to the ovary is likewise variable (figs. 15.57–15.59). Although rare, metastatic melanoma in the ovary may be differentiated from other masses in a patient with the appropriate history if melanin is present; in these cases, peripheral high T1 signal may be noted within the mass [135]. Krukenberg tumors generally have both cystic and solid components (fig. 15.58). The cystic components will be variable in signal on T1-weighted images, largely reflecting

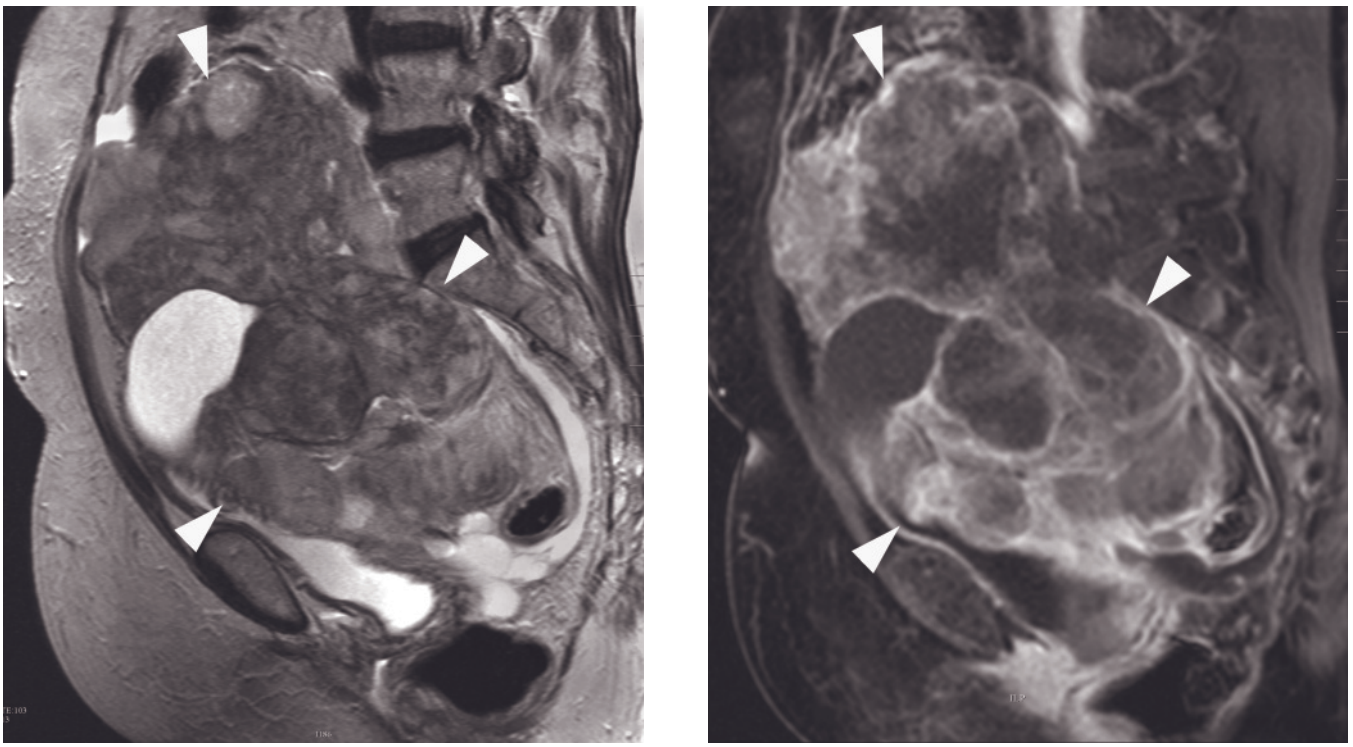

(*a*) (*b*)

FIG. 15.55 Ovarian carcinosarcoma. Sagittal T2-weighted ETSE (*a*) and gadolinium-enhanced fat-suppressed T1-weighted (*b*) images show a large, predominantly solid mass (arrowheads) with heterogeneous enhancement and areas of necrosis. Also known as malignant mixed mesodermal tumor, this rare aggressive primary ovarian cancer responds poorly to platinum-based chemotherapy compared to serous cystadenocarcinoma.

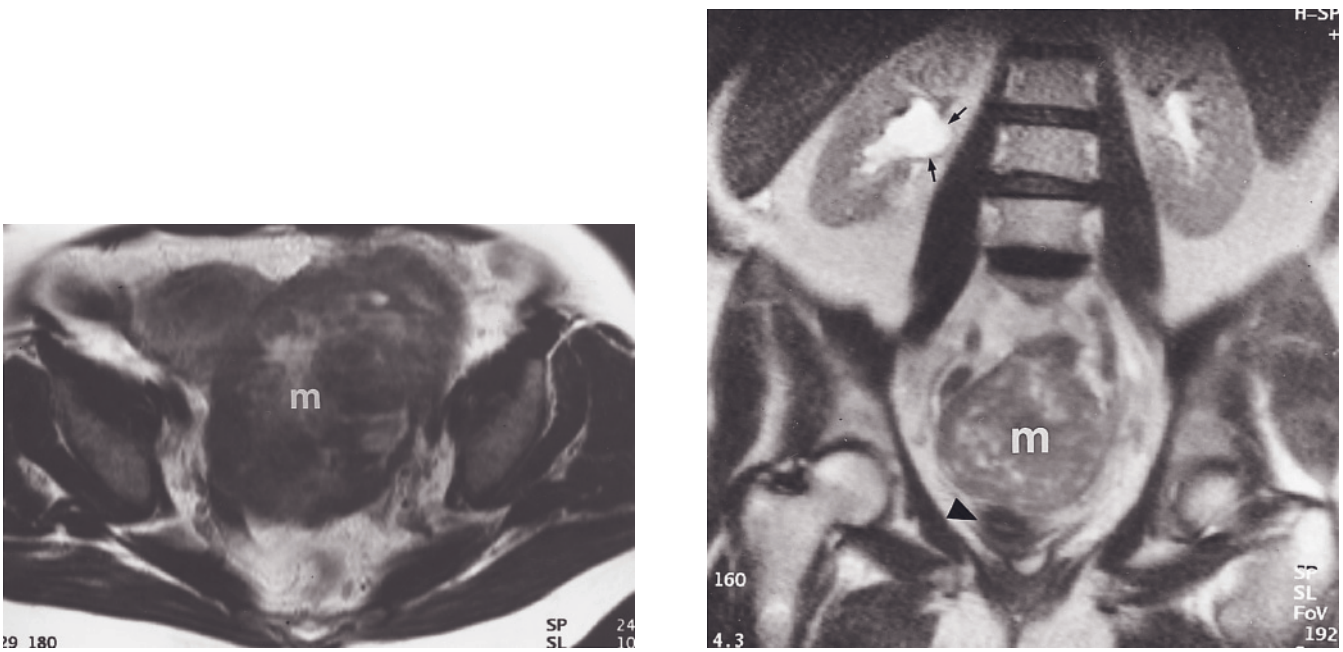

(*a*) (*b*)

FIG. 15.56 Disseminated lymphoma. Transverse 512-resolution T2-weighted ETSE (*a*), coronal T2-weighted SS-ETSE (*b*, *c*), and transverse gadolinium-enhanced fat-suppressed T1-weighted gradient-echo (*d*) images in a woman with disseminated lymphoma. Primary lymphoma of the ovary is rare, and ovarian involvement usually is seen in the setting of diffuse disease. A large mass (m, *a–d*) occupies the pelvis and obstructs the right distal ureter. Contiguous coronal SS-ETSE images highlight the pelvocaliectasis and proximal ureterectasis (arrows, *b*, *c*). After contrast, the lymphomatous mass enhances in a mildly intense and

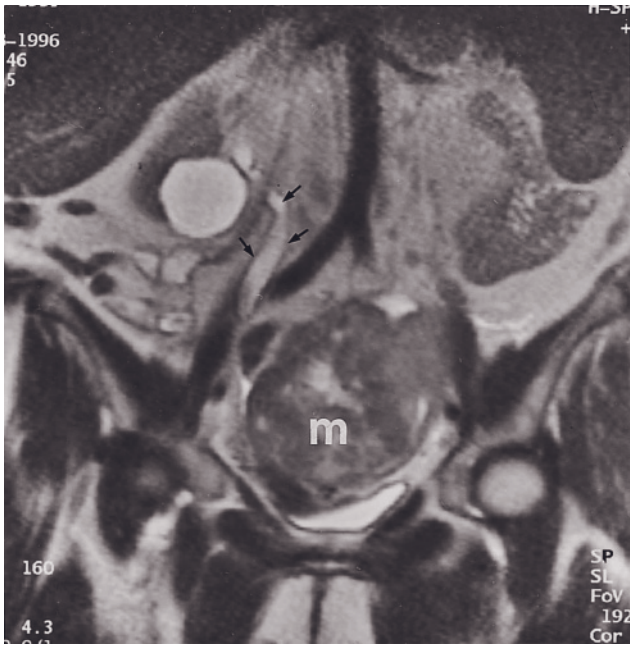

(*c*)

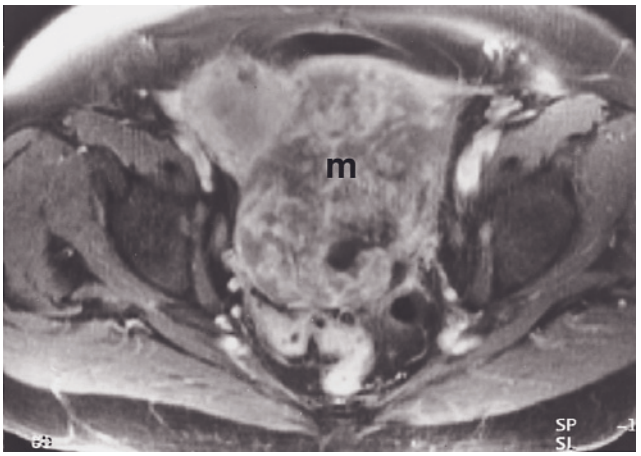

(*d*)

FIG. 15.56 (*Continued*) heterogeneous fashion. The uterus is displaced inferiorly (arrowhead, *b*). Discrete ovaries were not identified on any of the imaging sequences. At surgery, disseminated non-Hodgkin lymphoma with invasion of the adnexa was found. This pattern of enhancement is typical of lymphoma with mild enhancement and slight heterogeneity, with usually negligible necrosis despite large tumor size (compare to cystic ovarian cancers).

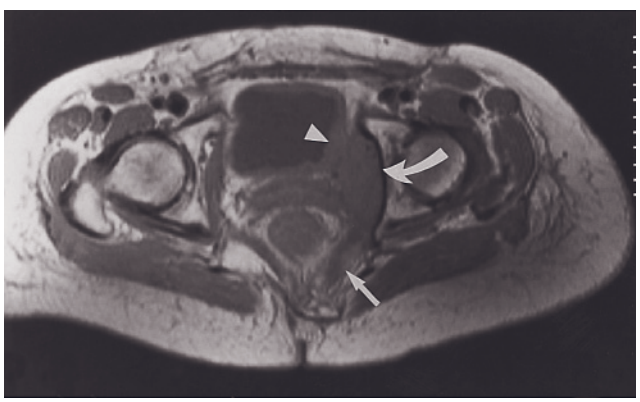

(*a*)

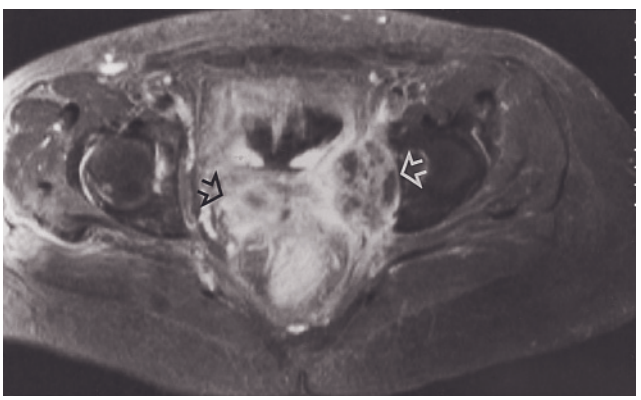

(*b*)

FIG. 15.57 Recurrent müllerian duct cancer metastatic to the ovaries. Proton density (*a*) and gadolinium-enhanced T1-weighted fat-suppressed SE (*b*) images in a woman with recurrent müllerian-duct cancer. Note the left pelvic mass, which invades the obturator externus muscle (curved arrow, *a*).Associated thickening of the left bladder wall (arrowhead, *a*) and levator ani muscle (straight arrow, *a*) suggests that the imaging findings may be related to previous radiotherapy. However, at a slightly higher level after contrast, bilateral adnexal masses are present that demonstrate heterogeneous enhancement, consistent with metastases to the ovaries (open arrows, *b*). Cancers of uterine origin are among the more common primary tumors to metastasize to the ovaries.

the content of mucin and or blood, both of which will appear high signal. Cystic regions are generally high signal on T2 but may be variable for the same reasons as T1, and the cystic component will show lack of enhancement on postgadolinium images. The solid components may be hypointense on T1-and T2-weighted images; this corresponds to areas of dense collagenous stroma (fig. 15.59). The solid components may show intense enhancement after gadolinium [136–138].

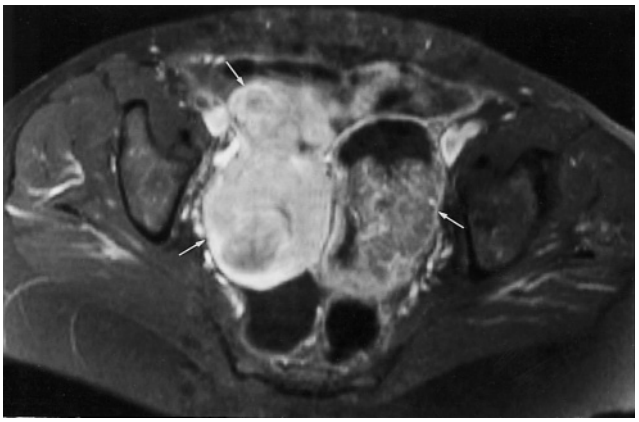

FIG. 15.58 Krukenberg tumors. Gadolinium-enhanced T1-weighted fat-suppressed SE image in patient with malignant signet cell metastases to the ovaries from primary colon cancer. Malignancies that cause Krukenberg tumors include gastric, pancreas, breast, colon, and gallbladder carcinomas. Involvement is often bilateral; the ovaries are enlarged but retain an ovoid morphology (arrows). The metastases are primarily solid, though cystic regions are common. Gadolinium-enhanced T1-weighted fat-suppressed technique is helpful to demonstrate ovarian involvement as well as coexisting peritoneal disease.

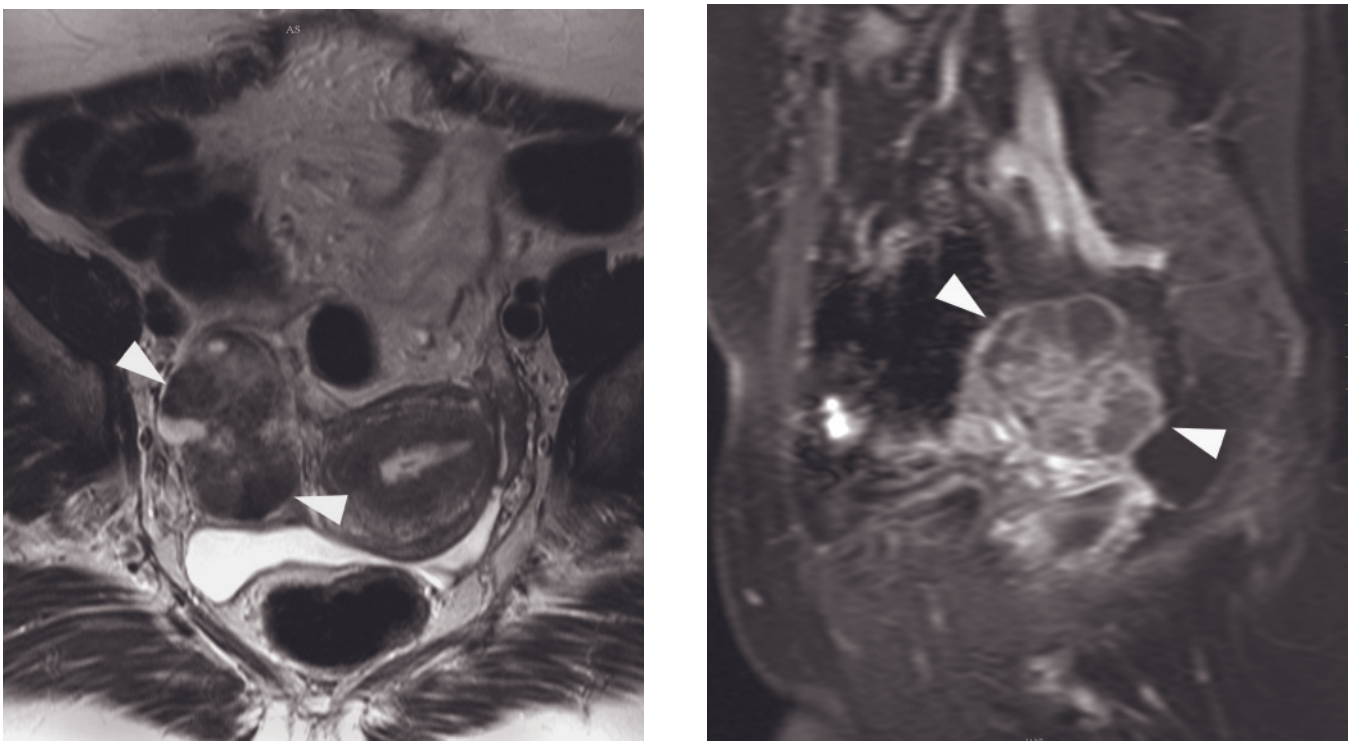

(*a*) (*b*)

FIG. 15.59 Krukenberg tumor. Transverse T2-weighted ETSE (*a*) and sagittal gadolinium-enhanced fat-suppressed T1-weighted gradient-echo (*b*) images in a patient with colon cancer show a heterogeneous right ovarian mass (arrowheads, *a*, *b*) with areas of low signal intensity on T2-weighted images (*a*) and heterogeneous enhancement (*b*). A smaller metastasis to the left ovary was present (not shown).

Malignant Disease of the Fallopian Tube

Primary Fallopian Tube Carcinoma

Primary fallopian tube carcinoma is a rare disease entity with a reported incidence in the United States of 3.6 cases per million women per year [139]. It comprises only 0.5% of all gynecologic tumors. The most common histology is adenocarcinoma; sarcomas (leiomyosarcoma, carcinosarcomas, and mixed müllerian tumors) and choriocarcinoma are even more rare. The typical patient is older (average age 55) and presents with such nonspecific symptoms as abdominal pain, abnormal vaginal bleed-

ing, and vaginal discharge [140]. The poor prognosis of fallopian tube malignancies relates to the late stage at diagnosis rather than to a particular aggressiveness of the tumor; the average 5-year survival is less than 50%. At presentation most women have widespread disease; the tumor can spread directly through the fimbriated end of the tube, through the wall of the tube, or via the lymphatics to the para-aortic, iliac, and lumbar nodes as well as to the ovaries, other pelvic organs, or more distant sites. The prognosis is dependent on disease burden at diagnosis. Both FIGO staging and an alternative similar to the Duke classification for colon cancer have been advocated [139]. Treatment is primarily surgical; adjuvant chemotherapy is also used. Radiation therapy at present does not appear to confer additional benefit.

The MR appearance of fallopian tube carcinoma has been described, and the tumor has been diagnosed preoperatively [141]. Typically, a small adnexal mass is seen with low T1 signal and high T2 signal. Enhancement is seen after the administration of gadolinium (fig. 15.60). Associated findings include hydrosalpinx, peritumoral ascites, and intrauterine fluid [140].

Metastases

Metastatic disease involving the fallopian tube is more common than primary carcinoma and is generally the result of direct extension from the ovary, endometrium, or cervix. Tumors arising outside of the genital system that can metastasize to the tubes include breast and gastrointestinal cancers. Lymphatic spread accounts for the majority of this involvement. The appearance of metastatic disease to the fallopian tubes has not been described in series. Anecdotal reports suggest that the appearance is similar to that of ovarian metastatic disease (fig. 15.61).

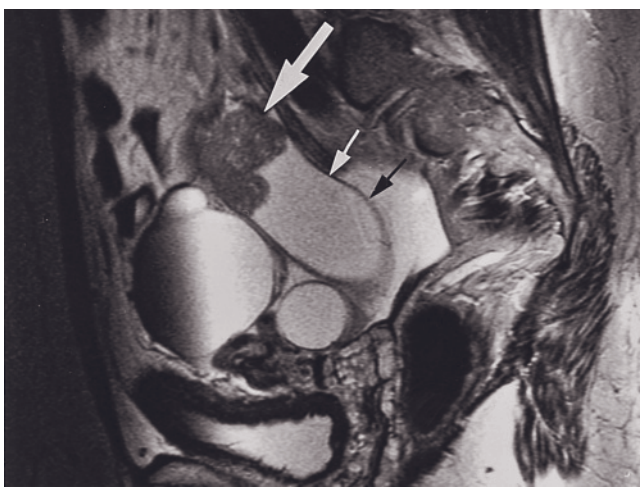

(*a*)

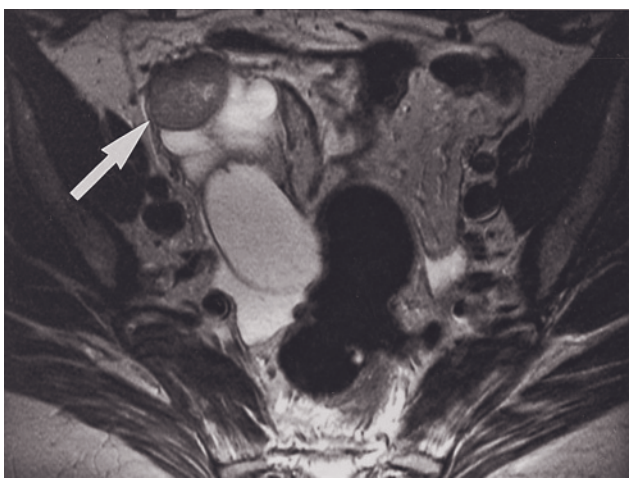

(*b*)

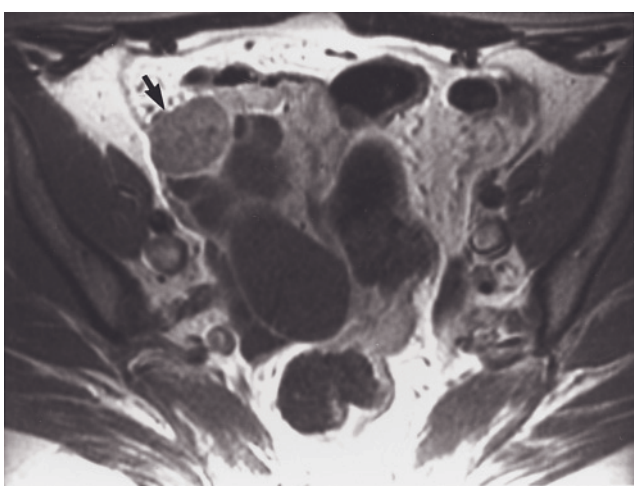

(*c*)

FIG. 15.60 Fallopian tube adenocarcinoma. Sagittal (*a*) and transverse (*b*) 512-resolution T2-weighted ETSE and gadolinium-enhanced T1-weighted SE (*c*) images. The fallopian tube is shown as a dilated tubular structure (arrows, *a*) that contains solid tumor components (large arrow, *a*, *b*). Heterogeneous enhancement of the tumor nodules is present (arrow, *c*) after gadolinium administration.

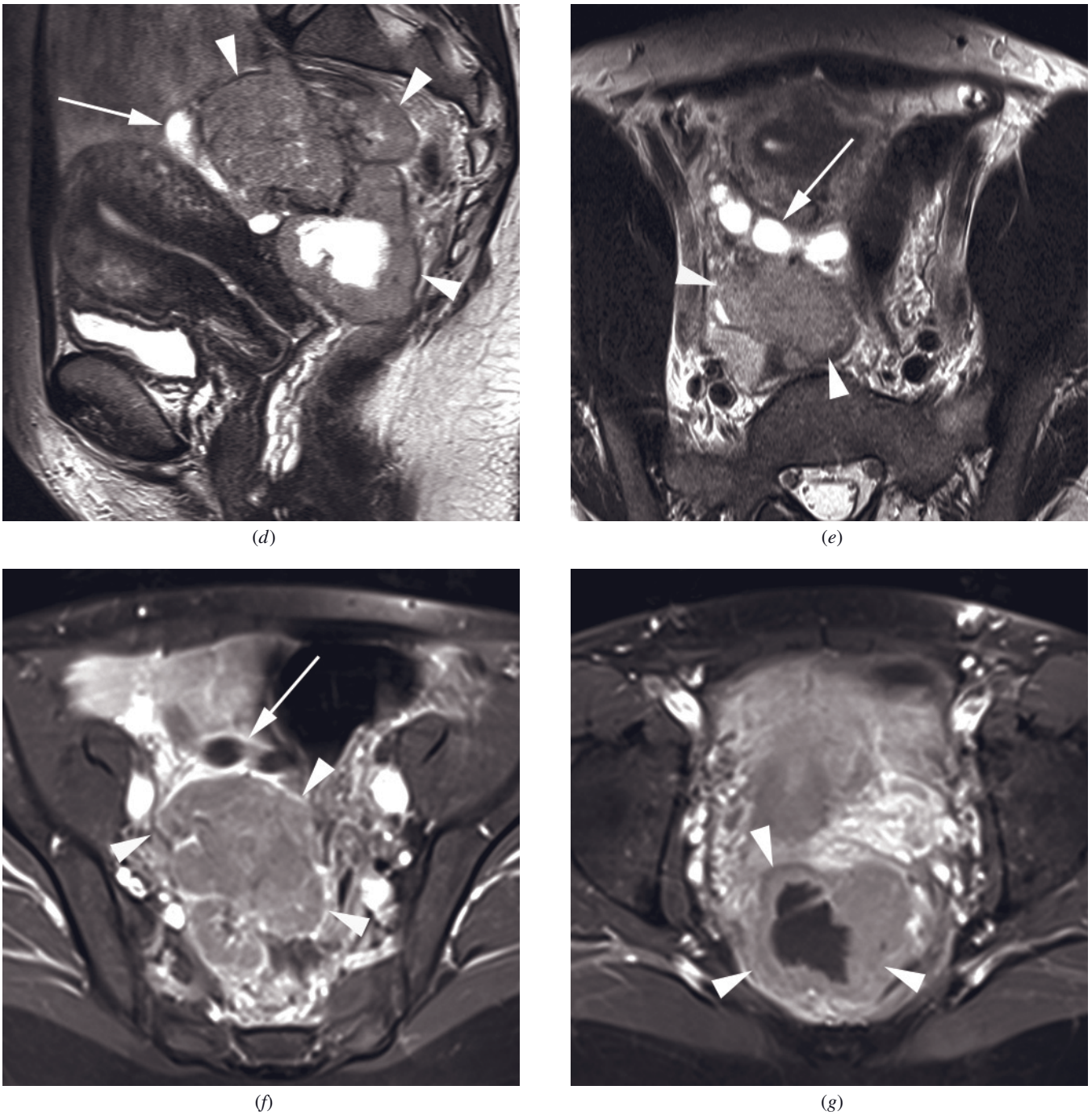

FIG. 15.60 (*Continued*) **Fallopian tube papillary serous carcinoma.** Sagittal (*d*) and transverse (*e*) T2-weighted ETSE and transverse gadolinium-enhanced fat-suppressed T1-weighted gradient-echo (*f*, *g*) images in a different patient show a heterogeneous and necrotic pelvic mass (arrowheads, *d*–*g*). A portion of the dilated fallopian tube is seen (arrow, *d*–*f*).

CONCLUSION

MRI offers distinct advantages over other modalities in the characterization of adnexal lesions, not only with regard to their organ of origin but also with regard to their pathology. Teratomas, endometriomas, simple and hemorrhagic cysts, fibromas, and hydrosalpinges can be diagnosed with a high degree of confidence. MRI may also be the most sensitive technique for the detection of peritoneal spread of ovarian carcinoma. In women of childbearing age and in women who are pregnant, the lack of ionizing radiation and the safety

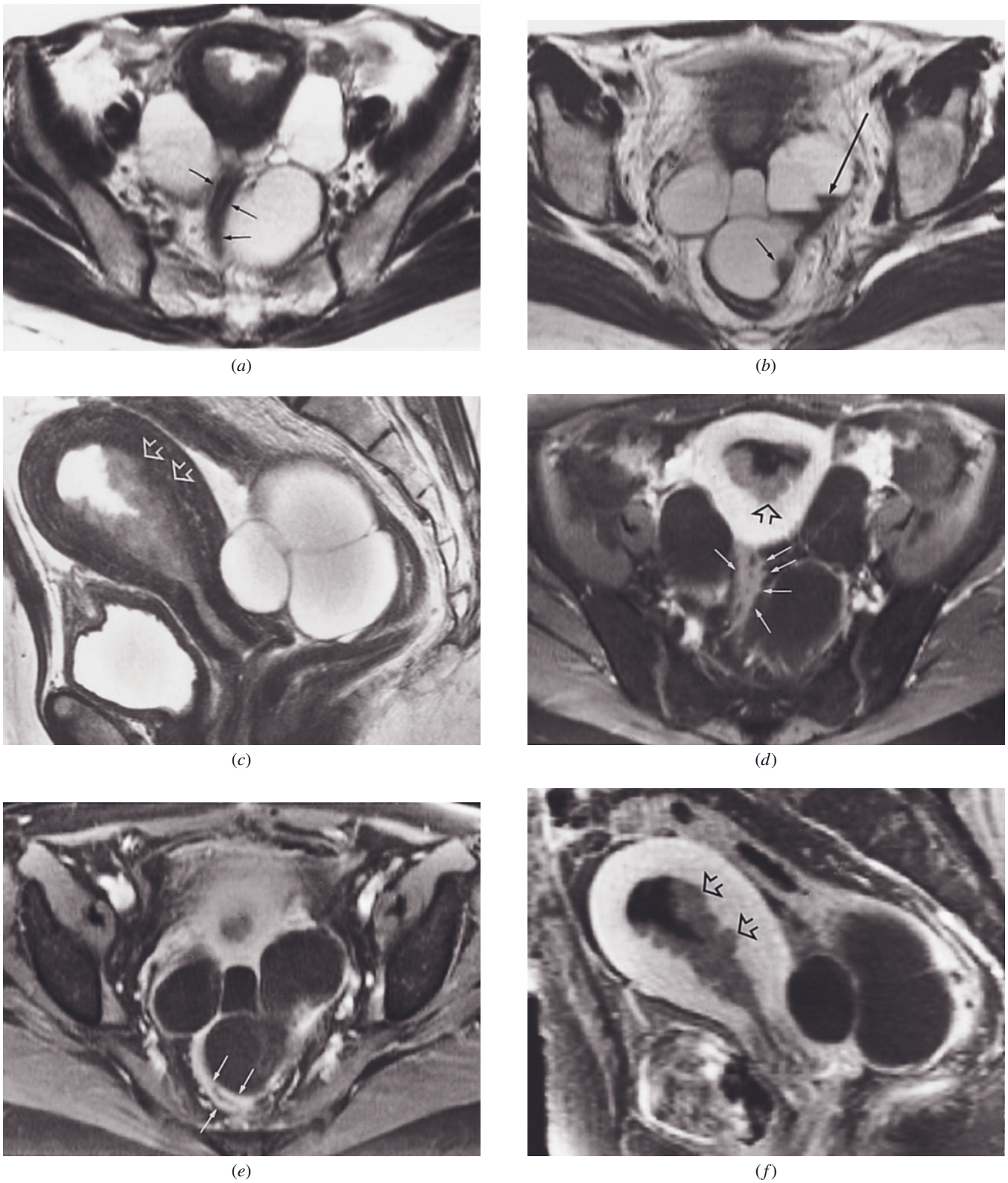

FIG. 15.61 Endometrial carcinoma metastatic to the fallopian tubes. Transverse (*a*, *b*) and sagittal (*c*) high-resolution T2-weighted ETSE and transverse (*d*, *e*) and sagittal (*f*) gadolinium-enhanced T1-weighted fat-suppressed gradient-echo images in a woman with metastatic mixed papillary serous and clear cell endometrial carcinoma complaining of a change in bowel habits. The endometrium is expanded and contains intermediate- and high-signal-intensity elements on the T2-weighted image (*c*). The junctional zone is effaced posteriorly (open arrows, *c*). Bilateral adnexal cystic masses compress and surround the sigmoid colon (arrows, *a*). The contents of the left fallopian tube appear complex; there is blood dependently (hematosalpinx) (long arrow, *b*) and nodularity of the tube wall (short arrow, *b*). The ovaries (not shown) were displaced anteriorly and superiorly by the diseased tubes. After contrast, the viable endometrial tumor enhances and scallops the posterior myometrium (open arrows, *d*, *f*). The compressed wall of the sigmoid colon is tethered and adherent to the dilated fallopian tubes (solid arrows, *d*, *e*).

of gadolinium are of paramount importance. Several studies have attempted to address the possible cost savings of MRI in the management of women with a variety of gynecological disorders [142–144]. Further work is needed in this era of rising health care costs to determine the best utilization of this technique.

REFERENCES

1. Curtis M, Hopkins MP, Zarlingo T et al. Magnetic resonance imaging to avoid laparotomy in pregnancy. *Obstet Gynecol* 82: 833–836, 1993.
2. Kier R, McCarthy SM, Scoutt LM et al. Pelvic masses in pregnancy: MR imaging. *Radiology* 176: 709–713, 1990.
3. Colleti P, Sylvestre PB. Magnetic resonance imaging in pregnancy. *Magn Reson Imaging Clin N Am* 2: 291–307, 1994.
4. Smith RC, Reinhold C, McCauley TR et al. Multicoil high resolution fast spin-echo MR imaging of the female pelvis. *Radiology* 184: 671–675, 1992.
5. Hayes CE, Dietz MJ, King BF et al. Pelvic imaging with phased-array coils: quantitative assessment of signal-to-noise ration improvement. *J Magn Res Imaging* 2: 321–326, 1992.
6. Heurtas CP, Brown MA, Semelka RC. MR Imaging of the adnexa. *Magn Reson Imaging Clin N Am* 14: 471–487, 2006.
7. McCauley TR, McCarthy S, Lange R. Pelvic phased-array coil: image quality assessment for spin-echo MR imaging. *Magn Reson Imaging* 10: 513–522, 1992.
8. Outwater EK, Mitchell DG. Magnetic resonance imaging techniques in the pelvis. *Magn Reson Imaging Clin N Am* 2: 161–188, 1994.
9. Tempany MC, Fielding JR. Female pelvis. In Edelman RR, Hesselink JR, Zlatkin MB (eds.). *Clinical Magnetic Resonance Imaging.* Philadelphia: WB Saunders, 1996, p. 1432–1465.
10. Hussain SM, van den bos IC, Oliveto JM, Martin JR. MR imaging of the female pelvis at 3T. *Magn Reson Imaging Clin N Am* 14: 537–544, 2006.
11. Haller JO, Freidman AP, Schaffer R et al. The normal and abnormal ovary in childhood and adolescence. *Semin Ultrasound* 4: 206, 1983.
12. Zaloudek C. The ovary. In Gompel C and Silverberg SG (eds.). *Pathology in Gynecology and Obstetrics*, Philadelphia: Lippincott, 1994, p. 313–413.
13. Outwater EK, Talerman A, Dunton C. Normal adnexa uteri specimens: anatomic basis of MR imaging features. *Radiology* 201: 751–755, 1996.
14. Outwater EK, Mitchell DG. Normal ovaries and functional cysts: MR appearance. *Radiology* 198: 397–402, 1996.
15. Levine D, Gosink B, Wolf SL et al. Simple adnexal cysts: the natural history in postmenopausal women. *Radiology* 184: 653–659, 1992.
16. Outwater EK, Dunton CJ. Imaging of the ovary and adnexa: clinical issues and applications of MR imaging. *Radiology* 194: 1–18, 1995.
17. O'Neill MJ, Yoder IC, Connolly SA, Mueller PR. Imaging evaluation and classification of developmental anomalies of the female reproductive system with emphasis on MR imaging. *AJR Am J Roentgenol* 173: 407–416, 1999.
18. Rowling SE, Ramchandani P. Imaging of the fallopian tubes. *Semin Roentgen* 31: 299–311, 1996.
19. Gambino J, Caldwell B, Dietrich R et al. Congenital disorders of sexual differentiation: MR findings. *AJR Am J Roentgenol* 158: 363–367, 1992.
20. Choi HK, Cho KS, Lee HW, Kim KS. MR imaging of intersexuality. *Radiographics* 18: 83–96, 1998.
21. Secaf E, Hricak H, Gooding CA et al. Role of MRI in the evaluation of ambiguous genitalia. *Pediatr Radiol* 24: 231–235. 1994.
22. DeCherney AH, Cholst I, Naftolin F. Structure and function of the fallopian tubes following exposure to diethylstilbestrol DES during gestation. *Fertil Steril* 36: 741–745, 1981.
23. Outwater EK, Huang AB, Dunton CJ et al. Papillary projections in ovarian neoplasms: appearance on MRI. *JMRI* 7: 689–695, 1997.
24. Outwater EK, Schiebler ML, Owens RS et al. MRI characterization of hemorrhagic adnexal masses: a blinded reader study. *Radiology* 186: 489–494, 1993.
25. Berkowitz RS, Goldstein DP. Gestational trophoblastic disease. In Hoskins WJ, Perez CA, Young RC (eds.). *Principles and Practice of Gynecologic Oncology.* Philadelphia: Lippincott, 2000, p. 1117–1138.
26. Hricak H, Demas BE, Braga CA et al. Gestational trophoblastic neoplasm of the uterus: MR assessment. *Radiology* 161: 11–16, 1986.
27. Barton JW, McCarthy SM, Kohorn EL et al. Pelvic MR imaging findings in gestational trophoblastic disease, incomplete abortion, and ectopic pregnancy: are they specific? *Radiology* 186: 163–168, 1993.
28. Kier R. Nonovarian gynecologic cysts: MR imaging findings. *AJR Am J Roentgenol* 158: 1265–1269, 1992.
29. Kurachi H, Murakami T, Nakamura H et al. Imaging of peritoneal pseudocysts: value of MR imaging compared with sonography and CT. *AJR Am J Roentgenol* 160: 589–591, 1993.
30. Jain KA. Imaging of peritoneal inclusion cysts. *AJR Am J Roentgenol* 174: 1559–1563, 2000.
31. Gompel C, Silverberg SG. Endometriosis. In Gompel S, Silverberg SG (eds.) *Pathology in Gynecology and Obstetrics* (4th edition). Philadelphia: Lippincott, 1994, p. 425–431.
32. Miyakoshi K, Tanaka M, Gabionza D et al. Decidualized ovarian endometriosis mimicking malignancy. *AJR Am J Roentgenol* 171: 1625–1626, 1998.
33. Nezhat F, Nezhat C, Allan CJ et al. Clinical and histological classification of endometriomas: implication for a mechanism of pathogenesis. *J Reprod Med* 37: 771–776; 1992.
34. Clement PB. Pathology of endometriosis. In: Rosen PP, Fechner RE (eds.) *Pathology Annual Vol. 25.* Norwalk, CT: Appleton and Lange, 1990, p. 245–295.
35. Gerbie AB, Merrill JA. Pathology of endometriosis. *Clin Obstet Gynecol* 31: 779–786, 1988.
36. Weitzman GA, Buttram VC. Classification of endometriosis. *Obstet Gynecol Clin N Am* 16: 61–77, 1989.
37. Woodward PJ, Sohaey R, Mezzetti TP Jr. Endometriosis: radiologic-pathologic correlation. *Radiographic* 21: 193–216, 2001.
38. Bulletti C, De Ziegler D, Polli V, Del Ferro E, Palini S, Flamigni C. Characteristics of uterine contractility during menses in women with mild to moderate endometriosis. *Fertil Steril* 77: 1156–1161, 2002.
39. Sugimura K, Okizuka H, Iamaoka I et al. Pelvic endometriosis: detection and diagnosis with chemical shift MR imaging. *Radiology* 188: 435–438, 1993.
40. Ha HK, Lim YT, Kim HS et al. Diagnosis of pelvic endometriosis: fat supressed T1-weighted vs. conventional MR images. *AJR Am J Roentgenol* 163: 127–131, 1994.
41. Ascher SM, Agrawal R, Bis KG et al. Endometriosis: appearance and detection with conventional and contrast-enhanced fat-suppressed spin-echo technique. *J Magn Reson Imaging* 5: 251–257, 1995.
42. Togashi K, Nishimura K, Kimura I et al. Endometrial cyst: diagnosis with MR imaging. *Radiology* 180: 73–78, 1991.

43. Scoutt LM, McCarthy SM, Lange R et al. MR evaluation of clinically suspected adnexal masses. *JCAT* 18: 609–618, 1994.
44. Thurnher S, Hudler J, Baer S et al. Gadolinium DOTA-enhanced MR imaging of adnexal tumors. *JCAT* 14: 939–949, 1990.
45. Thurnher SM. MR imaging of pelvic masses in women: contrast-enhanced vs. unenhanced images. *AJR Am J Roentgenol* 159: 1243–1250, 1992.
46. Siegelman ES, Outwater EK, Wang T et al. Solid pelvic masses caused by endometriosis: MR imaging features. *AJR Am J Roentgenol* 163: 357–361, 1994.
47. Stratton P, Winkel C, Premkumar A et al. Diagnostic accuracy of laparoscopy, magnetic resonance imaging, and histopathologic examination for the detection of endometriosis. *Fertil Steril* 79: 1078–85, 2003.
48. Bazot M, Darai E, Hourani R et al. Deep pelvic endometriosis: MR imaging for diagnosis and prediction of extension of disease. *Radiology* 232: 379–89, 2004.
49. Guzick DS. Polycystic ovary syndrome. *Obstet Gynecol* 103: 181–193, 2004.
50. Franks S. Polycystic ovary syndrome. *N Engl J Med* 333: 853–861, 1995.
51. Outwater EK, Schiebler ML. Magnetic resonance imaging of the ovary. *Radiol Clin North Am* 2: 245–274, 1994.
52. Kimura I, Togashi K, Kawakami S et al. Polycystic ovaries: implications of diagnosis with MR imaging. *Radiology* 201: 549–552, 1996.
53. Jain KA. Magnetic resonance imaging findings in ovarian torsion. *Magn Reson Imaging* 13: 111–113, 1995.
54. Kimura I, Togashi K, Kawakami S et al. Ovarian torsion: CT and MR imaging appearances. *Radiology* 190: 337–341, 1994.
55. Dohke M, Watanabe Y, Okumura A et al. Comprehensive MR imaging of acute gynecologic diseases. *Radiographics* 20: 1551–1556, 2000.
56. Ghossain MA, Hachem K, Buy JN et al. Adnexal torsion: magnetic resonance findings in the viable adnexa with emphasis on stromal ovarian appearance. *J Magn Reson Imaging* 20: 451–462, 2004.
57. Rha SE, Byun JY, Jung SE et al. CT and MR imaging features of adnexal torsion. *Radiographics* 22: 283–294, 2002.
58. Kilickesmez O, Tasdelen N, Yetimoglu B, Kayhan A, Cihangiroglu M, Gurman N. Diffusion-weighted imaging of adnexal torsion. *Emerg Radiol* 16: 399–401, 2009.
59. Lee AR, Kim KH, Lee BH et al. Massive edema of the ovary: imaging findings. *AJR Am J Roentgenol* 161: 343–344, 1993.
60. Umesaki N, Tanaka T, Miyana M et al. Successful preoperative diagnosis of massive ovarian edema aided by comparative imaging study using magnetic resonance and ultrasound. *Eur J Obstet Gynecol Reprod Biol* 89: 97–99, 2000.
61. Kramer LA, Lalani T, Kawashima A. Massive edema of the ovary: high resolution MR findings using a phased-array pelvic coil. *J Magn Reson Imaging* 7: 758–760, 1997.
62. Dohke M, Watanabe Y, Okumura A et al. Comprehensive MR imaging of acute gynecologic diseases. *Radiographics* 20: 1551–1566, 2000.
63. Tukeva TA, Aronen HJ, Karjalainen PT et al. MR imaging in pelvic inflammatory disease: comparison with laparoscopy and US. *Radiology* 210: 209–216, 1999.
64. Ha HK, Lim GY, Cha ES et al. MR imaging of tubo-ovarian abscess. *Acta Radiol* 36: 510–514, 1995.
65. Outwater EK, Siegelman ES, Chiowanich P et al. Dilated fallopian tubes: MR imaging characteristics. *Radiology* 208: 463–469, 1998.
66. Ha HK, Jung JK, Kang SK et al. MR imaging in the diagnosis of rare forms of ectopic pregnancy. *AJR Am J Roentgenol* 160: 1229–1232, 1993.
67. Outwater EK. Magnetic resonance imaging of acute and chronic pelvic pain disorders. In Fleischer AC, Javitt MC, Jeffrey RB, Jones HW (eds.). *Clinical Gynecologic Imaging*. Philadelphia, Lippincott-Raven, 1997, p. 263–271.
68. Kataoka ML, Togashi K, Kobayashi H et al. Evaluation of ectopic pregnancy by magnetic resonance imaging. *Hum Reprod* 14: 2644–2650, 1999.
69. Nishino M, Hayakawa K, Kawamata K, Iwasaku K, Takasu K. MRI of early unruptured ectopic pregnancy: detection of gestational sac. *J Comput Assist Tomogr* 26: 134–137, 2002.
70. Gullo G, Russ PD. Pelvic varices diagnosed with endorectal surface coil magnetic resonance imaging: case report. *Can Assoc Radiologists J* 51: 23–27, 2000.
71. Nascimento AB, Mitchell DG, Holland G. Ovarian veins: magnetic resonance imaging findings in an asymptomatic population. *J Magn Reson Imaging* 15: 551–556, 2002.
72. Coakley FV, Varghese SL, Hricak H. CT and MRI of pelvic varices in women. *JCAT* 23: 429–434, 1999.
73. Kim HS, Malhotra AD, Rowe PC, Lee JM, Venbrux AC. Embolotherapy for pelvic congestion syndrome: long-term results. *J Vasc Interv Radiol* 17: 289–297, 2006.
74. Morrow CP, Curran JP. Tumors of the ovary: classification; the adnexal mass. In Morrow CP, Curran JP (eds.). *Synopsis of Gynecological Oncology*. New York: Churchill Livingstone, 1998, p. 215–232.
75. Ghossain MA, Buy JN, Ligneres C et al. Epithelial tumors of the ovary: comparison of MR and CT findings. *Radiology* 181: 863–870; 1991.
76. Kinoshita T, Ishii K, Naganuma H et al. MR findings of ovarian tumors with cystic components. *Br J Radiol* 73: 333–339, 2000.
77. Outwater EK, Siegelman ES, Talerman A, Dunton C. Ovarian fibromas and cystadenofibromas: MRI of the fibrous component. *JMRI* 7: 465–471, 1997.
78. Cho SM, Byun JY, Rha SE, Jung SE, Park GS, Kim BK, Kim B, Cho KS, Jung NY, Kim SH, Lee JM. CT and MRI findings of cystadenofibromas of the ovary. *Eur Radiol* 14: 798–804, 2004.
79. Moon WJ, Koh BH, Kim SK et al. Brenner tumor of the ovary: CT and MR findings. *JCAT* 24: 72–76, 2000.
80. Outwater EK, Siegelman ES, Kim B et al. Ovarian Brenner tumors: MR imaging characteristics. *Magn Reson Imaging* 16: 1147–1153, 1998.
81. Koonings PP, Campbell K, Mishell DR Jr, Grimes DA. Relative frequency of primary ovarian neoplasms: a 10-year review. *Obstet Gynecol* 74: 921–926, 1989.
82. Isoda H, Setoh H, Oka A et al. Squamous cell carcinoma arising in a mature teratoma with metastasis to the urinary bladder. *Comput Med Imaging Graphics* 23: 223–225, 1999.
83. Dooms BC, Hricak H, Tscholakoff D. Adnexal structures: MR imaging. *Radiology* 158: 639–646, 1986.
84. Kido A, Togashi K, Konishi I et al. Dermoid cyst of the ovary with malignant transformation: MR appearance. *AJR Am J Roentgenol* 172: 445–449, 1999.
85. Togashi K, Nishimura K, Itoh K et al. Ovarian cystic teratomas: MR imaging. *Radiology* 162: 669–673, 1987.
86. Mitchell DG, Mintz MC, Spritzer CE et al. Adnexal masses: MR imaging observations at 1.5 T with US and CT correlation. *Radiology* 162: 319–324, 1987.
87. Stevens SK, Hricak H, Campos Z. Teratomas versus cystic hemorrhagic adnexal lesions: differentiation with proton-selection fat saturation MR imaging. *Radiology* 186: 481–488, 1993.
88. Kier R, Smith RC, McCarthy SM. Value of lipid- and water-suppression MR images in distinguishing between blood and lipid within ovarian masses. *AJR Am J Roentgenol* 158: 321–325, 1992.
89. Yamashita Y, Torashima M, Hatanaka Y et al. Value of phase-shift gradient-echo MR imaging in the differentiation of pelvic lesions with high signal intensity at T1-weighted imaging. *Radiology* 191: 759–764, 1994.

90. Mitchell DG. Chemical shift magnetic resonance imaging: applications in the abdomen and pelvis. *Top Magn Res Imaging* 4: 46–63, 1992.
91. Matsumoto F, Yoshioka H, Hamada T et al. Struma ovarii: CT and MR findings. *JCAT* 14: 310–312, 1990.
92. Dohke M, Watanabe Y, Takahashi A et al. Struma ovarii: MR findings. *JCAT* 21: 265–267, 1997.
93. Yamashita Y, Hatanaka Y, Takahashi M et al. Struma ovarii: MR appearances. *Abdom Imaging* 22: 100–102, 1997.
94. Joja I, Asakawa T, Shirakawa M. Uterus and ovary. *Jpn J Diag Imaging* 18: 291–299, 1998.
95. Matsuki M, Kaji Y, Matsuo M, Kobashi Y. Struma ovarii: MRI findings. *Br J Radiol* 73: 87–90, 2000.
96. Ojada S, Ohaki Y, Kawamura T et al. Cystic struma ovarii: imaging findings. *JCAT* 24: 413–415, 2000.
97. Murase E, Siegelman ES, Outwater EK et al. Uterine leiomyomas: histopathologic features, MR imaging findings, differential diagnosis, and treatment. *Radiographics* 19: 1179–1197, 1999.
98. Kim JC, Kim SS, Park YJ. "Bridging vascular sign" in the MR diagnosis of exophytic uterine leiomyoma. *JCAT* 24: 57–60, 2000.
99. Kitajima K, Kaji Y, Sugimura K. Usual and unusual MRI findings of ovarian fibroma: correlation with pathologic findings. *Magn Reson Med Sci* 7: 43–48, 2008.
100. Stevens SK, Hricak H, Stern JL. Ovarian lesions: detection and characterization with gadolinium-enhanced MR imaging at 1.5 T. *Radiology* 181: 481–488, 1991.
101. Schwartz RK, Levine D, Hatabu H, Edelman RR. Ovarian fibroma: findings by contrast-enhanced MRI. *Abdom Imaging* 22: 535–537, 1997.
102. Ueda J, Furukawa T, Higashino K et al. Ovarian fibroma of high signal intensity on T2-weighted MR image. *Abdom Imaging* 23: 657–658, 1998.
103. Troiano RN, Lazzarini KM, Scoutt LM et al. Fibroma and fibrothecoma of the ovary: MR imaging findings. *Radiology* 204: 795–798, 1997.
104. Yerli H, Agildere AM, Bilezikci B, Karadeli E. Sclerosing stromal tumor of the ovary with torsion. MRI features. *Acta Radiol* 44(6): 612–615, 2003.
105. Kim KA, Park CM, Lee JH, Kim HK, Cho SM, Kim B, Seol HY. Benign ovarian tumors with solid and cystic components that mimic malignancy. *AJR Am J Roentgenol* 182: 1259–1265, 2004.
106. Tanaka YO, Tsunoda H, Kitagawa Y, Ueno T, Yoshikawa H, Saida Y. Functioning ovarian tumors: direct and indirect findings at MR imaging. *Radiographics* 24 Suppl 1: S147–S166, 2004.
107. Torricelli P, Caruso Lombardi A, Boselli F, Rossi G. Sclerosing stromal tumor of the ovary: US, CT, and MRI findings. *Abdom Imaging* 27: 588–591, 2002.
108. Ihara N, Togashi K, Todo G et al. Sclerosing stromal tumor of the ovary: MRI. *J Comput Assist Tomogr* 23: 555–557, 1999.
109. Ozols RF, Rubin SC, Thomas GM, Robboy S. Epithelial ovarian cancer. In Hoskins WJ, Perez CA, Young RC (eds.). *Principles and Practice of Gynecologic Oncology.* Philadelphia: Lippincott, 2000, p. 981–1058.
110. American Cancer Society. *Cancer Facts and Figures: 1998.* Atlanta, GA: American Cancer Society, 1998, p. 13.
111. Yamashita Y, Torashima M, Hatanaka Y et al. Adnexal masses: accuracy of characterization with transvaginal US and precontrast and postcontrast MR imaging. *Radiology* 194: 557–565, 1995.
112. Komatsu T, Konishi I, Mondai M et al. Adnexal masses: transvaginal US and gadolinium-enhanced MR imaging assessment of intratumoral structure. *Radiology* 198: 109–115, 1996.
113. Yamashita Y, Hatanaka Y, Torashima M et al. Characterization of sonographically indeterminate ovarian tumors with MR imaging—a logistic regression analysis. *Acta Radiologica* 38: 572–577, 1997.
114. Jain KA, Friedman DL, Pettinger TW et al. Adnexal masses: comparison of the specificity of endovaginal US and pelvic MR imaging. *Radiology* 186: 697–704, 1993.
115. Hricak H, Chen M, Coakley FV et al. Complex adnexal masses: detection and characterization with MR imaging—multivariate analysis. *Radiology* 214: 39–46, 2000.
116. Sohaib SA, Sahdev A, Van Trappen P, Jacobs IJ, Reznek RH. Characterization of adnexal mass lesions on MR imaging. *AJR Am J Roentgenol* 18: 1297–1304, 2003.
117. Stevens SK, Hricak H, Stern JL. Ovarian lesions: detection and characterization with gadolinium-enhanced MR imaging at 1.5T. *Radiology* 181: 481–488, 1991.
118. Semelka RC, Lawrence PH, Shoenut JP et al. Primary ovarian cancer: prospective comparison of contrast-enhanced CT and pre- and postcontrast fat-suppressed MR imaging with histologic correlation. *J Magn Imaging* 3: 99–106, 1993.
119. Jeong YY, Outwater EK, Kang HK. Imaging of ovarian masses. *Radiographics* 20: 1445–1470, 2000.
120. Kurtz AB, Tsimikas JV, Tempany CMC et al. The comparative values of Doppler and conventional US, CT and MR imaging correlated with surgery and histopathologic analysis: report of the Radiological Diagnostic Oncology Group. *Radiology* 212: 19–27, 1999.
121. Tempany CMC, Zou KH, Silverman SG et al. Staging of advanced ovarian cancer: comparison of imaging modalities—report of the Radiological Diagnostic Oncology Group. *Radiology* 215: 761–767, 2000.
122. Low RN, Saleh F, Song SYT et al. Treated ovarian cancer: comparison of MR imaging with serum CA-125 level and physical examination—a longitudinal study. *Radiology* 211: 519–528, 1999.
123. Sutton CL, McKinney CD, Jones JE, Gay SB. Ovarian masses revisited: radiologic and pathologic correlation. *Radiographics* 12: 853–877, 1992.
124. Wagner BJ, Buck JL, Seidman JD, McCabe KM. Ovarian epithelial neoplasms: radiologic-pathologic correlation. *Radiographics* 14: 1351–1274, 1994.
125. Okamoto Y, Tanaka YO, Tsunoda H, Yoshikawa H, Minami M. Malignant or borderline mucinous cystic neoplasms have a larger number of loculi than mucinous cystadenoma: a retrospective study with MR. *J Magn Reson Imaging* 26: 94–99, 2007.
126. Matsuoka Y, Ohtomo K, Araki T, Kojima K, Yoshikawa W, Fuwa S. MR imaging of clear cell carcinoma of the ovary. *Eur Radiol* 11: 946–951, 2001.
127. Morrow CP, Curtin JP. Tumors of the ovary: sex cord stromal tumors and germ cell tumors. In Morrow CP, Curtin JP (eds.). *Synopsis of Gynecologic Oncology.* New York: Churchill Livingstone, 1998, p. 281–306.
128. Ko SF, Wan YL, Ng SH et al. Adult granulosa cell tumors: spectrum of sonographic and CT findings with pathologic correlation. *AJR Am J Roentgenol* 172: 1227–1233, 1999.
129. Morikawa K, Hatabu H, Togashi K et al. Granulosa cell tumor of the ovary: MT findings. *JCAT* 21: 1001–1004, 1997.
130. Koulouris CR, Peson RT. Ovarian stromal and germ cell tumors. *Semin Oncol* 36: 126–136, 2009.
131. Kohno A, Yoshikawa W, Yunoki M et al. MR findings in degenerated ovarian leiomyoma. *Br J Radiol* 72: 1213–1215, 1999.
132. Ferrozzi F, Tognini G, Bova D, Zuccoli G. Non-Hodgkin lymphomas of the ovaries: MR findings. *JCAT* 24: 416–420, 2000.
133. Mitsumori A, Joja I. MRI appearance of Non-Hodgkin's lymphoma of the ovary. *AJR Am J Roentgenol* 173: 245, 1999.
134. Young RH, Scully RE. Metastatic tumors in the ovary. In Blaustein A (ed.). *Pathology of the Female Genital Tract.* New York: Springer-Verlag, 1994, p. 939–974.

135. Moselhi M, Spencer J, Lane G. Malignant melanoma metastatic to the ovary: presentation and radiological characteristics. *Gynecologic Oncology* 69: 165–168, 1998.
136. Kim SH, Kim WH, Park KJ et al. CT and MR findings of Krukenberg tumors. Comparison with primary ovarian tumors. *JCAT* 20: 393–398, 1996.
137. Cho JY, Seong CK, Kim SH. Krukenberg tumor findings at color and power Doppler US; correlation with findings at CT, MR, and pathology. *Acta Radiologica* 39: 327–329, 1998.
138. Ha HK, Baek SY, Kim SH et al. Krukenberg's tumor of the ovary: MR imaging features. *AJR Am J Roentgenol* 164: 1435–1439, 1995.
139. Gompel C, Silverberg SG. The fallopian tube. In Gompel C, Silverberg SG (eds.). *Pathology in Gynecology and Obstetrics*. Philadelphia, Lippincott, 1994, p. 284–311.
140. Kawakami S, Togashi K, Kimura I et al. Primary malignant tumor of the fallopian tube: appearance at CT and MR imaging. *Radiology* 186: 503–508, 1993.
141. Takagi H, Matsunami K, Noda K, Furui T, Imai A. Primary fallopian tube carcinoma: a case of successful preoperative evaluation with magnetic resonance imaging. *J Obstet Gynaecol* 23: 455–456, 2003.
142. Schwartz LB, Panageas E, Lange R et al. Female pelvis: impact of MR imaging on treatment decisions and net cost analysis. *Radiology* 192: 55–60, 1994.
143. Yu KK, Hricak H. Can MRI of the pelvis be cost effective? *Abdom Imaging* 22: 587–601, 1997.
144. Hardesty LA, Sumkin JH, Nath ME et al. Use of preoperative MR imaging in the management of endometrial carcinoma: cost analysis. *Radiology* 215: 45–49, 2000.

CHAPTER 16

PREGNANCY AND FETUS

LORENE ROMINE, REENA CHOPRA, KATARINA KOPRIVSEK, WAQAS QURESHI, RICHARD C. SEMELKA, AND MICHÈLE A. BROWN

The choice of diagnostic imaging techniques in pregnant patients is limited by the potential risks to the fetus. Because low-dose irradiation of a fetus may increase the likelihood of childhood cancer, the use of ionizing radiation during pregnancy should be avoided whenever possible. As magnetic resonance imaging (MRI) does not employ ionizing radiation and there is no evidence of teratogenic or other adverse fetal effects to date [1–5], it is being increasingly used for imaging pregnant women. Ultrasonography is routinely used in the initial evaluation of the fetus and pregnant woman because it is safe, inexpensive, and widely available. In experienced hands, ultrasound is highly accurate in the diagnosis of maternal complications associated with pregnancy; however, if ultrasound findings are unclear or additional information is desired, MRI may be helpful (figs. 16.1 and 16.2). For fetal assessment, the role of MRI has increased with the advent of ultrafast sequences. Fast MR imaging techniques provide excellent resolution for imaging of the fetal and maternal anatomies without the need for sedation, and multiple studies have reported encouraging results regarding MRI in the evaluation of fetal and maternal disorders [6–12].

MRI SAFETY

At present, there is no clinical or experimental evidence of teratogenic or other adverse fetal effects from MR imaging in pregnancy [1, 3, 4, 13, 14], although a few studies have demonstrated that prolonged or high-level exposure to electromagnetic radiation might result in disorders of embryogenesis and teratogenicity in laboratory animals [14, 15]. In a survey of female MR workers, no substantial increase in adverse pregnancy outcome was found [16]. The safety concern arises from radiofrequency pulses, which result in energy deposition and potential tissue heating that are maximum at the body surface and approach zero near the body core [17]. The FDA regulates the amount of energy deposited by MR imaging, referred to as the specific absorption rate (SAR). No adverse fetal effects have been documented from MR imaging using routine sequences, even those associated with relatively high SAR. Several studies have failed to show any adverse long-term effects of fetal MR in children who were imaged as fetuses [14, 18–20].

It is generally suggested that MR be used in pregnant patients only when ultrasound cannot answer the

Abdominal-Pelvic MRI, Third Edition, edited by Richard C. Semelka. Copyright © 2010 John Wiley & Sons, Inc.

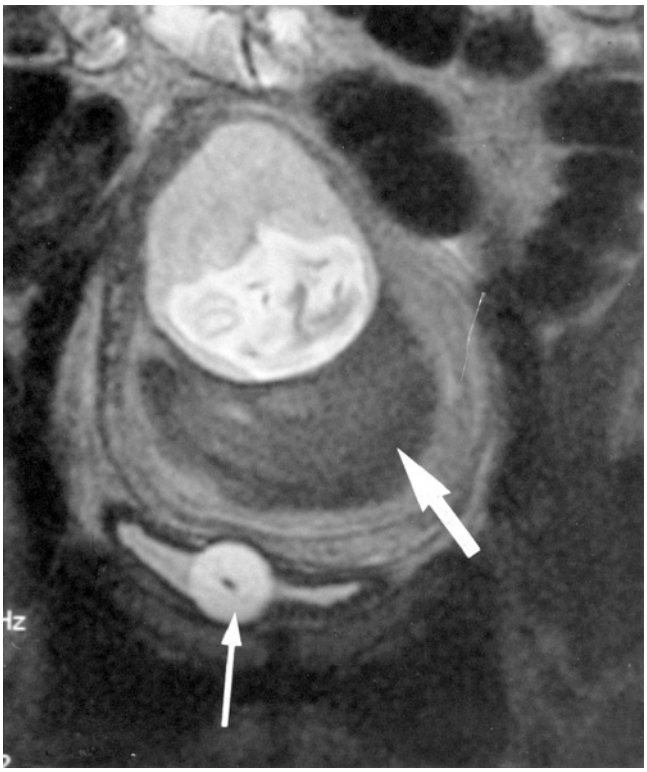

FIG. 16.1 Uterine hematoma in a cornual pregnancy at 12 weeks of gestation. Coronal SS-ETSE image through the maternal pelvis shows a hypointense uterine hematoma (large arrow). Intrauterine growth retardation of the fetus was also present because of cornual implantation. A Foley catheter is seen in the maternal urinary bladder (small arrow).

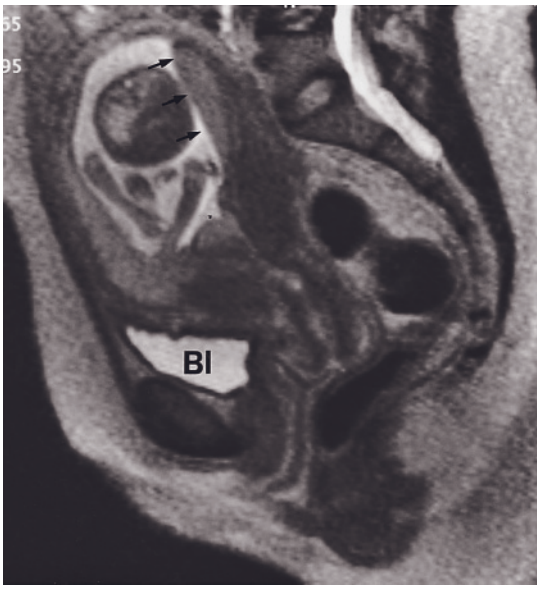

(*a*)

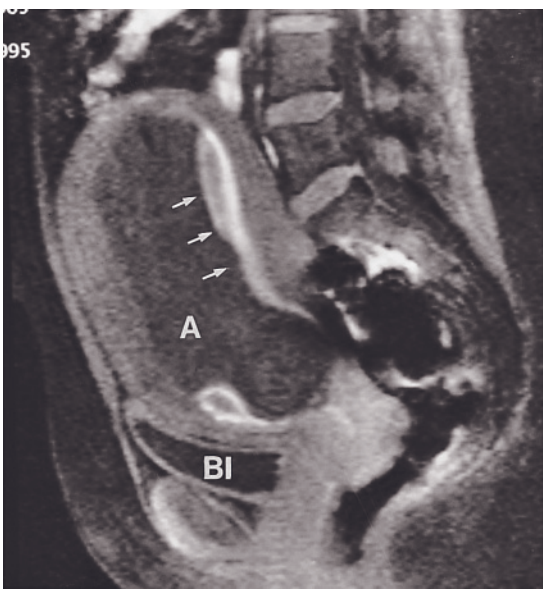

(*b*)

FIG. 16.2 Subchorionic hematoma. Sagittal SS-ETSE (*a*) and fat-suppressed SGE (*b*) images through the maternal pelvis show lenticular area of decreased signal intensity on the T2-weighted image (arrows, *a*) and moderately high signal on the SGE image (arrows, *b*), consistent with a subchorionic hematoma. Note the peripheral rim of higher signal intensity on the SGE sequence indicating subacute hemorrhage. A, amniotic fluid; Bl, maternal bladder.

clinical question and the benefits of MR are felt to outweigh theoretical risks [22]. Because of organogenesis, even greater caution should be used in the first trimester. A statement from the National Institutes of Health Consensus Development Conferences on MRI indicated that "MRI should be used during the first trimester of pregnancy only when there are clear medical indications and when it offers a definite advantage over other tests" [23]. It is important to remember, however, that the single greatest factor in morbidity and mortality of the pregnant patient with acute abdominal disease is delay in diagnosis [24].

Gadolinium-based contrast agents (GBCAs) used in MRI have been demonstrated to cross the placental barrier when injected into primates. These agents are then excreted by the fetal urinary tract into the amniotic cavity, and subsequently swallowed by the fetus [25]. The gadolinium-chelate molecules remain in the amniotic fluid for an indeterminate amount of time and may undergo dissociation during this time, releasing toxic free gadolinium ions into the amniotic fluid [26]. This raises concerns that the gadolinium may be incorporated into the developing fetal tissues, as free gadolinium has been shown to be taken up by liver and bone in rodents after intravascular administration of GBCA [27] and by bone in humans [28]. The impact of this is as yet unknown, and the American College of Radiology has recommended that gadolinium be administered in pregnancy only when there is "an overwhelming poten-

tial benefit to the patient or fetus outweighing the theoretic but potentially real risks of long-term exposure of the developing fetus to free gadolinium ions" [26]. Although a study performed in pregnant mice with gadopentetate dimeglumine injected into the peritoneal cavity failed to demonstrate any adverse effects [29], GBCAs have been shown to increase skeletal malformations in animal studies and are considered pregnancy category C drugs by the FDA [30].

For these reasons, initial noncontrast MR images should be reviewed in all cases before the decision to administer contrast is made. If the use of gadolinium-based contrast agents is deemed essential, specific avoidance of linear nonionic GBCAs (i.e., Omniscan and Optimark) is strongly recommended. These agents have a lower conditional stability than the other GBCAs and therefore have a greater tendency to dissociate, with free gadolinium identified as being deposited in bone [27, 28]. Macrocyclic agents have the highest stability (ProHance, Dotarem, and Gadovist) and may be preferred, and agents with higher T1 relaxivity and good stability (MultiHance) may be considered as they can be administered in lower dose [31]. Long-term animal studies have not been performed to evaluate the carcinogenic potential of GBCAs, but no carcinogenic effects have yet been demonstrated. When contrast is needed, informed consent should be obtained.

MRI TECHNIQUE

Although no specific patient preparation is absolutely required, patients may be best imaged with an empty bladder after fasting for at least 4 hours. A distended bladder may produce motion-related artifact in the phase-encoding direction. However, some investigators recommend drinking a negative oral contrast agent 1 hour before the study in order to negate any signal within the bowel lumen on T1- and T2-weighted images [24]. Imaging is performed with the patient supine unless she is in late pregnancy, in which case a decubitus position is preferred to decrease pressure on the inferior vena cava. A phased-array coil should be used. It is helpful to place a saturation band over the fat in the anterior abdominal wall to minimize artifact on non-fat-suppressed sagittal images, and it may be helpful to use an anterioposterior frequency-encoding direction for axial images.

For evaluation of fetal anomalies, ultrafast sequences such as T2-weighted single-shot echo-train spin-echo and T2-/T1-weighted steady-state free-precession gradient echo are used. If there is concern for hemorrhage, a T1-weighted sequence is added. Some centers are now using diffusion-weighted imaging (DWI) and MR spectroscopy to further evaluate the fetal brain. Diffusion-weighted imaging can be rapidly obtained in less than a half a second, and is particularly useful in evaluating hypoxic/ischemic injury [32]. DWI has also shown promise for evaluation of fetal lung maturity, as well as assessing for cystic renal disease and renal function [32, 33]. In cases of suspected appendicitis, a fat-saturated T2-weighted image is helpful to better visualize inflammatory fluid. Thick-slab T2-weighted echo train spin-echo images are used for MR urography as well as MR cholangiography in cases of suspected maternal disease.

MATERNAL IMAGING

MRI has been shown to be useful in the diagnosis of maternal complications during pregnancy. Physical examination in pregnancy is impaired by the presence of the gravid uterus, making assessment of abdominal or pelvic pathology difficult. Although CT is well established in the evaluation of acute abdominal pain, this exposes the fetus to ionizing radiation and should be avoided if possible. Ultrasonography remains the primary imaging modality; however, its value is limited by the enlarged uterus as well as lack of tissue specificity. MRI provides excellent anatomic detail without ionizing radiation and therefore is a useful adjunct in the characterization of abdominal and pelvic disease. MR has been shown to be helpful in evaluation of acute appendicitis, adrenal gland pathology, pancreatitis, inflammatory bowel disease, uterine fibroids, and adnexal masses [24, 34].

Acute appendicitis is the most common nonobstetric surgical condition in pregnant patients [35, 36]. Physical exam and imaging evaluation are made difficult by the enlarging uterus, which often displaces the appendix cephalad. In pregnant patients, fetal loss rate has been reported as <2% without rupture and 30% with ruptured appendicitis [37]. Pregnant patients with acute appendicitis may be misdiagnosed because the location of pain is not typical [38], and because symptoms and signs of appendicitis such as nausea, vomiting, and leukocytosis may occur physiologically during pregnancy. The MR appearance of appendicitis includes an enlarged appendix, periappendiceal fluid or inflammation, and/or abscess formation (fig. 16.3). MR can also demonstrate the normal appendix, which helps exclude the diagnosis of acute appendicitis. In retrospective studies evaluating pregnant patients with MRI, the appendix was seen in 83–91% of the patients in four studies [39–42] but in only 52% of patients in a recent study [43]. Although the appendiceal detection rate is rather low in the more recent study, this still represents a significant improvement over ultrasound, where the appendix was demonstrated in only 22% of the same

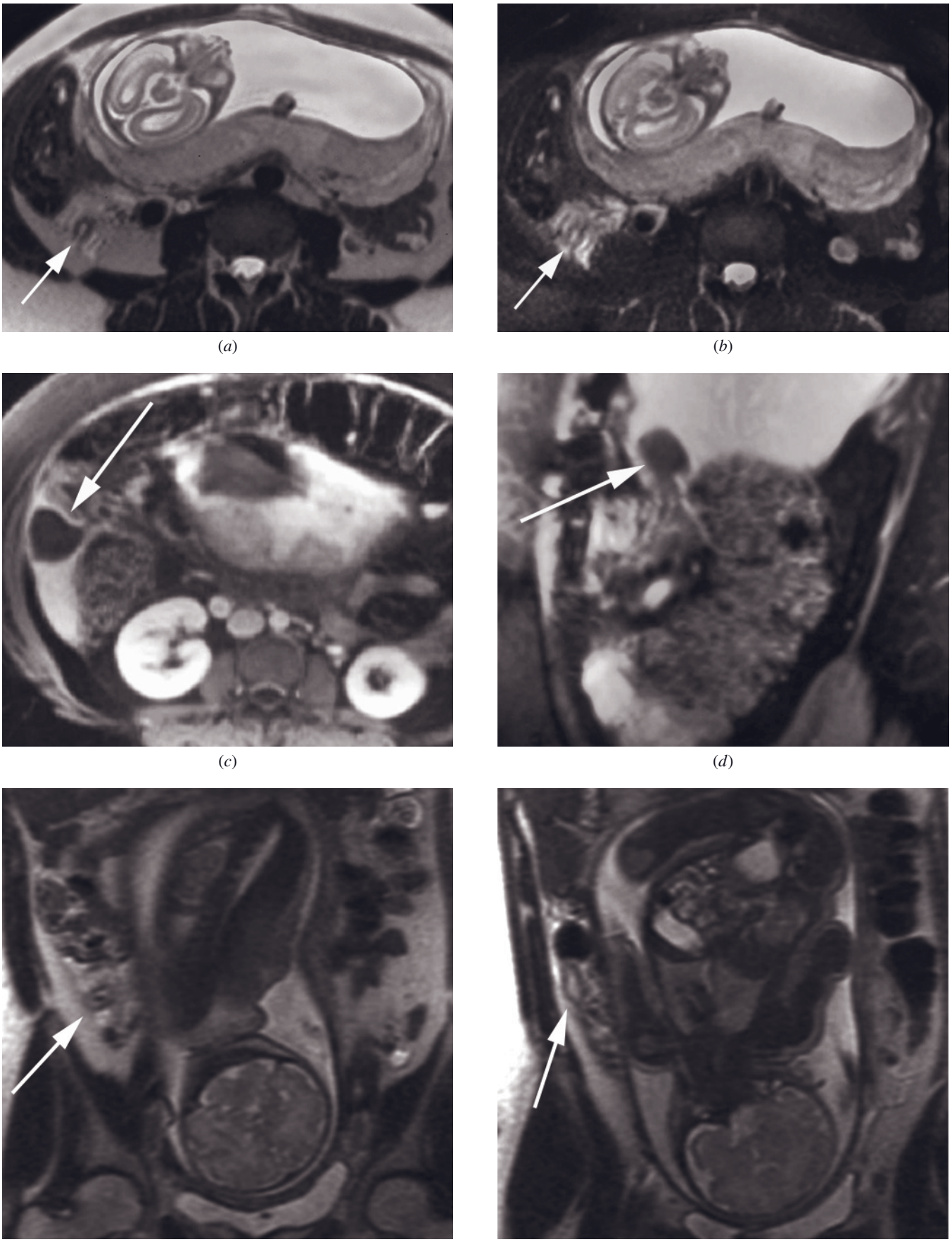

FIG. 16.3 Acute appendicitis in pregnancy. Transverse T2-weighted SS-ETSE (*a*) and fat-suppressed T2-weighted SS-ETSE (*b*) images in a pregnant patient with right lower quadrant pain show an enlarged appendix (arrow) with periappendiceal inflammation. Fat-suppressed T2-weighted sequences (*b*) help increase the conspicuity of inflammation while avoiding gadolinium. In a different patient, transverse (*c*) and sagittal (*d*) gadolinium-enhanced fat-suppressed T1-weighted gradient echo images demonstrate appendicitis with a subhepatic abscess (arrow, *c*, *d*). In a third patient, coronal (*e*, *f*) and transverse (*g*) T2-weighted SS-ETSE images

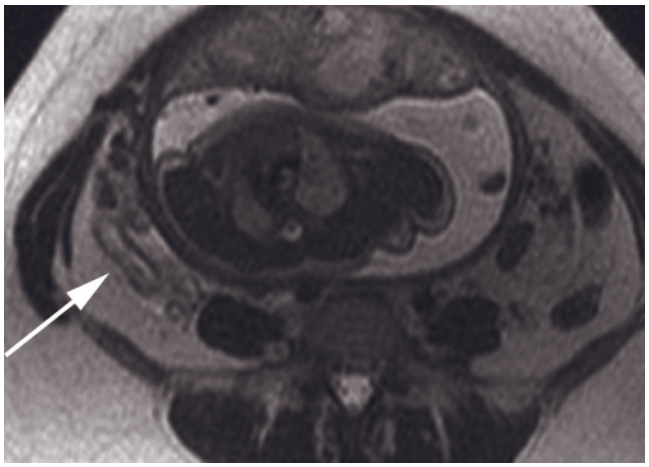

(*g*)

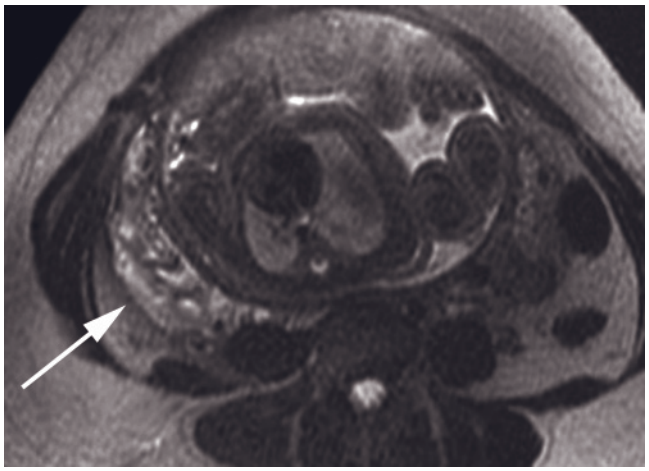

(*h*)

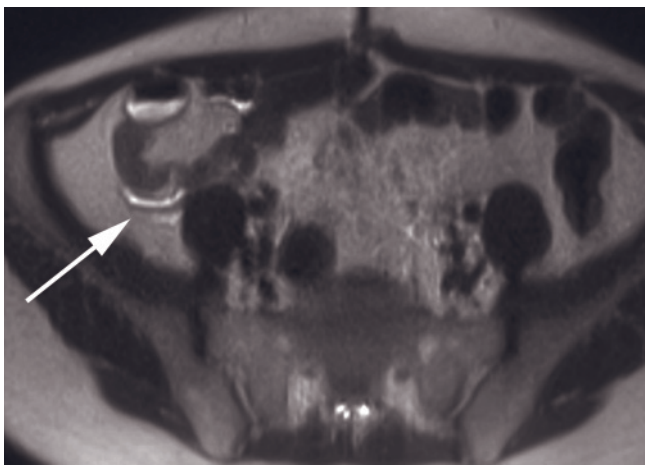

(*i*)

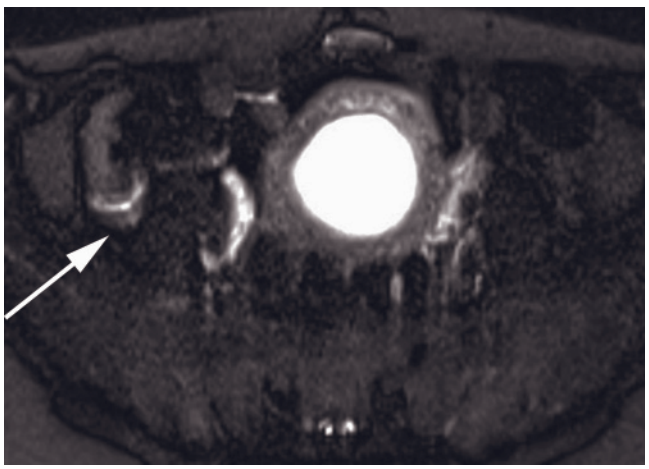

(*j*)

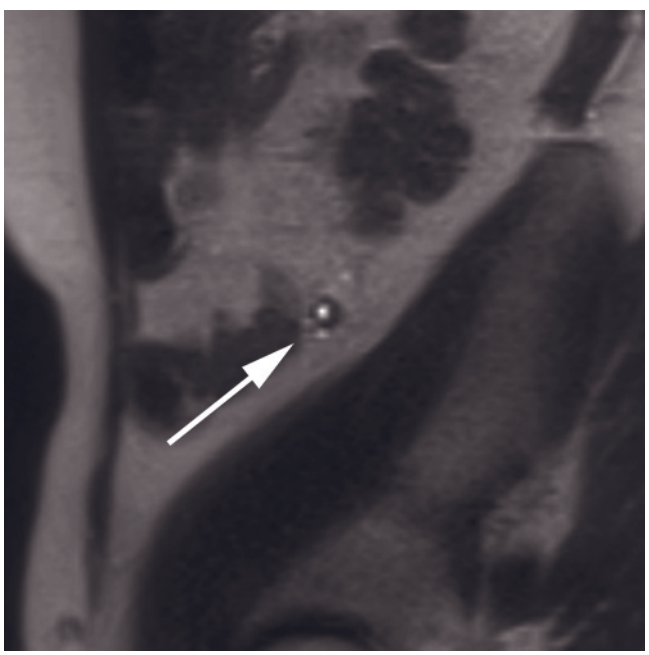

(*k*)

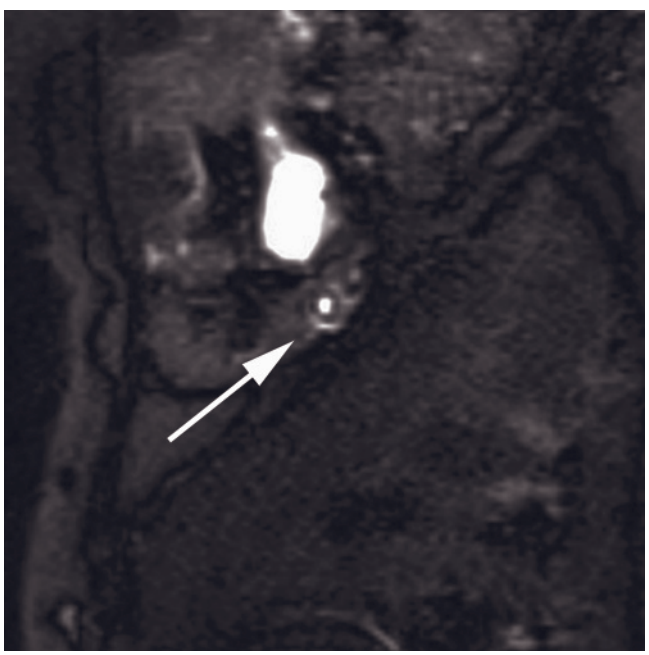

(*l*)

Fig. 16.3 (*Continued*) and transverse fat-suppressed T2-weighted SS-ETSE image (*h*) again show an enlarged appendix (arrows) with periappendiceal inflammation in the third trimester of pregnancy. Transverse (*i*, *j*), sagittal (*k*, *l*), and coronal (*m*) T2-weighted SS-ETSE (*i*, *k*, *m*) and fat-suppressed T2-weighted SS-ETSE (*j*, *l*) images from a fourth patient demonstrate more subtle findings of

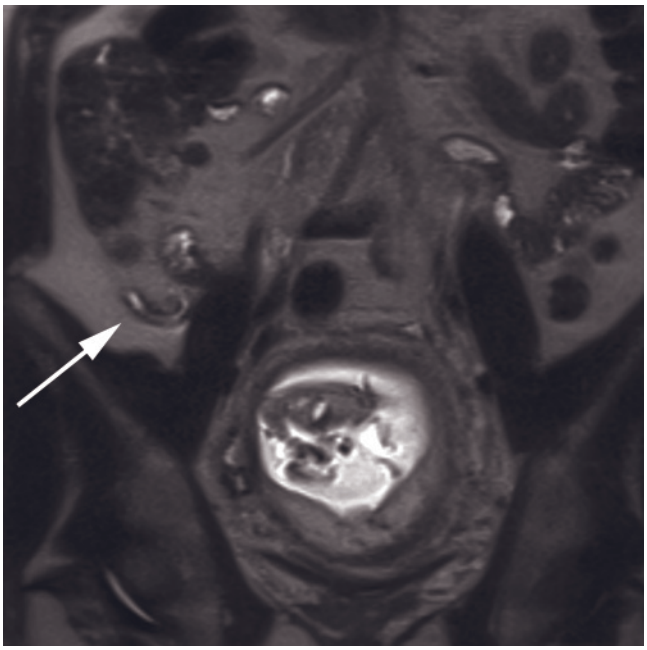

(*m*)

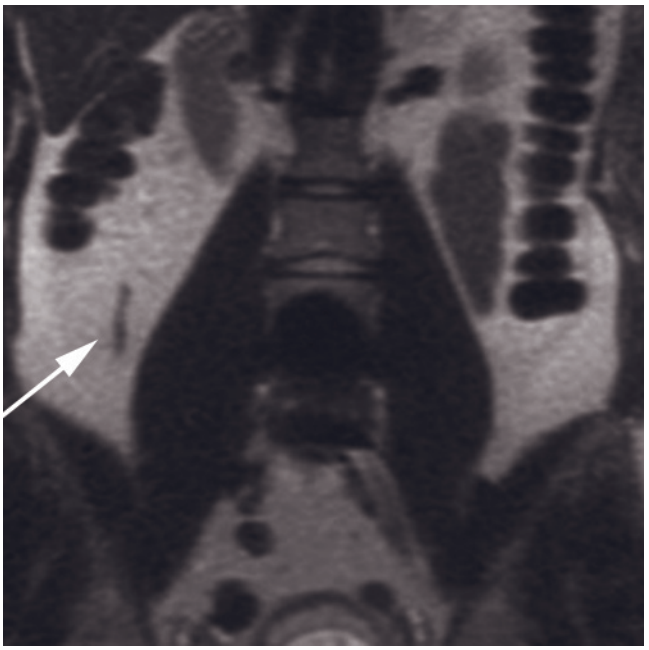

(*n*)

FIG. 16.3 (*Continued*) acute appendicitis. The fluid-filled appendix is mildly dilated (arrows) with a small amount of periappendiceal fluid. Normal appendix (arrow, *n*) in a pregnant patient for comparison. Coronal T2-weighted SS-ETSE image shows a nondilated appendix with no adjacent inflammation.

patients. To date, two studies have estimated the sensitivity, specificity, and negative predictive values for MRI in pregnant patients with suspected appendicitis at 80–100%, 93.6–100%, and 94–97%, respectively. Positive predictive value estimation has been inconsistent, reported as 1.4–100% in these studies, with the lower rate influenced by the low incidence of positive cases [40, 43].

MRI may also elucidate other gastrointestinal disorders as the cause of abdominal pain during pregnancy (fig. 16.4). Identification of those patients who might require immediate intervention, such as those with bowel obstruction, abscess, toxic megacolon, or bleeding, is important. Bowel obstruction is well depicted with MR imaging, particularly with single-shot echo-train spin echo-sequences. The etiology of obstruction, whether adhesion, inflammatory bowel disease, intussuception, or other, may also be evident with MRI. Cholelithiasis is easily diagnosed with ultrasound; however, the diagnosis of choledocholithiasis is more difficult. MR cholangiopancreatography (MRCP) is an accurate method for detecting stones in the ductal system. Pancreatitis secondary to gallstones may be diagnosed clinically; however, MRI may be helpful in identifying complications [24].

Hydronephrosis is common during pregnancy, because of smooth muscle relaxation in the ureters and hormonal changes as well as extrinsic compression by the gravid uterus [40]. This usually requires no intervention. It is occasionally necessary to exclude obstructing ureteral stone as the cause of hydronephrosis, and this may be difficult with ultrasound. On MR urography, physiologic hydroureter appears as a tapered narrowing at the sacral promontory with a collapsed pelvic ureter (fig. 16.5), while an obstructing stone appears as a convex filling defect at the midureter or vesicoureteral junction with a dilated ureter proximally [44, 45]. It is often helpful in these cases to position the patient with the symptomatic side up to decrease uterine pressure on the pelvic brim, which could potentially hinder identification of a distal ureteral stone. Pyelonephritis is more common in pregnant than nonpregnant patients because of urinary stasis (fig. 16.6, see Chapter 9). While the diagnosis is usually made based on clinical parameters, MR imaging is useful to detect or exclude complications that require intervention such as perinephric abscess.

Uterine leiomyomas demonstrate the same imaging characteristics during pregnancy as in the nongravid uterus. However, they may outgrow their vascular supply, resulting in degeneration. Most commonly hemorrhagic infarction and necrosis, the so-called red degeneration, will be seen and the leiomyoma thus presents with peripheral or diffuse high signal intensity

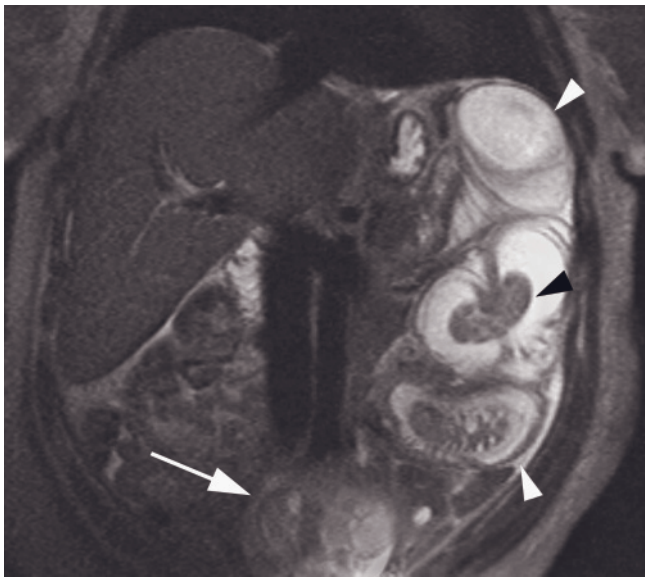

(*a*)

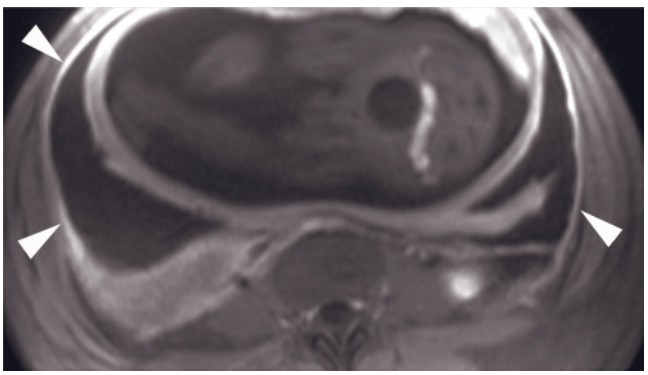

(*b*)

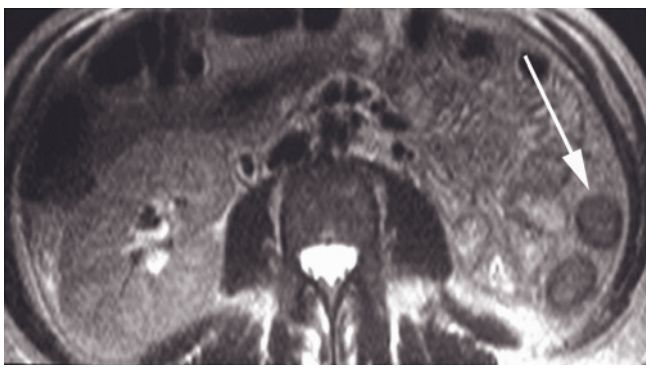

(*c*)

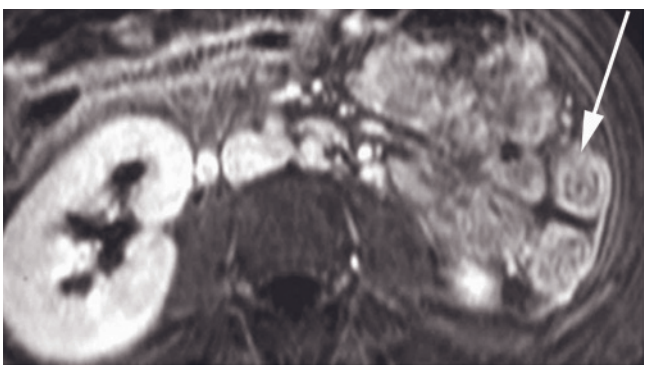

(*d*)

(*e*)

FIG. 16.4 Acute gastrointestinal disease in four different pregnant patients. Coronal T2-weighted SS-ETSE image (*a*) shows multiple dilated loops of small bowel (white arrowheads) with an unusual filling defect (black arrowhead). Surgery revealed intussusception. The gravid uterus is partially seen in the pelvis (arrow). In a second patient, who was known to have Crohn disease, transverse gadolinium-enhanced fat suppressed T1-weighted gradient echo image (*b*) shows free fluid with diffuse enhancement of the peritoneum (arrowheads) consistent with peritonitis. In a third patient, known to have ulcerative colitis, transverse T2-weighted SS-ETSE (*c*) and gadolinium-enhanced fat-suppressed T1-weighted gradient-echo (*d*) images show abnormally thickened colon (arrow, *c*, *d*) with marked enhancement (*d*). Coronal T2-weighted SS-ETSE image (*e*) in another patient shows multiple dilated loops of small bowel (arrow) to the right of the gravid uterus in a patient small bowel obstruction at 36 weeks of gestation.

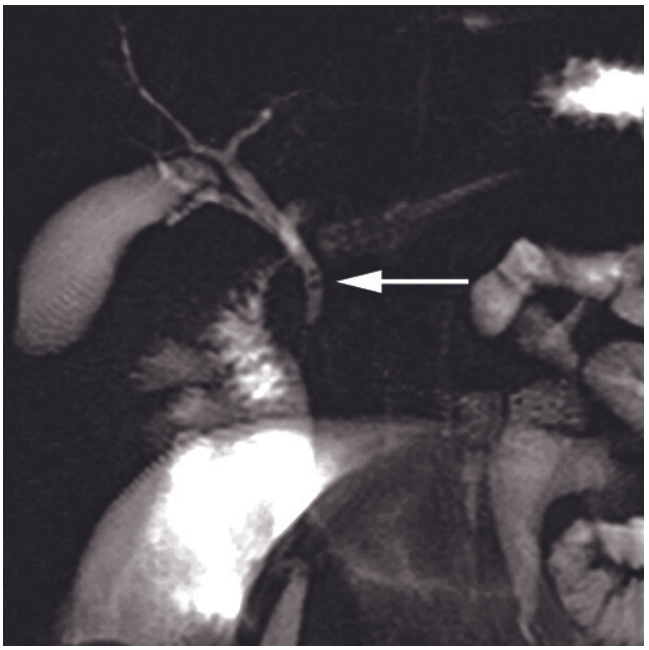

(*f*)

FIG. 16.4 (*Continued*) Oblique coronal thick slab MRCP image (*f*) shows two small stones in the common bile duct (arrow). Note the amniotic fluid in the gravid uterus and mild hydronephrosis.

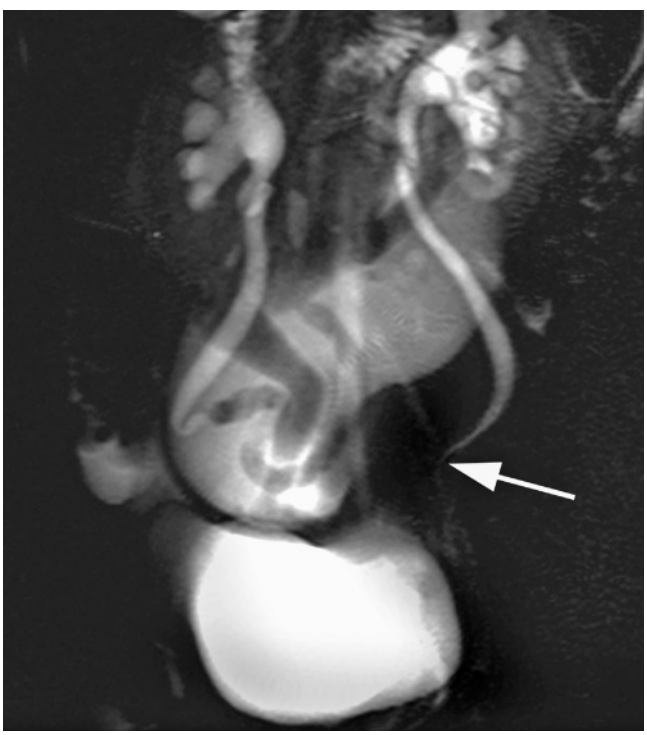

FIG. 16.5 Physiological hydronephrosis in a pregnant patient. Oblique coronal MR urography image shows bilateral hydronephrosis and smooth tapering of the left ureter at the pelvic brim (arrow) without dilation of the pelvic ureter, consistent with physiological hydronephrosis rather than ureteral stone.

FIG. 16.6 Pyelonephritis. Coronal T2-weighted SS-ETSE image in a patient 21 weeks pregnant with right upper abdominal pain and fever reveals right perinephric fluid (arrowheads) consistent with the clinical diagnosis of pyelonephritis.

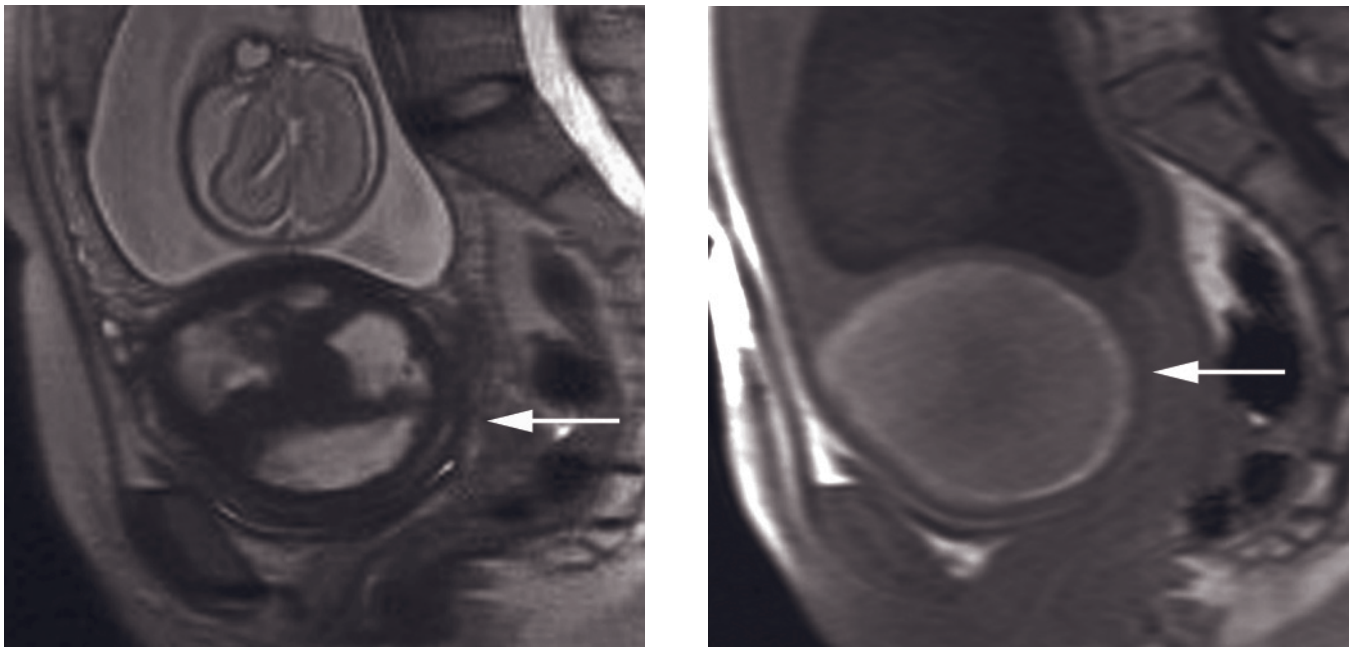

(*a*) (*b*)

FIG. 16.7 Red degeneration of leiomyoma during pregnancy. Sagittal T2-weighted SS-ETSE (*a*) and T1-weighted gradient echo (*b*) images reveal an 11-cm subserosal leiomyoma in the lower uterine segment (arrows). The leiomyoma demonstrates mixed signal on T2-weighted images and diffuse hyperintensity on T1-weighted images, consistent with red degeneration. Gravid uterus with 23-week fetus is partially visualized.

on T1-weighted images and variable signal intensities with or without low-signal-intensity rim on T2-weighted images (fig. 16.7) [46–48]. Leiomyomas may cause pain during pregnancy because of rapid growth, degeneration, or torsion. Large leiomyomas that undergo hemorrhagic infarction may lead to significant pain and premature labor [49]. MRI has been shown to be useful in characterizing uterine leiomyomas during pregnancy [50]. Degenerating leiomyomas are characterized by central high signal intensity on T2-weighted images. Central necrosis may also contain high signal intensity on T1-weighted images due to hemorrhagic components. Subserosal fibroids can undergo torsion as well as degeneration during pregnancy (fig. 16.8). Precise mapping of all leiomyomas should be performed with ultrasound early during pregnancy because evaluation will become more difficult during the second and third trimesters. When the gestational contents preclude accurate assessment with ultrasound, MRI is indicated. When multiple or large leiomyomas are present in the lower uterine segment, a decision may be made to perform cesarean section (fig. 16.9). By means of MRI, a leiomyoma might be identified as the source of a suspected adnexal mass (fig. 16.10).

The diagnosis of an adnexal mass during pregnancy poses a diagnostic challenge. The most common adnexal

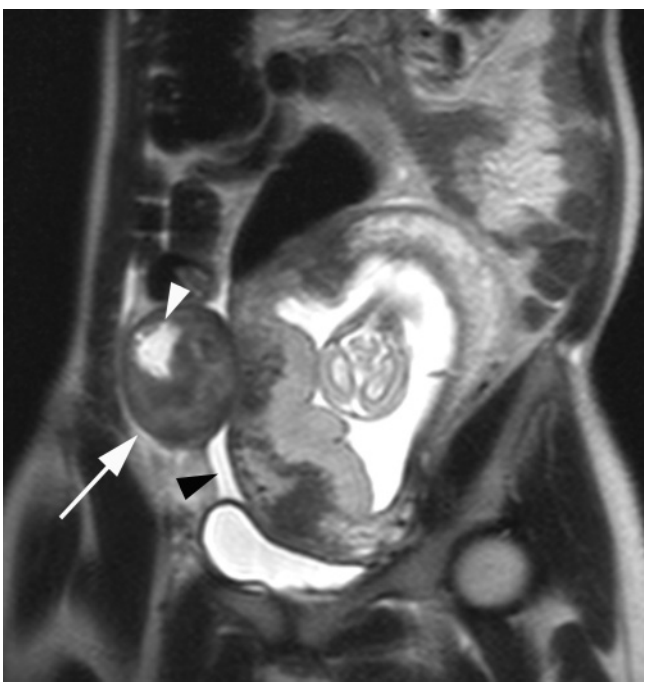

FIG. 16.8 Torsed subserosal fibroid in a pregnant patient. Coronal T2-weighted SS-ETSE image in a patient with severe right lower quadrant pain shows a subserosal fibroid (arrow) with evidence of degeneration (white arrowhead) and a small amount of adjacent fluid (black arrowhead). At surgery, a pedunculated fibroid was found to be twisted 270°.

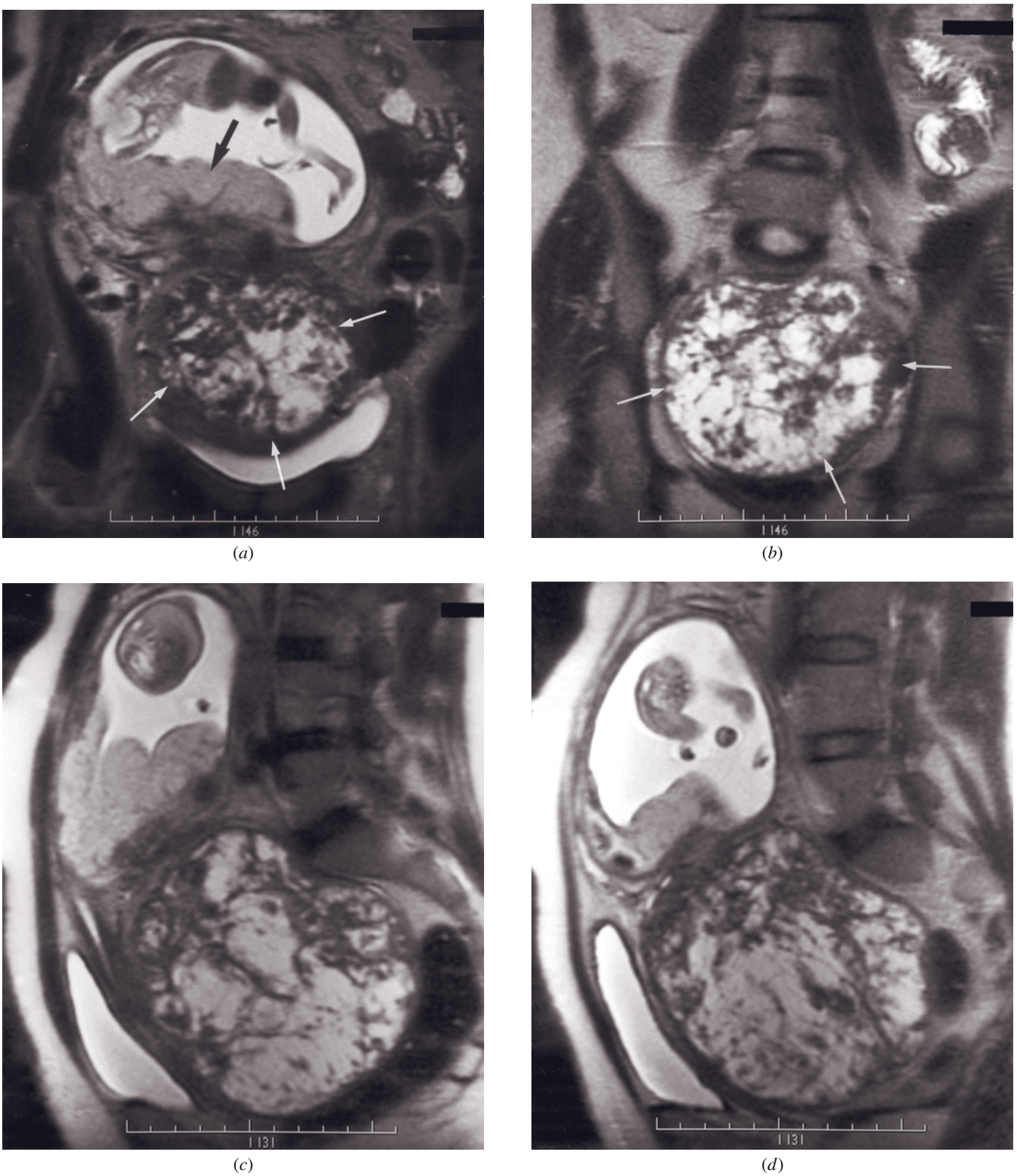

(*a*) (*b*) (*c*) (*d*)

FIG. 16.9 Large uterine leiomyoma in two pregnant patients. Coronal (*a*, anterior; *b*, posterior) and sagittal (*c*, *d*) T2-weighted SS-ETSE images.The large uterine leiomyoma (arrows, *a*, *b*) shows multiple foci of increased signal intensity corresponding to areas of degeneration. Note also the normal pregnancy and placenta (black arrow, *a*). Coronal SS-ETSE (*e*) and coronal

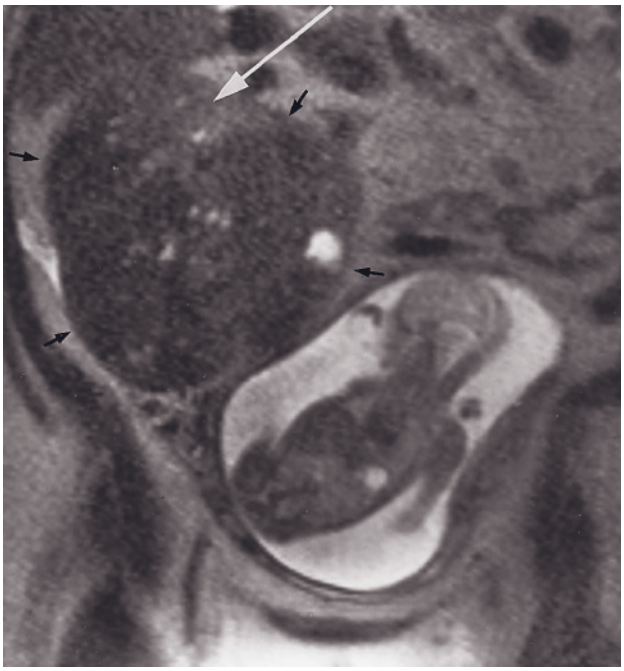

(*e*)

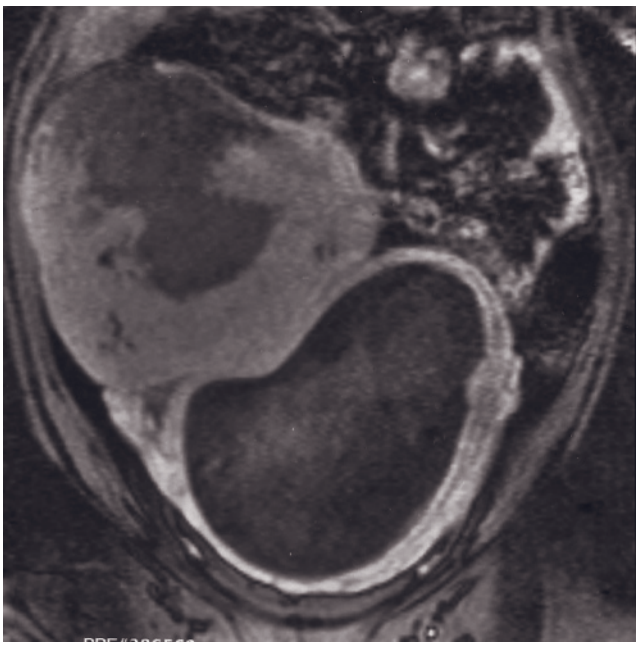

(*f*)

FIG. 16.9 (*Continued*) gadolinium-enhanced fat-suppressed SGE (*f*) images in a second patient. An 8-cm leiomyoma arises from the right superolateral aspect of the uterus. The leiomyoma is low in signal intensity and well defined on the SS-ETSE image (black arrows, *e*), which is the typical appearance for a leiomyoma. Ill-defined subtle high signal intensity (white arrow, *e*) is appreciated on the T2-weighted image (*e*), which corresponds to a region of lack of gadolinium enhancement on the gadolinium-enhanced fat-suppressed SGE image (*f*), reflecting degeneration. Clear definition of the uterine origin of the mass was appreciated on images obtained in multiple planes. Gadolinium was administered in this patient because of clinical concern of malignant disease. Note that even though data acquisition is 20 s with the breath-hold SGE sequence (*f*), fetal motion blurs out definition of the fetus. In contrast, the 1-s data acquisition of SS-ETSE freezes fetal motion, rendering the fetus clearly defined.

mass in a pregnant patient is a corpus luteal cyst. It usually measures less than 6 cm in size and does not enlarge during pregnancy. The criteria to differentiate benign and malignant ovarian lesions are described in Chapter 15, *Adnexa*. MRI allows differentiation of simple cysts from more complex lesions, and the relationship between the mass and the pregnant uterus can be established (fig. 16.11). Subserosal fibroids can be confused for adnexal masses, as discussed above, and MRI is helpful in making the distinction. Because of the increased pressure in the pelvic cavity, adnexal masses may undergo extrinsic compression, hemorrhage, or torsion and lead to exquisite abdominal pain [51]. Torsion is more common during pregnancy and may occur with or without an underlying mass. On MR imaging, a torsed ovary appears enlarged and edematous with increased stromal signal intensity on T2-weighted images [52] (fig. 16.12).

Cervical carcinoma in association with pregnancy is rare, with an incidence of approximately 1 per 1200–10,000 pregnancies. The association of cervical carcinoma with pregnancy, however, raises difficult management issues. MRI is currently the best imaging modality for evaluating pregnant patients with cervical carcinoma (fig. 16.13). With close surveillance, deliberate delay of therapy to achieve fetal maturity is a reasonable option for patients with early-stage cancer, since tumor characteristics and maternal survival are not adversely affected by pregnancy [53]. Other cervical masses may also be elucidated with MRI, such as cervical fibroids (fig. 16.14) or cervical endometriosis, visualization of which may be enhanced with utilization of vaginal gel [54]. MR signal characteristics are varied, but endometriomas of the cervix often demonstrate intermediate to high signal intensity on T1-weighted images and lower signal intensity on T2-weighted images because of the presence of hemorrhage (fig. 16.15).

Other pelvic masses may also be further characterized with MRI (fig. 16.16). Of particular note in pregnancy is abdominal fibromatosis, a subset of abdominal desmoid tumors that occur in pregnancy, in the first

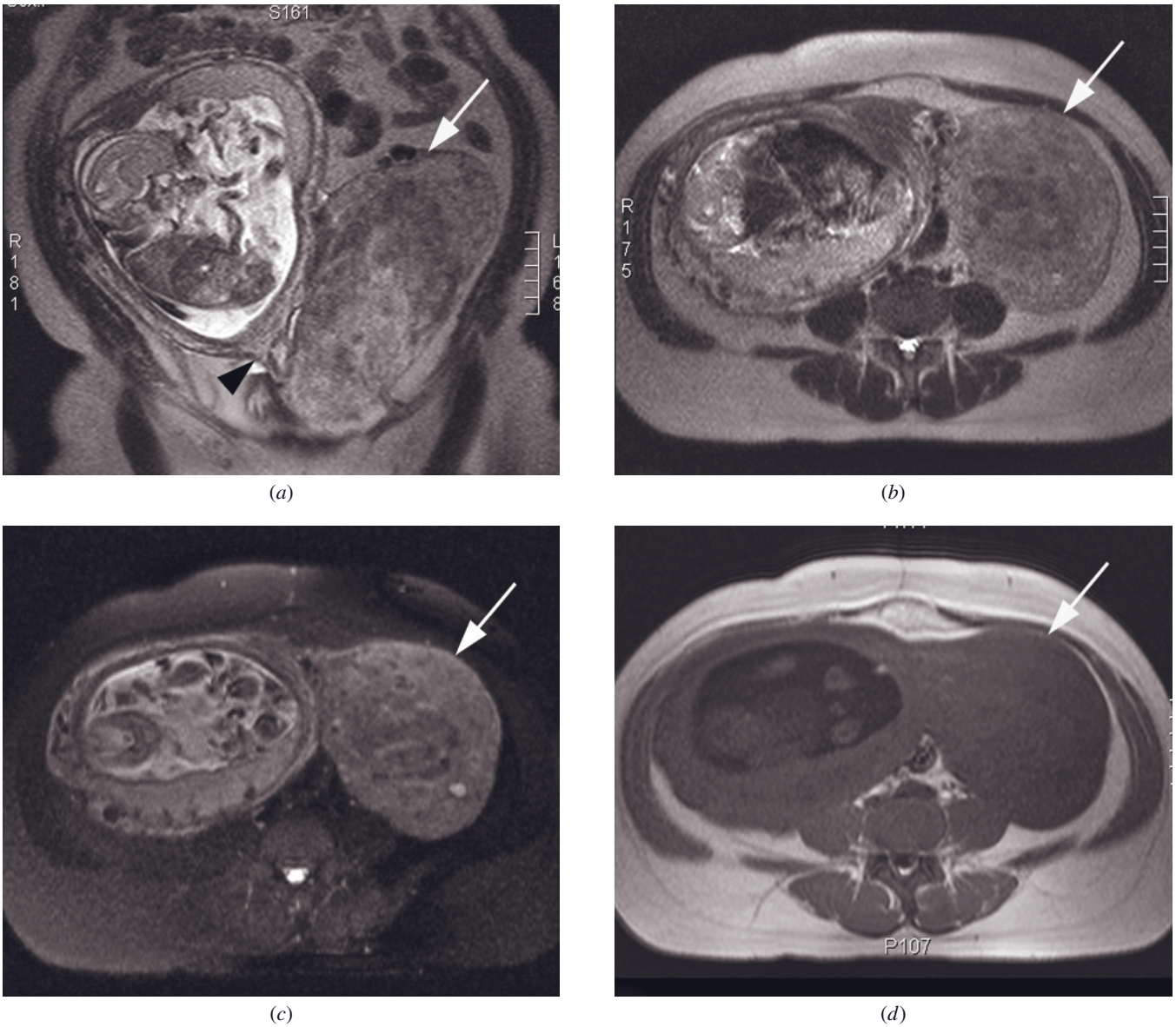

(*a*) (*b*) (*c*) (*d*)

FIG. 16.10 Large subserosal leiomyoma mimics an ovarian mass in a pregnant patient. Coronal (*a*) and transverse (*b*) T2-weighted SS-ETSE, fat-suppressed T2-weighted SS-ETSE (*c*), and T1-weighted gradient-echo (*d*) images show a large mass arising from the uterus (arrow). Although signal intensity on T2-weighted images (*a–c*) is higher than seen in a typical fibroid, the myometrium is splayed (arrowheads) around the mass, indicating uterine origin. A fat plane is not observed between the mass and the uterus on the T1-weighted image (*d*).

year postpartum, and in women taking oral contraceptives (fig. 16.17). It is thought that estrogen serves as a growth factor for these tumors. The most frequent locations are the rectus abdominus and internal oblique muscles of the anterior abdominal wall. On MRI, these lesions are typically heterogeneous in signal intensity. Lesions in the early stage are more cellular and demonstrate T2 hyperintensity. As the lesion evolves, it contains more collagen and less extracellular space and thus becomes less intense on T2-weighted images. Bands of T2 hypointensity are seen in the majority of cases. Treatment is with wide excision; nonoperable tumors may be treated with radiation and chemotherapy. There is a high rate of local recurrence. Spontaneous regression has been reported to occur after menopause or oophorectomy [55, 56].

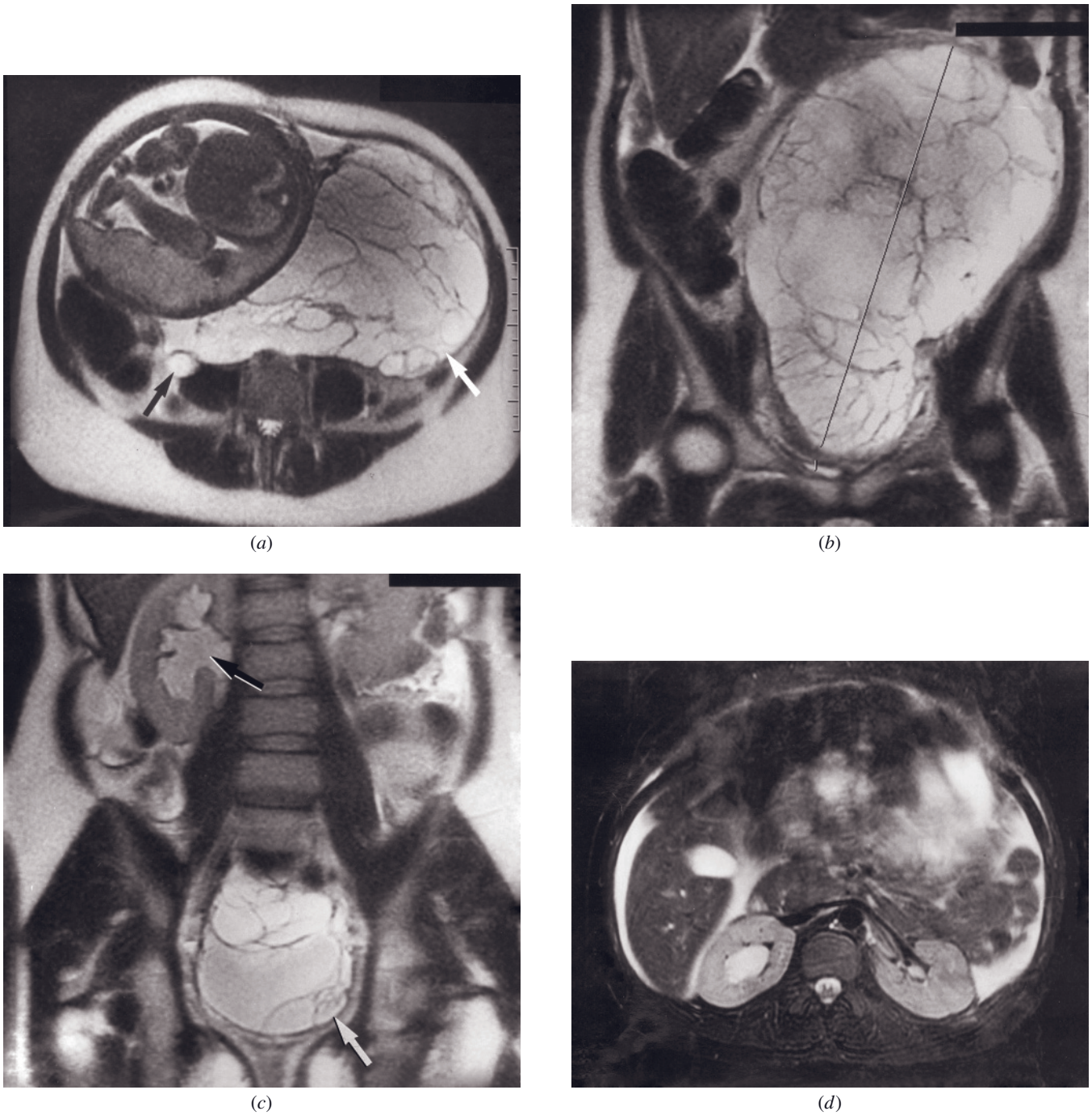

FIG. 16.11 Ovarian carcinoma in a pregnant patient at 28 weeks of gestation. Transverse (*a*) and coronal (*b*, *c*) T2-weighted single-shot ETSE and transverse fat-suppressed T2-weighted ETSE (*d*) images of the maternal abdomen. A large mainly cystic lesion with a maximal diameter of 27 cm is seen (white arrows, *a*, *c*); the pregnant uterus is displaced to the right. Ascites is present (*d*). Maternal hydronephrosis and dilated ureter (black arrows, *a*, *c*) are seen on the right side.

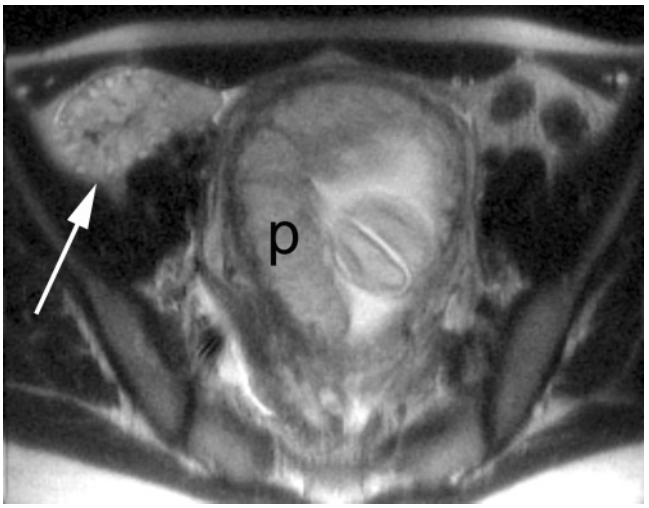

FIG. 16.12 Ovarian torsion in a pregnant patient. Transverse T2-weighted SS-ETSE shows an enlarged, edematous right ovary (arrow) with small peripheral follicles (p, placenta).

(*a*)

(*b*)

FIG. 16.13 Cervical carcinoma. Sagittal T2-weighted ETSE (*a*) and gadolinium-enhanced fat-suppressed T1-weighted gradient-echo (*b*) images in a pregnant patient at 12 weeks of gestation. A 3-cm mass within the anterior cervix is of intermediate T2 signal intensity and enhances to a lesser degree than the adjacent cervix and myometrium. On transverse images, there was no definite evidence of parametrial extension (not shown). Note distension of vagina with vaginal gel (Surgilube), which improves visualization of cervical mass.

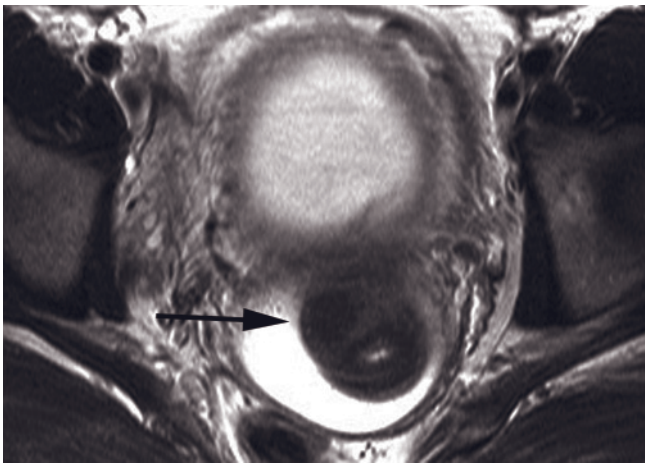

(*a*)

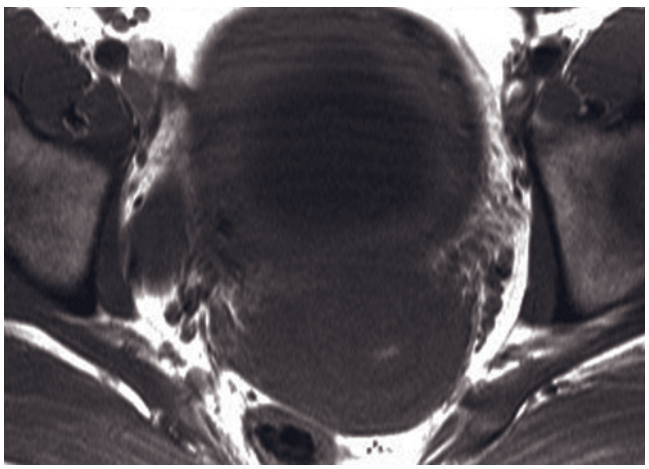

(*b*)

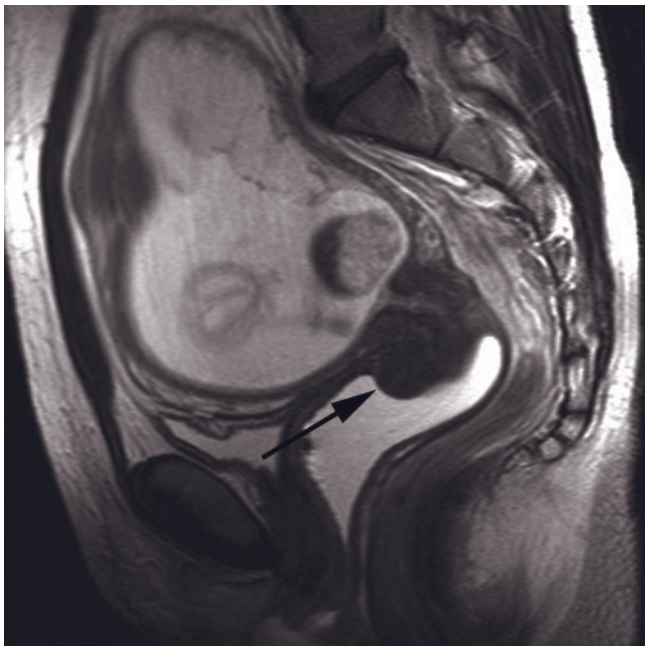

(*c*)

FIG. 16.14 Cervical fibroid. Transverse T2-weighted (*a*), transverse T1-weighted (*b*), and sagittal T2-weighted (*c*) TSE images in a pregnant patient at 14 weeks of gestation performed to evaluate cervical lesion seen on ultrasound. A well-circumscribed slightly T2-hypointense, T1-isointense mass is seen within the right anterior cervix (arrows, *a*, *c*), consistent with a cervical fibroid.

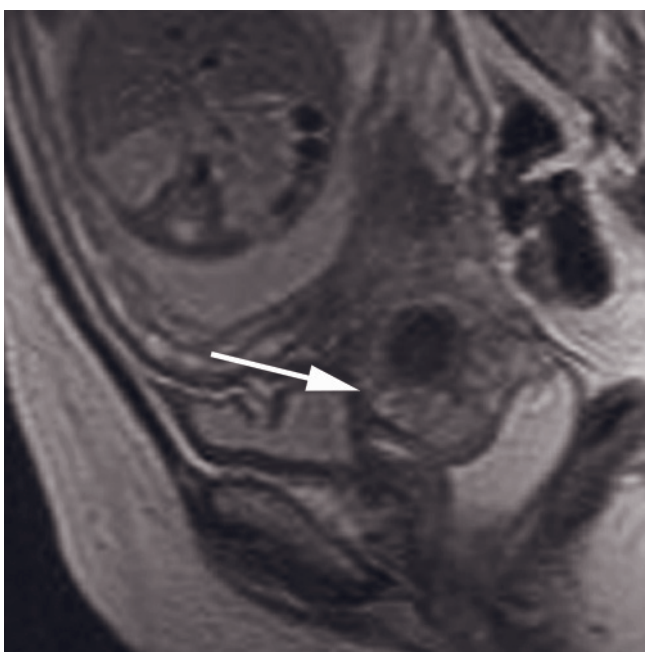

(*a*)

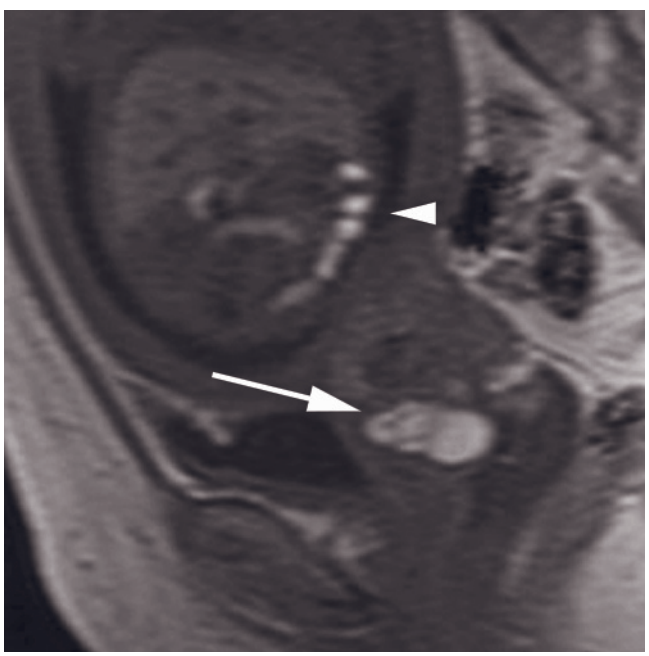

(*b*)

FIG. 16.15 Cervical endometriosis. Sagittal T2-weighted (*a*), sagittal T1-weighted (*b*), transverse T2-weighted (*c*), and transverse T1-weighted (*d*) TSE images of the cervix in a patient 26 weeks pregnant who presented with vaginal bleeding. A polypoid cervical mass was seen on physical exam. Images demonstrate a multilobulated mass centered at the posterior and right lateral cervix that extends into the posterolateral fornix. This demonstrates predominantly T2 hyperintensity and areas of T1 hyperintensity. Some blood products are noted in the cervical canal. Note also T1 hyperintense meconium in the fetal bowel (arrowhead, *b*).

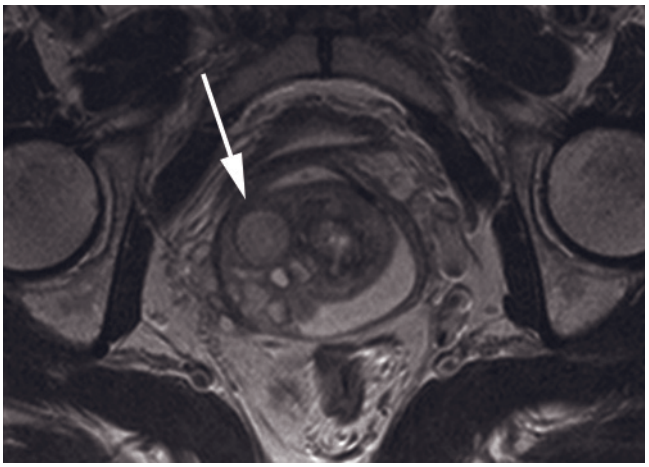

(*c*)

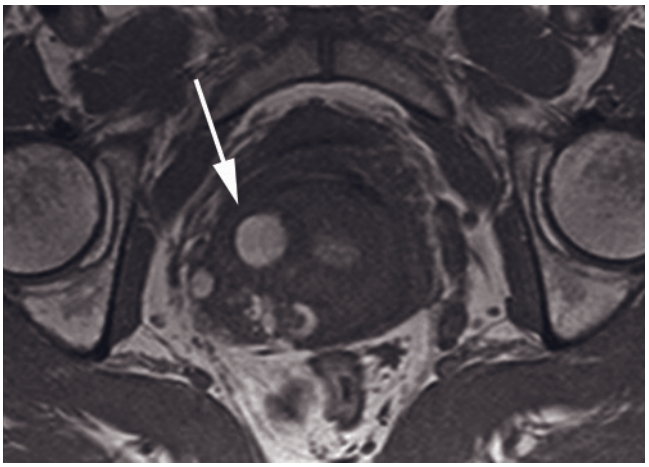

(*d*)

FIG. 16.15 (*Continued*)

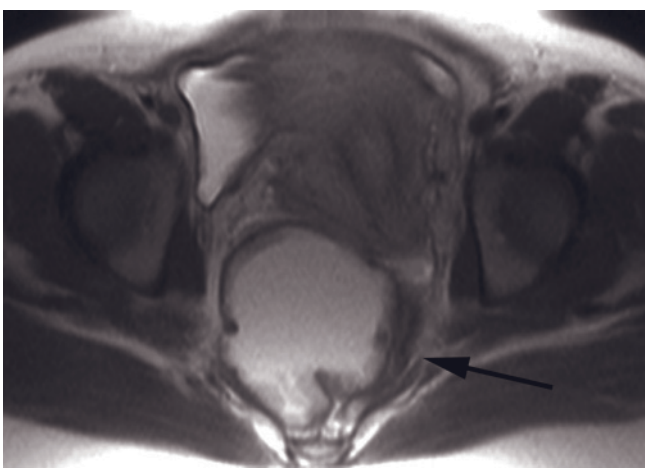

(*a*)

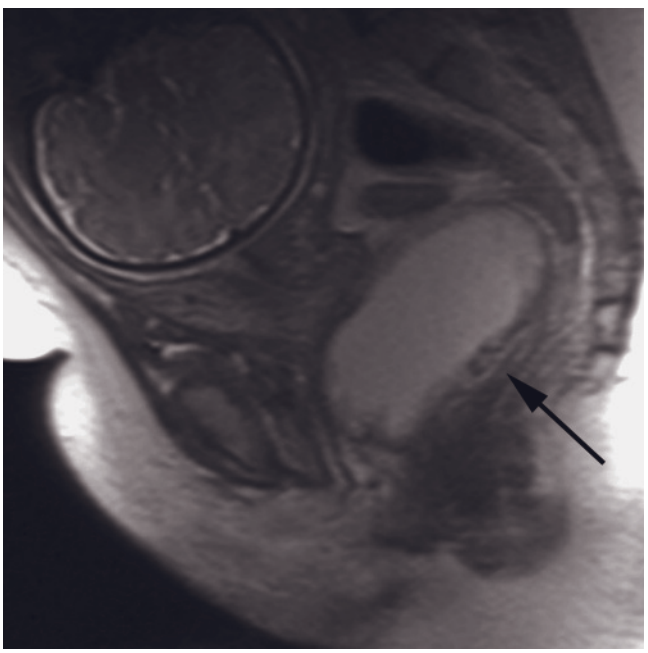

(*b*)

(*c*)

FIG. 16.16 Pelvic masses in two different patients. Transverse (*a*) and sagittal (*b*) T2-weighted SS-ETSE images and transverse fat-suppressed T1-weighted 3D gradient-echo image (*c*) in a patient 37 weeks pregnant. An irregular, 10-cm lobulated mass posterior to the vagina and anterior to the rectum (arrows) extends into the right ischiorectal fossa and demonstrates high fluid content and a thick wall. Increased T1 signal is present within the periphery of the mass. Pathology revealed a perivaginal sacrococcygeal teratoma. Coronal T2-weighted SS-ETSE images (*d*, *e*) to evaluate abdominal pain in a patient 18 weeks pregnant with a history of malignant peripheral nerve sheath tumor reveals peritoneal carcinomatosis. There is a large volume of ascites and nodular thickening along the peritoneum. Gravid uterus is noted (U, *e*).

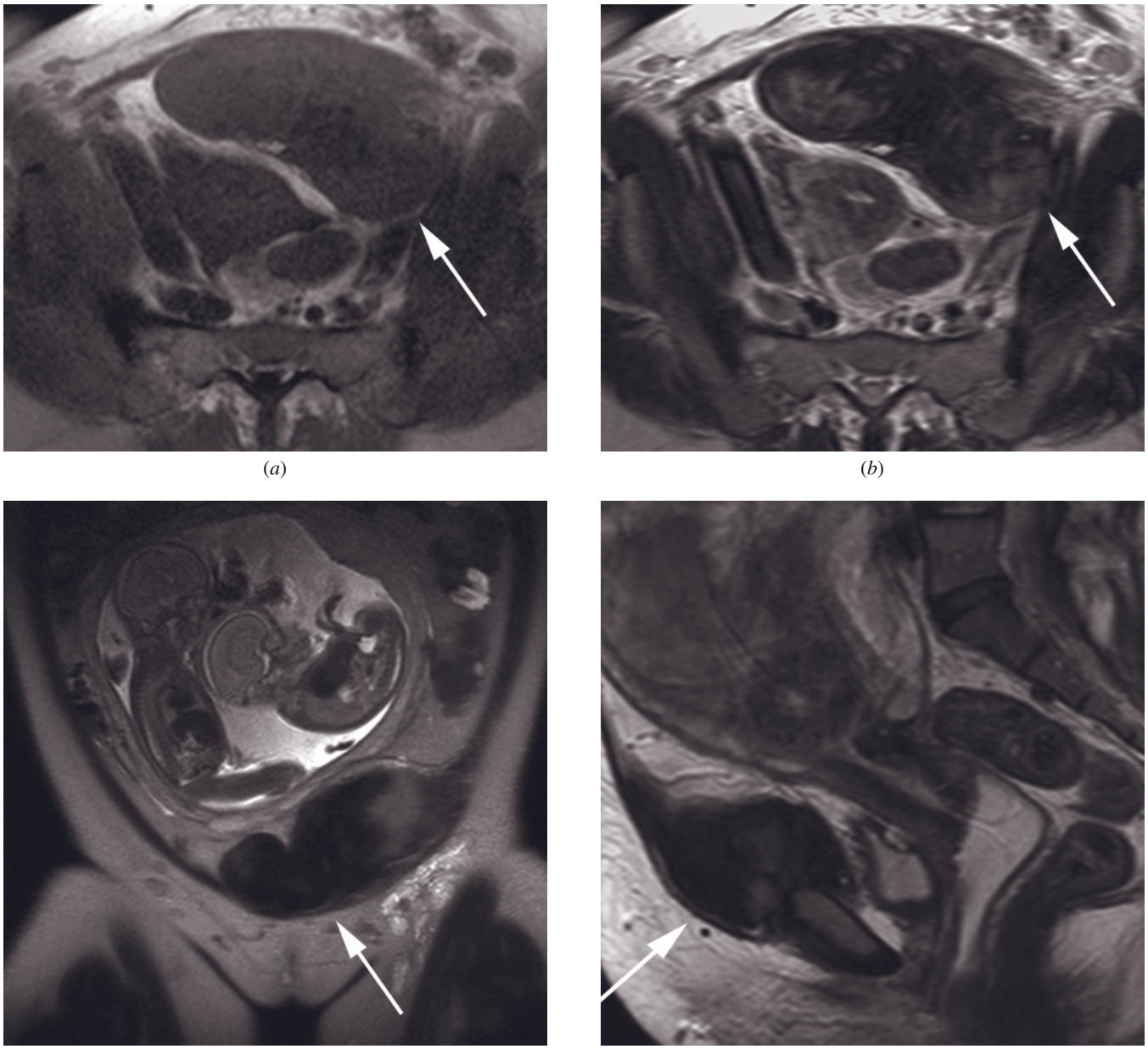

(*a*) (*b*) (*c*) (*d*)

FIG. 16.17 Abdominal fibromatosis. Transverse T1-weighted (*a*) and transverse (*b*), coronal (*c*), and sagittal (*d*) T2-weighted images demonstrate a mass arising from the anterior abdominal wall musculature (arrows) that is predominantly hypointense on both T1- and T2-weighted images. Twin gestation is visualized (*c*).

POSTPARTUM UTERUS

The greatest reduction in size of the uterine corpus and cervix occurs within 1 week after delivery. The uterus has returned to its normal size by 6 months (fig. 16.18). The presence of acute or subacute blood in the endometrial cavity is a common occurrence in the immediate postpartum period and resolves usually within 1 week. The junctional zone will be visualized again 2 weeks after delivery, with a complete reconstitution after 6 months. A small amount of free pelvic fluid is a normal finding in the postpartum patient [57, 58].

In women undergoing cesarean section, the incision is typically seen as an area of moderately high signal intensity on both T1- and T2-weighted sequences, suggesting the presence of a subacute hematoma within the myometrium, although the signal intensity may be variable [57] (fig. 16.19).

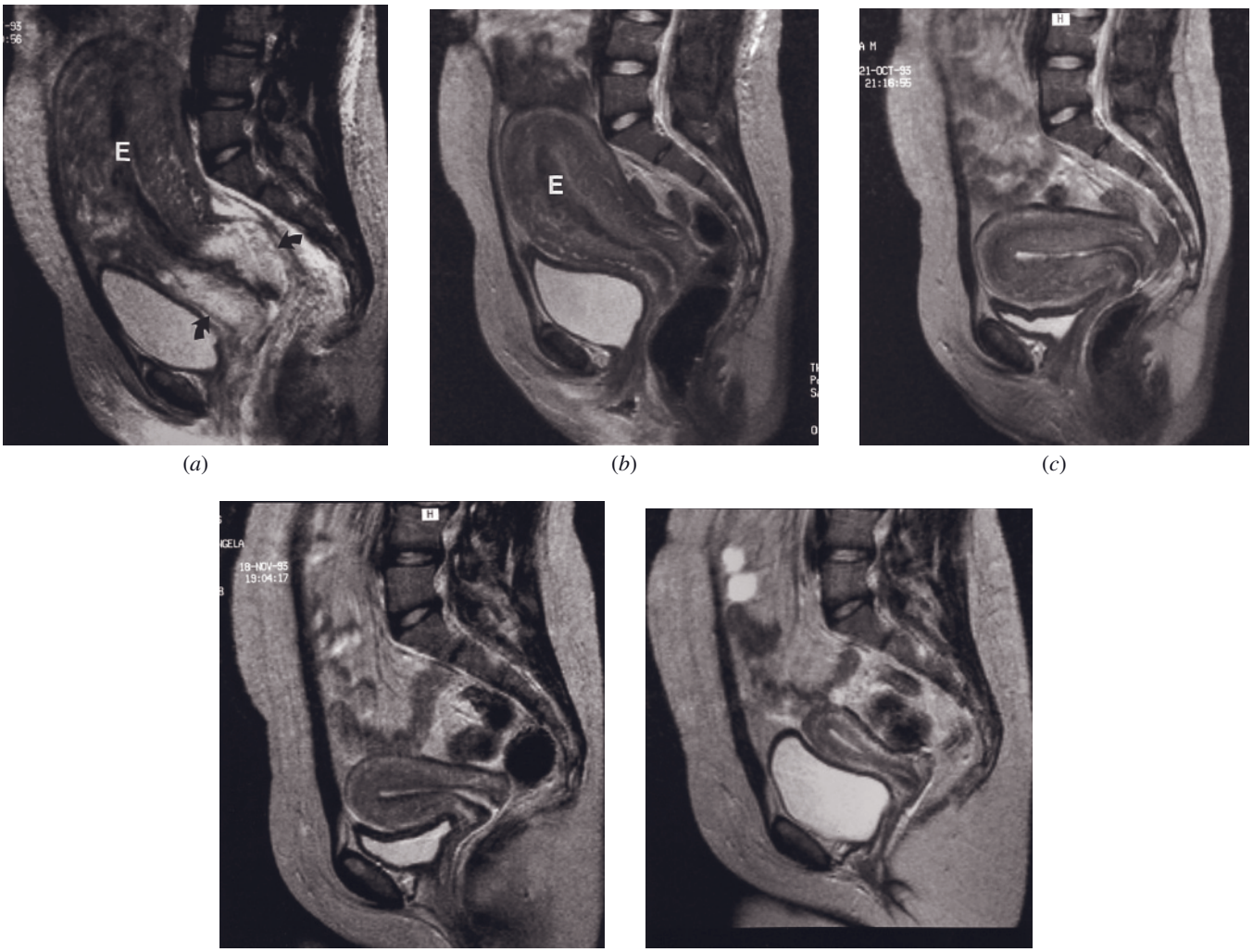

FIG. 16.18 Postpartum uterus. Sagittal T2-weighted echo-train spin-echo sequence (*a*) 24 hours, (*b*) 1 week, (*c*) 1 month, (*d*) 2 months and (*e*) 6 months after delivery.Acute and/or subacute blood is shown within the endometrial cavity (E) in the first week postpartum (*a,b*).The outer cervical stroma or smooth-muscle layer is hyperintense (curved arrows, *a*) in the first 30 hours after delivery. The inner fibrous stroma, however, remains hypointense throughout the postpartum period (*a–e*). The myometrium is of intermediate and heterogeneous signal intensity during the early postpartum period (*a–c*). By 6 months, complete reconstitution of the junctional zone (JZ) is evident (*e*). Note the gradual decreases in size of the uterus from (*a*) to (*e*).

FIG. 16.19 Postcesarean section uterus. Sagittal T2-weighted fat-suppressed echo-train spin-echo sequence in a patient 5 days after cesarean section. A hypointense scar is visible in the lower uterine segment (small arrows), as well as a bladder flap (curved arrow). The low signal intensity of the endometrial cavity (E) is due to the presence of acute and/or subacute blood. The lack of zonal differentiation of the myometrium are normal findings in the early postpartum period. Bl, bladder.

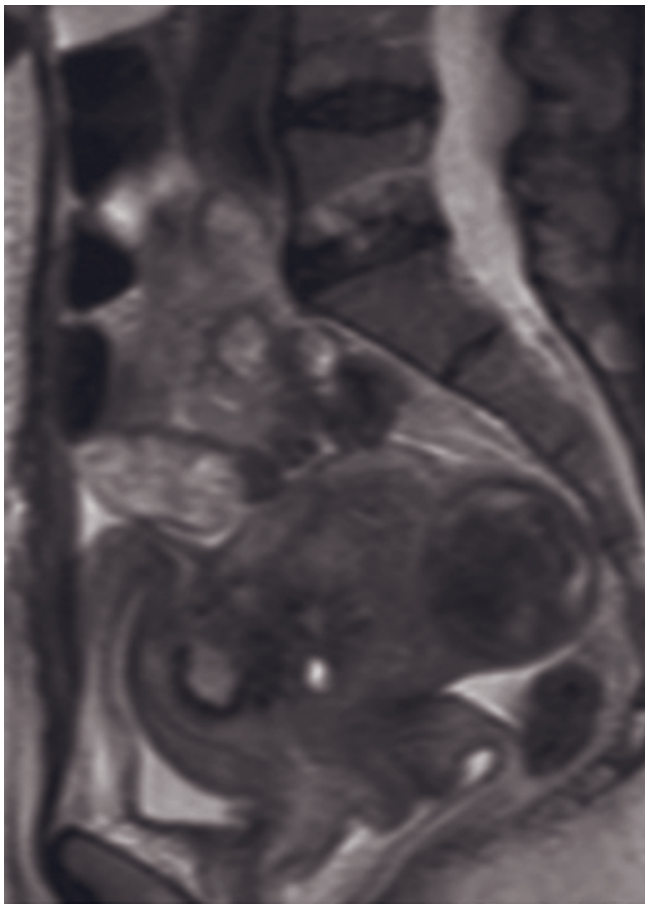

(*a*)

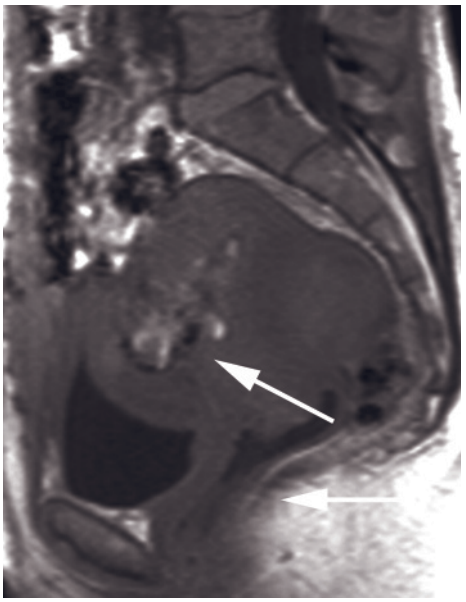

(*b*)

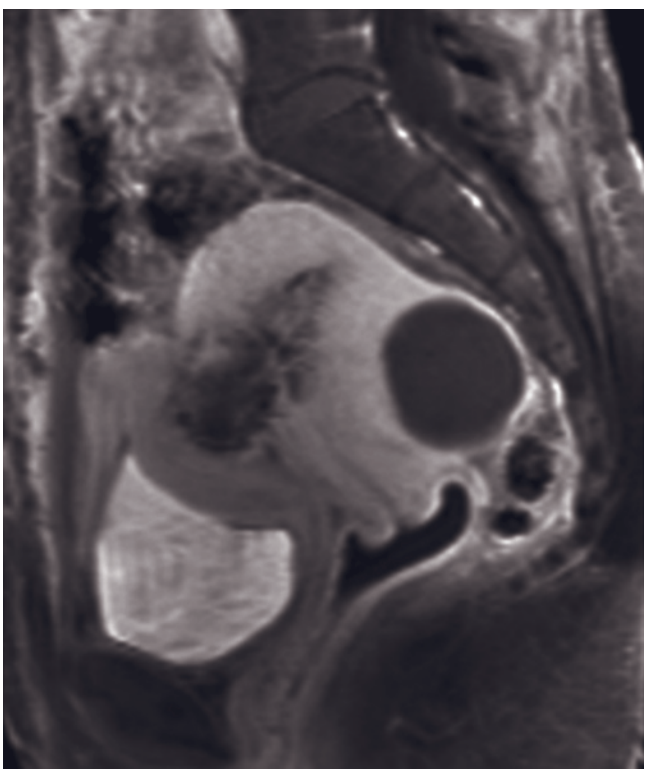

(*c*)

FIG. 16.20 Uterine dehiscence. Sagittal T2 (*a*)-, precontrast T1 (*b*)-, and delayed postcontrast fat-suppressed T1 (*c*)-weighted images in a patient with pain and fever after cesarean section. A large defect is present in the anterior uterine wall at the site of prior caesarean section. Blood products with T1 hyperintensity are seen extending through this defect before contrast administration (arrow, *b*). Postcontrast image clearly shows the large gap in enhancing myometrium. A nonenhancing uterine fibroid is incidentally noted posteriorly.

During the postpartum period, uterine dehiscence may occur at the site of cesarean section (fig. 16.20). This is well depicted on MRI as a transmural gap at the section site in the anterior uterus, and may be complicated by hematoma or abscess formation. An imaging plane perpendicular to the incision best illustrates the myometrial gap [59].

A prominent cesarean section scar may be identified in the anterior lower uterine segment on MRI (fig. 16.21), with marked thinning of the myometrium and fluid within the scar, consistent with a cesarean scar defect as described on ultrasound [60]. A cesarean scar pregnancy (fig. 16.22) is a rare form of ectopic pregnancy that may occur after cesarean section. In this

FIG. 16.21 Cesarean scar defect. Sagittal T2-weighted SS-ETSE image demonstrates a prominent scar with marked myometrial thinning in the anterior lower uterine segment, at site of prior caesarean section (arrow).

case, the gestational sac is completely surrounded by myometrium and fibrous scar tissue, likely due to invasion of the myometrium via a microtubular tract between the cesarean section scar and the endometrial canal. These have a high risk of uterine rupture and associated hemorrhage. Severe abdominal pain and profuse vaginal bleeding suggest impending rupture, and hemodynamic instability or collapse suggests rupture [61].

Ovarian vein thrombosis is a relatively rare complication, often associated with postpartum endometritis. It occurs most commonly in the right ovarian vein. The diagnosis of ovarian vein thrombosis is frequently difficult with ultrasound, and MRI is a good alternative to CT in such cases [57, 62]. Retained products of conception are often readily detected by ultrasound, but if ultrasound is limited or indeterminate, MRI provides accurate diagnosis (fig. 16.23). Retained products of conception are extremely hypervascular and seen together with blood products in the endometrial canal. Dynamic gadolinium-enhanced imaging is important for diagnosis. Gestational trophoblastic disease may have a similar appearance; however, the differentiation is easily made by β-human chorionic gonadotropin hormone levels. Retained products of conception may also appear as a hypervascular mass in the myometrium, mimicking acquired uterine arteriovenous malformation. The latter is an important diagnosis to consider because treatment with dilatation and curettage may aggravate rather than end uterine hemorrhage [63].

FETAL IMAGING

At present, ultrasonography is an inexpensive and widely available real-time investigation and remains the imaging technique of choice for prenatal assessment of the fetus. Since the development of ultrafast sequences, the role of fetal MRI has increased. MRI demonstrates fetal anatomy in detail. Major developmental structures of the fetus, particularly the central nervous system (CNS), lungs, and major abdominal viscera, can be adequately evaluated by MRI as early as the beginning of the second trimester. Its diagnostic accuracy is superior to sonography in selected cases, and in complex fetal disorders [8, 9, 12, 64, 65]. MRI is particularly helpful in CNS anomalies and, to a lesser extent, thoracic anomalies [12, 65, 66]. As a result, the majority of clinically indicated obstetric MR imaging involves either further evaluation of the fetal brain or the assessment of complex malformations and syndromes. MRI is also helpful for planning in utero surgical intervention.

Ultrafast T2-weighted sequences and T2-/T1-weighted steady-state free-precession images are the main techniques used for fetal MRI. No fetal sedation is needed. Additional imaging with T1-weighted gradient echo is helpful in certain cases for tissue characterization or detection of hemorrhage. T2*-weighted gradient-echo sequences may also help confirm the presence of blood [67]. Some centers are using diffusion-weighted imaging and MR spectroscopy for further evaluation of the fetal brain. MR fetography (a heavily T2-weighted thick slab adapted from MRCP) may be used as a scout sequence and provides information about fetal contours, extremities, and spinal dysraphia [21]. Gadolinium is generally not recommended for fetal imaging, but may be indicated for maternal disease. Before contrast administration, images should be reviewed, and there must be careful consideration of potential benefit to the pregnant patient versus theoretical risk to the fetus. When contrast is needed, informed consent should be obtained.

Normal Anatomy

Central Nervous System

Changes in fetal brain maturation proceed through different stages in a predictable fashion that can be reliably evaluated with fast T2-weighted imaging or steady-state free-precession images such as True-FISP. At 12–23 weeks of gestation, the brain demonstrates a smooth surface except for the interhemispheric fissure (fig. 16.24). Two or three layers in the cerebral cortex can be delineated at this time. At 24–26 weeks, the immature cortex, the intermediate zone, and the germinal matrix can be differentiated. The germinal matrix appears as a band of T2 hypointensity/T1 hyperintensity

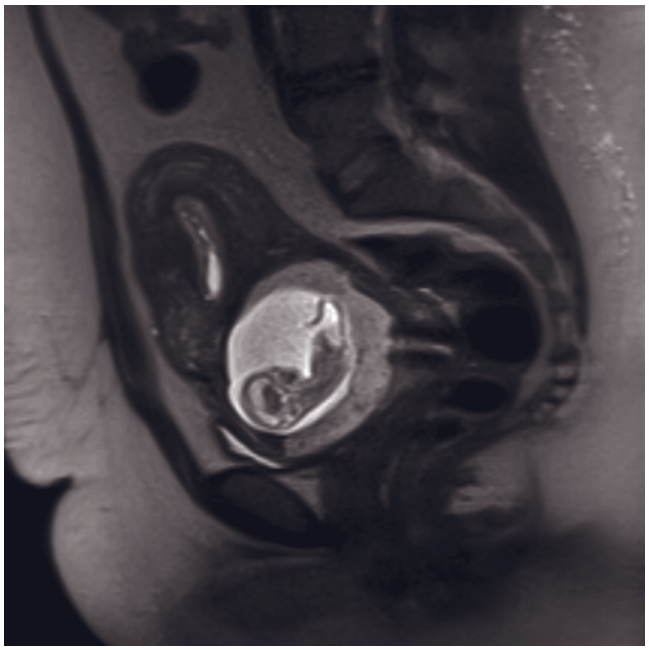

(*a*)

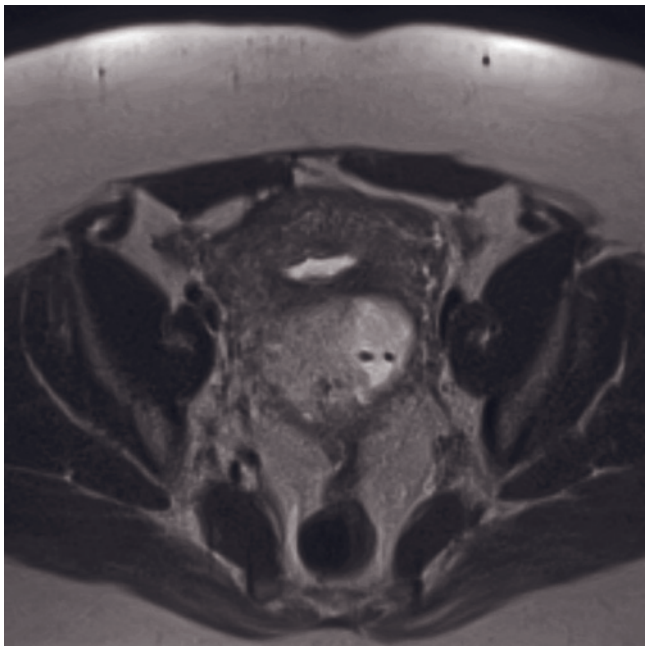

(*b*)

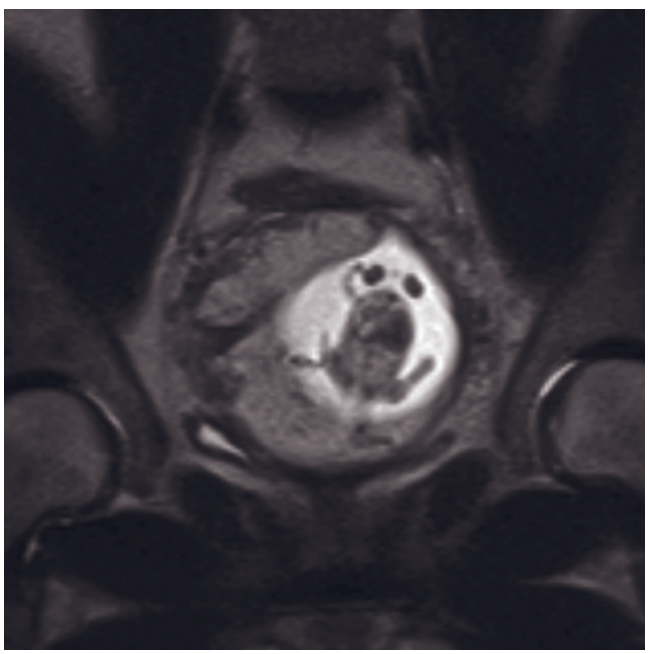

(*c*)

FIG. 16.22 Cesarean scar pregnancy. Sagittal (*a*), transverse (*b*), and coronal (*c*) T2-weighted SS-ETSE images demonstrate a gestational sac containing a fetus ectopically located within the lower uterine segment of the uterus. The gestational sac is surrounded by myometrium and uterine scar tissue rather than being located within the endometrium, as is seen with scar pregnancies.

surrounding the ventricles in early gestation until the third trimester, when it gradually regresses to be present only in the caudothalamic groove at term. The cortical plate is seen as a band of T2 hypointensity/T1 hyperintensity at the periphery of the brain. The intervening parenchyma is of higher signal intensity on T2-weighted images but contains three visible layers as well, usually discernable between 20 and 28 weeks of gestational age [67].

The sylvian fissure appears first as a smooth, curved, wide infolding of the brain before 18 weeks and progresses to a more angulated appearance by 23 weeks (figs. 16.24 and 16.25). Delay in maturation of the sylvian fissure is a sign of abnormal development [67]. This is best assessed on coronal and axial images. The parieto-occipital sulcus may be seen by 22–23 weeks, followed by the calcarine and cingulate sulcus at 24–25 weeks and the central sulcus at 27 weeks [21]. Sulcation

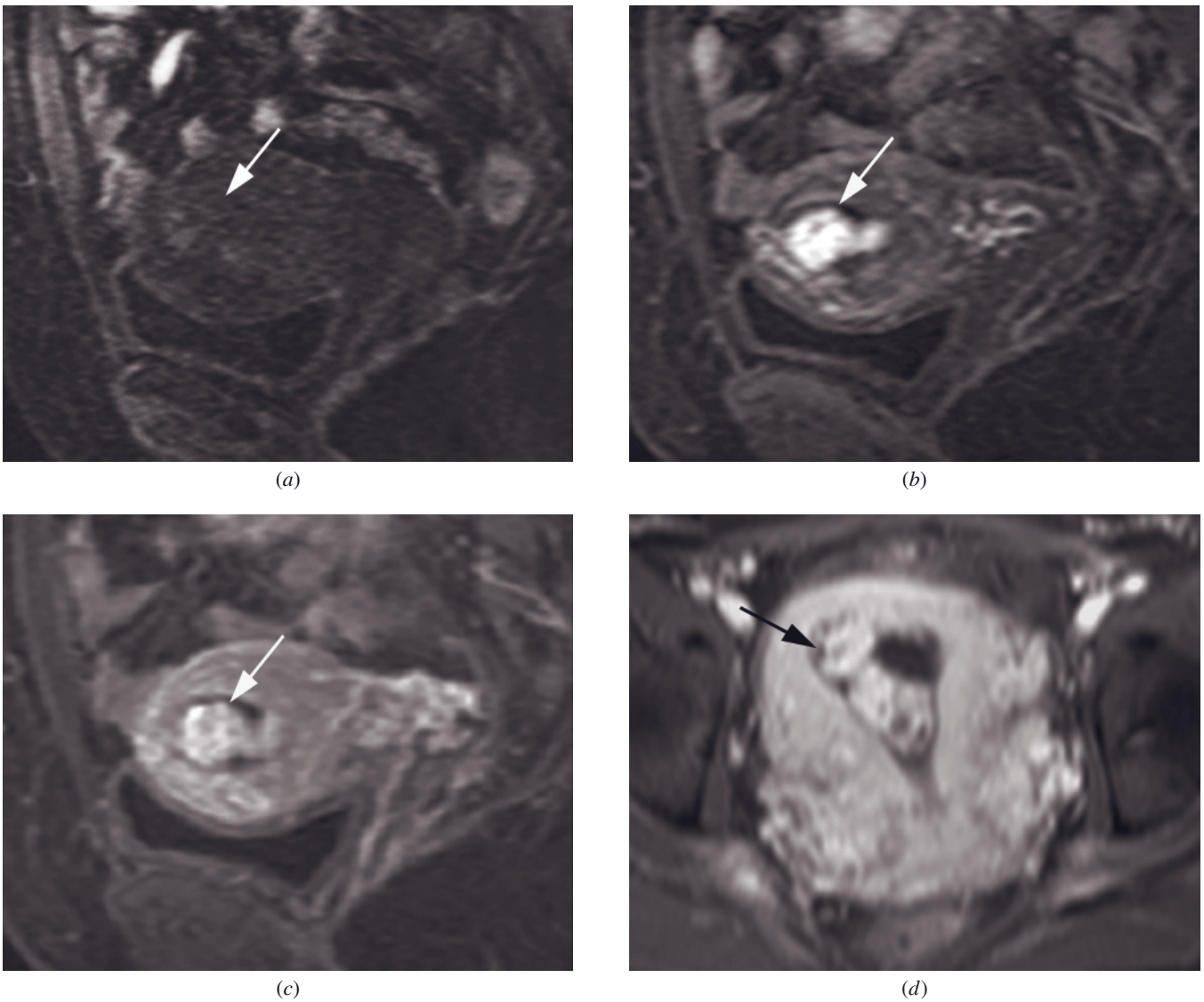

FIG. 16.23 Retained products of conception. Sagittal fat-suppressed T1-weighted gradient echo images pre- (*a*) and post-gadolinium in arterial (*b*) and venous (*c*) phases, and transverse delayed postgadolinium fat suppressed T1-weighted gradient echo image (*d*) in a postpartum patient with vaginal bleeding. There is mass within the endometrial canal that is low signal intensity pre-contrast (arrow, *a*) and shows early and intense enhancement (arrow, *b*).The mass retains contrast on delayed images (arrow, *c*, *d*).

in the whole cerebral cortex is seen from 30 weeks on, whereas infolding of the cortex and opercular formation will not be seen before 33 weeks (fig. 16.25).

At 23 weeks, cerebral ventricles appear relatively large, corresponding to the normal fetal hydrocephalus, gradually becoming smaller thereafter. The atria of the lateral ventricles remain relatively stable in size from 15 to 35 weeks gestation. There is general agreement that the size of the fetal lateral ventricles should be less than 10 mm at the level of the atria when measured in an axial plane by ultrasound [68–70]. In comparing sonographic and MR measurements of the atria, MR tends to result in a slightly smaller measurement; however, the definition of ventriculomegaly remains unchanged at >10 mm when a cutoff of 2 standard deviations above the mean is employed [71]. Sonographic measurements of the third ventricle in the axial plane have revealed an upper limit of normal ranging from 1.0–1.2 mm at 12 weeks to 3.5–3.6 mm at term [72, 73], although no MR correlation has yet been performed. The cisterna magna may be difficult to visualize in the third trimester with ultrasound because of attenuation from the calvarium at the skull base; however, this is well visualized with MRI throughout the second and third trimesters [71].

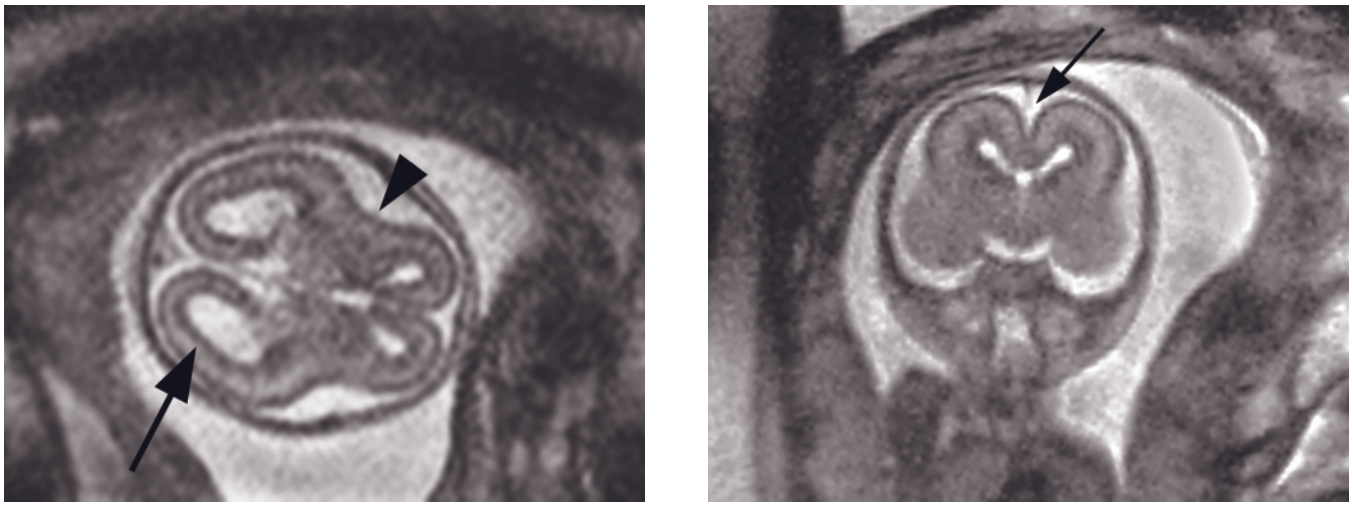

(*a*) (*b*)

FIG. 16.24 Normal fetal brain, 18 weeks of gestation. Transverse (*a*) and coronal (*b*) images through the fetal brain show three cortical layers, a smooth cortex with slight concavity at the sylvian fissure (arrowhead, *a*) and normal prominence of the lateral ventricles (arrow, *a*), which decreases after 23 weeks. The falx is partially visualized (arrow, *b*) superior to the interhemispheric fissure.

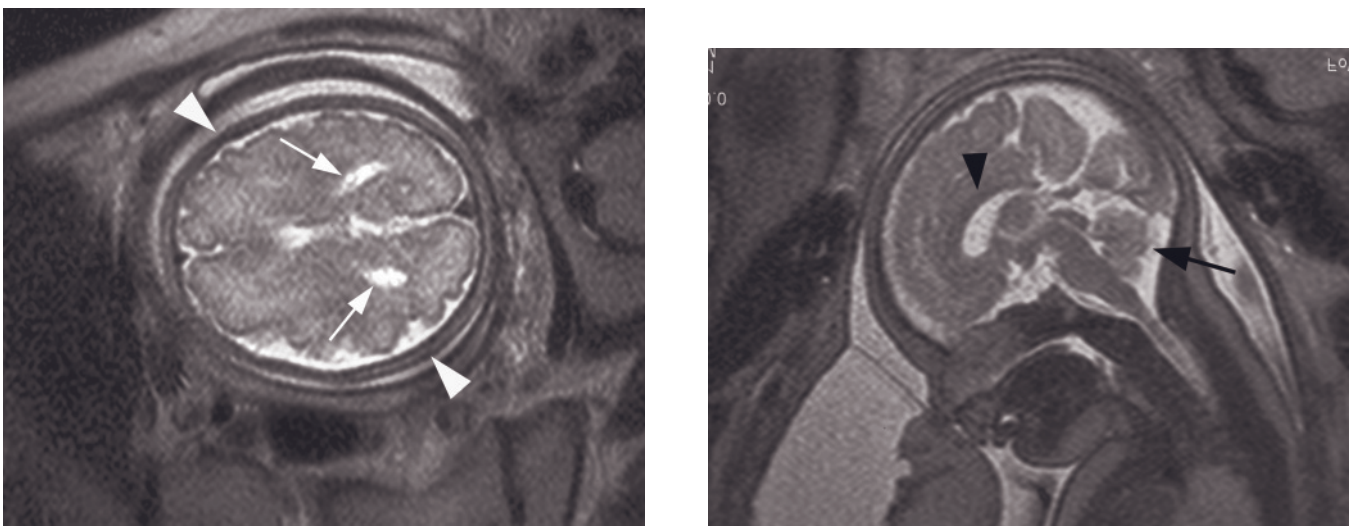

(*a*) (*b*)

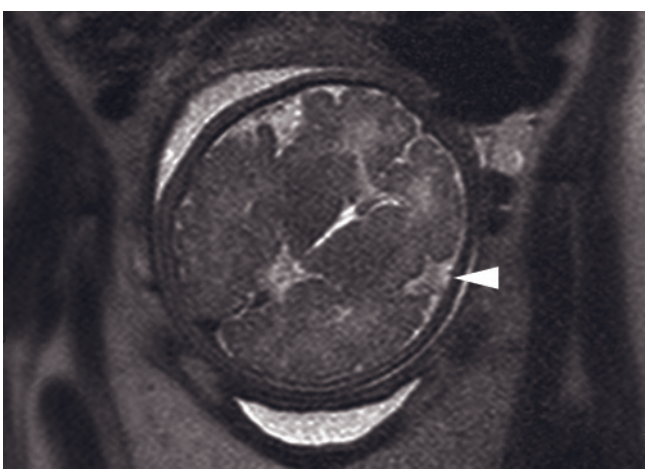

(*c*)

FIG. 16.25 Normal fetal brain, third trimester. Transverse (*a*) and sagittal (*b*) SS-ETSE images of the fetal head. The fetal skull (arrowheads, *a*) and the cerebral hemispheres are well delineated. Cerebral ventricles appear relatively smaller than in the second trimester (arrows, *a*), and gyral formation is seen. A normal cerebellum is seen (arrow, *b*) as well as a normal corpus callosum (arrowhead, *b*). Transverse SS-ETSE image (*c*) of the fetal head in a different patient shows the normal angulation of the sylvian fissure in the third trimester. Compare this to the smooth, wide curve of the 18-week brain in fig. 16.24*a*.

The subarachnoid space overlying the cortical convexities is slightly dilated at all gestational ages, most markedly at 21–26 weeks of gestation [11, 74].

The corpus callosum develops between 8 and 20 weeks of gestational age. With MR, the corpus callosum is normally visible by 20 weeks of gestation as a subtle T2 hypointensity (fig. 16.26). The corpus callosum forms in an orderly progression from genu to splenium, with the rostrum being formed last.

The cerebellar vermis is well depicted on midline sagittal and coronal images, whereas the cerebellar hemispheres may be better evaluated on axial or coronal views [67]. By 17.5 weeks of gestation, the primary fissure of the vermis should be visible, as should a normal fastigial point with an acute angle (fig. 16.27). The prepyramidal fissure is visible by 21 weeks, the preculminate fissure by 21–22 weeks, and the secondary fissure by 24 weeks. By 27 weeks, all vermian lobules and fissures are visible. The craniocaudal length of the vermis reaches that of the cerebellar hemispheres by 18–19 weeks. The vermis extends caudally to cover the roof of the fourth ventricle, completely covering it by

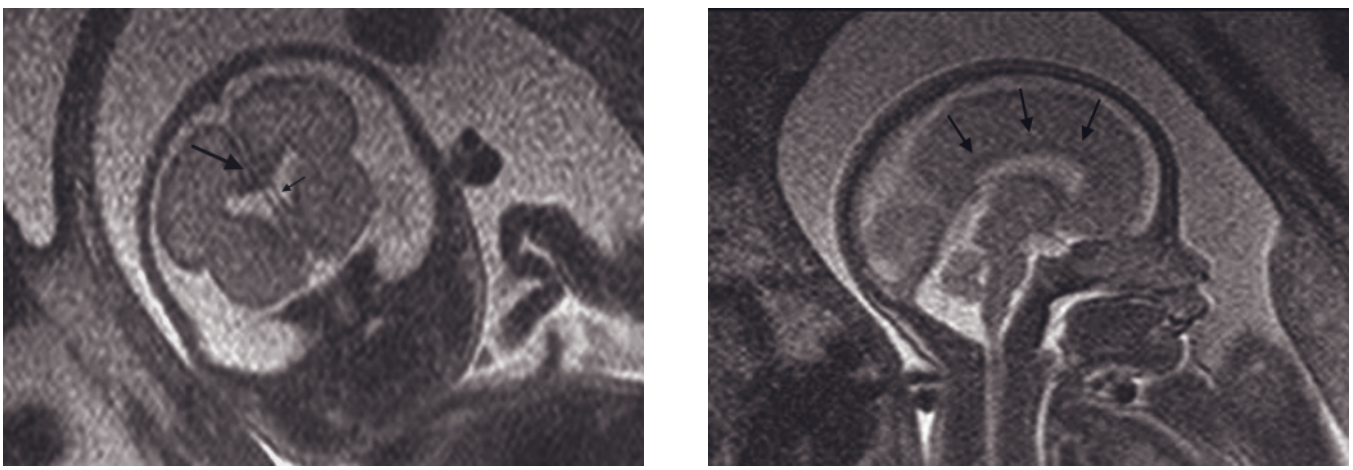

(*a*) (*b*)

FIG. 16.26 Normal corpus callosum. Coronal (*a*) and sagittal (*b*) T2-weighted SS-ETSE images of the fetal head demonstrate a normal corpus callosum at 25 weeks of gestation. The normal corpus callosum is seen as a subtle band of T2 hypointensity (large arrows, *a*, *b*). Note the normal cavum septum pellucidum (small arrow, *a*).

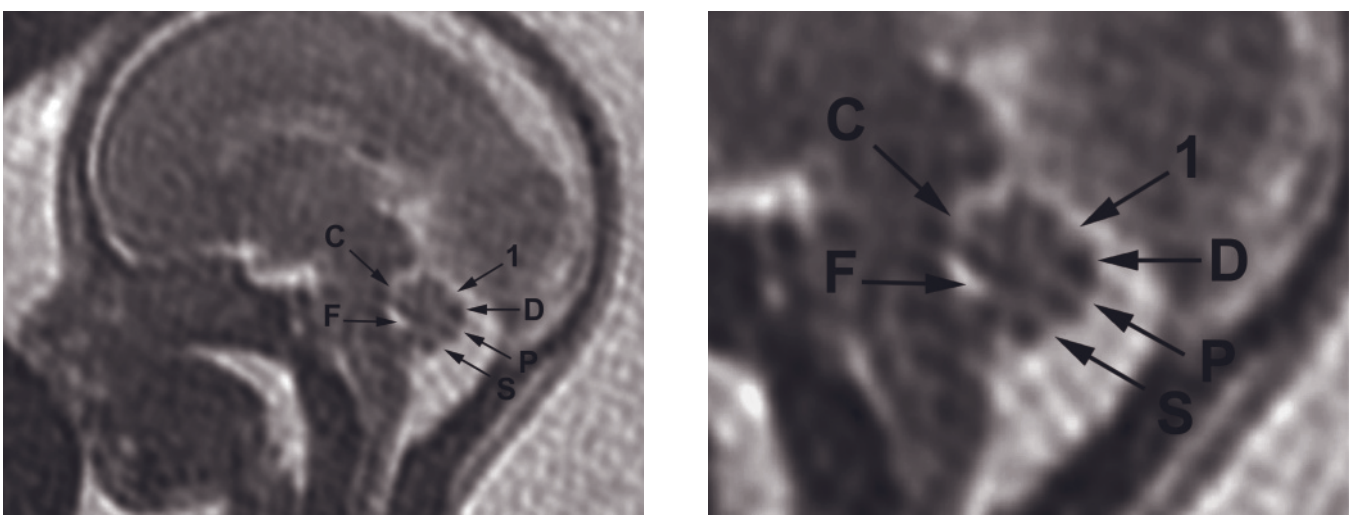

(*a*) (*b*)

FIG. 16.27 Normal cerebellar vermis. Sagittal T2-weighted SS-ETSE image of the cerebellar vermis (*a*) with magnified view for detail (*b*). Note the fastigial point (F), primary fissure (1), prepyramidal fissure (P), preculminate fissure (C), and secondary fissure (S) in this 19-week fetus.

22–24 weeks. The declive is the first lobule posterior to the primary fissure and appears as a focus of T2 hypointensity, important as a landmark for measuring the craniocaudal extent of the vermis [75].

Head and Neck

The nasopharynx and oropharynx are filled with amniotic fluid and are therefore hyperintense on T2-weighted images and hypointense on T1-weighted images [76]. On T2-weighted images, the normal palate appears as a hypointense stripe extending from the frenulum of the upper lip posteriorly to the nasal choanae where the nasopharynx and the oropharynx join together [77] (fig. 16.28). The thyroid gland is not well visualized on single-shot fast spin-echo sequences as it is isointense to surrounding structures; however it is visible as a hyperintense structure on T1-weighted fast spin-echo images [76].

Thorax

In the thorax, the lung and tracheobronchial tree, both filled with amniotic fluid, are hyperintense on T2-weighted imaging. The normal lungs are hyperintense to chest wall musculature and hypointense to amniotic fluid [12] (fig. 16.29). Sagittal and coronal images of the fetus at the level of the diaphragm clearly allow distinction between structures of the thorax and abdomen. The heart, pulmonary vasculature, and great vessels of the thorax appear as hypointense structures. At present, the value of fetal MRI for assessment of the heart is limited, because of the small size of the organ, the lack of flow information, and the fact that the fetal heart rate commonly exceeds 140 beats per minute, resulting in blurring of associated with cardiac pulsation [78]. The thymus is visible with intermediate signal intensity on single-shot fast spin-echo images [76].

Abdomen and Pelvis

The esophagus, stomach, and duodenum are filled with swallowed amniotic fluid, which acts as an intrinsic T2-hyperintense, T1-hypointense contrast agent. The distal ileum and colon are filled with T1- hyperintense, T2-hypointense meconium [21] (fig. 16.30). Between these two bowel segments mixing of these two fluids causes a gradual shift in signal intensities. With advancing gestational age, the amount of meconium gradually increases. The pattern of signal characteristics is helpful for identifying bowel segments and thereby estimating

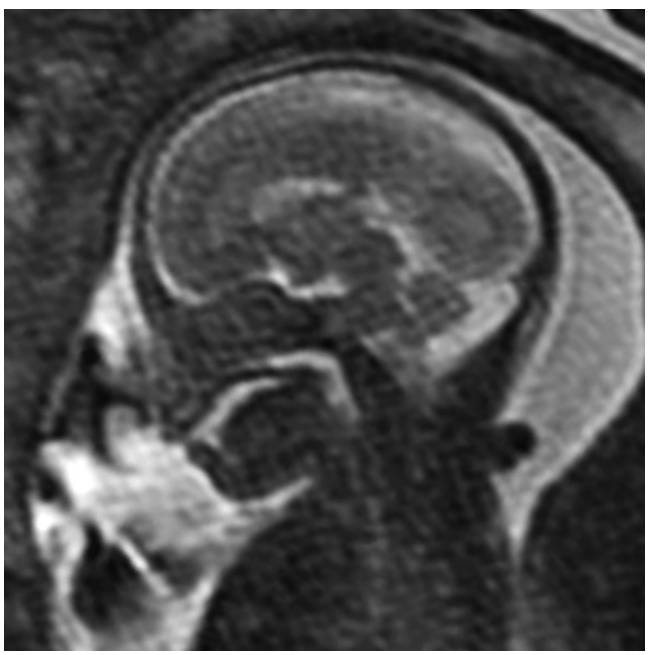

FIG. 16.28 Normal palate. Sagittal T2-weighted ETSE image shows the normal palate extending posteriorly from the frenulum of the upper lip as a continuous T2 hypointense arch, outlined by the normal fluid-filled nasopharynx and oropharynx. The palate continues posteriorly to the nasal choanae, where the nasopharynx and oropharynx meet.

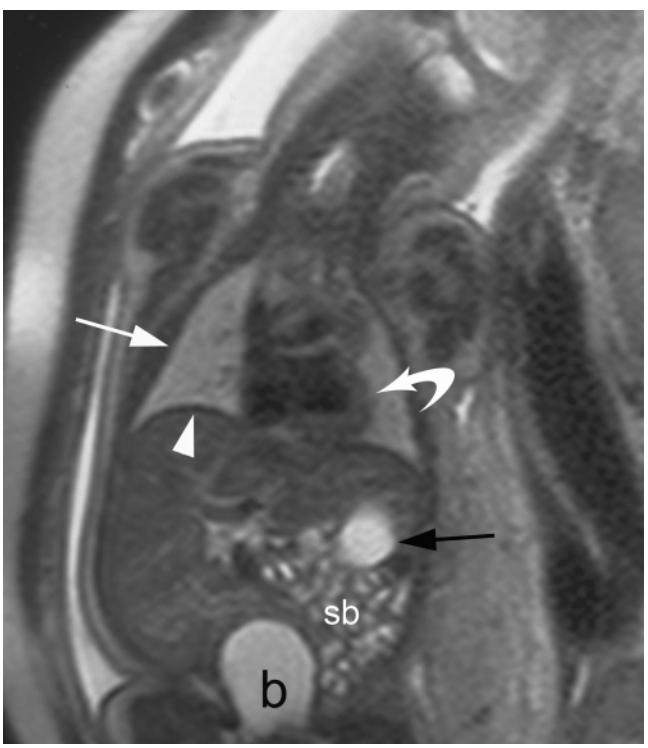

FIG. 16.29 Normal fetal torso, third trimester. Coronal T2-weighted SS-ETSE image of the fetus (rotated for orientation) show the fetal lungs (arrow), which are high signal intensity because of high fluid content, on either side of the thorax. The heart is visible, and the contrast between the signal-void area generated by the circulating blood and the intermediate signal intensity of the myocardium (curved arrow) allows assessment of ventricular wall thickness. The lung-liver interface outlines the diaphragm (arrowhead). The fetal stomach (black arrow), small bowel (sb), and bladder (b) are seen.

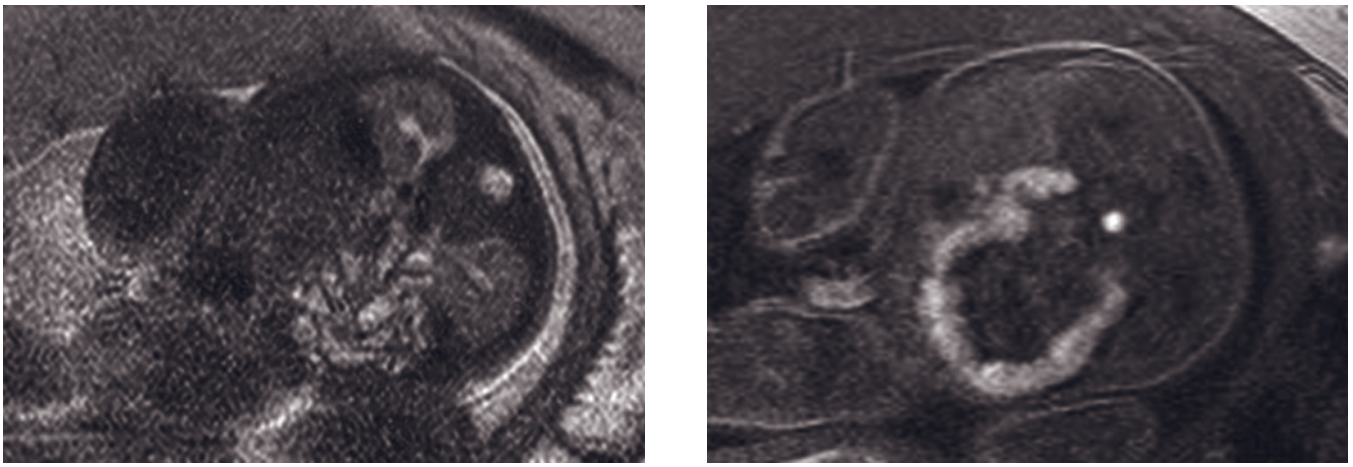

(*a*) (*b*)

FIG. 16.30 Normal bowel. Transverse T2-weighted ETSE (*a*) and transverse T1-weighted gradient echo (*b*) images of the fetal abdomen at 30 weeks show normal appearance to the bowel, with T2 hyperintense small bowel seen centrally that is T1-hypointense. The more distal, peripherally-located bowel demonstrates T1 hyperintensity and T2 hypointensity due to the presence of meconium.

the level of a suspected atresia. In addition, the high signal intensity of the colon relative to the abdominal organs on T1-weighted images allows maximal intensity projections of the colon [80].

The fetal gallbladder is also visible as a fluid-filled structure in the right upper quadrant of the abdomen [21]. The fetal liver is the largest organ in the body and is iso- to slightly hyperintense on T1-weighted images and of low to intermediate signal intensity on T2-weighted images. Early in development, the right and left lobes are symmetric in size owing to the distribution of the fetal circulation, whereas later in gestation the right lobe increases in size relative to the left [78, 80]. The spleen is similar in signal intensity to the liver and situated lateral to the stomach (fig. 16.31) [79].

The normal fetal kidneys are well defined and of intermediate signal intensity with hyperintense collecting systems on T2-weighted images (fig. 16.32). As the fetus matures, the lower-signal-intensity renal cortex becomes more readily distinguished from the higher-signal-intensity renal medulla [81]. The normal urinary bladder is also filled with fluid and easily identified on T2-weighted images. Occasionally, signal voids may be seen within the bladder because of ureteral jets [82]. The fetal adrenal glands may be identified in the suprarenal fossae and are of relatively lower T2 signal intensity.

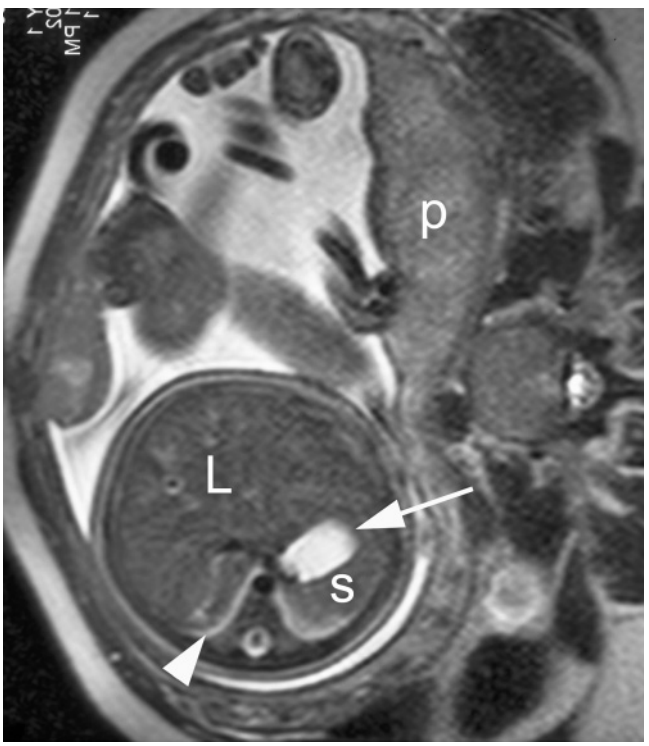

FIG. 16.31 Normal fetal abdomen, third trimester. Transverse SS-ETSE image through the fetal abdomen shows the low- to intermediate-signal-intensity liver (L), spleen (s), and adrenal gland (arrowhead). The fluid-filled stomach (arrow) is hyperintense. The placenta (p) is seen in a posterior location.

Fetal Anomalies

Central Nervous System

MRI is useful in further evaluating abnormalities seen or suspected on ultrasound and has been shown to be particularly helpful in cases of agenesis of the corpus callosum, posterior fossa anomalies, migrational disorders, cortical dysgenesis, intracranial hemorrhage, porencephaly, absent cavum septum pellucidum, ventriculomegaly, myelomeningocele, and space-occupying lesions [66, 83, 84]. MR imaging is often performed in families with a

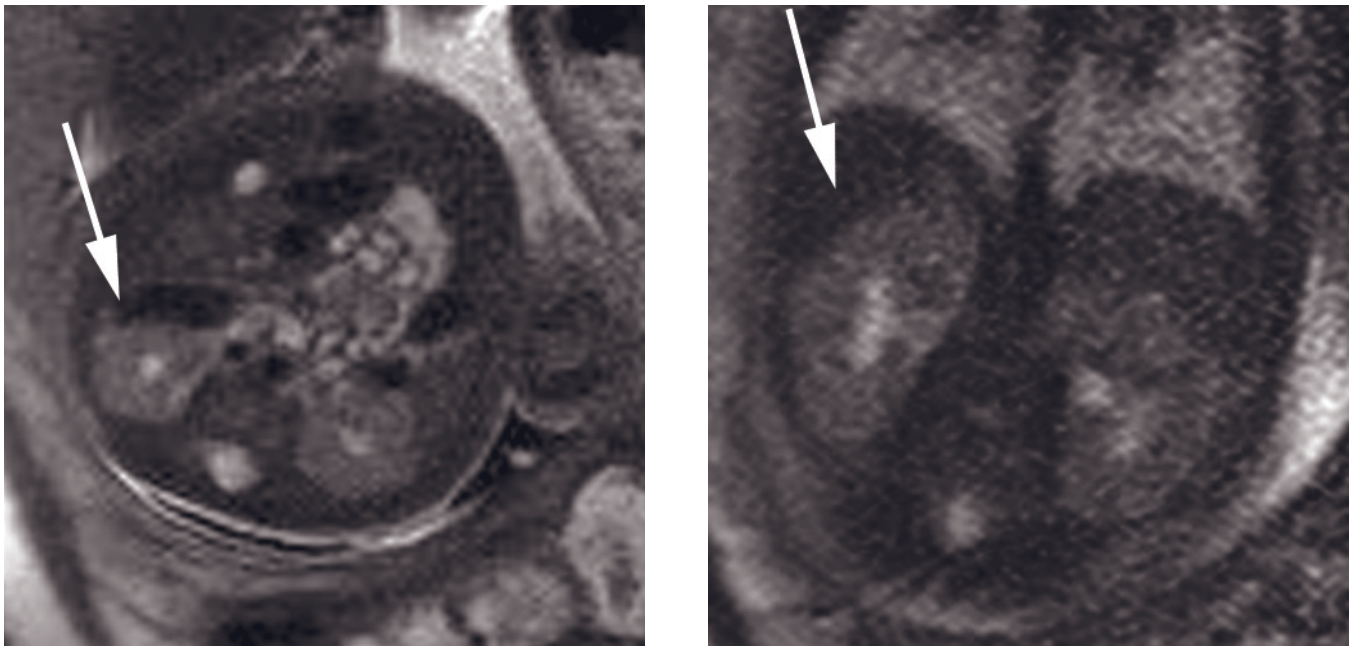

(*a*) (*b*)

FIG. 16.32 Normal kidneys. Transverse (*a*) and coronal (*b*) T2-weighted SS-ETSE images of fetal kidneys at 30 weeks (arrows). The renal parenchyma is intermediate in signal intensity, surrounding the hyperintense collecting system bilaterally.

history of prior pregnancy with CNS anomaly or genetic disorder, and in those at risk for destructive lesion, as malformations may be more difficult to detect with sonography. Monochorionic twins with twin-twin transfusion syndrome or cotwin demise are also often evaluated with MR imaging because of the higher risk of neurodevelopmental abnormality [85]. MRI is also helpful in difficult cases in which the abnormality is poorly characterized, or when the brain is difficult to see with sonography because of maternal body habitus, oligohydramnios, or advanced gestational age. Furthermore, fetal MRI performed to further evaluate sonographic abnormalities of the central nervous system has been shown to change diagnosis and management in many cases, with a change in diagnosis reported in up to 32%, prenatal counseling in 50%, and care in 19% [86].

Assessment of Ventriculomegaly. Ventriculomegaly is a frequent indication for fetal MRI, both to assess for associated anomalies and to further evaluate etiology, which may be related to disordered CSF dynamics, congenital malformation, or an obstructive lesion. Up to 80% of fetuses have been reported to have associated anomalies, with 18% demonstrating karyotype anomalies. Prognosis is worse with associated anomalies and in cases of progressive ventriculomegaly [67, 87]. Associated CNS anomalies include neural tube defects, agenesis of the corpus callosum, holoprosencephaly, aqueductal stenosis, Dandy–Walker complex, periventricular nodular heterotopias, polymicrogyria, lissencephaly, and destructive lesions such as subependymal and intraventricular hemorrhages, periventricular leukomalacia, multicystic encephalomalacia, and porencephaly [67, 88]. Mortality rates have been quoted as high as 62–85%, depending on associated anomalies. Developmental delay has been reported in 84% of those with associated anomalies and in 37% of those with isolated ventriculomegaly [67]. With mild ventriculomegaly, variably defined in the literature as an atrial width of 10–12 mm or 10–15 mm on axial sonogram, prognosis is better, although developmental delay has been reported in 50–56% of those with associated anomalies and in 0–36% of those with isolated mild ventriculomegaly [67, 87]. Detection of associated anomalies is therefore important for prenatal counseling. MRI plays an important role in this evaluation and has demonstrated sonographically occult CNS anomalies in up to 40–50% of cases of ventriculomegaly [67]. Half of the cases of ventriculomegaly are due to aqueductal stenosis, Chiari II malformation, or Dandy–Walker complex [89]. Dandy–Walker complex is further discussed under *Posterior Fossa.*

Aqueductal stenosis is characterized by dilated lateral and third ventricles with a normal-sized fourth ventricle, typically with marked and progressive dilatation (fig. 16.33). This may be congenital, due to X-linked or autosomal recessive disorders, or acquired from in utero infection or hemorrhage, although most cases are

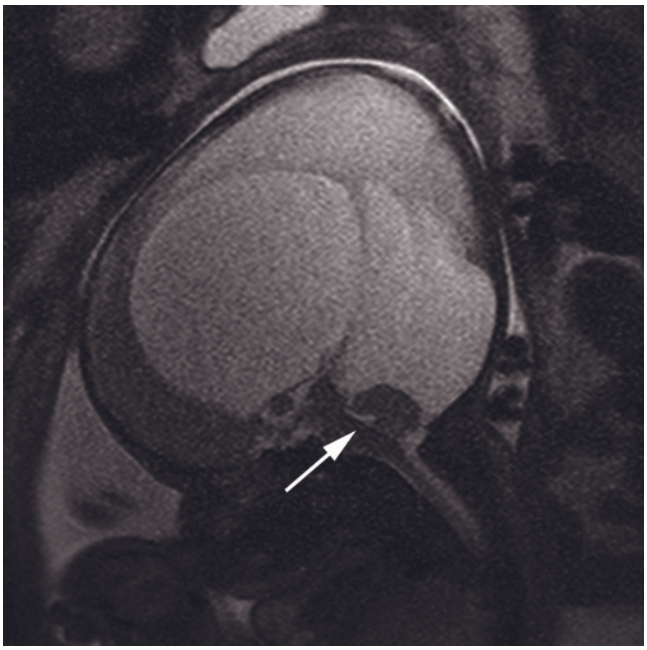

(*a*)

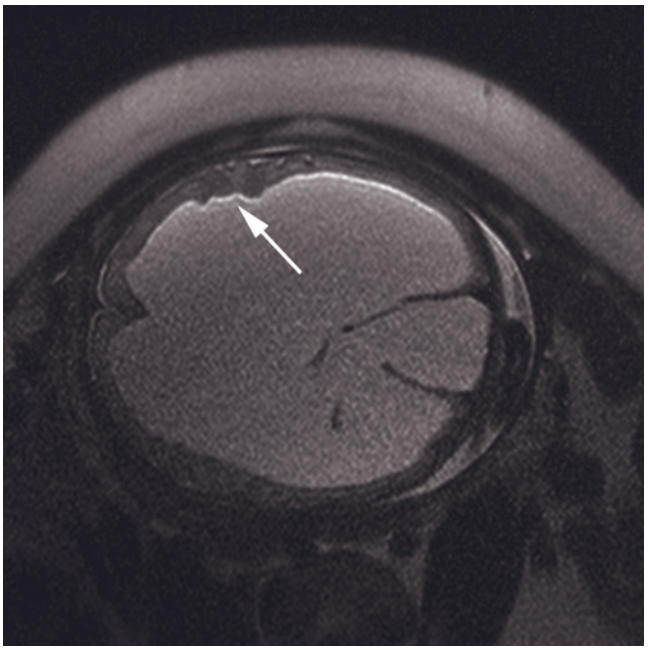

(*b*)

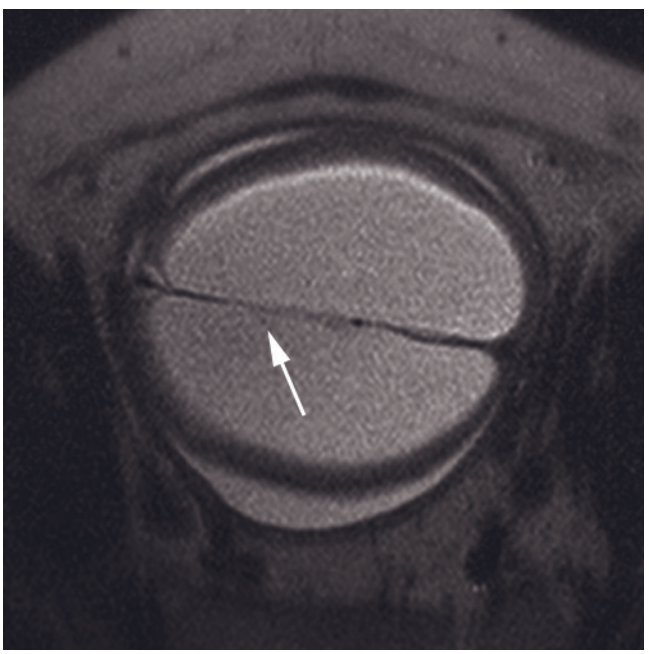

(*c*)

FIG. 16.33 Aqueductal stenosis. Sagittal (*a*) and transverse (*b*, *c*) images of the fetal brain at 36 weeks gestation. There is massive hydrocephalus of the lateral and third ventricles with normal-appearing fourth ventricle (arrow, *a*). A thin rim of residual cerebral tissue (arrow, *b*) and an intact falx (arrow, *c*) support the diagnosis of aqueductal stenosis rather than hydranencephaly or holoprosencephaly.

considered multifactorial and are without identifiable cause. Normal cognition has been reported in 24–86% of cases of aqueductal stenosis; however, a recent study evaluating prenatally diagnosed cases found only 10% to have normal cognition and reported a 27% mortality rate [90]. Furthermore, when the etiology is X-linked, there is consistently severe mental retardation. Half of those with X-linked aqueductal stenosis will have adduction of the thumbs, which may be a clue to the diagnosis [89].

Chiari II malformation is seen in practically all cases of myelomeningocele to varying degrees, and is a constellation of malformations that is most prominent in the hindbrain (fig. 16.34). Inferior herniation of the cerebellar tonsils, vermis, and caudal brainstem through an enlarged foramen magnum is demonstrated, frequently with medullary kinking. The posterior fossa is small, the tentorium is low, and the cerebellar hemispheres and superior vermis are displaced cranially. Tectal beaking, an enlarged massa intermedia, and dysgenesis

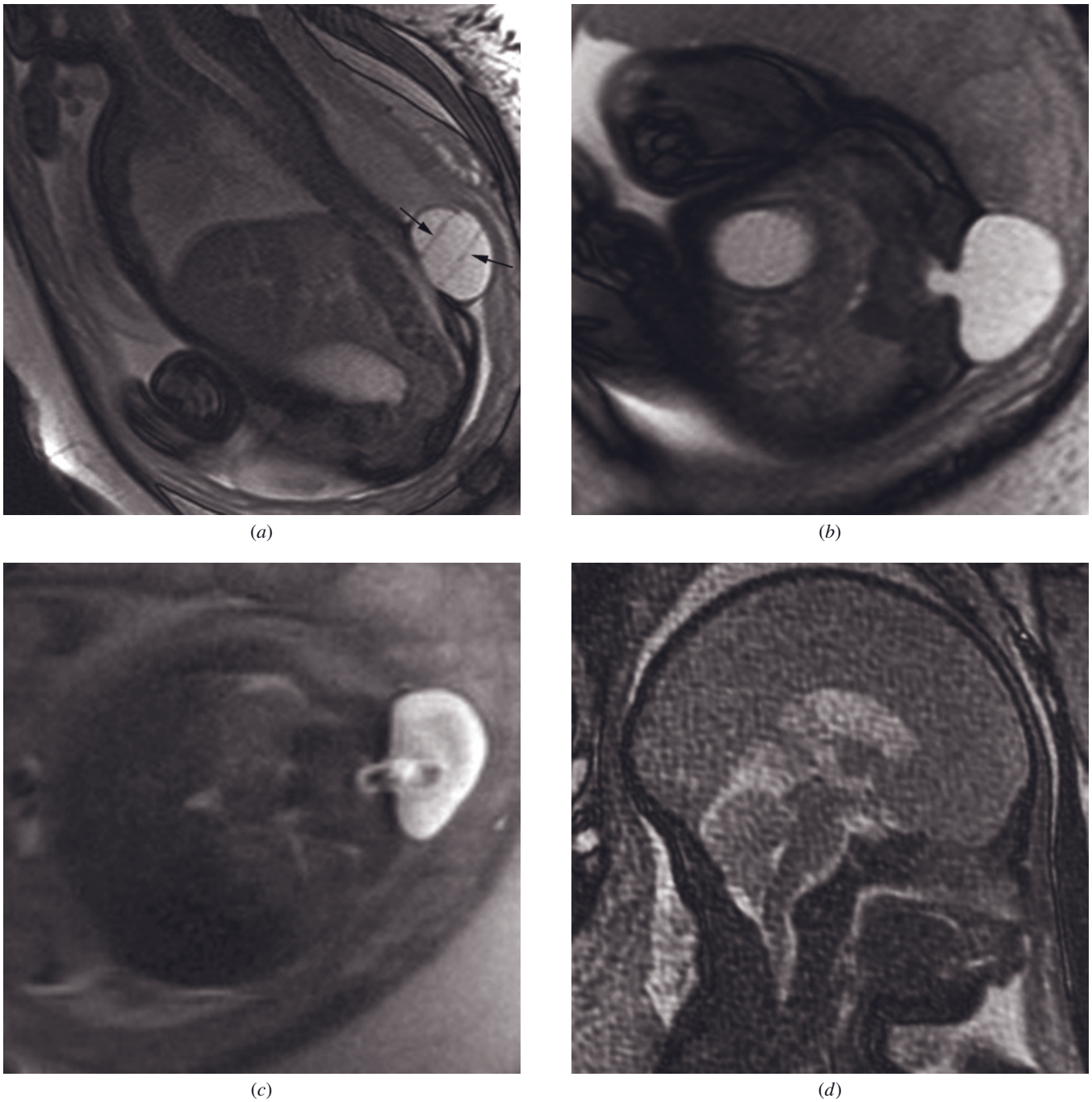

FIG. 16.34 Myelomeningocele and Chiari II malformation. T1-/T2-weighted steady-state free-precession images in the sagittal (*a*) and transverse (*b*) planes show a 3.7-cm myelomeningocele extending from the lumbar spinal canal. Linear hypointensities seen in the sagittal plane are consistent with nerve roots (arrows, *a*). Flow-related artifact on T2-weighted SS-ETSE images (*c*) precluded confident identification of the nerve roots with this sequence (compare *c* to *b*). Sagittal T1-/T2-weighted steady-state free-precession image of the brain (*d*) shows Chiari II malformation, with herniation of cerebellar tonsils through an enlarged foramen magnum and a small posterior fossa. Transverse T2-weighted SS-ETSE image (*e*) demonstrates ventriculomegaly, with the lateral ventricles measuring 2 cm at the atria.

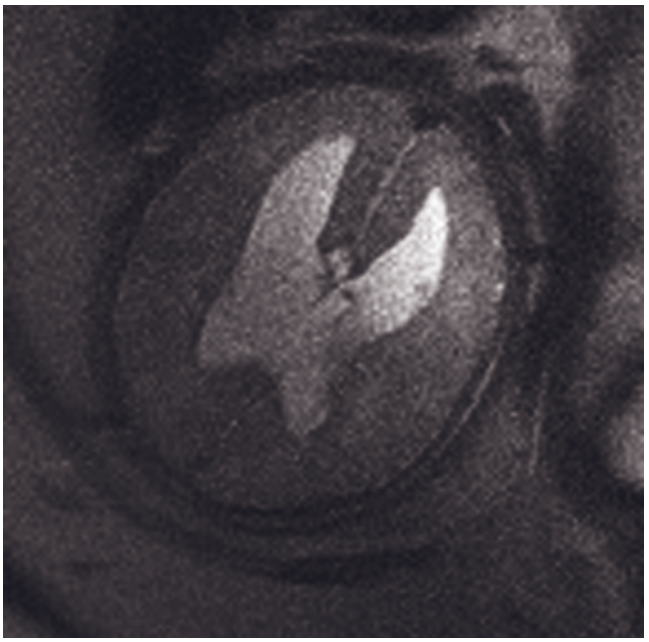

FIG. 16.34 (*Continued*) (*e*)

or agenesis of the corpus callosum are present. Polygyria and heterotopias are common. The fourth ventricle and aqueduct are small, the third ventricle is angulated, and the lateral ventricles may be normal or distorted and enlarged. Osseous abnormalities include lückenschädel, scalloping of the petrous pyramid, and shortening of the clivus. One-third of children develop symptoms of brainstem compression by the age of 5, and of these, one-third do not survive [91, 92]. Although Chiari II malformations and myelomeningoceles are usually identified with ultrasound, MRI is helpful when the sonogram is limited by maternal body habitus, oligohydramnios, and fetal positioning. Although MRI has not shown any benefit in localizing the level of spinal dysraphism, MRI can better identify the callosal abnormalities, heterotopias, and associated spinal cord anomalies such as diastematomyelia and syringohydromyelia, as well as evaluate the extent of hindbrain herniation [85, 93, 94]. Sagittal images of the fetal head and spine are helpful to evaluate cerebellar tonsillar herniation, fetal skin defect, and myelomeningocele, which may be seen as a mass posterior to the spine.

MRI depicts the normal and abnormal corpus callosum, which should be visible by 20 weeks of gestation (fig. 16.35), and MRI has been shown to have greater sensitivity and specificity than ultrasound for callosal abnormalities [85]. Abnormalities of the corpus callosum may result from karyotype anomalies, X-linked syndromes such as Aicardi syndrome, metabolic disorders, or insults such as infection during development [95, 96]. Although agenesis of the corpus callosum may be seen in isolation, associated anomalies are present in up to 85% of cases, detection of which is important for parental counseling as this increases the likelihood of a poor prognosis. In a recent study, MRI identified sonographically occult anomalies in 63% of cases and, in addition, detected a normal corpus callosum in 20% of cases referred for suspected callosal agenesis on ultrasound [95]. Associated lipomas and interhemispheric cysts may be seen with MR (fig. 16.36). Additional associated anomalies include Dandy–Walker malformation, Chiari II malformation, holoprosencephaly, gray matter heterotopia, schizencephaly, and encephalocele [88]. The clinical presentation is variable, ranging from normal to developmental delay, seizures, abnormal muscle tone, psychotic disorders, feeding problems, and social/behavioral problems [89, 97]. On MRI, an abnormal or absent corpus callosum may be seen directly, in addition to the indirect findings of agenesis seen with ultrasound, which include colpocephaly with a teardrop configuration to the lateral ventricles, a high-riding and enlarged third ventricle, and absent cavum septum pellucidum [98].

Holoprosencephaly is classically subdivided into alobar, semilobar, and lobar types, in decreasing order of severity. Holoprosencephaly may result from a variety of etiologies, including chromosomal, genetic, and syndromic, or be an isolated abnormality resulting from a variety of insults. Clinical features include seizures, choking, spasticity, developmental delay, fluctuating behavior, sleeping problems, and brainstem dysfunction. Involvement of the hypothalamus and basal ganglia leads to choreoathetoid movements, endocrinopathies, especially diabetes insipidus, and temperature dysregu-

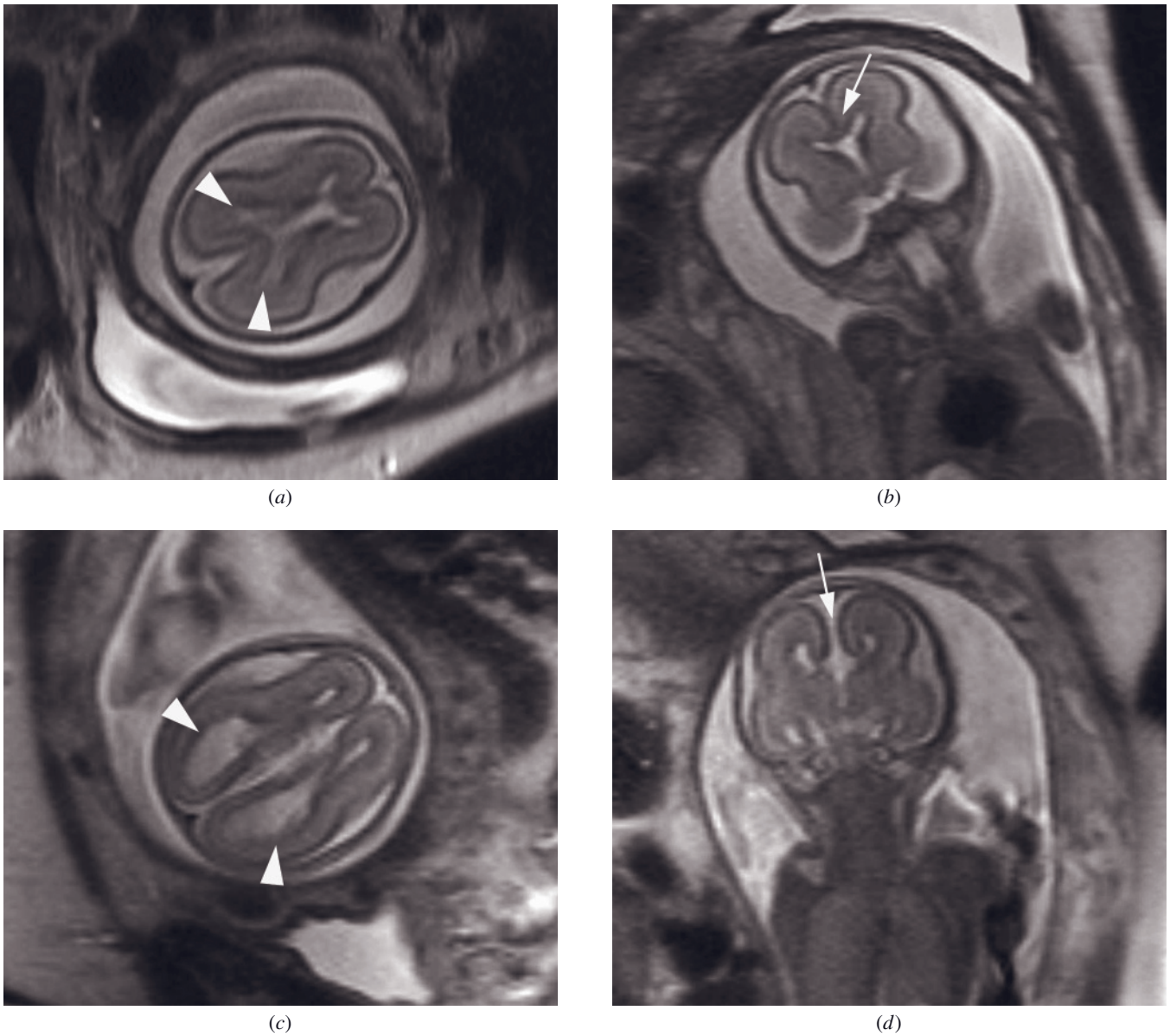

FIG. 16.35 Normal corpus callosum and absent corpus callosum at 22 weeks of gestation. Transverse (*a*) and coronal (*b*) T2-weighted SS-ETSE images through a normal fetal brain at 22 weeks of gestational age. The lateral ventricles are normal in size (arrowheads, *a*) with a normal intervening distance, and there is a visible corpus callosum (arrow, *b*). Transverse (*c*) and coronal (*d*) T2-weighted SS-ETSE images through a different fetal brain at 22 weeks of gestational age. There is dilatation and increased distance between the lateral ventricles (arrowheads, *c*) and absence of connecting fibers between the cerebral hemispheres (arrow, *d*).

lation [99, 100]. Diagnosis of alobar holoprosencephaly may be straightforward with ultrasound; however, diagnosis of lobar or semilobar forms may be quite difficult. Alobar holoprosencephaly is characterized by the presence of a monoventricle; absence of the cavum septum pellucidum, falx, third ventricle, corpus callosum, and olfactory bulbs and tracts; nonseparated deep gray nuclei; and usually a dorsal sac or cyst. The dorsal sac or cyst is caused by cystic extension of the monoventricle resulting from blocked cerebrospinal flow due to thalamic noncleavage. Associated facial malformations are present in the majority, which may include a proboscis, cyclopia, hypo- or hypertelorism, arrhinia, cleft lip and palate, single nostril, flattened nose, and central maxillary incisor. Infants typically die within the first year, though survival to 11 years has been reported.

Semilobar holoprosencephaly (fig. 16.37) is characterized by partial separation of the cerebral hemispheres posteriorly with partial falx and nonseparated, underdeveloped frontal lobes, monoventricle, absent cavum

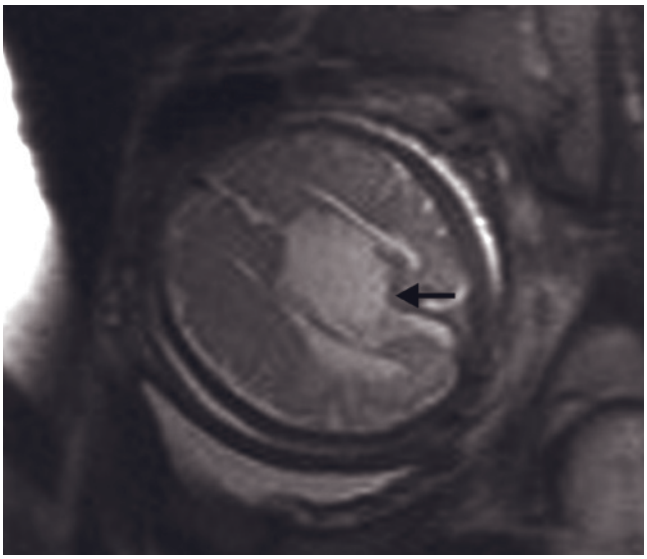

(*a*)

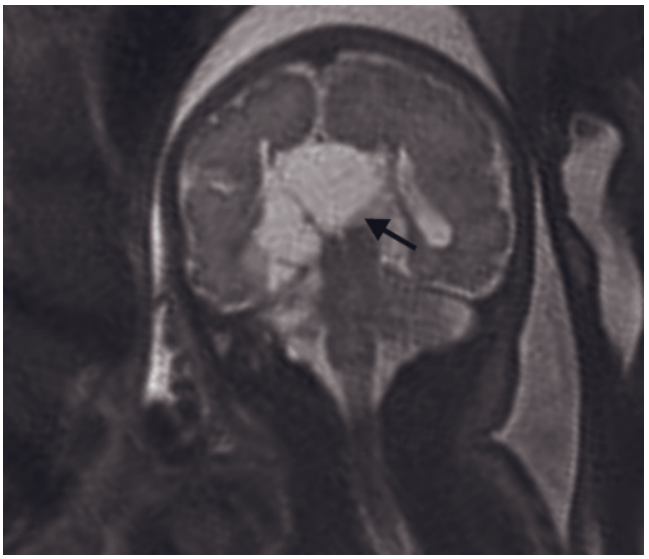

(*b*)

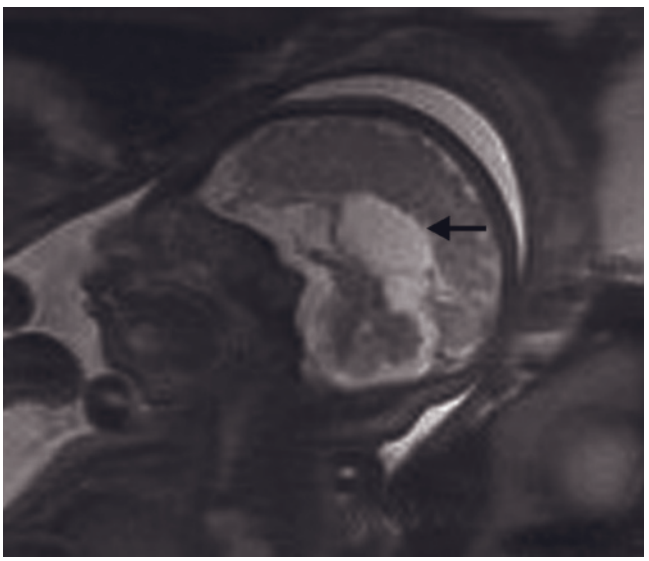

(*c*)

FIG. 16.36 Agenesis of the corpus callosum with interhemispheric cyst. Axial (*a*), coronal (*b*), and sagittal (*c*) T2-weighted SS-ETSE images of the fetal brain demonstrate a lobulated interhemispheric cyst (arrows, *a–c*) extending asymmetrically to the right associated with agenesis of the corpus callosum. An intact corpus callosum is not identified, and the lateral ventricles have a parallel configuration with colpocephaly (*a*).

septum pellucidum, partially or completely nonseparated deep gray nuclei, and malformed corpus callosum. Facial malformations are less prominent, and a dorsal sac is less commonly seen. Lobar holoprosencephaly is characterized by hypoplasia of the inferior frontal lobes and anterior falx with incomplete separation of the frontal lobes and absence of the cavum septum pellucidum. Compared with the other subtypes, there tends to be better formation of the corpus callosum, third ventricle, and frontal horns of the lateral ventricles in lobar holoprosencephaly. Dorsal cysts are uncommon with the lobar subtype. Semilobar and lobar subtypes generally survive longer than those with alobar holoprosencephaly, with survival into the teens [99–103].

In the middle interhemispheric (MIH) variant of holoprosencephaly (fig. 16.38), there is midline continuity of the posterior frontal and parietal lobes, with separation of the basal forebrain, anterior frontal lobes, and occipital lobes. The genu and splenium of the corpus callosum are relatively spared, but the body is absent. The thalami are less commonly fused, and a dorsal cyst is therefore less commonly seen with this variant compared with alobar holoprosencephaly. The deep gray nuclei are widely separated. No severe midline craniofacial defects are associated; however, cleft lips and palates, single central incisors, and hypertelorism may be seen. Clinically, these children fare better than those with classical holoprosencephaly in terms of expressive skills and upper extremity control. The deficits seen with MIH

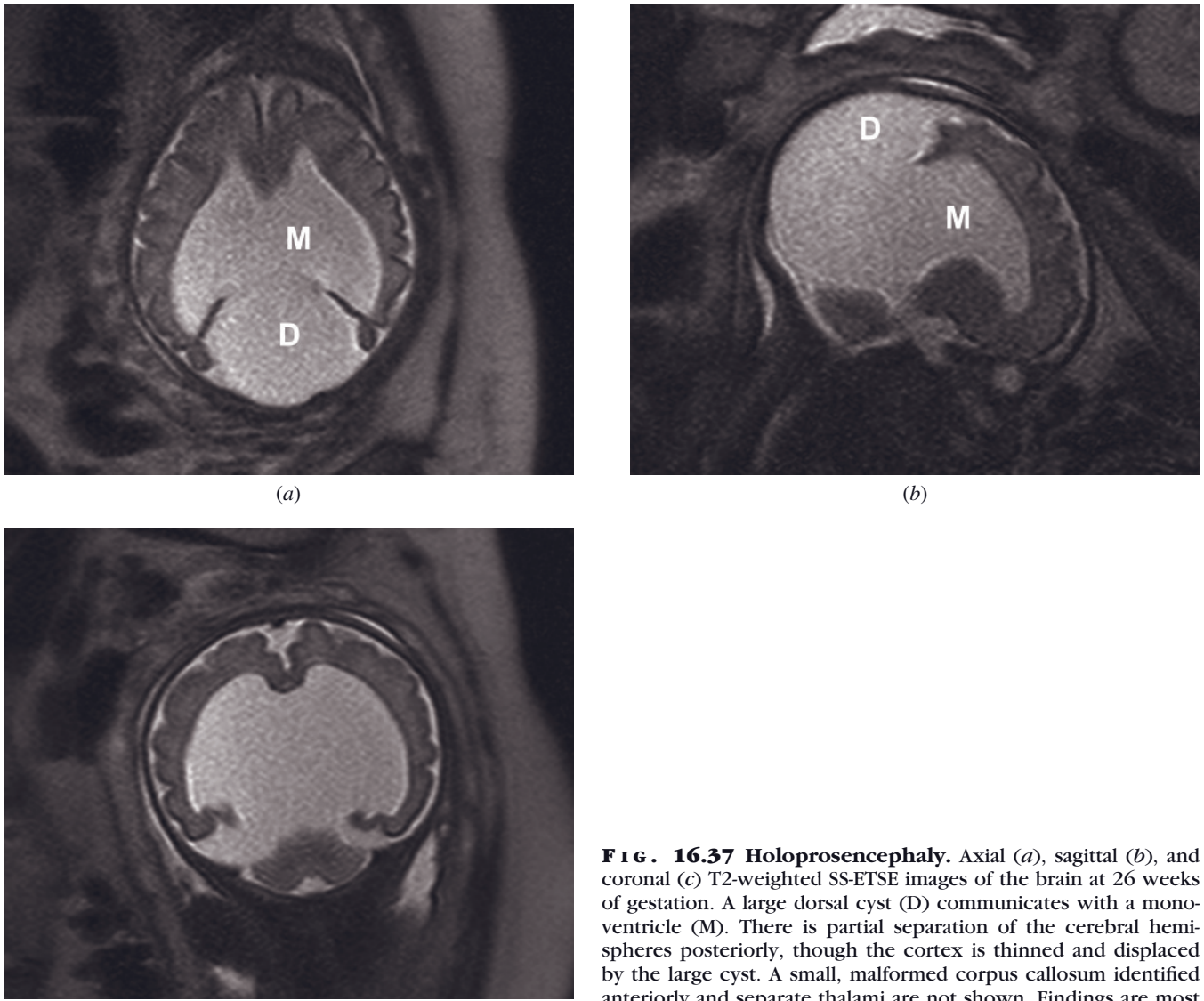

(*a*) (*b*) (*c*)

Fig. 16.37 Holoprosencephaly. Axial (*a*), sagittal (*b*), and coronal (*c*) T2-weighted SS-ETSE images of the brain at 26 weeks of gestation. A large dorsal cyst (D) communicates with a monoventricle (M). There is partial separation of the cerebral hemispheres posteriorly, though the cortex is thinned and displaced by the large cyst. A small, malformed corpus callosum identified anteriorly and separate thalami are not shown. Findings are most consistent with a semilobar variety of holoprosencephaly.

are related to the predominant involvement of motor cortex, including spasticity, dystonia, hypotonia, and oromotor deficits affecting speech and feeding [99, 104].

Posterior Fossa. The posterior fossa is well-evaluated with MRI. Assessment of vermian hypoplasia is performed on sagittal images. The tegmento-vermian angle may be used to assess vermian angulation and is defined as the angle between a line drawn along the dorsal brain stem parallel to the tegmentum and a second line drawn along the ventral vermis. A normal angle is close to 0, and an elevated angle is defined as >40°. An abnormal angle is often associated with vermian and cerebellar hypoplasia; however, it may also be seen in isolated elevation or rotation of the vermis due to a persistent Blake pouch cyst, which may have a good prognosis if not associated with supratentorial abnormalities or uncontrolled or progressive hydrocephalus [75, 105]. The craniocaudal extent of the vermis can be measured and compared to published norms. To measure, a line is drawn through the fastigial point and declive (the first lobule posterior to the primary fissure; fig. 16.27) and the craniocaudal extent is measured perpendicular to this. Relative growth of the superior and inferior vermian lobes can also be assessed by comparing the length above and below the line, which should be symmetric. In general, the degree of vermian lobulation correlates with prognosis [75].

The Dandy–Walker continuum includes Dandy–Walker malformation, Dandy–Walker variant, and mega cisterna magna. Outcomes are widely variable based on the degree of vermian hypoplasia and associated

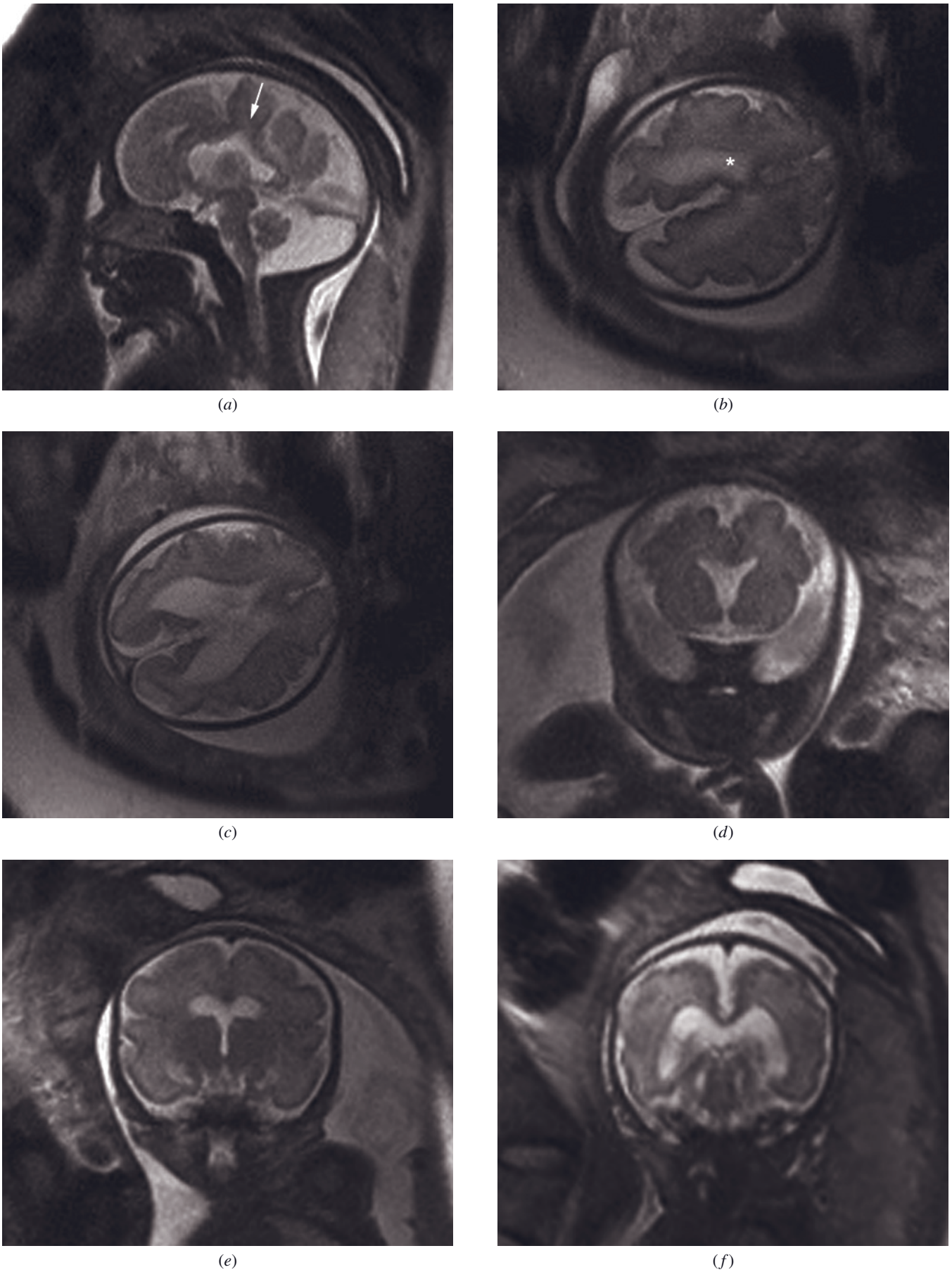

FIG. 16.38 Middle interhemispheric variant of holoprosencephaly. T2-weighted SS-ETSE images of the fetal brain at 32 weeks in the sagittal (*a*), axial (*b*, *c*), and coronal (*d–f*) planes demonstrate abnormal fusion of the posterior frontal/parietal lobes across the midline (*, *b*) with separation of the anterior and posterior cerebral hemispheres (*c*). Subjacent to the abnormal fusion, the body of the corpus callosum is malformed (arrow, *a*) but intact anterior and posterior to this. The cavum septum pellucidum is absent (*d–f*).

anomalies. Structural, genetic, and chromosomal anomalies may be present, including agenesis of the corpus callosum, polymicrogyria, neuronal heterotopias, occipital encephaloceles, facial anomalies, cardiac defects, polydactyly, and syndactyly, and portend a worse prognosis. Dandy–Walker malformation is defined as complete or partial vermian agenesis, cystic dilatation of the fourth ventricle, and enlargement of the posterior fossa with associated elevation of the tentorium, torcula, and transverse sinus [75, 85] (fig. 16.39). Dandy–Walker variant includes milder forms of vermian hypoplasia with a more normal-appearing posterior fossa (fig. 16.40). Visualization of a normal vermis can distinguish a mega cisterna magna from a Dandy–Walker variant.

Other posterior fossa abnormalities may also be detected with MRI. Joubert syndrome may be seen with an aplastic, hypoplastic, or cleft vermis with distorted fastigial point, absent primary fissure, and "molar tooth" configuration of the mesencephalon. Clinical features include mild-moderate mental retardation, abnormal eye movements, rhythmic tongue protrusion, motor delays, and transient neonatal hyperpnea. Rhomboencephalosynapsis is an abnormal fusion of the cerebellar hemispheres with absent vermis. The cerebellar folia are seen continuing across the midline on MR imaging. This is a heterogeneous clinical entity with presentation correlating with supratentorial abnormalities. Severe pontocerebellar and vermian hypoplasia may also be

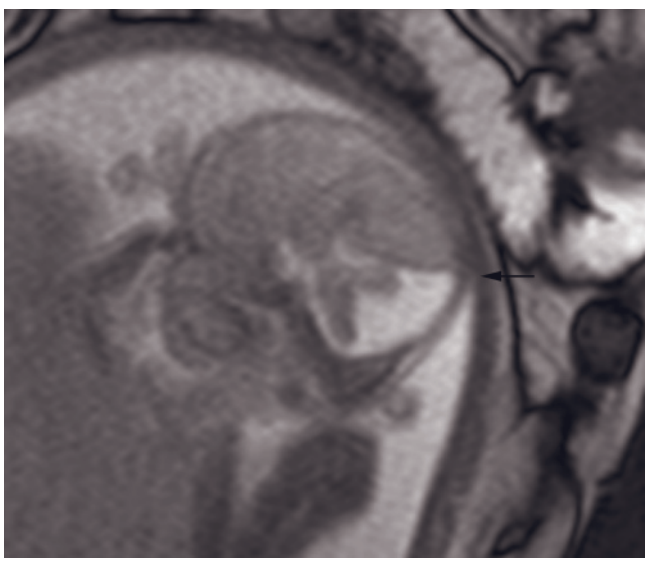

(*a*)

(*b*)

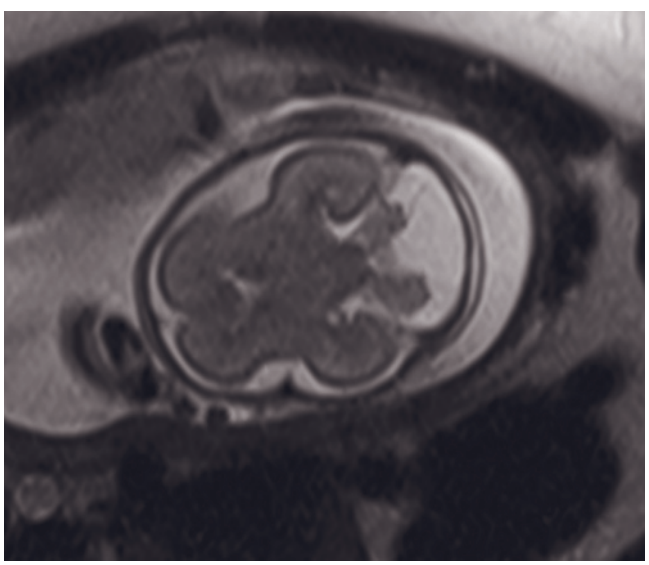

(*c*)

FIG. 16.39 Dandy–Walker malformation. Sagittal (*a*) and coronal (*b*) T1-/T2-weighted steady-state free-precession and axial T2-weighted SS-ETSE (*c*) images in a fetus at 23 weeks of gestational age. There is marked enlargement of the posterior fossa with superior displacement of the venous confluence (elevation of the torcula Herophili, arrow, *a*). Note the severe vermian hypoplasia associated with a retrocerebellar cerebrospinal fluid collection that appears continuous with the fourth ventricle.

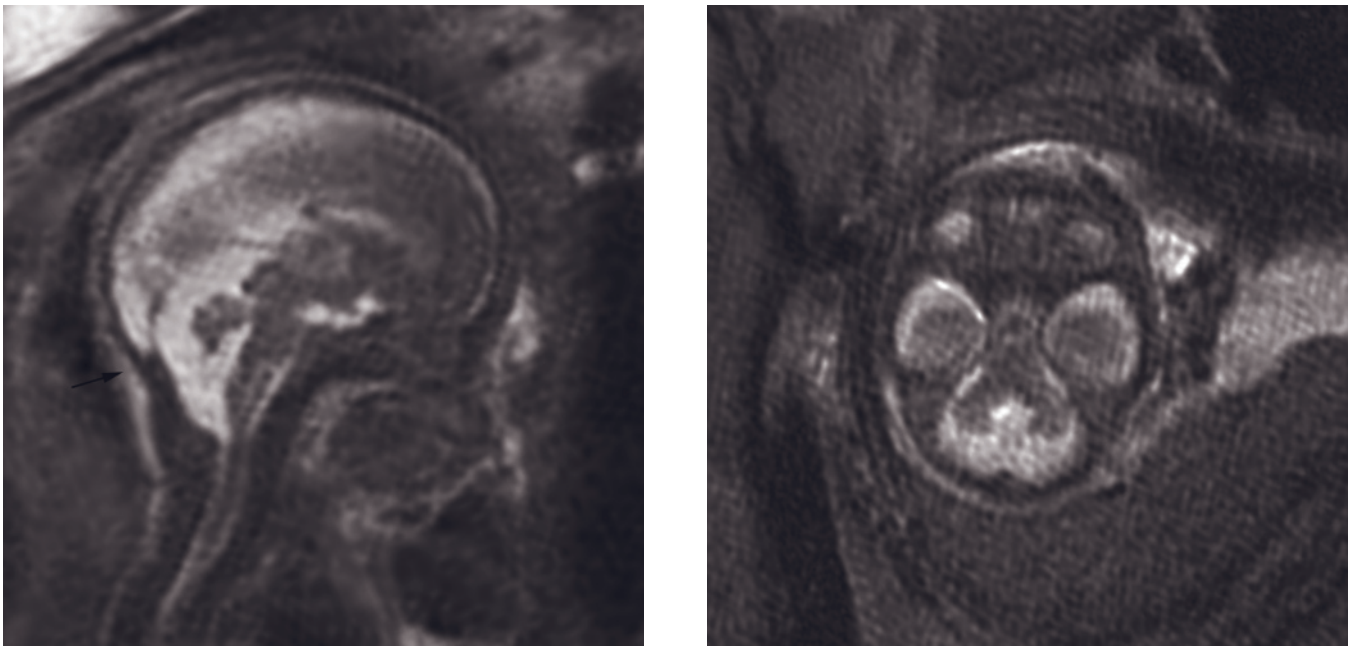

(*a*) (*b*)

FIG. 16.40 Dandy–Walker variant in two different patients. Sagittal (*a*) and transverse (*b*) T2-weighted SS-ETSE images of fetuses in the second trimester demonstrate a hypoplastic inferior vermis with communication of the fourth ventricle with an enlarged cisterna magna. The posterior fossa is normal in size, with normal position of the torcula Herophili (arrow, *a*).

seen with muscular dystrophies and microlissencephaly, both of which have poor prognoses [75].

Arachnoid cysts (fig. 16.41) are benign, space-occupying congenital lesions filled with cerebrospinal fluid and are usually easily diagnosed with ultrasound. MRI is helpful in evaluating the extent of the cyst and adjacent brain compression [83]. Most are located along the surface of the brain at the major fissures. Arachnoid cysts of the posterior fossa may compress the brainstem or cerebellum and lead to ventriculomegaly. Fetal arachnoid cysts may also be associated with chromosomal anomalies or agenesis of the corpus callosum [106].

Other Developmental Anomalies. A role for fetal MRI has been proposed in cases of absent cavum septum pellucidum in which the etiology is not readily apparent with ultrasound. Absence may be secondary to holoprosencephaly, septo-optic dysplasia, agenesis of the corpus callosum, schizencephaly, or encephalocele, or in cases of secondary destruction such as severe hydrocephalus, porencephaly, hydranencephaly, and valproic acid embryopathy. Isolated cases of absence of the cavum septum pellucidum also exist and are particularly difficult to differentiate from septo-optic dysplasia with ultrasound. These isolated cases may have no neurologic manifestations, although prenatal diagnosis is controversial as there may be cytoarchitectural distortions of the cortical layers that cannot yet be detected with MRI [107–109].

Septo-optic dysplasia is characterized by absent or hypoplastic cavum septum pellucidum and hypoplastic or dysplastic optic nerves (fig. 16.42). Two subtypes have been described, one of which includes schizencephaly, a cavum septum pellucidum remnant, and normal-sized ventricles. These patients tend to present with seizures and/or decreased visual acuity. The second type is not associated with schizencephaly, but instead demonstrates diffuse white matter hypoplasia, complete absence of the cavum septum pellucidum, and ventriculomegaly, and presents with symptoms related to hypothalamic-pituitary dysfunction. It has been suggested that this second type may represent a mild form of lobar holoprosencephaly. In general, associated anomalies are seen in over half of patients and include cortical malformations, holoprosencephaly, and agenesis of the corpus callosum. Clinical features are widely variable and also include developmental delay. Although prenatal diagnosis is possible with MRI, optic nerve hypoplasia is difficult to detect prenatally, and it has been suggested that only half of affected fetuses are recognized [107–111].

Encephaloceles are herniations of brain and meninges through a cranial defect (fig. 16.43). In the western world, occipital encephaloceles are the most common. These may be associated with syndromes such as

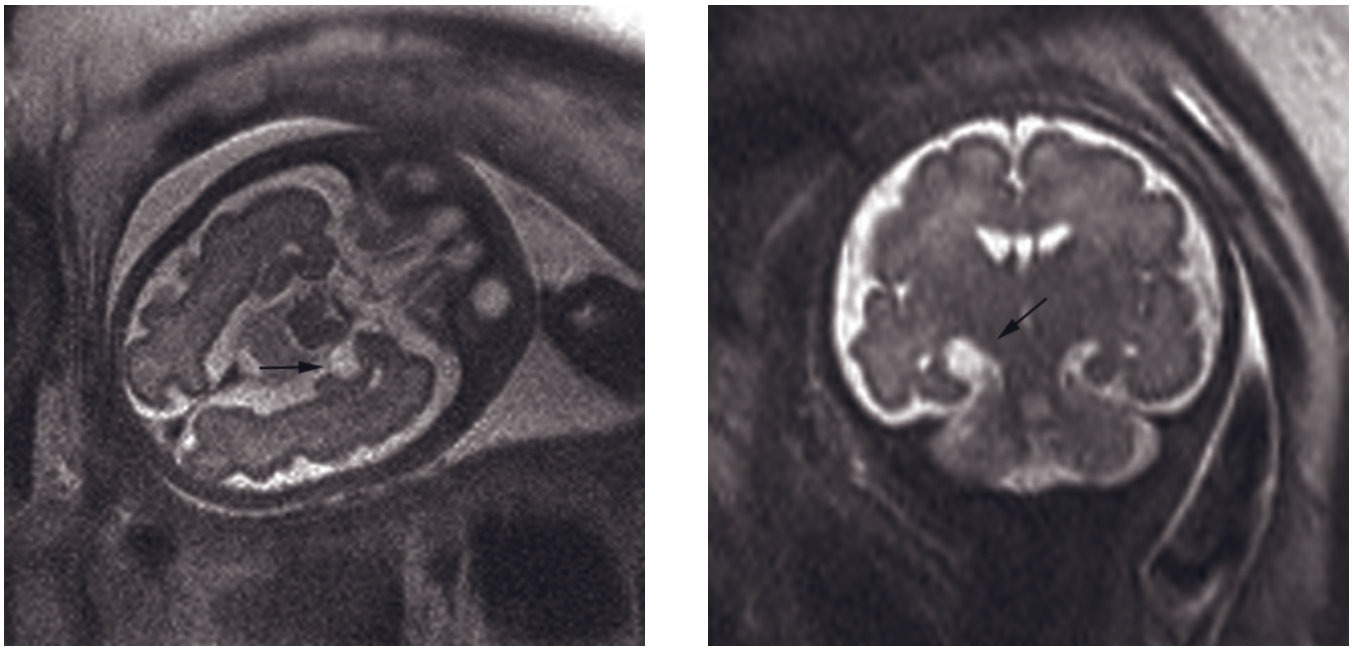

(*a*) (*b*)

FIG. 16.41 Arachnoid cyst of choroidal fissure. Transverse (*a*) and coronal (*b*) T2-weighted SS-ETSE images of the fetal brain at 34 weeks demonstrates a well-circumscribed, extra-axial, hyperintense cyst in the right choroidal fissure, consistent with an arachnoid cyst.

Meckel–Gruber syndrome (see *Cystic Renal Disease*, fig. 16.60), amniotic band syndrome, or Walker–Warburg syndrome, or associated with karyotype anomalies, in particular trisomies 13 and 18. In southeast Asia, frontal encephaloceles are more common. Karyotype anomalies have been found in up to 44% of fetuses with encephaloceles. In cases of isolated encephalocele, the amount of herniated brain is the most important prognostic factor. Polyhydramnios may be seen secondary to impaired swallowing or oligohydramnios secondary to associated anomalies in various syndromes [112, 113]. MRI may be helpful for evaluation of encephaloceles, in particular for characterization of small frontal encephaloceles.

Malformations of Cortical Development. Malformations of cortical development such as schizencephaly, gray matter heterotopias, polymicrogyria, and lissencephaly are better demonstrated with MRI than ultrasound [85]. In schizencephaly, a cleft lined by gray matter extends from the subarachnoid space to the lateral ventricle. Schizencephaly is described as closed-lip if the lips of the cleft are in contact with one another and as open-lip if the lips are separated [114, 115]. Symptoms vary depending on bilaterality and type and extent of cleft, with some unilateral closed-lip cases discovered incidentally showing few or no symptoms. Bilateral open-lip cases usually demonstrate seizures, paralysis, and profound developmental delay with little cerebral function [115]. MRI clearly demonstrates the clefts, with the gray matter lining the clefts evident as a band of T2 hypointensity, allowing distinction from porencephaly. The cavum septum pellucidum is absent in two-thirds of cases, and the corpus callosum may be focally thin or absent. Heterotopias, polymicrogyria, and septo-optic dysplasia may also be present [114].

Subependymal heterotopia is seen as periventricular nodules isointense to the germinal matrix, which are indistinguishable from the subependymal nodules of tuberous sclerosis [67]. A search for other features of tuberous sclerosis is therefore important. Cortical tubers are seen as low-signal-intensity foci on T2-weighted images that are of high signal intensity on T1-weighted images. Prenatal diagnosis of tuberous sclerosis has been reported with MRI as early as 21 weeks of gestational age [116]. Polymicrogyria may be localized or generalized and is characterized by lack of normal sulcation with multiple abnormal infoldings of the cerebral cortex.

Lissencephaly is characterized by shallow sylvian fissures, absent or reduced sulcation for gestational age, and absence of the normal layered appearance of the brain, with a large, thick band of neurons located within the white matter instead [85]. The most common clinical features of lissencephaly include severe psychomotor retardation, developmental delay, seizures, and failure

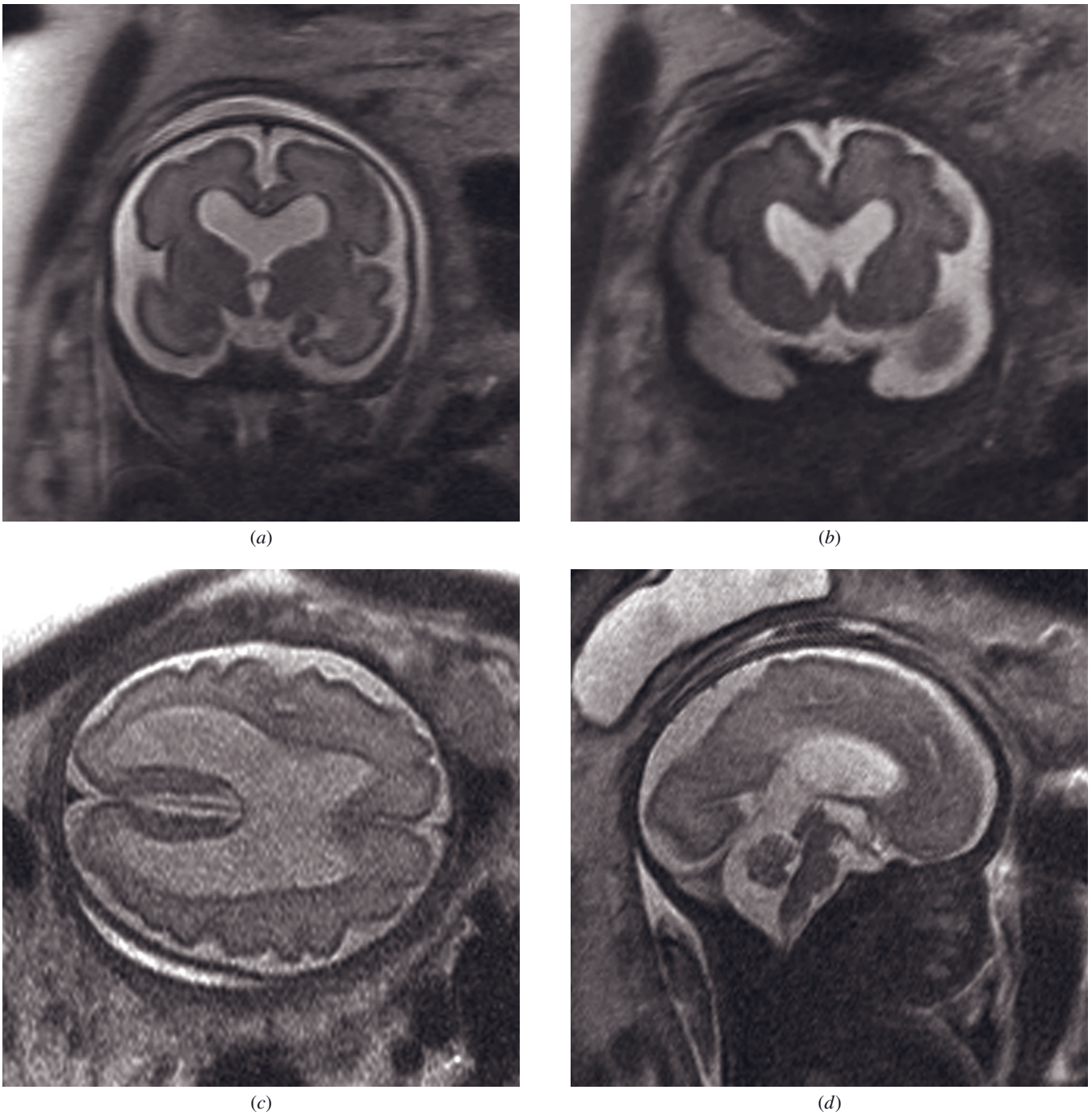

FIG. 16.42 Septo-optic dysplasia. T2-weighted SS-ETSE images in a fetus at 28 weeks of gestational age. The coronal (*a*, *b*) and axial (*c*) images show complete absence of the cavum septum pellucidum, with flattening of the roof of the lateral ventricles and inferior pointing of the frontal horns. On the sagittal image (*d*), the low position of fornices is observed. Optic nerve hypoplasia is identified on coronal (*a*) and sagittal (*d*) images. Note the enlarged lateral ventricles.

to thrive, with prognosis depending on the degree of failed cortical development. Death may occur in infancy or early childhood among those severely affected [117].

Destructive Lesions. Destructive lesions are also better seen with MRI than ultrasound. Fetal cerebral ischemia may result from placental, fetal, or maternal causes, including maternal hypovolemia, hypoxia, shock, abdominal trauma, hypotension, hypertension, and drug use, as well as fetal infection, twin-twin transfusion syndrome, and, rarely, inherited metabolic diseases [118, 119]. Areas of hemorrhage may result from

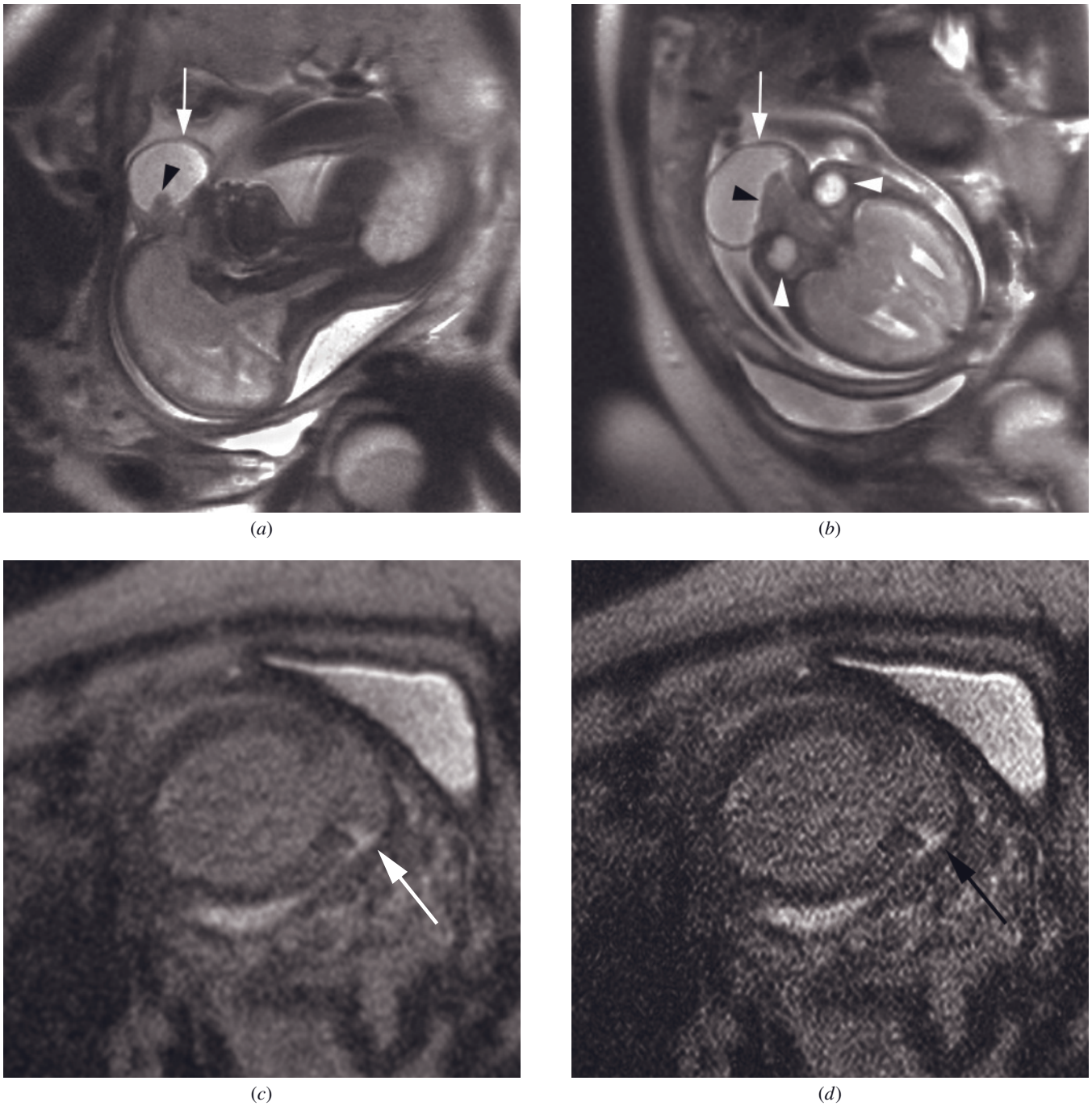

FIG. 16.43 Encephalocele. Sagittal (*a*) and transverse (*b*) T2-weighted SS-ETSE images through the fetal head show a frontal encephalocele. A round fluid-filled structure (arrow, *a*, *b*) is seen anterior to the fetal orbits (white arrowheads, *b*) and face. Intermediate signal intensity within the lesion (black arrowhead, *a*, *b*) continuous with the fetal brain indicates that the encephalocele contains neural tissue. Occipital encephalocele (*c*, *d*) in a fetus at 34 weeks. A posterior calvarial defect is demonstrated, with herniation of brain tissue through the defect (arrows).

hypoxia or ischemia related to maternal trauma, drug use, or infection, or in a fetus with a clotting disorder, hydrops, or underlying vascular malformation [85, 88].

Acute cerebral injury may manifest as white matter edema with T2 hyperintensity that may resolve or progress to necrosis. Acute white matter abnormalities may also manifest as loss of the intermediate layer of white matter seen in young fetuses or as leukomalacia, seen as subcortical T2 hyperintensity. Chronic changes of gliosis may be indirectly demonstrated with MR as

ventricular dilatation, thickened or irregular ventricular wall, or diffuse T2 hyperintensity/T1 hypointensity. Chronic changes of ischemia also include thickened or irregular germinal matrix, atrophy or necrosis, parenchymal cystic cavity (focal T2 hyperintensity), ependymal cyst (focal periventricular T2 hyperintensity), calcification (T2 hypointensity, T1 hyperintensity), and cortical malformations such as polymicrogyria or schizencephaly. Necrosis may appear as loss of normal signal contrast, area of T2 hyperintensity, volume loss with sharp delineation, porencephaly, or hydranencephaly (figs. 16.44 and 16.45). Laminar necrosis and some forms of periventricular leukomalacia may be seen as T1 hyperintensities. Cortical malformations, calcification, and ependymal cysts may also be seen with in utero infection [118, 119].

Hydranencephaly (fig. 16.45) is due to cerebral destruction in the bilateral internal carotid artery distribution in utero, usually during the second trimester, resulting in replacement of the majority of the cerebral hemispheres by cerebrospinal fluid covered with meninges. The falx is present as the insult occurs after formation of the brain and ventricles. The choroid plexus, thalami, basal ganglia, midbrain, cerebellum, brainstem, and portions of the occipital lobes are intact because of the unaffected posterior circulation. During the destructive phase, an abnormal mass of tissue and hemorrhage may be seen. Bilateral internal carotid artery occlusion is felt to be the usual cause, although in utero infection has also been implicated. Most infants die within the first year of life, and those that survive have severe mental retardation [89, 120, 121].

Parenchymal hemorrhage may be seen as T2 hypointensity/T1 hyperintensity, although the signal intensity varies with age of hemorrhage. Intraventricular debris or focal hematoma may be seen with intraventricular hemorrhage [67] (fig. 16.46). Subependymal hemorrhage may be difficult to see on routine images because of the similar signal intensity of the germinal matrix; however, this may be seen on T2*-weighted gradient-echo images as a focal area of hypointensity relative to the germinal matrix [67]. Subdural hemorrhage may also be seen in utero and has been reported in association with dural arteriovenous fistulas [85].

Neoplasms. Intracranial masses may be further characterized with fetal MRI. Intracranial teratoma accounts for about half of fetal intracranial tumors. Other fetal brain tumors include astrocytomas, lipomas, choroid plexus papillomas, craniopharyngiomas, and primitive neuroectodermal tumors, in order of decreasing incidence. The majority of fetal brain tumors are supratentorial, as opposed to the more common infratentorial pediatric tumors. With the exception of lipomas and choroid plexus papillomas, prognosis for fetal brain tumors is overall very poor. These tumors tend to bleed and obstruct the ventricular system and may present with hydrocephalus. There may be decreased swallowing due to hypothalamic dysfunction with resulting polyhydramnios [84, 122]. Apart from lipomas and choroid plexus papillomas, fetal brain tumors may grow quite rapidly, and the site of origin may not be discernable; however, most arise from the pineal gland, suprasellar area, or cerebellar hemispheres. Approximately 14% will have associated anomalies, the most common of which is a cleft lip or palate.

It is usually difficult to discern the type of fetal brain tumor with prenatal imaging. Teratomas are complex cystic and solid masses, often with calcification, usually midline and rapidly enlarging (fig. 16.47). Most with intracranial teratomas die in utero or in the neonatal period. Likewise, primitive neuroectodermal tumors, craniopharyngiomas, and glioblastomas are almost always fatal. Low-grade astrocytomas and gangliogliomas have a slightly better prognosis [122].

Choroid plexus papillomas usually arise in the lateral ventricles. Because of the overproduction of cerebrospinal fluid and/or decreased resorption, there is associated hydrocephalus. MRI may depict the hypertrophic choroid. Because of the early hydrocephalus, infants usually present with vomiting, lethargy, convulsions, and papilledema [123].

Lipomas are benign fatty tumors that are often asymptomatic. They are usually located in the midline or in association with a lateral ventricle and are smaller than other brain tumors, with an average diameter of 1.6 cm. Those located in the midline are strongly associated with agenesis of the corpus callosum. MRI is helpful to confirm the fatty nature of the lesion and to evaluate the corpus callosum [122].

Head and Neck

MRI allows evaluation of abnormalities involving the fetal head and neck. Cystic hygromas are benign congenital lesions due to sequestered lymphatic sacs that are usually in the neck and face, most often in the posterior cervical triangle (fig. 16.48). Depending on location, large lesions may compress the airway and MRI is useful in evaluating airway compromise and the need for EXIT (ex utero intrapartum treatment) procedure planning at delivery. MRI is also helpful in delineating the extent of the lesion for surgical planning [124]. MRI may also be helpful in evaluation of anterior neck masses to distinguish a goiter from teratoma or hemangioma. Goiters will demonstrate homogeneous hyperintensity on T1-weighted images and will be indistinct on T2-weighted images as opposed to the typically heterogeneous mass seen with teratomas [76].

Teratomas (fig. 16.49) may arise from the nasopharynx, palate, or thyrocervical area and are often large masses of cystic and solid components. Calcifications

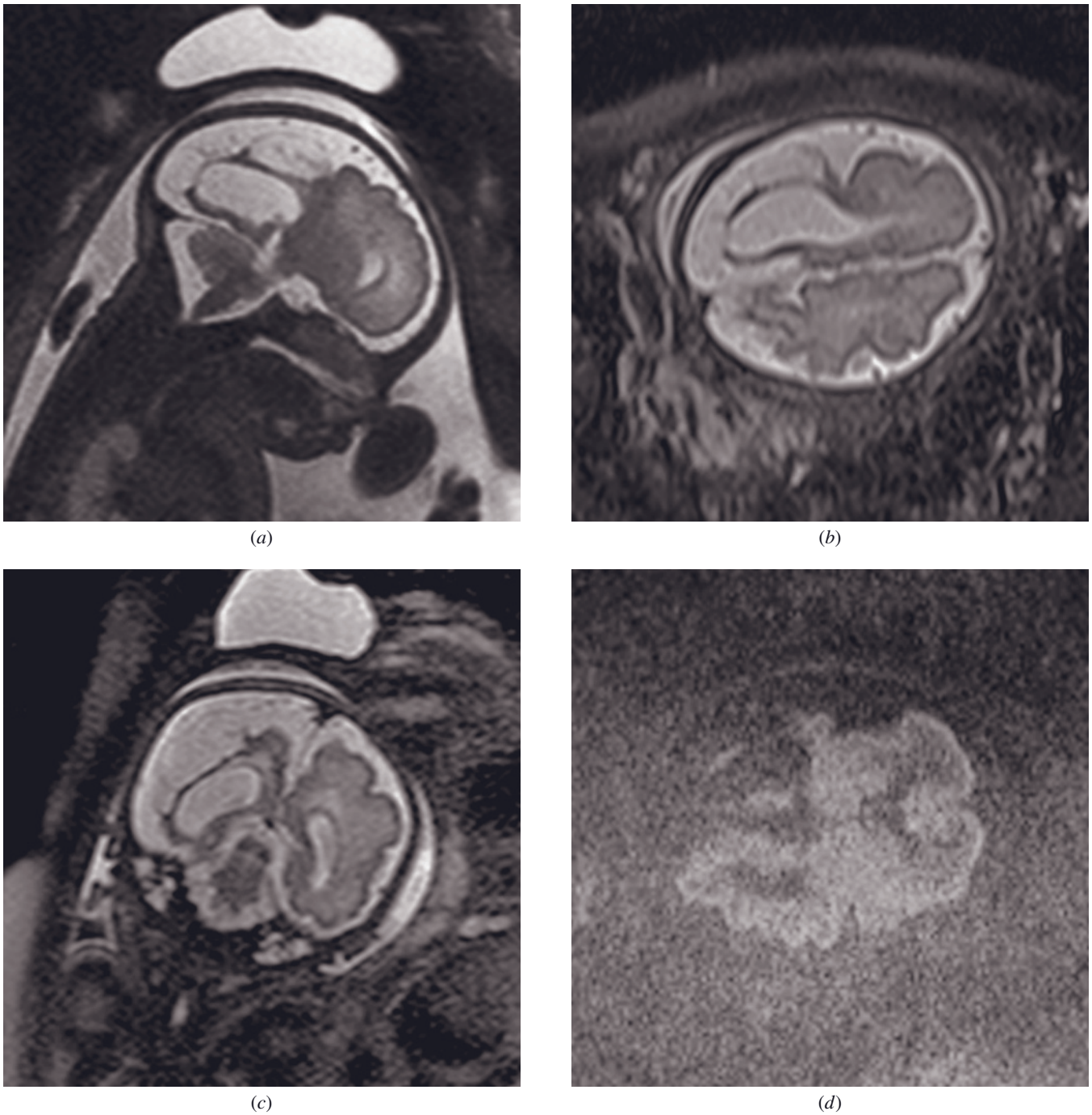

FIG. 16.44 Fetal stroke associated with elevated maternal anticardiolipin antibodies. T2-weighted SS-ETSE images in sagittal (*a*), axial (*b*), and coronal (*c*) planes show a large area of cystic encephalomalacia in the left parietal lobe, resulting from a left middle cerebral artery infarction in a fetus at 32 weeks of gestation. A smooth-walled cystic cavity isointense to CSF and containing thin septations is associated with ex vacuo enlargement of the right lateral ventricle. Axial diffusion-weighted image (*d*) reveals neither focal nor diffuse DWI hyperintensity, excluding acute infarction/ischemia.

are present in approximately 50% of cases and when present are virtually diagnostic. These masses may result in hyperextension of the fetal neck, with resulting malpositioning and dystocia. Those arising from the mouth are referred to as epignathi, most commonly originating from the palate, and typically extend out through the mouth. Transphenoidal intracranial extension can occur with epignathus. Polyhydramnios is common with cervical and oral teratomas because of impaired swallowing [122].

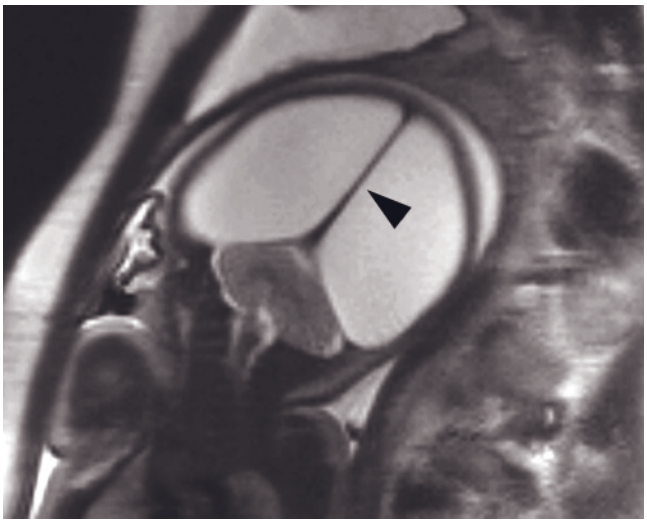

(*a*)

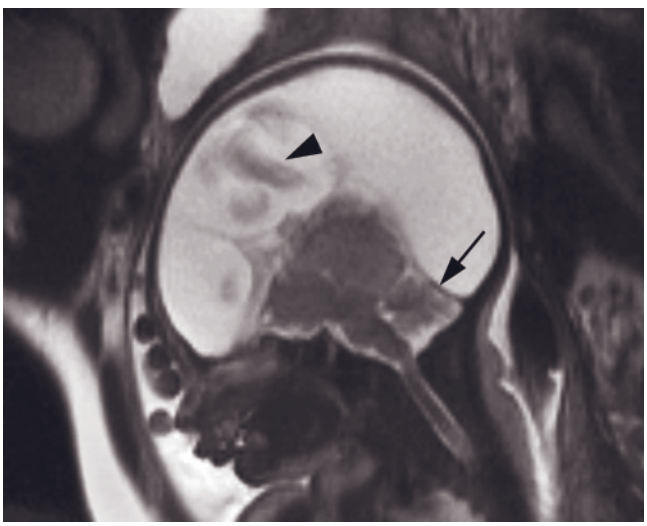

(*b*)

(*c*)

Fig. 16.45 Hydranencephaly. Coronal (*a*) and sagittal (*b*) T2-weighted SS-ETSE and sagittal T2/T1-weighted steady-state free precession (*c*) images of the fetal brain show replacement of the cerebral hemispheres with cerebrospinal fluid and no residual cerebral cortex.The falx is seen (arrowhead, *a*), and the midbrain and cerebellum (arrow, *b*) are preserved. Flow-related dephasing artifact is seen on SS-ETSE images within the amniotic fluid and fetal head (arrowhead, *b*). Note that the steady-state free precession technique (*c*) is devoid of this artifact.

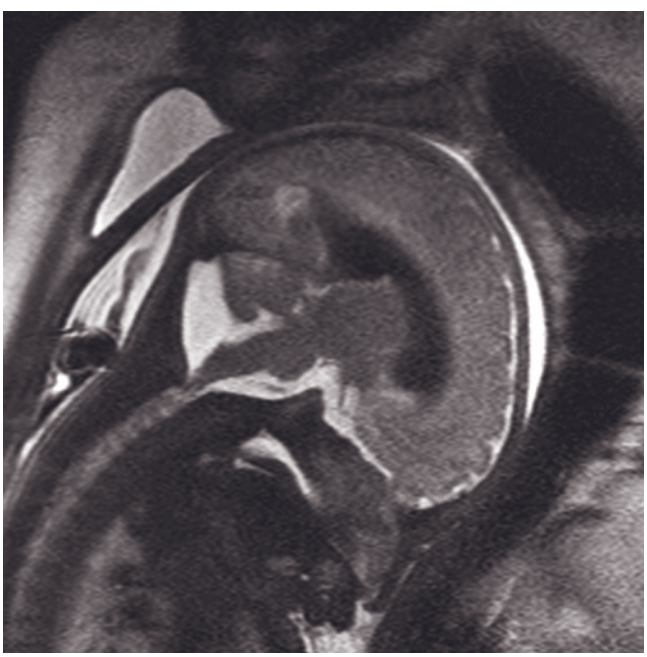

(*a*)

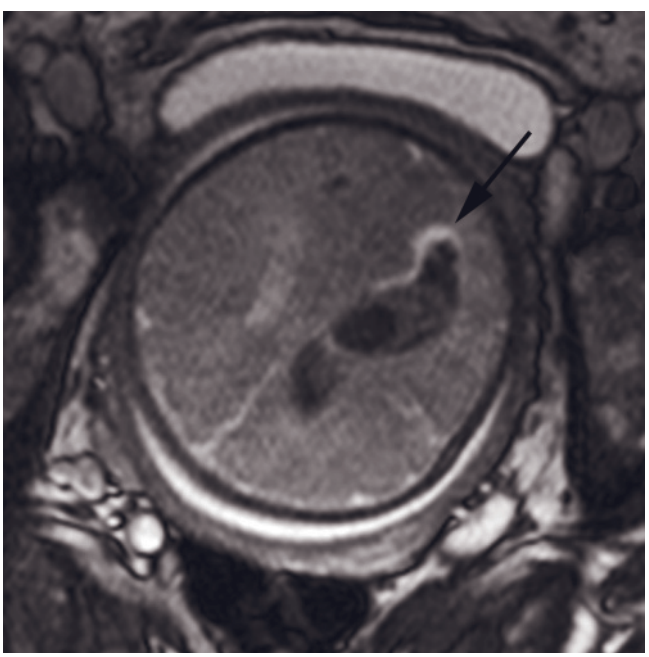

(*b*)

Fig. 16.46 Intraventricular hemorrhage. Sagittal T2-weighted SS-ETSE (*a*) and axial T2-/T1-weighted steady-state free-precession (*b*) images in a fetus at 32 weeks of gestation are shown. There is intraventricular hemorrhage with mild dilatation of the left lateral ventricle, manifested as hypointensity with peripheral rim of high signal intensity (arrow, *b*). Note the presence of

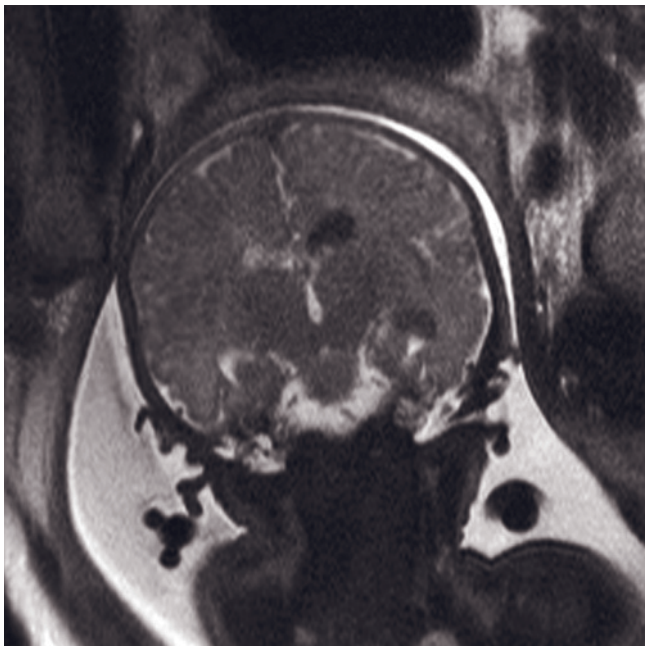

(*c*)

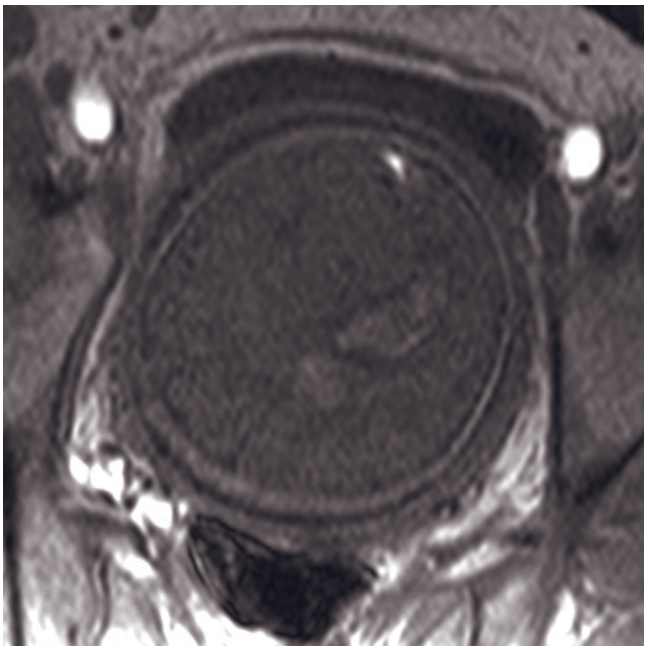

(*d*)

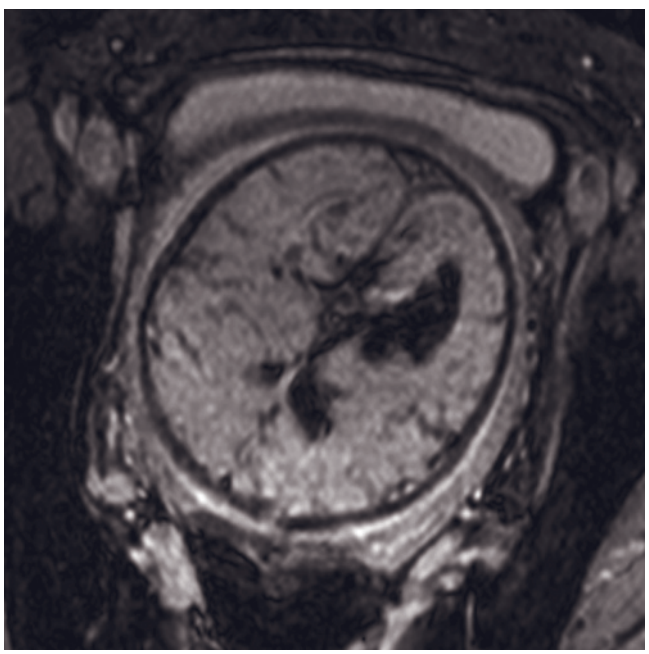

(*e*)

Fig. 16.46 (*Continued*) a small hemorrhagic collection in the frontal horn of the right lateral ventricle, anterior to the foramen of Monro, on the coronal T2-weighted SS-ETSE image (*c*). Subacute stage of bleeding is suggested, because of the signal characteristics on spin-echo and gradient-echo MR sequences: high signal intensity on T1-weighted image (*d*) and prominent low signal intensity on gradient echo T2* image (*e*).

Congenital epulis (fig. 16.50) is a rare, benign soft tissue tumor that arises from the gingival mucosa of the alveolar ridge of the fetus and is usually an isolated finding. These tumors have an 8:1 predilection for female fetuses. Although these lesions arise from the maxilla, the unerupted teeth are not involved by the tumor. No growth of the tumor is seen after birth, and there have been occasional reports of spontaneous regression postnatally. MRI can aid in narrowing the differential, which includes teratoma and hemangioma. These tumors are well circumscribed and usually pedunculated and demonstrate homogeneous T2 hypointensity. Prenatal detection is important for delivery planning as large tumors can potentially cause postnatal respiratory complications from airway obstruction [125, 126].

Detection of clefts of the lip and palate with sonography is highly variable and operator dependent, largely based on sonographer experience and type of cleft.

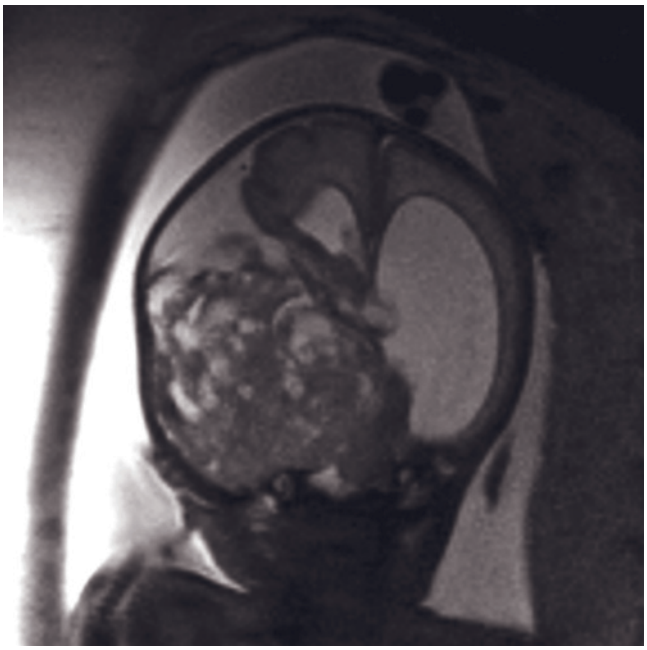

(*a*)

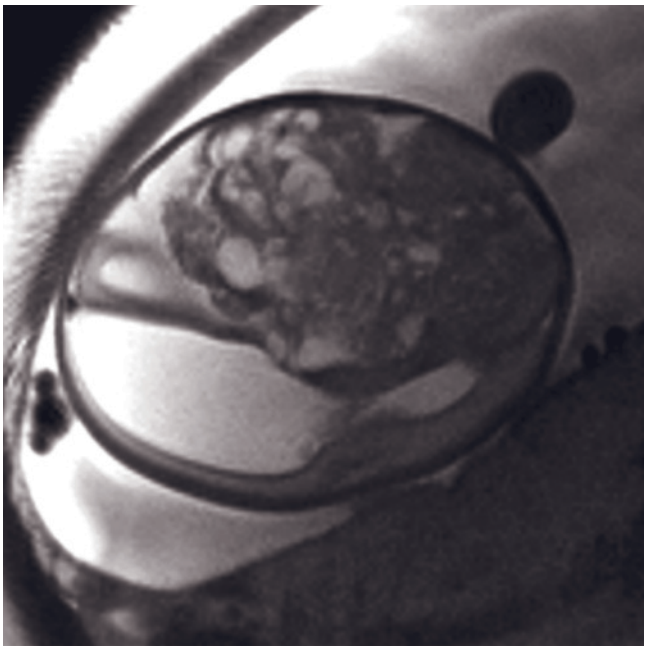

(*b*)

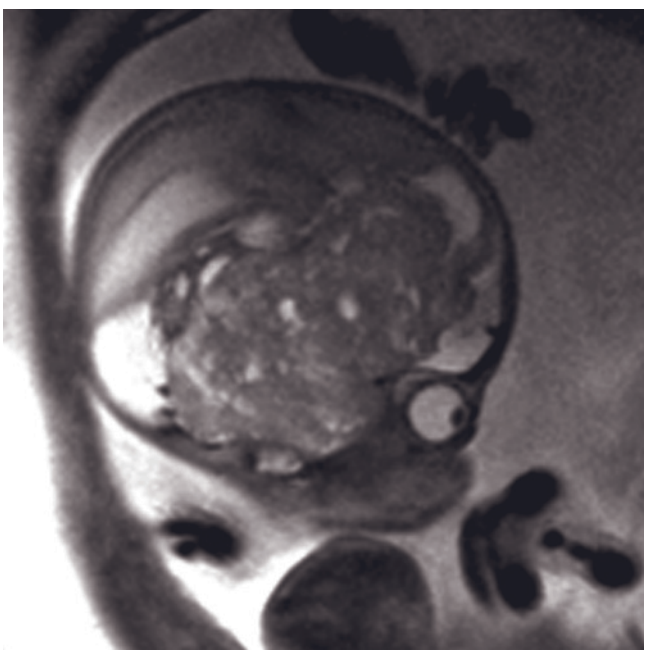

(*c*)

FIG. 16.47 Intracranial teratoma. Coronal (*a*), axial (*b*), and sagittal (*c*) T2-weighted SS-ETSE images of the fetal head demonstrate a large complex intracranial mass with both cystic and solid components occupying the majority of the right cerebral hemisphere. There is resulting midline shift and hydrocephalus.

Isolated cleft palate is particularly difficult to detect sonographically because of artifact from adjacent facial bones and the tongue. The primary palate lies anterior to the incisive foramen and includes the alveolar ridge; the secondary palate lies posterior to the incisive foramen and includes most of the hard palate and the soft palate. Clefts of the secondary palate are generally not well visualized with standard sonography. Clefts involving both the lip and palate and clefts involving the secondary palate are associated with a higher risk of karyotype anomalies. Median facial clefts are associated with holoprosencephaly. Isolated clefts of the palate may be syndromic or nonsyndromic. In addition, infants with cleft palate are at risk for chronic otitis media, hearing loss, abnormal speech, and midfacial retrusion, as opposed to isolated cleft lips. In general, the more posterior the cleft and the greater the involvement of the palate, the more complicated the surgical

(*a*)

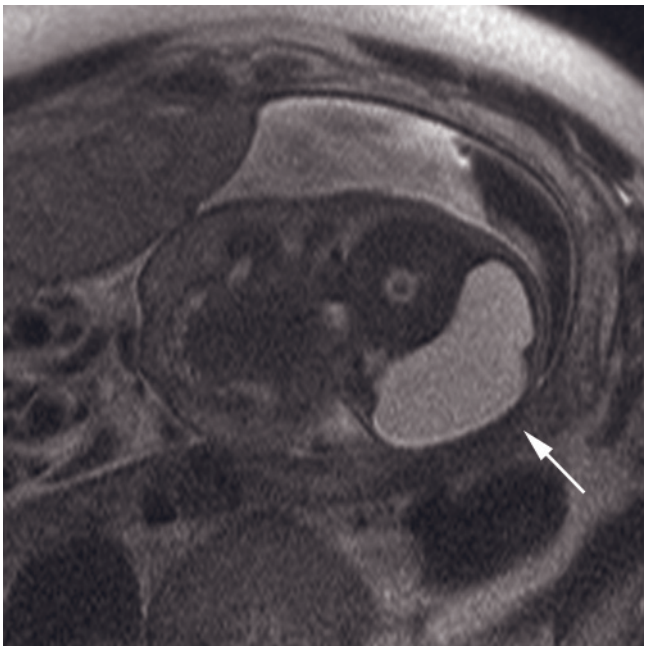

(*b*)

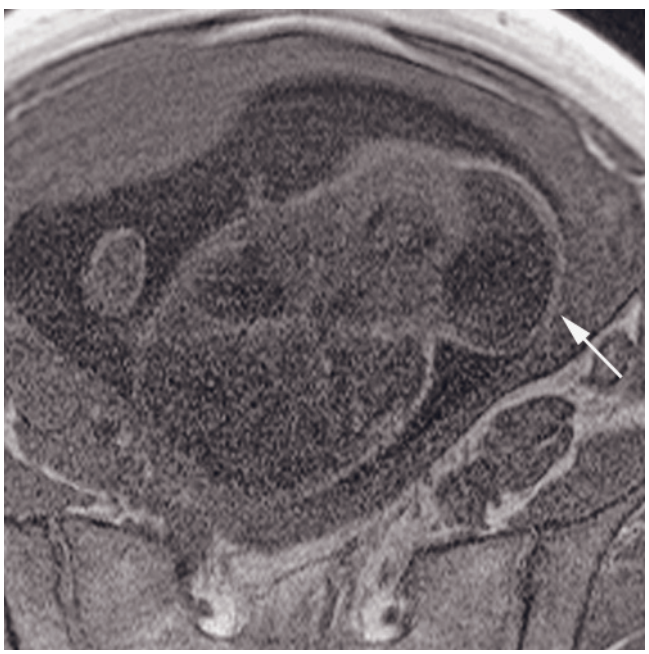

(*c*)

FIG. 16.48 Lymphangioma/cystic hygroma. Coronal (*a*) and axial (*b*) T2-weighted SS-ETSE images and axial T1-weighted image (*c*) show a single large T2-hyperintense/T1-hypointense cyst, extending from the mandible into the neck (arrows, *b*, *c*).

repair is. MRI allows visualization of the lip and both the primary and secondary palate [127, 128]. On T2-weighted images, the normal palate appears as a hypointense stripe extending from the frenulum of the upper lip posteriorly to the nasal choanae where the nasopharynx and the oropharynx join together [77] (fig. 16.28). Cleft lip is well seen in the coronal and axial planes, and cleft palate is best evaluated in the axial and sagittal planes (fig. 16.51). Abnormally elevated tongue position and communication of the oro- and nasopharynx are secondary signs of cleft secondary palate [127]. With routine MR imaging, fetal movement may limit visualization of the palate, which may be overcome by real-time MR imaging. As the secondary palate may be best visualized in the midsagittal plane when the oropharynx is distended with fluid, real-time SSFSE imaging may be performed every 3–4 s until the fetus swallows, allowing this distension [128].

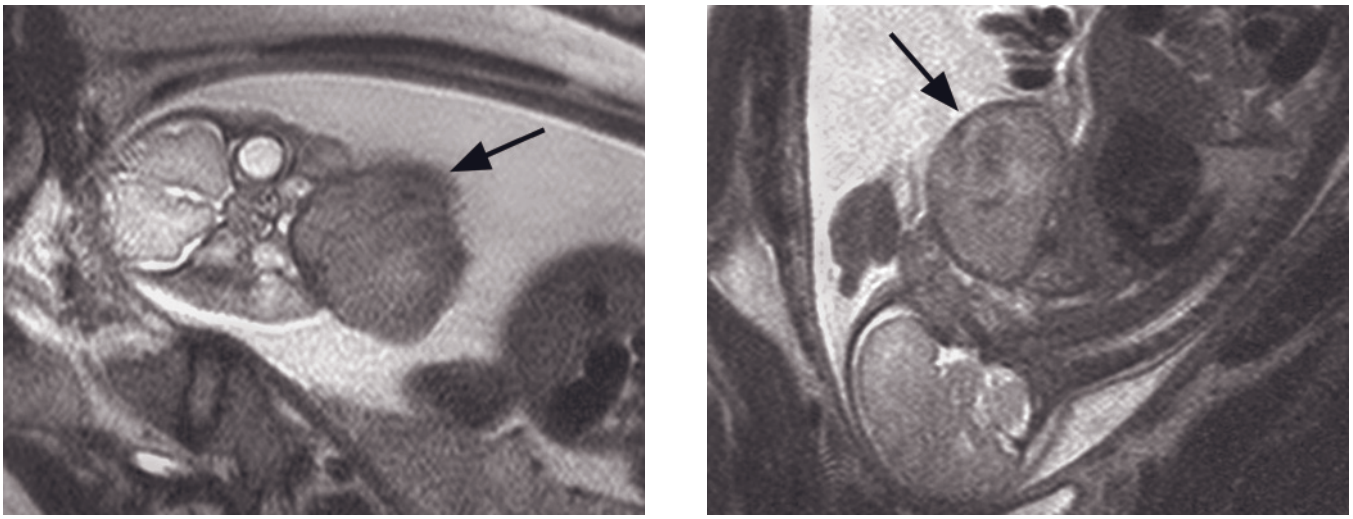

(*a*) (*b*)

FIG. 16.49 Teratoma of the fetal mouth. Coronal (*a*) and sagittal (*b*) T2-weighted SS-ETSE images through the fetal head and neck show a large, heterogeneous mass (arrow, *a*, *b*) arising from the fetal mouth.

Dacryocystocele is a benign cyst resulting from prenatal obstruction of the lacrimal system both proximally and distally (fig. 16.52). The lacrimal sac dilates with mucus and amniotic fluid due to obstruction, and the dilatation usually extends intranasally to the nasolacrimal duct, forming a nasal cyst. Cystic dilatation confined to the distal nasolacrimal duct may also be seen, in which case the superior portion of the nasolacrimal duct and the lacrimal sac are unaffected. Although spontaneous rupture occurs in most cases during the first month of life, prenatal detection is important because bilateral dacryocystoceles are a potential cause of neonatal nasal obstruction. Unilateral cysts must be differentiated from other abnormalities in this location, such as encephalocele, nasal glioma, rhabdomyosarcoma, dermoid cyst, or hemangioma. Dacryocystoceles may be associated with various syndromes or an isolated finding. MRI can accurately depict the three components of dacryocystoceles, all of which demonstrate T2 hyperintensity [129, 130].

Congenital hemangiomas (fig. 16.53) progress in utero, unlike infantile hemangiomas, which typically appear after birth. Congenital hemangiomas may be subdivided into rapidly involuting (RICH) and noninvoluting (NICH) types. RICH is more frequent, especially on the skull and in the peri-auricular region, and typically presents as a raised tumoral lesion. These lesions typically resolve by 14 months of age. On T2-weighted images, the majority of cases described demonstrate marked or slight hyperintensity; however, some cases have demonstrated hypointensity. Evidence of blood products may be seen with foci of T1 hyperintensity/T2 hypointensity. Flow voids may be seen. MRI is useful in characterizing the lesion and excluding encephalocele [131–134].

Thorax

MRI has been shown to be useful in assessment of hypoplastic lung in cases of congenital diaphragmatic hernia and the spine in cases of mediastinal cysts [12, 66, 135]. MRI has also been helpful in distinguishing congenital diaphragmatic hernias and other less common pulmonary lesions from adenomatoid-cystic pulmonary malformation (CCAMs) to better advantage than ultrasound [12]. MRI offers an advantage in determining whether liver is involved in a congenital diaphragmatic hernia, which may be difficult with ultrasound. MRI changed the diagnosis in nearly 50% of lung masses diagnosed sonographically in one study [12]. In another study evaluating a variety of thoracic abnormalities, the diagnosis was changed in 38% and affected management in 8% [136].

Congenital Diaphragmatic Hernia. Congenital diaphragmatic hernia is more common posterolaterally on the left than the right side. The stomach, small intestine, and colon herniate more frequently than liver, gallbladder, and spleen. Herniation of liver portends a worse prognosis, and it may be difficult to determine whether liver has herniated with ultrasound. With MRI, the liver, intestines, and lung are clearly differentiated based on signal characteristics and the location of the liver is more readily assessed (fig. 16.54). Recent MR studies have shown a worsening prognosis with increasing volume of liver herniated [137, 138]. A recent study found an 86% neonatal mortality if 20% or more of the

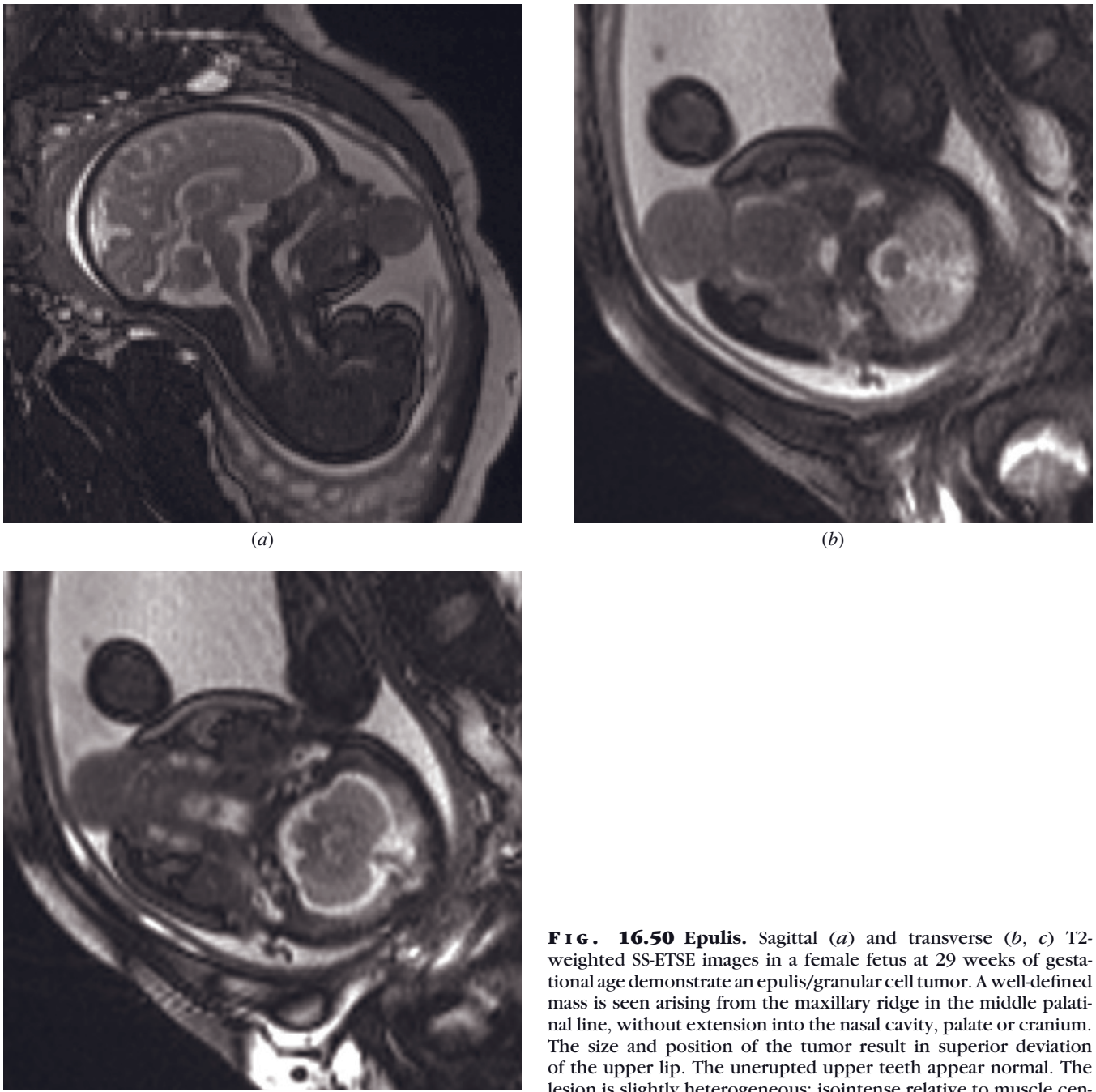

(*a*) (*b*) (*c*)

FIG. 16.50 Epulis. Sagittal (*a*) and transverse (*b*, *c*) T2-weighted SS-ETSE images in a female fetus at 29 weeks of gestational age demonstrate an epulis/granular cell tumor. A well-defined mass is seen arising from the maxillary ridge in the middle palatinal line, without extension into the nasal cavity, palate or cranium. The size and position of the tumor result in superior deviation of the upper lip. The unerupted upper teeth appear normal. The lesion is slightly heterogeneous: isointense relative to muscle centrally, with a peripheral hyperintense rim.

thoracic volume was occupied by liver as opposed to 13% mortality if less than 20% (as measured in the axial plane on MRI) [137]. There is a high rate of associated anomalies with congenital diaphragmatic hernia, which increase the mortality rate. Pulmonary hypoplasia is the primary cause of morbidity and mortality. On T2-weighted images, compressed lung is of intermediate signal intensity, hypointense to the noncompressed lung [12, 139]. MRI can provide an estimation of the residual lung volume, which may be important in predicting pulmonary hypoplasia. MRI thus plays an important role in prenatal counseling.

Pulmonary Malformations. Cystic adenomatoid malformations (CCAM) are hamartomatous pulmonary malformations that contain both cystic and solid tissue. Three types have been described pathologically, with decreasing cyst size from type I to type III. Prenatally,

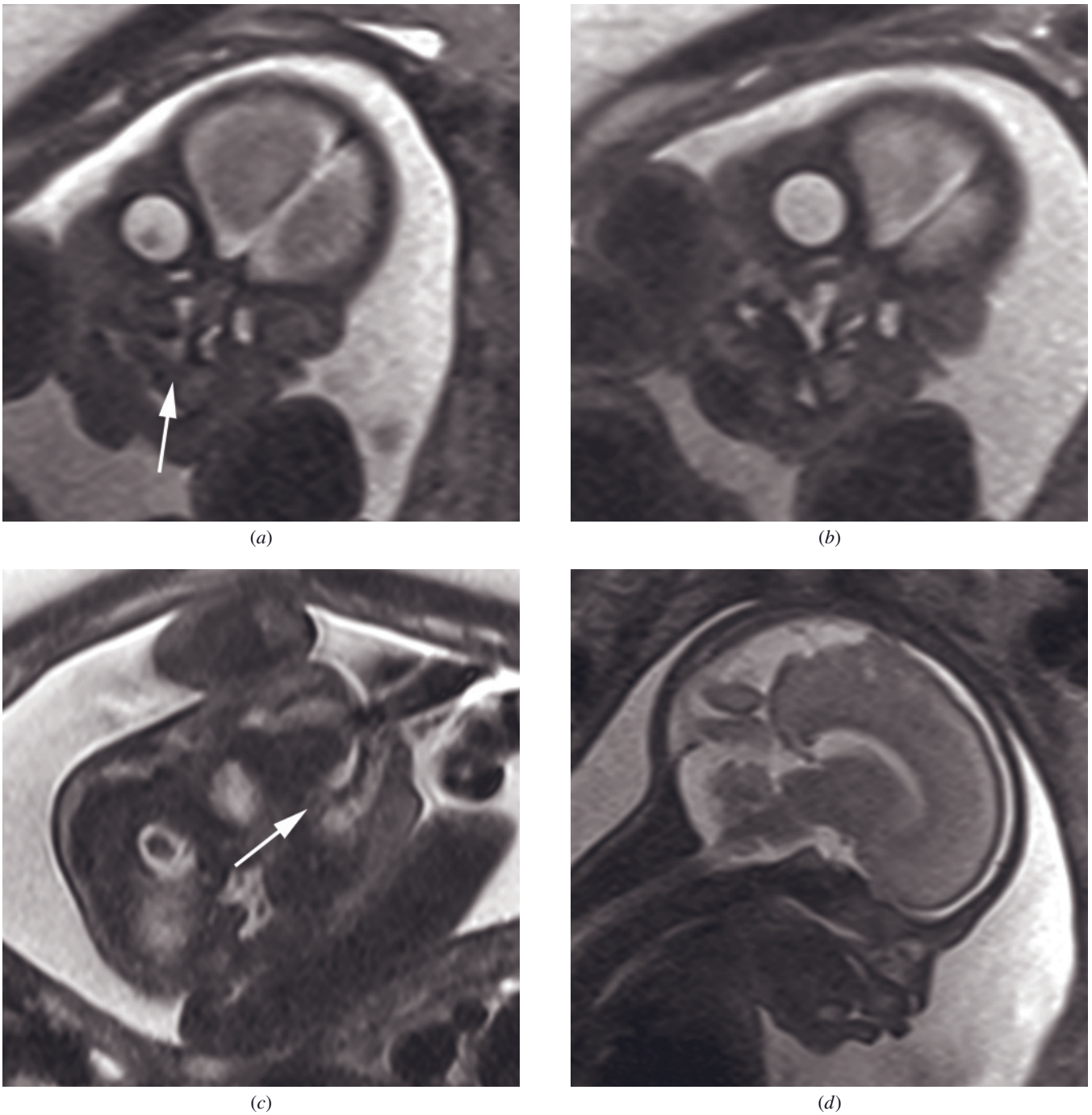

FIG. 16.51 Unilateral cleft lip and palate. T2-weighted SS-ETSE oblique coronal (*a*, *b*), transverse (*c*), and sagittal (*d*) images show complete unilateral clefts of the lip and palate on the right side. The cleft extends through the upper lip to the nose, forming a channel filled with amniotic fluid.

these are sonographically classified as macrocystic and microcystic, with the macrocystic having a better prognosis. MR features are variable, ranging from multiple large cysts with discrete walls to solid-appearing lesions; however, all have markedly higher signal intensity than normal lung on fluid-sensitive sequences (fig. 16.55). Lesions may enlarge or regress during the pregnancy. Development of hydrops portends a poor prognosis and is an indication for fetal intervention [12, 139].

Bronchopulmonary sequestration is abnormal pulmonary tissue that is not connected to the tracheobronchial tree. Two subtypes are described, based on the presence (extralobar) or absence (intralobar) of a

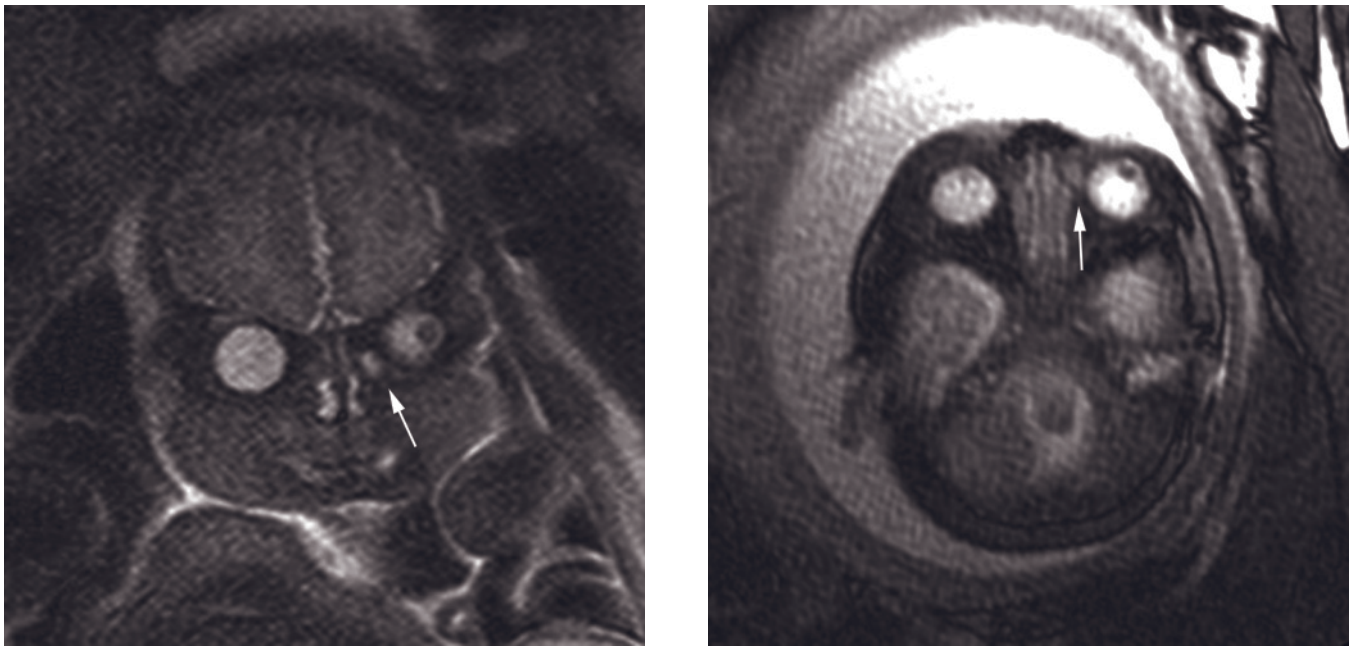

(*a*) (*b*)

FIG. 16.52 Dacryocystocele. Sagittal (*a*) and transverse (*b*) T2-weighted SS-ETSE images of the fetal head demonstrate a well-circumscribed, T2 hyperintense cyst at the inferomedial aspect of the left orbit, consistent with a dacryocystocele, confirmed at birth.

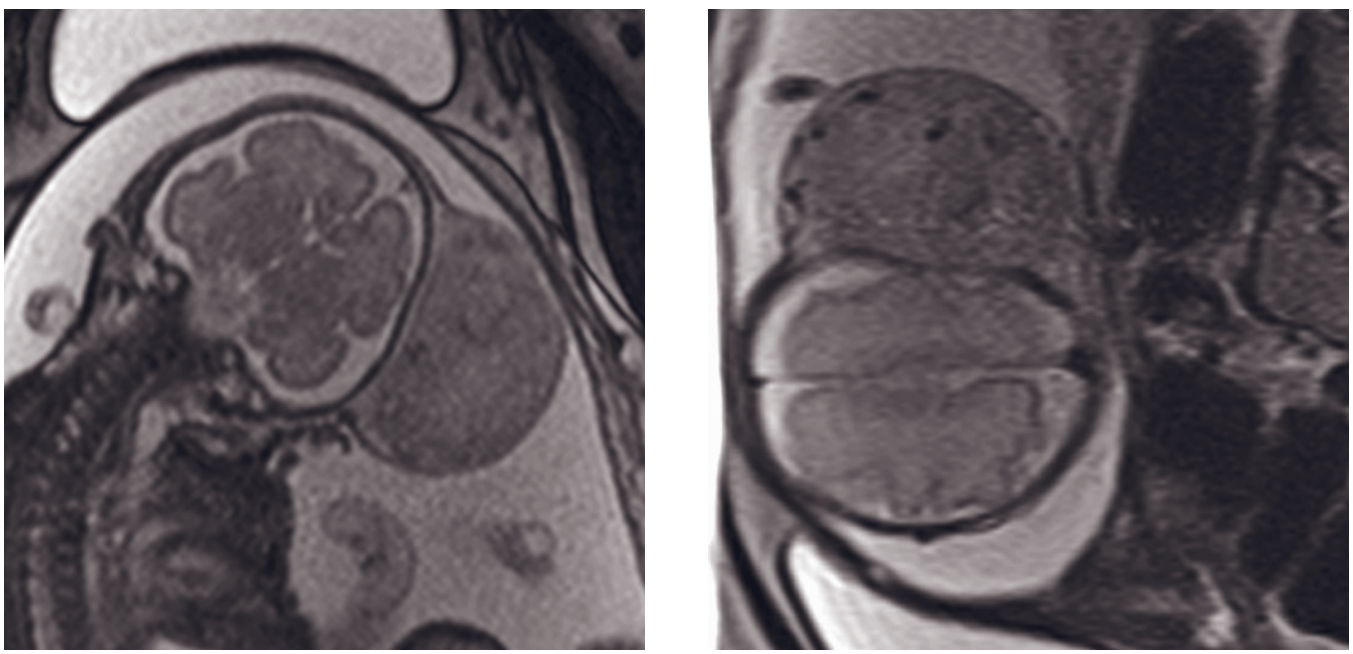

(*a*) (*b*)

FIG. 16.53 Congenital hemangioma. T2-weighted SS-ETSE images in coronal (*a*), axial (*b*), and sagittal (*c*) planes demonstrate a scalp hemangioma in a male fetus at 27 weeks of gestational age. There is a well-circumscribed extracranial mass originating from the soft tissues of the scalp. The underlying parietal bone and frontotemporal squama are intact. The mass is iso-/hyperintense with a hypointense pseudocapsule and prominent peripheral flow voids.

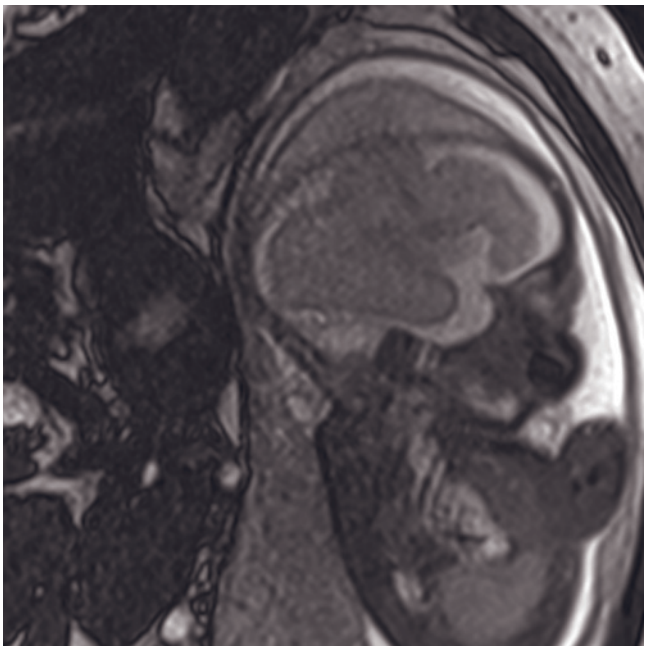

FIG. 16.53 (*Continued*) (*c*)

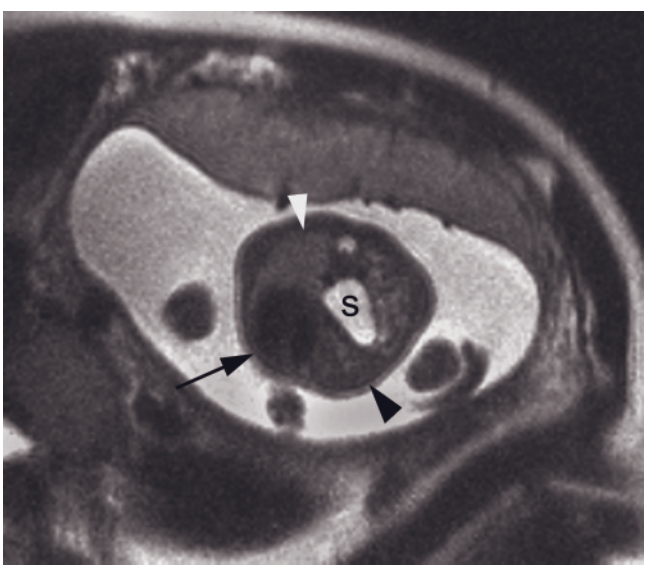

(*a*)

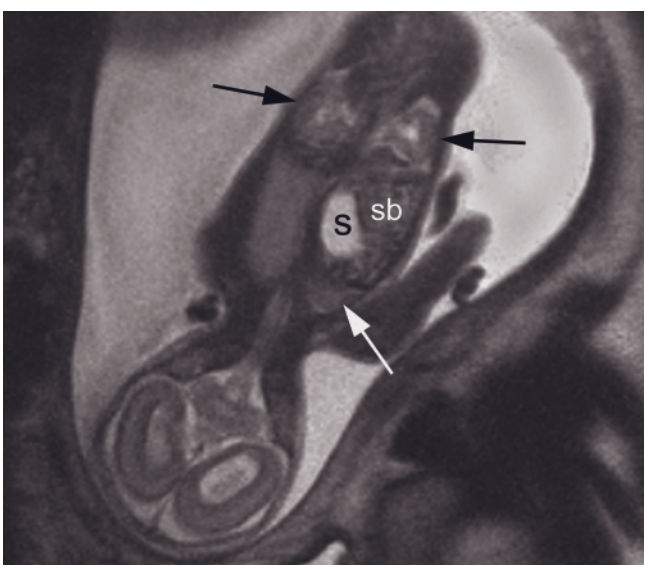

(*b*)

FIG. 16.54 Congenital diaphragmatic hernia. Transverse (*a*) and coronal (*b*) T2-weighted SS-ETSE images through the fetal torso in the second trimester show stomach (s, *a*, *b*) and small bowel (sb, *b*) in the left fetal chest. A small portion of fetal lung (white arrow, *b*) is seen at the apex. The transverse image shows the heart (black arrow, *a*) abnormally located in the right chest and the right lung (white arrowhead, *a*) posteriorly. The hernia contains liver (black arrow, *a*), which is associated with a worse outcome. Note normal second-trimester fetal kidneys (black arrows, *b*). Coronal T2-weighted SS-ETSE images (*c* and *d*) in a different

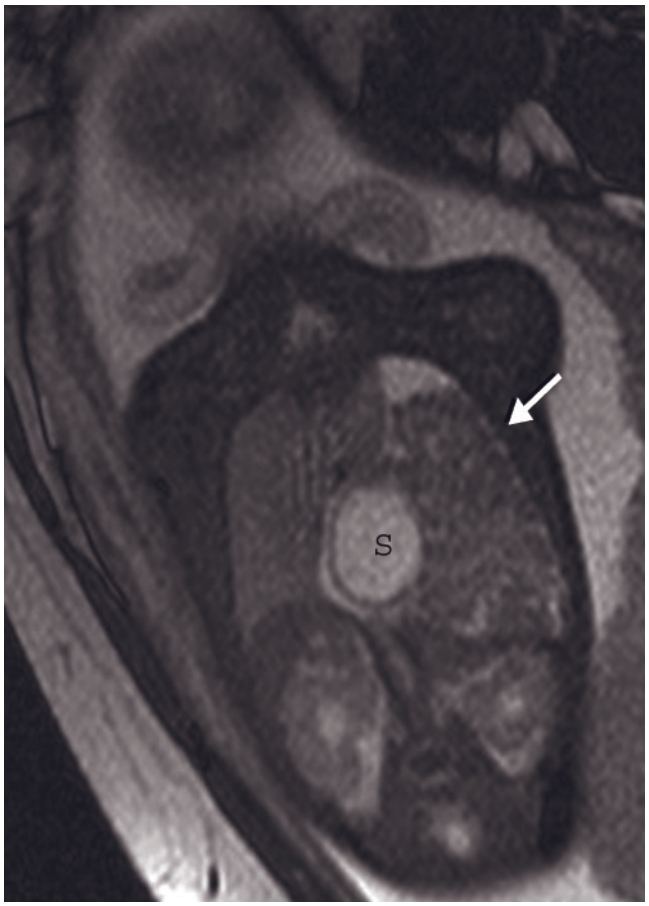

(*c*)

(*d*)

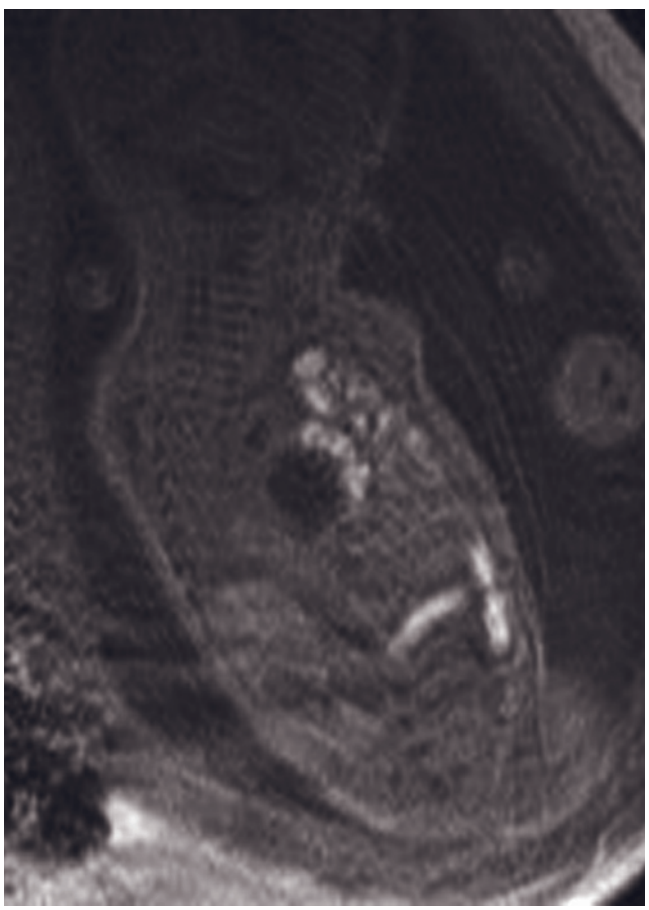

(*e*)

Fig. 16.54 (*Continued*) fetus at 30 weeks of gestational age demonstrate herniation of stomach and bowel above the diaphragm, occupying the left side of the fetal chest. A small amount of liver is also seen within the left hemithorax. Slightly obliqued coronal T1-weighted GRE image (*e*) in a third patient at 28 weeks of gestation demonstrates bowel within the left fetal hemithorax as evidenced by the hyperintense meconium in the distal bowel lumen.

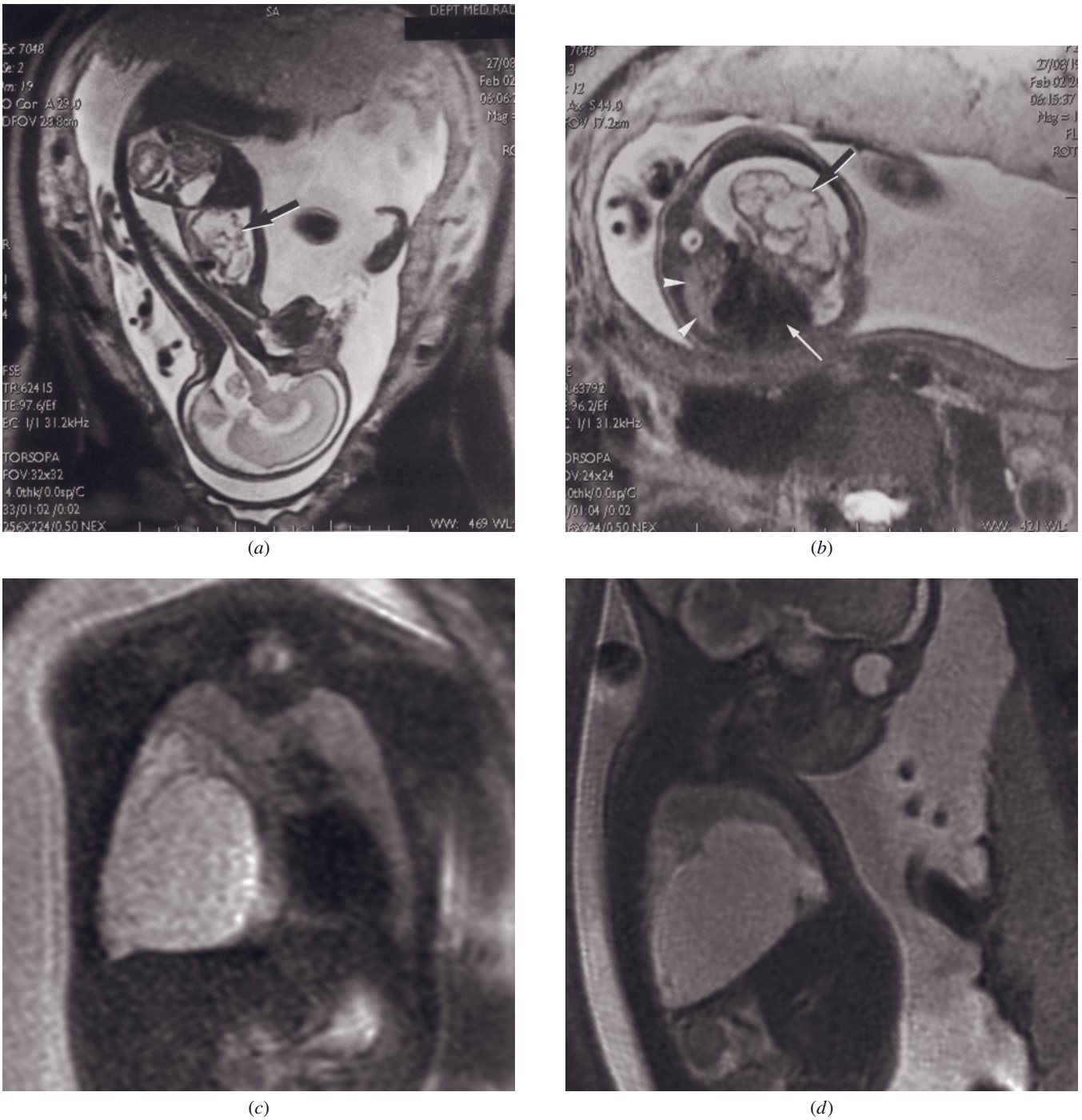

(*a*) (*b*) (*c*) (*d*)

FIG. 16.55 Cystic adenomatoid malformation. Sagittal (*a*) and transverse (*b*) T2-weighted SS-ETSE images of a fetus at 28 weeks of gestation reveal a mainly cystic, hyperintense lesion within the left hemithorax (black arrows). The heart (white arrow) is pushed to the contralateral side. Hypoplasia of the right lung (arrowheads) and associated polyhydramnios were seen. Coronal (*c*), sagittal (*d*), and transverse (*e*) T2-weighted SS-ETSE images of a different fetus at 30 weeks of gestation demonstrate a large

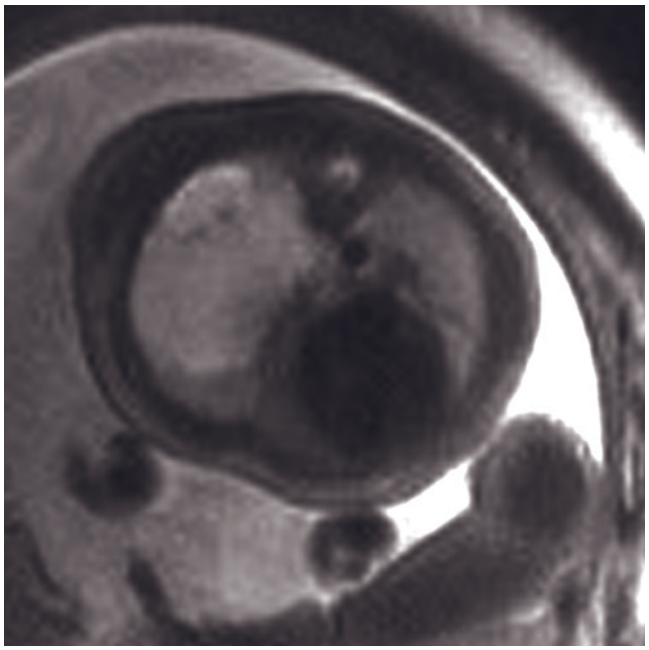

(*e*)

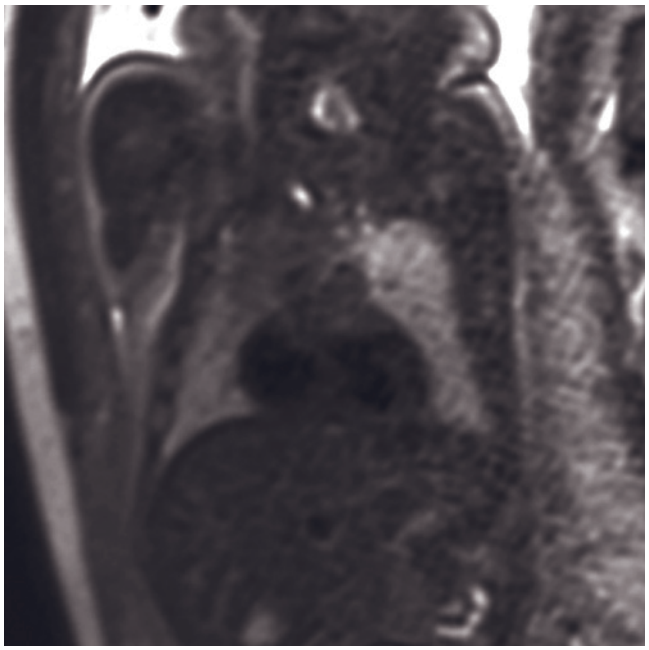

(*f*)

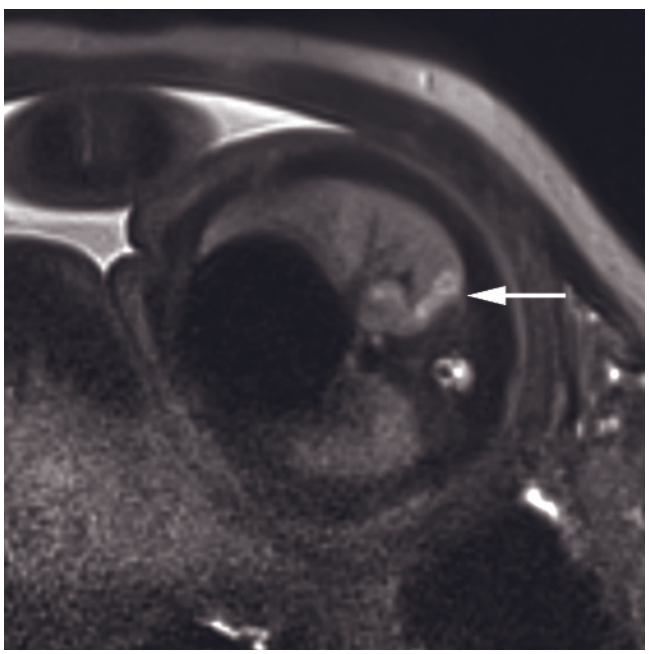

(*g*)

FIG. 16.55 (*Continued*) hyperintense lesion within the right hemithorax that appears macrocystic. Coronal (*f*) and transverse (*g*) T2-weighted SS-ETSE images in a third fetus with suspected congenital cystic adenomatoid malformation in the lung. There are 3 hyperintense foci (arrow, *g*) in the right lower lobe, well-visualized on the transverse SS-ETSE. The coronal image shows these foci to a lesser extent, but clearly depicts the intact diaphragm, excluding congenital diaphragmatic hernia.

separate pleural envelope. Intralobar sequestration drains via the pulmonary veins; extralobar sequestration drains to a systemic vein in 75%. Arterial supply is systemic for both types, usually from a branch off the aorta. Both are most commonly located in the lower lobes. Extralobar sequestrations are more often on the left and may be either above or below the diaphragm. Intralobar sequestrations are not commonly diagnosed in utero. Prenatally diagnosed sequestrations generally have a favorable prognosis; many regress in utero. Pleural effusions may develop and progress to tension hydrothoraces with resulting hydrops, an indication for intervention. On MRI, sequestrations appear as a homogeneously hyperintense mass with well-defined margin on fluid-sensitive sequences [12, 139]. Occasionally, the systemic arterial supply may be demonstrated (fig. 16.56).

Other pulmonary malformations may be seen on fetal MRI as well. Bronchial stenosis may be identified,

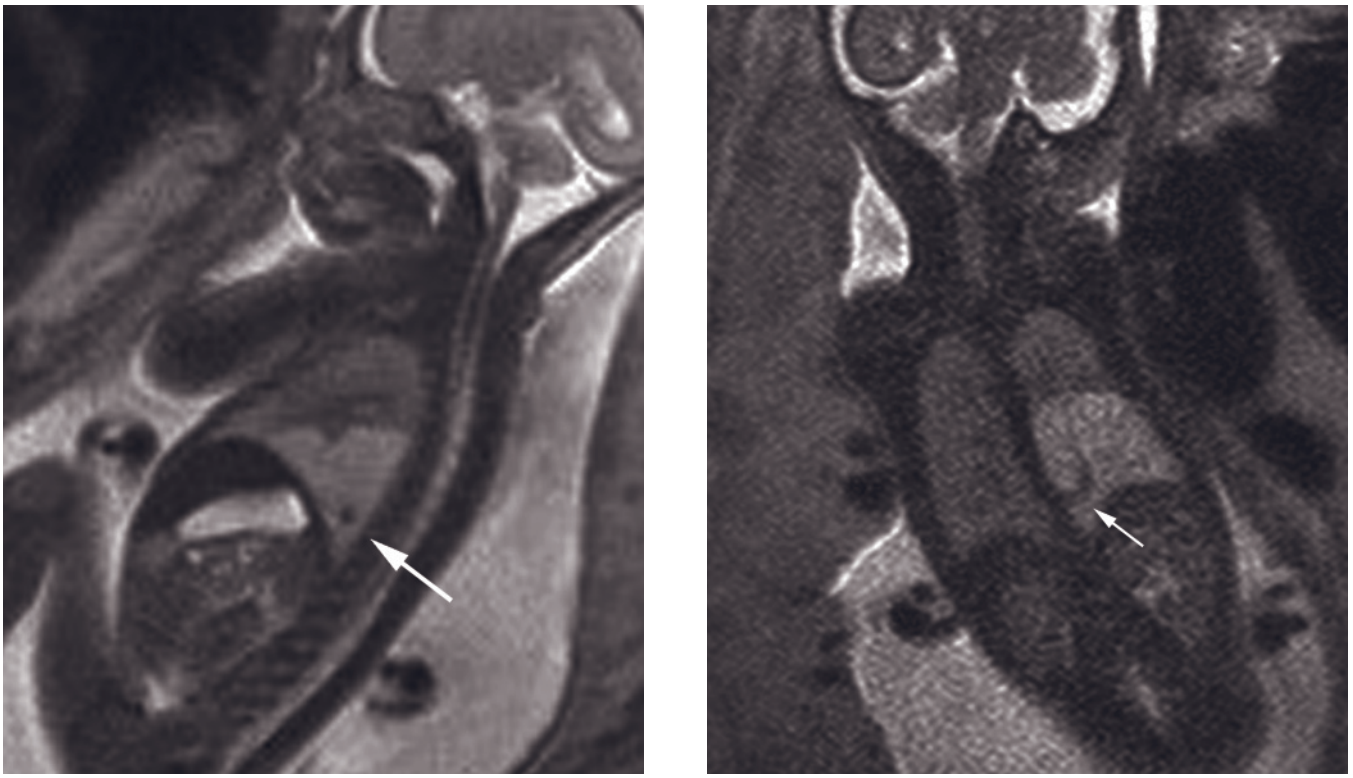

(*a*) (*b*)

FIG. 16.56 Bronchopulmonary sequestration. Sagittal (*a*) and coronal (*b*) T2-weighted SS-ETSE images in a fetus at 25 weeks of gestation demonstrate a mildly hyperintense mass in the left lower lobe. A flow void extends from the aorta into the pulmonary mass (arrows), suggesting systemic arterial supply to a bronchopulmonary sequestration.

with the affected lobe demonstrating homogeneously increased signal intensity relative to adjacent normal lung on fluid-sensitive sequences, but less intense than that of CCAMs [12]. Congenital high airway obstruction (CHAOS) may be demonstrated as well; tracheal atresia results in uniform T2 hyperintensity throughout bilaterally enlarged lungs, with fluid visible in the dilated trachea and eversion of the diaphragm [12].

Thoracic Cysts. Mediastinal masses and foregut cysts have occasionally been diagnosed as well. Bronchogenic cysts appear as T2 hyperintensities that are usually located in the middle mediastinum but may be intraparenchmyal as well. Neurenteric cysts are T2 hyperintensities located posteriorly, in communication with the meninges [139].

Neoplasms. Intrapericardial and mediastinal teratomas are uncommon. These tend to be mixed cystic and solid lesions demonstrating mixed signal intensity and may be quite large. In large masses, the origin of the mass may be difficult to discern, and the presence of calcifications is helpful in distinguishing mediastinal teratomas from pulmonary masses [12].

Abdomen and Pelvis

Kidneys. Oligohydramnios is frequently seen with renal anomalies and has been reported in 50% of cases referred for further evaluation of suspected renal anomalies [140]. Although fetal renal anomalies are often well depicted with ultrasound, the presence of associated oligohydramnios or anhydramnios can make sonographic evaluation very difficult, as can maternal body. Detection of severe renal anomalies in utero can potentially affect prenatal management, given the poor prognosis with pulmonary hypoplasia. MRI is not dependent on the quantity of amnionic fluid that is present and is able to depict both normal and abnormal anatomy accurately, despite maternal body habitus. MRI can therefore play an important role in prenatal counseling. In studies evaluating the role of MRI in sonographically suspected renal anomalies, MRI has been shown to change or narrow the diagnosis in 36% and to change management in one case (3%), allowing continuation of a pregnancy with a resulting normal neonate [141]. Another study evaluating sonographically suspected bilateral renal anomalies and cases of inadequate sonographic evaluation found MRI changed the diagnosis in 31% of patients and affected

continuation or termination of the pregnancy in 25% of patients [142].

Renal Agenesis. Renal agenesis may be a unilateral or bilateral process. When the process is bilateral, anyhdramnios results (fig. 16.57); when unilateral, the amniotic fluid status is variable, depending on the presence of contralateral renal anomalies. The sensitivity of ultrasound decreases as the amniotic fluid volume decreases, and MRI is therefore helpful for detection and further characterization of renal anomalies. MRI can confirm absence of a kidney in the renal fossa and can depict renal ectopia. Confirmation of bilateral renal agenesis is particularly important as this condition is universally fatal, and early detection can impact counseling and management of the pregnancy. With unilateral renal agenesis, MRI is helpful in evaluating the structure and morphology of the contralateral kidney, assessing fluid status, and evaluating the signal intensity of the lungs as an indicator of pulmonary maturation. Association of renal agenesis with VACTERL complex should prompt a meticulous evaluation for other fetal anomalies.

Renal Ectopia and Fusion Abnormalities. Sonographic detection of an ectopic kidney can prove challenging; however, renal ectopia can be readily demonstrated with MRI either with T2-weighted images or diffusion-weighted imaging [143]. Axial T2-weighted images will demonstrate extension of renal tissue across the midline, anterior to the spine, in cases of horseshoe kidney.

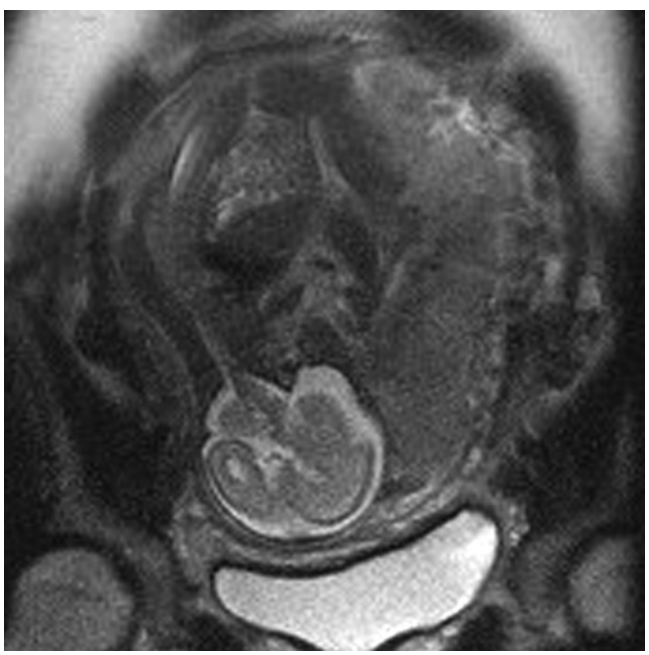

FIG. 16.57 Anhydramnios secondary to renal agenesis. Coronal T2-weighted SS-ETSE image of a fetus at 24 weeks of gestation reveals no visible amniotic fluid. No kidneys could be found.

Renal duplication is the most common morphologic anomaly of the kidneys [144]. Distension of the collecting system is often seen, related to the Weigert–Meyer rule that describes obstruction of the upper pole moiety and reflux into the lower pole moiety. An added benefit of MRI in these instances is that the path of the ureters can be followed, particularly the insertions into the bladder, where an associated ureterocele can sometimes be demonstrated.

Hydronephrosis. Mild pelviectasis, or central renal pelvis dilatation, can be a normal variant in the fetus. Different threshold measurements have been described in the sonographic literature to indicate hydronephrosis. While absolute numbers are important, the presence of caliectasis has been described as the most important factor, as this finding doubles the risk of needing surgery for hydronephrosis [145]. Fetal hydronephrosis can have many causes, the most common of which include ureteropelvic junction (UPJ) obstruction, vesicoureteral reflux, and posterior urethral valves [146]. Other less common etiologies may lead to upper tract dilatation as well, including ureterovesical obstruction, ureteroceles with or without duplicated collecting system, urethral atresia, megaureter, megacystis-microcolon hyperperistalsis syndrome, and extrinsic compression related to pelvic masses [143]. The dilated, fluid-filled collecting system is readily apparent on T2-weighted sequences.

In congenital UPJ obstruction, the renal pelvis is significantly dilated, with less striking dilatation of the calyces and a nondilated ureter. With continued progression of the obstruction, cystic parenchymal dysplastic changes will be seen, mainly in the periphery of the kidney.

Posterior urethral valves, an entity seen in male fetuses, will result in a ballooned appearance of the posterior urethra, distension of the urinary bladder, and, depending on the severity, varying degrees of hydroureteronephrosis. The typical "keyhole" deformity seen on ultrasound is also well-depicted with T2-weighted images.

Prune belly syndrome occurs almost exclusively in males and is characterized by abdominal wall laxity, distended urinary bladder and renal collecting systems, and cryptorchidism. The dilated renal collecting systems and dilated bladder are well visualized on T2-weighted images. The abdomen appears distended; however, clear evaluation of the abdominal wall and the rectus muscles is beyond the resolution of MR images [143].

Megacystis-microcolon hyperperistalsis syndrome is an autosomal recessive condition that is typically lethal

within the first year. It is characterized by a markedly enlarged bladder and dilatated urinary collecting system without obstruction, microcolon, and decreased gastrointestinal peristalsis. On MRI, visualization of an enlarged bladder and a very thin colon should raise suspicion for possible megacystis-microcolon hyperperistalsis syndrome. In comparison to ultrasound, the colon can be more easily discerned from small bowel with MRI by the presence of T1-hyperintense meconium [143, 147, 148].

Cystic Renal Disease. Multicystic dysplastic kidney (MCDK) is a nonfunctioning kidney replaced by noncommunicating cysts of varying sizes, scattered throughout the kidney (fig. 16.58). On ultrasound, the numerous cystic lesions in the abdomen may at times be difficult to distinguish from dilated loops of bowel, and MRI can play a confirmatory role in diagnosis. Unilateral MCDK is associated with contralateral renal anomalies, in particular UPJ obstruction and vesicoureteral reflux. The diagnosis is of great importance as bilateral MCDK is invariably fatal [149].

Autosomal recessive polycystic kidney disease (ARPKD) is an inherited disorder characterized by renal tubular malformation with nonobstructive cystic dilatation of the renal collecting tubules. The kidneys become enlarged and replaced by innumerable tiny cysts that may be resolved on T2-weighted sequences (fig. 16.59) or present as T2 hyperintensity. Liver fibrosis is also a feature of this disease. There is a wide spectrum of severity of both renal and hepatic involvement, and prognosis likewise ranges from pulmonary hypoplasia and neonatal death to survival into adulthood and variable development of renal failure and portal hypertension [150].

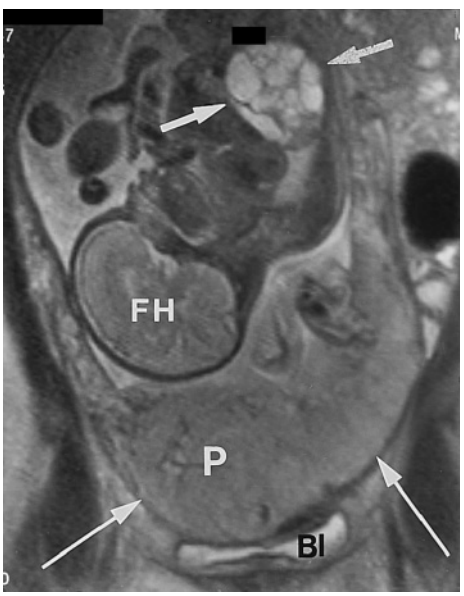

FIG. 16.58 Multicystic dysplastic kidney disease. Coronal SS-ETSE sequence through the maternal pelvis. Fetal kidney (arrows) shows multiple high-signal-intensity cysts, which is consistent with multicystic dysplastic renal disease. In addition, a complete placenta previa is demonstrated (long thin arrows). FH, fetal head; P, placenta; Bl, maternal bladder.

Meckel–Gruber syndrome is a fatal, autosomal recessive disorder, characterized by a triad of markedly enlarged polycystic kidneys, occipital encephalocele, and postaxial polydactyly. Many additional associated anomalies may be present as part of the syndrome, involving the brain, extremities, face, heart, and genitalia, among others. The presence of two of the classical features with a normal karyotype is suggestive of this entity (fig. 16.60). These classical findings may be seen with ultrasound, although sometimes the findings are equivocal, particularly the ability to definitively distinguish an encephalocele from a cystic hygroma or in the setting of marked oligohydramnios. Additionally, the encephalocele may sometimes be very small and not detected on ultrasound. In these cases, when polydactyly is suggested on ultrasound along with the finding of cystic kidneys MRI is very useful to evaluate the brain and skull, as the possibility of Meckel–Gruber should be considered in this setting [151].

Persistent Cloaca. Persistent cloaca is a rare anomaly in which the embryologic cloaca does not divide and a single perineal opening is present for the genital, urinary, and gastrointestinal tracts. This may be associated with ambiguous genitalia, obstructive uropathy, and pulmonary hypoplasia. There is significant anatomical variation with this entity; however, aberrant drainage of urine may lead to ascites if drainage occurs via the fallopian tubes and obstruction may lead to pelvic cystic structures, hydroureter, and oligohydramnios. The colon and vagina may also dilate because of accumulation of urine. The mixing of urine with meconium may lead to intraluminal calcified meconium. Cardiac and vertebral anomalies and intrauterine growth restriction may coexist. Diagnosis early in the second trimester is associated with a worse prognosis, with renal failure in childhood and pulmonary hypoplasia. In those fetuses that survive to delivery, a good postnatal outcome is expected with appropriate surgical intervention. Prenatal diagnosis is important for prenatal counseling and delivery planning. MRI may play a role in delineating the anatomy in these cases and in distinguishing isolated hydrocolpos from that associated with persistent cloaca [152–154].

Fetal Gastrointestinal System. Nonvisualization of the stomach with ultrasound can be caused by multiple etiologies, among them esophageal atresia, difficulty swallowing from various causes, and inadequate amni-

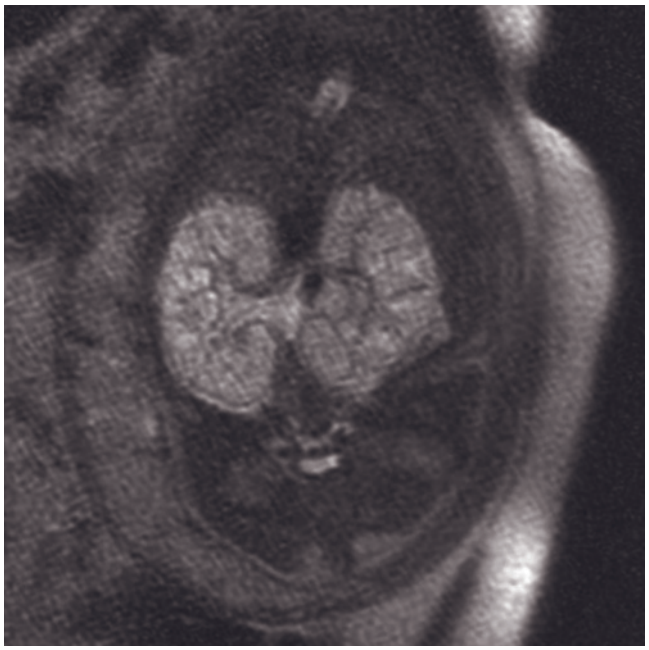

(*a*)

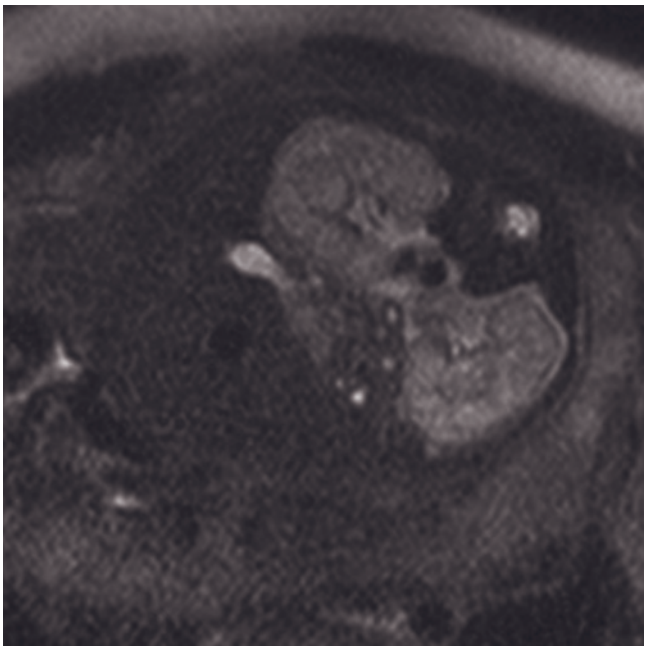

(*b*)

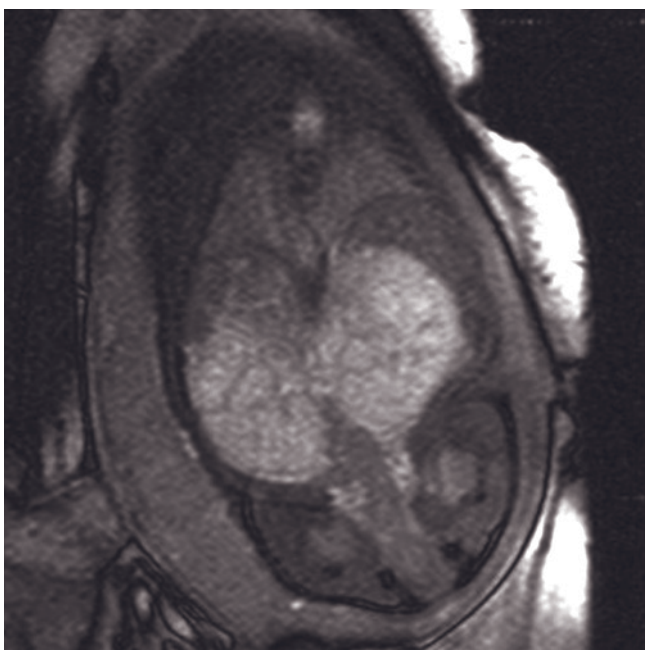

(*c*)

FIG. 16.59 Polycystic kidney disease. Sagittal (*a*) and transverse (*b*) T2-weighted SS-ETSE images show bilaterally enlarged kidneys, measuring 5.6 cm at 29 weeks of gestation. The kidneys are diffusely hyperintense, without clearly discernible cysts, consistent with polycystic kidneys. There is associated anhydramnios. Coronal T1-/T2-weighted steady-state free-precession image (*c*) shows relatively small chest in comparison to abdomen, suggesting possible pulmonary hypoplasia.

otic fluid volume. The stomach may be malpositioned in the chest, as in the case of congenital diaphragmatic hernia, or it may be on the right side of the abdomen as in heterotaxy syndromes. MRI may be helpful if the prenatal ultrasound has technical limitations.

In cases of small bowel dilatation, the approximate level of a small bowel atresia may be inferred by the signal intensity of the intraluminal contents proximal to the obstruction. If dilated small bowel is predominantly T2 hyperintense and T1 hypointense, a proximal obstruction such as jejunal atresia should be suspected. If dilated small bowel is mainly T2 hypointense and T1 hyperintense, then a distal atresia, such as ileal atresia, should be suspected [80, 155].

Abdominal Wall Defects. The abdominal wall closes once the midgut returns to the abdominal cavity after physiologic herniation, a process that is complete by the 12th week of gestation [80]. Abdominal wall abnormalities include omphalocele, gastroschisis,

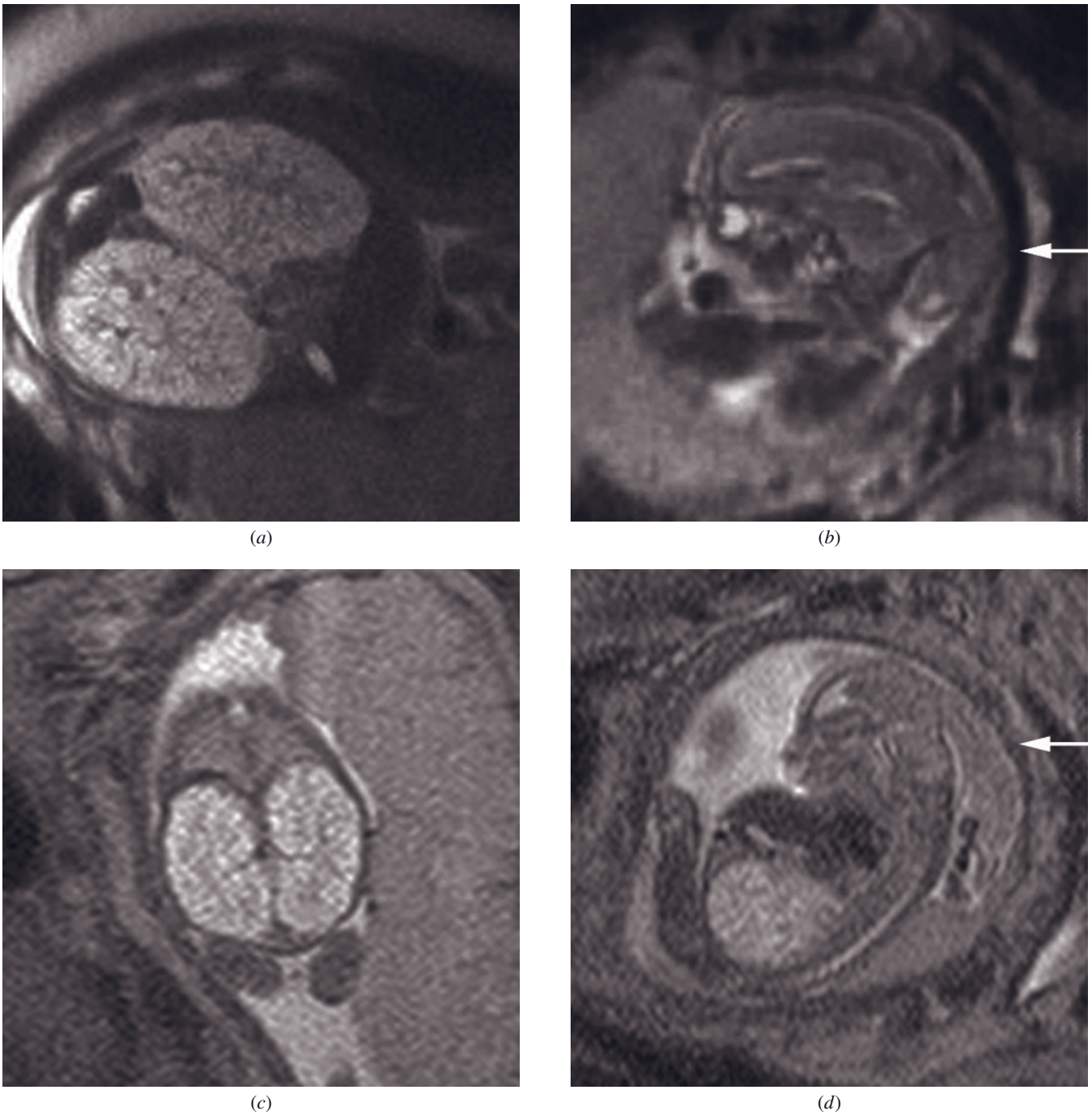

FIG. 16.60 Meckel–Gruber syndrome. Coronal T2-weighted SS-ETSE image of the kidneys in a 20-week fetus (*a*) demonstrates enlarged, hyperintense kidneys bilaterally measuring 5.7 cm, with innumerable small cysts. Sagittal T2-weighted SS-ETSE image of the fetal head (*b*) demonstrates herniation of brain tissue posteriorly (arrow), consistent with an occipital encephalocele. Coronal T2-weighted SS-ETSE image of the kidneys in a different fetus at 17 weeks of gestation (*c*) also reveals polycystic kidneys with enlarged, hyperintense kidneys bilaterally containing innumerable small cysts. Sagittal T2-weighted SS-ETSE image of the fetal head (*d*) also demonstrates an occipital encephalocele (arrow).

limb-body wall complex, amniotic bands, pentalogy of Cantrell, and bladder extrophy. The two main differential considerations when herniated contents are seen outside the abdominal cavity on ultrasound are omphalocele and gastroschisis. Although usually distinguishable on ultrasound, there are occasions when the distinction is difficult. On MRI, the herniated contents can be easily depicted [156]. The contents of the herniation are important, as generally omphaloceles carry a higher risk of karotype anomalies. Furthermore, with regard to omphaloceles, the presence of herniated liver has important prognostic implications [79].

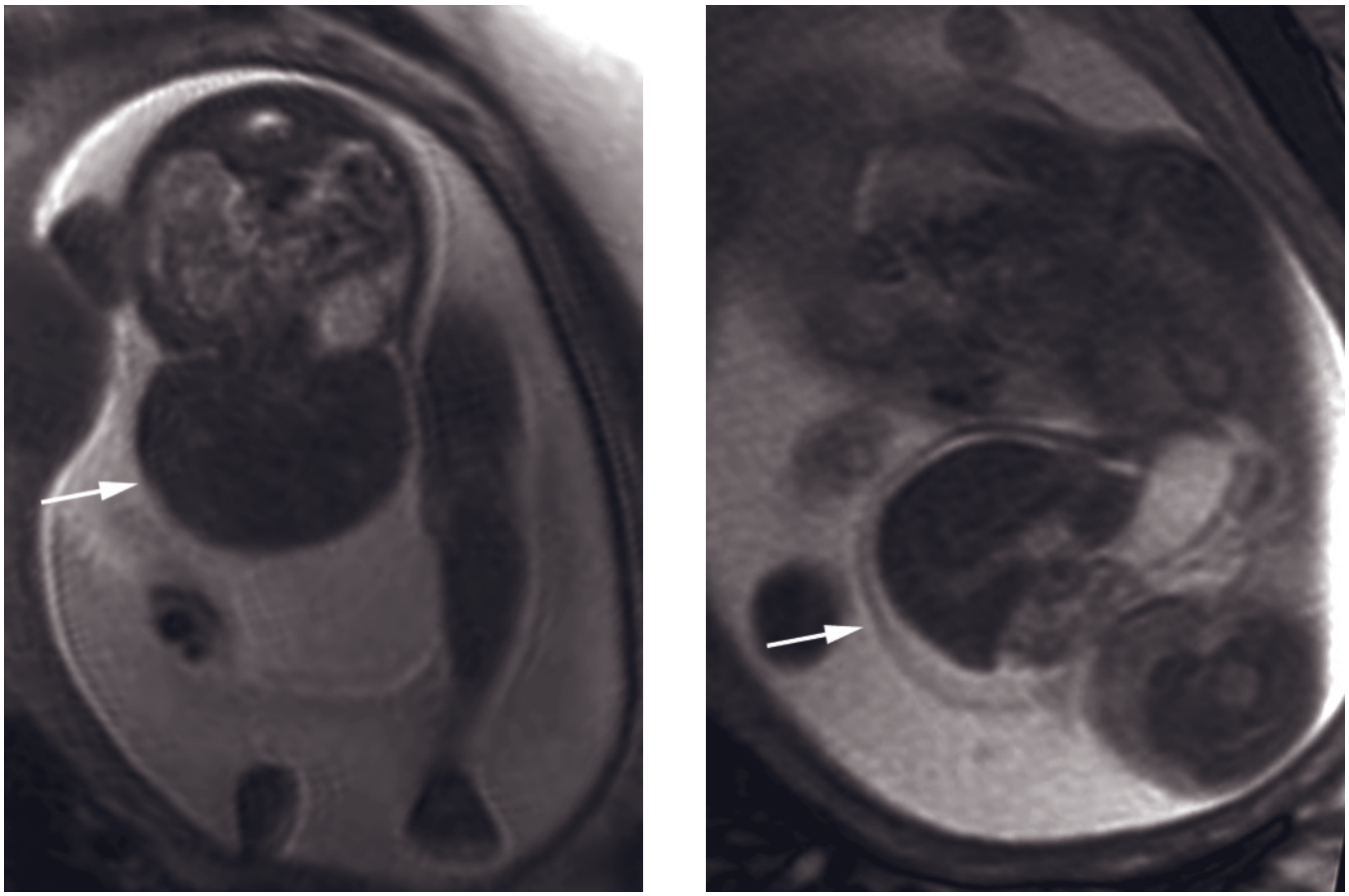

(*a*) (*b*)

FIG. 16.61 Omphalocele. T2-weighted ETSE images of a 25-week fetus obtained in the transverse and sagittal planes demonstrate a herniation of the anterior abdominal wall containing liver, stomach, and bowel (arrows). Note the covering membrane (*a*) and midline herniation, characteristic of omphalocele.

Omphalocele is an anterior abdominal wall defect with herniation of intra-abdominal contents through the base of the umbilical cord (fig. 16.61). Liver and small bowel are often herniated and are surrounded by a covering membrane, which on occasion may be difficult to detect with ultrasound. MRI is able to depict the contents of the hernia sac, which include amnion, Wharton jelly, viscera, and peritoneum [156]. There is a high incidence of other associated anomalies in the presence of an omphalocele.

Gastroschisis, in contradistinction to ompalocele, is herniation of abdominal contents without a covering membrane. The herniation occurs lateral to the umbilical cord insertion, usually to the right. Although gastroschisis is usually not associated with chromosomal or other anomalies, the neonatal prognosis depends on the condition of the herniated bowel. MRI may have a role in determining the condition of the bowel, specifically for the evaluation of bowel wall thickness, dilatation, and atresia. A study in 2006 suggested promise in the use of 3D MRI for evaluation of the bowel loops in gastroschisis [157].

Bladder exstrophy is a rare malformation describing the combination of an infraumbilical abdominal wall defect and exposure of the posterior bladder wall to the external environment (fig. 16.62). MRI will depict an infraumbilical solid mass protruding outside the abdominal cavity and nonvisualization of the bladder [158].

Abdominal/Pelvic Cysts. Cysts are easily discerned on MRI, because of the presence of T2 hyperintense fluid. Determination of the location of a cyst and the sex of the fetus allows narrowing of the differential diagnosis. MRI may help determine whether a cyst arises or is separate from the kidney. Enteric duplication cysts, due to improper recanalization of the gut, may occur at any point along the alimentary tract; most in the abdomen involve the ileum [159] (fig. 16.63). Meconium pseudocysts may be distinguished from enteric cysts on MRI, as the former demonstrate intermediate T1 signal intensity [84].

Neoplasms. MRI is helpful in determining the origin of abdominal masses. Sacrococcygeal teratoma

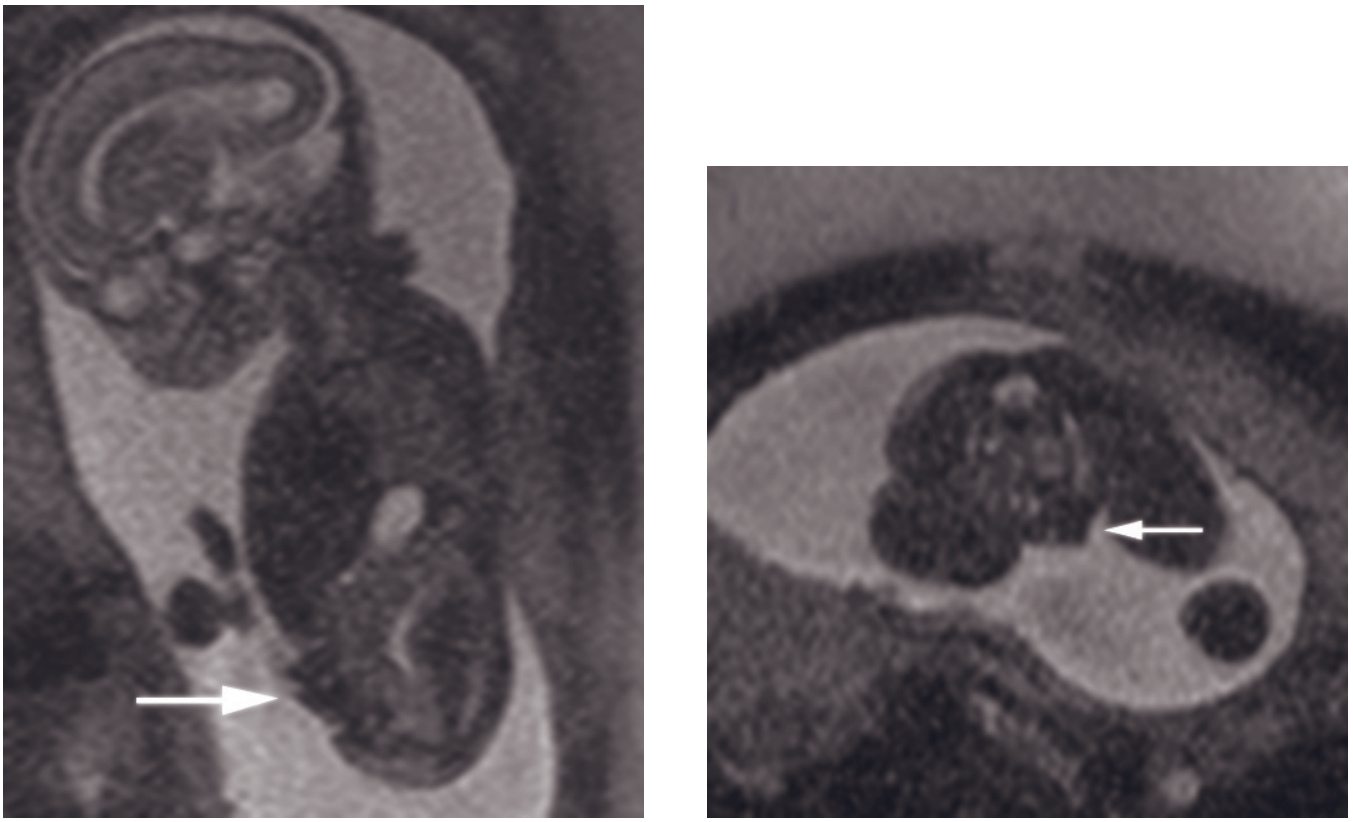

(*a*) (*b*)

FIG. 16.62 Bladder extrophy. Sagittal (*a*) and transverse (*b*) T2-weighted SS-ETSE images of a fetus at 20 weeks of gestation reveal no normal urinary bladder. An irregular, infraumbilical anterior abdominal mass is seen, suggestive of bladder extrophy.

(fig. 16.64) is the most common fetal and neonatal tumor. Prenatal diagnosis is associated with a nearly 50% mortality rate, as opposed to the 5% mortality rate of infants diagnosed neonatally. If not diagnosed before birth, complications include preterm labor, dystocia, hemorrhage into the tumor, and tumor avulsion with fetal exsanguination. Sacrococcygeal teratomas are divided into four types based on the relative amount of tumor located internally and externally. Type I is external with no or minimal internal component, type II is predominantly external with extension into the presacral space, type III is both external and internal with extension into the abdominal cavity, and type IV is completely internal. Intraspinal extension may occur. The size of the solid component of the tumor is the most important feature for prognosis, with predominantly cystic masses having a much better prognosis. Solid tumors can be very vascular and result in arteriovenous shunting, high-output cardiac failure, and hydrops. In addition, intratumoral hemorrhage may result in fetal anemia and also lead to high-output cardiac failure, the distinction of which is important for management. Polyhydramnios is often present and may elicit preterm labor. Conversely, oligohydramnios may rarely develop because of compression of the urinary tract. MRI is superior to ultrasound in evaluating the internal and intraspinal extent of the teratoma, in distinguishing a solid tumor from intratumoral hemorrhage or a microcystic tumor, and in detecting the presence and effects of compression of adjacent organs. MRI features vary and depend on the relative cystic and solid components, as well as the presence of associated hemorrhage. Associated anomalies include undescended testes, hydronephrosis, renal dysplasia, urethral atresia, hydrocolpos, and, less commonly, hip dislocation, clubbed feet, and rectal atresia or stenosis. Fetal surgery may be considered in cases with high-output cardiac failure because of the poor prognosis [122, 160]. The uncommon fetus in fetu is a retroperitoneal teratoma that is an encapsulated, pedunculated mass with highly organized features containing a rudimentary vertebrae or notochord. Some believe that this is the result of abnormal twinning rather than a well-developed teratoma [122].

Neuroblastoma is the most common congenital malignancy, representing 30% of all fetal tumors. These tumors are found anywhere along the sympathetic chain, with >90% arising from the adrenal gland. Prenatal

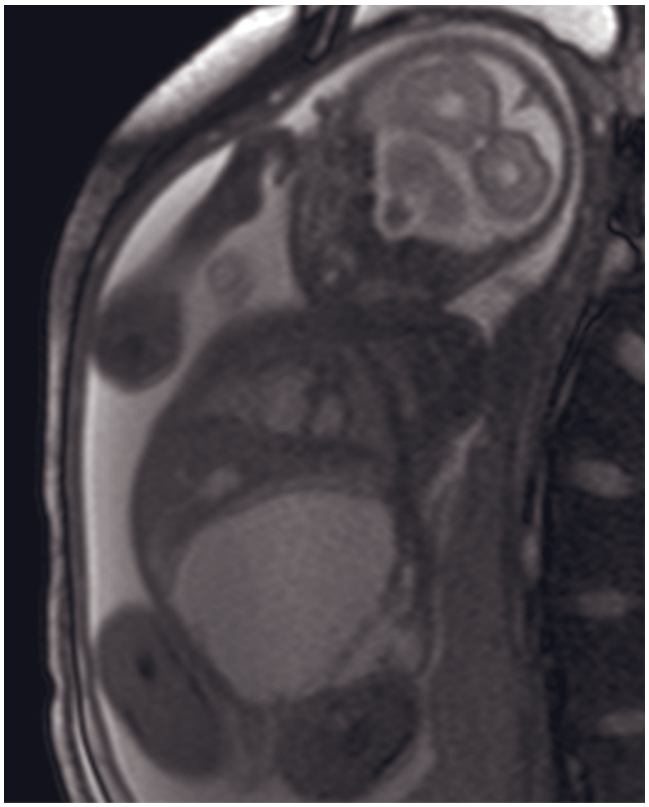

(*a*)

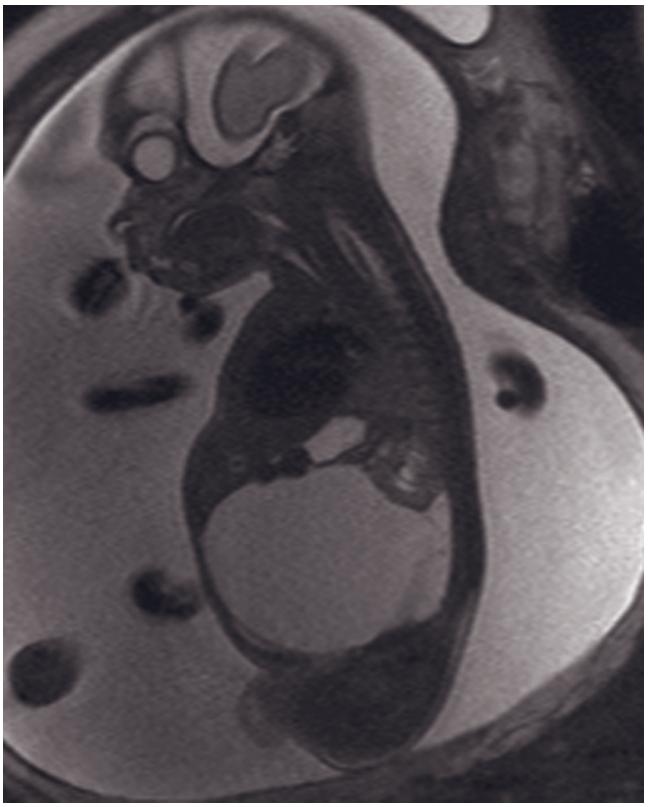

(*b*)

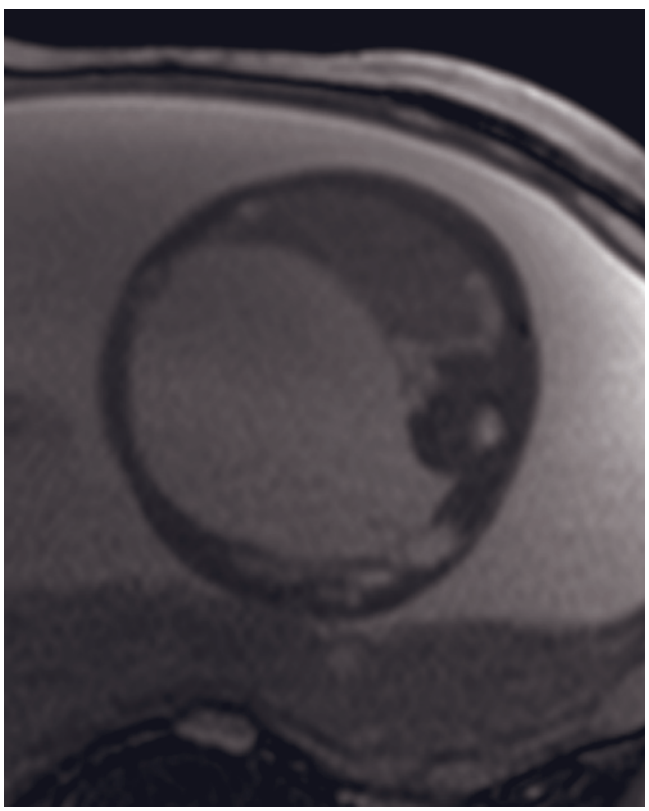

(*c*)

FIG. 16.63 Enteric duplication cyst. Coronal (*a*), sagittal (*b*), and axial (*c*) T2-weighted SS-ETSE images of a male fetus at 26 weeks of gestation reveal a large, well-demarcated, mainly left-sided single cyst, separate from the liver, kidneys, and bladder. The signal intensity of the cyst is slightly lower than simple fluid on T2-weighted images. Enteric duplication cyst was confirmed at surgery.

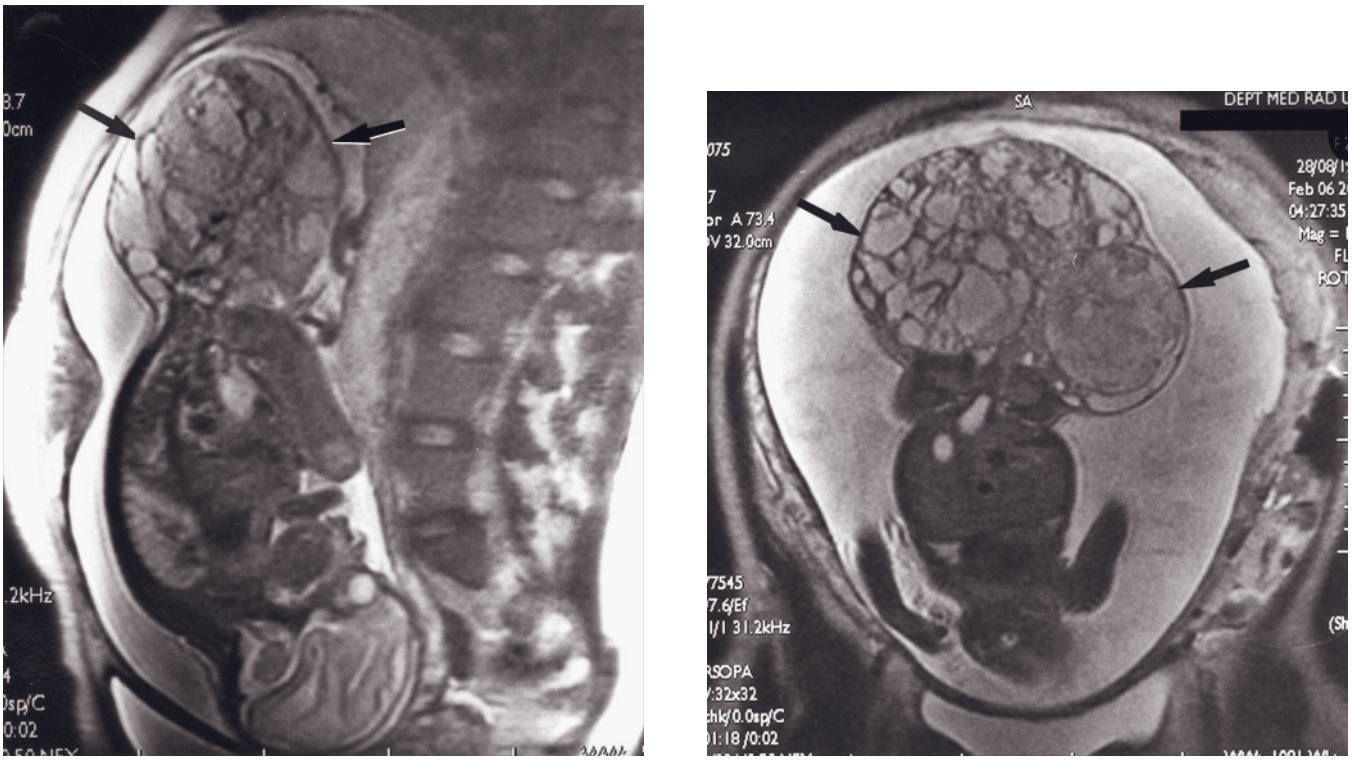

(*a*) (*b*)

FIG. 16.64 Fetus with sacrococcygeal teratoma at 28 weeks of gestation. Sagittal (*a*) and coronal (*b*) T2-weighted SS-ETSE images of the fetus show a large, mainly cystic, hyperintense lesion in the sacral region (arrows, *a*, *b*). Associated polyhydramnios is seen.

diagnosis portends a more favorable prognosis than postnatal diagnosis, with a 90–96% survival rate. MRI plays a role in determining the extent of the tumor. Approximately half of the tumors are cystic. Solid tumors are more likely to metastasize, with the liver the most common site. Liver metastases are present in 25% of fetal cases and may be diffusely infiltrative or focal masses. A normal fetal MRI does not exclude involvement as the infiltrative form may be difficult to demonstrate prenatally. Hepatomegaly or hydrops should raise suspicion of hepatic metastases. In the absence of metastatic disease, it may be difficult to distinguish neuroblastoma from adrenal hemorrhage. Paraspinal tumors may infiltrate the intervertebral foramina and result in neurological compromise. MRI has been shown to be beneficial in assessment of this extension and may prompt early delivery to preserve some neurological function [122, 161].

Mesoblastic nephroma is the most common fetal renal neoplasm. It is a benign, well-circumscribed renal tumor that tends to involve at least half of the kidney and is associated with polyhydramnios and, therefore, premature labor. It usually presents in the third trimester with rapid increase in amniotic fluid. These are often highly vascular, with the potential for hydrops. Tumors are predominantly solid, although they may have cystic areas. Prognosis is excellent after resection. The advantage of MRI is primarily in assessing organ of origin. Fetal Wilms tumor is more rare, but cannot be reliably distinguished with prenatal imaging [122, 162, 163].

Hepatic masses include hemangioendothelioma, mesenchymal hamartoma, hepatoblastoma, and metastases, primarily from neuroblastoma or leukemia. Hemangioendothelioma is a vascular tumor and arteriovenous shunting predisposes to high-output heart failure and hydrops. Kasabach–Merritt sequence (hemolytic anemia, thrombocytopenia, and consumptive coagulopathy) may also develop. These masses naturally regress after 6 months of life; however, treatment with corticosteroids may be necessary if symptomatic [122]. Mesenchymal hamartoma is a benign, usually cystic and multiseptated hepatic mass that is well-visualized on MRI. Hydrops may develop from rapid shift of fluid into the cyst. Surgery is curative [164].

Extremities

The extremities are easily recognized on T2-weighted images as low-signal-intensity structures within the high-signal-intensity amniotic fluid. MRI can provide accurate assessment of their dimensions. A disadvantage compared to ultrasonography, however, is the lack of real-time information, that is, the prenatal assessment

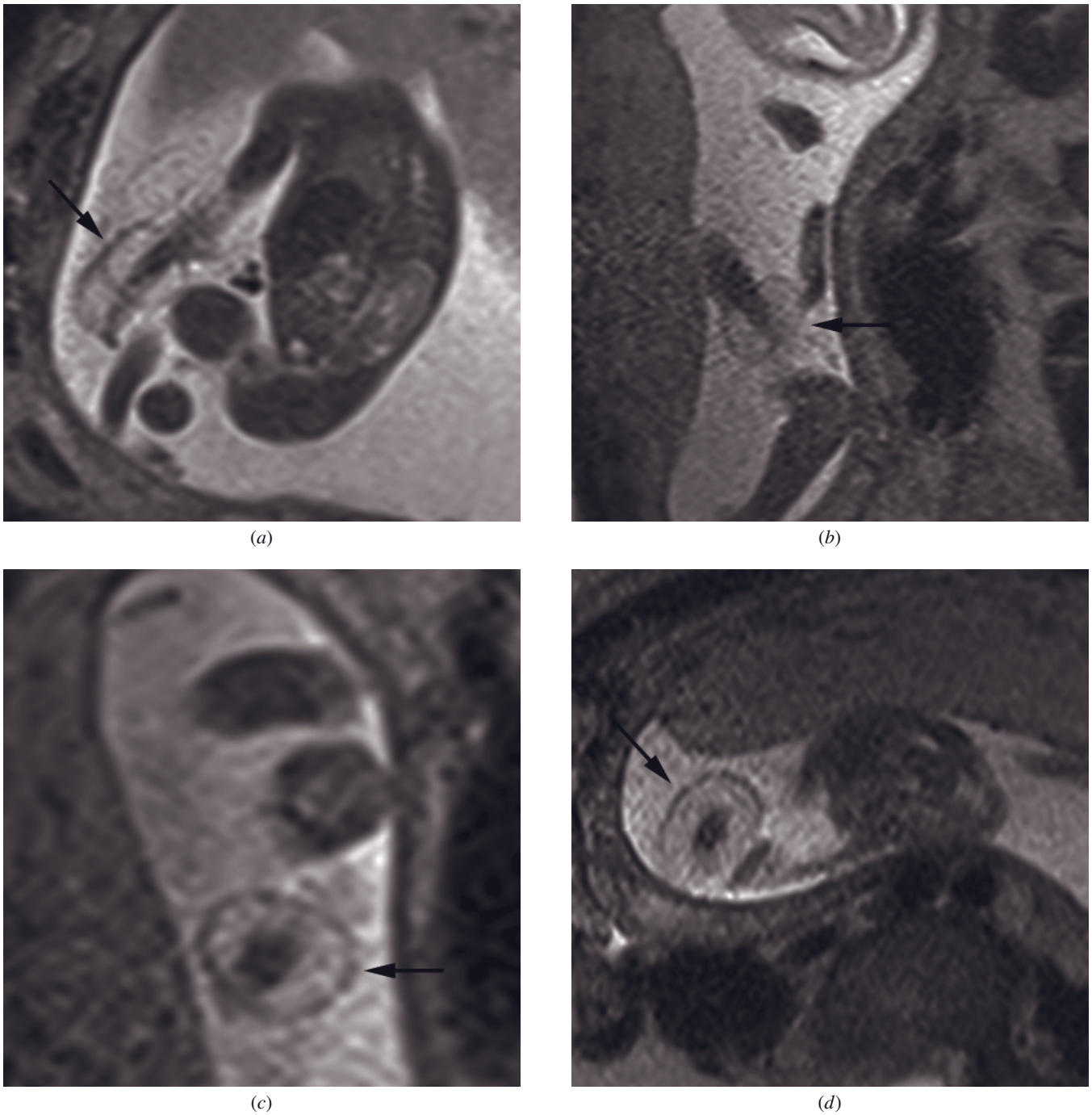

FIG. 16.65 Amniotic band of upper extremity with associated hand edema. T2-weighted SS-ETSE sequence performed in four planes (*a–d*) to evaluate upper extremity reveals a cystic mass surrounding the right forearm and extending to the distal interphalangeal joints (arrows). There is edema of the hand; however, the remainder of the arm is of normal caliber, similar to the contralateral normal-appearing arm. Contrast enhancement (not shown) demonstrated no flow within this cystic mass.

of function, of importance for example in cases of myelomeningocele [8, 78].

Amniotic band syndrome is a complex collection of abnormalities that ranges in severity from minor constriction rings causing extremity lymphedema, to amputation of digits, to severe, lethal deformities such as acrania. Amniotic bands can result from early rupture of membranes, leading to entrapment of fetal structures with resultant defects (fig. 16.65) [165]. If amniotic bands are suspected, SS-ETSE images may be difficult to interpret because of flow-related dephasing artifact, and steady-state free-precession sequences are helpful.

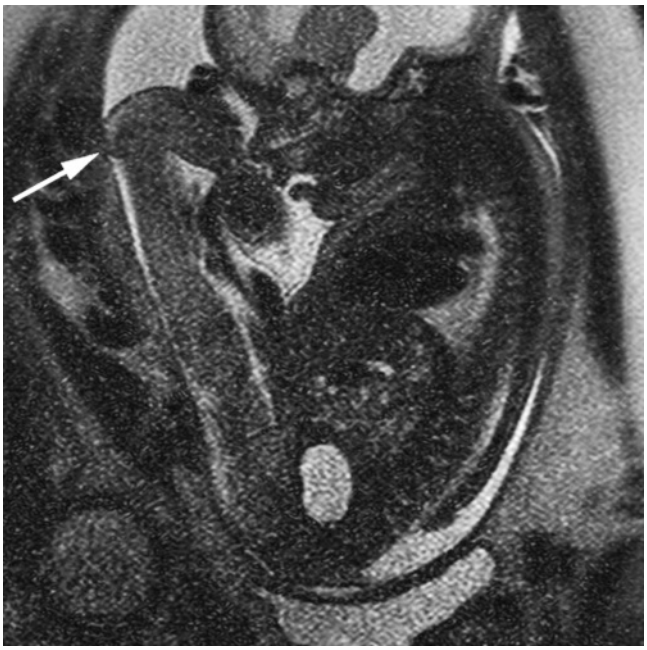

FIG. 16.66 Clubfoot. Sagittal T2-weighted SS-ETSE image of a fetus at 35 weeks of gestation demonstrates a clubfoot (arrow). Bilateral clubfeet were seen in this fetus with a Chiari II malformation.

Clubfoot, or talipes equinovarus (fig. 16.66), is an abnormality of the foot characterized by inversion and medial rotation of the foot. The diagnosis can be made by detecting abnormal alignment of the tibia and fibula with the bones of the foot, such that these bones are all visualized in the same plane. Although it may be an isolated finding, is not uncommonly associated with other abnormalities such as neural tube defects, and as such careful attention to the remainder of the fetal anatomic survey is necessary [166]. In addition, fetuses with clubfoot abnormality have a higher risk of associated aneuploidy, and this risk should be discussed with the family [167].

Fetal Weight and Amniotic Fluid

Accurate assessment of fetal weight during and at the end of pregnancy is useful for the management of labor and the neonatal period, since both intrauterine growth retardation and fetal macrosomia increase the risks of perinatal morbidity and mortality. MRI has been shown to be of value for the intrauterine assessment of growth retardation. Baker et al. [168] demonstrated that a single measurement of fetal liver volume with echoplanar imaging could accurately identify fetuses with a birth weight below the 10th percentile. Furthermore, it was shown that measurements of total fetal volume obtained with MRI correlate as well or better with actual birth weight than those obtained with ultrasonography, since

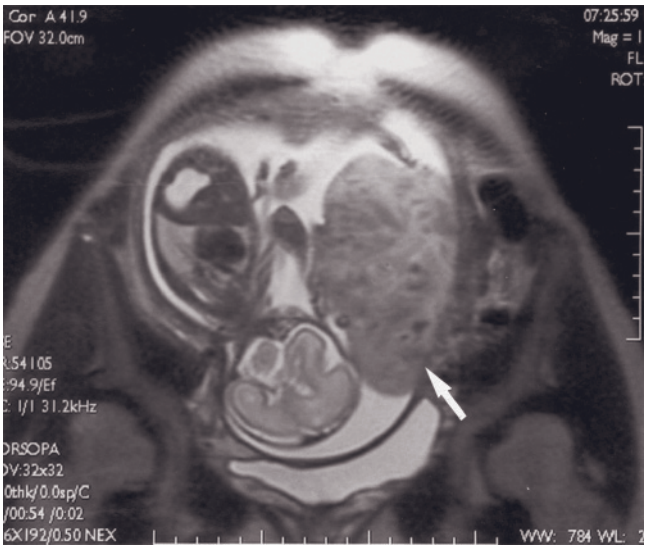

(*a*)

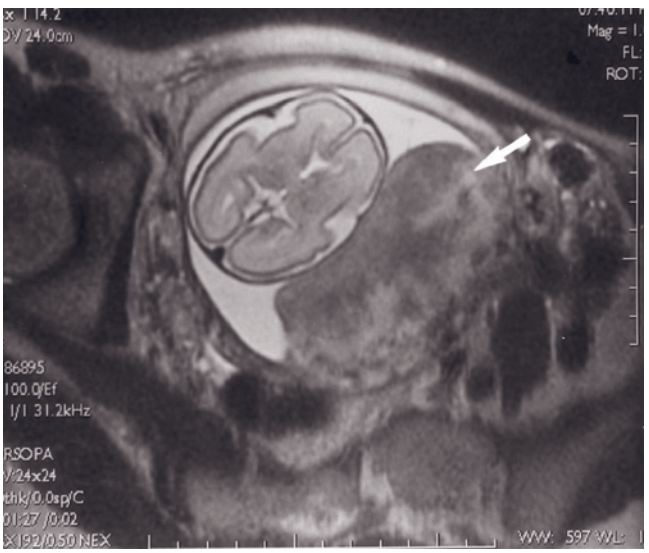

(*b*)

FIG. 16.67 Intrauterine growth retardation of a fetus of 26 weeks of gestation caused by placental infarction. Sagittal (*a*) and transverse (*b*) T2-weighted SS-ETSE images show an atypical compact shape of the placenta with inhomogeneous signal intensity (arrows, *a*, *b*). There is intrauterine growth retardation of the fetus. Placental infarction was diagnosed at time of delivery.

ultrasound can only measure fetal weight indirectly from anatomic measurements, for example, fetal head circumference, abdominal circumference, and femur length [14, 169]. Furthermore, MRI clearly demonstrates the lie of the fetus [78, 169]. In fetal growth retardation, MRI may occasionally reveal a cause such as placental infarction (fig. 16.67).

Normal amniotic fluid, similar to other simple biologic fluids, is hypointense on T1-weighted sequences and hyperintense on T2-weighted sequences. Volume

measurements of the amniotic fluid can be performed with MRI, which allows detection of oligohydramnios and polyhydramnios [169]. MRI can also visualize the umbilical cord and its insertion.

Multiple Gestation

MRI may be helpful in cases of multiple gestation to confirm the number, size, and location of placentas and evaluate for complications. The large field of view provided by MRI allows for global assessment (fig. 16.68). Twin-twin transfusion syndrome develops in diamniotic monochorionic twins (or multiples) in which there is an abnormal placental vascular anastomosis resulting in unbalanced blood flow between the fetuses, with a donor twin and a recipient twin. The donor twin develops oligohydramnios and the recipient polyhydramnios. This then progresses to renal failure of the donor twin with absent bladder filling, abnormal Doppler studies, congestive heart failure with hydrops, and fetal demise. Without intervention, there is nearly 100% perinatal mortality [170]. MRI has been reported to be helpful in assisting preoperative planning for endoscopic treatment of twin-twin transfusion [171]. In addition, these twins are at increased risk of cerebral ischemia and MRI plays a role in this evaluation. In conjoined twins, MRI may help delineate shared organs to determine prognosis and plan delivery (fig. 16.69).

Placental Imaging

MRI, because of its multiplanar capabilities, allows exact assessment of the placental position size and volume. Because of its ability to image the long axis of the entire cervical canal, MRI has been shown to be highly accurate in the diagnosis of placenta previa and might thus be an important adjunct to ultrasound in inconclusive cases (fig. 16.70) [172, 173]. Placenta previa is diagnosed when the placenta covers a portion or all of the internal cervical os and usually presents with painless vaginal bleeding during the course of the third trimester. A related placental condition is placenta accreta, which is a leading cause of emergent peripartum hysterectomy. Placenta accreta is caused by lack of decidua basalis, which normally prevents villous invasion of the myometrium; any cause of uterine scarring, such as cesarean section or myomectomy, can lead to abnormal placental attachment. Prior cesarean section is by far the most common risk factor. Uterine defects can be seen in many women after cesarean section (fig. 16.71). Three types of placenta accreta are described: placenta accreta vera (adherence to the myometrium), placenta increta

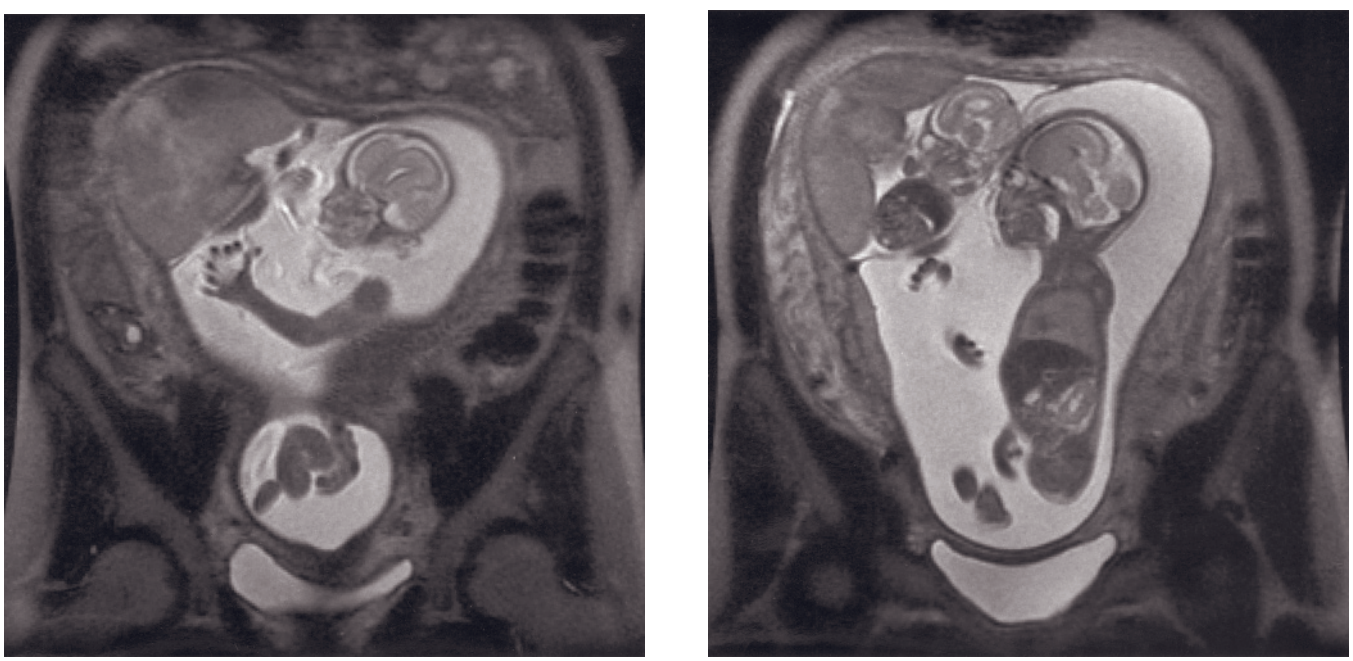

(*a*) (*b*)

FIG. 16.68 Twin pregnancy at 21 weeks of gestation. Intrauterine growth retardation of 1 fetus caused by hemodynamic impairment. Coronal T2-weighted SS-ETSE images (*a*, *b*) demonstrate the growth retardation of 1 twin. The placenta of this twin is very compact. (Reprinted with permission from Kubik-Huch RA,Wildermuth S, Cettuzzi L, Rake A, Seifert B, Chaoui R, Marincek B: Fetus and uteroplacental unit: fast MR imaging with three-dimensional reconstruction and volumetry—feasibility study. *Radiology* 219(2): 567–573, 2001.)

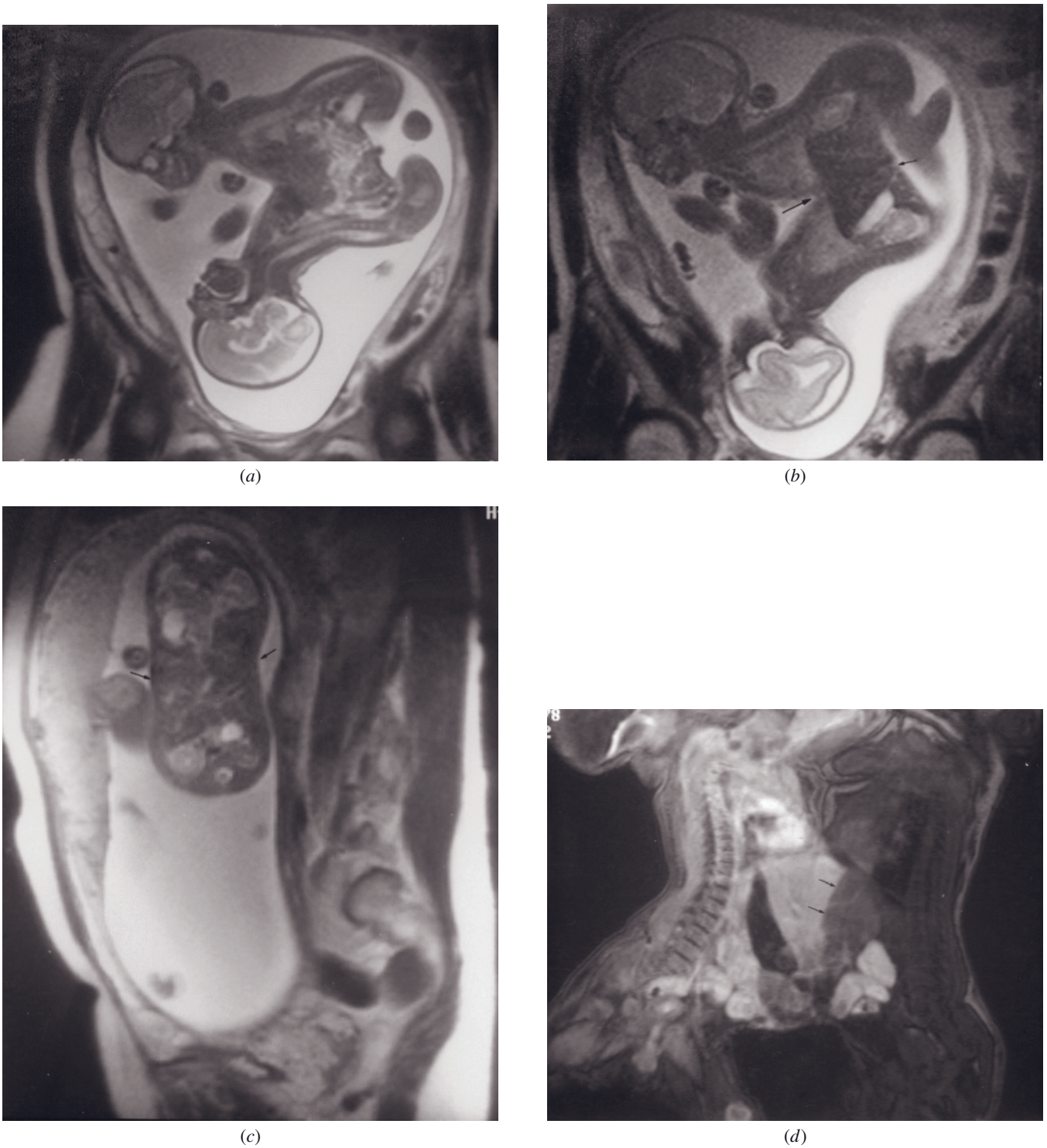

FIG. 16.69 Conjoined twins. Sagittal (*a*, *b*) and axial (*c*) T2-weighted SS-ETSE images demonstrate in utero conjoined twins. The peritoneal cavities of the conjoined twins are in continuity, and the livers are attached (arrows, *b*, *c*). Interstitial-phase gadolinium- enhanced fat-suppressed gradient-echo image (*d*) after gadolinium was administered to 1 neonate 1 day after birth demonstrates sharp demarcation of enhancing and nonenhancing livers (arrows, *d*), signifying that the hepatic vasculature of the twins is separate.

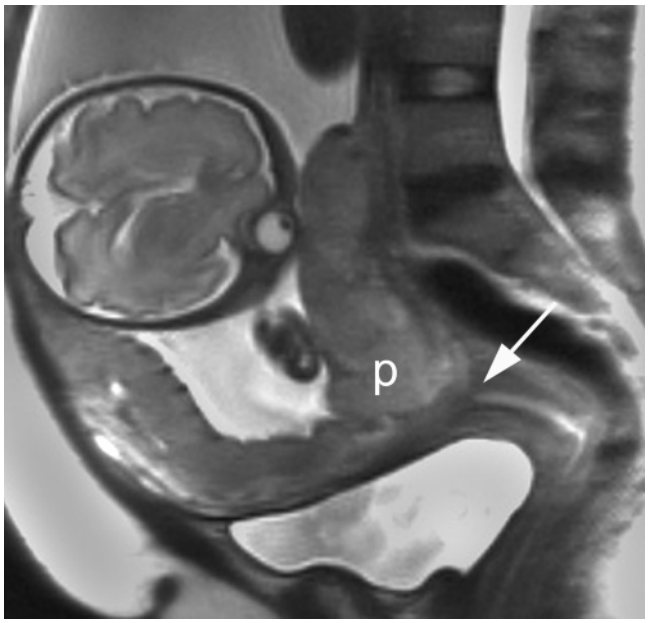

FIG. 16.70 Complete placenta previa. Sagittal T2-weighted SS-ETSE image through the maternal pelvis shows that the placenta (p) completely covers the internal cervical os (arrow).

FIG. 16.71 Uterine scar caused by prior Cesarean section. Sagittal T2-weighted ETSE image shows focal protrusion of endometrium (arrow) into the myometrial defect in the lower uterine segment.

(invasion into the myometrium), and placenta percreta (invasion of the uterine serosa). Because emergency hysterectomy is associated with substantial maternal morbidity and mortality, there have been increased efforts to improve the prenatal diagnosis of invasive placenta. While ultrasound often identifies placenta accreta, it may be falsely positive because of maternal vascularity or falsely negative because of posterior or fundal placental position [174, 175]. In cases of complex placenta percreta, ultrasound provides limited evaluation of extrauterine involvement, which may be extensive. MRI is particularly helpful to determine the extent of placental invasion, which is critical for presurgical planning. MRI may increase diagnostic confidence when ultrasound is suspicious and confirm or exclude placenta accreta when ultrasound is indeterminate. This is important because the diagnosis leads to changes in management. Cesarean section is planned at 35 weeks with gynecological oncology assistance. Many centers also perform prophylactic internal iliac artery balloon occlusion to control hemorrhage, and accurate diagnosis is important for proper patient selection.

MRI has shown promise as an accurate means of early diagnosis of placenta accreta. Diagnosis depends largely on multiplanar T2-weighted images, which may be obtained as single-shot echo-train spin echo. Some investigators use dynamic gadolinium, while others do not. On T1-weighted images, the normal placenta is intermediate in signal intensity and homogeneous in appearance. On T2-weighted echo-train spin-echo images, the placenta demonstrates moderately high signal intensity and fine internal architecture. MR findings suggestive of placenta accreta include myometrial thinning, irregularity, or focal disruption. MR findings of the more severe placenta percreta include dark placental bands on T2-weighted images, focal thinning of myometrium, disorganized architecture of the adjacent placenta, focal exophytic mass, and in cases of anterior placental invasion involving the bladder, thinning of the uterine serosal-bladder interface (figs. 16.72–16.74). The normal enhancement characteristics of the placenta with dynamic gadolinium imaging have been described. Third-trimester placentas often show early enhancement in a lobular patchy pattern along the maternal surface, while second-trimester placentas may enhance more heterogeneously. This appearance of lobular enhancement has been proposed to represent gadolinium in placental intervillous spaces, as a result of cotyledon formation during the third trimester [176]. On postgadolinium images, early arterial-phase hyperintense lobular enhancement of the placenta is particularly helpful in delineating the placental border. MR findings of placenta accreta vera may be subtle, since no frank myometrial invasion is present.

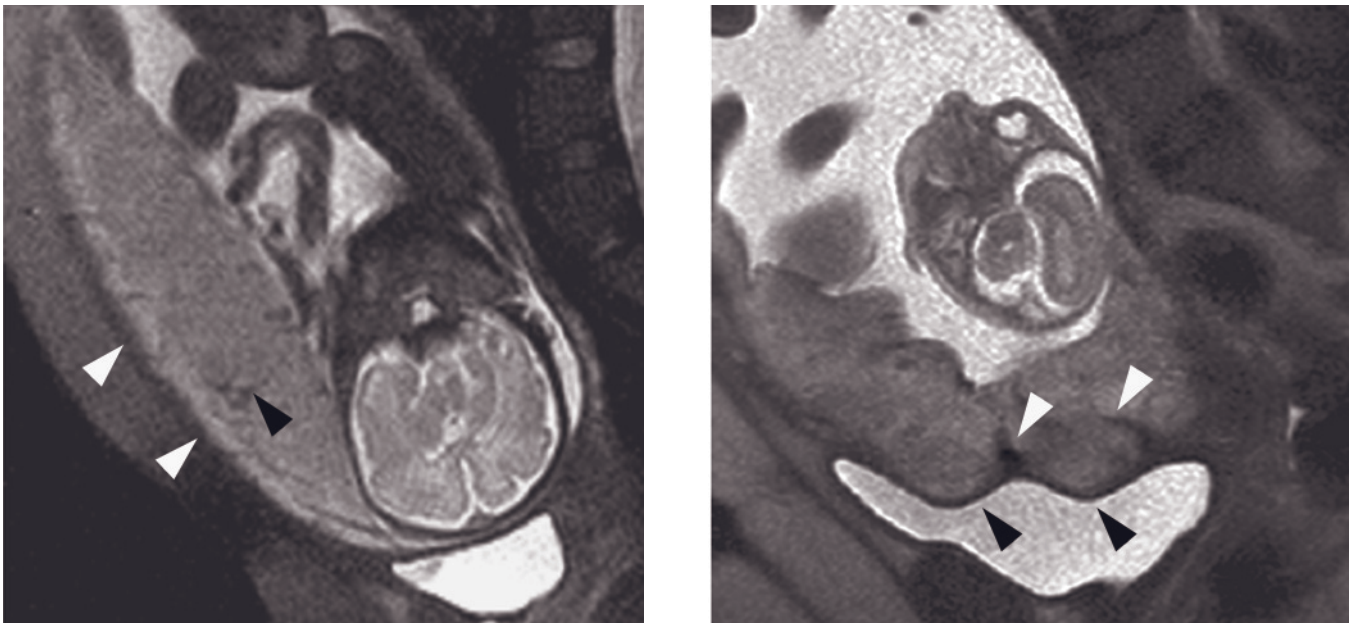

(*a*) (*b*)

FIG. 16.72 Normal placenta and invasive placenta, second trimester. Sagittal T2-weighted SS-ETSE images in 2 patients show a normal placenta (*a*) and an invasive placenta (*b*). The normal placenta (*a*) has a smooth outer contour (white arrowheads, *a*) and homogeneous moderately high signal intensity. Dark vessels (black arrowhead, *a*) can be seen coursing through the placenta. In contrast, the invasive placenta (*b*) is more heterogeneous, with a lobulated outer contour (black arrowheads, *b*) and dark bands (white arrowheads, *b*) that do not represent vessels. Placenta percreta was found at surgery.

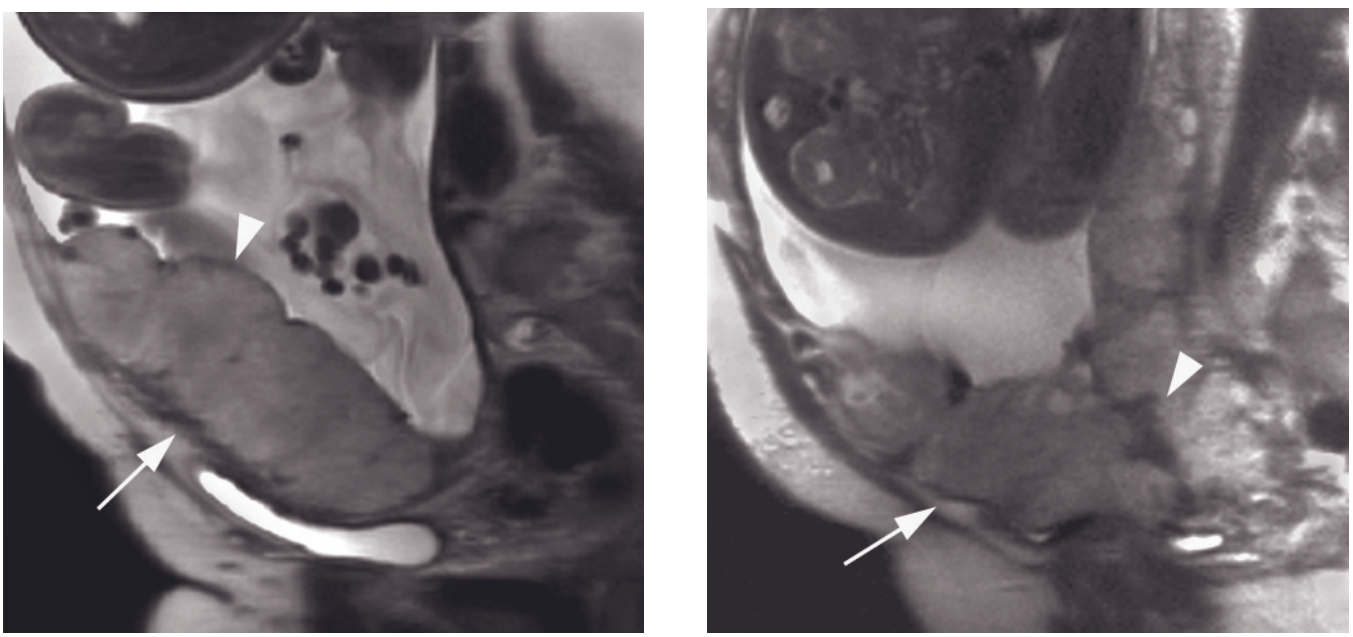

(*a*) (*b*)

FIG. 16.73 Normal placenta and invasive placenta, third trimester. Sagittal T2-weighted SS-ETSE images in 2 patients show a normal placenta (*a*) and an invasive placenta (*b*). The normal placenta (*a*) is of moderately high signal intensity, and the inner contour of the third-trimester placenta is lobulated in a regular and organized fashion, reflecting cotyledons (arrowhead, *a*) whereas the outer contour remains smooth (arrow, *a*). In contrast, the invasive placenta (*b*) is more heterogeneous, with distorted internal architecture, dark nonvascular bands (arrow, *b*), and lobulated outer contour (arrow, *b*). Placenta percreta was found at surgery.

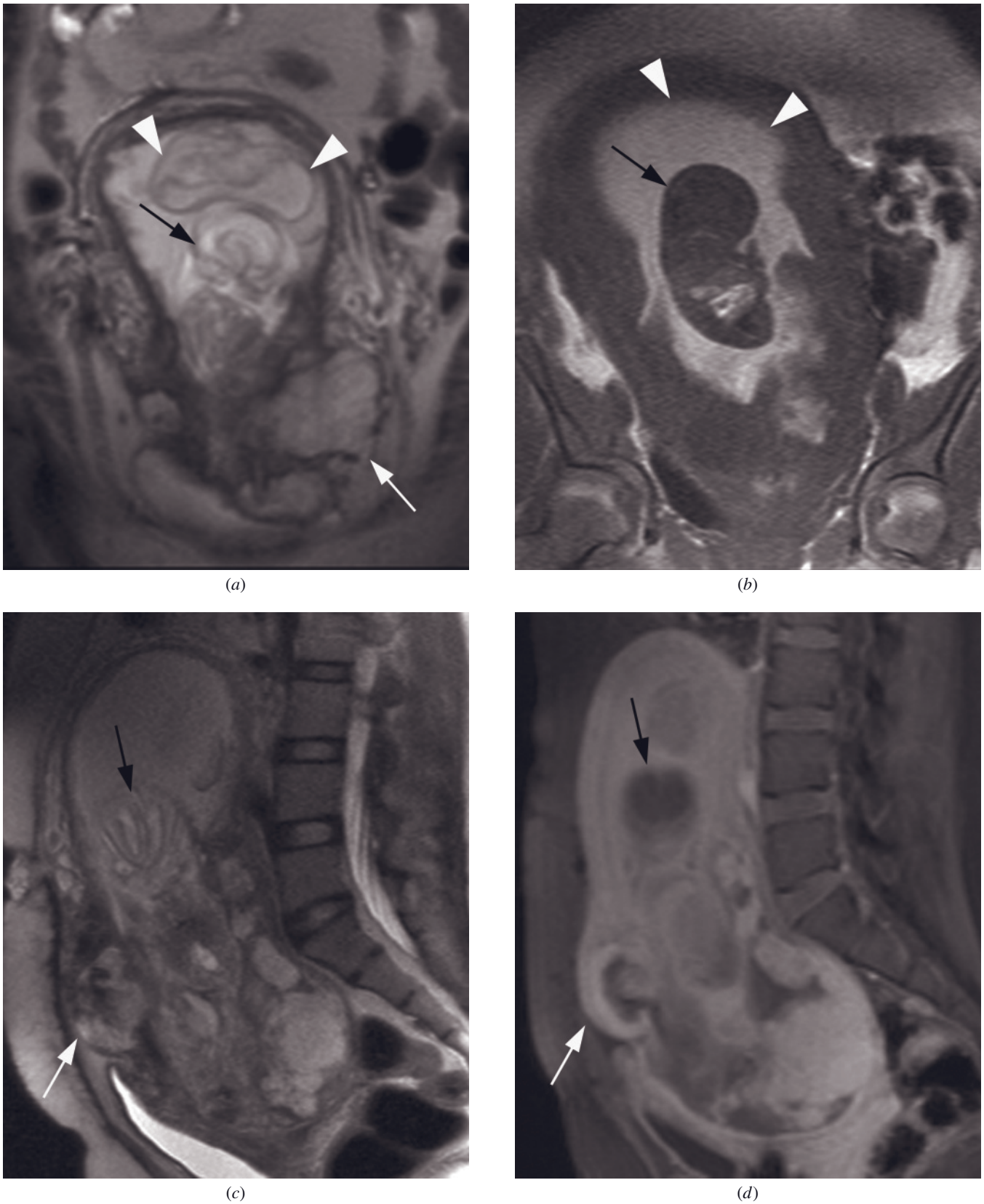

FIG. 16.74 Invasive placenta with fetal demise. Coronal T2-weighted SS-ETSE (*a*) and T1-weighted gradient-echo (*b*) and sagittal T2-weighted SS-ETSE (*c*) and gadolinium-enhanced fat-suppressed T1-weighted gradient-echo (*d*) images show an abnormal heterogeneous placenta extending outside the expected location of the uterine wall (white arrow, *a*, *c*, *d*). The uterus contains a fetus (black arrow, *a–d*) as well as blood (arrowheads, *b*) and sloughed membranes (arrowheads, *a*).

Gestational Trophoblastic Disease

The term gestational trophoblastic disease (GTD) includes a variety of disease entities, including complete or partial hydatidiform mole, invasive mole, and choriocarcinoma. Clinically, a molar pregnancy is suspected in a patient with hyperemesis gravidarum, severe preeclampsia before 24 weeks of gestation, a large-for-date uterus, or first-trimester bleeding. Laboratory findings are diagnostic with markedly elevated levels of β-human chorionic gonadotropin (β-hCG). The most common form is a complete hydatidiform mole, characterized by trophoblastic proliferation without the development of an embryo. A partial hydatidiform mole is a distinct entity, and both mole and fetus exhibit a triploid karyotype. Whereas patients with partial hydatidiform rarely develop an invasive mole or a choriocarcinoma, invasive moles are seen in approximately 10% of patients treated for complete hydatidiform mole and are characterized by myometrial invasion. Approximately 50% of choriocarcinomas arise from a preexisting molar pregnancy, whereas the other 50% will develop after any gestational event including abortion and ectopic or term pregnancy. Choriocarcinomas metastasize most frequently to the maternal lung.

The role of imaging in this patient population is limited, since the diagnosis and follow-up of patients with GTD is primarily based on β-hCG testing [177]. Computed tomography is the imaging procedure of choice for the detection of extrapelvic metastases. MRI besides ultrasonography might be used to evaluate the primary uterine disease, for example, the degree of myometrial invasion in patients with invasive moles or choriocarcinomas (fig. 16.75). In complete hydatidiform moles, MRI demonstrates a heterogeneous mass with multiple cystic spaces

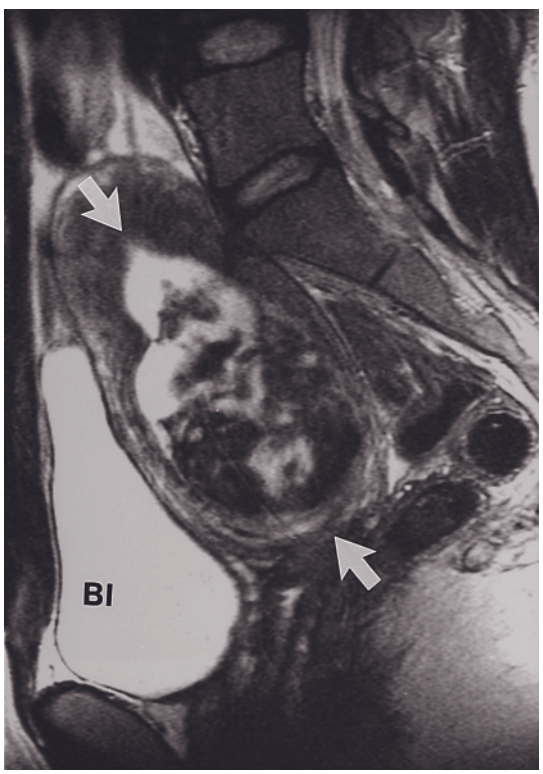

(*a*)

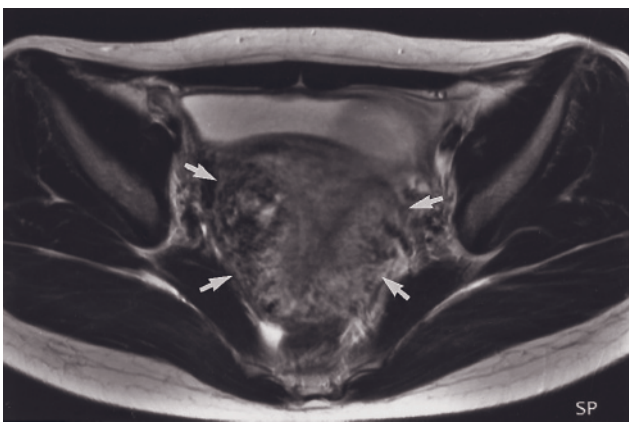

(*b*)

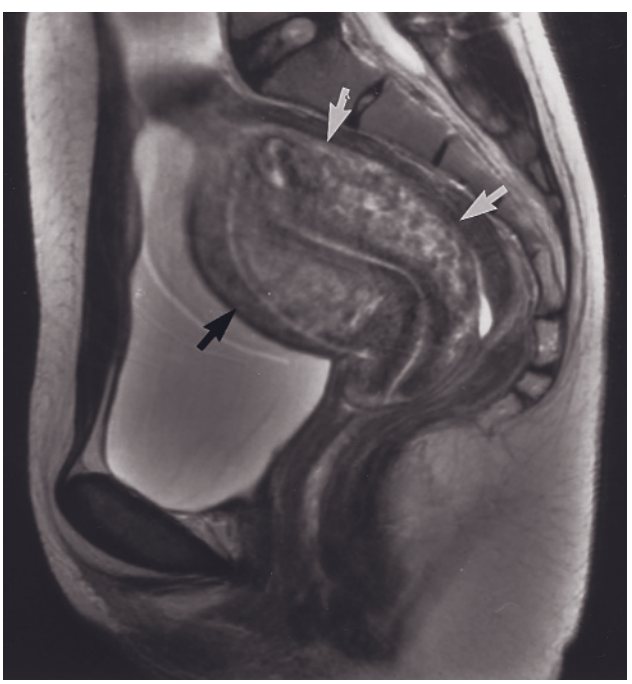

(*c*)

FIG. 16.75 Hydatidiform mole and invasive mole. Sagittal T2-weighted echo-train spin-echo image (*a*) in a patient with a partial hydatidiform mole. A large, heterogeneous mass is seen within the endometrial cavity (arrows, *a*) in a patient with elevated serum β-HCG levels. Note that there is no definite evidence of myometrial invasion. Transverse (*b*) and sagittal (*c*) T2-weighted echo-train spin-echo images in a second patient who has an invasive mole. Note that in distinction from the patient with the hydatid mole there is diffuse heterogeneous high signal intensity of the myometrium consistent with invasion (arrows *b*, *c*). Bl, bladder

distending the endometrial cavity. A rim of hypointense myometrium may be visible at the periphery of a molar pregnancy. The uterine zones are distorted or obliterated, and an irregular boundary between the tumor and the myometrium is seen. On T1 sequences, foci of high signal intensity corresponding to areas of hemorrhage may be seen. The mole is hypervascular and thus enhances intensely after gadolinium administration [178–180].

Pelvimetry

Pelvimetry is performed in patients who desire a trial of labor if the fetus is in breech presentation, if they have a history of secondary cesarean section due to dystocia, or if they present with pelvic deformity.

The use of X-ray pelvimetry has decreased steadily in the last two decades. MRI offers the benefit of accurate measurements of the bony structures of the pelvis without exposure to ionizing radiation (fig. 16.76). Furthermore, MRI can clearly delineate the soft tissues of the maternal pelvis. The use of gradient-echo sequences has been advocated for MR pelvimetry, since acquisition times are shorter compared to T1-weighted spin-echo sequences and they are characterized by a relatively low specific absorption rate [181–185].

Cervical Incompetence

Ultrasound remains the primary means of evaluating cervical competence in pregnancy; however, the cervix is

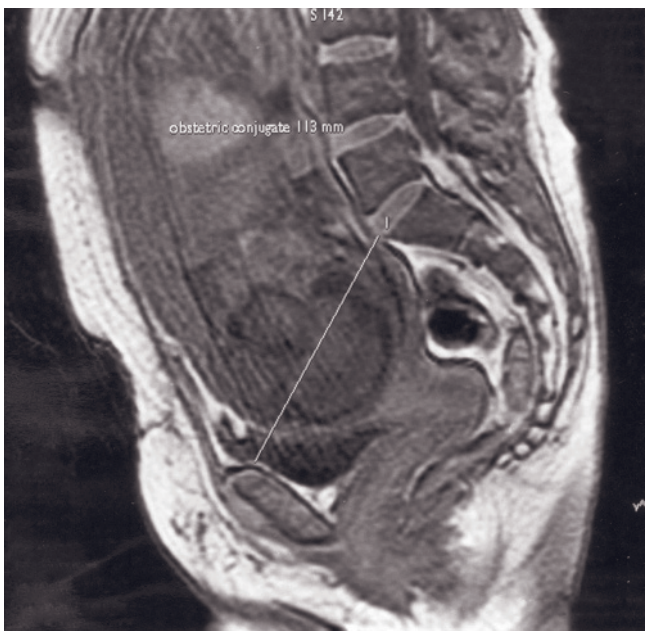

(*a*)

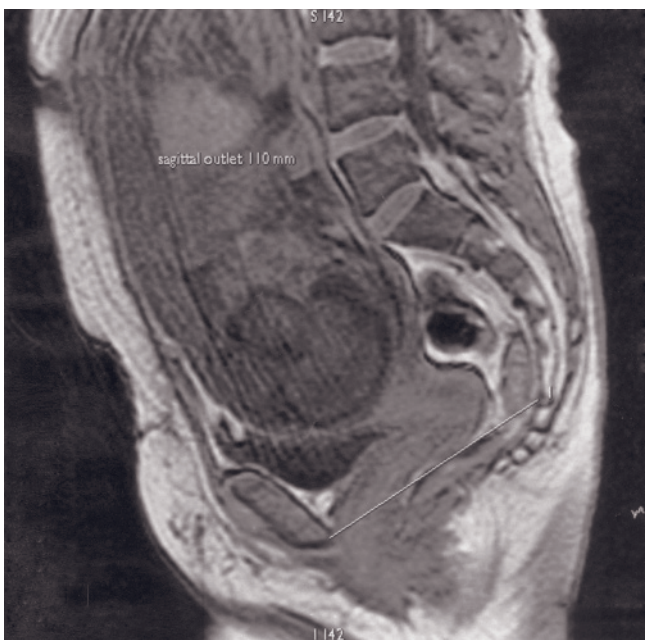

(*b*)

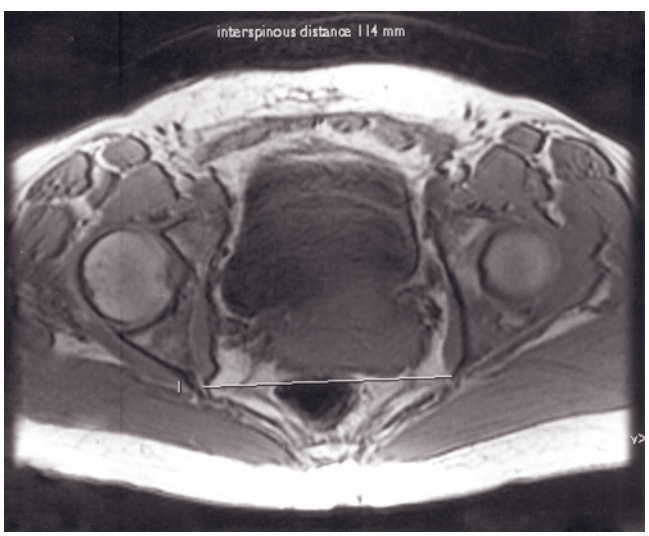

(*c*)

FIG. 16.76 MR pelvimetry performed in a pregnant patient. T1-weighted gradient echo sequences: Obstetric conjugate (*a*) and sagittal outlet (*b*) are measured on a midsagittal plane, interspinous distance (*c*) and intertuberous distance (*d*) on axial planes.

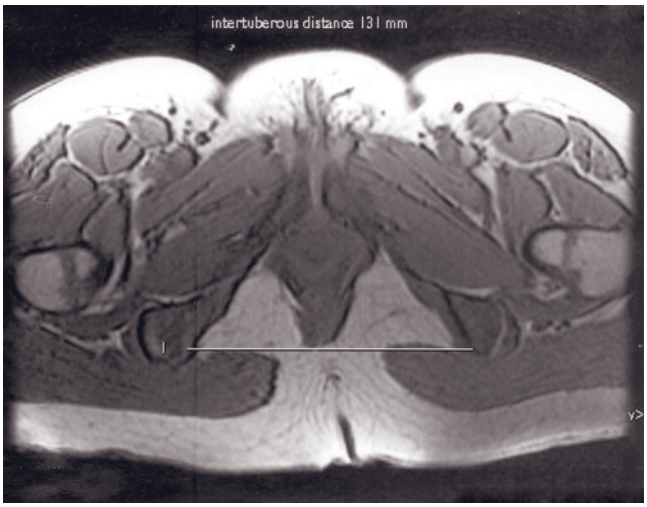

(*d*)

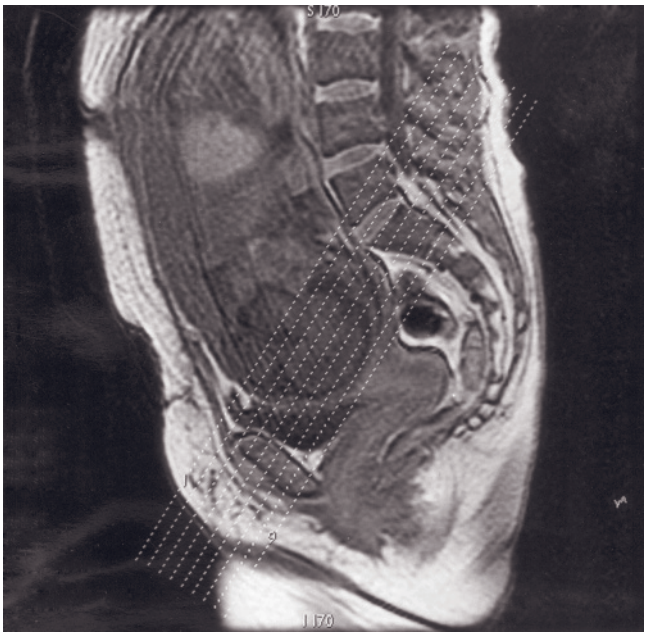

(*e*)

(*f*)

FIG. 16.76 (*Continued*) The transversal distance (*f*) is measured on an oblique plane acquired as shown on the localizing image (*e*).

well-depicted on MRI and unsuspected cervical incompetence may be detected (fig. 16.77). Evaluation of normal cervical length has revealed that at 24 weeks, the tenth percentile measurement is 25 mm, and measurements of this length or shorter were associated with a sixfold increase preterm delivery. Funneling may be seen with dilation of the internal os and amniotic fluid or membranes bulging into the proximal endocervical canal; funneling involving 60% of the total cervical length has also been associated with preterm delivery [186, 187]. Patients with multiple gestations have shorter cervical lengths for gestational age, and nomograms exist for comparison.

CONCLUSION

Because of the lack of ionizing radiation, MRI is well suited to evaluation of the pregnant patient and

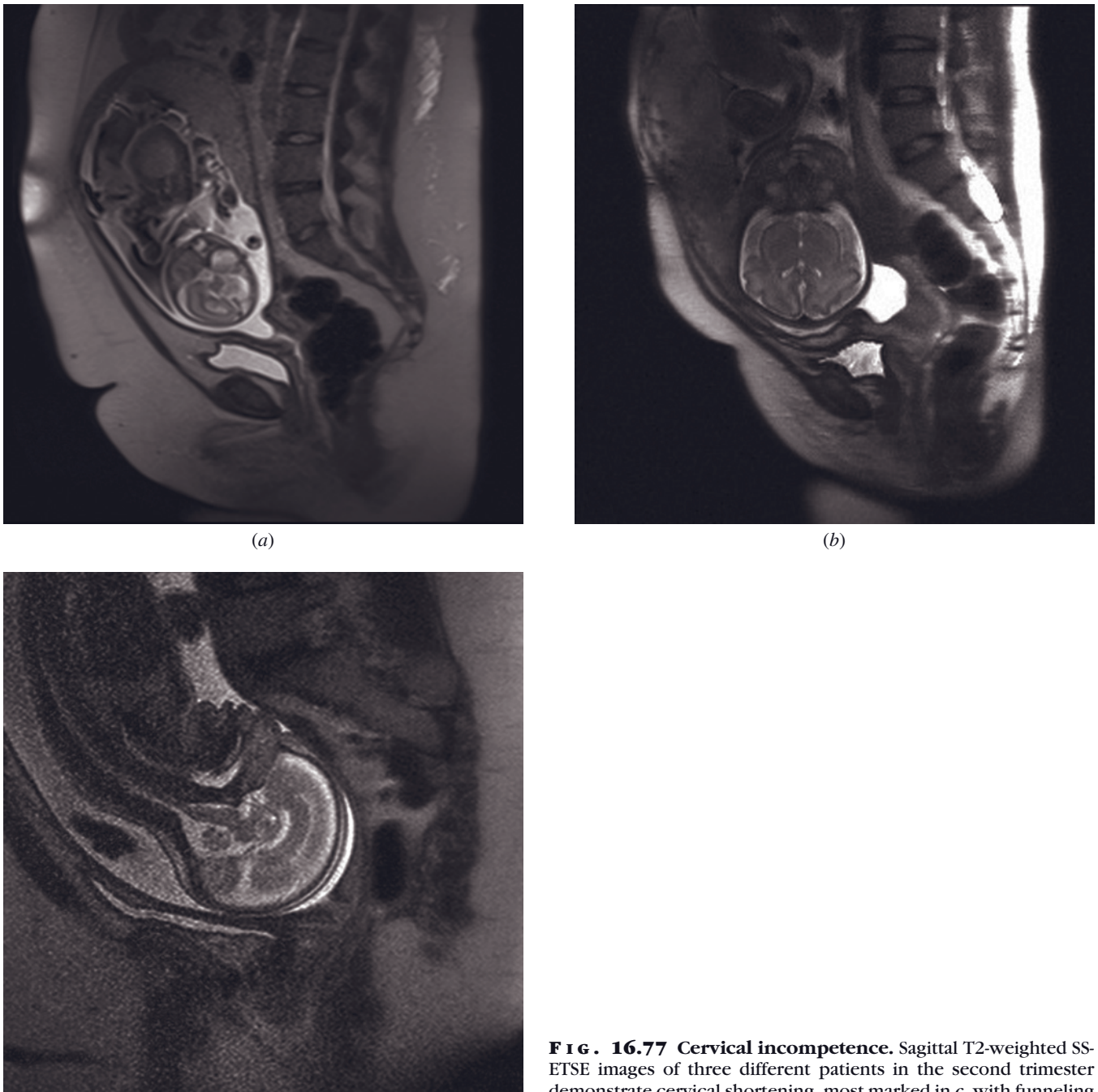

(*a*) (*b*) (*c*)

FIG. 16.77 Cervical incompetence. Sagittal T2-weighted SS-ETSE images of three different patients in the second trimester demonstrate cervical shortening, most marked in *c*, with funneling in *a* and *b*.

fetus when sonographic evaluation is limited, abnormalities are complex, or better anatomical detail is needed. As fetal interventions increase, the indications for fetal MRI are expected to increase as well. Because of safety concerns, MRI should be avoided in the first trimester if possible, and gadolinium should be given only if the benefits outweigh the risks to the fetus.

REFERENCES

1. Budinger TF. Nuclear magnetic resonance (NMR) in vivo studies: known thresholds for health effects. *J Comp Assist Tomogr* 5: 800–811, 1981.
2. Reid A, Smith FW et al. Nuclear magnetic resonance imaging and its safety implications: follow-up of 181 patients. *Br J Radiol* 55: 784–786, 1982.

3. McRobbie D, Foster MA. Pulsed magnetic field exposure during pregnancy and implications for NMR foetal imaging: a study with mice. *Magn Reson Imaging* 3: 231–234, 1985.
4. Heinrichs WL, Fong P et al. Midgestational exposure of pregnant BALB/c mice to magnetic resonance imaging conditions. *Magn Reson Imaging* 6: 305–313, 1988.
5. Baker PN, Johnson IR et al. Fetal weight estimation by echoplanar magnetic resonance imaging. *Lancet* 343: 644–645, 1994.
6. Levine D, Barnes PD et al. Fetal fast MR imaging: reproducibility, technical quality, and conspicuity of anatomy. *Radiology* 206: 549–554, 1998.
7. Kubik Huch RA, Wisser J et al. Prenatal diagnosis of fetal malformations by ultrafast magnetic resonance imaging. *Prenat Diagn* 18: 1205–1208, 1998.
8. Kubik Huch RA, Huisman TA et al. Ultrafast MR imaging of the fetus. *Am J Roentgenol* 174: 1599–1606, 2000.
9. Levine D, Barnes PD et al. Fetal central nervous system anomalies: MR imaging augments sonographic diagnosis. *Radiology* 204: 635–642, 1997.
10. Yamashita Y, Namimoto T et al. MR imaging of the fetus by a HASTE sequence. *AJR Am J Roentgenol* 168: 513–519, 1997.
11. Levine D, Barnes PD. Cortical maturation in normal and abnormal fetuses as assessed with prenatal MR imaging. *Radiology* 210: 751–758, 1999.
12. Hubbard AM, Adzick NS, Crombleholme TM, Coleman BG, Howell LJ, Haselgrove JC, Mahboubi S. Congenital chest lesions: diagnosis and characterization with prenatal MR imaging. *Radiology* 212: 43–48, 1999.
13. Schwartz JL, Crooks LE. NMR imaging produces no observable mutations or cytotoxicity in mammalian cells. *AJR Am J Roentgenol* 139: 583–585, 1982.
14. Baker PN, Johnson IR, Harvey PR, Gowland PA, Mansfield P. A three year follow-up of children imaged in utero with echoplanar magnetic resonance. *Am J Obstet Gynecol* 170(1): 32–33, 1994.
15. Tyndall DA and Sulik KK. Effects of magnetic resonance imaging on eye development in the C57BL/6J mouse. *Teratology* 43: 263–275, 1991.
16. Kanal E, Gillen J et al. Survey of reproductive health among female MR workers. *Radiology* 187: 395–399, 1993.
17. Kanal E. Pregnancy and the safety of magnetic resonance imaging. *Magn Reson Imag Clin N Am* 2: 309–317, 1994.
18. Clements H, Dunca KR, Fielding K, Gowland PA, Johnson IR, Baker PN. Infants exposed to MRI in utero have a normal paediatric assessment at 9 months of age. *Br J Radiol* 73: 190–194, 2000.
19. Kok RD, deVries MM, Heerschap A, van den Berg PP. Absence of harmful effects of magnetic resonance exposure at 1.5T in utero during the third trimester of pregnancy: a follow-up study. *Magn Reson Imaging* 22: 851–854, 2004.
20. Myers C, Duncan KR, Gowland PA, Johnson IR, Baker PN. Failure to detect intrauterine growth restriction following in utero exposure to MRI. *Br J Radiol* 71: 549–551, 1998.
21. Huisman, TAGM. Fetal magnetic resonance imaging. *Semin Roentgenol* 43(4): 314–336, 2008.
22. Food and Drug Administration. Magnetic resonance diagnostic device: panel recommendation and report on petitions for MR reclassification. *Fed Reg* 53: 7575–7579, 1998.
23. American Joint Committee on Cancer. *Manual for Staging of Cancer (3rd ed.).* Philadelphia: Lippincott, 1988, p. 151–153.
24. Brown MA, Birchard KR, Semelka RC. Magnetic resonance evaluation of pregnant patients with acute abdominal pain. *Semin Ultrasound CT MRI* 26: 206–211, 2005.
25. Panigel M, Wolf G et al. Magnetic resonance imaging of the placenta in rhesus monkeys, *Macaca mulatta. J Med Primatol* 17: 3–18, 1998.
26. Kanal E et al. ACR guidance document for safe MR practices: 2007. *AJR Am J Roentgenol* 188: 1447–1474, 2007.
27. Tweedle MF, Wedeking MS, Kumar K. Biodistribution of radiolabeled, formulated gadopentetate, gadoteridol, gadoterate, and gadodiamide in mice and rats. *Invest Radiol* 30(6): 372–380, 1995.
28. White GW, Gibby WA, Tweedle MF. Comparison of Gd(DTPA-BMA) (Omniscan) versus Gd(HP-DO3A) (ProHance) relative to gadolinium retention in human bone tissue by inductively coupled plasma mass spectroscopy. *Invest Radiol* 41(3): 272–278, 2006.
29. Rofsky NM, Pizzarello DJ et al. Effect on fetal mouse development of exposure to MR imaging and gadopentetate dimeglumine. *J Magn Reson Imaging* 4: 805–807, 1994.
30. Omniscan package insert. Princeton, NJ: GE Healthcare, 2007.
31. Lin S-P, Brown JJ. MR contrast agents: physical and pharmacologic basics. *J Magn Reson Imaging* 25: 884–899, 2007.
32. Brugger PC, Stuhr F, Lindner C, Prayer D. Methods of fetal MR: beyond T2-weighted imaging. *Eur J Radiol* 57(2): 172–181, 2006.
33. Thoeny HC, DeKeyzer F, Oyen RH, Peeters RR. Diffusion-weighted MR imaging of kidneys in healthy volunteers and patients with parenchymal diseases: initial experience. *Radiology* 235(3): 911–917, 2005.
34. Weinreb JC, Brown CE et al. Pelvic masses in pregnant patients: MR and US imaging. *Radiology* 159: 717–724, 1986.
35. Cappell MS, Friedel D. Abdominal pain during pregnancy. *Gastroenterol Clin* 32: 1–58, 2003.
36. Stone K. Acute abdominal emergencies associated with pregnancy. *Clin Obstet Gynecol* 45: 553–561, 2002.
37. Mazze RI, Kallen B. Appendectomy during pregnancy: a Swedish registry study of 778 cases. *Obstet Gynecol* 77: 835–840, 1991.
38. Mourad J, Elliot JP, Erickson L et al. Appendicitis in pregnancy: new information that contradicts long-held clinical beliefs. *Am J Obstet Gynecol* 184: 954–957, 2000.
39. Cobben LP, Groot I, Haans L et al. MRI for clinically suspected appendicitis during pregnancy. *AJR Am J Roentgenol* 183: 671–675, 2004.
40. Pedrosa I, Levine D, Eyvassadeh AD, Siewert B, Ngo L, Rofsky NM. MR imaging evaluation of acute appendicitis in pregnancy. *Radiology* 238: 891–899, 2006.
41. Oto A, Ernst RD, Shah R, Koroglu M, Chaljub G, Gei AF, Zacharias N, Saade G. Right-lower-quadrant pain and suspected appendicitis in pregnant women: evaluation with MR imaging—initial experience. *Radiology* 234(2): 445–451, 2005.
42. Lee KS, Rofsky NM, Pedrosa I. Localization of the appendix at MR imaging during pregnancy: utility of the cecal tilt angle. *Radiology* 249(1): 134–141, 2008.
43. Israel GM, Malquria N, McCarthy S, Copel J, Weinreb J. MRI vs. ultrasound for suspected appendicitis during pregnancy. *J Magn Reson Imaging* 28(2): 428–433, 2008.
44. Roy C, Saussine C et al. Fast imaging MR assessment of ureterohydronephrosis during pregnancy. *Magn Reson Imaging* 13: 767–772, 1995.
45. Spencer JA, Chahal R, Kelly A et al. Evaluation of painful hydronephrosis in pregnancy: magnetic resonance urographic patterns in physiological dilatation versus calculous obstruction. *J Urol* 171: 256–260, 2004.
46. Boni RA, Hebisch G et al. Multiple necrotic uterine leiomyomas causing severe puerperal fever: ultrasound, CT, MR, and histological findings. *J Comput Assist Tomogr* 18: 828–831, 1994.
47. Murase E, Siegelman ES et al. Uterine leiomyomas: histopathologic features, MR imaging findings, differential diagnosis, and treatment. *Radiographics* 19: 1179–1197, 1999.
48. Kawakami S, Togashi K et al. Red degeneration of uterine leiomyoma: MR appearance. *J Comput Assist Tomogr* 18: 925–928, 1994.

49. Coronado GD, Marshall LM, Schwartz SM. Complications in pregnancy labor, and delivery with uterine leiomyomas: a population based study. *Obstet Gynecol* 95: 764–769, 2000.
50. Sherer DM, Maitland CY, Levine NF et al. Prenatal MRI assisting in differentiating between large degenerating intramural leiomyoma and complex adrenal mass during pregnancy. *J Mat Fetal Med* 9: 186–189, 2000.
51. Curtis M, Hopkins MP et al. Magnetic resonance imaging to avoid laparotomy in pregnancy. *Obstet Gynecol* 82: 833–836, 1993.
52. Forstner R, Kalbhen CL, Filly RA et al. Abdominopelvic MR imaging in the non-obstetric evaluation of pregnant patients. *AJR Am J Roentgenol* 166: 1139–1144, 1996.
53. Nguyen C, Montz FJ et al. Management of Stage I cervical cancer during pregnancy. *Gynecol Surv* 55: 633–643, 2000.
54. Brown MA, Mattrey RF, Stamato S, Sirlin CB. MRI of the female pelvis using vaginal gel. *AJR Am J Roentgenol* 185: 1221–1227, 2005.
55. Dinauer PA, Brixey CJ, Moncur JT, Fanburg-Smith JC, Murphey MD. Pathologic and MR imaging features of benign fibrous soft-tissue tumors in adults. *Radiographics* 27(1): 173–187, 2007.
56. Durkin AJ, Korkolis DP, Al-Saif O, Zervos EE. Full-term gestation and transvaginal delivery after wide resection of an abdominal desmoid tumor during pregnancy. *J Surg Oncol* 89(2): 86–90, 2005.
57. Woo GM, Twickler DM et al. The pelvis after cesarean section and vaginal delivery: normal MR findings. *AJR Am J Roentgenol* 161: 1249–1252, 1993.
58. Willms AB, Brown ED et al. Anatomic changes in the pelvis after uncomplicated vaginal delivery: evaluation with serial MR imaging. *Radiology* 195: 91–94, 1995.
59. Leyendecker JR, Gorengaut V, Brown JJ. MR imaging of maternal diseases of the abdomen and pelvis during pregnancy and the immediate postpartum period. *Radiographics* 24(5): 1301–3016, 2004.
60. Armstrong V, Hansen WF, Van Voohis BJ, Syrop CH. Detection of cesarean scars by transvaginal ultrasound. *Obstet Gynecol* 101(1): 61–65, 2003.
61. Ash A, Smith A, Maxwell D. Caesarean scar pregnancy. *BJOG* 114(3): 253–263, 2007.
62. Kubik Huch RA. Female pelvis. *Eur Radiol* 9: 1715–1721, 1999.
63. Kido A, Togashi K, Koyama T, Ito H, Tatsumi K, Fujii S, Konishi J. Retained products of conception masquerading as acquired arteriovenous malformation. *J Comput Assist Tomogr* 27: 88–92, 2003.
64. Coakley FV, Hricak H et al. Complex fetal disorders: effect of MR imaging on management—preliminary clinical experience. *Radiology* 213: 691–696, 1999.
65. Frates MC, Kumar AJ, Benson CB, Ward VL, Tempany CM. Fetal anomalies: comparison of MR imaging and US for diagnosis. *Radiology* 232: 398–404, 2004.
66. Rajeswaran, R, Chandrasekharan, A, Joseph, S, Venkata Sai, PM, Dev, B, Reddy, S. Ultrasound versus MRI in the diagnosis of fetal head and trunk anomalies. *The Journal of Maternal-Fetal and Neonatal Medicine* 22(2): 115–123, 2009.
67. Glenn OA, Barkovich AJ. Magnetic resonance imaging of the fetal brain and spine: an increasingly important tool in prenatal diagnosis, part 1. *Am J Neuroradiol* 27: 1604–1611, 2006.
68. Cardoza JD, Goldstein RB, Filly RA. Exclusion of fetal ventriculomegaly with a single measurement: the width of the lateral ventricular atrium. *Radiology* 169: 711–714, 1988.
69. Farrell TA, Hertzberg BS, Kliewer MA, Harris L, Paine, SS. Fetal lateral ventricles: reassessment of normal values for atrial diameter at US. *Radiology* 193: 409–411, 1994.
70. Alagappan R, Browning PD, Laorr A, McGahan JP. Distal lateral ventricular atrium: reevaluation of normal range. *Radiology* 193: 405–408, 1994.
71. Twickler DM, Reichel T, McIntire DD, Magee KP, Ramus RM. Fetal central nervous system ventricle and cisterna magna measurements by magnetic resonance imaging. *Am J Obstet Gynecol* 187(4): 927–931, 2002.
72. Hertzberg BS, Kliewer MA, Freed KS, McNally PJ, DeLong DM, Bowie JD, Kay HH. Third ventricle: size and appearance in normal fetuses through gestation. *Radiology* 203: 641–644, 1997.
73. Sari A, Ahmetoglu A, Dinc H, Saglam A, Kurtoglu U, Kandemir S, Reit GH. Fetal biometry: size and configuration of the third ventricle. *Acta Radiol* 46(6): 631–663, 2005.
74. Lan LM, Yamashita Y et al. Normal fetal brain development: MR imaging with a half-Fourier rapid acquisition with relaxation enhancement sequence. *Radiology* 215: 205–210, 2000.
75. Robinson AJ, Blaser S, Toi A, Chitayat D, Halliday W, Pantazi S, Gundogan M, Laughlin S, Ryan G. The fetal cerebellar vermis: assessment for abnormal development by ultrasonography and magnetic resonance imaging. *Ultrasound Quarterly* 23: 211–223, 2007.
76. Shinmoto SH, Kashima K, Yuasa Y, Tanimoto A, Morikawa Y, Ishimoto H, Yoshimura Y, Hiramatsu K. MR imaging of non-CNS fetal abnormalities: a pictorial essay. *Radiographics* 20(5): 1227–1243, 2000.
77. Ghi T, Tani G, Savelli L, Colleoni GG, Pilu G, Bovicelli L. Prenatal imaging of facial clefts by magnetic resonance imaging with emphasis on the posterior palate. *Prenatal Diagn* 23(12): 970–975, 2003.
78. Amin RS, Nikolaidis P et al. Normal anatomy of the fetus at MR imaging. *Radiographics* 19: 201–214, 1999.
79. Shinmoto H, Kuribayashi S. MRI of fetal abdominal abnormalities. *Abdom Imaging* 28(6): 877–886, 2003.
80. Huisman TA, Kellenberger CJ. MR imaging characteristics of the normal fetal gastrointestinal tract and abdomen. *Eur J Radiol* 65(1): 170–181, 2008.
81. Huppert BJ, Brandt KR, Ramin KD, King BF. Single-shot fast spin-echo MR imaging of the fetus: a pictorial essay. *Radiographics* 19 Spec No: S215–S227, 1999.
82. Levine D, Stroustrup Smith A, McKenzie C. Tips and tricks of fetal MR imaging. *Radiol Clin N Am* 41(4): 729–745, 2003.
83. Huisman TAGM, Wisser J, Martin E, Kubik-Huch R, Marincek B. Fetal magnetic resonance imaging of the central nervous system: a pictorial essay. *Eur Radiol* 12(8): 1952–1961, 2002.
84. Laifer-Narin S, Budorick NE, Simpson LL, Plat LD. Fetal magnetic resonance imaging: a review. *Curr Opin Obstet Gynecol* 19(2): 151–156, 2007.
85. Glenn OA, Barkovich J. Magnetic resonance imaging of the fetal brain and spine: an increasingly important tool in prenatal diagnosis: part 2. *Am J Neuroradiol* 27(9): 1807–1814, 2006.
86. Levine D, Barnes PD, Robertson RR, Wong G, Mehta TS. Fast MR imaging of fetal central nervous system abnormalities. *Radiology* 229(1): 51–61, 2003.
87. Mehta TSS, Levine D. Imaging of fetal cerebral ventriculomegaly: a guide to management and outcome. *Semin Fetal Neonatal Med* 10(5): 421–428, 2005.
88. Dietrich RB, Cohen I. Fetal MR imaging. *Magn Reson Imaging Clin N Am* 14(4): 503–522, 2006.
89. Zimmerman RA, Bilaniuk LT. Magnetic resonance evaluation of fetal ventriculomegaly-associated congenital malformations and lesions. *Semin Fetal Neonatal Med* 10(5): 429–443, 2005.
90. Levitsky DB, Mack LA, Nyberg DA, Shurtleff DB, Shields LA, Nghiem HV, Cyr DR. Fetal aqueductal stenosis diagnosed sonographically: how grave is the prognosis? *AJR Am J Roentgenol* 164(3): 725–730, 1995.
91. Stevenson KL. Chiari type II malformation: past, present, and future. *Neurosurg Focus* 16(2): E5, 2004.
92. McLone DG, Dias MS. The Chiari II malformation: cause and impact. *Childs Nerv Syst* 19: 540–550, 2003.

93. Appasamy M, Roberts D, Pilling D, Buxton N. Antenatal ultrasound and magnetic resonance imaging in localizing the level of lesion in spina bifida and correlation with postnatal outcome. *Ultrasound Obstet Gynecol* 27: 530–536, 2006.
94. Von Koch CS, Glenn OA, Goldstein RB, Barkovich AJ. Fetal magnetic resonance imaging enhances detection of spinal cord anomalies in patients with sonographically detected bony anomalies of the spine. *J Ultrasound Med* 24(6): 781–789, 2005.
95. Glenn OA, Goldstein RB, Li KC, Young SJ, Norton ME, Busse RF, Goldberg JD, Barkovich AJ. Fetal magnetic resonance imaging in the evaluation of fetuses referred for sonographically suspected abnormalities of the corpus callosum. *J Ultrasound Med* 24: 791–804, 2005.
96. Marszal E, Jamroz E, Pilch J, Kluczewska E, Jablecka-Deja H, Krawczyk R. Agenesis of corpus callosum: clinical description and etiology. *J Child Neurol* 15(6): 401–405, 2000.
97. Schell-Apacik CC, Wagner K, Bihler M, Ertl-Wagner B, Heinrich U, Klopocki E, Kalscheuer VM, Muenke M, von Voss H. Agenesis and dysgenesis of the corpus callosum: clinical, genetic and neuroimaging findings in a series of 41 patients. *Am J Med Genet Part A* 146A(19): 2501–2511, 2008.
98. D'Ercole C, Girard N, Cravello L, Boubli L, Potier,A, Raybaud C, Blanc B. Prenatal diagnosis of fetal corpus callosum agenesis by ultrasonography and magnetic resonance imaging. *Prenatal Diagn* 18: 247–253, 1998.
99. Pulitzer SB, Simon EM, Crombleholme TM, Golden JA. Prenatal MR findings of the middle interhemispheric variant of holoprosencephaly. *Am J Neuroradiol* 25(6): 1034–1036, 2004.
100. Wong AM-C, Bilaniuk LT, Ng K-K, Chang Y-L, Chao A-S, Wai Y-Y. Lobar holoprosencephaly: prenatal MR diagnosis with postnatal MR correlation. *Prenatal Diagn* 25: 296–299, 2005.
101. Plawner LL, Delgado MR, Miller VS, Levey EB, Kinsman SL, Barkovich AJ, Simon EM, Clegg NJ, Sweet VT, Stashinko EE, Hahn JS. Neuroanatomy of holoprosencephaly as predictor of function: beyond the face predicting the brain. *Neurology* 59: 1058–1066, 2002.
102. Filly RA, Chinn DH, Callen PW. Alobar holoprosencephaly: ultrasonographic prenatal diagnosis. *Radiology* 151: 455–459, 1984.
103. Barr M Jr, Cohen MM Jr. Holoprosencephaly survival and performance. *Am J Med Genet C Semin Med Genet* 89(2): 116–120, 1999.
104. Lewis AJ, Simon EM, Barkovich AJ, Clegg NJ, Delgado MR, Levey E, Hahn JS. Middle interhemispheric variant of holoprosencephaly: a distinct cliniconeuroradiologic subtype. *Neurology* 59: 1860–1865, 2002.
105. Calabro F, Arcuri T, Jinkins JR. Blake's pouch cyst: an entity within the Dandy-Walker continuum. *Neuroradiology* 42: 290–295, 2000.
106. Chen C-P. Prenatal diagnosis of arachnoid cysts. *Taiwanese J Obstet Gynecol* 46(3): 187–198, 2007.
107. Malinger G, Lev D, Kidron D, Heredia F, Hershkovitz R, Lerman-Sagie T. Differential diagnosis in fetuses with absent septum pellucidum. *Ultrasound Obstet Gynecol* 25: 42–49, 2005.
108. Weinstein AS, Goldstein RB. Case 12. Absent septum or septo-optic dysplasia (magnetic resonance imaging not yet performed). *J Ultrasound Med* 21(5): 598, 617, 2002.
109. Lepinard C, Coutant R, Boussion F, Loisel D, Delorme B, Biquard F, Bonneau D, Guichet A, Descamps P. Prenatal diagnosis of absence of the septum pellucidum associated with septo-optic dysplasia. *Ultrasound Obstet Gynecol* 25: 73–75, 2005.
110. Hung J-H, Shen S-H, Guo W-Y, Chen C-Y, Chao K-C, Yang M-J, Hung C-YS. Prenatal diagnosis of schizencephaly with septo-optic dysplasia by ultrasound and magnetic resonance imaging. *J Obstet Gynaecol Res* 34(4 Part II): 674–679, 2008.
111. Barkovich AJ, Fram EK, Norman D. Septo-optic dysplasia: MR imaging. *Radiology* 171(1): 189–192, 1989.
112. Budorick NE, Pretorius DH, McGahan JP, Grafe MR, James HE, Slivka J. Cephalocele detection in utero: sonographic and clinical feature. *Ultrasound Obstet Gynecol* 5(2): 77–85, 1995.
113. David DJ, Proudman TW. Cephaloceles: classification, pathology, and management. *World J Surg* 13(4): 349–357, 1989.
114. Oh KY, Kennedy AM, Frias AE Jr, Byrne JL. Fetal schizencephaly: pre- and postnatal imaging with a review of the clinical manifestations. *Radiographics* 25(3): 647–657, 2005.
115. Huang WM, Monteagudo A, Bennett GL, Fowkes ME, Timor-Tritsch IE. Schizencephaly in a dysgenetic fetal brain: prenatal sonographic, magnetic resonance imaging, and postmortem correlation. *J Ultrasound Med* 25(4): 551–554, 2006.
116. Levine D, Barnes P, Korf B, Edelman R. Tuberous sclerosis in the fetus: second-trimester diagnosis of subependymal tubers with ultrafast MR imaging. *AJR Am J Roentgenol* 175: 1067–1069, 2000.
117. Ghai S, Fong KW, Toi A, Chitayat D, Pantazi S, Blaser S. Prenatal US and MR imaging findings of lissencephaly: review of fetal cerebral sulcal development. *Radiographics* 26(2): 389–405, 2006.
118. Garel C, Delezoide A-L, Elmaleh-Berges M, Menez F, Fallet-Bianco C, Vuillard E, Luton, D, Oury J-F, Sebag G. Contribution of fetal MR imaging in the evaluation of cerebral ischemic lesions. *Am J Neuroradiol* 25: 1563–1568, 2004.
119. Brunel H, Girard N, Confort-Gouny S, Viola A, Chaumoitre K, D'Ercole C, Figarella-Branger D, Raybaud C, Cozzone P, Panuel M. Fetal brain injury. *J Neuroradiol* 31: 123–137, 2004.
120. De Laveaucoupet J, Audibert F, Guis F, Rambaud C, Suarez B, Boithias-Guerot C, Musset D. Fetal magnetic resonance imaging (MRI) of ischemic brain injury. *Prenatal Diagn* 21: 729–736, 2001.
121. Kurtz AB, Johnson PT. Case 7: hydranencephaly. *Radiology* 210: 419–422, 1999.
122. Woodward PJ, Sohaey R, Kennedy A, Koeller KK. From the archives of AFIP: a comprehensive review of fetal tumors with pathologic correlation. *Radiographics* 25(1): 215–242, 2005.
123. Romano F, Bratta FG, Caruso G, DiNaro E, Serio R, Resta M, Loizzi P. Prenatal diagnosis of choroid plexus papillomas of the lateral ventricle. A report of two cases. *Prenatal Diagn* 16: 567–571, 1996.
124. Teksam M, Ozyer U, McKinney A, Kirbas I. MR imaging and ultrasound of fetal cervical cystic lymphangioma: utility in antepartum treatment planning. *Diagn Interv Radiol* 11: 87–89, 2005.
125. Kim SK, Won HS, Lee SW, Kim JK, Shim JY, Lee PR, Kim A. Prenatal diagnosis of congenital epulis by three-dimensional ultrasound and magnetic resonance imaging. *Prenat Diagn* 26(2): 171–174, 2006.
126. Roy S, Sinsky A, Williams B, Desilets V, Patenaude YG. Congenital epulis: prenatal imaging with MRI and ultrasound. *Pediatr Radiol* 33(11): 800–803, 2003.
127. Smith AS, Estroff JA, Barnewolt CE, Mulliken JB, Levine D. Prenatal diagnosis of cleft lip and cleft palate using MRI. *AJR Am J Roentgenol* 183: 229–235, 2004.
128. Kazan-Tannus, JF, Levine, D, McKenzie, C, Lim, K-H, Cohen, B, Farrar, N, Busse, RF, Mulliken, JB. Real-time magnetic resonance imaging aids prenatal diagnosis of isolated cleft palate. *Journal of Ultrasound in Medicine* 24: 1533–1540, 2005.
129. Bianchini E, Zirpoli S, Righini A, Rustico M, Parazzini C, Triulzi F. Magnetic resonance imaging in prenatal diagnosis of dacryocystocele: report of 3 cases. *J Comput Assist Tomogr* 28(3): 422–427, 2004.
130. Goldberg H, Sebire NJ, Holwell D, Hill S. Prenatal diagnosis of bilateral dacryocystoceles. *Ultrasound Obstet Gynecol* 15(5): 448–449, 2000.

131. Elia D, Garel C, Enjolras O, Vermouneix L, Soupre V, Oury J-F, Guibaud L. Prenatal imaging findings in rapidly involuting congenital hemangioma of the skull. *Ultrasound Obstet Gynecol* 31: 572–575, 2008.
132. Kashima H, Unno N, Hyodo H, Hyodo HM, Takagi K, Nakamura T, Kondoh Y, Noguchi M, Konishi I. Antenatal sonographic and magnetic resonance images of a giant hemangioma of the fetal skull. *Ultrasound Obstet Gynecol* 25(5): 522–52, 2005.
133. Richard F, Garel C, Cynober E, Soupre V, Bénifla JL, Jouannic JM. Prenatal diagnosis of a rapidly involuting congenital hemangioma (RICH) of the skull. *Prenat Diagn* 29(5): 533–535, 2009.
134. Miyakoshi K, Tanaka M, Matsumoto T, Hattori Y, Minegishi K, Ishimoto H, Yoshimura Y. Occipital scalp hemangioma: prenatal sonographic and magnetic resonance images. *J Obstet Gynaecol Res* 34(4 Pt 2): 666–669, 2008.
135. Duncan KR, Gowland PA et al. Assessment of fetal lung growth in utero with echo-planar MR imaging. *Radiology* 210: 197–200, 1999.
136. Levine D, Barnewolt CE, Mehta TS, Trop I, Estroff J, Wong G. Fetal thoracic abnormalities: MR imaging. *Radiology* 228: 379–388, 2003.
137. Worley, KC, Dashe, JS, Barber, RG, Megison, SM, McIntire, DD, Twickler, DM. Fetal magnetic resonance imaging in isolated diaphragmatic hernia: volume of herniated liver and neonatal outcome. *Am J Obstet Gynecol* 200: 318.e1–318.e6, 2009.
138. Walsh DS, Hubbard AM, Olutoye OO, Howell LJ, Crombleholme TM, Flake AW, Johnson MP, Adzick NS. Assessment of fetal lung volumes and liver herniation with magnetic resonance imaging in congenital diaphragmatic hernia. *Am J Obstet Gynecol* 183(5): 1067–1069, 2000.
139. Johnson AM, Hubbard AM. Congenital anomalies of the fetal/neonatal chest. *Semin Roentgenol* 39(2): 197–214, 2004.
140. Poutamo J, Vanninen R, Partanen K, Kirkinen P. Diagnosing fetal urinary tract abnormalities: benefits of MRI compared to ultrasonography. *Acta Obstet Gynecol Scand* 79: 65–71, 2000.
141. Barseghyan K, Jackson HA, Chmait R, DeFilippo RE, Miller DA. Complementary roles of sonography and magnetic resonance imaging in the assessment of fetal urinary tract anomalies. *J Ultrasound Med* 27: 1563–1569, 2008.
142. Cassart M, Massez A, Metens T, Rypens F, Lambot MA, Hall M, Avni FE. Complementary role of MRI after sonography in assessing bilateral urinary tract anomalies in the fetus. *AJR Am J Roentgenol* 182: 689–695, 2004.
143. Hormann M, Brugger PC, Balassy C, Witzani L, Prayer D. Fetal MRI of the urinary system. *Eur J Radiol* 57(2): 303–311, 2006.
144. Jeffrey RJ Jr, Laing FC, Wing VW, Hoddick W. Sonography of the fetal duplex kidney. *Radiology* 153(1): 123–124, 1984.
145. Grignon A, Filion R, Filiatrault D, Robitaille P, Homsy Y, Boutin H, Leblond R. Urinary tract dilatation in utero: classification and clinical applications. *Radiology* 160(3): 645–647, 1986.
146. Thomas DFM. Prenatally detected uropathy: epidemiological considerations. *Br J Urol* 81(Suppl 2): 8–12, 1998.
147. Garel C, Dreux S, Phillipe-Chomette P, Vuillard E, Oury J-F, Muller F. Contribution of fetal magnetic resonance imaging and amniotic fluid digestive enzyme assays to the evaluation of gastrointestinal tract abnormalities. *Ultrasound Obstet Gynecol* 28: 282–291, 2006.
148. White SM, Chamberlain P, Hitchcock R, Sullivan PB, Boyd PA. Megacystis-microcolon-intestinal hypoperistalsis syndrome: the difficulties with antenatal diagnosis. Case report and review of the literature. *Prenat Diagn* 20(9): 697–700, 2000.
149. Hussain S, Begum N. Multicystic dysplastic disease of kidney in fetus. *J Ayub Med Coll Abbottabad* 19(2): 68–69, 2007.
150. Lonergan GJ, Rice RR, Suarez ES. Autosomal recessive polycystic kidney disease: radiologic-pathologic correlation. *Radiographics* 20(3): 837–55, 2000.
151. Gupta P, Jain S. MRI in a fetus with Meckel-Gruber syndrome. *Pediatr Radiol* 38(1): 122, 2008.
152. Morikawa M, Yamada T, Cho K, Yamada H, Minakami H. Prenatal diagnosis and therapy of persistent cloaca. a case report. *Fetal Diagn Ther* 21(4): 343–347, 2006.
153. Warne S, Chitty LS, Wilcox DT. Prenatal diagnosis of cloacal anomalies. *BJU Int* 89(1): 78–81, 2002.
154. Picone O, Laperelle J, Sonigo P, Levaillant JM, Frydman R, Senat MV. Fetal magnetic resonance imaging in the antenatal diagnosis and management of hydrocolpos. *Ultrasound Obstet Gynecol* 30(1): 105–109, 2007.
155. Garel C, Dreux S, Phillippe-Chomette P, Vuillared E, Oury J-F, Muller F. Contribution of fetal magnetic resonance imaging and amniotic fluid digestive enzyme assays to the evaluation of gastrointestinal tract abnormalities. *Ultrasound Obstet Gynecol* 28(3): 282–291, 2006.
156. Sugai Y, Hosoya T. MR imaging of fetal omphalocele: a case report. *Magn Reson Med Sci* 7(4): 211–213, 2008.
157. Sasaki Y, Miyamoto T, Hidaka Y, Satoh H, Takuma N, Sengoku K, Sugimori H, Inaoka T, Aburano T. Three-dimensional magnetic resonance imaging after ultrasonography for assessment of fetal gastroschisis. *Magn Reson Imaging* 24(2): 201–203, 2006.
158. Hsieh K, O'Loughlin MT, Ferrer FA. Bladder exstrophy and phenotypic gender determination on fetal magnetic resonance imaging. *Urology* 65(5): 998–999, 2005.
159. McNamara A, Levine D. Intraabdominal fetal echogenic masses: a practical guide to diagnosis and management. *Radiographics* 25: 633–645, 2005.
160. Danzer E, Hubbard AM, Hedrick HL, Johnson MP, Wilson RD, Howell LJ, Flake AW, Adzick NS. Diagnosis and characterization of fetal sacrococcygeal teratoma with prenatal MRI. *AJR Am J Roentgenol* 187(4): W350–W356, 2006.
161. Blackman SC, Evenson AR, Voss SD, Barnewolt CE, Puder M. Prenatal diagnosis and subsequent treatment of an intermediate-risk paraspinal neuroblastoma: case report and review of the literature. *Fetal Diagn Ther* 24: 119–125, 2008.
162. Irsutti M, Puget C, Baunin C, Duga I, Sarramon J-F, Guitard J. Mesoblastic nephroma: prenatal ultrasonographic and MRI features. *Pediatr Radiol* 30: 147–150, 2000.
163. Chen W-Y, Lin C-N, Chao, C-S, Lin, MY-S, Mak C-W, Chuang S-S, Tzeng C-C, Huang K-F. Prenatal diagnosis of congenital mesoblastic nephroma in mid-second trimester by sonography and magnetic resonance imaging. *Prenatal Diagn* 23: 927–931, 2003.
164. Laberge J-M, Patenaude Y, Desilets V, Cartier L, Khalife S, Jutras L, Chen M-F. Large hepatic mesenchymal hamartoma leading to mid-trimester fetal demise. *Fetal Diagn Ther* 20: 141–145, 2005.
165. Ryu JK, Cho JY, Choi JS. Prenatal sonographic diagnosis of focal musculoskeletal anomalies. *Korean J Radiol* 4(4): 243–251, 2003.
166. Mammen L, Benson CB. Outcome of fetuses with clubfeet diagnosed by prenatal sonography. *J Ultrasound Med* 23: 497–500, 2004.
167. Shipp TD, Benacerraf BR. The significance of prenatally identified isolated clubfoot: is amniocentesis indicated? *Am J Obstet Gynecol* 178: 600–602, 1998.
168. Baker PN, Johnson IR et al. Measurement of fetal liver, brain and placental volumes with echo-planar magnetic resonance imaging. *Br J Obstet Gynaecol* 102: 35–39, 1995.
169. Kubik Huch RA, Wildermuth S et al. Fetus and utero-placental unit: fast MR imaging with three-dimensional reconstruction and volumetry-feasibility study. *Radiology* 219: 567–573, 2001.
170. Quintero RA. Twin-twin transfusion syndrome. *Clin Perinatol* 30: 591–600, 2003.
171. Luks FI, Carr SR, Ponte B, Rogg JM, Tracy TF Jr. Preoperative planning with magnetic resonance imaging and computerized

volume rendering in twin-to-twin transfusion syndrome. *Am J Obstet Gynecol* 185: 216–219, 2001.
172. Powell MC, Buckley J et al. Magnetic resonance imaging and placenta previa. *Am J Obstet Gynecol* 154: 565–569, 1986.
173. Kay HH, Spritzer CE. Preliminary experience with magnetic resonance imaging in patients with third-trimester bleeding. *Obstet Gynecol* 78: 424–429, 1991.
174. Levine D, Hulka CA, Ludmir J, Li W, Edelman RR. Placenta accreta: evaluation with color Doppler US, power Doppler US, and MR imaging. *Radiology* 205: 773–776, 1997.
175. Maldjian C, Adam R, Pelosi M, Pelosi M 3rd, Rudelli RD, Maldjian J. MRI appearance of placenta percreta and placenta accreta. *Magn Reson Imaging* 17: 965–971, 1999.
176. Marcos HB, Semelka RC, Worawattanakul S. Normal placenta: gadolinium-enhanced, dynamic MR imaging. *Radiology* 205: 493–496, 1997.
177. Wagner BJ, Woodward PJ et al. From the archives of the AFIP. Gestational trophoblastic disease: radiologic-pathologic correlation. *Radiographics* 16: 131–148, 1996.
178. Hricak H, Demas BE et al. Gestational trophoblastic neoplasm of the uterus: MR assessment. *Radiology* 161: 11–16, 1986.
179. Barton JW, McCarthy SM et al. Pelvic MR imaging findings in gestational trophoblastic disease, incomplete abortion, and ectopic pregnancy: are they specific? *Radiology* 186: 163–168, 1993.
180. Powell MC, Buckley J et al. Magnetic resonance imaging and hydatidiform mole. *Br J Radiol* 59: 561–564, 1986.
181. Levine D, Barnes PD et al. Obstetric MR imaging. *Radiology* 211: 609–617, 1999.
182. Stark DD, McCarthy SM et al. Pelvimetry by magnetic resonance imaging. *AJR Am J Roentgenol* 144: 947–950, 1985.
183. Weinreb JC, Lowe TW et al. Magnetic resonance imaging in obstetric diagnosis. *Radiology* 154: 157–161, 1985.
184. Pfammatter T, Marincek B et al. MR-pelvimetrische Referenzwerte. *Rofo Fortschr Geb Rontgenstr Neuen Bildgeb Verfahr* 153: 706–710, 1990.
185. Sigmund G, Bauer M et al. [A technic of magnetic resonance tomographic pelvimetry in obstetrics] Original title: Technik der kernspintomographischen Beckenmessung in der Geburtshilfe. *Rofo Fortschr Geb Rontgenstr Neuen Bildgeb Verfahr* 154: 370–374, 1991.
186. Doyle NM, Monga M. Role of ultrasound in screening patients at risk for preterm delivery. *Obstet Gynecol Clin N Am* 31(1): 125–139, 2004.
187. Wong G, Levine D. Sonographic assessment of the cervix in pregnancy. *Semin Ultrasound CT MR* 19(4): 370–380, 1998.

CHAPTER 17

PEDIATRICS

WAQAS QURESHI, NACIYE TURAN, THUY VU, MOHAMED ELAZZAZI, CARLOS GONZALEZ, RAFAEL DE CAMPOS, AND RICHARD C. SEMELKA

INTRODUCTION

Over the past decade, the role of body MR imaging in pediatrics has defined new practices. As the technology is improving each year, it has started to play an important role in clinical decision making. Body MRI has an important role in the diagnosis and management of a wide range of pediatric illnesses, including evaluation of abdominal masses, staging of local disease, identifying distant metastases, and monitoring response to therapy [1–4]. The elements of high-quality imaging, reproducibility of image quality and good conspicuity of disease, lie in the use of reliable sequences that minimize or avoid artifacts (figs. 17.1–17.4; Table 17.1).

MR is a noninvasive test with high intrinsic soft tissue contrast, few risks, and no exposure to ionizing radiation, all important factors in pediatric imaging [5, 6]. However, there has not been as strong an emphasis on pediatric MR imaging as on adult body MR. This is due in part to the lack of expertise in the field and in part to the challenges in imaging pediatric patients because of the level of cooperation and long imaging times needed in MRI studies. Although the majority of this book is dedicated to adult body MR imaging, we address broader aspects of pediatric MR imaging in this chapter. We foresee that the usage of pediatric MR will become widespread in the years to come. Chapter 1 gives a comprehensive account of diagnostic approach to protocoling and interpreting MR studies of the abdomen and pelvis. The unique aspects of pediatric MR are discussed in this chapter.

MRI TECHNIQUE

Imaging Sequences

T1-Weighted Sequences

Spin-Echo Sequence. Unlike in the adult patient, spin-echo imaging plays an important role in pediatric patients because they are more likely to be sedated or asleep, which is a useful status for image quality to be consistent for the long-duration, breathing-averaged sequence. Furthermore, the high intrinsic signal-to-noise ratio (SNR) of this sequence is important for imaging small individuals. Fat suppression is routinely applied in order to improve the dynamic range of tissue signal intensities.

Abdominal-Pelvic MRI, Third Edition, edited by Richard C. Semelka. Copyright © 2010 John Wiley & Sons, Inc.

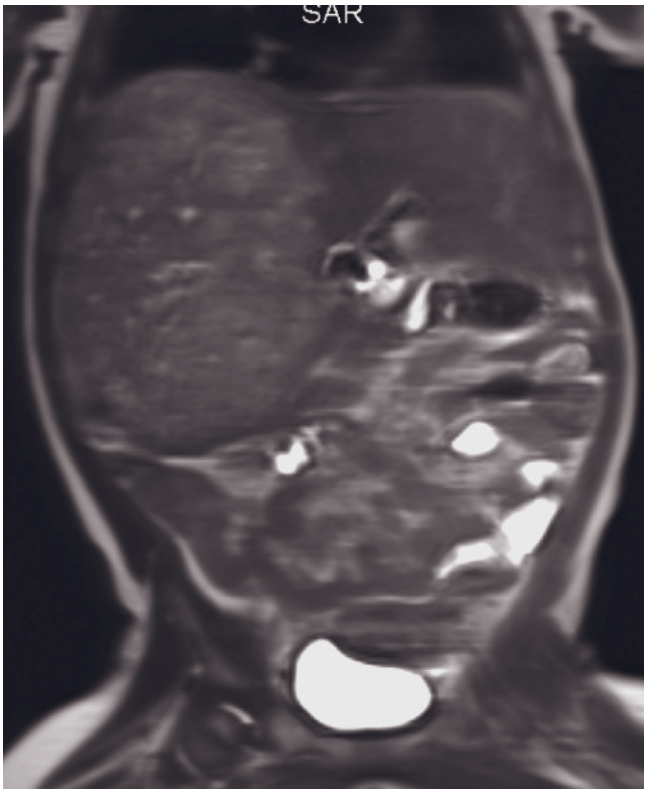

(*a*)

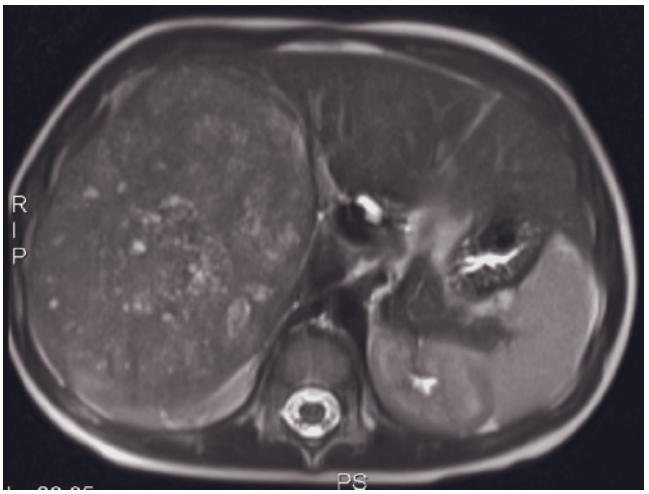

(*b*)

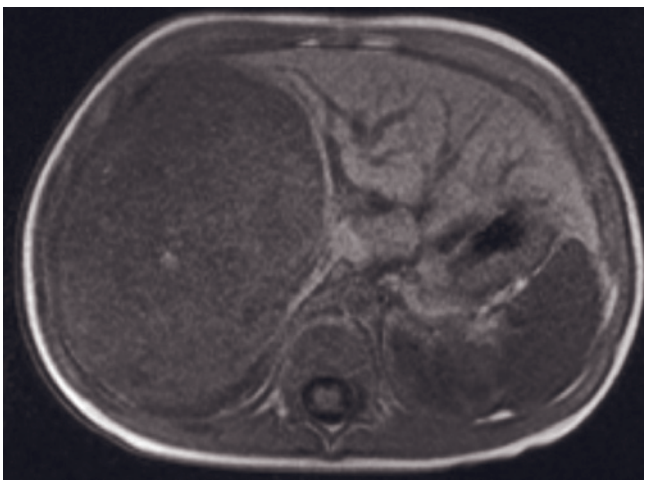

(*c*)

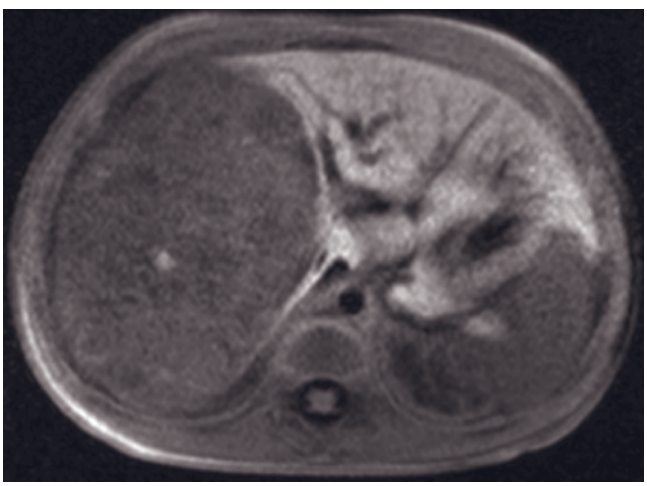

(*d*)

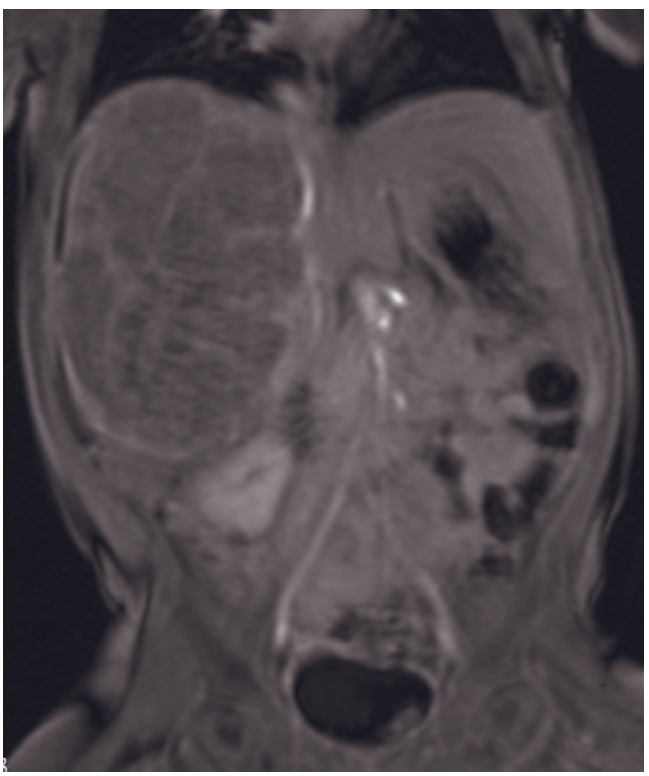

(*e*)

Fig. 17.1 Breathing-averaged (sedated patient) protocol in an 13-month-old female at 3.0 T. Coronal T2-weighted single-shot echo-train spin-echo (*a*), axial T2-weighted single-shot echo-train spin-echo (*b*), axial T1-weighted MR-RAGE (*c*), axial T1-weighted water-excitation MP-RAGE (*d*), coronal T1-weighted 90-s postgadolinium fat-suppressed 3D-GE(*e*), axial T1-weighted water-excitation MP-RAGE postgadolinium (*f*) images of a 13-month-old female with hepatoblastoma. The breathing motion artifact is minimal when such a protocol is observed while using 3.0 T systems.

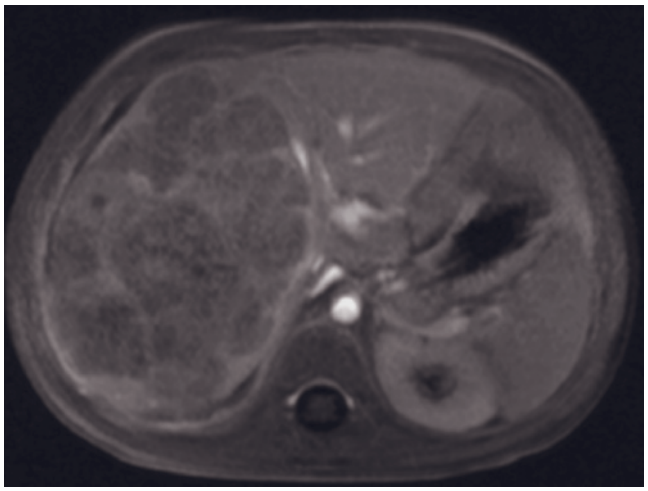

(*f*)

FIG. 17.1 (*Continued*)

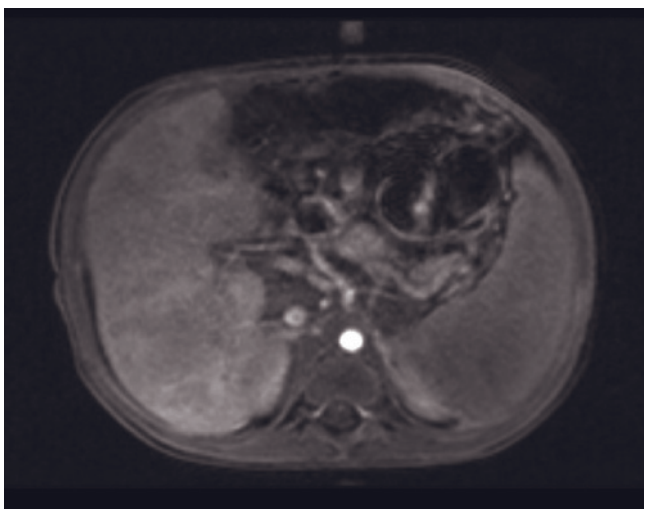

(*a*)

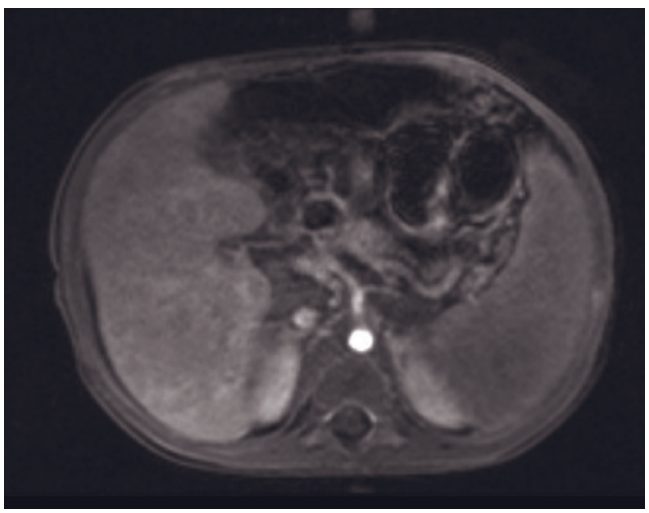

(*b*)

FIG. 17.2 Respiration-arrested protocol at 3.0 T. Axial T1-weighted immediate postgadolinium fat-suppressed 3D-GE images of adjacent slices (*a*, *b*) of a 10-month-old male. This respiration-arrested 3D gradient echo shows high spatial resolution with no breathing in an intubated infant. Note excellent demonstration of a diminutive portal vein and normal hepatic artery. Timing of respiration suspension is a careful choreography between the MR technologist and the anesthesia team.

2D-Spoiled Gradient-Echo Sequence. 2D-SGE sequences provide true T1-weighted imaging and, with the use of phased-array multicoil imaging, achievs good signal-to-noise ratio and short-duration sequence acquisition.

3D-Gradient-Echo Sequence. 3D-gradient-echo imaging has distinct advantages over 2D-gradient echo, primarily the ability to acquire thinner sections (because of the higher intrinsic signal) and fewer problems with phase artifacts from breathing and blood flow. Fat suppression should be routinely used to provide superior quality images.

Magnetization-Prepared Rapid-Acquisition Gradient-Echo Sequence. Spoiled gradient-echo imaging is sensitive to motion and requires patient cooperation with breath holding; as a result, in younger children the image quality is poor. This is the reason that in the pediatric age group motion-resistant imaging is often critical. The most commonly employed T1-weighted breathing-independent snap-shot sequence is termed magnetization-prepared rapid-acquisition gradient-echo (MP-RAGE). Current versions of MP-RAGE are limited because of low-signal to-noise ratio, varying signal intensity and contrast between sections, and the presence of signal-nulling effects caused by inverting 180°

(*a*)

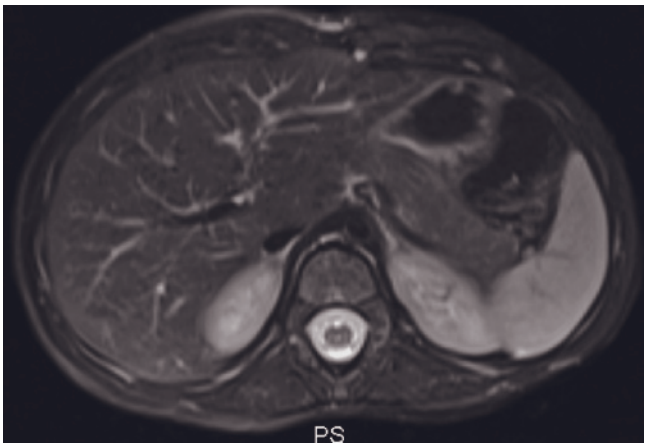

(*b*)

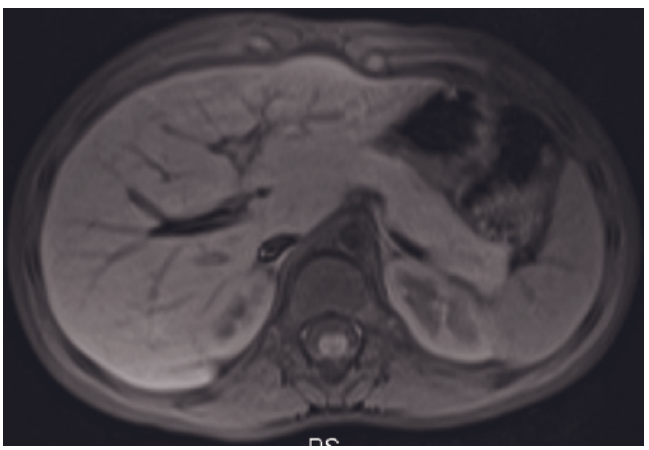

(*c*)

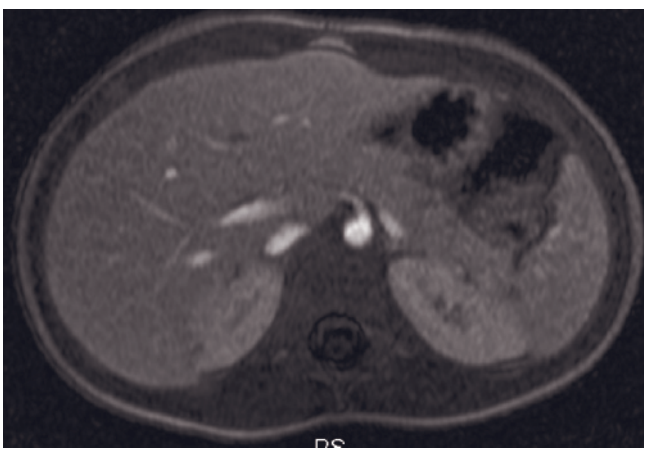

(*d*)

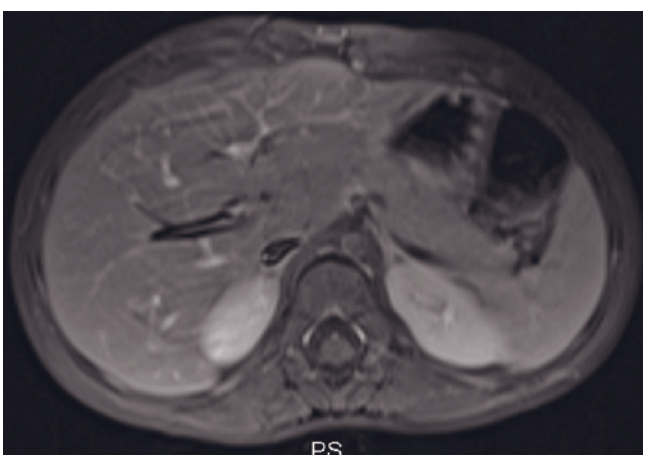

(*e*)

FIG. 17.3 Breathing-averaged (sedated patient) protocol MRI of the abdomen in a 3-year-old female at 1.5 T. Coronal water-excitation MP-RAGE (*a*), axial T2-weighted breathing-averaged fat suppressed spin-echo (*b*), axial T1-weighted fat-suppressed spin-echo (*c*), axial immediate postgadolinium MP-RAGE (*d*), and interstitial-phase T1-weighted fat-suppressed spin-echo (*e*) images. Note that *d* has a grainier appearance than the same sequence at 3.0 T(see fig. 17.1*d*), reflecting the lower signal-to-noise ratio of MP-RAGE at 1.5 T. **Motion-resistant protocol in a 2-year-old female at 3.0 T.** Coronal T2-weighted single-shot echo-train

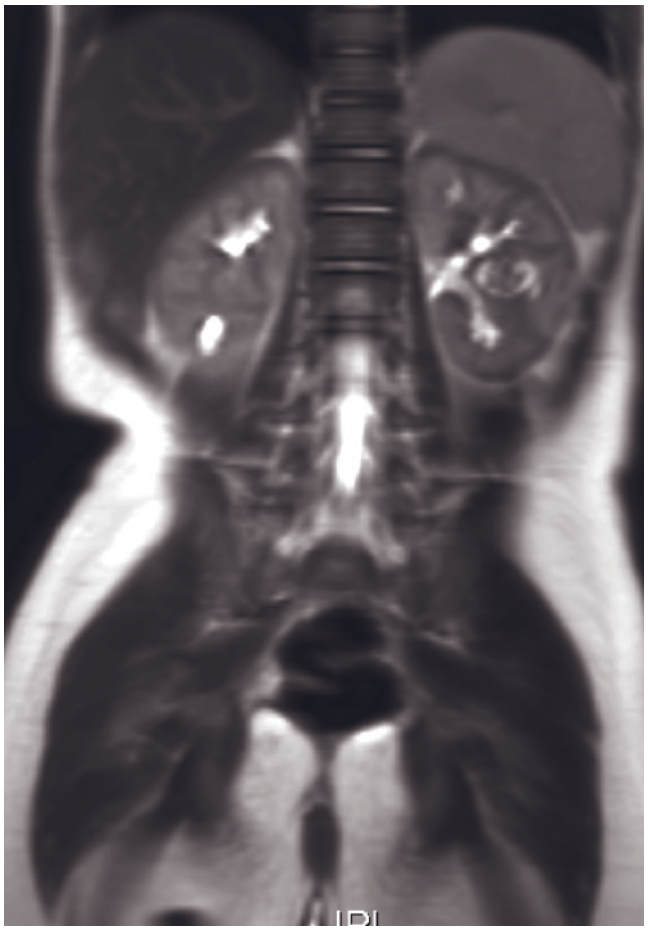

(*f*)

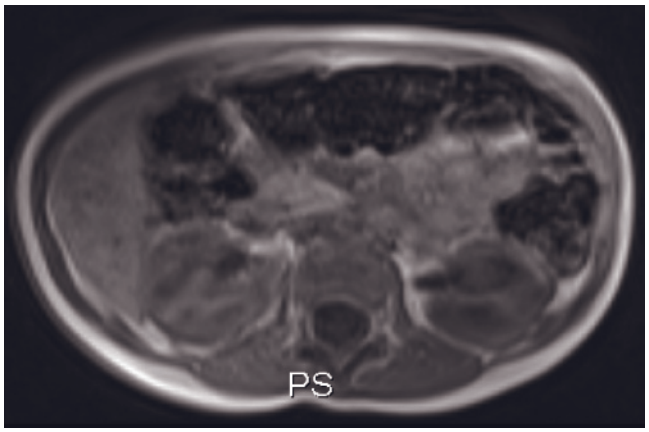

(*g*)

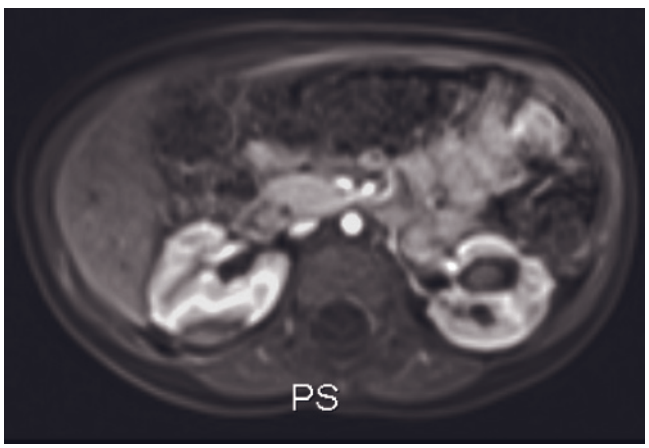

(*h*)

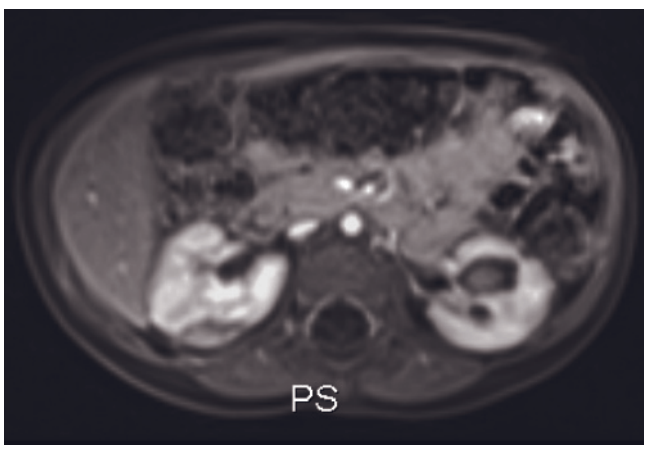

(*i*)

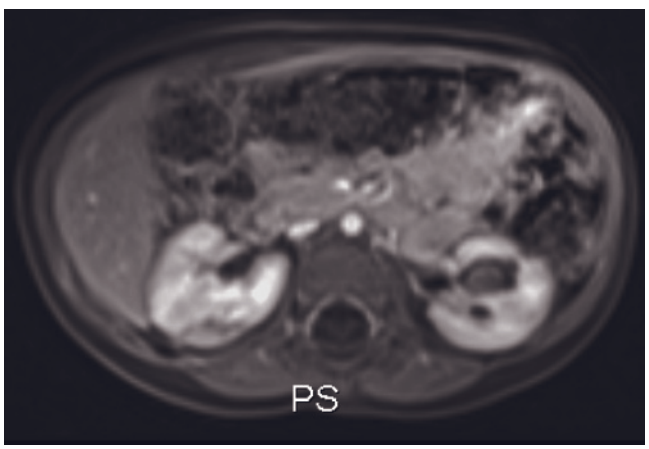

(*j*)

FIG. 17.3 (*Continued*) spin-echo (*f*), axial T1-weighted MPRAGE (*g*), axial T1-weighted immediate postgadolinium WE-MPRAGE (*h*), axial T1-weighted 60-s postgadolinium fat-suppressed WE-MPRAGE (*i*), and axial T1-weighted 90-s postgadolinium WE-MPRAGE (*j*) images of a 2-year-old female with nephroblastomatosis.

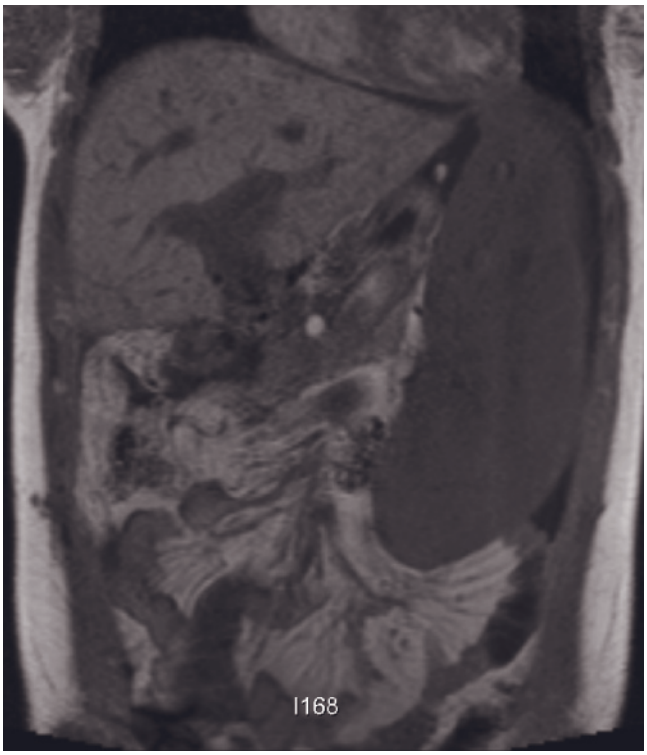

(*a*)

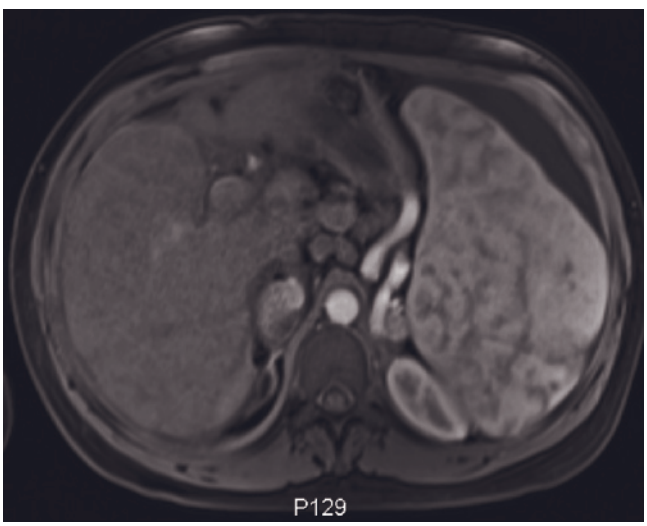

(*d*)

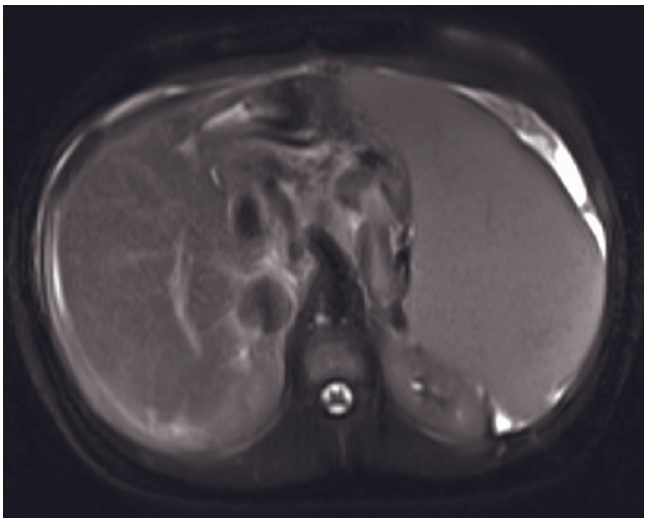

(*b*)

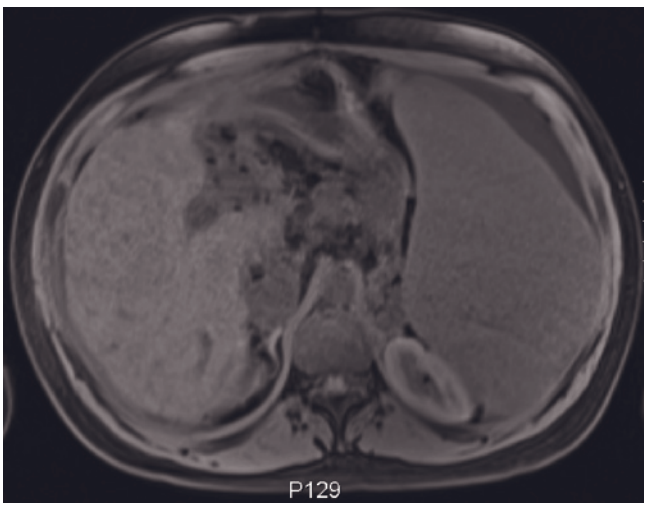

(*c*)

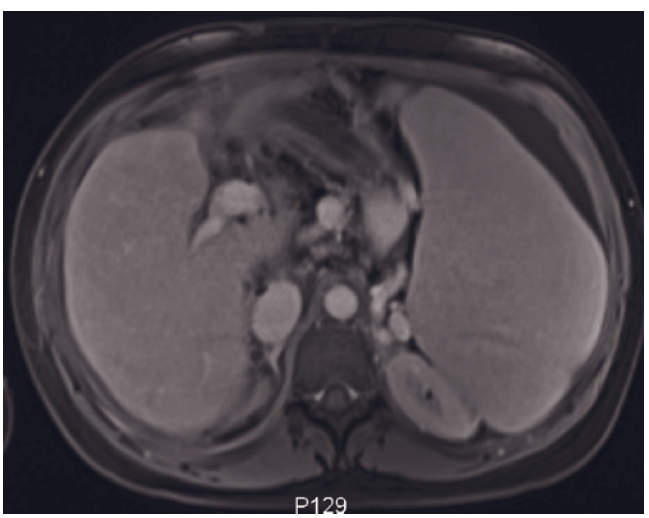

(*e*)

FIG. 17.4 Standard breath hold cooperative protocol MRI of the abdomen in a 17-year-old female with cirrhosis and portal hypertension at 1.5 T. Coronal water-excitation MP-RAGE (*a*), axial T2-weighted single-shot echo-train spin-echo (*b*), axial T1-weighted 3D gradient-echo (*c*), axial immediate (*d*), and 60-s (*e*) and 2-min (*f*) coronal fat-suppressed post-gadolinium 3D gradient-echo images. Image quality is extremely high on all sequences, with clear demonstration of chronic liver disease and features of portal hypertension, such as varices and splenomegaly.

(*f*)

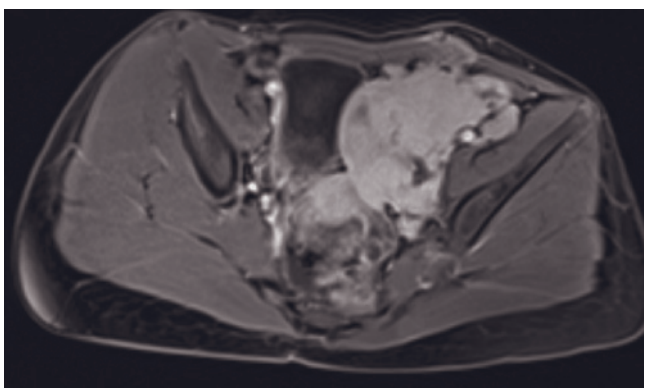

(*i*)

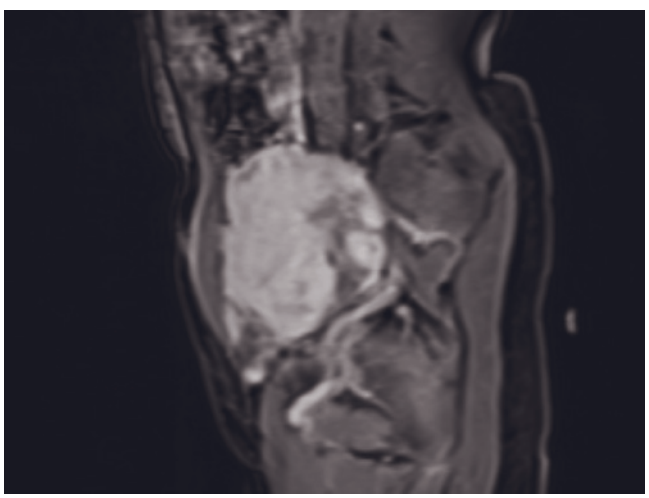

(*k*)

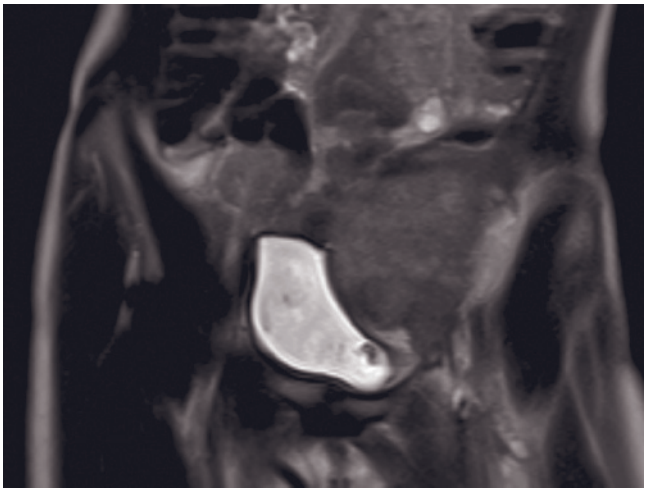

(*g*)

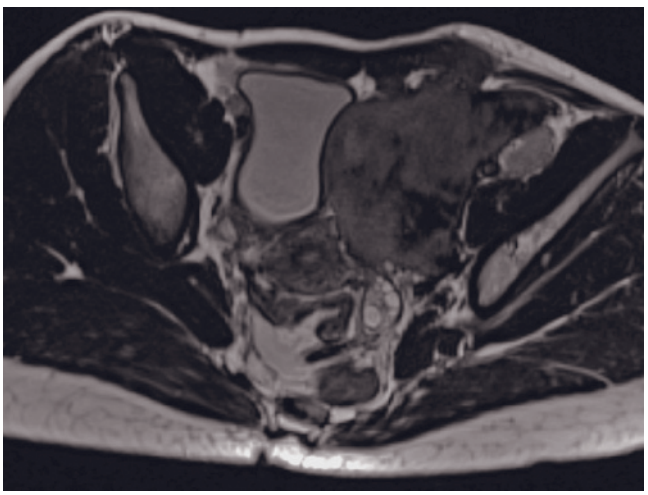

(*h*)

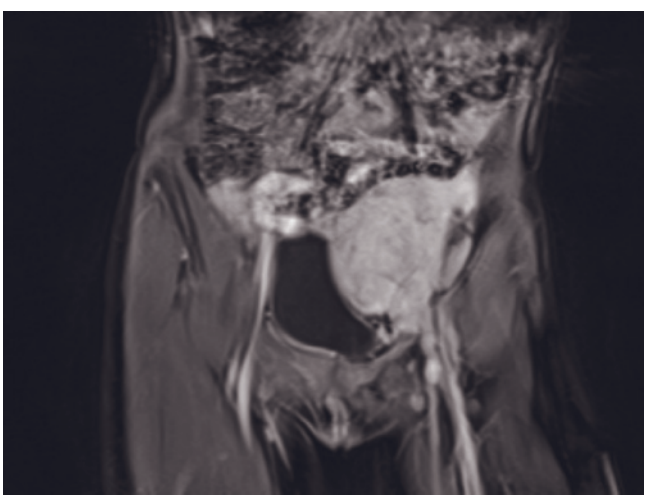

(*j*)

FIG. 17.4 (*Continued*) **Dermoid tumor in a 12-year-old female at 3.0 T.** Coronal T2-weighted single-shot echo-train spin-echo (*g*), axial T2-weighted echo-train spin-echo (*h*), axial T1-weighted fat-suppressed immediate postgadolinium 3D-GE (*i*), coronal T1-weighted postgadolinium fat-suppressed 3D-GE image (*j*), and sagittal postgadolinium T1-weighted fat suppressed 3D-GE (*k*) images from a 12-year-old female. The images show a large left pelvic heterogeneously enhancing dermoid tumor that is extending into the femoral canal and abuts the left pelvic side wall.

Table 17.1 Imaging Protocol Used at 1.5T and 3.0T

MR Sequence	Imaging Plane	Acquisition Time (s)
Breath Hold Protocol		
T2-SS-ETSE†	Coronal	~45
In-/out-of-phase T1-GE	Axial	<20
T2-SS-ETSE FS	Axial	~45
MRCP	Coronal	5
3D-GE‡	Axial	<20
3D-GE postgadolinium		
1. Hepatic arterial	Axial	<20
2. Portal venous	Axial	<20
3. Interstitial	Axial	<20
4. Interstitial	Coronal	<20
Breathing-Independent (Motion resistant) Protocol		
T2-SS-ETSE	Coronal	~45
In-/out-of-phase T1-GE	Axial	<40
T2-SS-ETSE FS	Axial	~45
WE-MPRAGE°	Axial coronal	<40 <40
MRCP	Coronal	5
WE-MPRAGE	Axial	90
WE-MPRAGE postcontrast		
1. Hepatic arterial	Axial	~35
2. Portal venous	Axial	~35
3. Interstitial	Coronal	~35
Breathing-Averaged Protocol		
T2-SS-ETSE	Coronal	~30
T2-SS-ETSE FS	Axial	30
MRCP	Axial	5
T2-ETSE-FS	Axial	240
T1-SE FS	Axial	270
WE-MPRAGE	Axial Coronal	<40 <40
In-/out-of-phase T1-GE	Coronal	<20
WE-MPRAGE	Axial	~100
WE-MPRAGE postgadolinium		
1. Hepatic arterial	Axial	~35
2. Portal venous	Axial	~35
3. Interstitial	Coronal	~35
4. T1-SE FS	Axial	290

†T2-SS-ETSE: T2-single-shot echo-train spin echo.
‡3D-GE: 3D gradient echo.
°WE-MPRAGE: water-excitation-magnetization-prepared rapid gradient echo. This fast echo sequence uses an inversion before application in order to achieve better T1 weighting.

pulses, which limit image quality on 1.5 T systems. Performing body MRI studies in children at 3 T allows for improved image quality because of the higher intrinsic signal of the system that offsets the low signal of the sequence. Water excitation is a recommended addition to the sequence as it improves the dynamic range of signal intensities of the various tissues.

T2-Weighted Sequences

Echo-Train Spin-Echo Sequence. Breathing-averaged echo-train spin echo results in consistent image quality in patients who are sedated. Since fat is very high in signal intensity on these sequences, usually fat suppression is required to optimize the soft tissue contrast between various tissues. Fat suppression should generally be applied in at least one set of images of the liver to ensure optimal contrast of high-signal abnormalities such as cystic masses or fluid collections adjacent to intraabdominal fat, and to improve liver lesion detection in the setting of fatty liver.

Single-Shot Echo-Train Spin-Echo Sequence. This sequence uses very long echo train lengths and half-Fourier imaging to provide high-quality images in a short duration of time [17–21]. This sequence is routinely used in all body MRI studies but is especially important in children, as it does not require breath-holding cooperation. It is routinely useful to acquire single-shot ETSE without and with fat suppression [22]. This facilitates identification of lesions in fatty liver, and can also be used to identify the presence of fat in a variety of structures.

Data Acquisition Parameters

Magnetic Field Strength

Over the last 5 years, one of the major advances in clinical MR imaging has been the more widespread use of 3.0 T imaging systems. Compared to 1.5 T systems, 3.0 T provides higher signal-to-noise ratio, higher spatial resolution, higher speed, and better fat suppression. The high signal-to-noise ratio is crucial in younger children because of their smaller size [5, 6, 23–26]. Artifacts are, however, more common at 3.0 T compared to 1.5 T [5, 6, 11, 23, 27, 28]. Standing wave artifacts are more evident at 3.0 T than 1.5 T and result in central signal loss in images obtained of the abdomen, which is made even worse in the setting of ascites. The smaller size of children and the infrequent occurrence of ascites result in less common and less severe standing wave artifacts than is observed in adults.

Receiver Coil

High spatial resolution and SNR are crucial. Receiver coils minimize the noise from nonimaged parts of the body, thereby improving the signal-to-noise ratio. Phased array coils, which contain multiple elements in contrast to the single channel coil, are now commonly used [5]. The coils used for 1.5 T and 3.0 T are different and may not be substituted for one another. Newer coil designs, such as 32-channel coils, hold the promise of

dramatically shortening data acquisition, such that standard sequences can be performed with less patient cooperation. This may increase substantially the role of MRI in children in a variety of settings.

MRI Examination

In the pediatric population, we generally aim for scanning times of approximately 20 minutes for upper abdominal studies and 35 minutes for abdomen and pelvis studies (Table 17.1). For the purpose of categorizing appropriate strategies, we have broadly classified children into three age groups based on their general level of cooperativeness:

1. Infants (<1.5 year of age)
2. Small children (1–6 years of age)
3. Older children (6–18 years of age)

Approaches to these three groups are described separately.

Infants (<1.5 Years of Age)

Infants comprise the pediatric population of age less than 1.5 years. The main challenge faced for MR imaging is physical movement and breathing activity of the patient. For minimizing these artifacts, the use of various protocols for sedation and general anesthesia in the pediatric population is widespread (Figs. 17.1 and 17.2). The choice of protocol strongly depends on the radiologist's training and the availability of trained nursing staff and anesthesiologists. Imaging of infants may often be performed without sedation by organizing their feeding and sleep schedules according to the timing of the MRI study. In general, imaging of infants is better at 3.0 T than at 1.5T. This is essentially due to the small size of the organs in this group. The higher signal-to-noise ratio (SNR) of 3.0 T allows for thinner sections and higher image quality of water excitation T1-weighted magnetization-prepared gradient-echo imaging (WE-MPRAGE) [10, 11]. A compelling feature of WE-MPRAGE is that it is a single-shot technique and therefore does not require patient cooperation [11]. For identical reasons, the single-shot T2-weighted echo-train spin-echo sequence is used in all MR protocols. Because of their higher intrinsic SNR, and because patients are generally sedated, breathing-averaged T1- and T2-weighted sequences form an important part of an MR imaging strategy in infants. Image quality and soft tissue contrast resolution are often improved with the use of fat suppression [10]. Fat suppression, as described above in the sequences section, provides significant signal difference between diseased tissue and normal tissue. As a time-saving device, T2-weighted sequences should be performed as echo-train sequences, which may also be considered on T1-weighted sequences. It may be essential to use fat suppression on T2-weighted echo-train spin-echo sequences for liver imaging [7, 8, 12]. Fat suppression ensures optimal contrast between high-signal abnormalities such as fluid collections or cystic masses and adjacent intra-abdominal or pelvic fat [13]. The basic MRI protocol in infants includes multiplanar noncontrasted fat-suppressed T1-weighted spin-echo and fat suppressed T2-weighted echo-train spin-echo sequences, then gadolinium administration, and finally WE-MPRAGE images in both the transverse and coronal planes.

In selected patients in which thin section and more dynamic imaging is required after gadolinium administration, patients will undergo general anesthesia and may be imaged with respiration-suspended 3D gradient-echo imaging. In this approach, breathing is arrested while the patient is intubated and under general anesthesia. This approach must be carefully choreographed with the anesthesiology team in order to accurately time the suspension of respiration with the data acquisition.

Small Children (1–6 Years of Age)

Since the anatomy in this age group is larger than in infants, it is not as crucial to image these patients with 3.0 T. Adequate preparation of the small child involves gentle description of the upcoming procedure and recruitment of the parent or guardian for comforting. However, this age group is generally more alert and anxious, and therefore more likely to require pharmaceutical sedation and restraints (Fig. 17.3). Pillows, Velcro straps, foam sponges, and tape are used to immobilize the child. Sedated patients can be swaddled in prewarmed blankets.

Because many of these patients will require at least moderate sedation, the imaging protocol is essentially identical to that performed in infants. Suspended respiration imaging may also be indicated in selected individuals. Older children within this age group may be sufficiently cooperative to undergo standard body MRI protocols without sedation. This is especially true if they are adequately prepared and coached, such as by child life specialists.

Older Children (6–18 Years of Age)

Older children are generally sufficiently cooperative (especially teenagers) to be imaged with standard body MR protocols. On modern MRI equipment the basic protocol includes single-shot T2-weighted echo-train spin echo (standard and with fat suppression), T1-weighted in-phase/out-of-phase gradient echo, fat-suppressed 3D T1-weighted gradient echo, gadolinium administration, and three passes using transverse 3D T1-weighted gradient echo (Figs. 17.4). Adequate preparation and instructions to the patients improve their ability to cooperate fully with breath hold instructions [9]. When patients are properly prepared and coached,

the best quality of body MRI studies can be anticipated in children between 12 and 18 years of age.

Sedation Technique

Sedation may play an important role in pediatric imaging; however, there is an overall lack of conformity in the choice of technique, medication(s), and the level of sedation. Different hospitals have different protocols for sedation. It is important to form a strategy based on age, developmental level, and type of study ordered before the MRI procedure.

Many newborns and infants can be successfully imaged without the need for sedation if the study is scheduled around the patients' feeding and sleeping schedules. Many older children (ages 6–18) may not require sedation; a child life specialist or a supportive parent may be useful in allaying anxieties and improving cooperation. These alternative techniques require creativity, patience, and planning but are safer than sedation for certain patients.

For any sedation procedure, children should be NPO for at least 4 hours before the examination. Monitoring of vital signs is essential. A nurse remains in the procedure area throughout the study and periodically records vital signs (pulse oxygenation, ventilation, hemodynamics, and temperature). When conscious sedation is selected, the person sedating the patient should be trained in advanced life support. The use of midazolam is widespread for minimal sedation and anxiolysis. For moderate sedation, chloral hydrate in children <2 years of age and pentobarbital sodium for those >2 years old are used. Midazolam can also be used in conjunction if needed. Monitored conscious sedation is most appropriate for healthy children and short diagnostic examinations. Titration of medications is based on the sedation continuum described in Table 17.2.

Before moderately sedating a pediatric patient, it is critical to do a thorough assessment including patient history, baseline vital signs, weight, airway examination, oropharyngeal examination, and a cardiopulmonary examination. The goal of this presedation assessment is the recognition of factors that may place the patient at increased risk for complications. The health care provider can also utilize this time to educate the patient's caregivers and assess the patient's anxiety level, developmental level, and individual personality.

Most often general anesthesia is chosen when a pediatric patient has comorbidities that are contraindications to conscious sedation or when timed breathing suspension would assist in improving the diagnostic quality of the images [14–16]. The presence of an anesthesiologist is also essential for such procedures, and availability guides the frequency of general anesthesia.

Table 17.2 Summary of Commonly Used Strategies for Pediatric Patients Receiving Body MRI

Types of Sedation	Newborn to Infants <1 year	1–6 years old	6–12 years old
Coordinate Sleep/ Feed Schedule	X		
Child Life Specialist		X	X
Parent Support/ Assistance		X	X
Anxiolysis		X	X
Moderate Sedation	X	X	X
General Anesthesia	X	X	
Breathing Suspended General Anesthesia	X	X	

The presence of new MR-compatible monitoring technology and the availability of effective and short-acting drugs have resulted in anxiolysis and moderate sedation being more frequently used in the radiology setting by nonanesthesiologists. There are several classes of medications used for these purposes, including benzodiazepines, opioids, barbiturates, dissociative agents, and sedative hypnotic agents.

The induction of sedation must be timed with the availability of MRI technologists and the MR room. The caregivers may be allowed to stay in the sedation room with the patient to comfort him/her. If the medication is given intravenously, the initial amount administered should be a low, weight-based dose that is then titrated at timed intervals for the desired effect. When moderate sedation has been achieved, the patient may be then taken to the scanner, where MRI compatible monitoring equipment may be placed on the patient. The patient is carefully positioned to maximize ventilation and decrease stimulation.

The patient should be vigilantly monitored and assessed during the sedation induction, the MR examination, and the recovery period. This allows the health-care provider to intervene immediately if the patient has a change in vital signs or becomes restless during the MRI.

When the MRI is completed, the patient should be taken to a quiet area to recover and be given ample time to awaken before being discharged. Recovery time varies depending on the type and amount of drugs used. Most conventional discharge criteria require the patient to return to his/her baseline status with intact protective reflexes before discharge. The caregivers should be given verbal and written discharge instructions before leaving the facility. It is often helpful to make sure the caregivers have a contact number to

call with concerns or questions they may have after discharge.

Gadolinium-Based Contrast Agents

The physician should pay special attention to the choice of appropriate gadolinium-based contrast agents (GBCA) in children. Although the incidence of renal failure and hence the risk of nephrogenic systemic fibrosis (NSF) is considerably lower in the pediatric population, it is imperative to follow guidelines at least as stringent as with adults. An additional concern that is critical for children is the potential for osseous deposition of gadolinium. As a result, we do not recommend the use of nonionic linear GBCAs, which exhibit lower conditional stability [29, 30].

FOLLOW-UP IN PEDIATRIC PATIENTS

In settings where serial imaging follow-up of pediatric patients is desired, MRI is a preferred method to image them. The most important reason for this is the exposure to ionizing radiation that occurs with CT. An additional consideration is that the risk associated with a stable chelate GBCA is less than with an iodinated contrast agent. Patients who have chronic diseases or malignancies that will involve serial re-evaluations of disease activity should undergo MRI. Examples include: hepatoblastoma (fig. 17.5), neuroblastoma, Wilms tumor, lymphoma (fig. 17.6), and Crohn disease.

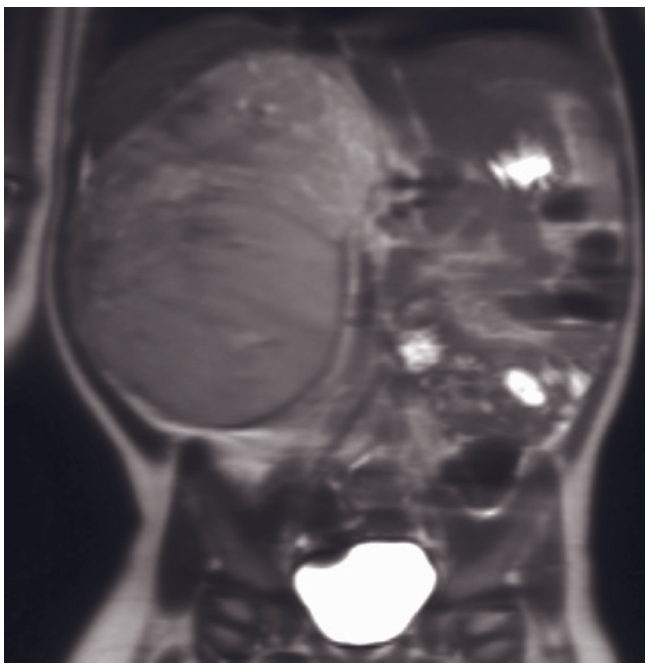

(*a*)

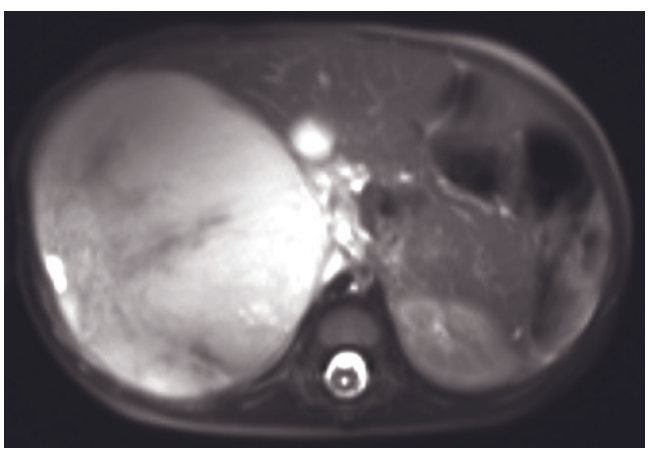

(*c*)

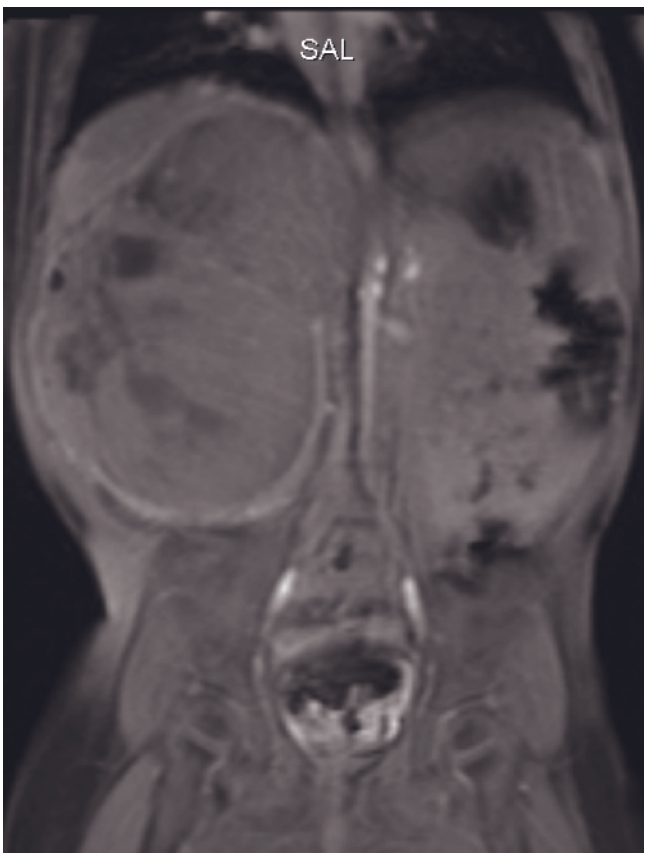

(*b*)

FIG. 17.5 Motion resistant protocol in an 18-month-old boy at 3 T. Coronal T2-weighted single-shot echo-train spin-echo (*a*), coronal water-excitation MP-RAGE (*b*), axial T2-weighted single-shot echo-train spin-echo (*c*), axial water-excitation T1-weighted MP-RAGE (*d*), and immediate (*e*) and 60-s (*f*) postgadolinium water-excitation MP-RAGE. All images show a large hepatoblastoma in the right lobe of the liver. All sequences are obtained without the requirement for breath holding. There is improved signal-to-noise ratio (SNR) with the use of 3 T magnet.

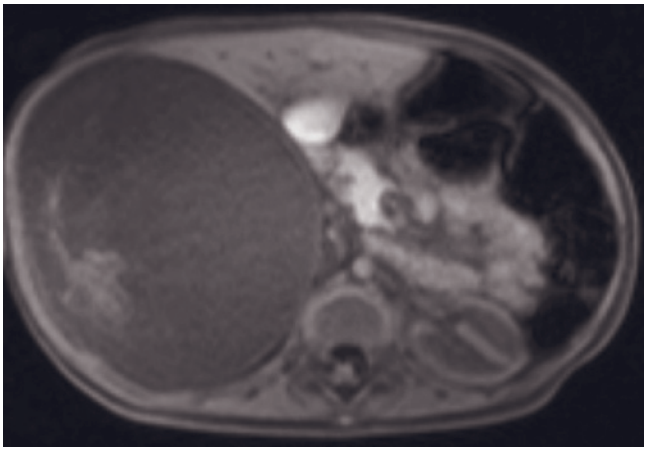

(*d*)

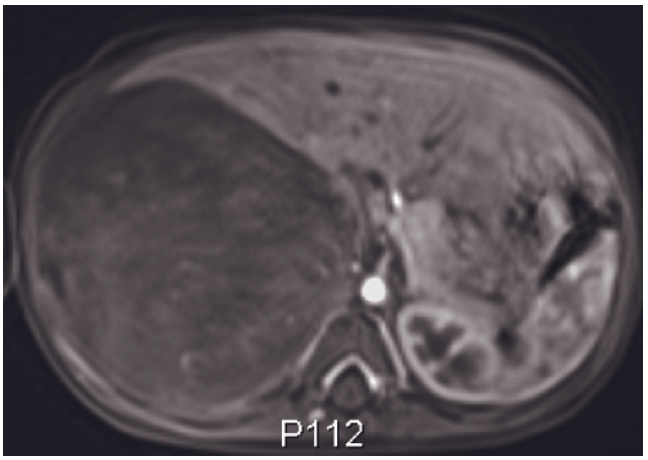

(*e*)

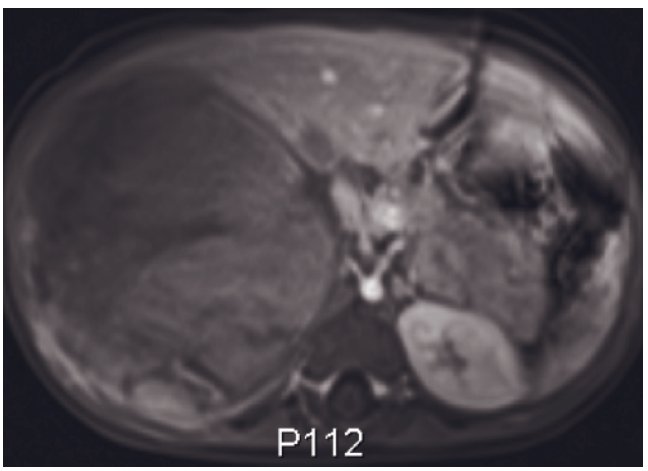

(*f*)

FIG. 17.5 (*Continued*) The high SNR of single-shot T1-weighted sequences at 3 T allow for consistent good-quality images (*d–f*), despite the use of intrinsically low signal sequences. Note the clear definition of the large malignancy due to the intrinsic high SNR at 3 T.

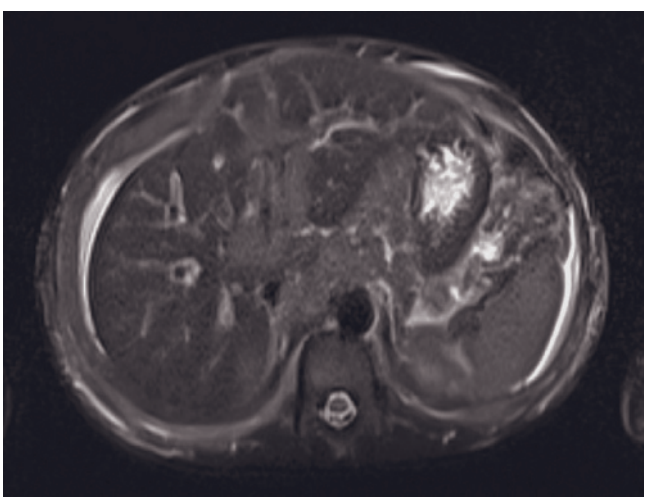

(*a*)

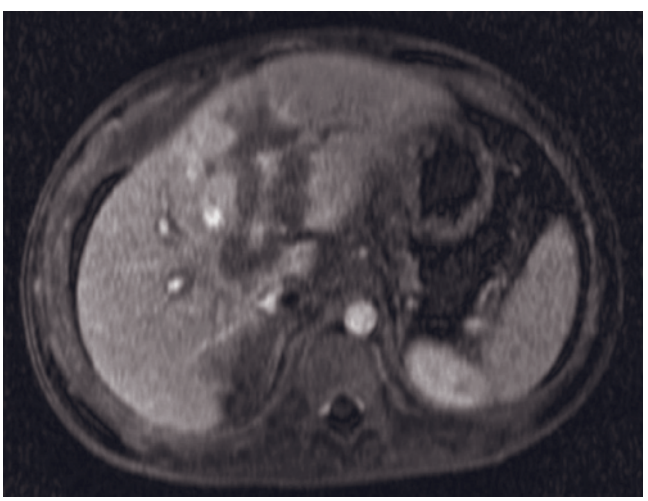

(*b*)

FIG. 17.6 Burkitt lymphoma. Transverse T2-weighted echo-train spin echo (*a*) and gadolinium-enhanced 3D gradient echo (*b*) of the liver and transverse 3D gradient echo of the pelvis (*c*). Extensive deposits of Burkitt lymphoma are noted in the liver, with prominent involvement of the periportal location, which is typical for lymphoma (*a*, *b*). In addition, peritoneal and

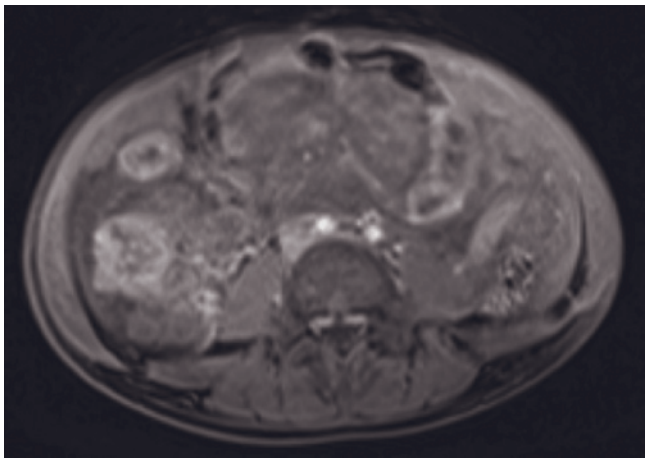

(*c*)

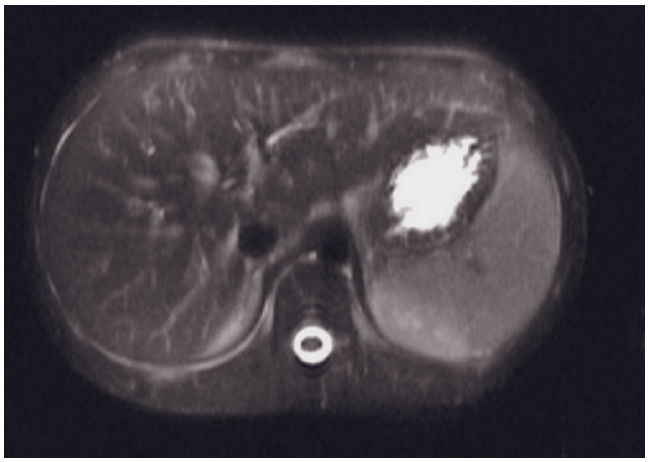

(*d*)

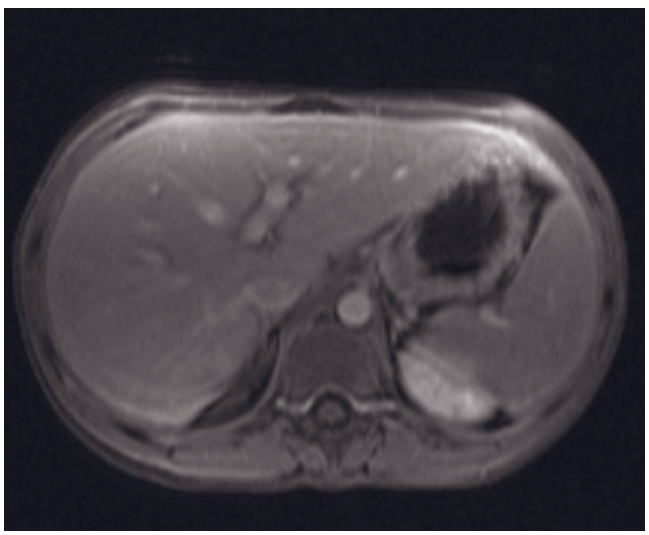

(*e*)

FIG. 17.6 (*Continued*) bowel involvement are also noted. Six months after the commencement of chemotherapy the lymphomatous deposits have largely resolved, as shown on transverse T2-weighted echo-train spin-echo (*d*) and gadolinium-enhanced fat suppressed 3D-GE sequences (*e*).

IMPORTANT DISEASE ENTITIES IN PEDIATRIC PATIENTS

The disease entities that afflict children are described in other chapters in the particular organs of interest. Rather than repeating these descriptions, we list the disease entities below with a description of where the entity is described in the text. A few illustrations will be made.

LIVER (Chapter 2)

1. Ciliated hepatic foregut cyst (pp. 60, 171)
2. Extramedullary hematopoiesis (pp. 67, 79–80)
3. Infantile hemangioendothelioma (pp. 106–109)
4. Hepatoblastoma (pp. 251, 253, 255)
5. Undifferentiated sarcoma of the liver (pp. 251, 256)
6. Wilson disease (pp. 315–317)
7. Cirrhosis in pediatric patients (pp. 317–318)
8. Mucopolysaccharidoses (pp. 384, 387)
9. Arteriovenous malformation in Rendu–Osler–Weber Syndrome (pp. 388, 392)

GALLBLADDER AND BILIARY SYSTEM (Chapter 3)

1. Cystic diseases of bile ducts (pp. 505–511)
2. Choledochal cyst (pp. 505, 508–510)
3. Choledochocele (pp. 505, 511)
4. Caroli disease (pp. 505, 511–513)

PANCREAS (Chapter 4)

1. Annular pancreas (pp. 541–544)
2. Congenital absence of dorsal pancreatic anlage (p. 542)
3. Short pancreas in the polysplenia syndrome (pp. 544, 546)
4. Cystic fibrosis (pp. 544–547)

5. Primary hemochromatosis (pp. 546, 548–549)
6. Von Hippel–Lindau syndrome (pp. 549–550, 606)
7. Autoimmune pancreatitis (pp. 656–666)

SPLEEN (Chapter 5)
1. Accessory Spleens (p. 681)
2. Asplenia (pp. 681, 685)
3. Polysplenia (pp. 681, 683, 685)
4. Gaucher disease (p. 683)
5. Sickle cell disease (pp. 683, 687)

GASTROINTESTINAL TRACT (Chapter 6)
1. Esophageal duplication cysts (pp. 726, 728)
2. Gastric duplication cysts (p. 736)
3. Congenital heterotopias (p. 736)
4. Congenital diverticula (pp. 736, 770)
5. Polyposis syndromes (pp. 829, 832, 837)
6. Rotational abnormalities (p. 770)
7. Diverticulum (pp. 736–737, 770–773)
8. Meckel diverticulum (pp. 736, 770, 774)
9. Intestinal atresia and stenosis (p. 770)
10. Colonic duplication (pp. 827, 832)
11. Anorectal anomalies (pp. 827, 869)

ADRENAL GLANDS (Chapter 8)
1. Congenital adrenal hyperplasia (p. 970)
2. Neuroblastoma (p. 998, 1006, 1012–1017)

KIDNEYS (Chapter 9)
1. Persistent fetal lobulation (p. 1031)
2. Ectopic kidney (p. 1032)
3. Horseshoe kidney (pp. 1032, 1034)
4. Crossed fused ectopia (pp. 1032, 1034)
5. Duplication of the collecting system (pp. 1032, 1036)
6. Hypoplastic kidney (pp. 1032, 1036)
7. Pelvic kidney (pp. 1032–1033, 1035, 1050)
8. Malrotation (p. 1031)
9. Medullary cystic disease (pp. 1049, 1059–1060)
10. Tuberous sclerosis (pp. 1066, 1069–1070)
11. Wilms tumor (pp. 1102–1105)

RETROPERITONEUM (Chapter 10)
1. Embryonal rhabdomyosarcoma (p. 1272)
2. Vascular malformations (pp. 1230, 1274)

BLADDER (Chapter 11)
1. Congenital diverticulum (pp. 1299–1300)
2. Rhabdomyosarcoma (p. 1316)

MALE PELVIS (Chapter 12)
1. Partial aplasia of corpora cavernosa (p. 1376)
2. Testicular hypoplasia and aplasia (p. 1386)
3. Cryptorchidism (pp. 1386–1388)
4. Hydrocele (pp. 1388–1392)

FEMALE URETHRA AND VAGINA (Chapter 13)
1. Duplication (pp. 1403, 1410, 1412)
2. Ectopic ureterocele (p. 1403)
3. Urethral diverticulum (pp. 1403, 1405–1407)
4. Vaginal agenesis and partial agenesis (pp. 1410–1412)
5. Vaginal atresia with hematometra (p. 1412)
6. Mayer–Rokitansky–Küster–Hauser syndrome (pp. 1411, 1413)
7. Abnormalities of gonadal differentiation (Differentiation and gender assignment are well shown by MR examination. MR shows homogenous structure of testis and follicles in ovaries. It also recognizes the bulb of penis distinctively) (pp. 1410–1415)
8. Ambiguous genitalia (pp. 1410, 1415)
9. Low transverse vaginal septum and hematocolpos (p. 1414)
10. Gartner duct cyst (pp. 1416, 1418–1419)
11. Cavernous hemangioma (pp. 1416, 1420)

UTERUS AND CERVIX (Chapter 14)
1. Müllerian duct anomalies (pp. 1439–1448)
2. Congenital disorders of sexual differentiation (p. 1448)

ADENEXA (Chapter 15)
1. Müllerian duct anomalies (pp. 1500, 1503–1504)

CONCLUSION

MRI has an important role in imaging the pediatric population, which will only continue to increase with faster imaging capabilities. At the same time, the use of CT in pediatrics has known health risks that may become manifest. Abdominal MR is a powerful tool for the diagnosis and management of many pediatric illnesses. It provides excellent anatomic information, especially with the use of 3.0 T MR systems, and does not utilize ionizing radiation, an important factor in pediatric imaging. MR has the potential to become a commonly used imaging modality for a wide range of pediatric illnesses, especially focal liver disease. Scanning protocols and sedation techniques are two important factors that must be carefully established in order to consistently obtain high-quality images.

REFERENCES

1. Semelka RC, Worawattanakul S, Kelekis NL, John G, Woosley JT, Graham M, Cance WG. Liver lesion detection, characterization, and effect on patient management: comparison of single phase spiral CT and current MRI techniques. *J Magn Reson Imaging* 7(6): 1040–1047, 1997.

2. Ichikawa T, Haradome H, Hachiya J, Nitatori T, Ohtomo K, Kinoshita T, Araki T. Pancreatic ductal adenocarcinoma: preoperative assessment with helical CT versus dynamic MR imaging. *Radiology* 202(3): 655–662, 1997.
3. Semelka RC, Shoenut JP, Kroeker MA, MacMahon RG, Greenberg HM. Renal lesions: controlled comparisons between CT and 1.5-T MR imaging with non enhanced and gadolinium-enhanced fat-suppressed spin-echo and breath-hold FLASH techniques. *Radiology* 182(2): 425–430, 1992.
4. Semelka RC, Kelekis NL, Molina PL, Sharp TJ, Calvo B. Pancreatic masses with inconclusive findings on spiral CT: is there a role of MRI? *J Magn Reson Imaging* 6(4): 585–588, 1996.
5. MacKenzie JD, Vasanawala SS. Advances in pediatric MR imaging. *Magn Reson Imaging Clin N Am* 16(3): 385–402, 2008.
6. Siegel MJ, Chung EM, Conran RM. Pediatric liver: focal masses. *Magn Reson Imaging Clin N Am* 16(3): 437–452, 2008.
7. Semelka RC, Martin DR, Balci NC. Magnetic resonance imaging of the liver: how I do it. *J Gastroenterol Hepatol* 21(4): 632–637, 2006.
8. Semelka RC, Simm FC, Recht M, Deimling M, Lenz G, Laub GA. T1 weighted sequence for MR imaging of liver: comparison of three techniques for single breath, whole volume acquisition at 1.0 and 1.5 T. *Radiology* 180(3): 629–635, 1991.
9. Semelka RC, Balci NC, Beeck BO, Reinhold C. Evaluation of a 10-minute comprehensive MR imaging examination of upper abdomen. *Radiology* 211(1): 189–195, 1999.
10. Ramalho M, Altun E, Herédia V, Zapparoli M, Semelka R. Liver MR imaging: 1.5T versus 3T. *Magn Reson Imaging Clin N Am* 15(3): 321–347, 2007.
11. Altun E, Semelka RC, Dale BM, Elias J Jr. Water excitation MPRAGE: an alternative sequence for postcontrast imaging of the abdomen in noncooperative patients at 1.5 Tesla and 3.0 Tesla MRI. *J Magn Reson Imaging* 27(5): 1146–1154, 2008.
12. Zapparoli M, Semelka RC, Altun E, Tsurusaki M, Pamuklar E, Dale BM, Gasparetto EL, Elias J Jr. 3.0-T MRI evaluation of patients with chronic liver diseases: initial observations. *J Magn Reson Imaging* 26(5): 650–660, 2008.
13. Tsurusaki M, Semelka RC, Zapparoli M, Elias J Jr., Altun E, Pamuklar E, Sugimura K. Quantitative and qualitative comparison of 3.0T and 1.5T MR imaging of the liver in patients with diffuse parenchymal liver disease. *Eur J Radiol* Epub 2008 Sep 12.
14. Mason KP, Zurakowski D, Connor L, Karian VE, Fontaine PJ, Sanborn PA, Burrows PE. Infant sedation for MR imaging and CT: oral versus intravenous pentobarbital. *Radiology* 233(3): 723–728, 2004.
15. Mason KP, Sanborn P, Zurakowski D, Karian VE, Connor L, Fontaine PJ, Burrows PE. Superiority of pentobarbital versus chloral hydrate for sedation in infants during imaging. *Radiology* 230(2): 537–542, 2004.
16. Weisenbach J, Vadon G, Storcz J. Sedation and sleep induction instead of anesthesia in infants and young children during CT and MRI examinations. *Orv Hetil* 137(12): 629–632, 1996.
17. Kelekis NL, Semelka RC, Worawattanakul S, deLange EE, Ascher SM, Ahn IO, Reinhold C, Remer EM et al. Hepatocellular carcinoma in North America: a multi-institutional study of appearance on T1-weighted, T2-weighted, and serial gadolinium enhanced gradient-echo images. *AJR Am J Roentgenol* 170(4): 1005–1013, 1998.
18. Huang J, Raman SS, Vuong N, Sayre JW, Lu DS. Utility of breath-hold fast-recovery fast spin-echo T2 versus respiratory triggered fast spin-echo T2 in clinical hepatic imaging. *AJR Am J Roentgenol* 184(3): 842–846, 2005.
19. Huang IH, Emery KH, Laor T, Valentine M, Tiefermann J. Fast-recovery fast spin-echo T2-weighted MR imaging: a free-breathing alternative to fast spin-echo in the pediatric abdomen. *Pediatr Radiol* 38(6): 675–679, 2008.
20. Semelka RC, Kelekis NL, Thomasson D, Brown MA, Laub GA. HASTE MR imaging: description of technique and preliminary results in the abdomen. *J Magn Reson Imaging* 6(4): 698–699, 1996.
21. Gaa J, Hutabu H, Jenkins RL, Finn JP, Edelman RR. Liver masses: replacement of conventional T2-weighted spin echo MR imaging with breath-hold MR imaging. *Radiology* 200(2): 459–464, 1996.
22. Grattan-Smith JD, Little SB, Jones RA. MR urography in children: how we do it. *Pediatr Radiol* 38: Suppl 1: S3–S17, 2008.
23. Anupindi S, Jaramillo D. Pediatric magnetic resonance imaging techniques. *Magn Reson Imaging Clin N Am* 10(2): 189–207, 2002.
24. Schenk JP, Friebe B, Ley S, Baudendistel K, Schoebinger M, Hähnel S, Mehrabi A, Tröger J, Hallscheidt P. Visualization of intrarenal vessels by 3.0-T MR angiography in comparison with digital subtraction angiography using renal specimens. *J Pediatr Radiol* 36(10): 1075–1081, 2006.
25. Hecht EM, Lee RF, Taouli B, Sodickson DK. Perspectives on body MR imaging at ultrahigh field. *Magn Reson Imaging Clin N Am* 15(3): 449–465, 2007.
26. Soher BJ. Dale BM, Merkle EM. A review of MR physics: 3T versus 1.5T. *Magn Reson Imaging Clin N Am* 15(3): 277–290, 2007.
27. Murkle EM, Dale BM, Paulson EK. Abdominal MR imaging at 3T. *Magn Reson Imaging Clin N Am* 14(1): 17–26, 2006.
28. Kuhl CK, Traber F, Schild HH. Whole-body high-field-strength (3.0-T) MR imaging in clinical practice. Part I. Technical considerations and clinical applications. *Radiology* 246(3): 675–696, 2008.
29. Wertman R, Altun E, Martin DR, Mitchell DG, Leyendecker JR, O'Malley RB, Parsons DJ, Fuller ER 3rd, Semelka RC. Risk of nephrogenic systemic fibrosis: evaluation of gadolinium chelate contrast agents at four American universities. *Radiology* 248(3): 799–806, 2008.
30. White GW, Gibby WA, Tweedle MF. Comparison of Gd (DTPA-BMA) (Omniscan) versus Gd (HP-DO3A) (ProHance) relative to gadolinium retention in human bone tissue by inductively coupled plasma mass spectroscopy. *Invest Radiol* 41(3): 272–278, 2006.

CHAPTER 18

CHEST

ERSAN ALTUN, JORGE ELIAS, JR., KATHERINE R. BIRCHARD, BUSAKORN VACHIRANUBHAP, VASCO HEREDIA, AND RICHARD C. SEMELKA

Lung cancer is the number one cause of cancer death in both men and women in the United States. More than 35 million people are living with chronic lung disease, including emphysema and asthma. Medical imaging of lung disease is a critical component of patient management. Chest X-ray and multidetector CT have been the mainstays of lung imaging. In the past, MRI of the lungs has been limited because of the low proton density of the lung parenchyma. This, in addition to magnetic susceptibility effects created by structural air-soft tissue interfaces in the lung, motion artifact, and long imaging times, has limited the success of lung MR. However, the development of faster sequences in conjunction with the use of advanced hardware and high-field-strength MR systems has significantly improved image quality. The lack of ionizing radiation may in the near future make MRI of the lungs ideal for those who must undergo serial imaging, for pediatric patients, and as a potential screening tool. In this chapter, we discuss current techniques, clinical applications, and future directions in MRI of the chest, excluding the heart.

CURRENT TECHNIQUES

MR has an established role in evaluation of intrathoracic processes such as pleural effusions and disease of the mediastinum, chest wall, and thoracic inlet [1–4]. Historically, the lung parenchyma has not been well visualized on MR because the signal from normal lung is not much greater than background air when conventional spin-echo, turbo spin-echo, and gradient-echo sequences are used. However, with fast T2-weighted sequences, images of the lung are improved [5–7]. In particular, single-shot T2-weighted echo-train spin-echo (ETSE) sequences are useful because they are generally motion insensitive and have little magnetic susceptibility or phase artifacts. T1-weighted 3D gradient echo (GRE) is the other effective sequence for lung imaging and has been shown to be beneficial in detection of small pulmonary nodules [8]. T2-weighted ETSE images tend to have the least artifact but have less spatial resolution compared to 3D-GRE. In one study, 3D-GRE was shown to have fewer false positives than T2-weighted ETSE in the detection of pulmonary nodules [9]. When they are

Abdominal-Pelvic MRI, Third Edition, edited by Richard C. Semelka. Copyright © 2010 John Wiley & Sons, Inc.

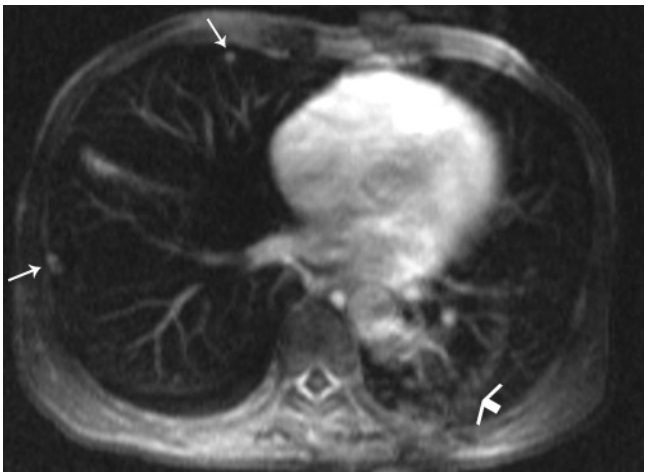

FIG. 18.1 Artifact. Fat-suppressed 2D-GRE image in a patient with lung metastases. Two small metastases are seen in the peripheral right lung (small arrows). Substantial phase artifact from cardiac motion makes evaluation of the left lower lobe impossible (large arrow).

used in combination, the accuracy of these techniques in the detection of pulmonary lesions has been shown to be quite high [10, 11].

Gadolinium-enhanced images are also necessary for MR assessment of the lungs. Gadolinium-enhanced 3D-GRE images are preferred over 2D-GRE images because of reduced motion artifact [12–14]. Although peripheral nodules or peripheral disease may be well visualized with the 2D-GRE technique, substantial phase artifact in the retrocardiac region obscures portions of the lung parenchyma, making it a less useful technique (fig. 18.1). The 3D-GRE technique is free of this artifact, allowing for better evaluation of all portions of the lung (fig. 18.1). Inflammatory changes in interstitial lung disease, mediastinal and hilar adenopathy, and malignant nodules can be evaluated with contrast-enhanced GRE images [15–18]. The pulmonary vasculature can also be evaluated with 3D-GRE sequences because of its high spatial resolution, which enables reconstruction of high-quality 3D MIP and multiplanar reformatted images (fig. 18.2). Therefore, 3D-GRE sequence is particularly advantageous for the chest examination because this sequence can evaluate the lung parenchyma, mediastinum, and vessels. 3.0T MR imaging has also improved the image quality of postgadolinium 3D-GRE sequences particularly, because of its higher signal-to-noise ratio. Higher signal-to-noise ratio can be translated into higher spatial and temporal resolution. Therefore, 3.0T MRI allows the acquisition of higher-spatial resolution images faster. This is particularly advantageous for 3D-GRE soft tissue sequences and 3D-GRE MR angiography (MRA) sequences. In summary, axial and coronal single-shot T2-weighted echo-train spin-echo, and pre- and postcontrast axial and coronal 3D-GRE images are currently the most useful sequences for evaluating the lung parenchyma (fig. 18.2).

PRIMARY LUNG CANCER

Primary lung cancer can be detected and staged with MRI [19]. The combined use of T2-weighted ETSE and gadolinium-enhanced 3D-GRE images provides high-quality images of lung cancer, regardless of location (fig. 18.3). High soft tissue contrast resolution allows consistent demonstration of chest wall invasion with MR (fig. 18.4). This has been shown to be especially helpful in evaluating chest wall extension of Pancoast tumors because of the additional benefit of direct coronal imaging (fig. 18.5). T2-weighted echo-train spin echo has been shown to be useful in differentiation between tumor and atelectatic lung [8].

PULMONARY NODULES

Virtually all studies comparing MR to CT in the detection of pulmonary nodules report similar performance, with CT being slightly better in the detection of small lesions. Sensitivity and specificity of detection of pulmonary nodules with MR have been reported as high as 93% and 96.2% compared to CT, but this varies depending on the size of lesion and the sequence used [19, 20]. Nodules as small as 3 mm can be seen with MRI [9, 15]. Tiny nodules that are missed on MR but seen on CT are often calcified or scarred (fibrotic), and thus have intrinsically low proton density and low signal. However, often CT cannot distinguish benign from malignant lesions at this size [21], and frequently the confirmation of benignity or malignancy can only be made by follow-up examinations. There are data to suggest that dynamic contrast-enhanced MR imaging can delineate kinetic and morphologic differences in vascularity and perfusion between benign and malignant pulmonary nodules, with washout being highly specific for malignancy [16]. On state-of-art MR systems, with phased-array torso coil, the combination of T2-weighted ETSE and gadolinium-enhanced fat-suppressed 3D-GRE techniques provides consistent and high-quality images of pulmonary nodules greater than or equal to 3 mm at 3.0T and greater than or equal to 4 mm at 1.5T (fig. 18.6). At 3.0T, the lower limit of lesion size for detection is lower, reflecting the higher spatial resolution. In most cases, the gadolinium-enhanced 3D-GRE image sequence shows metastases most conspicuously. In some cases, metastases that presumably have high fluid content and diminished vascularity may be better visualized on T2-weighted ETSE.

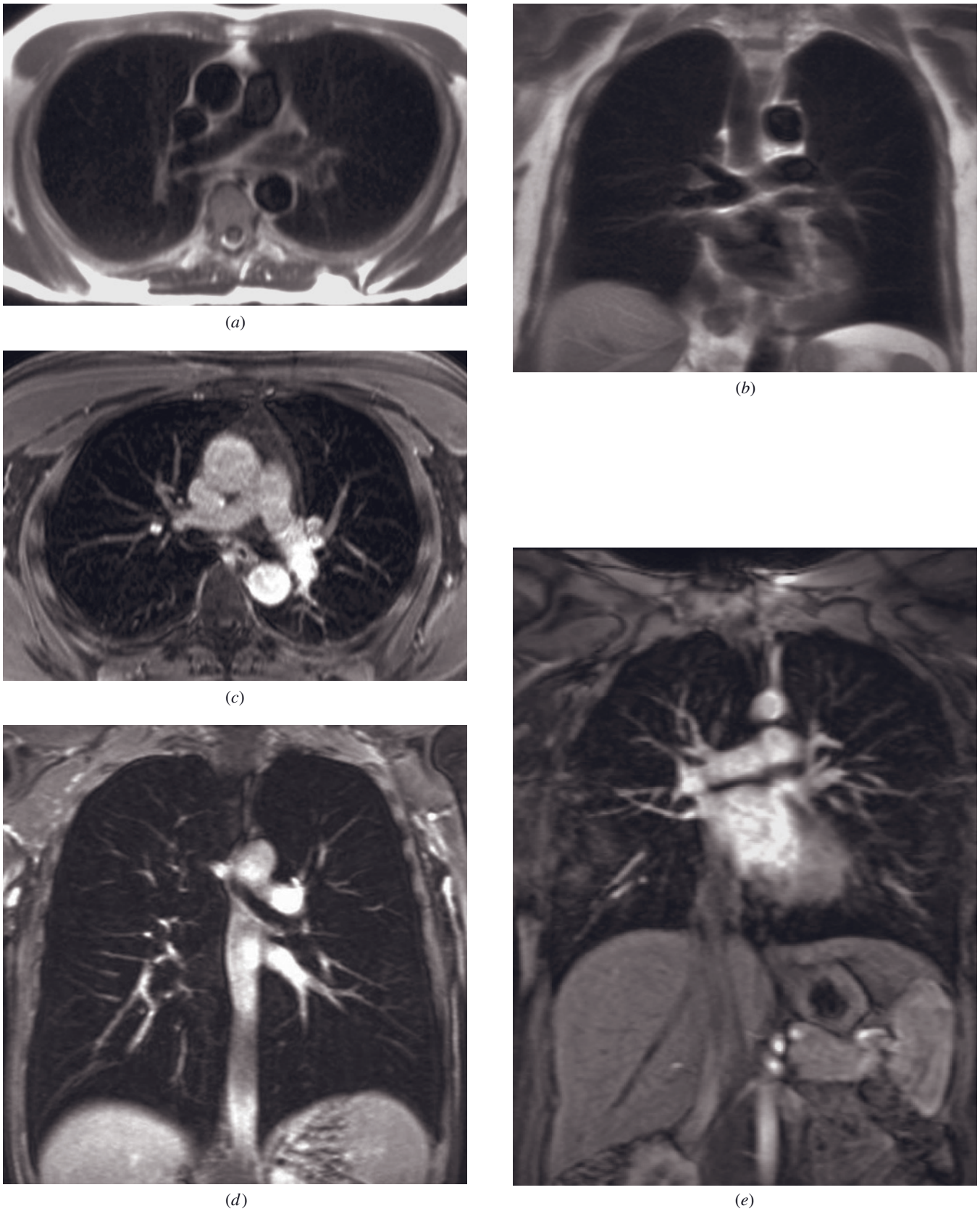

FIG. 18.2 Normal chest. Transverse (*a*) and coronal (*b*) T2-weighted ETSE images and transverse (*c*) and coronal (*d*) post-contrast fat-suppressed 3D-GRE images in a normal subject. Note the lack of phase artifacts in the retrocardiac region. Coronal T1-weighted postgadolinium fat-suppressed 3D-GE images (*e*, *f*), transverse T1-weighted postgadolinium fat-suppressed 3D-GE

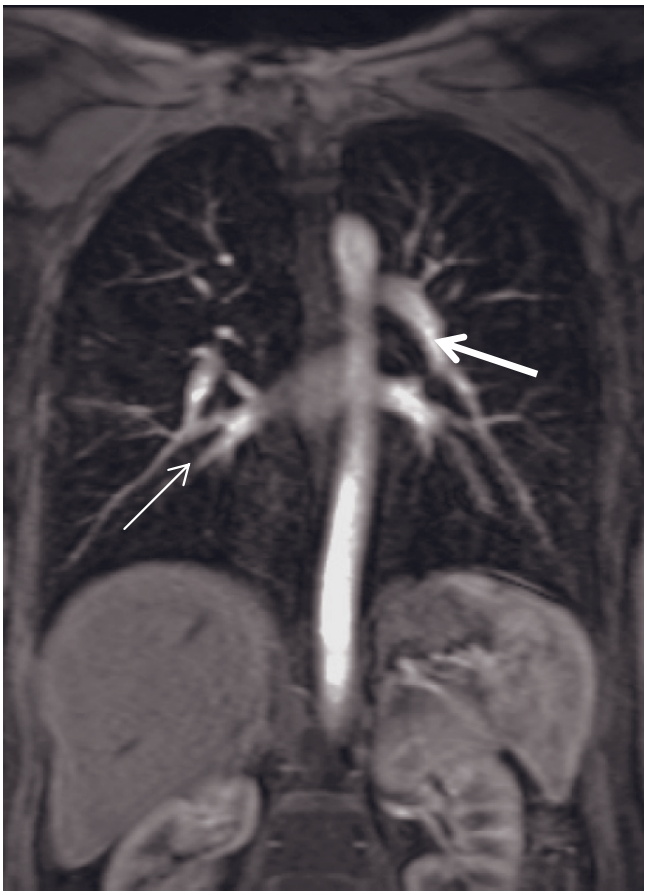

(*f*)

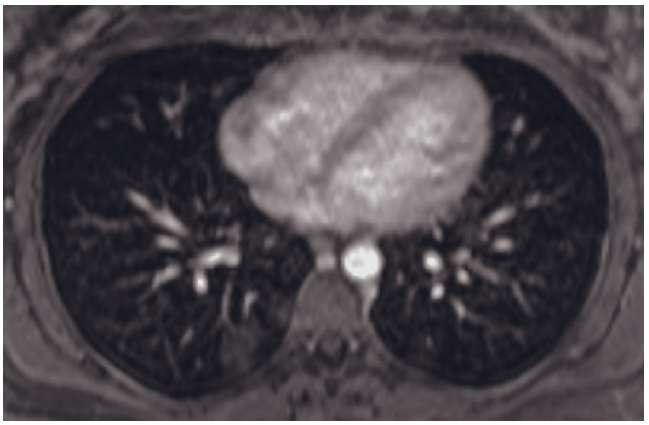

(*g*)

(*h*)

FIG. 18.2 (*Continued*) image (*g*), coronal T1-weighted postgadolinium subtracted 3D-GE images (*h*, *i*), and reconstructed 3D MIP image (*j*) in another patient with normal findings demonstrate lung parenchyma and vascular structures including pulmonary vasculature. Pulmonary arteries (thick arrows, *f*, *i*) and pulmonary veins (thin arrows, *f*, *i*) are shown. Minimal pulsation artifact over the right lung (*e*), which is due to cardiac pulsation, impairs the evaluation of lung parenchyma. However, transverse image shows there is no parenchymal abnormality in that region. Therefore, transverse and coronal images should be assessed together for the evaluation of lung parenchyma and pulmonary vascular structures.

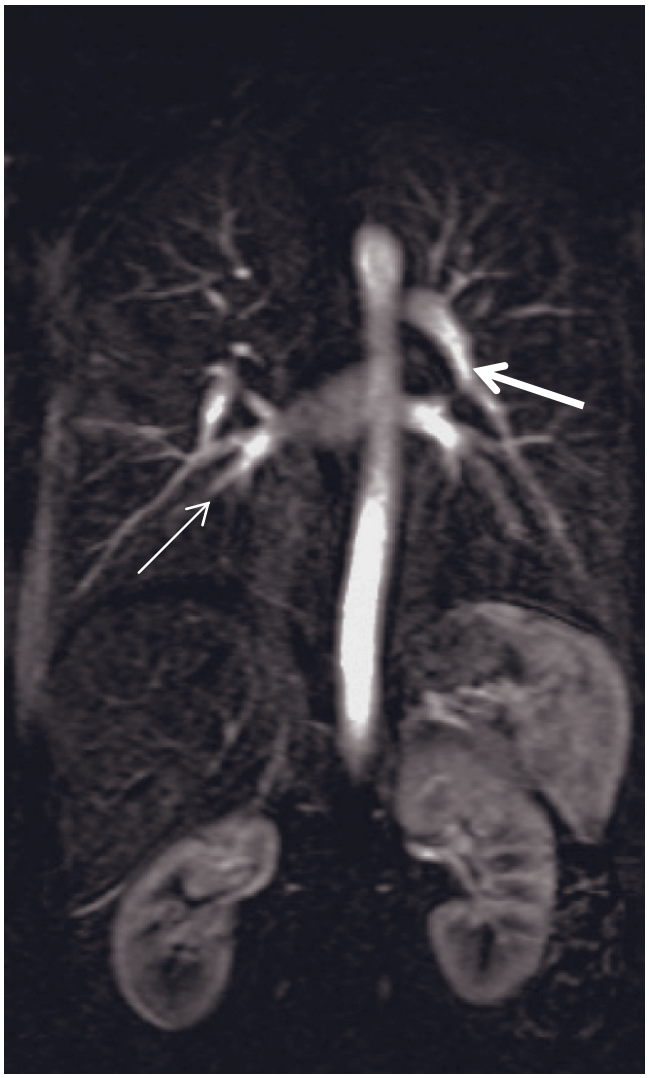

(*i*)

(*j*)

FIG. 18.2 (*Continued*)

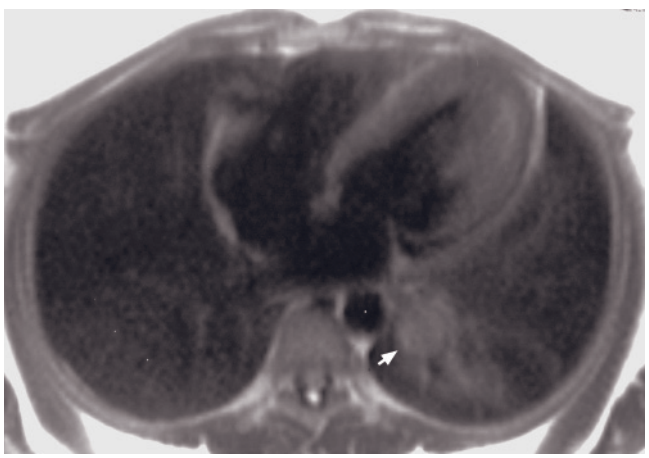

(*a*)

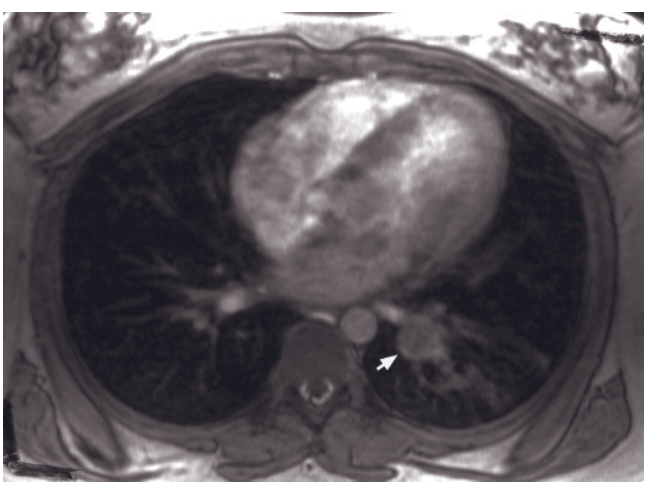

(*b*)

FIG. 18.3 Primary lung cancer. T2-weighted ETSE (*a*) and postgadolinium fat-suppressed 3D-GRE image (*b*) in a patient with lung cancer (arrows, *a*, *b*); T1-weighted postgadolinium fat-suppressed 3D-GRE images (*c*, *d*) in a second patient show primary

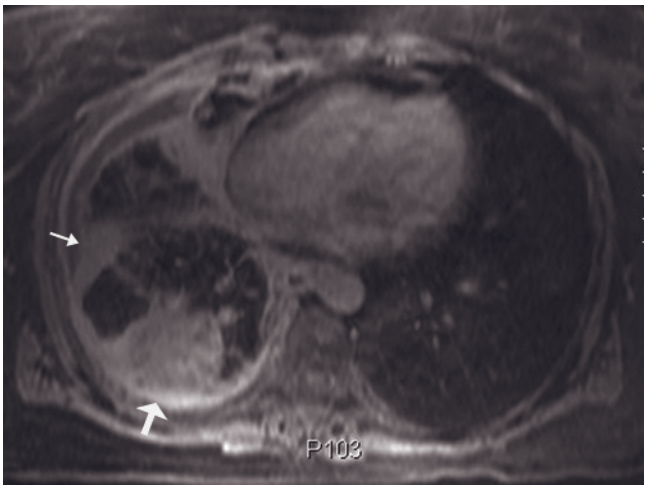

(*c*)

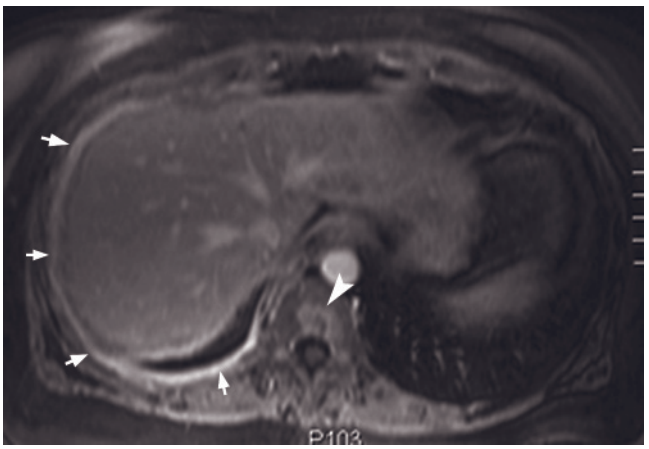

(*d*)

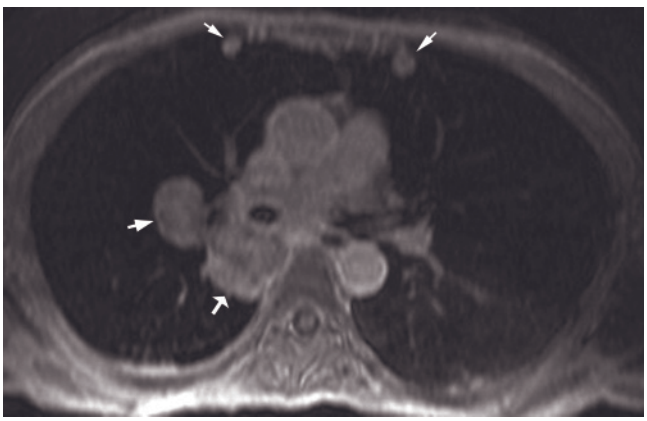

(*e*)

(*f*)

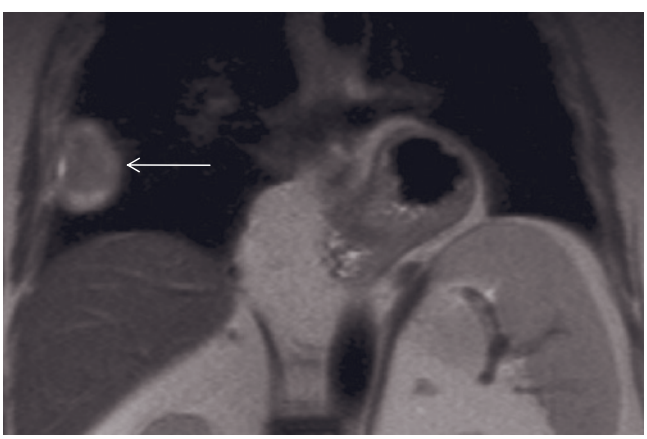

(*g*)

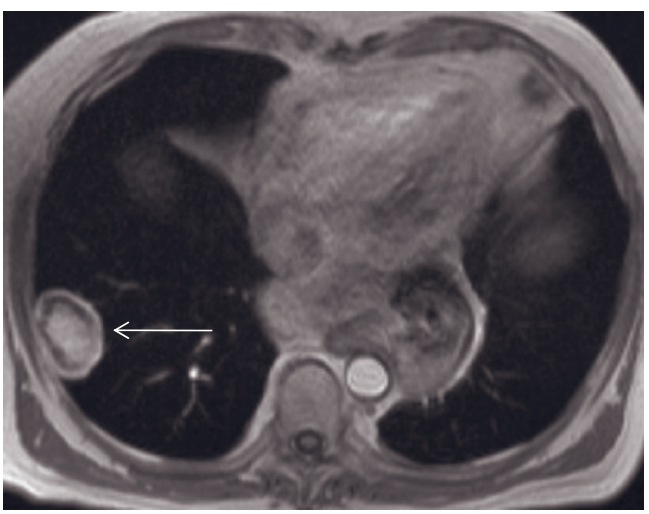

(*h*)

FIG. 18.3 (*Continued*) lung cancer (large arrow, *c*), pleural metastases (small arrows, *c*, *d*), and bone metastases (arrowhead, *d*). Transverse (*e*) and coronal (*f*) postgadolinium fat-suppressed 3D-GRE images in a third patient. The combination of the two techniques demonstrates the primary lung cancer, lymphadenopathy, and metastases consistently and well, regardless of location (arrows, *e*, *f*). Coronal T2-weighted single-shot echo-train spin-echo (*g*), transverse T1-weighted postgadolinium SGE (*h*), and transverse T1-weighted postgadolinium fat-suppressed 3D-GE (*i*) images demonstrate the primary lung cancer (arrows, *g*–*i*) located at the periphery of the right lung in another patient. The tumor shows progressive enhancement on postgadolinium images (*h*, *i*).

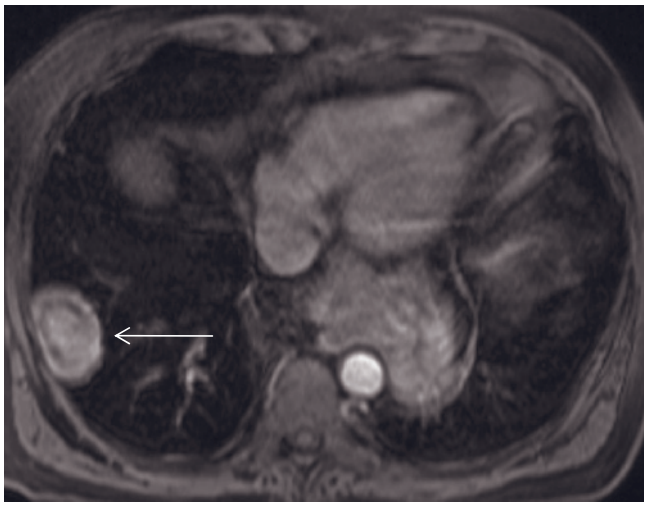

(*i*)

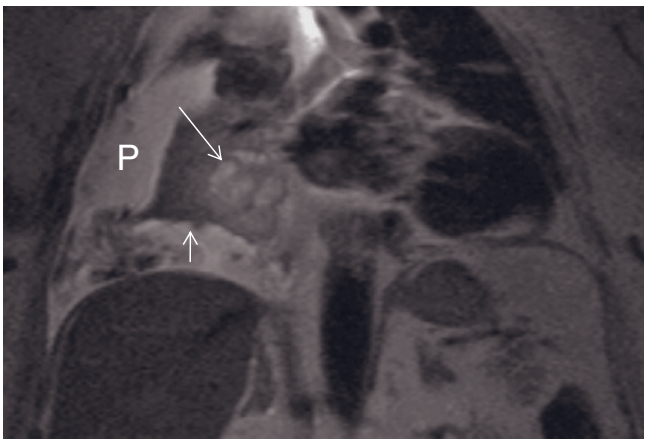

(*j*)

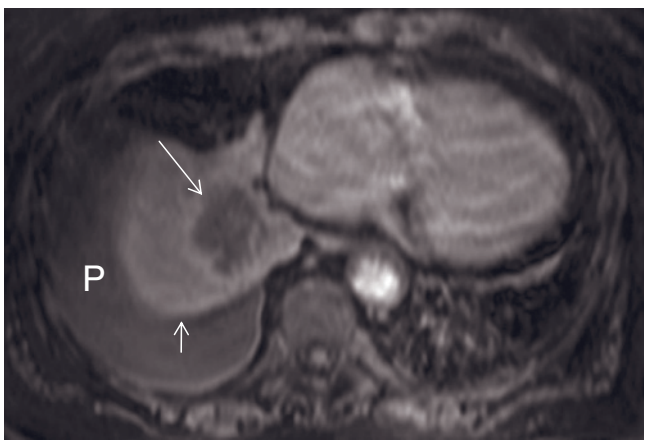

(*k*)

FIG. 18.3 (*Continued*) Note the paraesophageal hiatal hernia. Coronal T2-weighted single-shot echo train spin echo (*j*) and transverse T1-weighted postgadolinium fat-suppressed 3D-GE (*k*) images show the primary lung cancer (long arrows, *j*, *k*) in another patient. The tumor is located in the partially atelectatic right lung (short arrows, *j*, *k*). The mediastinum and the heart are deviated to the left side. Pleural effusion (P, *j*, *k*) is also noted. It should be noted in these examples that on early post contrast images, the primary tumor enhances less than adjacent collapsed lung, facilitating the diagnosis of malignancy.

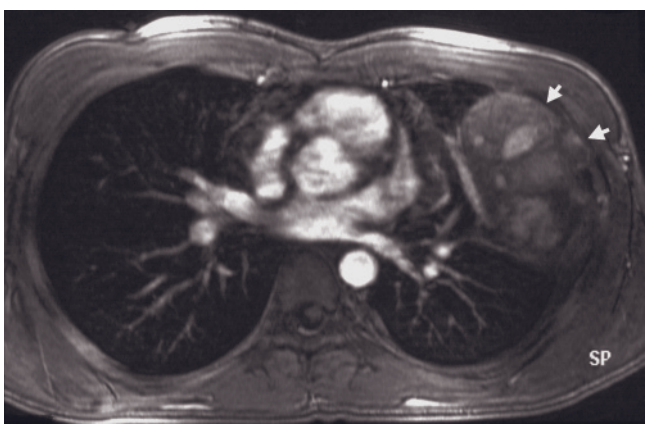

(*a*)

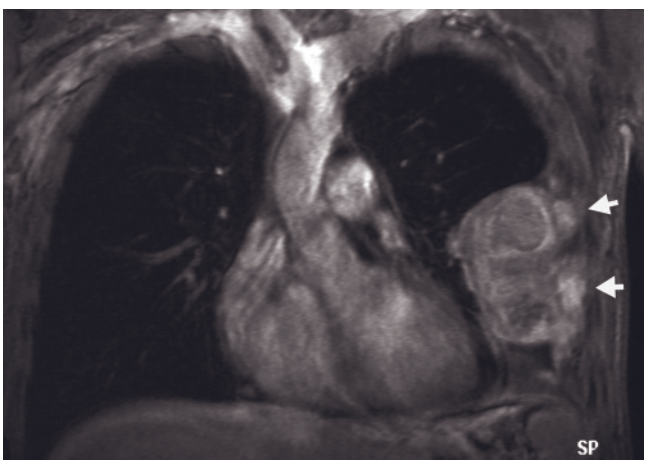

(*b*)

FIG. 18.4 Primary lung cancer with chest wall invasion. Transverse (*a*) and coronal (*b*) T1-weighted postgadolinium fat-suppressed 3D-GRE images in a patient with a large peripheral lung cancer that invades the chest wall (arrows, *a*, *b*). Transverse

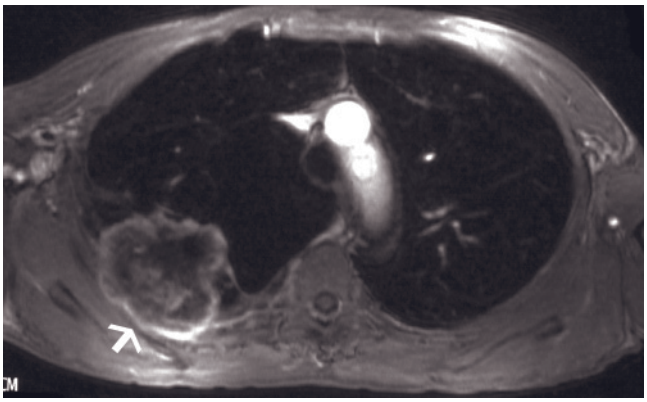

(*c*)

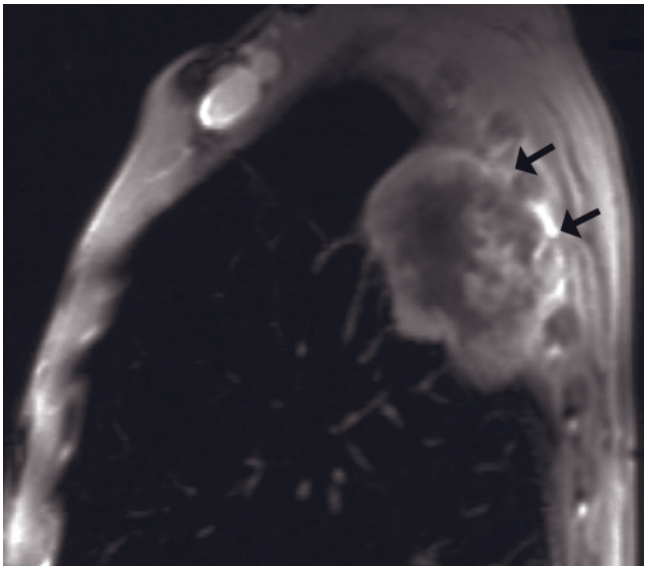

(*d*)

FIG. 18.4 (*Continued*) (*c*) and sagittal (*d*) T1-weighted postgadolinium fat-suppressed 3D-GRE images in a second patient show chest wall invasion (arrows, *c*, *d*).

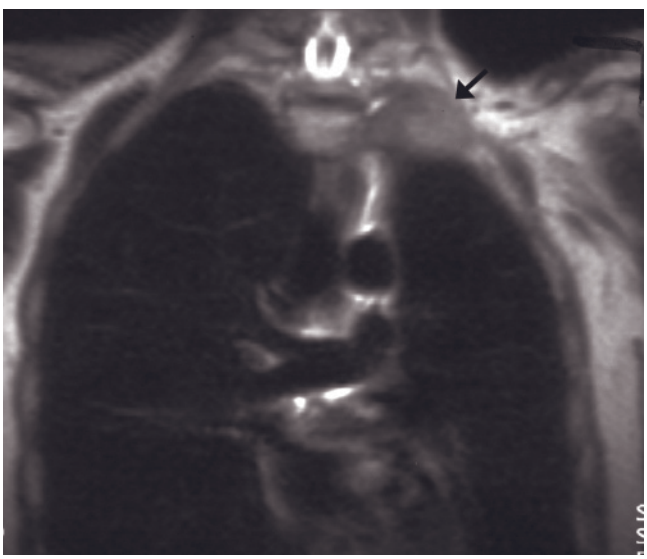

(*a*)

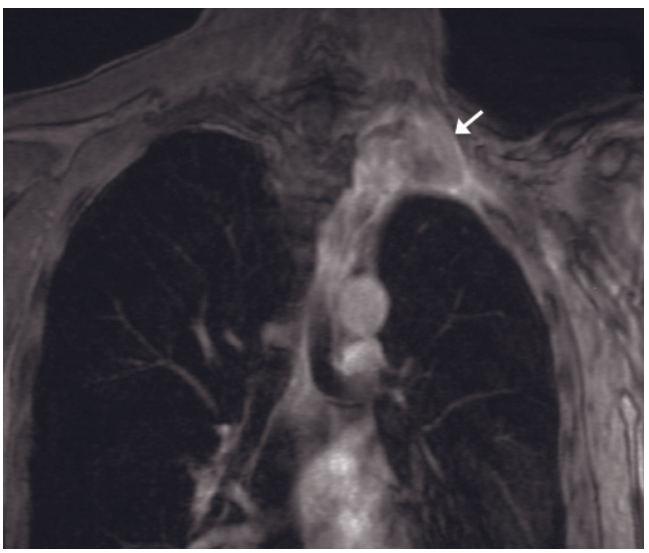

(*b*)

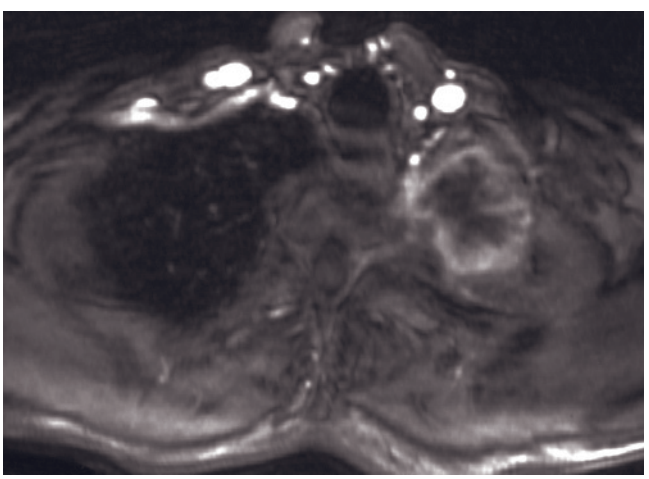

(*c*)

FIG. 18.5 Pancoast tumor. Coronal T2-weighted ETSE (*a*) and coronal (*b*), transverse (*c*), and sagittal (*d*) T1-weighted postgadolinium fat-suppressed 3D-GRE in patient with Pancoast tumor (arrows, *a*, *b*, *d*). Coronal (*e*) and transverse (*f*) T1-weighted

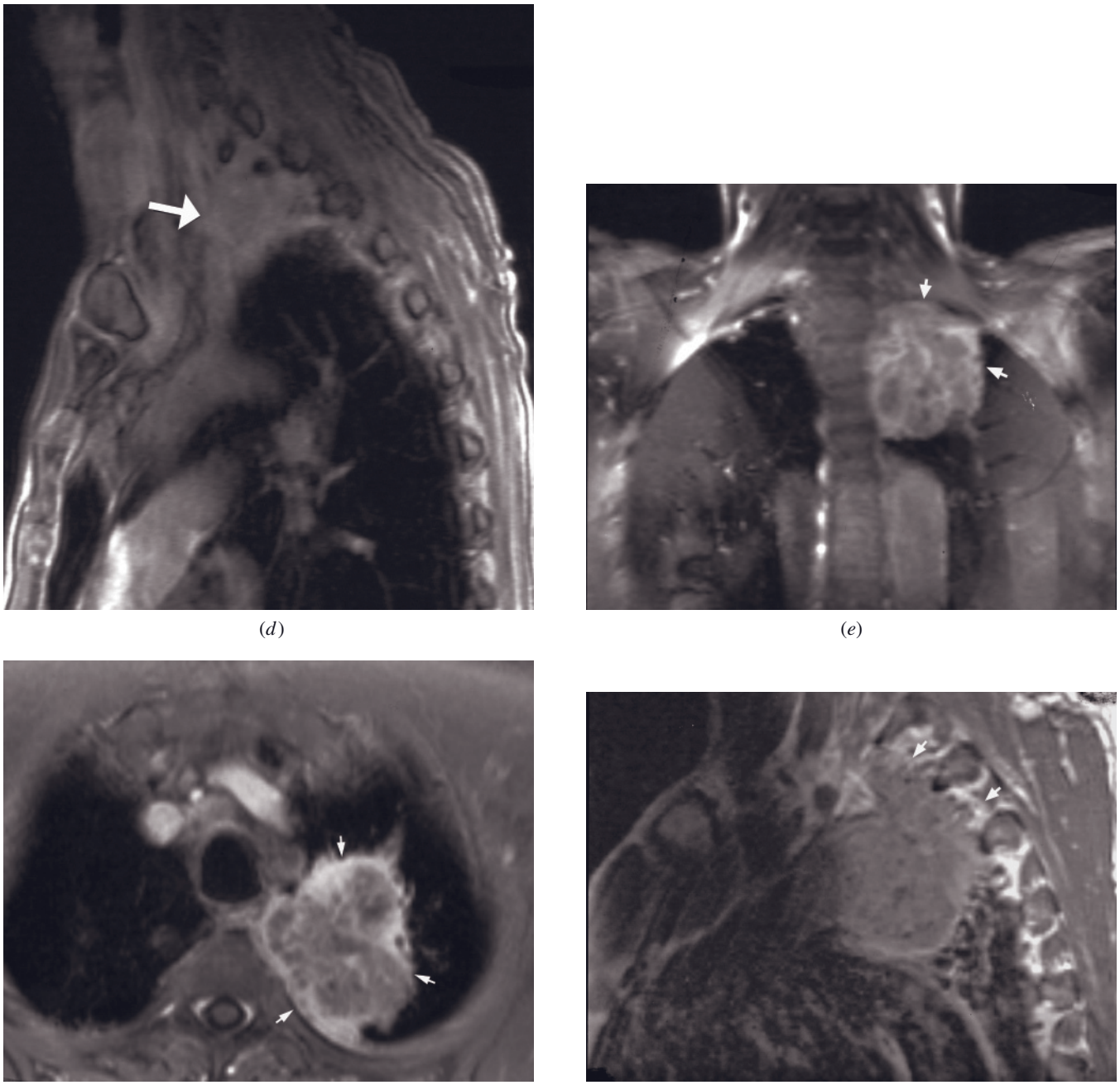

(*d*) (*e*)

(*f*) (*g*)

FIG. 18.5 (*Continued*) postgadolinium fat-suppressed 3D-GRE images and T1-weighted postgadolinium spin-echo image (*g*) in a second patient with Pancoast tumor. The combination of multiplanar imaging and high soft tissue contrast resolution results in excellent evaluation of Pancoast tumors. Soft tissue invasion at the thoracic inlet is well shown on direct coronal and sagittal imaging (arrows, *a*, *b*, *d*–*g*).

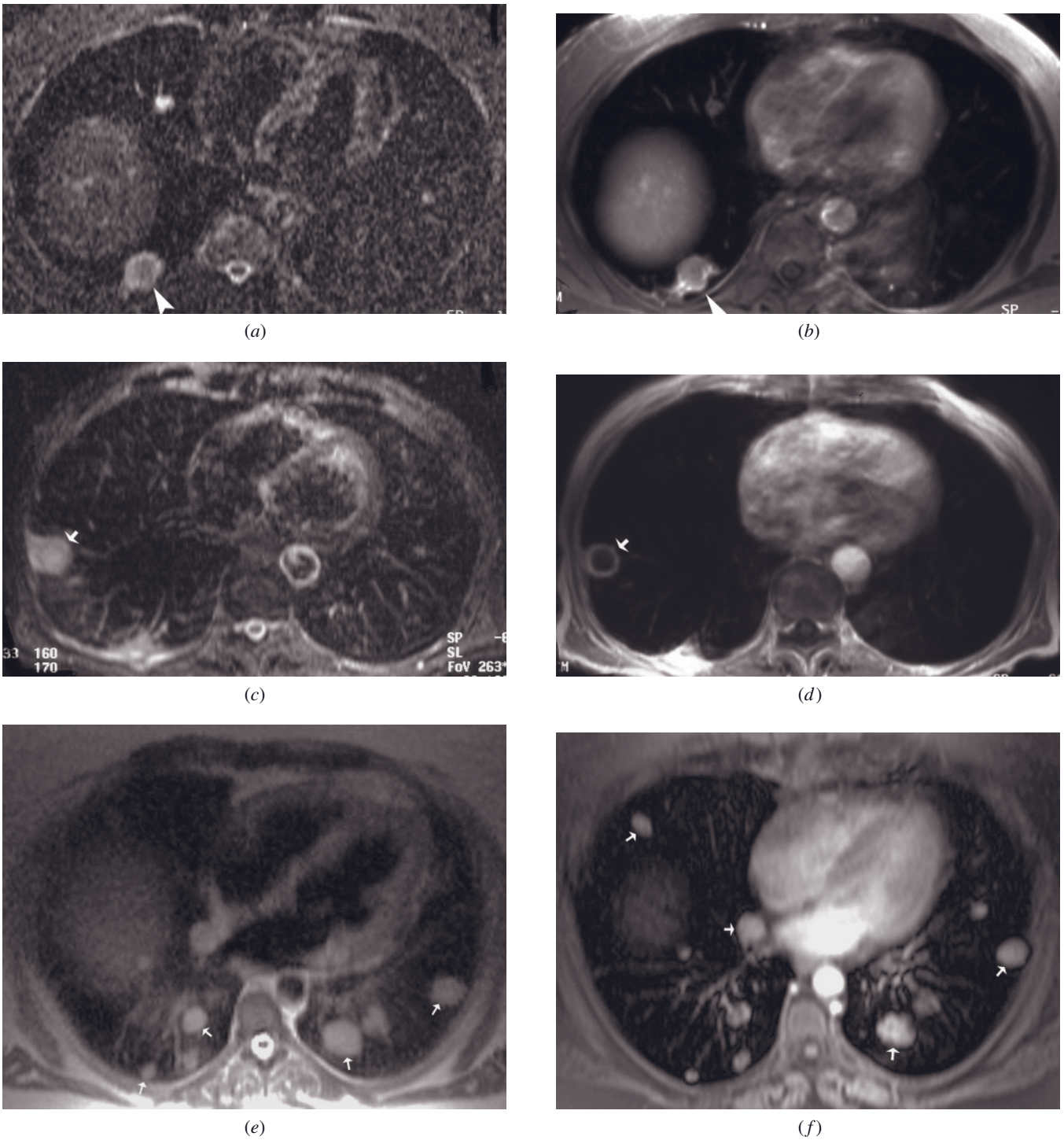

FIG. 18.6 Pulmonary nodules. Small lung metastases in ten patients (*a–s*). T2-weighted ETSE (*e*, *g*, *m*, *n*), fat-suppressed ETSE (*a*, *c*, *k*, *l*, *o*, *u*), and short tau inversion recovery (*t*) and multiplanar gradient-echo images (*b*, *d*, *f*, *h*, *i*, *j*, *p–s*, *v*, *w*) in ten patients

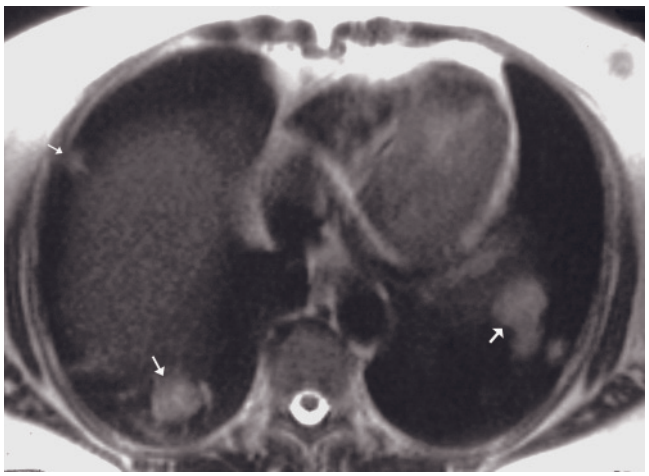

(*g*)

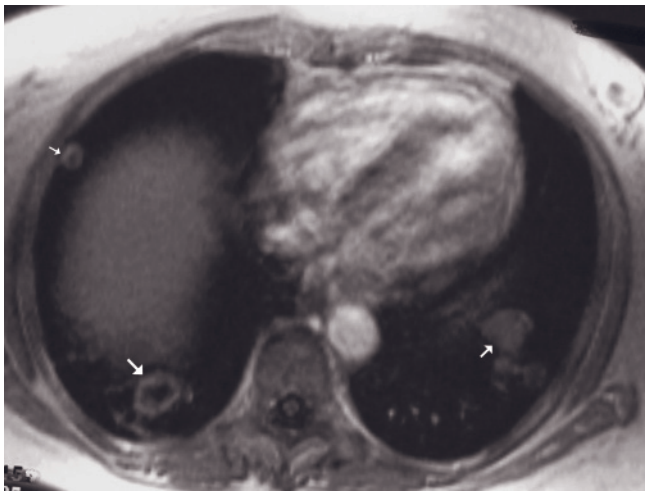

(*h*)

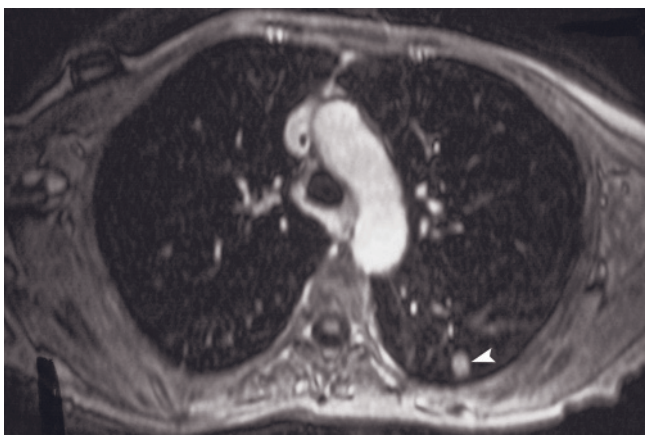

(*i*)

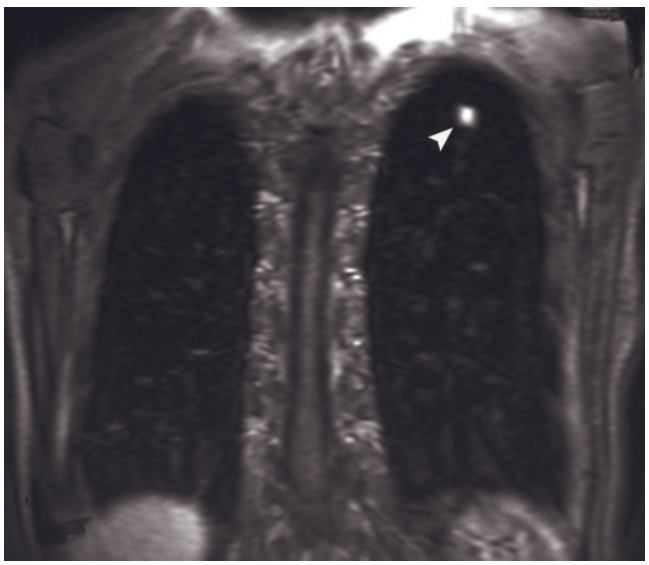

(*j*)

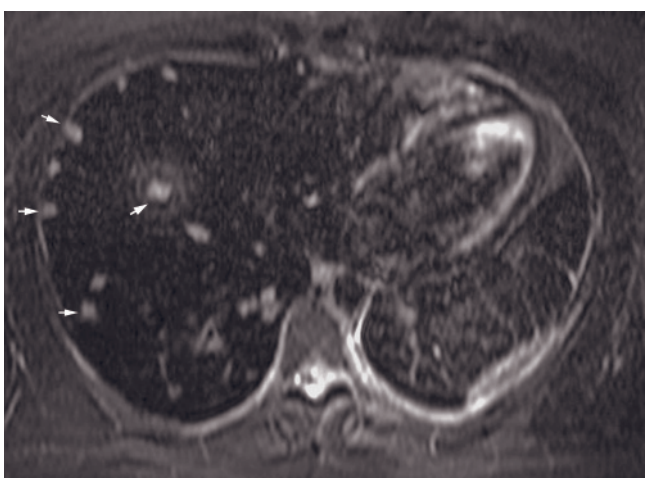

(*k*)

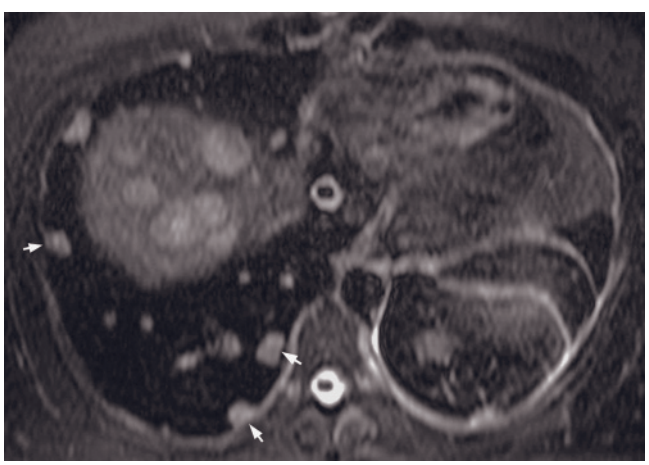

(*l*)

Fig. 18.6 (*Continued*) are shown: patient 1 (*a*, *b*); patient 2 (*c*, *d*); patient 3 (*e*, *f*); patient 4 (*g*, *h*); patient 5 [*i*, *j* (coronal)]; patient 6 (*k*, *l*); patient 7 (*m–p*); patient 8 (*q*, *r*); patient 9 (*s*); patient 10 (*t–w*). T2-weighted single-shot echo-train spin-echo

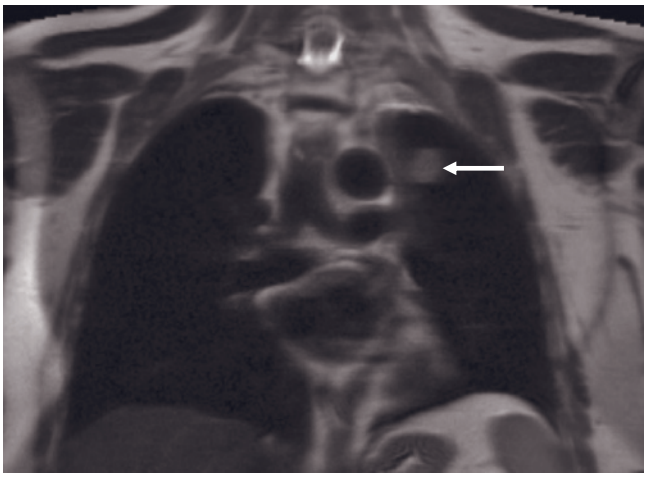

(*m*)

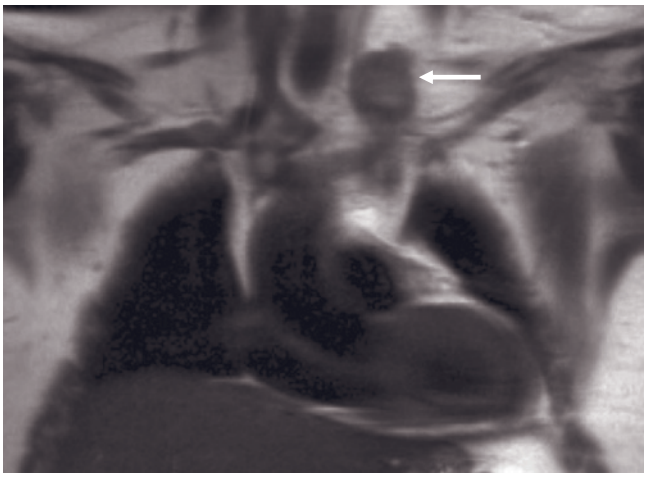

(*n*)

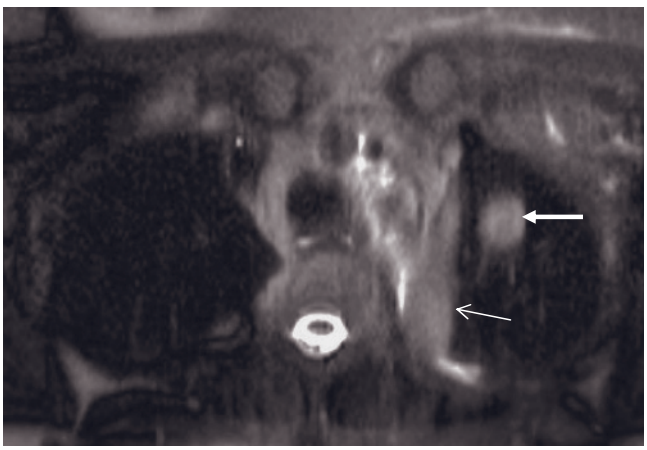

(*o*)

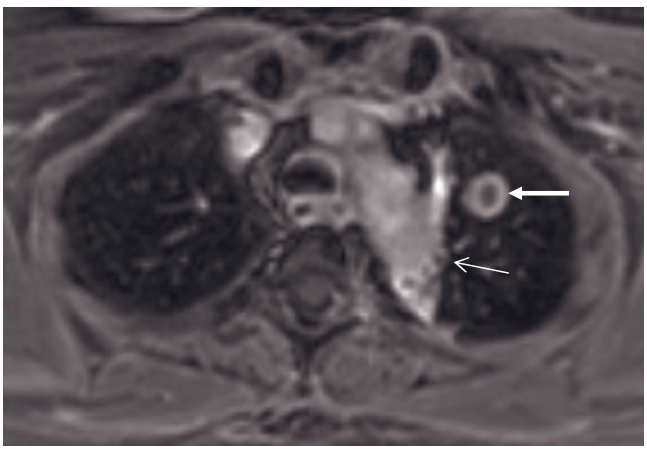

(*p*)

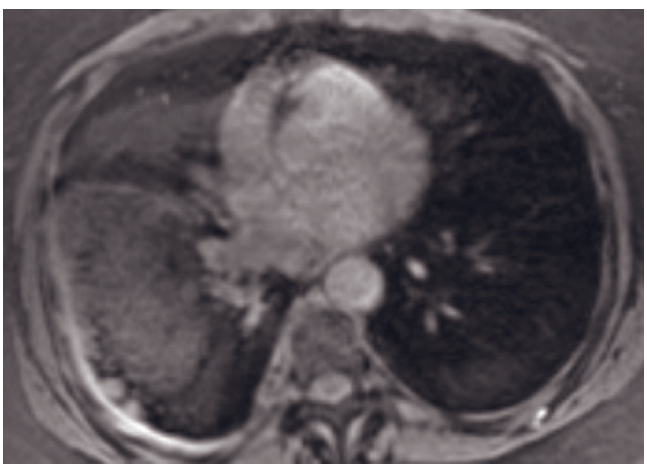

(*q*)

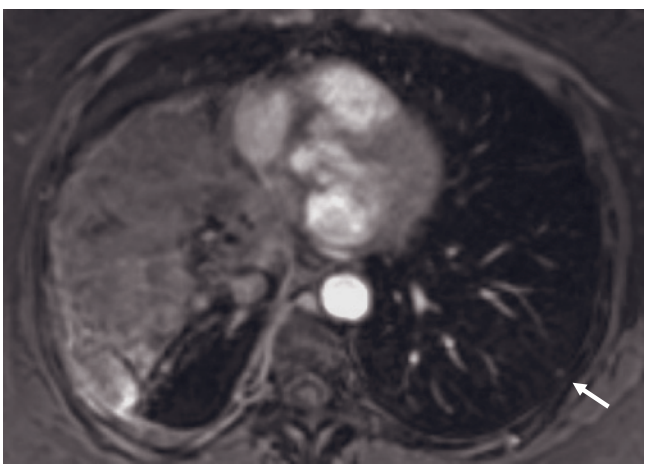

(*r*)

FIG. 18.6 (*Continued*) coronal (*m*, *n*) and transverse (*o*) and transverse T1-weighted fat-suppressed postgadolinium 3D-GE (*p*) images demonstrate the left lung (thick arrows, *m*, *o*, *p*) and subclavian lymph node (arrow, *n*) metastases in patient 7 with endometrial cancer. The lung metastasis show intense peripheral enhancement (thick arrow, *p*) on postgadolinium image (*p*). Note that there is an infiltrate (thin arrows, *o*, *p*) in the left lung. **Transverse T1-weighted postgadolinium fat-suppressed 3D-GE images (*q*, *r*) at 3.0T** demonstrate right pleural metastases and pleural metastatic thickening and a very small left lung metastasis (arrow, *r*) in patient 8 with HCC.

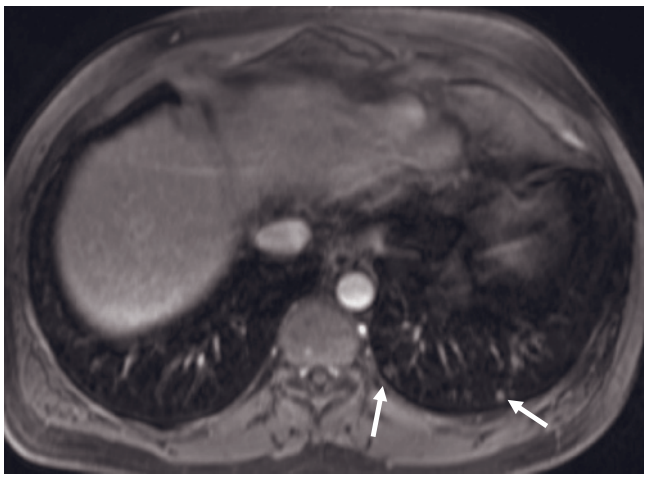

(*s*)

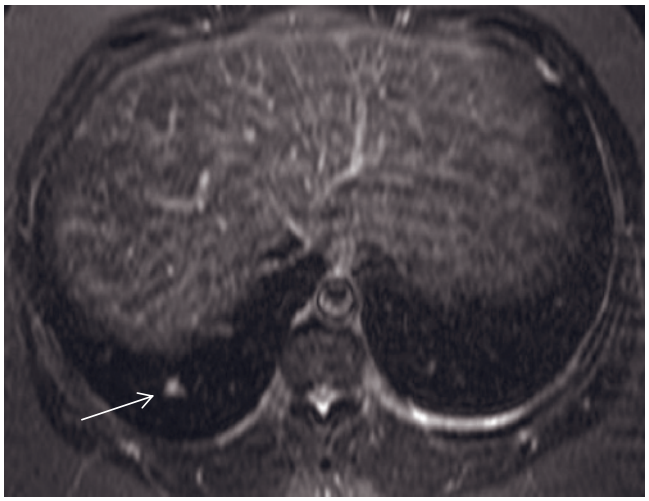

(*t*)

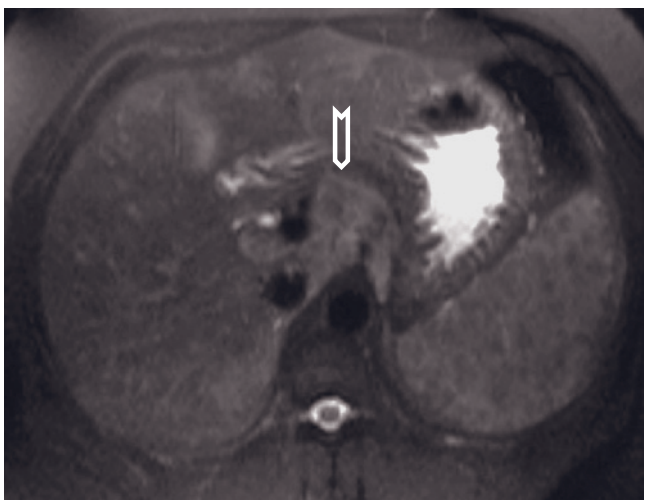

(*u*)

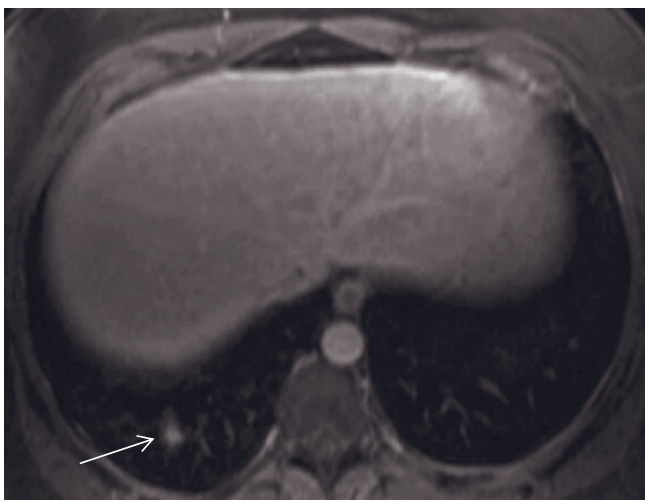

(*v*)

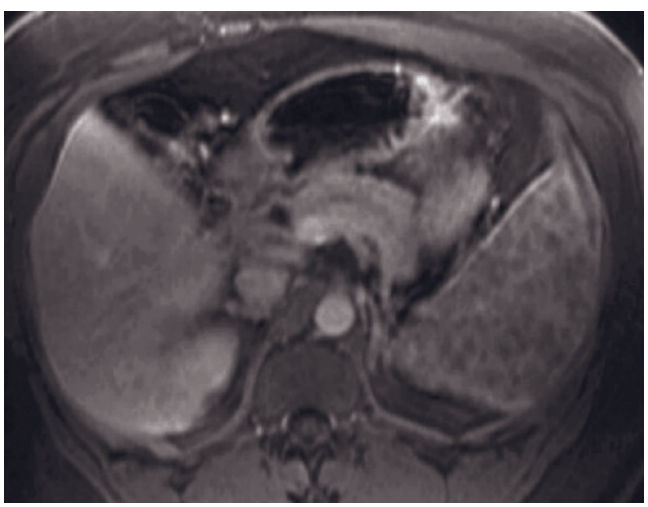

(*w*)

FIG. 18.6 (*Continued*) Transverse T1-weighted postgadolinium fat-suppressed 3D-GE image (*s*) at 1.5T demonstrates two small metastases in patient 9 with HCC. The metastatic lesions show prominent enhancement. Transverse T2-weighted short tau inversion recovery (*t*), fat-suppressed T2-weighted single-shot echo-train echo (*u*), and fat-suppressed T1-weighted postgadolinium 3D-GE (*v*, *w*) images demonstrate a left lung nodule (arrows, *t*, *v*) in patient 10 with sarcoidosis. Multiple diffuse granulomas, which show low signal on T2-weighted images and lower enhancement compared to the surrounding parenchyma, are detected in the liver and spleen. Note that there are multiple lymph nodes (open arrow, *u*) in the para-aortic, paracaval, and portacaval regions.

HILAR AND MEDIASTINAL ADENOPATHY

It is well supported in the literature that MR can be reliably used in the evaluation of mediastinal and hilar metastases [22–24]. Hilar adenopathy can be well imaged with gadolinium-enhanced 3D-GRE images [17]. The high spatial resolution of these images can be helpful for differentiating between nodes and vessels and is improved with the use of fat suppression (fig. 18.7). Promising new data suggest that short tau inversion recovery (STIR) echo-train spin-echo images of mediastinal and hilar lymph nodes can be evaluated for the presence of metastases based on quantitative and qualitative signal intensity [25].

PULMONARY INFILTRATES

Pulmonary infiltrates with a high fluid volume or prominent granulation tissue may be well shown on combined T2-weighted sequences (fluid detection) and gadolinium enhanced 3D-GRE (granulation tissue detection). Airspace and reticulonodular interstitial infiltrates may be adequately shown (fig. 18.8). Differentiating features of interstitial pneumonias are poorly demonstrated at the present time, however.

PLEURAL DISEASE

Pleural effusions may be evaluated on MR images and are best shown on T2-weighted images. Motion artifact from inspiration can result in variations in the signal of pleural effusions, and care must be taken not to confuse motion artifact with complex fluid. Motion-induced signal changes vary from slice to slice, whereas true complex effusions result in comparable appearance from slice to adjacent slice. The complexity of pleural fluid collections may be particularly well shown on MR images, especially single-shot T2-weighted images, in which higher-protein-content complex fluid appears lower signal than simple pleural fluid (fig. 18.9). Increased enhancement of inflamed pleura or abscess wall is well shown on fat-suppressed gadolinium-enhanced images. Pleural metastases, similar to peritoneal metastases, demonstrate moderately intense enhancement and irregular pleural thickening on gadolinium-enhanced fat-suppressed 3D-GRE images (fig. 18.10).

CHEST WALL MASS LESIONS

Similar to mass lesions of the wall of the abdomen and pelvis, chest wall masses can be well depicted and the extent of the mass well shown on MR images. Sequences that perform well at showing chest wall lesions are non-contrast T1-weighted GRE, fat-suppressed T2-weighted single-shot echo-train spin echo, and gadolinium-enhanced fat-suppressed T1-weighted 3D-GRE images. On older MR systems, the proximity of air-filled lung has posed challenges to obtaining homogenous fat suppression because of magnetic susceptibility effects, which has limited the role of MRI. On newer systems, homogeneous fat-suppression is more readily achieved, allowing

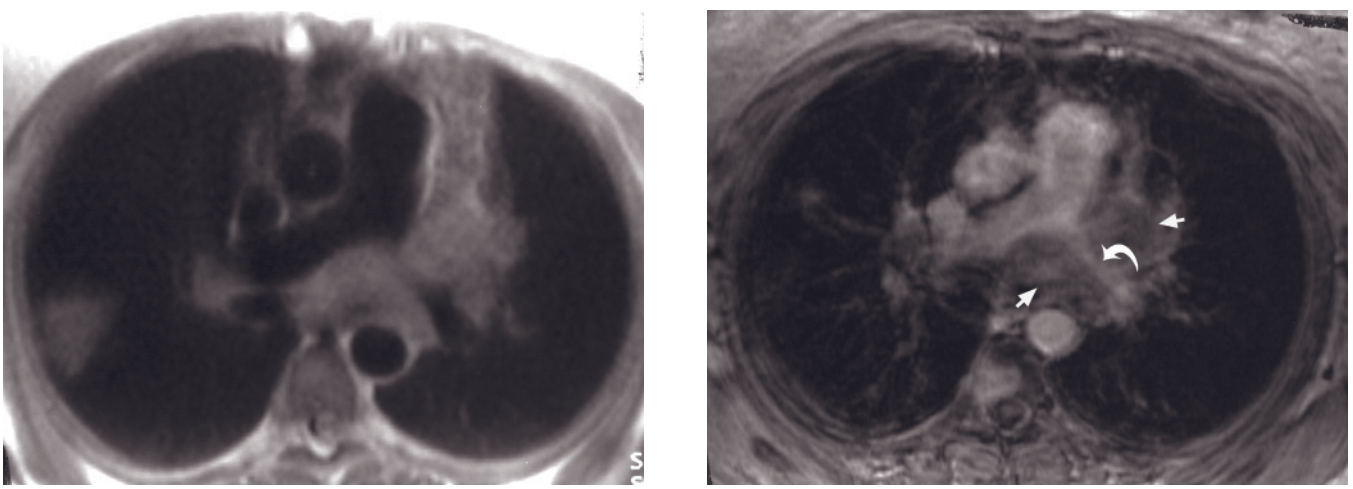

(*a*) (*b*)

FIG. 18.7 Mediastinal lymphadenopathy. T2-weighted ETSE (*a*) and postgadolinium fat-suppressed 3D-GRE (*b*) images demonstrate enlarged mediastinal lymph nodes (arrows, *b*) and left hilar adenopathy compressing the left pulmonary artery (curved arrow, *b*). T2-weighted ETSE (*c*) and postgadolinium 3D-GRE (*d*) images in a different patient demonstrate a large right

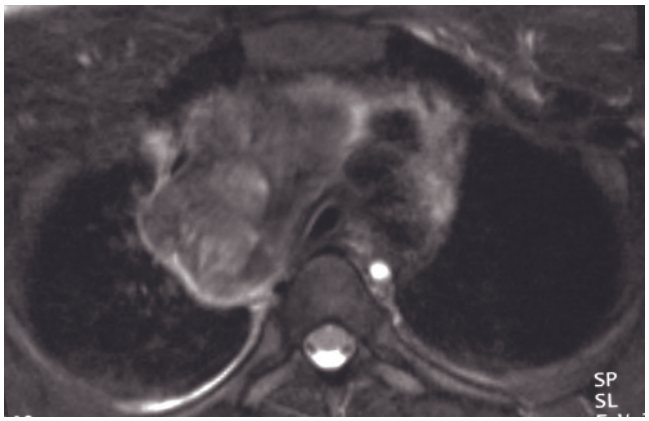

(*c*)

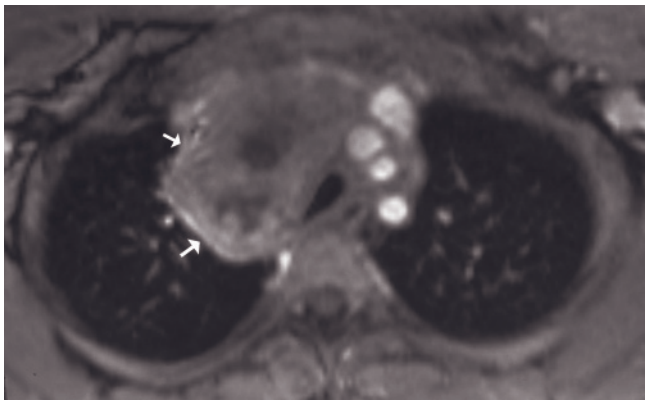

(*d*)

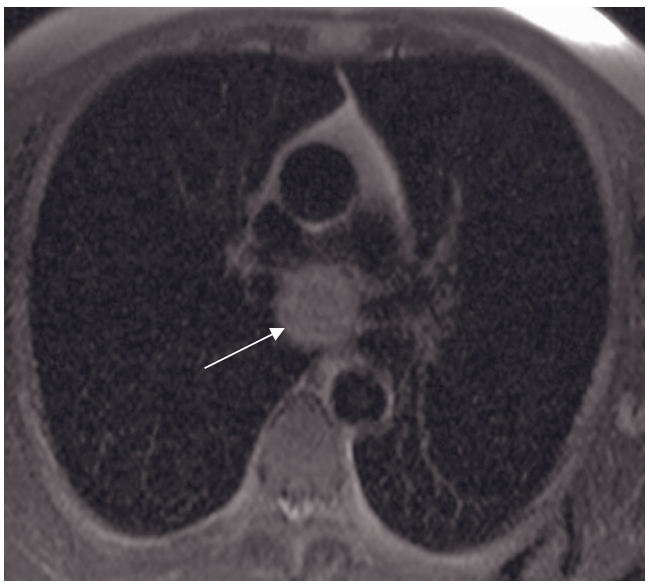

(*e*)

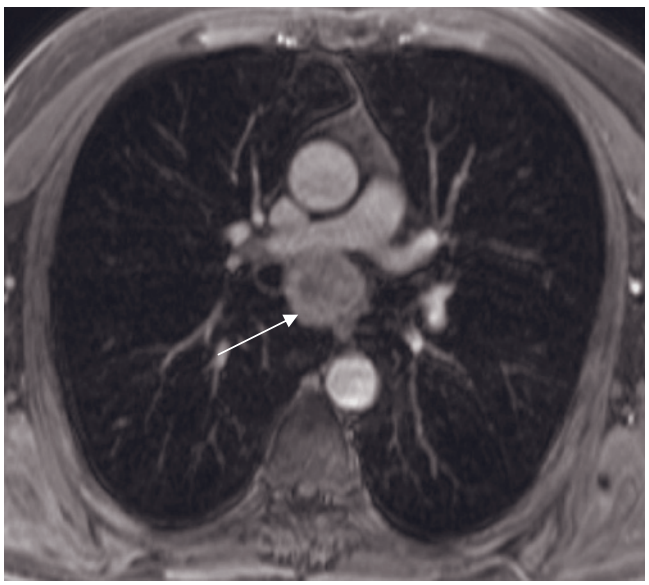

(*f*)

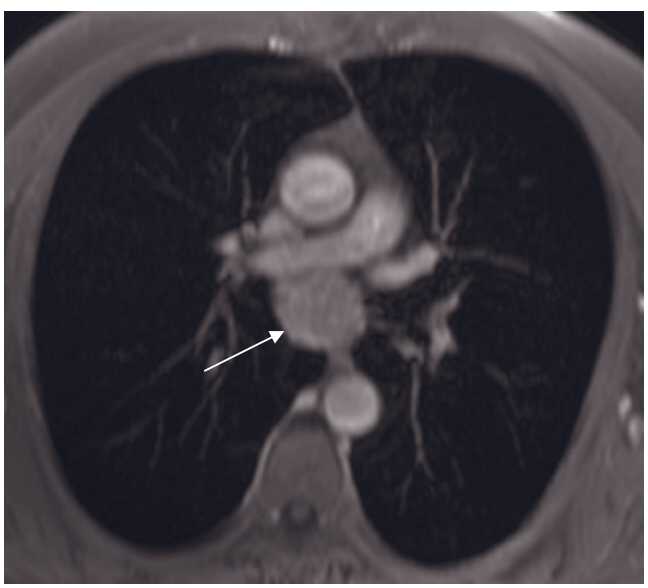

(*g*)

FIG. 18.7 (*Continued*) paratracheal lymph node (arrows, *d*). Transverse T2-weighted fat-suppressed single-shot echo-train spin-echo (*e*) and T1-weighted postgadolinium fat-suppressed 3D-GE (*f*, *g*) images demonstrate subcarinal lymph node metastasis (arrows, *e–g*) in another patient with gastrinoma.

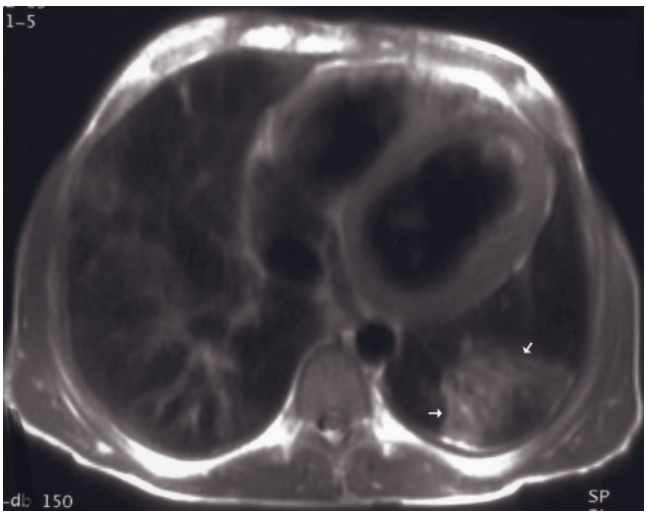

(*a*)

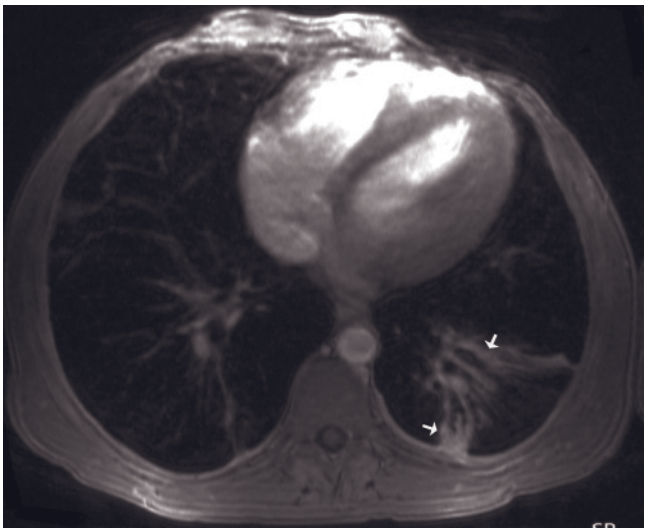

(*b*)

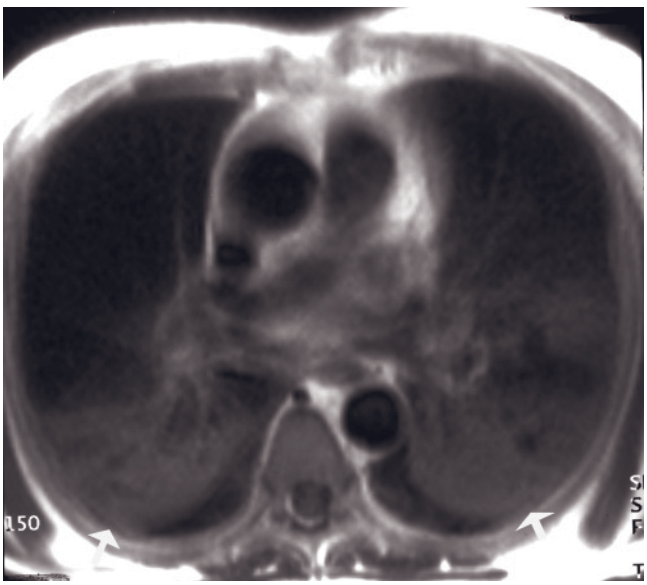

(*c*)

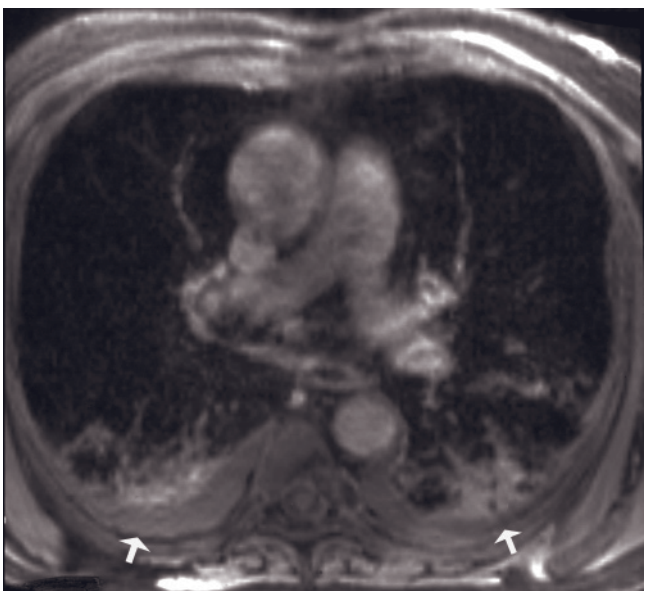

(*d*)

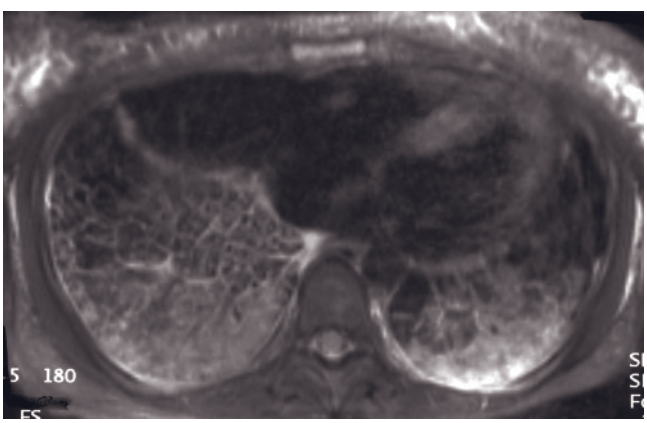

(*e*)

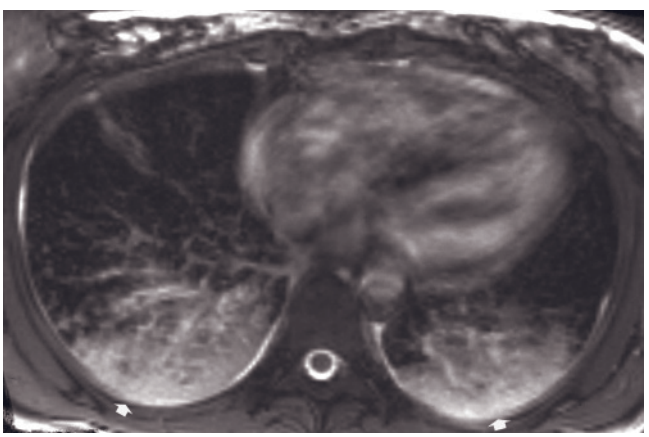

(*f*)

FIG. 18.8 Pulmonary infiltrate. T2-weighted ETSE (*a*, *c*, *o*, *s*), T2-weighted fat-suppressed ETSE (*e*, *f*, *m*, *p*, *t*), and post-gadolinium fat-suppressed 3D-GRE images (*b*, *d*, *g*, *h*, *j*, *k*, *l*, *n*, *q*, *r*, *u*) in nine patients with pulmonary infiltrates (arrows):

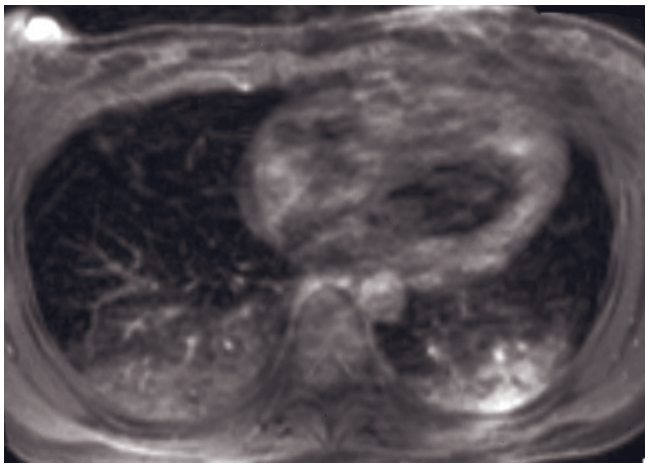

(*g*)

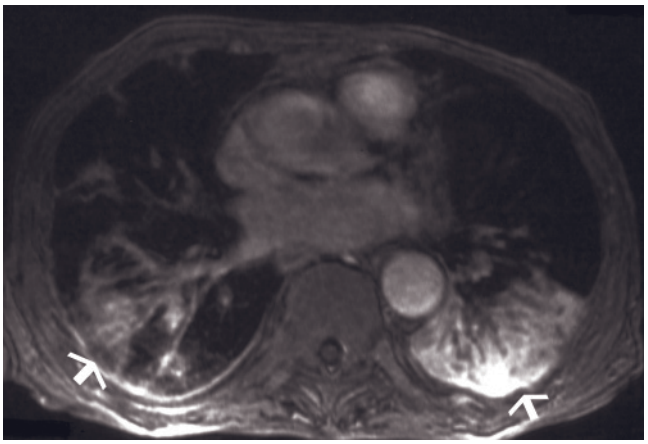

(*h*)

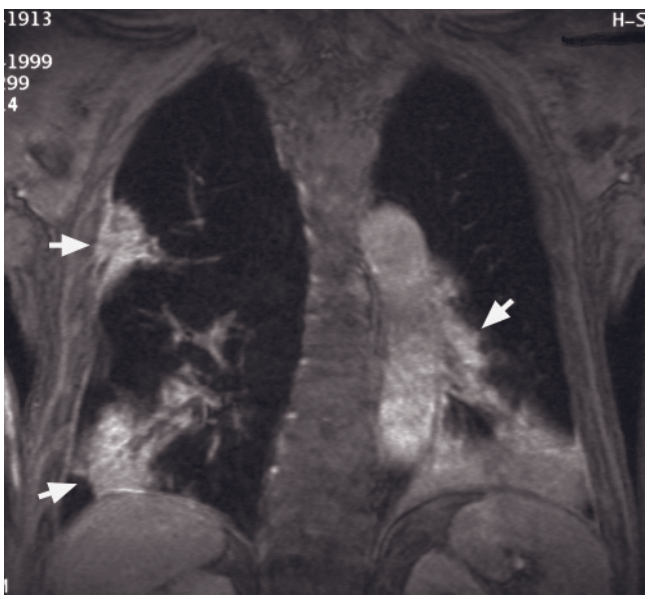

(*i*)

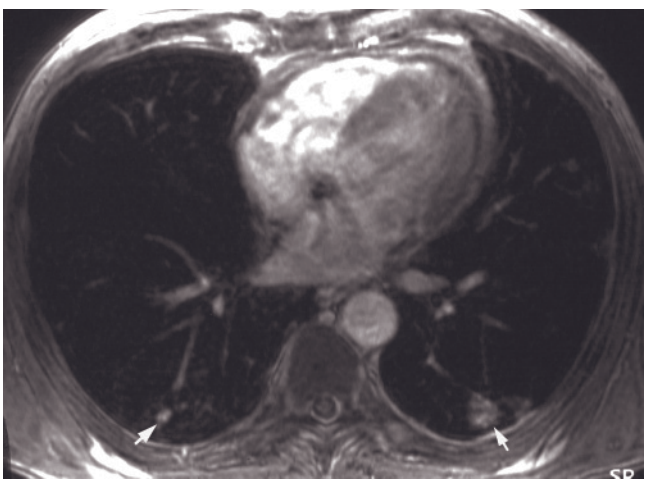

(*j*)

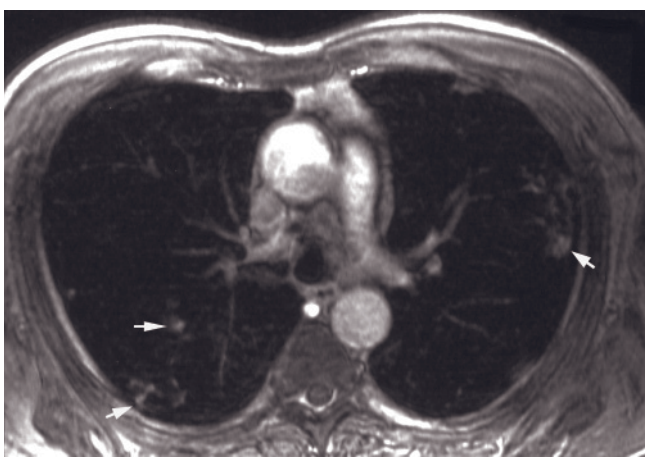

(*k*)

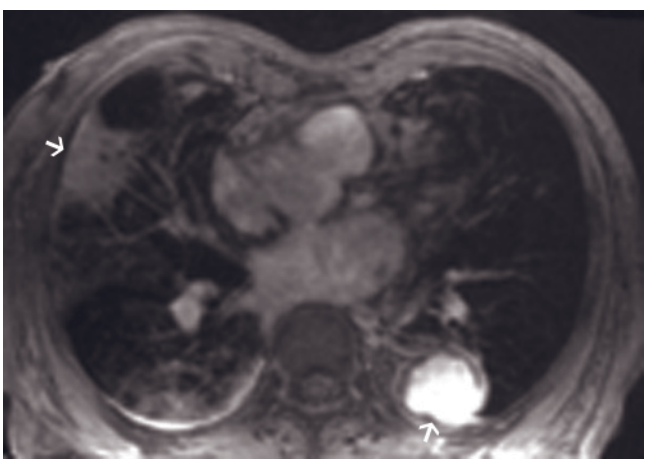

(*l*)

FIG. 18.8 (*Continued*) patient 1 (*a*, *b*); patient 2 (*c*, *d*); patient 3 (*e–g*); patient 4 [*h*, *i* (coronal)]; patient 5 (*j*, *k*); patient 6 (*l*); patient 7 (*m*, *n*); patient 8 (*o–r*); patient 9 (*s–u*). Transverse T2-weighted fat-suppressed single-shot echo-train spin-echo (*m*) and

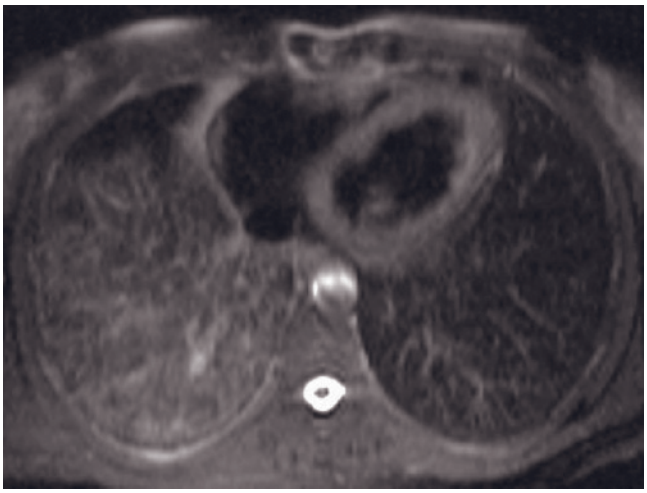

(*m*)

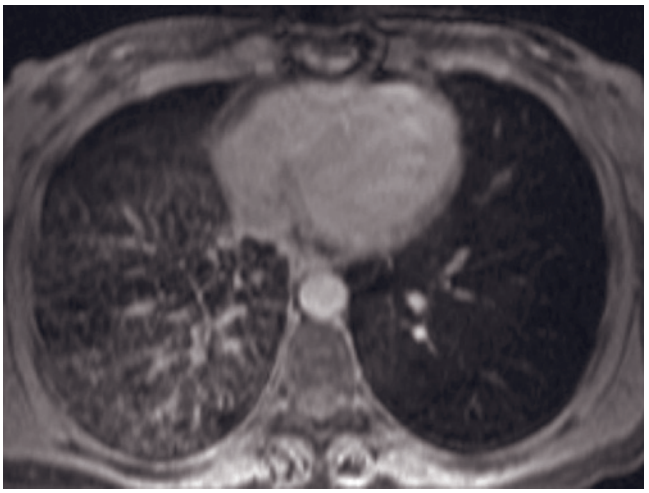

(*n*)

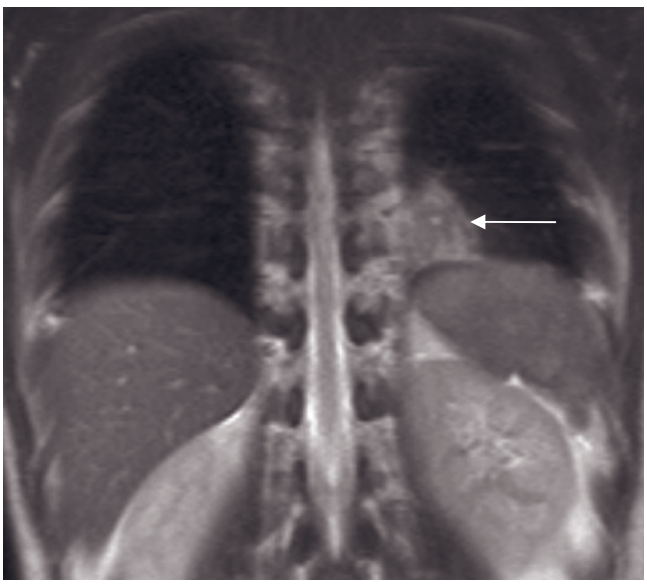

(*o*)

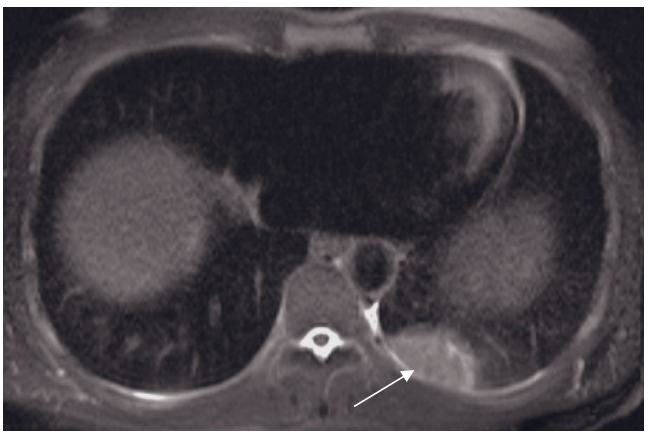

(*p*)

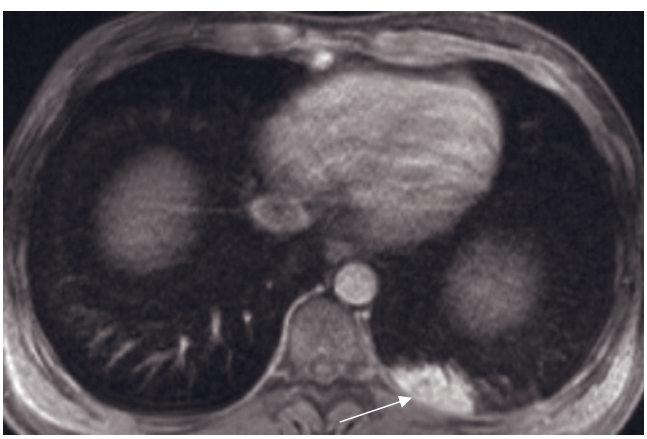

(*q*)

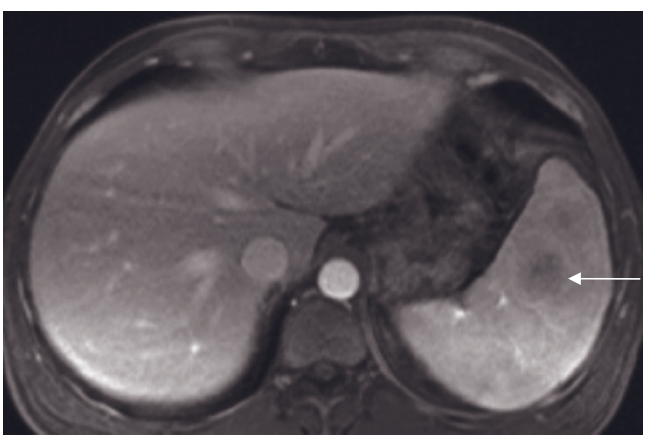

(*r*)

FIG. 18.8 (*Continued*) T1-weighted fat-suppressed postgadolinium 3D-GE (*n*) images demonstrate lymphangitic spread in the right lung in patient 7 with lung cancer. Coronal T2-weighted single-shot echo-train spin-echo (*o*), transverse T2-weighted fat-suppressed single-shot echo-train spin-echo (*p*), and transverse T1-weighted postgadolinium fat-suppressed 3D-GE (*q*, *r*) images demonstrate a consolidation (arrows, *o*–*q*) in the left lung in patient 8 with AIDS and disseminated *Cryptococcus neoformans* infection. There is minimal left pleural effusion seen as high signal intensity adjacent to the aorta. Note that there are multiple infectious foci seen as low-signal-intensity structures (arrow) in the spleen on postgadolinium image (*r*).

(*s*)

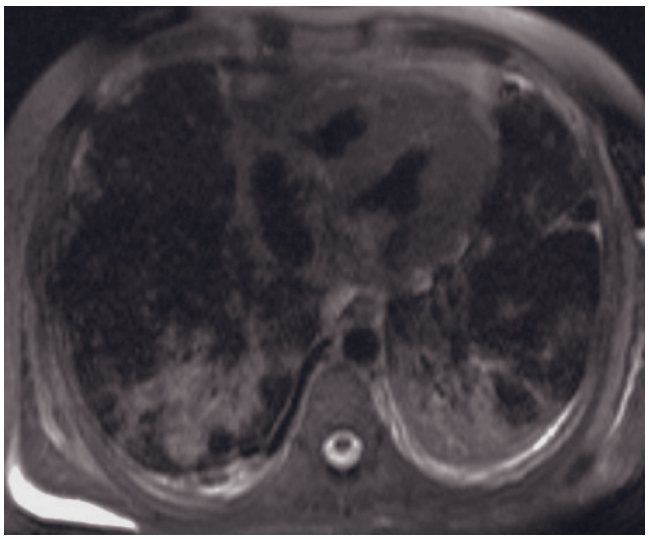

(*t*)

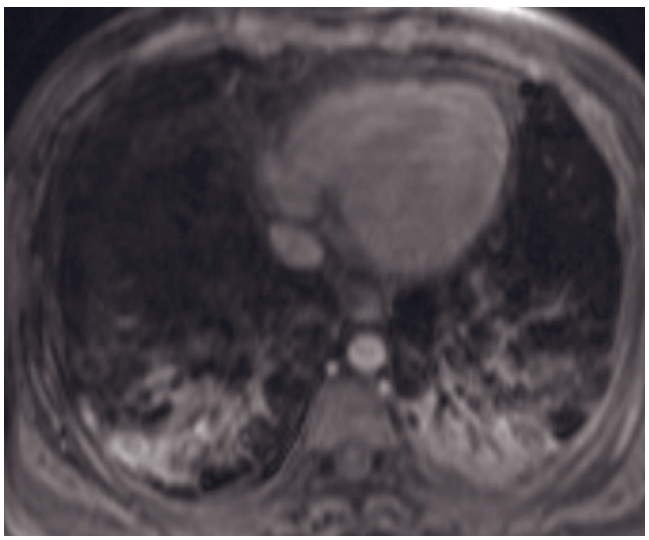

(*u*)

FIG. 18.8 (*Continued*) T2-weighted coronal (s) and transverse fat-suppressed (*t*) single-shot echo-train spin-echo, and transverse T1-weighted postgadolinium fat-suppressed 3D-GE (*u*) images demonstrate bilateral pulmonary infiltrates and pleural effusions in patient 9 with cystic fibrosis. Note that the pleural effusion extends into the minor fissure on the right side.

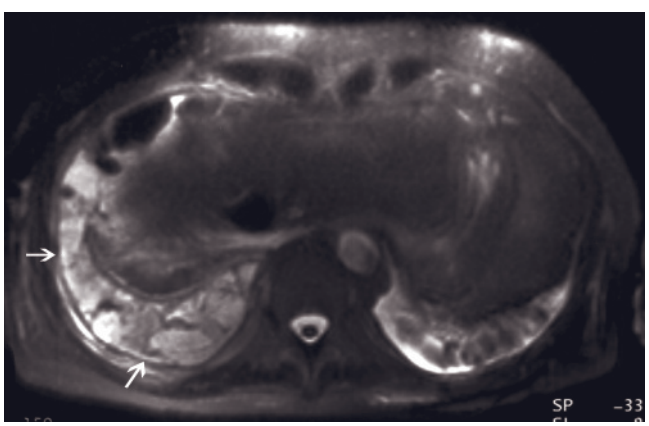

(*a*)

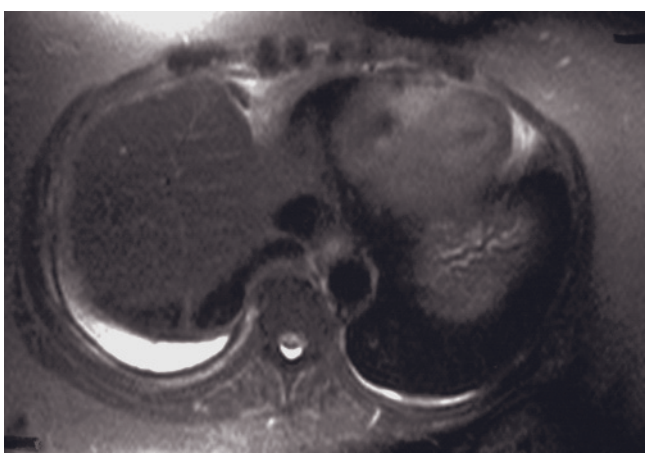

(*b*)

FIG. 18.9 Pleural disease. T2-weighted fat-suppressed ETSE image (*a*) demonstrates complex pleural effusion with numerous low-signal regions (arrows). In a second patient, T2-weighted fat-suppressed ETSE (*b*) and postgadolinium fat-suppressed 3D-GRE (*c*) images show bilateral pleural effusions. Split pleura sign is well demonstrated on postgadolinium image (arrows, *c*). T2-weighted

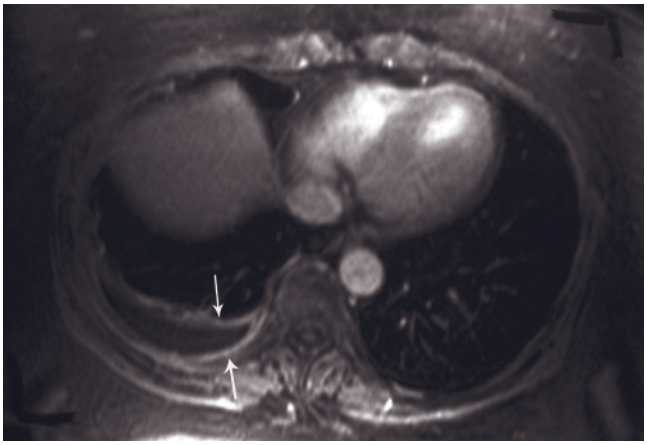

(*c*)

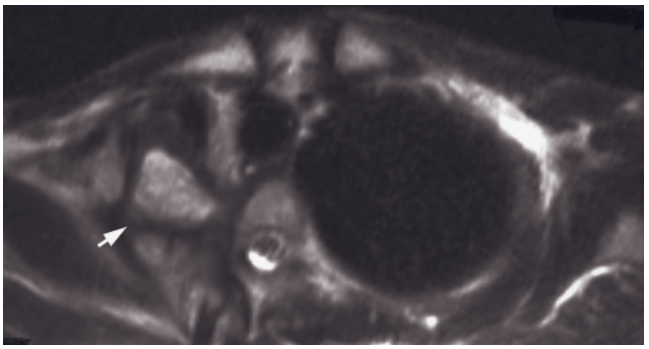

(*d*)

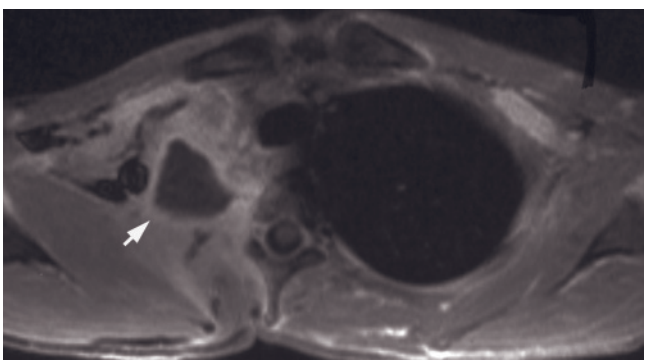

(*e*)

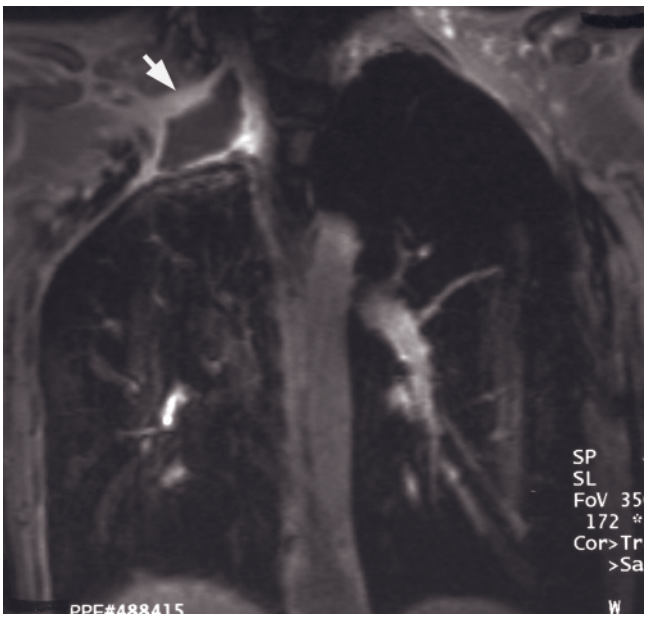

(*f*)

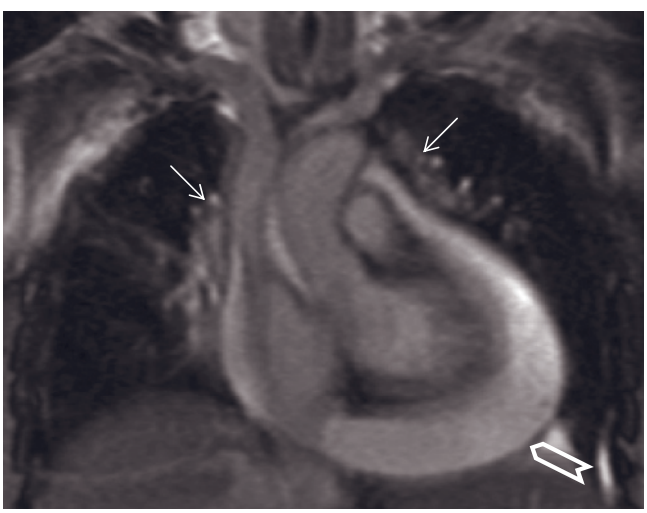

(*g*)

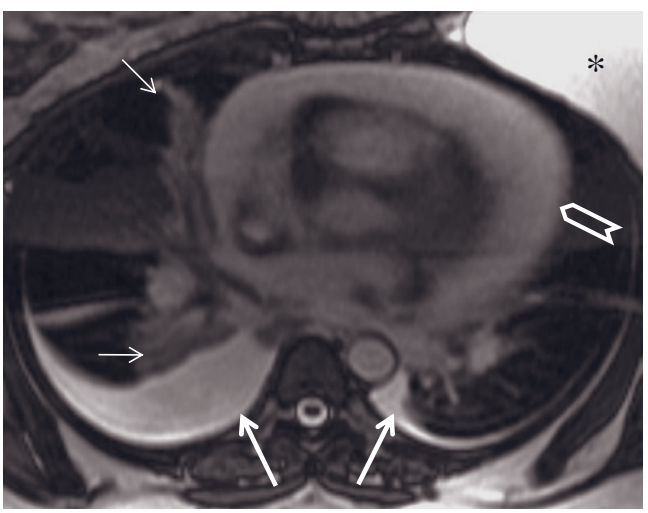

(*h*)

FIG. 18.9 (*Continued*) fat-suppressed ETSE (*d*) and postgadolinium 3D-GRE transverse (*e*) and coronal (*f*) images in a third patient status post lobectomy show a complex collection with intense enhancement, consistent with an abscess (arrows, *d–f*). Coronal (*g*) and transverse (*h*) T2-weighted true fast imaging with steady-state precession (True-FISP) images demonstrate bilateral effusion (long arrows, *g*, *h*), pericardial effusion (open arrow, *g*, *h*), and bilateral pulmonary infiltrates (short arrows, *g*, *h*) in another patient with pregnancy. True-FISP sequence is a bright-blood technique and does not require contrast administration, and therefore can be used for the evaluation of suspected pulmonary embolism in pregnant patients. Note that there is a breast implant (*, *h*).

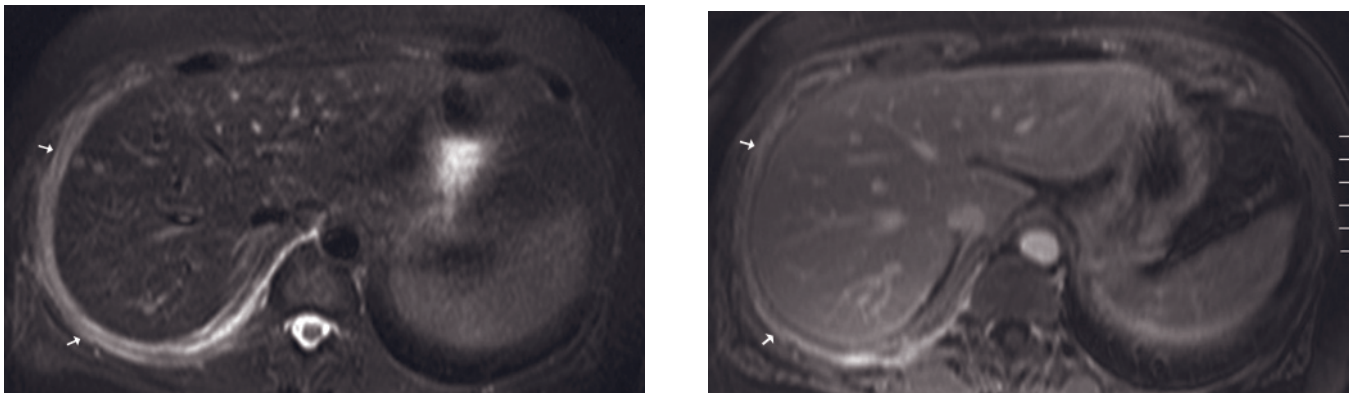

(*a*) (*b*)

FIG. 18.10 Pleural metastases. T2-weighted fat-suppressed ETSE (*a*) and postgadolinium 3D-GRE (*b*) images show enhancement and thickening of the pleura consistent with pleural metastases (arrows, *a*, *b*).

for high-image-quality studies that make use of the high soft tissue contrast of MRI (fig. 18.11).

PULMONARY MRA AND PULMONARY EMBOLI

Thousands of CT pulmonary angiographies (CTPA) and ventilation-perfusion (V/Q) studies are performed every year for the detection of pulmonary emboli. CTPA is the first-line imaging modality for the assessment of pulmonary arterial vasculature and has high accuracy for the detection of pulmonary emboli. However, the incidence of pulmonary emboli is relatively low in the young patient population. Our unpublished data show that only 5% of our patient population who were between 18 and 45 years of age and had suspected pulmonary embolism had positive findings of pulmonary embolism on CTPA studies. While 35% of this young patient population have no pathologic findings on CTPA studies, 60% have other findings. Because CTPA and V/Q studies contain ionizing radiation and the incidence of pulmonary embolism is particularly low in young patients, MRI studies including soft tissue MRI sequences and/or MRA sequences may be a good alternative first-line imaging modality for the evaluation of pulmonary embolism in young patients (fig. 18.12). Additionally, true fast imaging with steady-state precession (True-FISP) sequences, a bright-blood technique that does not require the use of gadolinium-containing contrast agents, may be used as first-line imaging studies for the evaluation of pulmonary embolism in pregnant patients or in patients who are at risk for nephrogenic systemic fibrosis or do not have venous access (fig. 18.12). Our unpublished data show that the use of True-FISP is feasible for the evaluation of pulmonary vasculature. The use of parallel imaging, in conjunction with MRA sequences or other soft tissue MR sequences, allows for dramatic shortening of data acquisition and thus a shorter breath hold. Therefore, MRI and MRA are feasible in dyspneic patients as well. Gadolinium-enhanced 3D-GRE MRA is effective in evaluating the pulmonary arteries and produces high-quality images (fig. 18.12). The sensitivity and specificity of MR angiography with parallel imaging in the detection of pulmonary emboli are similar to CT, and higher than ventilation-perfusion scintigraphy [26–28]. An additional advantage of gadolinium-enhanced pulmonary MRA over CTPA is that gadolinium has a larger window of visibility in the pulmonary vessels than iodine on CT images, which renders timing of data acquisition less critical. This is particularly true if gadobenate dimeglumine (MultiHance) or gadofosveset trisodium (Vasovist) is employed, as these exhibit protein binding and persist in the vascular space for a longer duration than other standard gadolinium agents. This may prove to have an even greater improvement in MRA of the pulmonary vessels [29, 30]. Additionally, the use of 3D-GRE sequences can also detect pulmonary embolism in the pulmonary arteries including lobar and segmental arteries as well as parenchymal pathologies (fig. 18.12) [31].

THORACIC MRA

MRA has an established role in the assessment of thoracic vascular abnormalities. Common applications include the evaluation of congenital anomalies such as aortic coarctation, vascular rings, and arteriovenous malformations. In patients with suspected vascular anomalies who are not dyspneic, gadolinium-enhanced 3D MRA results in high-quality images and definition of these abnormalities (figs. 18.13 and 18.14). Thoracic

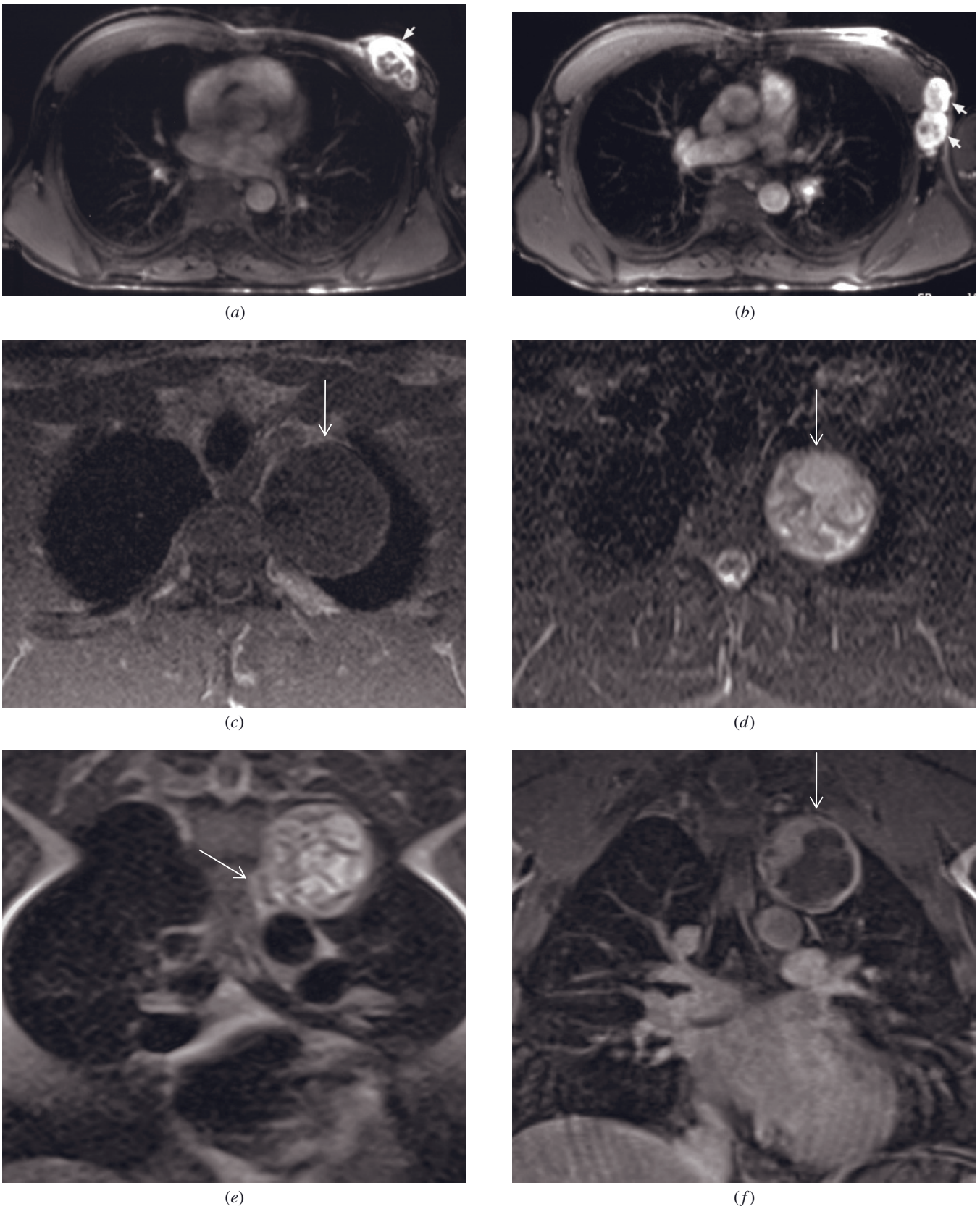

FIG. 18.11 Chest wall mass. Postgadolinium fat-suppressed 3D-GRE images (*a*, *b*) demonstrate multiple nerve sheath tumors in the left chest wall (arrows). Transverse T1-weighted fat-suppressed 3D-GE (*c*), transverse T2-weighted short tau inversion recovery (*d*), coronal T2-weighted single-shot echo-train spin-echo (*e*), and coronal T1-weighted fat-suppressed postgadolinium 3D-GE (*f*) images demonstrate a left paraspinal neurogenic tumor (arrows, *c*, *d*, *f*) in another patient. The tumor is located in the apical region and has a neural forminal extension (arrow, *e*). The tumor shows heterogeneous very bright signal on T2-weighted images and heterogeneous enhancement on postgadolinium images. There are cystic or necrotic regions in the tumor.

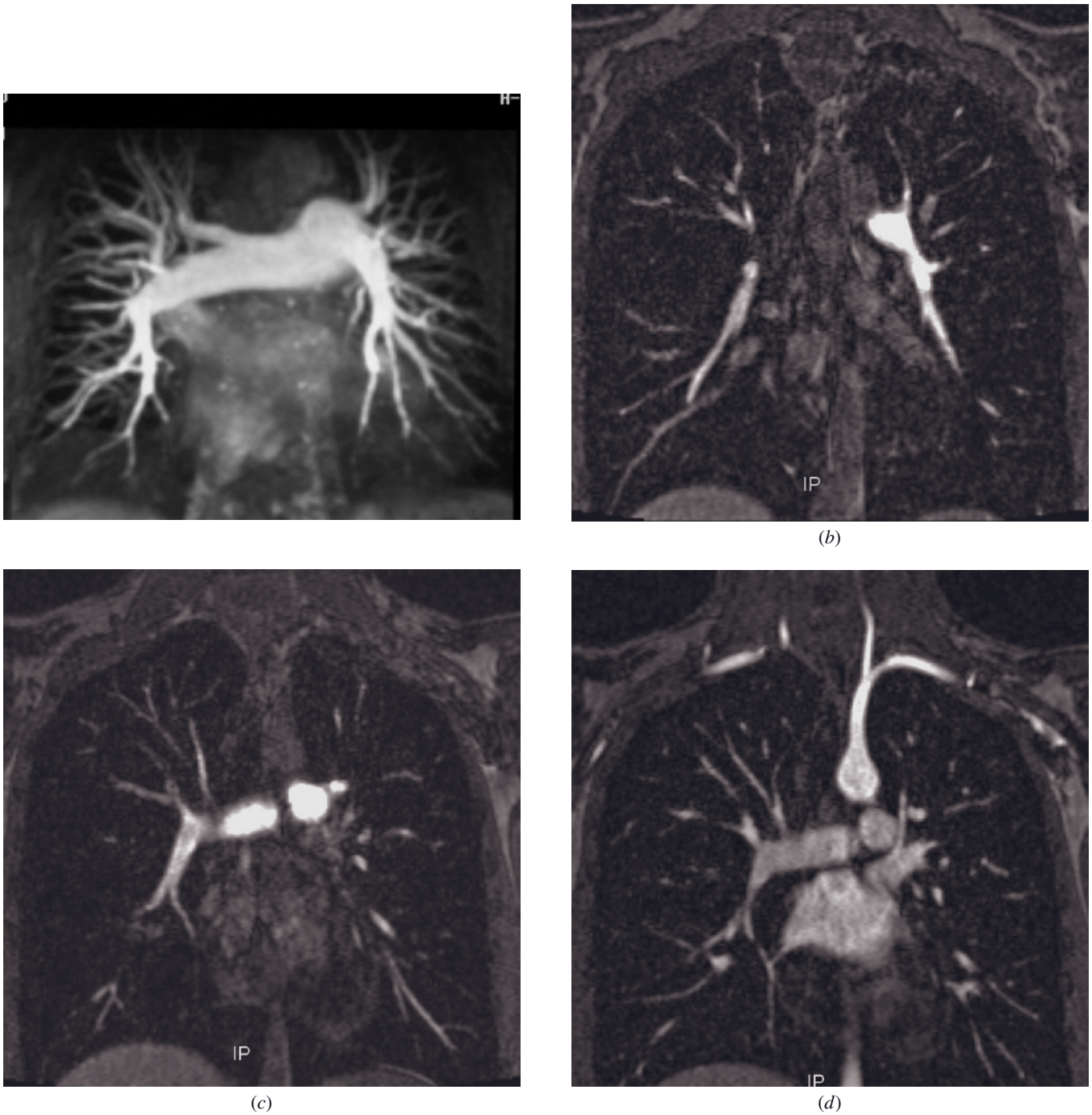

(*b*)

(*c*)

(*d*)

FIG. 18.12 Pulmonary MRA. Coronal maximum intensity projection (MIP) image (*a*) of postgadolinium 3D-MRA demonstrates excellent depiction of the pulmonary arteries. Coronal fat-suppressed 3D-GE MRA source images (*b–d*) and reconstructed 3D MIP

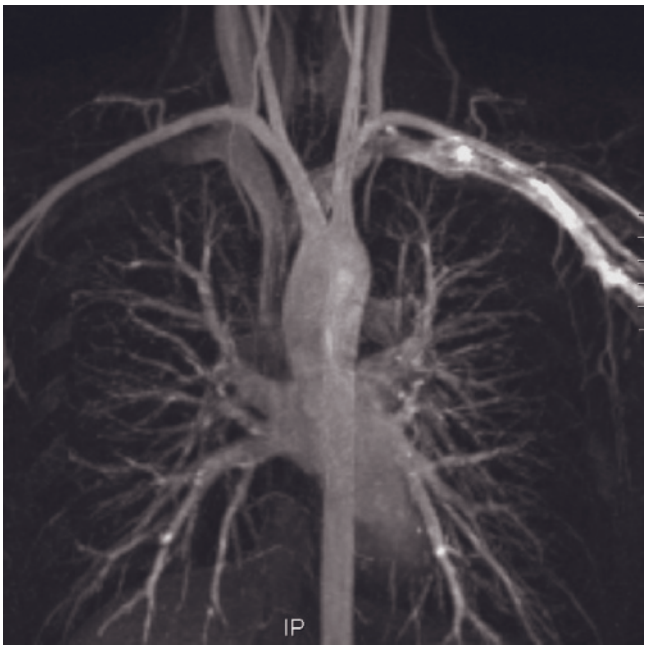

(*e*)

(*f*)

(*g*)

(*h*)

FIG. 18.12 (*Continued*) MRA image (*e*) demonstrate normal pulmonary vasculature at 3.0 T in another patient. Note that segmental and subsegmental pulmonary arteries can be visualized with pulmonary MRA, and 3.0 T MR imaging is particularly helpful because of high spatial and temporal resolution. Coronal T2-weighted true fast imaging with steady-state precession (True-FISP) images (*f*, *g*) demonstrate normal lobar and segmental pulmonary arteries in a pregnant patient. **Pulmonary Emboli.** Coronal T2-weighted single-shot echo-train spin-echo (*h*) and coronal (*i*) and transverse (*j*) T1-weighted postgadolinium fat-suppressed 3D-GE

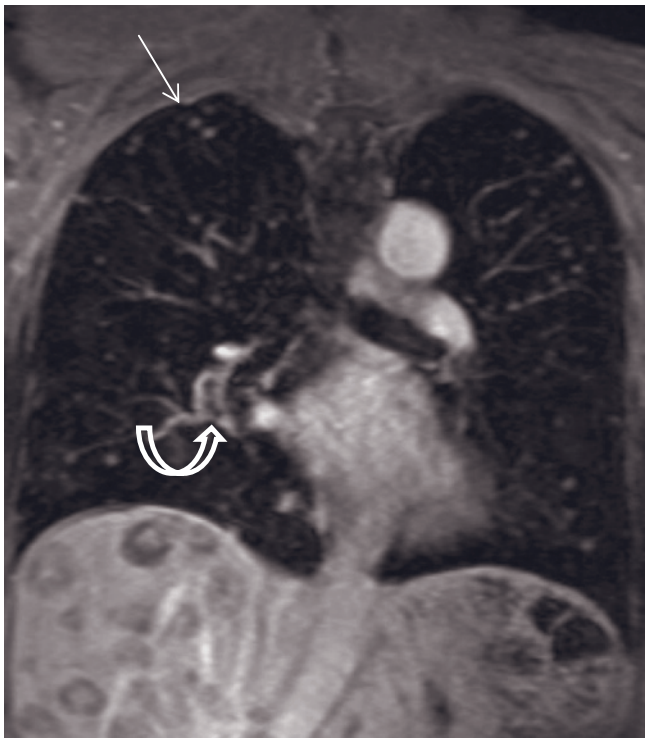

(*i*)

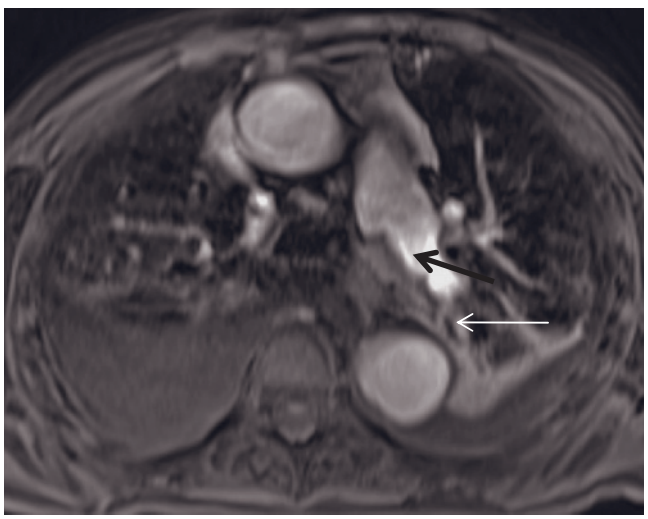

(*l*)

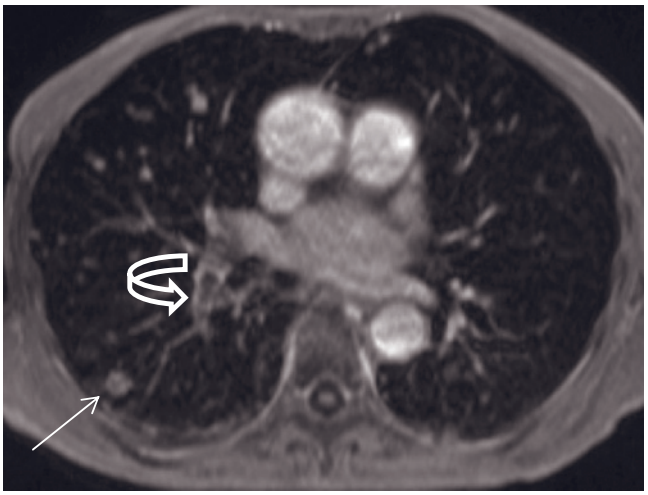

(*j*)

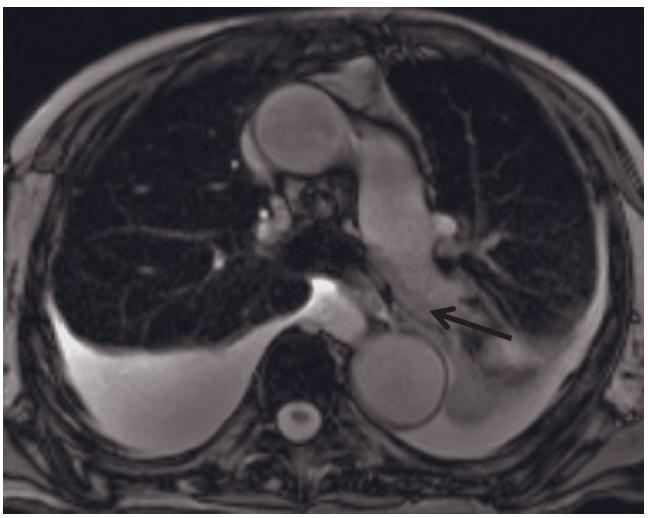

(*k*)

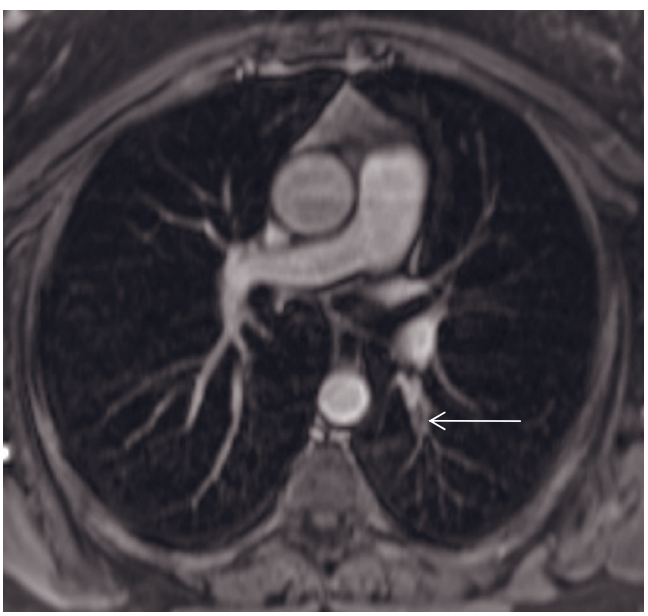

(*m*)

FIG. 18.12 (*Continued*) images demonstrate pulmonary emboli (curved arrows, *i*, *j*) involving right interlobar artery and its branches and multiple liver (arrow, *h*) and lung (arrows, *i*, *j*) metastases in another patient with unknown primary. Transverse T2-weighted true fast imaging with steady-state precession (True-FISP) (*k*) and transverse T1-weighted postgadolinium fat-suppressed 3D-GE (*l*) images demonstrate the thrombus (black arrows, *k*, *l*) as a filling defect located in the left pulmonary artery extending into the left lower lobe artery (white arrow, *l*) in another patient. Note that there are bilateral pleural effusions and left lower lobe atelectasis. Transverse T1-weighted postgadolinium fat-suppressed 3D-GE image (*m*) shows the thrombus (arrow) as a filling defect in the segmental artery of the left lower lobe.

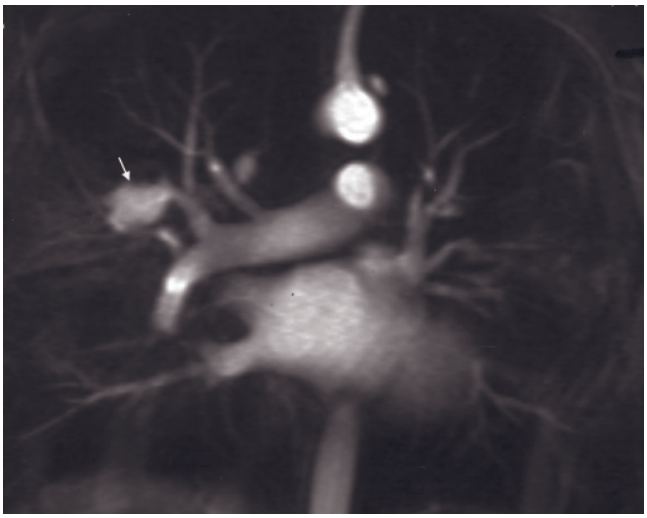

(*a*)

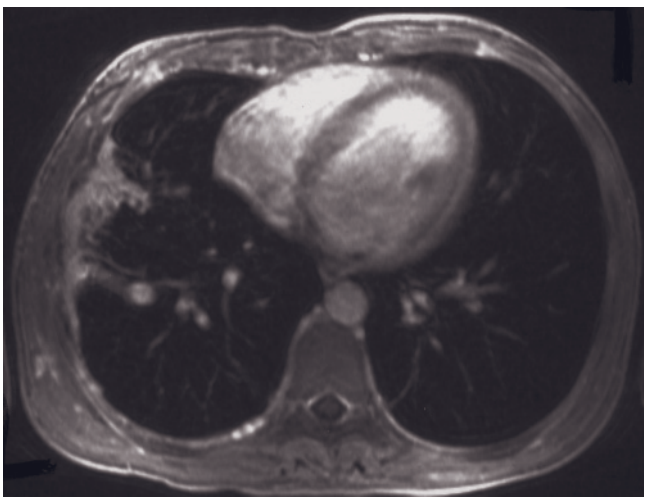

(*c*)

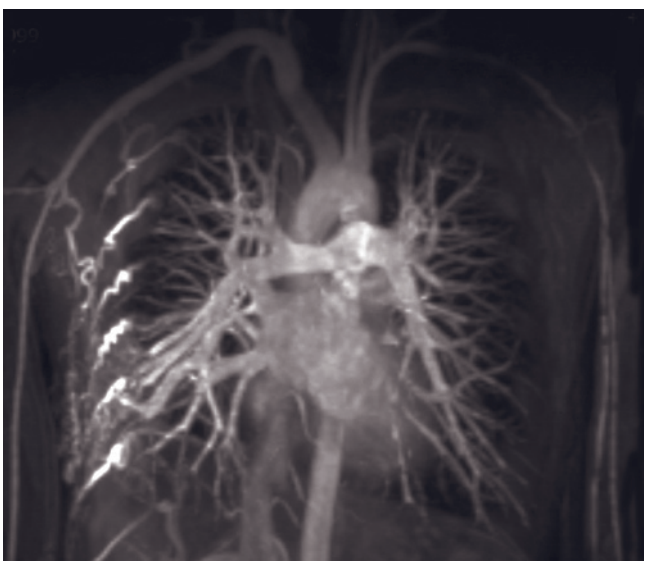

(*d*)

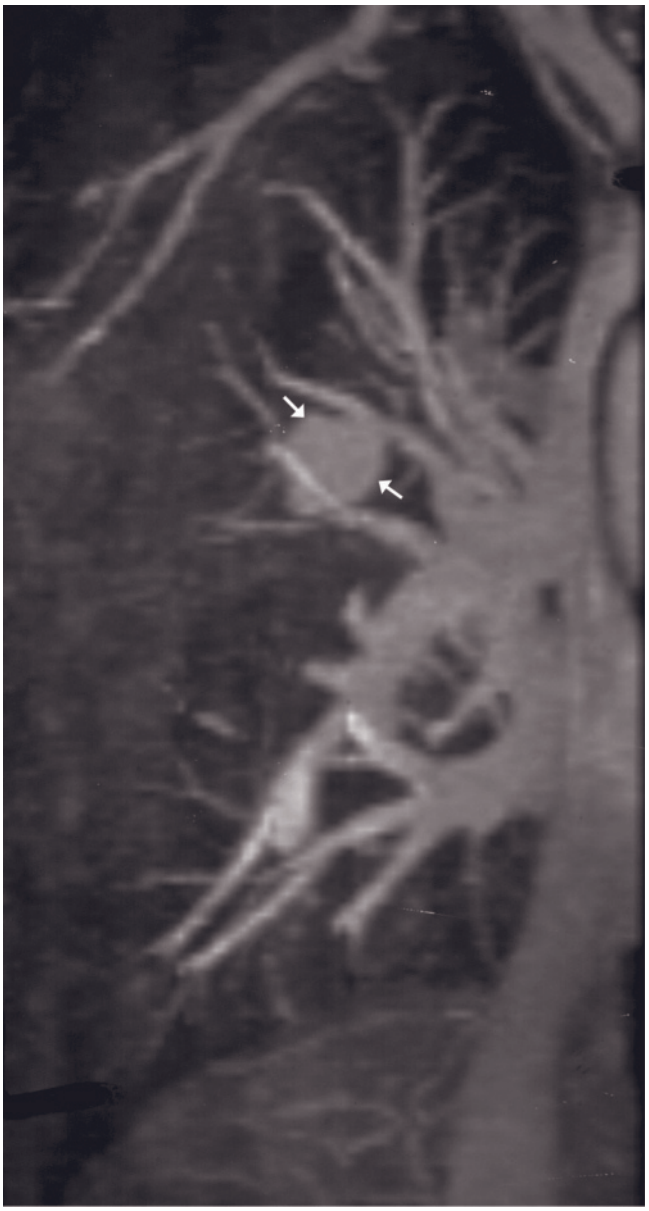

(*b*)

FIG. 18.13 MRA of vascular abnormalities. Coronal (*a*) and sagittal MIP (*b*) images of postgadolinium 3D-MRA of the chest demonstrate a pulmonary artery aneurysm (arrows). In a second patient, T1-weighted fat-suppressed 3D-GRE (*c*) and coronal MIP (*d*) images of postgadolinium 3D-MRA show a posttraumatic arteriovenous fistula involving pulmonary arteries and intercostal veins. Coronal postgadolinium 3D-GE images (*e*, *f*) demonstrate

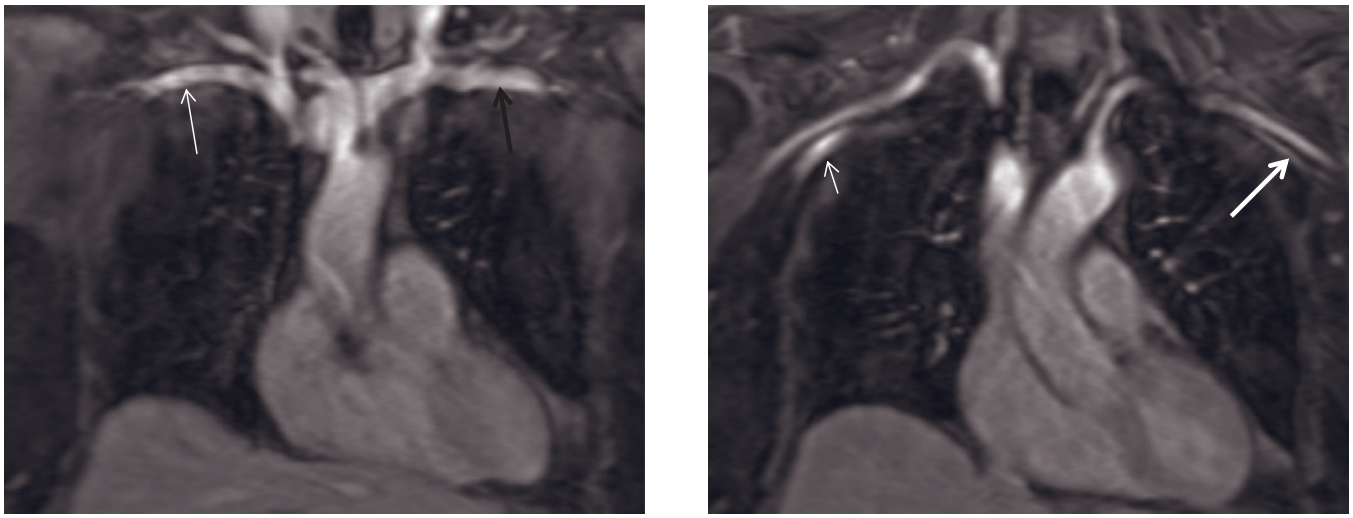

(*e*) (*f*)

FIG. 18.13 (*Continued*) decreased caliber of the left axillary vein (white long thick arrow, *f*) due to a proximal stenotic lesion in another patient. Note the normal calibers of the right subclavian (white long thin arrow, *e*), axillary (white short thin arrow, *f*), and left subclavian (black long thick arrow, *e*) veins.

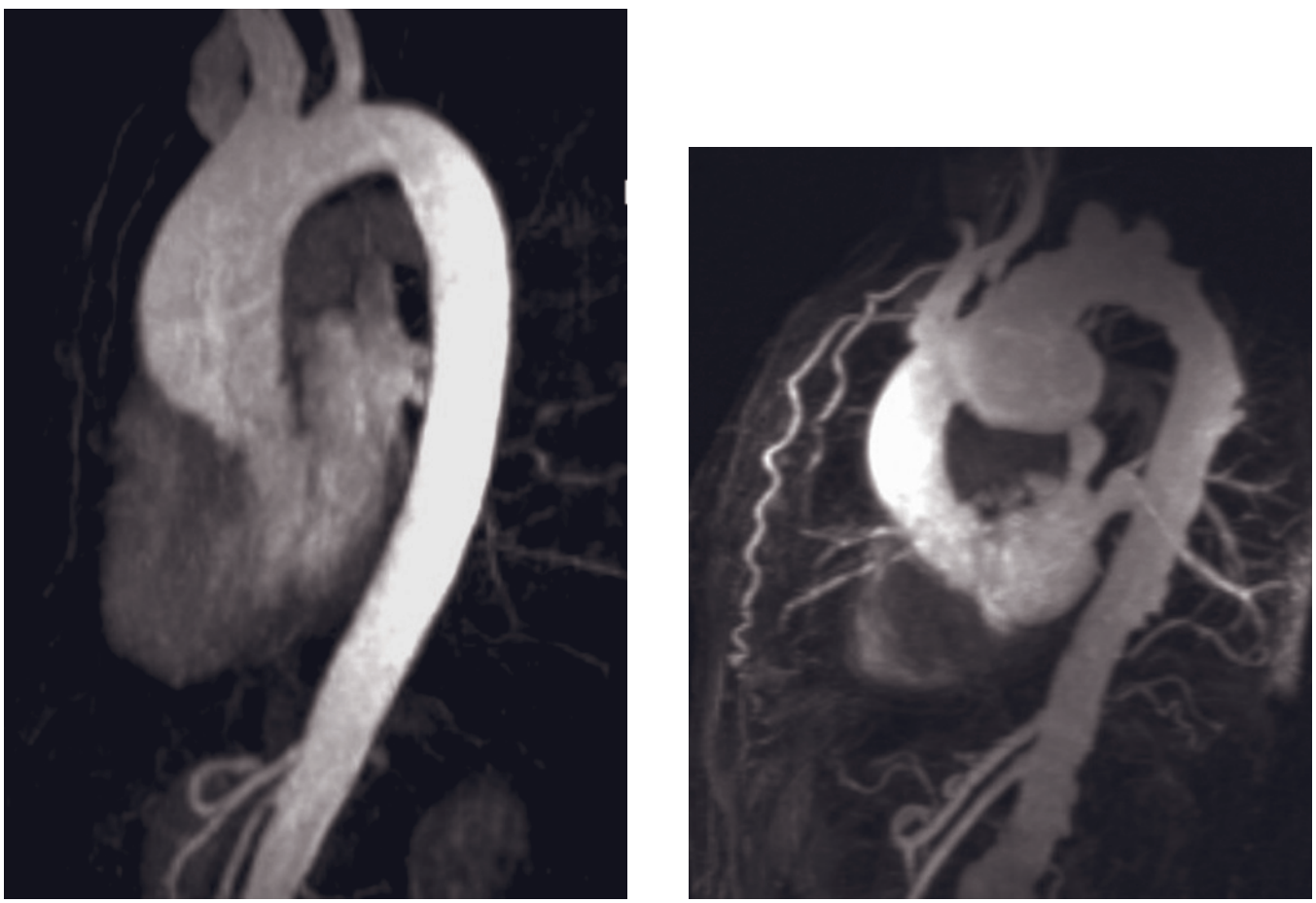

(*a*) (*b*)

FIG. 18.14 Thoracic aorta. Parasagittal (LAO) MIP images (*a*, *b*, *d*) of postgadolinium 3D-MRA, source image (*c*), and multiplanar reformatted (MPR) transverse image (*e*). Patient 1 (*a*) is normal, and patients 2 (*b*, *c*) and 3 (*c*, *d*) have aortic disease.

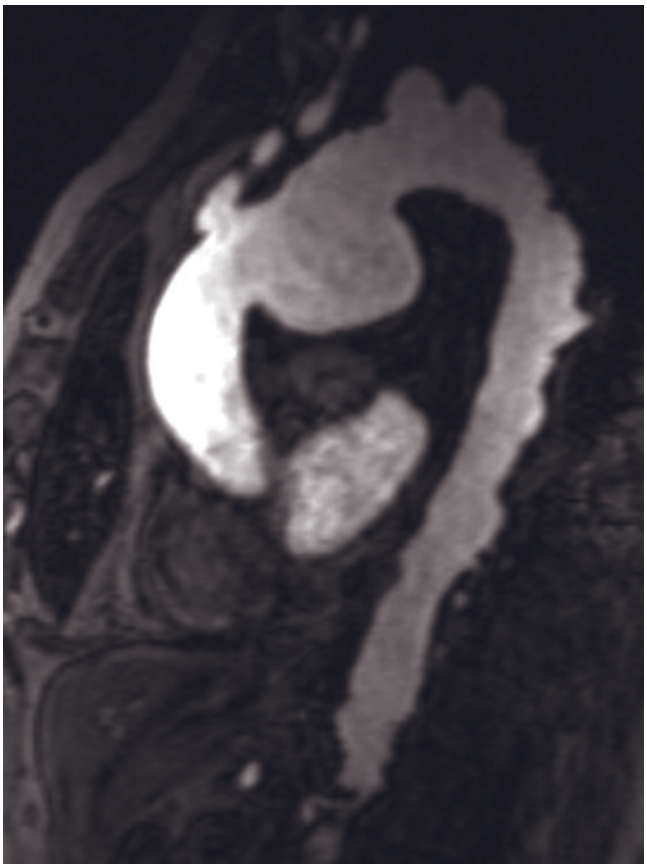

(*c*)

(*d*)

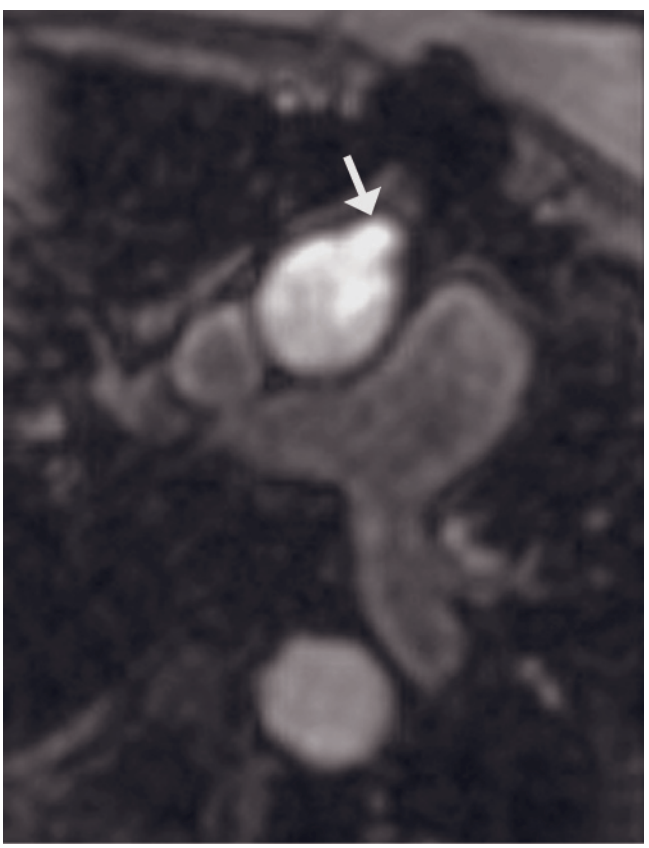

(*e*)

FIG. 18.14 (*Continued*) Patient 2 has diffuse atherosclerotic changes and saccular aneurysm originating from the inferior surface of the aortic arch, and patient 3 has a pseudoaneurysm of the ascending aorta (arrows, *d*, *e*). The large vessels of the thoracic aorta are optimally studied with MRA employing a dynamic gadolinium-enhanced MRA technique. It is always essential to look at the source images (*c*) in addition to the reconstructed images (*d*), and it is quite often useful to perform MPR reconstructions in additional planes (*e*), especially for smaller vascular abnormalities. Sagittal 3D reconstructed MIP image (*f*) and coronal T1-weighted postgadolinium fat-suppressed 3D-GE image (*g*) demonstrate saccular aortic aneurysm (black arrow, *f*; curved arrow, *g*) originating from the inferior surface of the aortic arch and diffuse atherosclerotic changes in another patient. Coronal (*h*) and sagittal (*i*)

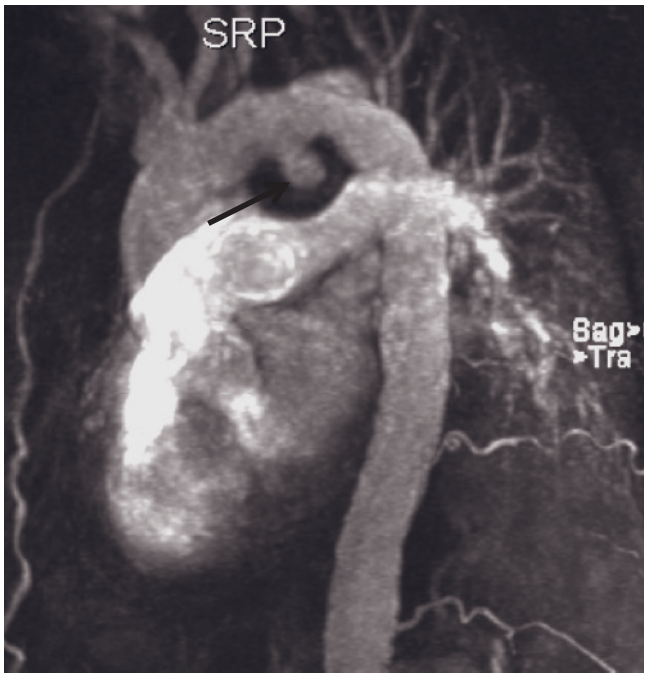

(*f*)

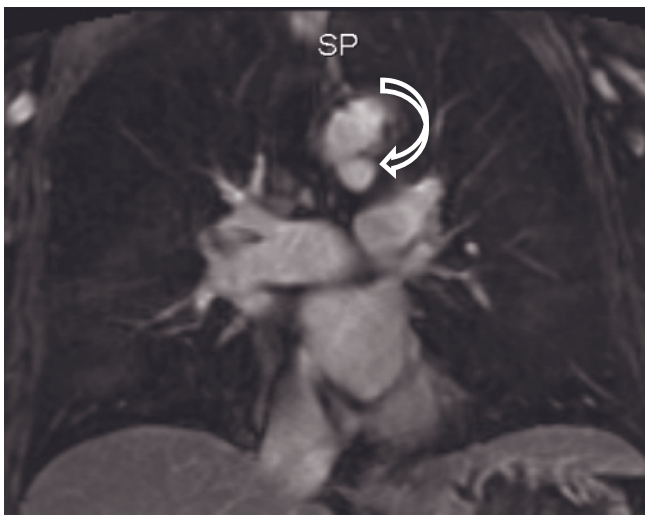

(*g*)

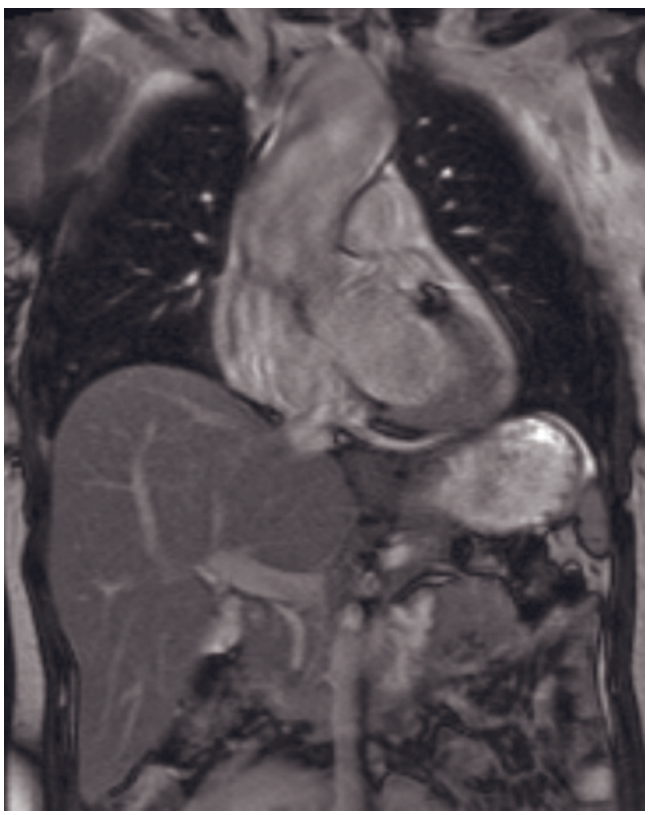

(*h*)

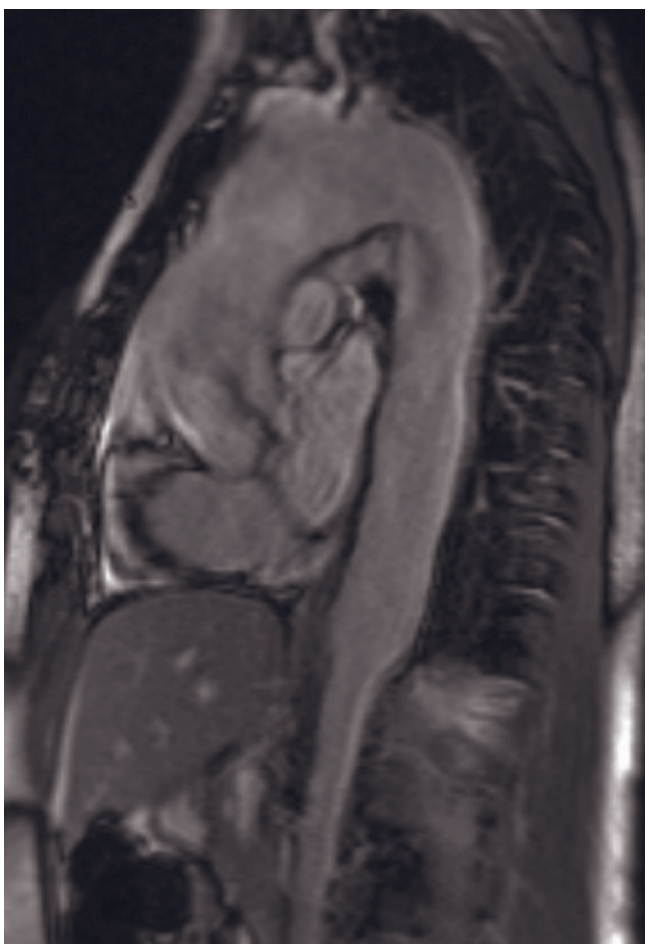

(*i*)

Fig. 18.14 (*Continued*) T2-weighted true fast imaging with steady-state precession (True-FISP) images demonstrate abdominal aortic aneurysm involving ascending and descending aorta in another patient. Note that the left ventricle wall is hypertrophied. Sagittal 3D-GE MRA images (*j–l*) and transverse reformatted image (*m*) demonstrate type B dissection in another patient.

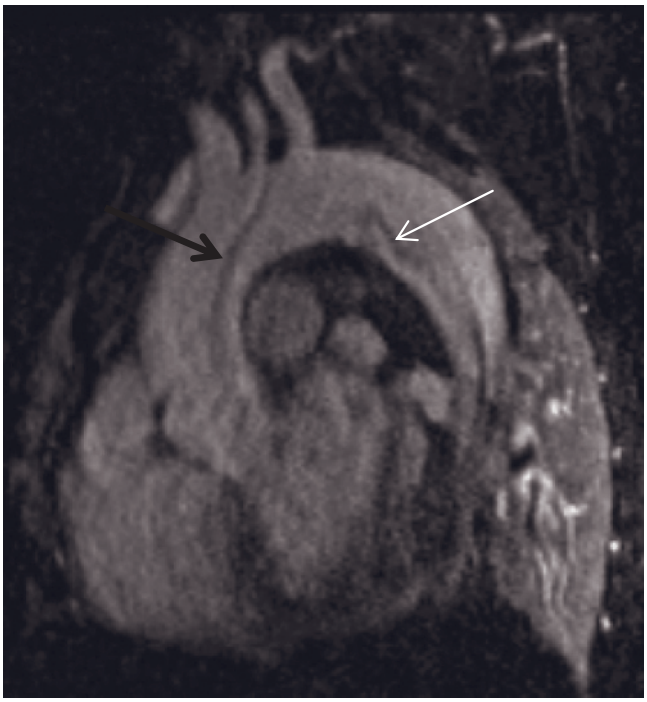

(*j*)

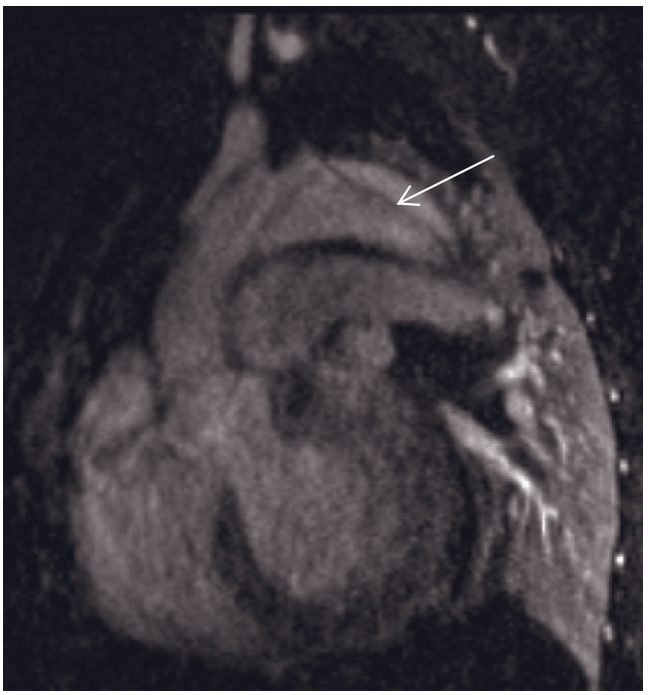

(*k*)

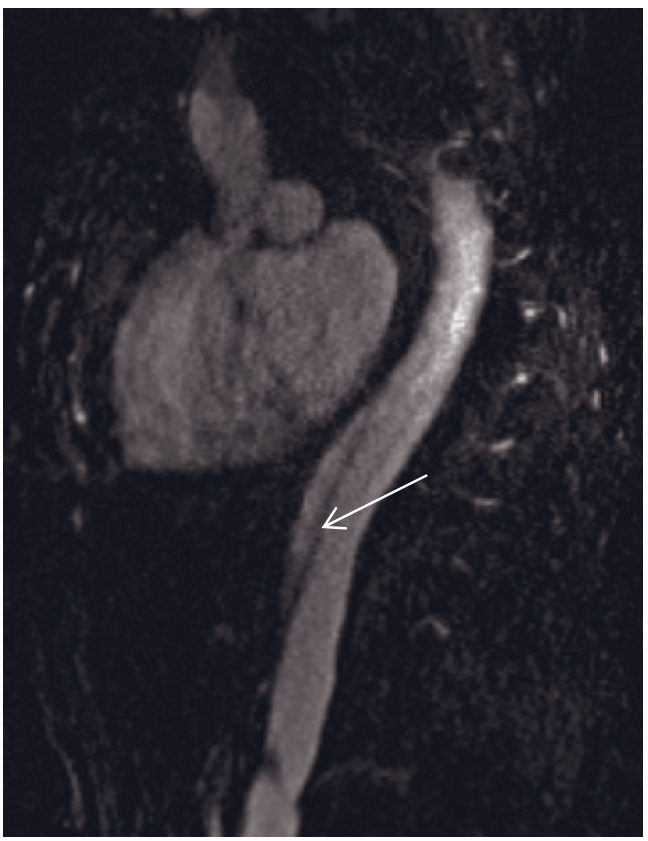

(*l*)

FIG. 18.14 (*Continued*) The dissection flap is seen as intraluminal hypointense structure (white arrows, *j–m*). The dissection starts distal to the subclavian artery and extends to the abdominal aorta. Note that there is an artifact (black arrows, *j*, *m*) simulating a dissection flap, which is parallel to the aortic wall. Sagittal 3D-GE MRA image (*n*) demonstrates type A dissection in another patient.

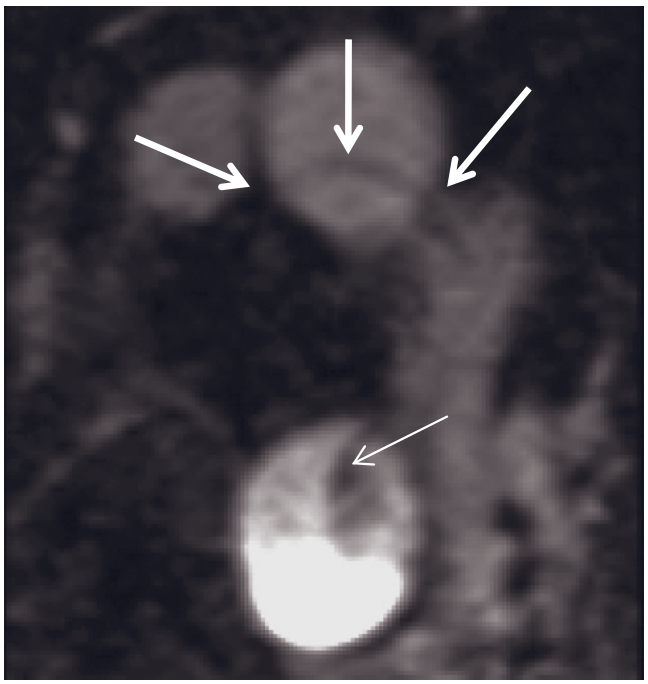

(*m*)

(*n*)

(*o*)

Fig. 18.14 (*Continued*) The dissection flap is seen as hypointense intraluminal structure (white arrows, *n*), and the dissection involves the ascending, descending, and abdominal aorta. Parasagittal 3D reconstructed MIP images (*o*, *p*) demonstrate aortic coarctation in another patient.

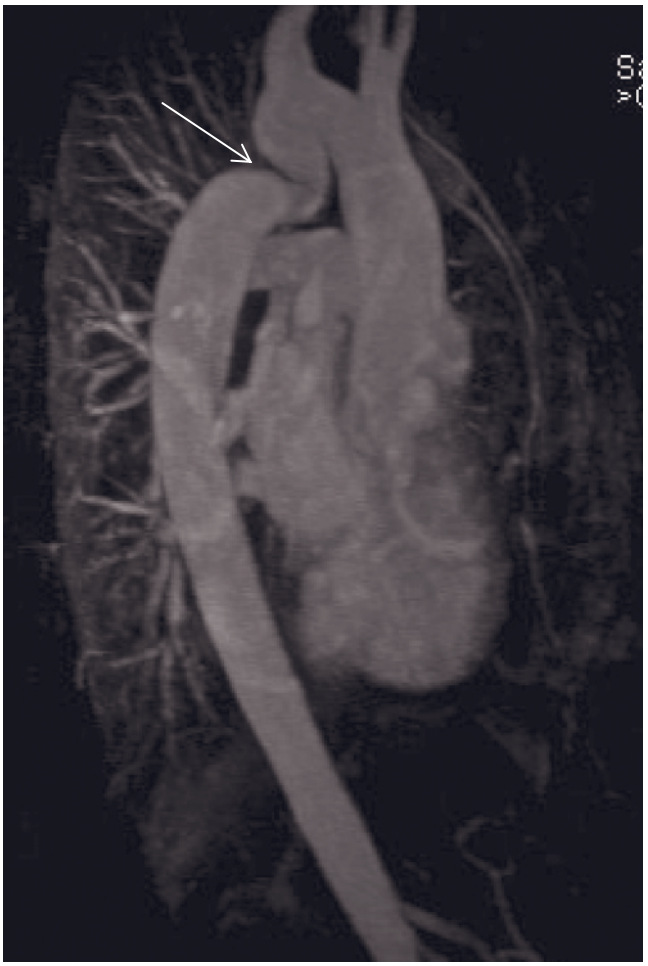

FIG. 18.14 (*Continued*) (*p*)

MRA is often performed for evaluation of aortic aneurysms and aortic dissection. Dissections of the aorta, including Stanford type A or B dissections, are well studied with MRA using an LAO projection data acquisition that follows the course of the aorta (fig. 18.14). More detailed discussion of MRA of the thoracic aorta is beyond the scope of this chapter and is well described in other sources [32].

SCREENING

On January 31, 2005, the Department of Health and Human Services listed, for the first time, ionizing radiation as a known human carcinogen in the 11th Report on Carcinogens. Screening for disease with MR, which does not use ionizing radiation, may be more desirable. Two studies evaluated the use of MR as a screening tool for pulmonary metastases as part of a whole-body screening protocol and made comparisons with multidetector CT. In one study, the rates of detection of pulmonary metastases on MR and CT were the same [33]. In the other study, all pulmonary metastases visualized on MR were also seen on CT, but additional pulmonary metastases were shown on CT [5]. However, in those patients in whom additional metastases were depicted by CT, the clinical management would have remained the same because of the presence of other lung metastases. Most of the metastases missed had a fibrotic or scar component that made them difficult to visualize on MR. Comparison of MR with conventional chest X-ray has also been performed. ECG-triggered single-shot echo-train spin echo was shown to be more reliable in the detection of pulmonary nodules than chest X-ray [21] and may play a role in screening certain populations. This sequence has a short acquisition time and does not require the use of gadolinium.

FUTURE DIRECTIONS

In the near future one major hardware advance that has the potential to impact substantially on imaging of the lungs is the use of 32-channel (or higher) torso coils

that will facilitate high parallel imaging short-duration sequences. The benefit of this may be observed with pulmonary MRA. High-field MRI using 3.0T systems may offer particular advantages for imaging the lungs as the high signal may be necessary to adequately demonstrate small nodules and different parenchymal disease. Pronounced differences in signal between normal lung and diseased lung result in a higher contrast between the two when a 3.0T scanner is used. Initial studies demonstrate that diffuse parenchymal diseases, including emphysema, sarcoid, pulmonary fibrosis, and cystic fibrosis, can be visualized [34]. Inhaled hyperpolarized gases as contrast agents are used for pathophysiologic evaluation of the lungs. MR imaging of the lungs can be performed with inhaled noble gases helium-3 and xenon-129 [35]. Inhaled hyperpolarized gases provide high temporal and spatial resolution images of the lung airspaces. The technique can be used to evaluate ventilation/perfusion defects and to evaluate regional gas exchange. Its applications may include evaluation of patients with asthma, emphysema, cystic fibrosis, and lung transplant. Currently, the technique is only performed at a limited number of institutions and for research purposes. Research studies have also described the use of inhaled aerosolized particulate gadolinium contrast agents that may better reflect airway dynamics [36].

REFERENCES

1. Davis SD, Henschke CI, Yankelevitz DF et al. MR imaging of pleural effusions. *J Comput Assist Tomogr* 14(2): 192–198, 1990.
2. Musset D, Grenier P, Carette MF et al. Primary lung cancer staging: prospective comparative study of MR imaging with CT. *Radiology* 160(3): 607–611, 1986.
3. Heelan RT, Demas BE, Caravelli JF et al. Superior sulcus tumors: CT and MR imaging. *Radiology* 170(3 Pt 1): 637–641, 1989.
4. Webb WR, Gatsonis C, Zerhouni EA et al. CT and MR imaging in staging non-small cell bronchogenic carcinoma: report of the Radiologic Diagnostic Oncology Group. *Radiology* 178(3): 705–713, 1991.
5. Lauenstein TC, Goehde SC, Herborn CU et al. Whole-body MR imaging: evaluation of patients for metastases. *Radiology* 233(1): 139–148, 2004.
6. Hatabu H, Gaa J, Tadamura E et al. MR imaging of pulmonary parenchyma with a half-Fourier single-shot turbo spin-echo (HASTE) sequence. *Eur J Radiol* 29(2): 152–159, 1999.
7. Yamashita Y, Yokoyama T, Tomiguchi S et al. MR imaging of focal lung lesions: elimination of flow and motion artifact by breath-hold ECG-gated and black-blood techniques on T2-weighted turbo SE and STIR sequences. *J Magn Reson Imaging* 9(5): 691–698, 1999.
8. Both M, Schultze J, Reuter M et al. Fast T1- and T2-weighted pulmonary MR-imaging in patients with bronchial carcinoma. *Eur J Radiol* 53(3): 478–488, 2005.
9. Schafer JF, Vollmar J, Schick F et al. [Detection of pulmonary nodules with breath-hold magnetic resonance imaging in comparison with computed tomography]. *Rofo* 177(1): 41–49, 2005.
10. Thompson BH, Stanford W. MR imaging of pulmonary and mediastinal malignancies. *Magn Reson Imaging Clin N Am* 8(4): 729–739, 2000.
11. Chung MH, Lee HG, Kwon SS et al. MR imaging of solitary pulmonary lesion: emphasis on tuberculomas and comparison with tumors. *J Magn Reson Imaging* 11(6): 629–637, 2000.
12. Semelka RC, Cem Balci N, Wilber KP et al. Breath-hold 3D gradient-echo MR imaging of the lung parenchyma: evaluation of reproducibility of image quality in normals and preliminary observations in patients with disease. *J Magn Reson Imaging* 11(2): 195–200, 2000.
13. Bader TR, Semelka RC, Pedro MS et al. Magnetic resonance imaging of pulmonary parenchymal disease using a modified breath-hold 3D gradient-echo technique: initial observations. *J Magn Reson Imaging* 15(1): 31–38, 2002.
14. Karabulut N, Martin DR, Yang M et al. MR imaging of the chest using a contrast-enhanced breath-hold modified three-dimensional gradient-echo technique: comparison with two-dimensional gradient-echo technique and multidetector CT. *AJR Am J Roentgenol* 179(5): 1225–1233, 2002.
15. Semelka RC, Maycher B, Shoenut JP et al. Dynamic Gd-DTPA enhanced breath-hold 1.5T MRI of normal lungs and patients with interstitial lung disease and pulmonary nodules: preliminary results. *Eur Radiol* (2): 576–582, 1992.
16. Schaefer JF, Vollmar J, Schick F et al. Solitary pulmonary nodules: dynamic contrast-enhanced MR imaging—perfusion differences in malignant and benign lesions. *Radiology* 232(2): 544–553, 2004.
17. Hasegawa I, Eguchi K, Kohda E et al. Pulmonary hilar lymph nodes in lung cancer: assessment with 3D-dynamic contrast-enhanced MR imaging. *Eur J Radiol* 45(2): 129–134, 2003.
18. Ohno Y, Adachi S, Motoyama A et al. Multiphase ECG-triggered 3D contrast-enhanced MR angiography: utility for evaluation of hilar and mediastinal invasion of bronchogenic carcinoma. *J Magn Reson Imaging* 13(2): 215–224, 2001.
19. Yi CA, Jeon TY, Lee KS et al. 3-T MRI: usefulness for evaluating primary lung cancer and small nodules in lobes not containing primary tumors. *AJR Am J Roentgenol* 189(2): 386–392, 2007.
20. Vogt FM, Herborn CU, Hunold P et al. HASTE MRI versus chest radiography in the detection of pulmonary nodules: comparison with MDCT. *AJR Am J Roentgenol* 183(1): 71–78, 2004.
21. Seemann MD, Seemann O, Luboldt W et al. Hybrid rendering of the chest and virtual bronchoscopy [corrected]. *Eur J Med Res* 5(10): 431–437, 2000.
22. Gamsu G, Webb WR, Sheldon P et al. Nuclear magnetic resonance imaging of the thorax. *Radiology* 147(2): 473–480, 1983.
23. Webb WR, Gamsu G, Stark DD et al. Magnetic resonance imaging of the normal and abnormal pulmonary hila. *Radiology* 152(1): 89–94, 1984.
24. Kim HY, Yi CA, Lee KS et al. Nodal metastasis in non-small cell lung cancer: accuracy of 3.0-T MR imaging. *Radiology* 246(2): 596–604, 2008.
25. Ohno Y, Hatabu H, Takenaka D et al. Metastases in mediastinal and hilar lymph nodes in patients with non-small cell lung cancer: quantitative and qualitative assessment with STIR turbo spin-echo MR imaging. *Radiology* 231(3): 872–879, 2004.
26. Ohno Y, Higashino T, Takenaka D et al. MR angiography with sensitivity encoding (SENSE) for suspected pulmonary embolism: comparison with MDCT and ventilation-perfusion scintigraphy. *AJR Am J Roentgenol* 183(1): 91–98, 2004.
27. Kluge A, Luboldt W, Bachmann G. Acute pulmonary embolism to the subsegmental level: diagnostic accuracy of three MRI techniques compared with 16-MDCT. *AJR Am J Roentgenol* 187(1): W7–W14, 2006.
28. Ersoy H, Goldhaber SZ, Cai T et al. Time-resolved MR angiography: a primary screening examination of patients with suspected pulmonary embolism and contraindications to administration of

iodinated contrast material. *AJR Am J Roentgenol* 188(5): 1246–1254, 2007.
29. Fink C, Goyen M, Lotz J. Magnetic resonance angiography with blood-pool contrast agents: future applications. *Eur Radiol* 17 Suppl 2: B38–B44, 2007.
30. Meaney JF, Goyen M. Recent advances in contrast-enhanced magnetic resonance angiography. *Eur Radiol* 17 Suppl 2: B2–6, 2007.
31. Altun E, Heredia V, Pamuklar E et al. Feasibility of postgadolinium 3D gradient-echo sequence to evaluate the pulmonary arterial vasculature in patients with suspected pulmonary embolism and other diseases involving the chest. *Magn Reson Imaging* 2009, in press.
32. Schneider G, Prince MR, Meaney JM et al. *Magnetic Resonance Angiography: Techniques, Indications, and Practical Applications.* Milan, Italy: Springer, 2005.
33. Goehde SC, Hunold P, Vogt FM et al. Full-body cardiovascular and tumor MRI for early detection of disease: feasibility and initial experience in 298 subjects. *AJR Am J Roentgenol* 184(2): 598–611, 2005.
34. Lutterbey G, Gieseke J, von Falkenhausen M et al. Lung MRI at 3.0T: a comparison of helical CT and high-field MRI in the detection of diffuse lung disease. *Eur Radiol* 15(2): 324–328, 2005.
35. Moller HE, Chen XJ, Saam B et al. MRI of the lungs using hyperpolarized noble gases. *Magn Reson Med* 47(6): 1029–1051, 2002.
36. Hirsch W, Wenkel R, Eichler G et al. Pulmonary resorption of inhaled gadobutrol in an animal model: usage to determine lung diffusion in MRI examinations. *Magn Reson Imaging* 22(4): 489–493, 2004.

CHAPTER 19

BREAST

DRAGANA DJILAS-IVANOVIĆ, HELMUTH SCHULTZE-HAACK, DAG PAVIC, AND RICHARD C. SEMELKA

INTRODUCTION

Breast cancer is the second most common type of cancer after lung cancer, and therefore a major health problem all over the world. It accounts for almost 40,000 deaths among American women per year. The large number of women at risk for this disease makes a broad-based screening of the population necessary.

Mammography has long been used for early detection and screening for breast cancers. With optimal technique and patient conditions, it has a reported sensitivity between 69% and 90% and specificity between 10% and 40%. Many factors (i.e., younger patients, implants, and postsurgical state), including breast tissue density, can affect these values. The use of mammography alone is believed to miss between 10% and 30% of all breast cancers. Sensitivity is variable even if double reading, either by computer-aided detection (CAD) software or by another radiologist, is employed as standard procedure [1–3].

Ultrasound has been used as an adjunct to mammography, with particular value in differentiating cystic from solid lesions and in facilitating guided biopsy of suspicious areas. However, ultrasound has limitations, including the possibility of missing microcalcifications [associated with ductal carcinoma in situ (DCIS)], and high level of operator dependence [1, 4].

The clinical importance of magnetic resonance imaging (MRI) in the detection of breast cancer with a contrast-enhanced MRI protocol has been established [5–7]. MRI is emerging as the most sensitive modality available for the detection of primary or recurrent breast cancer. The published sensitivity ranges between 89% and 100% [8–19]. The specificity of breast MRI has been reported to be more variable, overall ranging between 20% and 100% [8–15], with more recent studies yielding 70–90%. Since there is no radiation exposure, which represents a risk factor for cancer development, MRI is the ideal tool for periodic clinical examinations.

NORMAL ANATOMY

The breast is a modified skin gland enveloped in fibrous fascia. The adult breast lies between the 2nd and 6th ribs in the vertical axis and between the sternal edge

Abdominal-Pelvic MRI, Third Edition, edited by Richard C. Semelka. Copyright © 2010 John Wiley & Sons, Inc.

and the midaxillary line in the horizontal axis. It is attached to the dermis by fibrous bands called suspensory (Cooper) ligaments anteriorly, and the posterior surface is the pectoral fascia. Approximately three-quarters of the breast lie on the pectoralis major muscle (superior and medial portions).

The breast tissue is divided into upper outer, upper inner, lower outer, and lower inner quadrants, the subareolar area, and the axillary tail of the upper outer quadrant. The arterial blood supply is derived from the axillary, intercostal, and internal mammary arteries, and venous drainage is into the axillary and internal mammary veins. Lymphatic drainage is to the axillary, subclavicular, and internal mammary lymph nodes. While drainage from the upper outer quadrant is predominantly to the axillary lymph nodes (75–90%), drainage from the inner quadrants is to the internal mammary chain of nodes. The nerves are branches of the thoracic segmentals [20, 21].

The breast is composed of three major structures: skin, subcutaneous tissue including fat, and breast tissue. The breast parenchyma consists of 15–20 segments (lobes) radially distributed around the nipple. The nipple is the centrally located structure surrounded by the areola. Within the areolar dermis exist numerous sebaceous glands (the glands of Montgomery) and apocrine glands, as well as lactiferous ducts, which course through the dermis and open into the nipple epidermis. Each segment is drained by a collecting duct. These are about 2 mm wide. and they connect the nipple with lactiferous sinuses. Segmental (lactiferous) and subsegmental (major) ducts connect lactiferous sinuses with terminal duct-lobular units (TDLUs). Lobules are composed of terminal ducts and acini and their specialized supporting stroma. All these structures constitute the breast parenchyma, surrounded by a variable amount of adipose tissue, depending on the age and individual body habitus (adolescent women typically have dense, fibrous breasts, while postmenopausal women have predominantly fatty breasts). Abundant fibrous tissue makes radiographic evaluation more challenging because tumors also contain fibrous tissue, creating an appearance similar to normal tissue in a mammogram [20–22].

The premenopausal breast is a hormone-responsive organ. Estrogens cause increased blood flow through breast parenchyma in the second half of a cycle [23, 24]. In pregnancy, there is also a pronounced hormonally induced increase in the number of terminal ducts. The lobular epithelium increases at the expense of fibrofatty stroma. During lactation, the breast epithelial cells become vacuolated and lobular glands are distended with secretions.

Postmenopausal breast involution is generally characterized by regression of the parenchymal TDLUs. Breasts of postmenopausal women contain mostly fatty and fibroconnective tissue, with a marked reduction in the amount of glandular tissue [25, 26].

BREAST MRI

Because of the high spatial resolution of MRI, the anatomy of the breast can be exquisitely visualized (fig. 19.1).

Over the past decade, there has been a marked increase in the use of MRI of the breast. Multiple research studies have confirmed improved cancer detection, diagnosis, and evaluation of response to therapy with breast MRI compared to mammography and ultrasound.

Conventional noncontrast MR exam alone is not useful for the screening or diagnosis of breast cancer, because the differences in T1 and T2 relaxation times of benign and malignant breast lesions are not significant. The only indication for noncontrast breast MRI is detection and evaluation of implant rupture (fig. 19.2). For silicone implant evaluation, T2-weighted fast spin-echo sequences using inversion recovery for fat suppression and chemical saturation of the water signal are often sufficient [27].

Gadolinium-based contrast agent (GBCA) is essential for breast MRI (fig. 19.3). In cancers, early and significant increase in signal intensity after contrast injection is often seen, due to the increased density and leakiness of microvessels in tumor tissue [27]. Contrast-enhanced MRI has been shown to help in the differentiation of benign and malignant lesions, as rate and extent of enhancement reflect tumor-mediated angiogenesis [1, 4]. When invasive breast cancers grow beyond a size of a few millimeters, their high metabolic demand for oxygen and nutrients exceeds the supply provided by diffusion through normal vessels of fibroglandular tissue. The gap between demand and supply increases with increasing tumor size and causes the formation of new vessels or the sprouting of existing capillaries in the peritumoral stroma—a process referred to as angiogenesis or neoangiogenesis [28–30]. This angiogenic activity is therefore the basis of breast cancer detection and differential diagnosis with MRI. However, the signal enhancement does not depend linearly on the local concentration of contrast agent, but is also influenced by other factors such as T1 relaxation time of different tissues, diffusion rate of the contrast agent used, relaxivity of the contrast agent, and other factors [30].

Angiogenic activity is not pathognomonic for malignant tissue, but is also found in other conditions, including inflammatory changes or during wound healing [30]. Microcalcifications, which represent one of the most

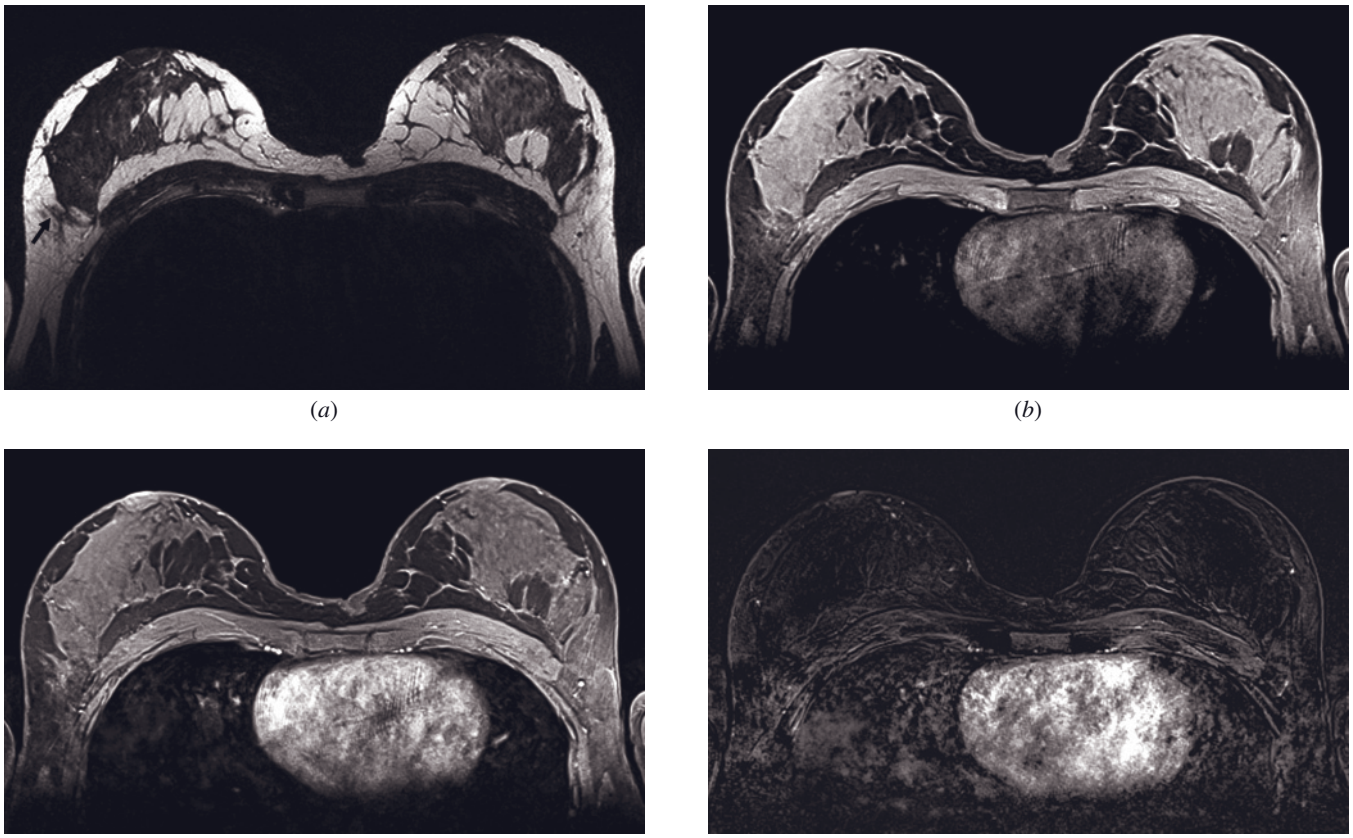

(*a*) (*b*)

(*c*) (*d*)

FIG. 19.1 Normal anatomy of the breast. The exquisite image quality in depicting the entire breast anatomy was possible with the 3T MRI unit with the 8-channel dedicated breast coil. Axial T2-weighted (*a*) and 3D gradient echo with fat suppression [volume imaging with enhanced water signal (VIEWS)] (*b*) images show normal breast anatomy. Fibroglandular tissue appears as dark, hypointense signal, and fat is shown as bright, hyperintense signal on T2-weighted image. 3D gradient recalled echo (GRE) images show hyperintense fibroglandular tissue and low-intensity fat tissue. On postcontrast GRE (*c*) and subtracted (*d*) images, there is no significant increase in signal enhancement of the breast tissue, indicating MRI background enhancement type 1. Note the small amount of T2-weighted hypointense scar tissue in the upper outer quadrant of the right breast (arrow, *a*), as a consequence of prior benign surgery.

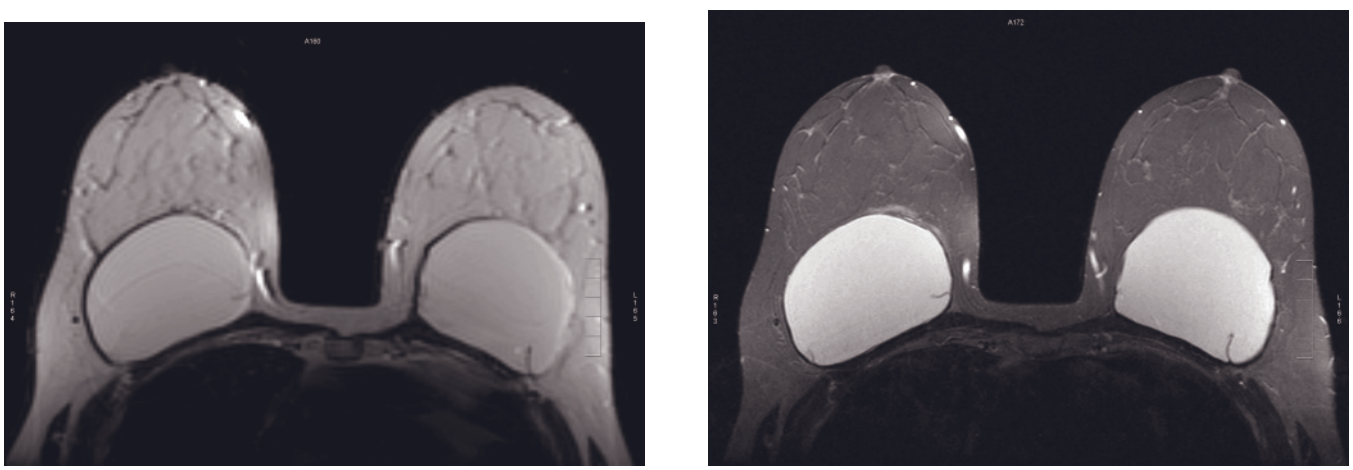

(*a*) (*b*)

FIG. 19.2 Silicone implant extracapsular rupture. Axial T2-weighted (*a*) and axial short tau inversion recovery (STIR) with chemical saturation of water-silicone specific (*b*) images show bilateral subglandular implants. Radial folds are seen bilaterally (*b*) as curved hypointense lines, perpendicular to the capsule (posterolateral aspect of the left breast implant and medial aspect of the right breast implant). In anteromedial aspect of the right breast implant a subcapsular line is seen, indicating implant rupture. Ill-defined, high-signal anterior to the implant and adjacent to it corresponds to extracapsular silicone, best appreciated in *b*.

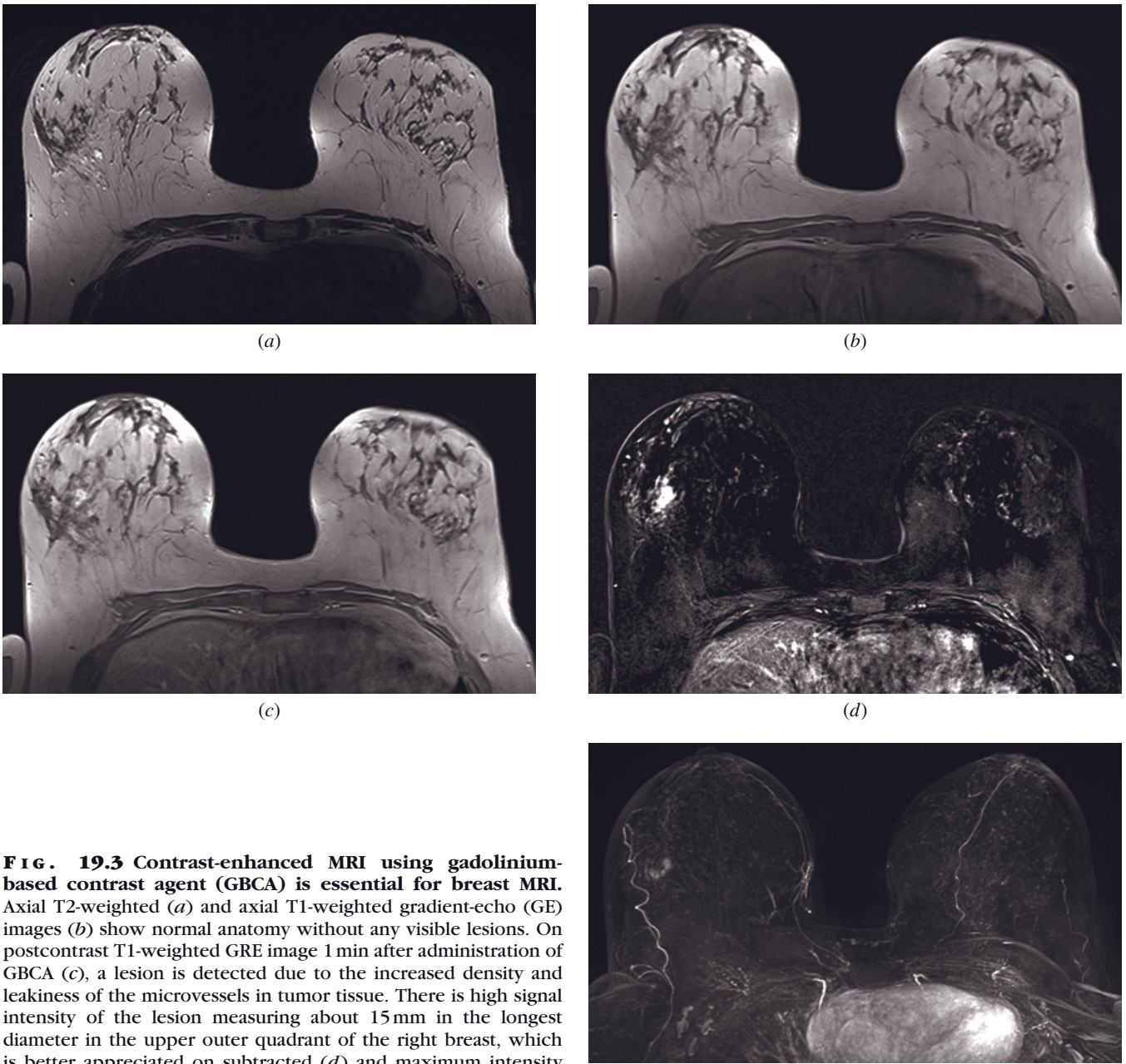

FIG. 19.3 Contrast-enhanced MRI using gadolinium-based contrast agent (GBCA) is essential for breast MRI. Axial T2-weighted (*a*) and axial T1-weighted gradient-echo (GE) images (*b*) show normal anatomy without any visible lesions. On postcontrast T1-weighted GRE image 1 min after administration of GBCA (*c*), a lesion is detected due to the increased density and leakiness of the microvessels in tumor tissue. There is high signal intensity of the lesion measuring about 15 mm in the longest diameter in the upper outer quadrant of the right breast, which is better appreciated on subtracted (*d*) and maximum intensity projection (MIP) (*e*) images.

common findings related to breast cancer seen on mammograms, are usually not detectable on MRI, except occasionally, as tiny signal voids [27]. Despite the fact that many benign and malignant entities enhance on GBCA-enhanced MRI, their enhancement kinetic profiles and morphologic characteristics help to narrow the differential diagnosis [31].

Close and consistent correlation between invasive growth and angiogenic activity explains the high sensitivity for the detection of invasive breast cancer that is afforded by MRI; in contrast, the weak or inconsistent angiogenic activity that can be associated with invasive lobular cancers and pure intraductal cancer explains the diagnostic difficulties in detecting these conditions [30].

In many cases, the observation of enhancement as a function of time permits distinction between benign and malignant lesions. Neoangiogenesis of most malignant lesions is reflected by early intense enhancement and faster washout times (the time it takes for clearance of the contrast material from the lesion). Most breast cancers will show more than 70% increase in signal intensity within 2 min after intravenous administration

of GBCA. This enhancement behavior can be demonstrated with fast dynamic T1-weighted sequences. Fairly high temporal resolution is required in order to obtain multiple scans during the optimal imaging period. Dynamic imaging includes a precontrast reference scan and multiple identical scans acquired after contrast injection in such a way that the first postcontrast scan is most sensitive to contrast and signal (center of k-space) at 60–90 s after onset of contrast injection. The whole dynamic contrast-enhanced series should last until about 10 min after contrast.

In postprocessing of dynamic imaging, it is useful to obtain time versus enhancement intensity curves from a representative region of interest (ROI). The size of the ROI should be greater then three pixels, and it should be placed over the most intense enhancement seen on the first postcontrast image. If multiple ROIs are applied in the same lesion, the most suspicious curve should be reported [32]. Commercially available computer-aided diagnosis (CAD) packages for breast MRI automate this process, as the whole breast is evaluated for pattern of enhancement on a pixel-by-pixel basis, resulting in parametric images. Color-coded overlay can be displayed over the original or subtracted scans. As with mammography CAD, color coding pinpoints the most suspicious areas and thus guides subsequent evaluation with time-intensity curves.

Time-intensity curves can be divided into three groups (fig. 19.4). Type I curves are characterized by a gradual and constant increase in enhancement over time (persistent enhancement) and support the finding of benign behavior. Type II curves are characterized by an initial rise in enhancement intensity followed by a plateau and can represent either benign or malignant lesions. Type III curves are the classic washout curves; a rapid initial rise in enhancement followed by marked decrease of signal intensity usually indicates malignancy [33]. However, some types of malignant lesions such as DCIS may sometimes exhibit Type I curves, whereas benign lesions such as intramammary lymph nodes, papilloma, or even fibroadenoma may at times show Type III curves. Therefore, enhancement curve type should be treated as ancillary or complementary information in evaluation of breast lesions.

Some studies have shown that architectural features like irregular tumor margins, peripheral enhancement, local area enhancement, and enhancement in segmental distribution favor the diagnosis of breast carcinoma [7]. On the other end of the spectrum, masses with lobular and smooth margins and with hypointense internal septations are consistent with fibroadenomas [17]. For accurate assessment of the architecture, high spatial resolution in breast MRI is mandatory.

In the early adoption of MRI in breast imaging, two approaches were established, one focusing on the rapid acquisition of images of both breasts after contrast injection (high temporal resolution of the "dynamic" school) and the other focusing on three-dimensional gradient-echo imaging with thin slices through one breast (high spatial resolution of the "static" school). The dynamic school put emphasis on evaluation of various enhancement profiles over time, while the static school stressed morphologic features in differentiation between malignant and benign lesions [34]. By 2000, most radiologists agreed that both high temporal and high spatial resolution are needed in the diagnostic process, to gain information about both the pharmacokinetics and the morphology of breast lesions [35].

High temporal resolution (i.e., acquisition speed) is required not only for the assessment of the enhancement kinetics of the lesion during dynamic imaging but also because only in the early postcontrast phase is the analysis of subtle morphologic features feasible. The challenge of current breast MRI is to compromise between the diverging demands of high spatial resolution and high temporal resolution. Recent technological advances in MRI such as parallel imaging and commercially available MR units with high-strength magnetic fields (3 T or more) combined with fast switching, strong gradient systems, provide both high spatial resolution and high temporal resolution [30].

Indications for Breast MRI

Breast MRI is indicated for:

- Evaluation of silicone implants
- Screening in high-risk patients (family risk, prior chest irradiation, prior breast cancer)
- Lesion characterization in selected cases
- Staging of known breast cancer before therapy
- Screening of the contralateral breast in patients with a new breast malignancy
- Searching for occult carcinoma (unknown primary)
- Monitoring treatment response of preoperative chemotherapy
- Differentiation between postoperative changes and recurrent tumor
- MRI-guided interventions (biopsy, preoperative wire localization)
- Mammographically dense breasts

Breast MRI is not at present indicated for:

- Replacement for mammography and/or ultrasound (they are complementary)
- Evaluation of mastitis/abscess formation
- Evaluation of calcifications
- Nipple discharge

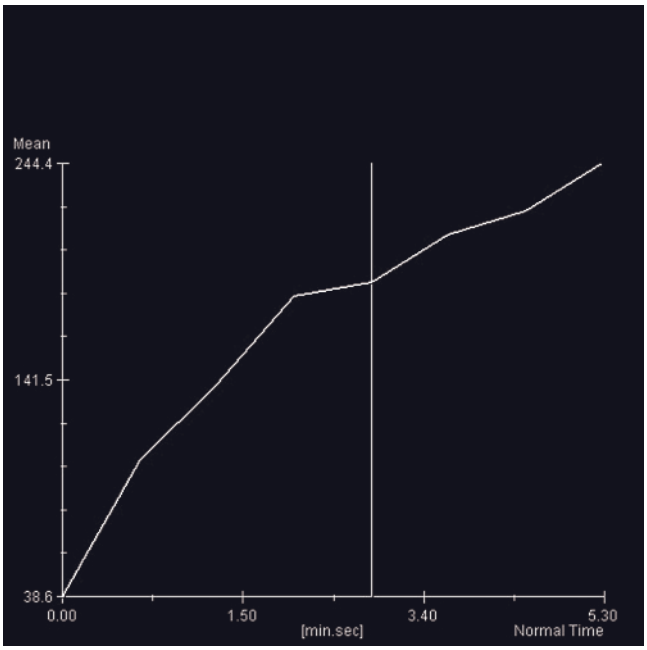

(*a*)

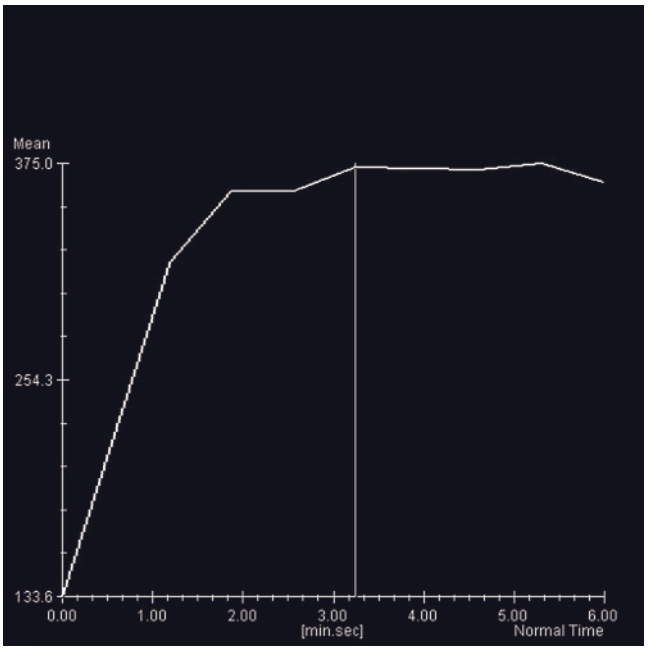

(*b*)

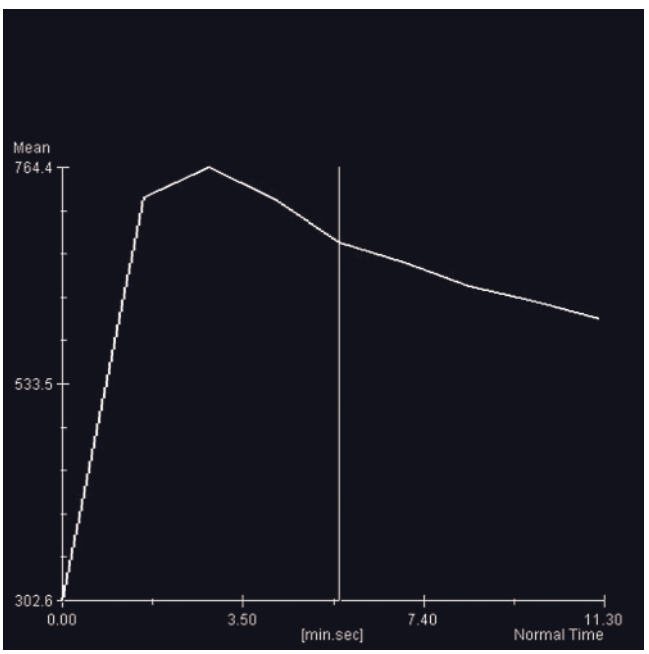

(*c*)

FIG. 19.4 The analysis of dynamic MR images helps to distinguish between benign and malignant lesions. The increase in signal intensity can be demonstrated with recurring fast dynamic T1-weighted sequences starting before contrast injection and ending about 6–10 min after GBCA application. Postprocessing of dynamic images with region of interest (ROI) analysis is applied to display time-intensity curves. The ROI positioned over the most enhancing part of the lesion can show a Type I (persistent enhancement; *a*), Type II (plateau; *b*), or Type III (washout; *c*) curve.

Technical Requirements

Magnetic Field Strength

The magnetic field strength (B_0) and signal-to-noise-ratio (SNR) are linearly dependent: An increase of B_0 results in higher SNR, and, as a result, higher-spatial-resolution images can be obtained in a relatively short acquisition time, if appropriate pulse sequences are used. The magnetic field should be homogeneous across the entire field of view (FOV) to allow optimal image quality when fat suppression sequences are used [30]. MRI scanners with low to intermediate field strengths (less than 1.0 T) should not be used, in order to ensure the best image quality and diagnostic accuracy, as spatial and temporal resolution and fat-water separation are all suboptimal [31]. According to recently published studies, the majority of cancers that went undetected at MRI were imaged with 1.0 T systems [36,

37]. A recently published intraindividual comparative study [38] showed that image quality was slightly but significantly higher at 3.0 T than at 1.5 T.

Gradient System

The strength, that is, the maximum amplitude and the rise time (slew rate), of the gradient system that manipulates the magnetic field for image creation plays a key role in providing high spatial and temporal resolution scans. With a strong gradient system, the field strength limitation can largely be overcome.

Imaging Coils

Breast MR exams are performed with the patient in a prone position, using dedicated breast surface coils (fig. 19.5). The closer the receiver coil is to the breasts, the better the SNR. All coils in use today are for bilateral imaging, covering both breasts with extension into the axilla. In addition, many dedicated breast surface coils have an open design, allowing access to the breast for MRI-guided interventions such as preoperative wire localizations and needle biopsies [35]. However, the open configuration comes at the expense of some SNR. Multichannel coils (currently 2–16 channels) may also provide a higher SNR and are compatible with current parallel imaging techniques [31].

Imaging Plane

The choice of imaging plane has different considerations and proponents. Nowadays, many radiologists prefer the transverse (axial) imaging plane, for various reasons. Its major advantage lies in the simultaneous demonstration of both breasts, and it is helpful in delineating or excluding chest wall invasion. The generation of maximum intensity projection (MIP) images of an axial image data set allows a presentation similar to the cranio-caudal (CC) view of routine mammograms. The theoretical advantage of coronal imaging is a significant reduction (50%) in acquisition time [because they can be acquired with a 50% rectangular field of view (FOV)], but more sections would be needed to cover the entire volume of the breast in the anterior-posterior dimension. In addition, coronal-plane imaging suffers from greater artifacts due to respiratory motion and pulsation artifacts. Another advantage of the coronal imaging plane, straightforward lesion localization in o'clock fashion, is now outdated. High-quality coronal reconstructions are easily obtained from axial or sagittal scans, especially if these had isotropic voxels.

Some may still advocate using the sagittal imaging plane, because of its similarity to a mammogram. This is rarely true, since the closest routine mammogram view would be the medio-lateral-oblique (mlo), which

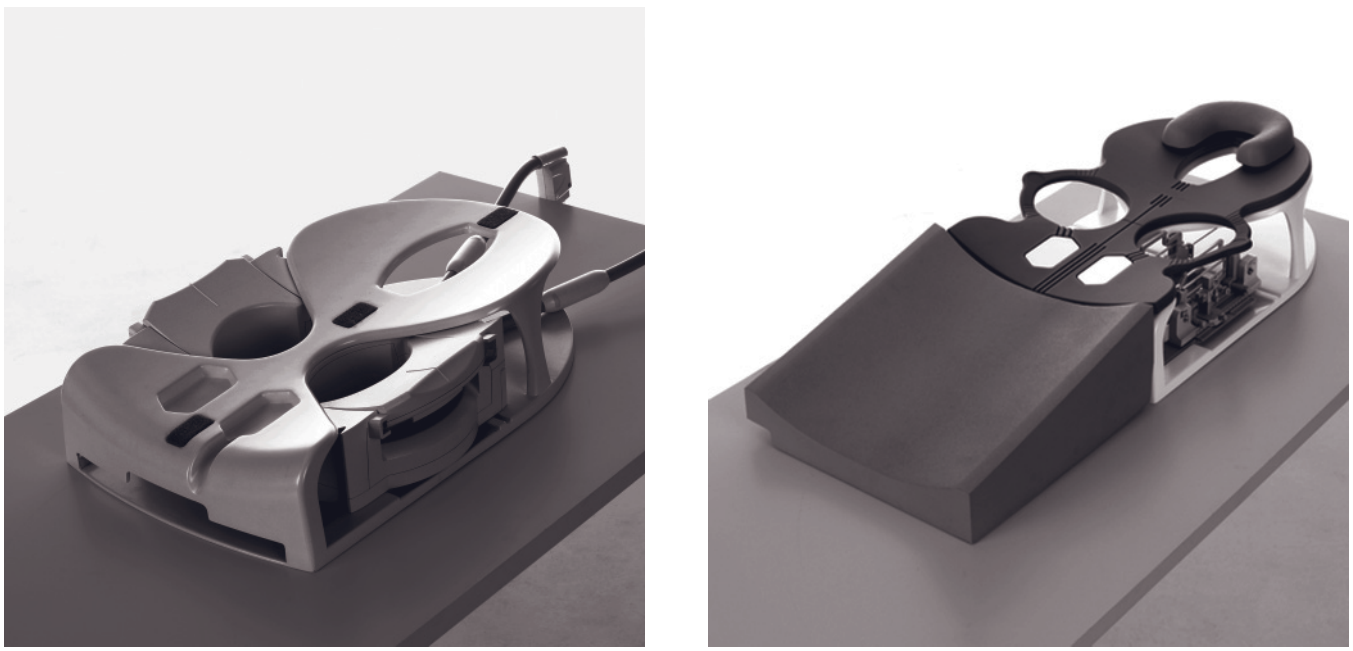

(*a*) (*b*)

FIG. 19.5 Dedicated open surface coils for breast MRI. A 16-channel dedicated breast coil is shown in *a*. The coil shown in *b* is used for both imaging and MR-guided interventions. There is a pillar-and-post type compression plate placed under the opening for the right breast.

is not a true sagittal view. The sagittal imaging plane has the technical advantage of a relatively small FOV, which is sufficient to cover the breast and makes a homogeneous magnetic field more easily achievable. The main disadvantage of sagittal imaging is that in order to maintain near-isotropic voxels far too many sections are necessary to cover both breasts. Simultaneous bilateral imaging allows the assessment of breast asymmetry, increases the conspicuity of asymmetric diffuse enhancement, and diminishes the number of false-positive findings resulting from heterogeneous enhancement that occasionally is observed in hormonally active breasts. It is essential for the detection of a synchronous and otherwise occult cancer in the contralateral breast, which occurs in approximately 3–5% of women with a diagnosis of breast cancer [39].

Patient Preparation and Positioning

Before starting the examination, it is extremely important to provide the patient with all the necessary information in order to achieve adequate psychological preparation. Her contribution to a successful outcome of the examination is more important than in any other MR examination. The MRI technologist or radiologist should inform the patient of the approximate duration of the image acquisition, of the ability to communicate via intercom, and finally of the crucial importance of remaining still during the entire image acquisition period since multiple dynamic image data sets are subtracted from each other. Any patient motion will prevent optimal results. The patient must feel comfortable during the examination as this will improve compliance and prevent excessive motion. The arms of the patient should be positioned above her head or along her body, always stabilized in order to prevent wraparound artifacts, when the left-right phase encoding direction is selected for transverse imaging. With small breasts it is usually better to have the arms alongside the body and breast coil padding removed in order to have the breasts deeper in the coil. This is especially important when performing MRI-guided interventions. If an infusion line is placed in the medial antecubital vein it too will be more secure. Sometimes it is useful to gently confine the extension of the breasts in the cranio-caudal direction, if transverse imaging is employed in order to reduce the number of images and improve spatial resolution. Hard compression of the breasts should, however, be avoided since the tumor vessels are thin walled, pliable, and easily constricted, preventing contrast medium inflow. The patient's head should be supported by a head holder or pillow, primarily for comfort but also to avoid wraparound artifacts if the superior-inferior phase-encoding direction is chosen for sagittal imaging [31]. It is advisable to check the position of the breasts once more before starting the acquisition to ensure that each breast is hanging as deeply as possible within the coil opening with the nipples centered and pointing straight down. In this way, the possibility of signal hot spots, due to distortions of breast tissue or partial placement in the coil, and of poor image quality along the chest wall and axilla, will be reduced to a minimum.

Contrast Administration

Breast MRI performed to evaluate a patient for breast cancer requires the use of a GBCA. Applications of either a single dose of 0.1 mmol/kg body weight or a double dose of 0.2 mmol/kg body weight have been described. To date, no strong data are available to support the advantage of double dosing for improved diagnostic accuracy. Therefore, because of concerns of tissue deposition, most notably nephrogenic systemic fibrosis, a single dose is recommended. It is administered via an indwelling catheter as a bolus injection followed by a 20-ml saline flush [27]. It is recommended to use a power injector at a rate of 2 ml/s to achieve consistency in the timing of contrast enhancement, if possible [31]. A saline flush is needed to push the contrast medium through the tubing and ensure that the full contrast dose has been delivered.

Imaging Protocol

The initial sequence should be T2-weighted echo-train spin echo or a short TI inversion recovery (STIR) as T2 characteristics of a breast lesion could be crucial for differential diagnosis [40]. STIR images show cysts, effusion, and inflammatory processes as bright, while suppressing signal from fat. For contrast-enhanced T1-weighted imaging we employ a 3D spoiled gradient-echo sequence with a short repetition time, a very short echo time, and a shallow flip angle [31]. There is an important choice between two-dimensional (2D) and three-dimensional (3D) imaging. 3D imaging indicates that phase encoding, frequency encoding, and section encoding are achieved by applying suitable gradients during image acquisition. For 2D imaging, section encoding is achieved by means of selective excitation. 3D imaging has a significant advantage of a higher inherent SNR, which allows thinner sections to be acquired and overall increased spatial resolution in a given acquisition time [30]. Most current 1.5 T and higher field systems have excellent homogeneity, sufficient gradient strength and speed, and computer capability to provide good 3D image quality. Near-isotropic voxels, 1 mm or better, can be obtained. The 3D acquisition is also more forgiving in regard to breathing artifacts. Often some type of fat suppression is employed in order to facilitate the detection of enhancement.

One precontrast T1-weighted gradient-echo sequence is acquired immediately before the contrast agent is

administered, followed by four or more additional acquisitions using the same sequence with identical parameters. The ideal temporal resolution is 60–120 s per acquisition. This ensures that uptake and washout of the contrast agent can be measured accurately even in the most rapidly enhancing lesions [31]. Since high spatial resolution is necessary, the largest imaging matrix achievable within this acquisition should be used, namely, 512 × 512 matrix size for bilateral transverse or coronal imaging and 256 × 256 matrix size for unilateral imaging with smaller FOV. Translated into an in-plane pixel size, this means 0.5 × 0.5 to 0.8 × 0.8 mm and a through-plane section thickness of 1–3 mm. For best multiplanar reconstructions a near-isotropic submillimeter voxel size may be desirable.

Phase encoding direction should never be anterior-posterior in order to avoid cardiac and respiratory motion artifacts through the breasts. Instead, the frequency encoding direction should be anterior-posterior. For sagittal and coronal imaging, the phase encoding direction should therefore be superior-inferior, while for the transverse plane imaging it should be in the left-right direction.

Fat Suppression

Uniform fat suppression minimizes the signal of the surrounding adipose tissue and makes enhancing soft tissue lesions more obvious. Active fat saturation eliminates the signal from fatty tissue by means of additional radiofrequency pulses or by choosing selective water excitation. Both require a very homogenous magnetic field across the entire FOV [30]. A similar effect of fat suppression can be achieved by subtraction during postprocessing. It does not require extra acquisition time, nor is it influenced by magnetic field inhomogeneities. Its only disadvantage is the high sensitivity to patient motion [31], which might render the study nondiagnostic. Thus a combination of fat-suppressed acquisitions and subsequent postprocessed subtractions provide the best results.

Artifacts

The importance of achieving a homogenous magnetic field across the field of view has already been emphasized.

There are a number of technical artifacts that can potentially degrade image quality and consequently limit the interpretation of the images.

Motion artifacts can degrade image quality even to the extent of being nondiagnostic. The reduced signal intensity of a moving structure as well as blurring can obscure lesions. Physiologic motion may result from respiration and gastrointestinal peristalsis, and be rendered more conspicuous by the presence of fluid (pleural, bowel, or blood in vessels). Periodic motion from pulsation of vessels (**ghosting**) has the appearance of mirror-artifact signal intensity projected in the phase-encoding direction. Cardiac motion is another major source of phase artifact. Nonphysiologic motion artifacts are caused by patient motion, which can be reduced by proper patient preparation and firm but comfortable fixation of the breasts [41]. Wraparound artifacts result in appearance of portions of anatomic structures where they do not normally belong [41].

Table 19.1 MRI Artifact Categories

MRI Artifact Category 1	No motion/subtraction artifacts
MRI Artifact Category 2	Minor motion/subtraction artifacts
MRI Artifact Category 3	Distinct motion/subtraction artifacts
MRI Artifact Category 4	Unacceptable motion/subtraction artifacts

Misregistration is a type of artifact specific to subtraction imaging. It occurs in subtraction images when there is movement between the images to be subtracted. The term **edge artifact** describes the color mapping artifact caused by subtle misregistration in computer-aided detection. It is suppressed by reformatting multiplanar images [41]. **Magnetic susceptibility** artifacts may appear near metallic or surgical clips, caused by degradation of the magnetic field uniformity in the vicinity of ferromagnetic materials [31]. A related artifact is **chemical shift**. Fat and water have slightly different magnetic properties and may be displayed with a shift in their location resulting in bright and dark lines along the frequency encoding direction.

Finally, there are artifacts due to body habitus, which include artifacts from breast tissue outside the coil, breast touching the coil, the width of the patient, etc. [41].

To standardize the influence on image quality classification of various artifacts, all the artifacts are categorized into four levels of severity (Table 19.1) [42].

MR Protocol for Improved Specificity

Despite the fact that dynamic contrast-enhanced (DCE) breast MRI has high sensitivity, the specificity remains relatively low [8–19]. Strategies to reduce the number of unnecessary interventions have stimulated research to improve noninvasive techniques of magnetic resonance. T2*-weighted perfusion MRI [43, 44] and hydrogen ^{1}H MR spectroscopy [45–48] have been examined as promising tools for improving the specificity in the detection of breast malignancy. T2*-weighted perfusion imaging is based on measurements of increased perfusion, which is typical in malignant tumors.

^{1}H MR spectroscopy is based on the detection of the ^{1}H nuclear MR of choline-containing compounds (Cho), which serve as markers of active tumors [49]. It has recently been reported that specificity improved to 87% with the addition of ^{1}H MR spectroscopy and to 100% with the further addition of perfusion MRI [50].

It has been shown that ^{1}H MR spectroscopy can reveal markedly elevated Cho peaks not only in cancers, but also in some cases of benign lesions (fibroadenomas). Still, this method has high negative predictive value for invasive cancers. In clinical practice, ^{1}H MR spectroscopy can help avoid breast biopsies in cases when Cho is not elevated, consistent with benign disease. MR spectroscopy has also been incorporated to evaluate response to neoadjuvant chemotherapy.

Diffusion-weighted MRI (DWI) produces in vivo images of biological tissues weighted with the local microstructural characteristics of water diffusion. DWI is based on the brownian motion of molecules, which is restricted in tumors. Diffusion has generally been shown to decrease in tissues with high cellularity such as malignant tumors [51, 52]. Recent studies using DWI have shown that apparent diffusion coefficient (ADC) values can be useful in differentiating benign and malignant breast lesion even without contrast administration. If DWI is used in combination with other MRI findings (especially margins and kinetic analysis), the sensitivity and specificity can be improved up to 92% and 86%, respectively [52].

Breast MR Image Interpretation

The first task in analyzing MR images is to detect the presence of lesions. A lack of enhancement of the lesion is strongly predictive of benignity, with negative predictive value for invasive cancer of 94–96%. It should be noted that the absence of observed enhancement at MRI does not necessarily exclude a cancer. It has been reported that those cancers that did not enhance were either very small or had small or no invasive component [39].

Once detected, lesions need to be classified by the type of enhancement. In 2003, the fourth edition of the manual for the American College of Radiology Breast Imaging Reporting and Data System (BI-RADS®) included a section dedicated to the performance and reporting of breast MRI [53]. The committee acknowledged that reporting of breast MRI should include field strength, precontrast and postcontrast sequences used, method of fat suppression, and postprocessing performed (subtractions, axial, sagittal, coronal reconstructions, and/or maximum intensity projections).

The BI-RADS MRI lexicon for breast imaging includes detailed language for describing morphology and kinetics of lesions. All suspicious enhancing areas should be described as 1) focus, 2) mass, or 3) non-masslike enhancement (Table 19.2).

Table 19.2 Diagnostic Features at Breast MRI (7)

Architectural Features	
Finding	Feature
Focal mass	Margin
	Shape
	Homogeneity
	Enhancement
	Initial magnitude
	Enhancing rim
	Nonenhancing internal septation
	Internal septation on T2-weighted images
	T2 signal intensity
	Associated area enhancement
Area enhancement	
	Distribution: segmental, regional, or diffuse
	Form: stippled, clumped, or confluent
Ductal enhancement	
	Branching
Border	

Foci are typically less than 5 mm in diameter, which is considered to be too small to be further characterized. Masses have defined convex margins. All mass descriptions should include reporting of mass shape, margin, and internal enhancement. Non-masslike enhancement means that enhancement occurs in an area of the fibroglandular tissue that appears normal on precontrast images; descriptions should include distribution, internal enhancement, and symmetry.

Associated findings (such as edema, adenopathy, cysts, and skin or chest wall involvement) should be reported and kinetic curve assessment of all lesions described. Kinetic curve assessment should include initial peak enhancement within the first 2 min after injection (slow, medium, or rapid) and delayed-phase (persistent, plateau, or washout) analyses [35, 53].

To quantify enhancement, the increase in signal intensity (SI) relative to baseline precontrast signal intensity is determined according to

$$(SI_{post} - SI_{pre})/SI_{pre}$$

where SI_{pre} is the signal intensity before the injection of the contrast agent and SI_{post} is the signal intensity after the injection of the contrast agent.

The most important features in classifying focal masses are considered to be margins and initial enhance-

ment intensity (at 2 min or less after contrast agent injection), followed by the qualitative assessment of the kinetic curve. The relative risk of cancer for a lesion that has a washout curve as compared with the risk for a lesion that has a persistent curve is approximately five to one. In some cases a rim enhancement of the lesion or associated area enhancement can be observed, which highly correlates with a cancer diagnosis [39].

For lesions with area enhancement, the distribution appears to be most predictive of diagnosis: Low-level stippled enhancement in a regional distribution indicates benignity, while segmental or clumped enhancement is cause for concern [35]. While enhancement kinetics are useful for the further differential diagnosis of morphologically equivocal masses, they may be misleading and should therefore not be used (or used only in cases in which enhancement is consistent with cancer) for the further classification of non-masslike enhancement. The reason is that in non-masslike enhancement the differential diagnosis includes DCIS and lobular cancers, known to exhibit inconsistent angiogenic activity. Symmetry is helpful in the further characterization of non-masslike enhancement but is not usually assessed in masses. Bilateral symmetric non-masslike enhancement in any distribution is more often caused by benign changes than by malignant lesions [30]. Table 19.3 summarizes the above points.

Table 19.3 Morphological and Kinetic MRI Features Suggestive of Diagnosis

Morphological and Kinetic Features	
Suggestive of Benignity	Suggestive of Malignancy
• A non-irregular shaped mass with a smooth margin; hypointense internal septations; no enhancement or homogeneous enhancement without a washout pattern on time-intensity curve.	• An irregular shaped mass with an irregular or spiculated margin, heterogeneous enhancement (rim enhancement) with a fast initial enhancement and a washout pattern on time-intensity curve. A "plateau" curve can also be observed in invasive carcinomas.
• A non-masslike stippled enhancement (regional, multiple regions) or diffuse and symmetric enhancement.	• A non-masslike clumped enhancement with a ductal or segmental spatial distribution.
Caution! False negatives: lobular cancers, DCIS	**Caution!** False positives: lymph nodes

Reporting System and Assessment Categories

According to the ACR BI-RADS lexicon [53], the report must be organized and presented with the following structure:

- Clinical data
- Comparison with old studies and standard imaging
- A detailed description of the technical MRI factors
- An overall description of the breast composition (similar to that of mammography lexicon)
- A clear description of any significant abnormal enhancement (which breast and lesion type):
  - Focus/foci
  - Mass: size, location, morphologic, data and internal enhancement characteristics, associated findings
  - Non-masslike enhancement: size, location, spatial distribution, and type of enhancement, associated findings
  - Symmetric or asymmetric (bilateral scans)
- A clear description of kinetic enhancement features of the abnormality
- Any important finding found on other post-processing techniques
- An overall impression with each lesion fully categorized

The report also must indicate whether a short-term follow-up or a biopsy should be considered. If the MRI study is not conclusive, a suggestion for the next course of action should be given (repeat MRI, second-look ultrasound, mammography, etc.).

Seven assessment categories are described:

Category 0: Need for additional imaging evaluation

Category 1: Negative (no abnormal enhancement found)

Category 2: Benign finding. In this category nonenhancing fibroadenomas, cysts, scars, fat-containing lesions, implants are described.

Category 3: Probably benign finding. Short-time interval follow-up suggested. A lesion placed in this category has a very high probability of being benign.

Category 4: Suspicious abnormality. Biopsy should be considered. A lesion placed in this category does not exhibit typical features of breast cancer but does have a low to moderate probability of being malignant.

Category 5: Highly suggestive of malignancy. Appropriate action should be taken.

Category 6: Known biopsy-proven malignancy. Appropriate action should be taken. This category is very useful for describing a known cancer during a breast MR study performed for local staging and therapy planning and monitoring.

The use of the BI-RADS MRI lexicon offers a logical approach for analyzing breast MRI studies by using

a standardized description that also includes an accepted quality standard. This standardization enables efficient communication with colleagues all over the world.

Difficulties in Breast MR Image Interpretation

Important causes of diagnostic difficulties include multiple small enhancing foci and areas of non-masslike enhancement that most commonly occur in premenopausal women. In the majority of cases, these foci will be due to proliferation of glandular tissue (adenosis) or to hormonal stimulation of normal breast parenchyma [30]. The differentiation from a small breast cancer or DCIS will at times be difficult if not impossible. Dynamic curves obtained from these lesions could complicate differential diagnosis even more if washout or plateau patterns are observed (which is not rare).

To avoid observing an unnecessary increase in enhancement due to hormonal stimulation, breast MRIs should be performed in the first half of the menstrual cycle, because the luteal phase of the menstrual cycle (second half), with the associated increase in estrogen and progesterone levels, leads to the stroma being edematous [4]. The ideal time for breast MRI is between days 5 and 10 after onset of menses, long enough after the luteal phase to decrease any residual enhancement [54, 55]. If MRI is performed in the correct phase of the cycle but there are still many enhancing foci symmetrically distributed in both breasts, one should consider repeating the MRI procedure in 2 weeks (waiting for change of hormonal situation) or in 3 months in the same phase of the cycle as the first time. For similar reasons, the use of hormone replacement therapy in postmenopausal women may lead to focal or diffuse enhancement. In such cases, it may be necessary to repeat the MRI examination 2 or 3 months after stopping hormone therapy to obtain optimal results [1, 56]. Similarly, pregnancy or lactation can hide or simulate malignant behavior.

As mentioned above, various benign conditions of the breasts can be difficult to distinguish from malignant lesions. Such processes as fibrocystic disease of the breast, fibroadenomas, sclerosing adenosis, atypical ductal hyperplasia, lobular carcinoma in situ (LCIS), and breast papillomas can all produce contrast enhancement patterns that are hard to distinguish from malignant lesions. MRI should not be performed to establish benign disease in those patients who have suspected benign breast tumors or proliferative changes (BI-RADS 3 lesions) [1, 4]. On the other hand, if these benign lesions are initially described at MRI, comparison with mammography and/or a second-look ultrasound should be performed. If this does not resolve the differential diagnostic problem, repeating MRI in 6 months time is recommended (for BI-RADS 3 lesions) [57, 58].

It has been published that the likelihood of malignancy in MRI-detected breast lesions increases significantly with increasing lesion size; thus biopsy is generally not warranted for MRI-detected lesions less than 5 mm because of the low (3%) frequency of malignancy in these lesions (Table 19.5). However, the final decision regarding biopsy recommendation should be based not only on lesion size but on other lesion features (e.g., morphology, kinetics, and enhancement pattern), patient risk factors, and clinical history [57].

Although overlooking invasive breast cancer on MR images is rare, it does occur [2, 30, 37]. Nonenhancing invasive breast cancers are exceedingly rare [59]. More often, the reason for failure to diagnose invasive cancer with breast MRI is early and strong enhancement in the surrounding normal fibroglandular tissue that may mask the enhancing cancer. Therefore, if strong background enhancement is present, it will be crucial to put in the report "MR imaging–dense breast" so that referring physicians understand that the high sensitivity that they may expect from a breast MR study may not be available in this particular case [30]. Even more, ACR categorization of background enhancement can be used (categories 1–4) according to mammographic breast density categorization (fig. 19.6) [53].

The degree of the enhancement depends on the amount of glandular (relative to fibrous and fatty) tissue and the patient's hormonal status. The term **background enhancement** refers to the enhancement in presumably normal fibroglandular tissue [30]. According to the American College of Radiology (ACR), the extent of background enhancement of the breast is graded into four types, marked as ACR categories 1–4 (Table 19.4) [53]. The different degree of background enhancement has certain implications on overall sensitivity and specificity in breast cancer detection, which decreases with increasing breast density. Therefore, it is important to rate background enhancement in every breast MRI report to communicate the degree of diagnostic confidence for breast cancer detection [30]. Bilateral symme-

Table 19.4 Management of MRI Detected Lesions According to BI-RADS Categorization and Size

Size	BI-RADS	Biopsy decision
<5 mm	—	Repeat MRI in 6 months
>5 mm	3	Repeat MRI in 6 months
<10 mm	4–5	BIOPSY
>10 mm	3	BIOPSY
	4–5	BIOPSY

try of background enhancement needs to be evaluated and can contribute to the diagnostic accuracy.

In earlier studies, the sensitivity for diagnosing DCIS was considered to be lower than that for diagnosing invasive cancers, which was explained by the lack of angiogenesis (obtained kinetic curves were not typical for malignant lesions) and the inability of MRI to detect microcalcifications (which were thought to be the main radiological characteristic of DCIS). Several recent studies reported the opposite: high sensitivity of MRI in detecting DCIS, especially DCIS with high nuclear grade with detection rate of up to 98% [60, 61], also revealing that MRI morphology of DCIS differs significantly from that of invasive carcinoma. Although breast MRI is currently the most sensitive tool for assessing invasive breast cancer, for the diagnosis of ductal carcinoma in situ it must be considered complementary information to conventional mammography. However, as the spatial resolution of MRI increases, the evaluation of DCIS should improve.

Table 19.5 ACR—MRI Density Types

MRI Density type 1	No enhancement of the parenchyma
MRI Density type 2	Patchy enhancement of the parenchyma
MRI Density type 3	Widespread patchy enhancement of the parenchyma
MRI Density type 4	Strong enhancement of the parenchyma

If breast MRI reveals a lesion that was not detected with previous, standard procedures (mammography, ultrasound, or clinical examination), the radiologist should try to localize the lesion with second-look ultrasound in order to perform US-guided biopsy or, at least, localization of a suspicious lesion. Second-look ultrasound can detect up to 75% of those lesions if it is performed on the basis of the MRI [58]. This is one of the reasons why the radiologist who is performing breast MRI should be familiar with all breast imaging procedures. If the lesion could not be localized with US, MR-guided biopsy is recommended. The procedure is rather simple to perform if the coil for breast biopsies

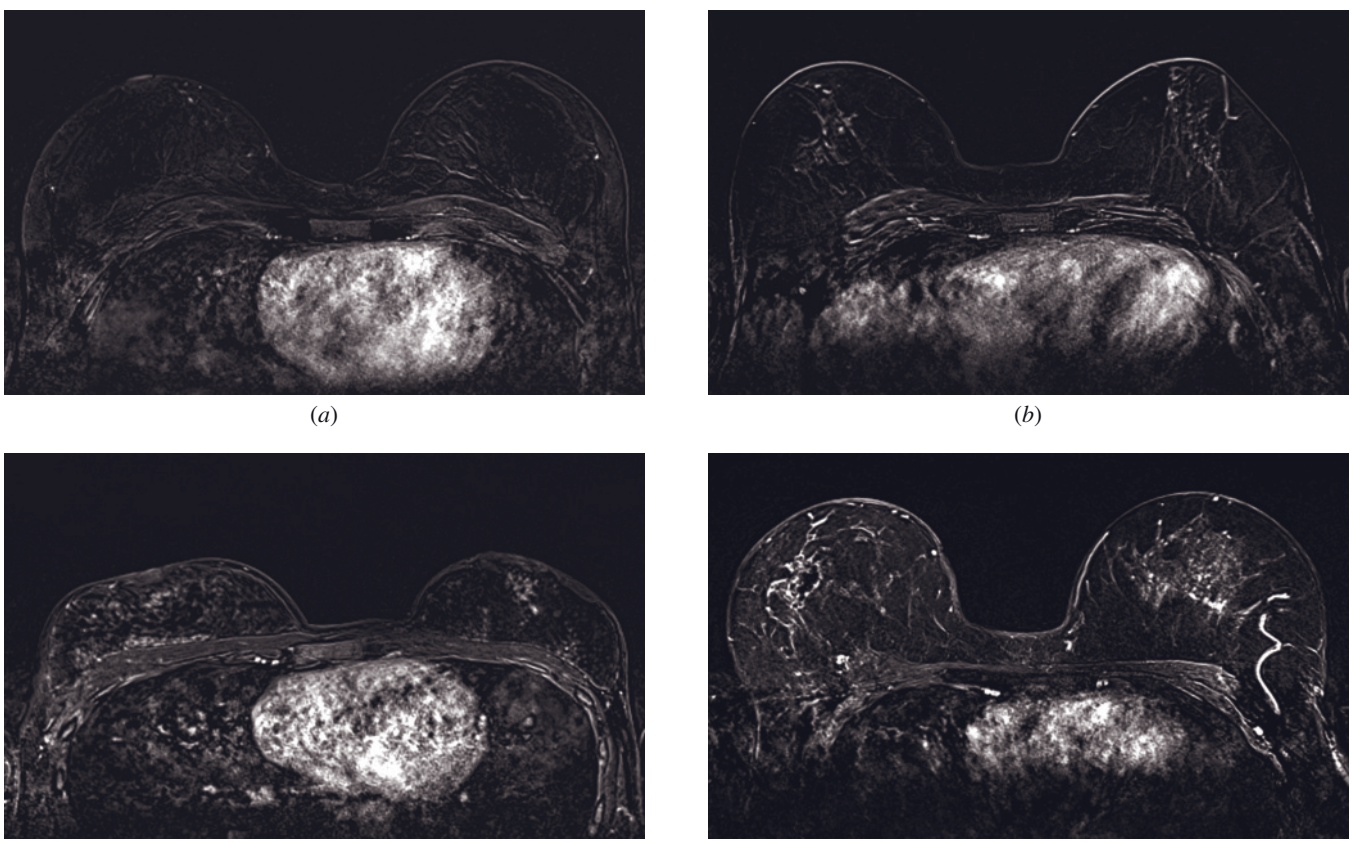

Fig. 19.6 Degree of the background enhancement in the breast is scaled into 4 levels, marked as ACR categories 1–4. This designation is important since the background enhancement affects MRI overall sensitivity and specificity in breast cancer detection. MRI background enhancement types 1–4 are shown on respective subtracted images (*a–d*).

and other standard MR compatible biopsy devices are available.

ANOMALIES OF THE BREAST

In the breast, as in the other organs, a few congenital anomalies can be found, most commonly asymmetry of the breasts and polythelia (fig. 19.7). Breast asymmetry is commonly present to some degree in almost every woman and thus considered predominantly a cosmetic problem (fig. 19.8). Polythelia represents the presence of one or more rudimentary nipple(s) along the milk ridge, from axilla to groin. Less common are athelia (complete absence of one or both nipples) and amastia (congenital absence of the breast, rare and usually unilateral). Hypoplasia of the breast is more common and manifests as small normal breast(s). Large breasts appear in two types of anomalies: juvenile hypertrophy [large breast(s) with a rapid growth during puberty] and macromastia [62].

BENIGN BREAST LESIONS

Although evaluation of benign diseases of the breast is not an indication for contrast-enhanced breast MRI, understanding and recognizing typical and some atypical benign features is of great importance for the radiologist, since these findings are very frequent and may cause diagnostic challenges.

MASS LESIONS

Cysts

Cysts are frequently identified lesions on MRI of the breast. They can be solitary or multiple within fibromicrocystic or fibromacrocystic changes of the breast tissue. They do not carry increased risk for breast cancer.

The pathohistology of cysts reveals dilatation of a duct (TDLUs), filled with liquid, with a thin layer of

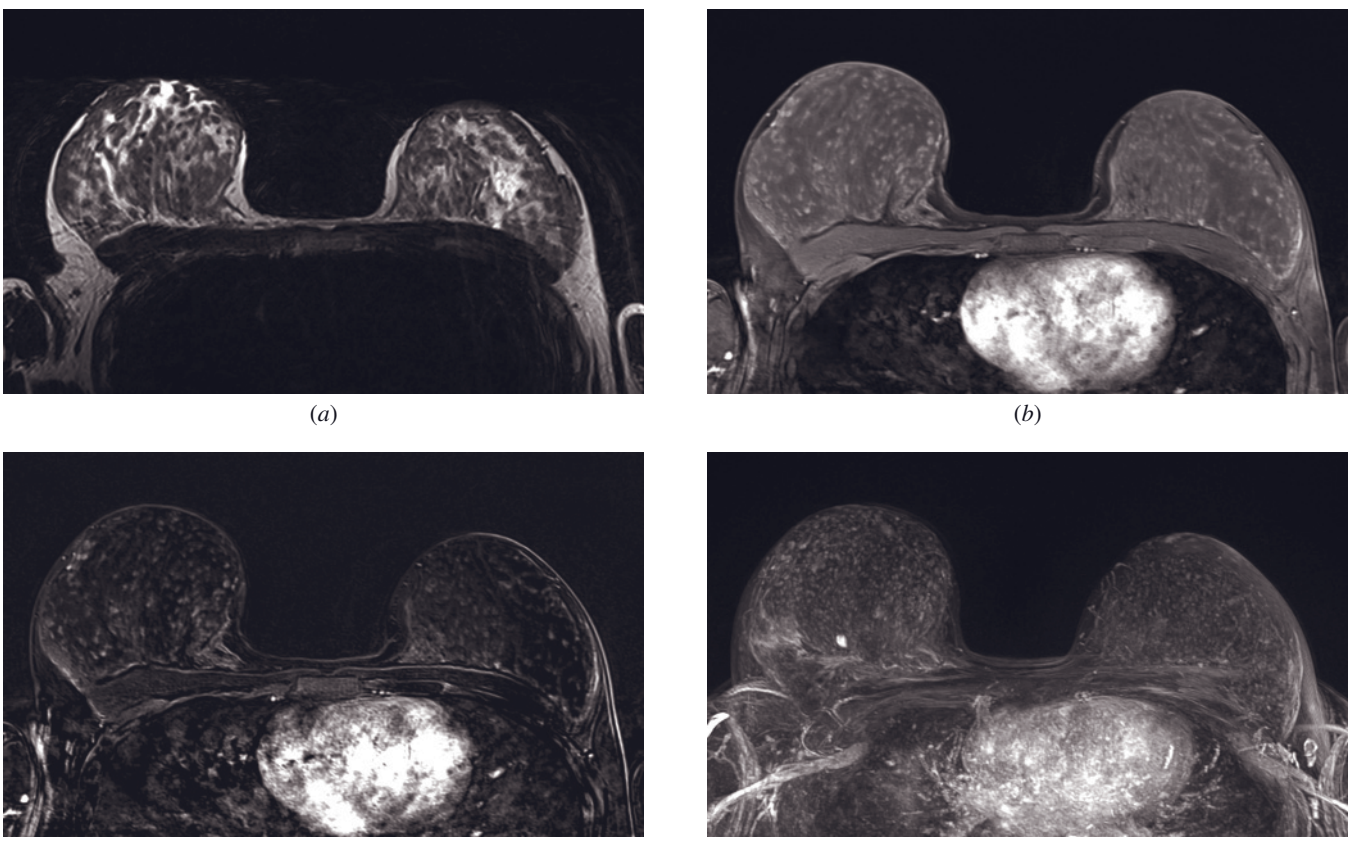

FIG. 19.7 Breast asymmetry. Axial T2-weighted image (*a*) shows an asymmetry with a larger amount of fibroglandular tissue in the right breast. Axial postcontrast dynamic GRE (*b*) and axial subtracted (*c*) images display multiple enhancing foci within the fibroglandular tissue, diffusely distributed in both breasts. The postcontrast MIP image (*d*) of this patient shows a small enhancing benign lesion (fibroadenoma) in the right breast.

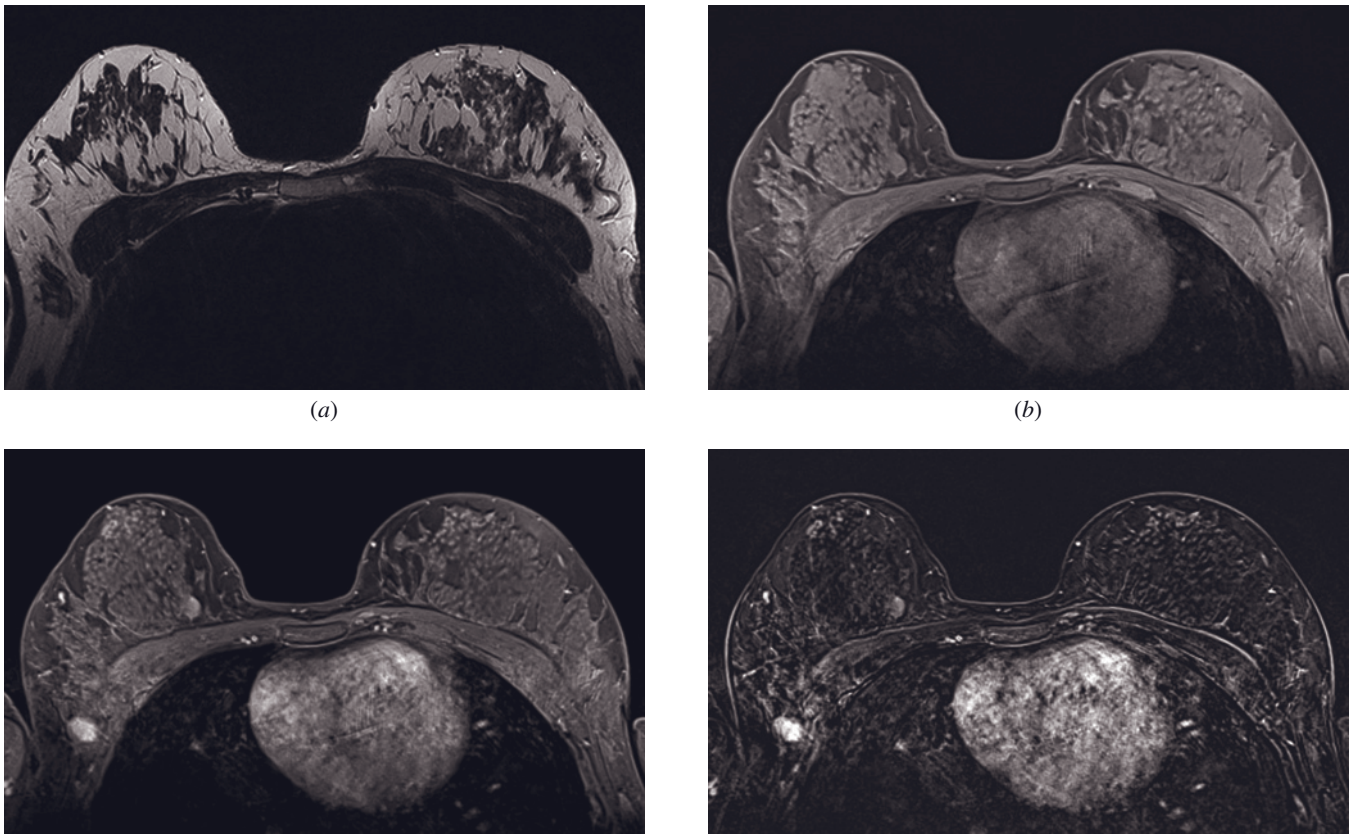

FIG. 19.8 Fibroadenoma in accessory breast tissue. Axial T2-weighted (*a*) and dynamic GRE images (*b*) show breast asymmetry with accessory fibroglandular tissue in the axillary tail of the right breast. Axial postcontrast VIEWS (*c*) and subtracted (*d*) images reveal hyperintense lobulated mass located in the accessory tissue, with hypointense internal septations, characteristic for fibroadenoma.

ductal epithelium. Most commonly, it occurs in women in the fourth decade, caused by hormonal changes in the menstrual cycle. Sometimes, cysts can exhibit thicker walls, with elements of inflammation (cells and fibrosis), and they can also contain blood or mucinous fluid (diluted or layered).

On precontrast T1- and T2-weighted images, cysts have signal characteristics that are most often consistent with fluid: very high on STIR and T2 images, low on T1, and intermediate to low on T2 with fat suppression. They are well-circumscribed lesions with a thin wall, and they usually do not enhance on postcontrast T1 images (fig. 19.9). Exceptions to the rule are inflamed cysts, with rim enhancement of the wall (fig. 19.10). It is crucial to recognize that the enhancement is smooth, present only around the cyst, and that there is no enhancement within the lesion (the differential diagnosis to rim enhancement with internal inhomogeneities, which is typical for breast cancers) [20].

If the content of a cyst has high signal intensity on postcontrast T1-weighted images (with or without fat suppression), it is very important to analyze precontrast T1 images or subtracted images, to exclude intrinsic high signal from blood or high protein content in cystic fluid.

Typical cysts with high T2 signal and no postcontrast enhancement are categorized as BI-RADS 2, without any need for dynamic analysis. Cysts with irregular, partially thick enhancing rim or papillary intracystic formation need further categorization with kinetic analysis; if the obtained curve is persistent or plateau type, it should be classified as "probably benign" or BI-RADS 3 lesion; if it shows washout type of enhancement it should be categorized as suspicious (BI-RADS 4), and biopsy should be recommended (we recommend US-guided if reliably seen on second-look ultrasound).

Hydatid cysts are very rare in the breast. They usually occur as a part of disseminated disease. In 0.27% of cases, the breast is the primary site of disease [63]. The typical MRI appearance includes a hypointense capsule on T2-weighted images corresponding with the pericyst and internal membranes [64]. Breast hydatid

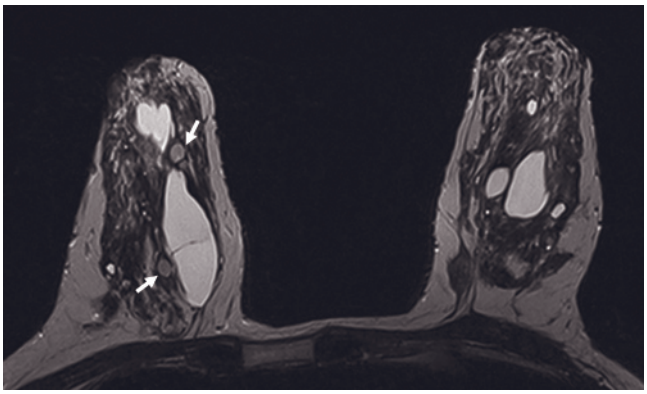

(*a*)

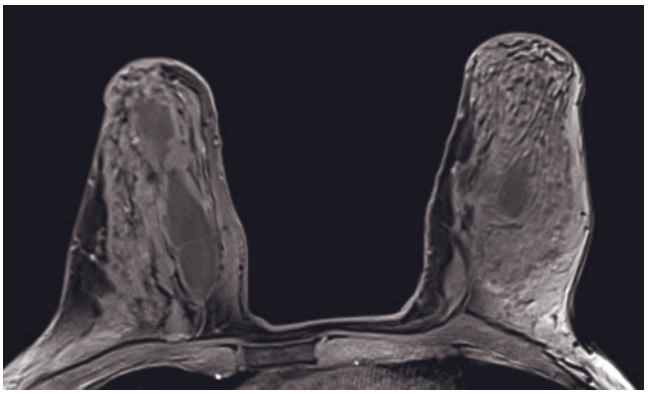

(*b*)

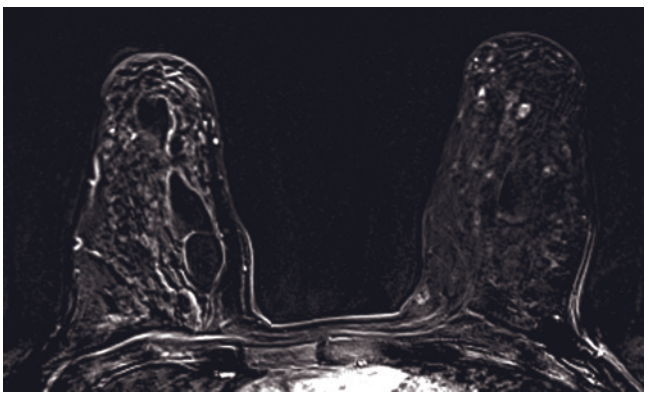

(*c*)

FIG. 19.9 Cysts. On axial T2-weighted images (*a*) most cysts have very high signal intensity. They are well-circumscribed lesions with a thin wall, and tiny septations are sometimes seen. They usually do not enhance on postcontrast images (*b*). Note two small cysts in the right breast (arrows, *a*) showing lower signal intensity on T2-weighted image and intermediate signal intensity on the GRE image (*c*), due to high proteinaceous and/or cellular content (there is no enhancement on postcontrast subtracted image).

may mimic a breast abscess, or a complicated cyst, with thick enhanced wall and internal septations.

Fibroadenoma

The most common benign neoplasm of the breast is the fibroadenoma (FA), a biphasic (fibroepithelial) tumor that originates from TDLU, most frequently in young women in the second or third decade of life.

The FA is a sharply demarcated, round, firm or rubbery tumor with a grayish-white cut surface. Their size is usually between 2 and 3 cm, but giant fibroadenomas larger than 10 cm can also be found [20, 22]. They are stimulated by estrogen and progesterone, pregnancy, and lactation, and they undergo atrophic changes in menopause [65].

They are comprised of epithelial (containing terminal ducts and lobules) and stromal elements (containing connective tissue) surrounded by a pseudocapsule [21]. Myxoid change or calcifications may occur. The stromal component may show focal or diffuse hypercellularity or extensive myxoid or mucinous change, transforming the tumor to a gelatinous nodule. A myxoid FA can grossly, microscopically, and radiologically be mistaken for a mucinous (colloid) carcinoma. FAs with significant myxoid stroma occurring in women younger than 40 years of age are more likely to be associated with multiple recurrences [20].

FAs do not have malignant potential, but rare cases of infiltrating carcinoma arising in an FA have been documented [22, 66]. Approximately 16% of FAs are complex. Complex fibroadenomas are smaller and appear at an older age. Sclerosing adenosis is the most frequent finding related to complexity and is found in 57% of complex FAs [67]. Atypical epithelial proliferations such as ductal intraepithelial neoplasia (DIN; ADH/DCIS) and lobular intraepithelial neoplasia (LIN; ALH/LCIS) can rarely be identified within the FA [68].

Concerning the interpretation of such lesions, one should be more conservative as long as these neoplastic lesions are confined to the FA (with no evidence of intraepithelial neoplasia outside of the FA). Such FAs associated with DIN have an excellent prognosis after excision, without a significantly increased risk for recurrences or subsequent invasive carcinomas [68].

Fibroadenomas may grow up to 20% in maximal linear dimension over 6 months for women of all ages. Growth of this magnitude does not necessarily indicate progression to phyllodes or malignancy; however, excision is recommended for growth beyond this limit [69].

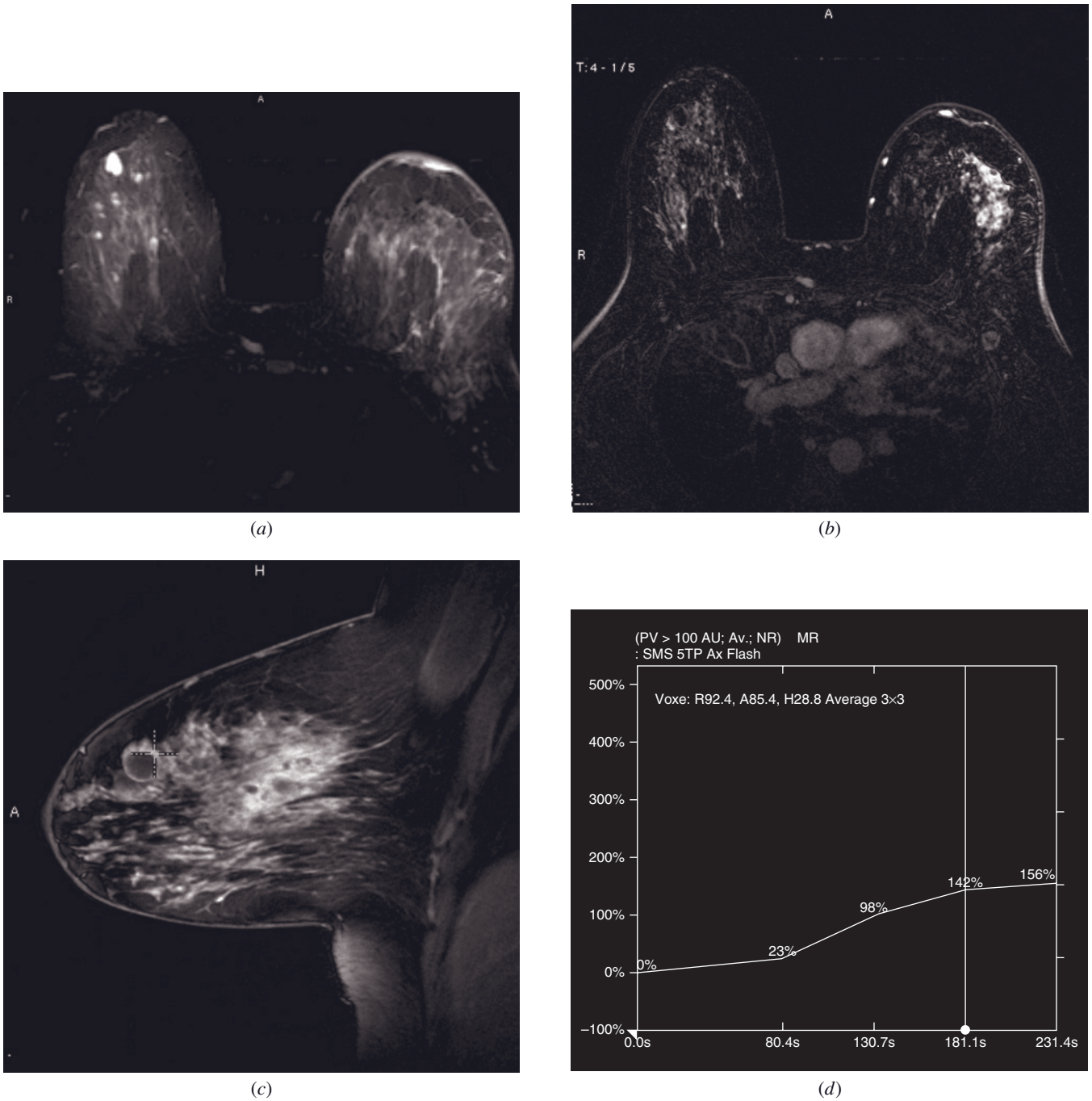

FIG. 19.10 Inflamed cyst. Axial T2 Fat Sat image (*a*) demonstrates several small round and oval masses with high signal in the lateral aspect of the right breast. There is a lobulated, high-signal mass anteriorly. Subtracted T1-weighted postcontrast image (*b*) demonstrates rim enhancement, thin and uniform throughout the whole circumference. The same appearance is demonstrated on the sagittal T1 weighted postcontrast scan (*c*), which was used to illustrate persistent enhancement on the corresponding Type I time-intensity curve (*d*). Note the enhancing IDC in the lateral aspect of the left breast on the MIP image (*b*).

MRI appearances of FAs are varied. They are usually round, oval, or lobular in shape with low-signal-intensity internal septa seen on postcontrast images and are found in up to 60% of all FAs [70] (fig. 19.11). These dark septations are caused by its internal lobulated composition. Although the presence of septations increases the diagnostic confidence (NPV 98%), recent studies revealed that 47% of malignant tumors also had nonenhancing internal septa [39, 71].

On T2-weighted images cellular and myxoid FAs are found to be hyperintense (caused by high fluid content) (fig. 19.12). On postcontrast images, they

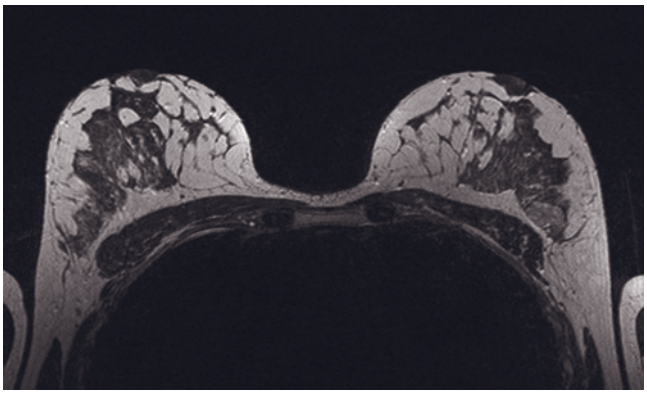

(*a*)

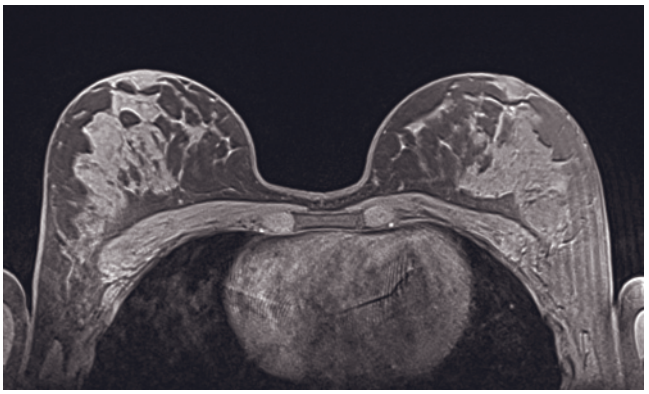

(*b*)

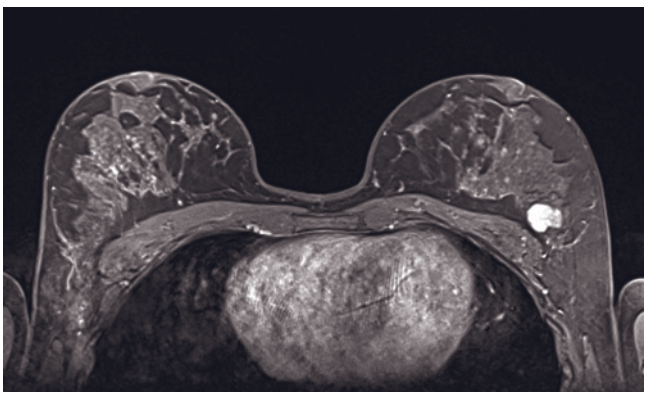

(*c*)

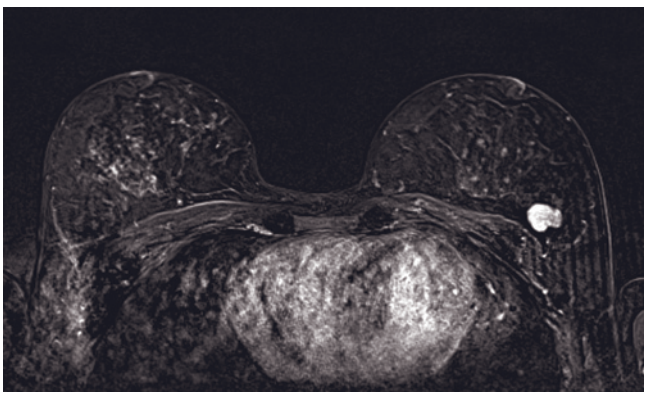

(*d*)

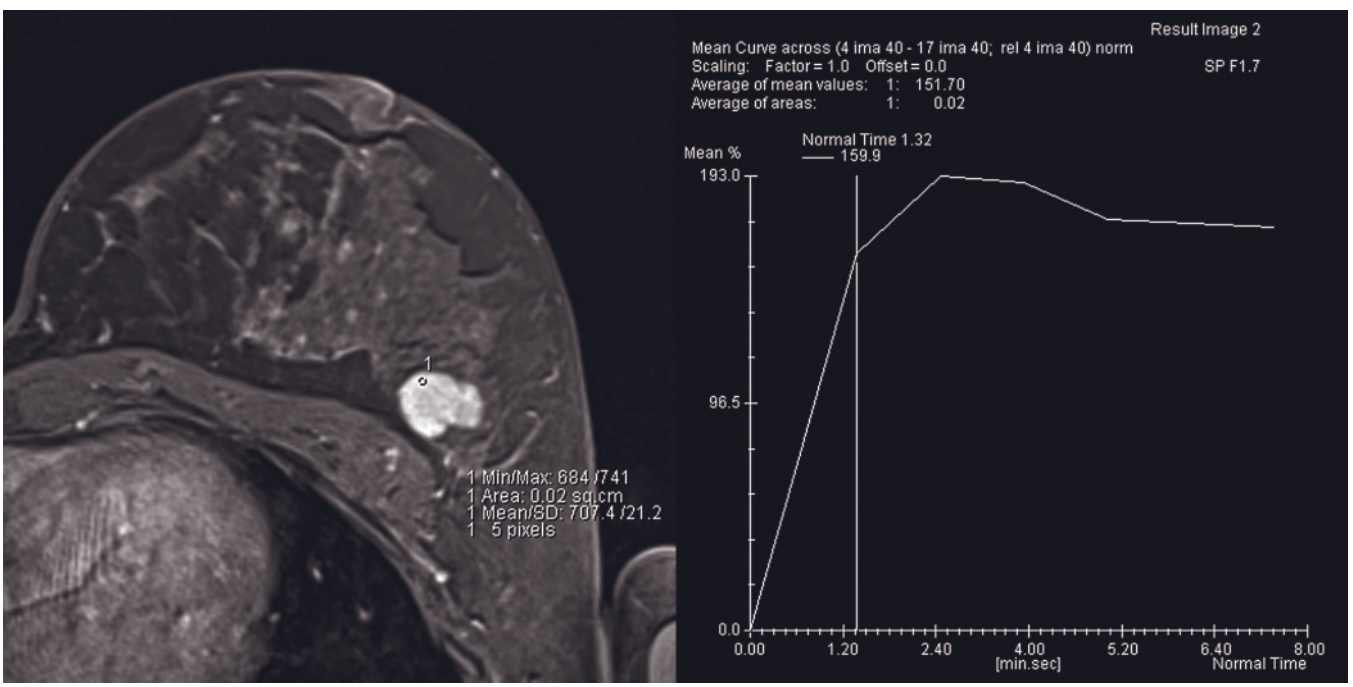

(*e*)

FIG. 19.11 Fibroadenoma (FA). Axial T2-weighted image (*a*) of a typical fibroadenoma reveals isointense lesion with irregular hypointense central sections due to the fibrous components of the FA. On axial precontrast GRE image (*b*), the lesion appears isointense to the surrounding parenchyma. Axial postcontrast GRE (*c*) and subtracted (*d*) images show enhancing lesion with slightly inhomogeneous central part. ROI analysis with time-intensity curves (*e*) shows a typical plateau curve (Type II) reaching a maximum enhancement (193%) 2.5 min after GBCA administration. This curve with typical morphology of FA does not influence BI-RADS categorization, and the lesion is categorized as BI-RADS 2. The mass remained mammographically stable after the 2-year follow-up.

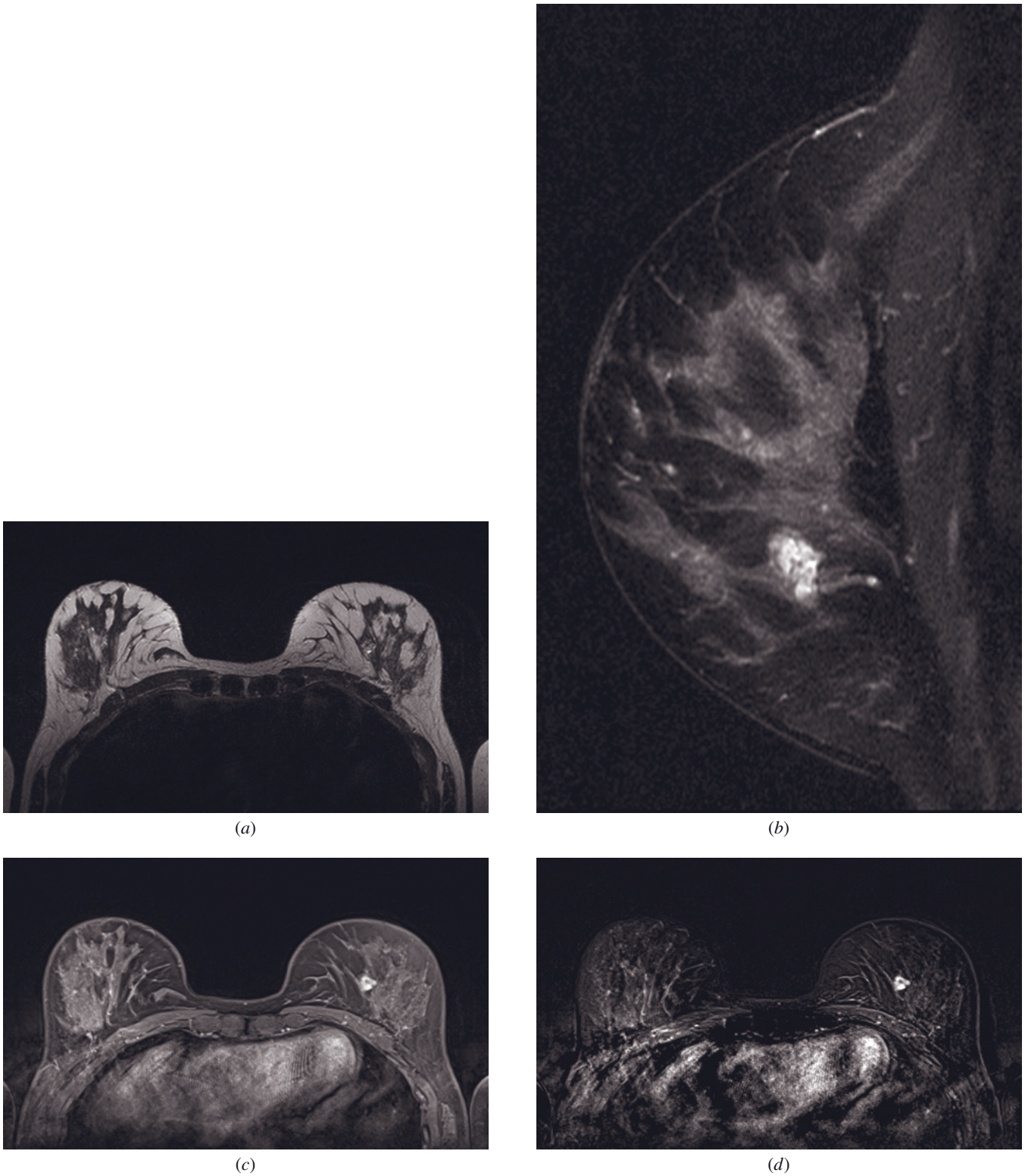

FIG. 19.12 Fibroadenoma (FA). Axial T2-weighted (*a*) and sagittal fat-saturated T2-weighted (*b*) images show a lobulated hyperintense lesion with low-signal-intensity internal septations. On axial T1-weighted postcontrast GRE (*c*) and subtracted (*d*) images, this mass strongly enhances, but there are nonenhancing septations, indicating a typical FA architecture.

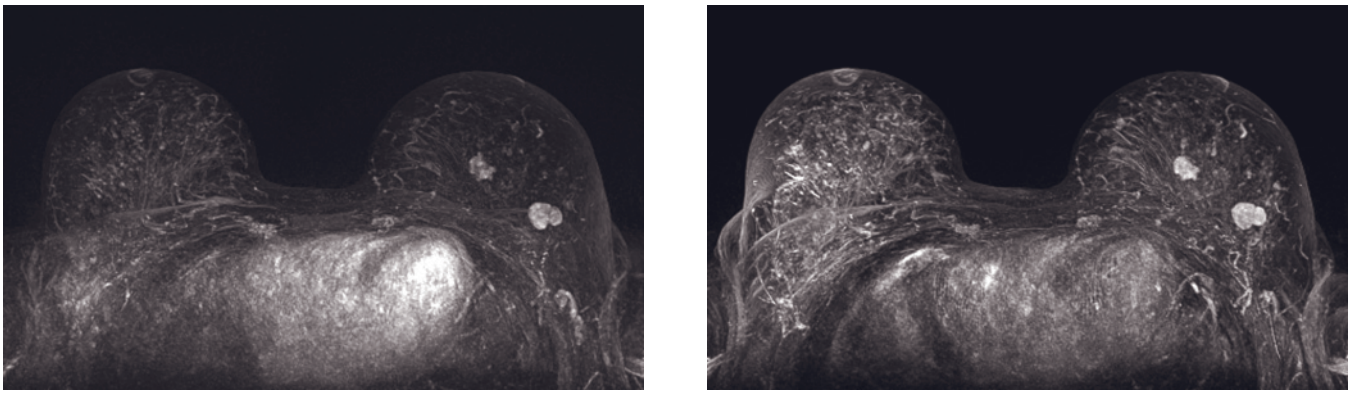

(*a*) (*b*)

FIG. 19.13 Fibroadenoma (FA). MIP images depict gradual increase in enhancement of 2 FAs in the left breast at 1 min (*a*) and 6 min (*b*) after application of GBCA, typical for benign lesions.

usually enhance to some extent, the intensity depending on the degree of fibrosis and hormonal stimulation, with persistent curve type usually observed (fig. 19.13). Plateau or washout types of curves are rarely seen. Less cellular and sclerotic FAs usually exhibit low signal intensity at T2-weighted sequences, without significant postcontrast enhancement.

Typical FAs are characterized as BI-RADS 2 lesion. If a lesion has an oval/round shape and a clear, smooth border with internal benign architecture, kinetic analysis will not influence the diagnosis. But if a lesion does not show typical internal architecture for FA, kinetic analysis should be performed: With persistent or plateau type of enhancement, 6-month follow-up is recommended (BI-RADS 3); with washout type, biopsy is recommended (BI-RADS 4). If ^{1}H MR spectroscopy is negative (no detectable Cho peak at 3.32 ppm) in cases of FAs with washout type of enhancement, categorization should be downgraded to BI-RADS 3, and the patient should be spared an unnecessary biopsy procedure [50, 52].

Phyllodes Tumor

The phyllodes breast tumor is a variant of fibroadenoma that constitutes 0.3–1.0% of all breast tumors [72, 73].

Histologically, phyllodes tumors (PTs) are similar to cellular intracanalicular fibroadenomas. They are distinguished by the presence of epithelium-lined clefts and their rapid growth [21, 27]. The tumors may be small or very large, ranging in size from 1 to 20 cm and more. The majority of PTs are well circumscribed and grayish-white, yellow, or pink, with foci of necrosis and hemorrhage in the larger tumors. Mucoid changes and calcifications can be present [20].

The current (2003) WHO classification of tumors of the breast and female genital organs divides phyllodes tumors into benign, borderline, and malignant categories based on mitotic activity, type of margin, stromal overgrowth, and cellular pleomorphism [74]. For practical purposes, benign and borderline tumors can be viewed as low-grade PTs. Malignant tumors represent high-grade PTs [20].

Although it has been shown that tumors smaller than 4 cm in diameter and pushing margins have a lower rate of recurrence [75], the behavior of phyllodes tumors cannot be predicted in an absolute way [20]. Approximately 30% of these tumors develop recurrences, and 10% metastasize hematogenously within 2–3 years after surgery. Lymph node metastases are very rare (<1% of high-grade PTs) [20].

On T2-weighted images, PTs are bright because of both cellular and cystic components, whereas low signal intensity is observed at T1. Cysts and hemorrhage are described as typical features of PTs, influencing both T1- and T2-weighted characteristics [76, 77] (fig. 19.14). Heterogeneous internal structure may be caused by regressive changes during tumor growth. Large phyllodes breast tumors may have a typical morphology with smooth margins, internal cysts, septations, and hemorrhage or perifocal or unilateral edema, but a reliable differentiation of phyllodes tumors and fibroadenomas is not possible according to imaging alone [76].

Both phyllodes breast tumors and fibroadenomas may have a contrast enhancement pattern suggestive of malignancy, in up to one-third of cases [76].

Mass shape, margin, and internal enhancement pattern do not correlate significantly with histologic grade of phyllodes breast tumor. Yabuucchi et al. [78] showed that areas in PTs with low ADC on diffusion-weighted images corresponded to stromal hypercellularity in intermediate and malignant phyllodes tumors. Accordingly, MRI can be used to guide the selection of an appropriate biopsy site, but several histologic find-

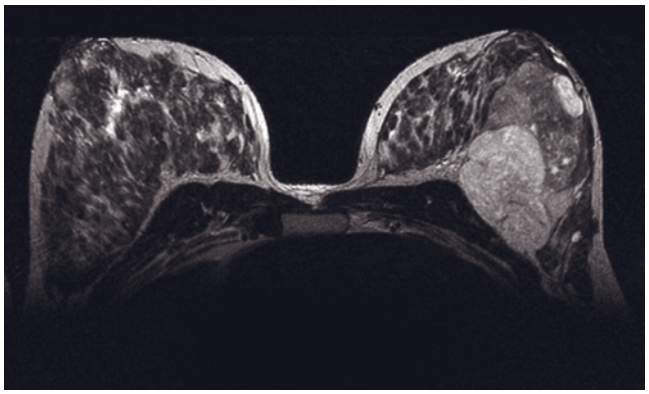

(*a*)

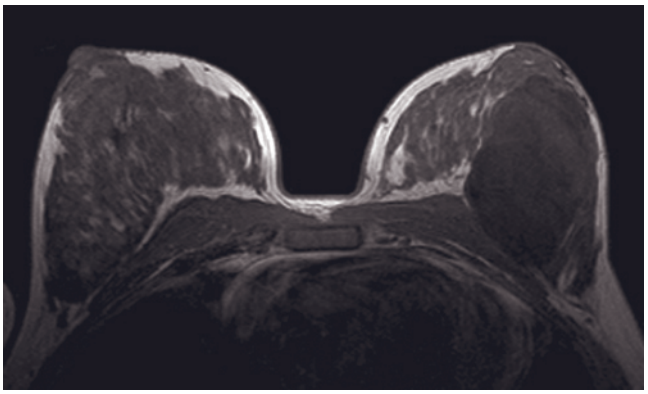

(*b*)

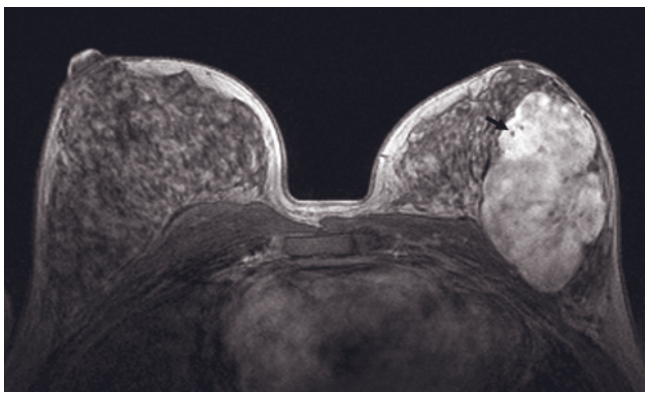

(*c*)

FIG. 19.14 Phyllodes tumor (PT). PTs are usually seen as a large, lobulated mass with smooth margins and internal septations. T2-weighted axial image (*a*) shows high-intensity areas in the tumor that result from both cellular and cystic components, whereas low signal intensity is observed on the T1-weighted image (*b*). Axial postcontrast T1 image (*c*) shows inhomogeneous, strongly enhancing lesion with small hypointense foci due to intratumoral calcifications (arrow).

ings must be used to help determine the histologic grade of phyllodes tumor of the breast [78].

Treatment of both benign and malignant phyllodes tumors requires complete surgical excision with 1- to 2-cm-wide margins [78–80]. However, some authors proposed a simple mastectomy for tumors larger then 5 cm in diameter and those of any size found to be malignant or intermediate [78, 81].

Papilloma

Intraductal papilloma is a common tumor located in major ducts and the subareolar region that can present diagnostic dilemma to the radiologist, pathologist, and surgeon. They usually measure 2–3 mm in diameter and can extend along the duct for several centimeters, causing dilatation of the duct and often a substantial bloody nipple discharge.

The lesion must be distinguished from papillomatosis, the form of epithelial hyperplasia that occurs in the peripheral ducts as a component of proliferative fibrocystic change [82]. The term "papillary lesion" is used to describe a spectrum of neoplasia (both benign and malignant) that develops within the breast [82]. It is used for every intraductal mass that is attached to the duct wall.

Papillomas consist of a double layer of epithelial cells and a fibrous stroma with a vascular core connected to the duct wall by a stalk [22, 27]. Secondary changes can occur within papillomas, such as infarction, hemorrhage, or fibrosis.

Areas of hyperplasia, DCIS, or invasive carcinomas may be found in papillomas, with an incidence as high as 20% [82, 83]. Thus the diagnosis of papilloma in a core needle biopsy (CNB) should lead to excisional biopsy of the entire lesion [82, 20]. Malignant papillary lesions tend to remain confined within the breast, and distant metastases are rare [84].

Conventional ductography (also termed galactography) has long been used to detect intraductal lesions. The detection of papilloma is possible with MRI, with limited sensitivity for small lesions. Papillomas visualized by MRI usually appear as well-circumscribed masses, directed toward the nipple, homogeneously enhanced in the early phase with washout seen on delayed scans, except if they are sclerosed (fig. 19.15). Dilated ducts, often hyperintense on T1- and T2-weighted images, represent one of the most important findings in intraductal papilloma [85–88]. Likely explanations for the high signal include hemorrhage or high protein content of the duct.

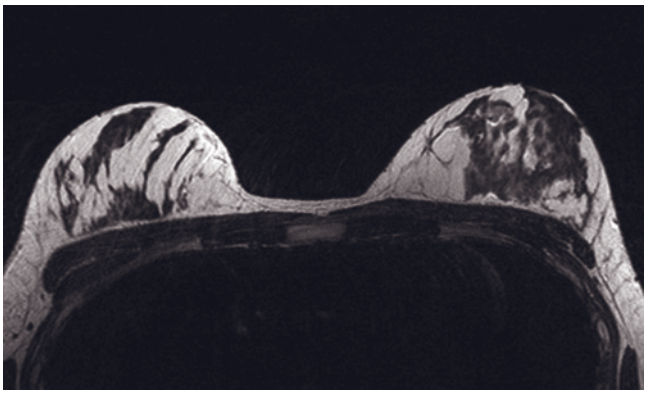

(*a*)

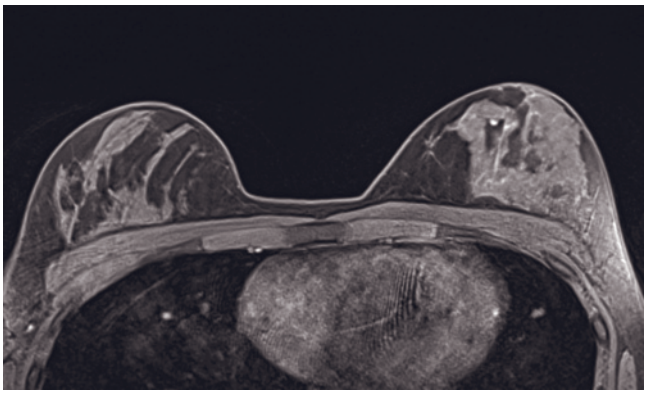

(*b*)

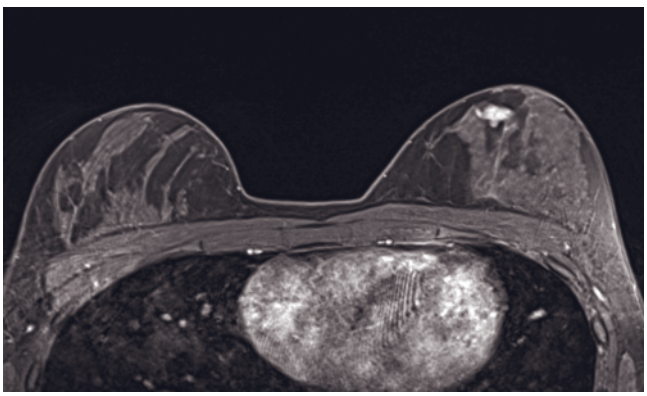

(*c*)

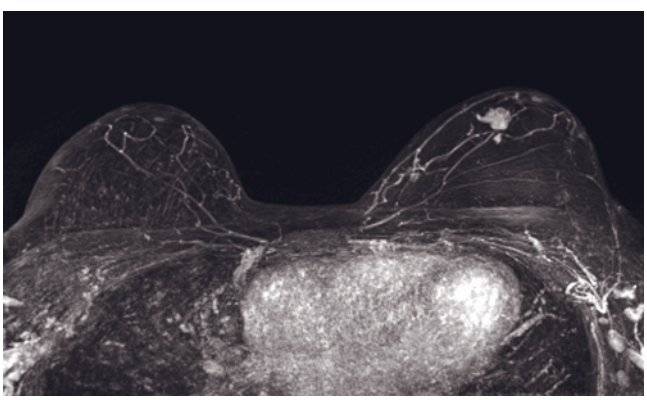

(*d*)

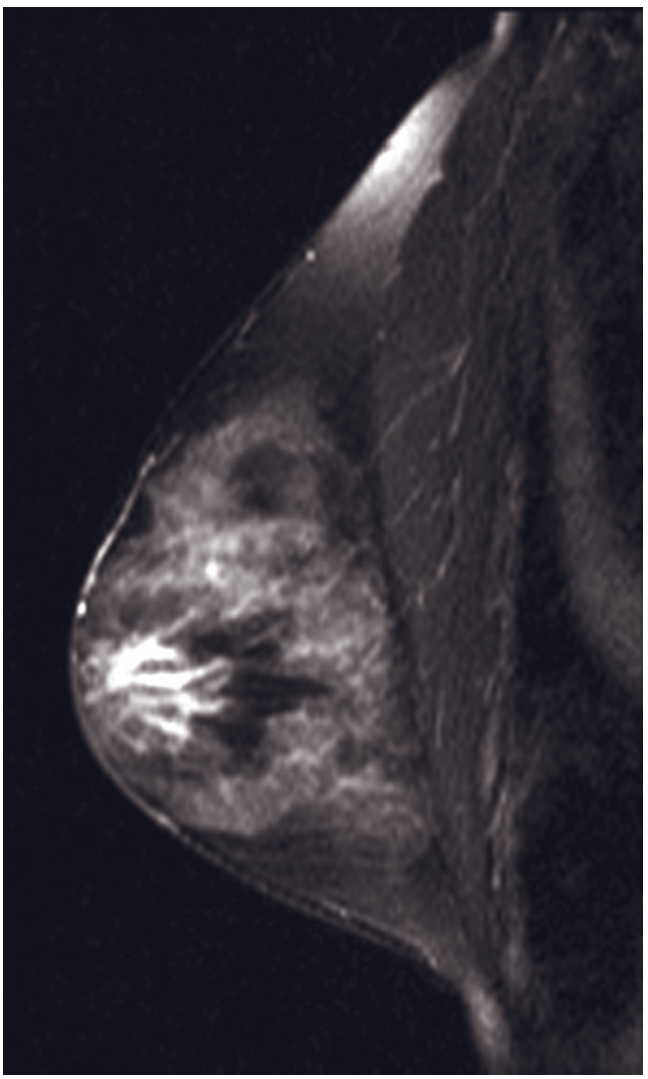

(*e*)

FIG. 19.15 Papilloma. Axial T2-weighted (*a*) and axial GRE (*b*) images show a well-circumscribed, oval, isointense mass located just below the subareolar region. On postcontrast GRE (*c*) and MIP (*d*) images it is seen as a strongly enhancing, slightly heterogeneous, lobulated mass. Papillomas are usually accompanied by dilated ducts as shown on the sagittal fat-saturated T2-weighted image (*e*). An ROI analysis of the dynamic images reveals a type III (washout) curve (*f*) that increases in signal intensity by 127%

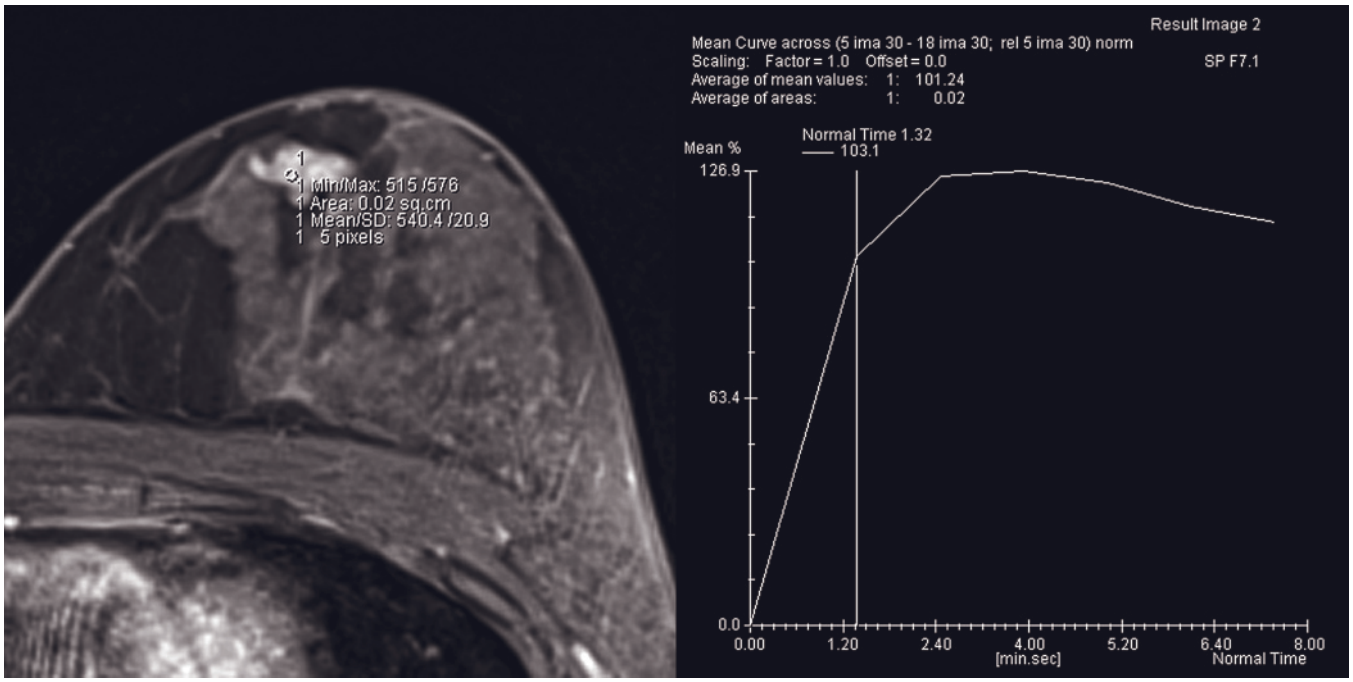

(*f*)

FIG. 19.15 (*Continued*) at 1.5 min after contrast injection, indicating BI-RADS 4 lesion. US-guided core needle biopsy (CNB) revealed papilloma.

MR ductography using microscopic coils has recently been proposed as a method that offers better detection of small intraductal papillomas. It has been reported that this method can show ducts measuring 0.8 mm in diameter and intraductal tumors as small as 1.0 mm. It also revealed a similar enhancing pattern for even the smallest lesions (3 mm) [85, 89].

A malignant papillary lesion is most reliably suggested by spiculation and rim enhancement, but no specific features can be used to diagnose a malignant process [82].

Multiple Papillomatosis

Multiple papillomatosis (MP) should be considered a risk factor for breast carcinoma, because of the proven significant association of MP with DCIS and invasive carcinoma [90, 91]. Gutman et al. [92] recently reported that the risk may not be greater than that with a solitary papilloma.

MRI is most useful in the preoperative planning of wide local excision margins in patients with MP [82], revealing multiple postcontrast enhancing irregularly shaped lesions in a single breast or both breasts with various types of kinetics (fig. 19.16).

Complete surgical excision is considered the treatment of choice for both solitary papillomas and multiple papillomatosis, with wire localization before surgery if necessary. Annual follow-up with mammography and ultrasound is recommended after excision of any papillary lesion [82, 83].

Hamartoma (Fibroadenolipoma)

Hamartoma is a well-circumscribed, usually encapsulated nodule, consisting of all breast tissue components, usually described as "breast within breast" on mammography. It consists of various proportions of fibroglandular and adipose components within the lesion with a pseudocapsule of compressed breast tissue [20].

Hamartoma has a typical mammographic appearance, and MRI is usually not needed for the diagnosis. The MRI appearance of this tumor depends on its histology, reflecting different amounts of fatty tissue and enhancing fibroglandular tissue. Recognition of the fatty capsule on non-fat-suppressed images can favor the diagnosis. However, correlation with mammography is recommended. ^{1}H MR spectroscopy of hamartoma is usually negative (no detectable Cho peak at 3.32 ppm) (fig. 19.17). Although ductal hyperplasia, apocrine metaplasia, calcifications, and adenosis may be associated with a hamartoma [20], surgery is not necessary in the vast majority of cases.

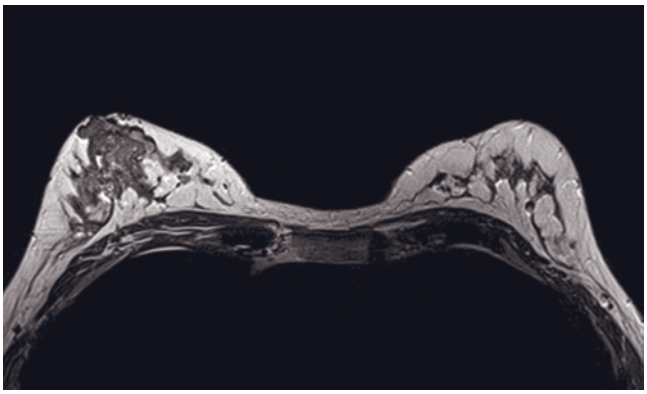

(*a*)

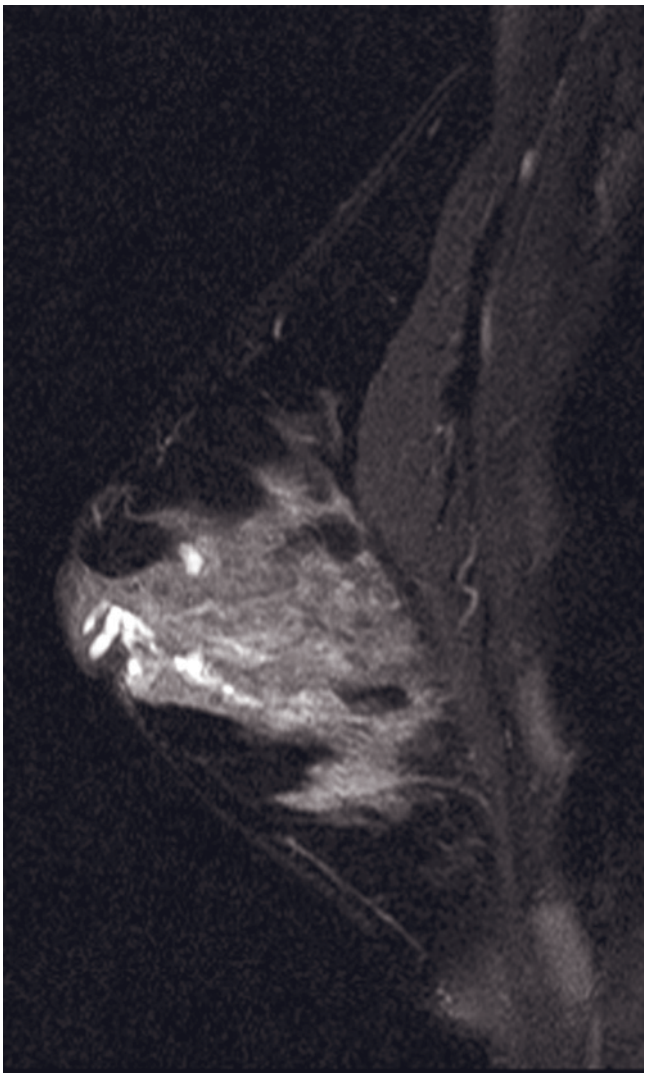

(*b*)

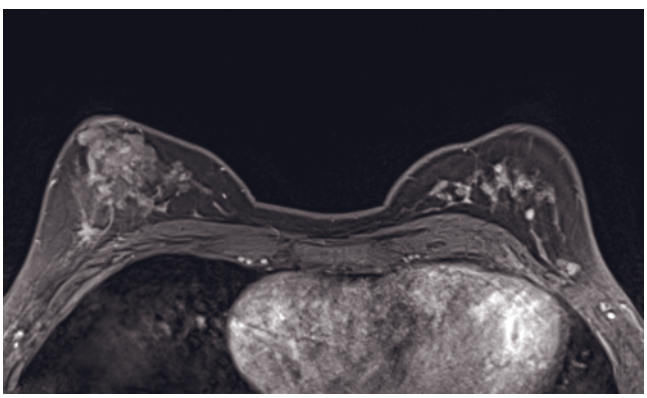

(*c*)

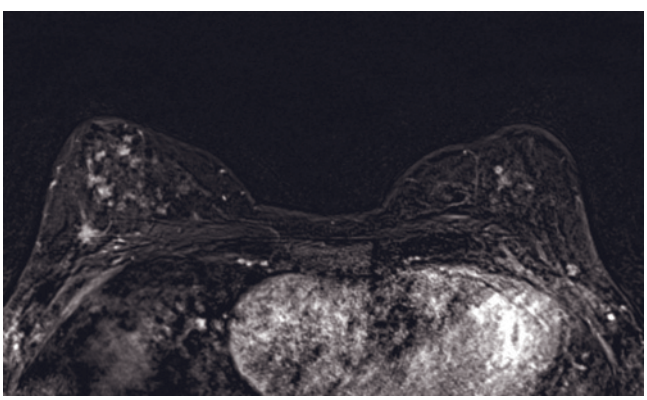

(*d*)

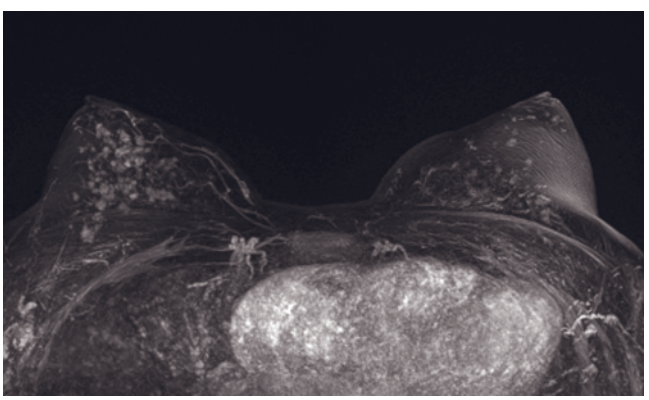

(*e*)

FIG. 19.16 Multiple papillomatosis. T2-weighted (*a*) and sagittal fat-saturated T2-weighted (*b*) images show dilated ducts in the right breast. Axial postcontrast GRE (*c*), subtracted (*d*), and MIP (*e*) images reveal multiple enhancing, irregularly shaped lesions in both breasts, showing washout kinetics (*f*), thus indicating BI-RADS 4 lesions. US-guided core needle biopsy (CNB) of both breasts verified multiple papillomatosis.

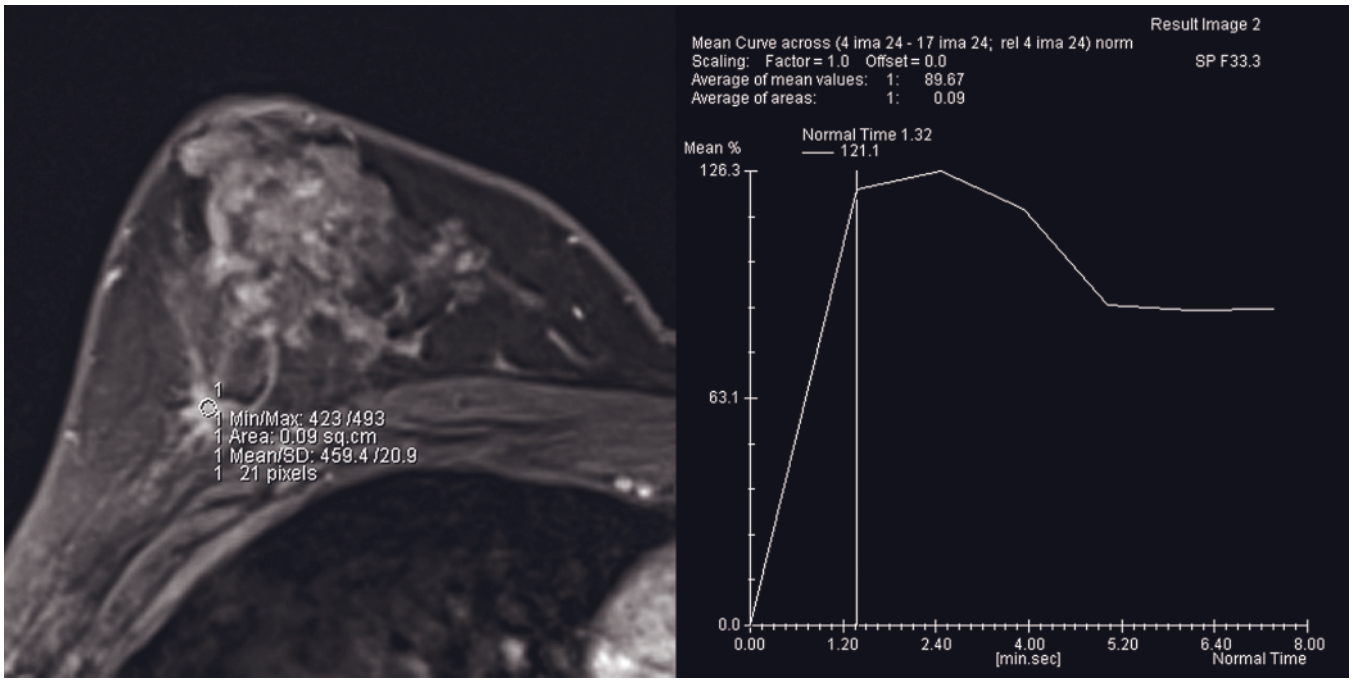

(*f*)

FIG. 19.16 (*Continued*)

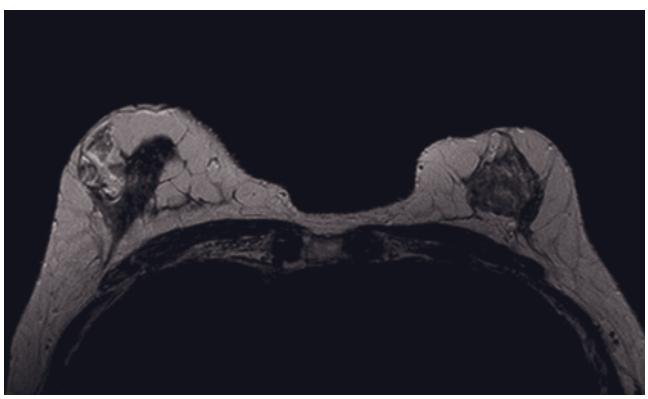

(*a*)

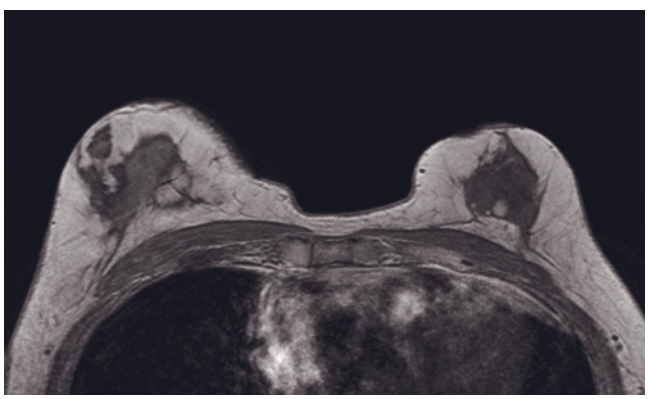

(*b*)

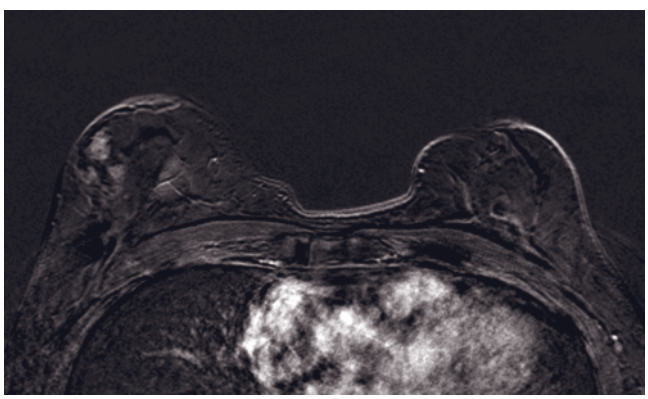

(*c*)

FIG. 19.17 Hamartoma. Axial T2-weighted (*a*) and T1-weighted (*b*) images reveal a well-circumscribed, heterogeneous mass, mainly hyperintense because of predominantly fatty content. There are also small, hypointense areas present, representing fibroglandular tissue, that show mild enhancement on a postcontrast subtracted image (*c*). Since ^{1}H MR spectroscopy (*d*) of hamartoma shows only a small Cho peak at 3.2 ppm, a benign nature of the lesion is confirmed. (Courtesy of Natasa M. Prvulovic, M.D., Diagnostic Imaging Center, Oncology Institute of Vojvodina, Serbia.)

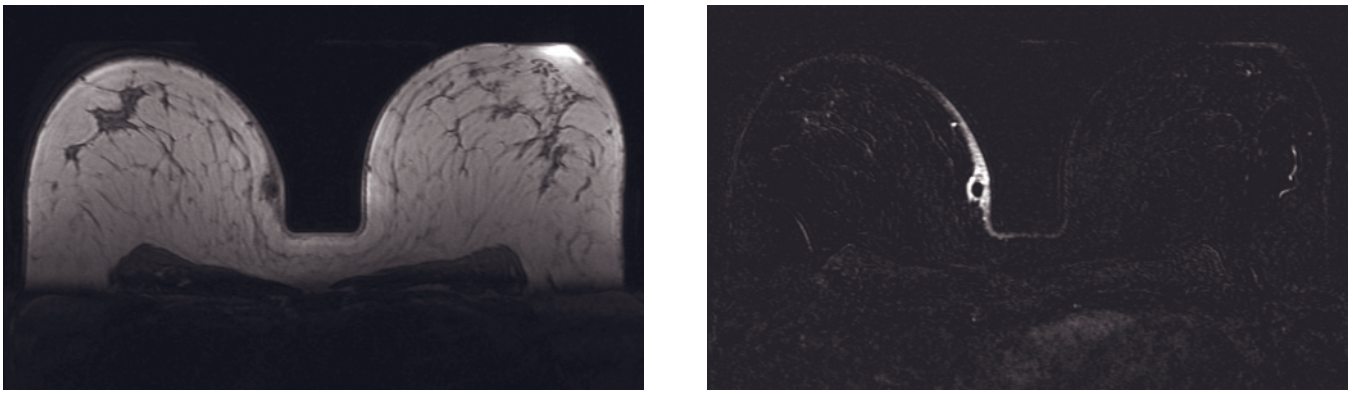

(*a*) (*b*)

FIG. 19.18 Abscess. Axial T2-weighted image (*a*) reveals an oval, well-circumscribed subcutaneous mass, surrounded by perifocal inflammatory changes and skin thickening, located in the medial aspect of the right breast. Strong ringlike and skin enhancement is seen on the axial postcontrast subtracted image (*b*).

Abscess

Breast abscess is an inflammatory condition usually located in the subareolar or periareolar region that can develop in both lactating and nonlactating women [20]. Mastalgia, subareolar lump, and overlying skin inflammation are noted with or without nipple discharge. Later, a fluctuant abscess can be palpated that yields pus spontaneously or on incision. If the abscess becomes chronic, fistula and nipple inversion frequently occur [93]. About 20% of cases are bilateral, and recurrences develop in almost 90% of patients [20]. Subareolar abscesses are particularly challenging, both from a therapeutic and an imaging perspective. For achieving a radical cure of the subareolar abscess, adequate surgical excision is desired.

On MRI, the most frequent finding is focal or diffuse signal intensity changes, hypointense on T1-weighted images and hyperintense on T2-weighted images (fig. 19.18). The abscess wall enhances gradually and progressively on dynamic postcontrast T1-weighted images, with abscess cavities visualized as irregular hypointense lesions and fistulas visualized with enhanced walls and heterogeneous content.

Standard MRI technique may often fail to exhibit some subtle structures of a subareolar abscess. To overcome this limitation, a microscopy coil has been suggested, which can provide a comprehensive view of inverted nipples, abscess cavities, fistulas, and inflammation around the lesion [93].

In rare cases of idiopathic granulomatous mastitis, MRI usually shows heterogeneously enhancing areas with or without multiple ringlike enhanced abscesses with a benign pattern of time-intensity curve [94]. Masslike enhancement and nodular enhancement may be found, and the time-intensity curves can vary from lesion to lesion [95].

Lymph Nodes

Lymph nodes are part of the normal anatomy of the breast, most commonly found in the axilla and axillary tail of the breast, but they can occasionally be found in any other part of the breast tissue.

On conventional MRI, lymph nodes appear as T2 hyperintense focal lesions with smooth margins. Since they show rapid enhancement with a washout curve in the early phase of dynamic postcontrast imaging, they can easily be confused with malignant foci. Reniform shape, fatty hilum, T2 hyperintensity, and typical mammographic appearance can confirm the diagnosis (fig. 19.19).

Nodes with a short-axis diameter of more than 1 cm are more common in malignant disease [96]. Nonuniform cortex thickening and loss of fatty hilum is suggestive of malignant involvement. The role of MRI in preoperative assessment of metastatic spread to lymph nodes is not reliable (with 36% sensitivity and 94% specificity). The sensitivity and specificity may improve up to 100% if ultrasmall superparamagnetic iron oxide (USPIO) contrast agents are used [97].

NONMASS LESIONS

Fibrocystic Changes and Sclerosing Adenosis

Fibrocystic changes (FCC) are benign alterations of the breast consisting of cystic dilatation of TDLU, with relative increase in fibrous stroma and proliferation of epithelial elements caused by hormonal imbalances [20, 22]. About 30% of women between the age of 20 years and menopause show some clinical evidence of FCC, although FCC can be identified in 60–80% of all

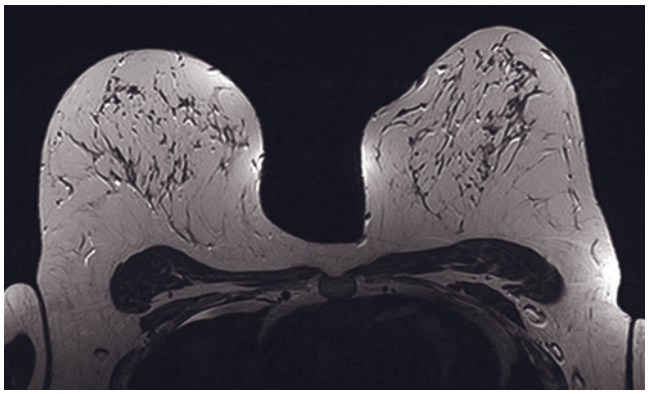

(*a*)

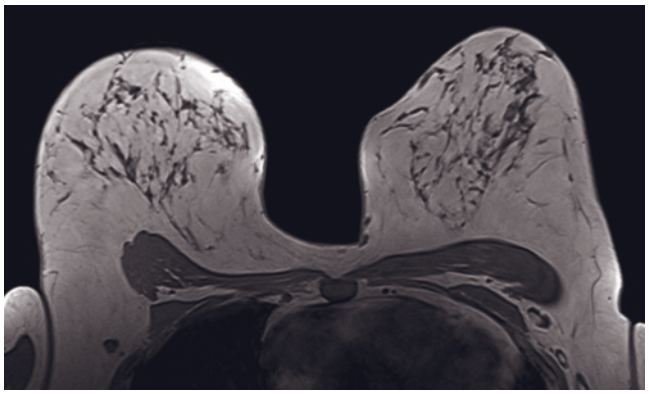

(*b*)

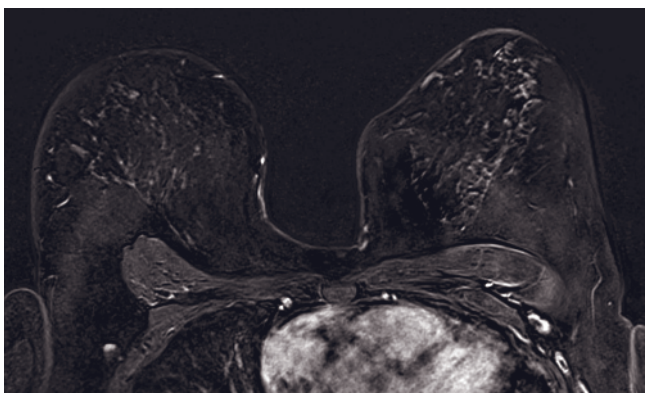

(*c*)

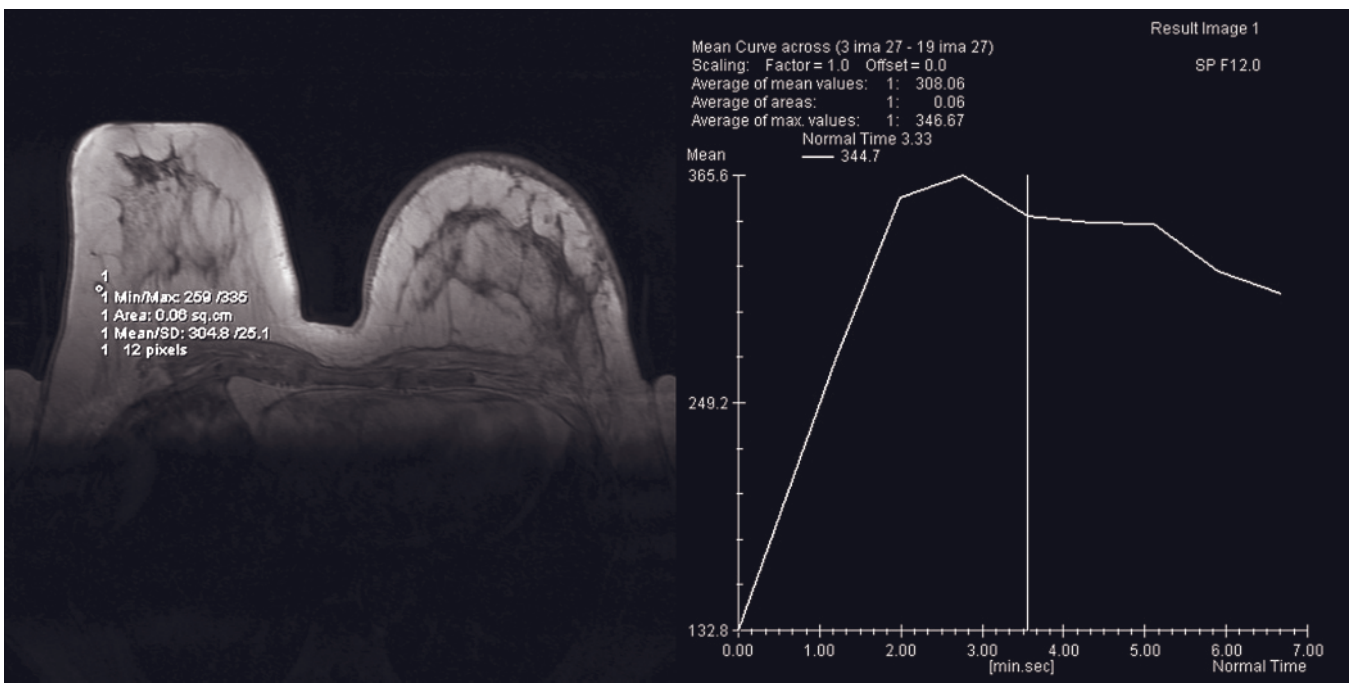

(*d*)

FIG. 19.19 Lymph nodes. Reniform shape and fatty hilum on T2-weighted (*a*) and T1-weighted (*b*) images make the typical morphology of lymph nodes seen bilaterally in axillas. After application of GBCA, peripheral enhancement is usually present (*c*). Another case is depicted in *d* and *e*. ROI analysis of the postcontrast dynamic images (*d*) often shows rapid enhancement followed by an early washout, resulting in type III curve. Typical MR morphology or mammographic (*e*) appearance is suggestive of diagnosis.

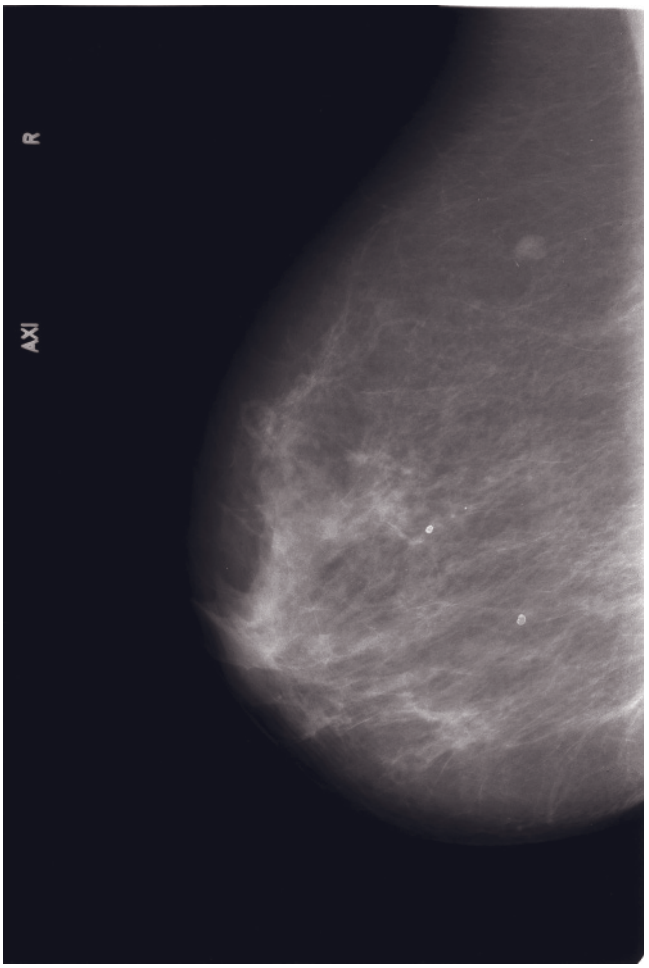

(*e*)

FIG. 19.19 (*Continued*)

autopsies [22]. FCC is frequently a multifocal, bilateral mammary alteration [20]. Premenstrual breast pain and palpable lumps in the breast correlate poorly with FCC [22].

A combination of cysts with a diameter of 1–2 mm (microcysts) and larger cysts of 1–2 cm in diameter (macrocysts) are characteristic findings in FCC. Nonproliferative FCCs are not associated with an increased cancer risk. FCCs with atypical apocrine metaplasia seem to be associated with a significant increased risk for breast cancer in women older than 60 years [98].

Sclerosing adenosis is a less common variant of proliferative FCC, characterized by a proliferation of small ducts and myoepithelial cells, associated with fibrosis. It carries a 4–5 times increased risk for cancer, even in the contralateral breast that may be unaffected with the condition [22].

In FCC (fig. 19.20) and sclerosing adenosis (fig. 19.21), MR reveals often bilaterally symmetric distribution of enhancing foci or areas of non-masslike enhancement that usually do not follow the ductal system, which is the most important feature in the differentiation from DCIS or invasive lobular carcinoma. Enhancement characteristics should not be taken into account, since they often exhibit washout-type curves, which is misleading in establishing the correct diagnosis [30].

Radial Scar

Radial scar (RS) is a sclerosing benign breast lesion consisting of a central fibroelastic core surrounded by radiating ducts [20]. It often mimics a carcinoma (clinically, radiologically, and pathologically) because of the stellate or nodular appearance, making the diagnosis challenging. The ductules around the central scarred zone can be associated with any type of intraductal proliferation (usual ductal hyperplasia, ADH, DCIS), or even invasive cancers, making RS a lesion with increased risk for cancer [20, 99]. Biopsy is mandatory for diagnosis. The diagnosis of RS established by a CNB should lead to complete excision of the lesion [100].

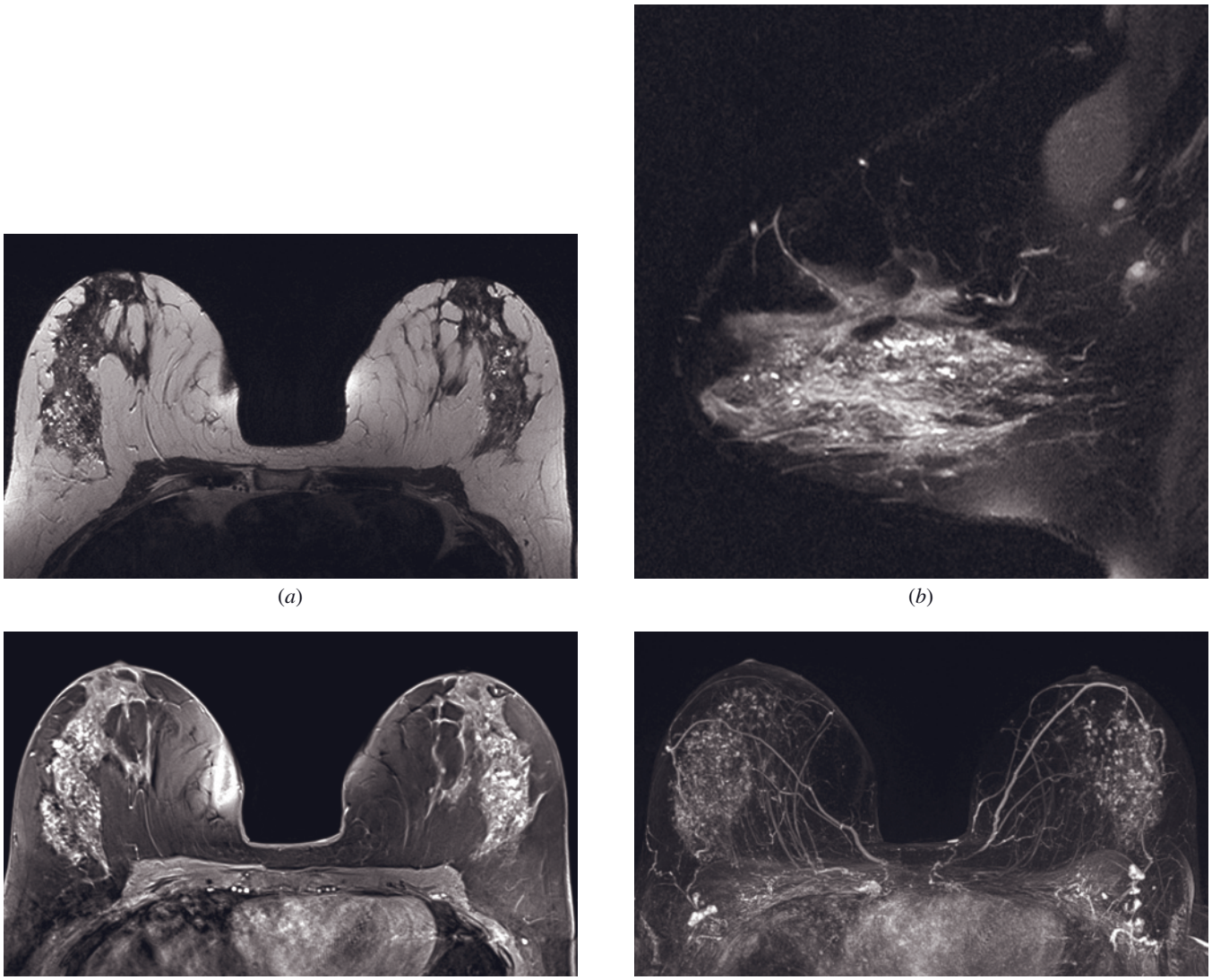

(*a*) (*b*) (*c*) (*d*)

FIG. 19.20 Fibrocystic changes (FCC). Axial T2-weighted (*a*) and sagittal T2 fat-saturated (*b*) images show multiple high-intensity foci scattered in both breasts within the fibroglandular tissue. Axial postcontrast GRE (*c*) and MIP (*d*) images reveal a non-masslike stippled enhancement of fibroglandular tissue, which is symmetrically distributed in both breasts, with innumerable enhancing foci.

On MRI, contrast-enhanced T1-weighted images show an enhancing irregular or spiculated mass that may be indistinguishable from carcinoma. Dynamic study usually shows heterogeneous enhancement patterns, regardless of the diagnosis and associated histologic features (fig. 19.22).

Ductal Carcinoma in Situ

Traditionally, carcinoma in situ has been considered the preinvasive form of cancer, with several histological types: intraductal, lobular, and papillary carcinoma in situ. Also, all intraductal proliferative lesions of the breast are divided into three categories: usual ductal hyperplasia (UDH), atypical ductal hyperplasia (ADH), and ductal carcinoma in situ (DCIS). The risk for subsequent development of invasive breast cancer ranges from approximately 1.5 times that of the reference population for UDH, to 4- to 5-fold for ADH, and 8- to 10-fold for DCIS [101]. The current data suggest that these entities share a few similarities, and that there may be no justification in separating them.

To overcome several disadvantages of the traditional classification system and replace it with a more meaningful system, an alternative terminology of ductal intraepithelial neoplasia (DIN) has been proposed

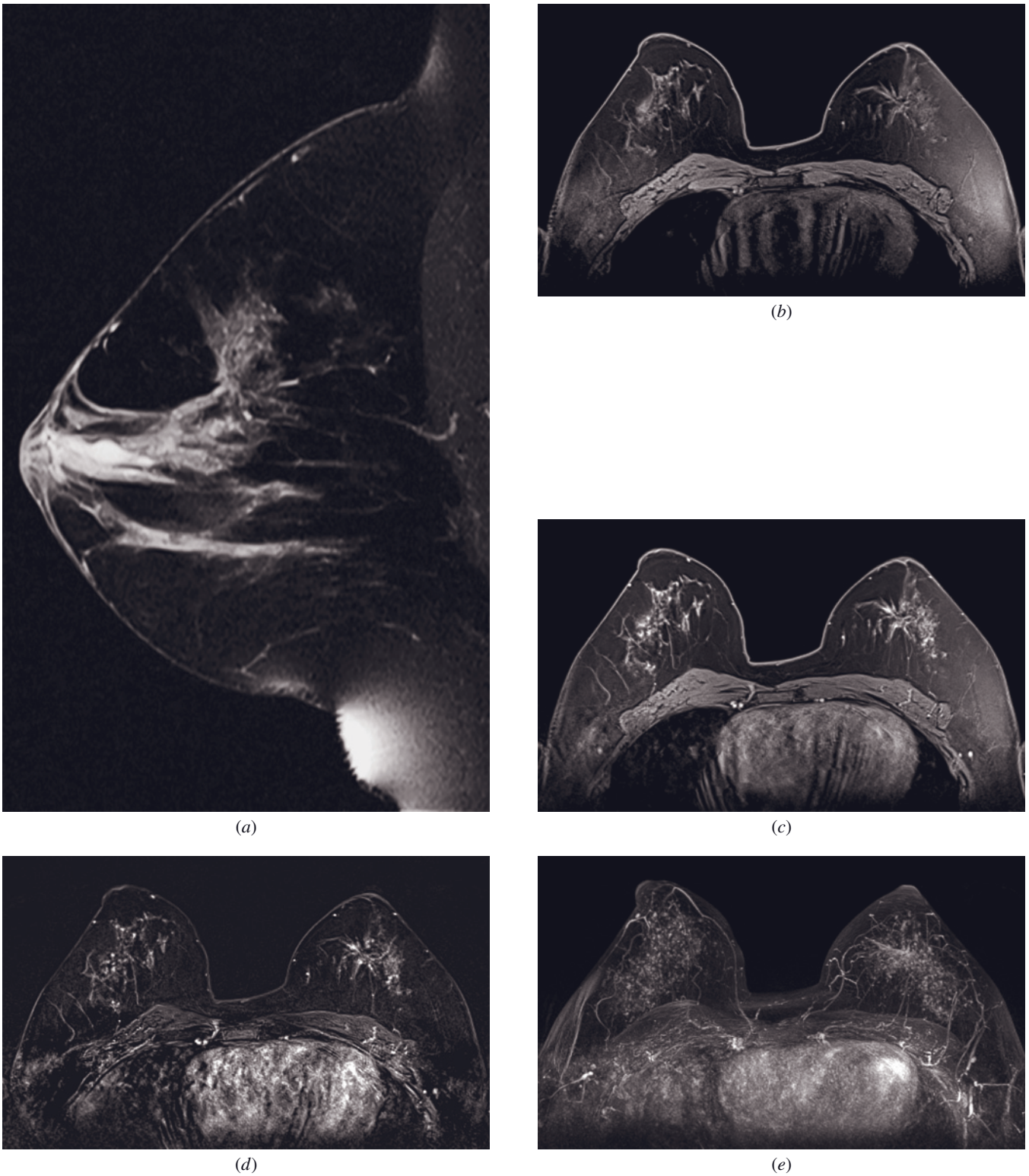

FIG. 19.21 Adenosclerosis. Sagittal fat-saturated T2-weighted (*a*) and axial GRE (*b*) images show an isointense lesion with long, radially distributed spicules in the upper inner quadrant of the left breast (BI-RADS 4 lesion). There is no significant enhancement on postcontrast GRE (*c*) and subtracted (*d*) images. Only architectural distortion with MRI background enhancement type 3 of the breast parenchyma is seen on the MIP image (*e*). Excisional biopsy revealed blunt duct adenosis (adenosis partim atypica).

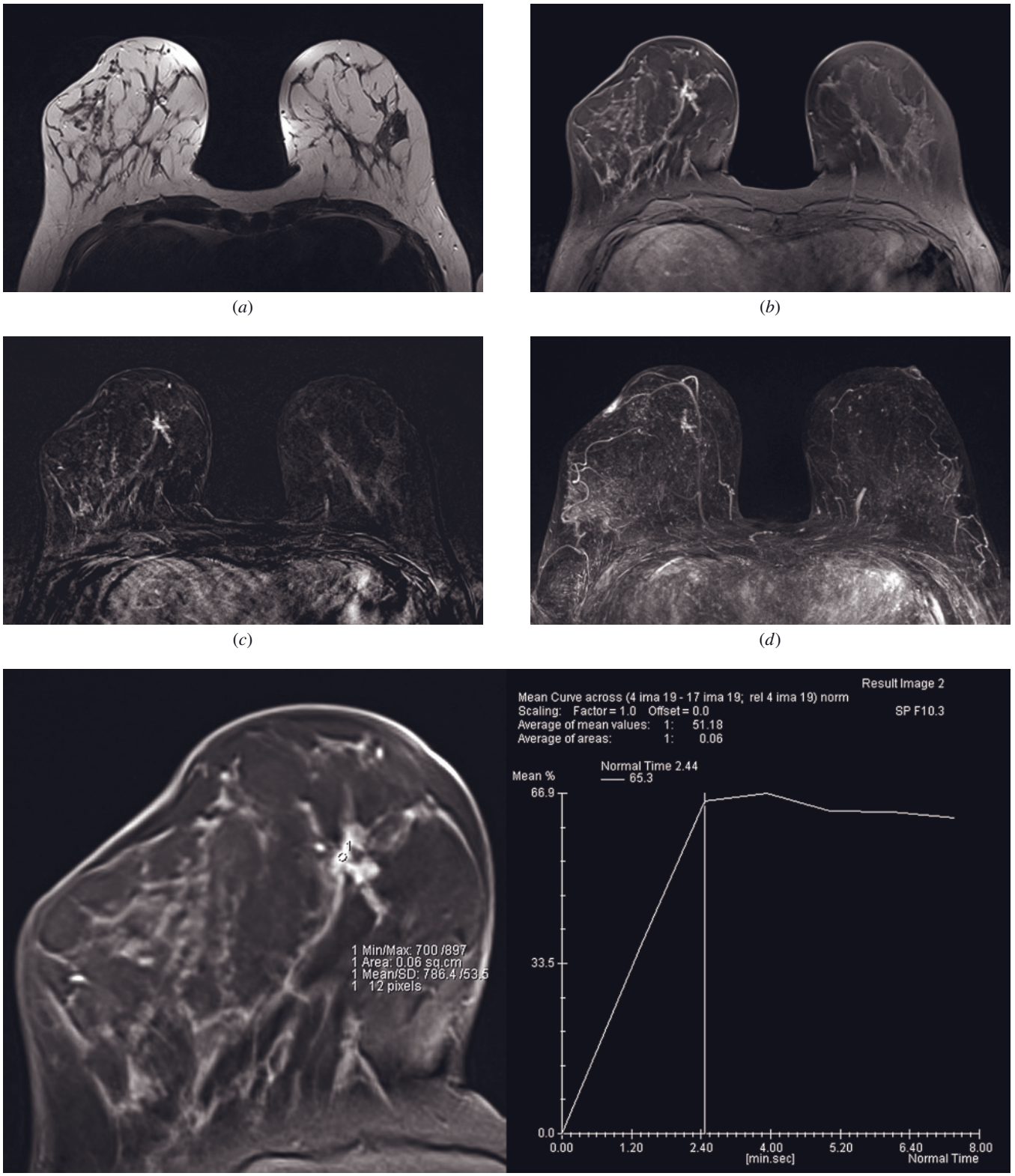

FIG. 19.22 Radial scar. Axial T2-weighted image (*a*) reveals a hypointense spiculated lesion in the right breast showing enhancement on postcontrast GRE (*b*), subtracted (*c*), and MIP images (*d*) with morphology that is indistinguishable from carcinoma. However, the dynamic curve (*e*) demonstrates a plateau pattern (Type II) with moderate initial enhancement and maximum signal increase of 67% at 4 min after administration of GBCA. The moderate enhancement rate in the first 2 min categorizes this lesion as a BI-RADS 4 despite its morphology. Excisional biopsy revealed a radial scar.

[20, 102]. The current *World Health Organization Classification of Tumours of the Breast* (2003) includes the DIN terminology in addition to the traditional system [101]. The classification of intraductal proliferative lesions may be modified as additional molecular, genetic, and clinical data become available [20].

Ductal carcinoma in situ (DCIS) itself is considered a heterogeneous group divided into low-grade (G1), intermediate-grade (G2), and high-grade (G3) lesions [22]. Whereas high-grade DCIS is likely to progress to high-grade invasive cancer, low-grade DCIS can be more indolent or might progress to only certain types of cancer, usually well differentiated. There is agreement that DCIS should be treated (at least) by local excision to avoid recurrence or progression to invasive breast cancer [60, 103, 104].

DCIS is visible on breast MR images. The sensitivity for diagnosing DCIS is lower than that for diagnosing invasive cancers, ranging from 30% to 90%, and morphology of DCIS on MRI differs significantly from that of invasive carcinoma [60, 61, 105, 106]. The typical DCIS appears as asymmetric (unilateral) non-masslike enhancement that follows segmental, linear, or ductal distribution [105, 106]. Only the minority of DCIS (14%) appear as mass lesions [61]. Internal enhancement is usually heterogeneous, with a so-called clumped or stippled architecture.

Although approximately 70% of DCIS exhibit rapid early enhancement (fig. 19.23), delayed enhancement is variable. Relatively benign enhancement kinetics of DCIS are probably the reason for the low sensitivity of breast MRI for DCIS shown in earlier studies [107, 108]. Therefore, any segmental or ductal enhancement on MR images suggests the presence of an intraductal pathologic condition. In turn, diffuse or multiple areas of regional enhancement on MR images favor the diagnosis of benign nonmass lesions [30] (fig. 19.24).

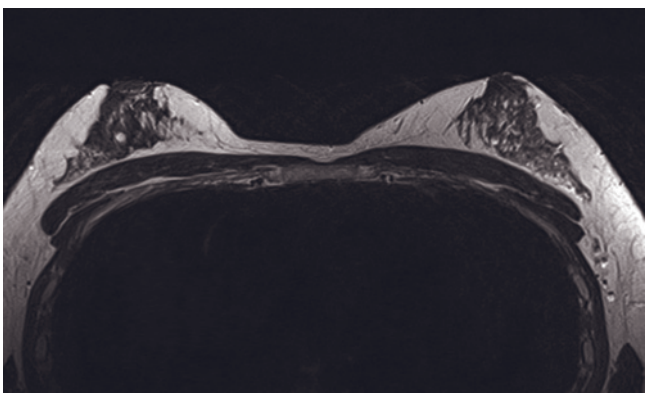

(*a*)

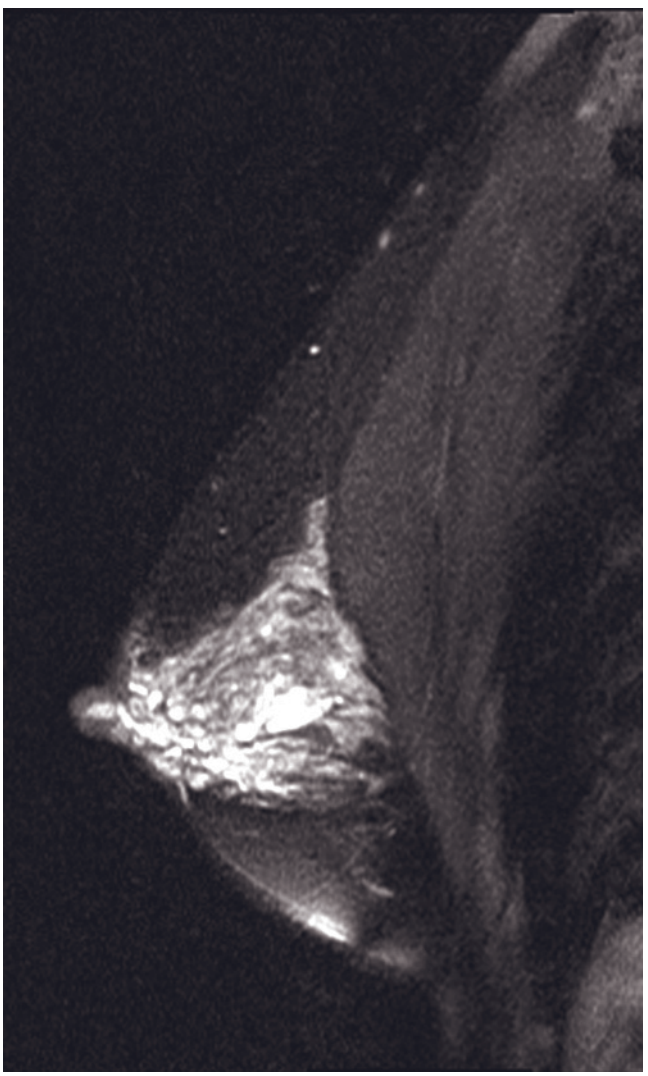

(*b*)

FIG. 19.23 Ductal carcinoma in situ (DCIS). Axial T2-weighted image (*a*) shows subtle architectural distortion with irregular, isointense lesions in the lateral part of the left breast. Sagittal T2-weighted fat-saturated image (*b*) reveals irregularly dilated ducts. On postcontrast GRE (*c*), subtracted (*d*), and MIP (*e*) images non-masslike enhancement in segmental distribution is seen, with a washout kinetic curve (Type III) indicating high-grade DCIS.

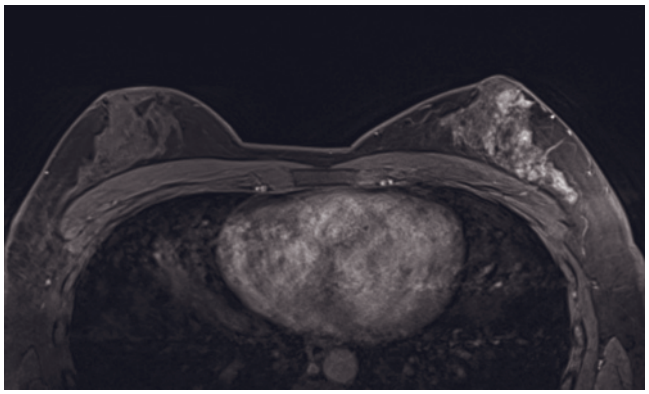

(*c*)

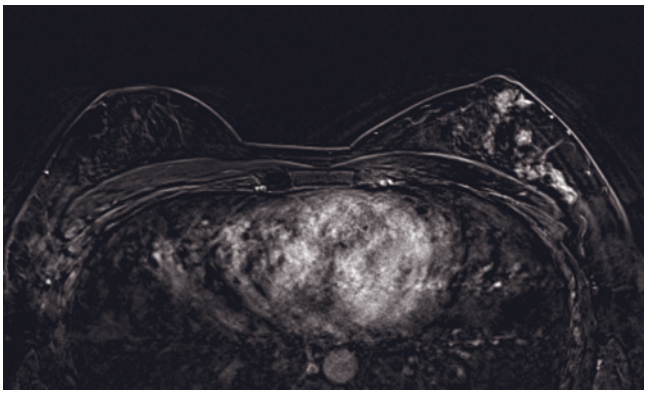

(*d*)

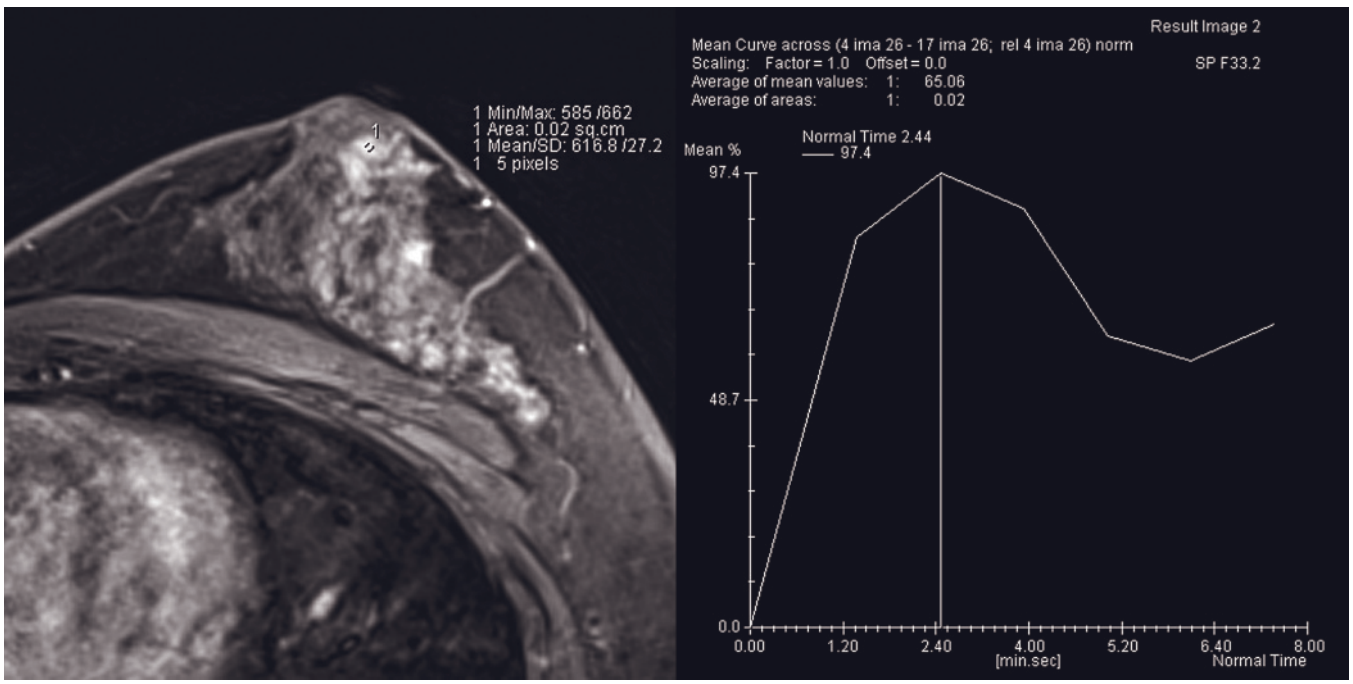

(*e*)

FIG. 19.23 (*Continued*)

MR imaging and mammography are complementary for diagnosing DCIS. According to more recent publications, about 10% of DCIS cases that are diagnosed with the aid of mammography would be missed with MR alone because of the absence of any abnormal enhancement. In turn, today up to 40% of DCIS cases are diagnosed only with breast MRI (fig. 19.25). Recent studies have shown that sensitivity rates of MRI for mammography-detected DCIS are high [60, 109–112].

Most breast cancers (at least 70–80%) arise in mammary ducts [21] and may have imaging patterns that reflect this ductal origin. According to one study [105] ductal enhancement accounted for 21% of MRI detected cancers that were subsequently biopsy proven, with a positive predictive value of 26%. The differential diagnosis for ductal enhancement includes DCIS, infiltrating carcinoma, atypical ductal hyperplasia (ADH), lobular carcinoma in situ (LCIS), and benign findings such as FCC, ductal hyperplasia, and fibrosis. ADH and LCIS, considered to be high-risk lesions, constitute 9% and 10% of suspicious linear ductal enhancement, respectively. It has been shown that at MRI, even LCIS has features suspicious for malignancy (fig. 19.26).

There is increasing evidence to suggest that breast MRI may be more sensitive for the diagnosis of high-grade DCIS, because the enhancement pattern on breast MRI has been shown to correlate with significantly higher vessel density in more aggressive DCIS, which can be prognostically relevant [30, 60, 113–117].

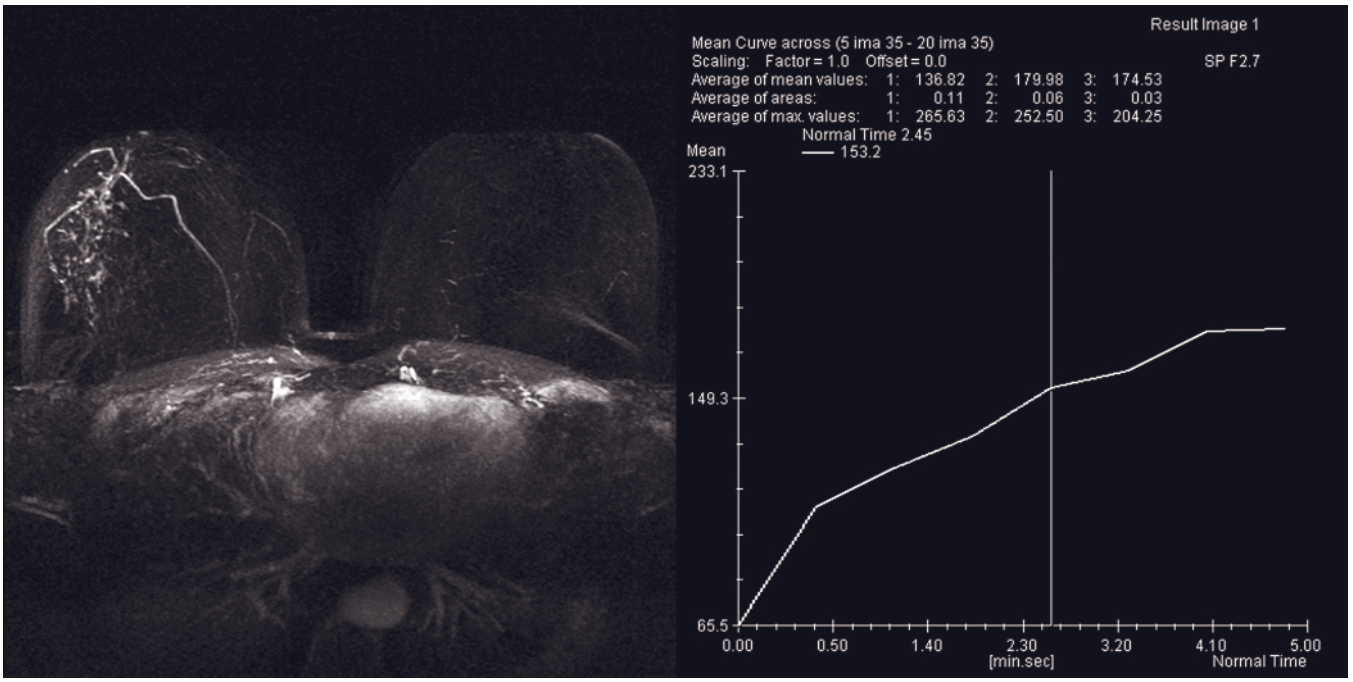

(*a*)

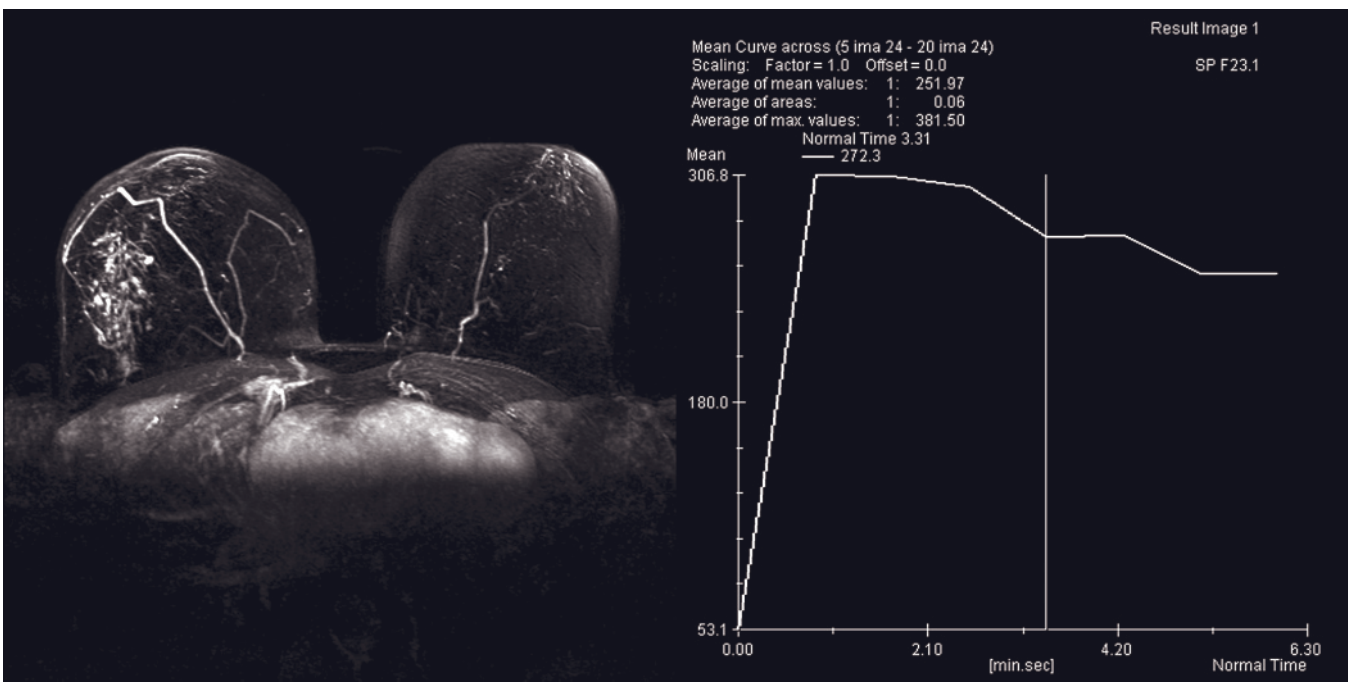

(*b*)

FIG. 19.24 Ductal carcinoma in situ (DCIS). MIP image (*a*) shows a non-masslike enhancement in segmental distribution within the right breast, with persistent kinetic curve. Since the patient refused biopsy, follow-up with another MRI study was performed after 6 months (*b*) showing significant increase in the non-masslike segmental enhancement typical for DCIS. Furthermore, the ROI analysis of this study reveals the alteration from persistent (Type I) to washout (Type III) type curve. Subsequent biopsy verified high-grade DCIS with multiple small foci of invasive ductal carcinoma (IDC).

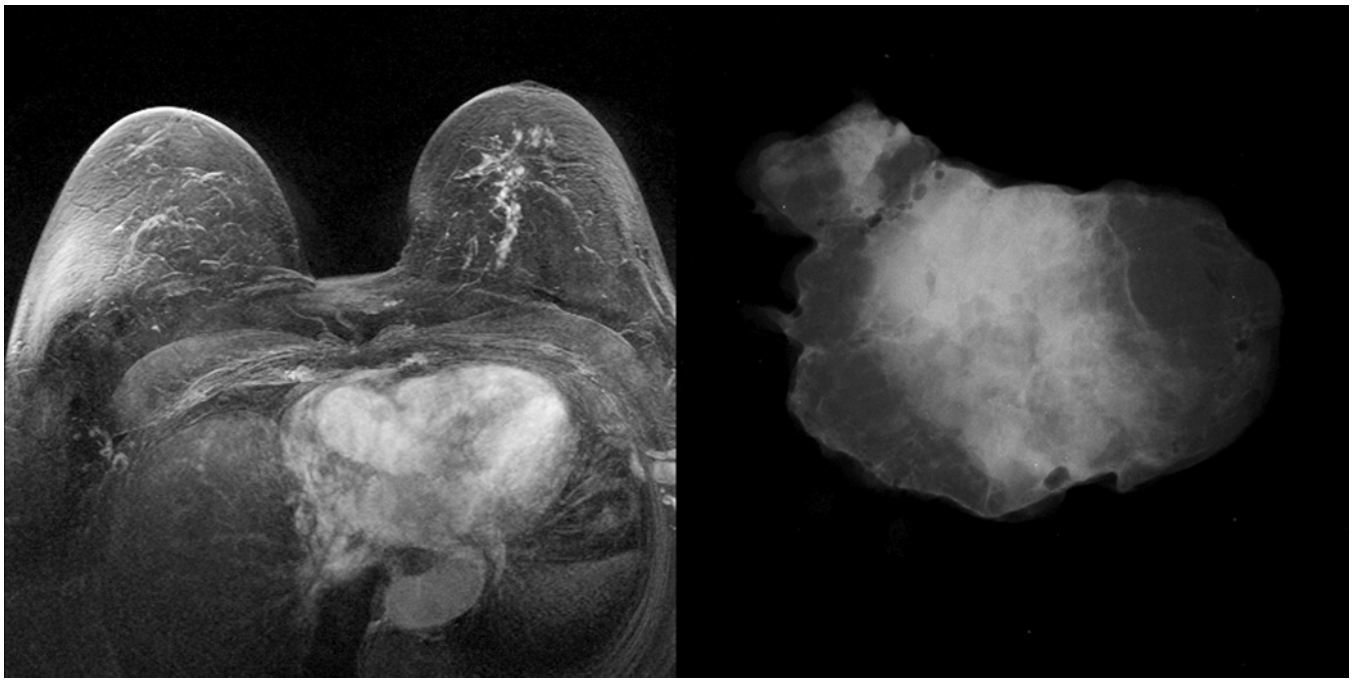

FIG. 19.25 Ductal carcinoma in situ (DCIS). MIP image (*a*) shows a non-masslike enhancement in ductal distribution occupying a significant area within central and deep subareolar regions of the left breast, indicating DCIS. Specimen radiography (*b*) reveals opacity that corresponded to DCIS. Microcalcifications seen in the lower right quadrant of the specimen were associated with benign epithelium.

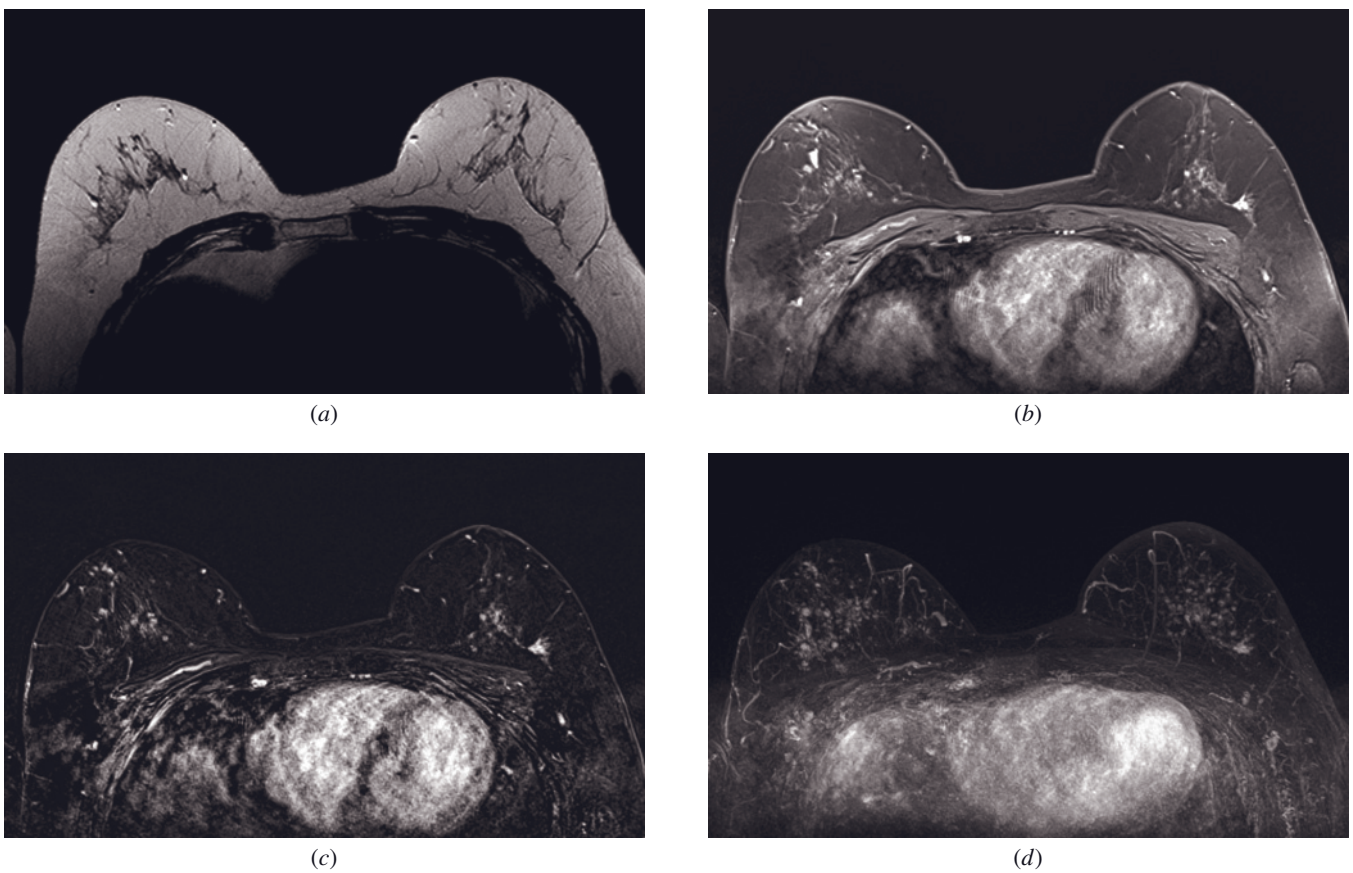

FIG. 19.26 Lobular carcinoma in situ (LCIS). Axial T2-weighted image (*a*) shows a hypointense stellate lesion in the lateral part of the left breast with moderate enhancement on the postcontrast dynamic GRE (*b*) and subtracted (*c*) images. MIP image (*d*) indicates many additional enhancing foci symmetrically distributed in both breasts. Analysis of the dynamic data set shows a washout

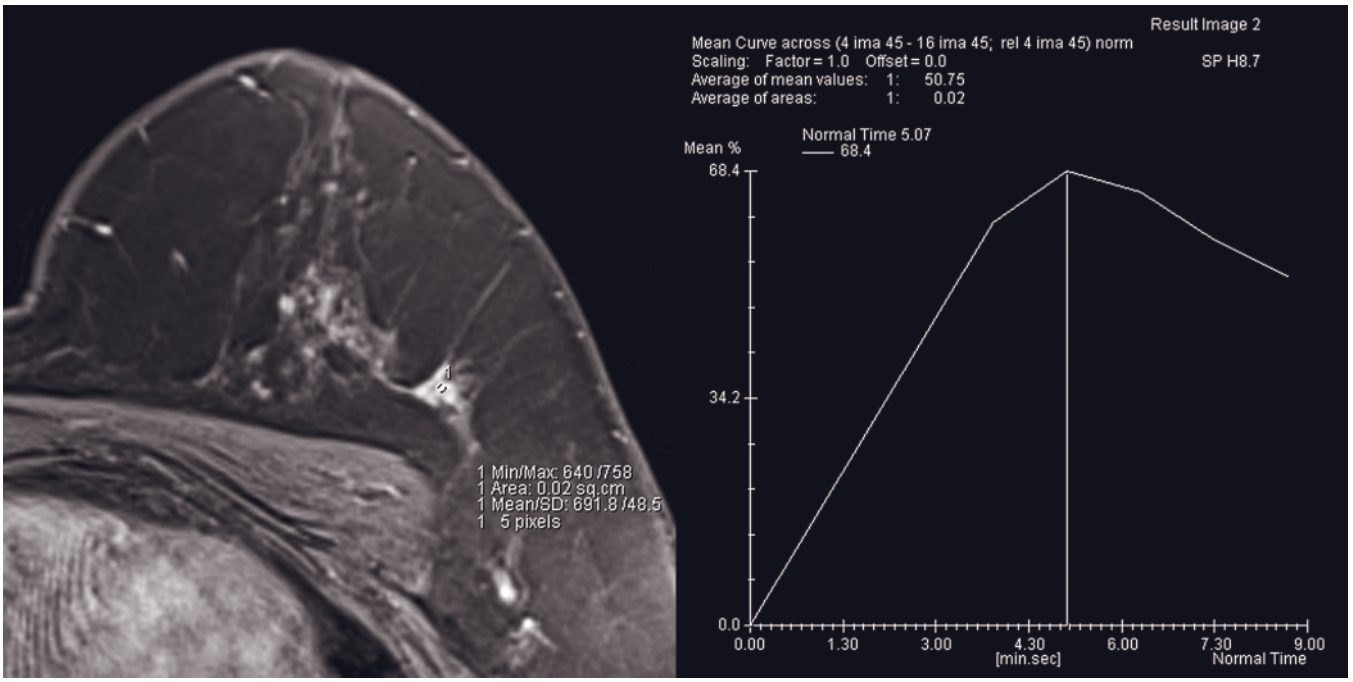

(*e*)

FIG. 19.26 (*Continued*) curve (*e*) with maximum enhancement increase of 68.4% five minutes after GBCA injection. Biopsy revealed LCIS in both breasts.

Table 19.6 CNB Underestimation
DCIS
High-risk/borderline lesions (B3): • Papillary lesions • Radial sclerosing lesions • Atypical ductal hyperplasia (ADH) • Lobular neoplasia (ALH and LCIS) • Cellular fibroepithelial tumors • Mucocele-like lesions • Columnar cell atypia

Percutaneous CNB is considered to be an accurate method for the histopathologic evaluation of breast lesions. Occasional underestimation happens in cases of DCIS and high-risk lesions. With one of these findings in CNB samples, complete excision of the lesion is recommended (Table 19.6).

The contexts of CNB underestimation are listed in Table 19.6.

MALIGNANT BREAST LESIONS

Breast Cancer

Breast cancer is the most common malignancy in women, and mortality from this malignancy is second only to lung cancer. The annual incidence rate in the US has remained stable over the last decade, at approximately 110 per 100,000. Before that, a relative increase in the breast cancer incidence rate may have resulted partly from an increased use of screening mammography, which revealed small cancers in preclinical stage. The incidence of breast cancer increases throughout a woman's life, reaching the plateau before menopause.

The pathogenesis of breast cancer is unknown, but many factors have been shown to be associated with increased risk for breast cancer, such as family history of breast cancer (including positive test for breast cancer gene *BRCA1/BRCA2* mutation), personal history of breast biopsy, diagnosis of high-risk lesions (ADH, LCIS), prior exposure to radiation, long period of menstruation (early menarche, late menopause), and nulliparity or older age at first-time pregnancy. Despite known risk factors, approximately 75% of breast cancers develop in women with no evident risk [118].

Genetic predisposition accounts for an estimated 5–10% of all breast cancers [119]. Since half of the women with *BRCA1* mutation develop breast cancer by the age of 50, when the breast density is higher [120], and those cancers do not tend to be associated with DCIS and microcalcifications, mammography alone may be insufficient to detect breast cancer at an early stage [121]. In the last decade, many researchers have proposed that screening MRI of the breast should be offered

to these patients [121–123]. However, with *BRCA2* carriers DCIS is more prevalent, and mammography remains a valuable screening tool in detecting microcalcifications. A recent study has shown that screening MRI allowed detection of more cancers in high-risk women than screening ultrasound or mammography [121]. The benefits include a predicted added cancer yield of 23 cancers per 1000 high-risk women screened with MRI, with less then 5% unnecessary biopsies. Although the specificity of screening MRI is lower than that of mammography or clinical examination (90%, 95%, and 98%, respectively), the overall accuracy is significantly higher [121]. Nowadays, breast MRI is considered an important complement to mammography in screening women at high risk.

The most common malignant breast tumors are of epithelial origin (adenocarcinomas) arising from TDLUs, with ductal carcinoma in 60–75% and lobular in 10% of all cases. Other subtypes account for 10–12% and include medullary, mucinous, papillary, and tubular cancers [21]. Tumors of mesenchymal origin are very rare.

Diagnostic Features of Invasive Cancers at Breast MRI

Gadolinium-based contrast-enhanced (GBCE) breast MRI provides accurate information about the morphology and enhancement kinetics of invasive cancers that can be used as strong predictors of malignancy. An important feature is the presence of enhancement of any type. However, a recent multicenter study showed that the absence of enhancement does not exclude invasive cancer with a negative predictive value of nonenhancement for invasive cancer of 94%. In that study, 16% of DCIS lesions and 3% of invasive cancers showed no appreciable enhancement [39].

Once detected, a lesion should be categorized by the type of enhancement as **mass or nonmass enhancement**. The **margins** of the focal mass (categories: smooth, lobulated, irregular, or spiculated) is the single most predictive feature in breast MRI interpretation (fig. 19.26). The **initial qualitative enhancement intensity** (at 2 min or less after contrast agent injection) is also highly predictive, followed by the type of kinetic curve (risk of cancer for a lesion that has a washout curve is 5 times higher than for lesions with plateau type). **Rim enhancement** and **associated area enhancement** are features that are rarely seen, but are highly indicative for malignancy. Associated area enhancement, explained as peritumoral inflammation of the tissue, sometimes cannot be distinguished from nonmass enhancement of FCC or DCIS. If an enhancing focal mass shows spiculated margins or rim enhancement it should be characterized as BI-RADS 5 lesion, irrespective of enhancement kinetics. The **distribution of area enhancement** is most predictive of diagnosis: Segmental and clumped distribution are associated with 78% and 60% likelihood of cancer, respectively, while low-level stippled enhancement in a regional distribution indicates benignity [39]. When a nonmass enhancement shows a segmental or clumped distribution with rapid enhancement and a washout, it is categorized as BI-RADS 5. With the benign type of kinetics (plateau or persistent), it is BI-RADS 4 lesion.

Secondary signs, if present, increase suspicion for carcinoma. The common signs detected at breast MRI are perilesional edema, architectural distortion, lymphadenopathy, skin thickening, or desmoplastic reaction (hook sign) recognized as a hypointense line from the lesion toward the pectoral muscle (fig. 19.27).

Asymmetric increase in breast vascularity in the breast that contains a cancer can often be observed, increasing diagnostic confidence, especially in searching for occult carcinoma. Possible explanations include reduced flow resistance in tumor tissue, high metabolic rate, and angiogenic stimulation of the whole breast in which a cancer is growing [124].

Classification and Staging

The American Joint Committee on Cancer (AJCC) staging system [125] provides a strategy for grouping patients with respect to prognosis. Therapeutic decisions are formulated in part according to staging categories but primarily according to lymph node status, estrogen and progesterone receptor levels in the tumor tissue, menopausal status, and the general health of the patient.

The AJCC has designated staging by TNM classification (Table 19.7).

One of the major applications of MRI in breast imaging is staging of breast cancer. MRI has been shown to be more accurate than mammography or ultrasound in detecting the size and extent of the lesion [126]. MRI tumor size correlates with pathology size; however, a significant overestimation exists, particularly for tumors larger than 2.0 cm. Clinicians should therefore use caution in relying on MRI tumor size in determining candidacy for breast conservation therapy (BCT) [127]. In addition, MRI is useful in the identification of multicentric disease (fig. 19.28), which may have an impact on the type of therapy (radical mastectomy vs. BCT). The sensitivity of MRI in detecting multicentric disease ranges from approximately 89% to 100% with bilateral imaging. Occult breast cancers are identified with MRI in 15–27% of patients, while unsuspected synchronous cancer in the opposite breast can be found with MRI in 3–6% of patients [39, 128, 129].

MRI is helpful in detecting pectoral muscle (fig. 19.29) and chest wall involvement of breast cancer.

Table 19.7 TNM Classification

Primary tumor (T):
- TX: Primary tumor cannot be assessed
- T0: No evidence of primary tumor
- Tis: Carcinoma in situ; intraductal carcinoma, lobular carcinoma in situ, or Paget disease of the nipple with no associated tumor
  Note: Paget disease associated with a tumor is classified according to the size of the tumor.
- T1: Tumor 2.0 cm or less in greatest dimension
  - T1mic: Microinvasion 0.1 cm or less in greatest dimension
  - T1a: Tumor more than 0.1 but not more than 0.5 cm in greatest dimension
  - T1b: Tumor more than 0.5 cm but not more than 1.0 cm in greatest dimension
  - T1c: Tumor more than 1.0 cm but not more than 2.0 cm in greatest dimension
- T2: Tumor more than 2.0 cm but not more than 5.0 cm in greatest dimension
- T3: Tumor more than 5.0 cm in greatest dimension
- T4: Tumor of any size with direct extension to (a) chest wall or (b) skin, only as described below.
  - T4a: Extension to chest wall
  - T4b: Edema (including peau d'orange) or ulceration of the skin of the breast or satellite skin nodules confined to the same breast
  - T4c: Both of the above (T4a and T4b)
  - T4d: Inflammatory carcinoma*
  - Note: Chest wall includes ribs, intercostal muscles, and serratus anterior muscle but not pectoral muscle.

Regional lymph nodes (N):
- NX: Regional lymph nodes cannot be assessed (e.g., previously removed)
- N0: No regional lymph node metastasis
- N1: Metastasis to movable ipsilateral axillary lymph node(s)
- N2: Metastasis to ipsilateral axillary lymph node(s) fixed to each other or to other structures
- N3: Metastasis to ipsilateral internal mammary lymph node(s)

Pathologic classification (pN):
- pNX: Regional lymph nodes cannot be assessed (not removed for pathologic study or previously removed)
- pN0: No regional lymph node metastasis
- pN1: Metastasis to movable ipsilateral axillary lymph node(s)
  - pN1a: Only micrometastasis (none larger than 0.2 cm)
  - pN1b: Metastasis to lymph node(s), any larger than 0.2 cm
  - pN1bi: Metastasis in 1 to 3 lymph nodes, any more than 0.2 cm and all less than 2.0 cm in greatest dimension
  - pN1bii: Metastasis to 4 or more lymph nodes, any more than 0.2 cm and all less than 2.0 cm in greatest dimension
  - pN1biii: Extension of tumor beyond the capsule of a lymph node metastasis less than 2.0 cm in greatest dimension
  - pN1biv: Metastasis to a lymph node 2.0 cm or more in greatest dimension
- pN2: Metastasis to ipsilateral axillary lymph node(s) fixed to each other or to other structures
- pN3: Metastasis to ipsilateral internal mammary lymph node(s)

Distant metastasis (M):
- MX: Presence of distant metastasis cannot be assessed
- M0: No distant metastasis
- M1: Distant metastasis present (includes metastasis to ipsilateral supraclavicular lymph nodes)

AJCC stage groupings

Stage 0	Tis, N0, M0
Stage I	T1,* N0, M0
Stage IIA	T0, N1, M0
	T1, N1, M0
	T2, N0, M0
Stage IIB	T2, N1, M0
	T3, N0, M0
Stage IIIA	T0, N2, M0
	T1, N2, M0
	T2, N2, M0
	T3, N1, M0
	T3, N2, M0
Stage IIIB	T4, Any N, M0
	Any T, N3, M0
Stage IV	Any T, Any N, M1

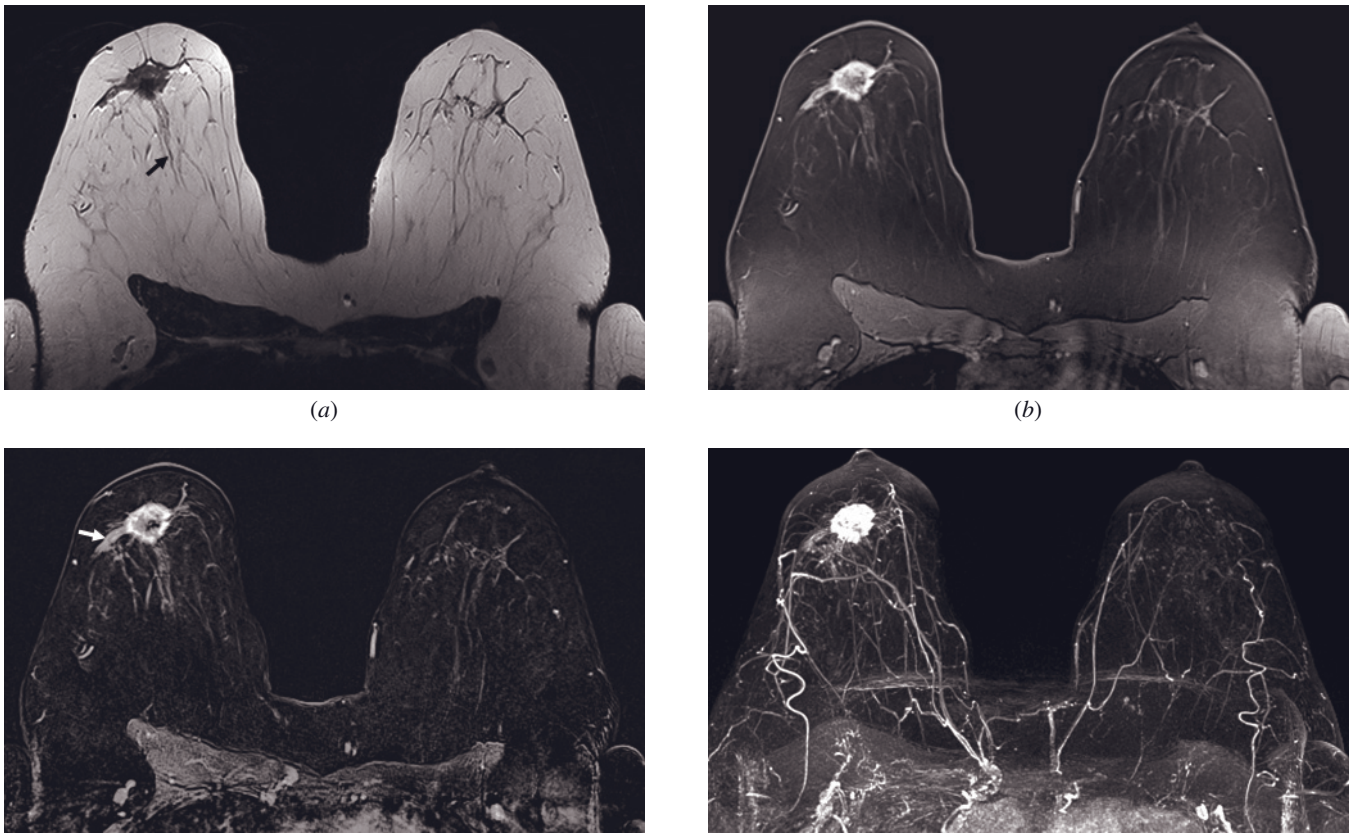

FIG. 19.27 Invasive ductal carcinoma (IDC). Axial T2-weighted image (*a*) shows an irregular, heterogeneous, hypointense mass with spiculated margins and a "hook sign" (black arrow) in the subareolar region of the right breast. On postcontrast GRE (*b*) and subtracted (*c*) images, two parallel areas of non-masslike enhancement in ductal distribution extending from the cancer (white arrow, *c*) depict the morphologic pattern suggestive of DCIS. MIP image (*d*) shows a more prominent vascularity of the right breast compared to the left.

Although involvement of the pectoral muscle does not increase the stage from T3 (T4 is when the serratus or intercostal muscles are involved), it might affect surgical therapy. Nipple involvement can also be clarified with MRI with a sensitivity of 80%, which is important when planning subcutaneous mastectomy [125]. In a study from Fisher et al. [130] the rate of recurrent tumor in the same breast was significantly lower in patients who had preoperative MRI for staging, compared to those who did not (1.2% and 6.8%, respectively).

Invasive Ductal Carcinoma

Invasive ductal carcinoma (IDC) is the most common type of breast carcinoma (60–75% of all mammary invasive carcinomas). It generally cannot be subclassified histologically (not otherwise specified, or NOS). The tumors can have an irregular, stellate shape or a nodular configuration with bulging margins. At gross pathology, these tumors usually show a grayish-white cut surface with hard consistency, with sizes ranging from a few millimeters to 10 cm or more [20]. Vascular and perineural invasion can be present, but with no prognostic significance. In the majority of cases, areas of ductal intraepithelial neoplasia DCIS and/or LCIS may be present. The immunohistochemistry for estrogen receptors (ER), progesterone receptors (PR), and human epidermal growth factor receptor 2 (HER2) needs to be performed for treatment planning as well as for the prognostic estimate [131]. Breast cancer characterized by negativity for ER, PR, and HER2 (triple-negative breast cancer) is associated with aggressive histologic features, poor prognosis, unresponsiveness to the usual endocrine therapies, and shorter survival.

At MRI, IDC appears as an irregular-shaped or oval focal mass, often with spiculated margins (fig. 19.28), with heterogeneous internal architecture. Tumors are usually hypointense or isointense on T1- and T2-weighted images, showing rapid postcontrast enhancement followed by washout or plateau type of time-intensity curve. Rim enhancement and/or spiculated borders are most indicative features for the diagnosis (figs. 19.29 and

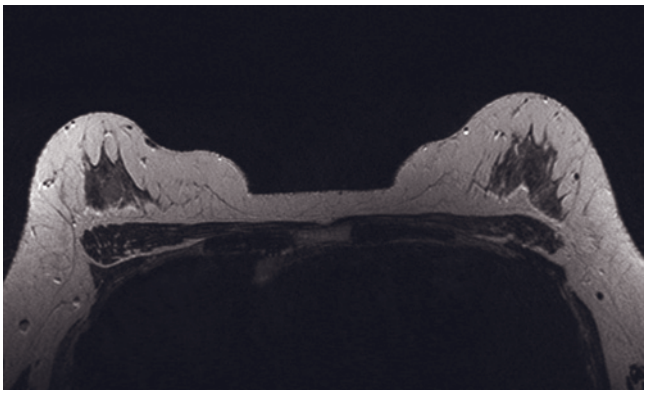

(*a*)

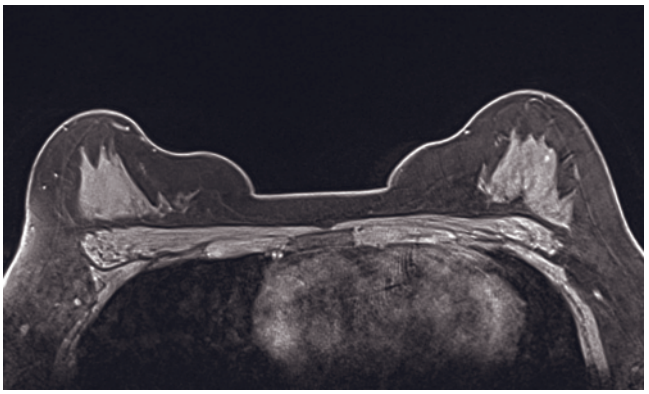

(*b*)

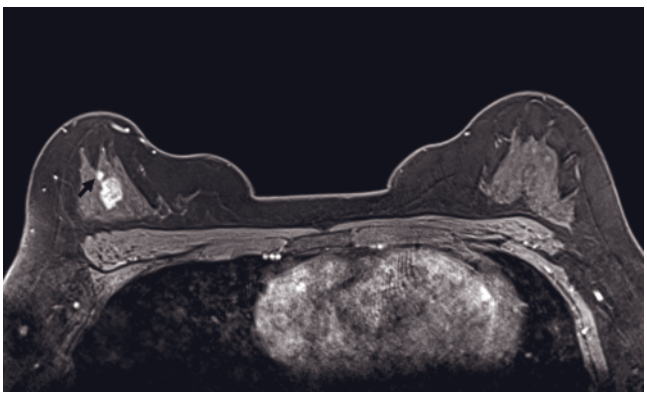

(*c*)

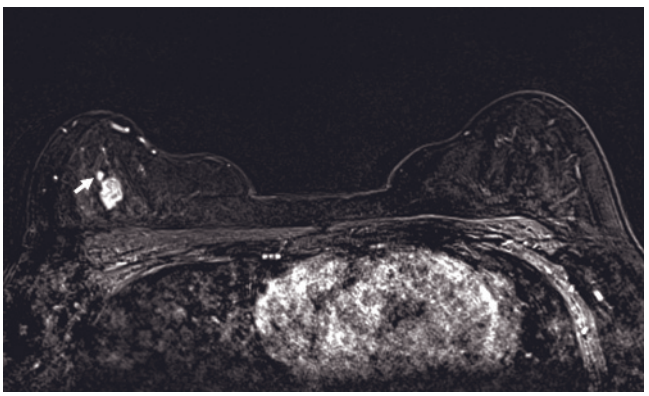

(*d*)

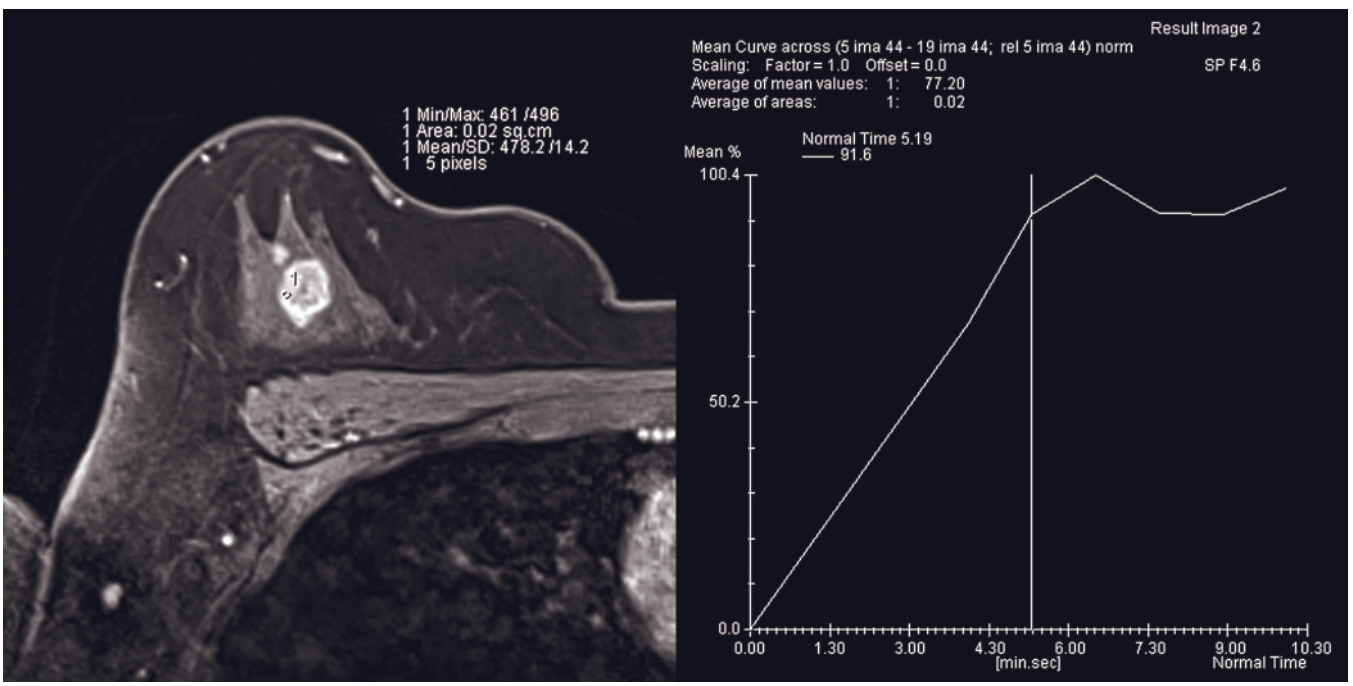

(*e*)

FIG. 19.28 Invasive ductal carcinoma (IDC). Axial T2-weighted image (*a*) shows a very subtle, slightly hyperintense oval mass with irregular margins in the right breast. On the axial precontrast GRE image (*b*), the mass is completely obscured, because it is of the same signal intensity as the surrounding parenchyma. Postcontrast GRE (*c*) and subtracted (*d*) images reveal a strongly enhancing mass with angulated, irregular margins and heterogeneous internal enhancement, suggestive of IDC. ROI analysis of the dynamic data set (*e*) shows a plateau curve (Type II), indicating BI-RADS 5 categorization. Small enhancing mass (arrows, *c* and *d*) anterior to the IDC represents a focus of high-grade DCIS with the same type of kinetics (*f*).

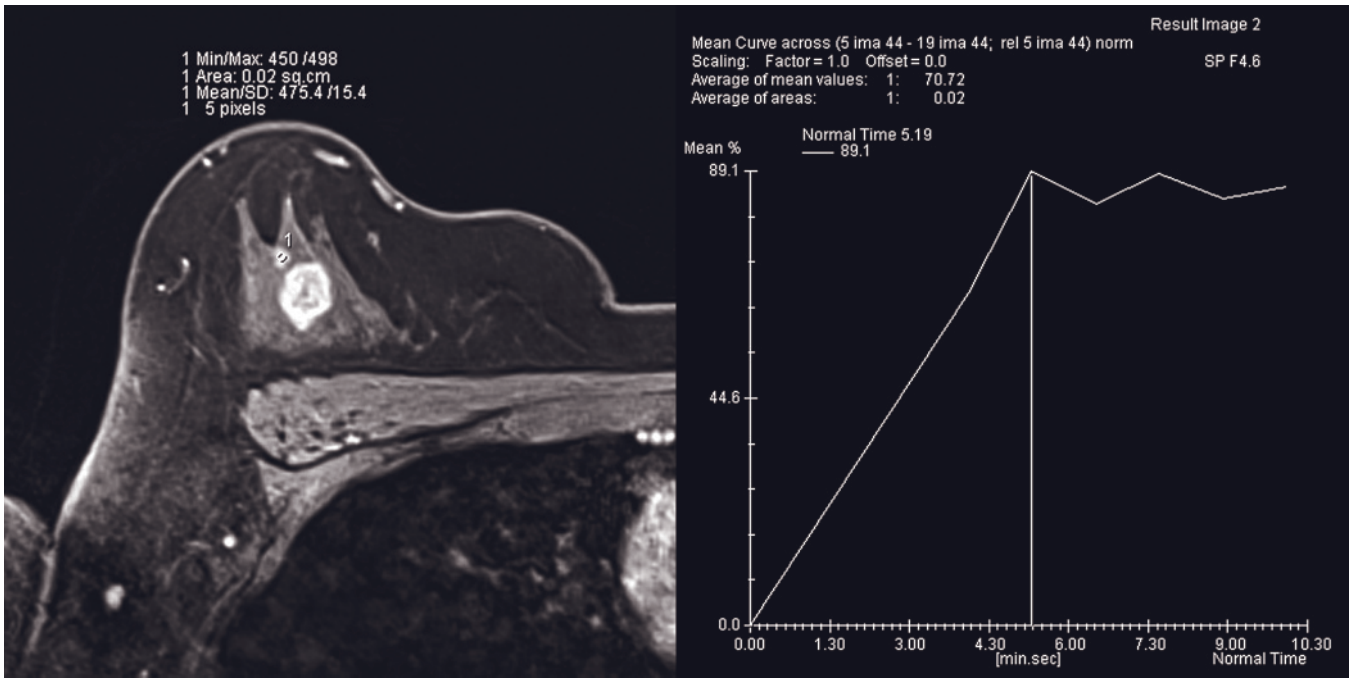

(*f*)

FIG. 19.28 (*Continued*)

19.30). They are often accompanied with ductal or segmental type of area enhancement due to the presence of DCIS. Multicentric and/or bilateral disease can be present and is well shown on MRI (figs. 19.31 and 19.32).

Uematsu et al. [132] recently showed that MRI findings of a unifocal lesion, mass lesion type, smooth mass margin, heterogeneous rim enhancement, persistent enhancement pattern, and very high signal intensity on T2-weighted images can be used to detect triple-negative breast cancer. Although triple-negative breast cancer can mimic lesions with a benign morphology, the early MR imaging recognition of triple-negative breast cancer could assist in both pretreatment planning and prognosis.

Invasive Lobular Carcinoma

Invasive lobular carcinoma (ILC) can present a diagnostic challenge because of its variable presentation, both at clinical exam and on imaging. Tumor may not be grossly visible because neoplastic cells grow in linear fashion, eliciting little or no desmoplastic reaction and mimicking normal breast parenchyma. Another gross manifestation of ILC is the formation of numerous small, hard nodules mimicking sclerosing adenosis. At least 5% of invasive breast carcinomas cannot be classified as ductal or lobular with certainty, or even as mixed ductal and lobular type. Immunohistochemistry can be helpful for classifying some of these primary breast carcinomas. Variants of ILC include solid, alveolar, histiocytoid, and tubulolobular carcinomas [20].

Histologically, ILC is characterized by an infiltrating pattern of small or medium-sized uniform epithelial cells, showing linear arrangement of carcinoma cells in a circumferential fashion around ducts and lobules ("targetoid" growth).

Because of its diffuse infiltrative growth pattern, ILC often does not appear as a focal mass on MRI, but as non-masslike enhancement. The narrow columns of diffusely infiltrating cancer cells may be fed by diffusion, supplied from preexisting fibroglandular capillaries, which likely explains why lobular invasive cancers may be accompanied with only weak angiogenic activity. Accordingly, lobular invasive breast cancer may exhibit only weak and persistent (misleading!) enhancement kinetics, and MRI may be reported as falsely negative [133, 134] (fig. 19.33). This is one of the reasons why, in non-masslike enhancement, enhancement kinetics should be used with caution [30]. The common appearance of ILC on MRI is an ill-defined mass that is near isointense on T1- and T2-weighted images and shows minimal postcontrast enhancement (fig. 19.34).

The likelihood of finding an additional site of cancer in the ipsilateral or contralateral breast at MRI is reported to be higher in women with ILC compared to other cancer histologies [127] (fig. 19.35). Accordingly,

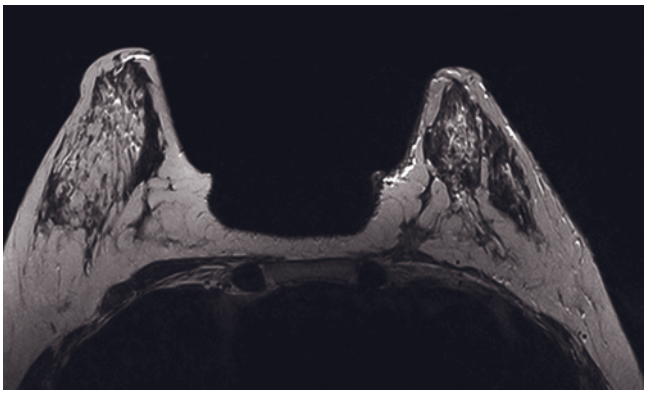

(*a*)

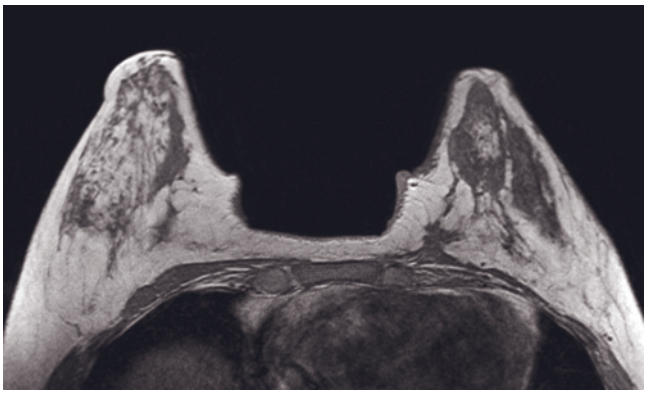

(*b*)

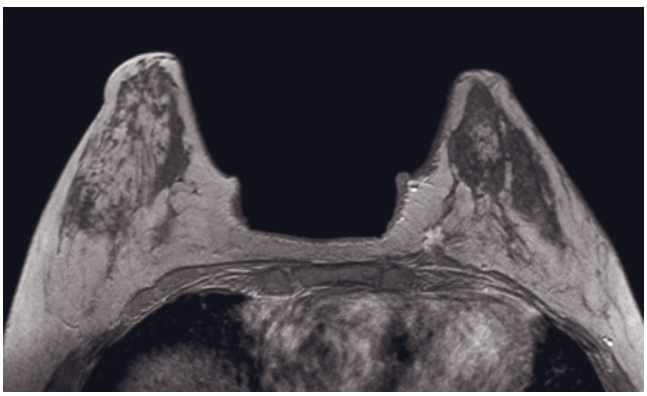

(*c*)

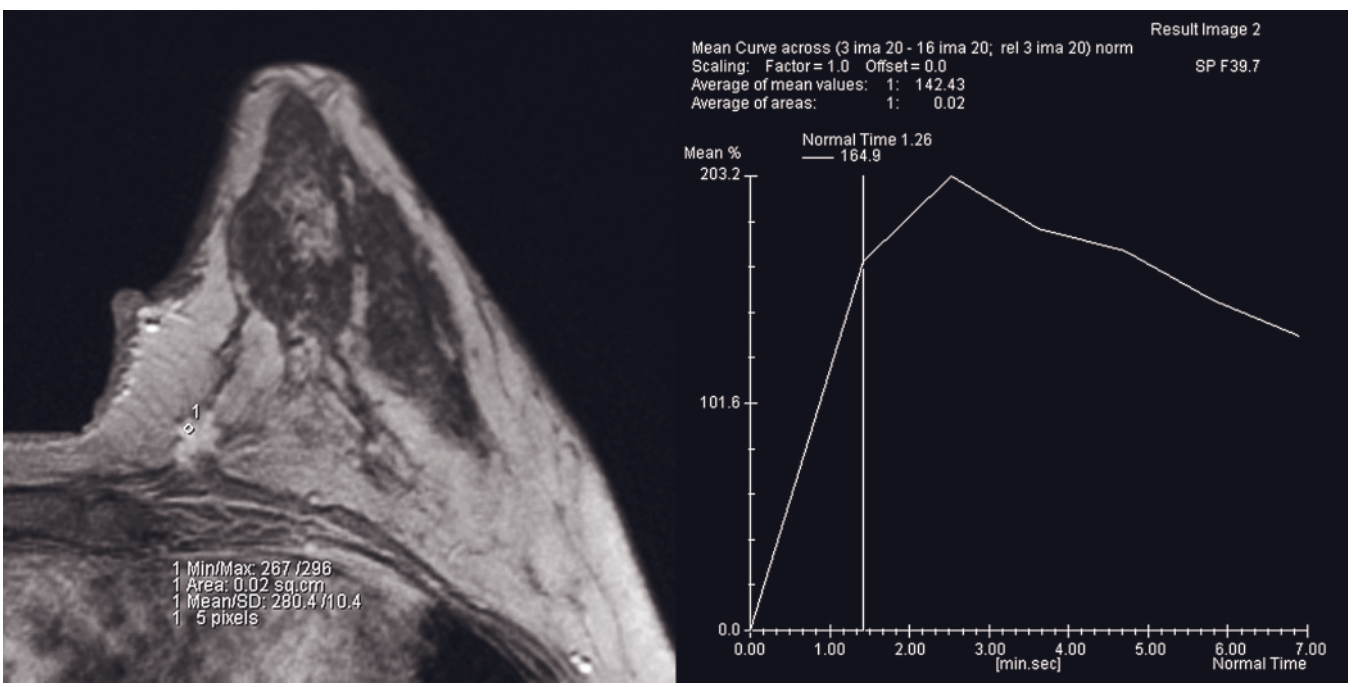

(*d*)

FIG. 19.29 Invasive ductal carcinoma (IDC). Follow-up MRI examination 1 year after breast conserving therapy (BCT) of the left breast revealed a small mass in posterior aspect of medial left breast. Axial T2-weighted (*a*) and T1-weighted GRE (*b*) images depict a heterogeneous, hypointense mass with spiculated margins, showing rapid postcontrast enhancement (*c*) and exhibiting a washout type of kinetic curve (*d*). There is obvious invasion of the pectoral muscle with loss of the posterior fat plane and disruption of pectoral fascia (*a–c*). A neighboring non-masslike area of enhancement is best appreciated on MIP image (*e*).

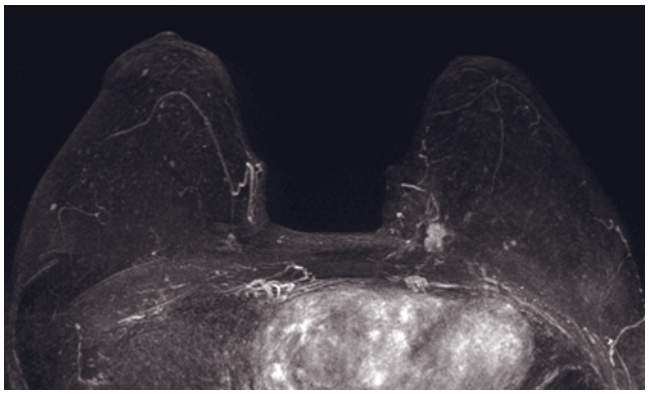

(*e*)

FIG. 19.29 (*Continued*)

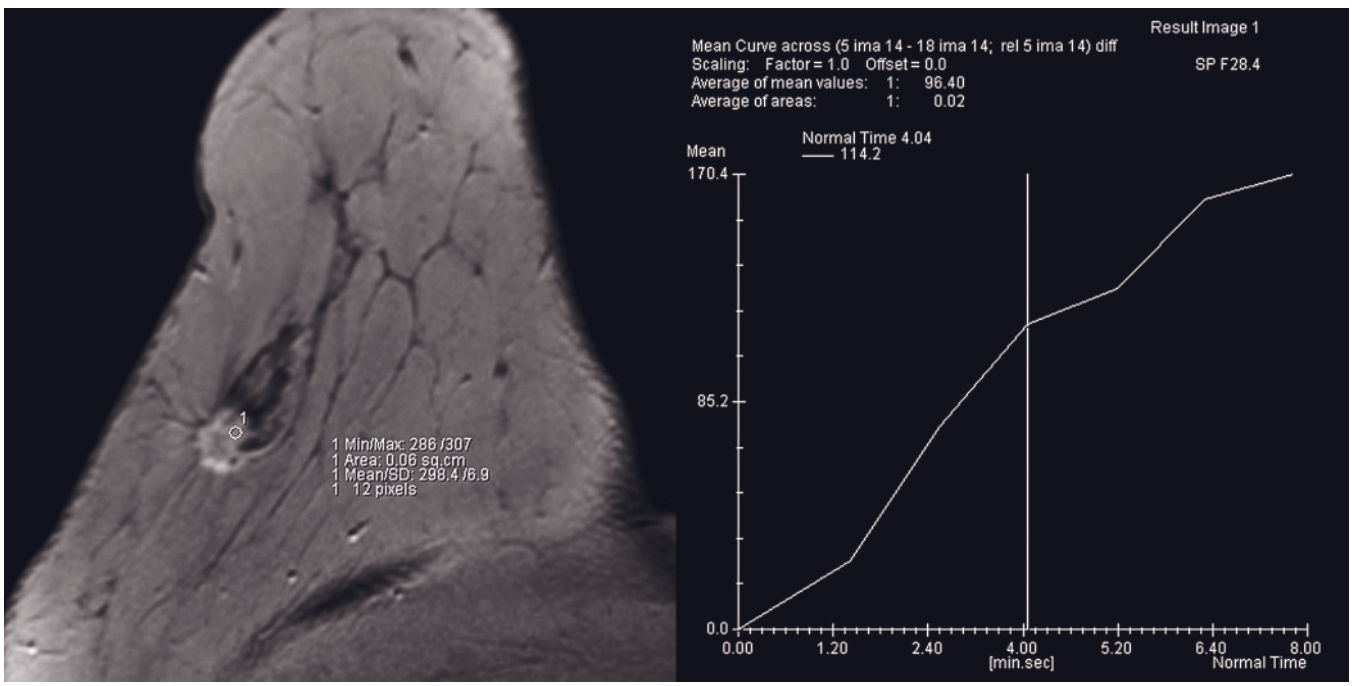

(*a*)

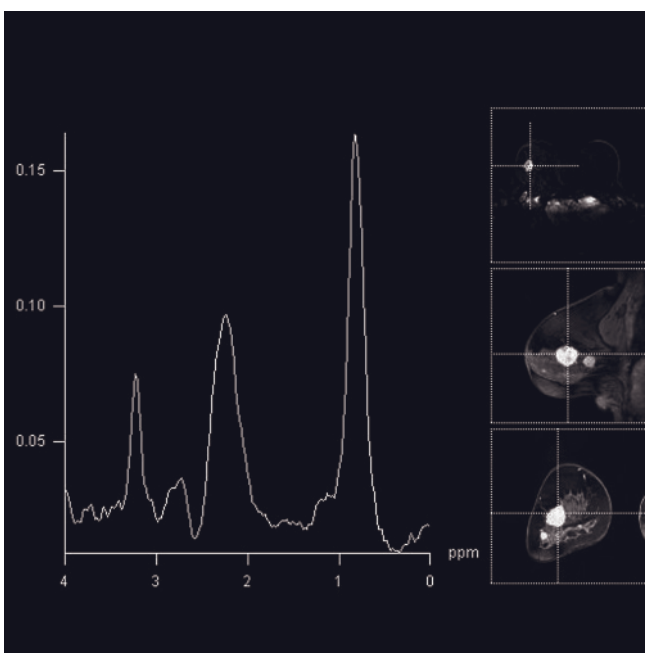

(*b*)

FIG. 19.30 Invasive ductal carcinoma (IDC). Rim enhancement and/or spiculated borders represent the most indicative features, even in the presence of a persistent type (Type I) of time-intensity curve (*a*). ^{1}H MR spectroscopy shows a prominent Cho peak at 3.2 ppm, indicating malignant nature of a lesion (*b*) (Courtesy of Natasa M. Prvulovic, M.D., Diagnostic Imaging Center, Oncology Institute of Vojvodina, Serbia.)

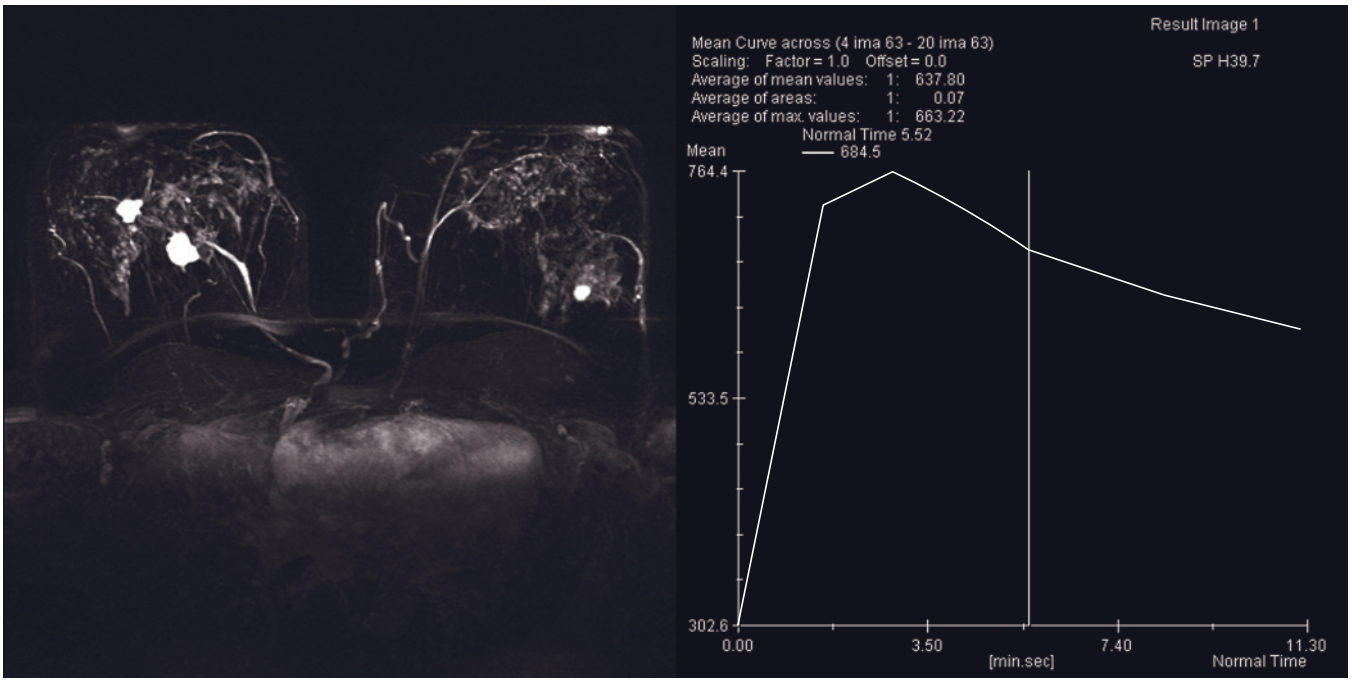

FIG. 19.31 Multicentric invasive ductal carcinoma (IDC). MIP image shows two enhancing lesions in the right breast and one in the left breast with washout kinetics—Type III time-intensity curve.

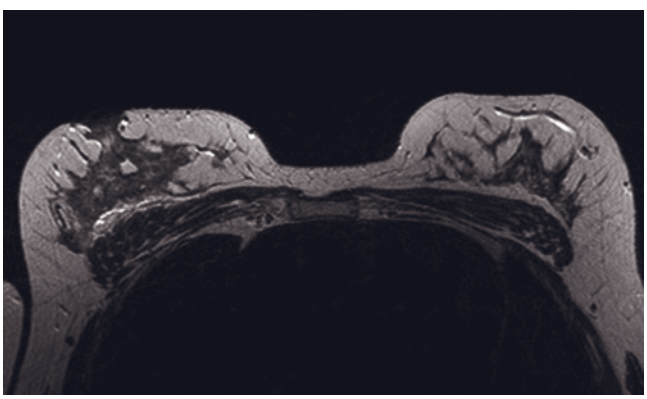

(*a*)

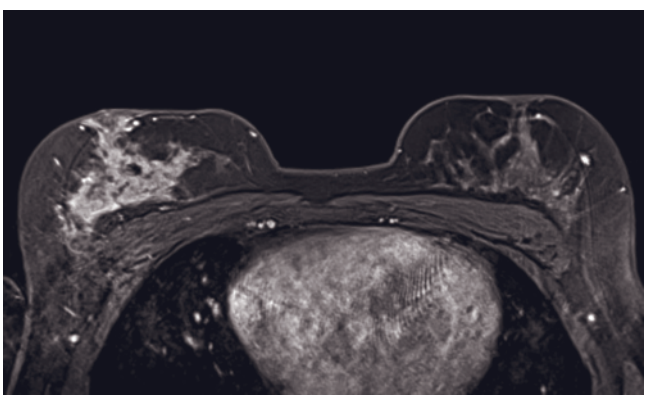

(*b*)

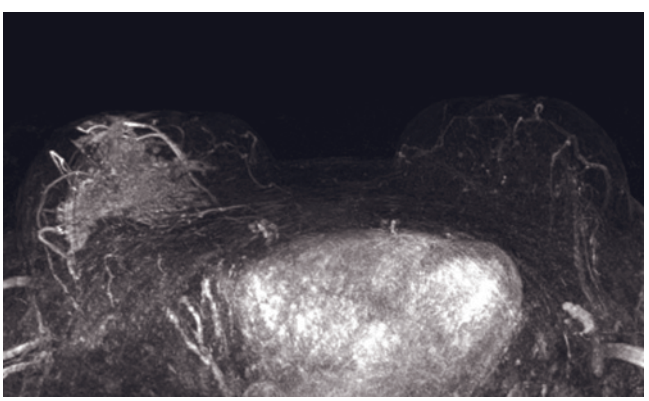

(*c*)

FIG. 19.32 Multicentric invasive ductal carcinoma (IDC). Extensive multicentric invasive ductal carcinoma (IDC) that completely infiltrates fibroglandular parenchyma of the right breast and invades the nipple seen on T2-weighted (*a*), postcontrast T1-weighted 3D GRE axial (*b*), and MIP (*c*) images. Enlarged,

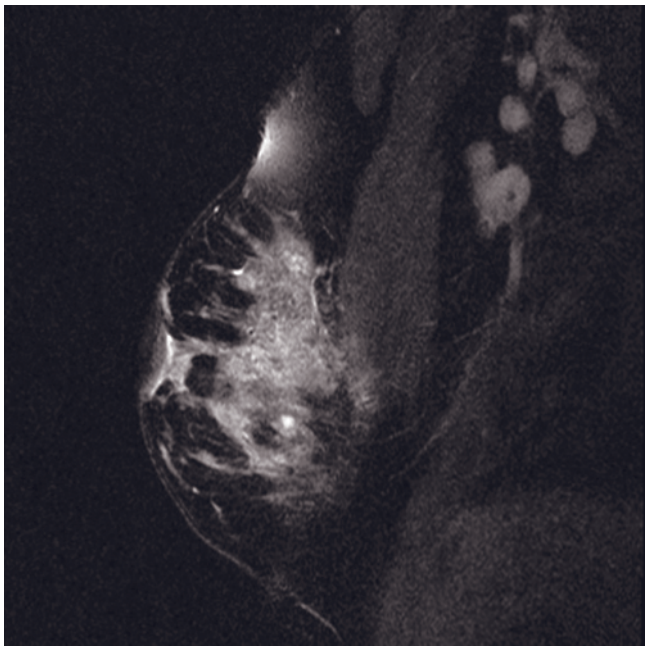

(*d*)

FIG. 19.32 (*Continued*) metastatic lymph nodes in the right axilla are seen on the fat-saturated T2-weighted sagittal image (*d*). Note a high-signal breast coil artifact at the skin of the upper portion of the breast.

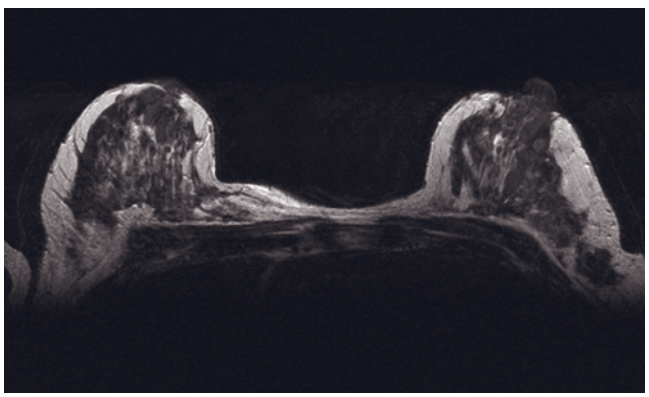

(*a*)

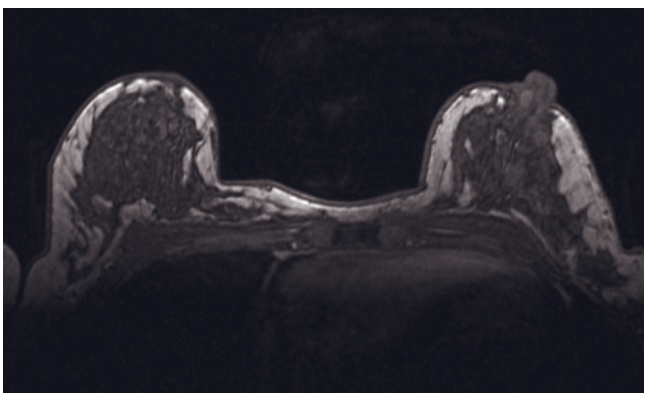

(*b*)

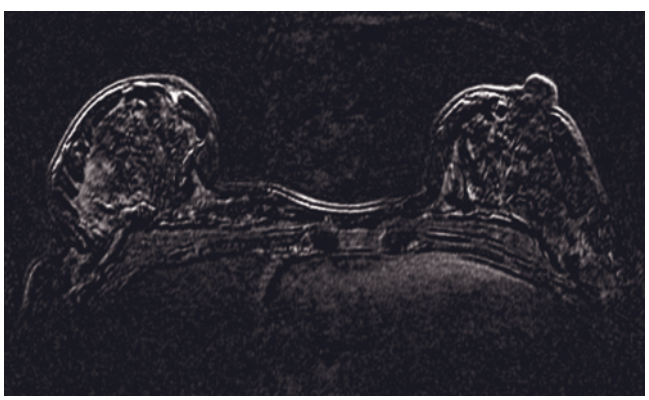

(*c*)

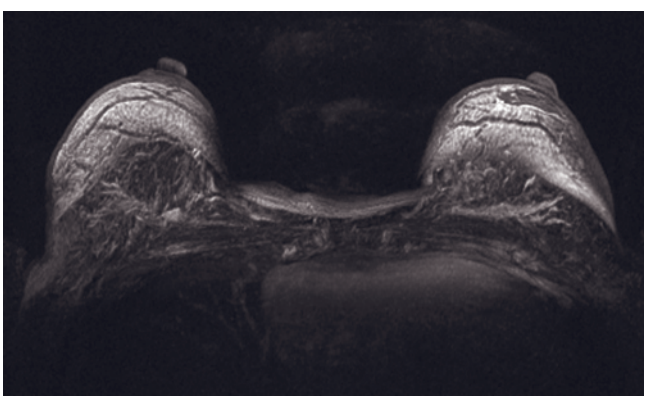

(*d*)

FIG. 19.33 Invasive lobular carcinoma (ILC). Axial T2-weighted (*a*) image reveals breast asymmetry seen as an additional hypointense area with irregular borders in the axillary tail of the left breast. Postcontrast T1-weighted GRE 3D (*b*), subtracted (*c*), and MIP (*d*) images did not show any enhancing lesions in the breast. This was thought to represent an accessory fibroglandular tissue. Both subtracted and MIP image quality was degraded by motion (imaging was performed at 1.5 T MR unit). There is also a heart motion-related artifact, best seen in *c*, indicating that the anterior-posterior phase-encoding direction was inappropriately chosen. Because of the lack of postcontrast enhancement MRI was reported as false negative. Biopsy revealed multicentric lobular cancer in the left breast with metastasis in the lymph nodes of the ipsilateral axilla.

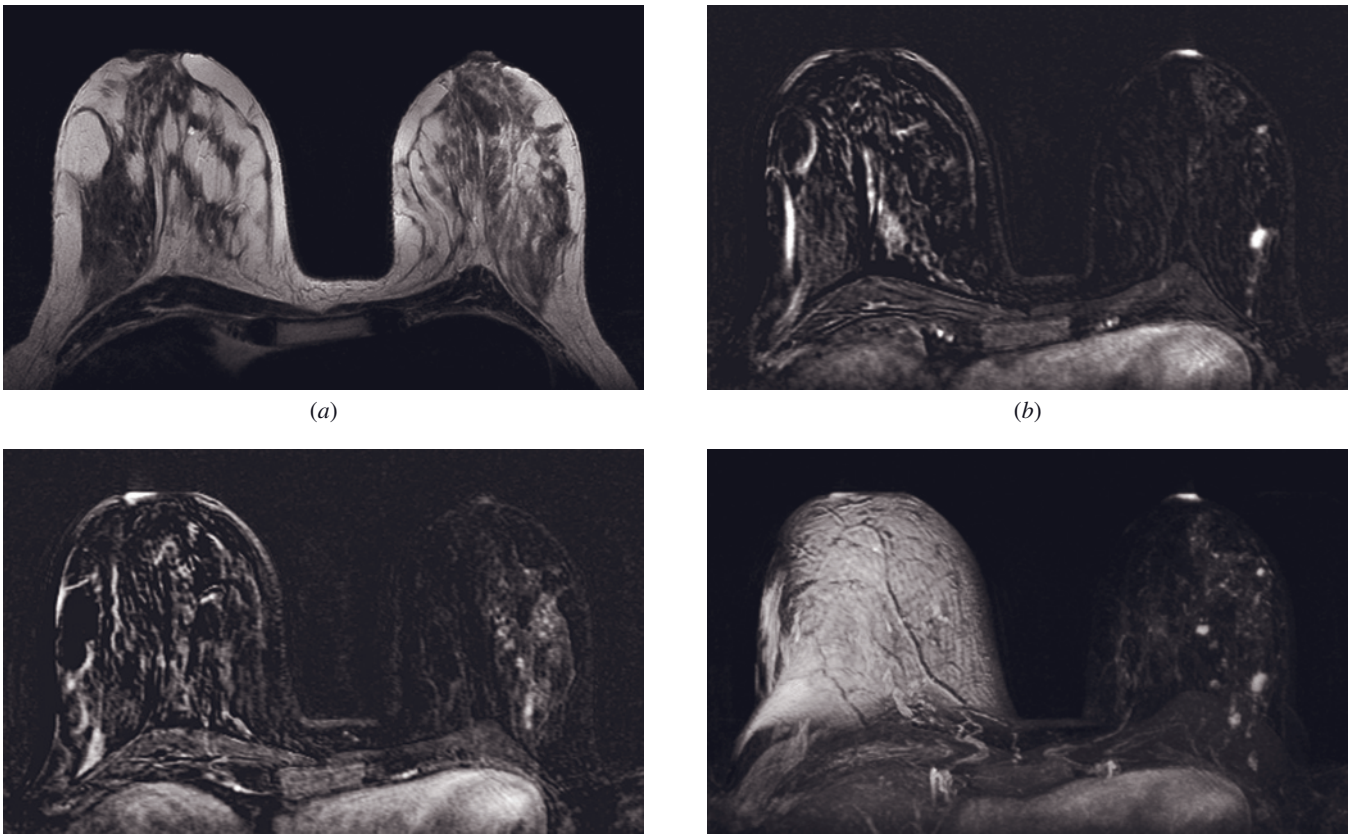

(*a*) (*b*) (*c*) (*d*)

FIG. 19.34 Multicentric invasive lobular carcinoma (ILC). Axial T2-weighted (*a*) image shows a single hypointense mass in the upper outer quadrant of the left breast, located between fibroglandular and subcutaneous fat tissue. Postcontrast subtracted images at the same (*b*) and different (*c*) levels and MIP image (*d*) show several irregularly shaped and oval enhancing subcentimeter lesions in segmental distribution within the left breast. ROI analysis of the dynamic data set (not shown) demonstrated a plateau curve (Type II). Both subtracted and MIP image quality was altered by motion artifacts (imaging was performed at 1.5 T MR unit). Note complete obscuration of the right breast on the MIP image (*d*) due to motion and misregistration. Biopsy revealed multicentric lobular cancer in the left breast (pT1).

preoperative breast MRI for the assessment of extent of disease and MRI follow-up after breast conserving treatment (BCT) is recommended.

Medullary Carcinoma

Medullary carcinoma is considered to be a subtype of IDC that accounts for 5–10% of invasive cancers. Histologically it appears as a circumscribed mass, composed of sheets of highly pleomorphic cells with a high mitotic index, surrounded by a peripheral lymphoid infiltrate. Despite a highly malignant histology, it has a better prognosis than IDC or ILC. Cystic degeneration inside a tumor may be present [22].

Imaging features of this tumor are often indistinguishable from fibroadenoma. At MRI, a medullary carcinoma usually appears as a well-circumscribed oval lesion with cystic degeneration, hence presenting a moderately low signal on T1-weighted and a moderately high signal on T2-weighted images, showing moderate nonspecific enhancement kinetics (fig. 19.36).

Colloid Carcinoma

Colloid or mucinous carcinoma is a histologically distinctive subtype of IDC that accounts for 2% of all invasive cancers. Histologically, it is characterized by small clusters of epithelial cells swimming in pools of mucin. If the tumor is not mixed with other types of invasive cancer, it has a better prognosis than IDC or ILC [22].

On MRI, the tumor does not show appreciable differences from IDC [14]. On occasion, it can mimic the appearance of a benign tumor because of its oval shape, areas of T2 hyperintensity, and smooth margins (fig. 19.37).

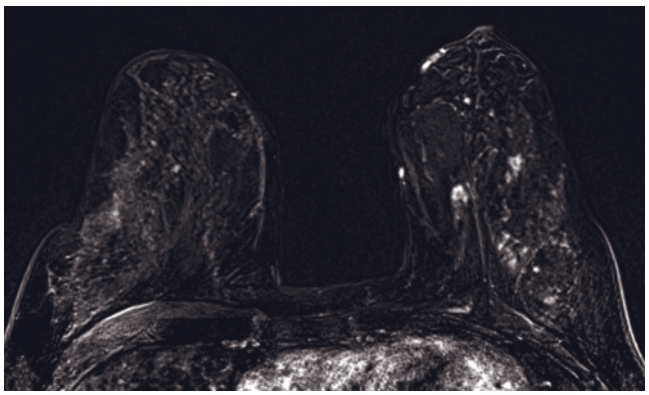

(*a*)

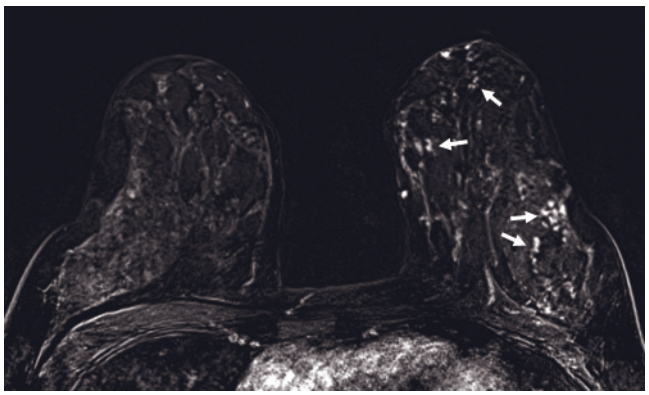

(*b*)

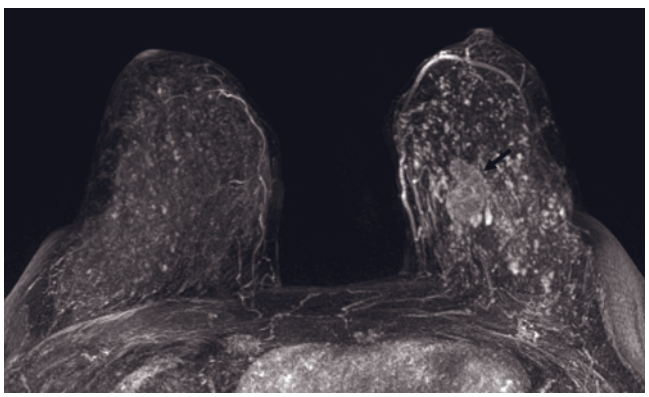

(*c*)

FIG. 19.35 Multicentric invasive lobular carcinoma (ILC). Postcontrast T1-weighted subtracted (*a*, *b*) and MIP (*c*) images show a well-circumscribed enhancing tumor measuring 3 cm in the central region of the left breast (black arrow, *c*) and multiple enhancing lesions measuring from few millimeters to 1 cm (white arrows, *b*) distributed diffusely in the entire breast. Pathology revealed multicentric ILC and many additional foci of LCIS.

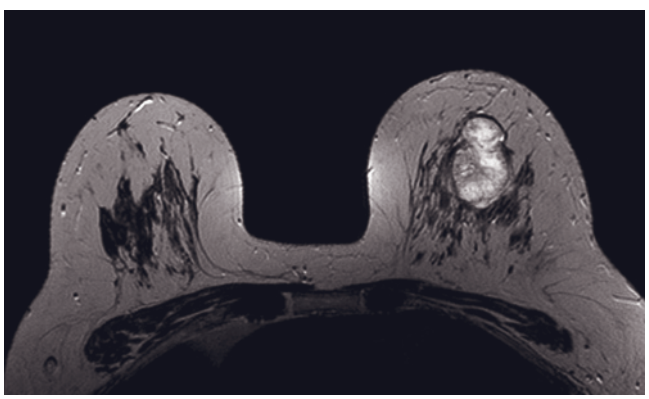

(*a*)

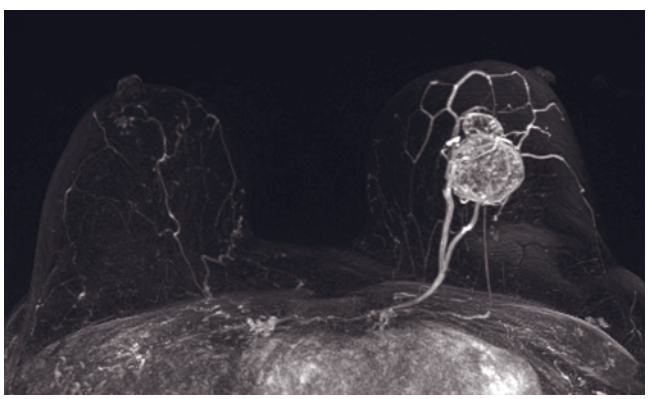

(*b*)

FIG. 19.36 Medullary carcinoma. Medullary carcinoma is depicted as an oval mass with smooth margins, mostly T2 hyperintense (*a*) with moderate to strong heterogeneous postcontrast enhancement as seen on the MIP image (*b*). In addition, striking increase in the vascularity of the left breast is evident (*b*) as the secondary sign of a malignancy.

Tubular Carcinoma

Tubular carcinoma, a subtype of IDC, accounts for 2% of all breast cancers. It consists of randomly arranged small ducts with only one or two layers of small cells. It rarely metastasizes to axillary lymphnodes, and the prognosis is excellent [22]. The MRI appearance is similar to IDC (figs. 19.38 and 19.39).

Papillary Carcinoma

Papillary carcinoma is a subtype of IDC, which accounts for 1–2% of breast cancers, in which the tumor components form papillary structures. Absence of a myoepithelial layer distinguishes papillary carcinomas from papillomas [21]. They usually remain noninvasive, even if they reach sizes of more then 2–3 cm.

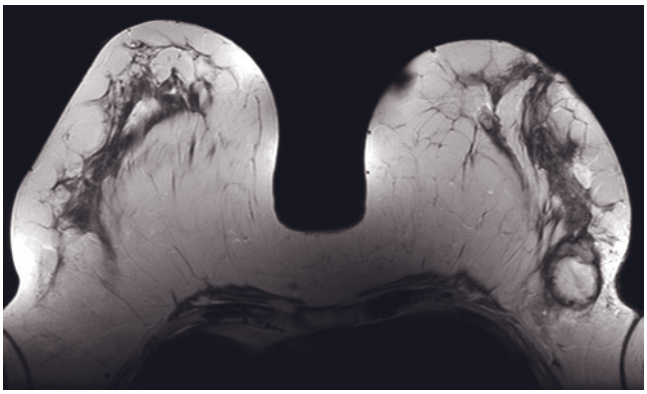

(*a*)

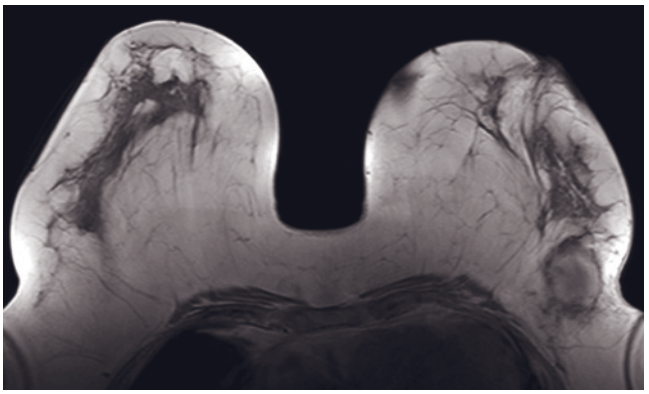

(*b*)

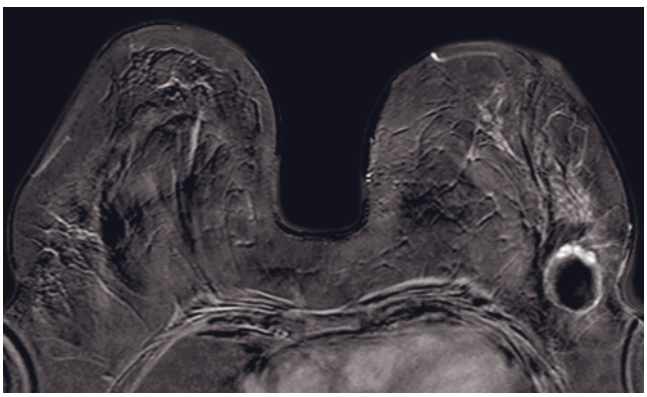

(*c*)

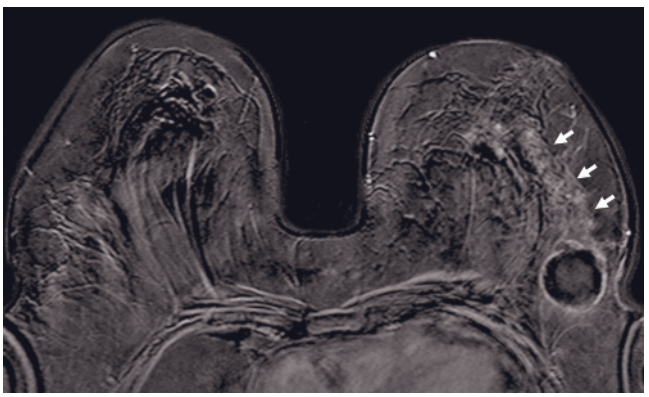

(*d*)

FIG. 19.37 Colloid (mucinous) carcinoma. Axial T2-weighted (*a*) and T1-weighted (*b*) images show an oval mass in the lateral aspect of the left breast, with smooth margins. It is mostly hyperintense on T2-weighted and T1-weighted images, with a few smaller confluent nodular lesions (T2 hypo-, T1 hyperintense) at its anterior border. On postcontrast T1-weighted (*b*), subtracted (*c*, *d*), and MIP (*e*) images a rim enhancement of the mass with strong enhancement of nodular portion of the tumor is seen. Biopsy demonstrated a colloid cancer measuring 3.5 cm with partial necrosis (pT2N1Mx). In addition, subtle architectural distortion within the fibroglandular parenchyma of the left breast is seen, with diffuse non-masslike enhancement in segmental distribution (arrows, *d*) showing persistent contrast kinetics (Type 1 curve). Pathology revealed low-grade DCIS and multiple papillomatosis.

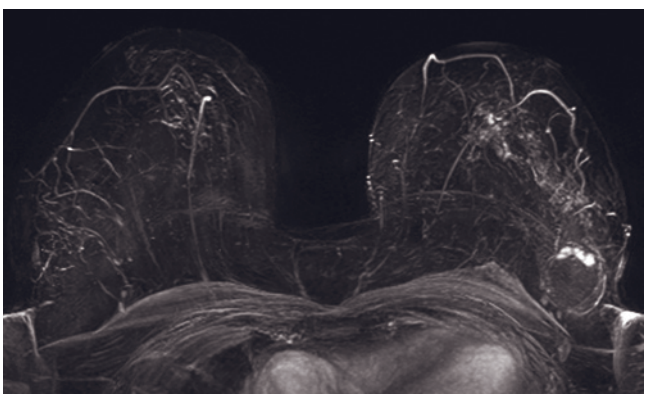

(*e*)

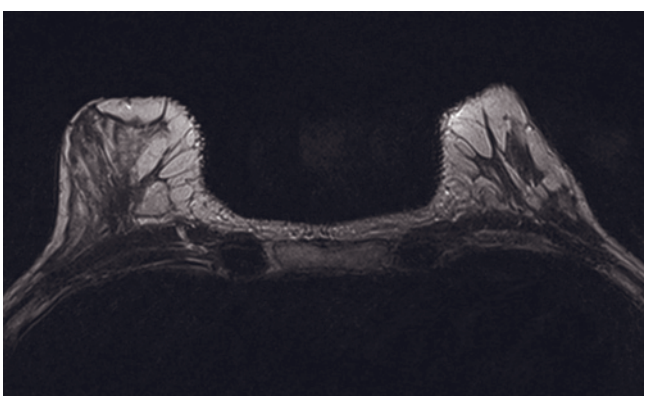

(*a*)

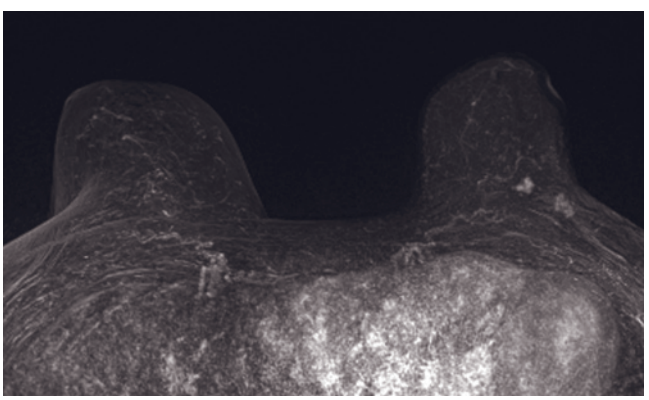

(*b*)

FIG. 19.38 Tubular carcinoma. Axial T2-weighted image (*a*) shows an irregular hyperintense mass with irregular margins in the upper outer quadrant of the left breast. On postcontrast MIP images (*b*), two lesions with similar characteristics are seen.

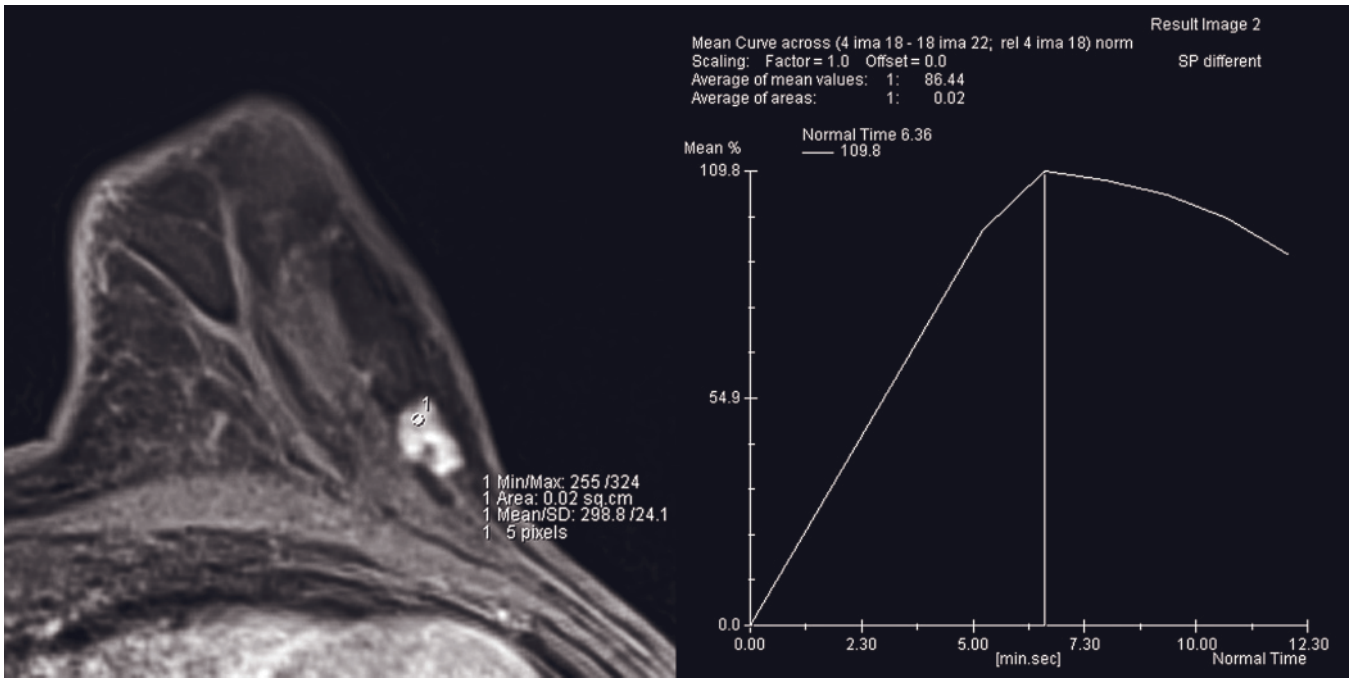

(*c*)

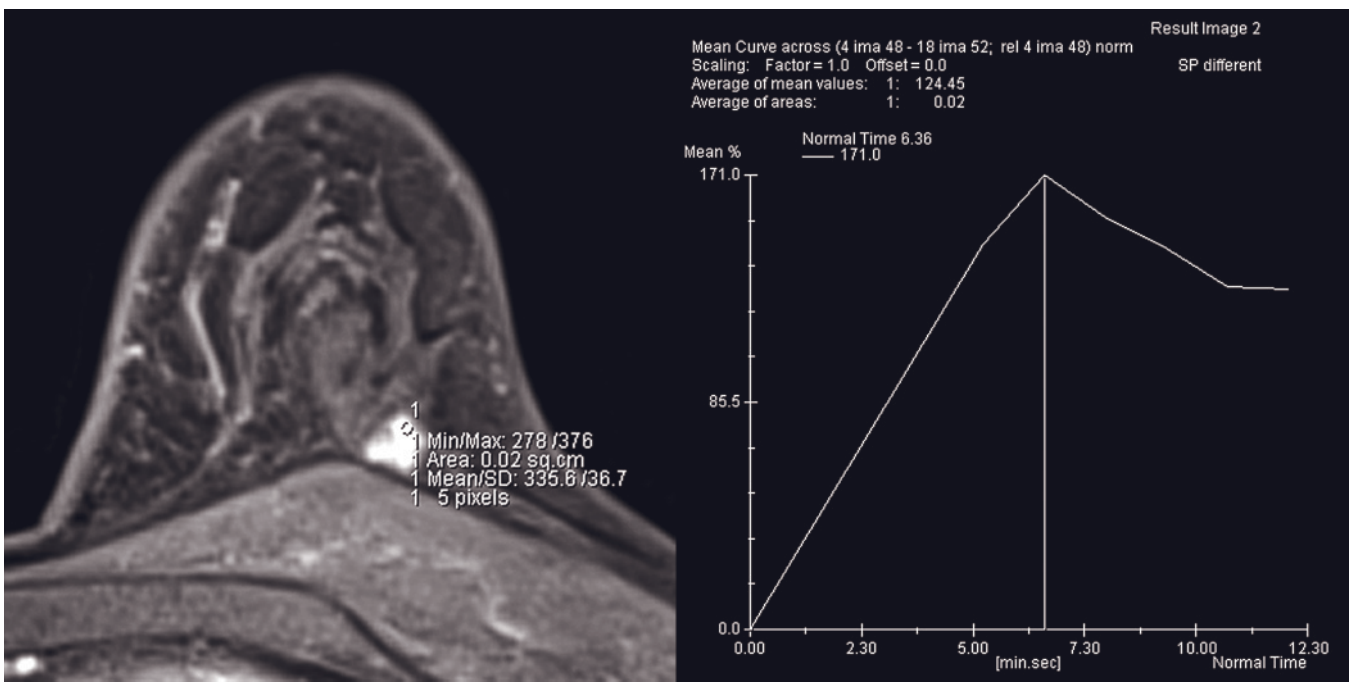

(*d*)

FIG. 19.38 (*Continued*) ROI analysis of the dynamic data set (*c*, *d*) demonstrates contrast washout (Type III curve), with maximum relative enhancement of 110% at the fifth minute after GBCA administration, indicating malignancy. However, on the

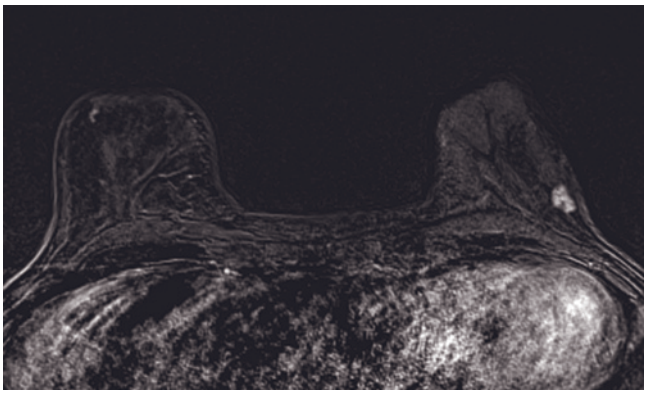

(*e*)

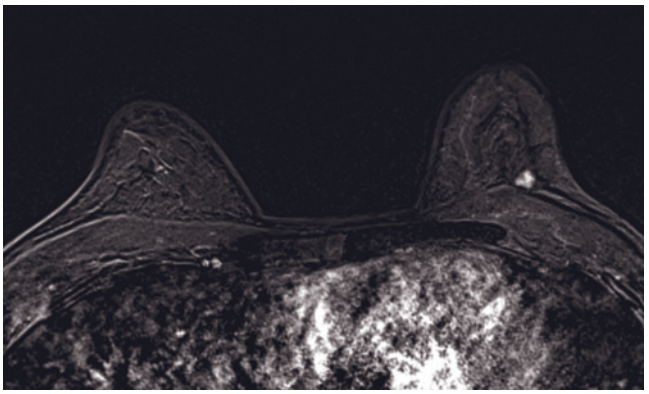

(*f*)

FIG. 19.38 (*Continued*) first postcontrast subtracted images (*e*, *f*) the lobulated shape of both lesions with low-intensity septations is demonstrated, which was not considered typical for malignant lesions. Biopsy revealed two tubular cancers (pT1N0M0) with low malignant potential.

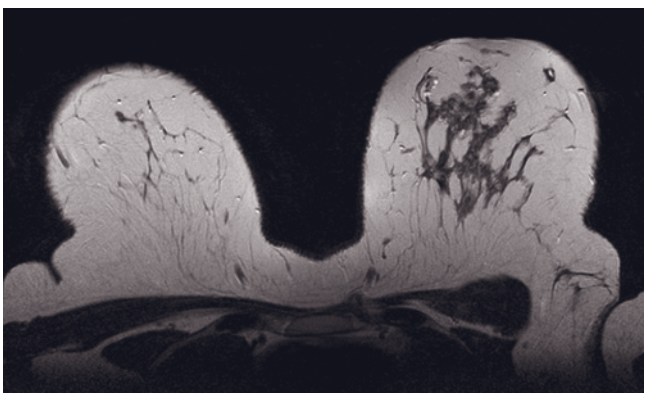

(*a*)

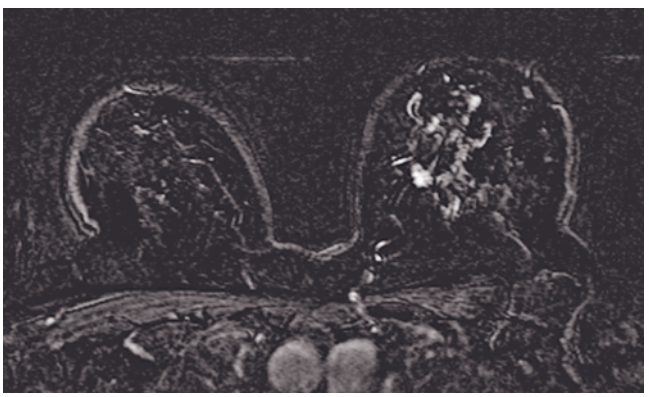

(*b*)

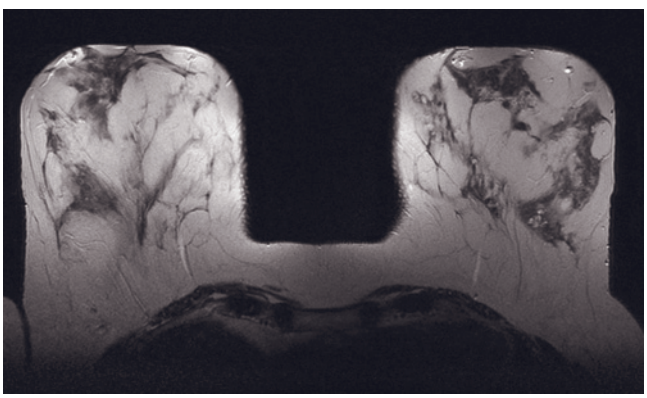

(*c*)

(*d*)

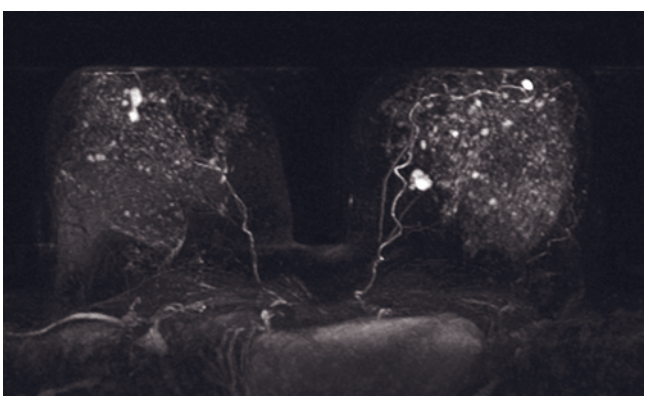

(*e*)

FIG. 19.39 Tubular carcinoma and IDC. T2-weighted image (*a*) shows a spiculated hypointense lesion in the lower inner quadrant of the left breast. On postcontrast subtracted (*b*) and MIP (*e*) images, lobulated shape and low-intensity septations within the tumor are seen. Biopsy revealed tubular cancer. In the subareolar region of the contralateral breast, another well-circumscribed hypointense lesion with ductal shape (*c*) and strong postcontrast enhancement (*d*, *e*) was incidentally found; biopsy revealed IDC. There is an enhancing oval mass in subareolar region of the left breast, which represented papilloma, as confirmed at the ultrasound-guided core biopsy (*e*). (Courtesy of Dragana Bogdanovic-Stojanovic, M.D., Diagnostic Imaging Center, Oncology Institute of Vojvodina, Serbia.)

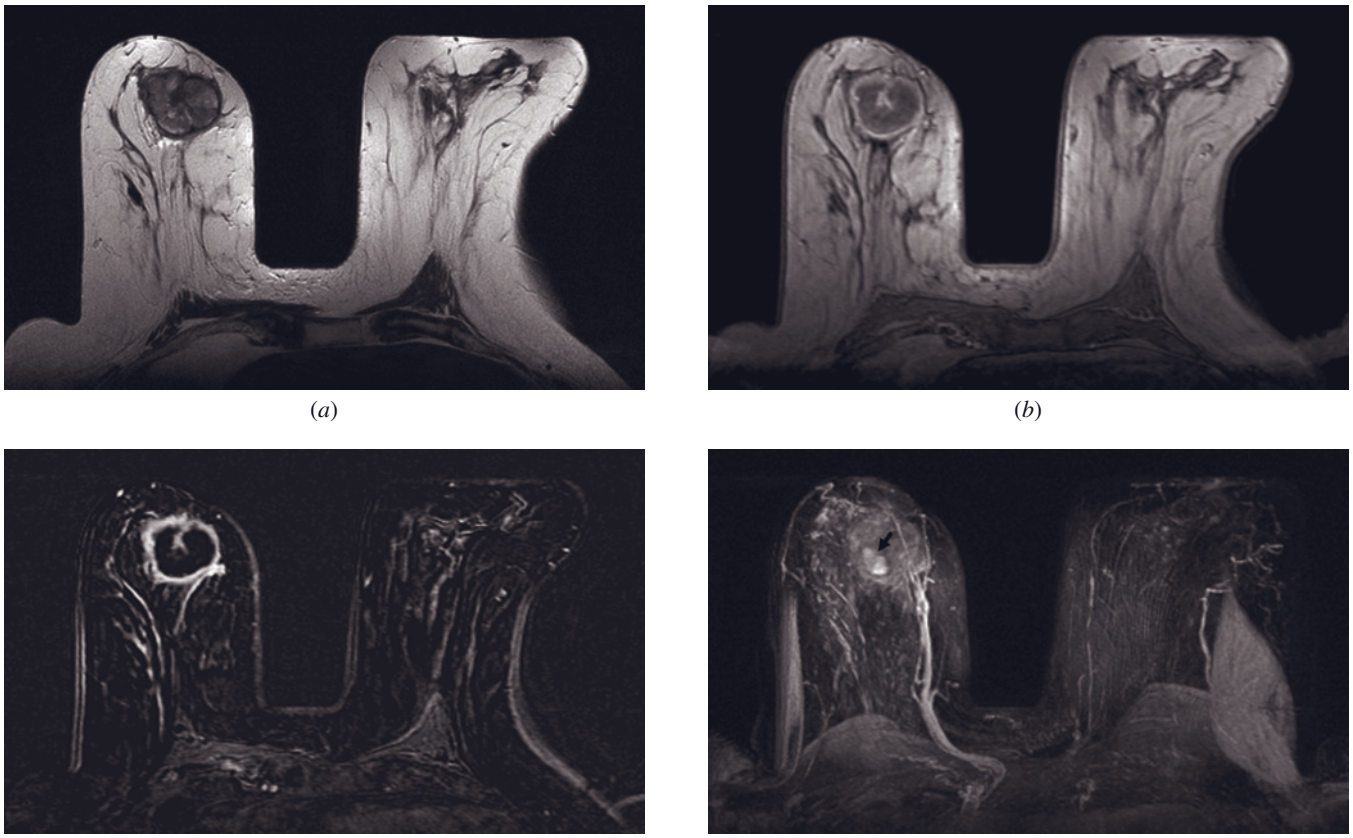

(*a*) (*b*) (*c*) (*d*)

FIG. 19.40 Papillary carcinoma. Axial T2-weighted image (*a*) shows a 35-mm oval mass in the subareolar region of the right breast, with heterogeneous, mostly T2 hypointense internal architecture and low-intensity capsule. The mass enhances strongly on postcontrast T1-weighted GRE 3D (*b*) and subtracted (*c*) images, showing typical rim-enhancing pattern (highly suspicious for malignancy) with thick irregular enhancing rim. An internal branching enhancement is seen coming from the anterior border of the mass. MIP image (*d*) reveals a well-circumscribed part of the tumor that shows stronger enhancement than the rest of the tumor (arrow), which correlates with pathology-proven IDC, measuring 2 cm in diameter, located within the papillary cancer.

Reported MRI characteristics are moderately enhancing masses with irregular borders and nonenhancing internal septations (fig. 19.40) [14]. In our experience, it is often hard to distinguish these tumors from benign papillary lesions if typical invasive morphology, that is, irregular, spiculated margin, is absent. Negative Cho peak on ^{1}H MR spectroscopy may aid the differential diagnosis, indicating a benign lesion (fig. 19.41).

Paget Disease

Paget disease (PD) of the breast consists of infiltration of the nipple–areolar complex epidermis by adenocarcinoma cells, and accounts for approximately 2% or 3% of breast carcinomas. Clinically, this is observed as an eczematous eruption of the nipple that may be associated with erosion or ulceration. It is often associated with underlying DCIS, which may also have an infiltrating component [135, 136].

Clinical examination and mammography are normal in 10–50% of cases and do not demonstrate the underlying neoplasia [135–137].

The value of MRI lies in its ability to show abnormal morphology and enhancement of the nipple–areolar complex (fig. 19.42), as well as the detection of possible associated underlying neoplastic foci in the breast [135]. Negative preoperative imaging, even with MRI, does not reliably exclude an underlying cancer, but MRI may be essential to perform because of the increased sensitivity to detect otherwise occult disease. In the setting of negative mammography, MRI can facilitate treatment planning for patients with PD [137].

Inflammatory Carcinoma

Clinical features of inflammatory breast carcinoma (IBC) include diffuse erythema, edema extending to greater than two-thirds of the breast, peau d'orange,

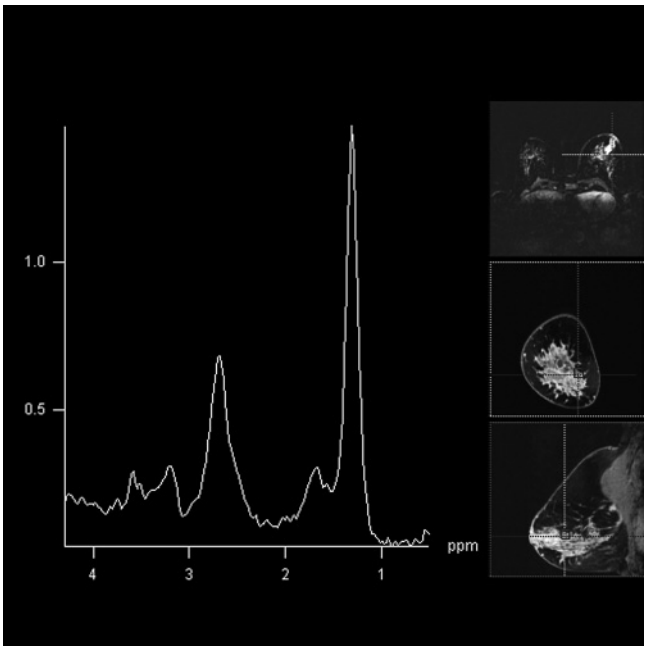

FIG. 19.41 Intraductal papilloma. The absence of a significant Cho peak at 3.2 ppm at ^{1}H MR spectroscopy indicates benign nature of lesion despite its rapid initial enhancement. Biopsy revealed intraductal papilloma in the left breast. (Courtesy of Natasa M. Prvulovic, M.D., Diagnostic Imaging Center, Oncology Institute of Vojvodina, Serbia.)

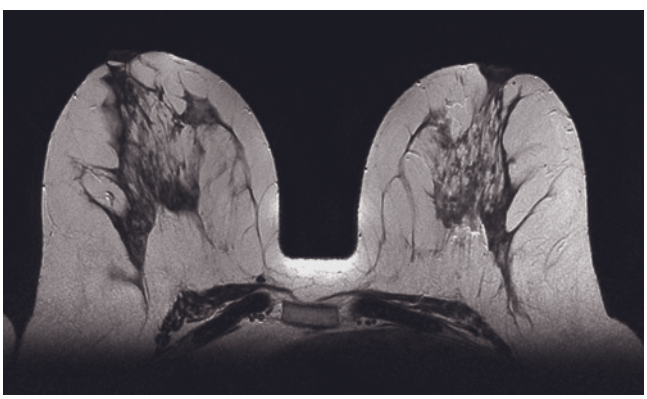

(*a*)

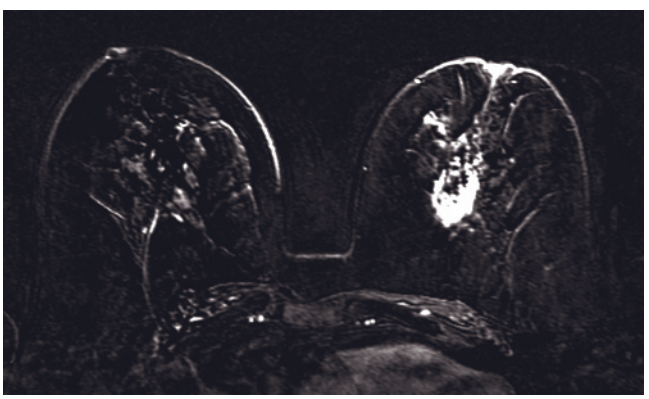

(*b*)

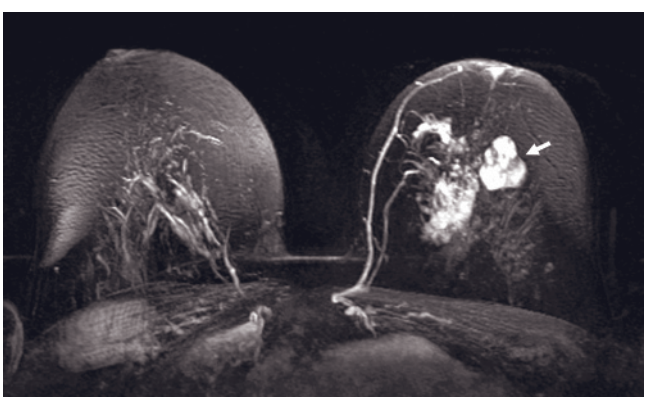

(*c*)

FIG. 19.42 Paget disease. Abnormal morphology, retraction, and strong enhancement of the nipple-areolar complex are seen on T2-weighted (*a*) and postcontrast subtracted (*b*) axial images. Additional enhancing lesions (*b*, *c*) in the central and medial part of the breast represent high-grade DCIS with multicentric foci of microinvasion (T1N0Mx). A well-circumscribed, lobulated mass (arrow) seen lateral to median plane in the left breast on MIP image (*c*) represents a hamartoma (incidental finding).

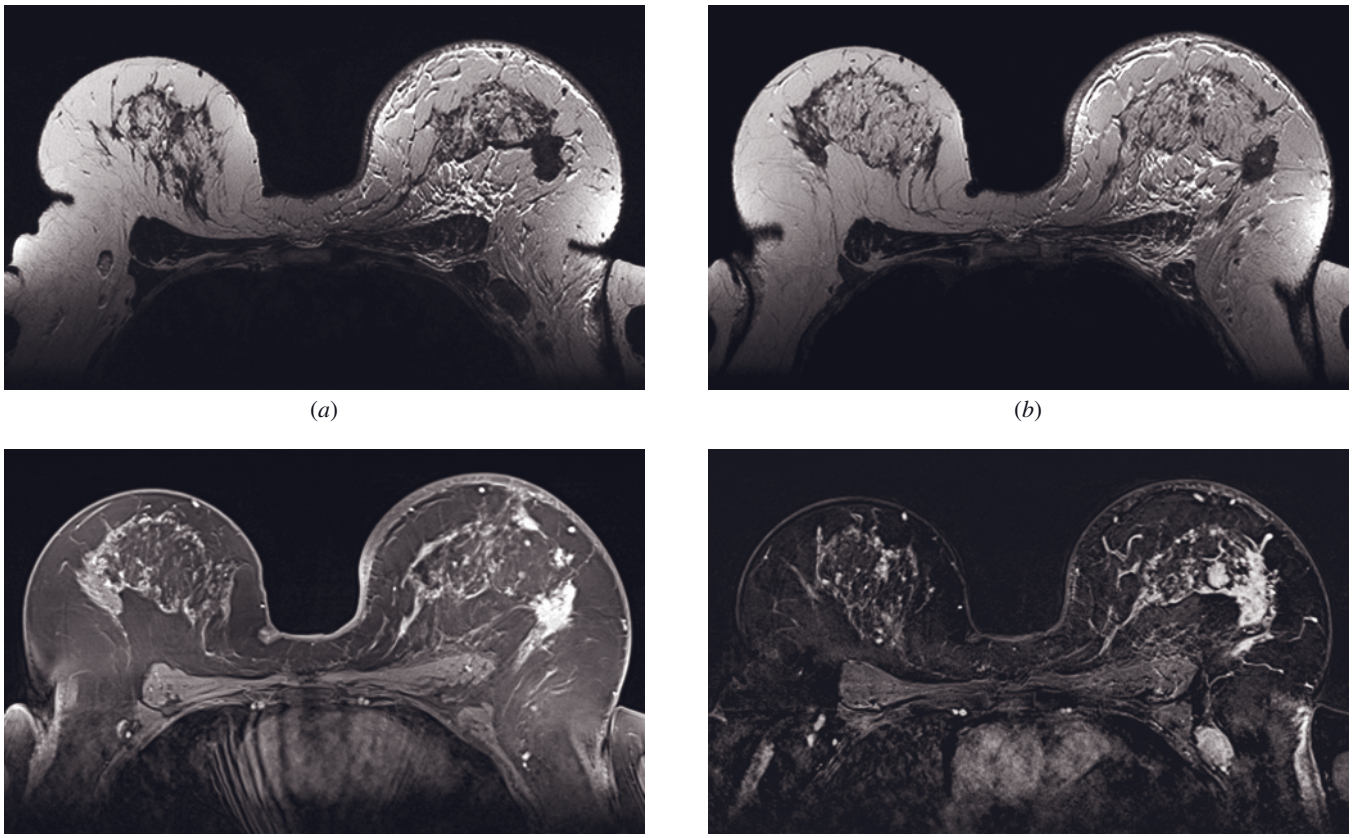

(*a*) (*b*) (*c*) (*d*)

FIG. 19.43 Inflammatory breast carcinoma (IBC). T2-weighted axial (*a*, *b*) and postcontrast GRE (*c*) and subtracted (*d*) axial images reveal left breast enlargement, diffuse skin thickening, abnormal nipple configuration, prominent vessels, and diffuse, cutaneous/subcutaneous, periareolar, pre- and subpectoral edema with an enlarged axillary lymph node. Multicentric tumors with spiculated margins are seen in the central and lateral aspect of the left breast, with washout kinetics.

tenderness, induration, warmth, and diffuse extent of tumor by palpation. Pathohistology reveals the presence of malignant tumor cells in the dermal lymphatics—lymphangiosis carcinomatosa cutis. In some cases, histopathology reveals lymphatic involvement of the skin, but there are no clinical signs of inflammatory carcinoma. Such tumors have been classified as "occult" inflammatory breast carcinomas [20]. Clinically diagnosed IBC follows a more aggressive course with a poorer prognosis (pT4) than the majority of breast cancers.

The discrimination between acute mastitis (AM) and IBC remains a diagnostic challenge because of overlapping clinical and imaging features. However, the combination of multiple dynamic and morphologic MRI criteria has the potential to establish the correct diagnosis. In both IBC and AM, MRI reveals breast enlargement, diffuse skin thickening, abnormal nipple configuration, prominent vessels, and cutaneous/subcutaneous, periareolar, and diffuse edema with enlarged axillary lymph nodes (fig. 19.43). A recent study [138] has shown that some MR findings significantly differ between the two: Masses with a greater average size were detected in IBC, T2 hypointensity of masses (IBC/AM, 77%/18%), blooming sign (62%/32%), infiltration of pectoralis major muscle (interruption of fat plane: 54.2%/16.7%). Perifocal (66.7%/33.3%) and prepectoral (73%/31%) edema were more often seen in IBC than in AM. The main localization of AM was subareolar, while localization of IBC was central or dorsal.

MESENCHYMAL TUMORS

Benign and malignant tumors of mesenchymal elements of the breast have imaging appearances similar to those at other sites in the body. They include benign tumors such as lipoma (fig. 19.44), myofibroblastoma, angiolipoma, and fibromatosis. Malignant tumors include liposarcoma, angiosarcoma, fibrosarcoma, dermatofibrosarcoma (fig. 19.45), and malignant fibrous

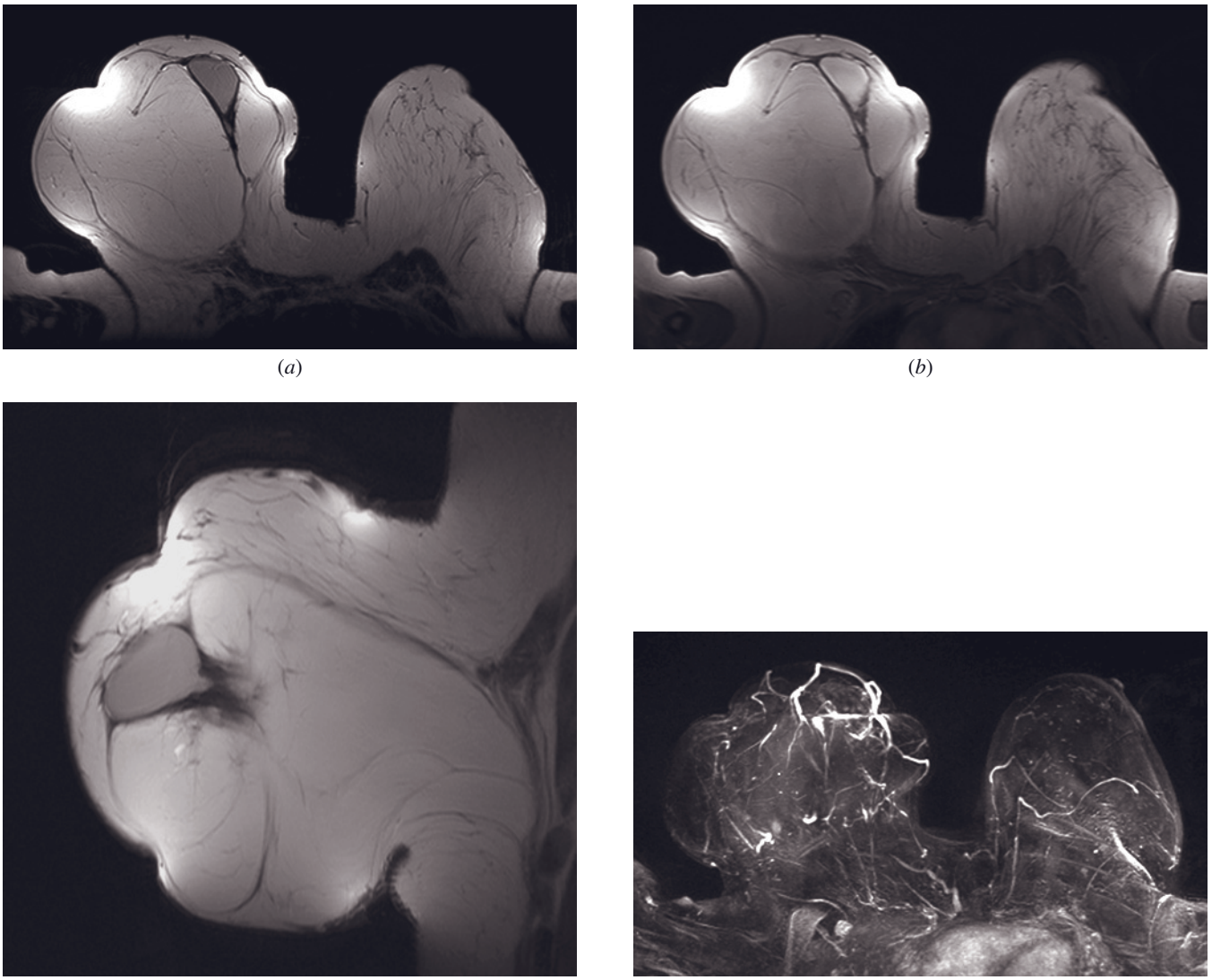

FIG. 19.44 Lipoma and galactocele. Axial T2-weighted (*a*) and T1-weighted (*b*) images reveal large (20 cm) encapsulated, homogeneous lipomatous tumor in the right breast that reaches the pectoral muscle without invasion, as shown on sagittal T2-weighted fat-saturated image (*c*). The well-circumscribed oval, T2 hypointense part of a tumor, measuring about 5 cm in diameter, shows high signal intensity on T1-weighted axial image (*b*) and no contrast enhancement (*d*). Fine needle aspiration (FNA) revealed galactocele (patient presented 2 years after breast-feeding cessation).

histiocytoma. When they occur in the breast they must be distinguished from breast cancer. Typically, more aggressive lesions show heterogeneous, rapid enhancement. In our experience, a negative Cho peak at ^{1}H MR spectroscopy in these lesions may mislead the radiologist to believe that the lesion could be benign, delaying the biopsy decision [139]. ^{1}H MR spectroscopy may be useful in the characterization of epithelial (carcinoma) but not of nonepithelial (mesenchymal) tumors (fig. 19.45). Wide local excision with clear margins, coupled with removal of the core biopsy tract, is necessary to avoid local recurrences.

Angiosarcoma

Although primary angiosarcomas are rare and account for 0.04% of all malignant breast tumors, the breast is one of the most common sites to develop angiosarcoma [140]. Primary angiosarcomas of the breast occur sporadically in young women, while secondary angiosarcomas occur most frequently after breast-conserving therapy with radiation therapy, usually after a latency period of 5 years [141]. Tumors often grow rapidly, reaching a size of up to 20 cm within 12 months. The main clinical sign is bluish skin and palpable tumor

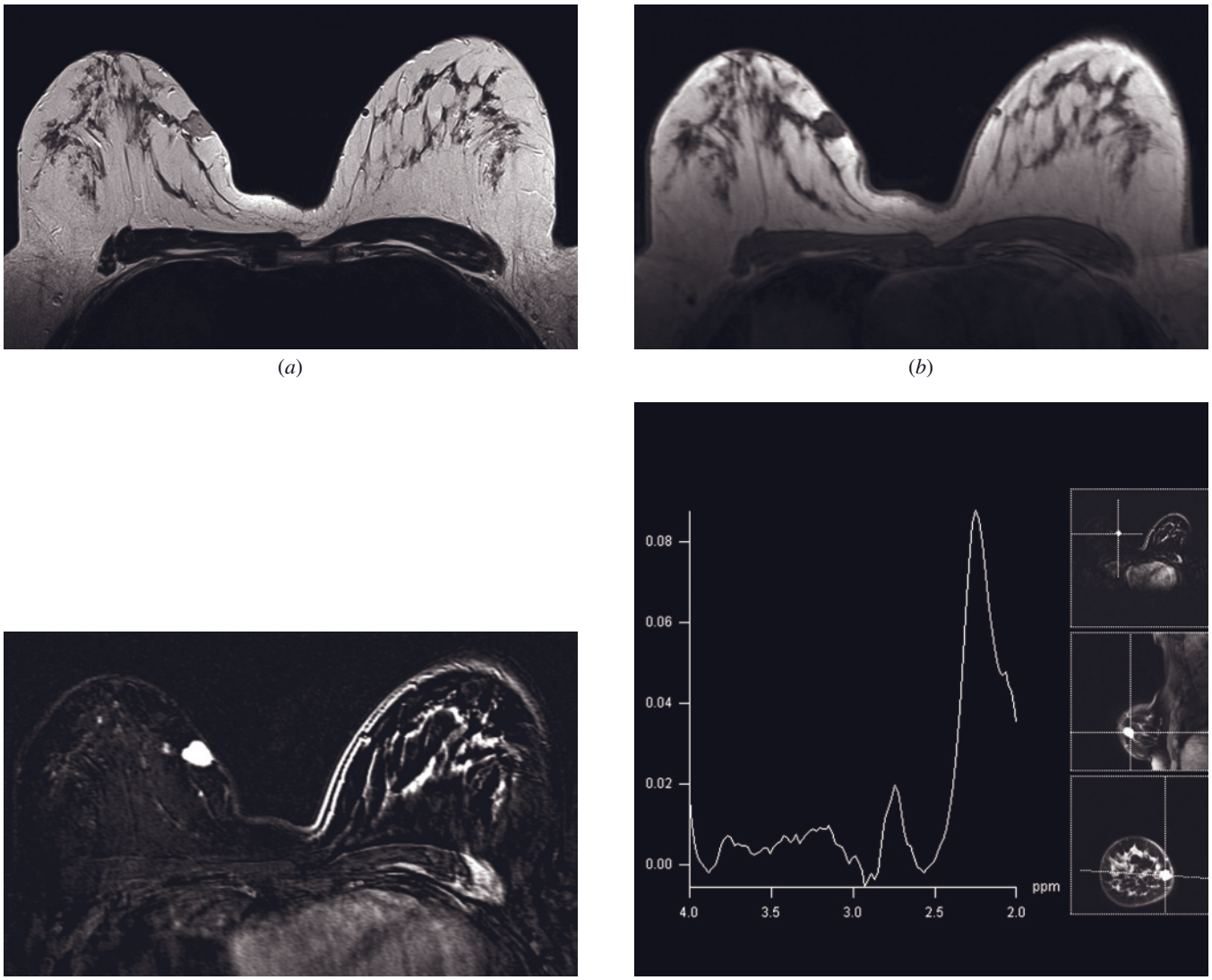

FIG. 19.45 Dermatofibrosarcoma protuberans (DFSP). DFSP in the breast presented as a strongly enhancing, lobulated mass with smooth margins, abutting the skin. Mass has intermediate to low intensity on both axial T2-weighted (*a*) and T1-weighted (*b*) images, with T2 hypointense foci in the central part of the tumor. It showed rapid initial enhancement with washout kinetics (*c*). The lesion was categorized as BI-RADS 4. ^{1}H MR spectroscopy was performed with a voxel size of 0.5 cm^3 (*d*). No apparent Cho peak was detected in a voxel placed in the lesion (*d*). Nevertheless, biopsy was performed, and pathology confirmed DFSP.

mass [142]. Surgical resection with mastectomy is the usual treatment. Recurrence rate depends on the tumor grade, and it is often accompanied by distant metastases [141].

MRI of angiosarcoma shows a heterogeneous mass with low signal intensity on T1-weighted and high signal intensity on T2-weighted images [143], with areas of hemorrhage or venous lakes with large draining vessels in the high-grade lesions (fig. 19.46). Enhancement depends on tumor grade, ranging from a progressive kinetics in low-grade angiosarcomas to rapid washout in high-grade angiosarcomas [144]. MRI may be used to determine lesion extent.

BREAST LYMPHOMA

Fewer than 0.5% of all lymphomas primarily affect the breast tissue. Primary and secondary lymphomas of the breast constitute approximately 0.15% of all malignant mammary neoplasms. The diagnosis of a primary breast lymphoma is established when there is no evidence of systemic lymphoma or leukemia at the time of detection of breast involvement. Primary lymphoma involves the breast only or the breast with ipsilateral axillary lymph nodes. Secondary breast lymphoma has an extramammary origin and has a typical presentation of multiple breast lesions (similar to the findings in other organs).

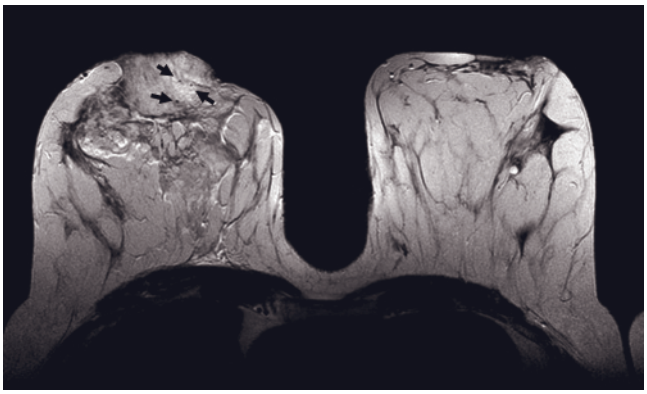

(*a*)

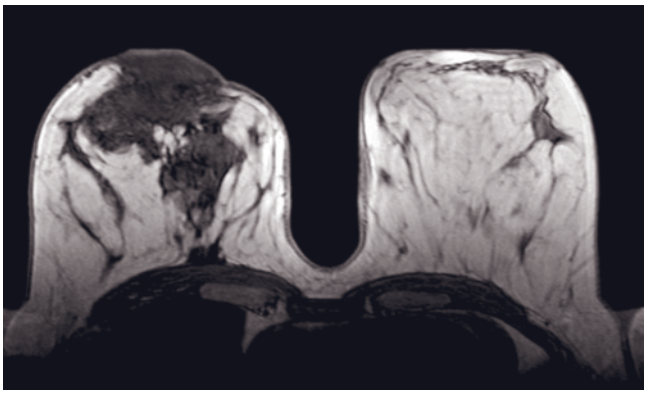

(*b*)

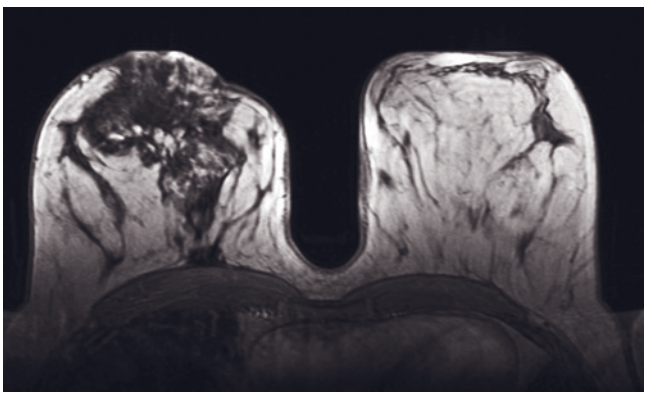

(*c*)

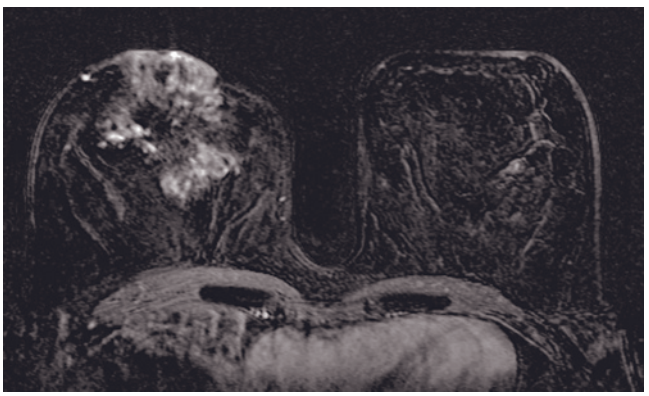

(*d*)

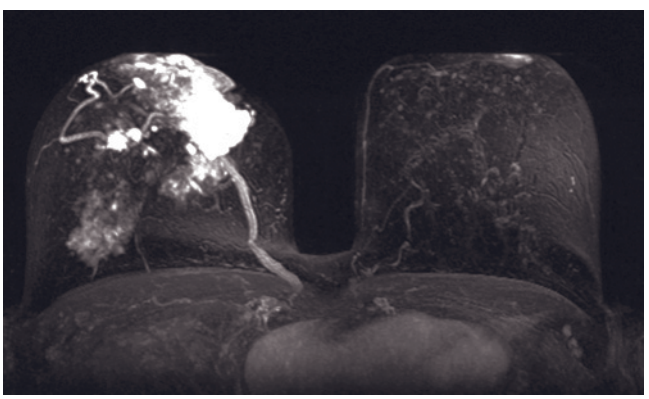

(*e*)

FIG. 19.46 Angiosarcoma of the breast. Extensive heterogeneous multifocal masses with skin invasion (main clinical sign was bluish skin) and tiny flow voids (arrows) are shown on T2-weighted axial image (*a*). The masses demonstrated low signal intensity on T1-weighted GRE image (*b*) and rapid heterogeneous enhancement on postcontrast (*c*) and subtracted (*d*) images. MRI was used to determine lesion extent, revealing that one-third of the breast tissue was involved, as seen on MIP image (*e*); large draining vessels are considered indicative of high tumor grade.

The majority of breast lymphomas are B-cell type, and only rarely are T-cell or histiocytic lymphomas found.

The age distribution is bimodal, with peaks in the 4th and 7th decades, without significant difference between primary and secondary lymphomas. Unilateral involvement is more common, showing a slight predominance for the right breast (60 : 40). Bilateral synchronous breast lymphoma is observed in approximately 10%, while metachronous contralateral disease occurs in 15% of cases.

The most frequent symptom is a palpable mass in the breast, sometimes painful, most commonly located in the upper outer quadrant. Rarely, skin fixation and cutaneous inflammatory changes can be detected. Enlarged axillary lymph nodes are clinically evident in 30–50% of the patients.

Typical MR findings include intensely and heterogeneously enhancing mass(es) (fig. 19.47) with rapid initial increase and a plateau or washout kinetics in dynamic study [145].

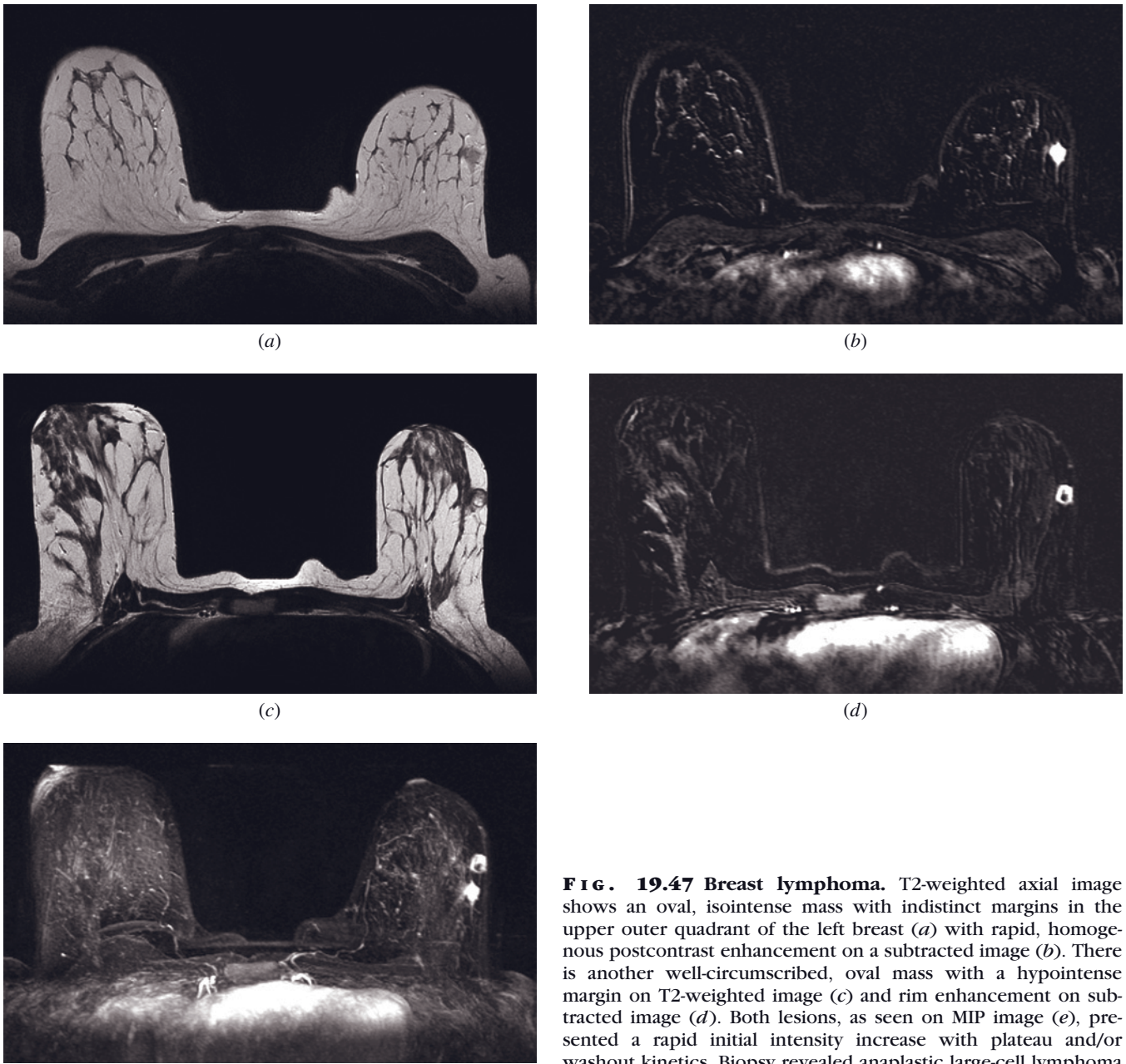

(*a*) (*b*) (*c*) (*d*) (*e*)

FIG. 19.47 Breast lymphoma. T2-weighted axial image shows an oval, isointense mass with indistinct margins in the upper outer quadrant of the left breast (*a*) with rapid, homogenous postcontrast enhancement on a subtracted image (*b*). There is another well-circumscribed, oval mass with a hypointense margin on T2-weighted image (*c*) and rim enhancement on subtracted image (*d*). Both lesions, as seen on MIP image (*e*), presented a rapid initial intensity increase with plateau and/or washout kinetics. Biopsy revealed anaplastic large-cell lymphoma (mixed-cell variant).

RADIATION-INDUCED CARCINOMA

Radiation is a well-recognized carcinogen. One of the best-documented, and most commonly encountered, radiation-induced cancers is the development of breast cancer after irradiation therapy for Hodgkin lymphoma, with a time delay between radiation and cancer development of 10–25 years [146]. There are two important distinguishing features. First, the age of diagnosis is usually in the early 40s, compared with the early 60s for breast cancer in the general population. Second, the incidence of bilateral disease, either synchronous or metachronous, is significantly higher (10–22%).

METASTASES IN THE BREAST

Breast is rarely the site of metastatic disease, which is responsible for only 0.4–6.6% of breast tumors. The most common metastases are those from cancer in the

contralateral breast, followed by metastases of melanoma, lung carcinoma, carcinoid tumor, lymphoma, and leukemia [147].

Regardless of their primary origin, metastatic breast lesions generally have some MR features in common. Usually, oval masses with well-defined borders are found, unlike the spiculated appearance of primary breast cancer. Lesions are commonly multicentric and bilateral, showing ring enhancement with centripetal progression and a washout type of dynamic curve [148].

The MR appearances of metastatic melanoma of the breast are variable depending on the amount of melanin pigment in the metastatic lesions. Since melanin possesses stable paramagnetic radicals, T1 and T2 relaxation times are shortened. Therefore, melanotic melanoma metastasis demonstrates a high signal on T1-weighted and often a low signal on T2-weighted images (fig. 19.48) [149].

Posttherapeutic MRI of the Breast

Breast-conserving therapy (BCT) followed by radiation therapy and chemotherapy is the treatment of choice for early-stage breast carcinoma. Neoadjuvant chemotherapy (NCT) is a systemic therapy initiated before the loco-regional treatment, indicated in patients with locally advanced or inflammatory breast cancers as well as in patients with operable breast cancer who were not candidates for BCT [150]. MRI is the most sensitive and reliable modality for local assessment (fig. 19.49) [127, 151, 152].

MRI Assessment of Postoperative Changes

Residual carcinoma is suspected when the initial attempt at surgical resection is incomplete. Recurrence may occur in a treated breast after lumpectomy with negative margins, with a recurrence rate of 1–2% per year [150].

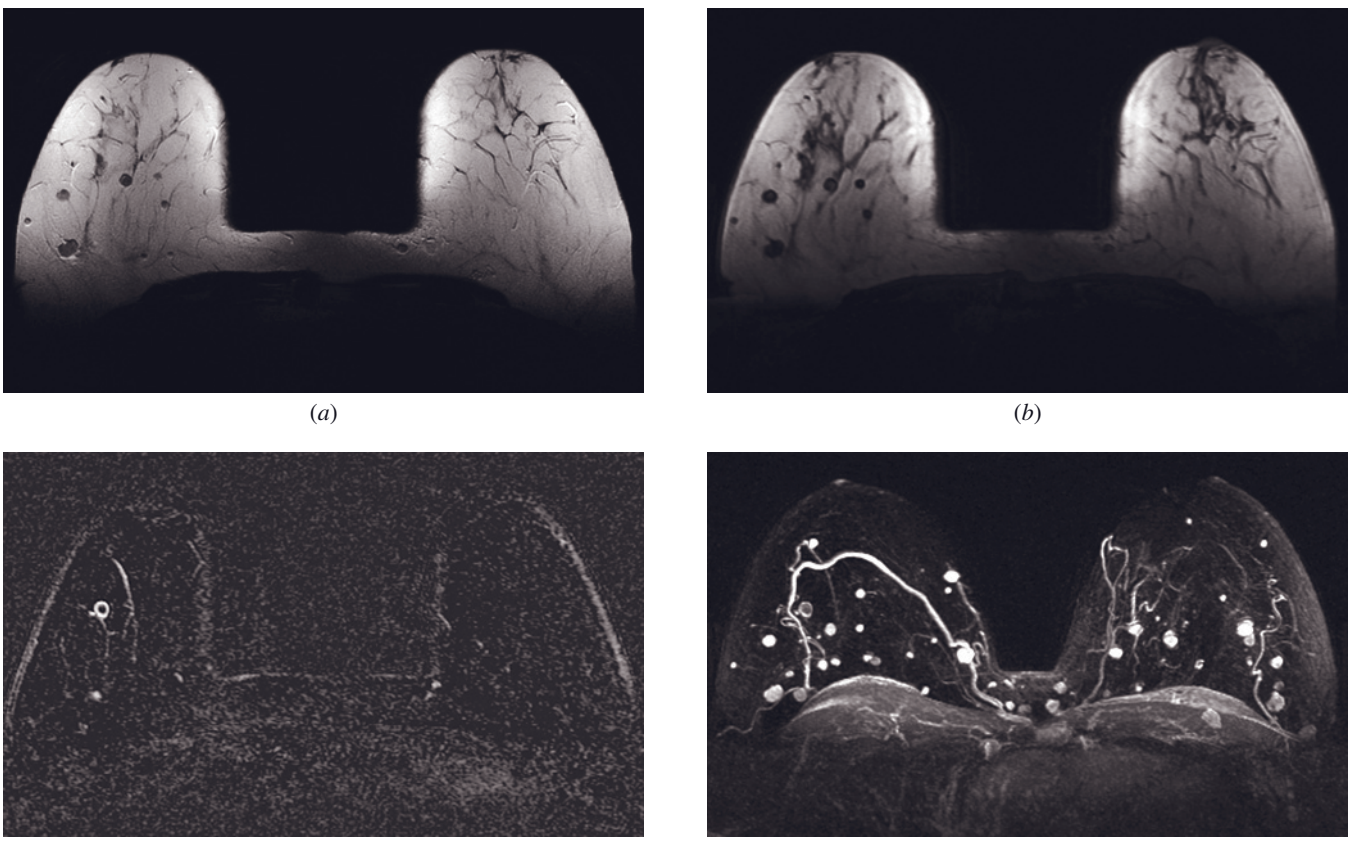

FIG. 19.48 Metastatic melanoma of the breast. Multicentric, bilateral round and oval masses are seen with low signal on T2-weighted image (*a*) and intermediate signal intensity with low-intensity rim on T1-weighted images (*b*). Lesions are well defined, showing typical ring enhancement on subtracted images (*c*) with centripetal progression (*d*, MIP image) and a washout-type dynamic curve.

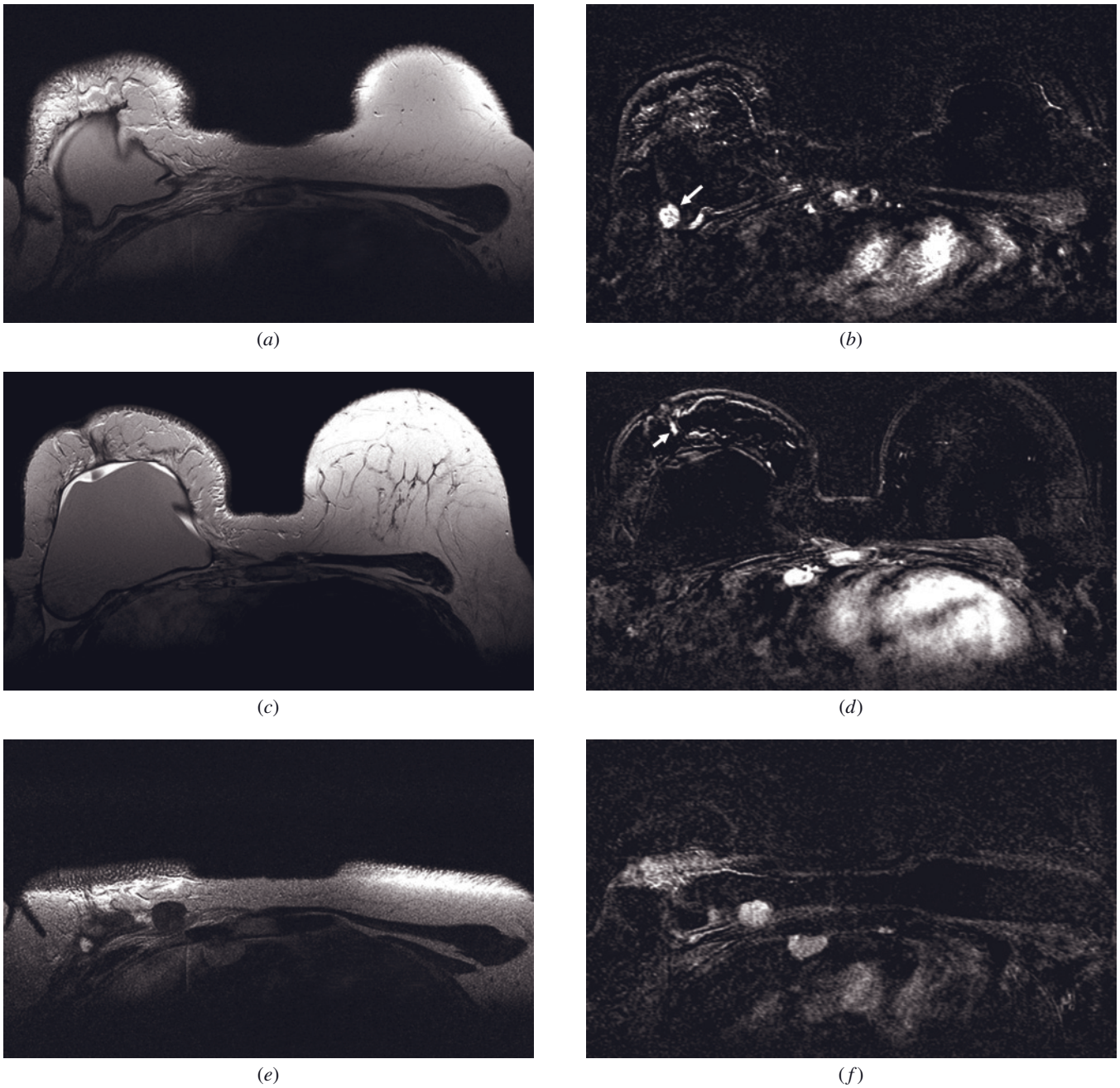

FIG. 19.49 MRI of the breast after subcutaneous mastectomy with silicone implant endoprosthesis in right breast. Axial T2-weighted image (*a*) shows hypointense lesion lateral to the implant with strong postcontrast enhancement on subtracted image (arrow, *b*) corresponding to tumor recurrence. In the subareolar region, DCIS is seen as clumped, ductal enhancement on subtracted (arrow, *d*) image, while T2-weighted image (*c*) was negative. In addition, enlarged ipsilateral infraclavicular and parasternal lymph nodes are seen (*d–f*). MRI is considered the most sensitive and reliable imaging modality for local assessment after breast cancer treatment. Note the nonuniform fat suppression of the right breast (*c*), a frequent but not diagnostically disturbing observation.

Although it has been reported that the recurrence rate was significantly lower in patients who underwent preoperative MRI for breast cancer staging (fig. 19.50) compared to those who did not [127], the findings are not yet conclusive. Recent studies have reported that the use of MRI at the time of initial diagnosis and evaluation of patients with early-stage breast carcinoma may not be associated with an improvement in outcome after BCT [153]. Recurrence may arise due to multifocal/multicentric tumor that was not detected at the time of

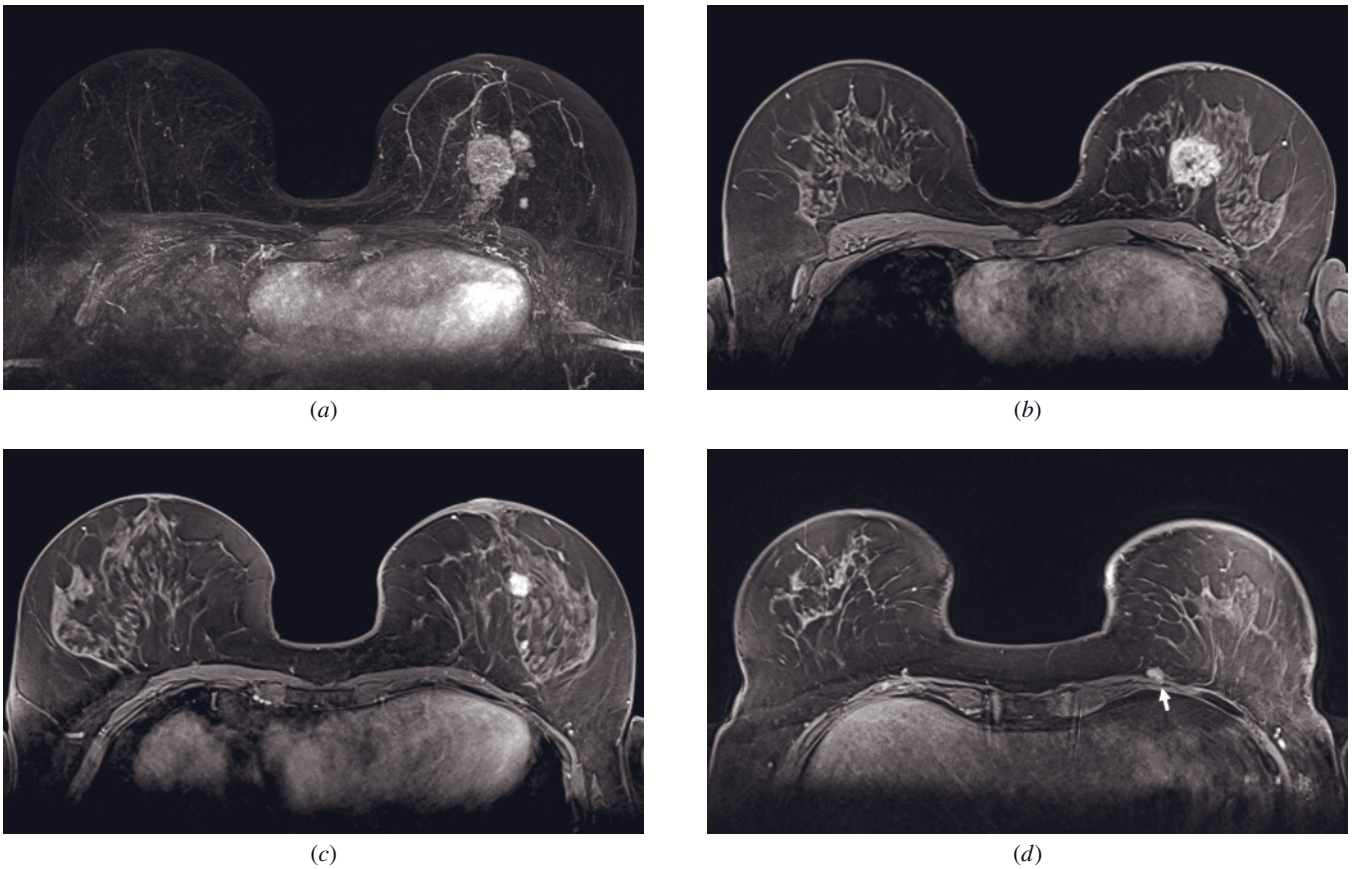

FIG. 19.50 Multicentric IDC at postoperative MRI. Multicentric IDC is shown at preoperative MRI exam on the MIP image (*a*) in the left breast. Postcontrast GRE images (*b*, *c*) show typical morphology of invasive cancers and obvious invasion of the pectoral muscle (arrow, *d*), influencing surgical approach.

diagnosis (fig. 19.51). The correct detection of multicentricity at preoperative MRI, however, in select cases results in improved management (switching from BCT to mastectomy), whereas erroneous classification of multiple foci of enhancement of benign tissue as multicentric disease may result in overtreatment. Information derived from MRI on local extent must be used appropriately, and simply transferring guidelines developed for mammographic staging to patients with MR-demonstrated multicentric cancer may not always work [154].

In general, breast MRI for the postoperative assessment of residual disease should be performed 28 days or more after surgery [155]. However, patients with positive surgical margins, whose further surgery should not be delayed, may benefit from immediate postoperative MRI to determine the extent of disease beyond the surgical site. Postoperative site may demonstrate enhancement up to 6 months after surgery without radiation therapy (fig. 19.52), and up to 18–24 months after radiation therapy [156]. MRI may not be useful for excluding small foci of residual disease, but it may be helpful for identifying gross residual disease or multicentricity of disease (fig. 19.52).

Findings suggestive of residual tumor include thickening beyond 5 mm of the enhancing wall of the seroma and an irregular or nodular enhancing rim around the resection cavity (fig. 19.53) [155]. Lack of enhancement at the lumpectomy site does not obviate re-excision if the surgical margin is positive. Re-excision or mastectomy is performed when initial margins of resection are positive or additional tumor foci are found. Breast MRI following surgery most commonly reveals fibrosis (fig. 19.54), scar tissue, seroma, hematoma and/or fat necrosis. Care is required in evaluating the postoperative breast as postsurgical changes can overlap in appearance with recurrent disease.

Fat Necrosis

Fat necrosis (FN) commonly occurs after BCT and CNB, as well as after radiation therapy for carcinoma. Early on, the lesion has the appearance of hemorrhage in indurated fat. After several weeks, it appears as a firm

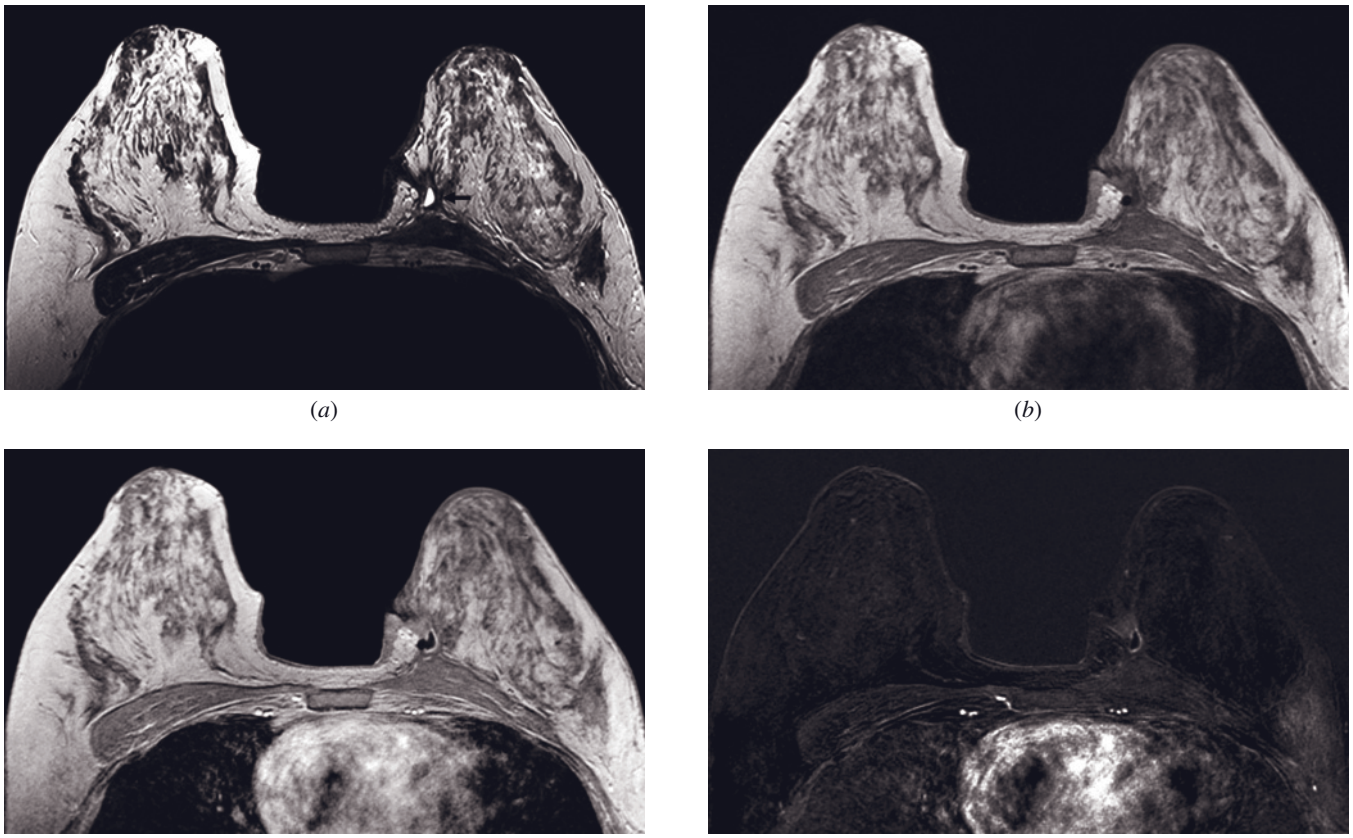

(*a*) (*b*)

(*c*) (*d*)

FIG. 19.51 Postoperative site after BCT and radiation therapy of the breast. Postoperative site may show postcontrast enhancement up to 18–24 months after BCT and radiation therapy of the breast. Postoperative scarring with skin thickening and a small seroma (arrow, *a*) in the medial aspect of the left breast are shown on the axial T2-weighted (*a*) and T1-weighted GRE (*b*) images. Postcontrast T1-weighted GRE (*c*) and subtracted (*d*) images demonstrate thin, regular enhancing margin of the postsurgical cavity 1 year after surgery and irradiation, without any signs of residual cancer.

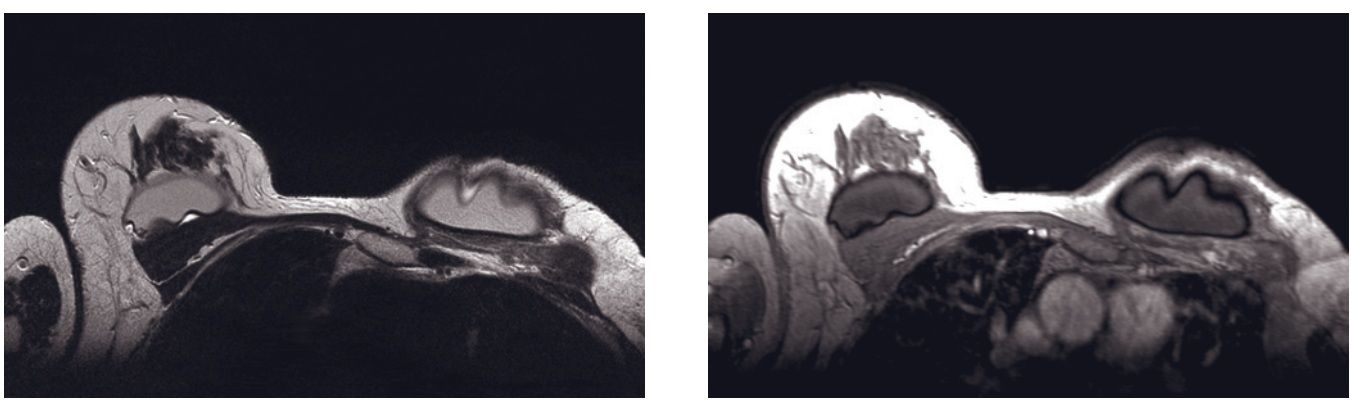

(*a*) (*b*)

FIG. 19.52 Postoperative breast MRI after subcutaneous mastectomy with implant endoprosthesis. Postoperative breast MRI after subcutaneous mastectomy with implant endoprosthesis shows infiltration of the pectoral muscle behind the implant (arrows, *c* and *d*) and along the lateral side of the implant on the axial T2-weighted (*a*), T1-weighted GRE (*b*), subtracted (*c*), and MIP (*d*) images.

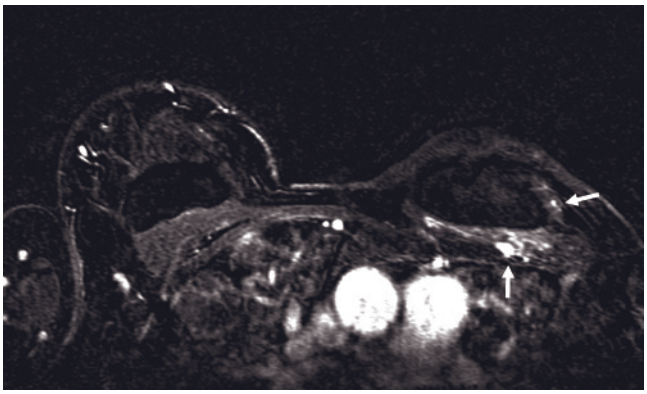

(*c*)

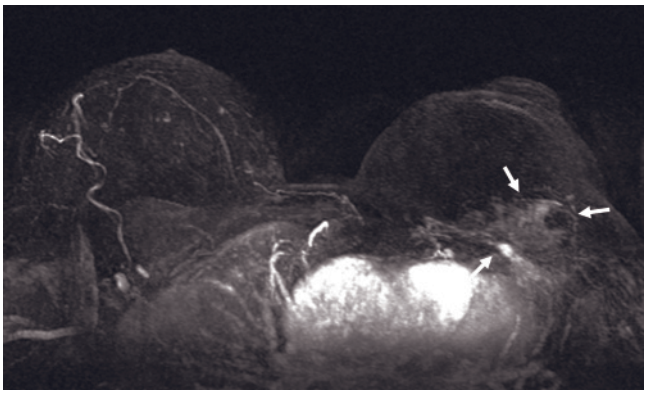

(*d*)

FIG. 19.52 (*Continued*)

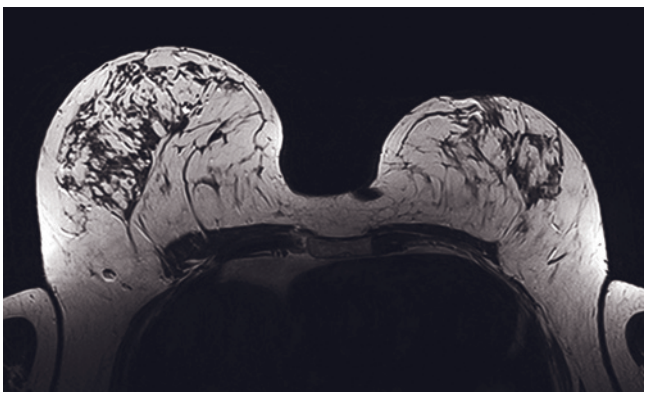

(*a*)

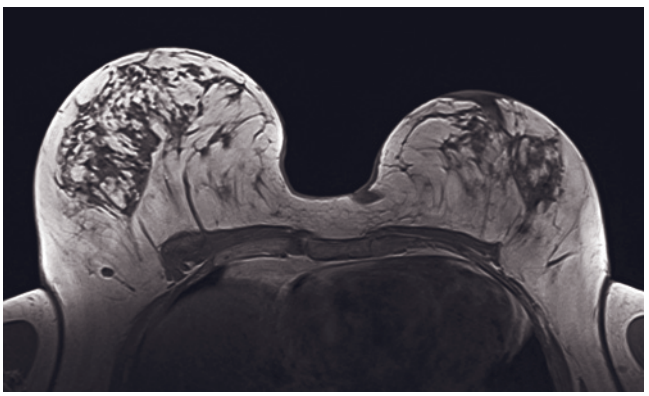

(*b*)

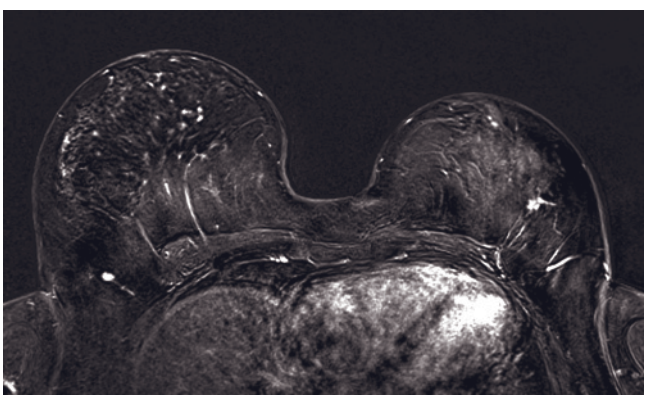

(*c*)

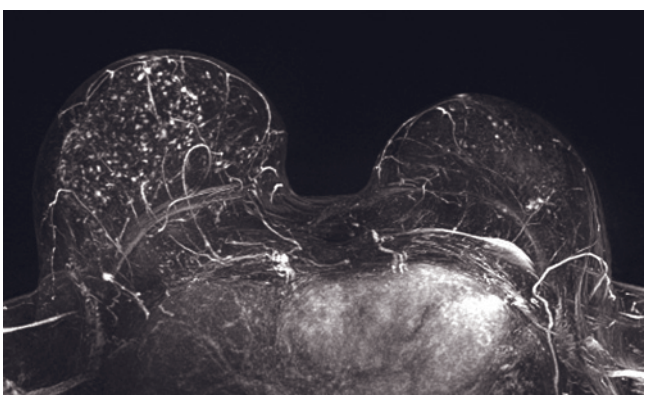

(*d*)

FIG. 19.53 Postoperative breast MRI 6 months after BCT. Axial T2-weighted (*a*) and T1-weighted GRE (*b*) images demonstrate only small irregular hypointense lesion. Findings suggestive of residual tumor include irregular enhancing rim (arrows) around the resection cavity, greater than 5 mm in size, seen on subtracted (*c*) and MIP (*d*) images. Biopsy revealed residual IDC, and re-excision was performed.

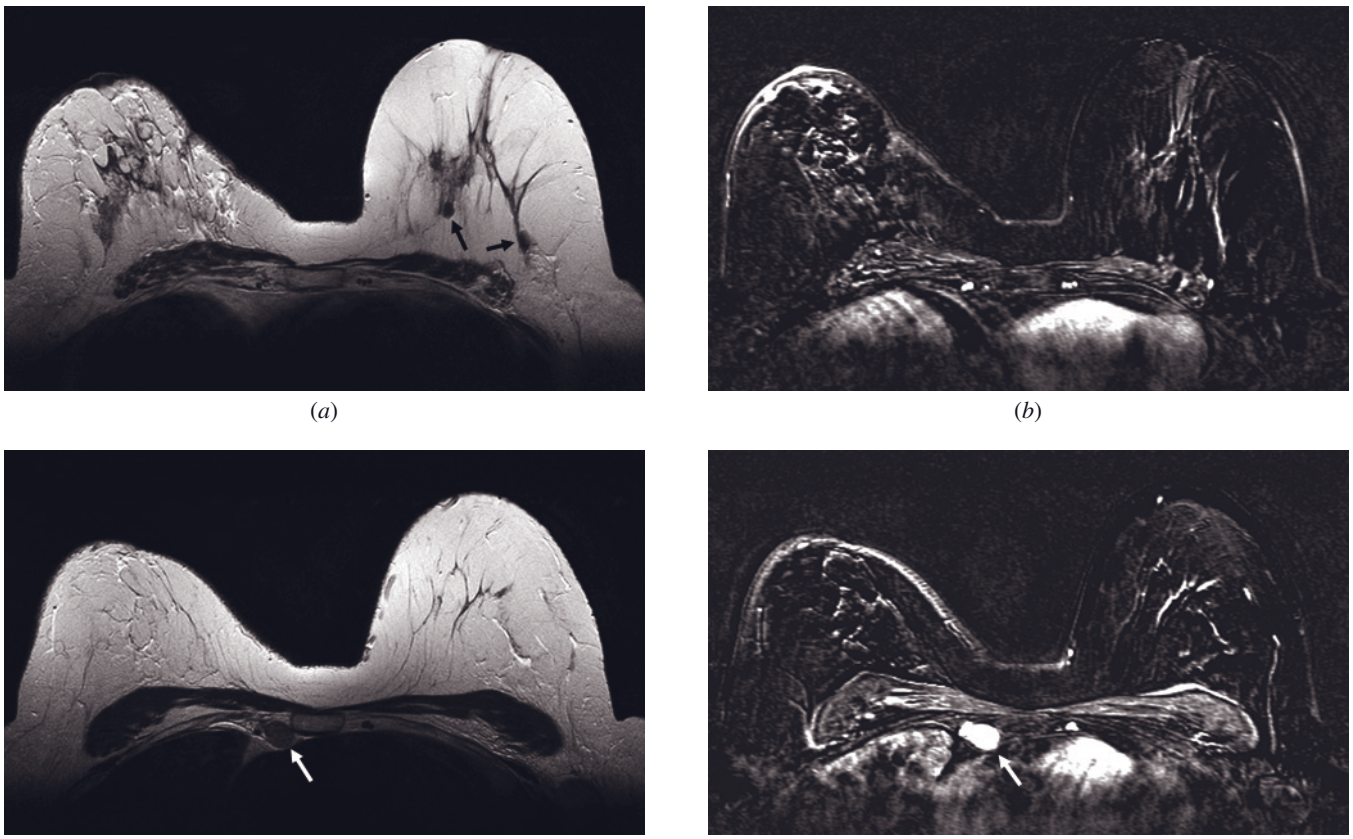

(*a*) (*b*) (*c*) (*d*)

FIG. 19.54 Breast MRI after BCT. Breast MRI after BCT most commonly reveals fibrosis, scar tissue, skin thickening, and lymphedema, as shown on axial T2-weighted (*a*) and subtracted (*b*) images without residual cancer. However, enlarged parasternal lymph nodes (white arrows) are seen (*c*, *d*), necessitating restaging. Note 2 small T2-weighted hypointense oval masses (*a*) with no postcontrast enhancement (*b*) in the right breast corresponding to hyalinized fibroadenomas (black arrows, *a*).

nodule with a well-delineated round border. The end stage of the process may show a dense scar [20]. Cystic degeneration may develop in the center, which often contains oily fluid with calcifications in the cyst wall, creating a specific mammographic appearance. However, clinical, mammographic, and ultrasound appearance may be indistinguishable from residual carcinoma.

On MRI, T1-weighted images without fat suppression can be extremely helpful to establish the diagnosis of FN by revealing bright fat signal centrally within the enhancing lesion (fig. 19.55). The appearance of fat necrosis on postcontrast T1-weighted images is variable, because of the various stages in maturation. Usually, a central unenhanced area (hypointense on fat-suppressed images) with thick enhanced rim is present (fig. 19.56). However, FN may mimic malignancy with varying appearances on MRI (fig. 19.57). Suspicious morphologic and kinetic features may be present (fig. 19.58), necessitating biopsy to exclude new or recurrent breast cancer [157]. Additionally, comparison with the mammogram can be invaluable.

Monitoring Efficacy of Neoadjuvant Chemotherapy

During or after neoadjuvant chemotherapy, diagnostic imaging studies are performed to 1) monitor early response to treatment and 2) identify possible residual disease.

The major aim of MRI is the comparative measurement of the tumor volume. With the WHO classification criteria, the tumor should be measured by multiplication of the largest perpendicular diameters of the tumor and for multiple lesions by the sum of the products of the perpendicular diameters. The response is evaluated by comparative measurements of the primary lesion (fig. 19.59). Four grades are usually used to describe the response: complete, partial, stable, or progressive disease. Complete response is defined as the disappearance of all known disease, partial response is defined as a decrease of 50% or more in the size of the lesion, and progressive disease as a 25% or more increase in the size of one or more measurable lesions, or the

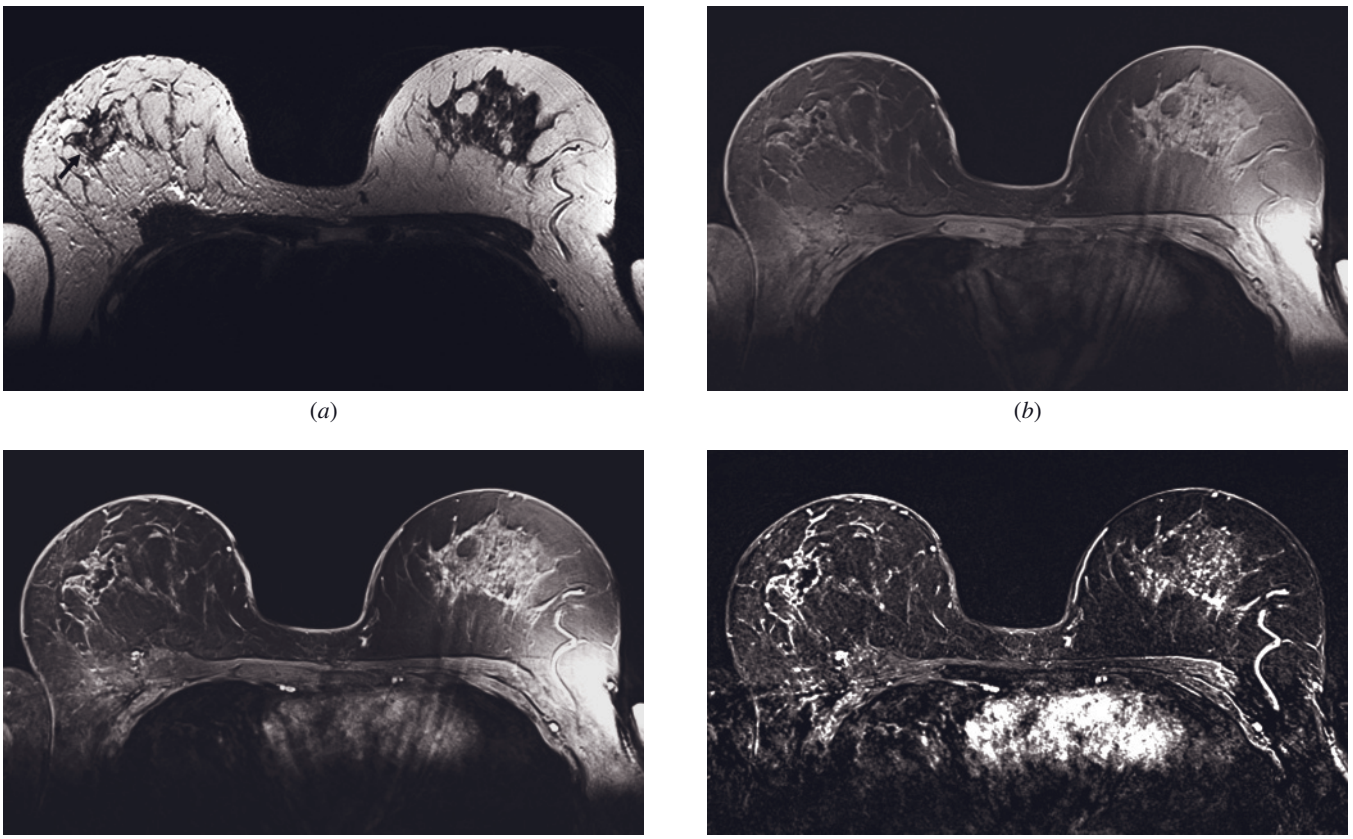

(*a*) (*b*) (*c*) (*d*)

FIG. 19.55 Fat necrosis 1 year after BCT. Axial T2-weighted image (*a*) shows heterogeneous, hyper- and isointense, well-circumscribed lesion with hypointense rim located in the lateral aspect of the right breast (arrow). Axial GRE image (*b*) reveals signal intensity of fat in the central area that does not enhance on postcontrast GRE (*c*) and subtracted (*d*) images. Enhancing lobulated rim is present.

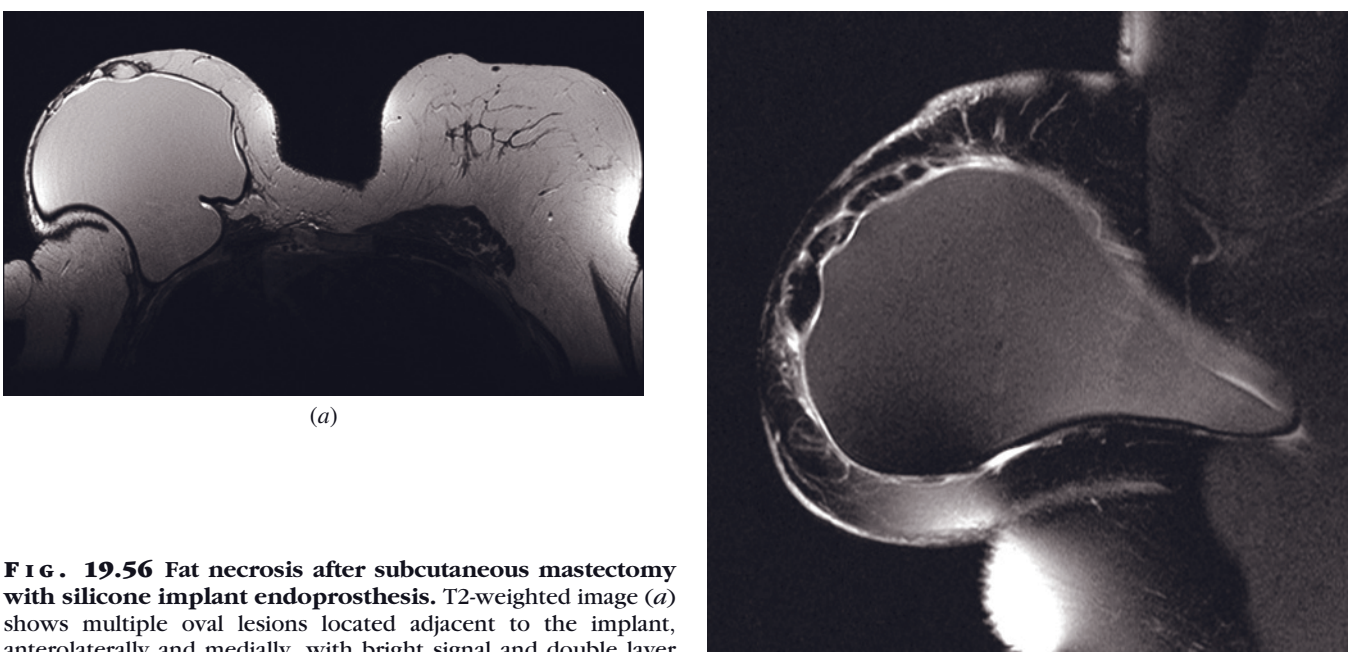

(*a*) (*b*)

FIG. 19.56 Fat necrosis after subcutaneous mastectomy with silicone implant endoprosthesis. T2-weighted image (*a*) shows multiple oval lesions located adjacent to the implant, anterolaterally and medially, with bright signal and double layer rim: iso- and hypointense. On fat-saturated T2-weighted sagittal (*b*)

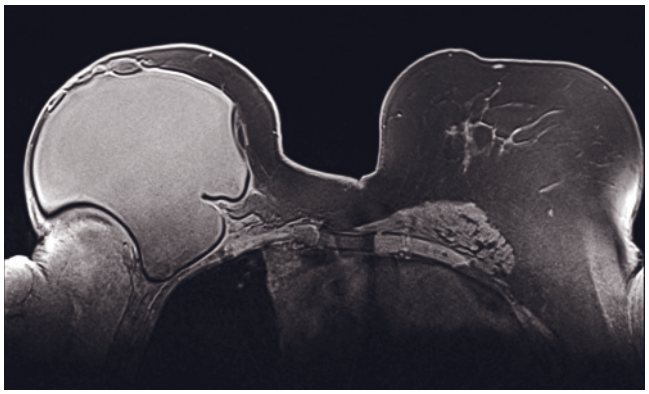

(*c*)

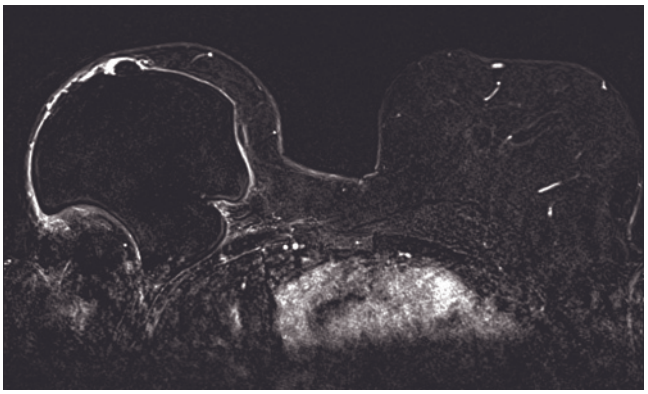

(*d*)

FIG. 19.56 (*Continued*) and axial GRE (*c*) images the fat signal is low. Postcontrast subtracted image (*d*) shows only thin, marginal enhancement of lesions, definitely excluding recurrent cancer.

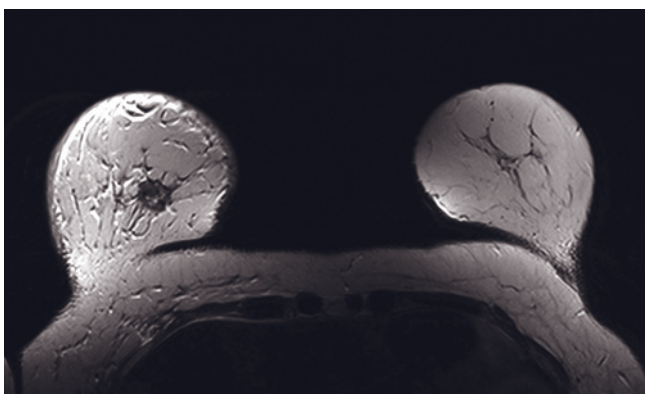

(*a*)

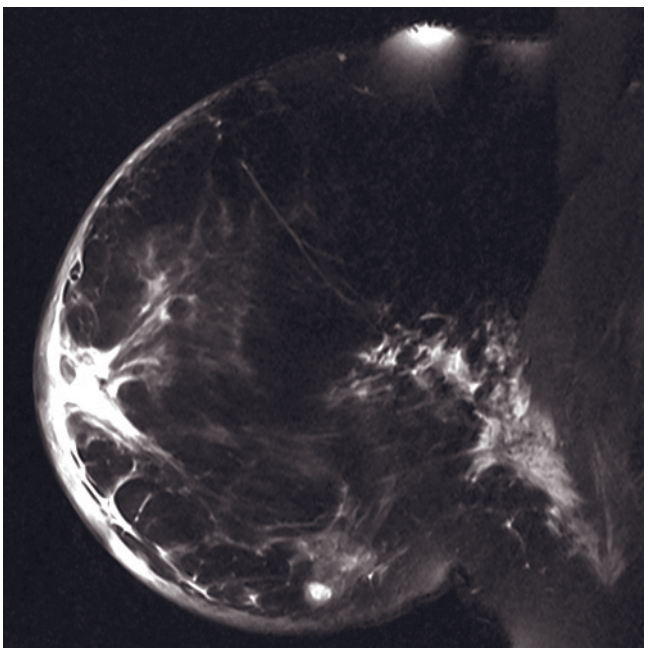

(*b*)

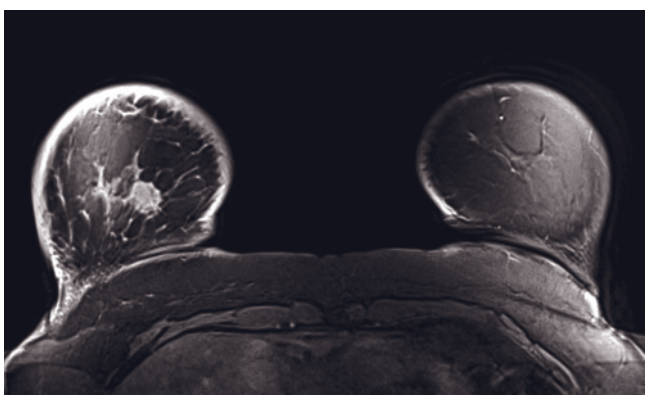

(*c*)

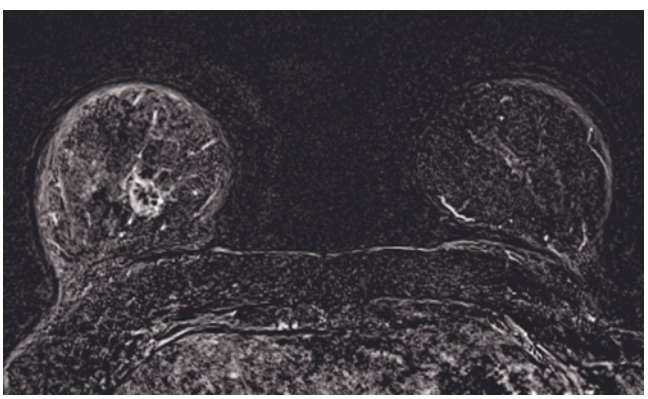

(*d*)

FIG. 19.57 Fat necrosis 6 months after BCT—diagnostic difficulties. An irregular mass of heterogeneous signal intensity with a hint of chemical-shift artifact is seen in the lower aspect of the right breast on axial T2-weighted image (*a*). On sagittal fat-saturated T2-weighted image (*b*), there is a persistent signal from the mass, which now looks lobulated and shows a small hyperintense oval part, likely due to cystic degeneration. Note the high T2 signal in the pectoralis muscle, consistent with postradiation changes. On the axial GRE image (*c*), the mass is of isointense signal with irregular borders. The postcontrast subtracted image (*d*) shows rim enhancement with enhancing incomplete septations, making this mass suspicious for malignancy. Type I time-intensity

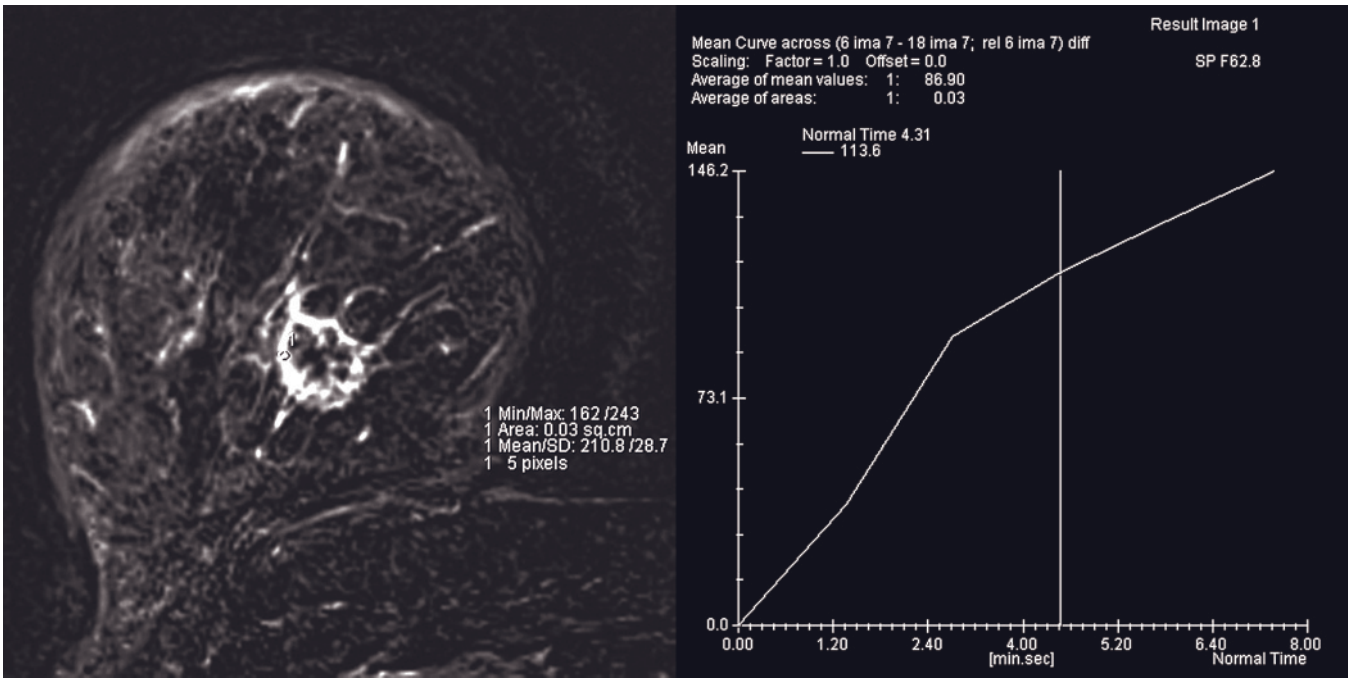

(*e*)

FIG. 19.57 (*Continued*) curve (*e*) was the most benign feature of this lesion on breast MRI. Mammographic and sonographic appearances of the lesion were consistent with fat necrosis. Fine needle aspiration (FNA) revealed oily content, confirming the benign nature of the lesion. It was categorized as BI-RADS 3, and 6 months follow-up was recommended.

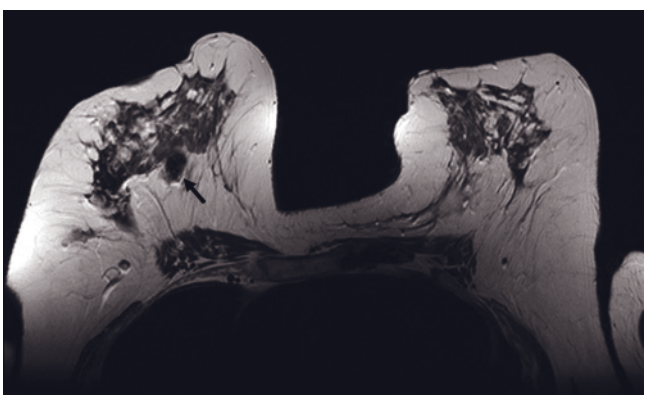

(*a*)

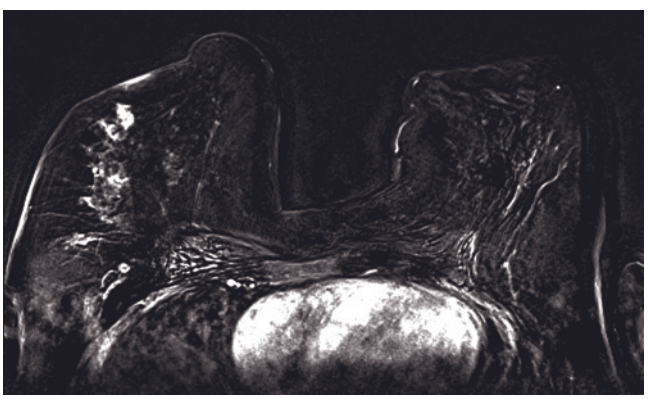

(*b*)

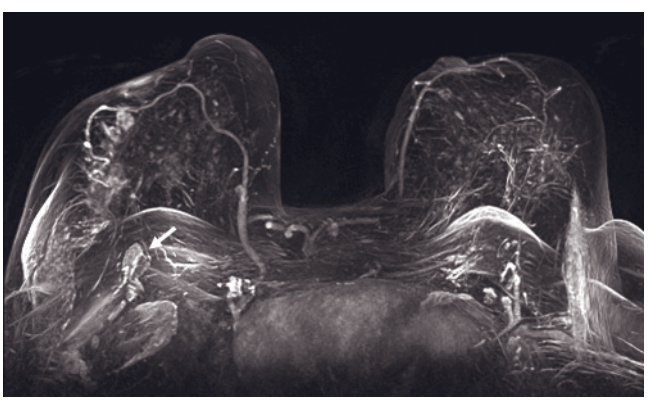

(*c*)

FIG. 19.58 Fat necrosis in the right breast 6 months after BCT. Clinical, mammographic, and sonographic appearances were indistinguishable from residual carcinoma. Breast MRI revealed extensive heterogeneous area in segmental distribution in the lateral right breast on T2-weighted image (*a*) that showed heterogeneous non-masslike postcontrast enhancement as seen on subtracted image (*b*). This was categorized as BI-RADS 4 lesion. Enlarged axillary lymph node (white arrow) is seen on MIP image (*c*). Biopsy revealed fat necrosis, and MRI follow-up after 3 months showed a decreased size of the enhancing lesion. Note hypointense hyalinized fibroadenoma (black arrow) in the central part of the right breast (*a*).

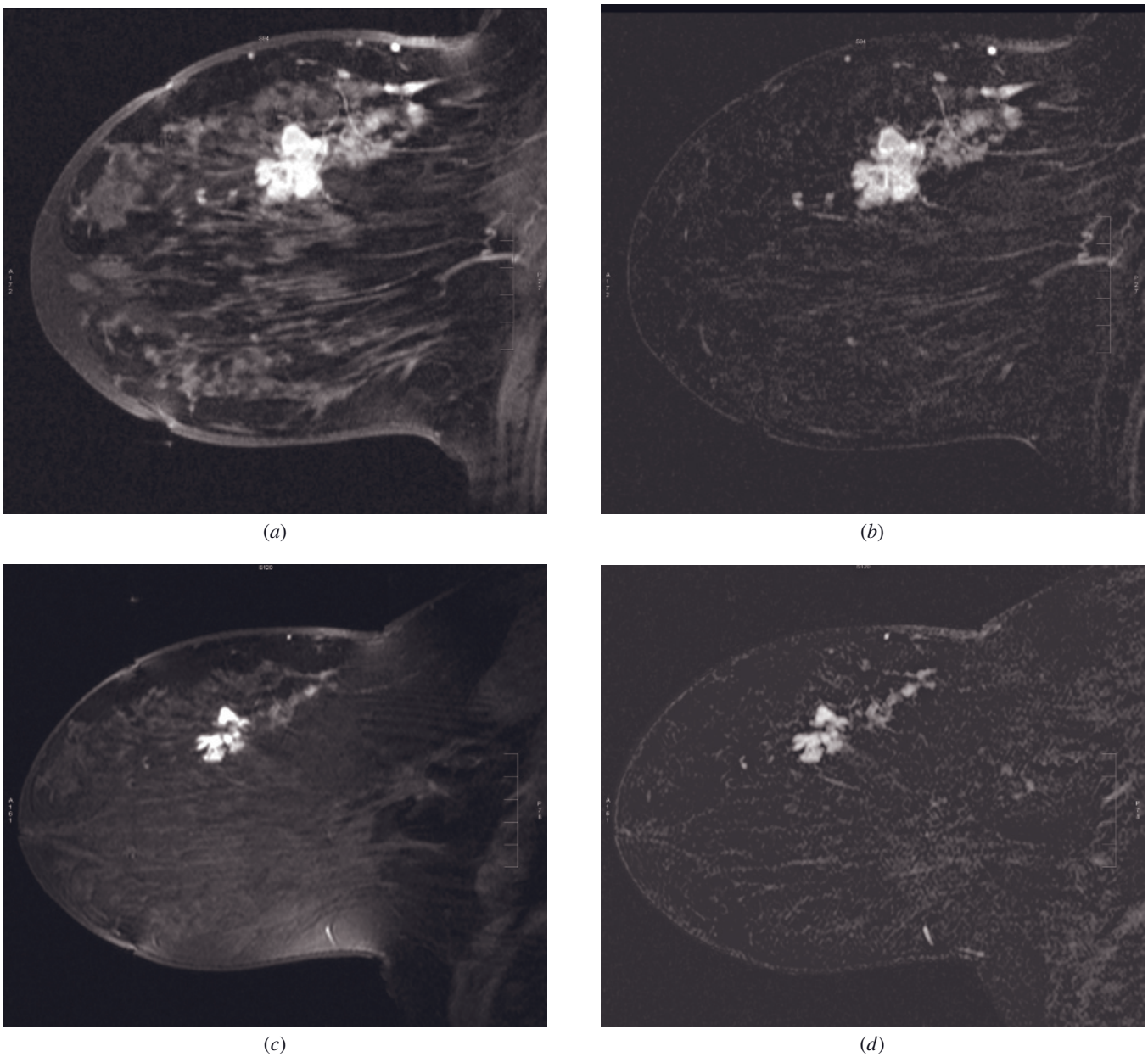

FIG. 19.59 Altering IDC appearance in course of neoadjuvant chemotherapy. Multiple MR exams in the sagittal plane, postcontrast 3D GRE T1-weighted scans, without and with subtraction, at approximately the same level. Initial study (*a*, *b*) demonstrates an irregular, strongly enhancing mass with irregular borders and rim enhancement. There is associated non-masslike enhancement in a segmental distribution posterior to the mass and an area of clumped enhancement in a ductal distribution at the posterior and superior border of this area, compatible with DCIS. Diffuse skin thickening is evident, most pronounced at the nipple-areolar complex. Note bright coil artifacts on the skin. The second study was performed at the middle point of chemotherapy (*c*, *d*): the mass is significantly smaller, non-masslike area of enhancement and clumped ductal enhancement reduced in size. The third study after completion of the 8 cycles of chemotherapy, before surgery (*e*, *f*), shows partial response.

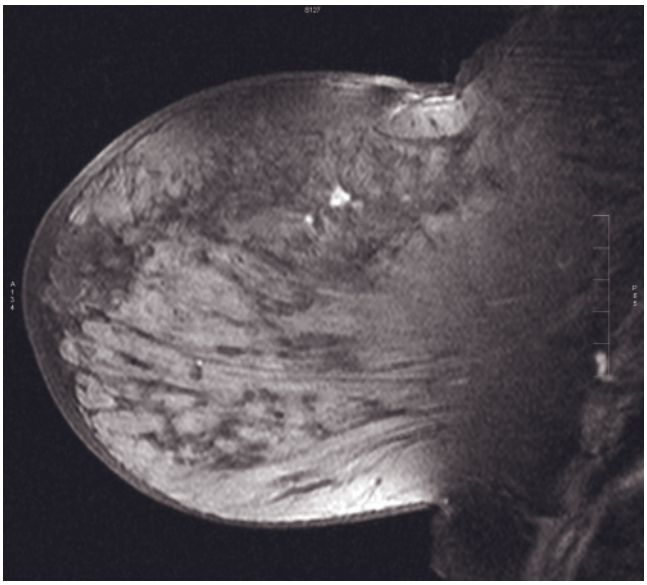

(*e*)

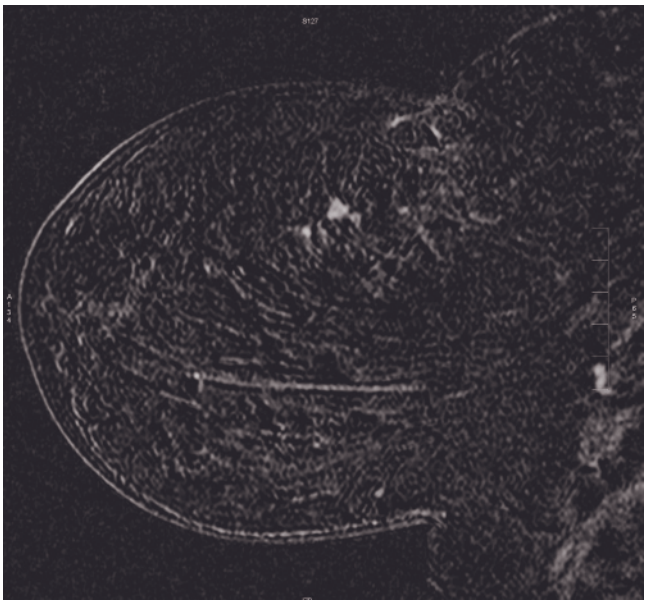

(*f*)

FIG. 19.59 (*Continued*) The mass is now fragmented and shrunken, and there are residual foci of enhancement scattered in the area of previously seen associated non-masslike enhancement. Skin thickening is decreased.

appearance of new lesions. Stable disease is defined as a stability or variation in measurements less than that of a partial response [150, 158, 159].

At dynamic GBCE breast MRI, a change in tumor volume and enhancement kinetics can be observed (slower wash in rate, absence of washout pattern, or flattening of the enhancement curve), as the earliest sign of response, which may be observed within several weeks of commencing therapy. The use of MRI may be justified to identify responders as early as 6 weeks after the first chemotherapy cycle [154, 160–162].

Proton ^{1}H MR spectroscopy, in particular at higher magnetic field strength, and diffusion-weighted imaging can help distinguish responders and nonresponders even earlier, as soon as 24 h after the first cycle of chemotherapy [163–165]. In ^{1}H MR spectroscopy, breast cancers typically exhibit an elevated Cho peak at 3.2 ppm (Cho is a marker of cellular proliferation). A reduction of the Cho peak seems to provide a very early sign of response. Predicting early response reduces unnecessary harm to a patient as well as the costs of inefficient therapy [154].

Although MRI may be superior to other methods, viable tumor remnants may be identified in up to 30% of patients, even if an MR study was negative. The underestimation of residual disease is probably due to the antivascular effects of chemotherapeutic agents, which may exceed the cytotoxic effects (especially with taxanes) [166–168].

MRI OF BREAST IMPLANTS

The two major indications for implant assessment by breast MRI are the evaluation of silicone implant rupture and the detection of breast cancer. If MRI is being performed to assess silicone implant rupture, a noncontrast study for the evaluation of the internal structure of the implant is optimal. If, however, MRI is used to detect possible neoplasm in the breast, a GBCE MRI study with the use of fat suppression and subtraction is necessary.

Types of Implants

Breast implants can be classified according to their location in relation to the pectoral muscle and their composition. In terms of location, there are **subglandular** (i.e., **retroglandular, retromammary, prepectoral**) and **submuscular** (**retropectoral, subpectoral**) implants. The implant location is individually chosen for each patient according to the patient's need, request, and body habitus [169]. Subglandular implants are situated behind the glandular tissue and in front of the pectoral muscle (fig. 19.60), which maximizes the augmentation effect, whereas submuscular location (fig. 19.61) allows for better evaluation of the breast tissue at mammography, while its cosmetic effect is not as pronounced.

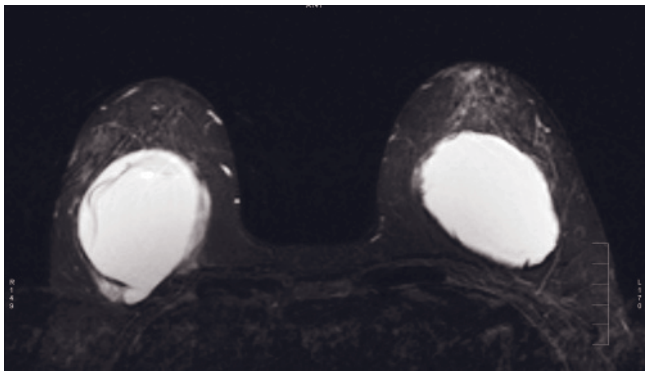

(*a*)

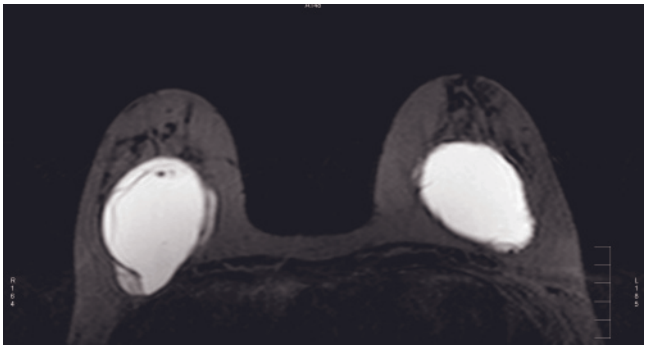

(*b*)

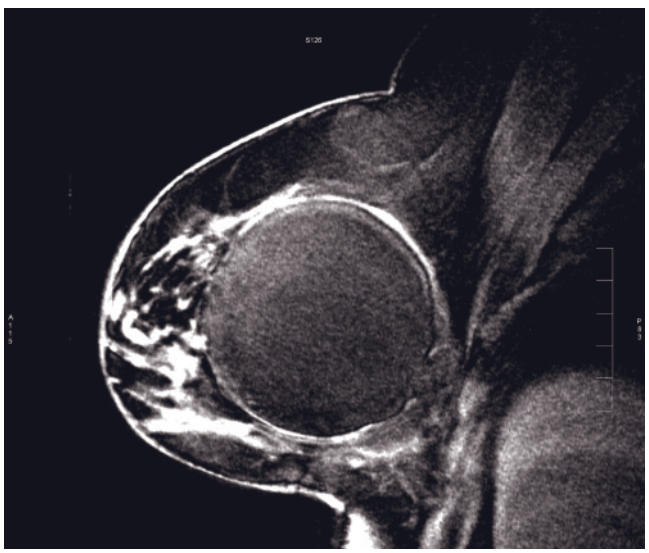

(*c*)

FIG. 19.60 Implant rupture. On axial fat-saturated T2-weighted (*a*) and silicon-specific IR (*b*) images, there are bilateral extracapsular ruptures of subglandular silicone implants. There is high signal from both silicone and fibroglandular tissue on *a*, and it is not possible to accurately differentiate free extracapsular silicone from the fibroglandular tissue at the anteromedial border of the implant in the left breast. With silicone-specific sequence (*b*) high signal persists, confirming the extracapsular rupture with the presence of extracapsular silicone. In the right breast, there is a focal bulge posteriorly with extracapsular silicone seen just lateral to it and at the medial border of the implant (*b*). Partly collapsed elastomer shell is well seen on the right as hypointense lines within the lateral and anterior aspect of the implant (*a*, *b*). A droplet of fluid is seen within the implant anteriorly, demonstrating the high signal in *a* and signal void in *b*. On fat-suppressed T1-weighted contrast enhanced sagittal image, a posterior focal bulge is clearly seen (*c*). Note the motion artifacts in phase-encoding direction in *a*.

Implants are divided by their composition into three categories: saline, silicone, and a combined saline-silicone. Furthermore, they can contain a single lumen or multiple lumens—two or more (fig. 19.62). Multiple lumen implants can consist of one lumen within another (silicone within saline, i.e., double lumen) or one lumen behind the other (i.e., stacked). Expander type implants consist of a single saline or a double saline-silicone lumen. The outer envelope of the implant also may vary depending on the material. Most contemporary implants have a silicone elastomer shell. A textured surface and a layer of polyurethane are incorporated in order to decrease the likelihood of contracture.

All implants are eventually surrounded by a host fibrous capsule, which forms as a response of the body to the foreign material of the implant. It is formed soon after the placement of the implant and represents a thin layer of scar tissue, which not uncommonly calcifies or, rarely, ossifies. This capsule may contract around the implant as early as a few weeks after placement, causing capsular contracture, one of the most common potential complications of implants. In addition, breast pain, hematoma, and infection may occur. Several papers have suggested a possible link between silicone implants and connective tissue disorders, but without strong supporting evidence. Finally, an important possible complication is implant failure.

Implant Failure

The functional definition of implant rupture is the failure of an implant to contain its silicone gel [169]. Gel bleed is the term used to describe the normal transudation of microscopic amounts of silicone gel through an intact shell. This term should not be used when there is any sign of a discontinuity in the shell. To avoid misinterpretation and miscommunication, some authors suggest the discontinuation of the term [169].

Implant rupture can be classified according to the degree of collapse. The first degree is termed gel leak or **uncollapsed rupture**, representing a small amount of silicone gel that is detected usually as a 0.5-mm-thick

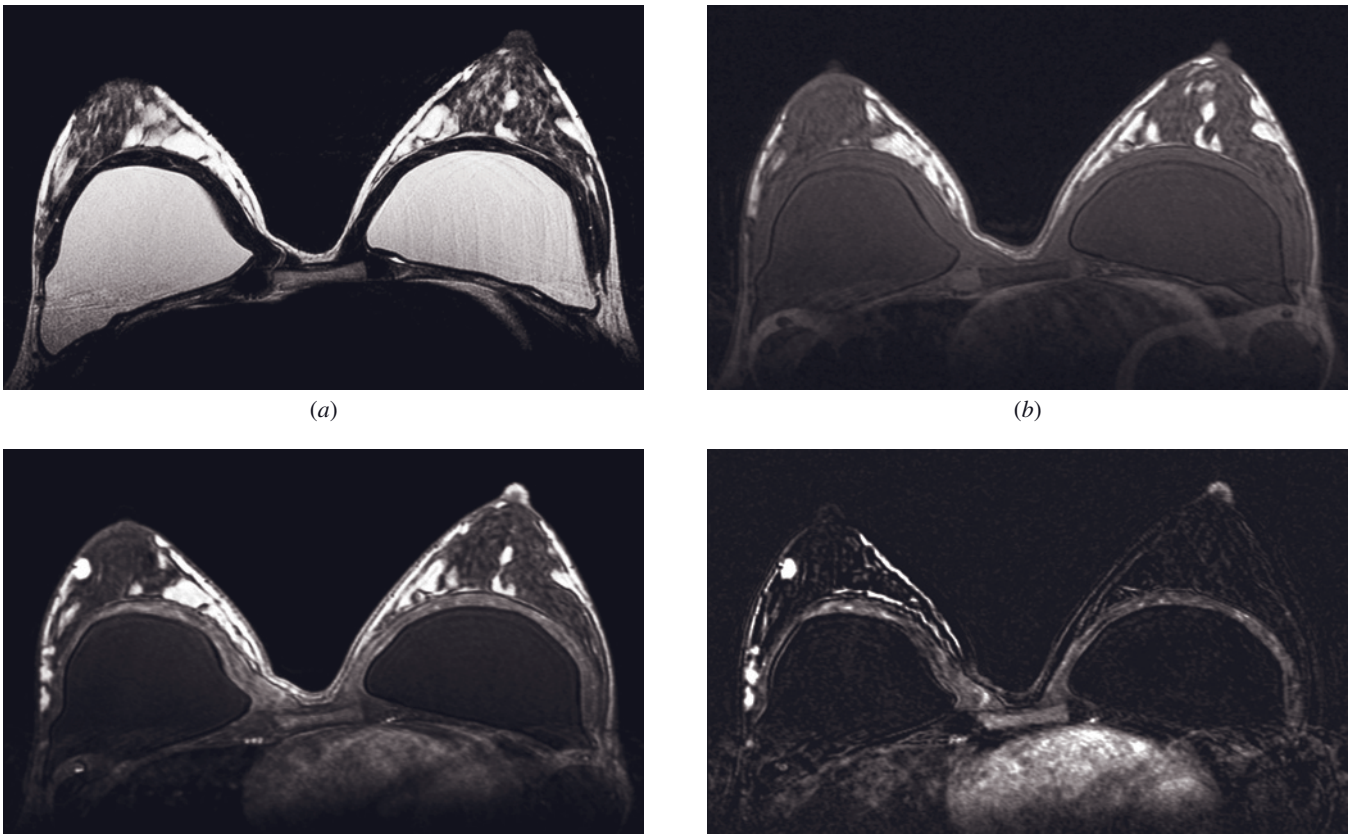

(*a*) (*b*) (*c*) (*d*)

FIG. 19.61 Multifocal IDC in patient with silicone implants. Subpectoral silicone implants are seen on axial T2-weighted (*a*) and T1-weighted GRE (*b*) images. Multiple enhancing masses are seen in the lateral aspect of the right breast on postcontrast T1-weighted GRE (*c*) and subtracted (*d*) images. Biopsy revealed multifocal IDC (Courtesy of Dragana Bogdanovic-Stojanovic, M.D., Diagnostic Imaging Center, Oncology Institute of Vojvodina, Serbia.)

layer on the surface of the implant (fig. 19.63). After a careful search, a small hole or other opening in the shell can be detected. The next degree can be classified as an **intracapsular rupture**, when silicone gel from a ruptured implant is still contained within the fibrous capsule and the shell collapses into the gel to a variable degree (fig. 19.62). The final degree of intracapsular rupture is a **fully collapsed implant**, where the shell is effectively fully collapsed within the gel (fig. 19.64). **Extracapsular rupture** refers to the circumstance in which silicone gel escapes through a defect in the fibrous capsule into adjacent tissues, either into the anatomic space where the implant was originally placed or, rarely, into neighboring anatomic spaces (fig. 19.60). For single-lumen silicone gel-filled implants, the definitions of rupture and collapse are relatively straightforward, while for double- and triple-lumen implants there are many possible configurations of rupture.

Implants may rupture for a variety of reasons: traumatic stress, such as manual compression to break up a painful capsule (closed capsulotomy), accidents, gunshot wounds, insertion of pleural tubes, and even mammographic compression [170]. Most ruptures, however, occur with no identifiable cause. Berg and Nguyen [171] reported that the mean age of ruptured implants was 13.4 years, while for intact implants it was 7.7 years. This led to a supposition that the main predisposing factor for rupture is the age of the implant, with an increasing possibility of rupture in older implants.

Approximately 77–89% of ruptures are classified as intracapsular, and between 11% and 13% are classified as extracapsular. The migration of silicone gel in extracapsular rupture is usually detected within the breast parenchyma, but sometimes silicone gel can migrate intraductally, through the nipple or transcutaneously through the skin. Distant localization includes axillary lymph nodes, pleura, chest wall, ribs, or even extremities, inguinal region, or liver. As a response to silicone migration, the body produces silicone granuloma around the foreign body.

The symptoms of implant rupture are usually minor and clinically silent. They may include pain or a palpable

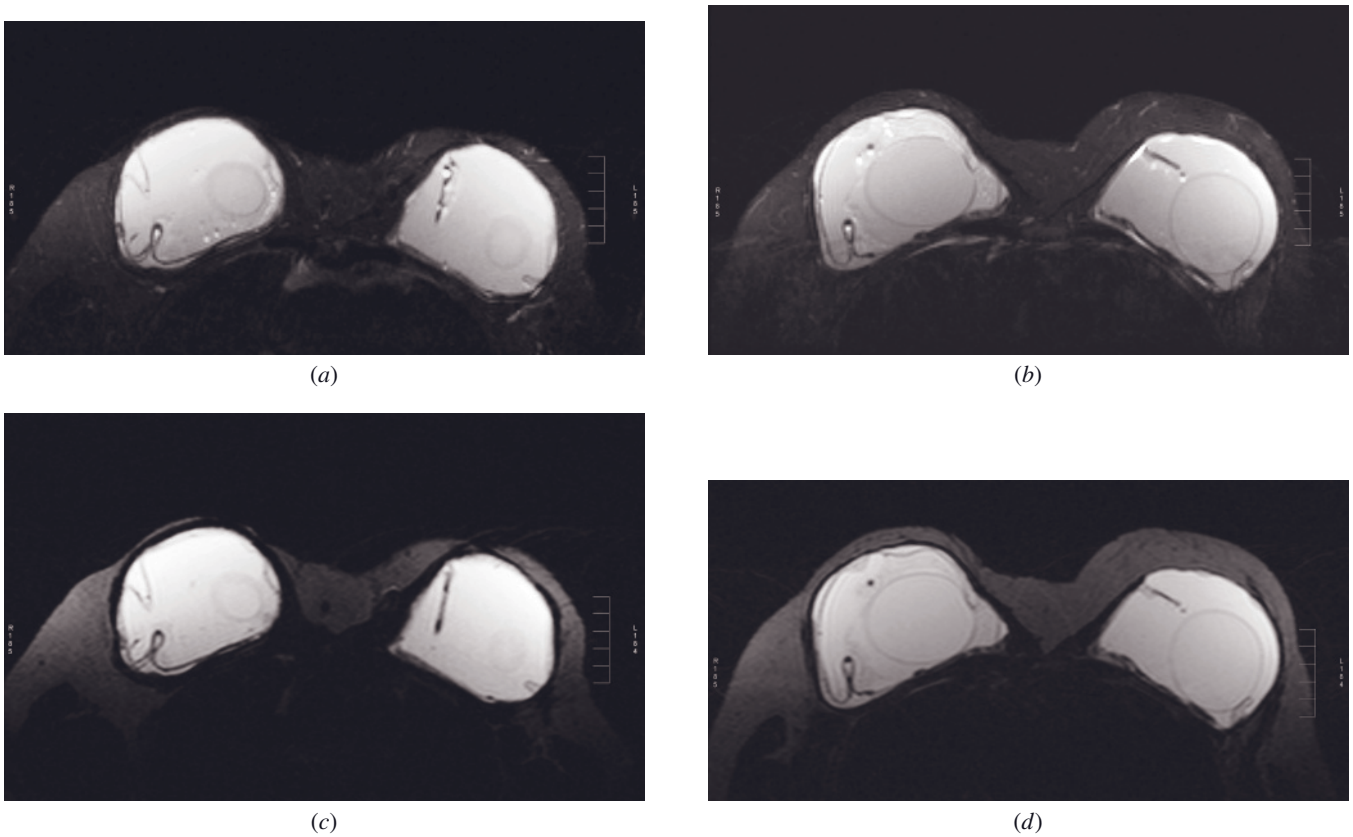

FIG. 19.62 Intracapsular rupture of outer lumen of double-lumen silicone-silicone implants. Bilateral axial fat-saturated T2-weighted (*a*, *b*) and corresponding silicone-specific (*c*, *d*) images demonstrate various signs of implant rupture. Keyhole sign is seen in the posterolateral aspect of the right breast implant, while there is a noose sign in the same area on the opposite side. There is pull-away sign in the anterolateral aspect of the right breast implant. Salad-oil sign is also seen as high signal foci within the gel (*a*, *b*), which are suppressed on silicone-only sequences (*c*, *d*), indicating fluid/serum influx, likely through a defect capsule. Note the rounded shape of the inner lumen components bilaterally, reflecting higher silicone pressure within them, which is a normal finding.

mass in the axilla, breast, or chest wall, but also changes in the morphology of the breast (asymmetry, size, shape) might occur. There are no supporting data for the use of screening imaging of asymptomatic women for implant rupture, but imaging studies, including mammography, ultrasound, and MRI, are undoubtedly useful in establishing the diagnose of implant failure.

Magnetic Resonance Imaging Technique

In women with silicone implants, breast MR is performed with a dedicated breast coil in the prone position. For sagittal acquisitions the phase encoding should be in the supero-inferior direction. High-resolution fast spin-echo T2-weighted imaging has a reported sensitivity of 95–98% for the detection of implant rupture. Sensitivity is somewhat lower in cases of subtle uncollapsed ruptures (about 50%).

The most common pulse sequences to image breast implants and soft tissue silicone are T2-weighted fast spin echo and fast inversion recovery (IR) with water saturation. In the first sequence, water and waterlike fluids, as well as silicone, look bright with fat of intermediate signal and allow an excellent appreciation of the internal structure of the implant. The latter sequence is a "silicone-only" sequence since it allows silicone to be bright whereas fat is suppressed (STIR) and water is dark (saturated), which provides excellent visualization of extracapsular silicone.

On T2-weighted fast spin-echo images, the intact single-lumen implant demonstrates a high signal surrounded by a thin hypointense layer of elastomer shell and fibrous capsule. Curvilinear hypointense lines within the implant that are continuous with the outer capsule are called radial folds or invaginations and are part of the normal appearance of an intact implant. They can be simple, traveling, branched, or with a crook-neck appearance; they can extend across the implant in a simple or complex pattern, short or long, single or multiple, and also have the appearance of free

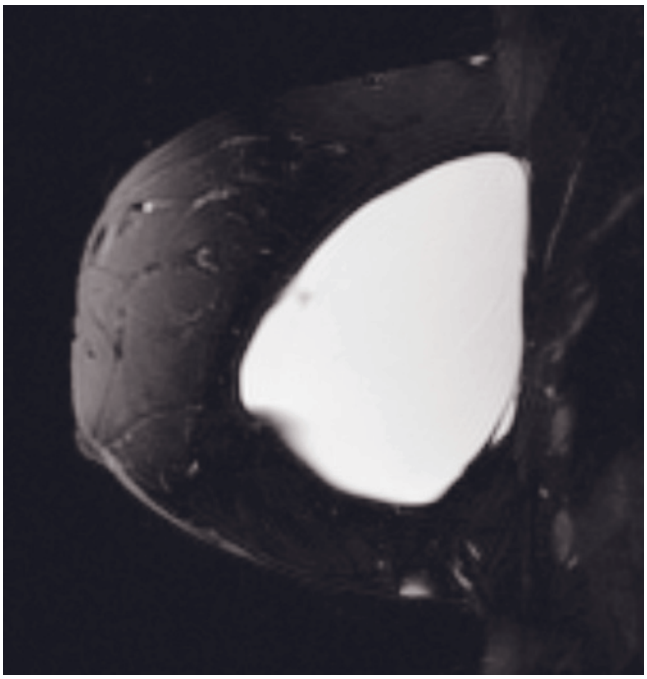

(*a*)

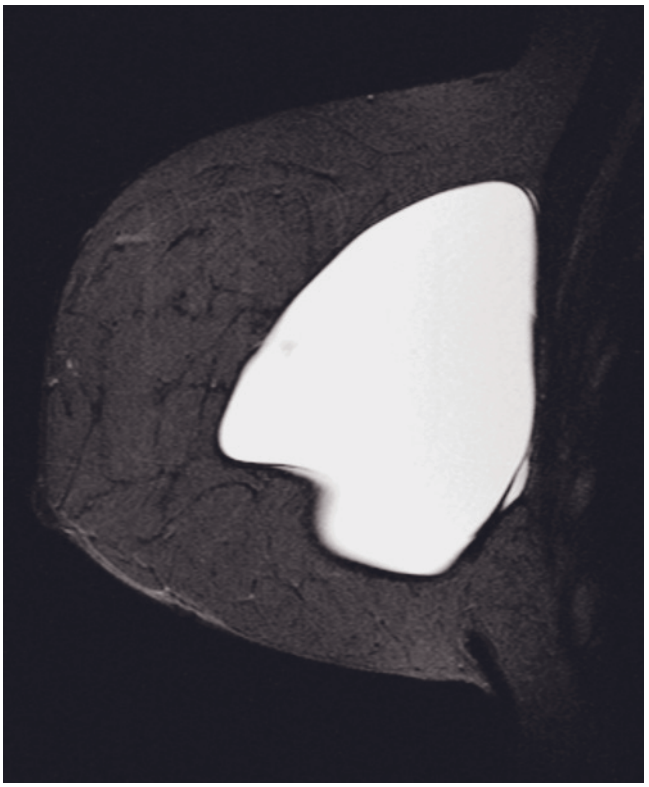

(*b*)

FIG. 19.63 Gel leak—uncollapsed rupture. Sagittal fat-saturated T2-weighted (*a*) and silicone-specific (*b*) images demonstrate small amount of silicone outside the inner shell at the posterior and superior border of the silicone implant. Note the indistinct anteroinferior border due to partial volume effect and complex radial fold. There were no signs of elastomer shell collapse.

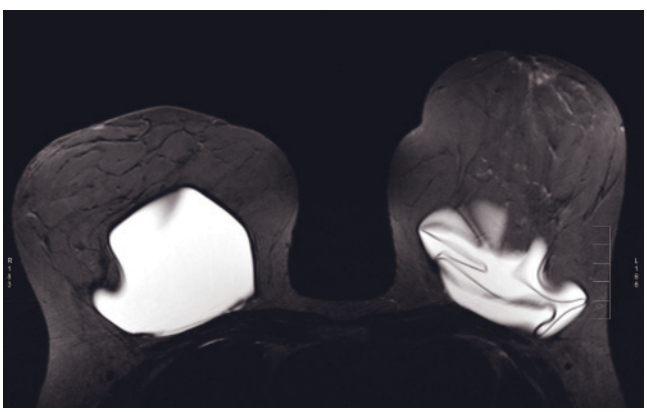

(*a*)

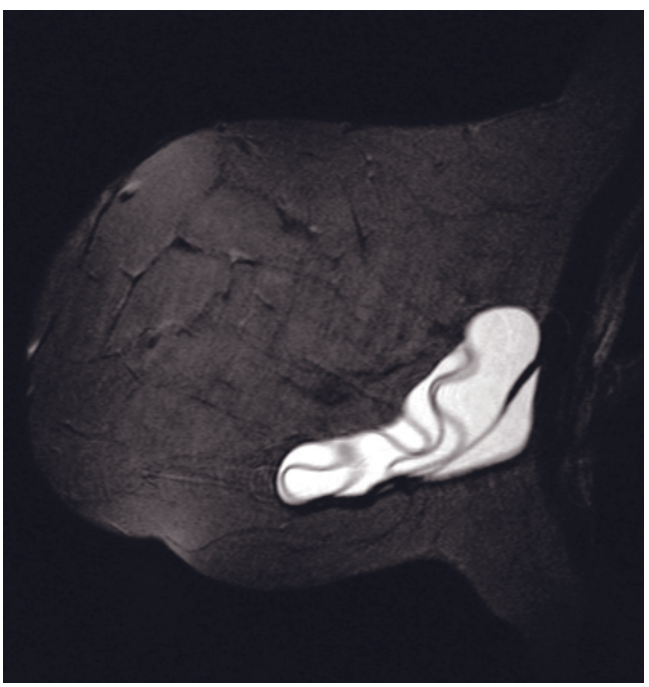

(*b*)

FIG. 19.64 Intracapsular rupture. Silicone-specific bilateral axial (*a*) and sagittal image of the left breast (*b*) demonstrate multiple curvilinear hypointense lines corresponding to completely collapsed elastomer shell—linguine sign. There is no extracapsular silicone, indicating that this is an intracapsular rupture. Note the subcapsular line at the posterior aspect of the right breast implant indicative of early, noncollapsed, intracapsular rupture (the same case as in fig. 19.63).

floating (which they are not) [169]. Contour variations have a wide spectrum of appearances, occurring also in the setting of rupture. Variation in the contour of the margins occurs when there is no capsule contracture, related to patient positioning. Others include medial bunching, superior feathering, and folding around the pectoralis major and are important only as a potential pitfall in establishing the diagnosis of an implant rupture. In the setting of a contracture, small focal bulges, with a diameter of 2 cm or less, can occur, with no predictive value for future rupture. Fluid droplets may be seen within the silicone in a single-lumen implant because of injection of saline or other material for custom-fit sizing. Waterlike fluid collections can sometimes be seen between the implant and the inner surface of the fibrous capsule, often in textured-surface implants, with no known cause or significance.

On MRI, first-degree implant rupture, silicone leakage, appears as tiny amounts of gel adjacent to the uncollapsed inner capsule–implant shell (fig. 19.63). Further leakage gives the **subcapsular line sign** of a minimally collapsed rupture, seen as a thin layer of gel between the implant shell and the outer, fibrous capsule (fig. 19.64).

Second-degree implant rupture, intracapsular rupture, corresponds to the implant shell rupture, but with the outer capsule still intact. Silicone can be trapped within the folds of the shell, described as **inverted teardrop, keyhole,** or **noose sign** (the sides of the infolding shell touch in the middle) (fig. 19.62); **pull-away sign** (similar to the keyhole sign, but more silicone is present in the fold so that the sides no longer touch); **pince-nez sign** (rare appearance near the tips of double keyholes), and **parallel-line sign** (silicone outside the implant shell is found between the layers of a larger infolding of the shell). The pitfalls with these signs are related to incorrect interpretation of variants in the implant shell appearance. One certain sign of intracapsular rupture is **linguine sign**. The shell is collapsed and folded in itself, which is visualized as stacked, hypointense curvilinear lines fully surrounded by the silicone gel (fig. 19.64).

The third degree, or extracapsular rupture, demonstrates free silicone that can be found outside the implant lumen and fibrous capsule, extending beyond the capsule into the breast parenchyma or axilla [170]. Except in the very rare cases of intentional surgical placement of free silicone, this represents the main sign of gross extracapsular rupture of the implant [169]. This condition is best appreciated with "silicone-only" sequences (water-suppressed inversion recovery with inversion time TI = 150–180 ms at 1.5 T and 220–250 ms at 3 T). Five main pitfalls may occur in the case of extracapsular rupture. Calcifications of the fibrous capsule may lead to a false-negative examination, more commonly encountered when using ultrasound. Another pitfall is when silicone from a prior rupture is mistakenly considered to indicate rupture of the current implant. In this case, taking an adequate and detailed implant history is essential. Yet another potential pitfall is mistaking fatty infiltration or edema for silicone granuloma. MRI is extremely useful in establishing the diagnoses of seroma or hematoma versus extracapsular rupture, when a patient is a surgical candidate. A fifth pitfall is differentiation between small focal extrusion of silicone gel versus a small nearby silicone gel cyst, which is uncommon [169].

In the setting of a double-lumen implant rupture or expander implant rupture, the shell can also be visualized in different degrees of collapse. Isolated failure of the shell that separates the two lumens results in saline mixing with the gel, described as a **salad oil sign**, and has no known clinical importance. An isolated outer saline lumen failure mimics an intact implant, and also does not have an important clinical consequence.

Breast Cancer Detection in Patients with Implants

MRI is the modality of choice to detect breast cancer in women with breast implants (fig. 19.61) In current practice, the MR protocol of choice for imaging breast cancer in women with implants consists of imaging both breasts in the transverse plane with a dedicated breast coil in order to obtain high in-plane resolution thin-slice images, with the highest possible temporal resolution for contrast-enhanced sequences.

An important issue that has been investigated carefully over the last decade is whether breast implants increase the incidence of breast cancer, and to date there have been no strong data to support this claim [169]. It is presently unknown whether breast cancer occurring within silicone-containing tissue can be missed and defined as "normal-appearing" silicone.

GBCE breast MRI is helpful as an ancillary tool to mammography in depicting breast cancer in women with breast implants. False positive findings include misclassifying the normally slow-enhancing fibrous capsule or silicone granuloma as cancer. In addition, in silicone-containing lymph nodes slow and regular contrast enhancement has been reported, without any signs of malignant cells present in the lymph nodes. The advantage of breast MRI compared with conventional mammography will be in the use of a contrast agent that helps visualizing cancer that is obscured by the implant on the mammogram and the clear visualization of posterior tissues [170]. Furthermore, the lack of need for compression, which carries a potential risk of rupture, with MRI compared to mammography is advantageous.

MR-Guided Interventions

In breast imaging, full use of any modality requires that it can be used for tissue sampling guidance. When an unsuspected lesion is seen on breast MRI, and cannot be confidently described as benign, the first step in further evaluation is targeted, so-called second-look breast ultrasound.

Location of the lesion within the breast must be accurately determined from the MRI scans. The ultrasound exam is then tailored to focus on that particular area in the breast. Because of the mobility of the breast and the supine position during an ultrasound exam, compared to the prone position in MRI, an examiner might face great difficulties in correlating MRI and ultrasound findings. This is often the case with a small lesion in a breast of larger size. Every effort should be made to confirm that the ultrasound finding, if any, corresponds to the initial MRI-detected lesion. When in doubt, ultrasound-guided biopsy should be performed and a marker clip placed at the biopsy site. The patient should then be scheduled for an MRI-guided biopsy. If, at the time of biopsy, the signal void from the marker clip is seen within the lesion on the preprocedural scan, this confirms that MRI and ultrasound have detected the same lesion, and MRI-guided biopsy can be canceled. MRI-guided biopsy should be reserved only for the lesion demonstrated exclusively by MRI. If a lesion can be reliably depicted by ultrasound or mammography, those modalities should guide the sampling.

In the early era of breast MRI, when a suspicious lesion was seen exclusively by MRI the only option was to perform an MRI-guided wire localization and surgical biopsy. Initially this was performed by a free-hand technique, with a vitamin E capsule as a skin marker to determine puncture position.

Currently, with the development of MRI-compatible biopsy devices, MRI-guided interventions have entered the mainstream of modern breast imaging. There are several vendors that offer MRI-guided biopsy systems, including dedicated hardware and software packages. A common feature is that the breast coil must be open, that is, curved on its sides, enabling access to the breast. Most modern breast coils follow this design. While it is possible to perform a biopsy with a coaxial sheath and a spring-loaded biopsy gun, vacuum-assisted 12–9G biopsy needles are most commonly used.

Proper patient positioning is of utmost importance for successful MRI-guided breast intervention. For lesions located closer to the chest wall, padding on the coil might have to be removed in order to position the breast deep enough in the coil. To facilitate targeting, the breast must be compressed. Dedicated solid and perforated compression plates are used for this purpose.

A sterile perforated or grid compression plate is usually placed over the lateral aspect of the breast, as the lateral approach provides easier access. A solid plate is placed on the opposite side of the breast, to achieve a firm support to the breast. If necessary, it is possible to use a medial approach as well. In that case, the contralateral breast coil opening is blocked, thus keeping the contralateral breast supported away from the access path. This approach is more difficult for the physician, as all the manipulation takes place deep under the patient, both hard to reach and hard to see.

The extent of compression should immobilize the breast, but not to the degree that the bloodflow would be compromised, as that would interfere with contrast delivery.

Technical details of performing the intervention, either preoperative wire localization or biopsy, are different with different vendor systems. In general, the procedure starts with noncontrast scans. When the proper breast positioning is confirmed, the contrast enhanced dynamic scans are run, usually with only two postcontrast sequences, most commonly using the sagittal imaging plane.

After the lesion is visualized, a coordinate system is introduced to determine the puncture site on the skin and the depth to the lesion. While this can be cumbersome with a free-hand technique, it is more straightforward with a dedicated biopsy system. Special, high MR

FIG. 19.65 MRI-guided core biopsy. MRI-guided core biopsy and marker clip placement was performed with a dedicated biopsy system and a workstation. Postcontrast T1-weighted axial (*a*) and subtracted (*b*) images demonstrate an enhancing mass in the subareolar region. Note that to facilitate the biopsy the breast was positioned to maximize the breast thickness anteriorly, where the targeted lesion was located. A sagittal postcontrast T1-weighted scan (*c*, *d*) was then obtained to plan the biopsy. A grid compression plate can be seen as a mash of rectangular signal voids at the skin surface (*d*). This plate contains high-signal markers (not shown here, seen on different images) that were selected on-screen to define a three-dimensional frame of reference. After the target was identified and marked on the postcontrast images, its location, i.e., the skin incision coordinates in the grid relative to the marker position, and the target's depth from the surface were automatically calculated. The stylet was introduced through the coaxial sheath and then replaced with a plastic localizing obturator. An obturator is seen as a round (*e*), or linear (*f*) signal void. Its position relative to the targeted enhancing mass can be easily determined. On the sagittal scan (*e*), it is located within the mass. On the axial scan (*f*), it is obvious that its tip passed the lesion. Therefore, the coaxial sheet had to be retracted about 4 mm before the obturator was replaced by the biopsy needle and biopsy was performed. After the biopsy, a marker clip was placed at the biopsy site. A marker clip's signal void is seen on both sagittal (*g*) and axial (*h*) postprocedural scans. The marker clip is located at the medial edge of the enhancing mass (*h*). The obturator is again seen (*h*), now pulled back even more. Pathology confirmed IDC.

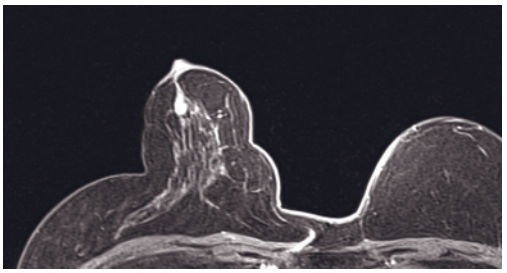

(*a*)

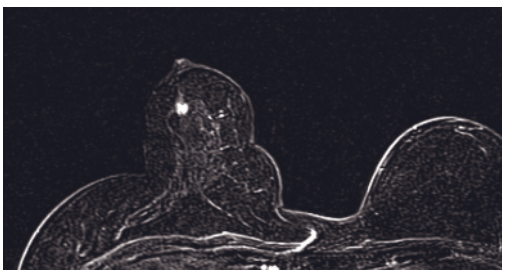

(*b*)

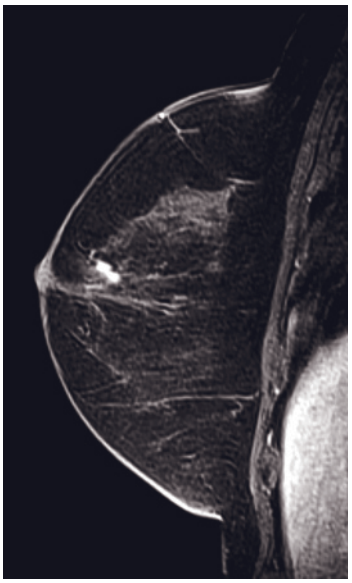

(*c*)

(*d*)

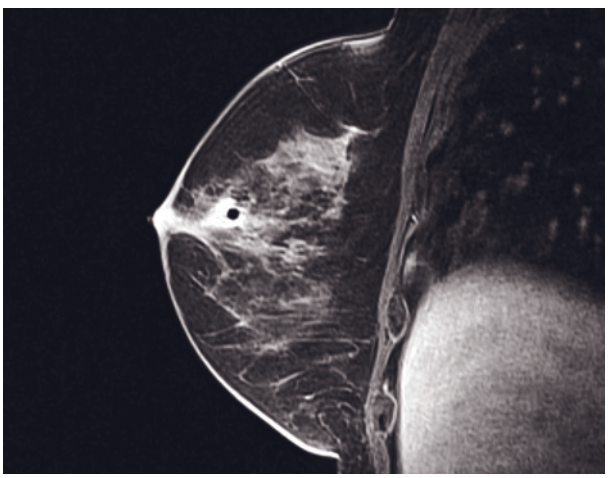

(*e*)

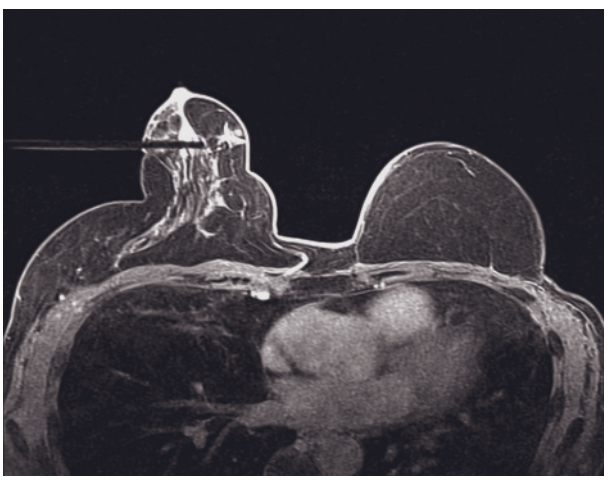

(*f*)

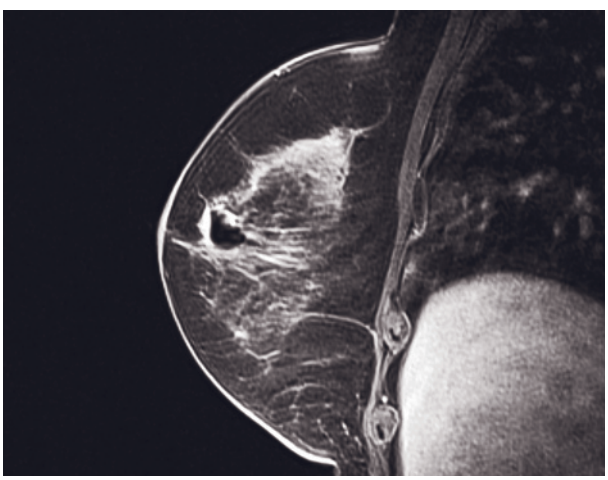

(*g*)

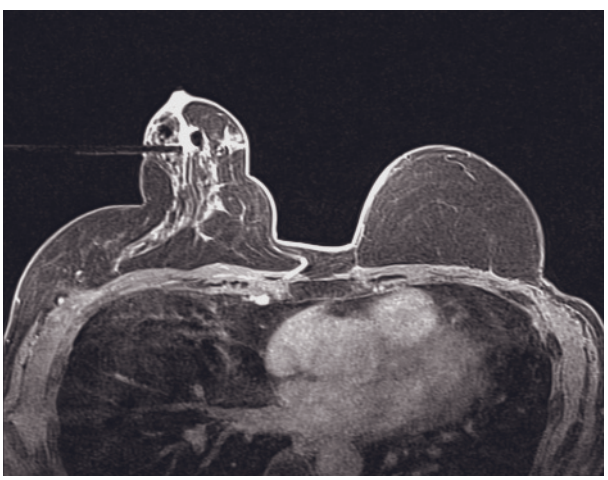

(*h*)

signal-producing reference points on the compression plate and the particular pattern of its openings can serve as a guide. Topical anesthetic is used to infiltrate the skin at the puncture site and the tissue along the anticipated needle track.

In the case of wire localization, a needle is introduced and its position is confirmed on the subsequent scan. Then a localization wire is placed and the needle is removed. The procedure is completed with the last scan demonstrating the final position of the localizing wire. The signal void of the wire is usually well seen. Before surgery, mammograms are obtained and the approximated position of the MR-detected lesion marked, to present the road map for the surgeon. Currently, there is no way to confirm by specimen imaging that the targeted area was indeed removed at surgery.

In case of an MRI-guided biopsy (fig. 19.65), an introducer stylet coupled with a thin coaxial sheath is advanced through the skin up to the targeted depth. It is then removed and replaced by an MR-safe, usually plastic, localizing obturator, while leaving the coaxial sheath in place for the duration of the procedure. The correct positioning is confirmed on the next scan. The obturator is then removed, and the vacuum-assisted core biopsy needle is introduced through the coaxial sheath to perform the biopsy. After the tissue samples are obtained, a marker clip is placed at the biopsy site. The placement of the clip can be confirmed on the final MR scan and with mammograms. It is important to document the clip's position to prevent possible subsequent surgical failure due to clip migration.

An MRI-guided vacuum-assisted biopsy has a low complication rate and has been shown to represent a reliable alternative to MRI wire localization of suspicious lesions [172–175].

ACKNOWLEDGMENTS

We thank Jasmina M. Konstantinovic, M.D., and Vladimir M. Ivanovic, BScEE, for invaluable assistance.

REFERENCES

1. Shinil K, Shah BS, Greatrex KV. Current role of magnetic resonance imaging in breast imaging: a primer for the primary care physician. *J Am Board Fam Pract* 18: 478–490, 2005.
2. Majid AS, de Paredes ES, Doherty RD et al. Missed breast carcinoma: pitfalls and pearls. *Radiographics* 23: 881–895, 2003.
3. Doi K, MacMahon H, Katsuragawa S et al. Computer-aided diagnosis in *radiology*: potential and pitfalls. *Eur J Radiol* 31: 97–109, 1997.
4. Rankin SC. MRI of the breast. *Br J Radiol* 73: 806–818, 2000.
5. Mansfield P, Morris P, Ordidge R, Coupland R, Bishop H, Blamey R. Carcinoma of the breast imaged by nuclear magnetic resonance (NMR). *Br J Radiol* 52: 242–243, 1979.
6. Heywang SH, Wolf A, Pruss E et al. MR imaging of the breast with Gd-DTPA: use and limitations. *Radiology* 171: 95–103, 1989.
7. Schnall MD, Blume J, Bluemke DA et al. Diagnostic architectural and dynamic features at breast MR imaging: multicenter study. *Radiology* 238: 42–53, 2006.
8. Kaiser W, Zeitler E. MR imaging of the breast: fast imaging sequences with and without Gd-DTPA. *Radiology* 170: 681–686, 1989.
9. Gilles R, Guinebretiere JM, Lucidarme O et al. Nonpalpable breast tumors: diagnosis with contrast-enhanced subtraction dynamic MR imaging. *Radiology* 191: 625–631, 1994.
10. Boetes C, Barentsz JO, Mus RD et al. MR characterization of suspicious breast lesions with a gadolinium-enhanced turbo-FLASH subtraction technique. *Radiology* 193: 777–781, 1994.
11. Chenevert TL, Helvie MA, Aisen AM et al. Dynamic three-dimensional imaging with partial k-space sampling: initial application for gadolinium-enhanced rate characterization of breast lesions. *Radiology* 196: 135–142, 1995.
12. Kelcz F, Santyr GE, Cron GO, Mongin SJ. Application of a quantitative model to differentiate benign from malignant breast lesions detected by dynamic, gadolinium-enhanced MRI. *J Magn Reson Imaging* 6: 743–752, 1996.
13. Muller-Schimpfle M, Ohmenhauser K, Sand J, Stoll P, Claussen CD. Dynamic 3D-MR mammography: is there a benefit of sophisticated evaluation of enhancement curves for clinical routine? *J Magn Reson Imaging* 7: 236–240, 1997.
14. Nunes LW, Schnall MD, Orel SG et al. Correlation of lesion appearance and histologic findings for the nodes of a breast MR imaging interpretation model. *Radiographics* 19: 79–92, 1999.
15. Yen YF, Han KF, Daniel BL et al. Dynamic breast MRI with spiral trajectories: 3D versus 2D. *J Magn Reson Imaging* 11: 351–359, 2000.
16. Fischer U, Kopka L, Brinck U, Korabiowska M, Schauer A, Grabbe E. Prognostic value of contrast-enhanced MR mammography in patients with breast cancer. *Eur Radiol* 7: 1002–1005, 1997.
17. Nunes LW, Schnall MD, Orel SG et al. Breast MR imaging: interpretation model. *Radiology* 202: 833–841, 1997.
18. Kuhl CK, Mielcareck P, Klaschik S et al. Dynamic breast MR imaging: are signal intensity time course data useful for differential diagnosis of enhancing lesions? *Radiology* 211: 101–110, 1999.
19. Schnall MD, Rosten S, Englander S, Orel SG, Nunes LW. A combined architectural and kinetic interpretation model for breast MR images. *Acad Radiol* 8: 591–597, 2001.
20. Moinfar F. *Essentials of Diagnostic Breast Pathology.* Berlin: Springer-Verlag, 2007.
21. Rosen PP. *Rosen's Breast Pathology*, 2nd Ed. Philadelphia, PA: Lippincott Williams & Wilkins, 2001.
22. Rubin R. *Rubin's Pathology: Clinicopathologic Foundations of Medicine*, 5th Ed. Philadelphia, PA: Lippincott Williams & Wilkins, 2007.
23. Zeppa R. Vascular response of the breast to estrogen. *J Clin Endocrinol Metab* 29: 695–700, 1969.
24. Vogel PM, Geariade NG, Fetter BF et al. The correlation of histologic changes in the human breast with the menstrual cycle. *Am J Pathol* 104: 23–24, 1981.
25. Huston SW, Cowen PN, Bird CC. Morphologic studies of age-related changes in normal human breast and their significance in the evolution of mammary cancer. *J Clin Pathol* 38: 281–287, 1985.
26. Folkman J, Klagsbrun M. Angiogenic factors. *Science* 235: 442–447, 1987.
27. Hylton NM. Breast magnetic resonance imaging techniques. In: Morris EA and Liberman L, eds. *Breast MRI: Diagnosis and Intervention.* New York: Springer-Verlag, 2004, p. 7–22.

28. Folkman J, Watson K, Ingbr D, Hanahan D. Induction of angiogenesis during the transition from hyperplasia to neoplasia. *Nature* 339: 58–61, 1989.
29. Schneider BP, Miller KD. Angiogenesis of breast cancer. *J Clin Oncol* 23: 1782–1790, 2005.
30. Kuhl CK. Current status of breast MR imaging. Part I. Technical issues. *Radiology* 244: 356–378, 2007.
31. Rausch DR, Hemdrick ER. How to optimize clinical breast MR imaging practices and techniques on your 1.5T system. *Radiographics* 26: 1469–1484, 2006.
32. Kinkel K, Helbich TH, Esserman LJ et al. Dynamic high-spatial-resolution MR imaging of suspicious breast lesions: diagnostic criteria and interobserver variability. *AJR Am J Roentgenol* 175: 35–43, 2000.
33. Morris EA. Breast cancer imaging with MRI. *Radiol Clin NAm* 40: 443–466, 2002.
34. Kuhl CK, Schild HH. Dynamic image interpretation of MRI of the breast. *J Magn Reson Imaging* 12: 965–974, 2000.
35. Lehman CD, Schnall MD. Imaging in breast cancer: magnetic resonance imaging. *Breast Cancer Res* 7: 215–219, 2005.
36. Berg WA, Gutierrez L, NessAiver MS et al. Diagnostic accuracy of mammography, clinical examination, US, and MR imaging in preoperative assessment of breast cancer. *Radiology* 233: 830–849, 2004.
37. Teifke A, Hlawatsch A, Beier T et al. Undetected malignancies of the breast: dynamic contrast-enhanced MR imaging at 1.0T. *Radiology* 224: 881–888, 2002.
38. Kuhl C, Jost P, Morakkabati N, Zivanovic O, Schild H, Gieseke J. Contrast-enhanced MR imaging of the breast at 3.0T and 1.5T in the same patients; initial experience. *Radiology* 239: 666–676, 2006.
39. Lehman CD, Gatsonis C, Kuhl CK et al. MRI evaluation of the contralateral breast in women with recently diagnosed breast cancer. *N Engl J Med* 356: 1295–1303, 2007.
40. Schnall MD, Blume J, Bluemke DA et al. Diagnostic architectural and dynamic features at breast MR imaging: multicenter study. *Radiology* 238: 42–53, 2006.
41. Ojeda-Fournier H, Choe KA, Mahoney MC. Recognizing and interpreting artifacts and pitfalls in MR imaging of the breast. *Radiographics* 27: 147–164, 2007.
42. Fischer U, Baum F. *Mammography Case Book. 100 Studies in the Breast Imaging*. Stuttgart: Thieme, 2006.
43. Kvistad KA, Rydland J, Vainio J et al. Breast lesions: evaluation with dynamic contrast-enhanced T1-weighted MR imaging and with T2*-weighted first-pass perfusion MR imaging. *Radiology* 216: 545–553, 2000.
44. Kuhl CK, Bieling H, Gieseke J et al. Breast neoplasm: T2* susceptibility-contrast, first-pass perfusion MR imaging. *Radiology* 202: 87–95, 1997.
45. Roebuck JR, Cecil KM, Schnall MD, Lenkinski RE. Human breast lesions: characterization with proton MR spectroscopy. *Radiology* 209: 269–275, 1998.
46. Gribbestad IS, Singstad TE, Nilsen G et al. In vivo ^{1}H MRS of normal breast and breast tumors using a dedicated double breast coil. *J Magn Reson Imaging* 8: 1191–1197, 1998.
47. Yeung DK, Yang WT, Tse GM. Breast cancer: in vivo proton MR spectroscopy in the characterization of histopathologic subtypes and preliminary observations in axillary node metastases. *Radiology* 225: 190–197, 2002.
48. Yeung DK, Cheung HS, Tse GM. Human breast lesions: characterization with contrast-enhanced in vivo proton MR spectroscopy—initial results. *Radiology* 220: 40–46, 2001.
49. Negendank W. Studies of human tumors by MRS: a review. *NMR Biomed* 5: 303–324, 1992.
50. Huang W, Fisher PR, Dulaimy K, Tudorica LA, O'Hea B, Button TM. Detection of breast malignancy: diagnostic MR protocol for improved specificity. *Radiology* 232: 585–591, 2004.
51. Rubesova E, Grell AS, Maertaeler VD, et al. Quantitative diffusion imaging in breast cancer: a clinical prospective study. *J Magn Reson Imaging* 24: 319–324, 2006.
52. Yabuuchi H, Matsuo Y, Okafuji T et al. Enhanced mass on contrast-enhanced breast MR imaging: lesion characterization using combination of dynamic contrast-enhanced and diffusion-weighted MR images. *J Magn Reson Imaging* 28: 1157–1165, 2008.
53. American College of Radiology. *Breast Imaging Reporting and Data System (BI-RADS) Atlas*. Reston, VA: American College of Radiology, 2003.
54. Kuhl CK, Bieling HB, Gieseke J et al. Healthy premenopausal breast parenchyma in dynamic contrast-enhanced MR imaging of the breast: normal contrast medium enhancement and cyclical-phase dependency. *Radiology* 203: 137–144, 1997.
55. Müller-Schimpfle M, Ohmenhauser K, Stoll P, Dietz K, Claussen CD. Menstrual cycle and age: influence on parenchymal contrast medium enhancement in MR imaging of the breast. *Radiology* 203: 145–149, 1997.
56. Heywang-Kobrunner SH, Veiweg P, Heinig A, Kuchler C. Contrast-enhanced MRI of the breast: accuracy, value, controversies, solutions. *Eur J Radiol* 24: 94–108, 1997.
57. Liberman L, Mason G, Morris EA, Dershaw DD. Does size matter? Positive predictive value of MRI-detected breast lesions as function of lesion size. *AJR Am J Roentgenol* 186: 426–430, 2006.
58. Teifke A, Lehr HA, Vomweg TW, Hlawatsch A, Thelen M. Outcome analysis and rational management of enhancing lesions incidentally detected on contrast-enhanced MRI of the breast. *AJR Am J Roentgenol* 181: 655–662, 2003.
59. Fisher U, Kopka L, Grabbe E. Invasive mucinous carcinoma of the breast missed by contrast-enhancing MR imaging of the breast. *Eur Radiol* 6: 929–931, 1996.
60. Kuhl CK, Schrading S, Bieling HB, Wardelmann E, Leutner CC, Koenig R, Kuhn W, Schild HH. MRI for diagnosis of pure ductal carcinoma in situ: a prospective observational study. *Lancet* 370: 485–492, 2007.
61. Rosen EL, Smith-Foley SA, DeMartini WB, Eby PR, Peacock S, Lehman CD. BI-RADS MRI enhancement characteristics of ductal carcinoma in situ. *Breast J* 13: 545–550, 2007.
62. Simmons PS. Anomalies of the adolescent breast. *Paediat Child Health* 18: 5–7, 2008.
63. Vega A, Ortega E, Cavada A, Garijo F. Hydatid cyst of the breast: mammographic findings. *AJR Am J Roentgenol* 162: 825–826, 1994.
64. Sinha A, Sharma R, Kandpal H, Seenu V, Sharma M. Imaging appearance of parasitic infestations of the breast: a report of two cases and review of the literature. *Acta Radiol* 49: 506–509, 2008.
65. Kuijper A, Mommers EC, van der Wall E, van Diest PJ. Histopathology of fibroadenoma of the breast. *Am J Clin Pathol* 115: 736–742, 2001.
66. Dupont WD, Page DL, Parl FE et al. Long-term risk of breast cancer in women with fibroadenoma. *N Engl J Med* 331: 10–15, 1994.
67. Sklair-Levy M, Sella T, Alweiss T et al. Incidence and management of complex fibroadenomas. *AJR Am J Roentgenol* 190: 214–218, 2008.
68. El-Wakeel H, Umpleby HC. Systematic review of fibroadenoma as a risk factor for breast cancer. *Breast* 12: 302–307, 2003.
69. Gordon PB, Gagnon FA, Lanzkowsky L. Solid breast masses diagnosed as fibroadenoma at fine needle aspiration biopsy: acceptable rates of growth at long-term follow-up. *Radiology* 229: 233–238, 2003.
70. Liberman L, Morris E, Lee MJY et al. Breast lesions detected at MRI: features and positive predictive value. *AJR Am J Roentgenol* 179: 171–178, 2002.

71. Macura KJ, Ouwerkerk RM, Jacobs MA, Bluemke DA. Patterns of enhancement on breast MR images: interpretation and imaging pitfalls *Radiographics* 26: 1719–1734, 2006.
72. Palmer ML, de Risi DC, Pelikan A et al. Treatment options and recurrence potential for cystosarcoma phyllodes. *Surg Gynecol Obstet* 170: 193–196, 1990.
73. Rowell MD, Perry RR, Hsiu JG, Barranco SC. Phyllodes tumours. *Am J Surg* 165: 376–379, 1993.
74. Tavassoli FA, Devilee P, eds. World Health Organization classification of tumours. *Pathology and Genetics. Tumours of the Breast and female Genital Organs. Fibroepithelial Tumours.* Lyon: IARC Press, 2003.
75. Norris HJ, Taylor HB. Relationship of histologic features to behavior of cystosarcoma phyllodes. *Cancer* 20: 2090–2099, 1967.
76. Wurdinger S, Herzog AB, Fischer DR et al. Differentiation of phyllodes breast tumors from fibroadenomas on MRI. *AJR Am J Roentgenol* 185: 1317–1321, 2005.
77. Kinoshita T, Fukutomi T, Kubochi K. Magnetic resonance imaging of benign phyllodes tumors of the breast. *Breast J* 10: 232–236, 2004.
78. Yabuuchi H, Soeda H, Matsuo Y et al. Phyllodes tumor of the breast: correlation between MR findings and histologic grade. *Radiology* 241: 702–709, 2006.
79. Rowell MD, Perry RR, Hsju JG et al. Phyllodes tumors. *Am J Surg* 165: 376–379, 1993.
80. Mangi AA, Smith BL, Gadd MA et al. Surgical management of phyllodes tumors. *Arch Surg* 134: 487–492, 1999.
81. Buchanan EB. Cystosarcoma phyllodes and its surgical management. *Am Surg* 61: 350–355, 1995.
82. Brookes MJ, Bourke AG. Radiological appearances of papillary breast lesions. *Clin Radiol* 63: 1256–1273, 2008.
83. Liberman L, Tornos C, Huzjan R et al. Is surgical excision warranted after benign, concordant diagnosis of papilloma at percutaneous breast biopsy? *AJR Am J Roentgenol* 186: 1328–1334, 2006.
84. Nassar H, Quareshi H, Volkanadsay N et al. Clinicopathological analysis of solid papillary carcinoma of the breast and associated invasive carcinomas. *Am J Surg Pathol* 30: 501–507, 2006.
85. Bhattarai N, Kanemaki Y, Kurihara Y et al. Intraductal papilloma: features on MR ductography using a microscopic coil. *AJR Am J Roentgenol* 186: 44–47, 2006.
86. Rovno S, Sigelman ES, Reynolds C et al. Solitary intraductal papilloma: findings at MR imaging and MR galactography. *AJR Am J Roentgenol* 172: 151–155, 1999.
87. Orel SG, Dougherty CS, Reynolds C et al. MR imaging in patients with nipple discharge: initial experience. *Radiology* 216: 248–254, 2000.
88. Daniel LB, Gardner WR, Birdwell LR et al. Magnetic resonance imaging of intraductal papilloma of the breast. *Magn Reson Imaging* 21: 887–892, 2003.
89. Kamemaki Y, Kurihara Y, Itoh D et al. MR mammary ductography using a microscopic coil for assessment of intraductal lesions. *AJR Am J Roentgenol* 182: 1340–1342, 2004.
90. Ali-Fehmi R, Carolin K, Wallis T et al. Clinocopathologic analysis of breast lesions associated with multiple papillomas. *Hum Pathol* 34: 234–239, 2003.
91. Hajit K, Willsher PC, Bennett M et al. Multiple papillomas of the breast: is current management adequate? *Breast* 15: 777–781, 2006.
92. Gutman H, Schachter J, Wasserberg N et al. Are solitary benign papillomas entirely benign? *Arch Surg* 138: 1330–1333, 2003.
93. Fu P, Kurihara Y, Kanemaki Y et al. High-resolution MRI in Detecting subareolar breast abscess. *AJR Am J Roentgenol* 188: 1568–1572, 2007.
94. Kocaoglu M, Somuncu I, Ors F et al. Imaging findings in idiopathic granulomatous mastitis. A review with emphasis on magnetic resonance imaging. *J Comput Assist Tomogr* 28: 635–641, 2004.
95. Ozturk M, Mavili E, Kahriman G et al. Granulomatous mastitis: radiological findings. *Acta Radiol* 48: 150–155, 2007.
96. Malich A, Fischer DR, Wurdinger S et al. Potential MRI interpretation model: differentiation of benign from malignant breast masses. *AJR Am J Roentgenol* 185: 964–970, 2005.
97. Harada T, Tanigawa N, Matsuki M et al. Evaluation of lymph node metastases of breast cancer using ultrasmall superparamagnetic iron oxide-enhanced magnetic resonance imaging. *Eur J Radiol* 63: 401–407, 2007.
98. Seidman JD, Ashton M, Lefkowitz M. Atypical apocrine adenosis of the breast: a clinicopathologic study. *Cancer* 77: 2529–2537, 1996.
99. Patterson JA, Scott M, Anderson N, Kirk SJ. Radial scar, complex sclerosing lesion and risk of breast cancer. Analysis of 175 cases in Northern Ireland. *Eur J Surg Oncol* 30: 1065–1068, 2004.
100. Fasih T, Jain M, Shrimankar J et al. All radial scars/complex sclerosing lesions seen on breast screening mammograms should be excised. *Eur J Surg Oncol* 31: 1125–1128, 2005.
101. Tavassoli FA, Hoefler H, Rosai J et al. "Intraductal proliferative lesions. In: Tavassoli FA, Devilee P, eds. *World Health Organization Classification of Tumours. Pathology and Genetics. Tumours of the Breast and Female Genital Organs.* Lyon: IARC Press, 2003, p. 63–75.
102. Tavassoli FA. Breast pathology: rationale for adopting the ductal intraepithelial neoplasia (DIN) classification. *Nat Clin Pract Oncol* 2: 116–117, 2005.
103. Morrow M. The certainties and the uncertainties of ductal carcinoma in situ. *J Natl Cancer Inst* 96: 424–425, 2004.
104. Baxter NN, Virnig BA, Durham SB, Tuttle TM. Trends in the treatment of ductal carcinoma in situ of the breast. *J Natl Cancer Inst* 96: 443–448, 2004.
105. Liberman L, Morris EA, Dershaw DD et al. Ductal enhancement on MR imaging of the breast. *AJR Am J Roentgenol* 2003 181: 519–525.
106. Morakkabati-Spitz N, Leutner C, Schild H et al. Diagnostic usefulness of segmental and linear enhancement in dynamic breast MRI. *Eur Radiol* 2005 15: 2010–2017.
107. Fischer U, Westerhof JP, Brinck U et al. Das duktale in-situ-karzinom in der dynamischen MR-mammographie bei 1,5 T. *Rofo* 164: 290–294, 1996.
108. Westerhof JP, Fischer U, Moritz JD, Oestmann JW. MR imaging of mammographically detected clustered microcalcifications: is there any value? *Radiology* 207: 675–681, 1998.
109. Boetes C, Strijk SP, Holland R et al. False-negative MR imaging of malignant breast tumors. *Eur Radiol* 7: 1231–1234, 1997.
110. Berg WA, Gutierrez L, NessAiver MS et al. Diagnostic accuracy of mammography, clinical examination, US, and MR imaging in preoperative assessment of breast cancer. *Radiology* 233: 830–849, 2004.
111. Kriege M, Brekelmans CT, Boetes C et al. Efficacy of MRI and mammography for breast-cancer screening in women with a familial or genetic predisposition. *N Engl J Med* 351: 427–437, 2004.
112. Bazzocchi M, Zuiani C, Panizza P et al. Contrast-enhanced breast MRI in patients with suspicious microcalcifications on mammography: results of a multicenter trial. *AJR Am J Roentgenol* 186: 1723–1732, 2006.
113. Furman-Haran E, Schechtman E, Kelcz F et al. Magnetic resonance imaging reveals functional diversity of the vasculature in benign and malignant breast lesions. *Cancer* 104: 708–718, 2005.
114. Ottinetti A, Sapino A. Morphometric evaluation of microvessels surrounding hyperplastic and neoplastic mammary lesions. *Breast Cancer Res Treat* 11: 241–248, 1988.

115. Guidi AJ, Schnitt SJ, Fischer L et al. Vascular permeability factor (vascular endothelial growth factor) expression and angiogenesis in patients with ductal carcinoma in situ of the breast. *Cancer* 80: 1945–1953, 1997.
116. Brown LF, Guidi AJ, Schnitt SJ et al. Vascular stroma formation in carcinoma in situ, invasive carcinoma, and metastatic carcinoma of the breast. *Clin Cancer Res* 5: 1041–1056, 1999.
117. Esserman LJ, Kumar AS, Herrera AF et al. Magnetic resonance imaging captures the biology of ductal carcinoma in situ. *J Clin Oncol* 24: 4603–4610, 2006.
118. Griff SK, Dershaw DD. Breast cancer. In: Bragg DG, Rubin P, Hricak H, eds. *Oncologic Imaging*. New York: WB Saunders, 2002, p. 265–293.
119. Genetics of breast and ovarian cancer (PDQ). National Cancer Institute Web site. http://www.cancer.gov/cancerinfo/pdq/genetics/breast-and-ovarian. Accessed February 1, 2006.
120. Easton DF, Ford D, Bishop DT. Breast and ovarian cancer incidence in BRCA1-mutation carriers. Breast Cancer Linkage Consortium. *Am J Hum Genet* 56: 265–271, 1995.
121. Lehman CD, Isaacs C, Schnall MD et al. Cancer yield of mammography, MR, and US in high-risk women: Prospective Multi-Institution Breast Cancer Screening Study1. *Radiology* 244: 381–188, 2007.
122. Regence: The Regence Group Medical Policy, Radiology Section: MR of the Breast. The Regence Group Web site. http://www.regence.com/trgmedpol/radiology/rad43.html. Accessed February 2, 2006.
123. Blue Cross Blue Shield: Magnetic resonance imaging of the breast in screening women considered to be at high genetic risk of breast cancer. http://www.bcbst.com/mpmanval/whstart.com. Accessed February 2, 2006.
124. Sardanelli F, Fausto A, Menicagli L, Esseridou A. Breast vascular mapping obtained with contrast-enhanced MR imaging: implications for cancer diagnosis, treatment and risk stratification. *Eur Radiol* 17: 48–512007.
125. http:\\www.cancerstaging.org
126. Kinkel K, Vlastos G. MR imaging: breast cancer staging and screening. *Semin Surg Oncol* 20: 187–196, 2001.
127. Onesti JK, Mangus BE, Helmer SD, Osland JS. Breast cancer tumor size: correlation between magnetic resonance imaging and pathology measurements. *Am J Surg* 196: 844–848, 2008.
128. Lee SG, Orel SG, Woo IJ et al. MR imaging screening of the contralateral breast in patients with newly diagnosed breast cancer: preliminary results. *Radiology* 226: 773–778, 2003.
129. Liberman L, Morris EA, Kim CM et al. MR imaging findings in the contralateral breast of women with recently diagnosed breast cancer. *AJR Am J Roentgenol* 180: 333–331, 2003.
130. Fischer U, Zachariae O, Baum F et al. The influence of preoperative MRI of the breasts on recurrence rate in patients with breast cancer. *Eur Radiol* 14: 1725–1731, 2004.
131. Helin EJ, Helle MJ, Kollioniemi OP et al. Immunohistochemical determination of estrogen and progesterone receptors in human breast carcinoma. Correlation with histopathology and DNA flow cytometry. *Cancer* 63: 1761–1767, 1989.
132. Uematsu T, Kasami M, Yuen S. Triple-negative breast cancer: correlation between MR imaging and pathologic findings. *Radiology* 250: 638–647, 2009.
133. Qayyum A, Birdwell RL, Daniel BL et al. MR imaging features of infiltrating lobular carcinoma of the breast: histopathologic correlation. *AJR Am J Roentgenol* 178: 1227–1232, 2002.
134. Szabo BK, Aspelin P, Wiberg MK, Bone B. Dynamic MR imaging of the breast. Analysis of kinetic and morphologic diagnostic criteria. *Acta Radiol* 44: 379–386, 2003.
135. Echevarria JJ, Lopez-Ruiz JA, Martin D et al. Usefulness of MRI in detecting occult breast cancer associated with Paget's disease of the nipple–areolar complex. *Br J Radiol* 74: 1036–1039, 2004.
136. Ikeda DM, Helvie MA, Frank TS, Chapel KL, Andersson IT. Paget disease of the nipple: radiologic-pahologic correlation. *Radiology* 189: 89–94, 1993.
137. Morrogh M, Morris EA, Liberman L et al. MRI identifies otherwise occult disease in select patients with Paget disease of the nipple. *J Am Coll Surg* 206: 316–321, 2008.
138. Renz DM, Baltzer PA, Böttcher J et al. Magnetic resonance imaging of inflammatory breast carcinoma and acute mastitis. A comparative study. *Eur Radiol* 18: 2370–2380, 2008.
139. Djilas-Ivanovic D, Prvulovic N, Bogdanovic-Stojanovic D, et al. Dermatofibrosarcoma of the breast: mammographic, ultrasound, MRI and MRS features. *Arch Gynecol Obstet* 280: 827–830, 2009.
140. Yang WT, Hennessy BT, Dryden MJ et al. Mammary angiosarcomas: imaging findings in 24 patients. *Radiology* 242: 725–734, 2007.
141. Brenn T, Fletcher CD. Postradiation vascular proliferations: an increasing problem. *Histopathology* 48: 106–114, 2006.
142. Glazebrook KN, Magut MJ, Reynolds C. Angiosarcoma of the breast. *AJR Am J Roentgenol* 190: 533–538, 2008.
143. Liberman L, Dershaw DD, Kaufman RJ, Rosen PP. Angiosarcoma of the breast. *Radiology* 183: 649–654, 1992.
144. Glazebrook KN, Morton MJ, Reynolds C. Vascular tumors of the breast: mammographic, sonographic, and MRI appearances. *AJR Am J Roentgenol* 2005 184: 331–338.
145. Yang WT, Lane DL, Le-Petross HT et al. Breast lymphoma: imaging findings of 32 tumors in 27 patients. *Radiology* 245: 692–702, 2007.
146. Alm El-Din MA, El-Badawy SA, Taghian AG. Breast cancer after treatment of Hodgkin's lymphoma: general review. *Int J Radiat Oncol Biol Phys* 72: 1291–1297, 2008.
147. Vergier B, Trojani M, De Mascarel I et al. Metastases to the breast: differential diagnosis from primary breast carcinoma. *J Surg Oncol* 48: 112–116, 1991.
148. Jakovljevic B, Stevanovic O, Bacic G. Metastases to the breast from small-cell lung cancer: MR findings. *Acta Radiol* 44: 485–488, 2003.
149. Ho LWC, Wong KP, Chan JHM, Chow LWC, Leung EYF, Leong L. MR appearance of metastatic melanotic melanoma in the breast. *Clin Radiol* 55: 572–573, 2000.
150. Tardivon AA, Ollivier L, El Khoury C, Thibault F. Monitoring therapeutic efficacy in breast carcinomas. *Eur Radiol* 16: 2549–2558, 2006.
151. Tillman BGF, Orel SG, Schnall MD et al. Effect of breast magnetic resonance imaging with early-stage breast carcinoma. *J Clin Oncol* 20: 3413–3423, 2002.
152. Berg WA, Gutierrez L, Ness Aiver MS et al. Diagnostic accuracy of mammography, clinical examination, US, and MR imaging in preoperative assessment of breast cancer. *Radiology* 233: 830–849, 2004.
153. Solin LJ, Orel SG, Hwang WT et al. Relationship of breast magnetic resonance imaging to outcome after breast-conservation treatment with radiation for women with early-stage invasive breast carcinoma or ductal carcinoma in situ. *J Clin Oncol* 26: 386–391, 2008.
154. Kuhl CK. Current status of breast MR imaging. Part II. Clinical applications. *Radiology* 244: 672–691, 2007.
155. Frei KA, Kinkel K, Bonel HM et al. MR imaging of the breast in patients with positive margins after lumpectomy: influence of the time interval between lumpectomy and MR imaging. *AJR Am J Roentgenol* 175: 1577–1584, 2000.
156. Lee CH. Problem solving MR imaging of the breast. *Radiol Clin N Am* 42: 919–924, 2004.
157. Daly CP, Jaeger B, Sill DS. Variable appearances of fat necrosis on breast MRI. *AJR Am J Roentgenol* 191: 1374–1380, 2008.
158. Therasse P, Arbuck SG, Eisenhauer EA et al. New guidelines to evaluate the response to treatment in solid tumors. *J Natl Cancer Inst* 92: 205–216, 2002.

159. Ollivier L, Vanel D, Leclère J. Monitoring tumour response. *Cancer Imaging* 3: 5–6, 2002.
160. Rieber A, Brambs HJ, Gabelmann A et al. Breast MRI for monitoring response of primary breast cancer to neo-adjuvant chemotherapy. *Eur Radiol* 12: 1711–1719, 2002.
161. El Khoury C, Servois V, Thibault F et al. MR quantification of the washout changes in breast tumors under preoperative chemotherapy: feasibility and preliminary results. *AJR Am J Roentgenol* 184: 1499–1504, 2005.
162. Delille JP, Slanetz PJ, Yeh ED et al. Invasive ductal breast carcinoma response to neoadjuvant chemotherapy: noninvasive monitoring with functional MR imaging pilot study. *Radiology* 228: 63–69, 2003.
163. Meisamy S, Bolan PJ, Baker EH et al. Neoadjuvant chemotherapy of locally advanced breast cancer: predicting response with in vivo ^{1}H MR spectroscopy—a pilot study at 4T. *Radiology* 233: 424–431, 2004.
164. Meisamy S, Bolan PJ, Baker EH et al. Adding in vivo quantitative ^{1}H MR spectroscopy to improve diagnostic accuracy of breast MR imaging: preliminary results of observer performance study at 4.0 T. *Radiology* 236: 465–475, 2005.
165. Roth Y, Tichler T, Kostenich G et al. High b-value diffusion-weighted MR imaging for pretreatment prediction and early monitoring of tumor response to therapy in mice. *Radiology* 232: 685–692, 2004.
166. 166, Wasser K, Sinn HP, Fink C et al. Accuracy of tumor size measurement in breast cancer using MRI is influenced by histological regression induced by neoadjuvant chemotherapy. *Eur Radiol* 13: 1213–1223, 2003.
167. Denis F, Desbiez-Bourcier AV, Chapiron C et al. Contrast enhanced magnetic resonance imaging underestimates residual disease following neoadjuvant docetaxel based chemotherapy for breast cancer. *Eur J Surg Oncol* 30: 1069–1076, 2004.
168. Rieber A, Zeitler H, Rosenthal H et al. MRI of breast cancer: influence of chemotherapy on sensitivity. *Br J Radiol* 70: 452–458, 1997.
169. Middleton MS, McNamara MP Jr. Breast implant classification with MR imaging correlation. *Radiographics* 20(3): E1, 2000.
170. Liberman L, Berg WA. Magnetic resonance imaging in women with breast implants. In: Morris EA and Liberman L, eds. *Breast MRI: Diagnosis and Intervention*. New York: Springer-Verlag, 2004, p. 238–255.
171. Berg WA, Nguyen TK. MR imaging of extracapsular silicone from breast implants: diagnostic pitfalls. *AJR Am J Roentgenol* 178: 465–472, 2002.
172. Orel SG, Rosen M, Mies C, Schnall MD. MR imaging-guided 9-gauge vacuum-assisted core-needle breast biopsy: initial experience. *Radiology* 238: 54–61, 2006.
173. Lehman CD, DePeri ER, Peacock S, McDonough MD, DeMartini WB, Shook J. Clinical experience with MRI-guided vacuum-assisted breast biopsy. *AJR Am J Roentgenol* 184: 1782–1787, 2005.
174. Liberman L, Morris EA, Dershaw DD, Thornton CM, Van Zee KJ, Tan LK. Fast MRI-guided vacuum-assisted breast biopsy: initial experience. *AJR Am J Roentgenol* 181: 1283–1293, 2003.
175. Perlet C, Heinig A, Prat X et al. Multicenter study for the evaluation of a dedicated biopsy device for MR-guided vacuum biopsy of the breast. *Eur Radiol* 12: 1463–1470, 2002.

CHAPTER 20

CONTRAST AGENTS

ERSAN ALTUN, DIEGO R. MARTIN, AND RICHARD C. SEMELKA

The number of advanced imaging studies, CT and MRI, that are performed in the U.S. continue to increase at a fast rate. It is estimated that 70 million CT studies and 30 million MR studies were performed in 2006. Almost half of these studies involve the use of intravenous contrast agents: Iodine-based contrast agent (IBCAs) are used in CT, and gadolinium-based contrast agents (GBCAs) are used in MRI. Complications from the use of IBCAs have been recognized for many years, with contrast-induced nephropathy (CIN) and anaphylactoid reactions being the most important and best-known complications. GBCAs had long been considered safe because of their reported much lower incidence of anaphylactoid reactions and CIN. Therefore, they were preferred over IBCAs in patients with renal impairment because of their presumed lower nephrotoxicity [1]. However, by October 2006, it was recognized by sufficient publications that use of GBCAs could result in the condition nephrogenic systemic fibrosis (NSF) in patients with renal impairment [1].

The discovery of the association of GBCAs with the development of NSF demonstrates and reminds us that all contrast agents should be used with caution in all patients [1]. Therefore, this chapter focuses on the categorization, enhancement and pharmacokinetic properties, toxicities and complications of administration, and practical guidelines for administration of MRI contrast agents.

CATEGORIZATION OF MRI CONTRAST AGENTS

MR contrast agents in clinical use are classified into three main types: 1) GBCAs, 2) iron-based contrast agents, and 3) manganese-based contrast agents.

GBCAs

GBCAs are by far the most commonly used MR contrast agents. They are essential for the detection and characterization of tumors, detection of inflammation and fibrosis, assessment of organ perfusion, and delineation of vessels and related vascular pathologies. Recognition of the phases of enhancement are critical for the detection and differentiation of these entities with the administration of GBCAs.

Abdominal-Pelvic MRI, Third Edition, edited by Richard C. Semelka. Copyright © 2010 John Wiley & Sons, Inc.

Classification of GBCAs

GBCAs in clinical use are classified into three types according to their distribution in the body as follows: 1) extracellular agents, 2) combined extracellular and intracellular agents, and 3) blood pool agents. GBCAs are classified into two types according to the backbone structure of their amine group, linear or macrocyclic. Linear and macrocyclic GBCAs may be further subclassified according to their charges as ionic or nonionic. Table 20.1 displays the categorization of GBCAs according to generic/product/manufacturer name, distribution in the body, chemical structure, elimination pathway, protein binding, thermodynamic stability, and dissociation rate.

Extracellular agents are distributed into extracellular space, including vascular and interstitial spaces. They have been in the longest use and have been the most widely used GBCAs. Extracellular agents can be linear or macrocyclic and ionic or nonionic. All extracellular agents are eliminated by the kidneys and do not exhibit protein binding. They are generally used at their standard dose, which is 0.1 mmol/kg. Extracellular agents can be used for the acquisition of hepatic arterial dominant, early hepatic venous, and interstitial phases of standard gadolinium-enhanced MRI images (fig. 20.1).

ProHance [gadoteridol, (Bracco Diagnostics, Milan, Italy)], Dotarem [gadoterate meglumine (Guerbet, Aulnay-sous-Bois, France)], and Gadovist [gadobutrol (Bayer Schering Pharma AG, Germany)] are the three macrocyclic GBCAs that are currently manufactured and in clinical use. Of the three, only ProHance is FDA approved for clinical use in the U.S. At the time of writing this chapter both Dotarem and Gadovist are in phase III clinical trials, under the observation of the FDA. As macrocyclic agents, all three of these contrast agents share the property of having the highest stability, in addition to being relatively pure nonspecific extracellular agents. There are, however, distinctive attributes of each agent, which may or may not be beneficial in their use.

ProHance is a nonionic macrocyclic agent that, in addition, has a low viscosity. The lower viscosity translates into easier and more rapid injection when administered by hand injection compared to other agents. This may be both advantageous (e.g., when only a small vein is cannulated this facilitates adequate injection) or potentially disadvantageous (e.g., more of a perceived "contrast rush" due to rapid injection).

Dotarem is an ionic macrocyclic agent, and therefore combines both the predominant stability factor of macrocyclic design with the ancillary factor of ionicity. Hence, from a theoretical standpoint of stability, Dotarem should be one of the safest GBCAs.

Gadovist is a nonionic macrocyclic GBCA. Gadovist has higher T1 relaxivity due to its structural difference. Marketed Gadovist solutions also have a double amount of gadolinium per volume due to their 1 molar (M) concentrations compared to 0.5 M concentrations of the other GBCAs. This agent can also be administered in a lower dose to achieve the same imaging effect, theoretically because of its higher T1 relaxivity.

We anticipate that by the time of the release of the next edition of this textbook both Dotarem and Gadovist will be FDA approved and on the U.S. market. The experience of NSF (discussed below) has taught all of us that GBCAs should not be considered completely innocuous, and that all agents are not the same. We have now developed a heightened awareness of differences and idiosyncrasies of these agents.

Combined extracellular and intracellular agents are distributed into the extracellular space including vascular and interstitial spaces, and intracellular spaces of hepatocytes. Therefore, these agents can also be termed combined extracellular and hepatocyte-specific agents. These agents are MultiHance [gadobenate dimeglumine (Bracco Diagnostics, Milan, Italy)] and Eovist [gadoxetic acid (Bayer HealthCare Pharmaceuticals, Wayne, NJ), in the US]/Primovist [gadoxetic acid (Bayer Schering Pharma AG, Germany), outside the US]. These agents are taken up by hepatocytes and excreted into bile ducts. Therefore, they have dual elimination including both renal and biliary elimination. The phase in which the liver shows uptake of these agents is termed the hepatocyte phase. These agents, which are linear and ionic, have also higher T1 relaxivity because of their structural difference and protein binding. Less than 5% of MultiHance and 15% of Eovist binds serum albumin transiently and reversibly. Hepatocyte uptake and higher T1 relaxivity make these agents advantageous for liver imaging and MR angiographies (MRAs). However, there are not sufficient data about the use of Eovist in MRAs. The hepatocyte phase is helpful for the detection of lesions that do not contain hepatocytes, including metastases, adenomas, and poorly differentiated hepatocellular carcinomas (HCCs) (figs. 20.2–20.4). This phase is particularly helpful for the differentiation of focal nodular hyperplasia (FNH) from adenoma. FNH contains hepatocytes and biliary canaliculi; therefore, hepatocyte-specific agents can be taken up and excreted into the bile ducts in FNH. However, hepatic adenomas do not contain normal hepatocytes and biliary canaliculi; therefore, hepatocyte-specific agents do not show uptake. Thus, while FNH enhances in the hepatocyte phase (fig. 20.2), hepatic adenomas do not (fig. 20.3). This phase is also helpful for the evaluation of liver function and the biliary system (figs. 20.5 and 20.6). Because of high T1 relaxivity, Eovist is used at one-fourth (0.025 mmol/kg) of the standard dose of extracellular GBCAs. However, there are not sufficient data demonstrating the diagnostic efficacy of this dose of

Table 20.1 Categorization of GBCAs According to Distribution in the Body, Chemical Structure, Elimination Pathway, Protein Binding, Thermodynamic Stability, and Dissociation Rate

Generic Name	Chemical Abbreviation	Product Name	Distribution	Amine Structure	Charge	Excretion	Protein Binding	FDA Approval	Standard Dosage	Thermodynamic Stability Constant	Dissociation Rate
Gadoversetamide	Gd-DTPA-BMEA	OptiMark (Mallinckrodt, St Louis, MO, USA)	Extracellular	Linear	Nonionic	Renal	None	Yes	0.1 mmol/kg	16.8	$>2.2 \times 10^{-2}$
Gadodiamide	Gd-DTPA-BMA	Omniscan (GE Healthcare, Amersham, United Kingdom)	Extracellular	Linear	Nonionic	Renal	None	Yes	0.1 mmol/kg	16.8	$>2 \times 10^{-2}$
Gadopentetate dimeglumine	Gd-DTPA	Magnevist (Bayer Schering Pharma AG, Germany)	Extracellular	Linear	Ionic	Renal	None	Yes	0.1 mmol/kg	22.2	1.2×10^{-3}
Gadobenate dimeglumine	Gd-BOPTA	MultiHance (Bracco Diagnostics, Milan, Italy)	Extracellular and intracellular (hepatocyte)	Linear	Ionic	Renal (%97), Biliary (%3)	<5%	Yes	0.1 mmol/kg*†	22.6	—**
Gadoxetic acid disodium	Gd-EOB-BOPTA	Eovist (Bayer HealthCare Pharmaceuticals, Wayne, NJ, USA); Primovist (Bayer Schering Pharma AG, Germany)	Extracellular and intracellular (hepatocyte)	Linear	Ionic	Renal (%50), Biliary (%50)	<15%	Yes	0.025 mmol/kg*	23.4	—**
Gadofosveset trisodium	Gd-DTPA	Vasovist (Epix Pharmaceuticals, Lexington, MA, USA)	Blood pool	Linear	Ionic	Renal (91%), Biliary (9%)	>85%	Yes	0.025 mmol/kg*	—**	—**
Gadobutrol	Gd-DO3A-butriol	Gadovist (Bayer Schering Pharma AG, Germany)	Extracellular	Macrocyclic	Nonionic	Renal	None	No	0.1 mmol/kg*‡	21.0	2.8×10^{-6}
Gadoteridol	Gd-HP-DO3A	ProHance (Bracco Diagnostics, Milan, Italy)	Extracellular	Macrocyclic	Nonionic	Renal	None	Yes	0.1 mmol/kg	23.8	6.4×10^{-5}
Gadoterate meglumine	Gd-DOTA	Dotarem (Guerbet, Aulnay-sous-Bois, France)	Extracellular	Macrocyclic	Ionic	Renal	None	No	0.1 mmol/kg	25.6	8.4×10^{-7}

*Gadobenate dimeglumine, gadoxetic acid, gadofosveset, and gadobutrol have higher T1 relaxivity compared to the other agents.
†Gadobenate dimeglumine has been reported to be diagnostically effective at its half-dose (0.05 mmol/kg).
‡Gadobutrol solution has double amount of gadolinium in its 1 molar (M) concentration compared to 0.5 M concentration of the other GBCAs' solutions.
**Not available.

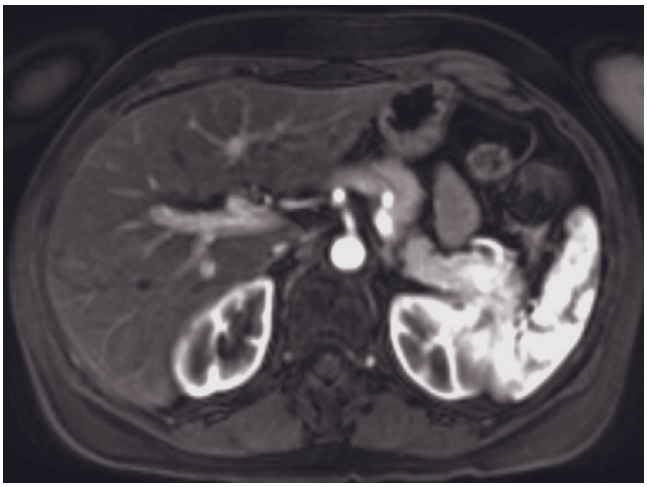

(*a*)

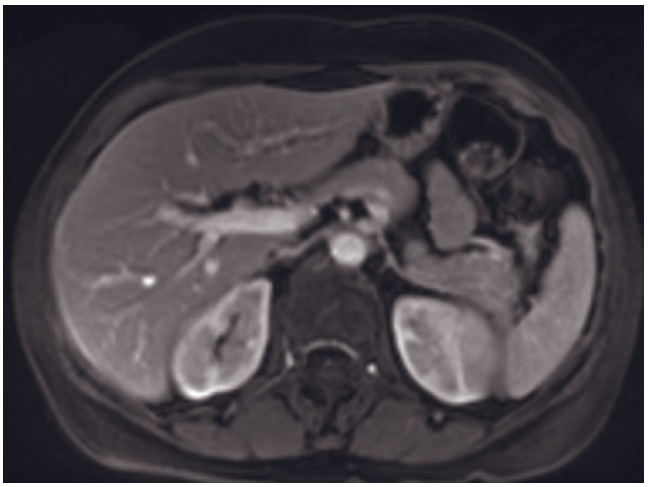

(*b*)

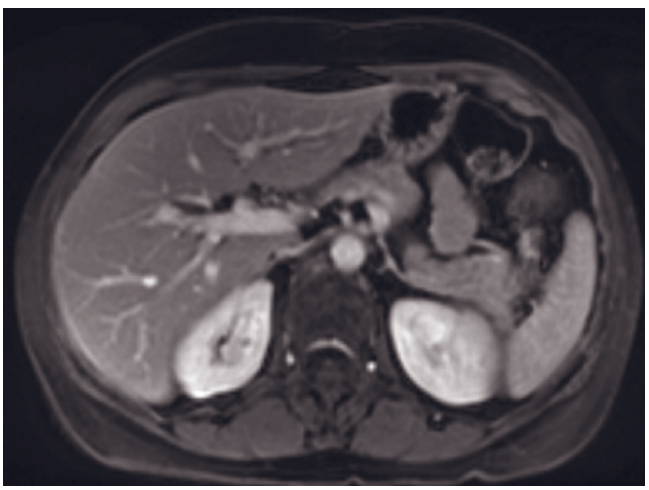

(*c*)

FIG. 20.1 Phases of enhancement. T1-weighted postgadolinium fat-suppressed hepatic arterial dominant phase (*a*), early hepatic venous phase (*b*), and interstitial phase (*c*) 3D-GE images at 3.0 T. Note that the contrast is present in the hepatic arteries and portal vein but not in the hepatic veins on the hepatic arterial dominant phase.

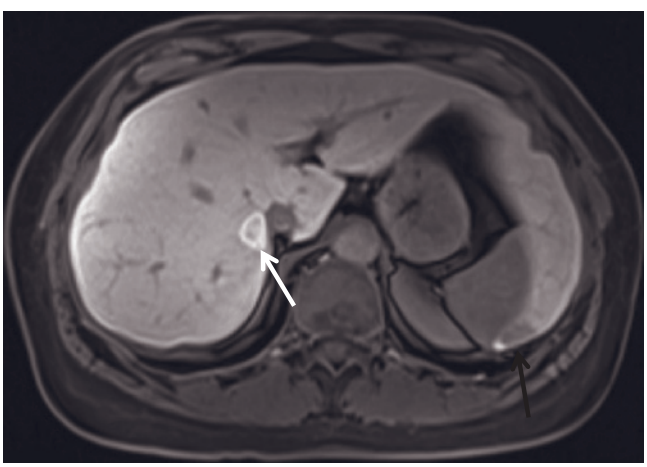

(*a*)

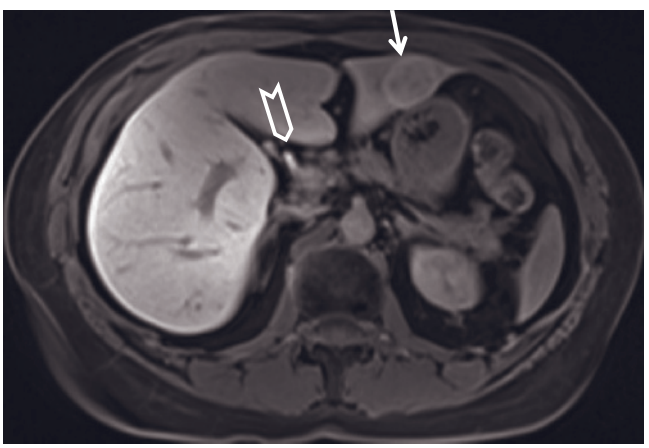

(*b*)

FIG. 20.2 Hepatocyte phase. T1-weighted postgadolinium 20-min hepatocyte phase fat-suppressed 3D-GE images (*a*, *b*) after administration of gadoxetic acid demonstrate two focal nodular hyperplasias (white arrows, *a*, *b*) and one hemangioma (black arrow, *a*). The liver and extrahepatic bile ducts (open arrow, *b*) are enhanced. Note that it is not possible to diagnose hemangioma based on hepatocyte phase findings; therefore, this phase should be used in combination with hepatic arterial dominant, early hepatic venous, and interstitial phases.

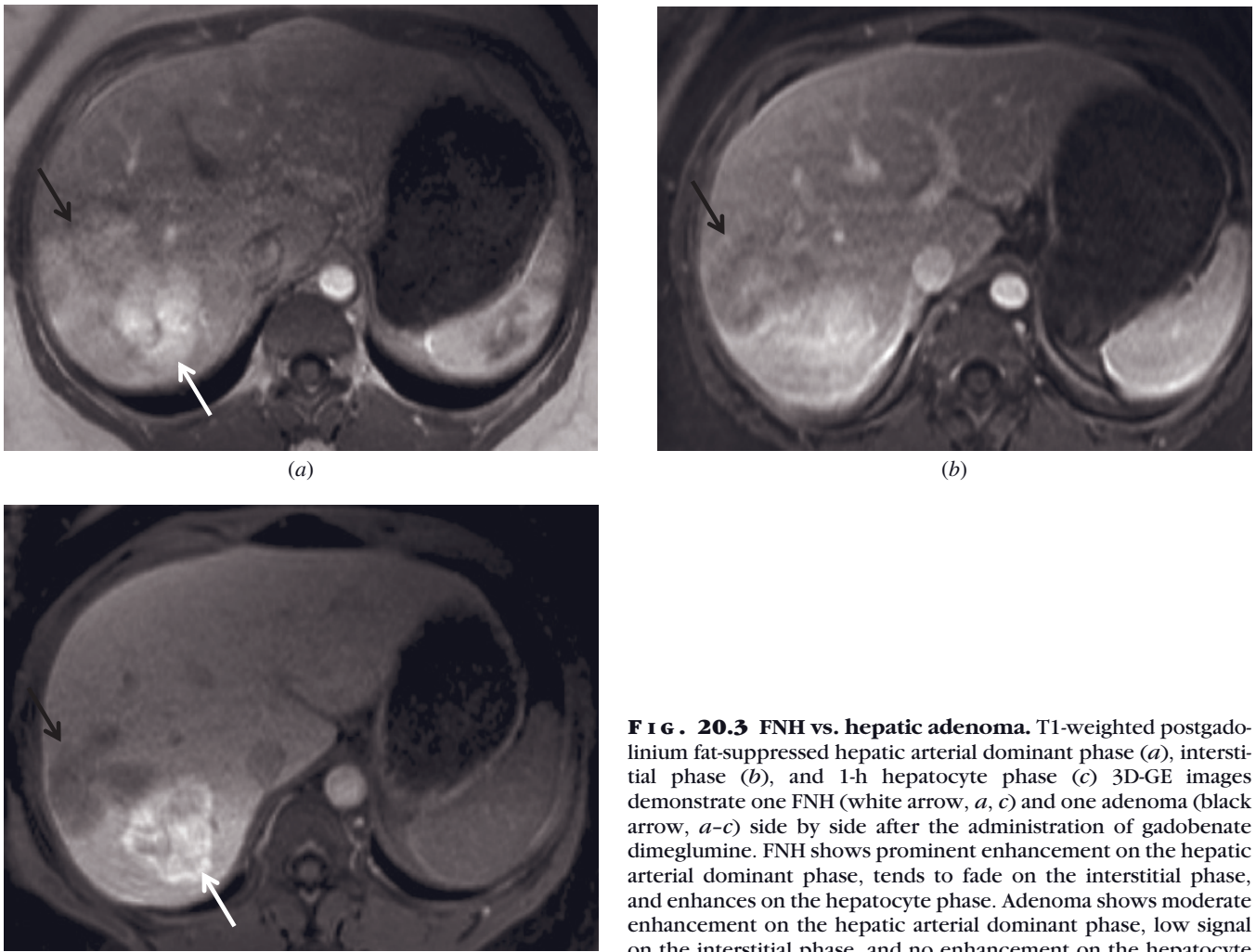

FIG. 20.3 FNH vs. hepatic adenoma. T1-weighted postgadolinium fat-suppressed hepatic arterial dominant phase (*a*), interstitial phase (*b*), and 1-h hepatocyte phase (*c*) 3D-GE images demonstrate one FNH (white arrow, *a*, *c*) and one adenoma (black arrow, *a*–*c*) side by side after the administration of gadobenate dimeglumine. FNH shows prominent enhancement on the hepatic arterial dominant phase, tends to fade on the interstitial phase, and enhances on the hepatocyte phase. Adenoma shows moderate enhancement on the hepatic arterial dominant phase, low signal on the interstitial phase, and no enhancement on the hepatocyte phase.

Eovist compared to the standard doses of extracellular GBCAs. MultiHance is approved for use at 0.1 mmol/kg; however, it has been shown that 0.05 mmol/kg (half-dose) of this agent has diagnostic efficacy comparable to the full dose of standard extracellular GBCAs. Combined extracellular and hepatocyte-specific agents can be used for the acquisition of the hepatic arterial dominant, early hepatic venous, interstitial, and hepatocyte phases of gadolinium-enhanced MRI studies.

An important difference between MultiHance and Eovist is the proportion that is eliminated through the biliary system in relation to renal clearance: approximately 5% of the administered dose of MultiHance is eliminated by the biliary system in patients with normal renal function, whereas approximately 50% of the dose of Eovist is eliminated by the biliary system. These proportions increase in the setting of renal failure, MultiHance to about 9% and Eovist to a fraction not yet established. In terms of image acquisition, this difference is manifest by the time of occurrence of the hepatocyte phase with these two agents: with MultiHance it is at about 1 hour (lasting for at least 4 hours), and with Eovist it is at about 20 minutes (lasting for about 4 hours). Biliary elimination with visualization of high signal contrast in the biliary tree is also more pronounced with Eovist. The earlier hepatocyte phase that is achieved with Eovist permits ready acquisition of an entire postcontrast study, including hepatic arterial dominant, early hepatic venous, and interstitial phases, with hepatocyte-phase, in one imaging session. To avoid excessive dead-time between the interstitial phase and hepatocyte phase, we recommend performing T2-weighted sequences after the interstitial phase and before the hepatocyte phase. Special note should be made that since the biliary elimination also results in T2 shortening, T2 sequence-based MRCP should not be performed after contrast administration but rather before it, as the T2 shortening can obscure the biliary tree. On the other hand, as the hepatocyte phase occurs at one hour with MultiHance, it is unavoidable that two imaging sessions

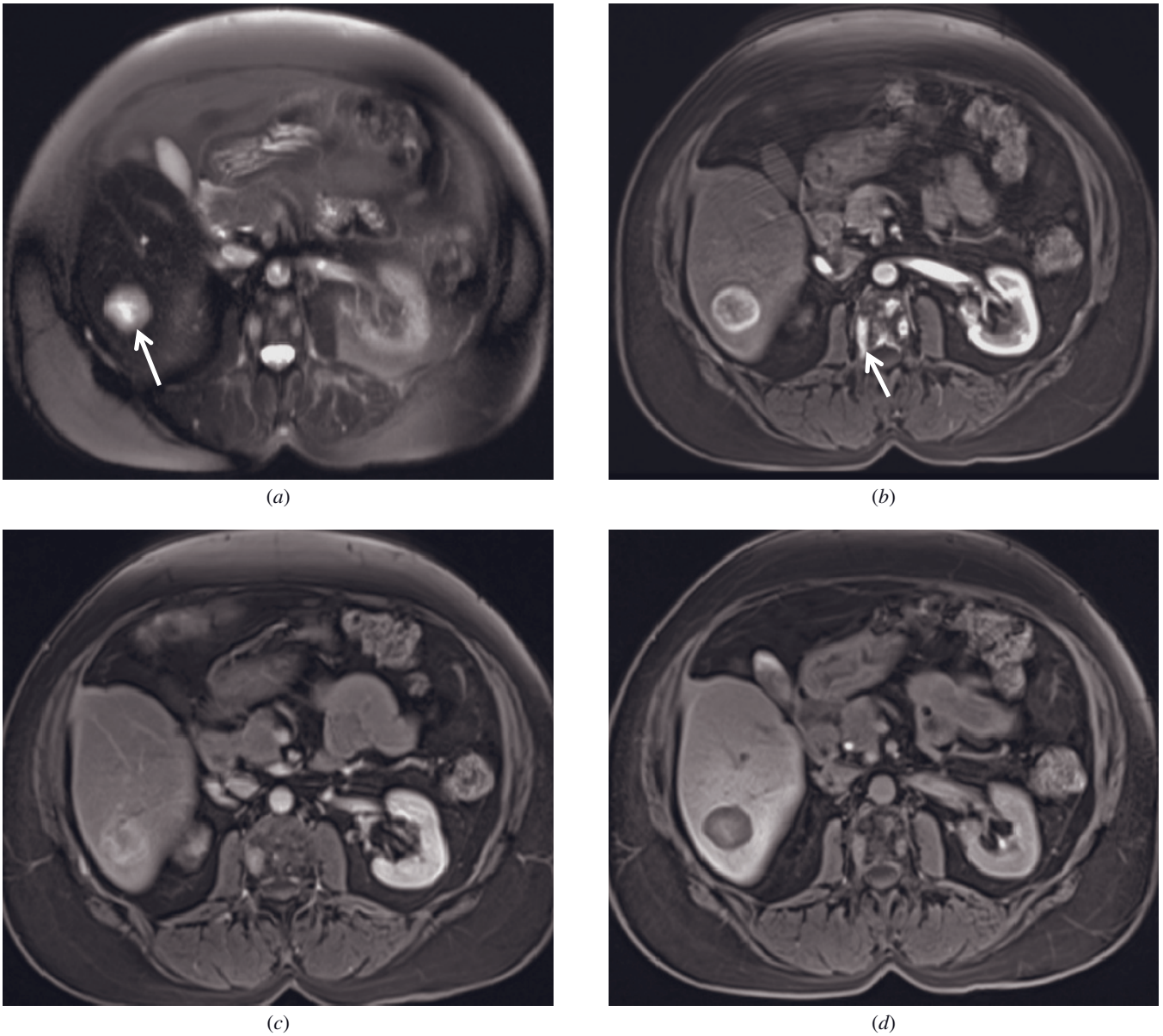

FIG. 20.4 Multiple myeloma metastases in the liver and vertebra. T2-weighted single-shot echo-train spin-echo (*a*), T1-weighted fat-suppressed 3D-GE hepatic arterial dominant phase (*b*), interstitial phase (*c*), and 20-min hepatocyte phase (*d*) images demonstrate liver metastasis (arrow, *a*) and multiple bone metastases (arrow, *b*) from multiple myeloma after the administration of gadoxetic acid. The liver metastases show prominent peripheral enhancement on the hepatic arterial dominant and interstitial phases and minimal enhancement on the hepatocyte phase. The bone metastases show prominent enhancement.

must be performed with a 1- to 2-hour delay between the full MR study and the delayed hepatocyte phase.

In making a decision between these agents for hepatocyte phase imaging other considerations must be entertained: Only Eovist is FDA approved for liver imaging, while the use of MultiHance is considered off-label, but on the other hand the cost of MultiHance is considerably less at the present time and at the current doses recommended by the manufacturers. MultiHance results in considerably greater signal increase on early postcontrast phases than Eovist (and our experience emphasizes the great importance of hepatic arterial dominant phase imaging); this is even the case if MultiHance is employed at half dose, as we routinely do because of NSF concerns.

Blood pool agents mainly stay in the vascular space. Vasovist [gadofosveset, (Epix Pharmaceuticals, Lexington, MA)] is a blood pool agent that has linear and ionic structure, and more than 85% of Vasovist binds serum albumin transiently and reversibly. A small amount of Vasovist is also distributed into the extracellular space. Binding to serum albumin provides higher

FIG. 20.5 Normal common bile duct. Coronal T1-weighted 20-min postgadolinium fat-suppressed 3D-GE image after administration of gadoxetic acid demonstrates the presence of contrast in the normal common bile duct.

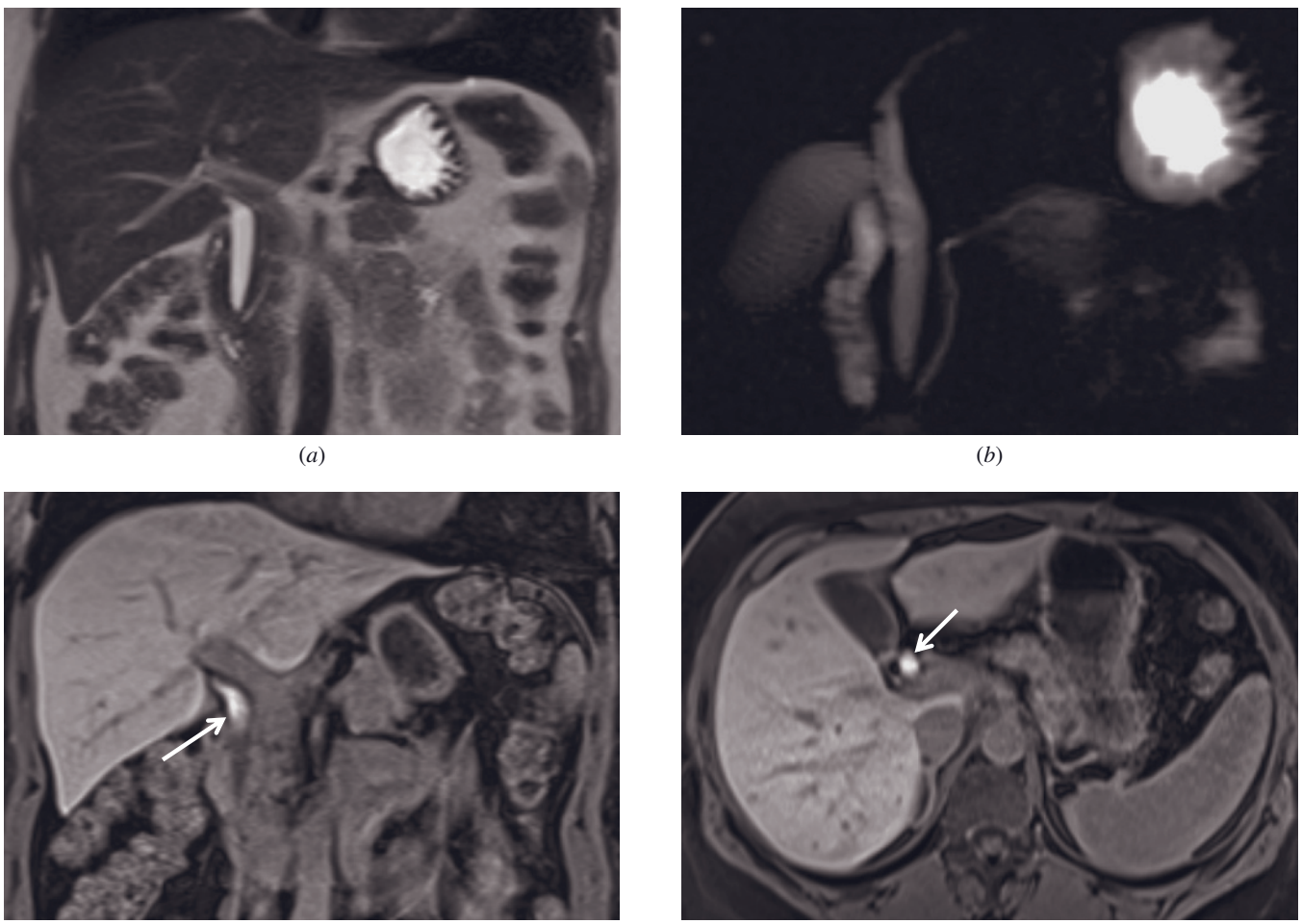

FIG. 20.6 Ampullary stenosis. Coronal T2-weighted single-shot echo-train spin-echo (*a*), coronal fast spin-echo thick-section MRCP (*b*), and coronal (*c*) and transverse (*d*) T1-weighted fat-suppressed 20-min hepatocyte phase 3D-GE images after administration of gadoxetic acid demonstrate dilated common bile duct and the presence of contrast in the dilated common bile duct. Note that the liver is enhanced.

T1 relaxivity and extended intravascular enhancement. Intravascular enhancement is higher and longer with Vasovist compared to the other protein-binding GBCAs (MultiHance and Eovist) because of tighter and longer-duration protein binding. A small amount of Vasovist is also taken up by hepatocytes and excreted into the bile ducts. Therefore, Vasovist has dual elimination including renal and biliary eliminations. Vasovist is administered at a dose of 0.025 mmol/kg. Blood pool agents may be advantageous for vascular imaging because of higher and longer intravascular enhancement; and Vasovist has recently been approved by FDA for body MRAs. However, the diagnostic role and safety profile of this agent need to be determined, and we have no clinical experience with this agent.

Phases of Enhancement

A critical aspect of the use of GBCAs is recognition of the importance of timing of data acquisition in order to maximize the information available regarding the dynamic handling of contrast by the vascular and extracellular spaces of various organs, tissues, and disease processes. These phases should include hepatic arterial dominant phase, early hepatic venous phase, interstitial phase, and hepatocyte phase (acquired only with hepatocyte-specific agents)

Hepatic Arterial Dominant Phase. Appropriate early timing of data acquisition immediately after contrast is the most critical aspect of timing. Three different techniques including empirical timing, test bolus, and bolus tracking methods are employed in order to acquire the optimal phase of early enhancement in a short time window of early postgadolinium imaging, which is the hepatic arterial dominant phase [2]. It has been recently reported that the arterial-phase bolus-track liver examination (ABLE) technique is a successful method for the acquisition of hepatic arterial dominant phase [3]. A bolus track sequence, which produces an image approximately every second, is used to detect the arrival of GBCAs to the level of the celiac axis. After 8 seconds, the liver is scanned with 3D-GE and standard ordered k space for a 16- to 20-second sequence. During the 8-second-period, the patient is given breathing instructions. This is also the technique that we routinely use now at our institution.

All these techniques depend on the estimation of circulation time of the contrast material from the site of injection or abdominal aorta to the liver [2]. Because the circulation time of the contrast material to the liver shows variation depending on a number of factors, different subphases of arterial phase enhancement other than the hepatic arterial dominant phase may be detected [2].

These subphases can be summarized based on vessel enhancement patterns and extent of organ enhancements, as displayed in Table 20.2. These subphases are as follows: 1) early hepatic arterial phase (EHAP), 2) mid-hepatic arterial phase (MHAP), 3) late hepatic arterial phase (LHAP), 4) splenic vein-only hepatic arterial dominant phase (SVHADP), and 5) hepatic arterial dominant phase (HADP).

1. EHAP is characterized by the presence of contrast in the arteries including the hepatic arteries; the absence of contrast in any venous structure; and the presence of no or only slight enhancement in the renal cortex, pancreas, spleen, and liver (fig. 20.7).
2. MHAP is characterized by the presence of contrast in the arteries, including the hepatic arteries; the

Table 20.2 Vessel and Organ Enhancement Patterns According to Su-phases of Early Enhancement

	EHAP	MHAP	LHAP	SVHADP	HADP
Vessel Enhancement					
All arteries	+	+	+	+	+
Renal veins	–	–	+	+	+
Portal vein	–	–	–	+	+
Splenic vein	–	–	–	+	+
Superior mesenteric vein	–	–	–	–	+
Suprarenal IVC	–	–	±	+	+
Hepatic vein	–	–	–	–	–
Organ Enhancement					
Renal cortex	No or slight	Mild or moderate	Moderate to intense	Moderate to intense	Moderate to intense
Spleen	No or slight	Mild or moderate	Moderate to intense	Moderate to intense	Moderate to intense
Pancreas	No or slight	Slight or mild	Mild or moderate	Moderate	Moderate
Liver	No or slight	Slight or mild	Slight or mild	Mild	Moderate

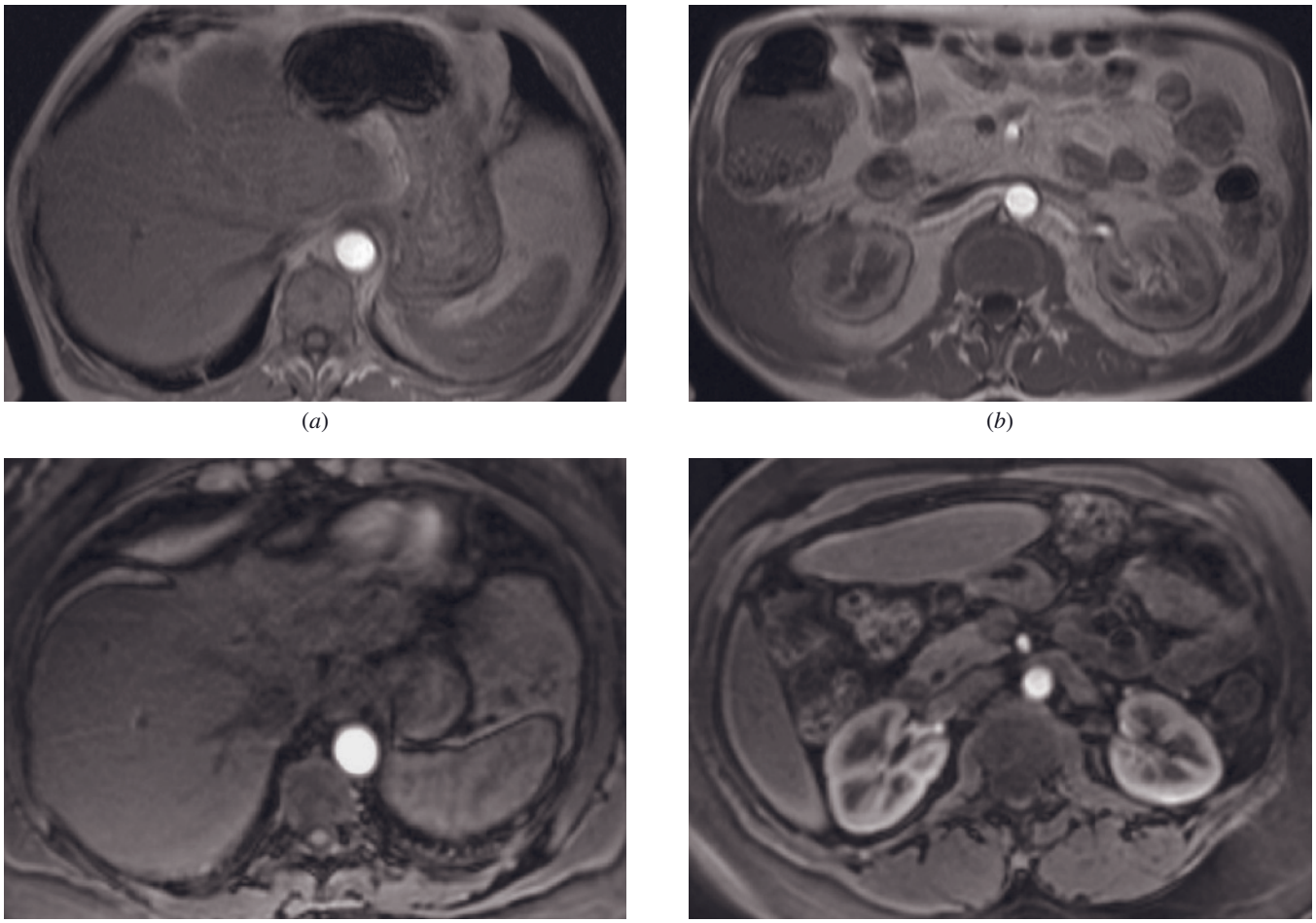

FIG. 20.7 EHAP and MHAP. The early hepatic arterial phase (EHAP) observed on transverse SGE images (*a*, *b*) acquired at 1.5 T. The mid-hepatic arterial phase (MHAP) observed on transverse 3D-GE images (*c*, *d*) acquired at 3.0 T. The contrast enhancement is seen in the aorta, renal arteries, and superior mesenteric artery, but there is no contrast enhancement in the veins on both EHAP and MHAP. The renal cortex, spleen, pancreas, and liver demonstrate slight enhancement on EHAP. The renal cortex and spleen show mild enhancement and the pancreas and liver shows slight enhancement on MHAP. The minimal enhancement of the normal pancreas reflects the too-early acquisition of data in these subphases.

absence of contrast in any venous structure; and the presence of mild to moderate enhancement in the renal cortex and the spleen and slight to mild enhancement in the pancreas and liver (fig. 20.7).

3. LHAP is characterized by the presence of contrast in the arteries, including the hepatic arteries, and renal veins; the presence or absence of contrast in the suprarenal IVC and the absence of contrast in the other venous structures; and the presence of moderate to intense enhancement in the renal cortex and the spleen, mild to moderate enhancement in the pancreas, and slight to mild enhancement in the liver (fig. 20.8).
4. SVHADP is characterized by the presence of contrast in the arteries, including the hepatic arteries, and in the portal vein, splenic vein, renal veins, and suprarenal IVC; the absence of contrast in the superior mesenteric vein and hepatic veins; and the presence of moderate to intense enhancement in the renal cortex and spleen, moderate enhancement in the pancreas, and mild enhancement in the liver (fig. 20.9).
5. HADP is characterized by the presence of contrast in the hepatic arteries, portal vein, renal veins, splenic vein, superior mesenteric vein. and suprarenal IVC; the absence of contrast in the hepatic veins; and the presence of moderate to intense enhancement in the renal cortex, spleen, and pancreas and moderate enhancement in the liver (fig. 20.9).

The enhancements of parenchymal organs demonstrate variations in these subphases [2]. It has been reported that the pancreas exhibits a capillary blush on the hepatic arterial dominant phase, which may act as

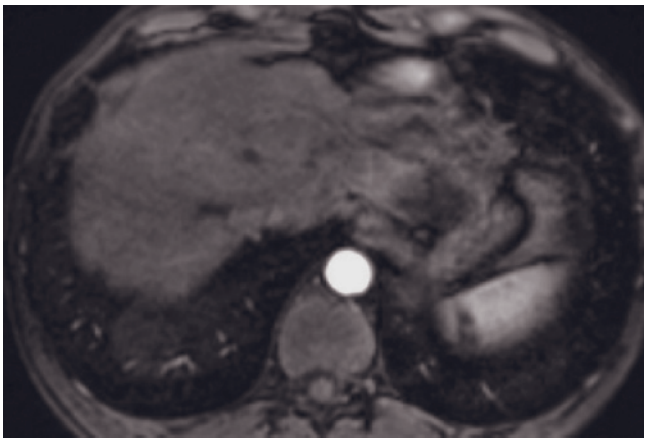

(*a*)

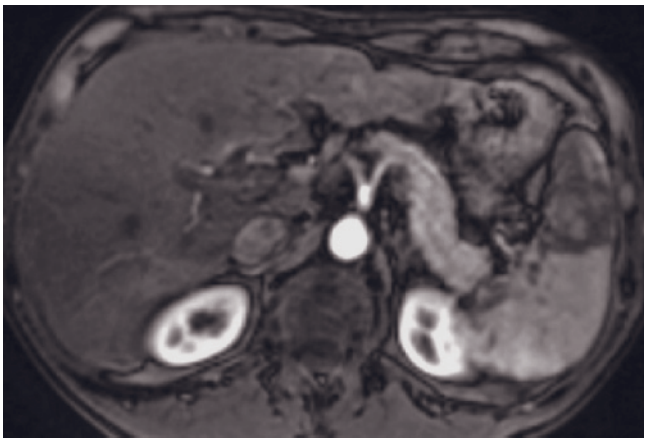

(*b*)

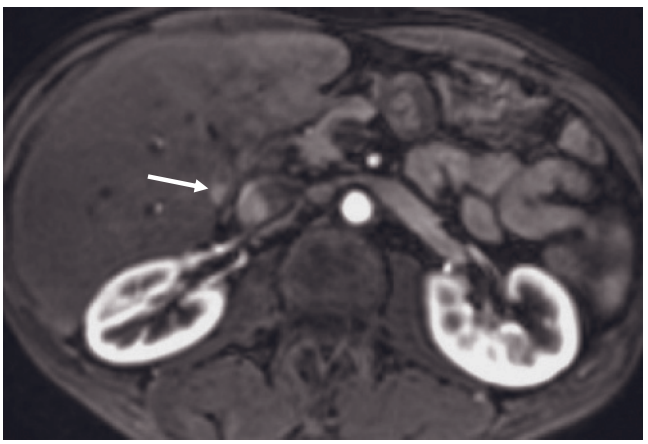

(*c*)

FIG. 20.8 LHAP. The late hepatic arterial phase (LHAP) observed on transverse 3D-GE images (*a*–*c*) acquired at 3.0 T. Contrast enhancement is seen in the aorta; celiac trunk; common hepatic artery and its branches; splenic, renal, and superior mesenteric arteries; and renal veins. The renal cortex demonstrates intense enhancement, the pancreas and spleen demonstrate moderate enhancement, and the liver shows mild enhancement on LHAP. The moderate enhancement of the normal pancreas reflects the adequate timing of enhancement of LHAP. Contour irregularity of the liver, splenomegaly, and patchy and nodular enhancement of the liver are also detected. Patchy enhancement of the liver is most pronounced in the left lobe (*b*, *c*) and is consistent with acute-on-chronic hepatitis. Small nodular enhancement (arrow, *c*) is consistent with a dysplastic nodule.

surrogate for the determination of the timing of the examination and for the enhancement of liver lesions [2]. Therefore, it can be accepted that the timing of enhancement is ideal when the pancreas shows a capillary blush [2]. It has been reported that the capillary blush is also observed in the LHAP and SVHADP subphases; and these phases are also adequate phases of early enhancement (fig. 20.10) [2]. However, EHAP and MHAP are not adequate phases of early enhancement because they are too early for the pancreas to show a capillary blush, and therefore these phases are too early for the evaluation of abdominal organs (fig. 20.10) [2].

In our clinical experience, if the portal vein is not enhanced it may be difficult to determine whether the timing of liver enhancement is in the MHAP (too early) or the LHAP (adequate timing) [2]. It has been reported that substantial enhancement of the pancreas is observed in combination with identification of the presence of contrast in renal veins in the LHAP [2]. Therefore, enhancement of the renal veins may also be used as a landmark for the determination of an adequate phase of enhancement, especially in the presence of pancreatic pathology that will reduce the enhancement of pancreatic tissue and preclude the use of the pancreas as a surrogate for ideal timing [2]. We do, however, anticipate that this observation of renal vein enhancement may be influenced by cardiac output, vascular resistance of the lung parenchyma, and renal function [2].

Early Hepatic Venous Phase. This phase should be acquired after the hepatic arterial dominant phase and is customarily referred to as the portal venous phase. However, early hepatic venous phase may be a more correct description, as contrast has just entered the hepatic veins at this time point.

Interstitial Phase. This phase should be acquired after the early hepatic venous phase, generally with 2–5 minutes after injection as the ideal time point, and is customarily referred to as the equilibrium phase. However, it may be more correctly referred to as interstitial phase, as no true equilibrium occurs, and the contrast is distributed into the interstitial space.

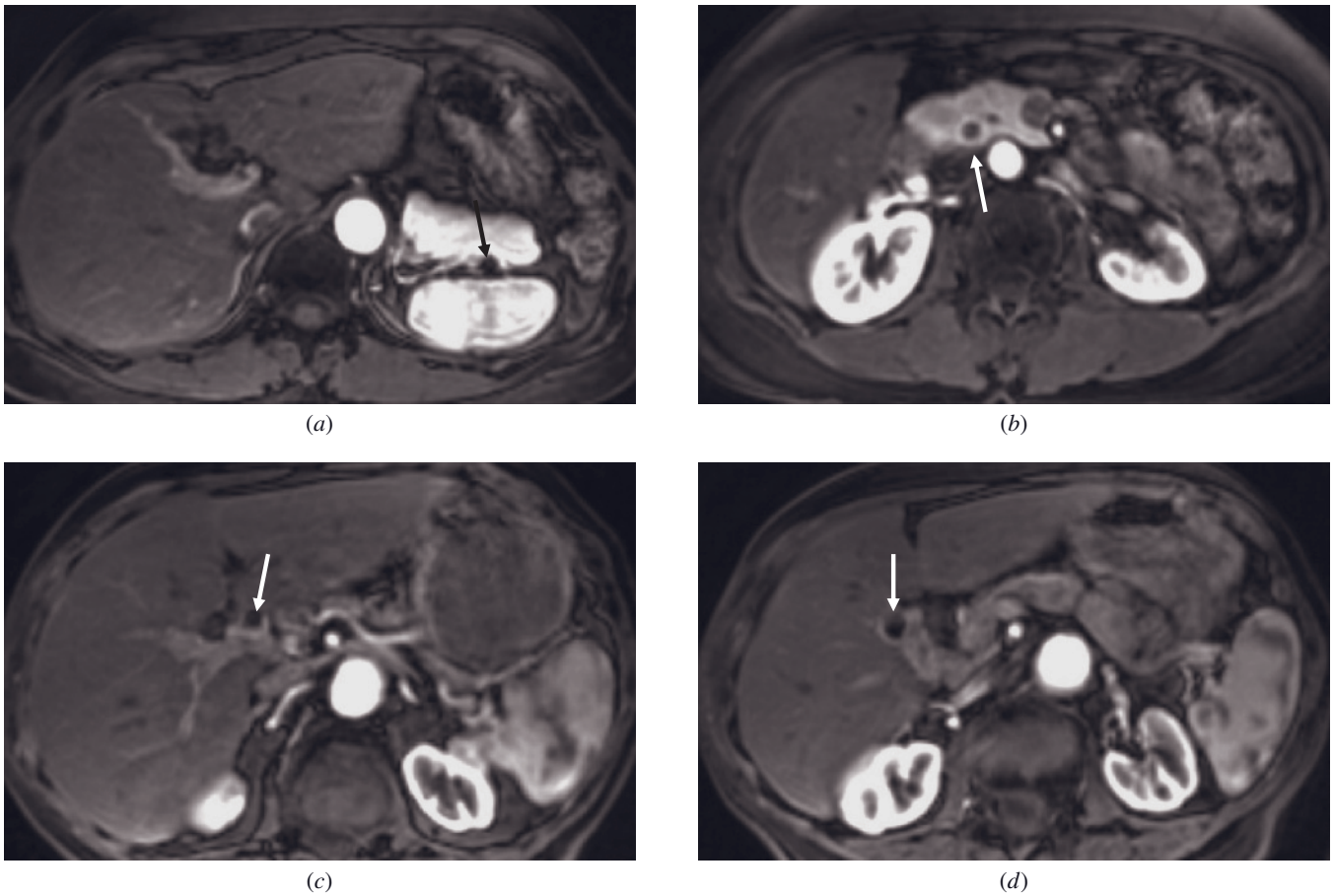

FIG. 20.9 SVHADP and HADP. The splenic vein-only hepatic arterial dominant phase (SVHADP) (*a*, *b*) and the hepatic arterial dominant phase (HADP) (*c*, *d*) observed on transverse 3D-GE images acquired at 3.0 T. Contrast enhancement is seen in the aorta, renal arteries, and splenic and superior mesenteric arteries and renal, splenic, and portal veins but not in the hepatic and superior mesenteric veins on SVHADP. The renal cortex and spleen demonstrate intense enhancement, the pancreas demonstrates moderate enhancement, and the liver shows mild enhancement on SVHADP. Although there are two pseudocysts located in the pancreatic tail (arrow, *a*) and head (arrow, *b*); the moderate enhancement of the pancreas reflects the adequate timing of enhancement on SVHADP. In addition to the contrast-enhanced vessels seen on SVHADP, contrast enhancement is also observed in the superior mesenteric vein on HADP. The renal cortex demonstrates intense enhancement, and the spleen, pancreas, and liver demonstrate moderate enhancement. The moderate enhancement of the normal pancreas reflects the adequate timing of enhancement of HADP. Note that there are benign cystic lesions in the liver parenchyma (arrows, *c*, *d*).

Hepatocyte Phase. This phase can only be acquired after the administration of combined extracellular and hepatocyte-specific agents including MultiHance and Eovist. These agents are taken up by hepatocytes and excreted into the bile ducts. The hepatocyte phase can be acquired after 1 hour following the administration of MultiHance and 20 minutes following the administration of Eovist.

Iron-Based Contrast Agents

Iron-based contrast agents, which include superparamagnetic iron oxide particles, and ultrasmall superparamagnetic iron oxide particles are selectively taken up by Kupffer cells of the reticuloendothelial system (RES). RES cells are primarily present in the liver, spleen, and lymph nodes. These agents exert their effects both on T1 and T2 relaxation times, and therefore postcontrast imaging can be performed with T1- and T2-weighted sequences. They are generally used for problem-solving in combination with GBCAs (fig. 20.11). Superparamagnetic iron oxide particles decrease the signal intensity of tissue containing RES cells on T1- and T2-weighted sequences and therefore increase the conspicuity of lesions that do not contain RES cells, such as metastases or primary tumors in the liver and spleen or hepatic fibrosis. Ultrasmall superparamagnetic iron oxide particles have been reported to be successful in the

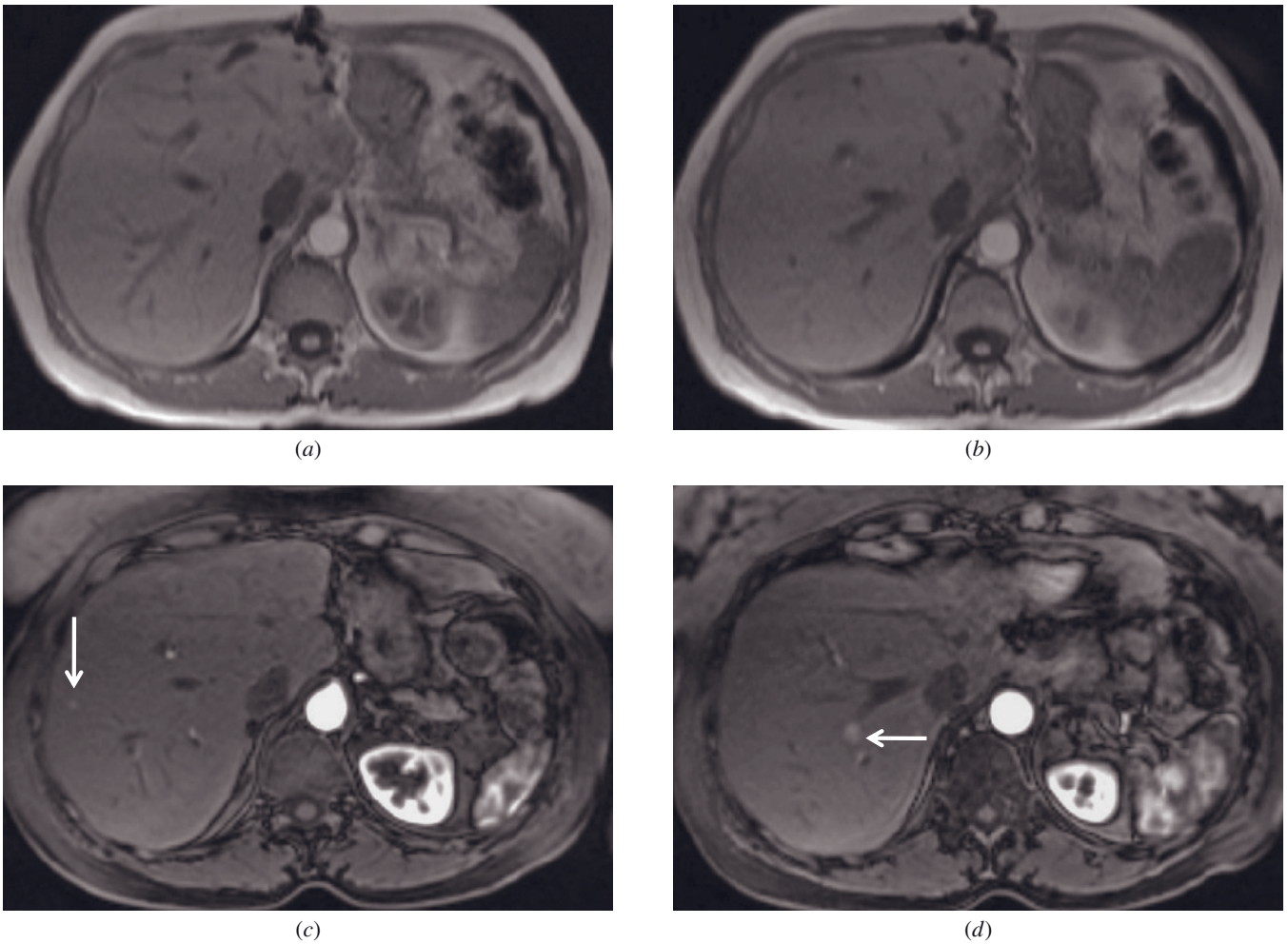

FIG. 20.10 EHAP vs. LHAP. T1-weighted postgadolinium EHAP SGE (*a*, *b*) and LHAP fat-suppressed 3D-GE (*c*, *d*) images demonstrate the importance of the timing of early enhancement. While no lesions are detected on EHAP images, two small metastases are detected on LHAP in the same patient.

diagnosis of lymph node metastases; however, this role is not yet well established.

Superparamagnetic iron oxide particles include ferumoxides [Feridex (Bayer Healthcare Pharmaceuticals, Wayne, NJ)] and ferucarbotran [Resovist (Bayer Schering Pharma AG, Berlin, Germany)]. Feridex is the only one of these agents that is FDA approved, but it is currently not available on the market. Ultrasmall superparamagnetic iron oxide particles include ferumoxtran (Combidex).

Ferumoxide particles are 50–180 nm in size, while ferucarbotran particles are about 60 nm in size [4]. Ferumoxide particles are coated with dextran, and ferucarbotran particles are coated with carboxydextran [4]. The smaller size of ferucarbotran particles increases the enhancement on T1-weighted sequences [4].

Resovist can be administered as a rapid bolus, and imaging can be performed immediately after administration, achieving T1-weighted-type organ enhancement. [4]. Both T1-weighted dynamic and T2-weighted delayed imaging can be performed; however, the T1-weighted perfusional enhancement compares poorly with GBCAs. Accumulation of Resovist in RES cells begins at 10 minutes and is present up to 8 hours after administration. Vasodilatation and paraesthesia are the most common adverse events [4].

Feridex is diluted with 100 ml of 5% dextrose solution administered as a slow infusion over 30 minutes. Postcontrast imaging can be performed from immediately after the infusion up to 3.5 hours. Leg and back pain are the most common adverse events [4].

Manganese-Based Contrast Agents

Mangafodipir trisodium (Mn-DPDP, Teslascan) is a liver-specific contrast agent, and postcontrast imaging is per-

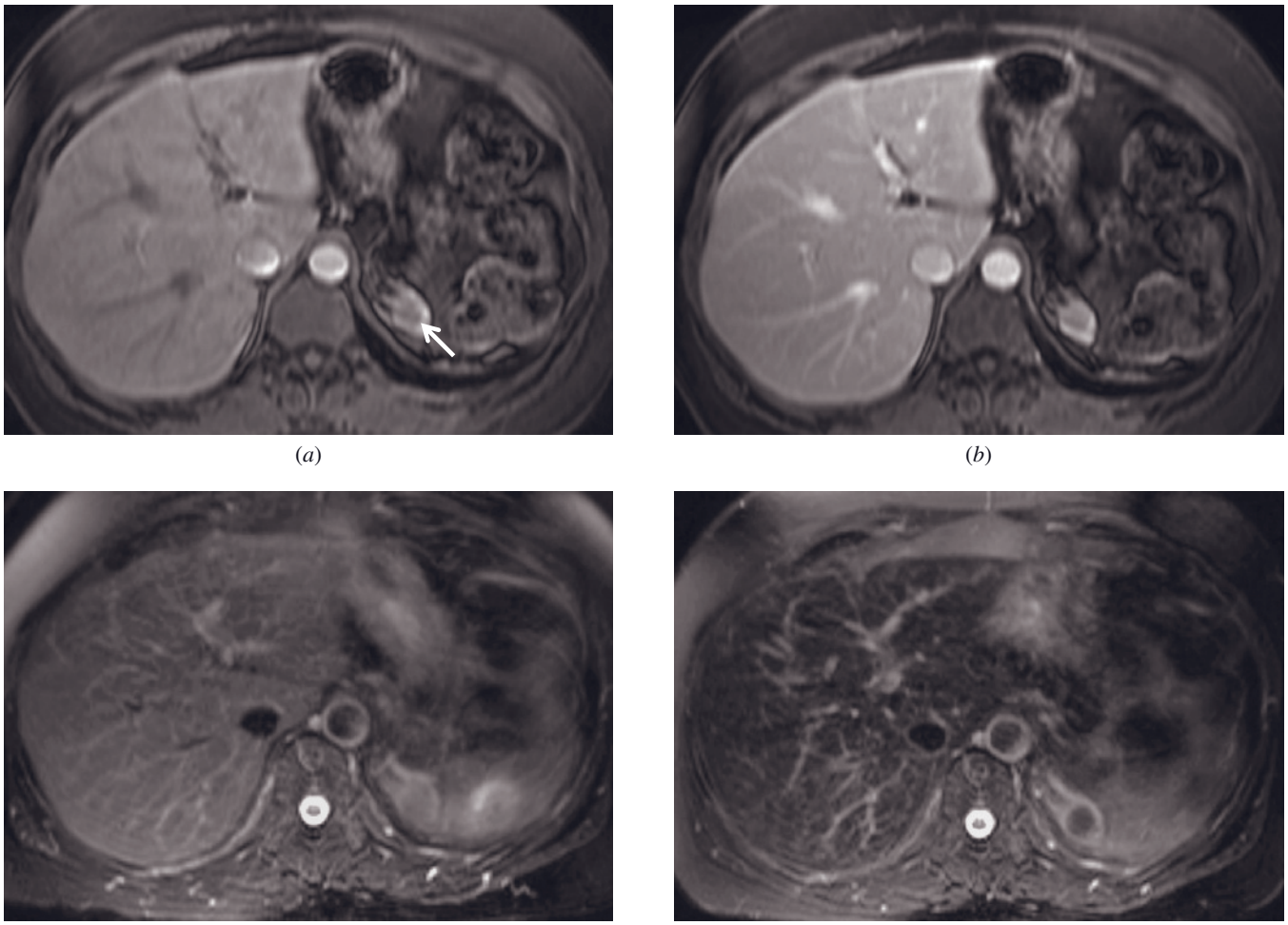

FIG. 20.11 Differentiation of pancreatic cancer from intrapancreatic splenule. T1-weighted postgadolinium fat-suppressed hepatic arterial dominant phase (*a*) and hepatic venous phase (*b*) 3D-GE images and T2-weighted pre-superparamagnetic iron oxide (SPIO) (*c*) and post-SPIO (*d*) images demonstrate a lesion in the pancreatic tail in a patient with splenectomy. The pancreatic tail is located in the splenic fossa due to the operation. The lesion shows low signal on postgadolinium T1-weighted images. The differential diagnosis includes pancreatic cancer based on the findings of postgadolinium imaging. However, the lesion shows lower signal after SPIO administration. Therefore, the diagnosis is consistent with intrapancreatic splenule.

formed with T1-weighted sequences. However, it has not been reported that it is more accurate in the diagnosis of liver lesions compared to GBCAs. Additionally, mangafodipir chelate readily dissociates after injection to yield free manganese (Mn) ions [4]. Free Mn is toxic, and therefore it has been considered that the instability of the chelate may lead to toxicity [4]. Chronic exposure to free Mn causes a Parkinsonism-like syndrome due to the accumulation in the brain [4]. Furthermore, the neurological risk increases in patients with chronic liver failure because of the decreased elimination of Mn by the liver [4]. Free Mn ions dissociated from Mn-DPDP have also been reported to cause a depressive action on heart function [4]. Teslascan was FDA approved but has been withdrawn from the market.

COMPLICATIONS OF GBCA ADMINISTRATIONS

Toxicity can generally be categorized as acute, subacute, and chronic, where the time of occurrence of the complication determines this categorization. Acute toxicity generally occurs within 48 hours (often within minutes) and is generally manifest clinically by adverse events that we classify as mild, moderate, and severe. Subacute toxicity generally occurs from 1 week to several months. The major subacute toxicity of GBCAs is the important disease process NSF. It is not known whether there is substantial chronic toxicity of GBCAs, and this may relate to bone deposition.

Acute Toxicity

The acute adverse reactions seen after GBCAs are allergy-like (urticaria, nausea, vomiting, headache, and altered taste sensation). They are uncommon and are usually mild to moderate in severity. Severe reactions, anaphylactoid types, are even more rare (0.001–0.01%), which is a factor of 10 more safe than IBCAs [5]. An increased frequency in adverse reactions has been observed in patients with a history of reactions to either GBCAs or IBCAs, and also a modest increased chance of adverse reactions is observed in patients with a history of allergies, as described with IBCAs. In patients with a history of previous GBCA reaction a different MR contrast agent should be used, and 12–24 hours of premedication with corticosteroids and antihistamines should be considered [5]. This would be most prudent in patients with a prior moderate to severe reaction, because second reactions to GBCAs tend to be more severe than the first [5]. Severe reactions should be treated very carefully and should require the assistance of a resuscitation team.

GBCAs are generally considered to have no nephrotoxicity at approved dosages for MR imaging [5]. However, CIN has been reported to be seen rarely after the administration of GBCAs, and the risk is particularly high with large volumes of GBCAs (100 ml and greater).

Subacute Toxicity

In 1997 Cowper et al. identified a scleromyxedema-like cutaneous disease in renal dialysis patients that they described in an initial series of fifteen patients in 2000 [6]. Subsequent to the observation of this condition in other subjects, this entity became initially described as nephrogenic fibrosing dermopathy [7]. In 2005, Daram et al. reported that this disease was not solely restricted to the skin and that systemic involvement may occur, and they proposed a new description as nephrogenic systemic fibrosis (NSF) [8]. Although the skin findings are similar to systemic sclerosis, NSF spares the face and lacks the serologic markers of systemic sclerosis [9].

In 2006, Dr. Thomas Grobner discovered an association between NSF development and Omniscan [gadodiamide, (GE Healthcare, Amersham, United Kingdom)], which is one of the GBCAs standard agents in contrast-enhanced MRI [10]. In this landmark study, Dr. Grobner found that all of his patients with NSF had been exposed to Omniscan before the development of NSF. Therefore, he proposed a triggering role for gadolinium in NSF development in patients with diminished renal function [10]. To date, several studies have confirmed the proposed role of GBCAs in NSF development [11–14].

Following these reports, the FDA published a box warning that the use of all GBCAs should be avoided in high-risk patients unless the diagnostic information is essential and not available with noncontrast MRI [15]. In Europe, the European Medicine Agency (EMEA) issued a similar warning with two clear distinctions, that only the use of specific GBCAs associated with the development of NSF are contraindicated in high-risk patients and that those specific GBCAs should also be cautiously used in low-risk patients including patients with stage 3 chronic kidney disease [16]. Both agencies have asked the manufacturers to include these warnings on the product labeling of GBCAs [15, 16].

GBCAs have long been considered safe, and preferred over IBCAs in patients with renal impairment [16]. However, the discovery of the association of GBCAs with the development of NSF demonstrates that GBCAs should also be used with caution in all patients, particularly in patients with renal impairment [16]. Because of the widespread use of GBCAs in MRI studies and the common occurrence of renal impairment in the general population, the medical community should therefore be familiar with NSF and the imaging management of patients at high risk for NSF.

NSF

Definition. NSF is a systemic disease characterized by widespread tissue fibrosis [6–8, 17]. To date, it has been exclusively seen in patients with renal impairment [6–8, 17]. The progressive fibrosis results from the deposition of collagen in tissues and initially and predominantly affects the skin [6–8, 17]. Systemic involvement, including the muscles, heart, pericardium, pleura, lungs, diaphragm, esophagus, kidneys, and testes, generally follows after skin involvement [6–8, 17, 18].

Epidemiology. There is no sex, age, or race predilection for the development of NSF [19]. It has been reported that the incidence of NSF varies according to the type of GBCA administered [20, 21]. The incidence of NSF has been reported to be 2–7% in patients with renal impairment following the use of Omniscan, which has been the agent most often reported to be associated with the development of NSF [14, 18]. However, because the determination of the incidence of NSF is largely based on reviews of databases, it is likely that mild cases may be overlooked and some deceased patients may have suffered from undiagnosed NSF. Therefore, it is probable that the incidence of NSF might be higher. Prior studies have observed the occurrence of NSF in patients with renal impairment who had prior unconfounded exposure to Omniscan [14, 18]. "Unconfounded" refers to the fact that the patient received only that agent, whereas "confounded" indicates that the patient received more than one type of agent. In a recent study, the benchmark incidences of NSF were also determined in general patient populations who underwent gadolin-

ium-enhanced MRI studies in four American universities, two each of which used Omniscan and Magnevist [gadopentetate dimeglumine, (Bayer Schering Pharma AG, Germany)]. These benchmark incidences of NSF have been reported to be 1 in 2913 patients for Omniscan and 1 in 44,225 for Magnevist [22]. This study also demonstrated that the incidence of NSF varies depending on the type of GBCA administered, and the risk of developing NSF is higher with the use of Omniscan compared to Magnevist [22].

Pathophysiology and Risk Factors. The pathophysiology of NSF is not completely understood [17, 21]. Diminished renal function and GBCAs are the two crucial factors necessary for the development of NSF [10–20]. Because NSF does not develop in all patients who have diminished renal function and prior GBCA exposure, it has been considered that additional cofactors might be involved in the pathophysiology [11, 14, 17]. Currently, it is considered that circulating fibrocytes play a critical role in the pathophysiology of NSF [23].

DIMINISHED RENAL FUNCTION. It has been shown that NSF develops after the use of standard and high-dose GBCAs in patients with severely decreased renal function [15, 20]. The severity of chronic kidney disease is classified according to the level of glomerular filtration rate (GFR) (Table 20.3) [24]. NSF is seen in patients with acute or chronic kidney disease (renal insufficiency), in whom GFR is less than 30 ml/min/1.73 m^2 [15, 20]. Additionally, NSF is also seen in patients with acute renal insufficiency of any severity due to hepatorenal syndrome or in patients with acute renal insufficiency of any severity in the perioperative liver transplantation period [15, 20].

Patients with GFR above 60 ml/min/1.73 m^2 have not been reported to develop NSF [20]. More than 95% of NSF patients have stage 4 and 5 chronic kidney disease, with the great majority of these having stage 5 chronic renal disease [15, 17]. The incidence of NSF in patients with stage 5 chronic kidney disease has been reported as 18% after the exposure of Omniscan in a recent study [25]. Whether NSF may occur in patients with stage 3 chronic kidney disease remains conjectural [20]. Diminished renal function has the effect of decreasing renal excretion of gadolinium, which results in an increased half-life in the body [14, 26]. The half-life of GBCAs in the body is about 90 minutes in healthy individuals with normal renal function, whereas the half-life of GBCAs in patients with diminished renal function is 50 hours or more depending on the severity of renal dysfunction [14, 26]. Because GBCAs can cross the placenta, enter the fetal circulation, and stay in the amniotic fluid for a long time, the half-life of gadolinium is longer in pregnant patients and in embryos or fetuses [20, 27]. The half-life of gadolinium is also longer in patients with fluid in third spaces such as seen in diffuse edema or ascites, as gadolinium shows delayed elimination in third space accumulation [28]. The half-life of gadolinium is likely longer in children under the age of 1 as well, because of their immature renal function [20]. The increased half-life of gadolinium in these settings increases the likelihood of gadolinium-chelate dissociation, with the resultant release of free gadolinium and its ligand, to trigger the processes leading to the development of NSF [14, 17, 21]. Additionally, the lever of renal dysfunction is correlated with the risk of developing NSF, and the severity of NSF, that is, the worse or more immature the renal function, the higher the risk and severity of NSF [15, 20, 29].

To summarize the categorization of risk, the highest-risk patients for NSF are defined as patients with stage 4 and 5 chronic renal disease, patients on dialysis, patients with acute renal failure, patients with hepatorenal syndrome, and patients in the perioperative liver transplantation period [20, 30]. Low-risk patients for NSF are defined as patients with stage 3 chronic renal disease, children under age of 1, and pregnant patients [20].

Table 20.3 Stages of Renal Diseases

Stage	Description	GFR* (ml/min/1.73 m^2)
1	Kidney damage with normal or increased GFR	≥90
2	Kidney damage with mildly decreased GFR	60–89
3	Moderately decreased GFR	30–59
4	Severely decreased GFR	15–29
5	Kidney failure	<15 (or dialysis)

Note: Chronic kidney disease is defined as either kidney damage or GFR lower than 60 ml/min/1.73 m^2 for more than 3 months.
*Glomerular filtration rate.

PHARMACOKINETICS OF GBCAS. Free gadolinium ion is toxic [31]. To ameliorate the toxicity of gadolinium, gadolinium ion is bound to a ligand to form a chelate [31]. However, gadolinium-chelate complexes dissociate to varying extents in solution based in the type of agent, both in vivo and in vitro [31]. Therefore; gadolinium-chelate complexes, free gadolinium ions, and free ligands exist as the components of an equilibrium reaction in solution [31]. Similarly, gadolinium-chelate complexes, free gadolinium ions, and free ligands exist in human tissues after administration of GBCAs [31].

Free gadolinium ion is an analog of zinc, calcium, iron, and copper, and the ions of these latter metals, found normally in the human body, compete with gadolinium ions in order to make bonds with the ligands via

transmetallation reactions [31, 32]. At this point it is uncertain to what extent transmetallation is active (i.e., zinc actively displacing gadolinium from the chelate) versus passive (i.e., zinc combining with the ligand from a gadolinium-chelate complex that has spontaneously disassociated). Transmetallation may increase the amount of free gadolinium ions in human tissues, which is made more likely when the half-life of gadolinium is increased because of diminished renal function [31, 32]. Free gadolinium is known to be deposited in human bone tissue in trace amounts in healthy individuals with normal renal function [33]. Recent studies have also identified the deposition of gadolinium in the skin of NSF patients but not in the skin of healthy individuals with normal renal function [34, 35]. These recent findings also emphasize that the deposition of free gadolinium in human tissues increases with decreasing renal function [34, 35].

The dissociation of gadolinium ions from gadolinium-chelate complexes varies for different types of GBCAs and can be defined by the thermodynamic stability constant and the dissociation constant [21, 31]. The thermodynamic stability constant determines the concentration at which gadolinium ions will dissociate from gadolinium-chelate complexes [21, 31]. The rate of this dissociation reaction is dependent on the dissociation constant [21]. Taken together, these two constants define the affinity of ligands for gadolinium ions at the physiological pH [21, 31]. Each GBCA has a different thermodynamic stability constant and dissociation rate (Table 20.1) [21, 31]. Because the specific type of GBCAs with lower thermodynamic stability and higher dissociation constants are more commonly associated with the development of NSF, the dissociation of gadolinium ion from gadolinium-chelate complexes has been considered as the trigger in NSF development [10, 17, 21]. GBCAs with higher thermodynamic stability constant and lower dissociation rate have an extremely low or nonexistent likelihood of NSF development [21]. Another factor associated with the risk of NSF development and the severity of the disease is the increased total volume of GBCA administered either as single or cumulative dose [14, 36].

GBCAs are classified into two types according to the backbone structure of their amine group, linear or macrocyclic [16, 21]. Linear and macrocyclic GBCAs may be further subclassified according to their charges as ionic or nonionic [16]. In contrast to the linear GBCAs, macrocyclic GBCAs create tighter bonds with gadolinium, as the structure resembles a cage, and therefore have higher thermodynamic stability constants and lower dissociation rates [16, 21]. This supports the observation that macrocyclic agents have a much lesser or near nonexistent association with the development of NSF compared to linear GBCAs [14, 21]. It has also been postulated that electrostatic charges present in ionic GBCAs cause tighter bonding than nonionic GBCAs, and therefore ionic GBCAs are more stable than nonionic GBCAs [37]. This may also be reflected in the lower incidence of NSF with ionic linear GBCAs (Magnevist) than nonionic linear GBCAs [Omniscan, Optimark (gadoversetamide, Mallinckrodt, St. Louis, MO)] [20, 22]. Our current belief is that agents that also exhibit hepatocyte elimination (MultiHance, Eovist) have an additional protective feature of a route of elimination when renal function is poor.

It is difficult or sometimes impossible to identify the specific GBCA associated with the development of NSF in each patient because of two reasons: 1) verifiable records of specific GBCAs administered to each patient usually have not been kept, (largely because these agents had all previously been considered so safe) and 2) more than one type of GBCA might have been administered to the patients with NSF. According to the current literature and NSF databases, the most common types of GBCAs associated with the development of NSF are as follows in decreasing order: 1) Omniscan 2), Optimark, and 3) Magnevist [15, 20]. All three of these gadolinium agents have linear amine structure [21]. Omniscan, which has one of the lowest thermodynamic stability constants and the highest dissociation rates, shows the highest degree of association with NSF development among these three GBCAs [15, 20, 21]. Moreover, marketed solutions of both Omniscan and Optimark include substantial amounts of the free chelating agent, 5% and 10%, respectively [9, 38, 39]. It is likely that free chelating agent has been added to these formulations in order to sequester free gadolinium when it is released by these slightly less stable chelates [9, 38]. It may be that the higher percentage of free chelate in Optimark may explain the lower association with NSF compared to Omniscan. Market solutions of the other GBCAs either contain no or only a very low amount of excess chelate [9]. The unconfounded associations of GBCAs with NSF development, other than the three mentioned above, have not been definitely confirmed [15, 20].

COFACTORS. Because NSF does not develop in all patients with renal impairment who have undergone GBCA exposure, it has been suggested that additional cofactors might be involved in the pathophysiology of NSF [11, 14, 17, 31, 36, 40]. Proinflammatory events present at the time of GBCA exposure, or that may develop after GGCA exposure, have been suggested to increase the risk of developing NSF [11, 14, 17, 36, 40]. Proinflammatory events include thromboembolic events; surgical interventions, particularly vascular surgical interventions and liver transplantations; systemic infections; and diseases associated with hypercoagulability [11, 14, 17]. Metabolic acidosis and high levels of eryth-

ropoietin have also been reported to be associated with NSF development [11, 14, 17, 36]. Furthermore, high levels of calcium, iron, zinc, copper, and phosphate ions have been suggested to increase the risk of NSF development, since these ions have affinity for complexing with the chelating ligand and displacing gadolinium ions [31, 40] or binding released gadolinium (phosphate). However, the necessity of cofactor presence for the development of NSF has not been definitely confirmed [40, 41].

CIRCULATING FIBROCYTE HYPOTHESIS. According to this hypothesis, free gadolinium can stimulate the migration of circulating fibrocytes, which are normally involved in wound healing, to the tissues (particularly to the dermis) by mechanisms that are not well understood [23, 42]. Consequently, the stimulated and migrated fibrocytes are considered to play a critical role in the development of fibrosis in tissues [23, 42]. It has been proposed that free gadolinium activates fibrocytes by means of transglutaminases and cytokines [42]. Further research is needed to confirm this hypothesis.

Clinical Findings. The symptoms and signs of NSF usually present in 2–3 months after the administration of GBCAs in the majority of patients [20]. However, presentation may arise within several days to years after the exposure of GBCAs [14, 22].

In general, NSF initially affects the skin of the extremities, especially the lower extremities, and may progressively involve the body [5–8, 20]. Initial symptoms and findings include pain, burning sensation, itching, swelling, and erythema [5–8, 20]. Skin thickening and hardening, red and brown plaques in the skin, and yellow spots in the sclera develop later [5–8, 20]. With the progression of NSF, joint stiffness and contractures as well as cachexia and fibrosis in the internal organs and muscles develop [17, 20]. Facial skin is characteristically spared to some extent [9].

Diagnosis. NSF is diagnosed with clinical findings, deep skin biopsy, and histopathology [14, 16, 20, 22]. The detection of gadolinium and fibroblasts producing procollagen and expressing CD-34 in the skin is helpful in the histopathological diagnosis [34, 43].

Treatment and Prognosis. There is no known effective treatment method for NSF [17, 44]. The correction of renal impairment with treatment or renal transplantation may either stop the progression of the disease or reverse the signs and symptoms [17, 44]. The role of dialysis has not yet been fully established in the treatment of NSF [17, 44]. The usefulness of hemodialysis in the prevention of NSF has not been shown definitely; however, in recent studies it has been reported that hemodialysis may protect against NSF at-risk patients [20, 30], and may also lessen the severity of disease. Currently, there is no medication with a proven efficacy for the treatment of NSF, although it has been reported that extracorporeal photopheresis and imatinib mesylate improved the clinical findings in some patients [17, 20, 44, 45, 46].

The rate of progression of NSF is variable and may range from slow to rapid [17]. The disease rarely remits spontaneously [17]. Fulminant progression of disease is seen in approximately 5% of patients, and may result in death in a short time period [17]. The mortality of NSF has been reported as 30%, although limited data are available [11]. There is increased mortality related to hemodialysis alone [12], which renders the specific mortality of NSF difficult to ascertain as most patients are on hemodialysis. The most common causes of NSF-related mortality include complications that develop secondary to restricted joint movement and respiratory insufficiency developing secondary to the involvement of respiratory muscles [17, 47].

Recommended Guidelines to Minimize the Risk of NSF

1. Pros and cons of the use of GBCAs should be assessed very carefully for high-risk patients before GBCA administration [15]. Noncontrast techniques including US, CT, or MRI should be used for the examination whenever the patient's medical problem can be evaluated safely and diagnostically with these techniques [15]. It should be remembered that even noncontrast CT carries with it the risk of radiation-induced malignancy; therefore, noncontrast ultrasound and MRI are generally the safest alternatives.
2. Omniscan, Magnevist, and Optimark should not be administered to patients with acute renal diseases, or chronic renal diseases of all stages, patients with hepatorenal syndrome, patients that are in the perioperative liver transplantation period, and children under age of 1 [15, 20].
3. When GBCA administration is considered diagnostically important for the evaluation of high-risk patients, GBCAs that do not have proven associations with NSF development should be used [20]. Macrocyclic GBCAs, because of their relatively stable structure or linear GBCAs with biliary elimination (MultiHance and Eovist), may be preferred in these high-risk patients [20].
4. The minimum dose of GBCA that generates a diagnostic MR examination should be administered to patients at high risk [20]. MultiHance and Eovist can be administered at lower doses than the standard doses of other GBCAs because of their high T1 relaxivity, and are therefore advantageous [48–51].

MultiHance and Eovist may be administered at 0.05 mmol/kg (half-dose of standard dose of gadobenate dimeglumine) and at 0.025 mmol/kg (standard dose of Eovist) to high-risk patients, respectively [49, 51]. There are insufficient data about the use of Eovist in subjects under age 18 [51]. An additional feature that causes these agents to possess low risk for NSF is that they have dual elimination by the kidneys and the biliary system [14].

5. GBCAs should not be administered in the first and second trimesters of pregnancy unless maternal survival may depend upon it [27]. The use of GBCAs is controversial in the third trimester of pregnancy and should be employed sparingly [27]. The pros and cons of GBCA administration to these patients should also be assessed very carefully; the most stable GBCAs should be administered at the lowest possible doses, if maternal well-being depends upon it [20, 27].
6. For traditional high-dose gadolinium procedures, such as MRA, GBCAs with high T1 relaxivity (e.g., MultiHance) should be used at doses as low as reasonable [20, 50].
7. a) All patients who are candidates for GBCA administration may theoretically be assessed for serum creatinine levels or estimated GFR (eGFR), which reflect renal function [27]. However, the calculation of eGFR may not be reasonable, necessary, or feasible in every patient [20, 27]. Therefore it has been reported that the determination of eGFR is not necessarily required when GBCAs other than Omniscan, Optimark, or Magnevist are used [20]. b) Kidney function diminishes with increasing age [52]. GFR below 60 ml/min/1.73 m^2 is observed in 11% of the population older than 60 years of age, and this circumstance may not be recognized in many patients [52]. As a result, patients should be questioned about their medical history, especially for renal diseases including solitary kidney, renal transplantation, renal tumors, and renal surgery; hypertension; and diabetes before MR examination [28]. Serum creatinine or eGFR values should be determined in these patients or perhaps also in patients over 60 years of age [28]. Whenever there is no information available on the renal function of patients who have a medical history of hypertension and diabetes, GBCAs with high T1 relaxivity should be administered at low doses.
8. There is no evidence about when a repeat GBCA-enhanced study should be performed in at-risk patients. It may be prudent to wait at least 48 hours between consecutive GBCA-enhanced examinations for patients who are not at risk to low risk, and at least one week, or perhaps longer, for patients who are at risk [20, 53].
9. Hemodialysis is effective at lowering the serum concentrations of GBCAs; however, hemodialysis is unlikely to be effective at eliminating GBCAs or deposited gadolinium in tissue [53–55]. It has been suggested that because there is a strong dose-response relationship between GBCAs and NSF development, GBCAs should be eliminated from the body as completely and quickly as possible before transmetallation and deposition of gadolinium in tissues occur, which is likely the triggering process for the development of NSF [53–55]. Therefore, since there is no consistent effective treatment for NSF, immediate hemodialysis after the administration of GBCAs, as a potential preventive approach, should be recommended for patients who are already on hemodialysis and receive GBCAs [53–55]. No patient should receive hemodialysis who is not already on hemodialysis, if the indication for dialysis is the MR study alone, because the mortality and morbidity of hemodialysis is higher than the risk of developing NSF following the exposure to stable GBCAs [20, 53–55]. Ongoing research suggests two sessions of hemodialysis spaced closely together (e.g., within 24 hours) may be important, as the first session may remove free chelate, which could also rebind with free gadolinium.
10. GBCAs should not be used in high dose as a substitute for iodinated contrast media on CT, on angiography, or on other X-ray procedures [20].
11. GBCAs should not be administered to patients who already have NSF [17].

Probabilistic Risk Assessment of NSF vs. CIN

CIN. Contrast induced nephropathy (CIN) is defined as iatrogenic renal function impairment following exposure to contrast media (CM), especially IBCAs, but also high-dose GBCAs [56–58]. CIN occurs more commonly subsequent to the administration of IBCAs compared to GBCAs, which may largely reflect a dose-related phenomenon [59–61]. CIN resulting from exposure to IBCAs is the third most common cause of acute renal failure in hospitalized patients, after impaired renal perfusion and the use of nephrotoxic drugs [56–59, 62].

The diagnosis of CIN includes three components: 1) an acute deterioration of renal function, 2) a temporal relationship with the parenteral administration of CM, and 3) the exclusion of alternative etiologic causes that may result in the acute deterioration of renal function [56–58]. The acute deterioration of renal function is described as a relative increase of 25% or more, or an absolute increase of 0.5 mg/dl or more from baseline in serum creatinine value [56–58]. The acute deterioration of renal function in CIN develops after the

first 24 hours in 80% of patients and within 48–72 hours in 20% of patients [56]. Recently, caution has been suggested in the interpretation of an elevation of serum creatinine values, as fluctuations may occur in the normal state of the patient independent of CM use [63].

The pathophysiology of CIN remains uncertain [64, 65]. The proposed mechanisms include toxic injury to renal tubules, ischemic injury, or decreased renal medullary perfusion [64, 65]. It has also been reported that different osmolality and viscosity of iodinated CM is also involved in the pathophysiology, with higher viscosity having a greater likelihood of causing this condition [66]. As the GFR decreases, the risk of CIN increases; and the risk particularly increases when the GFR is below 60 ml/min/1.73 m^2 [18, 56].

The incidence of CIN varies according to the type of IBCAs, stratified based on whether the IBCA is of high-, low- or iso-osmolality [66]. The incidence of CIN is two times higher with the use of high-osmolality IBCA (HOCM) compared to that of low-osmolality IBCA (LOCM) [59]. HOCM has been widely replaced with LOCM because of their higher nephrotoxicity and higher risk of adverse reactions [59].

The incidence of CIN following the intra-arterial or intravenous use of LOCM has been reported to vary between 0.6 and 2.3% in patients with normal renal function [56]. In patients with decreased renal function, the incidence of CIN following the intra-arterial and intravenous use of LOCM has been reported to vary between 3% and 50% and between 1% and 21%; respectively [59, 67]. The intra-arterial administration of LOCM has been reported to have a two times higher incidence of CIN compared to intravenous administration [67], which may in part reflect that administration is not as tightly controlled, and may be much higher than intravenous administration.

The incidences of CIN following the use of iso-osmolality CM (IOCM) and LOCM are similar in patients with normal renal function [59, 67]. Although the incidence of CIN with IOCM has been reported to be lower in patients with decreased renal function compared to LOCM in a few studies, other studies have shown the opposite effect, apparently in part influenced by the sponsor of the study. There is no definite evidence that IOCM are safer in patients with decreased renal function compared to LOCM [67, 68].

CIN is by definition an acute event, but the critical aspect of this condition is the long-term consequences and residual renal impairment. Residual renal impairment may be seen in 30% of patients with CIN [62]. CIN that requires dialysis is observed in 3% of patients who had underlying renal impairment [62]. Hospital mortality rate has been reported to be between 7% and 34% for in-patients with CIN, 15% for patients with underlying renal impairment alone, and 36% for patients requiring dialysis [62, 69]. One-year mortality rate has been reported to be 38% for patients with renal impairment and 45% for patients with renal impairment requiring dialysis [62]. These numbers are comparable to the mortality rates of NSF.

GBCA-induced CIN may also occur, as gadolinium is also a nephrotoxic agent [61]. However, the much lower incidence of CIN following exposure to GBCAs reflects that gadolinium is less nephrotoxic at MRI doses compared to IBCAs at the doses used for these agents, which are commonly 8–10 times the CM dose [59–61]. Therefore, GBCAs should not be used in large volumes (doses) intravenously for CIN reasons, in addition to the above-mentioned NSF reasons.

NSF vs. CIN. NSF is a disease process with high morbidity and probably mortality [11, 15, 17]. The risk of developing NSF is high in patients with stage 4 and 5 chronic renal disease and in patients with acute renal insufficiency, although most studies show that the great majority of patients have stage 5 disease and/or are on hemodialysis [15, 25]. Although the risk of developing NSF is unknown in patients with stage 3 chronic renal disease, it has been presumed that the risk is definitely much lower compared to stages 4 and 5 [20]. Additionally, NSF has not been reported in patients with GFR above 60 ml/min/1.73 m^2 [20]. More importantly, NSF develops after exposure to specific types of GBCAs including Omniscan, Optimark, and Magnevist [15, 20]. Other GBCAs have not been definitely associated with the development of NSF [20].

CIN also has a high morbidity and mortality [62]. The incidence of CIN is much higher than NSF [1, 14, 18, 56, 59]. CIN also is seen in patients of all renal functional levels, including patients with normal renal function, after exposure to IBCAs [56, 59, 70]. Importantly, the risk of developing CIN is also substantial in patients with stage 2 and 3 chronic renal diseases, and in patients with acute renal insufficiency [1, 18, 28, 56]. The risk of CIN increases as the GFR decreases [18, 56]. CIN develops after all types of IBCAs [52, 59]. Furthermore, it is recognized that further deterioration of renal function, even in patients on hemodialysis, by CIN worsens the patient's prognosis [62, 69].

In patients with acute renal failure, IBCAs should not be used, in order to preserve recoverable renal function [28]. However, the risk of NSF is also high in this patient group [28]. Therefore, if CM administration is necessary, the lowest doses of macrocyclic GBCAs, or linear GBCAs with high T1 relaxivity, should be used in these individuals [28].

The risk of CIN following the administration of IBCAs is much higher in patients with stage 2 and 3 chronic kidney disease, compared to the risk of NSF

following the administration of macrocyclic GBCAs, or linear GBCAs with high T1 relaxivity, which may in fact be nonexistent [1, 28, 71, 72]. The risk of CIN is higher in patients with stage 4 and 5 chronic kidney diseases, who have residual renal function and are not regularly on dialysis, compared to the risk of NSF following the administration of macrocyclic GBCAs, or linear GBCAs with high T1 relaxivity [28].

Thus both GBCAs and iodinated CM should be used cautiously in all patients, particularly in patients with renal impairment. Risk-benefit analysis should be performed before the administration of all CM, and the best combination of safety and diagnostic accuracy should be sought. Concern about NSF or CIN should not prevent the use of contrast agents in MRI or CT when they are deemed essential. The risk of NSF may be minimized or avoided with the use of GBCAs that are not associated with the development of NSF. The risk of CIN may also be reduced with the use of appropriate management techniques.

Our most recent multi-institutional study has shown that with a combination of a restrictive gadolinium policy and use of a more stable GBCA, the incidence of NSF, even if these studies are performed in patients with class V renal failure, may approach 0 [73].

Chronic Toxicity

It is not known whether or not there is chronic toxicity of GBCAs. There is no identified disease process related to chronic toxicity of GBCAs. Processes such as bone deposition of GBCA would fit into this category. At present, the importance of this is unknown. Liver deposition is also known to occur, and the importance of this is also unknown at present.

BREAST FEEDING AND GBCAs

The literature on the excretion into breast milk of GBCAs and the gastrointestinal absorption of these agents from breast milk is very limited. A review of the literature, however, reveals important facts: 1) less than 1% of the administered maternal dose of contrast agent is excreted into breast milk; and 2) less than 1% of the contrast medium in breast milk ingested by an infant is absorbed from the gastrointestinal tract. Therefore, the expected dose of contrast medium absorbed by an infant from ingested breast milk is extremely low [5]. Although there is consensus that a breast-feeding mother should consider using a pump to remove breast milk before contrast agent administration and then afterward she should use the pump and discard breast milk for 24 hours before resuming normal breast-feeding, this should be considered optional rather than mandatory. Since the biologic half-life of contrast agents is less than 120 minutes, the amount remaining in the mother (assuming her renal function is normal) after 24 hours is essentially undetectable [74].

REFERENCES

1. Martin DR, Semelka RC, Chapman A, Peters H, Finn JP, Thomsen, H. Nephrogenic systemic fibrosis versus contrast induced nephropathy: Risks and benefits of contrast enhanced MR and CT in renally impaired patients. *JMRI* 2009 (in press).
2. Goncalves Neto JA, Altun E, Vaidean G, Elazzazi M, Troy J, Ramachandran S, Semelka RC. Early contrast enhancement of the liver: exact description of subphases using MRI. *Magn Reson Imaging* 27:792–800, 2009.
3. Sharma P, De Becker J, Beck GM, Friel HM, Burrow B, Martin D. Arterial-phase bolus-track liver examination (ABLE): Optimization of liver arterial phase gadolinium enhanced MRI using centric re-ordered 3D gradient echo and bolus track real-time imaging. *Proc Intl Soc Mag Reson Med* 14: 3318, 2006.
4. Kirchin MA, Runge VM. Contrast agents for magnetic resonance imaging: safety update. *TMRI* 14: 426–435, 2003.
5. American College of Radiology Committee on Drugs and Contrast Media. *Manual on Contrast Media.* 5th ed. Reston, VA: American College of Radiology, 2004.
6. Cowper SE, Robin HS, Steinberg SM, Su LD, Gupta S, LeBoit PE. Scleromyxoedema-like cutaneous diseases in renal-dialysis patients. *Lancet* 356: 1000–1001, 2000.
7. Cowper SE, Su LD, Bhawan J, Robin HS, LeBoit PE. Nephrogenic fibrosing dermopathy. *Am J Dermatopathol* 23: 383–393, 2 001.
8. Daram SR, Cortese CM, Bastani B. Nephrogenic fibrosing dermopathy/nephrogenic systemic fibrosis: report of a new case with literature review. *Am J Kidney Dis* 46: 754–759, 2005.
9. Broome DR, Girguis MS, Baron PW, Cottrell AC, Kjellin I, Kirk AG. Gadodiamide-associated nephrogenic systemic fibrosis: why radiologists should be concerned. *AJR Am J Roentgenol* 188: 586–592, 2007.
10. Grobner T. Gadolinium—a specific trigger for the development of nephrogenic fibrosing dermopathy and nephrogenic systemic fibrosis. *Nephrol Dial Transplant* 21: 1104–1108, 2006.
11. Sadowski EA, Bennett LK, Chan RM et al. Nephrogenic systemic fibrosis: risk factors and incidence estimation. *Radiology* 243: 148–157, 2007.
12. Collidge TA, Thomson PC, Mark PB et al. Gadolinium-enhanced MR imaging and nephrogenic systemic fibrosis: retrospective study of a renal replacement therapy cohort. *Radiology* 245: 168–175, 2007.
13. Shabana WM, Cohan RH, Ellis JH et al. Nephrogenic systemic fibrosis: a report of 29 cases. *AJR Am J Roentgenol* 190: 736–741, 2008.
14. Lauenstein TC, Salman K, Morreira R et al. Nephrogenic systemic fibrosis: center case review. *J Magn Reson Imaging* 26: 1190–1197, 2007.
15. Public health advisory: gadolinium-containing contrast agents for magnetic resonance imaging (MRI). Omniscan, OptiMARK, Magnevist, ProHance, and MultiHance. U.S. Food and Drug Administration. "http://www.fda.gov/cder/drug/advisory/gadolinium_agents.htm" \t "1" www.fda.gov/cder/drug/advisory/gadolinium_agents.htm. Published June 8, 2006. Updated May 23, 2007. Accessed July 12, 2008.
16. Thomsen HS. Nephrogenic systemic fibrosis. *Imaging Decisions MRI* 11: 13–18, 2008.

17. Kuo PH, Kanal E, Abu-Alfa AK, Cowper SE. Gadolinium-based MR contrast agents and nephrogenic systemic fibrosis. *Radiology* 242: 647–649, 2007.
18. Thomsen HS. Enhanced computed tomography or magnetic resonance imaging: a choice between contrast medium-induced nephropathy and nephrogenic systemic fibrosis. *Acta Radiol* 48: 593–596, 2007.
19. Galan E, Cowper SE, Bucala R. Nephrogenic systemic fibrosis (nephrogenic fibrosing dermopathy). *Curr Opin Rheumatol* 18: 614–617, 2006.
20. Thomsen HS. ESUR Guideline: gadolinium-based contrast media and nephrogenic systemic fibrosis. *Eur Radiol* 17: 2692–2696, 2007.
21. Rofsky NM, Sherry DA, Lenkinski LE. Nephrogenic systemic fibrosis: a chemical perspective. *Radiology* 247: 608–612, 2008.
22. Wertman R, Altun E, Martin DR et al. Risk of nephrogenic systemic fibrosis: evaluation of gadolinium chelate contrast agents by four American universities. *Radiology* 248: 799–806, 2008.
23. Bucala R. Circulating fibrocytes: cellular basis for NSF. *J Am Coll Radiol* 5: 36–39, 2008.
24. National Kidney Foundation. K/DOQI clinical practice guidelines for chronic kidney disease: evaluation, classification, and stratification. *Am J Kidney Dis* 39: S46–S75, 2002.
25. Rydahl C, Thomsen HS, Marckmann P. High prevalence of nephrogenic systemic fibrosis in chronic renal failure patients exposed to gadodiamide, a gadolinium-containing magnetic resonance contrast agent. *Invest Radiol* 43: 141–144, 2008.
26. Joffe P, Thomsen HS, Meusel M. Pharmacokinetics of gadodiamide injection in patients with severe renal insufficiency and patients undergoing hemodialysis or continuous ambulatory peritoneal dialysis. *Acad Radiol* 5: 491–502, 1998.
27. Kanal E, Barkovich JA, Bell C et al. ACR Guidance document for safe MR practices: 2007. *AJR Am J Roentgenol* 188: 1–27, 2007.
28. American College of Radiology. Nephrogenic systemic fibrosis. In *Manual on Contrast Media Version 6*. 2008; p. 53–57.
29. Marckmann P. Nephrogenic systemic fibrosis: epidemiology update. *Curr Opin Nephrol Hypertens* 17: 315–319, 2008.
30. Prince MR, Zhang H, Morris M et al. Incidence of nephrogenic systemic fibrosis at two large medical centers. *Radiology* 248: 807–816, 2008.
31. Lin S-P, Brown JJ. MR contrast agents: physical and pharmacologic basics. *J Magn Reson Imaging* 25: 884–899, 2007.
32. Idee J-M, Port M, Raynal I, Schaefer M, Le Greneur S, Corot C. Clinical and biological consequences of transmetallation induced by contrast agents for magnetic resonance imaging: a review. *Fundam Clin Pharmacol* 20: 563–576, 2006.
33. Gibby WA, Gibby KA, Gibby WA. Comparison of Gd DTPA-BMA (Omniscan) versus Gd HP-DO3A (ProHance) retention in human bone tissue by inductively coupled plasma atomic emission spectroscopy. *Invest Radiol* 39: 138–142, 2004.
34. High WA, Ayers RA, Chandler J, Zito G, Cowper SE. Gadolinium is detectable within the tissue of patients with nephrogenic systemic fibrosis. *J Am Acad Dermatol* 56: 21–26, 2007.
35. High WA, Ayers RA, Cowper SE. Gadolinium is quantifiable within the tissue of patients with nephrogenic systemic fibrosis. *J Am Acad Dermatol* 56: 710–712, 2007.
36. Marckmann P, Skov L, Rossen K, Heaf JG, Thomsen HS. Case-control study of gadodiamide-related nephrogenic systemic fibrosis. *Nephrol Dial Transplant* 22: 3174–3178, 2007.
37. Morcos SK. Extracellular gadolinium contrast agents: differences in stability *Eur J Radiol* 66: 175–179, 2008.
38. Thomsen HS. Nephrogenic systemic fibrosis: a serious late adverse reaction to gadodiamide. *Eur Radiol* 16: 2619–2621, 2006.
39. Colletti PM. Nephrogenic systemic fibrosis and gadolinium: a perfect storm. *AJR Am J Roentgenol* 191: 1–4, 2008.
40. Grobner T, Prischl FC. Patient characteristics and risk factors for nephrogenic systemic fibrosis for gadolinium exposure. *Semin Dial* 21: 135–139, 2008.
41. Thomsen HS. Nephrogenic systemic fibrosis: a serious late adverse reaction to gadodiamide. *Eur Radiol* 16: 2619–2621, 2006.
42. Parsons AC, Yosipovitch G, Sheehan DJ, Sangueza OP, Greenberg CS, Sane DC. Transglutaminases: the missing link in nephrogenic systemic fibrosis. *Am J Dermatopathol* 29: 433–436, 2007.
43. Thakral C, Abraham JL. Gadolinium-induced nephrogenic systemic fibrosis is associated with insoluble Gd deposits in tissues: in vivo transmetallation confirmed by microanalysis. *J Cutan Pathol* Epub July 7, 2009.
44. Nainani N, Panesar M. Nephrogenic systemic fibrosis. *Am J Nephrol* 29: 1–9, 2008.
45. Mathur K, Morris S, Deighan C, Green R, Douglas KW. Extracorporeal photopheresis improves nephrogenic fibrosing dermopathy/nephrogenic systemic fibrosis: three case reports and review of literature. *J Clin Apher* 23: 144–150, 2008.
46. Kay J, High WA. Imatinib mesylate treatment of nephrogenic systemic fibrosis. *Arthritis Rheum* 58: 2543–2548, 2008.
47. Evenepoel P, Zeegers M, Segaert S, Claes K et al. Nephrogenic fibrosing dermopathy: a novel, disabling disorder in patients with renal failure. *Nephrol Dial Transplant* 19: 469–473, 2004.
48. Prokop M, Schneider G, Vanzulli A et al. Contrast-enhanced MR angiography of the renal arteries: blinded multicenter crossover comparison of gadobenate dimeglumine and gadopentate dimeglumine. *Radiology* 234: 399–408, 2005.
49. Schneider G, Maas R, Schultze Kool L et al. Low-dose gadobenate dimeglumine versus standard dose gadopentate dimeglumine for contrast-enhanced magnetic resonance imaging of the liver: an intra-individual crossover comparison. *Invest Radiol* 38: 85–94, 2003.
50. Volk M, Strotzer M, Lenhart M et al. Renal time-resolved MR angiography: quantitative comparison of gadobenate dimeglumine and gadopentate dimeglumine with different doses. *Radiology* 220: 484–488, 2001.
51. Huppertz A, Balzer T, Blakeborough A et al. Improved detection of focal liver lesions at MR imaging: multicenter comparison of gadoxetic acid—enhanced MR images with intraoperative findings. *Radiology* 230: 266–275, 2004.
52. Coresh J, Astor BC, Greene T, Eknoyan G, Levey AS. Prevalence of chronic kidney disease and decreased kidney function in the adult US population: Third National Health and Nutrition Examination Survey. *Am J Kidney Dis* 41: 1–12, 2003.
53. Shellock FG, Spinazzi A. MRI safety update 2008: Part 1, MRI contrast agents and nephrogenic systemic fibrosis. *AJR Am J Roentgenol* 191: 1–11, 2008.
54. Saab G, Abu-Alfa A. Will dialysis prevent the development of nephrogenic systemic fibrosis after gadolinium-based contrast administration? *AJR Am J Roentgenol* 189: W169, 2007.
55. Broome DR, Cottrell AC, Kanal E. Response to "Will dialysis prevent the development of nephrogenic systemic fibrosis after gadolinium-based contrast administration?" *AJR Am J Roentgenol* 189: W234–W235, 2007.
56. Mehran R, Nikolsky E. Contrast-induced nephropathy: definition, epidemiology, and patients at risk. *Kidney Int* 69: S11–S15, 2006.
57. Gleeson TG, Bulugahapatiya S. Contrast-induced nephropathy. *AJR Am J Roentgenol* 183: 1673–1689, 2004.
58. Murphy SW, Barrett BJ, Parfrey PS. Contrast nephropathy. *J Am Soc Nephrol* 11: 177–182, 2000.
59. Solomon R, Biguori C, Bettmann M. Selection of contrast media. *Kidney Int* 69: S39–S45, 2006.
60. Tombach B, Bremer C, Reimer P et al. Using highly concentrated gadobutrol as an MR contrast agent in patients also requiring hemodialysis: safety and dialysability. *AJR Am J Roentgenol* 178: 105–109, 2002.

61. Ergun I, Keven K, Uruc I et al. The safety of gadolinium in patients with stage 3 and 4 renal failure. *Nephrol Dial Transplant* 21: 697–700, 2006.
62. McCullough P, Adam A, Becker CR et al. Epidemiology and prognostic implications of contrast-induced nephropathy. *Am J Cardiol* 98: 5K–13K, 2006.
63. Bruce RJ, Djamali A, Shinki K, Michel SJ, Fine JP, Pozniak MA. Background fluctuation of kidney function versus contrast-induced nephrotoxicity. *AJR Am J Roentgenol* 192: 711–718, 2009.
64. Perrson PB, Tepel M. Contrast medium-induced nephropathy: the pathophysiology. *Kidney Int* 69: S8–S10, 2006.
65. Persson PB, Hansell P, Liss P. Pathophysiology of contrast medium-induced nephropathy. *Kidney Int* 68: 14–22, 2005.
66. Katzberg RW, Haller C. Contrast-induced nephrotoxicity: clinical landscape. *Kidney Int* 69: S3–S7, 2006.
67. Katzberg RW, Barrett BJ. Risk of iodinated contrast material-induced nephropathy with intravenous administration. *Radiology* 243: 622–628, 2007.
68. Thomsen HS, Morcos SK, Erley C et al. The ACTIVE trial: comparison of the effects on renal function of iomeprol-400 and iodixanol-320 in patients with chronic kidney disease undergoing abdominal computed tomography. *Invest Radiol* 43: 170–178, 2008.
69. Levy EM, Viscoli CM, Horwitz RI. The effect of acute renal failure on mortality. A cohort analysis. *JAMA* 275: 1489–1494, 1996.
70. Cheruvu B, Henning K, Mulligan J et al. Iodixanol: risk of subsequent contrast nephropathy in cancer patients with underlying renal insufficiency undergoing diagnostic computed tomography examinations. *J Comput Assist Tomogr* 31: 493–498, 2007.
71. Altun E, Martin DR, Wertman R, Lugo-Somolinos A, Fuller ER 3rd, Semelka RC. Nephrogenic systemic fibrosis: change in incidence following a switch in gadolinium agents and adoption of a gadolinium policy–report from two U.S. universities. *Radiology* 2009; Sep 29. [Epub ahead of print.]
72. Halvorsen RA. Which study when? Iodinated contrast-enhanced CT versus gadolinium-enhanced MR imaging. *Radiology* 249: 9–15, 2008.
73. Altun E, Martin DR, Wertman R, Lugo-Somolinos A, Fuller ER 3rd, Semelka RC. Nephrogenic systemic fibrosis: change in incidence following a switch in gadolinium agents and adoption of a gadolinium policy–report from two U.S. universities. *Radiology*, epub Sept 29, 2009.
74. Bettmann M. Frequently asked questions: iodinated contrast agents. *RadioGraphics* 24: S3–S1, 2004.

INDEX

For each index term, the volume number(s) for the page entries is given (*V1*, *V2*).

Abdominal cysts, fetal assessment, *V2*: 1617, 1619
Abdominal fibromatosis, in pregnancy, maternal imaging, *V2*: 1569–1570, 1575
Abdominal imaging:
  abdominal wall hernia, *V2*: 904, 908–909
  abscess, *V2*: 951, 955–959
  aortic aneurysm, *V2*: 1200–1207
  fetal assessment:
    anomalies, *V2*: 1612–1617
    neoplasms, *V2*: 1617–1620
    normal development, *V2*: 1583–1585
  MR strategies for, *V1*: 20–24
    3T general abdomen, *V1*: 23–24
Abdominal-pelvic imaging, protocol for, *V1*: 20, 22
Abdominal wall:
  endometriosis, *V2*: 1504–1507, 1513
  fetal assessment, congenital defects, *V2*: 1615–1617
  MR imaging techniques:
    benign neoplasms, *V2*: 1274, 1281–1283
    hernias, hematomas, and other lesions, *V2*: 904, 908–909, 1274, 1290–1293
    malignant neoplasms, *V2*: 1274, 1284–1290
  in pregnancy, maternal imaging, *V2*: 1570, 1574–1575
Abdominoperineal resection, postsurgical infection, *V1*: 892, 894–895
Ablative therapies, liver metastases, *V1*: 278–287
Abscess(es):
  appendiceal, *V1*: 874, 881
    in pregnancy, maternal imaging, *V2*: 1561–1564
  breast, *V2*: 1712
  enteric, gastrointestinal tract imaging, *V1*: 725
  infectious colitis, *V1*: 888
  intraabdominal, *V1*: 874, 884–885
  kidney, *V2*: 1142, 1144, 1149–1152
    renal transplants, *V2*: 1177, 1180–1181
  large intestine, *V1*: 874, 876–877, 881–886
    pericolonic abscess, diverticulitis, *V1*: 874, 877
  liver:
    amebic (nonpyogenic), *V1*: 430
    metastases, secondary infection, *V1*: 180, 188, 191–192
    pyogenic, *V1*: 418, 422–432
  ovarian abscess, *V2*: 1514, 1516–1517
  pancreas, pancreatic transplants, *V1*: 671–673
  pelvic, *V1*: 874, 884–886
  peritoneal, *V2*: 949, 951, 954–959
  Pouch of Douglas, *V1*: 874, 882–883
  prostate gland, *V2*: 1373–1374
  psoas muscle, *V2*: 1273–1274, 1276–1279
  rectal carcinoids, *V1*: 867–868
  spleen infection, *V1*: 710–711
  testicular, *V2*: 1397–1398
Accessory spleens, MR imaging, *V1*: 681–685
Achalasia, MR imaging, *V1*: 729–730, 732, 734
Acinar cell carcinoma, MR imaging, *V1*: 589
Acquired cystic disease of dialysis, *V2*: 1049, 1052, 1061–1062
Acquired immunodeficiency syndrome (AIDS). *See also* Human immunodeficiency virus (HIV)
  cholangiopathy, *V1*: 505
  esophageal infection, *V1*: 732–733
  infectious colitis, *V1*: 884, 888–892
  infectious enteritis, *V1*: 810, 813–814
  Kaposi sarcoma, *V1*: 748, 756
  mycobacterium avium intracellulare, *V1*: 433–435
ACTHoma, MR imaging, *V1*: 601, 605
Acute cholecystitis, magnetic resonance cholangiopancreatography, *V1*: 468–475
  chemoembolization-induced, *V1*: 468, 476
Acute hepatitis, *V1*: 321–329
Acute mastitis, inflammatory breast carcinoma, differential diagnosis, *V2*: 1739
Acute myelogenous leukemia, spleen infection, *V1*: 710–711
Acute pancreatitis:
  alcohol-related, *V1*: 625
  gallstone-related, *V1*: 625, 632
  MR imaging, *V1*: 625, 628, 631, 636–647
Acute pyelonephritis, *V2*: 1142, 1147–1149
  renal transplants, *V2*: 1177, 1179–1180
Acute tubular necrosis, *V2*: 1120, 1122
Addison disease, adrenal glands, *V2*: 1020
Adenocarcinoma:
  appendiceal, *V1*: 843
  bladder, *V2*: 1316, 1319–1320
  endometroid, *V2*: 1474, 1478
  esophagus, *V1*: 729–731
  fallopian tubes, *V2*: 1551
  female urethra, *V2*: 1403–1404
  gastric, *V1*: 738, 741, 743–751
  large intestine (*See also* Rectal cancer; specific cancers, e.g., Colon cancer)
    imaging studies, *V1*: 843–865
    mucocele, *V1*: 838, 841–842
  liver metastases, imaging studies, *V1*: 151, 153, 157–158
    undifferentiated tumors, *V1*: 162, 164, 177–179
  ovarian malignancies, undifferentiated neoplasms, *V2*: 1533, 1541
  pancreas, *V1*: 552–553, 556–589
  prostate cancer, *V2*: 1352, 1356–1373
  renal metastases, *V2*: 1112, 1115
  small bowel, *V1*: 777, 781–782
  uterus, *V2*: 1488–1491
  vaginal malignancies, *V2*: 1416, 1420–1426
Adenofibromas, benign ovarian neoplasm, *V2*: 1520, 1522–1523
Adenoma malignum, cervix, *V2*: 1489–1491
Adenomatoid tumor, testes, *V2*: 1386, 1388, 1390
Adenomatosis, liver, *V1*: 114–118
Adenomatous polyps:
  gastric polyps, *V1*: 736, 739–741
  rectum, *V1*: 829, 832, 835
  small intestine, *V1*: 775, 777–778
Adenomyomatosis:
  benign prostatic hyperplasia, *V2*: 1349
  endometrial carcinoma, *V2*: 1474–1475
  gallbladder neoplasms, *V1*: 480, 484

Abdominal-Pelvic MRI, Third Edition, edited by Richard C. Semelka. Copyright © 2010 John Wiley & Sons, Inc.

Adenomyosis, uterine, *V2*: 1456, 1466–1470
Adenosclerosis, benign breast lesions, *V2*: 1714, 1716
Adhesions, peritoneal, ovarian cysts, *V2*: 1504, 1508
Adiabatic pulses, fat-suppressed echo-train spin-echo sequences, *V1*: 9–10
Adnexa:
  fallopian tubes:
    carcinoma, *V2*: 1550–1552
    metastases to, *V2*: 1551–1553
    normal anatomy, *V2*: 1500, 1503
  metastases to, endometrial carcinoma, *V2*: 1474, 1476–1477
  MR imaging techniques, *V2*: 1499–1500
  ovary:
    benign neoplasms, *V2*: 1518–1531
      epithelial origin, *V2*: 1518–1523
      germ cell origin, *V2*: 1520–1521, 1526–1529
      sex cord-stromal origin, *V2*: 1525–1526, 1530–1531
    congenital anomalies, *V2*: 1503
    cysts, *V2*: 1500, 1502–1503
      functional cysts, *V2*: 1500, 1502, 1504–1506
      paraovarian/peritoneal cysts, *V2*: 1504, 1508
      theca-lutein cysts, *V2*: 1504, 1507–1508
    ectopic pregnancy, *V2*: 1517
    endometriosis, *V2*: 1504–1513
    hydrosalpinx, *V2*: 1517
    malignant neoplasms, *V2*: 1518
      carcinosarcoma, *V2*: 1545, 1548
      clear cell carcinoma, *V2*: 1533, 1538–1540
      epithelial origin, *V2*: 1531–1533
      germ cell origin, *V2*: 1533–1534, 1540–1544
      lymphoma, *V2*: 1545, 1548–1549
      mucinous tumors, *V2*: 1533, 1536–1538
      primary ovarian carcinoma, *V2*: 1526–1527, 1531
      serous tumors, *V2*: 1533–1536
      sex cord-stromal origin, *V2*: 1540, 1542, 1545–1547
    metastases to, *V2*: 1546–1547, 1549–1550
    normal anatomy, *V2*: 1500–1501
    ovarian torsion, *V2*: 1509–1510, 1514–1516
    pelvic inflammatory disease/tubo-ovarian abscess, *V2*: 1514, 1516–1517
    pelvic varices, *V2*: 1517–1518
    polycystic ovaries, *V2*: 1507, 1509, 1514
    transposed ovary, *V2*: 1500–1502
  pediatric imaging, *V2*: 1650
  in pregnancy, maternal imaging, masses, differential diagnosis, *V2*: 1567, 1569–1570
Adrenal cortex. *See* Adrenal glands, benign and malignant cortical lesions
  carcinoma, *V2*: 998, 1002–1006
Adrenal glands:
  Addison disease, *V2*: 1020
  benign cortical lesions:
    adenomas, *V2*: 969, 971–985
      bilateral, *V2*: 971, 974–976, 981, 984
      capillary blush, *V2*: 971–973, 978–979
      Dixon technique, *V2*: 971, 979
      hyperfunctioning adenomas, *V2*: 971
      minor hemorrhage, *V2*: 971, 982–984
      out-of-phase imaging, *V2*: 971, 983
      signal drop, *V2*: 971, 974, 982–983
    aldosteronomas, *V2*: 977, 986–987
    cysts and pseudocysts, *V2*: 980–981, 984, 991–993
    hemangioma, *V2*: 993–994
    hyperplasia, *V2*: 969–970, 977, 986–987
    myelolipoma, *V2*: 977–980, 988–990
  hemorrhage, *V2*: 1019–1020
  inflammatory disease, *V2*: 1019
  lesion classification and pattern recognition, *V2*: 969
  malignant cortical lesions:
    adrenal cortical carcinoma, *V2*: 998, 1002–1006
    metastastes, *V2*: 994–1002
  medullary masses:
    ganglioma, *V2*: 1006, 1013, 1017
    ganglioneuroblastoma to, *V2*: 1006, 1013, 1017–1018
    lymphoma, *V2*: 1017, 1019
    neuroblastoma, *V2*: 1006, 1012–1017
    pheochromocytoma, *V2*: 998, 1005–1111
    schwannoma, *V2*: 1006
  metastases (*See also* specific types of cancer)
    adenomas, differential diagnosis, *V2*: 964–968, 971
    hepatocellular carcinoma, *V1*: 192, 199
    imaging techniques, *V2*: 994–1002
  MR imaging techniques, *V2*: 963–968
  normal anatomy, *V2*: 963–968
  pediatric imaging, *V2*: 1650
Adrenal insufficiency, Addison disease, *V2*: 1020
Aggressive fibromatosis, *V2*: 912–914
Aicardi syndrome, fetal assessment, *V2*: 1588–1592
Air bubble artifacts:
  bile duct imaging, *V1*: 489, 493–494
  peritoneum, postsurgical air and fluid, *V2*: 936, 940
Aldosteronomas, *V2*: 977, 986–987
Allergy, gastric wall edema, *V1*: 761, 764
Alobar holoprosencephaly, fetal assessment, *V2*: 1588–1592
α1-Antitrypsin deficiency, imaging studies, *V1*: 315, 317
α-fetoprotein (AFP), hepatocellular carcinoma, venous thrombosis, *V1*: 235
Ambiguous genitalia, *V2*: 1415–1416
Amebic abscess, hepatic, *V1*: 430
American College of Radiology (ACR), breast MRI interpretation guidelines, *V2*: 1696–1700
American Joint Committee staging:
  breast cancer, *V2*: 1723–1725
  prostate cancer, *V2*: 1358, 1368
  testicular cancer, *V2*: 1392–1396
Amniotic band syndrome, fetal assessment, *V2*: 1621
Amniotic fluid, MR imaging and, *V2*: 1622–1623
Ampullary adenoma, MR imaging, *V1*: 511, 516
Ampullary carcinoma, bile duct imaging, *V1*: 518, 520, 527–530
Ampullary fibrosis, MRCP imaging, *V1*: 489, 495–496
Ampullary stenosis (bile duct):
  gadolinium-based contrast agent imaging, *V2*: 1771–1773
  MRCP imaging, *V1*: 489
Amyloid, urethra diffuse disease, *V2*: 1377–1380
Amyloidosis, seminal vesicles, *V2*: 1382, 1385
Anal canal:
  anorectal anomalies, *V1*: 827, 831, 833–834
  anorectal melanoma, *V1*: 867, 869
  cloacal repair, *V1*: 827, 833
  normal anatomy, *V1*: 824, 827, 831
  perianal fistula, *V1*: 883, 887–888
  squamous cell carcinoma, *V1*: 860, 866
Androgen exposure, female pseudohermaphroditism, *V2*: 1415–1416
Anesthesia, pediatric MRI, *V2*: 1638–1639, 1645
Aneurysms:
  abdominal aortic, *V2*: 1200–1207
  magnetic resonance angiography, *V2*: 1673, 1684
  renal artery disease, *V2*: 1133, 1135–1136
  renal vein, *V2*: 1138
  splenic artery aneurysm, *V1*: 706–709
Angioimmunoblastic lymphadenopathy, splenic involvement, *V1*: 700–702
Angiomas, spleen, *V1*: 688, 694
Angiomyolipomas:
  fatty liver differential diagnosis, *V1*: 383
  kidney, *V2*: 1063–1068
  liver lesions, *V1*: 67, 70, 80–81
  tuberous sclerosis and, *V2*: 1066, 1069–1071
Angiomyxoma, vulvar malignancies, *V2*: 1421
Angiosarcoma:
  breast cancer, *V2*: 1740–1741
  inferior vena cava, *V2*: 1237–1241
  liver metastases, *V1*: 240, 242, 249
  spleen, *V1*: 704, 706
Angiotropic intravascular lymphoma, liver metastases, *V1*: 238, 242
Anhydramnios, renal agenesis, *V2*: 1613

Annular pancreas, MR imaging, *V1*: 541–544
Anterior urethra, normal anatomy, *V2*: 1375–1376
Antiphospholipase deficiency, renal artery, *V2*: 1137
Aorta:
magnetic resonance angiography, *V2*: 1673, 1679–1684
normal anatomy:
MIP reconstruction, *V2*: 1198–1200
phase mapping, *V2*: 1194
retroperitoneal imaging, *V2*: 1200–1227
aortic aneurysm, *V2*: 1200–1207
aortic dissection, *V2*: 1201, 1208–1212
aortoiliac atherosclerotic disease/thrombosis, *V2*: 1204, 1207, 1214–1223
penetrating ulcers/intramural dissecting hematoma, *V2*: 1201, 1204, 1213
postoperative graft evaluation, *V2*: 1207, 1214, 1216, 1224–1227
Aortic atheroemboli, renal artery disease, *V2*: 1137, 1143
"Aortic cobwebs," aortic dissection, *V2*: 1201, 1208–1212
Aortic dissection:
magnetic resonance angiography, *V2*: 1673, 1684
renal artery disease, *V2*: 1133, 1135
Aortobifemoral graft:
infection, *V2*: 1214, 1216, 1226
postsurgical evaluation, *V2*: 1207, 1214, 1216, 1224–1225
Aortoiliac atherosclerotic disease/thrombosis, retroperitoneal imaging, *V2*: 1204, 1207, 1214–1223
"Aphtoid" ulcerations, Crohn disease, *V1*: 785
Apparent diffusion coefficient (ADC), breast imaging, *V2*: 1696
Appendicitis:
diagnostic imaging, *V1*: 874, 879–881
infectious enteritis, differential diagnosis, *V1*: 810, 813–814
in pregnancy, maternal imaging, *V2*: 1561–1564
Appendix:
abscess, peritoneal inflammation, *V2*: 951, 956
adenocarcinoma, *V1*: 843
carcinoma, peritoneal metastases, *V2*: 918, 923–924, 926
mucocele, *V1*: 832, 841–842
Aqueductal stenosis, fetal assessment, *V2*: 1585–1592
Arachnoid cysts, fetal assessment, *V2*: 1594–1595
Arciform enhancement, spleen, *V1*: 678–681
Arcuate uterus, *V2*: 1441, 1444, 1448
Arterial-phase bolus-track liver examination (ABLE) technique, hepatic arterial dominant phase (HADP) contrast agent, *V2*: 1774–1777
Arterial thrombosis, pancreatic transplants, *V1*: 671, 673
Arteriovenous fistulas, liver imaging, *V1*: 388–392
Arteriovenous malformations, abdominal wall, *V2*: 1274
Ascending colon:
adenocarcinoma, *V1*: 843–844
lipoma, *V1*: 832
Ascites:
intraperitoneal, *V2*: 936, 940–942
benign, *V2*: 936, 942
high-protein-content, *V2*: 936, 941
MRI signal intensity and, *V1*: 1–2
ovarian:
malignant epithelial tumors, *V2*: 1532–1533
theca-lutein ovarian cysts, *V2*: 1504, 1507–1508
Ashkenazi Jews, Crohn disease in, *V1*: 784
Asplenia syndrome, MR imaging, *V1*: 681, 685
Atherosclerotic disease:
abdominal aortic aneurysm, *V2*: 1201–1207
aortoiliac atherosclerotic disease/thrombosis, *V2*: 1204, 1207, 1214–1223
magnetic resonance angiography, *V2*: 1673, 1679–1684
penetrating aortic ulcers, *V2*: 1201, 1204, 1213
renal arterial disease, *V2*: 1128–1129, 1131–1144
Atresia, intestinal, *V1*: 770, 774
Atypical ductal hyperplasia (ADH), benign breast lesions, *V2*: 1715
Autoimmune diseases, chronic liver disease, *V1*: 303–304, 306–315
autoimmune hepatitis, *V1*: 311–314
primary biliary cirrhosis, *V1*: 314–315
primary sclerosing cholangitis, *V1*: 303–304, 306–311
Autoimmune pancreatitis, MR imaging, *V1*: 656, 664, 666
Autosomal dominant polycystic kidney disease (ADPKD):
hepatic cysts, *V1*: 67, 71–72
renal cell carcinoma, *V2*: 1098, 1101
renal cysts, *V2*: 1044, 1047, 1051–1056
Autosomal recessive polycystic kidney disease (ARPKD):
cystic lesions, *V2*: 1047, 1056–1058
fetal assessment, *V2*: 1614–1616

B1 inhomogeneities, 3T MR imaging, *V1*: 33
Background enhancement, breast MRI, *V2*: 1698–1700
"Backwash ileitis," *V1*: 799, 806
Bacterioides spp., tubo-ovarian abscess, *V2*: 1514, 1516–1517
Balloon dilation, achalasia, *V1*: 729–730, 732, 734
Barium studies:
Crohn disease, *V1*: 791
intestinal atresia and stenosis, *V1*: 770, 774
large intestine imaging, negative oral contrast agents, *V1*: 896–897
Bartholin glands:
carcinoma, *V2*: 1421
cysts, *V2*: 1416–1418
Basal cell carcinoma, vulvar malignancies, *V2*: 1421
"Beading," primary sclerosing cholangitis, MRCP imaging, *V1*: 497–499
Beckwith-Wiedemann syndrome, Wilms tumor and, *V2*: 1103–1106
Behçet disease, urethrovaginal fistulas, *V2*: 1408
"Bell clapper" deformity, testicular torsion, *V2*: 1396–1397
Bence Jones proteinuria, renal tubular blockage, *V2*: 1120, 1123–1124
Benign prostatic hyperplasia (BPH), *V2*: 1349–1354
prostate adenocarcinoma, differential diagnosis, *V2*: 1352, 1356–1358
Bezoar, gastric imaging, *V1*: 738, 742
Bicornuate uterus, *V2*: 1441, 1444, 1446
Bile, intraperitoneal, *V2*: 942, 945–946
Bile duct:
abnormal bile signal, *V1*: 460, 463
biliary cystadenoma/cystadenocarcinoma, liver lesions, *V1*: 67, 77–78
cystic disease, *V1*: 489, 493–494, 505, 508–511
diseases:
benign disease:
AIDS-related cholangiopathy, *V1*: 505
ampullary adenoma, *V1*: 511, 516
ampullary fibrosis, *V1*: 489, 495–496
ampullary stenosis, *V1*: 489
Caroli disease, *V1*: 505, 511–513
cholecdocholithiasis, *V1*: 488–492
choledochal cyst, *V1*: 505, 508–510
choledochocele, *V1*: 505, 511
cysts, *V1*: 489, 493–494, 505
infectious cholangitis, *V1*: 499, 502–507
mass lesions, *V1*: 511, 514–520
papillary adenoma, *V1*: 511, 515
papillary dysfunction, *V1*: 489, 493, 497
postsurgical complications, *V1*: 511, 514–515, 517–520
primary sclerosing cholangitis, *V1*: 494, 497–502
sclerosing cholangitis, *V1*: 493–494
imaging studies, *V1*: 483–488
pitfalls, *V1*: 489, 493–494
malignant disease:
carcinoma, intrahepatic/peripheral metastases, *V1*: 238–240, 242, 247–249
cholangiocarcinoma, *V1*: 515–518, 521–526
metastases to, *V1*: 530

Bile duct: (*Continued*)
periampullary/ampullary carcinoma, *V1*: 518, 520, 527–530
gadolinium-based contrast agent imaging, *V2*: 1768, 1770–1773
giant cell tumor, *V1*: 511, 514
magnetic resonance cholangiopancreatography, *V1*: 457, 463–464
normal anatomy, *V1*: 456–460
obstruction:
hepatic transplantation, *V1*: 292, 299
hepatocellular carcinoma, *V1*: 202, 224
pancreatic cancer, obstruction of, *V1*: 552, 562–564
T1-weighted magnetic resonance cholangiopancreatography, *V1*: 460–461
Bilharziosis, bladder calculi, *V2*: 1305
Biliary anastomoses, coronal imaging, *V1*: 464, 466–467
Biliary hamartoma, liver lesions, *V1*: 67, 73–77
colon cancer metastasis, *V1*: 67, 76–77
multiple, *V1*: 67, 74–75
solitary, *V1*: 67, 73
Biliary papillomatosis, MR images, *V1*: 514–515
Biliary system (tree):
air in, liver imaging, *V1*: 411, 413–414
gadolinium-based contrast agents, *V2*: 1771
magnetic resonance cholangiopancreatography, *V1*: 456–457
pancreatic adenocarcinoma, *V1*: 562–563, 566
pediatric imaging, *V2*: 1649
postsurgical complication, *V1*: 511, 514–515, 517–520
stricture, hepatic transplantation, *V1*: 292, 299
Billroth cords, splenic anatomy, *V1*: 677–678
Bilomas:
bile duct imaging, *V1*: 511, 517–518
hepatic transplantation, *V1*: 292, 296–298
infected, pyogenic hepatic abscess, *V1*: 418, 426–427
intraperitoneal, *V2*: 942, 944–945
Black-blood techniques:
aortic imaging, *V2*: 1200
abdominal aortic aneurysm, *V2*: 1201–1207
inferior vena cava, *V2*: 1216, 1223, 1229
congenital anomalies, *V2*: 1223, 1228–1230
portal venous thrombosis, *V1*: 388
vessel imaging, *V2*: 1194–1200
Bladder. *See also* Exstrophic bladder
benign masses:
calcifications, *V2*: 1304–1306
hemangiomas, *V2*: 1304
inflammatory myofibroblastic tumor, *V2*: 1304
leiomyoma, *V2*: 1300, 1302–1303
neurogenic tumors, *V2*: 1304–1305
papilloma, *V2*: 1300–1301
pheochromocytoma, *V2*: 1303
benign prostatic hyperplasia and, *V2*: 1349, 1351–1352
congenital disease, *V2*: 1298–1301
cystitis, *V2*: 1326–1328
cystitis cystica, *V2*: 1326, 1329–1330
cystitis glandularis, *V2*: 1326
edema, *V2*: 1324
endometriosis, *V2*: 1326
fistulas, *V2*: 1326, 1331–1335
cervical cancer metastases, *V2*: 1486, 1489
granulomatous disease, *V2*: 1326
hemorrhagic cystitis, *V2*: 1326, 1329
hypertrophy, *V2*: 1324–1325
malignant masses (*See* Bladder cancer)
metastases to:
cervical cancer, *V2*: 1486, 1488–1489, 1492–1495
vaginal carcinoma, *V2*: 1416, 1423
MR imaging techniques, *V2*: 1297–1298
artifacts, *V2*: 1298–1299
normal anatomy, *V2*: 1297–1298
pediatric imaging, *V2*: 1650
pelvic lipomatosis, *V2*: 1326, 1329–1330
postoperative evaluation, *V2*: 1331, 1335
radiation changes, *V2*: 1331, 1337
reconstruction, *V2*: 1331, 1335–1336
Bladder cancer:
adenocarcinoma, *V2*: 1316, 1319–1320
differential diagnosis, *V2*: 1298–1299
incidence and epidemiology, *V2*: 1305–1306
lymphoma and chloroma, *V2*: 1316, 1321
metastases, *V2*: 1320–1324
nonepithelial neoplasms, *V2*: 1316
primary urothelial neoplasm:
carcinosarcoma, *V2*: 1316
squamous cell carcinoma, *V2*: 1316–1318
transitional cell carcinoma, *V2*: 1306–1316
prostate cancer metastases, *V2*: 1358–1373
urachal carcinoma, *V2*: 1316
Blake pouch cyst, fetal assessment, *V2*: 1591
Bland thrombus, portal venous thrombosis, *V1*: 391, 396–397
Blood imaging, intraperitoneal, *V2*: 936, 943–944. *See also* Black-blood techniques; Bright-blood techniques
Blood pool agents, gadolinium-based, *V2*: 1768, 1772–1774
Blood thrombus, portal venous thrombosis, *V1*: 391, 396
Bochdalek hernia, *V2*: 904–905
Bolus-chase technique, vessel imaging, *V2*: 1195–1200
Bone metastases:
adrenal gland neuroblastoma, *V2*: 1013–1017
bladder cancer, transitional cell carcinoma, *V2*: 1307–1316
body wall tumors, *V2*: 1274, 1288–1290
gadolinium-enhanced T1-weighted images, *V1*: 13
prostate cancer, *V2*: 1358, 1367–1373
rectal adenocarcinoma, *V1*: 852, 861–863
Bourneville disease, renal cysts, *V2*: 1066, 1069–1071
Bowel imaging, fetal assessment, normal development, *V2*: 1583–1585
Bowel obstruction, in pregnancy, maternal imaging, *V2*: 1564
Bowel peristalsis:
abdominal-pelvic MRI artifacts, fast scanning, *V1*: 1–2
adnexal imaging artifacts, *V2*: 1499
Brain imaging:
fetal assessment:
neoplasms, *V2*: 1598
normal anatomy, *V2*: 1578–1583
whole body imaging, *V1*: 36, 40–42
BRCA1/BRCA2 gene, breast cancer, *V2*: 1722–1723
Breast:
benign lesions:
abscess, *V2*: 1712
cysts, *V2*: 1700–1703
fibroadenoma, *V2*: 1702–1706
hamartoma (fibroadenolipoma), *V2*: 1709, 1711
multiple papillomatosis, *V2*: 1709–1711
papilloma, *V2*: 1707–1709
phyllodes tumor, *V2*: 1706–1707
benign mesenchyma tumors, *V2*: 1739–1741
biopsy, MRI guidance and intervention, *V2*: 1760–1762
biopsy, MRI-guided interventions, *V2*: 1760–1762
fat necrosis in, *V2*: 1746, 1749–1752
implants, *V2*: 1754–1759
cancer and, *V2*: 1759
categories, *V2*: 1754–1755
failure, *V2*: 1687–1689, 1755–1757
fat necrosis, *V2*: 1746, 1749–1752
imaging techniques, *V2*: 1757–1759
postoperative MRI, *V2*: 1744–1749
lymph nodes, *V2*: 1712–1714
metastases to, *V2*: 1743–1744
MR imaging techniques:
artifacts, *V2*: 1695
coil systems, *V2*: 1693
congenital anomalies, *V2*: 1700–1701
contrast agents, *V2*: 1694
fat suppression, *V2*: 1695
gradient system, *V2*: 1693
imaging plane, *V2*: 1693–1694
imaging protocol, *V2*: 1694–1695
indications for imaging, *V2*: 1691
interpretation guidelines, *V2*: 1696–1700
magnetic field strength, *V2*: 1692–1693
morphological/kinetic diagnostic features, *V2*: 1697
normal anatomy, *V2*: 1687–1691

patient preparation and positioning, *V2*: 1694
region of interest, *V2*: 1691
reporting system and assessment categories, *V2*: 1697–1698
silicone implant rupture, *V2*: 1687–1689
specificity improvement, *V2*: 1695–1696
nonmass lesions
ductal carcinoma in situ, *V2*: 1715, 1718–1721
fibrocystic changes and sclerosing adenosis, *V2*: 1712, 1714–1716
lobular carcinoma in situ, *V2*: 1721–1722
radial scar, *V2*: 1714–1715, 1717
posttherapeutic MRI, *V2*: 1744–1749
Breast cancer:
angiosarcoma, *V2*: 1740–1742
bile duct/ampulla metastases, *V1*: 520
breast implants and, *V2*: 1759
classification and staging, *V2*: 1723–1725
colloid carcinoma, *V2*: 1732, 1734
dermatofibrosarcoma protuberans, *V2*: 1739, 1741
gallbladder metastases, *V1*: 483, 487
implants, detection in, *V2*: 1759
incidence and prevalence, *V2*: 1722–1723
inflammatory carcinoma, *V2*: 1737, 1739
intraductal papilloma, *V2*: 1736, 1738
invasive diagnostic features, MR imaging, *V2*: 1723
invasive ductal carcinoma, *V2*: 1725–1731, 1736
invasive lobular carcinoma, *V2*: 1727, 1731–1733
liver metastases:
benign lesions, differential diagnosis, *V1*: 177, 190
hemangiomas and, *V1*: 90
infiltrative pattern, *V1*: 162, 172
miliary pattern, *V1*: 173–175
post-radiation recurrence, *V1*: 257, 262–263
pre- and post-chemotherapy, *V1*: 257, 266–268
primary site studies, *V1*: 162, 171–175
ring enhancement imaging, *V1*: 162, 171
lymphoma, *V2*: 1741–1743
medullary carcinoma, *V2*: 1732–1733
mesenchymal tumors, *V2*: 1739–1741
metastases, *V2*: 1743–1744
invasive lobular carcinoma, *V2*: 1727, 1731–1733
MR imaging techniques, *V2*: 1688–1691
neoadjuvant chemotherapy monitoring, *V2*: 1749, 1753–1754
Paget disease, *V2*: 1737–1738
pancreatic metastases, *V1*: 619, 625, 630
papillary carcinoma, *V2*: 1733, 1737
postoperative residual carcinoma, *V2*: 1744–1749
radiation-induced carcinoma, *V2*: 1743
small intestine metastases, *V1*: 782, 792
splenic metastases, *V1*: 701, 703–706
stomach metastases, *V1*: 760
subcutaneous body wall metastases, *V2*: 1274, 1284
tubular carcinoma, *V2*: 1733–1736
Breast-conserving therapy (BCT):
fat necrosis, *V2*: 1746, 1749–1752
posttreatment MRI, *V2*: 1744–1749
Breast feeding, gadolinium-based contrast agents and, *V2*: 1786
Breast Image Reporting and Data System (BI-RADS®):
breast cancer imaging, *V2*: 1723
breast cysts, *V2*: 1701–1703
breast MRI interpretation guidelines, *V2*: 1696–1700
fibroadenomas, *V2*: 1706
lesion management protocols, *V2*: 1698–1700
reporting system and assessment categories, *V2*: 1697–1700
Breath-hold imaging:
1.5T *vs.* 3T imaging motion sensitivity, *V1*: 35
adrenal glands, *V2*: 964–968
aortic dissection, *V2*: 1201, 1208–1212
gradient echo sequences, motion artifact reduction, *V1*: 2–3
inferior vena cava, *V2*: 1216, 1223, 1229
kidneys, multicystic dysplastic kidney, *V2*: 1048–1049, 1058
noncooperative patients, *V1*: 25
pancreas, *V1*: 536
acute pancreatitis, *V1*: 625, 628, 634–647
islet-cell tumors, *V1*: 591–598
mucinous cystadenoma/cystadenocarcinoma, *V1*: 612–616
serous cystadenoma, *V1*: 606–607, 609–612
pediatric MRI, *V2*: 1637, 1639, 1642–1643
older children, *V2*: 1645–1646
peritoneal inflammation, abscess, *V2*: 951, 954–959
peritoneal metastases, intraperitoneal seeding, *V2*: 918–924
peritoneum, ascites, *V2*: 936, 940–942
renal cell carcinoma, *V2*: 1073–1095
retroperitoneal imaging, *V2*: 1194
small intestine, *V1*: 767–770
spleen, *V1*: 678–681
spoiled gradient echo sequences, *V1*: 3
T1-weighted magnetic resonance cholangiopancreatography, *V1*: 460–461
uterus and cervix, *V2*: 1434
Breathing-averaged protocol, pediatric MRI, *V2*: 1637–1638, 1640
Brenner tumors, benign ovarian neoplasms, *V2*: 1518, 1520–1523
"Bridging vascular sign," ovarian leiomyomas, *V2*: 1525–1526
Bright-blood techniques:
aortic imaging, *V2*: 1200
abdominal aortic aneurysm, *V2*: 1201–1207
inferior vena cava, *V2*: 1216, 1223, 1229
congenital anomalies, *V2*: 1223, 1229–1230
malignancies *vs.* thrombus, differential diagnosis, *V2*: 1240–1241
portal venous thrombosis, *V1*: 388
pulmonary emboli, *V2*: 1673, 1675–1677
vessel imaging, *V2*: 1194–1200
Broad ligament:
leiomyoma of, *V2*: 1449, 1453–1454
paraovarian cysts, *V2*: 1504, 1508
Bronchial stenosis, fetal assessment, *V2*: 1611–1612
Bronchogenic cysts, fetal assessment, *V2*: 1612
Bronchopulmonary sequestration, fetal assessment, *V2*: 1606, 1611–1612
Buck fascia fibrosis, *V2*: 1380–1381
Budd-Chiari syndrome:
acute-onset, *V1*: 398, 401
chronic, *V1*: 401, 406–407
cirrhosis, regenerative nodules, *V1*: 340
hepatic venous thrombosis, *V1*: 398, 401–405
primary sclerosing cholangitis, differential diagnosis, *V1*: 311
subacute, *V1*: 398, 402–405
Burkitt lymphoma:
gallbladder metastases, *V1*: 483, 487
pancreas, *V1*: 619, 624–625
pediatric patient imaging, *V2*: 1648–1649
retroperitoneal malignant masses, *V2*: 1253, 1257
Buttram-Gibbons classification system:
Müllerian duct anomalies, *V2*: 1440–1448
müllerian duct defects, *V2*: 1503

Cadaveric liver assessment, hepatic transplantation protocol, *V1*: 287, 292
Calcifications:
bladder calculi, *V2*: 1304–1306
breast, *V2*: 1688, 1690
breast implants, *V2*: 1759
prostate gland, *V2*: 1371, 1373
renal cysts, *V2*: 1042, 1048
seminal vesicles, *V2*: 1382, 1385
Calculi:
bladder, *V2*: 1304–1306
renal, *V2*: 1159, 1166–1169
Calyceal diverticulum, *V2*: 1164, 1172
Campylobacter jejuni, infectious enteritis, differential diagnosis, *V1*: 810, 813–814
Candida albicans:
esophageal infection, *V1*: 731–734
hepatic parenchyma fungal infection, *V1*: 433, 435–438
spleen infection, *V1*: 710–711

Candidiasis:
hepatic parenchyma, *V1*: 433, 435–438
renal, *V2*: 1155
Capillary phase enhancement:
adrenal glands, *V2*: 964–968
adrenal adenoma, *V2*: 971–973, 975, 978–979
gadolinium-enhanced images, *V1*: 2
T1-weighted sequences, *V1*: 10–13
hepatic arterial dominant phase imaging, gadolinium-based contrast agent, *V2*: 1775–1777
kidneys:
adenoma, *V2*: 1068
oncocytomas, *V2*: 1068, 1072
pancreatic imaging, *V1*: 536
acute pancreatitis, *V1*: 628, 636–647
chronic pancreatitis, *V1*: 648–665
pancreatic adenocarcinoma, *V1*: 553, 557–559, 564–565
spoiled gradient echo sequences, *V1*: 3–4
"Carcinoid syndrome," small intestine carcinoids, *V1*: 779, 790–791
Carcinoid tumors:
ileal, *V1*: 779, 789
kidney, *V2*: 1109–1110
liver metastases, *V1*: 164, 183–185
transcatheter arterial chemoembolization, *V1*: 270, 273
pancreas, *V1*: 602, 607–608
peritoneal metastases, *V2*: 936, 939–940
rectum, *V1*: 867–868
small intestine, *V1*: 779, 790–791
stomach, *V1*: 756, 759
terminal ileum, *V1*: 779, 790–791
Carcinosarcoma:
bladder, *V2*: 1316
endometriosis, *V2*: 1504, 1513
ovarian, *V2*: 1545, 1548
uterine, *V2*: 1475, 1479–1481
Cardiac gating:
esophageal imaging, *V1*: 726–727
vessel imaging, *V2*: 1194–1200
Cardiac motion artifacts, breast MRI, *V2*: 1695
Caroli disease, bile duct cysts, *V1*: 505, 511–513
Caruncle, female urethra, *V2*: 1407
Castleman disease, retroperitoneal benign lymphadenopathy, *V2*: 1249–1250
Catheterization:
bladder imaging, *V2*: 1298–1299
intraperitoneal, *V2*: 945
Cauliflower-type imaging, liver metastases, *V1*: 161–162, 168–170
Cavernous hemangioma, *V2*: 1416, 1420
Cavum septum pellucidum, absence, fetal assessment, *V2*: 1594
Cecum:
adenocarcinoma, *V1*: 843
lipoma, *V1*: 832, 839
lymphoma, *V1*: 860, 867
Celiac disease/sprue, small intestine, *V1*: 799, 807–809
Central nervous system, fetal imaging:
anomalies, *V2*: 1584–1585
normal anatomy, *V2*: 1578–1583
ventriculomegaly, *V2*: 1585–1592
Cerebellar vermis, fetal assessment, MRI, *V2*: 1578–1583
Cerebral ischemia, fetal assessment, *V2*: 1596–1601
Cervical cancer:
adenocarcinoma, undifferentiated carcinoma/sarcoma, *V2*: 1488–1491
adenoma malignum, *V2*: 1489–1491
bladder metastases, *V2*: 1320–1324
carcinoma, *V2*: 1482–1489
recurrence and posttreatment change, *V2*: 1492–1495
endometrial carcinoma, *V2*: 1472–1481
FIGO staging, *V2*: 1482–1488
in pregnancy, maternal imaging, *V2*: 1569, 1572
recurrent carcinoma and posttreatment change, *V2*: 1492–1494
retroperitoneal fibrosis, *V2*: 1249, 1252–1253
urethral metastases, *V2*: 1405
Cervical incompetence, *V2*: 1629–1631
Cervix:
benign disease, nabothian cysts, *V2*: 1467–1468, 1471
congenital anomalies, *V2*: 1441, 1444, 1447–1449
diethylstilbestrol exposure, *V2*: 1448
endometriosis, in pregnancy, *V2*: 1569, 1573–1574
fibroids, in pregnancy, maternal imaging, *V2*: 1569, 1573
metastases to, *V2*: 1492
MR imaging techniques, *V2*: 1433–1434
normal anatomy, *V2*: 1434–1437, 1436–1437
pediatric imaging, *V2*: 1650
in pregnancy:
cervical incompetence, *V2*: 1629–1631
endometriosis, *V2*: 1569, 1573–1574
stenosis, endometriosis and, *V2*: 1506, 1510
Cesarean scar pregnancy, *V2*: 1577–1580
Cesarean section:
placental imaging and, *V2*: 1623, 1625–1627
postpartum uterus imaging, *V2*: 1575–1580
Chagas disease, achalasia, *V1*: 732, 734
Charcot's triad, infectious cholangitis, *V1*: 499
Chemical shift imaging:
3T MR imaging, *V1*: 31–32
bladder artifacts, *V2*: 1298–1299
breast MRI, *V2*: 1695
gradient echo sequences, *V1*: 3
Chemoembolization:
acute cholecystitis, *V1*: 468, 476
transcatheter arterial chemoembolization, liver metastases, *V1*: 268, 270–278
Chemotherapy:
breast cancer, neoadjuvant, posttreatment MRI, *V2*: 1744–1753
liver metastases, *V1*: 257, 264–270
gadolinium-enhanced T1-weighted images, hepatic arterial dominant (capillary) phase, *V1*: 11–13
hemangiomas, differential diagnosis, *V1*: 101, 177, 190
pancreatic cancer, *V1*: 589–590
pancreatitis from, *V1*: 666–667
peritonitis and, *V2*: 949, 953
small intestine, toxicity enteritis, *V1*: 810, 817
spleen lymphomas, *V1*: 700, 702–703
tubulointerstitial kidney disease, *V2*: 1120–1121
Chest-abdominal-pelvic imaging:
protocol for, *V1*: 20, 23
whole body imaging, *V1*: 36, 39–40
Chest imaging. *See also* Lung cancer; Pulmonary disease
future research issues, *V2*: 1684–1685
hilar and mediastinal lymphadenopathy, *V2*: 1666–1667
mass lesions, *V2*: 1666, 1673–1674
mestastases to, *V2*: 1654, 1659–1660, 1662–1665, 1673–1674
MR imaging techniques, *V2*: 1653–1654
normal chest, *V2*: 1655–1657
pleural disease, *V2*: 1666, 1671–1672
protocol for, *V1*: 20, 22
pulmonary infiltrates, *V2*: 1666, 1668–1671
pulmonary MRA:
pulmonary emboli, *V2*: 1673, 1675–1677
vascular abnormalities, *V2*: 1673, 1678–1684
screening applications, *V2*: 1684
Chiari II malformation, fetal assessment, ventriculomegaly, *V2*: 1585–1592
Child-Turcotte-Pugh scale, primary sclerosing cholangitis, *V1*: 304, 311
Chlamydia trachomatis, tubo-ovarian abscess, *V2*: 1514, 1516–1517
Chloroma:
bladder, *V2*: 1316, 1321
kidney, *V2*: 1109, 1111
Cholangiocarcinoma:
bile duct imaging, *V1*: 515–518, 521–526
diffuse hepatocellular carcinoma, differential diagnosis, *V1*: 235
extrahepatic, *V1*: 516–518, 525–527
liver metastases, *V1*: 238–240, 242, 247–249
oriental cholangitis, differential diagnosis, *V1*: 502, 507
peritoneal metastases, *V2*: 918, 923–925

portal venous compression, *V1*: 391
primary sclerosing cholangitis, *V1*: 499
Cholangiopathy, AIDS-related, *V1*: 505
Cholangitis, infectious:
hepatic abscess, *V1*: 418, 424–425
MRCP imaging, *V1*: 499, 502–507
Cholecystectomy, bile duct complications, *V1*: 511, 514–515
Cholecystitis:
acute cholecystitis, *V1*: 468–475
chemoembolization-induced, *V1*: 468, 476
acute on chronic cholecystitis, *V1*: 468, 475
chronic, *V1*: 475, 477–478
hemorrhagic, *V1*: 475–477
xanthogranulomatous, *V1*: 477
Cholecystolithiasis, sonographic imaging, *V1*: 464
Choledochal cysts, MR imaging, *V1*: 505, 508–510
Choledochocele:
ampullary carcinoma and, *V1*: 520, 530
MR imaging, *V1*: 505, 511
small intestine, *V1*: 775–776
Choledocholithiasis:
magnetic resonance cholangiopancreatography, *V1*: 488–492
in pregnancy, maternal imaging, *V2*: 1564
Cholestasis, primary sclerosing cholangitis, MRCP imaging, *V1*: 494, 497–502
Choline levels:
breast NMR spectroscopy, *V2*: 1696
prostate cancer, adenocarcinoma, *V2*: 1352, 1356–1373
Chordoma, abdominal wall metastases, *V2*: 1274, 1289–1290
Choroid plexus papillomas, fetal assessment, *V2*: 1598–1599
Chronic cholecystitis, magnetic resonance cholangiopancreatography, *V1*: 475, 477–479
Chronic liver disease:
autoimmune diseases, *V1*: 303–304, 306–315
autoimmune hepatitis, *V1*: 311–314
primary biliary cirrhosis, *V1*: 314–315
primary sclerosing cholangitis, *V1*: 303–304, 306–311
genetic diseases, *V1*: 315–317
α1-antitrypsin deficiency, *V1*: 315, 317
Wilson disease, *V1*: 315–318
hemangiomas, *V1*: 101, 103–106
hepatitis:
acute on chronic, *V1*: 321, 327
chronic, *V1*: 321
hepatocellular carcinoma, incidence and prevalence, *V1*: 190, 192
nonalcoholic fatty liver disease, *V1*: 317, 319–320
radiation-induced hepatitis, *V1*: 321, 331
viral hepatitis, *V1*: 319, 321–330
Chronic lymphocytic leukemia (CLL), splenomegaly, *V1*: 700–701
Chronic membranous glomerulonephritis, *V2*: 1117, 1119
Chronic pancreatitis, *V1*: 640, 648–665
acute on chronic pancreatitis, *V1*: 656, 657–663
pancreatic adenocarcinoma:
differential diagnosis, *V1*: 575
risk for, *V1*: 552, 562–564
pancreatic adenocarcinoma imaging, differential diagnosis, *V1*: 575
Chronic prostatis, *V2*: 1373
Chronic pyelonephritis, *V2*: 1126, 1128, 1130
Chronic renal failure:
glomerular disease, *V2*: 1117–1120
renal cell carcinoma, *V2*: 1098–1101
Ciliated foregut hepatic cysts, *V1*: 60, 66–70
Circulating fibrocyte hypothesis, nephrogenic systemic fibrosis, *V2*: 1783
Cirrhosis:
autosomal dominant polycystic kidney disease, hepatic cysts, *V1*: 67, 72
biliary:
primary sclerosing cholangitis, *V1*: 304, 306–309, 311, 314–315, 497–502
regenerative nodules, *V1*: 333–334, 339–345
diffuse hyperperfusion and focal hyperperfusion abnormalities in, *V1*: 411, 414–415
dysplastic nodules, *V1*: 340, 342, 346–354
fatty infiltration, *V1*: 333–334
hemangiomas and, *V1*: 101, 103–106
hepatocellular carcinoma incidence and prevalence, *V1*: 188–189, 192
iron-containing nodules, *V1*: 334, 340, 344–346
iron overload, *V1*: 370
liver metastases, differential diagnosis, *V1*: 257, 270
macronodular regenerative nodules, *V1*: 331–333, 339–340
MR imaging studies, *V1*: 331–362
nonalcoholic fatty liver disease, *V1*: 317, 319–320
omental metastases, differential diagnosis, *V2*: 923–924
pathophysiology, *V1*: 321, 331
in pediatric patients, *V1*: 317–318
pediatric patients, imaging protocols, *V2*: 1637, 1642
portal hypertension, *V1*: 348, 351, 359–362
primary biliary cirrhosis, *V1*: 314–315
small intestine, hypoproteinemia, *V1*: 816, 824
subcutaneous varices, *V2*: 1274, 1290–1291
Cisterna chyli dilation, *V2*: 1237
Citrate levels, prostate cancer, *V2*: 1352
Clear cell carcinoma:
endometriosis, *V2*: 1504, 1513
malignant ovarian neoplasms, *V2*: 1533, 1538–1540
vaginal malignancies, *V2*: 1416, 1420–1421
Cleft palate, fetal assessment, *V2*: 1595–1596
head and neck imaging, *V2*: 1601–1607
Cloaca, persistent:
fetal assessment, *V2*: 1614
surgical repair, *V1*: 827, 833
vaginal agenesis/partial agenesis, *V2*: 1410–1411
Cloacogenic carcinoma, liver metastases, *V1*: 128, 137
Clostridium difficile, pseudomembranous colitis, *V1*: 883–884, 892
Clubfoot, fetal assessment, *V2*: 1622
Cocoon formation, intraperitoneal, *V2*: 945, 947
Coil systems, breast MRI, *V2*: 1693
Collagen injections, pelvic floor relaxation, *V2*: 1408–1410
Colloid carcinoma, breast cancer, *V2*: 1732, 1734
Colon cancer. *See also* Ascending colon; Proximal descending colon; Rectosigmoid colon; Sigmoid colon; Transverse colon
adenocarcinoma, *V1*: 843–865
cecum, *V1*: 843
multifocal adenocarcinoma, *V1*: 848, 853
diverticulitis, differential diagnosis, *V1*: 869, 878–879
duodenal metastases, *V1*: 779, 782, 791
imaging protocol for, *V1*: 16, 19–20
liver metastases:
biliary hamartoma, *V1*: 67, 76–77
low-fluid-content metastases, *V1*: 149, 154–155
MR imaging:
contrast agents, *V1*: 52–58
primary site studies, *V1*: 161, 165–171
post-chemotherapy, *V1*: 257, 269
post-resection recurrence, *V1*: 256, 261–262
lymphoma, *V1*: 860, 867
melamona, *V1*: 867, 869
pancreatic metastases, *V1*: 619, 625, 628
peritoneal metastases, *V2*: 918, 923–924, 926
polyps, MR colonography screening, *V1*: 848, 851
squamous cell carcinoma, *V1*: 860, 866
stomach metastases, *V1*: 760
ulcerative colitis and, *V1*: 867
Colonic duplication, *V1*: 827, 832
Colonic fistulae, *V1*: 883, 887–888
Colonic lipoma, *V1*: 832, 840
Colorectal adenocarcinoma, adenomatous polyps, *V1*: 829
Colostomy, peristomal hernia, *V2*: 904, 909

Combined extracellular-intracellular gadolinium-based contrast agents, *V2*: 1768
Common bile duct (CBD). *See* Bile duct
Common hepatic duct (CHD), normal anatomy, *V1*: 456
Computed tomography (CT):
acute pancreatitis, *V1*: 628, 631
adrenal gland imaging:
metastases, *V2*: 998–1002
MR imaging *vs.*, *V2*: 971
bladder cancer, transitional cell carcinoma, *V2*: 1308–1316
chronic pancreatitis imaging, *V1*: 648–665
Crohn disease, *V1*: 791
iodine-based contrast agents, *V2*: 1767
kidneys:
chronic renal failure, *V2*: 1098
MRI *vs.*:
Bosniak classification allteration, *V2*: 1037
calcified renal cysts, *V2*: 1042
liver imaging:
focal nodular hyperplasia, MR imaging *vs.*, *V1*: 121, 129
hepatic transplantation protocol, *V1*: 292
hepatocellular carcinoma, *V1*: 192
MRI *vs.*, *V1*: 192, 203–205
metastases:
computed tomography arterial portography *vs.* MRI, *V1*: 143, 145–147
spiral CT *vs.* MRI, *V1*: 128, 141–144
mycobacterium avium intracellulare, *V1*: 433–435
pancreatic cancer:
adenocarcinoma, *V1*: 552, 558–559
gastrinomas, *V1*: 591
macrocystic serous cystadenoma, *V1*: 607, 611–612
peritoneal metastases, *V1*: 575, 581–583
renal cell carcinoma, MR imaging *vs.*, *V2*: 1098–1099, 1102
whole body imaging, *V1*: 41–42
Computed tomography arterial portography (CTAP), liver imaging:
hemangiomas, *V1*: 88, 100
metastases imaging, MRI *vs.*, *V1*: 143, 145–147
coexistent cysts, *V1*: 190
portal venous thrombosis, *V1*: 397, 399–400
Computed tomography pulmonary angiography (CTPA), *V2*: 1673
Computer-aided diagnosis, breast cancer, *V2*: 1691
Concurrent disease, imaging protocol for, *V1*: 16, 19–20
Congenital adrenal hyperplasia, female pseudohermaphroditism, *V2*: 1415–1416
Congenital heterotopias, stomach, *V1*: 736
Congestive heart failure, liver imaging, *V1*: 407, 411–413
Conjoined twins, imaging studies, *V2*: 1623–1624
Connective tissue disease, cortical necrosis, renal artery, *V2*: 1137, 1142
Conn syndrome, adrenal gland adenomas and hyperplasia, *V2*: 977, 986–987
Contrast agents:
amniotic fluid as, *V2*: 1583–1585
bladder imaging, *V2*: 1298–1299
breast MRI, *V2*: 1694
categorization, *V2*: 1767–1779
contrast-induced nephropathy risk *vs.* nephrogenic system fibrosis risk assessment, *V2*: 1784–1786
gadolinium-based, *V2*: 1767–1777
classification, *V2*: 1768–1774
complications, *V2*: 1779–1786
early hepatic venous phase, *V2*: 1776
enhancement phases, *V2*: 1774
hepatic arterial dominant phase, *V2*: 1774–1777
hepatocyte phase, *V2*: 1777
interstitial phase, *V2*: 1776
gastrointestinal tract imaging, *V1*: 725
intraluminal, large intestine imaging, *V1*: 892, 895–897
iron-based, *V2*: 1777–1779
liver imaging, *V1*: 50–58
manganese-based, *V2*: 1778–1779
pediatric imaging, *V2*: 1647
Contrast-induced nephropathy (CIN):
nephrogenic systemic fibrosis risk *vs.*, *V2*: 1784–1786
risk factors, *V2*: 1767
Core needle biopsy:
breast lesion underestimation, *V2*: 1722
intraductal papilloma, *V2*: 1707, 1709
multiple papillomatosis, *V2*: 1707–1710
radial scar, *V2*: 1714
Coronal plane imaging:
biliary anastomosis, *V1*: 464, 466–467
breast MRI, *V2*: 1693–1694
female urethra, normal anatomy, *V2*: 1401–1403
hepatic transplantation, *V1*: 287, 289
liver:
hepatic cysts, *V1*: 60, 63–64
hypovascular cystic metastases, *V1*: 152
metastases, *V1*: 128, 137–138, 143, 148
Reidel lobe, *V1*: 58–59
viral hepatitis, *V1*: 321, 323–324
magnetic resonance cholangiopancreatography, *V1*: 456, 459
biliary anastomoses, *V1*: 464, 466–467
normal biliary tree, *V1*: 464–465
renal cell carcinoma, stage 3a, *V2*: 1076–1077, 1079–1081
vagina, *V2*: 1409–1410
Corpus callosum, fetal assessment, MRI, *V2*: 1578–1583
agenesis, *V2*: 1585–1592
Corpus cavernosa:
diffuse disease, *V2*: 1377–1380
inflammatory disease, *V2*: 1380–1381
normal anatomy, *V2*: 1375–1376
Corpus luteal cysts, *V2*: 1500, 1503, 1504
in pregnancy, maternal imaging, *V2*: 1569
Corpus spongiosum:
diffuse disease, *V2*: 1377–1380
normal anatomy, *V2*: 1375–1376
Corrosive esophagitis, *V1*: 731
Cortical development malformation, fetal assessment, *V2*: 1595–1596
Cortical necrosis, renal artery disease, *V2*: 1137, 1142
Corticomedullary differentiation (CMD):
acute tubular necrosis, *V2*: 1120, 1122
crossed fused ectopia, *V2*: 1032, 1034
renal artery disease, *V2*: 1133
renal function, *V2*: 1112, 1116–1117
renal parenchymal disease, *V2*: 1112–1124
obstruction, *V2*: 1121, 1125–1126, 1128–1129
renal transplants, *V2*: 1178–1184
Cost issues, whole body MR imaging, *V1*: 41–42
Cranio-caudal view, breast MRI, *V2*: 1693–1694
"Creeping" fat, Crohn disease, *V1*: 785
Crohn collitis, *V1*: 869, 872–874
Crohn disease:
acute on chronic, *V1*: 796, 803–804
Crohn colitis, large intestine, *V1*: 869, 872–874
dilated stagnant bowel loop, *V1*: 796, 805
entero-vesical fistulae, *V1*: 810, 813
infectious enteritis, differential diagnosis, *V1*: 810, 813–814
mild to moderate, *V1*: 795–796
moderate, *V1*: 797
pelvic fistulae, *V1*: 810–812
in pregnancy, *V1*: 796, 802
primary sclerosing cholangitis, MRCP imaging, *V1*: 494, 497–502
severe, *V1*: 793–794, 798–799
severity criteria, *V1*: 796, 802
small intestine, *V1*: 784–785, 791, 793–805
ulcerative colitis, differential diagnosis, *V1*: 785, 867–869, 870–874
urethrovaginal fistulas, *V2*: 1408
Crohn Disease Activity Index (CDAI), *V1*: 796
Cronkhite-Canada syndrome, colonic hamartomas, *V1*: 832
Crossed fused kidney ectopia, *V2*: 1032, 1034–1035
Cryotherapy:
liver metastases, *V1*: 278, 286–287
prostate cancer, *V2*: 1368–1373
Cryptococcal abscess, spleen, *V1*: 710–711
Cryptococcus, spleen infection, *V1*: 710–711

Cryptorchidism, *V2*: 1386–1388
fetal assessment, *V2*: 1613–1614
Cryptosporidium parvum, infectious enteritis, *V1*: 810, 813–814
Cushing syndrome, adrenal glands:
adenomas, *V2*: 971, 982–983
cortical hyperplasia, *V2*: 969–971
Cystadenofibroma, ovarian tumors:
benign neoplasm, *V2*: 1520–1523
borderline malignancy, *V2*: 1531–1532
Cystectomy, bladder reconstruction, *V2*: 1331, 1336
Cystic adenomatoid malformation (CCAM), fetal assessment, *V2*: 1604–1606, 1610–1612
Cystic ectasia, benign prostatic hyperplasia, *V2*: 1349–1354
Cystic fibrosis, pancreatic imaging, *V1*: 544–548
Cystic hygromas, fetal assessment, *V2*: 1598, 1603
Cystic nephroma, *V2*: 1060, 1063–1064
Cystic teratoma, benign ovarian neoplasms, *V2*: 1520–1521, 1523–1528
Cystitis, bladder, *V2*: 1326–1328
hemorrhagic, *V2*: 1326, 1329
Cystitis cystica, bladder, *V2*: 1326, 1329–1330
Cystitis glandularis:
adenocarcinoma, *V2*: 1316, 1319–1320
bladder, *V2*: 1326
Cystoceles, female urethra, *V2*: 1408–1410
Cysts. *See also* Pseudocysts
abdominal/pelvic, fetal assessment, *V2*: 1617, 1619
adrenal glands, *V2*: 980–981, 984, 991–993
pheochromocytoma, *V2*: 1005–1111
arachnoid, fetal assessment, *V2*: 1594–1595
bile duct, *V1*: 489, 493–494, 505, 508–513
choledochal cyst, *V1*: 505, 508–510
Blake pouch cyst, fetal assessment, *V2*: 1591
body wall, *V2*: 1274, 1280–1283
breast, *V2*: 1700–1703
cervix, nabothian cysts, *V2*: 1467–1468, 1471
choledochal cysts, MR imaging, *V1*: 505, 508–510
dacryocystocele, fetal assessment, *V2*: 1604, 1607
esophagus, duplication cysts, *V1*: 726, 728
fetal assessment:
arachnoid cysts, *V2*: 1594–1595
dacryocystocele, *V2*: 1604, 1607
thoracic, *V2*: 1612
ventriculomegaly, *V2*: 1590–1592
gastric duplication cysts, *V1*: 736
hepatic:
autosomal dominant polycystic kidney disease, *V1*: 67, 71–72
ciliated foregut, *V1*: 60, 66–70
ciliated foregut cysts, *V1*: 60, 66–70
coexistent metastases, *V1*: 165, 190
hemorrhagic cyst, *V1*: 60, 65
hydatid cyst, echinococcal disease, *V1*: 430–431
multilocular cyst, *V1*: 60, 65–66
solitary (nonparasitic), *V1*: 60–66
unilocular cyst, *V1*: 60–61
hydatid cyst:
liver imaging, *V1*: 430–431
spleen, *V1*: 683, 687–690
mesenteric cysts, *V2*: 907, 910
ovarian, *V2*: 1500, 1502–1503
dermoid cyst, *V2*: 1520–1521, 1526–1529
endometriotic cyst, *V2*: 1520, 1522–1523
functional cysts, *V2*: 1502, 1504–1506
paraovarian/peritoneal cysts, *V2*: 1504, 1508
in pregnancy, differential diagnosis, *V2*: 1567, 1569–1570
theca-lutein cysts, *V2*: 1504, 1507–1508
prostate, *V2*: 1344, 1347–1349
renal, *V2*: 1035, 1037–1064
acquired dialysis-related cystic disease, *V2*: 1049, 1052, 1061–1062
angiomyolipoma, *V2*: 1063–1068
autosomal dominant polycystic kidney disease, *V2*: 1044, 1047, 1052–1056
autosomal recessive polycystic kidney disease, *V2*: 1047, 1056–1058
calcified cysts, *V2*: 1042, 1048
complex cysts, *V2*: 1037, 1040–1041
fetal assessment, *V2*: 1614–1616
hemhorragic/proteinaceous cysts, *V2*: 1037, 1042–1047
medullary cystic disease, *V2*: 1049, 1059–1060
medullary sponge kidney, *V2*: 1049, 1060
multicystic dysplastic kidney, *V2*: 1047–1049, 1058
multilocular cystic nephroma, *V2*: 1060, 1063–1064
perinephric pseudocysts (parapelvic cysts), *V2*: 1042, 1044, 1050
septated cysts, *V2*: 1042, 1047
simple renal cysts, *V2*: 1035, 1037
thickened wall and infiltration, *V2*: 1043, 1049
tuberous sclerosis, *V2*: 1066, 1069–1071
von Hippel-Lindau disease, *V2*: 1066, 1068, 1072
seminal vesicles, *V2*: 1382, 1384
spleen:
epidermoid cysts, *V1*: 683, 688
hydatid cyst, *V1*: 683, 687–690
testes, scrotum and epididymis, *V2*: 1386, 1389
thoracic, fetal assessment, *V2*: 1612
urachal, *V2*: 1300–1301
vaginal:
Bartholin glands cyst, *V2*: 1416–1418
cavernous hemangioma, *V2*: 1416, 1420
Gartner duct cysts, *V2*: 1416, 1418–1419
Cytomegalovirus:
esophageal infection, *V1*: 731–734
infectious colitis, *V1*: 888
splenomegaly and, *V1*: 709–711

Dacryocystocele, fetal assessment, *V2*: 1604, 1607
Dandy-Walker complex, fetal assessment:
posterior fossa anomalies, *V2*: 1591, 1593–1597
ventriculomegaly, *V2*: 1585–1592
Denys-Drash syndrome, Wilms tumor and, *V2*: 1103–1106
Dermatofibrsarcoma protuberans, breast cancer, *V2*: 1739–1741
Dermoid cyst:
benign ovarian neoplasms, *V2*: 1520–1521, 1526–1529
pediatric patient, imaging protocol, *V2*: 1637, 1643
Desmoid tumor, *V2*: 912–914
Gardner syndrome, *V2*: 1274, 1280–1283
Diabetes mellitus, seminal vesicle calcification, *V2*: 1382, 1385
Dialysis, acquired cystic disease, *V2*: 1049, 1052, 1061–1062
Diaphragm:
fetal assessment:
anomalies, *V2*: 1604, 1612
hernia, *V2*: 1604–1605, 1608–1609
hernias in, *V2*: 904–909
Didelphys uterine anomaly, *V2*: 1441, 1444–1446
vaginal duplication, *V2*: 1412, 1414–1415
Diethylstilbestrol (DES) exposure:
ovarian anomalies, *V2*: 1503
uterine anomalies, *V2*: 1448
vaginal malignancies, *V2*: 1416, 1420–1426
Diffuse hyperperfusion abnormality, liver imaging, *V1*: 389–391, 411, 414–415
Diffuse infiltrative gastric adenocarcinoma, *V1*: 738, 741
Diffuse infiltrative hepatocellular carcinoma, *V1*: 212, 227, 234–238
Diffuse pancreatic adenocarcinoma, *V1*: 570, 576
Diffusion-weighted imaging (DWI), breast, *V2*: 1696
Diffusion-weighted single-shot echo planar imaging:
fetal assessment, *V2*: 1561
non-fat-suppressed *vs.* fat-suppressed images, *V1*: 35–37
Dilated stagnant bowel loop, Crohn disease, *V1*: 796, 805
Direct tumor invasion:
renal cell carcinoma metastases, *V2*: 1082, 1084–1085
splenic metastases, *V1*: 704–705

Disease-based strategies:
MR imaging sequences, *V1*: 14–24
screening applications, *V2*: 1684
whole body imaging, *V1*: 41–42
Disease conspicuity, abdominal-pelvic MRI, signal intensity differences and, *V1*: 1–2
Distal esophagomyotomy, achalasia, *V1*: 732, 734
Distribution of area enhancement, breast cancer imaging, *V2*: 1723
Diverticula, congenital:
bladder, *V2*: 1299–1301
female urethra, *V2*: 1405–1407
small intestine:
duodenal, *V1*: 770, 772–774
Meckel diverticulum, *V1*: 770, 774
stomach, *V1*: 736–738
Diverticular abscess, *V1*: 874, 876–877
Diverticulitis, *V1*: 869, 874–879
pericolonic abscess, *V1*: 874, 877
Diverticulosis, *V1*: 869, 874
Dixon breath-hold imaging technique, adrenal glands:
adenoma, *V2*: 971, 979
normal anatomy, *V2*: 964–968
Donor assessment, hepatic transplantation protocol, *V1*: 287–291
Dotarem gadolinium-based contrast agent, *V2*: 1768
"Double duct sign," pancreatic cancer, bile duct obstruction, *V1*: 552, 562–564
Double-echo out-of-phase imaging, adrenal glands, *V2*: 963–968
Double surface coils, bladder imaging, *V2*: 1298–1299
Drug toxicity, small intestine, *V1*: 810, 817
Ductal carcinoma in situ (DCIS):
benign masses, *V2*: 1715, 1717–1721
breast cancer, risk and prevalence, *V2*: 1723
diagnostic criteria, *V2*: 1699–1700
intraductal papilloma, differential diagnosis, *V2*: 1707–1709
Ductal intraepithelial neoplasia (DIN):
ductal carcinoma in situ, benign lesions, *V2*: 1715, 1718–1721
fibroadenomas, *V2*: 1702–1706
Duct-ectatic mucin-producing tumor, MR imaging, *V1*: 614–621
Duke colon cancer classification, fallopian tube carcinoma, *V2*: 1551, 1554
Duodenum:
adenocarcinoma, *V1*: 777, 781–782
Peutz-Jeghers syndrome, *V1*: 832
colon cancer metastases, *V1*: 779, 782, 791
Crohn disease in, *V1*: 785, 799
diverticulum, *V1*: 770, 772–774
hematoma, *V1*: 816, 823
inflammatory disease (duodenitis), *V1*: 810, 813–814
leiomyoma, *V1*: 775, 780
MALToma, *V1*: 779, 786
neurofibroma, *V1*: 775, 779
varices, *V1*: 775, 781
Duplication anomalies:
cervix, *V2*: 1441, 1444, 1447–1449
colonic duplication, *V1*: 827, 832
enteric duplication cyst, fetal assessment, *V2*: 1617, 1619
esophageal, *V1*: 726, 728
female urethra, *V2*: 1403
gastric duplication cysts, *V1*: 736
kidney, *V2*: 1613
vagina, *V2*: 1412, 1414–1415
Dynamic contrast-enhanced breast MRI, *V2*: 1695–1696
Dysgerminomas, ovarian malignancies, *V2*: 1533
Dysplastic nodules (DNs):
cirrhosis, *V1*: 340, 342, 346–354
hepatocellular carcinoma, *V1*: 189, 198, 202, 212, 357–358
Dysproteinemia, angioimmunoblastic lymphadenopathy, splenic involvement, *V1*: 700–702

Early hepatic arterial dominant phase (EHADP) imaging, gadolinium-based contrast agent, *V2*: 1774–1777
Echinococcal disease, liver imaging, *V1*: 430–433
Echo time (TE):
3T MR imaging, *V1*: 32–36
adrenal gland imaging, *V2*: 963–968
kidney imaging, paroxysmal nocturnal hemoglobinuria, *V2*: 1121, 1127
magnetic resonance cholangiopancreatography, *V1*: 456
small intestine imaging, *V1*: 767–770
whole body imaging, *V1*: 40–42
Echo-train short-tau inversion recovery (Echo-train-STIR) imaging, liver imaging:
focal nodular hyperplasia, *V1*: 121–127
hemangiomas, *V1*: 88, 97–99
hepatic cysts, *V1*: 60, 63
hepatocellular carcinoma, *V1*: 192, 195–197
metastases characterization, *V1*: 128, 140–141
primary sclerosing cholangitis, *V1*: 304, 306–308
Echo-train spin-echo (ETSE) sequences:
abdominal-pelvic imaging, *V1*: 6–10
fat-suppressed echo-train spin-echo sequences, *V1*: 7–10
single-shot echo-train spin-echo sequences, *V1*: 7–8
adnexa, *V2*: 1499–1500
aortic dissection, *V2*: 1201, 1208–1212
bladder, *V2*: 1298
chest imaging, *V2*: 1653–1654
colon cancer, *V1*: 848, 854–857
Gaucher disease, *V1*: 683
imaging parameters, *V1*: 23–24
kidney imaging, *V2*: 1029–1031
lung cancer, pulmonary nodules, *V2*: 1654, 1657, 1662–1665
magnetic resonance cholangiopancreatography, *V1*: 456–461
male pelvis, *V2*: 1343–1344
noncooperative patients, *V1*: 25
pediatric patients, *V2*: 1644
peritoneal inflammation, abscess, *V2*: 951, 954–959
placental imaging, *V2*: 1625–1627
rectal adenocarcinoma, *V1*: 848–850, 852, 857–860
fibrosis, *V1*: 852, 861–865
rectum, *V1*: 824, 827
retroperitoneum imaging, *V2*: 1194
benign lymphadenopathy, *V2*: 1247–1250
malignant metastatic lymphadenopathy, *V2*: 1258–1263
primary neoplasms, *V2*: 1266, 1271
uterine-cervical MRI, *V2*: 1434
Eclampsia, liver imaging, *V1*: 407, 410–411
Ectopic kidney, *V2*: 1032–1033
fetal assessment, *V2*: 1613
Ectopic pregnancy:
cesarean scar pregnancy, *V2*: 1577–1580
sites for, *V2*: 1517
theca-lutein ovarian cysts, *V2*: 1504, 1507–1508
Edema:
bladder, *V2*: 1324
ovarian torsion, *V2*: 1514–1516
Edge artifact, breast MRI, *V2*: 1695
Ejaculatory duct, cysts, *V2*: 1344, 1347–1349
Embryonal carcinoma, testes lesions, *V2*: 1390–1396
Embryonal rhabdomyosarcoma, retroperitoneal imaging, *V2*: 1266, 1272
Encephalocele, fetal assessment, *V2*: 1594–1595, 1597
Endarteritis, small intestine, radiation enteritis, *V1*: 816, 818
Endodermal sinus tumors, ovarian malignancies, *V2*: 1533–1534, 1542–1544
Endoluminal aortic graft placement, *V2*: 1214, 1216, 1224–1227
Endoluminal coil imaging, uterus, *V2*: 1433
Endometrial cancer:
adrenal metastases, *V2*: 994–995, 998–999
carcinoma, *V2*: 1468, 1470–1481
endometriosis, *V2*: 1504, 1513
fallopian tube metastases, *V1*: 155, 1551
hemorrhagic ovarian cyst, *V2*: 1500, 1503
polycystic ovarian syndrome, *V2*: 1509, 1514
liver metastases, imaging studies, *V1*: 149, 151

Endometrial hyperplasia, *V2*: 1448–1450
malignant ovarian neoplasms and, *V2*: 1542, 1545–1547
Endometrial polyps, *V2*: 1448–1450
malignant ovarian neoplasms and, *V2*: 1542, 1545–1547
Endometrioid tumors:
benign ovarian neoplasm, *V2*: 1520–1523
malignant ovarian neoplasms, *V2*: 1533, 1538
Endometrioma:
overian benign neoplasms, *V2*: 1504–1505, 1509, 1512–1513
pregnancy-related, *V2*: 1504, 1513, 1569, 1574–1575
Endometriosis, *V2*: 911
abdominal wall, *V2*: 1504–1507, 1513
bladder involvement, *V2*: 1326
body wall masses, *V2*: 1274, 1282
ovarian benign disease, *V2*: 1504–1507, 1510–1513
in pregnancy, cervical, *V2*: 1569, 1573–1574
Endometritis, postpartum uterus, *V2*: 1578–1580
Endometrium, vaginal agenesis/partial agenesis, *V2*: 1410–1413
Endorectal coil MRI:
bladder, *V2*: 1298–1299
coil imaging, rectal adenocarcinoma, *V1*: 850, 857
female urethra, normal anatomy, *V2*: 1401–1403
male pelvis, *V2*: 1343–1344
rectum, *V1*: 824, 827
vagina, *V2*: 1410
Endoscopic retrograde cholangiopancreatography (ERCP):
biliary anastomoses, *V1*: 464, 466–467
choledocholithiasis, MRCP *vs.*, *V1*: 488–489
intraductal papillary mucinous neoplasms, *V1*: 615
MR imaging *vs.*, *V1*: 455
pancreas divisum, *V1*: 541
pancreatic adenocarcinoma, bile duct obstruction, *V1*: 552, 562–564
primary sclerosing cholangitis, *V1*: 497–502
T2-weighted MRCP, *V1*: 456–457
Endothelial cysts, adrenal glands, *V2*: 981, 984, 991–993
Endovaginal coil imaging:
female urethra:
diverticulum, *V2*: 1405, 1407
normal anatomy, *V2*: 1401–1403
uterus, *V2*: 1433
vagina, *V2*: 1410
Endovascular graft, postsurgical evaluation, *V2*: 1214, 1216, 1226
End-stage kidney disease, hypertension, *V2*: 1146–1147
Entamoeba histolytica, hepatic abscess, *V1*: 430
Enteric abscesses, gastrointestinal tract imaging, *V1*: 725
Enteric duplication cyst, fetal assessment, *V2*: 1617, 1619
Enteric fistulae, gastrointestinal tract imaging, *V1*: 725
Enteritis:
radiation-induced, large intestine, *V1*: 888, 892–894
small intestine:
infectious, *V1*: 810, 813–814
radiation enteritis, *V1*: 815–816, 818
Enterobacter spp., prostate infection, *V2*: 1373–1374
Enteroceles, female urethra, *V2*: 1408–1410
Enterocystoplasty, bladder reconstruction, *V2*: 1331, 1335
Entero-vesical fistulae, Crohn disease, *V1*: 810, 813
Eosinophilic gastroenteritis, small intestine, *V1*: 809
Eovist gadolinium-based contrast agent, *V2*: 1768, 1771–1772
Epidermoid cysts, spleen, *V1*: 683, 688
Epididymis:
congenital anomalies, *V2*: 1386
cystic lesions, *V2*: 1386, 1389
infectious disease, *V2*: 1397–1398
MR imaging, *V2*: 1385
normal anatomy, *V2*: 1383–1384
Epignathi, fetal assessment, *V2*: 1599
Epispadias, *V2*: 1376
Epithelial ovarian neoplasms:
benign tumors, *V2*: 1518–1523
malignant tumors, *V2*: 1531–1533
primary peritoneal carcinoma, differential diagnosis, *V2*: 912, 917
Epithelioid hemangioendothelioma (EHE), liver metastases, *V1*: 251–253
Epstein-Barr virus, splenomegaly and, *V1*: 709–711
Epulis, congenital, fetal assessment, *V2*: 1601, 1605
Erectile dysfunction, congenital anomalies and, *V2*: 1376
Erythropoietin levels, nephrogenic systemic fibrosis and, *V2*: 1782–1783
Escherichia coli, prostate infection, *V2*: 1373–1374
Esophageal varices:
cirrhosis, portal hypertension, *V1*: 351, 361
MR imaging, *V1*: 727
Esophagitis:
radiation-induced, *V1*: 730–731
reflux, *V1*: 729–730, 732
Esophagus. *See also* Lower esophageal sphincter
benign masses, leiomyomas, *V1*: 726–728
duplication cysts, *V1*: 726, 728
infectious disease, *V1*: 731–734
inflammatory disease:
corrosive esophagitis, *V1*: 731
radiation esophagitis, *V1*: 730–731
reflux esophagitis, *V1*: 729–730, 732
malignant masses, *V1*: 729–731
metastases to:
achalasia, *V1*: 732, 734
esophageal cancer, differential diagnosis, *V1*: 729, 731
MR imaging, *V1*: 726
normal anatomy, *V1*: 725–726
Estrogen receptors, invasive ductal carcinoma, *V2*: 1723–1727
Ewing sarcoma, pelvic metastases, *V2*: 1274, 1288
Examination duration, MR imaging strategies and, *V1*: 14–24
Exophytic focal nodular hyperplasia (FNH), MR imaging, *V1*: 121, 133–134
Exophytic gastric adenocarcinoma, *V1*: 738
Exstrophic bladder, *V2*: 1299
adenocarcinoma, *V2*: 1316, 1319–1320
fetal assessment, *V2*: 1617–1618
Extracellular contrast agents, gadolinium-based, *V2*: 1768–1774
Extrahepatic ducts, variations, *V1*: 460, 464
Extramedullary hematopoiesis (EH):
kidney myelofibrosis, *V2*: 1068, 1073
liver MR imaging, *V1*: 67, 79–80
retroperitoneal masses, *V2*: 1249, 1251
Extrarenal pelvis, *V2*: 1164, 1170
Extremeties, fetal MRI, *V2*: 1620–1622
Ex utero intrapartum treatment (EXIT), fetal head and neck anomalies, MRI, *V2*: 1598–1699, 1601–1607

Fallopian tubes:
carcinoma, *V2*: 1550–1552
endometriosis, *V2*: 1505
hydrosalpinx, *V2*: 1517
metastases to, *V2*: 1551–1553
normal anatomy, *V2*: 1500, 1503
paraovarian cysts of Morgagni, *V2*: 1504, 1508
tubo-ovarian abscess, *V2*: 1514, 1516–1517
Familial adenomatous polyposis syndrome, *V1*: 829, 832, 837–838
Fast spin-echo sequences, *V1*: 6
breast, silicone implants, *V2*: 1688–1689, 1757–1759
vaginal metastases, *V2*: 1421–1426
Fat detection:
adrenal gland myelolipoma, *V2*: 979–980, 988–990
adrenal gland pheochromocytoma, *V2*: 1005–1111
echo-train spin-echo sequences, *V1*: 6–7
gradient echo sequences, *V1*: 3
hepatocellular carcinoma, *V1*: 192, 209–212
liver imaging:
angiomyolipomas, *V1*: 67, 70, 80–81
hepatocellular adenoma, *V1*: 107, 109–114
iron deposition coexistence, *V1*: 371, 376

Fat detection: (*Continued*)
out-of-phase (opposed-phase) spoiled gradient echo sequences, *V1*: 4–5
ovaries, benign germ cell tumors, *V2*: 1520–1521, 1526–1529
pancreas, uneven fatty infiltration, *V1*: 542, 545
Fat necrosis (FN), breast-conserving therapy, *V2*: 1746, 1749–1752
Fat-suppressed (FS) echo-train spin-echo sequences:
abdominal-pelvic imaging, *V1*: 7–10
adrenal gland imaging, *V2*: 963–968
neuroblastoma, *V2*: 1013–1017
breast MRI, *V2*: 1695
chronic pancreatitis, *V1*: 649, 652, 653–654
esophageal imaging, *V1*: 726–727
gastrointestinal tract, *V1*: 725
hepatic transplantation, ischemic changes, *V1*: 287, 290–292
liver imaging, *V1*: 46–48
angiomyolipomas, *V1*: 67, 70, 80–81
computed tomography *vs.*, *V1*: 128, 141–144
hepatocellular carcinoma, diffuse infiltrative, *V1*: 212, 227, 234–238
hypovascular metastases, *V1*: 149, 155–157
metastases, *V1*: 128, 138–139
mycobacterium avium intracellulare, *V1*: 433–435
primary sclerosing cholangitis, *V1*: 304, 309–311
viral hepatitis, *V1*: 321, 323–325
pediatric patients, *V2*: 1637
renal function, *V2*: 1112, 1116–1117
renal function assessment, *V2*: 1112, 1116–1117
retroperitoneum:
benign lymphadenopathy, *V2*: 1247–1250
lymphoma, *V2*: 1253–1257
malignant metastatic lymphadenopathy, *V2*: 1258–1263
Fat-suppressed gradient echo sequences:
adnexa, *V2*: 1499–1500
adrenal glands, *V2*: 963–968
adrenal cortical carcinoma, *V2*: 998, 1002–1006
metastases, *V2*: 995–1002
aortic graft evaluation, *V2*: 1214, 1216, 1224–1227
aortoiliac atherosclerotic disease/thrombosis, *V2*: 1204, 1207, 1214–1223
basic principles, *V1*: 4
bile duct, papillary adenoma, *V1*: 511, 515
bladder, *V2*: 1298
fistulas, *V2*: 1331–1335
transitional cell carcinoma, *V2*: 1307–1316
breast MRI, *V2*: 1695
cavernous hemangioma, *V2*: 1416, 1420
cirrhosis, portal hypertension, *V1*: 348, 351, 359–362
colon cancer, *V1*: 843–865
esophageal imaging, esophageal varices, *V1*: 727, 729
esophagus, malignant masses, *V1*: 729–731
kidneys:
angiomyolipomas, *V2*: 1063–1068
renal function assessment, *V2*: 1112, 1116–1117
large intestine:
lipomas, *V1*: 832, 839–840
ulcerative colitis, *V1*: 867–868, 870–871
liver imaging:
hepatic cysts, *V1*: 60–62, 64
metastases detection and characterization, *V1*: 128, 137–143
magnetic resonance cholangiopancreatography, *V1*: 460–461
ovaries:
endometriomas, *V2*: 1506, 1509–1512
pelvic inflammatory disease, *V2*: 1514, 1516–1517
pancreas, *V1*: 536–541
acute pancreatitis, *V1*: 628, 636–647
annular pancreas, *V1*: 542–544
chronic pancreatitis, *V1*: 648–665
cystic fibrosis, *V1*: 545–548
islet-cell tumors, *V1*: 590–598
pancreatic adenocarcinoma, *V1*: 552, 555–556, 570, 577–578
peritoneal inflammation:
abscess, *V2*: 949, 951, 954–959
pancreatitis, *V2*: 940–942, 946, 949
peritoneal metastases, *V2*: 923–924
pleural disease imaging, *V2*: 1666, 1671–1672
rectum, techniques, *V1*: 827, 831
renal function, *V2*: 1112, 1116–1117
retroperitoneum, *V2*: 1193–1194
scrotal hernia, *V2*: 1390
small intestine, *V1*: 775, 781
adenocarcinoma, *V1*: 777, 781–782
Crohn disease, *V1*: 785, 791, 793–805
gastrointestinal stromal tumor, *V1*: 779, 783–785
infectious enteritis, *V1*: 810, 813–814
ischemia and hemorrhage, *V1*: 816, 819–823
polyps, *V1*: 775, 777–778
radiation enteritis, *V1*: 816, 818
stomach, *V1*: 734
gastric adenocarcinoma, *V1*: 743
gastrointestinal stromal tumors, *V1*: 743, 748, 752–758
vessel imaging, inferior vena cava thrombus, *V2*: 1229–1237
Fat suppression effects:
3T MR imaging, ETSE *vs.* SGE sequences, *V1*: 33
magnetic resonance imaging variables, *V1*: 13–15
single-shot echo-train spin-echo *vs.* single-shot echo planar imaging, *V1*: 33–34
Fatty liver:
focal nodular hyperplasia and, *V1*: 379
hepatocellular carcinoma and, *V1*: 380
imaging studies, *V1*: 371, 373, 377–387
adenomatosis, *V1*: 114–115
fat-suppressed echo-train spin-echo sequences, *V1*: 7–10
focal imaging, *V1*: 371, 377
focal nodular hyperplasia, MRI *vs.* CT, *V1*: 121, 129
focal sparing, *V1*: 377, 384–385
hemangiomas, *V1*: 106
hepatic transplantation, *V1*: 299, 303
metastases, *V1*: 128, 140–142
adenoma, *V1*: 128, 142
mild infiltration, *V1*: 377, 380
minimal infiltration, *V1*: 377, 380
moderately severe diffuse infiltration, *V1*: 377, 381–382
multiple small foci, *V1*: 371, 378–379
nonalcoholic fatty liver disease, *V1*: 317, 319–320
segmental variation, *V1*: 377, 386–387
severe infiltration, *V1*: 377, 382–383
pediatric patients, *V2*: 1644
Feridex, iron-based contrast agent, *V2*: 1778–1779
Ferric ammonium citrate, positive intraluminal contrast agents, large intestine imaging, *V1*: 895
Ferumoxide contrast agents, *V2*: 1778–1779
Ferumoxtran contrast agents, *V2*: 1778–1779
Fetal assessment:
anomalies:
abdominal/pelvic cysts, *V2*: 1617–1620
abdominal wall defects, *V2*: 1615–1617
central nervous system, *V2*: 1584–1585
congenital hemangioma, *V2*: 1604, 1607
cortical development anomalies, *V2*: 1595–1596
cystic renal disease, *V2*: 1614–1616
destructive lesions, *V2*: 1596–1601
developmental, *V2*: 1594–1595
gastrointestinal system, *V2*: 1614–1615
head and neck, *V2*: 1598–1599, 1601–1607
hernia, *V2*: 1604–1605, 1608–1609
hydronephrosis, *V2*: 1613–1614
kidneys, *V2*: 1612–1613
persistent cloaca, *V2*: 1614
posterior fossa, *V2*: 1591, 1593–1597
pulmonary maformations, *V2*: 1605–1606, 1610–1612
renal agenesis, *V2*: 1613
renal ectopia and fusion abnormalities, *V2*: 1613
thoracic cysts, *V2*: 1612
thorax, *V2*: 1604, 1612
ventriculomegaly, *V2*: 1585–1592

extremities, *V2*: 1620–1622
fetal weight and amniotic fluid, *V2*: 1622–1623
MR imaging techniques, *V2*: 1561, 1578
multiple gestation, *V2*: 1623–1624
neoplasms:
abdominal, *V2*: 1617–1620
brain, *V2*: 1598–1599, 1600–1607
thoracic, *V2*: 1612
normal anatomy:
abdomen and pelvis, *V2*: 1583–1585
central nervous system, *V2*: 1578–1583
head and neck, *V2*: 1583
thorax, *V2*: 1583
placental imaging, fetal demise, *V2*: 1623, 1625–1627
safety and procedures, *V2*: 1559–1561
Fetal demise, invasive placenta, *V2*: 1625, 1627
Fetal weight, MR imaging and, *V2*: 1622–1623
Fibroadenolipoma, *V2*: 1709, 1711
Fibroadenoma (FA), breast, *V2*: 1702–1706
Fibrocystic breast changes (FCC), *V2*: 1712, 1714–1716
Fibroids, uterine, *V2*: 1456, 1462–1464. *See also* Leiomyomas
in pregnancy, maternal imaging, *V2*: 1567
Fibrolamellar carcinoma, imaging studies, *V1*: 238–239
Fibromas:
benign ovarian neoplasms, *V2*: 1525–1526, 1529–1530
malignant ovarian neoplasms, *V2*: 1540, 1542, 1545–1547
Fibromatosis, aggressive, *V2*: 912–914
Fibromuscular dysplasia, renal arteries and, *V2*: 1133, 1137
Fibrosarcoma, abdominal wall metastases, *V2*: 1274, 1287
Fibrosis:
bladder, transitional cell carcinoma recurrence, differential diagnosis, *V2*: 1308, 1316
chronic pancreatitis, *V1*: 648–665
cirrhosis and, *V1*: 333, 335–338
varices, *V1*: 351, 362
Crohn disease, *V1*: 785
liver:
autoimmune hepatitis and, *V1*: 312–314
chronic hepatitis, *V1*: 321, 330
diffuse hepatocellular carcinoma, differential diagnosis, *V1*: 235
fetal assessment, renal cysts, *V2*: 1614–1616
hepatic transplantation, *V1*: 299, 304
hepatocellular adenoma, *V1*: 113
ovarian, endometriosis, *V2*: 1506–1507, 1509–1512
penis and urethra inflammatory disease, *V2*: 1380–1381
primary sclerosing cholangitis, *V1*: 497–502
rectosigmoid colon adenocarcinoma, *V1*: 852, 858, 861–865
retroperitoneum:
benign masses, *V2*: 1240, 1242–1244
lymphoma, *V2*: 1253–1257
malignant masses, *V2*: 1249, 1252–1253
Fibrothecoma:
benign ovarian neoplasms, *V2*: 1525–1526
malignant ovarian neoplasms, *V2*: 1540, 1542, 1545–1547
Fibrous histiocytoma:
abdominal wall metastases, *V2*: 1274, 1286
inferior vena cava, *V2*: 1240–1241
Fibrous stromal tumors, benign ovarian neoplasms, *V2*: 1518–1523
Field-focusing effect, 3T MR imaging, *V1*: 33
Field of view (FOV):
breast MRI, *V2*: 1692–1693
parallel MR imaging, *V1*: 29–31
three-dimensional gradient echo sequences, *V1*: 3
uterine-cervical MRI, *V2*: 1434
whole body imaging, *V1*: 36, 38
FIGO (International Federation of Gynecology and Obstetrics) classification:
cervical cancer, *V2*: 1482–1488
endometrial carcinoma, *V2*: 1470, 1472–1474
fallopian tube carcinoma, *V2*: 1551
ovarian cancer, epithelial tumors, *V2*: 1532–1533
vaginal malignancies, *V2*: 1416, 1420–1426
Fistulae:
arteriovenous fistulas, liver imaging, *V1*: 388–392
bladder, *V2*: 1326, 1331–1335
cervical cancer metastases, *V2*: 1486, 1489
colonic fistulae, *V1*: 883, 887–888
Crohn disease:
entero-vesical, *V1*: 810, 813
pelvic, *V1*: 810–812
enteric, gastrointestinal tract imaging, *V1*: 725
female urethra, *V2*: 1407–1408
peritoneal, pelvic abscess and, *V2*: 951, 959
small intestine, *V1*: 810–813
vaginal, *V2*: 1421, 1426, 1429–1430
Floating gallstones, T2-weighted imaging, *V1*: 464, 469
Focal hyperperfusion abnormality (FHA), liver imaging, *V1*: 414–415
Focal nodular hyperplasia (FNH):
Budd-Chiari syndrome, *V1*: 403, 406–407
fatty liver and, *V1*: 379
hemangiomas and, *V1*: 90
hepatocellular adenoma, differential diagnosis, *V1*: 113
hepatocyte-specific contrast agents, imaging studies, *V2*: 1768, 1770–1771
hypervascular liver metastases, differential diagnosis, *V1*: 177, 180
liver metastases, differential diagnosis, *V1*: 177, 180
MR imaging, *V1*: 119, 121–136
contrast agents, *V1*: 54, 55–58
exophytic FNH, *V1*: 121, 133–134
fatty infiltration, *V1*: 121, 130–132
in fatty liver, CT comparison, *V1*: 121, 129
large-sized FNH, *V1*: 121, 127
medium-sized FNH, *V1*: 121, 123–126
Foldover artifacts, parallel MR imaging, *V1*: 29–30
Follow-through MR imaging, small intestine:
Crohn disease, *V1*: 796
enteroclysis, *V1*: 767–770
Foregut hepatic cysts, *V1*: 60, 66–70
Foreign bodies, intraperitoneal, *V2*: 945–947
Frequency-selective fat-suppression methods, gradient echo sequences *vs.*, *V1*: 3
Fungal infection:
hepatic parenchyma, *V1*: 433, 435–438
hepatic transplantation, *V1*: 299, 305
renal candidiasis, *V2*: 1155
spleen, *V1*: 710–711

Gadofosveset trisodium (Vasovist), vessel imaging, *V2*: 1198–1200
Gadolinium-based contrast agents (GBCAs), *V2*: 1767–1777
breast feeding and, *V2*: 1786
chronic toxicity, *V2*: 1876
classification, *V2*: 1768–1774
complications, *V2*: 1779–1786
early hepatic venous phase, *V2*: 1776
enhancement phases, *V2*: 1768, 1770, 1774
hepatic arterial dominant phase, *V2*: 1774–1777
hepatocyte phase, *V2*: 1768, 1770, 1777
interstitial phase, *V2*: 1776
nephrogenic systemic fibrosis, *V2*: 1780–1786
pharmacokinetics, *V2*: 1781–1782
toxicity studies, *V2*: 1779–1786
Gadolinium-enhanced imaging. *See also* MultiHance contrast agent (Gd-BOPTA); Primivist (Gd-EOB-DTPA)-enhanced imaging
acute cholecystitis, *V1*: 468, 470–475
adnexa, *V2*: 1499–1500
adrenal glands, *V2*: 963–968
metastases, *V2*: 995–1002
aorta, *V2*: 1200–1227
aortic dissection, *V2*: 1201, 1208–1212
aortic graft evaluation, *V2*: 1214, 1216, 1224–1227
aortoiliac atherosclerotic disease/thrombosis, *V2*: 1204, 1207, 1214–1223

Gadolinium-enhanced imaging (*Continued*)
appendicitis diagnostic imaging, *V1*: 874, 879–881
bile duct, cholangiocarcinoma, *V1*: 517–518, 521–526
bladder, *V2*: 1298
congenital anomalies, *V2*: 1299–1301
cystitis, *V2*: 1326–1328
fistulas, *V2*: 1331–1335
neurofibromas, *V2*: 1304–1305
papilloma, *V2*: 1300–1301
radiation changes, *V2*: 1337
squamous cell carcinoma, *V2*: 1316–1319
transitional cell carcinoma, *V2*: 1307–1316
breast, *V2*: 1688, 1690–1691
breast cancer, *V2*: 1723
chest imaging, *V2*: 1654
hilar and mediastinal lymphadenopathy, *V2*: 1666–1667
pulmonary emboli, *V2*: 1673, 1675–1677
cirrhosis, portal hypertension, *V1*: 348, 351, 359–362
colon cancer, *V1*: 843–865
lymphoma, *V1*: 860, 867
melanoma, *V1*: 867, 869
perirectal/peritoneal metastases, *V1*: 848, 854–857
contrast agents, *V2*: 1767–1777
disease detection and characterization, *V1*: 2
esophageal imaging, *V1*: 726–727
esophageal varices, *V1*: 727, 729
leiomyomas, *V1*: 726–728
malignant masses, *V1*: 729–731
reflux esophagitis, *V1*: 730, 732
fat effects and, *V1*: 13–15
fat-suppressed gradient echo sequences, *V1*: 4
female urethral diverticulum, *V2*: 1405–1407
gallbladder:
acute cholecystitis, *V1*: 472–475
adenomyomatosis, *V1*: 480, 484
carcinoma, *V1*: 481, 485–486
neoplastic polyps, *V1*: 480, 482–483
gastrointestinal tract, *V1*: 725
hepatic abscess, pyogenic, *V1*: 418, 422–432
hepatic transplantation, ischemic changes, *V1*: 287, 290–292
hepatocyte targeting, contrast agents, *V1*: 50–58
kidneys, *V2*: 1029–1031
fibromuscular dysplasia, *V2*: 1133, 1136–1137
hemodialysis effects, *V2*: 1102
hypertrophic kidney, *V2*: 1032, 1037
iron deposition, *V2*: 1121, 1125–1127
lymphoma, *V2*: 1106–1110
myelofibrosis, *V2*: 1073
pelvic kidney, *V2*: 1032
perinephric pseudocyst, *V2*: 1042, 1044, 1050
persistent fetal lobulation, *V2*: 1031
prominent columns of Bertin, *V2*: 1031
renal artery disease, *V2*: 1129, 1131–1144
renal collecting system dilation, *V2*: 1164, 1172
renal filling defects, *V2*: 1159, 1166–1169
renal function, *V2*: 1173–1177
transplants, *V2*: 1177–1184
trauma, *V2*: 1172–1174
Wilms tumor, *V2*: 1103–1106
large intestine:
abscesses, *V1*: 881–886
colonic adenomatous polyps, *V1*: 832, 835–838
colonic fistulae, *V1*: 883, 887–888
diverticulitis, *V1*: 869, 874–879
infectious colitis, *V1*: 888
mucocele, *V1*: 838, 841–842
positive intraluminal contrast agents, *V1*: 895
rectosigmoid carcinoma, *V1*: 850, 857–860
rectosigmoid colon adenocarcinoma, *V1*: 852, 863–865
techniques, *V1*: 824
ulcerative colitis, *V1*: 867–868, 870–871
liver, *V1*: 46, 49–50
arteriovenous fistulas, *V1*: 388–392
autoimmune hepatitis, *V1*: 312–314
bile duct carcinoma, intrahepatic/peripheral metastases, *V1*: 239–240, 242, 247–249
Budd-Chiari syndrome, hepatic venous thrombosis, *V1*: 398, 401–405
contrast agents, *V1*: 54, 55–58
hepatic cysts, solitary (nonparasitic) cysts, *V1*: 60, 64
metastases detection and characterization, *V1*: 128, 137–143
mycobacterium avium intracellulare, *V1*: 433–435
porta hepatis lymphadenopathy, *V1*: 352, 354, 359, 362–365
pyogenic abscess, *V1*: 418, 422–432
transcatheter arterial embolization, *V1*: 268, 270–278
undifferentiated sarcoma, *V1*: 251, 256
magnetization-prepared rapid-acquisition gradient echo sequences, *V1*: 5–6
male pelvis, *V2*: 1343–1344
ovaries:
endometrial implants, *V2*: 1506
endometrioma, *V2*: 1504–1505, 1509, 1513
germ cell tumors, *V2*: 1521
Krukenberg tumor, ovarian metastases, *V2*: 1547, 1550
mucinous cystadenocarcinoma, *V2*: 1533, 1536–1537
pelvic inflammatory disease, *V2*: 1514, 1516–1517
primary ovarian carcinoma, *V2*: 1531
sex cord-stromal tumors, *V2*: 1525–1526, 1529–1531
pancreas, *V1*: 536–541
acute pancreatitis, *V1*: 631
annular pancreas, *V1*: 542–544
autoimmune pancreatitis, *V1*: 664, 666
chronic pancreatitis, *V1*: 648–665
insulinomas, *V1*: 601, 603
mucinous cystadenoma/cystadenocarcinoma, *V1*: 612–616
pancreatic adenocarcinoma, *V1*: 552, 558–559, 562–564
pancreatic transplants, *V1*: 671–673
pediatric patients, *V2*: 1647
pelvic varices, *V2*: 1518
penis and urethra:
inflammatory disease, *V2*: 1380–1381
normal anatomy, *V2*: 1375–1376
peritoneal inflammation:
abscess, *V2*: 949, 951, 954–959
pancreatitis, *V2*: 940–942, 946, 949
peritoneal metastases, intraperitoneal seeding, *V2*: 918–924
portal venous thrombosis, *V1*: 393–398
in pregnancy, *V2*: 1560–1561
placental imaging, *V2*: 1625–1627
postpartum uterus, *V2*: 1578–1580
primary sclerosing cholangitis, MRCP imaging and, *V1*: 499–502
prostate cancer, adenocarcinoma, *V2*: 1357–1373
rectum:
adenocarcinoma, *V1*: 848–850, 858
rectal carcinoid tumors, *V1*: 867–868
techniques, *V1*: 827, 831
renal cell carcinoma, *V2*: 1099, 1102
staging, *V2*: 1073, 1077, 1079–1082, 1084–1087
retroperitoneum, *V2*: 1193–1194
benign lymphadenopathy, *V2*: 1247–1250
small intestine, *V1*: 767–770
adenocarcinoma, *V1*: 777, 781–782
carcinoid tumors, *V1*: 779, 790–791
Crohn disease, *V1*: 785, 791, 793–805
gastrointestinal stromal tumor, *V1*: 779, 783–785
infectious enteritis, *V1*: 810, 813–814
metastases to, *V1*: 782, 791–792
pancreatitis, *V1*: 810, 815
polyps, *V1*: 775, 777–778
radiation enteritis, *V1*: 816, 818
spleen, lymphomas, *V1*: 693–694, 699–703
stomach, *V1*: 734
gastric adenocarcinoma, *V1*: 738, 741, 743–751
gastrointestinal stromal tumors, *V1*: 743, 748, 752–758
postoperative evaluation, *V1*: 761, 766

T1-weighted magnetic resonance cholangiopancreatography, *V1*: 460–461
T1-weighted sequences, *V1*: 10–13
hepatic arterial dominant (capillary) phase, *V1*: 10–13
hepatic venous (interstitial) phase, *V1*: 11
portal venous/early hepatic venous phase, *V1*: 11
testes, scrotum and epididymis, *V2*: 1385
benign neoplasms, *V2*: 1388, 1390
infectious disease, *V2*: 1397–1398
three-dimensional gradient echo sequences, *V1*: 4
uterus:
endometrial hyperplasia/polyps, *V2*: 1449–1450
leiomyomas, *V2*: 1449, 1455–1457
vaginal malignancies, *V2*: 1416, 1420–1426
vessel imaging, *V2*: 1195–1200
inferior vena cava thrombus, *V2*: 1229–1237
signal intensity, *V1*: 14
whole body imaging, *V1*: 39–42
Gadovist gadolinium-based contrast agent, *V2*: 1768
Galactocele, breast cancer, *V2*: 1739–1740
Galactography, intraductal papilloma, differential diagnosis, *V2*: 1707–1709
Gallbladder:
bile layering, *V1*: 460, 464
cirrhosis regenerative nodules, *V1*: 334, 343
diffuse wall thickening, *V1*: 480–481
fetal assessment, normal development, *V2*: 1584–1585
gallstone disease:
acute cholecystitis with, *V1*: 468, 473–475
floating gallstones, *V1*: 464, 469
hyperintense gallstones, *V1*: 464, 469
neoplastic disease:
adenomyomatosis, *V1*: 480, 484
gallbladder carcinoma, *V1*: 480–481, 485–486
gallbladder polyps, *V1*: 480, 482–483
metastases to, *V1*: 483, 487
nonneoplastic disease:
acute cholecystitis, magnetic resonance cholangiopancreatography, *V1*: 468–475
chemoembolization-induced, *V1*: 468, 476
acute on chronic cholecystitis, *V1*: 468, 475
chronic cholecystitis, *V1*: 475, 477–478
gallstone disease, *V1*: 464–465, 467–469
hemorrhagic cholecystitis, *V1*: 475–477
xanthogranulomatous cholecystitis, *V1*: 477
normal anatomy, *V1*: 456
variants, *V1*: 460, 462–464
pediatric imaging, *V2*: 1649
porcelain gallbladder, *V1*: 477, 480
T1-weighted magnetic resonance cholangiopancreatography, *V1*: 460–461
Gallstones, acute pancreatitis and, *V1*: 625, 632
Gamna-Gandy bodies:
cirrhosis and, *V1*: 353
heterozygous thalassemia, *V1*: 374
spleen, *V1*: 711, 714
Ganglioma, adrenal glands, *V2*: 1006, 1012–1017
Ganglioneuroblastoma:
adrenal glands, *V2*: 1006, 1013, 1015–1017
retroperitoneum, *V2*: 1266
Ganglioneuromas, bladder lesions, *V2*: 1304–1305
Gardner syndrome:
colonic adenomatous polyps, *V1*: 829, 832
desmoid tumor, *V2*: 1274, 1280–1283
Gartner duct cyst, *V2*: 1416, 1418–1419
Gas bubbles, liver imaging, post-ablative therapies, *V1*: 286–287
Gastric adenocarcinoma, *V1*: 738, 741, 743–751
antrum, *V1*: 741, 747–748
body, *V1*: 741, 745–746
cardia, *V1*: 741, 744–745
colon cancer, differential diagnosis, *V1*: 843
extensive carcinomatosis, *V1*: 738, 751
pylorus, *V1*: 741, 749
TNM staging, *V1*: 738, 741–742
Gastric banding, *V1*: 761, 766
Gastric bowel imaging, protocol for, *V1*: 20, 22
Gastric diverticulum, imaging studies, *V1*: 736–738
Gastric duplication cysts, imaging studies, *V1*: 736
Gastric neurofibromas, *V1*: 739
Gastric outlet, Crohn disease obstruction, *V1*: 785, 799
Gastric polyps, imaging studies, *V1*: 736, 739–741
Gastric schwannoma, *V1*: 736, 740
Gastric ulceration, *V1*: 761–764
Gastric varices:
cirrhosis, *V1*: 348, 351, 359
MR imaging, *V1*: 738, 742
Gastric wall edema, *V1*: 761, 764
Gastric wall hyperplasia, MR imaging, *V1*: 601
Gastrinomas:
extrapancreatic, *V1*: 591, 593, 599–600
liver metastases, *V1*: 164, 180
transcatheter arterial chemoembolization, *V1*: 270, 272
pancreatic cancer, *V1*: 591, 593, 598–602
multiple, *V1*: 593, 600
Gastrinoma triangle, islet cell tumor imaging, *V1*: 598
Gastrin secretion, stomach carcinoids, *V1*: 759
Gastritis, *V1*: 761–764
atrophic, *V1*: 761, 763
Gastroduodenal pseudoaneurysm, *V2*: 1200–1201, 1205–1206
Gastroenteritis, eosinophilic gastroenteritis, small intestine, *V1*: 809
Gastroesophageal reflux disease (GERD), imaging studies, *V1*: 729–730, 732
Gastrointestinal juvenile polyposis, colonic hamartomas, *V1*: 832
Gastrointestinal stromal tumors (GISTs):
colorectal metastases, *V1*: 860, 866
imaging studies, *V1*: 743, 748, 752–758
high-grade GIST, *V1*: 748, 756
intermediate-to high-grade, *V1*: 748, 757
leiomyomas, *V1*: 726–728
liver metastases, sarcomas, *V1*: 147–150
low grade, *V1*: 748, 757–758
small intestine, *V1*: 777, 779, 783–785
Gastrointestinal tract. *See also* Stomach; specific segments, e.g., Esophagus
fetal assessment, *V2*: 1614–1615
MR imaging, *V1*: 725
pediatric imaging, *V2*: 1650
in pregnancy, maternal imaging, *V2*: 1564–1565
Gastrojejunostomy, *V1*: 761, 766
Gastroschisis, fetal assessment, *V2*: 1617
Gaucher disease, spleen imaging and, *V1*: 683
Genetic disease:
breast cancer, *V2*: 1722–1723
hemochromatosis:
liver imaging, *V1*: 354, 362, 365–368
pancreas, *V1*: 546, 548–549
liver, *V1*: 315–318
α1-antitrypsin deficiency, *V1*: 315, 317
Wilson disease, *V1*: 315–318
pancreas:
cystic fibrosis, *V1*: 544–548
primary hemochromatosis, *V1*: 546, 548–549
von Hippel-Lindau syndrome, *V1*: 549–550
Genitalia. *See also* Gonadal differentiation anomalies; Vagina; specific male and female organs, e.g., Penis
ambiguous, *V2*: 1415–1416
Germ cell tumors:
benign ovarian neoplasms, *V2*: 1520–1521, 1526–1529
malignant ovarian neoplasms, *V2*: 1533–1534, 1540–1544
testes lesions, *V2*: 1390–1396
Gestational trophoblastic disease, *V2*: 1628–1629
postpartum uterus, *V2*: 1578–1580
theca-lutein cysts, *V2*: 1504
Ghosting artifacts, breast MRI, *V2*: 1695

Giant cell tumor:
abdominal wall metastases, *V2*: 1274, 1289, 1290
bile duct, *V1*: 511, 514
Giant lymph node hyperplasia, retroperitoneal benign lymphadenopathy, *V2*: 1249–1250
Giardia lamblia, infectious enteritis, differential diagnosis, *V1*: 810, 813–814
Gleason score, prostate cancer, *V2*: 1368
Glomerular disease, *V2*: 1117–1120
renal vein thrombosis, *V2*: 1137, 1144
Glomerular filtration rate (GFR), nephrogenic systemic fibrosis, *V2*: 1781
Glucagonoma, MR imaging, *V1*: 601, 604
Glucocerebroside accumulation, Gaucher disease, *V1*: 683
Gluten-sensitive enteropathy (GSE), small intestine, *V1*: 799, 807–809
Goiter, fetal assessment, *V2*: 1598
Gonadal differentiation anomalies, vagina, *V2*: 1415
Gonadal dysgenesis:
gonadal differentiation anomalies, *V2*: 1415
ovarian anomalies, *V2*: 1503
uterine anomalies, *V2*: 1441–1442
Gonadoblastoma, ovarian anomalies, *V2*: 1503
Gossypiboma, intraperitoneal, *V2*: 945–947
Gradient echo sequences:
abdinomal-pelvic imaging, advantages, *V1*: 2–3
adrenal glands, *V2*: 963–968
aortic dissection, *V2*: 1201, 1208–1212
chest imaging, *V2*: 1654
fat-suppressed gradient echo sequences, *V1*: 4
kidneys:
iron deposition, *V2*: 1121, 1125–1127
renal collecting system dilation, *V2*: 1164, 1172
liver imaging:
contrast agents, *V1*: 51–58
fat/iron deposition, *V1*: 371, 376
fatty liver, *V1*: 371, 373, 377–387
metastases detection and characterization, *V1*: 128, 137–143
portal venous thrombosis, *V1*: 391, 393–400
magnetization-prepared rapid-acquisition gradient echo sequences, *V1*: 5–6
out-of-phase gradient echo sequences, *V1*: 4–5
pancreatic cancer:
adenocarcinoma, staging, *V1*: 575, 577–587
gastrinomas, *V1*: 591, 598–602
pediatric pateients, *V2*: 1637
renal artery disease, *V2*: 1136, 1139–1140
serial MRI examination, *V1*: 24–28
spoiled gradient echo sequences, *V1*: 3–4
T1-weighted magnetic resonance cholangiopancreatography, *V1*: 460
vessel imaging, *V2*: 1195–1200
Gradient system, breast MRI, *V2*: 1693
Graft failure:
aortic graft, postoperative evaluation, *V2*: 1207, 1214, 1216, 1224–1227
hepatic transplantation, *V1*: 287, 292
liver abnormalities, *V1*: 299, 303–306
Graft-*versus*-host disease, small intestine, *V1*: 816–817, 828–829
Gram-negative bacterial, prostate infection, *V2*: 1373–1374
Granulocytic sarcoma:
bladder, *V2*: 1316, 1321
kidney, *V2*: 1109, 1111
Granulomatous disease:
bladder, *V2*: 1326
breast abscess, *V2*: 1712
Granulosa cell tumors, malignant ovarian neoplasms, *V2*: 1540, 1542, 1545–1547
Gynecological malignancies:
bladder metastases, *V2*: 1320–1324
peritoneal metastases, *V2*: 923–924, 932

Half-Fourier acquisition single shot turbo spin-echo (HASTE) sequence:
abdominal pelvic imaging, *V1*: 7
adrenal gland imaging, *V2*: 963–964, 966
adenomas, *V2*: 971, 982–983
aldosteronomas, *V2*: 977, 986–987
cyst/pseudocyst, *V2*: 980–981, 984, 992–993
hypovascular adrenal metastases, *V2*: 994–995, 998, 1000
myelolipoma, *V2*: 977–980, 988–990
bladder imaging, *V2*: 1298
magnetic resonance cholangiopancreatography, *V1*: 456, 460
pancreatic imaging, *V1*: 536–539
pediatric patients, *V2*: 1644
retroperitoneal imaging, *V2*: 1194
scrotal hernia, *V2*: 1390
stomach, *V1*: 734–736
vessel imaging, *V2*: 1200
Hamartomas:
breast, *V2*: 1709, 1711
colonic polyps, *V1*: 832
gastric polyps, *V1*: 736, 739–741
mesenchymal, *V2*: 1620
small intestine polyps, *V1*: 775, 777–778
spleen, *V1*: 690, 693, 695–697
Head imaging, fetal assessment:
anomalies, *V2*: 1598–1599, 1601–1607
normal development, *V2*: 1583
Helicobacter pylori infection:
gastric ulceration and gastritis, *V1*: 761–764
stomach carcinoids, *V1*: 759
HELLP syndrome. *See* Hemolytic anemia, elevated liver function tests, and low platelets (HELLP) syndrome
Hemangioendothelioma, fetal assessment, *V2*: 1620
Hemangiomas:
adrenal glands, *V2*: 993–994
bladder lesiosn, *V2*: 1304
cavernous, *V2*: 1416, 1420
congenital, fetal assessment, *V2*: 1604, 1607
large intestine, infiltration, Kippel-Trenaunay syndrome, *V1*: 832, 841
liver lesions:
capsule-based, *V1*: 90, 101
central filling, *V1*: 73, 84–85
exophytic, *V1*: 101–103
Gd-EOB-DTPA-enhanced imaging, *V1*: 52, 54
giant hemangioma, *V1*: 88, 97–99
liver lesions, *V1*: 70, 72–73, 81, 83–106
metastases, differential diagnosis, *V1*: 165, 177, 190
multiple, *V1*: 72–73, 83
perilesional enhancement, *V1*: 90, 101
metastases, differential diagnosis, *V1*: 147–150
portal vein compression, *V1*: 88, 100, 391
type 1 enhancement, *V1*: 85, 87
type 2 enhancement:
central nodular lesion, *V1*: 85, 91
medium-sized lesion, *V1*: 85, 89–91
small lesion, *V1*: 85–86
small-sized slow-enhancing, *V1*: 88, 94–95
type 3 enhancement:
medium-sized lesion, *V1*: 88, 92–94
small lesion, *V1*: 85, 88
small-sized slow-enhancing, *V1*: 88, 95–96
pancreatic islet cell tumors, differential diagnosis, *V1*: 593
pelvic, *V2*: 1274, 1291–1292
spleen, *V1*: 687–688, 691–693
Hemangiopericytoma, retroperitoneal imaging, *V2*: 1266, 1273
Hematocele, testes, scrotum and epididymis, *V2*: 1388, 1390
Hematocolpometra:
didelphys uterine anomaly, *V2*: 1441, 1444–1446
vaginal duplication, *V2*: 1412, 1414
Hematogenous metastases:
body wall, *V2*: 1274, 1284–1290
ovarian endodermal sinus tumor, *V2*: 1534, 1542
peritoneum, *V2*: 924
Hematomas:
abdominal wall, *V2*: 1274
duodenal, *V1*: 816, 823
hepatic transplantation, *V1*: 292, 294–295
iliacus muscle, *V2*: 1274, 1279–1280

intramural dissecting, *V2*: 1201, 1204, 1213
liver trauma, *V1*: 438–442
pelvic, *V2*: 936, 944
perirenal, *V2*: 1156, 1158
postmyomectomy, *V2*: 1456, 1465
retroperitoneal, *V2*: 1249, 1251
splenic laceration, *V1*: 715, 716–717
subchorionic, in pregnancy, *V2*: 1559–1560
uterine, in pregnancy, *V2*: 1559–1560
postpartum uterus, *V2*: 1575–1580
Hematometra, vaginal agenesis/partial agenesis, *V2*: 1411–1412
Hemochromatosis:
primary:
liver, *V1*: 354, 362, 365–368
pancreas, *V1*: 546, 548–549
secondary, liver imaging, *V1*: 368–374
Hemodialysis:
acquired cystic disease, *V2*: 1049, 1052, 1061–1062
nephrogenic systemic fibrosis prevention, *V2*: 1783
Hemolytic anemia:
adrenal gland myelolipoma, *V2*: 977, 979–980, 988–990
liver imaging, *V1*: 368, 374–375
Hemolytic anemia, elevated liver function tests, and low platelets (HELLP) syndrome, liver imaging, *V1*: 407, 410–411
Hemorrhage:
acute pancreatitis, *V1*: 632, 639–640
adrenal glands, *V2*: 1019–1020
adenomas, *V2*: 971, 982–983
metastases, *V2*: 994–995, 998, 1000
pseudocysts, *V2*: 984, 991–994
cholecystitis, *V1*: 475–477
fetal assessment:
destructive lesions, *V2*: 1596–1601
intraventricular, *V2*: 1598, 1600–1601
hemangiomas and, *V1*: 88, 101, 103
hepatocellular adenoma, *V1*: 51, 107, 110–114
kidney, *V2*: 1156, 1158
liver metastases, *V1*: 165
ovaries:
clear cell carcinoma malignancies, *V2*: 1533, 1540
endometriosis, *V2*: 1506–1507, 1509–1512
hydrosalpinx, *V2*: 1517
paraovarian cysts, *V2*: 1504, 1508
pelvic inflammatory disease, *V2*: 1514, 1516–1517
sex cord-stromal tumor malignancies, *V2*: 1542, 1545–1547
prostate cancer therapy and, *V2*: 1368, 1370
psoas muscle, *V2*: 1274, 1276–1277
renal cell carcinoma, *V2*: 1088–1094
chronic renal failure, *V2*: 1098–1101
retroperitoneum, imaging techniques, *V2*: 1193–1194
small intestine, *V1*: 816, 819–823
stages, *V1*: 442
uterus, leiomyoma, *V2*: 1456, 1458–1459
Hemorrhagic cystitis, bladder, *V2*: 1326, 1329
Hemorrhagic ovarian cysts, *V2*: 1500, 1503
Hemorrhagic/proteinaceous renal cysts, *V2*: 1037, 1042–1047
angiomyolipomas, *V2*: 1063, 1066
dialysis, *V2*: 1049, 1052, 1062
Hemorrhagic pseudocysts:
chronic pancreatitis, *V1*: 656, 665
spleen, *V1*: 683, 687–690
Hemorrhagic telangiectasia, hepatic arteriovenous fistulas, *V1*: 388–392
Hemorrhoids, rectal varices and, *V1*: 838
Hemosiderin deposition:
bladder, hemorrhagic cysts, *V2*: 1326, 1329
spleen imaging, *V1*: 678–681
Hepatectomy, liver regeneration after, *V1*: 256, 259
Hepatic alveolar echinococcosis (HAE), *V1*: 430, 432–433
Hepatic arterial dominant phase (HADP) imaging, gadolinium-based contrast agent, *V2*: 1774–1777
Hepatic artery(ies):
adrenal gland imaging, capillary phase enhancement, *V2*: 964–968
gadolinium-enhanced SGE images, *V1*: 46, 49
gadolinium-enhanced T1-weighted sequences, *V1*: 10–13
hepatic transplant complications, *V1*: 287, 292
hepatocellular carcinoma, *V1*: 192, 198, 202
imaging protocol for, *V1*: 16–20
Mn-DPDP-enhanced SGE imaging, *V1*: 46, 50
obstruction, *V1*: 405, 407–408
Hepatic cysts:
autosomal dominant polycystic kidney disease, *V1*: 67, 71–72
ciliated foregut cysts, *V1*: 60, 66–70
coexistent metastases, *V1*: 165, 190
hemorrhagic cyst, *V1*: 60, 65
hydatid cyst, echinococcal disease, *V1*: 430–431
multilocular cyst, *V1*: 60, 65–66
solitary (nonparasitic), *V1*: 60–66
unilocular cyst, *V1*: 60–61
Hepatic parenchyma:
chronic liver disease:
autoimmune diseases, *V1*: 303–304, 306–315
autoimmune hepatitis, *V1*: 311–314
primary biliary cirrhosis, *V1*: 314–315
primary sclerosing cholangitis, *V1*: 303–304, 306–311
genetic diseases, *V1*: 315–317
α1-antitrypsin deficiency, *V1*: 315, 317
Wilson disease, *V1*: 315–318
hemangiomas, *V1*: 101, 103–106
nonalcoholic fatty liver disease, *V1*: 317, 319–320
radiation-induced hepatitis, *V1*: 321, 331
viral hepatitis, *V1*: 319, 321–330
diseases:
benign masses, *V1*: 60–121
angiomyolipomas, *V1*: 67, 70, 80–81
autosomal dominant polycystic kidney disease, *V1*: 67, 74–77
biliary cystadenoma/cystadenocarcinoma, *V1*: 67, 77–78
ciliated hepatic foregut cysts, *V1*: 60, 66–70
extramedullary hematopoiesis, *V1*: 67, 79–80
focal nodular hyperplasia, *V1*: 119, 121–136
hemangiomas, *V1*: 70, 72–73, 81–106
hepatocellular adenoma, *V1*: 107, 109–118
infantile hemangioendothelioma, *V1*: 106–109
lipomas, *V1*: 70, 82
peliosis hepatis, *V1*: 114–115, 119–120
solitary (nonparasitic cysts), *V1*: 60–66
malignant masses, *V1*: 121, 128, 137–287 (*See also* Liver, metastases)
ablative therapies, *V1*: 278–287
angiosarcoma, *V1*: 240, 242, 249
epithelioid hemangioendothelioma, *V1*: 251–253
fibrolamellar carcinoma, *V1*: 238–239
hepatoblastoma, *V1*: 251, 253–255
hepatocellular carcinoma, diffuse, *V1*: 212, 227–238
hepatocellular carcinoma, focal, *V1*: 188–189, 192–233
intrahepatic/peripheral bile duct carcinoma (cholangiocarcinoma), *V1*: 238–240, 242, 247–249
liver metastases, *V1*: 121, 128, 137–188
lesional/perilesional enhancement, *V1*: 147–150
MRI detection and characterization, *V1*: 127, 128, 137–143
MRI *vs.* CT, *V1*: 141–144
MRI *vs.* CTAP, *V1*: 143, 145–147
primary site features, *V1*: 161–162, 164–192
T1 *vs.* T2 images, *V1*: 143, 147
vascularity and degree of enhancement, *V1*: 149, 151–164
lymphoma, *V1*: 238, 240–245
malignant mesothelioma, *V1*: 242, 250–251

Hepatic parenchyma: (*Contnued*)
multiple myeloma, *V1*: 238, 245–246
postradiation therapy, *V1*: 257, 262–263
posttreatment lesions, *V1*: 256
resections, *V1*: 256–262
systemic chemotherapy, *V1*: 257, 264–270
transcatheter arterial chemoembolization, *V1*: 268, 270–278
undifferentiated sarcoma, *V1*: 251, 256
hepatic arterial dominant phase imaging, gadolinium-based contrast agent, *V2*: 1775–1777
infectious disease:
amebic (nonpyogenic) abscess, *V1*: 430
echinococcal disease, *V1*: 430–433
fungal infection, *V1*: 433, 436–438
metastases, secondary infection, *V1*: 180, 188, 191–192
mycobacterium avium intracellulare, *V1*: 433–435
mycobacterium tuberculosis, *V1*: 433
pyogenic abscess, *V1*: 418, 422–432
inflammatory disease:
hepatic transplantation complication, *V1*: 299–300
inflammatory myofibroblastic tumor (pseudotumor), *V1*: 415, 418–422
sarcoidosis, *V1*: 414–416
Hepatic transplantation:
bile duct obstruction following, *V1*: 292, 299
donor and recipient assessment, *V1*: 287–292
fibrosis, *V1*: 299, 304
fungal infection, *V1*: 299, 305
graft failure, *V1*: 287, 292
liver abnormalities, *V1*: 299, 303–306
hepatic arterial obstruction, *V1*: 405, 407–408
hepatocellular carcinoma recurrence, *V1*: 299, 302
inflammation following, *V1*: 299–300
lymphoma, *V1*: 238, 241
magnetic resonance cholangiopancreatography, bile duct anastomoses, *V1*: 519–520
MR imaging, *V1*: 287–305
posttransplant lymphoproliferative disorder, *V1*: 299–301
vascular complications, *V1*: 292–298
Hepatic venous system:
gadolinium-enhanced T1-weighted imaging:
early phase, *V1*: 11
interstitial phase, *V1*: 13
hepatic transplantation, *V1*: 292–294
hepatocellular carcinoma, *V1*: 192, 198–202
thrombosis, Budd-Chiari syndrome, *V1*: 398, 401–405
Hepatitis:
acute hepatitis, *V1*: 321–324
acute on chronic, *V1*: 321, 327–329
autoimmune hepatitis, *V1*: 311–314
chronic, *V1*: 321, 330
diffuse hepatocellular carcinoma, differential diagnosis, *V1*: 235
hepatitis B, *V1*: 321, 325
hepatitis C, *V1*: 321, 325–327
nonalcoholic steatohepatitis, *V1*: 319–320
radiation-induced, *V1*: 321, 331
viral hepatitis:
hepatocellular carcinoma, *V1*: 202, 212
imaging studies, *V1*: 319, 321, 330
Hepatoblastoma, *V1*: 251, 253–255
Hepatocellular adenoma (HCA):
adenomatosis, *V1*: 114–118
fatty liver and, *V1*: 380, 383
hepatocyte-specific contrast agents, differential diagnosis, *V2*: 1768, 1770–1771
hypervascular liver metastases, differential diagnosis, *V1*: 177, 180
imaging studies, *V1*: 107, 109–118
liver metastases, differential diagnosis, *V1*: 177, 180
carcinoid tumor, *V1*: 164, 183–185
Hepatocellular carcinoma (HCC):
adrenal metastases, *V1*: 192, 199
biliary cystadenoma/cystadenocarcinoma, differential diagnosis, *V1*: 67, 77–78
body wall metastases, *V2*: 1274, 1284–1285
carcinoid tumor, differential diagnosis, *V1*: 164, 183–185
cholangiocarcinoma, differential diagnosis, *V1*: 239–240, 242, 245–247
cirrhosis, differential diagnosis, *V1*: 333
dysplastic nodules, *V1*: 342, 346–354, 357–358
venous thrombosis formation, *V1*: 333
diffuse infiltrative, *V1*: 212, 227, 234–238
fatty liver and, *V1*: 380
genetics, *V1*: 189
hemochromatosis and, *V1*: 354, 367–368
hepatic transplantation and recurrence of, *V1*: 299, 302
hepatic vein thrombosis, *V1*: 405
hepatocyte-specific contrast agents, imaging studies, *V2*: 1768
hypervascular tumors, *V1*: 198, 202, 218–223
hypovascular tumors, *V1*: 192–194, 198, 215–217
incidence and prevalence, *V1*: 188–189, 192
mixed HCC-cholangiocarcinoma, *V1*: 238–240, 242, 248–249
MRI *vs.* CT imaging, *V1*: 192, 203–205
multifocal tumors, *V1*: 192, 194–198, 203–205
peritoneal metastases, *V1*: 192, 200–201; *V2*: 918, 923–924, 931
pleural metastases, *V1*: 192, 202
radiofrequency ablation, *V1*: 278, 280–286
recurrence, *V1*: 256, 260–261
solitary hypovascular tumor, *V1*: 192–194
transcatheter arterial chemoembolization, *V1*: 270, 274–278
venous thrombosis, *V1*: 202, 212, 224–232, 234–238
cirrhosis differential diagnosis, *V1*: 333
well-differentiated tumors, *V1*: 192, 205–212
Hepatocyte function:
hepatocellular carcinoma, *V1*: 189
MRI contrast agent targeting, *V1*: 50–58
gadolinium-based contrast agents, *V2*: 1777
Hepatocyte-specific gadolinium-based contrast agents, *V2*: 1768, 1770–1772, 1777
Hepatomegaly, Reidel lobe, differential diagnosis, *V1*: 58–60
Hepatosplenic candidiasis:
acute, *V1*: 433, 435–436
subacute, *V1*: 433, 436–437
Hepatosplenic sarcoidosis, imaging studies, *V1*: 414–416
Hepatosplenorenal histoplasmosis, *V1*: 709–711
Herlyn-Werner-Wunderlich syndrome, Gartner duct cyst, *V2*: 1416, 1418–1419
Hermaphroditis, gonadal differentiation anomalies, *V2*: 1415
Hernias, *V2*: 904–909
abdominal wall, *V2*: 904, 908–909, 1274
Bochdalek hernia, *V2*: 904–905
fetal assessment, *V2*: 1604–1605, 1608–1609, 1612
congenital diaphragmatic, *V2*: 1604–1605, 1608–1609
hiatus and internal, *V2*: 904, 906–907
scrotal, *V2*: 1390
small intestine, *V1*: 816, 827
Herpes simplex virus (HSV), esophageal infection, *V1*: 731–734
Heterotopias, congenital:
fetal assessment:
Chiari II malformation, *V2*: 1588–1592
subependymal, *V2*: 1595
stomach, *V1*: 736
Heterozygous thalassemia, liver imaging, *V1*: 370, 374–375
Hiatus hernia, *V2*: 904, 906–907
Hilar lymphadenopathy, *V2*: 1666–1667
Histiocytomas, retroperitoneal neoplasms, *V2*: 1265, 1271
Histoplasmosis, hepatosplenorenal histoplasmosis, *V1*: 709–711
Hodgkin lymphoma:
kidneys, *V2*: 1106–1110
liver metastases, *V1*: 238, 241
retroperitoneal lymphadenopathy, *V2*: 1253–1254
spleen malignancies, *V1*: 693–694, 700

Holoprosencephaly, fetal assessment, *V2*: 1585–1592
Homogeneous high-signal-intensity enhancement, spleen, *V1*: 678–681
Hormone therapy, prostate cancer, *V2*: 1368–1369
Horseshoe kidney, *V2*: 1032, 1034
Human chorionic gonadotropin:
  gestational trophoblastic disease, *V2*: 1578–1580, 1628–1629
  theca-lutein ovarian cysts, *V2*: 1504
Human epidermal growth factor receptor 2 (HER2), invasive ductal carcinoma, *V2*: 1723–1727
Human immunodeficiency virus (HIV):
  colonic lymphoma, *V1*: 860, 867
  lymphoma, liver metastases, *V1*: 238, 245
Human papillomavirus, vaginal malignancies, *V2*: 1416, 1420–1426
Hutch diverticula, bladder, *V2*: 1299
Hydatid cyst:
  breast cysts, *V2*: 1701–1703
  liver imaging, *V1*: 430–431
  paraovarian cysts of Morgagni, *V2*: 1504, 1508
  spleen, *V1*: 683, 687–690
Hydatidiform mole, gestational trophoblastic disease, *V2*: 1628–1629
Hydranencephaly, fetal assessment, *V2*: 1598, 1600
Hydrocele, testes, scrotum and epididymis, *V2*: 1388–1392
Hydrocephalus, fetal assessment, brain neoplasms, *V2*: 1598
Hydronephrosis:
  bladder neurofibromas, *V2*: 1304
  fetal assessment, *V2*: 1613–1614
  in pregnancy, maternal imaging, *V2*: 1564, 1566
Hydrops, mesoblastic nephroma, *V2*: 1620
Hydrosalpinx, *V2*: 1517
Hydroureter, in pregnancy, *V2*: 1564
21-Hydroxylase deficiency, female pseudohermaphroditism, *V2*: 1415–1416
Hypergastrinemia, stomach carcinoids, *V1*: 759
Hyperintense gallstones, T1-weighted imaging, *V1*: 464, 469
Hyperplastic kidney, *V2*: 1032, 1037
Hyperplastic polyps:
  gastric polyps, *V1*: 736, 739–741
  small intestine, *V1*: 775, 777–778
Hypersplenism, littoral cell angioma, *V1*: 688, 694
Hypertrophic bladder, *V2*: 1324–1325
Hypertrophic kidney, *V2*: 1032, 1037
Hypertrophic rugal folds, *V1*: 761, 765
Hypervascular liver metastases, *V1*: 128, 138–139. *See also* specific types of cancer
  chemotherapy-related, *V1*: 257, 264–270
  degree of enhancement and, *V1*: 149, 151–162
  focal nodular hyperplasia/hepatic adenocarcinoma, differential diagnosis, *V1*: 177, 180
  hepatocellular carcinoma, *V1*: 198, 202, 218–223
    small satellite tumors, *V1*: 217–218
  pancreatic adenocarcinoma, differential diagnosis, *V1*: 587–589
  perilesional enhancement, *V1*: 149–150
Hypervascular renal tumors, *V2*: 1084, 1086
Hypoplasia, breast, *V2*: 1700–1701
Hypoplastic kidney, *V2*: 1032, 1036
Hypoplastic uterus, *V2*: 1441
Hypoproteinemia, small intestine, *V1*: 816, 824
Hypospadias, *V2*: 1376
Hypovascular liver metastases:
  chemotherapy-related, *V1*: 257, 264–270
  hepatocellular carcinoma, *V1*: 192–194, 198, 215–217
  imaging studies, *V1*: 149, 152–156, 162
Hypovascular renal tumors, *V2*: 1084, 1087
Hysterectomy:
  adenomyosis, *V2*: 1467
  vaginal malignancy recurrence, *V2*: 1416, 1420–1426
Hysterosalpingography, uterus, congenital anomalies, *V2*: 1440

Idiopathic hemochromatosis:
  hepatocellular carcinoma and, *V1*: 354, 367–368
  liver imaging:
    advanced disease, *V1*: 354, 362, 365–366
    early stage, *V1*: 354, 362, 365
Ileal carcinoid, *V1*: 779, 789
Iliacus muscle:
  hematoma, *V2*: 1274, 1279–1280
  melanoma metastases, *V2*: 1273, 1276
Iliac vessels:
  MR imaging, *V2*: 1198–1200
  stenosis, *V2*: 1204, 1207, 1216–1218
  thrombosis, *V2*: 1204, 1207, 1222–1223
Imperforate anus, reconstruction, *V1*: 827, 834
Incisional hernia, abdominal wall imaging, *V2*: 904, 909
Indiana pouch, bladder reconstruction, *V2*: 1331, 1336
Infantile hemangioendothelioma (IHE), imaging studies, *V1*: 106–109
Infants (under 1.5 years), MR imaging techniques, *V2*: 1645
Infarct, splenic, *V1*: 719–722
Infectious colitis, *V1*: 883–884, 888–892
Infectious disease:
  cholangitis, *V1*: 499, 502–507
    cholangiocarcinoma incidence and, *V1*: 515
  esophagus, *V1*: 731–734
  female urethra, *V2*: 1407–1408
hepatic parenchyma:
  amebic (nonpyogenic) abscess, *V1*: 430
  echinococcal disease, *V1*: 430–433
  fungal infection, *V1*: 433, 436–438
  metastases, secondary infection, *V1*: 180, 188, 191–192
  mycobacterium avium intracellulare, *V1*: 433–435
  mycobacterium tuberculosis, *V1*: 433
  pyogenic abscess, *V1*: 418, 422–432
kidneys:
  abscess, *V2*: 1142, 1144, 1149–1152
  acute pyelonephritis, *V2*: 1142, 1147–1149
  malakoplakia, *V2*: 1153–1154
  pyonephrosis, *V2*: 1155–1156
  renal candidiasis, *V2*: 1155
  xanthogranulomatous pyelonephritis, *V2*: 1151–1152
large intestine:
  abdominoperineal resection, *V1*: 892, 894–895
  abscess formation, *V1*: 874, 876–877, 881–886
  appendiceal abscess, *V1*: 874, 881
  appendicitis, *V1*: 874, 879–881
  colonic fistulae, *V1*: 883, 887–888
  Crohn colitis, *V1*: 869, 872–874
  diverticulitis, *V1*: 869, 874–879
  infectious colitis, *V1*: 883–884, 888–892
  radiation enteritis, *V1*: 888, 892–894
  rectal surgery, *V1*: 892, 894–895
  ulcerative colitis, *V1*: 867–868, 870–871
pancreas, *V1*: 664–667
  pancreatic transplants, *V1*: 671–673
penis and urethra, *V2*: 1380
peritoneum:
  abscess, *V2*: 949, 951, 954–959
  mesenteric panniculitis, *V2*: 946, 950
  pancreatitis, *V2*: 940–942, 946, 949
  peritonitis, *V2*: 949, 951–953
prostate gland, *V2*: 1373–1374
seminal vesicles, *V2*: 1383
small intestine:
  Crohn disease, *V1*: 784–785, 791, 793–805
  drug toxicity, *V1*: 810, 817
  eosinophilic gastroenteritis, *V1*: 809
  fistula, *V1*: 810, 812–813
  gluten-sensitive enteropathy, *V1*: 799, 807–809
  graft-*versus*-host disease, *V1*: 816–817, 828–829
  hernia, *V1*: 816, 827
  hypoproteinemia, *V1*: 816, 824
  infectious enteritis, *V1*: 810, 813–814
  inflammatory bowel disease, *V1*: 782, 784
  intussusception, *V1*: 816, 825–826
  ischemia and hemorrhage, *V1*: 816, 819–823
  pancreatitis, *V1*: 810, 815
  pouchitis, *V1*: 810

Infectious disease: (*Continued*)
radiation enteritis, *V1*: 815–816, 818
scleroderma, *V1*: 809
ulcerative colitis, *V1*: 796, 799, 806
spleen, *V1*: 709–711
stomach, *V1*: 761–764
testes, scrotum and epididymis, *V2*: 1397–1398
tubo-ovarian abscess, *V2*: 1514, 1516–1517
Infectious enteritis, small intestine, *V1*: 810, 813–814
Inferior vena cava, retroperitoneal imaging, *V2*: 1216, 1223, 1229
congenital anomalies, *V2*: 1223, 1229–1230
primary malignant tumors, *V2*: 1237–1241
venous thrombosis, *V2*: 1229–1237
Inflammatory aortitis, *V2*: 1201, 1207
Inflammatory bowel disease (IBD):
gastrointestinal tract imaging, *V1*: 725
pregnancy and, *V1*: 868, 871
primary sclerosing cholangitis, *V1*: 494, 497–502
small intestine, *V1*: 782, 784
Inflammatory breast carcinoma (IBC), *V2*: 1737, 1739
Inflammatory disease:
adrenal glands, *V2*: 1019
bladder, *V2*: 1326–1330
esophagus:
corrosive esophagitis, *V1*: 731
radiation esophagitis, *V1*: 730–731
reflux esophagitis, *V1*: 729–730, 732
female urethra, *V2*: 1407–1408
hepatic parenchyma:
hepatic transplantation complication, *V1*: 299–300
inflammatory myofibroblastic tumor (pseudotumor), *V1*: 415, 418–422
sarcoidosis, *V1*: 414–416
large intestine:
abdominoperineal resection, *V1*: 892, 894–895
abscess formation, *V1*: 874, 876–877, 881–886
appendiceal abscess, *V1*: 874, 881
appendicitis, *V1*: 874, 879–881
colonic fistulae, *V1*: 883, 887–888
Crohn colitis, *V1*: 869, 872–874
diverticulitis, *V1*: 869, 874–879
infectious colitis, *V1*: 883–884, 888–892
radiation enteritis, *V1*: 888, 892–894
rectal surgery, *V1*: 892, 894–895
ulcerative colitis, *V1*: 867–868, 870–871
pancreas, *V1*: 625
miscellaneous conditions and infections, *V1*: 664–667
pancreatic transplants, *V1*: 671–673
pancreatitis, *V1*: 625
acute, *V1*: 625, 628, 636–647
autoimmune pancreatitis, *V1*: 656, 664, 666
chemtherapy-induced, *V1*: 664–667
chronic, *V1*: 640, 648–665
hemorrhagic, *V1*: 632, 640–641
mild, *V1*: 625, 632–635
pseudocyst, *V1*: 632, 642–647
pelvic inflammatory disease, tubo-ovarian abscess, *V2*: 1514, 1516–1517
penis and urethra, *V2*: 1380–1381
peritoneum:
abscess, *V2*: 949, 951, 954–959
mesenteric panniculitis, *V2*: 946, 950
pancreatitis, *V2*: 940–942, 946, 949
peritonitis, *V2*: 949, 951–953
primary sclerosing cholangitis, *V1*: 494, 497–502
prostate gland, *V2*: 1373–1374
small intestine:
Crohn disease, *V1*: 784–785, 791, 793–805
drug toxicity, *V1*: 810, 817
eosinophilic gastroenteritis, *V1*: 809
fistula, *V1*: 810–813, 812–813
gluten-sensitive enteropathy, *V1*: 799, 807–809
graft-*versus*-host disease, *V1*: 816–817, 828–829
hernia, *V1*: 816, 827
hypoproteinemia, *V1*: 816, 824
infectious enteritis, *V1*: 810, 813–814
inflammatory bowel disease, *V1*: 782, 784
intussusception, *V1*: 816, 825–826
ischemia and hemorrhage, *V1*: 816, 819–823
pancreatitis, *V1*: 810, 815
pouchitis, *V1*: 810
radiation enteritis, *V1*: 815–816, 818
scleroderma, *V1*: 809
ulcerative colitis, *V1*: 796, 799, 806
stomach, *V1*: 761–764
Inflammatory myofibroblastic tumor:
bladder lesions, *V2*: 1304
hepatic inflammatory disease, *V1*: 415, 418–422
Inflammatory polyps, small intestine, *V1*: 775, 777–778
Infrarenal aorta, thrombotic occlusion, *V2*: 1204, 1207, 1219–1221
Inguinal hernia:
abdominal wall imaging, *V2*: 904, 908
small intestine, *V1*: 816, 827
Initial qualitative enhancement, breast cancer imaging, *V2*: 1723
Insulinomas, pancreatic imaging, *V1*: 601, 603–606
Internal hernia, *V2*: 904, 906–907
International Organization for the Study of Inflammatory Bowel Disease (IOIBD), MRI criteria, *V1*: 796, 803
Interstitial phase imaging:
adrenal pheochromocytomas, *V2*: 1006–1111
gadolinium-based contrast agents, *V2*: 1776–1777
hypervascular liver metastases, *V1*: 149, 157–162
kidneys:
candidiasis infection, *V2*: 1155
medullary sponge kidney, *V2*: 1049, 1060
transitional cell carcinoma, *V2*: 1159–1165
xanthogranulomatous pyelonephritis, *V2*: 1152
renal artery disease, *V2*: 1137
Intraabdominal abscess:
imaging studies, *V1*: 874, 884
peritoneal inflammation, *V2*: 949, 951, 954–959
Intracellular agents, gadolinium-based, *V2*: 1768–1774
Intracranial neoplasms, fetal assessment, *V2*: 1598
Intraductal papillary mucinous neoplasms (IPMN), *V1*: 614
main duct type, *V1*: 614–617
serous cystadenoma, differential diagnosis, *V1*: 612
side-branch type, *V1*: 615, 618–621
Intraductal papilloma, breast imaging, *V2*: 1707–1709, 1738
Intraluminal contrast agent:
peritoneal abscess imaging, *V2*: 951, 954–959
rectal imaging, *V1*: 827, 831
intramural dissecting hematoma, *V2*: 1201, 1204, 1213
Intrapericardial neoplasms, fetal assessment, *V2*: 1612
Intraperitoneal varices, cirrhosis, *V1*: 348, 351, 359
Intrathoracic imaging techniques, *V2*: 1653–1654
Intrauterine contraceptive devices:
pelvic inflammatory disease, *V2*: 1514, 1516–1517
uterine imaging, *V2*: 1433
Intrauterine growth retardation, twin pregnancies, *V2*: 1623
Intravenous urography (IVU), magnetic resonance urography *vs.*,*V2*: 1188
Intussusception:
colonic duplication, *V1*: 827, 832
colonic lipoma, *V1*: 832, 840
large intestine lipomas, *V1*: 832, 839–841
small intestine:
inflammatory/infectious disease, *V1*: 816, 825–826
polyps, *V1*: 775, 777–778
Invasive ductal carcinoma (IDC):
breast implants, *V2*: 1754–1756
classification and staging, *V2*: 1723–1731
neoadjuvant chemotherapy, *V2*: 1749, 1753
postoperative MRI, *V2*: 1744, 1746–1749
Invasive lobular carcinoma (ILC), classification and staging, *V2*: 1727, 1731–1733

Inversion pulse:
fat-suppressed echo-train spin-echo sequences, *V1*: 9–10
magnetization-prepared rapid-acquisition gradient echo sequences, *V1*: 5–6
vessel imaging, *V2*: 1200
Inverted teardrop sign, breast implant rupture, *V2*: 1759
Iodine-based contrast agents, *V2*: 1767
Iron-based contrast agents, *V2*: 1777–1779
large intestine imaging, *V1*: 896–897
Iron-containing structures, out-of-phase (opposed-phase) spoiled gradient echo sequence detection, *V1*: 4–5
Iron deposition:
liver:
cirrhosis, *V1*: 370
coexisting fat and, *V1*: 371, 376
genetic idiopathic hemochromatosis, *V1*: 354, 362, 365–368
secondary hemochromatosis:
hemolytic anemia, *V1*: 368, 370, 374–375
transfusional iron overload, *V1*: 368–373
pancreas, primary hemochromatosis, *V1*: 546, 548–549
renal parenchyma, *V2*: 1121, 1125–1127
spleen imaging, *V1*: 678–681
Iron oxides. *See* Superparamagnetic iron oxide particles (SPIO); Ultrasmall paramagnetic iron oxide particles
Ischemia:
cerebral, fetal assessment, *V2*: 1596–1601
hepatic arterial obstruction, *V1*: 405, 407–408
small intestine, *V1*: 816, 819–823
Ischemic nephropathy, *V2*: 1129, 1131, 1134, 1139
Islet cell tumors:
accessory spleen, differential diagnosis, *V1*: 681–685
pancreatic, *V1*: 590–598
ACTHoma, *V1*: 601, 605
duct obstruction, *V1*: 592
gastrinomas, *V1*: 591, 598–600
glucagonoma, *V1*: 601, 604
insulinomas, *V1*: 601, 603
liver metastases, *V1*: 591, 593–596
somatostatinoma, *V1*: 601, 604–605
thrombus, *V1*: 591, 593, 597
undifferentiated, *V1*: 601
VIPomas, *V1*: 601, 606
pancreatic adenocarcinoma, differential diagnosis, *V1*: 587–589
Isovascular liver metastases:
hepatocellular carcinoma, *V1*: 198, 215–217
imaging studies, *V1*: 149, 151
Ivemark syndrome (asplenia), MR imaging, *V1*: 681, 685

Jejeunal atresia, fetal assessment, *V2*: 1615
Joubert syndrome, fetal assessment, *V2*: 1593–1597
Juvenile hypertrophy, breast, *V2*: 1700–1701
Juvenile polyposis syndrome, colonic adenomatous polyps, *V1*: 832
Juxtarenal process, *V2*: 1172–1173

Kaposi sarcoma, *V1*: 748, 756
Karyotype analysis, gonadal differentiation anomalies, *V2*: 1415
Kasabach-Merritt sequence, fetal assessment, *V2*: 1620
Kawasaki disease, retroperitoneal benign lymphadenopathy, *V2*: 1249–1250
Kidneys. *See also* Renal parenchyma
benign masses:
adenomas, *V2*: 1068
cysts, *V2*: 1035, 1037–1064
acquired dialysis-related cystic disease, *V2*: 1049, 1052, 1061–1062
angiomyolipoma, *V2*: 1063–1068
autosomal dominant polycystic kidney disease, *V2*: 1044, 1047, 1052–1056
autosomal recessive polycystic kidney disease, *V2*: 1047, 1056–1058
calcified cysts, *V2*: 1042, 1048
complex cysts, *V2*: 1037, 1040–1041
fetal assessment, *V2*: 1614–1616
hemhorragic/proteinaceous cysts, *V2*: 1037, 1042–1047
medullary cystic disease, *V2*: 1049, 1059–1060
medullary sponge kidney, *V2*: 1049, 1060
multicystic dysplastic kidney, *V2*: 1047–1049, 1058
multilocular cystic nephroma, *V2*: 1060, 1063–1064
perinephric pseudocysts (parapelvic cysts), *V2*: 1042, 1044, 1050
septated cysts, *V2*: 1042, 1047
simple renal cysts, *V2*: 1035, 1037
thickened wall and infiltration, *V2*: 1043, 1049
tuberous sclerosis, *V2*: 1066, 1069–1071
von Hippel-Lindau disease, *V2*: 1066, 1068, 1072
myelofibrosis, extramedullary hematopoiesis, *V2*: 1068, 1073
oncocytomas, *V2*: 1068, 1072
pattern recognition, *V2*: 1037
collecting system, filling defects, *V2*: 1159, 1166–1169
congenital anomalies, *V2*: 1031–1036
seminal vesicles and, *V2*: 1382, 1384
end-stage kidney disease, *V2*: 1138, 1146–1147
fetal assessment:
anomalies, *V2*: 1612–1613
normal development, *V2*: 1584–1585
hemorrhage, *V2*: 1156–1158
infectious disease:
abscess, *V2*: 1142, 1144, 1149–1152
acute pyelonephritis, *V2*: 1142, 1147–1149
malakoplakia, *V2*: 1153–1154
pyonephrosis, *V2*: 1155–1156
renal candidiasis, *V2*: 1155
xanthogranulomatous pyelonephritis, *V2*: 1152
malignant masses:
carcinoid tumor, *V2*: 1109, 1111
granulocytic sarcoma, *V2*: 1109, 1111
lymphoma, *V2*: 1103, 1106–1110
renal cell carcinoma, *V2*: 1073–1098
chronic renal failure, *V2*: 1098–1101
MR imaging, *V2*: 1098, 1102
radiofrequency ablation, *V2*: 1088–1089, 1095–1096
recurrence, *V2*: 1089, 1096–1097
staging, *V2*: 1073–1095
small cell carcinoma, *V2*: 1110, 1113
Wilms tumor (nephroblastoma), *V2*: 1102–1106
metastases to, *V2*: 1112, 1114–1115, 1159
MR imaging technique, *V2*: 1025–1031
normal anatomy, *V2*: 1025–1030
pediatric imaging, *V2*: 1650
renal collecting system dilation, *V2*: 1164, 1169–1172
renal function, *V2*: 1173, 1175–1177
transplants, *V1*: 671–673, 1173, 1177–1188
trauma, *V2*: 1172–1174
perinephric pseudocysts, *V2*: 1042
Kippel-Trenaunay syndrome, hemangiomatous infiltration, *V1*: 841
Klatskin tumors:
bile duct imaging, *V1*: 515–518, 522–526
biliary stent and, *V1*: 526–527
Klebsiella spp., prostate infection, *V2*: 1373–1374
Krukenberg tumor, ovarian metastases, *V2*: 1547, 1550

LAO projection data, magnetic resonance angiography, *V2*: 1684
Laparoscopic imaging, ovaries, MRI *vs.*, *V2*: 1506–1507
Large intestine. *See also* Colon cancer
benign masses:
hemangiomatous infiltration, Kippel-Trenaunay syndrome, *V1*: 841
lipomas, *V1*: 832, 839
mesenchymal neoplasms (miscellaneous), *V1*: 832, 841
mucocele, *V1*: 832, 838, 841–842
polyps/polyposis syndromes, *V1*: 829, 832, 835–838
varices, *V1*: 838

Large intestine (*Continued*)
congenital anomalies:
anorectal anomalies, *V1*: 827, 833
duplication, *V1*: 827, 832
malrotation, *V1*: 827
inflammatory and infectious disease:
abdominoperineal resection, *V1*: 892, 894–895
abscess formation, *V1*: 874, 876–877, 881–886
appendiceal abscess, *V1*: 874, 881
appendicitis, *V1*: 874, 879–881
colonic fistulae, *V1*: 883, 887–888
Crohn colitis, *V1*: 869, 872–874
diverticulitis, *V1*: 869, 874–879
infectious colitis, *V1*: 883–884, 888–892
radiation enteritis, *V1*: 888, 892–894
rectal surgery, *V1*: 892, 894–895
ulcerative colitis, *V1*: 867–868, 870–871
malignant masses (*See also* Rectal cancer; specific cancers, e.g. Colon cancer)
adenocarcinoma, *V1*: 843–865
TNM staging, *V1*: 843
metastases to, *V1*: 867, 869
gastrointestinal stromal tumors, *V1*: 860, 866
MR imaging techniques, *V1*: 824, 827
intraluminal contrast agents, *V1*: 892, 895–897
normal anatomy, *V1*: 823–824, 827, 830–831
Late hepatic arterial phase (LHAP), gadolinium-based contrast agent, *V2*: 1774–1777
Leiomyomas:
bladder, *V2*: 1300, 1302–1303
broad ligament, *V2*: 1449, 1453–1454
esophageal imaging, *V1*: 726–728
female urethra, *V2*: 1403
ovaries:
benign neoplasms, *V2*: 1525–1526
malignant transformation, *V2*: 1545, 1548
small intestine, *V1*: 775, 780
stomach, *V1*: 736
uterine, *V2*: 1449, 1451–1469
adenomyosis, differential diagnosis, *V2*: 1467, 1469
classification, *V2*: 1451
endometrial carcinoma, *V2*: 1468, 1470, 1473
hemorrhagic degeneration, *V2*: 1456, 1458–1459
intramural, *V2*: 1449, 1451
malignancy, *V2*: 1456, 1465–1466
MR imaging appearance, *V2*: 1452–1469
in pregnancy, maternal imaging, *V2*: 1564, 1567–1570
submucosal, *V2*: 1451–1452, 1454, 1456–1469
vaginal, *V2*: 1416, 1423
Leiomyosarcoma:
inferior vena cava, *V2*: 1237–1241
peritoneal metastases, *V2*: 918, 923–924, 930–931
retroperitoneal neoplasms, *V2*: 1265–1270
uterine, *V2*: 1456, 1465–1466
Lesser sac, intraperitoneal fluid, malignant disease, *V2*: 936, 941
Leukemia, bone metastases, *V2*: 1274, 1288–1290
Linear gadolinium-based contrast agents, *V2*: 1768–1774
Linguine sign, breast implant rupture, *V2*: 1759
Linitus plastica gastric carcinoma, *V1*: 738, 741, 750–751
Lipoleiomyoma, uterus, *V2*: 1456, 1464
Lipomas:
body wall masses, *V2*: 1274, 1283
breast cancer, *V2*: 1739–1740
cecal, *V1*: 832, 839
colonic, *V1*: 832, 840
fatty liver differential diagnosis, *V1*: 383
fetal assessment:
brain, *V2*: 1598–1599
ventriculomegaly, *V2*: 1588–1592
liver lesions, *V1*: 70, 82
pancreatic, *V1*: 551–556
peritoneal, *V2*: 910
small intestine, *V1*: 775
stomach, *V1*: 736, 738, 741
testicular, *V2*: 1386, 1388, 1390
Lipomatosis:
mesenteric, *V2*: 910
pelvic, bladder involvement, *V2*: 1326, 1329–1330
Liposarcoma, retroperitoneal, *V2*: 1265–1266, 1271
Lissencephaly, fetal assessment, *V2*: 1595–1596
Littoral cell angioma (LCA), spleen, *V1*: 688, 694
Liver. *See also* Hepatic cysts; Hepatic parenchyma; Hepatocellular carcinoma (HCC)
abscess:
amebic (nonpyogenic), *V1*: 430
infectious cholangitis, *V1*: 502, 506–507
metastases, secondary infection, *V1*: 180, 188, 191–192
pyogenic, *V1*: 418, 422–432
arteriovenous fistulas, *V1*: 388–392
biliary tree air, *V1*: 411, 413
cirrhosis, *V1*: 321, 331–362
iron overload, *V1*: 370
congestive heart failure, *V1*: 408, 411–413
contrast agents, *V1*: 50–58
diaphragmatic insertion imaging, *V1*: 58, 60
diffuse hyperperfusion abnormality, *V1*: 389–391, 411, 414–415
fat and iron deposition, *V1*: 371, 376
fatty liver, *V1*: 371, 373, 377–387
fetal assessment, *V2*: 1604, 1612
fibrosis, renal cysts, *V2*: 1614–1616
neoplasms, *V2*: 1620
focal hyperperfusion abnormality, *V1*: 414–417
gas bubbles, ablative therapies, *V1*: 286–287
genetic disease, *V1*: 315–318
α1-antitrypsin deficiency, *V1*: 315, 317
Wilson disease, *V1*: 315–318
hepatic arterial obstruction, *V1*: 405, 407–409
hepatic venous thrombosis:
hepatic vein thrombosis, *V1*: 405
hepatocellular carcinoma, *V1*: 202, 224–232
iron overload:
cirrhosis, *V1*: 370
genetic idiopathic hemochromatosis, *V1*: 354, 362, 365–368
secondary hemochromatosis:
hemolytic anemia, *V1*: 368, 370, 374–375
transfusional iron overload, *V1*: 368–373
laceration, hepatic transplantation complication, *V1*: 292, 296
lateral segment elongation imaging, *V1*: 58, 60
lesions:
pattern recognition, *V1*: 51
posttreatment, *V1*: 256
metastases to (*See also* Liver metastases under specific cancers)
ablative therapies, *V1*: 278–287
adrenal cortical carcinoma, *V2*: 998, 1006
adrenal gland neuroblastoma, *V2*: 1013–1017
angiosarcoma, *V1*: 240, 242, 249
avascular, *V1*: 149, 152
benign lesions, differential diagnosis, *V1*: 165, 177, 190
bile duct carcinoma (cholangiocarcinoma), *V1*: 238–240, 242, 247–249
biliary hamartoma, differential diagnosis, *V1*: 67, 73–77
capsule-based metastases, *V1*: 165, 189
hepatocellular carcinoma, *V1*: 202, 224, 232–233
chemotherapy-related, *V1*: 257, 264–270
coexistent cysts, *V1*: 165, 190
colon adenocarcinoma, *V1*: 843, 845, 858, 860
cryotherapy, *V1*: 278, 286–287
epithelioid hemangioendothelioma, *V1*: 251–253
in fatty liver, *V1*: 128, 140–142
fatty liver, imaging interference, *V1*: 371, 377–379
fibrolamellar carcinoma, *V1*: 238–239

focal nodular hyperplasia/hepatocellular adenoma, differential diagnosis, *V1*: 177, 180
hemangiomas, *V1*: 90, 101
hepatoblastoma, *V1*: 251, 253–255
hepatocellular carcinoma, *V1*: 188–189, 192–233
differential diagnosis, *V1*: 235
hypervascular metastases, *V1*: 128, 138–139
hypovascular cystic metastases, *V1*: 149, 152–153
insulinoma, *V1*: 601
islet cell tumors, *V1*: 594–597, 601, 604–606
lymphoma, *V1*: 238, 240–245
malignant mesothelioma, *V1*: 242, 250–251
melanoma, in fatty liver, *V1*: 128, 142
MR imaging techniques, *V1*: 121, 128, 137–147
computed tomography arterial portography *vs.*, *V1*: 143, 145–147
computed tomography *vs.*, *V1*: 141–144
coronal images, *V1*: 128, 143
detection and characterization, *V1*: 128, 137–143
lesional/perilesional enhancement, *V1*: 147–150
vascularity and degree of enhancement, *V1*: 149, 151–162
mucinous cystadenoma/cystadenocarcinoma, *V1*: 614–616
multiple myeloma, *V1*: 238, 245–246
pancreatic adenocarcinoma, *V1*: 552, 580, 584–587
pancreatic gastrinomas, *V1*: 591, 598–602
pancreatic islet cell tumors, *V1*: 591, 593–596
perfusional defect imaging, *V1*: 143, 147, 398–400
postradiation therapy, *V1*: 257, 262–264
posttreatment, *V1*: 256
pyogenic abscess, differential diagnosis, *V1*: 418, 430
rectal carcinoid tumors, *V1*: 867–868
resection, *V1*: 256–262
secondary infection, *V1*: 180, 188, 191–192
small intestine carcinoids, *V1*: 779, 790–791
transcatheter arterial chemoembolization, *V1*: 268, 270–278
undifferentiated sarcoma, *V1*: 251, 256
MR imaging:
basic technique, *V1*: 46–50
gadolinium-based contrast agents, *V2*: 1768, 1770–1772
gadolinium-enhanced T1-weighted images, hepatic arterial dominant (capillary) phase, *V1*: 10–13
protocol for, *V1*: 16–20
whole body imaging, *V1*: 36, 39
mucopolysaccharidoses, *V1*: 384, 387–388
normal anatomy, *V1*: 45–46
variations, *V1*: 58–60
pediatric imaging, *V2*: 1649
porta hepatis lymphadenopathy, *V1*: 352, 354, 362–364
portal venous air, *V1*: 411, 413
portal venous obstruction/thrombosis, *V1*: 388, 391, 393–400
hepatocellular carcinoma, *V1*: 202, 224–232
postradiation therapy, *V1*: 257, 262–264
preeclampsia and eclampsia, *V1*: 407, 410–411
resection, *V1*: 256–262
systemic chemotherapy, *V1*: 257, 264–270
transcatheter arterial chemoembolization, *V1*: 268, 270–278
transplantation, MR imaging, *V1*: 287–305
trauma, *V1*: 438–442
hepatic cysts, *V1*: 60, 65–66
Liver adenomatosis, *V1*: 114–118
Lobar/semilobar holoprosencephaly, fetal assessment, *V2*: 1589–1592
Lobular carcinoma in situ (LCIS), benign breast lesions, *V2*: 1719, 1721–1722
Lobular intraepithelial neoplasia (LIN), fibroadenomas, *V2*: 1702–1706
Lower esophageal sphincter (LES), achalasia, *V1*: 729–730
Lung cancer:
liver metastases, *V1*: 151, 161
squamous cell lung cancer, *V1*: 162, 175–176
MR imaging techniques, *V2*: 1654–1661
pancreatic metastases, *V1*: 619, 625, 629–630
pulmonary nodules, *V2*: 1654, 1657, 1662–1665
small intestine metastases, *V1*: 782, 792
splenic metastases, *V1*: 701, 703–706
stomach metastases, *V1*: 760
Lung imaging, fetal assessment, normal development, *V2*: 1583
Lymphadenopathy:
adrenal glands, retroperitoneal, *V2*: 1017, 1019
colon cancer, *V1*: 858, 860
lymphoma, *V1*: 860, 867
endometrial carcinoma, *V2*: 1474–1481
hilar and mediastinal, *V2*: 1666–1667
MRI signal intensity and, *V1*: 1–2
pancreatic adenocarcinoma, *V1*: 552, 577–578, 580, 584
peritoneal metastases, *V2*: 924–925, 934–935
porta hepatis lymphadenopathy, *V1*: 352, 354, 359, 362–364
retroperitoneum:
benign masses, *V2*: 1247–1250
Hodgkin lymphoma, *V2*: 1253–1254
malignant metastatic, *V2*: 1258–1263
spleen, lymphoma metastases, *V1*: 694, 699–703
Lymphangiomas:
fetal assessment, *V2*: 1598, 1603
pelvic, *V2*: 1274, 1291–1292
spleen, *V1*: 693
Lymphatic dissemination:
ovarian malignancies:
epithelial tumors, *V2*: 1532–1533
metastases to, *V2*: 1547, 1549–1550
peritoneal metastases, *V2*: 924–925, 934–935
carcinoid tumors, *V2*: 936–938
pseudomyxoma peritonei, *V2*: 936–938
testicular cancer, *V2*: 1391–1396
Lymph nodes:
adrenal gland neuroblastoma, *V2*: 1013–1017
bladder cancer, transitional cell carcinoma, *V2*: 1307–1316
breast, *V2*: 1712–1714
cervical cancer metastases, *V2*: 1486–1488
colon cancer imaging, *V1*: 843, 848
endometrial carcinoma, *V2*: 1474–1481
magnetic resonance lymphography, *V1*: 896–897
ovarian malignancies, epithelial tumors, *V2*: 1532–1533
pancreatic adenocarcinoma involvement, *V1*: 575, 578, 580, 584
prostate cancer metastases, *V2*: 1368–1373
psoas muscle tumors, *V2*: 1271, 1273–1274
retroperitoneal necrotic malignant, *V2*: 1258, 1262–1263
Lymphocele:
inferior vena cava thrombus, *V2*: 1237
renal transplants, *V2*: 1178, 1182, 1185
Lymphoma. *See also* Hodgkin lymphoma; Non-Hodgkin lymphoma
adrenal glands, *V2*: 1017, 1019
bile duct/ampulla metastases, *V1*: 520
bladder, *V2*: 1316, 1321
body wall, *V2*: 1274, 1284–1290
breast cancer, *V2*: 1741–1743
colorectal malignancies, *V1*: 860, 867
kidneys, *V2*: 1103, 1106–1110
liver metastases, *V1*: 238, 240–245
angiotropic intravascular, *V1*: 238, 242
Burkitt lymphoma, *V1*: 238, 243–244
HIV patient, *V1*: 238, 245
post-hepatic transplantation, *V1*: 238, 241
primary hepatic, *V1*: 238, 244
ovarian, *V2*: 1545, 1548–1549
renal pelvis and ureter, *V2*: 1159

Lymphoma (*Continued*)
retroperitoneal malignant masses, *V2*: 1253–1257
small intestine, *V1*: 779, 786–791
spleen malignancies, *V1*: 693–694, 699–703
direct tumor invasion, *V1*: 704–705
testicular, *V2*: 1395–1396
vaginal, *V2*: 1421, 1424

Macrocystic serous cystadenoma, MR imaging, *V1*: 607, 611–612
Macrocytic gadolinium-based contrast agents, *V2*: 1768–1774
Magnetic field strength:
breast MRI imaging, *V2*: 1692–1693
pediatric MRI, *V2*: 1644
Magnetic resonance angiography (MRA):
aortic imaging:
abdominal aortic aneurysm, *V2*: 1201–1207
aortic dissection, *V2*: 1201, 1208–1212
chest imaging, *V2*: 1654
hepatic transplantation protocol, *V1*: 287–289, 292
hepatocyte-specific contrast agents, *V2*: 1768
inferior vena cava, *V2*: 1223, 1228–1230
malignancies *vs.* thrombus, differential diagnosis, *V2*: 1240–1241
thrombus, *V2*: 1232–1237
insulinomas, *V1*: 601
kidney imaging, *V2*: 1029
transplants, *V2*: 1177–1184
liver, arteriovenous fistulas, *V1*: 388–392
pancreatic imaging, *V1*: 540
pancreatic transplants, *V1*: 671–673
pulmonary emboli, *V2*: 1673, 1675–1677
pulmonary vascular abnormalities, *V2*: 1673, 1678–1684
renal artery disease, *V2*: 1129, 1131–1133
retroperitoneal imaging, *V2*: 1194
vessels, *V2*: 1194–1200
small intestine, ischemia and hemorrhage, *V1*: 816, 819–823
thoracic, *V2*: 1673, 1679–1684
Magnetic resonance cholangiography, echo-train spin-echo sequences, *V1*: 7
Magnetic resonance cholangiopancreatography (MRCP). *See also* Secretin-enhanced MRCP
3T MR imaging, 8-channel torso coil, *V1*: 35–37
bile duct:
benign disease:
AIDS-related cholangiopathy, *V1*: 505
ampullary adenoma, *V1*: 511, 516
ampullary fibrosis, *V1*: 489, 495–496
ampullary stenosis, *V1*: 489
Caroli disease, *V1*: 505, 511–513
cholecdocholithiasis, *V1*: 488–492
choledochal cyst, *V1*: 505, 508–510
choledochocele, *V1*: 505, 511
cysts, *V1*: 505
infectious cholangitis, *V1*: 499, 502–507
mass lesions, *V1*: 511, 514–520
papillary adenoma, *V1*: 511, 515
papillary dysfunction, *V1*: 489, 493, 497
postsurgical complications, *V1*: 511, 514–515, 517–520
primary sclerosing cholangitis, *V1*: 494, 497–502
sclerosing cholangitis, *V1*: 493–494
imaging studies, *V1*: 483–488
pitfalls, *V1*: 489, 493–494
malignant disease:
carcinoma, intrahepatic/peripheral metastases, *V1*: 238–240, 242, 247–249
cholangiocarcinoma, *V1*: 515–518, 521–526
metastases to, *V1*: 530
periampullary/ampullary carcinoma, *V1*: 518, 520, 527–530
pitfalls of, *V1*: 489, 493–494
biliary anastomoses, *V1*: 464, 466–467
cholecystitis:
acute cholecystitis, *V1*: 468–475
chemoembolization-induced, *V1*: 468, 476
acute on chronic cholecystitis, *V1*: 468, 475
chronic, *V1*: 475, 477–478
hemorrhagic, *V1*: 475–477
xanthogranulomatous, *V1*: 477
gadolinium-based contrast agent, *V2*: 1771–1772
gallstone disease, *V1*: 464–465, 467–469
hepatic transplantation protocol, *V1*: 287–289
intestinal choledochocele, *V1*: 775–776
intraductal papillary mucinous neoplasms, *V1*: 615–621
intraductal papillary mucinous tumor, serous cystadenoma, differential diagnosis, *V1*: 612
MR imaging *vs.*, *V1*: 455
pancreatic imaging, *V1*: 536, 540
acute pancreatitis, *V1*: 625, 632
cystic fibrosis, *V1*: 546
pancreas divisum, *V1*: 541–542
trauma assessment, *V1*: 665, 668–671
in pregnancy, maternal imaging, *V2*: 1564
small intestine, adenocarcinoma, *V1*: 777
T2-weighted sequences, *V1*: 456–461
Magnetic resonance colonography, *V1*: 827
colon cancer polyps, *V1*: 848, 851–852
Magnetic resonance ductography, intraductal papilloma, differential diagnosis, *V2*: 1707–1709
Magnetic resonance imaging (MRI):
emerging developments in, *V1*: 25
liver imaging techniques, *V1*: 46–50
Magnetic resonance lymphography:
imaging contrast agents, *V1*: 896–897
retroperitoneum, malignant metastatic lymphadenopathy, *V2*: 1258–1263
Magnetic resonance spectroscopy:
male pelvis, *V2*: 1343–1344
prostate cancer, adenocarcinoma, *V2*: 1352, 1356–1373
Magnetic resonance urography:
echo-train spin-echo sequences, *V1*: 7
kidney imaging techniques, *V2*: 1184, 1188
perinephric pseudocyst, *V2*: 1042, 1044, 1050
transplants, *V2*: 1177–1184
in pregnancy, maternal imaging, *V2*: 1564, 1566
renal collecting system dilation, *V2*: 1164, 1170
Magnetic susceptibility artifact, breast MRI, *V2*: 1695
Magnetization-prepared rapid-acquisition gradient echo (MP-RAGE) sequences:
abdominal-pelvic imaging, *V1*: 5–6
pediatric patients, *V2*: 1637–1639, 1641–1644
Malakoplakia, *V2*: 1153–1154
Male pseudohermaphroditism, Wilms tumor and, *V2*: 1103–1106
Malignant mixed mesodermal/müllerian tumor:
bladder, *V2*: 1316
uterine sarcoma, *V2*: 1475, 1479–1481
Malrotation:
kidneys, *V2*: 1031
small intestine, *V1*: 770–771
Mammography:
ductal carcinoma in situ, benign lesions, *V2*: 1719–1721
MRI guidance and intervention, *V2*: 1760–1762
Manganese-based (Mn-DPDP (mangofodipir))-enhanced SGE imaging:
biliary tree, normal anatomy, *V1*: 460–461
contrast agenta, *V2*: 1778–1779
liver images, *V1*: 50
hepatocyte targeting, *V1*: 50–58
portal arteriorvenous system, *V1*: 46, 50
T1-weighted magnetic resonance cholangiopancreatography, *V1*: 460–461
Mass enhancement, breast cancer imaging, *V2*: 1723
Mastectomy:
postoperative MRI, *V2*: 1744–1749
prostheses, fat necrosis, *V2*: 1750–1752
Mastitis, inflammatory breast carcinoma, differential diagnosis, *V2*: 1739
Maternal imaging. *See also* pregnancy-related imaging under specific cancers and diseases
amniotic fluid assessment, *V2*: 1622–1623

anticardiolipin antibodies, fetal stroke, *V2*: 1598–1599
metastases in pregnancy, *V2*: 1561–1575
multiple gestation, *V2*: 1623–1624
placental imaging, *V2*: 1623, 1625–1627
postpartum uterus, *V2*: 1575–1580
pregnancy complications, *V2*: 1561–1575
Maximum-intensity projection (MIP):
aortic imaging, *V2*: 1200–1227
aortic dissection, *V2*: 1201, 1208–1212
breast MRI, *V2*: 1693–1694
ductal carcinoma in situ, *V2*: 1721
fibroadenomas, *V2*: 1703, 1706
chest imaging, *V2*: 1654
kidneys, renal artery disease, *V2*: 1129, 1131–1133
magnetic resonance cholangiopancreatography, *V1*: 456, 458–460
thoracic aorta, *V2*: 1679–1684
vessel imaging, *V2*: 1198–1200
inferior vena cava malignancies, *V2*: 1240–1241
Mayer-Rokitansky-Küster-Hauser syndrome:
uterine agenesis/hypoplasia, *V2*: 1441–1443
vaginal agenesis/partial agenesis, *V2*: 1411–1413
Mayo End-Stage Liver Disease (MELD) scale:
autoimmune hepatitis, *V1*: 314
primary sclerosing cholangitis, *V1*: 304, 311
Meckel diverticulum, *V1*: 770, 774
Meckel-Gruber syndrome:
encephalocele, fetal assessment, *V2*: 1595, 1597
renal cysts, fetal assessment, *V2*: 1614–1616
Meconium:
MR imaging, *V2*: 1583–1585
pseudocysts, *V2*: 1617
Mediastinal ascites, *V2*: 936, 942
Mediastinal lymphadenopathy, *V2*: 1666–1667
Medistinal neoplasms, fetal assessment, *V2*: 1612
Medium-vessel disease, renal artery, *V2*: 1136, 1138
Medulla, adrenal. *See* Adrenal glands, medullary masses
Medullary carcinoma, breast cancer, *V2*: 1732–1733
Medullary cystic disease, *V2*: 1049, 1059–1060
Medullary sponge kidney (MSK), *V2*: 1049, 1060
Megacystis-microcolon hyperperistalsis syndrome, fetal assessment, *V2*: 1613–1614
Meigs syndrome, benign ovarian neoplasms, *V2*: 1525–1526, 1529–1531
Melanoma:
anorectal, *V1*: 867, 869
breast metastases, *V2*: 1743–1744
iliacus muscle metastases, *V2*: 1273, 1276
metastases:
to bile duct/ampulla, *V1*: 520
to gallbladder, *V1*: 483, 487
to liver, *V1*: 164, 181–182
to pancreas, *V1*: 625, 628
ovarian metastases, *V2*: 1547, 1549–1550
splenic metastases, *V1*: 701, 703–706
stomach metastases, *V1*: 760
vulvovaginal malignancies, *V2*: 1421, 1424
Membranous nephropathy, glomerular disease, *V2*: 1117–1118
Menstruation, uterine changes, *V2*: 1437–1439
Merkel cell cancer, pancreatic metastases, *V1*: 625, 631
Mesenchymal hamartoma, fetal assessment, *V2*: 1620
Mesenchymal tumors, breast cancer, *V2*: 1739–1740
Mesenteric adenopathy, peritoneal metastases, *V2*: 924–925, 934–935
Mesenteric cysts, *V2*: 907, 910
Mesenteric lipodystrophy, *V2*: 946, 950
Mesenteric lipomatosis, *V2*: 910
Mesenteritis, *V2*: 946, 950
Mesoblastic nephroma, fetal assessment, *V2*: 1620
Mesorectum imaging, colon cancer, *V1*: 848
Mesothelioma, malignant:
liver metastases, *V1*: 242, 250–251
peritoneal diffusion, *V2*: 912, 915–917
Metabolic acidosis, nephrogenic systemic fibrosis and, *V2*: 1782–1783
Metallic artifacts:
bile duct MRCP, *V1*: 489, 493–494, 505
biliary papillomatosis, *V1*: 514–515
single-shot echo-train spin-echo sequences, *V1*: 7–8
Metastatic immature teratoma, peritoneal metastases, *V2*: 918, 923–924, 927
Methemoglobin:
bladder, hemorrhagic cysts, *V2*: 1326, 1329
renal cysts, hemhorragic/proteinaceous cysts, *V2*: 1037, 1046
Microcystic serous cystadenoma, *V1*: 606–607, 609–611
Microvarices, peritoneal, *V2*: 945–946, 948–949
Middle interhemispheric holoprosencephaly (MIH), fetal assessment, ventriculomegaly, *V2*: 1590–1592
Mid-hepatic arterial phase (MHAP) imaging, gadolinium-based contrast agent, *V2*: 1774–1777
Misregistration artifacts, breast MRI, *V2*: 1695
Monodermal teratoma, benign ovarian neoplasm, *V2*: 1521
Mosaic enhancement, liver imaging, congestive heart failure, *V1*: 407, 411–413
Motion-related artifacts:
1.5T *vs.* 3T imaging, *V1*: 35
adnexal imaging, *V2*: 1499–1500
breast MRI, *V2*: 1694–1695
chest imaging, *V2*: 1654
pleural disease, *V2*: 1666, 1671–1672
pregnancy-related MRI, *V2*: 1561
Motion-resistant imaging:
abdominal region, *V1*: 20–24
3T strategy, *V1*: 23–24
pediatric patients, *V2*: 1639, 1641, 1647–1648
Mucinous carcinoma, breast cancer, *V2*: 1732, 1734
Mucinous cystadenoma/cystadenocarcinoma, *V1*: 612–616
mucocele, large intestine, *V1*: 838, 841–842
ovaries:
benign neoplasms, *V2*: 1518–1520, 1521–1522
malignant neoplasms, *V2*: 1533, 1536–1537
Mucin-producing tumors, liver metastases, *V1*: 165, 185–186
Mucocele, appendix, *V1*: 832, 838, 841–842
Mucopolysaccharidoses, liver imaging, *V1*: 384, 387–388
Mucosa-associated lymphoid tissue (MALT), small intestine, *V1*: 779, 786–791
Müllerian duct:
adenocarcinoma, *V2*: 1488, 1491
cancer, ovarian metastases, *V2*: 1547, 1549
congenital anomalies, *V2*: 1439–1448
malignant mixed mesodermal/müllerian duct tumor, bladder, *V2*: 1316
ovarian anomalies, *V2*: 1503
prostate cysts, *V2*: 1344, 1348–1349
vaginal agenesis/partial agenesis, *V2*: 1410–1413
Multicystic dysplastic kidney, *V2*: 1047–1049, 1058
fetal assessment, *V2*: 1614–1616
MultiHance contrast agent (Gd-BOPTA):
classification, *V2*: 1768, 1771–1772
hepatocyt phase, *V2*: 1777
liver imaging, *V1*: 51–58
adenomatosis, *V1*: 114, 118
focal nodular hyperplasia, *V1*: 55–56, 121, 136
metastases characterization, *V1*: 128, 136
T1-weighted magnetic resonance cholangiopancreatography, *V1*: 460
Multilocular cystic nephroma, *V2*: 1060, 1063–1064
Multiplanar reformatting (MPR), renal artery disease, *V2*: 1131

Multiple endocrine neoplasia (MEN) type 1, stomach carcinoids, *V1*: 759
Multiple endocrine neoplasia (MEN) type IIA or IIB, pheochromocytoma, *V2*: 1005
Multiple gestation, MR imaging techniques, *V2*: 1623–1624
Multiple imaging variables, magnetic resonance imaging, *V1*: 13–14
Multiple myeloma:
  liver metastases, *V1*: 238, 245–246
  metastases, gadolinium-based contrast agent imaging, *V2*: 1771–1772
Mumps orchitia, *V2*: 1397–1398
Mural thrombus, abdominal aortic aneurysm, *V2*: 1200–1201, 1205
Mycobacterial infection, liver imaging, *V1*: 433–435
Mycobacterium avium intracellulare (MAI):
  hepatic involvement, *V1*: 433–435
  infectious colitis, *V1*: 884, 888, 891–892
  infectious enteritis, *V1*: 810, 813–814
  retroperitoneal benign lymphadenopathy, *V2*: 1247–1250
Myelofibrosis, kidney, extramedullary hematopoiesis, *V2*: 1068, 1073
Myelolipoma, adrenal glands, *V2*: 977–980, 988–990
Myelomeningocele, fetal assessment, Chiari II malformation, *V2*: 1586–1592
Myofibroblastic tumor, inflammatory:
  bladder lesions, *V2*: 1304
  hepatic inflammatory disease, *V1*: 415, 418–422
Myoglobinuria, renal tubular blockage, *V2*: 1120, 1124
Myometrial hematoma, postpartum uterus, *V2*: 1575–1580
Myometrial metastases, endometrial carcinoma, *V2*: 1470

Nabothian cysts, *V2*: 1467–1468, 1471
Nasopharynx. *See also* Cleft palate
  fetal assessment:
    anomalies, *V2*: 1598–1607
    normal development, *V2*: 1583
Neck imaging, fetal assessment:
  anomalies, *V2*: 1598–1599, 1601–1607
  normal development, *V2*: 1583
Necrosis:
  fetal assessment, destructive lesions, *V2*: 1598–1601
  ovarian fibroma, *V2*: 1526, 1530
Necrotizing granulomatous pancreatitis, inflammation or infection, *V1*: 665–666
Negative oral contrast agents, large intestine imaging, *V1*: 896–897
Neisseria gonorrhoeae:
  Bartholin glands cysts, *V2*: 1416–1418
  tubo-ovarian abscess, *V2*: 1514, 1516–1517
Neoadjuvant chemotherapy (NCT), breast cancer, posttreatment MRI, *V2*: 1744–1753
Neonatal ascites, *V2*: 936, 942
Nephrectomy:
  pancreatic imaging, *V1*: 540–541
  segmental, *V2*: 1142, 1146
Nephroblastoma (Wilms tumor), *V2*: 1102–1106
Nephrogenic systemic fibrosis (NSF):
  circulating fibrocyte hypothesis, *V2*: 1783
  contrast agents, *V2*: 1767
  contrast-induced nephropathy risk *vs.*, *V2*: 1784–1786
  definition, *V2*: 1780
  diagnosis, *V2*: 1783
  epidemiology, *V2*: 1780–1781
  gadolinium-based contrast agent toxicity, *V2*: 1780–1786
    cofactors, *V2*: 1782–1783
    pharmacokinetics, *V2*: 1781–1782
  pathophysiology and risk factors, *V2*: 1781
  pediatric imaging, contrast agents, *V2*: 1647
  pulmonary emboli imaging, *V2*: 1673, 1675–1677
  renal function, *V2*: 1781
  risk minimization guidelines, *V2*: 1783–1784
  treatment and prognosis, *V2*: 1783
  vessel imaging, *V2*: 1195–1200
Nephroma, mesoblastic, fetal assessment, *V2*: 1620
Nephropathy:
  ischemic, *V2*: 1129, 1131, 1134
  reflux nephropathy, *V2*: 1126, 1128, 1130
  Wilms tumor and, *V2*: 1103–1106
Nephrophthisis, *V2*: 1049, 1059–1060
Nephroscleroses, renal artery disease, *V2*: 1137
Nephrotic syndrome, *V2*: 1117, 1120
Neural tube defects, fetal imaging, *V2*: 1585–1592
Neurenteric cysts, fetal assessment, *V2*: 1612
Neurilemmoma, retroperitoneum, *V2*: 1240, 1245–1247
Neuroblastoma:
  adrenal glands, *V2*: 1006, 1012–1017
  fetal assessment, *V2*: 1618, 1620
  retroperitoneum, *V2*: 1266, 1273
Neuroendocrine carcinoma:
  pancreatic cancer, *V1*: 593
  stomach, *V1*: 759
Neurofibromas:
  bladder, *V2*: 1304
  retroperitoneum, plexiform, *V2*: 1240, 1245–1247
  small intestine, *V1*: 775, 779
Neurofibromatosis type 1:
  bladder lesions, *V2*: 1304–1305
  small intestine neurofibromas, *V1*: 775, 779
Neurogenic tumors:
  bladder, *V2*: 1304–1305
  small intestine neurofibromas, *V1*: 775, 779
  stomach, *V1*: 736, 738
Neurovascular bundles, prostate cancer invasion, *V2*: 1368–1373
Neutropenic colitis, *V1*: 884, 890
Nonalcoholic fatty liver disease (NAFLD), imaging studies, *V1*: 317, 319–320
Nonalcoholic steatohepatitis (NASH), *V1*: 319–320
Noncooperative patients, imaging protocols in, *V1*: 25–28
Nonepithelial tumors, bladder cancer, *V2*: 1316
Non-Hodgkin lymphoma:
  adrenal glands, *V2*: 1017, 1019
  colon, *V1*: 860, 867
  kidneys, *V2*: 1103, 1106–1110
  liver metastases, *V1*: 238, 240–245
  pancreas, *V1*: 619, 624–625
  peritoneal metastases, *V2*: 925
  retroperitoneal malignant masses, *V2*: 1253–1257
  small intestine, *V1*: 779, 786–791
  spleen, *V1*: 693–694, 699–703
  stomach, *V1*: 756, 758
Noninvoluting congenital hemangioma, fetal assessment, *V2*: 1604, 1607
Nonmass enhancement, breast cancer imaging, *V2*: 1723
Nonseminomatous tumors, testes, *V2*: 1390–1396
Non-slice selective inversion pulse, magnetization-prepared rapid-acquisition gradient echo sequences, *V1*: 5–6
Noose sign, breast implant rupture, *V2*: 1759
"Nutcracker syndrome," inferior vena cava thrombus, *V2*: 1232–1237

Obesity:
  nonalcoholic fatty liver disease, *V1*: 317, 319–320
  polycystic ovarian syndrome, *V2*: 1507, 1509, 1514
Oligohydramnios:
  encephalocele, fetal assessment, *V2*: 1595, 1597
  kidney anomalies, *V2*: 1612–1613
  twin-twin transfusion syndrome, *V2*: 1623–1624
Omental hypertrophy, cirrhosis, *V1*: 348, 351, 360
  intraperitoneal varices, *V2*: 923–924, 934
Omental metastases, peritoneal, interperitoneal seeding, *V2*: 923–924, 934–935
Omental varices, cirrhosis, *V1*: 348, 351, 359
Omphalocele, fetal assessment, *V2*: 1617
Oncocytomas, renal, *V2*: 1068, 1072
1.5T imaging:
  3T imaging *vs.*, *V1*: 31–36
    gastrointestinal tract, *V1*: 725
  adrenal glands, *V2*: 963–968

breast MRI, *V2*: 1694–1695
lung cancer, pulmonary nodules, *V2*: 1654, 1662
male pelvis, *V2*: 1343–1344
pediatric patients, *V2*: 1637, 1644
receiver coil, *V2*: 1644–1645
renal cell carcinoma, stage 4, 1082, 1084–1085
vaginal carcinoma, *V2*: 1416, 1422
Oral contraceptives:
abdominal fibromatosis, *V2*: 1570
primary ovarian carcinoma protection, *V2*: 1527
uterine changes, *V2*: 1439
Oral contrast agents:
large intestine imaging, *V1*: 892, 895–897
MR imaging strategies, *V1*: 20
pregnancy-related MRI, *V2*: 1561
retroperitoneum imaging, *V2*: 1194
Organs of Zuckerkandl:
benign neoplasms, *V2*: 1247
pheochromocytoma, *V2*: 1005–1111
Oriental cholangitis, MR imaging, *V1*: 502, 507
Oropharynx. *See also* Cleft palate
fetal assessment:
anomalies, *V2*: 1598–1607
normal development, *V2*: 1583
Out-of-phase (opposed-phase) spoiled gradient echo sequences:
adrenal glands, *V2*: 963–968
adenomas, *V2*: 971–985
metastases, *V2*: 998–1002
basic principles, *V1*: 4–5
kidneys, angiomyolipomas, *V2*: 1063–1068
pediatric patients, *V2*: 1645–1646
Ovarian arteries, uterine artery embolization, *V2*: 1456, 1464
Ovarian cancer:
carcinosarcoma, *V2*: 1545, 1548
clear cell carcinoma, *V2*: 1533, 1538–1540
colon metastases, *V1*: 867, 869
epithelial origin, *V2*: 1531–1533
primary peritoneal carcinoma, differential diagnosis, *V2*: 912, 917
gallbladder metastases, *V1*: 483, 487
germ cell origin, *V2*: 1533–1534, 1540–1544
imaging studies, *V2*: 1518
kidney metastases, *V2*: 1112, 1114
liver metastases, *V1*: 151, 158–160, 162, 164, 183–185, 187–188
lymphoma, *V2*: 1545, 1548–1549
mucinous tumors, *V2*: 1533, 1536–1538
peritoneal metastases, intraperitoneal seeding, *V2*: 918–924
in pregnancy, maternal imaging, *V2*: 1569, 1571
primary ovarian carcinoma, *V2*: 1526–1527, 1531
serous tumors, *V2*: 1533–1536
sex cord-stromal origin, *V2*: 1540, 1542, 1545–1547
small intestine metastases, *V1*: 779, 782, 792
uterine leiomyoma, differential diagnosis, *V2*: 1451
Ovarian hyperstimulation syndrome, theca-lutein ovarian cysts, *V2*: 1504, 1507–1508
Ovarian torsion:
paraovarian cysts, *V2*: 1504, 1508
in pregnancy, maternal imaging, *V2*: 1569, 1572
Ovarian vein thrombosis, postpartum uterus, *V2*: 1578–1580
Ovaries. *See also* Adnexa
benign neoplasms, *V2*: 1518–1531
epithelial origin, *V2*: 1518–1523
germ cell origin, *V2*: 1520–1521, 1526–1529
sex cord-stromal origin, *V2*: 1525–1526, 1530–1531
congenital anomalies, *V2*: 1503
cysts, *V2*: 1500, 1502–1503
dermoid cyst, *V2*: 1520–1521, 1526–1529
functional cysts, *V2*: 1500, 1502, 1504–1506
paraovarian/peritoneal cysts, *V2*: 1504, 1508
in pregnancy, differential diagnosis, *V2*: 1567, 1569–1570
theca-lutein cysts, *V2*: 1504, 1507–1508
ectopic pregnancy, *V2*: 1517
endometriosis, *V2*: 1504–1513
hydrosalpinx, *V2*: 1517
metastases to, *V2*: 1546–1547, 1549–1550
endometrial carcinoma, *V2*: 1474, 1476
normal anatomy, *V2*: 1500–1501
ovarian torsion, *V2*: 1509–1510, 1514–1516
pelvic inflammatory disease/tubo-ovarian abscess, *V2*: 1514, 1516–1517
pelvic varices, *V2*: 1517–1518
polycystic ovaries, *V2*: 1507, 1509, 1514
transposed ovary, *V2*: 1500–1502
Overlap syndrome, autoimmune liver disease, *V1*: 313–315
Ovotestes, MRI detection, *V2*: 1503

Paget disease:
of breast, *V2*: 1737–1738
vulvar carcinomas, *V2*: 1421
Palate imaging, fetal assessment, normal development, *V2*: 1583
Pancoast tumor, MR imaging, *V2*: 1654, 1660–1661
Pancreas:
3T MR imaging, *V1*: 35–37
cystic neoplasms, *V1*: 606–625 (*See also* Pancreatic cancer)
ductal dilatation:
chronic pancreatitis, *V1*: 648–652
trauma, *V1*: 665, 668–671
ductal stenosis, traumatic, *V1*: 665, 668–671
genetic disease:
cystic fibrosis, *V1*: 544–548
primary hemochromatosis, *V1*: 546, 548–549
von Hippel-Lindau syndrome, *V1*: 549–550
inflammatory disease, *V1*: 625
miscellaneous conditions and infections, *V1*: 664–667
pancreatitis, *V1*: 625
acute, *V1*: 625, 628, 636–647
autoimmune pancreatitis, *V1*: 656, 664, 666
chemtherapy-induced, *V1*: 664–667
chronic, *V1*: 640, 648–665
hemorrhagic, *V1*: 632, 639–641
mild, *V1*: 625, 632–635
pseudocyst, *V1*: 632, 642–647
metastases to, *V1*: 619, 625–631 (*See also* specific cancers, e.g., Breast cancer)
MR imaging, *V1*: 536–541
mucinous cystadenocarcinoma, liver metastases, *V1*: 165, 185–186
neoplasms (*See also* Pancreatic cancer)
benign solid, lipoma, *V1*: 551–556
focal lesions, pattern recognition, *V1*: 551
malignant solid, *V1*: 552–608
normal anatomy, *V1*: 535–536
pediatric imaging, *V2*: 1649–1650
transplants, *V1*: 671–673
trauma, *V1*: 665, 668–671
Pancreas divisum, MR imaging, *V1*: 541–542
Pancreatic anlage, congenital anomalies, *V1*: 542, 545
Pancreatic cancer:
acinar cell carcinoma, *V1*: 589
ACTHoma, *V1*: 601, 605
adenocarcinoma, *V1*: 552–553, 556–570, 556–589
diffuse, *V1*: 552, 576, 588
staging, *V1*: 575, 577–587
in tail, *V1*: 552, 574–575
vessel involvement, *V1*: 575, 577–578
adrenal gland metastases, *V2*: 998–1002
carcinoid tumors, *V1*: 602, 607–608
chemotherapy and radiation therapy and, *V1*: 589–590
chemotherapy/radiation-treated ductal adenocarcinoma, *V1*: 589–590
chronic pancreatitis, differential diagnosis, *V1*: 648, 656
cystic neoplasms:
cystic fibrosis, *V1*: 546
intraductal papillary mucinous neoplasms, *V1*: 614
main duct type, *V1*: 614–617
side-branch type, *V1*: 615, 618–621
lymphoma, *V1*: 619, 624–625
metastases, *V1*: 619, 625–632
mucinous cystadenoma/cystadenocarcinoma, *V1*: 612–616

Pancreatic cancer: (*Continued*)
pancreatic adenocarcinoma and, *V1*: 564
serous cystadenocarcinoma, *V1*: 612
serous cystadenoma, *V1*: 606–607, 609–612
solid/papillary epithelial neoplasm (papillary cystic neoplasm), *V1*: 619, 622–623
developmental anomalies, *V1*: 541–546
annular pancreas, *V1*: 541–544
pancreas divisum, *V1*: 541–542
pancreatic anlage, congenital absence, *V1*: 542, 545
short pancreas, polysplenia syndrome, *V1*: 544, 546
uneven fatty infiltration, *V1*: 542, 545
ductal adenocarcinoma, liver metastases, *V1*: 162
gastrinomas, *V1*: 591, 598–602
glucagonoma, *V1*: 601, 604
insulinomas, *V1*: 601, 603–604
iron-based contrast agents, differential diagnosis, *V2*: 1778–1779
islet cell tumors, *V1*: 590–598
pancreatic, *V1*: 590–598
gastrinomas, *V1*: 591, 598
undifferentiated, *V1*: 601
pancreatic adenocarcinoma, differential diagnosis, *V1*: 587–589
undifferentiated, *V1*: 590, 597–601
lymphoma, *V1*: 619, 624–625
peritoneal metastases, *V2*: 918, 923–924, 928
schwannoma, *V1*: 594–597, 601
somatostatinoma, *V1*: 601, 604–605
undifferentiated carcinoma, *V1*: 589
VIPoma, *V1*: 601, 606
Pancreatitis, *V1*: 625–667
acute, *V1*: 625, 628, 636–647
autoimmune pancreatitis, *V1*: 656, 664, 666
chemtherapy-induced, *V1*: 666–667
chronic, *V1*: 640, 648–665
pancreatic adenocarcinoma:
differential diagnosis, *V1*: 575
risk for, *V1*: 552, 562–564
focal pancreatitis, *V1*: 649, 652, 665
hemorrhagic, *V1*: 632, 639–641
mild, *V1*: 625, 632–635
necrotizing granulomatous, *V1*: 665–666
pancreas divisum and risk of, *V1*: 541
peritoneal inflammation, *V2*: 940–942, 946, 949
pseudocyst, *V1*: 632, 642–647
small intestine effects, *V1*: 810, 815
Papillary adenoma, bile duct, *V1*: 511, 515
Papillary carcinoma, breast cancer, *V2*: 1733, 1737
Papillary cystic neoplasm, pancreas, *V1*: 619, 622–623
Papillary dysfunction, bile duct, MRCP imaging, *V1*: 489, 493, 497
Papillary epithelial neoplasm, pancreas, *V1*: 619, 622–623
"Papillary lesions," intraductal papilloma, differential diagnosis, *V2*: 1707–1709
Papillary serous carcinoma:
fallopian tube metastases, *V2*: 1551–1552
uterus, *V2*: 1474, 1477
Papilloma:
bladder lesions, *V2*: 1300–1301
intraductal, *V2*: 1707–1709
Papillomatosis, intraductal papilloma, differential diagnosis, *V2*: 1707–1709
Papilomatosis, multiple, diagnostic imaging, *V2*: 1709–1711
Paraesophageal hiatal hernias, *V2*: 904, 906–907
Paraesophageal varices, cirrhosis, *V1*: 351, 361
Parallel-line sign, breast implant rupture, *V2*: 1759
Parallel MR imaging:
evolution of, *V1*: 25, 29–31
non-fat-suppressed *vs*. fat-suppressed images, *V1*: 35–37
pulmonary emboli, *V2*: 1673, 1675–1677
Paramagnetic contrast agents, liver imaging, *V1*: 50–51
Parametrium:
cervical cancer metastases, *V2*: 1486–1487
normal anatomy, *V2*: 1437
papillary serous carcinoma, *V2*: 1474, 1477
Paramtrium, normal anatomy, *V2*: 1437
Paraovarian cysts, *V2*: 1504, 1508
Parapelvic cysts, *V2*: 1042, 1044, 1050
Paraumbilical hernia, abdominal wall imaging, *V2*: 904, 909
Paraumbilical varices, cirrhosis, *V1*: 348, 351, 361
Parenchymal hemorrhage, fetal assessment, *V2*: 1598–1601
Paroxysmal nocturnal hemoglobinuria, iron deposition, renal parenchyma, *V2*: 1121, 1127
Patient preparation and positioning:
breast MRI, *V2*: 1694
MRI guidance and breast intervention, *V2*: 1760–1762
Pediatric patients:
cirrhosis in, *V1*: 317–318
MR imaging techniques, *V2*: 1637–1644
1.5T and 3.0T sequences, *V2*: 1639, 1644
adnexa, *V2*: 1650
adrenal glands, *V2*: 1650
bladder, *V2*: 1650
data acquisition parameters, *V2*: 1644–1645
echo-train spin-echo sqeuence, *V2*: 1644
female urethra/vagina, *V2*: 1650
follow-up procedures, *V2*: 1647–1649
gadolinium-based contrast agents, *V2*: 1647
gallbladder/biliary system, *V2*: 1649
gastrointestinal tract, *V2*: 1650
infants (under 1.5 years), *V2*: 1645
kidneys, *V2*: 1650
liver, *V2*: 1649
magnetic field strength, *V2*: 1644
magnetization-preparied rapid-acquisition gradient-echo sequences, *V2*: 1639, 1644
male pelvis, *V2*: 1650
older children (6–18 years), *V2*: 1645–1646
pancreas, *V2*: 1649–1650
receiver coil, *V2*: 1644–1645
retroperitoneum, *V2*: 1650
sedation technique, *V2*: 1646–1647
single-shot echo-train spin-echo sequence, *V2*: 1644
small children (1–6 years), *V2*: 1641, 1645
spin-echo sequences, *V2*: 1637
spleen, *V2*: 1650
T1-weighted sequences, *V2*: 1637, 1639–1644
T2-weighted sequences, *V2*: 1644
three-dimensional gradient-echo sequences, *V2*: 1639
two-dimensional spoiled gradient echo sequences, *V2*: 1639
uterus and cervix, *V2*: 1650
Peliosis hepatis, *V1*: 114–115, 119–120
Pelvic congestion syndrome, *V2*: 1517–1518
Pelvic floor relaxation, female urethra, *V2*: 1408–1410
Pelvic inflammatory disease (PID), ovarian abscess, *V2*: 1514, 1516–1517
Pelvic kidney, *V2*: 1031–1035
Pelvimetry, MR imaging techniques, *V2*: 1629
Pelvis:
abscesses, *V1*: 874, 884–886
peritoneal inflammation, *V2*: 951, 957–958
Burkitt lymphoma, retroperitoneal malignant masses, *V2*: 1253, 1257
cervical cancer invasion of, *V2*: 1486–1488
Ewing sarcoma pelvic metastases, *V2*: 1274, 1288
extrarenal, *V2*: 1164, 1170
female pelvis (*See* Vagina; specific organs, e.g., Uterus)
bowel peristalsis artifacts, *V2*: 1499
in pregnancy, maternal imaging, *V2*: 1570, 1574
uterine peristalsis, *V2*: 1437–1439
varices, *V2*: 1517–1518
fetal assessment:
anomalies, *V2*: 1612–1617
cysts, *V2*: 1617, 1619
normal development, *V2*: 1583–1585
lipomatosis, bladder involvement, *V2*: 1326, 1329–1330

male pelvis (*See also* specific organs, e.g., Prostate)
MR imaging technique, *V2*: 1343–1344
pediatric imaging, *V2*: 1650
postprostatectomy, *V2*: 1349, 1354
metastases, bladder involvement, *V2*: 1320–1322
protocol for, *V1*: 16–19, 21
whole body imaging, *V1*: 36, 40
Penis:
benign masses, prostheses, *V2*: 1376–1377
congenital anomalies, *V2*: 1376
diffuse disease, *V2*: 1377–1380
infectious disease, *V2*: 1380
inflammatory disease, *V2*: 1380–1381
metastases to, *V2*: 1376–1380
normal anatomy, *V2*: 1375–1376
primary tumors, *V2*: 1377–1380
trauma, *V2*: 1382
Percentage mural enhancement (MRP), Crohn disease imaging criteria, *V1*: 796, 803
Percutaneous gastrostomy tube, *V1*: 761, 766
Perfusional defect imaging, liver metastases, *V1*: 143, 147, 398–400
Periampullary carcinoma, bile duct imaging, *V1*: 518, 520, 527–530
Perianal fistula, *V1*: 883, 887–888
Perilesional enhancement:
liver imaging:
hemangiomas, *V1*: 90, 101
metastases, differential diagnoses, *V1*: 147–150
pancreatic adenocarcinoma, *V1*: 580, 587
uterine leiomyomas, *V2*: 1452–1469
Perinephric pseudocysts, *V2*: 1042, 1044, 1050
Perinephric stranding, renal abscess, *V2*: 1144, 1149–1152
Perineum, carcinomas, *V2*: 1421
Perioarterial lymphoid sheath (PALS), splenic anatomy, *V1*: 678
Periportal halo sign, primary biliary cirrhosis, *V1*: 314–315
Perisplenic varices, splenomegaly and, *V1*: 706–709
Peristalsis. *See* Bowel peristalsis; Uterine peristalsis
Peristomal hernia, abdominal wall imaging, *V2*: 904, 909
Peritoneum. *See also* Retroperitoneum
benign masses:
cysts, *V2*: 907, 910
desmoid tumor (aggressive fibromatosis), *V2*: 912–914
endometriosis, *V2*: 911
lipomas and mesenteric lipomatosis, *V2*: 910
cholangiocarcinoma metastases, *V1*: 520, 526
cirrhosis and enhancement of, *V1*: 348, 351, 360
colon cancer metastases, *V1*: 843, 847–848, 854–858, 860
congenital anomalies, *V2*: 904–907
foreign bodies, *V2*: 945–947
hepatocellular carcinoma metaseses, *V1*: 192, 200–201
hernias, *V2*: 904–909
abdominal wall, *V2*: 904, 908–909
Bochdalek hernia, *V2*: 904–905
hiatus and internal, *V2*: 904, 906–907
inflammatory disease:
abscess, *V2*: 949, 951, 954–959
mesenteric panniculitis, *V2*: 946, 950
pancreatitis, *V2*: 940–942, 946, 949
peritonitis, *V2*: 949, 951–953
intraperitoneal fluid:
ascites, *V2*: 936, 940–942
bile, *V2*: 942
biloma, *V2*: 942, 944–945
blood, *V2*: 936, 943–944
lesser sac involvement, *V2*: 936, 941
postsurgical, *V2*: 936, 940
urine, *V2*: 942
malignant masses:
diffuse malignant mesothelioma, *V2*: 912, 915–917
primary peritoneal carcinoma, *V2*: 912, 917
metastases to, *V2*: 912, 914, 918–936 (*See also* specific cancers)
carcinoid tumors, *V2*: 936, 939–940
contiguous spread, *V2*: 912
hematogenous spread, *V2*: 924
intraperitoneal seeding, *V2*: 914, 918–935
lymphatic dissemination, *V2*: 924–925, 934–935
ovarian cancer, *V2*: 1504–1505, 1533, 1535–1536
ovarian endodermal sinus tumor, *V2*: 1542
pseudomyxoma peritonei, *V2*: 936–938
MR imaging technique, *V2*: 902–903
normal anatomy, *V2*: 901–902
normal variants, *V2*: 904
ovarian cysts, *V2*: 1504, 1508
pancreatic adenocarcinoma metastases, *V1*: 575, 581–583
vascular disease, *V2*: 945–946, 948–949
Peritonitis, *V2*: 949, 951–953
Persistent fetal kidney lobulation, *V2*: 1031
Peutz-Jagers syndrome, colonic adenomatous polyps, *V1*: 832
Peyronie disease, *V2*: 1380–1381
Phase-cancellation artifact, out-of-phase (opposed-phase) spoiled gradient echo sequences, *V1*: 4–5
Phased-array multicoil imaging:
3T MR imaging, 4-channel *vs.* 8-channel, *V1*: 33–34
adnexa, *V2*: 1499
bladder, *V2*: 1298–1299
colon cancer, *V1*: 848
lung cancer, pulmonary nodules, *V2*: 1654, 1657, 1662–1665
male pelvis, *V2*: 1343–1344
pancreatic adenocarcinoma, *V1*: 559
pediatric patients, *V2*: 1644–1645
in pregnancy, *V2*: 1561
retroperitoneal neoplasms, *V2*: 1266
spoiled gradient echo sequences, *V1*: 3
uterus, *V2*: 1433
vessel imaging, *V2*: 1195, 1198–1200
Pheochromocytoma:
adrenal medullary masses, *V2*: 998, 1005–1111
bladder, *V2*: 1303
Phyllodes tumor, *V2*: 1706–1707
Picture archival computing system, vessel imaging, *V2*: 1200
Pince-nez sign, breast implant rupture, *V2*: 1759
Placenta, MR imaging techniques, *V2*: 1623, 1625–1627
Placenta accreta, MR imaging techniques, *V2*: 1623, 1625–1627
Placenta previa, MR imaging techniques, *V2*: 1623, 1625–1627
Pleural disease:
chest imaging, *V2*: 1666, 1671–1672
metastases, *V2*: 1673–1674
Pleural metastases, hepatocellular carcinoma, *V1*: 192, 202
Polycystic ovarian syndrome (PCOS), *V2*: 1507, 1509, 1514
Polygyria, fetal assessment, Chiari II malformation, *V2*: 1588–1592
Polyhydramnios:
encephalocele, fetal assessment, *V2*: 1595, 1597
fetal assessment:
brain neoplasms, *V2*: 1598
epignathi, *V2*: 1599
mesoblastic nephroma, *V2*: 1620
twin-twin transfusion syndrome, *V2*: 1623–1624
Polyorchia, *V2*: 1386
Polyposis coli, *V1*: 829, 832, 838
Polyposis syndromes:
gastric polyps, *V1*: 736, 739–741
large intestine, *V1*: 829, 832, 835–836
small intestinal polyps, *V1*: 775, 777–778
Polyps:
colonic, *V1*: 829, 832, 835–838
endometrial, *V2*: 1448–1450
gallbladder, *V1*: 480, 482–483
gastric, *V1*: 736, 739–741
small intestine, *V1*: 775, 777–778
Polysplenia syndrome:
MR imaging, *V1*: 681, 683, 686
short pancreas, *V1*: 544, 546
Polythelia, breast imaging, *V2*: 1700–1701
Porcelain gallbladder, *V1*: 477, 480
Porta hepatis lymphadenopathy:
hepatitis C and, *V1*: 327, 330
imaging studies, *V1*: 352, 354, 359, 362–365

Portal hypertension:
cirrhosis, *V1*: 348, 351, 359–362
esophageal varices, *V1*: 727, 729
gastric varices, *V1*: 738, 742
omental metastases, differential diagnosis, *V2*: 923–924
pediatric patients, imaging protocols, *V2*: 1637, 1642
rectal varices, *V1*: 838
splenomegaly, *V1*: 706–709
Portal venous system:
biliary tree, air in, *V1*: 411, 413–414
cirrhosis:
cavernous transformation, *V1*: 348, 351, 359
portal hypertension, *V1*: 348, 351, 359–362
gadolinium-enhanced T1-weighted images, *V1*: 11
hemangioma compression, *V1*: 88, 100
hepatic arterial dominant phase imaging, gadolinium-based contrast agent, *V2*: 1776–1777
hepatic transplantation complications, *V1*: 292–294
hepatocellular carcinoma, *V1*: 192, 194–198
MR imaging techniques, *V1*: 46–47, 50
porta hepatis lymphadenopathy, *V1*: 352, 354, 359
thrombosis, *V1*: 388, 391, 393–400
hepatocellular carcinoma, *V1*: 202, 212, 224–232, 234–238
infectious cholangitis, *V1*: 502, 506–507
pancreatic adenocarcinoma, *V1*: 566
Positive intraluminal contrast agents, large intestine imaging, *V1*: 895
Posterior fossa anomalies, fetal assessment, *V2*: 1591, 1593–1597
Posttransplant lymphoproliferative disorder (PTLD):
hepatic transplantation, *V1*: 299–301
renal transplants, *V2*: 1177, 1182, 1184–1185
Pouchitis, *V1*: 810
Pouch of Douglas abscess, *V1*: 874, 882–883
Preeclampsia, liver imaging, *V1*: 407, 410–411
Pregnancy. *See also* Fetal assessment; Gestational trophoblastic disease; Maternal imaging
amniotic fluid assessment, *V2*: 1622–1623
appendicitis diagnostic imaging, *V1*: 874, 880–881, *V2*: 1561–1564
cervical carcinoma in, *V2*: 1482–1483
cervical incompetence, *V2*: 1629–1631
cesarean scar pregnancy, *V2*: 1577–1580
Crohn disease in, *V1*: 796, 802
ectopic pregnancy, *V2*: 1517
endometrioma during, *V2*: 1504, 1513
fetal weight and amniotic fluid, *V2*: 1622–1623
inflammatory bowel disease and, *V1*: 868, 871
intussusception, *V1*: 816, 826
MRI safety in, *V2*: 1559–1561
multiple gestation, *V2*: 1623–1624
ovarian torsion during, *V2*: 1509–1510, 1514–1516
ovarian venous compression and thrombosis, *V2*: 1232, 1237
pelvimetry, *V2*: 1629
placental imaging, *V2*: 1623, 1625–1627
septate uterus, *V2*: 1441, 1447
subchorionic hematoma in, *V2*: 1559–1560
uterine hematoma in, *V2*: 1559–1560
Primary aldosteronism, aldosterone-secreting adrenal adenomas, *V2*: 977, 986–987
Primary biliary cirrhosis (PBC), *V1*: 314–315
Primary hemochromatosis:
liver, *V1*: 354, 362, 365–368
pancreas, *V1*: 546, 548–549
Primary peritoneal carcinoma (PPC), *V2*: 912, 917
Primary sclerosing cholangitis (PSC):
imaging studies, *V1*: 303–304, 306–311
MRCP imaging, *V1*: 494, 497–502
Primovist (Gd-EOB-DTPA) contrast agent, *V2*: 1768
liver imaging, *V1*: 51–58
focal nodular hyperplasia, *V1*: 121, 135
metastases characterization, *V1*: 128, 135
Proctitis:
infectious colitis, *V1*: 888
radiation-induced, *V1*: 888, 893–894
ProHance gadolinium-based contrast agent, classification, *V2*: 1768
Prominent columns of Bertin, kidney anomalies, *V2*: 1031
Prostate cancer:
adenocarcinoma, *V2*: 1352, 1356–1373
anaplastic state, *V2*: 1358, 1366
recurrence, *V2*: 1352, 1354
stage 2, *V2*: 1352, 1356–1357
American Joint Committee staging, *V2*: 1358, 1368
American Urological Committee staging, *V2*: 1368
benign prostatic hyperplasia and, *V2*: 1349–1352
bladder metastases, *V2*: 1320–1323
capsular extension, *V2*: 1352, 1358, 1359–1363, 1367–1373
prostatectomy, *V2*: 1368–1373
radiation therapy, *V2*: 1368–1373
rhabdomyosarcoma, *V2*: 1352, 1355
sarcoma, *V2*: 1352, 1356
squamous cell carcinoma, *V2*: 1352, 1355
Prostatectomy:
bladder changes, *V2*: 1331, 1335
prostate cancer treatment, *V2*: 1368–1373
prostate scarring, *V2*: 1352–1354
Prostate gland:
benign lesions, *V2*: 1349–1354
congenital anomalies, *V2*: 1344, 1347–1349
inflammatory and infectious disease, *V2*: 1373–1374
metastases to, *V2*: 1368–1373
MR imaging techniques, *V2*: 1343–1344
normal anatomy, *V2*: 1344–1346
trauma, *V2*: 1374–1375
Prostatis, chronic, *V2*: 1373
Prostheses:
breast, fat necrosis, *V2*: 1750–1752
breast implants, *V2*: 1754–1759
categories, *V2*: 1754–1755
failure, *V2*: 1687–1689, 1755–1757
fat necrosis, *V2*: 1746, 1749–1752
imaging techniques, *V2*: 1757–1759
postoperative MRI, *V2*: 1744–1749
penile, *V2*: 1376–1377
testicular, *V2*: 1386
Protein synthesis, liver metastases, *V1*: 165, 186
Proteus spp., prostate infection, *V2*: 1373–1374
Proton NMR spectroscopy, breast imaging, *V2*: 1696
fibroadenolipoma, *V2*: 1709, 1711
Proximal descending colon, adenocarcinoma, *V1*: 843, 845
Prune belly syndrome:
bladder anomalies, *V2*: 1299
fetal assessment, *V2*: 1613–1614
wandering spleen and, *V1*: 681
"Pruning," primary sclerosing cholangitis, MRCP imaging, *V1*: 497–502
Pseudoaneurysms:
aorta, *V2*: 1201–1207
renal artery disease, *V2*: 1133, 1135
Pseudocysts:
adrenal glands, *V2*: 980–981, 984, 991–993
intraperitoneal cocoon, *V2*: 945, 947
pancreatic:
acute on chronic pancreatitis, *V1*: 656, 659–664
acute pancreatitis, *V1*: 625, 628, 637, 642–647
hemorrhagic pancreatitis, *V1*: 656, 665
trauma, *V1*: 665, 668–671
perinephric (parapelvic), *V2*: 1042, 1044, 1050
peritoneal, *V2*: 910
ovarian cysts, *V2*: 1504, 1508
peritonitis, *V2*: 949, 951–953
spleen, *V1*: 683, 687–690
Pseudohermaphrodites, *V2*: 1415–1416
Pseudomembranous colitis, *V1*: 883–884, 889
Pseudomonas spp., prostate infection, *V2*: 1373–1374
Pseudomyxoma peritonei:
mucocele, large intestine, *V1*: 838, 841–842
peritoneal metastases, *V2*: 936–938
"Pseudopolyps," ulcerative colitis, *V1*: 867

Pseudotumor:
hepatic inflammatory disease, *V1*: 415, 418–422
retroperitoneal inflammatory, *V2*: 1247
testes, scrotum and epididymis, *V2*: 1388, 1390
Psoas muscle:
abscess, *V2*: 1273–1274, 1276–1279
MR imaging, *V2*: 1271, 1273–1280
neurogenic tumor, *V2*: 1271, 1273
Pulmonary emboli, magnetic resonance angiography, *V2*: 1673, 1675–1677
Pulmonary hyperplasia, fetal assessment, *V2*: 1605
Pulmonary infiltrates, *V2*: 1666, 1668–1671
Pulmonary nodules, MR imaging, *V2*: 1654, 1657, 1662–1665
"Pure gonadal dysgenesis," *V2*: 1415
Pyelonephritis:
acute, *V2*: 1142, 1147–1149
renal transplants, *V2*: 1177, 1179–1180
chronic, *V2*: 1126, 1128, 1130
in pregnancy, maternal imaging, *V2*: 1564, 1566
xanthogranulomatous, *V2*: 1152
Pyeloureteral anastomosis, renal transplants, *V2*: 1184
Pyogenic abscesses, hepatic, *V1*: 418, 422–432
Pyonephrosis, *V2*: 1155–1156
Pyosalpinx. *See* Tubo-ovarian abscess (TOA)

Radial scarring, breast lesions, *V2*: 1714–1715, 1717
Radiation therapy:
bladder changes, *V2*: 1331, 1337
breast cancer, post-therapy imaging, *V2*: 1744, 1747
breast carcinoma from, *V2*: 1743
cervical cancer metastases:
bladder fistulae, *V2*: 1486, 1489
recurrence and posttreatment change, *V2*: 1493–1495
Crohn disease, *V1*: 791
esophagitis, *V1*: 730–731
gastric ulceration and gastritis, *V1*: 761, 763
hepatitis, *V1*: 321, 331
large intestine:
enteritis, *V1*: 888, 892
proctitis, *V1*: 888, 893–894
liver metastases following, *V1*: 257, 262–264
pancreatic cancer and, *V1*: 589–590
peritoneal metastases, differential diagnosis, *V2*: 923–924
prostate cancer, *V2*: 1368–1373
rectosigmoid colon adenocarcinoma, *V1*: 852, 858, 861–865
small intestine, metastases *vs.*, *V1*: 815–816, 818
vaginal effects, *V2*: 1421, 1428
Radiofrequency ablation:
hepatocellular carcinoma, *V1*: 278, 280–286
liver metastases, *V1*: 278–280
renal cell carcinoma, *V2*: 1088–1089, 1095–1096
Radiofrequency power deposition, 3T MR imaging, *V1*: 31
Radiological Diagnostic Oncology Group (RDOG), ovarian cancer, epithelial tumors, *V2*: 1533
Rapid acquisition with relaxation enhancement (RARE) sequences, *V1*: 6
magnetic resonance cholangiopancreatography, *V1*: 456, 460
Rapidly involuting congenital hemangioma (RICH), fetal assessment, *V2*: 1604, 1607
Real-time ("on-the-fly") bolus-tracking method, liver imaging protocol, *V1*: 20
Receiver coil, pediatric MRI, *V2*: 1644–1645
Recipient assessment, hepatic transplantation protocol, *V1*: 287, 291–292
Reconstructive surgery:
bladder, *V2*: 1331, 1335–1336
imperforate anus, *V1*: 827, 834
Rectal cancer:
adenocarcinoma, *V1*: 843, 848–850, 852, 855–857
bone metastases, *V1*: 858, 861–863
bone metastases and sacral invasion, *V1*: 852, 861–863
endorectal coil imaging, *V1*: 850, 857
recurrent, *V1*: 850, 857–866
bladder metastases from, *V2*: 1320, 1323–1324
carcinoid tumors, *V1*: 867–868
MR imaging techniques, *V1*: 843, 848, 850, 852–865
penis and urethra metastases, *V2*: 1376–1377
vaginal metastases, *V2*: 1426–1427
Rectoceles, female urethra, *V2*: 1408–1410
Rectosigmoid colon:
adenocarcinoma, *V1*: 843, 848
fibrosis and, *V1*: 852, 861–863
recurrence rates, *V1*: 850, 857–860
bladder metastases from, *V2*: 1320, 1323–1324
lymphoma, *V1*: 860, 867
Rectourethral fistulas, *V2*: 1408
Rectovaginal fistula, *V2*: 1421, 1426, 1429–1430
Rectum:
anorectal anomalies, *V1*: 827, 831, 833–834
cloacal repair, *V1*: 827, 833
metastases to:
cervical cancer, *V2*: 1492–1495
gastrointestinal stromal tumors, *V1*: 860, 866
vaginal carcinoma, *V2*: 1416, 1423
MR imaging techniques, *V1*: 824, 827
normal anatomy, *V1*: 824, 827, 831
perforation and abscess, *V1*: 874, 886
postsurgical infection, *V1*: 892, 894–895
varices, *V1*: 838
Recurrent malignant disease imaging, echo-train spin-echo sequences, *V1*: 6–7
Recurrent pyogenic cholangitis, MR imaging, *V1*: 502, 507
Redundant sequences, MR imaging strategies and, *V1*: 16–24
Reflux nephropathy, *V2*: 1126, 1128, 1130
Regenerative nodules (RNs), cirrhosis, *V1*: 333–334, 339–345
iron-containing, *V1*: 334, 340, 344–346
Reidel lobe, MR imaging, *V1*: 58–60
Relaxation times, 3T MR imaging, *V1*: 32–36
Reliability issues, parallel MR imaging, *V1*: 29, 31
Remote table motion, MR imaging strategies, *V1*: 20
Renal adenomas, *V2*: 1068
Renal agenesis, fetal assessment, *V2*: 1613
Renal arterial disease, *V2*: 1128–1129, 1131–1133
abdominal aortic aneurysm, *V2*: 1201–1207
renal transplants, *V2*: 1177, 1182–1183
Renal blood flow evaluation, *V2*: 1173
Renal calculi, *V2*: 1159, 1166–1167
Renal cell carcinoma (RCC):
adrenal gland metastases, *V2*: 998–1002
autosomal dominant polycystic kidney disease and, *V2*: 1098, 1101
bilateral cancer, *V2*: 1088, 1093
chronic renal failure, *V2*: 1098–1101
cystic changes with, *V2*: 1088, 1090–1092
cystic disease, differential diagnosis, *V2*: 1052, 1061–1062
granulocytic sarcoma (chloroma), differential diagnosis, *V2*: 1109, 1111
hemorrhage, *V2*: 1088–1094
chronic renal failure, *V2*: 1098–1101
hypervascular tumors, *V2*: 1084, 1086
imaging protocol for, *V1*: 16, 19–20
infiltrative, *V2*: 1088, 1095
metastases, pancreas, *V1*: 619, 625
MR imaging, *V2*: 1098, 1102
radiofrequency ablation, *V2*: 1088–1089, 1095–1096
recurrence, *V2*: 1089, 1096–1097
renal cysts, differential diagnosis, *V2*: 1053, 1098
renal transplants, *V2*: 1177, 1181, 1184
staging, *V2*: 1073–1095
stage 1, *V2*: 1073–1077
stage 2, *V2*: 1076, 1078, 1087–1089
stage 3a, *V2*: 1076–1077, 1079–1081
stage 3b, *V2*: 1077, 1081
stage 3c, *V2*: 1082–1083
stage 4, *V2*: 1082, 1084–1085
subtraction image, *V2*: 1037, 1040
von Hippel-Lindau syndrome, *V1*: 549–550

Renal collecting system:
dilation, *V2*: 1164, 1169–1172
filling defects, *V2*: 1159, 1166–1169
Renal cortical infarcts, *V2*: 1137, 1143–1144
Renal ectopia. *See* Ectopic kidney
Renal filling defects, *V2*: 1159, 1166–1169
Renal function:
imaging studies, *V2*: 1173–1177
nephrogenic systemic fibrosis, *V2*: 1781
renal parenchymal disease, *V2*: 1112, 1116–1117
Renal parenchyma:
acute obstruction, paroxysmal changes, *V2*: 1121, 1127–1130
arterial disease, *V2*: 1127, 1129, 1131–1143
diffuse disease, *V2*: 1112–1124
acute tubular necrosis, *V2*: 1120, 1122
glomerular disease, *V2*: 1117–1120
renal function decline, *V2*: 1112, 1116–1117
tubular blockage, *V2*: 1120, 1123–1124
tubulointerstitial disease, *V2*: 1120–1121
iron deposition, *V2*: 1121, 1124–1127
lesions, pattern recognition, *V2*: 1031, 1037
obstruction, *V2*: 1121, 1125–1126, 1128–1129, 1170–1172
reflux nephropathy and chronic pyelonephritis, *V2*: 1126, 1128, 1130
renal arterial disease, *V2*: 1128–1129, 1131–1144
renal scarring, *V2*: 1128, 1138, 1145–1146
renal vein aneurysm, *V2*: 1138
renal vein thrombosis, *V2*: 1137, 1144
Renal pelvis and ureter:
calyceal diverticulum, *V2*: 1164, 1172
collecting system dilatation, *V2*: 1164, 1169–1172
filling defects, *V2*: 1159, 1166–1169
lymphoma, *V2*: 1159
metastases to, *V2*: 1159
squamous cell carcinoma, *V2*: 1159, 1165
urothelial carcinoma, *V2*: 1155, 1159–1165
Renal vein:
congenital anomalies, *V2*: 1223, 1228–1230
thrombosis, *V2*: 1137–1138, 1144
inferior vena cava thrombus and, *V2*: 1232–1237
nephrotic syndrome, *V2*: 1117, 1120
Rendu-Osler-Weber syndrome, hepatic arteriovenous fistulas, *V1*: 388–392
Repetition time (TR):
3T MR imaging, *V1*: 32–36
small intestine imaging, *V1*: 767–770
Resovist, iron-based contrast agent, *V2*: 1778–1779
Respiration artifacts:
abdominal-pelvic MRI, fast scanning and avoidance of, *V1*: 1–2
magnetic resonance cholangiopancreatography, *V1*: 460
Reticuloendothelial system (RES):
iron-based contrast agents, *V2*: 1777–1779
MRI contrast agent targeting, *V1*: 50–58
spleen imaging, *V1*: 678–681
Retractile mesenteritis, *V2*: 946, 950
Retroperitoneum:
benign masses:
extramedullary hematopoiesis, *V2*: 1249, 1251
fibrosis, *V2*: 1240, 1242–1244
lymphadenopathy, *V2*: 1247–1250
adrenal glands, *V2*: 1017, 1019
retroperitoneal neoplasms, *V2*: 1240, 1245–1247
bladder cancer metastases, transitional cell carcinoma, *V2*: 1308–1316
body wall:
benign neoplasms, *V2*: 1274, 1281–1283
hernias, hematoms, and other lesions, *V2*: 1274, 1290–1293
malignant neoplasms, *V2*: 1274, 1284–1290
malignant masses:
carcinoma, *V2*: 1265–1266
embryonal rhabdomyosarcoma, *V2*: 1265, 1271–1272
hemangiopericytoma, *V2*: 1265, 1271, 1273
leiomyosarcomas, *V2*: 1265–1270
liposarcoma, *V2*: 1265, 1271
lymphadenopathy, *V2*: 1258–1263
adrenal glands, *V2*: 1017, 1019
lymphoma, *V2*: 1253–1257
retroperitoneal fibrosis, *V2*: 1249, 1252–1253
testicular cancer, *V2*: 1258, 1263–1265
MR imaging technique, *V2*: 1193–1194
normal anatomy, *V2*: 1193
pediatric imaging, *V2*: 1650
psoas muscle, *V2*: 1271, 1273–1280
vessel imaging:
aorta, *V2*: 1200–1227
aortic aneurysm, *V2*: 1200–1207
aortic dissection, *V2*: 1201, 1208–1212
aortoiliac atherosclerotic disease/thrombosis, *V2*: 1204, 1207, 1214–1223
penetrating ulcers/intramural dissecting hematoma, *V2*: 1201, 1204, 1213
postoperative graft evaluation, *V2*: 1207, 1214, 1216, 1224–1227
inferior vena cava, *V2*: 1216, 1223, 1229
congenital anomalies, *V2*: 1223, 1229–1230
primary malignant tumors, *V2*: 1237–1241
venous thrombosis, *V2*: 1229–1237
magnetic resonance angiography, *V2*: 1194–1200
Rhabdomyosarcoma:
bladder cancer, *V2*: 1316
embryonal, retroperitoneal imaging, *V2*: 1266, 1272
prostate cancer, *V2*: 1352, 1355
vulvar malignancies, *V2*: 1421, 1423
Rhomboencephalosynapsis, fetal assessment, *V2*: 1593–1597
Ring enhancement imaging:
colon adenocarcinoma, *V1*: 843, 845
colon melanoma, *V1*: 867, 869
hepatosplenic candidiasis, *V1*: 433, 436
liver metastases:
breast cancer, *V1*: 162, 171
gastrinomas, *V1*: 164, 180
hepatocellular carcinoma, *V1*: 202, 232–233
lesional/perilesional enhancement, *V1*: 147–150
ovaries, endometriomas, *V2*: 1506, 1509–1512
pancreas:
insulinomas, *V1*: 601, 603
metastases to, *V1*: 625, 630–631
pancreatic islet cell tumors, *V1*: 593
Robson's renal cell carcinoma classification, *V2*: 1073–1095
Rokitansky-Aschoff sinuses:
gallbladder adenomyomatosis, *V1*: 480, 484
xanthogranulomatous cholecystitis, *V1*: 477

Sacral invasion, rectal adenocarcinoma, *V1*: 852, 861–863
Saddlebag urethral diverticulum, *V2*: 1405, 1407
Safety issues:
3T MR imaging, *V1*: 33
gadolinium-based contrast agents, *V2*: 1779–1786
MRI in pregnancy, *V2*: 1559–1561
whole body MR imaging, *V1*: 41–42
Sagittal-plane imaging:
bladder:
fistulas, *V2*: 1331–1335
metastatic neoplasms, *V2*: 1320–1324
breast MRI, *V2*: 1693–1694
female urethra, malignant masses, *V2*: 1403–1404
renal cell carcinoma:
stage 3a, *V2*: 1076–1077, 1079–1081
stage 4, *V2*: 1082, 1084–1085
vaginal metastases, *V2*: 1421–1426
"Sandwich sign," lymphatic dissemination, peritoneal metastases, *V2*: 925, 935
Santorini ducts, pancreas divisum, *V1*: 541–542

Sarcoidosis:
liver imaging, *V1*: 414–416
retroperitoneal benign lymphadenopathy, *V2*: 1249–1250
spleen, *V1*: 711–713
Sarcoma:
body wall, *V2*: 1274, 1284–1290
granulocytic, kidney, *V2*: 1109, 1111
liver metastases, undifferentiated, *V1*: 251, 256
perirectal metaseses, *V2*: 1274, 1287
peritoneal metastases, *V2*: 918, 923–924, 929–930
prostate cancer, *V2*: 1352, 1356
retroperitoneal, *V2*: 1265–1271
uterine, *V2*: 1475, 1479–1481
undifferentiated, *V2*: 1488–1491
Sarcomatoid carcinoma, bladder, *V2*: 1316
Saturation pulse, fat-suppressed echo-train spin-echo sequences, *V1*: 9–10
Scan time reduction, gradient echo sequences, *V1*: 2–3
Schistosoma baematobium, bladder calculi, *V2*: 1305
Schizencephaly, fetal assessment, *V2*: 1595–1596
Schwannoma:
adrenal glands, *V2*: 1006
gastric, *V1*: 740
pancreatic cancer, *V1*: 594–597, 601
Scleroderma:
reflux esophagitis, *V1*: 730
small intestine, *V1*: 809–810
Sclerosing adenosis, breast changes, *V2*: 1712, 1714, 1716
Sclerosing cholangitis. *See also* Primary sclerosing cholangitis (PSC)
MRCP imaging, *V1*: 493–494
Sclerosing hemangiomas, spleen, *V1*: 688, 693
Sclerosing mesenteritis, *V2*: 946, 950
Sclerosing stromal tumor, ovaries, *V2*: 1525–1526
Scrotum:
benign masses, *V2*: 1388–1392
congenital anomalies, *V2*: 1386
hernia, *V2*: 1390
MR imaging, *V2*: 1385
normal anatomy, *V2*: 1383–1384
Secondary infection, liver metastases, *V1*: 180, 188, 191–192
Secretin-enhanced magnetic resonance cholangiopancreatography (MRCP), chronic pancreatitis imaging, *V1*: 648–649, 652, 655
Sedated patients:
MRI imaging in, *V1*: 25–27
pediatric patients:
age categories, *V2*: 1645
T1-weighted imaging, *V2*: 1637, 1639–1644
technique, *V2*: 1646–1647
Semilobar holoprosoencephaly, fetal assessment, *V2*: 1589–1592
Seminal vesicles:
benign masses, *V2*: 1382
congenital anomalities, *V2*: 1382, 1384
hypoplasia, *V2*: 1344, 1348–1349
malignant masses, *V2*: 1382, 1384–1385
normal anatomy, *V2*: 1382–1384
prostate cancer metastases, *V2*: 1344, 1349, 1363–1365, m1384–1385
hemorrhage, *V2*: 1368, 1370–1372
Seminomas, testes lesions, *V2*: 1390–1396
Sensitivity encoding (SENSE):
parallel MR imaging, *V1*: 25, 29
small intestine imaging, *V1*: 767–770
Septated renal cysts, *V2*: 1042, 1047
Septated vagina, *V2*: 1412, 1414–1415
uterus didelphys, *V2*: 1441, 1444–1446
Septate uterus, *V2*: 1441, 1444, 1447–1449
Septo-optic dysplasia, fetal assessment, *V2*: 1594, 1596
Sequence technology, whole body imaging, *V1*: 40–42
Serial MRI examination, *V1*: 24–25
adrenal glands, *V2*: 964–968
Serosal metastases:
intraperitoneal seeding, *V2*: 923–924
small bowel obstruction, *V1*: 779, 782, 792
Serous cystadenocarcinoma, *V1*: 612
ovarian:
malignant tumors, *V2*: 1533–1535
metastases, *V2*: 1504–1505, 1533, 1535–1536
Serous cystadenoma:
benign ovarian neoplasms, *V2*: 1518–1523
MR imaging, *V1*: 606–607, 609–612
Serpiginous (arciform) enhancement, spleen, *V1*: 678–681
Serratia spp., prostate infection, *V2*: 1373–1374
Sertoli-Leydig cell tumors, malignant ovarian neoplasms, *V2*: 1540, 1542, 1545–1547
Serum creatinine levels, renal function and, *V2*: 1112, 1116–1117
Sex cord-stromal tumors:
benign ovarian neoplasms, *V2*: 1525–1526
malignant ovarian neoplasms, *V2*: 1540, 1542, 1545–1547
Sexual differentiaton disorders:
testicular feminization, *V2*: 1415, 1448
uterine anomalies, *V2*: 1448
Short-tau inversion recovery (STIR):
breast, silicone implants, *V2*: 1757–1759
breast imaging, *V2*: 1694–1695
cysts, *V2*: 1701–1703
cavernous hemangioma, *V2*: 1416, 1420
fat-suppressed echo-train spin-echo sequences, *V1*: 7–10
hepatic cysts, *V1*: 60, 63
liver imaging:
hemangiomas, *V1*: 88, 97–99
hepatic cysts, *V1*: 60, 63
mycobacterium avium intracellulare, *V1*: 433–435
pancreatic adenocarcinoma imaging, *V1*: 573
retroperitoneal lymphoma, *V2*: 1253–1257
spleen, *V1*: 678–681
Sickle cell disease:
hepatic iron overload, *V1*: 368, 370, 374–375
iron deposition, renal parenchyma, *V2*: 1121, 1124–1126
spleen imaging, *V1*: 683, 687
Siderosis, transfusional, liver imaging, *V1*: 368–373
Sigmoid colon:
adenocarcinoma, *V1*: 843, 846–848, 852
lipoma, *V1*: 832
Signal intensity index:
adrenal gland imaging:
adenomas, drop in, *V2*: 971, 974, 982–984
hemangiomas, *V2*: 993–994
metastases, *V2*: 994–1002
pheochromocytoma, *V2*: 1005–1111
breast MRI interpretation guidelines, *V2*: 1696–1700
vessel imaging, *V1*: 14
Signal-to-noise ratio (SNR):
3T imaging, uterus and cervix, *V2*: 1434
3T MR imaging *vs.* 1.5T, *V1*: 31–36
breast MRI, *V2*: 1692–1693
coil systems, *V2*: 1693
liver imaging techniques, *V1*: 46–50
male pelvis imaging, *V2*: 1343–1344
pancreatic imaging, *V1*: 536
parallel MR imaging, *V1*: 29
pediatric patient imaging:
receiver coil, *V2*: 1644–1645
spin-echo sequence, *V2*: 1637
prostate cancer, adenocarcinoma, *V2*: 1352, 1356–1373
Signal-void air, large intestinal abscess imaging, *V1*: 881–886
Silicone breast implants, *V2*: 1754–1759
rupture, *V2*: 1687–1689, 1755–1757
Simultaneous acquisition of spatial harmonics (SMASH), parallel MR imaging, *V1*: 25, 29–31
Single-shot echo-train spin-echo (SS-ETSE) sequences:
abdominal-pelvic imaging, *V1*: 6–8
abdominal wall hernia, *V2*: 904, 908–909
bile duct abnormalities, MRCP imaging, *V1*: 489, 493, 497
colon cancer, *V1*: 843–865
esophagus, *V1*: 726, 728
female urethra, pelvic floor relaxation, *V2*: 1408–1410
fetal assessment, *V2*: 1561
amniotic band syndrome, *V2*: 1621
cleft palate, *V2*: 1603–1607
normal development, *V2*: 1583
gastrointestinal tract, *V1*: 725
gluten-sensitive enteropathy, *V1*: 799, 807–809
hypertrophic rugal folds, *V1*: 761, 765
kidney imaging, *V2*: 1025–1031
filling defects, *V2*: 1159, 1166–1169
multicystic dysplastic kidney, *V2*: 1049, 1058
pyonephrosis, *V2*: 1155–1156

Single-shot echo-train spin-echo (SS-ETSE) sequences: (*Continued*)
large intestine:
abscesses, *V1*: 883–886
diverticulitis, *V1*: 869, 878–879
mucocele, *V1*: 838, 841–842
techniques, *V1*: 824
liver imaging, *V1*: 46–48
echinococcal disease, *V1*: 431–433
hepatic cysts, solitary cysts, *V1*: 60–64
Reidel lobe, differential diagnosis, *V1*: 58–60
unilocular cysts, *V1*: 60–63
magnetic resonance cholangiopancreatography, *V1*: 456–461
noncooperative patients, *V1*: 25
non-fat-suppressed *vs.* fat-suppressed images, *V1*: 35–37
pancreatic imaging, *V1*: 536–539
acute pancreatitis, *V1*: 625, 628, 635–647
pediatric patients, *V2*: 1644
infants, *V2*: 1645
older children, *V2*: 1645–1646
peritoneal metastases, intraperitoneal seeding, *V2*: 918–924
pleural disease imaging, *V2*: 1666, 1671–1672
in pregnancy, maternal imaging:
bowel obstruction, *V2*: 1564
conjoined twins, *V2*: 1623–1624
renal calculi, *V2*: 1159, 1166–1169
retroperitoneum:
lymphoma, *V2*: 1253–1257
primary neoplasms, *V2*: 1271
serial MRI examination, *V1*: 24–28
small intestine:
intussusception, *V1*: 816, 825–826
ischemia and hemorrhage, *V1*: 816, 819–823
small intestine imaging, *V1*: 767–770
adenocarcinoma, *V1*: 777, 781–782
choledochocele, *V1*: 775–776
Crohn disease, *V1*: 785, 791, 793–805
intestinal atresia and stenosis, *V1*: 770, 774
stomach, *V1*: 734–736
duodenal diverticulum, *V1*: 770, 772–774
postoperative evaluation, *V1*: 761, 766
uterine-cervical MRI, *V2*: 1434
Sjögren syndrome, autoimmune pancreatitis, *V1*: 664
Skene glands, urethrovaginal fistulas, *V2*: 1408
"Skip lesions," Crohn disease, *V1*: 785, 791, 797–799
Slice-selective inversion pulse, magnetization-prepared rapid-acquisition gradient echo sequences, *V1*: 5–6
Sliding hernia, *V2*: 904, 906–907
Slow enhancement techniques, liver hemangiomas, *V1*: 88, 90, 95–96
Small bowel. *See* Small intestine
Small cell carcinoma:
kidney, *V2*: 1109, 1111–1113
liver metastases, undifferentiated tumors, *V1*: 164, 177–179
Small intestine:
benign lesions:
leiomyomas, *V1*: 775, 780
lipomas, *V1*: 775
neurofibromas, *V1*: 775, 779
polyps, *V1*: 775, 777–778
varices, *V1*: 775, 781
congenital lesions, *V1*: 770–776
atresia and stenosis, *V1*: 770, 774
choledochocele, *V1*: 775–776
duodenal diverticulum, *V1*: 770, 772–774
Meckel diverticulum, *V1*: 770, 774
rotational abnormalities, *V1*: 770–771
fetal assessment, *V2*: 1615
inflammatory, infectious, and diffuse disease:
Crohn disease, *V1*: 784–785, 791, 793–805
drug toxicity, *V1*: 810, 817
eosinophilic gastroenteritis, *V1*: 809
fistula, *V1*: 810–813, 812–813
gluten-sensitive enteropathy, *V1*: 799, 807–809
graft-*versus*-host disease, *V1*: 816–817, 828–829
hernia, *V1*: 816, 827
hypoproteinemia, *V1*: 816, 824
infectious enteritis, *V1*: 810, 813–814
inflammatory bowel disease, *V1*: 782, 784
intussusception, *V1*: 816, 825–826
ischemia and hemorrhage, *V1*: 816, 819–823
pancreatitis, *V1*: 810, 815
pouchitis, *V1*: 810
radiation enteritis, *V1*: 815–816, 818
scleroderma, *V1*: 809–810
ulcerative colitis, *V1*: 796, 799, 806
leiomyosarcoma, hypervascular liver metastases, *V1*: 161, 163
malignant masses:
adenocarcinomas, *V1*: 777, 781–782
carcinoid tumors, *V1*: 779, 790–791
gastrointestinal stromal tumor, *V1*: 777, 779, 783–785
lymphoma, *V1*: 779, 786–791
metastases to, *V1*: 779, 782, 791–793
MR imaging, *V1*: 767–770
follow-through and enteroclysis, *V1*: 767–770
oral contrast agents, *V1*: 20
normal anatomy, *V1*: 765, 767
polyps, *V1*: 775, 777–778
Small-vessel disease, renal artery, *V2*: 1136–1141
renal transplants, *V2*: 1182, 1184
Solid epithelial neoplasm, pancreas, *V1*: 619, 622–623
Somatostatinoma, MR imaging, *V1*: 601, 604–605
Specific absorption rate (SAR):
echo-train spin-echo sequences, *V1*: 7
MRI in pregnancy, *V2*: 1559–1561
single-shot echo-train spin-echo sequences, *V1*: 36
Spectral (fat)-selective adiabatic inversion pulses (SPAIR), T2-weighted imaging, *V1*: 9–10
Spermatocele, testes, scrotum and epididymis, *V2*: 1388, 1390
Sphincter of Oddi:
abnormalities, MRCP imaging, *V1*: 489, 493, 497
pancreatic anatomy, *V1*: 536
Spigelian hernia, abdominal wall imaging, *V2*: 904, 909
Spin-echo sequence, pediatric patients, *V2*: 1637
Spiral computed tomography (CT):
liver imaging:
hemangiomas, *V1*: 88, 101–102
metastases imaging:
coexistent cysts, *V1*: 190
MR imaging *vs.*, *V1*: 128, 142–147
pancreas, pancreatic adenocarcinoma, *V1*: 552–553, 558–559, 564–565
peritoneal metastases, intraperitoneal seeding, *V2*: 918
renal filling defects, *V2*: 1159, 1166–1169
Spleen:
accessory and wandering spleens, *V1*: 681–685
asplenia, *V1*: 681, 685
benign mass lesions:
cysts, *V1*: 683, 687–690
hamartomas, *V1*: 690, 693, 695–697
hemangiomas, *V1*: 687–688, 691–693
littoral cell angioma, *V1*: 688, 694
lymphangiomas, *V1*: 693
pattern recognition, *V1*: 688
Gamna-Gandy bodies, *V1*: 711, 714
Gaucher disease, *V1*: 683
genetic hemochromatosis and, *V1*: 354
infarcts, *V1*: 719–722, *V2*: 1121
infectious disease, *V1*: 709–711
malignant masses:
lymphoma/hematologic malignancies, *V1*: 693–694, 698–703
metastases to, *V1*: 701, 703–706
angiosarcoma, *V1*: 704, 706
direct tumor invasion, *V1*: 704–705
metastases to:
colonic lymphoma, *V1*: 860, 867
glucagonoma/somatostatinoma, *V1*: 601, 604–605
imaging studies, *V1*: 701, 703–706
islet cell tumors, *V1*: 601, 604–606
MR imaging technique, *V1*: 678–681
normal anatomy, *V1*: 677–678
pediatric imaging, *V2*: 1650
polysplenia, *V1*: 681, 683, 686
portal and splenic thrombosis, *V1*: 388, 391, 394–395
sarcoidosis, *V1*: 711–713
sickle disease, *V1*: 683, 687

splenomegaly and vascular pathologies, *V1*: 706–709
subscapular fluid collection, *V1*: 715, 717
trauma, *V1*: 715–716
Splenic artery aneurysm, splenomegaly and, *V1*: 706–709
Splenic vein:
pancreatic anatomy, *V1*: 535
spleen, normal anatomy, *V1*: 677–678
thrombosis:
esophageal varices, *V1*: 727, 729
gastric varices, *V1*: 738, 742
pancreatic adenocarcinoma, *V1*: 575, 579
splenomegaly and, *V1*: 706–709
Splenic vein-only hepatic arterial phase (SVHADP), gadolinium-based contrast agent, *V2*: 1774–1777
Splenomegaly:
chronic lymphocytic leukemia (CLL), *V1*: 700
lymphoma metastases, *V1*: 694, 699–703
pathology, *V1*: 706–709
Splenorenal shunt, splenomegaly, *V1*: 706–709
Splenosis, *V1*: 715, 717–719
Splenules, MR imaging, *V1*: 681, 684–685
iron-based contrast agents, differential diagnosis, *V2*: 1778–1779
Spoiled gradient echo (SGE) sequences:
abdominal-pelvic imaging, *V1*: 3–4
adnexa, *V2*: 1499–1500
adrenal glands, *V2*: 963–968
appendicitis diagnostic imaging, *V1*: 874, 879–881
bladder, transitional cell carcinoma, *V2*: 1308–1316
chronic pancreatitis imaging, *V1*: 656–665
esophageal imaging, esophageal varices, *V1*: 727, 729
esophagus, malignant masses, *V1*: 729–731
gadolinium-enhanced T1-weighted images, hepatic arterial dominant (capillary) phase, *V1*: 11–13
image parameters, *V1*: 3
large intestine:
abscesses, *V1*: 881–886
colonic adenomatous polyps, *V1*: 832, 835–838
diverticulitis, *V1*: 869, 874–879
infectious colitis, *V1*: 888
liver imaging techniques, *V1*: 46–50
autoimmune hepatitis, *V1*: 312–314
colon cancer metastases, *V1*: 149, 154–155
computed tomography *vs.*, *V1*: 128, 141–144
contrast agents, *V1*: 52–58
diaphragmatic insertion, *V1*: 58, 60
focal nodular hyperplasia, *V1*: 121, 123–125, 127–128
hepatic cysts, solitary cysts, *V1*: 60–64
hepatocellular carcinoma, *V1*: 192–198, 213–217
hypervascular metastases, *V1*: 149, 157–158
hypovascular metastases, *V1*: 149, 153
metastases characterization, *V1*: 128, 137–143
Reidel lobe, differential diagnosis, *V1*: 58–60
squamous cell carcinoma metastases, *V1*: 162, 165–171
unilocular cysts, *V1*: 60–66
viral hepatitis, *V1*: 321–322
male pelvis, *V2*: 1343–1344
noncooperative patients, *V1*: 25
out-of-phase (opposed-phase) spoiled gradient echo sequences, *V1*: 4–5
pancreatic imaging, *V1*: 536–541
pancreatic adenocarcinoma, *V1*: 552, 554–556, 572, 574–575
psoas muscle metastases, *V2*: 1273, 1275
rectal adenocarcinoma, *V1*: 848–850
renal cell carcinoma, *V2*: 1073–1095
retroperitoneum, *V2*: 1193–1194
fibrosis, benign *vs.* malignant, *V2*: 1240, 1242–1244
malignant metastatic lymphadenopathy, *V2*: 1258–1263
small intestine, *V1*: 767–770
gastrointestinal stromal tumor, *V1*: 779, 783–785
metastases to, *V1*: 782, 791–792
polyps, *V1*: 775, 777–778
varices, *V1*: 775, 781
spleen, *V1*: 678–681
hamartomas, *V1*: 693, 695–697
lymphoma metastases, *V1*: 694, 699–703
splenic metastases, *V1*: 701, 703–706
stomach, gastric adenocarcinoma, *V1*: 743
three-dimensional imaging quality improvements, *V1*: 16
TR/TE/flip angle variations, *V1*: 23–24
vessel imaging:
aorta, *V2*: 1200–1227
abdominal aortic aneurysm, *V2*: 1201–1207
aortic dissection, *V2*: 1201, 1208–1212
aortoiliac atherosclerotic disease/thrombosis, *V2*: 1204, 1207, 1214–1223
inferior vena cava, *V2*: 1216, 1223, 1229
inferior vena cava thrombus, *V2*: 1229–1237
"Spoke wheel" pattern, renal oncocytomas, *V2*: 1068, 1072
Squamous cell carcinoma:
anal canal, *V1*: 860, 866
bladder cancer, *V2*: 1316–1318
esophagus, *V1*: 729–731
lung cancer, liver metastases, *V1*: 162, 175–176
prostate cancer, *V2*: 1352, 1355
renal pelvis and ureter, *V2*: 1159, 1165
vaginal malignancies, *V2*: 1416, 1420–1426
vulva, *V2*: 1421, 1427
"Stained glass" lesions, mucinous cystadenocarcinoma, ovarian malignancy, *V2*: 1533, 1536–1537
Steatosis. *See* Fatty liver
Stenosis:
ampullary (bile duct), *V1*: 489
gadolinium-based contrast agent, *V2*: 1771–1773
aqueductal, fetal assessment, *V2*: 1585–1592
bronchial, fetal assessment, *V2*: 1611–1612
cervical, endometriosis and, *V2*: 1506, 1510
iliac arteries, *V2*: 1204, 1207, 1216–1218
intestinal, *V1*: 770, 774
pancreatic duct, *V1*: 665, 668–671
renal artery disease, *V2*: 1131–1132
renal transplants, *V2*: 1178, 1183–1184
Stomach:
benign masses:
bezoar, *V1*: 738, 742
gastric polyps, *V1*: 736, 739–740
leiomyomas, *V1*: 736
neurogenic tumors and lipomas, *V1*: 736, 738, 740–742
varices, *V1*: 738, 742
congenital lesions, *V1*: 736
diverticula, *V1*: 736–738
gastric duplication cysts, *V1*: 736
heterotopias, *V1*: 736
fetal assessment, *V2*: 1615
infectious disease, *V1*: 761–764
inflammatory disease, *V1*: 761–764
malignant masses:
adenocarcinoma, *V1*: 738, 741, 743–751
Peutz-Jeghers syndrome, *V1*: 832
carcinoids, *V1*: 756, 759
carcinomas, *V1*: 741
gastrointestional stromal tumor, *V1*: 743, 748, 752–758
Kaposi sarcoma, *V1*: 748, 756
lymphoma, *V1*: 756, 758
TNM staging, *V1*: 742
metastases to, *V1*: 741, 759–760
MR imaging technique, *V1*: 734–736
normal anatomy, *V1*: 734–735
postoperative conditions, *V1*: 761, 766
Streak gonads:
ovarian anomalies, *V2*: 1503
vaginal anomalies, *V2*: 1415
Streptococcal infection, pyogenic hepatic abscess, *V1*: 418, 427
Stricture:
biliary tree, *V1*: 292, 299
female urethra, *V2*: 1407

Strongoloides stercoralis, infectious enteritis, differential diagnosis, *V1*: 810, 813–814
Struma ovarii, benign ovarian neoplasms, *V2*: 1521, 1528–1529
Subcapsular line sign, breast implant imaging, *V2*: 1759
Subchorionic hematoma, in pregnancy, *V2*: 1559–1560
Subependymal heterotopia, fetal assessment, *V2*: 1595
Subglandular breast implants, *V2*: 1754–1759
Submucosal hemorrhage, small intestine, *V1*: 816, 822–823
Submucosal imaging, ulcerative colitis, *V1*: 867–868, 870
Submucosal leiomyomas, uterine, *V2*: 1449, 1451–1469
Submuscular breast implants, *V2*: 1754–1759
Subscapular fluid collections, splenic trauma, *V1*: 715–717
Subtraction imaging, renal cysts, *V2*: 1037, 1040
Superior mesenteric artery:
  aortic dissection into, *V2*: 1201, 1212
  chronic pancreatitis imaging, *V1*: 648–665
  pancreatic adenocarcinoma involvement, *V1*: 575, 577–578
  vascular graft, branch vessel, *V2*: 1214, 1216, 1227
Superior mesenteric vein, thrombosis, small intestine ischemia and hemorrhage, *V1*: 816, 822
Supernumerary scrotal testes, *V2*: 1386
Superparamagnetic iron oxide particles (SPIO):
  characteristics, *V2*: 1777–1779
  liver imaging, reticuloendothelial system targeting, *V1*: 50, 54–58
  prostate cancer metastases, *V2*: 1368–1373
  spleen imaging, *V1*: 678–681
    accessory/wandering spleens, *V1*: 681–685
    lymphoma metastases, *V1*: 700
    splenic metastases, *V1*: 701, 703–706
Surface coils:
  bladder imaging, *V2*: 1298–1299
  colon cancer imaging, *V1*: 848
  whole body imaging, *V1*: 40–42
Surgical sponge retention, intraperitoneal, *V2*: 945–947
Susceptibility artifact, 3T MR imaging, *V1*: 31–32

T1-relaxivity agents, vessel imaging, *V2*: 1197–1200
T1-weighted imaging:
  abdominal-pelvic disease, *V1*: 2–6
    fat-suppressed gradient echo sequences, *V1*: 4
    gradient echo sequences, *V1*: 3–4
    magnetization -prepared rapid-acquisition gradient echo sequences, *V1*: 5–6
    out-of-phase gradient echo sqeuences, *V1*: 4–5
adnexa, *V2*: 1499–1500
adrenal glands:
  adrenal cortical carcinoma, *V2*: 998, 1002–1006
  metastases, *V2*: 994–1002
  myelolipoma, *V2*: 979–980, 988–990
  neuroblastoma, *V2*: 1013–1017
  pheochromocytoma, *V2*: 1005–1111
  techniques, *V2*: 963–968
aortic dissection, *V2*: 1201, 1208–1212
aortic grafts, *V2*: 1214, 1216, 1224–1227
bile duct:
  ampullary fibrosis, *V1*: 489, 495–496
  cholangiocarcinoma, *V1*: 517–518, 521–526
  infectious cholangitis, *V1*: 502–507
  primary sclerosing cholangitis, *V1*: 499–502
bile duct and parenchymal lesions, *V1*: 460–461
bladder, *V2*: 1298
  congenital anomalies, *V2*: 1299–1301
  hemorrhagic cystitis, *V2*: 1326, 1329
  leiomyomas, *V2*: 1300, 1302–1303
  metastatic neoplasms, *V2*: 1320–1324
  neurofibromas, *V2*: 1304–1305
  squamous cell carcinoma, *V2*: 1317–1319
  transitional cell carcinoma, *V2*: 1307–1316
breast:
  cysts, *V2*: 1701–1703
  fat necrosis, *V2*: 1749
breast cancer:
  invasive ductal carcinoma, *V2*: 1723–1727
  melanoma metastases, *V2*: 1743–1744
cervix, *V2*: 1434
colon cancer:
  melanoma, *V1*: 867, 869
  rectosigmoid carcinoma, *V1*: 850, 857–860
disease conspicuity and, *V1*: 1–2
esophagus, *V1*: 726, 728
  leiomyomas, *V1*: 726–728
female urethra:
  diverticulum, *V2*: 1405–1407
  malignant masses, *V2*: 1403–1404
  normal anatomy, *V2*: 1401–1403
fetal assessment:
  abdomen and pelvis, *V2*: 1583–1585
  brain imaging, *V2*: 1578–1583
  congenital hemangiomas, *V2*: 1604, 1607
  destructive lesions, *V2*: 1598–1601
  head and neck, *V2*: 1583
gadolinium-enhanced images, *V1*: 10–13
  hepatic arterial dominant (capillary) phase, *V1*: 10–13
  hepatic venous (interstitial) phase, *V1*: 11
  portal venous/early hepatic venous phase, *V1*: 11
gallbladder, *V1*: 460, 463
  acute cholecystitis, *V1*: 469–475
  carcinoma, *V1*: 481, 485–486
  gallstone disease, *V1*: 464–465, 467–469
  hemorrhagic cholecystitis, *V1*: 475–477
  polyps, *V1*: 480, 482–483
iron-based contrast agents, *V2*: 1777–1779
kidneys:
  acquired cystic disease, hemodialysis-induced, *V2*: 1052, 1061–1062
  angiomyolipomas, *V2*: 1063–1068
  cysts with thickened walls, *V2*: 1042, 1049
  hemorrhagic/proteinaceous cysts, *V2*: 1037, 1042–1044, 1046
  lymphocele, *V2*: 1182
  perinephric pseudocyst, *V2*: 1042, 1044, 1050
  renal function assessment, *V2*: 1112, 1116–1117
  small-cell carcinoma, *V2*: 1112–1113
  techniques, *V2*: 1025–1031
  trauma, *V2*: 1172–1174
  Wilms tumor, *V2*: 1103–1106
large intestine:
  colonic fistulae, *V1*: 883, 887–888
  intraluminal contrast agents, *V1*: 892, 895–897
  lipomas, *V1*: 832, 839–840
  mucocele, *V1*: 838, 841–842
liver, *V1*: 46–50
  ablative therapies, *V1*: 278–287
  angiosarcoma, *V1*: 242, 249
  bile duct carcinoma, intrahepatic/peripheral metastases, *V1*: 239–240, 242, 247–249
  Budd-Chiari syndrome, hepatic venous thrombosis, *V1*: 398, 401–405
  carcinoid tumor metastases, *V1*: 164, 183–185
  chemotherapy-related metaseases, *V1*: 257, 264–270
  cirrhosis, *V1*: 333–362
    dysplastic nodules, *V1*: 340, 342, 346–354
    regenerative nodules, *V1*: 333–334, 339–345
  contrast agents, *V1*: 51–58
  echinococcal disease, *V1*: 431–433
  fatty liver, *V1*: 371, 373, 377–387
  fibrolamellar carcinoma, *V1*: 238–239
  focal nodular hyperplasia, *V1*: 121
    hepatocellular adenoma, differential diagnosis, *V1*: 177, 180
  fungal infection, *V1*: 437–438
  hemangiomas, *V1*: 73, 81, 83, 85, 87
    chronic liver disease, *V1*: 103–105
    hepatocellular carcinoma, differential diagnosis, *V1*: 106
  hepatic abscess, pyogenic, *V1*: 418, 422–432

hepatic cysts:
foregut hepatic cysts, *V1*: 60, 66–70
solitary (nonparasitic), *V1*: 60–66
hepatic transplantation, *V1*: 292, 299
hepatocellular adenoma, *V1*: 107, 109–113
hepatocellular carcinoma, *V1*: 192, 198, 202–214
diffuse infiltrative, *V1*: 212, 227, 234–238
hypervascular metastases, *V1*: 151–162
inflammatory myofibroblastic tumor, *V1*: 418–422
lesional/perilesional enhancement, *V1*: 147–150
lymphomas, *V1*: 238, 240–245
melanoma metastases, *V1*: 164, 181–182
mesothelioma, malignant, *V1*: 242, 250–251
metastases detection and characterization, *V1*: 128, 137–143
mucin-producing tumors, *V1*: 165, 185–186
multiple myeloma, *V1*: 238, 245–246
pancreatic ductal adenocarcinoma metastases, *V1*: 162
porta hepatis lymphadenopathy, *V1*: 352, 354, 359, 362–365
portal venous air, *V1*: 411, 413
postradiation metastases, *V1*: 257, 262–264
primary biliary cirrhosis, *V1*: 314–315
primary sclerosing cholangitis, *V1*: 304, 306–311
radiation-induced hepatitis, *V1*: 321, 331
resection, metastases following, *V1*: 256–262
squamous cell carcinoma metastases, *V1*: 162, 165–171
T2 images *vs.*, *V1*: 143–147
techniques, *V1*: 46–50
transcatheter arterial embolization, *V1*: 268, 270–278
transfusional iron overload, *V1*: 368–373
trauma, *V1*: 442
undifferentiated sarcoma, *V1*: 251, 256
magnetic resonance cholangiopancreatography, *V1*: 460–461
ovaries:
benign neoplasms:
epithelial origin, *V2*: 1518–1523
germ cell tumors, *V2*: 1520–1521, 1526–1529
sex cord-stromal tumors, *V2*: 1525–1526, 1529–1531
cysts, functional cysts, *V2*: 1500, 1504–1506
endometriomas, *V2*: 1506
functional cysts, *V2*: 1504–1506
hydrosalpinx, *V2*: 1517
lymphoma, *V2*: 1545, 1548–1549
metastases to, *V2*: 1547, 1549–1550
ovarian torsion, *V2*: 1510, 1514–1516
pelvic inflammatory disease, *V2*: 1514, 1516–1517
polycystic ovarian syndrome, *V2*: 1507, 1509, 1514
pancreas, *V1*: 536–541
acute pancreatitis, *V1*: 628, 636–647
annular pancreas, *V1*: 542–544
autoimmune pancreatitis, *V1*: 664, 666
chronic pancreatitis, *V1*: 648–665
cystic fibrosis, *V1*: 545–548
gastrinomas, *V1*: 591, 598–602
insulinomas, *V1*: 601, 603
islet-cell tumors, *V1*: 590–598
metastases to, *V1*: 619, 625–631
mucinous cystadenoma/cystadenocarcinoma, *V1*: 612–616
pancreatic adenocarcinoma, *V1*: 552, 554–558, 562–564, 570, 572, 574–575, 577–587
liver metastases, *V1*: 580, 584–587
lymph node metastases, *V1*: 580, 584
primary hemochromatosis, *V1*: 546, 548–549
serous cystadenoma, *V1*: 607, 611–612
pediatric patients, *V2*: 1637, 1639–1646
pelvic varices, *V2*: 1517–1518
penis and urethra:
inflammatory disease, *V2*: 1380–1381
metastases, *V2*: 1376–1377
normal anatomy, *V2*: 1375–1376
primary tumors, *V2*: 1377–1380
peritoneum:
ascites, *V2*: 936, 940–942
intraperitoneal blood, *V2*: 936, 943–944
in pregnancy, *V2*: 1561
cervical fibroids, *V2*: 1569, 1573
fetal weight and amniotic fluid, *V2*: 1622–1623
postpartum uterus, *V2*: 1575–1580
prostate cancer, *V2*: 1352, 1356–1373
adenocarcinoma, *V2*: 1352, 1356–1373
prostate gland:
benign prostatic hyperplasia, *V2*: 1349–1354
inflammation and infection, *V2*: 1373–1374
normal anatomy, *V2*: 1344–1346
trauma, *V2*: 1374–1375
rectum, *V1*: 827, 831
renal cell carcinoma, *V2*: 1084, 1086
retroperitoneum:
benign lymphadenopathy, *V2*: 1247–1250
primary neoplasms, *V2*: 1265–1271
seminal vesicles:
cysts, *V2*: 1382, 1384
diffuse disease, *V2*: 1382–1383, 1385
normal anatomy, *V2*: 1382–1834
small intestine, *V1*: 767–770
carcinoids, *V1*: 779, 790–791
spleen, *V1*: 678–681
cysts, *V1*: 683, 687–690
hamartomas, *V1*: 690, 693, 695–697
hemangiomas, *V1*: 687–688, 691–693
littoral cell angioma, *V1*: 688, 694
lymphomas, *V1*: 693–694, 699–703
stomach, *V1*: 734
carcinoids, *V1*: 759
gastric adenocarcinoma, *V1*: 738
T3-weighted imaging *vs.*, *V1*: 32–36
testes, scrotum and epididymis, *V2*: 1385
benign neoplasms, *V2*: 1386, 1388–1390
cryptorchidism, *V2*: 1386–1388
infectious disease, *V2*: 1397–1398
malignant tumors, *V2*: 1392–1396
testicular prostheses, *V2*: 1386
trauma, *V2*: 1397
uterus, *V2*: 1434
endometrial carcinoma, *V2*: 1471–1481
endometrial hyperplasia/polyps, *V2*: 1449–1450
leiomyomas, *V2*: 1452–1469
uterine corpus, *V2*: 1434–1436
vagina, *V2*: 1409–1410
Bartholin glands cysts, *V2*: 1416–1418
Gartner duct cyst, *V2*: 1416, 1418–1419
radiation effects, *V2*: 1421, 1428
vaginal malignancies, *V2*: 1420–1426
vessel imaging, *V2*: 1194–1200
inferior vena cava malignancies, *V2*: 1237–1241
T2-weighted imaging:
3T MR imaging, *V1*: 33–36
abdominal-pelvic disease, *V1*: 6–10
adnexa, *V2*: 1499–1500
adrenal glands, *V2*: 964–968
adrenal cortical carcinoma, *V2*: 998, 1002–1006
metastases, *V2*: 994–1002
myelolipoma, *V2*: 979–980, 988–990
neuroblastoma, *V2*: 1013–1017
pheochromocytoma, *V2*: 1005–1111
ambiguous genitalia, *V2*: 1415–1416
aortic grafts, *V2*: 1214, 1216, 1224–1227
bile duct:
ampullary fibrosis, *V1*: 489, 495–496
cholangiocarcinoma, *V1*: 517–518, 521–526
infectious cholangitis, *V1*: 502–507
bile ducts, primary sclerosing cholangitis, *V1*: 499–502
biliary system, gadolinium-based contrast agents, *V2*: 1771
bladder, *V2*: 1298
congenital anomalies, *V2*: 1299–1301
cystitis, *V2*: 1326–1328
hemorrhagic cystitis, *V2*: 1326, 1329
hypertrophic bladder, *V2*: 1324–1325
leiomyomas, *V2*: 1300, 1302–1303
metastatic neoplasms, *V2*: 1320–1324
neurofibromas, *V2*: 1304–1305
transitional cell carcinoma, *V2*: 1307–1316

T2-weighted imaging: (*Continued*)
breast:
cysts, *V2*: 1701–1703
fibroadenomas, *V2*: 1703–1706
phyllodes tumor, *V2*: 1706–1707
protocol, *V2*: 1694–1695
silicone implants, *V2*: 1688–1689, 1757–1759
breast cancer:
invasive ductal carcinoma, *V2*: 1723–1727
melanoma metastases, *V2*: 1743–1744
cervical cancer, *V2*: 1483–1488
cervix, *V2*: 1434
chest, *V2*: 1653–1654
pleural disease, *V2*: 1666, 1671–1672
colon cancer, *V1*: 843–865
disease conspicuity and, *V1*: 1–2
echo-train spin-echo sequences, *V1*: 6–7
esophagus, *V1*: 726, 728
leiomyomas, *V1*: 726–728
fat-suppressed echo-train spin-echo sequences, *V1*: 7–10
female urethra:
diverticulum, *V2*: 1405–1407
malignant masses, *V2*: 1403–1404
normal anatomy, *V2*: 1401–1403
pelvic floor relaxation, *V2*: 1408–1410
fetal assessment:
abdomen and pelvis, *V2*: 1583–1585
central nervous system, *V2*: 1578–1583
congenital hemangiomas, *V2*: 1604, 1607
destructive lesions, *V2*: 1598–1601
head and neck, *V2*: 1583
kidney anomalies, *V2*: 1613
renal cysts, *V2*: 1614–1616
gallbladder:
acute cholecystitis, *V1*: 472–475
carcinoma, *V1*: 481, 485–486
gallstone disease, *V1*: 464–465, 467–469
hemorrhagic cholecystitis, *V1*: 475–477
normal gallbladder, *V1*: 460, 462
polyps, *V1*: 480, 482–483
iron-based contrast agents, *V2*: 1777–1779
kidneys:
adenoma, *V2*: 1068
granulocytic sarcoma (chloroma), *V2*: 1109, 1111
hemorrhagic/proteinaceous cysts, *V2*: 1037, 1042–1044, 1046
iron deposition, *V2*: 1121, 1125–1127
lymphocele, *V2*: 1182
lymphoma, *V2*: 1106–1110
multilocular cystic nephroma, *V2*: 1060, 1063–1064
perinephric pseudocyst, *V2*: 1042, 1044, 1050
simple cysts, *V2*: 1037–1039
techniques, *V2*: 1025–1031
Wilms tumor, *V2*: 1103–1106
large intestine:
colonic fistulae, *V1*: 883, 887–888
intraluminal contrast agents, *V1*: 892, 895–897
mucocele, *V1*: 838, 841–842
rectosigmoid carcinoma, *V1*: 850, 857–860
techniques, *V1*: 824
liver, *V1*: 46–50
ablative therapies, *V1*: 278–287
adenocarcinoma, undifferentiated tumors, *V1*: 162, 164, 177–179
angiosarcoma, *V1*: 242, 249
autoimmune hepatitis, *V1*: 312–314
bile duct carcinoma, intrahepatic/peripheral metastases, *V1*: 239–240, 242, 247–249
Budd-Chiari syndrome, hepatic venous thrombosis, *V1*: 398, 401–405
carcinoid tumor metastases, *V1*: 164, 183–185
chemotherapy-related metaseases, *V1*: 257, 264–270
cirrhosis, *V1*: 333–362
dysplastic nodules, *V1*: 340, 342, 346–354
regenerative nodules, *V1*: 333–334, 339–345
iron-containing, *V1*: 334, 340, 344–346
computed tomography *vs.*, *V1*: 128, 141–144
echinococcal disease, *V1*: 431–433
fat/iron deposition, *V1*: 371, 376
fatty liver, *V1*: 379–387
fibrolamellar carcinoma, *V1*: 238–239
focal nodular hyperplasia, *V1*: 121–126
hepatocellular adenoma, differential diagnosis, *V1*: 177, 180
fungal infection, *V1*: 437–438
hemangiomas, *V1*: 73, 81, 83, 85–86, 89–91
central nodular lesion, *V1*: 85, 91
chronic liver disease, *V1*: 103–105
hepatocellular carcinoma, differential diagnosis, *V1*: 106
hypervascular metastases, differential diagnosis, *V1*: 90, 101–103
medium-sized lesion, *V1*: 85, 89–91
small lesion, *V1*: 85–86
small-sized slow-enhancing, *V1*: 88, 94–95
hepatic abscess, pyogenic, *V1*: 418, 422–432
hepatic arterial obstruction, *V1*: 407
hepatic cysts:
foregut hepatic cysts, *V1*: 60, 66–70
solitary (nonparasitic), *V1*: 60–66
hepatic transplantation, *V1*: 292, 299
hepatocellular adenoma, *V1*: 107, 109–113
hepatocellular carcinoma, *V1*: 192, 198, 202–214
diffuse infiltrative, *V1*: 212, 227, 234–238
hypervascular metastases, *V1*: 151–162
inflammatory myofibroblastic tumor, *V1*: 418–422
lobe abnormalities, *V1*: 58–60
lymphomas, *V1*: 238, 240–245
melanoma metastases, *V1*: 164, 181–182
mesothelioma, malignant, *V1*: 242, 250–251
metastases detection and characterization, *V1*: 128, 137–143
T1 images *vs.*, *V1*: 147–150
multiple myeloma, *V1*: 238, 245–246
mycobacterium avium intracellulare, *V1*: 433–435
pancreatic ductal adenocarcinoma metastases, *V1*: 162
porta hepatis lymphadenopathy, *V1*: 352, 354, 359, 362–365
portal venous air, *V1*: 411, 413
portal venous thrombosis, *V1*: 391, 393–400
postradiation metastases, *V1*: 257, 262–264
preeclampsia and eclampsia, *V1*: 407, 410–411
primary biliary cirrhosis, *V1*: 314–315
primary sclerosing cholangitis, *V1*: 304, 306–311
radiation-induced hepatitis, *V1*: 321, 331
Reidel lobe, differential diagnosis, *V1*: 58–60
secondary infection, metastases, *V1*: 188, 191–192
transcatheter arterial embolization, *V1*: 268, 270–278
transfusional iron overload, *V1*: 368–373
trauma, *V1*: 442
viral hepatitis, *V1*: 321–330
magnetic resonance cholangiopancreatography, *V1*: 456–461
ovaries:
benign neoplasms:
epithelial origin, *V2*: 1518–1523
germ cell tumors, *V2*: 1520–1521, 1526–1529
sex cord-stromal tumors, *V2*: 1525–1526, 1529–1531
cysts, functional cysts, *V2*: 1500, 1504–1506
endometriomas, *V2*: 1506, 1509–1512
functional cysts, *V2*: 1504–1506
hydrosalpinx, *V2*: 1517
lymphoma, *V2*: 1545, 1548–1549
normal anatomy, *V2*: 1500–1501
ovarian torsion, *V2*: 1510, 1514–1516
pelvic inflammatory disease, *V2*: 1514, 1516–1517
polycystic ovarian syndrome, *V2*: 1507, 1509, 1514
pancreas:
acute pancreatitis, *V1*: 628, 636–647
autoimmune pancreatitis, *V1*: 664, 666
chronic pancreatitis, *V1*: 649, 665
gastrinomas, *V1*: 591, 593, 598–602

insulinomas, *V1*: 601, 603
islet-cell tumors, *V1*: 591–598
metastases to, *V1*: 619, 625–631
mucinous cystadenoma/cystadenocarcinoma, *V1*: 612–616
pancreatic adenocarcinoma, *V1*: 552–557
lymph node metastases, *V1*: 580, 584
primary hemochromatosis, *V1*: 546, 548–549
serous cystadenoma, *V1*: 606–607, 609–612
pediatric patients, *V2*: 1644
pelvic varices, *V2*: 1517–1518
penis and urethra:
inflammatory disease, *V2*: 1380–1381
metastases, *V2*: 1376–1377
normal anatomy, *V2*: 1375–1376
primary tumors, *V2*: 1377–1380
prostheses, *V2*: 1376–1377
peritoneum:
ascites, *V2*: 936, 940–942
intraperitoneal blood, *V2*: 936, 943–944
in pregnancy, *V2*: 1561
abdominal fibromatosis, *V2*: 1570
cervical fibroids, *V2*: 1569, 1573
fetal weight and amniotic fluid, *V2*: 1622–1623
postpartum uterus, *V2*: 1575–1580
prostate cancer, *V2*: 1352, 1356–1373
adenocarcinoma, *V2*: 1352, 1356–1373
prostate gland:
inflammation and infection, *V2*: 1373–1374
normal anatomy, *V2*: 1344–1346
trauma, *V2*: 1374–1375
psoas muscle, *V2*: 1271, 1273–1280
rectum, techniques, *V1*: 827, 831
renal cell carcinoma, *V2*: 1084, 1086
recurrence, *V2*: 1089, 1096–1097
retroperitoneum:
fibrosis, benign *vs.* malignant, *V2*: 1240, 1242–1244, 1249, 1252–1253
malignant metastatic lymphadenopathy, *V2*: 1258–1263
neurofibromas, *V2*: 1240, 1245–1247
primary neoplasms, *V2*: 1266–1271
seminal vesicles:
cysts, *V2*: 1382, 1384
diffuse disease, *V2*: 1382–1383, 1385
normal anatomy, *V2*: 1382–1834
single-shot echo-train spin-echo sequences, *V1*: 7–8
small intestine:
carcinoids, *V1*: 779, 790–791
Crohn disease, *V1*: 785, 791, 793–805
spleen, *V1*: 678–681
accessory/wandering spleens, *V1*: 681–685
cysts, *V1*: 683, 687–690
hamartomas, *V1*: 690, 693, 695–697
hemangiomas, *V1*: 687–688, 691–693
littoral cell angioma, *V1*: 688, 694
lymphangiomas, *V1*: 693
lymphomas, *V1*: 693–694, 699–703
stomach, *V1*: 734–736
carcinoids, *V1*: 759
gastric adenocarcinoma, *V1*: 738, 741, 743
gastrointestinal stromal tumors, *V1*: 743, 748, 752–758
testes, scrotum and epididymis, *V2*: 1385
benign neoplasms, *V2*: 1386, 1388, 1390
cryptorchidism, *V2*: 1386–1388
infectious disease, *V2*: 1397–1398
malignant tumors, *V2*: 1392–1396
testicular prostheses, *V2*: 1386
trauma, *V2*: 1397
uterus, *V2*: 1434
adenomyosis, *V2*: 1466–1470
endometrial carcinoma, *V2*: 1471–1481
endometrial hyperplasia/polyps, *V2*: 1448–1450
leiomyomas, *V2*: 1452–1469
menstrual changes, *V2*: 1437–1439
vagina:
agenesis/partial agenesis, *V2*: 1411–1412
Bartholin glands cysts, *V2*: 1416–1418
duplication anomalies, *V2*: 1412, 1414–1415
Gartner duct cyst, *V2*: 1416, 1418–1419
normal anatomy, *V2*: 1409–1410
radiation effects, *V2*: 1421, 1428
vaginal malignancies, *V2*: 1420–1426
vessel imaging, *V2*: 1194–1200
inferior vena cava malignancies, *V2*: 1237–1241
Takayasu arteritis, ischemic nephropathy, *V2*: 1136, 1139
Talipes equinovarus, fetal assessment, *V2*: 1622
Tamoxifen:
endometrial carcinoma, ovarian metastases, *V2*: 1474, 1476
uterine changes, *V2*: 1439–1440
Technetium (^{99m}Tc-pertechnetate) scintigraphy, Meckel divedrticulum, *V1*: 770, 774
Teratomas:
fetal assessment:
fetal mouth, *V2*: 1598, 1604
intracranial, *V2*: 1598–1599, 1602
sacrococcygeal teratoma, *V2*: 1617–1620
ovarian malignancies, *V2*: 1534, 1540, 1543–1544
Terminal duct-lobular units (TDLUs):
breast cancer, risk and prevalence, *V2*: 1723
breast cysts, *V2*: 1700–1703
fibroadenomas, *V2*: 1702–1706
fibrocystic breast changes, *V2*: 1712, 1714–1716
normal breast, *V2*: 1688
Testes:
benign masses:
cystic lesions, *V2*: 1386, 1389
neoplasms, *V2*: 1386, 1388, 1390
testicular prostheses, *V2*: 1386
congenital anomalies, *V2*: 1386
cryptorchidism, *V2*: 1386–1388
infectious disease, *V2*: 1397–1398
malignant masses, *V2*: 1390–1396
MR imaging, *V2*: 1385
normal anatomy, *V2*: 1383–1384
torsion, *V2*: 1396–1397
trauma, *V2*: 1397
Testicular cancer, retroperitoneal imaging, *V2*: 1258, 1263–1265
Testicular feminization, *V2*: 1415
uterine anomalies, *V2*: 1448
Thalassemia:
adrenal gland myelolipoma, *V2*: 977, 979–980, 988–990
hepatic iron overload, *V1*: 368, 370, 374–375
α-Thalassemia, liver imaging, *V1*: 370, 375
Theca-lutein ovarian cysts, *V2*: 1504, 1507–1508
Thecomas, benign ovarian neoplasms, *V2*: 1525–1526, 1531
Thin-collimation source images, magnetic resonance cholangiopancreatography, *V1*: 456, 460
Thorax:
fetal assessment:
anomalies, *V2*: 1604, 1612
normal development, *V2*: 1583
magnetic resonance angiography, *V2*: 1673, 1679–1684
Three-dimensional gradient echo sequences (3D-GE):
adnexa, *V2*: 1499–1500
adrenal glands, *V2*: 963–968
bladder, *V2*: 1298
transitional cell carcinoma, *V2*: 1307–1316
breast imaging, *V2*: 1694–1695
capillary phase imaging, *V1*: 2
chest imaging, *V2*: 1653–1654
hilar and mediastinal lymphadenopathy, *V2*: 1666–1667
pulmonary emboli, *V2*: 1673, 1675–1677
pulmonary infiltrates, *V2*: 1666, 1668–1671
colon cancer, *V1*: 843–865
peritoneal metastases, *V1*: 848, 854–857
dynamic contrast-enhanced imaging, *V1*: 3
esophageal imaging, *V1*: 726, 728
esophagus, malignant masses, *V1*: 729–731
fat-suppressed gradient echo sequences, *V1*: 4

Three-dimensional gradient echo sequences (3D-GE): (*Continued*)
gadolinium-enhanced T1-weighted images, hepatic arterial dominant (capillary) phase, *V1*: 11–13
gastrointestinal tract imaging, *V1*: 725
kidneys:
complex cysts, *V2*: 1037, 1040
fibromuscular dysplasia, *V2*: 1133, 1136–1137
horseshoe kidney, *V2*: 1032, 1034
renal blood flow evaluation, *V2*: 1173
renal filling defects, *V2*: 1159, 1166–1169
techniques, *V2*: 1025–1031
large intestine:
abscesses, *V1*: 881–886
colonic adenomatous polyps, *V1*: 832, 835–838
infectious colitis, *V1*: 888
techniques, *V1*: 824
ulcerative colitis, *V1*: 867–868, 870–871
liver imaging techniques, *V1*: 46–50
lung cancer, pulmonary nodules, *V2*: 1654, 1657, 1662–1665
male pelvis, *V2*: 1343–1344
pancreatic imaging, *V1*: 536–541
pancreatic adenocarcinoma, *V1*: 559, 564–566
pediatric patients, *V2*: 1637
older children, *V2*: 1645–1646
quality improvements, *V1*: 16
rectal adenocarcinoma, *V1*: 848–850
rectal carcinoid tumor, *V1*: 867–868
renal artery disease, *V2*: 1129, 1131–1133
renal cell carcinoma, stage 4, *V2*: 1082, 1084–1085
retroperitoneum, *V2*: 1193–1194
fibrosis, benign *vs.* malignant, *V2*: 1240, 1242–1244
malignant metastatic lymphadenopathy, *V2*: 1258–1263
small intestine, *V1*: 767–770
adenocarcinoma, *V1*: 777, 781–782
gastrointestinal stromal tumor, *V1*: 779, 783–785
infectious enteritis, *V1*: 810, 813–814
metastases to, *V1*: 782, 791–792
pancreatitis, *V1*: 810, 815
polyps, *V1*: 775, 777–778
radiation enteritis, *V1*: 816, 818
varices, *V1*: 775, 781
spleen, *V1*: 678–681
spoiled gradient echo (SGE) sequences, abdominal-pelvic imaging, *V1*: 3–4
stomach, *V1*: 734
gastric adenocarcinoma, *V1*: 743
vessel imaging, *V2*: 1195–1200
aorta, *V2*: 1200–1227
abdominal aortic aneurysm, *V2*: 1201–1207
aortic dissection, *V2*: 1201, 1208–1212
aortic graft evaluation, *V2*: 1214, 1216, 1224–1227
aortoiliac atherosclerotic disease/thrombosis, *V2*: 1204, 1207, 1214–1223
inferior vena cava, *V2*: 1216, 1223, 1229
thrombus, *V2*: 1229–1237
whole body imaging, *V1*: 40–42
Three-dimensional spin echo sequences, *V1*: 7
magnetic resonance cholangiopancreatography, *V1*: 456–461
single-shot echo-train spin-echo sequences, *V1*: 7–8
3.0T imaging:
adnexa, *V2*: 1500
adrenal glands, *V2*: 964–968
aorta, *V2*: 1200–1227
comparisons to 1.5T, *V1*: 31–36
female urethra, normal anatomy, *V2*: 1402–1403
gastrointestinal tract, *V1*: 725
kidney, renal cell carcinoma, stage 4, *V2*: 1082, 1084–1085
kidneys, *V2*: 1029–1031
liver imaging, hemangiomas, *V1*: 81, 83, 85, 88, 92–94, 96–97
lung cancer, pulmonary nodules, *V2*: 1654, 1662
male pelvis, *V2*: 1343–1344
pediatric patients, *V2*: 1637–1644
adnexa, *V2*: 1650
adrenal glands, *V2*: 1650
bladder, *V2*: 1650
data acquisition parameters, *V2*: 1644–1645
female urethra/vagina, *V2*: 1650
follow-up procedures, *V2*: 1647–1649
gadolinium-based contrast agents, *V2*: 1647
gallbladder/biliary system, *V2*: 1649
gastrointestinal tract, *V2*: 1650
imaging protocol, *V2*: 1637, 1644
infants (under 1.5 years), *V2*: 1645
kidneys, *V2*: 1650
liver, *V2*: 1649
magnetic field strength, *V2*: 1644
male pelvis, *V2*: 1650
older children (6–18 years), *V2*: 1645–1646
pancreas, *V2*: 1649–1650
receiver coil, *V2*: 1644–1645
retroperitoneum, *V2*: 1650
sedation technique, *V2*: 1646–1647
small children (1–6 years), *V2*: 1641, 1645
prostate cancer, adenocarcinoma, *V2*: 1352, 1356–1373
uterus and cervix, *V2*: 1434
vagina, vaginal carcinoma, *V2*: 1416, 1422
Thrombotic microangiopathy, renal artery disease, *V2*: 1133, 1137, 1141
Time-intensity curves, breast imaging, *V2*: 1691
Time-of-flight techniques, vessel imaging, *V2*: 1194–1200
TNM staging:
breast cancer, *V2*: 1723–1725
colon cancer, *V1*: 843
female urethral carcinoma, *V2*: 1403
gastric adenocarcinoma, *V1*: 738, 741–742
prostate cancer, *V2*: 1368
renal cell carcinoma (RCC), *V2*: 1073
testicular cancer, *V2*: 1392–1396
transitional cell carcinoma, bladder cancer, *V2*: 1307–1316
vaginal malignancies, *V2*: 1416, 1421
vulvar carcinomas, *V2*: 1421, 1427
Torsion, testicular, *V2*: 1396–1397
Toxicity studies, gadolinium-based contrast agents, *V2*: 1779–1786
Toxic megacolon:
Crohn colitis, *V1*: 869, 872–874
ulcerative colitis and, *V1*: 867–868, 870–781
Trachelectomy, cervical cancer, *V2*: 1493–1495
Transcatheter arterial chemoembolization, liver metastases, *V1*: 268, 270–278
Transfusional iron overload, liver imaging, *V1*: 368–373
Transfusional siderosis, liver imaging, *V1*: 368–373
Transhepatic signal intensity differences (THID), *V1*: 414–415
Transient hepatic arterial defects, *V1*: 414–415
Transitional cell carcinoma (TCC):
bladder:
advanced disease, *V2*: 1308, 1313–1314
diverticulum anomalies and, *V2*: 1300
invasive, *V2*: 1307–1308, 1312
recurrence, *V2*: 1308, 1316
superficial invasion, *V2*: 1307–1312
urothelial neoplasms, *V2*: 1306–1316
pancreatic metastases, *V1*: 619, 625, 627
renal pelvis and ureter, *V2*: 1155, 1159–1165
Transplant procedures:
hepatic transplantation:
bile duct obstruction following, *V1*: 292, 299
donor and recipient assessment, *V1*: 287–292
fibrosis, *V1*: 299, 304
fungal infection, *V1*: 299, 305
graft failure, *V1*: 287, 292
liver abnormalities, *V1*: 299, 303–306
hepatic arterial obstruction, *V1*: 405, 407–408
hepatocellular carcinoma recurrence, *V1*: 299, 302

inflammation following, *V1*: 299–300
lymphoma, *V1*: 238, 241
magnetic resonance cholangiopancreatography, bile duct anastomoses, *V1*: 519–520
MR imaging, *V1*: 287–305
posttransplant lymphoproliferative disorder, *V1*: 299–301
vascular complications, *V1*: 292–298
pancreatic transplants, *V1*: 671–673
renal transplants, *V1*: 671–673, *V2*: 1173, 1177–1188
Transposed ovaries, *V2*: 1500–1502
Transurethral resection of prostate (TURP):
bladder changes, *V2*: 1331, 1335
prostate defects, *V2*: 1352–1354
Transvaginal ultrasound:
pelvic inflammatory disease, *V2*: 1514, 1516–1517
uterus, congenital anomalies, *V2*: 1440
Transverse colon, adenocarcinoma, *V1*: 843, 845
Transverse echo train-STIR imaging, liver, hepatic cysts, *V1*: 60, 63
Transverse mesocolon, pancreatic adenocarcinoma involvement, *V1*: 575, 580
Trauma:
female urethra, *V2*: 1407
fetal assessment, destructive lesions, *V2*: 1596–1601
kidney, *V2*: 1172–1174
liver, *V1*: 438–442
pancreas, *V1*: 665, 668–671
penis and urethra, *V2*: 1382
prostate gland, *V2*: 1374–1375
renal artery injury, *V2*: 1133, 1136
spleen, *V1*: 715–719
testes, scrotum and epididymis, *V2*: 1397
True-FISP. *See* Two-dimensional steady-state precession-balanced echo MRI
Trypsin, pancreatitis and, *V1*: 625
Tuberculosis:
adrenal glands, *V2*: 1019
genitourinary, bladder involvement, *V2*: 1326
mycobacterium tuberculosis, hepatic involvement, *V1*: 433
renal abscess, *V2*: 1144
Tuberculous peritonitis, *V2*: 949, 951
Tuberous sclerosis:
fetal assessment, *V2*: 1595
renal cysts, *V2*: 1066, 1069–1071
Tubo-ovarian abscess (TOA), *V2*: 1514, 1516–1517
Tubular blockage, kdineys, *V2*: 1120, 1123–1124
Tubular carcinoma, breast cancer, *V2*: 1733–1736
Tubular ectasia:
medullary sponge kidney, *V2*: 1049, 1060
testes, scrotum and epididymis, cystic lesions, *V2*: 1386, 1389
Tubulointerstitial kidney disease, *V2*: 1120–1121
Tunnel cluster, endometrial hyperplasia/polyps, *V2*: 1448–1450
Turbo fast low-angle shot (TurboFLASH), abdominal-pelvic imaging, *V1*: 5
Turbo spin-echo sequences, *V1*: 6
magnetic resonance cholangiopancreatography, *V1*: 460
Turner syndrome:
gonadal dysgenesis, *V2*: 1415
uterine hypoplasia, *V2*: 1441–1442
Twin-twin transfusion syndrome, *V2*: 1623–1624
Two-dimensional spin echo sequences, *V1*: 7
breast imaging, *V2*: 1694–1695
magnetic resonance cholangiopancreatography, *V1*: 456–461
pediatric patients, *V2*: 1637
Two-dimensional spoiled gradient echo sequences:
capillary phase imaging, *V1*: 2
kidneys, techniques, *V2*: 1025–1031
magnetization-prepared rapid-acquisition gradient echo sequences, *V1*: 5–6
male pelvis, *V2*: 1343–1344
pancreatic imaging, *V1*: 536–541
spoiled gradient echo (SGE) sequences, abdominal-pelvic imaging, *V1*: 3
vessel imaging, *V2*: 1195–1200
Two-dimensional steady-state precession-balanced echo (True-FISP) MRI:
esophagus, *V1*: 726
esophageal varices, *V1*: 727, 729
fetal assessment, central nervous system, *V2*: 1578–1583
gastrointestinal tract imaging, *V1*: 725
glomerular disease, *V2*: 1117–1120
large intestine, techniques, *V1*: 824
nephrotic syndrome, *V2*: 1117–1120
pulmonary emboli, *V2*: 1673, 1675–1677
small intestinal varices, *V1*: 775, 781
uterus and cervix, *V2*: 1434
vessel imaging, *V2*: 1195–1200
Typhlitis, *V1*: 884, 890

Ulcerated gastric adenocarcinoma, *V1*: 738
Ulcerative colitis:
Crohn disease, *V1*: 785, 867–868, 870–871
differential diagnosis, *V1*: 785, 869, 872–874
large intestine, *V1*: 867–868, 870–871
primary sclerosing cholangitis, *V1*: 494, 497–502
small intestine, *V1*: 797, 806
Ulcers:
aortic, penetrating, *V2*: 1201, 1204, 1213
gastric, *V1*: 761–764
Ultrasmall paramagnetic iron oxide particles:
characteristics, *V2*: 1777–1779
endometrial carcinoma, *V2*: 1474–1481
liver imaging, reticuloendothelial system targeting, *V1*: 50, 54–58
Umbilical vein, cirrhosis and varices in, *V1*: 348, 351, 361
Undifferentiated sarcoma of the liver (USL), *V1*: 251, 256
Undifferentiated uterine carcinoma, *V2*: 1488–1491
Unicornuate uterus, *V2*: 1441, 1444
Uniform low signal intensity enhancement, spleen, *V1*: 678–681
Urachal carcinoma, *V2*: 1316, 1320
Urachal cyst, *V2*: 1300–1301
Uremic medullary cystic disease complex, *V2*: 1049, 1059–1060
Ureter anastomosis, renal transplantation, *V2*: 1182
Ureteric calculi, *V2*: 1159, 1168–1169
Ureterocele:
female urethra, *V2*: 1403
renal duplication, *V2*: 1613
Ureteropelvic junction, fetal assessment, hydronephrosis, *V2*: 1613–1614
Urethra:
female:
caruncles, *V2*: 1407
congenital anomalies, *V2*: 1402
diverticulum, *V2*: 1405–1407
duplication anomaly, *V2*: 1403
leiomyoma, *V2*: 1403
malignant masses, *V2*: 1403–1404
metastases to, *V2*: 1405
MR imaging, *V2*: 1401–1402
normal anatomy, *V2*: 1401–1403
pediatric imaging, *V2*: 1650
pelvic floor relaxation, *V2*: 1408–1410
trauma and strictures, *V2*: 1407
urethritis and fistulae, *V2*: 1407–1408
fetal assessment, hydronephrosis, *V2*: 1613–1614
male:
congenital anomalies, *V2*: 1376
diffuse disease, *V2*: 1377–1380
infectious disease, *V2*: 1380
inflammatory disease, *V2*: 1380–1381
male, normal anatomy, *V2*: 1375–1376
membranous rupture, *V2*: 1373–1374
metastases, *V2*: 1376–1377
primary tumors, *V2*: 1377–1380
trauma, *V2*: 1374–1375, 1382
Urethral carcinoma, female urethra, *V2*: 1403–1404
Urethritis, female urethra, *V2*: 1407–1408
Urethrography, femal urethral diverticulum, *V2*: 1405
Urethrovaginal fistulas, *V2*: 1408
Urinary incontinence, periurethral collagen injection, *V2*: 1408–1409
Urine, intraperitoneal, *V2*: 942
Urinoma, renal transplants, *V2*: 1182, 1184

Urothelial neoplasm:
bladder cancer:
carcinosarcoma, *V2*: 1316
squamous cell carcinoma, *V2*: 1316–1318
transitional cell carcinoma, *V2*: 1306–1316
renal pelvis and ureter carcinoma, *V2*: 1155, 1159–1165
Urthroscopy, femal urethral diverticulum, *V2*: 1405
Usual ductal hyperplasia, benign breast lesions, *V2*: 1715
Uterine artery embolization (UAE):
adenomyosis, *V2*: 1467, 1470
leiomyomas, *V2*: 1451, 1456, 1459–1463
Uterine peristalsis, menstrual cycle and, *V2*: 1437–1439
Uterus:
benign disease:
adenomyosis, *V2*: 1456, 1466–1470
endometrial hyperplasia/polyps, *V2*: 1448–1450
fibroids, *V2*: 1456, 1462–1463
leiomyomas, *V2*: 1449, 1451–1469
lipoleiomyoma, *V2*: 1456, 1464
congenital anomalies:
arcuate uterus, *V2*: 1441, 1444, 1448
bicornuate uterus, *V2*: 1441, 1444, 1446
didelphys uterus, *V2*: 1441, 1444–1446
diethylstilbesterol exposure, *V2*: 1448
Müllerian duct anomalies, *V2*: 1439–1448
segmental agenesis/hypoplasia, *V2*: 1441
septate uterus, *V2*: 1441, 1444, 1447–1449
sexual differentiation disorders, *V2*: 1448
unicornuate uterus, *V2*: 1441, 1444
contractions, *V2*: 1437–1439
dehiscence, postpartum uterus, *V2*: 1577
duplication anomalies, vaginal duplication and, *V2*: 1412, 1414–1415
hematoma, in pregnancy, *V2*: 1559–1560
malignant disease:
adenocarcinoma, undifferentiated carcinoma/sarcoma, *V2*: 1488–1491
endometrial carcinoma, *V2*: 1468, 1470–1481
sarcoma, *V2*: 1475, 1479–1481
menstrual changes, *V2*: 1437–1439
metastases to, *V2*: 1482
leiomyosarcoma, *V2*: 1456, 1465–1466
MR imaging techniques, *V2*: 1433–1434
normal anatomy, uterine corpus, *V2*: 1434–1436
pediatric imaging, *V2*: 1650
in pregnancy, maternal imaging:
leiomyomas, *V2*: 1564, 1567–1570
placental imaging, *V2*: 1623, 1625–1627
postpartum uterus, *V2*: 1575–1580
subserosal leiomyoma, *V2*: 1567, 1570
tamoxifen-induced changes, *V2*: 1439–1440
Utricular cysts, prostate, *V2*: 1344, 1347

Vagina:
agenesis/partial agenesis, *V2*: 1410–1413
ambiguous genitalia, *V2*: 1415–1416
benign masses, *V2*: 1416–1420
Bartholin glands cyst, *V2*: 1416–1418
cavernous hemangioma, *V2*: 1416, 1420
Gartner duct cysts, *V2*: 1416, 1418–1419
cervical cancer metastases, *V2*: 1486–1487
congenital anomalies and variants, *V2*: 1410
duplication/partial duplication, *V2*: 1412, 1414–1415
fistulas, *V2*: 1421, 1426, 1429–1430
gonadal differentiation abnormalities, *V2*: 1415
malignant masses, *V2*: 1416, 1420–1426
staging, *V2*: 1421
metastases to, *V2*: 1420, 1424–1426
cervical cancer, *V2*: 1405
urethral adenocarcinoma, *V2*: 1403–1404
vulvar/perineal carcinomas, *V2*: 1421, 1426–1428
MR imaging techniques, *V2*: 1409–1410
normal anatomy, *V2*: 1401–1403, 1408–1411
pediatric imaging, *V2*: 1650
radiation changes, *V2*: 1421, 1428
Vaginoplasty, vaginal agenesis/partial agenesis, *V2*: 1411
Vanillylmandelic acid (VMA), pheochromocytoma, *V2*: 1005
Varicella virus, splenomegaly and, *V1*: 709–711
Varices:
cirrhosis:
esohpageal, *V1*: 351, 361
fibrosis and, *V1*: 351, 362
gastric, *V1*: 348, 351, 359
subcutaneous, *V2*: 1274, 1290–1291
pelvic, *V2*: 1517–1518
periduodenal/duodenal, *V1*: 775, 781
peritoneal, *V2*: 945–946, 948–949
rectal, *V1*: 838
small intestine, *V1*: 775, 781
splenomegaly and, *V1*: 706–709
Varicocele, testes, scrotum and epididymis, *V2*: 1388–1390, 1392
Vascular disease:
abdominal wall imaging, *V2*: 1274
magnetic resonance angiography, *V2*: 1673, 1679–1684
penis and urethra, *V2*: 1380–1381
peritoneal, *V2*: 945–946, 948–949
renal artery disease, *V2*: 1133–1144
Vascular endothelial growth factor (VEGF), hepatocellular carcinoma, *V1*: 202
Vascular graft, branch vessel, *V2*: 1214, 1216, 1227
Vasculitis, renal artery disease, *V2*: 1136–1137
Vas deferens:
congenital anomalies, *V2*: 1386
cysts, *V2*: 1344, 1347–1349
Vasovist contrast agent, *V2*: 1772, 1774
Venous embolotherapy, pelvic varices, *V2*: 1518
Venous thrombosis:
hepatic venous thrombosis, *V1*: 398, 401–405
hepatocellular carcinoma, *V1*: 202, 212, 224–232, 234–238
inferior vena cava, *V2*: 1229–1237
tumor *vs.* blood thrombus, *V2*: 1229–1237, 1240–1241
nephrotic syndrome, *V2*: 1117, 1120
pancreatic transplants, *V1*: 671–673
portal venous system, obstruction/thrombosis, *V1*: 388, 391, 393–400
renal vein, *V2*: 1137, 1144
splenic vein, pancreatic adenocarcinoma, *V1*: 575, 579
splenomegaly and, *V1*: 706–709
superior mesenteric vein, small intestine ischemia and hemorrhage, *V1*: 816, 822
Ventriculomegaly, fetal imaging, *V2*: 1585–1592
Vermian hypoplasia, fetal assessment, posterior fossa anomalies, *V2*: 1591, 1593–1597
Vesicocervical fistulas, bladder involvement, *V2*: 1331–1335
Vessel imaging:
retroperitoneum:
aorta, *V2*: 1200–1227
aortic aneurysm, *V2*: 1200–1207
aortic dissection, *V2*: 1201, 1208–1212
aortoiliac atherosclerotic disease/thrombosis, *V2*: 1204, 1207, 1214–1223
penetrating ulcers/intramural dissecting hematoma, *V2*: 1201, 1204, 1213
postoperative graft evaluation, *V2*: 1207, 1214, 1216, 1224–1227
inferior vena cava, *V2*: 1216, 1223, 1229
congenital anomalies, *V2*: 1223, 1229–1230
primary malignant tumors, *V2*: 1237–1241
venous thrombosis, *V2*: 1229–1237
magnetic resonance angiography, *V2*: 1194–1200
signal intensity, *V1*: 14

Villous adenoma, large intestine, *V1*: 829, 832, 835–836
VIPoma, MR imaging, *V1*: 601, 606
Viral hepatitis:
  hepatocellular carcinoma, *V1*: 202, 212
  imaging studies, *V1*: 319, 321–330
Von Hippel-Lindau syndrome:
  pancreas, *V1*: 549–550
  renal cysts, *V2*: 1066, 1068, 1072
Von Meyenburg complexes, biliary hamartoma, *V1*: 67, 73–77
Von Recklinghausen disease:
  bladder lesions, *V2*: 1304–1305
  small intestine neurofibromas, *V1*: 775, 779
Vulva:
  carcinomas, *V2*: 1421, 1427–1428
  perivulvar cavernous hemangioma, *V2*: 1416, 1420
  squamous cell carcinoma, *V2*: 1421, 1427

WAGR syndrome, Wilms tumor and, *V2*: 1103–1106
Walker-Warburg syndrome, encephalocele, fetal assessment, *V2*: 1595, 1597
Wandering spleen, MR imaging, *V1*: 681–685
Water excitation T1-weighted magnetization-prepared gradient-echo imaging (WE-MPRAGE), pediatric patients, *V2*: 1645–1650
Weigert-Meyer rule, renal duplication, *V2*: 1613
Whipple procedure, pancreatic adenocarcinoma, *V1*: 588
Whole body imaging:
  3T MR imaging, safety issues, *V1*: 33
  pediatric patients, *V2*: 1637–1650
  performance improvements in, *V1*: 36, 38–42
  protocol for, *V1*: 20, 23
Wilms tumor, *V2*: 1102–1106
Wilson disease, imaging studies, *V1*: 315–318
Wirsung ducts, pancreas divisum, *V1*: 541–542
Wraparound artifacts, breast MRI, *V2*: 1695
Xanthogranulomatous cholecystitis, magnetic resonance cholangiopancreatography, *V1*: 477
Xanthogranulomatous pyelonephritis, *V2*: 1152
X-linked recessive disorder:
  fetal assessment, corpus callosum agenesis, *V2*: 1588–1592
  testicular feminization, *V2*: 1415

Yersinia enterocolitica infection, enteritis, *V1*: 810, 813–814
Yolk sac tumor, peritoneal metastases, *V2*: 918, 923–924, 927

Zellballen masses, pheochromocytoma, adrenal medullary masses, *V2*: 998, 1005–1111
Zollinger-Ellison syndrome:
  hypertrophic rugal folds, *V1*: 761, 765
  pancreatic cancer, *V1*: 591, 598–602
  stomach carcinoids, *V1*: 759